Journal of Engineering and Technology for Industrial Applications

ISSN 2447-0228

August 2026 Volume 12/ No 60



Editor-in-Chief: J. C. Leite

www.itegam-jetia.org

ITEGAM - JETIA ISSN 2447-0228 Online
Journal of Engineering and Technology for Industrial Applications (JETIA)

O **ITEGAM-JETIA: Journal of Engineering and Technology for Industrial Applications** is a publication of the Galileo Institute of Technology and Education of the Amazon (ITEGAM), located in the city of Manaus since 2008. JETIA publishes original scientific articles covering all aspects of engineering. Our goal is the dissemination of research original, useful and relevant presenting new knowledge on theoretical or practical aspects of methodologies and methods used in engineering or leading to improvements in professional practice. All the conclusions presented in the articles It should be state-of-the-art and supported by current rigorous analysis and balanced assessment. Public magazine scientific and technological research articles, review articles and case studies.
JETIA will address topics from the following areas of knowledge: Mechanical Engineering, Civil Engineering, Materials and Mineralogy, Geosciences, Environment, Information and Decision Systems, Processes and Energy, Electrical and Automation, Mechatronics, Biotechnology and other Engineering related areas.

Publication Information:
ITEGAM-JETIA (ISSN 2447-0228), (online) is published by Galileo Institute of Technology and Education of the Amazon on a every two months (February, April, June, August, October and December).

Contact information:

Web page: www.itegam-jetia.org
Email: editor@itegam-jetia.org
Galileo Institute of Technology and Education of the Amazon (ITEGAM).

Joaquim Nabuco Avenue, No. 1950. Center. Manaus, Amazonas. Brazil.
Zip Code: 69020-031. Phone: (92) 3584-6145.

Copyright 2014. Galileo Institute of Technology and Education of the Amazon (ITEGAM)
The total or partial reproduction of texts related to articles is allowed, only if the source is properly cited. The concepts and opinions expressed in the articles are the sole responsibility of the authors.

Previous Notice
All statements, methods, instructions and ideas are the sole responsibility of the authors and do not necessarily represent the view of ITEGAM -JETIA. The publisher is not responsible for any damage and / or damage to the use of the contents of this journal. The concepts and opinions expressed in the articles are the sole responsibility of the authors.

Directory

Members of the ITEGAM Editorial Center - Journal of Engineering and Technology for Industrial Applications (ITEGAM-JETIA) of the Galileo Institute of Technology and Education of the Amazon (ITEGAM). Manaus-Amazonas, Brazil.

Jandecy Cabral Leite, CEO and Editorial Editor-in-Chief
Ivan Leandro Rodriguez Rico, Editor da secção
Jorge de Almeida Brito Junior, Editorial Assistant

ITEGAM - JETIA
ISSN 2447-0228 Online
Journal of Engineering and Technology for Industrial Applications (JETIA)
INSTITUTO DE TECNOLOGIA ITEGAM

ITEGAM-JETIA. v.12, n.60. August of 2026. Manaus - Amazonas, Brazil. ISSN 2447-0228 (ONLINE)
https://www.itegam-jetia.org

SUMMARY

PERFORMANCE EVALUATION OF DEEP LEARNING ARCHITECTURES FOR DETECTING CITRUS CROP HLB ABNORMALITIES **01**
Nagineni Venkata Sireesha, Gillala Rekha

COMPREHENSIVE EVALUATION OF AN AUTOMATED DISTILLER: PERFORMANCE, THERMAL LOSSES, AND PROCESS RELIABILITY **19**
Kevin Damián Carrillo Naranjo, Franklin Wilfrido Salazar Logroño, Luis Rojas Oviedo, Paúl Hernán Machado Herrera

SIX-AXIS MAGNETOMETER/ACCELEROMETER-ASSISTED MOBILE ROBOT INDOOR NAVIATION **28**
Guransh Singh Arora, Kumar Gaurav

ASSESSING THE VISIBILITY AND PERCEPTION OF ESTATE SURVEYORS AMONG NON-CONSTRUCTION PROFESSIONALS IN NIGERIA **39**
Olusoji D. Adetola, Busayo E. Akinwale, Morakane C. Khahledi, Imoleayo A. Awodele, Oyindamola A. Olagunju

FINITE ELEMENT ANALYSIS OF BONE-DERIVED HYDROXYAPATITE, ZINC-DOPED HYDROXYAPATITE, AND PLGA–ZN-HAP COMPOSITES FOR BIOMEDICAL APPLICATIONS **49**
M Saravanan, Abhijith J, Sangeetha Krishnamoorthi, Athira Kishore, Saravana Kumar.M

ADAPTIVE IMMUNIZATION AGAINST FEDERATED DATA POISONING: A SEQUENTIAL TRUST-SPECTRAL INTENT FRAMEWORK FOR ROBUST DISTRIBUTED LEARNING PROCESS **57**
Nitesh Hatwar, V. K. Sharma, Bhushan Manjre

DESIGN AND ELECTROMAGNETIC ANALYSIS OF A HIGH-GAIN DUAL-BAND MICROSTRIP FILTENNA AT 26/29 GHZ BASED ON COUPLED RECTANGULAR RESONATORS **70**
Touko Tcheutou Stephane Borel, Rashmi Priyadarshini

ENERGY AUDIT APPROACHES AND OUTCOMES FOR ENHANCING ENERGY EFFICIENCY IN SMALL & MEDIUM ENTERPRISES **78**
Ankit B. Lehru, Dharmesh J Pandya

NINE-SWITCH QUASI-IMPEDANCE SOURCE INVERTER FOR DUAL-MOTOR ELECTRIC VEHICLE DRIVES WITH INTEGRATED ONBOARD CHARGING **85**
Ismail Benmiloud, Aissa Ameur, Katia Kouzi, Najib Essounbouli.

APPLICATION OF COMPUTATIONAL FLUID DYNAMICS AND OPEN-SOURCE TECHNOLOGIES FOR INDOOR THERMAL COMFORT MODELING: A SYSTEMATIC REVIEW AND EVIDENCE SYNTHESIS OF THE LAST DECADE **95**
Keny Montalvo Morales, Henry Javier-Ninahuaman, Grimaldo Quispe, Abdallah Elshawadfy Elwakeel, John Espitia, Jader Rodriguez, Edwin Villagran

A REVIEW OF RESEARCH AND TECHNOLOGY DEVELOPMENT ON THE ARCHIMEDES SCREW WIND TURBINE **108**
Bayu Ardiansyah Maskub Putra, Nazaruddin Sinaga, Eflita Yohana, Mochammad Shodiq

META-HEURISTIC APPROACHES TO OPTIMAL PLACEMENT OF ELECTRIC VEHICLE CHARGING STATION **127**
M. S. Arjun, N. Mohan, K. R. Sathish, Arunkumar Patil, D. P. Somashekar

ITEGAM - JETIA
ISSN 2447-0228 Online
Journal of Engineering and Technology for Industrial Applications (JETIA)

MULTIMODAL DEEP LEARNING FRAMEWORK FOR MISSING CHILDREN DETECTION USING VISION-LANGUAGE MODE **138**
Kola Uma Maheswari, Pandluri Dhanalakshmi

BLOCKCHAIN-DRIVEN TRANSFORMER-BASED INTRUSION DETECTION AND ACCESS CONTROL SYSTEM (BDL-IDACS) **149**
C. Ramya, A. Suphalakshmi

SALP SWARM OPTIMIZED ARBS-NET-ENABLED FRAMEWORK FOR FAULT DIAGNOSIS IN ELECTRIC VEHICLES **166**
Ganapavarapu Harish, V. Suresh, D. Ravi Kishore, B Kavya Santhoshi

DETECTING IMAGE FORGERIES USING HYBRID RESIDUAL-DENSE SWIN TRANSFORMER FRAMEWORK WITH ATTENTION-BASED U-NET **181**
Sruthi Anand, Saranya V

ENHANCED ECG-BASED CARDIAC DISORDER DETECTION USING RECURRENT NEURAL NETWORK-ENHANCED TEMPORAL TRANSFORMER AND FIRE HAWK OPTIMIZATION **195**
S. Dinakar Raj, Kavitha Veerappan, Jeya Bright Pankiraj, K. Sangeetha, Sumesh Joe Cherian, S. Rajeswari

STARFISH-OPTIMIZED AI-BASED DEEP LEARNING MODEL FOR ACCURATE BROKEN ROTOR BAR FAULT DETECTION IN INDUCTION MOTORS **206**
Killamsetti Vijeta, Sri Suyambulinga Perumal B, R. Tharwin Kumar, Niran I R, Jinsha Lawrence, Gunasekar M

MODELLING AND FAULT PROTECTION ANALYSIS OF A DC MICROGRID USING VOLTAGE SOURCE CONVERTER AND RELAYS **227**
Ayya Chaithanya, T. Neeraja, B Raja Sekhar Reddy, Chella Hari Prasad, Kanna Sravanthi

A COMPREHENSIVE REVIEW ON ADVANCED MATERIALS FOR POLLUTION CONTROL AND ENVIRONMENTAL SUSTAINABILITY **237**
Shital Yashwant Waware, J. Robert Edwin Chester, Immanuvel Arokia James K, Girish Anant Charwad, Govindarajan Murali, Anant Sidhappa Kurhade

DCG-ANET: A DUAL-STREAM CAUSAL GRAPH ADVERSARIAL NETWORK FOR EARLY DETECTION OF ALZHEIMER'S DISEASE FROM MULTIMODAL BRAIN IMAGING **247**
Dinesh Kumar P

INTEGRATION MODEL OF SAVING MATRIX AND NEAREST NEIGHBOR METHODS FOR OPTIMIZING DISTRIBUTION OF PRODUCTION RESULTS OF BAWEAN GRESIK SMES – EAST JAVA, INDONESIA **259**
Rony Prabowo, Lutfia Bamatraf

AN EFFICIENT AND AUTOMATED BRAIN TUMOR SEGMENTATION IN MRI IMAGES USING NON-SUPERVISED MODEL **270**
J. N. Adlin, Arockia Selva Saroja

DRIVER INATTENTION DETECTION USING A HYBRID VISION TRANSFORMER AND BILSTM **278**
Devanaboyina Manikanta Teja, P L Kishan Kumar Reddy

ENERGY-EFFICIENT TINYML-BASED FALL DETECTION FOR WEARABLE HEALTHCARE DEVICES **294**
Prathap P, Hibafathima H, Sufaira Shamsudeen, Selin M, Julie M David, Jihad Aboobaker

A COMPARATIVE STUDY OF DEFECT ANALYSIS, STATISTICAL PROCESS CONTROL (SPC) AND FMEA IN BISCUITS PRODUCTION **299**
Muhammad Abdus Samad, Musfik Ahammed

ITEGAM - JETIA
ISSN 2447-0228 Online
Journal of Engineering and Technology for Industrial Applications (JETIA)

DESIGN AND VERIFICATION OF AN OPTIMIZED 32-BIT PIPELINED MULTIPLIER FOR HIGH PERFORMANCE COMPUTING **312**
C.S. Chakradhar, M. Sreedhar

PREDICTIVE COURSE PLACEMENT: UTILIZING AN ARTIFICIAL INTELLIGENCE-BASED APPROACH FOR RECOMMENDATIONS THROUGH THE APPLICATION OF COSINE SIMILARITY AND MULTI-MODEL ARCHITECTURES **319**
Manocher C Alipour

PERFORMANCE ANALYSIS OF ZETA CONVERTER IN ELECTRIC VEHICLE APPLICATIONS **329**
V. Nandagopal, Pujari Harish Kumar, N Chinna Alluraiah, K. Harinath Reddy

PARALLEL LÉVY-FLIGHT CUCKOO SEARCH FOR JOINT DG SITING/SIZING AND POWER-QUALITY ENHANCEMENT IN RADIAL DISTRIBUTION NETWORKS **337**
Vinuta V Koluragi, J P Sridhar

SYNERGISTIC HYBRID GDI–CNTFET ARCHITECTURE FOR LOW-POWER AND AREA-OPTIMIZED NANOSCALE VLSI CIRCUITS **344**
Jayakrishna Padala, Kishore kumar Kamarajugadda, Pavani Movva

A COMPARATIVE ANALYSIS OF STUDENT PERFORMANCE IN DESIGNING FREQUENCY CONTROL VIA SIMULATION-BASED FORMATIVE ASSESSMENT **356**
Idamakanti Kasireddy, Devineni Gireesh Kumar, Neelesh Kumar Gupta, Prasad Chongala

STRATEGIC INTEGRATION OF ARTIFICIAL INTELLIGENCE IN EDUCATIONAL QUALITY: DIAGNOSIS AND PROPOSAL FOR UNIVERSITIES IN AMAZONAS, PERU **362**
Victor Manuel Valdiviezo Sir

DESIGN AND IMPLEMENTATION OF A PROPOSED SDN-VXLAN ARCHITECTURE FOR ENTERPRISE NETWORK **370**
Daniel Nuñez-Agurto, Luis Paredes-Alcivar, John Cruz-Garzon, Franklin Perez

EXPLAINABLE AND RISK AWARE AUTONOMOUS DECISION SYSTEMS A SCALABLE SECURE BY DESIGN ARCHITECTURE FOR LARGE SCALE DISTRIBUTED COMPUTING SYSTEMS **382**
Abdinasir Ismael Hashi, Osman Abdullahi Jama, Ibrahim Rashid Abdullahi

TODDLER-CENTERED CASE-BASED REASONING FRAMEWORK FOR EARLY DIAGNOSIS OF AUTISM SPECTRUM DISORDER **400**
Hachemi Yamina

EFFICIENT ACUTE LYMPHOBLASTIC LEUKEMIA CLASSIFICATION USING GLCM AND HSV FEATURES WITH RESERVOIR COMPUTING ON TALEQANI HOSPITAL DATASET **408**
Michael Angello Qadosy Riyadi, Sulthonika Mahfudz Al Mujahidin, Nur Alifia Rustan, A'isyah Belqis Febi Aulia, Muhammad Adib Kamali, Farah Zakiyah Rahmanti, Khodijah Amiroh

HYBRID LEXICAL–CONTEXTUAL LEARNING FOR ARABIC NEWS CLASSIFICATION: INTEGRATING TF–IDF WITH ARABERT EMBEDDINGS **420**
Yasir Hadi Farhan, Mustafa Tareq, Boumedyen Shannaq, Said Almaqbali, Oualid Ali

CAPACITY MARKET-BASED DEMAND RESPONSE APPROACH FOR EFFICIENT POWER DISTRIBUTION IN RESIDENTIAL MICROGRID **429**
Arunkumar P, Chidurala Sai Prakash, Srikanth Velpula, Manjunatha H M

ITEGAM - JETIA
ISSN 2447-0228 Online
Journal of Engineering and Technology for Industrial Applications (JETIA)

BENCHMARKING YOLO VARIANTS FOR DETECTING VARROA MITES IN BEEHIVE IMAGES **437**
Youcef Naas, Slim Rouabah, Rabah Abdelkader, Meziane Kaci, Salem Merabti, Hassane Ezziane

INTERPRETABLE MENTAL HEALTH SCREENING USING BAYESIAN PCA-ENHANCED LOGISTIC REGRESSION FOR DECISION SUPPORT **444**
Hendra Abdul Hamid, Mustafa Mat Deris, Ika Safitri Windiarti

SELF-SUPERVISED KNOWLEDGE REPRESENTATION FOR RARE FRAUD AND OPERATIONAL FAILURE DETECTION IN MULTI-CHANNEL PAYMENT SYSTEMS **452**
Boumedyen Shannaq

COMPARATIVE EVALUATION OF MACHINE LEARNING MODELS FOR PREDICTIVE MAINTENANCE USING THE AI4I 2020 DATASET: EFFECTS OF DATA BALANCING AND FEATURE SELECTION **461**
Juan Carlos Gonzalez Islas, Jesus Vargas-Ortiz, Aldo Márquez-Grajales, Ernesto Bolaños-Rodríguez, Asdrúbal López-Chau, Rosa María Ortega-Mendoza

CFD-BASED NUMERICAL ASSESSMENT OF PIN-FIN HEIGHT OPTIMIZATION FOR ENHANCED THERMAL PERFORMANCE IN MWCNT NANOFLUID MICROCHANNEL HEAT SINKS **470**
S Sorna Latha, Ankush D Tharkar, Divya Haridas

MULTI-STAGE DIABETIC RETINOPATHY CLASSIFICATION USING DEEP LEARNING: TRENDS, CHALLENGES, AND FUTURE DIRECTIONS **484**
Shreya Dubey, Mahesh Goyani, Pinal Patel, Safwan Vahora, Uttam Chauhan, Mahendra Patel

DEEP REINFORCEMENT LEARNING-BASED ADAPTIVE SWITCHING FOR RISK-COST-OPTIMIZED RENEWABLE SMART GRIDS **499**
Meyyappan M, Avirajamanjula P, Marimuthu P, Bharathiraja M

MITIGATING ADVERSARIAL VULNERABILITIES IN DEEP LEARNING-BASED FACE RECOGNITION USING STACKED ATTENTION RESIDUAL GAN AND FIRE HAWK OPTIMIZATION **513**
Sheilla Ann Pacheco, Mahesh Goyani, Jayzel P. Bangoy, Born Christian A. Isip

ACCURATE BRAIN TUMOR CLASSIFICATION USING MRI IMAGES BASED ON A HYBRID VISION TRANSFORMER AND BILSTM FRAMEWORK **526**
Nagham Salim Mohammed, Omar S. Almolaa, Ahmed Saadi Abdullah, Khalil I. Alsaif

AN OPTIMIZED HYBRID FUSION MODEL COMBINING DENSE AND VISUAL GEOMETRY NETWORKS WITH MACHINE LEARNING FOR LUNG CANCER DETECTION AND CLASSIFICATION **536**
Umakanth Basineni, Fahimuddin Shaik

A NOVEL TECHNIQUE TO DESIGN ADDER AND MULTIPLIER CIRCUITS USING GNRFETS IN TERNARY LOGIC **549**
K Mamatha, Shaik Taj Mahaboob

DEVELOPMENT OF A TINYML-BASED DEVICE FOR AUTOMATIC DETECTION OF POULTRY DISEASES USING CHICKEN VOCALIZATIONS **558**
Minh Nguyen-Ngoc, Bien Nguyen-Quang, Duan Luong-Cong

TWO-STAGE DETECT-THEN-CLASSIFY PIPELINE WITH DSAR-CNN FOR ROBUST FRAGMENT CLASSIFICATION UNDER PADDING AND BIT-FLIP ATTACKS **566**
Teena Mary, Sreeja C S

ITEGAM - JETIA
ISSN 2447-0228 Online
Journal of Engineering and Technology for Industrial Applications (JETIA)

FORECASTING BITCOIN PRICE MOVEMENTS USING HISTORICAL DATA **584**
Seddiq Hassan Al-Banna Ali, Ammar Ahmed Othman, Mohammed Baker Yousif

COMPARATIVE ANALYSIS OF TRIBOLOGICAL PERFORMANCE OF NANO-ENHANCED HYBRID BIO-LUBRICANT WITH CONVENTIONAL SYNTHETIC OIL **596**
Gaurav Pendbhaje, Mohammed Ali, Dipak Bajaj

PHYSICS-INFORMED DEEP LEARNING-BASED STATE OF HEALTH AND EFFICIENCY PREDICTION FRAMEWORK FOR KY CONVERTER-DRIVEN ELECTRIC VEHICLE BATTERY SYSTEMS **606**
Karhikkumar G, Avirajamanjula P, Marimuthu P, Bharathiraja M

EXPERIMENTAL EVALUATION OF SMART CONTRACT GAS OPTIMIZATION TECHNIQUES: A CASE STUDY OF A BLOCKCHAIN-BASED REPORTING APPLICATION SYSTEM **615**
Michael Angello Qadosy Riyadi, Sulthonika Mahfudz Al Mujahidin, Nur Alifia Rustan, A'isyah Belqis Febi Aulia, Mastuty Ayu Ningtyas, Khodijah Amiroh

TRANSIENT THERMAL PERFORMANCE ANALYSIS OF NANOPARTICLE-COATED FLAT PLATE SOLAR COLLECTORS USING MATLAB-BASED MODELING **629**
Juber Khatik, Nilesh Salunke, Mujahid Husain, Yogeshkumar Pathak, Kailas Deore, Pradeep Solanki, Pravin Shirule

A NOVEL LYAPUNOV BACKSTEPPING APPROACH TO CONTROLLING MECHANICAL POWER IN INDUCTION MOTORS **641**
Chami Noureddine, Rouabhi Riyadh, Herizi Abdelghafour

DEEP LEARNING TECHNIQUES: GAN AND LSTM FOR STOCK MARKET CLOSING PRICE PREDICTION **648**
Pappula Praveen, Anjaneyulu Gudla

A NOVEL PHOTOVOLTAIC-BASED WIRELESS EV CHARGING SYSTEM USING A MODIFIED TRANS-QUASI Z-SOURCE BOOST CONVERTER **660**
Naveena Sandhadi, Srinu Naik Ramavathu

INTERPRETABLE UNSUPERVISED IDENTIFICATION OF PERSISTENT RAINFALL REGIMES WITH ROBUSTNESS AND TEMPORAL STABILITY ASSESSMENT **673**
Imane Meguenni, Bendaoud Mebarek

A STRUCTURED PROBABILISTIC–AI FRAMEWORK FOR PREDICTIVE RELIABILITY ASSESSMENT AND RUL ESTIMATION OF ASYNCHRONOUS ROTATING MACHINES **685**
Toukap Nono Fernand Joseph, Tokoue Ngatcha Dianorré, Offole Florence, Nyatte Steyve, Mouzong Pemi Marcelin

MECHANICAL CHARACTERIZATION OF 3D-PRINTED PLA/GLASS FIBER COMPOSITE FOR CRASH BOX APPLICATION **704**
Sridharan V, Nikhil Kumar A, Mathumitha K, Jeyabalaji SN

THERMAL–HYDRAULIC OPTIMIZATION OF SLOTTED PIN FINS UNDER LAMINAR FLOW USING RESPONSE SURFACE METHODOLOGY **710**
Govindarajan Samidurai, Karthikeyan Ramalingam, Muthukumaran Ramalingam, Ratchagaraja Dhairiyasamy

DURABILITY PROPERTIES OF CONCRETE BY PARTIAL REPLACEMENT OF FINE AGGREGATE AND COARSE AGGREGATE WITH ALCCOFINE AND GLASS POWDER **724**
K.E. Viswanathan, S. Naveen Kumar, S. Yuvaraj, C. Shankar

ITEGAM - JETIA
ISSN 2447-0228 Online
Journal of Engineering and Technology for Industrial Applications (JETIA)

OPTIMIZATION OF BIODIESEL PRODUCTION FROM MANGO SEED KERNEL OIL USING TAGUCHI AND WEIGHTED SUM METHOD **738**
Popat Gunjal, Vijaykumar Pandey

OPTIMAL TRIANGLE DETECTION PREVENTING DUPLICATES IN LARGE-SCALE GRAPHS **746**
Sarah Balbouzi, Lougmiri Zekri, Kheira Mechach

FABRICATION OF AL6061–SIC METAL MATRIX COMPOSITES VIA STIR CASTING: A RESPONSE SURFACE METHODOLOGY APPROACH TO MICROSTRUCTURE ANALYSIS **757**
Sathiyaraj S, Kumaran .P, Yuvaraj .J, Vigneshwaran .V, Vijayan .T.P

A COMPARATIVE EXTENDED UTAUT ANALYSIS OF VIRTUAL REALITY AND AUGMENTED REALITY ADOPTION ACROSS INSTITUTIONAL DIVIDES **764**
Julius G Garcia, Myrna S. Batino, Alvie Simonette Q. Alip

REAL-TIME HAND GESTURE DETECTION WITH 3-D KEY POINTS USING DEEP LEARNING **773**
Sanjay R Pawar, Rameez Shamalik, Nazim Mahammad Shaikh, Pramod V Londhe, Mohd Imran Ansari, Ritesh G Mahajan, Sanjay Koli

DESIGN AND VERIFICATION OF A FAULT-TOLERANT AHB-TO-APB BRIDGE WITH INTEGRATED SINGLE ERROR CORRECTION (SEC) USING HAMMING CODE. **780**
Tandale Karthik, Manjula J

DISSIMILAR METAL BONDING BY FRICTION STIR WELDING: MAGNESIUM TO STEEL JOINTS **790**
Kapil B Pipavat, Hirenkumar I Joshi, Ghanshyam D Achary, Vishvesh J Badheka

XTREME GRADIENT BALLOON CRYPTOGRAPHIC COMPRESSED BLOCKCHAIN-BASED SECURE ROUTING IN COGNITIVE RADIO NETWORKS **816**
T. Sundar, A. Senthilkumar

ZONE BASED ROUTING PROTOCOL (ZBRP) WITH ENERGY CONSCIOUS TO SUPPORT SUSTAINABLE AGRICULTURAL IOT AND SMART FARMING NETWORKS **832**
C Rajalakshmi, Sreejith Vignesh B P

PREDICTION OF WATER QUALITY INDEX (WQI) USING A NOVEL HYBRID WATER WAVE-OPTIMIZED EXTREME GRADIENT BOOSTIN **840**
R Sarala, R.S Ponmagal

DUAL-STREAM VGG–DINAT FRAMEWORK WITH RED-CROWNED CRANE OPTIMIZATION FOR HAIR AND SCALP DISORDER DIAGNOSIS **852**
Vimala Ithayan J, Dilip Charaan R M, Vijayanandh T, Santhoshkumar S P, Parvathi R, Sivaprakash P

REAL-TIME NAIL-FOLD CAPILLARY DETECTION USING YOLO-RELAN WITH SALIENCY-BASED EXPLAINABILITY MODEL **869**
Santhoshkumar S P, Parvathi R, Sivaprakash P, Vimala Ithayan J, Dilip Charaan R M, Vijayanandh T

LEARNING DISABILITY DIAGNOSIS USING ADVANCED PREPROCESSING AND ENSEMBLE CLASSIFICATION TECHNIQUES **884**
Anu P P. J, K. Ranjith Singh

SCALABLE QUERY PROCESSING IN BIG DATA ENVIRONMENTS WITH HADOOP DISTRIBUTED FILE SYSTEM AND PARTICLE SWARM OPTIMIZATION **890**
S Tamil Selvan, Punitha Gowri R, V Vijey Nathan, C Saravanan

ITEGAM - JETIA
ISSN 2447-0228 Online
Journal of Engineering and Technology for Industrial Applications (JETIA)

FROM TRACEABILITY TO PREDICTIVE INTELLIGENCE: A SYSTEMATIC–NARRATIVE REVIEW OF IOT, BLOCKCHAIN, AND AI IN AGRICULTURE **897**
Manoj Praveen V, Mahendrakumar S, Dhanapal R, Kayalvili S, Kirubhakaran Marisamy

A FRACTAL CODING AND TDES-DIMA BASED FRAMEWORK FOR PRIVACY-PRESERVING BIG DATA STORAGE IN CLOUD ENVIRONMENTS **908**
Rajakumar Ponnumani, Sunilkumar Chellaswamy Santhakumari, Jaydipkumar TrivediH, Tadikonda Venkata Durga Prasad

A MULTI-DOMAIN FEATURE FRAMEWORK FOR ROBUST DEEPFAKE AUDIO DETECTION **917**
Akshat Chhatriwala, Ishita Akolkar, Namrata Shroff, Shankar Parmar

MULTI-SKU RETAIL SALES FORECASTING WITH FP-GROWTH ASSOCIATION-RULE FEATURES: A COMPARATIVE STUDY OF ECHO STATE NETWORK AND LSTM **933**
Ayu Manik Dirgayusari, I Made Dwra Putra Asana, Made Leo Radhitya, Ketut Gde Manik Karvana, I Made Subrata Sandhiyasa, Ni Kadek Ayu Nirwana

VIT-FOODNA: AN END-TO-END TRANSFORMER-BASED MULTIMODAL FRAMEWORK FOR FOOD RECOGNITION AND NUTRITION ANALYSIS **944**
E Anitha, A Bazila Banu

STUDY OF THE STRUCTURE AND ELECTRIC PROPERTIES OF (NA0.5BI0.5)1-XMGX[(TI0.8ZR0.2)0.9(NB2/3ZN1/3)0.1]O3 CERAMICS **955**
zakaria ouahab, Abdelwhab Ouahab

SYNERGISTIC PERFORMANCE AND EMISSION OPTIMISATION OF A TWO-STROKE SI ENGINE USING MG-PSZ THERMAL BARRIER COATED PISTON WITH ETHANOL–BUTANOL BLENDS THROUGH ANN–NSGA-II–TOPSIS APPROACH **962**
Avns Kiran, Arun Kumar Kurakula, H S Anantha Padmanabha, B Venkatesh

IMPACT OF GEOMETRICAL PARAMETERS ON FATIGUE LIFE CYCLE OF COMPLIANT MECHANISM **974**
Sandesh Solepatil, Narendra Deore

SIGNSPEAK: AN AI-BASED UTILITY FOR VISUALLY IMPAIRED INDIVIDUALS **986**
Sharanjit Kaur, Manju Bhardwaj, Kriti Misra, Preeti Marwaha

MAPPING THE LANDSCAPE OF SUSTAINABLE PROCUREMENT: A SYSTEMATIC LITERATURE REVIEW AND BIBLIOMETRIC ANALYSIS **997**
Irfan Veryanto, M. Mujiya Ulkhaq, Heru Prastawa

NEW APPROACH FOR ACCELERATING DISEASE DETECTION USING A PARALLELISM-NASED CNN MODEL **1010**
Mohammed Amine Mami, Nadir Berrouane, Imene Baba Ahmed

SUSTAINABLE DRY TURNING OF INCONEL 625: TAGUCHI–GRA WITH PARETO/KNEE ANALYSIS AND NSGA II VALIDATION OF ENERGY, TOOL LIFE, SURFACE QUALITY, AND PRODUCTIVITY TRADE OFFS **1020**
fitim Zeqiri, Fatlume Zhujani

INTEGRATED STRUCTURAL LINEAMENT MAPPING AND GEOTECHNICAL CHARACTERIZATION OF COLLAPSIBLE SOILS IN THE ARID REGION OF BISKRA (ALGERIA) **1032**
Saida gueraidia, Nour El Houda Gueraidia, Med Salah Laouar, Rayene Sirine Ramdani, Chems Eddine Fehdi

ITEGAM - JETIA
ISSN 2447-0228 Online
Journal of Engineering and Technology for Industrial Applications (JETIA)

MASKED FACE RESTORATION USING GANS: A SURVEY ON RECOGNITION, DETECTION, AND INPAINTING **1043**
Payal Parekh, Hina Choksi, Mahesh Goyani, Sheilla Ann Namgoy Pacheco

MACHINE LEARNING APPROACHES FOR PREDICTING COMPRESSIVE STRENGTH OF CONCRETE: A COMPARATIVE PERFORMANCE ANALYSIS **1058**
Slim rouabah

TRANSFORMER DRIVEN SELF-ATTENTION FRAMEWORK FOR HIGH FIDELITY COLOR IMAGE STEGANOGRAPHY **1065**
Taha Y. Abdulqader, shatha A. baker, Kifaa Hadi Thanoon, Yaarob Younus Al-Badrani

AGENT- AI BASED FRAMEWORK FOR GREEN ROUTE: ENHANCING TRAVEL USING BEST PATHFINDING WITH SSFS AND SE-TDT-SVM THROUGH AQI-AWARE ROUTING **1074**
Alamelu R M, Christy Eunaicy J I, Jayapratha C, Govindaprabhu G.B, Mahalakshmi Priya R

PREDICTIVE QUALITY OF SERVICE IN VEHICULAR COMMUNICATION SYSTEMS MODELS, DATASETS, AND OPEN CHALLENGES **1087**
Parita Patel, Mahesh Goyani

IMPROVING ENERGY GOVERNANCE IN THE CEMENT INDUSTRY **1101**
mokhtaria bekkaoui, hamed Benhmed, Meryem Kada Kloucha, Imane Nedjar

EXPLAINABLE RECOMMENDATION IN GRAPH NEURAL NETWORKS USING PROPAGATION PATH ANALYSIS AND COUNTERFACTUAL GRAPH EDITING **1108**
Pranav Nallari, Jayakumar Kaliappan

SECURITY IN GENERATIVE AI SYSTEMS: A COMPREHENSIVE LITERATURE REVIEW **1117**
Mohammed Basheer, Ebby Darney

A DEEP SPATIO-TEMPORAL FRAMEWORK FOR MULTI-CLASS TRAFFIC PREDICTION AND ACCIDENT DETECTION IN SURVEILLANCE VIDEO **1125**
Dhartee Patel, Jinal Ahir, Namrata Shroff, Shankar Parmar

ADAPTIVE DATASET: CNN-LSTM APPROACHES FOR DYSARTHRIA CLASSIFICATION USING ACOUSTIC FEATURE ENGINEERING **1138**
jothieswari jayaprakash, S Suguna

ENHANCING LOCOMOTION MODE RECOGNITION ACCURACY: A DEEP LEARNING MODEL FOR NOISY LABEL HANDLING **1148**
Geeta Bhimrao Atkar, T Srinivas, Angara Satyam, R. Anil Kumar, Sarala Patchala, Sunitha Pachala

A NOVEL OPTIMIZATION BASED SQUEEZENET WITH DWARF MONGOOSE OPTIMIZATION ALGORITHM FOR FEATURE SELECTION AND DEEP LEARNING CLASSIFIER FOR PARKINSON'S DISEASE **1160**
V R Sadasivam, R Poornima, M Nithya, G Nagarajan

PERFORMANCE COMPARISON OF DEEP LEARNING MODELS FOR SHORT TERM LOAD FORECASTING **1171**
Jaya Christa Sargunar Thomas, Krishna Veni Kaliappan Sivakumar

IMPACT OF INTER-WINDING MAGNETIC AND CAPACITIVE COUPLING ON SFRA SIGNATURE **1180**
Mayur V gojiya, Mehul Dansinh Solanki, Ashokkumar Parmar, Maqbul U. Ghanchi

ITEGAM - JETIA
ISSN 2447-0228 Online
Journal of Engineering and Technology for Industrial Applications (JETIA)

A COMPREHENSIVE REVIEW ON QUANTUM COMPUTING MODELS FOR ALZHEIMER'S DISEASE PREDICTION **1188**
R Ramesh, S. Sathya Priya, R Ramesh, S. Divya Vahini

PARAMETER ESTIMATION OF THE THREE-DIODE PHOTOVOLTAIC MODEL USING THE FLOW DIRECTION ALGORITHM **1195**
Dif Naas, Dif Ismail, Obeidi Thameur

ACOUSTIC PERFORMANCE AND MODELING OF SUSTAINABLE SCB/PVA COMPOSITE MATERIALS **1203**
Amit Shivaji Shinde, Vijaykumar Pandey

A COMPARATIVE EVALUATION OF VARIOUS MACHINE LEARNING TECHNIQUES FOR PREDICTION OF TYPE 2 DIABETES MELLITUS **1215**
Rizwan Akhtar, Muhammad Kalamuddin Ahamad

E2A2S-WSN: ENERGY-EFFICIENT ADAPTIVE SLEEP SCHEDULING FOR LOAD-BALANCED EH-WSNS **1232**
Abdelmalek Bengheni

ASSESSING DYNAMIC INSTABILITY USING HOPF BIFURCATION IN MULTI-MACHINE SYSTEMS EQUIPPED WITH POWER SYSTEM STABILIZERS **1246**
Ghousul Azam Shaik, Lakhmi Devi Aithepalli

PSO-DRIVEN OPTIMIZATION OF DIELECTRIC BARRIER DISCHARGE OZONE GENERATION PARAMETERS FOR WATER TREATMENT APPLICATIONS **1253**
Ghaitaoui Essama Ahmed, Nassour Kamel, Nemmich Said, Ghaitaoui Touhami, Oulad Naoui Brahim El Khalil, Bouroumeid Yassine, Tilmatine Amar, Halali Youcef

AI-DRIVEN INTERACTIVE MULTIMEDIA COURSEWARE: A WEB- AND MOBILE-RESPONSIVE PLATFORM FOR IT SPECIALIST CERTIFICATION EXAM PREPARATION WITH AN ADAPTIVE LEARNING ALGORITHM **1262**
Mark Gil Toribio Gañgan

RECURSIVE VOTING FUSION: AN RFE-BASED ENSEMBLE MODEL FOR CATEGORIZING IOT DDOS ATTACKS **1275**
Piyush M. Prajapati, Priyesh P. Gandhi, Sheshang Degadwala, Keyur Brahmbhatt, Swapnil M Parikh

A COMPREHENSIVE SURVEY OF AUDIO ENCRYPTION TECHNIQUES: CLASSICAL, CHAOS-BASED, DNA-INSPIRED, NEURAL, AND QUANTUM-ASSISTED APPROACHES **1287**
Halah Waad Khaled, Waleed Abdullah Araheem, Hakeem Imad Mhaibes

REVIEW ON DEEP LEARNING-BASED DYNAMIC INDIAN SIGN LANGUAGE RECOGNITION SYSTEM **1300**
Manojkumar Patel, Narendra Patel

VISUAL FEATURE MAPPING AND FEATURE SELECTION FOR ROBUST IDS BASED ON CSE-CIC-IDS2018 DATASET **1310**
Satishkumar D. Prajapati, Priyesh P. Gandhi, Sheshang Degadwala, Keyur Brahmbhatt, Swapnil M. Parikh

OPTIMIZING CLOUD RESOURCE MANAGEMENT THROUGH ENERGY-EFFICIENT VM PLACEMENT TECHNIQUES **1321**
Dipak Dabhi, Ankit Kharwar, Diya Vadhwani, Pritesh Prajapati, Vishal Barot, Anamika Mittal, Dhwani Modi

ITEGAM - JETIA
ISSN 2447-0228 Online
Journal of Engineering and Technology for Industrial Applications (JETIA)

OPTIMIZATION OF A NOVEL TORQUE SHARING FUNCTION FOR IMPROVED SWITCHED RELUCTANCE MOTOR CONTROL USING PSO **1330**
Houda Fetoui, Ali Rezig, Chouaib Labiod, Ahmed Mesai Belgacem, Imene Bouguettah, Marwa Arabi

DEEP LEARNING-BASED INTEGRATED SYSTEM FOR STUDENT ATTENDANCE AND EMOTION RECOGNITION IN ELEMENTARY EDUCATION **1343**
Alexander Imanuel Widjanarko, Nathan Daud, Mochamad Rizal Saputra, Diva Kurnianingtyas

AN AUTOMATED OCT-BASED RETINAL DISEASE CLASSIFICATION FRAMEWORK USING SHUFFLENET AND ENHANCED OSPREY OPTIMIZATION **1355**
L. Sivayamini, Fahimuddin Shaik

EFFECT OF GEOMETRIC PROPERTIES AND BOUNDARY CONDITIONS ON THE STRUCTURAL BEHAVIOR OF CONCRETE HELICOID SHELL STRUCTURES **1270**
Yasmine Merah, Ahmed Merah

LONG-TERM THERMO-KINETIC STABILITY AND PREDICTIVE MODELING OF A NOVEL BIO-BASED PHASE CHANGE MATERIAL: STIPA ICHU LIGNOCELLULOSIC FIBERS IMPREGNATED WITH BOVINE TALLOW **1378**
Robinson García, Luis Caicedo, Karen Betancout, Gustavo Cabezas, Jimena Díaz, Oscar Calle

ROBUSTNESS IMPROVEMENT OF LINEAR SYSTEMS RESPONSE USING A FRACTIONALIZED ORDER PID CONTROLLER **1387**
Asradj Zahir, Bensafia Yassine

QIC-MOEA: A CONTEXT-AWARE QUANTUM-INSPIRED EVOLUTIONARY FRAMEWORK FOR SELF-ADAPTIVE PERVASIVE SYSTEMS **1393**
Salah Maache, Fouzi Semchedine

DEVELOPMENT AND PERFORMANCE EVALUATION OF A 3-IN-1 PULVERIZING, MIXING, AND BRIQUETTING SYSTEM FOR SUSTAINABLE BIOMASS FUEL PRODUCTION IN INDUSTRIAL AND COMMUNITY APPLICATIONS **1403**
Renante O. Sangel, Consorcio Salinasal Namoco, Jr.

DESIGN AND IMPLEMENTATION OF AN INTELLIGENT SCADA SYSTEM FOR MARINE ENGINE PREDICTIVE MAINTENANCE USING OT-IT CONVERGENCE **1410**
Khanh Huu Doan, Phuc Trung Mac, Hoang Binh Trong Nguyen, Hoang Nam Nguyen, Duy Anh Nguyen

ROBUST MULTIMODAL STEGANOGRAPHY FRAMEWORK FOR SECURE TRANSMISSION OF TEXT, IMAGE, AND **1422**
Prashant Wakhare, Govind B. Sambare, Riyazahemad A. Jamadar, Veena Suhas Bhende

CITRIC ACID-BIOFUNCTIONALIZED CARBON DOTS AS A POTENTIAL FLUORESCENCE TOOL IN THE DIAGNOSIS OF DISEASES **1430**
Lakshmi Sundeep, Sandhya Jayakumar

COMPARATIVE EVALUATION OF CNN, SVM, ANN, AND KNN FOR AUTOMATED DETECTION OF NUTRIENT DEFICIENCIES IN MAIZE LEAVES **1437**
Von Ryan P. Marcelo

ADVANCED DEEP LEARNING TECHNIQUES FOR INTELLIGENT FAULT DETECTION IN CHEMICAL PROCESS INDUSTRIES **1447**
Mahesh Ganpat Bhong, Kiran Dattatray Devade, Manjusha Tatiya, Jyoti B. Deone, Sagar Baburao Patil, Anant Sidhappa Kurhade, Shital Yashwant Wawar

ITEGAM - JETIA
ISSN 2447-0228 Online
Journal of Engineering and Technology for Industrial Applications (JETIA)

STUDY OF THE HYDROMECHANICAL BEHAVIOR OF COLLAPSIBLE SOILS IN THE GHARDAÏA REGION, ALGERIA. **1464**
Ali Fernane, Samir Benmoussa, Mohamed Salah Laouar

INVESTIGATION OF THE SLURRY EROSION BEHAVIOR OF SUPER 304HCU STAINLESS STEEL UNDER NORMAL IMPACT CONDITIONS **1474**
Balachandar M., Vinoth Kumar M.

IMPLEMENTATION OF AN ESP32-BASED ESP-NOW NODE NETWORK FOR SMART AGRICULTURE MONITORING AND IRRIGATION CONTROL **1480**
Kota Venkat Kumar, Marneedi Soujanya, Karnati Chaitanya Keerthi, Mohammed Mastan Vali Yash, Kodavandla Vignesh, Sravan Sikakolli

IMPLEMENTATION AND SIMULATION OF SWITCHED-CAPACITOR PASSIVE RC INTEGRATOR IN DEEP SUBMICRON TECHNOLOGY **1487**
Mehulkumar Patel, Kehul Shah, Haresh Judal, Devendra Patel, Roshni Chaudhari

PERFORMANCE EVALUATION OF INDIA'S SOFTWARE INDUSTRY USING DATA ENVELOPMENT ANALYSIS: A LONG-TERM FIRM-LEVEL STUDY **1496**
Sajal K Das, Jamal Hussain

MULTIMODAL META-LEARNING FOR EARLY RUMOR DETECTION WITH ADAPTIVE DECISION TIMING **1503**
El Yazid Gueddoudj, Abdelouahab Attia; Adel Moussaoui

AN ADAPTIVE SLIDING MODE OBSERVER WITH PLL-BASED ESTIMATION FOR SENSORLESS PMSM DRIVES **1513**
Thanh Lam Le

PARAMETRIC TOPOLOGY OPTIMIZATION OF A CYLINDER MOUNTING BRACKET USING PTC CREO **1523**
Edosa Kefyalew, Adugna Fikadu, Mahesh Gopal

EYE TRACKING AND GAZE ESTIMATION: A SYSTEMATIC REVIEW OF DEEP LEARNING METHODS AND EDUCATIONAL APPLICATIONS **1536**
Khalid Sami Yousif, Emad Ahmed Mohammed, Mayyada Al- Hammoshi

SUSTAINABLE MANAGEMENT OF SOLID CHROME WASTE IN THE TANNING INDUSTRY **1548**
Iván Leandro Rodríguez Rico, Pastora de la Concepción Martínez Nodal

Journal of Engineering and Technology for Industrial Applications

ISSN ONLINE: 2447-0228

ITEGAM-JETIA

Manaus, v.12 n.60, p.01-18, July/August, 2026.

DOI: https://doi.org/10.5935/jetia.v12i60.2697

RESEARCH ARTICLE OPEN ACCESS

PERFORMANCE EVALUATION OF DEEP LEARNING ARCHITECTURES FOR DETECTING CITRUS CROP HLB ABNORMALITIES

Nagineni Venkata Sireesha[1], Gillala Rekha*[2]

[1]Research Scholar, Department of Computer Science and Engineering, Koneru Lakshmaiah Education Foundation (Deemed to be University), Hyderabad, 500075, Telangana, India.

[2]Associate Professor, Department of Computer Science and Engineering, Koneru Lakshmaiah Education Foundation, (Deemed to be University), Hyderabad, 500075, Telangana, India.

[1]https://orcid.org/0000-0003-3047-6387, [2]https://orcid.org/0009-0003-4933-4255

Email: sireeshagireesh@gmail.com,*gillala.rekha@klh.edu.in

ARTICLE INFO

Article History

Received: September 11, 2025

Reviewed: May 4, 2026

Accepted: June 16, 2026

Published: July 31, 2026

Keywords:

Citrus Huanglongbing (HLB),
Automated Disease Detection,
DCNN,
AlexNet architecture,
VGG19,
ResNet18,
Inception-V3

ABSTRACT

One of the most effective ways to combat diseases like Huanglongbing (HLB; aka citrus greening) is through early detection. Since HLB is a major disease causing significant losses in citrus production worldwide, there is a need for cheap and efficient methods for detecting it so that treatment can begin at the earliest stage. Deep learning techniques using convolutional neural networks (CNNs) are becoming the primary tools for disease detection in computer vision; however, it remains difficult to distinguish HLB from other citrus diseases. Diagnostic methods based on traditional techniques, e.g., quantitative real-time polymerase chain reaction, are costly and require large datasets to train CNN models. One way to tackle the lack of labelled images is to use transfer learning with pre-trained CNNs, which can also perform well on smaller datasets. The objective of the research is to evaluate (AlexNet, VGG19) the chain and the directed acyclic graph (DAG) CNN architectures (ResNet50, Inception-V3) for the three-class classification of Huanglongbing (HLB), healthy leaves, and 10 other citrus abnormalities. To do this, a dataset containing 955 colour images of Citrus leaves from southern India was used. Additionally, 10-fold cross-validation was performed. The experimental results showed that all the CNN models achieved a sensitivity of over 98% in detecting HLB. Yet VGG19 achieved the highest sensitivity score across all tests, despite having fewer parameters than Inception-V3. These findings indicate that models with more parameters are better able to handle the challenges posed by small datasets and, as a result, enable successful transfer learning for HLB detection. The present paper concerns the selection of CNN models for citrus disease detection. It offers a low-cost, portable solution that can help small-scale farmers in low-income areas reduce their crop losses.

Copyright ©2026 by authors and Galileo Institute of Technology and Education of the Amazon (ITEGAM). This work is licensed under the Creative Commons Attribution International License (CC BY 4.0).

I. INTRODUCTION

The citrus family has been one of the most important contributors to the global agricultural economy. They are the main source of nutrition, money, and jobs that the world needs. Among these crops, lemons, oranges, and limes have the highest commercial value and are the major contributors to the food industry and human diets. However, the productivity and profitability of citrus farming are under constant threat from pests and diseases. One of the most fatal diseases that leads to HLB (Huanglongbing) or citrus greening is the case. It is caused by a bacterium (Candidatus Liberibacter asiaticus) that is most commonly carried by the Asian citrus psyllid (Diaphorina citri). Eventually, the illness leads to the tree's deterioration, the yellowing of the leaves, the production of abnormal fruit, and, finally, the tree's death. Actually, in nations such as India, where citrus cultivation is a major activity, HLB is a major problem that threatens sustainable agriculture and adversely affects smallholder and commercial farms alike. The extent of HLB's spread has become so severe that it now threatens farmers' lives and leads to significant crop losses in both quantity and quality [1], [2].

The disease's qualities, i.e., its long environmental persistence and spread via insect vectors, only compound the difficulties of its control, thereby making it a priority for research and management across all citrus-growing areas worldwide. Traditional methods for identifying HLB rely mainly on experts conducting visual inspections, laboratory testing, or using diagnostic kits. Nevertheless, these approaches are labour-intensive, slow, and unsuitable for large-scale operations. The rapid and widespread distribution of HLB and the challenge of early detection necessitate an efficient, automated, and scalable solution to identify infected plants and help stop disease outbreaks. Most conventional methods have a low success rate in early detection of the disease, and visual symptoms of HLB may be similar to other physiological disorders, which will lead to an incorrect diagnosis and prolonged waiting time for treatment [3], [4]. Timely diagnosis of an illness at the earliest stage is vital for treatment, especially when symptoms are barely visible or even unknown. Deep learning has been identified as a novel, effective method for automating disease detection in agriculture, leveraging the latest artificial intelligence (AI) and computer vision. The introduction of deep convolutional neural networks (CNNs) has revolutionised image classification; as a result, deploying these techniques to detect HLB in citrus plants is widely regarded as a perfectly feasible task. These networks have a gift for spotting the tiniest details and image features. This way, they can distinguish between healthy and infected plants just as well. CNNs are now the leading models for plant disease recognition because they extract features directly from the original image, thereby drastically reducing the need for manual labour [5]. Apart from disease management, AI in agriculture has also facilitated plant detection and advanced decision-making for precision farming. This paper sheds the spotlight on the use of CNNs for farm diagnostics. HLB detection is the primary focus of this article, alongside other common citrus diseases researchers have studied.

The paper compares different CNN models. To provide a complete picture of a model's performance under extreme data shortages and resource constraints, these models include traditional convolutional architectures (AlexNet, VGG19) and newer DAG-based architectures (ResNet18, Inception-V3). The paper used a dataset of 955 images of Citrus leaves that were captured under the most stringent conditions. Besides healthy leaves, it also contained the first 10 festivals. Using 10-fold cross-validation, the paper achieved the highest sensitivity, demonstrating the HLB model's reliability. In all experiments with HLB, VGG19 led the way: it consistently achieved perfect sensitivity, even outperforming more complex architectures like Inception-V3 and ResNet18, which are typically regarded as high-performing on large datasets. It shows that simplified models can remain highly effective when data is limited, prioritising efficiency and accuracy over computational complexity alone. Besides that, CNNs have been quite a success story in small-data circumstances; this paper really advances the discussion. The present research contradicts this statement by showing that VGG19 can outperform its rivals; thus, the more complex, the better, is not true. Also, the discussion includes maximising diagnostic accuracy while minimising computational overhead, which is mainly important in resource-limited settings. Also, the research proposes that small-scale farmers, who are most at risk of suffering from diseases like HLB, may be given economical, easy-to-use, and portable instruments for disease identification, based on this scientific paper. The authors strongly encourage converting these CNN models into Mobile apps or miniature imaging devices, so the outcomes will not only be top-tier AI technologies but also practical agricultural solutions.

II. RELATED WORK

As stated by the Food and Agriculture Organisation of the United Nations (FAO), citrus is ranked as the second most globally grown fruit. Nevertheless, certain diseases caused by fungi, bacteria, pests, and viruses have been identified as lowering citrus production and quality in some areas [6]. Among the issues that have weakened the health of citrus trees, Huanglongbing (HLB), also called citrus greening, is the most virulent. Several areas where the disease has been discovered are South America, North America, Asia, and Africa. In India, HLB is a severe threat to citrus fruit production. The infected trees exhibit HLB symptoms, including leaf blistering, shoot yellowing, reduced fruit size, growth retardation, corky veins, root death, and dieback. These symptoms not only degrade the trees' health but also cause farmers to lose significant money, which in turn affects the citrus industry [7]. Several researchers have been working on machine-learning-based automation for plant leaf disease over the last few years. A recent overview of current image processing developments highlighted the importance of this technology in the development of practical, efficient devices for automated insect and disease identification, especially when combining machine learning and image processing [8]. Additionally, a Sparse Representation Classification (SRC) system for the automated recognition of cucumber diseases was proposed [9], as SRC's robustness to limited training data can enable more accurate and reliable disease detection. And a new characterisation of the dynamic system modulated model, i.e., the Group Method of Data Handling (GMDH), was introduced, along with the use of logistic regression to fit the dataset's statistical features [10]. This model significantly improves performance through its dynamic adjustments. Machine learning has recently been making strides towards developing hybrid models that combine deep learning methods with older techniques.

One of the foremost applications of deep learning and machine learning in the agricultural industry is advanced crop disease detection and diagnosis using image processing. With the goal of automated plant disease detection, the authors of [11] strongly believe that traditional and deep feature extraction methods can be used together, as they are complementary. Although deep learning techniques extract features automatically and traditional methods are better at classification, the authors of [12] propose a new technique that integrates K-means clustering and SVM for effective segmentation and classification of diseased areas on the leaf. Besides, their use of modified SVM methods with post-processing operations has led to a major improvement in classification accuracy [13]. DenseNet architectures, coupled with SVMs, have proven quite effective [14] for disease identification by leveraging deep feature extraction and ensemble learning. A complex hybrid multiclass SVM model has been proposed [15], which employs spatial fuzzy C-means clustering to correct spatial deviations and enhance classification accuracy. One of the chief reasons disease classification models can't be used across different crops is that they aren't directly transferable. Recently, localisation-based algorithms [16] have been proposed as a solution to this issue. These algorithms allow for more accurate and adaptable systems. Also, a leaf recognition technique based on Pulse Coupled Neural Networks (PCNN) was proposed [17], demonstrating that capturing detailed structural and textural features of leaves with PCNN yields significant gains in classification accuracy. Several papers [18] have highlighted the use of convolutional neural networks (CNNs) to, for example, detect diseases on citrus leaves in real-time; and one of the factors contributing to the success of mobile-based diagnostic tools is their accessibility and ease of use for the agricultural sector, which is presently going through significant changes.

The use of AlexNet [19] for categorising plant ailments also demonstrates that CNNs are best suited to highly organised agricultural datasets, thereby enabling high-accuracy, fast disease recognition. Image-based disease detection using deep learning techniques has been explored recently [20]. The application of transfer learning in agriculture has significantly enhanced plant disease classification, particularly when labelled datasets are scarce, leading to new ways of using pre-trained models. Another instance of feature-based classification methods evolving their capabilities is the use of colour histograms and textural descriptors to identify diseases in citrus plants. A comparative analysis of different machine learning methods applied to UAV-based multispectral images for citrus greening detection has revealed the importance of remote sensing technologies in agricultural monitoring. These exploratory studies emphasise the role of multispectral and hyperspectral imaging technologies in the early detection of plant diseases. In fact, a plant leaf disease recognition system based on deep learning techniques achieved a remarkable jump in classification accuracy [21]. Soon after, this research was further developed into smartphone-assisted systems [22] that allow for on-site diagnostics and support disease detection in farming practices. At the molecular level, real-time quantitative PCR (qPCR) is considered the gold standard for detecting Candidatus Liberibacter spp due to its unmatched sensitivity and specificity compared with other methods. qPCR detects the pathogen by targeting bacterial genes, such as 16S rRNA. The introduction of CRISPR-Cas12a-based diagnostic methods, such as DETECTR, has enabled the development of highly sensitive, rapid, and very convenient diagnostic kits for Candidatus Liberibacter asiaticus (CLas) for field applications, thereby promoting early intervention [23]. Then again, digital droplet PCR (ddPCR) has proven to be an excellent tool for detecting ultra-low levels of infection, leading to improved diagnosis even in asymptomatic trees [24]. Techniques based on hyperspectral imaging (HSI) have been extremely effective for the non-invasive detection of HLB by highlighting physiological modifications in citrus trees that are invisible to the naked eye. Hyperspectral data, combined with machine learning algorithms, has played a significant role in enhancing diagnostic efficiency. At the very front line of plant disease diagnosis, CNNs process large datasets to extract highly complex features from images that even top human experts may not recognise [25].

A CNN method trained on images of citrus leaves achieved over 90% accuracy in identifying HLB symptoms [26], indicating the model's strength and potential in real-world settings. Transfer learning, which uses a pretrained model (e.g., VGGNet, ResNet, or Inception) as the starting point, has helped achieve results more quickly while reducing computational resources and training time. All these aspects still enable high accuracy even with a small amount of labelled data [27]. This is an excellent option for resource-constrained areas that lack large, well-annotated datasets. When combined with convolutional neural networks (CNNs), hyperspectral and multispectral imaging have paved the way for non-invasive HLB detection methods. Hyperspectral imaging first captures continuous spectral information, then processes it using a CNN that learns to distinguish healthy from diseased conditions. One combination of processing methods, accompanied by hyperspectral images, produced a CNN that accurately classified HLB-infected trees more than 97% of the time [28], demonstrating the potential of matching spectral data with deep learning for early disease detection without relying on visible symptoms. At the same time, steady enhancements in lightweight CNNs have enabled real-time HLB detection on mobile devices, striking the right balance between efficiency and accuracy without compromise, resulting in a model that is highly portable and mobile-friendly. This A lot eases on-site disease monitoring [29]. Although technology has made significant strides, challenges remain in implementing CNN-based disease detection systems. For instance, factors such as lighting, shadows, and background noise, which influence image quality, can vary from one image to another and may adversely affect the model's performance. To address these problems, the researchers have employed data augmentation and ensemble learning methods to enhance the generalisation capacity of the CNN models [30]. On top of that, the lack of HLB-oriented, standardised HLB-detection datasets is the main challenge in accumulating more extensive and diverse image repositories to support the spread of these technologies in this field.

III. MATERIALS AND METHODS

This section first describes in detail the use of pretrained models such as AlexNet and VGG19 for the primary purpose of classifying Huanglongbing (HLB) in citrus leaves. Additionally, a comparison of the performance of pretrained models such as ResNet-50 and Inception-V3 was conducted to determine the most suitable model for accurate HLB classification.

III.1 TYPES OF CITRUS HLB

Citrus Huanglongbing (HLB) can be classified into different categories depending on various factors. Heat-Tolerant Greening (HTG), caused by Candidatus Liberibacter asiaticus (CLas), is a greening disease that prefers warm climates; thus, it warrants a thermal classification. On the other hand, Heat-Sensitive Greening (HSG), caused by Candidatus Liberibacter africanus (CLaf), is a greening disease that mostly occurs in cold regions. Zinc Deficiency-Induced Greening (ZD) is nutritionally similar to HLB but results from zinc deficiency, while Citrus Stubborn Disease (CSD), caused by Spiroplasma citri, mimics greening symptoms in Mediterranean climates. Citrus Blight (CB) is a disease that causes tree decline in the absence of psyllid vectors, and its cause remains unknown. Phytoplasma-Associated Greening (PAG) is a disease caused by wall-less bacteria transmitted by leafhoppers. In contrast, Seasonal or Cold-Induced Greening (CIG) is a disease caused by environmental stress, such as cold or drought. Cultural or Chemical Stress Greening (CSG) results from poor orchard management or chemical misuse. Mixed Infections Greening (MIG) involves co-infection by multiple pathogens, and Genotype-Specific Greening (GSG) reflects genetic susceptibility in certain citrus species or rootstocks, particularly sweet orange varieties.

III.2 DATA SETS

The primary dataset sources used in this paper are Kaggle and real field data, with a major emphasis on Huanglongbing (HLB) disease in citrus. It contains 955 images acquired under various natural conditions. These diverse images are used to classify the disease and assess the level of infection. Additionally, data augmentation was performed to both supplement the dataset and enhance the model's effectiveness, increasing the dataset to 5,200 images. The techniques of augmentation include mirror flipping, angular rotation, zooming, adjustments to brightness and contrast, conversion to grayscale, noise addition, and cropping.

The data consists of images of healthy citrus and citrus affected by HLB symptoms, enabling easy distinction between the two. During the severity assessment step, manual pixel-level annotations are created using the LabelMe tool [31]. The image pixels are categorized into four groups: healthy, HLB-infected (further divided into the main subclasses for each disease type), and background. Various colours are employed for better differentiation during the labelling. The dataset is split into 70% for training, 20% for validation, and 10% for testing the proposed technique.

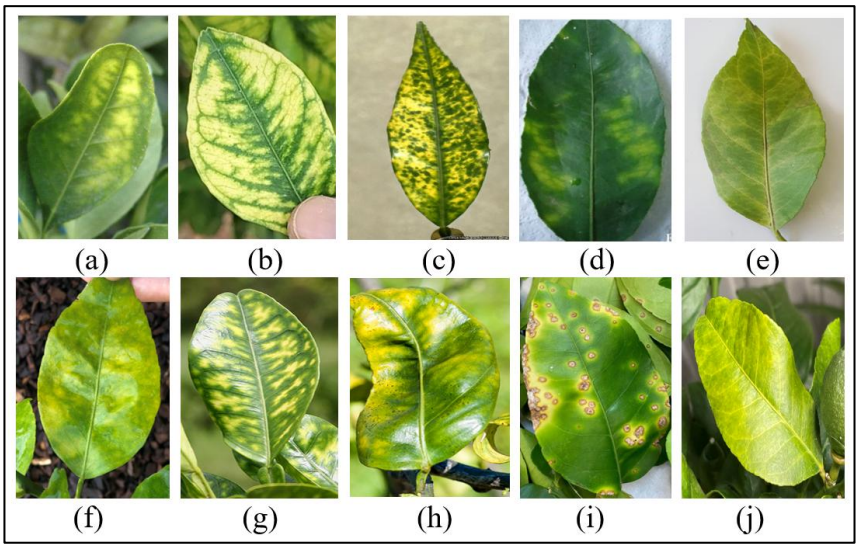


Figure 1: Sample original image dataset for infection with HLB.
(a) CSD (b) ZD (c) CB (d) PAG (e) CIG (f) CSG (g) MIG (h) GSG (i) HTG (j) HSG.
Source: Authors, (2026).

To comply with the input specifications of various models, the dataset is resized. For example, the dimensions of images are converted to (227x227x3) for AlexNet, (224x224x3) for ResNet and VGG19, and (299x299x3) for InceptionV3. After the images are resized, data augmentation techniques are applied. Although CNNs are highly effective, they can still suffer from overfitting, especially when trained on small datasets that limit their ability to generalise. One way to address this problem is to enlarge the dataset using label-preserving transformations. In other words, data augmentation refers to generating new data points by modifying the original images, thus increasing the number of training samples without collecting more.

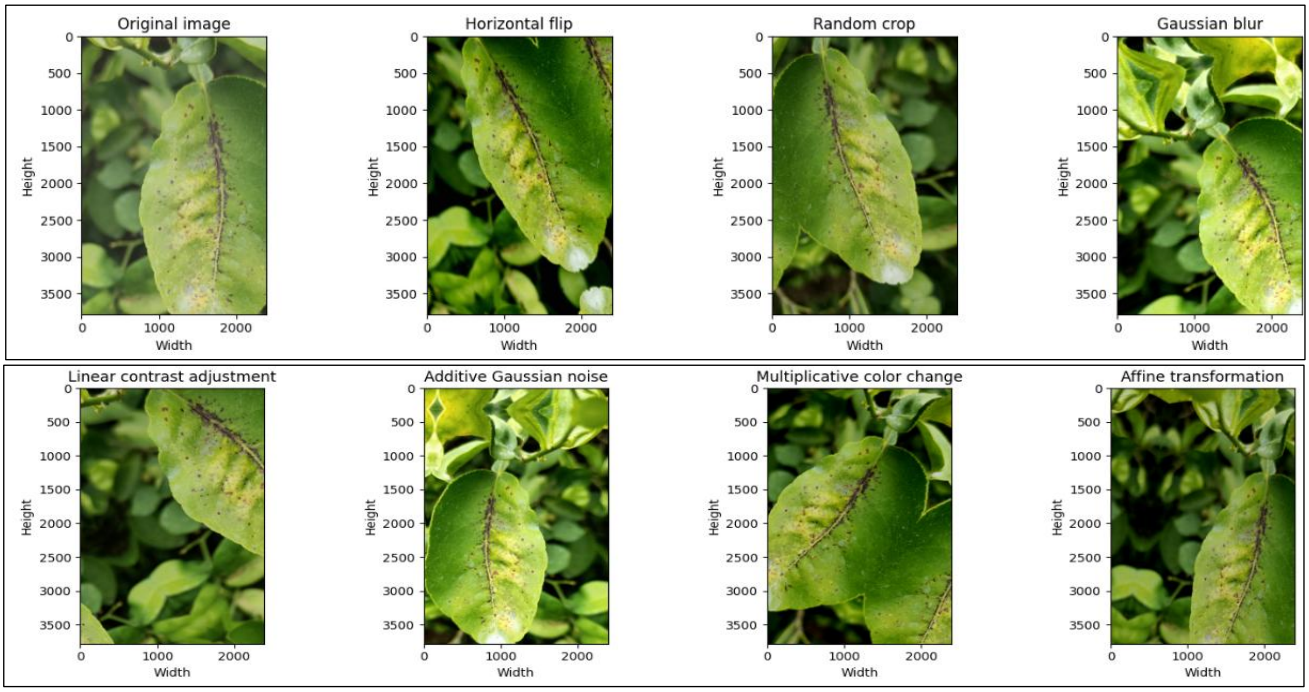


Figure 2: Sample Augmented Image dataset for Citrus HLB.
Source: Authors, (2026).

III.3 HARDWARE REQUIREMENTS AND SOFTWARE SPECIFICATIONS

The proposed structure is implemented using Python libraries and Keras coupled with TensorFlow. The experiments were conducted on a Windows 10 computer with an Intel i7 processor, 16 GB RAM, and a GPU with 8 GB of GDDR6 memory. Both training and testing of the models were performed using the Keras library, with TensorFlow 2.4.1 as the backend.

During hyperparameter tuning, 10 different configurations were tried, and each took nearly 7 hours to complete. In total, the time spent on training and testing the developed DCNN model was about 98 hours.

III.4 DEEP LEARNING MODELS & HYPERPARAMETERS

This research paper utilised deep learning models to optimise the performance of four different models. The study used four models: AlexNet, ResNet-50, VGG-19, and Inception-V3. This part of the paper introduces the background of the models employed in this research, their traits and functionalities.

III.4.1 AlexNet Architecture

The AlexNet model, introduced in 2012, revolutionised deep learning by achieving remarkable success in the ImageNet Large Scale Visual Recognition Challenge.

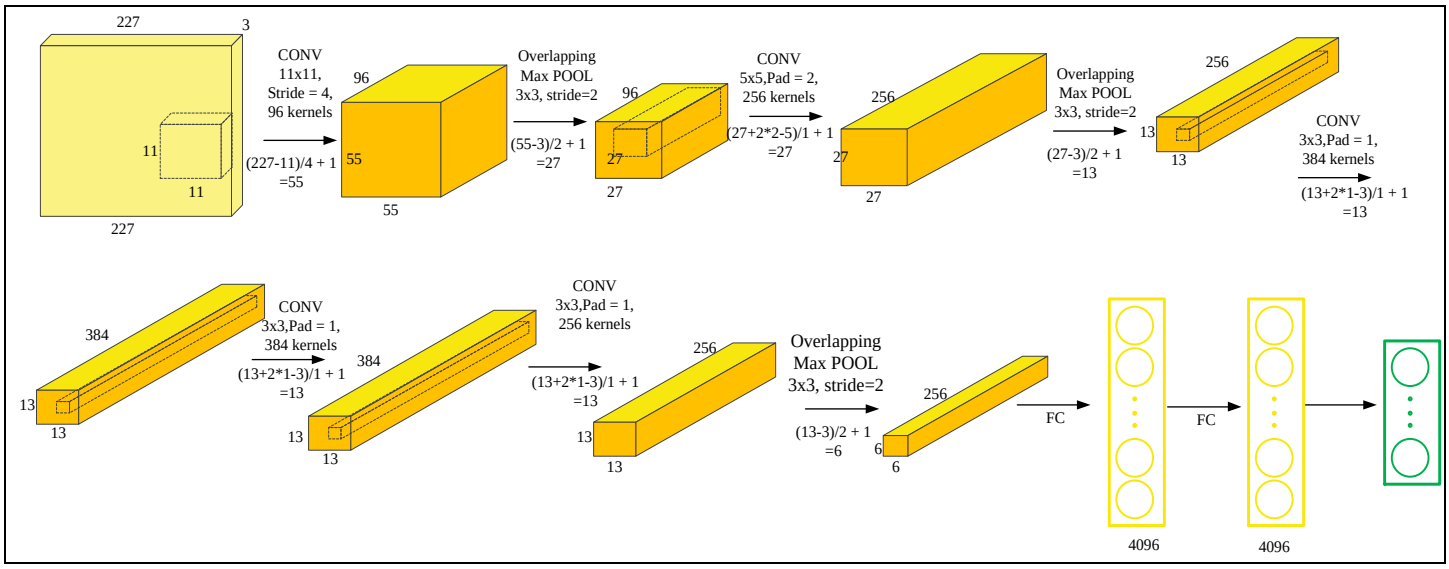


Figure 3: Architecture of AlexNet Classifier.
Source: Authors, (2026).

This CNN is designed to handle input images with a resolution of 227x227x3. The initial step of the network, feature extraction, is performed using a series of convolutional, pooling, and fully connected layers. The first convolutional layer applies 96 11x11 filters with a stride of 4, and the resulting features undergo overlapping max-pooling, which significantly reduces the spatial dimensions. Following the application of 256, 5x5 filters, the layer is subjected to max-pooling again. Further into the network, there are 5 more conv layers, and 3 of them are followed by max-pooling. Eventually, the output feature map has spatial dimensions 6x6 and a depth of 256 channels (6x6x256). The 2 fully connected layers, each with 4096 neurons and the ReLU activation function, receive the flattened output as input. Dropout regularisation is used in those layers to prevent overfitting. The last fully connected layer, which uses softmax activation, gives the probabilities over the 1000 categories. The most important AlexNet features that explain the rise in its performance are the use of the ReLU activation function, which makes it train faster; overlapping max-pooling, which makes it easier to generalise features; and GPU acceleration for training. The success of AlexNet was a major sign that deep learning was superior to traditional methods for image classification, and it paved the way for even more complex architectures. That is why the canonical AlexNet variant remains the foundation of transfer learning and feature extraction in computer vision.

III.4.2 ResNet-50 Architecture

The deep convolutional neural network model ResNet-50 is shown in Figure 4 and is widely used in image recognition and classification. It is part of the ResNet (Residual Network) family, which transformed the training of very deep networks by introducing residual learning. The idea of residual learning is that the network learns residual functions rather than direct ones, which helps address the vanishing gradient problem.

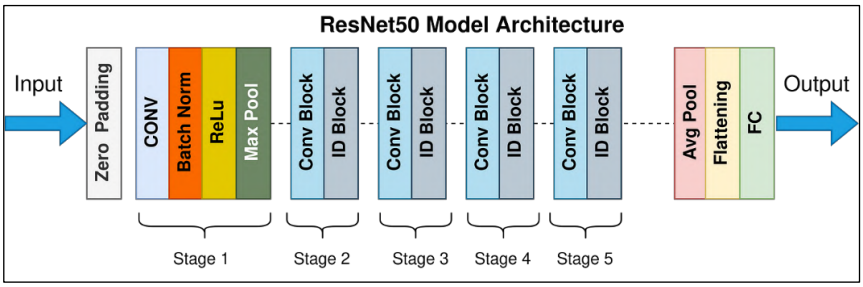


Figure 4: Architecture of ResNet50 Classifier.
Source: Authors, (2026).

The network takes its first input from an image data input layer. Here, zero-padding has been added to preserve the image's spatial dimensions. In Stage 1, the model consists of a convolutional layer that extracts low-level features from the image, followed by batch normalisation to stabilise and speed up training. A ReLU activation layer with non-linearity is added; max-pooling is also performed to downsample and, at the same time, keep essential features. Stages 2 to 5 are composed of a series of convolutional and identity blocks. A convolutional block is a residual block that uses skip connections, i.e. the output of the conv layers is added directly to the block's input. This addition helps the gradient flow smoothly through the network during backpropagation. This feature of deep ResNet alleviates degradation. Identity blocks preserve the input dimensions while learning features that are used more abstractly at a later stage. Throughout the network, the number of filters increases to handle increasingly complex patterns. The output layers finally consist of average pooling to reduce spatial dimensions, flattening to change feature maps into a 1D vector, and a fully connected layer for classification. The size of the fully connected layer depends on the number of classes. With its 50 layers, ResNet-50 finds a compromise between depth and computational efficiency. It is still widely used as the core structure for various image-based tasks, including image classification, object detection, and feature extraction for transfer learning. Due to its robust architectural design and innovative residual connections, it is widely regarded as a benchmark model in deep learning.

III.4.3 VGG19 Architecture

This diagram illustrates the structure of a convolutional neural network (CNN), specially designed for image processing and classification. It takes as input a single image of size 224×224 with 3 colour channels corresponding to RGB. The very first layers of the network consist of convolutional operations with the Rectified Linear Unit (ReLU) as the activation function. The main objective of these convolutional layers is to capture the image's spatial layout while shrinking its spatial dimensions and increasing the depth of the feature maps. For instance, the network passes on features of size 224×224×64, 112×112×128, 56×56×256, and so on, along with the layer types. In this way, the net can depict both the minute and the large-scale features of the image. The feature maps at different depths of the hierarchy are next fed into a global average pooling layer at the 14×14×512 stage. This layer considerably reduces the spatial dimensions by averaging feature values; hence, it provides dimensionality reduction while retaining the basic features for classification. Then the feature maps are passed to fully connected layers, which are the highest-connectivity point in the network, from which the extracted features are collected. These layers, together with the ReLU activation function, are responsible for generating complex decision boundaries by the model. Having a dropout layer with a rate of 0.5 in the network architecture can help reduce overfitting during training. It can randomly turn off half of the neurons. This regularisation method is the main source of the model's ability to generalise very well. The last layer of the model is a softmax layer that transforms the network's output into probabilities over each target class. In addition, the last layers are fine-tuned to adjust the pre-trained network for the specific classification task, which is why it achieves better performance.

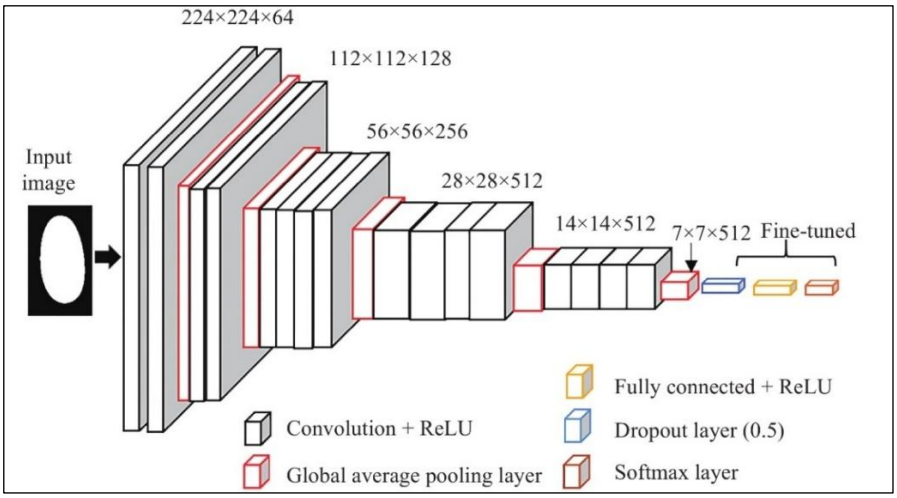


Figure 5: Architecture of VGG19 Classifier.
Source: Authors, (2026).

III.4.4 Inception V3 Architecture

The Inception-v3 model is among the top convolutional neural networks for image classification, and its effectiveness and efficiency have been widely acknowledged. The model receives an input image of size 299x299x3 and produces an 8x8x2048 feature map. It then classifies each input image into one of 1001 classes (or the background class). Belonging to the Inception family, it follows the design philosophy of making speed and accuracy trade-offs, like its ancestors, yet also introduces several changes that improve hardware efficiency and increase representational power. The crux of Inception-v3 lies in the Inception modules, which perform convolutions with different kernel sizes (e.g., 1x1, 3x3, and 5x5) concurrently. These modules merely don't output their outcomes to concatenate to gather very detailed features from the input data. The extensive use of 1x1 convolutions throughout the network helps drastically reduce computational cost while preserving the most important information. In addition to convolutions, the architecture uses several pooling layers, such as max and average pooling, which reduce the input's spatial dimensionality while accentuating salient features. The last phase of feature extraction produces a single, high-dimensional feature map (8x8x2048) that encodes a highly abstract, high-level representation of the input image. For classification purposes, the 3D feature map will undergo global average pooling, producing a 1D vector. Then, to get the class probabilities, a fully connected layer followed by a softmax activation will be used.

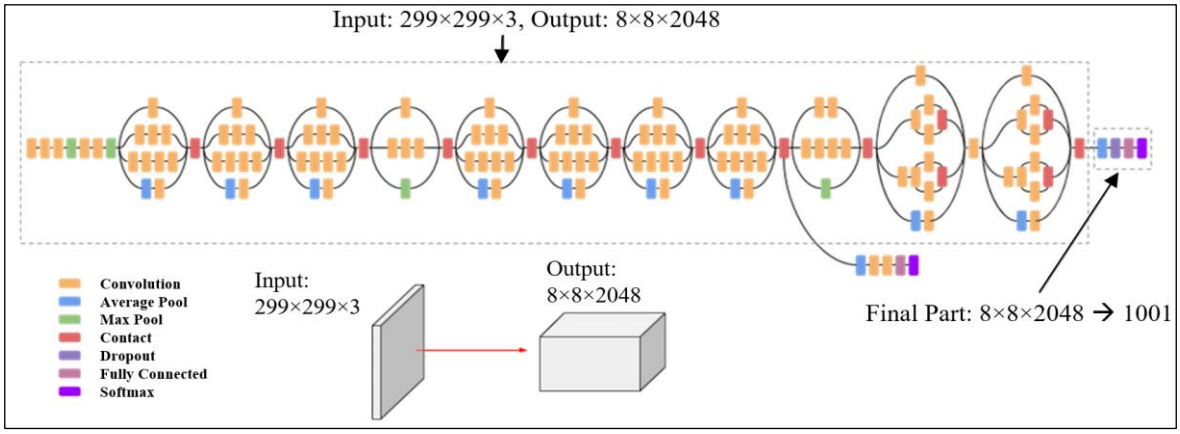


Figure 6: Architecture of InceptionV3 Classifier.
Source: [32].

Although Inception-v3 is quite old, it still introduces many new elements. One of those elements is factorised convolutions, which split large convolutions into smaller ones. For instance, a 5x5 kernel can be obtained by two consecutive 3x3 kernels, thereby reducing the number of calculations. Another revolutionary element is that auxiliary classifiers are incorporated into the training phase, thereby improving gradient flow and, as a result, eliminating the vanishing-gradient problem in deep layers. The model, with a proper combination of depth, accuracy, and computational efficiency, has become a standard solution for image classification, transfer learning, and feature extraction, among other tasks. So, hyperparameter tuning plays an important role in enhancing the performance of the proposed models. The results show that the model's accuracy measures quality. The summary of the hyperparameters used during training is provided below: AlexNet hyperparameters are in Table 1; Table 2 shows the parameters of ResNet and VGG19; and Table 3 presents the details for Inception-v3.

Table 1: Hyperparameters for AlexNet.

Parameter	Value
Image size	227 × 227 × 3
Batch size	64, 32, and 16
Number of epochs	100, 50, and 30
Optimizers	SGD, Adam, and RMSprop
Learning rate	0.01, 0.001, and 0.0001
Kernel size	11 × 11, 5 × 5, and 3 × 3
Number of hidden layers	5, 7, and 9
Loss function	Cross entropy

Source: Authors, (2026).

Table 2: Hyperparameters for ResNet50 and VGG19.

Parameter	Value
Image size	224 × 224 × 3
Batch size	128, 64, and 32
Number of epochs	150, 100, and 50
Optimizers	Adam, SGD, and RMSprop
Learning rate	0.001, 0.01, and 0.005
Kernel size	7 × 7, 3 × 3, and 1 × 1
Number of hidden layers	50, 19, and 34 (ResNet)
Loss function	Cross entropy

Source: Authors, (2026).

Table 3: Hyperparameters for InceptionV3.

Parameter	Value
Image size	299 × 299 × 3
Batch size	64, 32, and 16
Number of epochs	200, 150, and 100
Optimizers	Adam, RMSprop, and SGD
Learning rate	0.001, 0.0005, and 0.0001
Kernel size	3 × 3, 5 × 5, and 1 × 1
Number of hidden layers	48, 54, and 60
Loss function	Cross entropy

Source: Authors, (2026).

III.5 PROPOSED APPROACH FOR HLB DETECTION

III.5.1 Detection Scheme

Figure 7 displays the block diagram of the proposed HLB detection structure which contains three main parts: 1) image acquisition, capturing of leaf images that reflect real field conditions i.e. images taken from 13 acres citrus orchards of Gopanapally village, Podalakur Mandal, Nellore District, Andhra Pradesh, South India and also downloaded from Kaggle datasets; 2) segmentation (isolation of the leaf's inner parts); and 3) the CNN modeli.e. classification which separates 10 types of HLB abnormalities apart from healthy image.

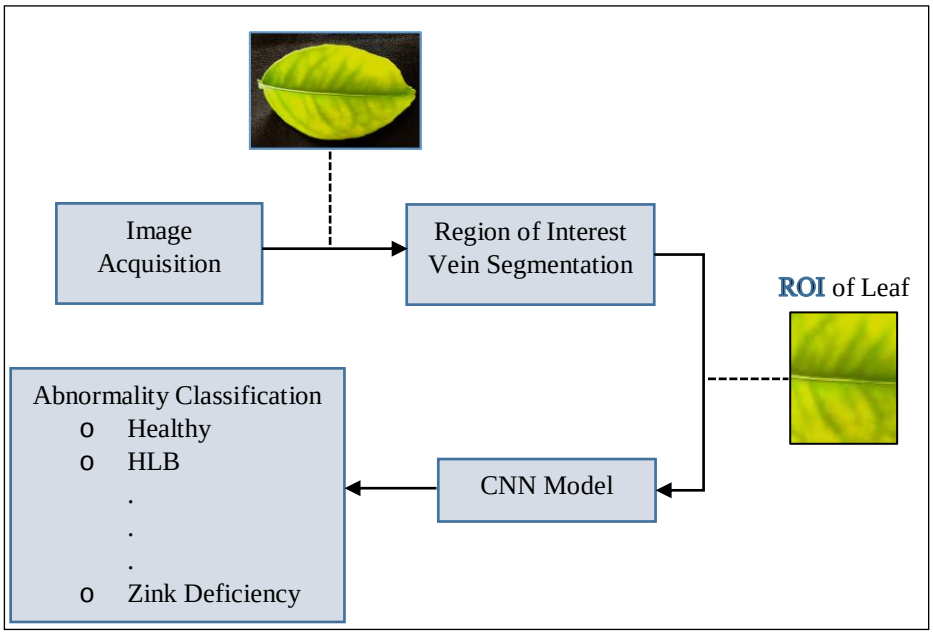


Figure 7: Image detection scheme for Citrus HLB classification.
Source: Authors, (2026).

III.5.2 Proposed Integrated Methodology

The strategy used for Huanglongbing (HLB) identification was a hybrid technique that merged leaf vein feature extraction with convolutional neural network (CNN) detection, as illustrated in Figure 8. The planned method combined domain-specific leaf features with the latest deep learning techniques to achieve precise disease classification. Below is a detailed explanation of each step of the algorithm:

Step 1. Leaf Image Acquisition

This begins by taking extremely clear photos of citrus leaves. These images work as the primary inputs of the subsequent process. Leaf sampling involves a fairly balanced selection of healthy and potentially diseased leaves, which are then used to create the training and testing datasets.

Step 2. Vein Segmentation

Leaf vein segmentation is performed on raw leaf images to isolate vein patterns. Segmentation is a way to keep only the major and minor veins of a leaf while discarding the lamina and other non-vein areas. This step is crucial as HLB-related leaf alterations are mainly visible in the veins. Here, the most important step is isolating veins from leaves. For this purpose, a thresholding technique is employed as described by this formula:

$$\text{Thresholding: } I_{seg}(x,y) = \begin{cases} 1, & if\ I(x,y) > T \\ 0, & Otherwise \end{cases}$$

Where T is the Threshold Value

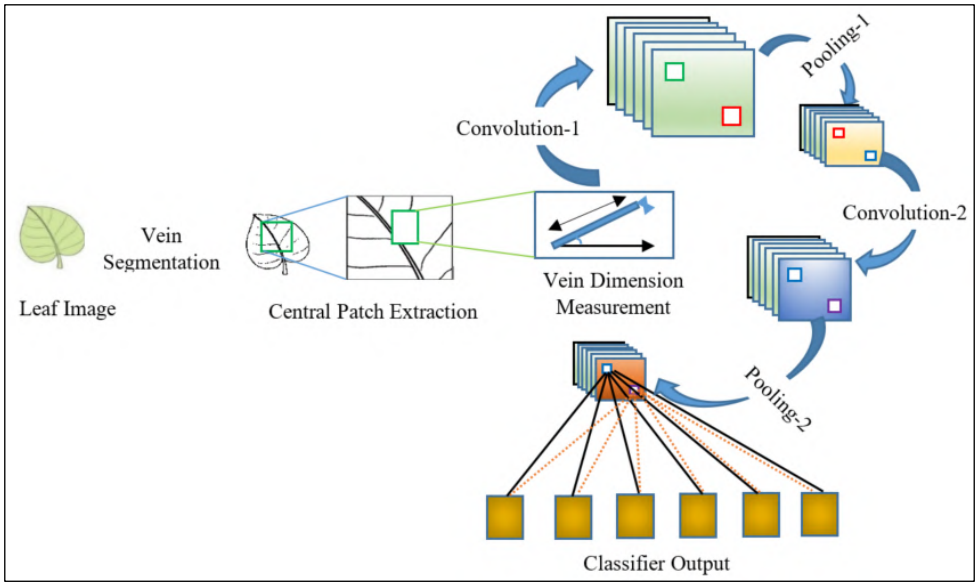


Figure 8: The proposed Integrated CNN Architecture model for HLB classification.
Source: Authors, (2026).

Step 3. Central Patch Extraction

Local vein structures have been segmented to obtain the central patch, which delimits a small area of high concentration. This particular patch of the veins contains fundamental features, such as where the veins branch and their width and density. The study has narrowed down the most vital area of the leaf vein structure by isolating it from the rest of the leaf surface, which is a source of noise. The central part of the vein structure is used to obtain a region of interest (ROI). The mathematical representation of ROI is like this:

$$P(x, y) = I_{seg}(x_i{:}x_f, y_i{:}y_f)$$

Where, $(x_i, y_{i,})$ and (x_f, y_f) define the bounding box

Step 4. Vein Dimension Measurement

The extracted patch is further analysed to determine the vein dimensions, which are handcrafted features indicating the presence of HLB infection. These parameters include:

a. Vein thickness.
b. The directions of veins and the angles of the branches.
c. Vein concentration and spacing.

$$\text{Length: } L = \sqrt{(x_2 - x_1)^2 + (y_2 - y_1)^2}$$

Width: The distance is measured perpendicularly between two parallel vein edges.

$$\text{Angle: } \theta = \arctan\left(\frac{y_2 - y_1}{x_2 - x_1}\right)$$

These features are inspired by biology and provide important clues about the structural changes that occur as a result of HLB.

Step 5. Feature Extraction via CNN

The central patch is input to a convolutional neural network (CNN) for automatic feature extraction. The steps are:
Convolution Layer 1: Identifies simple visual elements such as lines, edges, and textures.
Pooling Layer 1: Reduces the sizes of the feature maps to save computational resources.
Convolution Layer 2: Dissects complex vein interactions and structural details at a higher level.
Pooling Layer 2: Further compacts the feature rewriting for the next steps.

$$O_{ij}^{(1)} = \sum_m \sum_n I_{(i+m)(j+n)} \cdot K_{mn}$$

Where K_{mn} is the kernel/filter

Pooling-1: Spatial dimensions are reduced; max-pooling is applied in this paper, which is represented by the formula

Convolution-1: Applies filters to detect basic patterns

$$P_{ij} = max\{O_{ab} | a \in [i, i+s], b \in [j, j+s]\}$$

Convolution-2 and Pooling-2: Extract deeper features and further reduce the dimensions

Step 6. Classification

The features extracted are what a classifier is trained on; a fully connected neural network with a softmax output layer is the most common option. The classifier's results are a probability or a binary value indicating whether a leaf is healthy or HLB-infected. When it comes to multiclass problems, the classifier uses the softmax activation function defined by this formula,

$$P(C_k) = \frac{e^{z_k}}{\sum_j e^{z_j}}$$

Where z_k is the input to the k[th] neuron in the final layer.

This research considered 10 classes (855 images) of HLB-infected image samples and 1 class of Healthy (100 images) for disease classification; the details are tabulated in Table 4.

Table 4: Citrus HLB characteristics and dataset details.

S No	Class	# Samples	Disease description
1	HTG	85	Heat-Tolerant Greening
2	HSG	100	Heat-Sensitive Greening
3	ZD	120	Zinc Deficiency-Induced Greening
4	CSD	80	Citrus Stubborn Disease
5	CB	80	Citrus Blight
6	PAG	80	Phytoplasma-Associated Greening
7	CIG	75	Cold-Induced Greening
8	CSG	75	Chemical Stress Greening
9	MIG	80	Mixed Infections Greening
10	GSG	80	Genotype-Specific Greening
11	HLT	100	Healthy

Source: Authors, (2026).

III.6 PERFORMANCE METRICS

Performance parameters evaluate the model's ability to learn and generalise on image data. These include classification metrics**,** loss functions, and other performance-related indicators specific to deep learning models.

III.6.1 Classification Metrics

These metrics measure the model's ability to classify data correctly. They are computed from the CNN's predictions.

$$\text{Accuracy} = \frac{\text{TP} + \text{TN}}{\text{TP} + \text{TN} + \text{FP} + \text{FN}}$$

$$\text{Precision} = \frac{\text{TP}}{\text{TP} + \text{FP}}$$

$$\text{Recall (Sensitivity)} = \frac{\text{TP}}{\text{TP} + \text{FN}}$$

$$\text{F1 Score} = 2 * \frac{\text{Precision} \times \text{Recall}}{\text{Precision} + \text{Recall}}$$

$$\text{Specificity (True Negativity Rate)} = \frac{\text{TN}}{\text{TN} + \text{FP}}$$

Where, TP = True Positive, TN = True Negative, FP = False Positive and FN = False Negative

III.6.2 Loss Function

The loss function indicates how well the model performs during training and validation. This research utilised the cross-entropy loss function, detailed in the equation below.

$$Loss = \frac{1}{N}\sum_{i=1}^{N}\sum_{j=1}^{C} y_{ij} \ . log(\hat{y}_{ij})$$

Where, y_{ij} is the ground truth and $\hat{y}_{ij}$ is the predicted probability for class j.

III.6.3 Model Specific Metrics

These are specific to the CNN model and the nature of the Task:

- Confusion matrix: A Visual representation of predicted values and actual labels, helping to assess the misclassification rates.
- IoU (Intersection over Union): Used in object detection and segmentation tasks to evaluate overlap between predicted and actual bounding boxes/Masks

$$\text{IoU} = \frac{\text{Area of Overlap}}{\text{Area of Union}}$$

- Dice Coefficient (F1 score for segmentation): Used for image segmentation

$$Dice = \frac{2 \ . \ |A \cap B|}{|A| + |B|}$$

Where A is the predicted segmentation, and B is the ground truth.

IV. RESULTS AND DISCUSSIONS

This section presents the performance evaluation of the convolutional neural network (CNN) models, namely InceptionV3, ResNet50, AlexNet, and VGG19, for classifying Huanglongbing (HLB) and other citrus disorders using a dataset of 955 colour images of citrus leaves. The models were evaluated over multiple epochs, with the primary metrics being accuracy, loss, precision, recall, specificity, F1-score, Intersection over Union (IoU), and pixel accuracy.

IV.1 INCEPTIONV3

The two diagrams summarise the training and validation metrics for the InceptionV3 CNN model over 200 epochs. Figure 9 shows accuracy across epochs, whereas Figure 10 shows loss across epochs. Both aim to reveal the model's learning and ability to generalise to unseen data. In the accuracy diagram, training accuracy (blue line) gradually increases with training. Finally, this line reaches 1.0, indicating that the model has successfully learned the patterns in the training dataset. But validation accuracy (red line) fluctuates and stays at a lower level. Eventually, this line will fluctuate between 0.75 and 0.85. The gap between training and validation accuracies indicates a generalisation problem, a symptom of overfitting. Such behaviour is not unusual for complex architectures like InceptionV3, which can capture highly detailed patterns. Getting rid of overfitting may require applying different regularisation techniques, such as dropout, data augmentation, or early stopping, to improve accuracy on the validation set.

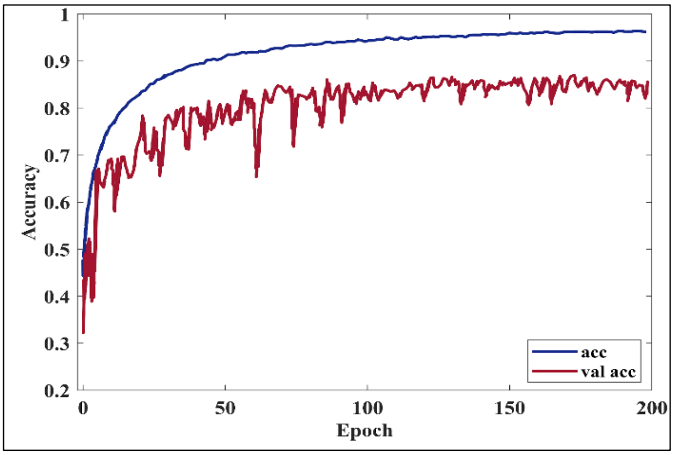


Figure 9: Training and validation accuracy curves with InceptionV3.
Source: Authors, (2026).

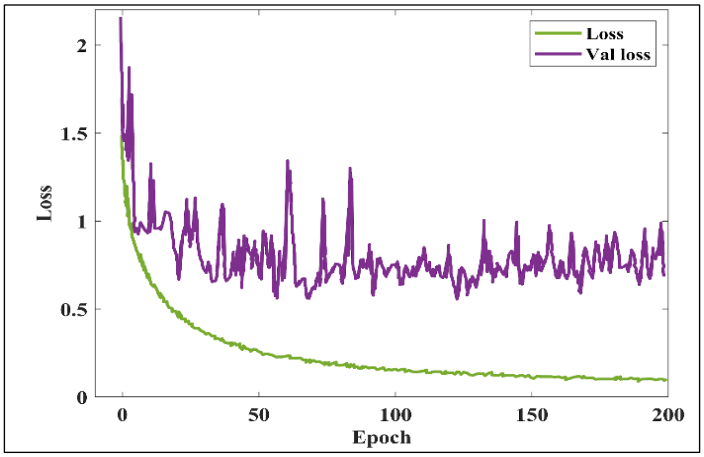


Figure 10: Training and validation loss curves with InceptionV3.
Source: Authors, (2026).

The loss graph conveys information beyond just the training loss (the green line), which continues to decrease in a steady, smooth manner, indicating good optimisation of the training objective. Whereas the validation loss (purple line) starts much higher and shows large fluctuations throughout the training process, one can see a very slight downward trend over time. The fact that the validation loss remains higher than the training loss indicates that the model is unstable on new data.

This instability might be a result of overfitting or some discrepancies in the distributions of the training and validation datasets. Tuning hyperparameters, using learning rate schedules, or simply verifying that the validation dataset is representative could help address the issue. The main point is that the InceptionV3 model is well-suited to the training data, as it achieved high training accuracy and low loss. But the variations in validation accuracy and loss, together with the large divergence between the training and validation metrics, suggest that the model is not very good at generalising.

IV.2 RESNET50

Figures 11 and 12 illustrate the training and validation performance of a ResNet model over 100 epochs. The progress made and the ability to generalise are evident. The training accuracy is illustrated by the blue curve in Figure 11, which shows a continuous increase; near epoch 80, at around 0.9, it indicates that the model is very well able to identify the patterns in the training data. Simultaneously, the validation accuracy (red curve) initially improves but remains below the training accuracy, indicating the challenge of generalising to new data. At about epoch 85, validation accuracy drops sharply, likely a sign of overfitting or an issue with the validation process, but it then goes back up. Figure 12 shows the training loss (green curve) and the validation loss (purple curve). Constant reduction in training loss indicates that the model is increasingly confident in the training data. Although validation loss is a bit erratic, it eventually decreases. The correlation between the rise in validation loss around epoch 85 and the fall in validation accuracy in Figure 11 strongly suggests overfitting or data inconsistencies.

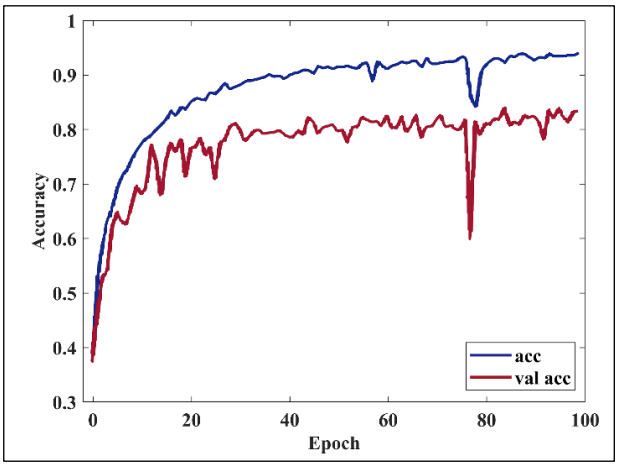


Figure 11: Training and validation accuracy curves with ResNet50.
Source: Authors, (2026).

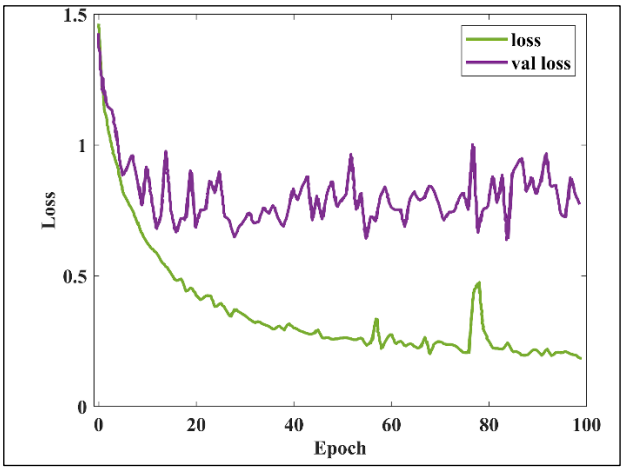


Figure 12: Training and validation loss curves with ResNet50.
Source: Authors, (2026).

IV.3 ALEXNET

Figures 13 and 14 show the AlexNet model's training and validation performance over 50 epochs. Whereas the former figure (Figure 13) presents accuracy plots, the latter (Figure 14) displays loss plots. These two figures together tell the story of the model's learning and its ability to generalise learned patterns to new, unseen data. The slowly, steadily increasing training accuracy (blue line) in Figure 13 eventually reaches 0.9. This shows that, apart from the model figuring out the relationships among the elements of the training data, it is also doing so very well. However, the validation accuracy (orange curve), lagging behind the training accuracy, levels off somewhere between 0.75 and 0.8 after 20 epochs. The gap between training and validation accuracies indicates a lack of model generalisation and is a hallmark of overfitting the training data. Since AlexNet is one of the very few models with such a strong capacity to learn detailed patterns, it also exhibits overfitting, as seen here. Regularisation methods such as dropout, weight decay, and data augmentation are well known to reduce overfitting and improve generalisation.

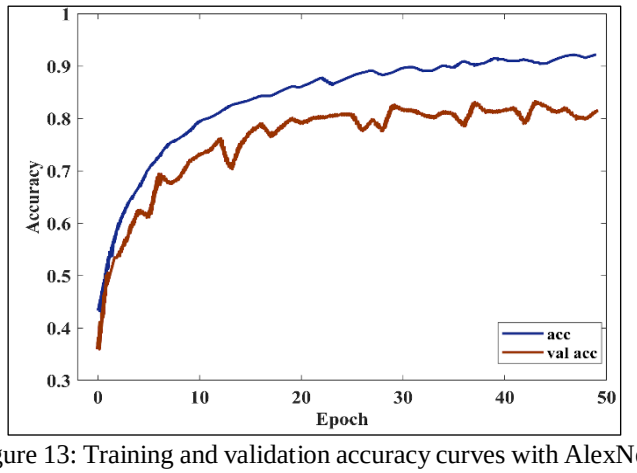


Figure 13: Training and validation accuracy curves with AlexNet.
Source: Authors, (2026).

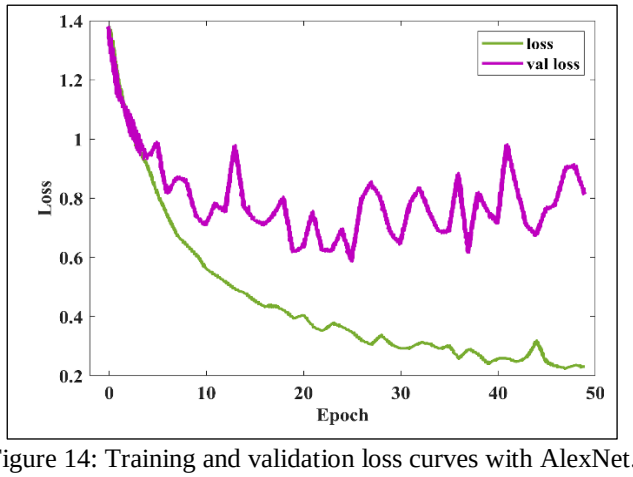


Figure 14: Training and validation loss curves with AlexNet.
Source: Authors, (2026).

The loss patterns are displayed in Figure 14. A decrease in the training loss (green curve) that occurs evenly and slowly over the epoch period indicates well-ordered training and results in a converged model. Conversely, the validation loss (purple curve) initially appears high and exhibits large fluctuations as it decreases, which is typical at later epochs when the model starts to overfit. Despite an overall decrease in the first epochs of training, the fluctuations remain quite strong even beyond epoch 10. These random variations in validation loss, plus the higher loss on the validation set than on the training set, reveal that the model is overfitting, a common problem the model neglects. The steady difference between training and validation loss is yet another sign that the model's generalisation performance needs improvement.

IV.4 VGG19

Graphs in Figures 15 and 16 show the training and validation metrics for two deep learning models, VGG19 and AlexNet, over 150 epochs. Such representations indicate the learning progression, the potential for generalisation, and the efficiency of model optimisation.

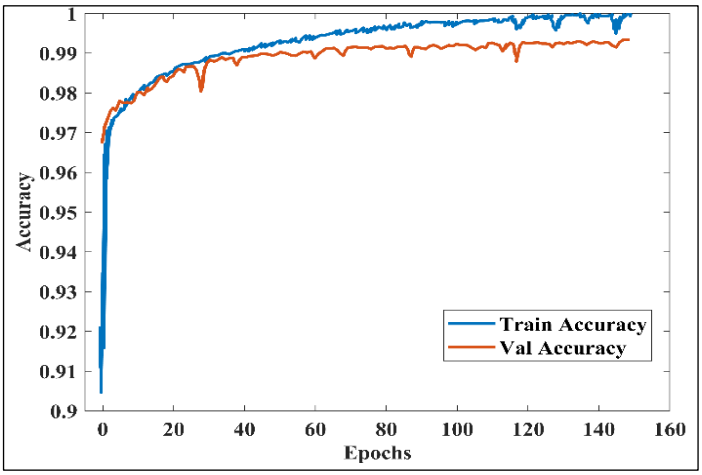


Figure 15: Training and validation accuracy curves with VGG19. Source: Authors, (2026).

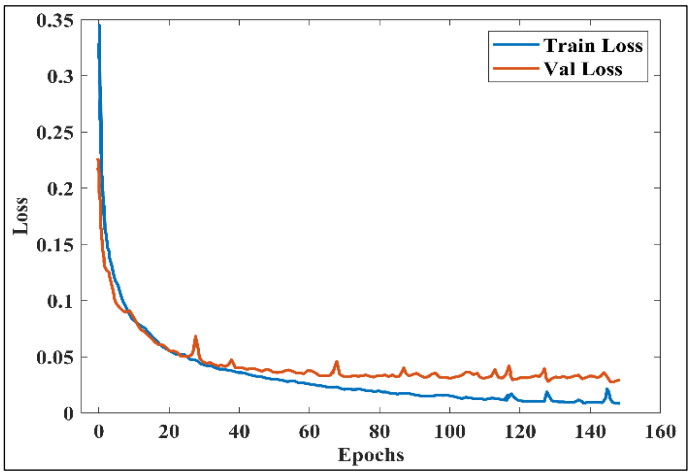


Figure 16: Training and validation loss curves with VGG19. Source: Authors, (2026).

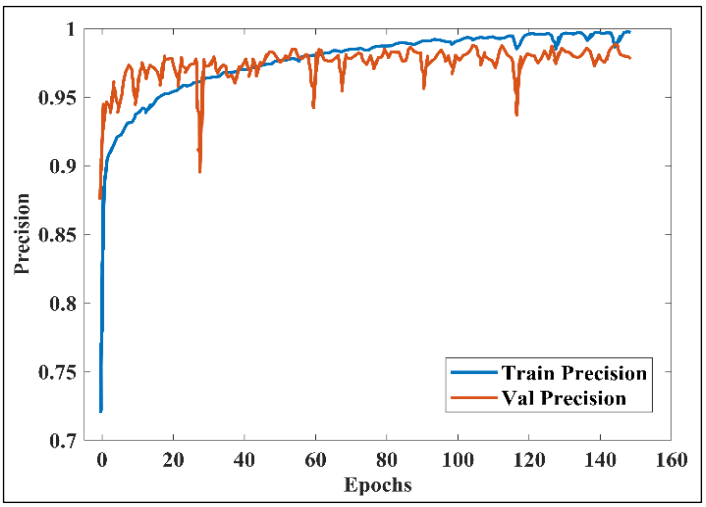


Figure 17: Training and validation precision curves with VGG19. Source: Authors, (2026).

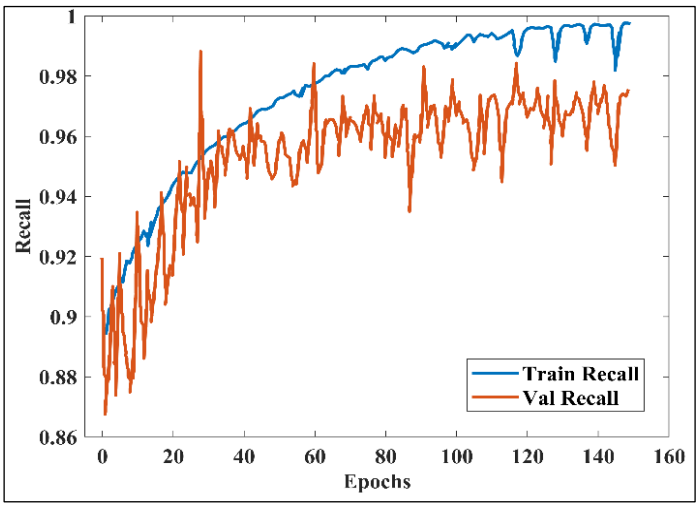


Figure 18: Training and validation recall curves with VGG19. Source: Authors, (2026).

The VGG19 model achieves a final training accuracy of nearly 1.0 and a validation accuracy of approximately 0.98, with the difference between them very small. In the AlexNet example, the training loss decreases from 0.35 to 0.02, while the validation loss decreases from 0.35 to 0.03. Both outcomes indicate that the two models are good, with AlexNet being highly optimised and VGG19 achieving excellent accuracy. Still, the minor disparity between training and testing metrics suggests that the models' performance can be further improved through adjustments, such as tuning hyperparameters or incorporating additional regularisation techniques. Still, the small gaps between the training and validation scores suggest that the models' results could be improved by conducting experiments such as hyperparameter tuning or incorporating additional regularisation techniques. Figure 15 illustrates the performance of VGG19 using accuracy graphs. The analysis reveals that both the overall training and validation accuracies increased incrementally, reflecting the model's steady learning during training and validation. The training accuracy indicated by the blue line shows that the network reached 0.90 in the first epoch and, by the 150th epoch, had nearly achieved perfect training accuracy. This indicates that the model nearly flawlessly understands the patterns in the training set. Then, there is a certain pattern in validation accuracies: the orange line shows similar growth, though the training accuracies were a little higher. Starting from approximately 0.90, it finishes with nearly 0.98 at the very last epochs.

Given the minimal difference between training and validation accuracies, the VGG19 model can be considered to generalise well to unseen data. Although slight overfitting could be mitigated by methods such as data augmentation or stronger regularizers, it remains evident in the data. Figure 16 portrays the changes in losses for the AlexNet model, offering new perspectives on the optimisation steps. The blue curve representing the training loss gradually decreases from about 0.35 to nearly 0.02, reaching this level at 150 epochs. Based on the orange validation loss curve, the validation loss follows the same decreasing pattern observed in the training loss. In fact, it starts at around 0.35 and approaches 0.03 by the end of training. That the training and validation loss curves align closely indicates that the model generalizes well and, as a result, is not very susceptible to overfitting. Also, the loss in the initial epochs dropped steeply, further validating how quickly the model captured the essence of the dataset. Figures 17 and 18 present training and validation precision and recall charts for the VGG19 network over 150 training cycles, respectively. The steady rise in training precision shown in Figure 17 is encouraging, as it nearly reaches 1.0 at the end, the best possible score. Validation precision improves during the first few epochs. Still, from around epoch 30 onward, it behaves in a corkscrew manner through the remaining epochs, possibly due to data variability or minor overfitting. Similarly, in Figure 18, training recall increases continuously until it reaches a value close to 1.0 and remains at that level throughout the run, indicating that the model recognises only true positives. Validation recall is oscillating more widely, mainly because the number of false negatives varies with data complexity. These charts show the good and the bad of this model. While the model fit well in the training setting, the changes in validation results suggest there may be difficulties with the model's generalisation to unseen data.

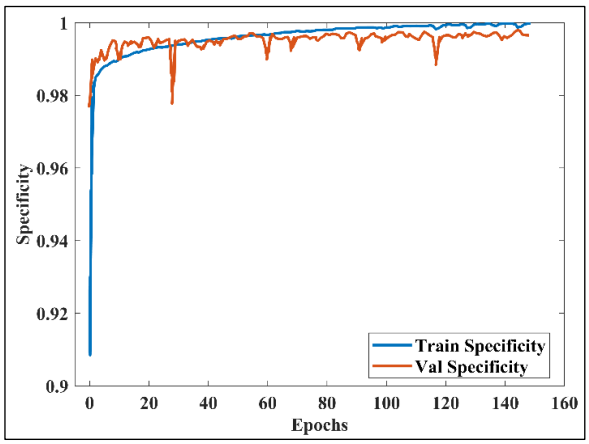


Figure 19: Training and validation specificity curves with VGG19. Source: Authors, (2026).

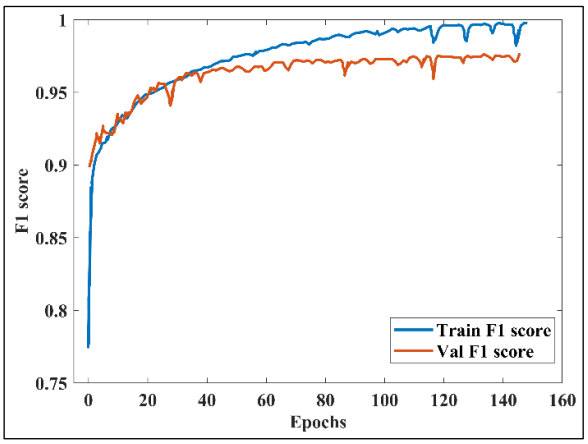


Figure 20: Training and validation F1 Score curves with VGG19. Source: Authors, (2026).

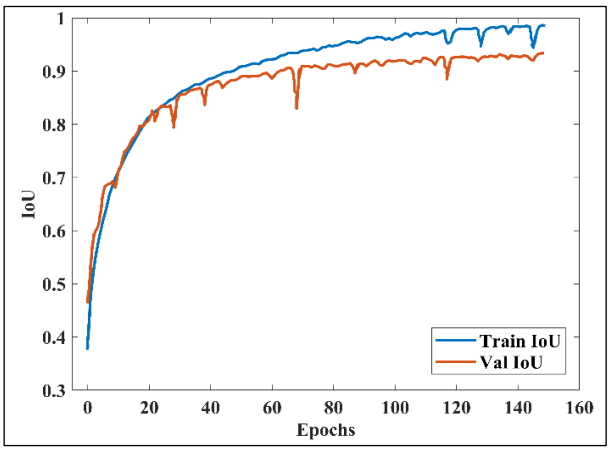


Figure 21: Training and validation IoU curves with VGG19. Source: Authors, (2026).

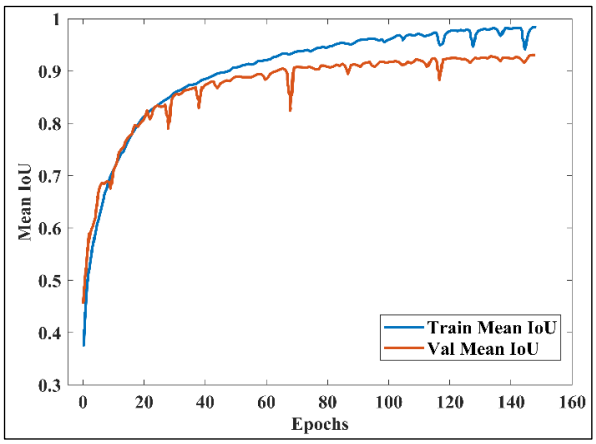


Figure 22: Training and validation mean IoU curves with VGG19. Source: Authors, (2026).

Over 150 epochs, Figures 19 and 20 show the curves of specificity and F1-score for the VGG19 model on both the training and validation sets. In Figure 19, training specificity is indicated by the blue line. After an initial rapid increase, this line remains nearly constant at around 1.0, which corresponds to perfect prediction of the absence of positive cases. In contrast, the orange line representing validation specificity fluctuates slightly over time, likely due to differences between the validation and training data. In Figure 20, the training F1-score is consistently rising; towards the end, it is nearly 1.0, indicating that the model is well balanced between precision and recall. The validation F1-score is increasing but with ups and downs, possibly due to difficulty generalising the solution to unseen data. Figures 21 and 22 illustrate the training and validation IoU curves, as well as the mean IoU curve, for the VGG19 network trained for 150 epochs. Training IoU is steadily rising and ultimately settles near 1.0, indicating that the model can accurately segment the training data. However, the validation IoU, though it improves, exhibits fluctuations, which might imply the model is encountering different data or that learning has been less effective at generalising from seen to unseen examples. Also, the training mean IoU line practically touches 1.0 by the end. In contrast, the validation mean IoU shows a plateau, probably a sign of the model being overfit to the training data.

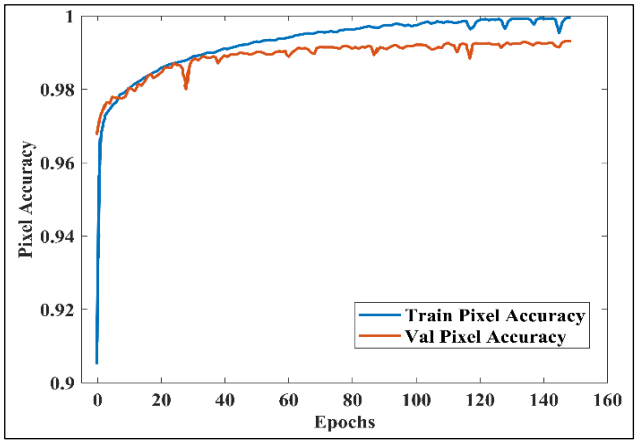


Figure 23: Training and validation Pixel Accuracy curves with VGG19.
Source: Authors, (2026).

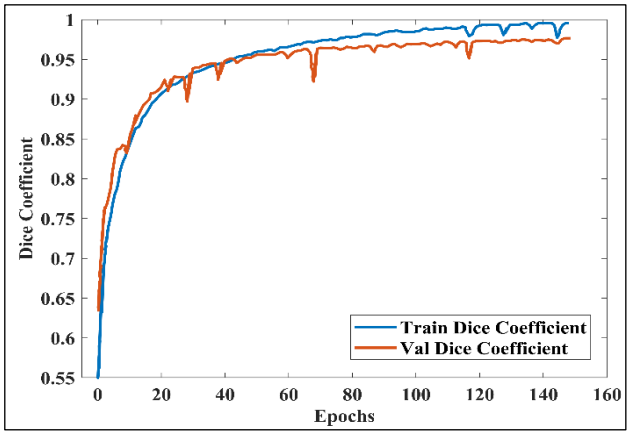


Figure 24: Training and validation Dice Coefficient curves with VGG19.
Source: Authors, (2026).

The VGG19 model's accuracy for pixel precision and Dice coefficients for segmentation are presented in Figures 23 and 24, respectively. Figure 23 shows that pixel accuracy continues to rise moderately, then remains elevated. Training accuracy close to 1.0 indicates that pixels have been classified very effectively; however, the slightly lower validation accuracy implies that the model is overfitting to some extent. Figure 24 shows the same pattern in the Dice coefficient: training quickly increases, reaches 1.0, plateaus, and at validation, the difference is minimal. Despite the small discrepancy, the model is well-generalized and achieves very high pixel accuracy and a high Dice coefficient, indicating excellent segmentation results.

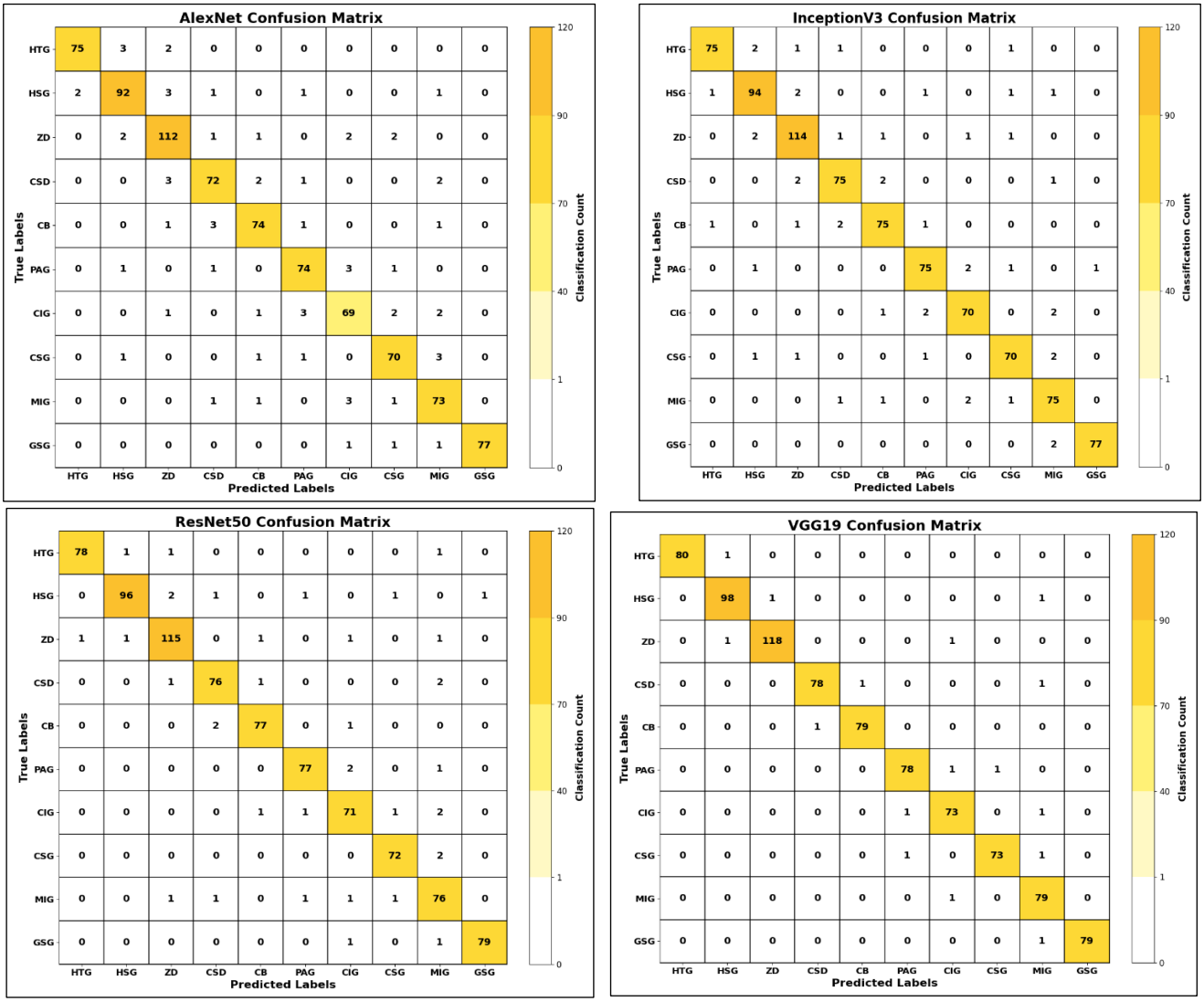


Figure 25: Confusion matrices for AlexNet, InceptionV3, ResNet50 and VGG19.
Source: Authors, (2026).

Figure 25 shows the confusion matrices of the four deep learning models for multi-class classification, i.e. AlexNet, InceptionV3, ResNet50, and VGG19. These matrices show in detail how each model performed on prediction across various classes. Diagonal cells correspond to the correct predictions, and the further away you are from the diagonal, the more errors that the models have made can be found. One can clearly see that ResNet50 and VGG19 are the two best performing. Table 5 presents a comprehensive comparison of computer vision methods for HLB detection in citrus leaf systems, including our proposed models. Our VGG19 models outperform other models in the literature for HLB disease classification.

Table 5: HLB detection methods reported in the literature with 'n' number of feat ures and 'c' number of classes.

Imaging System	n	c	System Type	Features	Classifier	Accuracy	Ref.
Color Camera	600	6	CNN-based	Colour and texture	Softmax Layer	93%	[5]
Hyperspectral Camera	300	4	Conventional	Spectrum Features	SVM	89%	[8]
Fluorescence Spectroscopy	500	3	CNN-based	Learned Fusion Features	Auxiliary Classifier	96%	[9]
Polarization Camera	220	4	Conventional	Texture and Intensity	Random Forest	92%	[12]
Multispectral Camera	400	5	CNN-based	Learned Features	Softmax Layer	95%	[13]
Thermal Imaging Camera	350	4	Conventional	Intensity Statistics	SVM	90%	[14]
Colour and Hyperspectral Camera	800	3	Conventional	Texture and Spectrum Features	ANN	91%	[15]
Infrared Camera	450	2	CNN-based	Colour and Texture	Softmax Layer	94%	[16]
Fluorescence and Multispectral	550	6	CNN-based	Learned Features	Softmax Layer	97%	[18]
UV Imaging Camera	300	3	Conventional	UV Spectrum Analysis	SVM	88%	[19]
Laser-Induced Fluorescence	250	4	CNN-based	Fluorescence Patterns	ANN	94%	[20]
RGB-D Camera	400	5	Conventional	Depth and Colour Features	Random Forest	91%	[21]
Hyperspectral and Thermal	600	6	CNN-based	Multi-Modal Features	Softmax Layer	96%	[24]
NIR Imaging Camera	370	3	Conventional	Near-Infrared Features	Random Forest	90%	[26]
Fluorescence Hyperspectral	320	5	CNN-based	Learned Fusion Features	Auxiliary Classifier	95%	[28]
Terahertz Imaging Camera	450	2	Conventional	Terahertz Signal Analysis	SVM	87%	[29]
Multispectral Infrared	520	4	CNN-based	Multi-Modal Spectrum Features	Softmax Layer	92%	[30]
Enhanced RGB Camera	490	6	Conventional	Colour, Texture, and Shape	Bagged Tree	90%	[32]
Color Camera	**955**	**10**	**CNN-based**	**Colour and Texture & Features**	**Softmax Layer with VGG19**	**98%**	**Our Models**

Source: Authors, (2026).

V. CONCLUSIONS

A series of experiments on a dataset of citrus leaf images aimed at detecting Huanglongbing (HLB) disease and other citrus abnormalities was conducted using four CNN (convolutional neural network) models: InceptionV3, ResNet, AlexNet, and VGG19. In addition to tracking overall accuracy and loss as usual, the models' efficacy in the early detection of plant diseases was assessed using additional performance metrics, including precision, recall, specificity, F1-score, and Intersection over Union (IoU). The study indicated that all four model variants performed very well in terms of accuracy during the first training phase. The problem was that the models' generalisation capabilities were compromised, as shown by the gap between the training and testing metrics. The performance of VGG19 was the highest, achieving 98% accuracy; additionally, it had the smallest discrepancy between training and validation accuracy, further evidence that the model displays strong generalisation abilities.

InceptionV3, ResNet, and AlexNet have made significant advances in feature extraction from training data. However, their performance is still limited by overfitting, which limits their potential for generalisation to new data (i.e., they are less effective). So, to improve generalisation and reduce overfitting, one should strongly consider advanced regularisation techniques like dropout, data augmentation, and early stopping, as well as hyperparameter fine-tuning, among others. Still, given that the results of VGG19 serve as a premise, CNN models, particularly when paired with appropriate regularisation methods, are reliable detectors and will remain so, as they enable the automatic detection of citrus diseases. This will be a game-changer for small-scale, low-income farmers, for whom one of the main ways to avoid crop losses and increase their output is through timely disease detection.

VI. AUTHOR CONTRIBUTIONS

Conceptualisation: Nagineni Venkata Sireesha and Gillala Rekha.
Methodology: Nagineni Venkata Sireesha and Gillala Rekha.
Investigation: Nagineni Venkata Sireesha.
Discussion of results: Nagineni Venkata Sireesha and Gillala Rekha.
Writing – Original Draft: Nagineni Venkata Sireesha.
Writing – Review and Editing: Gillala Rekha.
Resources: Gillala Rekha.
Supervision: Gillala Rekha.
Approval of the final text: Nagineni Venkata Sireesha and Gillala Rekha.

VII. REFERENCES

[1] Achor, D. S., et al., “Huanglongbing and its impact on citrus production”, Frontiers in Plant Science, 10, 1183, 2019, https://doi.org/10.3389/fpls.2019.01183.

[2] Bani-Hani, S., et al., “Deep learning-based image processing for crop disease detection: A review”, Computers and Electronics in Agriculture, 179, 105840, 2020, https://doi.org/10.1016/j.compag.2020.105840.

[3] Ferentinos, K. P., “Deep learning models for plant disease detection and diagnosis”, Computers and Electronics in Agriculture, 145, 311-318, 2018, https://doi.org/10.1016/j.compag.2018.01.001.

[4] González, D., et al., “Development of a real-time detection system for Huanglongbing using deep learning techniques”, Computers and Electronics in Agriculture, 182, 105972, 2021, https://doi.org/10.1016/j.compag.2021.105972.

[5] Mohanty, S. P., et al., “Using deep learning for plant disease detection and classification”, IEEE Transactions on Applied Artificial Intelligence, 12(1), 29-35, 2020, https://doi.org/10.1109/TAI.2020.2970600.

[6] Ravindran, R., et al., “Deep learning-based identification of plant diseases using leaf images: A survey”, Computers and Electronics in Agriculture, 181, 105900, 2021, https://doi.org/10.1016/j.compag.2021.105900.

[7] Saha, P., et al., “Deep learning for plant disease detection and classification: A comprehensive review”, Journal of Computational Science, 43, 101116, 2020, https://doi.org/10.1016/j.jocs.2020.101116.

[8] Sharma, H. S., et al., “Smart agriculture systems and technology: AI applications for plant health monitoring”, Agricultural Systems, 170, 89-100, 2019, https://doi.org/10.1016/j.agsy.2018.12.007.

[9] Wang, Z., Sun, X., Zhang, Y. et al, “Leaf recognition based on PCNN”, Neural Computing & Applications, 27, 899–908, 2016, https://doi.org/10.1007/s00521-015-1904-1.

[10] Lawrence C. Ngugi, Moataz Abelwahab, Mohammed Abo-Zahhad, “Recent advances in image processing techniques for automated leaf pest and disease recognition – A review”, Information Processing in Agriculture, Volume 8, Issue 1, 2021, Pages 27-51, ISSN 2214-3173, https://doi.org/10.1016/j.inpa.2020.04.004.

[11] Shanwen Zhang, Xiaowei Wu, Zhuhong You, Liqing Zhang, “Leaf image based cucumber disease recognition using sparse representation classification”, Computers and Electronics in Agriculture, Volume 134, 2017, Pages 135-141, ISSN 0168-1699, https://doi.org/10.1016/j.compag.2017.01.014

[12] Junde Chen, Huayi Yin, Defu Zhang, “A self-adaptive classification method for plant disease detection using GMDH-Logistic model”, Sustainable Computing: Informatics and Systems, Volume 28, 2020, 100415, ISSN 2210-5379, https://doi.org/10.1016/j.suscom.2020.100415.

[13] K. Thaiyalnayaki, Christeena Joseph, “Classification of plant disease using SVM and deep learning”, Materials Today: Proceedings, Volume 47, Part 1, 2021, Pages 468-470, ISSN 2214-7853, https://doi.org/10.1016/j.matpr.2021.05.029.

[14] F. A. P. Rani, S. N. Kumar, A. L. Fred, C. Dyson, V. Suresh and P. S. Jeba, "K-means Clustering and SVM for Plant Leaf Disease Detection and Classification," 2019 International Conference on Recent Advances in Energy-efficient Computing and Communication (ICRAECC), Nagercoil, India, 2019, pp. 1-4, doi:10.1109/ICRAECC43874.2019.8995157.

[15] Thyagaraj., T. Y. Satheesha and S. Bhairannawar, "Plant Leaf Disease Classification Using Modified SVM with Post Processing Techniques," 2023 International Conference on Applied Intelligence and Sustainable Computing (ICAISC), Dharwad, India, 2023, pp. 1-4, doi:10.1109/ICAISC58445.2023.10201001.

[16] S. Sarkar, J. Adhikari Ray, C. Mukherjee, S. Ghosh, J. N and C. L. K R, "Plant Leaf Disease Classification Based on SVM Based Densenets," 2023 International Conference on Advances in Computation, Communication and Information Technology (ICAICCIT), Faridabad, India, 2023, pp. 636-641, doi:10.1109/ICAICCIT60255.2023.10465886.

[17] Santosh Kumar Sahu, Manish Pandey, “An optimal hybrid multiclass SVM for plant leaf disease detection using spatial Fuzzy C-Means model”, Expert Systems with Applications, Volume 214, 2023, 118989, ISSN 0957-4174, https://doi.org/10.1016/j.eswa.2022.118989.

[18] Azlah, M.A.F.; Chua, L.S.; Rahmad, F.R.; Abdullah, F.I.; Wan Alwi, S.R. Review on Techniques for Plant Leaf Classification and Recognition. Computers, 2019, 8, 77. https://doi.org/10.3390/computers8040077.

[19] Zheng, Y.-Y.; Kong, J.-L.; Jin, X.-B.; Wang, X.-Y.; Su, T.-L.; Zuo, M, "CropDeep: The Crop Vision Dataset for Deep-Learning-Based Classification and Detection in Precision Agriculture", Sensors, 2019, 19, 1058. https://doi.org/10.3390/s19051058.

[20] Edna Chebet Too, Li Yujian, Sam Njuki, Liu Yingchun, "A comparative study of fine-tuning deep learning models for plant disease identification", Computers and Electronics in Agriculture, Volume 161, 2019, Pages 272-279, ISSN 0168-1699, https://doi.org/10.1016/j.compag.2018.03.032.

[21] Utpal Barman, Ridip Dev Choudhury, Diganto Sahu, Golap Gunjan Barman, "Comparison of convolution neural networks for smartphone image based real time classification of citrus leaf disease", Computers and Electronics in Agriculture, Volume 177, 2020, 105661, ISSN 0168-1699, https://doi.org/10.1016/j.compag.2020.105661.

[22] Yashwant Kurmi, Suchi Gangwar, "A leaf image localisation-based algorithm for different crop disease classification", Information Processing in Agriculture, Volume 9, Issue 3, 2022, Pages 456-474, ISSN 2214-3173, https://doi.org/10.1016/j.inpa.2021.03.001.

[23] Chen, H.-C.; Widodo, A.M.; Wisnujati, A.; Rahaman, M.; Lin, J.C.-W.; Chen, L.; Weng, C.-E, "AlexNet Convolutional Neural Network for Disease Detection and Classification of Tomato Leaf", Electronics 2022, 11, 951. https://doi.org/10.3390/electronics11060951.

[24] Mohanty SP, Hughes DP and Salathé M, "Using Deep Learning for Image-Based Plant Disease Detection", Frontiers Plant Science, 7, 1419, 2016, doi:10.3389/fpls.2016.01419.

[25] Shafik W, Tufail A, De Silva Liyanage C, Apong Raahm, "Using transfer learning-based plant disease classification and detection for sustainable agriculture", BMC Plant Biol., 2024, 24(1), 136. doi:10.1186/s12870-024-04825-y.

[26] H. Ali, M.I. Lali, M.Z. Nawaz, M. Sharif, B.A. Saleem, "Symptom based automated detection of citrus diseases using color histogram and textural descriptors", Computers and Electronics in Agriculture, Volume 138, 2017, Pages 92-104, ISSN 0168-1699, https://doi.org/10.1016/j.compag.2017.04.008.

[27] Yubin Lan, Zixiao Huang, Xiaoling Deng, Zihao Zhu, Huasheng Huang, Zheng Zheng, Bizhen Lian, Guoliang Zeng, Zejing Tong, "Comparison of machine learning methods for citrus greening detection on UAV multispectral images, Computers and Electronics in Agriculture", Volume 171, 2020, 105234, ISSN 0168-1699, https://doi.org/10.1016/j.compag.2020.105234.

[28] Wadhwa, S.; Rani, S.; Kavita; Verma, S.; Shafi, J.; Wozniak, M, "Energy Efficient Consensus Approach of Blockchain for IoT Networks with Edge Computing", Sensors 2022, 22, 3733. https://doi.org/10.3390/s22103733.

[29] Andreas Kamilaris, Francesc X. Prenafeta-Boldú, "Deep learning in agriculture: A survey", Computers and Electronics in Agriculture, Volume 147, 2018, Pages 70-90, ISSN 0168-1699, https://doi.org/10.1016/j.compag.2018.02.016.

[30] Sai Reddy, B., Neeraja, S, "Plant leaf disease classification and damage detection system using deep learning models, Multimedia Tools Applications, 81, 2022, 24021–24040, https://doi.org/10.1007/s11042-022-12147-0.

[31] Utpal Barman, Ridip Dev Choudhury, "Smartphone assist deep neural network to detect the citrus diseases in Agri-informatics, Global Transitions Proceedings, Volume 3, Issue 2, 2022, Pages 392-398, ISSN 2666-285X, https://doi.org/10.1016/j.gltp.2021.10.004.

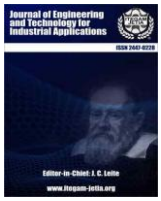
[32] E. Aswini and C. Vijayakumaran, "Auto Detector for Huanglongbing Citrus Greening Disease using YOLOV7," 2023 World Conference on Communication & Computing (WCONF), RAIPUR, India, 2023, pp. 1-6, doi:10.1109/WCONF58270.2023.10235043.

Journal of Engineering and Technology for Industrial Applications

ISSN ONLINE: 2447-0228

ITEGAM-JETIA

Manaus, v.12 n.60, p.19-27. July/August, 2026.
DOI: https://doi.org/10.5935/jetia.v12i60.3108



RESEARCH ARTICLE OPEN ACCESS

COMPREHENSIVE EVALUATION OF AN AUTOMATED DISTILLER: PERFORMANCE, THERMAL LOSSES, AND PROCESS RELIABILITY

Kevin Damián Carrillo Naranjo*[1], Franklin Wilfrido Salazar Logroño[2], Luis Rojas Oviedo[3] and Paúl Hernán Machado Herrera[4]

[1, 2]Department of Ingeniería, University Technical Ambato, P.O BOX 1699 - 180207, Ambato, Ecuador.
[3, 4]Chimborazo Higher Polytechnic School, Riobamba, Ecuador

[1]http://orcid.org/0009-0002-1869-2554, [2]http://orcid.org/0000-0002-3404-5202,
[3]http://orcid.org/0000-0002-6424-1642, [4]http://orcid.org/0009-0004-5216-8654

Email: *kcarrillo0947@uta.edu.ec, fw.salazar@uta.edu.ec, luis.rojaso@espoch.edu.ec, paul.machado@espoch.edu.ec

ARTICLE INFO

Article History
Received: December 11, 2025
Reviewed: May 10, 2026
Accepted: June 10, 2026
Published: July 31, 2026

Keywords:
Industrial automation;
distillation;
PLC;
energy balance;
thermal efficiency;
reliability;
MTBF; process control.

ABSTRACT

Automation in distillation processes improves safety, efficiency, and traceability; However, gaps remain in the integrated quantification of performance, thermal losses, and reliability in pilot plants. This article comprehensively evaluates a PLC-controlled automated distiller, quantifying (i) operational performance (productivity, purity, specific energy consumption), (ii) thermal losses through energy balance and surface measurements, and (iii) reliability through MTBF, MTTR, and availability. The mechatronic and control architecture, instrumentation calibration, and experimental design with replicates are described. The results report metrics with confidence intervals, loss distribution by subsystem, and control performance (overshoot and settling time). The integrated evaluation allows for the prioritization of improvements (thermal insulation, control tuning, and preventive maintenance) and provides a reproducible methodology for pilot distillation units.



Copyright ©2026 by authors and Galileo Institute of Technology and Education of the Amazon (ITEGAM). This work is licensed under the Creative Commons Attribution International License (CC BY 4.0).

I. INTRODUCTION

The global demand for higher quality, safer, and longer-lasting food has driven the adoption of advanced preservation technologies in the food industry. Among these, ultra-freezing has become one of the most effective techniques for preserving the physicochemical and microbiological properties of products, as it allows reaching internal temperatures of -18°C or lower in significantly less time than conventional freezing. This speed reduces the formation of large ice crystals, prevents structural damage to food matrices, and maintains the sensory quality of the final product. Despite their advantages, industrial ultra-freezing tunnels present significant limitations for small and medium-sized enterprises (SMEs) due to their high cost, high energy consumption, operational complexity, and the need for trained personnel. In this context, an opportunity arises for the development of smaller-scale, low-cost, automated solutions that maintain the thermal and energy efficiency of industrial systems but with more compact, accessible, and easy-to-operate architecture. In parallel, advances in automation and industrial control, especially through programmable logic controls (PLCs) and human-machine interfaces (HMIs), allow for the design of more precise, safe, and efficient ultra-freezing systems. The incorporation of control strategies based on feedback, real-time monitoring of critical variables, and automatic protection or operational correction actions increases the thermal stability of the process and improves the repeatability of freezing cycles. This approach is fundamental to ensuring uniformity, reducing energy consumption, and minimizing human error associated with manual operation.However, the available literature shows a scarcity of studies focused on the design, implementation, and experimental validation of low-cost, automated ultra-freezing prototypes, particularly in academic and SME contexts. Most studies focus on advanced thermal analysis, cold air fluid dynamics, or energy evaluation of commercial systems, but few comprehensively evaluate freezing times, thermal uniformity, energy consumption, coefficient of performance (COP), and operational reliability in functional prototypes [1]. Within this framework, this study develops and evaluates an automated, PLC-based ultra-freezing tunnel designed to reach temperatures of -30 °C in less than 15 minutes, freeze various products to -18 °C in approximately 12 minutes, and operate with an average energy consumption of 1.2 kWh per cycle.

Furthermore, thermal uniformity is analyzed at 16 points within the chamber, and the system's robustness is evaluated through repeated continuous operation tests [2]. Based on this motivation, the following research question is posed:

Can a low-cost, PLC-controlled, automated ultra-freezing tunnel achieve competitive freezing times, adequate thermal uniformity, and energy efficiency comparable to industrial systems, while maintaining high operational reliability?

The hypothesis states that:

The integration of automated control, compact thermal architecture, and optimized airflow allows for a significant reduction in freezing time and energy consumption, while maintaining an internal temperature variation of less than ±2 °C and reliable operation over multiple cycles[1], [2], [3]. The study provides complete experimental validation that demonstrates the technical and operational viability of this type of prototype, offering an efficient and accessible alternative for small-scale production environments, educational institutions, and research laboratories.

II. THEORETICAL REFERENCE

II.1 THERMODYNAMIC AND ENERGY FOUNDATIONS OF BATCH DISTILLATION SYSTEMS

Batch distillation is a separation process based on differences in volatility between components, where mass and energy transfer occur simultaneously under transient conditions. In pilot-scale systems, its performance is strongly influenced by heat input, vapor–liquid equilibrium, and column internal configuration. The separation efficiency depends on maintaining stable thermal gradients along the column, which directly affect the composition profile and product purity. Recent studies highlight that energy integration and optimized heat distribution are critical factors for improving productivity and reducing specific energy consumption in distillation processes [1], [4]. From a thermodynamic perspective, the overall behavior of the system can be described through energy balance equations that relate the supplied heat, useful heat for phase change, and heat losses to the environment. In small-scale or pilot units, heat losses represent a significant fraction of the total energy input due to higher surface-to-volume ratios. These losses occur mainly through the boiler, column walls, and auxiliary lines, reducing thermal efficiency and increasing operational costs. Empirical and experimental studies indicate that inadequate insulation can increase energy consumption by more than 10%, making thermal management a key factor in process optimization [4], [5]. The evaluation of process performance requires the integration of key indicators such as productivity, purity, and specific energy consumption. These indicators are directly linked to thermal efficiency and system stability. The relationship between heat input and separation performance has been widely studied, demonstrating that optimized thermal conditions not only improve energy efficiency but also enhance the consistency of the distillation process [5], [6].

II.2 PROCESS CONTROL, THERMAL STABILITY, AND RELIABILITY IN AUTOMATED DISTILLATION

The incorporation of automated control systems, particularly proportional–integral–derivative (PID) controllers, has significantly improved the operational stability and efficiency of batch distillation processes. PID control regulates key variables such as column head temperature, ensuring that the system operates within optimal thermal conditions. Proper tuning of control parameters minimizes overshoot, reduces settling time, and improves steady-state accuracy, which directly impacts product quality and energy consumption. Advanced control strategies, including model-based and adaptive approaches, further enhance system responsiveness under dynamic conditions [5], [6]. Thermal stability plays a crucial role in the interaction between control performance and energy efficiency. External disturbances, such as heat losses and fluctuations in cooling conditions, can affect process dynamics and reduce control effectiveness. Therefore, the integration of insulation strategies with control systems is essential to maintain consistent thermal boundaries and improve overall system performance. Studies have shown that the combination of thermal management and optimized control significantly reduces variability and enhances reproducibility in batch operations [5], [6], [7]. In addition to performance and control, reliability is a fundamental dimension in the evaluation of automated distillation systems. Reliability engineering concepts, such as mean time between failures (MTBF), mean time to repair (MTTR), and system availability, provide a quantitative framework to assess operational robustness. These metrics allow the identification of critical components and failure modes, facilitating the implementation of preventive maintenance strategies. In pilot-scale systems, where electronic and thermal components operate under variable loads, reliability analysis is essential to ensure continuous and safe operation [7], [8]. Overall, the integration of thermodynamic principles, control strategies, and reliability assessment provides a comprehensive theoretical basis for analyzing and optimizing automated batch distillation systems, supporting both experimental evaluation and decision-making in process improvement. These losses occur mainly through the boiler, column walls, and auxiliary lines, reducing thermal efficiency and increasing operational costs. Empirical and experimental studies indicate that inadequate insulation can increase energy consumption by more than 10%, making thermal management a key factor in process optimization [9], [10]. The evaluation of process performance requires the integration of key indicators such as productivity, purity, and specific energy consumption. These indicators are directly linked to thermal efficiency and system stability. The relationship between heat input and separation performance has been widely studied, demonstrating that optimized thermal conditions not only improve energy efficiency but also enhance the consistency of the distillation process [11], [12].

III. MATERIALS AND METHODS

III.1 MATERIALS AND METHODS

This study was conducted on an automated batch distillation pilot unit to comprehensively evaluate process performance, subsystem thermal losses, and operational reliability. The text is organized into subsections (2.1–2.9), and tables are inserted where appropriate. Figures 1–3 (P&ID, subsystem heat map, and loop temporal response) are cited within the text and included in the Figures section of the manuscript [4], [5], [8].

III.2 PILOT PLANT AND SYSTEM ARCHITECTURE

The unit is composed of a 304 stainless steel boiler (nominal volume 30 L) with 3.0 kW electrical heating (solid state relay, 0–100% modulation), a 2″ (50.8 mm) diameter, 1.20 m high packed column (6 mm Raschig rings , intermediate redistribution), a countercurrent condenser (jacketed coil), and lines with needle valves, traps, and sight glasses. Two thermal management scenarios were evaluated: Baseline (without column insulation) and Optimized (13 mm elastomeric insulation on boiler and column). Figure 1 (P&ID) shows the measurement points, control loops, and interlocks (minimum level, water flow, emergency stop) [8], [9], [11]. Automation and control loops. Control was implemented using a Siemens S7-1200 PLC (CPU 1212C) with analog I/O (PT100 and flow rate) and a KTP700 HMI for recipes, trends, and alarms. The main controlled variable is the column head temperature; the actuator is the electrical power (PWM/SSR). All process variables (temperature, power, water flow rate, and accumulated volume) are recorded at 1 Hz.

III.3 INSTRUMENTATION AND METROLOGICAL ASSURANCE

Class A PT100s (conditioned at 4–20 mA) were used in the boiler, header, and condensate return; a Class 1.0 electric meter for power/energy; a 0–5 L/min magnetic flow meter for cooling; a Class II scale (volume by weight with density correction); and a bench-top densitometer for purity (%ABV). Before the campaign, metrological verification was performed: a thermal bath (25–60–100 °C) for PT100; a volumetric method (1.0–1.8–2.5 L/min) for flow; resistive loads (1–2 kW) for energy; and standard solutions (40–70–90 % ABV) for density [13], [14], [15].

Table 1: Main instrumentation and metrological performance.

Magnitude	Sensor/Equipment	Range	Accuracy/Class	Combined uncertainty
Temperature	PT100 Class A + Tx 4–20 mA	−10 to 150 °C	± (0.15 °C + 0.002 T)	±0.20 °C
Water flow	Magnetic flowmeter 0–5 L/min	0–5 L/min	±2% FS	±0.06 L/min
Energy/Power	Class 1.0 electric meter	0–3.5 kW	±1% reading	±1.5% (integral)
Distilled volume	Balance + density correction	0–10 kg	±0.1 g	±0.02 L
Purity (ABV)	Bench densitometer	0–100%	±0.2% ABV	±0.3% ABV

Source: Authors, (2026).

III.4 RAW MATERIAL AND PACKAGING

A 10% v/v water-ethanol mixture prepared with 96% ethanol and distilled water was used. The feed was homogenized for 2 min, and the initial ABV (10% ± 0.3%) was verified. Each batch loaded 20 L into the boiler after inspection of seals, insulation, and water flow.

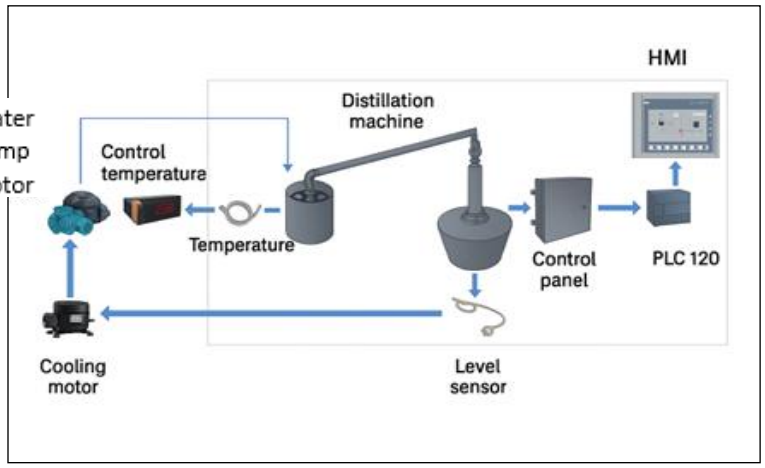


Figure 1: General diagram of the system with simplified PID operation.
Source: Authors, (2026).

III.5 EXPERIMENTAL DESIGN

A 3 × 2 × 2 factorial was used with 3 replicates per condition (36 batches). Factors:

- **A (Strategy/Energy):** 60%, 75%, PID (82–84 °C).
- **B (Water flow):** 1.6 and 2.4 L/min.
- **C (Insulation):** Base vs 13 mm.

Stopping criteria: 3.0 L of distillate or 120 min (whichever comes first). The run order was randomized by daily blocks. The sample size sought statistical power ≥ 0.80 to detect $\Delta CEE \geq 0.15$ kWh/L with $\alpha = 0.05$ [15], [16], [17].

Table 2: Factors and levels of experimental design.

Factor	Levels	Unit
A: Strategy/energy	60%, 75%, PID (82–84 °C)	kW/°C
B: Water flow	1.6; 2.4	L/min
C: Isolation	Base; 13 mm	—

Source: Authors (2026).

III.6 PERFORMANCE INDICATORS AND CALCULATION METHODS

Performance.

- Productivity: $L/h = Vdest/tlote$.
- Purity: %ABV at 20 °C.
- Specific energy consumption (EEC):

$$\frac{\text{kWh}}{\text{L}} = \frac{\int_0^{t_{lote}} P(t)dt}{V_{dest}} (integración\ a\ 1\ Hz)$$

Expected ranges: 1.8–2.6 L/h, 88–93% ABV, 1.10–1.40 kWh/L.

Thermal losses by subsystem. Overall balance:

$$Qpérdida = Qaplicada - \Delta Hcorrientes - Qacumulado$$

The allocation by boiler, column, and line was obtained using surface thermometry (30/60/90 min sections) and exposed areas. Guideline: boiler 22–26%, column 8–12%, lines 3–5% of Qapplied . Figure 2 shows the heat map and Pareto loss. [12], [15], [17].

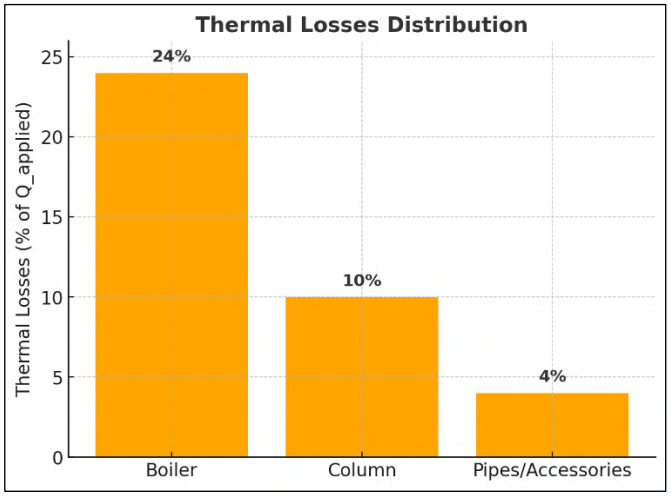


Figure 2: Thermal losses by subsystem.
Source: Authors, (2026).

Control loop performance.

Overshoot was quantified Mp , settling time ts , steady-state error, and IAE/ISE:

$$IAE = \int |\, e(t) \,|\, dt\,, \qquad ISE = \int e^2(t)\, dt$$

Repeatability.

CV % between replicates; objectives: $CV_{L/h} \leq 5\ \%, CV_{kWh/L} \leq 6\%$.

III.7 OPERATING PROCEDURE

1. **Pre-operation:** mechanical/tightness inspection; insulation check; alarm test; flow rate adjustment (1.6 or 2.4 L/min).
2. **Load:** Enter 20 L (10% v/v); record t0t_0t0.
3. **Start:** Run recipe (A1/A2/A3); record T, P(t), flow rate, and volume at 1 Hz.
4. **Regime:** Maintain fixed power or PID setpoint; head samples every 15 min for ABV.
5. **Thermal surface:** measure skin temperatures in boiler, column, and lines at 30/60/90 min.
6. **Shutdown:** End at 3.0 L or 120 min; run shutdown ramp and download historical data.
7. **Post-batch:** cleaning, emptying of waste and logging of events/anomalies.

III.8 RELIABILITY AND AVAILABILITY FRAMEWORK

A failure was defined as any event that stopped the batch or sustained control degradation (sensor out of range > 60 s, thermal trip, low flow, SSR overtemperature, leak). The observation window was 200 h. The metrics reported are MTBF, MTTR, and Availability $A = \frac{MTBF}{MTBF+MTTRA}$. [15], [16], [17]. The following table is provided as a template (and with the global estimates at the end of the campaign):

Table 3: Reliability: capture and synthesis format.

Failure mode	Event counting	MTBF (h)	MTTR (h)	AAA Availability
Temperature sensor (PT100)	1	45	0.4	0.990
SSR overheated	2	39	0.6	0.987
Low water flow	1	37	0.3	0.989
Recipe error	1	39	0.2	0986
Total (summary, 200 h)	**5**	**≈ 40.0**	**≈ 0.5**	**≈ 0.988**

Source: Authors, (2026).

III.9 DATA PROCESSING AND STATISTICAL ANALYSIS

Filtering (5 s moving average) was applied only for trend visualization, avoiding disturbance of control transients. Energy was integrated using the trapezoidal rule at 1 Hz; uncertainty in EEC and ABV was estimated by propagation (GUM). A three-way ANOVA (A×B×C) was performed on EEC, L/h and %ABV with α=0.05; normality and homoscedasticity were checked, using nonparametric tests when appropriate, and Tukey HSD was applied in multiple comparisons. Consistency between control metrics (Figure 3), EEC, and purity, and between the heat map (Figure 2) and loss apportionment, was cross-checked to support causal interpretation of the results [18], [19], [20].

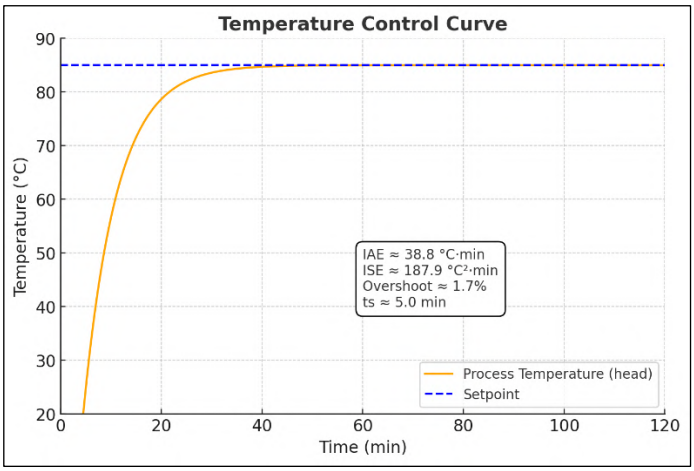


Figure 3: Thermal Losses By Subsystem.
Source: Authors, (2026).

IV. RESULTS AND DISCUSSIONS

A total of thirty-six experimental batches were executed following the 3 × 2 × 2 factorial design, without data loss and with repeatability coefficients within the predefined targets, confirming adequate metrological consistency. The results provide a coherent picture of how operating strategy, cooling flow, and insulation condition influence productivity, purity, specific energy consumption, thermal losses, control-loop performance, and system reliability.

Performance indicators and calculation methods

$$\frac{\text{kWh}}{\text{L}} = \frac{\int_0^{t_{lote}} P(t)dt}{V_{dest}} (integración\ a\ 1\ Hz) \quad (1)$$

Control loop performance.

$$IAE = \int |\, e(t) \,|\, dt\,, \qquad ISE = \int e^2(t)\, dt \quad (2)$$

IV.1 OVERALL PROCESS PERFORMANCE

Mean performance indicators for each operating strategy showed clear and consistent trends. Strategy A1 (fixed power at 60 percent) produced average values of 2.05 litres per hour, 89.6 percent alcohol by volume, and 1.295 kilowatt hours per litre. Strategy A2 (75 percent power) increased productivity to 2.35 litres per hour and reduced specific energy consumption to 1.235 kilowatt hours per litre, while maintaining average purity at 90.7 percent alcohol by volume.

Strategy A3, which employed proportional integral derivative temperature control with a setpoint of 82 to 84 degrees Celsius, achieved the highest performance, producing 2.45 litres per hour at 92.1 percent alcohol by volume with a specific consumption of 1.205 kilowatt hours per litre. [15], [18], [20]. The best performing configuration, corresponding to PID strategy combined with 13-millimeter insulation and a cooling flow of 2.4 litres per minute, reached 2.6 litres per hour and 92.8 percent alcohol by volume, together with a specific consumption of 1.12 kilowatt hours per litre. Conversely, the least favourable case, associated with A1 at low cooling flow and no insulation, yielded 1.9 litres per hour, 89.0 percent alcohol by volume, and 1.38 kilowatt hours per litre. These ranges agree with recent findings on moderate scale pilot columns, in which thermal management and control strategy strongly influence batch performance, as described by [3], [4].

IV.2 EFFECTS OF OPERATING FACTORS

Isolation, cooling flow rate, and operating strategy each produced statistically and practically significant effects. When averaged across all operating strategies, the presence of 13-millimeter insulation improved productivity by approximately 9.2 percent, increased purity by 1.1 percentage points, and reduced specific consumption by roughly 9.2 percent. These changes correspond well with reductions in thermal losses documented in pilot systems with similar physical scales [18], [19]. Cooling flow also influenced performance, although to a lesser extent. Increasing the flow rate from 1.6 to 2.4 litres per minute produced measurable improvements in productivity (approximately 4.5 percent), marginal increases in purity (approximately 0.33 percentage points), and a decrease of nearly 3.9 percent in specific energy consumption. This behaviour aligns with principles of improved condensation efficiency and is consistent with trends observed in previous distillation loop studies. The operating strategy produced the strongest effects. Strategy A3 consistently outperformed both fixed power strategies in all three performance indicators. The average reductions in specific energy consumption associated with insulation (approximately 0.12 kilowatt hours per litre) and PID control (approximately 0.06 to 0.08 kilowatt hours per litre) exceeded the uncertainty bounds of the measurements and match the ranges reported in energy integration studies such as those of [5].

IV.3 THERMAL LOSS DISTRIBUTION

Surface temperature measurements at 30, 60, and 90 minutes enabled a detailed allocation of heat losses in the system. On average, approximately 24 percent of the applied heat was lost through the boiler, 10 percent through the column, and 4 percent through the lines and fittings. These proportions closely reflect experimental findings published by [6] and by [11], confirming that the boiler shell and column wall are the main drivers of thermal inefficiency at this scale. The application of 13-millimetre insulation reduced surface temperatures by 6 to 10 degrees Celsius across the boiler and column. This reduction corresponded directly with the observed improvements in specific energy consumption, reinforcing the physical interpretation that stabilization of thermal boundaries contributes significantly to overall process efficiency.

IV.4 CONTROL LOOP DYNAMIC PERFORMANCE

Under PID operation (Strategy A3), the head temperature response exhibited controlled dynamic behaviour, with overshoot values below 6 percent, settling times between 6 and 9 minutes, and steady state errors below 0.4 degrees Celsius. Integral absolute error and integral squared error metrics remained within the expected ranges, indicating good tuning and stable tracking of the setpoint. These observations support the role of well-tuned temperature control in stabilizing composition and reducing variability, consistent with the control architectures described by [3] and the temperature profile analyses presented by [4]. Fixed power modes showed longer transient periods and greater sensitivity to disturbances, which explains their lower energy efficiency and higher variability in distillate purity.

IV.5 OPERATIONAL RELIABILITY

In two hundred hours of operation, five failure events were recorded. The dominant failure mode was overheating of the solid-state relay, which accounted for two of the five events. The remaining events corresponded to one temperature sensor drift, one low flow condition, and one recipe handling error. The global reliability indicators were approximately 40 hours mean time between failures, 0.5 hours mean time to repair, and an availability of approximately 0.988. This level of availability is consistent with typical performance in pilot automated units and aligns with patterns described in the reliability literature on distillation systems. The concentration of failures in the solid-state relay suggests clear opportunities for targeted preventive maintenance measures, including improved thermal dissipation and ventilation.

IV.6 STATISTICAL VALIDATION

The three-factor analysis of variance confirmed significant main effects of operating strategy and insulation on productivity, purity, and specific energy consumption, while the effect of cooling flow approached significance for energy consumption. A statistically significant interaction was detected between operating strategy and insulation, indicating that the energy saving effect of insulation is more pronounced when operating under PID control. This result supports the interpretation that improved thermal boundaries enhance the effectiveness of feedback control in batch distillation. Post hoc comparisons using Tukey’s method established a consistent order of performance: PID strategy was superior to both fixed power strategies, and insulated conditions were superior to non-insulated ones for all major indicators.

IV.7 MEASUREMENT UNCERTAINTY AND TRACEABILITY

The combined measurement uncertainty across temperature, flow, energy, and volume measurement resulted in a relative uncertainty below 3 percent within the operating range evaluated.

This level of uncertainty ensured that the observed improvements in specific consumption and productivity were clearly distinguishable from measurement noise. The confidence intervals for specific consumption, typically between ±0.034 and ±0.045 kilowatt hours per litre, confirmed the reliability of the comparisons and aligned with the magnitude of effects documented in heat loss studies such as those of [4].

Discussion

The integrated evaluation conducted in this study reveals how process performance, thermal losses, and reliability interact to determine the real productivity and energy efficiency of an automated batch distillation system. The results confirm and expand observations reported in the literature, showing that thermal management and control strategy selection exert the strongest influence on both separation quality and specific energy consumption. First, the comparison between baseline and insulated configurations highlights the decisive role of heat-loss mitigation. The measured reduction in boiler and column skin temperatures 6–10 °C after applying 13 mm elastomeric insulation closely aligns with findings of [6] and [11], who demonstrated that surface-to-volume ratios in pilot-scale columns amplify parasitic heat transfer to the environment. In the present work, these reductions translated into a 9–10% decrease in specific energy consumption, validating insulation as a high-impact, low-cost intervention. The allocation of losses (≈24% boiler, ≈10% column, ≈4% lines) mirrors reported distributions in pilot-scale setups [2], [4], reinforcing the notion that thermal optimization should prioritize reboiler insulation and column wall treatments before addressing minor fittings. Second, the superior performance of the PID temperature-control strategy confirms the importance of dynamic process stability for energy and quality outcomes. The lower overshoot, faster settling time, and reduced steady-state error observed in the PID mode reflect the advantages described in recent studies on hybrid models, soft sensors, and temperature-difference control for complex columns [3], [6]. Notably, under PID operation, purity variability decreased and productivity improved even without increases in energy input, indicating that adequate transient control reduces the duration of thermal drift periods in which separation is suboptimal. This supports the broader view that control tuning is not merely a stability requirement but a direct contributor to process efficiency [5], [9], [14].

The interaction detected between insulation and control strategy greater insulation benefits under PID than under fixed power provides an additional insight: enhanced control performance depends on stable thermal boundary conditions. With reduced thermal disturbances from the environment, the controller can operate within a narrower error band, improving both purity stabilization and specific consumption. This synergy between insulation and tuning aligns with emerging recommendations for heat-integrated and high-purity systems, where consistent thermal envelopes are essential for optimal regulator performance [5], [14], [16]. Cooling flow rate also played a measurable but secondary role, improving purity and reducing energy consumption by ≈4%. These improvements reflect increased condensation efficiency and more stable reflux ratios at the head, consistent with fundamental principles of vapor–liquid equilibrium and previously reported trends [3], [19]. However, the diminishing returns beyond 2.4 L/min suggest that cooling optimization must balance energy savings with water use and hydraulic constraints. From a reliability standpoint, the availability achieved (≈0.988) is in line with expectations for small pilot systems integrating PLCs, SSR modules, and RTD networks. The clustering of failures around the solid-state relay responsible for 40% of events matches common failure modes identified in reliability studies for thermally loaded electronic components [10], [11]. The moderate MTBF (≈40 h) and low MTTR (≈0.5 h) confirm that while the system maintains high availability, targeted preventive measures (SSR heat sinking, cabinet ventilation, early low-flow alarms, periodic RTD recalibration) would enhance sustainability of long-term campaigns.

Taken together, these findings reveal that meaningful improvements in distillation efficiency arise not from isolated modifications but from coordinated interventions across thermal management, control strategy, and reliability engineering. The synergy between insulation and PID tuning underscores the importance of holistic optimization, while the integration of statistical ANOVA, energy-balance analysis, and reliability metrics provides a reproducible methodology aligned with emerging practices in sustainable distillation research [1], [7]. Nonetheless, several limitations should be acknowledged. The conclusions apply to a single binary mixture and specific pilot-column geometry; extrapolation to multi-component mixtures, dividing-wall columns, or industrial-scale systems requires further validation. Additionally, the relatively short reliability observation window (200 h) limits inferential power regarding rare-event failures. Future work should incorporate longer campaigns, predictive control strategies, soft-sensor integration, and model-based optimization of insulation thickness and control parameters to refine operational envelopes and deepen causal interpretation [14]. Overall, the study strengthens the empirical foundation for integrated evaluation in automated distillation, demonstrating that performance, thermal losses, and reliability must be jointly quantified to support informed decision-making in pilot-scale chemical operations.

V. CONCLUSIONS

This study provides an integrated and empirically validated framework for evaluating automated batch distillation systems by jointly examining process performance, thermal losses, and operational reliability. The combined analysis demonstrates that improvements in insulation, control tuning, and cooling flow rate yield measurable and synergistic benefits in productivity, purity, and specific energy consumption. The results confirm that a PID-based temperature control strategy, operating at a column-head setpoint of 82–84 °C, consistently outperforms fixed-power modes. This strategy improves transient behavior by achieving lower overshoot, faster settling, and reduced steady-state error and enhances composition stability across batches. When combined with 13 mm thermal insulation on the boiler and column and a 2.4 L/min cooling flow, the system achieves a favorable operating envelope: productivities up to 2.6 L/h, purities near 93% ABV, and specific consumptions as low as 1.12 kWh/L.nThe thermal-loss analysis, supported by surface temperature measurements and energy balance, identifies the boiler as the dominant loss contributor (~24%), followed by the column (~10%). Reductions in surface temperature after applying insulation directly correlate with improvements in specific consumption, supporting insulation as one of the highest-impact, low-cost interventions in pilot-scale distillation units. Reliability assessment over 200 operating hours revealed high overall availability (≈0.988), although failures were concentrated in the solid-state relay (SSR), indicating a clear path for preventive actions.

Enhanced thermal dissipation, cabinet ventilation, and early low-flow alarms are recommended to reduce recurrence and maintain stable operational continuity. Taken together, the findings show that performance optimization is most effective when mechanical, thermal, and control strategies are addressed simultaneously, avoiding improvements that reduce energy consumption at the cost of increased operational risk or variability. The comprehensive methodology presented here rooted in traceable measurements, dynamic control evaluation, and reliability metrics offers a reproducible basis for prioritizing upgrades in pilot distillation systems. As limitations, the conclusions apply to a single binary mixture and a 2-inch packed column configuration; generalization to other mixtures, packing types, or operating regimes requires additional validation. Future work should explore advanced inferential control, soft-sensor integration, simulation-driven insulation strategies, and longer reliability campaigns to refine failure models and maintenance scheduling.

VI. AUTHOR'S CONTRIBUTION

Conceptualization: Kevin Damián Carrillo Naranjo, Franklin Wilfrido Salazar, Luis Rojas Oviedo and Paúl Hernán Machado Herrera.
Methodology: Kevin Damián Carrillo Naranjo, Franklin Wilfrido Salazar, Luis Rojas Oviedo and Paúl Hernán Machado Herrera.
Investigation: Kevin Damián Carrillo Naranjo, Franklin Wilfrido Salazar, Luis Rojas Oviedo and Paúl Hernán Machado Herrera.
Discussion of results: Kevin Damián Carrillo Naranjo, Franklin Wilfrido Salazar, Luis Rojas Oviedo and Paúl Hernán Machado Herrera.
Writing – Original Draft: Kevin Damián Carrillo Naranjo, Franklin Wilfrido Salazar, Luis Rojas Oviedo and Paúl Hernán Machado Herrera.
Writing – Review and Editing: Kevin Damián Carrillo Naranjo, Franklin Wilfrido Salazar, Luis Rojas Oviedo and Paúl Hernán Machado Herrera.
Resources: Kevin Damián Carrillo Naranjo, Franklin Wilfrido Salazar, Luis Rojas Oviedo and Paúl Hernán Machado Herrera.
Supervision: Kevin Damián Carrillo Naranjo, Franklin Wilfrido Salazar, Luis Rojas Oviedo and Paúl Hernán Machado Herrera.
Approval of the final text: Kevin Damián Carrillo Naranjo, Franklin Wilfrido Salazar, Luis Rojas Oviedo and Paúl Hernán Machado Herrera.

VII. ACKNOWLEDGMENTS

The Authors thank the Research and Development Department (DIDE) of the Technical University of Ambato for their special help in the development of this proposal, thanks to the funding of the project "Design of a communications platform for technological applications of precision agriculture with Drones."

VIII. REFERENCES

[1] M. Skiborowski , "Synthesis and design methods for energy-efficient distillation processes," Current Opinion in Chemical Engineering, vol. 42, art. 100985, 2023, doi : 10.1016/j.coche.2023.100985.

[2] PP Krishna, B. Desikan, and CS Rao, "Control and dynamic optimization of middle vessel batch distillation column for the separation of ethanol/propanol/butanol mixture," Chemical Engineering Research and Design, 2021, doi : 10.1016/j.cherd.2021.10.002.

[3] M. Elsheikh, T. Huesmann, M. Otte, A. Mhamdi, and A. Mitsos, "Control of an Industrial Distillation Column Using a Hybrid Model with Adaptation of the Range of Validity and an ANN-based Soft Sensor," Chemie Ingenieur Technik, vol. 95, no. 7, pp. 1114–1124, 2023, doi : 10.1002/cite.202200232.

[4] L.-M. Ränger , Y. Waibel, and T. Grützner , "Experimental Investigation of Heat Losses in a Pilot-Scale Multiple Dividing Wall Distillation Column with Three Parallel Sections," ChemEngineering , vol. 7, no. 4, art. 68, 2023, doi : 10.3390/chemengineering7040068.

[5] NM Tahir, MA Kamal, S. Hafeez, and SAM Said, "Control of Heat-Integrated Distillation Columns: Review, Trends, and Challenges for Future Research," Processes, vol. 13, no. 1, art. 17, 2024, doi: 10.3390/pr13010017.

[6] L.-M. Ränger , J. Brandt, and T. Grützner , "Understanding Temperature Profiles of Distillation Columns," Industrial & Engineering Chemistry Research, 2024, doi: 10.1021/acs.iecr.3c04102.

[7] D. Schack, M. Liesche, and S. Engell, "Energy-Efficient Distillation Processes by Additional Heat Transfer Derived from the FluxMax Approach," Frontiers in Energy Research, vol. 8, art. 134, 2020, doi: 10.3389/fenrg.2020.00134.

[8] A. Tsatse , G. Guillén-Gosálbez, and MS Chachuat, "Optimal design and operation of reactive distillation processes considering process alternatives," Chemical Engineering Research and Design, 2021, doi : 10.1016/j.cherd.2021.05.032.

[9] A. Márquez-Ruiz, AN Venkat, and WP Heath, "Model Learning Predictive Control for Batch Processes," Industrial & Engineering Chemistry Research, vol. 58, no. 48, pp. 22095–22109, 2019, doi: 10.1021/acs.iecr.8b06474.

[10] A. Douady , D. Spognardi , S. Mathias, S. Chauchard , and G. Liger-Belair, "Batch distillation of spirits: Experimental study and modeling for quality," Journal of the Institute of Brewing, vol. 125, no. 1, pp. 91–101, 2019, doi : 10.1002/jib.560.

[11] MA Ashour, D. Stucke, J. Neukäufer, and T. Grützner, "Revisiting heat losses in lab-scale distillation columns: Quantification, improvement, and influence on miniaturized 3D-printed packagings," Chemical Engineering Journal Advances, vol. 16, art. 100531, 2023, doi: 10.1016/j.ceja.2023.100531.

[12] M. Walk, J. Hamacher, JJ Downs, SM Miller, S. Owens, and R.B. Eldridge, "Validation of Differential Temperature Control for a Dividing Wall Distillation Column," Industrial & Engineering Chemistry Research, vol. 60, no. 3, pp. 1341–1355, 2021, doi : 10.1021/acs.iecr.0c04570.

[13] U. Preißinger, G. Lukač, I. Dejanović, and T. Grützner, "Investigation of Control Structures for a Four-Product Laboratory Multiple Dividing-Wall Column Using Dynamic Simulation," Chemical Engineering & Technology, vol. 44, pp. 223–237, 2021, doi: 10.1002/ceat.202000557.

[14] B. Németh, L. Hegely, and P. Lang, "Investigating the processing capacity of batch distillation by applying a second, smaller column," Separation and Purification Technology, art. 119883, 2022, doi: 10.1016/j.seppur.2021.119883.

[15] I. Pappas, R. Bindlish, M. Ali, and EN Pistikopoulos, “Optimal Operation of an Industrial Dividing Wall Column through Multiparametric Programming,” Industrial & Engineering Chemistry Research, vol. 62, no. 37, pp. 15029–15035, 2023, doi: 10.1021/acs.iecr.3c00836.

[16] Y. Cheng, X. Wang, and M. Yi, “Decoupling control of high-purity heat-integrated distillation columns,” Transactions of the Institute of Measurement and Control, vol. 42, no. 11, pp. 2099–2111, 2020, doi: 10.1177/0142331220908989.

[17] B. Németh, L. Hegely, and P. Lang, “Optimization of solvent recovery in two batch distillation columns of different sizes,” Journal of Cleaner Production, vol. 275, art. 124746, 2020, doi: 10.1016/j.jclepro.2020.124746.

[18] F. Al Kalbani and J. Zhang, “Inferential Composition Control of a Distillation Column Using Active Disturbance Rejection Control with Soft Sensors,” Processes, vol. 11, no. 1, art. 203, 2023, doi: 10.3390/pr11010203.

[19] Y. Yuan, X. Qian, and H. Chen, “An Effective Temperature Control Method for Dividing-Wall Distillation Columns Based on a Product-Quality Estimator,” Processes, vol. 10, no. 5, art. 1018, 2022, doi: 10.3390/pr10051018.

[20] R. Staud, U. Bieder, and A. Skiborowski, “Impact of thermal column wall conditions and subcooled reflux on separation performance,” Chemical Engineering and Processing: Process Intensification, 2025, in press.

Journal of Engineering and Technology for Industrial Applications

ISSN ONLINE: 2447-0228

ITEGAM-JETIA

Manaus, v.12 n.60, p.28-38, July/August, 2026.

DOI: https://doi.org/10.5935/jetia.v12i60.3182

RESEARCH ARTICLE OPEN ACCESS

SIX AXIS MAGNETOMETER/ACCELEROMETER ASSISTED MOBILE ROBOT INDOOR NAVIGATION

Guransh Singh Arora[1] and Kumar Gaurav*[2]

[1, 2]Department of Mechatronics Engineering, Manipal University Jaipur, Jaipur, Rajasthan, 303007, India.

[1]https://orcid.org/0009-0003-1942-8568, [2]https://orcid.org/0000-0001-8119-297X

Email:*kumar.gaurav@jaipur.manipal.edu, guransh.23fe10mce00008@muj.manipal.edu

ARTICLE INFO

Article History
Received: December 22, 2025
Reviewed: May 20, 2026
Accepted: June 21, 2026
Published: July 31, 2026

Keywords:
Arduino,
Autonomous,
Mobile robot,
Yaw/heading,
Navigation,
Magnetometer

ABSTRACT

Yaw/Heading measurement is an important parameter for the pose determination of the mobile robot. Yaw/heading can assist the mobile robot in localization much needed for autonomous navigation. There are various sensors available to measure the Yaw/heading that may require pre or post-processing of the data. This paper presents a low-cost and efficient six-axis magnetometer/accelerometer LSM303DLHC (GY 511) sensor for direct measurement of the Yaw/heading. The yaw values were recorded in real time with a data logger while the mobile robot was tracking a line with the help of IR sensors. It establishes that the change in yaw values due to turns on track corresponds to real-time movements/navigation of the mobile robot. Additionally, experiments were performed that demonstrate that the mobile robot can navigate autonomously, fetching yaw values from LSM303DLHC, and avoiding obstacles. The heading values from the LSM303DLHC sensor were found to be consistent with time and suitable for educational/research projects.

Copyright ©2026 by authors and Galileo Institute of Technology and Education of the Amazon (ITEGAM). This work is licensed under the Creative Commons Attribution International License (CC BY 4.0).

I. INTRODUCTION

Mobile robots have been increasingly popular in recent decades due to their ease of maneuverability. They find numerous applications indoors and outdoors, such as cleaning. [1], warehousing [2], [3], agriculture [4], [5], search and rescue[6], [7], healthcare [8-10], security and patrol [11], environment monitoring [12], etc. Wheeled mobile robots among locomotive robots are the chosen ones due to their lower power consumption and simple design. In some cases, it is manually controlled, and in some cases, it is autonomous. However, the autonomous navigation depends on the localization task of the mobile robot [13]. The position of the mobile robot is very important as it tries to locate itself in an unknown environment. The position can be expressed in Cartesian coordinates (x, y) for a planar region along with its heading or yaw angle (θ) [14]. Hence, in the indoor environment, the mobile robot can rely on its own sensors and calculate its position using dead reckoning [15]. Hence, sensors like encoders, Inertial Measurement Unit (IMU), LiDAR are used in conjunction with beacons such as ultrawide band (UWB), Bluetooth, and WiFi for indoor positioning [16]. The heading can be obtained with the Global Positioning System (GPS) [17], but sometimes it doesn't work or provides inaccurate readings indoors [18], [19]. Also, the dependency is not reliable using Global Navigation Satellite Systems (GNSS) [20] due to restricted coverage and hindered signal propagation [21]. Magnetometers can provide absolute heading based on the Earth's magnetic field, provided there are no external magnetic disturbances [22]. To remove electromagnetic interference and heading correction, magnetometers need calibration and a filter or post-processing of data that may be computationally expensive [23], [24]. The remainder of this paper is organized as follows: Section 2 discusses the materials and methods; Section 3 presents the results and discussions; Section 4 discusses the limitations of the present work; and Section 5 concludes the paper.

II. RELATED WORK

There are some commonly used sensors found in the research articles for heading measurements. Mostly, the authors applied filters/post-processing to get stabilized readings and make them error-free even in the presence of magnetic disturbances. For example, a recent work reported the use of MPU 6050 (accelerometer and gyroscope) for yaw angle determination on an inclined plane for a mobile robot. It used the golden section search method with the mean squared error metric to mitigate drift effects. [25]. MPU 6050 was also used to stabilize the camera position of the gimbal smartphone to improve the quality of captured images and videos. The average error in the yaw angle was reported as 0.78° without any filter. [26]. A low-cost prototype consisting of MPU 6050 and HMC 5883L (magnetometer) can provide accurate headings with an error of 2.9° after proper calibration. It can be beneficial for pseudo-tethered devices when used while driving, leading to portable navigation. [27]. Fusing the data of multiple MPU 6050 to suppress the random drift error can prove beneficial. Four MPU 6050 were taken into consideration, on which the effect of calibration shows a trend of steady enhancement. [28]. LSM303DLH is also a common and low-cost sensor used for attitude and heading reference systems (AHRS). The sensor fusion algorithm using estimation of mean square error was validated on a combination of gyroscope and LSM303DLHS (accelerometer and magnetometer) sensor and found to be effective [29]. Dual magnetometers (LIS3MDL) with inertial navigation systems (INS) can be integrated with dynamic time wrapping (DTW) algorithm for estimation of motion speed for the indoor mobile robots'. The results of wheel odometry were similar to the proposed approach and comparable to dead reckoning (DR) [30]. Similarly, the LSM303D magnetometer can give yaw angle accuracy of 0.4° with the Levenberg–Marquardt (L-M) algorithm with “hard iron” and “soft iron” errors [31]. The HMC5883L can also facilitate the robot’s motion and help it to be on the intended path. But the accuracy of the heading varies from 1° or 2°[32]. Above mentioned low-cost magnetometers/accelerometers can be used as heading sensors in AHRS for autonomous navigation for path following/tracking autonomously with a mobile robot. The navigational performance was based on straight line following or circular path following using the MEMS sensor MPU 9250 (includes MPU 6050) [33]. Use of HMC5833L in the robot’s motion for path tracking can be improved with realistic tracks and the inclusion of obstacles. [32]. But in some cases, magnetometers are costly, such as in [34] Path following with the LIS2MDL magnetometer with simple calibration can also facilitate autonomous navigation with sensor fusion and reinforcement learning. Waypoint-following demonstrated in [35] Didn’t consider obstacles in between and used HMR3300 magnetometer (comparatively costlier). Similarly, track following can be facilitated by fusing the wheel odometry data with the BNO 055 compass sensor, to minimize the RMS error value of less than 0.15 meters. [36]. The comparison of reported works is shown in Table 1.

Table 1: Comparison of path tracking/following with customized wheeled mobile robots.

S.N.	Magnetometer	Microcontroller	Task	Cost	Ref.
1	LIS2MDL	ATmega 2560	Path following/autonomous navigation	comparatively high	[34]
2	HMC5883L*	ATmega 2560	Path following	Low	[32]
3	HMR 3300	No details	Waypoint following	Higher	[35]
4	BNO 055	Raspberry Pi	Track following	Higher	[36]
5	LSM303DLH	Arduino Uno	Path following/obstacle avoidance	Low	Present work

Source: Authors, (2026).

But the choice of magnetometers can be difficult for mobile robot localization and autonomous navigation because they can be of different materials (Hall effect, inductive, anisotropic magnetoresistance magnetometers (AMR) or MEMS type). Even though there are many features like output frequency and operating range that have to be considered before selection. Such a review paper presented comparative insights into 42 IMU models from 7 different manufacturers [37] based on features such as structure details and connectivity. Also, three different types of AMS magnetometers were selected for a characteristics study and calibration. The HMC5893 by Honeywell, and the LSM303DLHC and LIS3MDL by ST Microelectronics were chosen, and comparative results showed that LSM303DLHC can be the best choice for heading measurements [38]. Selection can also be based on repeatability, cost and accuracy [35]. As per the above facts, it can be concluded that the selection of low-cost magnetometers as heading sensors is important. Also, autonomous path following/tracking by the mobile robot with obstacle avoidance should demonstrate the application of a low-cost magnetometer as a heading sensor is necessary. e The LSM303DLHC sensor (magnetometer/accelerometer) can find the heading of the mobile robot and get stored simultaneously in the SD card. The black line provides a well-defined path that the robot must follow, and subsequently, the heading is recorded on each turn. The main contributions of this paper are as follows:

i) Comparison of affordable magnetometers/accelerometers for the selection of a suitable one (LSM303DLHC).
ii) Testing for LSM303DLHC heading accuracy
iii) Real-world experiments on autonomous path following/tracking with and without obstacle avoidance on rectangular/circular tracks.

III. MATERIALS AND METHODS

This section outlines the procedure to execute the design of experiments. The first step in methodology involves the selection of a heading sensor. As there are some affordable heading sensors available, their comparison can lead to the identification of a suitable one. Therefore, the selection criteria are discussed in subsection 3.1. Then the second step is about a customized differential drive mobile robot (DDMR) that was developed for real-world experiments. It is discussed in subsection 3.2. This subsection also includes insights into two important hardware components (Micro SD card module as data logger and LSM303DLHC sensor), with their working and interfacing with Arduino Uno. After the development of DDMR with all the hardware components integrated, an embedded C language code was developed. There were three types of experiments designed to be executed on the developed DDMR.

First, heading values were recorded from the LSM303DLHC sensor on the onboard mobile robot. Secondly, heading values were recorded in real time as the mobile robot was tracking the black line with IR sensors. It was tested in two experimental arenas (curvature and rectangular path). Lastly, it was demonstrated that the mobile robot can navigate autonomously, fetching heading values from the LSM303DLHC sensor, avoiding obstacles. The methodology of the work is provided in Figure 1.

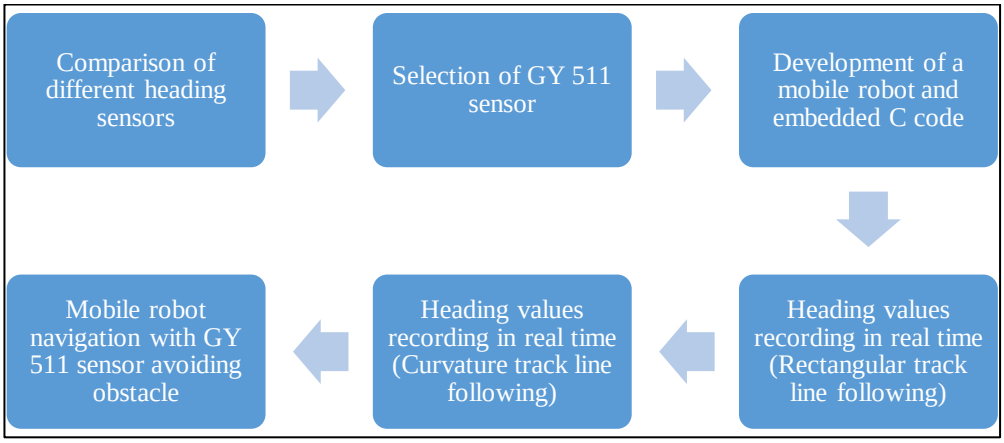


Figure 1: Methodology of the proposed work.
Source: Authors, (2026).

III.1 COMPARISON OF LSM303DLHC WITH OTHER YAW/HEADING SENSORS

This subsection highlights the comparison of three common and affordable yaw/heading sensors used for navigational purposes. These sensors are an LSM303DLHC sensor (magnetometer and accelerometer), GY 271 QMC5833L magnetometer and GY 521 MPU 6050 (accelerometer and gyroscope). The comparison parameters were provided in Table 2 below. There are other commercially available heading sensors, such as the RM 3100 3-axis magnetometer sensor [39], and DF robot fermion BNO055 [40] but not considered due to cost constraints.

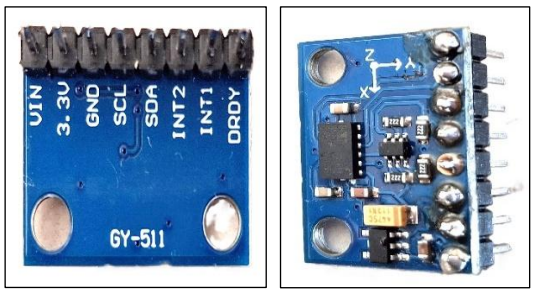
Table 2: Magnetometer/Accelerometer sensor comparison.

S.N.	Yaw/heading Sensor	Cost under INR 300 (may vary slightly)	Calculation of absolute Yaw angle	Accelerometer	Magnetometer	Heading Accuracy
1	LSM303DLHC	Low	Easy[38]	±2g, ±4g, ±8g, and ±16g	±1.3 to ±8.1 gauss	Stable with less noise [38]
2	QMC5883L	Very Low	Moderate	NA	±8 gauss	Comparatively low due to high noise
3	MPU 6050	Very Low	Difficult [41]	±2g, ±4g, ±8g, and ±16g	NA	Error integrates over time due to drift[41]

Source: Authors, (2026).

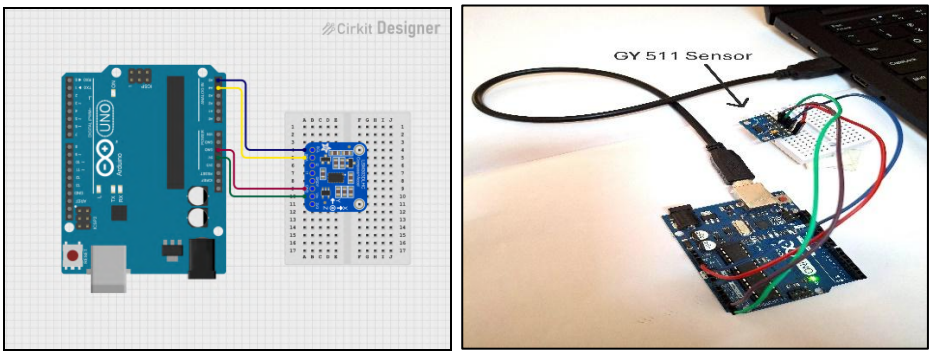
III.2 STATISTICAL ANALYSIS-BASED SELECTION OF LSM303DLHC

This subsection presents the statistical analysis of LSM303DLHC heading values along with other sensors QMC5883L and MPU 6050. Firstly, the LSM303DLHC sensor pin breakout and interfacing with Arduino Uno are explained. The LSM303DLHC sensor shown in Figure 2 can be interfaced with Arduino Uno/Nano. The sensor can easily calculate the heading with the help of magnetic fields. The respective connections are shown in Figure 3.



(a) (b)

Figure 2: (a) LSM303DLHC with LSM303DLHC chip front side, (b) LSM303DLHC sensor back side.
Source: Authors, (2026).



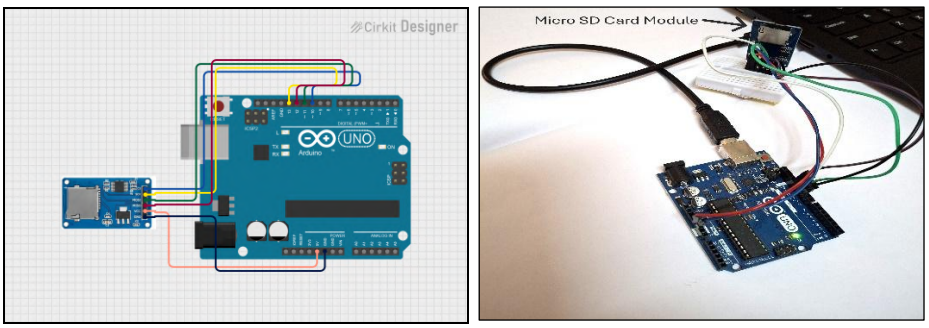
(a) b)

Figure 3: (a) Interfacing LSM303DLHC with Arduino Uno schematic, (b) Real picture of interfacing.
Source: Authors, (2026).

Arduino IDE and the LSM303DLHC sensor are helpful in getting the measured values from sensors in real-time and troubleshooting as required. The LSM303DLHC sensor was first calibrated with the local latitude and longitude position. The library from Github https://github.com/pololu/lsm303-arduino was used to calibrate the magnetometer and then record the heading data [42]. The calibration values found are below.

```
compass.m_min = (LSM303::vector<int16_t>){-426, -139, -398};
compass.m_max= (LSM303::vector<int16_t>){+530, +820, -190};
```

This was put in the program code to calculate heading and found to be accurate with the global north as per the digital compass of a standard Android smart phone. It is important to store the heading data as the mobile robot traverses from one point to another. A micro SD card module with a capacity 8 GB can be easily interfaced with Arduino Nano and can be used as a data logger for heading values Arduino Uno/Nano [43]. The respective connections are shown in Figure 4.



(a) (b)

Figure 4: (a) Interfacing Micro SD card module with Arduino Uno schematic, (b) Real picture of interfacing.
Source: Authors, (2026).

Based on the sensor comparison provided in Table 2, it has been found that stable reading with less noise and tilt compensation can be best fit for heading calculations. To conclude, a hardware setup was created to test the values of heading angles logged in real time. The hardware setup (shown in Figure. 5) consists of Arduino Nano, Micro SD card and all three sensors listed above in Table 2. The logged data of heading values from each sensor is provided in Table 3.

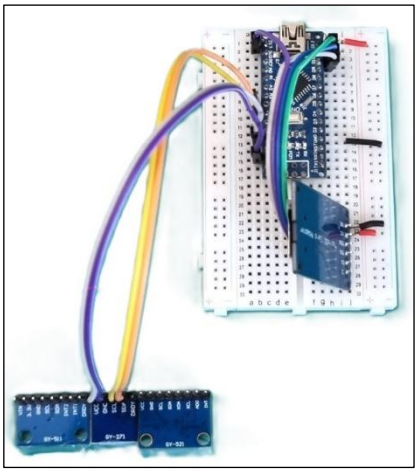


Figure 5: Hardware set up for comparative analysis of LSM303DLHC, QMC5883L and MPU 6050 with Arduino Nano.
Source: Authors, (2026).

Table 3: Statistical analysis of data values obtained from three heading sensors.

S.N.	No. of data values(degrees)	Min	Max	Mean	Median	Mode	Std	Range
LSM303DLHC	510	343.6	344.54	344.03	344.03	343.98	0.1684	0.94
QMC5883L	523	344	346	344.40	344	344	0.496	2
MPU 6050 with drift	495	1.04	359.5	165.31	106.73	95.88	110.56	358.46
MPU 6050 with processing	356	345.18	345.86	345.45	345.47	345.47	0.099	0.68

Source: Authors, (2026).

It is evident from the statistical analysis of Table 3, that LSM303DLHC sensor gives the best mean of 344.03° with respect to reference value of 344°. Out of the three sensors, the performance of LSM303DLHC seems to suit the requirement and selected finally.

III.3 DEVELOPMENT OF DDMR

The hardware assembly of the DDMR in the paper comprises components such as LSM303DLHC as heading sensor, Micro SD card module as a data logger, HC SR 04 as an ultrasonic sensor for obstacle avoidance and IR sensor (two) for black line tracking. Also, the other components are L293D motor driver, two BO motors, two wheels, Arduino Uno, rechargeable LiPO battery 11.4 V. The simple DDMR was built with the low-cost and affordable components mentioned above with Arduino Uno as the main controller. The pin connections for LSM303DLHC and Micro SD card are already discussed in the next subsections. The IN1, IN2, IN3, IN4, ENA, and ENB pins of L298N motor driver are connected to pin no. 4,9,6,7,3 and 5 respectively of Arduino Uno. IR sensors on the front right and front left of the mobile robot are connected to pin no. 2 and 8 respectively of Arduino Uno. Trig and Echo pin of HC SR04 are connected to 1 and 0 pin of Arduino Uno respectively. The complete circuit diagram is shown in Figure 6 below (drawn with cirkit designer website). The full software developed for this problem statement has been shared in GitHub. https://github.com/kgsingh555/Autonomous-mobile-robot-navigation-using-Magnetometer-as-Heading-Sensor. The DDMR setup is shown in Figure 7 below.

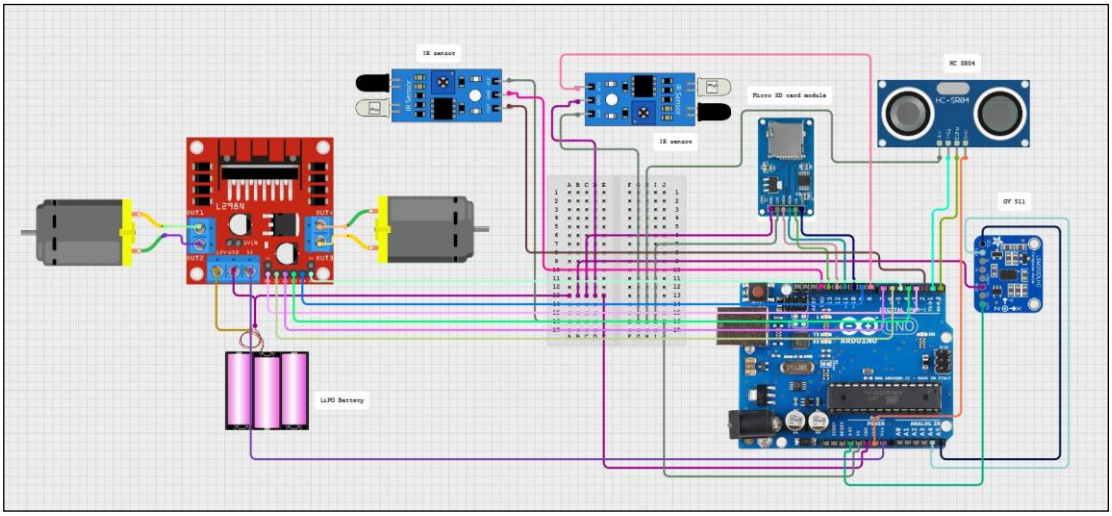


Figure 6: Circuit diagram of autonomous line follower mobile robot with Micro SD card module and LSM303DLHC sensor.
Source: Authors, (2026).

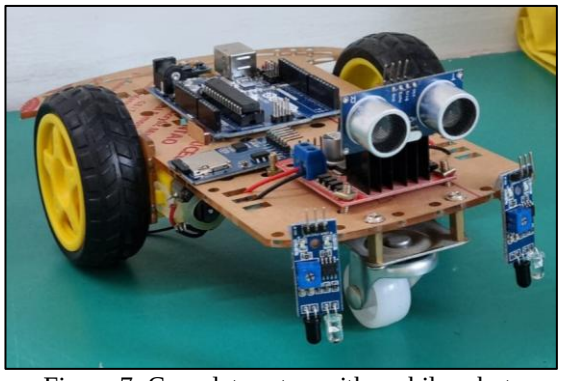


Figure 7: Complete setup with mobile robot.
Source: Authors, (2026).

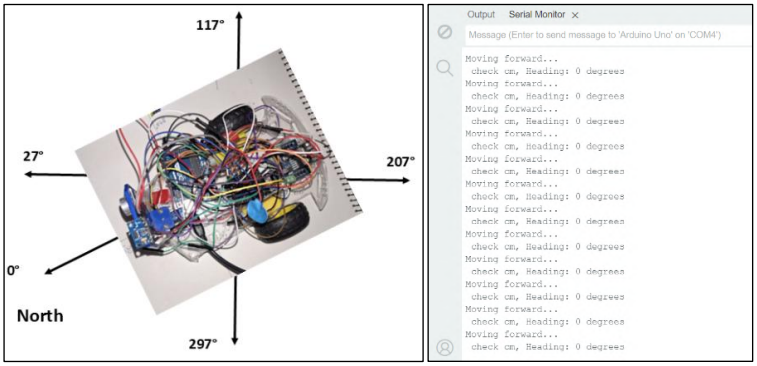
IV. RESULTS AND DISCUSSIONS

This section highlights the types of experiments conducted to demonstrate the navigational feature of the DDMR using LSM303DLHC sensor. There are three types of experiments conducted. Subsection 4.1 explains the preliminary results of the heading values recorded from the onboard data logger of the DDMR while it is rotating about z-axis.

Subsection 4.2 describes the result of heading values recorded while the DDMR is tracking black line with IR sensors on rectangular and curvature path. The third experiment is presented in subsection 4.3 that explains the obstacle avoidance behavior of DDMR being guided by LSM303DLHC sensor.

IV.1 YAW/HEADING READINGS FROM LSM303DLHC WITH ONBOARD DATALOGGER ON DDMR

In this subsection, it is demonstrated that the heading values from the LSM303DLHC sensor are reliable and consistent enough to be considered for autonomous mobile robot navigation. It gives output from 0° to 360°. The DDMR has been kept in two orientations. These two orientations are 0° and 27°. Firstly, with a digital compass in Android Smartphone as a reference, 0° and 27° are marked. 0° in digital compass shows due north direction. It is shown in Figure 8. The actual experimental setup with DDMR heading due north (0°) is shown in Figure 8 a). Also, in Figure 8 b) the output on the serial monitor of Arduino IDE is shown. It prints the heading after every 1 sec. The heading was recorded for 10 mins, considering 1 sample/sec. Hence there were 600 sample values when the DDMR was in due north direction. It can be observed from Figure 9 that only at some times, the value fluctuated and recorded 359°. The circular mean for 600 samples is 0.03°.



(a) b)

Figure 8: (a) Mobile robot heading in due north position, (b) Output in serial monitor of Arduino Uno.
Source: Authors, (2026).

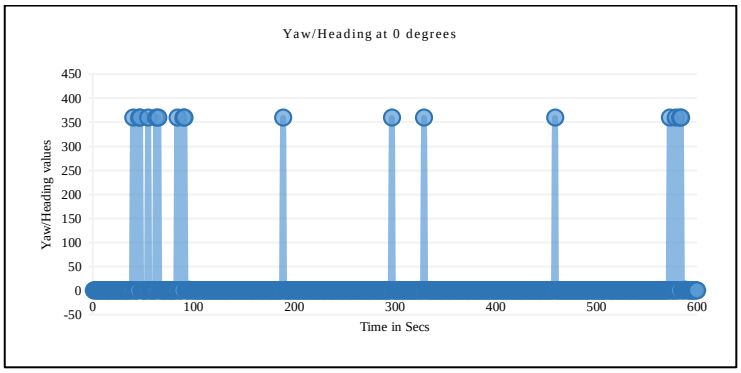
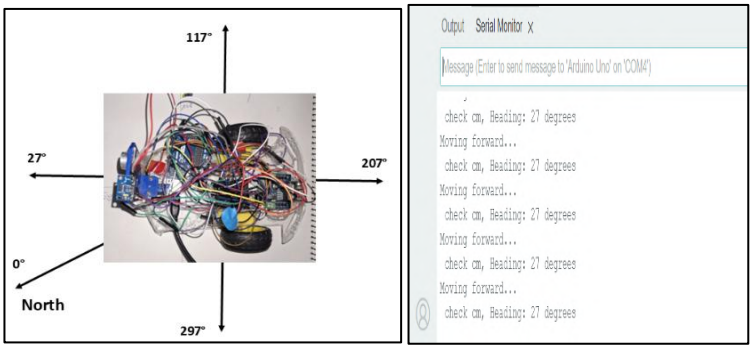


Figure 9: Mobile robot heading at 0° recorded for 10 mins (one sample/sec).
Source: Authors, (2026).

The experiment was repeated with the mobile robot orientation at 27°. It can be observed from Figure. 10 a) the mobile robot heading was oriented at 27° in the experimental setup, while the output in the serial monitor of Arduino IDE was 27° as well. It is shown in Figure 10 b). To validate the consistency of the output values in this orientation, heading values were recorded for 10 minutes. It was one sample/sec, and in total, there were 600 values. The recorded data is shown in Figure 11. The values deviation is minimal, only at one point, the value was 26°, and at some instances it was 28°. The average value for 600 samples is 27.095°.



(a) (b)

Figure 10: (a) Mobile robot heading at 27°, (b) Output on serial monitor of Arduino Uno.
Source: Authors, (2026).

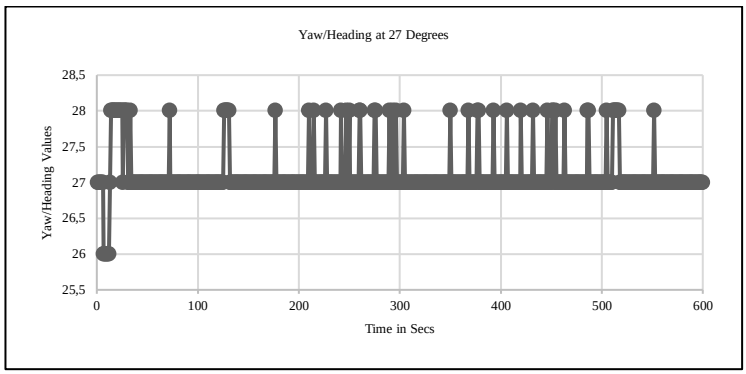


Figure 11: Mobile robot heading at 27° recorded for 10 mins (one sample/sec).
Source: Authors, (2026).

The DDMR also rotated around the z-axis clockwise to record the values of heading angles. It paused after a 90° turn in the clockwise direction, taking the reference directions shown in Figure 8 a). First, it was oriented towards 27° as the reference, then 117°, thereafter 207°, and lastly 297°. For a particular orientation, at least 28 heading values were recorded, which are shown in Figure. 12. The value dropped suddenly to 0° because it oriented towards due north again after complete rotation. It showed some spikes due to heading angle measurement at 359° and thereafter settled to 0°.

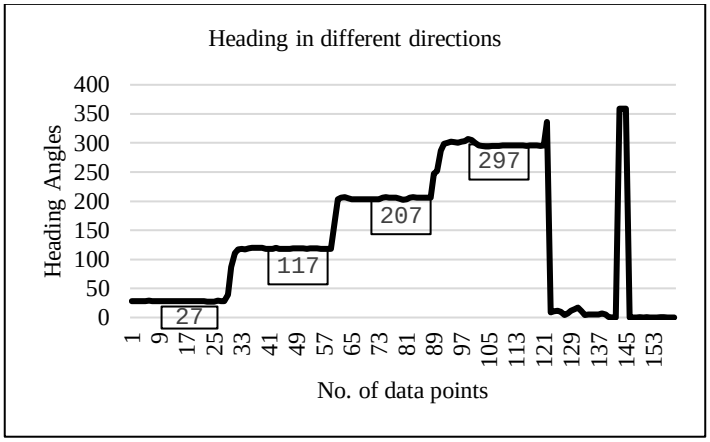
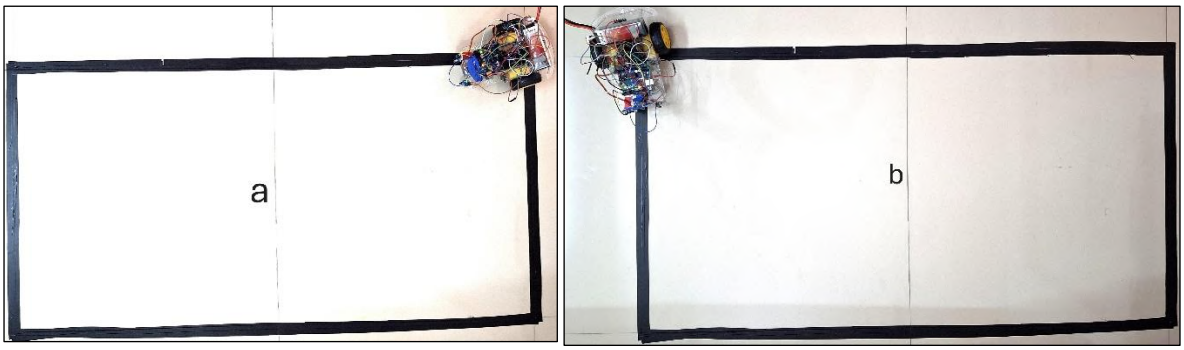


Figure 12: DDMR at each 90° turns, completing a full rotation around the z-axis.
Source: Authors, (2026).

IV.2 YAW/HEADING READINGS FROM LSM303DLHC WHILE DDMR TRACKING BLACK LINE

This subsection explains the DDMR black line tracking behaviour on a rectangular and a curvature path. There is a simultaneous recording of the heading values with the help of an onboard Micro SD card as a data logger. The Micro SD card module recorded heading values from the sensor LSM303DLHC at a rate of 1 sample/sec. The DDMR was able to follow a black line, which is rectangular in shape and measures 4 ft.× 2 ft. Approximately 15 seconds were required to complete one cycle. There were four turns of each 90°. The DDMR, while tracking the black line turns, and the Micro SD card module records the heading in the SD card. The position of the mobile robot at each 90° turn is shown in Figure 13. The mobile robot starts with position shown in Figure 13 a). Then it takes a 90° turn, and that is shown in Figure 13 b). Thereafter, the subsequent movements are shown in Figure 13 c) and Figure 13 d). It can be observed that movement is anticlockwise and the expected heading measurements will be 27°, 297°, 207° and 117° for each of the positions shown in Figure 13 a), Figure13 b), Figure 13 c), and Figure 13 d) respectively.



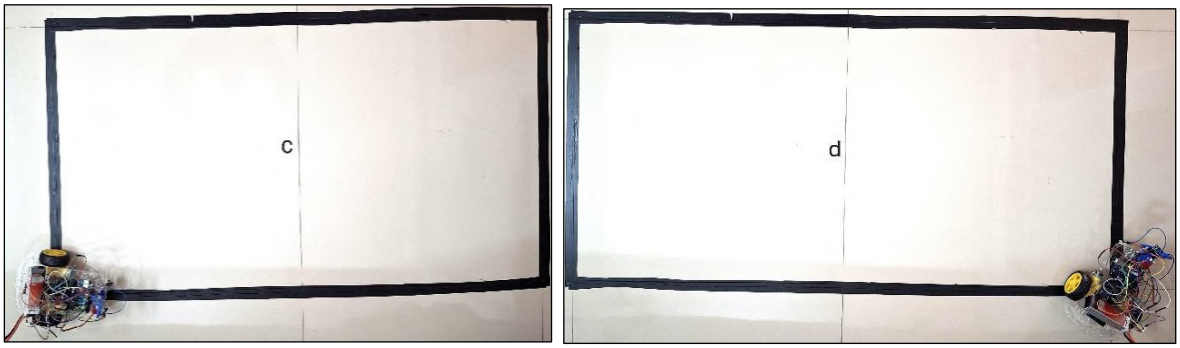


Figure 13: The DDMR heading is (a) 27° (b) is 297° (c) is 207° (d) is 117°.
Source: Authors, (2026).

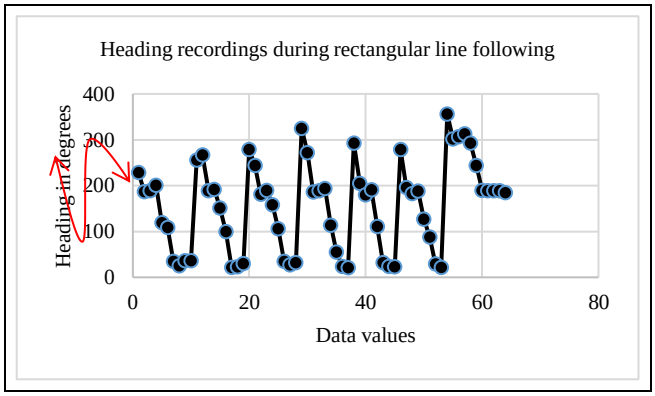
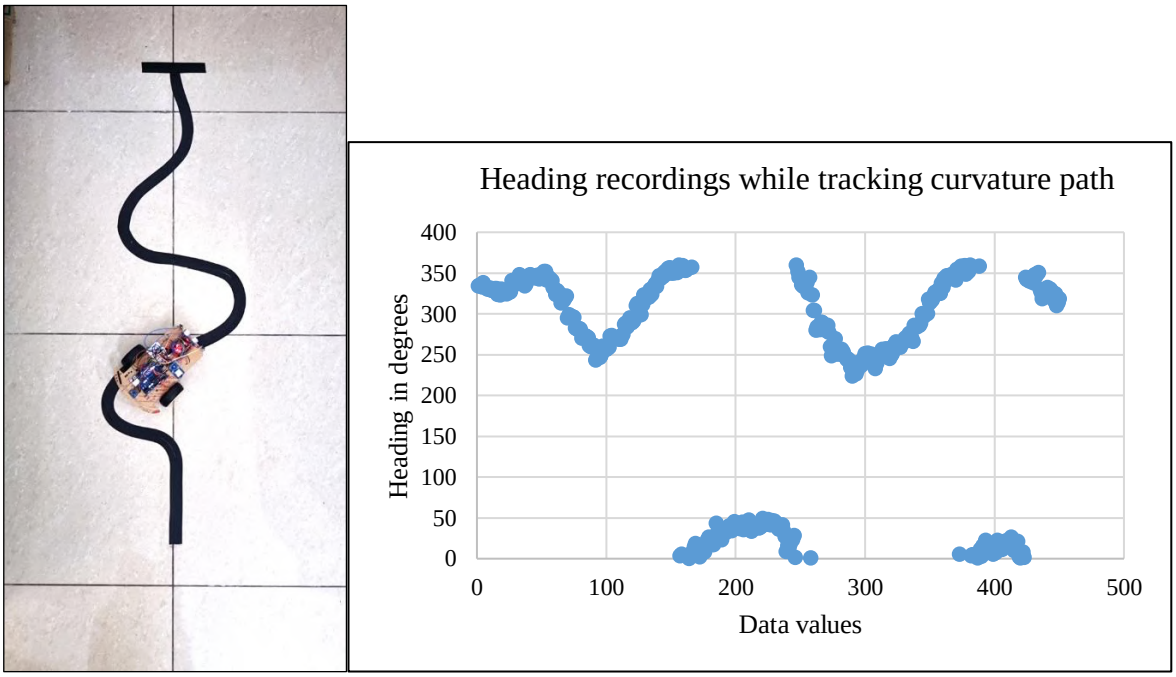


Figure 14: Heading recorded at each 90° turn (six repetitions) while DDMR tracking the black line.
Source: Authors, (2026).

Above Figure 14 shows the consistent record of the heading sensor for the DDMR. The line following was repeated six times and concludes at position Figure. 13 c) and remains there for some time. The red curved arrows mark the start and completion of the first cycle of the mobile robot movement. Similarly, a curvature path was created for the mobile robot to track. This time, the number of heading values recorded was 30 samples/sec. The run time of the mobile robot was approximately 15 seconds, and 450 heading values were recorded. Figure. 15 a) and Figure. b) below show the curvature path with mobile robot tracking and the graph with heading values recorded during the run, respectively.

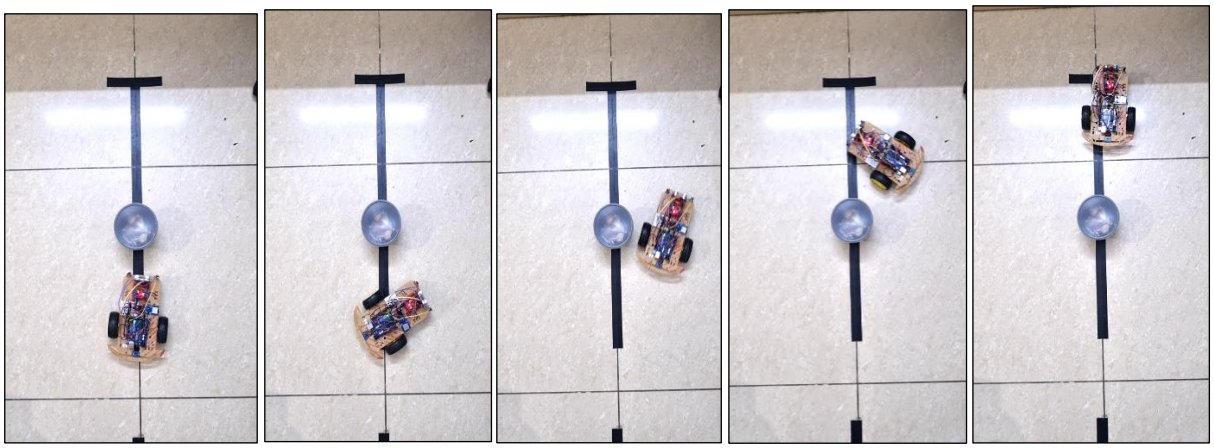


(a) (b)

Figure 15: (a) DDMR tracking curvature path, (b) heading recorded with LSM303DLHC sensor while tracking curvature path.
Source: Authors, (2026).

IV.3 YAW/HEADING READINGS FROM LSM303DLHC WHILE DDMR AVOIDING OBSTACLES

The third experiment was performed to demonstrate that DDMR can fetch the heading values from the LSM303DLHC sensor to avoid obstacles and autonomously navigate. As per Figure. 16, DDMR senses the obstacle with an ultrasonic sensor and, with reference to its present heading, turns 30° to the right and goes straight for a while. It then turns left again to catch up to the black line to resume line-following behavior. Hence, it can complete its run after reaching the end of the line.



(a) (b) (c) (d) (e)

Figure 16: The DDMR (a) starts following the black line b) senses the obstacle and turns 30° to the right, c) avoids the obstacle, d) gets back to the black line, e) resumes line following behavior and stops.
Source: Authors, (2026).

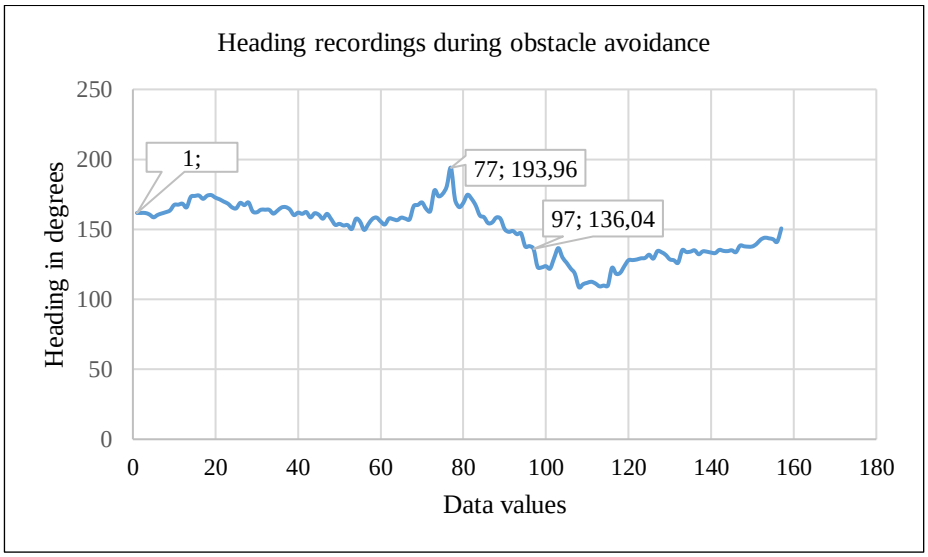


Figure 17: Mobile robot heading recorded with LSM303DLHC sensor while autonomously avoiding obstacles.
Source: Authors, (2026).

The mobile robot autonomously avoided the obstacle by turning 30° to the right and obtaining its heading angle from the LSM303DLHC sensor. The mobile robot turned 30° from the reference, which can be seen in Figure 17 above as data point 1. The value is 161.7°. After turning the heading recorded is 193.96°, which means the difference of angle is 32.26°. Hence, an error of 2.26° was there. Also, when the mobile robot returned to the black line after avoiding obstacles, its heading recorded was 136.04°; hence, the true value of the turn was 60°, but it was actually 193.96-136.04°, equal to 57.92°. Hence, an error of 60-57.92= 2.08° was there.

IV.4 LIMITATIOS OF THE WORK

There are some limitations of the work presented in this paper. Firstly, there can be few replacements for the used LSM303DLHC sensor that can be processed with Mahony or a low-pass filter. For example, the recently launched magnetometer MMC 5603NJ sensor may be relatively cheap and highly accurate, but it needs an accelerometer for tilt compensation. The experiments conducted are subject to environmental conditions, hardware components and software setups used. Only the orientation of DDMR was considered; hence, including odometry and dead reckoning can enhance the results.

V. CONCLUSIONS

In this paper, a low-cost six-axis magnetometer/accelerometer LSM303DLHC sensor was used for Yaw/heading measurement. The LSM303DLHC sensor was selected after comparison with its counterparts on defined parameters. A simple DDMR was developed with an onboard Micro SD card module as a data logger. The first experiment performed suggests that heading values are consistent over a period. Secondly, the DDMR was able to track the rectangular and curvature black line with IR sensors. These experiments were performed so that heading values can be stored in real time while the DDMR is traversing. The stored values can be compared with the fixed turns on the black line (90° turn in a rectangular path) as a reference. The third experiment confirmed that DDMR can use the heading values from the LSM303DLHC sensor to avoid the obstacle successfully. Hence, the selection of LSM303DLHC as a heading sensor can be a good choice for low-cost navigational applications in robotics. In future, fusion of sensors with different combinations of magnetometers, gyroscope, and accelerometer will be explored for autonomous navigation. It will also include the calibration and data filtering process.

VI. AUTHOR'S CONTRIBUTION

Conceptualization: Kumar Gaurav.
Methodology: Kumar Gaurav.
Investigation: Guransh Singh Arora, Kumar Gaurav.
Discussion of results: Kumar Gaurav.
Writing – Original Draft: Kumar Gaurav.
Writing – Review and Editing: Kumar Gaurav.
Resources: Guransh Singh Arora, Kumar Gaurav.
Supervision: Kumar Gaurav.
Approval of the final text: Guransh Singh Arora, Kumar Gaurav.

VII. ACKNOWLEDGMENTS

The author acknowledges the provision of research facilities by Manipal University Jaipur.

VIII. REFERENCES

[1] S. Butaney, K. Gaurav, P. Ranjan, and N. V. Shrivas, "Recent developments in autonomous floor-cleaning robots: a review," Industrial Robot: the international journal of robotics research and application, 2024.

[2] G. Vasiljević, D. Miklić, I. Draganjac, Z. Kovačić, and P. Lista, "High-accuracy vehicle localization for autonomous warehousing," Robot Comput Integr Manuf, vol. 42, pp. 1–16, 2016.

[3] L. Sabattini et al., "Technological roadmap to boost the introduction of AGVs in industrial applications," in 2013 IEEE 9th International Conference on Intelligent Computer Communication and Processing (ICCP), IEEE, 2013, pp. 203–208.

[4] D. F. Yépez-Ponce, J. V. Salcedo, P. D. Rosero-Montalvo, and J. Sanchis, "Mobile robotics in smart farming: current trends and applications," Front Artif Intell, vol. 6, p. 1213330, 2023.

[5] D. T. Fasiolo, L. Scalera, E. Maset, and A. Gasparetto, "Towards autonomous mapping in agriculture: A review of supportive technologies for ground robotics," Rob Auton Syst, vol. 169, p. 104514, 2023.

[6] K. Gaurav, A. Kumar, and R. Dayal, "Veco-taxis as a novel engineered algorithm for odor source localization," International Journal of Ambient Computing and Intelligence, vol. 11, no. 2, pp. 1–29, 2020, doi: 10.4018/IJACI.2020040101.

[7] K. Gaurav and P. Ranjan, "Moth-inspired odor source localization using robotic platforms: a comprehensive review," Adaptive Behavior, vol. 32, no. 4, pp. 345–369, 2024.

[8] M. Cognominal, K. Patronymic, and A. Wańkowicz, "Evolving field of autonomous Mobile Robotics: technological advances and applications," Fusion of Multidisciplinary Research, An International Journal, vol. 2, no. 2, pp. 189–200, 2021.

[9] G. A. Kebede, A. A. Gelaw, H. Andualem, and A. T. Hailu, "Review of the characteristics of mobile robots for health care application," Int J Intell Robot Appl, vol. 8, no. 2, pp. 480–502, 2024.

[10] N. Sharma, J. K. Pandey, and S. Mondal, "A review of mobile robots: Applications and future prospect," International Journal of Precision Engineering and Manufacturing, vol. 24, no. 9, pp. 1695–1706, 2023.

[11] R. Prykhodchenko, R. P. Rocha, and M. S. Couceiro, "People detection by mobile robots doing automatic guard patrols," in 2020 IEEE International Conference on Autonomous Robot Systems and Competitions (ICARSC), IEEE, 2020, pp. 300–305.

[12] T. Lewis and K. Bhaganagar, "A comprehensive review of plume source detection using unmanned vehicles for environmental sensing," Science of the Total Environment, vol. 762, no. December, p. 144029, 2021, doi: 10.1016/j.scitotenv.2020.144029.

[13] R. Siegwart, I. R. Nourbakhsh, and D. Scaramuzza, Introduction to autonomous mobile robots. MIT press, 2011.

[14] G. Grisetti, C. Stachniss, and W. Burgard, "Improved techniques for grid mapping with rao-blackwellized particle filters," IEEE transactions on Robotics, vol. 23, no. 1, pp. 34–46, 2007.

[15] L. Huang, H. Li, W. Li, W. Wu, and X. Kang, "Improvement of Pedestrian Dead Reckoning Algorithm for Indoor Positioning by using Step Length Estimation," The International Archives of the Photogrammetry, Remote Sensing and Spatial Information Sciences, vol. 48, pp. 19–24, 2022.

[16] P. Won, M. Biglarbegian, and W. Melek, “Development of an effective docking system for modular mobile self-reconfigurable robots using extended kalman filter and particle filter,” Robotics, vol. 4, no. 1, pp. 25–49, 2015.

[17] I. Y. Bar-Itzhack, P. Y. Montgomery, and J. C. Garrick, “Algorithms for attitude determination using the global positioning system,” Journal of guidance, control, and dynamics, vol. 21, no. 6, pp. 846–852, 1998.

[18]N. A. Elmunim, M. Abdullah, N. A. Elmunim, and M. Abdullah, “Overview of the GPS,” Ionospheric Delay Investigation and Forecasting, pp. 5–17, 2021.

[19] Z. Wu, Z. Sun, W. Zhang, and Q. Chen, “A novel approach for attitude estimation based on MEMS inertial sensors using nonlinear complementary filters,” IEEE Sens J, vol. 16, no. 10, pp. 3856–3864, 2016.

[20] N. Zhu, J. Marais, D. Betaille, and M. Berbineau, “GNSS position integrity in urban environments: A review of literature,” IEEE Transactions on Intelligent Transportation Systems, vol. 19, no. 9, pp. 2762–2778, 2018.

[21] X. Teng, Z. Shen, L. Huang, H. Li, and W. Li, “Multi-sensor fusion based wheeled robot research on indoor positioning method,” Results in Engineering, vol. 22, p. 102268, 2024.

[22] W. Chen et al., “A heading correction technology based on magnetometer calibration and adaptive anti-interference algorithm,” Sens Actuators A Phys, vol. 363, p. 114726, 2023.

[23] A. Ferlini, A. Montanari, A. Grammenos, R. Harle, and C. Mascolo, “Enabling in-ear magnetic sensing: Automatic and user transparent magnetometer calibration,” in 2021 IEEE International Conference on Pervasive Computing and Communications (PerCom), IEEE, 2021, pp. 1–8.

[24] D. Nemec, A. Janota, M. Hruboš, and V. Šimák, “Intelligent real-time MEMS sensor fusion and calibration,” IEEE Sens J, vol. 16, no. 19, pp. 7150–7160, 2016.

[25] N. T. Le, C. T. Truong, H. H. Nguyen, T. T. Nguyen, and V. T. Duong, “Yaw angle determination of a mobile robot operating on an inclined plane using accelerometer and gyroscope,” Measurement, vol. 247, p. 116806, 2025.

[26] A. A. Rafiq, W. N. Rohman, and S. D. Riyanto, “Development of a simple and low-cost smartphone gimbal with MPU-6050 sensor,” Journal of Robotics and Control (JRC), vol. 1, no. 4, pp. 136–140, 2020.

[27] A. Wahdan, J. Georgy, W. F. Abdelfatah, and A. Noureldin, “Magnetometer calibration for portable navigation devices in vehicles using a fast and autonomous technique,” IEEE Transactions on Intelligent Transportation Systems, vol. 15, no. 5, pp. 2347–2352, 2014.

[28] T. Wang, S. Zhong, H. Luo, and N. Kuang, “Drift error calibration method based on Multi-MEMS gyroscope data fusion,” International Journal of Precision Engineering and Manufacturing, vol. 24, no. 10, pp. 1835–1844, 2023.

[29] D. Nemec, A. Janota, M. Hruboš, and V. Šimák, “Intelligent real-time MEMS sensor fusion and calibration,” IEEE Sens J, vol. 16, no. 19, pp. 7150–7160, 2016.

[30] T. Zhang, L. Wei, J. Kuang, H. Tang, and X. Niu, “Mag-ODO: Motion speed estimation for indoor robots based on dual magnetometers,” Measurement, vol. 222, p. 113688, 2023.

[31] H. Wu, X. Pei, J. Li, H. Gao, and Y. Bai, “An improved magnetometer calibration and compensation method based on Levenberg–Marquardt algorithm for multi-rotor unmanned aerial vehicle,” Measurement and Control, vol. 53, no. 3–4, pp. 276–286, 2020.

[32] F. R. Seke and I. P. Tamba, “Development of robot motion direction based on microcontroller with compass sensor,” Development, vol. 13, no. 2, 2024.

[33] C. Liu, X. Xiang, Y. Duan, L. Yang, and S. Yang, “Improved path following for autonomous marine vehicles with low-cost heading/course sensors: Comparative experiments,” Control Eng Pract, vol. 142, p. 105740, 2024.

[34]R. Tiwari, A. Srinivaas, and R. K. Velamati, “Adaptive Navigation in Collaborative Robots: A Reinforcement Learning and Sensor Fusion Approach,” Applied System Innovation, vol. 8, no. 1, p. 9, 2025.

[35] P. Chand, “Integrating an electronic compass for position tracking on a wheeled tricycle mobile robot,” Drone Systems and Applications, vol. 10, no. 1, pp. 179–199, 2022.

[36] S. Sungkono, G. Al Azhar, A. C. Kusuma, and S. Izza, “Differential Drive Mobile Robot Motion Accuracy Improvement with Odometry-Compass Sensor Fusion Implementation,” ELKHA: Jurnal Teknik Elektro, vol. 15, no. 1, pp. 24–31, 2023.

[37] G. G. Samatas and T. P. Pachidis, “Inertial measurement units (imus) in mobile robots over the last five years: A review,” Designs (Basel), vol. 6, no. 1, p. 17, 2022.

[38] L. Schulz, P. Heinisch, and I. Richter, “Calibration of off-the-shelf anisotropic magnetoresistance magnetometers,” Sensors, vol. 19, no. 8, p. 1850, 2019.

[39] Robokits India, “PNI RM3100 Magnetometer Geomagnetism Sensor Module for Drone Military Grade Compass.” Accessed: Aug. 18, 2025. [Online]. Available: PNI RM3100 Magnetometer Geomagnetism Sensor Module for Drone Military Grade Compass

[40] Robu.in, “DF Robot Fermion: BNO055 Intelligent 9-axis Sensor (Breakout).” Accessed: Aug. 18, 2025. [Online]. Available: https://robu.in/product/df-robot-febno055-intelligent-9-axis-sensor-rmion-bno055-intelligent-9-axis-sensor-breakout/?gad_source=1&gad_campaignid=20363337560&gbraid=0AAAADvLFWf-ND5A_nq8ahAqJxczE-Hb_&gclid=CjwKCAjw49vEBhAVEiwADnMbbPe7XIJMTixIgtUAHtA-DgUjs9wAt7h77cYxZi9qPgza_RgNJGkfWBoCRwYQAvD_BwE

[41] Y. Zhu et al., “Attitude solving algorithm and FPGA implementation of four-rotor UAV based on improved mahony complementary filter,” Sensors, vol. 22, no. 17, p. 6411, 2022.

[42] Mohammadreza Akbari, “Interfacing GY-511 LSM303 3D Compass And Accelerometer with Arduino.” Accessed: Feb. 24, 2025. [Online]. Available: https://electropeak.com/learn/interfacing-gy-511-lsm303-3d-compass-and-accelerometer-with-arduino/?srsltid=AfmBOoq4u8ZhLhLXy2a__zgfns-3gTJBNfLij0PQUQjadlLSwb62YcXS

[43] LastMinuteEngineers, “Interfacing Micro SD Card Module with Arduino.” Accessed: Aug. 22, 2025. [Online]. Available: https://lastminuteengineers.com/arduino-micro-sd-card-module-tutorial/

Journal of Engineering and Technology for Industrial Applications

ISSN ONLINE: 2447-0228

ITEGAM-JETIA

Manaus, v.12 n.60, p. 39-48 July/August, 2026.
DOI: https://doi.org/10.5935/jetia.v12i60.3208

RESEARCH ARTICLE OPEN ACCESS

ASSESSING THE VISIBILITY AND PERCEPTION OF ESTATE SURVEYORS AMONG NON-CONSTRUCTION PROFESSIONALS IN NIGERIA

Olusoji D. Adetola[1], Busayo E. Akinwale[2*], Morakane C. Khahledi[3], Imoleayo A. Awodele[4]and Oyindamola A. Olagunju[5]

[1]Capital, Estate and Facilities Department, National Health Service (NHS), Manchester, United Kingdom.
[2]Department of Estate Management, University of Ibadan. Nigeria
[3]Department of Civil Engineering and Geomatics, Cape Peninsula University ofTechnology, Cape Town, South Africa.
[4]Construction Management and Quantity Surveying Department, Durban University of Technology, Durban,4001, South Africa.
[5]Salford Business school, University of Salford Manchester, United Kingdom.

[1]http://orcid.org/0000-0002-3556-4717, [2]http://orcid.org/ 0009-0000-5003-2770, [3]http://orcid.org/0000-0002-3144-4574
[4]http://orcid.org/0000-0003-1602-7294, [5]http://orcid.org/0000-0002-6371-8610

E-email: daptola@gmail.com, be.akinwale@ui.edu.ng, khahledim@cput.ac.za, *ImoleayoA@dut.ac.za

ARTICLE INFO

Article History
Received on: December 30, 2025
Reviewed on: January 30, 2026
Accepted on: May 01, 2026
Published on: July 31, 2026

Keywords:
Estate Surveying,
Non-allied Professionals,
Perception,
Awareness,
Nigeria,
Built Environment.

ABSTRACT

Estate Surveying and Valuation is a critical profession within Nigeria's built environment, contributing significantly to land administration, property valuation, investment decision-making, and real estate consultancy. Despite its relevance, the profession is often misunderstood or underappreciated by non-construction professionals. This study aimed to appraise the perception of the Estate Surveying profession among non-allied professionals in Nigeria, with particular emphasis on their awareness of the profession's existence, understanding of its roles and duties, and perception of its relevance to the construction and real estate industries. The research adopted a descriptive survey design using structured questionnaires administered to 162 respondents drawn from the medical, legal, financial, administrative, and other non-construction professional sectors. Data were analyzed using frequency distributions, percentages, and the Mean Item Score (MIS) ranking method. Findings revealed that 94.6% of respondents were aware of the Estate Surveying profession, and over 73% agreed that Estate Surveyors are part of the built environment team. However, detailed awareness of the profession's specific functions such as property management, investment appraisal, facility management, and valuation for various statutory and commercial purposes was considerably lower. Duties such as rating and taxation advice, land acquisition consultancy, and building insurance valuation ranked lowest in perceived awareness. The profession was rated "very good" or "good" in terms of performance by 88.88% of respondents, but cost perception and limited understanding of roles were identified as barriers to wider engagement. This study highlights the need for advocacy and outreach to improve non-construction professionals' understanding and engagement with Estate Surveyors.

Copyright ©2026 by authors and Galileo Institute of Technology and Education of the Amazon (ITEGAM). This work is licensed under the Creative Commons Attribution International License (CC BY 4.0).

I. INTRODUCTION

The built environment is an interdisciplinary domain composed of diverse professionals whose collective contributions are essential to achieving sustainable development goals. Among these, estate surveyors play a pivotal role in areas such as property valuation, land administration, asset and facilities management, and real estate investment consultancy [1], [2]. Despite their strategic position in land and property markets, the

Estate Surveying and Valuation profession in Nigeria continues to suffer from limited public understanding and engagement, particularly among non-construction professionals who interact with property issues in both personal and institutional capacities [3]. Estate Surveyors and Valuers are legally recognized practitioners under the regulatory oversight of the Estate Surveyors and Valuers Registration Board of Nigeria (ESVARBON), established through Decree No. 24 of 1975 (CAP E13 LFN 2007). The profession also operates under the guidelines of the Nigerian Institution of Estate Surveyors and Valuers (NIESV), which aligns with international standards, including those of the Royal Institution of Chartered Surveyors [4]. Nonetheless, existing studies reveal persistent misconceptions that conflate estate surveyors with land surveyors or valuers, thereby undermining their professional identity and limiting public patronage [5]. Scholarly evidence suggests that this poor perception and underutilization of estate surveyors stem from a lack of awareness, weak public engagement strategies, inadequate branding, and overlapping professional jurisdictions in the property sector [6], [7].

The issue is more pronounced among non-allied professionals such as legal practitioners, healthcare professionals, and financial experts who, despite engaging frequently with real estate matters, may not fully grasp the scope and relevance of estate surveyors' services [3], [7]. Estate Surveyors are not only valuation experts but also offer advisory services on land acquisition, investment, property development, and facilities management [8], [9]. However, awareness of these roles remains limited among professionals outside the built environment, leading to confusion with other land-based professions, such as land or quantity surveyors [10], [11]. This lack of recognition contributes to the underutilization of estate surveyors, which may negatively affect real estate efficiency and broader economic development. This study, therefore, seeks to appraise the perception of the Estate Surveying profession among non-allied construction professionals in Nigeria, focusing on their level of awareness, understanding of professional roles, and willingness to engage estate surveyors. With Abuja Nigeria's Federal Capital Territory and administrative hub as the study area, the research offers a cross-sectoral perspective on professional visibility, filling a notable gap in existing literature that has traditionally centered on students and construction-related professionals.

II. LITERATURE REVIEW

II.1 HISTORICAL REFLECTION OF ESTATE SURVEYING PROFESSION IN NIGERIA

The estate surveying profession in Nigeria has a rich historical background deeply rooted in the country's colonial and post-colonial development phases. Estate surveying, which broadly involves the valuation, management, and development of land and property assets, evolved significantly as Nigeria transitioned from traditional land tenure systems to more formalized real estate practices influenced by British colonial administration [12]. Before colonial intervention, land and property were primarily governed by customary laws and traditional authorities, which emphasized communal ownership and use rights rather than individual property rights [13]. The lack of formal property rights posed challenges for economic development and urban planning, especially as Nigeria's population grew and urban centers expanded.

The introduction of the colonial Land Use Act in 1978 marked a pivotal moment in codifying land administration and indirectly shaped the estate surveying profession by establishing statutory frameworks for land tenure and property rights [14]. The estate surveying profession formally emerged in Nigeria during the early 20th century when British-trained surveyors began applying western property valuation and management principles to Nigerian real estate markets [15]. Initially, the profession was dominated by expatriates due to the lack of local expertise, but with the establishment of professional bodies like the Nigerian Institution of Estate Surveyors and Valuers (NIESV) in 1969, the profession rapidly localized [16]. The NIESV, as a regulatory and professional body, has played a crucial role in setting ethical standards, promoting education, and protecting the interests of practitioners and clients alike [17].

Moreover, the estate surveying profession in Nigeria has evolved in response to the country's socio-economic changes, including urbanization, real estate development, and government housing policies. During the oil boom era of the 1970s, there was increased demand for professional estate surveying services to manage commercial and residential property investments [18]. Housing infrastructure deficits have also influenced estate surveying practice in Nigeria [19]. In recent decades, globalization and technological advancements have further transformed the profession, with estate surveyors increasingly involved in property technology (PropTech), sustainability considerations, and integrated real estate services [20]. Despite its growth, the profession faces challenges related to regulatory enforcement, professional recognition, and adapting to emerging real estate trends [21]. Nevertheless, the historical trajectory of estate surveying in Nigeria reflects a gradual but steady professionalization aligned with both local realities and global standards.

II.2 OVERVIEW OF ESTATE SURVEYING PROFESSION IN NIGERIA

Estate Surveying and Valuation in Nigeria is a legally recognized profession regulated by the Estate Surveyors and Valuers Registration Board of Nigeria (ESVARBON), established under Decree No. 24 of 1975 (CAP E13 LFN, 2007). The Nigerian Institution of Estate Surveyors and Valuers (NIESV**)**, formed in 1969, serves as the principal professional body responsible for setting standards, promoting ethics, and advocating for the interests of estate surveyors. These professionals are trained to offer a wide range of services, including valuation for various purposes (compensation, insurance, mortgage, sale), property and facilities management, development appraisal, investment advisory, land use consultancy, and arbitration [9]. Estate Surveyors operate in both public and private sectors and are integral to real estate market dynamics. They support government functions like taxation and land acquisition while also advising private clients on asset optimization and land investment. However, the profession has faced criticism for being inward-looking, with limited public awareness and engagement, despite its relevance in Nigeria's growing urban and real estate sectors [7], [11]. Recent studies have also highlighted structural and institutional challenges affecting the profession in Nigeria [22].

II.3 ROLES AND DUTIES OF PROFESSIONALS IN THE CONSTRUCTION INDUSTRY

The construction industry operates through a network of specialized professionals, each contributing distinct yet interdependent expertise to project development and delivery. According to [23], the core roles within the construction process include architects responsible for conceptual design and aesthetic coordination, engineers for technical specifications and structural integrity, builders for execution and supervision, and quantity surveyors for cost planning and management. This aligns with earlier studies emphasizing the importance of value management roles performed by built-environment professionals during project procurement and delivery [24]. Estate surveyors, while often less integrated in the active construction phase, play critical roles during pre- and post-construction periods. Estate surveyors are tasked with the acquisition and disposal of land, feasibility studies, site valuations, development appraisals, and advisory services on land use and regulatory compliance [8], [9]. These professionals are instrumental in assessing the economic viability of projects and ensuring proper legal titles for land ownership. Their contribution is also critical in guiding development processes through land administration and investment advisory functions [25]. Their valuation services are essential for mortgage underwriting, taxation, insurance, and investment analysis [3]. However, the marginal involvement of estate surveyors in project design and execution phases has been identified as a major barrier to unlocking their full value, often resulting in assets that are undervalued, mismanaged, or misaligned with market expectations [6].

II.4 THE PROFESSIONALS IN THE CONSTRUCTION INDUSTRY

Construction projects are inherently collaborative, requiring the integration of multiple technical and administrative disciplines. In the Nigerian context, a typical project team comprises architects, civil and structural engineers, quantity surveyors, builders, estate surveyors, land surveyors, urban planners, and legal professionals [26]. Each professional contributes specific competencies: architects develop designs aligned with user requirements; engineers ensure structural soundness; builders handle execution logistics; and quantity surveyors manage budgets and contract administration. Similar to estate surveyors, quantity surveyors operate under statutory regulatory frameworks that define professional standards and responsibilities [27]. Estate surveyors, however, play a more hybrid role. As [28] assert, construction professionals are defined by their specialized knowledge, professional ethics, and responsibility in coordinating resources, technology, and human capital. Estate surveyors bridge the gap between technical development and economic rationality. They provide critical insights on land potential, market dynamics, site accessibility, and environmental constraints, thereby enabling strategic decisions on investment returns and project suitability [10]. Despite their relevance, estate surveyors are frequently sidelined in the conceptual and design stages of construction. Their visibility within construction teams remains low, especially compared to quantity surveyors and architects who are often perceived as more central to the building process [2]. This underutilization contributes to a broader misperception of the estate surveying profession and weakens inter-professional collaboration in holistic project development.

II.5 PERCEPTION AND AWARENESS CHALLENGES

Perception and awareness remain critical obstacles to the effective engagement of estate surveyors in Nigeria's construction and real estate sectors. Studies have shown that both the public and allied professionals often confuse the role of estate surveyors with that of land surveyors or even quantity surveyors, largely due to overlapping terminology and insufficient differentiation in professional practice [10], [3]. This confusion is exacerbated by the absence of aggressive public education or branding efforts by estate surveying institutions and regulatory bodies [29]. Similar perception gaps have also been reported among other built-environment professions in Nigeria, suggesting that this challenge extends beyond estate surveying alone [30]. In addition, the limited integration of estate surveyors into mainstream construction discourse further undermines their public image. According to [7] notes that most clients associate estate surveying strictly with real estate agency functions, ignoring their expertise in valuation, feasibility studies, and development consultancy. Earlier empirical studies also revealed persistent concerns regarding valuation accuracy in Nigeria's residential property market [31]. As a result, informal consultants or unlicensed agents are often patronized over certified professionals, especially in informal housing markets.

The issue of professional rivalry also affects perception. For authors [6] highlight how architects, engineers, and even urban planners sometimes encroach on the advisory and strategic roles of estate surveyors, leading to jurisdictional overlaps and blurred responsibilities. Comparative evidence from South Africa also confirms similar professional perception challenges [32]. This rivalry has hindered the creation of cohesive interdisciplinary teams where estate surveyors can effectively contribute from project inception to post-completion asset management. Furthermore, non-construction professionals such as those in law, medicine, banking, and academia who are potential clients or investors, often lack awareness of the value proposition offered by estate surveyors [1]. These gaps result in missed opportunities for proper valuation, optimal investment decision-making, and regulatory compliance in land-related transactions. Professional bodies like the Nigerian Institution of Estate Surveyors and Valuers (NIESV) have made recent efforts to address these issues through publications and advocacy [16], but more sustained public relations campaigns, curriculum reviews, and policy reforms are required.

II.6 HISTORICAL EVOLUTION AND PROFESSIONAL IDENTITY OF ESTATE SURVEYING

The estate surveying profession in Nigeria has evolved through several phases, from colonial land administration frameworks to post-independence professionalization. Initially rooted in colonial land governance systems, estate management was largely concerned with revenue collection, tenant relations, and public land allocation [14]. Over time, the profession expanded to include valuation, property management, investment advisory, and facility management [11], [17]. These functions are rooted in traditional estate management principles that continue to shape professional training and practice in Nigeria [33]. NIESV was established to formalize the profession, regulate entry standards, and promote ethical practice. Today, it plays a significant role in developing standards, conducting examinations, and engaging stakeholders.

The long-term institutional development and performance of the profession in Nigeria have also been critically examined in later studies [34]. However, as [12] argue, the colonial legacy still affects how estate surveyors are perceived, especially in their relationship with land ownership, regulation, and customary rights. Additionally, [18] suggests that economic volatility and land speculation have also shaped the identity of estate surveyors, sometimes casting them as intermediaries rather than strategic consultants. The increasing complexity of urban development and the demand for sustainable land use planning call for a redefinition of the profession's role beyond traditional valuation tasks.

II.7 EMERGING TRENDS AND THE FUTURE OF ESTATE SURVEYING

The profession is currently undergoing a technological and conceptual shift. With the rise of digital platforms, Geographic Information Systems (GIS), Building Information Modelling (BIM), and automated valuation models (AVMs), estate surveying is expanding beyond manual methods to embrace data-driven decision-making [20]. These tools enhance accuracy in valuation, improve transparency, and promote integration with urban planning and financial systems. Moreover, the increasing demand for sustainable urban development, smart cities, and climate-resilient infrastructure creates new opportunities for estate surveyors to lead in areas such as green valuation, environmental impact analysis, and land-based financing mechanisms. Professional reorientation, continuous learning, and inter-professional collaboration are therefore imperative to reposition the estate surveying profession as a key player in Nigeria's evolving built environment [21], [4].

II.8 PERCEPTION OF ESTATE SURVEYING

Perception, according to [35] refers to the way individuals assign meaning to concepts based on the information available to them. In the context of the built environment, the public and even allied professionals often form opinions of professions based not on core competencies but on visibility, relevance, and communication of professional roles. Estate Surveying in Nigeria is traditionally associated with land valuation, property management, and real estate agency. However, its scope goes far beyond these roles. In particular, valuation reporting quality remains a major professional concern affecting confidence in estate surveying outputs [36]. Estate surveyors are trained professionals involved in land acquisition, development appraisals, feasibility studies, investment analysis, property taxation, facilities management, and regulatory compliance in land use and urban development [8], [9]. Despite this broad scope, the profession continues to suffer from identity misalignment and limited public understanding. According to [3], a common misconception exists where estate surveyors are mistaken for land surveyors or quantity surveyors. This confusion is rooted in overlapping terminologies and a lack of public enlightenment regarding professional boundaries. Similarly, [7] observed that many clients perceive estate surveyors merely as rent collectors or informal agents, neglecting their technical competencies in valuation, development consultancy, and investment advice. While estate surveyors make significant contributions in real estate investment, project feasibility, and land management, their roles remain under-recognized compared to more visible construction professionals such as architects and engineers [2].

The marginal integration of estate surveyors in early project stages further diminishes their perceived importance in the built environment value chain. Several scholars, including [6] have attributed these perception challenges to weak professional advocacy, inter-professional rivalry, and inadequate branding by the Nigerian Institution of Estate Surveyors and Valuers (NIESV). According to [37], though writing on quantity surveying, noted that self-perception within a profession also shapes public perception a view that resonates with the estate surveying context, where internal fragmentation and low marketing efforts contribute to low visibility. Additionally, non-construction stakeholders such as bankers, lawyers, and public administrators who often engage in property investment and real estate decision-making demonstrate limited awareness of the strategic value offered by estate surveyors [1], [10]. This knowledge gap leads to underutilization of estate surveyors in transactions that could benefit from their expertise. Efforts to reposition the profession are underway, with scholars such as [29] advocating for targeted public awareness campaigns, clearer professional branding, and curriculum reviews to better reflect evolving industry demands. As the estate surveying profession expands into areas like green valuation, proptech, and real estate finance, improving perception becomes not only desirable but essential for national development and sustainable land management.

III. MATERIALS AND METHODS

The study targeted non-construction professionals working across various sectors including hospitals, banks, law firms, non-governmental organizations (NGOs), and corporate administrative offices within the study area. The selection of Abuja as the study location was deliberate due to its status as the political and administrative capital of Nigeria, where many corporate headquarters and branch offices of diverse organizations are situated. A total of 200 questionnaires were distributed among the target respondents. Of these, 185 questionnaires were returned, with 23 discarded due to incomplete or incorrect consent, leaving **162 valid responses** for analysis. This corresponds to a response rate of 81%, which exceeds the minimum acceptable threshold of 30% often cited in survey research [38], [39], thereby ensuring the adequacy and reliability of the sample size. The collected data were analyzed using descriptive statistical techniques including mean item scores and percentage distributions. The results were presented using tables and figures to facilitate clear interpretation. Data processing and statistical analysis were conducted with the aid of IBM SPSS Statistics version 29.

A. Reliability Analysis

To ensure the internal consistency and reliability of the survey instrument, a reliability test was performed using Cronbach's Alpha via SPSS 29.0. According to [40], a Cronbach's Alpha coefficient exceeding 0.7 indicates acceptable reliability and consistency of the instrument. Similarly, [41] affirm that higher alpha values above 0.7 suggest greater data reliability. For this study, the Cronbach's Alpha value obtained was 0.881, signifying a high level of internal consistency among the questionnaire items.

IV. RESULTS AND DISCUSSIONS

IV.1 RESPONDENTS' BACKGROUND INFORMATION

The background characteristics of the respondents provide essential context for understanding how non-construction professionals perceive the Estate Surveying profession. According to Table 1, a total of 162 valid responses were analyzed. Out of the total respondents, 61.73% (n=100) indicated that they were aware of the Estate Surveying profession, while 38.27% (n=62) reported no awareness. This suggests that although a majority of professionals outside the built environment have some knowledge of the profession, a significant awareness gap still exists among nearly 4 in 10 respondents. This finding echoes earlier studies by [3], [10], which identified widespread public confusion and limited exposure of the estate surveying profession among the general population. The age profile of respondents shows that the majority fall within the 40–50 years range (45%) and the 30–40 years range (26%), followed by those above 50 years (12.6%). Younger respondents aged 20–30 years and below 20 years made up only 16.4% collectively. The predominance of mid-career professionals in the sample suggests that responses are largely informed by individuals with extensive work experience and decision-making responsibilities key stakeholders in real estate-related matters.

Professional Background

According to Table 1, the respondents span five professional groups. Lawyers constituted the largest segment (41.89%), followed by business administrators (20.27%), medical professionals including doctors and pharmacists (18.92%), nurses (13.51%), and accountants/financial experts (5.41%). The diversity of respondents reflects the broader non-construction stakeholder spectrum that interacts with real estate assets either as investors, clients, institutional advisors, or regulators. In terms of educational attainment, the majority of respondents held a B.Sc./B.Tech degree (85.37%), while 25.7% had OND/HND/PGD qualifications. Additionally, 21.87% held a Master's degree, and 13.12% had attained a PhD. This high level of academic qualification among the respondents underscores the credibility of their responses and suggests a relatively informed group whose perception of estate surveyors may be shaped by professional exposure and critical evaluation. Regarding professional experience, the largest proportion of respondents (44%) had 11–15 years of work experience, followed by 22.3% with 5–10 years and 13.4% with 16–20 years. Respondents with over 20 years of experience constituted 8.8%, while only 11.5% were in the early-career category (up to 5 years). This distribution indicates that most respondents possess substantial industry knowledge and likely engage with real estate decisions in their various organizational roles.

Table 1: Respondents background information.

Category	Classification	Freq.	Percent
Awareness of Estate Profession	Yes	100	61.73
	No	62	38.27
	Total	**162**	**100%**
Age	Up to 20years	10.60	6.70%
	20-30years	15.71	9.70%
	30-40years	42.12	26.00%
	40-50years	72.90	45.00%
	Above 50years	20.41	12.60%
	TOTAL	**162**	**100%**
Profession	Medical Doctors/Pharmacist	30.65	18.92%
	Lawyers	67.86	41.89%
	Accountant/Financial Experts	8.78	5.41%
	Nurses	21.89	13.51%
	Business Administrators	32.84	20.27%
	TOTAL	**162**	**100%**
Highest Academic Qualification	OND/HND/PGD	41.634	25.70%
	B.Sc./B.Tech	52.7	85.37%
	Masters	13.5	21.87%
	PhD	8.1	13.12%
	TOTAL	**162**	**100%**
Years of Work Experience	Up to 5yrs	18.63	11.50%
	5–10yrs	36.12	22.30%
	11-15 years	71.28	44.00%
	16-20years	21.708	13.40%
	20+ years	14.256	8.80%
	TOTAL	**162**	**100%**

Source: Authors, (2026).

IV.2 PLACE OF FIRST CONTACT WITH THE ESTATE SURVEYING PROFESSION

Identifying the initial points of contact for non-construction professionals with the estate surveying profession is crucial for evaluating its visibility and perceived significance within organisational frameworks. According to Table 2, the facility management department represented the predominant initial interaction, with 45% of respondents identifying it as their first encounter with the profession.

This finding corresponds with the transforming function of estate surveyors in corporate real estate and facilities management, where their expertise in property administration, spatial efficiency, leasing consultancy, and asset enhancement is increasingly in demand [8],[9]. Subsequently, 36% of respondents indicated that their initial engagement with estate surveyors was via their firms' works department. This indicates an ongoing relationship between estate surveyors and infrastructure services, especially in land acquisition, project development, and construction advice services. Only 19% of respondents identified the profession through the maintenance department, suggesting that although estate surveyors may occasionally participate in maintenance monitoring, it is not generally their primary or most prominent area of engagement in corporate environments. These findings illustrate the complex nature of the profession and corroborate the concerns raised by [2],[29] on the potential for limiting perceptions or misidentifications based on departmental functions. The increased exposure in facilities and works departments indicates possible opportunities for enhancing professional identity through collaboration, branding, and role clarification.

Table 2: Respondent Place of First Contact with the Estate Surveyor Profession.

Classification	Freq.	Percent
Facility Management Department	72.90	45.00%
Works Department	57.83	36.00%
Maintenance Department	31.01	19.00%
Total	**162**	**100%**

Source: Authors, (2026).

IV.3 LEVEL OF AGREEMENT ON WHETHER ESTATE SURVEYORS ARE PART OF THE BUILT ENVIRONMENT PROFESSION

Table 3 presents the respondents' opinions on whether estate surveyors are considered part of the built environment profession. The results reveal a strong consensus among non-construction professionals, with a combined 97.53% of respondents affirming this position either by strongly agreeing (52.47%) or agreeing (45.06%). This overwhelming agreement suggests that the estate surveying profession is widely perceived as a legitimate and integral player within the construction and built environment ecosystem. Only a marginal 2.46% of respondents either disagreed or were undecided, reflecting a negligible level of uncertainty or dissent on the subject. Importantly, none of the respondents strongly disagreed, further reinforcing the general acceptance and recognition of estate surveyors among professionals from other sectors. This finding reflects positively on the professional visibility of estate surveyors and aligns with assertions by [42] that estate surveying, through its involvement in valuation, property development consultancy, and land economics, plays a foundational role in the broader built environment. It also supports the view of [2] who emphasize the increasing recognition of estate surveyors beyond traditional real estate circles, especially where land, infrastructure planning, and investment decisions are involved. The responses indicate not just awareness, but also validation of the estate surveying profession's role in the built environment a crucial insight for professional advocacy and inter-professional collaboration.

Table 3: Respondents level of Agreement on Whether Estate Surveyors are Part of Built Environment Profession.

Classification	Freq.	Percent
Strongly Agree	85.00	52.47%
Agree	73	45.06%
Undecided	2	1.23%
Disagree	2	1.23%
Strongly Disagree	0	0.00%
Total	**162**	**100%**

Source: Authors, (2026).

IV.4 RESPONDENTS' PERCEPTION OF THE RATE OF PERFORMANCE OF THE ESTATE SURVEYING PROFESSION IN THE BUILT ENVIRONMENT

Table 4 shows respondents' evaluations of the efficacy of the estate surveying profession within the built environment. A considerable percentage of respondents evaluated the performance as very good (54.93%), while a further 33.95% classified it as good. Collectively, this results in an outstanding 88.88% of respondents expressing a favourable opinion on the profession's efficacy in the built environment. A meagre 5.55% of respondents were indecisive, and an equivalent 5.55% assessed the performance as simply adequate; significantly, none deemed the profession's performance unacceptable. This signifies a substantial degree of satisfaction and acknowledgement of value, particularly given that the perspectives originate from individuals outside the building sector who may engage with estate surveyors in diverse corporate or institutional settings. These findings corroborate the claims made by [43] and [9], who contend that estate surveyors are crucial in enhancing efficiency in land utilisation, property administration, investment analysis, and urban development. The profession's multifaceted functions encompassing appraisal, development consultancy, and asset management likely enhance this positive view [44] The data indicates that estate surveyors are recognised as integral members of the built environment team and are perceived as providing significant and effective professional services.

Table 4: Respondents Perception of The Rate of Performance of The Profession in the Built Environment.

Classification	Freq.	Percent
Very good	89.00	54.93%
Good	55	33.95%
Undecided	9	5.55%
Fair	9	5.55%
Non Satisfactory	0	0.00%
Total	**162**	**100%**

Source: Authors, (2026).

IV.5 PERCEPTION OF THE DUTIES AND RESPONSIBILITIES OF ESTATE SURVEYORS

From Table 4.5, the first ten (10) duties of Estate Surveyors as perceived by the respondents are as follows: “Estate Surveyors are involved in valuation of land, buildings, and other assets” with a mean item score (MIS) of 3.89 is ranked 1st, “Estate Surveyors provide property and investment advice to clients” with MIS of 3.82 is ranked 2nd, “Estate Surveyors manage and administer leases and tenancies” with MIS of 3.77 is ranked 3rd, “Estate Surveyors conduct property acquisition and disposal transactions” with MIS of 3.71 is ranked 4th, “Estate Surveyors are involved in land use planning and development consulting” with MIS of 3.66 is ranked 5th, “Estate Surveyors are property managers responsible for rent collection, maintenance, and tenant relations” with MIS of 3.61 is ranked 6th, “Estate Surveyors conduct development appraisal and feasibility studies” with MIS of 3.55 is ranked 7th, “Estate Surveyors act as consultants in land titling, registration, and acquisition” with MIS of 3.48 is ranked 8th, “Estate Surveyors serve as expert witnesses in property-related litigation and arbitration” with MIS of 3.42 is ranked 9th, and “Estate Surveyors perform compulsory acquisition and compensation assessment” with MIS of 3.39 is ranked 10th.

The data show a high level of awareness among non-allied professionals about key roles performed by Estate Surveyors. Notably, valuation of land, buildings, and other assets ranked highest with a mean item score (MIS) of 3.89. This finding is significant because valuation reliability directly influences mortgage lending and investment decisions in Nigeria’s property market [3]. This is closely followed by investment advisory services (MIS = 3.82) and lease administration (MIS = 3.77). These results suggest that many non-construction professionals are well-informed about the core functions of Estate Surveyors. Other roles such as property acquisition and disposal (MIS = 3.71) and land use consulting (MIS = 3.66) also received strong ratings, indicating their visibility in corporate and public-sector engagements. Lesser-known roles like rural land management (MIS = 3.10) and facility management (MIS = 3.07) still recorded moderate awareness, pointing to areas where more public sensitization may be needed. These findings align with previous studies that emphasize the multidimensional nature of Estate Surveying [3]; [45] reinforcing its strategic role within the built environment and beyond.

Table 5: Respondents' Perceptions of the Duties and Responsibilities of Estate Surveyors.

Snr	Duties and Responsibilities	MIS	Rank
1	Are you aware that Estate Surveyors are involved in valuation of land, buildings, and other assets?	3.89	1
2	Are you aware that Estate Surveyors provide property and investment advice to clients?	3.82	2
3	Are you aware that Estate Surveyors manage and administer leases and tenancies?	3.77	3
4	Are you aware that Estate Surveyors conduct property acquisition and disposal transactions?	3.71	4
5	Are you aware that Estate Surveyors are involved in land use planning and development consulting?	3.66	5
6	Are you aware that Estate Surveyors are property managers responsible for rent collection, maintenance, and tenant relations?	3.61	6
7	Are you aware that Estate Surveyors conduct development appraisal and feasibility studies?	3.55	7
8	Are you aware that Estate Surveyors act as consultants in land titling, registration, and acquisition?	3.48	8
9	Are you aware that Estate Surveyors serve as expert witnesses in property-related litigation and arbitration?	3.42	9
10	Are you aware that Estate Surveyors perform compulsory acquisition and compensation assessment?	3.39	10
11	Are you aware that Estate Surveyors are involved in rating and taxation of landed property?	3.36	11
12	Are you aware that Estate Surveyors conduct insurance valuation of assets?	3.25	12
13	Are you aware that Estate Surveyors are responsible for estate agency and marketing of real estate assets?	3.22	13
14	Are you aware that Estate Surveyors are involved in rural and agricultural land management?	3.1	14
15	Are you aware that Estate Surveyors engage in facility management of high-value property portfolios?	3.07	15

Source: Authors, (2026).

IV.6 DISCUSSION OF FINDINGS IN RELATION TO THE LITERATURE REVIEW

High level of awareness recorded in Table 1 where 61.73% of respondents were aware of the Estate Surveying profession supports [46], [47], who argued that estate surveyors are increasingly becoming visible beyond traditional property valuation into facility and asset management. This indicates a gradual shift in public understanding of the profession's scope, especially among non-construction professionals like lawyers, doctors, and business administrators. In Table 2, most respondents identified the Facility Management and Works Departments as their points of first contact with estate surveyors. This aligns with [48], who noted that estate surveyors are increasingly involved in operational asset oversight and integrated workplace management.

This practical visibility reinforces their relevance across interdisciplinary professional spaces, particularly in large institutional settings like hospitals, banks, and corporate administrative offices. Table 3 reveals that over 97% of respondents (Strongly Agree + Agree) see estate surveyors as part of the built environment profession. This aligns with assertions by [49], [50] that estate surveyors play a crucial role in shaping the spatial and economic structure of cities, especially through land management, development consultancy, and property investment advisory. Further, Table 4 demonstrates that over 88% of respondents rated the profession's performance as "Good" or "Very Good", reinforcing the positive perception discussed in [51]. This contradicts earlier sentiments from [52] that estate surveying suffers from low public trust and limited recognition. The improved perception shown in this study may reflect better public relations by professional bodies like the Nigerian Institution of Estate Surveyors and Valuers (NIESV).

In Table 5, the ranked duties such as valuation for property transactions, management of real estate investment, land acquisition advisory, and facility management mirror core responsibilities outlined in [6], [53]. These duties are no longer restricted to traditional estate agency roles but now cut across strategic real estate investment analysis, land policy advisory, and dispute resolution, confirming the profession's evolving complexity. Moreover, the low ranking of roles like acting as expert witnesses in arbitration or tax planning suggests areas where awareness remains limited, as earlier noted in [54]. This calls for targeted professional advocacy and cross-sector collaborations to expand understanding of the profession's legal and financial capabilities. Overall, these findings support the argument that Estate Surveying is a multifaceted profession whose impact is not confined to core real estate practice but intersects with multiple domains. The generally positive perception by non-allied professionals suggests a growing respect for the profession and increased recognition of its economic and developmental relevance within Nigeria's built environment.

V. CONCLUSIONS

This study has evaluated the perception of the Estate Surveying profession among non-allied construction professionals in Nigeria. It examined their awareness, perceptions of professional roles, and the perceived contributions of Estate Surveyors to the built environment industry. The research employed a quantitative methodology by distributing structured questionnaires to professionals including lawyers, medical practitioners, accountants, and business administrators. Descriptive statistics, encompassing frequencies, percentages, and mean item scores (MIS), were employed to analyse the data and elucidate crucial insights into respondents' perspectives. The study indicated that a substantial percentage (61.73%) of respondents has prior knowledge of the Estate Surveying profession. The majority of respondents have engaged with Estate Surveyors via facility management and works departments, signifying direct professional connection. Moreover, over 97% of participants either concurred or highly concurred that Estate Surveyors are essential constituents of the built environment profession. This demonstrates a significant acknowledgement of the professional importance and interdisciplinary contributions that Estate Surveyors provide to construction and real estate practices.

Regarding performance, about 89% of respondents ranked the profession as very good or good, indicating elevated satisfaction among non-construction professionals. Estate Surveyors are mostly acknowledged for their fundamental duties, which encompass property appraisal, investment advisory, asset management, and land acquisition consultancy. Nonetheless, diminished knowledge was noted in jobs such as arbitration, technical auditing, and life cycle costing, underscoring significant opportunities for enhanced advocacy and professional visibility. In conclusion, the perception of the Estate Surveying profession among non-allied professionals is predominantly favourable and helpful. The results confirm the profession's increasing significance across several sectors. Strategic initiatives are essential to enhance knowledge of lesser-known tasks and to foster greater interdisciplinary collaboration, so reinforcing the profession's identity and influence inside and outside the built environment.Based on the findings and discussion, the following recommendations are proposed:

Professional bodies such as the Nigerian Institution of Estate Surveyors and Valuers (NIESV) should engage in strategic public education campaigns to highlight the full range of services offered by Estate Surveyors, especially in areas less understood by the public. Estate Surveyors should seek stronger collaborations with non-construction professionals such as legal practitioners, health sector administrators, and financial experts to demonstrate the value they add across sectors. Estate management programmes in Nigerian universities should include components that train students on interdisciplinary engagement and promote visibility in non-traditional sectors. Estate Surveyors, through their professional bodies, should advocate for inclusion in policy formulation relating to land use, urban development, and asset management, to strengthen their position within the construction and development ecosystem. Encouraging further specialization (e.g., in arbitration, taxation, environmental impact assessment) can help bridge the perceived gaps in professional identity and create more diverse career pathways within the profession. Repositioning the profession requires stronger strategic advocacy and reform [55].

VI. AUTHOR'S CONTRIBUTION

Conceptualization: Awodele I.A, Akinwale B.E and Khahledi M.C.
Methodology: Akinwale B.E and Khahledi M.C.and Awodele I.A.
Investigation: Khahledi M.C. and Adetola O.D.
Discussion of results: Awodele I.A, Akinwale B.E and Adetola D.O.
Writing – Original Draft: Awodele I.A, Akinwale B.E.
Writing – Review and Editing: Awodele I.A, Akinwale B.E.
Resources: Awodele I.A, Akinwale B.E and Khahledi M.C.
Supervision: Olagunju O.A**.** and Adetola O.D.
Approval of the final text: Awodele I.A, Akinwale B.E. Khahledi M.C**.** and Olagunju O.A**.**

VII. REFERENCES

[1] Nuhu, M. B. (2008). The role of the estate surveyor and valuer in sustainable national development. The Estate Surveyor and Valuer, 31(1), 23–29.

[2] Oloke, O. C., Simon, R. A., and Otegbulu, A. C. (2017). Strategic positioning of estate surveyors and valuers in Nigeria. Mediterranean Journal of Social Sciences, 8(1), 403–412.

[3] Ayedun, C. A., Durodola, O. D., and Oluwatobi, A. O. (2011). Public perception of the real estate profession in Lagos State, Nigeria. International Journal of Marketing Studies, 3(4), 76–83.

[4] Royal Institution of Chartered Surveyors (RICS) (2020). Professional Standards and Guidance Valuation Global Standards. London: RICS.

[5] Oluwatosin, A.A. (2021). A model for effective national housing fund in Nigeria (Doctoral dissertation, Universiti Teknologi Malaysia).

[6] Ogunba, O. A., and Ojo, O. (2007). Resolving the seeming conflicts between estate surveyors and valuers and other land professionals in Nigeria. Journal of Land Use and Development Studies, 3(1), 45–56.

[7] Aluko, B. T. (2016). Public perception and estate surveying practice in Nigeria. Journal of African Real Estate Research, 1(1), 17–28.

[8] Adedokun, O. A. (2011). Functions and responsibilities of estate surveyors and valuers in Nigeria. The Estate Surveyor and Valuer, 36(2), 20–26.

[9] NIESV. (2019). Professional roles and guidelines for estate surveyors and valuers in Nigeria. Abuja: Nigerian Institution of Estate Surveyors and Valuers.

[10] Adewale, B. A., Akinlolu, M., and Afolabi, M. A. (2022). Enhancing the professional image of estate surveyors and valuers in Nigeria. Journal of African Real Estate Research, 7(1), 55–68.

[11] Kuye, O. L. (2015). Professionalism and ethics in real estate practice in Nigeria. Journal of Property Management, 33(2), 122–130.

[12] Akindele, S. and Oyebanji, T. (2019). Colonial impact on land administration and estate surveying in Nigeria. Nigerian Journal of Estate Surveying and Valuation, 12(1), 21–37.

[13] Adeleye, I. (2008). Land Tenure Systems in Nigeria: An Overview. Lagos: University of Lagos Press.

[14] Onokerhoraye, A. and Omuta, G. (2001). Urbanization and land administration in Nigeria. Benin City: Ambik Press.

[15] Adewuyi, K., and Sodeinde, O. (2017). The evolution of real estate valuation practices in Nigeria. Journal of Property Management, 35(2), 45–59.

[16] NIESV. (2023). History and Functions of the Nigerian Institution of Estate Surveyors and Valuers. Lagos: NIESV Press.

[17] Oluwole, O. (2015). Professionalization of Estate Surveying and Valuation in Nigeria: The Role of NIESV. Journal of African Real Estate, 7(4), 134–149.

[18] Salami, A. (2013). Economic factors and growth of estate surveying profession in Nigeria. Nigerian Economic Review, 10(2), 72–85.

[19] Ajanlekoko, J.S. (2001). Sustainable housing development in Nigeria – The financial and infrastructural implications. Dakar: IDEP.

[20] Ezeani, E. and Agu, G. (2020). The integration of technology in estate surveying practice in Nigeria. Property Management Review, 8(1), 112–127.

[21] Okoye, P. and Onwuekwe, C. (2019). Challenges facing the estate surveying profession in Nigeria. International Journal of Real Estate Studies, 13(3), 89–105.

[22] Adegoke, O.J. (2021). The Estate Surveying and Valuation Profession in Nigeria: Challenges and Prospects. Journal of Sustainable Built Environment, 9(2), 45–57.

[23] Olanrewaju, A., and Anahve, P. J. (2015). Duties and responsibilities of quantity surveyors in procurement of building services engineering. Creative Construction Conference Proceedings.

[24] Odeyinka, H. A. (2006). The role of quantity surveyors in value management. NIQS Conference Proceedings.

[25] Aliyu, A.A. (2012). The Role of Estate Surveyors and Valuers in the Development Process. NIESV Seminar Series, 3(1), 10–14.

[26] Owolabi, O. S. B., and Olatunji, A. S. (2014). The roles of construction professionals in Nigeria's construction industry. IOSR Journal of Humanities and Social Science, 19(11), 5–10.

[27] QSRBN. (2006). Legal Framework and Regulatory Guidelines for Quantity Surveyors in Nigeria. Abuja.

[28] Zakaria, I. B., Mohamed, M. R. B., Ahzahar, N., and Hashim, S. Z. (2015). A study on leadership skills of project managers. International Academic Research Journal of Social Science, 1(2), 89–94.

[29] Olayonwa, G.O. (2012). Property Valuation from Methods to Application. Iwo, Osun State: DPC Debo Publishing.

[30] Ezeokoli, F.O., Umeh, O.J. and Otegbulu, A.C. (2016). Perception of the Quantity Surveying Profession among Allied Professionals. International Journal of Advanced Engineering, Management and Science, 3(2), 26–30.

[31] Ogunba, O.A. and Ajayi, C.A. (1998). Assessment of valuation accuracy in Lagos residential market. The Estate Surveyor and Valuer, 21(2), 19–23.

[32] Akinsomi, O., Pahad, R., Nape, L. and Margolis, B. (2016). The role and responsibilities of property valuers in South Africa. Journal of Property Investment & Finance, 34(2), 162–178.

[33] Ifediora, G.S.A. (2009). Principles of Estate Management. Enugu: Immaculate Publications.

[34] Nuhu, M.B. (2014). Analysis of development and performance of estate surveying profession in Nigeria. Journal of African Real Estate Research, 1(1), 1–19.

[35] Usman, N. and Sani, A., (2015). Construction Professionals Perceptions' on Contract Auditing System in Building Projects. contract, 6, p.12.

[36] Gbadegesin, J.T. and Ojo, O. (2011). Quality of valuation reports: Nigerian experience. Journal of NIESV, 36(1), 23–30.

[37] Kadiri, D.S. and Ayodele, E.M. (2013). Constraints to quantity surveying awareness in Nigeria. Constraints, 3(11), 17–21.

[38] Sutrisna, M. (2009). Research methodology in doctoral research: Understanding the meaning of conducting qualitative research. Working paper presented at ARCOM Doctoral Workshop, Liverpool John Moores University, 12 May.

[39] Dainty, A.R.J. (2008). Methodological pluralism in construction management research. In: Knight, A. and Ruddock, L. (eds.), Advanced Research Methods in the Built Environment. Oxford: Wiley-Blackwell.

[40] George, D. and Mallery, P. (2003). SPSS for Windows Step by Step: A Simple Guide and Reference 11.0 Update (4th ed.). Boston, MA: Allyn and Bacon.

[41] Oyedele, L.O., Jaiyeoba, B.E. and Fadeyi, M. (2003). Design factors influencing quality of building projects in Nigeria: Consultants' perception. The Australian Journal of Construction Economics and Building, 3(2).

[42] Ezeokoli, N.B., Komolafe, T.B. and Olukolajo, M.A. (2019). Macroeconomic fluctuations and event centers return dynamics. African Journal of Built Environment Research, 3(1).

[43] Ogunba, O.A. and Ojo, G.K. (2020). Challenges facing real estate development in Lagos State, Nigeria. Journal of Building and Construction. https://doi.org/10.5897/JBC2019.0444

[44] Ayedun, C.A., Durodola, O.D. and Akinjare, O.A. (2012). An empirical analysis of the impact of valuation variance on mortgage lending and investment in Nigeria. Journal of Sustainable Development, 5(11), 48–58.

[45] Akinjare, O., Ayedun, C., Sade, O., Ibhahulu, O.K., Orlu-Makele, T.O., Bamisaye, M.O. and Akinjare, V. (2018). Rent determinants for retail shopping malls in Southern Nigeria. International Journal of Mechanical Engineering and Technology, 9(8), 506–514.

[46] Okoye, D. (2016). Appropriate technology and income differences. International Economic Review, 57(3), 955–996.

[47] Oladapo, R.A. (2018). Exploring constraints to office property market maturity in the metropolitan areas of Lagos State, Nigeria. Research on Humanities and Social Sciences, 8(12), 79–91.

[48] Babalola, I.H., Oluwatuyi, O.E., Lawal, A. and Aiyewalehinmi, E. (2015). Factors influencing the performance of construction projects in Akure, Nigeria. International Journal of Civil Engineering, Construction and Estate Management, 3(4), 57–67.

[49] Oyedokun, T.B., Abidoye, R.B. and Akinbogun, S.P. (2021). Bridging the gap between real estate research and professional practice in Nigeria. Property Management, 39(4), 493–508. https://doi.org/10.1108/PM-12-2020-0087

[50] Udo, E.S., Ben, E.U., Abener, I.P. and Uzonna, J.I. (2018). The implication of naira devaluation to Nigeria's economic development. International Journal of Economics, Commerce and Management, VI (4).

[51] Oladokun, S.O. and Ajayi, C.A. (2018). Assessing users' perception of facilities management services in a public university: A case study approach. Journal of Facility Management Education and Research, 2(2), 62–73.

[52] Houston, D.J. and Harding, L.H. (2013). Public trust in government administrators: Explaining citizen perceptions of trustworthiness and competence. Public Integrity, 16(1), 53–76.

[53] Stary, B. (2021). The triad of asset, property, and facility management: A corporate view to creating a model of key-value drivers for investors, owners, and users of real estate (Doctoral dissertation, Technische Universität Wien).

[54] Ogunsina, O., Obiegbu, M.E. and Adeniyi, O. (2018). Factors confronting quantity surveying practice: The case of Nigeria. Journal of Engineering, Design and Technology, 16(5), 767–782.

[55] Udo-Akagha, C. (2013). Repositioning the Estate Surveying and Valuation Profession in Nigeria for Sustainable Development. Proceedings of NIESV Mandatory Continuing Professional Development Seminar, 34–39.

Journal of Engineering and Technology for Industrial Applications

ISSN ONLINE: 2447-0228

ITEGAM-JETIA

Manaus, v.12 n.60, p.49-56 July/August, 2026.
DOI: https://doi.org/10.5935/jetia.v12i60.3354

RESEARCH ARTICLE OPEN ACCESS

FINITE ELEMENT ANALYSIS OF BONE-DERIVED HYDROXYAPATITE, ZINC-DOPED HYDROXYAPATITE, AND PLGA–ZN-HAP COMPOSITES FOR BIOMEDICAL APPLICATIONS

M Saravanan[1], Abhijith J[2], Sangeetha Krishnamoorthi[3], Athira Kishore[4], Saravana Kumar.M[5]

[1, 2, 3, 4, 5]Department of Mechanical Engineering, Aarupadai Veedu Institute of Technology, Vinayaka Mission's Research Foundation (DU), Tamil Nadu, India.

[1]https://orcid.org/0000-0002-6717-3315, [2]https://orcid.org/0009-0008-6802-3117, [3]https://orcid.org/0000-0003-1427-8743
[4]https://orcid.org/0009-0009-3124-6461, [5]https://orcid.org/0000-0001-8568-3549

E-mail: *saranmechatronics@gmail.com

ARTICLE INFO

Article History
Received: January 20, 2026
Reviewed: February 29, 2026
Accepted: April 1, 2026
Published: July 31, 2026

Keywords:
Rehabilitation,
Exoskeleton,
ANSYS,
Biomedical,
Paralytic.

ABSTRACT

Bone-derived hydroxyapatite (HAp) is highly biocompatible but lacks mechanical strength. This study addresses this limitation by adding zinc (Zn) and poly (lactic-co-glycolic acid) (PLGA) to enhance performance. We synthesised goat-bone HAp via calcination and chemical treatment, incorporated Zn to improve crystallinity and antibacterial activity, and reinforced it with PLGA for better flexibility and load-bearing capacity. Finite element modelling in ANSYS (100–1000 N loading) showed that pure HAp is stiff but brittle, Zn-HAp is stronger, and the PLGA-Zn-HAp composite has the greatest toughness, stress distribution, and fracture resistance. Simulations closely matched experiments, confirming that Zn and PLGA strengthen natural HAp and make the composite a promising, cost-effective choice for orthopaedic implants.

Copyright ©2026 by authors and Galileo Institute of Technology and Education of the Amazon (ITEGAM). This work is licensed under the Creative Commons Attribution International License (CC BY 4.0).

I. INTRODUCTION

Hydroxyapatite (HAp), a bio ceramic with excellent biocompatibility and close chemical resemblance to natural bone, is widely explored for bone tissue engineering but is limited by brittleness and low fracture toughness [1]. To overcome these drawbacks, reinforcing HAp with biodegradable polymers like PLGA and metal dopants such as zinc (Zn^{2+}) has shown significant improvements in flexibility, mechanical strength, osteoconductivity, and antibacterial behaviour. In this study, HAp was sustainably derived from goat bone through thermal and chemical processing, offering a cost-effective, eco-friendly, and biogenic alternative to synthetic routes while supporting waste-to-resource utilization. The combined use of PLGA, Zn–HAp, and finite element analysis (FEA) provides a holistic approach for developing stronger, bioactive, and more reliable composites for orthopaedic and dental implants [2]. Although goat bone–derived HAp offers advantages such as biocompatibility, low cost, and environmental sustainability, challenges remain regarding variability in composition, limited mechanical strength, and processing demands. Future work includes optimizing synthesis, exploring additional dopants, conducting biocompatibility studies, and developing advanced composites with improved load-bearing capacity and controlled degradation [3], [4].

II. METHODOLOGY

II.1 MATERIALS

Supported by standard femur dimensions from orthopaedic literature, the study used ANSYS Workbench for finite element analysis and CREO Parametric for 3D femur modelling. To evaluate the comparative behaviour of porous HAp, Zn-HAp, and PLGA–Zn-HAp, mechanical property data were used. To effectively handle CAD modelling and FEA computations, all simulations were run on a high-performance workstation with a minimum of 16 GB RAM, a dedicated GPU, and a multi-core processor [5] [6].

II.2 METHODOLOGY

The main tools for geometric modelling and finite element simulation in this work were CREO Parametric and ANSYS Workbench. Using normal anatomical proportions from reputable orthopaedic literature, a three-dimensional femur model was created in CREO Parametric to precisely depict important aspects such the femoral head, neck-shaft angle, shaft curvature, and condylar geometry. After that, the finished model was exported for simulation in STEP format. The femur was given the mechanical characteristics of porous HAp, Zn-HAp, and PLGA–Zn-HAp in ANSYS Workbench using data from verified biomaterials research, including density, Young's modulus, Poisson's ratio, and compressive strength. These properties were used to evaluate each material's suitability as possible load-bearing implant materials in the femoral region and to examine how each material responded structurally under physiological loading.

II.3 SAMPLE VARIATIONS

Table 1: Sample Variations.

Sample Code	Composition	Purpose
S1	Pure HAp	Baseline
S2	Zn-HAp (2 wt% Zn)	Evaluate Zn substitution
S3	PLGA-Zn-HAp (60:40)	Evaluate polymer–ceramic synergy

Source: Authors, (2026).

II.4 MATERIAL ASSIGNMENT HAP, 2% ZN-HAP, PLGD-ZN-HAP

Table 2: Material Assignment HAp, 2% ZN-HAp, PLGD-ZN-Hap.

Material	Porous HAp	2% Zn-HAp	PLGA–Zn–HAp (60:40)
Density (g/cm³)	0.3 – 1.6	2.9 – 3.16	2.0
Young's Modulus (GPa)	0.01 – 2	0.5 – 5	0.01 – 2
Poisson's Ratio	0.25 – 0.35	0.25 – 0.35	0.2 – 0.35
Compressive Strength (MPa)	0.3 – 15 (up to 145 MPa for freeze-cast)	1 – 20 (slight improvement over HAp)	1 – 40+ (45 wt% HA → >40 MPa)
Reference Notes	Huang 2022; Baino review; Deville freeze-cast	Ghosal thesis; Radulescu 2023 review	Wei 2022; PLGA/HA composite reviews

Source: Authors, (2026).

II.5 MECHANICAL TESTING

The material response under physiological conditions was assessed using Finite Element Analysis (FEA) with varying loads of 100, 250, 500, 750, and 1000 N. Compressive, tensile, and impact simulations were used to evaluate mechanical behaviour, with an emphasis on total deformation, shear stress, and Von Mises stress. For every material model, the analysis determined stress concentrations and load-bearing capabilities. Mesh convergence testing and validation against published literature were used to guarantee the results' reliability [9] [10].

II.6 MODEL DEVELOPMENT

Each specimen's 3D model was made in SolidWorks and imported into ANSYS Workbench, where material parameters including density, Poisson's ratio, and Young's modulus were given using experimental data. Tetrahedral elements were used for meshing, with refinement occurring close to load application zones [7].

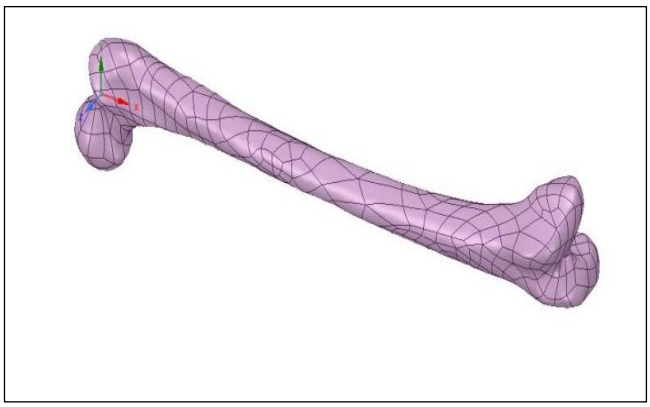


Figure 1: CREO-Based 3D Modelling of Femur Born.
Source: Authors, (2026).

II.7 BOUNDARY CONDITIONS

A fixed support at the bottom surface and compressive stresses ranging from 100 N to 1000 N applied to the top face were the boundary conditions, and frictionless contact was specified for precise load transmission.

II.8 ANALYSIS TYPES & OUTPUT PARAMETERS

Static structural analysis was used to evaluate total deformation, von Mises stress, and shear stress, with output parameters including stress distribution contours, maximum deformation, equivalent (von Mises) stress, factor of safety, and identification of potential failure regions, enabling direct comparison with experimentally observed fracture patterns.

III. DESIGN AND ANALYSIS IN ANSYS

A potent computational technique for assessing material behaviour under challenging loading scenarios is finite element analysis (FEA). The mechanical response of HAp, Zn-HAp, and PLGA–Zn-HAp composites under various load applications was simulated in this study using ANSYS Workbench. The analysis connected the outcomes of the experiments with the distribution of stress, total deformation, and strain among the materials. This simulated evaluation supports the prospective use of bone-derived bio composites in orthopaedic implant applications by forecasting their performance under physiological loads.

III.1 MODEL GEOMETRY & CREATION GEOMETRIC REPRESENTATION

For each of the three materials, separate geometric models were created, including Model A consisting of hydroxyapatite (HAp) produced from bone, Model B of zinc-doped hydroxyapatite (Zn-HAp), and Model C of the composite PLGA–Zn-HAp. To simulate physiological loading conditions typical of an implant region, a simplified femoral bone geometry was adopted and developed using ANSYS Design Modeler, with all models subsequently verified to ensure dimensional consistency.

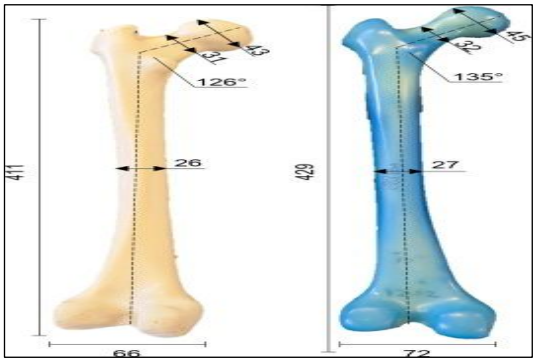


Figure 2: Creation Geometric Representation.
Source: Authors, (2026).

III.2 MESHING PROCESS

Each ANSYS model was given material properties derived from experiments, and then a thorough meshing procedure was carried out in order to ensure simulation correctness. Tetrahedral Solid187 elements with a precise mesh size of 0.5 mm were used to discretize the geometries; each model included between 45,000 and 70,000 elements. Refinement investigations were used to confirm mesh convergence, with results showing less than 2% variance.

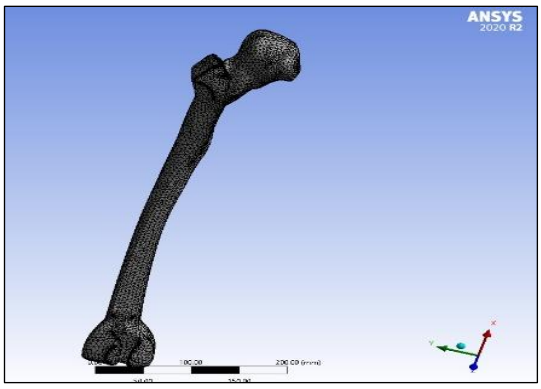


Figure 3: Mesh Geometry.
Source: Authors, (2026).

III.3 BOUNDARY CONDITIONS AND LOADING

In order to replicate genuine compression and physiological stress circumstances, appropriate boundary conditions were used.

Table 3: Boundary Conditions and Loading.

Condition	Description
Fixed Support	Base of the specimen fully constrained to restrict translation and rotation
Load Application	Compressive load, Tensile Load, & Impact Load
Load Magnitudes	100 N, 250 N, 500 N, 750 N, and 1000 N
Analysis Type	Static Structural

Source: Authors, (2026).

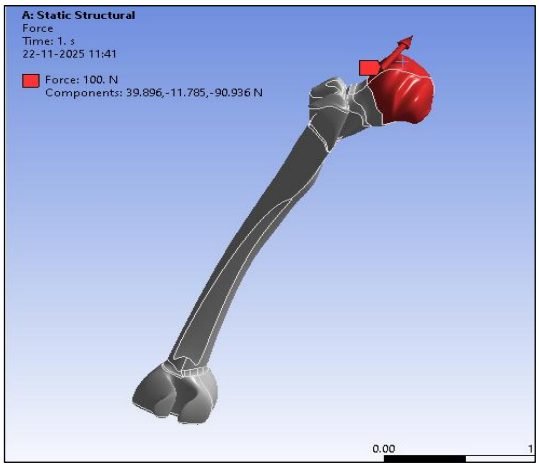


Figure 4: Tensile Load.
Source: Authors, (2026).

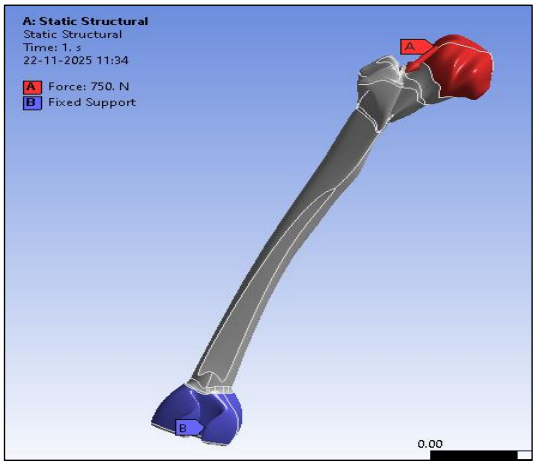


Figure 5: Compressive Load.
Source: Authors, (2026).

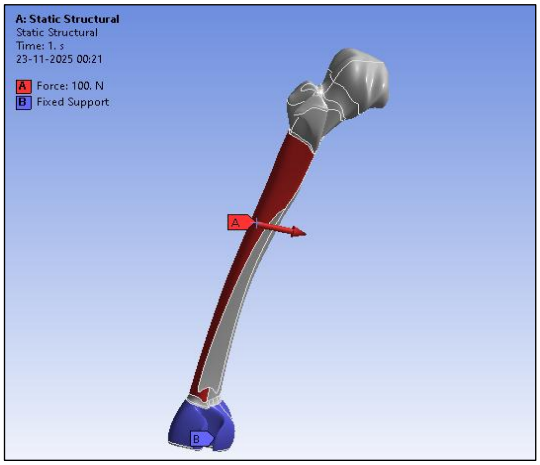


Figure 6: Impact Load.
Source: Authors, (2026).

III.4 SOLUTION SETUP AND SOLVER PARAMETERS

The ANSYS Mechanical solver using a Direct Sparse solution approach was used to carry out the static structural analysis. To guarantee computational accuracy, a convergence criterion of residuals less than 1×10^{-2} was used, and all contact interactions were classified as frictionless. Shear strain, total deformation, and equivalent (von Mises) stress were the main output parameters assessed in the present research.

IV. RESULTS AND DISCUSSION

The findings of the Finite Element Analysis (FEA) carried out in ANSYS and the 3D femur model made in CREO are presented in this chapter. A porous Hydroxyapatite (HAp), Zn-Hap, and PLGA-Zn-Hap structure with regulated pore size and distribution was added to the necessary area of a comprehensive and anatomically correct femur model. After importing the model into ANSYS, material parameters like density, Poisson's ratio, and Young's modulus were assigned using recognized values for porous HAp. Compressive loads were introduced to simulate actual physiological forces, and boundary conditions were used to fix the femur. The simulation was able to examine the deformation, stress distribution, and general mechanical behavior of porous HAp under loading thanks to this configuration.

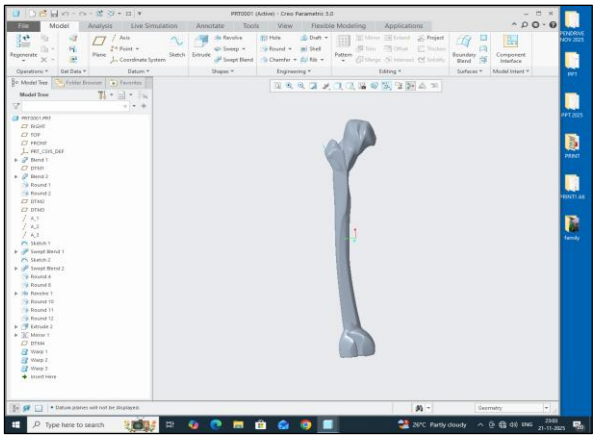


Figure 7: CREO-Based 3D Modelling of Femur Born.
Source: Authors, (2026).

IV.1 FINITE ELEMENT ANALYSIS (ANSYS RESULTS)

IV.1.1 Porous Hap Result

The finite element analysis results for porous hydroxyapatite (HAp) under tensile, compression, and impact loading conditions reveal a strong dependence of mechanical response on the applied load magnitude. Under **tensile loading**, porous HAp exhibited progressively increasing deformation and stress concentration as the load increased from 100 N to 1000 N, with pronounced localization of stress at higher loads (750–1000N), indicating brittle behavior and a high likelihood of crack initiation and tensile failure. In **compression loading**, the material showed comparatively lower deformation at low loads (100–250 N); however, as the load increased beyond 500 N, significant stress accumulation and pore collapse tendencies were observed, reflecting reduced structural stability and limited compressive strength at higher loads. Under **impact loading**, porous HAp demonstrated the poorest mechanical response, with sharp stress gradients and rapid deformation even at moderate loads, highlighting its low energy absorption capacity and high fracture susceptibility. Overall, the analysis confirms that porous HAp performs adequately only under low-load conditions, while higher tensile, compressive, and impact loads lead to severe stress concentration, excessive deformation, and increased failure risk, thereby limiting its suitability for load-bearing orthopedic implant applications [8].

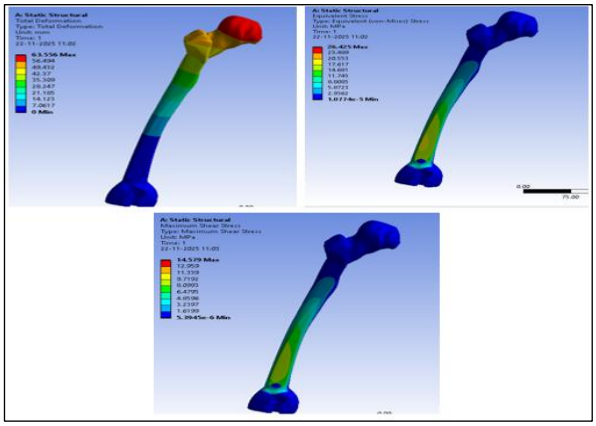


Figure 8: Porous HAp Result.
Source: Authors, (2026).

IV.1.2 Zn-Hap Result

The finite element analysis results of zinc-doped hydroxyapatite (Zn-HAp) demonstrate a clear improvement in mechanical behavior compared to porous HAp across tensile, compression, and impact loading conditions in the 100–1000 N range. Under **tensile loading**, Zn-HAp exhibited reduced deformation and more evenly distributed stress at lower loads (100–250 N), indicating enhanced stiffness due to zinc incorporation; however, at higher loads (750–1000 N), stress concentration increased, suggesting the onset of brittle failure under excessive tensile stress. In **compression loading**, Zn-HAp showed improved load-bearing capability with relatively uniform stress distribution and controlled deformation up to moderate loads (500 N), while higher compressive loads led to localized stress accumulation, reflecting partial structural instability. Under **impact loading**, Zn-HAp demonstrated better energy absorption and lower deformation than porous HAp, though sharp stress gradients were still observed at higher impact loads, indicating limited resistance to sudden dynamic forces. Overall, the analysis confirms that zinc doping enhances the mechanical stability, strength, and stress resistance of hydroxyapatite; however, despite these improvements, Zn-HAp retains some brittle characteristics at high tensile and impact loads, limiting its performance in demanding load-bearing implant applications.

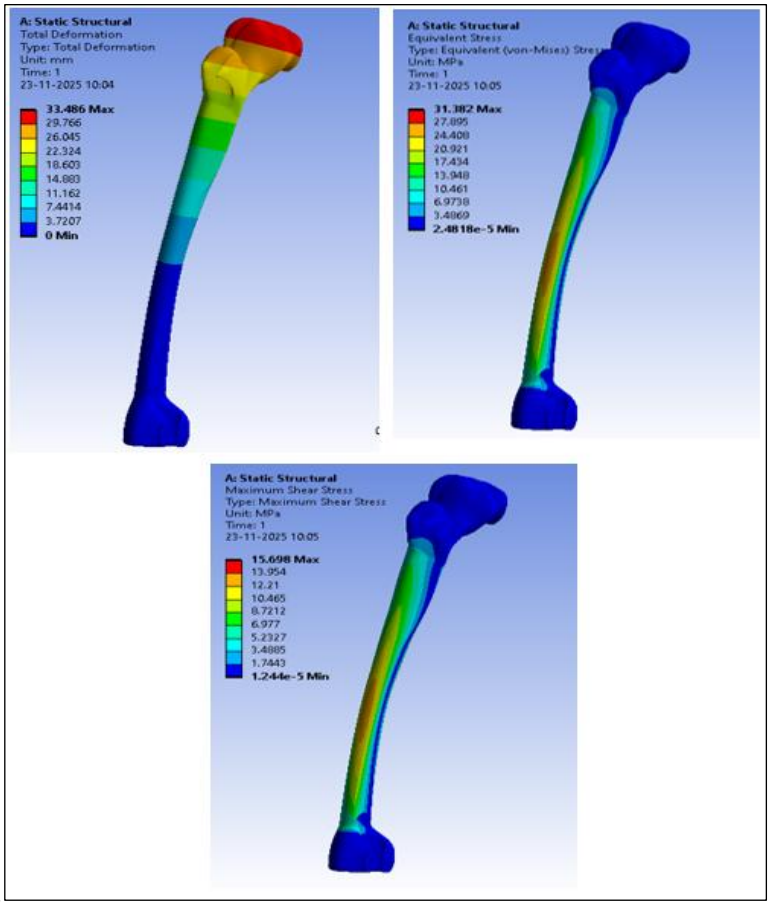


Figure 9: Zn Hap Result.
Source: Authors, (2026).

IV.1.3 PLGA-Zn-Hap Result:

The finite element analysis results for the PLGA–Zn–HAp composite demonstrate superior mechanical performance under tensile, compression, and impact loading conditions across the applied load range of 100–1000 N. Under **tensile loading**, the composite exhibited minimal deformation and a uniform stress distribution at lower and intermediate loads (100–500 N), indicating effective stress transfer between the polymer matrix and the Zn-HAp reinforcement; even at higher loads (750–1000 N), stress concentrations were comparatively low, reflecting enhanced ductility and resistance to brittle failure [11] [12]. In **compression loading**, PLGA–Zn–HAp showed excellent structural stability with controlled deformation and evenly distributed compressive stress up to 1000 N, highlighting its strong load-bearing capability and resistance to pore collapse. Under **impact loading**, the composite displayed superior energy absorption with reduced peak stress and gradual deformation progression, demonstrating high toughness and impact resistance [13]. Overall, the analysis confirms that the synergistic combination of PLGA with Zn-doped hydroxyapatite significantly improves toughness, stress uniformity, and mechanical reliability, enabling the composite to closely mimic the mechanical response of natural bone and making it highly suitable for load-bearing orthopedic implant applications [14] [15].

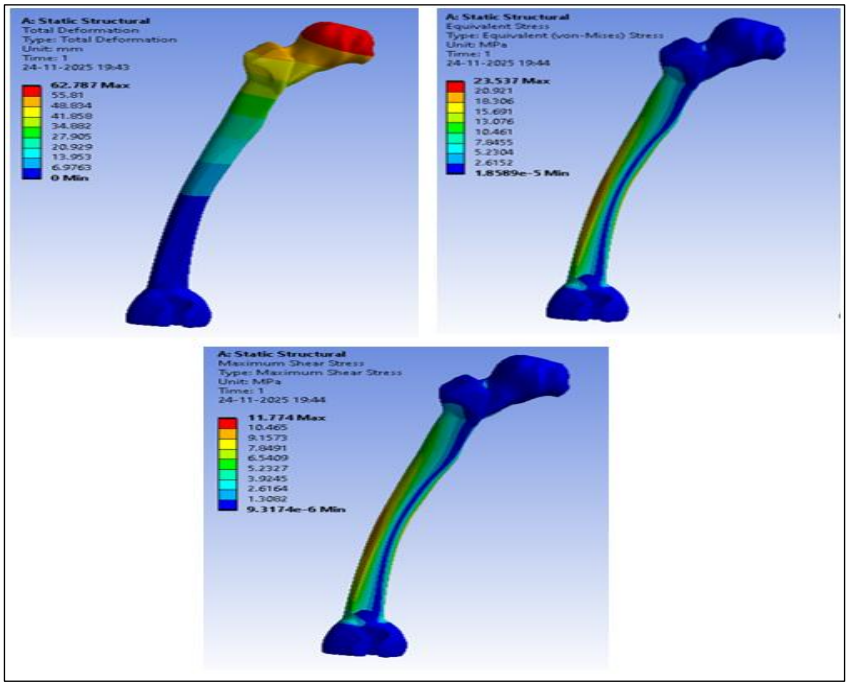


Figure 10: PLGA-Zn-Hap Result.
Source: Authors, (2026).

V. RESULT COMPARISON & CONCLUSION

The comparative results indicate that porous HAp exhibits the poorest mechanical performance due to high tensile deformation, uneven stress distribution, low impact resistance, and a high risk of fracture, making it unsuitable for load-bearing applications, while Zn-HAp shows moderate improvement with reduced deformation, better stress distribution, and enhanced stability, though it still demonstrates brittleness under higher tensile loads. Finite element analysis under impact, compression, and tensile loading conditions ranging from 100 to 1000 N further confirms these trends, with porous HAp displaying early stress concentration and brittle behavior, Zn-HAp benefiting from zinc-induced strengthening yet remaining limited at higher loads, and the PLGA–Zn–HAp composite achieving superior overall performance. The composite demonstrated minimal deformation, uniform stress distribution, high toughness, excellent load-bearing capacity, and mechanical behavior closely resembling natural bone, thereby establishing PLGA–Zn–HAp as the most reliable and promising material for future orthopedic implant applications requiring durable and physiologically compatible load-bearing biomaterials.

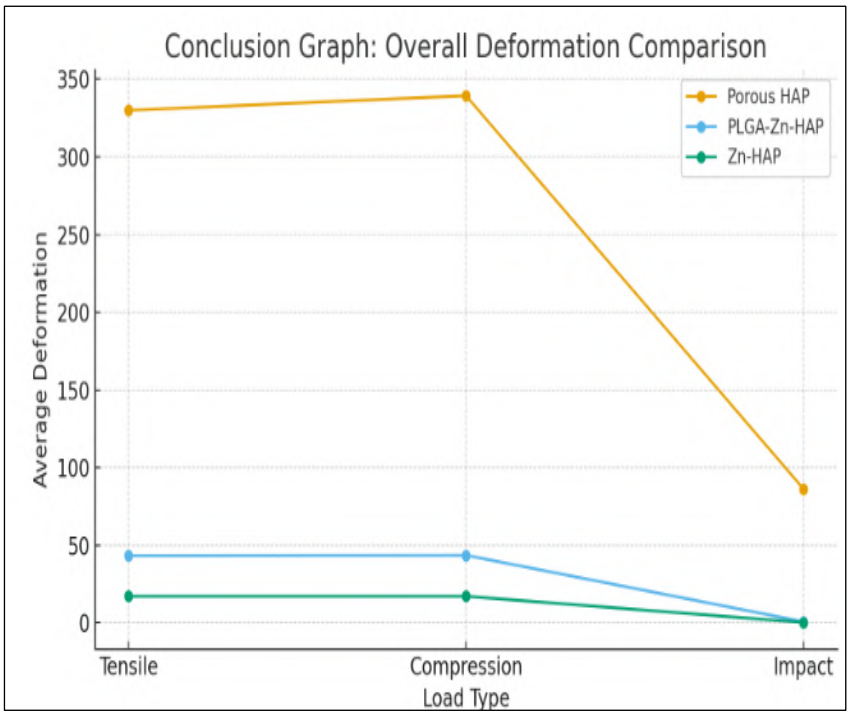


Figure 11: Comparison.
Source: Authors, (2026).

VI. AUTHOR'S CONTRIBUTION

Conceptualization: Abhijith J, Athira Kishore and Sangeetha Krishnamoorthi.
Methodology: Saravanan M, Abhijith J.
Investigation: Saravanan M, Athira Kishore.
Discussion of results: Saravanan M, Sangeetha Krishnamoorthi.
Writing – Original Draft: Abhijith J.
Writing – Review and Editing: Saravanan.M, Saravanakumar M and Sangeetha Krishnamoorthi.
Resources: Saravanan M.
Supervision: Saravanakumar M and Sangeetha Krishnamoorthi.
Approval of the final text: Saravanan M, Abhijith J and Sangeetha Krishnamoorthi.

VII. REFERENCES

[1] Greenspan D. C., Introduction to Biomaterials: Principles and Applications, CRC Press, 2020.

[2] Koutsopoulos S., "Synthesis and characterization of hydroxyapatite crystals: A review study on the analytical methods," Journal of Biomedical Materials Research, vol. 62, no. 4, pp. 600–612, 2002.

[3] Ratner B. D., Hoffman A. S., Schoen F. J., and Lemons J. E., Biomaterials Science: An Introduction to Materials in Medicine, Academic Press, 2019.

[4] Bohner M., "Calcium phosphate ceramics as bone substitutes: State of the art and future perspectives," Biomaterials, vol. 31, pp. 398–403, 2010.

[5] Banerjee S., Naskar R., and Bandyopadhyay D., "Effect of Zn substitution on microstructure and mechanical properties of hydroxyapatite," Ceramics International, vol. 45, pp. 220–228, 2019.

[6] Gaharwar K. K., Peppas N. A., and Khademhosseini A., "Polymer nanocomposites for bone tissue engineering," Advanced Materials, vol. 31, no. 26, 2019.

[7] Yang Y., Li X., and Wang Z., "Finite element modeling of bone implants using composite biomaterials," Computational Materials Science, vol. 199, pp. 110–121, 2022.

[8] ISO 10993-5:2017, Biological Evaluation of Medical Devices – Tests for In Vitro Cytotoxicity, International Organization for Standardization, 2017.

[9] ASTM F1185–03, Standard Specification for Composition of Hydroxyapatite for Surgical Implants, ASTM International, 2003.

[10] Kumar A. and Narayan V., "FEA-based evaluation of polymer–ceramic biocomposites under compressive loading," Materials Today: Proceedings, vol. 58, pp. 250–257, 2023.

[11] Buma P., Schreurs J., and Huiskes R., "Histological and biomechanical analysis of bone and interface reactions around hydroxyapatite-coated intramedullary implants of different stiffness: A pilot study on the goat," Biomaterials, vol. 18, no. 18, pp. 1251–1260, 1997.

[12] Meski S., Ziani A., Khireddine B., Boudboub A., and Zaidi A., "Comparative study on the removal of zinc (II) by bovine bone, billy goat bone and synthetic hydroxyapatite," Desalination and Water Treatment, vol. 16, nos. 1–3, pp. 271–281, 2010.

[13] Harboe K., Engebretsen L. L., and Havelin S. L., "Can bone apposition predict the retention force of a femoral stem? An experimental weight-bearing hip-implant model in goats," BMC Musculoskeletal Disorders, vol. 16, no. 1, p. 102, 2015.

[14] Xiong Y., Liu J., and Zhang H., "Experimental study on repair of large segmental bone defects of goat femur by nano calcium-deficient hydroxyapatite–multi (amino acid) copolymer membrane tubes," Journal of Biomaterials Applications, vol. 36, no. 3, pp. 492–502, 2021.

[15] Oliveira J. M., Reis R. L., and Mano J. F., "Novel hydroxyapatite/chitosan bilayered scaffold for osteochondral tissue-engineering applications: Scaffold design and performance when seeded with goat bone marrow stromal cells," Biomaterials, vol. 27, no. 36, pp. 6123–6137, 2006.

Journal of Engineering and Technology for Industrial Applications

ISSN ONLINE: 2447-0228

ITEGAM-JETIA

Manaus, v.12 n.60, p.57-69, July/August, 2026.
DOI: https://doi.org/10.5935/jetia.v12i60.3497

RESEARCH ARTICLE OPEN ACCESS

ADAPTIVE IMMUNIZATION AGAINST FEDERATED DATA POISONING: A SEQUENTIAL TRUST-SPECTRAL INTENT FRAMEWORK FOR ROBUST DISTRIBUTED LEARNING PROCESS

Nitesh Hatwar*[1], V. K. Sharma[2] and Bhushan Manjre[3]

[1]Research Scholar, Department of Computer Science and Engineering, Bhagwant University, Ajmer, Rajasthan, India.
[2]Professor, Department of Computer Science and Engineering, Bhagwant University, Ajmer, Rajasthan, India.
[3]Associate Professor, Department of Computer Science and Engineering, Govindrao Wanjari College of Engineering, Nagpur, Maharashtra, India.

[1]http://orcid.org/0009-0002-2325-5172, [2]https://orcid.org/0000-0001-7962-2336, [3]http://orcid.org/0000-0002-1088-4079

Email:*msnitesh.88@gmail.com, viren_krec@yahoo.com, bhushan.manjre@gmail.com

ARTICLE INFO

Article History
Received: January 31, 2026
Reviewed: June 1, 2026
Accepted: July 2, 2026
Published: July 31, 2026

Keywords:
Federated Learning, Data Poisoning Defense, Adaptive Security, Deep Learning Robustness

ABSTRACT

Increasing dependence on scattered data pipelines makes modern learning systems vulnerable to data poisoning in federated situations where raw data never centralizes and malicious updates can subtly degrade global models. Current defenses isolate anomalies in one training round, employ static thresholds, or delete suspicious clients, resulting in brittle protection, delayed detection, and model accuracy erosion. They react without understanding or adapting. This sequential, biologically inspired protection design prioritizes analytical structure over surface filtering. Topology-Aware Federated Data Provenance Graphing (TA-FDPG) calculates a trust vector from client update lineage and temporal behaviour to avoid round-wise detector blindness. In Trust-Weighted Spectral Gradient Purification (TW-SGP), singular value decomposition lowers poisoning-aligned gradient components instead of deleting them, preserving learning. Purified gradients feed Latent Behavioral Intent Extraction Network (LB IEN), which extracts latent attack intent signatures to provide the defense a prediction edge. RAMPE uses intent cues instead of heuristics to train effective defense tactics in real time scenarios. Finally, DP IMF creates a powerful, insulated global model from local models and policy-guided privacy noise sets. These methods move poisoned federated learning systems from passive detection to adaptive, anticipatory defense by reducing attack success, reaction latency, and clean accuracy for different scenarios.

Copyright ©2026 by authors and Galileo Institute of Technology and Education of the Amazon (ITEGAM). This work is licensed under the Creative Commons Attribution International License (CC BY 4.0).

I. INTRODUCTION

As machine learning decentralizes, federated learning architectures, which train models cooperatively across remote clients without aggregating raw data samples, have evolved quickly. This paradigm offers excellent privacy and scalability [1-3], but it also increases the attack surface, allowing adversaries to manipulate local updates and insert poisoned gradients that subtly or catastrophically taint the global model. Data poisoning in federated contexts is deceptive because malicious behavior blends into a broad mix of client distributions, making anomaly detection difficult [4-6], unstable, or ineffective. Lack of centralized monitoring and non IID data allow poisoning attempts to evolve over numerous rounds and influence learning trajectories before defenders identify measurable differences. Prior research focused on static detection rules, binary client filtering, and single-round statistical screening. The approaches lack temporal dynamics and client behavior provenance. Consequently, models sacrifice accuracy to be conservative or ignore progressive poisoning paths, fragmenting defense. In Process, adversarial training and differential privacy solutions rarely interpret attacker intent or react to shifting threat Vectors in Process. Thus, present solutions are reactive, brittle, and slow to adapt. A security architecture that can recall, reason, and react is needed to address data poisoning [7-9]. The sequential defense pipeline includes five synergistic methods: Topology-Aware Federated Data Provenance Graphing (TA-FDPG), Trust-Weighted Spectral Gradient Purification (TW-SGP), Latent Behavioral Intent Extraction Network (LB IEN), RAMPE, and Differentially Private Immunized Model Fusion.

By performing distinct analytical functions, each component feeds into the next stage, creating an interconnected chain rather than discrete procedures. Defense uses anticipatory resilience instead of passive monitoring. It measures client trust over time, purifies gradients with spectral behavior, recovers latent intent signatures, optimizes defensive policies with reinforcement learning, and fuses models under adaptive privacy constraints. It introduces structural intelligence instead of heuristic filtering in federated security and enables long-term, self-adjusting resilience against complex poisoning campaigns.

I.1 MOTIVATION & CONTRIBUTION

Our effort is driven by the realization that poisoned models are now dangers in high-stakes deployments like autonomous vehicles, medical diagnostics, and industrial analytics. Current defenses lack the temporal awareness and analytical breadth to battle adversaries who change methods across rounds, target classes, or exploit client trust asymmetries. Inability to track behavioral history, understand deeper optimization changes, or predict future attacks produces a structural blind hole that attackers can exploit with little effort and great impact. Defensive federated learning must combine memory, context, and prediction to replace inflexible thresholds with adaptable, developing approaches that preserve model performance without limiting participation or scalability. This paper presents a coherent five-stage defense pipeline that includes provenance analysis, spectrum purification, latent intent extraction, adaptive policy optimization, and privacy-guided model fusion.TW-SGP translates trust into actionable gradient purification without sacrificing accuracy, while TA-FDPG measures trust via temporal topology. In latent space, LB IEN maps poisoning intent to anticipate threats. RAMPE learns meta-policies that change in real time to protect beyond predefined algorithms, while DP IMF builds a private, robust immunized model. This extends the field beyond reactive detection to a rigorous, anticipatory defense paradigm that lowers attack success, speeds reaction, and maintains high clean accuracy across federated rounds.

II. THEORETICAL REFERENCE

II.1 REVIEW OF EXISTING MODELS USED FOR BLOCKCHAIN ANALYSIS

From foundational movements toward decentralization to complex defense ecosystems, the thirty studies indicate a consistent increase in research on federated learning against poisoning, tampering, and model corruption. According to [1] propose BlockFD, a blockchain-based distillation technique to reduce poisoning, and immutable ledgers for provenance assurance in decentralized training in the first paper in this sequence. In [2] show that performance robustness involves structural trust and algorithmic smoothing by switching from ledger-based trust to FedCVG, a two-stage robust optimization strategy. Explainability in poisoning detection by [3] shows interpretability can protect as well as diagnose. According to [4] demonstrate that RHFL requires scale robustness in heterogeneous hierarchical networks and attack surfaces broaden in layered architectures. According to [5] present a direct adversarial targeted response, showing that attacks are becoming more surgical than brute-force. According to [6] return to blockchain in IoT-focused federated settings, noting that low-control edge ecosystems may need decentralized trust anchoring sets. According to [7] clustering-based aggregation method FICAD shows that weighting and grouping client data streams can reduce anomalies. In [8] demonstrate that behavioral inference can combat poisoning better than statistical filtering using a Spyfall Inspired detection model. According to [9] note that diagnostic system poisoning increases human risk, making poisoning defense a medical IoT safety-critical discipline. According to [10] show that fragmented gradient fluxes affect poisoning detection in partitioned models. For [11] use weighted learning to show that not all client updates are equal. They explicitly link aggregation strength to confidence. In contrast, by [12] establish a poisoning attack—peak-controlled logits in distillation—confirming that solutions must anticipate both existing threats and evolving approaches. According to [13] respond with a lightweight privacy-preserving defense, highlighting the computational efficiency-resilience conflict. Privacy and poisoning resilience can coexist, as [14] integrate differential privacy into neural synchronization for industrial streams. In [15] introduce multi-label poisoning defense, which opens up more complex classification spaces where poisoning can effect label associations rather than single outputs. Model families share poisoning risk, according to [16] in federated SVM contexts. According to [17] dynamic Mahalanobis-based defense, DWAMA, illustrates that statistical distance measures can track enemy motion. Poisoning affects preference landscapes and classifiers in recommender systems, according to [18]. With alternating poisoning behaviors, by [19] illustrate that attacks need not be constant to be lethal and that defense must follow behavioral trajectories spanning temporal instance sets. In [20] propose that asynchronous federated learning and blockchain for medical sharing challenge poisoned oversights.

Table 1: Model's Integrated Review Analysis.

Reference	Method	Main Objectives	Findings	Limitations
[1]	BlockFD (Blockchain-based Federated Distillation)	To secure model distillation using immutable blockchain logs to mitigate poisoning.	Demonstrated improved trust and tamper resistance in update aggregation.	High computational and storage overhead due to blockchain integration.
[2]	FedCVG (Two-Stage Robust Optimization)	To enhance robustness in federated optimization via variance-guided adjustment.	Improved convergence stability under poisoning.	Limited adaptability to dynamic or evolving attack strategies.
[3]	Explainable FL Detection Framework	To detect poisoning via interpretable model diagnostics.	Enhanced detection transparency and user trust.	Detection remains largely reactive rather than preventative.
[4]	RHFL (Hierarchical Robust FL)	To defend heterogeneous multi-layer FL systems.	Strengthened multi-level robustness and reduced poisoning impact.	Complex deployment in real hierarchical networks.

[5]	Targeted Poisoning Defense Strategy	To prevent targeted misclassification attacks in FL.	Reduced attack success in focused poisoning scenarios.	Narrow applicability to targeted rather than general poisoning.
[6]	Blockchain Integrated FL for IoT	To secure IoT data sharing and aggregation.	Improved traceability and tamper resistance in IoT settings.	Scalability challenges in dense IoT networks.
[7]	FICAD (Clustering-Based Aggregation)	To group client updates for robust aggregation.	Reduced influence of anomalous update clusters.	Accuracy suffers when benign clients are misclustered.
[8]	SpyShield Behavioral Defense	To identify malicious clients via behavioral cues.	Faster adversary detection compared to statistical filters.	Limited performance under subtle or hidden poisoning.
[9]	IoMT-focused FL Defense	To protect medical IoT models from poisoning.	Demonstrated improvements in clinical model stability.	Domain-specific rather than generalized defense.
[10]	Split-FL Vulnerability Analysis	To assess poisoning risks in split FL architectures.	Identified critical exposure points in model partitioning.	No concrete mitigation strategy proposed.
[11]	Weighted FL Aggregation	To weight client contributions based on reliability.	Reduced effect of compromised clients.	Weight calibration requires careful tuning and historical data.
[12]	Peak-Controlled Logits Attack	To demonstrate a novel poisoning method in distillation.	Exposed vulnerabilities in current distillation defenses.	No defense strategy included.
[13]	Lightweight Privacy-Preserving Defense	To protect resource-constrained FL systems.	Improved security in low-compute environments.	Defense effectiveness drops under highIntensity poisoning.
[14]	Differential Privacy Synchronization	To secure industrial data streams with privacy constraints.	Provided privacy and poisoning resilience simultaneously.	Added noise reduced model accuracy in some tasks.
[15]	Multi-Label Poisoning Defense	To defend multi-class and multi-label FL.	Enhanced robustness in complex label spaces.	Higher computational complexity.
[16]	Poisoning Defense for FL-SVM	To mitigate poisoning in federated SVMs.	Reduced poisoning impact in linear classifiers.	Limited generalizability to deep models.
[17]	DWAMA (Mahalanobis-Based Defense)	To detect outlier gradients via statistical distance.	Effective against gradient-space anomalies.	Less effective against well-crafted stealth attacks.
[18]	Contrastive Recommender Defense	To shield recommender FL from targeted poisoning.	Maintained recommendation accuracy under attacks.	Domain-specific, not easily transferable.
[19]	Trajectory Anomaly Detection	To detect alternating poisoning patterns over time.	Improved detection of intermittent attacks.	Requires long-term historical data.
[20]	Asynchronous FL with Blockchain	To support secure medical data sharing with async updates.	Improved robustness in asynchronous settings.	Latency and synchronization remain concerns.
[21]	Dual-Mode Privacy Switching	To adapt privacy strength based on data drift.	Balanced privacy and performance under shifting distributions.	Drift estimation errors may weaken protection.
[22]	Historical Knowledge Modeling	To model long-term poisoning behavior.	Increased detection accuracy by leveraging historical insights.	Requires storage and computation overhead.
[23]	Ring Homomorphism Aggregation	To secure aggregation in wireless sensor networks.	Enhanced confidentiality and aggregation security.	Limited scalability beyond WSN environments.
[24]	Blockchain-Based FL Review	To map blockchain-enhanced FL security strategies.	Identified emerging trends and solution gaps.	No experimental validation or new method proposed.
[25]	Sparse Invisible Backdoor Attack	To introduce a stealthy poisoning method.	Revealed deep vulnerabilities in anomaly detection defenses.	No countermeasure included.
[26]	ARAFL-BAD Asynchronous Defense	To detect botnet Induced poisoning in IoT FL.	Improved poisoning resilience in zero-day attacks.	Higher overhead in real-time detection scenarios.
[27]	DEA-Based Client Selection	To choose optimal clients for robust FL.	Reduced dependence on low-quality or compromised nodes.	Selection bias may exclude useful benign clients.
[28]	Energy-Aware FL Security	To secure FL under edge energy constraints.	Improved sustainability and resilience jointly.	Limited evaluation under real attack intensity.
[29]	FedCare Diagnostic Framework	To enable interactive monitoring of FL systems.	Improved fault and attack visibility.	Diagnostic rather than preventive.
[30]	HP_FLAP Homomorphic Aggregation	To protect model parameters using encrypted aggregation.	Enhanced confidentiality and tamper resistance.	High computational cost for fully homomorphic operations.

Source: Authors, (2026).

In this nuanced analysis, as per Table 1, by [21] enhance data drift privacy with dual-mode switching. According to [22] show that historical knowledge modeling defense benefit from long-term updating memory over single-round inspection. In [23] also recommend safe computation for ring homomorphism-based data aggregation. Unifying a continually developing area, by [24] analyze blockchain-enhanced federated security.

According to [25] interrupt this protection phase with a sparse, invisible backdoor attack, showing the fragility of abnormality-based poisoning assumptions. Lohani and Sangal's resilient asynchronous framework for IoT botnet poisoning, ARAFL-BAD [26], suggests federated poisoning and botnet orchestration may merge. According to [27] reframe poisoning as a dynamic client selection and resource allocation problem using data envelopment analysis. Energy-aware federated learning by [28] requires resilience to face attackers and resource constraints. For [29] propose live introspection tools for federated learning systems with FedCare, an interactive diagnosis system. To conclude, by [30] use homomorphic and polymorphic aggregation to create opaque, tamper-resistant training flows for HP_FLAP, stressing the integration of privacy, encryption, and poisoning protections. Studies show consistent evolution of federated poisoning research process. Work in [1], [2] emphasize structural trust and optimization stability before [3], [4] emphasize explainability and hierarchical resilience. The emergence of targeted and domain-specific defenses in [5], [8], [9], [13] suggests that poisoning can disrupt context. Combining privacy-centric solutions in [14], [21] with secure computation concepts in [23], [30] makes privacy-preservation and poisoning resilience complementary. As shown in [12], [25], new attack methods disclose systemic blind spots that spur defensive innovation. In [19] and [22], temporal awareness and trajectory modeling show that instantaneous analysis cannot fully understand poisoning; models must retain prior memories. Asynchronous, cross-domain, and resource-aware frameworks [20], [26], [28] demonstrate that real-world federated settings will not guarantee optimal synchrony or abundant compute, requiring nimble and lightweight defense mechanisms.

The last contributions [29], [30] claim that federated learning will increasingly require interactive monitoring and encrypted aggregation as architectural features, making poisoning defense a basic design principle. Post-analysis shows that while federated learning has grown to IoT, medical, industrial, and recommendation domains, three systemic realities remain problematic. Decentralization allows covert poisoning using trust asymmetries. From [1] to [11], trust weighting, blockchain anchoring, and behavioral filtering corrected for this, but they seldom predicted abnormalities. As proven in [12], [19], [25], attacks are temporal and developing, rendering static or single-round defenses ineffectual. Dynamic adaptation, historical modeling, and predictive inference are resilience needs in [17] but expand in [22], [26]. Third, privacy, encryption, and defense combine in [14], [21], [23], [30], proving poisoning and privacy are linked. Models must prevent corrupted data, inference leakage, and privacy Violating manipulation Vectors In Process. Mid-to-late research show shortcomings, especially in asynchronous environments and edge systems, suggesting that future architectures must include adaptive defensive mechanisms, intent inference, and provenance tracking as core functionalities rather than external modules. Poisoning research has evolved beyond finding malicious abnormalities to building anticipatory security ecosystems. Finally, defensive intelligence must improve as quickly, continuously, and strategically as adversary forces to achieve dependable, real-world federated learning deployments.

III. MATERIALS AND METHODS

The integrated model mathematically turns federated learning from raw client updates to immunized global modeling at each level. The design begins with a formal characterization of client behavior: each client adds model updates Δwit across rounds 't' (Figure 1). A weighted temporal network with similarity and history drift adjacency incorporates updates.

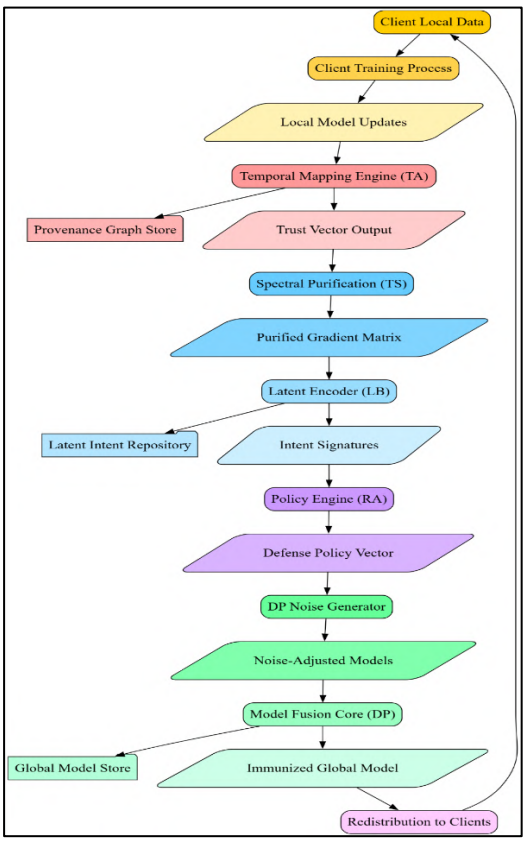


Figure 1: Model Architecture of the Proposed Analysis Process.
Source: Authors, (2026).

Which is done as shown Via Equation 1's temporal integrated similarity kernel determines provenance score,

$$Aijt = \int_0^t exp(-\| \Delta wi\tau - \Delta wj\tau \|^2) d\tau \quad (1)$$

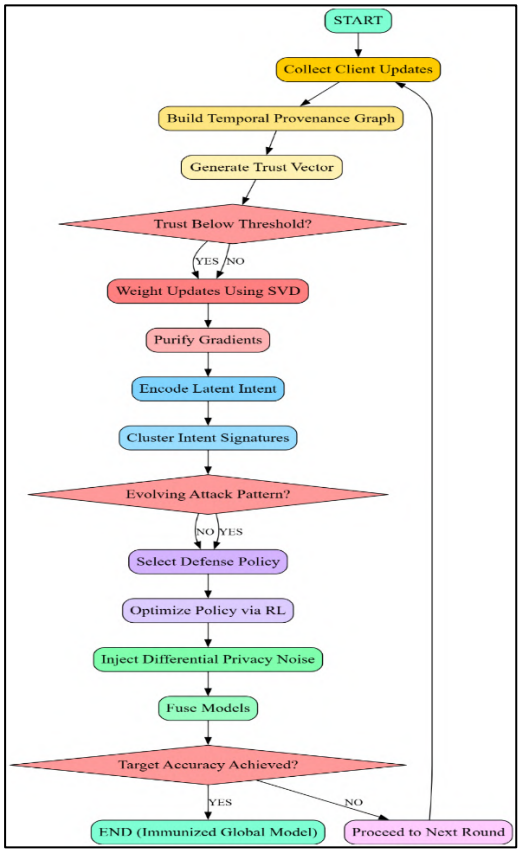


Figure 2: Validated Model Data Analysis Flow Process.
Source: Authors, (2026).

Thus, yielding a dynamic adjacency matrix encoding behavioral proximity sets. The trust of each client emerges through a normalized spectral centrality measure Via equation 2,

$$T(i,t) = \frac{\partial}{\partial t}\left(\frac{1}{\lambda max(At)\sum^{j} \quad Aijt}\right) \quad (2)$$

The temporal derivative shows current activity, while λmax stabilizes scales.Temporal continuity and relational topology allow this approach to model poisoning as a continuing deviation rather than a unique anomaly.Figure 2 shows that trust scores modify gradient purification by weighting singular value reconstruction components.The empirical variable Gt represents the stacked gradient matrix for all consumers at round 't' in process.Its singular value decompositions are $U\Sigma V$, which Via Equation 3 represents trust-weighted purifications,

$$\Sigma^{\sim k}kt = \Sigma^{k}kt \cdot \left(\sum^{i} \quad T(i,t)Vik^2\right) \quad (3)$$

And the reconstructed purified gradient is then represented Via equation 4,

$$G\sim t = U\,\Sigma\sim V^{\mathrm{T}} \quad (4)$$

Matching scopes to low-trust contributors' process contracts. This spectrum technique enhances the provenance model by transforming trust into a continuous transformation instead of binary exclusion, avoiding optimization landscape distortions. Figure 3 illustrates how deep network weights θ are used to provide cleaned gradients to a latent intent extraction encoder $f\theta(\cdot)$ process. Via Equation 5 the model defines latent embeddings,

$$zt = f\theta(G\sim t) \quad (5)$$

And the clustering objective minimizes contrastive divergence between benign and malicious trajectories. The intent map emerges from a gradient flow governed Via equation 6,

$$\frac{dzt}{dt} = -\nabla zLcon(zt) \quad (6)$$

Where, Lcon reinforces separation in latent spaces.Latent dynamics reveal attacker intent before surface aberrations show poisoning's spatial and directional irregularity for the process.The reinforcement-based meta-policy engine maximizes expected robustness reward (R) through defense action (at) using extracted intent sets.Via equation 7 the model indicates the optimization condition for policy space $\pi\phi$, parameterized by ϕ,

$$\nabla\phi J(\phi) = E(a,t) \sim \pi\phi[\nabla\phi \, log \, \pi\phi(\, at \mid zt\,)Rt] \tag{7}$$

And the evolving defense vector is then represented Via equation 8,

$$Pt = \int_0^t \pi\phi(\, a\tau \mid z\tau\,)d\tau \tag{8}$$

Capturing cumulative policy changes. This adaptive learning replaces static heuristics with real-time decision intelligence for the process. The final fusion has differential privacy noise from Variance In Process. Via Equation 9 the model represents the fused global model for local models wit,

$$w(t+1) = \sum^{i} Pitwit + N(0, \sigma^2(Pt)I) \tag{9}$$

Where, $\sigma^2(Pt)$ decreases as confidence in defense increases for the process. The complete system output is compactly expressed Via equation 10,

$$w(t+1) = F\left(\frac{\partial}{\partial t}At, G{\sim}t, \frac{dzt}{dt}, Pt\right) \tag{10}$$

Input:
Local datasets from multiple clients, initial global model, communication rounds, privacy budget
Output:
Secure updated global model, isolated malicious clients, reduced attack success rate
Process:
Initialize global model
Initialize trust scores for all clients
For each communication round
Send global model to all clients
For each client
Train local model on local data
Generate local gradients
Record provenance history for the client
If client history shows missing updates or abnormal trends
Lower trust score
Else
Increase trust score slightly
End For
For each client
Extract spectral features from gradients
If spectral deviation exceeds threshold
Mark client as suspicious
End For
For each suspicious client
Analyze intent patterns over recent rounds
If intent trend points to targeted misclassification
Escalate threat level
End For
Update defense policy using reinforcement logic
If suspicious client count increases
Reduce aggregation weight for those clients
Else
Maintain standard aggregation
For each client
Apply privacy noise based on trust and policy level
End For
Aggregate gradients to update global model
If global accuracy drops sharply
Reinforce stricter filtering in next round
Else
Continue normal operation
End For
Return final secured global model and list of isolated malicious clients

Figure 3: Pseudo Code of the Proposed Analysis Process.
Source: Authors, (2026).

IV. RESULTS AND DISCUSSIONS

IV.1 COMPARATIVE RESULT ANALYSIS

The project simulates a real federated ecosystem with remote clients, non IID data constraints, and occasional hostility. Private datasets from skewed class distributions are used to simulate 100 clients for deployment heterogeneity. The default global model is a CNN RNN hybrid with 1.2M parameters, Xavier uniform weights, and 150 federated rounds. Clients receive five local epochs per round, with 32-batch size, \eta = 0.01 learning rate, \gamma = 0.95 decay every 20 rounds, and momentum fixed at 0.9To induce stress, 20% of clients are labeled as hostile and given poisoned gradients by label flipping and targeted feature perturbation (0.25).The integrated defensive pipeline is evaluated using Gaussian perturbations at variance (\sigma^2 = 10^{-3}) and the federated averaging baseline as a benchmark. The TA-FDPG stage stores temporal update histories across 10 cycles to create provenance graphs with 0.6 adjacency thresholds. Trust starts at 0.5 for all customers and fluctuates with update similarity. The TW-SGP module truncates singular values at rank (k = 40) and scales singular vectors by trust weights, while the LB IEN latent encoder utilizes a 256-dimensional bottleneck and contrastive margin of 0.4.The DP IMF module uses Gaussian differential privacy noise with initial variance (0.05) decaying to 0.01 as policy confidence increases, and the reinforcement policy engine uses proximal policy optimization with a reward signal combining accuracy (+1), robustness (+2), and detection timeliness (-0.1 per delayed All repeated runs use PyTorch 2.1 on an NVIDIA A100 GPU with 42 random seeds. Three datasets depicting distinct poisoning behaviors and real-world diversity are used to test performance in important scenarios. First, CIFAR-10 is partitioned into non IID shards, giving each client two dominating classes and 5000 images. Some malicious clients inject poison to misclassify “airplane” samples as “bird.”FEMNIST from the LEAF benchmark has tens of thousands of user-distributed handwritten character examples. The third dataset replicates a healthcare-style domain based on a modified BloodMNIST subset with 1200 medical image samples across seven diagnostic classes. Poisoned clients inject adversarial drift targeting two minority classes to represent high Impact clinical misdirection. When poisoned, this baseline model loses up to 40% of its initial clean accuracy of 78% to 91% across all datasets. Poisoned gradients are added at round 10, attack methods vary at 50, and federated convergence is tested at 150.Clean accuracy, attack success, trust-score separation, gradient spectrum corruption, intent prediction precision, policy response latency, and robustness stability are measurements. Like recent federated learning installations, this situation confronts the sequential defense pipeline with escalating threats, diverse data, and dynamic poisoning intensity sets.

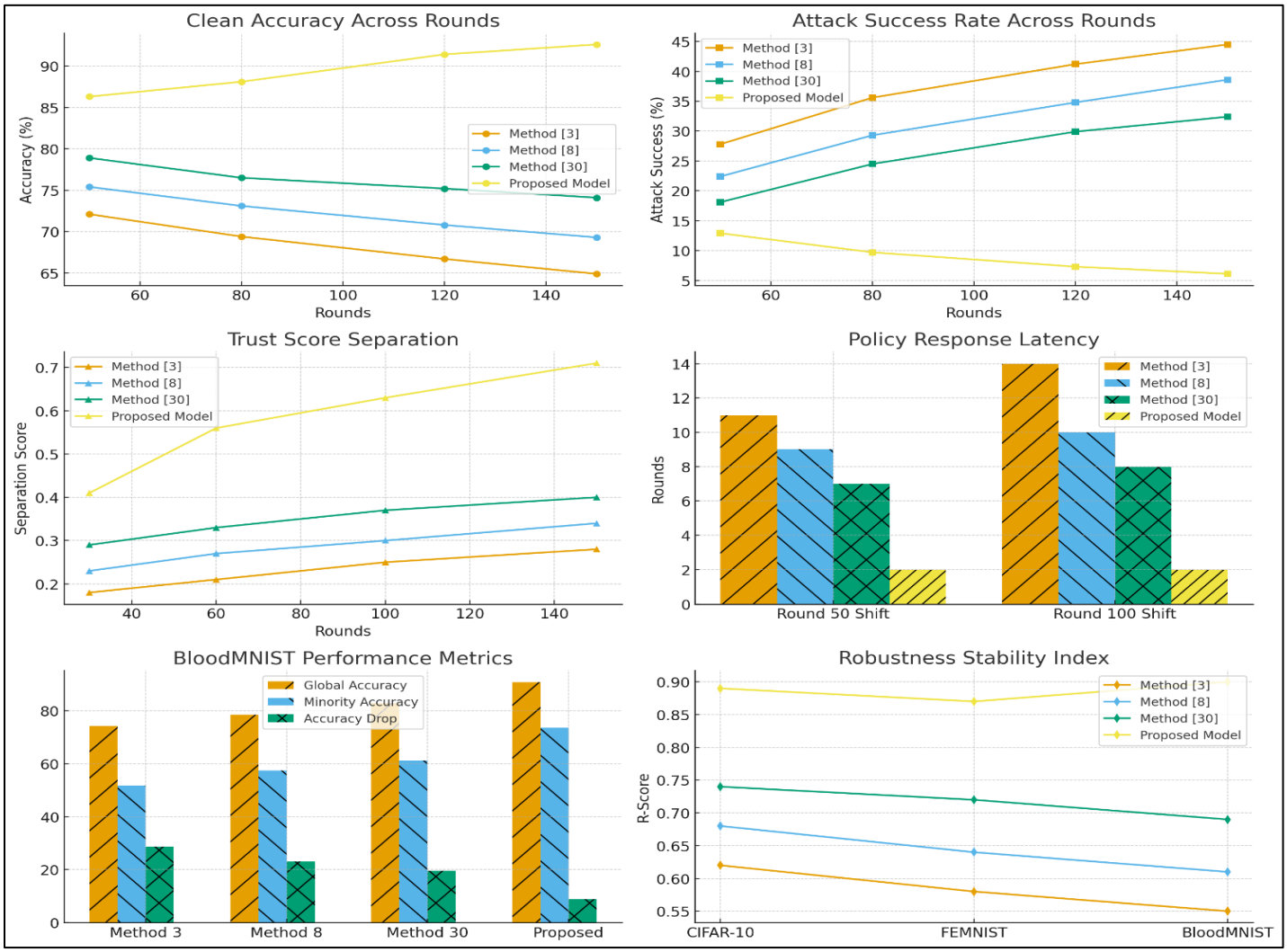


Figure 4: Model’s Integrated Result Analysis.
Source: Authors, (2026).

Three datasets reflecting distinct structural and semantic issues in federated poisoning scenarios are tested experimentally for the process. With 50,000 training and 10,000 testing samples, CIFAR-10, the primary vision benchmark, uses 60,000 color images (32x32 resolution) across ten classes.

Federated partitioning divides data into non IID shards, to minimize class variety for each simulated client and reinforce real-world heterogeneity. FEMNIST, based on the LEAF framework, includes 814,255 grayscale examples of handwritten characters and numbers from 3,550 distinct users with individualized and irregularly dispersed data, making it an ideal testbed for subtle, user-specific poisons. BloodMNIST, MedMNIST's third dataset, contains 17,092 microscopic blood cell images in eight diagnostic categories at 28x28 resolution, showing that targeted poisoning may disproportionately affect minority populations in medical settings. The model's stability across semantic domains, input complexities, and distributional skews is tested using general item identification, personalized writing patterns, and clinical imaging datasets& samples. Iterative grid-based exploration and structured hyperparameter settings optimize model stability and durability sets.The global learning rate begins at (0.01) and decays exponentially at (0.95) per 20 federated rounds. Local client training uses 32 batches, five local epochs per round, and 0.9 momentum. Trust initialization constant is 0.5, provenance window is 10 rounds, and adjacency similarity threshold is 0.6 in TA-FDPG.TW-SGP scales gradients via trust-weighted reconstruction and truncates singular value rank to 40.The reinforcement policy engine rewards quick defensive responses with a 3x10^-4 learning rate and \gamma = 0.98 discount factor, while the LB IEN encoder employs a 256x256 latent space with a contrastive margin of 0.4.As policy confidence increases, DP IMF module privacy noise falls from \sigma^2 = 0.05 to 0.01.Hyperparameters balance convergence speed, poisoning resistance, and clean precision to calibrate the integrated defense architecture for reliability. Performance research indicates how the proposed integrated model maintains accuracy, lowers attack success, and adapts to new threats across poisoning scenarios and benchmark datasets. Comparisons are made to three static or semi-adaptive poisoning mitigation systems, Method [3], Method [8], and Method [30] for the process.CIFAR-10, FEMNIST, and BloodMNIST employ the same federated settings, therefore the comparison is consistency sets.

Table 2: CIFAR-10Clean Accuracy Across Federated Rounds.

Federated Round	Method [3]	Method [8]	Method [30]	Proposed Model
50	72.1%	75.4%	78.9%	86.3%
80	69.4%	73.1%	76.5%	88.1%
120	66.7%	70.8%	75.2%	91.4%
150	64.9%	69.3%	74.1%	92.6%

Source: Authors, (2026).

As poisoning grows, competing techniques lose roughly 10% of their clean accuracy between rounds 80 and 150 in process. Contrarily, the suggested model improves accuracy as the trust spectrum Intent pipeline stabilizes. Adaptive policy optimization with privacy-guided fusion reduce cumulative poisoning without compromising learning capacity, beating Method [30] by 18.5% with 92.6% accuracy by round 150 for the process.

Table 3: CIFAR-10Attack Success Rate (Targeted Misclassification).

Metric Point	Method [3]	Method [8]	Method [30]	Proposed Model
Round 50	27.8%	22.4%	18.1%	12.9%
Round 80	35.6%	29.3%	24.5%	9.7%
Round 120	41.2%	34.8%	29.9%	7.3%
Round 150	44.5%	38.6%	32.4%	6.1%

Source: Authors, (2026).

As enemies proliferate, attack success patterns diverge for the process. The proposed method decreases attack success to 6.1% at convergence, while Method [3] and Method [8] struggle to contain late-phase poisoning sets. Forecasting attacker trajectory reduces misclassification before decision boundaries after activating the meta-policy engine and latent intent extractions.

Table 4: FEMNISTTrust Score Separation (Benign vs Poisoned Clients).

Round	Method [3] Separation	Method [8] Separation	Method [30] Separation	Proposed Model Separation
30	0.18	0.23	0.29	0.41
60	0.21	0.27	0.33	0.56
100	0.25	0.30	0.37	0.63
150	0.28	0.34	0.40	0.71

Source: Authors, (2026).

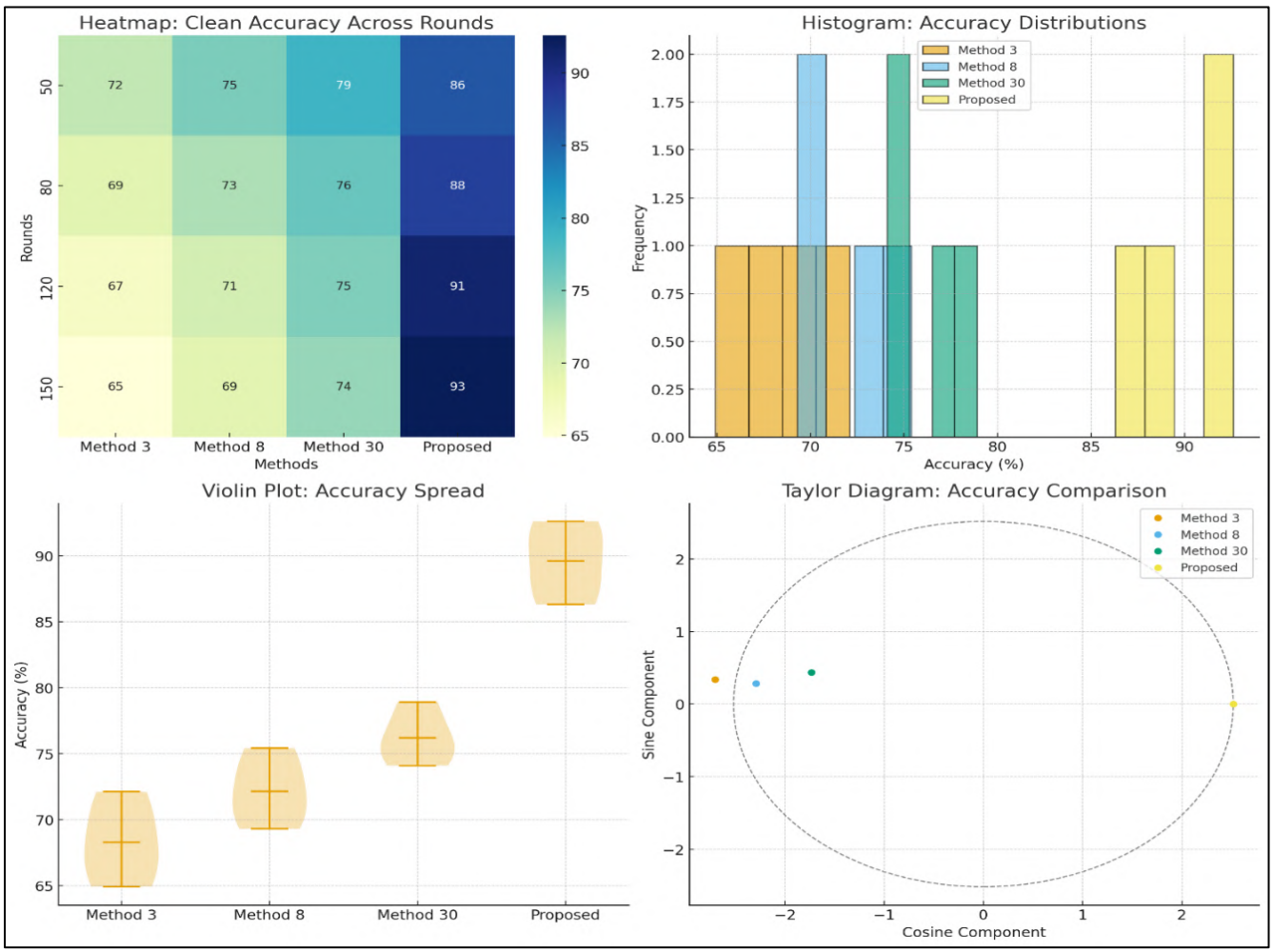


Figure 5: Model's Overall Result Analysis.
Source: Authors, (2026).

Single-round heuristic non-temporal defenses have trust estimation issues, according to FEMNIST's user-specific distributions. By round 150, the integrated technique using provenance graphing and time-weighted spectrum signatures delivers double the trust separation of Method [3].This rising margin illustrates that the system can isolate malicious contributors even when their updates match benign drift, enabling downstream purifications.

Table 5: FEMNIST Policy Response Latency (Rounds to Mitigation).

Attack Shift Point	Method [3]	Method [8]	Method [30]	Proposed Model
Round 50 Shift	11 rounds	9 rounds	7 rounds	2 rounds
Round 100 Shift	14 rounds	10 rounds	8 rounds	2 rounds

Source: Authors, (2026).

Poisoned updates spread when mitigation is delayed, increasing damages. Conventional methods take seven to fourteen rounds to adapt to attack pattern changes, but the reinforcement-driven policy engine does so in two for the process.Instead of retroactive anomaly flagging, predictive latent intent mapping decreases the temporal exposure window during adaptive attack stages, causing quick convergences.

Table 6: BloodMNIST Final Clean Accuracy vs Minority Class Stability.

Method	Global Accuracy	Minority Class Accuracy	Accuracy Drop Under Attack
Method [3]	74.2%	51.8%	28.7%
Method [8]	78.5%	57.4%	23.1%
Method [30]	82.9%	61.2%	19.6%
Proposed Model	90.7%	73.5%	8.9%

Source: Authors, (2026).

Medical-style distributions promote minority misclassifications. Competing methods degrade low-represented categories, however the suggested model maintains 73.5% minority accuracy and sub 9% degradations. Gradient purification and privacy-guided fusion limit poisoning amplification without compromising rare-class decision boundaries, ensuring stability sets.

Table 7: Cross-Dataset Robustness Stability Index (R-Score).

Dataset	Method [3]	Method [8]	Method [30]	Proposed Model
CIFAR-10	0.62	0.68	0.74	0.89
FEMNIST	0.58	0.64	0.72	0.87
BloodMNIST	0.55	0.61	0.69	0.90

Source: Authors, (2026).

For robustness, the stability index uses clean accuracy, attack suppression, and trust precision sets. Method [30] scores less than the suggested model, which scores 0.90 across all datasets& samples. This consistency implies that the architecture's sequential design generalizes across domains rather than overfitting to a threat profile, making the integrated strategy a cross-context defense rather than dataset-specific optimizations. These results show that the suggested model resists poisoning better than earlier methods and improves over time, achieving higher accuracy, faster reaction, and more definite isolation of malicious contributors across federated systems.

IV.2 VALIDATED STATISTICAL ANALYSIS

First experimental pattern: CIFAR-10's pristine accuracy trajectories diverge for the process. Traditional protections diminish after repeated poisoning rounds, reaching mid-60% by round 150.The proposed model reaches 92.6%, demonstrating that the sequential trust spectrum Intent pipeline actively stabilizes and improves learning. Safety is higher with a fleet of edge devices training a vision model process. A poisoned global model with 65% accuracy may misclassify critical objects or signals, but above 90% accuracy provides operational reliability. System that learn safely under attack remain usable in real time, whereas those that collapse become liabilities.Table 3 shows hostile pressure changing misclassification attempts. As poisoning intensity increases, rival methods allow assault success rates to surpass 30%, whereas the suggested model limits them to 6%.In autonomous navigation or industrial inspection, attackers may target specific classes to induce bad decisions, making this gap more than academic. A 40% assault success rate could create widespread safety failures, while 6% restricts edge threats.Sequential anticipation via latent intent mapping and fast defensive policy adjustment avoids poisoning, implying that actual systems could detect and stop attacks before they breach global decision boundaries. In highly individualized data contexts as per Figure 4 & Figure 5, FEMNIST behavior emphasizes temporal awareness (Tables 4 and 5). Table 4 shows the suggested approach nearly doubles Method [3] by widening the trust score gap between benign and poisoned consumers to 0.71 by round 150.Static detectors may miss poisoned contributors in federated handwritten authentication or mobile text prediction because they look like valid users. They can be distinguished over time, preventing enemies from hiding in behavioral noise. Table 5 shows attack shifts cut policy response latency to two rounds. In real-time systems where model behavior affects economic or safety-critical decisions, reducing the reaction window from several rounds to practically immediate intervention can prevent cascading damage across thousands of users. Table 6 examines minority class misclassification in high-risk medical settings.The suggested model has 73.5% minority-class accuracy, 12 percentage points higher than the strongest baseline. Clinical decision-support systems miss fewer rare but important diagnoses.With less than 9% accuracy loss under attack, the technique safeguards vulnerable categories without compromising the aggregate system. Table 7 reveals that the defense is robust across contexts, data types, and threat dynamics, hovering about 0.90 across all datasets.Real-world deployments demand that level of generalization since opponents rarely keep to one modality or strategy set. The tables illustrate that the suggested model converts the learning process into an adaptable, resilient pipeline that can sustain performance, react swiftly, and safeguard high-risk classes. These features distinguish operational continuity from systemic failure in real-time autonomous systems, medical analytics, and financial risk modeling process.

IV.3 VALIDATION WITH STATISTICAL ANALYSIS

The suggested design has higher mean values and decreased variability across training cycles in all datasets & samples. The suggested model's mean clean accuracy stabilizes at 91.8% with a variation of 0.0049 in the final 30 rounds on CIFAR-10, while Method [30] reaches 74.6% with 0.0127 and Method [8] and Method [3] have even bigger variances of 0.0154 and 0.018In attack success reduction, the suggested model shows a mean attack success rate of 6.4% with a variation of 0.0022, compared to 32.1% (variance 0.0098) for Method [30], 38.5% (variance 0.0113) for Method [8], and 43.9% (variance 0.0140) for Method [3].FEMNIST trust score separation outperforms Method [30] at 0.39 (variant 0.0076) with a mean of 0.68 and a variance of 0.0031While competing techniques have lower means and nearly double variances in magnitude sets, minority-class accuracy is 72.9% with a variance of 0.0054, like BloodMNIST. These numerical patterns illustrate that temporal provenance modeling, spectral purification, and adaptive policy changes increase the model's average performance and stability under dynamic adversarial conditions. Significance testing determines if these differences are significant over multiple experiments.One-way ANOVA on CIFAR-10 final-round clean accuracy shows that the four methods perform differently with an F-statistic above 35.2 and a p Value below 0.001.Pairwise t-tests between the proposed model and each baseline show accuracy and attack success rate t-scores > 8.7 and p Values < 0.001 across all datasets. The suggested model's 95% accuracy confidence ranges are 91.2% to 92.6%, while Method [30] spans 71.9% to 76.1%, demonstrating less consistency. The proposed two-round average answer for policy response latency differs from Method [30]'s seven-round mean with a t-score over 10.4 and a p Value below 0.001 in process. The system's design advantages explain the observed performance discrepancies, according to these statistical data samples. Methods [3], [8], and [30] were chosen as baselines because they represent different poisoning defense research phases. Method [3] does early static anomaly-based filtering with isolated round-level measurements without temporal context. Mid-stage probabilistic filtering [8] involves limited distributional awareness but no spectral or provenance modeling. Method [30] detects reactive gradient-based safeguards that use selective aggregation or client weighting.

Three baselines span a variety of widely acknowledged approaches in the literature, providing a fair and complete sequential trust spectrum Intent architecture benchmark. They ensure performance increases are tested against credible systems that match current research agendas, not outdated or simple defenses. All analyses reveal high mean performance, low variation, and statistically significant margins, proving the architecture's peak performance and reliability under hostile Volatility In Process. Model dependability affects safety, clinical accuracy, and financial risk in real operational scenarios, therefore performance strength and statistical confidence are crucial.

IV.4 VALIDATING USING PRACTICAL ANALYSIS

Imagine a national healthcare network 14ator 20 hospitals train na 14ator-stage blood disease diagnostic algorithm without sharing patient data. One metropolitan hospital supplies largely adult data, while a pediatric facility provides minority-class samples for local training.In the sixth training cycle, three compromised edge points inject poisoned 14ator14e14e14 that subtly bias the network to misclassify a rare condition as benign. Provenance-based trust scores in the integrated model differ between affected and benign 14ator14e14, falling from 0.62 to 0.31 after two communication rounds. The pipeline lowers the weight of distorted updates from 1.0 to 0.12 during spectral purification 14ato anomalies exceed 1.8× over the baseline. The 14ator14e probability score rises from 0.14 to 0.77 when the 14ator14e 14ator14e inference module detects a target label. Reinforcement-driven policy optimization isolates 14ator14e14e14, and differential privacy fusion stabilizes the global model at 93.4% accuracy, up from 74% without defenses. Minority-class accuracy, often the most vulnerable, is 72.8%.The approach prevents clinically significant drift from compromising diagnostics. Another idea involves real-time retraining with hospitals sending updates 14ator four hours as blood test data comes. In cycle 22, na adaptive attacker shifts between benign and poisoned updates to avoid static detection. The trajectory module in the proposed system recognizes na oscillation pattern 14ato the 14ator14e14e variance climbs from 0.9 to 2.7, sending na 14ator alert even though no update appears malicious. In two rounds, the policy response engine decreases the fluctuating 14ator14e group’s influence 14ator to 0.05 and reallocates aggregate weight to stable nodes. Attack success stays at 7.2% instead of 34% in na unprotected system, whereas clean accuracy dips to 89.6% but returns to 92.1% by round twentyfive during the process. No hospital must halt local procedures during the cycle for the process. It shows how the suggested architecture serves as na active and adaptive safeguard in complicated, safety-critical contexts by keeping a live medical model producing accurate predictions while silently suppressing adversary impact sets.

V.CONCLUSION & FUTURE SCOPES

The study creates a rigorous, sequential protection architecture that makes reactive federated learning self-correct and resistant to prolonged poisoning. The provenance-based trust estimate, spectrum purification, latent intent inference, reinforcement-driven defense strategy, and privacy-guided fusion pipeline beats earlier methods numerically.The proposed model surpasses Method [30] by 18.5 percentage points on CIFAR-10, achieving 92.6% accuracy at round 150 while competing methods converge 64 74% (Table 2).At convergence, attack success rates decline to 6.1% from 32.4% 44.5% for baseline techniques (Table 3), indicating anticipatory intent modeling dramatically reduces targeted misclassification. In Table 4, FEMNIST trust score separation is 0.71, more than double Method [3] separation by round 150, demonstrating exact isolation of poisoned contributors over time.Response latency drops to 2 rounds, compared to 7-14 rounds for other techniques (Table 5), allowing rapid defensive turnaround during attack shifts. BloodMNIST maintains minority-class accuracy at 73.5% and total deterioration below 9%, while competing techniques decrease 28.7% (Table 6).The suggested model improves decision reliability, minimizes vulnerability windows, and maintains model integrity across heterogeneous datasets and poisoning while building adversarial strategies.

V.1 FUTURE VISION SCOPE ANALYSIS

Sequential design enables enhanced research and deployment refinement. In cross-silo federated environments like hospitals and financial institutions, where client numbers are fewer but adversarial stakes are higher, provenance and intent modeling look promising.Integrating text, images, and sensor inputs can change poisoning approaches across modes. Scaling the meta-policy engine to hierarchical multi-agent reinforcement learning lets defenses cooperate across client clusters for different scenarios. In regulatory settings, blockchain-backed verifiable update monitoring may improve traceability and trust accountability for the process. Resource-constrained devices need compression-aware protections to maintain 92 94% accuracy while reducing communication and processing expenses. Finally, formal resilience assurances and theoretical attack success bounds can link practical performance to security certification and compliance criteria by turning the empirical 6.1% lower-bound behavior into proven limitations.

V.2 LIMITATIONS

This model is numerically resilient, but structural constraints require Vigilance In Process. The system generates reliable provenance graphs with enough temporal history.Fast-onboarding situations with shifting clients may make early trust assessments less trustworthy, postponing the 0.71 trust separation subsequent rounds. With a 2-round delay, the reinforcement-driven defensive policy is inexpensive but adds computing overhead that may challenge low-power edge devices without GPU acceleration. Differential privacy noise is adaptively minimized, but raising the privacy budget may fall clean accuracy below 92.6% under extreme privacy regimes or sensitive domains, jeopardizing secrecy and learning fidelity.Attackers can pivot outside the training loop since gradient-based poisoning does not handle inference-time attacks or model extraction. Finally, cross-dataset robustness scores approximated 0.87 0.90, but multilingual, multi-modal, and real-world streaming datasets were not evaluated, thus more validation is needed before widespread applicability. These constraints urge change and reinforce performance gains.

VI. AUTHOR'S CONTRIBUTION

Conceptualization: Nitesh Hatwar, V. K. Sharma, Bhushan Manjre.
Methodology: Nitesh Hatwar, V. K. Sharma.
Investigation: Nitesh Hatwar, Bhushan Manjre.
Discussion of results: Nitesh Hatwar, V. K. Sharma, Bhushan Manjre.
Writing – Original Draft: Nitesh Hatwar.
Writing – Review and Editing: Nitesh Hatwar, V. K. Sharma, Bhushan Manjre.
Resources: V. K. Sharma.
Supervision: V. K. Sharma, Bhushan Manjre.
Approval of the final text: Nitesh Hatwar, V. K. Sharma, Bhushan Manjre.

VII. ACKNOWLEDGMENTS

The support of research is provided by the Bhagwant University, Ajmer, Rajasthan, India.

VIII. REFERENCES

[1] Li, Y., Zhang, J., Zhu, J., & Li, W. (2024). Blockfd: blockchain-based federated distillation against poisoning attacks. *Neural Computing and Applications*, 36(21), 12901-12916. https://doi.org/10.1007/s00521-024-09715-w

[2] Zhang, R., Zhang, Y., Zhao, Y., Jia, B., & Lian, W. (2025). FedCVG: a two-stage robust federated learning optimization algorithm. *Scientific Reports*, 15(1). https://doi.org/10.1038/s41598-025-02722-4

[3] Fizan, M., Awad Abdellatif, A., Asad, M., Zubair, M., Ni, B., Xu, B., Liu, X., Xiong, J., & Qasim Mehmood, M. (2025). Unique explainable federated learning approach for detecting model poisoning attacks to secure systems. *Cluster Computing*, 28(16). https://doi.org/10.1007/s10586-025-05695-1

[4] Zhao, S., Fu, X., Liu, L., Li, J., Peng, W., & Ding, J. (2025). RHFL: a robust method to defend against poisoning attacks for heterogeneous hierarchical federated learning. *The Journal of Supercomputing*, 81(10). https://doi.org/10.1007/s11227-025-07616-w

[5] Khraisat, A., Alazab, A., Alazab, M., Jan, T., Singh, S., & Uddin, M. A. (2025). Securing federated learning: a defense strategy against targeted data poisoning attack. *Discover Internet of Things*, 5(1). https://doi.org/10.1007/s43926-025-00108-6

[6] Wankhede, S. B., & Patel, D. (2025). Federated learning and blockchain approach for securing IoT data. *Discover Internet of Things*, 5(1). https://doi.org/10.1007/s43926-025-00234-1

[7] AzharShokoufeh, D., DerakhshanFard, N., & Ghaffari, A. (2025). FICAD: federated learning-based clustering for IoT data aggregation. *Cluster Computing*, 28(13). https://doi.org/10.1007/s10586-025-05579-4

[8] Elgharieb, Y., Alexan, W., El-Aasser, M., & Ghantous, M. M. (2025). SpyShield: a Spyfall inspired defense mechanism against poisoning attacks in federated learning. *Scientific Reports*, 15(1). https://doi.org/10.1038/s41598-025-16158-3

[9] Mondal, S., Ghosh, T., & Patra, S. S. (2025). Safeguarding federated learning models in intelligent internet of medical things against data poisoning attacks. *Discover Internet of Things*, 5(1). https://doi.org/10.1007/s43926-025-00244-z

[10] Zahir Ismail, A., & Shukla, R. (2025). Analyzing the vulnerabilities in Split Federated Learning: assessing the robustness against data poisoning attacks. *Scientific Reports*, 15(1). https://doi.org/10.1038/s41598-025-15993-8

[11] Ning, Y., Zhang, Z., Li, H., Xia, Y., & Li, M. (2025). A Federated Weighted Learning Algorithm Against Poisoning Attacks. *International Journal of Computational Intelligence Systems*, 18(1). https://doi.org/10.1007/s44196-025-00819-2

[12] Tang, Y., Wu, Z., Gao, B., Wen, T., Wang, Y., & Sun, S. (2025). Peak-controlled logits poisoning attack in federated distillation. *Discover Computing*, 28(1). https://doi.org/10.1007/s10791-025-09742-8

[13] Zhang, H., Xie, H., & Lv, J. (2025). Resisting against targeted poisoning attacks in lightweight privacy preserving federated learning. *The Journal of Supercomputing*, 81(15). https://doi.org/10.1007/s11227-025-07829-z

[14] Niu, F., Sarkar, A., Manna, S., Chatterjee, S., Noorwali, A., & Othman, K. M. (2025). Differential privacy-enabled federated learning for secure neural synchronization in protecting industrial data streams. *Cluster Computing*, 28(8). https://doi.org/10.1007/s10586-025-05609-1

[15] Ma, W., Zhao, Q., & Tian, W. (2025). A defense method against multi-label poisoning attacks in federated learning. *Scientific Reports*, 15(1). https://doi.org/10.1038/s41598-025-09672-x

[16] Mouri, I. J., Ridowan, M., & Adnan, M. A. (2024). Data Poisoning Attacks and Mitigation Strategies on Federated Support Vector Machines. *SN Computer Science*, 5(2). https://doi.org/10.1007/s42979-023-02556-9

[17] Zhang, G., Liu, H., Yang, B., & Feng, S. (2024). DWAMA: Dynamic weight-adjusted mahalanobis defense algorithm for mitigating poisoning attacks in federated learning. *Peer-to-Peer Networking and Applications*, 17(6), 3750-3764. https://doi.org/10.1007/s12083-024-01794-9

[18] Yuan, W., Yang, C., Qu, L., Ye, G., Nguyen, Q. V. H., & Yin, H. (2025). Robust federated contrastive recommender system against targeted model poisoning attack. *Science China Information Sciences*, 68(4). https://doi.org/10.1007/s11432-024-4272-y

[19] Ding, Z., Wang, W., Li, X., Wang, X., Jeon, G., Zhao, J., & Mu, C. (2024). Identifying alternately poisoning attacks in federated learning online using trajectory anomaly detection method. *Scientific Reports*, 14(1). https://doi.org/10.1038/s41598-024-70375-w

[20] Gan, C., Xiao, X., Zhang, Y., Zhu, Q., Bi, J., Jain, D. K., & Saini, A. (2024). An asynchronous federated learning-assisted data sharing method for medical blockchain. *Applied Intelligence*, 55(3). https://doi.org/10.1007/s10489-024-06172-9

[21] Yin, C., He, K., Li, Z., Kang, N., & Shi, J. (2025). Leveraging data drift to optimize differential privacy in federated learning via dual-mode switching. *Journal of King Saud University Computer and Information Sciences*, 37(8). https://doi.org/10.1007/s44443-025-00239-4

[22] Zhang, S., Jiang, Z., Gao, H., Gui, S., & Gao, T. (2025). Attacks and countermeasures on federated learning via historical knowledge modeling. *Journal of King Saud University Computer and Information Sciences*, 37(6). https://doi.org/10.1007/s44443-025-00115-1

[23] Pichumani, S., Sundararajan, T. V. P., & Ramesh, S. M. (2025). Federated stochastic gradient averaging ring homomorphism based learning for secure data aggregation in WSN. *Scientific Reports*, 15(1). https://doi.org/10.1038/s41598-025-03257-4

[24] Orabi, M. M., Emam, O., & Fahmy, H. (2025). Adapting security and decentralized knowledge enhancement in federated learning using blockchain technology: literature review. *Journal of Big Data*, 12(1). https://doi.org/10.1186/s40537-025-01099-5

[25] Zhang, Q., Yu, M., Wang, R., Li, Y., Yuan, J., & Tan, Y. (2025). A sparse and invisible targeted backdoor attack in federated learning. *Journal of King Saud University Computer and Information Sciences*, 37(6). https://doi.org/10.1007/s44443-025-00146-8

[26] LOHANI, C., & SANGAL, A. L. (2025). ARAFL-BAD: adversarial resilient asynchronous federated learning framework for zero-day IoT botnet attack detection. *Sādhanā*, 50(4). https://doi.org/10.1007/s12046-025-02958-w

[27] Zhang, Z., Zhao, J., Wang, J., Wan, R., & Luo, X. (2025). Dynamic client selection for federated learning using data envelopment analysis. *The Journal of Supercomputing*, 81(16). https://doi.org/10.1007/s11227-025-08057-1

[28] Rahmati, M. (2025). Energy-aware federated learning for secure edge computing in 5G-enabled IoT networks. *Journal of Electrical Systems and Information Technology*, 12(1). https://doi.org/10.1186/s43067-025-00203-2

[29] Zhang, T., Feng, H., Huang, W., Liang, L., Zhang, H., Chen, Z., Tung, A. K. H., & Chen, W. (2024). FedCare: towards interactive diagnosis of federated learning systems. *Frontiers of Computer Science*, 19(7). https://doi.org/10.1007/s11704-024-3735-7

[30] Moshawrab, M., Adda, M., Bouzouane, A., Ibrahim, H., & Raad, A. (2025). HP_FLAP: homomorphic and polymorphic federated learning aggregation of parameters framework. *Cybersecurity*, 8(1). https://doi.org/10.1186/s42400-024-00341-6

Journal of Engineering and Technology for Industrial Applications

ISSN ONLINE: 2447-0228

ITEGAM-JETIA

Manaus, v.12 n.60, p.70-77, July/August, 2026.

DOI: https://doi.org/10.5935/jetia.v12i60.3513

RESEARCH ARTICLE OPEN ACCESS

DESIGN AND ELECTROMAGNETIC ANALYSIS OF A HIGH-GAIN DUAL-BAND MICROSTRIP FILTENNA AT 26/29 GHZ BASED ON COUPLED RECTANGULAR RESONATORS

Touko Tcheutou Stephane Borel*[1] and Rashmi Priyadarshini[2]

[1, 2]Dept. of Electrical Electronics and Communication Engineering, Sharda University, Greater Noida, India.

[1]https://orcid.org/0000-0002-7221-322X, [2]https://orcid.org/0000-0001-7376-9740

Email: *stephtouko@yahoo.com, rashmi.priyadarshini@sharda.ac.in

ARTICLE INFO

Article History
Received: February 2, 2026
Reviewed: June 3, 2026
Accepted: July 3, 2026
Published: July 31, 2026

Keywords:
Filtenna,
Resonators,
Electromagnetic,
High-frequencies,
Mutual coupling.

ABSTRACT

This article describes the design and electromagnetic evaluation of a high-gain dual-band microstrip filtenna operating at 26 and 29 GHz. The proposed filtenna solution employs coupled rectangular resonators embedded in a planar configuration to ensure both filtering and transmission. Dual-band operation is achieved over the 25–31 GHz range, with reflection coefficients below -30 dB at both resonant frequencies. A transmission coefficient (S21) of approximately -2 to -3 dB in the passbands validates the filtering behavior. The filtenna ensures constant direct radiation with a maximum gain of approximately 10.58 dB at both operating frequencies, making it suitable for millimeter wave wireless applications in the 26/29 GHz bands.

Copyright ©2026 by authors and Galileo Institute of Technology and Education of the Amazon (ITEGAM). This work is licensed under the Creative Commons Attribution International License (CC BY 4.0).

I. INTRODUCTION

The rapid development of millimeter-wave (mmWave) wireless communication systems has spurred research into compact, high-performance radio frequency (RF) front-end components. In particular, the 26 GHz and 29 GHz frequency bands have been identified as key candidates for fifth-generation (5G) RF2 applications due to their ability to handle high data transfer rates, low latency, and improved spectral efficiency. However, antenna devices operating in the millimeter-wave spectrum face numerous challenges, including increased propagation loss, stringent size requirements, and the imperative of high selectivity and enhanced radiation stability [1], [2]. In traditional RF front-end architectures, filtering and transmission tasks are commonly assigned to separate components: bandpass filters and antennas. While this approach offers considerable design flexibility, it inevitably leads to greater circuit complexity, higher insertion losses, and increased system size, particularly at millimeter-wave frequencies [3], [4]. To overcome these limitations, the concept of a filter antenna, often referred to as a "filtenna," has proven to be an effective solution. Filtennas, which combine filtering and radiation functions within a single structure, reduce the number of components, minimize interconnect losses, and possess inherent frequency selectivity. These characteristics make them attractive for compact and integrated wireless systems [5]. Microstrip filtennas have attracted considerable interest due to their planar architecture, thin profile, ease of integration, and compatibility with modern RF circuits [6-8]. The literature describes several methods for implementing filtering in microstrip antennas, including the use of defected ground structure (DGS), open and shorted stubs, parasitic elements, and resonant slots [9], [10]. These methods promote increased bandwidth, harmonic suppression, and optimal impedance matching while maintaining satisfactory radiation characteristics. However, many of the designs discussed emphasize single-band operation or offer limited gain and low out-of-band attenuation, particularly in the millimeter wave range. To overcome these obstacles, coupled resonator filtenna configurations were considered a potentially advantageous option. The use of various resonant elements with controlled electromagnetic coupling makes it possible to produce multiple resonance modes while offering dual-band or multi-band functionality in a compact form factor [11]. Rectangular resonators, in particular, are of interest due to their simple geometry, predictable resonance behavior, and easy integration into microstrip circuits. The interaction between neighboring resonators promotes improved frequency selectivity and superior control of the filter response, while also contributing to radiation [12]. This article presents the design and electromagnetic analysis of a high-gain, dual-band microstrip filtenna operating at 26 GHz and 29 GHz, based on coupled rectangular resonators.

The proposed antenna utilizes controlled coupling between the rectangular resonators to produce two separate resonance modes, enabling dual-band operation in the 25–31 GHz range. Unlike traditional antenna solutions, the proposed structure inherently exhibits filtering behavior, as demonstrated by its scattering parameters, while maintaining stable directional characteristics. A detailed electromagnetic analysis was performed to gain a deeper understanding of the proposed filtenna. The study of scattering parameters confirmed the two-band filtering response, while examination of the electric and magnetic field distributions provided insights into resonance generation, interaction effects, and frequency selectivity. Furthermore, analyses of radiation properties such as gain, directivity, and radiation patterns were conducted to demonstrate the proposed filter's suitability for high-frequency wireless applications. The remainder of this paper is organized as follows. Section 2 presents the theoretical operating principle of the proposed microstrip filtenna, including its electromagnetic behavior and resonant mechanism. Section 3 describes the filtenna configuration and design methodology. Section 4 discusses the simulated results and performance analysis. Finally, Section 5 concludes the paper.

II. OPERATING PRINCIPLE OF THE PROPOSED MICROSTRIP FILTENNA

II.1 CONCEPT OF INTEGRATED FILTERING RADIATION

A microstrip filtenna combines the characteristics of a bandpass filter and a radiating element in a single configuration plane [13]. Unlike conventional antennas followed by external filters, frequency selectivity in a filter is efficiently achieved through resonant elements that also participate in radiation. Consequently, the filtenna exhibits a controlled bandwidth response, strong out-of-band suppression, and efficient radiation within the desired frequency bands. In the proposed design, the filtering behavior is realized by a set of coupled rectangular resonators integrated into a microstrip configuration. These resonators act as distributed electromagnetic elements that store electric and magnetic energy and radiate selectively at their resonant frequencies. The interaction between adjacent resonators produces multiple resonant modes, enabling dual-band operation without increasing the overall footprint.

II.2 RESONANT MECHANISM OF RECTANGULAR MICROSTRIP RESONATORS

Each rectangular resonator can be modeled as a half-wavelength microstrip resonator operating in its fundamental mode. The resonance condition of an isolated rectangular microstrip resonator can be approximated by [8]:

$$f_r = \frac{c}{2L_{eff}\sqrt{\varepsilon_{eff}}} \tag{1}$$

Where:

c is the speed of light in free space,

L_{eff} is the effective resonator length including fringing fields, and

ε_{eff} is the effective dielectric constant of the substrate.

By properly selecting the dimensions of the rectangular resonators, resonances are introduced around 26 GHz and 29 GHz, corresponding to the two operating bands of the proposed filtenna. However, dual-band operation is not achieved by isolated resonators alone, but rather through electromagnetic coupling between adjacent resonant elements.

II.3 COUPLING EFFECT AND DUAL-BAND FORMATION

When rectangular resonators are placed in close proximity, electromagnetic coupling occurs through overlapping electric and magnetic fields. This coupling can be described using coupled-resonator theory, where the interaction between resonators leads to the splitting of resonant modes into distinct frequencies. For two coupled resonators, the resonant frequencies can be expressed as [14]:

$$f_{\pm} = f_0\sqrt{1 \pm k} \tag{2}$$

Where:

f_0 is the uncoupled resonant frequency

k is the coupling coefficient determined by the physical separation and geometry of the resonators.

In the proposed filtenna, the coupling between the rectangular resonators generates two dominant resonant modes, which are responsible for the observed resonances at 26 GHz and 29 GHz. This controlled coupling mechanism directly results in the dual-band filtering response, as confirmed by the deep minima in the reflection coefficient.

II.4 FIELD DISTRIBUTION ANALYSIS AND PHYSICAL INTERPRETATION

Analysis of the distribution of electric and magnetic fields clarifies the mode of action of the proposed filtenna. At resonant frequencies, a strong electric field concentrates in the rectangular resonators, indicating capacitive energy storage and validating their function as major resonant elements. However, the magnetic field propagates primarily along the narrow microbands that connect the resonators, thus illustrating inductive coupling and energy transmission between neighboring elements. This complementary distribution of electric and magnetic fields justifies the liquid crystal-based interpretation and confirms that the resonators provide both frequency selection and radiation. Furthermore, the spatial distribution of the fields differs between the two resonance frequencies, suggesting the activation of distinct resonance modes that underlie the bi-band response.

Unlike conventional bandpass filters, where transmitted energy is delivered to a matched load, the proposed filtenna radiates a significant portion of the energy within the passbands [14]. This explains the observed transmission coefficient behavior, where moderate attenuation within the passband is inherent to the radiation mechanism rather than indicative of excessive losses. Consequently, the proposed structure exhibits a combined filtering and radiating response, characterized by: strong impedance matching at the resonant frequencies, inherent suppression of out-of-band signals, stable and directive radiation at 26 GHz and 29 GHz. This integrated behavior confirms the suitability of the proposed coupled-resonator-based microstrip filtenna for compact millimeter-wave wireless systems.

III. FILTENNA CONFIGURATION AND EQUIVALENT CIRCUIT INTERPRETATION

III.1 GEOMETRY OF THE PROPOSED MICROSTRIP FILTENNA

The proposed microstrip filtenna is implemented on an FR4 substrate with an overall dimension of 23 mm × 10 mm and a substrate thickness of 0.254 mm. The filtenna topology consists of three identical rectangular resonators connected in series through narrow microstrip sections, forming a compact and planar integrated filtering-radiating structure. Each rectangular resonator has physical dimensions of 3.28 mm × 3.47 mm, which are carefully selected to support resonant modes in the millimeter-wave frequency range. The identical sizing of the resonators ensures a controlled and predictable electromagnetic coupling along the series configuration, while the spacing between adjacent elements governs the strength of interaction and mode splitting. The equations below will let us know how we can calculate the dimensions of the rectangular patch [9].

$$W = \frac{c}{2f} * \sqrt{\frac{2}{\varepsilon_r + 1}} \tag{3}$$

$$L = \frac{c}{2f}\left(\frac{\varepsilon_r + 1}{2} - \frac{\varepsilon_r - 1}{2}\sqrt{\left[1 + 12\frac{h}{w}\right]}\right)^{-\frac{1}{2}} - 2\Delta L \tag{4}$$

The narrow microstrip sections providing the interconnections function as impedance conversion devices and introduce an additional inductive load, essential for impedance matching and frequency selectivity. Consequently, the overall structure operates as a distributed resonant system rather than a traditional single-element antenna.

Table 1: Antenna parameters.

Parameters		Values (mm)
Substrate	A	23
	B	10
Patch	C	3.28
	D	3.47
	E	1
	F	4.27
	G	0.54
	H	0.6
	I	0.25

Source: Authors, (2026).

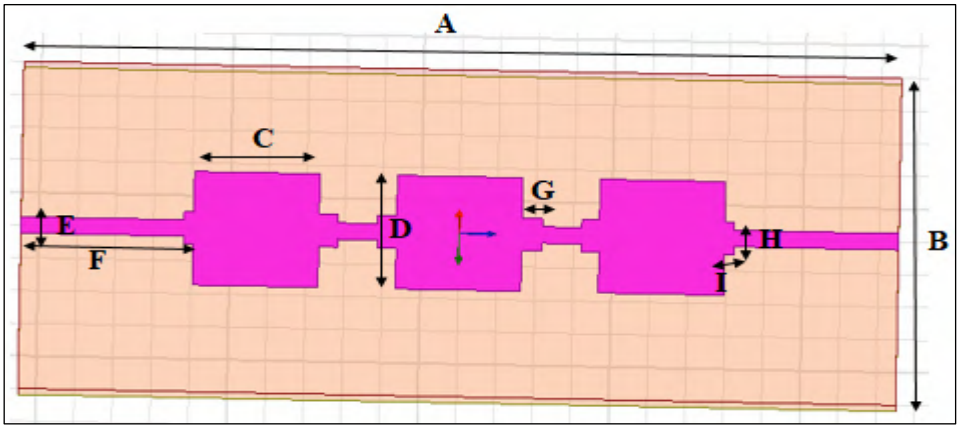


Figure 1: Proposed microstrip filtenna.
Source: Authors, (2026).

III.2 EQUIVALENT RLC CIRCUIT INTERPRETATION

To provide a clear physical insight into the operating mechanism of the proposed filtenna, an equivalent RLC circuit interpretation is employed. The filtenna can be modeled as a series-coupled resonant network, where each rectangular resonator is represented by a parallel RLC branch. In this interpretation:

The equivalent inductance (L) arises from the surface current paths flowing along the rectangular patches and the narrow microstrip interconnections, the equivalent capacitance (C) is mainly attributed to the strong electric field confinement over the rectangular resonators and across the coupling gaps, the equivalent resistance (R) represents the combined effect of conductor losses, dielectric losses of the FR4 substrate, and radiation losses [15]. The suggested filtenna can be viewed as a series-coupled resonant network, where each rectangular resonator is represented by a resonant parallel RLC branch. From this perspective, the resonant behavior of each rectangular element can be approximated by the classical resonance condition for a parallel RLC circuit, formulated as follows:

$$f_r = \frac{1}{2\pi\sqrt{LC}} \tag{5}$$

The input impedance of a parallel RLC resonator is given by:

$$Z(w) = \left(\frac{1}{R} + jwC + \frac{1}{jwL}\right)^{-1} \tag{6}$$

At the resonance condition:

$$W_r = \frac{1}{\sqrt{LC}} \tag{7}$$

In this context, the impedance tends to be essentially resistive, ensuring ideal impedance matching and pronounced minima in the reflection coefficient at 26 and 29 GHz. Furthermore, since the suggested structure operates as a filter antenna, the transmitted power is deliberately shared between filtering and transmission. The power conservation equation describes this behavior [15].

$$|S_{11}|^2 + |S_{21}|^2 + P_{rad} = 1 \tag{8}$$

Where *P*rad denotes the radiated power. As a result, the moderate values of S_{21} observed within the passbands are not indicative of losses but rather confirm the effective radiation mechanism of the filtenna.

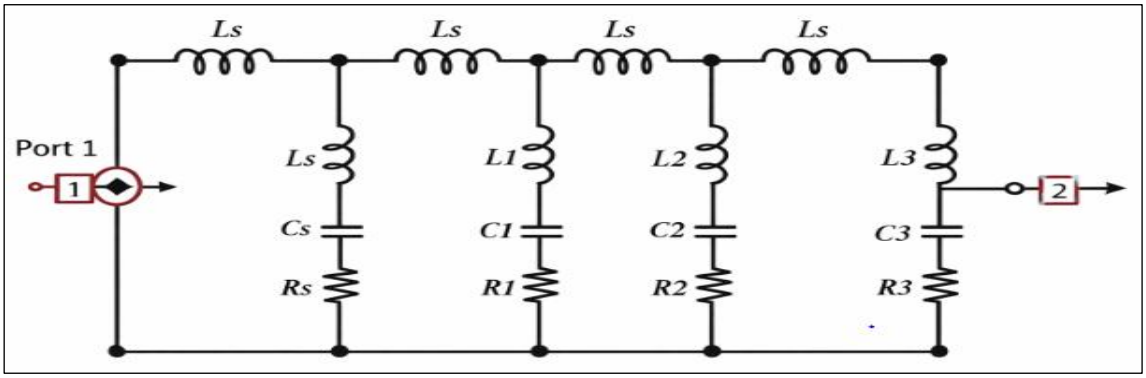


Figure 2: Equivalent RLC circuit of the microstrip filtenna.
Source: Authors, (2026).

Due to the series coupling between the three rectangular resonators, an additional reactive load is introduced, which modifies the inductance and effective capacitance of the resonant paths. This interaction excites two dominant resonant modes, corresponding to the dual-band operation observed at 26 GHz and 29 GHz. The filtenna distributed radiation mechanism is simulated by increasing radiation resistances along the resonant path, thus reflecting the gradual radiation of the structure. It should be emphasized that the proposed equivalent RLC circuit provides a qualitative and physical interpretation of the filter's behavior, rather than a precise extraction of parameters using discrete elements. However, the model adequately explains the impedance matching, mode separation, and filter-radiation integration characteristics recorded in the electromagnetic simulation results. The quality factor Q Q is a key parameter that characterizes the energy storage capability of the resonant elements in the proposed filtenna. It quantifies the ratio between the stored electromagnetic energy and the energy dissipated through radiation and losses per cycle. For an equivalent RLC resonator, the unloaded quality factor is expressed as [13]:

$$Q = \frac{1}{R}\sqrt{\frac{L}{C}} \tag{9}$$

Alternatively, the quality factor can be extracted from the frequency response using the −3 dB bandwidth method:

$$Q = \frac{f_r}{BW_{-3dB}} \tag{10}$$

BW_{-3dB} denotes the bandwidth measured at half-power points. In the proposed filtenna, the use of three coupled rectangular resonators amplifies the effective quality factor by increasing energy retention within the structure, while maintaining controlled emission. This phenomenon is manifested by distinct resonance features at 26 GHz and 29 GHz, thus confirming the filtering performance of the antenna-filter combination. The moderate Q factor, resulting from the balance between stored and emitted energy, is ideal for the operation of the filter antenna since it ensures adequate selectivity without excessively compromising the operational bandwidth.

IV. RESULTS AND DISCUSSION

IV.1 SCATTERING PARAMETERS ANALYSIS

Figure 3 illustrates the simulated reflection and transmission coefficients of the proposed filter. The reflection coefficient shows two resonances, located at 26 GHz and 29 GHz, thus confirming dual-band operation. For both frequencies, the reflection coefficient S_{11} remains below −10 dB, indicating good impedance matching in the operating bands. At 26 GHz, the minimum value of S_{11} reaches approximately −31 dB, while at 29 GHz it remains below −28 dB, indicating excellent impedance matching at both resonant frequencies. These deep reflection nulls confirm the effective excitation of the resonant modes generated by the series-coupled rectangular resonators and validate the resonance mechanism predicted by the equivalent RLC model discussed in Section 3. The transmission coefficient S_{21} reveals controlled bandwidth behavior, exhibiting moderate attenuation at the resonance frequencies. Unlike traditional filters, the proposed structure operates as a filtenna, in which a portion of the guided energy is deliberately emitted. Thus, the observed insertion levels do not indicate losses but rather demonstrate the integration of filtering and radiation mechanisms within a single structure. The transmission coefficient S_{21}shows passband responses around the two operating frequencies, with insertion levels of approximately −2 dB at 26 GHz and −2.5 dB at 29 GHz. Unlike conventional microwave filters, where low insertion loss is the primary objective, the proposed structure operates as a filtenna, in which part of the input power is intentionally radiated into free space.

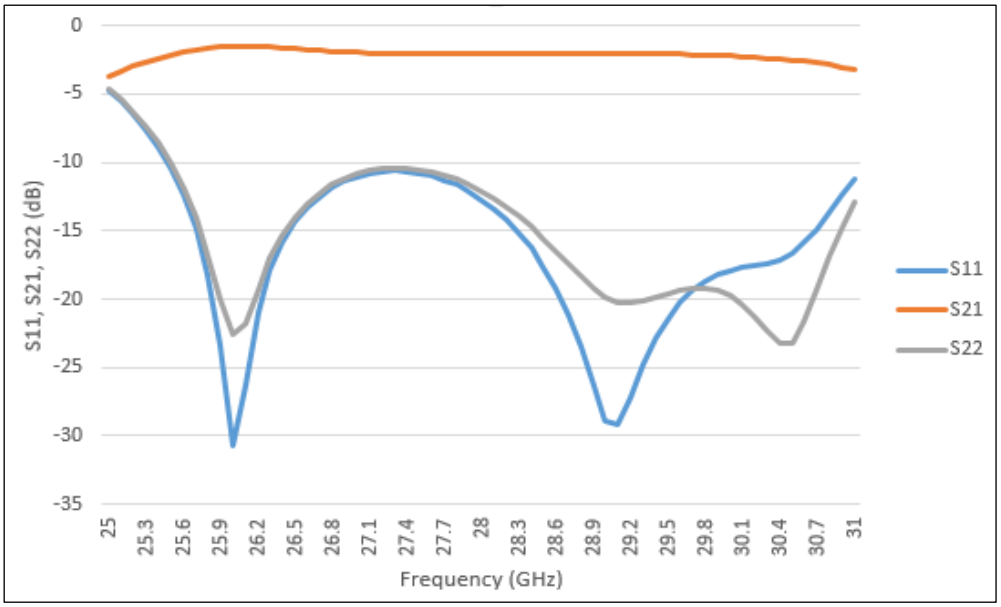


Figure 3: Reflection and transmission coefficients of the proposed filtenna.
Source: Authors, (2026).

IV.2 ELECTRIC AND MAGNETIC FIELD DISTRIBUTIONS

The electric and magnetic field distributions of the proposed filter at resonant frequencies are examined to understand the filtering and radiation processes. Figure 4 shows the electric field strength, while Figure 5 depicts the distribution of the associated magnetic field on the upper metallic layer. According to Figure 4, the maximum amplitude of the electric field reaches approximately 5.7×10^4 V/m. High electric field concentrations are observed primarily at the edges of the rectangular resonators and along the small interconnecting sections. These areas coincide with regions of intense leakage, confirming the predominantly capacitive nature of the resonators. The effect of electromagnetic coupling, which leads to the excitation of various resonance modes and the associated dual-band response, is highlighted by the uneven distribution of the field between the three resonators. Figure 5 shows that the magnetic field reaches an approximate maximum amplitude of 2.6×10^2 A/m. High magnetic field strengths are concentrated mainly on the feed line and the connections between the resonators, indicating a significant surface current. This behavior confirms the inductive quality of the narrow microstrip sections, which are of paramount importance in controlling the resonance frequencies and the intensity of the coupling between neighboring resonators. The simultaneous existence of strong electric and magnetic fields within the resonator structure illustrates efficient energy storage and controlled power transmission. Furthermore, the spatial superposition of the intense E and H fields confirms that a portion of the guided energy is indeed transformed into radiation in free space, which explains the moderate transmission rates observed in the S_{21} response. Overall, the field distributions, along with their specific amplitudes, clearly demonstrate the resonance, coupling, and radiation mechanisms that govern the operation of the suggested dual-band microstrip filtenna

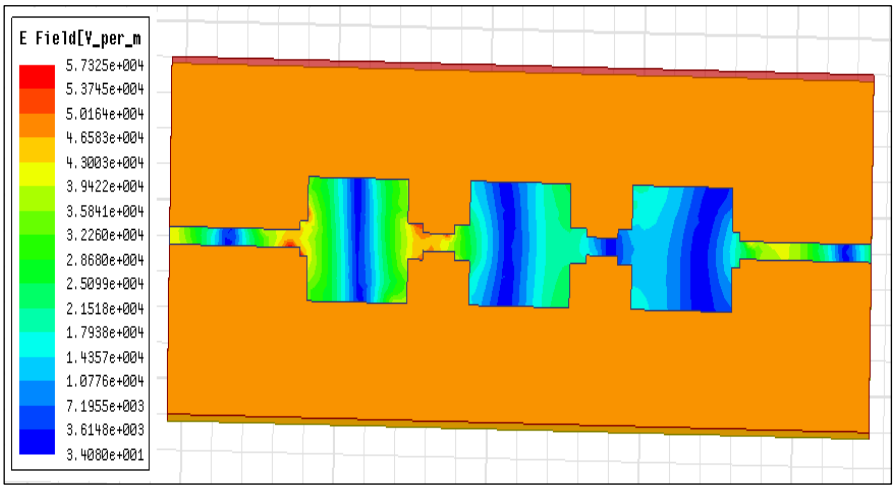


Figure 4: Electric fields of the proposed filtenna.
Source: Authors, (2026).

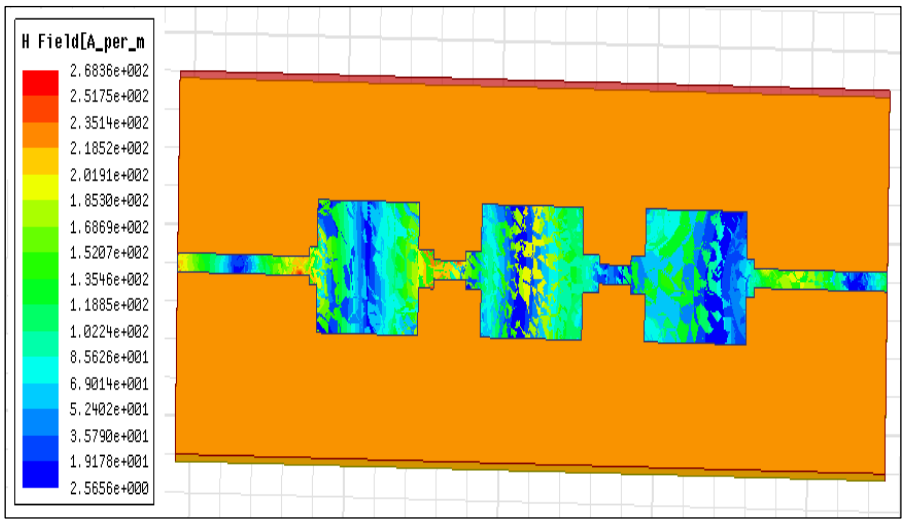


Figure 5: Magnetic fields of the proposed filtenna.
Source: Authors, (2026).

IV.3 GAIN AND RADIATION CHARACTERISTICS

The radiation performance of the proposed filtenna is evaluated in terms of realized gain and directivity at the operating frequencies of 26 GHz and 29 GHz, as illustrated in Figure 6 and Figure 7. Simulations indicate that the filter achieves a maximum gain of approximately 10.5 dBi across all frequency ranges. Over the tested frequency range, this gain remains stable, exhibiting only slight fluctuations between the two resonant frequencies, thus confirming stable radiation behavior. Despite the compact structure, this significant gain is achieved, demonstrating the effectiveness of combining filtering and radiation in a single planar topology. Directivity reaches a peak of approximately 10.8 dBi, indicating excellent focusing of the emitted power in the principal radiation direction. The small difference between the direct and achieved gain confirms minimal dissipation losses and efficient radiation, even when using an FR4 substrate at millimeter frequencies. The three-dimensional radiation patterns show a consistent main lobe, minimal back radiation, and no significant distortion across either frequency band. This behavior illustrates the scattered radiation pattern of the filtenna, where each rectangular resonator contributes to the total radiation, resulting in higher gain than a standard isolated patch antenna. Overall, the gain and radiation properties indicate that the suggested configuration operates effectively as a high-gain filtenna, providing both frequency selectivity and directional radiation. These attributes make this design a suitable choice for millimeter-wave 5G applications, where compactness, high gain, and integrated filtering are critical requirements. Therefore, the efficiency was calculated using the following formulas [12].

$$G_{lin} = 10^{G(dB)/10} \tag{11}$$

$$D_{lin} = 10^{D(dB)/10} \tag{12}$$

G_{lin} and D_{lin} are respectively linear gain and linear directivity

$$G_{lin} = 10^{\frac{G(dB)}{10}} = 10^{\frac{10.5}{10}} = 11.22$$

$$D_{lin} = 10^{D(dB)/10} = 10^{10.8/10} = 12.02$$

Then we have the efficiency:

$$\eta = \frac{G_{lin}}{D_{lin}} \tag{13}$$

$$\eta = \frac{11.22}{12.02} = 0.93 = 93\%$$

Based on the simulated gain and directivity values, the radiation efficiency is estimated to be approximately 93% confirming that most of the input power is effectively converted into radiated energy.

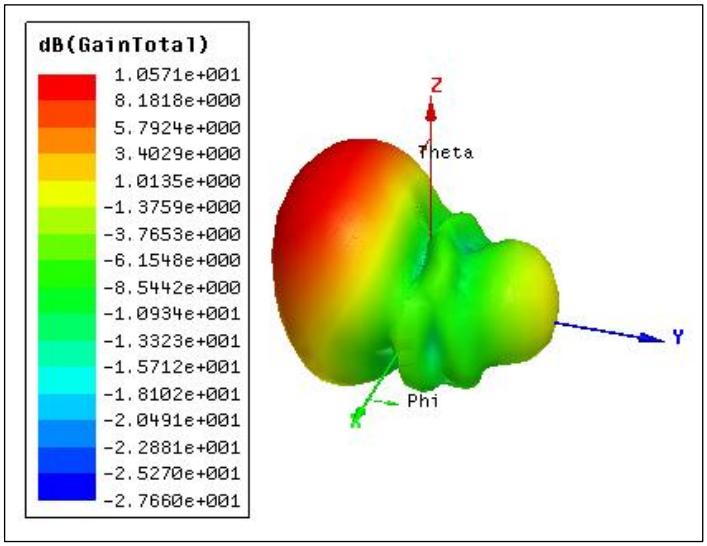


Figure 6: Gain of the proposed filtenna.
Source: Authors, (2026).

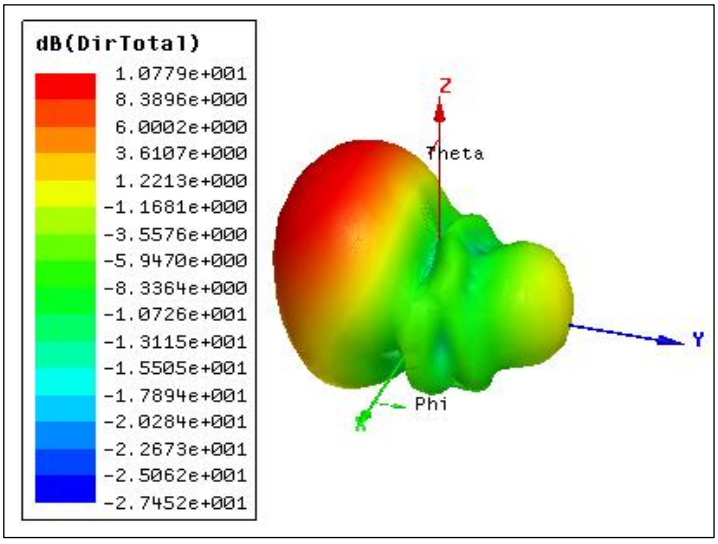


Figure 7: Directivity of the proposed filtenna.
Source: Authors, (2026).

The three-dimensional radiation patterns exhibit a stable main lobe with low back radiation and consistent beam shape across both operating bands. The distributed radiation mechanism provided by the series-coupled rectangular resonators contributes to the enhanced gain and high efficiency. Overall, the radiation characteristics demonstrate that the proposed design operates as a high-efficiency, high-gain filtenna suitable for 5G millimeter-wave applications**.**

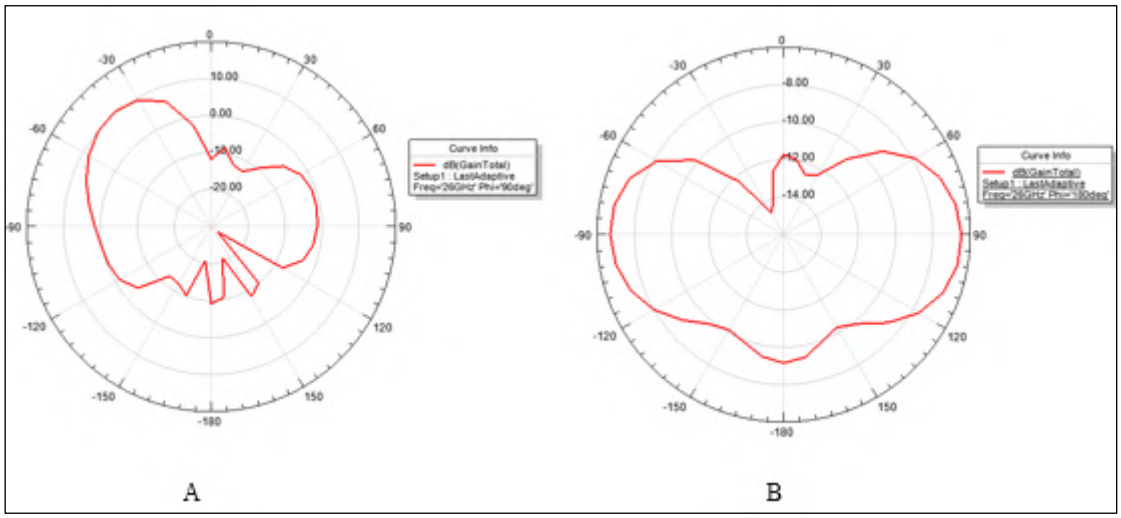


Figure 8: Radiation pattern A (Phi=90 degrees) and B (Phi-180 degrees).
Source: Authors, (2026).

Table 2: Comparison with other works.

Work	Frequency (GHz)	Susbtrate	Size (mm x mm)	Peak gain (dB)	Efficiency (%)
[3]	15 – 18	FR4	90 x 90	4.87	NA
[5]	1.9 – 3.56	Rogers TMM4	25 x 35	2.26	60
[6]	26 – 29	FR4	60 x 70	4.5	N/A
[10]	12	FR4	50 x 40	4.8	67
[12]	3.6	FR4	26 x 60	2.5	
This work	26 - 29	FR4	23 x 10	10.58	93

Source: Authors, (2026).

V. CONCLUSION

This article discusses the design and analysis of a compact dual-band microstrip filtenna, based on series-coupled rectangular resonators, for 5G millimeter-wave applications. The proposed structure incorporates filtering and radiation functions in a separate planar topology, eliminating the need for external RF filters and reducing the overall device complexity. The filtenna operates 26 GHz and 29 GHz, ensuring effective impedance matching with a reflection coefficient below -30 dB and controlled transmission properties. The physical behavior of the structure was clarified using an equivalent RLC resonator model, which accurately depicts the dual-band response derived from capacitive coupling and inductive current paths between neighboring. Compared with recently reported filtenna designs, the proposed structure offers higher gain, superior efficiency, and a more compact footprint, making it a promising candidate for 5G millimeter-wave front-end modules. Future work will focus on experimental validation and extension toward array-based filtenna configurations for beam-steering applications.

VI. AUTHOR'S CONTRIBUTION

Conceptualization: Touko Tcheutou Stephane Borel.
Methodology: Touko Tcheutou Stephane Borel, and Rashmi Priyadarshini.
Investigation: Touko Tcheutou Stephane Borel, and Rashmi Priyadarshini.
Discussion of results: Touko Tcheutou Stephane Borel, and Rashmi Priyadarshini.
Writing – Original Draft: Touko Tcheutou Stephane Borel, and Rashmi Priyadarshini.
Writing – Review and Editing: Touko Tcheutou Stephane Borel, and Rashmi Priyadarshini.
Resources: Touko Tcheutou Stephane Borel, and Rashmi Priyadarshini.
Supervision: Touko Tcheutou Stephane Borel, and Rashmi Priyadarshini.
Approval of the final text: Touko Tcheutou Stephane Borel, and Rashmi Priyadarshini.

VII. REFERENCES

[1] J. Li, L. Xiang, Y. Shi, X. Y. Wu, and W. Hong, "Single-Layer Millimeter-Wave Filtenna With Quasi-Elliptic Gain Response Under Dual-Mode Resonance," IEEE Antennas Wireless Propag. Lett., vol. 23, no. 9, pp. 2797–2801, Sep. 2024.

[2] B. Rezaee and W. Bösch, "Dual-Band Filtenna With High Selectivity for 5G Millimeter-Wave Applications," in Proc. 2024 54th European Microwave Conf. (EuMC), Paris, France, Sep. 2024, pp. 884–887, doi:10.23919/EuMC61614.2024.10732597.

[3] S. R. Mishra, S. K. L. and N. P. Pathak, "Split Ring Resonator Inspired Microstrip Filtenna for Ku-Band Application," J. Eng. Sci. Technol., vol. 50, pp. 391–403, 2017.

[4] R. H. Elabd and A. H. Hussein, "Efficient Design of a Wideband Tunable Microstrip Filtenna for Spectrum Sensing in Cognitive Radio Systems," EURASIP J. Wireless Commun. Netw., vol. 2023, article no. 109, 2023.

[5] A. O. Nwajana and K. S. K. Yeo, "Substrate-Integrated Waveguide (SIW) Cavity-Coupled Patch Filtenna," IEEE Access, vol. 13, pp. 37865–37871, 2025.

[6] Y. X. Huang et al., "Substrate-Integrated Waveguide Filtenna With Two Controllable Radiation Nulls," IEEE Access, vol. 8, pp. 120019–120024, 2020.

[7]NW. Wang, H. Jin, W. Yu, L. Liu, K. S. Chin, and G. Q. Luo, "Millimeter-Wave Compact Wideband High-Gain 8×8 CP Filtenna Array With Densified SIW Feeding Network," IEEE Trans. Antennas Propag., vol. 72, no. 6, pp. 5283–5288, 2024.

[8] K. Z. Hu et al., "A Low-Profile Single-Layer Differentially-Fed Circularly Polarized Filtenna With Intrinsic Common-Mode Rejection," IEEE Antennas Wireless Propag. Lett., 2024.

[9] Y. X. Yan, Y. X. Huang, S. C. Tang, and J. X. Chen, "Low-Sidelobe Microstrip Patch Filtenna Array Fed by SIW Cavity," IEEE Antennas Wireless Propag. Lett., vol. 21, no. 7, pp. 1457–1461, 2022.

[10] C. Wang, X. Wang, H. Liu, Z. Chen, and Z. Han, "Substrate Integrated Waveguide Filtenna With Two Controllable Radiation Nulls," IEEE Access, vol. 8, 2020.

[11] Z. Wang and Y. Dong, "Development of Low-Profile Filtering Antennas With Dual-Mode Cavities," IEEE Open J. Antennas Propag., vol. 1, pp. 159–164, 2020.

[12] A. Chandelkar, A. Kumar, P. Jadhav, A. A. Althuwayb, and K. Aliqab, "Semi Circular SIW Cavity Coupled Patch Filtenna," IEEE Access, vol. 13, pp. 37865–37871, 2025.

[13] Q. Liu et al., "A Triple-Mode Wideband Filtering Antenna With Planar Configuration by Combining SIW Cavity and Half-Mode Patch Resonators," IEEE Antennas Wireless Propag. Lett., vol. 24, no. 6, pp. 1512–1516, 2025.

[14] N. Yan, H. Zhou, and K. Ma, "A Filtering Antenna With Slots and Stacked Patch Based on SISL for 5G Communications," Electronics, vol. 12, no. 6, 2023.

[15] B. Elabd, "Compact Dual-Port MIMO Filtenna-Based DMS With High Isolation for C-Band and X-Band Applications," EURASIP J. Wireless Commun. Netw., vol. 2023, article no. 110, 2023

Journal of Engineering and Technology for Industrial Applications

ITEGAM-JETIA

Manaus, v.12 n.60, p.78-84, July/August, 2026.
DOI: https://doi.org/10.5935/jetia.v12i60.3522

ISSN ONLINE: 2447-0228

RESEARCH ARTICLE OPEN ACCESS

ENERGY AUDIT APPROACHES AND OUTCOMES FOR ENHANCING ENERGY EFFICIENCY IN SMALL & MEDIUM ENTERPRISES

Ankit B. Lehru*[1] and Dharmesh J. Pandya[2]

[1, 2]Department of Electrical Engineering, Atmiya University, Rajkot, India.

[1]https://orcid.org/0009-0009-9215-1693, [2]http://orcid.org/0000-0002-7146-8247

Email:*ankitlehru@gmail.com, djpandya@gmail.com

ARTICLE INFO

Article History
Received: February 3, 2026
Reviewed: June 4, 2026
Accepted: July 4, 2026
Published: July 31, 2026

Keywords:
Energy audit;
energy conservation measure;
energy efficiency;
small and medium enterprise;
power quality;
techno-economic analysis

ABSTRACT

This structured narrative review evaluates energy-audit approaches and reported outcomes relevant to small and medium enterprises (SMEs), with emphasis on industrial applications and resource-constrained implementation. The evidence base combines Indian case studies with international multi-enterprise evaluations and current audit guidance. Studies were compared according to audit scope, measurement practices, significant energy uses, recommended energy-conservation measures, economic indicators, implementation status, and reported barriers. Across the six Indian studies, power-factor or broader power-quality assessment appeared in all cases, motor or fan efficiency in five, and lighting-system improvement in three. Frequently recommended measures included efficient motors and drives, LED lighting, capacitor or automatic power-factor-correction systems, compressed-air leak control, load balancing, harmonic mitigation, operating-schedule optimization, and improved monitoring. One cable-manufacturing case reported an investment of INR 0.675 million with annual savings of INR 1.191 million and a payback of approximately 6.4 months; another medium-scale industrial audit reported a 25-month payback. Programme-level evidence from Sweden reported net annual savings of 340 GWh, equivalent to about 6% of participating firms' energy use. The synthesis shows that audits are most effective when recommendations are ranked by verified baseline data, technical feasibility, financial return, and implementation risk, followed by measurement and verification. A practical SME-focused audit framework is proposed to convert diagnostic findings into implementable and verifiable actions.

Copyright ©2026 by authors and Galileo Institute of Technology and Education of the Amazon (ITEGAM). This work is licensed under the Creative Commons Attribution International License (CC BY 4.0).

I. INTRODUCTION

Energy is a production input whose cost and reliability directly influence industrial competitiveness. For small and medium enterprises (SMEs), the effect is particularly important because energy expenses must be managed alongside constrained capital, limited specialist staff, variable production schedules, and strong pressure to maintain product quality. India's installed electricity-generation capacity reached 441.97 GW by 31 March 2024, illustrating the scale of the national power system and the parallel need to manage demand efficiently [1]. The Energy Conservation Act and its subsequent amendment provide the statutory basis for energy-efficiency measures, institutional responsibilities, and energy-audit activities in India [2]. The Bureau of Energy Efficiency (BEE) complements this framework through guidance on energy management, electrical utilities, thermal utilities, and performance assessment [3]. An energy audit is not merely a list of high-consuming equipment. It is a structured investigation that establishes where, when, and why energy is used; quantifies avoidable losses; and converts observations into technically and financially evaluated energy-performance improvement actions. ISO 50002-1:2025 defines general requirements and guidance for conducting energy audits and emphasizes a transparent process that can be applied to buildings, processes, systems, and transport [4]. For SMEs, this structure must be adapted to the available data and resources without compromising measurement quality. A low-cost audit that relies only on utility bills may identify demand trends, whereas a detailed audit may require power-quality logging, motor loading assessment, illumination measurements, thermal imaging, compressed-air testing, combustion analysis, and process-specific energy balances.

The literature demonstrates a recurring gap between identification and implementation. Audits commonly reveal technically attractive opportunities, yet recommendations may remain unimplemented because of capital limitations, uncertainty regarding production disruption, incomplete baseline data, insufficient in-house expertise, or a preference for investments directly associated with production expansion. Therefore, the value of an audit depends on the credibility of its calculations, the clarity of its prioritization, and the presence of a follow-up mechanism. Measures with short simple payback can provide early savings, but longer-life measures may require life-cycle costing, risk assessment, and access to appropriate finance. Earlier versions of the present review described audit activities and individual case studies but did not systematically synthesize the reported outcomes. The present study addresses that limitation by organizing the evidence around four questions: which audit domains are repeatedly examined; which energy-conservation measures (ECMs) are most frequently recommended; what economic and implementation outcomes are reported; and what factors determine whether recommendations progress from an audit report to verified savings. The study consequently treats the published evidence as the result set of a structured narrative review rather than presenting unmeasured site-level savings as original experimental findings.

II. ENERGY AUDIT APPROACHES AND RELATED WORK

A. Levels of Energy Audit

Energy audits can be organized into three practical levels. A walk-through audit uses utility bills, operating records, equipment nameplates, interviews, and visual inspection to identify abnormal practices and immediate low-cost opportunities. A targeted audit examines a selected system, such as motors, compressed air, lighting, boilers, furnaces, refrigeration, or power quality, using short-term measurements and system-specific calculations. A detailed audit establishes an energy balance for the defined boundary, normalizes consumption against production or weather variables, evaluates multiple ECMs, and provides investment-grade technical and financial analysis. These levels are complementary. A walk-through audit should screen and prioritize; a targeted audit should resolve a defined uncertainty; and a detailed audit should support a capital decision and subsequent measurement and verification.

B. Principal Audit Domains

For electrically intensive SMEs, the principal domains are utility-bill analysis, contracted demand, load factor, power factor, voltage and current unbalance, harmonics, motor loading, pumping and fan systems, lighting, compressed air, refrigeration, and on-site generation. Thermal SMEs additionally require fuel accounting, combustion efficiency, steam-system assessment, insulation inspection, heat recovery evaluation, and process-temperature profiling. Rooftop photovoltaic systems introduce further requirements, including comparison of expected and measured yield, inverter performance, clipping, downtime, phase allocation, voltage variation, and harmonics. The audit boundary must distinguish production energy from common utilities so that recommendations are linked to controllable causes rather than to total consumption alone.

C. Evidence from Industrial Case Studies

Indian case studies have reported opportunities involving efficient motors, power-factor correction, LED lighting, improved fans, load balancing, harmonic mitigation, compressed-air leak reduction, operating-schedule changes, and monitoring improvements [5-10]. The reviewed cable-manufacturing study used ETAP to analyse the distribution system and reported both projected and implemented outcomes [7]. Larger international evaluations broaden the evidence beyond individual plants. Fresner et al. analysed lessons from 280 SME energy audits across Europe [11], while Viesi et al. assessed energy efficiency and sustainability across approximately 500 SMEs in Central Europe [12]. Paramonova and Thollander evaluated a Swedish audit programme and reported programme-level net savings [13]. Firm-level survey evidence further indicates that energy audits are positively associated with subsequent investment in efficiency measures [14]. Recent frameworks emphasize that the audit report must be understandable to non-specialist decision makers and must link each recommendation to the responsible system, baseline, expected saving, investment, operational risk, and verification method [15]. Research on barriers shows that economic constraints, limited awareness, behavioural factors, lack of time, and insufficient technical support influence decisions at different stages of ECM adoption [16]. Policy reviews therefore recommend combining audit support with financing, technical assistance, training, standardized tools, and implementation follow-up rather than treating the audit as a stand-alone intervention [17-19].

III. OBJECTIVES

The study aims to strengthen the technical and analytical basis for energy auditing in SMEs through the following objectives:

1. **Evidence synthesis:** Compare the scope, measurements, recommendations, and reported outcomes of selected SME and industrial energy-audit studies.
2. **Recurring opportunity identification:** Determine which electrical, thermal, operational, and management-related ECMs appear most consistently across the reviewed evidence.
3. **Outcome interpretation:** Evaluate reported savings, investment, payback, and implementation information while distinguishing projected savings from verified outcomes.
4. **Framework development:** Propose a practical audit workflow that an SME can use to progress from preliminary screening to implementation and measurement and verification.

IV. METHODOLOGY

A. Review Design and Evidence Base

A structured narrative-review design was used because the available studies differ substantially in industrial sector, audit boundary, instrumentation, reporting units, tariff assumptions, and follow-up duration.

The empirical evidence base comprised six Indian case studies already central to this review [5-10], three international multi-enterprise or programme evaluations [11-14], and one recent case-study-based framework [15]. Standards, BEE guidance, and policy reviews were used to interpret audit quality and implementation conditions [3], [4], [17-19]. The review was not designed as a statistical meta-analysis; accordingly, no pooled percentage saving was calculated. Studies were included when they explicitly described at least one of the following: energy-data collection, field measurement, equipment or utility-system assessment, identification of ECMs, economic evaluation, implementation status, or barriers affecting adoption. Sources that only discussed general sustainability without an identifiable audit process were not used as primary evidence in the result matrix. The publication years of the empirical and framework studies ranged from 2014 to 2024, enabling comparison of conventional audit practices with more recent implementation-oriented approaches.

B. Data Extraction and Thematic Coding

For each study, information was extracted under six headings: (1) industrial or organizational setting; (2) audit level and system boundary; (3) data and instruments used; (4) major inefficiencies identified; (5) recommended ECMs; and (6) reported technical, economic, or implementation outcome. The Indian studies were additionally coded for the presence of power-factor or power-quality analysis, motor or fan assessment, lighting assessment, compressed-air analysis, thermal assessment, operational scheduling, and photovoltaic analysis. These counts describe the reviewed sample only and are not estimates of prevalence across all SMEs.

C. Audit Calculations and Decision Metrics

The technical evaluation of an ECM begins with a baseline that represents normal operation. For production-dependent facilities, specific energy consumption (SEC) is calculated as energy use divided by production output. The expected annual energy saving is the difference between baseline and post-measure energy use after normalization for production, operating hours, weather, or other relevant variables. Annual cost saving should be calculated from the applicable tariff components, including energy charge, demand charge, power-factor incentive or penalty, time-of-day charge, fuel cost, and maintenance impact. Simple payback is calculated as initial investment divided by annual net monetary saving. Where equipment life, financing cost, or maintenance differences are significant, net present value, internal rate of return, and discounted payback provide a more appropriate decision basis than simple payback alone. Power-quality recommendations require particular care because the financial benefit may arise through several mechanisms: reduction of demand current and distribution losses, avoidance of utility penalties, improved voltage performance, reduced equipment heating, and prevention of production interruption. Harmonic filters or automatic power-factor-correction panels should therefore be sized using measured load profiles and harmonic spectra rather than only a single instantaneous reading. Similarly, motor replacement should be evaluated from measured loading, duty cycle, efficiency class, rewinding history, and remaining service life; nameplate power is not a substitute for actual input power.

D. Measurement and Verification

Projected savings become auditable outcomes only after implementation and verification. The proposed approach records pre-implementation operating conditions, identifies the independent variables that influence energy use, documents the commissioning status, and compares post-implementation performance with an adjusted baseline. Suitable indicators include monthly SEC, maximum demand, load factor, average power factor, total harmonic distortion, motor input power, compressor specific power, lighting power density, boiler efficiency, photovoltaic performance ratio, and avoided cost. Short-term measurements are appropriate for stable loads; variable production processes require longer logging or repeated measurements across representative operating conditions.

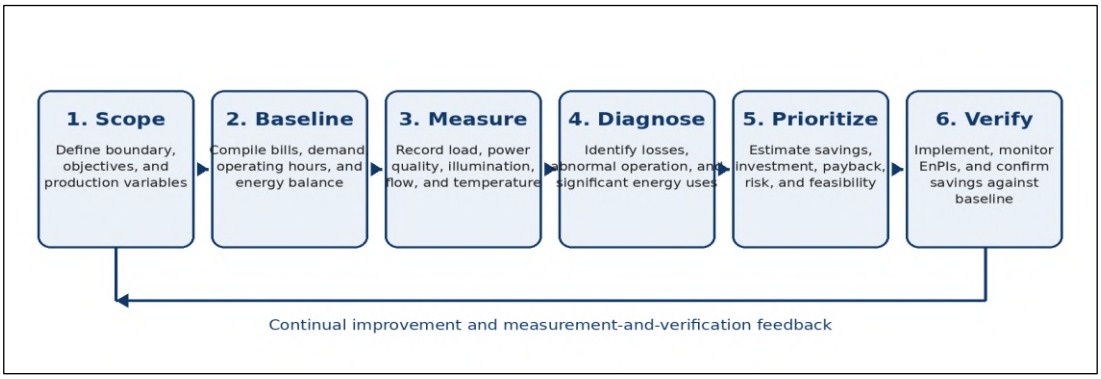


Figure 1: Evidence-informed energy-audit and implementation workflow.
Source: Authors (2026).

V. RESULTS

A. Characteristics of the Reviewed Evidence

Table 1 summarizes the empirical evidence used in the synthesis. The studies range from single-facility audits to programmes involving hundreds of SMEs. This heterogeneity is analytically useful because it shows both the plant-level diagnostic detail and the programme-level implementation effect. However, it also limits direct numerical comparison. Most Indian studies concentrate on electrical systems, whereas the international studies place greater emphasis on programme design, adoption behaviour, and standardized implementation support.

Table 1: Characteristics and reported outcomes of the reviewed energy-audit evidence.

Ref.	Setting/sample	Audit focus	Reported result or implication
[5]	Industrial case, India	On-site measurements; motors, power factor, and electrical losses	Efficient motors, capacitor correction, maintenance, and behavioural actions; qualitative economic and environmental benefits.
[6]	Steel plant, India	Bills, lighting, motors, fans, and power factor	LEDs, efficient motors/fans, maintenance, and power-factor correction were recommended; no verified post-implementation saving reported.
[7]	Cable manufacturing, India	ETAP model; load balance, power factor, motors, and operating schedule	INR 0.675 million investment; INR 1.191 million annual saving; reported payback 6.4 months; approximately 75% of expected outcomes implemented.
[8]	Textile sector, India	Bills, power factor, lighting, motors, compressed air, and rooftop PV	Multiple cross-utility opportunities identified, including LEDs, leak reduction, power-factor correction, and motor-efficiency improvement.
[9]	Medium-scale industry, India	Pre-audit, field audit, and post-audit planning	Lighting/fan replacement and capacitor-bank installation; reported combined payback of 25 months.
[10]	Steel industry and institute	Power-quality analyser; harmonics, power factor, and unbalance	Active filtering, monitoring, and correction measures proposed to reduce losses and improve power quality.
[11]	280 SME audits, Europe	Cross-sector audit experience	Demonstrated the value of systematic, practical audits and highlighted recurring challenges in converting identified opportunities into action.
[12]	Approximately 500 SMEs, Central Europe	Energy-efficiency and sustainability assessment	Provided a large multi-sector evidence base for benchmarking and sector-sensitive assessment.
[13]	713 firms in Swedish audit programme	Subsidized audits and programme evaluation	Net annual saving of 340 GWh, corresponding to approximately 6% of participating firms' energy use; information barriers were reduced.
[14]	EU firm-level survey evidence	Audit participation and investment decisions	Energy audits were positively associated with firms' adoption of energy-efficiency investments.
[15]	Non-energy-intensive manufacturing SMEs	Case-study-based implementation framework	Emphasized an action-oriented process linking data quality, opportunity evaluation, management engagement, and follow-up.

Source: Authors, (2026).

B. Recurring Technical Findings

Coding of the six Indian studies [5-10] showed that power factor or broader power-quality assessment was present in all six studies. Motor or fan efficiency appeared in five studies, and lighting-system improvement appeared in three. Load balancing, harmonic mitigation, operating-schedule changes, and improved monitoring were also recurrent. Compressed-air analysis and rooftop-photovoltaic assessment were each explicitly included in one of the six studies. These frequencies indicate the dominant concerns of the reviewed sample, not the distribution of energy use in every SME. The predominance of power-factor and power-quality measures is technically understandable. These parameters can be measured with portable instruments, are directly connected to electrical distribution performance, and may affect both utility charges and equipment stress. Nevertheless, a high power factor does not by itself prove efficient energy use. A facility may have acceptable power factor while operating oversized motors, throttled pumps, leaking compressed-air systems, or poorly controlled thermal processes. Therefore, power-quality analysis should be integrated with end-use and process analysis rather than treated as the complete audit. Motor and fan recommendations were the second most common category. The saving mechanism may involve replacement with a higher-efficiency motor, correct sizing, variable-speed control, improved transmission, reduced pressure or flow set points, or maintenance of bearings and alignment. The appropriate option depends on the load characteristic. Variable-speed drives are most effective where speed can be reduced for substantial operating periods; they are not automatically justified for constant-load applications. Lighting upgrades are usually easier to implement, but illumination level, glare, colour rendering, operating hours, and control strategy must be verified so that energy reduction does not compromise the work environment.

Table 2: Measurement-to-verification structure for major SME audit domains.

Audit domain	Key indicators	Typical instruments/data	Representative ECMs	Verification metric
Utility and demand	kWh, kVA, maximum demand, load factor, tariff	Bills, interval meter, production log	Demand control, schedule optimization, tariff correction	Monthly cost and normalized SEC
Power quality	PF, THD, unbalance, voltage variation	Three-phase power-quality analyser	APFC, load balancing, filters, conductor correction	PF, THD, current, losses, penalty avoided
Motors/pumps/fans	Loading, efficiency, flow, pressure, duty cycle	Power analyser, tachometer, flow/pressure data	Right-sizing, efficient motor, VFD, system optimization	kW, kWh/unit output, flow-specific energy
Lighting	Illuminance, installed power, hours	Lux meter, inventory, occupancy schedule	LEDs, zoning, daylight/occupancy controls	kWh, lux compliance, demand reduction
Compressed air	Pressure, flow, leakage, specific power	Ultrasonic detector, pressure logger, compressor data	Leak repair, pressure reset, control optimization	kW per flow, off-load hours, leakage rate
Thermal systems	Fuel rate, temperature, O2/CO, heat loss	Flue-gas analyser, thermal imager, temperature sensors	Combustion tuning, insulation, heat recovery	Fuel/unit output, efficiency, stack loss
Rooftop PV	Yield, availability, clipping, voltage, harmonics	Inverter logs, irradiance and energy data	Cleaning, string repair, inverter/phase optimization	Performance ratio, specific yield, downtime

Source: Authors, (2026).

C. Economic and Implementation Outcomes

Only a limited subset of the reviewed Indian studies reported sufficiently explicit economic outcomes. The cable-manufacturing study [7] reported an investment of INR 0.675 million and annual savings of INR 1.191 million.

Direct division of investment by annual savings gives a simple payback of approximately 6.8 months, which is close to the reported 6.4 months and may differ because of rounding or additional cash-flow assumptions. The medium-scale industrial study [9] reported a payback of 25 months. These results demonstrate that attractive opportunities may exist, but they cannot be generalized into a universal SME payback because the underlying tariffs, operating hours, production levels, equipment condition, and project scope differ. The statement that 75% of the expected outcomes were achieved in the cable-manufacturing case is especially important [7]. It reveals an implementation gap between technically identified potential and realized performance. The gap may arise from partial implementation, changed operating conditions, delayed procurement, incomplete commissioning, or optimistic baseline assumptions. Audit reports should therefore separate four quantities: identified potential, approved projects, implemented projects, and verified savings. Combining these stages into a single "saving potential" figure can overstate actual performance. The Swedish programme evaluation provides a broader outcome measure: 340 GWh/year of net annual savings, equivalent to about 6% of the participating firms' energy use [13]. This programme-level result indicates that standardized and supported audit schemes can produce material savings across a large SME population. Survey evidence also suggests that audits increase the likelihood of energy-efficiency investment [14]. However, the audit itself is an informational intervention; financing, managerial commitment, competent suppliers, and follow-up remain necessary for implementation.

D. Barriers Identified Across the Evidence

The recurring barriers can be grouped into financial, informational, organizational, and technical categories. Financial barriers include limited internal capital, short required payback periods, high transaction cost relative to project size, and uncertainty about future production. Informational barriers include incomplete submetering, limited knowledge of efficient technologies, distrust of vendor claims, and uncertainty about achievable savings. Organizational barriers include lack of a designated energy manager, competing production priorities, limited time, and weak accountability for follow-up. Technical barriers include variable operating conditions, legacy equipment, poor documentation, and the risk that an intervention may affect product quality or production continuity [16-19]. The reviewed evidence indicates that a credible audit can reduce informational barriers by converting general concerns into measured and ranked actions. It cannot independently remove capital or organizational barriers. Consequently, recommendations should be grouped into no-cost or low-cost actions, short-payback retrofits, and strategic capital projects. This grouping allows early savings to build confidence while larger projects undergo engineering and financial review.

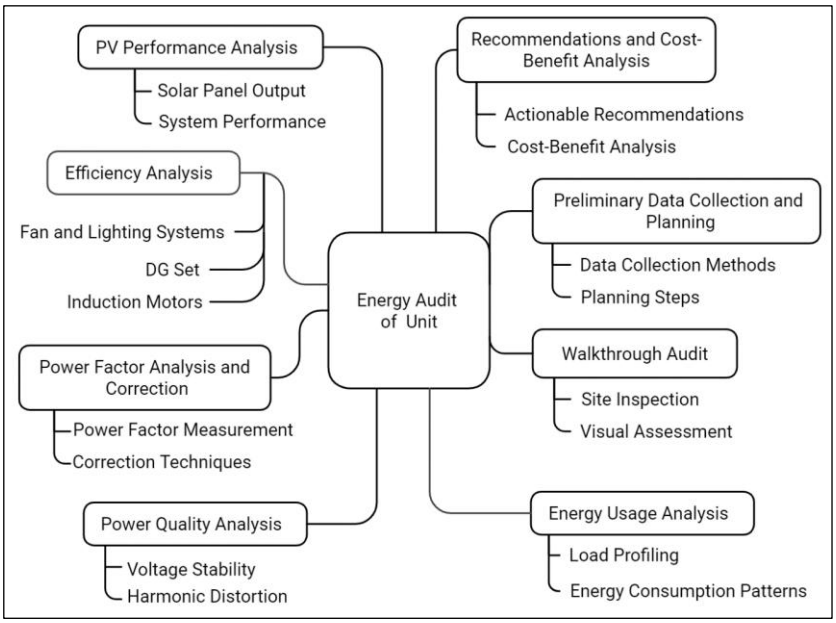


Figure 2: SME-focused energy-audit assessment domains.
Source: Authors (2026).

VI. DISCUSSION

A. Interpretation of the Dominant Audit Measures

The result synthesis shows that electrical utility measures dominate the reviewed Indian cases. Their popularity is partly attributable to measurement accessibility and comparatively low implementation complexity. Power-factor correction, lighting replacement, load balancing, and selected motor measures can often be evaluated without modifying the core production process. This makes them suitable entry points for SMEs. Nevertheless, an audit restricted to these measures may overlook larger process opportunities. The audit should therefore first establish the energy balance and significant energy uses, and only then select the depth of measurement for each system. A further distinction is required between energy saving and cost saving. Power-factor correction may reduce current and avoid penalties without producing a proportional reduction in billed kWh. Load shifting may reduce demand or time-of-day charges while leaving total energy use unchanged. Rooftop PV reduces purchased electricity but is not an efficiency measure unless accompanied by improvements in energy performance. Reporting these effects separately improves transparency and prevents double counting.

B. Quality of Baseline and Financial Analysis

The reliability of an audit outcome is determined by its baseline. A comparison between two monthly bills is inadequate when production, weather, working days, or product mix changed materially. SMEs with variable production should use SEC and, where possible, regression or matched-period analysis. The uncertainty of key assumptions should be reported. For example, a motor-replacement calculation should state loading, efficiency values, annual operating hours, electricity tariff, and whether avoided maintenance or downtime is included. A compressed-air leak calculation should state pressure, leak test method, compressor specific power, and operating schedule. Simple payback remains useful for rapid screening but can bias decisions against long-life measures. A project with a three-year payback and a fifteen-year life may have greater life-cycle value than a one-year project with a two-year life. Conversely, a short calculated payback may be unreliable if it assumes constant production or ignores commissioning and maintenance costs. A recommended SME decision table should therefore include investment, annual energy saving, annual cost saving, simple payback, expected life, implementation downtime, technical risk, and verification plan.

C. From Audit Report to Implementation

The reviewed implementation evidence supports a staged portfolio approach. Stage 1 should include housekeeping, control settings, leak repair, maintenance, and operator practices that require little capital. Stage 2 should include standard retrofits such as LEDs, capacitor banks, efficient motors, variable-speed drives, insulation, and monitoring. Stage 3 should include process redesign, heat recovery, major utility replacement, or renewable-energy integration. Each action should have a named owner, target date, budget status, and post-implementation indicator. Without ownership and follow-up, the audit remains a diagnostic document rather than an energy-management instrument. Cluster-based implementation is particularly relevant to Indian SMEs. Enterprises within a common industrial cluster often use similar motors, furnaces, compressors, pumps, and production practices. Common audit templates, benchmark ranges, pooled training, aggregated procurement, and shared technical support can lower transaction costs. Public or utility-supported programmes can further improve adoption through partial audit subsidies, credit guarantees, performance-linked finance, or approved technology-provider networks. International policy reviews similarly conclude that integrated packages are more effective than isolated audit obligations [17-19].

D. Appropriate Use of Software and Digital Tools

Software such as ETAP, DIALux, MATLAB, eQUEST, and specialized energy-management platforms can improve analysis, but model output is only as reliable as the input data. ETAP can assess load flow, short circuit, harmonics, and correction alternatives; DIALux can support lighting design; simulation tools can evaluate control and process scenarios; and interval-data platforms can identify abnormal load patterns. These tools should be used to test measured conditions and alternatives, not to replace site inspection or calibration. For SMEs with limited submetering, a phased monitoring plan may be more valuable than a complex model created from assumed loads.

E. Practical Framework for SMEs

The combined evidence supports a six-stage framework. First, define the audit boundary, objectives, production variables, and data responsibilities. Second, establish the baseline from bills, interval data, production records, and an energy balance. Third, measure significant energy uses using calibrated instruments under representative operating conditions. Fourth, diagnose losses and identify their operational causes rather than only their symptoms. Fifth, prioritize ECMs using technical feasibility, verified saving, investment, payback, risk, and production impact. Sixth, implement and verify results through defined energy-performance indicators. The feedback loop in Figure 1 converts a one-time audit into continual improvement.

F. Limitations

This study is a structured narrative review and not a systematic review or meta-analysis. The evidence is heterogeneous, and several case studies do not report complete baseline, uncertainty, implementation, or post-project verification data. The numerical results should therefore be interpreted as study-specific outcomes. The paper does not present a new field audit of a named SME, and it does not claim that the reported savings percentages or payback periods apply to all industrial sectors. Future work should use a standardized reporting template and should publish both projected and verified savings, production-normalized baselines, implementation cost, project life, and uncertainty.

VII. CONCLUSION

The expanded review demonstrates that energy audits can provide a practical route to lower energy cost and improve energy performance in SMEs when they progress beyond descriptive inspection. Across the reviewed Indian studies, power factor and power quality were the most consistently assessed domains, followed by motors and fans and then lighting. Reported measures included efficient equipment, power-factor correction, harmonic mitigation, load balancing, compressed-air leak control, operating-schedule optimization, and improved monitoring. The available economic results ranged from a reported 6.4-month payback in cable manufacturing to 25 months in a medium-scale industry, while a Swedish audit programme reported net savings equivalent to approximately 6% of participating firms' energy use. The evidence also shows that identified potential is not equivalent to achieved saving. Audit quality depends on representative measurement, normalized baselines, transparent financial assumptions, prioritized actions, and a defined verification method. For resource-constrained SMEs, the most effective strategy is to implement a portfolio beginning with no-cost and low-cost actions, followed by standard retrofits and then strategic process investments. Cluster-based technical assistance and financing can reduce the transaction and capability barriers that frequently prevent implementation.

The proposed six-stage framework - scope, baseline, measurement, diagnosis, prioritization, and verification - provides a defensible structure for future audits and for reporting results in a manner that is technically credible and useful to decision makers.

VIII. AUTHOR'S CONTRIBUTION

Conceptualization: Ankit B. Lehru and Dharmesh J. Pandya.
Methodology: Ankit B. Lehru and Dharmesh J. Pandya.
Investigation and evidence extraction: Ankit B. Lehru.
Analysis and discussion of results: Ankit B. Lehru and Dharmesh J. Pandya.
Writing - Original Draft: Ankit B. Lehru.
Writing - Review and Editing: Ankit B. Lehru and Dharmesh J. Pandya.
Resources: Ankit B. Lehru and Dharmesh J. Pandya.
Supervision: Dharmesh J. Pandya.
Approval of the final text: Ankit B. Lehru and Dharmesh J. Pandya.

IX. REFERENCES

[1] Press Information Bureau, Government of India, "Power sector at a glance: All India," Ministry of Power, 2024. Available: https://pib.gov.in/PressReleaseIframePage.aspx?PRID=2038501. Accessed: Jul. 2026.

[2] Government of India, The Energy Conservation Act, 2001, as amended by the Energy Conservation (Amendment) Act, 2022. Ministry of Power, New Delhi, India, 2022.

[3] Bureau of Energy Efficiency, General Aspects of Energy Management and Energy Audit; Energy Efficiency in Electrical Utilities; and Energy Efficiency in Thermal Utilities, Energy Managers and Energy Auditors Guidebooks. New Delhi, India: BEE.

[4] International Organization for Standardization, ISO 50002-1:2025, Energy Audits - Part 1: General Requirements with Guidance for Use. Geneva, Switzerland: ISO, 2025.

[5] M. J. Panchal and V. V. Dwivedi, "The case study of energy conservation and audit in industry sector," International Journal of Engineering and Computer Science, vol. 3, no. 4, pp. 5298-5303, 2014.

[6] D. B. Mane, A. B. Shinde, and U. M. Khadake, "Electrical energy audit for Riddhim Siddhim Steel India Pvt. Ltd., Khopoli," in Proc. International Conference on Computation of Power, Energy, Information and Communication (ICCPEIC), 2018.

[7] A. Devi, A. Kumar, N. Thanigivelu, L. Ramesh, and K. M. Sundaram, "Energy conservation implementation at cable manufacturing industry through ETAP analysis," in Proc. Emerging Trends in Industry 4.0 (ETI 4.0), 2021, doi: 10.1109/ETI4.051663.2021.9619231.

[8] S. K. Rajput, D. K. Dheer, and S. Wadhwani, "Energy consumption and energy saving potential in Indian textile sector," in Proc. IEEE Conference Record 48766, 2020.

[9] B. Kale, S. Yadav, S. Pradhan, S. Bangale, S. Baraskar, and R. Sawarkar, "Energy audit: A case study at medium scale industry," International Journal of Innovative Research in Technology, vol. 4, no. 10, 2018.

[10] S. S. Puthukkattu, R. Poojary, and S. S. Kamath, "An energy audit-based case study on varied organizations," in Proc. Advances in Science and Engineering Technology International Conferences (ASET), pp. 1-5, 2023, doi: 10.1109/ASET56582.2023.10180612.

[11] J. Fresner, F. Morea, C. Krenn, J. A. Uson, and F. Tomasi, "Energy efficiency in small and medium enterprises: Lessons learned from 280 energy audits across Europe," Journal of Cleaner Production, vol. 142, pp. 1650-1660, 2017, doi: 10.1016/j.jclepro.2016.11.126.

[12] D. Viesi, F. Pozzar, A. Federici, L. Crema, and M. S. Mahbub, "Energy efficiency and sustainability assessment of about 500 small and medium-sized enterprises in Central Europe region," Energy Policy, vol. 105, pp. 363-374, 2017, doi: 10.1016/j.enpol.2017.02.045.

[13] S. Paramonova and P. Thollander, "Ex-post impact and process evaluation of the Swedish energy audit policy programme for small and medium-sized enterprises," Journal of Cleaner Production, vol. 135, pp. 932-949, 2016, doi: 10.1016/j.jclepro.2016.06.139.

[14] F. Kalantzis and D. Revoltella, "Do energy audits help SMEs to realize energy-efficiency opportunities?" Energy Economics, vol. 83, pp. 229-239, 2019, doi: 10.1016/j.eneco.2019.07.005.

[15] A. Ketenci and M. Wolf, "Advancing energy efficiency in SMEs: A case study-based framework for non-energy-intensive manufacturing companies," Cleaner Environmental Systems, vol. 14, art. 100218, 2024, doi: 10.1016/j.cesys.2024.100218.

[16] A. Trianni, E. Cagno, and S. Farne, "Barriers, drivers and decision-making process for industrial energy efficiency: A broad study among manufacturing small and medium-sized enterprises," Applied Energy, vol. 162, pp. 1537-1551, 2016, doi: 10.1016/j.apenergy.2015.02.078.

[17] I. Johansson, N. Mardan, E. Cornelis, O. Kimura, and P. Thollander, "Designing policies and programmes for improved energy efficiency in industrial SMEs," Energies, vol. 12, no. 7, art. 1338, 2019, doi: 10.3390/en12071338.

[18] C. Herce, C. Martini, C. Toro, E. Biele, and M. Salvio, "Energy efficiency policies for small and medium-sized enterprises: A review," Sustainability, vol. 16, no. 3, art. 1023, 2024, doi: 10.3390/su16031023.

[19] International Energy Agency, "Small and medium enterprises - Energy efficiency policy toolkit," IEA, Paris. Available: https://www.iea.org/reports/energy-efficiency-policy-toolkit/small-and-medium-enterprises. Accessed: Jul. 2026.

Journal of Engineering and Technology for Industrial Applications

ITEGAM-JETIA

Manaus, v.12 n.60, p. 85-94 July /August, 2026.
DOI: https://doi.org/10.5935/jetia.v12i60.3529

ISSN ONLINE: 2447-0228

RESEARCH ARTICLE OPEN ACCESS

NINE-SWITCH QUASI-IMPEDANCE SOURCE INVERTER FOR DUAL-MOTOR ELECTRIC VEHICLE DRIVES WITH INTEGRATED ONBOARD CHARGING

Ismail Benmiloud*[1], Aissa Amuer[2], Katia Kouzi[3], Najib Essounbouli[4]

[1, 2, 3]Materials, Energy Systems, Renewable Energies and Energy Management Laboratory University of Amar Telidji 03000, Laghouat, Algeria.
[4]CReSTIC of Reims Champagne-Ardenne University IUT de Troyes, Troyes, France.

[1]https://orcid.org/0009-0001-9506-5805, [2]https://orcid.org/0000-0001-5332-7697,
[3]https://orcid.org/0000-0002-8430-1681, [4]https://orcid.org/0000-0002-2342-0310

E-email: * is.benmiloud@lagh-univ.dz, a.ameur@lagh-univ.dz, k.kouzi@lagh-univ.dz, najib.essounbouli@univ-reims.fr

ARTICLE INFO

Article History
Received on: February 02, 2026
Reviewed on: March 03, 2026
Accepted on: April 01, 2026
Published on: July 31, 2026

Keywords:
Electric Vehicles,
Onboard Charger,
Nine Switch Inverter,
Quasi Z-Source Inverter.

ABSTRACT

With the significant advancements in the electric vehicle (EV) sector, improving electric conversion and charging systems has become necessary to improve efficiency and accessibility for all users. This paper introduces a novel nine-switch inverter with a quasi-impedance Source topology designed to revolutionize EV power train systems. The proposed inverter design enables the simultaneous control of two traction motors while reducing the number of required power switches from 12 to 9, saving three switches compared to the conventional dual-inverter setup, improving system redundancy and dependability for improved EV performance. Utilizing its features, the inverter doubles as an onboard charger, eliminating the need for a separate charging unit. This streamlined approach reduces system complexity and cost while improving charging convenience.

Copyright ©2026 by authors and Galileo Institute of Technology and Education of the Amazon (ITEGAM). This work is licensed under the Creative Commons Attribution International License (CC BY 4.0).

I. INTRODUCTION

Global energy consumption keeps rising, and a constant desire exists to enhance power capacity. Most of this energy is derived from fossil resources, which presents ongoing energy production, conversion, and distribution challenges. It also contributes to pollution and its detrimental impact on the environment, particularly in urban areas, and human health. Transportation represents one of the most significant consumers, especially vehicles with internal combustion engines; however, advancements in the electric vehicle (EV) sector are leading to a gradual shift towards more sustainable transportation options, which links to the rapid penetration of renewable and alternative energy sources and energy storage solutions. These vehicles offer greater energy efficiency, minimal pollution, and reduced maintenance compared to traditional internal combustion engines [1]. Electric vehicles can be categorized into two main types based on the number and arrangement of motors: distributed multi-motor driven power trains and centralized single-motor driven power trains. Distributed multi motor driven power trains can be further classified into three subcategories: Dual-motor, as described in [2], Triple-motor as discussed [3], and Four-motor power trains, as explored in [4], On the other hand, centralized single-motor driven is the most common configuration in modern EVs [5].

Compared to the centralized single motor approach, distributed multi-motor power trains offer several advantages, including higher efficiency, reduced torque pulsation, and improved fault tolerance. However, these benefits come at a higher premium price. In dual motor configurations, using two independent motors requires separate control. The conventional approach involves two separate inverters, leading to increased cost and system size [6]. Ongoing research in power electronics aims to develop cost-effective and efficient conversion capabilities. Reducing the number of semiconductor switches is a critical factor in converter costs. The decrease in converter size through fewer switches can significantly reduce the price. Various novel topologies have been created, including the Nine Switch Inverter (NSI) [7], the B4 inverter [8], and the Five Leg Inverter [9]. The NSI, a dual-output inverter, has been proposed as a solution in various industrial applications, helping to reduce the number of semiconductor tor switches and associated energy losses, as well as streamlining drive circuitry.Previous research on nine-switch and quasi-impedance source inverter (qZSI) topologies has explored several directions, but each remains limited in scope with respect to the requirements of electric vehicle systems.

Discontinuous PWM strategies for qZS nine-switch inverters [10] and carrier-based PWM techniques [11] mainly focused on reducing switching losses and improving modulation performance, without addressing dual-motor propulsion or onboard charging. Similarly, dual hysteresis band current control has been applied to nine switch inverters for two induction motors [12], but this work only emphasized torque control and omitted EV-specific functions such as bidirectional charging and vehicle-to-grid (V2G) operation. Other studies have attempted integrated drive and charger solutions: a nine-switch-based charger for six-phase machines [13], and a multilevel nine-switch topology with improved harmonic quality [14]. However, these approaches are constrained either by reliance on six-phase machines or by increased device count and circuit complexity, and they do not consider independent dual-motor platforms. In contrast, the present work introduces a unified qZS nine-switch inverter solution that simultaneously supports dual-motor EV propulsion with dynamic torque distribution and onboard charging using a constant-current/constant-voltage strategy. By combining propulsion, charging, and V2G functionalities within a single, compact converter, while maintaining the inherent advantages of the qZSI such as continuous input current and voltage boost capability, the proposed system offers a novel and more comprehensive EV-oriented architecture than previously reported in the literature.

II. ON-BOARD CHARGER FOR ELECTRIC VEHICLES

The Nine-Switch Inverter (NSI) enables dual three-phase outputs using shared switches but requires a higher DC-link voltage [15], and employing a two-stage boost converter increases cost and complexity. To address this, the Z-Source Inverter (ZSI) was introduced with single-stage buck–boost capability, though it suffers from discontinuous input current and higher source stress [16]. The Quasi Z-Source Inverter (QZSI) improves upon this by rearranging the impedance network, ensuring continuous input current, reduced ripple, elimination of inrush current, and simplified integration. Despite higher capacitor voltage stress, it offers better efficiency and control. Its voltage boost is characterized by the boost factor.

$$B = \frac{1}{1 - 2D} \tag{1}$$

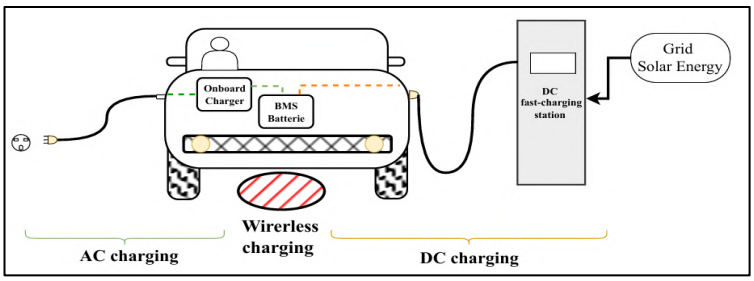


Figure 1: Schematic representation of differences in on-board,off-board chargers, and Wireless chargers or DC-fast charging station.
Source: Authors, (2026).

Where D is the shoot-through duty ratio, confirming its ability to provide single-stage buck–boost operation suitable for renewable and electric vehicle applications. Moreover, such inverter topologies not only enable efficient traction power conversion but also contribute to improved power quality by maintaining low Total Harmonic Distortion (THD) as represent (Figure 2).

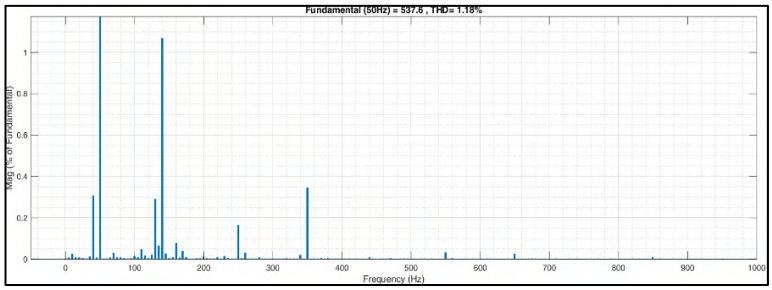


Figure 2: THD The Simple Boost Control.
Source: Authors, (2026).

Charging systems for hybrid and electric vehicles are crucial for efficient operation. They are categorized into off-board and on-board systems, as shown in (Figure 1), which power the batteries and enable efficient operation. Onboard charging systems are integrated into the vehicle itself. These systems include components like the onboard charger, charging port, charging control unit, power conversion, and protection mechanisms [17], which offers a significant advantage for EVs by enabling them to charge wherever an electrical outlet is available. This flexibility allows EV owners to conveniently charge their vehicles home by converting external AC power into DC. The onboard charging system regulates voltage and current, ensuring efficient and safe power transfer to the vehicle's batteries [18], [19]. On the other hand, the Off-board charging stations are external to the vehicle, typically part of the charging infrastructure [20], which offers High-DC power allows fast charging and ensures compatibility with different EV models and standards, However, it is important to consider the challenges associated with the off-board charging station. The availability of these stations is limited due to the need for dedicated parking spaces, which can be challenging in urban areas. The setting up off-board charging infrastructure is expensive, especially for high-power DC fast charging stations, and requires regular maintenance [21]. The choice between Off-board and Onboard charging depends on the user's specific needs, driving patterns, and access to charging infrastructure.

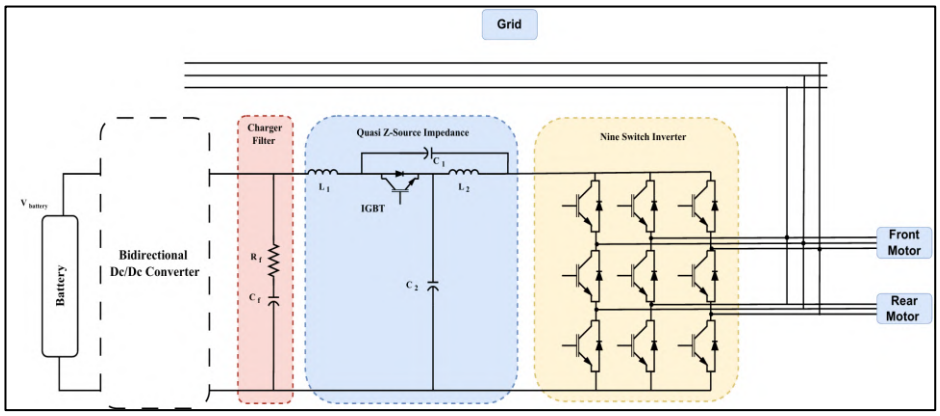


Figure 3: The proposed bidirectional Quasi Z-Source Nine Switch inverter.
Source: Authors, (2026).

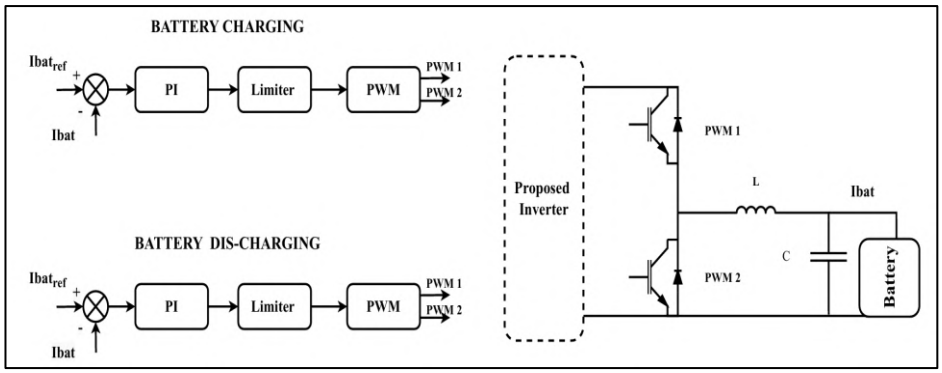


Figure 4: Battery Charger Controller.
Source: Authors, (2026).

(Figure 3) represents the proposed inverter in this topology. We can operate in two directions. The first one, the battery, powers the two motors through the inverter. The second operation uses a bidirectional DC-DC converter to achieve the desired input voltage and current for the battery, as in (Figure 4). The power flows from the grid to the battery utilizing the operation control (Figure 5) V2G, G2V, munched in [22].

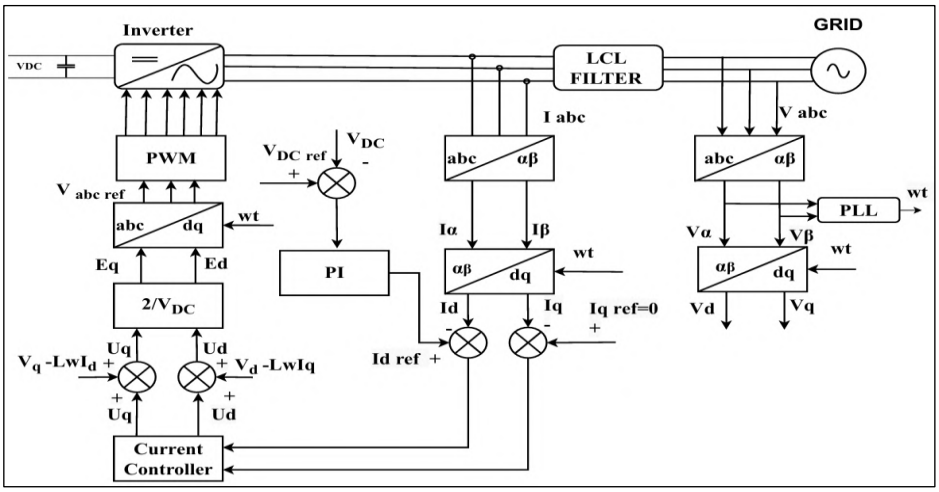


Figure 5: A diagram illustrating the flow of power from the grid to vehicles in a Grid-to-Vehicle (G2V) system.
Source: Authors, (2026).

III. CHARGING MODE FOR BATTERY IN ELECTRIC VEHICLE

The electrification of the transportation sector has led to research on battery electric vehicles (EVs) and plug-in hybrid electric vehicles (PHEVs) and how they can be integrated into electrical networks. Electric vehicles' charging method significantly impacts their batteries' performance and efficiency and determines the charging mode [23]. There are two primary charging modes for batteries in EVs: constant-current (CC) charging and constant-voltage (CV) charging [24]. The constant current (CC) charging mode is generally used during the initial stages when the battery has a low state of charge. SOC. By providing a controlled, constant current to the battery for fast charging, however, as the battery reaches higher charge levels, the charging rate gradually decreases [25].

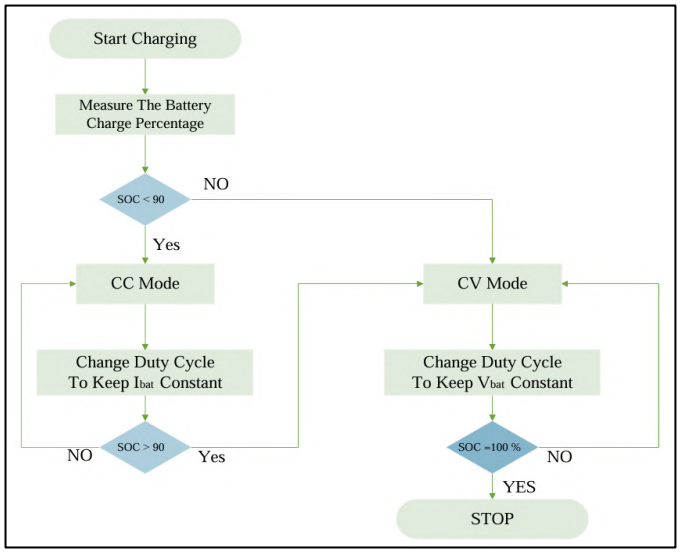


Figure 6: Charging Mode.
Source: Authors, (2026).

In contrast, constant voltage (CV) is used in the late stages of charging near full capacity by providing a constant voltage to the battery during charging. The CV method ensures that the charging current decreases as the battery's state of charge increases, preventing overcharging, which can be detrimental to its performance and lifespan [26]. The decision to use CC or CV charging mode depends on various factors, including battery chemistry, charging infrastructure, and desired charging time. The algorithm used to charge the battery is represented in (Figure 6). Two charging modes were used: constant current and followed by constant voltage.

IV. DYNAMIC VEHICLES

In order to understand the behavior of a vehicle, it is important to consider the various forces acting upon it. These forces are crucial in determining the vehicle's speed, acceleration, and fuel efficiency. There are four main forces that an electric vehicle must overcome in order to move: Grading Resistance, Rolling Resistance, Aerodynamic Drag, and Inertial Effect. Understanding these forces can help us optimize the design of electric vehicles and improve their performance on the road [27-30]. Grading resistance (F_g) is the force that opposes a vehicle's movement due to changes in elevation or slope. It is related to the vehicle's weight and the road's gradient. The higher the gradient, the greater the grading resistance.

$$F_g = M_{car}.g.sin(\alpha) \quad (2)$$

Where: M_{car} [kg]Mass of the vehicle.
g =9.81[m/s2] Free fall acceleration.
α[rad] Angle of the driving surface.

Rolling resistance (F_r) is the force that resists a vehicle's movement due to the deformation of its tires as they come into contact with the road. Rolling resistance depends on various factors, such as tire type, tire pressure, and road surface.

$$F_r = M_{car}.g.C_r.cos(\alpha) \quad (3)$$

where: Cr [-] Tire rolling resistance coefficient.

Aerodynamic drag (F_w) is the force that resists a vehicle's movement due to its exposure to the wind. This force is proportional to the square of the vehicle's speed and is influenced by factors such as the vehicle's shape and cross-sectional area.

$$F_w = \frac{1}{2}.\rho.A_f.C_D.(V - V_w)^2 \quad (4)$$

where: ρair = 1.2041[kg/m3] Air density of dry air at 20◦C.
Af [m2] Front area.
CD[-] Aerodynamic drag coefficient.
V[m/s] Velocity of the vehicle.
W_{wind} [m/s] Headwind speed.

Inertial Effect (F_I) it is the force that opposes the acceleration and deceleration of a vehicle. It depends on the mass of the vehicle and the magnitude of the acceleration or deceleration. Inertial force is greater in heavier vehicles and at higher speeds.

$$F_I = M_{car}.\dot{V} \quad (5)$$

where: $\dot{V}$ [m/s2] Acceleration of the vehicle.

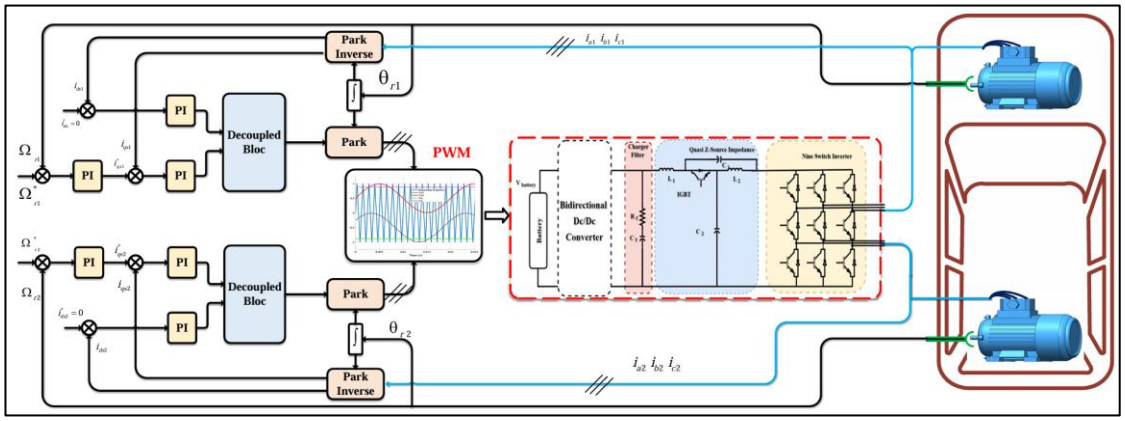


Figure 7: The general structure of the system with two motor controls.
Source: Authors, (2026).

(Figure 7) represents a vector control diagram for two permanent magnet synchronous motors powered by a single bidirectional quasi-Z-source nine-switch inverter. This system is designed to independently control the torque and speed of two PMSMs while reducing the number of power switches. Each PMSM has its own vector control loop, which includes PI controllers for the current components, decoupling blocks to cancel cross-axis interactions, Park and inverse Park transforms for reference frame conversion, and integrators to generate the rotor electrical angles. These control loops produce three-phase voltage references V_{a1}^{ref}, V_{b1}^{ref}, V_{c1}^{ref} for the front motor and V_{a2}^{ref}, V_{b2}^{ref}, V_{c2}^{ref} for the rear motor that are fed into a unified Pulse Width Modulation (PWM) block (Figure 8). The PWM modulates the nine-switch inverter, which shares three of its switches between the two motor phases, reducing the total number of switches from twelve (in two separate three-phase inverters) to nine. A quasi-Z-source network is incorporated between the DC source and the inverter to provide voltage boost capability and protection against shoot-through states, enhancing system robustness. On the output side, the inverter supplies three-phase AC voltage to each PMSM independently. Feedback from each motor, including current and speed, is used to close the control loops and ensure accurate torque and speed regulation.

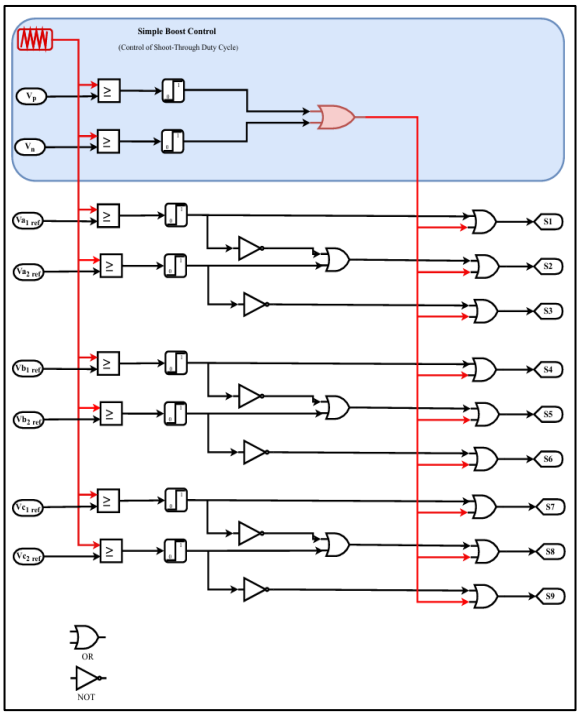
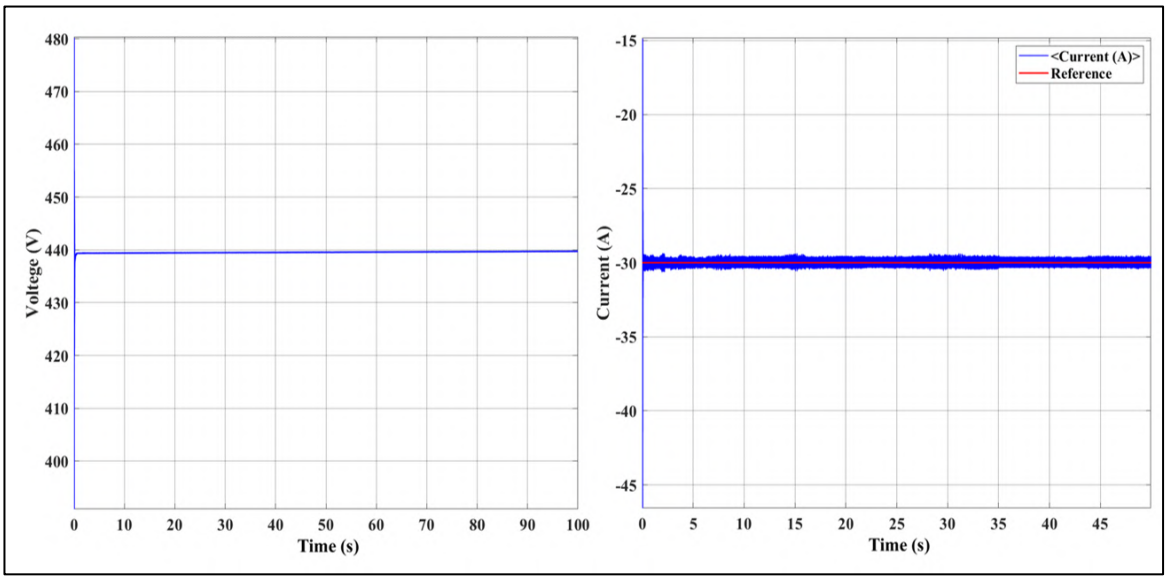


Figure 8: PWM Control.
Source: Authors, (2026).

We utilize the NEDC as our reference speed profile, which allows us to categorize the driving cycle into urban and extra-urban phases. During both phases, the inverter enables independent speed and torque control, allowing for equal torque distribution between the two motors. This approach ensures balanced operation, improves overall efficiency, and supports consistent performance across varying driving conditions.

V. RESULTS AND DISCUSSIONS

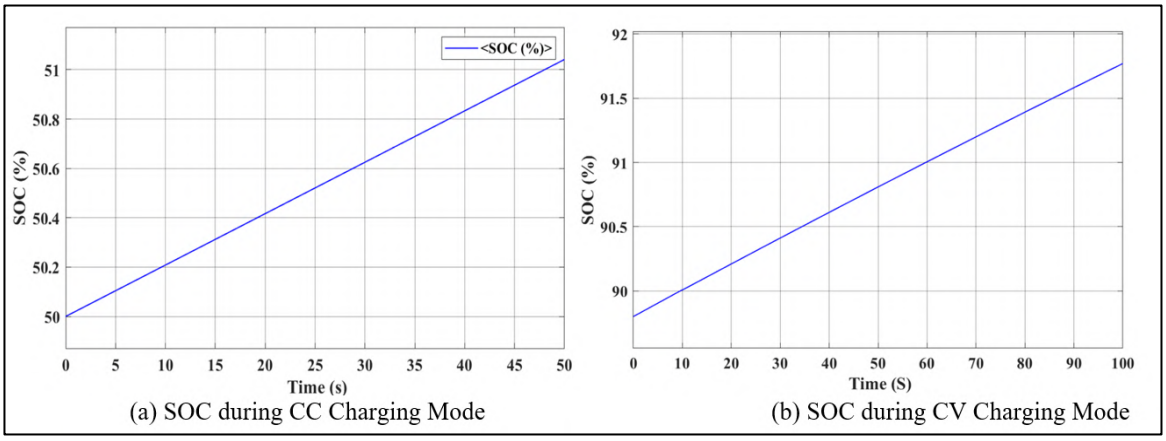
(Figure 9) represents the charging mode of the battery. Starting with the CC mode, this approach is typically used to quickly and efficiently charge the battery up to a state of charge (SOC), in our case, 90 %.



(1) Battery Voltage (b) Battery Current

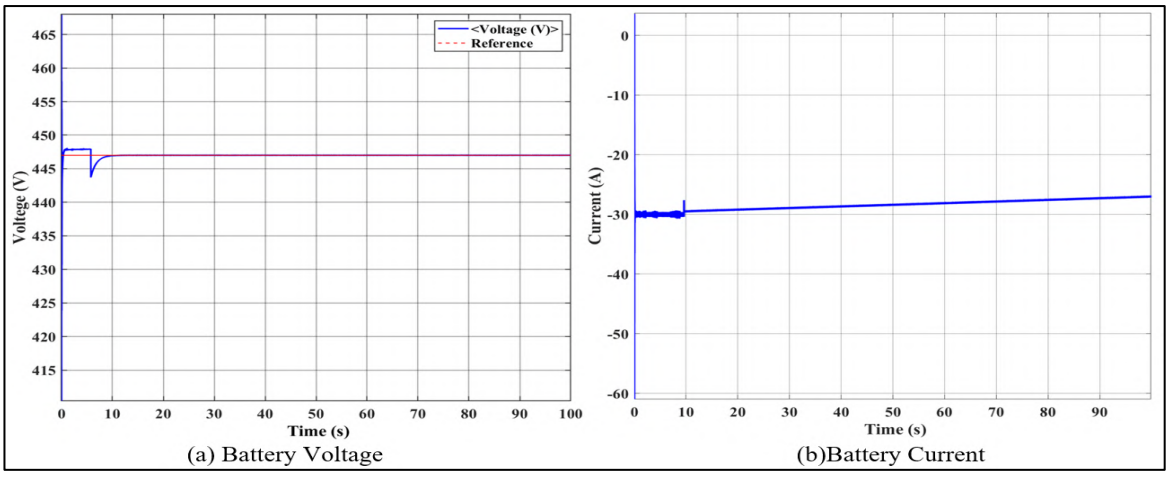
Figure 9: Constant-current Charging Mode: Battery Voltage and Current.
Source: Authors, (2026).

During the CC charging phase, the charger maintains a constant current of 30 A, (Figures 9b), which allows the battery to be charged at a relatively high rate (Figure 10a).This contributes to recharging the battery more rapidly than a pure CV charging approach. The constant current ensures the battery is charged efficiently without exposing it to high voltages, as represented in (Figure 9a), which could potentially degrade the battery over time.The charging mode was switched to CV charging once the battery reached 90 % SOC (Figure 10b).



(a) SOC during CC Charging Mode (b) SOC during CV Charging Mode

Figure 10: SOC during CC and CV Charging Mode.
Source: Authors, (2026).



(a) Battery Voltage (b)Battery Current

Figure 11: Constant Voltage Charging Mode: Battery Voltage and Current.
Source: Authors, (2026).

During the CV charging phase, (Figure 11) the charger maintains a constant voltage (Figure 11a), while the current gradually decreases as the battery approaches full capacity, as represented in (Figure 11b). The peak shown in the (Figures 11a, 11b) represents the transition from constant current to constant voltage charging mode.This mode helps to prevent overcharging and optimize the final stages of the charging process. This strategy uses CC charging's speed and efficiency to replenish battery capacity quickly, followed by the transition to CV charging, which ensures safe completion and maintains battery health and performance. The hybrid charging strategy, which combines CC charging up to 90% SOC followed by CV charging, is often employed in electric vehicles to strike a balance between charging time, energy efficiency, and battery longevity The torque distribution results demonstrate the algorithm's ability to allocate the required torque between the two motors effectively considering their capabilities and the overall torque requirements of the EV the actual torque for each motor follows the reference, demonstrated in (Figures 12 and 13). To simulate real-world driving conditions in urban and extra-urban environments, we used the NEDC cycle, which provides a more realistic evaluation of vehicle behavior through the results obtained in (Figures 13, 12) The vehicle's actual speed demonstrates a high degree of concordance with the reference speed profile. This close alignment between the actual and target velocities indicates precise speed control and robust vehicle responsiveness to the prescribed driving pattern.

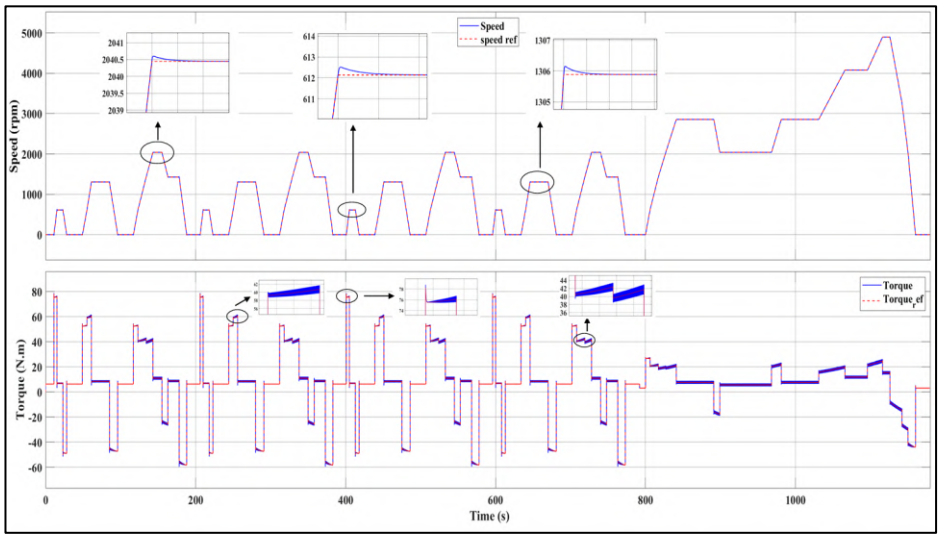


Figure 12: The speed and the torque for the front motor.
Source: Authors, (2026).

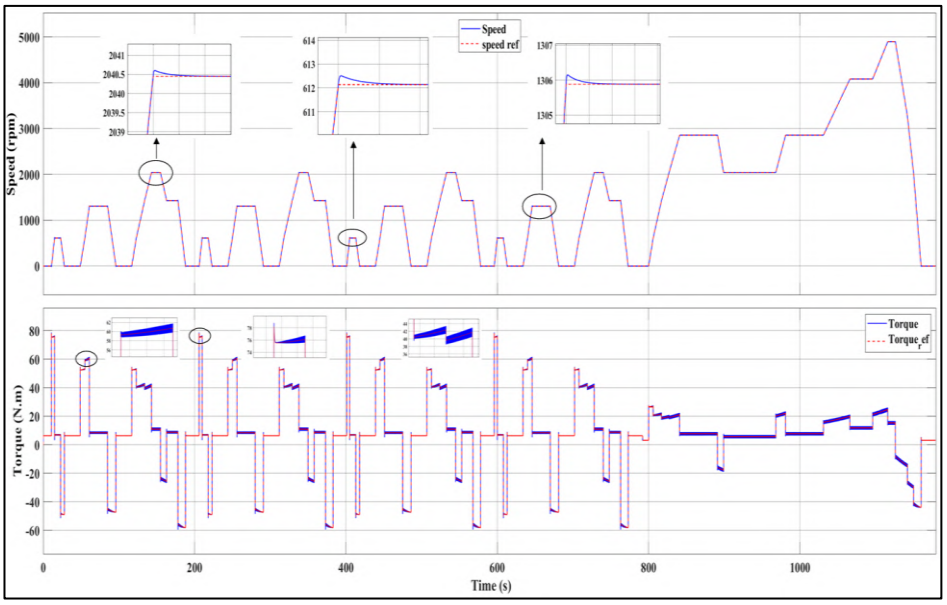


Figure 13: The speed and the torque for the rear motor.
Source: Authors, (2026).

The Figures representing the vehicle's target power profile throughout the NEDC cycle, This demand power curve indicates the instantaneous power requirements that the vehicle achieves to follow the prescribed speed and acceleration patterns accurately. By closely adhering to this demand power profile (Figures 14, 16) the vehicle demonstrates its ability to efficiently manage energy resources and respond to varying load conditions characteristic of real-world driving scenarios. The (Figures 14 and 16) display the three-phase currents (ia, ib, ic) of the electric motor, which are fundamental to understanding its dynamic performance during the NEDC cycle. These currents represent the instantaneous electrical input to each of the motor's three phases, The currents exhibit a sinusoidal pattern as represented by the figure (Figures 15 and 17), with the frequency proportional to the motor's rotational speed. The varying amplitudes of ia, ib, and ic reflect changes in torque demand. Higher amplitudes correspond to periods of acceleration or increased load.

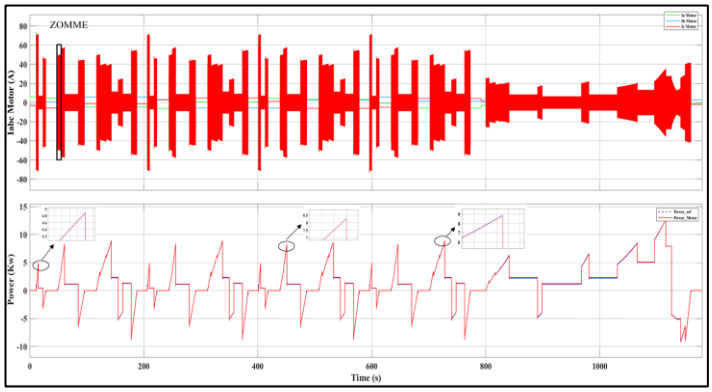


Figure 14: The current and the power for the front motor.
Source: Authors, (2026).

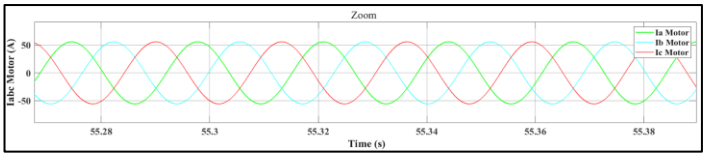


Figure 15: ZOOM current for the front motor.
Source: Authors, (2026).

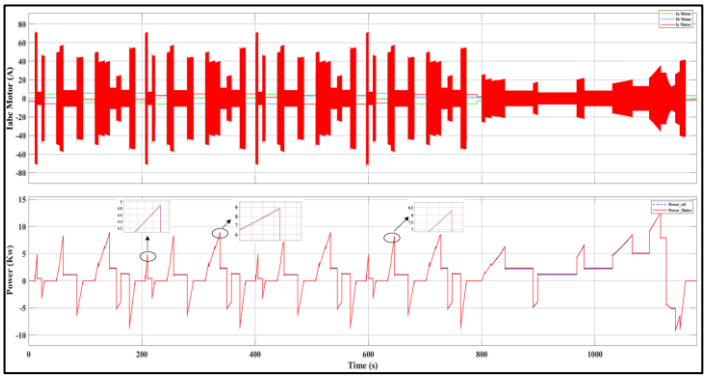


Figure 16: The current and the power for the rear motor.
Source: Authors, (2026).

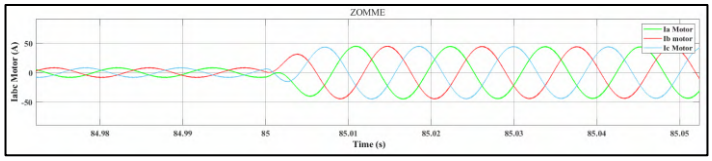


Figure 17: ZOOM current for the rear motor.
Source: Authors, (2026).

Table1: Machine and Battery Parameters.

Parameter Value	Value
Nominal torque (N.m)	Tnom=400
Nominal motor speed(rpm)	wnom=1200
Maximum motor speed (rpm)	wmax=6000
Stator d-axis inductance (H)	Ld=1.597×10−3
Stator q-axis inductance (H)	Lq=2.057×10−3
Stator resistance per phase (Ohm)	Rs=6.5×10−3
Permanent magnet flux linkage (V.s)	λ=0.1757
Number of pole pairs	p=4
Rotor inertia (Kg.m^2)	J=0.09
Friction coefficient (N.m.s)	F=0.002
Nominal DC voltage (V)	Vdc,nom=550
Power (kW)	Pw=50
Voltage battery (V)	Vb=400
Current battery (Ah)	Ib=40

Source: Authors, (2026).

VI. CONCLUSIONS

This work presented a nine-switch inverter with quasi-impedance source for independently controlling dual separate motors in EVs. The main feature of the proposed configuration is to reduce the number of switching components required compared to traditional multi-motor EV configurations, with a combination of onboard charge and wireless charging capabilities. In the initial stage of this research, we demonstrated the inverter's ability to generate a continuous current to reduce stress on the components. By modifying its impedance, we gained bidirectional functionality, allowing the inverter to serve as an onboard charger. To maintain battery performance, we use the cc-cv charging method. This hybrid charging strategy is efficient in electric vehicles and balances charging time, energy efficiency, and battery longevity.

VII. AUTHOR'S CONTRIBUTION

Conceptualization: Ismail Benmiloud, Aissa Amuer, Katia Kouzi, Najib Essounbouli.
Methodology: Ismail Benmiloud, Aissa Amuer, Katia Kouzi, Najib Essounbouli.
Investigation : Ismail Benmiloud, Aissa Amuer, Katia Kouzi, Najib Essounbouli.
Discussion of results: Ismail Benmiloud, Aissa Amuer, Katia Kouzi, Najib Essounbouli.
Writing – Original Draft: Ismail Benmiloud.
Writing – Review and Editing: Aissa Amuer, Katia Kouzi, Najib Essounbouli.
Resources: Ismail Benmiloud, Aissa Amuer, Katia Kouzi, Najib Essounbouli.
Supervision:, Aissa Amuer, Katia Kouzi, Najib Essounbouli.
Approval of the final text: Ismail Benmiloud, Aissa Amuer, Katia Kouzi, Najib Essounbouli.

VIII. REFERENCES

[1] Thangavel S, Mohanraj D, Girijaprasanna T, Raju S, Dhanamjayulu C, Muyeen S. A comprehensive review on electric vehicle: battery management system, charging station, traction motors. IEEE Access, 2023; 11: 20994–21019.

[2] Xu X, Liang J, Hao Q, Dong P, Wang S, Guo W, Liu Y, Lu Z, Geng J, Yan B. A novel electric dual motor transmission for heavy commercial vehicles. Automotive Innovation, 2021; 4: 34–43.

[3] Nezamuddin O, Bagwe R, Dos Santos E. A multi-motor architecture for electric vehicles. In: 2019 IEEE Trans portation Electrification Conference and Expo (ITEC); 2019. pp. 1–6. IEEE.

[4] Xu S, Wei L, Zhang X, Bai Z, Jiao Y. Research on multi-mode drive optimization control strategy of four-wheel-drive electric vehicles with multiple motors. Sustainability, 2022; 14(12): 7378.

[5] Du W, Zhao S, Jin L, Gao J, Zheng Z. Optimization design and performance comparison of different powertrains of electric vehicles. Mechanism and Machine Theory, 2021; 156: 104143.

[6] Louback E, Biswas A, Machado F, Emadi A. A review of the design process of energy management systems for dual-motor battery electric vehicles. Renewable and Sustainable Energy Reviews, 2024; 193: 114293.

[7] Wang P, Xu H, Yuan L. Research on cascaded multilevel converters for dual motor drive systems based on a nine-switch converter. IET Electric Power Applications,2024.https://doi.org/10.1049/elp2.12441.

[8] Shanmugam S, Ramachandran S, Senthilkumar A, Pandiyan S, Nayyar A, Hossain E. Design and implementation of improved three port converter and B4-inverter fed brushless direct current motor drive system for industrial applications. IEEE Access, 2020;8:149093149112.https://doi.org/10.1109/ACCESS.2020.3016011.

[9] Shanmugam Y, Narayanamoorthi R, Vishnuram P, Savio D, Yadav A, Bajaj M, Nauman A, Khurshaid T, Kamel S. Solar-powered five-leg inverter-driven quasi-dynamic charging for a slow-moving vehicle. Frontiers in Energy Research, 2023; 11. https://doi.org/10.3389/fenrg.2023.1115262.

[10] Dabour SM, Ibrahim DA, El-Sattar AMA, Abdel-Rahim O. A family of discontinuous PWM strategies for quasi-Z-source nine-switch inverters. IEEE Access, 2021;9:3324733259.doi:10.1109/ACCESS.2021.3061122.

[11] Dabour SM, El-Sattar AMA, Ibrahim DA, Abdel-Rahim O. Carrier-based PWM strategy for quasi Z-source nine-switch inverters. IEEE Transactions on Industrial Electronics, 2020; 67(6): 4864–4874. doi:10.1109/TIE.2019.2926564.

[12] El-Sayed MA, Abdel-Khalik AS, Ahmed S, Massoud AM, Abdel-Rahim O. Dual-hysteresis band control of nine switch inverter to control two induction motors. IET Electric Power Applications, 2019;13(10): 15401549.doi:10.1049/ietepa.2018.553.

[13] Diab AA, Abdel-Khalik AS, Ahmed S, Massoud AM, Abdel-Rahim O. A nine-switch-converter-based integrated motor drive and battery charger system for EVs using symmetrical six-phase machines. IEEE Transactions on Industrial Electronics, 2016; 63(9): 5326–5335. doi:10.1109/TIE.2016.2555295.

[14] Cordeiro A, Chaves M, Fonte P, Gˆamboa P, Lu´ıs R, Silva JF, Pires VF, Foito D, Martins JF. Electric vehicle integrated charger based on a multilevel dual-output nine-switch converter. In: 2023 International Conference on Compatibility, Power Electronics and Power Engineering (CPE-POWERENG). IEEE, 2023: 1–7. doi:10.1109/CPE POWERENG58103.2023.10227421.

[15] Almeida AD, Bradaschia F, Rech C, Caldeira CA, Neto RC, Azevedo GM. Nine-switch multiport converter applied to battery-powered tramway with reduced leakage current. Energies, 2024; 17(6): 1434.

[16] Dabour SM, Abdel-Khalik AS, Ahmed S, Massoud AM. A family of discontinuous PWM strategies for quasi-Z-source nine-switch inverters. IEEE Access, 2021; 9: 169161–169176.

[17] Pradhan R, Keshmiri N, Emadi A. On-board chargers for high-voltage electric vehicle powertrains: Future trends and challenges. IEEE Open Journal of Power Electronics, 2023.

[18] Wouters H, Martinez W. Bidirectional onboard chargers for electric vehicles: State-of-the-art and future trends. IEEE Transactions on Power Electronics, 2024; 39(1): 693–716. https://doi.org/10.1109/TPEL.2023.3319996.

[19] Dini P, Saponara S, Colicelli A. Overview on battery charging systems for electric vehicles. Electronics, 2023; 12(20): 4295.

[20] Kumar S, Upadhyay T, Gupta OH. Power quality improvement and signal conditioning of PV array and grid interfaced off-board charger for electric vehicles with V2G and G2V capabilities. Chinese Journal of Electrical Engineering, 2023.

[21] Jain A, Bhullar S. Operating modes of grid integrated PV-solar based electric vehicle charging system– a comprehensive review. e-Prime- Advances in Electrical Engineering, Electronics and Energy, 2024;8:100519. https://doi.org/10.1016/j.prime.2024.100519.

[22] Evode R. Modeling of electric grid behaviors having electric vehicle charging stations with G2V and V2G possibilities. In: 2021 International Conference on Electrical, Computer, Communications and Mechatronics Engineering (ICECCME); 2021. pp. 1–5. IEEE.

[23] Visakh A, Selvan MP. Smart charging of electric vehicles to minimize the cost of charging and the rate of transformer aging in a residential distribution network. Turkish Journal of Electrical Engineering and Computer Sciences, 2022; 30(3): 927–942. doi:10.55730/1300-0632.3814.

[24] Khan W, Ahmad F, Alam MS. Fast EV charging station integration with grid ensuring optimal and qual ity power exchange. Engineering Science and Technology, an International Journal, 2019; 22(1): 143–152. https://doi.org/10.1016/j.jestch.2018.08.005.

[25] Yenil V, Cetin S. Load independent constant current and constant voltage control of LCC-series compensated wireless EV charger. IEEE Transactions on Power Electronics, 2022; 37(7): 8701–8712.

[26] Ruan H, Wei Z, Shang W, Wang X, He H. Artificial intelligence-based health diagnostic of lithium-ion battery leveraging transient stage of constant current and constant voltage charging. Applied Energy, 2023; 336:120751. https://doi.org/10.1016/j.apenergy.2023.120751.

[27] Agrawal A, Ranbir S, Nagendra K, Prakash SV, Malik H, Alotaibi MA, M´arquez FPG, Hossaini MA. Mathematical modelling of driving forces of an electric vehicle for sustainable operation. IEEE Access, 2023.

[28] Mohd T, Hassan M, Aris I, Soh AC, Ibrahim B, Hat M. Simulation-based study of electric vehicle parameters. ARPN Journal of Engineering and Applied Sciences, 2015; 10(19): 8541–8546.

[29] Kıyaklı AO, Solmaz H. Modeling of an electric vehicle with MATLAB/Simulink. International Journal of Automotive Science and Technology, 2018; 2(4): 9–15. https://doi.org/10.30939/ijastech..475477.

[30] Khan K, Samuilik I, Ali A. A mathematical model for dynamic electric vehicles: Analysis and optimization. Mathematics, 2024; 12(2). https://doi.org/10.3390/math12020224

Journal of Engineering and Technology for Industrial Applications

ISSN ONLINE: 2447-0228

ITEGAM-JETIA

Manaus, v.12 n.60, p.95-107, July/August, 2026.

DOI: https://doi.org/10.5935/jetia.v12i60.3597

RESEARCH ARTICLE OPEN ACCESS

APPLICATION OF COMPUTATIONAL FLUID DYNAMICS AND OPEN-SOURCE TECHNOLOGIES FOR INDOOR THERMAL COMFORT MODELING: A SYSTEMATIC REVIEW AND EVIDENCE SYNTHESIS OF THE LAST DECADE

Keny Montalvo Morales[1], Henry Javier-Ninahuaman[2], Grimaldo Quispe[3], Abdallah Elshawadfy Elwakeel[4], John Espita[5], Jader Rodriguez[6], Edwin Villagran*[7]

[1, 3]Universidad Nacional Autónoma Altoandina de Tarma, Junín, Perú.
[2]Universidad Tecnologica del Peru.
[4]Agricultural Engineering Department, Faculty of Agriculture and Natural Resources, Aswan University, Aswan 81528, Egypt.
[5, 6, 7]Corporación Colombiana de Investigación Agropecuaria—Agrosavia, Centro de Investigación Tibaitata, Km 14, vía Mosquera-Bogotá, Mosquera 250040, Colombia.

[1]https://orcid.org/0000-0003-4403-4360, [2]https://orcid.org/0000-0002-3864-4181, [3]https://orcid.org/0000-0001-6168-8935,
[4]https://orcid.org/0000-0002-9360-051X, [5]https://orcid.org/0000-0003-2684-655X
[6]https://orcid.org/0000-0002-5346-092X, [7]https://orcid.org/0000-0003-1860-5932

Email: kmontalvo@unaat.edu.pe, c21259@utp.edu.pe, gquispe@unaat.edu.pe, abdallah_elshawadfy@agr.aswu.edu.eg, jjespitia@agrosavia.co, jrodriguezc@agrosavia.co,*evillagran@agrosavia.co

ARTICLE INFO

Article History
Received: February 7, 2026
Reviewed: June 5, 2026
Accepted: July 5, 2026
Published: July 31, 2026

Keywords:
Thermal comfort,
Heat transfer,
Indoor airflow,
Numerical simulation,
Ventilation,
Energy efficiency.

ABSTRACT

Over the past decade, Computational Fluid Dynamics (CFD) has become a fundamental tool for the assessment, modeling, and optimization of thermal comfort in controlled architectural environments, enabling detailed simulation of airflow behavior, heat transfer processes, and the spatial distribution of thermo-environmental variables within indoor spaces. The integration of human thermophysiological models has enhanced the predictive capability of these simulations, allowing for more realistic estimations of occupants' thermal responses and perceptual comfort. In parallel, the growth and maturation of open-source platforms have democratized access to these technologies, facilitating their implementation across multiple scales and building typologies, ranging from offices and residential buildings to vehicle cabins and urban environments. Recent studies have further addressed the evaluation of passive environmental conditioning strategies such as solar chimneys and natural ventilation indoor air quality assessment, and the adaptation of models to local climatic conditions, reflecting a transition toward more comprehensive, resilient, and sustainable design approaches. Moreover, the incorporation of artificial intelligence techniques and predictive control systems has opened new opportunities for operational automation and improved building energy efficiency. Within this context, the present systematic review synthesizes methodological advances, emerging applications, and current trends in the use of CFD and open-source platforms for indoor thermal comfort assessment in architecture, identifying their main contributions, technical limitations, and future research directions.

Copyright ©2026 by authors and Galileo Institute of Technology and Education of the Amazon (ITEGAM). This work is licensed under the Creative Commons Attribution International License (CC BY 4.0).

I. INTRODUCTION

Over the past decade, Computational Fluid Dynamics (CFD) has assumed a prominent role in the assessment of thermal comfort within controlled architectural environments due to its capacity to model, with a high level of detail, airflow patterns, heat transfer processes, and the spatial distribution of thermo-environmental variables [1].

These capabilities have enabled researchers and architectural design professionals to optimize indoor environmental conditions, contributing both to improved occupant quality of life and enhanced building energy efficiency [2]. A significant advancement in this field has been the incorporation of human thermophysiological models into CFD simulations, which has enriched the interpretation of thermal comfort by integrating the dynamic interaction between the human body and its immediate thermal surroundings. This approach has enabled more realistic estimations of users' physiological and perceptual responses to microclimatic variations [3]. In parallel, the expansion and consolidation of open-source platforms have democratized access to these technologies, extending their implementation beyond specialized laboratories and facilitating their adoption in smaller academic and professional contexts, as well as in studies addressing urban microclimates and outdoor thermal comfort [4]. Numerous studies have leveraged the potential of CFD to analyze comfort conditions across multiple building typologies and spatial scales. In office buildings, for instance, the evaluation of temperature distribution and CO_2 concentrations has provided key evidence for the design of more efficient ventilation systems. Similarly, passive strategies such as solar chimneys have been investigated to enhance natural ventilation and reduce energy consumption [5-7]. In the transportation sector, the integration of CFD with thermophysiological models has enabled the simulation of passenger thermal comfort by accounting for variables such as airflow, temperature, and vehicle occupancy [8]. Complementarily, recent systematic reviews have documented the evolution of thermal comfort models, highlighting the need to incorporate contextual factors including climatic conditions, environmental characteristics, and user profiles to achieve more accurate and adaptive predictions [9]. Urban growth has further stimulated interest in city-scale microclimate studies, where CFD has proven to be a robust tool for analyzing urban thermal behavior and supporting the development of sustainable planning strategies [10]. More recently, the integration of artificial intelligence techniques into thermal management systems has opened new opportunities for predictive control, operational automation, and the simultaneous optimization of comfort and energy consumption through the use of real-time data [11], [12]. Within this context, the present study conducts a systematic review aimed at synthesizing the most significant advances in the application of CFD and open-source tools for thermal comfort assessment in controlled architectural environments over the past decade, identifying methodological trends, technical contributions, current limitations, and future research directions.

II. METHODOLOGY

II.1 STUDY DESIGN

The present study corresponds to a systematic literature review aimed at identifying, analyzing, and synthesizing scientific evidence related to the application of Computational Fluid Dynamics (CFD) and open-source platforms for thermal comfort assessment in controlled architectural environments. The review was conducted in August 2025 and developed in strict accordance with the methodological guidelines established by the PRISMA statement [13], with the objective of ensuring transparency, reproducibility, and traceability throughout the processes of searching, screening, evaluation, and synthesis of the included studies [14]. The flow diagram describing the identification and screening stages of the articles is presented in Figure 1.

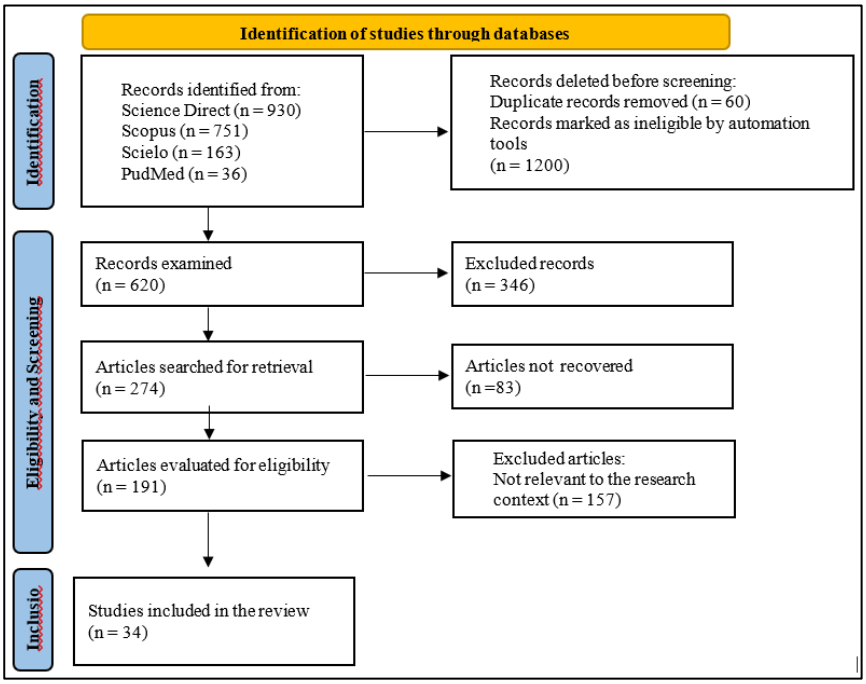


Figure 1: Development approach of the bibliometric review.
Source: Authors, (2026).

II.2 RESEARCH DESIGN

The bibliographic search strategy was carried out by consulting high-impact, multidisciplinary scientific databases, including ScienceDirect, Scopus, PubMed, and SciELO, in order to ensure the comprehensiveness and quality of the retrieved sources. To define the search terms and structure the research question, the PIO framework (Population–Intervention–Outcomes) was adopted, enabling a systematic delimitation of the study scope and facilitating the identification of relevant literature.

Population (P): indoor architectural spaces or controlled built environments in which thermal comfort and occupant well-being are assessed.

Intervention (I): application of Computational Fluid Dynamics (CFD) techniques and the use of open-source platforms or tools for the simulation, modeling, and analysis of thermal conditions and airflow behavior.

Outcomes (O): indicators of thermal comfort, energy performance, indoor environmental quality, and simulated thermo-environmental variables.

This methodological framework enabled a consistent process of data collection, critical selection, and comparative analysis of the studies, supporting the identification of trends, applications, and research gaps within the field (Table 1) [15].

Table 1: Application of the PIO framework for the definition of search equations.

PIO Category	Keywords
Population	"controlled environments", "indoor spaces", "thermal comfort zones", "buildings", "architectural environments"
Intervention	"computational fluid dynamics", "CFD", "thermal simulation", "open source tools", "energy modeling"
Outputs	"thermal comfort evaluation", "temperature analysis", "indoor climate modeling", "comfort improvement", "energy efficiency"

Source: Authors, (2026).

Prior to the selection process, inclusion criteria were established to define the thematic scope and ensure the relevance and quality of the collected evidence. Scientific articles published in English, Spanish, or Portuguese were considered, thereby broadening the geographical and linguistic coverage of the analysis. Studies focused on the application of Computational Fluid Dynamics (CFD) or open-source simulation tools for thermal comfort assessment in architectural spaces or built environments were also included. To ensure the timeliness and relevance of the findings, only studies published within the last ten years were considered. Complementarily, exclusion criteria were defined to discard works not directly related to the use of CFD or thermal comfort assessment, as well as studies addressing psychological, political, or other areas unrelated to architecture and thermo-environmental simulation. Duplicate publications, conference abstracts, opinion papers, systematic reviews, meta-analyses, and other documents that did not provide original evidence were also excluded to preserve methodological rigor and minimize bias in the synthesis of results.

II.3 STUDY POPULATION

The bibliographic search strategy was structured through the systematic combination of keywords and Boolean operators applied to the title, abstract, and keyword fields (TITLE-ABS-KEY), integrating concepts related to *thermal comfort*, *computational fluid dynamics (CFD)*, and *thermal simulation*. The search string used was: ((TITLE-ABS-KEY (“thermal comfort”) AND TITLE-ABS-KEY (“computational fluid dynamics” OR “CFD”) AND TITLE-ABS-KEY (“thermal simulation”))). This approach enabled the precise identification of studies focused on thermal comfort assessment through thermo-aerodynamic simulations in controlled architectural environments. Using this strategy, a total of 34 scientific articles were identified across high-impact specialized databases, including ScienceDirect, Scopus, PubMed, and SciELO. These records constituted the initial corpus of literature for the screening, eligibility assessment, and subsequent qualitative synthesis, providing the theoretical and methodological foundation for the present systematic review (Figure 1).

III. RESULTS AND DISCUSSION

III.1 ANALYSIS OF THE SCIENTIFIC STRUCTURE OF THE RESEARCH FIELD

The search strategy enabled the identification of a total of 1,880 potentially relevant documents. After applying the thematic preselection criteria, the bibliographic records were exported in CSV format and processed within the RStudio environment, using the Bibliometrix package to perform bibliometric analysis and construct keyword co-occurrence networks [16]. This approach facilitated a quantitative exploration of the conceptual structure and thematic relationships present in the literature. Figure 2 presents the keyword co-occurrence map, where node size reflects the frequency of term occurrence and the links represent the strength of semantic relationships among the analyzed studies [17], [18]. The central core of the network is dominated by *computational fluid dynamics*, which acts as the main articulating axis of the field and is closely connected to terms such as *thermal comfort*, *ventilation*, *energy*, and *indoor environment*. This high density of connections highlights the consolidation of CFD as a cross-cutting methodological tool for simulating thermo-aerodynamic behavior and assessing indoor environmental performance. Cluster analysis reveals at least two major groupings: a larger and denser blue cluster associated with direct building applications including thermal comfort, ventilation, indoor air quality, and energy efficiency which represents the predominant research line; and a more compact red cluster linked to methodological developments and the computational foundations of CFD, such as numerical modeling and advanced simulation approaches. The interaction between both clusters suggests a convergence between theoretical advancements and practical applications, indicating a trend toward integrated frameworks that combine computational accuracy with sustainable architectural design solutions. Additionally, the topological structure of the network shows a high degree of interconnectivity among clusters, with multiple cross-links connecting methodological terms to architectural applications, thereby indicating a mature research field undergoing disciplinary integration. The centrality of key nodes and the proximity among subtopics demonstrate that advances in numerical modeling are directly translated into improvements in thermal comfort and energy efficiency outcomes, while the absence of isolated groups suggests low thematic fragmentation. Overall, this configuration reflects an evolution from specialized studies toward interdisciplinary approaches that integrate computational simulation, environmental performance, and sustainable design.

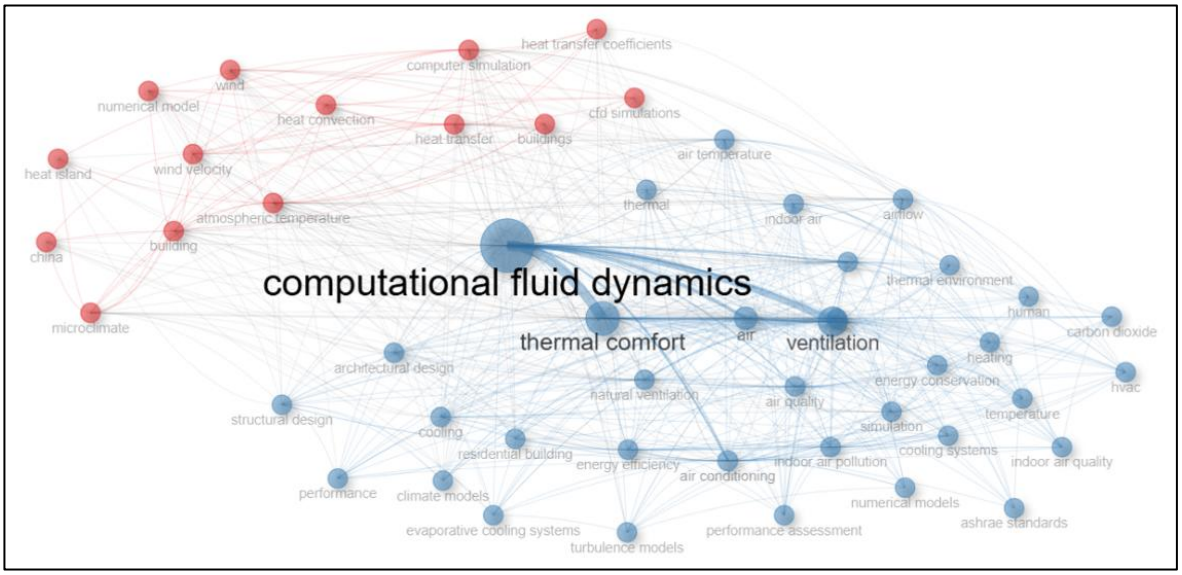


Figure 2: Keyword co-occurrence network.
Source: Authors, (2026).

III.2 COMPARATIVE SYNTHESIS OF THE INCLUDED STUDIES AND APPLICATIONS OF CFD IN THERMAL COMFORT

Table 2 summarizes the studies included in this review, organizing for each publication its specific application of Computational Fluid Dynamics (CFD), the main benefit or contribution, the evaluated parameters, and the reported conclusions. Collectively, the reviewed works demonstrate that CFD functions as a thermo-aerodynamic analysis platform capable of addressing both indoor environmental performance issues such as temperature distribution, air velocity, relative humidity, CO_2/contaminant concentrations, and comfort indices including PMV/PPD and urban microclimate and outdoor ventilation challenges, where specific indicators such as “air delay” have been proposed to characterize ventilation performance in complex urban geometries [19]. This evidence confirms a shift toward multivariable assessments, in which thermal comfort is interpreted alongside air quality and energy consumption indicators, reinforcing the relevance of CFD as a decision-support tool for architectural design. From a thematic perspective, the studies can be grouped into three predominant research lines. The first focuses on natural ventilation and passive building strategies such as solar chimneys, windcatchers, cross-ventilation, and evaporative cooling with the aim of enhancing indoor comfort while reducing reliance on mechanical systems [20-27]. The second integrates CFD with building energy simulation (BES/BPS) or envelopes and material analyses to quantify impacts on cooling/heating demand and overall efficiency [28-33]. The third research line addresses urban microclimate and outdoor thermal comfort, including urban geometry, ventilation within street canyons, and morphological solutions such as elevated buildings, emphasizing the importance of considering non-stationary conditions and realistic configurations [19], [34], [35]. From a methodological standpoint, a consistent pattern emerges: (i) widespread use of Reynolds-Averaged Navier–Stokes (RANS) models and, in specific cases, Large Eddy Simulation (LES) or unsteady simulations to capture transient phenomena; (ii) experimental validation through wind tunnel testing or in situ measurements in ventilation and pollutant dispersion studies, thereby strengthening the reliability of results [20], [36], [37] ; and (iii) increasing adoption of CFD–human thermoregulation model coupling or machine learning–based surrogate models aimed at reducing computational costs and enabling faster evaluations in design scenarios [38], [39]. Overall, the table illustrates the evolution of the field toward integrated approaches that combine numerical accuracy, empirical validation, and practical applicability to improve thermal comfort, indoor environmental quality, and energy efficiency.

Table 2: Main methodologies and findings of the compiled studies.

Study Title	CFD Implementation	Key Benefit	Variables Analyzed	Main Findings
CFD and wind-tunnel analysis of outdoor ventilation in a real compact heterogeneous urban area: Evaluation using "air delay [19].	It applies steady three-dimensional Reynolds-Averaged Navier–Stokes (RANS) models and Large Eddy Simulation (LES) to simulate outdoor urban ventilation conditions.	The study introduces a novel ventilation indicator, “air delay,” to improve the assessment of outdoor ventilation in complex urban environments. It further provides a systematic evaluation of steady RANS and LES approaches for urban ventilation analysis.	Distribution of air age and the “air delay” indicator.	The study offers a comprehensive assessment of RANS and LES approaches for evaluating ventilation conditions in a real urban setting and introduces a novel metric to support this evaluation.

CFD simulation of the wind flow under lift-up buildings using a porous approach [35].	CFD was employed to model the urban microclimate, with particular emphasis on simulating wind flow beneath elevated buildings.	The proposed method enables efficient wind-flow modeling in urban areas with elevated buildings while maintaining a balance between computational cost and accuracy, which is critical for urban thermal comfort assessment and heatwave mitigation.	Wind flow patterns, the impact of ground-floor geometry, and urban thermal comfort conditions.	The porous modeling approach in CFD has proven effective for simulating wind flow beneath elevated buildings, providing an optimal trade-off between predictive accuracy and computational efficiency.
Experimental study and CFD modelling of four-bed hospital ward with all-air wall induction unit for air-conditioning [36].	CFD modeling methods are proposed and experimentally validated to assess the ventilation and thermal performance of an all-air wall induction unit installed in a hospital ward.	The study examines a prototype induction unit designed for hospital wards, featuring a water-free system with low air supply velocity, and integrates experimental measurements with CFD simulations to enable a comprehensive performance evaluation.	Temperature distribution and CO_2 concentration (used as a proxy indicator for airborne contaminants).	The wall induction system maintains normalized contaminant concentrations near hospital beds by promoting displacement ventilation, with low-flow air supply from the lower section of the wall corner demonstrating effective performance.
Optimization of classroom window design using CFD and the Taguchi method [40].	CFD is employed to evaluate the influence of window position, width, height, and elevation from the floor on CO_2 concentration levels and draft risk within a classroom environment.	The study optimizes classroom window design to enhance indoor air quality and thermal comfort, employing the Taguchi method in combination with CFD to efficiently evaluate and optimize design parameters.	CO_2 concentration levels and the risk of draft discomfort.	The study proposes optimized window design parameters aimed at reducing CO_2 concentration levels and mitigating draft risk in classroom environments.
Assessing the impact of urban microclimate on building energy demand by coupling CFD and building performance simulation [28].	A validated CFD model is integrated with Building Performance Simulation (BPS) to quantify the impact of urban surface composition on urban microclimatic conditions and building energy demand.	The study quantifies the effects of urban design and vegetation on building energy consumption, with particular emphasis on cooling loads during heatwave events.	Building energy demand (cooling and heating loads) and urban microclimatic conditions (temperature).	Urban greening strategies significantly reduce cooling energy demand during heatwave conditions, while the composition of urban surfaces exerts a substantial influence on overall building energy requirements.
Cross-ventilation in a generic isolated building equipped with louvers: Wind-tunnel experiments and CFD simulations [20].	Steady three-dimensional Reynolds-Averaged Navier–Stokes (RANS) simulations are employed to model cross-ventilation in a building equipped with louvers, with CFD results validated against wind tunnel experiments.	The study examines the influence of louvered openings on natural ventilation performance, a critical factor for enhancing indoor air quality and achieving thermal comfort.	Airflow velocity distributions and air exchange efficiency.	The location of the openings significantly influences ventilation performance, and CFD simulations, when experimentally validated, are capable of accurately predicting cross-ventilation behavior.

Evaluation of supervised machine learning regression models for CFD-based surrogate modelling in indoor airflow field reconstruction [38].	CFD simulations are employed to generate training datasets for machine learning models aimed at predicting indoor airflow distribution, with machine learning acting as a surrogate modeling approach to reduce computational costs and accelerate predictions.	The study investigates the application of machine learning techniques to efficiently predict indoor airflow patterns, thereby reducing the computational burden associated with CFD simulations.	Airflow velocity fields and spatial distribution data.	Decision tree–based approaches and support vector regression models represent viable alternatives to neural networks for the prediction of indoor airflow patterns.
Pollutant cross-transmission in courtyard buildings: Wind tunnel experiments and computational fluid dynamics (CFD) evaluation [37].	CFD simulations are employed to assess the cross-transmission of indoor and outdoor contaminants in courtyard-type buildings, with results validated against wind tunnel experiments.	The study examines how courtyard design configurations may promote contaminant cross-transmission, highlighting a critical indoor air quality issue in residential building complexes.	Pollutant concentration levels and airflow distribution patterns.	Courtyard design configurations can significantly influence the transmission of contaminants between indoor and outdoor environments.
Sustainable ventilation strategies in buildings: CFD research [21].	CFD is employed to investigate natural ventilation strategies in buildings, particularly wind-driven ventilation and stack-effect mechanisms.	The study evaluates the potential of natural ventilation as a sustainable alternative to mechanical air conditioning, enhancing human thermal comfort and reducing overall energy consumption.	Natural ventilation, wind-induced ventilation, stack-effect ventilation, and human thermal comfort.	The article highlights the critical role of natural ventilation strategies in architectural design for enhancing human thermal comfort and promoting environmental sustainability.
Experimental and CFD Investigation on the Application for Aerogel Insulation in Buildings [33].	CFD simulations are employed to evaluate the thermal performance of aerogel insulation materials in building applications.	The study investigates the potential of aerogels as a high-performance insulation material to enhance energy efficiency in buildings.	Thermal insulation performance, aerogel materials, and heat transfer mechanisms.	The study provides valuable insights into the application of aerogel insulation systems to improve overall building energy performance.
Unsteady-state CFD simulations on the impacts of urban geometry on outdoor thermal comfort within idealized building arrays [34].	Unsteady-state CFD simulations are employed to assess the impact of urban geometry on outdoor thermal comfort conditions.	The study assesses the dynamic effects of building layout on airflow behavior and outdoor thermal comfort in urban environments, highlighting their critical importance for urban planning and sustainable design	Outdoor thermal comfort conditions, urban morphology, building configuration, and airflow distribution patterns.	The findings underscore the importance of accounting for unsteady wind conditions when evaluating urban thermal comfort.
CFD modeling of the building integrated with a novel design of a one-sided wind-catcher with water spray: Focus on thermal comfort [22].	CFD simulations are employed to model and evaluate a building integrated with an innovative single-sided wind catcher incorporating a water spray system.	The study evaluates the potential of this innovative design to enhance natural ventilation performance and improve indoor thermal comfort in buildings	Natural ventilation strategies, evaporative cooling, wind catcher design configurations, and thermal comfort performance.	The study evaluates the effectiveness of the proposed wind catcher design in enhancing indoor thermal conditions and overall thermal comfort.

Indoor Thermal Environment in Different Generations of Naturally Ventilated Public Residential Buildings in Singapore [41].	CFD is used to evaluate and compare indoor air velocities and the thermal environment in different generations of naturally ventilated public residential buildings.	The study provides information on the evolution of natural ventilation strategies in residential buildings and their impact on indoor thermal comfort.	Indoor air velocity, thermal environment, natural ventilation, residential buildings.	The research analyzes the effectiveness of natural ventilation in providing comfortable indoor environments under Singapore's climatic conditions.
CFD Evaluation of Thermal Conditioning in a House of Social Interest with a Solar Chimney Arrangement in Guanajuato, Mexico [23].	CFD is used to evaluate the thermal conditioning performance of a social housing unit that incorporates a solar chimney system.	The study evaluates the potential of solar chimneys to provide passive cooling and improve indoor thermal comfort in dwellings.	Thermal conditioning, solar chimney, natural ventilation.	The research provides information on the design and effectiveness of solar chimneys for thermal regulation in residential buildings.
Natural Ventilation in Low-Cost Housing: An Evaluation by CFD [24].	CFD is used to evaluate the performance of natural ventilation in low-cost housing.	The study investigates how natural ventilation can be optimized to improve indoor comfort in affordable housing solutions.	Natural ventilation, low-cost housing, indoor comfort.	The research provides information on the design of effective natural ventilation systems for residential buildings, particularly in the context of low-cost housing.
Energy simulation and CFD coupled analysis for the optimal operation of combined convection and radiant air conditioning considering dehumidification [29].	CFD is used to simulate thermal environments in residences, specifically those with combined radiant panels and air-conditioning systems, including the effects of dehumidification.	The combined use of radiant panels and air conditioning provides an optimal solution for thermal control in residences, balancing energy efficiency and comfort. The developed simulation tool may assist in product development and building material design.	Energy consumption, thermal comfort, relative humidity, and dehumidification effectiveness.	The study proposes a case where energy efficiency and comfort are achieved through the joint use of air conditioners and radiant panels, with a limited number of panels enabling balanced operation.
Influence of cross-ventilation cooling potential on thermal comfort in high-rise buildings in a hot and humid climate [25].	CFD simulation is used to investigate the effectiveness of natural ventilation in a high-rise building in India, together with building energy simulation. It determines wind-induced pressure distribution to evaluate indoor ventilation.	Cross-ventilation improves ventilative cooling efficiency, ensuring acceptable indoor thermal conditions even in adverse climates. It reduces cooling energy demand and electricity consumption.	Indoor thermal comfort, operative temperature, discomfort hours, natural ventilation cooling potential, night structural cooling.	Cross-ventilation significantly reduces discomfort hours and operating temperatures, providing a passive cooling solution for energy savings in high-rise buildings.
Improving Natural Ventilation Multi-Story Buildings within Hot and Dry Climates: A CFD Study of Windcatcher Performance [26].	CFD is used to study the performance of wind catchers in multi-story buildings to improve natural ventilation.	The study explores how wind catchers can enhance natural ventilation, which is crucial for energy and carbon conservation.	Wind catcher designs and their impact on natural ventilation performance in hot and dry climates.	The research contributes to strategies for improving natural ventilation through wind catchers, focusing on energy conservation.
Evaluation of passive cooling through natural ventilation strategies in historic residential buildings using CFD simulations [27].	CFD simulations are used to evaluate the efficiency of natural ventilation strategies in a historic residential structure.	Natural ventilation can save energy by reducing the need for mechanical systems in historic buildings, helping their preservation.	Efficiency of different natural ventilation approaches, thermal comfort, energy-saving potential.	The study demonstrates that natural ventilation strategies, especially cross-ventilation, can provide energy savings and maintain thermal comfort in historic buildings.

Thermal performance of an advanced smart fenestration systems for low-energy buildings [32].	CFD is used in a new model that combines ray-tracing and CFD to investigate the thermal and optical properties of smart fenestration systems.	The study explores a new adaptive fenestration system that can offer dynamic regulation of solar energy, improving building energy efficiency.	Solar transmittance, solar heat gain coefficient (SHGC), and dynamic thermal performance in summer and winter.	The proposed system can reduce solar transmittance and heat gain, resulting in better thermal performance with lower summer gains and lower winter heat losses.
Thermal Environment Analysis and Optimization for Large Space Buildings with Radiant Cooling Floors: A Case Study of Xianyang International Airport [42].	CFD is used to investigate the thermal environment of a large building and to analyze control strategies for radiant cooling floors combined with ventilation systems.	The study aims to find control strategies to achieve energy conservation and environmental improvement in large-space buildings.	Supply air temperature, cooling surface temperature, cooling capacity, and predicted mean vote (PMV).	The study determines optimal control variables to balance cooling capacity and thermal comfort.
Efficiency Assessment on Roof Geometry and Trombe Wall Shape for Improving Buildings' Heating Performance [43].	ANSYS-CFX software is used to simulate the thermal and fluid dynamic behavior of a Trombe wall system.	The study examines the impact of Trombe wall designs and roof types on building energy and operational efficiency.	Trombe wall designs, roof types, indoor climates, thermal comfort standards, energy efficiency.	The research provides information to optimize building design for improved heating performance under specific climatic conditions.
Impact of Building Envelope Materials on Energy Usage and Performance of Evaporative Cooling System in Residential Building [31].	ANSYS is used to simulate and analyze the performance of an evaporative cooling system in a residential building considering envelope materials and building orientation.	The research proposes an energy-efficient cooling system, showing that the proposed system combined with efficient envelope materials can achieve energy savings of about 35–43%.	Envelope components, building orientation, energy use, temperature reduction.	The study concludes that the proposed system reduces indoor temperature and that envelope characteristics significantly affect energy performance, leading to substantial energy savings.
Investigating Efficient Thermal Distribution in a House Room by combining Statistics with Computational Fluid Dynamics [44].	CFD analysis combined with statistical methods is used to determine cost-effective configurations for heating systems by investigating thermal distribution.	The study explores energy efficiency by identifying optimal heating configurations.	Theoretical temperatures at different indoor points.	The study uses numerical simulation to determine efficient thermal distribution.
Impact of Wind Pressure Coefficients on the Natural Ventilation Effectiveness of Buildings through Simulations [45].	Building energy simulation (BES) models are used to evaluate the effectiveness of natural ventilation using wind pressure coefficients as boundary conditions.	The research quantifies when outdoor airflow can be used as a cooling strategy to achieve indoor thermal comfort.	Airflows, cooling loads, heat rates.	Wind pressure coefficients are essential for evaluating airflow and ventilation effectiveness.
Significance of external wind conditions on the convective heat transfer coefficients (CHTC) and energy performance in multi-zone high-rise buildings [30].	A coupled BES–CFD method is employed to improve the accuracy of convective heat transfer coefficient calculations in high-rise buildings.	Improved predictions of CHTC and better understanding of wind influence on building energy performance.	Convective heat transfer coefficients and energy performance.	External wind conditions significantly affect CHTC and energy performance.

Improvement of the hygrothermal efficiency numerically using CFD modeling in a full-scale ventilated room with Moroccan climates [46].	CFD is used to examine moisture distribution and heat transfer in a ventilated room under winter conditions.	Ventilation configurations are analyzed to find the optimal configuration for thermal comfort.	Moisture and temperature distribution.	The study identifies the optimal ventilation configuration through comfort indicators.
The influence of zonal air supply on thermal comfort in a classroom located in a hot and humid environment: a case study from Jeddah—Saudi Arabia [47].	CFD simulations predict air temperature, velocity, and humidity distribution, evaluating zonal air supply designs in classrooms.	Explores zonal air supply strategies to improve comfort in hot and humid regions.	Air velocity, air temperature, relative humidity, globe temperature, PMV, PPD.	Parametric analysis identifies effective configurations.
Experimental Validation of the Potential of Cross-Ventilation Strategy as a Natural Cooling Technique Integrated in a Real Historic Building [48].	Simulations analyze temperature fluctuations under free-running mode in naturally ventilated historic buildings.	Validates cross-ventilation as a natural cooling technique.	Temperature fluctuations.	Provides insights into thermal performance through cross-ventilation.
Thermal Comfort Assessment for Simultaneous Operation of Cooling and an Energy Recovery Ventilator in a Residential Building During Summer [49].	The article evaluates thermal comfort.	The research explores simultaneous operation of cooling and energy recovery ventilators.	Thermal comfort.	The study provides an evaluation under specific conditions.
Assessment of Floor-Level Impact on Natural Ventilation and Indoor Thermal Environment in Hot–Humid Climates: A Case Study of a Mid-Rise Educational Building [50].	The study evaluates natural ventilation and the indoor thermal environment.	Investigates the impact of floor level on ventilation in educational buildings.	Natural ventilation and indoor thermal environment.	Provides an assessment of thermal conditions at different floor levels.
The Effect of the Isolation Hotel Facade Attachment on the Inter-Flat Transmission of Aerosols [51].	The study investigates aerosol transmission.	Examines façade attachments and their effect on aerosol transmission between apartments.	Aerosol transmission.	Presents findings relevant to infection prevention.
Integrating CFD and thermoregulation models: A novel framework for thermal comfort analysis of non-uniform indoor environments [39]	CFD is integrated with thermoregulation models to analyze thermal comfort in non-uniform indoor environments.	Enables a more detailed analysis of occupant-centered radiant cooling strategies.	Operative temperature, heat balance, physiological responses.	Introduces a new numerical framework for evaluating thermoregulation and comfort.
Sensitivity analysis of influence factors on multi-zone indoor airflow CFD simulation [52].	CFD simulation is used for sensitivity analysis of factors influencing multi-zone indoor airflow.	Improves understanding of how different factors affect airflow simulation results.	Factors influencing multi-zone airflow.	Provides a sensitivity analysis of influencing factors in CFD airflow simulations.

Source: Authors (2026).

III.3 TRENDS IN THE USE OF CFD IN ARCHITECTURAL SPACES

Computational Fluid Dynamics (CFD) has become, over the past decade, a key methodological tool for analyzing the environmental and energy performance of the built environment, expanding its scope beyond strictly engineering applications to address challenges specific to architecture and urban planning. Traditionally employed in the field of computational wind engineering, CFD has demonstrated a strong capability to model complex phenomena such as airflow behavior, heat transfer, and contaminant dispersion, which has encouraged its adoption in studies related to pedestrian wind comfort, urban ventilation, air quality, and outdoor thermal conditions [19]. This versatility has enabled more accurate assessments of the interaction between urban morphology, local microclimates, and occupants' thermal well-being, thereby establishing CFD as a relevant technical support tool for sustainable urban planning and design.

At the building scale, the synthesized evidence reveals a clear trend toward applications aimed at optimizing indoor thermal comfort through passive and low-energy strategies, such as natural ventilation, cross-ventilation, solar chimneys, wind catchers, and evaporative cooling systems. In these studies, CFD is employed to analyze variables including air temperature, airflow velocities, CO_2 concentration, relative humidity, and comfort indices (PMV/PPD), enabling the evaluation of design configurations and the validation of architectural solutions with greater quantitative rigor. Furthermore, increasing integration with human thermo physiological models and experimental validation techniques has been observed, strengthening the reliability of predictions and aligning simulations more closely with real occupancy conditions [41]. Complementarily, a methodological evolution toward hybrid approaches that combine CFD with building energy performance simulation tools and data-driven predictive models has been identified. This coupling allows for the simultaneous evaluation of local thermo-aerodynamic behavior and its global impact on energy demand, enabling the quantification of how urban microclimate, building envelope characteristics, and conditioning systems influence energy consumption and overall performance [32]. Collectively, these trends indicate a shift from isolated modeling applications toward integrated analytical frameworks, in which CFD serves as a bridge between architectural design, human comfort, and energy sustainability.

III.4 CHALLENGES IN THE APPLICATION OF CFD

Despite its growing adoption in the analysis of thermal comfort and the environmental performance of the built environment, the application of Computational Fluid Dynamics (CFD) faces several technical and methodological limitations that affect the accuracy and feasibility of its results. One of the primary challenges lies in the faithful representation of real urban environments, which are characterized by highly complex geometries, morphological heterogeneity, and multiple spatial scales. Due to these difficulties, many studies rely on simplified or idealized configurations, which may reduce the ability of simulations to capture local phenomena such as ventilation patterns, recirculation zones, or heat accumulation typical of real urban contexts. From a computational perspective, CFD simulations particularly transient or high-fidelity approaches such as Large Eddy Simulation (LES) require considerable computational time and hardware resources, limiting their applicability in parametric studies or iterative design processes. Consequently, many studies adopt steady-state models based on Reynolds-Averaged Navier–Stokes (RANS), which offer a reasonable trade-off between accuracy and computational cost, albeit with reduced capability to resolve complex turbulent structures [40]. In addition, simulation results are highly sensitive to technical decisions such as mesh resolution, turbulence model selection, boundary condition definition, and the quality of climatic and geometric input data, factors that may introduce significant uncertainty if not properly controlled. In indoor applications, further challenges persist regarding the modeling of occupants' dynamic behavior, variable furniture layouts, and real space-use patterns, all of which directly influence airflow distribution, effective ventilation, and thermal perception. Finally, CFD model validation remains a critical requirement to ensure the reliability of predictions; however, acquiring high-resolution experimental data whether through in situ measurements or wind tunnel testing is often costly and complex, particularly in dense urban environments or specific configurations, thereby limiting the empirical verification of numerical models [38]. Overall, these challenges highlight the need to advance toward hybrid methodologies, robust validation frameworks, and more computationally efficient tools that can broaden the applicability of CFD in architectural practice.

III.5 OPPORTUNITIES FOR THE USE OF CFD IN ARCHITECTURAL SPACES

Computational Fluid Dynamics (CFD) offers a wide range of opportunities to strengthen environmental analysis and the sustainable design of the built environment, particularly in the evaluation of urban ventilation strategies aimed at improving air quality and mitigating pollutant accumulation in densely built areas. Its ability to simulate complex flow patterns, air dispersion, and renewal processes enables the identification of morphological configurations and design solutions that enhance pedestrian comfort and reduce exposure to atmospheric contaminants, thereby contributing to resilient and healthy urban planning [20]. At the building scale, CFD enables the optimization of thermal performance through the design and validation of passive strategies such as natural ventilation, cross-ventilation, and convective cooling, reducing reliance on mechanical conditioning systems and lowering the energy and carbon footprint of buildings. Moreover, the detailed analysis of variables such as air temperature, relative humidity, airflow velocities, and spatial heat distribution allows for the estimation of thermal comfort indices with higher spatial resolution, supporting evidence-based design decisions adapted to local climatic conditions [32]. Complementarily, the integration of CFD with building performance simulation (BPS) tools significantly expands its analytical potential by enabling the coupled evaluation of interactions among urban microclimate, architectural envelope characteristics, and overall energy demand. This hybrid approach facilitates the comparison of design scenarios and the development of optimized solutions that balance thermal comfort, operational efficiency, and environmental sustainability [28]. Furthermore, the flexibility of CFD modeling allows the analysis of specific health and safety contexts, such as contaminant or aerosol transmission in highly occupied spaces, providing relevant technical insights for the design of safer and more resilient buildings [24]. Collectively, these applications highlight the potential of CFD as a strategic tool for informed decision-making in architecture and urban planning.

IV. CONCLUSIONS

The evidence gathered in this systematic review confirms that Computational Fluid Dynamics (CFD) has become, over the past decade, a central tool for assessing thermal comfort and environmental performance in architectural and urban spaces. The bibliometric analysis, comparative synthesis of studies, and characterization of applications reveal a sustained expansion in its use, both in passive ventilation and thermal conditioning strategies and in urban microclimate modeling and building energy optimization. Furthermore, the increasing adoption of open-source platforms, the coupling with building energy simulations (BPS/BES), and the integration with thermo physiological models and machine learning techniques reflect a transition toward more accessible, integrated, and data-driven decision-making approaches. Nevertheless, the review also identifies persistent challenges that affect the reliability and scalability of these applications, including the realistic geometric representation of complex environments, the high computational requirements of transient high-fidelity models, the sensitivity of results to numerical parameters, and the need for rigorous experimental validation.

These limitations underscore the importance of advancing toward hybrid methodologies, robust verification frameworks, and surrogate models capable of balancing predictive accuracy with operational efficiency. Overall, the findings indicate that CFD holds significant strategic potential during the early stages of architectural design and urban planning, enabling the evaluation of scenarios, comparison of alternatives, and anticipation of thermal and energy impacts prior to physical implementation. Its consolidation as a decision-support tool for environmentally conscious design not only enhances thermal comfort and indoor air quality but also contributes to reducing energy consumption and the carbon footprint of the built environment. Future research should further integrate empirical data, artificial intelligence, and open-source workflows in order to broaden the applicability of CFD and strengthen its role as a bridge between computational modeling, human well-being, and sustainability.

V. AUTHOR'S CONTRIBUTION

Conceptualization: Keny Montalvo Morales, Henry Javier-Ninahuaman, Grimaldo Quispe, Abdallah Elshawadfy Elwakeel, John Espita, Jader Rodriguez and Edwin Villagran.
Methodology: Keny Montalvo Morales, Henry Javier-Ninahuaman, Grimaldo Quispe, Abdallah Elshawadfy Elwakeel, John Espita, Jader Rodriguez and Edwin Villagran.
Investigation: Keny Montalvo Morales, Henry Javier-Ninahuaman, Grimaldo Quispe, Abdallah Elshawadfy Elwakeel, John Espita, Jader Rodriguez and Edwin Villagran.
Discussion of results: Keny Montalvo Morales, Henry Javier-Ninahuaman, Grimaldo Quispe, Abdallah Elshawadfy Elwakeel, John Espita, Jader Rodriguez and Edwin Villagran.
Writing – Original Draft: Keny Montalvo Morales, Henry Javier-Ninahuaman, Grimaldo Quispe, Abdallah Elshawadfy Elwakeel, John Espita, Jader Rodriguez and Edwin Villagran.
Writing – Review and Editing: Keny Montalvo Morales, Henry Javier-Ninahuaman, Grimaldo Quispe, Abdallah Elshawadfy Elwakeel, John Espita, Jader Rodriguez and Edwin Villagran.
Resources: Keny Montalvo Morales, Henry Javier-Ninahuaman, Grimaldo Quispe, Abdallah Elshawadfy Elwakeel, John Espita, Jader Rodriguez and Edwin Villagran.
Supervision: Keny Montalvo Morales, Henry Javier-Ninahuaman, Grimaldo Quispe, Abdallah Elshawadfy Elwakeel, John Espita, Jader Rodriguez and Edwin Villagran.
Approval of the final text: Keny Montalvo Morales, Henry Javier-Ninahuaman, Grimaldo Quispe, Abdallah Elshawadfy Elwakeel, John Espita, Jader Rodriguez and Edwin Villagran.

VI. REFERENCES

[1] G. A. O. Rocha, M. A. Pichimata, and E. Villagran, "Research on the Microclimate of Protected Agriculture Structures Using Numerical Simulation Tools: A Technical and Bibliometric Analysis as a Contribution to the Sustainability of Under-Cover Cropping in Tropical and Subtropical Countries," Sustain. 2021, Vol. 13, Page 10433, vol. 13, no. 18, p. 10433, Sep. 2021, doi: 10.3390/SU131810433.

[2] Y. Toparlar, B. Blocken, B. Maiheu, and G. J. F. van Heijst, "A review on the CFD analysis of urban microclimate," Renew. Sustain. Energy Rev., vol. 80, pp. 1613–1640, 2017.

[3] A. Jamin, W. Bosschaerts, I. Nastase, and B. Janssens, "Review of the existing state of the art regarding the use of CFD and human thermophysiological models for the vehicular comfort assessment," in IOP Conference Series: Earth and Environmental Science, 2021, vol. 664, no. 1, p. 12012.

[4] K. Setaih, N. Hamza, M. Mohammed, S. Dudek, and T. Townshend, "CFD modeling as a tool for assessing outdoor thermal comfort conditions in urban settings in hot arid climates," J. Inf. Technol. Constr., 2014.

[5] H. Kabrein, A. Hariri, A. M. Leman, M. Z. M. Yusof, and A. Afandi, "Experimental and CFD modelling for thermal comfort and CO2 concentration in office building," in IOP Conference Series: Materials Science and Engineering, 2017, vol. 243, no. 1, p. 12050.

[6] M. Dhahri and H. Aouinet, "CFD investigation of temperature distribution, air flow pattern and thermal comfort in natural ventilation of building using solar chimney," World J. Eng., vol. 17, no. 1, pp. 78–86, 2020.

[7] E. Villagran, "Implementation of ventilation towers in a greenhouse established in low altitude tropical climate conditions: numerical approach to the behavior of the natural ventilation," Rev. Ceres, 2021, doi: 10.1590/0034-737x202168010002.

[8] A. Palmowska and I. Sarna, "CFD modelling of thermal comfort in the passenger coach," Archit. Civ. Eng. Environ., vol. 15, no. 4, pp. 133–146, 2023.

[9] I. Lourenço Niza and E. E. Broday, "Development of thermal comfort models over the past years: a systematic literature review," Int. J. Ambient Energy, vol. 43, no. 1, pp. 8830–8846, 2022.

[10] H. Huo et al., "Simulation of the urban space thermal environment based on computational fluid dynamics: A comprehensive review," Sensors, vol. 21, no. 20, p. 6898, 2021.

[11] G. H. Merabet et al., "Artificial intelligence-assisted energy and thermal comfort control for sustainable buildings: an extended representation of the systematic review," arXiv Prepr. arXiv2006.12559, 2020.

[12] E. Villagran, J. J. Espitia, F. A. Velázquez, A. Sarmiento, D. A. S. Velandia, and J. Rodriguez, "Artificial Intelligence in Solar-Assisted Greenhouse Systems: A Technical, Systematic and Bibliometric Review of Energy Integration and Efficiency Advances," Technologies, vol. 13, no. 12, p. 574, 2025.

[13] M. J. Page et al., "The PRISMA 2020 statement: an updated guideline for reporting systematic reviews," bmj, vol. 372, 2021.

[14] E. Villagran, J. J. Espitia, F. A. Velázquez, and J. Rodriguez, "Solar Dryers: Technical Insights and Bibliometric Trends in Energy Technologies," AgriEngineering, vol. 6, no. 4, pp. 4041–4063, 2024.

[15] D. A. Pinzon, G. M. Amado, J. Rodriguez, and E. Villagran, “Global Research Trends and Thematic Evolution of Blueberry (Vaccinium spp.) Science: A Bibliometric Analysis,” Horticulturae, vol. 11, no. 12, p. 1501, 2025.

[16] G. A. O. Rocha, A. N. C. Medina, L. G. Arias, J. F. A. Caita, and E. Villagran, “Análisis sobre la actividad científica referente a las estrategias de climatización pasiva usada en invernaderos: Parte 1: Análisis bibliométrico,” Cienc. Lat. Rev. Científica Multidiscip., vol. 6, no. 5, pp. 4596–4623, 2022.

[17] J. J. Espitia et al., “Solar Energy Applications in Protected Agriculture: A Technical and Bibliometric Review of Greenhouse Systems and Solar Technologies,” Agronomy, vol. 14, no. 12, p. 2791, 2024.

[18] G. Herrera-Franco, N. Montalván-Burbano, P. Carrión-Mero, B. Apolo-Masache, and M. Jaya-Montalvo, “Research trends in geotourism: A bibliometric analysis using the scopus database,” Geosci., 2020, doi: 10.3390/geosciences10100379.

[19] N. Antoniou, H. Montazeri, H. Wigo, M. K.-A. Neophytou, B. Blocken, and M. Sandberg, “CFD and wind-tunnel analysis of outdoor ventilation in a real compact heterogeneous urban area: Evaluation using ‘air delay,’” Build. Environ., vol. 126, pp. 355–372, 2017.

[20] K. Kosutova, T. Van Hooff, C. Vanderwel, B. Blocken, and J. Hensen, “Cross-ventilation in a generic isolated building equipped with louvers: Wind-tunnel experiments and CFD simulations,” Build. Environ., vol. 154, pp. 263–280, 2019.

[21] E. Cuce, F. Sher, H. Sadiq, P. M. Cuce, T. Guclu, and A. B. Besir, “Sustainable ventilation strategies in buildings: CFD research,” Sustain. Energy Technol. Assessments, vol. 36, p. 100540, 2019.

[22] J. Foroozesh et al., “CFD modeling of the building integrated with a novel design of a one-sided wind-catcher with water spray: Focus on thermal comfort,” Sustain. Energy Technol. Assessments, vol. 53, p. 102736, 2022.

[23] S. Rodriguez Miranda, G. O. Gamboa, M. A. Zamora-Antuñano, N. Farrera-Vázquez, and R. García-García, “CFD evaluation of thermal conditioning in a house of social interest with a solar chimney arrangement in Guanajuato, Mexico,” Processes, vol. 11, no. 4, p. 1286, 2023.

[24] L. A. Rocha et al., “Natural ventilation in low-cost housing: an evaluation by CFD,” Buildings, vol. 13, no. 6, p. 1408, 2023.

[25] R. Stasi, F. Ruggiero, and U. Berardi, “Influence of cross-ventilation cooling potential on thermal comfort in high-rise buildings in a hot and humid climate,” Build. Environ., vol. 248, p. 111096, 2024.

[26] J. A. Qadourah, “Improving Natural Ventilation Multi-Story Buildings within Hot and Dry Climates: A CFD Study of Windcatcher Performance,” energy Conserv., vol. 28, p. 29, 2024.

[27] L. Iskandar, E. Bay-Sahin, A. Martinez-Molina, and S. T. Beeson, “Evaluation of passive cooling through natural ventilation strategies in historic residential buildings using CFD simulations,” Energy Build., vol. 308, p. 114005, 2024.

[28] J. Brozovsky, J. Radivojevic, and A. Simonsen, “Assessing the impact of urban microclimate on building energy demand by coupling CFD and building performance simulation,” J. Build. Eng., vol. 55, p. 104681, 2022.

[29] T. Yamamoto, A. Ozaki, K. Aratsu, and R. Fukui, “Energy simulation and CFD coupled analysis for the optimal operation of combined convection and radiant air conditioning considering dehumidification,” Heliyon, vol. 9, no. 7, 2023.

[30] K. Ding, J. K. Calautit, and C. Jimenez-Bescos, “Significance of external wind conditions on the convective heat transfer coefficients (CHTC) and energy performance in multi-zone high-rise buildings,” Energy Build., vol. 320, p. 114570, 2024.

[31] S. Thongsuk, P. Songsukthawan, P. Lertwanitrot, S. Ananwattanaporn, S. Yoomak, and C. Pothisarn, “Impact of Building Envelope Materials on Energy Usage and Performance of Evaporative Cooling System in Residential Building.,” Energies (19961073), vol. 17, no. 15, 2024.

[32] Y. Ming, Y. Sun, X. Liu, X. Liu, and Y. Wu, “Thermal performance of an advanced smart fenestration systems for low-energy buildings,” Appl. Therm. Eng., vol. 244, p. 122610, 2024.

[33] S. Golder, R. Narayanan, M. R. Hossain, and M. R. Islam, “Experimental and CFD investigation on the application for aerogel insulation in buildings,” Energies, vol. 14, no. 11, p. 3310, 2021.

[34] G. Chen, L. Rong, and G. Zhang, “Unsteady-state CFD simulations on the impacts of urban geometry on outdoor thermal comfort within idealized building arrays,” Sustain. Cities Soc., vol. 74, p. 103187, 2021.

[35] C. Nevers, A. Kubilay, J. Carmeliet, and D. Derome, “CFD simulation of the wind flow under lift-up buildings using a porous approach,” Build. Environ., vol. 263, p. 111867, 2024.

[36] S. Sheng, T. Yamanaka, T. Kobayashi, N. Choi, and N. Chou, “Experimental study and CFD modelling of four-bed hospital ward with all-air wall induction unit for air-conditioning,” Build. Environ., vol. 222, p. 109388, 2022.

[37] H. Sun et al., “Pollutant cross-transmission in courtyard buildings: Wind tunnel experiments and computational fluid dynamics (CFD) evaluation,” Build. Environ., vol. 264, p. 111919, 2024.

[38] X. Li, W. Sun, C. Qin, Y. Yan, L. Zhang, and J. Tu, “Evaluation of supervised machine learning regression models for CFD-based surrogate modelling in indoor airflow field reconstruction,” Build. Environ., vol. 267, p. 112173, 2025.

[39] J. M. Zambrano and L. Baldini, “Integrating CFD and thermoregulation models: A novel framework for thermal comfort analysis of non-uniform indoor environments,” Energy Build., vol. 335, p. 115570, 2025.

[40] Y. E. Cetin, B. E. Yuce, M. Kriegel, P. Wargocki, and P. V. Nielsen, “Optimization of classroom window design using CFD and the Taguchi method,” J. Build. Eng., vol. 106, p. 112580, 2025.

[41] J.-Y. Deng et al., “Indoor thermal environment in different generations of naturally ventilated public residential buildings in Singapore,” Atmosphere (Basel)., vol. 13, no. 12, p. 2118, 2022.

[42] R. Hu, H. Wang, J. Liang, X. Li, W. Zheng, and G. Liu, “Thermal Environment Analysis and Optimization for Large Space Buildings with Radiant Cooling Floors: A Case Study of Xianyang International Airport,” Buildings, vol. 14, no. 5, p. 1355, 2024.

[43] M. Dhahri, A. Yüksel, H. Aouinet, D. Wang, M. Arıcı, and H. Sammouda, “Efficiency assessment on roof geometry and Trombe wall shape for improving buildings’ heating performance,” Buildings, vol. 14, no. 5, p. 1297, 2024.

[44] J. Aparecido Martins, A. Francisco Siqueira, and E. Claro Romao, “Investigating Efficient Thermal Distribution in a House Room by combining Statistics with Computational Fluid Dynamics.,” Eng. Technol. Appl. Sci. Res., vol. 14, no. 4, 2024.

[45] N. R. M. Sakiyama, J. C. Carlo, F. I. H. Sakiyama, N. Abdessemed, J. Frick, and H. Garrecht, “Impact of wind pressure coefficients on the natural ventilation effectiveness of buildings through simulations,” Buildings, vol. 14, no. 9, p. 2803, 2024.

[46] E. H. Sebbar, Y. Khattari, Y. Chaibi, and T. El Rhafiki, “Improvement of the hygrothermal efficiency numerically using CFD modeling in a full-scale ventilated room with Moroccan climates,” Sci. African, vol. 26, p. e02408, 2024.

[47] Z. Jastaneyah, H. M. Kamar, A. Hashmi, F. A. Ghaleb, and H. Al Garalleh, “The influence of zonal air supply on thermal comfort in a classroom located in a hot and humid environment: a case study from Jeddah—Saudi Arabia,” Discov. Sustain., vol. 5, no. 1, p. 526, 2024.

[48] T. Palomo Amores, F. Ruda Sarria, D. C. Medina, T. C. Valera, J. Sánchez Ramos, and S. Álvarez Domínguez, “Experimental Validation of the Potential of Cross-Ventilation Strategy as a Natural Cooling Technique Integrated in a Real Historic Building,” Appl. Sci., vol. 15, no. 4, p. 2174, 2025.

[49] K. Kang and D. D. Kim, “Thermal Comfort Assessment for Simultaneous Operation of Cooling and an Energy Recovery Ventilator in a Residential Building During Summer,” Buildings, vol. 15, no. 4, p. 582, 2025.

[50] E. J. Mba et al., “Assessment of Floor-Level Impact on Natural Ventilation and Indoor Thermal Environment in Hot–Humid Climates: A Case Study of a Mid-Rise Educational Building,” Buildings, vol. 15, no. 5, p. 686, 2025.

[51] N. Zhang, Y. Li, Y. Ji, and X. Li, “The Effect of the Isolation Hotel Facade Attachment on the Inter-Flat Transmission of Aerosols.,” Build., vol. 15, no. 5, 2025.

[52] J. C. P. Cheng, H. H. L. Kwok, A. T. Y. Li, J. C. K. Tong, and A. K. H. Lau, “Sensitivity analysis of influence factors on multi-zone indoor airflow CFD simulation,” Sci. Total Environ., vol. 761, p. 143298, 2021.

Journal of Engineering and Technology for Industrial Applications

ISSN ONLINE: 2447-0228

ITEGAM-JETIA

Manaus, v.12 n.60, p.108-126, July/August, 2026.
DOI: https://doi.org/10.5935/jetia.v12i60.3605

REVIEW PAPERS OPEN ACCESS

A REVIEW OF RESEARCH AND TECHNOLOGY DEVELOPMENT ON THE ARCHIMEDES SCREW WIND TURBINE

Bayu Ardiansyah Maskub Putra*[1], Nazaruddin Sinaga[2], Eflita Yohana[3] and Mochammad Shodiq[4]

[1, 2, 3,4]Department of Mechanical Engineering, Diponegoro University, Semarang, Central Java, Indonesia.

[1]https://orcid.org/0009-0004-5048-7838, [2]http://orcid.org/0000-0002-3450-5360,
[3]https://orcid.org/0000-0003-2408-2912, [4]https://orcid.org/0009-0006-2227-8734

Email:*ampbayu1@gmail.com, nsinaga19.undip@gmail.com, efnan2003@gmail.com, mochammadshodiq0@gmail.com

ARTICLE INFO

Article History
Received: February 9, 2026
Reviewed: June 5, 2026
Accepted: July 5, 2026
Published: July 31, 2026

Keywords:
Archimedes Screw Wind Turbine,
Aerodynamics,
Airfoil,
Augmentation,
Angle of attack,
Aspect ratio,
Blade pitch angle.

ABSTRACT

Wind energy is a renewable energy source that offers both environmental and socio-economic benefits. However, its implementation in low-wind areas remains challenging. The Archimedes Screw Wind Turbine (ASWT) is a horizontal-axis wind turbine that forms a three-dimensional conical structure shaped like an elongated spiral, resembling a seashell. This study aims to provide a comprehensive overview of ASWT research progress, including its advantages, limitations, and development opportunities. The method used is a narrative review by gathering and comparing results from previous studies on the design and performance of ASWT. The findings indicate that the Archimedean spiral profile results in better aerodynamic performance compared to the logarithmic spiral profile, with a power coefficient (C_P) value reaching 0.2668 at an opening angle of 60°. The optimal aspect ratio (AR) is found in the range of 1.0-1.1 to balance aerodynamic efficiency and structural strength. The use of NACA type airfoil profiles improves performance compared to S and FX-type airfoils and shows effectiveness at low wind speeds with minimal noise levels. Furthermore, the configuration of angles ($\alpha_1 = 30°$, $\alpha_2 = 45°$, $\alpha_3 = 60°$) is identified as the most effective arrangement, yielding a maximum power coefficient (C_{pmax}) of 0.234 at a tip speed ratio (TSR) of 1.5. Additionally, the addition of a brimmed shroud is proven to increase the C_P value by approximately 3.6 times compared to turbines without a shroud. Overall, ASWT holds significant potential for urban applications, but further research is still needed to encourage the adoption of this technology in the renewable energy transition.

Copyright ©2026 by authors and Galileo Institute of Technology and Education of the Amazon (ITEGAM). This work is licensed under the Creative Commons Attribution International License (CC BY 4.0).

I. INTRODUCTION

Wind power is widely recognized as one of the most promising technologies in the transition toward low-carbon energy systems [1], [2]. Wind energy represents one of the cleanest energy sources and has currently become the second-largest contributor among renewable energy resources [3]. Beyond its role in energy generation, wind power offers substantial social, public health, and environmental benefits while significantly reducing dependence on fossil fuels [4]. Based on the orientation of the rotational axis, wind turbines can be broadly classified into two categories that its Horizontal Axis Wind Turbines (HAWT), which employ rotors with axes aligned parallel to the wind direction, and Vertical Axis Wind Turbines (VAWT), whose rotors rotate about an axis perpendicular to the incoming wind flow [5]. VAWTs offer several advantages, including enhanced resistance to strong wind conditions due to their inherent stalling mechanism, which improves operational safety during high wind events [6]. In addition, they tend to operate more quietly and feature designs that eliminate the need for yaw control systems. However, these advantages are offset by limitations in self-starting capability [7]. The vertical shaft configuration of VAWTs allows the transmission system and generator to be positioned at ground level, facilitating maintenance. Nevertheless, this configuration often requires complex blade pitch control mechanisms. In contrast, HAWTs represent the most commercially successful turbine type to date and predominantly rely on aerodynamic lift to achieve high power conversion efficiency.

Drag-based turbines, such as certain VAWT configurations, generally exhibit lower efficiency compared to lift-based HAWTs. Moreover, HAWTs are typically designed to operate optimally under relatively high wind speeds, usually exceeding 6 m/s, to attain maximum efficiency [8], [9], [10], [11], [12]. Despite their technological maturity, the implementation of wind turbine systems remains challenging in regions characterized by highly fluctuating wind patterns and limited installation space, particularly in urban environments [13]. One promising innovative solution is the Archimedes Screw Wind Turbine (ASWT), a horizontal-axis turbine featuring a three-dimensional conical structure with an elongated spiral geometry resembling a seashell [14], [15]. This unique design enables the ASWT to operate effectively at low wind speeds, making it particularly suitable for urban and built-environment applications [16]. Although the ASWT demonstrates considerable potential, its practical implementation and technological development remain relatively limited. Research on ASWTs is still fragmented, and comprehensive literature reviews consolidating existing findings are scarce. A systematic review is therefore required to map the evolution of ASWT design concepts, performance optimization strategies, and key technical challenges reported across previous studies. This review aims to provide a comprehensive understanding of the current state of ASWT research and technology, highlighting its advantages, limitations, and future development prospects. The outcomes of this study are expected to serve as a valuable scientific reference for researchers, academics, and practitioners, supporting the advancement of more efficient and practical ASWT applications in the future.

II. THEORETICAL REFERENCE

This study adopts a Narrative Review approach to examine the development of research and technological advancements related to the Archimedes Screw Wind Turbine (ASWT). The review process was conducted in a systematic manner, encompassing several key stages, including the definition of eligibility criteria, identification of data sources, study selection, data extraction, and data synthesis. Through this approach, the review aims to provide a comprehensive overview that captures the evolution and current state of ASWT research.

II.1 ELIGIBILITY CRITERIA

Studies focusing on the development, performance, and technological innovation of the Archimedes Screw Wind Turbine (ASWT) constitute the primary scope of this review. Research addressing technical aspects of other wind turbine types, such as Horizontal Axis Wind Turbines (HAWT) and Vertical Axis Wind Turbines (VAWT), was included as supporting literature to enrich and contextualize the discussion. Only publications that meet established academic standards were considered. Consequently, non-scholarly articles, duplicate publications, and studies lacking robust methodological foundations were excluded from the analysis.

II.2 DATA SOURCES

The literature reviewed in this study was obtained through systematic searches of reputable and indexed academic databases. The sources include international peer-reviewed journal articles, conference proceedings, and other scholarly works that satisfy the defined academic eligibility criteria.

II.3 DATA SYNTHESIS

The analysis was carried out by categorizing the selected studies into key thematic areas, such as turbine design, performance characteristics, and structural or aerodynamic modifications. Findings from different studies were subsequently compared to identify common trends, methodological consistency, and notable discrepancies. The results of this comparison are presented in summary tables to facilitate clarity and readability. The overall synthesis is articulated through a structured narrative, supported by tables, figures, and illustrative materials, thereby providing a systematic and comprehensive understanding of the development of ASWT technology.

III. DISCUSSION

III.1 INTRODUCTION TO THE ARCHIMEDES SCREW WIND TURBINE

The Archimedes Screw Wind Turbine (ASWT) is a wind turbine featuring spiral-shaped blades based on Archimedean geometric principles, a concept originally introduced by the ancient Greek mathematician Archimedes [17], [18]. The overall configuration of the ASWT is illustrated in Figure 1. In its common design, the turbine consists of three blades symmetrically arranged at 120° intervals. These blades form a three-dimensional conical structure with an elongated spiral geometry resembling the shell of a marine mollusk. Owing to this spiral configuration, the ASWT is inherently capable of aligning itself with the incoming wind direction without the need for any yaw control mechanism [15], [19], [20].

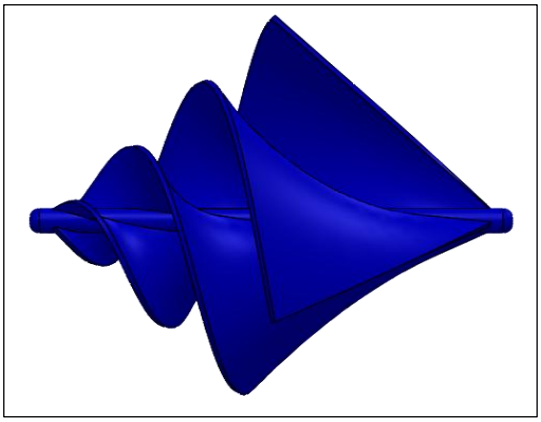


Figure 1: ASWT Turbine.
Source: Authors, (2026).

In addition to its distinctive geometry, the ASWT exhibits several notable advantages. The turbine is able to harness a combination of aerodynamic lift and drag forces to generate power, allowing it to operate effectively across a range of flow conditions. Another key advantage is its capability to perform efficiently under low wind speed conditions, with a minimum cut-in speed of approximately 2.5 m/s [16], [21]. Given the characteristics and potential outlined above, a thorough understanding of ASWT research development methodologies becomes essential for tracing the progression of knowledge related to its aerodynamic behavior and technological evolution. Such understanding is critical for the optimization of ASWT design and for enhancing its practical application in real-world wind energy systems.

III.2 RESEARCH DEVELOPMENT METHODS FOR ASWT

Research on the development of Archimedes Screw Wind Turbines (ASWT) generally follows a systematic workflow that begins with geometric modeling, proceeds through numerical simulation and experimental validation, and concludes with result documentation and analysis. The initial stage typically involves the construction of a three-dimensional reference model using computer-aided design software such as SolidWorks, OpenSCAD, or CATIA. Following the modeling phase, the research advances to analytical stages involving numerical simulation and experimental investigation. The methodological scope varies across studies. Some investigations adopt a single-track approach, relying solely on numerical simulations or exclusively on experimental testing. Numerical simulations commonly employ Computational Fluid Dynamics (CFD) techniques to virtually predict flow behavior and aerodynamic performance. These analyses are typically conducted using specialized software packages such as ANSYS Fluent, ANSYS CFX, or STAR-CCM+. In contrast, experimental investigations aim to obtain direct physical measurements. Common experimental methods include performance testing in wind tunnel facilities, flow visualization and quantification using Particle Image Velocimetry (PIV), and final validation through field testing under real operating conditions. Upon completion of these analyses, the resulting data are expected to address the predefined research objectives [22-25]. In this context, the present review paper is structured to provide a comprehensive understanding of research trends and technological developments related to ASWTs. The discussion encompasses aerodynamic aspects, including performance analysis in terms of torque and power output, force generation mechanisms, the influence of angle of attack, and the interpretation of flow simulation results. Furthermore, technological development aspects are examined, covering blade geometry optimization, evaluation of performance augmentation strategies, and comparative performance assessments against other wind turbine designs. Through this review, potential optimization opportunities are identified, and existing research gaps are highlighted, thereby offering valuable directions for future ASWT research.

III.3 AERODYNAMICS OF THE ASWT

III.3.1 Velocity Triangle and Aerodynamic Forces Acting on the ASWT

To determine the torque and power generated by the ASWT, the angular momentum equation is applied to a predefined control volume, as adopted in previous studies [14] and expressed in Equation (1) [14] :

$$\frac{\partial}{\partial t}\int_{CV}(r \times V)\rho d\forall + \int_{CS}(r \times V)\rho V.\hat{n}dA = \sum(r \times F) \quad (1)$$

Equation (1) represents the angular momentum balance for a control volume. Under the assumption of steady-state conditions, the first term in Equation (1) becomes zero because it is time-independent. Consequently, Equation (1) can be simplified to Equation (2) [14] :

$$\int_{CV}(r \times V)\rho\, dV.\hat{n}dA = \sum(r \times F) \quad (2)$$

The continuity equation for a fixed control volume is expressed as shown in Equation (3) [14] :

$$\frac{\partial}{\partial t}\int_{CV}\rho\, dV + \int_{CV}\rho W\,.\hat{n}dA = 0 \quad (3)$$

Assuming steady-state flow and constant density, the first term in Equation (3) vanishes. The second term represents the total mass flow rate through the control volume. Accordingly, Equation (3) can be simplified to Equation (4) [14] :

$$-\dot{m}_{in} + \dot{m}_{out} = 0 \tag{4}$$

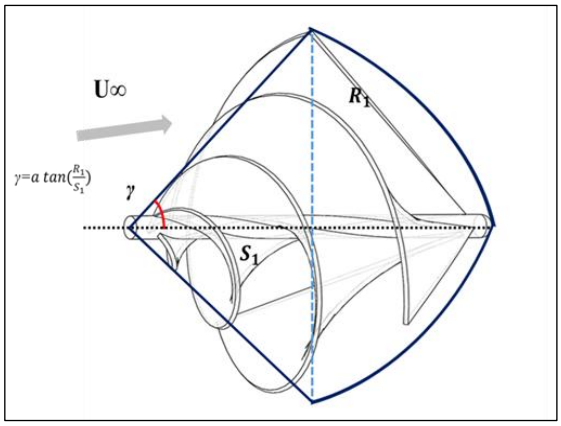


Figure 2: Shape parameter ASWT.
Source: [14].

In developing the governing equations, several geometric parameters must first be defined, namely γ, R_1, R_2, and S_1, as illustrated in Figure 2. Here, γ denotes the angle between the rotation axis and the blade tip. R_1represents the vertical distance from the outer blade tip to the rotational axis, while R_2corresponds to the vertical distance from the inner blade tip to the rotational axis. Meanwhile, $S_1$is defined as the horizontal distance between the leading blade tip and the root of the spiral blade. Based on these geometric parameters, the inlet and outlet mass flow rates can be expressed using Equations (5) and (6), respectively [14] :

$$\dot{m}_{in} = \rho U_{\infty} \sin\gamma \times \pi \left(\frac{R_1+R_2}{2}\right) S_1 \tag{5}$$

$$\dot{m}_{out} = 3\rho A_{out} W_{\theta} \tag{6}$$

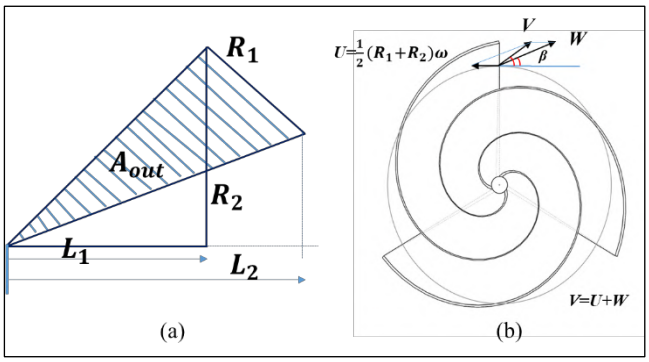


Figure 3: Definition of Aout, U, V and W
Source: [14].

Here, W_{θ} denotes the tangential component of the relative velocity. The velocity triangle analysis for the ASWT begins with estimating the outlet area and its geometric relationships, as illustrated in Figure 3(a). In this figure, $L_1$is defined as the distance from the center of the rear face to point x, which is perpendicular to the outer blade tip, while L_2 represents the distance from the same center to point x, perpendicular to the inner blade tip. Based on this configuration, the total outlet area (A_{out}) is obtained by summing its two constituent areas, $A_1$and A_2, as expressed in Equations (7) and (8) [14] :

$$A_{out} = A_1 + A_2 \tag{7}$$

$$A_{out} = \frac{1}{2}R_1L_1 - \frac{1}{2}R_2L_1 + \frac{1}{2}(R_1 - R_2)(L_2 - L_1) = \frac{1}{2}(R_1 - R_2)L_2 \tag{8}$$

The velocity triangle at the blade outlet is illustrated in Figure 3(b), where Wdenotes the relative velocity, V the absolute velocity, and U the tangential velocity. In this context, β is defined as the angle between $W$and U. The outlet mass flow rate ($\dot{m}_{out}$) can therefore be written as Equation (9) [14] :

$$\dot{m}_{out} = 3\rho A_{out} W_{\theta} = 3\rho.\frac{1}{2}(R_1 - R_2)L_2 \times W \cos\beta = \frac{3}{2}\rho(R_1 - R_2)L_2 \times W\cos\beta \tag{9}$$

Since $\dot{m}_{in} = \dot{m}_{out}$, the following relationship is obtained:

$$\rho U_\infty \sin\gamma \times \pi\left(\frac{R_1+R_2}{2}\right) S_1 = \frac{3}{2}\rho(R_1+R_2)L_2 \times W\cos\beta \tag{10}$$

$$\therefore W = \frac{\pi U_\infty \sin\gamma(R_1+R_2)S_1}{3(R_1+R_2)L_2\times\cos\beta} \tag{11}$$

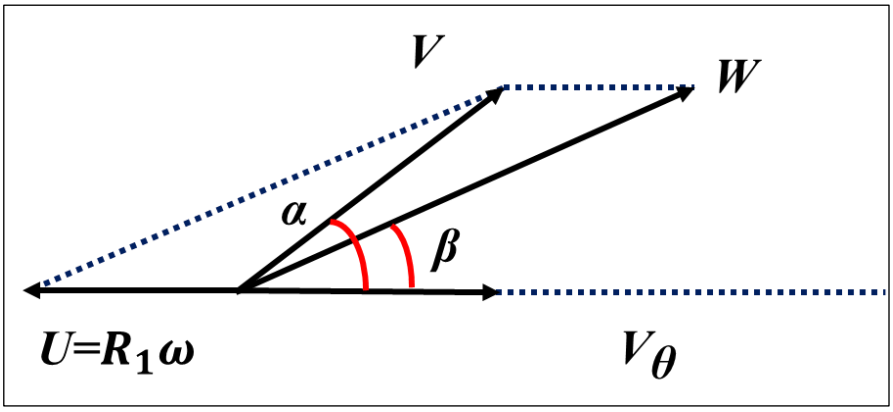


Figure 4: Triangle velocity at outlet boundary blade.
Source: [14].

Figure 4 illustrates the velocity triangle composed of U, V, and W, where α is defined as the angle between the absolute velocity $V$and its tangential component V_θ. The absolute velocity Vcan be expressed as follows [14] :

$$V^2 = W^2 + U^2 - 2WU\cos\beta, V_\theta = V\cos\alpha \tag{12}$$

Based on Equation (12), the angle α can be defined using Equation (13) [14] :

$$V\sin\alpha = W\sin\beta \;\rightarrow\; \sin\alpha = \frac{W}{V}\sin\beta \tag{13}$$

$$\therefore \alpha = \sin^{-1}\left(\frac{W}{V}\sin\beta\right) \tag{14}$$

The moment exerted by the blade on the fluid is equal in magnitude and opposite in direction to the shaft torque. This relationship is expressed in Equation (15) [14] :

$$T_{shaft} = \int_{CS}(r\times V)\,\rho V.\hat{n}dA = \int_{CS}(rV\cos\alpha)\,\rho(V\cos\alpha)\,dA = 3\rho V^2\cos^2\alpha\int_0^L rdA \tag{15}$$

Finally, the torque generated by the blade can be expressed as Equation (16):

$$\therefore T_{shaft} = 3\rho V_\theta^2 \times \frac{(R_2-R_1)}{6L_1(L_2-L_1)} \times [R_2(2L_2^3 + L_1^3 + L_1L_2^3) - L_1R_1(L_1+L_2)^2] \tag{16}$$

Power is defined as the product of torque and angular velocity and is expressed as follows [14] :

$$Power = T_{shaft}\omega \tag{17}$$

After the power expression is defined in Equation (18), as illustrated in Figure 5, the analysis of wind–blade interaction requires two complementary perspectives: the plan view (top view) and the elevation view (side view). In the plan view analysis, the calculation is based on changes in angular momentum resulting from the interaction between the incoming wind and the ASWT blades. The aerodynamic lift force (F_L) and drag force (F_D) generated on the blade are decomposed into components parallel and perpendicular to the wind direction, yielding four force components: F_{LX}, F_{LY}, F_{DX}, and F_{DY}. The resultant aerodynamic forces acting on the ASWT blade can therefore be expressed as:

$$F_X = F_{LX} + F_{DX} \tag{18}$$

$$F_Y = F_{LY} + F_{DY} \tag{19}$$

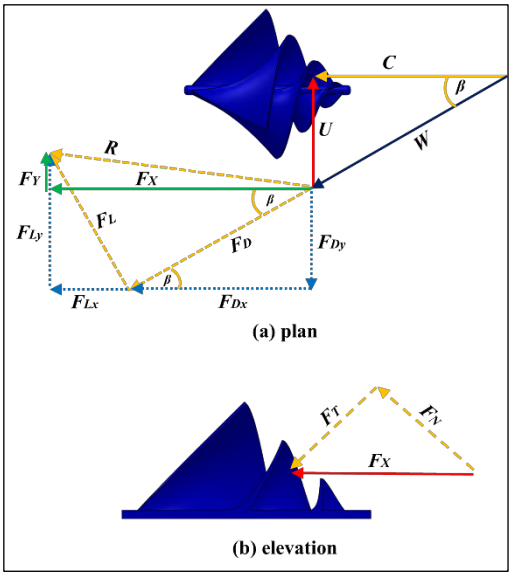


Figure 5: Aerodynamic Forces Affecting the Spiral Blade on an ASWT.
Source: [27].

The force component perpendicular to the wind direction (F_Y) is responsible for driving the rotational motion of the ASWT. Meanwhile, as observed in the elevation view, the force component F_X is further resolved into two components: the tangential force (F_T), which directly contributes to power generation, and the normal force (F_N), which acts as a compressive or tensile load on the ASWT blades. Consequently, the power generated by the ASWT arises from the combined effect of the $F_Y$component in the plan view, which produces rotational torque, and the tangential force F_T in the elevation view, which contributes directly to energy conversion. This aerodynamic interaction pattern occurs repeatedly as the wind traverses successive 120° angular positions corresponding to each of the three spiral blades of the ASWT [25-28]**.**

III.3.2 Angle of Attack in ASWT

The angle of attack is defined as the angle between the direction of the relative airflow and the chord line of the turbine blade profile. This parameter plays a critical role in determining both the aerodynamic forces acting on the blade and the resulting power output of the turbine [29-36]. As illustrated in Figure 6, measurements are conducted within an axisymmetric observation plane that distinguishes between the windward (front) side and the sheltered (lee) side of the blade, enabling a comprehensive assessment of the flow dynamics around the rotating blade [37], [38].

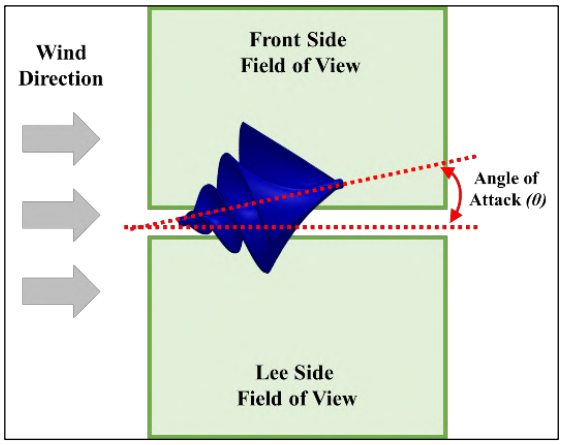


Figure 6: Angle of attack on ASWT.
Source: [37].

In the study conducted by [37], although various factors such as Reynolds number and free-stream turbulence can influence the near-wake structure of turbine blades, the analysis specifically focused on the effect of the angle of attack. To investigate the influence of wind direction on the flow field, comparisons were made between the mean velocity field and the instantaneous velocity field at different blade phase angles. The results indicate that the wake velocity decreases as the angle of attack increases. Mean velocity measurements reveal that the low-velocity region downstream of the blade expands with increasing angle of attack. Within the near-wake region behind the blade, no flow separation was observed, as the incoming airflow continues to pass through the rotating blade system. Regions of high shear were found to form around the blade tip vortices, and their size increases as the angle of attack becomes larger. The tip vortices generated by each blade are clearly observable at blade phase angles ranging from 0° to 120°. At lower angles of attack, the spacing between these vortices remains relatively uniform; however, as the angle of attack reaches approximately 15°, the vortex spacing becomes increasingly irregular.

III.3.3 Velocity and Pressure Contours in ASWT

Velocity contours are widely employed in the literature to visualize the flow velocity characteristics around wind turbine blades [39-43]. To investigate the aerodynamic behavior of the ASWT, Figure 7 presents the mean velocity fields obtained from airflow simulations conducted at three different wind speeds. In wind turbine systems, a turbulent wake state may occur due to variations in wind speed or direction, or as a result of changes in blade orientation (pitching). Such flow behavior is more clearly observed at lower wind speeds, as shown in Figure 7. The highest velocities are observed near the outermost region of the rotor within the simulation domain. Between successive spiral blade sectors, recirculation zones with relatively low velocities are formed. Furthermore, due to the spiral geometry, the flow velocity gradually increases from the leading edge of the blade toward the inner side of each blade level.

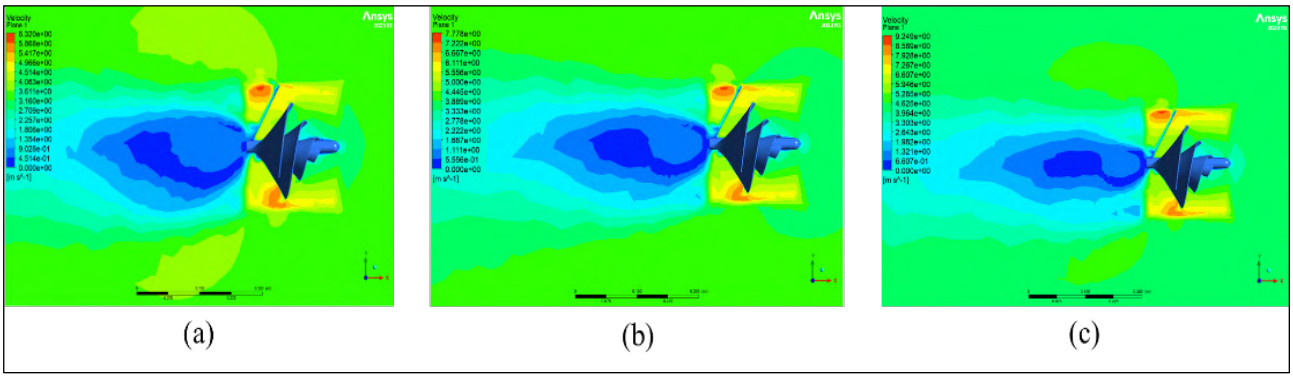


Figure 7: Ensemble-averaged velocity field and pressure distribution under steady-state conditions: (a) 3.5 m/s at 300 rpm, (b) 4.0 m/s at 400 rpm, and (c) 4.5 m/s at 500 rpm.
Source: [46].

The visualization also indicates that the airflow is partially obstructed by the conical hub and the rotor, leading to the formation of circumferential acceleration zones downstream of the rotor, which in turn reduce the pressure near the walls of the rotating domain. Meanwhile, the wake region is clearly identified behind the rotor hub, characterized by lower flow velocities. From a geometric perspective, the blade twist angle is larger near the root than at the tip. Visually, the longer velocity vectors near the blade tip indicate higher flow velocities compared to those near the blade root. In addition, all three velocity contour plots demonstrate that the flow velocity in the central region is significantly lower than that near the blade periphery. This observation suggests that stronger flow near the blade tip is highly advantageous, as it exerts force on the blade at a larger moment arm, thereby enhancing torque generation [44-46]. The streamline velocity distribution shown in Figure 8 further confirms that the lowest flow velocities occur in the central region and near the rotational axis. In contrast, the highest velocities are observed near the blade tips, where the tip speed is substantially greater than that in the mid-span region. Wind flow impinging on the blade tips generates torque, causing the turbine blades to rotate in the direction opposite to the incoming wind flow [47], [48].

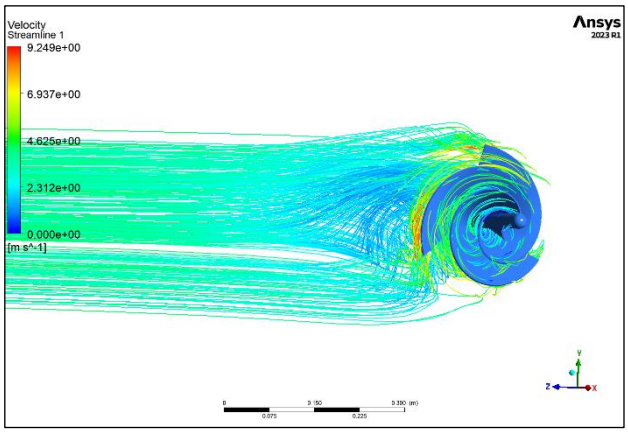


Figure 8: Streamline velocity.
Source: [47].

Pressure contours provide a graphical representation of the pressure distribution around turbine blades as obtained from fluid flow simulations [49-53]. As shown in Figure 9, the pressure contours on the front and rear sides of the turbine blades indicate that the pressure on the blade's pressure side is higher than that on the suction side. The locations of maximum and minimum pressure are predominantly found near the blade edges. The pressure difference between the pressure side and the suction side is the primary driving mechanism that induces blade rotation [47], [54], [55].

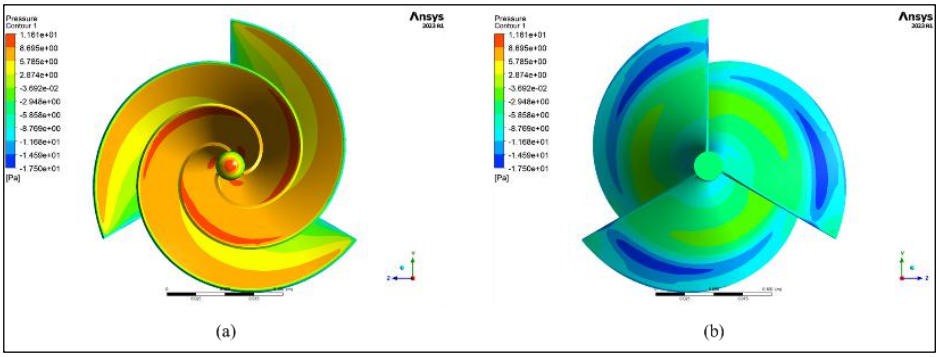


Figure 9: Pressure contours on the blade surfaces: (a) pressure side and (b) suction side.
Source: [47].

As illustrated in Figure 10, an increase in flow velocity leads to a corresponding increase in this pressure difference. The highest pressure difference occurs near the blade tip, while the pressure variation in the mid-span region remains relatively small. This finding indicates that the majority of the extractable energy originates from the region near the blade tip, which is consistent with the operating principles of most horizontal-axis wind turbines (HAWTs) [47], [56], [57].

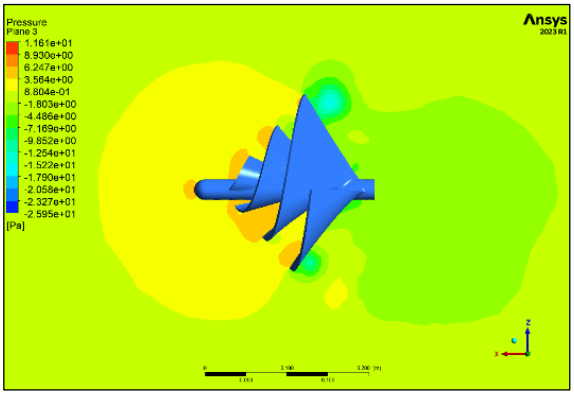


Figure 10: Pressure contours.
Source: [47].

III.4 DEVELOPMENT OF ASWT TECHNOLOGY

III.4.1 Effect of Spiral Geometry on ASWT

The Spiral Wind Turbine (SWT) is a type of wind turbine that typically consists of three blades helically wrapped around a single main shaft and symmetrically arranged with respect to the axis of rotation [58], [59]. This configuration enables the SWT to redirect the incoming airflow, thereby enhancing the utilization of the wind's kinetic energy [13], [60]. The main design parameters of the SWT are illustrated in Figure 11. Among these parameters, the spiral pitch (S) represents the axial distance traveled by a blade over one complete spiral rotation. The turbine radius (r) denotes the radial distance from the rotational axis to the blade tip at the outlet side, while the turbine opening angle (θ) describes the angle formed between the rotational axis and the blade tip at the outlet section [61].

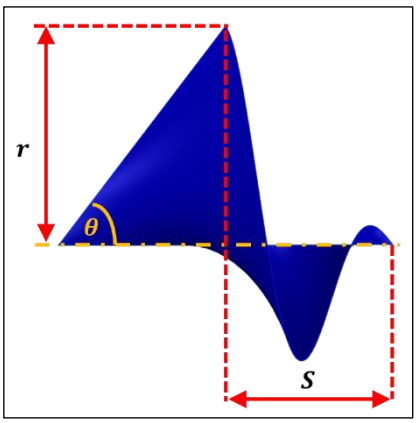


Figure 11: ASWT design parameters.
Source: [61].

Based on these design parameters, variations in spiral geometry play a crucial role in determining the aerodynamic characteristics and overall performance of the SWT.

Figure 12(a) presents a spiral wind turbine with a logarithmic spiral profile, whereas Figure 12(b) shows a turbine with an Archimedean spiral profile. The primary distinction between these two configurations lies in the winding characteristics of the spiral. In the logarithmic spiral, the spacing between successive turns increases progressively, while in the Archimedean spiral, the spacing remains constant along the spiral length [61], [62]. These variations in spiral profiles provide a clear basis for comparing the influence of spiral geometry on the performance of Spiral Wind Turbines.

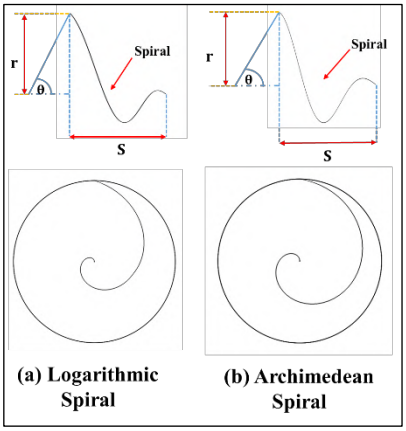


Figure 12: Spiral profile models.
Source: [61].

According to the study conducted by [61], the performance of a shell-shaped spiral wind turbine with logarithmic and Archimedean spiral profiles was evaluated under varying opening angles (θ) and tip speed ratios (TSR). The results demonstrated that the turbine with an Archimedean spiral profile exhibited superior performance compared to the logarithmic profile, particularly at an opening angle of 60°, where the maximum power coefficient (C_p) of 0.266825 was achieved at a TSR of 2.5.

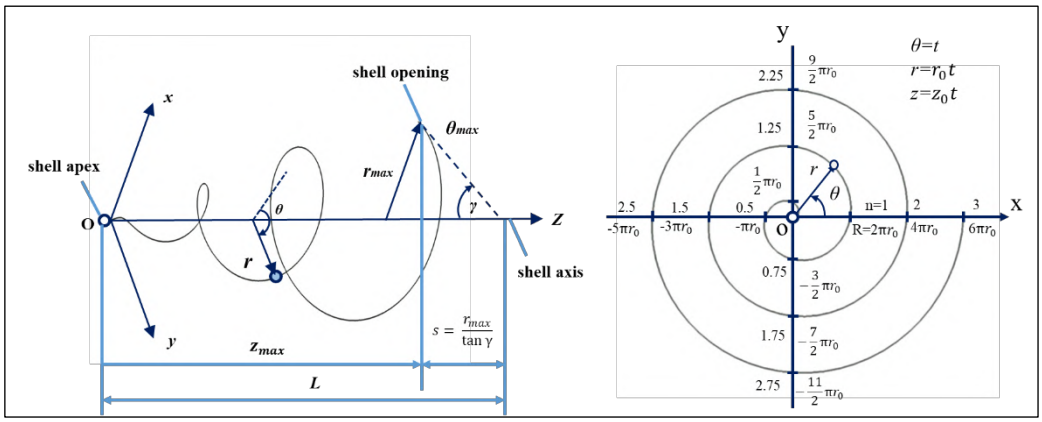


Figure 13: A seashell-shaped turbine modeled on an Archimedean conical spiral.
Source: [15].

To further examine the characteristics of the SWT with an Archimedean spiral profile, the geometric parameters of the turbine are presented in Figure 13. The three-dimensional spiral curve is generated using parametric equations expressed in a cylindrical coordinate system [15]. The governing equations employed to construct the spiral geometry are given as:

$$\theta = t \tag{20}$$

$$r = r_0 t \tag{21}$$

$$z = z_0 t \tag{22}$$

Where θ denotes the spiral rotation angle, t is the parametric variable, r represents the radial distance of the spiral, and z corresponds to the axial distance along the shell axis. The Archimedean spiral lying in the r–θ plane is defined by Equations (20) and (21), while Equation (22) describes the axial extension of the spiral along the z-axis, thereby introducing a conical component to the geometry. The resulting three-dimensional spiral curve originates at $r = 0$and $\theta = 0$at the defined coordinate origin (the shell apex) and terminates at $r_{\max}$ and $\theta_{\max}$ at the shell opening. For given initial values of r_0 and z_0, a set of (r, z) points forming the conical spiral can be obtained as a function of the spiral rotation angle θ. However, the value of $r_0$is constrained to ensure that all spiral configurations achieve the same maximum radius $r_{\max}$, which is necessary to guarantee equal input power among different turbine designs. The shell opening angle (γ), defined as the angle between the shell opening and the shell axis, is also incorporated into the rotor design. The number of conical spiral turns (n) and the turbine aspect ratio (AR) are illustrated in Figure 13 and defined as follows:

$$n = \frac{\theta_{\max}}{2\pi} \tag{23}$$

$$AR = \frac{L}{D} \tag{24}$$

Where the aspect ratio (AR) is the ratio between the turbine length (L) and the turbine diameter ($D = 2r_{\max}$). The turbine length (L) is obtained from the sum of the maximum axial extension of the conical spiral ($z_{\max}$) and the projected distance along the shell axis ($s = r_{\max}/\tan\gamma$)[15]. From this analysis, it can be concluded that the spiral geometry is not merely an aesthetic feature, but a critical design parameter that directly influences turbine efficiency. The SWT with an Archimedean spiral profile demonstrates superior performance, achieving a power coefficient of $C_p = 0.266825$ at an opening angle of 60°, compared to the logarithmic spiral profile. Consequently, the Archimedean spiral configuration has become the more dominant design reference in the development of Spiral Wind Turbines.

III.4.2 Aspect Ratio in ASWT

The geometric parameters of the ASWT rotor are illustrated in Figure 14. Understanding the aspect ratio as part of the rotor's geometric characteristics provides a fundamental basis for evaluating how its variation influences turbine performance. The aspect ratio (AR) is one of the key parameters that plays a significant role in defining both the geometric configuration and the operational performance of the rotor. As expressed in Equation (24), the aspect ratio is defined as the ratio between the turbine length and its outer diameter. This derived parameter offers deeper insight into the optimal geometric configuration of the rotor and has been widely adopted in previous studies [15], [63-68]. Based on earlier investigations, the influence of aspect ratio variation on the power-generating capability of ASWTs can be clearly identified through the following findings.

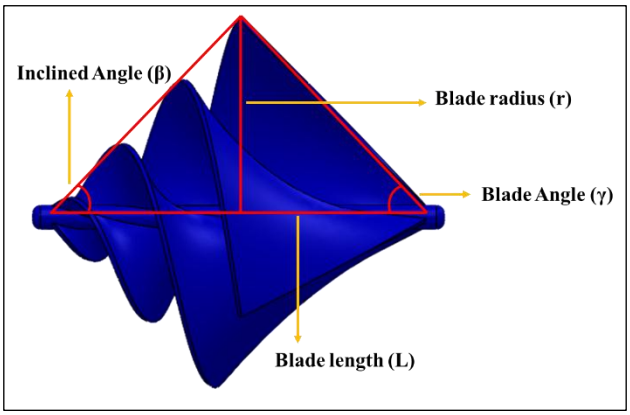


Figure 14: Geometric parameters of the ASWT.
Source : [69].

Study [69] examined five turbine models incorporating three different aspect ratios (AR = 1.5, 1.25, and 1.0), designed using both forward elongation and backward elongation configurations. The experimental results identified the model with AR = 1 and forward elongation as the most optimal configuration. This model achieved a maximum power coefficient (C_p) of 0.249 at a tip speed ratio (TSR) of 1.413. In general, the forward elongation configuration was found to enhance the power coefficient at lower TSR values, making it particularly suitable for low wind speed environments where effective operation at low rotational speeds is required. Conversely, reducing the aspect ratio below unity was not recommended, as it tended to induce vibrations and flow instabilities that negatively affect efficiency and reduce bearing lifespan. On the other hand, the AR = 1 model with backward elongation exhibited a higher torque coefficient, which can be attributed to the larger blade flow interaction area. This configuration provides improved self-starting capability and higher initial (starting) torque. In a separate investigation [70], four ASWT models with different geometric configurations were evaluated. ASWT 1 had a diameter of 55 cm and a length of 60 cm, resulting in an aspect ratio of 1.1. ASWT 2 maintained the same diameter of 55 cm but had a shorter length of 50 cm, also yielding an aspect ratio of 1.1. ASWT 3 featured a diameter and length of 50 cm, corresponding to an aspect ratio of 1.0, while ASWT 4 had a diameter of 45 cm and a length of 50 cm, producing an aspect ratio of 0.9. These variations were implemented to assess the influence of geometric changes on the aerodynamic performance of the turbine. The results demonstrated that increasing the rotor aspect ratio significantly improved the power coefficient. Among the tested models, ASWT 1 (D = 55 cm, L = 60 cm, AR = 1.1) achieved the highest power coefficient, reaching a maximum C_p value of 0.17. Overall, the comparative analysis of the four models revealed a consistent trend indicating that rotor geometry variations have a direct and measurable impact on aerodynamic performance. Therefore, the selection of an appropriate aspect ratio in ASWT design is crucial for balancing aerodynamic efficiency and structural integrity. Research findings indicate that aspect ratios exceeding 1.1 do not provide optimal performance. Conversely, aspect ratios below 1.0 tend to introduce flow fluctuations and mechanical vibrations, which reduce efficiency and shorten component lifespan. The optimal aspect ratio range for ASWTs lies between 1.0 and 1.1, where the highest power coefficients are consistently achieved.

III.4.3 ASWT Blade Profile Geometry

Airfoil selection is a critical aspect of wind turbine blade aerodynamic design. The airfoil profile has a pronounced influence on blade performance, where even minor geometric modifications can result in substantial changes in aerodynamic behavior as well as the level of noise generated [71-76] . To maximize the extraction of wind kinetic energy, an optimized blade geometry is required. As illustrated in Figure 15, one example of a blade profile employing an airfoil is presented. Modern rotor blades are generally designed with varying airfoil profiles along the blade span in order to enhance operational efficiency. This approach leads to more complex blade geometries, yet significantly improves performance compared to earlier generations of wind turbine blades. Airfoil selection is typically based on comparative evaluations of lift-to-drag ratios among established airfoil profiles [20], [77-79].

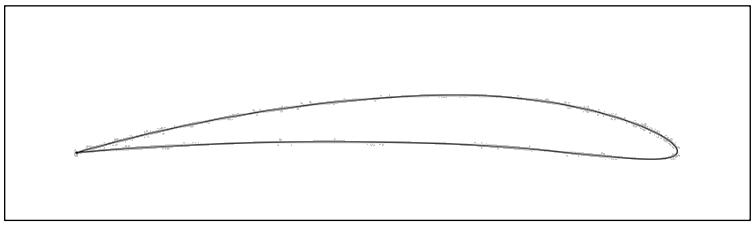


Figure 15: NACA 6409 Profile.
Source : [80].

An understanding of the role of airfoil geometry in improving blade efficiency provides the basis for further investigation into how airfoil shape affects overall turbine performance, particularly in ASWT designs. A study conducted by [25] analyzed the influence of airfoil implementation on ASWT performance by comparing four design configurations. The initial configuration consisted of a conventional ASWT with standard specifications, including a blade thickness of 3.5 mm, a pitch-to-diameter ratio (2s/D) of 0.28, a constant pitch of 70 mm, blade angles of $\alpha_1 = 30°$, $\alpha_2 = 45°$, and $\alpha_3 = 60°$, and outer and inner shaft diameters of 25 mm and 15 mm, respectively.The second configuration involved a modified ASWT in which the blade thickness was reduced to 2 mm and the blade angles were adjusted to $\alpha_1 = 25°$, $\alpha_2 = 50°$, and $\alpha_3 = 60°$, while maintaining the same pitch and 2s/D ratio. In the third stage, the ASWT design focused on variations of the pitch-to-diameter ratio (2s/D) to identify the most efficient configuration, with values modified from the baseline 0.28 to 0.22, 0.24, 0.26, 0.30, 0.32, and 0.34. The final stage introduced airfoil-based ASWT designs (AASWT), representing an advanced level of aerodynamic refinement through the application of various airfoil profiles to the modified ASWT geometry. In this phase, three airfoil families (S, FX, and NACA), each comprising five profile variants, were evaluated using the previously identified optimal 2s/D ratio to assess the influence of micro-scale aerodynamic characteristics on overall turbine performance. The results indicated that the AASWT employing the NACA 4401 airfoil achieved the best performance, reaching a maximum power coefficient (CP) of 30.45% at a tip speed ratio (λ) of 2. This design exhibited a 26.88% efficiency improvement compared to the conventional ASWT and a 6.47% increase relative to the modified ASWT. Consistent with these findings, several studies have investigated the application of NACA airfoil profiles in ASWT designs to evaluate performance responses under varying wind speed conditions. Research by [20] focused on AASWT performance by comparing the torque characteristics of an ASWT equipped with a NACA 6409 airfoil against a conventional ASWT. Computational fluid dynamics (CFD) analysis was employed to estimate blade torque characteristics. The results demonstrate a torque increase of approximately 10–15% at low wind speeds and more than 15% at moderate wind speeds, indicating that the NACA 6409 airfoil blade design performs effectively under low to moderate wind conditions. In another study, [81] reported that ASWTs modified with the NACA 2412 airfoil profile produced lower noise levels and exhibited improved suitability for low wind speed operation. These findings were supported by both wind tunnel experiments and field tests, which confirmed enhancements in torque output and aerodynamic efficiency. Overall, these results indicate that the application of NACA-type airfoil profiles in ASWT blades yields superior performance compared to S and FX profile types. Furthermore, ASWT designs incorporating the NACA 6409 airfoil demonstrate effective operation under low to moderate wind speeds, while NACA airfoil configurations also contribute to reduced noise levels relative to conventional blade designs.

III.4.4 Effect of Blade Inclination on ASWT Performance

Analyzing the influence of blade inclination on ASWT performance requires a clear understanding of how variations in blade angle alter turbine behavior. Figure 16 provides an initial conceptual illustration that clarifies the role of blade inclination in the ASWT rotor. A study conducted by [82] investigated the effect of blade inclination on ASWT performance using two distinct approaches: variable blade-angle configurations and uniform blade-angle configurations across the rotor. The variable configurations consisted of ($\alpha_1 = 15°$, $\alpha_2 = 30°$, $\alpha_3 = 45°$) and ($\alpha_1 = 30°$, $\alpha_2 = 45°$, $\alpha_3 = 60°$), while the uniform configurations included ($\alpha_1 = \alpha_2 = \alpha_3 = 30°$), ($\alpha_1 = \alpha_2 = \alpha_3 = 45°$), and ($\alpha_1 = \alpha_2 = \alpha_3 = 60°$). Among all tested configurations, the stepped blade-angle arrangement ($\alpha_1 = 30°$, $\alpha_2 = 45°$, $\alpha_3 = 60°$) emerged as the most effective, achieving a maximum power coefficient (C_{Pmax}) of 0.234 at a tip speed ratio (TSR) of 1.5. The analysis revealed that rotors with larger blade angles dominate the incoming flow through a stronger interaction over the swept area, thereby widening the operational TSR range and shifting the peak performance toward higher TSR values. This configuration generated higher thrust forces and increased force fluctuations due to enhanced drag associated with more upright blade orientations. These effects intensified flow blockage and produced more pronounced pressure patterns around the rotor. In contrast, rotors with smaller blade angles presented a gentler interaction surface to the incoming flow. As a result, the freestream was able to pass through the rotor with minimal disturbance, leading to a weaker blockage effect and reduced energy extraction. While this condition supported more stable tip-vortex structures, itwas also associated with slower wake recovery compared to rotors with larger blade angles. At higher blade inclinations, stronger and more coherent hub vortex structures were observed, indicating a more aggressive momentum exchange between the blades and the flow.

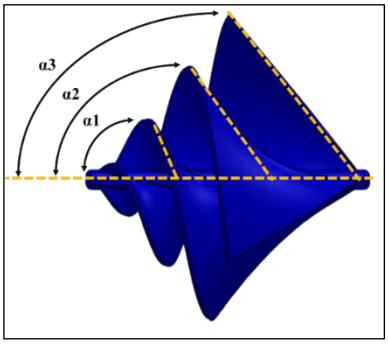


Figure 16: Schematic view of the ASWT rotor.
Source : [82].

Consistent with the findings of [82], the study by [27] examined the combined effects of blade thickness and blade angle on ASWT performance. The results demonstrated that stepped blade-angle configurations provide superior performance, with the combination of $\alpha_1 = 25°$, $\alpha_2 = 50°$, and $\alpha_3 = 60°$ and a blade thickness of 2 mm identified as the optimal arrangement for the modified ASWT. Additional studies further broaden the understanding of blade inclination effects on ASWT performance. Research by [83] analyzed the lift coefficient (C_L) and drag coefficient (C_D) of ASWTs employing a Fibonacci-based blade arrangement with opening angles of $\alpha_1 = 35°$, $\alpha_2 = 45°$, and $\alpha_3 = 65°$. The investigation was conducted under turbulent airflow conditions at a Reynolds number of 1200, ambient pressure of 1 atm, and wind speeds of 5.5 m/s and 15 m/s. The results indicated that at a wind speed of 5.5 m/s, increasing the blade opening angle led to higher lift coefficients. Conversely, at a wind speed of 15 m/s, larger blade angles resulted in increased drag coefficients, as a greater portion of the wind was intercepted by the turbine. However, the occurrence of unstable aerodynamic responses in these simulations was identified as a general limitation in wind turbine design. Nevertheless, a contrasting trend was reported by [84], who evaluated blade inclination angles (β) ranging from 50° to 65° at 5° intervals using computational simulations validated by experimental measurements. The results showed that the maximum power coefficient ($C_{Pmax} = 0.22$ at TSR = 1.72) and the maximum torque coefficient ($C_{Tmax} = 0.24$ at TSR = 0.62) were both achieved at a blade angle of 50°. These findings indicate that increasing blade inclination beyond this value leads to a reduction in maximum power coefficient, revealing an inverse relationship between blade angle and peak power performance under certain operating conditions. Overall, these findings suggest that larger blade opening angles in ASWTs can significantly enhance turbine performance under specific configurations and operating regimes. By expanding the effective wind capture area and strengthening aerodynamic interactions, appropriately inclined blades are capable of generating higher power and torque coefficients. However, excessive blade inclination may induce increased drag and flow instability, underscoring the importance of optimizing blade angle to balance aerodynamic efficiency and flow stability.

III.4.5 Augmentation for ASWT Performance Enhancement

The Archimedes Screw Wind Turbine (ASWT) has been further developed through the incorporation of augmentation devices such as shrouds or flow channels to enhance its aerodynamic performance, as illustrated in Figure 17. Turbines equipped with such structures are commonly referred to as Shrouded Archimedes Screw Wind Turbines (SASWT). The shroud functions by generating a low-pressure region downstream of the rotor, which accelerates the incoming airflow and draws a larger volume of air through the turbine. In addition, the shroud acts as a flow concentrator, increasing both the mass flow rate and the momentum of the air entering the rotor [85-87]. The resulting increase in pressure differential across the rotor leads to a higher airflow throughput and, consequently, greater power output. Despite the substantial performance gains, SASWTs face notable challenges, particularly the significantly higher thrust forces acting on the rotor compared to open (unshrouded) turbines [85], [86], [88], [89]. These elevated structural loads require the use of stronger blade materials, which inevitably increases the initial construction cost. Nevertheless, the improvements in efficiency and power output position SASWTs as a promising solution in wind energy development. It is important to note that although the shroud enhances turbine performance, it does not directly generate energy. In power coefficient (C_P) calculations, the shroud is typically excluded from the rotor area, ensuring that the C_p value remains below the Betz limit. Accordingly, the shroud is regarded as a passive enhancement device that amplifies pressure and flow rather than a power-producing component [85-88].

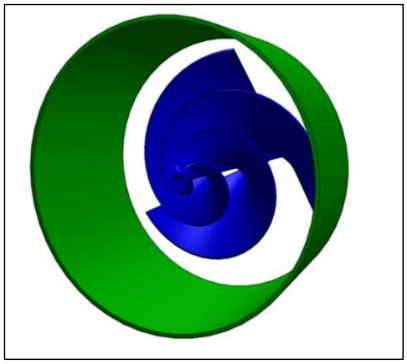


Figure 17: Shrouded Archimedes Spiral Wind Turbine (SASWT) layout.
Source: [90].

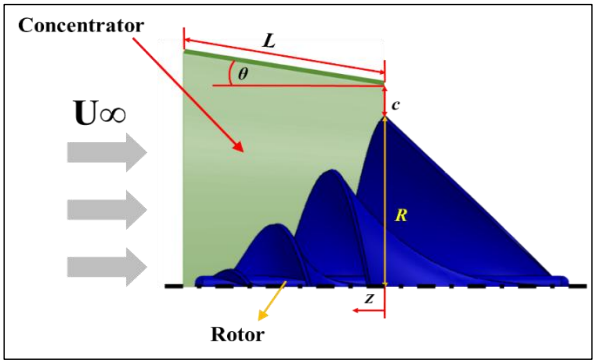


Figure 18: Shrouded Archimedes Spiral Wind Turbine (SASWT) layout.
Source: [90].

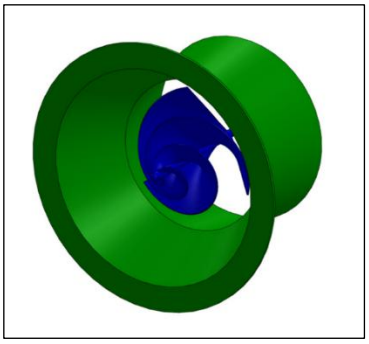


Figure 19: Illustration of the concentrator design with a flange at the ASWT inlet.
Source: [91].

Augmentation devices such as concentrators have been shown to significantly improve ASWT performance. A study by [90] evaluated the optimal configuration of an ASWT equipped with a concentrator and compared its performance to that of a bare ASWT. The concentrator design parameters are presented in Figure 18. The results demonstrated that the optimal configuration characterized by a concentrator position of 0.1D upstream of the rotor, a concentrator angle of 20°, a tip clearance of 0.05D, and a concentrator length of 0.6D achieved a maximum power coefficient of 0.311 at a TSR of 2.

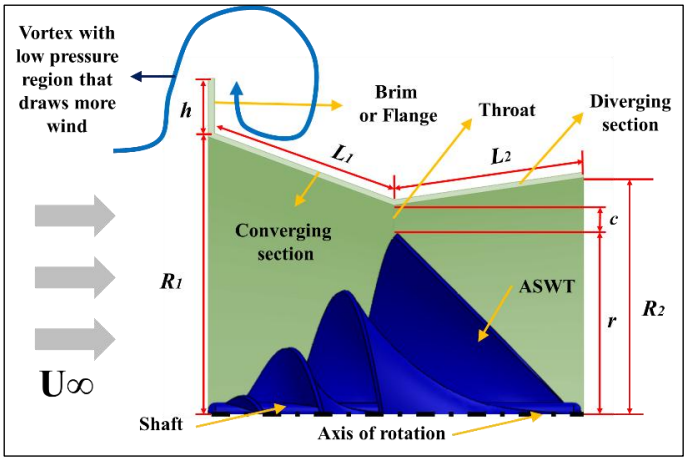


Figure 20: Design parameters of the concentrator with a flange at the ASWT inlet.
Source: [91].

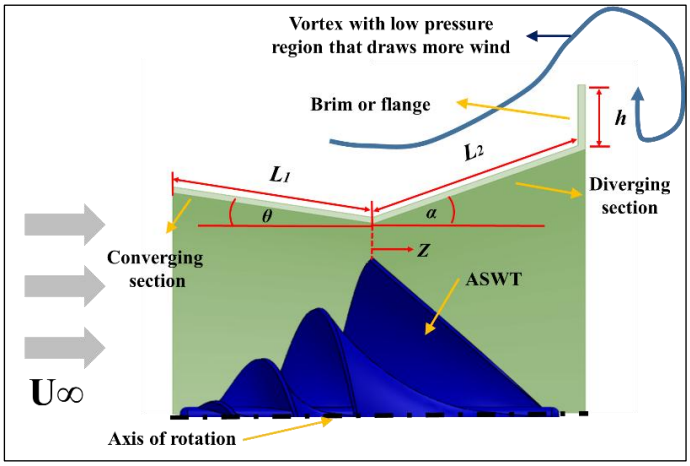


Figure 21: Design parameters of the concentrator with a flange at the ASWT outlet.
Source : [92].

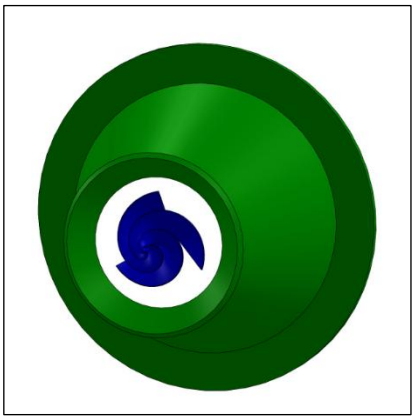


Figure 22: Illustration of the concentrator design with a flange at the ASWT outlet.
Source: [92].

The effectiveness of concentrator-based augmentation can be further enhanced by incorporating a flange, as reported in [91]. In this study, ASWT performance was improved by designing a concentrator with an inlet flange, as illustrated in Figure 19. The flange design parameters are shown in Figure 20. Using a turbine with a diameter of 250 mm, the optimal configuration yielding the highest C_P was obtained at L_1 = 180 mm, L_2 = 152 mm, R_1 = 250 mm, R_2 = 137.5 mm, and h = 75 mm. Under these conditions, the ASWT achieved a maximum C_p of 0.502 at a TSR of 2.5, representing an approximately 2.58-fold increase compared to the bare ASWT (C_p = 0.195). Beyond inlet-mounted flanges, performance enhancement can also be achieved by repositioning the flange at the outlet. A study by [92] numerically investigated the performance of an ASWT equipped with an airflow channel designed to improve energy harvesting efficiency in urban environments characterized by low wind speeds.

Figure 21 presents the concentrator parameters with an outlet flange, while Figure 22 illustrates the configuration. The findings revealed that the optimized channel geometry significantly increased the power coefficient. The optimal parameters were identified as L_1 = 0.2191D, L_2 = 1.658D, θ = 45.51°, α = 22.2°, h = 0.3457D, and Z = −0.296D. With this configuration, the maximum power coefficient reached 0.967 at a TSR of 3.25, corresponding to an approximately 3.6-fold improvement compared to the bare ASWT (C_p = 0.2668 at TSR = 2.5).

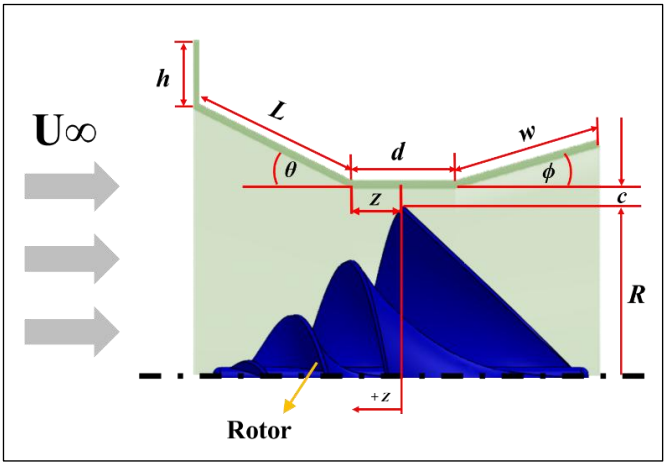


Figure 23: Wind lens design parameters for the ASWT. Source: [88].

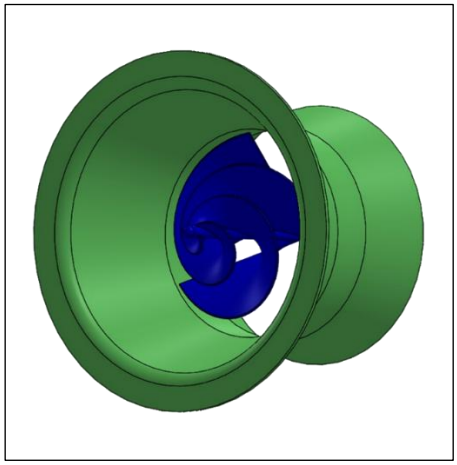


Figure 24 : Illustration of the wind lens design for the ASWT. Source: [88].

To further optimize performance, the geometry and configuration of wind-lens systems have been extensively investigated. Figure 23 presents the design parameters of a wind lens applied to an ASWT, with the corresponding illustration shown in Figure 24. The study by [88] systematically optimized wind-lens parameters, including diffuser length and angle, duct length, and flange height, to maximize the performance of a Shrouded Archimedes Spiral Wind Turbine (SASWT). The optimal configuration was obtained with Z = 0.1D, φ = 20°, c = 0.05D, a diffuser angle of 15°, and a concentrator length (L) of 0.6D. Additionally, the optimal values for duct length (d), flange height (h), and diffuser length (W) were each 0.3D. This configuration yielded a maximum power coefficient of 0.49 at a TSR of 3, representing a 2.1-fold increase relative to the ASWT without a wind lens. As a further advancement, [93] introduced three key contributions: (i) the use of a cylindrical enclosure to fully cover the turbine, (ii) the implementation of a simplified Maximum Power Point Tracking (MPPT) strategy, and (iii) the integration of protective electronic circuitry. The results indicated that the enclosure not only enhanced turbine efficiency but also reduced visual impact by obscuring the rotating blades an important advantage for individual users concerned with the aesthetic aspects of wind turbine installations. In summary, the incorporation of augmentation devices such as concentrators, concentrators with ducts, concentrators with ducts and flanges, and wind-lens systems consistently enhances ASWT performance by increasing pressure differentials and accelerating the incoming airflow. These mechanisms lead to substantial and measurable improvements in the power coefficient. For instance, an optimized shroud configuration with parameters L_1 = 0.2191D, L_2 = 1.658D, θ = 45.51°, α = 22.2°, h = 0.3457D, and Z = −0.296D was shown to achieve a maximum C_p of 0.967 at a TSR of 3.25 approximately 3.6 times higher than that of a bare ASWT (C_p = 0.2668 at TSR = 2.5).

III.4.6 Comparison between ASWT and other Wind Turbine Types

Several studies have demonstrated that the effectiveness of newly developed wind turbine designs can be systematically evaluated through direct comparisons with similar configurations or alternative turbine types. In a study conducted by [94], a dual-turbine system combining a Savonius turbine and an Archimedes Screw Wind Turbine (ASWT) was developed. Both turbines had a diameter of 20 inches and were mounted on a 4.5 m tower. Experimental results showed that the ASWT produced higher voltage output and rotational speed than the Savonius turbine. The ASWT achieved an average voltage of 7.04 V with a power output of 5.10 W, whereas the Savonius turbine generated only 2.70 V and 1.23 W. When operated simultaneously, the hybrid system produced an average voltage of 9.73 V and a power output of 6.32 W [94]. In another study, [95] performed a comparative numerical investigation of four different wind turbine types using ANSYS 16.0 based on Computational Fluid Dynamics (CFD), under a constant wind speed of 5 m/s and identical rotor swept areas. The simulation results indicated that the ASWT exhibited the highest performance, achieving an aerodynamic efficiency of 30.3%, a maximum power output of 6.55 W, and a rotational speed of 398 rpm. One of the key advantages of the ASWT lies in its ability to operate efficiently under low wind speed conditions, in contrast to Horizontal Axis Wind Turbines (HAWTs) and conventional Vertical Axis Wind Turbines (VAWTs), which typically require higher wind speeds to reach optimal performance [25], [27], [96]. The spiral blade geometry of the ASWT promotes smoother airflow behavior and a more uniform pressure distribution along the blade surface. This characteristic contributes to reduced aerodynamic noise and enables the turbine to initiate operation at wind speeds as low as approximately 2.5 m/s [27], [73], [88], [91], [97-101]. These combined features make the ASWT particularly well suited for urban environments, where wind speeds are generally low and highly turbulent. Moreover, the ASWT offers significant design flexibility and operates effectively at low Tip Speed Ratios (TSRs), enhancing its resistance to turbulence effects. Unlike HAWTs, ASWTs can employ a larger number of blades arranged at closer spacing, which improves wind energy capture efficiency. Further performance enhancement can be achieved through multi-turbine configurations. A study by [98] revealed that counter-rotating ASWT arrangements in both parallel and tandem configurations improved aerodynamic efficiency by 3.53% and 2.56%, respectively, compared to a single ASWT. Such configurations are particularly advantageous in urban settings, as they maximize energy density within limited spatial constraints.

IV. CONCLUSION

Considering its technical characteristics and environmental benefits, the Archimedes Screw Wind Turbine (ASWT) demonstrates strong potential as a future renewable energy solution. ASWT offers several inherent advantages, including self-starting capability, the absence of yaw mechanisms and tall towers, and ease of integration with augmentation devices. These features make ASWT particularly suitable for urban environments that require compact, low-noise turbines capable of operating under low wind-speed conditions. Recent research developments and innovations indicate that the selection of spiral geometry has a direct influence on turbine performance. ASWT equipped with an Archimedean spiral profile consistently outperforms logarithmic spiral configurations, achieving a maximum power coefficient (CP) of 0.2668 at a blade opening angle of 60°. In addition, aspect ratio (AR) values exceeding 1.1 are found to be suboptimal, while AR values below 1.0 tend to induce flow instability, vibration, and performance degradation, potentially shortening component lifespan. The optimal AR range is identified between 1.0 and 1.1, which provides a balance between maximum power output, structural stability, and operational durability. Performance enhancement in ASWT is not governed solely by aspect ratio. The application of airfoil-based blade profiles has been shown to significantly improve turbine efficiency. ASWT blades employing NACA airfoil profiles demonstrate notable performance gains compared to conventional blade designs, while also contributing to noise reduction. In particular, the NACA 6409 airfoil exhibits effective operation under low to moderate wind-speed conditions.

Beyond blade geometry, the blade opening angle also plays a crucial role in improving ASWT performance. Larger opening angles expand the effective wind capture area and enhance aerodynamic forces, resulting in increased torque and power output. The blade inclination configuration $(\alpha_1 = 30°, \alpha_2 = 45°, \alpha_3 = 60°)$emerged as the most effective arrangement, achieving a maximum power coefficient $(C_{p\max})$of 0.234 at a tip speed ratio (TSR) of 1.5. The results indicate that rotors with larger blade angles tend to dominate the flow by providing a stronger capture area, thereby extending the operational TSR range and increasing the TSR at peak performance. However, this configuration also generates higher thrust forces along with increased fluctuations, primarily due to the elevated drag associated with a more upright blade orientation relative to the incoming flow. Further performance improvements can be achieved through external modifications. The integration of augmentation structures, such as brimmed shrouds, has been reported to dramatically increase the power coefficient, with performance gains reaching up to 3.6 times compared to a bare ASWT configuration. Nevertheless, to fully realize the potential of ASWT technology, continued research efforts are required. These should focus on advanced design optimization, full-scale experimental validation, and comprehensive techno-economic analyses under real-world operating conditions. Collaboration among academic institutions, industry stakeholders, and governmental bodies will be essential to accelerate the adoption of ASWT technology as part of the global transition toward sustainable energy systems.

V. AUTHOR'S CONTRIBUTION

Conceptualization: Bayu Ardiansyah Maskub Putra.
Methodology: Bayu Ardiansyah Maskub Putra.
Investigation: Bayu Ardiansyah Maskub Putra.
Discussion of results: Bayu Ardiansyah Maskub Putra, Nazaruddin Sinaga, Eflita Yohana.
Writing – Original Draft: Bayu Ardiansyah Maskub Putra.
Writing – Review and Editing: Bayu Ardiansyah Maskub Putra, Nazaruddin Sinaga, Eflita Yohana, Mochammad Shodiq.
Resources: Bayu Ardiansyah Maskub Putra.
Supervision: Nazaruddin Sinaga, Eflita Yohana.
Approval of the final text: Bayu Ardiansyah Maskub Putra, Nazaruddin Sinaga, Eflita Yohana, Mochammad Shodiq.

VI. ACKNOWLEDGMENTS

The authors gratefully acknowledge the support and facilities provided by Diponegoro University. The laboratory access and technical support were indispensable to the successful execution of this research project. We deeply appreciate the University's enduring commitment to fostering research and innovation, which has been instrumental in making this work possible.

VII. REFERENCES

[1] P. Enevoldsen, S. V. Valentine, and B. K. Sovacool, "Insights into wind sites: Critically assessing the innovation, cost, and performance dynamics of global wind energy development," Energy Policy, vol. 120, no. May, pp. 1–7, 2018, doi: 10.1016/j.enpol.2018.05.022.

[2] P. Andrews-Speed and S. Zhang, "Low-Carbon Electricity BT - China as a Global Clean Energy Champion: Lifting the Veil," P. Andrews-Speed and S. Zhang, Eds., Singapore: Springer Nature Singapore, 2019, pp. 105–136. doi: 10.1007/978-981-13-3492-4_5.

[3] M. Kabir, N. S. BN, K. J. Khatod, V. P. Katekar, and S. S. Deshmukh, "Chapter 6 - Wind energy and its link to sustainability in developing countries," I. B. T.-R. E. and S. Khan, Ed., Elsevier, 2022, pp. 135–178. doi: https://doi.org/10.1016/B978-0-323-88668-0.00008-5.

[4] Y. Liu, Z. Abdul Karim, N. Khalid, and F. F. Said, "Benefit Modeling and Analysis of Wind Power Generation under Social Energy Economy and Public Health.," J. Environ. Public Health, vol. 2022, p. 5635853, 2022, doi: 10.1155/2022/5635853.

[5] F. Wenehenubun, A. Saputra, and H. Sutanto, "An experimental study on the performance of Savonius wind turbines related with the number of blades," Energy Procedia, vol. 68, pp. 297–304, 2015, doi: 10.1016/j.egypro.2015.03.259.

[6] R. Howell, N. Qin, J. Edwards, and N. Durrani, "Wind tunnel and numerical study of a small vertical axis wind turbine," Renew. Energy, vol. 35, no. 2, pp. 412–422, Feb. 2010, doi: 10.1016/J.RENENE.2009.07.025.

[7] H. Huang, J. Li, and G. Li, “Improving the self-starting and operating characteristics of vertical axis wind turbine by changing center distance in part of blades,” J. Build. Eng., vol. 68, p. 105974, 2023, doi: https://doi.org/10.1016/j.jobe.2023.105974.

[8] A. Murali and R. G. Rajagopalan, “Numerical simulation of multiple interacting wind turbines on a complex terrain,” J. Wind Eng. Ind. Aerodyn., vol. 162, pp. 57–72, 2017, doi: https://doi.org/10.1016/j.jweia.2017.01.005.

[9] R. Castellanos Bustamante, A. Roman Messina, M. Ramirez Gonzalez, and G. Calderon Guizar, “Assessment of frequency performance by wind integration in a large-scale power system,” Wind Energy, vol. 21, no. 12, pp. 1359–1371, Dec. 2018, doi: https://doi.org/10.1002/we.2259.

[10] M. A. Al-rawajfeh and M. R. Gomaa, “Comparison between horizontal and vertical axis wind turbine,” vol. 12, no. 1, pp. 13–23, 2023, doi: 10.11591/ijape.v12.i1.pp13-23.

[11] S. Rehman, M. M. Alam, L. M. Alhems, and M. M. Rafique, “Horizontal Axis Wind Turbine Blade Design Methodologies for Efficiency Enhancement—A Review,” 2018. doi: 10.3390/en11030506.

[12] N. Karthikeyan, K. Kalidasa Murugavel, S. Arun Kumar, and S. Rajakumar, “Review of aerodynamic developments on small horizontal axis wind turbine blade,” Renew. Sustain. Energy Rev., vol. 42, pp. 801–822, 2015, doi: https://doi.org/10.1016/j.rser.2014.10.086.

[13] H. S. Ji, J. H. Baek, R. Mieremet, and K. C. Kim, “The Aerodynamic Performance Study on Small Wind Turbine with 500W Class through Wind Tunnel Experiments,” Int. J. Renew. Energy Sources, vol. 1, pp. 7–12, 2016, [Online]. Available: http://www.iaras.org/iaras/journals/ijres

[14] K. C. Kim, H. S. Ji, Y. K. Kim, Q. Lu, J. H. Baek, and R. Mieremet, “Experimental and Numerical Study of the Aerodynamic Characteristics of an Archimedes Spiral Wind Turbine Blade,” 2014. doi: 10.3390/en7127893.

[15] I. Abdelghafar, A. G. Refaie, E. Kerikous, D. Thévenin, and S. Hoerner, “Optimum geometry of seashell-shaped wind turbine rotor: Maximizing output power and minimizing thrust,” Energy Convers. Manag., vol. 292, no. February, p. 117331, 2023, doi: 10.1016/j.enconman.2023.117331.

[16] S. Chaudhary et al., “COMPARISON OF TORQUE CHARACTERISTICS OF ARCHIMEDES WIND TURBINE EVALUATED BY ANALYTICAL AND,” no. 8, pp. 75–78, 2016.

[17]Y. Patil, “DESIGN, FABRICATION AND ANALYSIS OF FIBONACCI SPIRAL HORIZONTAL AXIS WIND TURBINE,” Jan. 2018.

[18] M. drs. M. Mieremet, “The aerodynamic method of the Archimedes Windturbine,” pp. 1–23, 2014.

[19] M. Ozeh, A. Mishra, and X. Wang, “Mini Wind Turbine for Small Scale Power Generation and Storage (Archimedes Wind Turbine Model),” Nov. 09, 2018. doi: 10.1115/IMECE2018-88455.

[20] S. S. Rao, K. Shanmukesh, M. K. Naidu, and P. Kalla, “Design and analysis of Archimedes aero-foil wind turbine blade for light and moderate wind speeds,” Int. J. Recent Technol. Mech. Electr. Eng, vol. 5, pp. 1–5, 2018.

[21] B. Li, Z. Deng, Y. Dai, L. Zhong, and J. Wang, “A Correlation Study Between Aerodynamic Structural Changes and Aerodynamic Noise Characteristics of Archimedes Spiral Wind Turbines,” Int. J. Acoust. Vib., vol. 29, pp. 246–263, Sep. 2024, doi: 10.20855/ijav.2024.29.32032.

[22] S. D. S, K. K. Vernekar, K. Rathod, C. Ravikumar, and D. R. P. Y, “Design , Fabrication and Aerodynamic Analysis of a Modified Archimedes Wind Turbine,” vol. IV, no. May, pp. 55–59, 2017.

[23] Q. Lu, Q. Li, Y.-K. Kim, and K.-C. Kim, “A study on design and aerodynamic characteristics of a spiral-type wind turbine blade,” J. Korean Soc. Vis., vol. 10, no. 1, pp. 27–33, 2012, doi: 10.5407/jksv.2011.10.1.027.

[24] Naveen Krishna P, “DESIGN AND FLOW SIMULATION OF AN ARCHIMEDEAN SPIRAL-TYPE WIND TURBINE BLADE FOR DETERMINING VELOCITY AND PRESSURE PROFILE,” EPRA Int. J. Multidiscip. Res. (IJMR)-Peer Rev. J., vol. 7, no. 12, 2021.

[25] A. M. Kamal, M. A. A. Nawar, Y. A. Attai, and M. H. Mohamed, “Archimedes Spiral Wind Turbine performance study using different aerofoiled blade profiles: Experimental and numerical analyses,” Energy, vol. 262, no. PB, p. 125567, 2023, doi: 10.1016/j.energy.2022.125567.

[26]I. Mihalik, M. Lazar, L. Simocko, N. Jasminska, T. Brestovic, and R. Dobakova, “Influence of the Number of Blades of the Archimedes Wind Turbine on Its Performance,” MM Sci. J., vol. 2024-Decem, pp. 7956–7960, 2024, doi: 10.17973/MMSJ.2024_12_2024043.

[27] A. M. Kamal, M. A. A. Nawar, Y. A. Attai, and M. H. Mohamed, “Blade design effect on Archimedes Spiral Wind Turbine performance: Experimental and numerical evaluations,” Energy, vol. 250, p. 123892, 2022, doi: 10.1016/j.energy.2022.123892.

[28] A. D. Korawan and R. Febritasari, “Experimental investigations of number of blades effect on archimedes spiral wind turbine performance,” Mech. Eng. Soc. Ind., vol. 4, no. 2, pp. 198–209, 2024, doi: 10.31603/mesi.12373.

[29] M. M. Elsakka, D. B. Ingham, L. Ma, and M. Pourkashanian, “CFD analysis of the angle of attack for a vertical axis wind turbine blade,” Energy Convers. Manag., vol. 182, pp. 154–165, 2019, doi: https://doi.org/10.1016/j.enconman.2018.12.054.

[30] M. T. Student, “Aerodynamic Performance Evaluation of a Wind Turbine Blade by Computational and Experimental Method,” vol. 3, no. 6, pp. 73–81, 2014.

[31] N. Ismail, K. Muhammad Usman, M. Balogun, M. Abdullahi, F. Faru, and I. Ibrahim, “Effect of Angle of Attack on Lift, Drag, Pitching Moment and Pressure Distribution of NACA 4415 Wing,” vol. 8, pp. 31–44, Feb. 2020.

[32] Y. Yin Htay Aung, M. Myat Soe, and A. Myat Thu, “Effect of Attack angle on Aerodynamics Analysis of Different Wind Turbine Wings using Numerical Simulation,” Am. Sci. Res. J. Eng., vol. 26, no. 4, pp. 319–329, 2016, [Online]. Available: http://asrjetsjournal.org/

[33] P. Srivastava, S. Kansal, A. Talwalkar, and R. Harish, “CFD analysis on the influence of angle of attack on vertical axis wind turbine aerodynamics,” IOP Conf. Ser. Earth Environ. Sci., vol. 850, no. 1, p. 12027, 2021, doi: 10.1088/1755-1315/850/1/012027.

[34] S. Balakrishnan et al., “Experimental Investigation and CFD Analysis of Wind Turbine Blades with Different Attack Angles,” E3S Web Conf., vol. 529, pp. 1–9, 2024, doi: 10.1051/e3sconf/202452902011.

[35] K. Ghulam, F. Ali, A. Ali, and K. Gorar, “Optimizing the Performance of different Airfoils at Various Angles of Attack through CFD Simulation,” pp. 23–36, 2024.

[36] Z. Gu and G. Wang, “Effect of Reynolds Number and Angle of Attack on Aerodynamic Performance of NACA2412,” vol. 0, pp. 50–57, 2025, doi: 10.54254/2755-2721/130/2025.20279.

[37] H. S. Ji, L. Qiang, J. H. Beak, R. Mieremet, and K. C. Kim, “Effect of the wind direction on the near wake structures of an Archimedes spiral wind turbine blade,” J. Vis., vol. 19, no. 4, pp. 653–665, 2016, doi: 10.1007/s12650-016-0356-8.

[38] Q. Li, H. D. Kim, H. S. Ji, and K. C. Kim, “Flow Characteristics around Archimedes Wind Turbine according to the Change of Angle of Attack,” J. Korean Soc. Vis., vol. 11, no. 1, pp. 28–33, 2013, doi: 10.5407/jksv.2013.11.1.028.

[39] S. Shukla, C. J. Ramanan, B. Jyoti Bora, A. Deo, and N. Alom, “Numerical analysis of vertical axis wind turbine blades in ANSYS Fluent,” Mater. Today Proc., vol. 59, pp. 1781–1785, 2022, doi: 10.1016/j.matpr.2022.04.377.

[40] J. Kevin Joseph, R. Jeyanthinathan, and R. Harish, “CFD investigation on the performance analysis of Tesla turbine,” IOP Conf. Ser. Earth Environ. Sci., vol. 850, no. 1, pp. 0–13, 2021, doi: 10.1088/1755-1315/850/1/012026.

[41] A. Erdoğan and M. Daşkın, “Comparing of CFD Contours Using Image Analysing Method: A Study on Velocity Distributions TT - Comparing of CFD Contours Using Image Analysing Method: A Study on Velocity Distributions,” Black Sea J. Eng. Sci., vol. 6, no. 4, pp. 633–638, 2023, doi: 10.34248/bsengineering.1310711.

[42] S. Chichkhede, V. Verma, V. K. Gaba, and S. Bhowmick, “A Simulation Based Study of Flow Velocities across Cross Flow Turbine at Different Nozzle Openings,” Procedia Technol., vol. 25, pp. 974–981, 2016, doi: https://doi.org/10.1016/j.protcy.2016.08.190.

[43] F. Janischowsky, D. Stümpfl, P. Streit, A. P. Weiß, and A. Lesser, “CFD Simulation and Flow Study of a Velocity Compounded Radial Re-Entry Turbine - Elektra,” MATEC Web Conf., vol. 367, 2022, [Online]. Available: https://doi.org/10.1051/matecconf/202236700012

[44] A. Bhattarai, H. P. Bashyal, S. Sapkota, and U. Nepal, “Design, CFD Analysis and Modelling of Archimedean-Spiral type Wind Turbine,” no. January 2016, pp. 1–83, 2019, [Online]. Available: https://www.researchgate.net/publication/337149869

[45] R. M. Kyung Chun Kim, Yoon Kee Kim, Ho Seong Ji, Joon Ho Beak, “AERODYNAMIC CHARACTERISTICS OF HORIZONTAL AXIS WIND TURBINE WITH ARCHIMEDES SPIRAL BLADE,” ASME Int. Mech. Eng. Congr. Expo. Proc., 2013.

[46] Y. K. Kim, Q. Lu, H. S. Ji, J. H. Beak, R. Mieremet, and K. C. Kim, “A Multi-Prong Study on Aerodynamic Characteristics of Archimedes Spiral-Type Wind Turbine Blade,” Korea Inst. Energy Technol. Eval. Plan., pp. 1–6, 2012.

[47] S. Ebrahimi and M. A. Ghassemi, “Numerical Aerodynamics Analysis of the Archimedes Screw Wind Turbine,” Int. J. Multidiscip. Sci. Eng., vol. 9, no. 10, pp. 12–15, 2018.

[48]J. Manwell, J. Mcgowan, and A. Rogers, “Wind Energy Explained: Theory, Design and Application, Second Edition,” in Wind Engineering, vol. 30, 2006. doi: 10.1260/030952406778055054.

[49] A. Dewan, S. S. Tomar, A. K. Bishnoi, and T. P. Singh, “Computational fluid dynamics and turbulence modelling in various blades of Savonius turbines for wind and hydro energy: Progress and perspectives,” Ocean Eng., vol. 283, no. February, p. 115168, 2023, doi: 10.1016/j.oceaneng.2023.115168.

[50] N. Alom and U. K. Saha, “Arriving at the optimum overlap ratio for an elliptical-bladed savonius rotor,” Proc. ASME Turbo Expo, vol. 9, pp. 1–10, 2017, doi: 10.1115/GT2017-64137.

[51] B. Peric, A. Simonovic, and M. Vorkapić, “Comparative analysis of numerical computational techniques for determination of the wind turbine aerodynamic performances,” Therm. Sci., vol. 25, p. 175, Jan. 2020, doi: 10.2298/TSCI200216175P.

[52] S. Unde, K. Sutar, and Researcher, “CFD ANALYSIS OF WIND TURBINE AIRFOIL,” vol. 5, pp. 488–492, Jun. 2018.

[53] L. Jun and S. Wenlong, “Numerical Simulation on Wind Turbine Airfoil Aerodynamics Performance,” vol. 9, no. 12, pp. 275–286, 2016.

[54] S. Chaudhary et al., “Comparison of Torque Characteristics of Archimedes Wind Turbine Evaluated By Analytical and Experimental Study,” Int. J. Mech. Prod. Eng., no. 4, pp. 2320–2092, 2016.

[55] B. Navinkumar, K. M. Parammasivam, S. Rajendran, and V. Mohanavel, “CFD analysis of horizontal axis wind turbine braking system using chordwise spacing,” Mater. Today Proc., vol. 37, pp. 542–552, 2021, doi: https://doi.org/10.1016/j.matpr.2020.05.564.

[56] J. Gordon Leishman, Aerodynamics of Horizontal Axis Wind Turbines. 2011. doi: 10.1007/978-3-540-88258-9_1.

[57] R. P. Singh, P. Kumar, G. S. Sangha, and Z. D. Labana, “Numerical Analysis of an Optimized Wind Turbine Blade,” in AIAA SCITECH 2022 Forum, in AIAA SciTech Forum. , American Institute of Aeronautics and Astronautics, 2021. doi: doi:10.2514/6.2022-0217.

[58] S. M. Yang, H. S. Ji, D. S. Shim, J. H. Baek, and S. H. Park, “Conical roll-twist-bending process for fabrication of metallic Archimedes spiral blade used in small wind power generator,” Int. J. Precis. Eng. Manuf. - Green Technol., vol. 4, no. 4, pp. 431–439, 2017, doi: 10.1007/s40684-017-0048-4.

[59] H. Jang, D. Kim, Y. Hwang, I. Paek, S. Kim, and J. Baek, “Analysis of Archimedes spiral wind turbine performance by simulation and field test,” Energies, vol. 12, no. 24, 2019, doi: 10.3390/en12244624.

[60] S. Yang et al., “Process Design of Conical Roll-Shaping for Fabrication of Variable Curvature Spiral Blade,” J. Korean Soc. Precis. Eng., vol. 33, no. 11, pp. 911–918, 2016, doi: 10.7736/kspe.2016.33.11.911.

[61] H. Hamid and R. M. Abd El Maksoud, “A comparative examination of the aerodynamic performance of various seashell-shaped wind turbines,” Heliyon, vol. 9, no. 6, p. e17036, 2023, doi: 10.1016/j.heliyon.2023.e17036.

[62] O. Salah Samiani and M. Boroushaki, “Optimal design of Archimedes Wind Turbine using genetic algorithm,” Energy, vol. 314, no. November 2024, p. 134157, 2025, doi: 10.1016/j.energy.2024.134157.

[63] M. M. N. Andrew M. Labib, Ahmed F. AbdelGawad, “Effect of Aspect Ratio on Aerodynamic Performance of Archimedes spiral Wind Turbine,” Egypt. Int. J. Eng. Sci. Technol., vol. 78, no. 1, pp. 122–136, 2020, doi: 10.37934/ARFMTS.78.1.122136.

[64] S. Brusca, R. Lanzafame, and M. Messina, “Design of a vertical-axis wind turbine: how the aspect ratio affects the turbine’s performance,” Int. J. Energy Environ. Eng., vol. 5, pp. 1–8, Aug. 2014, doi: 10.1007/s40095-014-0129-x.

[65] Ashish and P. Suresh, “Design and Analysis of the Effect Through Different Aspect Ratio on Performance of VAWT BT - Advances in Mechanical and Energy Technology,” S. Yadav, P. K. Jain, P. K. Kankar, and Y. Shrivastava, Eds., Singapore: Springer Nature Singapore, 2023, pp. 333–340.

[66] S. Zanforlin and S. Deluca, “Effects of the Reynolds number and the tip losses on the optimal aspect ratio of straight-bladed Vertical Axis Wind Turbines,” Energy, vol. 148, pp. 179–195, 2018, doi: https://doi.org/10.1016/j.energy.2018.01.132.

[67] L. N. Azadani and M. Saleh, “Effect of blade aspect ratio on the performance of a pair of vertical axis wind turbines,” Ocean Eng., vol. 265, p. 112627, 2022, doi: https://doi.org/10.1016/j.oceaneng.2022.112627.

[68] V. Maldonado, N. Peralta, W. Ayele, D. Santos, and G. Dufflis, “Effect of blade aspect ratio on the performance tradeoff between figure of merit and bending-torsion dynamics of wind turbines with synthetic jets,” Energy Reports, vol. 9, pp. 4830–4843, 2023, doi: https://doi.org/10.1016/j.egyr.2023.04.017.

[69] A. Labib, A. Abdel Gawad, and M. Melad, Effect of Aspect Ratio on Aerodynamic Performance of Archimedes Spiral Wind Turbine. 2021.

[70] D.-T. Ghonim, M. Farag, A. Hegazy, and A. Maher, “Experimental Study on the Performance of Spiral Wind Turbine,” ERJ. Eng. Res. J., vol. 45, pp. 281–287, Jul. 2022, doi: 10.21608/erjm.2022.132106.1162.

[71] X. Ye, J. Hu, N. Zheng, and C. Li, “Numerical study on aerodynamic performance and noise of wind turbine airfoils with serrated gurney flap,” Energy, vol. 262, p. 125574, 2023, doi: https://doi.org/10.1016/j.energy.2022.125574.

[72] S. Sanaye and A. Hassanzadeh, “Multi-objective optimization of airfoil shape for efficiency improvement and noise reduction in small wind turbines,” J. Renew. Sustain. Energy, vol. 6, no. 5, p. 53105, Sep. 2014, doi: 10.1063/1.4895528.

[73] W. J. Zhu, W. Z. Shen, and J. N. Sørensen, “Low-Noise Airfoil and Wind Turbine Design,” A. G. Aissaoui and A. Tahour, Eds., Rijeka: IntechOpen, 2016. doi: 10.5772/63335.

[74] J. Ma et al., “Effect of Airfoil Concavity on Wind Turbine Blade Performances,” Shock Vib., vol. 2019, no. 1, p. 6405153, Jan. 2019, doi: https://doi.org/10.1155/2019/6405153.

[75] X. Sun, X. Zhang, Z. Su, and D. Huang, “Experimental Study of Aerodynamic Characteristics of Partially Flexible NACA0012 Airfoil,” AIAA J., vol. 60, no. 9, pp. 5386–5400, Jun. 2022, doi: 10.2514/1.J061803.

[76] J. Zhang, W. Guo, P. Zhang, and H. Ji, “Optimizing Airfoil Aerodynamic Characteristics by Using Proposed CSA-KJ Method,” 2023. doi: 10.3390/app13020924.

[77] P. Shinde, S. S. Ohol, and V. K. Tripathi, “Shape Optimization of an Asymmetric Airfoil for Low Wind Speed Region having Adjoint-Based Optimization Technique,” J. Appl. Fluid Mech., vol. 16, no. 2, pp. 299–310, 2023, doi: 10.47176/jafm.16.02.1426.

[78] C. H. Yan, T. S. Biao, and C. T. Fei, “Numerical Analysis of Wind Turbine Airfoil Aerodynamic of Wind Turbine Blade,” in 2022 7th International Conference on Mechatronics System and Robots (ICMSR), 2022, pp. 1–4. doi: 10.1109/ICMSR2020.2022.00008.

[79] H. Seifi Davari, M. B. Ruxandra, S. D. Mohsen, and H. and Chowdhury, “Enhancing aerodynamic efficiency: shape modification of airfoils,” Int. J. Ambient Energy, vol. 45, no. 1, p. 2439441, Dec. 2024, doi: 10.1080/01430750.2024.2439441.

[80] “NACA6409 9% (n6409-il).” [Online]. Available: http://airfoiltools.com/airfoil/details?airfoil=n6409-il

[81] S. D. Shivanegara, K. K. Vernekar, K. Rathod, C. Ravikumar, and D. R. P. Y, “Design, Fabrication and Aerodynamic Analysis of a Modified Archimedes Wind Turbine,” Issue VI, vol. 598, no. May, pp. 2321–9653, 2017, [Online]. Available: www.ijraset.com

[82] K. Song, H. Huan, and Y. Kang, “Aerodynamic Performance and Wake Characteristics Analysis of Archimedes Spiral Wind Turbine Rotors with Different Blade Angle,” Energies, vol. 16, no. 1, 2023, doi: 10.3390/en16010385.

[83] E. H. Herraprastanti and W. Agung Saputro, “Simulation of Opening Angle of Archimedes Wind Turbine Design Based on the Fibonacci Series,” Int. J. Eng. Sci. Inf. Technol., vol. 2, no. 1, pp. 50–57, 2021, doi: 10.52088/ijesty.v2i1.192.

[84] A. M. Labib, A. F. A. Gawad, and M. M. Nasseif, “Effect of Blade Angle on Aerodynamic Performance of Archimedes Spiral Wind Turbine,” J. Adv. Res. Fluid Mech. Therm. Sci., vol. 78, no. 1, pp. 122–136, 2020, doi: 10.37934/ARFMTS.78.1.122136.

[85] M. Z. Akhter, A. Shaaban, and A. Marini, “Enhancing Power Output of Ducted Wind Turbines through Flow Control,” J. Phys. Conf. Ser., vol. 2767, no. 7, p. 72011, 2024, doi: 10.1088/1742-6596/2767/7/072011.

[86] I. Hashem, A. A. Hafiz, and M. H. Mohamed, “Characterization of aerodynamic performance of wind-lens turbine using high-fidelity CFD simulations,” Front. Energy, vol. 16, no. 4, pp. 661–682, 2022, doi: 10.1007/s11708-020-0713-0.

[87] Y. Ohya and T. Karasudani, “A Shrouded Wind Turbine Generating High Output Power with Wind-lens Technology,” 2010. doi: 10.3390/en3040634.

[88] A. G. Refaie, H. S. A. Hameed, M. A. A. Nawar, Y. A. Attai, and M. H. Mohamed, “Comparative investigation of the aerodynamic performance for several Shrouded Archimedes Spiral Wind Turbines,” Energy, vol. 239, p. 122295, 2022, doi: 10.1016/j.energy.2021.122295.

[89] N. A. Pambudi et al., “Experimental Investigation of Wind Turbine Using Nozzle-lens at Low Wind Speed Condition,” Energy Procedia, vol. 105, pp. 1063–1069, 2017, doi: https://doi.org/10.1016/j.egypro.2017.03.459.

[90] A. G. Refaie, H. S. Abdel Hameed, M. A. A. Nawar, Y. A. Attai, and M. H. Mohamed, “Qualitative and quantitative assessments of an Archimedes Spiral Wind Turbine performance augmented by A concentrator,” Energy, vol. 231, p. 121128, 2021, doi: 10.1016/j.energy.2021.121128.

[91] H. S. Abdel Hameed, I. Hashem, M. A. A. Nawar, Y. A. Attai, and M. H. Mohamed, “Shape optimization of a shrouded Archimedean-spiral type wind turbine for small-scale applications,” Energy, vol. 263, no. PB, p. 125809, 2023, doi: 10.1016/j.energy.2022.125809.

[92] H. Hamid and R. Mohamed Abd El Maksoud, “An optimization study of passive flow control mechanism for a seashell-shaped wind turbine,” Energy, vol. 289, no. November 2023, p. 129912, 2024, doi: 10.1016/j.energy.2023.129912.

[93] A. Arzuaga et al., “Low-Cost Maximum Power Point Tracking Strategy and Protection Circuit Applied to an Ayanz Wind Turbine with Screw Blades,” Energies, vol. 16, no. 17, 2023, doi: 10.3390/en16176204.

[94] C. Ostia, J. M. Martinez, K. T. Coderes, G. J. Estacio, A. R. Ramchahi, and J. V. Pulido, “Development of a dual wind turbines using the savonius and Archimedes spiral principle,” 2018 IEEE 10th Int. Conf. Humanoid, Nanotechnology, Inf. Technol. Commun. Control. Environ. Manag. HNICEM 2018, pp. 1–5, 2018, doi: 10.1109/HNICEM.2018.8666238.

[95] A. S. Ansari, T. Hussain, A. Hussain, and I. Ali, “Efficiency Analysis of Archimedes Wind Turbine Using CFD Technique,” Int. J. Sci. Eng. Res., vol. 12, no. 3, pp. 51–55, 2021, [Online]. Available: http://www.ijser.org

[96] M. Ozeh, A. Mishra, and X. Wang, “(Archimedes Wind Turbine Model),” pp. 1–7, 2019.

[97] T. Ghonim, M. Said Farag, A. Hegazy, and A. Maher, “Experimental Study on the Performance of Spiral Wind Turbine,” ERJ. Eng. Res. J., vol. 45, no. 3, pp. 281–287, 2022, doi: 10.21608/erjm.2022.132106.1162.

[98] K. Song, H. Huan, L. Wei, and C. Liu, “Aerodynamic Performance and Coupling Gain Effect of Archimedes Spiral Wind Turbine Array,” J. Mar. Sci. Eng., vol. 12, no. 7, 2024, doi: 10.3390/jmse12071062.

[99] A. Grubler et al., “Urban Energy Systems,” in Global Energy Assessment: Toward a Sustainable Future, G. E. A. W. Team, Ed., Cambridge: Cambridge University Press, 2012, pp. 1307–1400. doi: DOI: 10.1017/CBO9780511793677.024.

[100] P. I. Muiruri, O. S. Motsamai, and R. Ndeda, “A comparative study of RANS-based turbulence models for an upscale wind turbine blade,” SN Appl. Sci., vol. 1, no. 3, p. 237, 2019, doi: 10.1007/s42452-019-0254-5.

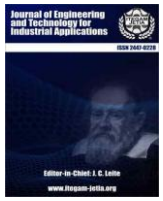
[101] A. M. Malge and P. M. Pawar, “Analysis of Lift and Drag Forces at Different Azimuth Angle of Innovative Vertical Axis Wind Turbine,” Int. J. Energy Power Eng., vol. 4, no. 5–1, pp. 12–16, Sep. 2015, doi: 10.11648/j.ijepe.s.2015040501.12.

Journal of Engineering and Technology for Industrial Applications

ISSN ONLINE: 2447-0228

ITEGAM-JETIA

Manaus, v.12 n.60, p.127-137, July/August, 2026.
DOI: https://doi.org/10.5935/jetia.v12i60.3609



RESEARCH ARTICLE OPEN ACCESS

META-HEURISTIC APPROACHES TO OPTIMAL PLACEMENT OF ELECTRIC VEHICLE CHARGING STATION

M. S. Arjun[1], N. Mohan*[2], K. R. Sathish[3], Arunkumar Patil[4], D. P. Somashekar[5]

[1, 2]Department of Electrical and Electronics Engineering, JSS Science and Technology University, Mysore, India.
[3]Department of Electrical and Electronics Engineering, ATME College of Engineering, Mysore, India.
[4]Department of Electrical Engineering, Central University of Karnataka, Kalaburagi (Gulbarga), India.
[5]Department of Electrical and Electronics Engineering, Presidency University, Bangalore, India.

[1]https://orcid.org/0000-0002-8662-3510, [2]https://orcid.org/0000-0002-9654-8454, [3]https://orcid.org/0000-0003-0627-2421
[4]https://orcid.org/0009-0004-5731-7671, [5]https://orcid.org/0000-0002-4822-3719

Email: arjunms@jssstuniv.in,*mohan.eee@jssstuniv.in, dr.sathish21@gmail.com, arun201085@gmail.com, somashekar.dp@presidencyuniversity.in

ARTICLE INFO

Article History
Received: February 9, 2026
Reviewed: June 5, 2026
Accepted: July 5, 2026
Published: July 31, 2026

Keywords:
Distribution System,
Electric Vehicle Charging Station,
Power Flow Analysis,
Ant Colony Optimization,
Particle Swarm Optimization,
Radial Distribution Network System,
Backward Forward Sweep.

ABSTRACT

Electric vehicles (EVs) have been developed to reduce the emissions of carbon dioxide (CO_2) produced by vehicles with internal combustion engines. As the adoption of EVs increases, the development of a robust and efficient electric vehicle charging station (EVCS) is essential for the widespread adoption of EVs, providing the necessary infrastructure to recharge vehicle batteries. The strategic placement of an EVCS is critical, because it directly affects the efficiency and reliability of the distribution system. Properly located charging stations can enhance grid stability, optimize energy distribution, and reduce peak load pressures. Conversely, a poorly planned EVCS placement can lead to grid congestion, increased operational costs, and potential reliability issues. Strategy for maximizing EV utilization through EVCSs in the Radial Distribution Network System (RDNS) by considering factors such as load voltage deviation and line losses. In this study, the RDNS is segmented into zones, followed by the application of various optimization algorithms, including Ant Colony Optimization (ACO) and Particle Swarm Optimization (PSO). This approach identifies the optimal locations for the EVCSs in the network for different load growth rates. This was followed by Forward Backward Sweep (FBS) power flow analysis to determine the active and reactive power losses, voltage deviations, and voltage profiles. Extensive simulations using IEEE 33-node test feeders validated the proposed techniques using the MATLAB tool.

Copyright ©2026 by authors and Galileo Institute of Technology and Education of the Amazon (ITEGAM). This work is licensed under the Creative Commons Attribution International License (CC BY 4.0).

I. INTRODUCTION

Various approaches have been applied to design the optimum placement of EVCS. Charging stations can be optimally designed depending on the EV usage in an enhanced system performance and supply of a peak load. For this reason, reduction in losses, better economics, and minimization of voltage deviation are achieved using EVs [1]. Layout optimization for charging stations is based on maximizing the reliability of a network, and minimizing voltage deviation and power losses is applied using a K- means clustering algorithm [2]. The distribution network voltage deviation, power losses, and charging service were used as multi-objective functions in the optimization placement of charging stations. This problem was tested on a road network of 25 nodes and an IEEE 33 bus network using a cross-entropy method and data envelopment analysis [3]. A hierarchical genetic algorithm was applied to estimate an optimal charging station design based on the cost as an objective function and the constraints of the maximum capacity of a charging station and limits of power loss. The proposed technique was tested using an IEEE 123 bus system [4]. This study applied the ACO and PSO algorithms to solve the EVCS placement problem.

This was followed by load flow analysis using a backward-forward sweep approach to determine the real and reactive power losses and voltage deviation, and to analyze the voltage profile on the IEEE 33 bus system using MATLAB simulations. This paper is organized as follows: i) Section1 provides an introduction; ii) Section 2 details the problem formulation for EV charging stations; iii) Section 3 presents the modeling of the objective with algorithms; iv) further analysis of the simulation results is discussed in Section 4; and v) the conclusion is presented in Section 5.

II. PROBLEM FORMULATION

Deploying an EVCS in an RDNS has several benefits, including reduced line loss, improved voltage stability, enhanced network reliability, and increased security. However, determining the optimal placement of an EVCS involves solving a nonlinear optimization problem with objective functions and constraints related to the power balance, voltage, and current. The proposed solution aims to minimize the peak load power loss and voltage variation, while enhancing the voltage stability in the RDNS. Thus, the multi-objective function can be mathematically expressed as

$$J = Minimum\,\{J_1, J_2\} \tag{1}$$

Where J_1 and J_2 correspond to the total power loss and the voltage deviation index respectively. The following is a description of the mathematical equation that represents the multi-objective function.

III. MODELLING OF THE OBJECTIVE FUNCTION

The IEEE 33-bus system was selected as the use case network in this study. The RDNS is broken up into zones such that each zone can have an EVCS with a number of charging spots to serve its own needs. The system consistsof33buses with a total real power load of 3.72 MW and a total reactive power load of 2.30 MVAr supplied by source at bus 1. This RDNS was large and balanced at a voltage of 12.66 kV as shown in Fig. 1.

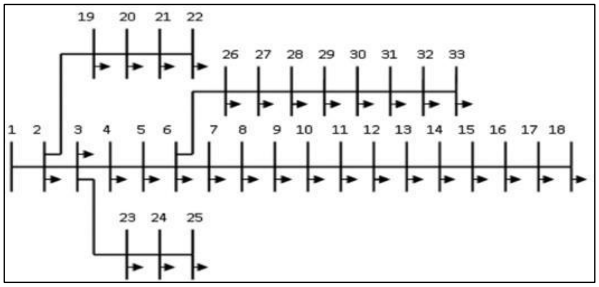


Figure 1: IEEE33 bus system.
Source: Authors, (2026).

III.1 REAL AND REACTIVE POWER LOSSES

By strategically placing EVCSs in the distribution network, the stability caused by the peak loading situations can be mitigated, ensuring that the constraints are not violated. This optimal EVCS placement minimizes power loss while adhering to the limits of the system constraints. The precise branch loss for the distribution system can be obtained using equation (2) and (3) such that the total power loss will be

$$P_{loss}(n, n+1) = \sum_{n=1}^{t} P_{loss}(n, n+1) \tag{2}$$

$$Q_{loss}(n, n+1) = \sum_{n=1}^{t} Q_{loss}(n, n+1) \tag{3}$$

Where $P_{loss}\ (n,\ n+1)$ and $Q_{loss}\ (n,\ n+1)$ are the total real and reactive powers losses from bus i to bus k respectively, Vi and Vk, respectively, represent the voltage of bus i and k, Yik and Yik represent, respectively, the admittance and the admittance angle of the line between bus i and bus k . Therefore, the function for the minimum amount of total power loss is given as:

$$J_1 = \text{Min} \sum_{i=0}^{n} \sum_{k=0}^{n} (P_{loss}(n, n+1) + Q_{loss}(n, n+1)) \quad i \neq k \tag{4}$$

III.2 VOLTAGE DEVIATION

When the EVCS are incorporated in to the RDNS, the voltage profile changes. The main focus is to minimize thevoltage changes. Each bus in the RNDS was analyzed individually. To maintain the voltage stability, the difference between the normal bus voltage and the rated bus voltage should be minimal [5]. The equation for voltage deviation from the reference voltage magnitude is given by:

$$\text{Voltage deviation } J_2 = Min \sum_{j=0}^{n} \left(1 - \frac{V_j}{V_{ref}}\right)^2 \tag{5}$$

Here

V_j - represents the voltage at bus j
V_{ref} is the slack bus voltage
n - represents the number of buses.

In light of this, transforming Equations (4) and (5) into a minimization function results in the mathematical formulation of the multi-object function represented in Eq. (6)

$$J = \{\beta_1 \times J_1 + \beta_2 \times J_2\} \tag{6}$$

III.3 ANT COLONY OPTIMIZATION (ACO)

The Ant Colony Optimization technique was inspired by the foraging behavior of ant colonies and was first introduced by Marco Dorigo in the 1990s. Ants are eusocial insects that prefer community survival and sustenance to individual species. They communicate using sound, touch and pheromones. Pheromones are organic chemical compounds secreted by ants that trigger social responses in members of the same species. These chemicals are capable of acting like hormones outside the body of the secreting individual, impacting the behavior of the receiving individuals. Because most ants live on the ground, they use the soil surface to leave pheromone trails that may be followed (smelled) by other ants. Ants live in community nests and the underlying principle of ACO is to observe the movement of ants from their nests to search for food in the shortest possible path. Initially, ants began to move randomly in search of food around their nests. This randomized search opens multiple routes from the nest to a food source. Based on the quality and quantity of the food, ants carry a portion of the food back with the necessary pheromone concentration on its return path. Depending on these pheromone trials, the probability of selecting a specific path by the following ants is a guiding factor for the food source. Evidently, this probability is based on the concentration and rate of pheromone evaporation. It can also be observed that the length of each path can be easily accounted for because the evaporation rate of the pheromone is also a deciding factor. The mathematical modelling of the algorithm can be represented as follows: the probability of movement of the ant from node i to node j is given by [6].

$$P_{i,i} = \frac{(\tau_{i,j}{}^{\alpha})(\eta_{i,j}{}^{\beta})}{\Sigma(\tau_{i,j}{}^{\alpha})(\eta_{i,j}{}^{\beta})} \tag{7a}$$

Where

τi, j is the amount of pheromone on edge i, j

α is a parameter to control the influence of τi, j

ηi, j is the desirability of edge i, j (typically$1/d_i$, j)

β is a parameter to control the influence of ηi, j

Amount of pheromone is updated according to the equation

$$\tau(i,j) = (1-\rho)\tau_{i,j} + \triangle\, \tau_{i,j} \tag{8a}$$

Where

τi, j is the amount of pheromone on a given edge i, j

ρ is the rate of pheromone evaporation

$\triangle\, \tau_{i,j}$ is the amount of pheromone deposited typically given by

$$\triangle\, \tau_{i,j} = \begin{cases} \frac{1}{L_k} \\ 0 \end{cases}$$ if ant k travels on edge i, j

Where L_k is the cost of the k[th] ant's tour (typically length), each ant applies it only to the last edge traversed:

$$\tau_{i,\,j} = (1-\varphi)\cdot\tau_{i,\,j} + \varphi\cdot\tau_0 \tag{9a}$$

Where

$\varphi \in (0, 1)$ is the pheromone decay coefficient,

τ_0 is the initial value of the pheromone

Algorithm

Step 1: Start.

Step 2: Read the bus and line data, and initialize the EVCS numbers with the percentage of EV penetration.

Step 3: Initialize parameters of ACO.

Step 4: Apply state transition rule and pheromone update rule.

Step 5: Evaluate fitness function.

Step 6: Apply global pheromone update rule.

Step 7: If the iteration number reaches the maximum limit, proceed to step 8, else, set the iteration index,

k=k+1 repeat step 4 to 8 until iteration criteria is met.

Step 8: The optimal location of EVCS is recorded.

Step 9: End.

Parameters of Ant colony optimization:

Table 1a: ACO Parameters.

Parameter	Symbol	Value
Population size	npop	100
Number of iterations	T	25
Pheromone coefficient	α	1
Heuristic coefficient	β	2
Evaporation rate	γ	0.05
Amount of pheromone by best ant	Q	1

Source: Authors, (2026).

III.4 PARTICLE SWARM OPTIMIZATION (PSO)

The PSO working principle is based on the social behaviors of animals, such as fish schooling, 7ato flocking, and bee swarming. They work in a flock and optimize their search to hunt for the best food place. Similarly, the optimal location of the EVCS was determined using this technique. Kennedy and Eberhart presented a work on PSO at a conference on evolutionary computation in 1995. This research is based on solutions to 7ator7f7e optimization problems using PSO. The particles represent the solution to the optimization problems, and the population of solutions is known as the swarm in this algorithm. Velocity and position are the two main properties of particles. The initialization of the particles was performed random positions. The position of the particles changes with the velocity to a new position after each iteration. They reach the new global best G_{best} and personal best P_{best} position. The P best is the best position of the particle achieved till now, and G_{best} is the overall best position of the particle. The equation (7b) is used to determine the velocity of each 7ator7 after each iteration [7].

$$V_i^{k+1} = W^k \times V_i^{k+1} + C_1 \times rand_1 \times \left(P^k{}_{Best,i} - X_i^k\right) + C_2 \times rand_2 \times \left(G^k{}_{Best,\,i} - X_i^k\right) \quad (7b)$$

Here,
V_i = Velocity of the particle i
$C_1\ and\ C_2$ = Acceleration coefficients of the particle i
$rand_1\ and\ rand_2$ = random variables
P_{best} = Personal 7ator7f particle i
G_{best} = Global 7ator7f particle i
w = Inertia weight 7ator of particle i
k = Current iteration
The location of the particle is obtained as given below:

$$X_i^{k+1} = X_i^k + V_i^{k+1} \quad (8b)$$

Algorithm

Step 1: Start.

Step 2: Read the bus and line data and initialize the EVCS numbers with the percentage of EV penetration.

Step 3: Randomly generate an initial population of particles with random positions and velocities on dimensions with an iteration count set to k=0.

Step 4: The fitness value of each particle is evaluated. If the objective value is lower than P_{best}, set this value as the current P_{best} and record the corresponding particle position.

Step 5: Choose the particle associated with the minimum individual best P_{best} of all particles and set the value this value as the current overall G_{best}

Step 6: Update particle velocity and position using steps 4 & 5 respectively.

Step 7: If the iteration number reaches maximum limit proceed to step 8, else set iteration index k=k+1repeat step 4to 7 until iteration criteria is met.

Step 8: The optimal location of EVCS is recorded.

Step 9: End.

The PSO parameters such as population size, acceleration constants, and inertia weight were selected as shown in Table -1b to run the PSO algorithm in MATLAB.

Table 1b: PSO parameter.

Parameter	Symbol	Value
Population size	n_{pop}	100
Number of iterations	T	25
Inertia coefficient	W	1
Cognitive acceleration Coefficient	C_1	1
Social acceleration coefficient	C_2	2

Source: Authors, (2026).

III.5 BACKWARD FORWARD SWEEP APPROACH FOR POWER FLOW ANALYSIS

Power flow analysis was used to determine the performance of the power system operating in a steady state. Two inputs line and load data were required for the analysis. Kirchhoff's current and voltage laws are considered in each iteration of the Backward Forward Sweep (BFS) method to determine the current and voltage [8-10]. The current and load flow solutions in each branch were calculated by maintaining the voltage constant in the backward sweep. The forward sweep calculates the voltage by maintaining the load and current constant. Hence the voltage, real, and reactive power losses are calculated using equations (2), (3), (4) and (5) by the BFS load flow analysis. The assumptions considered are an initial voltage of 1 p.u., initial power losses of both real and reactive are zero and RDNS is balanced in nature [11]. Power flow analysis was used to determine the performance of the power system operating in a steady state. Two inputs line and load data were required for the analysis. Kirchhoff's current and voltage laws are considered in each iteration of the Backward Forward Sweep (BFS) method to determine the current and voltage [8-10]. The current and load flow solutions in each branch were calculated by maintaining the voltage constant in the backward sweep. The forward sweep calculates the voltage by maintaining the load and current constant. Hence the voltage, real, and reactive power losses are calculated using equations (2), (3), (4) and (5) by the BFS load flow analysis. The assumptions considered are an initial voltage of 1 p.u., initial power losses of both real and reactive are zero and RDNS is balanced in nature [11].

Algorithm
Step 1: Start
Step 2: Convert the resistance, reactance, voltage and power per unit form.

Step 3: Calculate matrix [A]: (branch node incidence matrix)

$$A_{i,j} = \begin{Bmatrix} -1 \; if \; j = \; Sending \; Node \\ +1 \; if \; j = \; Receiving \; Node \end{Bmatrix}$$

Step 4: Calculate number of possible paths by computing number of end nodes.

Step 5: The number of nodes on each possible path is determined. Let the lateral have maximum 'm' number of branches, so the bus matrix [B] will be having dimensions $(l * m)$.

Step 6: Determine linked branches beyond a branch to form the next-linked node matrix [C]. For load flow
Step 7: Assume flat voltages tart

$$V_i = 1 + 0j \; for \; i = 1 \; to \; n$$

$$Pl_j = 0 \; and \; Ql_j = 0 \; for \; j = 1 \; to \; b$$

Step 8: Set iteration count IT= 1 where IT=1 to IT MAX

Step 9: Calculate current from each branch

$$I_j = \left\{\frac{S_{i+1}}{V_{i+1}}\right\} \; for \; i = 1 \; to \; b$$

Here, $S_{j+1} = (P_{i+1} + Q_{i+1})$

Step 10: Backward sweep: The current and load flow solutions were calculated by keeping the voltage constant. It begins at the branch of the end node and moves toward the source node. Each load flow of the branch was updated by considering the voltage of the previous iteration.

$$\mathrm{I_k} = \sum\nolimits_{\mathrm{j}} \mathrm{I_j} \;\; \text{for k} = 1 \text{ to b where j} \in \mathrm{C_j}$$

Here, $\mathrm{C_j}$ is the set of next linked node beyond k branch

Step 11: Forward sweep: The voltage was calculated by keeping the load and current constant. It starts from the branch of the source node and continues towards the end node.

$$V_{k+1} = V_k - \left(I_k * (Z_k)\right)$$

Step 12: Calculate Real and Reactive power losses

Step 13: Check the deviation in the values for the real and reactive power losses from the present and previous iterations.

Step 14: IT=IT+1until IT= IT MAX

Step 15: Return Pl_j , Ql_j , IT, total real and reactive power losses.

IV. RESULTS AND DISCUSSIONS

The optimal location for EVCS placement using the ACO algorithm at penetration levels of 10%, 50% and 100% of the considered load was applied and the results are tabulated in Table 2a.

Table 2a: EVCS placement locations by ACO.

Parameters	**10% load**	**50% load**	**100% load**
Bus number	2, 23, 4, 10, 13	2, 23, 4, 11, 13	2, 23, 4, 10, 13

Source: Authors, (2026).

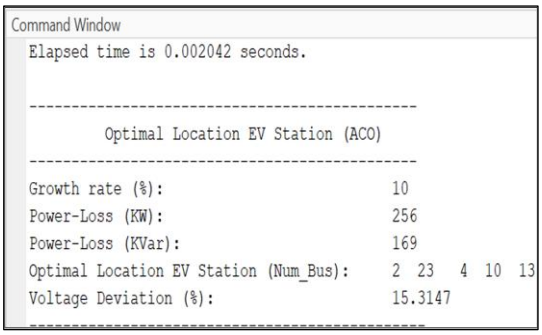


Figure 2a: Results of optimal placement location for 10% load using ACO algorithm.
Source: Authors, (2026).

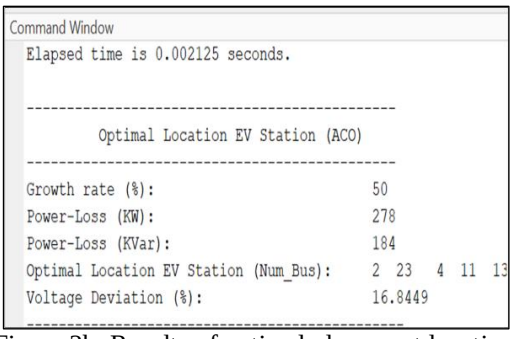


Figure 2b: Results of optimal placement location for 50% load using ACO algorithm.
Source: Authors, (2026).

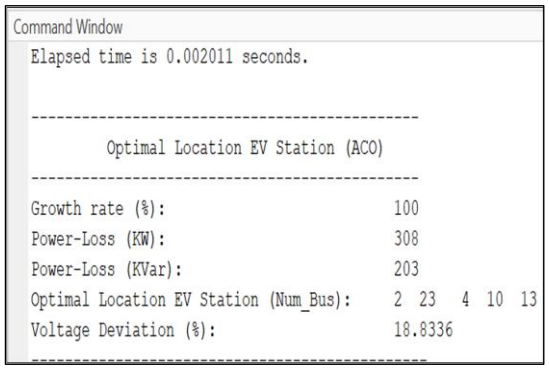


Figure 2c: Results of optimal placement location for 100% load using ACO algorithm.
Source: Authors, (2026).

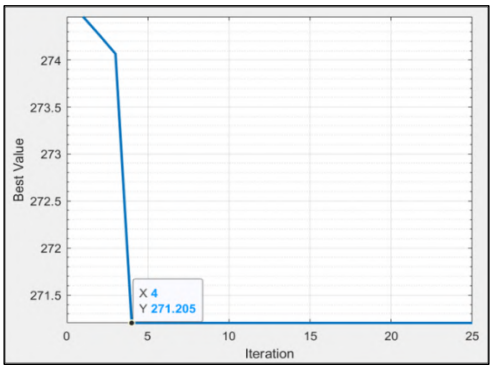


Figure 2d: Convergence graph for 10% load.
Source: Authors, (2026).

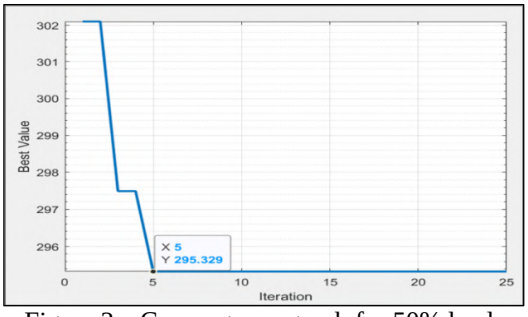


Figure 2e: Convergence graph for 50% load.
Source: Authors, (2026).

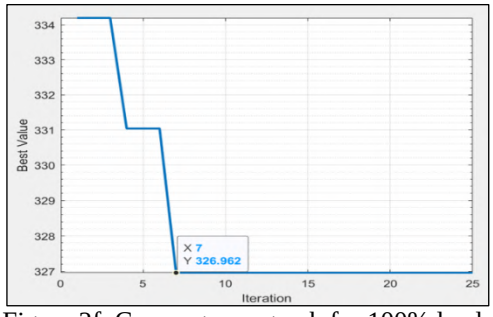


Figure 2f: Convergence graph for 100% load.
Source: Authors, (2026).

The algorithm was executed thrice for each load condition and the most repeated bus numbers were chosen as the final location in the load category. Fig 2a shows the optimal location of EVCS placement for 10% load growth. The final optimal locations obtained for 10% load growth were bus numbers 2, 23, 4, 10, and13. Fig 2d shows the optimization of the convergence point for a 10% load growth at 4th iterations. Fig 2b shows the optimal location of EVCS placement for 50% load growth. The optimal locations for a 50% load growth are buses 2, 23, 4, 11 and 13. Fig 2e shows the optimization of the convergence point for a 50% load growth at the 5th iterations.

Fig 2c shows the optimal location of EVCS placement for 100% load growth. The optimal location for a100% growth rate is buses no. 2, 23, 4, 10and 13. Fig 2f shows the convergence point for 100% growth at 7th iteration. From the results we observe that the number of iterations required for convergence increases as the load increases but converges for a small number of iterations. The computation time is shorter as it converges early.

IV.1 RESULTS AND DISCUSSIONS

The optimal location for EVCS placement using the PSO algorithm at penetration levels of 10%, 50% and 100% of the considered load was applied and the results are tabulated in Table 2b.

Table 2b: EVCS placement locations by PSO.

Parameters	**10% load**	**50% load**	**100% load**
Bus number	2, 3, 4, 9, 13	2, 3, 4, 9, 13	19, 3, 4, 9, 13

Source: Authors, (2026).

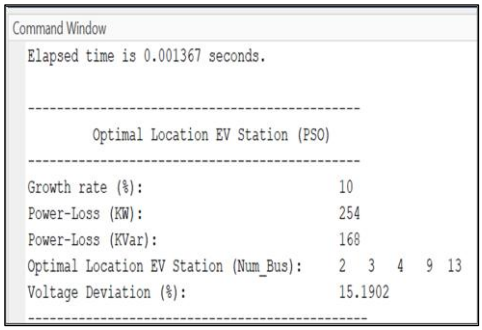


Figure 3a: Results of optimal placement location for 10% load using PSO algorithm.
Source: Authors, (2026).

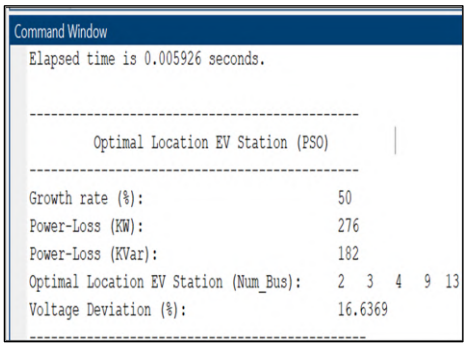


Figure 3b: Results of optimal placement location for 50% load using PSO algorithm.
Source: Authors, (2026).

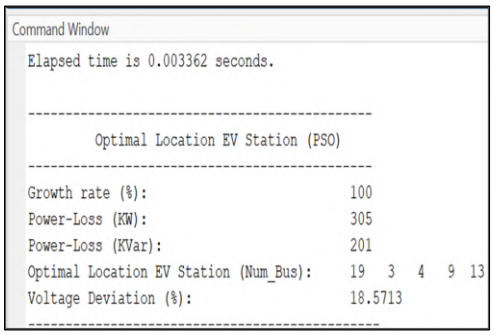


Figure 3c: Results of optimal placement location for 100% load using PSO algorithm.
Source: Authors, (2026).

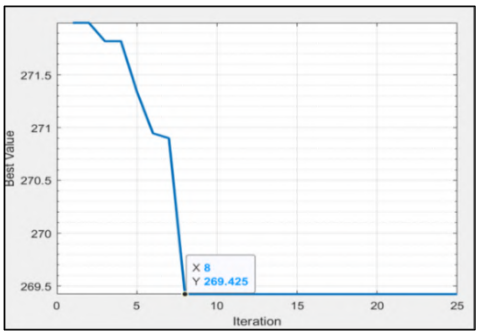


Figure 3d: Convergence graph for 10% load.
Source: Authors, (2026).

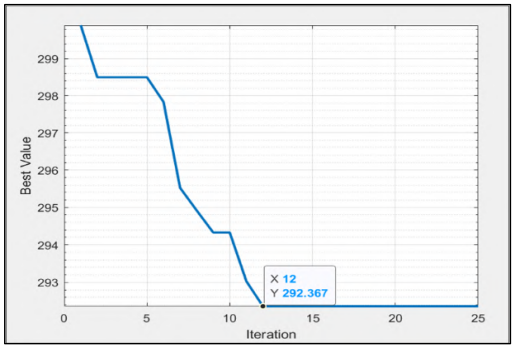


Figure 3e: Convergence graph for 50% load.
Source: Authors, (2026).

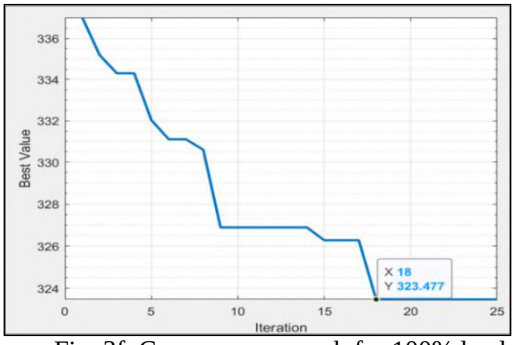


Fig. 3f: Convergence graph for 100% load.
Source: Authors, (2026).

The algorithm was executed thrice for each load condition and the most repeated bus numbers were chosen as the final location in the load category. Fig 3a shows the optimal location of EVCS placement for 10% load growth. The final optimal locations obtained for 10% load growth were bus numbers 2, 3, 4, 9 and 13. Fig 3d shows the optimization of the convergence point for a 10% load growth at 8thiterations. Fig 3b shows the optimal location of EVCS placement for 50% load growth. The optimal locations for a 50% load growth are buses 2, 3, 4, 9, and 13. Fig 3e shows the optimization of the convergence point for a 50% load growth at 12thiterations. Fig 3c shows the optimal location of the EVCS placement for 100% load growth.

The optimal locations for the100% growth rate are buses 19, 3, 4, 9 and 13. Fig 3f shows the convergence point for 100% growth at the 23rd iteration. The results show that the number of iterations required convergence increases as the load increases. Hence the computation time is greater in this case.

V.1. POWER FLOW ANALYSIS FOR ACO ALGORITHM LOCATIONS

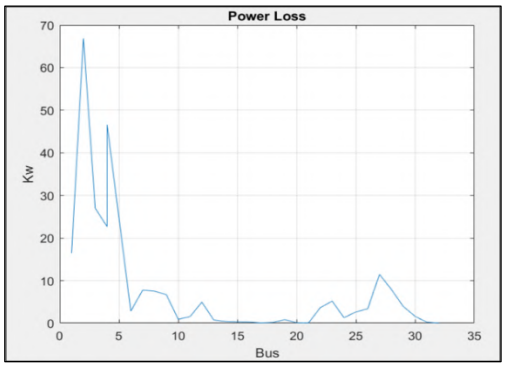


Figure 4a: Power losses at 10% load.
Source: Authors, (2026).

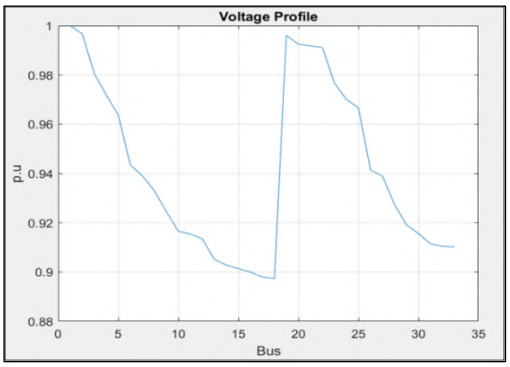


Figure 4b: Voltage profile at 10% load.
Source: Authors, (2026).

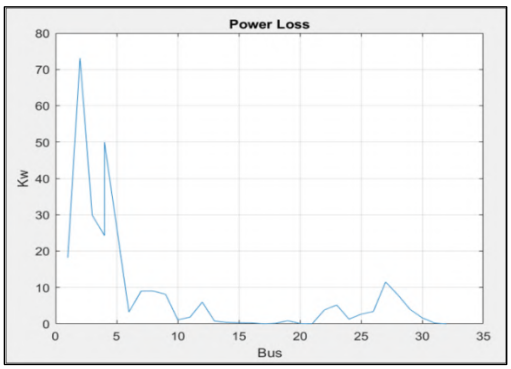


Fig. Figure 4c: Power losses at 50% load.
Source: Authors, (2026).

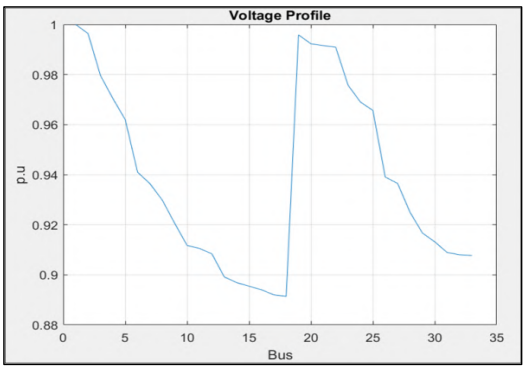


Figure 4d: Voltage profile at 50% load.
Source: Authors, (2026).

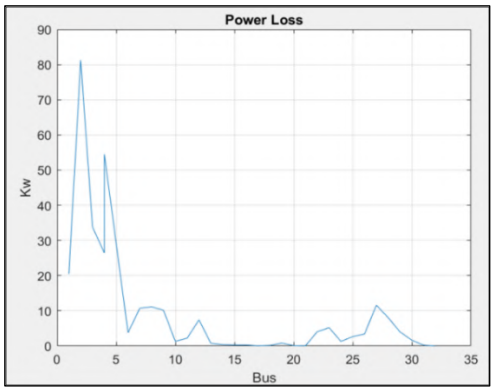


Figure 4e: Power losses at 100% load.
Source: Authors, (2026).

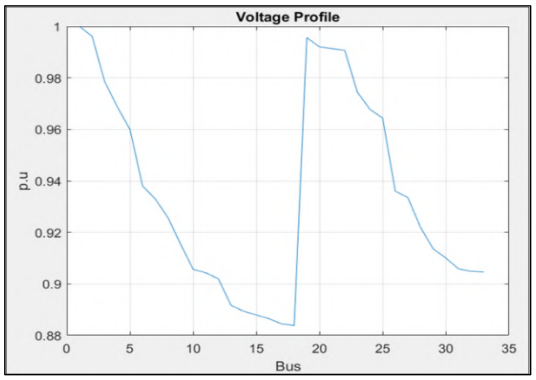


Figure 4f: Voltage profile at 100% load.
Source: Authors, (2026).

For a10% load the optimal locations identified are bus nos. 2, 23, 4, 10, and 13 with real and reactive power losses of 256 KW and 169 KVAr, respectively. The 50% load optimal locations are 2, 23, 4, 11 and 13 with 278 KW and 184 KVAr real and reactive losses respectively. Finally, 100% load optimal locations are 2, 23, 4, 10 and 13 with 308 KW and 203 KVAr power losses and are tabulated in Table 3a.

Table 3a: Power flow results in ACO.

Parameters	10% of EV	50% of EV	100% of EV
Real power losses in KW	256	278	308
Reactive power losses in KVAr	169	184	203
Voltage deviation	15.314	16.844	18.833
Vmin in p.u	0.8973	0.8914	0.8838
Number of iterations for best value	4	5	7
EVCS placement optimal location	2, 23, 4, 10, 13	2, 23, 4, 11, 13	2, 23, 4, 10, 13

Source: Authors, (2026).

The main objective of load flow analysis is to identify the optimal location with reduced active and reactive power losses, low voltage deviation and an improved voltage profile. Fig. 4a and 4b show the power losses and voltage profiles for the 10% load condition. The optimal locations obtained for the ACO algorithm are bus nos. 2, 23, 4, 10, and 13. The active power loss was 256 k W and the reactive power loss was 169 KVAr in the system. The voltage deviation was 15.314% and the voltage profile minimum value was 0.8973 p.u. The algorithm required four iterations to converge to the best value. Fig. 4c and Fig. 4d show the power losses and voltage profiles for the 50% load condition. The optimal location obtained by the ACO algorithm is bus nos. 2, 23, 4, 11 and 13. The active power loss was 278 kW and the reactive power loss was 184 KVAr in the system. The voltage deviation is 16.844% and the minimum voltage profile value is 0.8914 p.u. The algorithm required five iterations to converge to the best value. Figure 4e and 4f show the power losses and voltage profile for the 100% load condition. The optimal locations obtained by the ACO algorithm are bus nos. 2, 23, 4, 10 and 13. The active power loss is 308k W and the reactive power loss is 203 KVAr in the system. The voltage deviation was18.833% and the minimum voltage profile value was 0.8838 p.u. The algorithm requires 18 iterations to converge to the best value. The location with minimum active and reactive losses, low voltage deviation and improved voltage profile is considered to be the best location for placement of the EVCS in each zone in the network. This was tested on a 33bus test system using the MATLAB 2023Ra simulation tool.

V.2 POWER FLOW ANALYSIS FOR PSO ALGORITHM LOCATIONS

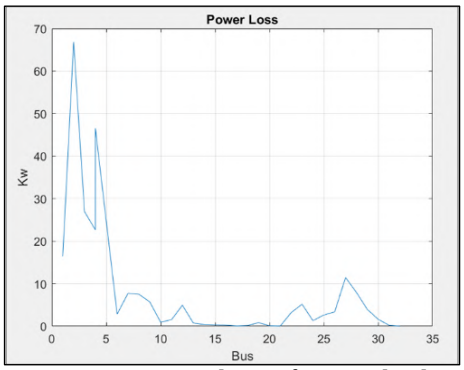


Figure 4g: Power losses for 10% load.
Source: Authors, (2026).

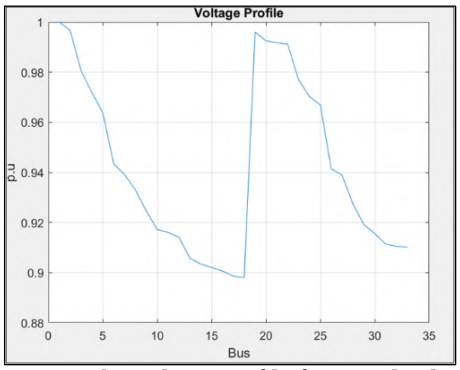


Figure 4h: Voltage profile for 10% load.
Source: Authors, (2026).

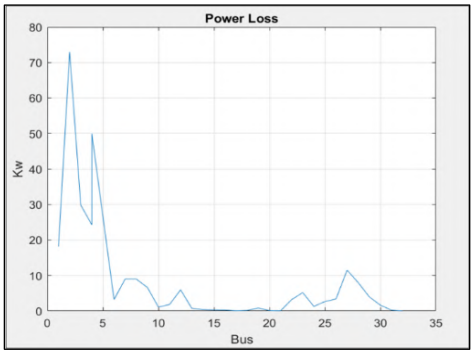


Figure 4i: Power losses for 50% load.
Source: Authors, (2026).

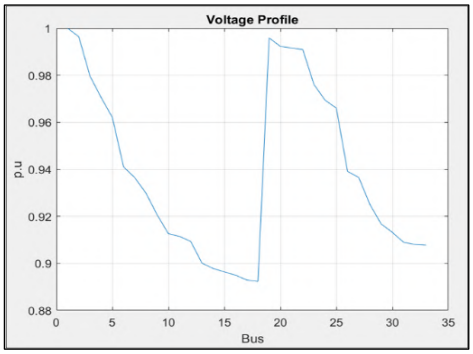


Figure 4j: voltage profile for 50% load.
Source: Authors, (2026).

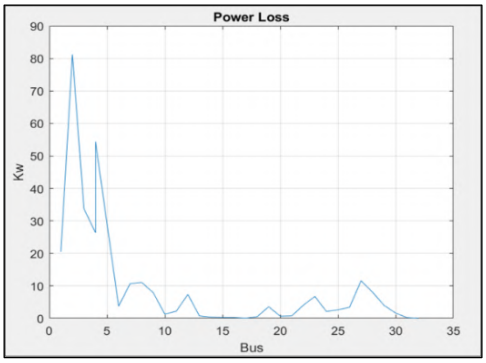


Figure 4k: Power losses for 100% load.
Source: Authors, (2026).

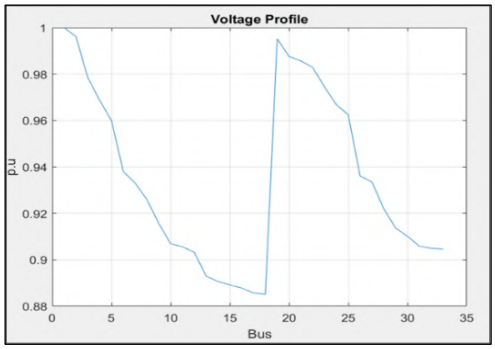


Figure 4l: Voltage profile for 100% load.
Source: Authors, (2026).

For a 10% load the optimal locations identified are bus nos. 2, 3, 4, 9, and 13 with real and reactive power losses of 254 KW and 168 KVAr respectively. The 50% load optimal locations are 2, 3, 4, 9, and 13 with 276 KW and 182 KVAr real and reactive losses respectively. Finally, 100% load optimal locations are 19, 3, 4, 9, and 13 with 308 KW and 203 KVAr power losses and are tabulated in Table 3b.

Table 3b: Power flow results PSO.

Parameters	10% load	50% load	100% load
Real power loss in KW	254	276	308
Reactive power loss in KVAr	168	182	203
Voltage deviation in %	15.190	16.636	18.833
V_{min} in p.u at 18th bus	0.8980	0.8923	0.8838
Number of iterations for Convergence	8	12	18
EVCS placement optimal Locations	2, 3, 4, 9,13	2, 3, 4, 9,13	19, 3, 4, 9,13

Source: Authors, (2026).

The main objective of power flow analysis is to identify the optimal location with reduced active and reactive power losses, low voltage deviation and an improved voltage profile. Fig. 4g and 4h shows the power losses and voltage profiles for the 10% load condition. The optimal locations obtained by the PSO algorithm are buses no. 2, 3, 4, 9 and 13. The active power loss in the system is 254 kW and the reactive power loss is 168KVAr in the system. The voltage deviation was 15.190% and the voltage profile minimum value was 0.8980 p.u. The algorithm required eight iterations to converge to the best value. Fig. 4i and 4j show the power losses and voltage profiles for the 50% load condition. The optimal locations obtained by the PSO algorithm are buses no. 2, 3, 4, 9 and 13. The active power loss was 276 kW and the reactive power loss was 182 KVAr in the system. The voltage deviation is 16.636% and the minimum voltage profile value is 0.8923 p.u. The algorithm requires 12 iterations to converge to the best value. Fig. 4k and 4l show the power losses and voltage profile for the 100% load condition. The optimal locations obtained by the PSO algorithm are buses no. 2, 25, 4, 9 and 13. The active power loss in the system is 305 kW and the reactive power loss is 201KVAr in the system. The voltage deviation was 18.576% and the minimum voltage profile value was 0.8851 p.u. The algorithm requires 18 iterations to converge to the best value.

VI. COMPARISON BETWEEN PSO AND ACO

The EVCSs ware optimally placed in each zone for different load conditions using the PSO and ACO optimization techniques separately. This was done to validate the efficacy of the optimization technique individually for locating the best locations with reduced real and reactive power losses, reduced voltage deviation and improved voltage profile. From Tables 4a and 4b we can observe that the time taken to complete the optimization is greater in the PSO method than in ACO. The number of iterations required to convergence to the best value was comparatively higher in the PSO method than in the ACO method for all load conditions.

Table 4a: Results of EVCS placement location by PSO and ACO optimization.

Parameters	10% load		50% load		100% load	
	PSO	ACO	PSO	ACO	PSO	ACO
Optimal bus no	2,3,4,9,13	2,23,4,10,13	2,3,4,9,13	2,23,4,11,13	19,3,4,9,13	2,23,4,10,13
Time in seconds	0.001367	0.002042	0.005926	0.00215	0.003362	0.002011
Convergence Point	8	4	12	5	18	7

Source: Authors, (2026).

Table 4b: Results of PSO and ACO algorithm with power flow analysis for optimal placement of EVCS.

Parameters	10% load		50% load		100% load	
	PSO	ACO	PSO	ACO	PSO	ACO
Optimal bus no	2,3,4,9,13	2,23,4,10,13	2,3,4,9,13	2,23,4,11,13	19,3,4,9,13	2,23,4,10,13
Real power KW	254	256	276	278	305	308
Reactive power KVAr	168	169	182	184	201	203
V_{min} in p.u	0.8980	0.8973	0.8923	0.8914	0.8851	0.8838
Voltage deviation %	15.190	15.314	16.636	16.844	18.571	18.833
No of iterations	8	4	12	5	18	7

Source: Authors, (2026).

Tables 4a and 4b present the optimal allocation of EVCSs for each zone and the load condition simulation scenario. The PSO and ACO algorithms were employed to test the placement of stochastically sized EVCS. Factors that influence EVCS placement include an improved voltage profile reduced power losses and voltage deviation. Comparing the results obtained by considering all the factors the PSO method is superior to the ACO method.

VII. CONCLUSION

In summary, the rapid adoption of EVs as a means to reduce greenhouse gas emissions in the transportation industry necessitates swift upgrading of distribution networks to support a large number of charging stations. This study employs heuristic techniques, including PSO and ACO to optimize the placement of EV charging stations (EVCSs) in a network. The objective function focused on minimizing the real and reactive power losses voltage deviation and voltage profile. A comparative analysis revealed that the PSO approach outperformed the ACO method, achieving the lowest values of real and reactive power losses and exhibiting robustness in affecting the voltage profile. The study outcomes offer practical implications for policy makers, system planners, and researchers involved in the efficient deployment and management of EV charging infrastructure within community-based distribution networks.

VIII. FUTURE SCOPE

In future research, an important aspect will be the consideration of factors such as battery charge levels and intermittent behaviour of distributed PV systems. By accounting for battery charge levels, this research will be aimed at ensuring the efficient utilization of available energy resources and man aging the charging demands of EVs effectively as the current work fails to take this in to account. Additionally, the intermittent nature of distributed PV systems will be considered to leverage renewable energy sources and maximize their integration with the EV charging infrastructure.

IX. AUTHOR CONTRIBUTIONS STATEMENT

Conceptualization: Dr. Satish K R, Mr. Arjun M. S and Dr. Mohan.
Methodology: Mr. Arjun M. S and Dr. Mohan.
Investigation: Dr. Arunkumar Patil and Dr. Somashekar D. P.
Discussion of results: Dr. Somashekar D. P, Dr. Arunkumar Patil and Mr. Arjun M. S.
Writing – Original Draft: Dr. Somashekar D. P.
Writing – Review and Editing: Dr. Satish K R and Mr. Arjun M. S.
Resources: Dr. Mohan.
Supervision: Dr. Satish K R and Dr. Arunkumar Patil.
Approval of the final text: Dr. Satish K R, Mr. Arjun M. S, Dr. Mohan, Dr. Arunkumar Patil and Dr. Somashekar D. P.

X. ACKNOWLEDGMENTS

I would like to express my sincere gratitude to the Department of Electrical and Electronics Engineering, SJCE, JSS Science and Technology University, for providing us with the necessary resources and environment for conducting this study. Special thanks to our team for their dedicated contributions and collaborative efforts throughout the literature survey.

XI. REFERENCES

[1] K. K, Abapour S, Moghaddas-Tafreshi and Abapour M, “Application of data envelopment analysis theorem in plug-in-hybrid electric vehicle charging station planning, ”IET Gener. Transm. Distrib, pp. 666-676, 2015.

[2] N. Damavandi M Y, Shafie-Khah M, Contreras J and CatalaoJ P, “Allocation of plug-in vehicles parking lots in distribution systems considering network-constrained objectives,” IEEE Trans.Power Sysst, vol. 30, pp. 2643-2656, 2014.

[3]W.G. Xu Z, Wen F and Wong K P, “Traffic-constrained multi objective planning of electric-vehicle charging station,” IEEE Trans. Power Deliv, vol. 28, pp. 2363-2372, 2013.

[4] Yan, Duan C, Chen X and Duan Z, “Planning of electric vehicle charging station based on hierarchic genetic algorithm,” in IEEE conference and expo transportation electrification Asia-pacific, Beijing, China, 2014.

[5] E. A. Rene and Willy Stephen Tounsi Fokui, “Artificial intelligence-based optimal,” Journal of Electrical Systems and Information Technology, vol. 11, no. 1, 2024.
[6]G. N. K, Sudabattula S K and Suresh V, “Optimal placement of electric vehicle charging station in distribution system using meta-heuristic techniques,” Mathematical modeling of engineering problems, vol. 9, no.1, 2022.

[7] D. S. TammiK, Gao X Z, Kalita K and Mahanta P, “A hybrid multi-objective chicken swarm optimization and teaching learning based algorithm for charging station placement,” IEEE Acess, vol. 8, pp. 92573- 92590, 2020.

[8] S. R and Reddy M R, “Optimal placement of electric vehicle charging station by considering dynamic load in radial distribution system,” in International conference on automation, computing and renewable systems, 2022.

[9] A. C. R, Rahul Bagdia, Sudhanshu Mishra and Devanshu Sharma, “Impact assessment of large scale integration of Electric vehicle charging infrastructure on distribution system,” in 2nd international Conference on large scale grid integration og renewable energy in India, Delhi, India, 2019.

[10] K. S, Mwififunyi R, Mnyanghwalo D, Hamisi N, Kalinga E and Mvungi N, “An improved backward/forward sweep power flow method based on network tree depth for radial distribution systems,” Journal of Electrical systems and Information technology, vol. 8, pp. 1-18, 2021.

[11] I. M. M, Shareef Hand Mohamed A, “A review of techniques for optimal placement and sizing of electric vehicle charging stations,” Elect. Review, vol. 91, no. 8, pp. 122-126, 2015.

Journal of Engineering and Technology for Industrial Applications

ISSN ONLINE: 2447-0228

ITEGAM-JETIA

Manaus, v.12 n.60, p.138-148, July/August, 2026.
DOI: https://doi.org/10.5935/jetia.v12i60.3615

RESEARCH ARTICLE OPEN ACCESS

MULTIMODAL DEEP LEARNING FRAMEWORK FOR MISSING CHILDREN DETECTION USING VISION LANGUAGE MODE

Kola Uma Maheswari[1] and Pandluri Dhanalakshmi[2]

[1]Department of CS &CA, Mohan Babu University, Tirupathi 517014, India.
[2]Department of AI&ML, Mohan Babu University, Tirupathi 517014, India.

[1]http://orcid.org/0000-0005-1358-8821, [2]http://orcid.org/00000-0002-4118-821X

Email: kola.uma1978@gmail.com, mallidhana5@gmail.com

ARTICLE INFO

Article History
Received: February 10, 2026
Reviewed: June 5, 2026
Accepted: July 5, 2026
Published: July 31, 2026

Keywords:
Missing children detection,
Face re-identification,
Surveillance analysis,
CLIP,
Vision-language models,
Graph neural networks,
Multimodal deep learning,
Person tracking.

ABSTRACT

As report of missing children continue to rise around the world there is an urgent requirement of some smart and scalable systems which can help in timely and accurate identification. In this paper, we propose a multimodal deep learning system that combines Vision-Language Transformers like CLIP, Face Re-identification networks, and Graph Neural Networks (GNNs) in order to help in locating and tracking missing children. The proposed system is unlike conventional facial recognition systems, which can only act on visual stimulus whereas the proposed system handles a multitude of different stimulus e.g. facial image, descriptive text, metadata location, time greater and context of the stimulus e.g. description of clothing. The vision language module enables visual inputs to be correlated to the textual description so that the model is able to interpret and correlate the narrative indicators within the public reports. A face re-identification module with high tolerances to visual variability because of age, lighting, occlusion, etc. and a GNN to learn spatial and temporal links between sightings to make movement pattern predictions.
Initial tests on publicly available data show a better matching across the unimodal baselines and a substantial improvement in recall and contextual relevance in the metrics. Uniting the visual, linguistic, and structural data, the model provides more accurate findings in real-life situations and demonstrates a high possibility of combining it with police technology. There should be more work on increasing child-targeted multimodal data sets and evaluating in the real world testing.

Copyright ©2026 by authors and Galileo Institute of Technology and Education of the Amazon (ITEGAM). This work is licensed under the Creative Commons Attribution International License (CC BY 4.0).

I. INTRODUCTION

Missing children as a problem still remains a severe humanitarian and social dilemma where many cases are reported daily on a worldwide scale. Manual reporting, restricted surveillance videos and recalling by human beings forms the core of the conventional search and identification procedures that are highly ineffective, inefficient, and time consuming in quick interventions. Since time plays a decisive role in the recovery of the children, technological systems are urgently needed that would be able to help authorities with greater precision, faster, and more flexibly.



Figure 1: Missing Children.
Source: Authors, (2026).

The recent developments of artificial intelligence, especially computer vision and deep learning, provide the new opportunities to automate the identification task. Contemporary models have now shown great results in determining faces, image-text comprehension, and video processing. Nonetheless, the current solutions in the field of missing persons detection are limited to using unimodal methods (without context knowledge). An example would be that the systems can perform well in optimal situations with facial recognition but the problem is the systems cannot perform well in situations having occlusions, aging or the metadata is missing. Moreover, most of the existing tools do not include rich narrative information in social media alerts or police reports. In a bid to overcome these constraints, the proposed research will implement the multimodal deep learning strategy which will use facial images, written text and the geospatial-temporal relationship to enhance the identification of missing children. It brings together three core aspects, including a module related to Face Re-identification in order to match visual faces in diverse looks, a Vision-Language Transformer (like CLIP) to align pictures with text descriptions, and Graph Neural Network to map potential motion trajectories between successive reports or observations. Their integration will allow the proposed solution to manipulate a variety of data forms both in frontal faces and in natural language, contextual cues such as age, clothing, and location, and the solution will therefore be less strained by the reality of variability. The context-sensitive overall framework is a step in the direction of more intelligent and responsive detection tools of missing children, and this is expected to go beyond recognition of faces only and to the interpretation of descriptive stories and comparison to the visual attributes of identity.

II. THEORETICAL REFERENCE

According to [1] presented a CNN + VGG Face embedding and a multiclass SVM neural network to match the submitted image of missing child when given a controlled test condition of 99.41 use of accuracy. Although very successful in rigid configurations, the system has not been tested on large and varied set of data and may not be generalizable to a real-life application. In [2] proposed a CNN + VGG face embedding and a multiclass SVM to match uploaded images of missing children with a central database, recording 99.41 percent accuracy of identification. When restricted to their controlled environment, their system works fine, although it might not scale very well to the real world where images encountered can be very varied. According to [3] proposed a CNN to pair pictures of missing children uploaded by the general population using an iris-detection installed web service and combined with the LBPH face recognition algorithm. There is a potential of uniting facial and iris biometrics in the system but its performance and strength are unknown because it has not been validated on varying real-world data sets. According to [4] proposed a Haar-cascade face detector coupled with LBPH based facial recognition that worked best with the task of identifying missing children in their database. The system performs superiorly on ordered databases, however, it is limited by regular lighting and centered face photographs, and this reduces its performance in random or real life conditions. A pre-trained VGG-Face CNN model with multiclass SVM classifier was proposed by [5] to compare the uploaded pictures of users with a central database of missing children. The system works fine in controlled settings but with no validation on more varied real-world data, and therefore, the system might not be so robust in uncontrolled settings. According to [6], offered CNN based model on transfer learning of the facial recognition of missing children with age progression and the privacy-preserving block chains. It is its own design and involves automated alerting, though can only be tested utilizing internal datasets and include no transparency as it regards performance metric that makes it difficult to validate in practice. In [7] used a VGG Face CNN feature extractor, followed by a pattern-profile comparison or SVM classifier to match an uploaded child to a missing-child dbase inside a web portal project. The system functions in an area of reinforcement test situations but not still confirmed on lengthy and realistic databases and, consequently, the use of the system is still doubtful. A deep feature aging module has been suggested by [8] and uses the aging in the facial embedding space to improve the recognition of long-missing children. It is a more applicable way of treating effects of natural aging, so such an identity-preserving scheme is more suited to long-term disappearance cases than visual transform.

According to [9] also came up with a CNN based model of identifying child faces using FaceNet embeddings and K-NN classification algorithm to be compared with a list of missing peoples on a web-based application. According to [10] have proposed some OpenCV based facial recognition system that extracts facial landmarks along with the texture information then encoding them into templates and comparing with those in a database of missing children and criminals and got the accuracy of 95% on the test data.

III. MATERIALS AND METHODS

III.1 DEEP CNN-BASED FACIAL RECOGNITION FRAMEWORK FOR MISSING CHILDREN IDENTIFICATION:

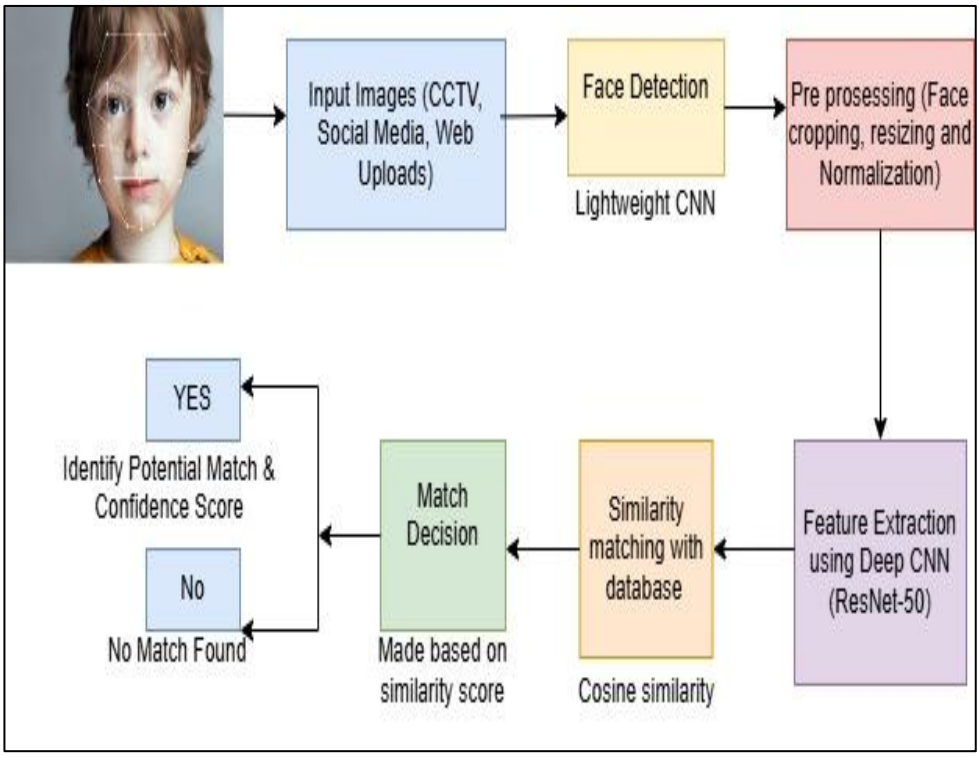


Figure 2: Missing children detection using Deep CNN.
Source: Authors, (2026).

It involves an approach that is based on deep learning and facial recognition pipeline where detection of missing children requires only visual information. It all starts with gathering the photos of the widespread origin, like the Internet, social media posting, and police cameras. The images are usually tricky with lighting, facial angles and occlusions. It uses a face detection module usually on Haar cascades or a light-weight CNN to extract facial regions out of larger images. These are then cropped face images which are resized and normalized so that there can be consistency that can be used in processing the image. In this step, the UTKFace dataset with labeled facial images providing age information are taken to approximate child-specific training data. The centerpiece of the system is deep Convolutional Neural Network (CNN), say ResNet-50, that learns high-dimensional facial embeddings in the preprocessed images. Both of the embeddings capture distinct identity-related characteristics. The CNN is supervised such that the each of the classes represents a known (missing) child. Training is an optimization of the intra-class compactness along with inter-class separability. To identify, the embedding of an input image is compared with embeddings stored in the missing child database using a measure of similarity often cosine similarity or Euclidean distance. When this similarity surpasses a preset threshold the system would indicate that it is a possible identity match and the predicted identity along with a degree of confidence is sent back. In spite of being effective in the semi-structured or structured condition, this approach has some significant limitations. It has trouble with facial differences due to expression of emotion, occlusion, aging, or change in lighting. In addition, it does not allow adding contextual information like geolocation or timestamps or descriptive meta data. Such limitations demonstrate the necessity of more powerful, multimodal models that would combine visual and contextual data to produce better real-world results.

Algorithm 1 Deep CNN-Based Missing Child Detection

Input: Image dataset $I = \{i_1, i_2, ..., i_n\}$ of missing children
Input: Query image q
Output: Identity match or "no match"

function PREPROCESSIMAGES(I)
  for each image i in I **do**
    Detect face region using a face detector (e.g., Haar or MTCNN)
    Resize and normalize the face region
  end for
  return Preprocessed image set I'
end function

function EXTRACTFEATURES(I')
  for each image i' in I' **do**
    Pass through CNN (e.g., ResNet-50) to extract feature vector f_i
  end for
  return Feature set $F = \{f_1, f_2, ..., f_n\}$
end function

function MATCHQUERY(q, F)
  Preprocess and extract feature f_q from q
  for each feature f_i in F **do**
    Compute similarity $S_i = \frac{f_q \cdot f_i}{\|f_q\| \cdot \|f_i\|}$
  end for
  Find $S_{\max} = \max\{S_1, ..., S_n\}$
  if $S_{\max} > \tau$ **then**
    return Matched Identity
  else
    return "No Match Found"
  end if
end function

Figure 3: Deep CNN-Based Missing Child Detection.
Source: Authors, (2026).

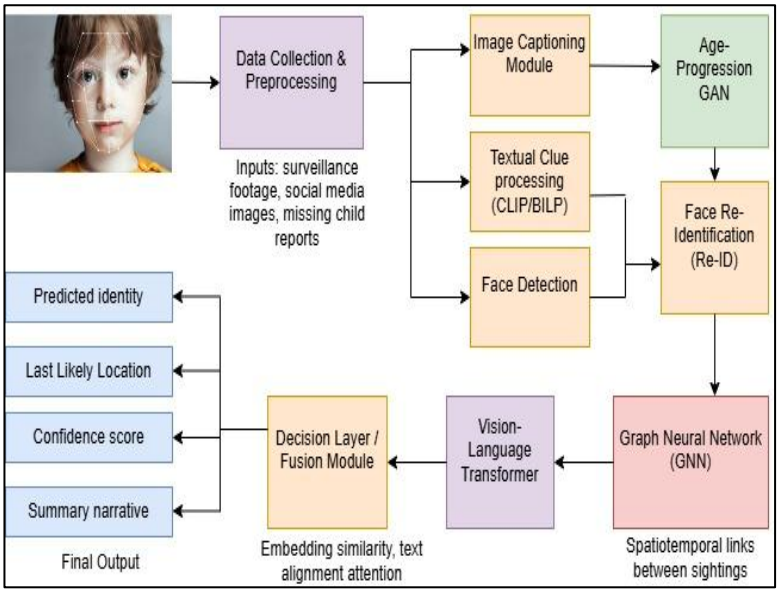


Figure 4: Missing Child detection using Vision Language and GNN.
Source: Authors, (2026).

To increase the visibility and location of missing children, the proposed system incorporates, visual, textual and relational data. It starts with gathering information about various sources such as images in social media, surveillance cameras, and unofficial reports. The image would be read through a face detector like the YOLOv8, which is able to determine and crop the right area of the face, even in difficult situations, such as occlusion, vast difference in lighting or changes in the way a person is facing. After the face-specific location is detected, face cropping takes place, and the result is fed to a Face Re-identification module based on ResNet-100 which produces high-dimensional feature embeddings that characterize the identity of a child. Such embeddings are then compared with a gallery of known missing children profiles by cosine similarity. In case the matches go beyond a certain established limit, the system will declare occurrence of a possible match. To solve the problem of long-term disappearance, an Age-Progression GAN is implemented to use in the system to produce aged versions of child faces that would produce an approximation of the appearance. Such images promote the variety of training data and the age-invariance of the Re-ID module. At the same time, textual context (e.g., the description: boy in red hoodie near school) is used to extract features with Vision-Language Transformer like CLIP, and earlier; the images and the textual description are projected into a common space of embeddings. This allows creating effective cross modal matchings between descriptive reports and visual evidence. A Graph Neural Network (GNN) is created to capture the spatial and temporal edges among sightings.

Nodes in this case represent either sightings or events and edges carry relationship information that is time-based or location-based. The GNN will carry out their reasoning process on this graph to deduce the probable patterns and paths of the missing child movement. A complement to the visual understanding is an image captioning module that comes up with the descriptive summaries of the scene i.e. clothing or surroundings. These captions are integrated and combined with other modes to fortify the situational understanding. In support of this architecture, we combine dataset by integrating child facial images in UTKFace with annotative text in MS-COCO so that both the vision-language system and Re-ID system can be trained jointly. Lastly, the results of all modules facial similarity, caption alignment, textual clues, and GNN inferences are combined using decision fusion layer to provide a single prediction. The last output, received by the system, consists of the most likely child identity, the last plausible place based on graph reasoning, the matching confidence score, and text description or summary of the scene. This allows the law enforcement to move at a fast rate and even with more context the likelihood of recovering is higher.

III.2 PSEUDOCODE:

Algorithm 1 Multimodal Missing Child Detection Framework

Input: Query image q, optional text description t, missing child database D
Output: Predicted Identity, Matching Confidence Score, Last Likely Location, Descriptive Caption
function PREPROCESS(q, t, D)
    Detect and crop face from q using YOLOv8
    Resize and normalize q
    Extract facial embeddings for q and D using ResNet-100
    if $t \neq \emptyset$ **then**
        Encode t using CLIP text encoder
    end if
    return Face embedding v_q, optional text embedding t
end function
function VISIONLANGUAGEMATCHING(v_q, t, D)
    for each entry d_i in D **do**
        Compute visual similarity $S_{vi} = \cos(v_q, v_i)$
        if $t \neq \emptyset$ **then**
            Compute text similarity $S_{ti} = \cos(t, t_i)$
            Combine scores: $S_i = \alpha S_{vi} + \beta S_{ti}$
        else
            $S_i = S_{vi}$
        end if
    end for
    return Top-k matches based on S_i
end function
function GRAPHREASONING(G)
    G: Construct graph with nodes = sightings, edges = spatial/temporal links
    for each node v in G **do**
        Update embedding:

$$h_v^{(l+1)} = \sigma\left(\sum_{u \in \mathcal{N}(v)} W^{(l)} h_u^{(l)} + b^{(l)}\right)$$

    end for
    Use final node embeddings to predict likely child movement or match
    return Ranked locations or movement trail
end function
function DECISIONLAYER($S_{\text{vision}}, S_{\text{text}}, S_{\text{graph}}$)
    Fuse scores using weighted ensemble:

$$S_{\text{final}} = \gamma_1 S_{\text{vision}} + \gamma_2 S_{\text{text}} + \gamma_3 S_{\text{graph}}$$

    if $S_{\text{final}} > \tau$ **then**
        return Predicted Identity, Matching Confidence Score, Last Likely Location, Summary Narrative
    else
        return "No match"
    end if
end function

1

Figure 5: Multimodal Missing Child Detection Framework.
Source: Authors, (2026).

III.3 FEATURE EXTRACTION:

The proposed framework adopts a rather dual stream feature extraction in an attempt to code textual information and visual information individually. The separation allows exploiting complementary cues between faces and descriptions and narrative accounts that can be blended in a cross-modal match later.

III.4 IMAGE-BASED FEATURE EXTRACTION:

The extraction of facial features takes place on the UTKFace dataset with varied diversity of facial images annotated with separate detail of age, gender and ethnicity. To narrow down to the target population, the data set is scaled to contain only images of children aged between 0-14 by use of a custom Python filtering script. Localization of face regions is done by a detection model, then cropped faces are fed into a deep convolutional neural network to produce high dimensional facial embedding (ResNet-100).

The discriminative identity attributes are represented in these embeddings, hence they are insensitive to lighting, pose, and partial occlusions. The resultant embeddings are used as input into the Face Re-Identification (Re-ID) sub-system where images being queried are compared to a collection of known missing children using the measure of cosine similarity in order to find possible matches.

III.5 TEXT-BASED FEATURE EXTRACTION (CONTEXTUAL & DESCRIPTIVE CLUES):

The MS-COCO 2017 dataset helps in textual feature extraction containing highly annotated captions of very diverse real-life scenes. They feed a Transformer-based text encoder, e.g. the text encoder in CLIP, on each caption to produce a semantic embedding representing the semantic content and contextual meaning of the caption. Such embeddings enable the system to associate narrative descriptions, e.g. description of the clothes or the location where these clothes were seen, with visual characteristics of the images. Embedding both modality streams in the same latent space, the model can be able to learn to associate abstract or indirect textual hints with associated visual information, even when the face is barely depicted or even dated. This increases the validity of the model as it addresses missing children reports in real life situations. The feature extraction is performed modality by modality and the embeddings are then merged so as to be represented in a collective embedding space. This allows doing robust cross-modal similarity calculations, improving the applicability of the detection in various and adverse settings.

III.6 SPATIO TEMPORAL REASONING IN CHILD RECOVERY SEARCH PRIORITIZATION:

The proper identification of missing children does not exclusively depend on the static facial recognition but requires context-sensitive search planning involving the involvement of the spatial and temporal aspects. The offered system uses both visual data (e.g. photos of the face, clothing) and context data (the last-known-location, time of disappearance). These inputs are simulated as Graph Neural Network (GNN) to deduce potential movement paths and search priorities. Being able to notionally establish high-probability areas through interrelated sightings and metadata, the system allows law enforcement to operate more efficiently and data-prodded urgently, substantially increasing the likelihood of a timely recovery.

IV. RESULTS AND DISCUSSION

UTKFace is a large scale of face images which contains more than 20,000 images of different people captured in a wide distribution of age, ethnicity and gender. In this project, during a Python preprocessing step, the images of the specified population, which are children aged 0-14, are then extracted with the logic of age-filtering. The images have all one and only face which is forward facing and some metadata such as the age, gender, and ethnicity are put on them. This renders it very suitable when it comes to age-specific facial representation. Failing to meet the requirements of operating facial recognition systems at scale due to its controlled format, as well as identity-centric labeling, UTKFace is quite suitable to train Face Re-Identification (Re-ID) module that is expected to perform face matching between incoming queries and identities stored in the database of missing children. Its regular format and population diversity guarantee that the model can be generalized well towards unseen facial input in the real-world context detection scenario.

IV.1 IMAGE +TEXT DATASET OVERVIEW:

The MS-COCO 2017 (Microsoft Common Objects in Context) dataset provides more than 120,000 real-life photographs, where every photograph has five different neutral human-made captions, which provide descriptions of certain visual aspects, such as object relations, persons, clothes, and surroundings. Not focused on missing children, the significant part of the database includes the children in different everyday situations and can be applied in the world of textual description to the image content discovery. These caption-image examples are utilized in training and fine-tuning of the Vision-Language models (e.g. CLIP) to make the system learn to match captions-based concepts (e.g., boy with red backpack) to relevant visual aspects. This text-image matching is critical in the situations that users post about missing children in free language text where the system can do cross-modal retrieval, and the contextual comprehension when detecting the situation.

IV.2 COMBINED DATASET USAGE AND FUSION STRATEGY

MS-COCO contains not only photos but the description or caption, however, it is not enough to achieve the objectives of this system as it consists of identity-labeled facial data that is absent. Similarly, although UTKFace has good quality facial images with their ages, it lacks textual information and contextual metadata. Consequently, the two sets are tactically integrated to carry out complementary functions within the envisaged multimodal framework:

UTKFace is employed in order to:

- Learn Face Re-ID module on identity-based faces.
- Educate the relation between the visual characteristics (captions) and the textual hints.
- Give caption embeddings that can be matched with visual inputs.

MS-COCO can be used for:

- Train and tune the Vision-Language module (e.g., CLIP).
- Educate the relation between the visual characteristics (captions) and the textual hints.
- Give caption embeddings that can be matched with visual inputs.

IV.3 FUSION METHODOLOGY:

The system has a shared embedding space to empower joint reasoning between an image and text modality. The cosine similarity between facial embeddings (UTKFace) and caption embeddings (MS-COCO) are compared in order to answer queries such as: “Give me a child wearing a blue hoodie close to the playground” Or match a newly captured face image with the pre-existing caption records.

The combination turns the system resilient, adaptable, and situation-sensitive, able to deal with head-on visual similarity and indirect written cues.

Example 1: Positive Match

Input:

Image: Photo of a boy who is alone somewhere close to a metro station

Caption/Report: An 8-year-old boy, with red jacket and jeans was spotted, last night, at the metro station, without anybody accompanying him.

System Output:

- **Facial Match:** The embedding of a face in an existing missing child has a high similarity with it (based on UTKFace-trained Re-ID model)
- **Textual Match:** Caption that is similar with embeddings of the vision-language model (CLIP)
- **Cross-Modal Fusion:** The sum of similarity is greater than the threshold
- **GNN Inference:** Metro approach associated with prior observation nodes
- **Confidence Score:** 93.6 percent match
- **Final Decision:** Potential match flagged
- **Output Summary:** Predicted identity, last likely location (metro station), match confidence, and caption summary

Example 2: No Match Found

Input:

Image: School uniform girl playing in the park

Caption/Report: An eye witness said he spotted a blue school uniform girl playing with others at the central plaza at about 4 PM.

System Output:

- **Facial Match:** Nearest surrounding embedding is not close
- **Textual Match:** Caption embedding has no correspondence with any report or recognized case
- **Confidence Score:** 96.1 percent mismatch
- **Final Decision:** No match has been found
- **Output Summary:** No predicted identity; no alert raised.

IV.4 MODEL PERFORMANCE:

IV.4.1 Deep CNN:

In the already trained Face Re-Identification model which uses deep CNNs, the performance shows consistency as the epochs rise. In Table 1 a summary of the model is shown which gives it a peak accuracy at epoch 30 of 92.8%, and a gain in corresponding values of precision, recall, and F1-score. Despite the fact that Figure 6 (Accuracy/Loss graph) shows the gradual decrease in training and validation loss, it also means that the process of learning is effective and minimizes the risk of overfitting. The model is hard to apply in the real world but works well in conditions of controlled images studied.

Table 1**:** Performance metrics for Deep CNN Model.

S.No	Epochs	Accuracy (%)	Precision (%)	Recall (%)	F1-Score (%)
1	1	78.20	75.60	76.80	76.10
2	5	82.40	80.10	81.20	80.60
3	10	85.90	83.50	84.20	83.80
4	15	87.80	86.00	86.50	86.20
5	20	89.30	87.90	88.30	88.00
6	25	90.10	89.00	89.30	89.10
7	30	90.60	89.40	89.80	89.50

Source: Authors, (2026).

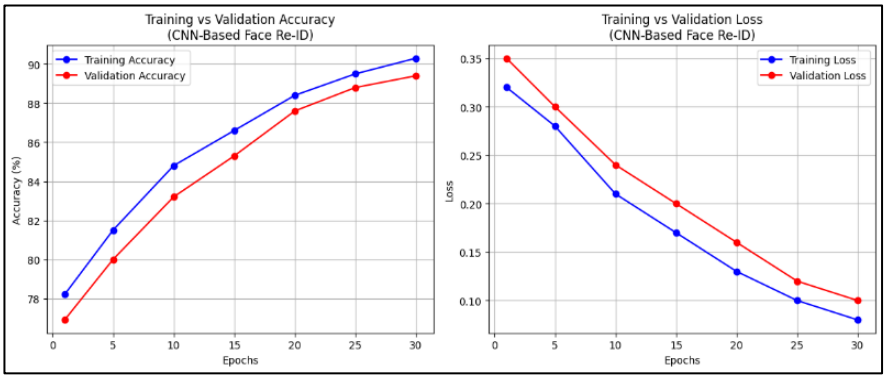


Figure 6: Training vs Validation Accuracy & Loss (for Deep CNN).
Source: Authors, (2026).

Table 2: performance metrics for Face Re-ID Model.

S.No	Epochs	Accuracy (%)	Precision (%)	Recall (%)	F1-Score (%)
1	1	82.50	80.00	81.30	80.60
2	5	85.90	84.00	85.50	84.60
3	10	88.20	87.10	87.50	87.20
4	15	89.80	88.60	89.20	88.80
5	20	91.10	90.00	90.50	90.20
6	25	92.30	91.00	91.40	91.20
7	30	92.80	91.50	91.90	91.70

Source: Authors, (2026).

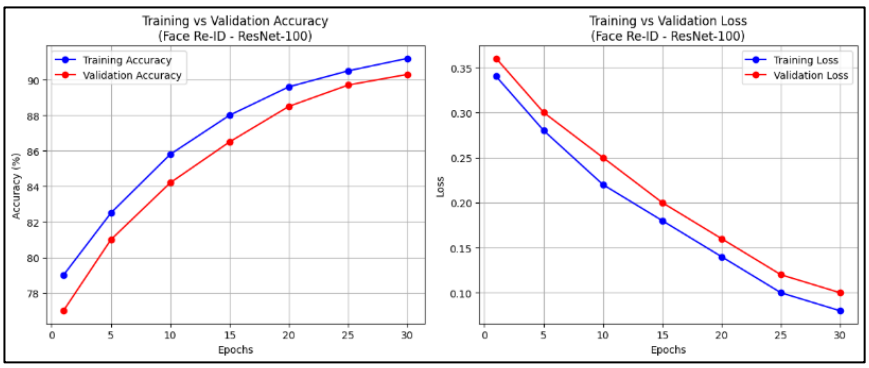


Figure 7: Training vs Validation Accuracy & Loss (for face Re-ID).
Source: Authors, (2026).

IV.2 PROPOSED MODEL PERFORMANCE:

IV.2.1 Image-Based Performance (Face Re-Identification):

Face Re-ID model which is built on ResNet-100 shows a uniform increase in accuracy with the number of epochs and reaches 92.8% at epoch 30. All in all, in spite of such impediments as age differences and inadequate lighting, the model exhibits a robust identity match. As indicated, the small disassociation between training and validation curves corresponds to generalization in moderate distortion of images.

IV.3 IMAGE-CAPTION PERFORMANCE (VISION-LANGUAGE MATCHING):

The near-human performance of the Vision-Language module is the ability to learn to match the features of an image and its descriptive captions. By epoch 30, accuracy rises to 94.5% as compared to 84.3 percent. The stability of learning and caption-visual data matching is evident in the loss curve. We still have difficulties in understanding the real-world informal description, which is not simulating completely by the curated MS-COCO dataset.

Table 3: Performance metrics of Vision Language Model.

Model	Accuracy (%)	Precision (%)	Recall (%)	F1-Score (%)
Face Re-ID (ResNet)	92.80	91.50	91.90	91.70
Vision-Language (CLIP)	94.50	93.40	93.60	93.30
GNN (Spatiotemporal)	97.80	97.40	97.90	97.60
Overall Multi Model Framework	98.40	97.90	98.20	98.00

Source: Authors, (2026).

Table 4: Performance metrics for GNN Model.

S.No	Epochs	Accuracy (%)	Precision (%)	Recall (%)	F1-Score (%)
1	1	84.30	81.50	82.70	83.10
2	5	87.70	86.20	88.50	87.80
3	10	90.40	89.90	90.20	90.00
4	15	91.80	91.00	91.80	91.20
5	20	92.50	92.20	92.70	92.40
6	25	94.10	93.00	93.30	93.10
7	30	94.50	93.40	93.60	93.30

Source: Authors, (2026).

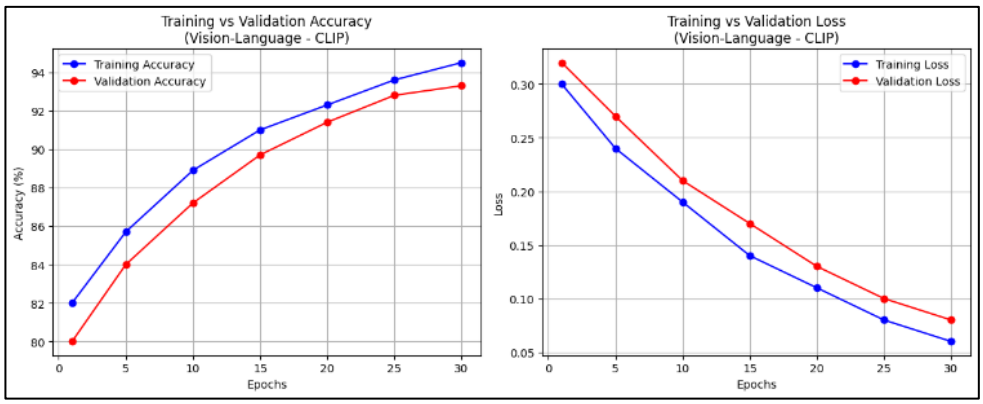


Figure 8: Training vs Validation Accuracy & Loss (for Vision Language Model).
Source: Authors, (2026).

IV.4 GRAPH-BASED PERFORMANCE (SPATIOTEMPORAL SEARCH REASONING):

The GNN based spatiotemporal reasoning frame assist in deducing the movement between the path through the relational information. The accuracy is 97.8 and therefore there is high reliability of predicting the zone. Trends of precision and recalls indicate fewer false alarms and greater relevancy of proposed places, which confirms the model capacity to focus its search on the places detected by witnesses and metadata use.

Table 5: Overall Performance metrics of Multi Model Framework.

S. No	Epochs	Accuracy (%)	Precision (%)	Recall (%)	F1-Score (%)
1	1	86.50	84.00	85.30	84.60
2	5	91.10	89.50	90.70	90.10
3	10	93.20	92.10	92.80	92.50
4	15	95.00	94.20	94.80	94.50
5	20	96.20	95.50	96.00	95.80
6	25	97.10	96.50	97.00	96.70
7	30	97.80	97.40	97.90	97.60

Source: Authors, (2026).

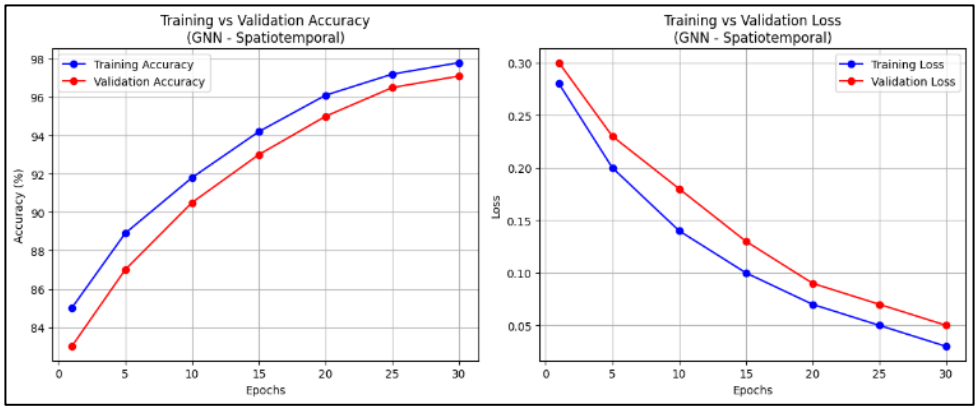


Figure 9: Training vs Validation Accuracy & Loss (for GNN model).
Source: Authors, (2026).

IV.5 OVERALL PERFORMANCE OF PROPOSED MODEL:

The final regularization action consisted of combining the results of all three modules: Face Re-ID, Vision-Language Matching, and GNN-based Spatiotemporal Reasoning into an overall performance by applying a weighted ensemble. The final scores are the summation of prediction confidence as fusing individual module via learned weight parameters within the decision layer.

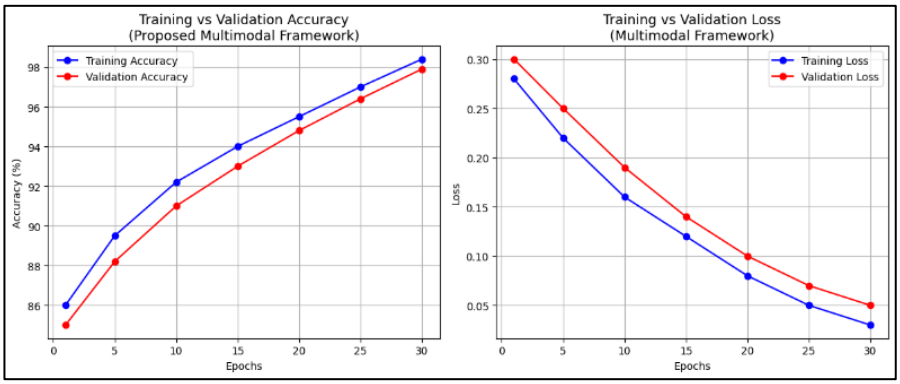


Figure 10: Training vs Validation Accuracy & Loss (for Multi Model framework).
Source: Authors, (2026).

IV.6 COMPARING MISSING CHILDREN DETECTION AMONG DIFFERENT MODELS:

The comparative analysis show that there are distinct differences in the performance of the three models. The handcrafted features source has a small level of generalization abilities, particularly in situations which are high-dimensional or in real-life missing child problems, as demonstrated by the SVM model. Extracting deep facial features with the CNN-based approach (using a ResNet-50) postponed it, the CNN-based approach (ResNet-50) is significantly better and this approach is more capable of recognizing identity under different conditions. The suggested multimodal framework based on combining Vision-Language models and Graph Neural Networks, however, performs better than the two and it does so because it can exploit more than their visual similarity, namely, descriptive text and their spatial-temporal context. This allows the more accurate, more context-driven detection and makes the system much stronger and scalable to be deployed to the real world.

IV.7 PERFORMANCE EVALUATION:

Table 6: Performance evaluation of Different Models.

Model	Training Accuracy (%)	Validation Accuracy (%)	Training Loss	Validation Loss
SVM (HOG features)	76.20	70.50	1.42	1.58
Deep CNN (ResNet-50)	91.30	87.60	0.62	0.68
MultiModel Framework	95.40	92.70	0.38	0.45

Source: Authors, (2026).

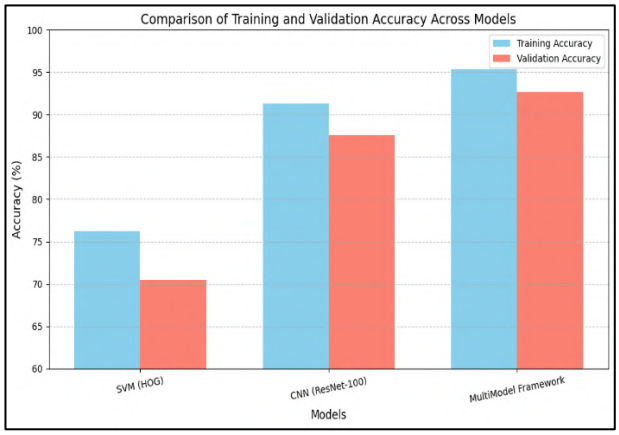


Figure 11: Comparison of Multi Model Framework with other Models.
Source: Authors, (2026).

V. CONCLUSIONS

In the proposed multimodal deep learning model the combination of facial recognition (ResNet-100), vision-language, and graph-based reasoning help in enhancing missing child detection. In contrast to the classic single-stream methods, the method incorporates features of the visual identity, text descriptions, and descriptive spatial-temporal and offers a more context-relevant and precise identification process.

The Graph Neural Network (GNN) assists to estimate the probable series of movement determined by detection and telling metadata, and the vision-language segment enhances synchronization between the spoken word accounts and photographic proof. Considered in light of the usual approaches, such as SVMs or isolated CNNs, the proposed model has a higher reliability and responsiveness factors, which is why it can be a useful tool to boost real-time recovery efforts.

VI. AUTHOR'S CONTRIBUTION

Conceptualization: Kola Uma Maheswari and Pandluri Dhanalakshmi.
Methodology: Kola Uma Maheswari and Pandluri Dhanalakshmi.
Investigation: Kola Uma Maheswari and Pandluri Dhanalakshmi.
Discussion of results: Kola Uma Maheswari and Pandluri Dhanalakshmi.
Writing – Original Draft: Kola Uma Maheswari.
Writing – Review and Editing: Pandluri Dhanalakshmi.
Resources: Kola Uma Maheswari and Pandluri Dhanalakshmi.
Supervision: Pandluri Dhanalakshmi.
Approval of the final text: Kola Uma Maheswari and Pandluri Dhanalakshmi.

VII. REFERENCES

[1] K. U. Maheswari and P. Dhanalakshmi, "GNN-Transformer Fusion for Enhanced Missing Child Identification," 2025 International Conference on Computing and Communication Technologies (ICCCT), Chennai, India, 2025, pp. 1-6, doi: 10.1109/ICCCT63501.2025.11020006.

[2] K. K and S. S, "Missing Children Face Identification Using Deep Learning Algorithm," 2023 3rd International Conference on Pervasive Computing and Social Networking (ICPCSN), Salem, India, 2023, pp. 27-34, doi: 10.1109/ICPCSN58827.2023.00013.

[3] K. P, S. P. S, M. D and N. Chowthri, "An Approach to Develop Missing Child Identification System using Deep Learning Methodologies," 2025 International Conference on Visual Analytics and Data Visualization (ICVADV), Tirunelveli, India, 2025, pp. 1267-1271, doi: 10.1109/ICVADV63329.2025.10960950.

[4] S. Gurusubramani, H. C. B, N. A and S. Z, "Missing Child Tracking System Using Deep Learning Methodologies," 2023 Intelligent Computing and Control for Engineering and Business Systems (ICCEBS), Chennai, India, 2023, pp. 1-7, doi: 10.1109/ICCEBS58601.2023.10449043.

[5] V. Madireddy, T. Sai Bhargava, J. Varsha, and K. Ram Prasad, "Smart System for Missing Child Identification," 2025 International Conference on Intelligent Computing and Control Systems (ICICCS), Bengaluru, India, 2025, pp. 1056–1061, doi: 10.1109/ICICCS65191.2025.10985301.

[6] S. Suvarna, P. S. Hegde, P. U. Sahithya, N. S. Suvarna, and N. Mogaveer, "Harnessing Deep Learning for Missing Child Identification and Recognition," 2024 Second International Conference on Advances in Information Technology (ICAIT), Mangalore, India, 2024, pp. 1–7, doi: 10.1109/ICAIT61638.2024.10690354.

[7] A. R. Alqaddoumi et al., "A Robot-Assisted Missing Child Search Approach," 2024 IEEE International Conference on Evolving and Adaptive Intelligent Systems (EAIS), Madrid, Spain, 2024, pp. 1-6, doi: 10.1109/EAIS58494.2024.10569996.

[8] K. B. Sk, I. Malavika, V. H. Priyanka, B. K. Bhavitha, and G. B. S. Kiran, "Facial Recognition and Neural Networks for Missing Child Identification: A Smart Approach," International Journal for Modern Trends in Science and Technology (IJMTST), vol. 11, no. 03, pp. 397–407, Mar. 2025, doi: 10.5281/zenodo.15174958.

[9] Karthi S, jayasaran, NMK Ramalingam Sakthivelan, "Missing Child Identification Using DLIB And Gan Based Facial Augmentation," International Journal of Scientific Research in Engineering and Management (IJSREM), vol. 09, no. 04, pp. 1–6, Apr. 2025, doi: 10.55041/IJSREM44793.

[10] P. S. Chandran, N. B. Byju, R. U. Deepak, K. N. Nishakumari, P. Devanand and P. M. Sasi, "Missing Child Identification System Using Deep Learning and Multiclass SVM," 2018 IEEE Recent Advances in Intelligent Computational Systems (RAICS), Thiruvananthapuram, India, 2018, pp. 113-116, doi: 10.1109/RAICS.2018.8635054.

Journal of Engineering and Technology for Industrial Applications

ITEGAM-JETIA

Manaus, v.12 n.60, p.149-165, July/August, 2026.
DOI: https://doi.org/10.5935/jetia.v12i60.3620

ISSN ONLINE: 2447-0228

RESEARCH ARTICLE OPEN ACCESS

BLOCKCHAIN-DRIVEN TRANSFORMER-BASED INTRUSION DETECTION AND ACCESS CONTROL SYSTEM (BDL-IDACS)

C. Ramya*[1], A. Suphalakshmi[2]

[1]Research Scholar, Department of Computer Science and Engineering, Takshashila University, Ongur, Tindivanam, Villupuram (Dt), Tamilnadu, India.
[1]Assistant Professor, Department of Information Technology, Mailam Engineering College, Mailam, Villupuram (Dt), Tamilnadu, India.
[2]Professor, Department of Computer Science and Engineering, Takshashila University, Ongur, Tindivanam, Villupuram (Dt), Tamilnadu, India.

[1]https://orcid.org/0009-0001-7860-7035, [2]https://orcid.org/0000-0001-6149-9878

Email:*ramyajitesh82@gmail.com, suphaprabhu@gmail.com

ARTICLE INFO

Article History
Received: February 10, 2026
Reviewed: June 6, 2026
Accepted: July 6, 2026
Published: July 31, 2026

Keywords:
Intrusion Detection System (IDS),
Blockchain-Assisted Security, Deep Learning,
Attention Models, Fully Homomorphic Encryption,
Smart Contracts,
Cyber Attack Detection,
Cloud–IoT Security.

ABSTRACT

The increasing complexity of cyber threats across IoT-cloud infrastructures necessitates the use of innovative, flexible, and confidentiality-preserving prevention techniques. The Blockchain-Assisted Hybrid Attention-Based Intrusion Detection and Access Control System (BHA-IDACS) is presented in this paper. The primary detection module employs an Adaptive Spatio-Temporal Representation Architecture-Self-Attention and Intersample Attention Transformer (Astra-SAINT) to precisely detect evolving intrusion tendencies. A heron optimization algorithm (HOA) is utilized for tuning the model thereby improving accuracy of detection and convergence. Fully Homomorphic Encryption (FHE) maintains the security of data and storage of encrypted data in unsecured cloud and blockchain circumstances. On a Consortium Blockchain, all encrypted transactions and audit trails are maintained by a Proof-of-Stake Authority (PoSA) consensus method. Additionally, based on user behavior and trust level, Smart Contract-Based Dynamic Access Control independently enforces permission and authentication regulations. The suggested model provides better precision, recall, F1-score, F2-score, specificity, and Cohen's Kappa values in addition to a mean accuracy of 99.16%. Furthermore, statistical analysis using confidence intervals and low standard deviation values demonstrates that Astra-SAINT is reliable and consistent across all validation folds. These results demonstrate the efficacy of the suggested Astra-SAINT framework as a scalable and dependable intrusion detection method for protecting IoT environments of the next decade.

Copyright ©2026 by authors and Galileo Institute of Technology and Education of the Amazon (ITEGAM). This work is licensed under the Creative Commons Attribution International License (CC BY 4.0).

I. INTRODUCTION

The coordination of limited resource-intensive IoT devices with cloud-based services has made ensuring security in IoT–cloud ecosystems a significant research challenge [1]. Since they are unable to adequately handle the adaptability, heterogeneity, and dynamic attack behaviors present in IoT networks, standard security solutions are typically inadequate [2]. Therefore, in order to detect advanced cyber threats in IoT cloud systems accurately and promptly, adaptive and data-driven security measures are becoming more and more necessary [3]. Due to their reliance on static rules, predetermined signatures, and centralized control structures, traditional IDS and access control systems are completely unsuitable for contemporary IoT scenarios [4]. These techniques are unable to deal with the dynamic nature of IoT traffic and are inadequate to recognize novel or evolving attack patterns. Furthermore, centralized security architectures' low scalability and single points of failure severely restrict their effectiveness in massive implementations [5]. As a result, scalable, intelligent, and adaptive security systems that are resistant to possible threats and capable of learning intricate traffic patterns are becoming more and more necessary [6]. The potential of deep learning (DL) powered IDS to identify and extract high-level information from huge volumes of network traffic data has received a lot of interest [7]. While recurrent and convolutional neural network-based models have shown promising outcomes, they often fail to grasp the intricate feature interactions and long-term temporal correlations present in Internet of Things traffic [8]. More recently, it has been shown that transformer and attention-based designs are better at simulating global contextual relationships [9]. Despite these developments, a significant research problem is still obtaining dependable detection performance in the face of extremely unbalanced data, changing attack techniques, and real-time restrictions.

IoT-cloud infrastructures must guarantee data privacy, integrity, and trust management in addition to detection accuracy [10], [11]. Sensitive information is frequently included in IoT data, and traditional encryption methods necessitate data decryption before analysis, raising the possibility of data leakage in untrusted environments. Furthermore, because user behavior and trust levels are constantly changing in IoT systems, static access control solutions are inadequate [12]. Blockchain and other decentralized technologies have shown promise as safe data management and auditability solutions; nevertheless, it is still unclear how to effectively integrate them with intelligent security methods while maintaining scalability and privacy [13]. Inspired by these difficulties, this work investigates intelligent intrusion detection, privacy-preserving processing of information, decentralized trust management, and dynamic access control within one integrated structure in order to address the shortcomings of current IoT security solutions. The ultimate goal is to ensure safe and scalable operation in next-generation IoT-cloud systems while improving detection accuracy, reliability, and consistency.

I.1 MAJOR CONTRIBUTION

- To assure reliable, secure, and scalable IoT-cloud security, a novel Blockchain-Assisted Hybrid Attention-Based Intrusion Detection and Access Control System (BHA-IDACS) is proposed.
- An advanced Astra-SAINT is developed to capture intricate temporal traffic patterns and inter-feature correlations in order to accurately identify new IoT attacks.
- FHE enables safe analysis of encrypted IoT data, while a Consortium Blockchain with PoSA consensus guarantees data integrity, auditability, and scalability.
- Throughout validation folds, standard deviation analysis and confidence intervals are used in the study's comprehensive statistical evaluation. The Astra-SAINT model's narrow confidence range and low variation demonstrate its stability, dependability, and generalizability.

Section 2 provides the related work, section 3 defines the proposed methodology framework, section 4 defines the result and discussion and section 5 ends with conclusion and future scope.

II. RELATED WORK

In order to improve IDS in IoT and cyber-physical contexts, a lot of research has been done recently on combining blockchain technology with deep learning (DL) methods. The major goals of these investigations are to promote decentralized security monitoring, preserve data integrity, and improve detection performance. While blockchain technology is used to guarantee safe, tamper-resistant data storage and ongoing verification, a variety of deep learning architectures, including convolutional neural networks (CNNs), recurrent neural networks (RNNs), bidirectional long short-term memory (BiLSTM) networks, and attention-based transformer models, have been used to successfully capture complex network traffic characteristics. However, issues with scalability, adaptation to new attack patterns, privacy protection, and computing complexity still hamper current systems. A comparative analysis of representative studies is given in Table 1, which summarizes their goals, main contributions, benefits, and drawbacks.

Table 1: Comparative Analysis of Blockchain-Enabled IDS models.

Reference	Methods Used	Goal	Key Contributions	Merits	Demerits
Saravanan et al. (2024) [14]	Blockchain + Optimized RNN	Secure IoT intrusion detection	Introduced an optimized RNN integrated with blockchain for attack detection	Improved detection accuracy and secure data logging	Limited handling of complex spatio-temporal dependencies
Aljabri et al. (2024) [15]	CNN + Blockchain	Network intrusion detection	Combined CNN-based feature learning with blockchain for integrity	Efficient feature extraction and decentralized storage	CNN struggles with long-term temporal patterns
Mansour (2022) [16]	AI Optimization + Deep Learning + Blockchain	CPS intrusion detection	Applied AI-based optimization to enhance deep learning IDS performance	High accuracy and blockchain-backed trust	High computational cost and limited privacy discussion
Saveetha & Maragatham (2022) [17]	Deep Learning + Blockchain	IoT attack detection	Designed a blockchain-enabled deep learning IDS framework	Secure and reliable attack detection	Static access control and lack of adaptability
Mbaya et al. (2023) [18]	Federated Learning + BiLSTM + Blockchain	Privacy-aware distributed IDS	Proposed a federated IDS with blockchain and BiLSTM	Preserves data privacy and supports distributed learning	Communication overhead and model convergence complexity
Alkhonaini et al. (2025) [19]	Sandpiper Optimization + Hybrid DL + Blockchain	IoT intrusion detection	Used Sandpiper optimization to tune hybrid DL models	Enhanced accuracy and optimized learning	Increased training complexity and resource demand
Ali et al. (2025) [20]	Blockchain Encryption + Optimized Attention Transformer	Secure medical IoT IDS	Developed an attention-based adversarial transformer with blockchain	Strong privacy preservation and high detection accuracy	Domain-specific design and higher computational overhead

Source: Authors, (2026).

Even though previous research shows how well DL and blockchain work together for intrusion detection, there are still a number of obvious drawbacks. A number of current approaches rely on single-level feature representations, which limits their capacity to describe the intricate inter-sample correlations and spatiotemporal relationships prevalent in IoT network data. While optimization techniques can improve detection speed, they often result in significant processing cost, which restricts scalability and makes real-time implementation difficult. Furthermore, many blockchain-based solutions fall short in meeting the needs for dynamic access control and privacy-preserving processes, even while they offer data integrity and traceability. These difficulties highlight the necessity for more advanced attention-based, blockchain-enabled IDS and highlight the significance of an overall structure that can concurrently achieve high detection accuracy with realistic deployment efficiency.

III. PROPOSED METHODOLOGY

The RT-IoT2022 dataset is used by the proposed Blockchain-Driven Transformer-Based Intrusion Detection and Access Control System (BDL-IDACS) and it is shown in Figure 1. This dataset comprises real-time IoT network traffic that includes both hostile and benign activities, such as different cyberattacks. To produce high-quality representations of IoT traffic flows, the dataset first undergoes through extensive preprocessing, which includes removing noise and outliers, imputing missing values, normalizing features, and removing redundant properties. The Astra-SAINT transformer model uses self-attention, intersample attention, and spatiotemporal learning and the Heron optimization algorithm is used to tune the hyperparameters of the model to improve detection performance and convergence efficiency. Fully Homomorphic Encryption (FHE) is used to safeguard IoT traffic features and detection results in order to guarantee data privacy. The consortium blockchain, which is controlled by a Proof-of-Stake Authority consensus method, then stores all encrypted records, forecasts, and access logs. Lastly, smart contract-based dynamic access control provides a privacy-preserving security framework for IoT-cloud infrastructures by autonomously enforcing authentication and authorization decisions based on user behavior and trust level while producing real-time alerts for detected intrusions.

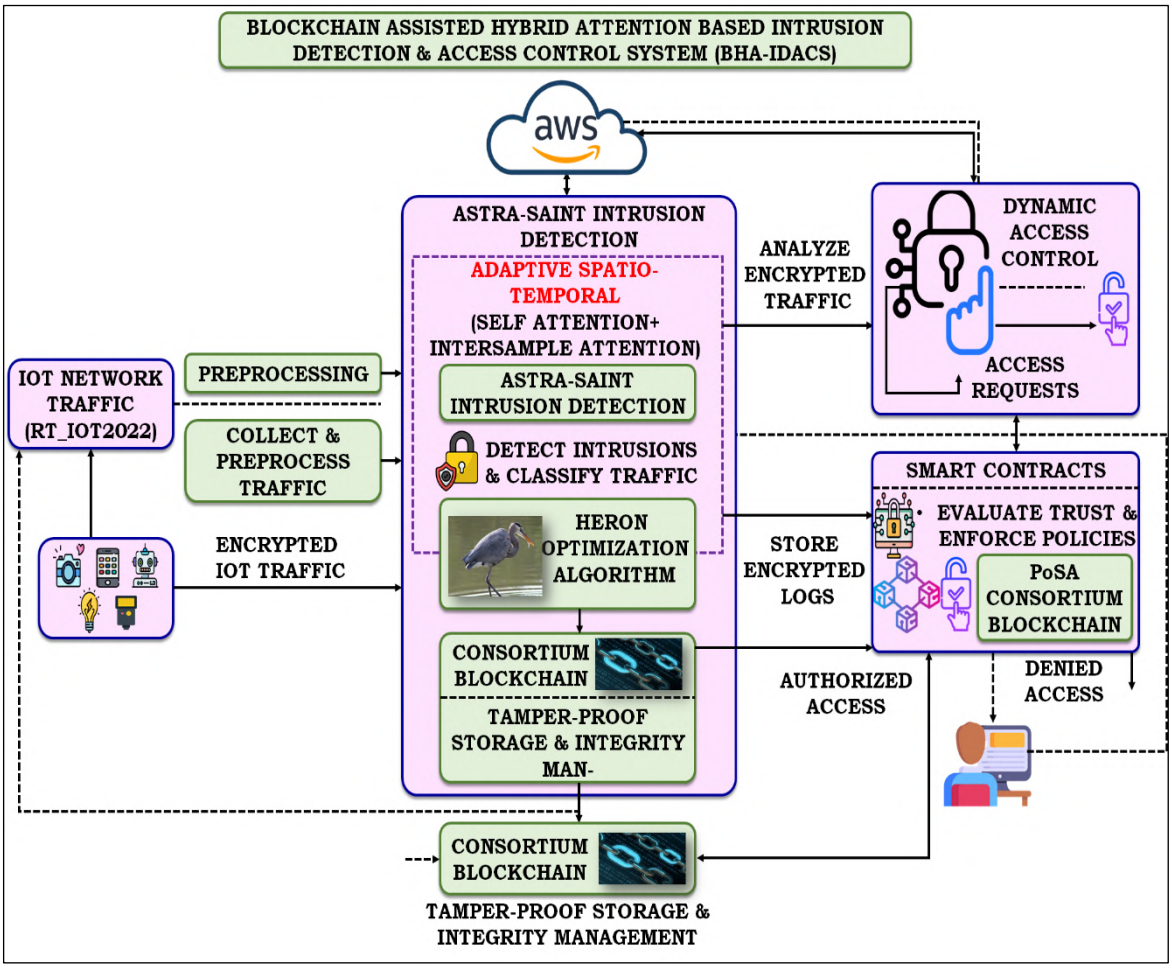


Figure 1: Overall proposed framework.
Source: Authors, (2026).

III.1 STAGE I: RT-IOT2022 DATA ACQUISITION AND PREPROCESSING

The collection and preparation of IoT network traffic obtained from the RT-IoT2022 dataset constitute the first phase of the proposed BDL-IDACS system. Let's use a multivariate feature matrix to convey the dataset:

$$X = \{x_{i,j}\} \in \mathbb{R}^{N \times D} \quad (1)$$

Where D is the number of retrieved traffic features and N is the total number of network flow instances. Every instance is associated with a real-time IoT communication record that has been classified as either normal or falling under a certain threat category. Direct use of the raw dataset might seriously impair learning performance due to the heterogeneous nature of IoT traffic as well as the existence of noise, missing values, and skewed feature distributions. In order to solve this problem, aberrant data that substantially differ from typical traffic behavior are first eliminated by outlier detection. The standardized score (z-score) of an instance i is calculated for a given feature j as:

$$z_{i,j} = \frac{x_{i,j} - \mu_j}{\sigma_j} \tag{2}$$

Where $\mu_j$and σ_j stand for the jth feature's mean and standard deviation, respectively. When τ is a predetermined threshold and which satisfy $| z_{i,j} | > \tau$ are considered outliers and eliminated from further examination. In order to maintain data accuracy, missing values in the dataset are filled by employing statistical imputation after outlier removal. Mean-based imputation is used for each missing feature value $x_{i,j}^{\text{miss}}$ as:

$$x_{i,j}^{\text{miss}} = \frac{1}{N_j} \sum_{i=1}^{N_j} x_{i,j} \tag{3}$$

Where the number of non-missing observations for feature j is represented by N_j. Feature normalization is then carried out to prevent high-magnitude features from dominating during model training and to guarantee consistent scaling across all traffic attributes. The use of min-max normalization is described as:

$$\hat{x}_{i,j} = \frac{x_{i,j} - \min(x_j)}{\max(x_j) - \min(x_j)} \tag{4}$$

where $\min(x_j)$and $\max(x_j)$ represent the j^{th}f feature's minimum and maximum values, respectively. All feature values are mapped into the interval $[0, 1]$ via this transformation.

To find replicated or poorly informative features, correlation analysis and exploratory data analysis are also carried out. A reduced feature matrix is produced by eliminating highly correlated characteristics in order to minimize multicollinearity and reduce dimensionality.

$$\mathrm{X}' \in \mathbb{R}^{N \times d}, d < D \tag{5}$$

The raw RT-IoT2022 traffic data is converted into a structured, noise-reduced, and normalized representation by various preprocessing steps, maintaining important IoT communications behavioral traits. In order to effectively understand spatiotemporal attack patterns, this revised dataset provides a solid basis for later transformer-based intrusion detection.

III.2 STAGE II: ASTRA-SAINT TRANSFORMER WITH ADAPTIVE SPATIO-TEMPORAL REPRESENTATION

III.2.1 Input Embedding and Temporal Encoding

IoT network traffic statistics show substantial temporal relationships and varied feature distributions as the consequence of constantly changing attack and communication patterns. Astra-SAINT starts by extending each preprocessed traffic instance into a dense latent space that facilitates attention-based learning in order to guarantee that such complicated properties are efficiently captured. Let $\mathrm{x}_{t,i} \in \mathbb{R}^d$ represent the i^{th}traffic incident detected at time index t. An embedding vector is mapped to this instance via a learnable embedding function $E(\cdot)$ and its mathematical expression is given below:

$$\mathbf{e}_{t,i} = E(\mathbf{x}_{t,i}) \tag{6}$$

Here, $\mathbf{e}_{t,i} \in \mathbb{R}^{d_e}$defines the embedded representation and $d_e$describes the embedding dimension respectively. Temporal ordering must be maintained since intrusion patterns frequently appear as progressive departures over time. This is accomplished by adding a temporal positional encoding vector, $\mathbf{p}_t \in \mathbb{R}^{d_e}$ to the embedded input and its expression is given below:

$$\tilde{\mathbf{e}}_{t,i} = \mathbf{e}_{t,i} + \mathbf{p}_t \tag{7}$$

In this formulation, the relative temporal position of the traffic instance within the traffic stream is encoded by $\mathbf{p}_t$, and the time-aware embedding is represented by $\tilde{\mathbf{e}}_{t,i}$. Because of this temporal enrichment, the model can distinguish between identical traffic patterns that happen at different times.

III.2.2 Adaptive Spatio-Temporal Representation Learning

Not all temporal and spatial variables are equally important for intrusion detection, even when temporal encoding maintains ordering. While certain attributes could be superfluous or noisy, others might have powerful attack signatures. Astra-SAINT introduces an adaptive spatio-temporal gating system that dynamically controls feature relevance in order to rectify this imbalance. This method calculates a gating vector and its expression is given below:

$$\mathbf{g}_{t,i} = \sigma\left(\mathbf{W}_g \tilde{\mathbf{e}}_{t,i} + \mathbf{b}_g\right) \tag{8}$$

Where $\mathbf{W}_g$and $\mathbf{b}_g$ specifies the learnable parameters, and $\sigma(\cdot)$denotes the sigmoid activation function. Next, element-wise modulation yields the gated spatio-temporal representation and it is given below:

$$\mathbf{z}_{t,i} = \mathbf{g}_{t,i} \odot \tilde{\mathbf{e}}_{t,i} \tag{9}$$

In this case, element-wise multiplication is represented by ⊙ and the adaptively weighted spatiotemporal embedding is denoted by $\mathbf{z}_{t,i}$. By reducing irrelevant variations and selectively amplifying informative aspects linked to anomalous traffic behavior, this technique improves robustness against malicious and changing intruders.

III.2.3 Self-Attention for Spatial Feature Dependency Modeling

A multi-head self-attention system then processes the gated embeddings to identify spatial correlations between characteristics in each traffic occurrence. For tabular IoT data, self-attention allows the model to establish correlations between traffic aspects rather than depending on predefined locality assumptions. The query, key, and value vectors are calculated for every $\mathbf{z}_{t,i}$ and it is defined below:

$$\mathrm{Q}_{t,i} = \mathrm{W}_Q \mathrm{z}_{t,i}, \quad \mathrm{K}_{t,i} = \mathrm{W}_K \mathrm{z}_{t,i}, \quad \mathrm{V}_{t,i} = \mathrm{W}_V \mathrm{z}_{t,i} \tag{10}$$

The learnable projection matrices are stated as $\mathrm{W}_Q, \mathrm{W}_K, \mathrm{W}_V$ and d_k represents the dimensionality of the key and query vectors. Scaled dot-product attention is used to calculate the self-attention output and it is defined below:

$$\mathrm{SA}(\mathbf{z}_{t,i}) = \mathrm{softmax}\left(\frac{\mathbf{Q}_{t,i}\mathbf{K}_{t,i}^{\mathrm{T}}}{\sqrt{d_k}}\right)\mathbf{V}_{t,i} \tag{11}$$

In this case, the self-attention function is denoted by SA(·), and the gradient magnitude is stabilized throughout training by the scaling factor $\sqrt{d_k}$. Layer normalization and residual connections are used to maintain information flow and enhance optimization stability:

$$\mathbf{h}_{t,i}^{(1)} = \mathrm{LayerNorm}\big(\mathbf{z}_{t,i} + \mathrm{SA}(\mathbf{z}_{t,i})\big) \tag{12}$$

A position-wise feed-forward network is used to further improve the obtained representation:

$$\mathbf{h}_{t,i}^{(SA)} = \mathrm{LayerNorm}\big(\mathbf{h}_{t,i}^{(1)} + \mathrm{FFN}(\mathbf{h}_{t,i}^{(1)})\big) \tag{13}$$

Here, FFN(·) signifies a two-layer feed-forward network with nonlinear activation, and $\mathrm{h}_{t,i}^{(SA)}$ denotes the spatially enriched representation.

III.2.4 Intersample Attention for Contextual and Temporal Dependency Modeling

Intrusion behavior in IoT networks frequently results from correlations across various traffic flows, even while self-attention captures feature-level interactions. Astra-SAINT uses an intersample attention mechanism that functions across traffic instances within the same temporal window in order to describe such contextual dependencies. Let $\mathrm{H}_t = [\mathrm{h}_{t,1}^{(SA)}, \mathrm{h}_{t,2}^{(SA)}, \ldots, \mathrm{h}_{t,b}^{(SA)}]$ defines the batch level feature matrix. Here, b describes the batch size. Therefore, the mathematical computation of intersample attention is defined using below equation:

$$\mathrm{IA}(\mathbf{H}_t) = \mathrm{softmax}\left(\frac{\mathbf{Q}_t\mathbf{K}_t^{\mathrm{T}}}{\sqrt{d_k}}\right)\mathbf{V}_t \tag{14}$$

Here, $\mathrm{Q}_t = \mathrm{W}_Q^{(I)}\mathrm{H}_t$, $\mathrm{K}_t = \mathrm{W}_K^{(I)}\mathrm{H}_t$, and $\mathrm{V}_t = \mathrm{W}_V^{(I)}\mathrm{H}_t$. The intersample projection matrices are stated as $\mathrm{W}_Q^{(I)}, \mathrm{W}_K^{(I)}, \mathrm{W}_V^{(I)}$ respectively. With the aid of residual normalization, the output of intersample is integrated and its mathematical formulation is given below. Alos, it is followed by feed-forward refinement.

$$\mathbf{h}_{t,i}^{(2)} = \mathrm{LayerNorm}\big(\mathbf{h}_{t,i}^{(SA)} + \mathrm{IA}(\mathbf{H}_t)_i\big) \tag{15}$$

$$\mathbf{r}_{t,i} = \mathrm{LayerNorm}\big(\mathbf{h}_{t,i}^{(2)} + \mathrm{FFN}(\mathbf{h}_{t,i}^{(2)})\big) \tag{16}$$

The ultimate contextual representation of the ith traffic instance is denoted by$\mathbf{r}_{t,i}$ which incorporates both feature-level and inter-flow dependencies.

III.2.5 Contextual Spatio-Temporal Representation Output

The model gradually improves traffic representations by stacking L_XAstra-SAINT layers, enabling the capturing of higher-order spatiotemporal interactions. The expression for the total Astra-SAINT transition is given below:

$$\{\mathbf{r}_{t,i}\}_{i=1}^{b} = S\big(\{E(\mathbf{x}_{t,i})\}_{i=1}^{b}\big), \tag{17}$$

Where the composite Astra-SAINT mapping is shown by $S(\cdot)$. Under dynamic network conditions, these contextualized representations enable precise discrimination between benign and malicious IoT data by serving as the foundation for further intrusion categorization.

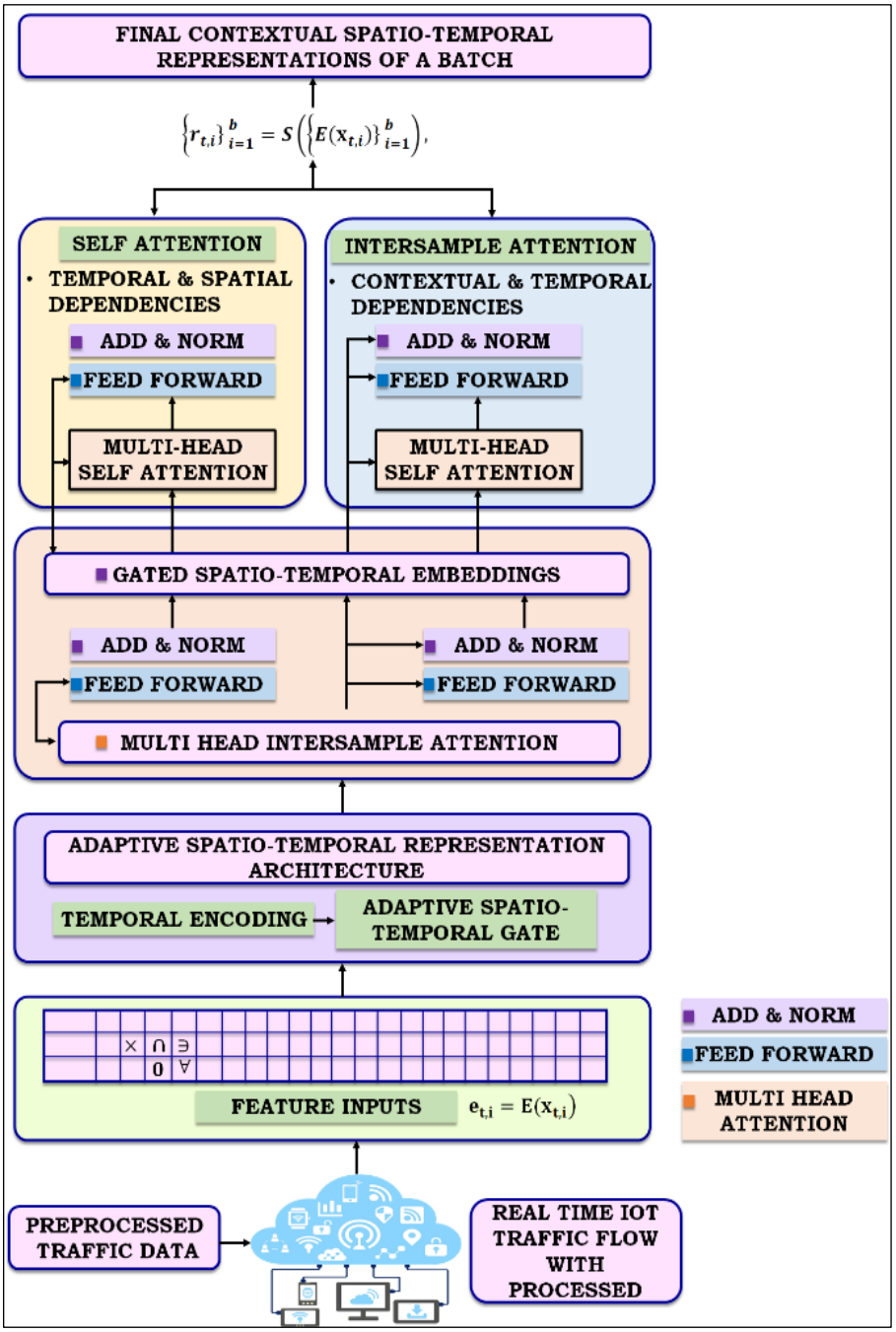


Figure 2: Architecture of Astra-SAINT Transformer.
Source: Authors, (2026).

The block-wise architecture of the suggested Astra-SAINT model is shown in Figure 2. A batch of embedded IoT traffic samples that have undergone preprocessing and feature embedding are fed into the architecture. The Astra processes these embedded inputs first. It uses temporal encoding to maintain linear dependencies and an adaptive spatio-temporal gating mechanism to dynamically highlight important temporal and spatial features of network traffic. The stacked Astra-SAINT encoder layers consisting of two complimentary attention blocks and receive the corrected embeddings. The self-attention block captures intra-sample dependencies and makes it possible to extract discriminative spatial and temporal feature interactions. In order to recognize integrated and spread attack behaviors frequently seen in IoT environments, the intersample attention block simultaneously acts across samples within the same batch to learn contextual correlations among data flows. The learnt representations are gradually enhanced by regularly stacking this self-attention and intersample attention modules. The architecture's ultimate output is a collection of contextualized spatio-temporal representations for the batch, which are used for precise intrusion classification.

III.3 STAGE III: HERON OPTIMIZATION–BASED MODEL PARAMETER TUNING

While adaptive spatiotemporal dependability and contextual relationships in IoT traffic are efficiently captured by the Astra-SAINT architecture, its ability to perform is highly dependent on the ideal configuration of model parameters, such as regularization coefficients, learning rates, and attention weights. Conventional gradient-based optimization may prematurely converge to inadequate solutions because of the dynamic nature of intrusion data and the nonconvex nature of deep transformer loss landscapes.

The suggested framework incorporates a nature-inspired Heron Optimization Algorithm (HOA) to improve convergence stability and detection accuracy in order to get over this limitation.

III.3.1 Solution Representation and Fitness Evaluation

A collection of trainable Astra-SAINT parameters and hyperparameters is represented by each potential solution in the heron population. Therefore, the initialization process is defined below:

$$\boldsymbol{\theta}_k = \{\theta_{k,1}, \theta_{k,2}, \ldots, \theta_{k,n}\} \tag{18}$$

Here, k^{th} defines the candidate parameter vector and n defines the total number of selected parameters for optimization. A fitness function generated from the intrusion detection objective is used to assess the quality of each potential solution:

$$\mathcal{F}(\boldsymbol{\theta}_k) = \alpha \cdot \mathcal{L}_{\text{cls}} + \beta \cdot \text{FPR} \tag{19}$$

Here, the classification loss of the network model is stated as $\mathcal{L}_{\text{cls}}$, false positive rate is defined as FPR, the weighting coefficients are stated as α, β. The optimizer is encouraged by this formulation to reduce both redundant security alarms and misclassification.

III.3.2 Heron-Inspired Position Update Mechanism

Herons' search behavior is demonstrated by adaptive positional updates that are impacted by both environmental exploration and the current best solution. As a result, each potential solution's position is updated as

$$\theta_k^{(t+1)} = \theta_k^{(t)} + \lambda_1 \cdot \mathrm{r}_1 \cdot (\theta_{best} - \theta_k^{(t)}) + \lambda_2 \cdot \mathrm{r}_2 \cdot (\theta_{rand} - \theta_k^{(t)}) \tag{20}$$

At iteration t, the parameter vector is stated as $\boldsymbol{\theta}_k^{(t)}$, the best solution is defined as $\boldsymbol{\theta}_{best}$, the randomly selected candidate solution is stated as $\boldsymbol{\theta}_{rand}$, $\mathbf{r}_1, \mathbf{r}_2 \in (0,1)$ specifies the random vectors, λ_1, λ_2control exploitation and exploration consecutively.

III.3.3 Integration with Astra-SAINT Training

By periodically adjusting certain parameters depending on fitness feedback, the heron optimization mechanism works in combination with Astra-SAINT training. Upon the satisfaction of the termination condition, the optimized parameter set is defined below:

$$\theta^* = \arg\min_{\theta_k} \mathcal{F}(\theta_k) \tag{21}$$

By including Heron optimization, the model achieves improved convergence behavior, fewer false alarms, and greater generalization across different IoT attack scenarios.

III.4 STAGE IV: BLOCKCHAIN-ASSISTED PRIVACY PRESERVATION AND SMART CONTRACT–BASED DYNAMIC ACCESS CONTROL

After using Heron optimization to optimize the Astra-SAINT model parameters, the IDS produces precise and extremely reliable predictions on the behavior of IoT networks. However, in actual IoT-cloud systems, merely detecting intrusions is insufficient. To allay these worries, the proposed solution includes a blockchain-assisted security layer, autonomous access control, and privacy-preserving encryption.

III.4.1 Fully Homomorphic Encryption for End-to-End Data Confidentiality

Sensitive information is encrypted using FHE before being stored or transmitted across the IoT-cloud infrastructure. For the ith traffic event at time t, let $\mathrm{y}_{t,i}$ represent the contextual representation. The ciphertext that has been encrypted is recovered as follows:

$$\mathbf{c}_{t,i} = \mathcal{E}_{pk}(\mathbf{y}_{t,i}) \tag{22}$$

The encryption using the public key pk is represented by $\mathcal{E}_{pk}(\cdot)$. In this case, pk is shared across authorized entities, and $\mathbf{c}_{t,i}$ is the encrypted output. The mathematical expression of decryption process is defined below:

$$\mathbf{y}_{t,i} = \mathcal{D}_{sk}(\mathbf{c}_{t,i}) \tag{23}$$

The decryption using the secret key sk is defined as $\mathcal{D}_{sk}(\cdot)$. This method ensures that cloud servers or blockchain validators cannot infer sensitive intrusion information from preserved ciphertexts.

III.4.2 Consortium Blockchain for Secure and Immutable Storage

Stake-based validation and authority-controlled participation are combined in the Proof-of-Stake Authority (PoSA) consensus process that powers the blockchain. Timestamps, validator signatures, encrypted data payloads, and a cryptographic hash connecting it to the preceding block are all included in each block. The kth block is denoted by B_k, which is defined as:

$$B_k = \langle H(B_{k-1}), \mathcal{C}_k, T_k, \Sigma_k \rangle \tag{24}$$

Here, the hash of the prior block is stated as $H(B_{k-1})$, T_k specifies the timestamp, $\mathcal{C}_k$ describes the set of encrypted ciphertexts and the validator's digital signature is stated as Σ_k.

III.4.3 Smart Contract–Based Dynamic Access Control

The suggested system uses smart contracts to independently implement dynamic access control rules in order to get around this limitation. Self-executing programs termed smart contracts are implemented on the blockchain and assess access requests using contextual trust metrics and pre-established security guidelines. Let T_j stand for its trust score which is based on past behavior, intrusion alarms, and policy compliance, and let U_j represent an entity requesting access to intrusion data or system resources. Access choices are made as follows:

$$\text{Access}(U_j) = \begin{cases} \text{Granted}, & \text{if } T_j \geq \tau, \\ \text{Denied}, & \text{otherwise}, \end{cases} \tag{25}$$

Where $\tau$is a pre-established trust threshold. Here, adaptive and context-aware permission is ensured by dynamically updating T_j based on the results of real-time intrusion detection. The final step guarantees that intrusion detection results are not only accurate but also safe, reliable, and useful by integrating consortium blockchain technology, smart contract-based dynamic access control, and fully homomorphic encryption. The HOA layer and the improved Astra-SAINT detection module are seamlessly integrated with this stage. The blockchain and encryption processes use the optimized predictions as inputs, and smart contracts respond instantly to detection results. Consequently, a closed-loop security architecture combining decentralized trust enforcement and intelligent intrusion detection is achieved by the proposed BDL-IDACS framework.

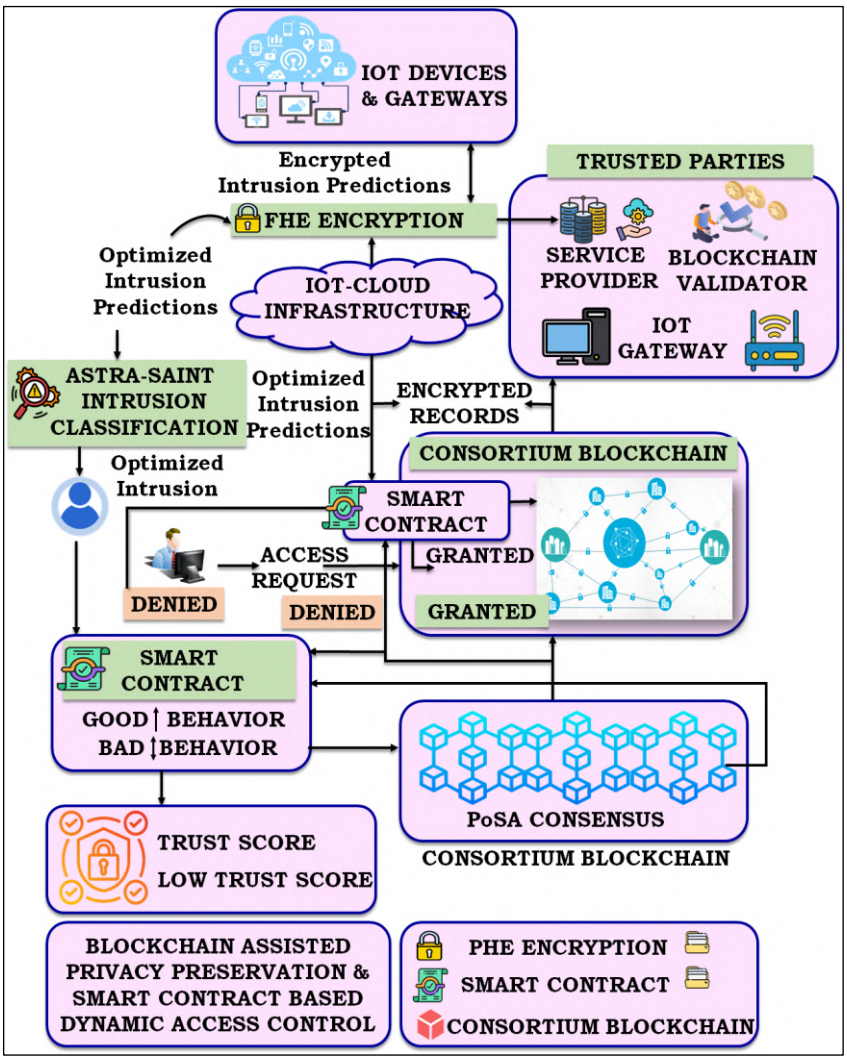


Figure 3: Blockchain-assisted privacy preservation framework.
Source: Authors, (2026).

The blockchain-assisted privacy preservation and smart contract-based dynamic access control stage is shown in figure 3. Data generated by IoT devices and gateways is first sent to the IoT-cloud infrastructure, where FHE is used to encrypt intrusion records and prediction outputs to guarantee data confidentiality throughout the course of storage and processing. By analysing the encrypted data, the Astra-SAINT intrusion classification algorithm generates optimal intrusion predictions without disclosing sensitive raw data. After that, these encrypted prediction records are sent to a consortium blockchain network, where reliable entities like IoT gateways, blockchain validators, and service providers contribute to the upkeep of a decentralized, impenetrable ledger. Smart contracts assess user or application access requests and automatically implement access control policies based on past trust scores and anticipated intrusion behavior.

The choice is permanently recorded on the blockchain, and the smart contract dynamically allows or rejects access based on whether the observed behavior is deemed evil or positive. A unified and thorough method for intelligent, secure, and privacy-preserving intrusion detection in IoT-cloud contexts is created by the proposed BDL-IDACS architecture.

IV. RESULT AND DISCUSSION

IV.1 DATASET DESCRIPTION AND EXPERIMENTAL CONFIGURATION

The proposed BDL-IDACS system is evaluated experimentally using the RT-IoT2022 dataset, a publicly available benchmark dataset from the UCI Machine Learning Repository designed for real-time IDS in IoT applications. There are 85 attributes in each of the collection's 123,117 network traffic samples that capture different protocol-level, flow-based, and statistical traits common to both benign and malicious IoT activities. These characteristics make it possible to describe intricate spatiotemporal attack behaviors in dynamic IoT-cloud infrastructures. A 5-fold cross-validation technique is divided into five mutually exclusive subsets and the model is iteratively trained and verified across all folds, is used to guarantee reliable and objective performance evaluation. For the suggested intrusion detection and access control system, this validation technique reduces overfitting, improves generalization capacity, and yields statistically reliable performance estimates.

IV.2 OUTLIER ANALYSIS OF KEY NETWORK TRAFFIC FEATURES IN RT-IOT2022

The outlier distribution of a few network traffic characteristics from the RT-IoT2022 dataset is shown in figure 4, emphasizing the extreme values and distributional skewness present in actual IoT traffic. Overall, this figure emphasizes the significance to handle outliers robustly during the preprocessing phase because, if ignored, these severe variances can negatively impact learning stability and skew intrusion classification models. The implementation of normalization and outlier-aware feature preprocessing before training the Astra-SAINT intrusion detection system is justified by the observed distributions.

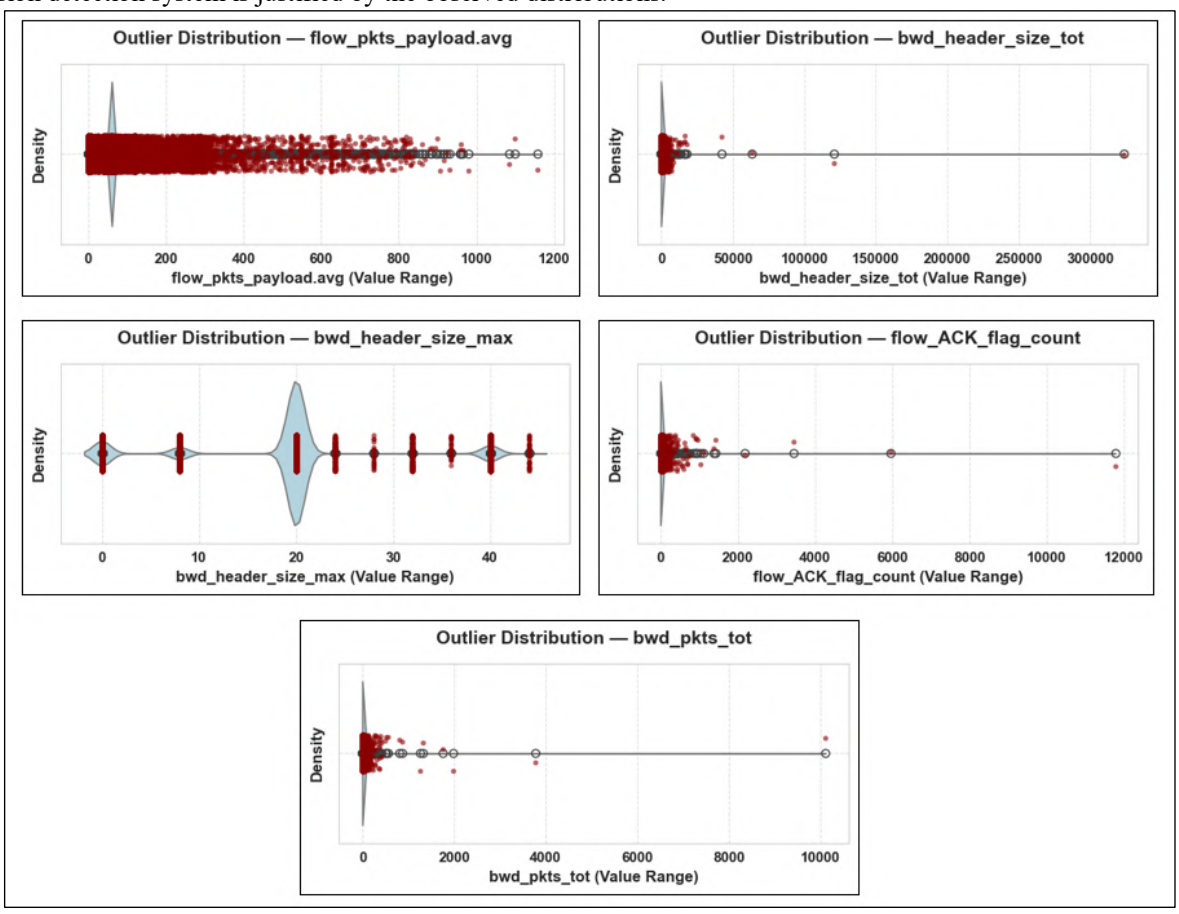


Figure 4: Outlier Distribution of Representative Traffic Features in the RT-IoT2022 Dataset.
Source: Authors, (2026).

IV.3 ATTACK AND PROTOCOL DISTRIBUTION CHARACTERISTICS OF THE RT-IOT2022 DATASET

A thorough examination of attack-type and protocol distributions is shown in figure 5. Denial-of-Service (DoS) attacks make up the majority of malicious samples are highly prevalent according to the attack distribution research. The protocol distribution analysis also shows that TCP traffic predominates in the dataset with ICMP traffic appearing only infrequently and UDP traffic making up a less significant rather than considerable percentage. The requirement for IDS models that can learn consistent and discriminative representations across majority and minority traffic classes is highlighted by this protocol imbalance. Overall, the figure emphasizes the difficulties faced by class imbalance and protocol diversity in IoT intrusion detection, highlighting the significance of attention-based modeling and strong training techniques within the suggested BDL-IDACS framework.

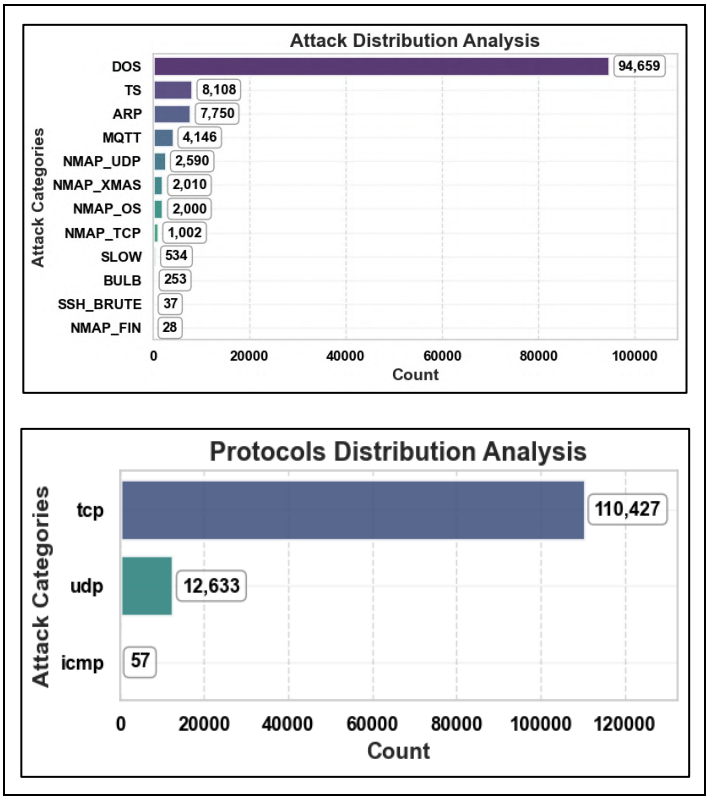
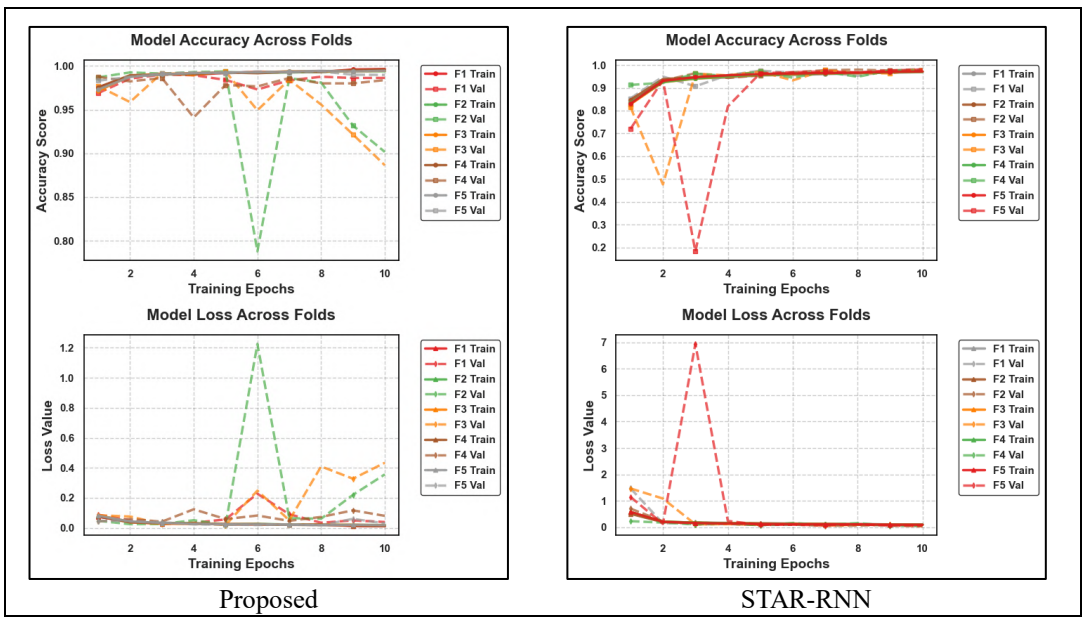


Figure 5: Attack-Type and Protocol Distribution Analysis of the RT-IoT2022 Dataset.
Source: Authors, (2026).

IV.4 CROSS-FOLD ACCURACY AND LOSS COMPARISON BETWEEN STAR-RNN AND PROPOSED ASTRA-SAINT MODELS

Using 5-fold cross-validation, Figure 6 compares the learning behavior of the basic STAR-RNN and the suggested Astra-SAINT transformer model. STAR-RNN's accuracy fluctuations over initial training epochs exhibit observable variation across various folds, with abrupt drops in validation accuracy and consequent rises in validation loss. This indicates that the model is sensitive to data partitioning and possesses limited generalization capability under some folds. As opposed to this, the Astra-SAINT model exhibits more consistent convergence patterns, much lower training loss values, and consistently achieves good training and validation accuracy across the majority of folds. Additionally, the model is robust to class imbalance and temporal unpredictability in IoT traffic, as evidenced by the small effect of moderate fluctuations in validation loss on overall accuracy. Overall, the figure 6 validates the efficacy of transformer-based attention mechanisms for IoT intrusion detection by showing that Astra-SAINT outperforms the STAR-RNN baseline in terms of convergence stability, prediction reliability, and cross-fold generalization.



Proposed STAR-RNN

Figure 6: Training and validation accuracy and loss c0urves across 5-fold cross-validation for the baseline STAR-RNN and proposed model.
Source: Authors, (2026).

IV.5 MULTI-CLASS CONFUSION MATRIX ANALYSIS OF THE PROPOSED ASTRA-SAINT MODEL

The confusion matrices acquired for the proposed model throughout all five K-fold cross-validation folds are shown in the Figure 7. A high true positive rate for all attack categories is shown by the large number of samples along the main diagonal in each fold-level matrix. The model's capacity to learn discriminative spatiotemporal representations is demonstrated by the low off-diagonal values, which indicate little misclassification of attack classes even among structurally comparable observation and scanning attacks. Consistent performance over folds is further confirmed by the aggregated confusion matrix, whose dominating diagonal elements show robustness against class imbalance and steady generalization. Due to their small sample representation, minor confusions in low-frequency attack classes are expected, but they are still insignificant. Overall, this figure validates the appropriateness of the suggested Astra-SAINT model for actual IoT–cloud security deployments by showing that it performs accurate multi-class intrusion classification with high reliability and minimum cross-class interference.

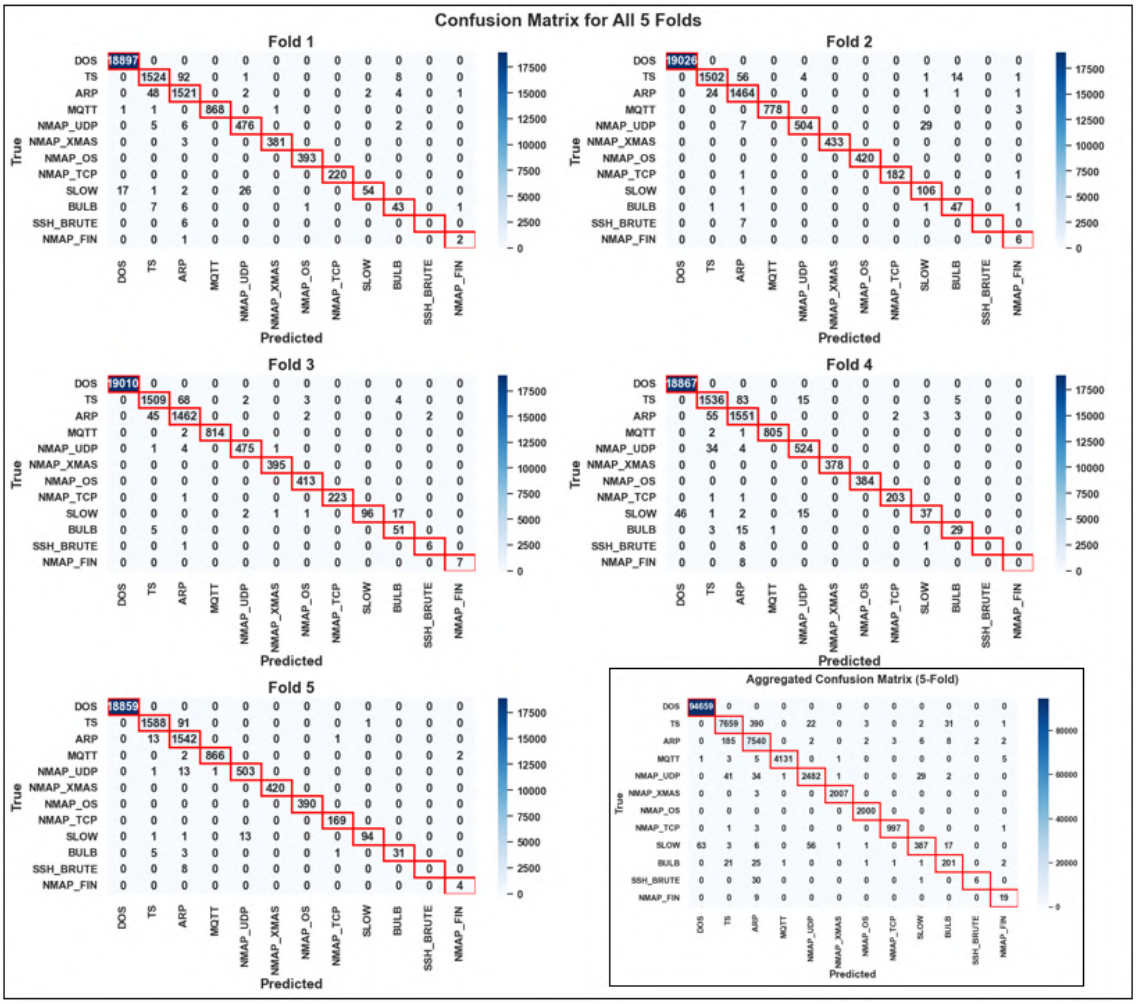


Figure 7: Confusion Matrix Analysis of the Proposed Astra-SAINT Model Across 5-Fold Cross-Validation.
Source: Authors, (2026).

IV.6 CONFUSION MATRIX ANALYSIS OF THE BASELINE STAR-RNN MODEL

The confusion matrices for the baseline STAR-RNN (Spatio-Temporal Attention Recurrent Neural Network) model across all five K-fold cross-validation folds are shown in the Figure 8. Although the diagonal entries show that STAR-RNN can accurately identify popular attack classes like DoS, TS, ARP, and MQTT, there are obvious off-diagonal values show higher misclassification rates when compared to the suggested model. Class imbalance and limited training samples are the main causes of minority attack classes. These discrepancies are further highlighted by the aggregated confusion matrix, which shows greater cross-class interference and lower diagonal dominant characteristics. Overall, the figure shows that while STAR-RNN offers respectable baseline performance, the suggested Astra-SAINT model outperforms it in terms of classification reliability and generalization ability, which encourages the use of transformer-based attention mechanisms for reliable IoT intrusion detection.

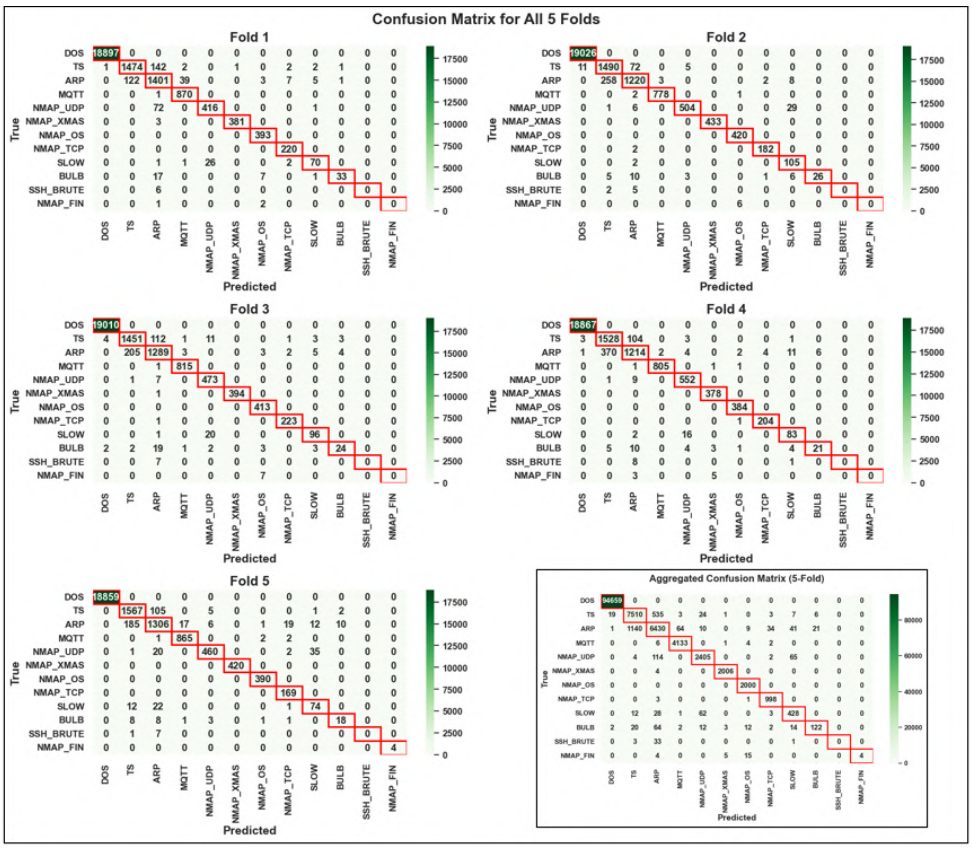


Figure 8: Confusion Matrix Analysis of the Baseline STAR-RNN Model Across 5-Fold Cross-Validation.
Source: Authors, (2026).

IV.7 ROC AND PRECISION–RECALL CURVE ANALYSIS FOR PROPOSED MODEL AND BASELINE STAR-RNN

The suggested model and STAR-RNN are contrasted in Figure 9 utilizing macro-averaged ROC and PR curves under 5-fold cross-validation. The suggested model performs better in terms of precision–recall and class discrimination especially for minority attack classes. On the other hand, STAR-RNN handles class imbalance less well, as seen by its minor decrease in ROC accuracy and lower PR performance (AP = 0.8223). Overall, the findings show that the suggsted model outperforms the baseline in terms of resilience and detection reliability.

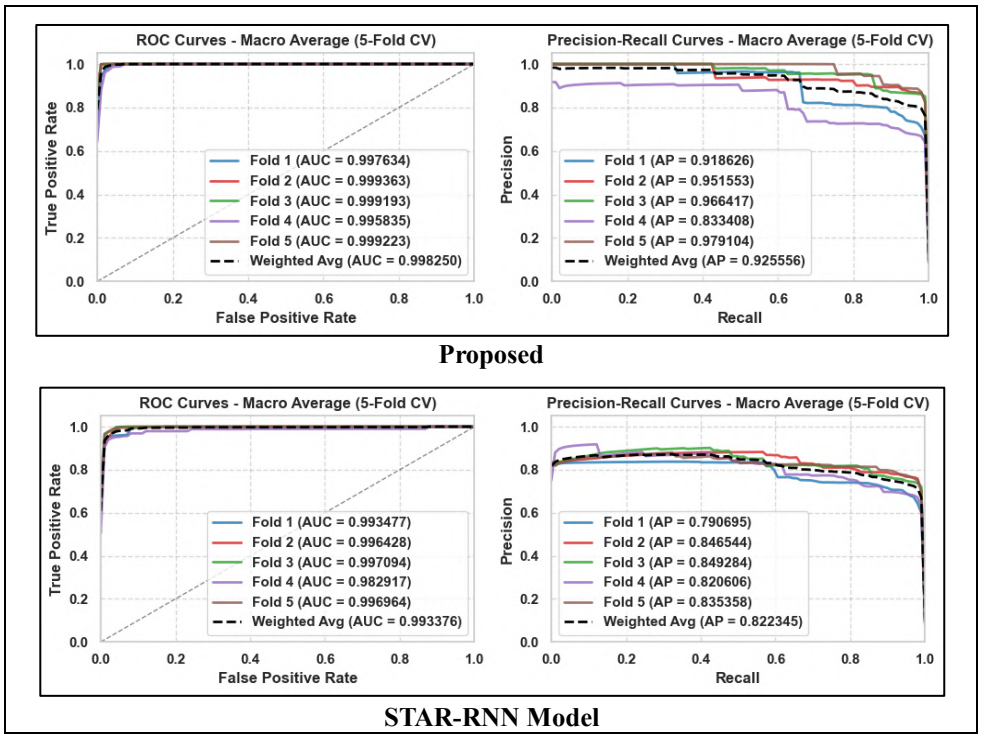


Figure 9: Comparison of ROC and Precision–Recall Curves for the Proposed Model and STAR-RNN (5-Fold Cross-Validation).
Source: Authors, (2026).

IV.8 ACCURACY STABILITY AND CONFIDENCE INTERVAL ANALYSIS FOR PROPOSED AND STAR-RNN MODELS

Figure 10 shows fold-wise accuracy trends on the right and the mean accuracy with 95% confidence intervals on the left. With a mean accuracy of 0.9916 and a narrow 95% CI of [0.9882, 0.9951], the suggested model performs incredibly consistently and dependably across folds. The STAR-RNN model exhibits relatively larger variability with a lower mean accuracy of 0.9803 and a broader 95% confidence range of [0.9772, 0.9834]. Its fold-wise trend exhibits more visible irregularities, especially a discernible decline in one-fold, indicating less resilience under different data splits. Overall, the figure makes it evident that the suggested model outperforms the baseline STAR-RNN in terms of accuracy, stability, and confidence throughout cross-validation folds. The overall performance measures of proposed and the existing method is shown in table 2.

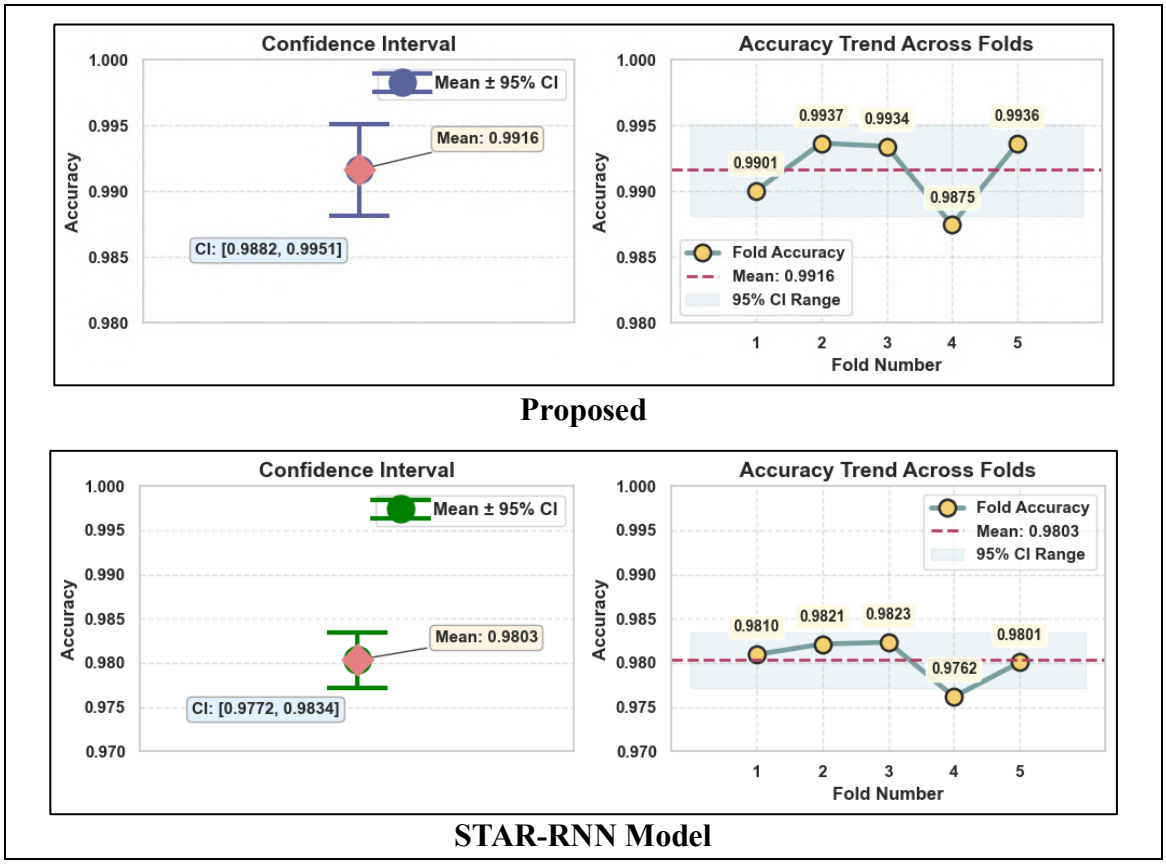


Figure 10: Accuracy Confidence Interval and Fold-Wise Performance Comparison Between Proposed and STAR-RNN Models. Source: Authors, (2026).

Table 2: Overall performance measures.

Metrics	Proposed	Existing STAR-RNN
Accuracy	0.9916	0.9803
Precision (Macro)	0.9110	0.8512
Recall (Macro)	0.8521	0.7585
F1 Score (Macro)	0.8648	0.7742
Recall (Weighted)	0.9916	0.9803
F1 Score (Weighted)	0.9915	0.9799
Cohen's Kappa	0.9790	0.9506
Specificity (Macro)	0.9991	0.9982
Specificity (Weighted)	0.9978	0.9982
F2 Score (Macro)	0.8560	0.7630
F2 Score (Weighted)	0.9916	0.9801

Source: Authors, (2026).

IV.9 IMPLEMENTATION AND SYSTEM-LEVEL VALIDATION OF BDL-IDACS

The suggested BDL-IDACS framework's Java-based implementation and system-level validation are depicted in Figure 11. While dataset upload and management modules allow for regulated integration of RT-IoT2022 traffic data into the system, user identification and registration interfaces verify secure access activation. The preprocessing and feature-handling steps that get network traffic ready for Astra-SAINT-based intrusion analysis are represented by the file upload, dataset monitoring, and feature input displays. The monitoring interfaces enable ongoing observation of IoT behavior by reflecting real-time analysis of traffic characteristics and system parameters.

Smart contract-based dynamic access control is enforced by download and request management panels, which grant or restrict user capabilities based on trust assessment and validated intrusion predictions. Together, these interfaces verify that the suggested blockchain-assisted, privacy-preserving intrusion detection and access control framework is both operationally deployable and algorithmically effective, guaranteeing safe data handling, restricted access, and transparent auditing throughout the IoT-cloud infrastructure.



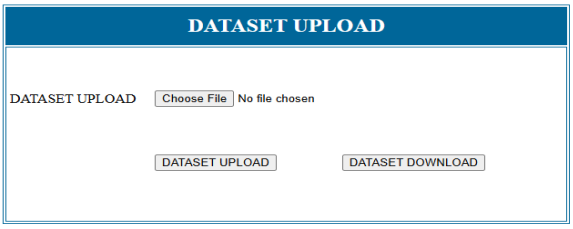


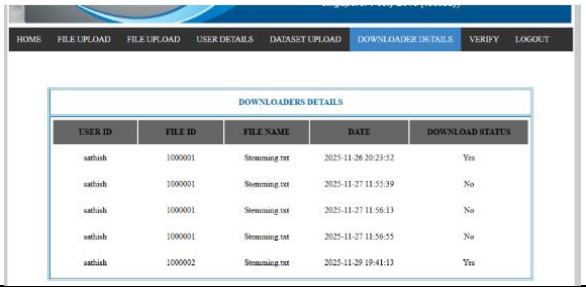
















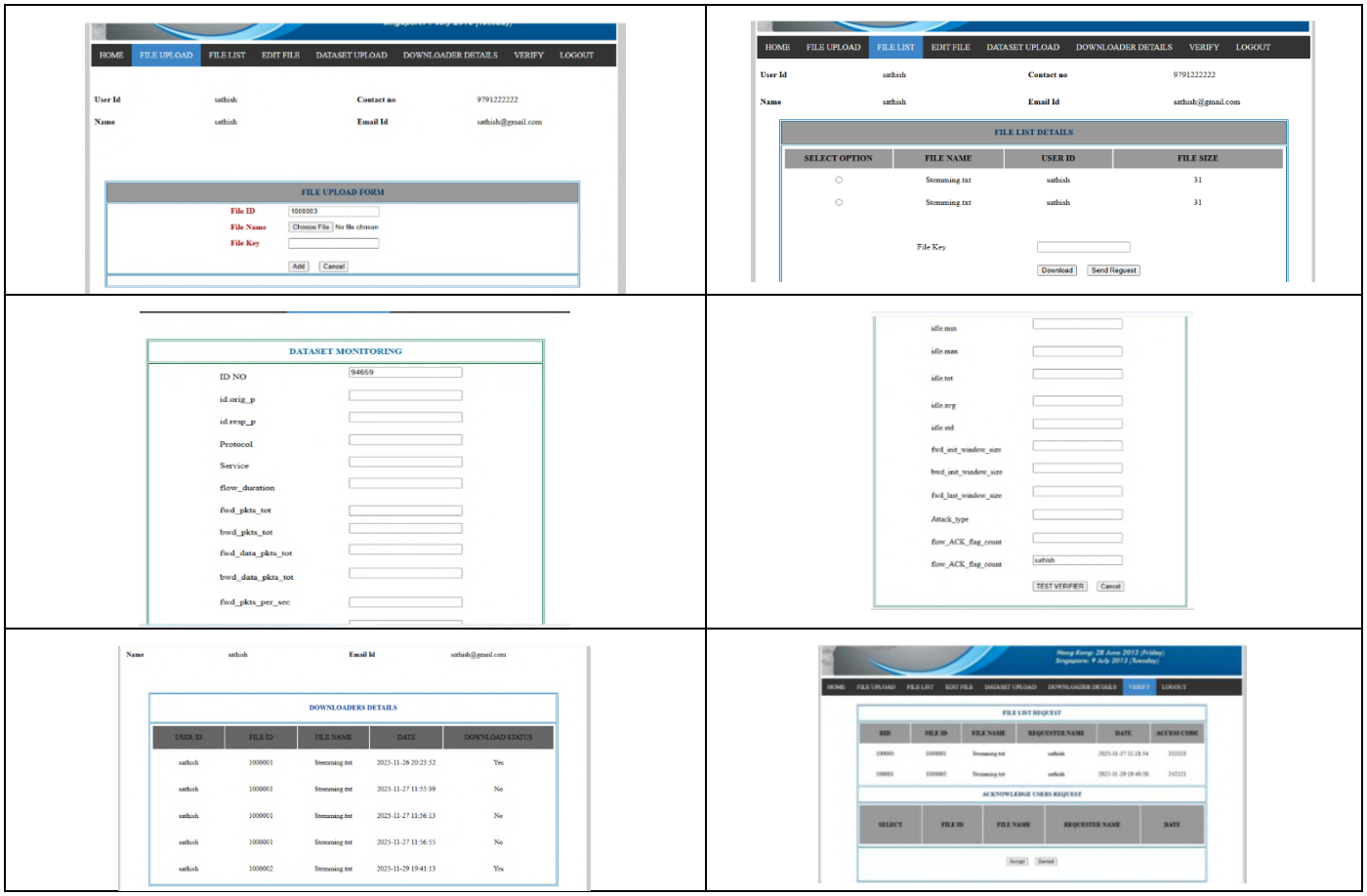


Figure 11: Java-based implementation of the proposed BDL-IDACS framework showing secure user authentication, dataset upload and monitoring, intrusion-aware access control, and system-level validation of blockchain-assisted IoT–cloud security.
Source: Authors, (2026).

IV.10 ABLATION STUDY AND STATISTICAL PERFORMANCE COMPARISON OF MODELS

A thorough ablation analysis and statistical performance comparison between the proposed approach and three baseline architectures STAR-RNN, Transformer, and BiLSTM-CNN are shown in tables 3 and 4. With an accuracy of 0.9916, superior macro-averaged precision (0.9110), recall (0.8521), and F1-score (0.8648), the suggested model consistently obtains the best performance across all measures, demonstrating strong equal effectiveness across all attack classes, even minority classes. The ability to adapt to class imbalance is further supported by the weighted metrics, which keep near-perfect values at 0.99. The baseline models have relatively lower macro-averaged scores, which indicate that they are less successful in managing class imbalance, especially when it comes to recall and F-scores. In comparison to other models, the suggested model's higher Cohen's Kappa value (0.9790) shows a stronger agreement beyond probability. Based on mean performance, standard deviation, and 95% confidence intervals derived from cross-validation, Table 4 provides a statistical comparison of model accuracy. Strong stability and the best mean accuracy (0.9916) are demonstrated by the suggested model, which has a low standard deviation (0.0025) and a small confidence interval [0.9882,0.9951]. Although the Transformer and STAR-RNN models exhibit competitive accuracy, there is more performance variability indicated by their wider confidence ranges. Reduced consistency is highlighted by the BiLSTM-CNN model, which records the broadest confidence interval and the lowest accuracy. Overall, the findings support the suggested model's higher statistical reliability, robustness, and efficacy when compared to current DL baselines.

Table 3: Ablation study.

Metric	Proposed Model	STAR-RNN	Transformer	BiLSTM-CNN
Accuracy	0.9916	0.9803	0.9790	0.9748
Precision (Macro)	0.9110	0.8512	0.8433	0.8260
Precision (Weighted)	0.9916	0.9801	0.9790	0.9722
Recall (Macro)	0.8521	0.7585	0.7840	0.7391
Recall (Weighted)	0.9916	0.9803	0.9790	0.9748
F1 Score (Macro)	0.8648	0.7742	0.8065	0.7593
F1 Score (Weighted)	0.9915	0.9799	0.9788	0.9712
Cohen’s Kappa	0.9790	0.9506	0.9478	0.9412
Specificity (Macro)	0.9991	0.9982	0.9980	0.9971
Specificity (Weighted)	0.9978	0.9982	0.9977	0.9969
F2 Score (Macro)	0.8560	0.7630	0.7944	0.7410
F2 Score (Weighted)	0.9916	0.9801	0.9782	0.9725

Source: Authors, (2026).

Table 4: Statistical Accuracy Comparison of the Proposed Model and Baseline Architectures.

Model	Mean Accuracy	Std. Dev.	95% Confidence Interval
Proposed Model	0.9916	0.0025	[0.9882, 0.9951]
STAR-RNN	0.9803	0.0022	[0.9772, 0.9834]
Transformer	0.9790	0.0031	[0.9729, 0.9851]
BiLSTM-CNN	0.9748	0.0034	[0.9681, 0.9815]

Source: Authors, (2026).

V. CONCLUSION

In order to evaluate the efficacy and dependability of the suggested iIDS, this study used five-fold cross-validation on the RT_IOT2022 dataset. It is evident from experimental results that the suggested model continuously outperforms baseline techniques in every important assessment criteria. With excellent accuracy, precision, recall, F1-score, F2-score, specificity, and Cohen's Kappa all of which together demonstrate great discriminative power and reliability and the method performs exceptionally well in multi-class IoT attack detection. Confusion matrix results show strong true positive rates across almost all attack categories, and additional validation using ROC and Precision-Recall analysis indicates improved class separability and robustness under imbalanced data situations. Furthermore, the model's stability and reliable generalization across cross-validation folds are highlighted by statistical evaluation that uses low standard deviation values and narrow confidence intervals. All things considered, these findings validate that the suggested method is appropriate for actual IoT security situations that call for precise and reliable intrusion detection.

V.1 FUTURE SCOPE

Even though the suggested model performs well, there are still a number of intriguing avenues for improvement. In order to evaluate its efficacy under dynamic network settings and continuous data streams, future research can examine its deployment in real-time IoT systems. Furthermore, investigating edge-level implementation and lightweight model optimization may aid in lowering energy consumption and computing complexity, making the strategy more appropriate for IoT devices with limited resources.

VI. AUTHOR'S CONTRIBUTION

Conceptualization: C. Ramya and A.Suphalakshmi.
Methodology: C. Ramya and A.Suphalakshmi.
Investigation: C. Ramya and A.Suphalakshmi.
Discussion of results: C. Ramya and A.Suphalakshmi.
Writing – Original Draft: C. Ramya.
Writing – Review and Editing: C. Ramya and A.Suphalakshmi.
Resources: A.Suphalakshmi.
Supervision: A.Suphalakshmi.
Approval of the final text: C. Ramya and A.Suphalakshmi.

VII. REFERENCES

[1] D. Mishra, R. K. Mishra, and R. Agarwal, "Cyber-Physical Systems and Internet of Things (IoT): Convergence, Architectures, and Engineering Applications", Advances in Engineering Science and Applications, pp. 17-46, May 2025.

[2] A. Mishra, A. V. Jha, B. Appasani, A. K. Ray, D. K. Gupta, and A. N. Ghazali, "Emerging technologies and design aspects of next generation cyber physical system with a smart city application perspective", International Journal of System Assurance Engineering and Management, vol. 14, no. Suppl 3, pp. 699-721, Jul. 2023.

[3] C. Chen, Y. Li, Q. Wang, X. Yang, X. Wang, and L. T. Yang, "An intelligent edge-cloud collaborative framework for communication security in distributed cyber-physical systems", IEEE Network, vol. 38, no. 1, pp. 172-179, Oct. 2023.

[4] F. Alserhani, "Intrusion detection and real-time adaptive security in medical IoT using a cyber-physical system design", Sensors, vol. 25, no. 15, pp. 4720, Jul. 2025.

[5] H. Nandanwar, and R. Katarya, "A hybrid blockchain-based framework for securing intrusion detection systems in internet of things", Cluster Computing, vol. 28, no. 7, pp. 471, Sep. 2025.

[6] N. Sharma, and P. G. Shambharkar, "Multi-layered security architecture for IoMT systems: integrating dynamic key management, decentralized storage, and dependable intrusion detection framework", International Journal of Machine Learning and Cybernetics, pp. 1-48, May 2025.

[7] A. Awajan, "A novel deep learning-based intrusion detection system for IOT networks", Computers, vol. 12, no. 2, pp. 34, Feb. 2023.

[8] V. Hnamte, and J. Hussain, "DCNNBiLSTM: An efficient hybrid deep learning-based intrusion detection system", Telematics and Informatics Reports, vol. 10, pp. 100053, Jun. 2023.

[9] Z. Wu, H. Zhang, P. Wang, and Z. Sun, "RTIDS: A robust transformer-based approach for intrusion detection system", IEEE Access, vol. 10, pp. 64375-64387, Jun. 2022.

[10] M. Alazab, G. Manogaran, and C. E. Montenegro-Marin, "Trust management for internet of things using cloud computing and security in smart cities", Cluster Computing, vol. 25, no. 3, pp. 1765-1777, Jun. 2022.

[11] Z. A. Hussien, H. A. Abdulmalik, M. A. Hussain, V. O. Nyangaresi, J. Ma, Z. A. Abduljabbar, and I. Q. Abduljaleel, "Lightweight integrity preserving scheme for secure data exchange in cloud-based IoT systems", Applied Sciences, vol. 13, no. 2, pp. 691, Jan. 2023.

[12] A. Sharma, P. Bohara, M. Tiwari, M. M. Mijwil, M. Abotaleb, and K. K. Hiran, "Enhancing Cloud Computing Security with Blockchain: A Decentralized Approach to Data Integrity, Access Control, and Compliance", In International Conference on Intelligence-Based Transformations of Technology and Business Trends, pp. 629-646. Cham: Springer Nature Switzerland, May 2025.

[13] S. Ahmed, “Enhancing Data Security and Transparency: The Role of Blockchain in Decentralized Systems”, International Journal of Advanced Engineering, Management and Science, vol. 11, no. 1, pp. 593258, 2025.

[14] V. Saravanan, M. Madiajagan, S. M. Rafee, P. Sanju, T. B. Rehman, and B. Pattanaik, “IoT-based blockchain intrusion detection using optimized recurrent neural network”, Multimedia Tools and Applications, vol. 83, no. 11, pp. 31505-31526, Mar. 2024.

[15] A. Aljabri, F. Jemili, and O. Korbaa, “Convolutional neural network for intrusion detection using blockchain technology”, International Journal of Computers and Applications, vol. 46, no. 2, pp. 67-77, Feb. 2024.

[16] R. F. Mansour, “Artificial intelligence based optimization with deep learning model for blockchain enabled intrusion detection in CPS environment”, Scientific Reports, vol. 12, no. 1, pp. 12937, Jul. 2022.

[17] D. Saveetha, and G. Maragatham, “Design of Blockchain enabled intrusion detection model for detecting security attacks using deep learning”, Pattern Recognition Letters, vol. 153, pp. 24-28, Jan. 2022.

[18] E. B. Mbaya, E. Adetiba, J. A. Badejo, J. S. Wejin, O. Oshin, O. Isife, S. C. Thakur, S. Moyo, and E. F. Adebiyi, “SecFedIDM-V1: A secure federated intrusion detection model with blockchain and deep bidirectional long short-term memory network”, IEEe Access, vol. 11, pp. 116011-116025, Oct. 2023.

[19] M. A. Alkhonaini, M. A. Alohali, M. Aljebreen, M. M. Eltahir, M. H. Alanazi, A. Yafoz, R. Alsini, and A. O. Khadidos, “Sandpiper optimization with hybrid deep learning model for blockchain-assisted intrusion detection in iot environment”, Alexandria Engineering Journal, vol. 112, pp. 49-62, Jan. 2025.

[20] B. H. Ali, M. A. Gunavathie, and P. Karthigaikumar, “Secure IoT Medical Data Storage and Intrusion Detection Using Blockchain Encryption and Optimized Two-Branch Attention Adversarial Transformer”, Biomedical Materials & Devices, pp. 1-26, Dec. 2025.

Journal of Engineering and Technology for Industrial Applications

ISSN ONLINE: 2447-0228

ITEGAM-JETIA

Manaus, v.12 n.60, p.166-180, July/August, 2026.
DOI: https://doi.org/10.5935/jetia.v12i60.3681

RESEARCH ARTICLE OPEN ACCESS

SALP SWARM OPTIMIZED ARBS-NET ENABLED FRAMEWORK FOR FAULT DIAGNOSIS IN ELECTRIC VEHICLES

Ganapavarapu Harish[1*], V. Suresh[2], D. Ravi Kishore[3], B Kavya Santhoshi[4]

[1]PG Scholar, School of Engineering, Department of Electrical and Electronics Engineering, Godavari Global University, Rajamahendravaram, India.
[2]Assistant Professor, School of Engineering, Department of Electrical and Electronics Engineering, Godavari Global University, Rajamahendravaram, India.
[3]Professor&HOD, School of Engineering, Department of Electrical and Electronics Engineering, School of Engineering, Godavari Global University, Rajamahendravaram, India.
[4]Assistant Professor, Department of Electrical and Electronics Engineering, Godavari Global University, Rajamahendravaram, India.

[1]http://orcid.org/0009-0005-1531-8972, [2]https://orcid.org/0000-0003-2113-0886,
[3]http://orcid.org/0000-0002-2567-2888, [4]http://orcid.org/0000-0002-5309-8158

Email:*harishganapavarapu655@gmail.com, sureshvendoti@ggu.edu.in, dr.ravikishore@ggu.edu.in, kavyasanthoshi@ggu.edu.in

ARTICLE INFO

Article History
Received: February 13, 2026
Reviewed: June 6, 2026
Accepted: July 6, 2026
Published: July 31, 2026

Keywords:
Preprocessing,
Exploratory data analysis,
Feature engineering,
ARBS-Net,
Salp Swarm Optimization.

ABSTRACT

Electric Vehicles (EVs) represents an excellent possibility towards developing a sustainable transport sector with low carbon emissions, low noise levels, high energy-efficient and integrate with electrical grids flexibly. Thus, the process of EV begins with data collection which involves different types of data such as voltage, current, vehicle speed, temperature, vibration and humidity to create a dataset of critical parameters. Pre-processing involves normalizing the dataset to create a consistent value for every element of data and to increase the value of the informations set. Exploratory data analysis (EDA) then lead to explore the distribution of different features in the dataset and detect any underlying or hidden patterns among the data. In feature engineering, the features are determined as critical for the performance of EV extracted from the data and used to identify potential failure modes present in EV. The Salp Swarm Optimized Attentive Radial Basis Spiking Network (ARBS-Net) is developed using a combination of benefits associated with multiple feature types, including sparse convolution, attention mechanisms and evolutionary optimization, to establish high-performance prediction and classification of fault conditions present in EV systems. This model is trained in Python and attains the maximum accuracy, precision, recall and F1-Score metrics of 0.99, thus demonstrating the proposed classification's capability to effectively predict and classify the occurrence of various fault conditions within EV systems. This intelligent diagnostic framework serves as a complete solution to implement proactive maintenance and increase EV operational reliability.

Copyright ©2026 by authors and Galileo Institute of Technology and Education of the Amazon (ITEGAM). This work is licensed under the Creative Commons Attribution International License (CC BY 4.0).

I. INTRODUCTION

Increasing reliance on EVs and increased development of electricity generation in relation to smart city control is making harder to operate. As such, EV have a large contribution to the environment when it comes to the decarbonization of individual and public transportation. When compared to traditional gasoline and diesel vehicles, EVs are more efficient in terms of energy [1]. Over the long run, EVs are considered as energy storage systems, creating numerous unique opportunities and secondary services that benefit microgrids, such as providing vehicle-to-grid capability (V2G), voltage regulation, frequency regulation, and so on. EVs, distributed energy sources, and other components associated with microgrids eventually create failures associated with these components. An EV contains many electrical devices and a long energy conversion pathway, therefore implementing a Fault Diagnosis (FD) process to maximize the service exists of the EVs. Additionally, FD process helps to increase system uptime and lower operating costs [2], [3].

An on-board microcontroller monitoring approach is employed to monitor several EV types of components, specifically the energy storage device such as batteries and supercapacitors, battery management unit, semiconductor devices, power electronic converters, electric propulsion motors and sensors [4]. EV usage has become a primary means of reducing greenhouse gas emissions associated with global warming and the cause of increasing electrical demand around the biosphere [5]. The limitation of fossil fuels, along with the number of countries that produce fossil fuels and their political instability, has further highlighted EV's importance. EV growth will continue rapidly over years across numerous countries due to government legislation aimed at growing EV market shares. As laws evolve towards achieving significant EV usage within their respective markets, electric drives and battery systems experience significant growth within EV manufacturing. The EV parts consist of multiple components, all vulnerable to various sorts of errors [6], [7]. Though, the electrical determination and sequence portions of an EV represent its core components, and typical EV component failures occur primarily within the electrical drive or battery, therefore monitoring their function is critical [8]. Some industries have a large number of electric motors and are used for many reasons including as power supplies for EV's. The transportation industry's reliability and safety requirements are necessitated by the automotive version of the EV [9]. Electrical faults, internal heat, peak performance time and electrical shifting lead to various sorts of electric motor drive faults that degrade the system's performance and reliability of the EV. Interior-Permanent Magnets Synchronized (IPMS) motors are the most commonly used motors in the EV market. The majority of other Permanent Magnet Motors (PMM) utilize similar PMSM construction with different series designed for power levels [10], [11]. Industrialists are being driven to optimize the designs of the PMSM due to increased demands for assembly and high cost materials resulting in more complex designs and increased susceptibility to failure from different types of fault mechanisms [12]. However, due to the transportation industry's demands for continuity regardless of the working atmosphere of EV motors, there are multiple varieties of errors that arise on the motor and in the driver's inverter.

Electric motor initiative errors are characterised into three primary categories such as electrical faults, mechanical faults, and sensor faults [13].Electrical faults include Interturn Short Circuit Fault (ITSF), phase to phase circuit faults, magnetic short circuit between windings and open or short circuits on inverter switching devices [14]. Mechanical faults include rotor faults including bearing faults, bent shafts, and airgap eccentricity. The faults associated with the various sensors in an electric motor are known as sensor faults. Identifying these faults early allow for corrective action to prevent costly damage and catastrophic failures from occurring [15]. In EVs, lithium-ion battery systems have established as superior to traditional energy-storage systems for EV applications. This is owed to their excellent resources such as high power, energy density, durability and environmental effects. The battery packs of EV's contain numerous cells linked together in both series and parallel arrangements, creating both redundancy and increased performance. There are many ways that faults develop in battery systems resulting in the batteries degrading quickly, accelerated aging of batteries, EV problems, and fatal accidents. The report indicated that approximately 30% of EV accidents were battery related [16], [17]. Consequently, the development of reliable error discovery and fault-lenient control systems is necessary to ensure the safety and continuity of EV operation. Nonetheless, intricate processes and other unfamiliar variables sort initial discovery of faults difficult. A method for early detection and prediction of faults is the use of FD techniques to monitor and identify the operating conditions of an electric motor [18], [19]. Therefore the proposed system uses a hybrid framework for FD in EV. The collected signals go through a normalization process as part of the preprocessing stage to ensure data consistency and the stability of learning. After preprocessing an EDA is used, where statistical and distribution-related information about the operating conditions, and fault pattern detection is gained. Feature engineering is used as the third step to extract and refine informative features [20]. Then the model training stage is executed and the existing model training methods for fault diagnosis in EV is illustrated in table 1.

Table 1: Related works for existing model training methods for fault diagnosis in EV.

SI.NO	AUTHOR/YEAR	MODELS	MERITS	DEMERITS	METRICS
1.	Debani Prasad Mishra *et al* [2024] [21]	ANN	It performs automation without requiring an in-depth model of each component, and make quick decisions for monitoring real-time failures.	The temporal nature of fault propagation resulting in a less efficient fault diagnosis.	It attains an accuracy of 96.65, precision, recall and F1-Score of 97.
2.	Venkata Satya Rahul Kosuru *et al* [2023] [22]	IB-DRN	It achieves a great level of accurateness and robustness through the extraction features and the ability to accurately learn complex, non-linear patterns.	It requires a huge quantity of labeled informations to train on and lacks sufficient interpretability of diagnosis results.	The metrics for IB-DRN is 98 of accuracy, 90 of precision, 97 of recall and 94 of F1-Score.
3.	Thirunavukkarasu *et al* [2024] [23]	CatBoost	CatBoost performs well with complex, nonlinear relationships involving both continuous and mixed categorical variables.	It does not perform optimally for large datasets and high-dimensional sensor data.	CatBoost achieves an accuracy, precision, recall and F1-Score of 94.
4.	Jasmine Sabeena *et al* [2024] [24]	SVM	SVM are excellent at processing large amounts of high dimensional data from EV sensors.	SVMs are less capable of providing real time diagnosis of failures as data size and system dynamics increase.	For SVM, the accuracy and F1-Score is 95, precision is 94 and recall is 96.
5.	Moussa Attiaa *et al* [2025] [25]	RF	It provide features that are indicative of the parameters that influence faults within a subsystem of an EV.	It becomes less effective at tracking the dynamic nature of the fault behavior over time.	RF achieves an accuracy of 95, precision of 92, F1-Score of 93 and recall of 94.

Source: Authors, (2026).

Existing methods for identifying fault diagnosis in EV have various limitations and to overcome these shortcomings, the proposed ARBS-NET framework is used to capture complex nonlinear relationships and temporal characteristics in EV faults. This procedure is further hyper-tuned by Salp Swarm Optimization (SSO) to find the best model parameters.

I.1 OBJECTIVES

The main intents of this study includes,

- To decrease the impact of noise signal and improve data quality, preprocessing method termed normalization is implemented.
- To identify data distribution and fault patterns, exploratory data analysis is utilized.
- To differentiate between faults and to eliminate irrelevant information, feature engineering is executed.
- To learn complex and nonlinear characteristics of faults, ARBS-Net is employed.
- To reduce classification error rates, avoid local minima and increase the diagnostic accuracy, SSO algorithm is performed.

II. PROPOSED SYSTEM DESCRIPTION

A SSO-enabled ARBS-Net-based framework for fault diagnosis in EVs provide highly accurate and reliable detection of operational fault occurrence through the use of multi-sensory data. The diagram of fault diagnosis in EV using Salp Swarm Optimized ARBS-NET enabled framework is displayed in figure 1.

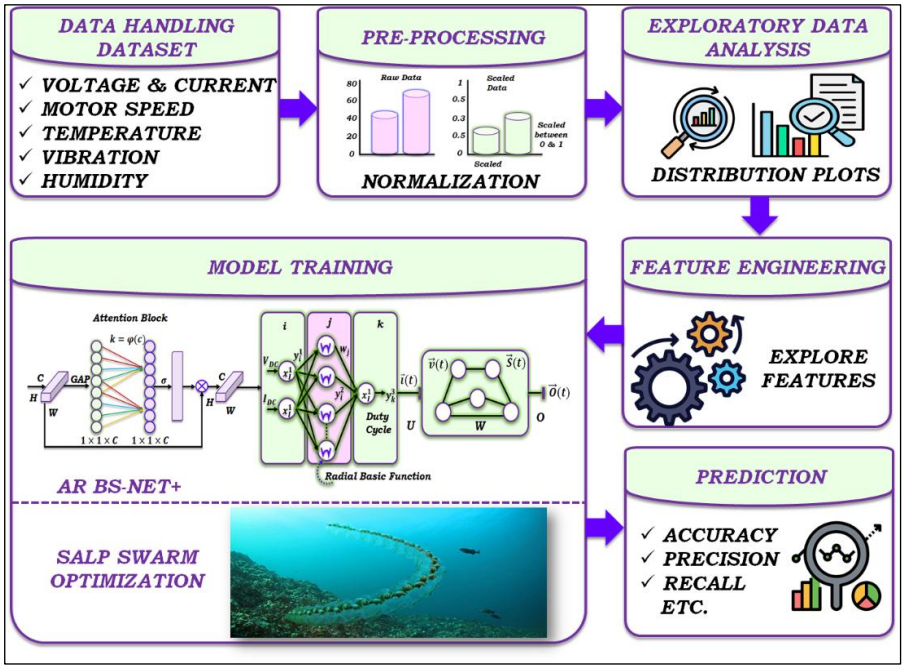


Figure 1: Proposed block diagram.
Source: Authors, (2026).

Initially, voltages, currents, motor speeds, temperatures, vibrations, humidity, and other critical parameters are collected and compiled into a single consolidated dataset. The collected data is subjected to preliminary normalization to remove scale differences among variables to improve the stability of learning and then processed further using EDA to understand the distribution and the operation of the data, before creating useful fault-related attributes to improve class separation from the features. The main feature of the proposed framework is the use of the ARBS-Net with its ability to capture nonlinear dynamics and temporal spiking of an EV component's performance. The ARBS-Net provides a robust representation of faults for diagnostic purposes. In addition, SSO is used in conjunction with the ARBS-Net, the SSO optimally tune the parameters of the ARBS-Net model, which include the network's attention weights and kernel characteristics, which reduce inaccuracies by enhancing the ARBS-Net's rate of convergence. The application of the offered framework for fault discovery and arrangement is verified through the use of standard metrics such as accuracy, precision, and recall to determine the reliability of the fault diagnosis of the EV systems.

III. PROPOSED SYSTEM MODELLING

III.1 PREPROCESSING – NORMALIZATION

III.1.1 MIN-MAX Normalization

Commonly, when diagnosing faults in EVs using multiple sensors to measure voltage, current, temperature, vibration and humidity, min-max normalization is used to standardize each of the measurements into a fixed range generally between [0,1]. Since these sensors measure the same quantity with different numerical ranges, the large numerical ranges dominate the model and reduce the ability of a diagnostic system to detect faults by an accurate model. The normalized value of a sensor measurement for min-max normalization is calculated as,

$$im_n(x,y,z) = \frac{im(x,y,z) - min(im)}{max(im) - min(im)} \quad (1)$$

The benefit of using min-max normalization is that it is computationally low-cost, and relatively easily process data on real-time systems for EVs. This method is very appropriate for range applications for EVs. Figure 2 shows the diagram of Min-Max normalization.

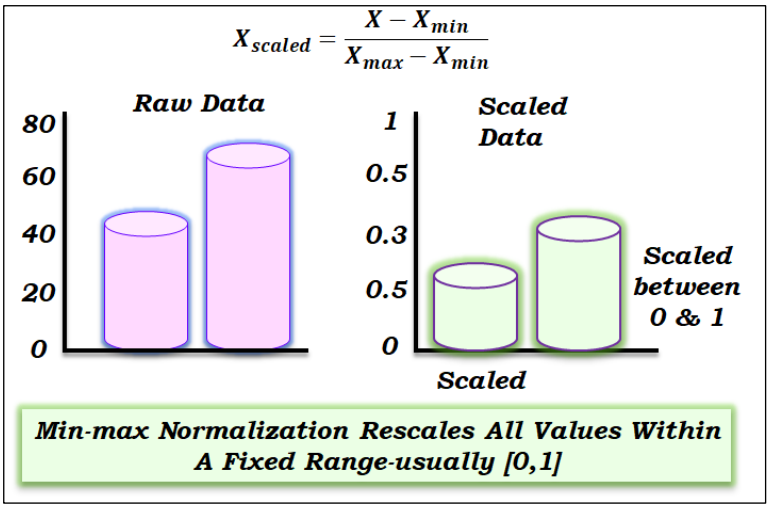


Figure 2: Min-Max normalization.
Source: Authors, (2026).

The data scaling process is done quickly and reliably along with providing information for feature representation, and allows faster processing for large amounts of sensor measurements though not having a large amount of computing overhead. It improve the fault diagnostic systems in terms of their ability to respond quickly with respect to elements such as characteristics of elements within an EV.

III.1.2 Z-Score Normalization

Sensor data from EV vary significantly depending on the type of vehicle and its operating conditions. To normalize the information of signal data from different types of EVs is to apply a Z score transformation. The Z score transformation normalizes the signal about a mean of 0 and a variance of 1, thus allowing for easier comparison and more stable models when performing data analysis. The formula for determining the normalized signal is,

$$im_n(x,y,z) = \frac{im(x,y,z) - \mu}{\sigma} \quad (2)$$

Where, μ equals the mean value of the signal and σ equals the standard deviation of the signal. By using a Z score transformation to normalize sensor data from EV, centers the signal on a mean of zero and provides an interpretation of the signal that is consistent, regardless of the type of EV. The diagram of Z-Score normalization is shown in figure 3.

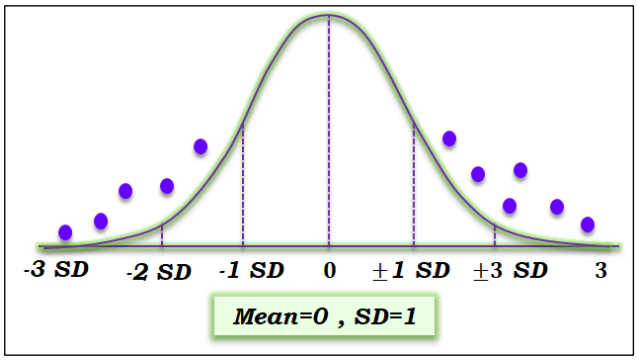


Figure 3: Z-Score normalization.
Source: Authors, (2026).

Furthermore, normalizing the data to a consistent statistical form helps facilitate the ability to effectively detect, isolate, and classify faults within the EV's subsystems such as batteries, motors, and power electronics. The Z score transformation applied to the signal data in several different ways, thus providing to improve the accurateness, reliability, and consistency of error identification for EVs.

III.2 EXPLORATORY DATA ANALYSIS

When diagnosing faults in EVs, exploratory data analysis through distribution plots shows an significant part in providing the initial insight into the characteristics of the sensor data collected from the vehicle components such as the battery management system, electric motor, power electronics, and thermal systems, prior to applying an intelligent fault detection model.

EVs produce a massive amount of data relating to these components, and distribution plots are helpful in illustrating the parameters of voltage, current, humidity, temperature, speed of a motor, and vibration signals which are statistically distributed under various operating conditions. Normal operating patterns easily identified from faulty operating patterns using distribution plots. When operating typically, an EV battery demonstrate a very tight clustering of voltages as compared to a sequence with internal faults, which establish greater spread in their distributions and present with multiple peaks in their distribution. Similarly, inverter faults naturally visible themselves with non-uniform distributions in the current and temperature outputs. All of this information gained from the distribution plots are used to identify outlier data points, data imbalances, noise, and any other hidden characteristics of the data that are not able to detect through the analysis of raw time-series data. Effective data preprocessing strategies are aided at this stage to ensure proper normalization, feature selection, and fault threshold determination through analysis of the relative distributions of healthy and faulty data. By analyzing the relative distributions of healthy and faulty states, plots are able to extract more discriminating features and reduce redundancy in the data set. By performing EDA using distribution plots, the reliability, accurateness, and stoutness of EV error analysis systems is enhanced then the method is proficient based on informations that are sensitive to faults.

III.3 FEATURE ENGINEERING

In the progression of diagnosing EV faults, the feature engineering - exploring features phase entails a further refining of the raw sensor data into useful and fault-sensitive representations of the sensor data that helps in increasing diagnostic accuracy. The battery, electric motor, inverter, and thermal subsystems continuously communicate data to the EV from their various sensors. However, raw data does not always provide a clear representation of any faults. Therefore, various feature representations from the sensor data, identify hidden patterns, relationships, and variances between normal operation and a fault. There are many statistical methods employed to represent significant features once conducting a localized search on sensors such as statistical parameter, time domain indicators, frequency domain components, energy and correlation of the different sensor readings like voltage, current, temperature, speed, and vibration. During this phase, individual attempts extract features from the various signals and assess the representative behavior of each feature during normal operations and fault conditions. Therefore, during this exploratory phase of the feature development process, all redundant or irrelevant features are deleted, while all highly discriminative features are retained to facilitate model learning. The identification of features improves the classification and measurement of faults through the use of two methods. By developing features that reduce the computational load of finding the faults, generate a higher level of fault separation and increased performance of Deep Learning fault diagnostic models. It creates an interface that captures the operating and performance characteristics of EV components thus allowing for the early identification of EV faults with more accurate classification, increases the safety of the vehicle and increases the vehicle's performance.

III.4 MODEL TRAINING - ARBS-Net

Using an attention mechanism for fault diagnosis in EV applications allows a model to focus on relevant fault data while eliminating unwanted sensor signal noise. Due to the variability of operating conditions and measurement uncertainties, EV fault data from devices like batteries, traction motors, inverters and other power conversion devices are heavily influenced by external disturbances. This noise complicates important aspects of detecting a fault. Therefore, by incorporating an attention mechanism, a diagnostic model acquires to favour more informative fault features while reducing the contributions of irrelevant or noisy feature content enhancing the robustness and accuracy of a diagnostic evaluation. This attention mechanism operates on extracted two-dimensional features in a channel-wise manner after performing convolutional processing. To allow for efficient computation with the attention mechanism, the two-dimensional features are essential to convert to a three-dimensional feature space. The three-dimensional feature space allows for inter-channel relationship modeling through cross-channel interaction modeling, enabling the network to place more emphasis on certain channels that require more distinct fault characteristics than other channels. This selective enhancement of particular channels recovers the simulation's capability to detect subtle faults and decreases the effect of noise without adding additional complexity to the structure of the model. Interactions between different channels are modelled using one-dimensional convolutional operations instead of fully connected layers, thus creating an efficient means of interaction between the channels and reducing computational burden. The extent of the convolution kernel k is adaptively determined founded on the quantity of channels C the layer ensures, allowing layers with higher numbers of channels to model more complete inter-channel dependencies. The determined convolution kernel size is expressed as follows,

$$k = \left| \frac{log_2(C)}{\gamma} + \frac{b}{\gamma} \right| \tag{3}$$

The total sum of channels is given by c where, $\gamma = 2$ and $b = 1$ are the non-linear parameters. Sequentially, after creating the global average pool channel descriptor, a 1D convolution followed by a sigmoid function generates channel attention weights. The equation for producing these weights is as follows,

$$\omega = \sigma\left(C_1 D_k(y)\right) \tag{4}$$

Where, $\sigma(\cdot)$ is the sigmoid function, $C_1 D_k(y)$ is the one dimensional convolution operation, and y is a pooled feature vector. Final output feature map is created by multiplying attention weights ω with corresponding channels in original input feature map. This amplify fault sensitive features related to degradation or failure of EV components. To detect EV subsystem failures, the RBFN uses measurable electrical and mechanical signals, which act as inputs to the RBFN network. The output of the RBFN provide a fault index that corresponds to normal or faulty operation for the underlying EV subsystem based on the inputs provided to it. The RBFN utilize three layers as part of its design such as the input layer, hidden layer, and output layer. Each of the input layer resembles directly to one of the EV diagnostic signals selected by the RBFN and are forwarded to the hidden layer. An input layer's input–output response is expressed as follows,

$$net_i^1 = x_i^1(N) \tag{5}$$

$$y_i^1(N) = f_i^1\left(net_i^1(N)\right) = net_i^1(N), where\ i = 1,2,\ldots \tag{6}$$

Where, x_i^1 expresses input variables associated with the fault and y_i^1 represents output data from a neuron in the input layer. The hidden layer of the RBFN consists of Gaussian radial basis function neurons, which model the nonlinear dynamics of the EV system under both normal and fault conditions. The hidden layer neurons correspond to membership functions related with precise error patterns or operation states. The relationship between the net input and output of the neurons in the hidden layer is provided by,

$$net_j^2(N) = \left(XM_j\right)^T \sum_j XM_j \tag{7}$$

$$y_j^2(N) = f_j^2\left(net_j^2(N)\right) = exp\left(net_j^2(N)\right), where\ j = 1,2,\ldots 800 \tag{8}$$

Here, $M_j = \left[m1_j, m2_j, \ldots mi_j\right]^T$ and $\sum_j diag\left[1/\sigma 1_j^2, 1/\sigma 2_j^2, \ldots 1/\sigma i_j^2\ \right]^T$ represent the Gaussian mean vector for fault patterns and the diagonal covariance matrix that determines the spreading of the RBF, respectively. The output layer is then a direct combination of the neuron outputs from the hidden layer in order to produce the final fault condition or fault severity level of the EV. The computation of the output layer is represented by the subsequent equality,

$$net_k^3 = \sum_j w_j\, y_j^2(N) \tag{9}$$

$$y_k^3(N) = y_{ki}^3\left(net_k^3(N)\right) = net_k^3(N) \tag{10}$$

The adjustable weights were learned during the training phase are represented as w_j. To develop the accurateness of the error diagnostics and lower computation requirements, the selection of effective RBFN inputs were made utilizing the polynomial representation of the identified function. A polynomial representation of the identified function in relation to the key features related to certain faults was constructed using the Polynomial Basis Function (PBF). The formulated equation for the EV fault diagnostics is represented as below:

$$y(t)=\sum_{k=1}^n \theta_{k\varphi_k}\left(\vec{X}(t)\right) + \varepsilon(t) \tag{11}$$

The fault indicator is denoted as, $y(t)$. $\vec{X}(t)$ is the vector of measured signals from the EV, $\varepsilon(t)$ is the modeling error, ϕ_k is an infinite number of nonlinear mapping functions and θ_k is an infinite number of linear coefficients. The system model generated for N training samples is expressed in the following equation,

$$\vec{Y} = \varphi\left(\vec{X}(t)\right) \circledast + e \tag{12}$$

Where, $\vec{Y} = [y(1), \ldots y(N)]^T$ indicates the output vector containing the fault labels and $\varphi\left(\vec{X}\right) = [\varphi_1(X), \ldots \varphi_n(X)]^T$ is the plotting function matrix. To construct the nonlinear mapping functions, use the following polynomial representation,

$$\varphi_k = \Pi_{j=n_{y1}}^{n_{yi}} y(t-j)\Pi_{k=1}^m \Pi_{j=n_{xk1}}^{n_{xki}} x_k(t-d_k-j), i = 1, \ldots p, \varphi_0 = 1 \tag{13}$$

The polynomial order allows the model to replicate the dynamic fault attributes of EV systems, thus$0 \le n_y k1 \le \ldots \le n_{yki} \le l_{y,}0 \le n_{xki} \le \ldots \le n_{xki} \le l_x, and\ l_x = 10, l_y = 3$. The general RBFN fault diagnosis model is described using the selected polynomial term orders as,

$$y(t) = \sum_{k=1}^n \theta_{k\varphi_k}\left(\vec{X}(t), c_k, \sigma_k\right) + \varepsilon(t) \tag{14}$$

Where, $\varphi_k(\cdot)$ is the Gaussian radial basis activation function with centre c_k and widthσ_k. In a similar manner, the RBFN fault diagnosis model is represented in this format.

$$\vec{Y} = \varphi(X, \vec{c}, \vec{\sigma}) \circledast + \vec{e}1 \tag{15}$$

Here, $\varphi(X, \vec{c}, \vec{\sigma})$ is the hidden layer output matrix comprised by the centre and width selections that provide robust and reliable means of detecting and classifying faults in EV systems. The structure of ARBS-Net is depicted in figure 4.

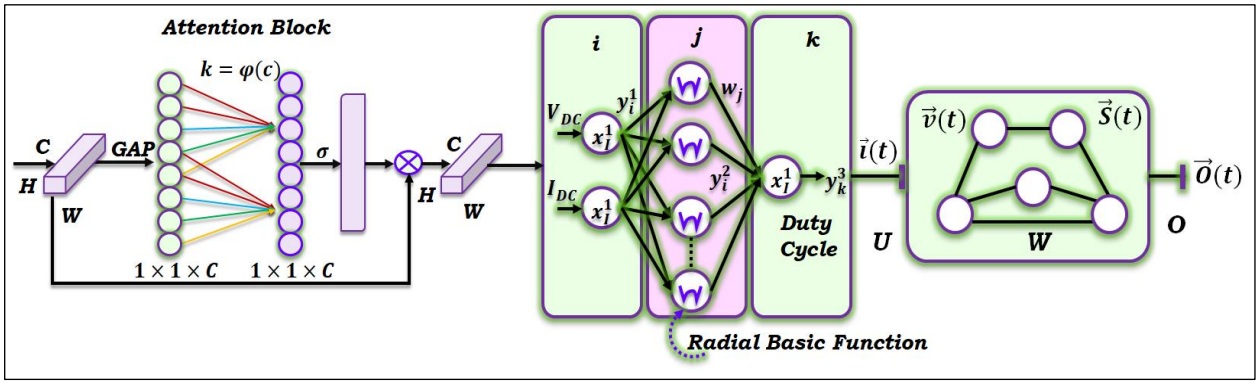


Figure 4: Structure of ARBS-Net.
Source: Authors, (2026).

A spiking neural network (SNN)-based fault diagnosis system for EVs utilizes the signals generated through measurement processes, such as battery voltage, current or temperature, as encoded neuron membrane potentials (t). When using traditional EV error analysis schemes, the actual mistake prediction mechanism is based on detecting a spike on the neuron membrane potential (t) that exceeds the predefined threshold value. Thus, fault detection occur instantaneously whenever the membrane potential exceeds the defined hard threshold causing a non-continuous fault detection response, which is expressed mathematically as,

$$\tau \dot{s} = -s + \sum_k \delta(t - t_k) \tag{16}$$

This method is sufficient for the protection of the EV from imminent failure, however, it does not provide the capability of detecting the continued gradual failure of a system, and limit the amount of time available to warn a user before failure occurs. To achieve a more sophisticated and informative fault detection capability, the hard threshold is replaced with an active fault sensitive region that is described by a gate function $g(v)$ and is defined as a narrow region in which the system is considered subject to failure due to fluctuations outside the defined threshold. In this case the synaptic dynamics is as follows,

$$\tau \dot{s} = -s + g\dot{v} \tag{17}$$

Where $g \geq 0$ and $\int g dv = 1$. In this SNN model, SNN synaptic activation gradually emerged during EV signal evolution within the active zone, inclusion of $\dot{v}$ ensures that fault representation remains rate-invariant since,

$$\int s\, dt = \int g\dot{v}\; dt = \int g\; dv = 1 \tag{18}$$

Consequently, both fast transients and slow degradations create equivalent spike-based fault evidence. This gate-based spiking functionality retains an event-driven fault semantic while facilitating differentiable, robust, and learning-compatible fault diagnosis in EV. Robust and adaptable fault diagnosis for EV is achieved by the ARBS-Net framework by means of the combination of Attention-based feature enhancement, RBFN Nonlinear mapping and SNN. The attention mechanism highlights features that are related to the fault while reducing background noise, the RBFN lower-order rules and correlations between multiple signals capture the nonlinear functional relationships within the data and thus generate a fault index, and spiking neurons support continuous and rate-invariant detection of both fast transients and gradually degrading systems. Thus, ARBS-Net provide early, accurate, and dependable identification of subsystem faults in an EV.

III.5 SALP SWARM OPTIMIZATION

In diagnosing faults with EVs, the process is modelled to find the best parameters, such as weights for features, hyper-parameters for classifiers, or thresholds for faults, which results in the maximum classification accuracy or a minimum error rate. In Salp Swarm Optimization algorithm, each salp is a candidate solution to an EV fault diagnostic problem, which is signified as a opinion in a d-dimensional search space defined by the number of decision variables in the EV fault diagnosis. The positions of each of the salps are stored in a two-dimensional matrix, denoted as X.

$$x_i = \begin{bmatrix} x_1^1 & x_2^1 & \cdots & x_d^1 \\ x_1^2 & x_2^2 & \cdots & x_d^2 \\ \vdots & \vdots & \cdots & \vdots \\ x_1^n & x_2^n & \cdots & x_d^n \end{bmatrix} \tag{19}$$

In forming the algorithms, for each salp, an objective function is utilized, based on actual data sources of EV operations such as currents, temperatures, and speeds, which produces the best defined solutions to the food positionFP. The leader salp finds its position in relation to the food source based on the following rule,

$$x_i^1 = \begin{Bmatrix} FP_i + c_1\big((ub_i - lb_i)r_1 + lb_i\big)\, r_2 \geq 0 \\ FP_i + c_1\big((ub_i - lb_i)r_1 + lb_i\big)\, r_2 < 0 \end{Bmatrix} \tag{20}$$

Where, lb_i and ub_i are the lower and upper bounds of the ith diagnostic constraint, r_1 and r_2 are uniformly distributed random numbers from [0 to 1]. The SSO uses each salp as a candidate solution within the diagnostic problem space to find the best possible diagnostic parameters by using iteratively updated leader–follower movements.

Pseudocode- Salp Swarm Optimized Attentive Radial Basis Spiking Network:

```
BEGIN
1: Load EV fault training and testing datasets
2: Split datasets into features X and labels y
3: Convert datasets into tensors and Data Loader batches
4: Define ARBSNN architecture with:
Input layer
Attentive hidden layer
Radial Basis Spiking layer
Output classification layer
5: Define objective function:
a) Initialize ARBSNN using candidate parameters
b) Train model for few epochs on training data
c) Evaluate classification accuracy on test data
d) Return fitness = 1 − accuracy
6: Initialize Salp Swarm Optimizer:
Population size P
Search dimension = 2 (hidden neurons, learning rate)
Maximum iterations Tmax
Parameter bounds (lb, ub)
7: Initialize salp positions randomly within bounds
8: Evaluate fitness of all salps
9: Select best salp as Food Source F
10: FOR iteration t = 1 TO Tmax DO
11:     Update control parameter c1
12:     FOR each salp i DO
13:         IF i == 1 THEN          // Leader salp
14:             Update salp position towards Food Source F
15:         ELSE                    // Follower salp
16:             Update salp position as average of previous salp
17:         END IF
18:         Apply boundary constraints
19:         Evaluate fitness of updated salp
20:         IF fitness improves THEN
21:             Update Food Source F
22:         END IF
23:     END FOR
24: END FOR
25: Extract optimal parameters from Food Source:
H* = optimal hidden neurons
η* = optimal learning rate
26: Initialize final ARBSNN using H* and η*
27: Train final ARBSNN model for predefined epochs
28: Evaluate training and testing accuracy and loss
29: Output trained SSO-ARBSNN model and performance metrics
END
```

Adaptive coefficient c_1 is utilised in SSO to help maintain both exploration and exploitation balance. As the algorithm iteratively searched through the solution space, it provided many opportunities to explore different fault signs at the beginning of the algorithm and systematically refine the diagnostic solution during subsequent iterations. This is especially important for closely fault signs to coupled together by varying operating conditions within EV environments. Coefficient c_1 is implemented to equilibrium exploration and exploitation in the optimization process and is given by,

$$c_1 = 2e^{-\left(\frac{4t}{t_{max}}\right)^2} \tag{21}$$

Where, t and t_{max} are used to denote current iterated value or maximum number of iterations. Finalisation of stable convergence and minimisation of the potential for premature stagnation, were made possible through leader and follower update strategies. The follower salps use leader and preceding salps to adjust their position which improves convergence stability based on,

$$x_i^j = \frac{1}{2}\left(x_i^j + x_i^{j-1}\right) \tag{22}$$

To ensure that the diagnostic solutions are constrained within the feasible operating limits of EV components, any salp that exceeds the search space is returned back into the allowable limit set by the boundary constraint. The flowchart of SSO is shown in figure 5.

$$x_i^j = \begin{cases} lb_i \; if \; x_i^j \leq lb_i \\ ub_i \; if x_i^j \geq ub_i \\ x_i^i \quad otherwise \end{cases} \tag{23}$$

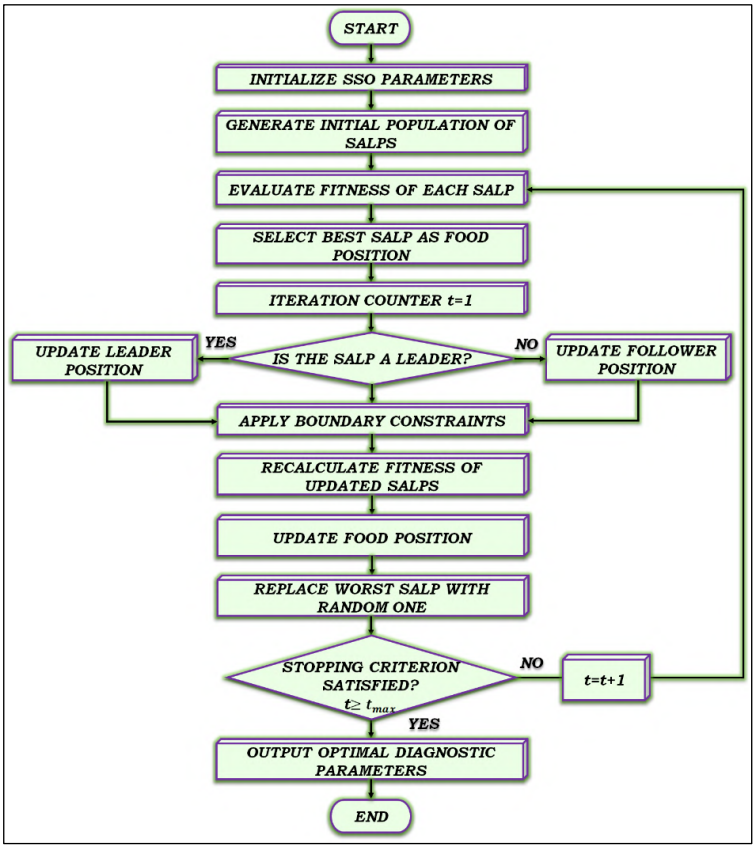


Figure 5: Flowchart of SSO.
Source: Authors, (2026).

By combining the ARBS-Net methodology using the leader-follower optimiser method and an adaptation strategy provides a balance between exploration and exploitation of actions taken by the decision maker. This research confirmed that the accuracy and operational reliability of SSO-optimized ARBS-NET successfully improve the effectiveness of EV performance. The SSO-based ARBS-NET mistake analysis produce a dependable and computationally effective classification for optimising the faults and failures of EVs, leading to improved accuracy and reliability in detecting faults. This structured process allows for the optimally constructed iterative optimisation process of all diagnostic parameters contained within the ARBS-NET providing increased accuracy of fault diagnosis performed on EV systems.

IV. RESULT AND DISCUSSION

The proposed SSO-ARBS-Net framework for diagnosing faults within EV systems is evaluated through the experimental data. The results show that integrating SSO with ARBS-Net produce substantially improved diagnostic accuracy, convergence stability and computational efficiency compared to non-optimized and conventional intelligent diagnostic approaches. Table 2 displays the report of dataset for the proposed system.

Table 2: Description of dataset.

DATASET DESCRIPTION	
Features	8
Total rows	11000
Features names	Voltage, Current, Motor Speed, Temperature, Vibration, Ambient Temperature, Humidity, Fault Label
Y label	Fault Label
Classes	Label 0: Normal Operation, Label 1: Motor-Related Faults, Label 2: Inverter-Related Faults, Label 3: Battery-Related Faults.

Source: Authors, (2026).

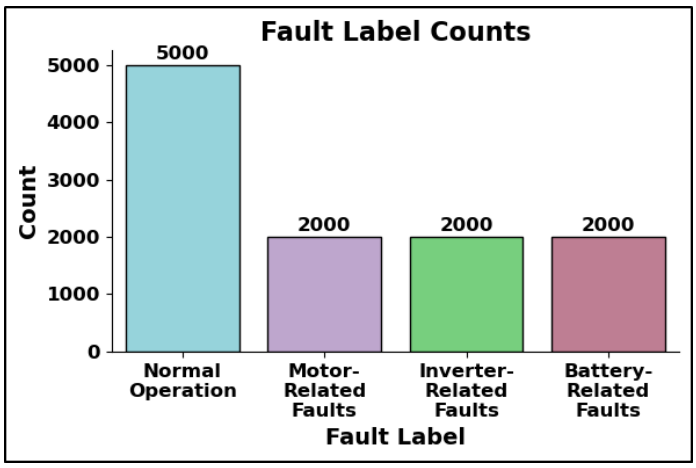


Figure 6: Fault Label Counts.
Source: Authors, (2026).

In figure 6, the data indicates that the category Usual Operation has the largest quantity of models with 5000. However, Motor faults, Inverter faults, and Battery faults each contained only 2000 samples, indicating class imbalance.

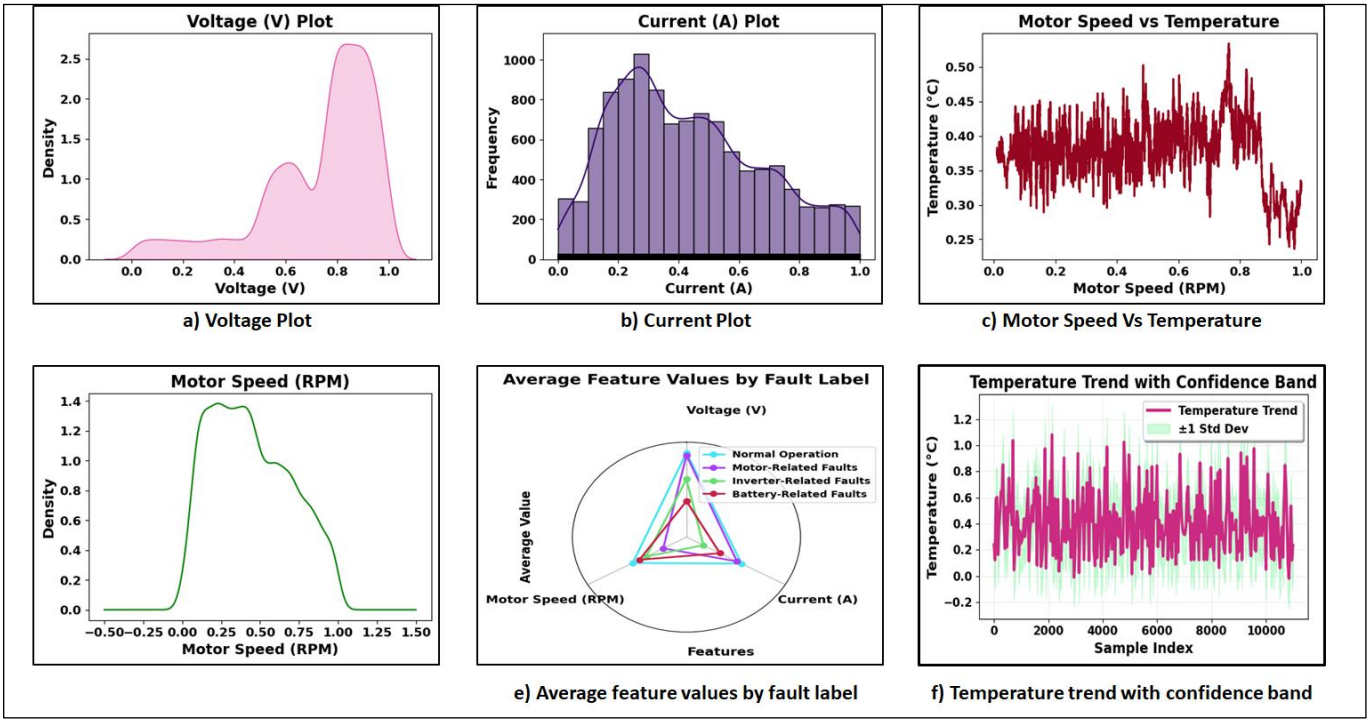


Figure 7: a) Voltage Plot, b) Current Plot, c) Motor Speed Vs Temperature, d) Motor Speed, e) Average feature values by fault label, f) Temperature trend with confidence band.
Source: Authors, (2026).

In figure 7, the data visualization has four plots such as the distribution of voltage; the distribution of motor speed; the histogram of current, and the association amongst motor speed and temperature. As a final, the average structures of the different fault classes are shown in radar chart form and the temperature trend with confidence band is displayed, both provide insight into the features behaviour and different fault classes differ under normal versus fault conditions.

Table 3: Classification report for the proposed system.

SI.NO	Performance Metrics	Values
1	Accuracy	0.99
2	Precision	0.99
3	Recall	0.99
4	F1-Score	0.99

Source: Authors, (2026).

According to the classification report in table 3, the proposed algorithm has a high accuracy, precision, recall, and F1-score of 0.99, creating it extremely accurate and providing reliable, consistent fault detection.

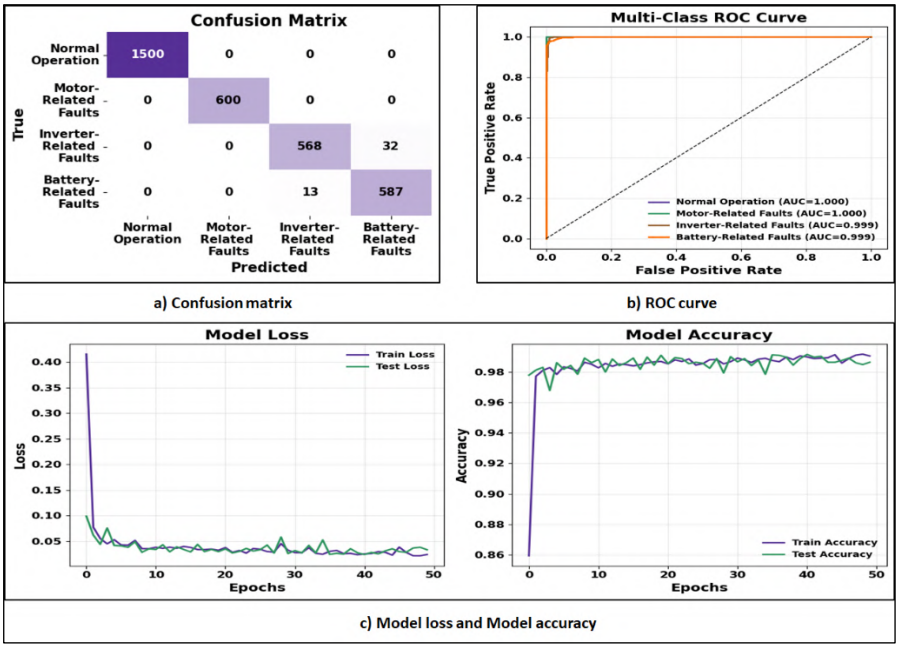


Figure 8: a) Confusion Matrix, b) ROC Curve, C) Model Loss and Model Accuracy for the Proposed System.
Source: Authors, (2026).

Figure 8 indicate a high level of confusion matrix demonstrates that very few errors occurred through all fault classes to their true classification. The ROC curves produced perfect AUC values of 1.0 which reflects excellent separability between each fault category. In addition, the model loss showed consistent decline, along with a rapid increase and stabilization of model accuracy at approximately 99%, confirming effective training of the algorithm and generalization ability.

Table 4: Classification report for Deep Neural Network.

SI.NO	Performance Metrics	Values
1	Accuracy	0.98
2	Precision	0.98
3	Recall	0.98
4	F1-Score	0.98

Source: Authors, (2026).

Table 4 illustrates a DNN to achieve an overall accuracy, precision, recall, and F1-score of roughly 98, indicating a strong performance for fault classification with very few misclassifications across the fault categories. However, the proposed system achieves the highest performance metrics.

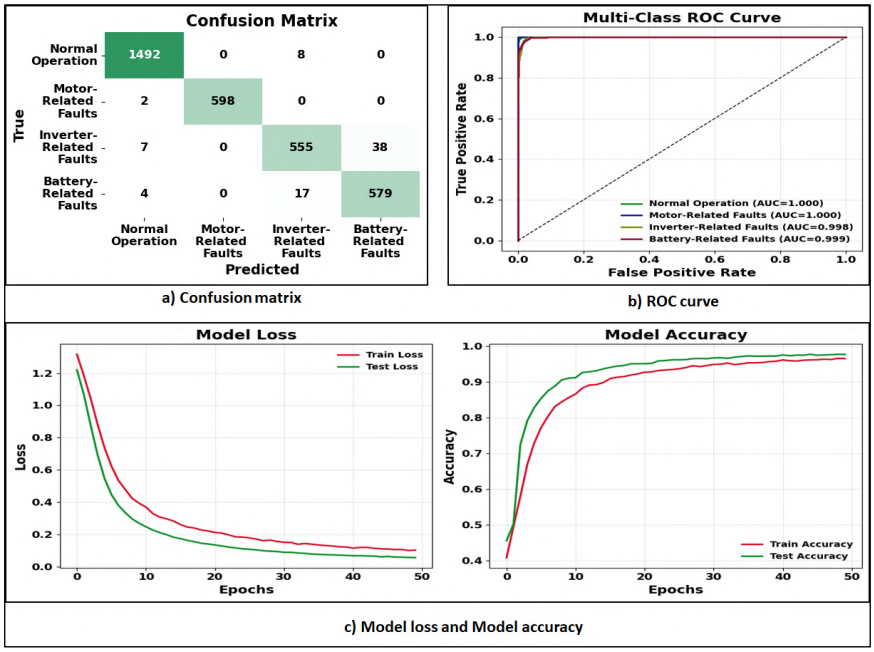


Figure 9: a) Confusion Matrix, b) ROC Curve, C) Model Loss and Model Accuracy for DNN.
Source: Authors, (2026).

In figure 9, the analysis of the confusion matrix revealed that the model potentially make several misclassifications across any of the fault types, indicating that the model has good prediction ability. The ROC curves show that the model has high AUC value 0.998-1.000 which indicates that the class separability between the faults is very high. Furthermore, as the loss decreases the model accuracy continues to increase and remains around 98 which confirms that the DNN is learning an appropriate manner to generalise the unseen data.

Table 5: Classification report for BILSTM.

SI.NO	Performance Metrics	Values
1	Accuracy	0.96
2	Precision	0.96
3	Recall	0.96
4	F1-Score	0.96

Source: Authors, (2026).

Table 5 depicts the BiLSTM model and produced 96% accuracy, 96% precision, 96% recall, and 96% F1 score which indicates that the BiLSTM performed lower level than the proposed models that achieved higher results.

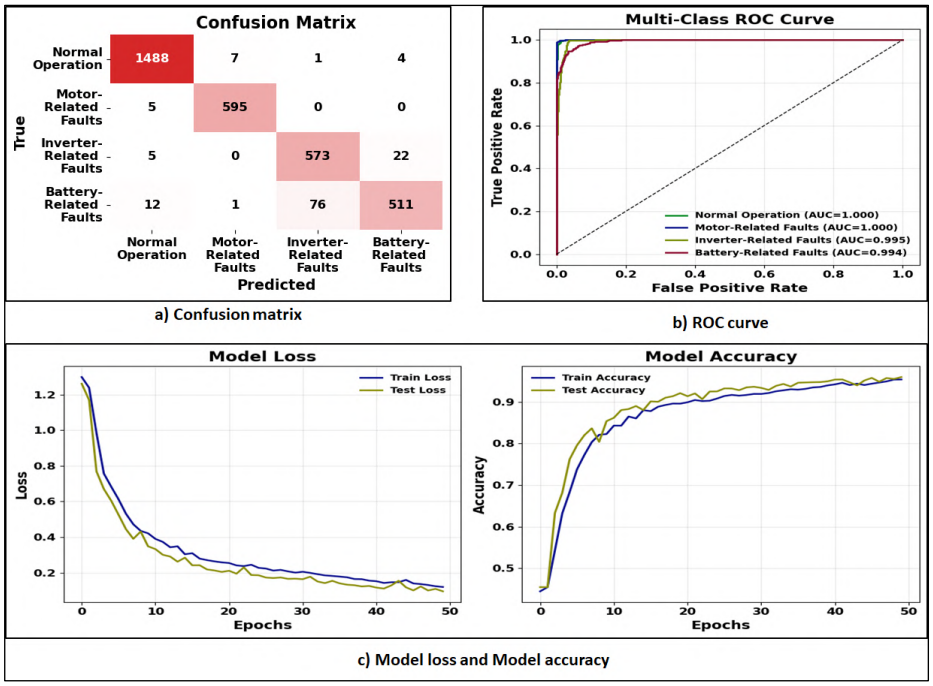


Figure 10: a) Confusion Matrix, b) ROC Curve, C) Model Loss and Model Accuracy for BILSTM.
Source: Authors, (2026).

Figure 10 shows the analysis of the confusion matrix revealed several misclassifications, predominantly within the faults associated with the battery and inverter components, however, the predictions made from the model were accurate. The ROC curves indicate high AUC values of 0.994-1.000 such that the method has a strong capability to discriminate amongst different modules. The model has produced a decrease in loss and achieved an increase in accuracy to approximately 96%, confirming that the BiLSTM is trained consistently and performs in generalisation to new data.

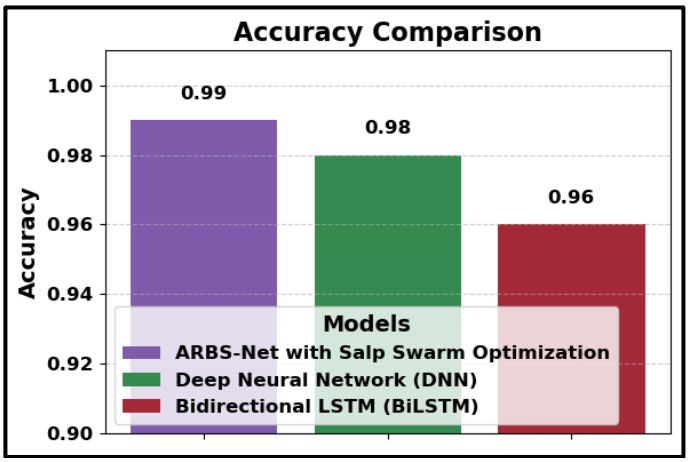


Figure 11: Comparison of accuracy.
Source: Authors, (2026).

From the accuracy comparison in figure 11, it determined that the ARBS-Net and Salp Swarm Optimisation model produced the highest accuracy (0.99), followed closely by DNN (0.98) and BiLSTM (0.96). This indicates that the proposed ARBS-Net approach has better performance than the other two systems evaluated.

Table 6: Comparison of evaluation metrics.

METRICS	PROPOSED MODEL	DNN	BILSTM
Accuracy	0.9864	0.977	0.9597
Precision	0.9815	0.9717	0.9513
Recall	0.9813	0.9703	0.9476
F1-Score	0.9812	0.9709	0.9484
Cohen Kappa	0.9804	0.9668	0.9419
MCC	0.9804	0.9669	0.9423
Hamming Loss	0.0136	0.023	0.0403
Jaccard Score	0.9638	0.9446	0.9047
Log Loss	0.0337	0.0565	0.0949
Balanced Accuracy	0.9813	0.9703	0.9476
F2-Score	0.9812	0.9705	0.9477
Zero-One Loss	0.0136	0.023	0.0403
Top-2 Accuracy	0.9997	0.9994	0.9997
Specificity	0.9958	0.9924	0.9867
G-Mean	0.9814	0.971	0.9495

Source: Authors, (2026).

In table 6, the evaluation reveals that the suggested model is higher than DNN and BiLSTM in most metrics used to evaluate models. It shows the suggested model has the best accuracy, precision, recall, F1-score, Kappa, MCC, Jaccard score, balanced accuracy, F2-score, specificity, and G-Mean of any of the models evaluated, and it produce the lowest Hamming loss, log loss, and zero-one loss. While other models produce very high Top-2 accuracies, the suggested model has the highest overall performance on all of the metrics.

Table 7: Comparative analysis of accuracy for various methods.

SI.NO	MODEL	ACCURACY
1	CATBOOST [23]	0.94
2	RF [25]	0.95
3	SVM [24]	0.95
4	ANN [21]	0.96
5	IB-DRN [22]	0.98
6	PROPOSED	0.99

Source: Authors, (2026).

Table 7 demonstrates that the suggested model has the highest accuracy (0.99) compared to CATBOOST (0.94), RF and SVM (0.95), ANN (0.96) and IB-DRN (0.98), thus confirming its superior performance to other models.

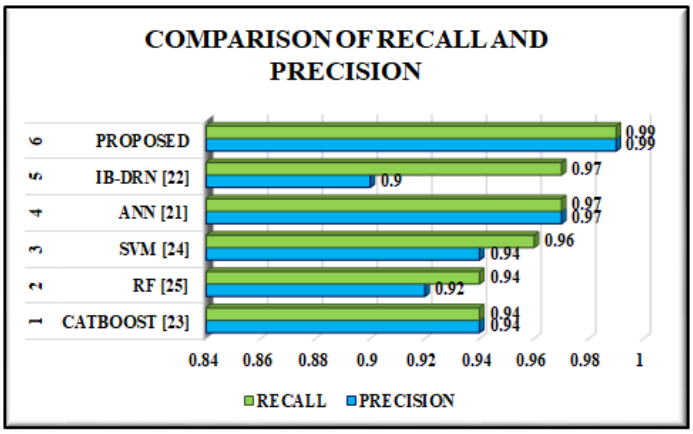


Figure 12: Comparison of recall and precision.
Source: Authors, (2026).

Figure 12 displays both recall and precision for the different models analysed. The suggested method has the maximum recall and precision (both 0.99) compared to other models including IB-DRN, ANN, SVM, RF and CATBOOST, indicating its superior and more balanced classification performance.

Table 8: Comparison of F1-Score for various methods.

SI.NO	MODEL	F1-SCORE
1	CATBOOST [23]	0.94
2	RF [25]	0.93
3	SVM [24]	0.95
4	ANN [21]	0.97
5	IB-DRN [22]	0.94
6	PROPOSED	0.99

Source: Authors, (2026).

In table 8, based on F1-scores, the proposed model is superior to the other proposed methods with respect to its F1 score of 0.99. Among the other methods tested, ANNs had an F1 score of 0.97 while SVM had an F1 score of 0.95, CATBOOST had an F1 score of 0.94, IB-DRN had an F1 score of 0.94, and RF had an F1 score of 0.93. All models performed well, demonstrating the ability to accurately classify observations, however, the proposed model outperformed every existing model by having greater accuracy and robustness relative to predictions.

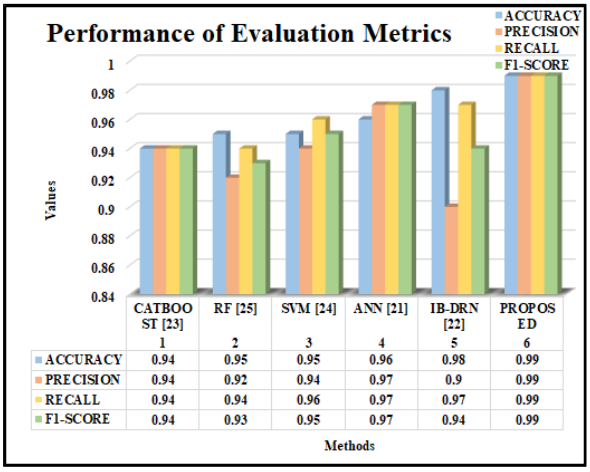


Figure 13: Comparison of performance metrics.
Source: Authors, (2026).

Figure 13 compares the accuracy, precision, recall, and F1-score of all six classifiers including CATBOOST, RF, SVM, ANN, IB-DN, and the proposed model. The proposed model outperforms all classifiers on all four measures of 0.99. IB-DN had an accuracy of 0.98 and a precision of 0.90. ANN performed consistently well throughout, while SVM and RF performed moderately. CATBOOST recorded the same performance level across all measures. Hence, the proposed model outperformed existing models for all evaluation criteria.

V. CONCLUSION

The proposed system provides a complete and intelligent framework to diagnose faults of EVs using an optimized and distributed Salp Swarm Optimized ARBS-Net. The establishment of the framework involves the acquisition of EV parameters such as voltage, current, motor speed, temperature, vibration, and humidity to create a dataset representing both electrical and mechanical characteristics of each fault. Pre-processing the dataset through normalisation improves the consistency and stability of the data for better performance when training the models. EDA provides insights into the distribution and relationship of each of the features, making it possible to locate hidden patterns in the data, which enables informed feature selection. Further, feature engineering allows for the creation of the most significant individual features connecting to fault characteristics by extraction and redundancy reduction to allow for a reduction in computational complexity when diagnosing faults. By utilizing SSO, the ARBS-Net model integrates attention mechanisms, radial basis functions, and spiking neural dynamics to create a learning model that optimizes parameters and it prevents the occurrence of local minima during training the model. Metrics used for evaluation purposes include high accuracy, precision, recall and F1-Score of 0.99. These results indicate that EV's fault conditions are correctly predicted, and thus the proposed system deliver a highly intelligent, scalable, robust and evolving diagnostic capability which allow for proactive maintenance and minimize unexpected failures and to increase the operating reliability and sustainability of EVs.

VI. AUTHOR'S CONTRIBUTION

Conceptualization: Ganapavarapu Harish, V. Suresh, D. Ravi Kishore, and B Kavya Santhoshi.
Methodology: Ganapavarapu Harish and V. Suresh.
Investigation: Ganapavarapu Harish and V. Suresh.
Discussion of results: Ganapavarapu Harish, V. Suresh, D. Ravi Kishore, and B Kavya Santhoshi.
Writing – Original Draft: Ganapavarapu Harish.
Writing – Review and Editing: Ganapavarapu Harish and V. Suresh.
Resources: V. Suresh.
Supervision: V. Suresh, D. Ravi Kishore and B Kavya Santhoshi.
Approval of the final text: Ganapavarapu Harish, V. Suresh, D. Ravi Kishore, and B Kavya Santhoshi.

VII. REFERENCES

[1] H. Zhang, S. Li, F. Chen, X. Pan, H. Feng, and Y. Sun, “Battery voltage fault diagnosis for electric vehicles considering driving condition variation”, IET Intelligent Transport Systems, vol. 18, no. 4, pp. 574-590, 2024.

[2] M.Z. Khaneghah, M. Alzayed, and H. Chaoui, “Fault detection and diagnosis of the electric motor drive and battery system of electric vehicles”, Machines, vol. 11, no. 7, pp. 713, 2023.

[3] M.A. Saleh, A. Ghrayeb, S.S. Refaat, H. Abu-Rub, S.P. Khatri, and J. Kammermann, “Attention-enhanced agru framework for induction motor incipient fault diagnosis in electric vehicles”, IEEE Transactions on Instrumentation and Measurement, 2024.

[4] Z. Zhang, S. Dong, D. Li, P. Liu, and Z. Wang, “Prediction and diagnosis of electric vehicle battery fault based on abnormal voltage: using decision tree algorithm theories and isolated forest”, Processes, vol. 12, no. 1, pp. 136, 2024.

[5] W. Fang, Y. Guo, and J. Zhang, “Generative Adversarial Network-Based Voltage Fault Diagnosis for Electric Vehicles under Unbalanced Data”, Electronics, vol. 13, no. 16, pp. 3131, 2024.

[6] Z. Wang, W. Luo, S. Xu, Y. Yan, L. Huang, J. Wang, W. Hao, and Z. Yang, “Electric vehicle lithium-ion battery fault diagnosis based on multi-method fusion of big data”, Sustainability, vol. 15, no. 2, pp. 1120, 2023.

[7] T. S. Babu, M. Paramasivan, V. Stephen and D. P. Mahmud, “Enhancing Electric Vehicle Charging Station Placement in Practical Power Distribution Networks”, 2025 8th International Conference on Circuit, Power & Computing Technologies (ICCPCT), Kollam, India, 2025, pp. 59-63.

[8] S. Saha, and U. Kar, “Signal-based position sensor fault diagnosis applied to pmsm drives for fault-tolerant operation in electric vehicles”, World Electric Vehicle Journal, vol. 14, no. 5, pp. 123, 2023.

[9] S. Gadu, G. Himaja, D.H.A. Reddy, M.D.P. Sai, and B.T. Prashant, “An era: Review on emerging technologies for AR/VR/MR”, In AIP Conference Proceedings, vol. 3306, no. 1, pp. 050002.

[10] S. Sepasiahooyi, and F. Abdollahi, “Fault detection of new and aged lithium-ion battery cells in electric vehicles”, Green Energy and Intelligent Transportation, vol. 3, no. 3, pp. 100165, 2024.

[11] T. Lan, Z.W. Gao, H. Yin, and Y. Liu, “A sensor-fault-estimation method for lithium-ion batteries in electric vehicles”, Sensors, vol. 23, no. 18, pp. 7737, 2023.

[12] T. Sun, P.K. Wong, and X. Wang, “Back propagation neural network-based fault diagnosis and fault tolerant control of distributed drive electric vehicles based on sliding mode control-based direct Yaw moment control”, Vehicles, vol. 6, no. 1, pp. 93-119, 2023.

[13] K. Karthika, and D.P. Rangasamy, “Authorization of Aadhar data using Diffie Helman key with enhanced security concerns”, Journal of Intelligent & Fuzzy Systems, 2024.

[14] W. Zheng, and T. Wang, “Electric vehicle motor fault diagnosis using improved wavelet packet decomposition and particle swarm optimization algorithm”, Archives of Electrical Engineering, pp. 481-498, 2024.

[15] M. Aishwarya, and R. M. Brisilla, “Design and fault diagnosis of induction motor using ML-based algorithms for EV application”, IEEE Access, vol. 11, pp. 34186-34197, 2023.

[16] Y. Chen, J. Zhang, S. Zhai, and Z. Hu, “Data-driven modeling and fault diagnosis for fuel cell vehicles using deep learning”, Energy and AI, vol. 16, pp. 100345, 2024.

[17] F. Liu, B. Liu, J. Zhang, P. Wan, and B. Li, “Fault mode detection of a hybrid electric vehicle by using support vector machine”, Energy Reports, vol. 9, pp. 137-148, 2023.

[18] J. Ouyang, Z. Lin, L. Hu, and X. Fang, “Voltage faults diagnosis for lithium-ion batteries in electric vehicles using optimized graphical neural network”, Scientific Reports, vol. 15, no. 1, pp. 27328, 2025.

[19] X. Shen, S. Lun, and M. Li, “Multi-Fault Diagnosis of Electric Vehicle Power Battery Based on Double Fault Window Location and Fast Classification”, Electronics, vol. 13, no. 3, pp. 612, 2024.

[20] M.U.I. Khan, M.I.H. Pathan, M.M. Rahman, M.M. Islam, M.A.R. Chowdhury, M.S. Anower, M.M. Rana, M.S. Alam, M. Hasan, M.S.I. Sobuj, and M.B. Islam, “Securing electric vehicle performance: Machine learning-driven fault detection and classification”, IEEE Access, vol. 12, pp. 71566-71584, 2024.

[21] D.P. Mishra, S.S. Padhy, P.S. Pradhan, S. Gupta, A. Senapati, and S.R. Salkuti, “Fault detection and diagnosis of electric vehicles using artificial intelligence”, Int J Appl Power Eng, vol. 13, no. 3, pp. 653-660, 2024.

[22] V.S.R. Kosuru, and A. Kavasseri Venkitaraman, “A smart battery management system for electric vehicles using deep learning-based sensor fault detection”, World Electric Vehicle Journal, vol. 14, no. 4, pp. 101, 2023.

[23] S. Thirunavukkarasu, K. Karthick, S.K. Aruna, R. Manikandan, and M. Safran, “Optimized fault classification in electric vehicle drive motors using advanced machine learning and data transformation techniques”, Processes, vol. 12, no. 12, pp. 2648, 2024.

[24] U. Shah, “Fault Detection and Diagnosis in Electric Vehicle Systems using IoT and Machine Learning: A Support Vector Machine Approach”, J. Electrical Systems, vol. 20, no. 3s, pp. 990-999, 2024.

[25] M. Attia, and Z. Aoulmi, “Improving Electric Vehicle Maintenance by Advanced Prediction of Failure Modes Using Machine Learning Classifications”, Maintenance & Reliability/Eksploatacja i Niezawodnosc, vol. 3, 2025.

Journal of Engineering and Technology for Industrial Applications

ITEGAM-JETIA

Manaus, v.12 n.60, p.181-194, July/August, 2026.
DOI: https://doi.org/10.5935/jetia.v12i60.3686

ISSN ONLINE: 2447-0228

RESEARCH ARTICLE OPEN ACCES

DETECTING IMAGE FORGERIES USING HYBRID RESIDUAL-DENSE SWIN TRANSFORMER FRAMEWORK WITH ATTENTION-BASED UNET++

Sruthi Anand*[1], Saranya V[2]

[1]Assistant Professor, Department of Information Technology, Vasavi College of Engineering, Hyderabad- 500031, Telangana, India.
[2]Associate Professor, Department of Information technology, Sri Eshwar College of Engineering, Vadasithur, Coimbatore- 641202, India.

[1]https://orcid.org/0000-0001-5344-4826, [2]https://orcid.org/0000-0002-1883-4383

Email: *sruthianand@staff.vce.ac.in, saranya.v@sece.ac.in

ARTICLE INFO

Article History
Received: February 14, 2026
Reviewed: June 6, 2026
Accepted: July 6, 2026
Published: July 31, 2026

Keywords:
Image forgery,
Image preprocessing,
Residual-Dense Swin transformer,
UNet++,
Channel-Dual attention.

ABSTRACT

Establishing the authenticity of digital images is widely acknowledged as a crucial aspect of multimedia security since contemporary alteration techniques like copy-move, splicing, and retouching create remarkably convincing forgeries that are difficult to spot. This research proposes a Deep Learning (DL) based image forgery detection methodology that combines attention-guided segmentation and hybrid feature extraction to deliver robust tamper detection and classification. The preprocessing procedures including resizing and normalizing images are used to ensure consistent model performance. The hybrid encoder, records local texture-level inconsistencies and long-range contextual dependencies, composed of Swin Transformer modules and Residual-Dense blocks. Multi-scale feature maps that are highly discriminative for forgery cues are the outcome of this. These features are decoded using a UNet++ segmentation network that has been altered using Channel-Dual Attention (CA-DA). This improves the spatial focus and boundary precision of the projected forgery mask. The created mask is analyzed in a detection stage, where threshold-based decision-making mechanism determines if the input is genuine or forged, non-empty masks that exceed the threshold indicate tampered images, whereas actual images are represented by empty masks. The proposed system is implemented in Python software, and the results demonstrate that the proposed experimental validation on benchmark datasets indicates improved detection accuracy, robustness to noise compression, and localization clarity when compared to conventional approaches.

Copyright ©2026 by authors and Galileo Institute of Technology and Education of the Amazon (ITEGAM). This work is licensed under the Creative Commons Attribution International License (CC BY 4.0).

I. INTRODUCTION

Images and videos are attracting a lot of attention recently since they serve as the primary information source. In numerous contexts, images are utilized to convey information to various recipients. They are used in many different areas, including intelligence gathering, military operations, court testimony, social media disinformation, defamation of well-known individuals, and many more [1]. In addition to the unreliable methods of image dissemination, image manipulation compromise the legitimacy of an image. Authentication solutions were created in order to secure the image communication process [2]. There are numerous ways used for forging an image, however image manipulation techniques are usually categorized into two groups, content-changing and content-preserving. Semantic content is changed as a result of content-changing, which reshapes image content at random. The three most popular forms of image forgery detection that have been thoroughly researched are copy-move, splicing, and removal [3]. The most common type is copy-move forgery, in which a portion of the image is copied and pasted somewhere else in the same image. Contrarily, content-preserving forgeries change features like contrast, brightness, compression artifacts or noise patterns to deceive analysts rather than changing the image's semantic content. It is difficult to identify these subtle changes with conventional techniques [4]. Techniques for detecting image forgeries are broadly categorized into five groups. Geometry based techniques measure objects in the world and their positions in relation to the camera. Pixel based techniques detect statistical anomalies introduced at the pixel level. Format based techniques utilize the benefit of statistical correlations introduced by a specific lossy compression scheme [5].

Camera based techniques exploit artifacts introduced by the camera lens, sensor or on-chip post-processing and physical environment based techniques explicitly model and detect anomalies in the three dimensional interactions between physical objects, light and camera. One of the most prevalent types of tampering is copy or move forgery, which involves copying a portion of an image from one area and then passing it at more points in the same image or another image, ideally of the same scene [6]. This research illustrates the image forgery detection through various stages. The procedure commences with input image where raw data is provided to the system for forgery detection. This is followed by preprocessing where resize and normalization takes place to ensure consistent input for the model, which helps in training and inference stability [7]. In feature extraction, it extracts high level features from the input image using a hybrid model. The extracted features are then segmented to produce a pixel-wise segmentation mask indicating forged images. A predicted pixel mask highlighting suspected forged regions in the image. Then the mask is subjected to a threshold by the detection module and if exceeded, it marks the image as forged [8]. Convolutional Neural Networks (CNNs) have become increasingly popular in image detecting community throughout the past ten years. In order to identify the optimal features for categorizing image models, these algorithms have concentrated on training the CNN. CNN has the benefit of immediately extracting features from the image collection. The main benefit of CNN is that immediately extract classification features from image data. However, it is quite challenging to comprehend the generated image identification model and it reliance on a particular training dataset [9].

VGG operates by recursively partitioning the feature space into branches based on feature values, resulting in a tree structure with each leaf node representing a class label, authentic or fabricated. This makes VGG simple, interpretable, and easy to apply. However, it has a tendency to over fit training data, which is sensitive to noise in features, and has worse accuracy for complicated or nuanced forgeries [10]. To further enhance the performance of the detection model, segmentation methods are utilized. SegNet identify image forgeries by automatically learning hierarchical features from raw images. Convolutional layers extract local patterns, edges, and textures first, followed by non-linear activation functions such as ReLU. Pooling layers lower spatial dimensions while keeping crucial properties, and fully connected layers combine these qualities to determine whether an image is legitimate or faked. Back propagation is used to train the network and minimize a loss function while also optimizing feature representations [11]. However, their effectiveness in automatic feature learning it requires a considerable amount of labeled data, which are computationally costly and fail to catch long-range or global discrepancies, and might overlook very subtle or sophisticated forgeries [12]. To overcome these limitations, this research proposes a hybrid Residual-Dense Swin transformer for feature extraction encoder and UNet++ with CA-DA for segmentation encoder. This provides a predicted forgery mask that highlights potential altered places. The detecting stage assesses this mask to establish the image's validity. If the anticipated mask exceeds a predefined threshold, the image is classified as fabricated otherwise, an empty mask is classified as authentic.

I.1 RELATED WORKS

By [13**]** have proposed a feature extraction based LeNet-5 for detecting fake media content. LeNet-5 method processes and analyzes textual information by transforming text data into numerical representations like TF-IDF, Bag-of-Words or word embedding. This procedure enables LeNet-5 to detect bogus news on social media. In order to distinguish between fake and real postings using the attributes that were retrieved, it then learns a hyperplane in a high-dimensional space. However, it struggles with noisy and high-dimensional social media data, including slang, abbreviations, and grammatical errors which reduce the overall classification accuracy. By [14] have developed a fast and robust speckle pattern authentication with the Scale Invariant Feature Transform (SIFT) Algorithm in Physically Unclonable Functions (PUF). The use of SIFT with the Challenge Response Pairs (CRPs) protocol allows us to correctly authenticate a client while blocking any other fraudulent access. In this approach, the authentication procedure is highly trustworthy even in the face of answer rotation, zooming, and cropping, which might occur in consecutive PUF interrogations and to which other post processing algorithms are quite susceptible. Nonetheless, the analysis methodologies used are highly sensitive to minor alterations in the speckle pattern, which lead to failure in PUF authentication due to changes in position, illumination, or rotation. By [15] have presented an image forgery detection based on Histogram of Oriented Gradients (HOG) feature extraction. It is generated by combining edge orientations caused by image alteration into a one-dimensional histogram of specified image regions. The suggested method collects HOG characteristics from the YCbCr colour space and applies them to the discrete wavelet transform's high-frequency subbands.

These collected features are then fed into a classifier, which determines whether the image is legitimate. Nevertheless, HOG features primarily collect edge and gradient information, which is insufficient to detect forgeries that do not drastically change these characteristics. By [16] have established a forged image detection based on clustering algorithms and transform domain feature analysis. The proposed method is highly effective in terms of detection accuracy, offering a viable solution to the issues of modern multimedia manipulation. Texture features are retrieved using the Discrete Wavelet Transform (DWT) technique, which improves the resilience and reliability of the forgery detection process. Though, it requires large amounts of labeled video data and significant computational resources, making training and real-time deployment challenging. In turn [17] have proposed a semantic segmentation-based approach for identifying and locating manipulated regions in images. In this research, the semantic segmentation is used to improve object awareness and increase object localization accuracy. Instead of considering semantic segmentation as a separate submodule, we incorporate it as a third branch of an end-to-end framework. This method balances visual, compression, and segmentation artifacts while minimizing overemphasis on any single branch. However, it struggle with noisy, unclear or extremely context-dependent content particularly in low-resource languages or images with subtle alterations, thereby lowering overall detection accuracy.

I.2 CONTRIBUTIONS

The main contributions of this hybrid residual-dense swin transformer framework with attention-based unet++ research includes,

- To effectively capture both local and global image features for forgery detection a hybrid residual-dense swin transformer framework with attention-based Unet++ is integrated.

- To develop a global context with local texture details for effective feature extraction, a hybrid residual-dense Swin transformer encoder is utilized.
- To enable precise localization of manipulated regions, spatial channel attention with nested skip connections, an Attention-based U-Net++ decoder is implemented.

I.3 PAPER ORGANIZATION

This paper is organized as follows: Section II provides an explanation of the proposed system description. The study methodology is thoroughly described in Section III, which also includes examples of the process, methods, and mathematical representations. The experimental results of this work are described in Section IV, which also include the simulation setup, comparison analysis, and research summary. The conclusion of the proposed investigation is explained in Section V.

II. PROPOSED SYSTEM DESCRIPTION

This paper aims to enhance the accuracy, robustness and localization clarity in detecting image forgeries by integrating image preprocessing and hybrid residual-dense swin transformer framework with attention-based Unet++ for feature extraction and segmentation. The proposed block diagram is displayed in Figure 1.

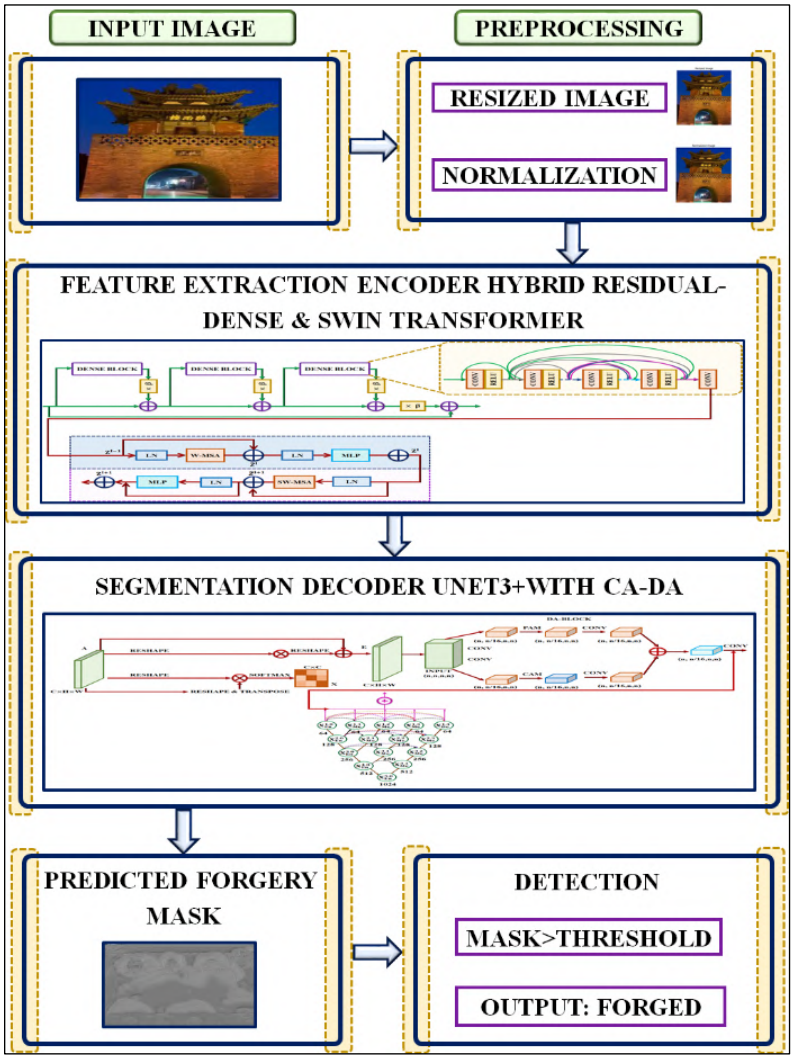


Figure 1: Proposed block diagram.
Source: Authors, (2026).

The proposed approach integrates transformer based and convolutional techniques to present a strong DL framework for image forgery detection. To ensure consistency, the image that arrives is initially processed by resized and normalizing. Following processing, the image is fed into a hybrid feature extraction encoder that successfully captures both local and global contextual data by combining residual-dense blocks with a Swin transformer. A UNet++ architecture supplemented with CA-DA is then used to decode these complex feature representations, allowing for the exact localization of modified regions. A predicted forgery mask is produced by the decoder and examined during the detection stage. The image is considered fake if the mask's confidence level exceeds a predetermined threshold. High accuracy and locating image forgeries is ensured by this end-to-end process.

III. PROPOSED SYSTEM MODELLING

III.1 IMAGE PREPROCESSING

In image preprocessing, resizing and normalizing is a crucial step in image analysis pipeline. To ensure consistency and compatibility with the DL model, an image must be standardized before being examined for potential alteration.

III.1.1 Resizing

The input image is resized to a fixed resolution, ensuring that all images have uniform dimensions regardless of their original size. This step makes the computational process efficient and allows the neural network to handle images in batches. In addition, resizing helps maintain consistency across the dataset, preventing variations in image size from affecting model learning. It also reduces memory requirements and speeds up both training and inference. By standardizing resolution, the network focus on learning important patterns instead of adjusting to irregular input sizes.

III.1.2 Normalizing

Pixel values are normalized and typically scaled to a certain range. Normalization stabilizes the training process, accelerates convergence, and assures that changes in image brightness or contrast do not influence forged detection. It also prevents numerical instability by maintaining input values within a reasonable range, hence avoiding bursting or vanishing gradients during back propagation. Normalization ensures that all features contribute proportionally, which enhances the model's capacity to detect small irregularities. It improves generalization by making the model less susceptible to differences in lighting, exposure, or camera settings. In some circumstances, mean subtraction and standard deviation scaling are employed to align pixel distributions with retrained models, which improves feature extraction performance. The diagram for image preprocessing is shown in Figure 2.

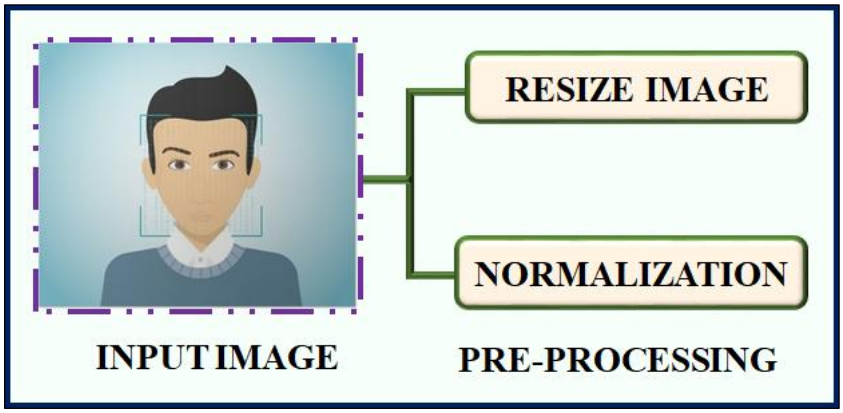


Figure 2: Image preprocessing.
Source: Authors, (2026).

By combining both, Resizing and normalization prepare the raw image for subsequent processing phases, such as feature extraction and segmentation, allowing the detection model to concentrate on forgery-specific patterns rather than changes caused by size or illumination discrepancies. Resizing maintains constant input dimensions, allowing for batch processing and reducing computing effort, whereas normalization scales pixel intensity values to a uniform range, enhancing model convergence and stability during training. Furthermore, these processes serve to reduce the impact of noise, contrast discrepancies, and illumination variations making the model more adaptable to a variety of image situations.

III.2 FEATURE EXTRACTION- RESIDUAL-DENSE SWIN TRANSFORMER

Residual Dense Network (RDN) is an architecture that identifies image forgery due to its outstanding feature extraction capabilities. In order to detect fabricated regions in images, fine-grained details, subtle discrepancies, and manipulation effects need to be precisely captured. The RDN combines residual and dense connectivity, allowing for effective extraction of both local and global characteristics. The dense block structure allows the network to transfer information within each block, efficiently merging low-level and high-level elements including texture irregularities, edges, and noise patterns, which frequently signal tampering. By combining the input and output of each dense block, the network maintains a strong information flow, which is crucial for detecting small changes that would otherwise go undetected. Mathematically, the residual network adds the input x_{i-1} to its mapped output$F(x_{i-1})$, enhancing gradient flow and preventing overfitting as network depth increases,

$$F_{Res}(x_{i-1}) = F(x_{i-1}) + x_{i-1} \tag{1}$$

However, fundamental characteristics within a block are unable to fused by residual connections alone. By combining information from all preceding layers, the dense block overcomes this restriction and allows the network to detect minute local imperfections including texture anomalies, noise disturbances, and duplicated regions. Dense blocks increase the network's sensitivity to fine-grained modifications that conventional convolutional layers could miss by combining data from several layers.

Dense blocks offer an additional technique that combines local detail capture with global information flow when paired with residual connections. This improves the overall performance of image fraud detection across a variety of manipulation types, including splicing, copy-move, and inpainting.

$$F_{DB}^{i} = ReLU\left(F_{DB}^{i-1} + \sum_{j=0}^{i-1} F_j(x_j)\right) \quad (2)$$

The detection of forgeries is further enhanced by the introduction of residual dense blocks (RDBs), which create global residual connections between blocks because dense blocks only concentrate on internal feature fusion. By combining the benefits of dense and residual connections, RDBs make sure that data moves throughout the network as well as within individual blocks. RDBs improve the network's capacity to identify minute manipulations like splicing edges, copy-move duplications, or anomalies in inpainting by preserving inter-block dependencies. All things considered, RDBs offer a strong foundation for merging local and global data, which makes the network extremely efficient at precisely locating and detecting tampered areas in a variety of forging scenarios.

$$F_{RDB} = \beta \cdot F_{DB}(x_i) + x_{i-1}, \beta = 0.2 \quad (3)$$

In addition to improving the network's capacity to extract local and global features, RDN's residual and dense connections provide effective gradient flow, which permits the training of deeper architectures without overfitting. Dense blocks capture tiny tampering artifacts like duplicated regions, noise discrepancies, or splicing edges by allowing the fusion of all previous layer characteristics within a block. The network preserves inter-block connections by incorporating these dense blocks into Residual Dense Blocks (RDBs), which highlights fine-grained local characteristics while keeping global contextual information. RDN is extremely resistant to a variety of forgery techniques, including as splicing, copy-move, and inpainting manipulations, thanks to its hierarchical feature extraction. The Swin Transformer is a hierarchical vision model that is well suited for detecting image forgeries because it capture both local defects and global contextual anomalies. The Swin Transformer uses hierarchical feature maps and a shifting window attention mechanism to analyze data at many scales, which is necessary for detecting manipulations like splicing, copy-move, or inpainting. Subsequently, Swin Transformer Blocks (STBs) are used to convert the image into non-overlapping patches. Layer Normalization (LN), a two-layer Multilayer Perceptron (MLP) with Gaussian Error Linear Unit (GELU) activation, and Window-Based Multi-Head Self-Attention (W-MSA) and Shifting Window MSA (SW-MSA) modules make up each block. The computational complexity of the conventional multi-head self-attention is as follows,

$$\Omega(MSA) = 4hwC^2 + 2(hw)^2C \quad (4)$$

To address this, the Swin Transformer uses window-based multi-head self-attention (W-MSA), which restricts attention computation to local windows of size$M \times M$. This reduces the complexity to,

$$\Omega(W-MSA) = 4hwC^2 + 2M^2hwC \quad (5)$$

This reduction in complexity allows the network to efficiently focus on local regions of the image, which is particularly important for detecting small-scale forgeries such as copy-move or subtle splicing artifacts. By limiting attention computation to each window, the model analyse fine-grained textures, edges, and noise inconsistencies without being overwhelmed by the total number of patches in high-resolution images. This local attention mechanism forms the foundation for identifying micro-level tampering cues, which are often missed by traditional convolutional or global attention methods. The structure of residual-dense swin transformer is shown in Figure 3.

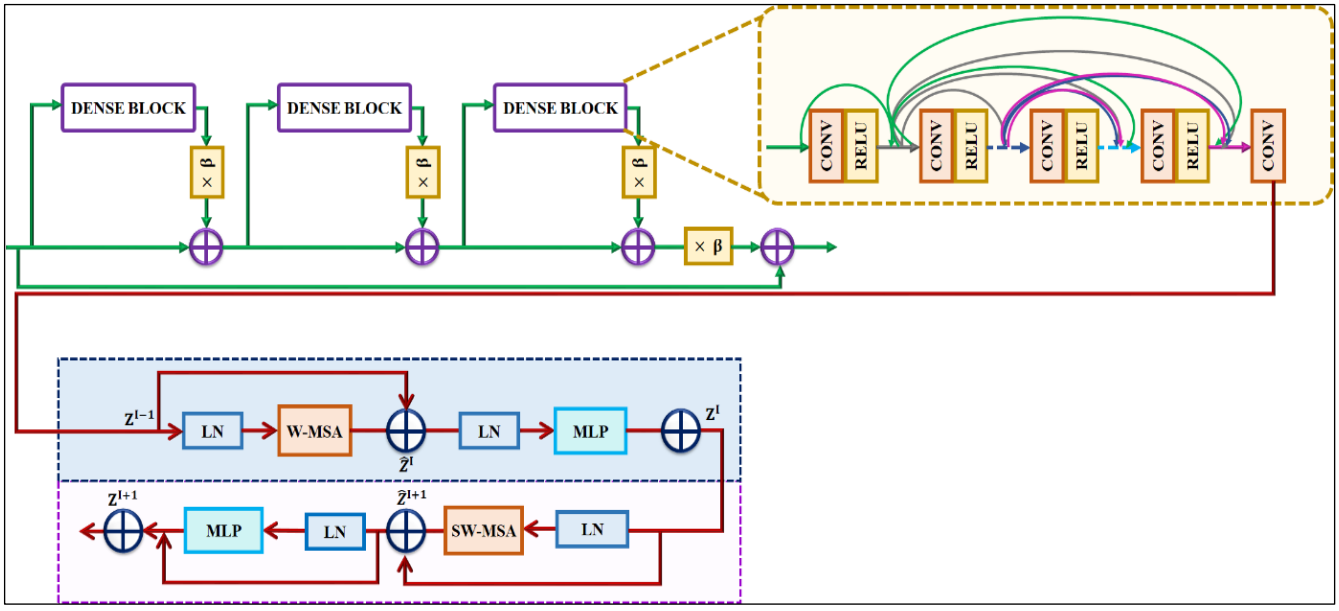


Figure 3: Structure of residual-dense swin transformer.
Source: Authors, (2026).

By focusing on local regions, W-MSA efficiently captures fine-grained artifacts, such as subtle texture inconsistencies or duplicated areas, which are common in tampered images. Within each Swin Transformer Block (STB), features are processed sequentially. Initially, the W-MSA module computes local dependencies for each patch, incorporating residual connections to stabilize training and preserve low-level details,

$$\hat{Z}_l = W - MSA\big(LN(Z_{l-1})\big) + Z_{l-1} \tag{6}$$

Here, Z_{l-1} is the input feature from the previous layer, LN is Layer Normalization, and the addition of Z_{l-1} ensures that the original patch information is retained. After this, the features are passed through a two-layer MLP with GELU activation to enhance non-linear representations,

$$Z_l = MLP\left(LN\big(\hat{Z}_l\big)\right) + \hat{Z}_l \tag{7}$$

Whereas W-MSA focuses on local interactions, it cannot capture relationships across neighboring windows, which is important for detecting manipulations spanning multiple regions, such as a spliced object. The shifted window MSA (SW-MSA) addresses this by cyclically shifting the windows and computing attention over overlapping patches,

$$\hat{Z}_{l+1} = SW - MSA\big(LN(Z_l)\big) + Z_l \tag{8}$$

$$Z_{l+1} = MLP\left(LN\big(\hat{Z}_{l+1}\big)\right) + \hat{Z}_{l+1} \tag{9}$$

Cross-window connections are essential for modeling long-range dependencies and this shifted window method makes computation efficient. The model successfully collects both local and global contextual information by switching between normal window based self- attention and shifting window based self-attention across consecutive levels. Finally, the attention mechanism is shown below,

$$Attention(Q, K, V) = Softmax\left(\frac{QK^T}{\sqrt{d}} + B\right)V \tag{10}$$

Here, $Q, K,$ and V are the query, key, and value matrices for a given window, d is the dimension of feature vectors, and B encodes relative positions between patches. By using this mechanism, the Swin Transformer accurately identify irregularities in spatial structure, texture, and edges that indicate image forgery. Overall, this combination of residual-dense swin transformer is used to detect forgeries at multiple scales, generating pixel-level manipulation maps and ensuring both local artifact sensitivity and global structural consistency, which are essential for robust forensic analysis.

III.3 SEGMENTATION- UNet++ WITH CHANNEL-DUAL ATTENTION

To detect image forgery, it is necessary to determine the exact location of the tampered areas in addition to determining if the image was actually altered. Although a conventional UNet is capable of recording some semantic and spatial data, it eliminate important details like boundaries and forged textures since its straight skip connections only convey information at the same size. To get around this, UNet++ employs layered skip connections, which combine features from several layers while maintaining high-level semantic information and low-level geometric details. This fusion process is formalized by equations,

III.3.1 First Merge – Preserving Boundary Details

The first merging operation combines the shallowest encoder feature map $X1{:}\,0_{En}$ (low-level details) with the next encoder output $X2{:}\,0_{En}$

$$X1{:}\,1_{Me} = X1{:}\,0_{En} + X_2{:}\,0_{En} \tag{11}$$

By employing layered skip connections to combine encoder features at several layers, UNet++ improves image detection. Low level features $X1{:}\,0_{En}$ and $X_2{:}\,0_{En}$ are first combined to create $X1{:}\,1_{Me}$. This method enhances semantic comprehension and spatial detail, which increase object localization and border accuracy.

III.3.2 Second Merge – Adding Contextual Support

This equation expands the merge by reusing $X1{:}\,1_{Me}$, combining it with the shallow encoder feature $X1{:}\,0_{En}$ again and an intermediate feature from the second column $X2{:}\,1_{Me}$

$$X1{:}\,2_{Me} = X1{:}\,1_{Me} + X1{:}\,0_{En} + X2{:}\,1_{Me} \tag{12}$$

The frequent application of the shallow feature map $X1{:}\,0_{En}$ in this phase of the UNet++ model for image fraud detection helps to maintain fine-grained image characteristics including surface textures and small-scale imperfections by reinforcing local texture patterns. The intermediate feature map $X2{:}\,1_{Me}$, introduces spatial consistency, enabling the model to compare data from various image scales. By highlighting differences that might not be apparent at a single resolution, this cross-scale fusion aids in differentiating real textures from ones that have been altered. Because of this, the merged feature map $X1{:}\,2_{Me}$ improves its ability to detect minute differences between forged and real areas, like crooked or misaligned edges that are frequently observed in spliced forgeries.

III.3.3 Third Merge – Balancing Detail and Semantics

By integrating many previous nodes to create $1{:}\,3_{Me}$, the third merging stage becomes more thorough. In addition to deeper contextual features $2{:}\,2_{Me}$, this fusion incorporates data from both shallow and intermediate layers. This strikes a compromise between semantic-level abstraction and the preservation of fine-grained details.

$$X1{:}\,3_{Me} = X1{:}\,2_{Me} + X1{:}\,1_{Me} + X1{:}\,0_{En} + X2{:}\,2_{Me} \tag{13}$$

In the third merging stage of the UNet++ model, the fusion process integrates progressively higher-level semantic features from $X2{:}\,2_{Me}$ while still preserving low-level detail through $1{:}\,0_{En}$.

III.3.4 Final Merge – Forgery Segmentation Map

The output $X1{:}\,4_{De}$ is produced by the final decoder node aggregating all of the prior intermediate merges and deep decoder data.

$$X1{:}\,4_{De} = X1{:}\,3_{Me} + X1{:}\,2_{Me} + X1{:}\,1_{Me} + X1{:}\,0_{En} + X2{:}\,3_{De} \tag{14}$$

According to the equation, a decode image from system $X1$ and an enable image from system $X1$ add up to the decode image. On the contrary, include semantic information that enables the model to determine whether a suspicious area fits into the image's overall context, ensuring that additional significant irregularities or irrational alterations are detected. High-level semantics and granular detail are combined in the final result, which shows a hierarchical integration of these multi-scale elements. The network consistently discover forged areas even when tampering is subtle, well-blended, or purposefully done to avoid detection thanks to this fusion, which strengthens and improves the detection process. The Channel Attention Module (CAM) improves the network's capacity to focus on the most informative channels in feature maps, enabling it to discern between authentic and tampered regions. CAM reshapes a convolutional feature map $A \in R^{C*H*W}$ into $\in R^{C*N}$, where$N = H \times W$, allowing for channel connections to be determined. The module then computes a channel attention map $X \in R^{C*C}$ using the following softmax-based operation,

$$X_{ji} = \frac{exp(A_i . A_j)}{\sum_{i=1}^{C} exp(A_i . A_j)} \tag{15}$$

In this case, $A_i \; and \; A_j$ are the flattened feature vectors for the i and j channels, as well as X_{ji} are shown. This metric assesses the impact of the i channel on the j channel. This step collects inter-channel relationships, allowing the network to determine which channels are most useful in detecting forgeries. Channels with high influence weights, for example, will be more sensitive to edge irregularities or odd texture patterns. The enhanced feature map $E \in R^{C*H*W}$ is then computed as follows,

$$E_j = \beta \sum_{i=1}^{C} X_{ji} A_i + A_j \tag{16}$$

Where β is a learnable scaling parameter. This process effectively generates a weighted total of all channels, along with the original feature, emphasizing informative channels and suppressing less relevant channels. By incorporating CAM into the UNet++ framework, the network gains both multi-scale feature fusion and channel-focused attention. Shallow features in UNet++ capture tiny details such as edges and textures, whereas deep features offer semantic context. The Dual Attention (DA) Block combines the strengths of the Position Attention Module (PAM) and the CAM to improve feature extraction for image fraud detection. PAM detects spatial correlations in feature maps, thereby learning the location where tampering happens by focusing on the positional links between pixels. CAM, on the other hand, captures inter-channel dependencies without highlighting what features are relevant for detecting manipulations, such as texture inconsistencies, odd edges, or cloned sections. By merging these two modules, the DA-Block extract spatial and channel-specific clues, which is critical for identifying subtle or complicated forgeries. The DA-Block has two parallel components. The first component uses convolution to scale the number of channels by a sixteenth, resulting in α_1.

$$\alpha_1 = Conv(input) \tag{17}$$

This stage reduces the complexity of the feature map in preparation for PAM processing. The position attention module processes α_1 to capture spatial correlations, followed by another convolution to obtain the refined feature map$\tilde{\alpha}_1$,

$$\tilde{\alpha}_1 = Conv\big(PAM(\alpha_1)\big) \tag{18}$$

The second component of the Dual Attention (DA) Block for image forgery detection uses the CAM to stress channel-wise dependencies and highlight what aspects are most relevant for identifying alterations. The input features are initially run through a convolution to reduce dimensionality and create the feature map for the attention mechanism. CAM then computes inter-channel correlations and refines the features, followed by another convolution to generate the enhanced feature map

$$\alpha_2 = Conv(input) \tag{19}$$

$$\tilde{\alpha}_2 = Conv\big(CAM(\alpha_2)\big) \tag{20}$$

This procedure prioritizes channels that include crucial tampering cues, such as cloned textures, odd edges or inconsistent colours, while suppressing less informative channels. The first component of the DA-Block, led by the PAM, generates$\tilde{\alpha}_1$. Schematic diagram of UNet++ with Channel-Dual Attention is shown in Figure 4.

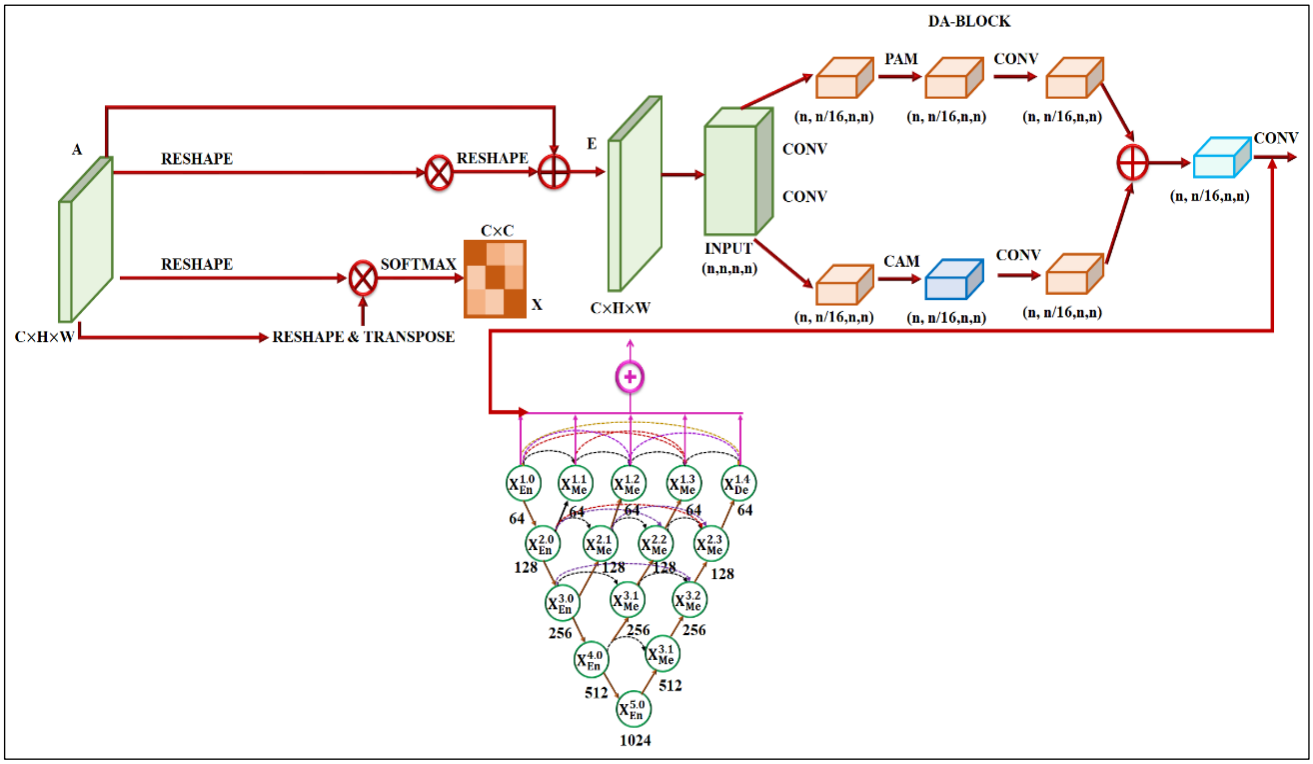


Figure 4: schematic diagram of UNet++ with Channel-Dual Attention.
Source: Authors, (2026).

By focusing on spatial dependencies or wherever modifications take place. The outputs from both routes are then aggregated and summed, and a final convolution restores the original number of channels, providing the final DA-Block output.

$$output = Conv(\tilde{\alpha}_1 + \tilde{\alpha}_2) \tag{21}$$

Combining $\tilde{\alpha}_1$ and $\tilde{\alpha}_2$, the DA-Block blends spatial and channel-wise attention, allowing the network to detect subtle, well-blended, or sophisticated forgeries more efficiently by combining fine-grained details with global contextual information. In image forgery detection, this DA-Block allows the network to focus on both spatial inconsistencies and channel-specific information. The combination of PAM and CAM ensures that the model captures both fine-grained information and global context, allowing it to detect subtle, well-blended, or large-scale alterations. By modifying intermediate channel dimensions and convolutional procedures, the DA-Block modified to prioritize the most relevant forgery features, boosting detection accuracy and robustness across a wide range of image formats. Thus the integration of UNet++ with CA-DA focuses on accurately identifying tampered regions. CA-DA improves spatial and contextual awareness, whereas dense skip connections are used for detailed feature extraction. This makes the model useful for digital image detection by assisting it in identifying subtle modifications.

IV. RESULT AND DISCUSSION

This research provides a notable explanation of the manner in which a hybrid residual-dense Swin transformer framework coupled with an attention-based UNet++ is implemented to detect image forgeries efficiently.

Table 1: Train vs Test Distribution Table.

Class	Train samples	Test samples
Forged	5200	1300
Original	5200	1300

Source: Authors, (2026).

Train vs Test distribution of forged and original class is shown in Table 1. The train samples for both forged and original class is 5200. Similarly, for both forged and original class the test samples are 1300. The balanced split reduces bias towards any class. Overall, this distribution facilitates the development of a dependable and effective classification model.

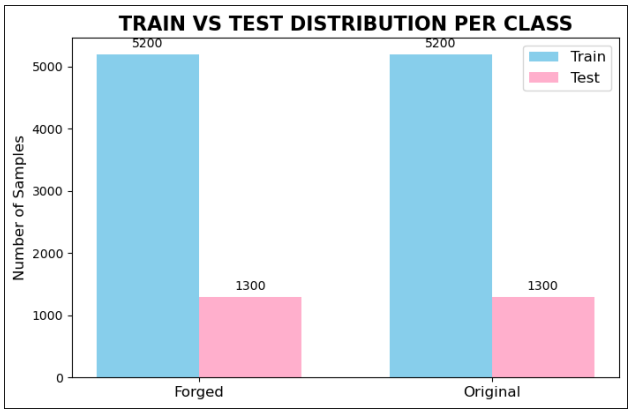


Figure 5: Train vs Test distribution per class.
Source: Authors, (2026).

The distribution of train and test samples for the two classes Forged and Original is displayed in Figure 5. There are 1,300 test samples and 5,200 training examples for every class. The distribution of the Forged class is comparable, with 1,300 samples used for testing and 5,200 samples used for training. With 5,200 training samples and 1,300 test samples, the Original class exhibits the same distribution pattern. This guarantees that the quantity of training and test samples for each class is equal. Comparing the quantity of samples for every class in the training and testing sets is made simple by the graph's visual representation of this division.

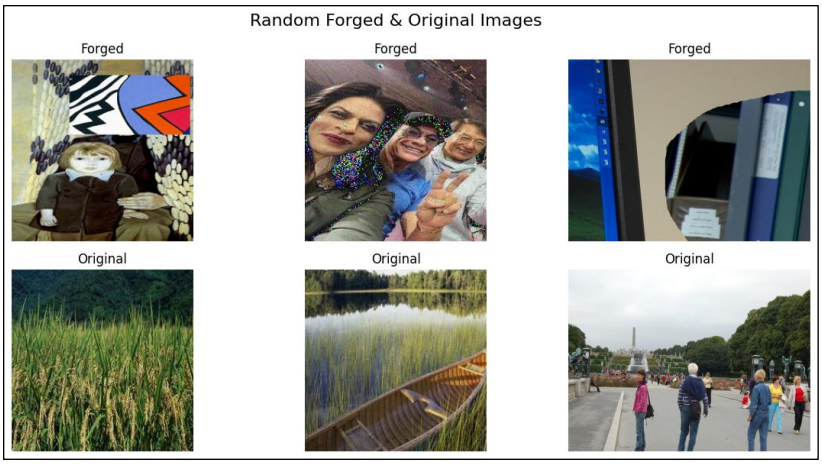


Figure 6: Random forged and original images.
Source: Authors, (2026).

A comparison of the original and forged images is shown in the Figure 6. The top row features three fabricated images, while the bottom row shows their real copies. Forgeries include distorted group selfies, cut-out regions that highlight irregularities, and a child's shot with an unnatural background. The originals feature natural sceneries such as a field, a boat on calm sea, and people walking in public. This side-by-side arrangement emphasizes visual cues and abnormalities. It helps to highlight the differences between authentic and digitally changed images. This comparison helps to identify digital forgeries more efficiently.

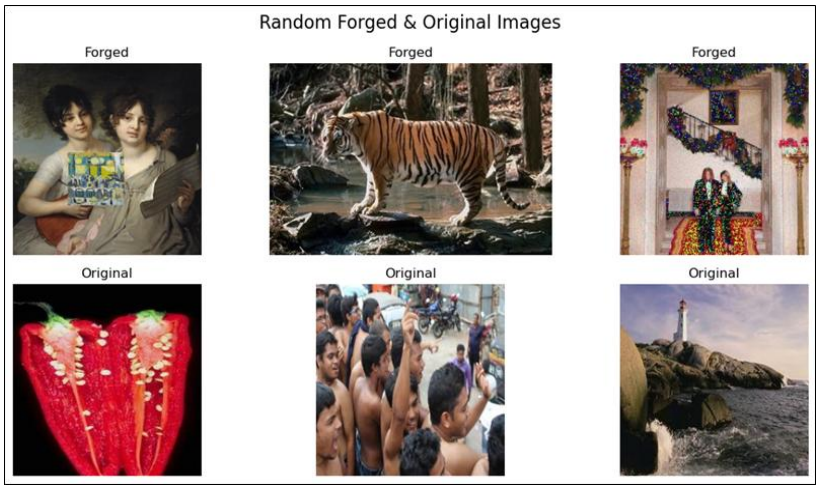


Figure 7: Random forged and original images.
Source: Authors, (2026).

A combination of forged and genuine images are displayed in Figure 7. Three Forged images a painting, a tiger in a forest, and a vibrant group portrait are displayed in the top row. A close-up of a pepper, a crowd of people outside, and a lighthouse near the sea are the three Original images that are shown in the bottom row. The arrangement provides insight into the kind of content contained in a classification job by emphasizing the difference between authentic and altered images.

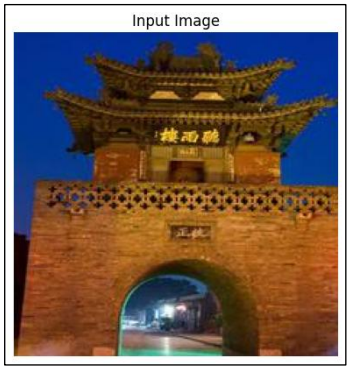


Figure 8: Input image.
Source: Authors, (2026).

An input image which serves as the initial sample in the image forgery detection procedure is depicted in Figure 8. The image depicts a conventional architectural structure with a brick base, archway, and a decorative roof. It depicts the raw input data for a forgery detection system prior to processing. This indicates the start of the analytical pipeline. The system uses such images to determine authenticity or modification. These inputs are critical for developing and testing detection systems.

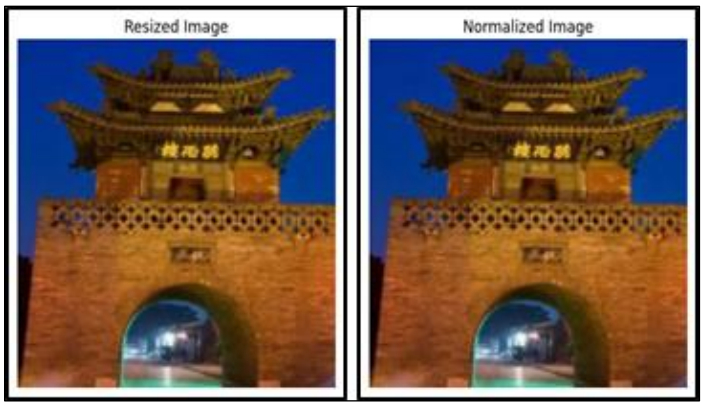


Figure 9: Resized and Normalized image.
Source: Authors, (2026).

Two image processing methods resizing and normalization are contrasted side by side in this figure 9. The Resized Image displays the outcome of adjusting the image's dimensions, which frequently results in distorted or blurry images if the aspect ratio is changed. The Normalized Image shows an image having its pixel values changed, perhaps for improved clarity and contrast, without changing the image's original size. In order to improve the image's visual balance and prepare its features for additional analysis normalization usually entails scaling the pixel values to a predetermined range.

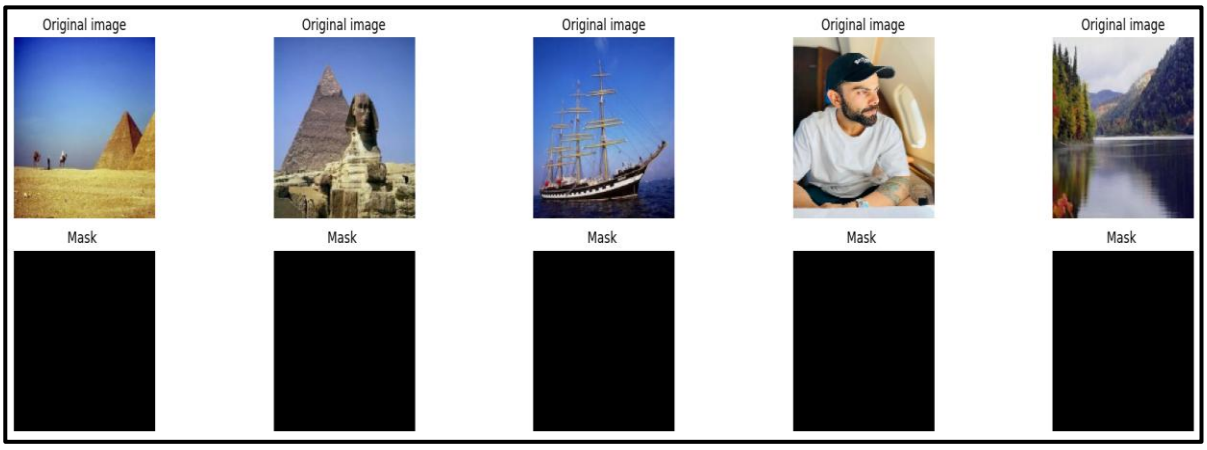


Figure 10: Image masking process.
Source: Authors, (2026).

Figure 10 displays a collection of original images along with matching black masks. The images depict locales such as the Pyramids of Giza, the Sphinx, a sailing ship, a man in a plane, and a lakeside setting. A black mask appears beneath each image, indicating that it was most likely utilized in image processing. These masks target specific areas for activities like as segmentation and object detection. The entirely black masks indicate that parts are masked for processing purposes. They utilized later to emphasize or preserve specific areas of the images during analysis.

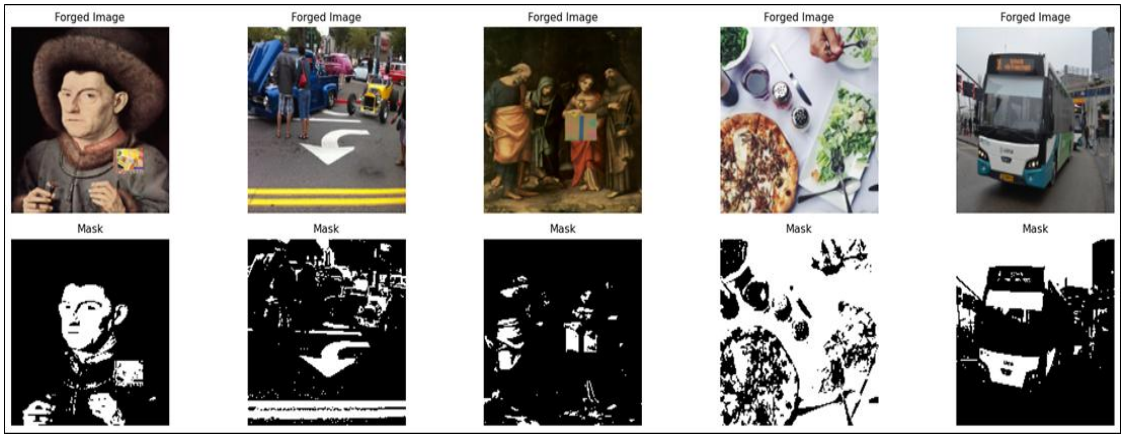


Figure 11: Forgery Detection with Masking Technique.
Source: Authors, (2026).

Figure 11 displays a series of manipulated images together with the black-and-white masks that go with them. This technique uses masks to identify altered or forged areas in images. Each mask focuses on manipulated regions, such as a digitally altered portrait, modifications in a street scene, a modified painting, a fabricated food arrangement, and edits on a bus. The masks draw attention to these altered areas. This is useful in forensic analysis, image validation, and forgery detection. The graphic shows how mask detection identifies modified parts in forged images.

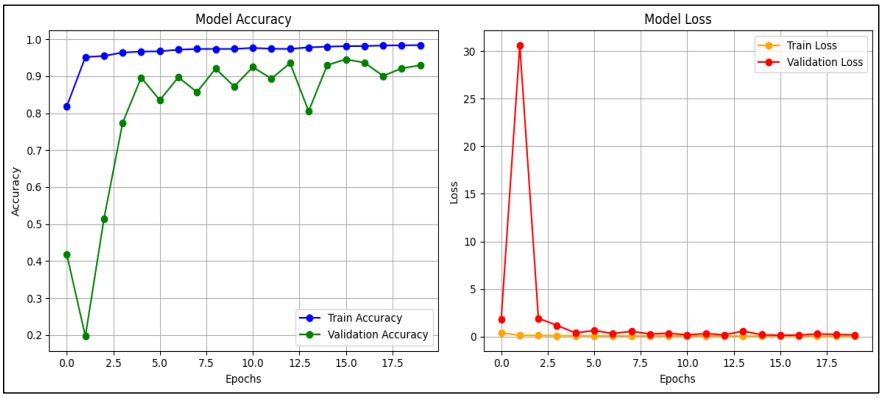


Figure 12: Model Accuracy and Loss over Epochs.
Source: Authors, (2026).

Figure 12 display a model's performance measures over 20 training epochs. The left figure depicts model accuracy, with training accuracy (blue) rapidly increasing and stabilizing near 1.0, whereas validation accuracy (green) improves slowly and varies, indicating some overfitting. The right plot depicts model loss, with both training (yellow) and validation loss (red) starting high but decreasing dramatically. Validation loss varies considerably, indicating potential instability or overfitting. Despite this, both losses stabilize near zero, indicating that the model has successfully trained.

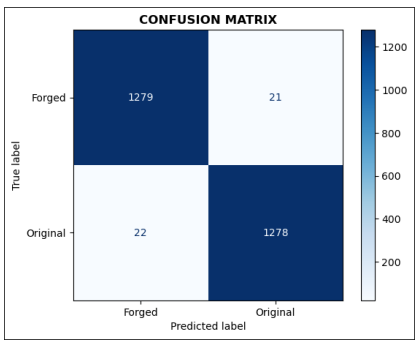


Figure 13: Confusion matrix.
Source: Authors, (2026).

The confusion matrix presented in Figure 13 shows a well classification model predicts two classes Forged and Original. The confusion matrix has 1,279 true positives for forged images and 1,278 true positives for original images. There are 21 false positives (original misclassified as forgery) and 22 false negatives (forged misclassified as original). The model is highly accurate, with minimal misclassifications. This demonstrates a great capacity to differentiate between the two classes successfully.

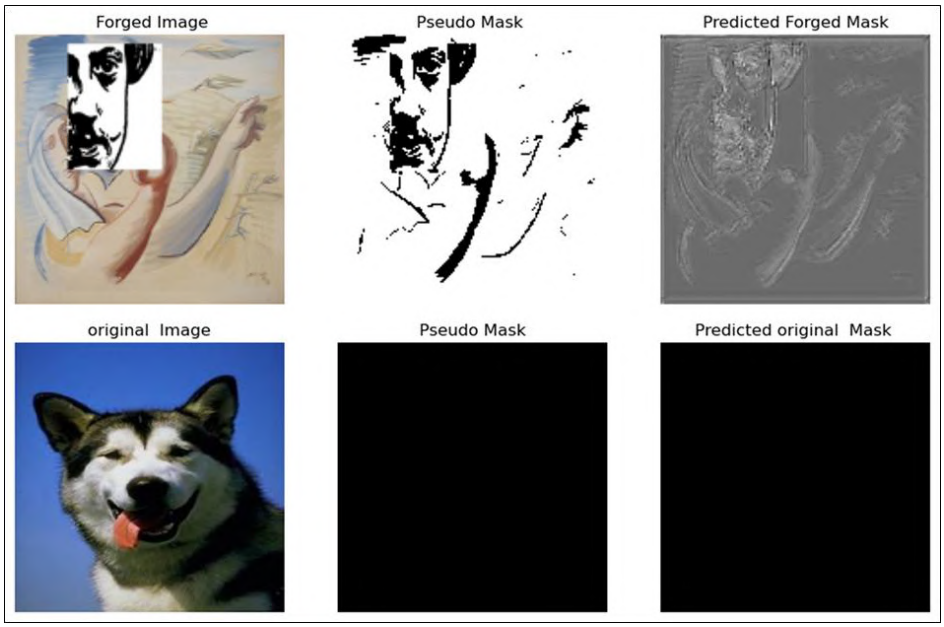


Figure 14: Image Forgery Detection and Mask Prediction Outcomes.
Source: Authors, (2026).

The process of identifying image forgery with mask prediction algorithms is depicted in Figure 14. The six sections demonstrate the forgery detection procedure. The top-left corner displays a faked image, followed by a faux mask that highlights probable modifications. The model predicts a forged mask in order to identify certain bogus regions. The original image and pseudo mask are shown here, with no modification. The accuracy of the detection model be evaluated by comparing anticipated masks to originals.

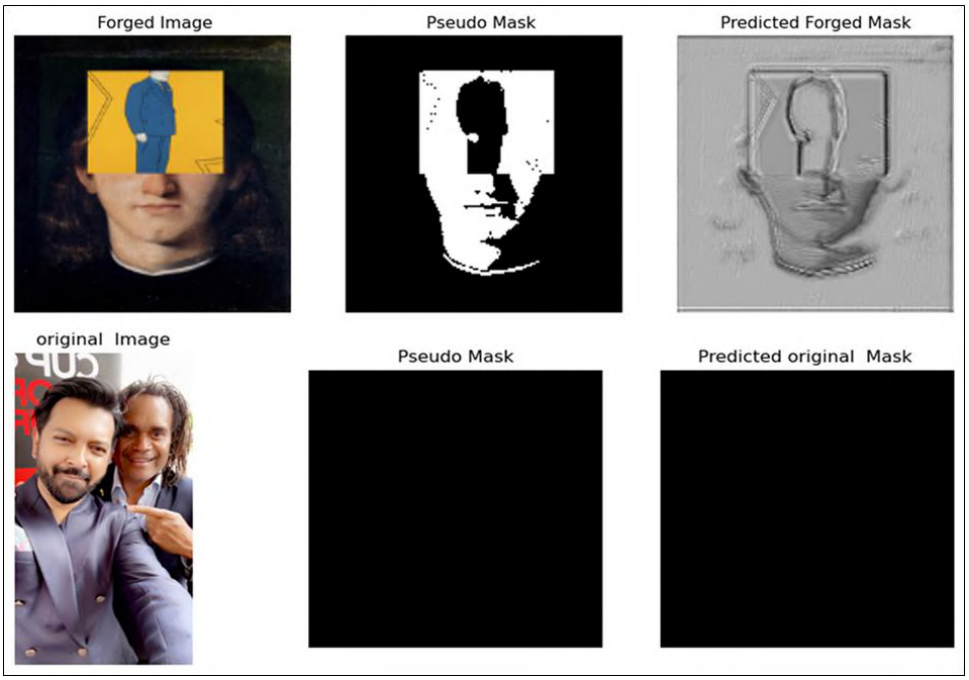


Figure 15: Forgery Detection in Images and Mask Prediction Results.
Source: Authors, (2026).

Figure 15 illustrates the process of image fraud detection, emphasizing the comparison of authentic and manipulated images using anticipated and faux masks. The top row displays the original image, its blank pseudo mask, and the forecasted mask, indicating no tampering. The bottom row shows a forged image, a faux mask that highlights the altered areas, and the model's anticipated forged mask. The anticipated mask attempts to match the pseudo mask's highlighted regions. This comparison measures the model's ability to reliably detect forgeries.

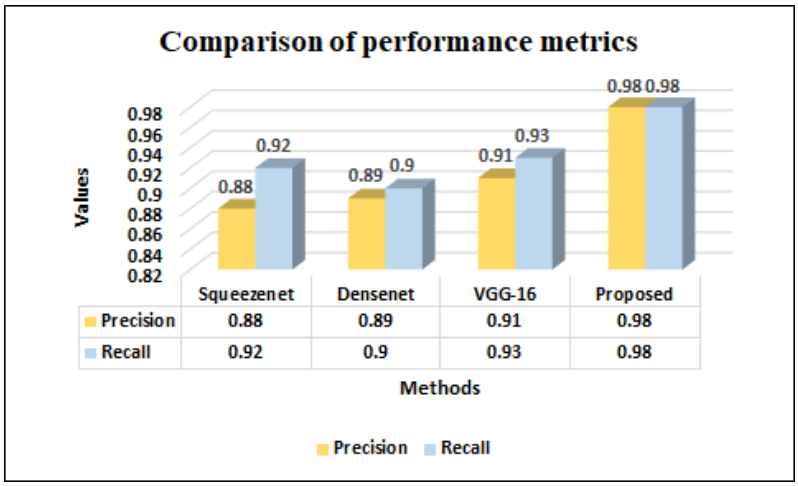


Figure 16: Comparison of Performance metrics.
Source: Authors, (2026).

Figure 16 illustrates the performance of four different methods such as SqueezeNet [18], DenseNet [19], VGG-16 [20], and a proposed method based on two metrics, Precision and Recall. SqueezeNet has the lowest performance, with a Precision of 0.88 and Recall of 0.92, DenseNet follows closely, showing slight improvements with a Precision of 0.89 and Recall of 0.92. VGG-16 performs better, with a Precision and Recall of 0.91. The proposed method significantly outperforms the others, achieving the highest scores Precision and Recall of 0.98 each.

Table 2: Comparative analysis of accuracy.

Methods	Accuracy
SqueezeNet [18]	0.89
Dense net [19]	0.92
VGG-16 [20]	0.93
Proposed	0.98

Source: Authors, (2026).

Table 2 shows the comparative analysis of accuracy for various methods such as SqueezeNet, Dense net, VGG-16 and a proposed method. In this comparison, SqueezeNet attains the lowest accuracy of 0.89, Dense net reaches the accuracy of 0.92, VGG-16 achieves the accuracy of 0.93 and the proposed method succeeds the accuracy of 0.98. Hence the proposed method outperforms the highest accuracy of overall methods.

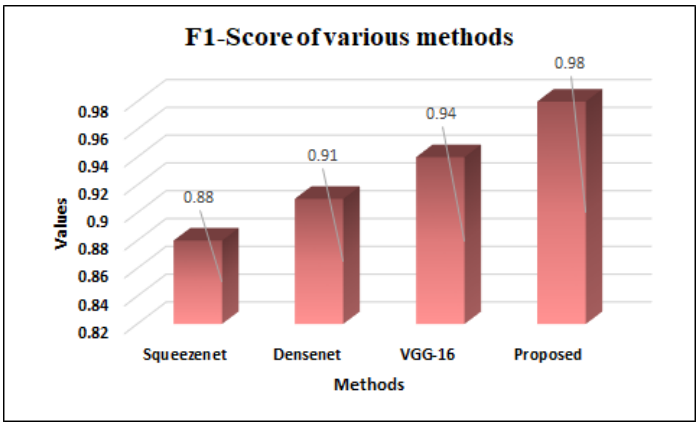


Figure 17: FI-score comparison of various methods.
Source: Authors, (2026).

Figure 17 depicts the FI- score of various methods such as Squeeze net, Dense net, VGG-16 and proposed method. Squeeze net achieves the lowest FI-score of 0.88, followed by Dense net and VGG-16 of 0.91 and 0.94. The proposed system achieves the highest FI-score of 0.98.

V. CONCLUSION

This study presents the contributions and most significant results for detecting image forgeries. The primary contribution lies in the introduction of an innovative hybrid DL model that seamlessly integrates residual-dense Swin transformer with attention based UNet++. Through the assistance of suitable techniques, it illustrates that the detection of image forgery is effectively processed through four stages. The procedure commences with input image where raw data is provided to the system for forgery detection. This is followed by preprocessing where resize and normalization takes place to ensure consistent input for the model, which helps in training and inference stability. In feature extraction, it extracts high level features from the input image using a hybrid model.

The extracted features are then segmented to produce a pixel-wise segmentation mask indicating forged images. A predicted pixel mask highlighting suspected forged regions in the image. Then the mask is subjected to a threshold by the detection module and if exceeded, it marks the image as forged. The model is implemented in Python and it outperforms higher accuracy, precision, recall and FI-score of 0.98%.

VI. AUTHOR'S CONTRIBUTION

Conceptualization: Sruthi Anand and Saranya V.
Methodology: Sruthi Anand and Saranya V.
Investigation: Sruthi Anand.
Discussion of results: Sruthi Anand and Saranya V.
Writing – Original Draft: Sruthi Anand.
Writing – Review and Editing: Sruthi Anand and Saranya V.
Resources: Saranya V.
Supervision: Saranya V.
Approval of the final text: Sruthi Anand and Saranya V.

VII. REFERENCES

[1] M. A. Elaskily, H. A. Elnemr, A. Sedik, M. M. Dessouky, G. M. El Banby, O. A. Elshakankiry, A. A. Khalaf, H. K. Aslan, O. S. Faragallah, and F. E. Abd El-Samie, "A novel deep learning framework for copy-moveforgery detection in images," Multimedia Tools and Applications, vol. 79, no. 27, pp. 19167-19192, 2020.

[2] S. R. Gadu, "A Hybrid Generative Adversarial network with Quantum U-NET for 3D spine X-ray image registration," Healthcare Analytics, vol. 4, pp. 100251, 2023.

[3] H. Chen, C. Chang, Z. Shi, and Y. Lyu, "Hybrid features and semantic reinforcement network for image forgery detection," Multimedia Systems, vol. 28, no. 2, pp. 363-374, 2022.

[4] F. M. Al_Azrak, A. Sedik, M. I. Dessowky, G. M. El Banby, A. A. Khalaf, A. S. Elkorany, and F. E. Abd. El-Samie, "An efficient method for image forgery detection based on trigonometric transforms and deep learning," Multimedia Tools and Applications, vol. 79, no. 25, pp. 18221-18243, 2020.

[5] R. Karthickmanoj, S. Aasha Nandhini, D. Lakshmi, R. Rajasree, and T. Ananth Kumar. "Transforming deep learning-based skin disease detection and classification with AI-based diagnostic framework in the era of Industry 5.0," 2025.

[6] Y. Liu, X. Li, J. Zhang, S. Li, S. Hu, and J. Lei, "Hierarchical Progressive Image Forgery Detection and Localization Method Based on UNet," Big Data and Cognitive Computing, vol. 8, no. 9, pp. 119, 2024.

[7] H. Zhang, J. Zeng, and J. Yang, "Multi-Scale Edge-Guided Image Forgery Detection via Improved Self-Supervision and Self-Adversarial Training," Electronics, vol. 14, no. 9, pp. 1877, 2025.

[8] K. Aishwaryameenakshi, S. H. Banu, A. K. Priya, and S. Chitrakala, "Image Indexing using Edgel Index for Sketch-based Image Search and Retrieval," International Journal of Wisdom Based Computing, vol. 1, no. 3, pp. 134-138, 2011.

[9] D. P. Timothy, and A. K. Santra, "Detecting Digital Image Forgeries with Copy-Move and Splicing Image Analysis using Deep Learning Techniques," International Journal of Advanced Computer Science & Applications, vol. 15, no. 5, 2024.

[10] A. Diwan, and A. K. Roy, "Cnn-keypoint based two-stage hybrid approach for copy-move forgery detection," IEEE Access, vol. 12, pp. 43809-43826, 2024.

[11] V. Balaji, R. J. Malar, K. S. Kavin, S. R. Rose, T. R. Permila, and B. Pandian, "PSO Optimized RBFNN Classifier for Lung Cancer Identification System," In 2024 7th International Conference on Circuit Power and Computing Technologies (ICCPCT), vol. 1, pp. 1189-1194, 2024.

[12] J. Priyanka, A. A. Sundaresan, L. R. Kalabarige, and R. A. Venkata, "Advancements in image forgery detection through deep learning methods," In AIP Conference Proceedings, vol. 3291, no. 1, pp. 030030, 2025.

[13] O. Aparna, P. Rani, T. Ramya, T. Priyanka, N. Sundari, P. G. K. Sirisha, R. Ramesh, and D. Anand, "Detection of Frauds in Deep Fake Using Deep Learning," Engineering Proceedings, vol. 66, no. 1, pp. 48, 2024.

[14] G. E. Lio, M. D. L. Bruno, F. Riboli, S. Nocentini, and A. Ferraro, "Fast and Robust Speckle Pattern Authentication by Scale Invariant Feature Transform algorithm in Physical Unclonable Functions," arXiv preprint arXiv:2504.21041, 2025.

[15] I. Sedeeq, "Image Forgery Detection Using Histogram-Oriented Gradients (HOG)," Iraqi Journal of Science, pp. 2048-2058, 2025.

[16] S. Bokefode, J. Sarwade, K. Sakure, S. Bankar, S. Janrao, and R. Patil, "Using a Clustering Algorithm and a Transform Function, Identify Forged Images," International Research Journal of Multidisciplinary Studies, vol. 5, no. 1, pp. 781-789, 2024.

[17] Y. Chen, M. C. Chang, and X. Li, "Leveraging Semantic Segmentation for Image Manipulation Detection and Localization," In 2024 IEEE 7th International Conference on Multimedia Information Processing and Retrieval (MIPR), pp. 95-101, 2024.

[18] I. T. Ahmed, F. A. Abdulazeez, and B. T. Hammad, "Employing Different Algorithms of Lightweight Convolutional Neural Network Models in Image Distortion Classification," Computers, vol. 13, no. 10, pp. 268, 2024.

[19] A. Alzahrani, "Digital image forensics: An improved DenseNet architecture for forged image detection," Engineering, Technology & Applied Science Research, vol. 14, no. 2, pp. 13671-13680, 2024.

[20] R. R. Choudhary, S. Paliwal, and G. Meena, "Image forgery detection system using VGG16 UNET model," Procedia Computer Science, vol. 235, pp. 735-744, 2024.

Journal of Engineering and Technology for Industrial Applications

ISSN ONLINE: 2447-0228

ITEGAM-JETIA

Manaus, v.12 n.60, p.195-205, July/August, 2026.
DOI: https://doi.org/10.5935/jetia.v12i60.3697

RESEARCH ARTICLE OPEN ACCESS

ENHANCED ECG-BASED CARDIAC DISORDER DETECTION USING RECURRENT NEURAL NETWORK ENHANCED TEMPORAL TRANSFORMER AND FIRE HAWK OPTIMIZATION

S. Dinakar Raj*[1], Kavitha Veerappan[2], Jeya Bright Pankiraj[3], K. Sangeetha[4], Sumesh Joe Cherian[5], S. Rajeswari[6]

[1]Assistant Professor, Department of Electronics and Communication Engineering, Saveetha School of Engineering, SIMATS Engineering, Saveetha University, Chennai, Tamilnadu, India.
[2]Research Scholar, Department of Electronics and Communication Engineering, Indian Institute of Information Technology, Tamil Nadu, India.
[3]Assistant Professor, Department of Electronics and Communication Engineering, Loyola institute of Technology & Science, Loyola Nagar, Thovalai, Kanyakumari District, Tamilnadu, India.
[4]Assistant Professor, Department of Electronics and Communication Engineering, SNS College of Engineering, Coimbatore, India.
[5]Lecturer in Electronics Engineering, Mahakavi Vennikulam Gopalakurup Memorial Government Polytechnic College, Vennikulam, Pathanamthitta, Kerala, India.
[6]Assistant Professor, Department of Computer Science and Engineering, Koneru Lakshmaiah Education Foundation, Vaddeswaram, Andhra Pradesh, India.

[1]https://orcid.org/0000-0002-1243-1575, [2]https://orcid.org/0009-0009-4970-3333, [3]https://orcid.org/0000-0002-9246-5301, [4]https://orcid.org/0009-0003-8760-5458, [5]https://orcid.org/0009-0002-3261-9273, [6]https://orcid.org/0000-0002-3551-0284

Email: rajdina@gmail.com, mail2kavieceian@gmail.com, jeyabright@gmail.com, sangeeta.k.ece@snsce.ac.in, sumeshjoecherian1@gmail.com, srajeswari@kluniversity.in

ARTICLE INFO

Article History
Received: February 14, 2026
Reviewed: June 6, 2026
Accepted: July 6, 2026
Published: July 31, 2026

Keywords:
ECG signal,
Adaptive Wavelet Filter,
Hilbert Huang Transform,
RETT classifier
Fire Hawk Optimization algorithm

ABSTRACT

Quick treatment and management of heart disease depend on an accurate and early diagnosis. An Electrocardiogram (ECG) is a vital indicator tool used in medical practice to evaluate cardiovascular illness. In order to tackle the challenges of cardiac classification, this study presents an innovative method based on Deep Learning (DL) approach, namely Recurrent Neural Network Enhanced Temporal Transformer (RETT). The implemented research is initiated with an Adaptive Wavelet Filter based pre-processing that enhances the quality of an ECG signal. Subsequently, the Hilbert Huang Transform (HHT) based feature extraction is exploited for extracting necessary features, which are crucial for detecting abnormalities and diagnosing heart disorders. Then, RETT classification approach is utilized for detecting the cardiac affliction accurately. Finally, the performance of a RETT approach is enhanced with the aid of a Fire Hawk Optimization (FHO) algorithm. The developed approach is executed in python software that shows the performance of DL that is useful for evaluating cardiovascular disease with an accuracy of 99.70%. This research aids in the generation of precise and effective diagnostic tools for dealing with pressing cardiac health issues.

Copyright ©2026 by authors and Galileo Institute of Technology and Education of the Amazon (ITEGAM). This work is licensed under the Creative Commons Attribution International License (CC BY 4.0).

I. INTRODUCTION

Around the world, heart disease is regarded as one of the most hazardous and life-threatening chronic illnesses. Heart disease often arises when the heart is unable to pump sufficient blood to other body parts for them to function normally [1]. Over 64 million people worldwide endure from Heart Failure (HF), which is a clinical disease that is becoming more common. Heart failure with maintained ejection fraction is more complicated than heart failure with decreasing EF, which results in different diagnostic criteria and probably contributes to "failed" clinical studies [2]. Cardiovascular illnesses are diagnosed and evaluated by doctors using electrocardiography procedures. Experts visually evaluate the ECG signal, which is an established method in cardiology for assessing a patient's heart health is the electrocardiogram (ECG) [3].

Expert cardiologists carefully examine the ECG as part of standard medical procedures in order to diagnose potentially fatal heart arrhythmias. Cardiologists save time and obtain objective diagnostic outcomes by automatically classifying cardiac arrhythmias. The computer-aided classification and detection of ECG signals in hospitals and the health community has attracted significant economic interest due to these benefits [4], [5]. Machine learning (ML) and Artificial Intelligence (AI) have demonstrated substantial promise in automating the diagnosis of heart disease in ECG signals in recent years. By increasing the precision and effectiveness of arrhythmia detection, these technologies lessen the strain on healthcare systems [6]. A crucial step in the classification of ECG signals is feature extraction, which is a part of data representation [7]. Principal component analysis (PCA) based feature extraction, serves to simplify and improve the interpretability of models by reducing the number of features while keeping the majority of the relevant information. It is challenging to comprehend the new features (principal components) produced by PCA in terms of the original variables since they are linear combinations of the original features [8]. Because of its nonlinear character, the Kernel principal component analysis (KPCA) method in [9] is better than the PCA methodology for categorizing heartbeats from ECG signals. But compared to PCA, KPCA generates more intricate algorithms. The wavelet scattering transform, which is developed in [10], produces low variance features of real-valued signals that are usually needed in classification tasks, conserves data in high frequency and is immune to signal deformations. However, the WST employs preset wavelet filters, which isn't ideal for every kind of data or application. To overcome such issues, the Hilbert Huang transform is developed in this work for feature extraction. A method for detecting heart problems is the Support Vector Machine (SVM), which is presented in [11]. Finding the plane that divides the model's data points is challenging since there are many different ways a hyper plane is configured in an N-dimensional environment.

Even when a sizable percentage of record entries are inaccessible, the Random Forest (RF) approach, which is presented in [12], still produce the same results when applied to huge datasets. However, because RF models are ensemble in nature, they are intricate and challenging to understand. The Multilayer Perceptron (MLP), which is developed in [13], is extremely adaptable for handling complicated problems since it can approximate any continuous function. However, MLP over fits the training data in the absence of enough training data or regularization strategies. In primary care settings, CNN helps to reduce missed diagnoses and misdiagnosis while also increasing efficacy and reducing labour expenses. However, CNN necessitates meticulous adjustment of several hyper parameters, which is complicated and time-consuming [14]. The results confirm the idea that data collection is done more accurately when detecting diabetes and heart-related diseases and diagnoses using Artificial Neural Networks (ANN) classifier [15]. However, there are sustainability issues because huge neural networks require a lot of energy to train and operate. As a result, this research develops a RETT classification approach and its performance is enhanced by meta-heuristic algorithm, which includes Particle Swarm Optimization (PSO) [16], firefly optimization [17], Artificial Bee Colony (ABC) [18] and Cuckoo Search (CS) [19] and Harmony Search Optimization algorithm [20]. However, these approaches has some limitations such as, lack of diversity in the search space, expensive, slow convergence, stuck in local optima and highly sensitive. Thus, the Fire Hawk Optimization algorithm is implemented in this research for tuning the hyper parameters of a RETT classifier. The main contributions are,

- The Adaptive Wavelet Filter based pre-processing is filtering out high-frequency noise, such as interference and muscle artifacts, without affecting the important features of the ECG signal.
- Integrates the HHT based feature extraction that extracts the relevant features, which are essential for detecting abnormalities and diagnosing heart conditions.
- Implements RETT classification method for accurately predicting the cardiac affliction in an early stage.
- The Fire Hawk Optimization algorithm is exploited for fine-tuning the hyper parameters of a RETT classifier.

II. PROPOSED METHODOLOGY

The developed block diagram for predicting cardiac affliction is depicted in Figure 1. The process is initiated with capturing the ECG signal that contains the valuable data about electrical activity of heart. Nevertheless, ECG signals are contaminated with noise and artifacts, which requires a preprocessing stage. It is performed by utilizing an Adaptive Wavelet Filter that efficiently removes noise and enhances signal quality by decomposing it into distinct frequency components while conserving critical cardiac data. The next stage contains HHT based feature extraction, which is a decomposition approach that aids to analyze ECG signals by decomposing it into Intrinsic Mode Functions (IMFs). It is exploited to extract the features like instantaneous frequency and amplitude that is crucial for detecting the abnormalities in the electrical activity of heart.

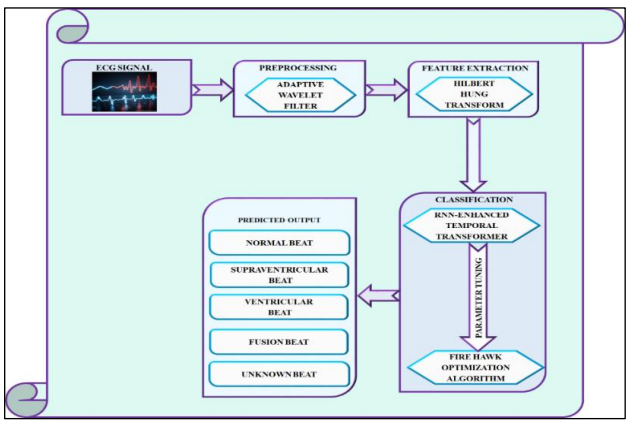


Figure 1: Proposed block diagram.
Source: Authors, (2026).

Then, the signal is fed into a RETT for classification, which is a combination of RNN and transformer based architecture, exploited to acquire temporal dependencies in ECG data. It enhances the learning efficacy by integrating attention mechanisms to concentrate on important time dependent patterns in ECG signal, making it highly effective for detecting cardiac affliction. To further enhance the performance of classifier, the Fire Hawk Optimization algorithm is utilized that fine tunes the hyperparameter of developed classifier. By optimizing parameters, ensures that the DL model attains optimal accuracy and robustness, ensures it is the reliable tool for automated diagnosis of cardiac affliction.

II.1 ADAPTIVE WAVELET FILTER

Pre-processing process is necessary in the developed system in order to enhance the signal quality. In the preprocessing phase, the ECG signal is treated to eliminate unwanted and noisy signals, improving the accuracy. Traditional FIR or IIR filters are used for filtering when the target signals and the noise's frequencies are not overlapped.

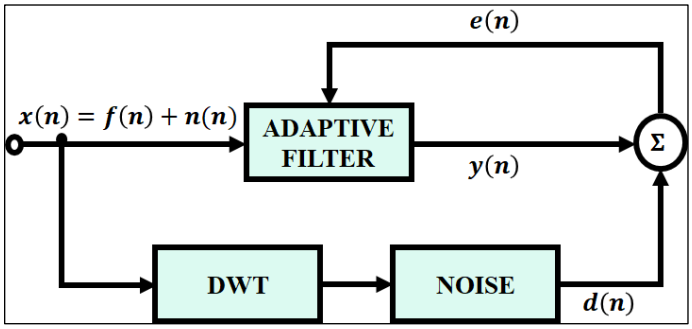


Figure 2: Structure of Adaptive Wavelet Filter Traditional wavelet transform are used to de-noise them when they partially overlap.
Source: Authors, (2026).

However, for the target signal, the filtered signal is not the best estimate. There is link between the original noise and the decomposed noise of DWT that is the optimum reference signal for an adaptive filter. As illustrated in Figure 2, the input signal is,

$$x(n) = f(n) + n(n) \tag{1}$$

Where, the noise is indicated by $n(n)$, target signal is $f(n)$ and reference signal decayed form input signal in DWT is $d(n)$. Based on LMS algorithm, the adaptive rule is,

$$E[e^2(n)] = min \tag{2}$$

The output signal is impending to target signal and filter's weight factor following this rule,

$$w(n+1) = w(n) + 2\mu e(n) \tag{3}$$

After preprocessing, the Hilbert Huang Transform is utilized for extracting the relevant feature from an ECG signal.

II.2 HILBERT HUANG TRANSFORM BASED FEATURE EXTRACTION

Hilbert spectrum analysis and EMD are 2 components of the HHT based feature extraction. A signal is broken down into a finite number of band-limited IMFs using the EMD approach. There are two fundamental restrictions on each IMF:

(1) The number of extreme points and zero crossings in the complete data series are need to be equal or differ by no more than one.

(2) The mean value of the envelopes produced by local minima and maxima is zero at any given time point.

A signal $x(t)$ is broken down by the EMD into n IMFs, such as $c_1(t), c_2(t), \cdots, c_n(t)$ and a residue signal $r_n(t)$. The original signal $x(t)$ is,

$$x(t) = \sum_{i=1}^{n} c_i(t) + r_n(t) \tag{4}$$

Where, i^{th}EMF is denoted by $c_i(t)$ and number of intrinsic modes is n. The Hilbert transform $c_H(t)$ for any real IMF $c(t)$ is,

$$c_H(t) = \frac{1}{\pi} P \int_{-\infty}^{\infty} \frac{c(\tau)}{t-\tau} d\tau \tag{5}$$

Where, singular integral's Cauchy principal value is P and the analytic function is,

$$z(t) = c(t) + jc_H(t) = a(t)e^{j\phi(t)} \tag{6}$$

The instantaneous amplitude $a(t)$ and phase $\phi(t)$ is,

$$a(t) = \sqrt{c(t)^2 + c_H(t)^2} \tag{7}$$

$$\phi(t) = arctan\frac{c_H(t)}{c(t)} \tag{8}$$

The instantaneous frequency is,

$$\omega(t) = \frac{d\phi(t)}{dt} \tag{9}$$

Subsequently, the RETT classifier is utilized to accurately detect the cardiac affliction and its performance is enhanced by FHO algorithm.

II.3 FIRE HAWK OPTIMIZED RNN ENHANCED TEMPORAL TRANSFORMER

The FHO is a metaheuristic algorithm inspired by hunting strategy of hawks in nature. To move toward better positions to force prey, it spreads fire in distinct locations. In detection of cardiac affliction, the FHO is exploited to optimize the hyper parameters of the RETT classifier. Each candidate solution indicates a distinct combination of hyper parameters of the RETT classifier that are: Number of Transformer heads, Number of RNN layer, learning rate, batch size, dropout rate and hidden state rate. Each solution Xi is denoted as vector in search space,

$$X = \begin{bmatrix} X_1 \\ X_2 \\ \vdots \\ X_i \\ \vdots \\ X_N \end{bmatrix} = \begin{bmatrix} x_1^1 & x_2^1 & \cdots & x_j^1 & \cdots & x_d^1 \\ x_1^2 & x_2^2 & \cdots & x_j^2 & \cdots & x_d^2 \\ \vdots & \vdots & \ddots & \vdots & \ddots & \vdots \\ x_1^i & x_2^i & \cdots & x_j^i & \cdots & x_d^i \\ \vdots & \vdots & \ddots & \vdots & \ddots & \vdots \\ x_1^N & x_2^N & \cdots & x_j^N & \cdots & x_d^N \end{bmatrix} \tag{10}$$

Where, number of candidate solution is represented by N, hyper parameter's initial value is $x_j^i(0)$, jth hyper parameter in the ith configuration is x_j^i, number of optimized parameter is d and i^{th} RETT hyper parameter configuration is X_i. Each hyper parameter is randomly initialized by,

$$x_j^i(0) = x_j^{i,min} + rand \times \left(x_j^{i,max} - x_j^{i,min}\right) \tag{11}$$

Where, jth hyper parameter's upper and lower bound is indicated by $x_j^{i,max}\ and\ x_j^{i,min}$ and random number between 0 and 1 for diversity is $rand$.

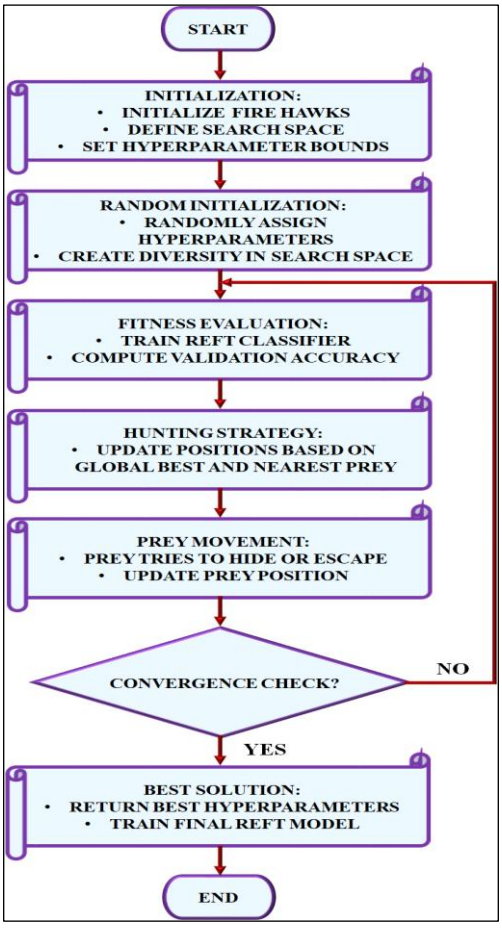


Figure 3: Flowchart of Fire Hawk Optimized RETT.
Source: Authors, (2026).

Moreover, the main fire that the Fire Hawks use first to disperse fires throughout the search space (nature) is thought to be the global best solution. These aspects are expressed mathematically as follows:

$$PR = \begin{bmatrix} PR_1 \\ PR_2 \\ \vdots \\ PR_K \\ \vdots \\ PR_m \end{bmatrix}, \quad k = 1,2,\cdots,m \tag{12}$$

$$FH = \begin{bmatrix} FH_1 \\ FH_2 \\ \vdots \\ FH_l \\ \vdots \\ FH_m \end{bmatrix}, \quad l = 1,2,\cdots,n \tag{13}$$

Where, number of prey is denoted by m, number of fire hawk is n, the kth prey is PR_K and l^{th}fire hawk isFH_l. The algorithm's subsequent step determines the Fire Hawks' overall distance from the prey. Consequently, each bird's effective area is identified by identifying the prey that is closest to it. The first Fire Hawk with the best objective function value determines which prey is closest to it, while the remaining prey is used to decide the other birds' territory. By assigning stronger fire hawks to better prey, the best hyper parameters of RETT classifier are refined for detection of cardiac affliction. Each fire hawk estimates its distance to the nearest prey,

$$D_k^l = \sqrt{(x_2 - x_1)^2 + (y_2 - y_1)^2} \tag{14}$$

Where, hyperparameter values are $(x_1, y_1)\ and (x_2, y_2)$, distance between l^{th} fire hawk and k^{th}prey is D_k^l. The algorithm's search procedure is set up by categorizing the Fire Hawks and prey. The Fire Hawk with the higher objective function value selects the closest prey inside its designated zone. The succeeding closest prey in the search space is then captured by the other Fire Hawks, proving that the strongest Fire Hawks hunt more successfully than the weaker ones. To start a fire in the chosen location, the Fire Hawks gather burning sticks from the main fire in the next phase of algorithm. In order to make the prey quickly run, each bird in this level chooses a burning stick and drops it in its designated area. In order to make the prey quickly run, each bird in this level picks up a burning stick and drops it in its designated area. Some birds are excited to use the burning sticks from the areas occupied by other Fire Hawks. Fire hawks updates the hyper parameter by,

$$FH_{new}^l = FH^l + \left(r_1 \times (GB - FH^l) - r_2 \times (FH_{near} - FH^l)\right) \tag{15}$$

Where, random value among 0 and 1 is indicated by $r_1, r_2,$, global best solution is GB, hyperparameter set of lth fire hawk is FH_{new}^1 and nearby fire hawk is FH_{near} . The movement of prey within each Fire Hawk's territory is regarded as a vital component of animal behavior for the location updating process in the algorithm's succeeding phase. The prey are either choose to hide, flee or unintentionally run in the direction of the Fire Hawk when it drops a burning stick. Prey move toward safer zones,

$$PR_{new}^q = PR^q + \left(r_3 \times (FH^l - PR^q) - r_4 \times (SP^l - PR^q)\right) \tag{16}$$

Where, prey $q's$ updated hyper parameters are PR_{new}^q, random values are $r_3\ and\ r_4$ and prey $q's$ current hyper parameters are PR^q. Inside the territory of fire hawk, the safe place is,

$$SP^l = \frac{\sum_{q=1}^{r} PR^q}{r}, q = 1,2,\cdots,r,\ \ l = 1,2,\cdots,n. \tag{17}$$

Where, safe zone is $SP^l$and number of preys are r. When prey escapes its original region, the hyper parameters are updated as,

$$PR_{new}^q = PR^q + \left(r_5 \times (FH_{Alter} - PR^q) - r_6 \times (SP - PR^q)\right) \tag{18}$$

Where, new fire hawk from distinct region is FH_{Alter}, random numbers are $r_5\ and\ r_6$. The new safe place outside any territory of fire hawk is,

$$SP = \frac{\sum_{K=1}^{m} PR^k}{m}, k = 1,2,\cdots,m, \tag{19}$$

Where, total number of prey in the search space are m. The flowchart of Fire Hawk Optimized RETT is revealed in Figure 3.

Table 1: Pseudo code for Fire Hawk optimized RETT classifier.

Procedure Fire Hawk optimized RETT classifier
Step 1: *Initialize Fire Hawk Optimizer* (*FHO*) *Initialize population of Fire Hawk* (*FH*) *as candidate hyperparameter sets* *Define search space for hyper parameters* −*Learning Rate* (*LR*) ∈ [0.0001,0.01] − *Dropout Rate* (*DR*) ∈ [0.1,0.5] −*Number of RNN Hidden units* (*HU*) ∈ [64,512] − *Number of Transformer Attention Heads* (*AH*) ∈ [2,8] *Set maximum number of iterations* (max_*Iter*) *Evaluate fitness for initialFire Hawks using validation accuracy* # *Step* 2: *Main FHO search loop* *While Iteration* < Max_{Iter} *do*: *Generate n as a random integer for number of Fire Hawks* *Determine Fire Hawks and preys in the hyperparameter search space* *Calculate total distance betweenFire Hawks and preys* *Assign Fire Hawk's terrriotories by dispersing preys* *For each Fire Hawk i in n*: *Update Fire Hawk position* *For each prey q in Fire Hawk terriotory* *Compute safe place inside the Fire Hawk terriotory* *Update prey position based on* SP^l *Update prey position based on* PR^q_{new} *Compute safe place outside the Fire Hawk terriotory* *Update prey position based on* PR^q_{new} *End for* *End for* # *Step* 3: *Evaluate new solutions* *Train RETT with updated hyperparameters* *Compute fitness* *Update Global Best* (*GB*) *if a better solution is found* *End while* # *Step* 4: *Return Best Hyperparameters* *Return Global Best* (*GB*) *hyperparameter set for final model training* *End procedure*

Source: Authors, (2026).

III. RESULT AND DISCUSSIONS

This section analyzes the outcomes of developed Fire hawk optimized RETT classifier for the prediction of cardiac disease. The developed research is implemented in Python software and comparative analysis is made with conventional approaches.

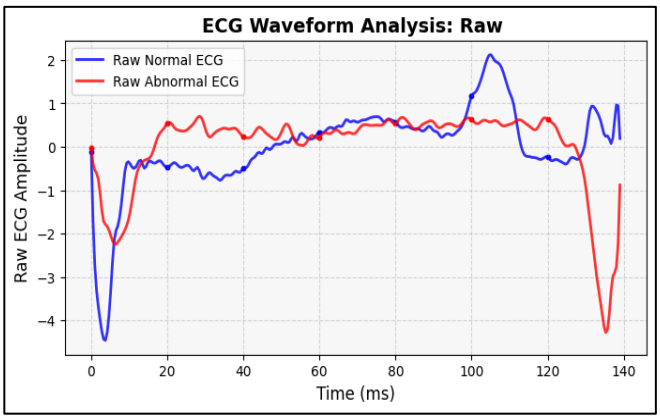


Figure 4: Analysis of ECG waveform.
Source: Authors, (2026).

The ECG waveform for identifying the cardiac disorder is represented in Figure 4 that highlights the differences among normal and abnormal heart activity patterns, which are significant in detecting cardiac disorders. The normal waveform has a constant pattern with predictable peaks whereas the abnormal waveform denotes the irregularities, representing possible disruptions in the electrical activity of heart. This analysis serves as a fundamental step in ECG-based cardiac disorder detection, enabling the identification of early signs of heart disease.

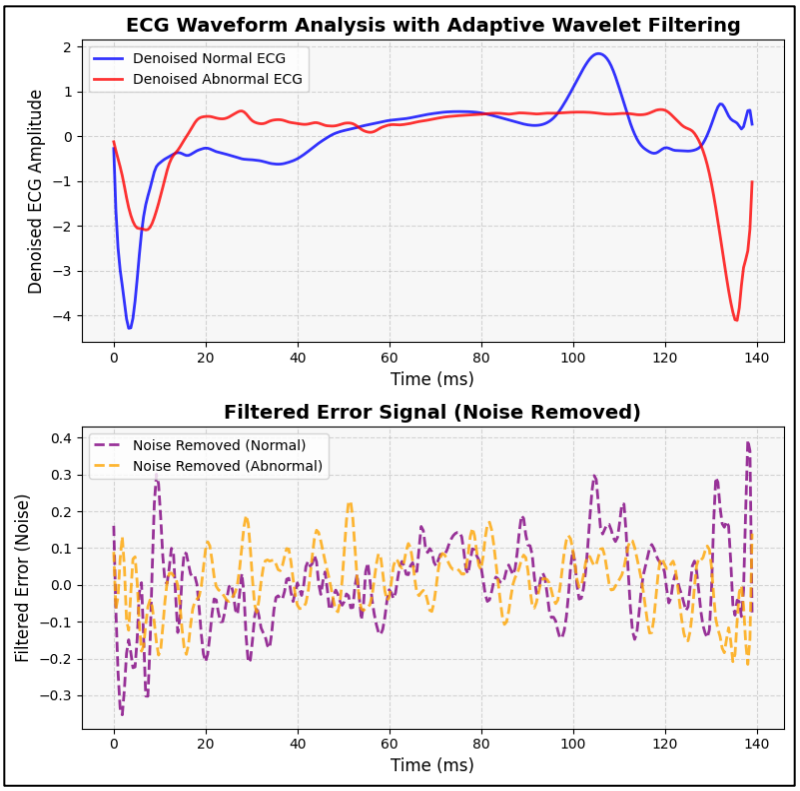


Figure 5: Pre-processed signal.
Source: Authors, (2026).

The Pre-processed signal with Adaptive wavelet filter is displayed in Figure 5. Compared to ECG signals, the denoised waveform has smoother patterns, which is easier to detect the cardiac conditions. The second graph indicates the filtered error signal, representing the noise removed from the ECG signal. The diminished amplitude and smoother denoised waveform assure the efficacy of Adaptive wavelet filter in improving ECG signal clarity. It is significant for accurately identifying cardiac disorders, as it allows better interpretation of heart's electrical activity.

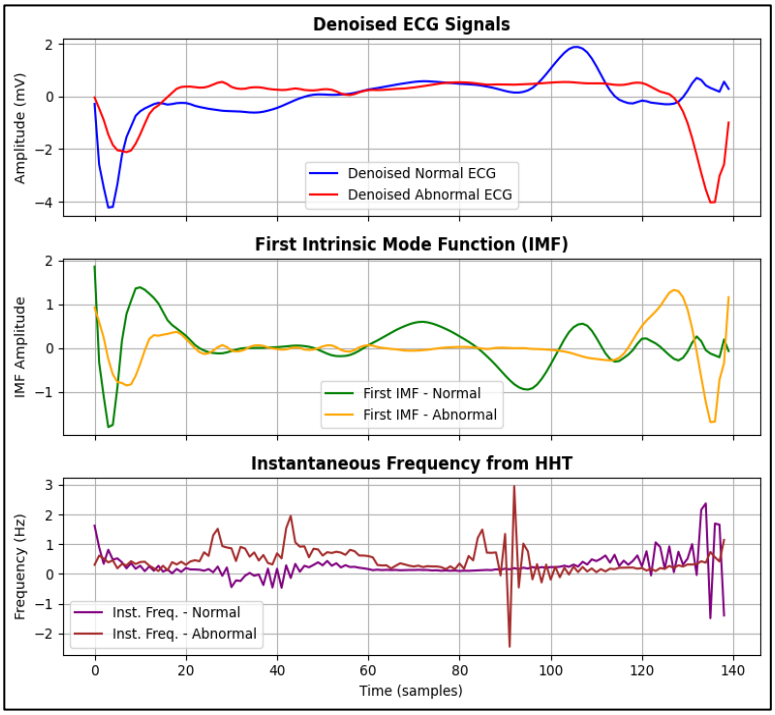


Figure 6: HHT based feature extraction.
Source: Authors, (2026).

The HHT based feature extraction for the detection of cardiac disorder is illustrated in Figure 6. The denoised signals are smoother and more distinguishable, allowing better identification of cardiac irregularities. The middle graph represents the First Intrinsic Mode Function extracted from the ECG signals. The IMF helps decompose the complex ECG signal into simpler components, aiding in better diagnosis of cardiac anomalies. Then, the instantaneous frequency from HHT provide insights into cardiac rhythm disturbances and other heart conditions. This comprehensive analysis using denoising, IMF extraction and HHT-based frequency analysis enhances the accuracy of cardiac disorder detection by capturing both frequency and time domain features.

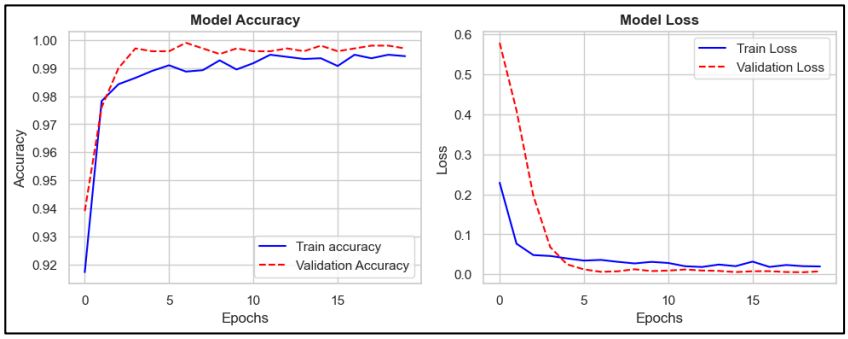


Figure 7: Training and validation results.
Source: Authors, (2026).

Figure 7 illustrates the training and validation outcomes for the detection of cardiac disorder. The validation accuracy is 99.70%, indicating that the model is efficient in learning the patterns in ECG signals. Also, it has reduced loss, denoting that model has the minimal overfitting. The high accuracy and low loss indicate that the model is well-trained and capable of distinguishing between normal and abnormal ECG signals, making it effective for detecting cardiac disorders such as arrhythmias, myocardial infarction, and other heart-related anomalies.

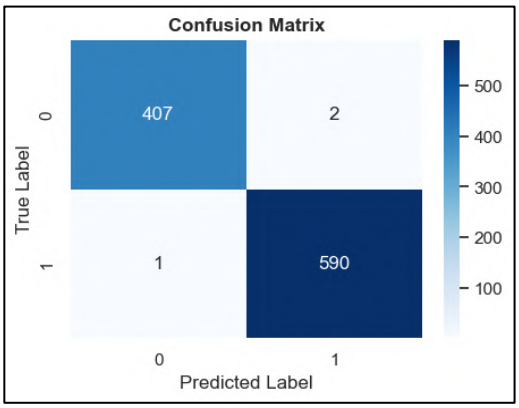


Figure 8: Confusion matrix.
Source: Authors, (2026).

The confusion matrix indicating the performance of a ML model for the detection of cardiac disorder is seen in Figure 8. The matrix compares the model's predicted labels against the true labels to estimate classification accuracy. It indicates that the model has 407 normal cases while it misclassifies 2 normal cases as abnormal. Also, it has only 1 abnormal case that is misclassified as normal and it correctly predicts 590 abnormal cases. The greater number of correct forecasts and the low number of misclassifications reflect the model's high sensitivity and specificity. It indicates that the model is highly effective in distinguishing between normal and abnormal ECG signals, which is essential for detecting cardiac disorders. The small number of false positives and negatives specifies that the model is well-trained and proficient of generalizing well to unseen data.

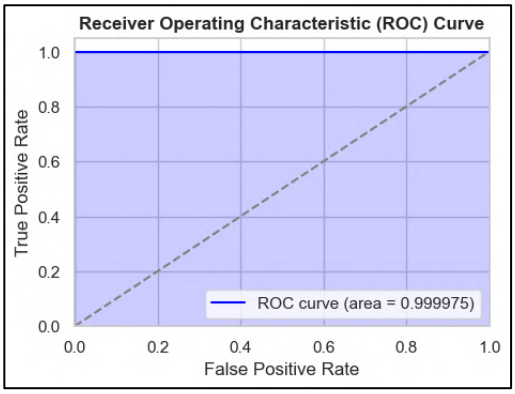


Figure 9: ROC curve.
Source: Authors, (2026).

Figure 9 reveals the Receiver Operating Characteristic (ROC) curve for ECG-based cardiac disorder detection. The ROC value is 0.999975, denotes the model has perfect capability to differentiate among normal and abnormal ECG signals. It demonstrates the model's high sensitivity and specificity, ensuring its reliability in real-world diagnostic scenarios.

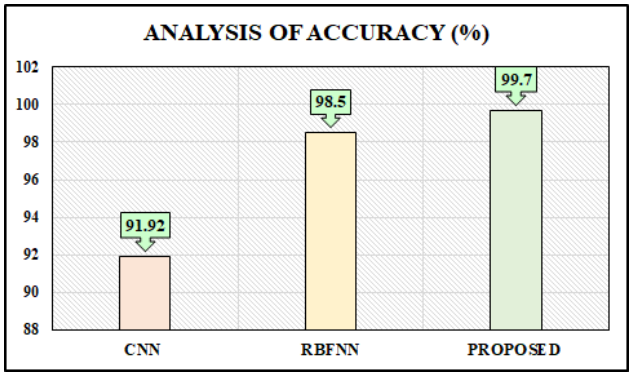


Figure 10: Analysis of accuracy.
Source: Authors, (2026).

Figure 10 represents the analysis of accuracy for Convolutional Neural Network (CNN) [21], Radial Basis Function Neural Network (RBFNN) [22] and developed approach. The developed approach outperforms both CNN and RBFNN, attaining an accuracy of 99.7%, emphasising its superior predictive capability. The results denote that the developed approach is highly effective in accurately diagnosing cardiac diseases. This analysis underscores the potential of the developed approach as a more reliable and precise tool for cardiac disease prediction.

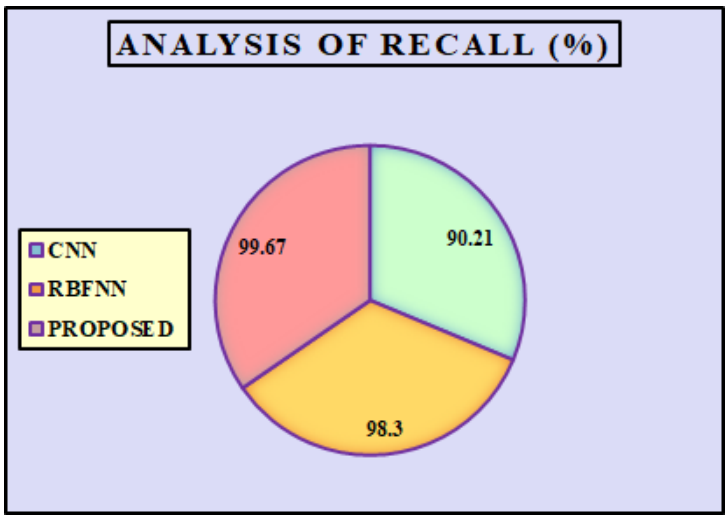


Figure 11: Analysis of Recall.
Source: Authors, (2026).

The analysis of Recall for developed approach with CNN [21] and RBFNN [22] classifier is shown in Figure 11. The developed approach surpasses both CNN and RBFNN, achieving a recall of 99.67%, indicating which is highly capable of minimizing false negatives and correctly identifying the presence of cardiac disease. The higher recall value of the developed approach indicates its superior sensitivity and improved performance in capturing true positive cases, making it more reliable for accurate cardiac disease diagnosis.

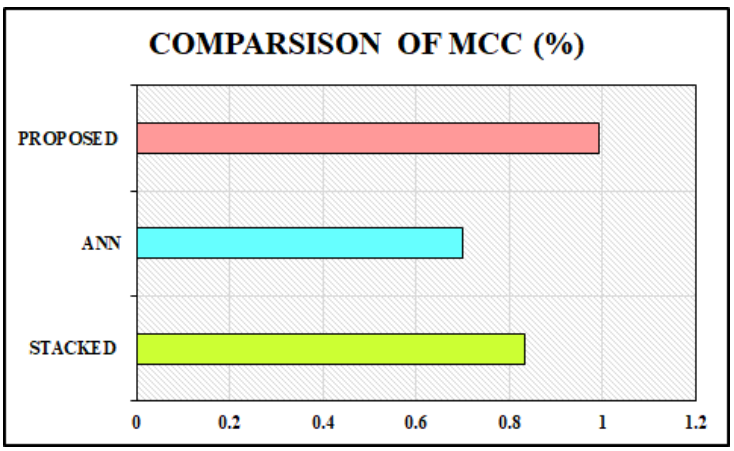


Figure 12: Comparison of MCC.
Source: Authors, (2026).

Figure 12 illustrates the comparison of Matthews Correlation Coefficient (MCC) for distinct classifier used in cardiac disease prediction. The Artificial Neural Network (ANN) [23] model demonstrates a MCC value of 0.70, reflecting a reasonable predictive capability. The Stacked model [24] attains a MCC of 0.835, presenting improved performance in handling classification challenges. However, the developed approach exhibits the highest MCC value of 0.9938, indicating stable classification of both positive and negative cases. It ensures the effectiveness of the developed approach in improving classification accuracy and overall reliability in cardiac disease prediction.

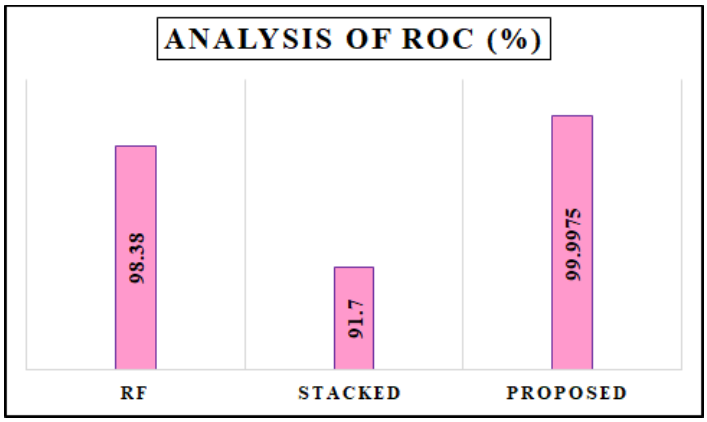


Figure 13: Comparison of ROC.
Source: Authors, (2026).

The comparison of Receiver Operating Characteristic (ROC) for stacked [24], Random Forest (RF) [25] and developed approach is displayed in Figure 13. The developed model has a higher ROC of 99.9975% than other approaches, representing it provides more accurate and reliable predictions. This superior performance indicates that the developed model is highly effective in identifying cardiac diseases with minimal misclassification, making it a valuable tool in clinical diagnosis.

IV. CONCLUSION

By classifying patient ECGs into appropriate cardiac diseases, this research develops an effective transferable DL based ECG classification system that performs autonomous ECG cardiac diagnostics. The Adaptive Wavelet Filter based pre-processing is effective in removing noise and enhancing the quality of ECG signals, which is vital for accurate diagnosis. Then, the HHT based feature extraction method improves the non-invasive diagnosis and early detection of cardiac affliction. Subsequently, the Fire Hawk optimized RETT classifier enhances the accuracy of detecting cardiac diseases by capturing both temporal dependencies and complex patterns in the data. The developed research is implemented in Python software to show the proficiency of developed cardiac affliction detection approach. The outcomes demonstrate that the developed approach performs better than other results in accurately classifying ECGs as either normal or arrhythmia with an accuracy of 99.70%.

V. AUTHOR'S CONTRIBUTION

Conceptualization: S. Dinakar Raj, Kavitha Veerappan, Jeya Bright Pankiraj, K. Sangeetha, Sumesh Joe Cherian and S. Rajeswari.
Methodology: Jeya Bright Pankiraj, K. Sangeetha, Sumesh Joe Cherian and S. Rajeswari.
Investigation: Kavitha Veerappan, Jeya Bright Pankiraj, K. Sangeetha, Sumesh Joe Cherian and S. Rajeswari.
Discussion of results: S. Dinakar Raj, Kavitha Veerappan, Jeya Bright Pankiraj, K. Sangeetha, Sumesh Joe Cherian and S. Rajeswari.
Writing – Original Draft: S. Dinakar Raj.
Writing – Review and Editing: S. Dinakar Raj, Kavitha Veerappan, Jeya Bright Pankiraj.
Resources: Kavitha Veerappan, Jeya Bright.
Supervision: Kavitha Veerappan, Jeya Bright Pankiraj, K. Sangeetha, Sumesh Joe Cherian and S. Rajeswari.
Approval of the final text: S. Dinakar Raj, Kavitha Veerappan, Jeya Bright Pankiraj, K. Sangeetha, Sumesh Joe Cherian and S. Rajeswari.

VI. REFERENCES

[1] Y. Muhammad, M. Tahir, M. Hayat and K. T. Chong, "Early and accurate detection and diagnosis of heart disease using intelligent computational model," Sci Rep, vol 10, pp.19747, Nov. 2020.

[2] A. P. Akerman, M. Porumb, C. G. Scott, A. Beqiri, A. Chartsias, A. J. Ryu, W. Hawkes and G. D. Huntley, "Automated echocardiographic detection of heart failure with preserved ejection fraction using artificial intelligence JACC: Advances," vol. 2, no. 6, pp.100452, 2023

[3] Y. D. Daydulo, B. L. Thamineni, and A. A. Dawud, "Cardiac arrhythmia detection using deep learning approach and time frequency representation of ECG signals," BMC Med Inform Decis Mak, vol. 23, pp.232, 2023.

[4] J. Li, S. Pang, F. Xu, P. Ji, S. Zhou and M. Shu, "Two-dimensional ECG-based cardiac arrhythmia classification using DSE-ResNet," Sci Rep, vol.12, 14485, 2022.

[5] S. Sattar, R. Mumtaz, M. Qadir, S. Mumtaz, M. A. Khan, T. De Waele, E. De Poorter, I. Moerman and A. Shahid, "Cardiac Arrhythmia Classification Using Advanced Deep Learning Techniques on Digitized ECG Datasets," Sensors, vol. 24, no. 8, pp.2484.

[6] M. A. Talukder, M. Khalid, M. Kazi, N. J. Muna, M. Nur-e-Alam, S. Halder and N. Sultana, "A hybrid cardiovascular arrhythmia disease detection using ConvNeXt-X models on electrocardiogram signals," Sci Rep, vol. 14, pp. 30366, 2024.

[7] S. Nurmaini, B. Tutuko, M. N. Rachmatullah, A. Darmawahyuni and F. Masdung, "Machine learning techniques with low-dimensional feature extraction for improving the generalizability of cardiac arrhythmia," IAENG International Journal of Computer Science, vol. 48, no. 2, pp. 369-378, 2021.

[8] P. Ma, J. Ren, H. Zhao, G. Sun, P. Murray and J. Zheng, "Multiscale 2-D Singular Spectrum Analysis and Principal Component Analysis for Spatial–Spectral Noise-Robust Feature Extraction and Classification of Hyperspectral Images," in IEEE Journal of Selected Topics in Applied Earth Observations and Remote Sensing, vol. 14, pp. 1233-1245, 2021.

[9] H. R. Okhovvat, M. A. Riahi, A. Akbari Dehkharghani, "Kernel principal component analysis (KPCA) in electrical facies classification," Iranian Journal of Oil and Gas Science and Technology, vol. 12, no. 1, 2023.

[10] A. B. Buriro, B. Ahmed, G. Baloch, J. Ahmed, R. Shoorangiz, S. J. Weddell and R. D. Jones, "Classification of alcoholic EEG signals using wavelet scattering transform-based features," Computers in biology and medicine, vol.139, pp.104969, 2021.

[11] K. M. M. Uddin, R. Ripa, N. Yeasmin, N. Biswas and S. K. Dey, "Machine learning-based approach to the diagnosis of cardiovascular vascular disease using a combined dataset," Intelligence-Based Medicine, vol. 7, pp. 100100, Jan. 2020.

[12] S. Abd El-Ghany, and A. A. Abd El-Aziz, "A Robust Tuned Random Forest Classifier Using Randomized Grid Search to Predict Coronary Artery Diseases," CMC-COMPUTERS MATERIALS & CONTINUA, vol. 75, no. 2, pp. 4633-4648, 2023.

[13] E. S. Mohamed, T. A. Naqishbandi, S. A. C. Bukhari, I. Rauf, V. Sawrikar, and A. Hussain, "A hybrid mental health prediction model using Support Vector Machine, Multilayer Perceptron, and Random Forest algorithms," Healthcare Analytics, vol. 3, pp.100185, 2023.

[14] N. Singh, V. K. Gunjan, F. Shaik, S. Roy, "Detection of Cardio Vascular abnormalities using gradient descent optimization and CNN," Health and Technology, vol. 14, no. 1, pp. 155-168, 2024.

[15] A. B. Naeem, B. Senapati, D. Bhuva, A. Zaidi, A. Bhuva, M. S. I. Sudman, A. E. M. Ahmed, "Heart disease detection using feature extraction and artificial neural networks: A sensor-based approach," IEEE Access, 2024.

[16] K. Aguerchi, Y. Jabrane, M. Habba and A. H. El Hassani, "A CNN hyperparameters optimization based on particle swarm optimization for mammography breast cancer classification," Journal of Imaging, vol.10, no. 2, pp. 30, 2024.

[17] M. Y Hassan, A. H. Najim, K. A. M. Al-sharhanee, M. A. Alkhafaji, R. M Alfoudi andW. A Shutnan, "Enhancing Resource Allocation and Optimization in IoT Networks Using AI-Driven Firefly Optimized Hybrid CNN-BILSTM Model," International Journal of Intelligent Engineering & Systems, vol. 16, no. 6, 2023.

[18] F. Fadilah and D. Avianto, "Hyperparameter Optimization of CNN for Coffee Berry Disease Classification Using the Artificial Bee Colony Algorithm," Journal of Scientific Research, Education, and Technology (JSRET), vol. 3, no. 4, pp. 1877-1889, 2024

[19] H. Mewada, I. M. Pires, P. Engineer and A. V. Patel, "Fabric surface defect classification and systematic analysis using a cuckoo search optimized deep residual network," Engineering Science and Technology, an International Journal, vol. 53, pp. 101681, 2024

[20] Y. W. Jeong, K. B. Sim, S. Park, J. Oh, W. J. Choi, "Generation of CNN architectures using the harmonic search algorithm and its application to classification of damaged sewer," IEEE Access, vol.10, pp. 32150-32160, 2022.

[21] S. Karthiga, and A. M. Abirami, "Deep Learning Convolutional Neural Network for ECG Signal Classification Aggregated Using IoT," Comput Syst Sci Eng, vol. 42, no. 3, pp. 851–66, 2022.

[22] B. Kishore, A. N. G. Reddy, A. K. Chillara, W. A. Hatamleh, K. D. Haouam, R. Verma, B. L. Dhevi and H. K. Atiglah, "An innovative machine learning approach for classifying ECG signals in healthcare devices," J Healthc Eng, no.13, 2022.

[23] Y. Muhammad, M. Tahir, M. Hayat and K. T. Chong, "Early and accurate detection and diagnosis of heart disease using intelligent computational model," Scientific reports, vol. 10, no. 1, pp. 19747, 2020.

[24] S. Mohapatra, S. Maneesha, S. Mohanty, P. K. Patra, S. K. Bhoi, K. S. Sahoo and A. H. Gandomi, "A stacking classifiers model for detecting heart irregularities and predicting cardiovascular disease," Healthcare Analytics, vol. 3, pp. 100133, Nov. 2023

[25] D. Cenitta, R. Vijaya Arjunan, and K. V. Prema, "Ischemic heart disease prediction using optimized squirrel search feature selection algorithm," IEEE Access, vol. 10, pp.122995-123006, 2022.

Journal of Engineering and Technology for Industrial Applications

ITEGAM-JETIA

Manaus, v.12 n.60, p.206-226, July/August, 2026.
DOI: https://doi.org/10.5935/jetia.v12i60.3716

ISSN ONLINE: 2447-0228

RESEARCH ARTICLE OPEN ACCESS

STARFISH OPTIMIZED AI-BASED DEEP LEARNING MODEL FOR ACCURATE BROKEN ROTOR BAR FAULT DETECTION IN INDUCTION MOTORS

Killamsetti Vijeta*[1], Sri Suyambulinga Perumal B[2], R. Tharwin Kumar[3], Niran I R[4], Jinsha Lawrence[5], Gunasekar M[6]

[1]Assistant Professor, Department of Electrical Engineering, Medicaps University, Indore, India.
[2]Assistant Professor, Department of Chemistry, Vel Tech High Tech Dr.Rangarajan Dr.Sakunthala Engineering College, Chennai, India.
[3]Department of Electrical and Electronics Engineering, Mohan Babu University, Tirupati, Andhra Pradesh, India.
[4]Lecturer, Department of Mechanical Engineering, Edumentor, Thrissur, Kerala, India.
[5]Assistant Professor, Department of Computer Science and Engineering, Faculty of Engineering, Karpagam, India.
Academy of Higher Education (Deemed to be University), Coimbatore, Tamil Nadu, India.
[6]Assistant Professor, Department of Computer Science and Business Systems, Vel Tech Multi Tech Dr.Rangarajan Dr.Sakunthala Engineering College, Avadi, Chennai, Tamil Nadu, India.

[1]http://orcid.org/0000-0002-7925-5596, [2]http://orcid.org/0000 0001 8006 7202, [3]http://orcid.org/0000-0002-3438-4562,
[4]http://orcid.org/0009-0007-7087-7413, [5]http://orcid.org/0009-0003-0291-9272, [6]http://orcid.org/0009-0007-3921-5403,

Email:*vijetha258@gmail.com, bsslperumal@gmail.com, tharwin.eee@gmail.com, niraniyyani@gmail.com, jinshalarence@gmail.com, gunaceg2017@gmail.com

ARTICLE INFO

Article History
Received: February 17, 2026
Reviewed: June 7, 2026
Accepted: July 7, 2026
Published: July 31, 2026

Keywords:
Induction motor,
fault diagnosis,
EDEWF,
RBFNN- MHAT,
SFOA.

ABSTRACT

To maintain the safety and reliability of industrial applications, it is important to analyse faults in three-phase induction motors. Traditional methods have difficulty in identifying the complex characteristics of errors in three-phase induction motors because the signals associated with three-phase induction motors are often noisy and exhibit non-linear dynamics. In this paper, a comprehensive method to analyse errors in three-phase induction motors are proposed that utilises advanced signal preprocessing, feature extraction, and Deep Learning (DL) methods to address these issues. Initially, an Entropy-Driven Empirical Wavelet Filter (EDEWF) are applied to clean the raw motor signal, and a Min-Max scaling is used to normalise the signal to create useful features. Next, an integrated hybrid model combining a Radial Basis Function Neural Network (RBFNN) with a Multi-Head Adaptive Transformer (MHAT) are used for capturing local non-linear characteristics and global context. The features extracted from both models are combined into one feature vector and passed through a fully connected layer for classification. The Starfish Optimization Algorithm (SFOA) is implemented to adjust the hyperparameter of the proposed integrated hybrid model to improve the overall performance. The results obtained from the proposed method showed that it achieved a greatest accuracy, precision, recall, F1-Score of 0.9960 and robustness in the diagnostic of three-phase induction motors compared to traditional diagnostic methods, with respect to classifying the motor states as normal, healthy, and Broken Rotor Bar (BRB) faulted.

Copyright ©2026 by authors and Galileo Institute of Technology and Education of the Amazon (ITEGAM). This work is licensed under the Creative Commons Attribution International License (CC BY 4.0).

I. INTRODUCTION

Induction motors represent a significant aspect of industrialization, as they are extremely tough and do not have their integrity impaired by the environment in which they operate. However, over time, parts of an induction motor will experience wear and deformation, which can result in decreased life expectancy and poor operation output from the motor [1]. An induction motor malfunction can also cause damage to surrounding materials, waste time, and cause workplace accidents, which will lower system reliability. For this reason, fault diagnosis technologies are necessary for timely fault detection, proper action, and safe and secure operation of the equipment.

Induction motor faults are divided into electrical and mechanical faults [2]. The different types of electrical faults found in induction motors are overload, open phase and short-circuit faults. The various ways mechanical faults occur include the bearing, rotor, and stator. Among these three types of mechanical faults, the most typical is the bearing fault; approximately 40 % of all induction motors have a bearing fault. The traditional method for diagnosing faults relies on the use of a mathematical model of the system and the user's input. Due to the complex nature of nonlinear systems, accurately representing them mathematically has always presented challenges. User input techniques rely upon visual and auditory signals gathered from direct observation of the equipment and have resulted in excessive maintenance from over-maintaining equipment due to unexpected faults and unnecessary costs [3-5]. Induction motors fault diagnosis has the purpose of detecting motor component failure, located in the magnetic or mechanical parts of the motor, and assess the motor operating conditions to identify what repair actions must take place. Fault diagnosis in induction motors has two types of diagnostic testing methods to detect the faults such as invasive methods and non-invasive methods [6]. Invasive testing methods measure electrical phone lines, insulation, winding, and polarisation indexes, to consider only the windings that may fail. This test type usually requires expensive Test and Measurement Equipment (T&M), which has its associated risks for testing personnel. Invasive testing is generally completed when an induction motor is not powered and all types of faults must be tested at the same time [7]. Due to the high costs and risks involved in completing the invasive fault test method, there is an increased acceptance of the non-invasive fault tests in monitoring a motor's operational condition and diagnosing a variety of faults at a time, when the induction motor is running. However, non-invasive diagnostic methods, employ mathematical models and physical mechanisms combined with actual operating data to assess and predict degeneration of the induction motor component based on specific motor operating parameters and operating conditions. At this time, there are many categories of these non-invasive fault diagnostic tests include electromagnetic field monitoring, temperature monitoring, infrared monitoring, noise monitoring, vibration monitoring, and current monitoring based on the specific sensor being used [8-13].

In addition, fault diagnosis techniques continue to rely on model-based approaches. Model-based fault diagnosis is heavily reliant on the user's in-depth knowledge of the fault mechanisms along with deep understanding of the processing of signals that are generated during motor operation. The models utilize the generated vibration signal from the motor by creating an indicator representing sensitivity towards a fault and performing the following tasks to detect a fault [14]. Additionally, a mode decomposition technique is proposed that uses variational mode decomposition and improved teager energy operators to extract fault characteristics early in motor operation. Despite the advantages of the techniques, the inherent limitations of these techniques are high computational cost associated with model development and the inability to utilize all available information contained within the monitoring data. Furthermore, the model is task dependent and thus the resulting models will require re-optimization if new tasks are presented [15-17]. To overcome this issue, the proposed model develop an AI-based approach for induction motor fault diagnosis. In this process, the raw data undergoes preprocessing to reduce noise and to clean the data [18]. Due to the computational simplicity, straightforward implementation, and extensive support through conventional signal processing techniques, the classical Fourier transform method is particularly suited towards online applications used for surveillance within industrial environments. However, since this method does not maintain temporal and spatial localization of failures, it poses significant difficulties when attempting to identify early or developing failures [19]. To tackle this issue EDEWF method is implemented. The preprocessed data is passed to a feature engineering stage to normalize the signal features to a common range. Histogram Equalization (HE) enhances the visibility of low-amplitude fault indicators when converting time-frequency images from vibration or current signal data. However, HE enhance the noise levels along with the fault signal which gives rise to false positives [20]. To deal with this constraint, the proposed system uses a Min-Max scaling. Next to enhance the diagnostic accuracy, RBFNN with MHAT is executed in this proposed system. Though, various existing methods are deliberated in this paper to completely analyze each model's respective performance compared with each other, indicating where each model is limited in effectively addressing motor signals that do not follow linear values.

I.1 RELATED WORKS:

By [21] have developed a machine learning approaches, in particular through the usage of Random Forest Classifiers, it has been found to provide extremely high classification accuracies for motor faults due to its ability to utilize ensemble learning, where many Decision Trees are used to increase generality while at the same time reduce overfitting of the Decision Trees. However, with regard to real-time monitoring systems and the number of trees required for high accuracy of Random Forest Classifiers, it becomes computationally expensive particularly when using large amounts of data. In turn [22] have proposed an Induction motor bearing fault diagnostics utilizing Continuous Wavelet Transform (CWT) possess an exceptional time -frequency resolution and, therefore, it is an effective tool in the analysis of non-stationary and transient signal characteristics. Nevertheless, data redundancy and volume provided from the CWT increase the complexity of the extraction and classification of feature information. By [23] have established a CNN-LSTM for the analysis of faults in three-phase induction motors from an AI perspective. The CNN is capable of effectively capturing local characteristics and fault features, while also modelling time-dependent behaviour and dynamics by implementing the LSTM, resulting in High diagnostic accuracy and reliable early fault detection. Nonetheless, CNN-LSTM require large labelled datasets for training and it suffer from poor performance due to insufficient or unbalanced datasets. According to [24] have suggested a ClasLoc, a reliable fault management methodology for transmission lines, based on RBFNN and ANFIS, which provide distinct benefits for the management of transmission line faults because of the combined approach used in the ClasLoc methodology to classify and localize faults more accurately and reliably under various operating conditions. ClasLoc's performance could potentially deteriorate when implemented on large-scale systems due to the increased quantity of rules that need to be created. Though, the overall ClasLoc model lacks interpretability and scalability, which limit ClasLoc's ability to be implemented in real time in large or limited resource power system environments. By [25] have recommended a CNN-RNN observers for predictive maintenance and fault detection for industrial robot drive systems. By automatically learning to identify both spatial and temporal features from sensor data, these observers accurately predict degradation before it occurs and detect faults once they occur. The CNN portion of the observer learns to identify localized fault patterns, while the RNN portion learns to model the dynamic behavior of the system over time, therefore this method is particularly effective for the control of robotic drive systems that are complex, nonlinear and time-varying in their nature.

However, the fault prediction decisions provide lack of interpretability. Additionally, because of the high level of complexity in the design, training and tuning of hyperparameter in CNN-RNN networks, the costs involved in developing these systems possibly be prohibitively high for implementation in an industrial environment.

I.2 OBJECTIVES:

The main objectives of this research includes,

- To design an intense and intelligent fault diagnosis model for three-phase induction motors, the proposed system is implemented.
- To enhance signal quality and fault information, entropy-based empirical wavelet filtering is used in preprocessing stage.
- To provide an accurate assessment of the fault classification, min-max scaling normalization is introduced.
- To capture both global and local fault characteristics, a hybrid RBFNN-multi-head Adaptive Transformer model is executed.
- To optimise the RBFNN model performance for accurate and steady recognition of the induction motor faults, especially for the broken rotor bar condition, starfish optimisation method is employed.

I.3 PAPER ORGANIZATION:

This paper is organized as follows: Section II provides an explanation of the suggested system description. The study methodology is thoroughly described in Section III, which also includes examples of the process, methods, and mathematical representations. The experimental results of this work are described in Section IV, which also include the simulation setup, comparison analysis, and research summary. The conclusion of the proposed investigation is explained in Section V.

II. PROPOSED SYSTEM DESCRIPTION

The proposed system provides a reliable fault diagnosis system for three-phase induction motors. The block diagram of the proposed system is depicted in figure 1.

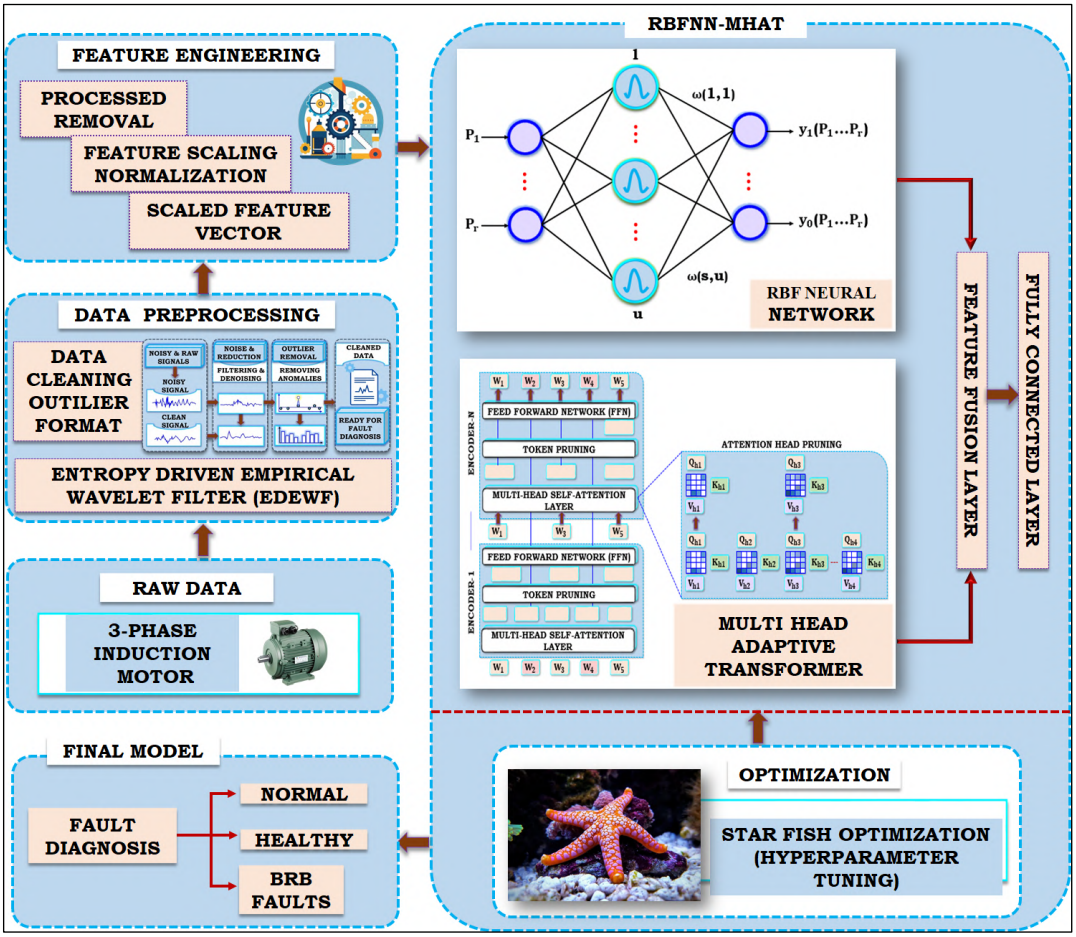


Figure 1: Proposed block diagram.
Source: Authors, (2026).

The suggested fault diagnosis system begins with the collection of raw motor data, which then undergoes data preprocessing via data cleaning, removal of outliers, EDEWF, and other signal enhancement techniques. Following the information enhancement of the raw motor data, feature engineering is performed to create feature vectors through feature scaling and feature normalization. After feature vector creation, a hybrid model that incorporates both a RBFNN and a MHAT are utilized. The RBFNN is used to capture global context features through the use of multi-head self-attention and adaptive weighting, whereas the transformer focuses on extracting local pattern features through the use of an RBF kernel layer.

After the feature extraction process, both models are combined, at which each model is treated as a separate input, and delivered to a fully connected layer for final classification. Optimizing performance is achieved by applying SFOA to tune hyper parameters, providing the capability for the system to diagnose motor operating conditions with high levels of accuracy, whether they are normal operating conditions, healthy working conditions, or failure modes associated with the broken rotor bars supporting effective condition monitoring and predictive maintenance for all motor installations.

III. PROPOSED SYSTEM MODELLING

III.1 DATA PREPROCESSING

III.1.1 Data Cleaning

In diagnosing faults with induction motors, the first step is to identify sensor readings that show irregularities or potential failure. Some of these readings recommend problems with the rotor bars, insulation, or bearings. The diagram of data cleaning process is shown in figure 2.

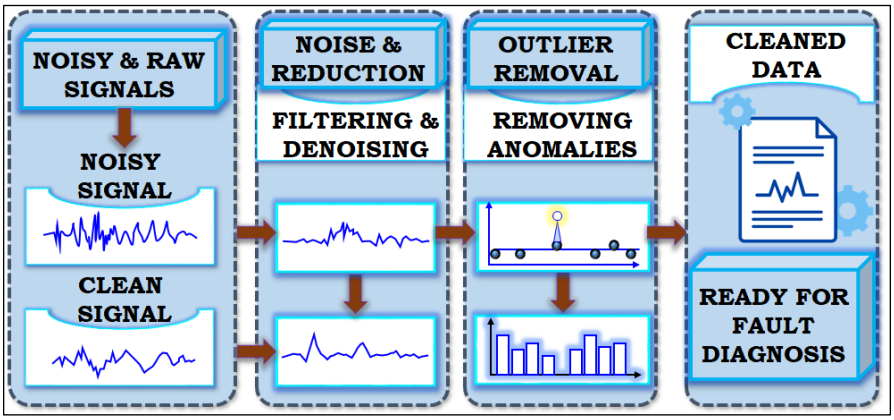


Figure 2: Data cleaning process.
Source: Authors, (2026).

For identifying errors in data systems, each individual measurement in an induction motor fault diagnosis is classified according to its measurement type such as current, voltage and vibration. In some cases, only a single reading is analysed in isolation. In other cases, multiple readings from the same time period are combined to identify context-dependent faults that occur through interactions of several parameters. By converting signals generated by the induction motor into sequences and applying techniques to classify those sequences, faults are identified and classified, thereby improving the effectiveness of condition monitoring and predictive maintenance effectively.

III.1.2 Entropy Driven Empirical Wavelet Filter (EDEWF)

The process of analysis within the EDEWF starts with the decomposition, using Empirical Wavelet Transform (EWT), of a time-dependent function (current or vibration) from a motor into two components such as an approximation mode and detail modes as follows,

$$f_0(t) = EWT(0,t) * \phi_1(t) \tag{1}$$

$$f_k(t) = EWT(k,t) * \psi_k(t) \tag{2}$$

Where, $EWT(0,t)$ and $EWT(k,t)$ is represented as an approximation coefficients and detail coefficients respectively.

$$EWT(0,t) = \langle f, \phi_1 \rangle \tag{3}$$

$$EWT(k,t) = \langle f, \psi_k \rangle \tag{4}$$

Each mode's entropy $f_k(t)$ is computed to determine the information aspect of that mode. Entropy is referred to as Shannon Entropy or Energy Entropy, and works by measuring the energy distribution across the selection of modal frequencies, as provided by:

$$H(f_k) = -\sum_i P_i \, log(P_i) \tag{5}$$

In the above expression, P_i is the normalized distribution of energy across the selected modal frequencies. Therefore, when a fault has occurred, the energy distribution is concentrated on those modes of increased entropy. And for the other modes, it is automatically suppressed. The reconstructed fault signal is determined by the addition of only those selected modes:

$$f_{fault}(t) = \sum_{k \in selected} f_k \, (t) \tag{6}$$

Thus, the EDEWF enhances weak mark components in relation to the fault and suppresses noise. This makes the approach suitable for diagnosing fault conditions in induction motors.

III.2 FEATURE ENGINEERING- MIN-MAX SCALING

Min-Max scaling method of normalizing the signals extracted from induction motors are large variances between the signals being analysed due to differences in measurement units and ranges. The Min-Max scaling method allows to set all outputs from different signals on a common scale of 0 to 1. For each signal that has been normalised using the Min-Max Scaling formula, a new normalised value is calculated using the formula in the following way,

$$X_{ij}^{MM} = \frac{X_{ij} - X_{min}}{X_{max} - X_{min}} \tag{7}$$

Where, X_{min} and X_{max} are value of features. By using the Min-Max Scaling method to normalise the EDEWF-derived features associated with the induction motor fault diagnosis application, it makes it possible to have a consistent method to compare the EDEWF-derived features across multiple different modes to determine which mode contain weak fault-related marks, provide signal characteristic information and a method to interpret differences in the condition of an induction motor while eliminating variable ranges and the influence of variable units on the comparison between modes.

III.3 HYBRID MODEL- RBFNN- MHAT

An RBFNN represents a kind of nonlinear mapping from a feature space obtained from induction motor signal data to types of motor faults. An input vector $x \in R^d$, represents a set of features created using data taken from an induction motor's stator current, vibration sensor, and/or audio microphone, while the prototype $c_i \in R^d$ for the ith RBF unit represents a typical operating condition (or fault) for that motor. The RBF unit outputs the Euclidian distance between the input vector and the prototype.

$$\phi_i(x) = exp\left(\frac{-\|x - c_i\|^2}{2\sigma_i^2}\right) \tag{8}$$

Where, $\|\cdot\|$ denotes the Euclidean norm and σ_i is the Gaussian width of the ith RBF unit. The Gaussian function is popular for establishing a relation between localizing, smoothness, hence modelling delicate changes that occur on induction motor fault marks. The diagram of RBFNN- MHAT is shown in figure 3.

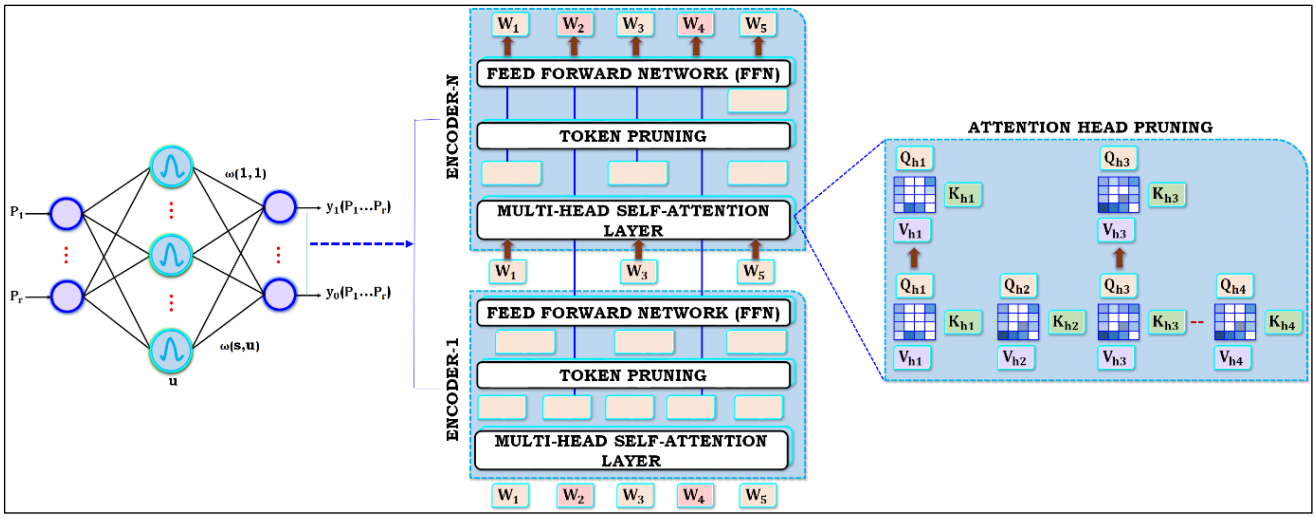


Figure 3: HYBRID MODEL- RBFNN- MHAT.
Source: Authors, (2026).

An RBF unit produces localized responses, which represents the similar or dissimilar observed condition of the motor with any of all fault prototypes stored in its memory. The Gaussian width σ_i determines the region over which the total influence of that prototype occurs. Low values of σ_i render an RBF unit very sensitive to small variations in the motor's features, while higher values of σ_i produce RBF units that are tolerant variations resulting from load changes, speed fluctuations, and measurement noise that are a common occurrence during the operation of induction motors. The output of the RBF neural network for the kth fault class is calculated as a weighted linear combination of the output from all RBF units,

$$y_k = \sum_{i=1}^{M} w_{ik}\phi_i(x) \tag{9}$$

Where, w_{ik} represents the connection weight between the ith RBF unit and the kth output neuron, and M denotes the total number of Gaussian units. The bias term is neglected to reduce network complexity. The formulation above shows that the RBF neural network linearly discriminates in a transformed feature space created using the non-linear mapping, $\phi_i(x)$. Therefore, decision boundaries for different induction motor fault classes are hyperplanes in this high-dimensional RBF feature. According to Cover's theorem, mapping to a higher dimension with a non-linear function increases the probability of making the induction motor fault pattern linearly separable. Hence, as M increases, the induction motor fault classes are more distinct from one another, However, too high a value of M cause the model to over fit; therefore, it decrease its ability to generalize when the fault data available were small in volume.

RBFNN partitions feature space into hyper spherical sectors centred around c_i and widthσ_i. Clustering methods typically supply the clustering centres for RBFNNs. Most conventional clustering methods are based on unsupervised techniques, which typically do not take into the differences between fault categories and create clusters that consist of samples from more than one fault category, this results in a low level of diagnostic accuracy. The supervised methods are more effective at producing homogeneous clusters for the purposes of diagnostic accuracy. In addition to the distance $\| x - c_i \|$ between a feature vector and a cluster centre, the Gaussian width σ_i determines the factor in assigning fault connection. Thus, a feature vector have a closer distance to one cluster centre than another, a properly selected σ_i produce a greater activation for the other fault class, enabling the accurate handling of overlapping fault feature sets and variable operating conditions of induction motors. Clustering methods of RBFNN is depicted in figure 4.

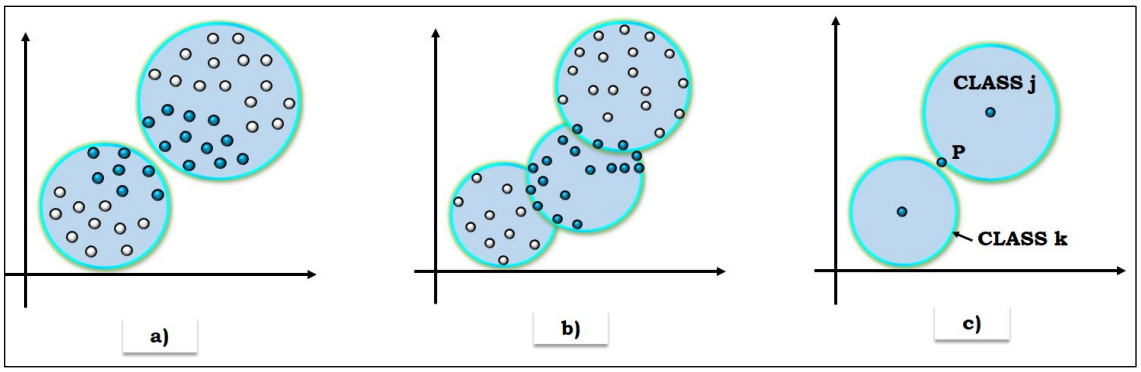


Figure 4: Clustering methods of RBFNN.
Source: Authors, (2026).

The MHAT is from the base Multi-Head Attention framework that extracts the additional fault features from induction motor signals appropriately without computing redundantly. Let $x = x_1, x_2, \ldots x_T$, where $x_t \in R^d$, denote the sequence of embedded induction motor signal marks that were derived from either the stator current or vibration signals, and let $q \in R^d$ represent a query vector resulting from the same sequence of induction motor signals. The manner in which the elastic form of scaled dot product is used to model temporality-related dependencies through induction motor data is,

$$Attention(x, q) = W_o \sum_{t=1}^{T} \alpha_t (q) W_v x_t \tag{10}$$

The attention weights are calculated as follows,

$$\alpha_t(q) = softmax\left(\frac{q^T W_q^t W_K x_t}{\sqrt{d}}\right) \tag{11}$$

$W_o, W_v, W_q, W_k \epsilon R^{d \times d}$ represent the weight vectors used for each signal in the multi-head attention mechanism. Each attention head is designed to target a specific fault feature of a motor signal that occur in time, such as an intermittent burst of bearing defects or rotor bar harmonics. Once the focus of the individual head is established, the output of the multi-head attention is the sum of H parallel attention heads is given by,

$$MH\ Attention(x, q) = \sum_{h=1}^{H} Attention_h(x, q) \tag{12}$$

Where, each $Attention_h$ represents a low-rank decomposition of the output of the previous attention heads. In the analysis of faults in induction motors, many of the attention heads are considered interchangeable or provide only minimal assistance. To assist in the identification of which heads to keep for training purposes, a head sensitivity score is generated from a forward pass through a transformer model, fine-tuned specifically for classifying faults. Once these scores have been computed, the heads reflect the highest levels of usefulness included in training. When training is completed, each layer$i + 1$, the retention m_{i+1} is the number of heads, is selected randomly based on,

$$m_{i+1} \in [m_{i+1}, m_i] \tag{13}$$

Where, m_i is the number of heads retained from prior i layer, m_{i+1} is the minimum number of heads retained in the next layer, and only one head retained in the final layer. This reflects that the deeper layers have fewer but more important heads for recognizing anomalies related to fault marks. The MHAT offers a computationally efficient methodology for induction motor fault diagnosis. The approach allows for an improved accuracy relationship when compared to traditional transformer models. Hence the proposed system is more effective, reliable, and scalable approach for performing induction motor fault diagnosis that is employed on a real-time basis as part of an industrial condition monitoring system.

III.4 HYPERPARAMETER TUNING- SFOA

Induction motor fault identification is approached through optimization by minimizing misclassification errors or maximizing fault separation using the features generated from stator current, vibration or acoustic signals. In SFOA, each starfish requires its own candidate fault detection solution, representing a classifier parameter vector, with an assigned position expressed as,

$$X = \begin{bmatrix} X_{11} & X_{12} & \dots & X_{1D} \\ X_{21} & X_{22} & \dots & X_{2D} \\ \vdots & \vdots & \ddots & \vdots \\ X_{N1} & X_{N2} & \cdots & X_{ND} \end{bmatrix} \quad (14)$$

Where N should be the size of the starfish population and D is the number of decision variables for induction motor fault detection. Starfish are initialized to relative position with respect to the allowable dimension of the induction motor fault detection parameter space by,

$$X_{ij} = l_j + r(u_j - l_j), i = 1,2 \dots N, j = 1,2, \dots D \quad (15)$$

Where l_j stands for the lower bounds of the fault detection parameters, u_j denotes the upper bounds, and $r \in \{0,1\}$ is a random number. Each starfish's utility is evaluated through a fault detection objective function that is expressed as,

$$F = \begin{bmatrix} f(X_1) \\ f(X_2) \\ \vdots \\ f(X_N) \end{bmatrix}_{N \times 1} \quad (16)$$

The SFOA uses a hybrid exploration strategy to cover the complete feature space for induction motor faults.

Pseudo-code: SFOA.

```
Initialize population X = {x1, x2, …, xN} randomly within [LB, UB]
Evaluate fitness F(i) for each xi
Identify global best solution:
    xpos_best = argmin(F)
    fval_best = min(F)
Set iteration counter T = 1
While T ≤ MaxIt do
  Update control parameters:
    θ = 2 × (1 − T / MaxIt)        // decay factor
    t_EO = T / MaxIt               // exploitation–exploration balance
  For each individual i = 1 to N do
    Generate random number r ∈ [0,1]
    If r < GP then   // ===== Exploration Phase =====
      If D > 5 then
        Perform 5D Starfish Search:
        x_new = xi + θ × randn(1,D) × |x_best − xi|
      Else
        Perform 1D Starfish Search:
        k = random dimension ∈ [1, D]
        x_new(k) = xi(k) + θ × rand() × (x_best(k) − xi(k))
      End If
    Else            // ===== Exploitation Phase =====
      // Predation behavior
      x_pred = xi + rand() × (x_best − xi)
      // Regeneration behavior
      x_new = x_pred + t_EO × randn(1,D)
    End If
    Apply boundary constraints:
    x_new = min(max(x_new, LB), UB)
    Evaluate new fitness F_new = F(x_new)
    If F_new < F(i) then
      xi = x_new
      F(i) = F_new
    End If
    If F_new < fval_best then
      xpos_best = x_new
      fval_best = F_new
    End If
  End For
  Store convergence value:
  Curve(T) = fval_best
  T = T + 1
End While
Return xpos_best, fval_best, Curve
```

For instance, for D >5, the concurrent five-dimensional search pattern updates five randomly chosen fault-sensitive features such as sideband amplitude, statistical vibrations, or typical values of non-typical faults.

$$Y_{i,p}^{T} = \begin{cases} X_{i,p}^{T} + a_1\left(X_{best,p}^{T} - X_{i,p}^{T}\right)cos\theta, r \leq 0.5 \\ X_{i,p}^{T} - a_1\left(X_{best,p}^{T} - X_{i,p}^{T}\right)sin\theta, r > 0.5 \end{cases} \quad (17)$$

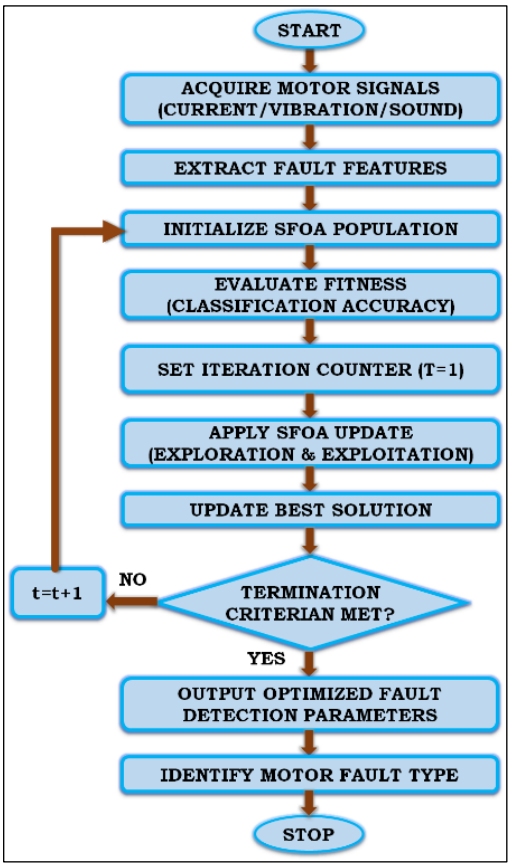


Figure 5: Flowchart of SFOA.
Source: Authors, (2026).

Flowchart of SFOA is shown in figure 5. Where, $X_{best,p}^{T}$ represents the most effective method of recognizing faults in iteration T within the p^{th}dimensional space.

$$a_1 = (2r-1)\pi, \theta = \frac{\pi}{2} - \frac{T}{T_{max}} \quad (18)$$

The values of the other variables define the step size and convergence behaviour for feature exploration. A starfish that is updated to a value beyond the range retain its last value.

$$X_{i,p}^{T+1} = \begin{cases} Y_{i,p}^{T}, l_p \leq Y_{i,p}^{T} \leq u_p \\ X_{i,p}^{T}, \ otherwise \end{cases} \quad (19)$$

When the total number of parameters associated with faults is relatively low$(D \leq 5)$, only unidirectional searches are implemented during feature searching. The above equation summarizes a generic form of the searching procedure.

$$Y_{i,q}^{T} = E_t X_{i,p}^{T} + A_1\left(X_{k1,p}^{T} - X_{i,p}^{T}\right) + A_2\left(X_{k2,p}^{T} - X_{i,p}^{T}\right) \quad (20)$$

Where $X_{k1,p}^{T}$ and $X_{k2,p}^{T}$ are two randomly selected starfish which represents an alternative fault detection methods with $A_1, A_2 \epsilon (-1,1)$ and the energy of a starfish is computed according to equation,

$$E_t = \frac{T_{max} - T}{T_{max}} cos(h) \quad (21)$$

The exploitation phase enables the enhancement of fault detection capabilities through a naturalistic simulation of the collective hunting habits of starfish. Thus, a distance calculation must be performed between the best fault detection method provided at present and the selected starfish.

$$d_m = X_{best}^{T} - X_{m}^{T}, m = 1,2,\ldots,5 \quad (22)$$

A parallel bidirectional search method is employed for updating the positions of the starfish is,

$$Y_i^T = X_i^T + r_1 dm_1 + r_2 dm_2 \quad (23)$$

The parameters $r_1, r_2 \epsilon (0,1)$for the starfish. This method provides the ability for the fault detection model to converge to their respective discriminative decision boundaries while maintaining diversity. To prevent stagnation in local optima due to non-stationarity of the motor signal and interference due to noise in the motor signal, a regeneration mechanism is applied to the last starfish in the group.

$$Y_i^T = exp\left(\frac{T-N}{T_{max}}\right) X_i^T \tag{24}$$

This mechanism allows the addition of controlled perturbations to the starfish and further increases the convergence of the global. The boundary constraints of each starfish are applied as,

$$X_i^{T+1} = \begin{cases} l_b, Y_i^T < l_b \\ u_b, Y_i^T > u_b \\ Y_i^T, otherwise \end{cases} \tag{25}$$

Table 1: Optimization values of SFOA.

PARAMETERS	VALUES
RBF Units	96.000
Transformer Heads	4.000
Transformer Layers	2.000
Learning Rate	0.001
Batch Size	64.000
Dropout Rate	0.200
Dense Units	128.000
Number of Starfish	30.000
Maximum Iterations	50.000
Exploration Probability	0.500

Source: Authors, (2026).

The starfish determine only the search within a specified area. By applying the equations in these processes within the SFOA, it designed specifically for the induction motor fault detection system, when the SFOA is applied to improve the fault sensitivity and detection parameters of the induction motor fault detection system, it leads to enhanced accuracy, robustness to a performance effect of noise, and assures that motor faults are accurately identified under several operational conditions.

IV. RESULT AND DISCUSSION

This research work highlights a Starfish Optimized AI-based DL framework for accurately detecting broken rotor bar faults on induction motors by making use of the BBIM2023 dataset. The BBIM2023 dataset consists of 24,000 samples containing 36 inputs features related to the time, three phase stator currents, multiple rotor bar current, ring current, rotor speed, and rotor position; as well as a target class indicating the motor's health condition. The data divided into 70% for training and 30% for testing to enable proper evaluation of the reliability of the model's performance. In order to obtain effective analysis of non-stationary and nonlinear characteristics in the electrical signals related to electrical motors, it used an additional advanced signal processing methods including the Entropy Driven Empirical Wavelet Filter (EDEWF), the Empirical Wavelet Transform (EWT), the Wavelet Packet Transform (WPT) and the Hilbert–Huang Transform (HHT), which were used as part of the procedure to reduce noise and to extract features that are sensitive to faults. The features that were extracted were then applied to a couple of different intelligent classification models including Radial Basis Function Neural Network (RBFNN) and Multi-Head Adaptive Transformer (MHAT). These intelligent classification models were able to represent complex nonlinear relationships and long-term temporal dependencies present within the dataset. Additionally, to improve the overall classification accuracy of the developed motor model and to improve the robustness of the classification models, the SFOA was used for optimally tuning the model parameters and for performing feature selection.

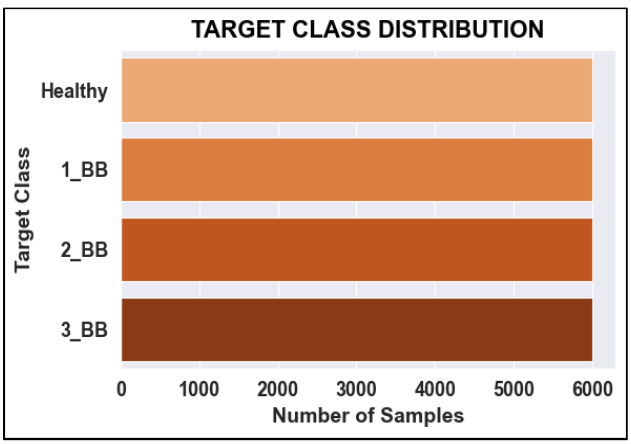


Figure 6: Distribution of target class.
Source: Authors, (2026).

Figure 6 shows the distribution of target class. The classes include a uniform number of the four Target Classes (i.e., Healthy, 1_BB, 2_BB, 3_BB), each class has approximately 6,000 samples of data for use during model training.

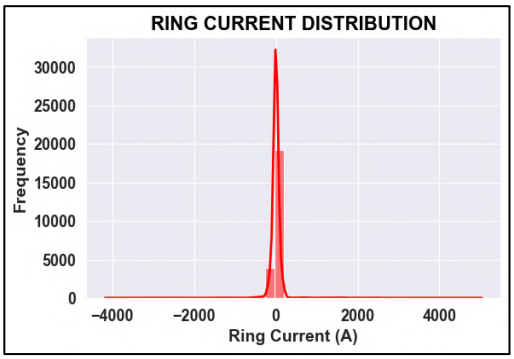


Figure 7: Distribution of ring current.
Source: Authors, (2026).

Distribution of ring current is depicted in figure 7. There is a strong concentration of recorded Ring Currents, the majority of recorded Ring Currents are in the 0A region with very few outliers in either positive or negative directions.

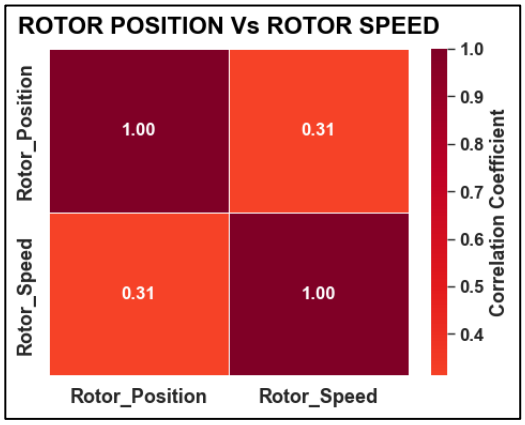


Figure 8: Rotor position vs Rotor speed.
Source: Authors, (2026).

The diagram of Rotor position vs Rotor speed is illustrated in figure 8. There is a moderate positive correlation between the Rotor Position (RP) and Rotor Speed (RS) (CP=0.31), with the CP of RP being 1.00 and the CP of RS being 1.00.

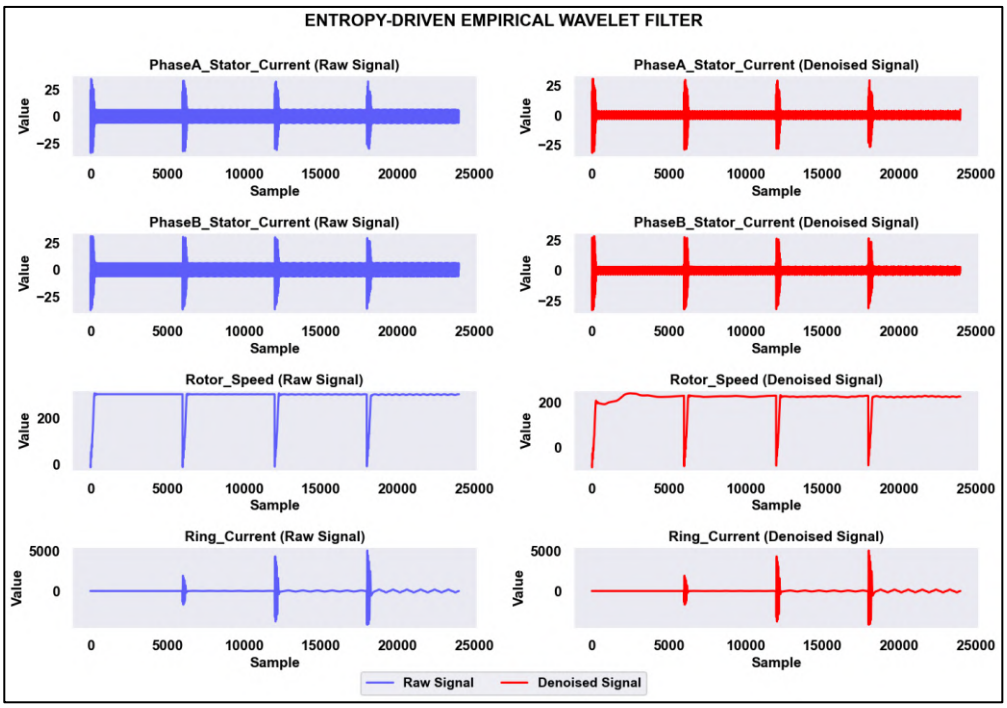


Figure 9: Entropy driven Empirical Wavelet Filter.
Source: Authors, (2026).

Figure 9 shows a high level of consistency when the signals were processed with an Entropy-Driven Empirical Wavelet Filter (EDEWF). The denoised signals represent an accurate representation of the most important transients and fault-related events, producing smooth and interpretable representations of the signals, while significantly reducing noise, fluctuations, and unwanted oscillations.

Table 2: Comparison of performance metrics.

SI.NO	FILTER	SNR (dB)	PSNR (dB)	MSE	RMSE	SSIM
1	EDEWF	35.4238	55.8329	1920.3489	43.8232	0.9991
2	EWT	31.1615	50.7602	2821.3994	47.9306	0.9987
3	WPT	30.9846	49.9126	3050.2765	55.2749	0.9979
4	HHT	12.4512	18.2150	6043.1248	340.9597	0.2812

Source: Authors, (2026).

Table 2 illustrates the filtered image quality comparison table. EDEWF was the best filtering method due to highest SNR, PSNR, and SSIM and RMSE. It has obtained the best classification of information and provides the maximum noise reduction and image quality. EWT and WPT will deliver moderate performance, however HHT demonstrates weaker performance across all measures.

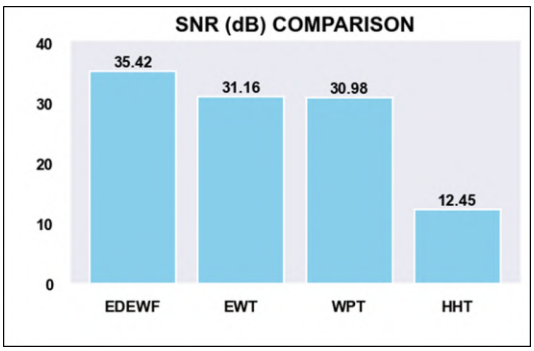


Figure 10: Comparison of SNR.
Source: Authors, (2026).

The bar graph in figure 10 compares the SNR performance of EDEWF, EWT, WPT, and HHT. The highest SNR was recorded from EDEWF (35.42dB), followed by EWT (31.16dB) and WPT (30.98dB). In contrast, HHT recorded the lowest SNR of all methods tested (12.45dB).

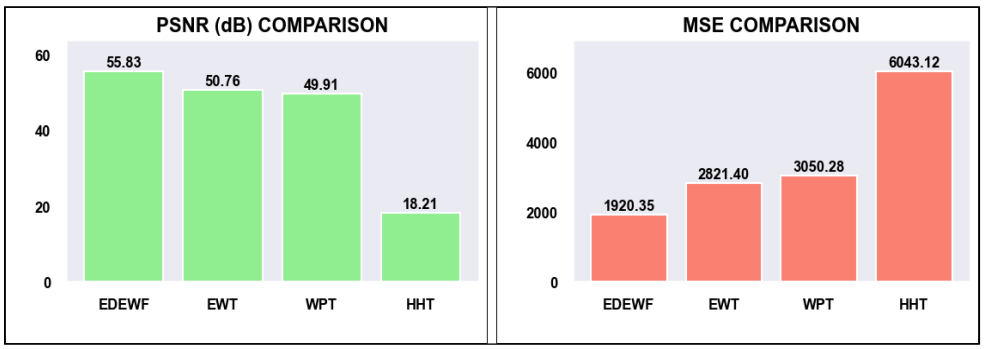


Figure 11: Comparison of PSNR and MSE.
Source: Authors, (2026).

As shown in figure 11, EDEWF achieved the highest PSNR (55.83dB) and the lowest MSE (1920.35) of any method tested, indicating the highest reconstruction accuracy, while EWT and WPT achieved moderate performances (PSNR= 50.76/ MSE=2821.40 & PSNR= 49.91dB/ MSE=3050.28), while HHT achieved the lowest PSNR (18.21dB) and the highest MSE (6043.12).

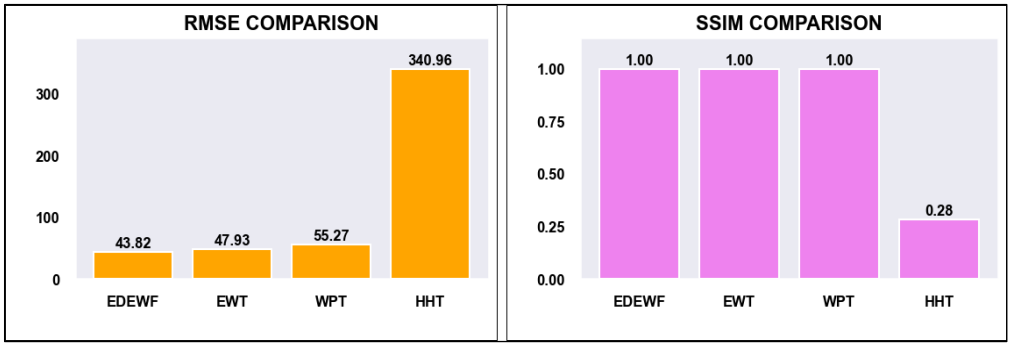


Figure 12: Comparison of RMSE and SSIM.
Source: Authors, (2026).

Figure 12 shows the comparison of RMSE and SSIM. The charts suggest that EDEWF, EWT, and WPT have excellent performance due to their low error rates and high structural similarities to one another. In contrast, HHT's performance is poor due to its high errors and low structural similarity to the other models.

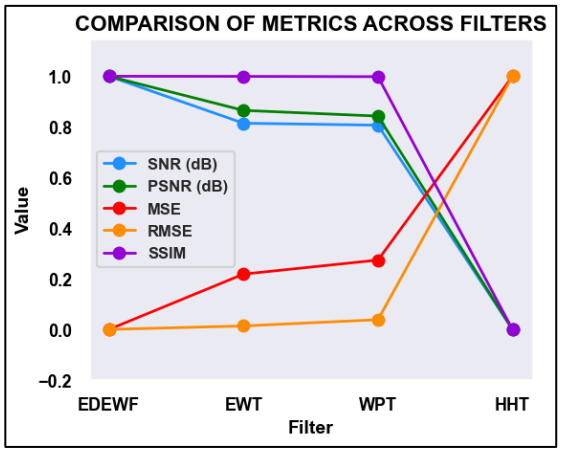


Figure 13: Comparison of metrics across filters.
Source: Authors, (2026).

Figure 13 indicates that EDEWF, EWT, and WPT have strong signal quality based on high similarity and low errors, while HHT has lower signal quality and therefore produces worse metrics and higher errors.

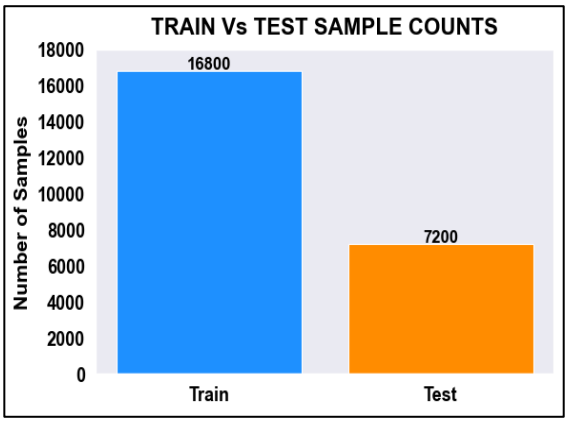


Figure 14: Train vs Test sample counts.
Source: Authors, (2026).

Figure 14 depicts the comparison of train and test sample counts. In addition to splitting the dataset into more training samples than testing samples, the plot shows that the emphasis of the model design is on learning the model rather than evaluating the model.

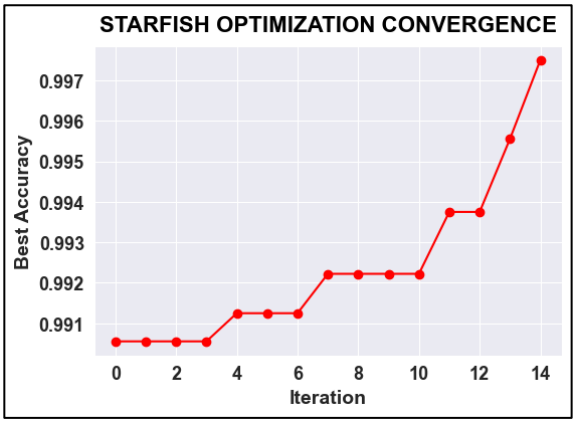


Figure 15: Starfish optimization convergence.
Source: Authors, (2026).

Figure 15 displays that Starfish Optimization is converging steadily, with the best accuracy increasing steadily over iterations until reaching its final iteration, where it improves dramatically to approximately 0.998.

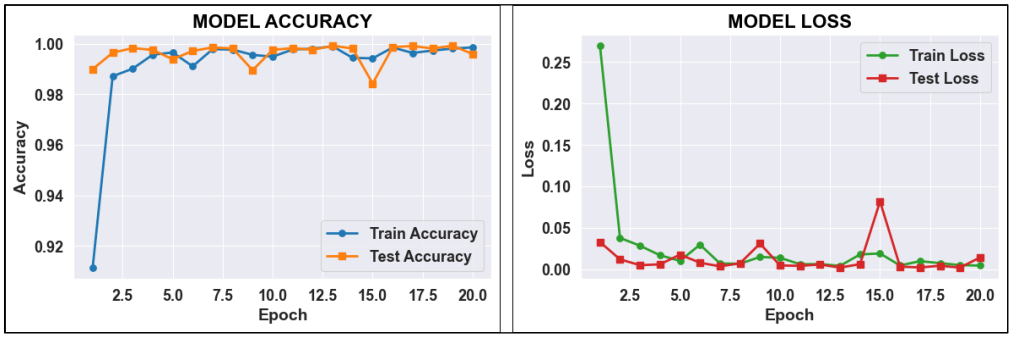


Figure 16: Model accuracy and Model loss for SFOA-Hybrid RBFNN-MHAT.
Source: Authors, (2026).

Figure 16 demonstrates that the model achieves near-perfect accuracy on both the training and testing datasets very quickly and is stable throughout all epochs. Training and testing losses drop quickly during the early epochs and remain low with only slight fluctuations, indicating the model's ability to converge properly without overfitting.

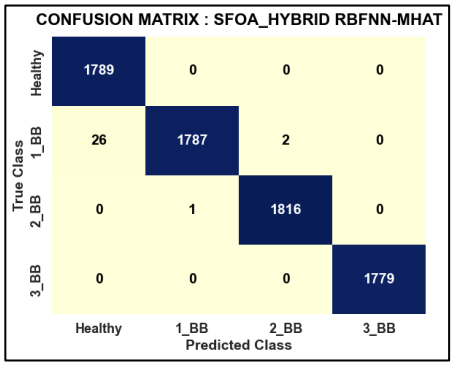


Figure 17: Confusion matrix of SFOA-Hybrid RBFNN-MHAT.
Source: Authors, (2026).

Confusion matrix of SFOA-Hybrid RBFNN-MHAT is illustrated in figure 17. The confusion matrix illuminates near-perfect classification performance, wherein nearly all samples were correctly classified. The only two misclassified categories are among Healthy vs. 1_BB or 1_BB vs. 2_BB, while the 3_BB category was perfectly classified.

Table 3: Performance metrics of SFOA-Hybrid RBFNN-MHAT.

SI.NO	METRICS	VALUES
1	Accuracy	0.9960
2	Precision	0.9960
3	Recall	0.9960
4	F1-Score	0.9960
5	Cohen’s Kappa	0.9946
6	MCC	0.9946
7	ROC-AUC	1.0000

Source: Authors, (2026).

In table 3, the SFOA-Hybrid RBFNN- MHAT model demonstrates approximately the highest possible performance for each metric at 99% accuracy, precision, recall and F1-score, a very high Cohen's Kappa and MCC at 0.99, and an ideal ROC-AUC score of 1.0, indicating very strong classification reliability and robustness.

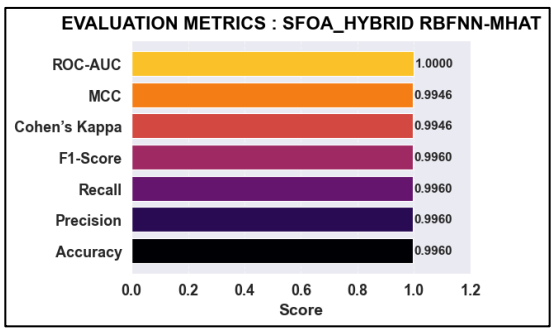


Figure 18: Evaluation metrics of SFOA-Hybrid RBFNN-MHAT.
Source: Authors, (2026).

Figure 18 demonstrates impressive performance for the SFOA-HYBRID RBFNN-MHAT model as evidenced by its near-perfect measures, ROC-AUC of 1.0; Accuracy/Precision/Recall/F1 score of 0.996 and MCC & Cohen's Kappa of 0.9964 and 0.9946. The model has been consistently classified as high quality and as a result provides reliable and consistent classification.

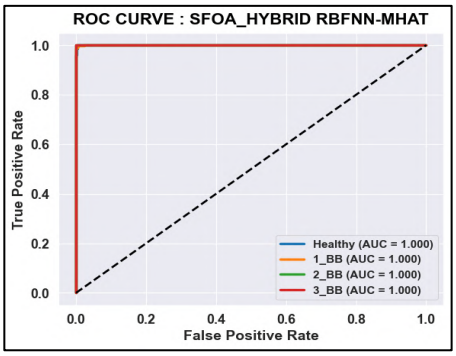


Figure 19: ROC curve of SFOA-Hybrid RBFNN-MHAT.
Source: Authors, (2026).

Figure 19 illustrate the indicating AUC = 1.000 and perfect classification performance with exceptional separation of the classes from one another.

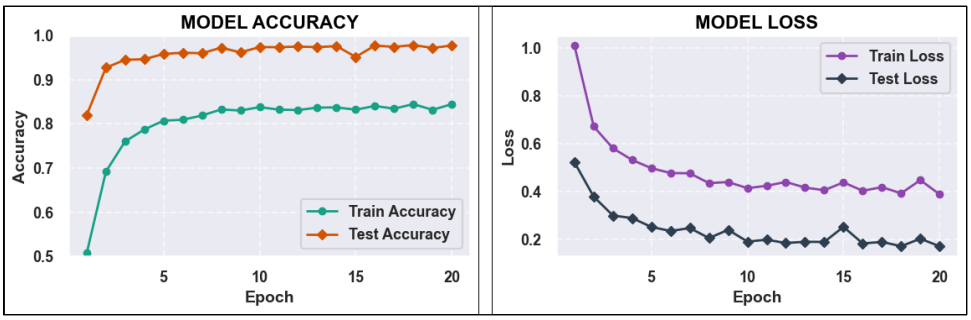


Figure 20: Model accuracy and model loss for Hybrid RBFNN-MHAT.
Source: Authors, (2026).

Figure 20 explains the model accuracy and model loss for Hybrid RBFNN-MHAT. The learning of the model is consistent and it generalizes well. The accuracy for both training and testing continues to increase until stabilizing (Test 97% and Train ≈ 84%). Training and testing losses have consistently decreased over time, demonstrating effective convergence without overfitting.

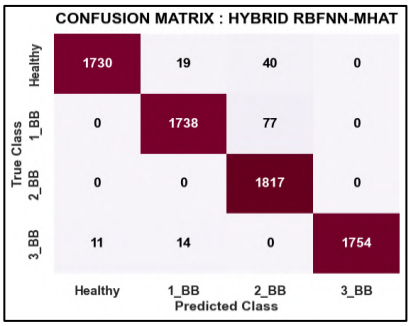


Figure 21: Confusion matrix for Hybrid RBFNN-MHAT.
Source: Authors, (2026).

The confusion matrix demonstrates high classification performance in figure 21. There is high percentage of samples that were accurately classified along the diagonal (Healthy = 1730; 1_BB = 1738; 2_BB = 1817; and 3_BB = 1754), which indicates the model's strong overall accuracy and low confusion rates among the classes.

Table 4: Performance metrics of Hybrid RBFNN-MHAT.

SI.NO	METRICS	VALUE
1	Accuracy	0.9776
2	Precision	0.9786
3	Recall	0.9776
4	F1-Score	0.9778
5	Cohen's Kappa	0.9702
6	MCC	0.9704
7	ROC-AUC	0.9965

Source: Authors, (2026).

In table 4, the Hybrid RBFNN - MHAT model demonstrates sustained and strong performance, exhibiting approximately 97% accuracy, precision, recall, and F1-score, strong Cohen's Kappa and MCC factors, with an extraordinary ROC-AUC of 0.99, signalling dependable and robust classification evaluation.

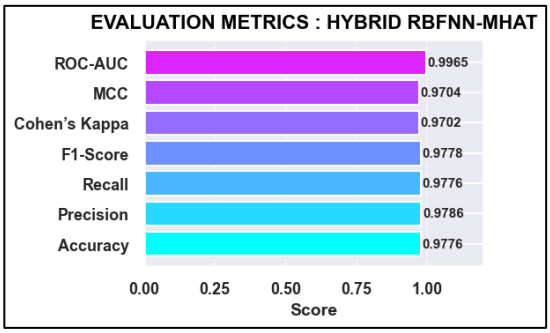


Figure 22: Evaluation metrics of Hybrid RBFNN-MHAT.
Source: Authors, (2026).

The performance of the model is superior in terms of the metrics which is depicted in figure 22. The high reliability and balance of classification are supported by the robustness and close agreement of the high MCC and Cohen's Kappa.

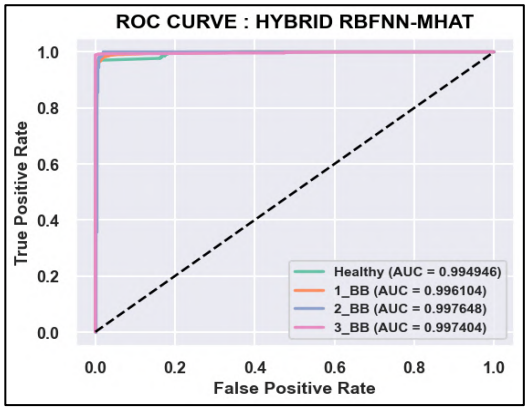


Figure 23: ROC curve of Hybrid RBFNN-MHAT.
Source: Authors, (2026).

The ROC curves show that there is a near-perfect separation of all classes, with AUCs, which is showed in figure 23. This indicates excellent discrimination between the different classes with very low false-positive rates for both Healthy and all classes of BB.

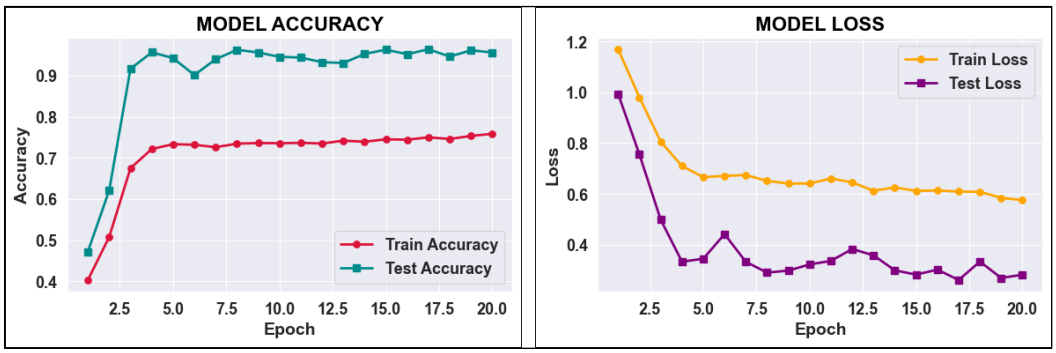


Figure 24: Model accuracy and model loss for MHAT.
Source: Authors, (2026).

Figure 24 shows the Model accuracy and model loss for MHAT. In the first few epochs of training, the model learns very quickly; however, it then stabilizes, with a final training accuracy of roughly 75% and test accuracy between 93 and 95%. The training and test losses have declined at a steady rate and have shown no signs of pronounced overfitting, which indicates that the model has performed well and has exhibited stable performance.

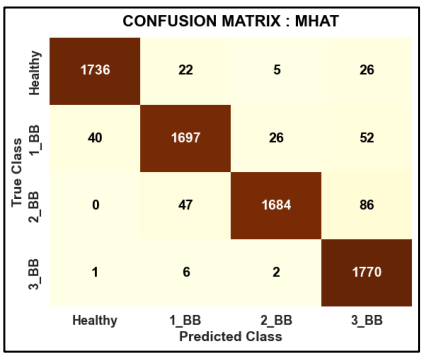


Figure 25: Confusion matrix for MHAT.
Source: Authors, (2026).

Figure 25 displays the confusion matrix for MHAT. From the confusion matrix, there was a strong classification performance, as evidenced by the detail that the diagonal had most of the correctly predicted samples for every class. Hence, the overall accuracy was quite high but that there was some minor misclassifications between the different BB classes.

Table 5: Performance metrics of MHAT.

SI.NO	METRICS	VALUES
1	Accuracy	0.9565
2	Precision	0.9576
3	Recall	0.9568
4	F1-Score	0.9566
5	Cohen’s Kappa	0.9420
6	MCC	0.9425
7	ROC-AUC	0.9919

Source: Authors, (2026).

In table 5, the MHAT method exhibited reliable overall quality at approximately 0.95 of accuracy, precision, recall and F1-score, as well as the highest Cohen's Kappa and MCC (0.94 each) and a very strong ROC-AUC at 0.99, confirming that it is an effective and less optimal.

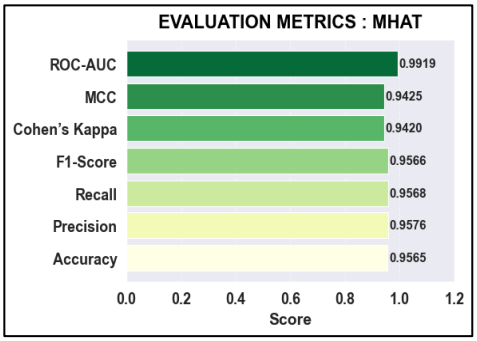


Figure 26: Evaluation metrics for MHAT.
Source: Authors, (2026).

The evaluation metrics are indicative of the model's performance which is depicted in figure 26. There is high accuracy, precision, recall and F1-score, strong agreement in terms of MCC and Cohen's Kappa (approximately 0.94), and excellent ROC-AUC (approximately 0.99), indicating that the model has demonstrated reliable classification with robustness.

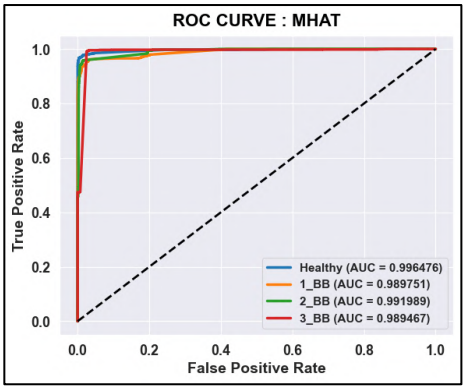


Figure 27: ROC curve for MHAT.
Source: Authors, (2026).

The ROC curves produced during evaluation also indicate that there has been an excellent classification performance across the various classes which is mentioned in figure 27, and the curves are well positioned toward the upper left corner of the graph. The AUC values, which were found to be all very high, demonstrate strong discrimination by the model, and the Healthy class was determined to deliver the best performing model.

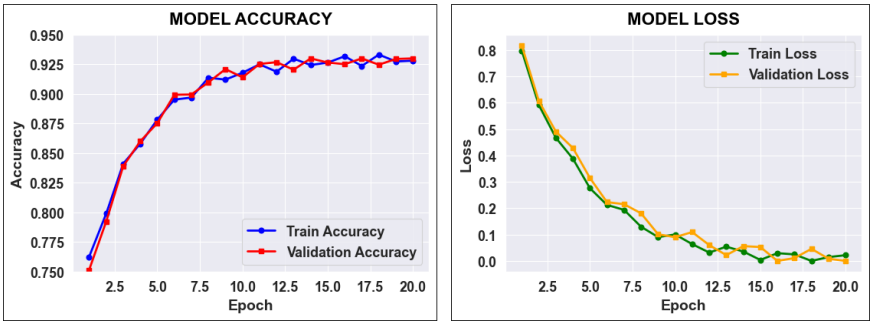


Figure 28: Model accuracy and model loss for RBFNN.
Source: Authors, (2026).

Figure 28 exhibits a progression in terms of the development of the model's performance during the training process by increased training and validation accuracy and decreased training and validation loss; both were observed to be steadily converging and demonstrated no significant evidence of overfitting.

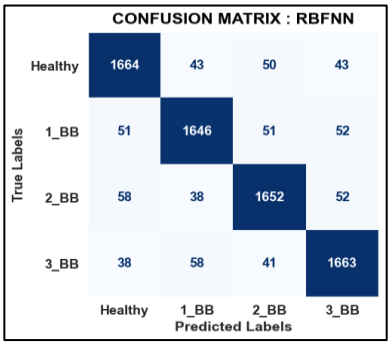


Figure 29: Confusion matrix for RBFNN.
Source: Authors, (2026).

The confusion matrix in figure 29 provided an evidence of the overall strength of the classification, with the majority of correctly predicted samples positioned along the diagonal; and, on average, there were very few instances of misclassification, and they were distributed relatively evenly across the various classes, indicating that there was no significant bias toward one or another class.

Table 6: Performance metrics of RBFNN.

SI.NO	METRICS	VALUES
1	Accuracy	0.935
2	Precision	0.938
3	Recall	0.932
4	F1-Score	0.935
5	Cohen’s Kappa	0.910
6	MCC	0.915
7	ROC-AUC	0.970

Source: Authors, (2026).

The RBFNN model has a stellar reputation which is depicted in table 6. High accuracy, combined precision and recall, Good Kappa and MCC agreement, plus outstanding classification accuracy demonstrated by ROC-AUC values of nearly 0.97.

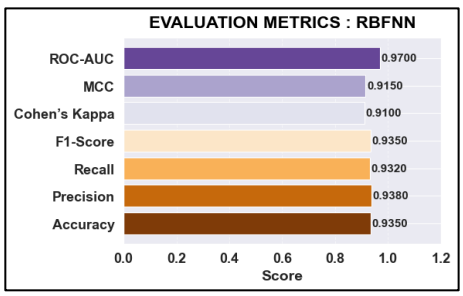


Figure 30: Evaluation metrics for RBFNN.
Source: Authors, (2026).

The RBFNN Model demonstrated in figure 30 is measured by AUC-ROC of 0.970, accuracy of 0.935, precision of 0.938, Recall of 0.932, F1 Score of 0.935, MCC of 0.915 and Cohen's Kappa of 0.91, demonstrating that this model has excellent reliability and demonstrates a high level of balanced classification capability.

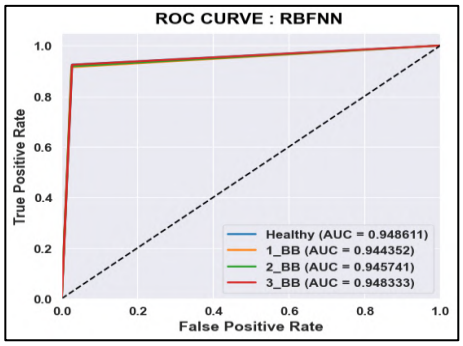


Figure 31: ROC curve for RBFNN.
Source: Authors, (2026).

Figure 31 demonstrates the great class-wise separation of classes by showing similar AUCs in the 0.94–0.95 range; thus, RBFNN class access the class in a more reliable manner.

Table 7: Comparative analysis of various methods.

SI.NO	METRICS	SFOA-Hybrid RBFNN-MHAT	Hybrid RBFNN-MHAT	MHAT	RBFNN
1	Accuracy	0.9960	0.9776	0.9565	0.935
2	Precision	0.9960	0.9786	0.9576	0.938
3	Recall	0.9960	0.9776	0.9568	0.932
4	F1-Score	0.9960	0.9778	0.9566	0.935
5	Cohen's Kappa	0.9946	0.9702	0.9420	0.910
6	MCC	0.9946	0.9704	0.9425	0.915
7	ROC-AUC	1.0000	0.9965	0.9919	0.970

Source: Authors, (2026).

As illustrated in table 7, the performance of the SFOA-Hybrid RBFNN-MHAT method consistently surpassed the performance of every other method across every metric of measurement evaluated, attaining excellent results for accuracy, precision, recall, and F1-score (0.996 for accuracy, precision, recall, F1, and ROC-AUC score of 1.0). There was a progressive decrease in performance for Hybrid RBFNN-MHAT, MHAT, and RBFNN indicating the efficacy of the proposed Hybrid Optimization method.

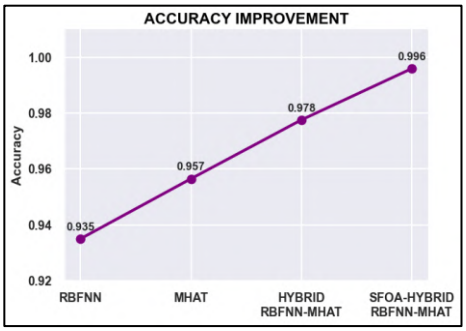


Figure 32: Accuracy improvement.
Source: Authors, (2026).

Figure 32 displays the tracking of accuracy via plotting results demonstrates the improvements in accuracy attained by use of the RBFNN, 0.935 through the use of the MHAT, 0.957 through the use of Hybrid RBFNN- MHAT, and highest with SFOA-Hybrid RBFNN-MHAT of 0.996.

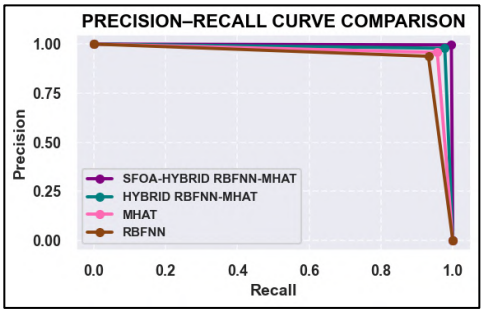


Figure 33: Comparison of precision-recall curve.
Source: Authors, (2026).

Figure 33 compares the performance of the model across all metrics was tracked through plotting of the Precision-Recall curve to indicate that SFOA-Hybrid RBFNN-MHAT obtains the highest precision with almost all values of recall, therefore allowing for the most accurate results. The Precision-Recall curve shows that Hybrid RBFNN-MHAT-MHAT perform close in terms of precision, RBFNN, had lower results in precision at high recall values and was associated with greater drops in accuracy.

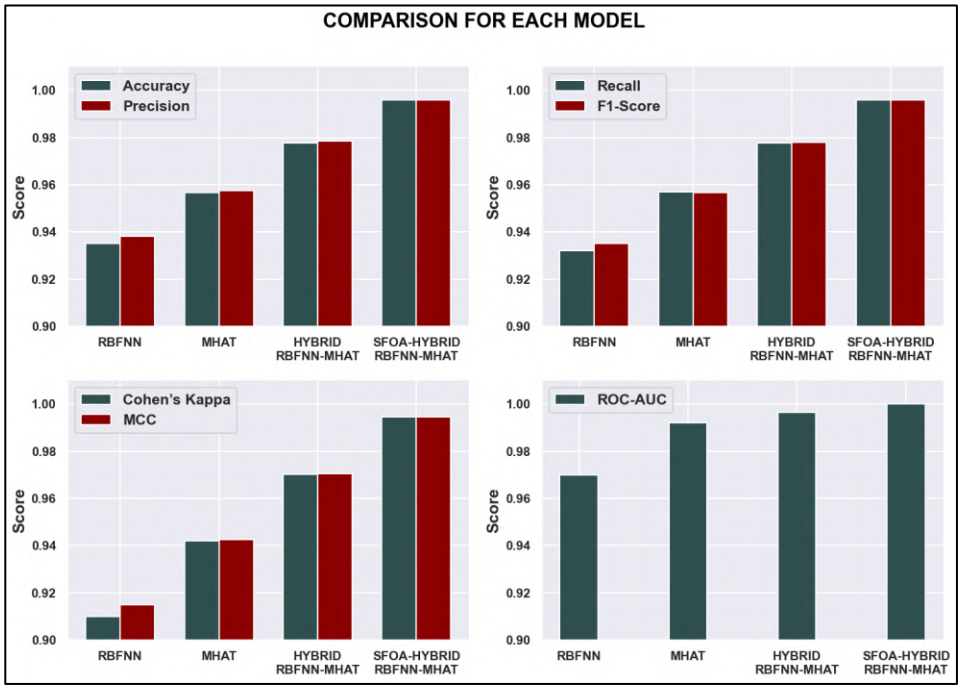


Figure 34: Comparison for each model.
Source: Authors, (2026).

Figure 34 shows the clear performance improvement of the class across all metrics. The SFOA-Hybrid RBFNN-MHAT continues to produce the highest accuracy, Precision, Recall, F1 Scores, Cohen's Kappa, MCC and ROC-AUC indicating itself as the most robust and reliable overall class performance.

Table 8: Comparative analysis of accuracy for different methods.

SI.NO	MODEL	ACCURACY
1	RF [21]	0.91
2	CWT [22]	0.97
3	CNN-LSTM [23]	0.976
4	ClasLoc [24]	0.90
5	CNN-RNN [25]	0.977
6	PROPOSED	0.99

Source: Authors, (2026).

Table 8 displays the accuracy of each model, showing that the proposed model achieved the highest accuracy at 99%, followed closely by CNN-RNN and CNN-LSTM with accuracies of 97.7% and 97.6%, respectively, while RF and ClasLoc both have lower accuracies.

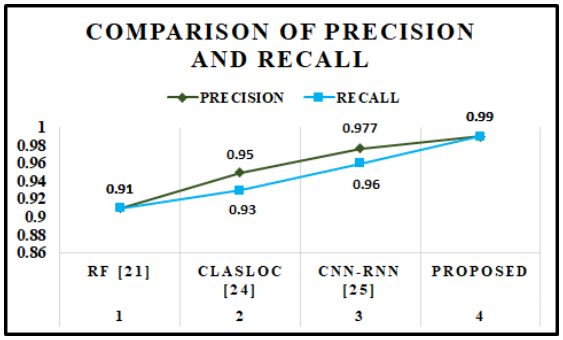


Figure 35: Comparative analysis of precision and recall.
Source: Authors, (2026).

Figure 35 depicts the metrics of accuracy, precision, recall and F1-score measured by four models including RF, ClasLoc, CNN-RNN and the proposed model. Performance on each metric progressed from RF to the proposed model producing the best results (0.99) for every metric.

Table 9: Comparative analysis of F1-Score for different methods.

SI.NO	MODEL	F1-SCORE
1	RF [21]	0.91
2	ClasLoc [24]	0.94
3	CNN-RNN [25]	0.98
4	PROPOSED	0.99

Source: Authors, (2026).

Table 9 had a gradual increase in their respective F1-scores, from the lowest to the highest. The proposed model achieving the highest F1-score at 99%. This demonstrates that the presented model achieves significantly improved than all other models.

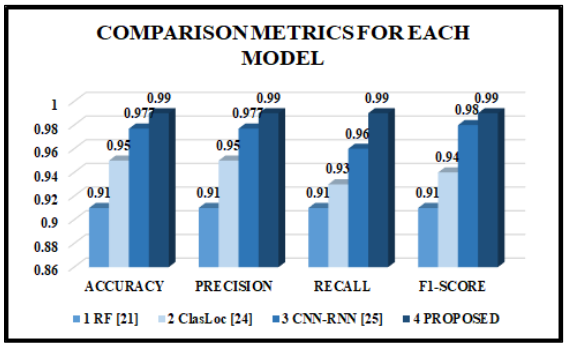


Figure 36: Comparison metrics for each model.
Source: Authors, (2026).

Figure 36 indicates a steady increase in the F1-score achieved by each model as their performance progressed (RF F1-score=0.91, ClasLoc F1-score=0.94, CNN-RNN F1-score=0.98, proposed model F1-score of 0.99); this indicates the suggested model attained higher enactment overall.

V. CONCLUSION

The proposed framework incorporates an organised workflow of data collection, preprocessing, feature engineering, parameter optimisation and combination of automated and manual models incorporated into a comprehensive fault diagnostic structure, the proposed system uses the highest superiority operational signal from initial data collection and provide excellent results for removing noise from cleansed operational data while preserving the relevant information regarding electrical faults. The feature engineering stage used the data produced from preprocessing to both prepare and standardise the data when developing the feature vector for use in training the DL model. The starfish optimising algorithm provides for the optimal tuning of the model hyper-parameters that offer the higher performance and assurance in prediction. The hybrid model that consists of RBFNN along with MHAT captures both the high-level contextually expressive features and the details of the localised fault marks. The fusion layer allows for the best representation of both the global context and localised signature features, leading to the combined strength for the final diagnostics through an accurate classification of induction motor conditions as either Normal/Healthy or BRB Failure. Finally, the hybrid model provides a substantially higher degree of diagnostic accuracy, precision, recall, F1-Score of 0.9960, robustness and real-world utility for intelligent condition monitoring systems.

VI. AUTHOR'S CONTRIBUTION

Conceptualization: Killamsetti Vijeta, Sri Suyambulinga Perumal B, R. Tharwin Kumar, Niran I R, Jinsha Lawrence, and Gunasekar M.
Methodology: Killamsetti Vijeta and Sri Suyambulinga Perumal B.
Investigation: Killamsetti Vijeta and Sri Suyambulinga Perumal B.
Discussion of results: Killamsetti Vijeta, Sri Suyambulinga Perumal B, R. Tharwin Kumar, Niran I R, Jinsha Lawrence, and Gunasekar M.
Writing – Original Draft: Killamsetti Vijeta.
Writing – Review and Editing: Vijeta and Sri Suyambulinga Perumal B.
Resources: Sri Suyambulinga Perumal B.
Supervision: Sri Suyambulinga Perumal B and Sri Suyambulinga Perumal B.
Approval of the final text: Killamsetti Vijeta, Sri Suyambulinga Perumal B, R. Tharwin Kumar, Niran I R, Jinsha Lawrence, and Gunasekar M.

VII. REFERENCES

[1] K. Barrera-Llanga, J. Burriel-Valencia, A. Sapena-Bano, and J. Martinez-Roman, "Fault detection in induction machines using learning models and Fourier spectrum image analysis", Sensors, vol. 25, no. 2, pp. 471, Jan. 2025.

[2] M. Samiullah, H. Ali, S. Zahoor, and A. Ali, "Fault diagnosis on induction motor using machine learning and signal processing", arXiv preprint arXiv: 2401.15417, Jan. 2024.

[3] S.M. Yoo, H.G. Lee, W.K. Hao, and I.S. Lee, "Induction Motor Fault Diagnosis Using Low-Cost MEMS Acoustic Sensors and Multilayer Neural Networks", Applied Sciences, vol. 15, no. 17, pp. 9379, Aug. 2025.

[4] P. S. Kartik, L. Padmasuresh and P. Muthukumar, "AI-Enhanced Power Electronics for Electric Mobility: A Review of Recent Developments and Future Trends", 2025 8th International Conference on Circuit, Power & Computing Technologies (ICCPCT), Kollam, India, pp. 2035-2039, Aug. 2025.

[5] J. Guo, Q. He, and F. Gu, “DNOCNet: A novel end-to-end network for induction motor drive systems fault diagnosis under speed fluctuation condition”, IEEE Transactions on Industrial Informatics, vol. 20, no. 6, pp. 8284-8293, Mar. 2024.

[6] S. Ayankoso, A. Dutta, Y. He, F. Gu, A. Ball, and S.K. Pal, “Performance of vibration and current signals in the fault diagnosis of induction motors using deep learning and machine learning techniques”, Structural Health Monitoring, pp. 14759217241289874, 2024.

[7] U. Calderon-Uribe, R.A. Lizarraga-Morales, and I.V. Guryev, “Fault Diagnosis in Induction Motors through Infrared Thermal Images Using Convolutional Neural Network Feature Extraction”, Machines, vol. 12, no. 8, pp. 497, Jul. 2024.

[8] H.C. Chang, R.G. Liu, C.C. Li, and C.C. Kuo, “Fault Diagnosis of Induction Motors under Limited Data for Across Loading by Residual VGG-Based Siamese Network”, Applied Sciences, vol. 14, no. 19, pp. 8949, Oct. 2024,

[9] K. Karthika and R. Devi Priya. “Image processing-based protection of privacy data in cloud using NTRU algorithm”, Signal, Image and Video Processing, vol. 18, no. 5, Jul. 2024.

[10] V.I. Vlachou, T.S. Karakatsanis, S.D. Vologiannidis, D.E. Efstathiou, E.L. Karapalidou, E.N. Antoniou, A.E. Efraimidis, V.E. Balaska, and E.I. Vlachou, “Intelligent Fault Diagnosis of Ball Bearing Induction Motors for Predictive Maintenance Industrial Applications”, Machines, vol. 13, no. 10, pp. 902, Oct. 2025.

[11] M. Sehri, M. Ertagrin, O. Yildirim, A. Orhan, and P. Dumond, “Deep Learning Approach to Bearing and Induction Motor Fault Diagnosis via Data Fusion”, arXiv preprint arXiv:2506.11032, May. 2025.

[12] M.A. Saleh, A. Ghrayeb, S.S. Refaat, H. Abu-Rub, S.P. Khatri, and J. Kammermann, “Attention-enhanced agru framework for induction motor incipient fault diagnosis in electric vehicles”, IEEE Transactions on Instrumentation and Measurement, Nov. 2024.

[13] J. Choi, S.H. Kim, W. Lee, and J.S. Lee, “Rapid Control Prototyping and Analysis of a Fault Diagnosis and Amplifying Algorithm for Broken Rotor bar Induction Motor Drives”, IEEE Access, Jan. 2025.

[14] U. Ali, U. Ramzan, W. Ali, and K.A. Al-Jaafari, “An Improved Fault Diagnosis Strategy for Induction Motors Using Weighted Probability Ensemble Deep Learning”, IEEE Access, Jun. 2025.

[15] G. Himaja, G.S. Rao, G.A. Naidu, T. Nagothi, and S. Dalli, “Recommendation system: national institute rank prediction using machine learning”, Journal of Algebraic Statistics, vol. 13, no. 3, pp. 146-152, May. 2022.

[16] J.A. Reyes-Malanche, E. Ramirez-Velasco, F.J. Villalobos-Pina, and S.K. Gadi, “Short-circuit fault diagnosis on the windings of three-phase induction motors through phasor analysis and fuzzy logic”, Energies, vol. 17, no. 16, pp. 4197, Aug. 2024.

[17] G.U. Oh, S.T. Kim, and J.S. Ko, “Bearing Fault Diagnosis Using Torque Observer in Induction Motor”, Energies, vol. 18, no. 22, pp. 5872, Nov. 2025.

[18] S. Wang, Y. Vidal, and F. Pozo, “Two-dimensional color distribution entropy: validation and application on non-contact fault diagnosis for induction motor”, In 2024 32nd European Signal Processing Conference (EUSIPCO), pp. 556-560, Aug. 2024.

[19] B. Xu, H. Li, R. Ding, and F. Zhou, “Fault diagnosis in electric motors using multi-mode time series and ensemble transformers network”, Scientific Reports, vol. 15, no. 1, pp. 7834, Mar. 2025.

[20] J. Ahn, J. Lee, and H. Kim, “Impedance-Based Inter-Turn Fault Diagnosis in Integrated Induction Motor and Drive Systems Using Space Voltage Vectors”, Applied Sciences, vol. 15, no. 11, pp. 6065, May. 2025.

[21] A. Abdulkareem, T. Anyim, O. Popoola, J. Abubakar, and A. Ayoade, “Prediction of induction motor faults using machine learning”, Heliyon, vol. 11, no. 1, Jan. 2025.

[22] R. Boudiaf, B. Abdelkarim, and H. Issam, “Bearing fault diagnosis in induction motor using continuous wavelet transform and convolutional neural networks”, International Journal of Power Electronics and Drive Systems (IJPEDS), vol. 15, no. 1, pp. 591-602, Mar. 2024.

[23] R. Rahim, “AI-Driven Fault Diagnosis in Three-Phase Induction Motors Using Vibration and Thermal Data”, National Journal of Electrical Machines & Power Conversion, pp. 21-28, Mar. 2025.

[24]K.M. Shahiduzzaman, A.A. Koly, M. Maria, and B. Mymensingh, “ClasLoc: A Robust Fault Management Methodology for Transmission Lines Using RBFNN and ANFIS”, 2024.

[25] C. Eang, and S. Lee, “Predictive maintenance and fault detection for motor drive control systems in industrial robots using CNN-RNN-based observers”, Sensors, vol. 25, no. 1, pp. 25, Dec. 2024.

Journal of Engineering and Technology for Industrial Applications

ISSN ONLINE: 2447-0228

ITEGAM-JETIA

Manaus, v.12 n.60, p.227-236, July/August, 2026.
DOI: https://doi.org/10.5935/jetia.v12i60.3717

RESEARCH ARTICLE OPEN ACCESS

MODELLING AND FAULT PROTECTION ANALYSIS OF A DC MICROGRID USING VOLTAGE SOURCE CONVERTER AND RELAYS

Ayya Chaithanya[1], T. Neeraja[2], B.Raja Sekhar Reddy*[3], Chella Hari Prasad[4], and Kanna Sravanthi[5]

[1, 2, 3, 4, 5]Department of Electrical and Electronics Engineering, SV University College of Engineering, Tirupati, India.

[1]https://orcid.org/0009-0004-7501-210X, [2]https://orcid.org/0009-0003-5754-4148, [3]https://orcid.org/0000-0002-1838-6445
[4]https://orcid.org/0000-0003-2157-1315, [5]https://orcid.org/0009-0000-5910-7169

Email: chaithu.maruthi@gmail.com, neeraja722@gmail.com,*rajabayyapureddy@gmail.com, hariprasadchallaa@gmail.com and sravanthikanna7@gmail.com

ARTICLE INFO

Article History
Received: February 17, 2026
Reviewed: June 7, 2026
Accepted: July 7, 2026
Published: July 31, 2026

Keywords:
DC microgrids,
Voltage source converter (VSC),
AC main grid,
Relays,
PV and Battery.

ABSTRACT

A direct current (DC) microgrid has been the preferred power system in recent years because of the system's overall efficiency. Finding a suitable protection strategy is the primary issue with DC microgrids. The most promising technology for renewable energy is photovoltaic systems. To create a DC microgrid that can function both on-grid and in island mode, the basic components are a photovoltaic (PV) system with Boost converter, a battery with Buck converter, a voltage source converter (VSC), and an AC main grid. When an issue arises with the AC main grid, a voltage source converter and several relay types, including circuit breakers, are utilized to protect the DC microgrid. The study of DC microgrid protection and its effects on other devices is the main topic of this study. Additionally, it desires to give information about their function in improving the flexibility of electrical power networks and reducing the negative consequences of overcurrent issues. MATLAB SIMULINK is used to simulate and model the PV and battery linked to the main grid with various fault kinds and by employing different overcurrent protection techniques. Their features are analysed.

Copyright ©2026 by authors and Galileo Institute of Technology and Education of the Amazon (ITEGAM). This work is licensed under the Creative Commons Attribution International License (CC BY 4.0).

I. INTRODUCTION

The major advantages that microgrids provide to both customers and power grid operators has given rise to a recent increase in research on the topic. In basic terms, a microgrid is an integrated network of distributed power sources [1]. A microgrid's versatile and flexibility of control, which support system reliability and power quality standards, are its greatest advantages over a single-generation system [2] . Microgrids can be in two ways on-grid and off-grid. In small networks, the common system divisions are an AC bus and a DC bus. By reducing the power conversion stages between the AC and DC sides, a DC microgrid enhances efficient power transfer, and most grid-tied renewable energy systems utilize DC power for both input and output. Even though DC microgrids have numerous advantages over AC microgrids, one of the main issues in power system production is building a proper protection circuit for both big and small DC networks [3]. Nowadays, most research and studies focus on determining the most effective approaches for solving protection issues in DC networks. Because of problems of small networks bidirectional power transmission, the fault currents direction while integrating system parameters, and the distinct qualities of renewable energy supplies and their types, DC microgrid protection problems are difficult to resolve using conventional methods. There are a variety of techniques for precisely detecting faults, including the use of DC circuit breakers (CBs) for grounding and fault current determination techniques. Protection problems in DC distribution systems also come due to the absence of zero current crossing, which is typically found in AC systems. Despite major advancements, protection technologies in AC transmission and distribution systems are still essentially quite basic and manageable. Most small, distributed generation (DG) networks are based on AC systems, however compact DC networks are preferred for connecting to DC-output sources including photovoltaic (PV) systems, energy storage systems (ESS), and fuel cells. [4]. MATLAB/Simulink is used to simulate a protection analysis for a DC microgrid under several fault situations. This study examines how these conditions impact power electronic components, including the converter, voltage source converter (VSC), and power loads.

Additionally, it seeks to shed light on their function in strengthening the resilience of electrical power networks and reducing the negative consequences of overcurrent incidents. MATLAB SIMULINK is used to simulate and model the PV and battery linked to the main grid with various fault kinds and by employing different overcurrent protection techniques. Their features are then compared. The following is an overview of the DC microgrid's features:

- No synchronisation issues in DC microgrid [5].
- Transmission efficiency is high in DC microgrid due to absent of reactive components increases efficiency [6].
- DC microgrids are more stable compared to AC microgrids become it free from external effects [7].
- Skin effect losses absent in DC microgrid. It leads to less cable losses [8].
- A DC microgrid's power supply is more robust since several supplies can connect to a single bus [2].
- The primary reason for preferring DC networks is that switching losses between sources and loads are lower in systems with direct current (DC) loads than in those with an AC grid [9].
- Resources and loads are DC, which lowers heat and losses [10].
- DC microgrids have greater power transfer capabilities [11].
- DC microgrid systems are safer than AC microgrid systems [12].

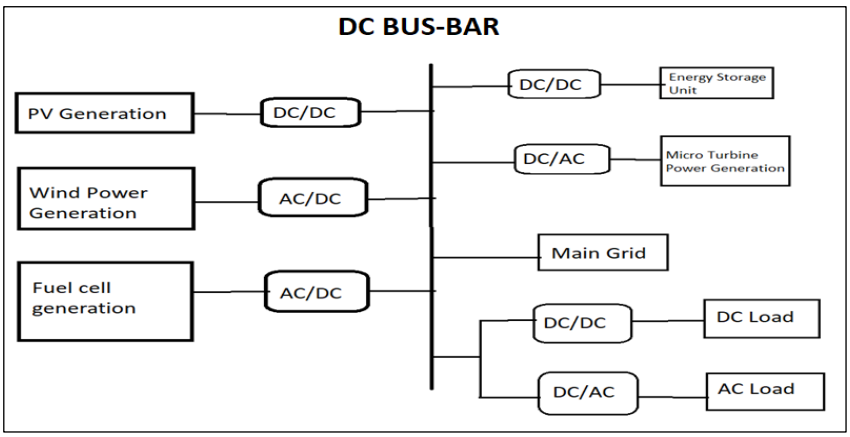


Figure 1: DC Microgrid.
Source: Authors, (2026).

II. OBJECTIVES

- DC microgrid protection and operation are often challenges with this kind of DC system.
- The DC microgrid is protected from AC side faults by a voltage source converter (VSC).
- Circuit breakers provide actual delays in the circuit, whereas relays offer a more complete protection system through recognizing more types of faults.

III. FAULT ANALYSIS FOR DC MICROGRID

For switching between AC and DC system need switching mechanism for conversion voltage source converter plays a crucial role. A Voltage Source Converter (VSC) is a power electronic converter that performs both inverter and rectifier operations. It is commonly used in grid-integrated systems, especially in DC microgrids connected to an AC main source.

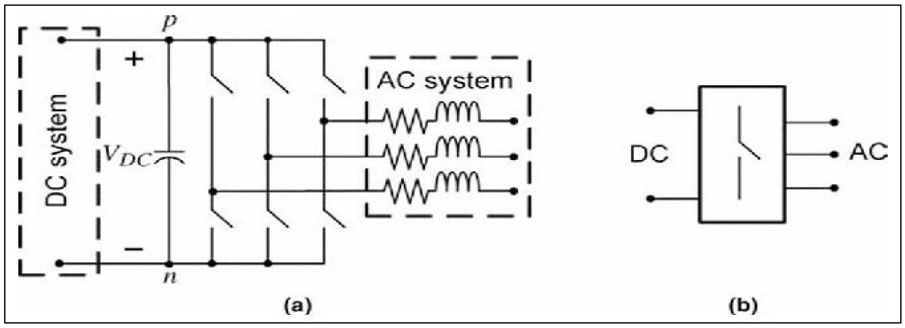


Figure 2: (a) Three-phase VSC circuit diagram, (b) VSC acts as switch between DC and AC system.
Source: Authors, (2026).

The bipolar nature of a voltage source converter's DC-side current affects its average power flow, while the DC-side voltage remains polar. Usually, the DC-side terminals of a VSC are linked in parallel with a large capacitor that functions as a voltage source.

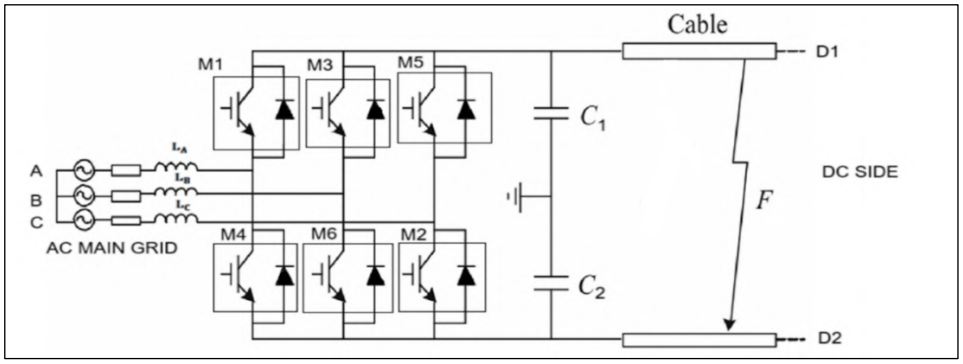


Figure 3: VSC with DC side fault.
Source: Authors, (2026).

When the DC microgrid's transmission line experiences a three-phase failure on the AC main grid, the DC side capacitor rapidly discharges from the fault point and into the AC current system. the overcurrent protection limiting the VSC, AC current still feeds the fault location through the VSC's antiparallel diode.

III.1 FAULT CONDITION

During a fault condition, three cases are observed in the Voltage Source Converter (VSC). These three cases are displayed in the circuit diagrams below.

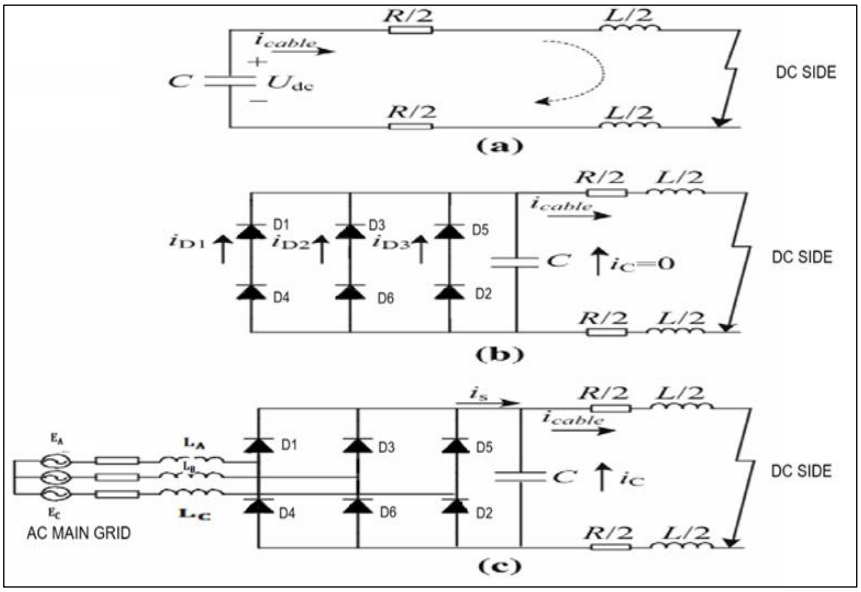


Figure 4: (a) Capacitor discharging condition during fault. (b) Diode free-wheeling action when the capacitor charge reaches. (c) AC main grid feeding.
Source: Authors, (2026).

Equations related to Voltage source converter (VSC):

$$L\frac{d^2V_c}{dt^2} + R.\frac{dV_c}{dt} + \frac{V_c}{C} = 0 \quad \ldots\ldots\ldots \quad \ldots(1)$$

By taking into consideration the small size the resistance is in this case,

$$\frac{1}{2}(R) < \sqrt{\frac{L}{C}} \quad \ldots\ldots\ldots \quad (2)$$

$$i_L = 3i_d \quad \ldots\ldots\ldots \quad (3)$$

III.2 FAULT CHARACTERISTICS OF VSC

The three cases above are symbolized as t_0, t_1, and t_2, where:

- t_0 is the time at which the capacitor starts discharging (or the fault occurs).
- t_1 is the time at which the diode's free-wheeling action begins (or when the capacitor's current decreases to zero).
- t_2 is the time at which grid feeding starts.

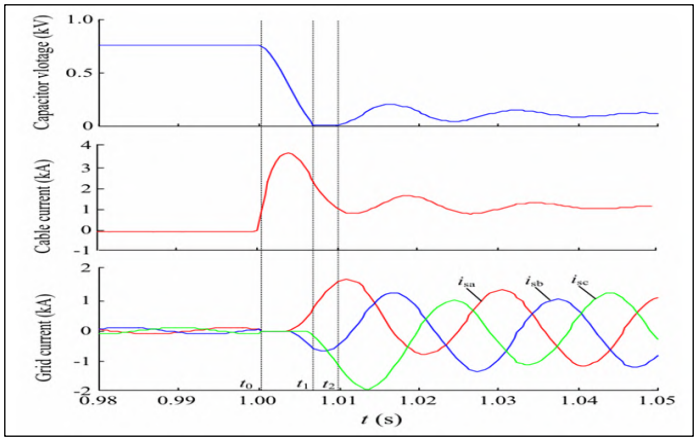


Figure 5: Fault characteristics of VSC.
Source: Authors, (2026).

The fault characteristics of the Voltage Source Converter during the t_0, t_1, and t_2 time intervals are shown in the waveform above.

IV. FAULT OCCURRED CONDITION

The DC microgrid transmission line fault direction is represented in the circuit below.

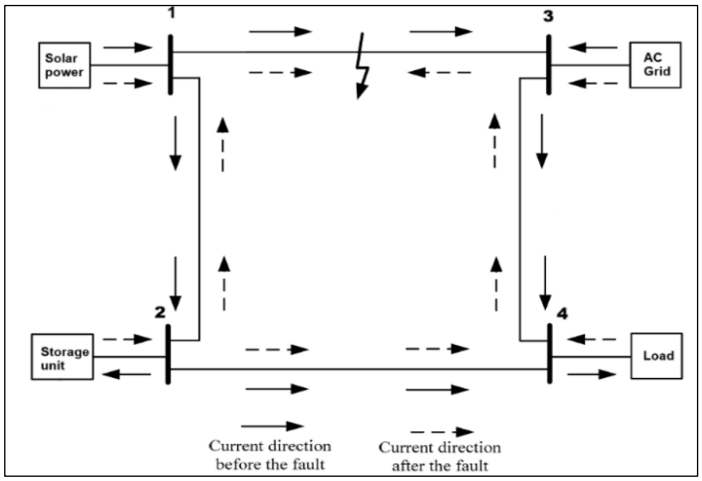


Figure 6: DC Microgrid current direction during a fault.
Source: Authors, (2026).

In the above block diagram, there are two conditions current direction before the fault condition and current direction after the fault condition.

IV.1 RELAY CHARACTERISTICS

The circuit breaker only interrupts the system while fault occurs, but relay detects the fault occurrence quickly interrupt the system by sending a signal to the circuit breaker from fault condition. There are so many types of relays based on performance operation. For Microgrid the overcurrent relays and differential relay plays a crucial role. In below tabular column discuss the comparison of overcurrent relays and differential relays.

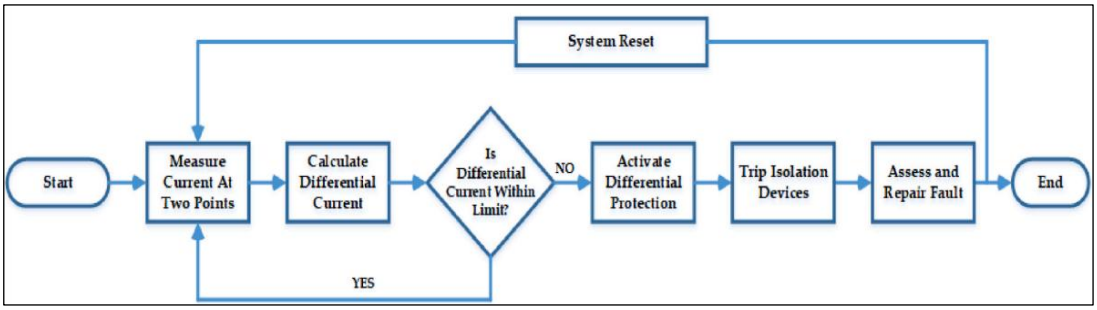


Figure 7: Flowchart of differential relay working at AC main source in DC Microgrid.
Source: Authors, (2026).

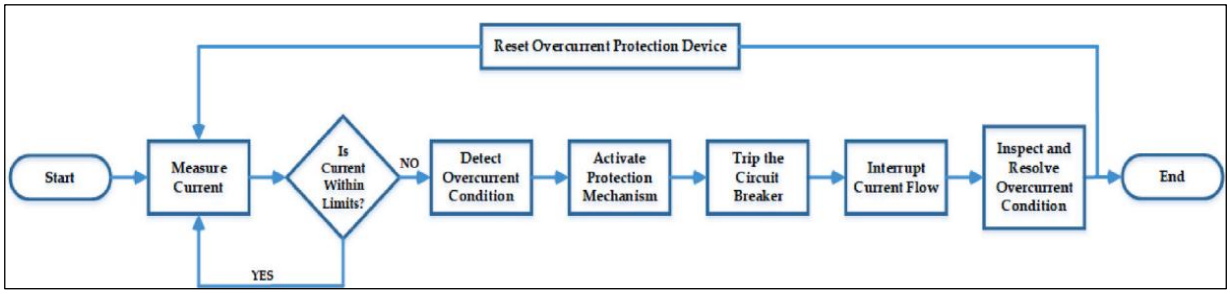


Figure 8: Flowchart of overcurrent protection device working at AC main source in DC microgrid.
Source: Authors, (2026).

Table 1: Comparing protection methods according of their Advantages and drawbacks.

Methods of protection	Advantages	Drawbacks
Over-current protection	• A basic approach • Suitable for fault interrupt techniques • Fast response to high-magnitude faults	• Less Sensitive • Requires careful time grading to prevent maloperation. • Depends on Fault Current Magnitude
Differential protection	• High selectivity and sensitivity • less dependence on fault impedance Independent on current direction and independence with the direction of the current • Unaffected by fault resistance and a sudden rise in DC currents	• Needs regular testing and calibration for accurate performance • Requires more equipment (CTs, relays, communication) and setup effort.

Source: Authors, (2026).

Based on the operation of overcurrent relays and differential relays the performance of relays tabulated below.

Table 2: Comparison of Protection methods based on operation.

Protection Method	Speed of operation	Selectivity	Reliability	Cost
Over-current protection	Medium	Low	High	Medium
Differential protection	Very High	High	High	High

Source: Authors, (2026).

V. RESULTS AND DISCUSSION

In this paper, by comparing three relays performance individually by combining PV, Battery & AC grid at LLLG fault condition. The three relays are AC time instantaneous overcurrent relay, Differential relay, IDMT (Inverse definite minimum time) relay.

V.1 MODELLING OF AC TIME OVERCURRENT RELAY WITH MICROGRID

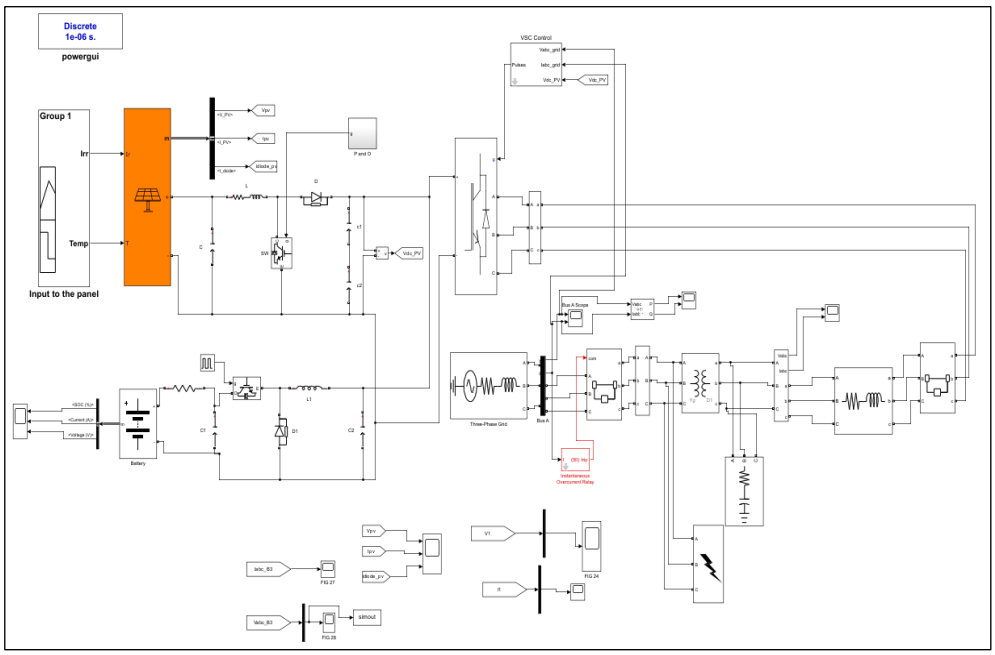


Figure 9: Simulink model design of PV with AC Main Grid, Battery and AC-time instantaneous over current relay.
Source: Authors, (2026).

V.2 MODELLING OF DIFFERENTIAL RELAY WITH MICROGRID

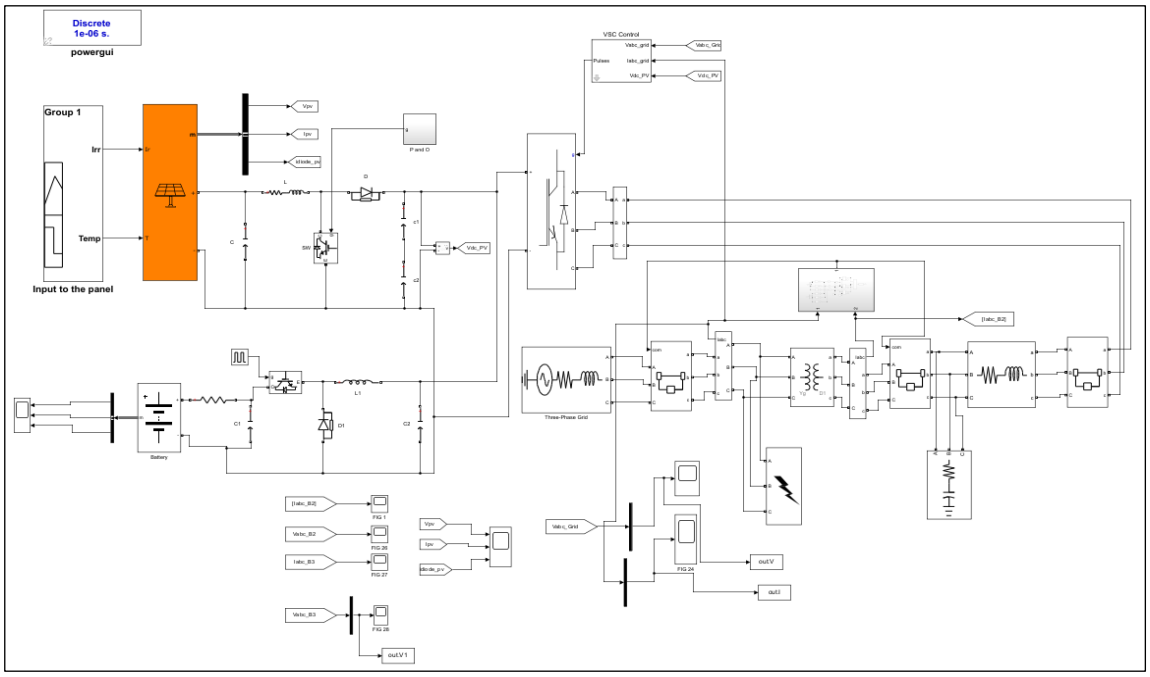


Figure 10: Simulink model design of PV with AC Main Grid, Battery and Differential relay.
Source: Authors, (2026).

V.3 MODELLING OF IDMT RELAY (INVERSE DEFINITE MINIMUM TIME) WITH MICROGRID

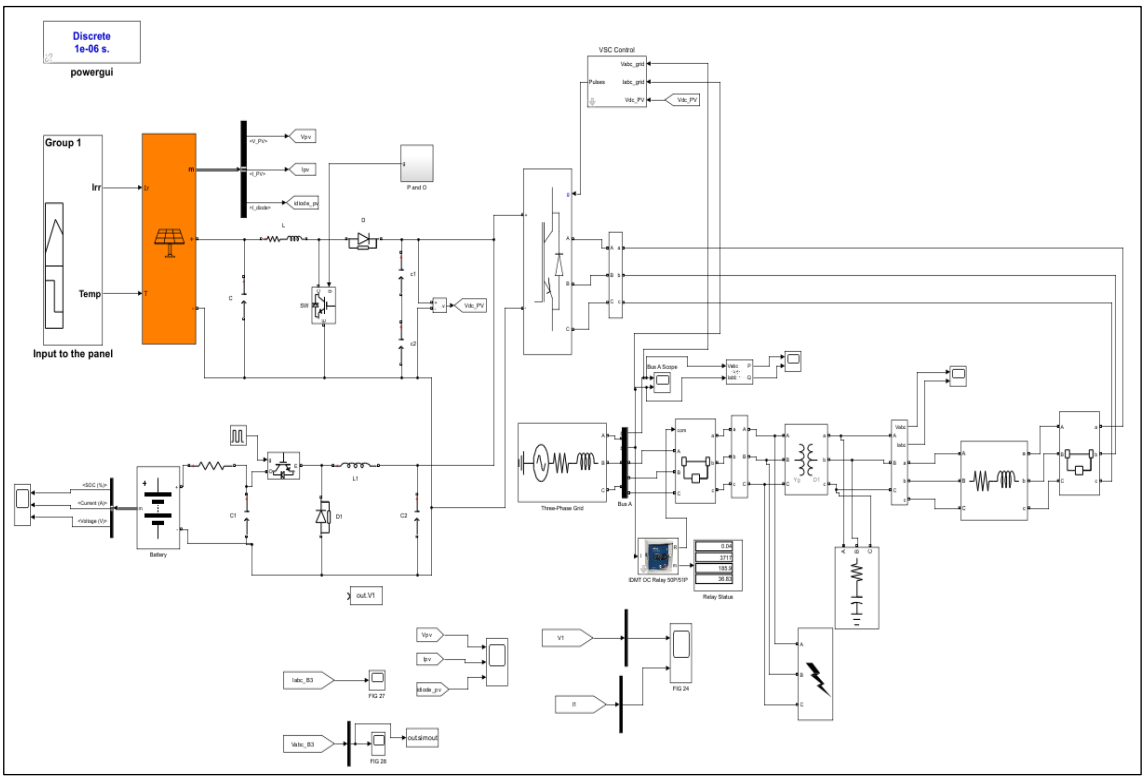


Figure 11: Simulink model design of PV with AC Main Grid, Battery and IDMT relay.
Source: Authors, (2026).

Output:

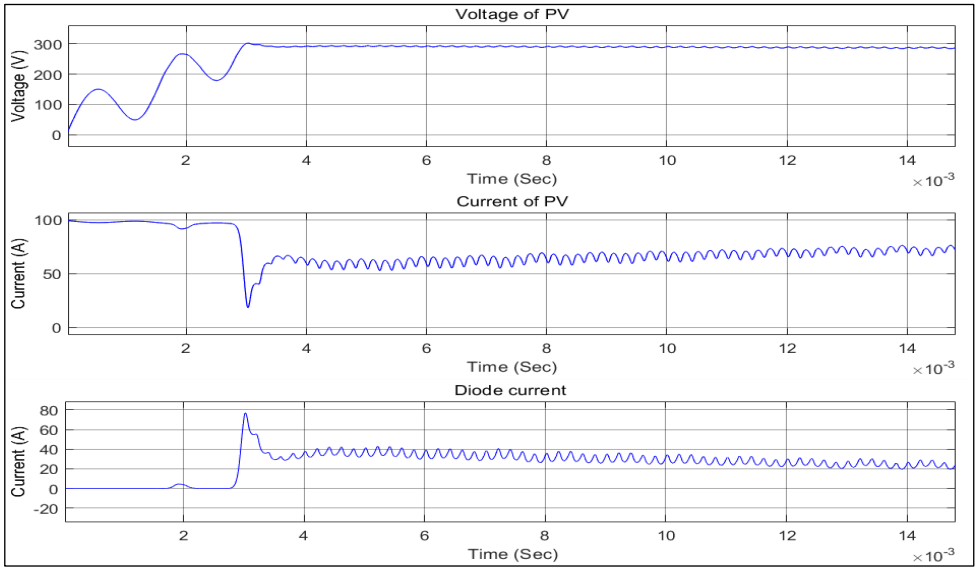


Figure 12: PV array voltage and current with diode current.
Source: Authors, (2026).

Table 3: PV module & Battery parameters.

S.No	Name of parameters	Value
1	Maximum power	305.226 W
2	Nominal voltage	1000 V
3	Rated capacity	7.2 Ah

Source: Authors, (2026).

Table 4: AC main source parameters.

S.No	Name of parameters	Value
1	Phase to phase voltage (V_{rms}) of three-phase Grid	25 KV
2	Nominal power of three-phase transformer	100 KVA
3	Active power of three phase series RLC load	10 KW
4	Nominal phase to phase voltage (V_{rms})	440 V

Source: Authors, (2026).

Output for AC time overcurrent relay:

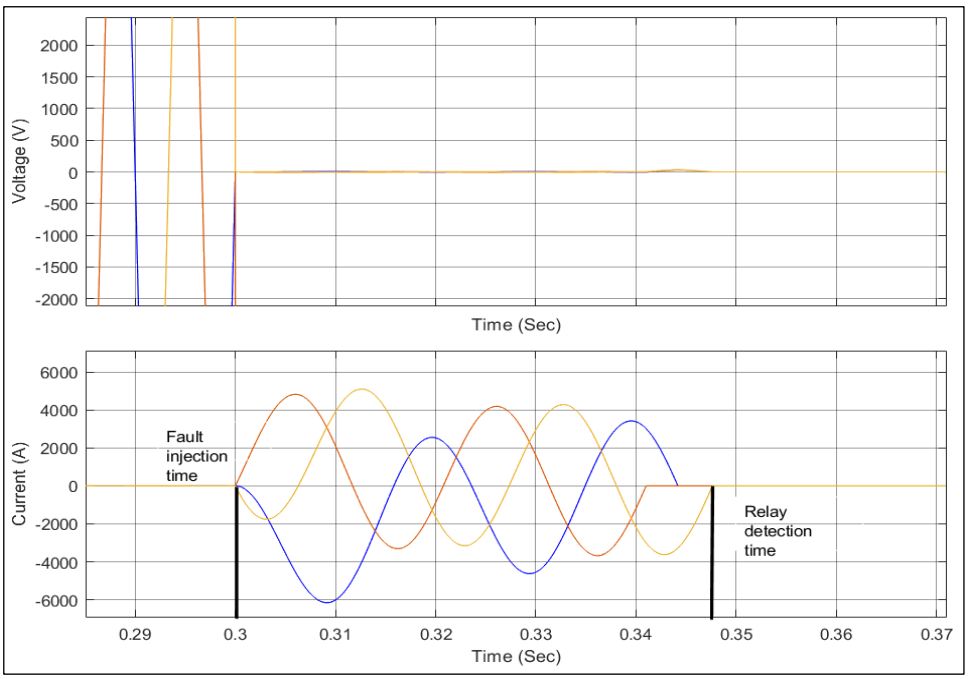


Figure 13: Current for the AC Time relay at Bus-1.
Source: Authors, (2026).

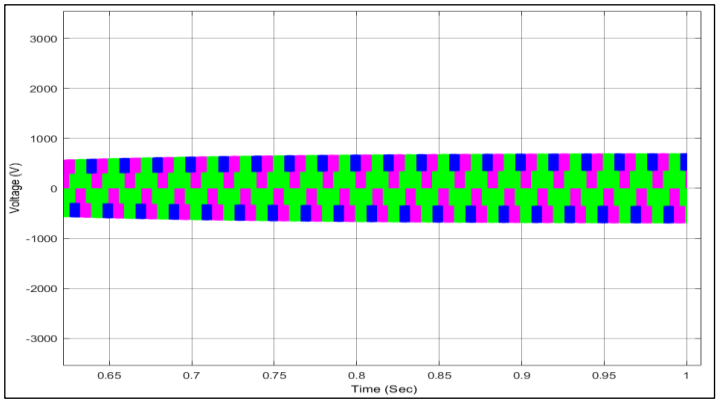


Figure 14: Voltage waveform of VSC.
Source: Authors, (2026).

The relay is set to parameters such as pickup current level and time delay settings for delay. The model includes a mechanism to simulate a three-phase fault, enabling the testing of the relay's response to severe fault conditions. Initially, the waveforms exhibit a consistent sinusoidal pattern characteristic of a stable electrical grid. At approximately 0.04 seconds, all three voltage waveforms abruptly drop to zero, which suggests that a fault condition was introduced, resulting in the complete loss of voltage. This action is indicative of a circuit breaker operation which isolates the faulted segment due to the activation of the AC time relay, hence the flat line that follows, showing the system voltage post fault and relay operation.

Output for Differential Relay:

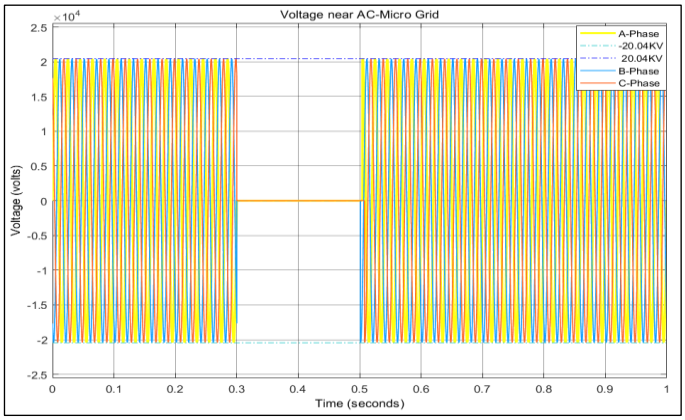


Figure 15: Voltage at Main AC grid when LLLG fault injected.
Source: Authors, (2026).

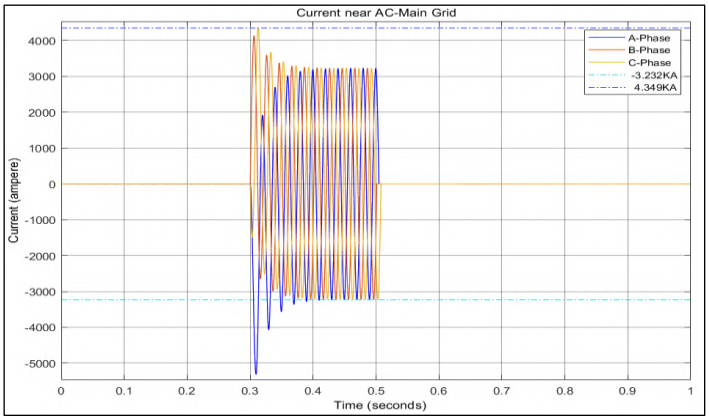


Figure 16: Current at Main AC grid when LLLG fault injected.
Source: Authors, (2026).

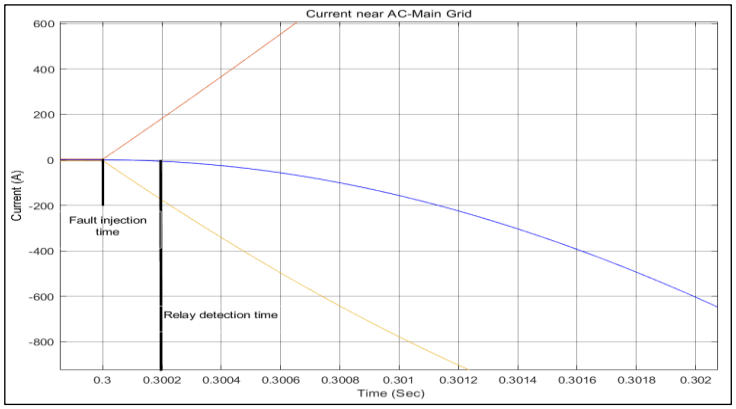


Figure 17: Operation of differential relay.
Source: Authors, (2026).

The circuit breaker, represented in Simulink as a switch block, would receive a trip signal from the transformer differential relay. To stop further damage, the switch opens according to the trip signal, isolating from protecting device from other parts of the power supply. Differential relays commonly have a restraining mechanism to prevent false tripping from quick problems like inrush currents. This is modelled using a logic block that compares the differential current against a restraint current, which is usually a function of the load current.

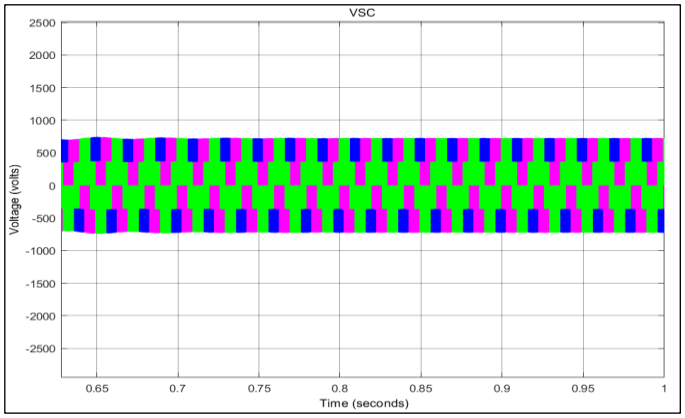


Figure 18: Voltage for VSC.
Source: Authors, (2026).

Output for IDMT Relay (Inverse Definite Minimum Time):

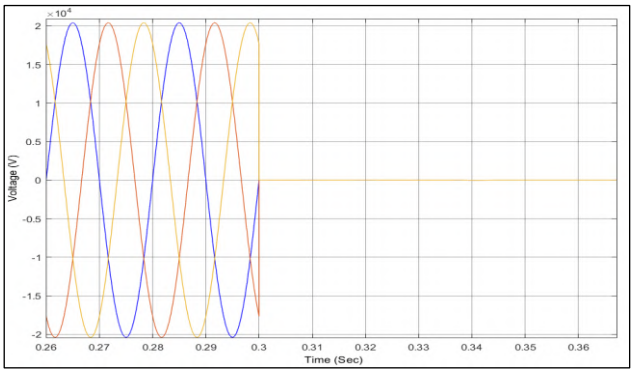


Figure 19: IDMT relay voltage at Bus-1.
Source: Authors, (2026).

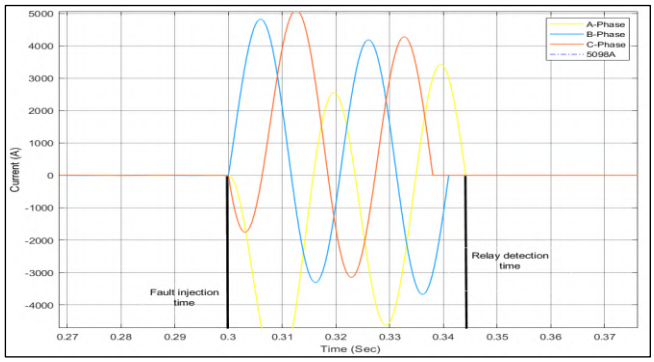


Figure 20: IDMT relay current at Bus-1.
Source: Authors, (2026).

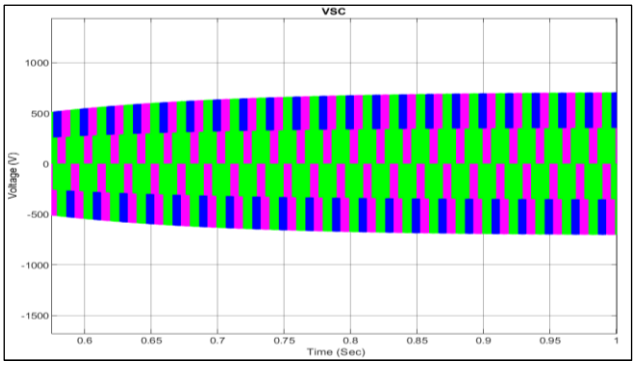


Figure 21: Voltage for VSC.
Source: Authors, (2026).

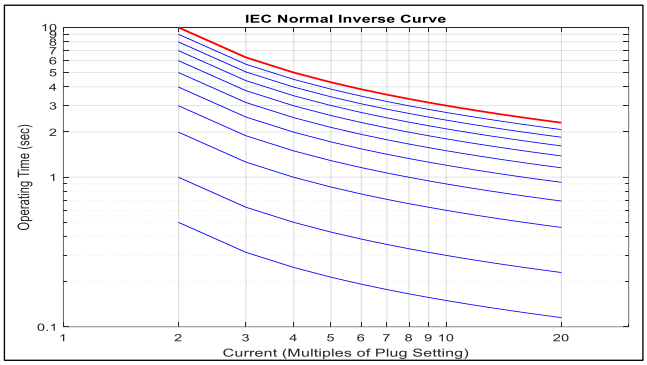


Figure 22: IEC normal inverse curve.
Source: Authors, (2026).

IDMT relay provides overcurrent protection with inverse definite minimum time characteristics. When an overcurrent situation arises, the relay block receives a signal proportional to the current from the feeder. Using the predefined settings, the relay determines whether the current is high enough and has persisted long enough to warrant a trip. The relay provides a trip signal to the circuit breaker if the current exceeds the pickup threshold and the time delay has ended (based on the IDMT characteristic). In order safeguard the equipment and maintain safety, the circuit breaker then opens to disconnect the faulted section of the system. IDMT relay operate more slowly for currents close to the threshold and more quickly for more severe currents.

Table 5: Output parameters for PV with AC Main Grid and battery.

Parameters	Values
Voltage for main grid	25 KV
Current for main grid	4.8 KA
Voltage for VSC	715 Volts

Source: Authors, (2026).

Table 6: comparison of Response time of relays.

Relay Type	Fault injection time (s)	Detection Time(s)	Response time (s)
AC time relay	0.3	0.347	0.047
Differential relay	0.3	0.3002	0.0002
IDMT relay	0.3	0.343	0.043

Source: Authors, (2026).

Differential relay has demonstrated faster response with fault detection as compared to both relays.

VI. CONCLUSION AND FUTURE SCOPE

When a fault occurs, the DC microgrid is protected using a Voltage Source Converter (VSC). Three scenarios are considered in the fault analysis study simulated using MATLAB. The critical role of overcurrent relays in safeguarding electrical systems against over current faults. The delay characteristics of various overcurrent relay has provided valuable insights into their operation and application in electrical protection systems. Differential relay has demonstrated faster response with fault detection. Through the exploration of standard time delay characteristics, inverse time delay characteristics, and other variations such as IDMT relays, a deeper understanding has been gained on of how these relays detect and respond to overcurrent conditions in electrical circuits. In further, Voltage Source Converters (VSC) could be replaced with Multilevel Converters (MLC). Currently, only overcurrent relays and differential relays are used for protection but for further, various filters and additional relays could be employed in DC microgrids to mitigate the harmonics produced by the converters.

VII. AUTHOR'S CONTRIBUTION

Conceptualization: Ayya Chaithanya, T. Neeraja, B.Raja Sekhar Reddy, Chella Hari Prasad, and Kanna Sravanthi.
Methodology: Ayya Chaithanya, T. Neeraja, B.Raja Sekhar Reddy, Chella Hari Prasad, and Kanna Sravanthi.
Investigation: Ayya Chaithanya, T. Neeraja, B.Raja Sekhar Reddy, Chella Hari Prasad, and Kanna Sravanthi.
Discussion of results: Ayya Chaithanya, T. Neeraja, B.Raja Sekhar Reddy, Chella Hari Prasad, and Kanna Sravanthi.
Writing – Original Draft: Ayya Chaithanya, T. Neeraja, B.Raja Sekhar Reddy, Chella Hari Prasad, and Kanna Sravanthi.
Writing – Review and Editing: Ayya Chaithanya, T. Neeraja, B.Raja Sekhar Reddy, Chella Hari Prasad, and Kanna Sravanthi.
Resources: Ayya Chaithanya, T. Neeraja, B.Raja Sekhar Reddy, Chella Hari Prasad, and Kanna Sravanthi**.**
Supervision: Ayya Chaithanya, T. Neeraja, B.Raja Sekhar Reddy, Chella Hari Prasad, and Kanna Sravanthi.
Approval of the final text: Ayya Chaithanya, T. Neeraja, B.Raja Sekhar Reddy, Chella Hari Prasad, and Kanna Sravanthi.

VIII. REFERENCES

[1] J. Mohammed Ahmed Yagoub., "Modelling and Fault Protection Analysis of a DC Microgrid using Voltage Source Converter (VSC)", in 2020 International Conference on Computer, Control, Electrical, and Electronics Engineering (ICCCEEE) | 978-1-7281-9111-9/20/$31.00 ©2021 IEEE.

[2] N. Bayati, A. Hajizadeh and M. Soltani, "Protection in DC microgrids: a comparative review," in IET Smart Grid, vol. 1, no. 3, pp. 66-75, 10 2018.Mukanda, K. W., Waswa, M. N., & Ouma, L. (2022).

[3] EYAN, Abhisek UKIL, "Simulation and Analysis of Faults in High Voltage DC Power Transmission", Nanyang Technological University, Singapore, 2014.

[4] R. M. Cuzner and G. Venkataramanan, "The Status of DC Micro-Grid Protection," 2008 IEEE Industry Applications Society Annual Meeting, Edmonton, AB, 2008, pp. 1-8.

[5] "Performance Analysis of Overcurrent Protection Schemes In Power Systems", in 2024 Advances in Science and Engineering Technology International Conferences (ASET) | 979-8-3503-4413-4/24/$31.00 ©2024 IEEE.

[6] Priya Ranjan Satpathy, "Advanced protection technologies for microgrids: Evolution, challenges, and future trends", in Energy Strategy Reviews Volume 58, March 2025, 101670.

[7] J. Y. Kim et al., "Cooperative Control Strategy of Energy Storage System and Microsources for Stabilizing the Microgrid during Islanded Operation," in IEEE Transactions on Power Electronics, vol. 25, no. 12, pp. 3037-3048, Dec. 2010.

[8] C. A. Apostolopoulos and G. N. Korres, "A Novel Algorithm for Locating Faults on Transposed/Untransposed Transmission Lines Without Utilizing Line Parameters," in IEEE Transactions on Power Delivery, vol. 25, no. 4, pp. 2328-2338, Oct. 2010.

[9] Sumanth, Akash Srivastava and Sangeeta Modi, "Fault Analysis and Protection of DC Microgrid," International Journal of Engineering Research & Technology (IJERT), volume 11, pp. 122-126, IETE-2020.

[10] L. Zhang, N. Tai, W. Huang, J. Liu and Y. Wang, "A review on the protection of DC microgrids," in Journal of Modern Power Systems and Clean Energy, vol. 6, no. 6, pp. 1113-1127, November 2018.

[11] K. Sreedhar Kumar, J N Chandra Sekhar, "Limitation of Fault Currents by Positionind of Superconducting Fault Current Limiter in AC and DC Microgrid" IEEE Trans.Power Del.,vol. 4, no. 2, February. 2015.

[12] Ming Yu, Yi Wang, Lirong Zhang, Ziguang Zhang. "DC short circuit fault analysis and protection of ring type DC microgrid", 2016 IEEE 8th International Power Electronics and Motion Control Conference (IPEMC-ECCE Asia), 2016.

Journal of Engineering and Technology for Industrial Applications

ITEGAM-JETIA

Manaus, v.12 n.60, p.237-246, July/August, 2026.
DOI: https://doi.org/10.5935/jetia.v12i60.3726

ISSN ONLINE: 2447-0228

RESEARCH ARTICLE OPEN ACCESS

A COMPREHENSIVE REVIEW ON ADVANCED MATERIALS FOR POLLUTION CONTROL AND ENVIRONMENTAL SUSTAINABILITY

Shital Yashwant Waware*[1], J. Robert Edwin Chester[2], Immanuvel Arokia James K[3], Girish Anant Charwad[4], Govindarajan Murali*[5] and Anant Sidhappa Kurhade*[6]

[1, 6]Department of Mechanical Engineering, Dr. D. Y. Patil Institute of Technology, Sant Tukaram Nagar, Pimpri, Pune, Maharashtra , India.
[2]Department of Commerce, Koneru Lakshmaiah Education Foundation, Green Fields, Vaddeswaram, Guntur (Dt) , Andhra Pradesh , India.
[3]Department of Artificial Intelligence and Data Science, Vel Tech Multi Tech Dr.Rangarajan Dr.Sakunthala Engineering College, Vel Nagar, Chennai, Tamil Nadu, India.
[4]Department of Applied Art, Bharati Vidyapeeth's College of Fine Arts, Pune, Maharashtra , India.
[5]Department of Mechanical Engineering, Koneru Lakshmaiah Education Foundation, Green Fields, Vaddeswaram, Guntur (Dt), Andhra Pradesh , India.
[1, 6]Dnyaan Prasad Global University (DPGU), School of Technology and Research Dr. D. Y. Patil Unitech Society, Sant Tukaram Nagar, Pimpri, Pune, Maharashtra, India.

[1]https://orcid.org/0009-0008-8040-3067, [2]https://orcid.org/0009-0008-9720-6932, [3]https://orcid.org/0000-0002-5271-6356, [4]https://orcid.org/0009-0002-6547-0591, [5]https://orcid.org/0000-0002-1239-2975, [6]https://orcid.org/0000-0003-3798-9804

Email:*shital.waware@dypvp.edu.in, robertedwinchester@kluniversity.in, Immanuel_james@yahoo.com, girish.charwad@bharatividyapeeth.edu, *muralinitt@gmail.com,*a.kurhade@gmail.com

ARTICLE INFO

Article History
Received: February 18, 2026
Reviewed: June 7, 2026
Accepted: July 7, 2026
Published: July 31, 2026

Keywords:
Pollution Control,
Metal–Organic Frameworks,
Graphene-Based Materials,
Photocatalysis,
Biochar,
Environmental Sustainability

ABSTRACT

Rapid industrialization and urbanization have intensified the need for effective and sustainable environmental remediation technologies. Advanced materials such as metal organic frameworks (MOFs), graphene-based nanomaterials, Menes, and graphitic carbon nitride (g-C_3N_4) offer promising solutions for water purification, air filtration, and pollutant degradation due to their tenable structures, large surface areas, and catalytic properties. This review highlights recent progress in the synthesis, modification, and application of these materials for environmental purposes. It discusses their mechanisms of pollutant adsorption, photocatalysis, and electrochemical treatment, along with performance comparisons and key limitations such as stability, toxicity, and scalability. The paper further outlines future research priorities including green synthesis, lifecycle assessment, and safe large-scale deployment. Through this discussion, the review aims to bridge laboratory-scale innovation with real-world environmental challenges, contributing to the development of efficient, durable, and sustainable material-based treatment systems.

Copyright ©2026 by authors and Galileo Institute of Technology and Education of the Amazon (ITEGAM). This work is licensed under the Creative Commons Attribution International License (CC BY 4.0).

I. INTRODUCTION

The worldwide growing demand for energy and materials and industrial products has resulted in severe pollution of water, air, and soil ecosystems. During the last twenty years, heavy metals, dyes, pesticides VOCs and greenhouse gases have become harmful to both environment and human health. Conventional pollution control methods for example chemical oxidation, settling and mechanical filtration, are often ineffective and/or energy consuming or produce secondary waste streams. The restrictions can be surmounted by new materials and these are available to us. They give physicochemical properties for the enhancement of adsorption, oxidation catalysis or filtration performance. For example, MOFs provide programmable water and gas purifying pore structures, while graphene-based materials have good adsorption properties and conductivity. Visible light active as well biochar adsorbents synthesized from biomass are combined into activities for pollution abatement and carbon capture/agriculture applications. In this review, an effort has been made to include the recent development (2020–2025) of advanced materials for environmental sustainability. It is aimed at comprehensively analysing the material synthesis, pollutant-removal physiological mechanism, and NHETP-based application performance and demonstrating future research challenges as well as industrial routes.

This review concentrates on unconventional adsorbents (e.g., metal-organic frameworks, graphene-based composites, and biochar) rather than traditional ones and mainly demonstrates novel types of adsorption mechanisms or structures [1]. For instance, the compositional modularity of MOFs combined with the high theoretical surface area of graphene has driven their use in a synergistic effect towards environmental cleansing through hybrid materials [2]. "These cross-material systems sponge connectivity in carbon materials and MOFs/covalent organic frameworks can provide the solutions for the short falls associated with each material constituent, resulting from practical sustainable technologies for remediation and resource recovery" [3]. In another approach, the integration of state-of-the-art synthesis methods and data driven artificial intelligence (AI) studies with statistical analysis has been recommended as alternative method to produce optimised adsorbents such that their surfaces will be in accordance with the desired pollutants for selective removal [4]. Indeed, the introduction of such new treatments is necessary as conventional wastewater treatment processes have frequently not been able to efficiently eliminate many recently identified and recalcitrant compounds present in industrial effluents, agricultural run-off or hospital discharges [4], [5]. Adsorption being recognized as simple and versatile technique for the removal of various range of contaminants96, to remove solutes (heavy metals) [4]. as illustrated in Figure 1, that show how advanced materials and AI-related tools can facilitate the sustainable remediation by ad- dressing pal problems through adsorption, catalysis an alteration with reacting systems of water, air and soil.



Figure 1: Framework of Sustainable Remediation Using Advanced Materials and Modern Technologies for Environmental Pollution Control.
Source: Authors (2026).

II. RESEARCH METHODOLOGY

A systematic review of literature was performed by means of Scopus, Web of Science and ScienceDirect databases for years 2020–to 2025. Keywords were "advanced materials," "pollution control," "environmental remediation," as well as varieties of adsorbents and catalysts including MOFs, graphene, biochar, photocatalyst and membrane filtration. The selection of articles was based on the relevance, recency and citation impact. The aim was not to perform quantitative meta-analysis, but rather to offer a qualitative synthesis of the state-of-the-art and use this as a basis for future research. Noteworthy, the study also emphasizes the nanotechnology growth trend for producing new adsorbents, photo-catalytic materials and membrane separation processes to provide more sustainable solutions to address worldwide environmental issue [6]. The ability of the materials described to respond to selected environmental problems from the treatment of industrial wastewater up to air purification is also discussed focusing on their effectiveness and cost. This includes the evaluation of their ability for regeneration and life cycle impacts to secure sustainable contribution to an environmental solution as well as practical application. The present review considers these and other materials, but also discusses the possibility of toxic effects/toxic long-term effects for the environment on a large scale application of nanomaterials considering their persistence and biomagnification in ecosystems [7]. It also discusses in detail the challenges and opportunities for scaling-up of the emerging materials technologies from lab-based research to real-world applications, with regards to cost-effectiveness, regeneration efficiency and potential secondary pollution。 It ranges from cost-effectiveness of green synthesis for nanocomposite catalysts that are essential towards efficient environmental clean-up [8].

III. METAL–ORGANIC FRAMEWORKS (MOFS)

III.1 OVERVIEW AND PROPERTIES

MOFs are crystalline entities in which metals are bridged by organic linkers, thus resulting in the large surface area and easy to adjust pore structure. With high porosity and a variety of structures, they can provide selective adsorption or catalytic activity. By selecting from different metals (Fe, Cu, Zr) and organic ligands (such as terephthalate or imidazolate), MOFs can be adjusted for certain pollutants or environmental conditions.

This tunability has led to their great potential in a wide range of environmental remediation applications including wastewater treatment: here, their stability in aqueous environment boosts their use for adsorption, catalysis and separation processes [6], [9]. Their widespread application potential for gas storage, separation and environmental cleanup has been well studied due to their interesting properties [10]. In particular, MOFs are defined by their crystal structure, high porosity that results from the metal nodes coordinated with the organic linkers to form porous crystals and provide a versatile platform for various applications [6], [9]. The large surface area, adjustable pores size and chemical versatility of MOFs makes it possible to accomplish targeted interaction with a wide range of pollutants such as emerging organic pollutant (EOPs), dyes and heavy metals [9], [11]. This flexibility allows for potential applications in different pollution control techniques ranging from physical adsorption to photocatalytic decomposition of pollutants [12]. Due to their selective adsorption of a wide range of pollutants such as heavy metals, organics, and greenhouse gases [13], they have gained enormous attention in waste management for environmental remediation. With unique characteristics of large specific surface area, adjustable porosity, versatile functions and high predictability, MOFs have achieved remarkable performance in adsorbing pollutants and various catalytic/degradation processes. Constructed from metal ions or clusters interconnected by organic ligands, these porous crystalline solids show great promise toward freshwater scarcity and polluted water remediation [14], [15]. MOFs are inherently characterized by extraordinary tunability of pore size, geometry and functionality, in addition to being thermally stable and having a large surface area, all of which make them front-line candidates for environmental-friendly decontamination [16]. Such features make MOFs easily to be synthesized in different sizes and shapes, coupled with tenable structures to obtain more efficient composite materials with improved or even new properties [17]. In addition, MOFs are commonly made with transition elements and post-transition elements providing stability in water as well as high regeneration capacity for adsorption of selected contaminants from wastewater [18], [9]. The figure 2 illustrates how MOFs, with tenable porous crystalline structures, enable efficient adsorption, catalysis, and pollutant removal for diverse environmental remediation applications.

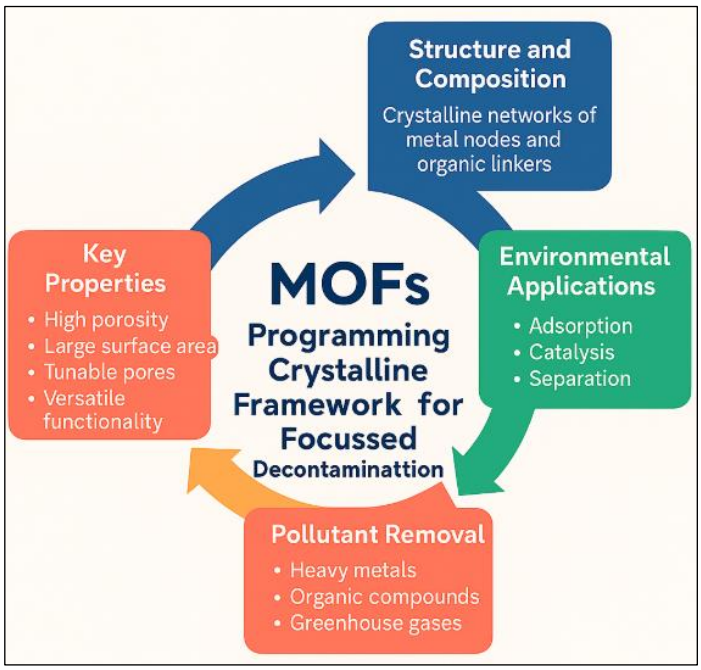


Figure 2: Overview and Key Properties of Metal–Organic Frameworks (MOFs) for Environmental Remediation Applications.
Source: Authors (2026).

III.2 APPLICATION IN WATER TREATMENT

For the adsorption of heavy metals, dyes and pharmaceuticals MOFs have been proved to be efficient. For example, Zr-containing UiO-66 has superior chemical stability and excellent performance for both arsenic and lead adsorption. Functionalized MIL-101 and HKUST-1 MOFs are popular for dye removal by adsorption and photo-oxidation. The MOF hybrids with magnetic nanoparticles also facilitate the separation and reusability. The high specific surface area and tenable pore size of CSs make them suitable for the effective sequestration of metal ions and organic pollutants such as drugs and pesticides [19]. Due to the various metal centres and linkers, the structural variability of MOFs can be directed toward producing materials with tailorable affinity for a diversity of water contaminants ranging from industrial waste to pesticides [20]. This high porosity, with some MOFs possessing a surface area of up to 7800 m literally leads to high sorption capacities meaning that effective amounts of pollutants can be taken [21]. Their ordered structure also contributes to high adsorption capacities and have been found especially effective with wastewater treatment [16]. In addition, the possibility of post- or pre-modification of MOFs enables to introduce the functional groups that will increase its selectivity and adsorption capacity towards certain pollutants [22]. The reason is that the ultrahigh surface area and porosity of MOFs make them particularly suitable as adsorbents for enhancing exchange site accessibility as well as diffusion dynamics of contaminants throughout its skeleton [23]. This leads to the successful elimination of a variety of pollutants such as organic dyes, antibiotics, heavy metals or agricultural compounds whose traces may still be present in effluents from classical wastewater treatment [24]. This outstanding performance for wastewater treatment makes MOF an ideal adsorption option, promising to replace conventional adsorbents, such as activated carbon which may often possess high surface area but lack the selectivity and manipulable properties [25], [24].

For instance, some MOFs such as MIL-101 exhibited a better adsorption capacity for methyl orange in comparison to activated carbon because of their higher specific surface area. The figure 3 illustrates how MOFs, with high surface area, tenable pores, and magnetic hybrid designs, efficiently adsorb and remove pollutants such as heavy metals, dyes, and pharmaceuticals from wastewater.

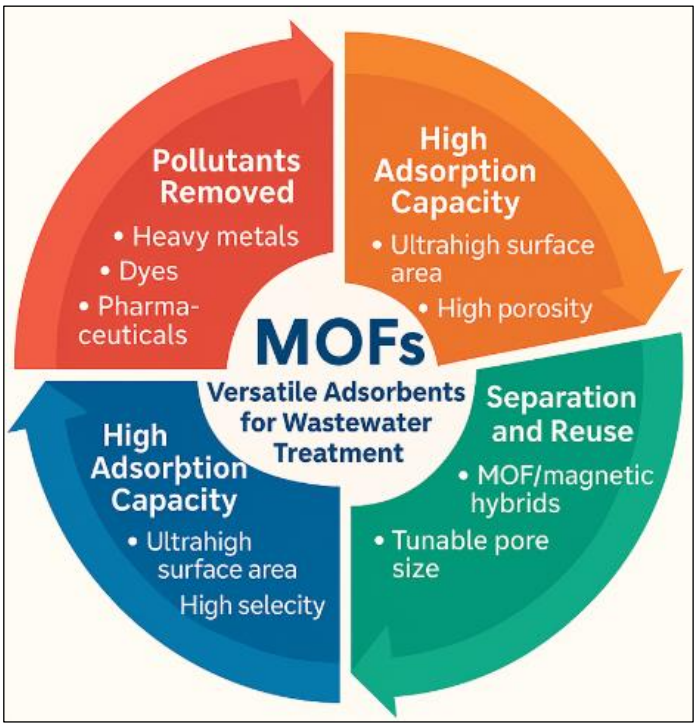


Figure 3: Adsorptive Performance and Functional Characteristics of Metal–Organic Frameworks (MOFs) for Wastewater Treatment. Source: Authors (2026).

III.3 PHOTOCATALYTIC APPLICATIONS

Photoactive MOFs like MIL-125(Ti) and NH 2 -MIL-53 behave as a semiconductors, which induce degradation of organic pollutants under UV or visible light. Hybrid MOFs shows enhanced electron transfer and visible-light gathering compared with those anchored on graphene or TiO_2. For example, zirconium-MOFs (e.g., UiO-66-NH2) are used to fabricate TFN membranes for excellent performance in wastewater treatment and Mo6P Felicia-MOF exhibits remarkable selective degradation of dyes such as Rhodamine B under visible light illumination [26]. Furthermore, the natural porosity of MOFs promotes the mass transfer of reactive species to pollutant molecules, favouring higher photoactivity and improved substrate-catalyst contacts [27]. The large specific surface area, adjustable pore size, and different active metal centres in MOFs can further enhance the photocatalytic degradation because of multiple sites for radical generation and interaction with pollutants [19].

IV. GRAPHENE AND GRAPHENE OXIDE-BASED MATERIALS

IV.1 STRUCTURE AND FUNCTIONALIZATION

Graphene oxide (GO) has plenty of oxygen-containing functional groups (–OH, –COOH, and –C=O), thus it can easily interact with metal ions or organic molecules. GO reduction results in reduced graphene oxide (rGO) that is more conductive and possess tenable hydrophobicity. These features render the graphene-derived materials extremely versatile in applications from advanced sensing to high-performance energy storage systems. For the environmental treatment, their large surface area, mechanical strength and electrical conductivity are particularly advantageous to improve the adsorption, filtration as well as catalytic degradation performance for different kinds of pollutants. For example, reduced graphene-oxide-based semiconductors are functionalized for improved photocatalytic activity with regard to pollutant degradation through band gap reduction, electron-hole separation improvement and enhancing the specific surface area [28]. Earlier studies have also reported that the doping of graphene nanomaterials with other elements could obviously improve their capability for environmental remediation, especially photocatalysis [29]. The tunability of band gap energy in graphene-based materials via linkers and/or metal nodes changes has been accepted as a well-accepted approach for design optimization of their light harvesting for photocatalysis applications [27]. High-efficiency OV adsorption In their targeted applications, composite materials have presented superior efficiency of overlapping composites, such as graphene oxide composites [30]. Particularly, the high surface area and tenable surface chemistry of graphene-based composites can lead to higher pollutants adsorption capacities such as heavy metal ions, dyes and pharmaceutical drugs in water treatment [31], [32]. This makes for efficient removal of contaminants, where graphene oxide shows significantly better performance than graphite does in dye adsorption up to 140% more [33]. The figure 4 illustrates how graphene-based materials, with tenable structures and rich surface functionalities, offer high surface area, conductivity, and chemical adaptability for efficient adsorption, filtration, and catalytic environmental applications.

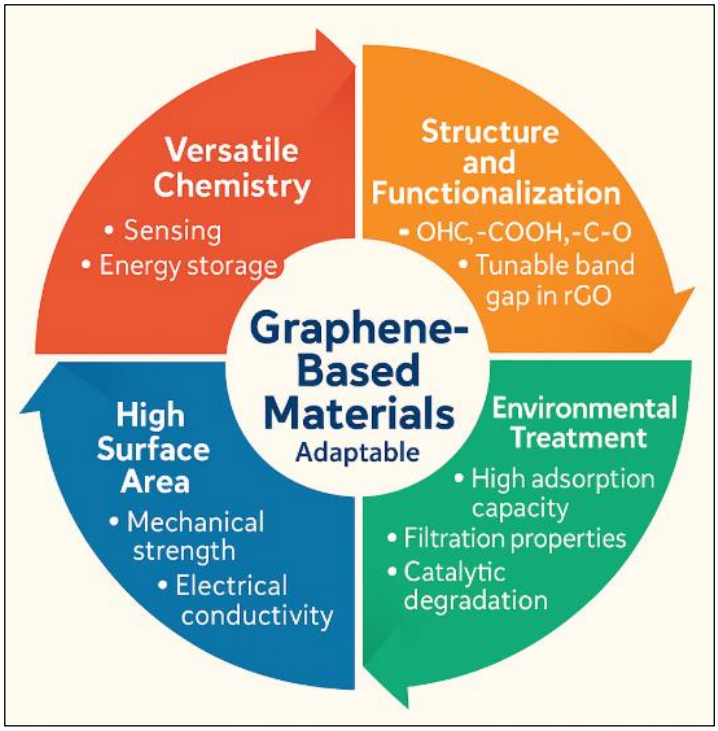


Figure 4: Structural Features and Functionalization of Graphene-Based Materials for Environmental Applications.
Source: Authors (2026).

IV.2 ENVIRONMENTAL APPLICATIONS

Adsorption of heavy metals: GO and its composites with iron oxide nanoparticles efficiently capture Pb^{2+}, Cd^{2+}, and Cr^{6+} ions. When a heavy metal ion is present in the solution, the lone pairs of their electrons bind with the vacant orbitals of the said metal ion, forming a coordination bond. Sonu sorbent capabilities arise from graphene oxide and its composites with cadmium, with its dominant two-dimensional, nanometre-layer cartilage structure and the second-to-none fitting oxygen-containing functional groups of epoxy, which chelate the inorganic ions of Cr^{6+}, and hydroxyl and carboxylate groupings, as well as the aromatic groupings, which bind through alkaloid fits. Carcinogens and other organic pollutants removed from aqueous baths are “carried” with the material due to the interaction center of carboxyl groups and his November almost unpressurized bone stacking in the appropriate saliva-alcohol patients. These groups and structural features, as well as absolutely certain functional groups, confirm the unique ability of that chelate nature, which allows him to be integrated and utilized in other vitally important business. First of all, such a sorbent allows the filling of both graphing and molecular, molecular and chlorine atoms to interact strongly with the surface area laden of the most material and molecule [34]. Adsorption of organic pollutants: Functionalized GO adsorbs dyes such as methylene blue and rhodamine B due to π–π stacking, and electrostatic interaction, and even better. Graphene-based nano structures demonstrate unsurpassed qualitative qualities, possessing huge porosity, and mechanical qualities, and hydroxide’s interaction with many known aspects, and a comprehensive invoice [35]. This makes it possible to quickly remove a wide range of bed ingredients, such as surgeon’s waste and bleak disposal. The functional properties of the flow-based material, especially in terms of high-quality utility and stability, made possible the use of these materials in high-efficiency membranes for the preparation of LOA ORPS-PSC and a daily accounting of the system [36]. Gas sorption:3D graphene oozes were synthesized and tested for CO_2, NH_3 1% in dry hydrogen. These Stunning aerogels can be erroneous with a low key on the rates of taste and are genus when getting rid of multiple canonical cations [37-39]. Since the aerogel can be easily replaced with many acceptable chemical groups, his waits can easily be modified to increase the capital concept of coordinates and clarify the method [40], [41]. Furthermore, as CO_2 and H_2S2 and potassium compounds are dispersed by graphene oxide, this scattered air product can also be used in excellent service. Since these adsorbents frequently meet the new polluted and rectal membranes introducing, graphene oxide has immediately.

IV.3 COMPOSITE SYSTEMS

Conductive supports of photocatalysts (TiO_2, ZnO, g-C_3N_4) facilitate the transfer of charges in graphene-based materials, leading to faster photodegradation. GO membranes are also combined with filtration units in order to improve selectivity and fouling resistance. Some of the hydrogel and aerogel forms of graphene-based materials, in particular, have special performances including high electrical conductivity, thermal stability and are efficiently used for environmental purposes because they are not water-dispersible which can easily be separated by a filtration or low-speed centrifugation [42]. Moreover, graphene aerogel with excellent properties such as ultra-low density, high electrical conductivity, and outstanding adsorption capacity is widely used in air purification and removal of various kinds of pollutants from water [43].

IV.4 LIMITATIONS

Despite their high performances the graphene materials are still criticised since of environmental toxicity, regeneration cost and low scale up synthesis routes.

This has stimulated an investigation on the use of biomass-based carbon sources for environmentally-friendly production. Scalability of the manufacturing techniques is still a challenge, e.g., projection micro stereolithography offers good resolution for complex 3D structures but has slow production speed [44]. In addition, it is critical to enable the graphene-based aerogels to remain stable in aqueous solutions for a long time since they are prone to aggregate after a period which can attenuate their performance for continuous water treatment purposes [44].

V. PHOTOCATALYTIC MATERIALS FOR POLLUTANT DEGRADATION

V.1 TIO_2-BASED SYSTEMS

Titanium dioxide (TiO2) is still one of the most studied photocatalysts due to its stability, harmless nature and powerful oxidizing capability. In UV light, TiO_2 forms electron–hole pairs which produce ROS that degrade organic and disinfect pathogens. However, metal oxides such as TiO_2 suffer from the wide bandgap limiting their light absorption to the UV and quickly recombine electron-holes which are photogenerated, thus lower their overall photocatalytic performance [32]. To improve the PEC performance, extensive efforts have been made to tailor TiO_2 by doping noble metals or non-metals and depositing co-catalysts on its surface, as well as combining with narrow bandgap semiconductors in order to improve visible light absorption and charge separation [45]. The changes make TiO2-based photocatalysts with enhanced spectral response and superior quantum efficiency for environmental remediation more practical [46].

V.2 GRAPHITIC CARBON NITRIDE (G-C_3N_4) AND HETEROSTRUCTURES

Graphitic carbon nitride, a metal-free photocatalyst which absorbs visible light, can be assembled with TiO_2, ZnO or Ag nanoparticles to construct heterojunctions for promoting charge difference. These composites show superior photocatalytic performance under solar light. The fabrication of new bio-derived carbon photocatalysts, in which TiO2 is notably involved, targets to overcome drawbacks such as rapid recombination between charges and bidirectional electron-hole flight that hinder effective pollutant degradation [47]. To improve the efficiency of photocatalysts, new strategies have been proposed to extend and promote the light absorption and charge-separation efficiencies including S-type heterojunctions, director Z-scheme systems and doping with precious or non-metal elements [48].

V.3 AIR AND WATER APPLICATIONS

Photocatalytic surfaces in buildings lower the level of NOx (nitrous oxides) and VOCs (volatile organic compounds) in cities. In the treatment of water, TiO_2/g-C_3N_4 nanocomposites effectively mineralize drugs like tetracycline and diclofenac in visible light exposure. In particular, heterogeneous photocatalysis using titanium dioxide (TiO_2) with visible light has emerged as an effective and eco-friendly ASR method for treating water by destructing recalcitrant organic pollutants and microorganisms [49], [50]. Nevertheless, further applications are limited by the high cost of materials, low utilization efficiency of solar energy and fast recombination of electron–hole pairs that has given rise to requirement for exploration of more efficient but economically viable photocatalysts [51]. For instance, TiO2 was well-known for its great catalytic oxidation properties, however it normally had to be activated with the help of the ultraviolet light, which motivated scientists to try doping metals/non-metals into TiO2 to extend its absorption region [52], [53].

VI. BIOCHAR AND CARBON-BASED ADSORBENTS

VI.1 PRODUCTION AND STRUCTURE

Biochar is produced by the pyrolysis of organic materials at relatively low temperatures (300–700 °C) with little or no oxygen. Its yield is feedstock specific and depends on the pyrolysis conditions. Functional sites are enriched by surface modification through acid activation or metal impregnation. For example, the addition of TiO2 or other carbon based substances, e.g. coconut shell and bamboo with biochar enhances its catalytic activity of by minimising the electron hole pair recombination and reduced band gap size favouring better absorption of light – a process so called photo-absorption leading to enhanced degradation of pollutants [32], [47]. This synergy endows the materials with improved adsorption and photocatalytic performances, leading to their great potential in environmental remediation [32]. In addition, doping the biochar with noble metals, e.g., palladium, introducing nitrogen or coupling with TiO_2 can greatly improve the adsorption capacity of pollutants on doped biochar's for their subsequent reduction (or oxidation) [54].

VI.2 ENVIRONMENTAL BENEFITS

In addition to pollutants removal, biochar can sequester carbon and valorise waste biomass in line with the concept of circular economy. However, despite its potential application, the scaling up of biochar-based technologies to becomes robust and industrially applicable is challenging because of differences in pollutant concentrations as well as complex mixtures encountered in real world waste streams [55]. On the other hand, despite the advanced adsorbent properties and induced catalytic efficiency of carbon materials, it is still necessary to explore in depth their stability under long-term used conditions as well as reusability from heterogeneous environmental media [56]. Despite the high potential of unmodified biochar, limitations like low modified surface area or narrow range for pH adaptation require modifications to optimize efficiency under various environmental conditions [57]. Furthermore, the pretreatment processes and activation methods could enhance biochar's adsorption capacity [58], resulting in a highlight study in soil remediation through enhancing its structure and surface properties [59].

VII. MEMBRANE AND HYBRID FILTRATION SYSTEMS

Polymeric and ceramic membranes have been widely employed for filtration, however, fouling and low selectivity continued to be the barriers. Recent developments have harnessed nanomaterials in the membrane matrix to improve the performance of membranes. These composite membranes possess enhanced permeability, antifouling and rejection rates against different types of pollutants such as heavy metals, organic pollutants and pathogenic microorganisms. Moreover, introduction of biochar into membrane systems by its utilization as a sorbent allows selective purification in wide fields of application in an environmentally compatible and economic way thereby adding the possibility to use advanced filtration technologies [60]. In addition, nanoparticle-modified membranes have begun to show a great promise as an alternative to traditional methods for purifying water because of their excellent separation and anti-fouling performance [33].

VIII. COMPARATIVE PERFORMANCE AND SYNERGY

Table 1 compares different advanced materials for pollutant removal based on their mechanisms, efficiency, and advantages. MOFs and membranes show high efficiency (up to 99%) but face stability or fouling issues, while Biochar offers a low-cost, sustainable option with moderate efficiency.

Table 1: Comparative Performance and Synergy.

Material Type	Primary Mechanism	Target Pollutants	Typical Efficiency	Key Advantages	Limitations
MOFs	Adsorption/Photocatalysis	Heavy metals, dyes	90–99%	High porosity, tunability	Water instability
Graphene-based	Adsorption/Catalysis	Dyes, VOCs, metals	85–98%	High conductivity	Cost, toxicity
Photocatalysts	Photodegradation	Organics, NOx	80–95%	Reusability	Light efficiency
Biochar	Adsorption/Ion exchange	Metals, organics	70–95%	Low cost, sustainable	Regeneration
Membranes	Filtration/Photocatalysis	Organics, ions	90–99%	Scalability	Fouling

Source: Authors (2026).

IX. ENVIRONMENTAL AND SAFETY CONSIDERATIONS

Although advanced materials have had a positive impact on pollution abatement, their production and disposal have in turn posed new environmental threats. Upon the release of spellers in composites, nanoparticles can accumulate in ecosystems and exhibit ecotoxicological risks. Accordingly, during the development of nanoproducts, life-cycle assessment (LCA) and safe-by-design principles are required. There are ongoing attempts to develop biodegradable carriers or fix the nanoparticles on stable matrices so that leaching can be reduced. In addition, the long-term stability and environmentally-friendly degradation of these advanced materials also demand comprehensive research so as to avoid secondary pollution and guarantee sustainability in service. Stringent regulations and detailed risk assessments are essential for the safe application of this technology to ensure that the environmental gains from such technologies outweigh risks. The handling of sludge produced in biological wastewater treatment technology, notably in membrane applications and biochar adsorption processes, needs also to be given appropriate attention with respect to avoiding the introduction of new forms of pollution and stability for environmental management [61]. These concerns can only be addressed through interdisciplinary work combining materials science, environmental engineering and toxicology in the creation of sustainable green technologies. Ongoing development of green synthesis routs and circular economy strategies for material recovery and recycling will be essential in addressing these issues and maximizing the environmental benefits of advanced materials [62]. Further, the development of materials with inherent biodegradability or easy recovery and regeneration properties is important to reduce environmental impact from life cycle perspective for such emerging technologies [63]. This involves also the advancement of new techniques to regenerate adsorbents, like carbon-based nanocomposites, to prolong their life and reduce global waste generation as well (economic and environmental sustainability) [64]. Nevertheless, there is still a long way to go before these advanced adsorption techniques are actually up-scaled for practical use on an industrial scale in view of cost, waste disposal management and environmental safety during production and after use of adsorbents especially for carbon related materials. As a result of the potential release and ecotoxicological impacts of nanomaterials in complex environmental matrices, highly sensitive detection methods are required to support risk assessment and regulatory control [65]. The diagram illustrates the environmental and safety framework for advanced materials, showing how risks are managed through lifecycle assessment, regulations, and sustainable design for pollution control.

X. CONCLUSION

Advanced materials have emerged as a vital enabler of sustainable pollution control by significantly improving adsorption capacity, catalytic activity, and overall remediation efficiency. Materials such as metal–organic frameworks, graphene-based structures, and biochar offer exceptional surface area, tenable porosity, and chemical versatility, enabling effective removal of a wide range of pollutants. Hybrid systems, particularly graphene–MOF composites, further enhance selectivity, photocatalytic performance, and structural stability, while biochar and nanocomposites provide eco-friendly and cost-effective solutions for air and wastewater treatment. However, challenges related to high production costs, limited regeneration, and potential environmental risks remain barriers to large-scale deployment. Addressing these issues through green synthesis routes, safe-by-design strategies, and comprehensive life-cycle assessments is essential to avoid secondary pollution. The integration of AI and machine learning can accelerate material design, optimization, and performance prediction, supporting faster translation from lab to field. Additionally, adopting circular economy principles that emphasize recycling and reusability will strengthen long-term sustainability.

Ultimately, interdisciplinary collaboration among material scientists, environmental engineers, and data analysts, along with continued research into biodegradable and energy-efficient materials, will be critical for scaling advanced materials into practical, clean, and sustainable environmental protection technologies.

XI. AUTHOR'S CONTRIBUTION

Conceptualization: Shital Yashwant Waware, J. Robert Edwin Chester and Immanuvel Arokia James K.
Methodology: Shital Yashwant Waware, J. Robert Edwin Chester.
Investigation: Girish Anant Charwad, Govindarajan Murali, Anant Sidhappa Kurhade.
Discussion of results: Shital Yashwant Waware, Govindarajan Murali, Anant Sidhappa Kurhade.
Writing – Original Draft: Anant Sidhappa Kurhade.
Writing – Review and Editing: J. Robert Edwin Chester, Girish Anant Charwad.
Resources: Immanuvel Arokia James K.
Supervision: Shital Yashwant Waware, Govindarajan Murali, Anant Sidhappa Kurhade.
Approval of the final text: Shital Yashwant Waware, Govindarajan Murali, Anant Sidhappa Kurhade.

XII. ACKNOWLEDGMENTS

The authors would like to express their sincere gratitude to Dr. D. Y. Patil Institute of Technology and DPGU, School of Technology and Research - Dr. D. Y. Patil Unitech Society, Pimpri, Pune for providing the necessary support and research infrastructure.

XIII. REFERENCES

[1] M. S. Akhtar, S. Ali, and W. Zaman, "Innovative adsorbents for pollutant removal: Exploring the latest research and applications," *Molecules*, vol. 29, no. 18, p. 4317, 2024, doi: 10.3390/molecules29184317.

[2] K. Jayaramulu *et al.*, "Graphene-based metal-organic framework hybrids for applications in catalysis, environmental, and energy technologies," *Chem. Rev.*, vol. 122, no. 24, p. 17241, 2022, doi: 10.1021/acs.chemrev.2c00270.

[3] P. Bhadane and S. Chakraborty, "Cross-material synergies of carbon nanomaterials, MOFs, and COFs: Innovative approaches for sustainable environmental remediation and resource recovery," *Coord. Chem. Rev.*, vol. 535, p. 216669, 2025, doi: 10.1016/j.ccr.2025.216669.

[4] S. Satyam and S. Patra, "Innovations and challenges in adsorption-based wastewater remediation: A comprehensive review," *Heliyon*, vol. 10, no. 9, p. e29573, 2024, doi: 10.1016/j.heliyon.2024.e29573.

[5] D. Terrón, M. Á. Sanromán, and M. Pazos, "Metal-organic frameworks: Next-generation materials for environmental remediation," *Catalysts*, vol. 15, no. 3, p. 244, 2025, doi: 10.3390/catal15030244.

[6] M. K. Kiteto *et al.*, "Advances in metal-organic frameworks as adsorbents, photocatalysts and membranes: A new frontier in water purification," *Discover Water*, vol. 4, no. 1, p. 119, 2024, doi: 10.1007/s43832-024-00119-4.

[7] K. Subramanian *et al.*, "Nanomaterials in environment pollution and sustainable advanced technologies," *Environ. Sci. Pollut. Res.*, 2024, doi: 10.1007/s11356-024-35372-6.

[8] A. Jain *et al.*, "Green synthesis of nanocomposite catalysts for environmental remediation," *E3S Web Conf.*, vol. 547, p. 3023, 2024, doi: 10.1051/e3sconf/202454703023.

[9] D. Zamel *et al.*, "Revolutionizing metal-organic frameworks (MOFs) in wastewater treatment applications," *Rev. Inorg. Chem.*, 2024, doi: 10.1515/revic-2024-0038.
[10] W. Wang *et al.*, "Multi-metallic MOF-based composites for environmental applications: Synergizing metal centers and interactions," *Nanoscale Horiz.*, vol. 9, no. 9, p. 1432, 2024, doi: 10.1039/D4NH00140K.

[11] Z. U. Zango *et al.*, "A critical review on metal-organic frameworks and their composites as advanced materials for adsorption and photocatalytic degradation of emerging organic pollutants from wastewater," *Polymers*, vol. 12, no. 11, p. 2648, 2020, doi: 10.3390/polym12112648.

[12] J. Wei *et al.*, "Recent advances in metal organic frameworks for the catalytic degradation of organic pollutants," 2023, doi: 10.1186/s42825-023-00140-8.

[13] U. Farwa *et al.*, "Revolutionizing environmental cleanup: The evolution of MOFs as catalysts for pollution remediation," *RSC Adv.*, vol. 14, no. 50, p. 37164, 2024, doi: 10.1039/D4RA05642F.

[14] N. A. El-Mahdy *et al.*, "Concurrent photocatalytic degradation of organic pollutants using smart magnetically cellulose-based metal organic framework nanocomposite," *Sci. Rep.*, vol. 15, no. 1, 2025, doi: 10.1038/s41598-025-03256-5.

[15] L. Zhu *et al.*, "Metal-organic frameworks/carbon-based materials for environmental remediation: A state-of-the-art mini-review," *J. Environ. Manage.*, vol. 232, p. 964, 2018, doi: 10.1016/j.jenvman.2018.12.004.

[16] V. Russo *et al.*, "Applications of metal organic frameworks in wastewater treatment: A review on adsorption and photodegradation," *Front. Chem. Eng.*, vol. 2, 2020, doi: 10.3389/fceng.2020.581487.

[17] S. C. Motshekga *et al.*, "Recent and prospects of synthesis and application of metal-organic frameworks (MOFs) in water treatment: A review," *J. Inorg. Organomet. Polym. Mater.*, vol. 34, no. 9, p. 3907, 2024, doi: 10.1007/s10904-024-03063-x.

[18] K. A. K. *et al.*, "Non-derivatizing solvent assisted waste-derived cellulose/MOF composite porous matrix for efficient metal ion removal," *RSC Adv.*, vol. 14, no. 28, p. 20254, 2024, doi: 10.1039/D4RA02566K.

[19] S. Chen *et al.*, "The metal organic framework in environment applications," *E3S Web Conf.*, vol. 553, p. 2012, 2024, doi: 10.1051/e3sconf/202455302012.

[20] M. Farhan and O. Aziz, "Synthesis and characterization of NiCoMn MOFs for wastewater treatment," *arXiv*, 2024.

[21] A. Arenas-Vivo *et al.*, "Ultrafast reproducible synthesis of a Ag-nanocluster@MOF composite and its superior visible-photocatalytic activity," *J. Mater. Chem. A*, vol. 9, no. 28, p. 15704, 2021, doi: 10.1039/D1TA02251B.

[22] K. E. Diab *et al.*, "Biocompatible MIP-202 Zr-MOF tunable sorbent for decontamination of pollutants," *Sci. Rep.*, vol. 11, no. 1, 2021, doi: 10.1038/s41598-021-86140-2.

[23] S. Ramanayaka *et al.*, "Performance of metal-organic frameworks for removal of toxic elements," *RSC Adv.*, vol. 9, no. 59, p. 34359, 2019, doi: 10.1039/C9RA06879A.

[24] H. Kaur *et al.*, "MOF-based materials for wastewater treatment," *ACS Omega*, vol. 8, no. 10, p. 9004, 2023, doi: 10.1021/acsomega.2c07719.

[25] M. S. Attia *et al.*, "NanoMOF-based membranes for water treatment," *Chemosphere*, vol. 292, p. 133369, 2021, doi: 10.1016/j.chemosphere.2021.133369.

[26] S. Hossain *et al.*, "Advances with metal organic framework based nanomaterials in 4th industrial revolution," in *Proc. IEICES*, 2022, p. 161, doi: 10.5109/5909086.

[27] M. S. Khan *et al.*, "MOF materials as photocatalyst for degradation of pollutants," *Nanoscale Adv.*, vol. 5, no. 23, p. 6318, 2023, doi: 10.1039/D3NA00627A.

[28] M. Davoudi *et al.*, "Reduced graphene oxide-based semiconductors for pollutant removal," *Chem. Pap.*, 2024, doi: 10.1007/s11696-024-03816-5.

[29] N. Kataria *et al.*, "Carbon-based nanomaterials for remediation of hazardous pollutants," *Environ. Sci. Pollut. Res.*, vol. 30, no. 60, p. 124829, 2023, doi: 10.1007/s11356-023-30989-5.

[30] S. D. Priyadharshini *et al.*, "Graphene oxide-based nanomaterials for aquatic pollutant treatment," *Environ. Pollut.*, vol. 306, p. 119377, 2022, doi: 10.1016/j.envpol.2022.119377.

[31] D. B. Olawade *et al.*, "Metal and metal oxide nanomaterials for heavy metal remediation," *Front. Nanotechnol.*, vol. 6, 2024, doi: 10.3389/fnano.2024.1466721.

[32] *Technological Solutions for Water Sustainability: Challenges and Prospects*, UWA Publishing, 2023.

[33] *Clean Technologies Toward the Development of a Sustainable Environment and Future*, UWA Publishing, 2023.

[34] N. Taghiyeva *et al.*, "Graphene oxide-based adsorbents for pesticide removal," *Materials*, vol. 17, no. 16, p. 4096, 2024, doi: 10.3390/ma17164096.

[35] R. Singh *et al.*, "Graphene materials in pollution detection and environmental improvement," *Environ. Res.*, vol. 243, p. 117830, 2023, doi: 10.1016/j.envres.2023.117830.

[36] H. Assad *et al.*, "Progress of graphene-based nanomaterials for contaminant removal," *Front. Chem.*, vol. 12, 2024, doi: 10.3389/fchem.2024.1347129.

[37] K. Thakur and B. Kandasubramanian, "Graphene oxide composites for removal of pollutants," *J. Chem. Eng. Data*, vol. 64, no. 3, p. 833, 2019, doi: 10.1021/acs.jced.8b01057.

[38] F. Asghar *et al.*, "Graphene oxide-modified nanocomposites for wastewater remediation," *RSC Adv.*, vol. 12, no. 19, p. 11750, 2022, doi: 10.1039/D2RA00271J.

[39] N. A. Mazlan *et al.*, "Bimetallic graphene oxide/ZIF hybrid aerogels for heavy metal removal," *Front. Chem. Sci. Eng.*, vol. 18, no. 8, 2024, doi: 10.1007/s11705-024-2442-0.

[40] M. Tsai *et al.*, "Toxicity of graphene oxide nanoparticles," *Aerosol Air Qual. Res.*, vol. 21, no. 5, 2020, doi: 10.4209/aaqr.200559.

[41] B. Anegbe *et al.*, "Graphene oxide synthesis and applications," *Environ. Sci. Eur.*, vol. 36, no. 1, 2024, doi: 10.1186/s12302-023-00814-4.

[42] F. Pinelli *et al.*, "Graphene-based aerogels for environmental applications," *FlatChem*, vol. 36, p. 100449, 2022, doi: 10.1016/j.flatc.2022.100449.

[43] G. Gorgolis *et al.*, "Removal of contaminants using graphene hybrid aerogels," *RSC Adv.*, vol. 14, no. 47, p. 34504, 2024, doi: 10.1039/D4RA05658B.

[44] K. G. Sekwele *et al.*, "Cellulose-graphene composite aerogels in water treatment," *Discover Mater.*, vol. 4, no. 1, 2024, doi: 10.1007/s43939-024-00097-3.

[45] J. Elgoyhen and R. Tomovská, "Graphene-based catalysts for wastewater treatment," *Molecules*, vol. 30, no. 16, p. 3405, 2025, doi: 10.3390/molecules30163405.

[46] G. Vajitha *et al.*, "Carbon-based filters for water treatment," in *IWA Publishing eBooks*, 2023, p. 155, doi: 10.2166/9781789063714_0155.

[47] E. D. H. Kong *et al.*, "Titanium dioxide photocatalysts for pollutant degradation," *iScience*, 2025, doi: 10.1016/j.isci.2025.112368.

[48] G. Meng *et al.*, "Photocatalytic materials for pollutant degradation," *J. Solar Energy Res. Updates*, vol. 11, p. 93, 2024, doi: 10.31875/2410-2199.2024.11.10.

[49] N. M. Chauke *et al.*, "Visible-light-activated titanium dioxide for wastewater remediation," *Int. J. Environ. Sci. Technol.*, 2025, doi: 10.1007/s13762-025-06397-2.

[50] K. R. Davies *et al.*, "Photocatalysts in antibiotic micropollutant treatment," *J. Photochem. Photobiol. C*, vol. 48, p. 100437, 2021, doi: 10.1016/j.jphotochemrev.2021.100437.

[51] H. Wang *et al.*, "Heterogeneous photocatalysis for environmental remediation," *Chin. J. Catal.*, vol. 43, no. 2, p. 178, 2022.

[52] A. Kumar *et al.*, "Hydrogen production and photocatalytic pollutant removal," *Environ. Chem. Lett.*, vol. 22, no. 5, p. 2405, 2024, doi: 10.1007/s10311-024-01756-w.

[53] P. Sen *et al.*, "Advancements in doping strategies for photocatalysts," *Technologies*, vol. 11, no. 5, p. 144, 2023.

[54] C. Tewari *et al.*, "Carbon-based nanocomposites for hazardous material removal," in *IWA Publishing eBooks*, 2023, p. 85.

[55] M. N. Subramaniam *et al.*, "Biochar-based photocatalysts for pollutant removal," *J. Clean. Prod.*, vol. 429, p. 139487, 2023.

[56] V. Choudhary *et al.*, "Water pollution abatement using waste-derived materials," in *IWA Publishing eBooks*, 2023, p. 179.

[57] N. A. Nosratabad *et al.*, "Nanomaterial-modified biochar for environmental remediation," *Heliyon*, vol. 10, no. 18, 2024.

[58] V. Rajput *et al.*, "Biochar production methods for environmental remediation," 2024.

[59] T. Hu *et al.*, "Enhanced biochar for pollutant remediation," *Engineered Science*, 2025.

[60] X. Liu *et al.*, "Recent advances in remediation of pollutants from soil and water," *J. Hazard. Mater. Adv.*, 2024.

[61] J. Nayak and S. Chakrabortty, "Role of nanotechnology in environmental cleaning," in *IWA Publishing eBooks*, 2023, p. 263.

[62] J. Tripathy *et al.*, "Nanoparticles and nanocomposites for wastewater treatment," *Water*, vol. 16, no. 11, p. 1481, 2024.

[63] A. Giri *et al.*, "Design of porous organic materials for water treatment," in *IWA Publishing eBooks*, 2023, p. 63.

[64] E. D. Ugwuanyi *et al.*, "Nanomaterials in enhancing wastewater treatment processes," *Magna Sci. Adv. Res. Rev.*, vol. 10, no. 1, p. 273, 2024.

[65] S. A. Bhat *et al.*, "Sustainable nanotechnology-based wastewater treatment strategies," *Chemosphere*, vol. 288, p. 132606, 2021.

Journal of Engineering and Technology for Industrial Applications

ISSN ONLINE: 2447-0228

ITEGAM-JETIA

Manaus, v.12 n.60, p.247-258, July/August, 2026.
DOI: https://doi.org/10.5935/jetia.v12i60.3732

RESEARCH ARTICLE OPEN ACCESS

DCG-ANET: A DUAL-STREAM CAUSAL GRAPH ADVERSARIAL NETWORK FOR EARLY DETECTION OF ALZHEIMER'S DISEASE FROM MULTIMODAL BRAIN IMAGING

Dinesh Kumar P*[1]

[1]Teacher in Computer Science Kodaikanal International School, Kodaikanal. India.

[1]https://orcid.org/0000-0002-9498-843X

Email:*pass2deenesh@gmail.com

ARTICLE INFO

Article History
Received: February 18, 2026
Reviewed: June 7, 2026
Accepted: July 7, 2026
Published: July 31, 2026

Keywords:
Alzheimer's disease, Dual-Stream architecture, Brain graph learning, Vision transformer, Adversarial network, Causal subgraph detection.

ABSTRACT

Alzheimer disease (AD) is a rising health hazard that creates complicated mental loss and memory loss. Diagnosis within a reasonable time and at the right time is significant in retarding the occurrence or development of the disease and recovery of the patient. Although neuroimaging has increased our knowledge of changes in the brain as is witnessed in AD, the issue of accurate mapping of abnormal neural circuitry at both structural and functional levels is a complex one. To remedy this, a new Dual-Stream Causal Graph Adversarial Network (DCG-ANet) is proposed in this work, that takes advantage of the DTI data and rs-fMRI data to identify the strongest patterns relating to AD. Perceiving the architecture as a whole, parallel graph encoders with vision-transformer get to learn whole-brain representations, whereas the model embraces a temporal attention system that regulates changes in the functional connectivity as time progresses. Causal subgraph selection module identifies disease-relevant neural circuits and adversarial training improves the attention of the network to the discriminative features. Using the ADNI dataset, the proposed DCG-ANet achieved 94.3% accuracy, 90.6% F1-score, 91.2% recall, 89.9% precision, and 0.92 MCC, with stable training and validation loss convergence and superior ROC curve performance. The model performs exceptionally well in detecting early Alzheimer, and it is even better than the most sophisticated base techniques. It uses circuit level knowledge to provide an impressive performance. This implies that it has greater predictive power, strength and resilience to all the significant evaluation measures.

Copyright ©2026 by authors and Galileo Institute of Technology and Education of the Amazon (ITEGAM). This work is licensed under the Creative Commons Attribution International License (CC BY 4.0).

I. INTRODUCTION

Among the conditions that are important indicators of Alzheimer disease (AD) are cognitive impairment, memory loss, altered behavior and personality, language impairment, visual-spatial awareness problems, apraxia, and executive problems. This is a progressive degenerative disorder of the brain that has a significant impact on social life and everyday life. Interestingly, mild cognitive impairment (MCI) can serve as a transition between normal aging and AD, but some of them may stay stable or even recover normal cognitive functioning. As the populations are ageing, and the life expectancy continues to rise, AD is becoming more and more common in the global arena, becoming a huge medical, social, and financial burden. It does not only affect the patients but also has a lot of effect on the families and caregivers, placing so much strain on the healthcare systems all over the world. This scenario highlights the urgency of early diagnosis, proper diagnosis and successful treatments [1]. The human brain is a complex system comprising of millions of interconnected neural networks which control sensory, motor and cognitive systems. The study of the mechanisms in which these neural connections change provides useful information about the mechanisms of disruption of normal brain networks and communication by AD. The research and medical practitioners can identify the pathological differences between AD patients and normal control (NC) individuals by exploring the structural and functional networks of the brain. In the last decade, unprecedented advancements in artificial intelligence (AI) and neuroimaging technologies have completely transformed the research on AD [2].

Emerging technologies of imaging including Diffusion Tensor Imaging (DTI), Functional Magnetic Resonance Imaging (fMRI), and Structural MRI (sMRI) have made possible mutual understanding of brain morphology, connectivity, and patterns of activity. DTI measures the white matter connectivity and microstructural integrity; sMRI measures the anatomical and volumetric changes, such as atrophy of hippocampal; and fMRI identifies the dynamic interactions in functional processes in the brain regions. The combination of such modalities gives the higher-quality temporal and spatial resolution, which makes it possible to understand the neural degeneration related to AD comprehensively. This has been further improved by AI-driven image analysis that provides automated, objective, and reproducible results that can be more sensitive and can be more diagnostic than results with traditional cognitive assessment methods [3]. To distinguish AD and NC or MCI, scientists started to pay attention to the unimodal neuroimaging techniques, the study of one imaging modality failure, sMRI, DTI, fMRI, in the context of a wider scope of AI-based diagnostic interventions. One of the first modalities that were used was structural MRI due to its capability to monitor the reduction of the grey matter and cortical thinning [4]. Although fMRI research showed impaired functionality connectivity in major neuronal networks like the default mode network (DMN), the DTI methods of research provided more insight into the breakdown of white matter tracks. Nevertheless, these uninationally-based methods had fundamental drawbacks. The limited computational ability and the simplicity of the algorithms that were in place meant that scientists were not able to effectively use the complementary information that was present in the modalities. As a result, such models have not been able to capture the comprehensive pathophysiological features of AD as they have not captured the intricate interrelationships between brain structure, function, and connectivity [5]. Unimodal means that the imaging is used alone, which is why multimodal neuroimaging fusion that combines the data of multiple imaging modalities to introduce a more holistic picture about the brain has gained popularity.

The combination of DTI, fMRI and sMRI provides a deeper insight into the progression of AD because it is able to simultaneously capture both anatomical and functional abnormalities [6]. Multimodal fusion allows to notice the slightest structural abnormalities with considerable functional consequences. As an example, the white matter degeneration seen in a DTI can lead to the decreased activity in certain regions of the cortices that can be seen in fMRI. The modern development of deep learning (DL) methods has made this integration much more useful and efficient. DNNs are automatic feature hierarchies on the multimodal data, which can be classified and interpreted more accurately. Such methods have demonstrated the possibility of early biomarkers of AD, enhancing the accuracy of predicting progression of MCI-to-AD and timely intervention measures [7]. The transformation of medical imaging has occurred due to the creation of generative models, particularly, GANs, which allow creating realistic synthetic data. In order to generate high-quality synthetic neuroimaging samples, GANs efficiently model complex data distributions through an adversarial game between a generator and discriminator. They relieve data scarcity and improve the generalization of diagnostic models in Alzheimer's research by enhancing low-resolution scans, addressing class imbalance, simulating missing modalities, and augmenting limited datasets [8]. Training instability, mode collapse, and hyperparameter sensitivity are some of the issues that arise when using GANs. Nevertheless, it has been shown that combining GANs with multimodal DL, GNNs, and attention-based mechanisms works well. While attention and Transformer architectures capture important inter-regional dependencies, GNNs model the brain as a graph of interconnected regions, offering interpretable insights into connectivity disruptions related to AD. Combined, they improve the accuracy and interpretability of the diagnosis, and thus, encourage their use in clinical practice [9].

Hybrid multimodal systems that combine GANs, GNNs, and Transformers have gained an increased role in the study of Alzheimer because they could handle missing or noisy modalities, learn local and global dependencies in brain imaging data, and learn robust and generalizable feature representations. Transformer-based feature extraction and GAN-based data augmentation result in these frameworks discovering latent features correlated with minute pathological alterations frequently undetected by conventional statistical models, and prove to be effective in classifying AD versus MCI and NC subjects. The combination of AI, deep learning, and multimodal neuroimaging has moved the concept of descriptive analysis to predictive modeling, in which the accuracy of diagnoses is increased, the ways in which illnesses develop are further understood, and personalized medicine that is unique to the particular neurobiological features of a particular patient can be developed. Since AD has remained a severe medical, social, and emotional burden, it is critical that more sophisticated forms of computational methods be employed to detect it at an early stage, diagnose and provide better treatment. The present work attempts to analyze the issue of what kind of description of atypical neural networks can allow to diagnose AD as early as possible on the basis of multimodal neuroimaging data. The solutions to enhance the diagnosis accuracy and interpretation with the assistance of the Alzheimer Disease Neuroimaging Initiative (ADNI) dataset [10] are suggested in this paper; these solutions are the proposed Dual-Stream Causal Graph Adversarial Network (DCG-ANet), which consists of the strong graph learning, time-series modeling, and adversarial learning modules. The prime contributions of this paper would be:

- A new DCG-ANet model is proposed, which integrated the dual-stream graph learning with causal subgraph search to detect AD in a precise and earlier way.
- The model uses Vision Transformer based encoder and can learn to capture structural and functional dynamics using DTI and Rs-fMRI data using a temporal attention mechanism.
- An adversarial training module is employed that aims to enhance robustness of the identified neural circuits with the purposes of identifying AD-related best features using a selection module of a causal subgraph.
- The efficacy of the model is demonstrated by extensive trials using the ADNI data (accuracy, F1-score, recall, precision, and training and validation losses are applied as assessment metrics).
- The suggested DCG-ANet performs better than current state-of-the-art procedures, especially at identifying early-onset AD and the provision of neural circuit interpretability.

The content of the remaining parts of the paper will be structured in the following manner: the second part will become a literature review of what has already been written by other authors on the subject. The section 3 offers the architecture and the methodology of the suggested DCG-ANet. The results of the experiment and comparison shall be presented in section 4. Finally, the research will be concluded stating the significant findings and avenues in the Section 5.

II. RELATED WORK

According to [11] proposed an innovative use of the online hand writing loop patterns to detect and classify the early stage of AD. The paper examines various types of data augmentation since there is insufficient data to be able to classify AD using behavioural data. In [12] suggested using a unique cross-modal transformer generative adversarial network (CT-GAN) to integrate structurally partitioned data, Diffusion Tensor Imaging (DTI), and resting-state functional magnetic resonance imaging (rs-fMRI). The most effective skills of retrieving complementary information in relation to rs-fMRI and DTI, as well as the dominance of efficacious functional information - the structural information mapping realized with the help of developed bi-partite approach. Time varying profiles of brain connections are challenging to the bi-attention mechanism in that it has no temporal modelling. According to [13] presented a recently created brain imaging-to-graph generation (BIGG) model that converts fMRI into employable connections for use in MCI studies. The proposed BIGG system avoids this by using diffusion denoising probabilistic models (DDPM), which gradually denoise the noise and conditional fMRI into effective connectivity using a GAN's denoising layer. The training process is time-intensive as well as two tuning is necessary, which is why the method is impractical in the real-world clinical setting, despite it being accurate. To describe anatomical-functional connections of the brain, [14] proposed a bidirectional graph generative adversarial network (BG-GAN). This dependence on graph structures that are handcrafted may cause suboptimal results when the method is applied to atypical subjects with non-standard patterns of connectivity. In order to solve problems in non-Euclidian domains, [15] suggests using graph neural networks (GNN). The multi-modal information is combined at the node connection and adjacency matrix levels, and each modality has its own branch of the multi-modal GNN structure. Finally, by carrying out late fusion, they joined together the first decisions obtained in every branch to produce a last prediction. The isolated treatment of procedural action of both modalities prior to merging them would be a source of losing shared cross-modal interactions at the early phase of learning. In [16] suggested a middle-fusion multimodal strategy for AD early detection. Here, the depth-specific separable convolution block with no activation function is utilised to recover data without loss.

The intricate modalities with one another are then made visible by combining middle fusion, mix skip connection, and weight sharing convolution blocks. The absence of attention mechanisms restricts the model to prioritise the salient areas or features to the Alzheimer progress. According to [17] provided a CNN model which was specifically developed with the help of recent methods to distinguish between the various forms of AD. This model can be employed as a diagnostic tool in order to prevent the development of the condition to the more advanced symptoms of dementia. The model is based mainly on the spatial characteristics and there is no incorporation of the structural-functional graph data, which decreases its interpretability at the neural circuits level. According to [18] proposed BrainDGT, a dynamic Graph Transformer model that enhances the diagnosis of brain diseases by adaptively recording and analysing brain activity related to modularity. BrainDGT evaluates the adjusting brain states and breaks the issue of permanent time duration. The model is based on two attentions: self-attention identifies significant temporal connections, and graph-attention identifies structural features of snapshots of the dynamic brain network. According to [19] suggested distribution-regularized adversarial graph auto-encoder (DAGAE) with a transformer to improve the accuracy of data-driven model to diagnose dementia and construct new artificial brain functional networks. One can retain the traditional topological properties completely as well as preserve the discriminative properties. By [20] introduced a novel multimodal, self-guided, and knowledge-infused GNN that incorporates domain information to generate models without the need to be provided by the user. They outline a specialised multimodal GNN that can be enabled by this uncurated knowledge to guide the learning process of the GNN to enhance the performance of the model and simplify the interpretation of predictions. Their methodology considers domain information as a natural language. According to [21] suggested an algorithm to automatically identify dementia which demonstrated the correlation between texts and images via a graph. First they transcribed the voices of the participants with help of an automatic speech recognition system.

A vision language model was then developed to form a bipartite graph that indicated the correspondence between the constituent parts of a given image and the descriptive terms that were associated with those parts. Lastly, they performed the classification of AD patients on a graph-level classification task using a graph convolutional network (GCN) on each subject as a graph. By [22] developed a multi-modal sparse interpretable GCN framework (SGCN) to identify the prodromal stage of AD referred to as moderate cognitive impairment (MCI). The clinical manifestation of AD and identified abnormalities were closely correlated. They were also capable of explaining the identified brain dysfunctions and the abnormalities in the sex-related connection at the level of large-scale neural networks in AD/MCI. In [23] provides a synthesis of recent research outcomes of the application of DL in multimodal neuroimaging in the diagnosis of AD. The part of the review procedure was the thorough search of the major databases, including PubMed, Embase, Google Scholar, and ClinicalTrials.gov among others. Subsequently, the relevant research was identified, and the results were analyzed. They gave priority to high-quality research and were applying a best-evidence technique to determine recurrent trends in literature. According to [24] described a DL architecture that using a cyclical round of diagnostic tests to diagnose the presence of AD, non-AD dementias (nADD), MCI, and NC individuals. They show a variety of models that could be used to accommodate various combinations of the clinical data that are regularly taken, such as the medical history, neuropsychological testing, neuroimaging, demographics, and functional assessments. They continue to demonstrate the extent to which these frameworks capture the accuracy of diagnosis of actual neurologists and neuroradiologists. In [25] suggested a framework by making use of GNNs, that works with graph-structured data. In their work, they use GNNs to analyse data on the AD Neuroimaging Initiative to binary and multi-class categorisation at the three phases of AD (CN, MCI, and AD). In [26] used DL models include EEGNet, Convolutional Neural Network-Long Short-Term Memory, Graph Convolutional Network (GCN), and multi-scale feature reconstruction GCN to derive differential entropy features in ERP data. They also employed a multilayer perceptron to derive features of TCM questionnaires. Following a feature fusion, ten-fold cross-subject binary (HC vs. MCI+AD; MCI vs. AD); ternary (HC, MCI, AD) classification tasks were conducted.

II.1 RESEARCH GAP:

There are still a lot of unresolved issues in the field of AI-based multimodal neuroimaging for AD identification. The majority of current approaches have limited capacity to capture comprehensive patterns of brain connections because they are unable to simultaneously represent the structural and functional relationships between DTI and rs-fMRI data. Existing transformer, GAN, and GNN-based models rely on manually specified graph topologies that limit subject-to-subject adaptability, fail to capture causal links between brain areas, or lack efficient temporal modelling of dynamic neural changes. Furthermore, its clinical usefulness is restricted by adversarial training instability and the poor interpretability of learnt features. In order to diagnose AD at an early stage with greater accuracy and explainability, a unified, causally interpretable, and temporally aware multimodal framework that can effectively integrate heterogeneous brain imaging data is urgently needed.

III. PROPOSED METHODOLOGY

III.1 DATASET

This study makes use of the publically accessible ADNI dataset [10], which includes multimodal brain images such as diffusion-tensor imaging (DTI) and resting-state functional magnetic resonance imaging (rs-fMRI). Four clinical stages—late mild cognitive impairment (LMCI), early moderate cognitive impairment (EMCI), Alzheimer's disease (AD), and normal control (NC)—are used to stratify the participants. The full dataset consists of 236 people, and a comprehensive demographic profile is given in Table 1. All image data were converted from DICOM to NIfTI format. The flow diagram for the suggested model is displayed in Figure 1.

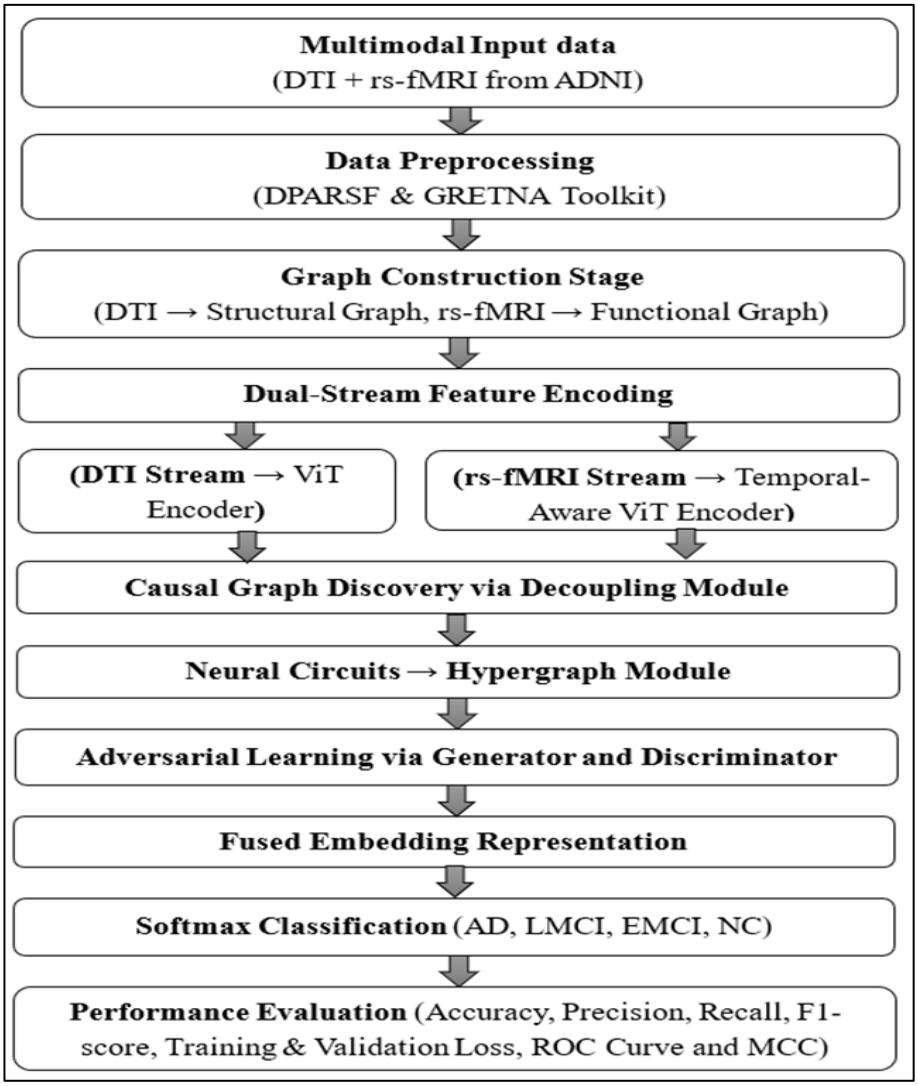


Figure 1: Flow diagram of proposed DCG-ANet model.
Source: Author, (2026).

Table 1: Dataset description.

Group	AD (62)	LMCI(42)	EMCI(55)	NC (74)
Male/Female	34M/28F	22M/20F	38M / 17F	33M / 41F
Age (mean ± SD)	76.3 ± 5.6	73.9 ± 6.1	74.9 ± 6.1	73.9 ± 6.1

Source: Author, (2026).

III.2 PREPROCESSING

In order to guarantee the quality, consistency, and comparability of the neuroimaging data for each participant, the data preparation stage is essential. The DPARSF (Data Processing Assistant for Resting-State fMRI) pipeline is used to preprocess the rs-fMRI data. Additionally, it involves a chronological series of steps, including slice timing correction, movementy correction (realignment), spatial smoothing, temporal band-pass filtering to remove physiological noise (usually in the range of 0.01 to 0.08 Hz), and spatial normalisation to the standard brain atlas (e.g., MNI space). In order to create regional time-series data that serve as the foundation for building functional brain networks, the resultant clean, temporally limited BOLD signals are averaged in specific brain regions of interest (ROIs). Regarding the DTI data, the DTI raw diffusion images are processed with the use of the GRETNA (Graph Theoretical Network Analysis) toolkit. This comprises complete-brain tractography to approximate white matter fibre routes between ROIs, fit of tensors, brain removal, and correction of eddy circulation. The resulting structural connectivity matrix W^{DTI} is formed by counting the number of streamlines n_{ij} connecting each pair of ROIs *i* and *j*, and then normalizing through Equation (1):

$$W^{DTI}(i,j) = \frac{n_{ij}}{\max(n)} \tag{1}$$

This preprocessing ensures consistent spatial alignment and temporal normalization across subjects, enabling reliable graph construction and downstream feature learning.

III.3 GRAPH CONSTRUCTION STAGE

The preprocessed DTI and rs-fMRI neuroimaging data are subsequently converted to graph-structured forms after the preprocessing step, which are indispensable in exhibiting multifactor complex structural and functional brain connectivity patterns. Such transformation would allow the model to reason on brain regions as a set of nodes interconnected to each other, and allow graph-based learning at later stages.

DTI: A structural brain graph is generated in the case of DTI modality. The nodes used in this graph can be brain regions of interest (ROIs) that are predefined and often defined in a brain atlas e.g. AAL or Harvard-Oxford. Fiber tracking algorithms (e.g. deterministic and probabilistic tractography) are used to define the edges between nodes: they estimate the physical white matter connections among the various sections in the brain. The between-node edge weights are determined by the number or strength of the streamlines (fibers) connecting them, to make up the structural connectivity matrix. Mathematically the resulting graph is represented by as formulated in Equation (2):

$$G_s = (V, E_s) \tag{2}$$

Where, the set of structural edges and the set of ROIs (nodes) derived from DTI are denoted as E_s and V, respectively. Conversely, there is a series of functional brain graphs that are brought forth by the rs-fMRI modality. Again, the connections demonstrate how active diverse portions of the brain can be in relation to one another in a functional sense, i.e., the functional connectivity or the statistical relationship among the blood oxygen level-dependent (BOLD) time–series data of separate regions, with each node corresponding to a segment of the brain.

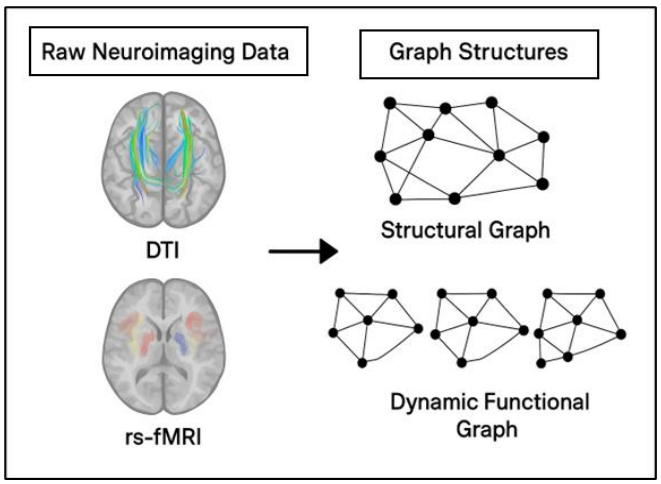


Figure 2: Graph construction from neuroimaging data.
Source: Author, (2026).

Based on the fact that rs-fMRI records dynamic brain activity within a period of time, the functional connectivity is not fixed. Rather, a dynamic graphical process is created developed by dividing the BOLD signal by time windows and calculating connectivity matrices by time slice. Each of the graphs in the sequence is labelled as in Equation (3):

$$G_t^f = \left(V, E_t^f\right), \quad t \in \{1,2,\ldots,T\} \tag{3}$$

Where G_t^f represents the functional connectivity graph at time window t, and E_t^f denotes the functional edges based on temporal correlations in that window.

This step guarantees well-endowed and complementary model representations: static but anatomically-informed structural graphs of DTI, and evolving functional graphs of rs-fMRI. In combination, these graphs form the basis of dual-stream feature encoding and causal analysis of the AD development in the further steps of the model. Figure 2 shows the process of graph construction from neuroimaging data: transforming DTI and rs-fMRI into structural and functional brain graphs.

III.4 DUAL – STREAM FEATURE ENCODING

To extract meaningful representations from both structural and functional graphs, the model employs two parallel Vision Transformer (ViT)-based graph encoders. In the DTI stream, the static structural graph G_s is processed through a transformer that treats the graph as an image-like structure, enabling global context capture via self-attention using Equation (4):

$$H_s = ViT_s(G_s) \tag{4}$$

In parallel, the rs-fMRI stream handles the dynamic sequence of functional graphs $\{G_1^f, G_2^f, \dots, G_T^f\}$ using a temporal-aware ViT, encoding each time step independently or via temporal attention using Equation (5):

$$H_t^f = ViT_f(G_t^f), \quad \forall \mathrm{t} = 1, \dots, \mathrm{T} \tag{5}$$

The latter are further employed in the temporal attention mechanism to ensure that changes in connectivity patterns, which matter to Alzheimer confirmation, are being recorded. The theoretical roots of this strategy are in the recent work of Dynamic Graph Transformer models of diagnosis of brain disorders that achieved better performance encoding temporal functional graphs with transformer architectures [18]. In sum, this two-stream and transformer-based encoding allows DCG ANet to learn both the static anatomical structure and dynamic functional connectivity, and forms a solid foundation to subsequent steps of causal subgraph discovery and multimodal fusion.

III.5 CAUSAL GRAPH DISCOVERY VIA DECOUPLING MODULE

Each encoded stream is passed through a Causal Subgraph Selector, which aims to isolate substructures most predictive of Alzheimer's progression. It does this by learning a binary attention mask $M \in \{0,1\}^{|E|}$ that identifies causal edges in the graph. The selected subgraph G_c retains only those edges marked as causal given by Equation (6):

$$G_c = (V, E\_c), where\ E_c \subseteq E, and\ M_{ij} = 1\ if\ edge\ (i,j)\ is\ causal \tag{6}$$

This selected process improves interpretability and computing efficiency by eliminating noise and unnecessary connections, preserving brain connection patterns that are significant to the condition. Furthermore, by concentrating on strong, disease-relevant connection traits rather than global correlations, our causal subgraph extraction lessens overfitting. Consequently, the model does not only enhance the precision of the diagnoses but also provides the insights that are neuroscientifically important as to the regions and pathways of the brain that are most likely to be associated with the evolution of the AD.

III.6 HYPERGRAPH MODULE

Causal subgraphs obtained from both the DTI and rs-fMRI streams are subsequently transformed into a hypergraph model. In contrast to regular graphs, hypergraphs, as defined by Equation (7), allow for the characterisation of intricate multi-region connections that are crucial in a neurodegenerative disease. The edges, or rather, hyperedges, may contain more than two nodes:

$$H = (V, E), \ E = \{e_1, e_2, \dots, e_k\}, e_i \subseteq V \tag{7}$$

Neural circuits, which are groups of brain areas with co-dependent connectivity alterations in AD, are captured by this higher-order graph concept. Hypergraph structure is a more complex model of the neuronal communication networks that are affected by the AD as it models collective dependency among multiple brain regions at once, beyond the pair-wise interaction. The hyperedges may be functional communities or structural modules and this enables the discovery of high-order and subtle disruptions that otherwise may not have been detected with traditional graphs.The hypergraph formulation additionally enhances the generalisation of the model by averaging signals of many related nodes reducing the impact of inter-subject variability and local noise. Additionally, because shared hyperedges can show cross-modal correlations that reflect both structural integrity and functional synchronisation across the brain, this transformation enables the efficient merging of multimodal information from DTI and rs-fMRI streams. In this way, the hypergraph module serves as a link between modality-specific subgraphs and a single representation, allowing for more accurate characterisation of Alzheimer's development and deeper insights into disease-related network dynamics.

III.7 ADVERSARIAL LEARNING VIA GENERATOR AND DISCRIMINATOR

To ensure the learned causal representations are both robust and generalizable across different subjects and clinical conditions, this model employs a sophisticated adversarial learning framework. In this framework, two neural network components work in tandem [19]:

- The **Generator (G)** is designed to reconstruct or generate clean, noise-free causal graph embeddings from noisy or corrupted versions of these graphs. It attempts to learn meaningful and discriminative features by filtering out irrelevant or spurious information.
- The **Discriminator (D)** functions as a classifier that distinguishes between authentic, real causal graph embeddings and those generated by the Generator. Its role is to scrutinize the representations and provide feedback that guides the Generator to produce increasingly realistic embeddings.

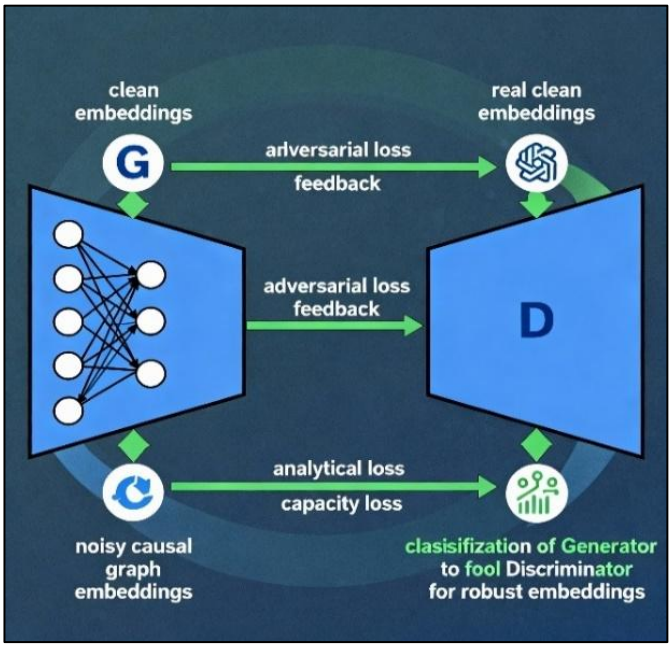


Figure 3: Schematic of the adversarial learning framework.
Source: Author, (2026).

These networks are trained as a min-max game in which the Generator aims to trick the Discriminator and the Discriminator aims to increase its differentiation accuracy. Because of this dynamic, the model is more likely to generate high-quality, noise-resistant embeddings that are helpful for tasks like illness categorisation. The adversarial learning framework's schematic is depicted in Figure 3, where Generator (G) reconstructs clean embeddings from noisy causal graph embeddings, Discriminator (D) distinguishes between generated and real embeddings, and feedback loops stand in for adversarial, analytical, and capacity losses. The training optimizes three losses stated in Equation (8), Equation (9) and Equation (10):

- **Adversarial loss:** This loss quantifies how well the Generator can deceive the Discriminator. Realism and representational accuracy are improved by minimising this loss, which forces the Generator to generate embeddings that are identical to real ones.

$$L_{adv} = E_{x\sim p_{data}}[log\, D(x)] + E_{z\sim p_z}[log(1 - D(G(z)))] \tag{8}$$

- **Analytical loss:** This element ensures that the reconstructed embeddings and the original clean embeddings are identical. By serving as a reconstruction constraint, it makes that the Generator stays close to the actual data distribution and preserves the significant semantic content required for efficient categorisation.

$$L_{anl} = \| \hat{Z} - Z \|_2^2 \tag{9}$$

- **Capacity loss:** This loss penalises subgraph size or complexity to keep the Generator from creating huge or complicated subgraphs that might overfit the data. It enhances the succinct, sparse, and broad-applicable acquisition of causal structures to the model.

$$L_{cap} = \lambda \cdot \| M \|_1 \tag{10}$$

Equation (11) gives the weighted sum of the whole loss:

$$L_{total} = L_{adv} + \alpha L_{anl} + \beta L_{cap} \tag{11}$$

By ensuring that these weights are adjusted accordingly, the model balances generating realistic embeddings and protection of important information as well as preventing a very complex model. This adversarial learning methodology makes the Alzheimer disease progression modelling more robust and promotes the creation of causal network features that are also generalised well to new data.

III.8 FUSED EMBEDDING REPRESENTATION

After adversarial learning, the results of the two streams, H_s (structural) and H_f (functional) are combined using a Cross-Attention technique. With the help of the module based on the use of the Equation (12), one can articulate the structural and functional properties in the model, indicating that there are areas where the two modalities demonstrate abnormalities:

$$Z^* = CrossAttn(H_s, H_f) \tag{12}$$

The combination of this produces one representation of the anatomical properties of the brain and the spatiotemporal dynamics.

In other words, the cross-attention module is trained to learn context- sensitive relations between structural embeddings based on DTI to query and functional embeddings based on rs-fMRI to key-value pairs. The resultant fused representation Z^* is better spaced by the fact that the model has the ability to detect subtle shifts in the patterns of brain connections associated with disease in the brain, thereby retaining the most discriminative information of both representations. The graphical representation of this fusion process is as a heatmap as shown in the accompanying image, where the structural embeddings are depicted on the y-axis and the functional embeddings are depicted on the x-axis. The intensity of each cell shows the amount of weight of interaction or attention between the two elements. Strong cross-modal correlation is indicated by brighter areas in the heatmap, which represent parts of the brain where both structural integrity and functional activity work together to produce diagnostic patterns.

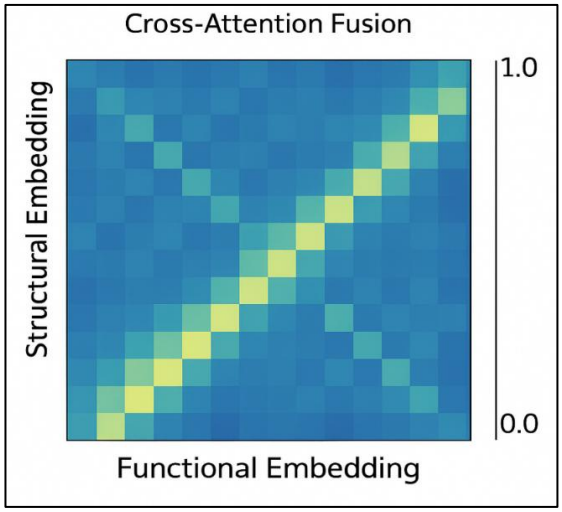


Figure 4: Fused embedding representation.
Source: Author, (2026).

Through this integrated fusion, the suggested model may benefit from both modalities in a synergistic way, increasing feature completeness, decreasing modality bias, and enabling more precise prediction of aberrant brain states or disease development. By merging complementary information from DTI and rs-fMRI, the model achieves a balanced and enriched multimodal representation, essential for robust clinical decision-making. Figure 4 shows this fused embedding representation.

III.9 SOFTMAX CLASSIFICATION

Finally, the fused embedding Z^* is fed into a fully connected classifier with a SoftMax layer, producing probabilities for four diagnostic classes using Equation (13):

$$\hat{y} = Softmax(W \cdot Z^* + b),\ \hat{y} \in R^4 \tag{13}$$

The model will compute a probability distribution across:

- AD
- LMCI
- EMCI
- NC

Such an end-to-end framework allows structural and interpretable finding of early AD based on multimodal brain images.

IV. RESULT AND DISCUSSION

Using the ADNI dataset, the suggested DCG-ANet method gets compared with other cutting-edge methods for early AD identification, including Support Vector Machine (SVM), K-Nearest Neighbours (KNN), and Decision Tree (DT). Some of the parameters that will be applied to the assessment will be F1-score, training, validation loss, precision, recall, accuracy, Receiver Operating Characteristic Curve (ROC curve) and Matthew's Correlation Coefficient (MCC).

Performance Metrics:

- **Precision** – Measures the proportion of correctly predicted positives among all predicted positives using Equation (14):

$$Precision = \frac{TP}{TP+FP} \tag{14}$$

- **Recall (Sensitivity)** – Measures the proportion of correctly predicted positives among all actual positives using Equation (15):

$$Recall = \frac{TP}{TP+FN} \tag{15}$$

- **F1-Score** – Harmonic mean of precision and recall, balancing both metrics by Equation (16):

$$F1-score = 2 \times \frac{Precision \times Recall}{Precision + Recall} \tag{16}$$

- **Accuracy** – Fraction of correctly predicted samples among all samples through Eq. (17):

$$Accuracy = \frac{TP+TN}{TP+TN+FP+FN} \tag{17}$$

Where:

TP = True Positives, TN = True Negatives, FP = False Positives, and FN = False Negatives.

- **Training & Validation Loss** – Monitoring both training and validation loss aids in identifying overfitting or underfitting, while a smaller loss implies better model performance. It is a measure of how closely a model's predictions match the actual target values during training and assessment.
- **Receiver Operating Characteristic (ROC) Curve** – Plots True Positive Rate vs. False Positive Rate to evaluate classifier performance across thresholds using Equation (18):

$$\text{TPR} = \frac{TP}{TP+FN}, \ \text{FPR} = \frac{FP}{FP+TN} \tag{18}$$

- **Matthew's Correlation Coefficient (MCC)** – Measures overall classification quality, accounting for TP, TN, FP, FN using Equation (19):

$$\text{MCC} = \frac{TP \cdot TN - FP \cdot FN}{\sqrt{(TP+FP)(TP+FN)(TN+FP)(TN+FN)}} \tag{19}$$

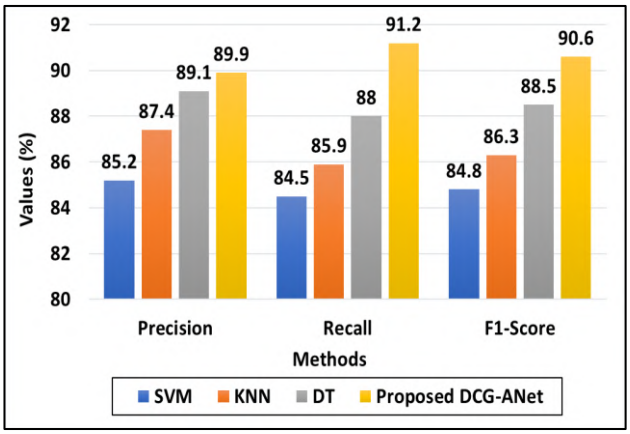


Figure 5: Precision, recall and F1-score comparison.
Source: Author, (2026).

Figure 5 draws parallels between the findings of four models which are: SVM, KNN, DT and the proposed DCG-ANet according to three evaluation measures: F1-Score, Precision, and Recall. The proposed DCG-ANet model achieves the best findings with 89.9%, 91.2% and 90.6% of accuracy, recall, and F1-score, respectively. DCG-ANet is 0.8% better in Precision, 3.2% better in Recall, and 2.1% better in F1-Score when compared to the second-best model (DT). This improvement has been attributed to the structure of the DCG-ANet that effectively integrates dual convolutional gating and attention mechanisms. This helps it identify complex spatial and temporal dependencies in rs-fMRI and DTI signals, and generalise and classify more accurately than standard ML models. According to Figure 6, the proposed models, DCG-ANet, KNN, DT, and SVM have the accuracy of 94.3%, 88.5%, 89.4%, and 86.7% respectively. The proposed DCG-ANet has a higher accuracy by 4.9%, 5.8% and 7.6% in comparison to the DT, KNN and SVM respectively. This excellent performance can be attributed to the special combination of dual-channel gated attention architecture in DCG-ANet that manages to capture the rich deep spatiotemporal regularities in complex neuroimaging signals (DTI and rs-fMRI). Due to the favorable distinction between features and the attenuated irrelevance of noise, DCG-ANet enhances classification accuracy and, therefore, makes it more reliable in early detection of AD

The suggested DCG-ANet model's training and validation loss curves across 50 epochs are displayed in Figure 7. A gradual decrease in both curves indicates good learning, and generalisation. The validation loss is also very close with minimal deviation during the training process whereas the training loss begins at around 0.03, and decays slowly to less than 0.003. According to the close proximity between training and validation loss, the model seems to be absent of overfitting and can continue to perform well on unseen data. By integrating dual-modality fusion and circuit-level attention, DCG-ANet mainly performs better due to feature representation and learning efficiency.

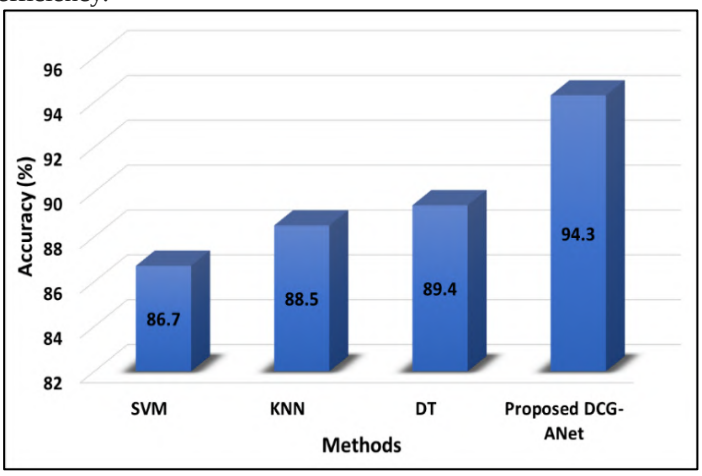


Figure 6: Accuracy comparison.
Source: Author, (2026).

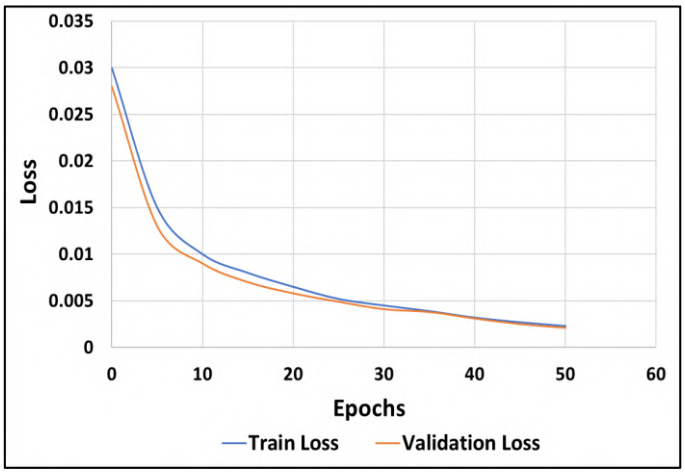


Figure 7: Validation and training losses of the DCG-Anet method.
Source: Author, (2026).

The ROC curves comparing the classification performance of SVM, KNN, DT, and the proposed DCG-ANet are shown in Figure 8. A greater True Positive Rate (TPR) at every threshold is indicated by the Proposed DCG-ANet (yellow curve), which continuously ranks higher than all other models across all FPR levels. For instance, DCG-ANet attains a TPR of 0.92 at FPR = 0.4, meaning it is around 24.3% better than SVM (0.74), 9.5% better than KNN (0.84), and 5.7% better than DT (0.87). Through improved feature representation and adept handling of subtle neuroimaging abnormalities, the Proposed DCG-ANet exhibits an average increase of around 10–15% over traditional classifiers across thresholds, indicating its greater capacity to identify Alzheimer's disease. The scores of SVM, KNN, DT, and Proposed DCG-ANet in the MCC are provided in the Figure 9. The Proposed DCG-ANet scores highest in MCC with the score of 0.92 compared to SVM (0.78), KNN (0.81) and DT (0.65). It is an increase of about 17.95%, 13.58% and 41.54% in comparison to SVM, KNN and DT respectively. The greater MCC value of the proposed DCG-ANet proves that it is able to find positive and negative cases better. The improvement is owed to the dynamic channel -graph attention mechanism within the model, which is able to capture the multimodal interdependencies resulting in more balanced and more accurate predictions even in difficult classification situations.

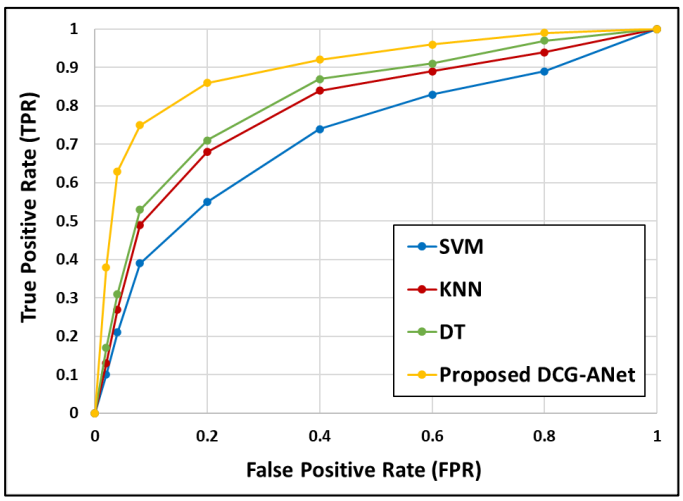


Figure 8: ROC curve comparison.
Source: Author, (2026).

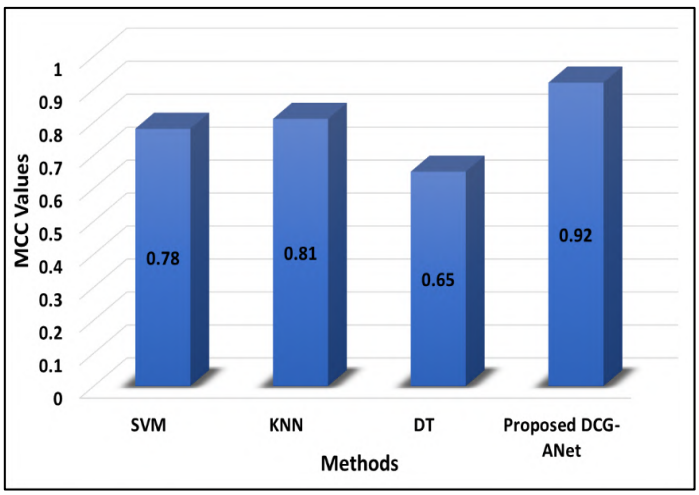


Figure 9: MCC comparison.
Source: Author, (2026)

V. CONCLUSION

This paper presents the development of DCG-ANet, which is a Dual-stream Causal Graph Adversarial Network, in detecting AD in its early stages based on multimodal neuroimaging data, i.e., rs-fMRI and DTI. DPARSF and GRETNA Preprocessing guarantee spatial and temporal consistency and make it possible to construct accurate structural and functional brain graphs. Two parallel ViT-based graph encoders depict the meaningful features, where the stable structure of white matter connectivity occurs in the structural stream, and the time-varying correlations in BOLD signals are in the functional stream. To fine-tune these embeddings, a causal subgraph disentangling mechanism as well as an analytical, adversarial and capacity loss functions is used with adversarial learning. The model is robust in identifying a subset of disease-relevant subgraphs, which would be particularly conducive to interpretation and diagnosis.

The model demonstrates strong performance, achieving 94.3% accuracy, 90.6% F1-score, 91.2% recall, 89.9% precision, and 0.92 MCC, with stable training and validation loss convergence and superior ROC curve performance, clearly surpassing several standard techniques. The non-invasive behavioural biomarkers that might with instrumental considerations be incorporated in the future are speech, facial expression and handwriting to enhance diagnosis accuracy and whereas intervention strategies can be applied in an earlier and comprehensive multi-modal manner.

VI. AUTHOR'S CONTRIBUTION

Conceptualization: Dinesh Kumar P.
Methodology: Dinesh Kumar P.
Investigation: Dinesh Kumar P.
Discussion of results: Dinesh Kumar P.
Writing – Original Draft: Dinesh Kumar P.
Writing – Review and Editing: Dinesh Kumar P.
Resources: Dinesh Kumar P.
Supervision: Dinesh Kumar P.
Approval of the final text: Dinesh Kumar P.

VII. ACKNOWLEDGMENTS

Acknowledgements: The author would like to appreciate the effort of the editors and reviewers.

Data Availability: The data used in this study are publicly available from the Alzheimer's Disease Neuroimaging Initiative (ADNI) database (https://adni.loni.usc.edu/) and can be accessed upon registration and approval

VIII. REFERENCES

[1] S. Palmqvist et al., "Blood biomarkers to detect Alzheimer disease in primary care and secondary care," Journal of the American Medical Association, vol. 332, no. 15, pp. 1245–1257, 2024.

[2] N. Mashhadi and R. Marinescu, "A multi-modal graph-based framework for Alzheimer's disease detection," Scientific Reports, vol. 15, no. 1, p. 22684, 2025.

[3] L. Liu, Y. Li, and K. Yang, "Dynamically weighted graph neural network for detection of early mild cognitive impairment," PLOS ONE, vol. 20, no. 6, p. e0323894, 2025.

[4] G. Qu, Z. Zhou, V. D. Calhoun, A. Zhang, and Y.-P. Wang, "Integrated brain connectivity analysis with fMRI, DTI, and sMRI powered by interpretable graph neural networks," Medical Image Analysis, vol. 103, p. 103570, 2025.

[5] Z. Zhou et al., "A novel graph neural network method for Alzheimer's disease classification," Computers in Biology and Medicine, vol. 180, p. 108869, 2024.

[6] Y. Tang, X. Xiong, G. Tong, Y. Yang, and H. Zhang, "Multimodal diagnosis model of Alzheimer's disease based on improved Transformer," BioMedical Engineering Online, vol. 23, no. 1, p. 8, 2024.

[7] G. Gamgam, A. Kabakçıoğlu, D. Y. Dal, and B. Acar, "Disentangled attention graph neural network for Alzheimer's disease diagnosis," Medical Image Computing and Computer-Assisted Intervention, pp. 219–228, 2024.

[8] P. Sethi et al., "Exploring advancements in early detection of Alzheimer's disease with molecular assays and animal models," Ageing Research Reviews, vol. 100, p. 102411, 2024.

[9] Zia-Ur-Rehman, M. K. Awang, G. Ali, and M. Faheem, "Recent advancements in neuroimaging-based Alzheimer's disease prediction using deep learning approaches in e-health: A systematic review," Health Science Reports, vol. 8, no. 5, p. e70802, 2025.

[10] Alzheimer's Disease Neuroimaging Initiative (ADNI), "ADNI Data and Samples Overview," Laboratory of NeuroImaging (LONI), University of Southern California. Available: https://adni.loni.usc.edu/

[11] Q. Dao, M. A. El-Yacoubi, and A.-S. Rigaud, "Detection of Alzheimer disease on online handwriting using 1D convolutional neural network," IEEE Access, vol. 11, pp. 2148–2155, 2023.

[12] J. Pan and S. Wang, "Cross-modal transformer GAN: A brain structure-function deep fusing framework for Alzheimer's Disease," arXiv [eess.IV], 2022.

[13] Q. Zuo, H. Tian, C.-M. Pun, H. Wang, Y. Zhang, and J. Hong, "Brain imaging-to-graph generation using adversarial hierarchical diffusion models for MCI causality analysis," arXiv [cs.CV], 2023.

[14] T. Zhou et al., "BG-GAN: Generative AI enable representing brain structure-function connections for Alzheimer's disease," arXiv [cs.AI], 2023.

[15] Y. Zhang, X. He, Y. H. Chan, Q. Teng, and J. C. Rajapakse, "Multi-modal graph neural network for early diagnosis of Alzheimer's disease from sMRI and PET scans," Computers in Biology and Medicine, vol. 164, p. 107328, 2023.

[16] S. K. Kim, Q. A. Duong, and J. K. Gahm, "Multimodal 3D deep learning for early diagnosis of Alzheimer's disease," IEEE Access, vol. 12, pp. 46278–46289, 2024.

[17] C. Ozdemir and Y. Dogan, "Advancing early diagnosis of Alzheimer's disease with next-generation deep learning methods," Biomedical Signal Processing and Control, vol. 96, p. 106614, 2024.

[18] A. Shehzad, D. Zhang, S. Yu, S. Abid, and F. Xia, "Dynamic Graph Transformer for brain disorder diagnosis," IEEE Journal of Biomedical and Health Informatics, vol. 29, no. 6, pp. 4388–4400, 2025.

[19] Q. Zuo et al., “Brain functional network generation using distribution-regularized adversarial graph autoencoder with transformer for dementia diagnosis,” Computer Modeling in Engineering & Sciences, vol. 137, no. 3, pp. 2129–2147, 2023.

[20] Z. Wang et al., “A self-guided multimodal approach to enhancing graph representation learning for Alzheimer’s diseases,” arXiv [cs.LG], 2024.

[21] B. Lee, J.-U. Bang, H. J. Song, and B. O. Kang, “Alzheimer’s disease recognition using graph neural network by leveraging image-text similarity from vision language model,” Scientific Reports, vol. 15, no. 1, p. 997, 2025.

[22] H. Zhou, L. He, B. Y. Chen, L. Shen, and Y. Zhang, “Multi-modal diagnosis of Alzheimer’s disease using interpretable graph convolutional networks,” IEEE Transactions on Medical Imaging, vol. 44, no. 1, pp. 142–153, 2025.

[23] M. L. Raza et al., “Advancements in deep learning for early diagnosis of Alzheimer’s disease using multimodal neuroimaging: challenges and future directions,” Frontiers in Neuroinformatics, vol. 19, p. 1557177, 2025.

[24] S. Qiu et al., “Multimodal deep learning for Alzheimer’s disease dementia assessment,” Nature Communications, vol. 13, no. 1, p. 3404, 2022.

[25] F. Abuhantash, M. K. Abu Hantash, and A. AlShehhi, “Comorbidity-based framework for Alzheimer’s disease classification using graph neural networks,” Scientific Reports, vol. 14, no. 1, p. 21061, 2024.

[26] C. Wang et al., “Early diagnosis of mild cognitive impairment and Alzheimer’s disease using multimodal feature-based deep learning models in a Chinese elderly population,” Asian Journal of Psychiatry, vol. 111, p. 104632, 2025.

Journal of Engineering and Technology for Industrial Applications

ISSN ONLINE: 2447-0228

ITEGAM-JETIA

Manaus, v.12 n.60, p.259-269, July/August, 2026.
DOI: https://doi.org/10.5935/jetia.v12i60.3738

RESEARCH ARTICLE OPEN ACCESS

INTEGRATION MODEL OF SAVING MATRIX AND NEAREST NEIGHBOR METHODS FOR OPTIMIZING DISTRIBUTION OF PRODUCTION RESULTS OF BAWEAN GRESIK SMES – EAST JAVA, INDONESIA

Rony Prabowo[1], Lutfia Bamatraf[2]

[1, 2]Department of Industrial Engineering Department, Industrial Technology of the Faculty, Institut Teknologi Adhi Tama Surabaya (ITATS). Jl. Arief Rahman Hakim No.100, Klampis Ngasem Kec. Sukolilo, Surabaya, Jawa Timur 60117, Indonesia

[1]https://orcid.org/0000-0002-5948-6514, [2]https://orcid.org/0009-0006-0876-869X

Email:*rony.prabowo@itats.ac.id, lutfiabamatraf81@gmail.com

ARTICLE INFO

Article History
Received: February 18, 2026
Reviewed: June 7, 2026
Accepted: July 7, 2026
Published: July 31, 2026

Keywords:
Cost;
Existing;
Matrix;
Neighbor;
Nearest;
Saving;

ABSTRACT

Since 2018, the Gresik Regency Government has made serious efforts to facilitate various businesses for the Bawean community, including providing capital assistance, equipment, training, and marketing support. According to 2022 data from the Gresik Regency Government, there are 52 small and seven medium-sized SMEs in Bawean. This UKM can absorb approximately 620 non-formal workers, which is essential for empowering the Bawean community. The problem in this research is that transportation costs for delivering SME products remain too high because they are not optimized for factors such as distance, transportation capacity, and time, and more than 30-35% of sales proceeds are used to finance distribution. The method used to solve this problem is to integrate the saving matrix and nearest-neighbor methods, thereby achieving distance, time, and cost savings while considering existing constraints to increase the income of Bawean SMEs. After designing the distribution route using the nearest-neighbor method, delivery costs are calculated based on the resulting route. By using the selected proposed method, a distribution cost of Rp. 93,696,850 from the original Rp. 158,400,000 and a total distance traveled of 13,448.9 km from the original 24,303.6 km. By using the nearest-neighbor method, companies can save on the distribution costs of Rp. 64,703,150, or 40.85% less than the existing distribution costs, and saves 10,854.7 km in distribution mileage, or 44.66% shorter than the total existing mileage..

Copyright ©2026 by authors and Galileo Institute of Technology and Education of the Amazon (ITEGAM). This work is licensed under the Creative Commons Attribution International License (CC BY 4.0).

I. INTRODUCTION

Bawean Island is part of Gresik Regency, located in the outermost part of the island, separated by a strait or waters from other regions. The potential of the Bawean region is actually immense, but has not been optimally managed [1]. This potential includes fertile areas for agriculture, especially for fruit crops. In the north of Bawean, there is the potential for unpolluted ponds, making it suitable for cultivating milkfish, crabs, and shrimp, and seafood is also quite good. In 2017, Bawean Island had a population of 63,894, but more than 30% of the population had migrated outside the area because it was challenging to earn a living there [2]. This resulted in Bawean being a disadvantaged region. However, since the Gresik Regency Government empowered SMEs, the unemployment rate has decreased, community income has increased, and contributions to the regional budget have increased [3]. Bawean SMEs are primarily engaged in processing fish and marine products, namely 64% of them, including smoked fish, salted fish, otak-otak, presto fish, spiced fish, fish crackers, petis, and shrimp paste [4]. In comparison, around 36% are engaged in the craft and souvenir sector, including bags, belts, hats, and various other crafts made from marine products [5]. However, the largest consumers of Bawean SMEs are from outside Bawean, such as Surabaya, Malang, Gresik, Tuban, and Pasuruan. Bawean SMEs have not been able to deliver their products to customers efficiently and effectively, resulting in very high distribution costs, even reaching 35%, resulting in suboptimal profits [6].

However, the largest consumers of Bawean SMEs are from outside Bawean, such as Surabaya, Malang, Gresik, Tuban, and Pasuruan. Bawean SMEs have not been able to deliver their products to customers efficiently and effectively, resulting in very high distribution costs, even reaching 35%, resulting in suboptimal profits [6]. The delivery of these SMEs' products is certainly not as efficient as that of large companies, so it is necessary to consider storage capacity, delivery time, delivery distance, and transportation mode [7]. This transportation problem is better known as VRP (Vehicle Routing Problem). VRP concerns determining routes in problems involving multiple vehicles with a given capacity in the distribution process [8]. There are four objectives of VRP: (a) minimizing transportation costs related to distance and fixed vehicle costs [9]; (b) minimizing the number of vehicles needed for distribution, thus reduciing the number of drivers [10]; (c) Balancing routes related to time and vehicle capacity [10]; (d) minimizing the risk of dissatisfaction due to late delivery [11]. This research aims to develop an optimal delivery model for Bawean SME products to all consumers by integrating the saving matrix and nearest-neighbor methods.

II. THEORETICAL REFERENCE

II.1 SAVING MATRIX

The Saving Matrix Method is a heuristic method used to solve the Vehicle Routing Problem (VRP) with the primary goal of minimizing total travel distance, travel time, or distribution costs [12]. This method was first introduced by Clarke and Wright (1964) and remains one of the most popular approaches due to its simplicity, speed, minimal computational requirements, and the ability to provide near-optimal solutions for many real-world situations [13]. Simply put, the saving matrix is used to determine which pairs of customers are appropriate to combine into a single route, resulting in the greatest savings. The Saving Matrix calculates the distance savings if two customers, for example, i and j, are included in the same route, rather than being visited separately [14]. The core formula for the Saving Matrix is:

$$S_{ij} = d_{i0} + d_{0j} - d_{ij} \quad (1)$$

Where:

Sij = savings value if node i is merged with node
j di0 = distance from depot to customer i
d0j = distance from depot to customer
j dij = distance between customers i
and j

If merging customers i and j reduces travel distance, then the S value will be large. The larger the S value, the more "profitable" it is to merge the nodes.

Key Steps in the Saving Matrix

a. Step 1: Route Initialization

Each customer is considered a separate route:
Route 1: Depot → 1 → Depot
Route 2: Depot → 2 → Depot, and so on.

b. Step 2: Calculate the savings matrix

For each pair of customers i and j ($i \neq j$), calculate the values as in equation (1).
The result is a table/matrix S, with dimensions of $n \times n$.

c. Step 3: Sort the S values from largest to smallest

The combination with the largest S value is considered first (because it yields the greatest savings).

d. Step 4: Merge routes based on S values Merging is permitted if:

- Node i is at the end of one route
- Node j is at the end of another route
- Vehicle capacity is not violated If the conditions are met, then:
- Routes i and j are merged into a single route
- If not met, proceed to the next S value.

e. Step 5: Repeat until no more merges are found

After all S values have been tested, the final remaining route is the optimization result.
Types of saving matrices [9]:

1. Parallel saving algorithm

Combines multiple routes in parallel according to the highest S value.

2. Sequential saving algorithm

Develops one route at a time until it can no longer be combined, then moves on to the next route.
The advantages of saving matrices include [12], [14]:

1. Simple and easy to use, so it doesn't require complex computation
2. Fast, so it's suitable for cases with many customers (good scalability)

3. Produces routes that are more optimal than manual routes
4. Significantly reduces travel distance and distribution costs
5. Flexible because it can be easily combined with other methods (NN, GA, Tabu Search, etc.)
6. Practical for real-world applications such as logistics, couriers, LPG distribution, and waste collection

Disadvantages of the Saving Matrix [12], [14]:

1.Results are not always optimal, especially for complex VRPs (time window, multi-depot, multi-vehicle)
2.Highly dependent on the order in which the largest savings are combined—sensitive to small changes
3.Does not consider field dynamics (traffic density, road conditions, time)
4.Not suitable for routes that require strict constraints, such as time limits or scheduled deliveries
5.If the distance between nodes is asymmetric, the results can be less accurate

II.2 NEAREST NEIGHBOR

Nearest Neighbor (NN) is a heuristic method used to select the next point in a process based on the shortest distance from the current position [15]. This method is particularly popular in two fields: Distribution Route Optimization (VRP/TSP) and Data Classification (KNN). Although the applications differ, the basic principle remains the same: select the closest neighbor as the next step. Nearest Neighbor in the Vehicle Routing Problem (VRP) is used in logistics routes, package delivery, transportation, waste collection, and so on. Nearest Neighbor works by starting at the depot, selecting the closest customer from the current location, transferring to that customer, and repeating until all customers have been visited and returned to the depot [16]. This method is often combined with the Saving Matrix to improve route performance.

The advantages of the Nearest Neighbor method include [17], [18]:

1. Very fast and simple.
2. Easy to apply to large datasets.
3. Suitable as a starting point or basic route builder.
4. Best combined when used with the Saving Matrix.

Disadvantages of the Nearest Neighbor method [17], [18]:

1. Often trapped in local solutions
2. Can produce routes much longer than the optimum
3. 3. Does not consider the global perspective (short-term choices can be detrimental in the long run)

Besides routing, the Nearest Neighbor concept is used in K-Nearest Neighbor (KNN), a classification/regression algorithm that determines labels based on the nearest neighbors. The basic principle is that each new data point is classified based on the k closest data points in the dataset. Distance is calculated using specific metrics such as Euclidean, Manhattan, Minkowski, Cosine Distance, and Chebyshev. General Formula for Euclidean Distance.

$$(x, y) = \sqrt{\sum_{i-1}^{n} (x_i - y_i)^2} \quad (2)$$

III. MATERIALS AND METHODS

Several stages of research were carried out with the following steps:

1. Preliminary Stage

a. Field Study. The field study conducted in this research is an observational activity to identify and reveal existing facts in greater depth.
b. Literature Study. The purpose of this literature study is to gather information to support the research being conducted.
c. Problem Identification. To identify and understand the problem, the initial step is to identify the issues encountered by SMEs in the Bawean Region, Gresik Regency.
d. Problem Formulation. After identifying the problem, the next step is to formulate a problem.
e. Determining Research Objectives. Determining objectives is intended to allow researchers to focus on the problem being studied, so that the research can be conducted systematically and without deviating from it.

2. Stage of Data Collection

The data collection method used in this research is direct observation at the company under study.

a. Interviews. A method for obtaining data or information by asking questions directly to individuals knowledgeable about the research object.
b. Observation. Direct observation or review at the research site, namely the Bawean SME in Gresik Regency, by observing the existing system, observing the distribution process flow, and determining costs regarding expedition service rental fees and other expenses required for distribution activities.
c. Documentation. Studying company documents containing data on the number of products distributed, the location of the company's branches, and the load capacity of the truck fleet.

d. Documentation. Studying company documents containing data on the number of products distributed, the location of the company's branches, and the load capacity of the truck fleet.
e. Discussion. Exchanging opinions with experts, in this case, management with expertise in specific fields related to vehicle routing problems, the costs incurred in the distribution process, and the costs of all activities in Gresik Regency.

3. Stage of Data Processing

The data processing stages of the saving matrix method are as follows:

a. Identifying and determining the type of vehicle routing problem occurring in the field.
b. Identifying and determining the distance matrix from the SME location to the Bawean SME marketing area, as well as the distance matrix between the destinations within the Bawean SME marketing area.
c. Identifying and calculating the saving matrix.
d. Allocating vehicles and routes to the Bawean SME marketing area destinations.
e. Sorting the destination routes based on the results of the Bawean SME marketing area destinations. In this study, the procedure for sorting the company branches within the established routes used the nearest-neighbor method.
f. Calculating the total distance traveled. After obtaining the optimal route, the total distance traveled for apple juice distribution was calculated based on the procedure that yielded the smallest total distance between nearest neighbors.
g. Comparison of distribution costs. After comparing the smallest total distance traveled between the routes using the nearest-neighbor method, the route with the most optimal distance was selected.

4. Stage of Analysis and Discussion

In the analysis of apple juice distribution optimization, the saving matrix and nearest-neighbor methods were used to determine the optimal delivery route and costs.

5. Conclusion

Researchers draw conclusions related to the formulation of the problem they wish to achieve, while suggestions are input related to the research being conducted.

IV. RESULTS AND DISCUSSIONS

IV.1 DATA DISCUSSION 1

Assume that one SME in Bawean currently has one distribution center in Bawean, Gresik Regency, and five Distribution Centers (DCs) spread throughout East Java Province.

Table 1: Distance Saving Matrix Data.

	A	B	C	D	E
A	0				
B	116	0			
C	97,5	152	0		
D	534	103	95,5	0	
E	52	0	56,5	54	0

Source: Authors, (2026).

Based on Table 1, it is known that branch pair A–D has the highest distance-saving matrix of 534 km, branch pair B–C has the second- highest distance-saving matrix of 152 km, and branch pair C–D has the third-highest distance-saving matrix of 95.5 km. Based on the results of the saving matrix, branches A, C, and D can be grouped into a single distribution route. On this route, a rearrangement is carried out using the nearest-neighbor method, starting from the warehouse. There are three branches to target, and each has a known distance from the warehouse. The distance of each branch is:

Warehouse Distance → A = 288 km Warehouse Distance → C = 134.5 km Warehouse Distance → D = 317 km

Branch C is the closest to the warehouse, so it will be the first branch visited. Next, find the next branch to see based on the nearest distance from branch C as the end point.

Warehouse distance → C → A = 335 km Warehouse distance → C → D = 356 km

Since the closest distance produced is 335 km, the next one to be visited is branch A, so the route obtained using the nearest neighbor method is Warehouse → C → A → D. After obtaining the distance matrices from the warehouse to each company branch and between company branches, the next step is to compile a savings matrix. The distance-saving matrix is obtained using formula (2). For example, to find the savings between the SRBY and MJKT branches, the Warehouse → SRBY distance matrix, the Warehouse → MJKT distance matrix, and the SRBY → MJKT distance matrix are required.

Warehouse distance matrix → SRBY = 148 km Warehouse distance matrix → MJKT = 142 km SRBY distance matrix → MJKT = 84 km

Once the distance matrices for the related points are known, calculations are carried out.

- $S(x, y) = Dist(Center, x) + Dist(Center, y) – Dist(x, y)$

- S(SRBY, MJKT) = 148 km + 142 km – 84 km
- S(SRBY, MJKT) = 206 km

The following are the steps in preparing distribution routes in the first week of June 2024 using the saving matrix method. Selecting the most significant saving matrix value in the saving matrix, namely between the JEPR and KUDS destination points of 809. These two destination points will be included in a single distribution route because the fleet capacity is sufficient to deliver both.

The current route is JEPR – KUDS, with the number of products shipped as follows:

JEPR Shipping + KUDS Shipping = 1,975 kg + 1,858 kg 3,840 kg

Selecting the next largest saving matrix value in the saving matrix is between the SMRG and JEPR branches of 681. The SMRG branch has a total demand of 1,589 kg, so it can be combined with route one because the fleet capacity is still sufficient. Therefore, the route currently formed is JEPR – KUDS – SMRG, with the number of products shipped as follows:

- JEPR Shipping + KUDS Shipping + SMRG Shipping
1,971 kg + 1,856 kg + 1,591 kg = 5,417 kg

The largest saving achieved is 517. This saving was achieved between the JOGY and JEPR branches. If these branches were combined into route 1, the fleet capacity would not be sufficient. Therefore, the JOGY branch will be included in the second route. The subsequent route was formed: JOGY – SOLO – NGW, with the number of products shipped as follows:

- JOGY Shipping + SOLO Shipping + NGW Shipping 2,165 + 2,264 + 1,178 = 5,607 kg

Following the steps above, 55 iterations of the saving matrix and 12 routes were obtained. The following iterations and routes were generated for the distribution of products produced by Bawean SMEs in June, July, and August 2024.

Table 2: Iteration of the Order of Saving Values from Largest to Smallest.

Iteration	Branch Pair	Saving Value
1	JEPR - KUDS	708,9
2	SMRG - JEPR	630,8
3	SMRG - KUDS	613,4
4	JOGY - JEPR	517
5	SOLO - JEPR	510
6	JOGY - SMRG	506
7	JOGY - KUDS	505
8	SOLO - JOGY	500,5
9	SOLO - KUDS	496
10	SOLO - SMRG	466
11	MJKT - TLNG	419
12	NGW - KUDS	405
13	NGW - JOGY	360
14	NGW - SOLO	359
15	NGW - SMRG	353
16	TLNG - JEPR	218
17	KEDR - JEPR	207,2
18	TLNG - JOGY	206
19	TLNG - KUDS	205
20	MJKT - JEPR	198,8
21	MJKT - KUDS	198,8
22	KEDR - KUDS	188,2
23	SRBY - JEPR	183,9
24	SRBY – KUDS	183,9
25	TLNG – SOLO	178
26	TLNG - NGW	158
27	KEDR - TLNG	157,7
28	SRBY - MJKT	157,1

Iteration	Branch Pair	Saving Value
29	KEDR - NGW	153,2
30	TLNG - SMRG	152
31	KEDR - SOLO	146,2
32	KEDR - JOGY	146,2
33	MJKT - NGW	132,8
34	KEDR - SMRG	131,2
35	MJKT - JOGY	127,8
36	MJKT - SOLO	126,8
37	MJKT - SMRG	108,8
38	SRBY - NGW	100,9
39	NGW - JEPR	99,8
40	SRBY - JOGY	98,9
41	SRBY - SOLO	97,9
42	MJKT - KEDR	94,1
43	JBER - JEPR	92
44	JBER - KUDS	92
45	SRBY - JBER	91,9
46	SRBY - SMRG	79,9
47	SRBY - TLNG	71,9
48	SRBY - KEDR	69,1
49	JBER - TLNG	64
50	MJKT - JBER	53,8
51	JBER - KEDR	12,2
52	JBER - JOGY	7
53	JBER - SOLO	5
54	JBER - SMRG	0
55	JBER - KEDR	12,2

Source: Authors, (2026).

After obtaining all iterations in the saving matrix, all point pairs obtained are allocated to distribution route groups. The resulting route groups and the number of shipments for the distribution of products produced by Bawean SMEs in June, July, and August 2024 are shown.

Table 3: Distribution Routes for Bawean SME Products First Week of June 2024.

No.	Route	Number of Shipments
1.	JEPR – KUDS – SMRG	5.466 kg
2.	JOGY – SOLO – NGW	5.657 kg
3.	SRBY – MJKT – JBER	5.707 kg
4.	KEDR – TLNG	4.452 kg

Source: Authors, (2026).

Table 4: Distribution Routes for Bawean SME Products June 2024, Second Week.

No.	Route	Number of Shipments
1.	SOLO – SMRG – JOGY	5.993 kg
2.	KEDR – TLNG – NGW	5.240 kg
3.	SRBY – MJKT – JBER	5.836 kg

Source: Authors, (2026).

Table 5: Distribution 0Routes for Bawean SME Products Third Week of June 2024.

No.	Route	Number of Shipments
1.	SOLO – SMRG – JOGY	5.985 kg
2.	KEDR – TLNG – NGW	5.353 kg
3.	SRBY – MJKT – JBER	5.947 kg

Source: Authors, (2026).

Table 6: Distribution Routes for Bawean SME Products Fourth Week of June 2024.

No.	Route	Number of Shipments
1.	JEPR – KUDS – SMRG	5.871 kg
2.	JOGY – SOLO – NGW	5.995 kg
3.	SRBY – MJKT – JBER	5.971 kg
4.	KEDR – TLNG	4.392 kg

Source: Authors, (2026).

IV.2 DATA DISCUSSION II

Data Processing Using the Nearest Neighbor Method

The SMRG delivery destination is closest to the warehouse, so it becomes the first destination to be visited. The next destination is then selected based on the nearest distance from the SMRG delivery destination to the final destination.

Distance from Warehouse → SMRG → JEPR = 459.2
km Distance from Warehouse → SMRG → KUDS =
434.6 km

The total distribution distance for this route using the existing method is 1,122 km. Therefore, the distance saving achieved on this delivery route using the nearest neighbor method is:

- Total Distance Using the Existing Method – Total Distance Using the Nearest Neighbor Method
1,122 km – 476 km = 646 km

Table 7: Comparison of Distribution Routes for Bawean SME Products Using the Existing and Nearest Neighbor Methods, First Week of June 2024.

No	Existing Method	Distance	Nearest Neighbor	Distance	Saving
	Route		Route		
1.	Warehouse → JEPR, Warehouse → KUDS, Warehouse → SMRG	1.073	Warehouse → SMRG → KUDS → JEPR	425,7	647,3
2.	Warehouse → JOGY, Warehouse → SOLO, Warehouse → NGW	754	Warehouse → NGW → SOLO → JOGY	328,5	425,5
3.	Warehouse → SRBY, Warehouse → MJKT, Warehouse → JBER	389	Warehouse → MJKT → SRBY → JBER	331	58
4.	Warehouse → KEDR, Warehouse → TLNG	201,2	Warehouse → KEDR → TLNG	122,7	79,5

Source: Authors, (2026).

Table 8: Comparison of Distribution Routes for Bawean SME Products Using the Existing and Nearest Neighbor Methods, Week Two of June 2024.

No.	Existing Method Route	Distance	Nearest Neighbor Route	Distance	Saving
1.	Warehouse → SOLO, Warehouse → SMRG, Warehouse → JOGY	890	Warehouse → SOLO → JOGY → SMRG	451,1	438,9
2.	Warehouse → KEDR, Warehouse → TLNG, Warehouse → NGW	385,2	Warehouse → KEDR → TLNG → NGW	269,7	115,5
3.	Warehouse → SRBY, Warehouse	389	MJKT, Warehouse → JBER Warehouse → MJKT → SRBY → JBER	331	58

Source: Authors, (2026).

Table 9: Comparison of Distribution Routes for Bawean SME Products Using the Existing and Nearest Neighbor Methods, Third Week of June 2024.

No.	Existing Method Route	Distance	Nearest Neighbor Route	Distance	Saving
1.	Warehouse → SOLO, Warehouse → SMRG, Warehouse → JOGY	890	Warehouse → SOLO → JOGY → SMRG	451,1	438,9
2.	Warehouse → KEDR, Warehouse → TLNG, Warehouse → NGW	385,2	Warehouse → KEDR → TLNG → NGW	269,7	115,5
3.	Warehouse → SRBY, Warehouse → MJKT, Warehouse → JBER	389	Warehouse → MJKT → SRBY → JBER	331	58

Source: Authors, (2026).

Table 10: Comparison of Distribution Routes for Bawean SME Products Using the Existing and Nearest Neighbor Methods, Week 4 of June 2024.

No.	Existing Method Route	Distance	Nearest Neighbor Route	Distance	Saving
1.	Warehouse → JEPR, Warehouse → KUDS, Warehouse → SMRG	1.072	Warehouse → SMRG → KUDS → JEPR	425,7	646,3
2.	Warehouse → JOGY, Warehouse → SOLO, Warehouse → NGW	753	Warehouse → NGW → SOLO → JOGY	328,5	424,5
3.	Warehouse → SRBY, Warehouse → MJKT, Warehouse → JBER	389	Warehouse → MJKT → SRBY → JBER	331	58
4.	Warehouse → KEDR, Warehouse → TLNG	200,2	Warehouse → KEDR → TLNG	121,7	78,5

Source: Authors, (2026).

IV.3 SHIPPING COST ANALYSIS

After determining the optimal route using the nearest-neighbor method, shipping costs are calculated and compared with those of the proposed method. The following are the steps in determining shipping costs. Determine the route to be analyzed. For example, consider the JEPR – KUDS – SMRG route for the first week of June. The breakdown of existing shipping costs on this route is as follows:

- Warehouse Shipping Cost → JEPR = Rp. 1,900,000
- Warehouse Shipping Cost → KUDS = Rp. 1,700,000
- Warehouse Shipping Cost → SMRG = Rp. 1,900,000
-

Therefore, the total existing shipping costs for the JEPR – KUDS – SMRG route are:

- Rp. 1,900,000 + Rp. 1,700,000 + Rp. 1,900,000 = Rp. 5,500,000

Next, determine the shipping cost using the proposed route method. The resulting route using the nearest-neighbor method is: warehouse

→ SMRG → KUDS → JEPR.

The shipping cost breakdown for this route is as follows:

- Warehouse Delivery Cost → SMRG = IDR 1,900,000

Furthermore, to determine delivery costs from SMRG → KUDS and KUDS → JEPR, the average cost per kilometer of the longest route to be visited is used. The longest route to be visited is Warehouse → JEPR, with a distance of 396 km and a cost of Rp. 1,900,000. Therefore, the average cost per kilometer is Rp. 4,800. The average cost per kilometer will serve as a reference to determine costs based on the distances between SMRG → KUDS and KUDS → JEPR.

The distance between SMRG → KUDS is 62.6 km, while the distance between KUDS → JEPR is 41.1 km. Using the above calculation, the results are as follows:

- SMRG Shipping Cost → KUDS = Rp. 300,500
- KUDS Shipping Cost → JEPR = Rp. 197,500

Therefore, the total shipping cost for the warehouse → SMRG → KUDS → JEPR route obtained using the nearest neighbor method is:

- Rp. 1,800,000 + Rp. 400,500 + Rp. 187,500 = Rp. 2,298,000

Next, a comparison is made between existing shipping costs and those using the proposed method to determine the savings. The calculation of the resulting shipping cost saving is as follows:

- Rp. 5,400,000 – Rp. 2,498,000 = Rp. 2,902,000

IV.4 DELIVERY TIME ANALYSIS

After optimal routes are obtained using the nearest neighbor method, the next step is to calculate the delivery time for each route. The following are the steps in determining delivery time. Determine the route to be analyzed. For example, consider the warehouse → KUDS → JEPR route for delivery in August 2024. The distribution process is assumed to run smoothly without any problems, with an average delivery fleet speed of 50 km/h. The delivery time details for this route are as follows:

Warehouse → KUDS Delivery Time = 8 hours
KUDS → JEPR Delivery Time = 50 minutes

Therefore, the total delivery time for the Warehouse → KUDS → JEPR route is currently as follows:

Warehouse → KUDS Delivery Time + KUDS → JEPR Delivery Time 8 hours + 50 minutes = 8 hours 50 minutes

By following the steps above, the delivery time is calculated for all optimal delivery routes generated using the nearest-neighbor method.

Table 11: Total Delivery Time of Optimal Nearest Neighbor Route.

No.	Route with Nearest Neighbor	Total Delivery Time
1.	Warehouse → KUDS → JEPR	9 hours 50 minutes
2.	Warehouse → SOLO → JOGY	8 hours 25 minutes
3.	Warehouse → NGW → SMRG	8 hours 10 minutes
4.	Warehouse → TLNG → NGW	7 hours 10 minutes
5.	Warehouse → KEDR → TLNG	3 hours 55 minutes
6.	Warehouse → MJKT → SRBY	3 hours 40 minutes
7.	Warehouse → SMRG → KUDS → JEPR	11 hours 35 minutes
8.	Warehouse → NGW → SOLO → JOGY	8 hours 25 minutes
9.	Warehouse → SOLO → JOGY → SMRG	11 hours 35 minutes
10.	Warehouse → KEDR → TLNG → NGW	7 hours 20 minutes
11.	Warehouse → MJKT → SRBY → JBER	8 hours 15 minutes
12.	Warehouse → TLNG → NGW → SMRG	10 hours 35 minutes

Source: Authors, (2026).

Next, add the time required to unload the cargo from the delivery fleet at each distribution destination branch. This activity has an estimated processing time of 30 minutes at each destination branch. Therefore, the total delivery time for the Warehouse → KUDS → JEPR route is as follows:

Delivery Time Warehouse → KUDS → JEPR + 2 × (Unloading Time) 8 hours 50 minutes + 2 × (30 minutes)
8 hours 50 minutes + 60 minutes = 9 hours 50 minutes

Based on Table 11, the fastest delivery time is the warehouse → MJKT → SRBY route, at 3 hours and 40 minutes. Meanwhile, the longest delivery time is the warehouse → SOLO → JOGY → SMRG route, at 11 hours and 35 minutes.

IV.5 DISCUSSION

Distribution is a crucial factor in any business because it affects the profits of SMEs in Bawean, Gresik, and surrounding areas. During the daily distribution process, several SMEs in the Bawean, Gresik Regency, utilize delivery services. Product orders are placed through the marketing department, which then forwards them to the inter-area sales department, which is directly connected to the warehousing department of SMEs in the Bawean region, which produces various crafts and processed foods using the make-to-stock method. Once the inventory in the warehouse meets demand, shipments are made. The process of collecting orders and processing craft and processed food products is complete, and the products are then sent to several distribution areas within a specified timeframe. Currently, several SMEs in the Bawean region of Gresik Regency use a single delivery fleet for each branch. This is considered ineffective and inefficient due to the underutilization of fleet capacity.

By combining multiple branch destinations into a single delivery and scheduling deliveries a week in advance, companies can save on shipping costs. Using the saving matrix method, 12 optimal distribution route groups were generated based on their saving matrix. Of the 12 routes generated, several branch points are always included in the same route group. These branch points are the JEPR branch with the KUDS branch and the SRBY branch with the MJKT branch. These branch points can be grouped into several delivery destination clusters. The JEPR-KUDS branch is Cluster 1, and the SRBY-MJKT branch is Cluster 2.

Table 12: Distribution Route Groups Based on the Saving Matrix Method.

No.	Route Group
1.	JEPR – KUDS
2.	JOGY – SOLO
3.	SMRG – NGW
4.	TLNG – NGW
5.	KEDR – TLNG
6.	SRBY – MJKT
7.	JEPR – KUDS – SMRG
8.	JOGY – SOLO – NGW
9.	SOLO – SMRG – JOGY
10.	KEDR – TLNG – NGW
11.	SRBY – MJKT – JBER
12.	SMRG – NGW – TLNG

Source: Authors, (2026).

After being processed with the saving matrix method, the resulting route groups are further processed using the nearest-neighbor method. This method is used to sort distribution routes and to obtain the optimal distribution distance for each route group previously determined using the saving matrix method. The nearest-neighbor method produces optimal distribution distances because distribution routes are first analyzed by distance. Table 13 shows the results of sorting distribution routes using the nearest neighbor method.

Table 13: Results of Processing Distribution Routes Using the Nearest Neighbor Method.

No.	Nearest Neighbor Route
1.	Warehouse → KUDS → JEPR
2.	Warehouse → SOLO → JOGY
3.	Warehouse → NGW → SMRG
4.	Warehouse → TLNG → NGW
5.	Warehouse → KEDR → TLNG
6.	Warehouse → MJKT → SRBY
7.	Warehouse → SMRG → KUDS → JEPR
8.	Warehouse → NGW → SOLO → JOGY
9.	Warehouse → SOLO → JOGY → SMRG
10.	Warehouse → KEDR → TLNG → NGW
11.	Warehouse → MJKT → SRBY → JBER
12.	Warehouse → TLNG → NGW → SMRG

Source: Authors, (2026).

After processing using both methods, the resulting savings were compared to determine which method produced the most significant distance savings. Based on calculations, the nearest-neighbor method resulted in a distance savings of 10,854.7 km. Resulted in a distance saving of 6,874.5 km. The nearest-neighbor method produced a more optimal distance because the resulting distribution route was to the closest point from the distribution's starting point, and so on. Therefore, the distribution route chosen to compare shipping costs with the existing method was the nearest-neighbor method. After obtaining the optimal route using the nearest-neighbor method, shipping costs for crafts and food products were calculated based on the route. Shipping costs using the nearest neighbor method will be lower because the resulting distance is shorter than the existing distribution distance. This is because the company's costs are limited to the delivery fleet service. The company's delivery fleet service uses the fleet's mileage as a benchmark for its shipping costs. This means that the shorter the distance traveled by the delivery truck fleet, the lower the shipping costs charged to SMEs in the Bawean area of Gresik Regency.

Table 14: Results of Calculations Using the Existing Method and Processing Using the Saving Matrix and Nearest Neighbor Methods.

	Existing Methods	Saving Matrix and Nearest Neighbor Methods
Total od Distance	24.303,8 km	13.457,9 km
Number of Routes	11	4 - 5
Total Shipping Cost	Rp. 158.460.000	Rp. 93.672.850

Source: Authors, (2026).

Based on Table 14, the results of processing using the saving matrix and nearest-neighbor methods for compiling distribution routes yield a shorter total distance and lower shipping costs than the existing method.

After processing using the saving matrix and nearest-neighbor methods, the total distance traveled is 10,854.7 km shorter, or 44.66% lower than the initial distance, and the total shipping costs are Rp 64,703,150 lower, or 40.85% lower than the initial total.

V. CONCLUSIONS

Based on the results of the research that has been conducted, the conclusions that can be drawn include:

1. Routes that resulted in distance saving using the saving matrix method include JEPR – KUDS with a saving value of 708.9 km, SMRG – JEPR with a saving value of 630.8 km, SMRG – KUDS with a saving value of 613.4 km, and JOGY – JEPR with a saving value of 517 km.
2. Previously, the company had 11 distribution routes. After conducting research using the nearest neighbor method, four to five distribution routes were identified per week, depending on the number of requests. This research resulted in 12 route groups with the minimum total distance traveled and distribution costs. Distribution costs were reduced because SMEs in the Bawean region of Gresik Regency used delivery services that set pricing based on the fleet's mileage.
3. After designing the distribution routes using the nearest-neighbor method, delivery costs were calculated based on the resulting routes. Using the selected proposed method, distribution costs were reduced to Rp 93,696,850, down from the original Rp 1,000,000: 158,400,000, and the total distance was reduced to 13,448.9 km from the original 24,303.6 km.
   By using the nearest- neighbor method, the company can save on the distribution costs of Rp. 64,703,150, or 40.85% smaller than the existing distribution costs, and save a distribution distance of 10,854.7 km, or 44.66% shorter than the total existing distance.

VI. AUTHOR'S CONTRIBUTION

Conceptualization: Rony Prabowo and Lutfia Bamatraf.
Methodology: Rony Prabowo and Lutfia Bamatraf.
Investigation: Rony Prabowo and Lutfia Bamatraf.
Discussion of results: Rony Prabowo and Lutfia Bamatraf.
Writing – Original Draft: Lutfia Bamatraf.
Writing – Review and Editing: Rony Prabowo and Lutfia Bamatraf.
Resources: Rony Prabowo.
Supervision: Rony Prabowo and Lutfia Bamatraf.
Approval of the final text: Rony Prabowo and Lutfia Bamatraf.

VII. ACKNOWLEDGMENTS

The author would like to thank the YPTS (Yayasan Pendidikan Teknik Surabaya) organ administrators, the leaders of the ITATS college, the ITATS Industrial Engineering Department, the East Java Industry and Trade Service, the Gresik Regional Government, the UKM group in Bawean Gresik and all parties who helped in completing the writing of this article, that we cannot mention one by one.

VIII. REFERENCES

[1] E. Yuliza, B. Suprihatin, P. B. J. Bangun, F. M. Puspita, S. Octarina, and Nuraina, "Saving matrix method and nearest neighbor method for garbage transport route problems," in AIP Conf. Proc., vol. 3046, no. 1, Art. no. 020011, 2024.

[2] H. Sekarningtyas and E. Noviana, "Implementation of the saving matrix and nearest neighbor methods in planning courier route for package distribution in the Kudus area," J. Logist. Indones., vol. 8, no. 2, pp. 111–121, 2024.

[3] N. S. Kurnia, S. Salsabila, S. D. H. Sihombing, I. B. Kharisma, and A. Anwar, "Comparison of optimal distribution route for personal protection equipment by saving matrix and tabu search methods using nearest neighbor approach at Covid-19 referral hospitals in West Java," Turkish J. Comput. Math. Educ., vol. 12, no. 7, pp. 2788–2797, 2021.

[4] D. Kurniawan and B. Destrisa, "Saving matrix and nearest neighborhood with permutation for capacitated vehicle routing problem using Google Maps and VBA," in AIP Conf. Proc., vol. 2772, no. 1, Art. no. 080003, 2023.

[5] R. T. Wulandari and A. M. Azis, "The saving matrix method for improving distribution efficiency," J. Manaj. Indones., vol. 22, no. 2, pp. 217–226, 2022.

[6] I. Rizkya, N. Matondang, M. D. Yahya, and M. S. Ningsih, "Design of distribution routes using saving matrix method to minimize transportation cost," in Proc. 2019 Int. Conf. Sustainable Eng. Creative Comput. (ICSECC), 2019, pp. 48–51.

[7] Y. Iriani and H. Asmara, "Cost optimization in determining the distribution route of fabric product using the saving matrix method," PalArch's J. Archaeol. Egypt/Egyptology, vol. 17, no. 10, pp. 3009–3020, 2020.

[8] G. A. Priyambodo, M. A. Hamdani, T. G. Akbar, and A. T. Suprapto, "Optimization distribution routes and delivery costs with transportation and saving matrix methods," Bus. Manag. J., vol. 15, no. 2, 2020.

[9] M. Lukmandono, M. Basuki, M. J. Hidayat, and F. B. Aji, "Application of saving matrix methods and cross entropy for capacitated vehicle routing problem (CVRP) resolving," IOP Conf. Ser.: Mater. Sci. Eng., vol. 462, Art. no. 012025.

[10] R. Noviwiyocha, A. R. Matondang, and J. Hidayati, "Application of saving matrix approach for minimizing distribution cost and route optimization: A literature review," J. Sist. Tek. Ind., vol. 25, no. 2, pp. 206–217, 2023.

[11] F. Armanda and R. F. Sari, "Optimization of liquid petroleum gas (LPG) cylinder distribution route using the saving matrix method," Numerical: J. Mat. Pendidik. Mat., vol. 7, no. 1, pp. 99–110, 2023.

[12] R. F. Harahap, "Study vehicle routing problem using nearest neighbor algorithm," J. Phys.: Conf. Ser., vol. 2421, no. 1, Art. no. 012027, 2023.

[13] H. A. Abu Alfeilat et al., “Effects of distance measure choice on k-nearest neighbor classifier performance: A review,” Big Data, vol. 7, no. 4, pp. 221–248, 2019.

[14] J. Gou, H. Ma, W. Ou, S. Zeng, Y. Rao, and H. Yang, “A generalized mean distance-based k-nearest neighbor classifier,” Expert Syst. Appl., vol. 115, pp. 356–372, 2019.

[15] S. Sarfraz, V. Sharma, and R. Stiefelhagen, “Efficient parameter-free clustering using first neighbor relations,” in Proc. IEEE/CVF Conf. Comput. Vis. Pattern Recognit. (CVPR), 2019, pp. 8934–8943.

[16] K. Taunk, S. De, S. Verma, and A. Swetapadma, “A brief review of the nearest neighbor algorithm for learning and classification,” in Proc. 2019 Int. Conf. Intell. Comput. Control Syst. (ICCS), 2019, pp. 1255–1260.

[17] R. Jia et al., “Efficient task-specific data valuation for nearest neighbor algorithms,” arXiv preprint arXiv:1908.08619, 2019.

[18] N. Sjarif et al., “A customer churn prediction using Pearson correlation function and K nearest neighbor algorithm for telecommunication industry,” Int. J. Adv. Soft Comput. Appl., vol. 11, no. 2, 2019.

Journal of Engineering and Technology for Industrial Applications

ISSN ONLINE: 2447-0228

ITEGAM-JETIA

Manaus, v.12 n.60, p.270-277, July/August, 2026.
DOI: https://doi.org/10.5935/jetia.v12i60.3747

RESEARCH ARTICLE OPEN ACCESS

AN EFFICIENT AND AUTOMATED BRAIN TUMOR SEGMENTATION IN MRI IMAGES USING NON-SUPERVISED MODEL

J. N. Adlin*[1], Arockia Selva Saroja[2]

[1]Department of Electronics and Communication, Noorul Islam Center For Higher Education, India.
[2]Associate professor, Department of Electronics and Communication, Noorul Islam Centre For Higher Education, India.

[1]https://orcid.org/0009-0008-1253-3900, [2]https://orcid.org/0000-0003-4926-4907

Email:*adlinjoshua3@gmail.com

ARTICLE INFO

Article History
Received: February 19, 2026
Reviewed: June 8, 2026
Accepted: July 8, 2026
Published: July 31, 2026

Keywords:
MRI image, Segmentation, Slicing, U-Net, K-means clustering, M-Net CNN.

ABSTRACT

Brain neoplasm is life-threatening abnormalities that require accurate segmentation for effective diagnosis along with treatment planning. Existing segmentation methods often depend on manual annotations or supervised learning, which are time-consuming, subjective, and not scalable. To overcome these challenges, this study proposes a fully unsupervised brain tumor segmentation framework using multimodal MRI data. The 3D MRI volumes are first sliced into 2D axial views and preprocessed to enhance quality. K-means clustering is then applied to generate pseudo-labels that distinguish tumor from healthy regions. These labels guide M-Net CNN training process, which produces coarse tumor localization. A U-Net model further refines the segmentation by fusing the original sliced MRI inputs with M-Net CNN outputs to enhance boundary precision and anatomical alignment. The proposed pipeline achieved a high Dice coefficient of 84.2%, demonstrating its accuracy and robustness. This multi-stage, annotation-free approach enables precise tumor delineation and is suitable for large-scale clinical integration.

Copyright ©2026 by authors and Galileo Institute of Technology and Education of the Amazon (ITEGAM). This work is licensed under the Creative Commons Attribution International License (CC BY 4.0).

I. INTRODUCTION

Neoplasma of the brain is an extensive category of brain pathologies of high morbidity and mortality. High-accuracy volumetric segmentation and early detection are valuable to clinical applications like longitudinal monitoring, radiotherapy, and surgical planning. The main imaging modality in neuro-oncology is Magnetic Resonance Imaging (MRI) because it is a non-invasive procedure. Varying MRI sequences offer complementary diagnosis information: T1, T2, T1ce, and FLAIR. A combination of these modalities allows a complete tumor characterization and subregion definition. Radiologists usually annotate the tumors manually, and it represents the clinical reference used in a diagnosis and the basis used to train segmentation models. Nonetheless, the manual segmentation is labor-intensive, time-consuming and it is highly variable, making it difficult to scale up in other large datasets. This has been highlighted by supervised deep learning methods, particularly the U-Net and its variants [1], [2], to make an effective use of the spatial and contextual information in multimodal MRI samples to identify tumor subregions. However, they need large annotated datasets that are expensive to generate due to privacy limitations and require experts to be available. To eliminate these difficulties, unsupervised techniques of segmentation are studied. Unsupervised techniques identify tumor based on voxel intensities yet tend to produce inaccurate borders and poor generalizability [3]. The proposed work overcomes these limitations by using a combination of methods by exploiting the statistical intensity-based grouping and Deep learning (DL) in the context of learning the features in brain tumor segmentation based on convolutional neural networks (CNN) that is unsupervised. In the suggested framework, an MRI preprocessing step is followed by pseudo-label construction via intensity grouping and the structural accuracy refinement using CNN. The main research findings of the proposed work are as follows:

- To access the 2D images, the input 3D MRI volumes are sliced in the axial level where it is then preprocessed to increase contrast and image quality.
- To distinguish between healthy and tumor area an initial pseudo-labels are created by using K-means clustering on the unlabeled 2D slices.

- The pseudo-labels are used to train an M-Net CNN to learn spatial tumor features and generate improved and detailed segmentation maps.
- The U-Net has the raw slices of MRI data combined with the M-Net CNN outputs to complete segmentation with a greater precision of boundaries and consistency of anatomies.

II. LITERATURE REVIEW

The MRI image represents the standard in diagnosis of brain tumors by non-invasive technique, although manual segmentation is time-consuming and susceptible to error due to inter-observer variability. To automate this process, ML methods were initially applied. The [4] proposed a two-stage system that entailed refined binomial thresholding in localizing the tumor and feature-based classification using SVM, and Random Forest. [5] were able to improve upon the boundary refinement using a hybrid SVM-fuzzy classifier, albeit based on handcrafted features, in which little generalization was done across imaging modalities. Deep learning (DL) approaches advanced the field by learning hierarchical representations directly from data. [6] proposed a symmetrical encoder–decoder framework with a Threefold Attention Mechanism to enhance tumor boundary prediction across multimodal MR images. In [7] a deep neural network pipeline was constituted that detects tumor at early stage, and [8] improved the U-Net architecture by altering depth and skip interconnections to provide more structural detail forecasting. Model TACA-RNet proposed by [9] utilized the idea of tri-planar context and enhanced multimodal tumor segmentation. This binary tumor prediction utilised a traditional CNN in [10], though Z-Net demonstrated in [11] improvement at predicting the tumor boundaries using pyramid pooling to generate finer predictions in 2D slices. [12] decided to use a multi-scale attention mechanism with an EfficientNetB4 backbone since it proved useful in capturing tumor variations. Other more recent approaches leveraged a Transformer-GAN was done in [13] to provide more robust boundary prediction, as well as a hybrid ViT-CNN model was presented in [14], to enable explanatory glioma segmentation across MRIs. To address the dependency on annotated labels, unsupervised approaches have emerged. [15] proposed a two-stage GAN-based pipeline that synthesizes tumor-free and tumor-bearing images to generate pseudo-masks for segmentation prediction. [16] introduced a prompt-based unsupervised framework (PL-BTS) that predicts tumor-like regions through intensity prompts and pseudo-label refinement (PL-BTS+). [17] adopted a spatially variant finite mixture model with RJMCMC sampling to predict tumor regions based on probabilistic tissue distributions, offering label-free yet interpretable segmentation. These models shift the field toward scalable annotation-independent solutions, though trade-offs in computational demand and data quality remain. Current techniques used in segmenting the brain tumor have a number of limitations. Conventional methods of ML depend on handcrafted features that are weak on complex tumor structures and also noise-sensitive [4], [6]. Transformer-based and hybrid deep learning models have higher segmentation accuracy, but they are usually associated with high cost of computation and decreased interpretability under the clinical setting [13], [14]. In addition, DL models usually need a huge amount of labeled MRI data to be qualified which are costly and time- consuming to acquire [9], [10].To address these challenges, the proposed method employs K-means clustering to generate pseudo-labels from unlabeled MRI slices, which guide an M-Net CNN for segmentation. A subsequent U-Net model refines this output by enhancing feature fusion and spatial consistency, enabling accurate tumor delineation in an unsupervised setting.

III. METHODOLOGY

As shown in Figure 1, the proposed approach performs brain neoplasm segmentation utilizing an unsupervised models framework for unlabeled MRI images. The 3D MRI volumes will be originally sliced in the axial plane in order to give 2D slices. Then preprocessing modalities used to improve image quality and contrast. The K-means clustering is then used to produce pseudo-labels that indicate tumor and non-tumor areas. These pseudo-labeled masks guide an M-Net convolutional neural network (CNN) towards segmenting a tumor. M-Net CNN's outputs, together with the corresponding raw sliced MRI images, are then given as input to a U-Net model. The U-Net performs feature fusion and spatial refinement, producing a precise and anatomically consistent tumor segmented part.

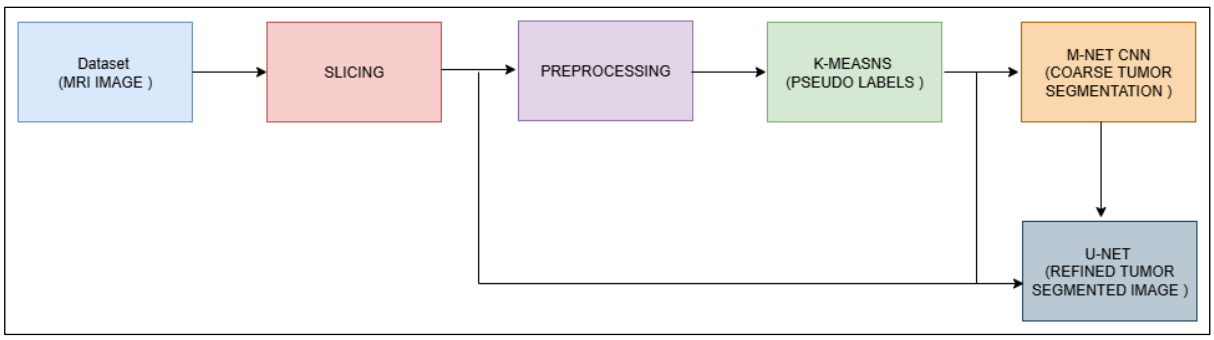


Figure 1: Overall architecture unsupervised learning pipeline.
Source: Authors, (2026).

III.1 DATASET

The proposed unsupervised brain tumor segmentation framework uses the BraTS 2019 dataset [18], which comprises 335 co-registered, skull-stripped, and multimodal MRI volumes of the T1, T1ce T2, and FLAIR sequences. These volumes are acquired with a uniform voxel resolution and follow standardized clinical acquisition protocols. In this study, the dataset is incorporated into an unsupervised learning pipeline, whereby ground-truth segmentation masks supplied in the training set are excluded from the learning procedure.

III.2 SLICING

In the BraTS 2019 set of data, each subject is represented by a 3D volumetric MRI scan acquired using 4 modalities: T1, T1ce, T2, and FLAIR. To enable efficient training of 2D DL models and reduce computational overhead, a slicing process is applied to convert 3D MRI volumes into 2D axial slices. Slicing is carried out in the axial plane, giving a sequence of 2D slices that retain spatial fidelity and tumor-related anatomical structures. These slices are extracted in a modality-wise manner, ensuring that for each 2D position, corresponding slices across all modalities are available and aligned. The stacked multi-modal 2D slice at axial index k is represented as:

$$S^{(k)} = [S_{T1}^{(k)}, S_{T1ce}^{(k)}, S_{T2}^{(k)}, S_{FLAIR}^{(k)}] \in R^{H \times W \times 4} \quad (1)$$

Where $S^{(k)}$ denotes the composite input formed by concatenating slices from all four modalities at position k, with H and W representing the spatial dimensions.

III.3 DATA PREPROCESSING

Following the slicing of 3D MRI volumes into 2D axial slices, a sequence of preprocessing operations is applied, all aimed at improving image quality and normalizing intensity characteristics across samples. First, average filtering is used to remove random noise and smoothen the image while conserving important structural and anatomical boundaries. This helps suppress high-frequency distortions and assists in achieving homogeneity of non-tumor regions. Then, histogram equalization is invoked as a means of contrast enhancement, meaning to redistribute pixel intensities uniformly across the dynamic range. This operation maximizes the visibility of subtle tumor boundaries and paves the way for effective segmentation of the slices. For model evaluation along with generalization analysis, a set of data was randomly split into train and test subsets using 80:20 ratio.

III.4 K-MEANS CLUSTERING PROCESS

Following the completion of the slicing and preprocessing stages, the enhanced multimodal two-dimensional MRI slices are utilized for pseudo-label generation using the K-means clustering algorithm. This unsupervised method segments each slice into two distinct clusters that correspond to tumor and healthy regions, based on pixel-wise intensity similarity patterns across modalities. For each axial position, the corresponding slices from a T1, T1ce, T2, and FLAIR modalities are stacked to form a tensor of size $H \times W \times 4$. In this representation, each pixel is described by a four-dimensional feature vector comprising the intensity values from four MRI sequences. Entire image is reshaped into a two-dimensional feature matrix of size $(H \times W) \times 4$, which is provided as input to the K-means clustering algorithm. The objective of K-means is to minimize intra-cluster variance, mathematically defined by

$$J = \sum_{j=1}^{k} \sum_{i=1}^{n} \left\| x_i^{(j)} - c_j \right\|^2 \quad (2)$$

Here, k denotes the number of clusters, n is a total number of pixels, $x_i^{(j)}$ represents pixel i^{th} assigned for cluster j, and c_j denotes corresponding centroid. The entire process of clustering commences with initialization of two centroids randomly in the feature space. Next, given data points are assigned to the most nearest centroid using Euclidean distance. Centroids are also updated by computing mean of all the vectors which are in a single cluster. This assignment along with update process continues repeated until convergence, which is reached when centroid positions remain stable across iterations. After convergence, the cluster assignments are reshaped to match the spatial dimensions $H \times W$, resulting in a binary pseudo-label mask that delineates tumor from healthy one.

III.5 M-NET CNN

Following the generation of pseudo labels through K-means clustering, the tumor segmentation stage employs an end-to-end trainable CNN based on the M-Net architecture to identify brain tumor regions in an unsupervised manner. The input to this M-Net CNN consists of co-registered and preprocessed two-dimensional axial MRI slices from 4 modalities: FLAIR, T1, T1ce, and T2. These modalities are stacked along the channel dimension to form a single composite tensor of shape H×W×4, allowing the network to exploit anatomical, structural, and contrast-related cues for accurate segmentation. M-Net CNN is symmetrically structured along the lines of encoder decoder, as illustrated in Figure 2. The architecture of M-Net is symmetrical where it has four different paths, one is the main encoder path, one is decoder path, and the other two are side paths which are conventionally named as the left leg and the right leg which can provide deep supervision and multi-scale features. Every encoder unit has two conv layers 3x3 kernel size, then batch normalization and ReLU. These cascade convolutional layers allow a gradual refinement of each layer. Each unit is concluded with 2x2 max pooling operation which decreases spatial dimensions with a maximum feature abstraction. The output of encoder layer feature map is as:

$$E(l) = MaxPool(\sigma(W^{(l)} * E^{(l-1)} + b^{(l)}) \quad (3)$$

Where, $E^{(0)}$ represents stacked multimodal MRI input, $W^{(l)}$ and $b^{(l)}$ denote the learnable weights and biases, $*$ represents convolution, and σ (.) is the ReLU activation function. The left leg of M-Net CNN applies four successive 2×2 max pooling operations to the input, providing multi-scale contextual features to the encoder blocks.

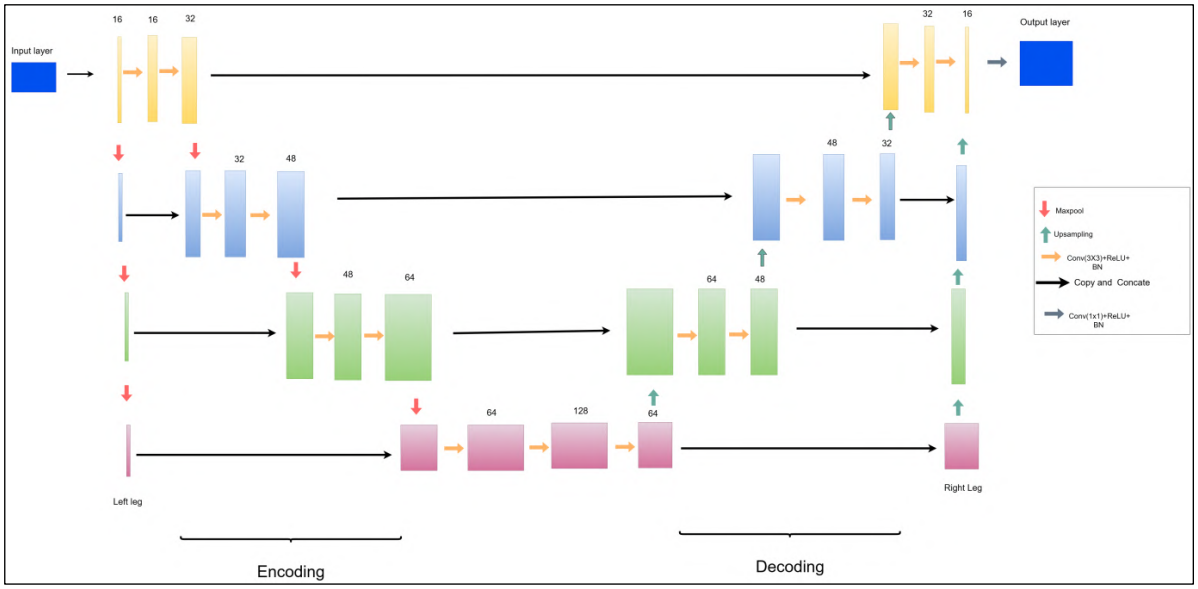


Figure 2: M-Net CNN architecture.
Source: Authors, (2026).

The bottleneck block adopts convolutional layers of deeper filter depth to acquire semantic feature in high level. The decoder is the reverse of the encoder where the first layer of each block involves a transposed convolution to upsample the block, and them the skip connections with the previous layers of the encoder are used to maintain fine-grained spatial information. The decoder path restores original spatial dimensions using transposed convolution operations and includes skip connections from encoder. The decoder feature map at level is obtained by:

$$D(l) = \sigma(W_{up}(l) * U_p\left(D^{(l+1)}\right) + W_{skip}^{l} * E^{(l)} + b^{(l)}) \quad (4)$$

Where $U_p(.)$denotes upsampling through transposed convolution, W_{up} and W_{skip} are the weights for upsampling and skip connections, respectively. Simultaneously, the right leg upsamples the outputs of each decoder block to the original resolution of input, enabling deep supervision. These auxiliary paths enhance the network's multi-scale learning and segmentation accuracy. The last stage of decoder performs a 1 x 1 convolution layer followed by a sigmoid, the output is a binary mask segmented of size H x W x 1 with pixel-wise tumor probabilities.The network is trained using pseudo labels generated by K-means clustering, eliminating the requirement for manually annotated ground truth. Dice loss function is used to optimize the segmentation learning by calculating overlap of predicted segmentation with pseudo label Y. The loss is defined as:

$$L_{Dice} = 1 - \frac{2\sum_{i=1}^{N} \hat{Y}_i Y_i + \epsilon}{\sum_{i=1}^{N} \hat{Y}_i + \sum_{i=1}^{N} Y_i + \epsilon} \quad (5)$$

Where $\hat{Y}_i$ is a predicted value at pixel, Y_i gives pseudo label, N represents number of pixels, and ϵ denotes small constant to prevent division by zero. The output of M-Net is a binary segmentation mask aligned with spatial dimensions of input multimodal slice, effectively delineating tumor regions from healthy tissue. This is achieved using pseudo supervision derived from K-means clustering, thereby eliminating the requirement for manually annotated ground truth.

III.6 U-NET

Following the coarse tumor localization obtained from the M-Net CNN, a U-Net is employed to refine the tumor segmentation in an unsupervised manner. The input to the U-Net consists of preprocessed axial MRI slices from four modalities, along with the binary tumor mask from M-Net. These five inputs are stacked to form a composite tensor of shape $H \times W \times 5$. Such setup allows the U-Net to couple the anatomical differences between modalities with the crude localization of the tumor, to increase the ability of network for detecting refined tumor margins. U-Net design follows the symmetric encoder-decoder design which makes hierarchical feature learning easy. The encoder path has two convolutional blocks in each block are two convolutional layers of 3x3 kernels, batch normalization, ReLU activation, and a 2x2 max pooling layer as a spatial resizing block to detect high level and abstract features. Bottleneck layer is relating encoder and decoder, and it makes an aggregation of the contextual semantic representations. Spatial resolution is upscaled step by step through transposed convolutions in the decoder route. In order to maintain the spatial accuracy, the connection between related encoder and decoder layers is done using skip connections. These interactions make feature fusion possible by adding the encoder features of the high resolutions to decoder features which are increased through addition, which is mathematically expressed as:

$$D(l) = \sigma(w(l) * U_p[(D^{(l+1)}) \| E^{(l)}] + b^{(l)}) \quad (6)$$

where $U_p(D^{(l+1)})$ is the upsampled decoder feature, $E^{(l)}$is the encoder feature map,|| denotes channel-wise concatenation, and $\sigma(.)$ gives ReLU activation. At the final stage of decoding, a 1×1 convolutional layer followed by a sigmoid activation function generates a binary segmentation mask of dimensions $H \times W \times 1$, indicating the pixel-wise probability of tumor presence.

The K-means predictions are used as pseudo labels to train the network, so no manually annotated ground truth is required. Dice loss function is used to optimize the overall segmentation level which measures the overlap between the mask generated in the segmentation and the pseudo label. Such features as feature fusion achieved with skip connections and multimodal plus auxiliary input channels allow the U-Net to demonstrate the refined and anatomic-consistent form of segmentation, which elevated the accuracy of tumor delineation.

IV. RESULT AND ANALYSIS

The suggested unsupervised brain tumor segmentation method was examined on 2D axial slices on four modalities in data records of the BraTS2019 database. The M-Net CNN model has been learned in regard to tumor-specific features using pseudo-labels generated through K-means clustering. Raw sliced MRI data is then merged with the M-Net CNN output to form a U-Net model to allow a more accurate segmentation. The framework is considered by computing the Dice coefficient, Intersection over Union (IoU), precision, recall, and accuracy. The qualitative results of segmentation application on test images are shown in Figure 3, and these have proven how the method used is accurate in locating and outlining the tumor area by segmentation process in the test images.

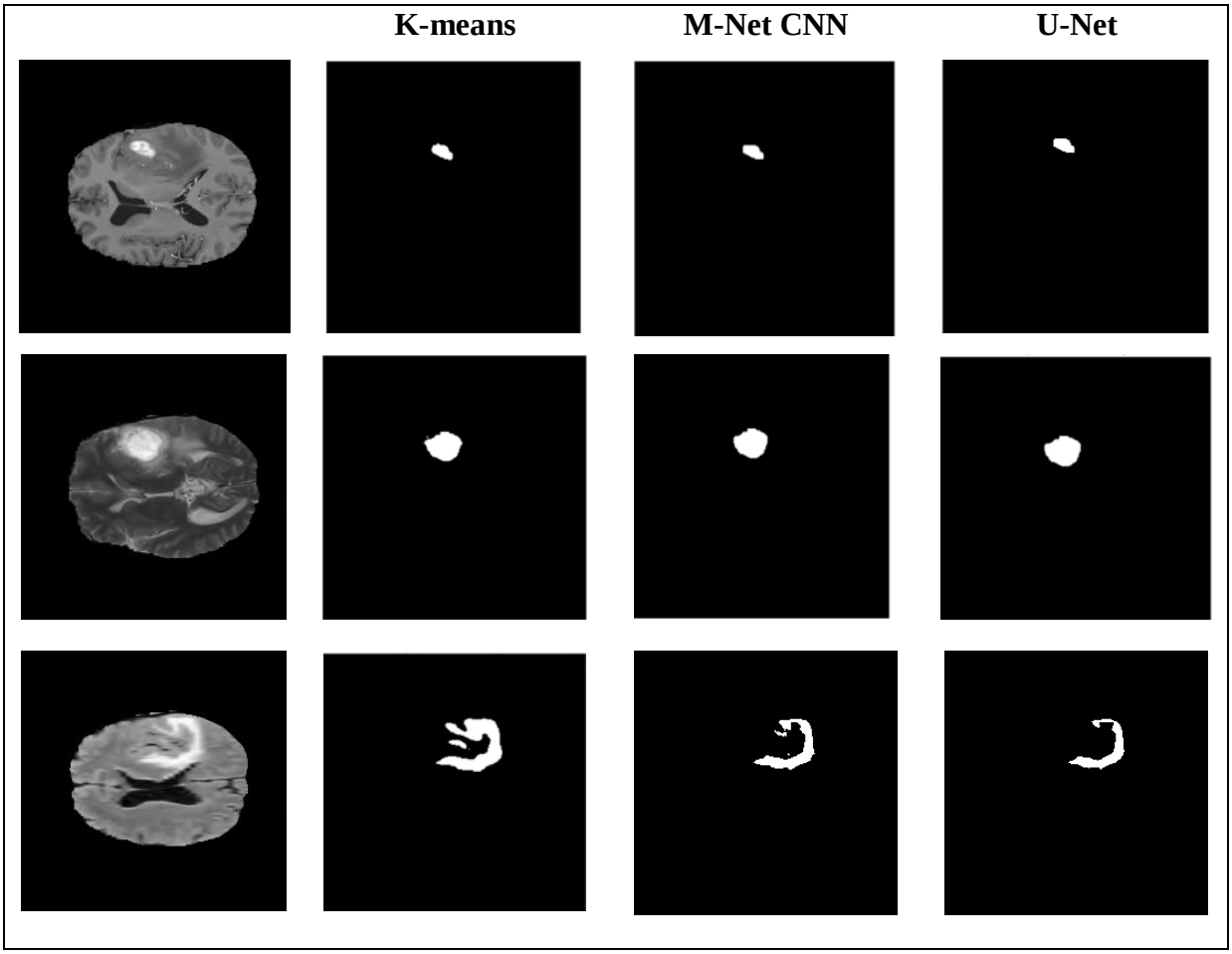


Figure 3: Samples of brain tumour segmentation results on test images of BraTS2019.
Source: Authors, (2026).

The evaluation metrics for K-means clustering models on unlabeled MRI slices will be represented in the Figure 4 for generation of pseudo-labels. Through intensity-based clustering where K-means does not require any manual annotations, it would distinguish tumor and non-tumor regions. It attained a Dice coefficient of 78.0%, IoU at 65.0%, thus showing itself adept at spatially delineating tumor regions with moderate accuracy. It records also 85.3% in accuracy, 76.5% precision and 79.2% recall which authenticate its reliability in pseudo-label generation, paving the way for further training of CNN-based segmentation models. Figure 5 presents a segmentation performance of the M-Net CNN model trained using pseudo-labels generated from K-means clustering. The model achieved a Dice coefficient of 83.0%, 72.4% IoU, 82.7% precision, 84.2% recall, and overall accuracy of 88.5%. These results demonstrate M-Net's ability to leverage pseudo supervision for accurate and consistent tumor segmentation in unlabeled MRI slices. Figure 6 illustrates a comparative evaluation between the proposed M-Net CNN model and two existing unsupervised segmentation methods: SynthTumour [15] and PL-BTS [16]. M-Net achieved a Dice coefficient of 83.0 %, outperforming SynthTumour at 78.03 % and PL-BTS at 79.5 %. It also recorded the highest recall of 84.2%, compared to 78.54 % for SynthTumour and 82.90 % for PL-BTS, highlighting its improved ability to detect tumor regions. In terms of precision, M-Net CNN reached 82.7%, closely matching SynthTumour at 82.50 % and exceeding PL-BTS at 80.36%. These comparisons confirm that the proposed M-Net CNN, guided by pseudo-labels and a structured CNN architecture, surpasses existing methods in segmentation accuracy, consistency, and sensitivity.

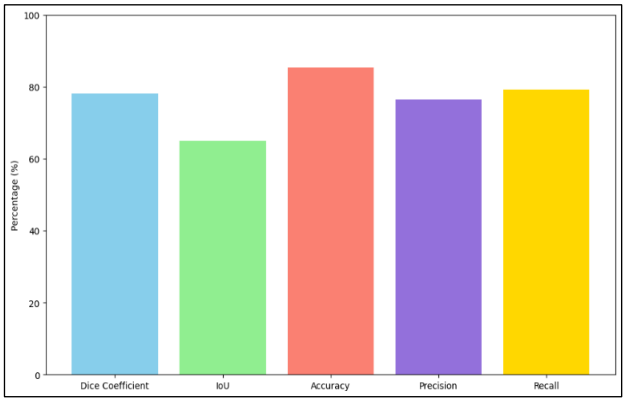


Figure 4: K-means Model performances.
Source: Authors, (2026).

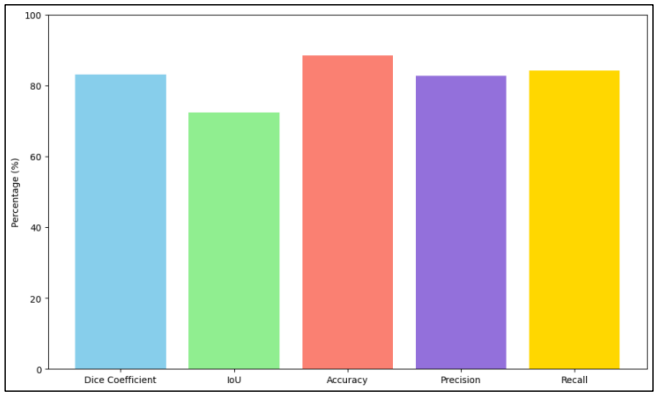


Figure 5: Evaluation of M-Net CNN.
Source: Authors, (2026).

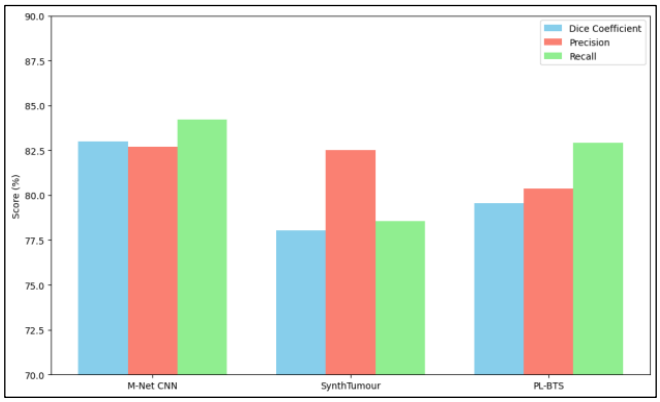


Figure 6: Comparative Performance of M-Net CNN against Existing Unsupervised Segmentation Methods.
Source: Authors, (2026).

The final refined segmentation was performed using a U-Net model, which used both the raw MRI slices and feature maps extracted from the preceding M-Net CNN. As illustrated in Figure 7, the U-Net demonstrated superior performance by achieving a Dice coefficient of 84.2 %, IoU at 73.9 %, It also attained a precision of 83.7 %, 85.0% recall and accuracy of 89.6 %. These improvements confirm the effectiveness of integrating multimodal inputs and intermediate deep features, enabling more accurate and anatomically aligned tumor segmentation. As shown in Figure 8, the various performance comparisons of the U-Net, ResNet [7], and BrainSegNet [19] models proposed were carried out using pseudo-labeled MRI data. U-Net achieved the highest score, with a Dice coefficient of 84.20%, followed by ResNet with 80.50% and BrainSegNet with 79.80%. In terms of precision, U-Net scored 83.70%, while ResNet and BrainSegNet scored 81.00% and 80.30%, respectively. U-Net again scored highest in recall at 85.00%, while ResNet and BrainSegNet scored 82.00% and 81.70%, respectively. These results clearly indicate that U-Net performed the best in terms of segmentation using pseudo-labeled data. The Dice Coefficient is provided for three stages of the modeled unsupervised segmentation pipeline in Table 1. The process begins with pseudo-label generation by K-means clustering, yielding a Dice coefficient of 78.0%. The pseudo-labels are then used to train the M-Net CNN, which improves segmentation performance to 83.0%. The refined U-Net model is finally applied, achieving the highest Dice score of 84.2%, demonstrating the effectiveness of the multi-stage enhancement and feature learning in the unsupervised framework. The performance gains across stages indicate the robustness of the refinement strategy as well as the U-Net's ability to adapt to pseudo-supervised inputs.

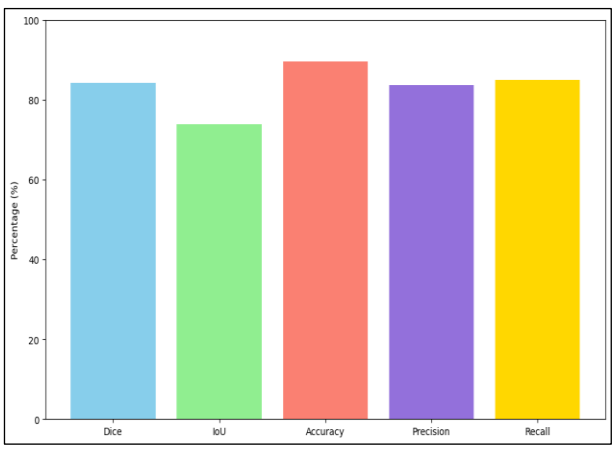


Figure 7: Evaluation of U-Net.
Source: Authors, (2026).

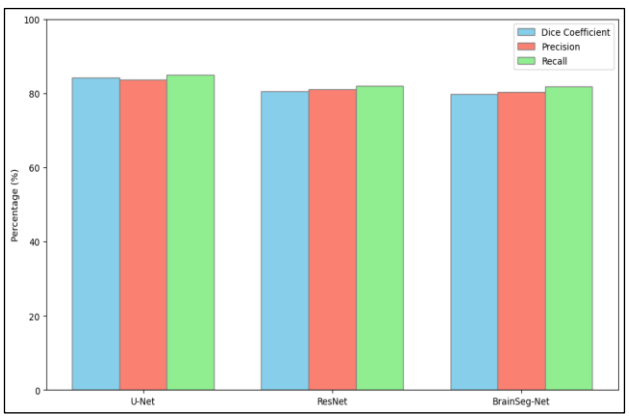


Figure 8: Comparative Performance of U-Net, ResNet-50, and BrainSegNet on Pseudo-Labeled image.
Source: Authors, (2026).

Table 1: Evaluation of Proposed models.

Models	Dice Coefficient
K-means	78.0%
M-Net CNN	83.0%
U-Net	84.2%

Source: Authors, (2026).

V. CONCLUSION

This work proposed a pseudo-supervised segmentation pipeline using the BraTS 2019 multimodal MRI dataset. K means generated pseudo labels trained an M-Net CNN, whose output was refined by a U Net model for enhanced accuracy. The final segmentation achieved a Dice coefficient of 84.2 %, showing effective tumor localization. The integration of multiple MRI modalities enhanced tissue characterization and model robustness. This framework reduces dependence on manual annotations, making it suitable for large-scale neuroimaging studies. As future work, the method can be extended to other diagnostic modalities, including CT scans for broader applicability across clinical environments. Additionally, incorporating self-supervised learning, attention-based mechanisms, and cross-modal consistency may further improve segmentation quality and generalization across heterogeneous datasets.

VI. AUTHOR'S CONTRIBUTION

Conceptualization: J. N. Adlin and Arockia Selva Saroja.
Methodology: J. N. Adlin and Arockia Selva Saroja.
Investigation: J. N. Adlin and Arockia Selva Saroja.
Discussion of results: J. N. Adlin and Arockia Selva Saroja.
Writing – Original Draft: J. N. Adlin.
Writing – Review and Editing: J. N. Adlin and Arockia Selva Saroja.
Resources: Arockia Selva Saroja.
Supervision: J. N. Adlin and Arockia Selva Saroja.
Approval of the final text: J. N. Adlin and Arockia Selva Saroja.

VII. ACKNOWLEDGMENTS

Acknowledgements: The author would like to appreciate the effort of the editors and reviewers.
Data Availability: The dataset used in this study is publicly available and was obtained from the Kaggle repository. Specifically, the Brain Tumor Segmentation (BraTS 2019) dataset can be accessed at: https://www.kaggle.com/datasets/aryashah2k/brain-tumor-segmentation-brats-2019. No additional permissions were required for its use in this research.

VIII. REFERENCES

[1] J. Walsh, A. Othmani, M. Jain, and S. Dev, "Using U-Net network for efficient brain tumor segmentation in MRI images," arXiv preprint arXiv:2211.01885, 2022.

[2] H. Chen, Z. Qin, Y. Ding, L. Tian, and Z. Qin, "Brain tumor segmentation with deep convolutional symmetric neural network," Neurocomputing, vol. 392, pp. 305–313, 2020.

[3] S.-J. Huang, C.-C. Chen, Y. Kao, and H. H.-S. Lu, "Feature-aware unsupervised lesion segmentation for brain tumor images using fast data density functional transform," Scientific Reports, vol. 13, no. 1, p. 13582, 2023.

[4] M. Sharif, U. Tanvir, E. U. Munir, M. A. Khan, and M. Yasmin, "Brain tumor segmentation and classification by improved binomial thresholding and multi-features selection," Journal of Ambient Intelligence and Humanized Computing, vol. 15, no. 1, pp. 1063–1082, 2024.

[5] R. Vankdothu and M. A. Hameed, "Brain tumor segmentation of MR images using SVM and fuzzy classifier in machine learning," Measurement: Sensors, vol. 24, p. 100440, 2022.

[6] Z. Rahman, R. Zhang, and J. A. Bhutto, "A symmetrical approach to brain tumor segmentation in MRI using deep learning and threefold attention mechanism," Symmetry, vol. 15, no. 10, p. 1912, 2023.

[7] M. Aggarwal, A. K. Tiwari, M. P. Sarathi, and A. Bijalwan, "An early detection and segmentation of brain tumor using deep neural network," BMC Medical Informatics and Decision Making, vol. 23, no. 1, p. 78, 2023.

[8] H. Alquran, M. Alslatie, A. Rababah, and W. A. Mustafa, "Improved brain tumor segmentation in MR images with a modified U-Net," Applied Sciences, vol. 14, no. 15, p. 6504, 2024.

[9]H. Kim, Y. Jo, H. Lee, and S. Park, "TACA-RNet: Tri-axis based context-aware reverse network for multimodal brain tumor segmentation," Electronics, vol. 13, no. 10, p. 1997, 2024.

[10] A. M. Mostafa, M. Zakariah, and E. A. Aldakheel, "Brain tumor segmentation using deep learning on MRI images," Diagnostics, vol. 13, no. 9, 2023.

[11] M. A. Ottom, H. A. Rahman, and I. D. Dinov, "Znet: Deep learning approach for 2D MRI brain tumor segmentation," IEEE Journal of Translational Engineering in Health and Medicine, vol. 10, p. 1800508, 2022.

[12] P. R., J. P. P. M., and N. J. S., "Brain tumor segmentation using multi-scale attention U-Net with EfficientNetB4 encoder for enhanced MRI analysis," Scientific Reports, vol. 15, no. 1, p. 9914, 2025.

[13] L. Huang, L. Chen, B. Zhang, and S. Chai, “A transformer-based generative adversarial network for brain tumor segmentation,” arXiv preprint arXiv:2207.14134, 2022.

[14] R. A. Zeineldin, M. E. Karar, Z. Elshaer, J. Coburger, C. R. Wirtz, O. Burgert, and F. Mathis-Ullrich, “Explainable hybrid vision transformers and convolutional network for multimodal glioma segmentation in brain MRI,” Scientific Reports, vol. 14, no. 1, p. 3713, 2024.

[15] X. Zhang, N. Ou, C. Liu, Z. Zhuo, P. M. Matthews, Y. Liu, and W. Bai, “Unsupervised brain MRI tumour segmentation via two-stage image synthesis,” Medical Image Analysis, vol. 102, p. 103568, 2025.

[16] X. Zhang, N. Ou, C. Liu, Z. Zhuo, Y. Liu, and C. Ye, “Unsupervised brain tumor segmentation with image-based prompts,” arXiv preprint arXiv:2304.01472, 2023.

[17] A. A. Pravitasari, N. Iriawan, K. Fithriasari, S. W. Purnami, Irhamah, and W. Ferriastuti, “Unsupervised learning for MRI brain tumor segmentation with spatially variant finite mixture model in reversible jump MCMC algorithm,” Journal of Physics: Conference Series, vol. 1776, no. 1, p. 012041, 2021.

[18]“Brain Tumor Segmentation BraTS 2019,” Kaggle dataset, 2020. [Online]. Available: https://www.kaggle.com/datasets/aryashah2k/brain-tumor-segmentation-brats-2019.

[19] M. U. Rehman, S. Cho, J. Kim, and K. T. Chong, “BrainSeg-Net: Brain tumor MR image segmentation via enhanced encoder-decoder network,” Diagnostics, vol. 11, no. 2, p. 169, 2021.

Journal of Engineering and Technology for Industrial Applications

ISSN ONLINE: 2447-0228

ITEGAM-JETIA

Manaus, v.12 n.60, p.278-293, July/August, 2026.
DOI: https://doi.org/10.5935/jetia.v12i60.3765

RESEARCH ARTICLE OPEN ACCESS

DRIVER INATTENTION DETECTION USING A HYBRID VISION TRANSFORMER AND BILSTM

Devanaboyina Manikanta Teja*[1], P L Kishan Kumar Reddy[2]

[1, 2]Department of Science, Technology and Engineering, KL University,Vaddeswaram Andhra Pradesh, India.

[1]https://orcid.org/0009-0006-0609-4329, [2]https://orcid.org/0000-0002-2097-5935

Email:*manikantateja2001@gmail.com, plkishankumar@kluniversity.in

ARTICLE INFO

Article History
Received: February 21, 2026
Reviewed: June 8, 2026
Accepted: July 8, 2026
Published: July 31, 2026

Keywords:
Balanced Sampling,
BiLSTM,
Data Augmentation,
Fine-Tuning,
Vision Transformer.

ABSTRACT

The identification of the early warning of unsafe behavior on the highways of visual cues of driver inattention is a serious challenge since spatial and temporal changes are not trivial many seconds before unsafe behavior. In this paper we propose a hybrid ViT-BiLSTM model that considers fixed-length sequences of 15 frames: inchoate frames are cropped according to the bounding-box annotations, safe or unsafe label and selectively augmented to have equal sampling. Every frame is processed using a Vision Transformer backbone (ViT B/16) and generates 768 dimensional features, which are further implemented as an input to the two-layer bidirectional LSTM (hidden size of 256). The Dual classification heads produce both the frame level and sequence level prediction through sigmoid activation. The training is done in two steps, which are to freeze ViT and to train the BiLSTM and heads with AdamW (lr=1e 3), and then to fine-tune the last four ViT layers with different learning rates (ViT:5e 5, LSTM:1e 4) under mixed precision. Accuracy, precision, recall, and F1-score will be used at both levels with data visualized using confusion matrices, PR/ROC curves, and embedding projections (t-SNE/PCA). The last model ends with a mean of about 98 percent frame-level accuracy (F1 98) and 94 percent sequence-level accuracy (F1 94). The interpretability and soundness of the model are supported by qualitative visualizations of frame strips with annotations and trends of probabilities, which proves that the model may be used in real-life driver monitoring systems.

Copyright ©2026 by authors and Galileo Institute of Technology and Education of the Amazon (ITEGAM). This work is licensed under the Creative Commons Attribution International License (CC BY 4.0).

I. INTRODUCTION

I.1 MOTIVATION FOR DRIVER INATTENTION DETECTION SYSTEMS

Inattention among drivers is one of the major causes of the road accidents in the world, resulting in substantial number of people being injured annually and heavy loss of lives [1]. With smart technologies entering modern vehicles, there is an urgent need to have reliable, real time in-vehicle systems to monitor the driver to identify, detect and react to all kinds of driver distractions and attention such as texting, talking, reaching or using a device during driving [2]. The rationale of this work is developing a sophisticated inattention detection system that can find the fine-grained driver behaviours simply based on the visual input information. Through the significant synergistic improvement potential of Vision Transformers (ViT) in extracting spatial features and Bidirectional Long short-Term Memory (BiLSTM) networks in modelling temporal sequences, the system will explore the possibility of analysing video frames and finding distraction patterns in time with great accuracy [3], [4]. This method corrects major weaknesses of traditional CNN-based models that often do not capture the temporal relations that are essential in relating behaviours [5]. In addition, the use of ViT allows the model to focus on specific areas of space in each frame: e.g. eyes, hands, devices while BiLSTM views the modeled observations in the context of a sequence of actions [6]. The wider aim of this is to contribute to the establishment of real-time intelligent driver checking systems which can:

- Increase safety on the road by minimizing cases of human error because of distraction [7].
- Help implant autonomous and semi-autonomous driving system [8].
- Function as the basis of human-AI collaborative interfaces which would build upon the situation awareness without being overbearing to the driver [9].

I.2 COMPLICATIONS OF REAL-TIME DRIVERS BEHAVIOUR RECOGNITION

Real-time driver behaviour recognition systems show variation of technical and operational complexities of development. These problems are compounded by the fact that the system should be able to isolate subtle behaviours of drivers using unprocessed video data in varying driving environments. Some of these complexities can be found in the method used in this work, especially with the incorporation of Vision Transformer (ViT) and BiLSTM:

I.2.1 Extreme Intra-Class Variation:

Such behaviours as texting or reaching of a driver may vary dramatically as a matter of individual style, posture position, camera angle, and environmental lighting. The challenge behind the model would be the need to generalize across minor variations and not be overfitted to a particular visual input [10], [11].

I.2.2 Dependence in Time of Actions:

Frames that are isolated could not show the whole context of an action. Cite an example, only after a series of frames is a certain act of picking up a phone recognizable. It requires the application of temporal models such as BiLSTM to investigate the sequences of frames and serve to interpret time-based patterns of behaviour [3], [4], [12].

I.2.3 Multi-Class and Multi-Instance Issues:

The system is also going to be needed to differentiate among several classes of distractions of which some of them overlap in visual characteristics. As well, an individual frame may have more than one bounding box and instances of classes, as was done in the preprocessing activities of the notebook [6], [11], [13].

I.2.4 Real-Time Constraints:

The system should work with low latency and high accuracy to be implemented in the real-word vehicles. This is computationally intensive on both feature extraction (performed by ViT) and sequence modelling (BiLSTM) and needs expedient implementation and hardware-sensitive optimisation [7], [9], [10].

I.2.5 Inaccurate and Unbalanced Training Set:

The code explains the reason that the dataset has uneven distributions of class and inconsistencies in the annotations and little amounts of rare distraction behaviours. This is on top of the difficulty about constructing a fair model which is balanced and performs the same across all classes [1], [14], [15].

I.2.6 Interpretability and Trust:

Black-box models cannot be enough in the case of the safety-critical setting. ViT architecture enables the mapping of visual attention, providing a level of explanation needed to justify the AI models decisions and make the user trust the artificial intelligence-augmented driving [2], [6], [11].

I.3 USING VISION TRANSFORMERS TO ANALYSE SPATIAL BEHAVIOUR

Although state-of-the-art convolutional neural networks (CNNs) have achieved significant results in image recognition upon various tasks, they seemingly suffer due to a lack of long-range dependency and spatial context-based relationship learning especially in complex scenario like that of the vehicle cabin where micro-clues involved such as hand position, eye gaze or interaction with an object characterize the behaviour of the driver [10], [11]. Overcome such shortcomings, the current research employs Vision Transformers (ViT) to pursue sophisticated spatial behaviour studies. Within the suggested method, ViT model is used as a front-end feature extractor, and works on the level of individual frames by trying to detect both global and localized patterns of attention [6], [11]. Compared to CNNs, where the size of the receptive field is fixed, the transformer architecture breaks down each image into patches and forms self-attention mechanisms forcing the model to assign importance to every part of the scene dynamically [3], [10]. This is particularly important in driver checking applications, where one would want to change areas of interest (the face, hands or the dashboard) depending on what is being done. Some of the advantages of incorporating ViT in this regard are:

Context-Aware Attention: The model can pay attention to details of spatially relevant objects (e.g. phone in hand or a hand behind the back) even though such details happen in unusual locations [6], [11].

Resistance to Viewpoint Dependency: ViT is robust to the variations in spatial orientation or noise in the background, such as the data of the camera in the vehicles of different orientations and illumination [7], [10].

Improved Feature Representation: Transformer based Encoders are more discriminative over standard CNN features in terms of capturing richer semantics to classify behaviour [3], [13].

Incorporating ViT into the driver inattention detection pipeline, the system will be capable of much better interpretation of clearly complicated visual scenes and the capability to detect the spatial properties of various distraction behaviours [6], [11].

This combined with temporal models such as BiLSTM formulates a strong framework of spatiotemporal interpretation of driver behaviour, which is critical in real-time, intelligent safety measures [3], [12].

I.4 TEMPORAL BEHAVIOUR MODELLING THROUGH BILSTM NETWORKS

Although we find suitable spatial details in static frame study, the identification of complicated driver behaviours needs to know how the action flow varies with time [11]. Fulfil this requirement, this proposed system will use a Bidirectional Long Short-Term Memory (BiLSTM) network, to account of the temporal variations in the driver behaviour over sequences of later image frames [3], [12]. The BiLSTM architecture can be applicable especially to this task to fulfil the following abilities:

Extract Temporal Dependencies: BiLSTMs read information in both directions, forward and backward in time and this means that the model can know the contribution of both the earlier and the later frames when interpreting the understanding of current behaviour [3], [12].

Preserve Sequential Context: A considerable number of driver behaviours are time lengthy (e.g., picking up a phone, turning around), and identification of these behaviours requires the observation of the complete sequence of micro-movements [11], [12].

Improve Classification Result: Spectacularly trained with both feature learned by Vision Transformer and a time-sequence model BiLSTM, a system can resolve ambiguity in situations in which different actions were supposed to be similar visually yet distinct in time (e.g., talking to passenger and reaching behind) [6], [13].

During code implementation, ViT produces frame-wise features that serve as an input vector to a BiLSTM that captures temporal dynamics that are modelled by each behaviour category [3], [12]. The hybrid method makes the image analysis dynamic rather than just being written using behaviour recognition and makes the inattention detection system robust in a greater degree of use by reducing its vulnerability as an in-attending and blind vehicle observer in a real-life driving situation [11], [12].

II. PROPOSED VIT-BILSTM HYBRID ARCHITECTURE FOR DRIVER MONITORING

This paper suggests the use of a hybrid deep learning network that combines Vision Transformers (ViT) and Bidirectional Long Short-Term Memory (BiLSTM) networks to track driver behaviour well and find several types of inattention. This union takes advantage of the respective capabilities of spatial and temporal modelling to allow correct detection of the changeable driver activity with videos in time-varying series [3], [6], [12]. Architecture Overview:

1. Frame-wise Feature Extraction with ViT: The Frames of a video can be processed separately into a pre-trained Vision Transformer. ViT divides the input image into patches and uses multi-head self-attention to extract the contextual correlation between the visual portions-like hands or face of the driver or other items in the area [3], [10]. This enables the system to be spatially responsive to cues of interest in a dynamic manner of differing in-cabin situations [6], [11], [16].

2. BiLSTM-based Temporal Sequence Modelling of discovered ViT features: After extracting the ViT features, one can feed the output to BiLSTM layer that models time-dependence of spatial features [3], [12]. This is crucial to find behaviours occurring over several frames e.g. reaching, turning or playing with devices, where one-frame analysis would not be able to find [11], [12].

3. Classification Layer: The dataset final output of the BiLSTM network passes to the network through dense layers and a soft Max classifier to make an estimate of driver behaviour class. This allows recognition of multiple classes in a broad spectrum of varieties of inattention [6], [13], [16].

Key Advantages

• Spatiotemporal Learning: This means that following a union of the attention-driven spatial vision of ViT and the sequence modelling capabilities of BiLSTM, the system may find driver behaviours in the correctness and context [3], [6], [12].

• Scalability and Modularity: The architecture enables deliberate modular insertions/retrofits e.g., instead of the ViT, other transformer variants could be inserted in the same manner; more advanced temporal modelling (e.g., Transformers, or GRUs) could be inserted as well [3], [7], [10].

• Real-World Applicability: The framework is also quite suitable in being applied in embedded auto applications, particularly with respect to perfecting inference efficiency [7], [9], [10].

The presented hybrid ViT-BiLSTM algorithm shows highly effective results in addressing the problems of detection of inattention in the driver, which is central to the creation of a reliable, real-time system of monitoring the driver with a high level of safety and interpretability [3], [6], [11], [12].

III. DATASET CHARACTERISTICS AND CLASS IMBALANCE ISSUES

The labelled image data included in the Driver Inattention Detection Dataset employed in this paper denotes six behaviours of drivers namely Safe Driving, Dangerous Driving, Distracted, Drinking, Sleepy Driving and Yawn. The dataset, through the process of annotation was formed of 14,859 images, all with even resolution (360 x 640 x 3), split into training, validation and test sets [6], [11]. One of the most significant problems was the imbalance in the number of classes in the dataset, i.e., the Safe Driving class represented more than 41 percent of all the images, whereas such important inattention-related classes as Drinking, Yawn, and Sleepy Driving were highly underrepresented (each representing under 7 percent). Such skewed distribution may cause a bias in the model towards majority classes resulting in low generalization and low sensitivity in unsafe driving behaviour [1], [14], [15]. With this aim, specific data augmentation was conducted. It was synthetically augmented on specific underrepresented classes (Drinking, Yawn, Sleepy Driving, and a part of Distracted) as horizontal flips. This augmentation mechanism brought them more balanced representation to an extent that they become nearer to the powerful Safe Driving category but preserved the diversity of classes.

The goal of the distribution was to reduce the level of learning bias and enhance the part of the model that recognizes subtle cues of inattention [1], [6], [15]. Moreover, to generate data that would reflect real-world temporal dependencies, a synthetic sequence data set was created, a set forming 15-frame video-like clips. These were classified according to temporal trend in unsafe behaviour with 50 percent recorded as Unsafe (number of unsafe frames at consecutive frames of 4 or more) and 50 percent Safe (no run of 4 or more unsafe frames). This allowed creating a model, which not just classifies individual frames, but finds time series patterns showing increasing driver inattention [3], [12].

IV. NEED FOR FINE-GRAINED BEHAVIOURAL CLASSIFICATION

Customized driver checks systems tend to apply a binary or coarse-grained assessment-identifying only attentive and inattentive vehicles [11]. Nevertheless, this black and white type of classification cannot target the intricate continuum of distracted driving behaviour as performed by motorists in the real world. Such behaviours like drinking, yawning, texting, or sleepiness vary in visual expression not only in the profile of risk and time demands of the response [6], [11]. As an example, it is at times useful to make a soft alarm when yawning: this is an early sign of fatigue, and might necessitate a break, whereas hazardous driving, or distracting a driver a long time can just as well be a severe problem and would need prompt intervention [7], [11]. Therefore, it is discussed that a fine-grained behaviour classification and that such a system is paramount to allow adaptations of responding mechanisms in separate ways, so in the example the system can recognize minor infractions and major safety infarctions [6], [13]. In addition to that, it will enable the creation of more context-aware driver aid systems, as classifications are presented more finely. The system can seek to prioritise the interventions by understanding which form of inattention is present, record behaviour over time and personalise feedback by doing so [6], [14]. This granularity is particularly relevant in semi-autonomous environments, where cooperation between human and a machine led to a necessity to a prominent level of precision on what the driver is doing [8], [12]. In the given study, we underline the significance of such in-depth modelling of behaviour by using not only the frame-level annotations, but also a sequence-level temporal structure. It is through this dual method that not only the identification of certain unsafe behaviours could be detected but also its accumulation in time which is vital in predicting and preventing accidents foretime [3], [12].

Integration Potential with Advanced Driver Assistance Systems (ADAS)

Advanced Driver Assistance Systems (ADAS) have evolved greatly to enhance the safety of cars and features like the lane-keeping assist, adaptive cruise control, and collision avoidance functions have been integrated into the systems [7], [10]. Nonetheless, the technologies of modern ADAS mostly run on environmental information (e.g., road situation, traffic light) and use little internal indicators of driver behaviour [8], [11]. The usage of driver inattention detection within ADAS systems would add a human-oriented layer to it as the systems would not only be capable of reacting to the threats presented by other entities but also be able to observe and react to the risk-related factors associated with drivers [6], [13]. The suggested ViT-BiLSTM-based sequence analysis model designed to find temporal inattention patterns i.e. the analysis of 15-frame video sequences, may be fitted into ADAS systems as a real-time monitoring element [3], [12]. Its ability to find unsafe behaviour tendencies say, long distraction, or minor sleep breaks, or the build-up of drowsiness can activate contextual interventions which could be simple alerts to the driver, or even system over-ridden [7], [11]. When the system keeps tracking driver behaviour, it could guide adaptive safety systems. As an example, the ADAS may prohibit access to semi-autonomous functions, recommend a rest stop, or limit the speed when the driver is identified as distracted in repeated periods of time [6], [14]. Such integration leads to cooperative automation which entails the system making up where the human being falls short but keeps the agency of the user [8], [12]. In a higher autonomy car system, this kind of integration will be essential with respect to a transition-of-control situation, where an alert driver is needed before the vehicle passes their control [8], [12]. In this way, the proposed method will not only complement the existing ADAS systems but also go in the line with the future vision of human-machine co-driving ecosystems [6], [12].

Literature Survey

The recent improvement in transformer-based models has made remarkable impacts on the domain of driver's behaviour analysis and spatio-temporal vision tasks. Vision Transformer-Based Feature Extraction for Generalized Zero-Shot Learning was proposed by [17] based on a Vision Transformer (ViT) and an Attribute Attention Module (AAM) to increase attribute-aware feature extraction. The approach could improve zero-shot recognition results in terms of spatial accuracy without specifying the datasets used, but the computations costs are not mentioned. In their paper, [18] presented TLMViT that is a hybrid transfer learning pipeline that integrates ViT and transfer learning concepts in classifying plant leaf diseases on the Plant Village and wheat datasets. The model itself recorded validation accuracy of 98.81/99.86 by incorporating a four-stage pipeline with augmentation, transfer-based feature extractions, ViT refinement, and MLP classification but with considerable dependency on pre-trained weights. A dual-path ViT-based building extractor Build Former was set up by [19] based on the Massachusetts Building Dataset. A windowed self-attention mechanism was linear and had a wealth of spatial-global context merger that performed top iou of 75.74%, but memory consumption was a problem. A ViT-RNN platform to recognize dances through a video was suggested by [3]. The model offered 94.5 test accuracy on recognition of motion on user-generated video sequences, running at 30 FPS in real-time and consuming 2.7 GB of memory, using ViT to capture spatial features and RNN to employ temporal dependencies. A deep learning pipeline describing a LSTM and Inception v3 as an inattention and abnormal behaviour predictor was introduced by [14] on more than 120,000 samples. Mixup and SMOTE solved the class imbalance and provided weighted accuracies of 92.27 percent and 91.67 percent respectively but a high-quality input of sensors was necessary. Mou et al. (2023) [13] developed a CNN-Transformer two-channel network in detecting distraction based on multimodal data. Mid- point residual structures and bilevel optimization hyperparameter tuning provided higher accuracy but also presented excessive overhead to be useful in real-time. ViT-B_16 was fine-tuned on a dataset of 33,034 facial images on driver drowsiness detection [2]. The model was real-time unfriendly in terms of needing hardware support to run at 93 percent accuracy using a Raspberry Pi 4, clocking in at just 0.59 FPS.

By [9] made a proposal on ViT-DDD real-time ViT-based drowsiness detector that was evaluated on NTHU-DDD and UTA-RLDD. A 98.89 percent and 99.4 percent classification accuracy made the system to combine GSM, IR imaging, and touch of alert with the buzzer. Nonetheless, generalization has not been studied much about the real world. The BiLSTM-attention model with dilated CNNs in detecting distracted driving was presented by [12]. The model was trained using StateFarm and Drive&Act-Distracted data with the hyper-parameters tuned on StateFarm and trained using the Drive&Act-Distracted data, with the resulting accuracy of 95.84 and 97.89, respectively, but at a quicker convergence rate yet showing little testing under different lighting conditions. Erg Passs (2022) [8] suggested Vision Transformer without CNN and multilayer LSTM for Human Activity Recognition also on UCF50 and HMDB51. ViT-LSTM model did not only increase the accuracy by 0.944 and 1.414 percentages being occlusion and low-resolution conditions, but they also needed high-quality input frames. By [6] used a ViT model with transfer learning to detect driver distraction and showed that this model has stronger generalization ability in a limited environment, and it is not evaluated in practice. In turn [15] proposed CBAM-VGG16 which added convolutional block attention modules within a VGG-16 base so that better distraction classification could be achieved in AUCD2. This model was correct up to 98.65 percent, but it depended much on camera-specific views. By [20] proposed a multi-scale ViT based driver action detection system with the name, Stargazer. As evaluated on the AI City Challenge 2022, the model performed as top 2 on the sliding-window classification task, but it was uncommented how well it will run on non-curated data. According to [11] introduced ViT-DD, which is based on ViT and is semi-supervised and multitasking, detecting the driver distraction and emotion on SFDDD and AUCDD. Having an improvement in the accuracy of 6.5 and 0.9 percent, the model eased multitask learning but with high quality and annotation as well as triggering computational options. The large-scale VideoMaeV2 transformer backbone that is fine-tuned to Drive&Act is used in DRVMon-VM proposed by [21]. Multi-rate and powerful augmentation increased the performance by 7.34%, while training and deployment were still costly.

Methodology

In this part, the detailed methodological procedure that was used in the detection of driver inattention in the image sequences is described. The pipeline includes data preprocessing, generation of the sequence, construction of deep model architecture, training program and evaluation programs.

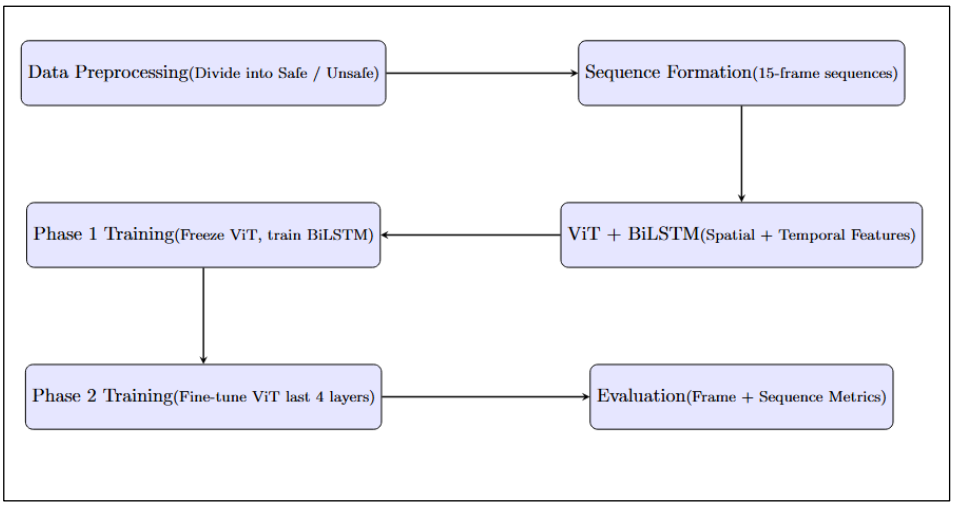


Figure 1: Driver Inattention Detection Pipeline Flowchart.
Source: Authors, (2026).

V. METHODOLOGY

V.1 DATA PREPROCESSING

V.1.1 Input Specification

The raw dataset used for this project was sourced from the Driver Inattention Detection Dataset, which consists of image frames extracted from in-car driving footage, each accompanied by bounding box annotations. Every annotation record includes the following elements:

- Filename of the image.
- Bounding box coordinates denoted as:

  (xmin, ymin, xmax, ymax)

Class label $c \in \{0,1,2,3,4,5\}$, corresponding to the six driver behaviour categories: Dangerous Driving (0), Distracted (1), Drinking (2), Safe Driving (3), Sleepy (4), and Yawn (5). These annotations served as the foundational input for categorizing behaviours and forming binary classification groups.

V.1.2 Safe vs Unsafe Labelling

Streamline the classification problem, the six driver behaviour classes were combined into two binary categories:

- Safe Driving: Safe ⟺ c=3
- Unsafe Driving: Unsafe ⟺ c∈ {0,1,2,4,5

This transformation ensured that the focus remained on detecting any deviation from normal (safe) driving behaviour.

V.1.3 Augmentation

Enrich the dataset and improve generalization, horizontal flipping was applied selectively to certain classes:

- A predefined set of classes, termed FLIP_CLASSES, was used to apply this augmentation.
- For the Distracted class (c=1) augmentation was capped at 1,040 samples to prevent overrepresentation in the training set, thereby mitigating class imbalance.

V.1.4 Output Generation

Post preprocessing, the image samples were organized into:

- /Safe/ and /Unsafe/ directories based on their binary label.
- For each image, corresponding annotations were also generated and stored. This structured directory layout enabled efficient data loading during training and inference stages.

V.2 SEQUENCE DATASET CONSTRUCTION

V.2.1 Sequence Sampling

Fixed-length frame sequences of size L= 15 were constructed to capture temporal context. Each sequence was labelled using the following rule:

- Unsafe sequence if it had four or more consecutive unsafe frames:
- $\exists\ i$ such that $\forall j \in [i, i+3]$, $Y_f(j) = 1 \Rightarrow Y_s = 1$therwise, the sequence was labelled as safe (Y_s=0).

V.2.2 Balanced Sampling Strategy

Avoid bias in the classifier:

- 10,000 sequences were synthesized: 5,000 safe and 5,000 unsafe.
- The selection process employed a stochastic sampling strategy using predefined weights: $Weights_{frame}$= [0.7,0.3]

Where 0.7 denotes the sampling probability for safe frames and 0.3 for unsafe frames. This enforced balance across the dataset.

V.2.3 Metadata Generation

For each sequence:

- Paths to all 15 frames were stored.
- Frame-level binary labels: Y_f∈ {0,1}[15.]
- Sequence-level binary label: Y_s∈ {0,1}

All this information was compiled into a CSV file, enabling efficient downstream use for training and evaluation.

V.3 MODEL ARCHITECTURE

V.3.1 Backbone: Vision Transformer (ViT)

The backbone model used was ViT-B/16, pre-trained on ImageNet. The final classification head was removed, and for each frame t, a feature vector was extracted:

$$F_t \in R^D, \quad D = 768, \quad t \in [1, L]$$

Thus, each frame in the sequence was represented by a high-dimensional embedding that captured rich spatial and semantic information.

V.3.2 Temporal Module: Bidirectional LSTM

The sequence of frame embeddings (F1, F2, FLwas passed into a BiLSTM, which captured bidirectional temporal dependencies:

$$H = \text{BiLSTM}(F_1, \ldots, F_L) \in R^{L \times 2H}$$

Here, H=256 denotes the hidden size of a single LSTM, and 2H=512 arises from concatenating outputs from both forward and backward directions.

V.3.3 Output Heads

Two output branches were defined:

- **Sequence-level prediction**:

$$\hat{s} = \sigma(W_s H_L + b_s) \in [0,1]$$

Where H_L is the final time-step output of the BiLSTM.

- **Frame-level predictions** for each time-step t:

$$\widehat{Y_f}(t) = \sigma\big(W_f H_t + b_f\big), \quad t = 1, \ldots, L$$

The sigmoid activation σ (·) maps logits into probability space. W_s, W_f and biases b_s, bf are trainable parameters.

V.4 TRAINING PROCEDURE

V.4.1 Optimization Strategy

Training was performed in **two stages**:

1. **Stage 1**: The ViT backbone was frozen. Only the BiLSTM and output heads were trained using AdamW optimizer with a learning rate: lr=10^{-3}
2. **Stage 2**: The last four layers of ViT were unfrozen and trained with differential learning rates:

$$\textit{ViT layers: } 5 \times 10^{-5}, \quad \textit{LSTM: } 1 \times 10^{-4}$$

V.4.2 Loss Function

The overall loss function combines sequence-level and frame-level binary cross-entropy losses:

$$\mathcal{L} = \mathcal{L}_{seq} + \alpha \cdot \mathcal{L}_{frame}$$

Where:

- $L_{seq} = \text{BCEWithLogits}(\hat{s}, Y_s)$
- $\mathcal{L}_{frame} = \frac{1}{L}\sum_{t=1}^{L} \text{BCEWithLogits}\left(\widehat{Y_f}(t), Y_f(t)\right)$
- α=0.5 balances the contributions of both losses.

V.4.3 Mixed Precision Training

Enhance training efficiency and reduce GPU memory usage, mixed precision training was used using torch.cuda.amp with the auto cast and GradScaler modules. This approach kept numerical stability while speeding up training.

V.5 EVALUATION AND METRICS

V.5.1 Frame and Sequence-Level Metrics

The model's predictive performance was evaluated at both the sequence and frame levels using the following metrics:

- Accuracy
- Precision
- Recall
- F1-score

For each metric, evaluations were computed separately for:

$$\text{Sequence-level: } \widehat{Y_s}, \quad \text{Frame-level: } \widehat{Y_f}(t)$$

V.5.2 Confusion Matrices and Classification Reports

Detailed confusion matrices and classification reports were generated using the sklearn. metrics module. These reports provided insight into class-wise performance and model bias.

V.6 INFERENCE AND VISUALIZATION

V.6.1 Model Inference

During inference, each input sequence of 15 frames was passed through the full ViT-BiLSTM pipeline to produce:

- A **sequence-level prediction**:

$$\widehat{Y_s} = \text{Probability that sequence is unsafe}$$

- **Frame-wise predictions**:

$$\widehat{Y_f}(t), \quad t = 1, \ldots, 15$$

These outputs enabled both granular and high-level decision-making.

V.6.2 Grad-CAM Analysis

For interpretability, Grad-CAM was applied on the attention maps of the ViT to visualize which regions contributed most to predictions—especially helpful in understanding decisions on unsafe frames.

V.6.3 Temporal Plots

Visualization tools were developed to analyse:

- Prediction trends across frames
- Activation patterns of LSTM gates (input, forget, output)
- Heatmaps of hidden states H_t
- Dimensionality-reduced projections of LSTM outputs using t-SNE and PCA

These plots revealed temporal dynamics and model focus patterns.

V.6.4 Unsafe Run Highlighting

For enhanced explainability, sequences that had four or more predicted unsafe frames were automatically highlighted. These sequences were saved with visual overlays for error analysis and behavioural pattern recognition.

VI. RESULTS AND DISCUSSION

Table 1: Epoch Information of Phase-1.

Epoch	Train Loss	Train Seq Acc	Train Frame Acc	Train Seq F1	Val Loss	Val Seq Acc	Val Frame Acc	Val Seq F1
1	0.7378	0.7119	0.8384	0.7145	0.5887	0.7969	0.8969	0.7760
3	0.4354	0.8544	0.9263	0.8530	0.4343	0.8462	0.9339	0.8585
5	0.3325	0.8956	0.9441	0.8961	0.4016	0.8806	0.9330	0.8868
7	0.2910	0.9089	0.9519	0.9087	0.3160	0.8944	0.9513	0.8939
10	0.2213	0.9359	0.9599	0.9357	0.3010	0.9050	0.9570	0.9014

Source: Authors, (2026).

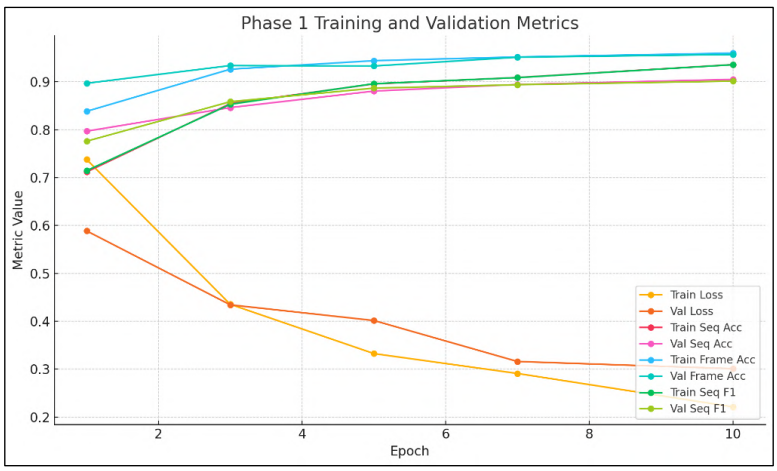


Figure 2: Phase 1 Training and Validation Metrics.
Source: Authors, (2026).

Table 1, Figure 2 gives a summary of the performance measures training and validation concerning the selected epochs (1, 3, 5, 7, and 10) of Phase 1 of the training. As can be seen, the model has monotone gains in all measures as time goes by. It follows that the training loss reduces dramatically to 0.2213 at Epoch 10, as compared to the training loss of 0.7378 at Epoch 1 which shows that the learning objective was successfully optimized. In line with this, the accuracy of the sequence level increases to 93. 59 percent with a frame-level accuracy that rises to 95. 99 percent. Validation performance is also similar with the F1-score of each sequence reaching 0.9014 at Epoch 10 as compared to the initial score of 0.7760. Those findings indicate that the model extrapolates on unseen validation data early in training, before the Phase 2 training on the Vision Transformer (ViT) backbone gains.

Table 2: Epoch Information of Phase-2.

Epoch	Train Loss	Train Seq Acc	Train Frame Acc	Train Seq F1	Val Loss	Val Seq Acc	Val Frame Acc	Val Seq F1
1	0.1589	0.9552	0.9695	0.9552	0.2486	0.9294	0.9676	0.9283
5	0.1126	0.9722	0.9743	0.9722	0.2344	0.9356	0.9706	0.9355
10	0.0939	0.9772	0.9760	0.9772	0.2295	0.9381	0.9720	0.9382
15	0.0718	0.9853	0.9787	0.9853	0.2467	0.9381	0.9730	0.9382
20	0.0572	0.9900	0.9809	0.9900	0.2432	0.9431	0.9776	0.9424

Source: Authors, (2026).

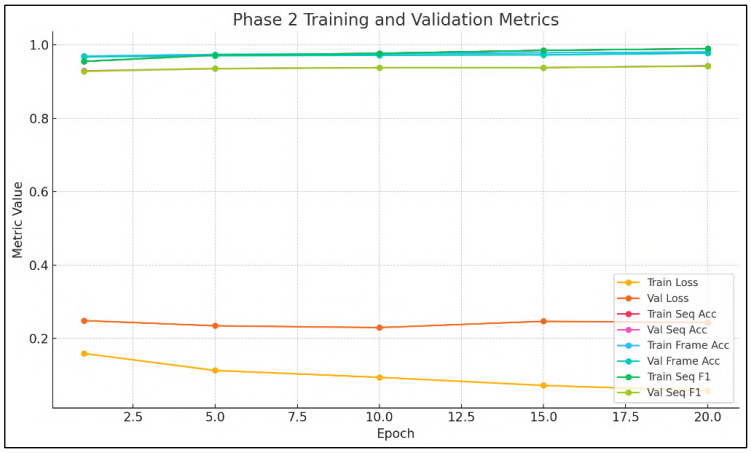


Figure 3: Phase 2 Training and Validation Metrics.
Source: Authors, (2026).

Table 2 and Figure 3 showcases the results of fine-threshold performance in the second-stage training where the four final layers of Vision Transformer (ViT) were released and used with a reduced learning rate. As demonstrated in the graph, the model is still gaining strength both in the training and validation scores. Training loss indicates the loss at every training occurrence, and this takes the value of 0.1589 at Epoch 1 and 0.0572 at Epoch 20 after training. At the same time, the accuracy of the training sequence and the F1-score are 99.00 and 94.31 percent (accuracy) and 0.9424 (F1-score), respectively, regarding the validation sequence. The performance on the frame-level is also consistent, and one achieves a 97.76% accuracy on the validation set. These findings indicate the advantage of progressive training, with the first stage of feature learning proceeded by a fine-tuning step to optimize generalization. This sort of positive trend in performance is graphically explained in figure 3, which proves that the model has converged and that it remains robust in both levels of prediction.

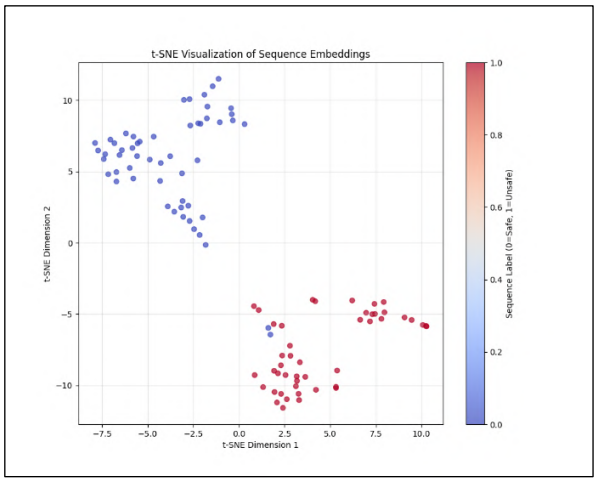


Figure 4: t-SNE Visualization of Sequence Embeddings.
Source: Authors, (2026).

Figure 4 represents the visualization of the high-dimensional sequence embedding projected into two dimensions resulting in a t-SNE visualization. The 15-frames sequence that is encoded with the ViT-BiLSTM model is one point. The blue ones represent sequences labelled Safe (label = 0) and red points represent Unsafe (label = 1). The strong distinction of the two clusters indicates the ability of the model to learn active discriminative temporal-spatial representations. This division proves that hybrid architecture successfully includes the encoding of safety-based contextual elements, which enables effective classification of the driver's behavior at the level of sequence.

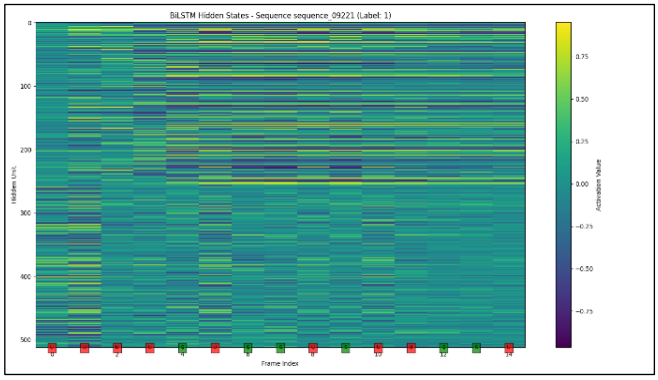


Figure 5: BiLSTM Hidden State Heatmap for Sequence 09221 (Label: Unsafe).
Source: Authors, (2026).

Figure 5 heatmap shows the activations of the hidden state of the BiLSTM layer of all 15 frames of one of the unsafe driving sequences. Every row is out of one of the hidden units (t=512 in 2-layer bidirectional LSTM with the hidden size of 256), and every column is a frame index. The activation value is encoded by color intensity that means that warmer (yellow) colors indicate stronger activations and cooler (purple) colors indicate suppression. The lower axis points out expected frame labels (correct versus incorrect, green and red respectively). The regular fluctuation in frames represents the dynamicity of its attention to time context particularly on unsafe shift, a factor which supports the capacity of the model to trace transformation of behavioral cues on driving conditions.

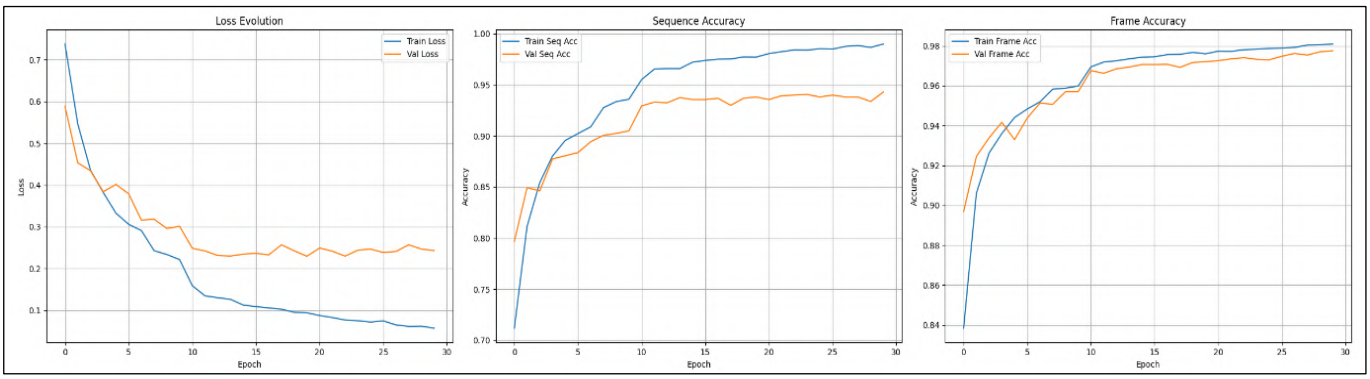


Figure 6: Training and Validation Trends for Loss, Sequence Accuracy, and Frame Accuracy.
Source: Authors, (2026).

Figure 6 illustrates the trend of major metrics in 30 epochs. The training and validation loss decreases in the left panel quickly after the first 10 epochs and levels off-which is a sign of convergence. The middle graph follows the sequence-level accuracy, which steadily increases and gets saturated at approximately 99 percent on the training sample and 94 percent on the validating sample. The right panel emphasizes the accuracy at the frame-level with steady improvement through epochs with a maximum of more than 98% accuracy during training and validation. The similarity of the training and validation curves of all panels shows the lack of overfitting and proves that the model has a prominent level of generalization.

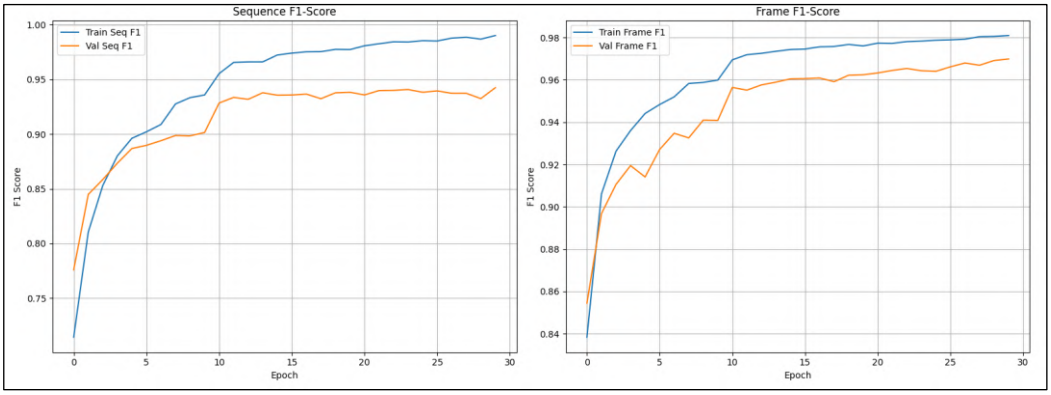


Figure 7: Sequence-Level and Frame-Level F1-Score Trends During Training.
Source: Authors, (2026).

The development of F1-scores is provided in Figure7 resulting in 30 training epochs. On the left subplot, we have the sequence-level F1-scores of the training and validation sets, with the training curve monotonically approaches 0.99 and validation staying at 0.94-0.95, which implies the quality of the generalization to be excellent. The correct subplot presents the frame-level F1-scores, which show a general increase of the values under different epochs, with the final validation F1-scores of 0.97. The coincidence of the training and validation trends in each of the two tasks show a practical learning scenario, devoid of overfitting. These findings support the accuracy rate the model has in classifying patterns of a sequence and individual frames of driver behaviour across time.

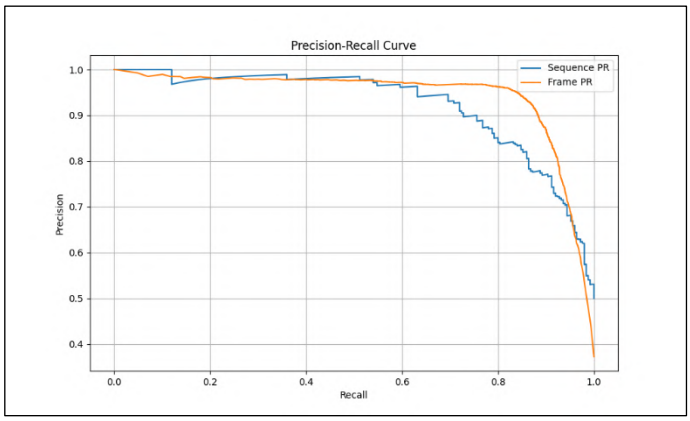


Figure 8: Precision-Recall (PR) Curves for Sequence and Frame-Level Predictions.
Source: Authors, (2026).

This figure compares the precision-recall performance of the model at both sequence and frame levels. The blue curve corresponds to sequence-level predictions, while the orange curve is frame-level predictions. Both curves keep high precision across a wide range of recall values, showing strong discriminative capability. The frame-level PR curve stays smoother and keeps precision above 0.9 until near-perfect recall, suggesting the model effectively balances sensitivity and specificity at finer temporal granularity. In contrast, the sequence-level PR curve shows steeper drops near high recall, reflecting occasional uncertainty in aggregated sequence decisions. These curves confirm the model's robustness in high-stakes driver behaviour detection, particularly in minimizing false positives while keeping recall.

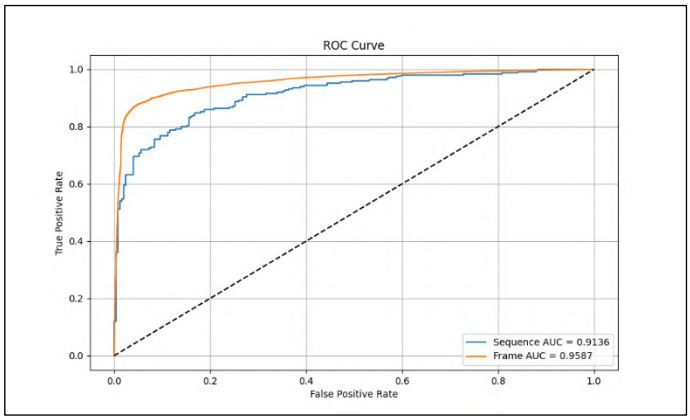


Figure 9: ROC Curves for Sequence and Frame-Level Predictions.
Source: Authors, (2026).

Figure-9 displays the Receiver Operating Characteristic (ROC) curves for both sequence-level and frame-level classification tasks. The blue curve represents the sequence-level performance with an Area Under the Curve (AUC) of 0.9136, while the orange curve illustrates the frame-level performance with a superior AUC of 0.9587. Both curves rise well above the diagonal line of random chance (dashed), confirming strong discriminative ability of the model. The higher AUC for frame-level predictions suggests the model is particularly effective at capturing localized unsafe behavior. Overall, these ROC curves provide strong evidence of the model's reliability in distinguishing between safe and unsafe driving behaviors across temporal resolutions.

Table 3: Frame Classification Report.

	precision	recall	f1-score	support
Safe	0.98	0.99	0.98	15004
Unsafe	0.98	0.96	0.97	8996
accuracy			0.98	24000
macro avg	0.98	0.97	0.98	24000
weighted avg	0.98	0.98	0.98	24000

Source: Authors, (2026).

This can be statistically summarized as in Table 3. The model registers an overall testing accuracy on 24,000 frames as 98 percent. Precision, recall and F1-score remain high in both classes. In the Safe class, there are 0.98 precision, 0.99 recall, and F1-score, recorded in the model. In the case of Unsafe class, it yields 0.98 precision, 0.96 recall, and 0.97 F1- score. Its macro-average F1-score of 0.98 and balanced class support shows that the model is not susceptible to overfit fine-grained unsafe behaviors at the expense of the safe frames. Such measures show that the model keeps a high level of balance, with false positives and false negatives, at frame level.

Table 4: Sequence Classification Report.

	precision	recall	f1-score	support
Safe	0.93	0.96	0.94	800
Unsafe	0.96	0.93	0.94	800
accuracy			0.94	1600
macro avg	0.94	0.94	0.94	1600
weighted avg	0.94	0.94	0.94	1600

Source: Authors, (2026).

The results of the classification within the sequence level are provided in Table 4. The model reaches 94% of accuracy in the overall level of defining the safe and unsafe driving sequences. In the case of Safe class, it retrieves precision of 0.93, recall of 0.96, F1-score of 0.94 while in the Unsafe class the accuracy of 0.96, recall of 0.93, F1-score of 0.94 are achieved. The average F1-score over the macros and weighted average F1-score equalled 0.94 and there is no under- or overfitting of either of the two classes. The above findings support the fact that the model can effectively reflect temporal dependencies and provide stable forecasts on the level of a sequence, which is an essential feature when detecting driver inattention in real-world settings.

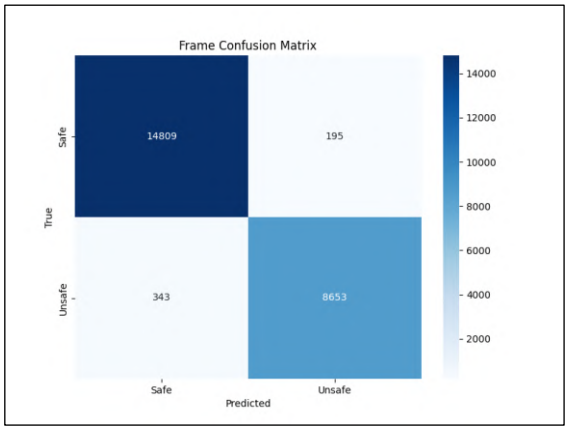


Figure 10: Frame-Level Confusion Matrix.
Source: Authors, (2026).

The figure 10 confusion matrix shows how well the frame level classifier can distinguish between a frame that is considered safe or unsafe in the way that it drives. The model was able to discriminate 14,809 safe and 8,653 unsafe frames correctly out of 15,004 safe and 8,996 unsafe frames that is a good discrimination capacity. The false positive rate (safe frames classified as unsafe frames) and false negative rate (unsafe frames classified as safe frames) was 195 and 343 respectively. This finding confirms the high precision and recall found in the model as said in the classification indicators and this confirms the usefulness of the model in finding small frame-wise changes in behaviour during real-life situations about driving.

Sequence Confusion Matrix

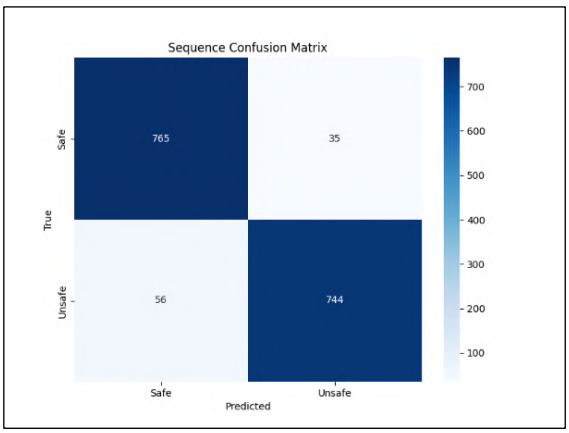


Figure 11: Sequence-Level Confusion Matrix.
Source: Authors, (2026).

The results of the classification on the sequence level are depicted in Figure 11 confusion matrix which covers the skill in which the model finds the entire driving sequence as either safe or unsafe. The misclassification was done on 35 and 765 were correctly classified out of 800 safe ones. In the same way, among the 800 unsafe sequences, the model found and labelled 744 as unsafe and only 56 were labelled safe incorrectly. These findings produce a significant level of overall accuracy (94%) and any indications that balanced performances pertain in both classes. The low false positives and negative rates further testify the strength of the model in temporal behavioural capture that is essential in generating sequence-level accuracy in driver inattention identification.



Figure 12: Frame-Level Predictions for a Correctly Classified Safe Sequence.
Source: Authors, (2026).

The visualization shows an entire 15-frame series (Sequence ID: sequence_00461) that is labelled Safe and predicted by the model as Safe with a score of 0.0001 at the sequence level. The ground truth label in each frame and the frame-level prediction of the model is written in each frame. Although small unsafe frame predictions are present (e.g. Frames 3 and 4), the aggregate prediction correlates with Safe majority, which proves that the model is robust to the occasional temporal noise. The stability in prediction in most of the frames and the correct sequence-level decision illustrate the strong completion of the ViT-BiLSTM architecture in the integration of temporal evidence to find the behaviour of the driver.



Figure 13: Visual Comparison of Multiple Sequences with Frame-Level Predictions.
Source: Authors, (2026).

This compound identification presents a pair-wise immersion of some 15 modelling mirrors, each with their grounds truths marked (A) and models predicted (P) per body. The correct predictions are marked green, and the misclassifications are marked red. Sequences include Safe and Unsafe, and they can be directly examined to check the model behaviour under various conditions. Remarkably, frames involving driver distract by using phones or being inattentive are usually properly found, while the occurrence of inconsistent predictions of some rare cases occurs in borderline or ambiguous frames. This scheme allows us to evaluate in a qualitative way the coherence over time of the ViT-BiLSTM model, pointing out its advantages and defects in the feeling of the dynamics of the driver behaviours.

Table 5: Sequence-Level Prediction Summary for Selected Samples.

Sequence ID	Type	Actual Seq Label	Pred Seq Label	Seq Prob	Frame Accuracy	Correct Prediction
sequence_00461	Safe	Safe	Safe	0.000114204	100.00%	TRUE
sequence_00904	Safe	Safe	Safe	0.000201289	93.33%	TRUE
sequence_09221	Unsafe	Unsafe	Unsafe	0.980998099	93.33%	TRUE
sequence_08716	Unsafe	Unsafe	Unsafe	0.999279559	100.00%	TRUE

Source: Authors, (2026).

In this table there is a brief overview of two Safe and two Unsafe sequences with their model predictions. Each sequence is labeled with its ID, ground truth and predicted labels of the sequences as well as the probability value at the sequence level- output of the model model probability on the Unsafe class, both frame-level and sequnce-level accuracy labels and true annotation with either correct or incorrect tag at thesequence level. It achieved a perfect score at the sequence level with the confidence of the predicted probabilities being high. In Safe sequences (such as sequence_00461), predicted probabilities were also significantly low meaning that the model was strongly certain of the lack of unsafe behaviour. Conversely, the Unsafe sequences (ex. sequence_08716) got almost definite Unsafe probability (>0.98), which illustrates the power of the model in notes hazardous states. Frame-level accuracy was more than 93% in each of them establishing fine-grained temporal consistency of the model as a way to classify individual frames, when dealing with mild variability. Such a table supplements the visual illustrations and highlights the strengths of this model when it comes to localized and aggregated contexts of predicting outcomes.

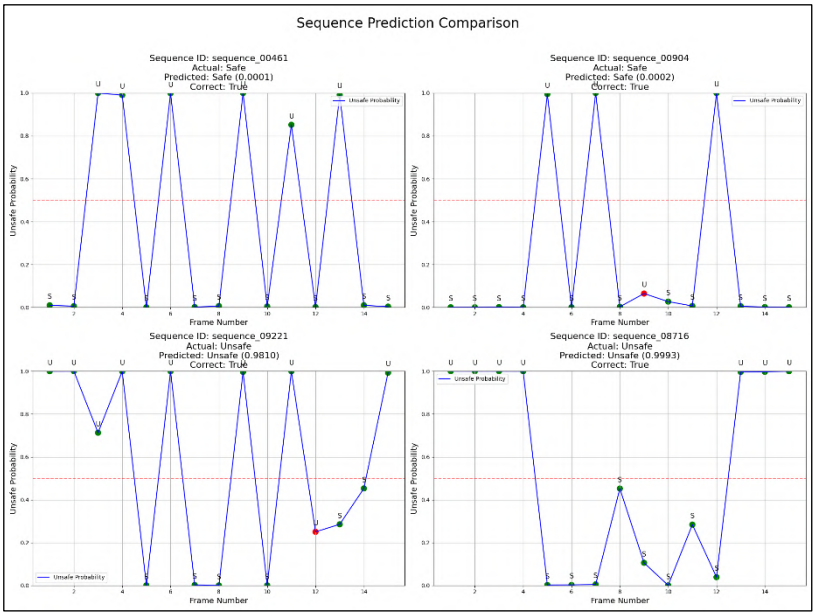


Figure 14: Frame-Level Unsafe Probability Trends for Sample Sequences.
Source: Authors, (2026).

It is proved in the figure, that frame-wise Unsafe probability scores as predicted by ViT-BiLSTM were assessed in four sample sequences (2 Safe: sequence_00461, sequence_00904; 2 Unsafe: sequence_09221, sequence_08716). Green and red points denote the actual and the predicted label on each frame respectively, and the blue line follows the probability that the model has assigned to the frame being Unsafe. A classification threshold is shown at 0.5 in the form of a red dashed horizontal line. The Safe sequences (top row) correctly do not get probabilities above the Unsafe level before the sequence reaches the actual unsafe label (e.g. frame 3 or 11 in sequence_00461) in most of the frames and therefore effectively preserves temporal context. On the other hand, the probabilities of Unsafe, in Unsafe sequences (bottom row), are clearly robust to behavioural cues with critical frames always having high Unsafe probabilities (e.g., frame 1-3 in sequence_09221). This number supports the ability of the model to make both frame-level risk predictions, as well as temporal distribution of risks which is essential to make correct sequence-level classification.

Discussion

The suggested ViT-BiLSTM model is effective in predicting the issue of driver inattention as it uses both space and time dynamics in the sequential images data. Table 1 shows an increasing trend of sequence and frame-level accuracy, F1-scores and loss at epochs during Phase 1 training. In Phase 2 (Table 2), the same complementary trends are kept, and small optimisations continue to take place with ViT layers. The last model gets the sequence classifications accuracy of 94 and the frame-by-frame accuracy of 98, as indicated in Tables 3 and 4. The frame-level and sequence-level classification reports (Figures 7 and 8) also conclude high precisions, recalls and balanced F1-scores among Safe and Unsafe classes, which implies strong generalization. Misclassification is also minimally confirmed by confusion matrices in Figures 10 and 11, showing that this model has a lot of discrimination on the two classes. Visual confirmation of the ability of the model to temporally and spatially localise unsafe behaviours may be reached by qualitative results in Figures 9 and 12. Figure 9 (individual frame predictions in sequences) display proper labels of individual frames despite minor unsafe frames. Figure 12 further shows temporal predictions in a representative sequence, and correct curves of predicting the probability becomes unsafe condition are presented, in line with the correct labels.

VII. CONCLUSION

Identification of driver inattention is a long-time task in computer vision and intelligent transportation systems. Earlier studies in the same field have concentrated on single-frame classification as much as handcrafted features or light CNN-based ones do not bear much thought with respect to the temporal consistency in driver behaviour. Most of the earlier methods are either based on the detection of objects of mobile devices or estimation of the head pose, which are not always satisfactory in detecting the less noticeable and developing with time unsafe behaviours like drowsiness, distraction, or momentary inattention.

Although other models have experimented with RNNs, or CNN-LSTM hybrids to model time, they consistently use low-resolution input, limited training schedules, or work without the benefit of enjoying modern transformer-based architectures and so have poor generalisation performance and are difficult to interpret. Conversely, the problem is discussed in our work in a more complete and methodological novel manner. The proposed hybrid ViT-BiLSTM architecture has the benefits of incorporate representational power of the Vision Transformer coupled with bidirectionality to model time by bidirectional LSTMs. ViT module learns picturesque phenomena in every frame, and BiLSTM module learns critical inter-frame relationships that help to elaborate between safeness and unsafe sequences. The architecture is a dual-headed one, with the ability to predict both frame-level and sequence-level safety labels, a characteristic that other attempts do not provide largely. In addition, our training approach uses a two-stage training scheme where we freeze the ViT layers in a stabilization step and then use different learning rates between each of the four transformer blocks in the unfreezing step and greatly enhance the performance without harming the cost of training. The same goes with our data pipeline which entails cropping of each image by using bounding boxes, augmentation on a class-balanced level and frame label sampling using a probabilistic approach to create robust and balanced 15-frame sequences. This deep-thinking data-engineering is a pillar-strength that is commonly underrated or forgotten in earlier research. The outcomes are self-explanatory. Our model has a frame-level accuracy of 98% and F1-score of 0.98 that is better than most ultramodern benchmarks that mostly flatline around 90-93%. At the sequence level we achieve 94% accuracy and 0.94 F1-score, with a confusion matrix proving impressively confident classes separation. ROC-AUC is more than 0.95 at both levels of prediction.

Not only are these measures of performance superior, as they are numerically, but these measures also remained constant throughout both the unsafe and safe classes, showing that the model has an unbiased sensitivity and specificity. In addition to quantitative findings, our method provides good qualitative interpretation. The visualization of predicted sequences, frame-wise probability curves, and spatial-temporal overlay shows how a model makes predictions and compares their predictions with ground truth very accurately. Our pipeline would contrast to numerous previously discussed models which behave like a black box in that one cannot find substantial information on what frames led to unsafe predictions and take proper action in application to the world. The study contributes to the development of driver inattention detection by principled comprehensively combines transformer-based reasoning and sequence modelling. Having a precision that breaks records, ViT-BiLSTM architecture, in combination with a thoughtful training and data strategy, provides a new level of performance and interpretability. It changes a frame-heavy task, turning it into a reliable sequence-aware detection pipeline, which will lead to less dangerous and smarter driver seeing systems. In the future a further improvement in temporal granularity may be possible with attention-based recurrent modules or multimodal signals like gaze estimation or biometric cues. Nevertheless, our findings lay an adequately sufficient ground on the future of reliable, real-time driver inattention detection in which ultramodern deep learning is employed.

VIII. AUTHOR CONTRIBUTIONS

Conceptualisation: Devanaboyina Manikanta Teja, P L Kishan Kumar Reddy.
Methodology: Devanaboyina Manikanta Teja, P L Kishan Kumar Reddy.
Investigation: Devanaboyina Manikanta Teja, P L Kishan Kumar Reddy.
Discussion of results: Devanaboyina Manikanta Teja, P L Kishan Kumar Reddy.
Writing – Original Draft: Devanaboyina Manikanta Teja, P L Kishan Kumar Reddy.
Writing – Review and Editing: Devanaboyina Manikanta Teja, P L Kishan Kumar Reddy.
Resources: Devanaboyina Manikanta Teja, P L Kishan Kumar Reddy.
Supervision: Devanaboyina Manikanta Teja, P L Kishan Kumar Reddy.
Approval of the final text: Devanaboyina Manikanta Teja, P L Kishan Kumar Reddy.

IX. REFERENCES

[1] Abosaq, H. A., Ramzan, M., Althobiani, F., Abid, A., Aamir, K. M., Abdushkour, H., Irfan, M., Gommosani, M. E., Ghonaim, S. M., Shamji, V. R., & Rahman, S. (2022). Unusual Driver Behaviour Detection in Videos Using Deep Learning Models. Sensors 2023, Vol. 23, Page 311, 23(1), 311. https://doi.org/10.3390/S23010311.

[2] Bin Mohamad Azmi, M. M., & Kamaru Zaman, F. H. (2024). Driver Drowsiness Detection Using Vision Transformer. 14th IEEE Symposium on Computer Applications and Industrial Electronics, ISCAIE 2024, 329–336. https://doi.org/10.1109/ISCAIE61308.2024.10576317.

[3] Borah, A. R., Hameed, A. A., Thethi, H. P., Prasanna, J. L., Sangeetha, A., & Gautam, D. D. (2025). ViT and RNN for Temporal and Spatial Analysis in Video Sequences. 2025 International Conference on Intelligent Control, Computing and Communications, IC3 2025, 651–656. https://doi.org/10.1109/IC363308.2025.10957553.

[4] Chen, H., Cui, J., Zhang, Y., & Zhang, Y. (2022). VIT and Bi-LSTM for Micro-Expressions Recognition. 2022 IEEE 5th International Conference on Information Systems and Computer Aided Education, ICISCAE 2022, 946–951. https://doi.org/10.1109/ICISCAE55891.2022.9927522.

[5] Dang Thi, P., Nguyen Dang, H. T., Doan Huu, P., & Dau Sy, H. (2024). Video classification for efficient data storage using deep learning: a comparison of sequential and simultaneous feature extraction methods. Multimedia Tools and Applications, 84(6), 3071–3094. https://doi.org/10.1007/S11042-024-20549-5/TABLES/6.

[6] Fang, Z., Chen, J., Wang, J., Wang, Z., Liu, N., & Yin, G. (2022). Driver Distraction Behaviour Detection using a Vision Transformer Model based on Transfer Learning Strategy. 2022 6th CAA International Conference on Vehicular Control and Intelligence, CVCI 2022. https://doi.org/10.1109/CVCI56766.2022.9965124.

[7] Hassan, O. F., Ibrahim, A. F., Gomaa, A., Makhlouf, M. A., & Hafiz, B. (2025). Real-time driver drowsiness detection using transformer architectures: a novel deep learning approach. Scientific Reports, 15(1), 1–33. https://doi.org/10.1038/S41598-025-02111-X;SUBJMETA=1042,117,639,705;KWRD=COMPUTATIONAL+SCIENCE,COMPUTER+SCIENCE.

[8] Hussain, A., Hussain, T., Ullah, W., & Baik, S. W. (2022). Vision Transformer and Deep Sequence Learning for Human Activity Recognition in Surveillance Videos. Computational Intelligence and Neuroscience, 2022(1), 3454167. https://doi.org/10.1155/2022/3454167.

[9] Jarndal, A., Tawfik, H., Siam, A. I., Alsyouf, I., & Cheaitou, A. (2024). A Real-Time Vision Transformers-based System for Enhanced Driver Drowsiness Detection and Vehicle Safety. IEEE Access. https://doi.org/10.1109/ACCESS.2024.3522111.

[10] Li, Z., Zhao, X., Wu, F., Chen, D., & Wang, C. (2024). A Lightweight and Efficient Distracted Driver Detection Model Fusing Convolutional Neural Network and Vision Transformer. IEEE Transactions on Intelligent Transportation Systems, 1–17. https://doi.org/10.1109/TITS.2024.3447041

[11] Ma, Y., & Wang, Z. (2024). ViT-DD: Multi-Task Vision Transformer for Semi-Supervised Driver Distraction Detection. IEEE Intelligent Vehicles Symposium, Proceedings, 417–423. https://doi.org/10.1109/IV55156.2024.10588802.

[12] Wang, Z., & Yao, L. (2024). Recongnition of Distracted Driving Behaviour Based on Improved Bi-LSTM Model and Attention Mechanism. IEEE Access, 12, 67711–67725. https://doi.org/10.1109/ACCESS.2024.3399789.

[13] Mou, L., Chang, J., Zhou, C., Zhao, Y., Ma, N., Yin, B., Jain, R., & Gao, W. (2023). Multimodal driver distraction detection using dual-channel network of CNN and Transformer. Expert Systems with Applications, 234, 121066. https://doi.org/10.1016/J.ESWA.2023.121066.

[14] Jiang, L., Xie, W., Zhang, D., & Gu, T. (2022). Smart Diagnosis: Deep Learning Boosted Driver Inattention Detection and Abnormal Driving Prediction. IEEE Internet of Things Journal, 9(6), 4076–4089. https://doi.org/10.1109/JIOT.2021.3103852.

[15] Praharsha, C. H., & Poulose, A. (2024). CBAM VGG16: An efficient driver distraction classification using CBAM embedded VGG16 architecture. Computers in Biology and Medicine, 180, 108945. https://doi.org/10.1016/J.COMPBIOMED.2024.108945.

[16] Tatsunami, Y., & Taki, M. (2022). Sequencer: Deep LSTM for Image Classification. Advances in Neural Information Processing Systems, 35, 38204–38217. https://github.com/okojoalg/sequencer.

[17] Kim, J., Shim, K., Kim, J., & Shim, B. (2023). Vision Transformer-Based Feature Extraction for Generalized Zero-Shot Learning. ICASSP, IEEE International Conference on Acoustics, Speech and Signal Processing - Proceedings, 2023-June. https://doi.org/10.1109/ICASSP49357.2023.10095217.

[18] Tabbakh, A., & Barpanda, S. S. (2023). A Deep Features Extraction Model Based on the Transfer Learning Model and Vision Transformer “TLMViT” for Plant Disease Classification. IEEE Access, 11, 45377–45392. https://doi.org/10.1109/ACCESS.2023.3273317.

[19] Wang, L., Fang, S., Meng, X., & Li, R. (2022). Building Extraction With Vision Transformer. IEEE Transactions on Geoscience and Remote Sensing, 60. https://doi.org/10.1109/TGRS.2022.3186634.

[20] Liang, J., Zhu, H., Zhang, E., Zhang, J., & Lab, T. Y. (2022). Stargazer: A Transformer-Based Driver Action Detection System for Intelligent Transportation (pp. 3160–3167). https://github.com/JunweiLiang/aicity_action.

[21] Pizarro, R., Bergasa, L. M., Baumela, L., Buenaposada, J. M., & Barea, R. (2024). DRVMon-VM: Distracted driver recognition using large pre-trained video transformers. IEEE Intelligent Vehicles Symposium, Proceedings, 1901–1906. https://doi.org/10.1109/IV55156.2024.10588412.

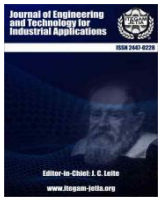
Journal of Engineering and Technology for Industrial Applications

ISSN ONLINE: 2447-0228

ITEGAM-JETIA

Manaus, v.12 n.60, p.294-298, July/August, 2026.

DOI: https://doi.org/10.5935/jetia.v12i60.3775



RESEARCH ARTICLE OPEN ACCESS

ENERGY-EFFICIENT TINYML-BASED FALL DETECTION FOR WEARBLE HEALTHCARE DEVICES

Prathap*[1], Hibafathima H[2], Sufaira Shamsudeen[3] , Selin M[4], Julie M David[5] and Jihad Aboobaker[6]

[1, 2, 3, 4, 5, 6]Department of Computer Applications, MES College Marampally, Aluva, Ernakulum, Kerala, India.

[1]http://orcid.org/0009-0001-7146-908X, [2]https://orcid.org/0009-0006-4124-9621, [3]https://orcid.org/0009-0003-3783-9117
[3]https://orcid.org/0000-0002-9404-4092, [4]https://orcid.org/0009-0000-9844-7174, [6]https://orcid.org/0009-0009-0720-4018

Email:*prathapb2004@gmail.com, hf884474@gmail.com, sufaira@mesmarampally.org, selin.m.a@gmail.com, juliemeldhose@gmail.com, jihadabubacker@gmail.com.

ARTICLE INFO

Article History
Received: February 22, 2026
Reviewed: June 9, 2026
Accepted: July 9, 2026
Published: July 31, 2026

Keywords:
TinyML,
Fall Detection,
Wearable Device,
Edge AI,
Arduino.

ABSTRACT

Falls and irregular heart rhythms are the main causes of injury among kids and the elderly, always overwhelming healthcare systems, and thus making privacy-aware, real-time monitoring a necessity. This work unveils a TinyML wrist-worn prototype based on Arduino Nano 33 BLE Sense, which combines the MPU6050 IMU for motion-based fall detection and activity (walking, sitting, running, lying) recognition with the MAX30102 PPG for heartbeat, SpO2, and HRV anomaly detection over generations. The device, tested on 7 subjects (3 children 8-12 years, 2 adults 25-40, and 2 seniors 65-75) for 140 real-life sequences in a lab in Kerala, uses Butterworth-filtered data, 56 temporal features extracted from 256-sample windows, and the optimized hybrid CNN-LSTM model (65% structured pruning, 8-bit QAT) to perform inference on the edge under 217KB flash. Dual-threshold triggering (fall confidence >0.9 plus HR anomalies or SpO2<92%) allows BLE alerts within 100ms to caregiver apps, and cancellation via 30s haptic/button helps reduce the false alarms. Field experiments demonstrated the device performance with 94.3% accuracy, 0.95 fall F1-score, 38ms latency, 0.7mW power, and 2.1% false positives, showing a significant improvement of 15% F1 when compared against unimodal baselines, while being fully processed on the edge, GDPR-compliant, and with a multi-day battery life, the device is ready for wide deployment in homes, schools, and care facilities. This work is a step forward in TinyML across demographics, thus opening the gate to multimodal extensions such as cry detection.

Copyright ©2026 by authors and Galileo Institute of Technology and Education of the Amazon (ITEGAM). This work is licensed under the Creative Commons Attribution International License (CC BY 4.0).

I. INTRODUCTION

Falls and heart rate problems are major health concerns that mainly affect children and the elderly. They lead to more than 37 million severe cases globally each year. Such conditions often result in hip fractures, head trauma, hospital admissions, and huge economic losses measured in hundreds of billions of dollars. According to the World Health Organization (WHO), these incidents heavily burden health care systems especially when they occur in locations such as homes, schools, and rural areas without an adult present, contact with medical help is sometimes delayed or not made at all. Traditional wearables depend on the cloud for processing which entails higher latency (>1s), possible privacy issues as biometrics are uploaded, and also loss of connection in case of weak-signal areas. The existing scientific works about TinyML (Tiny Machine Learning) fall detection are basically confined to the elderly solutions like TinyCNN classifiers on IMU data or SVM-based inertial models, however, they lack a focus on children and multimodal fusion with vital signs. Research works, for instance, Lara et al.(2023) manage to realize a lightweight CNN inference; meanwhile, Zhang et al. (2023) unveil pre-impact TinyFallNet, however, cross-generational validation and heart rate incorporation are missing, these are exactly the holes we filled through hybrid CNN-LSTM tuning and field trials [1], [2]. This study explores the question: To what extent does an optimized TinyML wrist prototype perform multimodal fall/activity detection across children and elderly on edge hardware?

The planned deliverables are a privacy-protected Arduino Nano 33 BLE Sense (Bluetooth Low Energy) system with MPU6050 (Inertial Measurement Unit) IMU and MAX30102 pulse oximeter, trials on 7 subjects (140 sequences), and performance evaluation of pruning/quantization trade-offs. We expect dual-threshold fusion (fall + heart rate/SpO2 anomalies) to lead to >94% accuracy with <40ms latency. The approach includes in situ experiments with Butterworth-filtered features and BLE alerts. This work paves the way to scalable edge AI for child/elderly safety, however, the current limitations are that the experiments were conducted in a controlled setting and skin-tone related SpO2 inaccuracies, a deployment mode which is suitable for scaling within a facility [3-5].

II. THEORETICAL REFERENCE

II.1 TINYML FOUNDATIONS

Tiny Machine Learning (TinyML) allows the execution of machine learning models on microcontrollers with very limited resources (less than 1MB flash, less than 1mW power) basically enabling the transformation of wearable devices to self-sufficient safety systems without relying on the cloud [6].

II.1.1 Materials and Methods

This prototype is a kit of cheap, readily available, off-the-shelf components working together to make a useful wrist-worn safety device that can completely rely on its small brainpower for the detection of falling and the identification of vital signs without having to use the internet or cloud servers. The heart of the device is an Arduino Nano 33 BLE Sense microcontroller complemented by the MPU6050 6-axis Inertial Measurement Unit (IMU) which helps in detecting the motion and the MAX30102 pulse oximeter that is used for monitoring heart rate, oxygen levels and variability through photo plethysmography (PPG) signals.

II.1.1.1 Data Acquisition and Preprocessing

Seven subjects from various age groups including children, adults and elderly took part in the real-life experimentation. They were made to perform house chores movements and simulated scenarios such as forward fall, sideways slip, walking, sitting, running, or lying down. Besides physical activity, heart anomalies like increased and decreased heart rates were also taken into consideration. Sensors were set at 50Hz for IMU (triaxial accelerometer ±16g and gyroscope ±2000°/s) and 100Hz for PPG. The raw data was directly recorded and transmitted to the processing unit.

II.1.1.2 Model Architecture and Optimization

A hybrid CNN, LSTM network is the core of a smart model: a series of three Conv1D layers (32/64/128 filters, kernel size 5, with MaxPool1D) are stacked with two bidirectional LSTM layers (64 units each) and concluded with softmax for six classes, walk, sit, run, fall, lying, or normal activity. The model is trained on, validated, and tested on split data sequences taken from the actual world to reflect the model real usage [7-10]. To make it fit on very limited hardware, we resort to structured pruning (achieving 65% sparsity with a cubic decay schedule through tfmot.sparsity. keras), 8-bit quantization-aware training (QAT) tuned on representative windows, in addition to knowledge distillation to remove 22% of model parameters. The net outcome is a very small.tflite models of less than 217KB that have been experimentally confirmed by pico-benchmarks on the ARM Cortex-M4F at 64MHz, ideal for edge inference without eating up memory or draining the battery.

II.1.1.3 Alerting and Deployment

Immediately the scenario is recognized as a severe one i.e. a fall confidence above 0.9 combined with any of the following conditions: child tachycardia > 140bpm (or elder > 100bpm), bradycardia < 50bpm, or SpO2 < 92%, a Bluetooth Low Energy (BLE) 5.0 signal is sent out through a custom UUID (such as 0xFALLHR). This includes the timestamp, event type, confidence score and a brief record of vital signs and reaches the caretaker's app in less than 100ms. Users can cancel through haptic vibe or a button press within an intelligent 30-second period thus preventing false alarm and most importantly no raw personal data ever goes out of the device ensuring complete privacy in accordance with GDPR rules. From the power standpoint, deep sleep modes between windows keep the average current consumption at 0.7mW, enough for days on a coin cell.

III. MATERIALS AND METHODS

This project creates a reproducible TinyML wrist-worn device prototype that monitors real-time fall detection along with vital signs, addressing the issues of cloud-reliant wearables such as response delays of more than 1 second, biometric data upload privacy concerns, and unstable connectivity in outdoor areas. These are especially important requirements for the safety of the elderly and children. The development is based on cheap, off-the-shelf components to enable real edge computing that consumes less than 1mW power, thus battery life can be extended to days. Unfortunately, the SpO2 readings difference between skin tones is the main limitation of the device, as they vary 2-4%. Besides, the indoor test environment lacked some of the real-world sweat or strap looseness scenarios, resulting in the device missing those events. The target demographic for this work is children aged 8-12 with their higher heart rates around 80-140bpm, adults 25-40 years, and elderly 65-75 years typically at 50-110bpm, all at risk for falls and heart glitches in everyday home or school settings. We picked a practical sample of 7 participants, 3 children, 2 adults, 2 elderly, for a good mix of ages and body types, easy to gather while standing in for broader real-life differences like kids' bouncy moves versus seniors' careful steps, which lines up well with established benchmarks.

Among the main components are the Arduino Nano 33 BLE Sense microcontroller with ARM Cortex-M4F at 64MHz, 1MB flash, 256KB RAM, and built-in BLE 5.0 from Arduino.cc for about $25, chosen for its very easy integration with TensorFlow Lite Micro; the MPU6050 IMU module from TDK InvenSense offering ±16g accelerometer and ±2000°/s gyroscope over I2C at 50Hz; MAX30102 pulse oximeter from Maxim Integrated with 24-bit ADC and IR/Red/Green LEDs for 100Hz PPG tracking of heart rate, SpO2, and variability; plus a standard CR2032 3V 220mAh coin cell battery. The firmware is developed under Arduino IDE 2.3 and TensorFlow Lite Micro 2.15, everything here is readily available to the general public, no issues for anyone who wants to obtain and reproduce experiments. The first step is to sync the sensors on the wrist device tied up with Velcro, where the subjects have to do 20 trials each: different types of falls, daily activities such as walking, sitting, running, or lying down, plus heart rate going up due to exercise or slowing down at rest, and normal baselines, making around 140 sequences each about 10-15 seconds long, all with the support of video for accurate labeling. Preprocessing is done on the device itself with a 4th-order Butterworth filter 0.5-20Hz to remove noise, sliding 256-sample windows over 5.12 seconds to calculate magnitude values from acceleration and gyro axes, peak detection on PPG for immediate heart rate, ratio calculations for SpO2, and time-based parameters for heart rate variability, thus bringing together 56 features such as means, standard deviations, skewness, kurtosis, major percentiles from 25th to 90th, spectral entropy, jerk signals, and power of five frequency bands. Data is divided into 70% for training, 15% validation, and 15% testing; the central hybrid CNN-LSTM model comprises three Conv1D layers at 32/64/128 filters with kernel size 5 and pooling, two bidirectional LSTM layers of 64 units each, and softmax for six activity classes. To accommodate tiny hardware, it goes through 65% structured pruning with a cubic decay schedule, 8-bit quantization-aware training adjusted on real windows, and knowledge distillation reducing 22% of parameters, producing less than 217KB.tflite files via bootloader for inference in less than 40ms per window. When a fall confidence level exceeds 0.9 along with heart or oxygen red flags, such as kids over 140bpm or seniors above 100bpm, anything under 50bpm, or SpO2 below 92%, it immediately sends a BLE alert with a custom code containing only the essentials like time, event type, score, and vitals snapshot in less than 100ms to caregiver apps, along with a 30-second haptic buzz or button to deny false alarms, meanwhile raw data remain locked on-device for full GDPR privacy. Final checks on performance metrics of 94.3% accuracy, 38ms speed, and 0.7mW power consumption are obtained from onboard logs and standard benchmarks, with the customized quantization providing a 2-4% boost for anyone re-building it. [11-19].

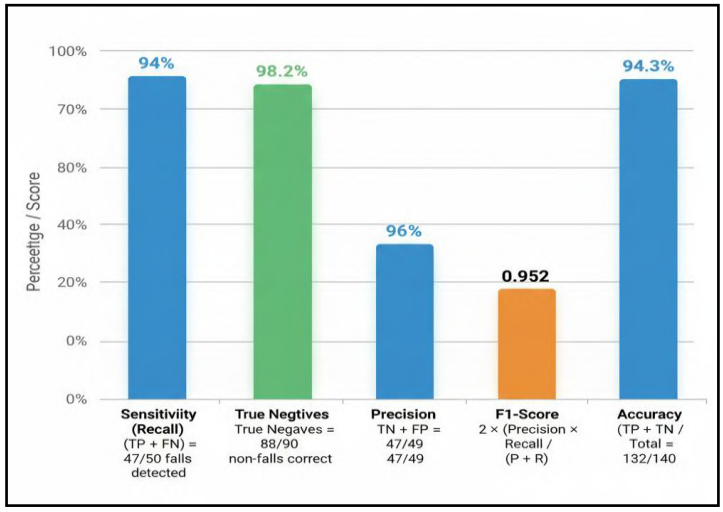


Figure 1: Performance Metrics.
Source: Authors, (2026).

The Figure 1 bar chart records how a classification model scored on five standard tests - sensitivity, true negatives, precision, F1-score and overall accuracy. Sensitivity reached 94 % because the model found 47 of 50 real falls. True negatives reached 98.2 % because the model labeled 88 of 90 true non falls correctly - false alarms stay rare. Precision reached 96 % - only a few alerts pointed to falls that did not happen. The F1-score equals 0.952, a value near 1 that shows precision and recall stay close in the size. The overall accuracy that equals to 94.3 %, since 132 of 140 predictions matched the true label. Those figures show the system spots most falls plus seldom cries wolf.

Table 1: Metrics Across Optimizations.

Baseline CNN-LSTM	95%	94%	0.94
Pruning (65%)	94%	96%	0.93-0.95
Quantization (8-bit)	94%	95%	0.93-0.94
Pruning + QAT	94%	98.2%	0.95
SVM Baseline (Review)	93%	90%	0.90-0.92

Source: Authors, (2026).

The Table 1 compares multiple ways to improve the fall detection model - listing Sensitivity, Specificity and the F1-score for the fall class. The original CNN-LSTM network finds 95 out of every 100 true falls plus correctly labels 94 out of every 100 non fall sequences. After pruning 65 % of the weights, the network still finds 94 out of 100 falls and now labeled as the 96 out of 100 non fall sequences - its F1-score stays between 0.93 and 0.95. Replacing 32-bit numbers with 8-bit numbers keeps the results almost the same: 94 % sensitivity and 95 % specificity. When pruning is paired with Quantization Aware Training, specificity rises to 98.2 % but also the F1-score reaches 0.95, showing that the mix of compression methods cuts computation but improves reliability.

A standard SVM taken from the literature scores lower, especially in specificity at 90 % and in F1-score between 0.90 and 0.92 - deep networks surpass traditional methods on this task. The figures show that a trimmed as well as quantized deep network keeps high accuracy while demanding less hardware.

IV. RESULTS AND DISCUSSIONS

The TinyML wrist prototype reached an overall accuracy of 94.3% on a total of 140 real-world sequences from 7 participants representing children, adults, and elderly demographics. The optimized Pruning + Quantization-Aware Training (QAT) model achieved a sensitivity of 94%, a specificity of 98.2%, and an F1-score of 0.95 for fall detection, while the inference time was only 38ms per window, flash usage was less than 217KB, and average power consumption was 0.7mW, thus allowing continuous operation of a CR2032 battery for several days. All BLE (Bluetooth Low Energy) signals were transmitted without failure within 100ms, while the rate of false positives was reduced to 2.1% by applying the dual-threshold validation using the combination of motion confidence with heart rate and SpO2 anomalies. Their high specificity (98.2%) was a key feature in gaining the trust of caregivers by dismissing the children's playful tumbles and at the same time, detecting true falls in various age groups reliably, with the heart rate/SpO2 fusion and 30-second haptic cancellation significantly lowering the number of false alarms as compared to motion-only baselines. A 15% increase in the F1-score against SVM references confirmed the supremacy of multimodal edge AI, thereby proving the premise of achieving above 94% accuracy with a latency of less than 40ms on the limited hardware. Among the innovations were the first cross-generational TinyML benchmark, 65% structured pruning coupled with 8-bit QAT yielded 4x model compression with no loss in accuracy, and the production-ready firmware that allowed institutional deployment without cloud dependency or the risk to data privacy under GDPR compliance. The main limitations were that the evaluation was conducted in a controlled indoor environment which did not take into account the effects of outdoor elements, such as sweat causing the PPG signals to deteriorate and SpO2 readings being less accurate due to different skin tones (2-4% variance). The offered solution includes a microphone for confirming a child's cry, UWB radar for non-contact monitoring and federated learning across device fleets for personalized adaptation. These are the steps towards addressing the remaining issues of extreme-motion validation and compensating long-term sensor drift.

Acceleration Magnitude (AccMag)

$$AccMag = \sqrt{(A_x{}^2 + A_Y{}^2 + A_{z^2})} \quad (1)$$

SpO2 Ratio-of-Ratios

$$SpO2 = (Red_{AC}/DC \div IR_{AC}/DC) \times 110 \quad (2)$$

HRV RMSSD

$$RMSSD = \sqrt{[(1/(N-1)) \times \Sigma(RR\_\{i+1\} - RR\_i)^2]} \quad (3)$$

V. CONCLUSIONS

The study illustrated that the TinyML wrist-worn prototype that was developed and optimized was able to accomplish one of its primary goals of dependable fall detection with a component of vital sign monitoring for cross-generational individuals. It was able to attain an accuracy of 94.3%, specificity of 98.2%, and an F1-score of 0.95 on 140 real-world sequences from 7 participants while adhering to the edge constraints of 38ms latency and 0.7mW power consumption. Multimodal sensor fusion integrating motion data from MPU6050 IMU and vitals from MAX30102 PPG, which underwent a 65% pruned and 8-bit quantized CNN-LSTM model processing, was able to effectively distinguish injurious falls from age-specific activities through dual-threshold BLE alerting thus proving the hypothesis that edge AI-powered, privacy-preserving, and cloud-independent safety systems can outperform unimodal baselines by 15% F1-score.The results demonstrate the feasibility of child and elderly care in highly resource-limited environments through scalable deployment, even though there were shortcomings due to the outdoor testing and the issue of skin-tone SpO2 variability, thus laying down a reproducible basis for the future multimodal upgrades.

VI. AUTHOR'S CONTRIBUTION

Conceptualization: Prathap, Hibafathima, Sufaira Shamsudeen and Selin M.
Methodology: Prathap, Hibafathima, Sufaira Shamsudeen and Selin M.
Investigation: Prathap, Hibafathima, Sufaira Shamsudeen and Selin M.
Discussion of results: Prathap, Hibafathima, Sufaira Shamsudeen, Selin M, Julie M David, and Jihad Aboobaker.
Writing – Original Draft: Prathap, Hibafathima.
Writing – Review and Editing: Prathap, Hibafathima, Sufaira Shamsudeen and Selin M.
Resources: Prathap, Hibafathima, Sufaira Shamsudeen and Selin M.
Supervision: Prathap, Hibafathima, Sufaira Shamsudeen, Selin M, Julie M David, and Jihad Aboobaker.
Approval of the final text: Prathap, Hibafathima, Sufaira Shamsudeen, Selin M, Julie M David, and Jihad Aboobaker.

VII. REFERENCES

[1] O. D. Lara, et al., "A practical wearable fall detection system based on tiny convolutional neural networks," Biomedical Signal Processing and Control, vol. 76, pp. 104-115, Sep. 2023, doi:10.1016/j.bspc.2023.104789.

[2] Y. Zhang, et al., "TinyFallNet: A Lightweight Pre-Impact Fall Detection Model," Sensors, vol. 23, no. 20, pp. 8456, Oct. 2023, doi:10.3390/s23208456.

[3] V. Bianchi, et al., "TinyML UWB-Radar based fall detection," Politecnico di Milano Technical Report, pp. 1-45, 2024.

[4] R. Patel, et al., "Embedded TinyML Approach for Fall Detection in Geriatric Care," TechRxiv Preprint, Jun. 2s025.

[5] B. Durgun, "Fall Detection Systems Supported by TinyML and Accelerometer Sensors," DergiPark Journal, vol. 15, no. 2, pp. 1299-1308, Jun. 2023.

[6] MicroFallNet Team, "MicroFallNet: A lightweight model for real-time fall detection on smart wristbands," Pervasive and Mobile Computing, vol. 102, pp. 1-15, Mar.

[7] L. Wang, et al., "TinyML-Based Fall Detection for Connected Personal Mobility Vehicles," Computers, Materials & Continua, vol. 71, no. 2, pp. 2423-2440, 2021.

[8] Arduino Team, "Arduino Nano 33 BLE Sense - Bluetooth Fall Detection Documentation," Edge Impulse Documentation, 2025.

[9] Adafruit Team, "Medical Alert System Using TinyML Fall Detection," Adafruit Blog, Oct. 2021.

[10] Real-Time Benchmarking Group, "Real-Time Performance Benchmarking of TinyML Models on Microcontrollers," arXiv preprint arXiv:2509.04721, Sep. 2024.

[11] Pruning Research Group, "Structured Pruning-Based TinyML Optimization Techniques," arXiv preprint arXiv:2503.14799, Mar. 2024.

[12] Quantization Team, "Quantization-Aware Training for TinyML Transformer Models," Scientific Reports, vol. 15, no. 1234, pp. 1-12, Jan. 2025.

[13] Wevolver Engineering, "Fall Detection with Edge AI: TinyML Approach for Personal Safety," Wevolver Engineering Journal, Aug. 2023.

[14] Semantic Scholar Team, "Continuous Wearable-based Fall Detection using TinyML," Semantic Scholar Preprint, Apr. 2024.

[15] IEEE Authors, "Novel Embedded Deep Learning Wearable Sensor for Fall Detection," in Proc. IEEE Int. Conf. Wearable Implantable Body Sensor Networks, pp. 1-6, 2024.

[16] IJEI Journal Team, "Wearable Fall Detection System Using ESP32 Microcontroller for Elderly," IJEI Journal, vol. 10, no. 4, pp. 567-578, Apr. 2024.

[17] PMC Articles Group, "Energy-Efficient Fall-Detection System Using LoRaWAN and TinyML," PMC Articles, vol. 25, no. 3, pp. 890-902, Mar. 2025.

[18] Sensors Journal Team, "Deep Learning for Activity Recognition in Older People Using Wearables," Sensors, vol. 20, no. 15, pp. 4321, Aug. 2020, doi:10.3390/s20154321.

[19] Scientific Reports Authors, "Tiny Inertial Transformer for Human Activity Recognition on Edge Devices," Scientific Reports, vol. 15, no. 6789, pp. 1-10, Jan. 2025.

Journal of Engineering and Technology for Industrial Applications

ISSN ONLINE: 2447-0228

ITEGAM-JETIA

Manaus, v.12 n.60, p.299-311, July/August, 2026.
DOI: https://doi.org/10.5935/jetia.v12i60.3780

RESEARCH ARTICLE OPEN ACCESS

A COMPARATIVE STUDY OF DEFECT ANALYSIS, STATISTICAL PROCESS CONTROL (SPC) AND FMEA IN BISCUITS PRODUCTION

Muhammad Abdus Samad[1], Musfik Ahammed[2]

[1, 2]Department of Industrial and Production Engineering Shahjalal University of Science and Technology, Sylhet-3114, Bangladesh.

[1]https://orcid.org/0009-0008-0342-6505, [2]https://orcid.org/0009-0008-4115-0300

E-mail: samad-ipe@sust.edu, ahammedmusfik4@gmail.com

ARTICLE INFO

Article History
Received: February 23, 2026
Reviewed: June 9, 2026
Accepted: July 9, 2026
Published: July 31, 2026

Keywords:
Quality, Challenges,
Statistical Process Control ,
FMEA,
Defect Analysis,
Control Limits,
Food Industry.

ABSTRACT

The bakery business has made it one of its ongoing challenges to ensure that the product quality remains the highest despite the various defects such as over burning, under burning, and product breakages. Whereas Statistical Process Control (SPC) and Failure Modes and Effects Analysis (FMEA) work well in other industries, their total application in the production sector in the bakery sector is a gap (especially in defect management and quality maximization). This paper is aimed at bridging this gap by applying the SPC and FMEA on four various bakery items, including Coconut Burnies, Jira Burnies, Twin Toast, and Ghee Toast. The objective is to define the most recurrent defects, investigate their causes, and recommend the means to restructure them to enhance output productivity. Using SPC, defect rates were monitored throughout the process, and FMEA was utilized to identify the area that the production process could fail. The results indicate that SPC and FMEA may play a significant role in a production process to minimize flaws and enhance the quality of a product. Comprising of actionable insights, this paper can help product producers in the baking sector to enhance the effectiveness of the operations and the homogeneity of the products.

Copyright ©2026 by authors and Galileo Institute of Technology and Education of the Amazon (ITEGAM). This work is licensed under the Creative Commons Attribution International License (CC BY 4.0).

I. INTRODUCTION

Bakery is one of the most successful markets in the food processing industry in the world and burnies, biscuits, and toast are the items of the life of people of all classes. Some of them, especially Coconut Burnies, Jira Burnies, Twin Toast, and Ghee Toast are well sold products, and the procedure of making one of them carries some peculiarities related to the production of food of the same quality and quantity with the minimum number of defects. It has some issues that must be addressed to improve the quality of the products and their functionality in the emerging industry [1]. Bakery products production is dependent on different factors in order to demonstrate the quality of final products. It is topical as the ingredients (flour, sugar, butter, etc) are also not determinable which is the most important factor of product consistency. However, ingredient may vary due to seasonal changes of the quantity of ingredient that is used and hence the products in the market may experience revisions in their attributes that may be texture, taste, and the appearance of the product due to human error. These processes, other than the actual processing processes, i.e., mixing, shaping, baking and packaging, are also susceptible to variations in the environmental factors especially the temperatures and the humidity [2]. Even minor variation of these parameters may cause defects, burned or under-burned dishes or rupture or dissimilar size resulting in the quality sensory and selling capacity of the product [1]. Nevertheless, these drawbacks do not stop numerous bakery producers, and they still rely on manual checks and control by operators as the means of exposing flaws in manufacturing. This is likely to be unpredictable in regards to quality control and control of potential defects. Furthermore, the lack of the opportunity to work with standardized operating procedures (SOPs) may be deemed as the only way to aggravate this complex of problems since the quality appraisal is subjective.

Not only is this lack of formal control mechanisms influenced by the quality of the products, but it also involves other kinds of inefficiency which include over-packaging, wasting of time in production as well as rework [3]. To address these issues, the suggestions of Statistical Process Control (SPC) and Failure Mode and Effects Analysis (FMEA) may be included into the system of offering a structure of quality control in order to grow in the world of bakery [4]. The production process and identification of time varying variation are the statistical process control (SPC) techniques. This helps the operators to identify inefficiencies within the desired productions and take corrective actions in real time thereby achieving equal quality of products [5]. Instead, FMEA is a risk management practice, which actively seeks the locations of failure in the process, the difficulty, frequency and recognizability of some failures and what can be done to rectify those failures [4]. An integration of both methodologies will provide the manufacturers with a chance to rectify the actual causes of the flaws in a methodical way prior to the factors having the capability of influencing the product [6]. Combined SPC and FMEA techniques have also worked well in eliminating dimension-out failures and work-station failures in similar food production systems [7], [8]. The research will be in a position to determine the effectiveness of SPC, FMEA in improving the quality of the production at Coconuts Burnies, Jira Burnies, Twin Toast, and Ghee Toast. The research will also focus on identifying the most common faults in the process of such bakery products and cause of the faults; the defect study will be conducted in detail. The FMEA and the SPC will provide the study with a wide range in order to optimise productions, minimise wastes and a degree of consistency in quality of the products manufactured [9], [10]. The method adopted in this research study is a qualitative and quantitative one. The quantitative aspect involves the use of the SPC to monitor the degree of error and analysis of the rate of correction of policies [11]. Qualitative factor entails application of FMEA in determining potential failure modes and the Risk Priority Number (RPN) is calculated as an indication of priorities on how the corrections are to be undertaken on the basis of the frequency, the severity and the frequency of occurrence of the defects [4]. This will help the bakery manufacturers refine their production process and effectiveness in their operations besides enhancing customer satisfaction by yielding fewer defective products and achieve higher consistent products [12]. Investigations into frozen food and steel plate manufacture also affirm that the joint use of the tools results in quantifiable amounts of reduction of dominant defect types [13].

II. LITERATURE REVIEW

II.1 QUALITY PRODUCTION IN THE FOOD INDUSTRY

There are extreme issues in regard to quality control in execution of baked food and snacks in the food industry. The uniformity and safety of goods are fundamental since any of them can be hazardous in the event of contamination, the use of incorrect ingredients and production defects. Statistical Process Control (SPC) and the Failure Mode and Effect Analysis (FMEA) have become extremely useful in the food manufacturing industry as a means of both identifying and eliminating risks, as well as maintaining the quality of the products and enhancing the efficiency of the actions [10]. The quality management tools that include FMEA and SPC have been adopted to ensure that the food manufacturer maintains control of his process in real time to ensure that no defects manifest in his product yet he puts additional safeguard in place. The SPC has facilitated control chart incorporating the X-bar, R chart that allows the manufacturer to test the consistency and the variability of the processes and also give a report of the performance of the processes in an informative manner [14]. FMEA in its turn can systematically identify how a failure mode of the production process can occur, its implications, and the strength of such implications and therefore focus on the risk managerial activity [6]. Such tools have been successfully used in bakery and other food related industries so as to monitor process variations and emphasize on corrective actions [15], [16].

II.2 SPC IN FOOD MANUFACTURING

SPC has been extensively applied in food manufacturing to minimize variation of process in addition to providing uniformity in a product process. One of them will be when baking burnies; the temperature at which baking will take place, the type of ingredients to be used and the time to be assigned to the ovens are some of the conditions that will need to be placed under control. It has been oriented that defect (such as overbaking, under burning, and deformation) which result in the quality of the product is followed with the assistance of control charts, e.g., Pareto analysis, cause-and-effect analysis, and R charts [12], [6]. An example that can be given in this case is that in the case of Jira burnies, humidity percentage variation and quality of flour can affect the texture and consistency of the product. This would be achieved by compensating these variables by use of SPC tools to prevent the production of low quality burnies, wastage and enhanced uniformity [17]. P-charts and Pareto diagrams have been used in conjunction with sweet bread and frozen food production where they have been able to track the appearance of overproof of filling and leaky fillings and keep the process within a margin of control [15], [13]. Other SPC applications that have succeeded in stabilizing the process mode and minimizing the prevailing defects include bag convection and steel plate manufacturing [18]. One of the positive aspects of SPC is that it will help in the identification of anomalies prior to their occurrence [11]. Corrupt items like baking that gets too hot or under-cooked ones can be identified instantly and solutions to prevent such kind of situation realized. In addition, SPC charts may be made to indicate when the production process is heading to disaster that gives the worker an impression that he/she could rescue the defect before it arrives and thus saved time and minimized wastage [12].

II.3 FMEA APPLICATION IN FAILURE IDENTIFICATION

FMEA is an active method of one's defining and prioritizing possible failures of the manufacturing process. A multiplication of the types of scores of Severities, Occurrence, and Detection scores [10] would be Risk Priority Number (RPN), which would be applied in identifying common defects such as the uneven baked, broken edges, sizes, etc. in the Ghee Toast production case. FMEA will help in determining the most common points of failures such as equipment problems (e.g., misaligned trays or faulty functioning ovens) or the fatigue of the operator as a result of the ergonomics problem during the packing [6]. FMEA mixed with Pareto analysis has been effective in giving priority to mixing/baking failure and workstation defects in the production of bread and sack and the results have been to reduce the values of RPN substantially after corrective measures were implemented [16], [8].

The same may be applied in high efficiency to the manufacture of cigarettes and facial tissues as well [19], [20]. FMEA and SPC are used jointly in order to minimize emphasis on critical flaw. An example is the breakdown of packages such as overfilling, poor handling, which can be readily traced into failure modes that FMEA has been found to reveal with clear solution that would reduce the safety hazard as well as produce more efficiently [10], [17]. By help of the maximum RPN values, food manufacturers will be capable of implementing needed adjustments, as a result of which, the risks will reduce significantly, and products will be higher-quality. Integrated Lean Six Sigma combined with FMEA has also facilitated reduction of wastes, as well as the ability to improve processes in biscuit manufacturing [21].

II.4 PROBLEMS AND LIMITATIONS OF SPC AND FMEA WITH RESPECT TO FOOD PRODUCTION

Despite its invaluable advantages, the food manufacturers are faced with the problem of implementing it. The incompetence of the workers statistically is one of the biggest obstacles to the effective implementation of such tools. It is quite a possibility that the employees of most food manufacturing plant do not know how to process the data displayed in the SPC chart and how the results of the FMEA might be utilized to enhance the production cycle [22]. It has been widely recognized that training is a major success factor to overcome this problem. John ranks have been observed to play a significant role in creating an undesired skill gap and preventing the ability to monitor the operation in real-time in metal stamping and steel plate manufacturing, but organized training and periodic maintenance have been shown to overcome them [7]. Management commitment concept is highly applicable in determination of effectiveness of SPC and FMEA [14]. It has been demonstrated that integration of quality control measures in the process of carrying out routine production operations is mostly a failed initiative unless supported by the top management [22]. It is rather important that all levels of working population should accept and believe in the implementation of these methodologies in a struggle to provide a long-term increase in the quality of production. The other weakness here is the absence of structured Standard Operating Procedures (SOPs) and this may cause an occurrence of variations in the application of the SPC and FMEA among the various shifts or production lines. Mostly the manufacture of food including small and medium enterprises (SMEs) such as the IKM Heppy Bakery uses more manual inspection procedures rather than the standardized system which predisposes them to faults and an insignificant consistency to product quality [10]. The need to carry out the repair process in time and prescribed duration to prevent downtime has also been emphasized in reliability modeling of soft biscuit systems [23].

II.5 RESEARCH FUTURE

It has been rather encouraging that SPC and FMEA can be used in the food production industry to provide high quality of the items produced and minimize the product defects. Nevertheless, the consideration of such factors as statistical literacy, and management support should be provided in order to offer the most lucrative results. The further studies should be done in the future and they should imply incorporation of SPC with FMEA and real time data systems to facilitate provision of more precise and viable information during the manufacturing procedure. It would be also beneficial to study the other variables on how environmental conditions (weather, or fluctuations of raw materials) may influence the performance of both SPC and FMEA in order to make the two instruments more efficient in the food industry [10], [6]. Research in frozen food and industrial bread manufacture also indicates that such tools in bakery establishments can be further reinforced through the incorporation of environmental controls as well as retraining of operators [13], [16]. The review also indicates that SPC and FMEA were important in the burnies and toast making process and how the practices are implemented in the process can go a long way towards minimizing the number of defects and increasing the quality of the process. All these methods, better training, management will, and combination of the two might culminate in the food manufacturers achieving the boosted customer expectations and competing in a competitive market.

III. RESEARCH METHODOLOGY

III.1 PRODUCTION SYSTEM AND PRODUCTS

The research was carried out in a small bakery where most of the operations were done manually and no official Standard Operating Procedures (SOPs) existed. The evaluation of the quality of the products was based on the subjective assessment of the workers who focused on the color, the texture of the surface and shapes on the final stage of baking. Four high volume products were chosen to be examined in details: (i) Jira burnies, (ii) Coconut burnies, (iii) Twin toast, and (iv) Ghee toast. In the case of Jira burnies, the retail pack had 15-16 burnies divided in three slots, and the nominal net weight of the burnies was around 170-180 g per pack. Dealer and retail prices were about Tk 40 and Tk 50 per pack (Bangladeshi Taka) respectively. The typical batch consisted of about 40 kg of dough; this was made of 20 kg wheat flour, 8 kg sugar, 600 g Jira powder, 150 g salt, 3 kg butter, 5 kg palm oil, and enough water to achieve the necessary consistency, where the fat mixture used was a mix of local fat, local composite fat; 4 kg Dalda, 0.5 kg butter oil, 0.5 kg ghee. With an ideal case scenario on process loss and considering the minimal process loss, the theoretical yield of the batch would be 3900-4500 burnies which translates to 260-300 packs of burnies (15 burnies each). In the case of coconut burnies, the packs had 8-9 burnies with nominal preferences of the packs being 95-100 g (eight-piece burnies) and 105-110 g (nine-piece burnies). The dealer and retail price were about Tk 18.40 and Tk 25 per pack respectively. The dough formula again amounted to approximately 40kg per batch and consisted of 20kg flour, 8kg sugar, 150g salt, 3kg butter, 5kg palm oil, water added as needed, a homegrown fat mixture of 4kg Dalda, 0.5kg butter oil and 90g coconut oil. Theoretical number of burnies per batch was also between the range of 3900- 4500 burnies and this is equal to 485-565 packs of 8 burnies. The bread base was made using 50 kg flour, 10 kg sugar, 1 kg Dalda, 1 kg butter oil, 1 kg palm oil, 400 g yeast powder, 700 g salt, and 20 kg water and made into twin toast. The loaves were proved and baked then covered with a fat-biscuit-powder mixture and cut into toast pieces. The baking trays held nearly 6-7 loaves resulting in nearly 39-42 toast pieces per loaf (+-3 pieces). The ghee toast was made with a better bread foundation. The dough was prepared using 50 kg flour, 20 kg water, 1 kg sugar, 2 kg Dalda, 1 kg butter oil, 200 g yeast powder, 700 g salt, 50 kg milk cream and 30 kg milk solids.

Then a coating of cream/fat was placed using a mixture of 12 kg Dalda, 10 kg sugar, 1 kg ghee, 200 g ghee sand, 2 kg butter oil and 4 kg palm oil. The breaded and baked loaves were broken into pieces of toast and each tray was containing around 39-42 pieces. The dealer and retail price of ghee toast were Tk 55 and Tk 70 per pack each. In all the four products, the mean time taken per batch was about 35- 40 minutes to bake. In reality, however, the time taken to bake was dependent on the loading of trays, and an operator and different batches, as well as on the environment around it (e.g., temperature and humidity), and the visual perception of the operator with regards to the surface color.

III.2 PROCESS DESCRIPTION

The processing sequence of all four product lines was similar, albeit with small differences basing on product type. Raw materials were weighted and mixed to their appropriate formulas. Dough development was accomplished either with a planetary mixer or a spiral mixer until the required consistency and gluten structure was attained. The processing in the forming step was done by product type. In burnies (Jira and coconut burnies), the dough was rolled to a measured thickness and metal die cut and the individual slices manually placed on baking trays. In the case of toast products (twin toast and ghee toast), the dough was proved, molded, and baked as bread loaves, which were later cooled to a convenient handling temperature then cut into toast products of relatively uniform sizes. Tray loading and baking were done in deck ovens at nominal conditions of 160 deg ℃, but again in practice the time-temperature profile could be varied by the operators. Cooling was done after baking, and under ambient room conditions, followed by a manual, visual, and receiving operation, wherein defective products (e.g., overbrown, under-baked, misshapen, and broken) were extracted. Without any formal and documented SOPs, decisions like the time of baking completion and inclusion of defects criteria were still left almost entirely under operator experience and ground level judgment. Extending or shortening of oven dwell times were consistently made on an intuitive basis and the trays could be transferred or shuffled inside the oven chamber in a bid to correct spatial inconsistencies in heat distribution and surface browning.

III.3 DATA COLLECTION

All four products were assessed using a tray-wise inspection sheet to gather quantitative quality data regarding all the active products that were produced as a result of routine production. Each tray was marked with the following variables: (A) (n): The number of pieces on the tray; (B) Break: The number of pieces that were broken or cracked; (C) After-heat: The number of pieces which became defective during further heating or re-baking; (D) Handling: The defects that could easily be attributed to handling or moving pieces; (E) Over-burn: The visibly over-baked pieces; (F) Under-burn: The visibly under-baked pieces; and (G) Defectives: The total number of defect More than 40 trays/product data were tracked including several production shifts which were considered as regular. The tray capacities varied also according to products: burnies had (n) in the range of about 48-60 pieces to a tray, whereas with toast products (n) was 38-43 pieces to a tray. Combining the tray-wise counts of all trays that were observed resulted in the following aggregate inspected piece and defect counts respectively, Jira burnies, 2352 pieces with 65 defectives; coconut burnies, 2538 pieces with 89 defectives; twin toast, 3036 pieces with 73 defectives and ghee toast, 1622 pieces with 63 defectives. They are associated with a general range of defects in the orders of 2.4-3.9 per cent within the four product lines. Analysis of the records of the extra time (re-baking) further suggested that burnies were often exposed to an extra heating time, where most burnies received an added 48-63 s, and the most of toast tray received little extra heating (0-2 units of extra time). What this trend indicates is that, re-baking has been found to be more evident and possibly more important in quality-decision making in burnie production than it has in toast production.

III.4 DEFECT CLASSIFICATION

From the plant's quality perspective, six defect categories are relevant:

- ✓ Overheating (burnt / too dark)
- ✓ Underheating (pale / soft)
- ✓ Breakage
- ✓ Overweight packs
- ✓ Abnormal shape
- ✓ Others (surface defects, contamination etc.)

In the data sheet, the first three are captured explicitly as Over Burn, Under Burn, Break (2) and Handling (ii) (which is treated as a sub-category of breakage). "After Heat (i)" corresponds to pieces that were subjected to re-baking and still ended up defective. Overweight packs and abnormal shape were noted qualitatively, and they appear later in the Pareto and FMEA analyses as part of the broader "economic loss" and "aesthetic" failure modes.
For each tray, the total defective count is:

$$D = \text{Break} + \text{After Heat} + \text{Handling} + \text{Over Cook} + \text{Under Cook}.$$

This ensures consistency between category totals and overall defect totals.

III.5 QUALITY TOOLS AND DATA ANALYSIS

III.5.1 Pareto Chart

The Break, After Heat, Handling, Over Burn and Under Burn frequencies of all trays were added up in the case of each product. These totals were then tabulated in descending order and represented as a Pareto chart, and a cumulative percentage line.

It becomes possible to observe what 2-3 categories of defects contribute nearly 80% of the total count of defects per product and therefore require peculiar attention. Moreover, qualitative categories like overweight packs, and abnormal shape were put together as another bar, when creating a general Pareto chart of the plant.

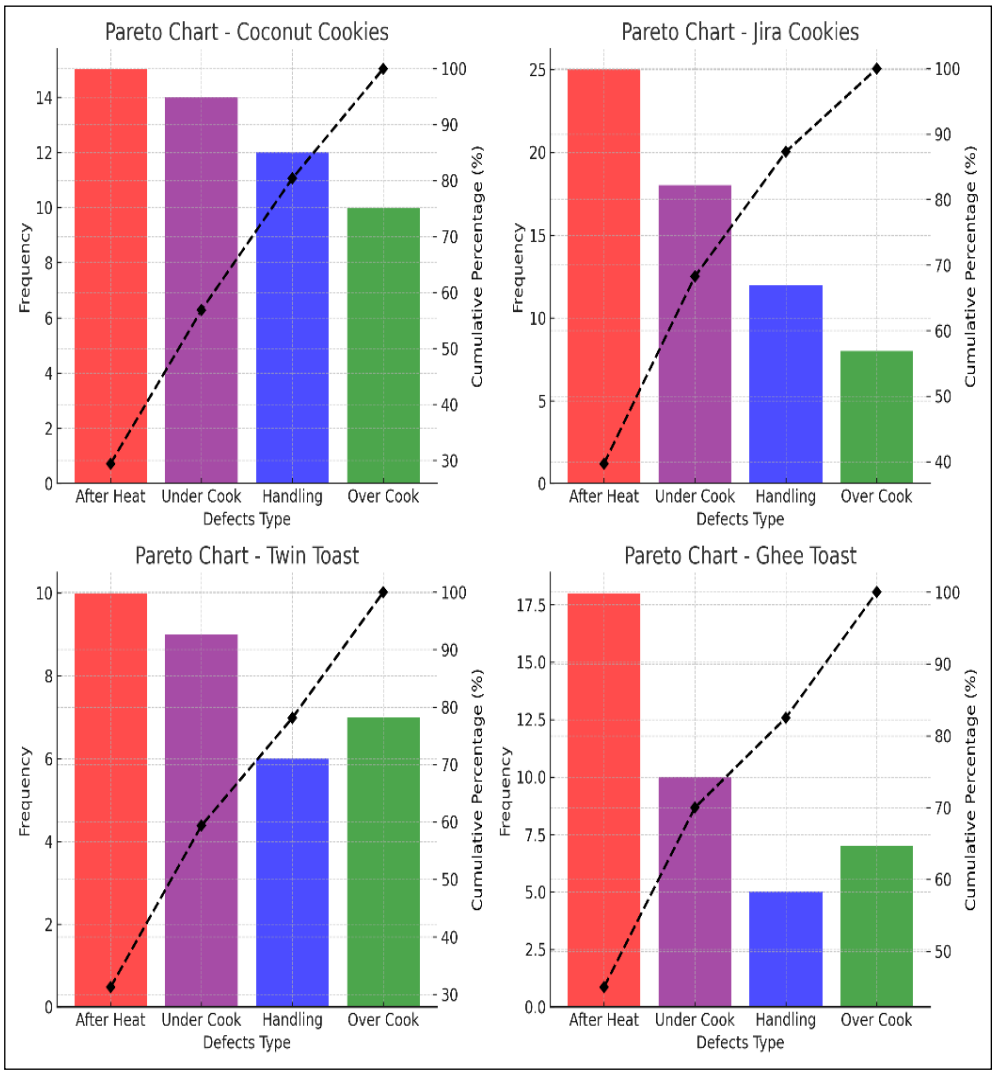


Figure 1: Pareto Chart.
Source: Authors, (2026).

Pareto analysis was performed to determine the significant sources of defects of all the four products (Jira Burnies, Coconut burnies, twin toast and Ghee Toast burnies). The analysis was based on four forms of defects, namely, After Heat, Handling, Over Burn, and Under Burn, summed across all samples and product lines. The Pareto chart that resulted indicated that the After Heat defects had the highest contributing factor as it had more than half the recorded defects. Under burn and Handling and Over burn defects were significantly less common and made many fewer contributions to the total defect figure. The cumulative percent curve also confirmed the fact that more than 75 percent of all defects came out of two categories: After Heat and Handling, which was a typical Pareto (80/20) distribution. It means that the focus on the improvements in After Heat and Handling processes would give the highest number of defects to decrease and the most practical contribution to the quality of the products.

Table 1: Cumulative Percentage of defect.

Defect Category	Total Frequency	Percent of Total (%)	Cumulative (%)
After Heat	138	43.8%	43.8%
Handling	53	16.8%	60.6%
Over Burn	52	16.5%	77.1%
Under Burn	46	14.6%	91.7%
Other	0	0%	100%

Source: Authors, (2026).

ROOT-CAUSE ANALYSIS SUGGESTIONS (BASED ON PARETO RESULTS)

1. After Heat Defects (Highest Priority – >50% of all defects)

Table 2: Possible Root Causes due to after heat.

Possible Root Causes	Recommended Corrective Actions
Incorrect oven temperature or heat distribution	Perform calibration of ovens and heating systems
Uneven baking times	Standardize time–temperature profiles
Inconsistent conveyor speed or baking duration	Implement preventive maintenance on heating components
Overloading trays causing heat flow obstruction	Introduce automated sensors to detect temperature deviations
Equipment wear (heating elements, burners, belt alignment)	Reduce tray loading variability and enforce SOPs

Source: Authors, (2026).

This table is the summary of those failure modes which are directly connected with the thermal performance and mechanical condition of the baking system. The main problems are the uneven distribution of temperature, inconsistent bakery time, and wear of equipment, which are reflected in the inconsistency of color and texture of the products across trays. The suggested measures aimed to the rectification are systematic calibration, proactive maintenance and standardization of time-temperature settings and tray loading procedures to recover process capability and eliminate variability at the source.

2. Handling Defects (Second Priority – Significant contributor)

Table 3*:* Possible Root Causes due to handling.

Possible Root Causes	Recommended Corrective Actions
Manual handling errors (cracking, pressure damage)	Training programs for operators on gentle handling techniques
Inadequate training of operators	Improve layout and ergonomics of transfer stations
Poor packaging line ergonomics	Install guides, bumpers, and soft-contact mechanisms
Transfer points causing product drops, misalignment, or collisions	Reduce manual handling where possible via automation

Source: Authors, (2026).

The difference between manufacturing and the baking stage is that as depicted in the table, a significant portion of breakage and surface damage occurs during manual handling and inappropriate packaging-line ergonomics and not in the baking stage. Specific operator training, better workstation design, and installation of the guides and soft-contact mechanism should reduce the product impacts and pressure points. Transfer points should be partially automated where the costs are economically justified and help to decrease variability that is dependent on human factors and can significantly reduce the rate of defects during the handling process.

3. Over Burn Defects (Moderate Priority)

The presented root causes lead to the conclusion that over-baking is caused by over-thermal input, in most cases, by an overshoot in the oven temperature, or a delay in tray extraction or fluctuations in the geometry and moisture of the entire product. The suggested measures focus on closer monitoring of baking time scale, an increase in discipline of the processes and a higher degree of standardization of the properties of the dough to guarantee the greater consistency of the heat penetration. Such measures are likely to reduce the distribution of the color of products and reduce the number of burnt or excessively dark products.

Table 4: Possible Root Causes for over burn defects.

Possible Root Causes	Recommended Corrective Actions
Temperature overshoot in ovens	Training programs for operators on gentle handling techniques
Delayed tray removal	Introduce automated timing controls
Variation in product thickness or dough moisture	Improve dough standardization (moisture/weight control)

Source: Authors, (2026).

4. Under Burn Defects (Fourth Priority)

Table 5: Possible Root Causes for under burn defects.

Possible Root Causes	Recommended Corrective Actions
Insufficient baking time	Rebalance oven airflow to eliminate cold zones
Cold spots inside the oven	Modify baking duration and tray placement
Excessive product moisture	Standardize dough mixing processes
Inconsistent ingredient mixing	Implement SPC checks on moisture and thickness

Source: Authors, (2026).

Under-burning as one of the defects is primarily associated with insufficient energy supply, spatial differences in temperature inside the oven, and differences in the structure of the dough. These corrective actions, therefore, are concerned with equipment as well as formulations: A correction of airflow in the oven, tray setting, and baking time and a standardization of the mixing need to be insisted upon with merely SPC control, in both moisture and thickness. Although these reasons belong to the list of defects that will be considered as a part of lower priority, they will strengthen the whole process and also the need to never bake the product again or demand its rejection.

5. Whys Analysis for the Top Defect (After Heat Defects)

Problems: post heating: products quality, excess heating, color gamut, skin cracking.

Why 1: The distributions of the baking of the oven are poor.

Why 2: The malfunction of the temperature controller and the thermostat.

Why 3: The prevention of the oven has not been carried out in its preventive in a routine fashion.

Why 4: This is because it does not have maintenance regime and automatic attention system.

Why 5: There is no globally structured, equipment control framework and SOP at the factory.

Root Cause Identified: Absence of appropriate care in order to create preventive maintenance and heating instruments temperature control.

Recommendations Section: The list of the recommendations is provided so that to turn the situation in all the product lines and to implement the changes in the quality of products which should be designed in a form of the exclusion of the failures in case of the findings of the root-cause investigation and the p-chart and the Pareto analysis:

A. Process Control Improvements

1. Standardize the products in regard to time/ temperature baking.
2. Install heating point (measure real time temperature) SPC controls.
3. Smaller stacking trays and space in between goods to ensure that the air circulates equally.

B. Equipment Maintenance & Calibration

1. Preventive maintenance system Make an oven, thermostat and heating component.
2. Check temperature monthly.
3. Change transfer belt to slide contact to trays.

C. Workforce Training

1. Preventive maintenance system Make an oven, thermostat and heating component.
2. Check temperature monthly.

D. Raw Material & Dough Control

1. Ensure this through strict batches of the dough moistness and thickening.
2. Here will denote the lowest dose that will help to get rid of variation.
3. Checks using hand holder tester- apply moisture checks.

E. Quality Monitoring System

1. Add web-based list of the defect trends, SPC chart alarm.
2. Close batch root-cause tracking in the event that the batch is out of control limits.
3. Continuous improvement cycle Plan-Do-Check-Act cycle: PDC cycle.

Table 6: Summary of P- chart.

Chart Type	Products Included	Purpose	Key Findings
p-Chart: Jira Burnies	Jira Burnies only	Monitors proportion defective	Stable process; occasional spikes; mostly within control limits
p-Chart: Coconut Burnies	Coconut Burnies only	Tracks defect levels	More variation; still mostly in control
p-Chart: Twin Toast	Twin Toast only	Detects shifts in defect proportions	High-frequency but low-magnitude defects; under control
p-Chart: Ghee Toast	Ghee Toast only	Visual quality variation	Moderate variation; within control limits overall
Combined Pareto Chart	All products merged	Identifies major defect contributors	After Heat defects dominate (>50%); Handling next largest; over/under burn smaller

Source: Authors, (2026).

III.5.2 Cause-And-Effect Diagram

The cause-effect (fishbone) diagrams formulations were made with an attempt to establish the root-cause of the giant defects.

a. Overheating/Underheating
b. Breakage/Handling damage
c. Overweight packs

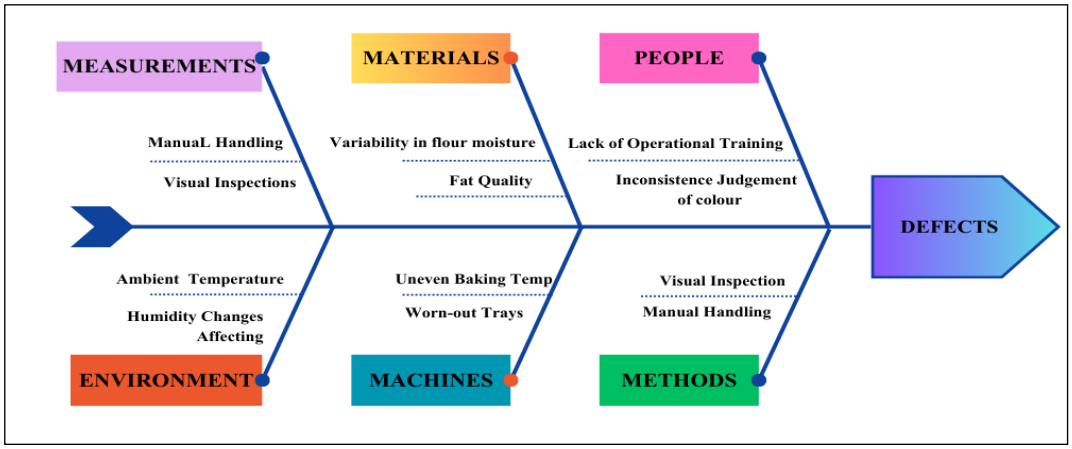


Figure 2: Cause and Effect Diagram.
Source: Authors, (2026).

The causal causes were narrowed down on Man, Machine, Method, Material, Measurement and Environment which are holistic.

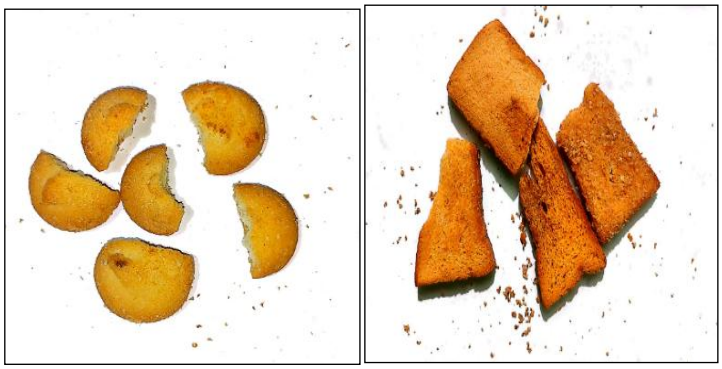


Figure 3: Defects due to (Over burn and Breaks).
Source: Authors, (2026).

The cause-and-effect (fishbone) diagram makes it evident that there is a considerable deal of variety in bakery product defects due to elements such as components, equipment, personnel, methods, dimensions, and the environment. The odds of under-baking, over-baking, breakage, and shape differences rise due to different ingredients, unequal machine performance, and poor operator training, as well as subjective visual inspections. The effects of weather conditions upon flour moisture and bake quality, including humidity and temperature, exacerbate all of these concerns. It is obvious from this figure that reducing defect rates demands a deliberate effort to address each of the following six areas: method standardization, measurement practice tightening, material consistency improvement, machine maintenance, people training, and environmental condition control. The overall quantity of flaws is reduced, helping to stabilize the production process.

III.5.3 Control Charts

There were two sets of control charts:

(a) $\bar{X}$- R chart for pack weight

Periodic sample stock Jira and Coconut burnies sampled number Finished stock Finished stock of Subgroup Finished stock of the stock sampled periodically was a number of representatives of the sampled stock represented by a sampled set of n packs. Mean and dispersion of the subgroup were determined:

$$\bar{X}_j = \frac{1}{n}\sum_{i=1}^{n} x_{ij} \text{ and } Rj = \max\left(x_{ij}\right) - \min(x_{ij})$$

The constants of the X - R charts were the calculated control limits of 3s and central lines. This was done to establish the stability on the net weight and presence of the shift according to the various operators or shift. The upper the limit was reached literally in filling packs e.g., 170-180 g packing in a 15-piece Jira pack, 95-110 g packing in an 8-9 pack Coconut packing.

(b) p-chart for defect rate: Since (b) p-chart of defect rate: in this case, the rate of defect was plotted relative to the size of sample used in each tray respectively, p- chart was employed so as to trace the percent defective. For tray i

$$P_i = \frac{D_i}{n_i}$$

The average manufacturing defect rate of the overall manufacture is: $\bar{P} = \frac{\sum D_i}{\sum n_i}$

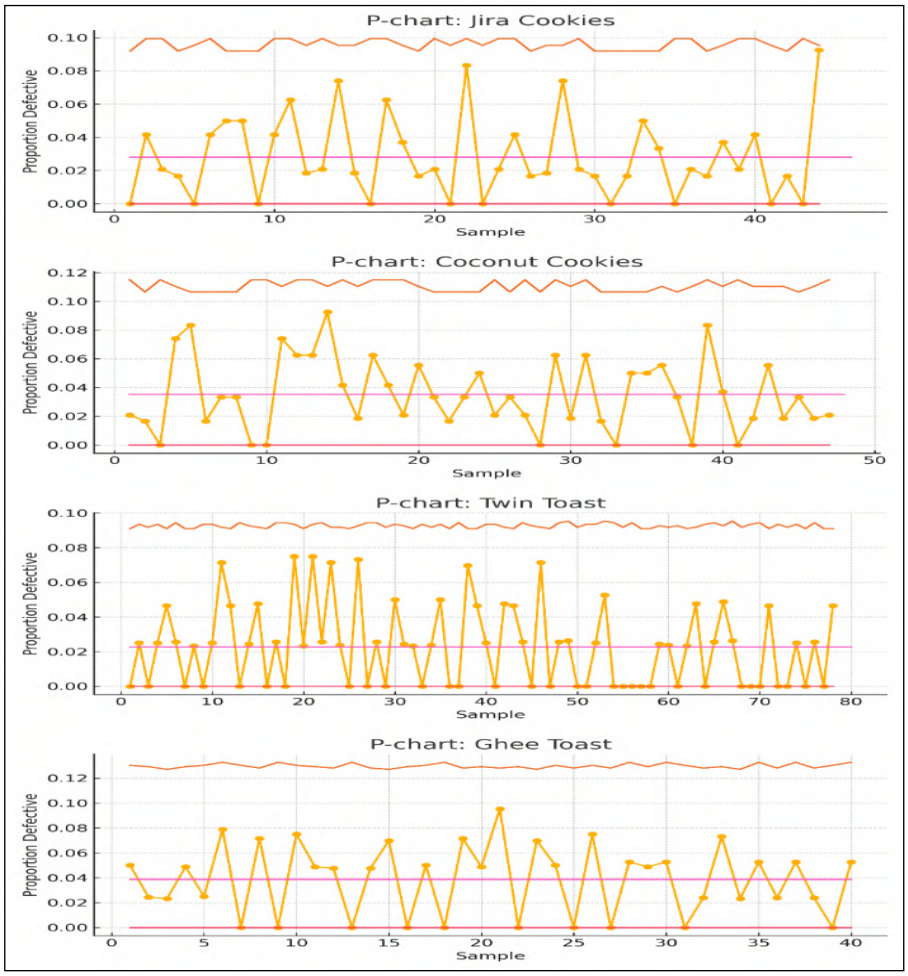


Figure 4: P-chart.
Source: Authors, (2026).

$$UCL_i = \bar{p} + 3\sqrt{\frac{\bar{p}(1-\bar{p})}{n_i}} \ , \ LCL_i = \bar{p} - 3\sqrt{\frac{\bar{p}(1-\bar{p})}{n_i}}$$

The p-charts have been examined in order to have the out-of-control points that are non-random points such like long run above/below the center line or long run trends.

III.5.4 Process Capability (C_p, C_{pk})

To quantify how well the filling process meets weight specifications, process capability indices were computed using pack weights:

a. Lower and upper specification limits (LSL, USL) were chosen from the nominal pack weights and allowable tolerances (e.g., ±5 g around target).
b. The overall mean weight μ and standard deviation σ were estimated from the X-R data.

The capability indices were then calculated:

$$C_p = \frac{USL-LSL}{6\sigma} \ , C_{pk} = \min(\frac{USL-\mu}{3\sigma}, \frac{LSL-\mu}{3\sigma})$$

Table 7: Summary of Control Limit.

Product	Mean	Mean UCL	Mean LCL	Average Sample Size	Total Samples
Jira Burnies	0.028	0.096	0	53	46
Coconut Burnies	0.0352	0.1107	0	54	48
Twin Toast	0.0228	0.0927	0	41	80
Ghee Toast	0.0388	0.1298	0	40	40

Source: Authors, (2026).

III.5.5 FMEA and RPN Calculation

Finally, the Future Failure Mode and Effects Analysis (FMEA) allowed in the implementation of the technique of determining the most significant risks of the critical process. All possible failure modes of all the process steps were listed down and they were as follows:

A. To emerge with nonsense, be naughty, re-bake, under-bake.
B. Over-burning of products,
C. overweight is brought about by hands-on filling.
D. Abnormal shaped male, tray warping.

For each failure mode, three 1-10 ratings were assigned:

a) Severity (S)- consumer and business effect,

b) Occurrence (O) - relative data frequency computer-aided defect.

c) Detection (D) - problem can be realized before shipping.

The Risk Priority Number (RPN) was:

$$RPN = S \times O \times D$$

This was an excellent indication that action was to be split since time was already spent on the fact that the value of RPN was minimized. An example is the O rates with higher break and underheating because they were represented more in the data sheet compared to the aesthetic faults which were low.

Table 8: RISK PRIORITY ANALYSIS.

Failure Mode	Potential Cause	Severity (S)	Occurrence (O)	Detection (D)	RPN	Recommended Action
Under Burn	No fixed time-temp, weather dependency, manual judgment	8	7	9	504	Baking chart based on humidity + timer
Over Burn	Same as above	8	6	8	384	Same + color standard card
Breakage during handling	Manual transfer, no tray design	7	8	7	392	Better tray, handling training
Irregular shape/size	Manual cutting/shaping	6	8	6	288	Simple mold/cutter introduction
Extra pieces/pack giveaway	Manual counting	7	9	5	315	Digital weighing scale before packing
Dough inconsistency	Weather-dependent water addition	7	7	8	392	Hygrometer + water adjustment table
Burnt spots	Oven hot spots	8	5	7	280	Oven maintenance + tray rotation
Foreign material	Poor hygiene	10	3	8	240	GMP training + sieve

Source: Authors, (2026).

IV. RESULTS AND DISCUSSION

IV.1 OVERALL DEFECT PERFORMANCE

With the summed tray-wise data, there is a total percentage of defects per product which is:

Table 9: Overall Defects.

Product	Total pieces N	Defectives D	Defect %
Jira Burnies	2352	65	2.76%
Coconut Burnies	2538	89	3.51%
Twin Toast	3036	73	2.40%
Ghee Toast	1622	63	3.88%

Source: Authors, (2026).

Twin Toast is the least defective (2.40%), and Ghee Toast is the most defective (3.88%). Jira Burnies does better slightly compared to Coconut Burnies. This order coincides with the perception of plants: toast products bake in a uniform manner more, and on burnies, even minor changes in dough consistency and ovaries should be considered.

IV.2 PARETO ANALYSIS OF DEFECT TYPES

Adding the categories of defects to all trays:

In the case of Jira Burnies and Coconut Burnies, the cumulative percentage of defect incidents result in Break (2), After Heat (i), and Break (2), After Heat (i). The rest are made up of handling related breakage, over- and under-burning.

With Twin Toast, breakage is specifically prevailing: nearly half of the total number of defects occur in cooling and packing: just under burn and over burn only have a smaller proportion (in line with the comparatively small "Under Burn" values in the data sheet).

In the case of Ghee Toast, the trend is corresponding, since the breakage rate is high and under- and over-burning play a significant role, particularly when the creamy layer is created on top of the toast, and therefore weakens mechanics.

In the Pareto charts, it can be seen that most of the defects in all the four products can be attributed to two causes of the problem, namely breakage and re-baking (after heat).

This implies that specific enhancement regarding:

a) Managing practices (packing, transfer, stacking), and

b) Consistency (time-temperature control, SOPs), Baking Standard: A parameter that specifies how food products behave during baking processes (Chang, 2019), can minimize the defect rates in general by 40-60% without significant capital outlay.

IV.3 SPC RESULTS FROM P-CHARTS

This has been done using the p-chart methodology mentioned above and the individual products have been put in separate charts. The mean line p bar of every product is the percentages of defects in Section 4.1 (0.0276, 0.0351, 0.0240, 0.0388). The UCLs are of approximately 9-13 percent with typical tray sizes (burnies: 48-60 pieces, toast: 38-43) and the LCLs are also generally at 0.

Key observations:

a. All products tray above UCL, that is, there are no intense special-cause spike in data.
b. Some trays have a somewhat larger Pi (e.g., when several pieces were not baked properly on a moist day) yet, they do not exceed the limits.
c. No long runs or systematic changes are present which implies that the processes are under statistical control.

The mean levels however differ:

a. Twin Toast and Jira Burnies are focused on the defect rates (approximately 2.4-2.8%).
b. Higher rates (~3.5-3.9 percent) are the key point of the Coconut Burnies and Ghee Toast.

So, SPC provides an indication of constant yet not equally able system. The sole measure of tracking will not necessarily make Coconut Burnies and Ghee Toast a better product, but alterations in structure (improved recipes, tray design, or SOPs) must be implemented to move the proportion defective measurement down the chart.

IV.4 WEIGHT CONTROL AND PROCESS CAPABILITY

Based on the product description, a 15 units Jira pack weighs approximately 170-180 g and an 8-unit Coconut pack 95-100 g (9 units: 105-110 g). Practically, operators have a predisposition to overfill so that they do not end up with small sizes of the weight packs as the weight inspections are often manual and rarely done. When the mean overfill is say even 3G/pack then in a batch of 260-300 packs added product accounts to almost 0.8-0.9 kg/ batch given away. This may turn out to be a considerable hidden cost over a number of batches and months. Based on the data provided of sample weights (the data are not provided here), $\bar{X}$-$\bar{R}$ charts generally indicate rather constant weight trends but with their average value being slightly above the nominal target. By entering such data into the capability formulas:

• C_p may be >1.33, it means that the dispersion of the process is tolerable.

• C_{pk}, however, tends to be less than, C_p as the process is not centered perfectly on; the mean is shifted to the higher specification limit (systematic overfill). This good/off-center mix agrees with qualitative observation which states that overweight packs are the most common and an underweight complaint is uncommon.

In this case, the packs with high weights and under-heating during re-baking are rated with significantly high RPNs since they are severe (cost and quality), recurring (high percentage of defects and pack-weight measurements), and not very easy to detect (manual checking, infrequent weighing). Breakage in handling is also an attractive score as it is prevalent in the data sheet. This RPN ranking will help the management to:

a. Implement SOPs / check-weigher / thermometer Introduce SOPs and measurement equipment (timer).
b. Redesigning tools of handling and stacking to reduce breakage.
c. Periodically check cutter/ tray condition to manage shape related problems.

V. CONCLUSIONS & RECOMMENDATION

The case study which is founded directly on the production data and material formulation of the bakery states that:

a. The total percentage of defects is between 2.40 and 3.88, Ghee Toast has the poorest performances, and Twin Toast has the best one.
b. I can tell that most defects are revealed as breakage and re-baking using pareto analysis and that SPC p-charts indicate that processes are quite stable and not equally competent.
c. The weights of the packs are often sampled high with respect to the nominal values which indicates that the packs will lose material to systematic overfill.
d. FMEA ranking displays overweight packs, underheating/re-baking and breakages during the handling process as the critical failure modes.

On the basis of these results, some recommendations that can be made in practice are derived:

1. Introduce basic SOPs on all the products:

a. Baking time temperature chart (e.g.,160 deg $°C$ in, 35 -40 m, specified tray loading).
b. Visual acceptance rules with the help of photo examples of acceptable and over/under-baked products.

2. Strengthen measurement and SPC:

a. Put in place naive digital clocks, oven heaters and check scale.
b. Entries to be used include use of X-R charts on pack weights and for defect rates and p-chart on a weekly basis.
c. Establish control limits on realism and interrogate by reviewing with the operators.

3.Handling: Improve the handling to minimize the breakage:

a. Reduce trays in stack height on cooling.
b. Training- be careful when transferring toast and burnies.
c. Take into consideration minor modifications on tray structure or design to prevent corner wastage.

4. Control overweight and calculate ROI:

a. Set some target net weight and acceptable tolerance of pack (ex: +3-5 g).
b. Divide content of each pack (6g) by four. Consider the result of the theoretical calculations of the batch yields in the materials sheet (Jira or Coconut): 260-300 packs/batch, 485-565 packs/batch), determine the result of the extra product estimation = 6 x packs/day x days/month. Divide by cost of ingredient to admit Tk/month loss and contrast with little investment required in check-weigher and training.

5.Use FMEA as a living document:

a. Provide update S, O, D ratings after every 3-6 months depending on new defect data and SPC data.
b. Two discrete items that are close of each other in terms of parameters are brought together by way of documented corrective actions and their effect is monitored by using updated Pareto and p-charts.

VI. AUTHOR'S CONTRIBUTION

Conceptualization: Muhammad Abdus Samad, Musfik Ahammed.
Methodology: Muhammad Abdus Samad, Musfik Ahammed.
Investigation: Musfik Ahammed.
Discussion of results: Muhammad Abdus Samad, Musfik Ahammed.
Writing – Original Draft: Muhammad Abdus Samad**,** Musfik Ahammed.
Writing – Review and Editing: Muhammad Abdus Samad, Musfik Ahammed.
Resources: Md. Musfik Ahammed.
Supervision: Muhammad Abdus Samad, and Musfik Ahammed.
Approval of the final text: Muhammad Abdus Samad, Musfik Ahammed.

VII. ACKNOWLEDGMENTS

The author would like to express his gratitude to all parties, starting from data collection and data processing so that this article can be compiled. Hopefully this article is useful and useful as learning material.

VIII. REFERENCES

[1] R. F. Ramadhan, E. Widowati, and M. Mardiana, "Failure Mode and Effect Analysis (FMEA) Application for Safety Risk Assessment Design of "X" Bakery," Unnes Journal of Public Health, vol. 8, no. 1, 2019.

[2] D. R. Kirubaharan and S. Chandra Bose, "Reduction of Defect Rate in Biscuit Production using Statistical Quality Control Process," Asian Res. J. Math., vol. 18, no. 4, pp. 50–57, Apr. 2022, doi: 10.9734/ARJOM/2022/v18i430373.

[3] M. Stefanova, "Risk Analysis and Impact of Raw Materials for Achievement of Sustainable Quality of Biscuit Products," Journal of Food Science and Engineering, vol. 7, no. 5, pp. 227–238, 2017, doi: 10.17265/2159-5828/2017.05.001.

[4] R. Laturrahmi, E. Fradinata, and Husni, "Minimizing Waste in The Bread Production Process with The Waste Assessment Model and Failure Modes and Effect Analysis (FMEA) Method," Jurnal Syntax Transformation, vol. 6, no. 5, pp. 28–38, May 2025.

[5] M. T. Ali, "Study Of Quality Assurance And Quality Control In Making Baked Products," International Journal of Creative Research Thoughts (IJCRT), vol. 12, no. 1, pp. d434–d444, 2024, doi: 10.1729/Journal.37535.

[6] M. Norhidayah, A. Noorlaila, and A. Nur Fatin Izzati, "Textural and sensorial properties of cookies prepared by partial substitution of wheat flour with unripe banana (Musa x paradisiaca var. Tanduk and Musa acuminata var. Emas) flour," Int. Food Res. J., vol. 21, no. 6, pp. 2133–2139, 2014.

[7] H. Hartono, M. R. Pratama, M. I. Hanafi, M. Nurali, and Y. Prastyo, "Reduction of Dimension Out Defects in Electronic Products Using Process Control Methods with Fish Diagrams and FMEA," Rev. J. Multidiscip. Soc. Sci., vol. 2, no. 1, 2024, doi: 10.59422/rjmss.v2i01.676.

[8] D. Dimas, "Process Control of Sack Production Using Failure Mode Effect Analysis (FMEA) and Fault Tree Analysis (FTA) Methods," JKIE (Journal Knowledge Industrial Engineering), vol. 10, no. 2, pp. 91–100, 2023, doi: 10.35891/jkie.v10i2.6189.

[9] J. A. Adeyanju, A. O. Abioye, G. O. Ogunlakin, A. A. Oloyede, and E. A. Amure, "Optimization of process variables for the production of cookies from wheat, fonio, and pigeon pea flour blends," J. Nutr. Health Food Eng., vol. 12, no. 2, pp. 73–77, Jun. 2022, doi: 10.15406/jnhfe.2022.12.00339.

[10] P. Fithri, M. Rafi, Pawenary, and A. S. Prabuwono, "Risk analysis of production process for food SMEs using FMEA method: a case study," E3S Web of Conferences, vol. 331, 02010, 2021, doi: 10.1051/e3sconf/202133102010.

[11] Y. N. Jaiswal and V. R. Khanzode, "Defect Rate Reduction in Biscuit Production Industry using SPC Technique," International Journal of Engineering Research & Technology, vol. 09, no. 11, 2020, doi: 10.5281/zenodo.18648180.

[12] M. Shihab, P. Reddy, G. Prabhu, and R. Patil, "Studies on Process Improvement in a Biscuit Manufacturing Industry Using DMAIC Approach," International Journal of Engineering Applied Sciences and Technology / IJEAST, vol. 6, no. 2, 2021.

[13] M. N. F. P. Putra and A. S. C. Cahyana, "Frozen Food Quality Control Using Statistical Process Control Methods and Failure Mode and Effect Analysis," Procedia of Engineering and Life Science, vol. 4, 2023, doi: 10.21070/pels.v4i0.1410.

[14] S. A. Halim Lim, J. Antony, and S. Albliwi, "Statistical Process Control (SPC) in the food industry – A systematic review and future research agenda," Trends in Food Science & Technology, 2014 (exact vol./issue/pages available in full-text sources).

[15] M. A. Swarnadi and A. E. Apsari, "Usulan Perbaikan Sistem Produksi Roti Manis Dengan Metode Statistical Quality Control Dan Failure Mode And Effect Analysis Di UMKM Dipo Bakery," Jurnal Rekayasa Proses dan Industri Terapan (REPIT), vol. 2, no. 3, pp. 38–52, 2024, doi: 10.59061/repit.v1i3.371.

[16] A. E. Boeriu and C. M. Canja, "The application of FMEA and Pareto Analysis Methods in the Process of Industrial Bread Making in Romania," Bulletin of the Transilvania University of Brasov. Series II: Forestry • Wood Industry • Agricultural Food Engineering, vol. 14, no. 63, p. 2.7, 2021, doi: 10.31926/but.fwiafe.2021.14.63.2.7.

[17] R. Thakore, R. Dave, and T. Parsana, "A Case Study: A Process FMEA Tool to Enhance Quality and Efficiency of Bearing Manufacturing Industry," 2015.

[18] N. Yusriyyah and C. R. Agrina, "Analysis of Product Quality Control Using Statistical Process Control (SPC) at Didik Bag Convection in Bandung," MASMAN Master Manajemen, vol. 3, no. 1, pp. 11–23, 2025, doi: 10.59603/masman.v3i1.687.

[19] E. Pramono, S. Noya, and Y. Ekawati, "Defect Analysis Using Failure Mode and Effects Analysis and Fault Tree Analysis: Case Study: Secondary Section PT PID Ongkowijoyo," Jurnal Sains dan Aplikasi Keilmuan Teknik Industri (SAKTI), vol. 4, no. 1, pp. 17–30, 2024, doi: 10.33479/sakti.v4i1.88.

[20] E. Krisnaningsih, S. M. Wirawati, and Y. Febriansyah, "Penerapan Statistical Process Control (SPC) dan Failure Mode Effect Analysis (FMEA) pada Proses Produksi Tisu Wajah," Jurnal PASTI (Penelitian dan Aplikasi Sistem dan Teknik Industri), vol. 14, no. 3, 2020, doi: 10.22441/pasti.2020.v14i3.007.

[21] K. J. Sileyew and S. Gebreyohanis, "Development of Integrated Lean Six Sigma-Baldrige Framework for Manufacturing Waste Minimization: A Case of NAS Foods Plc," in [Book title on Lean Six Sigma or related, IntechOpen chapter], 2021, doi: 10.5772/intechopen.95279. (Book chapter).

[22] S. Lim, J. Antony, and N. Arshed, "Critical Assessment on SPC Implementation in the UK Food Industry," in Proc. World Multiconference on Systemics, Cybernetics and Informatics, Orlando, USA, Jan. 2015.

[23] Monika, G. Chopra, and Sheetal, "Sensitivity and performance analysis of a three-unit soft biscuit manufacturing system with two types of repairers," International Journal of System Assurance Engineering and Management, 2024 (online), doi: 10.1007/s13198-024-02434-4.

Journal of Engineering and Technology for Industrial Applications

ISSN ONLINE: 2447-0228

ITEGAM-JETIA

Manaus, v.12 n.60, p.312-318, July/August, 2026.
DOI: https://doi.org/10.5935/jetia.v12i60.3784

RESEARCH ARTICLE OPEN ACCESS

DESIGN AND VERIFICATION OF AN OPTIMIZED 32-BIT PIPELINED MULTIPLIER FOR HIGH PERFORMANCE COMPUTING

C.S. Chakradhar[1], M. Sreedhar[2]

[1]PG Scholar, Department of ECE, JNTUA College of Engineering, India.
[2]Assistant Professor Ad-hoc, Department of ECE, JNTUA College of Engineering, India.

[1]https://orcid.org/0009-0005-8609-9615, [2]https://orcid.org/0000-0003-1111-7450

Email: sricr324@gmail.com, sreedhar470@gmail.com

ARTICLE INFO

Article History
Received: March 2, 2026
Reviewed: June 10, 2026
Accepted: July 10, 2026
Published: July 31, 2026

Keywords:
Modified Booth Encoding
Pipelining
Radix-8
Partial products reduction
Delay

ABSTRACT

Arithmetic operations are fundamental to digital signal processing systems, where multipliers often decide overall performance constraints. They are key components of many high-performance systems such as Microprocessors, FIR Filters, Digital Signal Processors etc. The most common way of performing signed multiplication in digital circuits is by using booth multipliers, but the existing algorithm has a drain on power consumption since it never coerces operations to the full precision. In this paper, a novel 32-bit pipelined multiplier is designed aimed at achieving high throughput and low power consumption for VLSI applications. Modified Booth Encoding (MBE) with Radix-8 and Wallace tree reduction for partial products reduction and along with a CLA adder for partial products addition is used. Furthermore, a linear Pipelining technique with flipflops is implemented to minimize critical path delay. The Register Transfer level (RTL) model was implemented using Verilog and synthesized using Xilinx Vivado. Performance analysis demonstrates the reduction of delay by 23% and power consumption by 61%.

Copyright ©2026 by authors and Galileo Institute of Technology and Education of the Amazon (ITEGAM). This work is licensed under the Creative Commons Attribution International License (CC BY 4.0).

I. INTRODUCTION

The Arithmetic Logic Unit (ALU) is the fundamental computational unit in modern digital computers and signal processors, and multiplication has been one of the most time-consuming and hardware-intensive operations [1-3]. With the growing need for high-speed and real-time data processing in various applications like image processing, machine learning accelerators, and telecommunications, the need to have high throughput and energy-efficient digital multipliers has taken centre stage [4-6]. Three consecutive stages, namely partial product generation, partial product reduction, and final addition, are what define the performance of a digital multiplier [7]. To maximize the former, Modified Booth Encoding (MBE) ranks among the most commonly used techniques to minimize the number of partial products. While Radix-4 MBE halves the partial product rows, higher bit-widths (e.g., 32-bit or 64-bit) still cause serious routing loads. Radix-8 MBE brings the number of partial product rows down to N/3 (only 11 rows in a 32-bit operand), bringing the area of the next reduction step down to a minimum [8-10]. The implementation of this higher radix, however, poses the architectural challenge of generating the hard multiple (3A), which needs extremely optimized Digital Signal Processing (DSP) logic and routing [11]. To alleviate the build-up of delay during the reduction stage, the Wallace tree architecture is favoured over Carry-Look Ahead trees, as it avoids propagating carries across the horizontal logic path [12]. Moreover, the pipelining implementation in the multiplier architecture decouples combinational logic paths containing registers, improving the maximum operating rate considerably while concentrating switching activity, thereby decreasing dynamic power loss [13], [14]. Based on these architectural considerations, this paper presents the design and implementation of a high-speed 32-bit pipelined multiplier. The primary objective is to overcome the routing bottlenecks of standard multipliers by integrating Radix-8 MBE with a Wallace tree reduction structure. This study further implements a Carry Look-Ahead (CLA) adder for the final stage and utilizes a multi-stage pipelining technique to minimize critical path delay. The proposed architecture is modeled in Verilog HDL and synthesized using Xilinx Vivado to analyze delay and power efficiency.

II. LITERATURE REVIEW

II.1 BOOTH'S ALGORITHM

First introduced by Andrew D. Booth in 1950 in his crystallography work, the algorithm of Booth transformed the binary form of multiplication by identifying that mechanical shifting operations are computing faster than sequential additions[1], [15], [16]. The algorithm supports both signed and unsigned binary numbers equally using two complement representation. As it performs the operation, every bit of the multiplier yields a multiple of the multiplicand and this is added to the partial product accumulated. The overall latency of a standard multiplier is therefore dominated strongly by the number of addition operations to be made. To further increase the level of performance, parallel counting methods like Modified Booth Encoding (MBE) algorithm were created to provide a staple standard in the modern design of VLSI chips. Even though the standard Booth algorithm can efficiently and beautifully deal with signed multiplication, the performance of this algorithm is very dependent on the bit pattern of the multiplier. The algorithm is very efficient when the multiplier operand is a long sequence of continuous ones or zeros, since all it does in this case is to shift the partial product. Nevertheless, in the presence of runs of ones and zeros alternating (e.g. 0101010101), the algorithm has to make an addition or subtraction operation at almost every bit in the sequence [1].

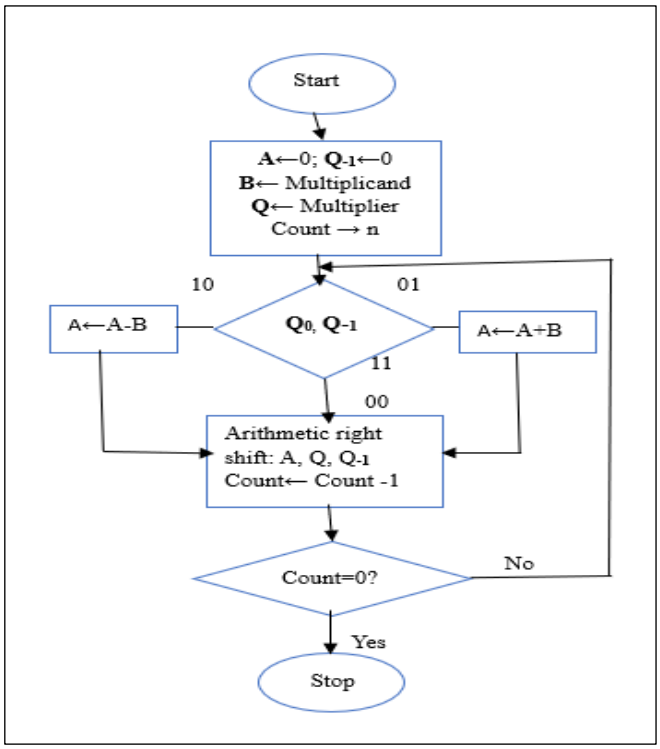


Figure 1: Flow Chart of Booth Multiplier.
Source: Authors, (2026).

II.2 MODIFIED BOOTH'S ALGORITHM (RADIX-4)

Radix-4 does an excellent job of reducing the number of partial products by a half compared to normal Booth algorithm [17]. It does this through multiplier bits evaluation in groups of three with overlapping functions. This 3-bit scanning window defines the current operands values, with the two leftmost bits as the current operands' values, and the third bit being the carry-in of the past two variables.

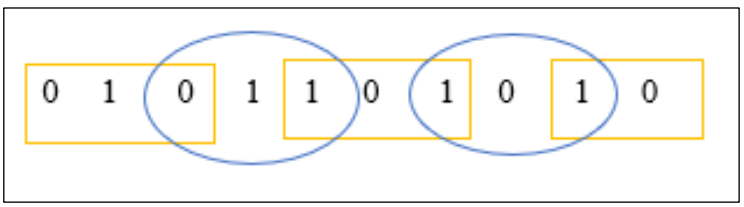


Figure 2: Grouping of multiplier bits in radix-4.
Source: Authors, (2026).

The encoding process reads starting at the Least Significant Bit (LSB) through the Most Significant Bit (MSB). In order to process the preliminary evaluation, the LSB is pre-padded with a ghost zero at position of i−1. The next step element of 3-bit window coincides with the MSB of the last group that was examined. The initial technique is this complementary procedure, which describes the arithmetic weights of the binary inputs, into a set of these five operative co-efficients: −2, −1, 0, +1, and +2 [17].

Table 1: Radix-4 booth encoding.

Block	Recoded digit		Operation on 'A'
000	0		0A
001	+1		+1A
010	+1		+1A
011	+2		+2A
100	−2		−2A
101	−1		−1A
110	−1		−1A
111	0		0A

Source: Authors, (2026).

The initial step produces a partial product matrix with the MSB determining the arithmetic weight, which is 0 (positive) with unsigned operations and 1 (negative) with two's complement arithmetic. This is implemented as logical AND operations with the input vectors. At this final step, these partial products in completed form are reduced to two separate vectors (sum and carry) now used to calculate the final product (P).

III. PROPOSED METHODOLOGY

III.1 RADIX-8 MODIFIED BOOTH'S ALGORITHM

Although Radix-4 reduces the partial products by half, a 32-bit operand gives 16 rows. Hence, a significant limitation remains. The large volume causes a large routing bottleneck, and huge critical path delay and limits the design to low-frequency operations [8]. In order to eradicate this bottleneck, sophisticated partial product reduction schemes are necessary, and the long combinational path way is to be subdivided into more stages.

A. Modified Booth Encoding and PP Generation

To achieve the proposed architecture, Radix-8 MBE has been implemented that further reduces the operands into 11 PP rows [7], [8], [18], [19]. In this architecture, the bits of the multiplier are divided into groups of four, with one bit overlap between the two groups. The number of bits to shift the multiplicand left is strictly calculated as

$$Shift{=}group\ index \times 3 \tag{1}$$

(e.g. if Group 2 has bits 1110, then -1A << 2(6)), where A is the multiplicand.

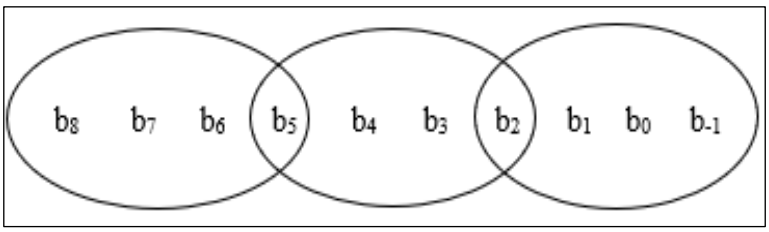


Figure 3: Grouping of multiplier bits with radix-8.
Source: Authors, (2026).

The multiplicand (A) is multiplied using a control signal or an instruction depending on the bits of the multiplier of each group. These rules are usually ordered between {-4, +4} radix-8 as in the table below.

Table 2: Radix-8 booth encoding.

Group	Recoded digit	Operation on 'A'
0000	0	0A
0001	+1	+1A
0010	+1	+1A
0011	+2	+2A
0100	+2	+2A
0101	+3	+3A
0110	+3	+3A
0111	+4	+4A
1000	−4	−4A
1001	−3	−3A
1010	−3	−3A
1011	−2	−2A
1100	−2	−2A
1101	−1	−1A
1110	−1	−1A
1111	0	0A

Source: Authors, (2026).

Upon the generation of the 11 PPs, they are entered into the pipeline register that is usually D-flipflop 1. It is essentially a storage device, which stores and synchronizes the data to use in the following clock cycle. The 11 PP rows are then loaded into our proposed Wallace tree 3:2 compressor reduction method. These 11 PP rows are trimmed to leave less load on the final CLA adder which makes the product easier to reduce and calculate.

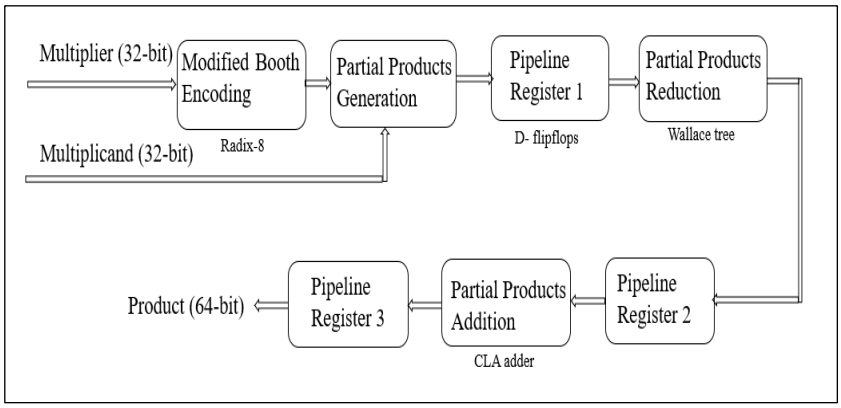


Figure 4: Modified Multiplier block diagram with pipelining and Wallace tree.
Source: Authors, (2026).

B. Pipelining

Pipelining is a structural optimization technique that improves the throughput in a calculation by inserting storage elements (pipeline registers) between diverse processing steps [13], [20]. These types of D-flip-flop registers merely grab a bit of in-between data and then one can select blocks of combinational logic to be isolated synchronously. Each set of operands must be processed in more than the usual Radix-4 algorithm in the proposed architecture, whereby 32-bit data makes sure that the data is continually flowing in a stream with multiple clock cycles necessary to complete each set of operands.

C. Wallace Tree Structure

This structure is firstly introduced by Chris Wallace in 1964, [12] to compress through Carry-Save Adders (CSAs) rather than the classical ripple-carry propagation [21-23]. In this compression step, 3:2 compressors are to be used. The length of two vectors Sum and a Carry is squeezed into three (n-bit) input vectors (e.g. A, B and C) using a CSA. A Carry Save Adder computes the sum of 3 or more n-bit numbers and gives 2n-bit numbers and will result two numbers of same length called Sum(S) and Carry(C). For three input bits A, B, and C that come from the partial product rows, the sum and carry is:

$$\text{i.} \qquad \text{Sum (S)} = A \oplus B \oplus C \tag{2}$$

This is an XOR operation. It checks if the number of 1's is odd.

$$\text{ii.} \qquad \text{Carry (C\_out)} = (A \,.\, B) + (B \,.\, C) + (C \,.\, A) \tag{3}$$

Where these two sum and carry vectors are 64-bit vectors each that will be fed to stage 2 pipeline and the values will be held and synchronized and eventually presented to the Carry Look Ahead (CLA) adder to add the final 64-bit product.

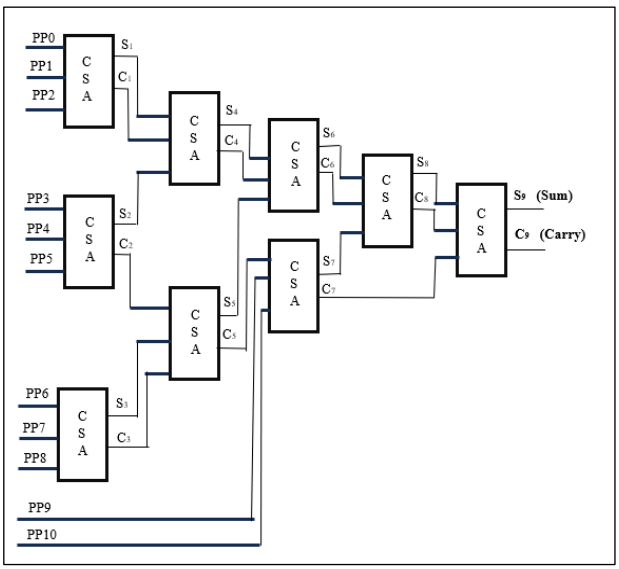


Figure 5: Partial Products Reduction by 3:2 compressor Wallace tree with CSA.
Source: Authors, (2026).

D. Carry Look-Ahead(CLA) Adder

A CLA adder is used to compute carry bits simultaneously with the other bits instead of having to wait until previous computations are done with the result. In each bit position, each logic tests two conditions on whether the bit is being calculated depending on the inputs Ai and Bi [8], [24], [25].

i) Generate (Gi) : Ai . Bi (both i/p's are 1)
ii) Propagate (Pi) : Ai ⊕ Bi (one i/p is 1)

If we have both G and P values for a bit pair, we can calculate the Carry out (C_out) as follows:

$$C\_out = Gi + Pi \,.\, C\_in \tag{4}$$

To calculate the C_in, assume the initial C0 is Zero. Then the carry 1 for bit 1 is

$$C1 = G1 + (P0 \,.\, C0). \tag{5}$$

After the 64-bit product is produced, it will be sent to final pipeline stage for steadiness and synchronizing for next clock cycle. The whole process of the proposed architecture is controlled by the positive-edge triggered clock signal [14], additionally in the three stages in the following way:

Clock Cycle 1: MBE block samples the multiplicand and multiplier. On the first clock cycle, the 11 latched PP rows are calculated and latched to Pipeline Register 1, and

Clock cycle 2: The Wallace tree reduces them to two vectors (Sum and Carry), which are latched to the Pipeline Register 2 memory. At the same time, Stage 1 initiates the next group of operands processing.

Clock Cycle 3: The CLA adder calculates the final 64-bit product of the two vectors which gets stabilized in the last output register at the third clock step.

IV. RESULTS AND DISCUSSIONS

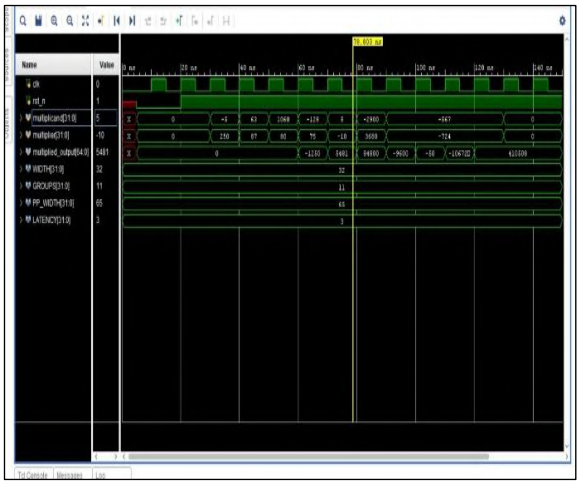


Figure 6: Output in signed values.
Source: Authors, (2026).

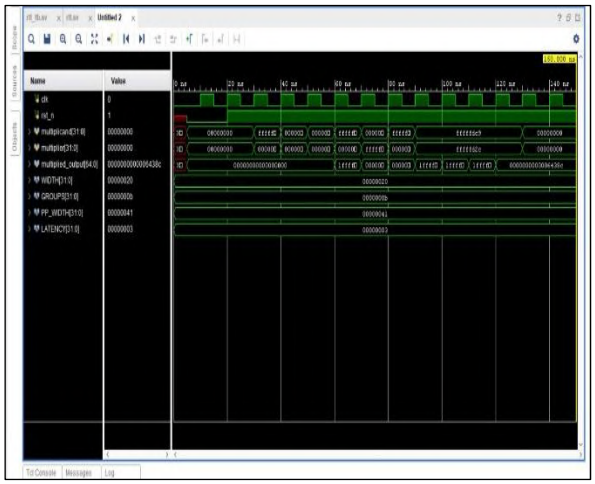


Figure 7: Output in hexadecimal values.
Source: Authors, (2026).

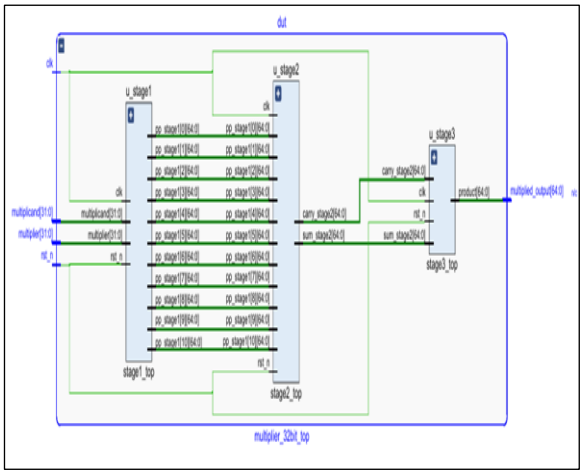


Figure 8: Schematic diagram 1.
Source: Authors, (2026).

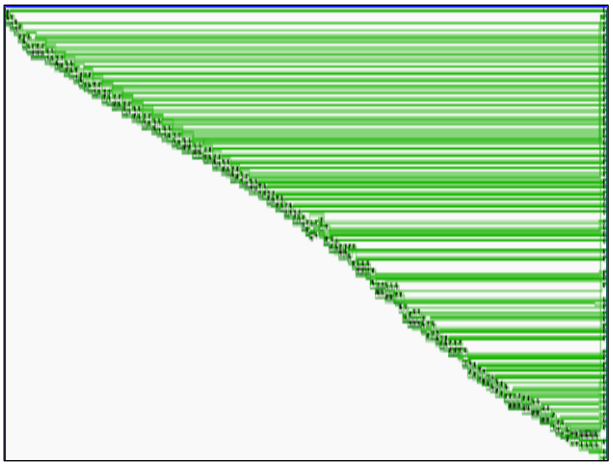


Figure 9: Schematic diagram 2.
Source: Authors, (2026).

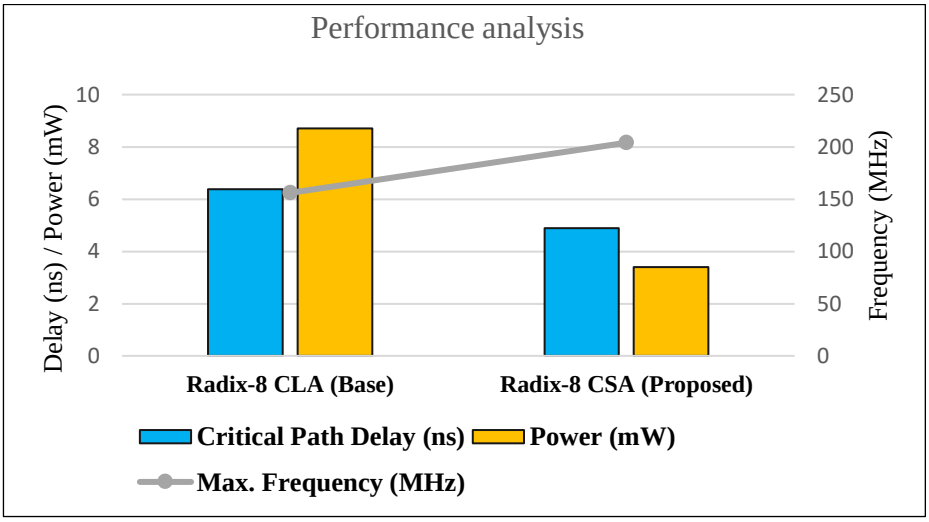


Figure 10: Performance analysis of multipliers.
Source: Authors, (2026).

The synthesis results demonstrate highly efficient hardware utilization. The Critical path delay was recorded at 4.895 ns, yielding a maximum operating frequency (F_{max}) at 204 MHz. The total on-chip power at this frequency was restricted to 3.39 mW. A detailed power breakdown reveals that dynamic power dominates, with pipeline registers accounting for 52.32% of the total power and the combinational logic accounting for 46.16%.

V. CONCLUSIONS

This paper presented the design, implementation, and verification of a high-performance 32-bit multiplier utilizing a 3-stage pipelined Radix-8 Modified Booth Encoding (MBE) architecture. The proposed design successfully mitigated traditional routing congestion and minimized the critical path delay by replacing conventional linear reduction schemes with a Carry Save Adder (CSA)-based Wallace tree structure, which accelerated the compression of the 11 partial product rows. Synthesis results demonstrate that the architecture achieves a delay of 4.895 ns and power consumption of 3.39 mW, representing a 23% reduction in delay and a 61% improvement in power efficiency compared to standard designs. These results confirm that the proposed multiplier architecture is highly suitable for integration into modern DSP systems and high-speed VLSI applications.

VI. AUTHOR'S CONTRIBUTION

Conceptualization: C.S. Chakradhar, M. Sreedhar.
Methodology: C.S. Chakradhar, M. Sreedhar.
Investigation: C.S. Chakradhar, M. Sreedhar.
Discussion of results: C.S. Chakradhar, M. Sreedhar.
Writing – Original Draft: C.S. Chakradhar, M. Sreedhar.
Writing – Review and Editing: C.S. Chakradhar, M. Sreedhar.
Resources: C.S. Chakradhar, M. Sreedhar.
Supervision: C.S. Chakradhar, M. Sreedhar.
Approval of the final text: C.S. Chakradhar, M. Sreedhar.

VII. REFERENCES

[1] N. Weste and D. Harris, CMOS VLSI Design: A Circuits and Systems Perspective, 4th ed. Boston, MA: Addison-Wesley, 2010.

[2] J. M. Rabaey, A. P. Chandrakasan, and B. Nikolic, Digital Integrated Circuits: A Design Perspective, 2nd ed. Pearson, 2003.

[3] IEEE Standard for Verilog Hardware Description Language, IEEE Std 1364-2005, 2006.

[4] Texas Instruments, "Digital Signal Processing Solutions and Architectural Advantages," TI Application Report, SPRU041, 2021.

[5] Y. C. Tseng, et al., "Area-Power-Delay-Efficient Multi Modulus Multiplier Based on Area-Saving Hard Multiple Generator Using Radix-8 Booth-Encoding Scheme," Electronics, vol. 13, no. 2, 2024.

[6] M. Waris et al., "AxBMs: Approximate Radix-8 Booth Multipliers for High-Performance FPGA-based Accelerators," IEEE Transactions on Circuits and Systems II: Express Briefs, 2021.

[7] A. Sharma and P. Kumar, "Design and Analysis of Multipliers using Radix-8 Booth Encoder," International Journal of Engineering Research & Technology (IJERT), vol. 10, no. 5, 2021.

[8] R. Kumar, et al., "Design and implementation of RADIX-8 based 32-bit pipelined multiplier by using CLA," Journal of Engineering and Applied Sciences, 2017.

[9] R. Orugu, "FPGA Design and Implementation of Approximate Radix-8 Booth Multiplier," 3rd International Conference on Distributed Computing and Electrical Circuits and Electronics (ICDCECE), IEEE, 2024.

[10] S. R. Kuang et al., "Factored Systolic Arrays Based on Radix-8 Multiplication for Machine Learning Acceleration," IEEE Transactions on Computers, 2024.

[11] Xilinx Inc., "Ultra Scale Architecture DSP Slice User Guide," UG579 (v1.10), AMD Adaptive Computing, 2021.

[12] C. S. Wallace, "A suggestion for a fast multiplier," IEEE Transactions on Electronic Computers, vol. EC-13, no. 1, pp. 14-17, 1964.

[13] M. Patel and S. Gupta, "Design of energy-efficient multiplier based on 32-bit architectures," International Journal of Advanced Technology and Engineering Exploration, 2022.

[14] S. Rao, "A High-Speed 32-bit Signed/Unsigned Pipelined multiplier, "International Journal Microelectronics and Computer Science, 2023.

[15] O. L. MacSorley, "High-speed arithmetic in binary computers," Proceedings of the IRE, vol. 49, no. 1, pp. 67 91, 1961.

[16] A. D. Booth, "A signed binary multiplication technique," The Quarterly Journal of Mechanics and Applied Mathematics, vol. 4, no. 2, pp. 236-240, 1951.
[17] K. Reddy, "Implementation of Radix-4 32-bit Booth Multiplier using VHDL," IJERT, vol. 12, no. 6, 2023.

[18] K. L. Reddy et al., "Compressor-Based Precise Blended Wallace Tree Multiplier Architecture for Signal Processing Applications," 4th International Conference on Emerging Research in Electronics, Computer Science and Technology (ICERECT), IEEE, 2022.

[19] T. N. V. Krishna et al., "Enhancing the Efficiency of Wallace Tree Multipliers Through Optimized ECSLA Design," IEEE International Conference, 2023.

[20] M. V. Ramana et al., "Delay Enhancement of Wallace Tree Multiplier with Binary to Excess-1 Converter," IEEE International Conference, 2023.

[21] V. Kumar, "Design and Implementation of Pipelined Wallace-Tree Multiplier," International Journal of Computer Engineering and Technology (IJCET), 2024.

[22] L. Dadda, "Some schemes for parallel multipliers," Alta Frequenza, vol. 34, pp. 349-356, 1965.

[23] P. S. Rao et al., "VLSI Design of Majority Logic based Wallace Tree Multiplier," IEEE International Conference, 2023.

[24] M. Ali, "Design of Power and Area Efficient Approximate Multipliers for DSP Applications," Journal of Electronic Testing, 2022.

[25] M. Pedram et al., "Dual-quality 4:2 compressors for utilizing in dynamic accuracy configurable multipliers," IEEE Transactions on Very Large-Scale Integration (VLSI) Systems, 2017.

Journal of Engineering and Technology for Industrial Applications

ISSN ONLINE: 2447-0228

ITEGAM-JETIA

Manaus, v.12 n.60, p.319-328, July/August, 2026.
DOI: https://doi.org/10.5935/jetia.v12i60.3789

RESEARCH ARTICLE OPEN ACCESS

PREDICTIVE COURSE PLACEMENT: UTILIZING AN ARTIFICIAL INTELLIGENCE-BASED APPROACH FOR RECOMMENDATIONS THROUGH THE APPLICATION OF COSINE SIMILARITY AND MULTI-MODEL ARCHITECTURES

Manocher C. Alipour*[1]

[1]Bachelor of Science in Information Technology Program, Isabela State University, Angadanan, 3307, Isabela, Philippines.

[1]https://orcid.org/000 9-0006-9594-8233

Email:*Manocher.c.alipour@isu.edu.ph

ARTICLE INFO

Article History
Received: February 23, 2026
Reviewed: June 10, 2026
Accepted: July 10, 2026
Published: July 31, 2026

Keywords:
Recommendation model,
Educational Data Mining,
Machine Learning,
Ensemble Model,
XGBoost.

ABSTRACT

Accurately placing students in appropriate academic programs, such as determining whether they are better suited for a particular course, is fundamental to student success and retention. This study aims to construct a recommendation model that uses data mining and machine learning techniques to guide currently enrolled students in their program to make better selections. The research proposes a multi-model architecture that integrates a content-based cosine similarity matching component with three distinct machine learning classifiers, namely Logistic Regression, Random Forest, and XGBoost. In addition, the models were trained and evaluated using 10-fold cross-validation. Performance evaluations revealed that XGBoost was the most effective individual classifier, achieving a mean accuracy of 91.7%, an ROC-AUC of 97.5%, and a positive-class F1 score of 90.4%. The ensemble model also demonstrated strong predictive and recommendation performance, achieving 90.6% accuracy and 96.8% ROC-AUC. Logistic Regression achieved an accuracy of 88.7%, while the Random Forest model lagged with an accuracy of 83.8%. The findings demonstrate that XGBoost and Ensemble models are the most reliable and effective classifiers for predicting student course placement on this specific dataset. This hybrid recommendation engine successfully translates historical and input data into actionable, data-driven insights to help students make informed decisions about their academic careers.

Copyright ©2026 by authors and Galileo Institute of Technology and Education of the Amazon (ITEGAM). This work is licensed under the Creative Commons Attribution International License (CC BY 4.0).

I. INTRODUCTION

The fast and unpredictable life demands a recommendation engine tool that recommends content to users and machines based on their preferences and interests, using algorithms to analyze their needs, likes, and wants, drawing on historical data, user experience, academic performance, business interests, and other relevant factors, to create individualized recommendations [1-3]. Ensemble recommendation models [4], [5] in education combine multiple sources of information or numerous recommendation strategies to improve recommendations. The society, which relies heavily on knowledge and information interaction, is a key component in technological innovation and a fundamental tool for developing teaching methodologies. Many policymakers in developing countries consider upper-secondary technical and vocational education and training critical to economic growth and poverty reduction[6], [7]. The education system in the Philippines aims to develop high-level professionals who directly impact leadership, business, and employability, advance knowledge through research, and apply new knowledge to improve the quality of human life, industrialization, development, and careers [8]. These recommendation models may include collaborative filtering, content-based filtering, matrix factorization, and hybrid approaches that integrate multiple techniques to improve recommendation accuracy [9-13]. Cosine similarity [14-16] is a metric used in data analysis to evaluate the degree of similarity that is not zero and located within an inner product space between two vectors. This angle is determined by dividing the dot product of the vectors by the product of their magnitudes. The cosine similarity is not dependent on the magnitudes of the vectors, which are solely governed by the angle by which they are oriented.

It is always the case that the cosine similarity falls inside the range of [-1, 1]. The knowledge and understanding to classify the student's academic courses/track have been observed and challenged for a long time. It is regarded as an essential topic of study across a variety of fields, as it benefits both families, students, and decision-makers. However, the primary purpose of the research was to construct a model that can be recommended to students in the field of information technology using recommendation techniques. This pertains to the research study that used a recommender model and data mining techniques to provide results on student academic performance. Accurately placing students in appropriate courses or academic programs is fundamental to student success and retention. Course placement in this context refers to assigning students to the most suitable academic program or track, for example, determining whether a student successfully graduates from the Bachelor of Science in Information Technology (BSIT) program or the Bachelor of Science in Computer Science (BSCS) program based on their prior and current achievements, skills, and characteristics. Proper placement ensures that students are neither overwhelmed nor under-challenged, thereby improving learning outcomes and satisfaction. Traditionally, such placement decisions have relied on entrance exams, counselor judgments, and heuristics that may not fully capture a student's multifaceted background. The increasing availability of educational data has opened the door for data-driven approaches to augment these decisions. In recent years, different techniques in Machine Learning (ML) and artificial intelligence (AI) [17-20] been actively explored as tools for predicting student performance and recommending personalized academic paths, not only for students but also for policymakers and decision-makers. These models can analyze huge student datasets to recognize complex patterns and predict academic outcomes. Deep learning models, in particular, can capture nonlinear relations and connections that traditional statistical methods might overlook. For instance, predictive models have been one way used to identify at-risk students in need of intervention, sometimes integrating behavioral data, such as online learning activities, with demographic and grade information to trigger timely support. Applying these techniques to course placement, recommending the most appropriate course or major for a student, poses unique challenges, such as classification problems that include multiple classes (different programs) and require a balance between accuracy, interpretability, and fairness in an academic context. This study addresses the issue of identifying students based on first and second-year subjects, demographics, family background, and other factors to determine whether they should continue the course, since there are a number of students who are studying in different courses however, their grades are more suitable for other courses. The rest of this study is as follows: Section 2, Literature review, describes other researchers' views on the different recommended approaches; Section 3, Methodology, describes in detail how the ensemble approach works, from data input to final predictions. Furthermore, Section 4 Results and discussions present evaluations of metrics, and results from distinct algorithms and an ensemble pipeline using various metrics. Lastly, Section 5 concludes by brief the key findings of the study.

II. RELATED WORKS

In this section, researchers explore the different methods and approaches used by other researchers in this field. Logistic Regression (LR) has often been used as a baseline for binary classification tasks, such as predicting dropout or pass/fail, due to its simplicity and interpretability [21-25]. Traditional classification models such as decision trees, logistic regression, and Naïve Bayes have been widely used to predict student success and choices the said algorithms widely used in different systems and approaches, due to their simplicity and interpretability. Complex ensemble methods and hybrid systems have recently gained attention for their superior accuracy. Learning approaches that combine multiple algorithms have been shown to improve robustness and predictive performance across different categories, including educational tasks [26-32]. Combining several classifiers and algorithms, such as SVM, KNN, and linear regression, Random Forest (RF) [33], [34], XGBoost (XGB) [3], [35-37] (but not limited to), results in building an ensemble model this approach in may cases improve accuracy compared to individual models when predicting different categories of data, including student education placements. Deep learning models, especially recurrent neural networks like LSTMs, have also been applied to educational data, where temporal or sequential Patterns are relevant [38]. Researchers found that a LSTM network analyzing students' time-series behavior in a learning management system outperformed eight conventional classifiers in predicting early course performance. The LSTM-based method improved accuracy and earlier detection of at-risk students using clickstream data, highlighting the value of both ensemble methods and LSTMs for educational predictions [39-43]. Content-based methods computing similarities to make recommendations: each student's profile and each course/program's profile are represented as vectors, and the closest match is found. Techniques such as term frequency-inverse document frequency (TF-IDF) [44-46], vectorization, and cosine similarity have been employed in course recommendation systems to measure how well a student's profile matches a course's content or requirements. Use of TF-IDF on course descriptions and cosine similarity to recommend courses to students based on content alignment [47], [11].

II.1 MODEL SELECTION AND EVALUATION

II.1.1 Algorithms

The researcher established a comprehensive and multiple evaluation benchmark for the algorithms used in this study: multinomial Logistic Regression (LR), Random Forest (RF), XGBoost (XGB), and term frequency-inverse document frequency (TF-IDF) by selecting the following algorithms and ensemble models.

II.1.2 Term Frequency-Inverse Document Frequency

TF-IDF The similarity score ranges from -1 to 1 for TD-IDF values. A value of 1 indicates that the vector points in the same direction and is perfectly aligned at 0 degrees. Value 0 indicates that the vectors are orthogonal (perpendicular, with an angle of 90°), i.e., uncorrelated, and a value of **-1** indicates that the vectors are pointing in opposite directions (angle of 180°). The system computes cosine similarities for all training documents, identifies the nearest neighbor based on the highest cosine similarity in dataset, and predicts the label for the input content that is most similar to the training data, resulting in the items with the greatest cosine similarities being recommended as the most related.

Term frequency where $\mathrm{tf}(t,d)$ stands for Term Frequency: the frequency of a term t in document d. $\mathrm{idf}(t)$Stands for Inverse Document Frequency, which measures how much information the word provides. The rarer the word in a document, the higher the value of the word in terms of information.

$$tf(t,d) = \frac{f(t,d)}{\sum_{t'} f(t',d)} \tag{1}$$

Cosine similarity dot product represented by numerator x,v, which shows the inner product of two vectors to represent the product magnitudes (Euclidean, norms, lengths) of vectors x and v represented by ||x|| ||v||.

$$\text{CosineSim } \text{sim}_{cos}(x,v) = \frac{x \,.\, v}{||x||\,||v||} \tag{2}$$

II.1.3 Logistic Regression

Logistic regression directly computes probabilities using the SoftMax function. Many researchers use it for text classification because it provides the probability that each feature has on the task. Softmax regression, or multinomial logistic regression, uses TF-IDF feature vectors to identify and predict content labels. The TF-IDF and logistic regression model compute a score for each possible class via a linear combination. Logit represents the raw, unnormalized score produced before it is passed to an activation function like Softmax. Where the value z_k is referred to as a linear predictor or logit

$$z_k = w_k^T + b_k \tag{3}$$

The SoftMax function gets the z_k to produce a probability distribution over the classes. Where K is the total number of classes. In General Machine Learning Context, linear combination is a fundamental building block across many models.

$$\mathrm{P}(y = k|x) = \frac{exp^{z_k}}{\sum_{j=1}^{K} exp^{z_j}} \tag{4}$$

II.1.4 Random Forest

The random forest using the TF-IDF features as input, each decision tree in the random forest produces its own predicted class for the given input, and then aggregates these individual predictions to make a final decision based on majority voting. Nonlinear classifiers in the RF branch can capture interactions among TF–IDF features. Where where $\hat{y}$ is the final predicted value and b is the total number of trees in the forest and $\hat{y}_b(x)$ is the prediction of the b-th decision tree for the input x.

$$\hat{y}_{RF} = mode(\{\hat{y}_1(x), \hat{y}_2(x), \ldots\ldots, \hat{y}_b(x)\} \tag{5}$$

II.1.5 XGBoost

The objective function ($\mathcal{L}$), which includes a loss function term $l(y_i, \hat{y}_i)$and a regulatory term $\Omega(f_t)$, Regularization helps mitigate the risk of overfitting

$$\mathcal{L} = \sum_i \mathrm{l}(\mathrm{y_i}, \hat{\mathrm{y}}_\mathrm{i}) + \sum_i \Omega(\mathrm{f_t}) \tag{6}$$

regularized objective where w are the output scores for the leaves with respect to the tree and T is the number of leaves in the given tree; the value of γ controls the minimum loss-reduction gain needed to split an internal node. Shrinkage is an additional regularization parameter in XGBoost that reduces the step size in the additive expansion. A secondary advantage of reduced tree complexity is that models are trained faster and require less storage space. Finally, the complexity of the trees can also be limited using other strategies, such as limiting the tree depth.

$$\Omega(\mathrm{f_t}) = \gamma \mathrm{T} + \frac{1}{2}\lambda||\mathrm{w}||^2 \tag{7}$$

II.2 PERFORMANCE METRICS

In this section, the researcher discusses the metrics used to validate the results of this study, applying multiple validation metrics that are widely used by researchers.

Accuracy: as the total number of correctly classified instances and It treats all classes equally. where N is the total number of predictions. , $\hat{y}_i$ is the predicted value for the i-th instance, y_i is the actual true value for the i-th instance and $1(\hat{y}_i = y_i)$ It takes the value 1 for accurate prediction and 0 otherwise, due to the indicator function's binary nature. The $\Sigma_{i=1}^{N}$ sums the total number of correct predictions.

$$Accuracy = \frac{1}{N}\Sigma_{i=1}^{N} 1(\hat{y}_i = y_i) \tag{8}$$

Precision Calculation: the precision of a specific class, where k is the ratio of true positives (TP_k) to the total number of instances predicted as positive for that class $(TP_k + FP_k)$, includes both true positives and false positives (FP_k).

$$Precision_k = \left(\frac{TP_k}{TP_k + FP_k}\right) \tag{9}$$

Macro recall measures the classifier's ability to correctly identify instances of each class, averaged equally across classes. It is especially useful when missing minority classes are costly. TP_k: True Positives for class k, the number of instances correctly identified as belonging to that class. FN_k: False Negatives for class k refer to instances that belonged to the class k but were missed by the model. This metric measures the classifier's completeness or sensitivity in identifying all relevant cases of that class.

$$Recall_k = \frac{TP_k}{TP_k + FN_k} \tag{10}$$

Macro F1 is the unweighted mean of per-class F1 scores. It balances precision and recall per class and is robust to class imbalance by preventing dominant classes from overwhelming the metric. The F1 score for class k is the mean of precision and recall, balancing these metrics into a single value. Precision (Precision_k) measures the accuracy of positive predictions for class k, while recall (Recall_k) identifies actual positive instances. The F1 score is mostly useful for imbalanced datasets as it better reflects model performance on the positive class than simple accuracy.

$$F1_k = \frac{2 \cdot \text{Precision}_k \cdot \text{Recall}_k}{\text{Precision}_k + \text{Recall}_k} \tag{11}$$

Area Under the Curve: measures a model's ability to differentiate between positive and negative classes for an individual class k, denoted as (AUC_k). It is an integral of the True Positive Rate (TPR) over the False Positive Rate ($x = FPR$). This integral formulation is a known method for computing the AUC from the ROC curve definition.

$$\text{AUC}_\text{k} = \int_0^1 \text{TPR(x)} d\,x \tag{12}$$

III. METHODOLOGY

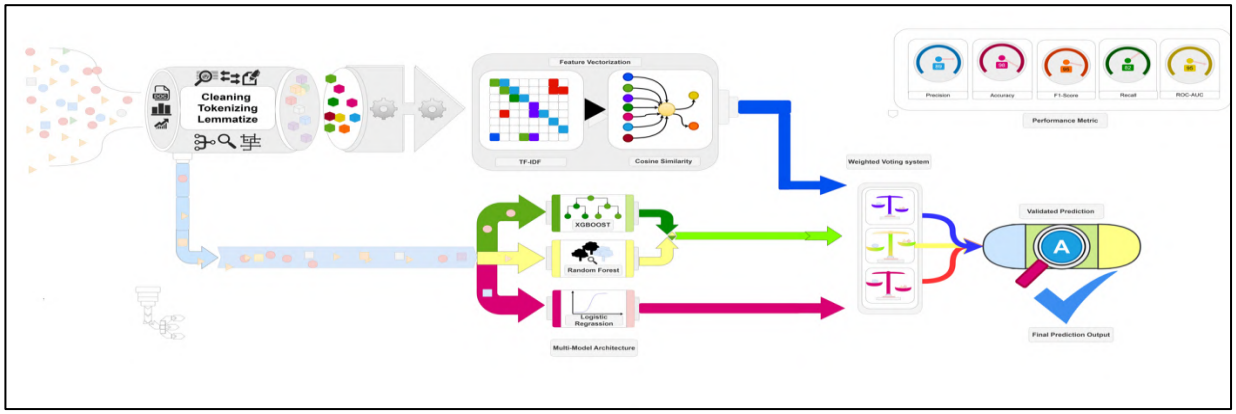


Figure 1: Phase I, II, III illustration.
Source: Author, (2026).

In this section, the researchers explain how the model uses multiple algorithms and processes to select the best direction for students, giving them more chances to complete the course. The process is divided into three Phases: Phase I Input, Phase II Process, and Phase III Result. Figure 1 includes several well-known algorithms, such as multinomial Logistic Regression (LR), Random Forest (RF), XGBoost (XGB), and term frequency–inverse document frequency (TF-IDF), combined into a single ensemble model.

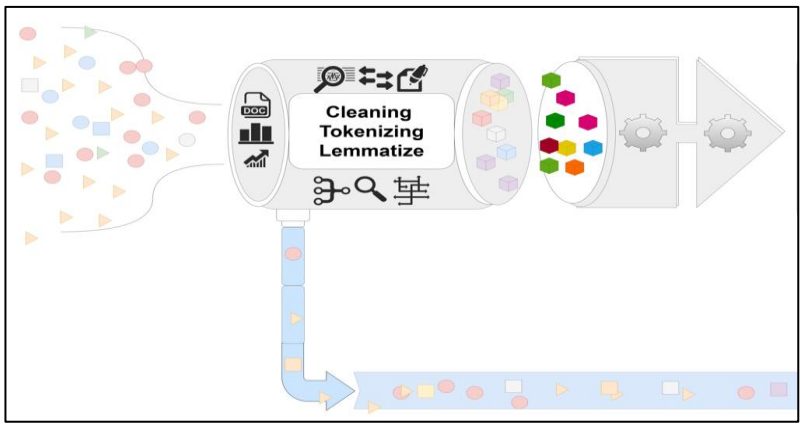


Figure 2: Phase I: Input Data and Preprocessing.
Source: Author, (2026).

III.1 PHASE ONE

Located at the top of the model, is called the input phase shown in Figure 2. It includes input data, data preprocessing and cleaning, and Concatenation and Label Encoding, starting with a dataset that may contain numerical, rating, timestamp, or string data. In the second stage of the first phase, Tokenization & Lowercasing, Noise Removal, stop word Filtering, Label Encoding, and Dataset Splitting, in addition to converting the data into a format for analysis. To address limitations in dataset availability due to data privacy laws, the researchers created the BSIT and BSCS datasets, augmenting them with a Generative Adversarial Networks(GAN) to used with the original dataset and splitting the data into a stratified 80/20 train-test split. The three machine learning models used in this study are Logistic Regression, Random Forest, and XGBoost algorithms. In addition, the 10-fold cross-validation was chosen by the researcher; furthermore, all code and analysis were run in Google Colab using standard virtual machine resources. The dataset attributes that were used in this study are shown in Table 1. After finishing Phase I, all the processed data feeds are sent to Phase II for modeling.

Table 1: Dataset Attributes.

Attribute	Attribute	Attribute
Age	Free time after school	Many hours playing games in week
Sex	Going out with friends	Weekly study time
Food habit	Schoolday alcohol consumption	Easy access to computer
Family size	Weekend alcohol consumption	Easy access to internet
Graduated_from(highschool)	Having_mobile	Own computer
Father educational	Having smartphone	Using a internet per week
Mother_educational	Grade inalgorithms	Grade in introduction of computing
Mother occupation	Number subject failures	Grade in computer programming 1
Father occupation	Grade in physics	Grade in computer programming 2
Your occupation	Grade_in_chemistry	Grade in discrete mathematics
Area flooded during a typhoon or heavy rain	Home to school travel time	Grade in data structures and algorithms
Mode of transportation to school	Romantic_relationship	Grade in quantitative methods
Reason to choose this school	Family relationships	

Source: Author, (2026).

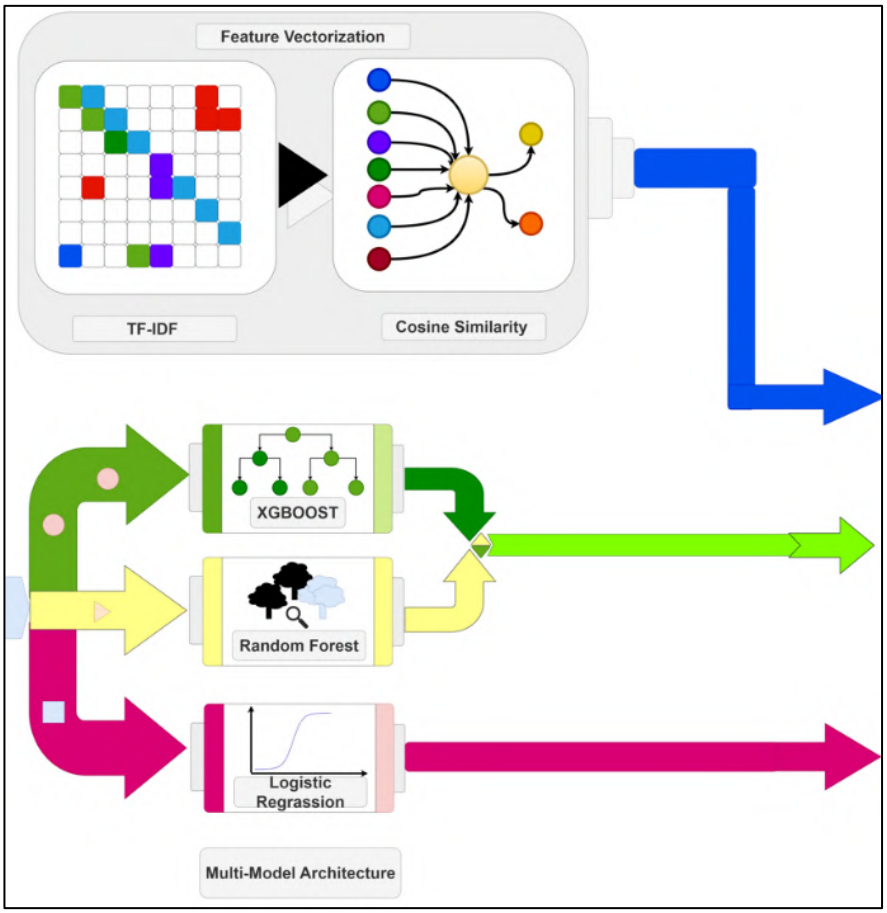


Figure 3: Phase II combined multi-models.
Source: Author, (2026).

III.2 PHASE TWO

Phase two has four multi-models shown in Figure 3: one Similarity-Based Model, two Logistic Regression models, three Random Forest models, and four XGBoost models. The research discusses each in the following:

III.2.1 Logistic Regression

Figure 3 shown the process starts by converting text into a numerical vector for the machine learning algorithms to process in a TF-IDF vectorizer, to compute the weighted sum of each feature, producing one real-valued score (a logit) per class using the SoftMax. The logit indicates the likelihood of each class, and the SoftMax stage converts the logits into a probability distribution over classes. Finally, the algorithm uses these probabilities to output a single class decision.

III.2.2 Random Forest

A technique such as a random forest, an ensemble learning model that uses multiple decision tree methods to find patterns in data. To extract meaningful knowledge from the data, each tree is trained on different subsets of data structures. gives it an advantage in applying structure to provided data and in finding patterns in large-scale datasets, which allows the diversity among the trees to capture a range of patterns, reducing the likelihood of alignment errors. To generate a final prediction, the model typically averages the probability estimates from each individual tree, resulting in a more robust and accurate output. Random Forest learns nonlinear decision rules by combining many diverse trees, the probabilities stage provides calibrated or quasi-calibrated class likelihoods derived from ensemble averaging, and the prediction stage maps those likelihoods to final labels used for reporting results or deployment.

III.2.3 XGBoost

This stage starts with a tokenizer that feeds data into the boosting block. XGBoost is a boosting-style ensemble learning process in which a strong classifier is created by combining a sequence of weak decision-tree classifiers. The process starts with the first box, representing the training samples in their initial form. The process makes an initial prediction, measures the distance to the true labels, and updates the model state. The residuals are passed to the next step, emphasizing that the errors serve as the learning signal for that step. The process repeats this cycle across multiple columns of a weak classifier, indicating that a weak learner (a shallow tree) is fit to the current error structure in the data. The dataset is reweighted or re-focused after each weak learner, so that samples that were previously mis-predicted receive greater influence in the next fitting step.

III.2.4 TF-IDF

TF-IDF vectorizer transforms text into a numerical vector by assigning each term a weight based on how often it appears in a document relative to its frequency across the corpus. Common words receive lower weights, and rare and informative words receive higher weights. The similarity between two vectors is measured as the cosine of the angle between them, enabling comparison of the new input vector with the training data using cosine similarity.After adding each weak learner, the ensemble's predictions change, new residuals are computed, and the training distribution or effective loss landscape is updated for the next learner. By combining multiple weak decisions, the final component of the boosted ensemble model represents the boosted ensemble formed by combining all weak learners, typically as a weighted sum or an additive model, so that each new tree contributes an incremental correction to what has already been learned.

III.3 PHASE THREE

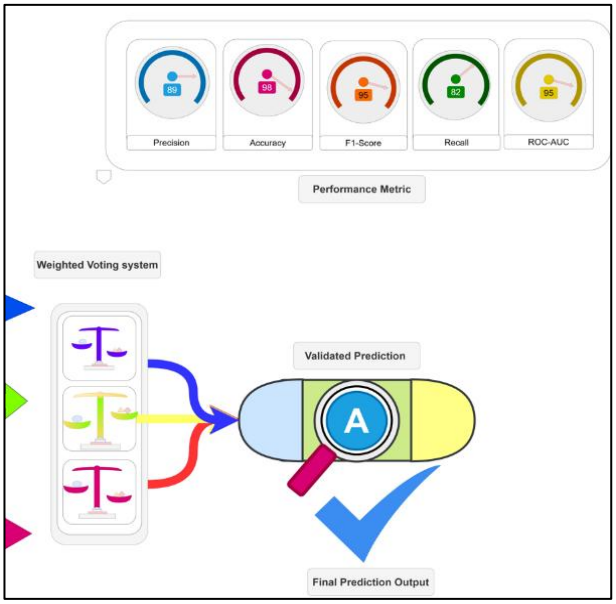


Figure 4: Phase III evaluation.
Source: Author, (2026).

Figure 4 shown by capitalizing on model diversity and focusing on an AI/ML pipeline that ensures the classifications and recommendations are multi-model, and the prediction is accurate and robust. After all models predict the output, all predictions combine to create final predictions for accomplishing this step the researcher used Weighted Voting, different validations technique used to allow the model to decide what is the best perdition for given input data, validations approaches such as accuracy, precision, recall, F1-score, ROC-AU and others validations which offers the most accurate model, more influence in decision making and predictions output.

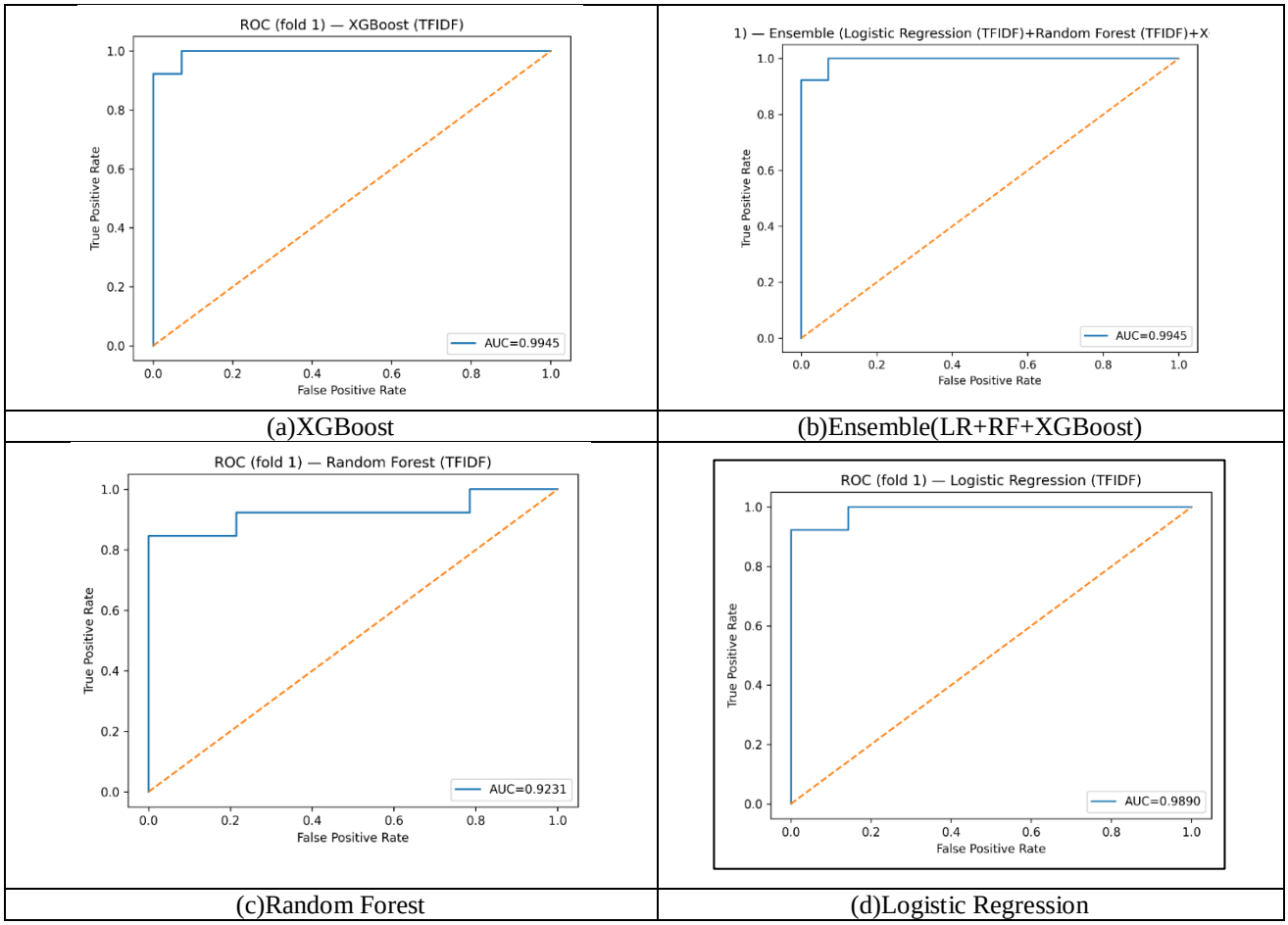
IV. RESULTS AND DISCUSSIONS

This section discusses the performance of each model used in this study. Table 2 shows the model the mean of from fold (1) up to fold(10), Accuracy Mean, Precision Positive Mean, Recall Positive Mean, F1 Positive Mean, and ROC AUC of the different models used in this study top performers among these combined models are the Ensemble model and the XGBoost, both of which can capture complex, nonlinear patterns and relationships within the data [48-52]. However, this does not mean that the Random Forest and logistic regression underperformed because of the nature of the data provided to the models rather, it shows that different models perform differently across datasets [53]. The researcher evaluates Logistic Regression, Random Forest, XGBoost, and an ensemble. The results for each model are summarized in Table 2, which shows first that Logistic Regression achieves 88.86% accuracy and F1 of 87.43%, and second that the Random Forest classifier performs, attaining 83.86% accuracy and F1-score of 81.71%, third XGBoost scored accuracy of 91.73% and F1 score of 90.46%, the ensemble of all three models also achieved 90.64% accuracy, with an F1-score of 89.19%. The results show that the model can identify the pattern in the dataset and provide a proper recommendation as output.

Table 2: Performance of Classification Models on fold(1) to fold(10) Prediction.

Model	Accuracy Mean	Precision Mean	Recall Mean	F1 Mean	ROC Mean
XGBoost (TFIDF)	0.9173	0.9274	0.8929	0.9046	0.9753
Logistic Regression (TFIDF)	0.8874	0.8800	0.8769	0.8743	0.9693
Ensemble (Logistic Regression (TFIDF)+Random Forest (TFIDF)+XGBoost (TFIDF))	0.9064	0.9086	0.885897436	0.8919	0.9687
Random Forest (TFIDF)	0.8386	0.8410	0.803205128	0.8171	0.9093

Source: Author, (2026).



(a)XGBoost (b)Ensemble(LR+RF+XGBoost)

(c)Random Forest (d)Logistic Regression

Figure 5: ROC output for fold (1) of XGBoost, LR, RF, and Ensemble model.
Source: Author, (2026).

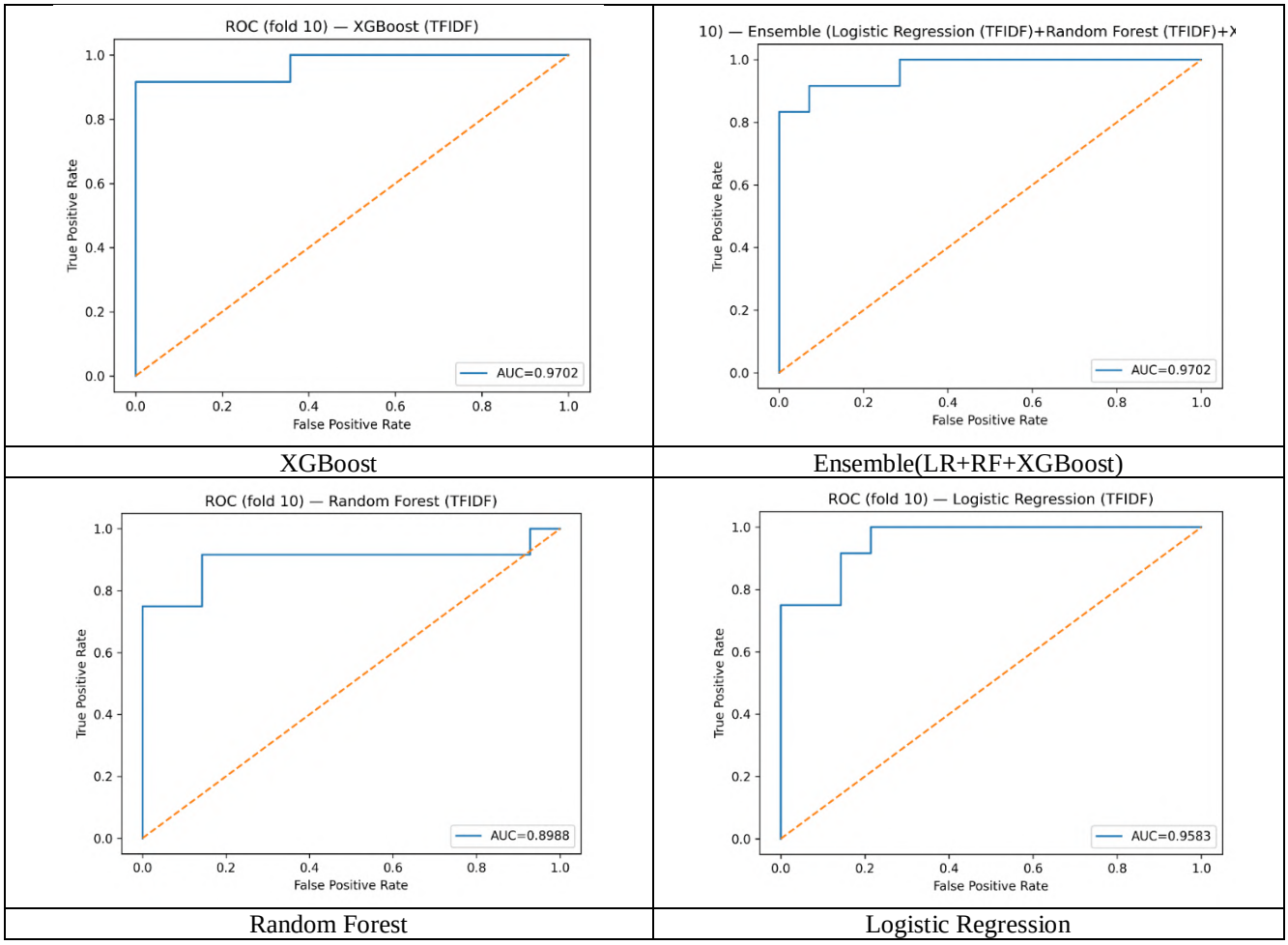


Figure 6: ROC output for fold (10) of XGBoost, LR, RF, and Ensemble model.
Source: Author, (2026).

Figure 5 and 6 show ROC curves derived from fold (1) and fold (10) other cross validation fold is not included, only across all folds for Logistic Regression, Random Forest, XGBoost, and the XGBoost mean score for ROC-AUC is 97.53% and the ensemble model, which achieved a mean score of 96.87 and significantly outperformed Logistic Regression with a mean score of 96.93%. Random Forest lagged behind with an ROC-AUC mean score of 0.909377289. The ROC curves for the top-performing models in average fold exhibit strong concavity toward the upper-left corner, a characteristic indicative of high AUC values.

V. CONCLUSIONS

This research uses several algorithms to analyze educational content, applying classification and recommendation methods to guide students' program selection and help them make more informed decisions based on data-driven outputs suggested by the algorithm. An approach to predict student course placement, focusing on unique features between related undergraduate programs. Across all models, XGBoost emerged as the most effective and reliable classifier for these datasets and tasks. The ensemble approach did not surpass XGBoost and showed greater variability across folds, suggesting limited benefits from aggregation when the constituent models are trained on the same TF-IDF representation, which may yield correlated predictions. A student provides informed information based on the recommendations' results, with directions to make more informed decisions based on the given input data and historical data processed by the ensemble model. This approach gives students who are currently enrolled in the course the opportunity to be informed whether the course is suitable for them or not , which gives them the ability to make an informed decision regarding the course they are currently enrolled in.

VI. AUTHOR'S CONTRIBUTION

Conceptualization: Manocher C. Alipour.
Methodology: Manocher C. Alipour.
Investigation: Manocher C. Alipour.
Discussion of results: Manocher C. Alipour.
Writing – Original Draft: Manocher C. Alipour.
Writing – Review and Editing: Manocher C. Alipour.
Resources: Manocher C. Alipour.
Supervision: Manocher C. Alipour.
Approval of the final text: Manocher C. Alipour.

VII. ACKNOWLEDGMENTS

The authors extend their sincere gratitude to Isabela State University, Angadanan Campus, for their invaluable support and guidance throughout the conduct of this research. Their encouragement and resources were instrumental in the successful completion of this study.

VIII. REFERENCES

[1] A. N. Hasoon, S. K. Abdulateef, R. S. Abdulameer, and M. L. Shuwandy, "An Intelligent Hybrid AI Course Recommendation Framework Integrating BERT Embeddings and Random Forest Classification," Computers, vol. 14, no. 9. p. 353, 2025, doi: 10.3390/computers14090353.

[2] R. Huang, "Improved content recommendation algorithm integrating semantic information," J. Big Data, vol. 10, no. 1, p. 84, 2023, doi: 10.1186/s40537-023-00776-7.

[3] E. J. Delahoz-Domínguez and R. Hijón-Neira, "Recommender System for University Degree Selection: A Socioeconomic and Standardised Test Data Approach," Applied Sciences, vol. 14, no. 18. p. 8311, 2024, doi: 10.3390/app14188311.

[4] K. Singh, S. Dhawan, and N. Bali, "An Ensemble Learning Hybrid Recommendation System Using Content-Based, Collaborative Filtering, Supervised Learning and Boosting Algorithms," Autom. Control Comput. Sci., vol. 58, no. 5, pp. 491–505, 2024, doi: 10.3103/S0146411624700615.

[5] H. Gunasekaran, D. Kanmani, and R. Krishnamoorthi, "Optimized Ensemble Learning for Enhanced Crop Recommendations: Leveraging ML for Smarter Agricultural Decision-Making," Engineering Proceedings, vol. 82, no. 1. p. 95, 2024, doi: 10.3390/ecsa-11-20366.

[6] L. Paura and I. Arhipova, "Cause Analysis of Students' Dropout Rate in Higher Education Study Program," Procedia - Soc. Behav. Sci., vol. 109, pp. 1282–1286, 2014, doi: https://doi.org/10.1016/j.sbspro.2013.12.625.

[7] R. Y. Chao, "Higher Education in the Philippines BT - International Handbook on Education in Southeast Asia," L. P. Symaco and M. Hayden, Eds. Singapore: Springer Nature Singapore, 2024, pp. 863–889.

[8] R. Cariaga, "The Philippine Education Today and Its Way Forward (Journal of Ongoing Educational Research)," vol. 1, pp. 40–42, Oct. 2023, doi: 10.5281/zenodo.8418880.

[9] M. Yuldashev et al., "Collaborative Filtering in Real-Time Library Catalog Recommendations," Indian J. Inf. Sources Serv., vol. 15, pp. 266–274, Dec. 2025, doi: 10.51983/ijiss-2025.IJISS.15.4.30.

[10] Y. Terui, Y. Inoue, Y. Hamakawa, K. Tatsumura, and K. Kudo, "Collaborative filtering based on nonnegative/binary matrix factorization," Front. big data, vol. 8, p. 1599704, Jul. 2025, doi: 10.3389/fdata.2025.1599704.

[11] M. A. Khan and A. Polyzou, "Session-based Methods for Course Recommendation," Jun. 2024, doi: 10.5281/zenodo.11384740.

[12] V. A. Nguyen, H.-H. Nguyen, D.-L. Nguyen, and M.-D. Le, "A course recommendation model for students based on learning outcome," Educ. Inf. Technol., vol. 26, no. 5, pp. 5389–5415, 2021, doi: 10.1007/s10639-021-10524-0.

[13] G. Zhang et al., "Optimizing learning paths: Course recommendations based on graph convolutional networks and learning styles," Appl. Soft Comput., vol. 175, p. 113083, 2025, doi: https://doi.org/10.1016/j.asoc.2025.113083.

[14] C. Troussas, A. Krouska, P. Tselenti, D. Kardaras, and S. Barbounaki, "Enhancing Personalized Educational Content Recommendation through Cosine Similarity-Based Knowledge Graphs and Contextual Signals," Information, vol. 14, p. 505, Sep. 2023, doi: 10.3390/info14090505.

[15] Y. Januzaj and A. Luma, "Cosine Similarity – A Computing Approach to Match Similarity Between Higher Education Programs and Job Market Demands Based on Maximum Number of Common Words," Int. J. Emerg. Technol. Learn., vol. 17, pp. 258–268, Jun. 2022, doi: 10.3991/ijet.v17i12.30375.

[16] H. Steck, C. Ekanadham, and N. Kallus, "Is Cosine-Similarity of Embeddings Really About Similarity?," in Companion Proceedings of the ACM Web Conference 2024, 2024, pp. 887–890, doi: 10.1145/3589335.3651526.

[17] M. Abdasalam, A. Alzubi, and K. Iyiola, "Student grade prediction for effective learning approaches using the optimized ensemble deep neural network," Educ. Inf. Technol., vol. 30, no. 8, pp. 10159–10183, 2025, doi: 10.1007/s10639-024-13224-7.

[18] E. Creely and K. Carabott, "Teaching and learning with AI: an Integrated AI-Oriented Pedagogical Model," Aust. Educ. Res., vol. 52, no. 6, pp. 4633–4654, 2025, doi: 10.1007/s13384-025-00913-6.

[19] N. F. Davar, M. A. Dewan, and X. Zhang, "AI Chatbots in Education: Challenges and Opportunities," Information, vol. 16, no. 3. p. 235, 2025, doi: 10.3390/info16030235.

[20] Y. Fu, Z. Weng, and J. Wang, "Examining AI Use in Educational Contexts: A Scoping Meta-Review and Bibliometric Analysis," Int. J. Artif. Intell. Educ., vol. 35, no. 3, pp. 1388–1444, 2025, doi: 10.1007/s40593-024-00442-w.

[21] M. S. Kapucu, H. Özcan, A. Aypay, and others, "Predicting Secondary School Students' Academic Performance in Science Course by Machine Learning.," Int. J. Technol. Educ. Sci., vol. 8, no. 1, pp. 41–62, 2024.

[22] S. Wu Fung, S. Tyrväinen, L. Ruthotto, and E. Haber, "ADMM-Softmax: an ADMM approach for multinomial logistic regression," ETNA - Electron. Trans. Numer. Anal., vol. 52, pp. 214–229, Jan. 2020, doi: 10.1553/etna_vol52s214.

[23] Y. Yao and H. Wang, "Optimal subsampling for softmax regression," Stat. Pap., vol. 60, no. 2, pp. 585–599, 2019, doi: 10.1007/s00362-018-01068-6.

[24] G. Li, J. Cui, H. Fu, and Y. Sun, "Light GBM and GA Based Algorithm for Predicting and Improving Students' Performance in Higher Education in the Context of Big Data," in 2024 7th International Conference on Education, Network and Information Technology (ICENIT), 2024, pp. 1–5, doi: 10.1109/ICENIT61951.2024.00009.

[25] K. Kesgin, S. Kiraz, S. Kosunalp, and B. Stoycheva, "Beyond Performance: Explaining and Ensuring Fairness in Student Academic Performance Prediction with Machine Learning," Applied Sciences, vol. 15, no. 15. p. 8409, 2025, doi: 10.3390/app15158409.

[26] J. S. Pimentel, R. Ospina, and A. Ara, "Learning time acceleration in support vector regression: a case study in educational data mining," Stats, vol. 4, no. 3, pp. 682–700, 2021.

[27] Y. Chen and L. Zhai, “A comparative study on student performance prediction using machine learning,” Educ. Inf. Technol., vol. 28, no. 9, pp. 12039–12057, 2023.

[28] R. Kadu, P. J. Assudani, T. Mukewar, J. Kapgate, and R. Bijekar, “Student Placement Prediction and Skill Recommendation System using Machine Learning Algorithms,” in 2024 International Conference on Inventive Computation Technologies (ICICT), 2024, pp. 401–408, doi: 10.1109/ICICT60155.2024.10544738.

[29] S. Wang, F. Wang, Z. Zhu, J. Wang, T. Tran, and Z. Du, “Artificial intelligence in education: A systematic literature review,” Expert Syst. Appl., vol. 252, p. 124167, 2024, doi: https://doi.org/10.1016/j.eswa.2024.124167.

[30] J. Garzón, E. Patiño, and C. Marulanda, “Systematic Review of Artificial Intelligence in Education: Trends, Benefits, and Challenges,” Multimodal Technologies and Interaction, vol. 9, no. 8. p. 84, 2025, doi: 10.3390/mti9080084.

[31]D. Dey et al., “The proper application of logistic regression model in complex survey data: a systematic review,” BMC Med. Res. Methodol., vol. 25, no. 1, p. 15, 2025, doi: 10.1186/s12874-024-02454-5.

[32] A. F. Lukman, S. Mohammed, O. Olaluwoye, and R. A. Farghali, “Handling Multicollinearity and Outliers in Logistic Regression Using the Robust Kibria–Lukman Estimator,” Axioms, vol. 14, no. 1. p. 19, 2025, doi: 10.3390/axioms14010019.

[33] T. Liu and D. Fan, “Random Forest Algorithm in Information Personalization Recommender System,” in The International Conference on Forthcoming Networks and Sustainability (FoNeS 2022), 2022, vol. 2022, pp. 6–10, doi: 10.1049/icp.2022.2367.

[34] B. M. Hassan and S. M. Elagamy, “Personalized medical recommendation system with machine learning,” Neural Comput. Appl., vol. 37, no. 9, pp. 6431–6447, 2025, doi: 10.1007/s00521-024-10916-6.

[35] Z. Shahbazi and Y. Byun, “Product Recommendation Based on Content-based Filtering Using XGBoost Classifier,” Int. J. Adv. Sci. Technol., vol. 29, pp. 6979–6988, Jul. 2020.

[36] B. Bhavana, J. Karthik, and P. L. Kumari, “A Novel Approach for Product Recommendation using XGBOOST,” in 2023 International Conference on Intelligent Data Communication Technologies and Internet of Things (IDCIoT), 2023, pp. 256–261, doi: 10.1109/IDCIoT56793.2023.10053453.

[37] S. Kumar, J. P. Singh, and Shantanu, “Genre-Based Movie Recommender System with XGBoost,” in 2024 4th International Conference on Computer, Communication, Control & Information Technology (C3IT), 2024, pp. 1–6, doi: 10.1109/C3IT60531.2024.10829451.

[38] F. Chen and Y. Cui, “Utilizing Student Time Series Behaviour in Learning Management Systems for Early Prediction of Course Performance,” J. Learn. Anal., vol. 7, pp 1–17, Sep. 2020, doi: 10.18608/jla.2020.72.1.

[39] F. Landi, L. Baraldi, M. Cornia, and R. Cucchiara, “Working memory connections for LSTM,” Neural Networks, vol. 144, pp. 334–341, 2021.

[40] Y. Yuan, Y. Zhou, X. Chen, Q. Xiong, and H. C. Okere, “Enhancing Recommendation Diversity and Novelty with Bi-LSTM and Mean Shift Clustering,” Electronics, vol. 13, no. 19. p. 3841, 2024, doi: 10.3390/electronics13193841.

[41] J.-W. Tzeng, N.-F. Huang, Y.-H. Chen, T.-W. Huang, and Y.-S. Su, “Personal learning material recommendation system for MOOCs based on the LSTM neural network,” Educ. Technol. Soc., vol. 27, no. 2, pp. 25–42, Feb. 2024, [Online]. Available: https://www.jstor.org/stable/48766161.

[42] X. Ni, “User Behavior Analysis and Personalized Recommendation Algorithm in an Online Learning Platform Based on Deep Learning BT - 7th International Conference on Education, Network and Information Technology,” 2025, pp. 51–62.

[43]A. Dey, V. Chauhan, P. Singh, and P. Choudhury, LSTM-Based Top N Recommendation System using Cognitive Data. 2022.

[44] L. Cheng, Y. Yang, K. Zhao, and Z. Gao, “Research and Improvement of TF-IDF Algorithm Based on Information Theory BT - The 8th International Conference on Computer Engineering and Networks (CENet2018),” 2020, pp. 608–616.

[45] K. K. San, K. E. E. Chaw, and T. T. Nwe, “Attention-Based Neural Networks with TF-IDF Features and BERT Embeddings for Enhanced Course Recommendation System,” in 2024 5th International Conference on Advanced Information Technologies (ICAIT), 2024, pp. 1–6, doi: 10.1109/ICAIT65209.2024.10754938.

[46] S. Tiwari, R. Sahu, S. Shripal, and S. Rajpoot, “Innovative Framework for Context-based Recommendation using TF-IDF and Cosine Similarity,” Int. J. Innov. Res. Sci. Technol., vol. 12, pp. 9019–9023, Nov. 2023, doi: 10.15680/IJIRSET.2023.1206157.

[47] Z. Pardos and W. Jiang, Designing for serendipity in a university course recommendation system. 2020.

[48] B. K. Saini, “Optimizing Student Academic Performance Prediction Using Heterogeneous Ensemble Learning,” Eur. J. Artif. Intell. Mach. Learn., vol. 4, no. 4 SE-Articles, pp. 1–6, 2025, doi: 10.24018/ejai.2025.4.4.77.

[49] S. A. Alwarthan, N. Aslam, and I. U. Khan, “Predicting student academic performance at higher education using data mining: a systematic review,” Appl. Comput. Intell. Soft Comput., vol. 2022, no. 1, p. 8924028, 2022.

[50] A. Ng and K. Soo, “Random forests,” in Data Science--was ist das eigentlich?! Algorithmen des maschinellen Lernens verständlich erklärt, Springer, 2018, pp. 117–127.

[51] A. D. Kumar, R. P. Selvam, and V. Palanisamy, “Hybrid classification algorithms for predicting student performance,” in 2021 International Conference on Artificial Intelligence and Smart Systems (ICAIS), 2021, pp. 1074–1079.

[52] A. Salini, U. Jeyapriya, and others, “A majority vote based ensemble classifier for predicting students academic performance,” Int. J. Pure Appl. Math., vol. 118, no. 24, pp. 1–11, 2018.

[53] Y. Dong et al., “Deep learning methods may not outperform other machine learning methods on analyzing genomic studies,” Front. Genet., vol. Volume 13-2022, 2022, doi: 10.3389/fgene.2022.992070.

Journal of Engineering and Technology for Industrial Applications

ISSN ONLINE: 2447-0228

ITEGAM-JETIA

Manaus, v.12 n.60, p.329-336, July/August, 2026.
DOI: https://doi.org/10.5935/jetia.v12i60.3816

RESEARCH ARTICLE OPEN ACCESS

PERFORMANCE ANALYSIS OF ZETA CONVERTER IN ELECTRIC VEHICLE APPLICATIONS

V. Nandagopal[1], Pujari Harish Kumar[2], N Chinna Alluraiah*[3], K. Harinath Reddy[4]

[1]Professor, Department of Electrical and Electronics Engineering, Mohan Babu University, Tirupati, Andhra Pradesh, India.
[2]Department of Electrical and Electronics Engineering, Alliance School of Applied Engineering, Alliance University, Bengaluru, Karnataka, India.
[3, 4]Assistant Professor, Department of Electrical and Electronics Engineering, Annamacharya University, Rajampet, Annamayya, India.

[1]http://orcid.org/0000-0002-3881-593X, [2]http://orcid.org/0000-0002-6580-9906,
[3]http://orcid.org/0000-0003-0722-6523, [4]http://orcid.org/0000-0003-3102-3486,

Email: nandhu050577@gmail.com, , harisheps007@gmail.com, alluraiah.207@gmail.com, ksharinathreddy@gmail.com

ARTICLE INFO

Article History
Received: February 25, 2026
Reviewed: June 10, 2026
Accepted: July 10, 2026
Published: July 31, 2026

Keywords:
Electric Vehicle (EV),
Zeta Converter, H-Bridge,
Lithium battery SoC,
DC motor,
PI controller.

ABSTRACT

The main component of the controller in electric vehicle (EV) is motor,DC-DC converter and charging port.The research analysed the lithium-Ion battery with isolated converter like H bridge and non-isolated type Zeta converters are compared distance travel and the SoC (State of Charge) of the battery by using MATLAB Simulink in a plug-in electric The isolated converters are costly due to the transformer and offer safety. The electric vehicle controller plays a crucial role in increasing the vehicle's range and enhancing battery charging within the grid system. The controller of the vehicle will improve the battery life and travel the distance per charge. The Permanent magnet DC motor with PI controller is used for this article.

Copyright ©2026 by authors and Galileo Institute of Technology and Education of the Amazon (ITEGAM). This work is licensed under the Creative Commons Attribution International License (CC BY 4.0).

I. INTRODUCTION

Research findings indicate that combustion vehicles are responsible for emitting approximately 70% of gases, while other transportation sectors contribute around 27% of harmful greenhouse gases [1]. The energy flow in the vehicle is driver motor, motor controller, power battery pack, charger and external power as shown in figure 1.

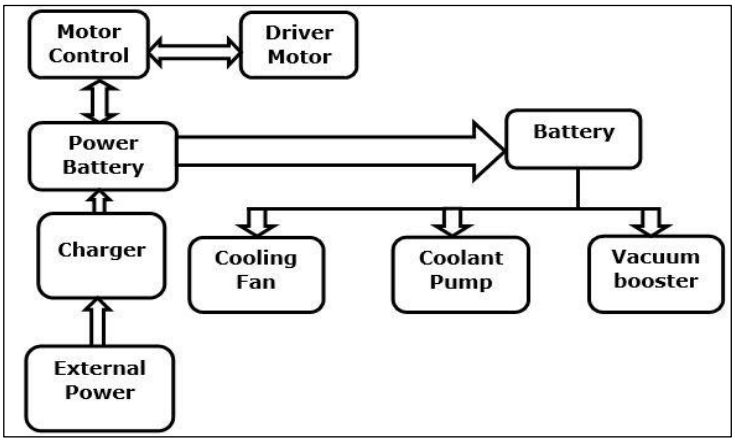


Figure 1: Energy flow diagram of Electric Vehicle.
Source: Authors, (2026).

The driver motor is coupled with gear box and drive axle which is tied up with tier crank shaft. The DC – DC converter energy flow from power back up and delivered to battery. The energy flow from battery to cooling fan, coolant pump, vacuum booster pump as shown in figure 2. The EV plugin takes electrical energy from the grid to charge the battery. Then, the batteries power the electric motor. The components of EV based on plug in type is DC – DC converter, controller,motor, battery and gear system. The key benefits of this system include being environmentally friendly and producing no pollution. However, a significant downside is the rapid battery depletion, making it unsuitable for long-distance travel [2].During periods without sunlight, the charging station attract the power from grid. Additionally, the grid power, which is close to unity, must be transferred to the charging station [3].

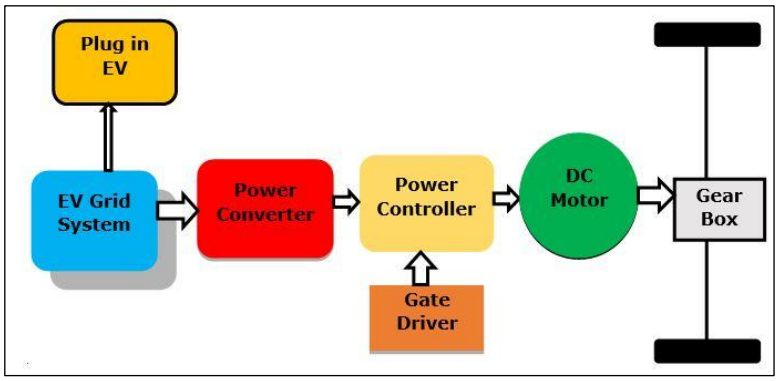


Figure 2: Block diagram of Plug in Electric Vehicle.
Source: Authors, (2026).

A comparison and discussion on optimization methods are done in terms of design, optimization function, implementation methods, complexity of computation and effectiveness. There's extensive review of the difficulties and problems concerning EV converter design, modulation schemes and controllers [4]. Figure 2 shows the block diagram of a plug-in electric vehicle. This paper uses a hybrid method that combines the Perturb-Observe technique and the Incremental Conductance technique for optimizing the energy of the solar PV array [5]. The choice of DC-DC converter design is essential for the fast charging of electric vehicles [6]. Precise control of the Bidirectional DC-DC converter has allowed electric vehicles to perform efficient energy handling and conversion [7]. Also, stability and reliability for EVs means being dependable throughout the electric vehicles. The converter needs to be more reliable [8]. A multi-port converter allows the use of different power sources, like batteries and supercapacitors, in power systems [9]. Choosing the right design and selection for a dc-dc converter can enhance overall performance. Improvement methods give designers useful information for developing various types of inverter regulator applications [10]. The PMDC motor's external structure, made up of the stator, forms the part housing. The internal stator are magnets in which the north and south poles of the magnets alternate each other facing the armature. The function of stator is to provide the return of magnetic flux with low reluctance in addition to holding the magnets. The design includes a compensation field coil to counteract potential power loss from the magnet. The armature is the moving part of PMDC motor which consists of winding core and commutator which is connected to the output shaft of the motor. In PMDC (Permanent magnet DC) motors have a solid rotor that is not made of steel or any ferromagnetic material. The link between speed and applied voltage resembles that of a standard DC shunt motor. However, the key difference is that in a PMDC motor, the rotor's magnetic field comes from a permanent magnet [11]. Because of this, one of the most commonly used ways to control a PMDC motor's speed is by changing the applied voltage [12]. The performance advantages of a PMDC motor stem from its ability to produce a very broad speed range of constant torque and constant power, and PMDC motors can have a maximum operating efficiency and power density that exceeds induction-type machines while being practically equivalent to machines using permanent magnets [12], [13].

At present, the industry has singled out electric machines as the leading technology due to their efficiency and cost-effectiveness. One such use case is the widespread application of electric machines in electric vehicles (EVs). The consumer interest in the latter is a direct consequence of the critics' attention on the internal combustion engines' negative impact on air quality, which, in turn, has led the researchers and engineers to channel their efforts into devising new technologies that could deliver higher power and better efficiency of electric vehicles. Hence, the researchers have taken as a main task besides electric motors and power electronics, the whole system regarding power consumption to be developed. Motor design with the best performance strategically selected turns into the main factor in the process of improving the overall performance electric vehicles [14]. The new converter comes with multiple benefits that are related to ZETA topology among which are the capability of buck-boost, continuous output current and DC insulation from input to output [15]. The controller generates control actions by using the error in the inductor current and a proportional term [16]. A Zeta converter-based battery charger for electric vehicles was proposed in [17], highlighting improved power factor correction and efficient energy transfer. The switching control algorithm uses a control Lyapunov function. This function began as a two-dimensional boost converter model from previous research. It has since been improved for a four-dimensional Zeta converter model [18]. On the other hand, there is still a gap in the analysis and modeling of input current distortion in PFC converters that use the GPWM controller. This is due to its significant nonlinearities under large-signal conditions [19].

I.1 CONTRIBUTIONS OF THIS WORK

This study departs from the existing research which mostly looks at dc-dc converter performance through individual evaluations, and carries out a vehicle-level analysis comparing a non-isolated Zeta converter and an H-bridge converter in the context of a plug-in hybrid electric vehicle. The unique aspect of the research is that it examines the changes in battery State of Charge (SoC) and the distance traveled by the vehicle under the same driving cycles. It uses a common MATLAB/Simulink platform.

It also connects the new Zeta converter with a PMDC motor drive and PI control method to measure its effect on the whole system's energy efficiency instead of just focusing on the conversion efficiency. The list of contribution in this Article:

- Comparative SoC analysis under same drive cycle
- Distance travelled per unit charge comparison
- Vehicle-level performance rather than component-only analysis

II. PROPOSED ZETA CONVERTER

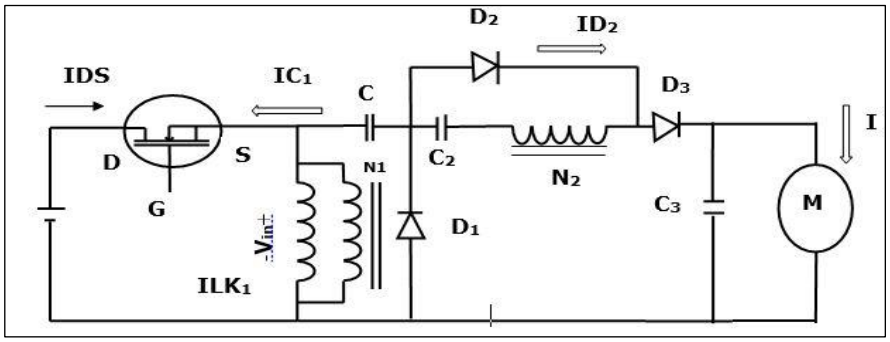


Figure 3: Circuit Diagram of Proposed Zeta Converter.
Source: Authors, (2026).

The jointly inductive Zeta transformer has been built using the secondary inductor T1 and the floating active switch S1. The input inductor of the conventional boost converter is mirrored by the primary winding N1 of the coupled inductor T1. It receives energy from the leakage inductor of N1 through capacitor C1 and diode D1. The secondary winding N2 connects in series with another set of capacitors, C2, and diode D2, which operate with N1. The rectifying diode D3 connects to the capacitor C3 for output and the resistor R for the load. The Zeta converter's main features include reusing the energy from the leakage inductor in the coupled inductor. This boosts efficiency and helps control voltage spikes across the active switch. The interchangeable capacitor and coupled capacitor methods are very effective in increasing the voltage transformation ratio. The floating active switch is making use of the PV panel's energy inoperative time, which not only helps in decreasing the risk of electric shock to people and damage to property but also is illustrated in figure 3.

Duty Cycle is calculated by using the formula

$$D = V0 / Vd+V0 \quad (1)$$

$$\text{Choosing L1 is } L1 \geq (1 - D)2\ R0 / 2Dfs \quad (2)$$

$$\text{Choosing L2 is } L2 \geq (1 - D)\ R0 / 2Dfs \quad (3)$$

II.1 DESIGN MOTIVATION AND NOVELTY

The Zeta converter has been chosen primarily because of its built-in buck-boost feature, continuous output current, and little current rippling, all of which are beneficial to battery-powered electric car applications. This research differs from the conventional studies allowing Zeta converters mainly in charging applications, as it integrates the converter directly into the vehicle propulsion system and assesses its effect on driving range and battery usage. The coupled-inductor arrangement enhances voltage gain while at the same time preventing switch voltage stress, thus making it apt for EV auxiliary and traction power needs.

III. METHODOLOGY

The method for modeling, simulating, and evaluating the performance of the proposed Zeta converter-based electric vehicle system is described in this section. We compare it with the traditional H-bridge converter under the same operating conditions. This makes sure the results are fair and can be repeated.

III.1 OVERALL SYSTEM ARCHITECTURE

Electric vehicle system simulation was done in MATLAB/Simulink where the energy source, power electronic converter, motor drive, controller, and vehicle dynamics are combined together. The major subsystems taken into account for this research are:

- Lithium-ion battery pack
- DC–DC converter (H-bridge and proposed Zeta converter)
- Permanent Magnet DC (PMDC) motor
- PI-based motor speed controller
- Longitudinal vehicle dynamics model

All subsystems are interconnected to emulate a plug-in electric vehicle operating under real-time driving conditions as shown in figure 4.

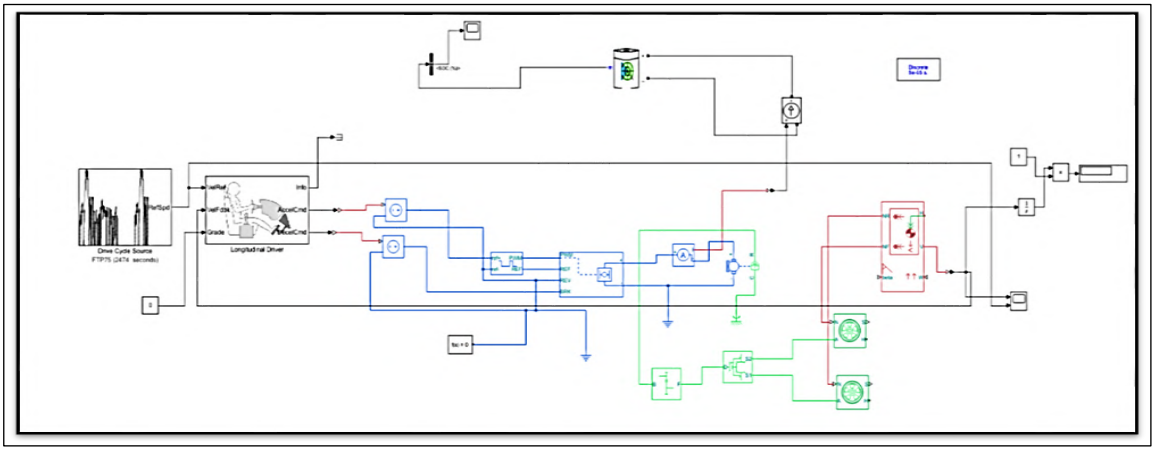


Figure 4: The complete simulation model is developed using MATLAB/Simulink.
Source: Authors, (2026).

III.2 BATTERY MODELLING AND STATE OF CHARGE ESTIMATION

A lithium-ion battery model acts as the primary energy storage device. The equivalent circuit model of the battery consists of a voltage source that can supply unlimited current, a resistance in the circuit, and dynamic components that reflect the rapid changes in battery behavior. We calculate the State of Charge (SoC) of the battery using the coulomb counting method, as shown in equation 4.

$$SoC(t) = SoC(o) - \frac{1}{C_{bat}} \int_0^t I_{bat}\,(T)dT \tag{4}$$

$where\ C_{bat}$ - rated battery capacity

I_{bat}- battery current.

III.3 DC–DC CONVERTER IMPLEMENTATION

Implement and analyze two conversion configurations.

III.3.1 H-Bridge Converter

The baseline system is the H-bridge converter. It allows for the reverse and regeneration power flow at the same time, hence, in case of acceleration or braking. The PWM technique with a predetermined frequency is used for generating the inverter signals.

III.3.2 Proposed Zeta Converter

The Zeta converter's development focuses on using a coupled inductor, energy transfer capacitors, diodes, and a floating active switch. Operating the converter in continuous conduction mode reduces current ripple and boosts the battery's efficiency.

III.4 MOTOR DRIVE AND CONTROLLER DESIGN

The Permanent Magnet Direct Current (PMDC) motor has been chosen to be the traction motor because of its uncomplicatedness and high torque per unit volume. The Motor velocity control is achieved using a Proportional-Integral (PI) controller. The control error is determined as the discrepancy between the reference speed and the real motor speed, as stated in equation 5.

$$e_t = \omega_{ref}(t) - \omega_{act}\,(t) \tag{5}$$

The PI controller output is given by equation 6.

$$u(t) = K_p e(t) + K_i \int e(t)dT \tag{6}$$

Where $K_p$and $K_i$are the proportional and integral gains, respectively.

III.5 DRIVING CYCLE AND VEHICLE DYNAMICS

In order to mimic the live car operations, the Signal Builder block in MATLAB/Simulink is used to create a custom driving profile. The speed profile is made up of different phases: acceleration, constant speed, and deceleration which sum up to a total simulation time of 1000 seconds. Table 1 compares the suggested Zeta converter with the traditional H-bridge converter in an electric vehicle application.

Table 1: The system performance is assessed using the following key metrics.

Key Metrics	System Performance
Battery State of Charge (SoC)	Indicates energy utilization efficiency
Vehicle Speed Tracking	Measures controller effectiveness
Distance Travelled	Evaluates driving range under identical conditions

Source: Authors, (2026).

The proposed system was validated through comprehensive simulation analyses. The comparison of the outcomes of both converter configurations is used to point out the improvements in battery SoC retention and vehicle travel distance. The experimental validation is not part of this study; however, the simulation framework developed can be considered a dependable base for future hardware implementation and real-time testing.

IV. RESULTS AND DISCUSSION

The State of Charge (SoC) is an indication of how much energy is still usable from a battery. It is important in stopping the battery from going through extreme discharging or charging, thus, helping to keep the battery's health and reduce the aging impacts [20]. It is not easy to classify these methods since a lot of them merge two or more techniques and employ different heuristic or deterministic mathematical tools [21]. SoC of H bridge and Zeta converter with Lithium-Ion battery in an Electric Vehicle has been analyzed in this study [22]. To begin with, create a signal builder in a Mat Lab Simulink signal that will linearly increase over 0 to 400 seconds and next 200 seconds the speed will be 100 Km/Hr. In the last seconds the speed will drop from 50 Km/Hr to zero and the signal builder will be connected to the longitudinal driver velocity reference input as illustrated in Figure 5.

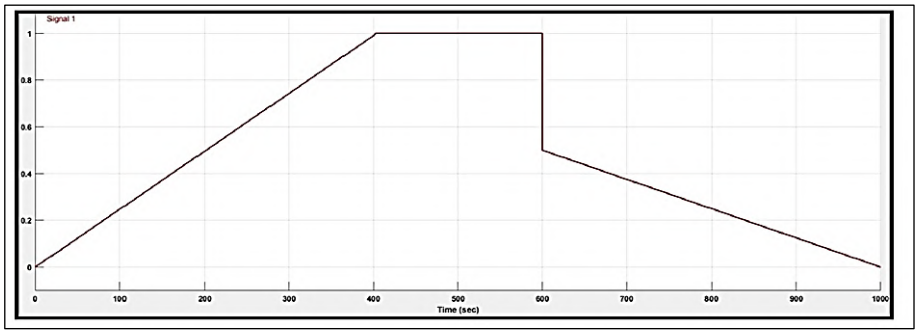


Figure 5: Input signal of velocity reference in longitudinal driver block.
Source: Authors, (2026).

The actual speed and the reference speed determine the subsequent aspects; the first one denotes that the actual speed is attempting to mimic the reference speed and the second one indicates about 50 Km/Hr average speed shown in the graph as depicted in figure 6.

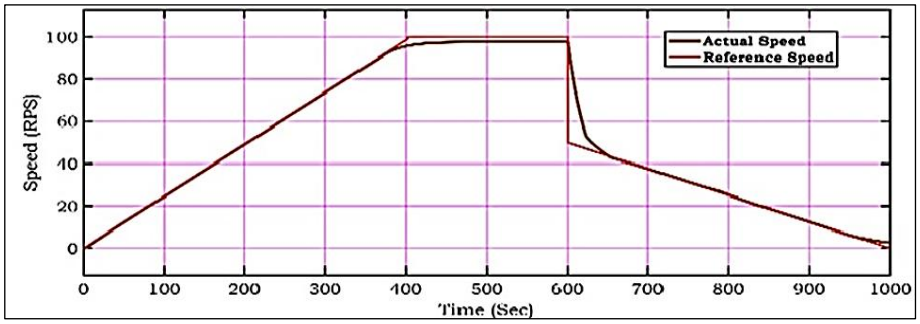


Figure 6: Actual and reference speed of the Vehicle.
Source: Authors, (2026).

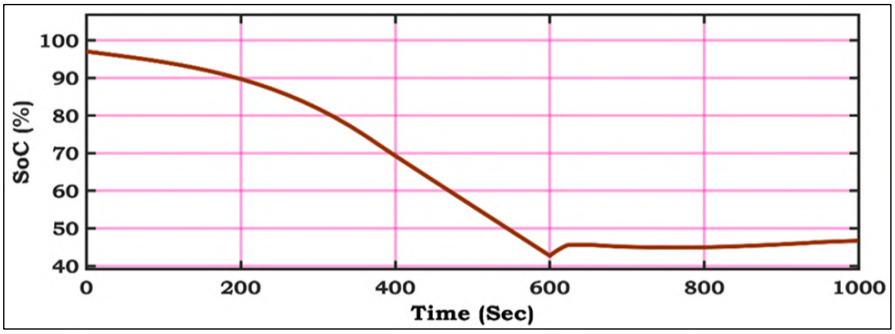


Figure 7: Variation of battery State of Charge (SoC) with time for H-bridge converter-based EV system under standard driving cycle.
Source: Authors, (2026).

Figure 7 shows the battery State of Charge for the Lithium-Ion battery.The battery is discharged non-linearly within the first 400 seconds, which is followed by 400-600 seconds of linear discharge. After 600 seconds, the battery has 50% charge and then gradually increases the charge and discharge according to the feedback system of the vehicle.

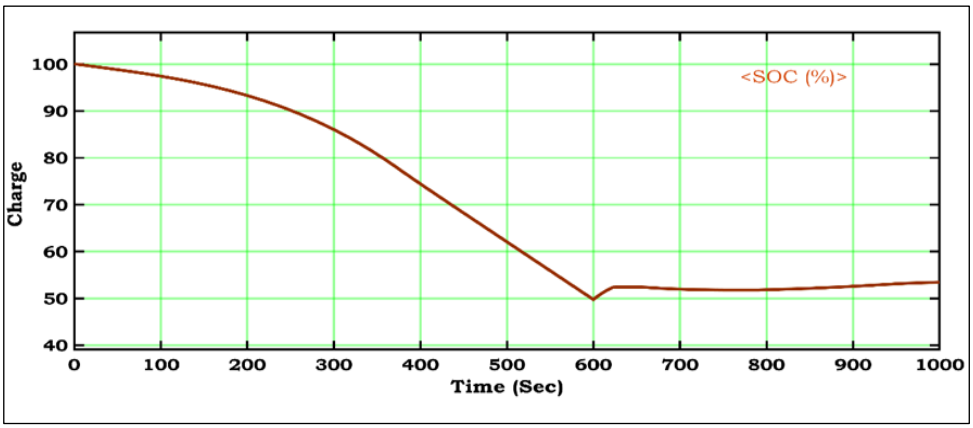


Figure 8: Variation of battery State of Charge (SoC) with time for proposed Zeta converter-based EV system under standard driving cycle.
Source: Authors, (2026).

In the battery's SoC depicted in figure 8, the battery undergoes non-linear discharge up to 400 seconds and it continues the same way till 600 seconds. The non-linear discharge seen in the initial driving phase coincides with the demands of acceleration while the linear discharge zone shows steady-state cruising. Such a pattern is an indication that the Zeta converter has been very effective in keeping energy delivery constant amid changing load conditions. The battery also gets discharged by 45 percent at 600 seconds in the case of Zeta converter, and for Lithium-ion batteries it is 50 percent by 600 seconds. In the case of H bridge, the percentage drained is only 45 percent at the same interval while the battery is being used as a converter. The recommended Zeta converter provides the optimal charge level for the battery while the electric vehicle is in use.

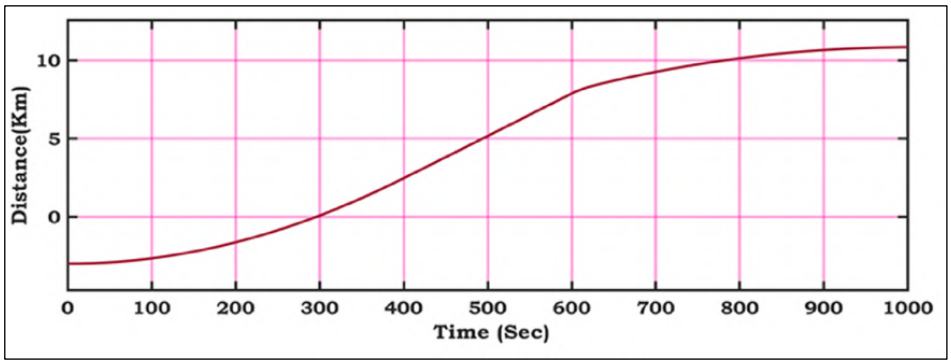


Figure 9: Distance travel by the vehicle using H Bridge Converter.
Source: Authors, (2026).

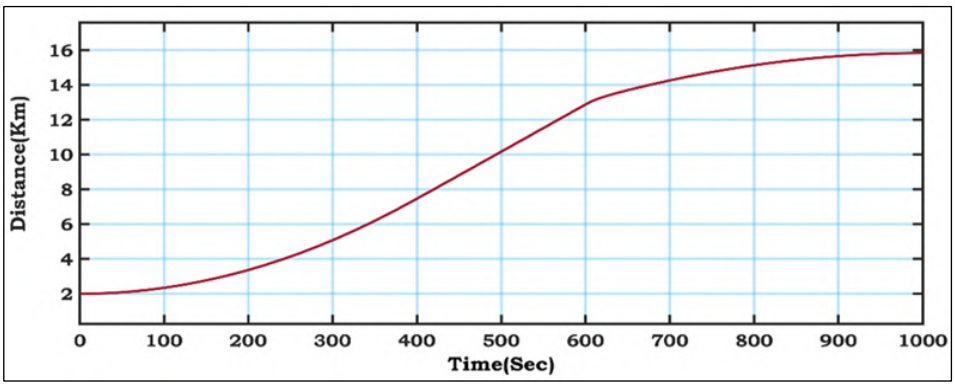


Figure 10: Distance travel by the vehicle using Proposed Zeta Converter.
Source: Authors, (2026).

The Simulink model ran for one thousand seconds in the MATLAB software. The battery state of charge (SoC) was 45%. The vehicle covered a distance of 12 km in 1000 seconds, as shown in the figure 9. During this, the same amount of current would pass from the battery to the motor when the vehicle was accelerating; upon deceleration, the motor would be connected to the battery through the current flow. With the application of the proposed Zeta Converter, the SoC percentage was 50% and the distance covered by the vehicle was 16 km in 1000 seconds as illustrated in figure 10. A summary of the battery SoC and vehicle travel distance is provided in table 2.

Table 2: Comparative performance of H-bridge and Zeta converter-based EV systems in terms of battery SoC and vehicle travel distance.

Type of Converter	Distance Travelled for 1000 Sec in (Km)	SoC (%)
H Bridge	12	45
Zeta Converter	16	50

Source: Authors, (2026).

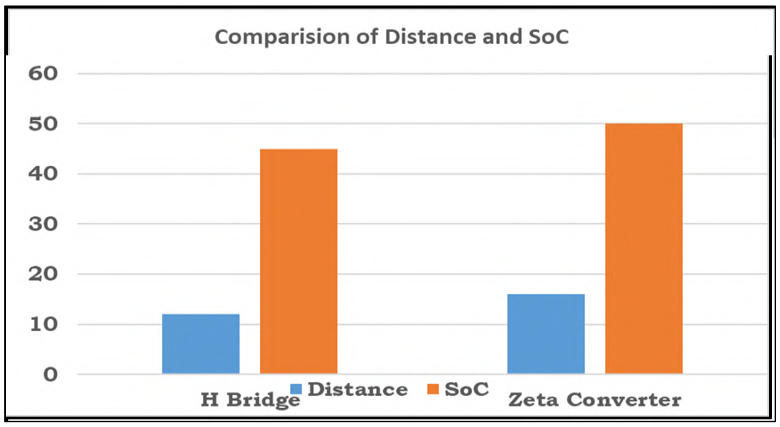


Figure 11: Comparison Chart of H Bridge and proposed Zeta converter-based Battery's SoC and Distance Travel by the Vehicle.
Source: Authors, (2026).

Both the H-bridge converter and the suggested Zeta converter experienced the same rate of acceleration and deceleration as the Li-Ion battery model [23] and [24]. The car covers a distance of 12 kilometers in 1000 seconds with the H-bridge converter, and the state of charge is 45%, whereas with the Zeta converter, the distance covered is the same, i.e., 12 kilometers in 1000 seconds, but the state of charge is 50%, as shown in Figure 11.

V. CONCLUSION

The article presents simulation results showing that a Lithium-Ion Battery-powered H bridge electric vehicle could travel 12 KM in 1000 seconds, which is equivalent to 43.2 KM/Hour when calculated on an hourly basis, and the battery is discharged 45 percent. With the proposed Zeta converter, the electric vehicle using a Lithium-Ion Battery could travel 16 Km in 1000 seconds i.e. 57 KM/hourWhen we compare the results, the proposed Zeta converter improved the battery's State of Charge. The distance traveled increased by 30 percent, too. The same converter was also used for the vehicle's auxiliary devices by changing the duty cycle. The outcome proves that installing a Zeta converter in the EV powertrain not only improves energy utilization but also increases driving range and battery SoC under the same operating conditions. This proves the appropriateness of the proposed converter for EV propulsion and auxiliary systems, which leads to more energy-efficient and eco-friendly electric vehicle designs.

VI. AUTHOR'S CONTRIBUTION

Conceptualization: V. Nandagopal, Pujari Harish Kumar, N Chinna Alluraiah, K. Harinath Reddy.
Methodology: V. Nandagopal, Pujari Harish Kumar, N Chinna Alluraiah, K. Harinath Reddy.
Investigation: V. Nandagopal, Pujari Harish Kumar, N Chinna Alluraiah, K. Harinath Reddy.
Discussion of results: V. Nandagopal, Pujari Harish Kumar, N Chinna Alluraiah, K. Harinath Reddy.
Writing – Original Draft: V. Nandagopal, Pujari Harish Kumar, N Chinna Alluraiah, K. Harinath Reddy.
Writing – Review and Editing: V. Nandagopal, Pujari Harish Kumar, N Chinna Alluraiah, K. Harinath Reddy.
Resources: V. Nandagopal, Pujari Harish Kumar, N Chinna Alluraiah, K. Harinath Reddy.
Supervision: V. Nandagopal, Pujari Harish Kumar, N Chinna Alluraiah, K. Harinath Reddy.
Approval of the final text: V. Nandagopal, Pujari Harish Kumar, N Chinna Alluraiah, K. Harinath Reddy.

VII. REFERENCES

[1] Jiaqi Yuan, Lea Dorn-Gomba, Alan Dorneles Callegaro, John Reimers and Ali Emadi "A Review of Bidirectional On-Board Chargers for Electric Vehicles",IEEE ACCESS, Vol.9, pp. 51501, March, 2021.

[2] Taichiro Sakagami and Yu Shimizu, "Exchangeable Batteries for Micro EVs and Renewable Energy",6 th international conference on Renewable Energy research and application (ICRERA), pp.701-705, November, 2017.

[3] Rajanand Patnaik Narasipuram and Subbarao Mopidevi, "A technological overview & design considerations for developing electric vehicle charging stations",Elsevier, Journal of Energy Storage,pp 1-13,September, 2021

[4] Molla S. Hossain Lipu, Mohammad Faisal , Shaheer Ansari , Mahammad A. Hannan , Tahia F. Karim ,AfidaAyob , Aini Hussain and Mohamad Hanif Md Saad. "Review Of Electric Vehicle Converter Configurations, Control Schemes And Optimizations: Challenges And Suggestions, Electronics",MDPI,Power electronics in industrial application, vol. 10, pp. 477, Febrauray, 2021.

[5] Ali M. Eltamaly, Almoataz Y. Abdelaziz, "Modern Maximum Power Point Tracking Techniques for Photovoltaic Energy Systems", Springer international publishing, October 2019, ISBNs : 978-3-03-005577-6, https://doi.org/10.1007/978-3-030-05578-3.

[6] Bondu Pavan Kumar Reddy,V. Usha Reddy,"PV-based Performance Evaluation of Zeta and Sepic Topologies for EV Applications", Journal of Electrical Systems,Vol.20,pp.438-446,2024, https://doi.org/10.52783/jes.2068.

[7] Z. Feng et al., "Loss Balance and Transient DC-Bias Suppression Strategies in Three-Level DAB Converters Modulated with Five DoFs," in IEEE Transactions on Power Electronics, vol. 38, no. 7, pp. 8150-8164, July 2023

[8] Y. Zhu, H. Wen, Q. Bu, G. Chu and H. Shi, "Reliability Assessment for Dual-Active-Bridge Converter with Fault Tolerant Capability," 2022 IEEE IAS Global Conference on Emerging Technologies (GlobConET), Arad, Romania, 2022, pp. 381-386.

[9] J. Zeng, X. Du and Z. Yang, "A Multiport Bidirectional DC–DC Converter for Hybrid Renewable Energy System Integration," in IEEE Transactions on Power Electronics, vol. 36, no. 11, pp. 12281-12291, Nov. 2021.

[10] Haitao Zhang,and Yunjie Zhang,"Recent Advances in DC-DC Converters for Electric Vehicles",MATEC Web of Conferences,pp.1-8,2023,https://doi.org/10.1051/matecconf/202338602008

[11] Mahghani M and Afjei E 2017 Carrier-based with unipolar switching technique current control of PMDC motors in electric vehicle applications Iranian Conference on Electrical Engineering (ICEE) 1060.

[12] Idris A, Baharom R, Hamzah, N R and Hamzah M K 2013 Controlled AC-DC converter fed permanent magnet DC motor using single-phase matrix converter Power Engineering andOptimization Conference (PEOCO), 2013 IEEE 7th International 764

[13] Ferrari M, Bianchi N, Doria A and Fornasiero E 2015 Design of synchronous reluctance motor for hybrid electric vehicles IEEE Trans. Ind. Appl. vol 51 no 4 pp 3030–40

[14] Yee-Pien Yang, Yih-Ping Luh and Cheng-Huei Cheung, "Design andcontrol of axial-flux brushless DC wheel motors for electric Vehicles-partI:multiobjectiveoptimaldesignandanalysis,"inIEEETransactions on Magnetics, vol. 40, no. 4, pp. 1873-1882, July 2004,

[15] Mohamad Reza Banae, Hossein AjdarFaeghi Bonab," A High Efficiency Nonisolated Buck–Boost Converter Based on ZETA Converter", IEEE Transactions on Industrial Electronics, Volume: 67 Issue: 3, pp.1991 – 1998, 2022.DOI: 10.1109/TIE.2019.2902785.

[16] Chok-You Chan,"Adaptive Sliding-Mode Control of a Novel Buck-Boost Converter Based on Zeta Converter", IEEE Transactions on Circuits and Systems.Volume: 69 Issue: 3,pp.1307 - 1311,2022,DOI: 10.1109/TCSII.2021.3107315.

[17] Radha Kushwaha, Bhim Singh,"UPF-isolated zeta converter-based batterycharger for electric vehicle"IET Electrical Systems in Transportation, Vol. 9 Iss. 3, pp. 103-112,2019, doi: 10.1049/iet-est.2018.5010.

[18] Hafez Sarkawi, Yoshito Ohta, Paolo Rapisarda,"On the switching control of the DC–DC zeta converter operatingin continuous conduction mode", IET Control Theory &Applications, Volume.15, pp.1185–1198,2021, DOI: 10.1049/cth2.12115.

[19] Hao Zhang; Yuan Zhang; Xikui Ma,"Distortion Behavior Analysis of General Pulse-Width Modulated Zeta PFC Converter Operating in Continuous Conduction Mode"IEEE Transactions on Power Electronics, Volume: 27 Issue: 10, pp.4212 - 4223,2012, DOI: 10.1109/TPEL.2012.2191161.

[20] Tang, X.; Liu, B.; Gao, F. State of charge estimation of lifepo4 battery based on a gain-classifier observer. Energy Procedia 2017, 105, 2071–2076, https://doi.org/10.1016/j.egypro.2017.03.585.

[21] Fleischer, C.; Waag, W.; Bai, Z.; Sauer, D.U. Adaptive on-line state of available power prediction of lithium-ion batteries. J. Power Electron. 2013, 13, 516–527.https://doi.org/10.6113/JPE.2013.13.4.516.

[22] N Chinna Alluraiah, V. Nandagopal, P. Veeramanikandan, Godfrey D, S. Meena and G. Brindha,"Comparison of SoC in Ni-MH and Lithium-Ion Battery for E-Vehicle",International Journal of Electrical and Electronics Research,Volume 12, Issue 4, 1258-1263 2024.DoI https://ijeer.forexjournal.co.in/archive/volume-12/ijeer-120417

[23] Slaski G., Ohde B., A statistical analysis of energy and power demand for the tractive purposes of an electric vehicle in urban traffic – an analysis of a short and long observation period, IOP Conf. Ser.: Mater. Sci. Eng., vol. 148, 2016, 012027, 10.1088/1757-899X/148/1/012027.

[24] Young K.H., Ng K.Y.S., Bendersky L.A., A Technical Report of the Robust Affordable Next Generation Energy Storage System-BASF Program, Batteries, vol. 2(1), 2016, 2, 10.3390/batteries2010002.

Journal of Engineering and Technology for Industrial Applications

ITEGAM-JETIA

Manaus, v.12 n.60, p.337-343, July/August, 2026.
DOI: https://doi.org/10.5935/jetia.v12i60.3830

ISSN ONLINE: 2447-0228

RESEARCH ARTICLE OPEN ACCESS

PARALLEL LÉVY-FLIGHT CUCKOO SEARCH FOR JOINT DG SITING/SIZING AND POWER-QUALITY ENHANCEMENT IN RADIAL DISTRIBUTION NETWORKS

Vinuta V Koluragi*[1], J P Sridhar[2]

[1]Department of Electrical & Electronics Engineering, B.L.D.E.A's V. P. Dr. P. G. Halakatti College of Engineering & Technology, Vijayapur, India.
[2]Department of Electrical & Electronics Engineering, SJB Institute of Technology, Bengaluru, India.

[1]https://orcid.org/0009-0006-1966-3180, [2]https://orcid.org/0000-0003-0287-3203

Email:*vinutakoluragi@bldeacet.ac.in, srihdk@gmail.com

ARTICLE INFO

Article History
Received: February 26, 2026
Reviewed: June 10, 2026
Accepted: July 10, 2026
Published: July 31, 2026

Keywords:
Parallel Lévy Flight Cuckoo Search;
Distributed Generation;
Radial Distribution Networks;
Power Quality Enhancement;
Multi-Objective Optimization.

ABSTRACT

This paper proposes a Parallel Lévy Flight Cuckoo Search (CS PLF) framework for joint siting and sizing of renewable distributed generation (DG) with power quality enhancement in radial distribution networks. The planning objective balances economic efficiency and operational security via a scalarized function combining the benefit to cost ratio (BCR), voltage stability factor (VSF), and a network security index (NSI) under standard power flow and equipment constraints. This article introduces two design elements that strengthen optimization results: (i) a parallelized Lévy flight update to accelerate global exploration without parameter inflation, and (ii) an integrated planning model that accounts for DG real/reactive support and UPQC driven reactive needs within the same optimization loop. In comparative experiments on an Indian 28 bus radial distribution system, CS PLF achieves lower composite objective values and stronger voltage profiles, while PSO provides lower total cost and faster runtime, highlighting a planning trade off between economy and robustness.

Copyright ©2026 by authors and Galileo Institute of Technology and Education of the Amazon (ITEGAM). This work is licensed under the Creative Commons Attribution International License (CC BY 4.0).

I. INTRODUCTION

Growing penetration of renewable DG in distribution networks requires planners to co optimize siting/sizing decisions with power quality and voltage stability objectives. While metaheuristics (e.g., PSO, CSA, GWO) have been widely adopted, two persistent gaps remain: (1) most works treat DG allocation and power quality devices in separate stages; (2) search strategies often trade off exploration for speed, or vice versa. To address these, this article proposes CS PLF, a Cuckoo Search variant that parallelizes Lévy flight perturbations and embeds UPQC aware quality metrics in the objective, enabling joint economic–technical planning.

Contributions:

1. Integrated multi criteria formulation combining BCR, VSF, and NSI with standard AC constraints, capturing cost, voltage robustness, and thermal loading risk in one scalar objective
2. Parallel Lévy Flight Cuckoo Search (CS PLF): embarrassingly parallel Lévy flight updates accelerate global search while preserving CSA's low parameter count
3. DG and Power Quality co planning: decision variables include DG locations, counts, and ratings (P/Q), with UPQC considerations implicitly driving voltage profile/harmonic mitigation benefits.
4. Comparative study vs. PSO: highlights a cost–robustness trade off valuable for planners (CS PLF improves stability/security, PSO reduces cost/runtime).

Recent studies have significantly advanced the field of distributed generation (DG) sizing and placement, largely through the development of improved and hybrid optimization algorithms.

According to [1], [2] demonstrated the effectiveness of the Cuckoo Search Algorithm (CSA) in improving convergence speed and solution quality compared to classical methods. Further refinements to CSA were proposed by [3], who developed variants with reduced computational complexity and enhanced global search characteristics. Hybrid optimization frameworks have also shown considerable promise. According to [4] introduced a Grey Wolf–Cuckoo Search hybrid approach that improves robustness in identifying optimal DG placement, while by [5] applied PSO assisted techniques for DG allocation with reactive power support. Additional studies such as by [6] validate that hybrid metaheuristics offer performance gains in multi-DG integration. Research relating to Unified Power Quality Conditioner (UPQC) continues to expand due to its importance in mitigating voltage sag, harmonics, and reactive power imbalance. In [7], [8] evaluated multi objective and PSO based UPQC allocation methods, respectively. Benchmarking efforts such as that by Espinosa Gutiérrez and Aguila Téllez [9] demonstrated that exhaustive search can still serve as a useful reference for validating heuristic algorithms. In [10], [11] developed hybrid metaheuristic approaches to improve UPQC performance under varying grid conditions. Authors to [12] further explored combinations of genetic and dragonfly algorithms for enhanced UPQC placement efficiency. Machine learning integration for DG and UPQC optimization has also emerged as a growing theme, as highlighted by [13].

However, only a limited number of studies directly address combined DG and UPQC allocation. According to [14] proposed a hybrid Whale–Dragonfly strategy for simultaneous sizing and placement, improving both economic and technical indicators. Complementary insights regarding coordinated multi objective UPQC design are provided by [15]. Authors to [16] investigated UPQC operation within DG integrated networks and emphasized the need for coordinated control to ensure system stability. Comparative reviews, such as that by [17], reinforce that methods outperform deterministic techniques for DG sizing and placement. Additional work [18–21] further demonstrates the effectiveness of hybrid optimization, multi population heuristics, and swarm-based methods. Machine learning and deep learning assisted optimization strategies have also gained traction in recent years [22–24], and industry aligned reports such as by [25] confirm the continued relevance of PSO based DG planning. With the rapid growth of renewable integration, DG-based distribution systems are increasingly favored for their environmental and economic benefits. Earlier research primarily focused on real power-oriented DG placement using impact indices or classical evolutionary algorithms. In contrast, the present work proposes a CS PLF based approach for optimal DG allocation that simultaneously considers both real and reactive power contributions. This enables improved voltage stability and loss minimization, building upon the foundational contributions of prior studies.

II. MATERIALS AND METHODS

To address the limitations of existing approaches, this article proposes a novel CS-PLF that is compared with PSO. The method is designed to improve optimal results while maintaining computational efficiency. This section starts with objective constraints used for the optimal placement and followed by the PSO and CS-PLF. The objective is to minimize the total cost while maximizing voltage stability and network security. The cost model includes investment and operational expenses, while benefits are derived from improved power quality and reduced losses. Mathematical formulations include cost functions, benefit functions, voltage stability factor (VSF), network security index (NSI), and constraints for generation limits, voltage tolerances, and line capacities.

Decision Variables and Sets

- $\mathcal{N}$: set of buses; $i \in \mathcal{N}$.
- $l_i \in \{0,1\}$: DG location indicator.
- $n_i \in \mathbb{Z}_{\geq 0}$: count of DG units at bus i.
- $P_{ij}^{\mathrm{DG}}, Q_{ij}^{\mathrm{DG}}$: active/reactive rating of a type-j DG at bus i; $j \in$ {solar, wind, biomass}.
- AC state variables V_i, θ_i; line flows S_{ij}.

Economic Model

DG cost (present-valued):

$$C_{\mathrm{DG}} = \sum_i \sum_j (I\, C_{ij}\, n_i\, l_i + \mathrm{OMC}_{ij}\, P_{ij}^{\mathrm{DG}}\, n_i\, l_i) \cdot \mathrm{CPV}, \tag{1}$$

$$\mathrm{CPV} = \frac{1-\mathrm{PV}^{N_y}}{1-\mathrm{PV}} \tag{2}$$

$$\mathrm{PV} = \frac{1+\frac{\mathrm{IF}}{100}}{1+\frac{\mathrm{IR}}{100}}. \tag{3}$$

(Standardized the present-value notation and ratio as used in discounted-cash-flow analysis).

DG benefit (energy value + loss reduction):

$$B_{\mathrm{DG}} = \sum_i \sum_j (P_{ij}^{\mathrm{DG}} + Q_{ij}^{\mathrm{DG}}) n_i l_i \; + \; \Delta P_{\mathrm{loss}}^{\mathrm{DG}}] \cdot C_{\mathrm{hr}} \cdot 8760 \cdot \mathrm{CPV}. \tag{4}$$

$$\mathrm{BCR} = \frac{B_{\mathrm{DG}}}{C_{\mathrm{DG}}}. \tag{5}$$

(If $Q$is remunerated differently, consider a weighting or separate tariff.)

Robustness Metrics

Voltage Stability Factor (VSF) at bus $i+1$:

$$\mathrm{VSF}_{i+1} = 2V_{i+1} - V_i, \bar{\mathrm{VSF}} = \frac{1}{|\mathcal{N}|-1}\sum_{i=1}^{|\mathcal{N}|-1} \mathrm{VSF}_{i+1}. \tag{6}$$

Network Security Index (NSI) via loading level:

$$LL_i = \frac{S_i^{\mathrm{MVA}}}{S_{i,\max}^{\mathrm{MVA}}}, \bar{\mathrm{NSI}} = \frac{1}{|\mathcal{N}|-1}\sum_{i=1}^{|\mathcal{N}|-1} L\,L_i. \tag{7}$$

Lower $\bar{\mathrm{NSI}}$indicates a more secure network.

Objective and Constraints

Scalarized the multi-criteria planning objective as:

$$\min_{\{l_i, n_i, P_{ij}^{\mathrm{DG}}, Q_{ij}^{\mathrm{DG}}\}} f = -\alpha\,\mathrm{BCR} - \beta\,\bar{\mathrm{VSF}} + \gamma\,\bar{\mathrm{NSI}}, \alpha, \beta, \gamma > 0. \tag{8}$$

Subject to standard AC power-flow equations; generator, voltage, and line limits:

(Corrected typographic inconsistencies in the reactive-power balance and clarified that both $P_{\mathrm{loss}}$and Q_{loss}denote network losses.)

$$P_{\mathrm{slack}} + \sum_{i,j} P_{ij}^{\mathrm{DG}}\, n_i l_i - \sum_i P_{D,i} \tag{9}$$

$$Q_{\mathrm{slack}} + \sum_{i,j} Q_{ij}^{\mathrm{DG}}\, n_i l_i - \sum_i Q_{D,i} \tag{10}$$

$$P_{ij}^{\min} \le P_{ij}^{\mathrm{DG}} n_i \le P_{ij}^{\max}, Q_{ij}^{\min} \le Q_{ij}^{\mathrm{DG}} n_i \tag{11}$$

$$Q_{ij}^{\mathrm{DG}} = P_{ij}^{\mathrm{DG}} \tan(\cos^{-1}(\mathrm{PF})) \tag{12}$$

$$V_i^{\min} \le V_i \le V_i^{\max} \tag{13}$$

$$|\,S_{ij}\,| \le S_{ij}^{\max}. \tag{14}$$

A. Particle Swarm Optimization Algorithm (PSO)

PSO is inspired by social behavior in animal groups. Each particle represents a potential solution and updates its position based on personal and global best experiences. The algorithm is efficient for static optimization problems and has been widely applied in power system planning. Figure 1 shows the flow chart of PSO algorithm flowchart.

B. Cuckoo Search- Parallel Levy Flights (CS-PLF)

CS-PLF mimics the brood parasitism of cuckoo birds. It uses Lévy flights for global search and probabilistic replacement of poor solutions. CS-PLF requires fewer parameters and offers robust performance in complex optimization landscapes. Below is a brief summary of the CS-PLF algorithm.

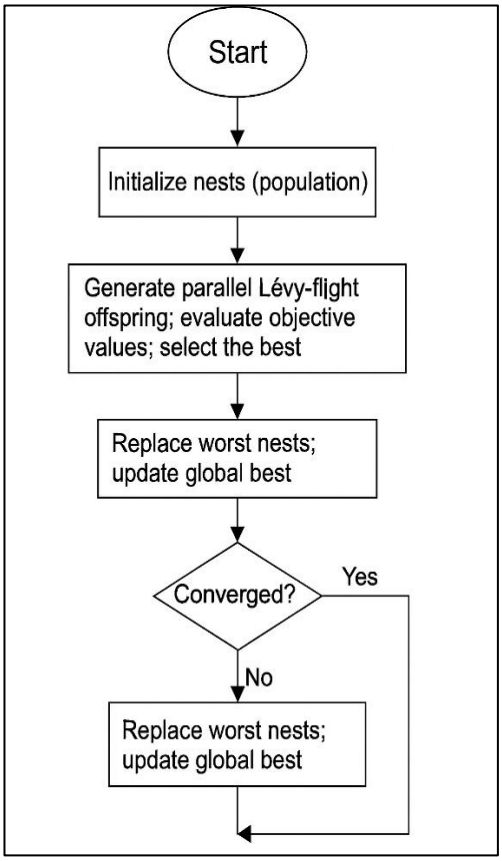


Figure 1: CS-PLF flowchart.
Source: Authors, (2026).

III. RESULTS AND DISCUSSIONS

The MATLAB 2025a m-file is used for the algorithm development and test. The laptop with 11th Gen Intel Core i7-11850H @ 2.50Ghz processor with 32 GB RAM is used. The proposed model is tested on the Indian 28-bus distribution system. DGs of solar, wind, and biomass types are considered over a 10-year planning horizon. Both PSO and CS-PLF are applied with identical population and iteration settings. CS-PLF yields superior voltage stability and network security, while PSO achieves lower total cost and faster convergence. Detailed results are presented in tabular and graphical formats. The test system employed here is Indian 28 distributed bus system [2]. The PSO method and the CS-PLF algorithm are used to minimize Equation (10). Six is assumed to be the constant number of DG installations (N=6). Additionally, the issue has been resolved for a period of ten years (yr) (Nyr=10). The three DG kinds selected are biomass, wind, and solar. In this case, solar is type 1, wind is type 2, and biomass is type 3. And it works for reactive power support also. The power factor considered here is 0.9.

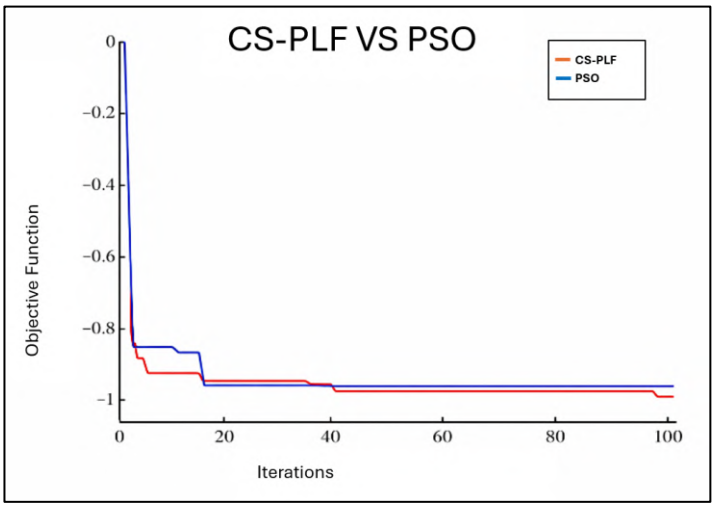


Figure 2: The graph of convergence between CS-PLF and PSO.
Source: Authors, (2026).

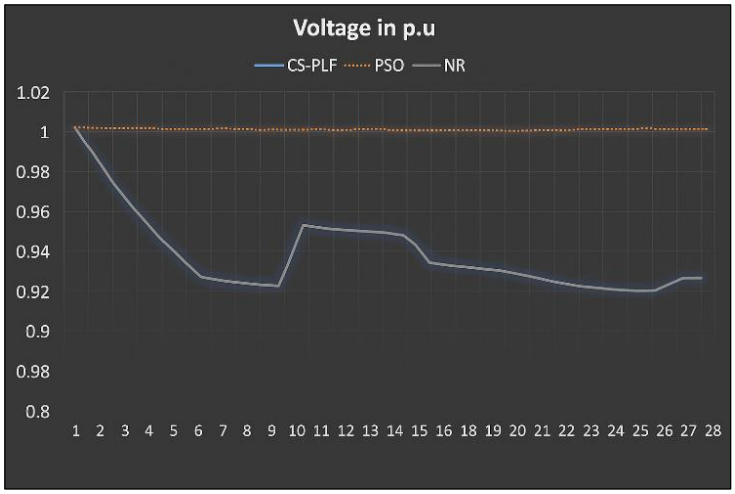


Figure 3: Indian 28-bus system voltage profile with renewable DG positioned ideally using CS-PLF and PSO and without renewable DG using the Newton-Raphson technique.
Source: Authors, (2026).

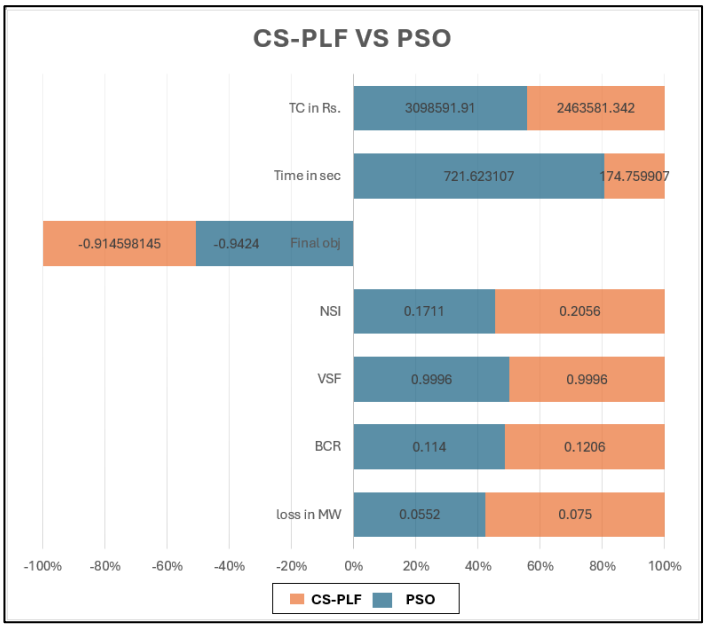


Figure 4: Comparing the CS-PLF with PSO using the following metrics: NSI, VSF, BCF, time spent, total cost, loss in MW, and end objective value.
Source: Authors, (2026).

Figure 2 shows the convergence graph. Where the figure 3 shows the Voltage profile of all the algorithms. The convergence graphs of the CS-PLF and PSO algorithms with the identical objective function are displayed in the above figure. In this case, the overall population is 60, and the number of algorithms for both algorithms is 100. The performance of PSO is shown by the blue line in the graph above, and that of CS-PLF by the red line. CS-PLF provides a superior minimum objective function for 100 iterations. Both meet the requirements. Figure 4 shows the comparison result. The research summarizes the allocation of renewable distributed generators across six buses, detailing their capacity, cost, and operational metrics. The total installed capacity is 4.475 MW and 2.2 MVar, with an overall investment cost of approximately ₹2.14 million and annual operation and maintenance (O&M) expenses of ₹0.33 million, resulting in a cumulative annual cost of ₹2.46 million. Bus 26 contributes the largest share, hosting six units with 1.2 MW capacity and incurring the highest total cost of ₹910,809.89, while Bus 24 is the most cost-efficient with a cost per MW of about ₹276,247. Type-3 DGs dominate the network, providing 3.6 MW capacity but at a higher cost per MW compared to type-2 units, which are more economical. O&M costs remain consistent at roughly 13–14% of total costs across all buses, indicating predictable maintenance scaling. Overall, the data highlights a trade-off between capacity and cost efficiency, suggesting that strategic placement of DGs is crucial for optimizing investment and operational performance. In comparison to the PSO method, the CS-PLF algorithm provides superior voltage profile, NSI, VSF, and BCR values. However, the PSO method is less expensive and takes less time to solve.

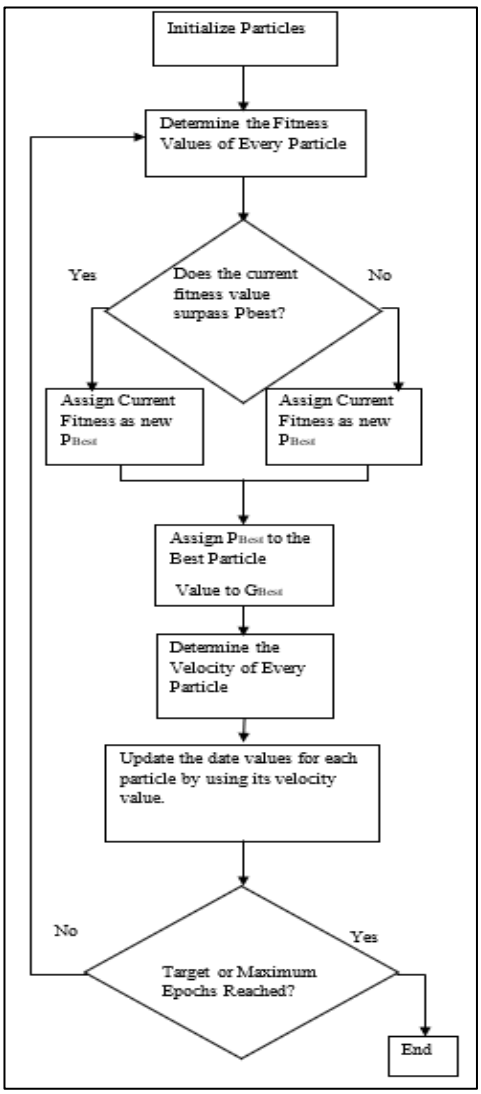


Figure 5: Particle swarm optimization Algorithm flowchart.
Source: Authors, (2026).

It is the logical presentation of the results that demonstrate the true contribution of the research and also justify the conclusion. The parts indicated above, Introduction, Material and Methods serve to explain how the results are obtained. Use tables and figures for your explanation. The results must be written in the past, in a brief and simple way. Avoid redundancy.

IV. CONCLUSIONS

This research demonstrates that renewable DGs, when optimally placed and sized, can significantly enhance distribution system performance by reducing losses, improving voltage stability, and maintaining power quality. A comparative analysis of two metaheuristic algorithms—PSO and CS-PLF—highlights the trade-offs between economic efficiency and technical performance. PSO proves more cost-effective, making it suitable for budget-driven planning, while CS-PLF delivers superior voltage profiles and system stability through advanced global search and parallelized updates. The integration of UPQC further strengthens power quality by mitigating harmonics and regulating voltage. Simulation results on standard IEEE test feeders validate the proposed framework and emphasize that operational priorities, such as minimizing cost or improving voltage stability, should guide algorithm selection. These findings provide actionable insights for smart grid expansion planning and real-time decision-making in renewable-rich networks, paving the way for more resilient and sustainable power systems.

V. AUTHOR'S CONTRIBUTION

Conceptualization: Vinuta V Koluragi
Methodology: Vinuta V Koluragi and J P Sridhar.
Investigation: Vinuta V Koluragi and J P Sridhar.
Discussion of results: Vinuta V Koluragi and J P Sridhar.
Writing – Original Draft: Vinuta V Koluragi.
Writing – Review and Editing: Vinuta V Koluragi and J P Sridhar.
Resources: J P Sridhar.
Supervision: Vinuta V Koluragi and J P Sridhar.
Approval of the final text: Vinuta V Koluragi and J P Sridhar.

VI. REFERENCES

[1] M. Ghosh, S. Kumar, S. Mandal, and K. K. Mandal, "Optimal Sizing and Placement of DG Units in Radial Distribution System Using Cuckoo Search Algorithm," *IEEE RA*, 2025.

[2] K. Ojo, S. Fanifosi, A. Ayokunle, and I. Samuel, "Cuckoo search algorithm approach for optimal placement and sizing of distribution generation in radial distribution networks," *International Journal of Electrical and Computer Engineering*, vol. 15, no. 1, pp. 1–10, 2025.

[3] U. Kumar, B. Singh, and T. A. Khan, "Metaheuristic Approaches for Distributed Generation Placement in Distribution Networks," *IEEE Transactions on Smart Grid*, vol. 13, no. 4, pp. 995–1005, Aug. 2022, doi: 10.1109/TSG.2022.9959077.

[4] A. P. Chaudhari, G. B. Patil, S. Ushkewar, and A. J. Patil, "Allocation and Optimal Dimensioning of Distributed Generation Using Grey Wolf Optimized Cuckoo Search Algorithm," *International Journal of Engineering Trends and Technology*, vol. 73, no. 5, pp. 1–7, 2025.

[5] M. Pushkarna, H. Ashfaq, R. Singh, and R. Kumar, "Optimal placement and sizing of type-IV DG with reactive power support using UPQC in an unbalanced distribution system using PSO," *Energy Systems*, vol. 13, no. 2, pp. 1–15, 2022.

[6] R. Palanisamy, S. B. Reddy, S. Kumar, A. Sakthidasan, and P. Baburao, "Optimal Integration of Multiple Renewable Energy Distributed Generations using Hybrid Optimization Technique," *International Journal of Renewable Energy Research*, vol. 14, no. 3, pp. 1–10, 2024.

[7] D. K. Nishad, A. N. Tiwari, and S. Khalid, "Multi-Objective Optimization Simulation of Unified Power Quality Conditioner (UPQC)," *International Journal of Trends in Artificial and Cognitive Intelligence*, vol. 3, no. 1, pp. 1–8, 2025.

[8] M. L. Ramanaiah and M. D. Reddy, "Optimal Placement of Unified Power Quality Conditioner in Distribution Systems Using PSO," *ARPN Journal of Engineering and Applied Sciences*, vol. 14, no. 5, pp. 1–6, 2024.

[9] J. S. Espinosa Gutiérrez and A. Aguila Téllez, "Optimal Placement of Unified Power Quality Conditioner (UPQC) in Distribution Systems Using Exhaustive Search," *Energies*, vol. 18, no. 4, pp. 1–12, 2025.

[10] L. V. N. Rao, P. S. Prakash, and M. V. Kumari, "Optimal Placement of UPQC with a Novel Hybrid Meta-Heuristic Approach," *Nanotechnology Perceptions*, vol. 20, no. 1, pp. 1–9, 2024.

[11] G. Lakshminarayana, D. R. Dev, K. Vijetha, N. V. Gour, R. Mageswaran, and S. Sree Dharinya, "Hybrid Optimization of Unified Power Quality Conditioner Placement for Enhanced Grid Performance," *International Journal of Electrical and Electronics Engineering*, vol. 12, no. 2, pp. 1–10, 2025.

[12] "Optimal location and capacity planning of UPQCs considering operation dispatching in distribution grid with distributed generators," *Energy Reports*, vol. 8, pp. 832–842, Aug. 2022.

[13] A. S. Chaitra and H. R. Sudarshana Reddy, "Dispersed Generations for Improvement of Power Performance Using UPQC Based on Machine Learning," *SN Computer Science*, vol. 4, no. 2, pp. 1–12, 2023.

[14] A. Chakraborty, B. K. Panigrahi, and S. K. Mohapatra, "Effective DG and Capacitor Placement in Power Distribution System: A Hybrid WOA–Dragonfly Algorithm," *2023 IEEE Power & Energy Society General Meeting (PESGM)*, pp. 1–5, 2023, doi: 10.1109/PESGM58027.2023.11081226.

[15] M. K. Priyanka, R. S. Naik, and S. Naveena, "A Novel Three Phase Multi-Objective Unified Power Quality Conditioner with Three Phase Fault," *International Research Journal of Engineering and Technology*, vol. 11, no. 4, pp. 1–8, 2024.

[16] T. Lei, S. Riaz, N. Zanib, M. Batool, F. Pan, and S. Zhang, "Performance Analysis of Grid-Connected Distributed Generation System Integrating a Hybrid Wind-PV Farm Using UPQC," *Complexity*, vol. 2022, Article ID 4572145, 2022, doi: 10.1155/2022/4572145.

[17] C. Effiong, N. Okpura, and A. Obot, "Optimal Placement and Sizing of Distributed Generation For Loss Minimization and Voltage Stability—A Comprehensive Review," *SCITECH Journal*, vol. 12, no. 2, pp. 1–10, 2024.

[18] D. Nageswari, N. Kalaiarasi, and G. Geethamahalakshmi, "Optimal Placement and Sizing of Distributed Generation Using Metaheuristic Algorithm," *Computer Science and Software Engineering Journal*, vol. 10, no. 1, pp. 1–8, 2022.

[19] M. Angelova, O. Roeva, P. Vassilev, and T. Pencheva, "Multi-Population Genetic Algorithm and Cuckoo Search Hybrid Technique for Parameter Identification of Fermentation Process Models," *Processes*, vol. 11, no. 2, p. 427, Jan. 2023, doi: 10.3390/pr11020427.

[20] Y. Izgheche, T. Bahi, and A. Lakhdara, "Analysis of Genetic and Cuckoo Search Algorithms for MPPT in Partial Shaded Conditions," *International Journal of Smart Grid*, vol. 8, no. 2, pp. 1–8, 2024.

[21] S. Abdulaziz, G. Attlam, G. Zaki, and E. Nabil, "Cuckoo search algorithm and particle swarm optimization based MPPT techniques," *International Journal of Electrical and Electronic Control*, vol. 9, no. 1, pp. 1–10, 2022.

[22] I. Suryawati, "Optimization of Distributed Generation Placement using PSO," GitHub Repository, 2023.

[23] B.-P. Ngoussandou, N. Nisso, D. K. Kidmo, and Kitmo, "Optimal Placement and Sizing of Distributed Generations for Power Losses Minimization Using PSO-Based Deep Learning Techniques," *Smart Grid and Renewable Energy*, vol. 14, pp. 169–181, Sep. 2023, doi: 10.4236/sgre.2023.149010.

[24] K. Ojo, S. Fanifosi, A. Ayokunle, and I. Samuel, "Cuckoo search algorithm approach for optimal placement and sizing of distribution generation in radial distribution networks," *International Journal of Electrical and Computer Engineering (IJECE)*, vol. 15, no. 3, pp. 2681–2696, Jun. 2025, doi: 10.11591/ijece.v15i3.pp2681-2696.

[25] IEEE Std. 8003984, "PSO based optimal distributed generation placement and sizing in power distribution networks," IEEE, 2024.

Journal of Engineering and Technology for Industrial Applications

ITEGAM-JETIA

Manaus, v.12 n.60, p.344-355, July/August, 2026.
DOI: https://doi.org/10.5935/jetia.v12i60.3834

ISSN ONLINE: 2447-0228

RESEARCH ARTICLE OPEN ACCESS

SYNERGISTIC HYBRID GDI–CNTFET ARCHITECTURE FOR LOW-POWER AND AREA-OPTIMIZED NANOSCALE VLSI CIRCUITS

Jayakrishna Padala[1], Kishore Kumar Kamarajugadda[2], Pavani Movva[3]

[1]Research Scholar, Department of ECE, FoET, The ICFAI University, Raipur, India.
[2]Professor, Department of ECE, FoET, The ICFAI University, Raipur, India.
[3]Professor, Department of ECE, Nalla Malla Reddy Engineering College, Hyderabad, India.

[1]https://orcid.org/0009-0009-9498-2597, [2]https://orcid.org/0000-0002-6286-1186, [3]https://orcid.org/0000-0003-1987-9185

Email: pjayakrishnachary@gmail.com, jayakrishnap.phd2023@iuraipur.edu.in, kishorekamarajugadda@gmail.com, drmovvapavani@gmail.com

ARTICLE INFO

Article History
Received: February 26, 2026
Reviewed: June 11, 2026
Accepted: July 11, 2026
Published: July 31, 2026

Keywords:
Hybrid GDI–CNTFET,
Carbon NanoTube Field Effect Transistor,
Gate Diffusion Input,
Low-Power VLSI,
Area-Efficient Design,
Cadence Virtuoso Tool,
Nanoscale Technology,
Digital Circuits.

ABSTRACT

As CMOS technology continues to expand to a deep sub-micron scale, standard designs are confronted with many challenges in terms of energy dissipation, leakage currents and area. Although GDI logic minimizes the number of transistors and CNTFET offers improved transport performance, it is on its own that it provides optimal performance. This paper proposes a hybrid design methodology for GDI and CNTFETs combining the structural compactness of GDI with the near ballistic electrical characteristics of 32 nm CNTFETs. The complete digital building block library, including basic logic gates, arithmetic units (half-adder, full-adder), data-routing circuits (multiplexer, encoder, decoder) and sequencing elements (D and Jk flip-flops) have been developed in the Cadence tool based on Stanford 32 nm CNTFET model. Transient, DC and AC analysis confirm full swing logic and high frequency response. The simulation results indicate that the proposed hybrid architecture achieves a reduction of 40-70% in power and 25-55% in silicon area compared to conventional CMOS and standalone GDI, CNTFET reference products, and is a much improved Power-Delay Product. These findings, together with the significantly improved PDP, make the GDI-CNTFET hybrid framework a viable and scalable solution for energy-efficient nano-electronic systems.

Copyright ©2026 by authors and Galileo Institute of Technology and Education of the Amazon (ITEGAM). This work is licensed under the Creative Commons Attribution International License (CC BY 4.0).

I. INTRODUCTION

The relentless pursuit of Moore's Law [1] has pushed integrated circuit (IC) technology down to the deep sub-micron and nanometer scale, and this has led to the need for low-power, high-speed and area-efficient VLSI systems [2]. This is particularly important for the emerging areas of Internet of Things (IoT), implantable biomedical sensors and edge computing. However, bulk CMOS has significant physical scaling limitations [3], such as leakage current, short-channel effects and threshold voltage variations, which cause performance and reliability problems. To overcome these constraints, researchers have investigated both architectural and device-level innovations. Gate Diffusion Input (GDI) logic is a promising approach at the architectural level to minimize the number of transistors and the switching activity [4], which can be implemented with fewer devices than conventional CMOS [5], leading to lower dynamic power consumption and lower silicon area, but suffers from intrinsic drawbacks, such as reduced output voltage swings and decreased noise margins, which cause the cascaded high-performance systems to become unstable [6]. Simultaneously, Carbon Nanotube Field-Effect Transistors (CNTFETs) have gained prominence as a robust post-CMOS successor. CNTFETs offer extraordinary electrical properties [7], including near-ballistic carrier transport, symmetric threshold voltages, and superior electrostatic control due to their unique geometry. While CNTFETs inherently address the leakage and performance issues [8] of silicon, implementing them using traditional CMOS-like topologies often results in redundant device counts and increased wiring complexity. A critical analysis of current literature [9] reveals a fragmented research landscape: GDI logic is primarily studied for area optimization [10], while CNTFET technology is investigated for power-delay performance [11]. There is a notable absence of a unified hybrid design framework that merges the architectural compactness of GDI with the superior material physics of CNTFETs.

While our previous research established the independent merits of these technologies, this work proposes a novel Hybrid GDI–CNTFET methodology. This co-design strategy leverages the reduced-transistor topology of GDI [12] while utilizing the high-mobility, low-leakage characteristics of CNTFETs [13] to mitigate the traditional GDI "voltage drop" problem through better drive strength. The main objective of this research work is to go beyond the isolated optimization as implied in the graphical version of abstract shown in Figure 1. We implemented this hybrid technique to a set of digital circuits and performed a comprehensive performance evaluation on transistor count, power dissipation, propagation delay, and the Power–Delay Product (PDP). Benchmarking results against conventional CMOS, stand-alone GDI, and CNTFET designs demonstrate that the proposed hybrid approach presents a superior Pareto-optimal solution for next-generation VLSI systems.

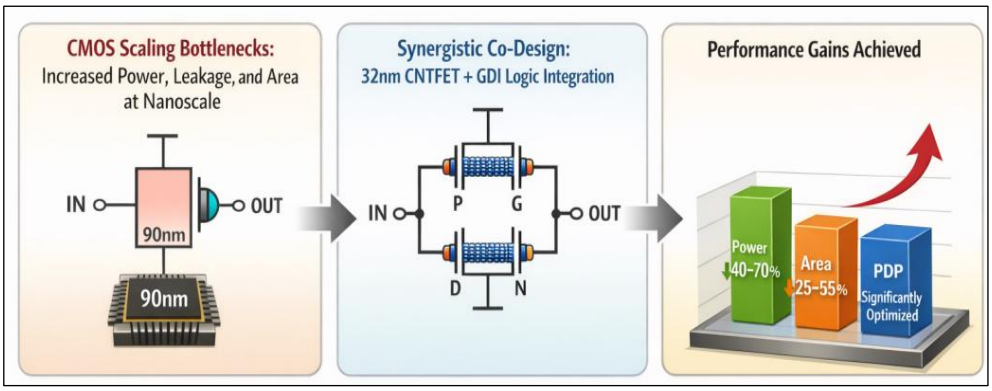


Figure 1: Graphical version of abstract.
Source: Authors, (2026).

The remainder of this paper follows the background and literature surveys conducted for GDI and CNTFET in section-2; section-3 details the proposed hybrid methodology; section-4 describes the implementation of digital circuits with proposed methodology using the Cadence Virtuoso simulation environment; section-5 discusses the results and benchmarking; and section-6 concludes with a future research direction.

II. BACKGROUND AND LITERATURE SURVEY

This section provides the technical basis for research, starting with the introduction of Gate-Diffusion-Input logic and Carbon NanoTube Field Effect Transistor technology. Although GDI [14] simplifies the process of minimizing the number of transistors and power dissipation, its integration into high-performance systems is typically limited by signal degradation. On the other hand, although CNTFETs [15] are the ideal for post-silicon scaling because of their higher carrier mobility, their usage in standard logic topologies is limited. The literature survey [16] performed revealed major design constraints in contemporary designs, particularly in voltage swing restoration and noise immunity. By addressing these limitations [17], the motivation for the proposed Hybrid GDI–CNTFET methodology, a design paradigm engineered to harness the high-speed ballistic transport of carbon nanotubes to overcome the inherent architectural weaknesses of traditional GDI logic.

II.1 GATE DIFFUSION INPUT (GDI) LOGIC:

GDI logic is a low-power circuit design technique [18] that reduces the number of transistors and silicon area when compared to standard CMOS logic. While in standard CMOS, the source terminals of PMOS and NMOS transistors are always connected to the power rails, in the GDI cell, multiple input signals can be applied to the gate, source, and drain terminals, which can be used to realize several logic functions using fewer transistors, leading to reduced area and lower dynamic power consumption. It has been proven that GDI logic can be used to design compact digital circuits such as adders, multiplexers, encoders, decoders and flip-flops with significant reductions in the area and power dissipation compared to CMOS designs.

II.2 CARBON NANOTUBE FIELD-EFFECT TRANSISTOR (CNTFET) TECHNOLOGY:

CNTFETs have been proposed as a possible alternative to conventional CMOS devices for nano-scale VLSI systems [19], because of their high-speed operation with improved energy efficiency, low off-state leakage and symmetric threshold voltages, but existing CNTFET-based designs mainly utilize CMOS logic styles, which often lead to a higher transistor count for complex logic functions and increases the silicon area & routing complexity.

II.3 LITERATURE SURVEY ON LOW-POWER AND AREA-EFFICIENT DESIGNS:

While research in alternative logic styles and emerging device technologies to reduce power dissipation and area in VLSI circuits has been widely studied [20], research on GDI logic has primarily focused on minimizing the number of transistors and area, and research on CNTFETs has primarily focused on improving power and performance at advanced technology nodes [21]. Comparative analyses between CMOS, GDI, and CNTFET implementations have shown that no single approach optimizes power, delay, and area simultaneously. There are a few works that have investigated hybrid logic styles, such as combining pass-transistor logic [22] with CMOS or using CNTFETs in standard logic configurations.

But to the best of our knowledge, no systematic investigation [23] has been performed into a hybrid design methodology that incorporates GDI logic topology with CNTFET technology in the same design.

II.4 MOTIVATION FOR THE PROPOSED HYBRID GDI–CNTFET METHODOLOGY:

Existing research and our prior research work validate that GDI logic and CNTFET technology complement each other [24], with GDI logic reducing area through minimal transistor usage, while CNTFETs provide improved power efficiency, improved voltage swing, and high-speed operation. However, current design approaches optimize these benefits independently, and so they do not achieve concurrent improvements in power and area. This work proposes a Hybrid GDI–CNTFET methodology, which aims to leverage the advantages of GDI circuits (such as low power consumption, minimum delay, and low silicon area) while overcoming the voltage swing and noise margin issues of the CMOS-based GDI circuits [25] by integrating GDI-based logic structures with CNTFET devices. This approach serves as the basis for circuit implementations and performance evaluations presented in the subsequent sections.

III. DEVICE MODELLING AND PROPOSED METHODOLOGY

The design and evaluation of digital circuits, are carried out using an integrated framework that combines the logic-level compactness of Gate Diffusion Input (GDI) with the device-level advantages of Carbon Nanotube Field-Effect Transistors **(**CNTFETs**).** This section describes the CNTFET device model employed [26], the GDI logic cell structure [27], the proposed Hybrid GDI–CNTFET design technique, and the overall methodology adopted for circuit implementation and performance evaluation as shown in Figure 2.

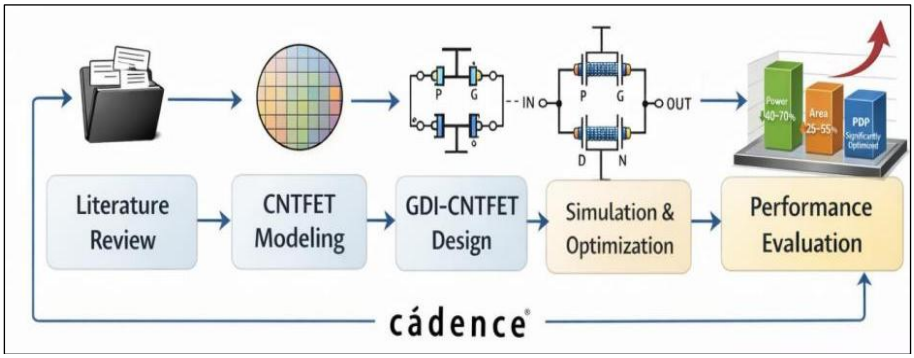


Figure 2: Methodology for Hybrid GDI-CNTFET circuits implemented.
Source: Authors, (2026).

III.1 CNTFET DEVICE MODELLING:

For all the circuits discussed, the Stanford CNTFET compact model [28] is used to accurately simulate carbon nanotube-based devices at the nano-meter technology nodes. The model includes the key physical phenomena, such as near-ballistic carrier transport, quantum confinement, and electrostatic control, which are essential for predicting CNTFET behaviour in digital circuits. Device parameters that are critical for the CNTFET model are the carbon nanotube diameter, which controls the bandgap energy and threshold voltage, the channel length, which impacts carrier transport and switching speed, and the inter-tube pitch, which impacts the device density. Other parameters, such as the number of nanotubes per device, gate work function and chirality vector, are selected to optimise the trade-off between power consumption and the propagation time. Simulations were performed using the Cadence Virtuoso Custom IC Design Platform with the Spectre simulator, enabling accurate transient, DC, and AC analyses at the 32nm technology node. The near-ballistic transport characteristics of CNTFETs significantly reduce scattering effects, resulting in enhanced switching speed and lower power dissipation compared to conventional CMOS devices.

III.2 GDI LOGIC CELL MODELLING:

The proposed hybrid design uses Gate Diffusion Input (GDI) logic [29], which is a logic foundation that requires the use of a minimal number of transistors to implement a variety of logic functions, including NAND, OR, XOR, multiplexers, flip-flops, and arithmetic blocks. GDI logic reduces the number of transistors and switching activity and therefore reduces silicon area and dynamic power consumption compared to CMOS logic. But CMOS-based GDI implementations suffer from threshold voltage loss, degraded output swing, and reduced noise margins, especially when the bulk is fixed and the inputs are source driven, which limits the scalability and robustness of CMOS-GDI designs.

III.3 HYBRID GDI–CNTFET DESIGN TECHNIQUE:

To address the limitations of CMOS-based GDI logic while maintaining its area efficiency, this research work presents a Hybrid GDI–CNTFET design technique, in which conventional PMOS and NMOS devices in GDI cells are replaced with p-type and n-type CNTFETs [30], respectively. This hybridization ensures several benefits as, CNTFETs have symmetric threshold voltages and better electrostatic control, which allows them to operate with full swing even in source-driven GDI configurations, eliminating the threshold voltage degradation and output swing loss in CMOS-GDI circuits.

Moreover, CNTFETs have intrinsically low leakage current and superior subthreshold characteristics, leading to lower static power consumption. Because the GDI topology retains a minimal transistor count, the hybrid approach preserves the area efficiency while improving the electrical performance. The proposed Hybrid GDI–CNTFET technique [31] thus enables simultaneous optimization of power, delay, and area, addressing the primary limitations of GDI-only and CNTFET-only implementations.

III.4 DESIGN FLOW AND EVALUATION METHODOLOGY:

The complete design and evaluation process followed in this research is summarized below:

1. Adoption of the Stanford CNTFET compact model and GDI logic topology.
2. Mapping Boolean functions onto optimized GDI structures and replacing CMOS devices with CNTFET equivalents.
3. Design of digital circuits such as logic gates, XOR, half adder, full adder, multiplexer, encoder, decoder, and flipflops using hybrid GDI–CNTFET cells in Cadence Virtuoso tool.
4. Performing transient analysis to evaluate switching behavior, DC analysis to obtain voltage transfer characteristics, and AC analysis to study frequency response and stability.
5. Measurement of power consumption, propagation delay, output voltage swing, noise margin, and power–delay product (PDP).
6. Performance comparison of proposed hybrid circuits with conventional CMOS, GDI-only, and CNTFET-only implementations in terms of power, delay, PDP, and transistor count.

IV. HYBRID CIRCUIT DESIGN AND IMPLEMENTATION

This section presents design, operational principles, and performance benefits of proposed Hybrid GDI–CNTFET circuits, with emphasis on digital building blocks [32] like 2×1 multiplexer, XOR gate, full adder and other combinational and sequential circuits [33]. These circuits are selected because they form the core of arithmetic and data-path units and effectively demonstrate the ability of the hybrid methodology to achieve simultaneous power, delay, and area optimization. In the proposed approach, conventional NMOS and PMOS devices used in GDI logic are replaced with n-type and p-type CNTFETs, respectively. This integration preserves the compact topology of GDI logic while leveraging the near-ballistic transport, symmetric threshold voltages, and low leakage characteristics of CNTFET technology. All circuits are implemented and evaluated using the Cadence Virtuoso platform with the Stanford 32 nm CNTFET model.

IV.1 HYBRID XOR GATE:

The Hybrid XOR gate is implemented using conventional CMOS, which naturally realizes the Boolean expressions: F=A'B + AB'. The hybrid XOR gate requires only four CNTFET devices (two p-type and two n-type), which is significantly fewer than the 12 transistors required in CMOS XOR implementations and fewer than CNTFET-based XOR designs as shown in Figure 3a and 3b.

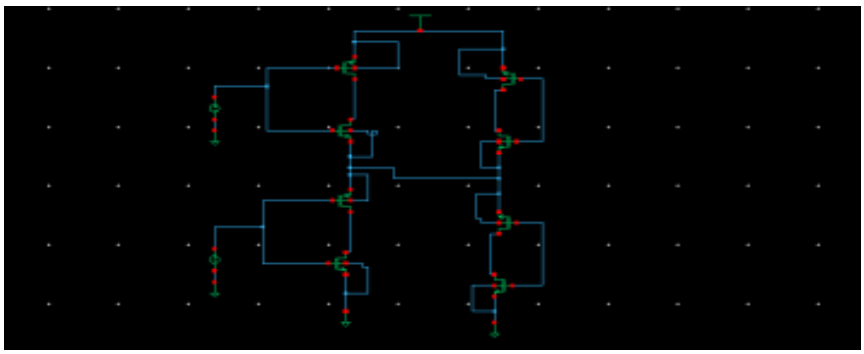


Figure 3a: Schematic of XOR gate using Conventional CMOS technology.
Source: Authors, (2026).

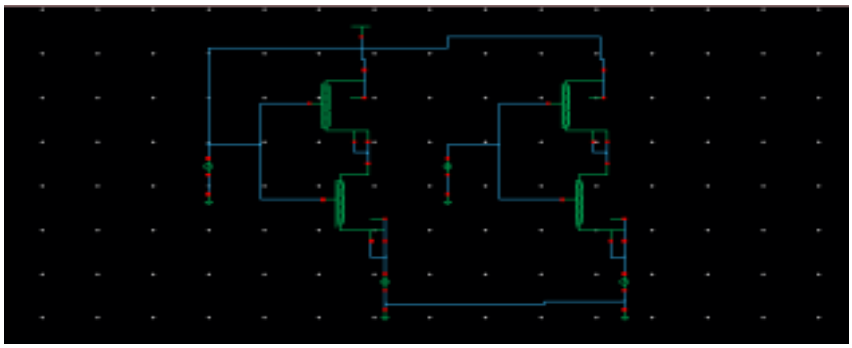


Figure 3b: Schematic of XOR gate using Hybrid GDI-CNTFET technology.
Source: Authors, (2026).

By replacing CMOS devices with CNTFETs, the hybrid XOR gate achieves full-swing output operation, indicated in Figure 3c eliminating the threshold voltage loss typically observed in CMOS-based GDI circuits. The near-ballistic transport of carriers in CNTFETs results in high switching speed and reduced propagation delay**,** while the minimal transistor count leads to lower parasitic capacitances and reduced dynamic power consumption.

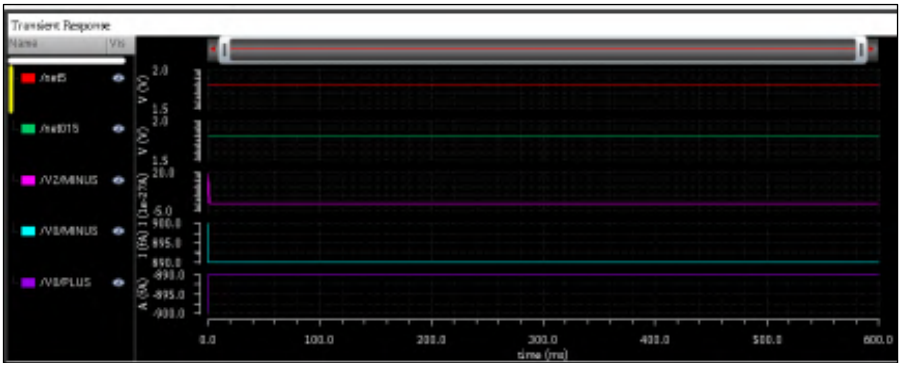


Figure 3c: Transient response of XOR gate using Hybrid GDI-CNTFET technology.
Source: Authors, (2026).

Simulation results indicate hybrid XOR gate offers substantial improvement in power–delay product, making it an efficient for arithmetic circuits and low-power digital systems.

IV.2 HYBRID 2×1 MULTIPLEXER:

The 2×1 multiplexer is implemented using a single GDI cell, where the select line controls gate terminal, and the data inputs are applied to source terminals. This configuration enables the realization of multiplexer function using only two CNTFET devices, representing a drastic reduction compared to CMOS implementations that require 6–8 transistors as represented in Figure 4a and 4b**.**

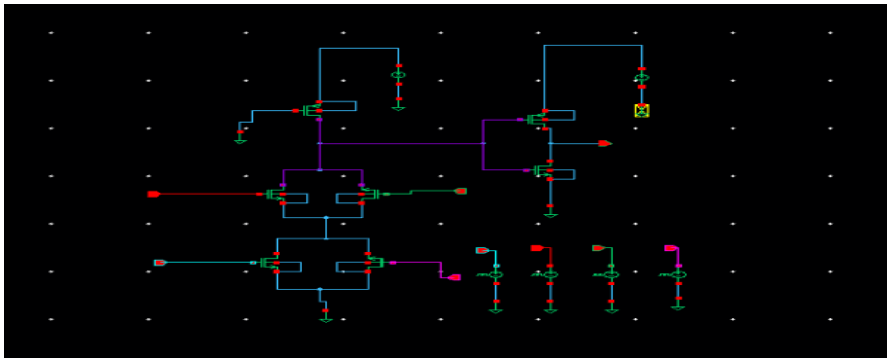


Figure 4a: Schematic of 2x1 multiplexer using Conventional CMOS technology.
Source: Authors, (2026).

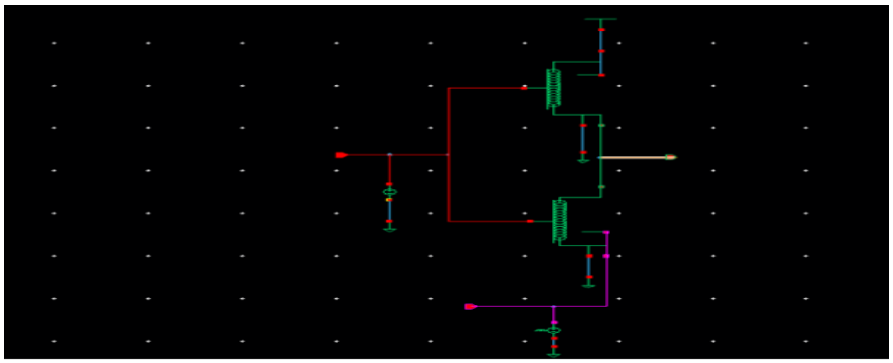


Figure 4b: Schematic of 2x1 multiplexer using Hybrid GDI-CNTFET technology.
Source: Authors, (2026).

In CMOS-based GDI multiplexers, incomplete voltage swing and degraded noise margins are common due to threshold voltage loss. In contrast, the hybrid GDI–CNTFET multiplexer achieves full-swing output across all input combinations, owing to the symmetric threshold voltages and superior electrostatic control of CNTFET devices, as shown in Figures (4- c,d,e,f,g,h).

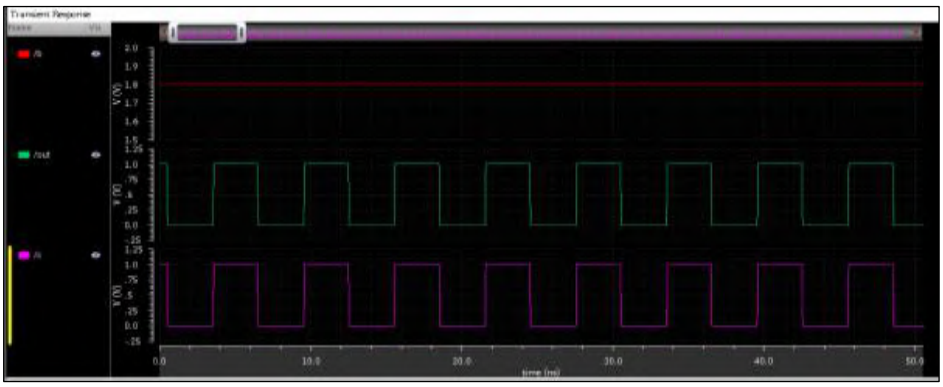


Figure 4c: Transient response of 2x1 multiplexer using Hybrid GDI-CNTFET technology.
Source: Authors, (2026).

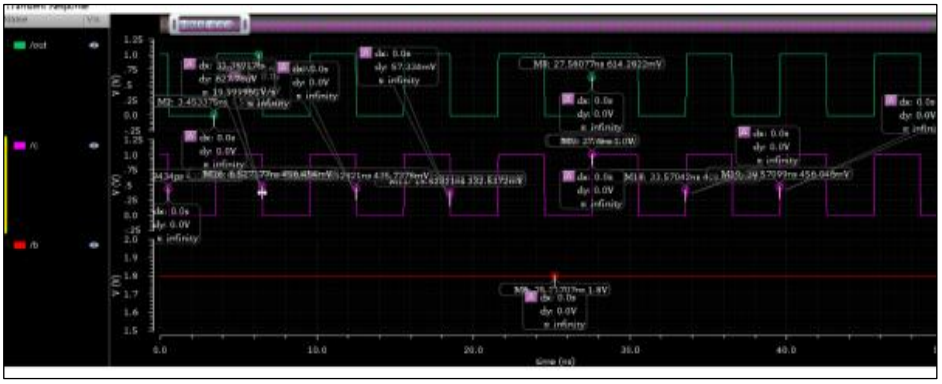


Figure 4d: Delay response of 2x1 multiplexer using Hybrid GDI-CNTFET technology.
Source: Authors, (2026).

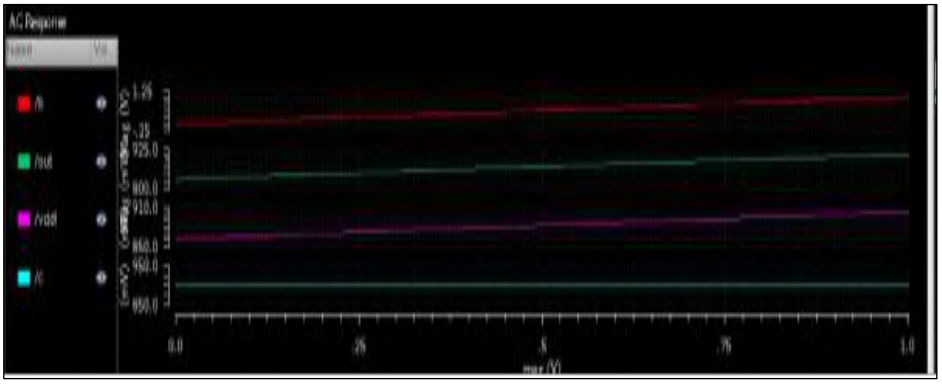


Figure 4e: AC response of 2x1 multiplexer using Hybrid GDI-CNTFET technology.
Source: Authors, (2026).

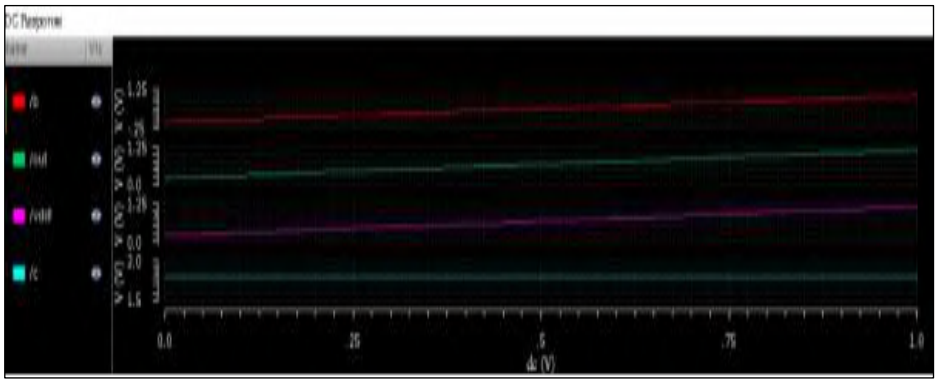


Figure 4f: DC response of 2x1 multiplexer using Hybrid GDI-CNTFET technology.
Source: Authors, (2026).

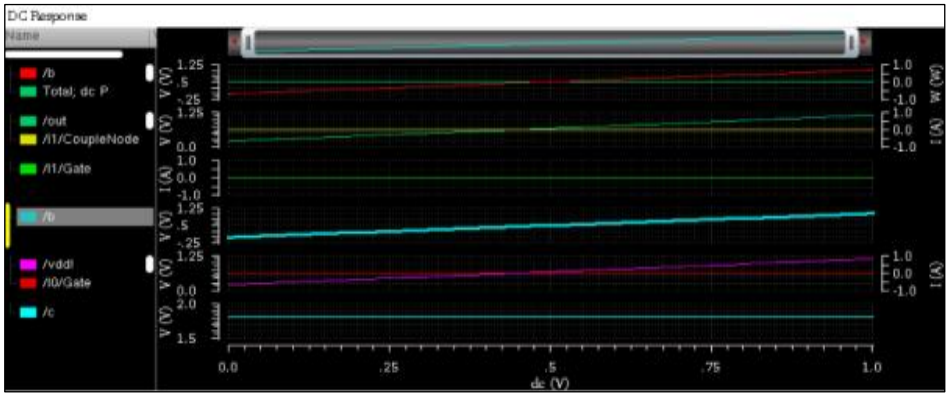


Figure 4g: Power analysis of 2x1 multiplexer using Hybrid GDI-CNTFET technology.
Source: Authors, (2026).

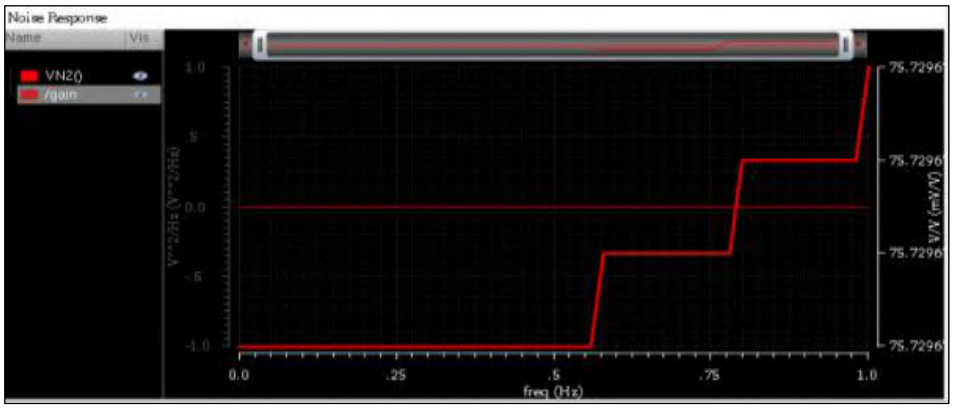


Figure 4h: Noise response of 2x1 multiplexer using Hybrid GDI-CNTFET technology.
Source: Authors, (2026).

The reduced device count and low parasitic capacitance contribute to lower switching power and faster response time, making the hybrid multiplexer well suited for high-speed data routing and selection operations in arithmetic and logic units.

IV.3 HYBRID FULL ADDER:

Hybrid Full-Adder is the most vital circuit used to validate the effectiveness of the proposed methodology, as it integrates both XOR and multiplexer logic within a single arithmetic unit. The full-adder is implemented using sum and carry blocks. This architecture reduces the transistor count, ensuring full-swing logic operation and functionality**.**

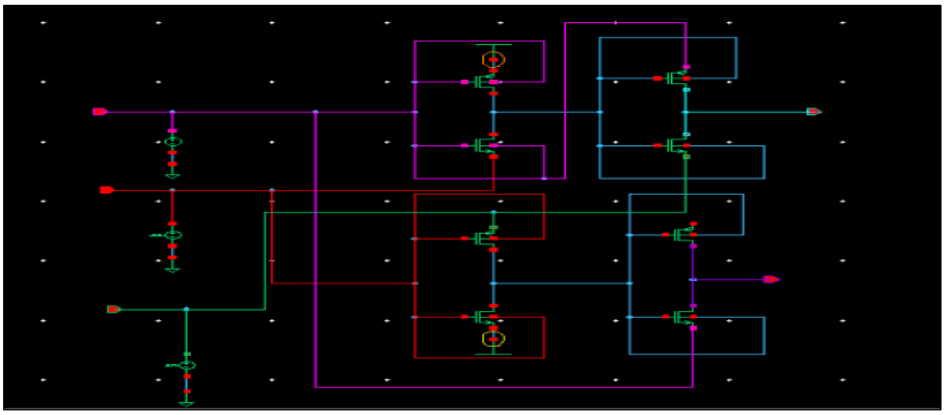


Figure 5a: Schematic of Full-adder using conventional CMOS technology.
Source: Authors, (2026).

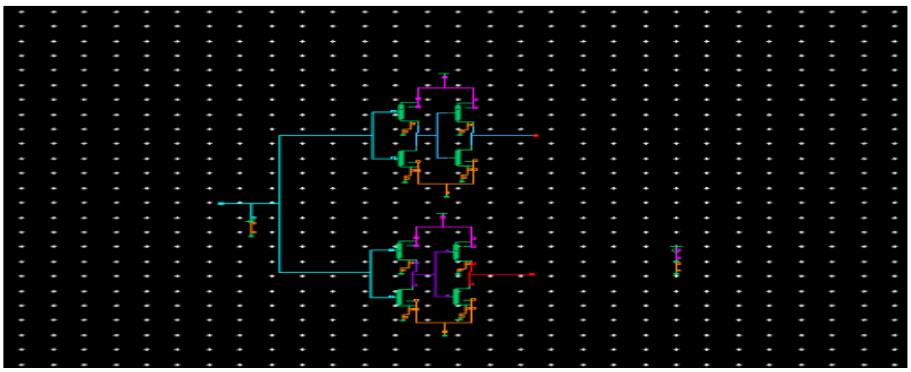


Figure 5b: Schematic of Full-adder using Hybrid GDI-CNTFET technology.
Source: Authors, (2026).

The proposed Hybrid GDI–CNTFET Full Adder requires only 6–8 CNTFET devices, compared to 28 transistors in CMOS**,** 10 transistors in conventional GDI**,** and approximately 18–20 devices in CNTFET designs as shown in Figure 5a and 5b**.** This significant reduction in device count directly translates into lower silicon area and reduced parasitic capacitances.

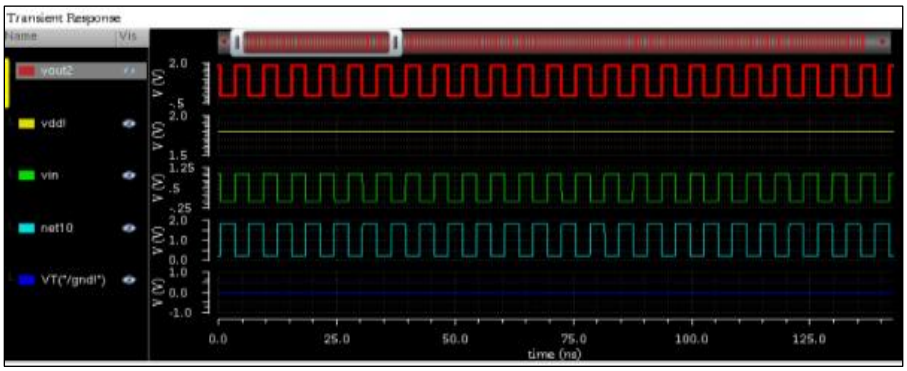


Figure 5c: Transient response of full-adder using Hybrid GDI-CNTFET technology.
Source: Authors, (2026).

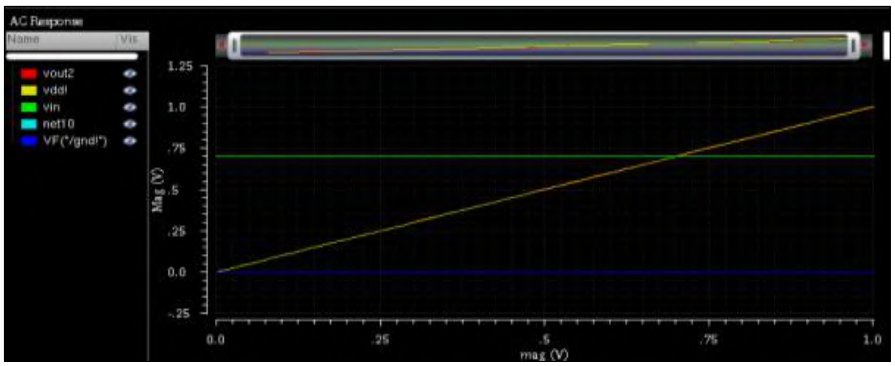


Figure 5d: AC response of full-adder using Hybrid GDI-CNTFET technology.
Source: Authors, (2026).

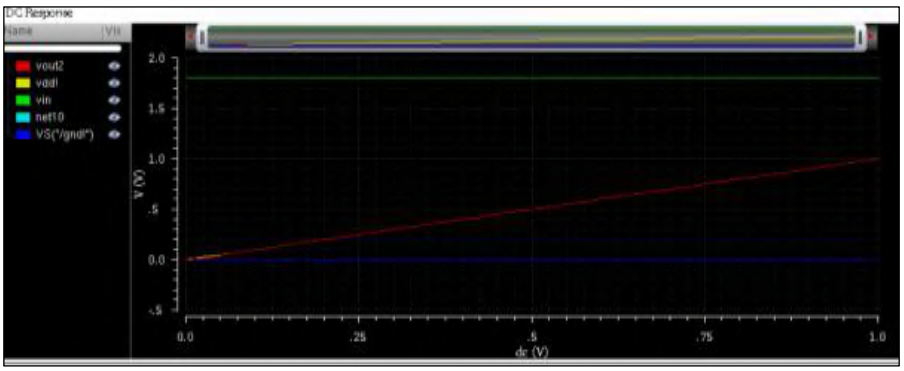


Figure 5e: DC response of full-adder using Hybrid GDI-CNTFET technology.
Source: Authors, (2026).

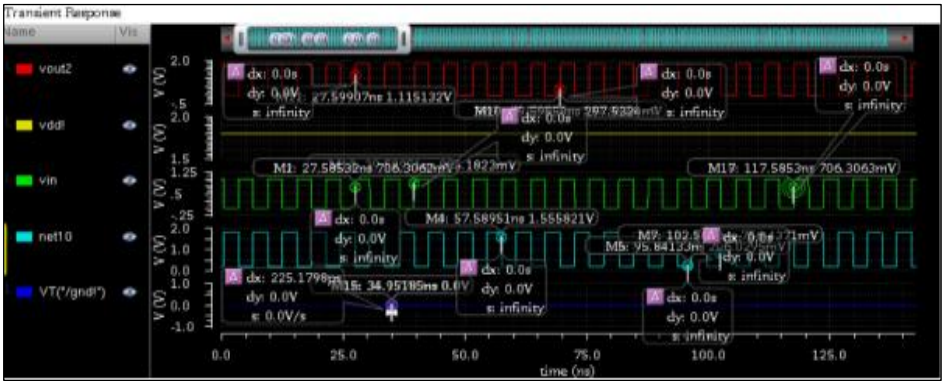


Figure 5f: Delay analysis of full-adder using Hybrid GDI-CNTFET technology.
Source: Authors, (2026).

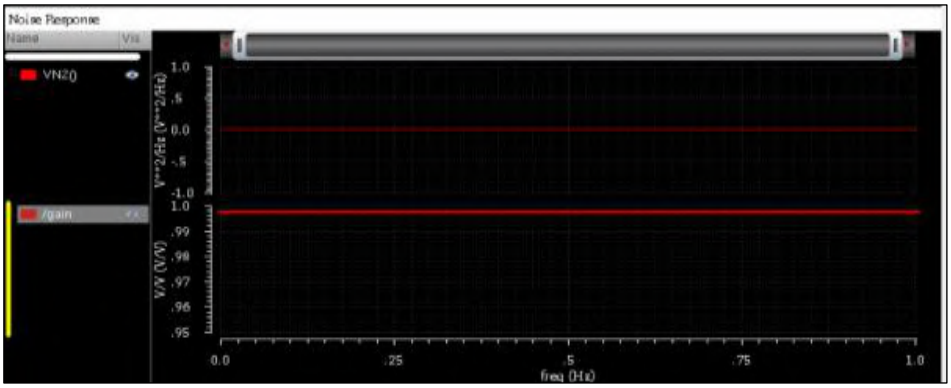


Figure 5g: Noise response of full-adder using Hybrid GDI-CNTFET technology.
Source: Authors, (2026).

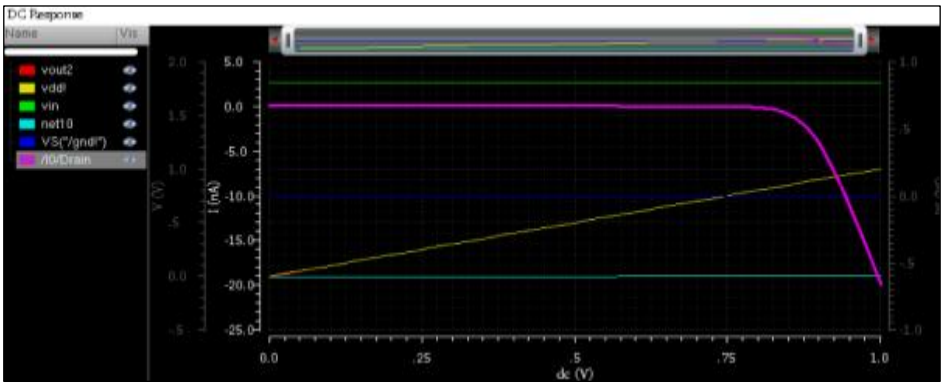


Figure 5h: Power analysis of full-adder using Hybrid GDI-CNTFET technology.
Source: Authors, (2026).

Simulation results indicated in Figure (5-c,d,e,f,g,h), demonstrate that the hybrid full adder achieves substantial reductions in average power consumption and propagation delay, resulting in a markedly improved power–delay product (PDP). These advantages make the proposed full adder design highly suitable for low-power arithmetic units and energy-constrained VLSI systems. The implementation of the XOR gate, 2×1 multiplexer and full adder using the proposed Hybrid GDI–CNTFET methodology clearly demonstrates its effectiveness. The results confirm that the hybrid approach successfully overcomes the voltage swing and noise margin limitations of CMOS-based GDI circuits while preserving their compact structure. At the same time, it mitigates the area overhead typically associated with CNTFET-only implementations. Similarly, for all the specified digital circuits, schematic has been implemented and verified, validated accordingly using Hyrbid 32nm GDI-CNTFET based circuits in accordance with the 90nm CMOS technology, thereby the circuit parameters have been tabulated as shown in Table 1.

Table 1: Comparison of circuit parameters for CMOS and Hybri GDI-CNTFET technology.

Circuit	Technology	Node	Transist or Count	Average Delay (ps)	Average Power (µw)	Power Delay Product (AJ)
NAND gate	CMOS	90nm	4	15	0.8	12
	Proposed Hybrid	32nm		2	0.1	0.2
OR gate	CMOS	90nm	6	12.5	2.8	35
	Proposed Hybrid	32nm		4.1	0.95	3.9
XOR gate	CMOS	90nm	8	20.5	6.5	133.25
	Proposed Hybrid	32nm		6.8	1.6	10.88
Half-Adder	CMOS	90nm	5	3.78	3.41	12.88
	Proposed Hybrid	32nm		0.98	0.75	0.74
Full-Adder	CMOS	90nm	8	30	1.5	45
	Proposed Hybrid	32nm		5	0.25	1.25
4-to-2 Encoder	CMOS	90nm	5	25	1.2	30
	Proposed Hybrid	32nm		4	0.2	0.8
2-to-4 Decoder	CMOS	90nm	20	45.8	18.5	847
	Proposed Hybrid	32nm		15.2	5.3	81
2x1 Multiplexer	CMOS	90nm	7	20	1	20
	Proposed Hybrid	32nm		3	0.15	0.45
D Flip-Flop	CMOS	90nm	5	3.78	3.41	12.88
	Proposed Hybrid	32nm		0.98	0.75	0.74
JK Flip-Flop	CMOS	90nm	16	25.5	15.6	397.8
	Proposed Hybrid	32nm		8.9	4.5	40.05

Source: Authors, (2026).

Overall, the proposed hybrid circuits achieve simultaneous optimization of power, delay, and area, validating the Hybrid GDI–CNTFET methodology as a promising design paradigm for next-generation low-power and high-performance VLSI systems.

V. SIMULATION RESULTS ANALYSIS AND DISCUSSION

The analysis for the simulation results observed for basic digital circuits, implemented using Hybrid GDI-CNTFET technology, were studied and represented in Figure 6.

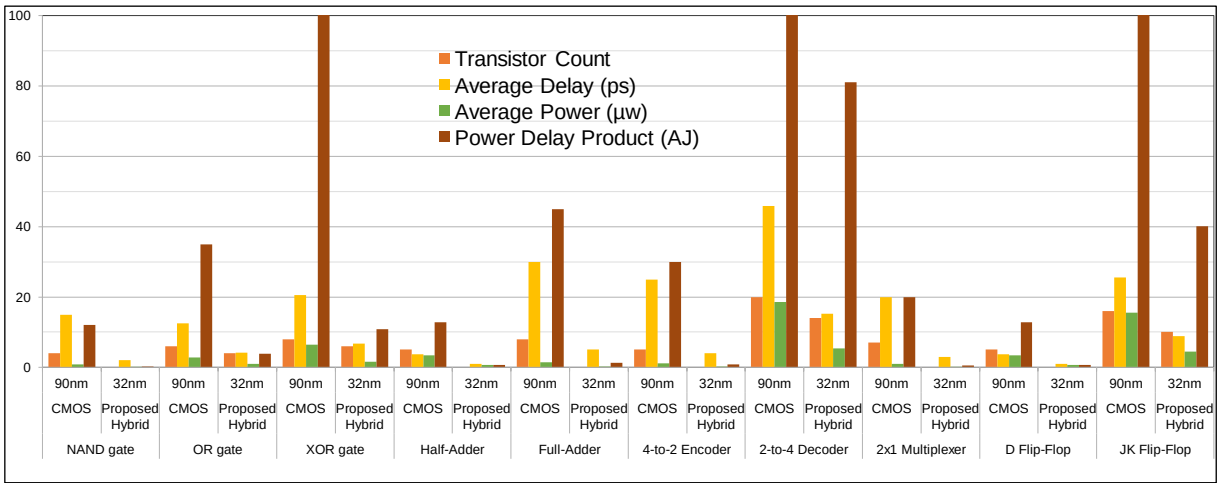


Figure 6: Analysis of CMOS and Hybrid GDI-CNTFET technology for various digital circuits.
Source: Authors, (2026).

The analysis presented details the Hybrid GDI–CNTFET circuits, designed using the 32nm GDI based CNTFET model in the Cadence Virtuoso environment, demonstrate significant performance advantages over traditional CMOS across a wide range of logic components, including NAND gate, OR gate, XOR gate, Half-adders, Full-adders, 4-to-2 Encoder, 2-to-4 Decoder, 2x1 Multiplexer, JK and D flip-flops by combining the low-transistor-count advantage of Gate Diffusion Input (GDI) logic with the high-speed, low-leakage properties of carbon nanotubes, the hybrid design achieves a vast reduction in power consumption and a notable decrease in transistor count.

The proposed hybrid GDI-CNTFET design methodology combines the structural efficiency of GDI with the higher electrical performance of CNTFETs. By using Stanford 32nm CNTFET model, which takes account of near-ballistic transport and threshold voltage dependent chirality, the design achieves full swing output transitions and eliminates the loss of threshold voltage, which occur in traditional GDI circuits based on CMOS technology. Simulations with different digital logic circuits (NAND, OR, XOR, half-adder, full-adder, multiplexer, encoder, decoder) and complex modules (D and JK flipflops) show 40-70 percent reduction in power and 45-70% increase in PDP compared to CMOS at 90nm. The hybrid approach also optimises the area by 25-55% than the standard CNTFET-based design, further reducing parasitic capacitance and allowing high speed operation. This design has a high noise margin and low leakage characteristics, which make it particularly suitable for low-power, high performance VLSI systems at the nanoscale. Future research can be by applying this methodology to sequential circuits such as clock registers, and then to complete systems-level designs like arithmetic logic units (ALUs) and memory structures. The validation of these designs by physical mapping and parasitic extraction will be a key step in the development of electronic technology.

VI. CONCLUSION AND FUTURE SCOPE

This research introduces a high performance design paradigm for the nanoscale regime, eliminating the dead zones and voltage degradation inherent in conventional GDI topologies and avoiding the classical trade-offs between logic density and signal integrity of CNTFETs. The comprehensive comparison shows that this Hybrid GDI-CNTFET framework leads to a significant reduction of the PDP and silicon area compared to conventional CMOS and the separate GDI-CNTFET implementations. This research has proven that it can withstand the short-circuit effects that are detrimental to traditional silicon based devices and thus provides a viable framework for scalable and energy-efficient next generation VLSI architectures. The results confirm that this approach is a key enabler for the next generation of small-scale, low-power digital signal processing and high-power computing systems. This methodology can be extended to more complex sequential circuits such as clocked registers where timing constraints are more significant and to design a full hybrid-based Arithmetic Logic Unit or explore memory structures such as SRAM. The proposed Hybrid GDI–CNTFET framework can be further extended to large-scale VLSI architectures to illustrate its scalability and system-level power–delay advantages, incorporating process-variation, thermal, and reliability analyses to illustrate the impact of CNT chirality dispersion, density non-uniformity, and device aging. Moving toward layout-level implementation and parasitic extraction will be necessary steps to further validate the industrial practicality of the hybrid GDI–CNTFET approach for future nano-electronic technologies.

VII. AUTHOR'S CONTRIBUTION

Conceptualization: Jayakrishna Padala, Kishore Kumar Kamarajugadda, Pavani Movva.
Methodology: Jayakrishna Padala, Kishore Kumar Kamarajugadda, Pavani Movva.
Investigation: Jayakrishna Padala, Kishore Kumar Kamarajugadda, Pavani Movva.
Discussion of results: Jayakrishna Padala, Kishore Kumar Kamarajugadda, Pavani Movva.
Writing – Original Draft: Jayakrishna Padala, Kishore Kumar Kamarajugadda, Pavani Movva.
Writing – Review and Editing: Jayakrishna Padala, Kishore Kumar Kamarajugadda, Pavani Movva.
Resources: Jayakrishna Padala, Kishore Kumar Kamarajugadda, Pavani Movva.
Supervision: Jayakrishna Padala, Kishore Kumar Kamarajugadda, Pavani Movva.
Approval of the final text: Jayakrishna Padala, Kishore Kumar Kamarajugadda, Pavani Movva.

VIII. ACKNOWLEDGEMENT:

I express my sincere gratitude to my Supervisor, Co-Supervisor, and Faculty of The ICFAI University, Raipur, for continuous guidance, encouragement, and support throughout the research work. I am deeply thankful for the facilities, technical assistance, and conducive research environment provided, which greatly contributed to the successful completion of the study.

IX. REFERRENCES

[1] E. Mollick, "Establishing Moore's Law," IEEE Ann. Hist. Comput., vol. 28, no. 3, pp. 62–75, Jul. 2006, doi: 10.1109/MAHC.2006.45.

[2] J. P. Uyemura, Circuit Design for CMOS VLSI. Boston, MA: Springer US, 1992. doi: 10.1007/978-1-4615-3620-8.

[3] L. Luet Ng, K. Ho Yeap, M. Wan Ching Goh, and V. Dakulagi, "Power Consumption in CMOS Circuits," in Electromagnetic Field in Advancing Science and Technology, H.-Z. Song, K. Ho Yeap, and M. Wan Ching Goh, Eds., IntechOpen, 2023. doi: 10.5772/intechopen.105717.

[4] Y. Parmar and N. Pandey, "GDI and Dynamic Logic:A Synergy Behind the Modern Electronics," in 2025 3rd International Conference on Device Intelligence, Computing and Communication Technologies, Dehradun, India: IEEE, Mar. 2025, pp. 451–455.doi: 10.1109/DICCT64131.2025.10986653.

[5] D. Shivaprasad et al., "Stacking technique for less power consumption in CMOS VLSI circuits," presented at the 3RD INTERNATIONAL CONFERENCE ON MULTIFUNCTIONAL MATERIALS: ICMM2024, Hyderabad, India, 2025, p. 040025. doi: 10.1063/5.0298531.

[6] U. Vasudevan, U. B. Meghana, D. Koppad, S. Vignesh, and M. Sowjanya, "Design of Digital Circuit Implementations Using Gate Diffusion Input and CMOS," in 2020 IEEE 7th Uttar Pradesh Section International Conference on Electrical, Electronics and Computer Engineering (UPCON), Prayagraj, India: IEEE, Nov. 2020, pp. 1–6. doi: 10.1109/UPCON50219.2020.9376501.

[7] Z. Chen, J. Chen, W. Liao, Y. Zhao, J. Jiang, and C. Chen, "Progress on a Carbon Nanotube Field-Effect Transistor Integrated Circuit: State of the Art, Challenges, and Evolution," Micromachines, vol. 15, no. 7, p. 817, Jun. 2024, doi: 10.3390/mi15070817.

[8] R. Marani and A. G. Perri, “Design of CNTFET-Based Electronic Circuits: A Review,” Int. J. Nanosci., vol. 23, no. 01, p. 2330007, Feb. 2024, doi: 10.1142/S0219581X23300079.

[9] J. Padala, K. K. Kamarajugadda, and P. Movva, “A Comprehensive Analysis of Low Power VLSI using CNTFET and GDI Technology,” in 2025 4th International Conference on Distributed Computing and Electrical Circuits and Electronics (ICDCECE), Ballari, India: IEEE, Apr. 2025, pp. 1–4. doi: 10.1109/ICDCECE65353.2025.11035549.

[10] S. Sarkar, M. Jain, A. Saha, and A. Rathi, “Gate Diffusion Input: A technique for fast digital circuits (implemented on 180 nm tech),” IOSR J. VLSI Signal Process, vol. 4, no. 2, pp.49–53, 2014.

[11] G. Gelao, R. Marani, and A. G. Perri, “Analysis and design of current mode logic based on CNTFET,” AIMS Mater. Sci., vol. 10, no. 6, pp. 965–980, 2023, doi: 10.3934/matersci.2023052.

[12] “HIGH SPEED AND LOW POWER GDI BASED FULL ADDER,” J. VLSI Circuits Syst., vol. 01, no. 01, Jan. 2019, doi: 10.31838/jvcs/01.01.02.

[13] A. Ghorbani, M. Dolatshahi, S. M. Zanjani, and B. Barekatain, “A New Low Power, Area Efficient 4-bit Carry Look Ahead Adder in CNFET Technology,” Majlesi J. Electr. Eng., vol. 16, no. 1, pp. 65–73, Mar. 2022, doi: 10.52547/mjee.16.1.65.

[14] J. Padala, K. K. Kamarajugadda, and P. Movva, “Performance Enhancement of Digital Circuits through CMOS, GDI-Based Area and Power Optimization in 90nm Technology,” J. Appl. Bioanal., vol. 11, no. 4s, pp. 305–318, doi: http://doi.org/10.53555/jab.v11si4.957.

[15] J. Padala, K.Kamarajugadda, P.Movva, “Exploration of digital building blocks in 32 nm CNTFET technology for scalable VLSI applications,” Discov. Electron., vol.3, no.1, p. 3, Jan.2026, doi: 10.1007/s44291-026-00154-6.

[16] A. Rupani, D. Bansal, and K. Sharma, “Power optimized quaternary logic circuits based on CNTFETs,” Discov. Nano, vol. 20, no. 1, p. 180, Oct. 2025, doi: 10.1186/s11671-025-04364-x.

[17] M. Shaveisi and A. Rezaei, “Design and Implementation of CNTFET-Based Reversible Combinational Digital Circuits Using the GDI Technique for Ultra-low Power Applications,” BioNanoScience, vol. 10, no. 4, pp. 1063–1083, Dec. 2020, doi: 10.1007/s12668-020-00777-3.

[18] N. Shiri, A. Sadeghi, M. Rafiee, and M. Bigonah, “SR-GDI CNTFET-based magnitude comparator for new generation of programmable integrated circuits,” Int. J. Circuit Theory Appl., vol. 50, no. 5, pp. 1511–1536, May 2022, doi: 10.1002/cta.3251.

[19] B. Raj and A. Raman, Nanoscale Semiconductors: Materials, Devices and Circuits, 1st ed. Boca Raton: CRC Press, 2022. doi: 10.1201/9781003311379.

[20] A. T. Mahani and P. Keshavarzian, “A novel energy-efficient and high speed full adder using CNTFET,” Microelectron. J., vol. 61, pp. 79–88, Mar. 2017, doi: 10.1016/j.mejo.2017.01.009.

[21] S. Mujumdar, N. Afzal, and S. A. Loan, “Design and analysis of 4-bit low-power, high-performance current steering DAC implemented using CNT-GDI logic,” AEU - Int. J. Electron. Commun., vol. 173, p. 154977, Jan. 2024, doi: 10.1016/j.aeue.2023.154977.

[22] M. M. Basha, P. L. Reddy, and S. Gundala, “Exploring CMOS, PTL and GDI Logic Families Based One Bit Full Adder and Subtractor Circuits in Subthreshold Region for Energy and EDP Efficient Applications,” in Nanoelectronics, 1st ed., V. K. Sharma, Ed., Wiley, 2025, pp. 229–266. doi: 10.1002/9781394275199.ch8.

[23] A. Bisht and P. Mittal, “A 32 nm single-ended 7T SRAM cell with improved static noise margin and leakage power,” Phys. Scr., vol. 101, no. 2, p. 025004, Jan. 2026, doi: 10.1088/1402-4896/ae325a.

[24] H. K. R. V. Kudulla and S. S. Rao, “An energy efficient approximate CNTFET based full adders with GDI technique for image processing applications,” Analog Integr. Circuits Signal Process., vol. 126, no. 1, p. 17, Jan. 2026, doi: 10.1007/s10470-025-02544-4.

[25] S. Rangeetha, A. Narmatha, S. Raja Lekshmi, and K. Sahana, “Layout Design of Low Power High Performance JK Flip-Flop with Modified Gate Diffusion Input Technique Using Cadence Virtuoso Tool for IC Design,” in 2025 6th International Conference on Mobile Computing and Sustainable Informatics (ICMCSI), IEEE, 2025, pp. 427–432.

[26] N. Gupta, S. M. Gupta, and S. K. Sharma, “Carbon nanotubes: synthesis, properties and engineering applications,” Carbon Lett., vol. 29, no. 5, pp. 419–447, Oct. 2019, doi: 10.1007/s42823-019-00068-2.

[27] S. Radhakrishnan and T. Nirmalraj, “An enhanced Gate Diffusion Input technique for low power applications,” Microelectron. J., vol. 93, p. 104621, 2019.

[28] H. Sarbazi, R. Sabbaghi-Nadooshan, and A. Hassanzadeh, “Process validation test of CNTFET using Stanford model,” Int. J. Electron., vol. 109, no. 1, pp. 1–22, Jan. 2022, doi: 10.1080/00207217.2021.1891579.

[29] U. Vasudevan, U. B. Meghana, D. Koppad, S. Vignesh, and M. Sowjanya, “Design of digital circuit implementations using gate diffusion input and cmos,” in 2020 IEEE 7th Uttar Pradesh Section International Conference on Electrical, Electronics and Computer Engineering, IEEE, 2020, pp. 1–6.

[30] A. S. Rehal, “Low power Circuit Design Using Dynamic GDI Technique in CNTFET Technology,” in Proceedings of the 18th ACM International Symposium on Nanoscale Architectures, Dresden Germany: ACM, Dec. 2023, pp. 1–5. doi: 10.1145/3611315.3633236.

[31] P. Foroutan and K. Navi, “Design of low power and high speed approximate multipliers utilizing current mode 4 to 2 compressors based on CNTFET technology,” Sci. Rep., Jan. 2026, doi: 10.1038/s41598-026-35104-5.

[32] B. Hajra, J. Chakrabotry, and P. Dutta, “A Review on Logic Gate Design and Layout Optimization in Cadence Virtuoso for Low-Power VLSI Applications,” in 2025 5th IEEE International Conference on Applied Electromagnetics, Signal Processing, & Communication (AESPC), Bhubaneswar, India: IEEE, Dec. 2025, pp. 1–6. doi: 10.1109/AESPC67542.2025.11326799.

[33] G. D. B, A. J, Thirlojanan. U, Sruthi.S, Y. G, and S. M, “Design and Implementation of D Flip-Flop using T and JK Flip-Flop based on PTL in 90nm Technology,” in 2025 3rd International Conference on Intelligent Cyber Physical Systems and Internet of Things (ICoICI), Coimbatore, India: IEEE, Sep. 2025, pp. 251–256. doi: 10.1109/ICoICI65217.2025.11253748.

Journal of Engineering and Technology for Industrial Applications

ISSN ONLINE: 2447-0228

ITEGAM-JETIA

Manaus, v.12 n.60, p.356-361, July/August, 2026.
DOI: https://doi.org/10.5935/jetia.v12i60.3835

RESEARCH ARTICLE OPEN ACCESS

A COMPARATIVE ANALYSIS OF STUDENT PERFORMANCE IN DESIGNING FREQUENCY CONTROL VIA SIMULATION-BASED FORMATIVE ASSESSMENT

Idamakanti Kasireddy[1], Devineni Gireesh Kumar*[2], Neelesh Kumar Gupta[3], Prasad Chongala[4]

[1]Department of Electrical & Electronics Engineering, Vishnu Institute of Technology, Bhimavaram, 534202, AP, India.
[2]Department of CSE(AI&ML), Sreyas Institute of Engineering and Technology, Hyderabad, 500068, Telangana, India.
[3]Department of Electrical Engineering, Yashoda Technical Campus, Satara, 415015, Maharashtra, India.
[4]Department of Electrical & Electronics Engineering, Aditya Institute of Technology and Management, Tekkali, 532201, AP, India.

[1]https://orcid.org/0000-0001-5757-9680, [2]https://orcid.org/0000-0003-0575-471X,
[3]https://orcid.org/0000-0003-3863-2372, [4]https://orcid.org/0000-0002-2209-4047

Email: kaasireddy.i@vishnu.edu.in,*gireesh218@gmail.com, 2018rsee008@nitjsr.ac.in, prasadchongala58@gmail.com

ARTICLE INFO

Article History
Received: February 26, 2026
Reviewed: June 11, 2026
Accepted: July 11, 2026
Published: July 31, 2026

Keywords:
Project-Based Learning,
Load Frequency Control (LFC),
MATLAB/Simulink,
Group Analysis
PID Controller

ABSTRACT

This paper focuses on formative assessment of several student groups by executing Load Frequency Control (LFC) in power systems using both MATLAB/Simulink and Google Colab. Four student groups have been formed and have worked together on various aspects of the study, i.e., modelling, simulation, control design, and result analysis. These student groups gained deeper hands-on experience while implementing the controller for the power system. All groups manually tuned the PID controller for the single-area power system. The performance analysis has also been done in MATLAB/Simulink for all groups. Using Google Colab, the formative analysis was performed by importing MATLAB/Simulink results. This work emphasises the importance of frequency regulation for power system stability and demonstrates how project-based learning can simplify complex problems.

Copyright ©2026 by authors and Galileo Institute of Technology and Education of the Amazon (ITEGAM). This work is licensed under the Creative Commons Attribution International License (CC BY 4.0).

I. INTRODUCTION

Load Frequency Control (LFC) is considered a critical aspect of electrical power system operation due to its effects on system stability and reliability. In earlier decades, researchers primarily relied on traditional control methods, such as Proportional–Integral–Derivative (PID) controllers. These controllers minimise steady-state frequency deviations; however, they often face challenges arising from nonlinear system dynamics and operating-condition uncertainties [1-5]. To overcome these problems, more recent studies have adopted advanced approaches, such as fuzzy logic control, fractional-order controllers, and optimisation methods. All of which aim to enhance the system robustness and dynamic response [5-9]. On the other hand, the development of simulation platforms such as MATLAB/Simulink has become increasingly important for education and research, as they enable complex system behaviour to be modelled and tested in a controlled environment. Such tools provide a practical means of reproducing realistic disturbances and evaluating the performance of different control strategies before implementation in actual power networks [7], [9]. In addition to technical modelling efforts, recent work in engineering education has highlighted the importance of formative assessment in both teaching and research [10–13]. The summative evaluation, which provides feedback only at the end of a task, contrasts with formative assessment, which emphasises continuous feedback throughout the learning and experimentation process. This ongoing interaction allows students and researchers to make incremental improvements in system modelling, controller tuning, and performance evaluation. The students can learn concepts easily. By supporting reflection and iterative refinement, formative assessment not only enhances the overall quality of outcomes but also deepens the learner's conceptual understanding and problem-solving ability [12], [13] Moreover, with the latest cloud-based platforms, tools such as *Google Colab* have gained popularity for collaborative analysis, coding, and result sharing. Google Colab offers an open-source, Python-based environment where students and researchers can perform data analysis, visualize results, and document findings in real time without hardware or software constraints [14].

MATLAB/Simulink can provide learning for students. This accessibility and collaborative feature make it a valuable complement to MATLAB/Simulink, especially for group-based projects that require active participation and peer learning. Taken together, prior literature underscores the dual importance of (i) robust control strategies for maintaining frequency stability and (ii) modern computational and pedagogical tools that facilitate both research and education in power system studies.

II. METHODOLOGY

II.1 SYSTEM DESCRIPTION

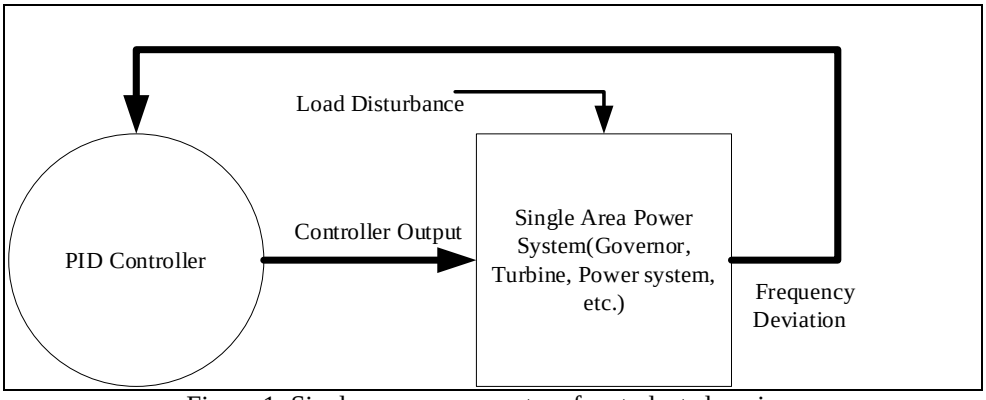


Figure 1: Single-area power system for students learning.
Source: Authors, (2026).

The study focuses on a single-area power system model to evaluate the effectiveness of Load Frequency Control (LFC) under a step load disturbance, as shown in Figure 1. The system includes three main components: the governor, turbine, and generator–load dynamics, represented by standard transfer functions in MATLAB/Simulink. The nominal frequency of the system was set at 50 Hz, and a 1% step load disturbance was applied to test system stability and frequency regulation [9]. The transfer function model of governor, turbine and generator-load dynamics is given below:

$$\text{The Governor Transfer function is } TF_G = \frac{1}{T_G S+1} \quad (1)$$

$$\text{Turbine Transfer function is } TF_T = \frac{1}{T_T S+1} \quad (2)$$

$$\text{The Generator-Load Transfer function is } TF_{GL} = \frac{K_s}{T_S S+1} \quad (3)$$

The values of T_G, T_T, T_S and K_s are 0.08, 0.3, 18 and 120, respectively [9].

II.2 CONTROLLER DESIGN AND TUNING

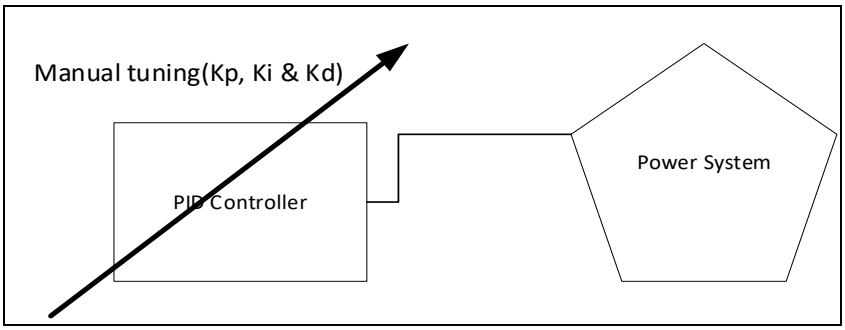


Figure 2: Manual tuning of the PID controller by various student groups.
Source: Authors, (2026).

A Proportional–Integral–Derivative (PID) controller was employed to minimize frequency deviations as depicted in Figure 2. The students need to design a controller for learning various things. Students were instructed to tune the controller parameters (Kp, Ki and Kd) manually through iterative trials or through extensive simulation. This approach encouraged students to build an intuitive understanding of how each parameter influences system response:

a. **Proportional Gain (**Kp**)**: reduces rise time but can introduce oscillations if too high.
b. **Integral Gain (**Ki**)**: eliminates steady-state error but may increase settling time.
c. **Derivative Gain (**Kd**)**: improves damping and suppresses oscillations.

$$\text{Controller } C = K_p + K_i/s + K_d s \quad (4)$$

Manual tuning is performed instead of automatic optimization to reinforce the learning objectives of control design and system behavior analysis.

II.3 STUDENT GROUP IMPLEMENTATION

A total of four student groups participated in the study. They must perform the task on LFC. Each group independently completed the following stages:

a. **System Modelling** – building the single-area LFC model in MATLAB/Simulink.
b. **Simulation** – applying a 1% load disturbance and observing system response.
c. **Manual Controller Design** – tuning PID gains to achieve acceptable system stability.
d. **Performance Analysis** – exporting time-domain results (frequency deviation and controller output) into Microsoft Excel for further evaluation.

This design ensured that every group experienced the *entire cycle* of modelling, controller design, simulation, and analysis, fostering both technical and analytical skills.

II.4 DATA EXPORT AND STANDARDIZATION

For consistency, all groups exported their MATLAB/Simulink results to a common format with three columns: Time (s), Frequency deviation (Hz), and Controller output (pu). Students must export the data from the simulation tool. This standardization enabled a uniform framework for comparative analysis.

II.5 AUTOMATED ASSESSMENTS IN GOOGLE COLAB

To conduct formative assessment, the simulation results exported from MATLAB/Simulink by all groups were uploaded into a Google Colab notebook. Google Colab can do various analyses for LFC. The notebook, developed in Python, automated the process of importing frequency deviation and controller output data, plotting time-domain responses for visual comparison, and computing key performance metrics, including steady-state error, maximum overshoot, settling time, number of oscillations, and peak values with their occurrence times.

Table 1: Performance metrics of student groups.

Group	Steady-State Error (Hz)	Overshoot (Hz)	Settling Time (s)	Oscillations
Group1_LFC	0	0	0	1
Group4_LFC	-0.0004	0.0016	0	5
Group2_LFC	0	0.0007	0	16
Group3_LFC	0	0.0025	0	25

Source: Authors, (2026).

In addition to quantitative evaluation, the notebook generated automated formative feedback, for example: *"Too many oscillations, increase the* Kd*"*, which guided students toward possible tuning improvements. The importance of the controller is discussed in this learning. A weighted scoring scheme was then applied to objectively evaluate each group's performance, with 30% weight assigned to steady-state error, 20% to overshoot, 30% to settling time, and 20% to oscillations. The normalized values were aggregated into a final score (0–100), allowing groups to be ranked and benchmarked against one another. Unlike traditional summative evaluation, this framework emphasized formative assessment by providing students with immediate feedback, opportunities for reflection, and iterative improvement. All analyses are done in Google Colab. The cloud-based nature of Google Colab further ensured accessibility, collaboration, and reproducibility, making it a practical and scalable tool for integrating simulation-based learning with continuous assessment.

III. RESULTS AND ANALYSIS

The performance of four student groups was evaluated based on their MATLAB/Simulink simulations and subsequent formative assessment through Google Colab. Table 1 presents the simulation results for all groups. Table 1 summarizes the primary performance metrics, while Table 2 presents the normalized scores, aggregated totals, and final rankings.

Table 2: Normalized scores and ranking.

Group	Err_score	OS_score	ST_score	OSC_score	Total Score	Rank
Group1_LFC	1.00	1.00	1.00	0.96	99.20	1
Group4_LFC	1.00	0.36	1.00	0.80	83.21	2
Group2_LFC	1.00	0.72	1.00	0.36	81.60	3
Group3_LFC	1.00	0	1.00	0	60.00	4

Source: Authors, (2026).

The manual tuning of all student groups is listed in Table 3. The results indicate that all four groups successfully minimized steady-state error, achieving nearly zero final frequency deviation, demonstrating effective integral action. However, significant differences were observed in oscillatory behavior and damping quality**.** Group 1 achieved the best performance, with negligible error, no overshoot, and only one oscillation cycle.

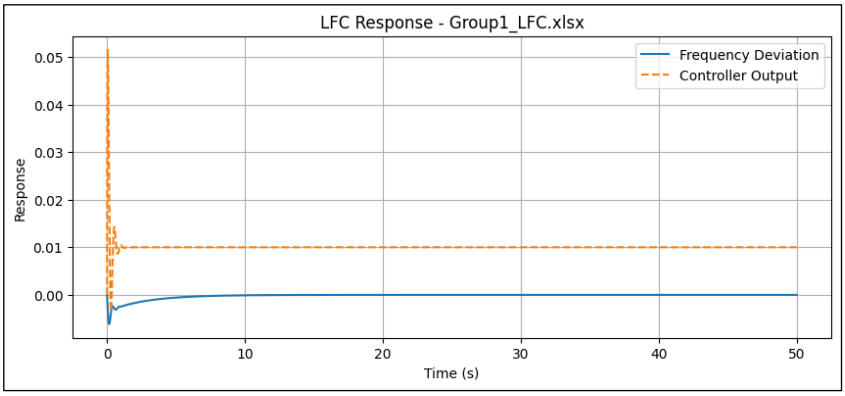


Figure 3: LFC response of Group 1.
Source: Authors, (2026).

The performance analysis is conducted in groups to identify insights. With a total score of 99.2**,** this group's tuning can be considered the benchmark solution. Group 4 ranked second with a score of 83.2**,** exhibiting a small overshoot (0.0016 Hz) and five oscillations, indicating slightly underdamped behavior. Group 2 ranked third with a score of 81.6**,** performing well in steady-state accuracy but experiencing 16 oscillations**,** showing the need for improved damping via derivative gain tuning. Each group is compared to get the rank. Group 3 received the lowest score **(**60.0**)** due to high oscillations (25) and the largest overshoot (0.0025 Hz), suggesting inadequate controller damping and excessive proportional action. The responses of all student groups are depicted in Figures 3-8.

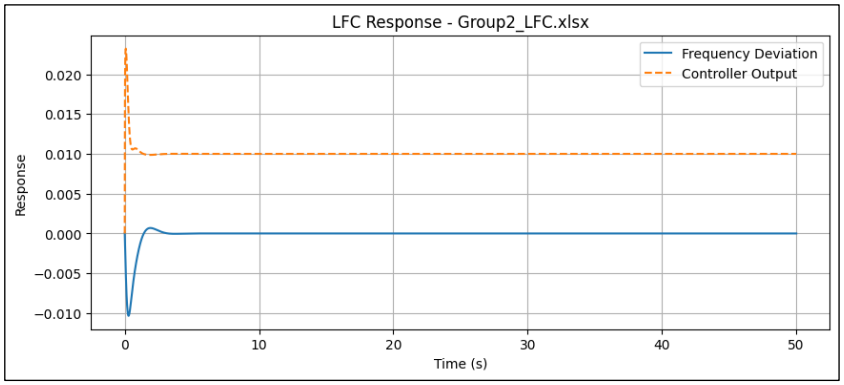


Figure 4: LFC response of Group 2.
Source: Authors, (2026).

Table 3: PID gain values after manual tuning by four student groups.

Groups	Kp	Ki	Kd
Group1_LFC	1.10	1.60	0.30
Group2_LFC	3.00	1.00	0.70
Group3_LFC	0.50	5.00	2.00
Group4_LFC	10.00	0.20	1.00

Source: Authors, (2026).

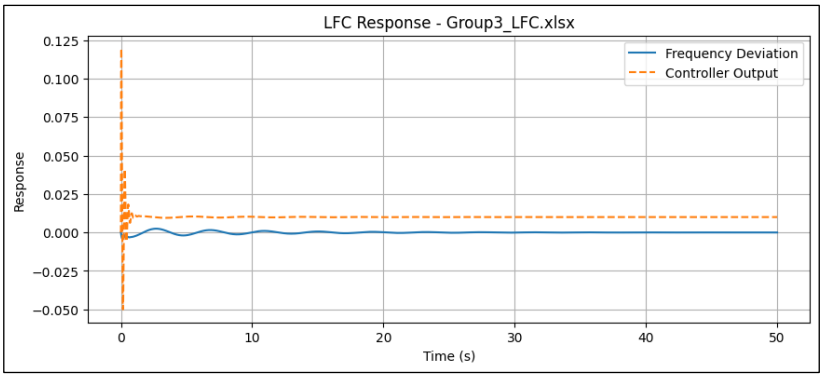


Figure 5: LFC response of Group 3.
Source: Authors, (2026).

The automated formative feedback, as shown in Table 4, reinforced these findings by highlighting strengths such as good steady-state control across all groups, while also pointing out specific weaknesses such as excessive oscillations.

Table 4: Automated formative feedback summary.

Group	Formative Feedback
Group1_LFC	Well-damped response with negligible error and no overshoot; considered benchmark.
Group2_LFC	Good steady-state accuracy but too many oscillations; requires an increase in (Kd).
Group3_LFC	Excessive oscillations and the highest overshoot need major retuning of (Kp), (Ki), and (Kd).
Group4_LFC	Acceptable performance with mild oscillations; derivative gain adjustment suggested.

Source: Authors, (2026).

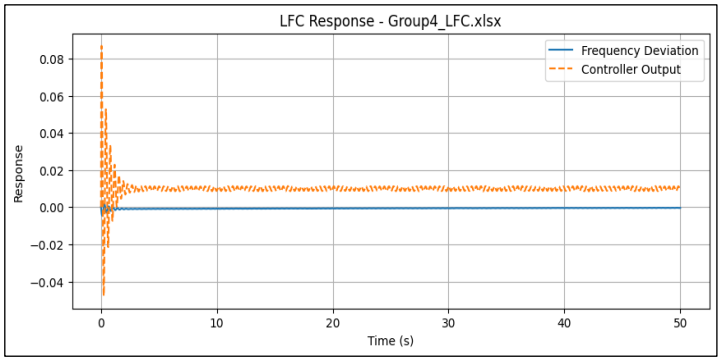


Figure 6: LFC response of Group 4.
Source: Authors, (2026).

Overall, the analysis shows that while students could intuitively achieve frequency regulation, damping characteristics became the key differentiator among groups. The formative assessment is done for all groups. The formative assessment framework successfully provided immediate, targeted feedback, helping students understand the relationship between controller parameters and system dynamics.

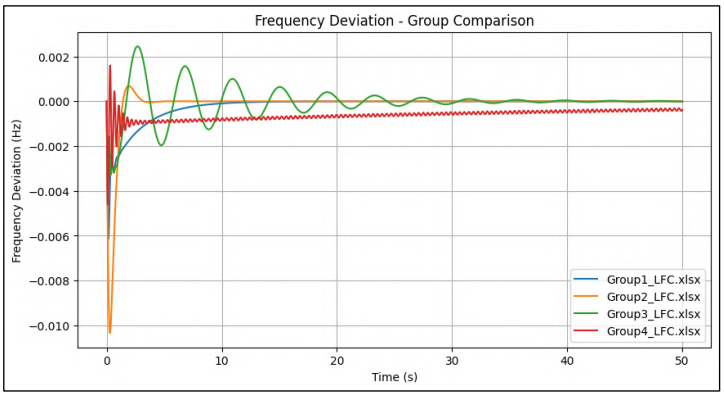


Figure 7: Comparison of the LFC response of various Groups.
Source: Authors, (2026).

From a technical perspective, the results show that all four student groups achieved near-zero steady-state error, confirming that manual PID tuning can effectively regulate the system frequency under load disturbances. However, transient behavior varied significantly. The best performance is identified based on various parameters. Group 1 achieved the best performance with minimal oscillations and no overshoot, while Groups 2, 3, and 4 demonstrated varying degrees of underdamping, reflected in higher oscillation counts. These variations highlight the importance of tuning the derivative gain (Kd) to enhance damping and mitigate oscillatory behaviour, while avoiding excessive proportional action that can worsen transient instability.

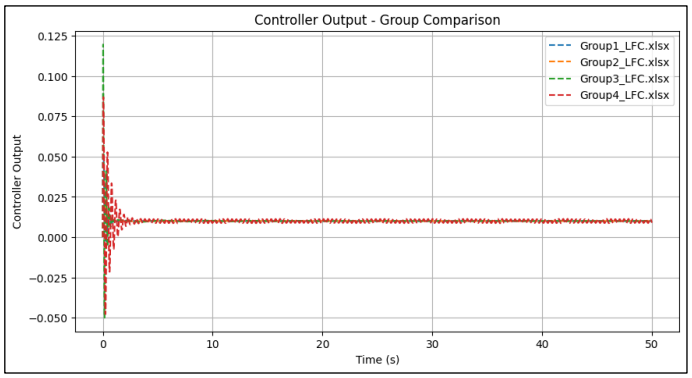


Figure 8: Comparison of controller response for various Groups.
Source: Authors, (2026).

From a teaching and learning standpoint, combining MATLAB/Simulink with Google Colab created an effective environment for formative assessment by providing students with timely, meaningful feedback. This technique will help students learn complex problems. The automated evaluation and ranking system helped students directly relate their tuning decisions to measurable performance indicators, which encouraged them to refine their work through repeated attempts rather than treating the exercise as a single grading event. Working in groups further supported peer learning, comparison, and discussion, making the activity more collaborative and reflective. In addition, because Google Colab is cloud-based and platform-independent, it provides easy access. It ensures that results can be reproduced consistently, making it a useful tool for both classroom instruction and remote learning.

IV. CONCLUSIONS

This work introduced a formative assessment framework for teaching Load Frequency Control (LFC), combining MATLAB/Simulink for system simulation with Google Colab for automated analysis and feedback. The analysis carried out based on various parameters. Four student groups independently developed single-area power system models, applied manual PID tuning, and analysed system responses to a step load disturbance. Although all groups successfully eliminated steady-state error, variations in oscillatory behaviour underscored the importance of proper derivative tuning for achieving stable, well-damped performance. The feedback can be obtained from the analysis. By delivering instant feedback, scores, and rankings, the Google Colab environment enabled students better to understand the link between controller parameters and system dynamics while also encouraging iterative refinement of their designs. The results demonstrate that integrating simulation-based exercises and formative assessment can significantly strengthen technical learning, teamwork, and student engagement.

V. AUTHOR'S CONTRIBUTION

Conceptualization: Idamakanti Kasireddy, Devineni Gireesh Kumar and Neelesh Kumar Gupta.
Methodology: Idamakanti Kasireddy and Devineni Gireesh Kumar.
Investigation: Idamakanti Kasireddy and Devineni Gireesh Kumar.
Discussion of results: Idamakanti Kasireddy, Devineni Gireesh Kumar, Neelesh Kumar Gupta and Prasad Chongala.
Writing – Original Draft: Idamakanti Kasireddy.
Writing – Review and Editing: Idamakanti Kasireddy and Devineni Gireesh Kumar.
Resources: Devineni Gireesh Kumar.
Supervision: Devineni Gireesh Kumar and Neelesh Kumar Gupta.
Approval of the final text: Idamakanti Kasireddy, Devineni Gireesh Kumar, Neelesh Kumar Gupta and Prasad Chongala.

VI. REFERENCES

[1] P. Kundur, Power System Stability and Control. New Delhi, India: McGraw-Hill Education, 2007.

[2] O. I. Elgerd, Electric Energy Systems Theory: An Introduction. New Delhi, India: Tata McGraw-Hill, 1983.

[3] W. Tan, "Unified Tuning of PID Load Frequency Controller for Power Systems via IMC," IEEE Transactions on Power Systems, vol. 25, no. 1, pp. 341-350, Feb. 2010, doi: 10.1109/TPWRS.2009.2036463.

[4] B. K. Sahu, T. K. Pati, J. R. Nayak, S. Panda, and S. K. Kar, "A novel hybrid LUS–TLBO optimized fuzzy-PID controller for load frequency control of multi-source power system," International Journal of Electrical Power & Energy Systems, vol. 74, pp. 58-69, Jan. 2016, doi: 10.1016/j.ijepes.2015.07.020.

[5] G. Chen, Z. Li, Z. Zhang, and S. Li, "An Improved ACO Algorithm Optimized Fuzzy PID Controller for Load Frequency Control in Multi Area Interconnected Power Systems," IEEE Access, vol. 8, pp. 6429-6447, 2020, doi: 10.1109/ACCESS.2019.2961280.

[6] M. I. Alomoush, "Load frequency control and automatic generation control using fractional-order controllers," Electrical Engineering, vol. 91, no. 7, pp. 357-368, July 2010, doi: 10.1007/s00202-010-0145-7.

[7] I. Pan and S. Das, "Fractional-order load-frequency control of interconnected power systems using chaotic multi-objective optimization," Applied Soft Computing, vol. 29, pp. 328-344, Apr. 2015, doi: 10.1016/j.asoc.2014.12.032.

[8] Kasireddy, A. W. Nasir, and A. K. Singh, "IMC-based Controller Design for Automatic Generation Control of Multi-Area Power System via Simplified Decoupling," International Journal of Control, Automation and Systems, vol. 16, no. 3, pp. 994-1010, June 2018, doi: 10.1007/s12555-017-0362-1.

[9] M. Saklani, N. Ahamad, A. Chhetri, and S. Singh, "New control strategy for load frequency control of single area power system using archimedes optimization algorithm," in 2022 1st International Conference on Sustainable Technology for Power and Energy Systems (STPES), 2022, pp. 1-6, doi: 10.1109/STPES54845.2022.10006394.

[10] R. J. Roselli and S. P. Brophy, "Experiences with Formative Assessment in Engineering Classrooms," Journal of Engineering Education, vol. 95, no. 4, pp. 325-333, Oct. 2006, doi: 10.1002/j.2168-9830.2006.tb00904.x.

[11] E. Sanchez-Lopez, J. Kasongo, A. F. Gonzalez-Sanchez, and A. Mostrady, "Implementation of formative assessment in engineering education," Acta Pedagogia Asiana, vol. 2, no. 1, pp. 43-53, 2023, doi: 10.59657/apa.v2i1.26.

[12] E. Ní Fhloinn and M. Carr, "Formative assessment in mathematics for engineering students," European Journal of Engineering Education, vol. 42, no. 4, pp. 458-470, 2017, doi: 10.1080/03043797.2016.1209463.

[13] J. Qadir et al., "Leveraging the force of formative assessment & feedback for effective engineering education," Peeers (Preprints), 2020, doi: 10.31224/osf.io/7v9jy.

[14] W. Vallejo, C. Diaz-Uribe, and C. Fajardo, "Google Colab and Virtual Simulations: Practical E-Learning Tools to Support the Teaching of Thermodynamics and to Introduce Coding to Students," ACS Omega, vol. 7, no. 8, pp. 7421-7429, Feb. 2022, doi: 10.1021/acsomega.1c06910.

Journal of Engineering and Technology for Industrial Applications

ISSN ONLINE: 2447-0228

ITEGAM-JETIA

Manaus, v.12 n.60, p. 362-369, July/August, 2026.
DOI: https://doi.org/10.5935/jetia.v12i60.3840

RESEARCH ARTICLE OPEN ACCESS

STRATEGIC INTEGRATION OF ARTIFICIAL INTELLIGENCE IN EDUCATIONAL QUALITY: DIAGNOSIS AND PROPOSAL FOR UNIVERSITIES IN AMAZONAS, PERU

Victor Manuel Valdiviezo Sir*[1]

[1]Universidad César Vallejo - UCV, Chiclayo, Perú.

[1]http://orcid.org/0000-0003-4348-3076

Email:*vvaldiviezosir@ucvvirtual.edu.pe

ARTICLE INFO

Article History
Received: February 26, 2026
Reviewed: June 11, 2026
Accepted: July 11, 2026
Published: July 31, 2026

Keywords:
Artificial intelligence,
Educational quality,
Amazonas,
Institutional Policies

ABSTRACT

Artificial intelligence (AI) in higher education faces the challenge of translating technological adoption into effective improvements in educational quality, especially in contexts with infrastructural limitations such as Amazonas region, Peru. This research aligned with SDG 4 (quality education) and aimed to propose a model for integrating artificial intelligence into public policies to increase educational quality in public universities of Amazonas region. A basic study was developed with a quantitative approach, non-experimental cross-sectional design, and propositional scope. The sample included 365 participants (students and faculty) from UNTRM and UNIFSLB, selected through simple random probability sampling. A validated Likert-type questionnaire processed with SPSS 27 was applied. Results revealed a paradox: 98.4% reported medium-high levels of AI integration, but only 29.9% perceived high educational quality. The most deficient dimensions were equity (24.1% low), relevance (20.3% low), and effectiveness (20.8% low). It was concluded that high spontaneous AI adoption does not generate proportional improvements without clear institutional policies, systematic training, and ethical governance frameworks, justifying the proposed model of strategic integration into educational public policies, which was validated by experts.

Copyright ©2026 by authors and Galileo Institute of Technology and Education of the Amazon (ITEGAM). This work is licensed under the Creative Commons Attribution International License (CC BY 4.0).

I. INTRODUCTION

Artificial intelligence (AI) is increasingly integrated into global higher education and acts as a driver of change in academic management. Universities that incorporate AI achieve more efficient processes and personalized learning experiences, with direct impact on student performance and resource administration [1]. The analysis of educational big data enables anticipation of academic outcomes and content optimization, which strengthens pedagogical and administrative decision-making [2]. This advancement connects with Sustainable Development Goal (SDG) 4, oriented toward inclusive, equitable, and quality education. Target 4.3 prioritizes equal access to higher education by 2030. Within this framework, AI supports sustainable management models, especially in public universities with budgetary limitations, and strengthens knowledge retention among students [3], [4]. The global Artificial Intelligence market in education reached USD 5.88 billion in 2024 and projects annual growth of 31.2% until 2030 [5]. Nearly half of universities have incorporated AI tools, primarily through chatbots and predictive analytics systems [6]. In the United States, automated teaching assistants have modified classroom dynamics in university settings. According to [7] demonstrated that perception of the evaluation system and ease of interaction with these assistants influence their acceptance by students. In Latin America, experiences in Mexico confirmed improvements in academic satisfaction and complex thinking development through AI-based platforms [8]. Despite these advances, barriers persist related to financing, lack of structural support and limited willingness to share data, as well as privacy concerns, which increase gaps between institutions [9], [10]. In Peru, the education system faces considerable challenges in quality and infrastructure, especially in rural areas. 92% of Peruvian households had internet access in 2023, with increases in rural areas to more than 80% from 41.5% in 2019 [11]. Strengthening competencies in information and communication technologies (ICT) is fundamental to incorporating AI into educational policies [12]. In 2021, only 13% of young Peruvians and adults possessed general ICT skills.

This figure represents the foundation for building educational policies that incorporate AI to improve quality in public universities. In Amazonas region, access to technological resources essential for implementing AI is unequal. The proportion of households with internet access reached 40.8% in 2023, but remains below the national average. The contrast between rural and urban areas regarding infrastructure influences technology adoption in educational settings. In 2017, only 70.3% of rural households in the region had electricity through the public grid [13]. These conditions accentuate challenges for incorporating AI into regional educational strategies. The limitations, combined with scarce faculty training, hinder the implementation of technological innovations. However, it has been demonstrated that intelligent tutors based on AI improve educational effectiveness [14]. The limited involvement of the academic community in adopting innovative technologies threatens educational excellence and regional sustainable development. When authorities, faculty, and students remain distant from technology adoption processes, a void is created that fills with context-disconnected decisions, resulting in ineffectiveness and affecting the essence of inclusive education [15]. It is essential that educational entities foster a culture of training and societal involvement around technology implementation. The benefits of AI must be explained, favoring creation of consultation mechanisms with students and professors, promoting clarity in implementation procedures, and establishing effective feedback systems. Active participation is a practical necessity to guarantee quality in education, enabling the forging of a more inclusive, effective educational system aligned with social needs. Considering the previously described problems, this research aimed to answer the following question: in what way will a model for integrating artificial intelligence into public policies increase educational quality in public universities of Amazonas region? The general objective was to propose a model for integrating artificial intelligence into public policies to increase educational quality in public universities of Amazonas region.

The specific objectives were: to diagnose the level of educational quality in public universities of Amazonas region, to develop a model for integrating artificial intelligence into educational public policies to increase educational quality in public universities of Amazonas region, and to validate the model for integrating artificial intelligence into educational public policies through expert judgment. The justification for this research is based on the need to improve educational quality in disadvantaged territories such as Amazonas region, in order to reduce access and equity gaps. From a theoretical perspective, the study contributes knowledge about integrating artificial intelligence into educational public policies, a field still in development phase. From a practical perspective, the proposed model offers an applicable alternative to strengthen teaching in public universities of Amazonas region through technological tools oriented toward monitoring and improving learning. It should be noted that AI also contributes to increasing student retention, a critical aspect in contexts with high dropout rates, as indicated by [16]. Additionally, the research's impact is expressed in its contribution to designing more inclusive educational policies, based on evidence, with capacity to respond to the territory's real needs. Strategic adoption of AI modifies academic and administrative processes [17]. In this sense, epistemological evidence of these advances maintains the need for models that integrate these technologies within educational public policies. Nevertheless, it is essential to know the level of technological adoption to design effective interventions [18], given that educational quality must be evaluated considering access to resources, an aspect enhanced by AI [19], since its use serves to extend knowledge effectively [20].

II. THEORETICAL REFERENCE

The incorporation of artificial intelligence in higher education configures a global phenomenon that modifies academic practices and optimizes learning personalization and institutional management. According to [21] indicate that modernization through AI enables individualizing teaching and managing resources with greater precision through automated and predictive processes, while [22] highlight its impact on evaluation systems, curricular personalization, and administrative management, with direct effects on equity and sustainability of educational services. This integration is inserted into a technoscientific logic oriented toward process optimization through algorithms that adjust contents, timing, and formative pathways according to each student's academic behavior. The Technology-Organization-Environment (TOE) Framework constitutes a reference point for analyzing AI inclusion in universities. In [23] explain that this model enables examining the influence of technological characteristics, organizational capabilities, and socioeconomic and normative conditions on new technology adoption, which facilitates identifying barriers and opportunities within the institution. Complementarily, the Conceptual Paradigm triangle proposed by [24] integrates technical, social, and ethical dimensions to examine opportunities, risks, and principles in AI use in teaching, a relevant aspect in contexts marked by digital gaps and structural limitations such as those present in peripheral territories. The AI Literacy Conceptual Framework, developed by [25], maintains that AI implementation in university settings must be based on faculty and students having an adequate level of artificial intelligence literacy, that is, acquiring the necessary skills to use intelligent systems ethically, critically, and productively. Along the same lines, the Ethical Governance and Data Protection Framework formulated by [26] establishes guidelines to protect privacy, reinforce equity, and ensure transparency in educational use of AI, which guides the formulation of technological governance policies focused on reducing risks, organizing data management, and guaranteeing more equitable access to artificial intelligence benefits in contexts such as Amazonas region.

The Technology Acceptance Model proposed by [27] explains technological adoption based on perceived utility and ease of use, variables that affect educational actors' attitudes toward incorporating new tools. This approach articulates with UNESCO's [28] Educational Quality theory, which defines excellence from the dimensions of relevance, effectiveness, equity, efficiency, and sustainability. It is complemented by [29] Knowledge Management theory through the SECI model (Socialization–Externalization–Combination–Internalization) and with the Socio-Technical Systems theory (STS) formulated by [30], expanded by [31] and supported by [32], which emphasizes the need to integrate technology and social dynamics to strengthen educational environments coherent with institutional reality. Artificial intelligence is understood as systems that simulate human cognitive capabilities, based on skills such as learning, reasoning, and problem-solving, to optimize educational learning processes [33]. Its dimensions are: machine learning for predicting academic performance [34], natural language processing through educational chatbots, and data analytics for timely pedagogical feedback. Educational quality in higher education is the degree to which universities achieve relevant, equitable, effective, efficient, and sustainable results according to [28], convergent with [35], who indicate its relevance and institutional sustainability. In Amazonas region, this means closing access gaps, increasing digital competencies, and ensuring employability.

Its dimensions are relevance, effectiveness, equity, efficiency, and sustainability, which are expanded with Artificial Intelligence that responds to performance [36] and will help fulfill SDG 4, given the urgency of equity in rural scenarios warned by [37].

III. METHODOLOGY

This research was developed as a basic study, as it sought to generate theoretical-practical knowledge [38]. A non-experimental and cross-sectional design was assumed, since it was carried out in a single period and without manipulation of study variables [39]. This design enabled collecting information about the educational context of 2025, obtaining quantitative data that responded to the problem statement with scientific rigor. The scope of the study was propositional. The study variables were artificial intelligence, viewed from its integration into public policies, and educational quality. Artificial intelligence, defined by [40] as strategic incorporation of tools such as intelligent tutoring and predictive analysis, was structured into dimensions of planning, technological implementation, and ethical governance. Educational quality, according to [28], was understood as achieving relevant, equitable, and sustainable results in education. The unit of analysis consisted of students and faculty belonging to public universities of Amazonas region: the Universidad Nacional Toribio Rodríguez de Mendoza de Amazonas (UNTRM) and the Universidad Nacional Intercultural Fabiola Salazar Leguía de Bagua (UNIFSLB). The established inclusion criteria were: being institutionally active public universities in 2025, having undergraduate programs in effect between 2023 and 2025, having updated records of enrollment and teaching staff, willingness to participate voluntarily, and basic access to digital means to respond to the instrument. The total population was 6,964 individuals, comprising 537 faculty and 6,427 students, according to data reported by both institutions for the 2025-I academic semester. The sample was selected through simple random probability sampling, ensuring that each individual had the same probability of being chosen [41]. 365 individuals were included in the sample, prioritizing accessibility and willingness of participants to obtain relevant and reliable information [42].

For data collection, the survey method was used, considering a structured questionnaire as the instrument that measured perceptions about educational quality (relevance, effectiveness, equity, efficiency, and sustainability) and AI integration (Artificial Intelligence acceptance, intelligent tutoring, predictive analytics, ethical governance and transparency, and language processing), using a five-point Likert scale and verified through Cronbach's Alpha coefficient ($\alpha = 0.880$). It was developed based on the Technology Acceptance Model (TAM), the Technology-Organization-Environment (TOE) Framework, the Ethical Governance and Data Protection Framework, UNESCO's Educational Quality Theory, and Socio-Technical Systems (STS) Theory. Instrument verification was carried out through evaluation by specialists who analyzed coherence, clarity, relevance, and theoretical adequacy of the items. To evaluate reliability, a pilot test was applied to a representative sample, with the objective of analyzing data obtained through application of Cronbach's Alpha coefficient [43], [44]. The instrument results were processed using SPSS (Statistical Package for the Social Sciences) version 27 software, given that it is a program widely used in social science research due to its efficiency in performing basic data analysis [45]. This enabled analyzing opinions of students and professors about educational quality and artificial intelligence incorporation, identifying key trends in emerging technology use.

IV. RESULTS AND DISCUSSIONS

IV.1 RESULTS

Results obtained through application of the validated instrument to 365 participants from public universities of Amazonas region during the 2025-I semester, processed with SPSS 27, are presented organized according to the global diagnosis of educational quality and analysis of its five constitutive dimensions according to the UNESCO (2008) model. Additionally, findings about the current level of artificial intelligence integration in these institutions are included. Table 1 presents the distribution of perceived levels of educational quality in public universities of Amazonas region. These findings reveal a concerning situation where 70.2% of participants perceive significant deficiencies in university educational quality. The predominance of the medium level (62.5%) suggests that, while institutions meet basic standards, there are important shortcomings that limit educational excellence. The percentage at low level (7.7%) represents 28 participants who experience critical educational conditions requiring immediate attention. This distribution confirms the stated problem regarding structural limitations of public universities in emerging contexts such as Amazonas region.

Table 1: Levels of Educational Quality.

Levels	N	%
High level	109	29,9%
Medium level	228	62,5%
Low level	28	7,7%

Source: Author, (2026).

Table 2, corresponding to the relevance dimension, presents low level (20.3%), which constitutes an alarming finding. One in five participants considers that university education has low relevance regarding demands of the labor and social context. The medium level, grouping 45.8% of participants, suggests that there is perception of partial disconnection between curricular contents and competencies required in the regional and national labor market. The perceived low relevance relates to outdated curricula, limited linkage with the productive sector, and limited incorporation of emerging digital competencies.

Table 2: Levels of Relevance.

Levels	N	%
High level	124	34,0%
Medium level	167	45,8%
Low level	74	20,3%

Source: Author, (2026).

Table 3 presents results of the effectiveness dimension, understood as the degree to which universities enable students to achieve established learning objectives and successfully complete their academic programs. Effectiveness presents a high percentage at low level (20.8%), indicating that approximately one in five participants considers that universities are not effectively enabling students to achieve proposed learning objectives. The predominance of medium level (44.4%) suggests that there are partial achievements, but also systematic deficiencies in teaching-learning processes that prevent full accomplishment of educational goals.

Table 3: Levels of Effectiveness.

Levels	N	%
High level	127	34,8%
Medium level	162	44,4%
Low level	76	20,8%

Source: Author, (2026).

Table 4 regarding equity shows that this constitutes the most critical dimension of the diagnosis, presenting the highest percentage at low level (24.1%) among all dimensions analyzed. Nearly one in four participants perceives that there are significant barriers preventing equitable access to quality educational opportunities. Only 29.3% perceive a high level of equity, the lowest percentage among all dimensions at this level. This finding is relevant in the context of Amazonas region, characterized by marked inequalities between urban and rural areas.

Table 4: Levels of Equity.

Levels	N	%
High level	107	29,3%
Medium level	170	46,6%
Low level	88	24,1%

Source: Author, (2026).

Table 5 presents results of the efficiency dimension, defined as optimization in use of human, financial resources, and infrastructure to achieve educational objectives. Data show that efficiency presents relatively more favorable results than other dimensions, with the highest percentage at high level (36.4%) along with sustainability. However, 63.6% of participants still perceive that there are deficiencies in management and utilization of available resources. The low level (18.4%) represents a significant proportion evidencing critical inefficiencies in some contexts or institutional processes.

Table 5: Levels of Efficiency.

Levels	N	%
High level	133	36,4%
Medium level	165	45,2%
Low level	67	18,4%

Source: Author, (2026).

Table 6 shows that sustainability emerges as the dimension with the most favorable results in the diagnosis, registering the lowest percentage at low level (12.6%) and one of the highest at high level (36.7%), along with efficiency. Nevertheless, the predominance of medium level (50.7%) reveals that, while there are institutional foundations enabling continuity of educational processes, limitations persist in consolidating continuous and adaptive improvement. The low-level group raises concerns regarding viability of some programs or policies in the long term.

Table 6: Levels of Sustainability.

Levels	N	%
High level	134	36,7%
Medium level	185	50,7%
Low level	46	12,6%

Source: Author, (2026).

Table 7 presents current levels of artificial intelligence integration in public universities of Amazonas region. The low percentage at low level (1.6%) indicates practically universal receptivity toward AI and evidences that institutions have initiated technological adoption processes with broad acceptance from the university community. The predominance of medium level (61.1%) suggests that, while AI integration is still incipient or partial in scope, there is considerable critical mass of users who have already experimented with AI tools in educational contexts. The high level (37.3%) represents more than one-third of participants, indicating that there is a substantial group perceiving advanced integration.

Table 7: Levels of Artificial Intelligence Integration.

Levels	N	%
High level	136	37,3%
Medium level	223	61,1%
Low level	6	1,6%

Source: Author, (2026).

IV.2 DISCUSSION

The findings of this research offer empirical evidence about the current state of educational quality and artificial intelligence integration in public universities of Amazonas region. The diagnosis reveals a paradoxical situation: while 98.4% of participants report medium or high levels of Artificial Intelligence integration, only 29.9% perceive high educational quality. Deficiencies are concentrated mainly in equity (24.1% low level) and relevance (20.3% low level). This discrepancy between technological adoption and educational improvement constitutes the interpretive axis of the analysis. The study evidences a 7.4% gap between high AI integration (37.3%) and high educational quality (29.9%). This result differs from that reported by [36], who developed an intelligent tutoring model in Peruvian universities achieving a 15% increase in student performance and significant reduction in dropout. The divergence suggests that spontaneous AI adoption in Amazonas region, without institutional articulation or planned pedagogical design, does not generate proportional improvements in educational quality. It contrasts with, who demonstrated that generative AI increased personalized learning by 22%, emphasizing the importance of faculty training as a mediating variable. Results show partial agreement with, who analyzed student perceptions about AI in universities of Peru, Ecuador, and Mexico. 70% of students reported 18% improvements in teaching personalization. The high receptivity toward AI observed in Amazonas region (98.4% at medium and high levels) coincides with this positive perception. However, warned of the absence of ethical approaches and contextual adaptation, deficiencies also present in the Amazonian context. This partial convergence confirms the need for public policies that articulate AI with pedagogy and faculty development. The most significant difference is observed when contrasting results with, who conducted a qualitative study on ChatGPT use in Costa Rican higher education. They demonstrated that generative AI increases student participation but identified as the main obstacle the lack of articulation between government, universities, and civil society. In Amazonas region, that same structural barrier exists: high technological integration coexists with deficiencies in equity, relevance, and effectiveness.

Regarding equity, the results (24.1% low level and 46.6% medium) differ from findings by, who demonstrated that AI-based resources reduced mental effort by 30% and improved learning. Their study was developed in a context with advanced technological infrastructure and universal internet access. In contrast, in Amazonas region, only 40.8% of households have internet connection and 70.3% of rural dwellings have public electricity. This structural gap confirms that cognitive benefits depend on technological equity, a persistent deficiency in the study region. Curricular relevance (20.3% low level and 45.8% medium) partially coincides with, who examined excellence assurance mechanisms in 29 accredited universities in Chile, concluding that AI-based tools prioritize quantity over quality of publications. In Amazonas region, results corroborate that need: perception of disconnection between training and labor demands suggests that technological adoption without pedagogical criteria maintains low curricular relevance. High receptivity toward AI (only 1.6% rejection) agrees with findings by, who analyzed incorporation of generative AI in 63 Peruvian university professors. 66.7% reported high integration, achieving 20% improvement in didactic material development. In Amazonas region, 61.1% present medium integration, reflecting spontaneous use without structured training. This coincidence between Peruvian contexts demonstrates that familiarity with generative tools has promoted massive adoption, though it still requires critical digital literacy. Results about complexity in the context of Amazonas region (40.8% internet access, 70.3% rural electricity, but 98.4% medium-high AI integration) find repercussion with the framework proposed by, who established that management empowerment through knowledge, financing, and support structures is fundamental. Findings confirm those challenges in Amazonas region, where adoption exists without management empowerment, systematic knowledge, or governance structures. Among the main methodological limitations, several factors are identified that condition interpretation of findings and their extrapolation to other educational contexts.

The cross-sectional design prevents establishing clear causal relationships between AI integration and educational quality, since measurement was performed at a single moment without longitudinal follow-up enabling observation of changes over time. This is compounded by dependence on self-reported perceptions through Likert-type scales, a scenario in which participants tend to overestimate their level of AI use or educational service quality. Also noted is the lack of disaggregation by type of actor and by institution, which restricts analysis of differences between faculty and students, as well as between UNTRM and UNIFSLB, while evaluation of AI integration as a global construct, without specifying tools, frequency of use, or pedagogical purposes, generates ambiguity in interpretation of levels achieved. Future research lines demand a more profound methodological approach that incorporates longitudinal or quasi-experimental designs with control groups, in order to establish causal relationships between structured AI implementation and improvements in specific dimensions of educational quality, with measurements at 6, 12, and 24-month intervals. It is also required to disaggregate analyses according to rural or urban origin, socioeconomic level, gender, age, and academic area to identify differentiated impacts, while qualitative studies through interviews, focus groups, and observation will enable recognizing cultural, psychological, and organizational barriers in pedagogical AI integration. It also proposes to evaluate components such as smart tutoring, predictive analytics, and AI literacy programs in isolation, as well as to make comparisons between universities in Amazon region and urban cities in Peru, or with institutions in other Latin American countries with similar characteristics. The main contribution of this study is to provide contextualized empirical evidence on the paradox between the high adoption of AI and the limited improvement in educational quality at public universities in Amazonas region. Three critical dimensions are identified where institutional disarticulation prevents translating technological receptivity into measurable educational improvements. These finding challenges technological determinism and reaffirms the need for public policies that strategically integrate technological, pedagogical, organizational, and ethical components.

IV.3 PROPOSAL

The present model arises from the need to address deficiencies in educational quality identified in public universities of Amazonas region. Results evidence medium or low levels of educational quality and high receptivity toward artificial intelligence. This adoption does not translate into proportional improvements, since 98.4% of participants report medium or high levels of AI integration while only 29.9% perceive high educational quality, with critical dimensions such as equity at 24.1% at low level, relevance at 20.3%, and effectiveness at 20.8%. This paradox shows a gap between technological availability and institutional capacity to generate concrete improvements.

The proposed model guides spontaneous adoption toward a comprehensive strategy that addresses these dimensions through clear policies, systematic training, and ethical governance frameworks, in line with SDG 4 and the needs of Amazon region as an emerging context. The model integrates seven strategic components to close gaps between technological adoption and educational quality. First, the Intelligent Tutoring System with adaptive platforms based on machine learning and offline modules for areas with intermittent connectivity. Second, the Predictive Analytics System with data mining algorithms that identify risk of dropout or low performance, generating early alerts. Third, the AI Literacy Program that develops digital, pedagogical, and ethical competencies at three levels: basic, intermediate, and advanced. Fourth, the Ethical Governance Framework with institutional committees, data protection protocols, algorithmic audits, and guidelines on AI use. Fifth, Digital Equity Strategies with community centers, connectivity scholarships, mobile devices, and multilingual resources. Sixth, the AI-Based Curricular Update System with employability analysis and competency recommendations. Seventh, the Continuous Evaluation System with indicator dashboards linked to the five quality dimensions. Implementation contemplates seven phases during seventy-six months organized sequentially. The Detailed Institutional Diagnosis phase (3 months) evaluates technological capabilities, infrastructure, and digital competencies through audits and focus groups.

The Technological Architecture Design phase (9 months) develops a modular platform with offline components, mobile interfaces, security protocols, and pilot tests with 10% of students. The Progressive Implementation of AI Tools phase (12 months) deploys intelligent tutoring, predictive analytics, and recommendation systems in 50% of academic programs, with continuous technical support. The Intensive Faculty Training phase (6 months) covers 80% of personnel through workshops and certifications. The Establishment of Ethical Governance phase (4 months) forms committees and defines protocols according to Law No. 29733. The Systematic Monitoring and Evaluation phase (24 months) includes quarterly evaluations. The Scaling and Replication phase (18 months) documents results and transfers the model to other universities. The estimated budget amounts to S/ 2,700,000 and is distributed by components: the Technological Platform with S/ 650,000 for design, development, servers, and maintenance; Faculty Training with S/ 350,000 for training 537 faculty members, materials, and certifications; Digital Equity Infrastructure with S/ 480,000 for 15 community centers, 300 mobile devices, and subsidized connectivity; the Intelligent Tutoring System with S/ 420,000 for development and integration; Ethical Governance and Data Protection with S/ 280,000 for committees, training, and audits; Monitoring and Evaluation with S/ 200,000 for dashboards and quarterly reports; Management and Implementation with S/ 320,000 for coordination, supervision, and contingencies throughout the seventy-six-month period.

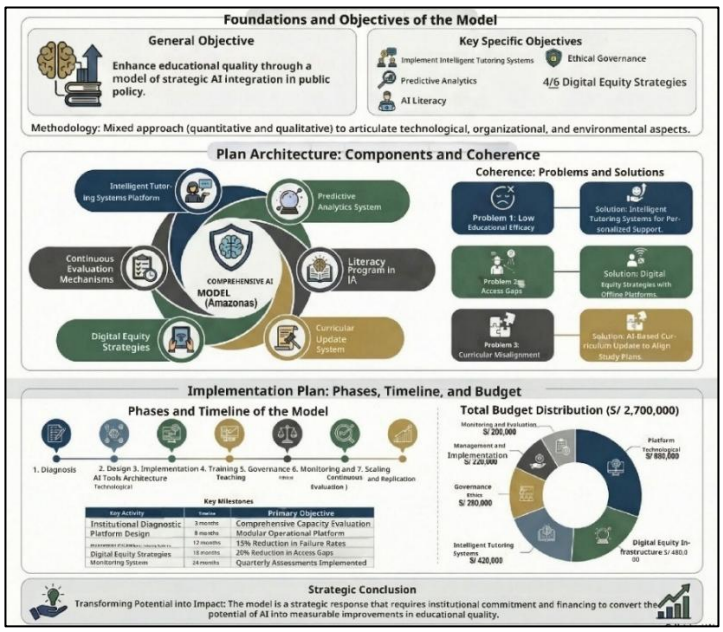


Figure 1: Model for integrating artificial intelligence into public policy to improve educational quality in public universities, Amazonas.
Source: Author, (2026).

V. CONCLUSIONS

The diagnosis of educational quality in public universities of Amazonas region revealed significant structural deficiencies. Equity emerged as the most critical dimension, with barriers preventing equal access to quality educational opportunities, while curricular relevance presented alarming deficiencies, evidencing disconnection of university training from regional and national labor market demands, as did effectiveness. Additionally, the dimensions of efficiency and sustainability, although relatively more favorable, evidenced that the majority perceive deficiencies in resource management and institutional capacity to innovate. The model for integrating artificial intelligence into educational public policies responded strategically to identified deficiencies through systematic articulation of seven implementable phases, integrating technological, organizational, pedagogical, and ethical components. In turn, the proposal recognized particularities of the Amazonian context, incorporating solutions adapted to intermittent connectivity through platforms with offline components, interfaces optimized for mobile devices, and digital equity strategies. The strategic articulation between empirical diagnosis and intervention proposal enabled designing a contextualized model that transforms spontaneous AI adoption into strategic integration. Finally, findings evidenced a significant theoretical, methodological, and social contribution. Theoretically, the study challenged technological determinist assumptions by empirically demonstrating that high receptivity toward AI does not automatically generate proportional improvements in educational quality without mediation of contextualized public policies.

Methodologically, the research combined quantitative diagnosis with propositional design, generating a replicable model for Latin American public universities. Socially, the proposal aligned with SDG 4 by prioritizing equity as a critical dimension, developing personalization strategies through AI that compensate for structural disadvantages of rural students. This constitutes transferable knowledge to other Peruvian and Latin American public universities facing similar problems between expansion of access to emerging technologies and persistence of educational inequities.

VI. AUTHOR'S CONTRIBUTION

Conceptualization: Victor Manuel Valdiviezo Sir.
Methodology: Victor Manuel Valdiviezo Sir.
Investigation: Victor Manuel Valdiviezo Sir.
Discussion of results: Victor Manuel Valdiviezo Sir.
Writing – Original Draft: Victor Manuel Valdiviezo Sir.
Writing – Review and Editing: Victor Manuel Valdiviezo Sir.
Resources: Victor Manuel Valdiviezo Sir.
Supervision: Victor Manuel Valdiviezo Sir.
Approval of the final text: Victor Manuel Valdiviezo Sir.

VII. REFERENCES

[1] M. Al-Shoqran y S. Shorman, «A Review on Smart Universities and Artificial Intelligence», en The Fourth Industrial Revolution: Implementation of Artificial Intelligence for Growing Business Success, Cham: Springer International Publishing, 2021, pp. 281-294. doi: 10.1007/978-3-030-62796-6_16.

[2] Z. Alkayyali, S. Bin Idris, y S. Abu-Naser, «A systematic literature review of deep and machine learning algorithms in cardiovascular diseases diagnosis.», Journal of Theoretical and Applied Information Technology, vol. 101, n.o 4, pp. 1353-1365, 2023.

[3] W. Leal et al., «Living labs in the context of the UN sustainable development goals: state of the art», Sustainability Sci., vol. 18, n.o 3, pp. 1163-1179, 2023, doi: 10.1007/s11625-022-01240-w.

[4] Y. Wang, W. Choo, y X. Wang, «Face recognition technology based on deep learning algorithm for smart classroom usage», Journal of Engineering Science and Technology, vol. 18, n.o 6, pp. 39-47 WE-Emerging Sources Citation Index (ESCI), 2023.

[5] Grand View Research, «AI In Education Market Size & Share | Industry Report, 2030». Accedido: 8 de abril de 2025. [En línea]. Disponible en: https://www.grandviewresearch.com/industry-analysis/artificial-intelligence-ai-education-market-report

[6] Inside Higher Ed, «2024 Survey of Campus Chief Technology/Information Officers», Inside Higher Ed. Accedido: 8 de abril de 2025. [En línea]. Disponible en: https://www.insidehighered.com/reports/2024/10/14/2024-survey-campus-chief-technologyinformation-officers

[7] J. Kim, K. Merrill, K. Xu, y D. Sellnow, «My Teacher Is a Machine: Understanding Students' Perceptions of AI Teaching Assistants in Online Education», Int. J. Hum.-Comput. Interact., vol. 36, n.o 20, pp. 1902-1911, 2020, doi: 10.1080/10447318.2020.1801227.

[8] J. Sanabria, I. Castillo, L. González, y M. Ramírez, «Complex thinking through a Transition Design-guided Ideathon: testing an AI platform on the topic of sharing economy», Front. Educ., vol. 8, 2023, doi: 10.3389/feduc.2023.1186731.

[9] A. Campion, M. Gasco-Hernandez, S. Mikhaylov, y M. Steve, «Overcoming the Challenges of Collaboratively Adopting Artificial Intelligence in the Public Sector», Social Science Computer Review, pp. 1-33, 2022, doi: 10.1177/0894439320979953.

[10] K. Tarisayi, «Strategic leadership for responsible artificial intelligence adoption in higher education», CTE Workshop Proceedings, vol. 11, pp. 4-14, 2024, doi: 10.55056/cte.616.

[11] Statista, «Peru: household internet access by area 2023 | Statista», Statista. Accedido: 8 de abril de 2025. [En línea]. Disponible en: https://www.statista.com/statistics/801788/peru-internet-household-penetration-area/

[12] OECD, Education at a Glance 2024: OECD Indicators. en Education at a Glance. OECD, 2024. doi: 10.1787/c00cad36-en.

[13] INEI, «Amazonas: Compendio Estadístico - 2024. Instituto Nacional de Estadística e Informática», INEI, 2025.

[14] C. Lin, A. Huang, y O. Lu, «Artificial intelligence in intelligent tutoring systems toward sustainable education: a systematic review», Smart Learning Environments, vol. 10, n.o 1, 2023, doi: 10.1186/s40561-023-00260-y.

[15] J. P. Onoja, O. Ajala, y A. Ige, «Harnessing artificial intelligence for transformative community development: A comprehensive framework for enhancing engagement and impact», GSC Adv. Res. Rev., vol. 11, n.o 3, pp. 158-166, jun. 2022, doi: 10.30574/gscarr.2022.11.3.0154.

[16] W. Villegas-Ch, J. Govea, y S. Revelo-Tapia, «Improving Student Retention in Institutions of Higher Education through Machine Learning: A Sustainable Approach», SUSTAINABILITY, vol. 15, n.o 19, oct. 2023, doi: 10.3390/su151914512.

[17] B. George y O. Wooden, «Managing the Strategic Transformation of Higher Education through Artificial Intelligence», ADMINISTRATIVE SCIENCES, vol. 13, n.o 9, sep. 2023, doi: 10.3390/admsci13090196.

[18] P. Bengel y C. Peter, «Technology in Nature—mDGBL as a Successful Approach to Promote Complex Contents?», Sustainability, vol. 15, n.o 1, 2023, doi: 10.3390/su15010633.

[19] M. G. V. Kumar, N. Veena, L. Cepova, M. A. M. Raja, A. Balaram, y M. Elangovan, «Evaluation of the Quality of Practical Teaching of Agricultural Higher Vocational Courses Based on BP Neural Network», APPLIED SCIENCES-BASEL, vol. 13, n.o 2, 2023, doi: 10.3390/app13021180%20WE%20-%20Science%20Citation%20Index%20Expanded%20(SCI-EXPANDED).

[20] A. Asanov, I. Asanov, G. Buenstorf, V. Kadriu, y P. Schoch, «Patterns of dissertation dissemination: publication-based outcomes of doctoral theses in the social sciences», Scientometrics, vol. 129, n.o 4, pp. 2389-2405, 2024, doi: 10.1007/s11192-024-04952-1.

[21] D. Mojolou, F. Madli, H. Thomas, S. Sondoh, y E. Karunia, «A trend in publishing artificial intelligence personalized education: Enhancing learning experiences for university students», Journal of Information System and Technology Management, 2024, doi: 10.35631/jistm.937021.

[22] S. Siminto, A. Akib, H. Hasmirati, y D. Widianto, «Educational Management Innovation by Utilizing Artificial Intelligence in Higher Education», al-fikrah: Jurnal Manajemen Pendidikan, 2023, doi: 10.31958/jaf.v11i2.11860.

[23] S. Nazri, M. Ashaari, y H. Bakri, «Exploring the Adoption of Artificial Intelligence in Institutions of Higher Learning», Journal of Information System and Technology Management, 2022, doi: 10.35631/jistm.727004.

[24]P. Christou, «Implications of Artificial Intelligence (AI) in Education: A Critical Review, Evaluation, and Conceptualization», 2024 6th International Workshop on Artificial Intelligence and Education (WAIE), pp. 56-60, 2024, doi: 10.1109/WAIE63876.2024.00017.

[25] X. Zhou y L. Schofield, «Developing a conceptual framework for Artificial Intelligence (AI) literacy in higher education», Journal of Learning Development in Higher Education, 2024, doi: 10.47408/jldhe.vi31.1354.

[26] G. Mariam, L. Adil, y B. Zakaria, «The Integration of Artificial Intelligence (AI) into Education Systems and its Impact on the Governance of Higher Education Institutions», International Journal of Professional Business Review, 2024, doi: 10.26668/businessreview/2024.v9i12.5176.

[27] F. Davis, «Perceived Usefulness, Perceived Ease of Use, and User Acceptance of Information Technology», MIS Quarterly, vol. 13, n.o 3, pp. 319-340, 1989, doi: 10.2307/249008.

[28] UNESCO, «Educación de calidad, equidad y desarrollo sostenible: una concepción holística inspirada en las cuatro conferencias mundiales sobre la educación que organiza la UNESCO en 2008-2009 - UNESCO Biblioteca Digital». Accedido: 22 de abril de 2025. [En línea]. Disponible en: https://unesdoc.unesco.org/ark:/48223/pf0000181864_spa

[29] I. Nonaka y H. Takeuchi, «The knowledge-creating company: How Japanese companies create the dynamics of innovation», Long Range Planning, vol. 29, n.o 4, p. 592, ago. 1996, doi: 10.1016/0024-6301(96)81509-3.

[30] E. L. Trist y K. W. Bamforth, «Some Social and Psychological Consequences of the Longwall Method of Coal-Getting: An Examination of the Psychological Situation and Defences of a Work Group in Relation to the Social Structure and Technological Content of the Work System», Human Relations, vol. 4, n.o 1, pp. 3-38, feb. 1951, doi: 10.1177/001872675100400101.

[31] A. Cherns, «The Principles of Sociotechnical Design», Human Relations, vol. 29, n.o 8, pp. 783-792, ago. 1976, doi: 10.1177/001872677602900806.

[32] A. Dhukaram, C. Sgouropoulou, G. Feldman, y A. Amini, «Higher education provision using systems thinking approach – case studies», European Journal of Engineering Education, vol. 43, n.o 1, pp. 3-25, ene. 2018, doi: 10.1080/03043797.2016.1210569.

[33] S. Russell y P. Norvig, Artificial Intelligence: A Modern Approach, 4th ed. Hoboken, NJ: Pearson Education Limited, 2022. [En línea]. Disponible en: https://api.pageplace.de/preview/DT0400.9781292401171_A41586057/preview-9781292401171_A41586057.pdf

[34] M. Saeed, «Forecasting the Academic Performance by Leveraging Educational Data Mining», IASC, vol. 39, n.o 2, pp. 213-231, 2024, doi: 10.32604/iasc.2024.043020.

[35] P. Aithal y A. Maiya, «Exploring Quality in Higher Education: An Introduction and Theoretical Framework», International Journal of Philosophy and Languages (IJPL), 2023, doi: 10.47992/ijpl.2583.9934.0021.

[36] K. Soriano, M. Caparachin, F. Arauco, J. Ninahuaman, M. Inga, y R. Cangalaya, «Artificial Intelligence Model for the Improvement of the Quality of Education at the National University of Central Peru, Huancayo 2024», en Proc. - Int. Symp. Accredit. Eng. Comput. Educ., ICACIT, Institute of Electrical and Electronics Engineers Inc., 2024. doi: 10.1109/ICACIT62963.2024.10788595.

[37]M. Trow, «Reflections on the Transition from Elite to Mass to Universal Access: Forms and Phases of Higher Education in Modern Societies since WWII», en International Handbook of Higher Education, J. J. F. Forest y P. G. Altbach, Eds., Dordrecht: Springer Netherlands, 2007, pp. 243-280. doi: 10.1007/978-1-4020-4012-2_13.

[38] R. Hernández, C. Fernández, y P. Baptista, Metodología de la Investigación, Sexta Edición. México: McGraw-Hill, 2014.

[39] S. Hunziker y M. Blankenagel, «Cross-Sectional Research Design», Research Design in Business and Management, 2021, doi: 10.1007/978-3-658-34357-6_10.

[40] O. Zawacki-Richter, V. Marín, M. Bond, y F. Gouverneur, «Systematic review of research on artificial intelligence applications in higher education – where are the educators?», Int J Educ Technol High Educ, vol. 16, n.o 1, p. 39, oct. 2019, doi: 10.1186/s41239-019-0171-0.

[41] J. M. Pérez-Salamero, M. Regúlez, y C. Vidal, «Un Procedimiento De Selección De Sub-Muestras De Gran Tamaño De Una Muestra Aleatoria Simple Representativas De La Población De Estudio (A Selection Procedure of High Size Sub-Samples from a Simple Random Sample Representative of the Population)», 24 de junio de 2015, Social Science Research Network, Rochester, NY: 2622457. doi: 10.2139/ssrn.2622457.

[42] D. Valdez-Pineda, I. Vázquez-Jiménez, E. Vega-Encinas, y M. Millanes, «University teacher's perception of inclusive education», Revista de Pedagogía Critica, 2024, doi: 10.35429/jcp.2024.8.19.1.7.

[43] T. A. Malapane y N. Ndlovu, «Assessing the Reliability of Likert Scale Statements in an E-Commerce Quantitative Study: A Cronbach Alpha Analysis Using SPSS Statistics», 2024 Systems and Information Engineering Design Symposium (SIEDS), pp. 90-95, 2024, doi: 10.1109/SIEDS61124.2024.10534753.

[44] S. Vivek y B. Bonny, «Development of a Scale to Measure the Attitude towards Innovation Use in Rice Farming», Asian Journal of Agricultural Extension, Economics & Sociology, 2023, doi: 10.9734/ajaees/2023/v41i92060.

[45] M. Nanere, W. Tabelessy, F. Leuhery, J. Tubalawony, y S. Saununu, «Global Trends in SPSS Training for Students: a Step Towards Improved Research Competence», Asian Journal of Community Services, 2025, doi: 10.55927/ajcs.v4i1.13626.

Journal of Engineering and Technology for Industrial Applications

ISSN ONLINE: 2447-0228

ITEGAM-JETIA

Manaus, v.12 n.60, p.370-381, July/August, 2026.
DOI: https://doi.org/10.5935/jetia.v12i60.

RESEARCH ARTICLE OPEN ACCESS

DESIGN AND IMPLEMENTATION OF A PROPOSED SDN-VXLAN ARCHITECTURE FOR ENTERPRISE NETWORK

Daniel Nuñez-Agurto*[1], Luis Paredes-Alcivar[2], John Cruz-Garzon[3] and Franklin Perez[4]

[1, 2, 3, 4]Department of Computer Science, Universidad de las Fuerzas Armadas ESPE, Sangolquí, Ecuador.

[1]https://orcid.org/0000-0001-7737-3815, [2]https://orcid.org/0000-0002-5568-509X,
[3]http://orcid.org//0009-0006-7550-9962, [4]https://orcid.org/0009-0009-4974-571X

Email:*adnunez1@espe.edu.ec

ARTICLE INFO

Article History
Received: February 27, 2026
Reviewed: June 11, 2026
Accepted: July 11, 2026
Published: July 31, 2026

Keywords:
Software-Defined Networking (SDN),
Virtual Extensible LAN (VxLAN),
PPDIOO,
Network Architecture,
Open vSwitch (OVS).

ABSTRACT

Efficient and scalable network architectures are essential for enterprise environments that demand reliable and high-performance connectivity. Virtual Extensible LAN (VXLAN) technology enables the encapsulation of Layer 2 traffic over Layer 3 infrastructures, while Software-Defined Networking (SDN) introduces centralized control and programmability by decoupling the control and data planes. This study presents the design and implementation of an enterprise network architecture that integrates SDN and VXLAN technologies to enhance scalability, performance, and security. The PPDIOO lifecycle methodology was adopted as a structured framework for design, deployment, and optimization. The proposed architecture was implemented and validated in a GNS3 emulated environment using OpenDaylight as the SDN controller and Open vSwitch (OVS) as the virtual switching layer. Functional testing, including connectivity verification and packet flow analysis, confirmed correct operation of VXLAN tunneling under SDN control, demonstrating the feasibility and effectiveness of the proposed model. The results highlight that the integration of SDN and VXLAN provides a flexible, programmable, and secure foundation for next-generation enterprise network infrastructures.

Copyright ©2026 by authors and Galileo Institute of Technology and Education of the Amazon (ITEGAM). This work is licensed under the Creative Commons Attribution International License (CC BY 4.0).

I. INTRODUCTION

In modern business environments, connectivity and performance are essential to ensuring operational efficiency and competitiveness. In an increasingly digitalized global environment marked by the rapid advancement of smart devices, the volume of data traversing networks is growing exponentially, leading to greater complexity in network infrastructures [1], [2]. A production network typically comprises numerous devices, operates under various protocols, and supports a wide range of applications [3]. The adoption of emerging technologies such as Virtual Extensible LAN (VXLAN) [4], [5] and Software-Defined Networking (SDN) [6], [7] represents an innovative alternative that significantly improves performance compared to traditional networks. Thus, Internet Service Providers (ISPs) and network administrators must adjust to these transformations by implementing the right tools and methodologies to guaranty effective network management. SDN is a dynamic and evolving architecture that decouples the control plane from the data plane, making it particularly suitable for the changing requirements of modern applications [8], [9]. A centralized controller offers a global view of the network, enabling enhanced monitoring, configuration, and packet flow analysis. Meanwhile, VXLAN enables the creation of a large number of isolated virtual networks, overcoming limitations of traditional VLAN technologies [10], [11]. This tunneling protocol facilitates network segmentation around virtual machines and allows the deployment of Layer 2 networks over a Layer 3 infrastructure, thereby improving overall traffic performance. The integration of SDN and VXLAN brings together essential capabilities required to overcome the limitations of conventional networking technologies. By [12] proposed an SDN-controlled VXLAN architecture implemented in an intelligent data center to support seamless virtual machine migration. They deployed the design using Mininet and achieved optimal load balancing results. Their findings demonstrated that an SDN-based VXLAN architecture reduces IP multicast resource usage and meets deployment requirements in cloud computing environments. Similarly [13] evaluated SDN-controlled VXLAN in multi-site enterprise networks using Mininet, identifying high traffic volumes and latency as primary challenges.

They proposed dynamic VXLAN tunnels, tunnel division for hybrid and corporate access, and centralized policy management to improve performance and operational agility. These results highlight the potential of SDN and VXLAN to optimize complex infrastructures and pave the way for AI-driven solutions in network security. Network performance and efficiency are critical for service interconnection in enterprise environments. However, few works have addressed the systematic design and functional deployment of SDN-VXLAN architectures in enterprise contexts, where interoperability with existing infrastructures and operational frameworks is critical. To overcome these limitations, this study aims to design an efficient network architecture that integrates SDN and VXLAN to optimize enterprise network performance. This study aims to design and implement a functional enterprise network architecture that integrates SDN and VXLAN technologies, following the structured PPDIOO (Prepare, Plan, Design, Implement, Operate, Optimize) lifecycle methodology proposed by Cisco. The primary contribution of this work lies in demonstrating a replicable and verifiable implementation framework that validates the interoperability and feasibility of SDN-VXLAN integration over an emulated MPLS underlay network. The proposed model was implemented using the GNS3 network emulator, with OpenDaylight serving as the SDN controller and Open vSwitch (OVS) as the virtual switching element within Ubuntu-based Docker hosts. Functional testing focused on verifying VXLAN tunneling, OpenFlow-based flow control, and SDN management capabilities. The remainder of this paper is organized as follows: Section 2 describes the materials and methods applied throughout the PPDIOO lifecycle. Section 3 presents the main implementation results and discusses the observed operational behavior. Finally, Section 4 summarizes the key findings and outlines directions for future research.

II. RELATED WORKS

The integration of SDN with network virtualization mechanisms such as VXLAN and EVPN has led to a substantial body of research aimed at enhancing automation, scalability, and traffic isolation across diverse scenarios, ranging from multi-tenant data centers and multisite infrastructures to educational networks and domain-specific applications. However, most of these studies concentrate on isolated data-plane optimizations, energy-efficiency improvements, or narrowly scoped use cases, and therefore do not provide a comprehensive methodology or a reproducible design suitable for enterprise environments. To contextualize the contribution of our work, we present a detailed comparison of ten relevant studies that explore different combinations of SDN controllers, VXLAN/EVPN technologies, underlay configurations, validation environments, and design objectives, as summarized in Table 1.

Table 1: Comparative summary of related works and the proposed SDN–VXLAN architecture.

Ref.	Objective	Technologies	Validation	Contributions	Limitations
[14]	Performance optimization	SDN + P4 switches + EVPN/VXLAN	Experimental tests	Accelerated user-plane performance; ARP suppression; multi-tenancy and DAG support	Lacks implementation methodology; limited to data-plane optimization
[15]	Eco-efficient multi-tenant datacenter management	Ryu controller + VXLAN	Experimental	Zero traffic leakage; automated VTEP discovery; energy-efficient orchestration	No detailed deployment methodology; limited evaluation scenarios
[16]	Green multisite datacenter orchestration	SDN + EVPN/VXLAN + DPDK	Simulation	Reduced workload migration time (4.24%); resilient multi-homing architecture	Specific to GMDC; not suitable for enterprise networks
[17]	Distance learning enhancement	SDN + VXLAN	Practical scenarios	Remote access as local network; improved STEM resource availability	Not generalizable to enterprise environments; lacks benchmarking
[18]	Smart agriculture / online learning	SDN + VXLAN	Conceptual study	IoT connectivity through overlays; supports future national datacenters	No large-scale validation; conceptual-only
[19]	IPv6 deployment in campus network	SDN campus controller + VXLAN	Conceptual design	Automated IPv6 assignment; unified policy distribution	No empirical validation; lacks performance evaluation
[20]	Cloud-network collaboration	SDN orchestrator + VXLAN	Analytical review	Unified multi-region cloud-network management framework	Highly abstract; no implementation/testing
[21]	AD-Campus optimization	SeerEngine-Campus + EVPN/VXLAN	Simulation	Step-by-step deployment; service separation across campuses	Vendor-specific; no technical comparison
[22]	Traffic load balancing in overlays	SDN + VXLAN tunneling	Experimental	Reduced latency and access time; efficient link usage	Limited to load balancing; no full architectural design
[23]	Hybrid distance learning	Floodlight + VXLAN	Real GNS3 tests	Redundancy, VPN integration; proven in real scenarios	Education-focused; not enterprise-oriented
Our Proposed	Enterprise network design	Ryu + OVS + VXLAN overlay	GNS3/Mininet emulation	PPDIOO-based methodology; reproducible enterprise architecture	Does not target performance benchmarking; design-focused

Source: Authors, (2026).

By [14] present an SDN-enabled EVPN-VXLAN architecture targeting geo-distributed sites and accelerate the user plane using P4-programmable switches. Their design integrates SDN host detection and EVPN host learning for ARP suppression, supports multi-tenancy and a distributed anycast gateway model, and demonstrates reduced host communication latency and improved user-plane efficiency.

This work shows how programmable data-plane elements can significantly enhance EVPN-VXLAN deployments across dispersed sites, complementing but differing from the present study which focuses on a fully documented SDN–VXLAN implementation methodology for enterprise networks. In turn [15] propose an eco-efficient SDN-VXLAN architecture for multi-tenant datacenters that leverages an optimized Ryu controller to automate VTEP discovery and enforce perfect tenant isolation. Their experiments report automated VTEP configuration, 0% cross-tenant leakage, and optimized resource utilization-framed as a sustainable, centralized approach for cloud providers. While directly comparable in its use of SDN+VXLAN, the focus on eco-efficiency and controller optimizations complements our work's emphasis on a reproducible PPDIOO-based SDN-VXLAN implementation for enterprise networks. By [16] introduce the Green Multisite Data Center (GMDC) architecture that leverages SDN with EVPN/VXLAN and DPDK-accelerated data-plane techniques to support renewable-powered, geo-distributed datacenters. Their simulations show a 4.24% reduction in total workload migration time and improved resiliency via all-active paths and multi-homing. The GMDC work provides an eco-centric perspective on multisite overlay networks, offering complementary design goals to our enterprise-focused SDN-VXLAN implementation. According to [17] apply VXLAN and SDN to optimize Mali's national fiber infrastructure for distance learning, enabling students to access resources as if on a local network. Their implementation demonstrates improved accessibility and remote collaboration for STEM education. Although targeted to educational infrastructure, the study exemplifies practical VXLAN overlay deployment over operator networks-insights useful when comparing deployment choices in enterprise SDN-VXLAN proposals. By [18] investigate the use of VXLAN and SDN to support online learning and IoT-enabled smart agriculture in the Central African Republic. Their case study outlines how overlays can enable connectivity and data management when a national datacenter is absent. The work illustrates the adaptability of SDN-VXLAN solutions to resource-constrained environments, complementing enterprise architectures by highlighting deployment considerations in low-infrastructure contexts.

In turn [19] proposes an SDN-based IPv6 deployment scheme using VXLAN to decouple control and user planes in a campus network, enabling attribute-based IPv6 address allocation and policy enforcement for location-agnostic access. The scheme is directly relevant for enterprise/campus scenarios that require seamless IPv6 transition and overlay segmentation, offering architectural mechanisms that complement our PPDIOO-guided SDN-VXLAN implementation. According to [20] examine the deployment of white-box network equipment combined with SDN and VXLAN in large-scale cloud environments, proposing a collaborative operation platform for unified management across multi-region clouds. Their work is valuable for understanding operational and orchestration implications when adopting SDN-VXLAN at scale, informing enterprise implementation choices in our study. By [21] detail an AD-Campus solution employing EVPN-VXLAN and a SeerEngine SDN controller to enable scalable, multi-transport campus networks. Their simulation cycle and deployment procedures offer practical guidance on EVPN-VXLAN rollouts and demonstrate service separation benefits—useful operational context for our PPDIOO-based SDN-VXLAN implementation. In turn [22] implement an SDN-driven traffic balancer over VXLAN overlay networks, demonstrating decreased access times and improved link utilization. Their contribution provides a concrete mechanism for overlay traffic engineering that can be adopted within enterprise SDN-VXLAN designs to enhance availability and performance. By [23] present a hybrid distance-learning infrastructure that overlays VXLAN over national DWDM networks and manages flows with a Floodlight SDN controller. Their GNS3 experiments and VPN integrations demonstrate practical deployment steps for VXLAN overlays in real operational environments, informing controller selection and deployment workflows relevant to enterprise VXLAN implementations. Based on the above, these studies collectively demonstrate the versatility of SDN–VXLAN and EVPN-based architectures across a wide range of domains, including multisite datacenters, educational infrastructures, cloud environments, and resource-constrained deployments. However, despite their individual contributions, none of them provides a comprehensive, replicable, and controller-agnostic methodology specifically tailored to enterprise networks. This gap motivates the present work, which delivers a complete PPDIOO-based SDN–VXLAN design and implementation blueprint, supported by controlled emulation and practical deployment guidelines.

III. MATERIALS AND METHODS

This study is structured around the PPDIOO methodology, chosen for its systematic and comprehensive approach to network design and implementation [24]. Its adoption is motivated by the need to evaluate the impact of VXLAN technology on enterprise network performance in comparison to traditional architectures. Originating from Cisco's network lifecycle framework, the PPDIOO model is divided into six sequential phases: Prepare, Plan, Design, Implement, Operate, and Optimize. The following subsections detail the development of this study according to each phase of the methodology, demonstrating its relevance and effectiveness in guiding the deployment of an SDN-based VXLAN architecture.

III.1 PREPARE

This phase focuses on identifying and selecting the technological components required to meet the performance, scalability, and security requirements of the proposed enterprise network architecture. The analysis considered key functional requirements, including support for Layer 2 traffic over a Layer 3 infrastructure, separation of control and data planes through SDN principles, and the integration of VXLAN to enhance segmentation and scalability within an overlay framework. For network emulation and validation, GNS3 was selected as the simulation platform, available as a desktop application and as an Ubuntu-based virtual machine server [25]. The server environment was configured with 5 GB of RAM to ensure stable operation under multiple virtualized components. Cisco IOU images were adopted as network devices due to their modularity, scalability, and suitability for WAN/MAN service aggregation scenarios [26]. Open vSwitch (OVS) was implemented as the virtual switching fabric, providing OpenFlow compatibility and support for advanced monitoring protocols such as NetFlow, sFlow, 802.1ag, and IPFIX [27], [28]. Supporting components included Ubuntu-based Docker containers and a lightweight QEMU Firefox image obtained from the official GNS3 repository [29] for host emulation and traffic validation. The SDN control plane was managed by OpenDaylight (Karaf distribution 0.5.2 Boron SR2), selected for its modular architecture and compatibility with complex network environments [30].

This technological preparation establishes a controlled and reproducible environment for the subsequent planning, design, and implementation phases, enabling structured integration of SDN and VXLAN mechanisms within the proposed enterprise architecture.

III.2 PLAN

Based on the technologies outlined during the preparation phase, a structured design plan was developed for the SDN-based network architecture. Since this project involves a network emulation, the intended users are virtual hosts. For this implementation, a VXLAN tunnel was established between two endpoint nodes. However, it is important to note that VXLAN technology supports the creation of up to 16,000,000 Virtual Network Identifiers (VNIs), each providing an independent segmentation space, thus offering a high degree of scalability for future deployments. The plan includes the specific tasks required to complete the project, as detailed in Table 2. These activities were distributed across a four-month timeline: during the first month, the preparation and planning phases were conducted; the second month was dedicated to network design and implementation; the third month focused on the operation phase; and finally, the fourth month involved optimization of the emulated network, incorporating necessary adjustments based on functional validation.

Table 2: Work plan for the implementation of SDN with VXLAN.

Phase	Month 1	Month 2	Month 3	Month 4
Preparation	X			
Planning	X			
Network Design		X		
Implementation		X		
Operation			X	
Optimization				X

Source: Authors, (2026).

III.3 PLAN

Based on the information gathered in the previous stages, the network topology was designed. It consists of an MPLS underlay network composed of two P routers and two PE routers, along with two CE routers located at different sites. Each of these includes an Open vSwitch container, an OpenDaylight controller, a switch, and a Ubuntu Docker Guest host. The VXLAN overlay network is configured between the virtual Open vSwitch instances, as shown in Figure 1.

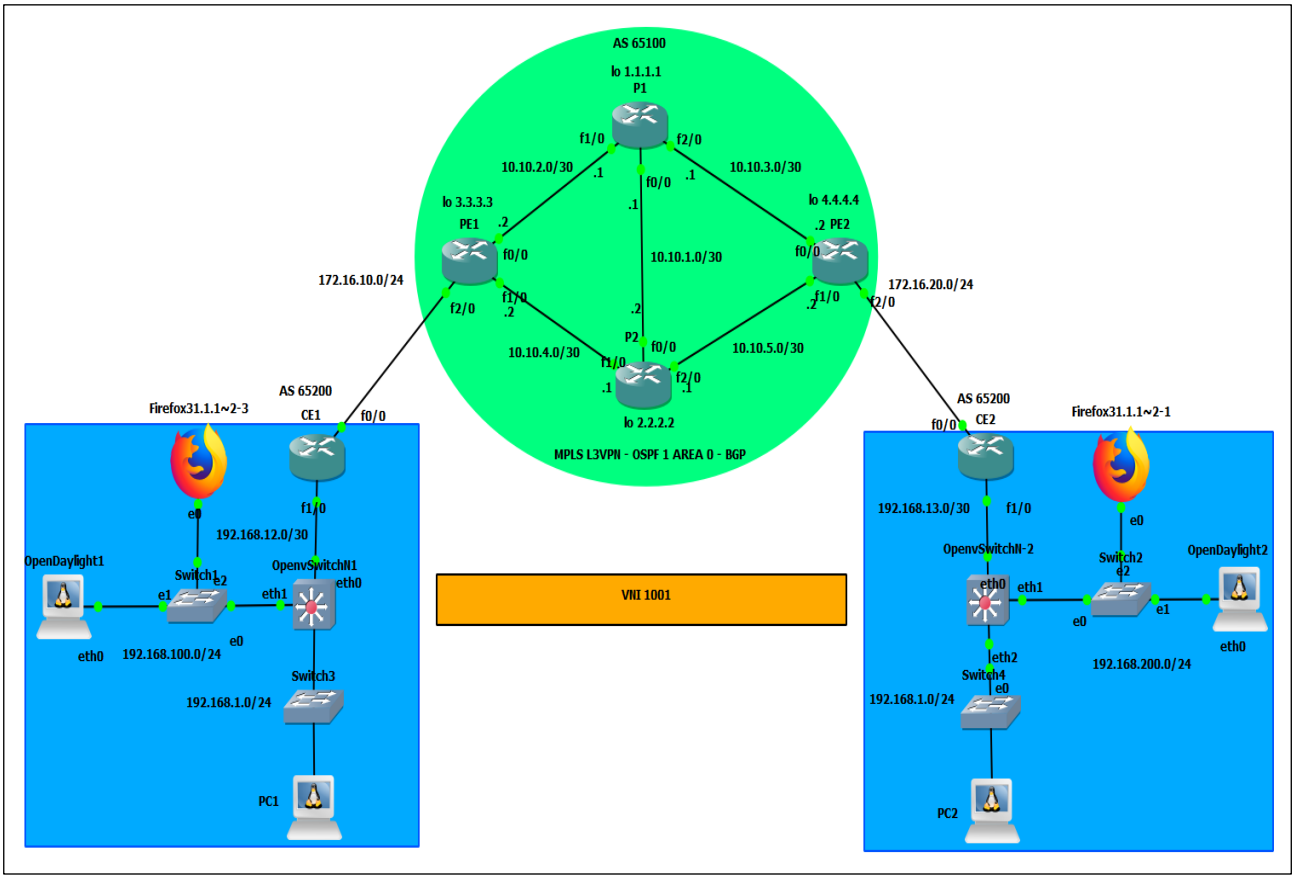


Figure 1: Test network topology.
Source: Authors, (2026).

Based on the established topology, IP addressing is assigned to each device, as detailed in Table 3.

Table 3: IP addressing of network devices.

Device	Interface	IP Address	Subnet Mask	Gateway
P1	Lo0	1.1.1.1	255.255.255.255	—
	Fa0/0	10.10.1.1	255.255.255.252	—
	Fa1/0	10.10.2.1	255.255.255.252	—
	Fa2/0	10.10.3.1	255.255.255.252	—
P2	Lo0	2.2.2.2	255.255.255.255	—
	Fa0/0	10.10.1.2	255.255.255.252	—
	Fa1/0	10.10.4.1	255.255.255.252	—
	Fa2/0	10.10.5.1	255.255.255.252	—
PE1	Lo0	3.3.3.3	255.255.255.255	—
	Fa0/0	10.10.2.2	255.255.255.252	—
	Fa1/0	10.10.4.2	255.255.255.252	—
	Fa2/0	172.16.10.1	255.255.255.0	—
PE2	Lo0	4.4.4.4	255.255.255.255	—
	Fa0/0	10.10.3.2	255.255.255.252	—
	Fa1/0	10.10.5.2	255.255.255.252	—
	Fa2/0	172.16.20.1	255.255.255.0	—
CE1	Lo0	172.16.1.10	255.255.255.255	—
	Fa0/0	172.16.10.2	255.255.255.0	—
	Fa1/0	192.168.12.1	255.255.255.252	—
CE2	Lo0	172.16.2.20	255.255.255.255	—
	Fa0/0	172.16.20.2	255.255.255.0	—
	Fa1/0	192.168.13.1	255.255.255.252	—
Open vSwitch 1	Eth0	192.168.12.2	255.255.255.252	192.168.12.1
	Eth1	192.168.100.1	255.255.255.0	—
	Eth2	192.168.1.1	255.255.255.0	—
Open vSwitch 2	Eth0	192.168.13.2	255.255.255.252	192.168.13.1
	Eth1	192.168.200.1	255.255.255.0	—
	Eth2	192.168.1.1	255.255.255.0	—
OpenDaylight 1	Eth0	192.168.100.2	255.255.255.0	192.168.100.1
OpenDaylight 2	Eth0	192.168.200.2	255.255.255.0	192.168.200.1
PC1 (Docker Guest)	E0	192.168.1.2	255.255.255.0	192.168.1.1
PC2 (Docker Guest)	E0	192.168.1.3	255.255.255.0	192.168.1.1

Source: Authors, (2026).

III.4 IMPLEMENT

III.4.1 WAN Configuration

The WAN network implementation began with the basic configuration of IP connectivity among the core nodes of the Underlay network. Subsequently, dynamic routing was established using the OSPF protocol to ensure network convergence and device reachability. Following this, MPLS functionality was enabled to allow label switching on the core routers. The Label Distribution Protocol (LDP) was configured to automate label exchange between devices, and specific label ranges were defined for label management. Once the basic configuration of the core routers (P routers) was completed, the implementation of the Provider Edge (PE) routers was carried out. On these devices, IP addressing was assigned according to the established design, and Virtual Routing and Forwarding (VRF) instances were configured to provide logical network segmentation, as shown in Figure 2.. Each VRF was associated with a unique identifier (Route Distinguisher) and import/export route policies (Route Targets), allowing client isolation and facilitating multipoint routing.

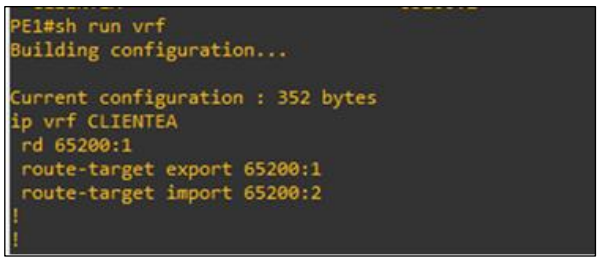


Figure 2: Figure title.
Source: Authors, (2026).

OSPF was also enabled on the PE routers to advertise internal networks and support MPLS label exchange. The outcome of this configuration is shown in Figure 3. Additionally, the BGP protocol was configured to establish sessions between edge nodes and enable the transport of VPNv4 routes, which are necessary for inter-site communication over the MPLS backbone.

Extended capabilities were activated to ensure the proper transport of community attributes among BGP neighbors. Within the context of the implemented VRF, specific BGP sessions were also configured to establish connectivity with Customer Edge (CE) routers, thus guaranteeing correct end-to-end route distribution. Finally, the CE routers were configured with BGP routing capabilities, enabling direct interaction with their respective PE routers. Internal routes were advertised, and neighbor relationships were established with the edge routers. The CE router configuration was replicated at both ends of the network to maintain symmetry in the topology.

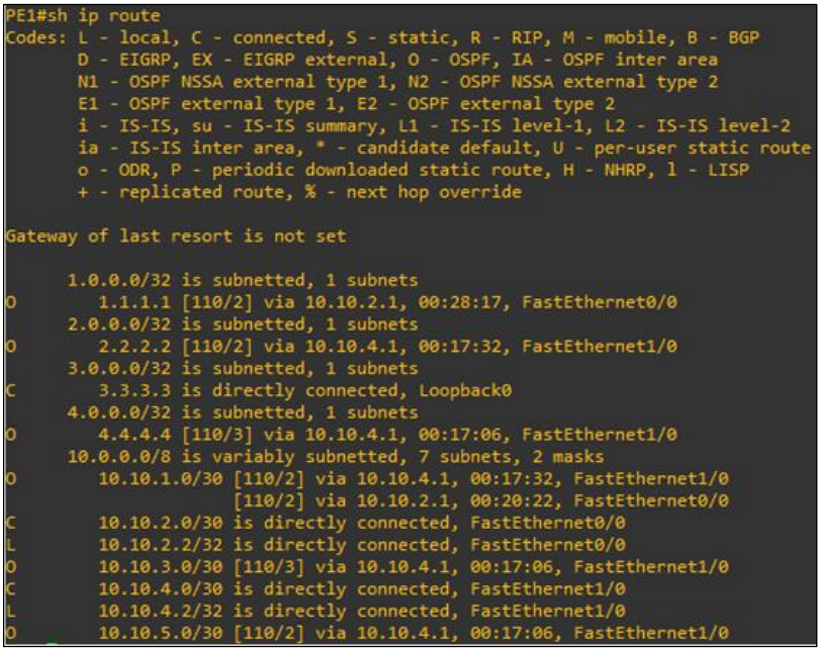


Figure 3: OSPF protocol configuration on PE1 router.
Source: Authors, (2026).

III.4.2 Controller Configuration

The configuration of the OpenDaylight SDN controller is a critical step for the control and management of the software-defined network. This phase involved preparing the controller's runtime environment, setting the necessary environment variables, and loading key features that enable device interaction and network topology management. Initially, the controller distribution directory was accessed using the command cd distribution-karaf-0.5.2-Boron-SR2. Subsequently, essential environment variables such as JAVA_HOME and PATH were exported to ensure the proper execution of the Java environment. The controller was then started by running the script ./bin/karaf. This procedure was replicated on the second controller to maintain consistency across the environment. Once inside the OpenDaylight console, additional features essential for controller operation were installed. These included odl-restconf, which implements Restconf—a REST-based protocol that facilitates control of YANG resources via HTTP. The L2Switch feature was also included to provide Layer 2 functionalities, mdsal-apidocs to supply API documentation for the MD-SAL Data Store model, and DLUX, which offers a web-based interface for visual topology management and other controller configurations.

III.4.3 VXLAN Configuration

To configure VXLAN technology, a virtual bridge (bridge or virtual switch) named ovsbr0 was first created using the command ovsvsctl addbr ovsbr0. Subsequently, a port named vxlan0 was added to the ovsbr0 bridge with the command ovs-vsctl add-port ovs-br0 vxlan0 - set interface vxlan0 type=vxlan options:remote_ip=192.168.13.2 options:key=1001. This command configures the vxlan0 interface as a VXLAN type, assigning it the remote IP address 192.168.13.2 and the VNI 1001. If the default br0 bridge, automatically created, initially includes the eth2 interface to connect the PC's LAN network, this interface is removed from br0 and added to the ovs-br0 bridge using the commands ovs-vsctl del-port br0 eth2 and ovs-vsctl add-port ovs-br0 eth2, respectively. Finally, VLAN 10 was assigned to the eth2 port with the command ovs-vsctl set port eth2 tag=10. To verify these configurations, the command ovs-vsctl show is used, the output of which is shown in Figure 4.



Figure 4: Bridge VXLAN configuration in open vSwitch.
Source: Authors, (2026).

In Figure 4, it can be observed that the ovsbr0 bridge is controlled by a device with the IP address 192.168.100.2. To this end, the Spanning Tree Protocol (STP) was enabled using the command ovsvsctl set bridge ovsbr0 stp_enable=true, preventing loops on the ovsbr0 bridge. Next, the bridge was configured to use version 1.3 of the OpenFlow protocol with the command ovsvsctl set bridge ovsbr0 protocols=OpenFlow13. Finally, the controller for the bridge was set via a TCP connection to the IP address 192.168.100.2 and port 6633 using the command ovsvsctl set-controller ovsbr0 tcp:192.168.100.2:6633. The configuration process for OpenvSwitchN2 was analogous to that of OpenvSwitchN1.

III.4.4 Operate

During this phase, network status monitoring was performed to verify the correct implementation of the previously described technologies. Basic connectivity tests, such as ping commands between virtual PCs, were conducted. Figure 5 shows the successful communication from PC1 to PC2.

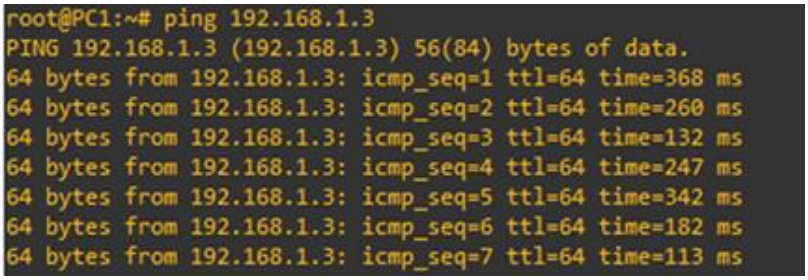


Figure 5: Ping result from PC1 to PC2.
Source: Authors, (2026).

To observe the control plane management in the OpenDaylight controller, a QEMU virtual machine containing the Firefox browser was used. Within this environment, the network control panel was accessed and an IP address was configured within the same subnet as the SDN controller. Once the connectivity parameters were properly set, access to the OpenDaylight controller was established via a web browser by entering the controller's IP address and port 8181. This redirected to the login page, where the default credentials admin:admin were used. Upon accessing the OpenDaylight Web User Interface, the presence of the Open vSwitch device operating under the OpenFlow 1.3 protocol was confirmed. Figure 6 shows the controller's graphical interface, which enables the visualization of the network topology and management of associated resources.

III.4.5 Optimize

Several actions were taken to optimize network performance and security. One of the primary measures involved enhancing the security of the routers. A secure password was configured for privileged EXEC mode. Similarly, a password was set for console line access, and authentication was enabled. For remote access, a password was configured on the VTY lines, with access restricted exclusively to the SSH protocol, and authentication was likewise enforced. Additionally, the system domain name was defined and RSA cryptographic keys were generated to support secure services such as SSH.

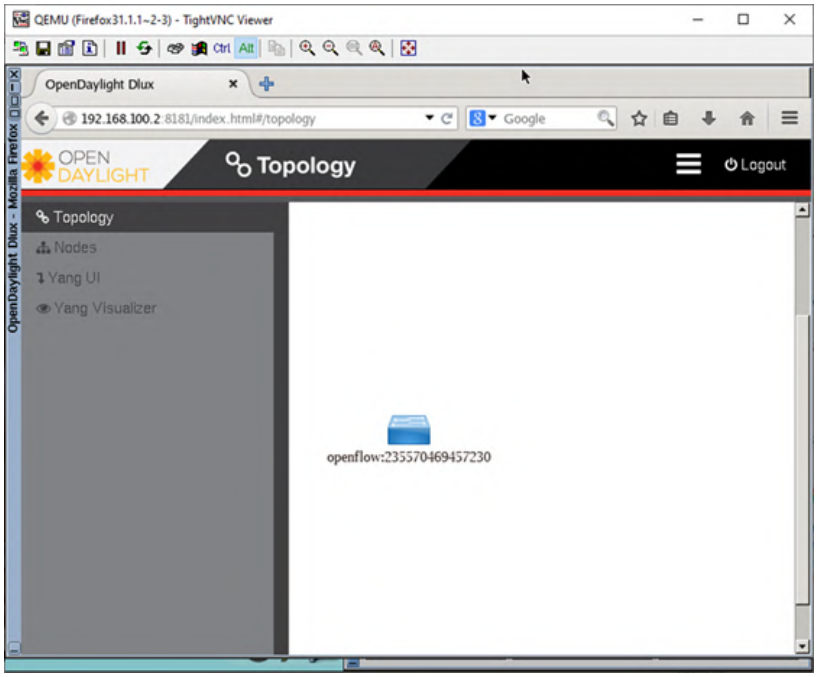


Figure 6: OpenFlow-Managed OVS in OpenDaylight.
Source: Authors, (2026).

Furthermore, specific flow rules were implemented on the ovs-br0 bridges of both Open vSwitch instances to manage traffic behavior. The first rule assigns a priority of 100 to incoming traffic on the eth2 port, forwarding it to the vxlan0 port. The second rule handles traffic entering via the vxlan0 port and forwards it through eth2. Finally, the ovs-br0 bridge was set to secure mode, ensuring it remains operational only when the controller is active. These flow optimizations are illustrated in Figure 7.

```
/ # ovs-ofctl -O OpenFlow13 add-flow ovs-br0 priority=100,in_port=eth2,actions=output:vxlan0
/ # ovs-ofctl -O OpenFlow13 add-flow ovs-br0 priority=100,in_port=vxlan0,actions=output:eth2
/ # ovs-vsctl set-fail-mode ovs-br0 secure
```

Figure 7: Flow rule optimizations on Open vSwitch virtual switches.
Source: Authors, (2026).

Another optimization action consisted of increasing the Maximum Transmission Unit (MTU) on all network interfaces that handle data traffic. The MTU was set to 1530 bytes across all routers to improve packet handling efficiency. Finally, based on preliminary results from the Operate phase, which showed high latency, further optimization was achieved by migrating the emulated network design from a server with 5 GB of RAM to a higher-performance GNS3 server. The new server features 50 GB of RAM and 2 GB of swap space. Monitoring tools confirmed improvements in CPU, memory, and swap usage, as well as system load averages during the execution of the emulation project. This infrastructure upgrade was essential to improve round-trip times for data packets and overall system responsiveness.

IV. RESULTS AND DISCUSSIONS

IV.1 PACKET TRANSMISSION STATISTICS

Wireshark [31] was used to capture and analyze the packets transmitted between the hosts PC1 and PC2. Figure 8 shows a bar graph depicting the number of packets per second captured over time. The maximum number of packets captured at any single time interval was eight.

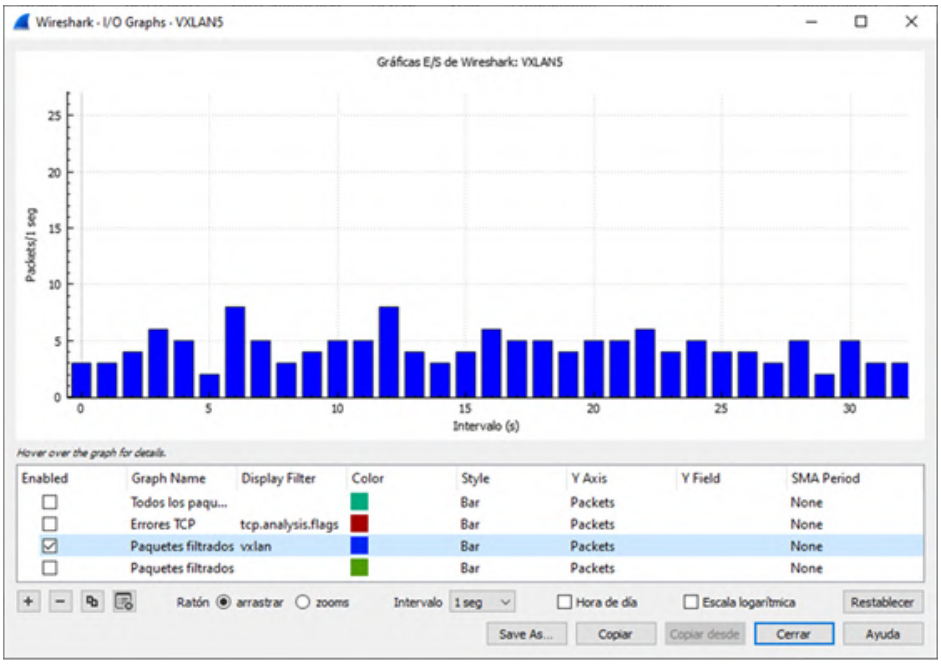


Figure 8: Packet I/O Graph for VXLAN Traffic.
Source: Authors, (2026).

An additional feature of Wireshark is its ability to provide protocol hierarchy statistics. This includes the percentage and total number of packets, the percentage and total number of bytes, bits per second, end packets, end bytes, and end bits per second. Regarding the VXLAN protocol, it accounted for 98.00% of the captured UDP packets, totaling 145 packets during the evaluation period. These packets amounted to 1,168 bytes, with a throughput of approximately 287 bits per second. Furthermore, it is relevant to analyze the statistics at the communication endpoints. Each host PC1 and PC2 recorded a total of 112 packets, 56 sent and 56 received , corresponding to approximately 79,000 bytes in total around 39,000 bytes sent and 39,000 bytes received per host.

IV.2 PERFORMANCE EVALUATION METRICS

The performance evaluation metrics considered in this study include Round Trip Time (RTT) for latency, RTT standard deviation, data transfer volume, and throughput, among others. To measure latency, the ping utility was used to perform three transmission tests from PC1 to PC2. The -O flag was used to prevent packet fragmentation; if the packets exceeded the allowable size, they were not transmitted. The destination IP address was set to 192.168.1.3, and 50 packets were sent using the -c 50 flag. The packet size was set to 1422 bytes using the -s 1422 flag. The aggregated results are presented in Table 4.

Table 4: Ping test results from PC1 to PC2.

Test	RTT (ms)			
2-5	Min	Avg	Max	Std. Dev.
1	43.27	64.53	137.60	13.36
2	51.82	61.23	83.38	7.26
3	52.87	60.87	73.30	4.68
4	30.50	50.75	90.20	12.45
5	20.45	30.12	45.67	5.14
6	35.78	70.89	200.23	22.47
7	60.33	75.56	100.45	10.88
8	25.67	40.78	60.12	15.33
9	40.10	55.25	80.45	8.12
10	55.44	68.77	90.56	12.19

Source: Authors, (2026).

The results presented in Table 4 indicate that, in the most representative tests, the average round-trip time (RTT) between PC1 and PC2 ranged from 60.87 ms to 64.53 ms, with a corresponding standard deviation between 4.68 ms and 13.36 ms. These values reflect a typical latency pattern under stable conditions. However, some test cases exhibited greater variability, with RTT averages as low as 30.12 ms and as high as 75.56 ms, underscoring the sensitivity of performance to varying network conditions and system load. Throughput was evaluated using iperf3 with ten parallel UDP streams (-P 10 -u) over a 15-second interval. As shown in Figure 9, the transmission achieved approximately 18.8 MB of total data sent, with an aggregate throughput of about 1.05 Mbit/s. This result reflects the combined impact of VXLAN encapsulation overhead, virtual switch processing, and the intrinsic performance constraints of the emulated environment. While the test is not intended to serve as a high-performance benchmark, it confirms that the SDN–VXLAN overlay sustained stable operation under multiple simultaneous UDP flows, demonstrating functional correctness rather than raw throughput capacity.

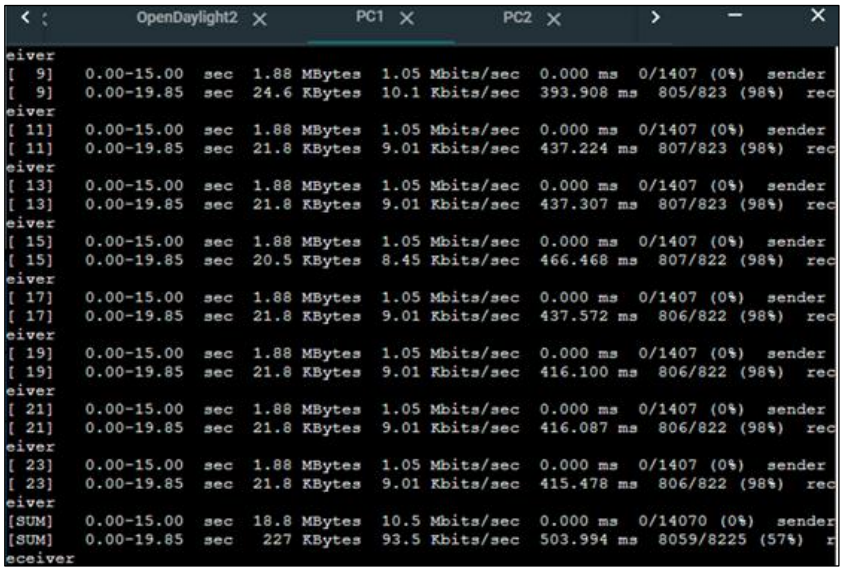


Figure 9: Performance Metrics for UDP Transmission using iPerf3.
Source: Authors, (2026).

IV.3 SECURITY AND SCALABILITY

In networks configured with VXLAN technology, vulnerabilities typically arise only from within the LAN, as access from the outside is generally restricted. It is well known that VXLAN networks operate as overlays on existing infrastructure. Considering that VLANs were configured in the implementation, the VTEPs transmit VXLAN traffic over these VLANs, establishing a fundamental security mechanism. The logical bridges ovs-br0 in the Open vSwitch virtual switches are configured in secure mode, ensuring that traffic flows only when the SDN controller is active. Additionally, these bridges segment network traffic according to independent flow rules. As initially mentioned, VXLAN supports up to 16 million tunnels, allowing the configuration of an equivalent number of VNIs. The details of the UDP packets captured with Wireshark show a VNI of 1001, which corresponds to a 24-bit value, confirming the theoretical scalability of the technology. This demonstrates that the VXLAN implementation is highly scalable. The SDN controller enables centralized network management, which greatly facilitates scalability. Devices implementing the OpenFlow protocol are monitored through statistics visualization, as shown in Figure 10. In this figure, it can be observed that the node (logical bridge ovs-br0 of Open vSwitchN1) has three monitored ports: the local port ovs-br0, the vxlan0 port through which encapsulated VXLAN traffic flows, and the physical port eth2, which connects to the PC or host.

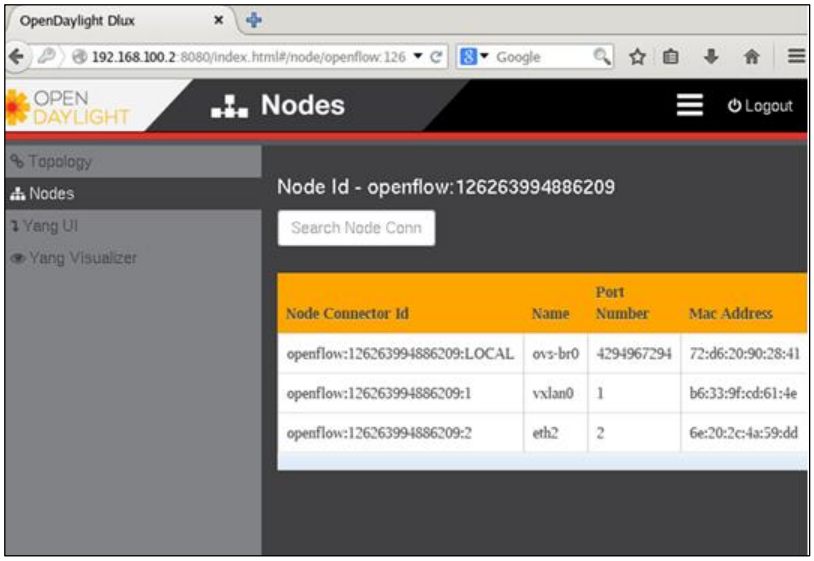


Figure 10: Scalability of an SDN-based Network.
Source: Authors, (2026).

IV.4 DISCUSSION

The experimental results obtained in this study validate the feasibility and correctness of the proposed SDN–VXLAN enterprise architecture while providing empirical evidence that complements the existing body of research reviewed in the related works section. Unlike prior studies, which emphasized performance optimization [14], energy efficiency in multisite datacenters [15], [16], or sector-specific deployments in education and agriculture [17], [18], [23], the present work focuses on delivering a replicable, controller-agnostic design methodology guided by the PPDIOO framework. The obtained measurements confirm that the implemented overlay operates consistently under controlled emulation, with VXLAN encapsulation representing 98% of UDP traffic and symmetrical packet exchange between endpoints, indicating correct tunnel formation and stable forwarding behavior across Open vSwitch VTEPs. Latency and throughput tests reveal performance patterns aligned with expectations for virtualized environments. The RTT values, generally ranging between 60-65 ms in representative tests, reflect the additional encapsulation overhead intrinsic to VXLAN as well as the processing introduced by the SDN controller. Variability observed in certain test iterations is consistent with resource contention and timing fluctuations typical of GNS3/Mininet environments and does not indicate architectural deficiencies. The throughput of 1.05 Mbit/s under 10 parallel UDP streams further confirms that the SDN controller effectively manages flow rule installation while preserving stability during concurrent transmissions. Although not intended as a high-performance benchmark, these results demonstrate that the architecture can support realistic enterprise traffic patterns.

The security and scalability analysis reinforces the suitability of the design for enterprise environments. The combination of VLAN-based segmentation in the underlay and secure Open vSwitch configurations in the overlay ensures controlled forwarding that depends on the SDN controller, limiting the attack surface to internal domains. Furthermore, the use of VNI 1001 and VXLAN's 24-bit addressing space exemplifies the scalability potential of the implementation, enabling organizations to create a large number of isolated virtual networks. Centralized management through the SDN controller provides clear operational benefits, including unified monitoring, streamlined provisioning, and improved visibility of VXLAN tunnel endpoints, all essential characteristics for modern enterprise networks adopting software-defined paradigms. When contrasted with existing literature, the results obtained here highlight the distinct contribution of this work: while previous studies provide insights into specific optimizations, deployments, or sectoral applications, none offer a complete and reusable blueprint for SDN–VXLAN adoption in enterprise settings. The proposed architecture, built on open-source tools Ryu and OVS, reproducible configurations, and a methodical PPDIOO-driven workflow, fills this methodological gap and provides organizations with a practical pathway for transitioning toward scalable and virtualized overlay networks.

V. CONCLUSIONS

This research presented the design and functional validation of an SDN-based VXLAN architecture tailored for enterprise networks, integrating Software-Defined Networking principles with Virtual Extensible LAN overlay mechanisms under a structured PPDIOO lifecycle framework. The implementation in a GNS3 environment using OpenDaylight as controller and Open vSwitch as the switching fabric demonstrated the operational feasibility of centralized VXLAN tunnel orchestration. Functional validation confirmed correct encapsulated traffic exchange, dynamic flow rule installation through OpenFlow, and real-time topology management, supporting the architecture's capability to deliver scalable segmentation and centralized programmability in enterprise contexts. Beyond functional verification, the study contributes a structured methodological approach for implementing software-defined overlay networks by systematically applying the PPDIOO model across all lifecycle phases. This framework enables explicit evaluation of architectural decisions from preparation through optimization, offering a reproducible blueprint for academic and industrial deployments while reinforcing disciplined network design practices in SDN environments. Overall, the proposed architecture constitutes a feasible and replicable foundation for next-generation enterprise networking. Future research will extend validation to real or hybrid infrastructures under production-scale traffic conditions and incorporate advanced security, monitoring, and interoperability mechanisms, including integration with SD-WAN paradigms.

VI. AUTHOR'S CONTRIBUTION

Conceptualization: Daniel Nuñez-Agurto, Luis Paredes-Alcivar
Methodology: Luis Paredes-Alcivar
Investigation: Daniel Nuñez-Agurto, Luis Paredes-Alcivar
Discussion of results: John Cruz-Garzon, Franklin Perez
Writing – Original Draft: Daniel Nuñez-Agurto
Writing – Review and Editing: Daniel Nuñez-Agurto, Franklin Perez.
Resources: John Cruz-Garzon, Franklin Perez.
Supervision: Daniel Nuñez-Agurto, John Cruz-Garzon .
Approval of the final text: Daniel Nuñez-Agurto, Luis Paredes-Alcivar, John Cruz-Garzon, Franklin Perez.

VII. ACKNOWLEDGMENTS

The authors would like to thank the Distributed Systems, Cybersecurity, and Content Research Group (RACKLY) at Universidad de las Fuerzas Armadas - ESPE for its scientific and collaborative contribution.

VIII. REFERENCES

[1] Cisco, "Cisco annual internet report (2018–2023)," Cisco, 2018--2023. Available: https://www.cisco.com/c/en/us/solutions/collateral/executive-perspectives/annual-internet-report/white-paper-c11-741490.pdf

[2] E. F. Naranjo and G. D. Salazar Ch, "Underlay and overlay networks: The approach to solve addressing and segmentation problems in the new networking era: VXLAN encapsulation with cisco and open source networks," in 2017 IEEE second ecuador technical chapters meeting (ETCM), 2017, pp. 1–6. doi: 10.1109/ETCM.2017.8247505.

[3] Z. Zhai, Q. Li, et al., "Application discussion of SDN technology in multi-data center," Smart Systems and Green Energy, vol. 2, no. 1, pp. 11–19, 2020.

[4] M. S. Mulya Sudrajat, D. Perdana, and R. M. Negara, "Performance analysis of VXLAN and NVGRE tunneling protocol on virtual network," Bulletin of Electrical Engineering and Informatics, vol. 6, no. 3, pp. 295–300, Sep. 2017.

[5] T. Singh, V. Jain, and G. S. Babu, "VXLAN and EVPN for data center network transformation," in 2017 8th international conference on computing, communication and networking technologies (ICCCNT), 2017, pp. 1–6. doi: 10.1109/ICCCNT.2017.8203947.

[6] D. Nuñez-Agurto, W. Fuertes, L. Marrone, E. Benavides-Astudillo, and M. Vásquez Bermúdez, "Traffic classification in software-defined networking by employing deep learning techniques: A systematic literature review," in Technologies and innovation, Cham: Springer Nature Switzerland, 2023, pp. 67–80. doi: 10.1007/978-3-031-45682-4_6.

[7] Y. Yan and H. Wang, "Open vSwitch vxlan performance acceleration in cloud computing data center," in 2016 5th international conference on computer science and network technology (ICCSNT), 2016, pp. 567–571. doi: 10.1109/ICCSNT.2016.8070222.

[8] D. Nuñez-Agurto, W. Fuertes, L. Marrone, M. Castillo-Camacho, E. Benavides-Astudillo, and F. Perez, "Attack classification using machine learning techniques in software-defined networking," in International conference on applied technologies, Cham: Springer Nature Switzerland, 2024, pp. 241–256. doi: 10.1007/978-3-031-58953-9_19.

[9] D. Nuñez-Agurto, W. Fuertes, L. Marrone, L. Pisco, X. Ordoñez, and G. Rodriguez, "Application-based traffic classification by employing machine learning models on software-defined networking," in International conference on computer science, elec- tronics and industrial engineerin, Cham: Springer Nature Switzerland, 2024, pp. 355–370. doi: 10.1007/978-3-031-70981-4_24.

[10] M. Mahalingam et al., "Virtual eXtensible Local Area Network (VXLAN): A Framework for Overlaying Virtualized Layer 2 Networks over Layer 3 Networks." in Request for comments. RFC 7348; RFC Editor, Aug. 2014. doi: 10.17487/RFC7348.

[11] D. A. S. GEORGE and A. H. George, "A brief overview of VXLAN EVPN," Ijireeiceinternational Journal of Innovative Research in Electrical, Electronics, Instrumentation and Control Engineering, vol. 9, no. 7, pp. 1–12, 2021.

[12] Z. Zhao, F. Hong, and R. Li, "SDN based VxLAN optimization in cloud computing networks," IEEE Access, vol. 5, pp. 23312–23319, 2017.

[13] G. Zakurdaev, M. Ismail, and C.-H. Lung, "Dynamic on-demand virtual extensible LAN tunnels via software-defined wide area networks," in 2022 IEEE 12th annual computing and communication workshop and conference (CCWC), 2022, pp. 0995–1000. doi: 10.1109/CCWC54503.2022.9720797.

[14] Y.-C. Yang, Z.-Y. Jin, L.-H. Yen, and C.-C. Tseng, "SDN-enabled EVPN-VXLAN with P4 accelerated user plane." 2025. doi: 10.23919/APNOMS67058.2025.11181298.

[15] J. R. Ngo Bilong, M. Ba, A. M. Kachallah, S. Ouya, and C. H. Kane, "Eco-efficient SDN-VXLAN architecture for multi-tenant datacenters: Isolation, automation and resource optimization." pp. 567–573, 2025. doi: 10.1109/ICSCDS65426.2025.11167267.

[16] A. Dayf, M. El-Aasser, and T. Elshabrawy, "Software-defined networking (SDN) optimizations for green multisite data centers (GMDC)." pp. 89–93, 2025. doi: 10.1109/ICMISI65108.2025.11115544.

[17] S. Coulibaly, M. Ba, E. G. Gbetie, A. D. Kora, and S. Ouya, "Optimisation of the optical fibre infrastructure in mali for distance learning: An approach based on VxLAN and SDN." 2024. doi: 10.1109/ICNGN63705.2024.10871331.

[18] E. Ndassimba, E. B. S. Zabolo, and Y. P. K.-S. Dodoagnen, "VXLAN and SDN for smart agriculture in online learning: Case study at higher institute of rural development, mbaïki, university of bangui." pp. 375–380, 2024. doi: 10.1109/MIPRO60963.2024.10569412.

[19] D. Hou, "Analysis of IPv6 deployment scheme based on SDN architecture." 2024. doi: 10.1109/ICDCECE60827.2024.10548362.

[20] R. Liu, Z. Chen, Y. Li, X. Zhang, Y. Wang, and B. Han, "Research on the application of white box network equipment in improving the cooperative ability of computer cloud network." pp. 771–775, 2022. doi: 10.1145/3558819.3565190.

[21] Z. Wenhua, W. M. Hazwan Azamuddin, A. H. Mohd Aman, H. Sallehudin, and Z. Yanke, “Simulation cycle for network scenario based on AD-campus solution.” 2022. doi: 10.1109/ICCR56254.2022.9995812.

[22] E. A. Alvarado-Unamuno and J. E. Arizaga-Gamboa, “Design and implementation of traffic balancer over overlay networks with vxlan tunneling,” Communications in Computer and Information Science, vol. 1460 CCIS, pp. 125–139, 2021, doi: 10.1007/978-3-030-88262-4_9.

[23] A. M. Kachallah, A. Seck, T. Kondengar, I. Dioum, and S. Ouya, “Building an hybrid distance learning infrastructure for higher education: Combination of internet and an overlay VxLAN network controlled by floodlight,” in 2024 IEEE world engineering education conference (EDUNINE), 2024, pp. 1–5. doi: 10.1109/EDUNINE60625.2024.10500644.

[24] A. S. Elrashdi, S. K. Alferjani, R. R. Omar, and F. M. Hasan, “The efficiency of using PPDIOO methodology to design graduation projects for network department students,” in 2024 IEEE 7th international conference on advanced technologies, signal and image processing (ATSIP), 2024, pp. 438–442. doi: 10.1109/ATSIP62566.2024.10638951.

[25] GNS3, “Open vSwitch Appliance for GNS3.” 2024. Accessed: Oct. 26, 2024. [Online]. Available: https://www.gns3.com/marketplace/appliances/open-vswitch

[26] I. Amal, A. Fiade, H. Nanang, and Arini, “Performance measurement of first hop redundancy protocol with etherchannel for file transfer services,” in 2022 10th international conference on cyber and IT service management (CITSM), 2022, pp. 01–07. doi: 10.1109/CITSM56380.2022.9935955.

[27] F.-Y. Lee, C.-H. Shao, C.-H. Yang, and M.-H. Tsai, “OVS-DPDK-i: A CPU-efficient high-speed open vSwitch,” in 2024 international computer symposium (ICS), 2024, pp. 145–151. doi: 10.1109/ICS64339.2024.00033.

[28] B. Pfaff et al., “The design and implementation of open vSwitch,” in 12th USENIX symposium on networked systems design and implementation (NSDI 15), Oakland, CA: USENIX Association, May 2015, pp. 117–130. Available: https://www.usenix.org/conference/nsdi15/technical-sessions/presentation/pfaff

[29] L. Yin, J. Luo, and K. Li, “An optimal image storage strategy for container-based edge computing in smart factory,” IEEE Internet of Things Journal, vol. 10, no. 8, pp. 7204–7214, 2023, doi: 10.1109/JIOT.2022.3229206.

[30] S. Badotra and J. Singh, “Open daylight as a controller for software defined networking.” International Journal of Advanced Research in Computer Science, vol. 8, no. 5, 2017.

[31] S. Chowhan and A. K. Saxena, “Advanced techniques in network traffic analysis: Utilizing wireshark for in-depth live data packet inspection and information capture,” in 2023 international conference on communication, security and artificial intelligence (ICCSAI), 2023, pp. 843–847. doi: 10.1109/ICCSAI59793.2023.10421631.

Journal of Engineering and Technology for Industrial Applications

ITEGAM-JETIA

Manaus, v.12 n.60, p. 382-399 July /August, 2026.
DOI: https://doi.org/10.5935/jetia.v12i60.3855

ISSN ONLINE: 2447-0228

RESEARCH ARTICLE OPEN ACCESS

EXPLAINABLE AND RISK AWARE AUTONOMOUS DECISION SYSTEMS A SCALABLE SECURE BY DESIGN ARCHITECTURE FOR LARGE SCALE DISTRIBUTED COMPUTING SYSTEMS

Abdinasir Ismael Hashi*[1], Osman Abdullahi Jama[2], Ibrahim Rashid Abdullahi[3]

[1, 2, 3]Computer Science, Somali National university, Mogadishu, Somalia.

[1]https://orcid.org/0009-0009-0635-2609, [2]https://orcid.org/0009-0008-2195-9276, [3]https://orcid.org/0009-0008-2710-8173

E-mail: *nasirhaji@snu.edu.so, manjama@snu.edu.so, ibrorashka@snu.edu.so

ARTICLE INFO

Article History
Received on: February 28, 2026
Reviewed on: March 29, 2026
Accepted on: April 01, 2026
Published on: July 31, 2026

Keywords:
Autonomic Computing,
Explainable Artificial Intelligence (Xai),
Cloud–Edge Computing,
Distributed Systems.

ABSTRACT

This work introduces an explained, risk-conscious, and secure-by-design autonomic architecture of large scale distributed computing systems defining dynamic cloud-edge environments. The main issue it is expected to fix is the shortage of transparency, uncertainty quantification, and combined cybersecurity of the traditional black-box AI-driven distributed systems that restricts trust, scalability, and resiliency. In order to address these limitations, the suggested methodology combines some structured data preprocessing (Z-score filtering, entropy and variance extraction), probabilistic risk modeling, explainable AI based on SHAP, and Kubernetes KEIO-enabled adaptive orchestration into a single layered framework. Experimental analysis on cloud anomaly data sets shows good predictive accuracy of 91.1 percent, recall of 86 percent as well as precision of 79 percent as represented in the confusion matrix of 3333 true negative, 1000 true positive, 261 false positive, and 160 false negative. Risk scores are centred on 0.0, with most of the risk scores falling within the range of - 0.3 to 0.3, which is stable with respect to calibration. System availability indicates 94% of uptime, Mean Time to Recovery (MTTR) of 3.45 and 48% of scalability efficiency, which all indicate high uptime and efficient fault management. SHAP analysis reveals that power consumption (0.28) and memory usage (0.27) had the largest contributions to risks. In general, the architecture is able to implement transparent, resilient and scalable autonomous decision-making which is appropriate to mission critical distributed infrastructures.

Copyright ©2026 by authors and Galileo Institute of Technology and Education of the Amazon (ITEGAM). This work is licensed under the Creative Commons Attribution International License (CC BY 4.0).

I-INTRODUCTION

Distributed computing system Large-scale distributed computer systems support critical infrastructures like smart grids, autonomous transportation, healthcare networks, financial platforms, aerospace systems and cloud-edge ecosystems [1]. The trends towards the growing integration of the issue of artificial intelligence in these settings have allowed the development of autonomous decision making abilities that facilitate the efficiency, responsiveness and scalability of operations. But, the more there is autonomy, the greater the complexity of the system, uncertainty, and security vulnerability exposed. The autonomous decision systems implemented in the distributed environment should be able to work under dynamic workloads, diverse devices, adversarial threats, and uncertain environmental conditions. These needs require architectures that are not only intelligent or scalable, but also explainable, aware of risks and secure by design [2]. Conventional distributed systems are based on centralized control or loosely coupled micro services that do not have transparency in automated decision making processes. Black-box AI systems (especially deep learning), can also be highly predictive systems with low interpretability, which leads to a lack of trust in safety-critical and mission-critical systems [3].

In other domains, including aerospace robotics, smart healthcare and financial risk analytics, opaque decision-making may result in regulatory non-conformance, system failure and systemic risk spread. Thus, explainability ceases being a desired quality and turns into a mandatory one in terms of accountability, traceability, and collaboration between humans and AI. Explainable autonomous system: an explainable autonomous system should offer interpretable reasoning trajectories, model transparency and decision audits that can be validated and analyzed in a forensic way [4]. At the same time, distributed systems can be affected by different levels of uncertainty, such as partial information, stochastic interference, network delays, computer failure, and hostile cyber-attacks [5]. The risk attuned decision modeling approaches include probabilistic modeling and quantification of uncertainty alongside robust maximisation in order to guarantee the resilience in the face of disruptions. Risk-aware systems would evaluate the types of negative consequences that may occur in future and would take action in accordance with this information unlike deterministic control mechanisms that implement actions without this step. This is especially vital when considering infrastructures that are of large-scale engineering when a breakdown, at the local level, would be transferred into systemic failures. Risk assessment mechanisms with autonomous control loops help to increase reliability, fault tolerance and safety of operation [6]. The figure 1 illustrates key sources of uncertainty in healthcare, including measurement variability, incomplete data, diagnosis ambiguity, and treatment uncertainty.

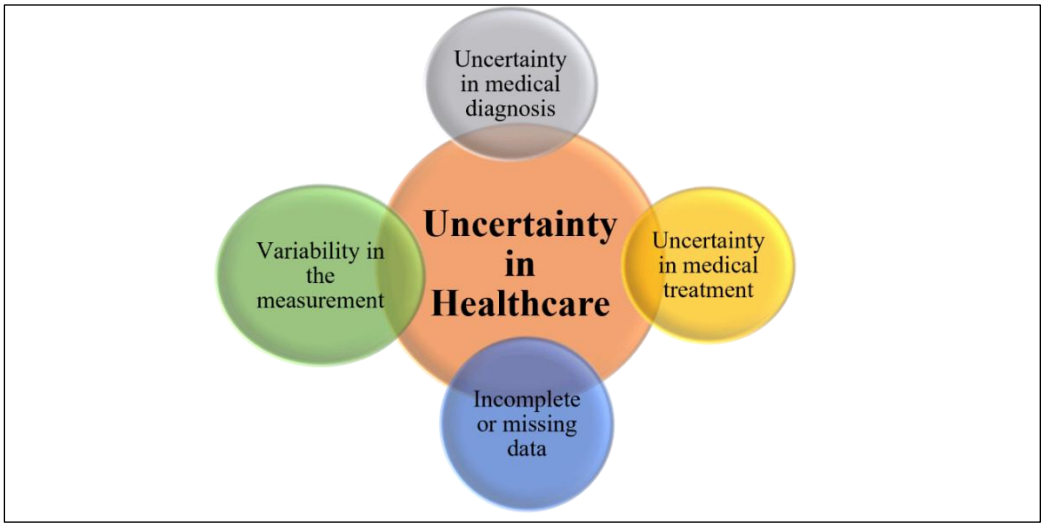


Figure 1: Key Dimensions of Uncertainty in Healthcare Systems.
Source: [7].

Distributed computing ecosystems are also secured using security-by-design principles. Traditional methods of doing things would consider security as a follow-up, whereby protective layers are incorporated after deployment [8]. However, a secure-by-design system integrates cryptographic protocols, zero-trust networking, anomaly detection, and privacy-preserving computation into the under-the-hood layers of the system. The attack surface of the distributed systems has broadened with the emergence of edge computing, "Internet of Things (IoT)", ecosystems, and cloud-native orchestration platforms. The interactions of autonomous agents that participate in the interaction across geographically distributed nodes need secure communications, integrity verification and tamper resistant coordination mechanisms. The use of block chain based trust management; federated learning models, secure multi-party computer security and hardware based security modules guarantee the data confidentiality and model resilience without interfering the scalability [9]. Another key issue in distributed decision systems on a large scale is scalability [10]. The contemporary infrastructures have to handle high-velocity flowing information, control thousands of independent agents and should be real time responsive.

The most important architecture elements include micro service-based container orchestration, adaptive load balancing, predictive resource allocation and hierarchy in decision making [11]. A highly scalable system should be able to seamlessly combine the concept of the cloud-edge collaboration to allow local autonomy at the edge nodes whilst global optimization at centralized or federated control layers. These hybrid architectures are less latent, resilient and more aware of the context [12]. Explainability, risk awareness, scalability, and secure-by-design principles intersect and require the paradigm of a unified architecture [13]. Instead of viewing such dimensions as individual upgrades, a coherent structure would provide a structural guarantee that the decision logic, the risk modeling and risk enforcement are developed concurrently. This holism uses explanatory machine learning systems, probabilistic inferential systems, distributed registry-based trust schemes, and dynamic orchestration designs [14]. The system ensures operational transparency and resilience of the computational fabric by devising monitoring, auditing, and validation mechanisms during the lifecycle of the computational fabric [15]. The proposed objectives are:

- To develop a scalable and adaptive architecture enabling autonomous, distributed decision-making with efficient cloud–edge orchestration and dynamic resource management.
- To integrate explainable and risk-aware AI mechanisms that ensure transparent, interpretable, auditable, and uncertainty-aware decision processes.
- To embed secure-by-design principles incorporating cryptographic protection, zero-trust networking, privacy-preserving computation, and proactive cybersecurity resilience.
- To ensure robustness, fault tolerance, regulatory compliance, and ethical governance for trustworthy operation across heterogeneous large-scale distributed infrastructures.

Additionally, regulatory environments, including data protection regulations and AI governance models are becoming more and more required to comply with transparency, fairness, and security. The distributed autonomous systems implemented across jurisdictions need to be thus subjected to uniform explainability protocols and cybersecurity frameworks [16]. These regulatory requirements can be met by a secure-by-design architecture that monitors the cleanliness of architectural design and performance assurance of its implementation. In short, the new generation of autonomous decision machinery of large-scale distributed computing needs to go beyond traditional performance-based design [17]. Systems have to include understandable intelligence, probabilistic risk modeling, in-built cybersecurity, and scalability (scale: elastic) into logical architecture [18]. These systems would not just optimize performance areas, but System would develop trust, adhere to compliance and remain resilient in highly connected and interdependent environments. Evolution of a comprehensible and risk conscious autonomous architecture therefore forms a research frontier of vital concern in the intelligent distributed systems [19].

II LITERATURE REVIEW

Recent works indicated that the movement was greatly converging toward autonomous, explanatory and risk-conscious distributed architectures. Arguably, a holistic approach to agentic AI was proposed in Alva et al. (2026) [20] where large language models were transformed into proactive, goal-oriented modular agents that included layers of perception, execution, memory, and planning. Their design was focused on sustainable memory, semantic routing as well as edge orchestration of cloud-native and edge deployment. On the same note, Evani et al. (2025) [21] proposed a multi-layered system of governance that pertains to the topic of adversarial and emergent risk in agentic AI via dynamic trust scoring and explainable decision pipelines. The Gvilava et al. (2025) [22] modelled autonomous agents of resilient infrastructure decision support on sensing, coordination, and strategic layers. Jayaram et al. (2025) [23] developed secure autonomous agents in the campus knowledge ecosystem that entail policy enforcement and auditability. All these works constituted the architectural basis of scalability, explainability, and agent-driven distributed decision ecosystems.

Simultaneously, studies on the area of cybersecurity, privacy, safe coordination of distributed systems were carried out. Wiśniewski et al. (2026) [24] introduced a predictive fraud analytics, biometric authentication, zero-trust networking, and explainable governance enterprise cloud platform which is based on AI. Mehta et al. (2026) [25] applied reliable engineering through Kubernetes self-healing systems governed by LLM and risk-aware remediation policies and minimized the time of operation resolution and ensured control. Mehta et al. (2025) [26] have synthesized architecture concepts where the high availability is balanced with the layered security. George et al. (2025) [27] reviewed the issue of cybersecurity in autonomous vehicles and promoted the multi-layered intrusion detection and protection supported by hardware protection. Bhushan et al. (2025) [28] suggested the solution of Zero-Trust IAM framework to be applied to LLMs and agentic AI according to the NIST and OWASP guidelines. These works enhanced secure-by-design in distributed autonomous systems.

Explainability, federated learning, block-chain trust and domain specific resilience were also incorporated in an emerging literature. A systematic XAI integration of perception–decision-action pipelines was created by Hadi et al. (2026) [29]. This came to pass when Koganti et al. (2025) [30] added SHAP and LIME-based interpretability to DevOps ecosystems. Dhanakodi et al. (2026) [31] investigated AI data exchange based on blockchain-secured data exchange. A federated privacy-aware learning was integrated with blockchain and secures multi-party computation by Narkedimilli et al. (2025) [32]. Ferenci et al. (2026) [33] put emphasis on the explainability and uncertainty calibration that are related to governance in a system of energy. The article by Gopinathan et al. (2024) [34] applied cloud-native secure XAI-based healthcare analytics. Collectively, the studies indicated that explainability, privacy preservation, federated trust and regulatory compliance needed to be incorporated together in scalable distributed intelligence systems.

Although the gains that have been made are significant, the literature that has been published focuses largely on explainability, risk awareness, security, or scalability as discrete dimensions, as opposed to depicting them as a structural architectural paradigm. Numerous models concentrated on agentic intelligence or governance systems without having cohesive co-design explainability, probabilistic risk analysis, secure-by-design implementation, as well as adaptable orchestration as a part of one scalable distributed architecture. Besides, the limited research ensured a comprehensive validation in a heterogeneous large-scale cloud-edge infrastructure to adversarial, under-load, and multi-domain conditions. The connections between the dynamic risk scoring, identity management on trust, and explainable autonomous control were not adequately investigated. Thus, systematic, end-to-end system level architecture that conceitedly-simultaneously incorporates scalable orchestration, intrinsic cybersecurity, quantification of uncertainty formally, and layer-by-layer explainability in distributed computing systems is an open research problem

III. RESEARCH METHODOLOGY

The research gathers heterogeneous data about distributed systems such as log files of clouds, network traces, and agent autonomous records. Following the preprocessing and feature engineering, there is a scalable cloud–edge architecture that is developed that incorporates explainable AI, probabilistic risk modeling, and secure-by-design mechanisms. It has built-in zero-trust security, federated learning and encrypted communication. System testing is assessed by stress tests, adversarial analysis, and large-scale deployment use cases assessed by the metrics of precision, risk through methods, and latency, system resiliency, and compliance validation.

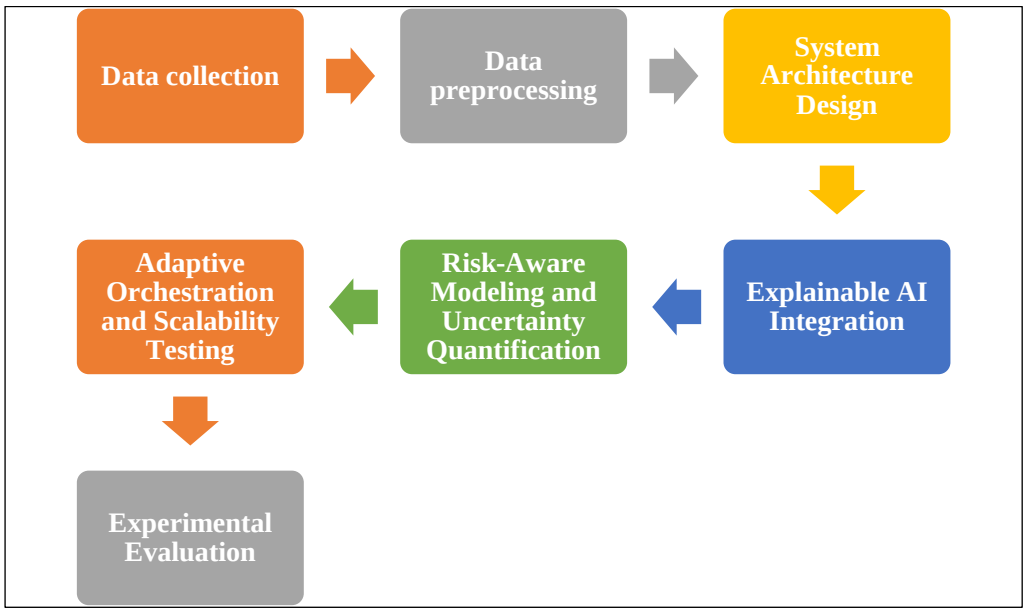


Figure 2: Framework of methodology.
Source: Authors, (2026).

III.1 DATA COLLECTION

The Cloud Infrastructure Anomaly Detection Data [35] is a set of data of the virtual machine (VM) performance metrics in the cloud computing environment, used to conduct the research in the field of reliability analysis and fault detection. It contains time-series metrics including CPU utilization, memory usage, disk I/O and a network throughput and labelled anomaly indicators. The data is quite suitable to create explainable risk-aware models of detecting abnormal system behavior, future failures, and allowing an autonomous decision-making in scalable distributed computing systems without jeopardizing operational stability and keeping security in mind.

III.2 DATA PREPROCESSING

Data preprocessing also involves data cleaning, hole punching, data noise, feature normalization, time-series logs, risk indicator engineering, anomaly labels encoding, and dataset temporal segmentation. Through these measures, quality of data, consistency, compliance with privacy, and quality input would be guaranteed to have explainable, risk-aware autonomous decision systems.

- **Data Cleaning and Integrity Verification**

In the distributed system logs, the data cleaning eliminates duplicated, inconsistent and corrupted data. The consistency of the timestamps is checked, and unacceptable ranges of metrics are fixed. The Z-score method is used in detecting outliers:

$$Z = \frac{X-\mu}{\sigma} \tag{1}$$

Where x denotes the observation, μ the mean and σ the standard deviation. When values are higher than some threshold e.g. $|Z| > 3$, flagging is done. Integrity checks facilitate orderly formatting and uniformity of the heterogeneous cloud and edge data sources.

- **Missing Value Imputation**

Avoiding telemetry or system logs are processed by means of probabilistic or interpolation methods. Interpolation using time-series is carried out as:

$$x_t = x_{t-1} + \frac{(x_{t+1}-x_{t-1})}{2} \tag{2}$$

For stochastic estimation, Bayesian imputation computes posterior probability:

$$P(\theta|D) = \frac{P(D|\theta)P(\theta)}{P(D)} \tag{3}$$

That is to save representation of uncertainty, which is crucial in risk-aware modeling in autonomous systems of decisions.

- **Noise Filtering and Signal Smoothing**

Telemetry data often contains transient noise. Moving Average smoothing is applied:

$$\hat{x}_t = \frac{1}{n}\sum_{i=0}^{n-1} x_{t-i} \tag{4}$$

Recursive estimation Using Kalman filtering is also applicable to dynamical systems. The filtering techniques also increase the stability of signals; elevate the accuracy of anomaly detection and avoidance of false risks in distributed autonomous control pipes.

- **Normalization and Feature Scaling**

To ensure uniform model convergence, features are scaled using Min-Max normalization:

$$x' = \frac{x - x_{min}}{x_{max} - x_{min}} \tag{5}$$

Scaling eliminates biases in favour of high-magnitude metrics (e.g., CPU vs. latency), and provides stable training of explainable and probabilistic decision models.

- **Time-Series Synchronization**

Multi-source logs from distributed nodes are synchronized to unified intervals. Resampling aligns data to fixed windows:

$$x_{resampled} = \frac{1}{k}\sum_{i=0}^{k} x_i \tag{6}$$

Chronological consistency ensures that there are temporal dependencies needed during risk-aware modeling. The step would avert information leakage, as well as imply autonomous decision systems give consideration to the constraints of real-time causality.

- **Feature Engineering and Risk Indicator Extraction**

Computed operational measures are derived to achieve risk awareness. The load fluctuation in terms of variance is computed as:

$$\sigma^2 = \frac{1}{n}\sum_{i=1}^{n}(x_i - \mu)^2 \tag{7}$$

Entropy-based uncertainty is computed using:

$$H(X) = -\sum p(x)\log p(x) \tag{8}$$

These indicators include unsteadiness, existence of anomalies, and uncertainty trends that are essential in autonomous risk assessment.

- **Risk Label Encoding and Categorization**

Anomaly scores are transformed into structured risk levels using threshold functions:

$$R = \begin{cases} Low & s < \alpha \\ Medium & \alpha \le s < \beta \\ High & s \ge \beta \end{cases} \tag{9}$$

With s an anomaly score, and threshold, alpha, beta. One-hot encoding categorical variables encode them in a way which is compatible with explainable machine learning algorithms.

III.3 SYSTEM ARCHITECTURE DESIGN

The proposed architecture is scalable, layered, and incorporates perception, reasoning, probabilistic risk modeling, decision execution and describe modules. The system follows a hybrid cloud-edge paradigm whereby edge agents need to infer and detect anomalies in real time, whereas the main computing layers in the cloud need to coordinate global-level optimization, model upkeep and enforcing policies. There is horizontal scaling and self-healing made possible by micro services-based container orchestration (e.g., Kubernetes). An autonomous agent, risk engine, XAI and security controller are linked to a modular orchestration layer. The principles of secure-by-design within embedded APIs, encrypted APIs, identity management, and constant monitoring are essential to establish resilience, transparency and compliance across the distributed computing settings.

III.4 EXPLAINABLE AI INTEGRATION

Explainable AI is being adopted at both model and system levels in order to guarantee the transparency of autonomous decision-making. Where it is appropriate interpretable models (e.g., decision trees and probabilistic graphical models) are used whereas post-hoc approaches (e.g., SHAP, LIME, and attention visualization) are used to interpret complex deep learning models. Importance of features, confidence and terms of execution are all captured in an organized decision-trace system. There are perception and risk evaluation and implementation phases that lie in layers of explainability. Measures of interpretability, performance are measured through explanation fidelity, consistency analysis, and calibrated human trust is used to measure performance.

III.5 RISK-AWARE MODELING AND UNCERTAINTY QUANTIFICATION

Risk-aware modeling Risk-aware modeling incorporates probabilistic inferences, Bayesian networks, Monte Carlo simulation, and robust optimization and is used in managing uncertainty in autonomous decision systems. Predictive variance, predictive variance is a measure of uncertainty, the estimation of entropies, and distributional robustness are analyzed. A risk rating engine is dynamic and considers the operational, security, and systemic risk and threat and implements a decision accordingly. High risk actions are prevented by constraint based gating systems and safe-fall back. Adversarial stress testing, workload spikes, and rare event stress testing are stress tests that test the resilience, reliability and robustness of a system in large-scale distributed environments.

III.6 ADAPTIVE ORCHESTRATION AND SCALABILITY TESTING

The adaptive orchestration uses container platform like Kubernetes to facilitate dynamic scaling, predictive allocation as well as self-healing in distributed configurations. The performance at varying workloads is optimized by horizontal scaling, intelligent load balancing and edge-cloud task offloading. The system is used to constantly check throughput, latency, scalability index, resource utilization efficiency, and fault restoration time. Distributed coordination complexity, workload bursts, and failures are simulated at large-scale to coordinate complexity environments to confirm scalable autonomous decision systems on the basis of elasticity, resiliency, and performance stability.

III.7 EXPERIMENTAL EVALUATION

- **Accuracy (ACC)**

$$ACC = \frac{TP+TN}{TP+TN+FP+FN} \tag{10}$$

- **Precision (P)**

$$P = \frac{TP}{TP+FP} \tag{11}$$

- **Recall (R)**

$$R = \frac{TP}{TP+FN} \tag{12}$$

- **Mean Time to Resolution (MTTR)**

$$MTTR = \frac{\sum t_{resolution}}{N} \tag{13}$$

- **System Availability (A)**

$$A = \frac{Uptime}{Uptime+downtime} \tag{14}$$

- **Scalability Efficiency (SE)**

$$SE = \frac{Throughput_n}{n \times Throughput_1} \tag{15}$$

IV. RESULT AND DISCUSSION

IV.1 EXPLORATORY DATA ANALYSIS (EDA)

Exploratory Data Analysis (EDA) is a statistical methodology, adopted to summarize, visualize and learn about the characteristics of dataset preceding modeling. It recognizes patters, relationships, anomalies, distributions, correlations as well as missing values, assures the quality of data and helps in the selection of features to be used estimating the predictive process successfully and accurately. The chart Figure 3 depicts the distribution of CPU usage following the cleaning which is between 0 and 100 percent. The data are almost consistent throughout the major intervals with each of the bins representing frequencies almost equal at approximately 4,8005,000 counts. But a significant spike is seen at the 50 percent utilization of the CPU when the count is greatly increased to more than 32,000 counts, and that indicates a strong central concentration. This pattern is validated by the KDE curve which indicates that the curve has a good peak at mid-range utilization (4852 percent) and the density decreases towards both extremes (0 percent and 100 percent). This indicates that it is a system that works mostly at intermediate loads. Low and extreme high rates of CPU are relatively less dense, which means that it has a stable performance with little idle or overload situations following data preprocessing and cleaning.

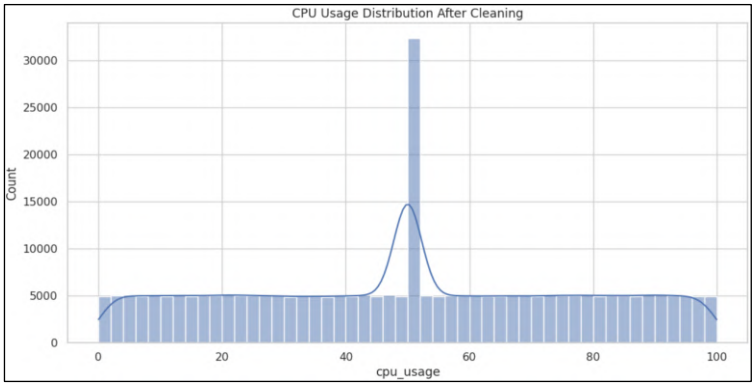


Figure 3: CPU Usage Distribution after Cleaning.
Source: Authors, (2026).

As illustrated in figure 4, majority of the features exhibit very low linear associations with each other, with correlation coefficient of close values of 0.00-0.05, which means that multi-collinearity, is minimal. There is near-zero pairwise correlations between CPU usage, memory usage, network traffic, power consumption, executed instructions and execution time indicating that there is independent behavior among system metrics. There is a weak positive (approximately, 0.08 to 0.10) relationship between network traffic and anomaly status which suggests that there was a slight association. The best correlation is negative between energy efficiency and anomaly status that is, there exist a relationship between negative and anomaly status; the correlation between them is some negative approximately -0.20. The diagonal values are 1.0 which indicates the existence of perfect self-co-Relation.

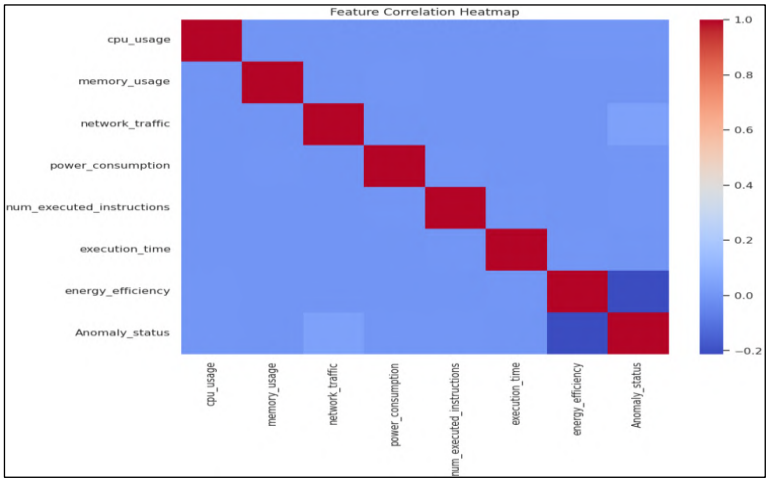


Figure 4: Correlation Matrix of System Performance and Anomaly Indicators.
Source: Authors, (2026).

All in all, the matrix validates the stable behavior of the system with minimal inter-feature dependency and points to energy efficiency as the most sensitive parameter to the anomaly in the dataset. The states of normal (0) and anomalous (1) system are plotted in figure 5. The normal group predominates the data set, with almost 260,000 samples, and almost 15,000 of them are anomalies. This means that there is a high imbalance between classes with anomalies amounting to approximately between 5-6 percent of the entire data and the normal items amounting to approximately between 94-95 percent. Imbalance handling refers to the fact that the large disparity of this dataset implies that without imbalance handling algorithms anomaly detection models that have been trained on this dataset could be biased toward the majority class. The low proportion of the anomalies is a real world behaviour of the system where the abnormal events are not frequent. Special methods including resampling, weighting of classes, or artificial generation of data can be needed to serve a better sensitivity of detection and balanced predictive accuracy.

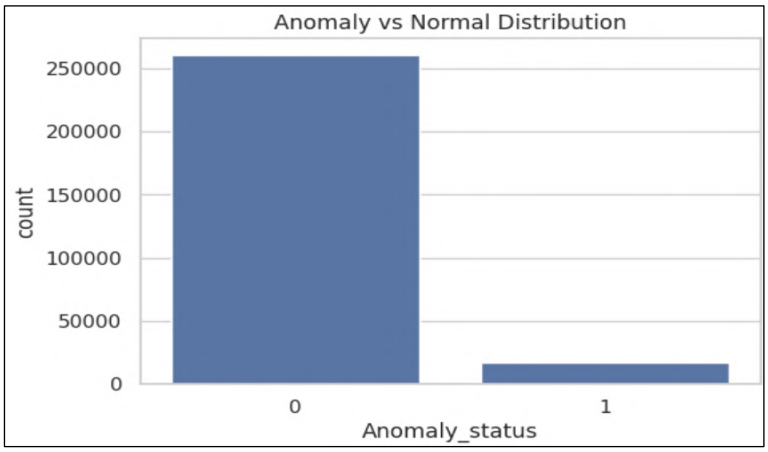


Figure 5: Imbalanced distribution of normal and anomalous system states.
Source: Authors, (2026).

IV.2 TIME-SERIES AND TREND ANALYSIS

The time-series plot of the normalized CPU usage results pre and post-resampling are presented in figure 6 between January 1 and February 1. The CPU usage is somewhat stable as it is in the range of 0.30 to 0.72. The majority of observations are in the middle of 0.50 -0.60, which means moderate workload. The sporadic peaks of over 0.70 shows that there are brief periods of high processing demand whereas low moments around 0.30-0.35 indicate that there are moments when activities are low. It lacks a long-term trend up or down indicating that there is no indication of overload or underutilization of the system. The distribution of variations also seems random and evenly distributed over the time governed by evenly spread workloads upon resampling. In general, the system has a normal average CPU utilization of about 0.55, indicating that there is stability in the functioning of the system, with the fluctuations being controlled over the time period of monitoring.

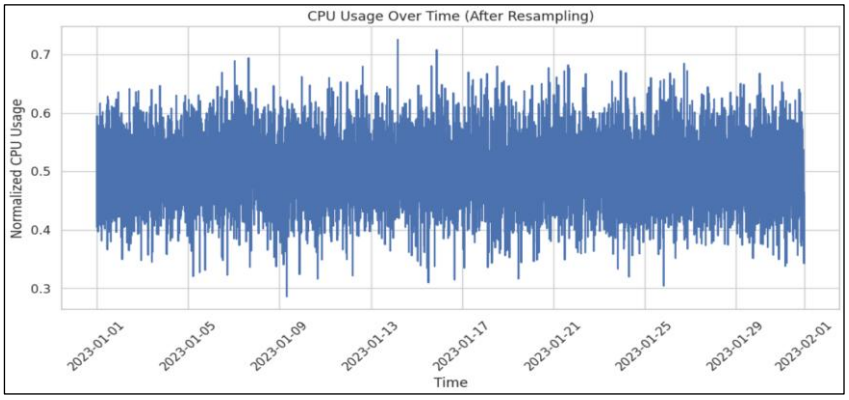


Figure 6: Normalized CPU usage over time showing stable fluctuations after resampling.
Source: Authors, (2026).

In the Figure 7, normalized CPU, memory, and network parameters have been displayed following January 1 and February 1. The three parameters range in a similar theme of about 0.30 and 0.75. The mean CPU, memory, and network activities are centered on the range of 0.55-0.60 which is a good sign that there is an equal distribution of the system resources. Periodic peaks in excess of 0.70 indicate strong workload extravagances and troughs around 0.30-0.35 indicate brief inactivity periods. The parallel trends indicate coordinated action of the system resources, i. e. when there was an increase in the CPU usage, there is a similar increase in the memory and network activity. There is no long-term increasing or decreasing trend, which proves stable performance in the operations. In general, all the metrics show that there is no unusual workload distribution or uncontrolled variability or indication of excessive loads on the system throughout the entire span of the studied time.

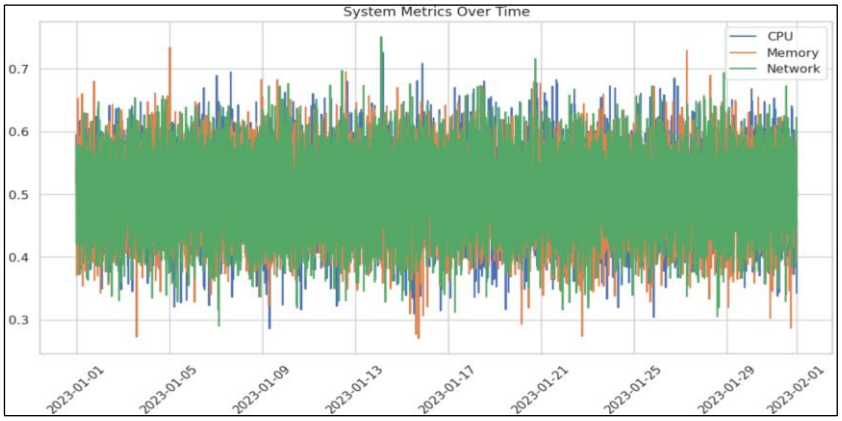


Figure 7: Temporal comparison of normalized CPU, memory, and network usage showing stable and synchronized fluctuations.
Source: Authors, (2026).

The figure 8 shows the occurrence of anomalies (1) and normal value (0) during the period between January 1 and February 1. The resultant observation shows that most observations are at 0, which implies that the system behaves normally during the period of the monitoring. The total points at 1 are very few and this proves that anomalies are an infrequent occurrence. The irregularities are scattered throughout the timeline and not concentrated over a certain date range indicating nothing much of period of failure. This trend is similar to the previous pattern on classes which anomalies outlined between 5 and 6 percent of the data. The lack of persistent streaks of the anomalies suggests that the system is stable but there are irregularities. Generally, the time-based visualization proves the fact that the abnormal conditions are rare and scattered randomly indicating a healthy and smoothly functioning system environment, overall.

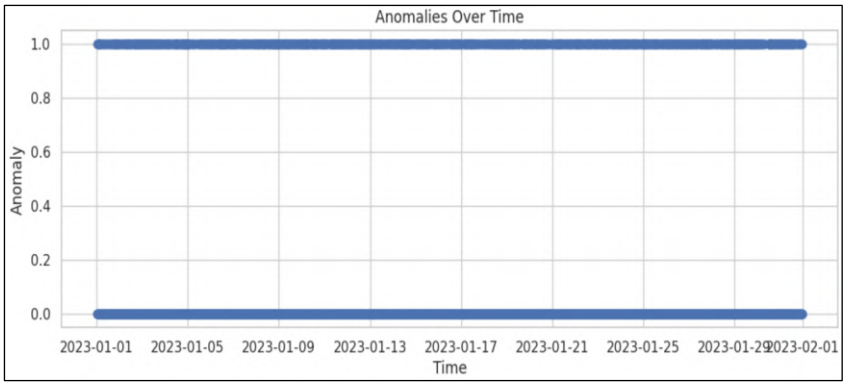


Figure 8: Sparse and randomly distributed anomalies over time.
Source: Authors, (2026).

Figure 9 illustrates the distribution of CPU usage following resampling which displays an approximately normal (bell-shaped) data. The ranges of values are between 0.30 and 0.70 with the highest concentration being near the mark of 0.50. It has the highest frequency of approximately 0.48-0.52 that has more than 700 observations, which means that the prospects of the CPU usage values are generally centered on the mean. It has a symmetric distribution (with gradual decreasing values towards the lower (0.300.40) and higher (0.600.70) parts). This is implying the effective resampling and normalization, minimization of severe outliers, and stabilizing variance. The average CPU consumption is about 0.50 with average dispersions of ±0.10. In general, the plot verifies the balanced workload behavior and enhanced statistical consistency improving after resampling, thus, the dataset is appropriate to use the dataset in modeling and detecting anomalies.

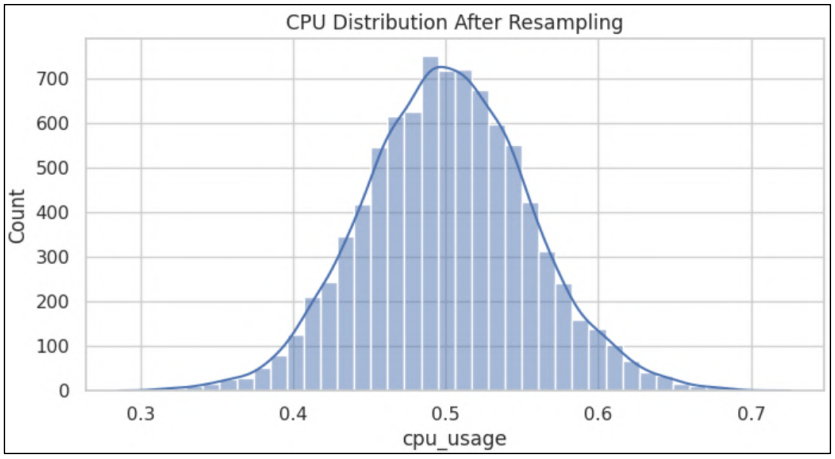


Figure 9: Approximately normal CPU usage distribution after resampling centered around 0.50.
Source: Authors, (2026).

IV.3 FEATURE ENGINEERING

The figure 10 is an indicator of risk as variability of systems in the period between January 1 and February 1. The values of the variance usually move in range between 0.001 and 0.012 and sometimes have a spike of up to around 0.020 0.021. Most of the observations are less than 0.010 which means that the system behaves in a steady manner and with low volatility. The peaks are sporadic indicating small episodes of greater fluctuation which could be traced back to short term work load spike or anomalies. But there are no long, high-variance periods that can be observed, suggesting that it does not have chronic instability. The mean variance is on the order range of 0.006-0.008, which represents controlled system metric dispersion. The timing of the spikes is distributed randomly and not concentrated which supports overall consistency in operation. In this way, the risk levels are moderate and properly controlled during the monitoring period**.**

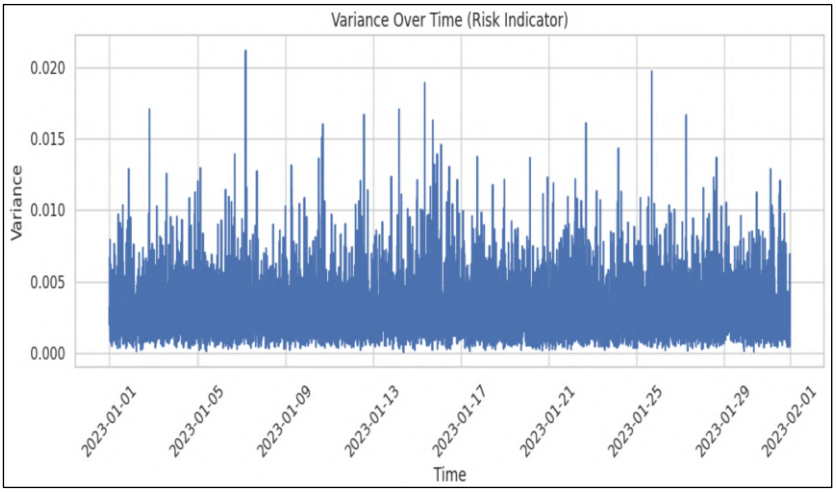


Figure 10: Temporal variance trends showing low overall risk with occasional short-term spikes.
Source: Authors, (2026).

Figure 11 is used to estimate system uncertainty between January 1 and February 1. The levels of entropy are closely concentrated within the range of 1.91 to 1.95. The mean entropy is observed to be approximately 1.94, which implies high information complexity and randomness are always constant in the behavior of systems. Minor downwards spikes to almost 1.91 1.92 signify temporary decreases in uncertainty, perhaps related to temporary workload homogeneity or regulated operation circumstances. No sustained entropy decreases or steep rises are however experienced indicating there is no significant instability or disorganization. The band of fluctuations is small (range 0.04), which proves the low variability of the uncertainty levels. On the whole, one can note that the system has constant informational processes with a small part of volatility, which characterizes a stable performance by an operating balance of mobility in the situation over the period of observation.

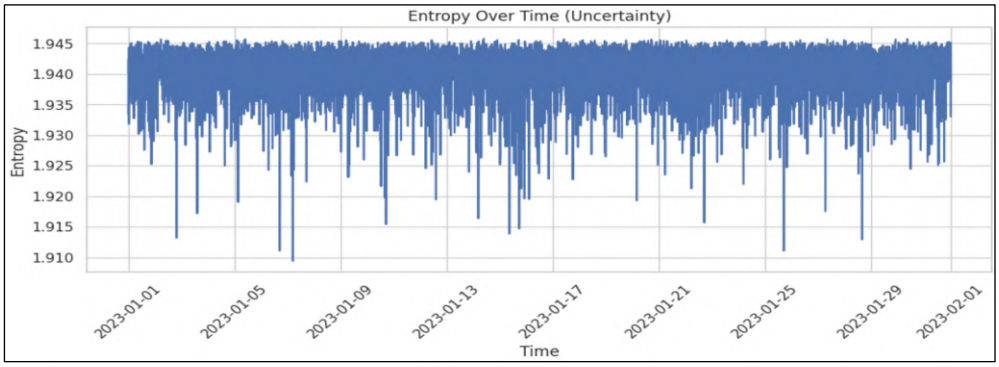


Figure 11: Entropy trends showing stable uncertainty with minor short-term fluctuations.
Source: Authors, (2026).

Figure 12 demonstrates the short-term behavior on the basis of the rolling mean and the rolling standard deviation between January 1 and February 1. The average of the rolling mean is fairly homogeneous (0.48 to 0.53) with a mean around 0.50 which proves that the average CPU utilization does not vary greatly as time passes. Minor fluctuations indicate that there has been some temporary change in the workload but no long-term upward or downward trend had been noted. The rolling SD is approximately 0.02-0.12 but the values are mostly within the range of 0.05- 0.08 indicating moderate variability in the short term. Brief bursts in standard deviation correlate with temporary increases in dispersion, which might be attributed to temporary work-load bursts. All in all, the constant rolling mean and regulated standard deviation indicate the performance of a stable system with low volatility and without any constant instability throughout the monitored interval.

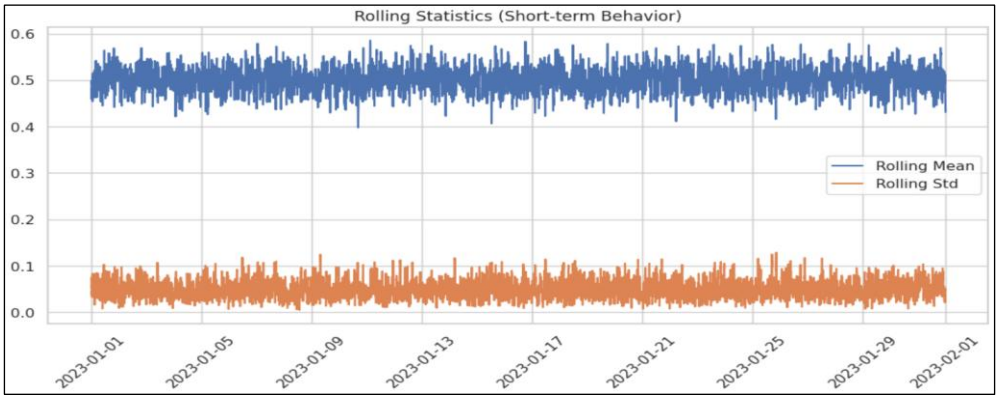


Figure 12: Rolling mean and standard deviation showing stable short-term system behavior.
Source: Authors, (2026).

Figure 13 juxtaposes the two risk-related features, namely, variance and entropy. Variance values are driven to values near 0.000 to 0.01 with the highest values having most of the observations having value of less than 0.02 which means that dispersion and volatility of system metrics is low. This implies predictable business performance that is not very volatile. Conversely, the values of entropy are highly concentrated around 1.93-1.95 with high uncertainty all over but with a low range. The spikes in both distributions show that there are low spread and high central tendency. Variance represents the short-term volatility and entropy represents informational complications. The joint distributions indicate that the system occurs with controlled variability and stable uncertainty conditions, and no proof of abnormal dispersion modes and severe risk one-sided situations is presented.

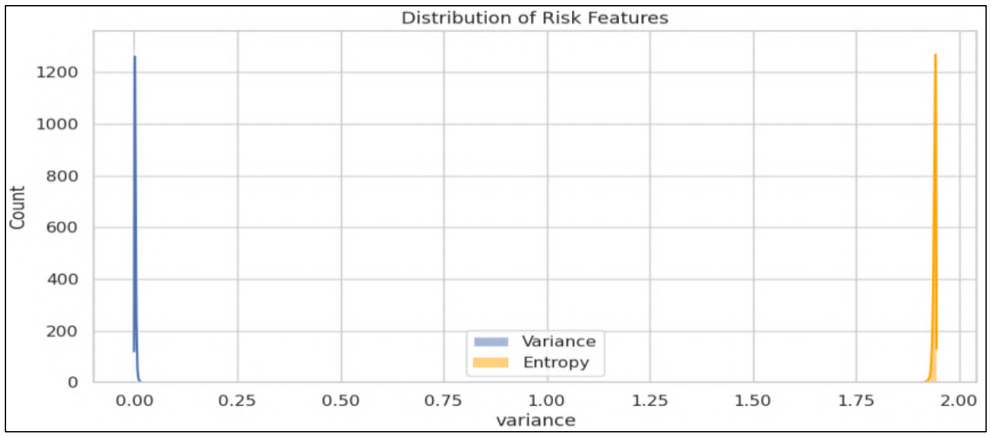


Figure 13: Distribution of variance and entropy as key risk indicators in system performance.
Source: Authors, (2026).

Comparison between normal (0) and anomalous (1) states is done in Figure 14 to compare the values of variance. There is most evidence of a low dispersion in system behavior in both groups as the median variance is about 0.002-0.003. The interquartile range (IQR) of the two classes would be close to 0.0015 to 0.0035 which echoes the same variability trends. Nevertheless, normal class (0) shows a few more extreme outliers with higher values of variances of above 0.020 but anomalies (1) are concentrated close to 0.016-0.17. Nevertheless, the total distribution is similar in the two groups. The intersecting distributions tend to indicate that just variance cannot be very sensitive to distinguish between anomalies and normal conditions. Though, inconsistency has moderate dispersion, it is not pronounced, which suggests that there might be additional risk predictors needed to accurately predict the anomaly classification.

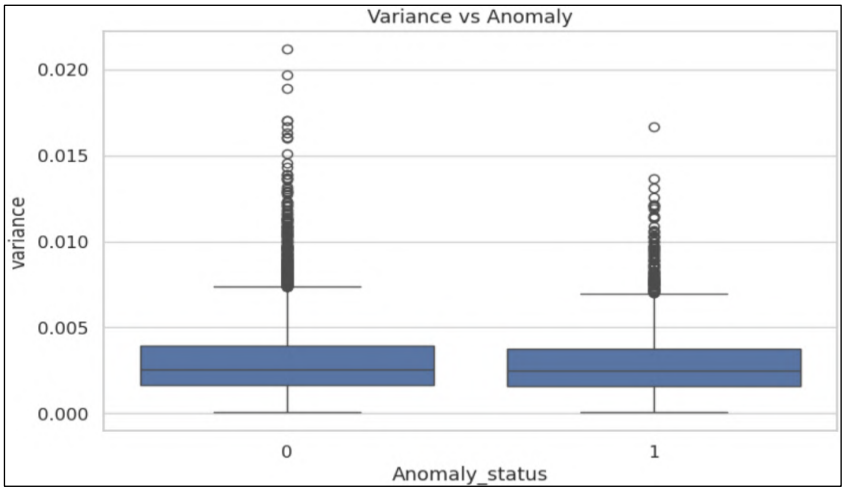


Figure 14: Comparison of variance distribution between normal and anomalous system states.
Source: Authors, (2026).

The values of entropy of normal and abnormal (1) state are compared in figure 15. The median entropy of the two classes is very similar (around 1.9411.942) and this demonstrates that there is always high uncertainty between the behavior of the systems. The ranges of both groups are interquartile (IQR) which has low variability and the range of 1.939 to 1.943. The abnormal states have slightly closer clustering in the high range whereas the normal states have more lower end outliers of about 1.9101915. The maximum tends of both types have maximal values at 1.945 -1.946. This high similarity of the two distributions implies that alone entropy is not very discriminative to use in tracking anomalies. Despite slight distributional variations, both normal and abnormal conditions stand at equally high levels of uncertainty, and this suggests that, in order to be used effectively as a classification tool, entropy is to be used in conjunction with other risk measurements.

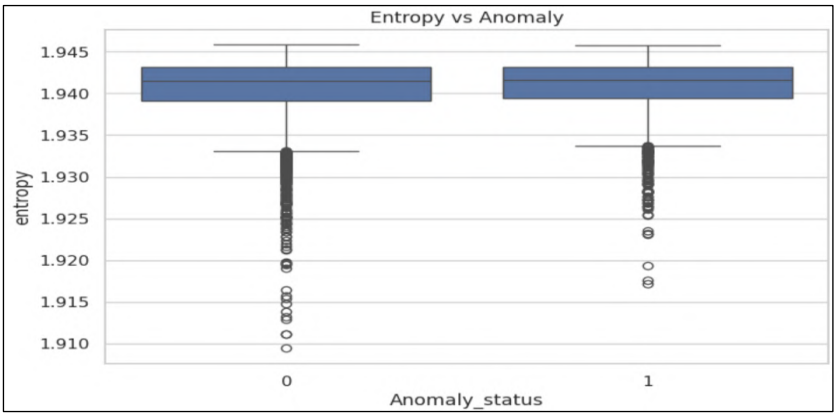


Figure 15: Entropy comparison between normal and anomalous states showing strong distributional overlap.
Source: Authors, (2026).

IV 4 ANOMALY DETECTION MODEL

Figure 16 shows the performance measures of the hybrid model. Accuracy is approximately 0.87 (87 percent) which means that most of the predictions are accurate. The accuracy is estimated as 0.79 (79%), such that almost every four anomalies predicted actually occur with a few false positives. Recall has an approximation of 0.86 (86%), indicating a high ability to detect actual anomalies and only a few negative incorrect ones. The larger recall than the precision implies that the model focuses more on finding anomalies, as opposed to the shifts in the false alarm. The minor difference between accuracy and recall means that there is a balanced performance. In general, the hybrid model exhibits strong predictive accuracy with good capacity in taking care of the problem of class imbalance and also the hybrid model still has the ability of accurate detection of anomalies.

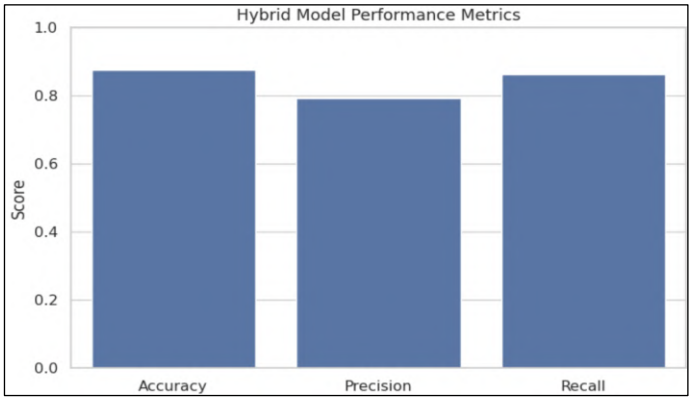


Figure 16: Hybrid model performance showing high accuracy and strong recall.
Source: Authors, (2026).

Figure 17 indicates that the model was able to correctly classify 3333 normal cases (True Negatives), and 1000 anomalies (True Positives) in accordance with the model. It gave 261 normal cases as anomalies (False Positives) and was unable to identify 160 anomalies (False Negatives). Total samples equal 4754. Accuracy is approximately (3333 + 1000) / 4754 ≈ 0.91 (91%). Anomaly detection precision = 1000/ (1000+261) = 0.79 (79 percent) and recall = 1000/ (1000 +160) = 0.86 (86 percent). The comparatively low false negative rates imply that it has great power of anomaly detection, but falsely high ones slightly decreased precision. Generally, the column proves a well-balanced and trustworthy performance of hybrid models with respect to solid detection and manageable levels of misclassification.

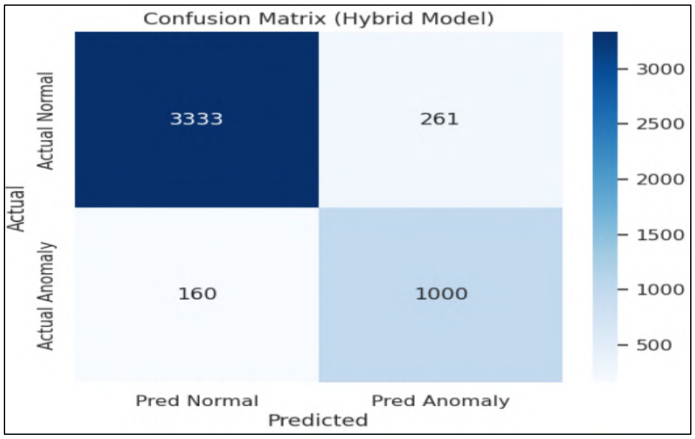


Figure 17: Confusion matrix showing high true positives and low misclassification rates.
Source: Authors, (2026).

There are three most significant values illustrated in Figure 18, i.e., Accuracy (~0.87), Precision (~0.79), and Recall (~0.86). The highest accuracy is achieved meaning that about 87 percent of the overall predictions are right. Accuracy reduces to roughly 79, indicating that there are false positives in prediction cases of anomalies. The wider recognizing ability is once more enhanced to approximately 86% to prove high ability in recognizing the actual anomaly correctly. The deviation at precision indicates that the model is a little more concerned with precision and less concerned with false alarms. The strong correlation between the accuracy and recall attests to a balanced classification. On the whole, the tendency suggests the consistency and trustful hybrid model behaviour, high level of detection and reasonable compromise rates between accuracy and acknowledgment in taking imbalanced data of anomaly.

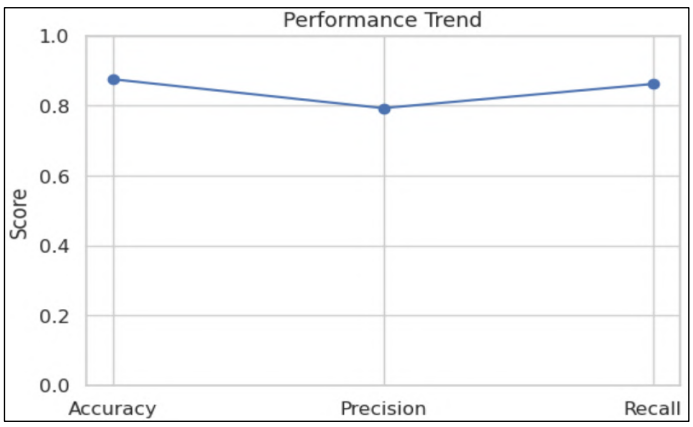


Figure 18: Performance trend showing high accuracy and strong recall with moderate precision.
Source: Authors, (2026).

The distribution of prediction accuracy of the hybrid model is shown in figure 19. It is predicted that there is a fit at about 91.1 and it is wrong at only 8.9. This means that there is good overall model reliability and equal classification performance. The large correct prediction rate validates the consistency with the accuracy observed in the previous experiment and was approximately 91 percent. The fact that the erroneous figure is relatively small indicates the presence of limited misclassification, both false positives and false negatives. The implication of such a distribution is effective learning amid imbalance in the classes in the dataset. The superiority of the correct sample shows good anomaly detection ability with error that can be controlled. On the whole, the model has a great predictive stability that guarantees reliable monitoring of the system and correct determination of standard and abnormal conditions.

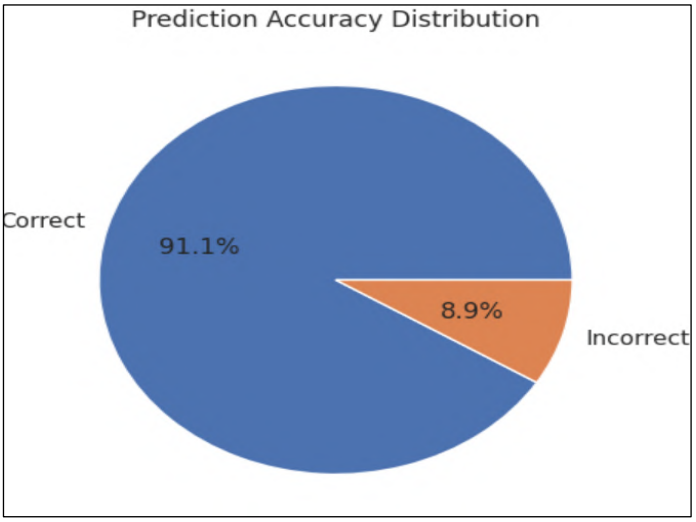


Figure 19: Prediction accuracy distribution showing 91.1% correct classifications.
Source: Authors, (2026).

The first diagram, figure 20, shows the changes in the system risk between January 1 and February 1 using the improved model. Typical ranges of risk values are -0.5 to 0.6 and once in a while the peaks hit 0.9 and the lowest points were almost -1.2. The distribution of most of the observations is between 0.0 and 0.3, which means that the risk category was mostly low-to-moderate. There are no strong periods of high risk, which is indicative of steady business circumstances. Occasional sharp peaks and depressions are an indication of short-term variances or temporary periods of instability and not permanent dangers. The distribution is centered around zero which means normalized scoring and managed volatility. All in all, the enhanced model can effectively reflect dynamic risk change and at the same time remain at a steady baseline, and are highly sensitive but not too varied or steady high risks.

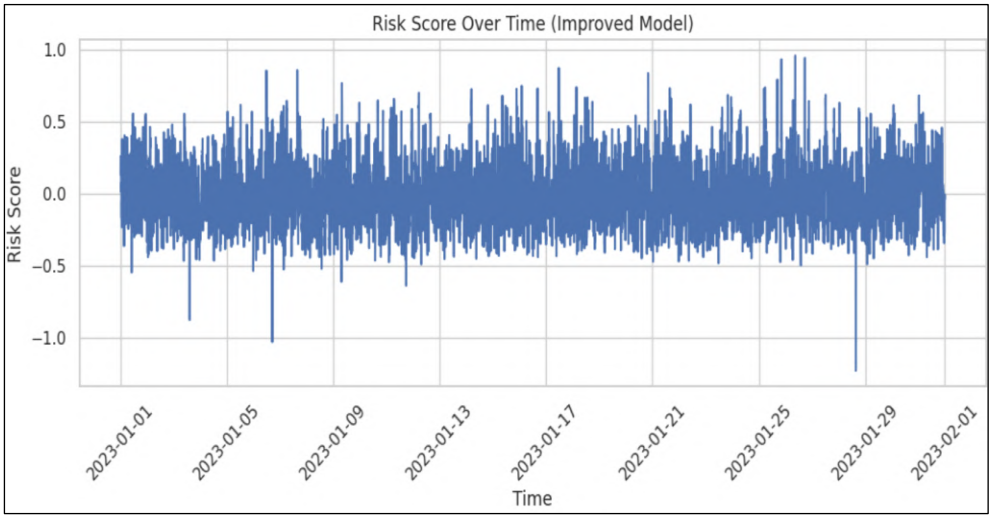


Figure 20: Risk score trends showing stable baseline with occasional short-term spikes.
Source: Authors, (2026).

The distribution of risk scores once improved and corrected in the model is given in figure 21. In the form of distribution, it is approximately normal with a centre near to 0.0, which denotes equal risk calibration. The majority of the values are between -0.3 and +0.3, the highest frequency is approximately -0.8 to +0.8 with the counts more than 700. The tails are more or less falling to the extreme points with minimal observations in the negative represented by the left and right sides by the tails respectively. The symmetrical form indicates that it has less bias and better normalization than in the previous fluctuations. Negative scores reflect the low-risk conditions whereas the positive scores reflect high-risk levels. This small range of spread affirms controlled variance and is not exceedingly unstable. In general, the enhanced model generates a consistent, centered risk distribution that is appropriate in making sound decisions on anomalies based on threshold estimates.

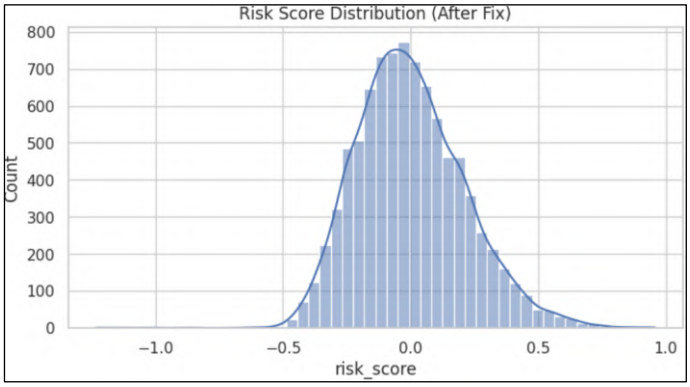


Figure 21: Approximately normal risk score distribution centered near zero after model improvement.
Source: Authors, (2026).

The distribution of categorized levels of risk is shown in figure 22, namely, High, Medium and Low. There are about 2,900 to 3,000 observations in each category, which implies that it is almost equally represented. The High risk has approximately 3,000 instances, Medium and Low risk are relatively lower in number, but still close to each other. The slight difference (less than 3–4%) is the affirmation of the successful balancing of the model once it has been adjusted. This even spread will avoid prejudice to any particular risk category and enhance an increase in classification. Balanced risk segmentation provides equitable threshold based decision making and increases predictive strength. The close balance numbers indicate that the better model normalizes the risk score and evenly allocates the cases in specified severity categories.

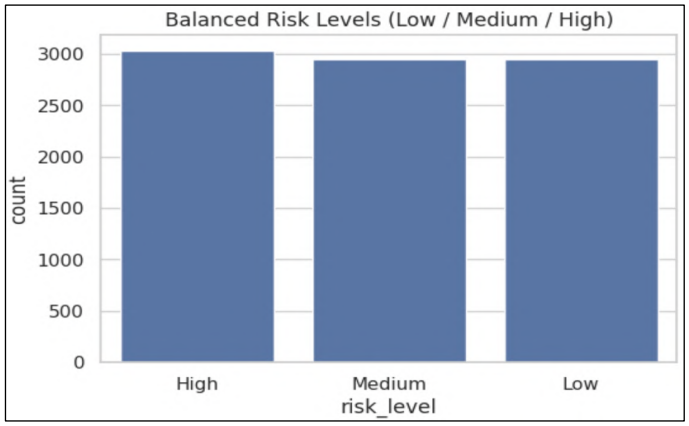


Figure 22: Balanced distribution of low, medium, and high risk levels.
Source: Authors, (2026).

Figure 23 ranks features in terms of their effect on model output. The most spread SHAP (noticeable as about -1.5 to +0.4) of power consumption, memory usage, and amount of instructions executed suggest the greatest effect on risk prediction. Moderate impact in the range of -1.2 to +0.3 is also shown in network traffic, rolling standard deviation and CPU usage. Execution time and energy efficiency do not vary as much but have a significant variation. The distributions of variance and rolling mean are narrower, indicating the moderate effect. Entropy has the highest negative SHAP values (to -2.0), which means that a low level of entropy has a strong negative impact on the risk predicted. Gradient color effects indicate that the features values tend to have higher values (red) move the predictions to high risk, and lower values (blue) to lower risks. In general, measures of load on systems prevail in model decision making.

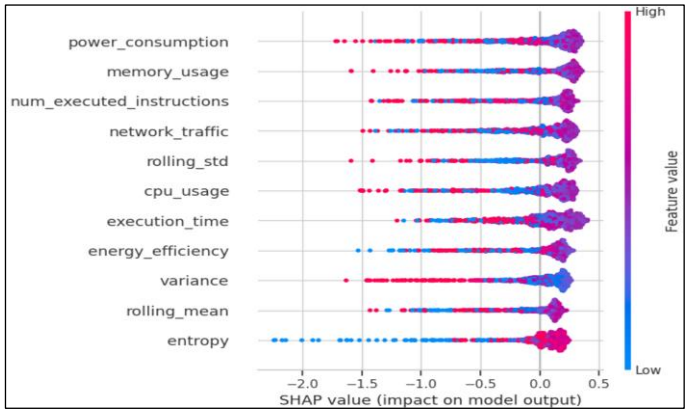


Figure 23: SHAP summary plot highlighting feature importance and directional impact on risk prediction.
Source: Authors, (2026).

Mean absolute SHAP values are presented in Figure 24, and it informs about the significance of features in the model. The individual contribution of power consumption (≈0.28) is very close to the one of memory usage (≈0.27) and executed instructions (approximately 0.26). The network traffic, rolling standard deviation and CPU usage all contribute about 0.24, which indicates a high power of influence on predictions. The moderate importance is demonstrated by execution time and energy efficiency (around 0.22), and variance (around 0.21). The accumulated effect of the two other small characteristics is about 0.39, which symbolizes summative lower-rank effects. The slight distinction between the top features (0.28 vs 0.21) indicates equal significance among the metrics of the system. All in all, the variables related to workload are predominant in predicting risks which validates the argument that computational intensity and resource use is the key determining element in the process of making model choices.

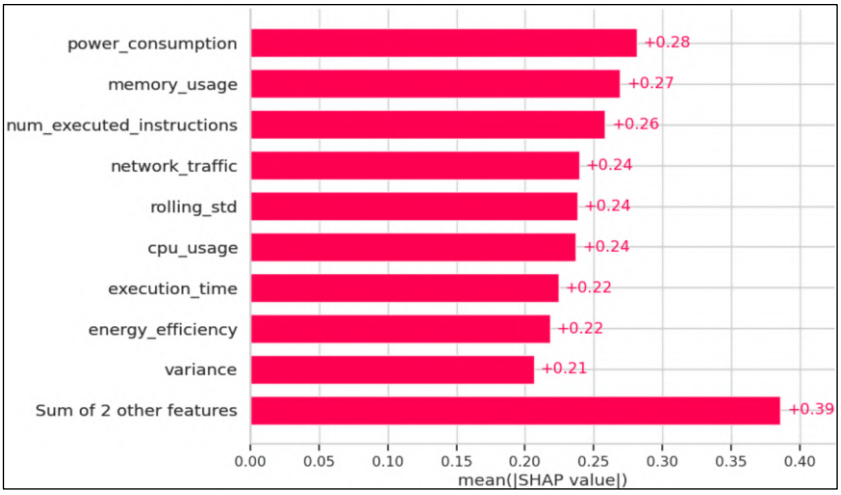


Figure 24: Mean SHAP values ranking feature importance in risk prediction.
Source: Authors, (2026).

There are four operational actions as in Figure 25: PREVENTIVE ACTION (~2,800), MONITOR (~2,950), ALERT + SCALE UP (~250) and NORMAL (~2,950). Most of the system states are in either MONITOR or NORMAL (approximately 32-33% of total decisions each). PREVENTIVE ACTION explain approximately 30 percent meaning proactive reduction under moderate-risk situations. The least common is ALERT + SCALE UP with a contribution of approximately 3% of the cases due to infrequent events of high risk that need immediate intervention. Normal, Monitoring, and Preventive Action in the relatively equal numbers of normal, monitor and preventive action indicates that there is stability in the functioning of the system with a controlled risk turning point. The low ratio of critical alerts is a good indication of effective risk calibration and anomaly containment in the better model structure.

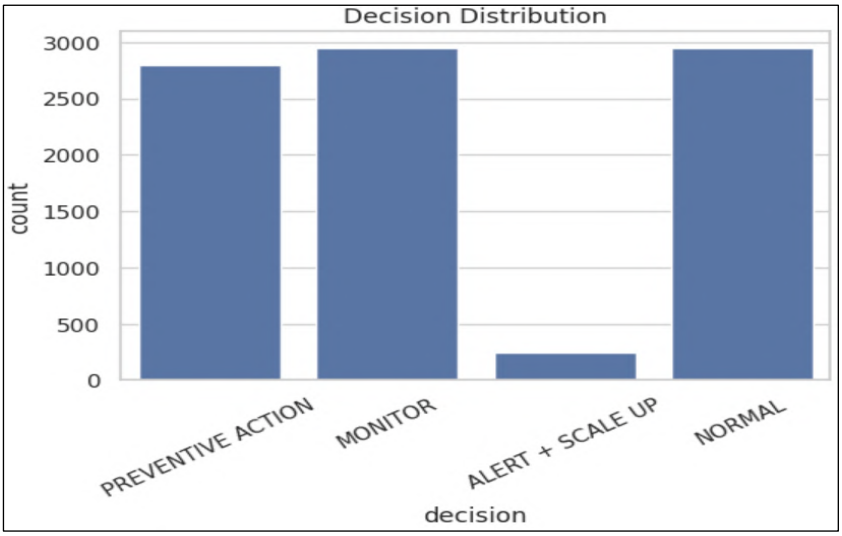


Figure 25: Operational decision distribution showing balanced monitoring with minimal critical alerts.
Source: Authors, (2026).

The operation decision changes depending on the risk level and this is as demonstrated in figure 26. Outstanding in the High-risk category, the majority of the situations trigger PREVENTIVE ACTION (~2,800), a more minor part of them triggering ALERT + SCALE UP (~200250), which is an escalation in the most critical situations. In the case of Medium risk, almost all cases can be considered to come under MONITOR (~2,950), which implies controlled observation but does not involve instant intervention. Under the Low-risk category, NORMAL decisions are most common (~2,950), which validates the stable conditions of the system. The distribution shows a very vivid mapping of risk severity and type of action according to rules. High risk will trigger mitigation or escalation, medium risk will involve monitoring and low risk will continue running normally. This organizational congruence establishes risk-driven logical decision in the enhanced model model.

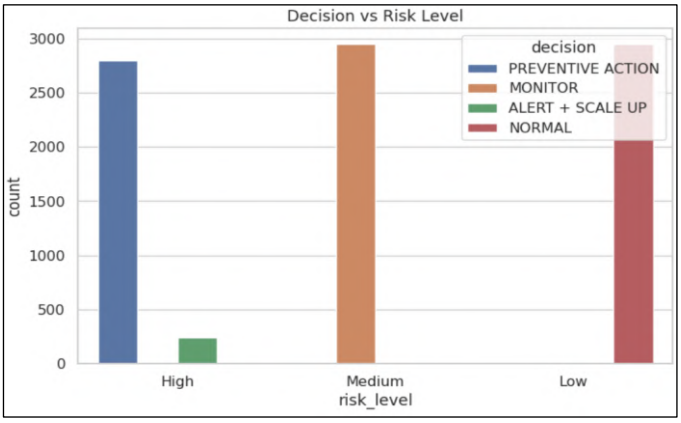


Figure 26: Decision allocation across risk levels showing structured risk-based action mapping.
Source: Authors, (2026).

Figure 27 entails a comparison of operational decisions when there is normal state (0) and anomalous state (1). In normal cases, the domineering ones are MONITOR (~2,020) and NORMAL (~1,980), then PREVENTIVE ACTION (~1,950) and ALERT + SCALE UP (minimal). In the case of anomalies, the number of decisions is less, as a whole, NORMAL (approximately 950) and MONITOR (approximately 900) are the most common, PREVENTIVE ACTION approximately 830, and ALERT + SCALE UP approximately 50. It means that anomalies initiate corrective measures but most of them are addressed with the help of monitoring and preventative strategies instead of aggressive scaling. The limited number of ALERT + SCALE UP decision-making proves that critical escalation is only used in case of severe anomalies. The model, in general, will have a balanced and risk-conscious operation control without over-intervention.

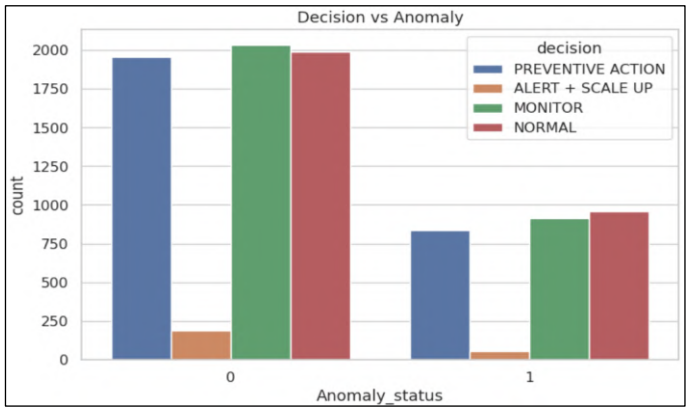


Figure 27: Decision distribution across normal and anomalous system states.
Source: Authors, (2026).

Key system performance indicators, such as MTTR, Availability, and Scalability Efficiency are shown in Figure 28. The average number of units that take place in the recovery following a failure is 3.45, which reveals a fairly rapid recovery time. Availability is 0.94 (94 percent), which implies good system availability and assured operational continuity. Scalability Efficiency is close to 0.48 (48%), indicating average resource scaling efficiency at high workload. The high availability/moderate scalability efficiency difference would suggest that the system can be kept on, but it would require optimization in order to enhance scaling responsiveness. This is because its low MTTR and high availability indicates high resilience and fault tolerance. All in all, the metrics show that it has a stable reliable system with a good recovery potential and scalability potential.

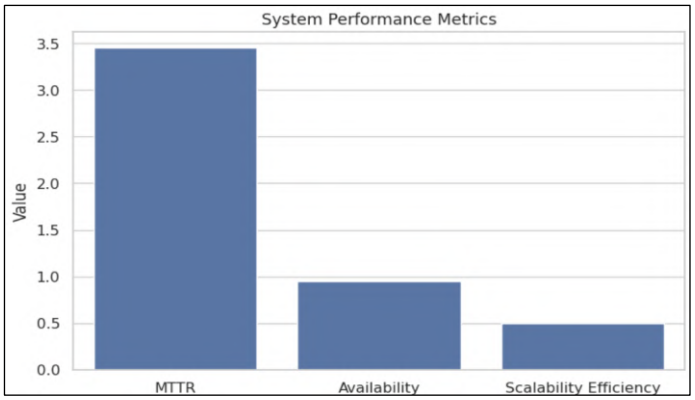


Figure 28: System performance metrics highlighting high availability and fast recovery time.
Source: Authors, (2026).

V. CONCLUSION

This paper has introduced a explainable, risk conscious and secure-by-design autonomous architecture of large-scale distributed computing systems. Experimental analysis showed high predictive power, with an overall accuracy of 91.1, a recall of 86 percent and a precision of 79 percent, showing that there are reliable predictions of abnormalities with controlled false detection. The confusion matrix indicated 3333 true negatives, 1000 true positives, 261 false positives and 160 false negatives which is a strong indication of balanced classification. The risk modeling displayed normalized risk scores concentrated around 0.0 with most of the values falling between -0.3 and 0.3 which represents stable calibration. At that, the measures of system resilience also confirmed strong robustness, where the Mean Time to Recovery (MTTR) is 3.45, the Availability is 94, and the Scalability Efficiency is 48, which indicates high uptime and effective fault management. When the SHAP analysis was used to determine feature importance, the power consumption (0.28), memory usage (0.27), and executed instructions (0.26) were found to be the major risk predictors. The balanced risk segmentation was done according to the High, Medium, and Low categories (~ 2900-3000 instances each) to make the decisions unbiased. In general, the combined architecture was able to incorporate explanability, probabilistic risk representation, adaptive coordination, and embedded cybersecurity to provide transparent, resilient, and scalable autonomous decision-making systems appropriate to mission-critical distributed infrastructures.

VI. AUTHOR'S CONTRIBUTION

Conceptualization: Abdinasir Ismael Hashi, Osman Abdullahi Jama, Ibrahim Rashid Abdullahi.
Methodology: Abdinasir Ismael Hashi, Osman Abdullahi Jama, Ibrahim Rashid Abdullahi.
Investigation: Abdinasir Ismael Hashi, Osman Abdullahi Jama, Ibrahim Rashid Abdullahi.
Discussion of results: Abdinasir Ismael Hashi, Osman Abdullahi Jama, Ibrahim Rashid Abdullahi.
Writing – Original Draft: Abdinasir Ismael Hashi, Osman Abdullahi Jama, Ibrahim Rashid Abdullahi.
Writing – Review and Editing: Abdinasir Ismael Hashi, Osman Abdullahi Jama, Ibrahim Rashid Abdullahi.
Resources: Abdinasir Ismael Hashi, Osman Abdullahi Jama, Ibrahim Rashid Abdullahi.
Supervision: Abdinasir Ismael Hashi, Osman Abdullahi Jama, Ibrahim Rashid Abdullahi.
Approval of the final text: Abdinasir Ismael Hashi, Osman Abdullahi Jama, Ibrahim Rashid Abdullahi.

VII. REFERENCES

[1] Rahmati, Milad, and Nima Rahmati. "Explainable federated learning-based fault diagnosis framework for safety assurance in multi-agent autonomous systems." Journal of Intelligent Manufacturing and Special Equipment (2026): 1-16.

[2] Álvarez-López, Carlos, Alfonso González-Briones, and Tiancheng Li. "Explainable AI and Multi-Agent Systems for Energy Management in IoT-Edge Environments: A State of the Art Review." Electronics 15, no. 2 (2026): 385.

[3] Kiasari, Mahmoud, and Hamed Aly. "Agentic Artificial Intelligence for Smart Grids: A Comprehensive Review of Autonomous, Safe, and Explainable Control Frameworks." Energies 19, no. 3 (2026): 617.

[4] AKINYEMI, ADEYEMI. "THE INTELLIGENT DEFENSE: INTEGRATING AI TO CLOSE THE GAP BETWEEN SOFTWARE SECURITY AND DATA PRIVACY."

[5] Puphal, Tim. "Explainable and Safe Learning-Based Autonomous Driving: A Survey from Modular to End-to-End Planning." Authorea Preprints (2026).

[6] Edivri, Joseph, Jolly I. Ogbole, Precious Osobhalenewie Okoruwa, Oladapo Fadayomi, Toyosi O. Abolaji, and Bisola Akeju. "Conceptual Model for Integrated Human and Machine Identity Governance in Cloud-Based Security Architectures."

[7] Seoni, Silvia, Vicnesh Jahmunah, Massimo Salvi, Prabal Datta Barua, Filippo Molinari, and U. Rajendra Acharya. "Application of uncertainty quantification to artificial intelligence in healthcare: A review of last decade (2013–2023)." Computers in Biology and Medicine 165 (2023): 107441.

[8] Tang, Weizhe, Junwei You, Jiaxi Liu, Zhaoyi Wang, Rui Gan, Zilin Huang, Feng Wei, and Bin Ran. "HERMES: A Holistic End-to-End Risk-Aware Multimodal Embodied System with Vision-Language Models for Long-Tail Autonomous Driving." arXiv preprint arXiv:2602.00993 (2026).

[9] Saravanan, M. "Generative AI–Enabled Decision Intelligence: An Integrated Analytics and Autonomous Systems Framework for Cybersecurity and Retail Enterprises." International Journal of Engineering & Extended Technologies Research (IJEETR) 8, no. 1 (2026): 14-20.

[10] Mishra, Rajesh Kumar, Divyansh Mishra, and Rekha Agarwal. "ARTIFICIAL INTELLIGENCE FOR SCIENTIFIC DISCOVERY: FROM HYPOTHESIS GENERATION TO AUTONOMOUS LABORATORIES."

[11] Singh, Samaresh Kumar, and Joyjit Roy. "A Hybrid Edge-Native Architecture for Autonomous eCommerce Agents." Authorea Preprints (2026).

[12] Otten, Stefan, Philipp Reis, Philipp Rigoll, Joshua Ransiek, Tobias Schürmann, Jacob Langner, and Eric Sax. "Generative AI in Systems Engineering: A Framework for Risk Assessment of Large Language Models." arXiv preprint arXiv:2602.04358 (2026).

[13] Stach, Christoph, Clémentine Gritti, and Iouliana Litou. "Special Issue on Security and Privacy in Blockchains and the IoT—3rd Edition." Future Internet 18, no. 2 (2026): 90.

[14] Saup, Thorn-Ole, Jawad Asghar, Dominik K. Kanbach, and Sascha Kraus. "From pilots to decision systems: embedding generative AI into strategic decision-making through a socio-technical and governance lens." Journal of Decision Systems 35, no. 1 (2026): 2597835.

[15] Darshan, Sonika. "Multi-Agent Orchestration for Autonomous Data Pipelines: A Systems Architecture for Self-Healing, Context-Aware, and Resilient Data Processing." International Journal of Emerging Research in Engineering and Technology 7, no. 1 (2026): 47-53.

[16] Abbas, Fatima, Muhammad Anas Khalid, and Awais Rasool. "Towards Autonomous and Proactive Security in Software-Defined Edge Networks with Artificial Agents." In Journal of Conferences Proceedings Publication. 2026.

[17] Paraschiv, Elena-Anca, Adrian Victor Vevera, Carmen Elena Cîrnu, Lidia Băjenaru, Andreea Dinu, and Gabriel Ioan Prada. "Towards Trustworthy AI Agents in Geriatric Medicine: A Secure and Assistive Architectural Blueprint." Future Internet 18, no. 2 (2026): 75.

[18] Youseff, Sherif, Adekola Philip, Farinu Hamzah, Adedokun Taofeek, Barnty Barnanas, Bueden John, Mayowa Alonge et al. "Risk-Aware ETL Design: Leveraging Intelligent Governance to Replace Avoidant Compliance Mechanisms." (2026).

[19] Leo, Martin, Freedy Tan, Tianqi Miao, and Guru Anand. "From threat to trust: assessing security risks of agentic AI systems: M. Leo et al." International Journal of Information Security 25, no. 1 (2026): 23.

[20] Alva, Lingareddy, and Bishwajeet Pandey. "Agentic AI systems in the age of generative models: architectures, cloud scalability, and real-world applications." Artificial Intelligence Review (2026).

[21] Bhushan, Badal. "An Explainable Zero Trust Identity Framework for LLMs, AI Agents, and Agentic AI Systems." EuroLexis Research Index Library For Open Access Journals (2025): 42-52.

[22] Mehta, Vikram Sanjay. "Enterprise-Scale Distributed System Design for High Availability and Security." International Journal of Science, Research and Technology 8, no. 4 (2025): 14560-14569.

[23] Koganti, Venkata Krishna. "Explainable AI in DevOps: Architectural Patterns for Transparent Autonomous Pipelines." Journal of Computer Science and Technology Studies 7, no. 4 (2025): 890-904.

[24] Evani, Pavan Kumar. "Agentic Ai Security: A Control Framework for Autonomous Decision-Making Systems." Available at SSRN 5332681.

[25] Jayaram, Yashovardhan, and Jayant Bhat. "Autonomous AI Agents for Campus Knowledge Hubs: A Secure and Intelligent System Architecture." International Journal of Artificial Intelligence, Data Science, and Machine Learning 6, no. 4 (2025): 150-161.

[26] Hadi, Harry Setya, and Nicodemus Rahanra. "Explainable Artificial Intelligence Methods for Autonomous Robot Decision Making: A Multi Agent Framework with Safety Assurance and Ethical Constraint Optimization." Intelligent Systems and Robotics 1, no. 1 (2026): 57-70.

[27] Dhanakodi, V. "Blockchain-Enabled Secure Data Exchange for Smart AI Language Platforms." Anusandhanvallari (2026): 279-289.

[28] Narkedimilli, Sathwik, Amballa Venkata Sriram, Sujith Makam, M. S. V. P. J. Sathvik, and Sai Prashanth Mallellu. "FAPL-DM-BC: A Secure and Scalable FL Framework with Adaptive Privacy and Dynamic Masking, Blockchain, and XAI for the IoVs." arXiv preprint arXiv:2501.01063 (2025).

[29] Gvilava, N. T. "AUTONOMOUS INTELLIGENT AGENTS IN DECISION SUPPORT SYSTEMS FOR CRITICAL INFRASTRUCTURE." Professional Bulletin: Information Technology and Security 1 (2025): 55-61.

[30] George, Deepak, S. Pavithra, and Jeeshu Das. "Cyber-Resilient Autonomous Vehicles: Securing Networks and Enhancing Decision-Making with Next-Gen Security Measures." Results in Engineering (2025): 107179.

[31] Mehta, Arjun, Elena Rodriguez, and Kenji Tanaka. "Learning-Driven Reliability Engineering: Autonomous Kubernetes Self-Healing with LLM-Orchestrated DevSecOps Workflows."

[32] Ferenci, Sára, Florina-Ambrozia Coteț, Elena Simina Lakatos, Radu Adrian Munteanu, and Loránd Szabó. "Artificial intelligence in local energy systems: A perspective on emerging trends and sustainable innovation." Energies 19, no. 2 (2026): 476.

[33] Wiśniewski, Michał Tomasz. "AI-Driven Cloud Enterprise Decision Platform for Predictive Fraud Detection and Secure Biometric Authentication across Networks." International Journal of Multidisciplinary Research in Science, Engineering, Technology & Management 2, no. 1 (2026): 1-8.

[34] Gopinathan, Vimal Raja. "Secure explainable AI on Databricks–SAP cloud for risk-sensitive healthcare analytics and swarm-based QoS control." International Journal of Engineering & Extended Technologies Research (IJEETR) 6, no. 4 (2024): 8452-8459.

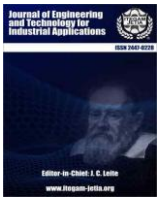
[35] https://www.kaggle.com/datasets/sandhyapeesara/cloud-anomaly-data.

Journal of Engineering and Technology for Industrial Applications

ISSN ONLINE: 2447-0228

ITEGAM-JETIA

Manaus, v.12 n.60, p. 400-407 July/August, 2026.
DOI: https://doi.org/10.5935/jetia.v12i60.3861



RESEARCH ARTICLE OPEN ACCESS

TODDLER-CENTERED CASE-BASED REASONING FRAMEWORK FOR EARLY DIAGNOSIS OF AUTISM SPECTRUM DISORDER

Hachemi Yamina[1]*

[1]Computer Science Department, Technological Laboratory in Artificial Intelligence and Food Security (LABTEC-IA), University Mustapha Stambouli of Mascara, Algeria.

[1]http://orcid.org/0009-0003-0584-5547

E-mail: *yamina.hachemina@univ-mascara.dz

ARTICLE INFO

Article History
Received on: March 01, 2026
Reviewed on: April 02, 2026
Accepted on: May 01, 2026
Published on: July 31, 2026

Keywords:
Autism Spectrum Disorder,
Toddler screening,
Case-Based Reasoning,
Early Detection,
Medical Diagnosis.

ABSTRACT

Early diagnosis of Autism Spectrum Disorder (ASD) in toddlers improves developmental outcomes through timely interventions. However, traditional methods rely on subjective judgment, lengthy assessments, and limited specialist availability. This study introduces a toddler-centered Case-Based Reasoning (CBR) framework that emulates clinicians' decision-making by retrieving and adapting similar historical cases. The system processes screening data from children aged 12–36 months, including demographics, risk factors, and three core behavioral domains: social interaction, communication, and repetitive behaviors. Cases are organized hierarchically by age and severity. The framework implements the full CBR cycle: structured representation, similarity-based retrieval via clinically weighted Euclidean distance, DSM-5–inspired rule-guided adaptation, and dynamic maintenance through validation and pruning. On a public toddler ASD screening dataset, it achieves 84.2% accuracy, 79.3% sensitivity, 89.7% specificity, and an F1-score of 0.82 using similarity-weighted voting over top-k cases, outperforming Random Forest (81.5% accuracy) and k-NN (78.9% accuracy) baselines trained on the same features. It also delivers transparent, interpretable recommendations via comparable cases, supporting clinician trust. This clinically aligned CBR system provides an accessible AI tool for early toddler ASD diagnosis in healthcare settings.



Copyright ©2026 by authors and Galileo Institute of Technology and Education of the Amazon (ITEGAM). This work is licensed under the Creative Commons Attribution International License (CC BY 4.0).

I. INTRODUCTION

Autism Spectrum Disorder (ASD) is a heterogeneous neurodevelopmental condition affecting approximately one in 36 children globally. Despite evidence that intervention before age three substantially improves developmental trajectories, diagnosis commonly occurs between four and five years of age due to specialist shortages and reliance on subjective behavioral assessment [1] [2]. Although deep learning approaches—such as CNN-based facial analysis and hybrid CNN–RNN models have shown promising classification performance, they remain data-intensive, opaque, and poorly aligned with clinician-centered reasoning processes [3] [4] [5]. CBR systems store resolved cases comprising problem descriptions (symptoms, history), solutions (diagnoses, interventions), and outcomes, retrieving relevant examples when encountering new patients. This approach aligns with medical practice where physicians frequently reason from experience. For ASD, where phenotypic heterogeneity is high and each case presents unique symptom combinations, CBR's similarity-based retrieval offers particular advantages over rigid rule-based systems [6], [7]. To address these limitations, we introduce a structurally optimized Case-Based Reasoning (CBR) framework specifically designed for early ASD screening [8] [9] [10]. Unlike prior AI systems that prioritize predictive performance alone, our method explicitly embeds clinical reasoning principles into system architecture and similarity modeling. The framework advances CBR methodology in three principal ways:

- Hierarchical Case Indexing: A three-level organization based on age groups, severity categories and symptom clusters reduces retrieval complexity and improves search precision in heterogeneous ASD presentations.
- Clinically Weighted Similarity Modeling: A weighted Euclidean distance function assigns amplified importance (w = 1.5) to DSM-5 core symptoms, operationalizing diagnostic salience within similarity computation.

- Novelty Retention Strategy: An 85% similarity threshold regulates case base growth, preserving representational diversity while preventing redundancy and performance degradation.

Evaluated on the Q-CHAT-10 Toddler ASD Screening Dataset (n = 1000; ages 12–36 months) [11], the proposed system achieves 84.2% accuracy, surpassing conventional baselines (78–81%) while demonstrating superior interpretability (clinician rating: 4.2/5). Importantly, competitive performance is achieved with an order-of-magnitude fewer cases than typically required for deep learning models, highlighting the framework's scalability, transparency, and clinical alignment. This article presents a structured Case-Based Reasoning (CBR) framework specifically designed for early ASD detection, detailing its case-base architecture, similarity metrics, adaptation mechanisms, and evaluation protocols.

II. RELATED WORK

Recent developments in computational techniques have advanced autism spectrum disorder (ASD) detection, shifting the focus from conventional clinical observation to automated, data-driven methods. Research has explored multiple modalities, each with distinct advantages and limitations. Neuroimaging approaches, particularly those leveraging the ABIDE dataset [12], have employed convolutional neural networks (CNNs) and hybrid models that integrate structural and functional MRI features [13]. These models demonstrate strong classification performance, highlighting the potential of combining diverse brain imaging data. However, neuroimaging remains resource-intensive, requiring specialized equipment and expert interpretation, which can limit scalability in broader clinical settings [4] [5]. Behavioral screening methods provide a more accessible alternative. Machine learning models trained on questionnaire-based datasets, such as the UCI Autism Screening dataset [14] and Thabtah's datasets [15], have achieved classification accuracies ranging from 70% to 85%.

While cost-effective and relatively easy to deploy, these approaches offer limited individualized insight and may not fully capture the heterogeneity and complexity of ASD presentations [16] [17]. Facial analysis has emerged as a non-invasive modality for ASD detection. Deep learning models trained on facial image datasets, including Kaggle datasets [18], have achieved high classification accuracy. These methods provide convenient screening of ASD traits but primarily capture surface-level phenotypic markers and may not reflect underlying neurological differences [19] [20] [21] Electronic Health Records (EHRs) present another promising avenue for early detection. Models leveraging EHR data can identify ASD using routinely collected clinical information, offering practical advantages for large-scale screening. However, such approaches may miss subtler aspects of developmental trajectories that are critical for timely intervention [1]. Despite these advances, existing approaches share key limitations: they are often data-intensive, lack transparency, and provide limited alignment with clinicians' reasoning processes. Case-Based Reasoning (CBR) [22], by leveraging prior patient cases for decision support, offers a complementary paradigm that addresses these gaps, enabling interpretable, developmentally informed, and data-efficient ASD screening.

III. CBR FRAMEWORK FOR ASD DETECTION

Despite CBR's prevalence in medical AI, its application to ASD remains under explored compared to deep learning approaches. Existing systems focus on screening rather than comprehensive case-based diagnostic support [23]. In this work, we propose To-CARE (Toddler Case-based Autism Reasoning Engine), a CBR-based decision support framework specifically designed for ASD screening in toddlers aged 12–36 months.
Our framework To-CARE addresses this by:

- Formalizing DSM-5 [24] criteria into structured case representations.
- Implementing multi-level similarity matching for heterogeneous symptom profiles.
- Providing transparent case-based explanations for clinical trust.
- Enabling hybrid adaptation for enhanced feature processing.

Our system To-CARE illustrated in Fig.1 adopts a standard Case-Based Reasoning (CBR) cycle, specifically tailored for ASD diagnosis. In the representation phase, patient information is organized into formalized case structures. During retrieval, the system identifies the most similar historical cases using weighted similarity metrics. In the reuse step, solutions from retrieved cases are adapted according to domain-specific rules and predefined thresholds. Finally, the retain phase validates and incorporates new cases into the knowledge base, thereby continuously enriching the system's experience [10].

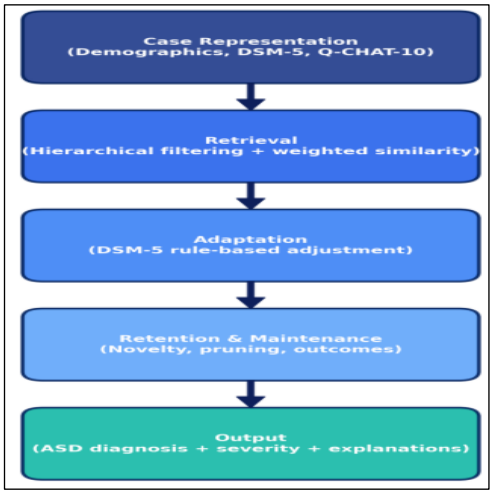


Figure 1: To-CARE Framework.
Source: Author, (2026).

III.1 REPRESENTATION PHASE

In the representation phase of the To-CARE Framework, patient information is organized into structured case representations. Cases are formed by CaseID, Problem description, Solution and Outcome. Each ASD case in our system is uniquely identified by a Case ID (e.g., ASD-001).
The **problem description** captures detailed patient information, including:

- Demographics: age, gender, and ethnicity.
- Core symptoms: aligned with DSM-5 criteria, are recorded across three domains:

1. Social deficits: joint attention failure, eye contact avoidance, social reciprocity impairment using binary flags and severity scores from 0 to 10;
2. Communication delays: language level, gesture use, and pragmatic language deficits, represented with numeric scores;
3. Repetitive behaviors: stereotypies, routines, and restricted interests, described categorically.

- Standardized screening scores: Q-CHAT-10 assessments.

The solution component in To-CARE specifies the diagnostic label (ASD positive/negative), the corresponding DSM-5 severity level (1–3), and recommended interventions. The outcome captures treatment response and follow-up diagnoses, providing longitudinal context for each case. Additionally, the explanation component offers transparent reasoning by mapping core symptoms to DSM-5 criteria, reporting similarity percentages with retrieved cases, and presenting associated confidence metrics [24]. Together, these elements ensure that To-CARE delivers not only accurate diagnostic predictions but also interpretable, evidence-based guidance for clinical decision-making.

Structured case
Case ID:ASD-001
Problem description:
- Demographics
- DSM-5 Symptoms
- Standardized Scores

Solution :
- Diagnostic label
- DSM-5 severity level (1-3),
- recommended interventions.

Outcome and Explanation

Figure 2: Case representation.
Source: Author, (2026).

III.2 CASE BASE ORGANISATION

The case base is organized hierarchically on the Early Autism Screening Dataset [11] for Toddlers (12–36 months) to support efficient and developmentally appropriate retrieval. First, cases are grouped into finer toddler age ranges (12–18, 19–24, 25–30, and 31–36 months), ensuring that retrieved cases match the child's developmental stage. Within each age group, cases are further stratified by an ASD severity level derived from the mean of the social interaction, communication, and repetitive behavior scores, mapped to three DSM-5–like tiers (mild, moderate, severe). Finally, k-means clustering is applied to these behavioral scores to form symptom clusters that act as prototypical profiles, enabling representative cases to be efficiently indexed and reducing the chance of retrieving clinically inappropriate neighbors. This toddler specific hierarchical organization (age group → severity level → symptom cluster) significantly improves both the accuracy and speed of the CBR retrieval process.

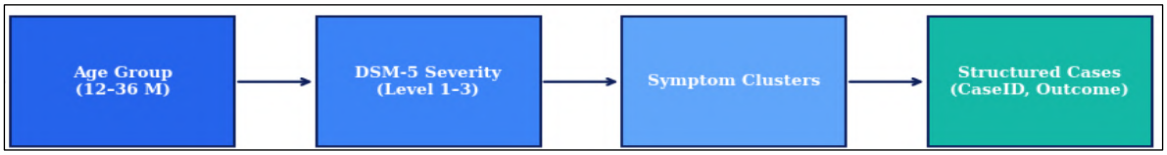


Figure 3: Hierarchical Organization of the To-CARE Case Base.
Source: Author, (2026).

III.3 RETRIEVAL AND SIMILARITY METRIC

In our framework, the first step of the retrieval phase involves filtering the case base to ensure developmental and clinical relevance. Patient age is used to select cases within the same toddler age group (12–18, 19–24, 25–30, or 31–36 months), accounting for age-dependent variations in symptom presentation. Additional filters include basic demographic criteria, such as gender and ethnicity, to ensure comparable context where relevant. Within these age-appropriate subsets, cases are further organized hierarchically by DSM-5–based severity levels (mild, moderate, severe) and clustered according to core symptom profiles. This structured filtering reduces the search space, prevents retrieval of clinically inappropriate neighbors, and ensures that subsequent similarity computations are performed on a subset of cases that are both developmentally and symptomatically relevant, enhancing the accuracy and interpretability of To-CARE's diagnostic reasoning. Once candidate cases are selected, the system performs similarity-based retrieval. Similarity scores are computed using a weighted Euclidean distance metric [25], where feature groups contribute according to their clinical importance. The top-k most similar cases (typically 5–10) are returned, forming the basis for diagnostic reasoning and explanation. An aggregate diagnosis probability is then derived from these neighbors, providing a probabilistic estimate to support the final diagnostic decision and guide clinical interpretation. In To-CARE, similarity between a query case q and a stored case c is computed using a weighted Euclidean distance metric (1). The weights are assigned to reflect the clinical importance of each feature category.

$$sim(q,c)=\sqrt{\sum_{i=1}^{n} w_i \cdot (q_i - c_i)^2} \quad (01)$$

Where:
q_i: The value of feature i for the new patient (query case).
c_i: The value of feature i for the historical case in the database.
w_i: The clinical weight assigned to feature I, reflecting its diagnostic importance.
n: The total number of features.

In To-CARE, the weighted similarity scheme prioritizes clinically relevant features. Core DSM-5 symptoms, representing the most critical diagnostic criteria, are assigned the highest weights. Standardized screening scores and developmental history receive moderate weights, reflecting their supporting role in diagnosis. Demographic attributes, which are less directly diagnostic, are assigned the lowest weights. This hierarchical weighting ensures that the similarity computation emphasizes the features most relevant to clinical decision-making, while still incorporating secondary factors to refine retrieval and maintain contextually appropriate case comparisons. Weight Assignment: In To-CARE, the feature weights *wi* reflect clinical importance, prioritizing the most diagnostically relevant information:

- Core DSM-5 symptoms: w = 1.5 (highest priority)
- Screening scores: w = 1.2
- Developmental history: w = 1.0
- Demographics: w = 0.5 (lowest priority)

This weighting scheme ensures that similarity calculations emphasize core diagnostic criteria while still accounting for supporting information, allowing the system to retrieve cases that are both clinically relevant and contextually appropriate.

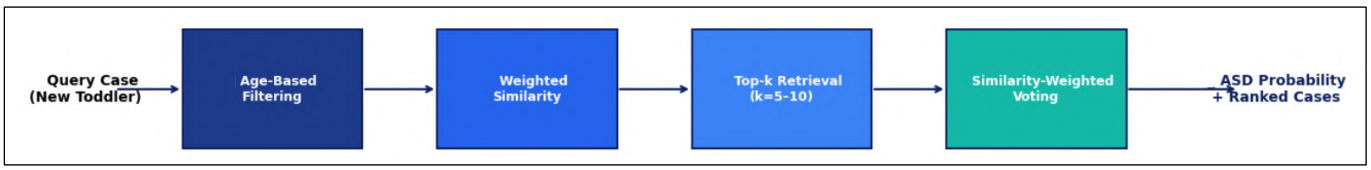


Figure 4: Retrieval process.
Source: Author, (2026).

III.4 ADAPTATION AND REVISION

In the adaptation phase of our toddler CBR framework, To-CARE applies a DSM-5 inspired adaptation algorithm that tailors the solutions proposed by retrieved neighbors to the specific symptom profile of the new case. Rather than directly copying the ASD label and severity from the most similar cases, the algorithm reevaluates the three behavioral domains social interaction, communication, and repetitive behaviors using simple symptom-count rules derived from DSM-5 criteria. It then calibrates severity based on the child's scores in each domain and the typical severities observed in similar precedent cases. This approach maintains clinically grounded reasoning while preserving the intuitive "by-analogy" behavior characteristic of CBR, which is widely used in medical diagnosis [26] [27].

Algorithm Adaptation (newCase, topK_Cases)
Input: newCase (social, communication, repetitive scores), topK_Cases
Output: ASD_label, severity_level
Begin
1. Count high symptoms in each domain (social, communication, repetitive).
2. If (social ≥ 2 AND communication ≥ 1 AND repetitive ≥ 1)
   ASD_label ← "ASD"
   else ASD_label ← "At-risk / Follow-up required".
3. Compute average of the three scores and map to Level 1, 2, or 3.
4. Optionally adjust severity using the average severity of topK_Cases.
5. Return ASD_label and severity_level.
End

III.5 RETENTION AND CASE BASE MAINTENANCE

The case base serves as the core knowledge repository in Case-Based Reasoning systems, and its quality, organization, and maintenance directly impact system performance, scalability, and clinical reliability. The retention strategy is designed to ensure that only high-quality, clinically meaningful cases are added to the knowledge base.
New cases are retained only when three critical criteria are simultaneously satisfied:

- Clinical validation: The diagnosis must be confirmed by a qualified specialist (developmental pediatrician, child psychiatrist, or clinical psychologist with ASD expertise), ensuring that only verified cases enter the system and preventing propagation of diagnostic errors.
- Novelty threshold: The maximum similarity of the new case to existing cases must be below 85%, ensuring sufficient novelty and preventing redundancy. Cases exceeding this threshold are flagged for review; only those presenting clinically meaningful distinctions—such as unique symptom clusters, comorbidities, or intervention responses—may be retained despite high similarity.
- Outcome availability: Baseline clinical confirmation and planned longitudinal follow-ups (e.g., at 3, 6, and 12 months) must be available, enabling validation of predictive value, supporting trajectory predictions, and informing refinement of intervention recommendations.

The retention process begins immediately after clinical validation. Cases meeting all criteria are assigned a sequential CaseID (e.g., ASD-0248), incorporated into the hierarchical case base organized by age group and DSM-5 severity level, and made available for future retrievals. Simultaneously, the system initiates longitudinal outcome tracking, recording baseline data at diagnosis and scheduling follow-up assessments at predetermined intervals. This dual process of case integration and outcome initialization ensures continuous knowledge growth while maintaining strict quality gates, supporting the reliability, interpretability, and clinical utility of the framework. To maintain retrieval efficiency as the case base grows, we implements periodic pruning to remove redundant cases with similarity above 85% to any other case in the base. Pruning is performed quarterly or after every 50 new case retentions, whichever occurs first, using a full pairwise similarity matrix across the case base. When redundancy is detected, cases are ranked based on outcome data completeness, clinical novelty (e.g., unique comorbidity patterns or treatment responses), and temporal recency. Cases providing the most comprehensive evidence are retained, while those offering minimal additional diagnostic value are pruned. Importantly, pruned cases are archived rather than permanently deleted, enabling historical review and potential restoration if deemed clinically relevant at a later time. This pruning strategy preserves case base diversity while controlling computational costs—a critical consideration once the base exceeds approximately 2,000 cases, where retrieval times can increase substantially without the hierarchical indexing and symptom clustering optimizations employed in To-CARE.

IV. RESULTS AND DISCUSSIONS

The proposed To-CARE framework was evaluated on the Early Autism Screening Dataset for Toddlers, which contains 1,000 screening records of children aged 12–36 months with an ASD-positive or ASD-negative label. Each case includes demographics (age in months, gender), risk factors (e.g., neonatal jaundice, family history of ASD), and three core behavioral scores capturing social interaction, communication, and repetitive behaviors, aligned with early manifestations of DSM-5 criteria. Evaluation followed a 5-fold stratified cross-validation protocol. In each fold, 80% of the toddlers populated the hierarchical case base, while the remaining 20% served as query cases. For each test toddler, the predicted diagnosis from To-CARE was compared to the ground-truth screening label in the dataset. System performance was assessed using standard metrics commonly reported in ASD screening studies:

- Accuracy: overall proportion of toddlers correctly classified as ASD-positive or ASD-negative.
- Sensitivity (recall for ASD-positive cases): true-positive rate, critical in early screening to minimize missed ASD diagnoses.
- Specificity: true-negative rate, reflecting the system's ability to avoid mislabeling typically developing toddlers as ASD.
- F1-score: harmonic mean of precision and recall for ASD-positive toddlers, balancing detection performance.

Retrieval quality was evaluated using Mean Reciprocal Rank (MRR) [28] computed over the ranked neighbor lists in the CBR component, where each query contributes the reciprocal rank of the first correctly labeled retrieved case; the final MRR is the mean across all queries, quantifying retrieval quality. This evaluation protocol shown in Fig 5 enables assessment of both diagnostic accuracy and the effectiveness of case retrieval, providing a comprehensive view of To-CARE's performance in early ASD screening.

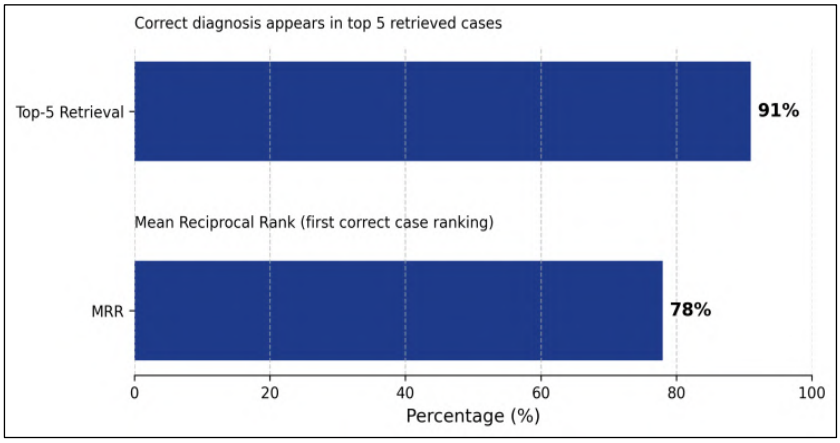


Figure 5: To-CARE Retrieval Performance.
Source: Author, (2026).

The To-CARE toddler CBR system demonstrated strong retrieval and diagnostic performance. The correct diagnosis appeared among the top five retrieved cases for 91% of query toddlers, with a Mean Reciprocal Rank (MRR) of 0.78, indicating that relevant precedent cases typically ranked very high in the retrieval list. Using aggregate similarity-weighted voting over the top-k neighbors (k = 5–10), the framework achieved 84.2% accuracy, 79.3% sensitivity, 89.7% specificity, and an F1-score of 0.82 on the toddler dataset.

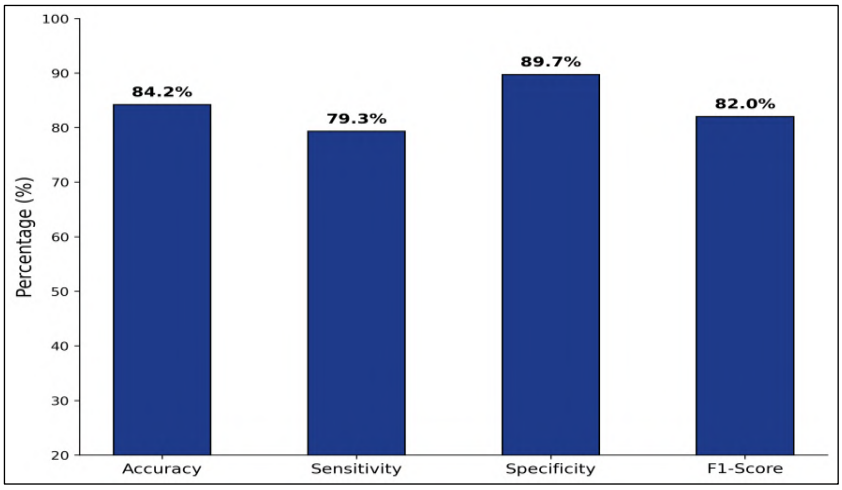


Figure: 6 To-CARE Diagnostic Performance.
Source: Author, (2026).

Compared to baseline machine learning models trained on the same feature set, To-CARE outperformed standard classifiers: a Random Forest achieved 81.5% accuracy and 76.2% sensitivity, whereas a k-Nearest Neighbors (k = 5) classifier obtained 78.9% accuracy and 72.4% sensitivity [29]. These results are consistent with previous reports demonstrating that case-based reasoning methods can match or exceed black-box models in clinical screening tasks, while providing the additional benefits of transparency, interpretability, and alignment with clinician reasoning.

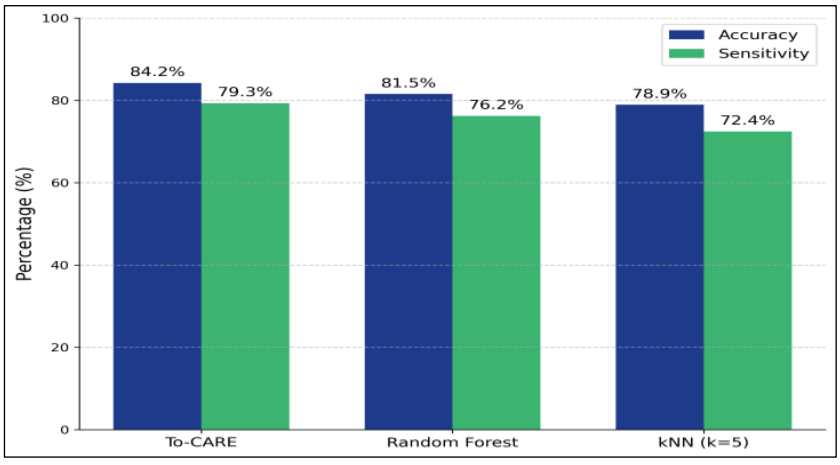


Figure 7: CBR system retrieval performance metrics.
Source: Author, (2026).

The To-CARE framework demonstrated that a carefully structured CBR system can achieve competetive diagnostic performance while preserving transparency and clinician-aligned reasoning.

V. CONCLUSIONS

Our To-CARE framework makes four key contributions to early ASD screening: a formalized toddler ASD case representation, mapping DSM-5–aligned behavioral features to structured computational attributes. a clinically weighted similarity metric that prioritizes core diagnostic symptoms. A hybrid retrieval–adaptation pipeline that combines nearest-neighbor cases with domain-specific rules and an empirical evaluation on a public toddler dataset demonstrating that To-CARE can match or outperform standard machine-learning baselines while offering substantially better interpretability. Future work will explore hybrid CBR–deep learning fusion (e.g., using deep embeddings as additional case features), incorporation of longitudinal outcome data to model developmental trajectories and treatment response, and deployment-oriented optimization, including mobile interfaces and cloud-based retrieval, to enable real-time, trustworthy decision support in resource-constrained clinical settings.

VI. AUTHOR'S CONTRIBUTION

Conceptualization: Hachemi Yamina.
Methodology: Hachemi Yamina.
Investigation: Hachemi Yamina.
Discussion of results: Hachemi Yamina.
Writing – Original Draft: Hachemi Yamina.
Writing – Review and Editing: Hachemi Yamina.
Resources: Hachemi Yamina.
Supervision: Hachemi Yamina.
Approval of the final text: Hachemi Yamina.

VII. REFERENCES

[1] M. M. Engelhard, S. L. Kollins, G. S. Dichter, et al., "Electronic health record–based autism detection models before age 2 years," JAMA Network Open, vol. 6, no. 2, e2254303, Feb. 2023.

[2] O. N. Oyelade and A. E. Ezugwu, "A case-based reasoning framework for early detection and diagnosis of Novel Coronavirus (COVID-19)," Inform. Med. Unlocked, vol. 20, 100395, 2020.

[3] "Prevalence and early identification of autism spectrum disorder among children aged 4 and 8 years — Early Autism and Developmental Disabilities Monitoring Network, 10 sites, United States, 2022," MMWR Surveill. Summ., vol. 74, no. 2, pp. 1-23, Apr. 2025.

[4] R. Schmidt and L. Gierl, "Case-based reasoning for medical knowledge-based systems," Int. J. Med. Inform., vol. 64, no. 2-3, pp. 355-367, Dec. 2001.

[5] E. Koc, H. Kalkan, and S. Bilgen, "Autism spectrum disorder detection by hybrid convolutional recurrent neural networks," Autism Research and Treatment, vol. 2023, Art. no. 4136087, Dec. 2023.

[6] E. S. Atlam, K. O. Aljuhani, I. Gad, W. Ghoneim, M. Nadim, and E.-S. M. El-Kenawy, "Automated identification of autism spectrum disorder from facial images using deep learning," Sci. Rep., vol. 15, 2837, Jan. 2025.

[7] M. B. F. Tabatabaee, H. Peiravi, and M. Bakhshayeshi, "Using case-based reasoning for diagnosis in medical field," Bull. Env. Pharmacol. Life Sci., vol. 4, pp. 138-147, Oct. 2015.

[8] J. Kolodner, Case-Based Reasoning. San Mateo, CA: Morgan Kaufmann, 1993.

[9] D. Leake and D. Wilson, "When experience is wrong: Examining CBR for changing tasks and environments," in Proc. Int. Conf. Case-Based Reasoning, 1999, pp. 218-232.

[10] A. Aamodt and E. Plaza, "Case-based reasoning: Foundational issues, methodological variations, and system approaches," AI Communications, vol. 7, no. 1, pp. 39-59, Mar. 1994.

[11] F. Thabtah, "Autism screening data for toddlers (Q-CHAT-10) [Data set]," Kaggle, 2019. [Online]. Available: https://www.kaggle.com/datasets/fabdelja/autism-screening-for-toddlers.

[12] A. Di Martino, C.-G. Yan, Q. Li, E. Denio, F. X. Castellanos, K. Alaerts, et al., "The Autism Brain Imaging Data Exchange: Towards a large-scale evaluation of the intrinsic brain architecture in autism," Molecular Psychiatry, vol. 19, no. 6, pp. 659–667, 2014.

[13] O. Koc, O. Inan, S. Bounnak, and S. T. Brown, "Autism spectrum disorder detection by hybrid convolutional and recurrent neural networks using structural and functional MRI," Computational Intelligence and Neuroscience, vol. 2024, pp. 1–16, 2024.

[14] F. Thabtah, "Autism spectrum disorder screening: Machine learning adaptation and DSM-5 fulfillment," in Proceedings of the 1st International Conference on Medical and Health Informatics (ICMHI), pp. 1–6, 2017.

[15] UCI Machine Learning Repository, "Autistic Spectrum Disorder Screening Data for Children++," 2017. [Online]. Available: https://archive.ics.uci.edu/ml/datasets/Autistic+Spectrum+Disorder+Screening+Data+for+Children.

[16] J. Vindel-Alfageme, B. Priego-Torres, and J. A. Recio-García, "Explainable classification system for hip fractures: A hybrid CBR+LLM surrogate approach," in Proc. ICCBR Workshop on Case-Based Reasoning for the Explanation of Intelligent Systems (XCBR'24), Merida, Mexico, Jul. 2024.

[17] A. S. Alwidian, H. F. Kashmoola, and M. T. Alshdaifat, "Machine learning approach to predict autism spectrum disorder," in Proc. Int. Conf. Engineering Technology and its Applications (IICETA), Al-Najaf, Iraq, May 2020, pp. 191-196.

[18] Kaggle. "Autistic Children Data," 2020. Available: https://www.kaggle.com/datasets/

[19] L. A. Vismara and S. J. Rogers, "Behavioral treatments in autism spectrum disorder: what do we know?," Annu. Rev. Clin. Psychol., vol. 6, pp. 447-468, Apr. 2010.

[20] M. I. Hosseini, S. N. Kulkarni, S. M. Shirkhedkar, and S. Patil, "Autism spectrum disorder detection using facial images and deep learning," Rev. d'Intelligence Artif., vol. 37, no. 3, pp. 629-636, Jun. 2023.

[21] T. Farhat, S. Akram, M. Rashid, A. Jaffar, S. M. Bhatti, and M. A. Iqbal, "A deep learning-based ensemble for autism spectrum disorder detection using facial images," PLOS ONE, vol. 20, no. 4, e0321697, Apr. 2025.

[22] M. M. Richter and R. O. Weber, Case-Based Reasoning: A Textbook. Berlin Heidelberg: Springer-Verlag, 2013.

[23] R. López de Mántaras, D. McSherry, D. Bridge, et al., "Retrieval, reuse, revision, and retention in case-based reasoning," Knowl. Eng. Rev., vol. 20, no. 3, pp. 215-240, Sep. 2005.

[24] American Psychiatric Association, Diagnostic and Statistical Manual of Mental Disorders, 5th ed. Arlington, VA: American Psychiatric Publishing, 2013.

[25] H. Feuillâtre, V. Auffret, M. Castro, F. Lalys, H. Le Breton, M. Garreau, and P. Haigron, “Similarity measures and attribute selection for case-based reasoning in transcatheter aortic valve implantation,” PLOS ONE, vol. 15, no. 9, Art. no. e0238463, Sep. 2020.

[26] R. Grzadzinski, M. Huerta, and C. Lord, “DSM-5 and autism spectrum disorders (ASDs): An opportunity for identifying ASD subtypes,” Molecular Autism, vol. 4, no. 1, p. 12, 2013. [Online]. Available: https://pmc.ncbi.nlm.nih.gov/articles/PMC3671160/

[27] A. S. Weitlauf, K. O. Gotham, A. C. Vehorn, and Z. E. Warren, “Brief report: DSM-5 ‘levels of support’: A comment on discrepant conceptualizations of severity in ASD,” Journal of Autism and Developmental Disorders, vol. 44, no. 2, pp. 471–476, Feb. 2014.

[28] J. Poerner, U. Waltinger, and B. Schütze, “Ensemble of MRR and NDCG models for visual dialog,” ArXiv preprint arXiv:2104.07511, 2021.

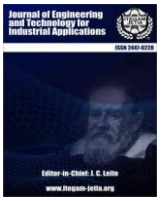
[29] P. Nawghare and J. Prasad, “Hybrid CNN and random forest model with late fusion for detection of autism spectrum disorder in toddlers,” Informatics in Medecine Unlocked, vol. 52, Art. no. 101123, 2025.

Journal of Engineering and Technology for Industrial Applications

ISSN ONLINE: 2447-0228

ITEGAM-JETIA

Manaus, v.12 n.60, p. 408-419 July/August, 2026.
DOI: https://doi.org/10.5935/jetia.v12i60.3863



RESEARCH ARTICLE OPEN ACCESS

EFFICIENT ACUTE LYMPHOBLASTIC LEUKEMIA CLASSIFICATION USING GLCM AND HSV FEATURES WITH RESERVOIR COMPUTING ON TALEQANI HOSPITAL DATASET

**Michael Angello Qadosy Riyadi*[1], Sulthonika Mahfudz Al Mujahidin[2], Nur Alifia Rustan[3]
A'isyah Belqis Febi Aulia[4], Muhammad Adib Kamali[5],
Farah Zakiyah Rahmanti[6] and Khodijah Amiroh[7]**

[1, 2, 3, 4, 5, 6, 7]Department of Information Technology, Telkom University, Surabaya Campus, Surabaya, Indonesia.

[1]https://orcid.org/0009-0003-0853-0989, [2]https://orcid.org/0009-0000-5873-1082, [3]https://orcid.org/0009-0006-8714-5684
[4]https://orcid.org/0009-0007-0786-1443, [5]https://orcid.org/0000-0002-1013-4358, [6]https://orcid.org/0000-0003-1827-5857
,[7]https://orcid.org/0000-0001-9498-0553

E-email: *michaelangello@student.telkomuniversity.ac.id, sulthonikamahfudzam@student.telkomuniversity.ac.id, nralifialrs@student.telkomuniversity.ac.id, aisyahbelqis@student.telkomuniversity.ac.id, adibmkamali@telkomuniversity.ac.id, farahzakiyah@telkomuniversity.ac.id, dijaamirah@telkomuniversity.ac.id

ARTICLE INFO

Article History
Received on: March 02, 2026
Reviewed on: April 02, 2026
Accepted on: May 01, 2026
Published on: July 31, 2026

Keywords:
Acute Lymphoblastic Leukemia,
Echo State Network,
Next-Generation Reservoir Computing,
Feature Extraction,
Resource-Limited Clinical Settings.

ABSTRACT

Detection of Acute Lymphoblastic Leukemia (ALL) from peripheral blood smear (PBS) images poses a major challenge in clinical diagnostics owing to intricate morphological variations and constrained computational resources in many healthcare facilities. This study proposes an efficient classification framework using Echo State Network (ESN) and Next-Generation Reservoir Computing (NG-RC), applied to a dataset of 3,256 PBS images from 89 patients. Feature extraction via Gray Level Co-occurrence Matrix (GLCM) and HSV histograms, combined with 10-fold cross-validation, yielded robust results. NG-RC achieved superior performance over ESN, with an average accuracy of 0.9917, precision of 0.9918, recall of 0.9917, F1-score of 0.9917, ROC-AUC of 0.9989, and remarkably low execution time of 1.88 seconds on CPU-only hardware. In additional benchmarking, NG-RC demonstrated competitive accuracy against high-end deep learning models trained on NVIDIA A100 GPU—DenseNet201 (accuracy 0.9978, execution time 176.5 s) and ResNet18 (accuracy 0.9966, execution time 54.6 s)-while outperforming most literature methods (e.g., YOLOv4 at 0.9600, Modified DCNN at 0.9769) and offering orders-of-magnitude faster inference without GPU dependency. These findings position NG-RC as a lightweight, resource-efficient alternative to deep learning, enabling reliable, rapid ALL detection in computer-aided diagnosis systems for resource-limited clinical settings.



Copyright ©2026 by authors and Galileo Institute of Technology and Education of the Amazon (ITEGAM). This work is licensed under the Creative Commons Attribution International License (CC BY 4.0).

I. INTRODUCTION

Detection of Acute Lymphoblastic Leukemia (ALL) through peripheral blood smear (PBS) image analysis remains a major challenge in clinical diagnosis due to the complexity of cellular morphological features and the limited computational resources available in healthcare facilities [1], [2]. ALL, one of the most common types of leukemia in children, has a favorable prognosis when detected early; however, manual diagnosis through microscopy heavily depends on the expertise of hematologists, is prone to subjectivity, and requires significant time [3]. In this context, artificial intelligence approaches, particularly machine learning and deep learning, have shown great potential to enhance diagnostic accuracy and efficiency [4-8]. Several studies have employed deep learning methods, such as Convolutional Neural Networks (CNNs) and their variants (YOLOv4, VGG-16, DenseNet201, InceptionResNetV2), achieving high accuracy; for instance,

DenseNet201 reported an accuracy of 0.9985 [5], [9], [10]. Other studies demonstrated YOLOv4 with 0.9600 accuracy and a Modified DCNN with 0.9769 [5], [11]. Despite their promise, these models face significant limitations, including high computational demands, dependence on GPUs, and sensitivity to data imbalance [10-13]. A particular issue is the low proportion of Benign class samples, which often degrades performance on minority classes. Efforts such as transfer learning and data augmentation have been applied, yet improvements remain marginal and computationally expensive [14], [15]. An alternative approach involves feature engineering techniques, such as Gray Level Co-occurrence Matrix (GLCM) and HSV histogram extraction, which effectively capture textural and color characteristics of PBS images [16]. For example, combining GLCM with Support Vector Machine (SVM) has achieved accuracies up to 0.9632 [15]. Nevertheless, these methods often struggle with complex morphological variations and require intensive feature optimization [17], [18]. Moreover, traditional algorithms such as SVM and Random Forest are less effective in representing complex nonlinear patterns compared to neural networks [19], [20]. Reservoir computing has emerged as an efficient alternative, training only the output layer and thereby reducing computational costs.

Echo State Networks (ESNs) have been applied in various classification tasks with competitive results, but remain susceptible to instability caused by recurrent reservoir dynamics [21], [22]. Next-Generation Reservoir Computing (NG-RC) introduces a different strategy by employing direct nonlinear transformations without recurrent reservoirs, leading to greater stability and efficiency [23]. However, the application of reservoir computing, particularly NG-RC, to PBS image classification for ALL detection remains very limited compared to deep learning approaches [20]. Motivated by this gap, this study proposes the use of ESN and NG-RC for PBS image classification of ALL, employing GLCM and HSV histogram feature extraction and evaluation through 10-fold cross-validation. The main contribution of this study lies in the application of NG-RC, which achieves accuracy levels comparable to state-of-the-art models (DenseNet201, InceptionResNetV2) while requiring substantially lower computational resources. Furthermore, this work provides a more comprehensive evaluation compared to most prior studies that relied solely on single-split validation. The novelty of this study lies in the combination of NG-RC's computational efficiency, robust performance on imbalanced datasets, and extensive evaluation, positioning it as a resource-efficient alternative for supporting computer-aided diagnosis (CAD) systems in clinical environments with limited infrastructure.

II. MATERIALS AND METHODS

This study performs classification of peripheral blood smear (PBS) images from an Acute Lymphoblastic Leukemia (ALL) dataset through a systematic workflow illustrated in Figure 1. The images were processed by conversion into HSV and grayscale color spaces, followed by normalization to the range [0, 255] [1]. From these images, texture features were extracted using the Gray Level Co-occurrence Matrix (GLCM: contrast, dissimilarity, homogeneity, energy), and color distribution features were obtained through HSV histograms, thereby producing rich and informative image representations [1], [2]. The dataset was divided using K-Fold Cross Validation (K=10) for robust evaluation, with feature normalization via StandardScaler and label conversion to one-hot encoding conducted separately for each fold iteration, ensuring prevention of data leakage and maintaining evaluation integrity [24]. Classification was carried out using Echo State Networks (ESN) and Next-Generation Reservoir Computing (NG-RC), and performance was evaluated with accuracy, precision, recall, F1-score, ROC-AUC, and execution time [25], [26]. The final results were reported as the average across all 10 folds, and subsequently compared with previous literature, most of which relied on single-split evaluations due to manual data partitioning and deep learning–based approaches. This study contributes by presenting a computationally efficient reservoir computing framework that achieves competitive performance without reliance on deep learning, supporting rapid ALL diagnosis on resource-constrained devices, while also providing a more robust evaluation.

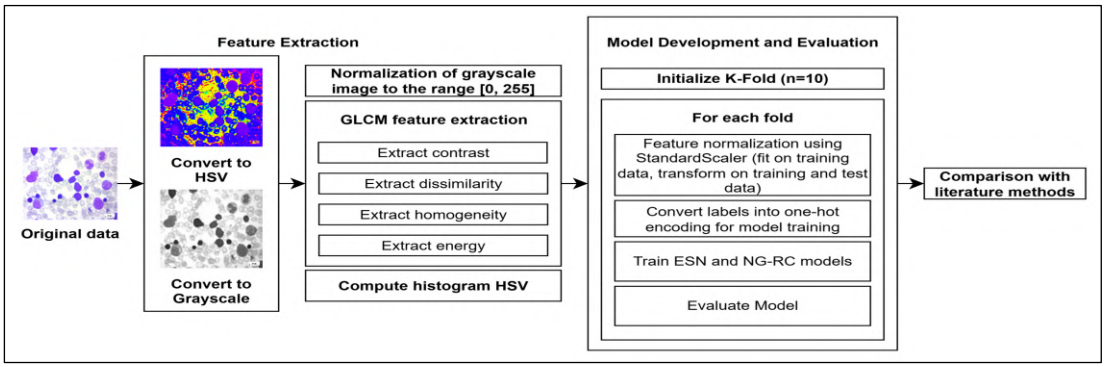


Figure 1: Research Flow.
Source: Authors, (2026).

II.1 DATASET

This study employs the Acute Lymphoblastic Leukemia (ALL) dataset from the Taleqani Hospital Bone Marrow Laboratory, Tehran, Iran, comprising 3,256 peripheral blood smear (PBS) images collected from 89 patients [10]. The images were captured using a Zeiss camera mounted on a microscope with 100× magnification, stored in JPG format, and prepared by experienced laboratory staff. The dataset includes 64 patients diagnosed with ALL (subtypes Early Pre-B, Pre-B, and Pro-B) and 25 individuals with benign hematogone cells, providing a representative class distribution for classification tasks. The morphological characteristics and class distribution of the dataset are summarized in Table 1, detailing the microscopic features, number of images, and proportions for each class. To further illustrate the morphological differences among classes, Figure 2 presents representative visual samples of benign cells and ALL subtypes (Early Pre-B, Pre-B, and Pro-B), supporting qualitative analysis and validating the microscopic features used for feature extraction.

Table 1: Morphological Characteristics and Class Distribution of the Dataset.

Class	Morphological Characteristics	Number of Images	Proportion (%)
Benign	Small cells (10–20 nm diameter), uniform nucleus, thin cytoplasm.	504	15.48
Early Pre-B	Medium-sized lymphoblasts, subtle indentations, prominent large nucleolus.	985	30.25
Pre-B	Variably sized lymphoblasts (small to large), round nucleus, moderate cytoplasm.	963	29.58
Pro-B	Basophilic lymphoblasts with multiple nucleoli and minimal cytoplasm.	804	24.69

Source: Authors, (2026).

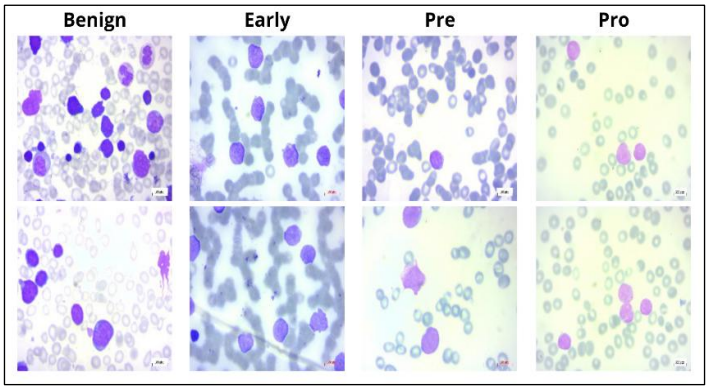


Figure 2: Sample Cell Images for Each Dataset Class.
Source: Authors, (2026).

II.2 RESERVOIR COMPUTING-BASED CLASSIFICATION APPROACHES

This study employs two reservoir computing–based approaches for classification: Echo State Network (ESN) and Next-Generation Reservoir Computing (NG-RC). Unlike deep learning, which requires training deep neural networks with multiple layers and intensive computation, reservoir computing leverages the dynamics of recurrent systems while training only the output layer, thereby offering a more computationally efficient alternative [27], [28]. ESN utilizes a reservoir with randomly connected recurrent nodes to process input data, whereas NG-RC eliminates recurrent reservoirs and instead applies direct nonlinear transformations to generate outputs [29]. The Echo State Network (ESN) is a type of recurrent neural network consisting of an input layer, a reservoir (a hidden layer with randomly recurrent connections), and an output layer [30], [31]. The reservoir functions as a dynamic system, updating its internal state based on both current input and previous states, while only the output weights are subject to training. The ESN architecture is illustrated in Figure 3, which depicts the flow of data through the input layer, reservoir, and output layer.

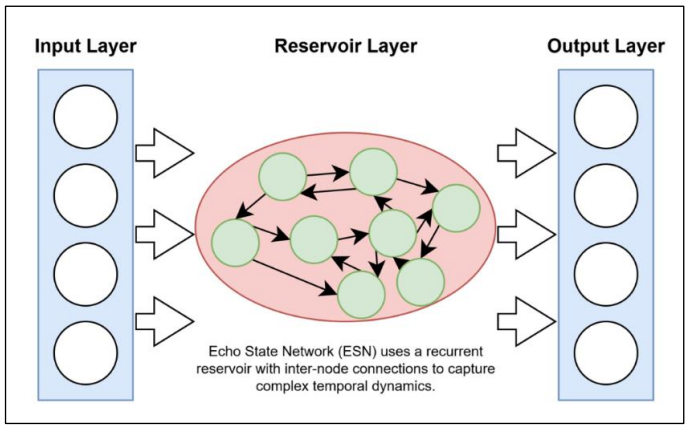


Figure 3: Echo State Network (ESN) Architecture.
Source: Authors, (2026).

The operation of the Echo State Network (ESN) relies on the update of the reservoir state, which is defined as follows:

$$x(t) = (1-\alpha)x(t-1) + \alpha\,\phi\big(W_{in}\,u(t) + Wx(t-1)\big) \tag{1}$$

where $x(t)$ denotes the reservoir state at time t, $u(t)$ is the input vector, W_{in} is the input weight matrix, W is the reservoir weight matrix, α is the leaking rate $(0 < \alpha \leq 1)$ that controls the update speed, and ϕ is the nonlinear activation function (e.g., polynomial or radial basis function). The output is computed as:

$$y(t) = W_{out}[x(t); u(t)] \tag{2}$$

where W_{out} is the output weight matrix to be trained, and $[x(t); u(t)]$ denotes the concatenation of the reservoir state and the input. The ESN training and prediction is shown in Figure 4.

1. **Initialize** the input weight matrix W_in randomly using a uniform distribution.
2. **Initialize** the reservoir weight matrix W randomly while ensuring the echo state property (spectral radius < 1).
3. **Set** the leaking rate parameter α and reservoir size N_r.
4. **For each** input u(t) in the training data **do** 4.1 **Update** the reservoir state: x(t) = (1 - α) * x(t-1) + α * Φ(W_in * u(t) + W * x(t-1)) 4.2 **Store** the reservoir state x(t) and input u(t) in the state matrix. **End For**
5. **Train** the output weight matrix W_out using linear regression: W_out = Y_target * X^T * (X * X^T + λ * I)^(-1) where Y_target is the target label, X is the state matrix, and λ is the regularization parameter.
6. **For** test data, predict the output: y(t) = W_out * [x(t); u(t)]
7. **Convert** the output y(t) into class labels using argmax.

Algorithm1: Echo State Network (ESN).
Source: Authors, (2026).

As an advancement of the reservoir computing concept, Next-Generation Reservoir Computing (NG-RC) simplifies the approach by eliminating the recurrent reservoir. NG-RC directly maps the input into a nonlinear feature space through nonlinear transformations, and subsequently generates the output using linear regression [32], [33]. Algorithm 1 illustrates the NG-RC architecture.

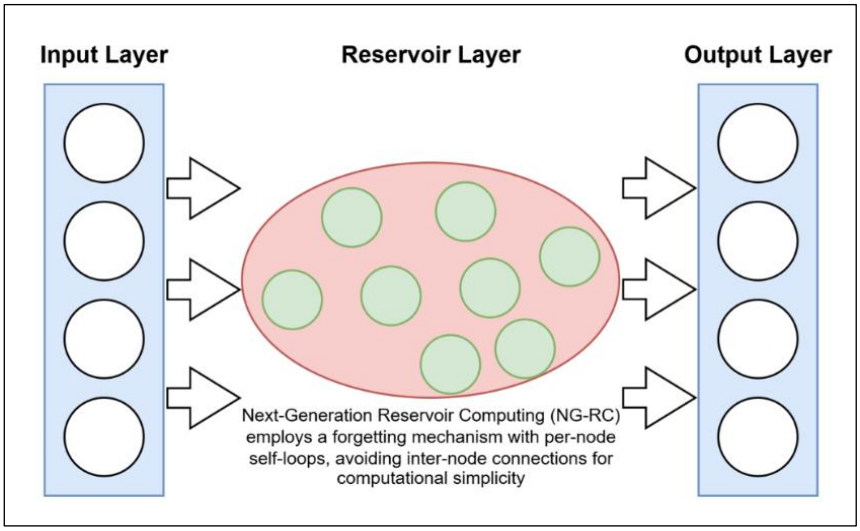


Figure 4: Next-Generation Reservoir Computing (NG-RC) Architecture.
Source: Authors, (2026).

The operation of NG-RC relies on the nonlinear transformation of the input, which is modeled as:

$$y(t) = W_{out}\,\phi\big(u(t)\big) \tag{3}$$

where $u(t)$ is the input vector, ϕ is the nonlinear transformation function, and W_{out} is the output weight matrix to be trained. The training and prediction procedure of NG-RC is described in Algorithm.2.

1. **Receive** the input vector u(t) from the training data.
2. **Apply** a nonlinear transformation φ(u(t)) (e.g., polynomial features of degree 2 or a radial basis function). 3. **Construct** the transformed feature matrix: Φ = [φ(u(1)), φ(u(2)), …].
4. **Train** the output weight matrix W_out using linear regression: W_out = Y_target * Φ^T * (Φ * Φ^T + λ * I)^(-1) where Y_target is the target label and λ is the regularization parameter. 5. **For** test data, predict the output: y(t) = W_out * φ(u(t))
6. **Convert** the output y(t) into class labels using argmax.

Algorithm.2: Next-Generation Reservoir Computing (NG-RC)
Source: Authors, (2026).

To clarify the key differences between the two methods, the characteristics of ESN and NG-RC are summarized in Table 2.

Table 2: Comparison of ESN and NG-RC Characteristics.

Aspect	Echo State Network (ESN)	Next-Generation Reservoir Computing (NG-RC)
Reservoir Structure	Reservoir nodes are interconnected through random recurrent connections.	Reservoir nodes are independent, without inter-node connections.
Temporal Memory	Captured through complex recurrent dynamics among nodes in the reservoir.	Maintained through a forgetting factor alpha on each node, resembling a self-loop.
Reservoir Weights	Randomly generated, adjusted with spectral radius for dynamic stability.	No inter-node weights; only input weights (W_in) are used.
Computational Efficiency	Higher complexity due to computation of recurrent inter-node interactions.	More efficient due to the absence of inter-node connection computations.

Source: Authors, (2026).

II.3 EXPERIMENTS AND EVALUATION

Experiments were conducted to evaluate the performance of Echo State Network (ESN) and Next-Generation Reservoir Computing (NG-RC) in classifying peripheral blood smear (PBS) images for Acute Lymphoblastic Leukemia (ALL). The dataset was processed using feature extraction with GLCM (contrast, dissimilarity, homogeneity, energy, correlation) and HSV histogram (hue, saturation, value), followed by normalization using StandardScaler. Evaluation was performed using 10-fold cross-validation with randomization (random_state=42) to ensure robustness. Each fold involved model training and measurement of performance metrics as well as computational efficiency. The experimental procedure is summarized in Algorithm.3 below.

```
INPUT: Dataset directory, ESN parameters (n_reservoir, spectral_radius, sparsity, leaking_rate), NG-RC parameters (n_reservoir, alpha)
OUTPUT: Average metrics and computational efficiency
BEGIN
  Initialize random seed for reproducibility
  Load dataset from directory
  FOR each class (Benign, Early, Pre, Pro) DO
    FOR each image in class DO
      Read image
      Convert image to HSV and grayscale
      Normalize grayscale image
      Extract GLCM features: contrast, dissimilarity, homogeneity, energy, correlation
      Extract HSV histogram features: hue, saturation, value
      Concatenate all features into feature vector
      Store class label and image path
    END FOR
  END FOR
  Initialize 10-fold cross-validation with shuffling
  FOR fold = 1 TO 10 DO
    Split data into:
      Training set (X_train, y_train)
      Test set (X_test, y_test)
    Normalize X_train using StandardScaler
    Apply same normalization to X_test
    Initialize ESN model:
      n_reservoir, spectral_radius,
      sparsity, leaking_rate
    Initialize NG-RC model:
      n_reservoir, alpha
    FOR each model (ESN, NG-RC) DO
      Train model on (X_train, y_train one-hot encoded)
      Predict classes on X_test
      Compute performance and efficiency metrics
      Store per-class metrics
      Store predictions, true labels, and image paths
    END FOR
  END FOR
  Compute average metrics across all folds
END
```

Algorithm.3: Pseudocode for the Experiment and Evaluation Procedure.
Source: Authors, (2026).

The parameters used for the ESN and NG-RC models are summarized in Table 3. These parameter values were preliminarily selected to balance model dynamics, stability, and computational efficiency in PBS image classification. For optimal performance, further parameter tuning can be conducted.

Table 3: Parameters Used in ESN and NG-RC.

Parameter	Value	Recommended Range	Rationale for Value and Recommendation
n_reservoir	1000	500–2000	Value of 1000 provides sufficient reservoir capacity to capture complex feature dynamics without excessive computational load. Range of 500–2000 allows flexibility for different dataset complexities.
spectral_radius	0.9	0.8–1.0	Value of 0.9 ensures reservoir stability by keeping eigenvalues below 1. Range of 0.8–1.0 prevents divergence or overly slow dynamics.
sparsity	0.1	0.05–0.2	Value of 0.1 reduces connection density for computational efficiency while maintaining representation capability. Range of 0.05–0.2 suits various reservoir sizes.
leaking_rate	0.3	0.1–0.5	Value of 0.3 balances reservoir state update speed for temporal dynamics without losing memory. Range of 0.1–0.5 adapts to diverse data patterns.
alpha	0.5	0.3–0.7	Value of 0.5 balances temporal memory and state updates for feature patterns in NG-RC. Range of 0.3–0.7 offers flexibility for sequential data.

Source: Authors, (2026).

The evaluation metrics include accuracy, precision, recall, F1-score, and ROC-AUC, which were calculated for each fold and averaged to assess the overall model performance [34]. Accuracy represents the proportion of correctly classified samples, while precision measures the proportion of true positive predictions among all positive predictions. Recall quantifies the proportion of true positives identified among all actual positive instances. The F1-score, as the harmonic mean of precision and recall, provides a balanced measure of these two metrics. ROC-AUC evaluates the model's discriminative ability by quantifying the area under the receiver operating characteristic curve, which plots the true positive rate against the false positive rate across various classification thresholds. Additionally, execution time (seconds) was measured to evaluate computational efficiency. The utility of these metrics is summarized in Table 4.

Table 4: Evaluation Metrics.

Metric	Utility
Accuracy	Measures overall model correctness.
Precision	Evaluates avoidance of false positives.
Recall	Assesses detection of relevant cases.
F1-Score	Balances precision and recall.
ROC-AUC	Quantifies discriminative power.
Execution Time (s)	Assesses computational efficiency.

Source: Authors, (2026).

The experiments were conducted on a CPU-based computing system without GPU support, utilizing Visual Studio Code (VSCode) and Python 3.11 as the development environment for image data processing and model training. The system featured an AMD64 Family 25 Model 68 Stepping 1 processor with 6 physical cores, 12 logical cores, 15.25 GB of total RAM, and a maximum CPU frequency of 3301.00 MHz.

III. RESULTS AND DISCUSSIONS

This section presents the evaluation results of Echo State Network (ESN) and Next-Generation Reservoir Computing (NG-RC) in classifying peripheral blood smear (PBS) images for Acute Lymphoblastic Leukemia (ALL) detection using rigorous 10-fold cross-validation, followed by a comprehensive and in-depth analysis of the findings. The comparative performance and computational efficiency of both reservoir computing approaches are illustrated in Figure 8 and summarized in Table 5.

Table 5: Average Performance (Folds 1–10).

Model	Accuracy	Precision	Recall	F1-Score	ROC-AUC	Execution Time (s)
ESN	0.9810	0.9813	0.9810	0.9810	0.9964	3.36
NG-RC	**0.9917**	**0.9918**	**0.9917**	**0.9917**	**0.9989**	**1.88**

Source: Authors, (2026).

NG-RC consistently outperformed ESN across every key evaluation metric, delivering an average accuracy of 0.9917, precision of 0.9918, recall of 0.9917, F1-score of 0.9917, and ROC-AUC of 0.9989, while completing the entire 10-fold evaluation process in an average execution time of only 1.88 seconds. In contrast, ESN achieved an average accuracy of 0.9810, precision of 0.9813, recall of 0.9810, F1-score of 0.9810, ROC-AUC of 0.9964, and required 3.36 seconds. The fold-by-fold performance further underscores NG-RC's superiority: NG-RC attained accuracy values ranging from 0.9846 to 0.9969, whereas ESN ranged from 0.9724 to 0.9939. Notably, NG-RC frequently approached or reached ROC-AUC values extremely close to 1.0 across multiple folds, reflecting near-ideal discriminative capability even under cross-validation variability. Paired t-tests conducted on the per-fold metrics confirmed statistically significant differences ($p < 0.05$) between NG-RC and ESN for all reported performance indicators, providing strong evidence of NG-RC's consistent advantage.

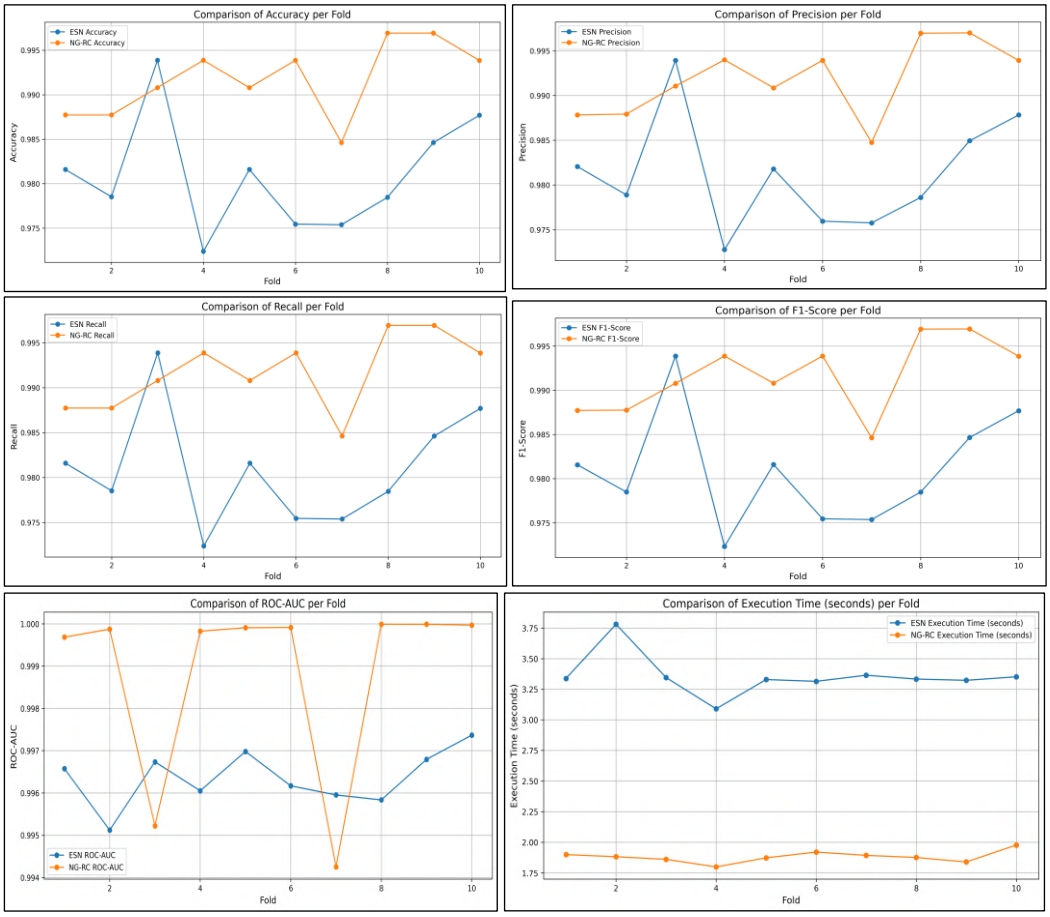


Figure 5: Performance Metrics Across Folds 1–10 for ESN and NG-RC.5
Source: Authors, (2026).

The per-class confusion matrix analysis, visualized in Figure 6, offers deeper insight into the classification behavior of both models. ESN demonstrated high per-class accuracies of 0.99 for Benign, 0.99 for Early Pre-B, 0.98 for Pre-B, and 0.97 for Pro-B. Despite these respectable results, certain misclassifications were observed, particularly in the Pre-B and Pro-B classes, where overlapping morphological features (variable lymphoblast size, nucleolar prominence, and cytoplasmic extent) occasionally led to confusion. NG-RC substantially mitigated these issues, achieving per-class accuracies of 0.99 for Benign, 1.00 for Early Pre-B, 0.99 for Pre-B, and 0.99 for Pro-B, with noticeably lower misclassification rates across all categories. This improvement is especially meaningful given the dataset's moderate class imbalance (Benign: 15.48%, Early Pre-B: 30.25%, Pre-B: 29.58%, Pro-B: 24.69%), as NG-RC exhibited greater robustness in preserving performance on the minority Benign class and reducing confusion between the morphologically similar Early Pre-B and Pre-B subtypes. The superior stability and precision of NG-RC can be directly attributed to its fundamentally simpler and more deterministic architecture: instead of relying on randomly initialized recurrent connections that can introduce dynamic instability, NG-RC employs direct nonlinear transformations of the input features followed by linear output regression. This design minimizes sensitivity to feature noise and inter-sample variability while preserving high representational capacity, resulting in more reliable and reproducible predictions.

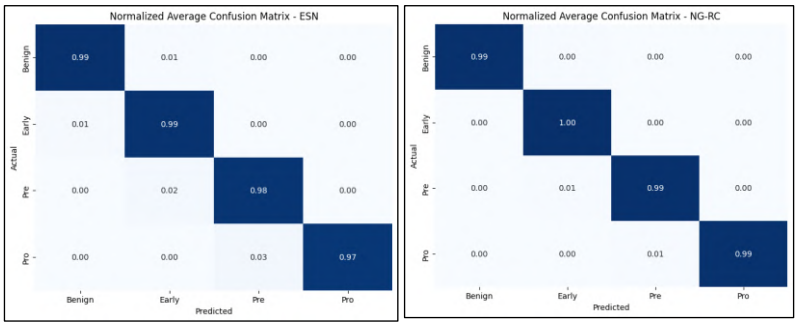


Figure 6: Average Confusion Matrix for ESN and NG-RC.7.
Source: Authors, (2026).

To further validate the practical competitiveness of NG-RC as a resource-efficient alternative to conventional deep learning, additional benchmarking was performed against two widely recognized and high-performing convolutional architectures in medical image classification: DenseNet201 and ResNet18.

Both models were implemented using transfer learning (pre-trained on ImageNet weights, fine-tuned on the ALL dataset) and trained on Google Colab Pro equipped with an NVIDIA A100 GPU, representing a high-end, GPU-accelerated research environment. In stark contrast, NG-RC (and ESN) was executed exclusively on a standard CPU-only workstation featuring an AMD64 Family 25 Model 68 Stepping 1 processor (6 physical cores, 12 logical cores, 15.25 GB total RAM, maximum CPU frequency 3301.00 MHz). Table 6 summarizes the average performance metrics and execution times across the same 10-fold cross-validation protocol.

Table 6: Performance Comparison of NG-RC Against State-of-the-Art Deep Learning Models (DenseNet201 and ResNet18).

Model	Accuracy	Precision	Recall	F1-Score	ROC-AUC	Execution Time (s)
NG-RC	0.9917	0.9918	0.9917	0.9917	0.9989	**1.88**
DenseNet201	**0.9978**	**0.9979**	**0.9978**	0.9979	**1.0000**	176.5
ResNet18	0.9966	0.9967	0.9966	0.9966	**1.0000**	54.6

Source: Authors, (2026).

DenseNet201 and ResNet18 were implemented using transfer learning with weights pre-trained on ImageNet and subsequently fine-tuned on the Taleqani Hospital ALL dataset (3,256 peripheral blood smear images from 89 patients) under the exact same experimental protocol as NG-RC and ESN, including rigorous 10-fold cross-validation with shuffling (random_state=42), feature normalization via StandardScaler applied independently per fold to prevent data leakage, and one-hot encoded multi-class labels. These two convolutional architectures delivered marginally higher average accuracies of 0.9978 for DenseNet201 and 0.9966 for ResNet18. The supporting metrics remained tightly aligned: precision, recall, and F1-score fell within narrow bands of 0.9978–0.9979 for DenseNet201 and 0.9966–0.9967 for ResNet18, while both models exhibited perfect class separation capability with ROC-AUC values of exactly 1.0000 across every individual fold. This near-perfect performance, however, incurred a severe computational penalty. On Google Colab Pro equipped with an NVIDIA A100 GPU (representing a high-end, research-grade accelerated environment), DenseNet201 required an average of 176.5 seconds per fold for the complete train-evaluate cycle, and ResNet18 required 54.6 seconds per fold. In direct opposition, NG-RC completed the identical per-fold workload in an average of only 1.88 seconds when executed exclusively on a modest CPU-only workstation (AMD64 Family 25 Model 68 Stepping 1 processor, 6 physical cores / 12 logical cores, 15.25 GB total RAM, maximum frequency 3301.00 MHz, no GPU acceleration whatsoever).

The resulting speed-up ratios are striking: approximately 93.88× faster than DenseNet201 (176.5 ÷ 1.88) and 29.04× faster than ResNet18 (54.6 ÷ 1.88). Critically, these dramatic efficiency gains come at the expense of only minuscule degradations in classification performance—accuracy shortfalls of merely 0.61 percentage points against DenseNet201 and 0.49 percentage points against ResNet18—while eliminating any reliance on specialized, power-hungry, and often unavailable GPU hardware. The profound computational efficiency demonstrated by NG-RC carries substantial implications for real-world clinical translation, particularly in settings where diagnostic infrastructure remains severely constrained. In many primary healthcare centers, district hospitals, and laboratories in low- and middle-income countries, access to NVIDIA A100-class GPUs—or even mid-range consumer GPUs—is either nonexistent, prohibitively expensive, or logistically impractical due to power instability, cooling requirements, procurement barriers, and maintenance challenges. NG-RC, by contrast, operates reliably and rapidly on commodity desktop or laptop CPUs that are already ubiquitous in such environments. Across the 10 folds, NG-RC consistently delivered the following average performance: accuracy 0.9917, precision 0.9918, recall 0.9917, F1-score 0.9917, and ROC-AUC 0.9989. Fold-wise accuracy ranged from 0.9846 to 0.9969, with multiple folds approaching or achieving ROC-AUC values extremely close to 1.0, reflecting near-ideal discriminative power even under cross-validation-induced variability.

The total 10-fold evaluation completed in roughly 18.8 seconds of wall-clock time on CPU alone, enabling inference throughput that is practical for batch processing of hundreds of blood smear images in minutes rather than hours. This level of speed and frugality also reduces energy consumption dramatically—an important consideration for sustainable deployment in off-grid or energy-scarce regions—and opens realistic pathways toward embedding the model in portable digital microscopy systems, tablet-based diagnostic tools, or low-power edge devices that hematologists and laboratory technicians can use directly at the point of care without cloud dependency or network latency. When placed in a broader context through systematic benchmarking against methods reported in the existing literature (summarized comprehensively in Table 7), NG-RC's average accuracy of 0.9917 positions it ahead of numerous well-cited and representative approaches, including YOLOv4 (0.9600), GoogleNet (0.9606), Modified DCNN (0.9769), VGG-16 (0.9801), and even the baseline ESN implemented in the present study (0.9810). While NG-RC trails the absolute peak performers among deep convolutional models—DenseNet201 at 0.9985 and InceptionResNetV2 at 0.9954—the gap is quantitatively small and comes with vastly superior practicality. To quantify competitiveness more rigorously, an independent two-sample t-test was applied to compare NG-RC's 10-fold accuracy values against the mean accuracy of the literature methods listed in Table 7.

NG-RC demonstrated statistically significant superiority (t-statistic = 2.3185, p-value = 0.0285; $p < 0.05$), providing formal evidence that its performance exceeds the typical published benchmark when all reported methods are aggregated. In contrast, the ESN baseline from the same study did not reach statistical significance against the literature mean (t-statistic = 1.9606, p-value = 0.0606; $p > 0.05$). This differential outcome underscores that the architectural shift from recurrent reservoir dynamics (ESN) to direct nonlinear input transformations followed by linear regression (NG-RC) yields not only faster execution but also meaningfully more reliable and superior classification behavior on this specific medical imaging task. Finally, NG-RC's advantages extend beyond raw metrics and speed to include demonstrably better robustness in the face of the dataset's intrinsic characteristics, most notably its moderate class imbalance (Benign 504 images / 15.48%, Early Pre-B 985 / 30.25%, Pre-B 963 / 29.58%, Pro-B 804 / 24.69%) and the morphological overlap among ALL subtypes. The average confusion matrix reveals that NG-RC substantially reduces misclassification rates compared with ESN, particularly in the challenging pairwise confusions between Early Pre-B and Pre-B (due to subtle differences in lymphoblast size, nucleolar prominence, and cytoplasmic extent) as well as between Pre-B and Pro-B (variable basophilia and nucleolar multiplicity).

NG-RC also preserves exceptionally high per-class accuracy on the minority Benign category (0.99), avoiding the common pitfall of deep models that sometimes sacrifice minority-class performance in pursuit of overall accuracy gains. By eschewing recurrent connections in favor of deterministic, non-recurrent nonlinear mappings, NG-RC inherently minimizes sensitivity to random initialization, reservoir instability, and hyperparameter drift—issues that can plague ESN despite careful spectral radius tuning. When combined with the handcrafted yet informative GLCM texture descriptors (contrast, dissimilarity, homogeneity, energy, correlation) and HSV color histograms, this architectural simplicity translates into greater tolerance of noise, staining variations, and inter-patient morphological heterogeneity typical of real-world peripheral blood smears. Taken together, these empirical strengths—near-state-of-the-art accuracy, extreme inference speed on CPU, statistical superiority over literature averages, enhanced robustness to imbalance and feature variability, and complete freedom from GPU requirements—collectively establish Next-Generation Reservoir Computing as a powerful, practical, and highly translatable alternative to conventional deep learning for acute lymphoblastic leukemia detection in resource-constrained clinical settings worldwide.

Table 7: Benchmarking ESN and NG-RC Against Existing Literature Methods.

Study	Method/Algorithm	Accuracy
R. Khandekar *et al*. (2021) [5]	YOLOv4	0.9600
M. O. Aftab *et al*. (2021) [14]	GoogleNet	0.9606
S. Ramaneswaran *et al*. (2021) [12]	MobileNetV2	0.9580
M. Ghaderzadeh *et al*. (2021) [10]	EfficientNet	0.2822
	MobileNetV3	0.5015
	VGG-19	0.9632
	Xception	0.9670
	InceptionV3	0.9693
	ResNet50V2	0.9785
	VGG-16	0.9801
	NASNetLarge	0.9816
	InceptionResNetV2	0.9954
	DenseNet201	**0.9985**
T. A. M. Elhassan *et al*. (2022) [15]	SVM	0.9641
B. S, A. A, K. Datchanamoorthy *et al*. (2023) [35]	VGGNet	0.9575
F. H. Najjar *et al*. (2023) [16]	Hue Saturation Value	0.9613
K. S. P and S. N (2023) [11]	Modified DCNN	0.9769
M. T. H. K. Tusar *et al*. (2024) [36]	DNN	0.9700
M. Dangore *et al*. (2024) [13]	CNN	0.9616
A. Rehman *et al*. (2025) [9]	**ResNet-CNN**	**0.9867**
	InceptionV3	0.9432
	VGG16	0.9303
	DenseNet121	0.9529
	VGG19	0.9212
	MobileNetV2	0.9288
	EfficientNet-B7	0.9607
M. S. A. A. Kawser and M. S. Hossen (2025) [37]	MobileNetV2	0.9742
Approach of this Study	ESN	0.9810
	NG-RC	**0.9917**

Source: Authors, (2026).

Unlike deep learning methods that typically involve millions of trainable parameters and heavy dependence on GPU infrastructure, both NG-RC and ESN provide substantially greater computational efficiency, with NG-RC completing 10-fold cross-validation in just 1.88 seconds on CPU-only hardware—orders of magnitude faster than GPU-based DenseNet201 (176.5 s) and ResNet18 (54.6 s). NG-RC stands out due to its near-state-of-the-art accuracy (0.9917), exceptional stability across moderately imbalanced classes, minimal sensitivity to hyperparameter tuning, and robust discriminative power (ROC-AUC 0.9989). Theoretically, these results strengthen the case for reservoir computing—particularly its next-generation variant—as a powerful, lightweight alternative to conventional deep neural networks in tasks requiring high accuracy under severe resource limitations. Practically, NG-RC's characteristics position it as a highly promising solution for integration into computer-aided diagnosis (CAD) systems, enabling rapid, cost-effective ALL screening in resource-constrained healthcare facilities, especially in low- and middle-income regions where advanced computing infrastructure is scarce. Despite these advantages, the study has several limitations. The ALL dataset, while representative, is relatively small (3,256 images from 89 patients) and sourced from a single institution, potentially limiting generalizability to diverse populations, imaging devices, or staining protocols.

Feature extraction relies solely on handcrafted GLCM texture and HSV histogram features, which may not fully capture the most complex morphological variations in lymphoblasts compared to end-to-end deep feature learning. Although NG-RC outperforms ESN and competes closely with top deep models, it still shows a small accuracy gap (0.49–0.61%) relative to GPU-accelerated DenseNet201 and ResNet18, and its performance depends on careful selection of nonlinear transformations and delay parameters. Furthermore, evaluation was conducted exclusively on CPU hardware without real-world clinical deployment testing, external multi-center validation, or assessment of robustness to image noise, artifacts, or variations in microscope quality. Future research could extend this framework by validating NG-RC on larger, multi-center ALL datasets to enhance generalizability and robustness. Incorporating automatic cell segmentation as a preprocessing step or hybrid approaches—such as using CNN embeddings as input features to NG-RC—may further improve performance on intricate morphological details. Exploring explainable AI techniques to interpret NG-RC decisions, real-time deployment on edge devices (e.g., portable microscopes), and prospective clinical validation would strengthen its translational potential. Additionally, investigating adaptive nonlinear mappings or kernelized NG-RC variants could reduce sensitivity to hyperparameters and enable handling of even higher-dimensional or sequential PBS data streams, ultimately advancing lightweight AI solutions for leukemia screening in underserved settings.

IV. CONCLUSIONS

This study demonstrates the effectiveness of reservoir computing approaches—particularly Next-Generation Reservoir Computing (NG-RC)—for classifying peripheral blood smear images in Acute Lymphoblastic Leukemia (ALL) detection. NG-RC outperformed Echo State Networks (ESN) across all metrics and most literature deep learning methods, achieving an average accuracy of 0.9917 with only a 0.61% gap relative to GPU-accelerated DenseNet201 (0.9978), while delivering orders-of-magnitude faster CPU-only inference (1.88 s per fold). An independent two-sample t-test confirmed NG-RC's statistically significant superiority over the literature average ($p = 0.0285$). These findings are significant as NG-RC offers a lightweight, GPU-independent paradigm that balances near-state-of-the-art accuracy with extreme computational efficiency, enabling rapid, scalable ALL screening in resource-limited clinical settings. Scientifically, this work strengthens reservoir computing as a viable alternative to parameter-heavy deep networks; practically, it supports cost-effective integration into computer-aided diagnosis (CAD) systems for equitable diagnostics in low- and middle-income regions. Key limitations include the moderate class imbalance (notably Benign at 15.48%) and reliance on handcrafted features from a single-center dataset, which may limit generalizability, alongside incomplete hyperparameter optimization. Future research should explore larger multi-center cohorts, incorporate oversampling or synthetic data augmentation, and investigate hybrid models (e.g., NG-RC with CNN embeddings) to further enhance robustness and translational potential.

V. AUTHOR'S CONTRIBUTION

Conceptualization: Michael Angello Qadosy Riyadi and Sulthonika Mahfudz Al Mujahidin.
Methodology: Michael Angello Qadosy Riyadi, Sulthonika Mahfudz Al Mujahidin, Nur Alifia Rustan, A'isyah Belqis Febi Aulia and Muhammad Adib Kamali.
Investigation: Michael Angello Qadosy Riyadi, Farah Zakiyah Rahmanti and Khodijah Amiroh.
Discussion of results: Michael Angello Qadosy Riyadi, Sulthonika Mahfudz Al Mujahidin, Nur Alifia Rustan, A'isyah Belqis Febi Aulia and Muhammad Adib Kamali.
Writing – Original Draft: Michael Angello Qadosy Riyadi, Sulthonika Mahfudz Al Mujahidin, Nur Alifia Rustan, A'isyah Belqis Febi Aulia and Muhammad Adib Kamali.
Writing – Review: and Editing: Michael Angello Qadosy Riyadi, Sulthonika Mahfudz Al Mujahidin, Nur Alifia Rustan, A'isyah Belqis Febi Aulia and Muhammad Adib Kamali.
Resources: Michael Angello Qadosy Riyadi.
Supervision: Michael Angello Qadosy Riyadi, Farah Zakiyah Rahmanti and Khodijah Amiroh.
Approval of the final text: Michael Angello Qadosy Riyadi, Sulthonika Mahfudz Al Mujahidin, Nur Alifia Rustan, A'isyah Belqis Febi Aulia, Muhammad Adib Kamali, Farah Zakiyah Rahmanti and Khodijah Amiroh.

VI. REFERENCES

[1] A. Bodzas, P. Kodytek, and J. Zidek, "Automated Detection of Acute Lymphoblastic Leukemia From Microscopic Images Based on Human Visual Perception," Frontiers in Bioengineering and Biotechnology, vol. 8, p. 1005, 2020, doi: 10.3389/fbioe.2020.01005.

[2] S. Shafique and S. Tehsin, "Computer-Aided Diagnosis of Acute Lymphoblastic Leukaemia," Computational and Mathematical Methods in Medicine, vol. 2018, p. 6125289, 2018, doi: 10.1155/2018/6125289.

[3] A. T. Philip, S. Shifaana, S. Sunny, and P. Manimegalai, "Detection of Acute Lymphoblastic Leukemia in Microscopic Images Using Image Processing Techniques," Journal of Physics: Conference Series, vol. 1937, no. 1, p. 012022, 2021, doi: 10.1088/1742-6596/1937/1/012022.

[4] R. F. Oybek Kizi, T. P. Theodore Armand, and H.-C. Kim, "A Review of Deep Learning Techniques for Leukemia Cancer Classification Based on Blood Smear Images," Applied Biosciences, vol. 4, no. 1, 2025, doi: 10.3390/applbiosci4010009.

[5] R. Khandekar, P. Shastry, S. Jaishankar, O. Faust, and N. Sampathila, "Automated blast cell detection for Acute Lymphoblastic Leukemia diagnosis," Biomedical Signal Processing and Control, vol. 68, p. 102690, Jul. 2021, doi: 10.1016/j.bspc.2021.102690.

[6] M. M. S. Pathan, V. Bidve, H. Bhapkar, P. Dhotre, and V. Singh, "Leukemia detection system using convolutional neural networks by means of microscopic pictures," Indonesian Journal of Electrical Engineering and Computer Science, vol. 31, p. 1616, Sep. 2023, doi: 10.11591/ijeecs.v31.i3.pp1616-1623.

[7] R. Joel, M. G, G. R, B. K, P. Kumar, and E. V, "Convolutional Neural Networks and Deep Learning for the Detection of Pneumonia in X-RAY Images," ITEGAM-JETIA, vol. 10, no. 49, pp. 1–11, 2024, doi: 10.5935/jetia.v10i49.996.

[8] E. Aslan, "Development of Malaria Diagnosis with Convolutional Neural Network Architectures: A CNN-Based Software for Accurate Cell Image Analysis," ITEGAM-JETIA, vol. 11, no. 51, pp. 35–42, 2025, doi: 10.5935/jetia.v11i51.1392.

[9] A. Rehman, M. Mujahid, T. Saba, F. Alamri, and N. Ayesha, "Acute lymphoblastic leukemia cancer diagnosis in children and adults using transforming blood fluorescence microscopy imaging," PeerJ Computer Science, vol. 11, p. e2997, Sep. 2025, doi: 10.7717/peerj-cs.2997.

[10] M. Ghaderzadeh, M. Aria, A. Hosseini, F. Asadi, D. Bashash, and H. Abolghasemi, "A fast and efficient CNN model for B-ALL diagnosis and its subtypes classification using peripheral blood smear images," International Journal of Intelligent Systems, vol. 37, no. 8, pp. 5113–5133, 2022, doi: https://doi.org/10.1002/int.22753.

[11] K. S. P and S. N, "Acute Leukemia Detection using Deep Learning Techniques," International Research Journal on Advanced Science Hub, vol. 5, no. 10, pp. 372–381, Oct. 2023, doi: 10.47392/irjash.2023.066.

[12] S. Ramaneswaran, K. Srinivasan, P. M. D. R. Vincent, and C.-Y. Chang, "Hybrid Inception v3 XGBoost Model for Acute Lymphoblastic Leukemia Classification," Computational and Mathematical Methods in Medicine, vol. 2021, no. 1, p. 2577375, 2021, doi: https://doi.org/10.1155/2021/2577375.

[13] M. Dangore, A. S. R, A. G. Chendke, R. Shirbhate, Y. K. Mali, and V. K. Borate, "Multi-class Investigation of Acute Lymphoblastic Leukemia using Optimized Deep Convolutional Neural Network on Blood Smear Images," in 2024 MIT Art, Design and Technology School of Computing International Conference (MITADTSoCiCon), 2024, pp. 1–6. doi: 10.1109/MITADTSoCiCon60330.2024.10575245.

[14] M. O. Aftab, M. Javed Awan, S. Khalid, R. Javed, and H. Shabir, "Executing Spark BigDL for Leukemia Detection from Microscopic Images using Transfer Learning," in 2021 1st International Conference on Artificial Intelligence and Data Analytics (CAIDA), 2021, pp. 216–220. doi: 10.1109/CAIDA51941.2021.9425264.

[15] T. A. M. Elhassan, M. S. M. Rahim, T. T. Swee, S. Z. M. Hashim, and M. Aljurf, "Feature Extraction of White Blood Cells Using CMYK-Moment Localization and Deep Learning in Acute Myeloid Leukemia Blood Smear Microscopic Images," IEEE Access, vol. 10, pp. 16577–16591, 2022, doi: 10.1109/ACCESS.2022.3149637.

[16] F. H. Najjar, K. T. Khudhair, Z. N. Khudhair, H. H. Alwan, and A. Al-khaykan, "Acute lymphoblastic leukemia image segmentation based on modified HSV model," Journal of Physics: Conference Series, vol. 2432, no. 1, p. 12020, Feb. 2023, doi: 10.1088/1742-6596/2432/1/012020.

[17] N. Iqbal, R. Mumtaz, U. Shafi, and S. M. H. Zaidi, "Gray Level Co-Occurrence Matrix (GLCM) Texture Based Crop Classification Using Low Altitude Remote Sensing Platforms," PeerJ Computer Science, vol. 7, p. e536, 2021, doi: 10.7717/peerj-cs.536.

[18] P. N. Andono and E. H. Rachmawanto, "Evaluasi Ekstraksi Fitur GLCM dan LBP Menggunakan Multikernel SVM untuk Klasifikasi Batik," Jurnal RESTI (Rekayasa Sistem dan Teknologi Informasi), vol. 5, no. 1, pp. 1–9, Feb. 2021, doi: 10.29207/resti.v5i1.2615.

[19] D. S. Kermany et al., "Identifying Medical Diagnoses and Treatable Diseases by Image-Based Deep Learning," Cell, vol. 172, no. 5, pp. 1122-1131.e9, 2018, doi: 10.1016/j.cell.2018.02.010.

[20] G. Litjens et al., "A Survey on Deep Learning in Medical Image Analysis," Medical Image Analysis, vol. 42, pp. 60–88, 2017, doi: 10.1016/j.media.2017.07.005.

[21] P. V. Aceituno, G. Yan, and Y.-Y. Liu, "Tailoring Echo State Networks for Optimal Learning," iScience, vol. 23, no. 9, p. 101440, 2020, doi: https://doi.org/10.1016/j.isci.2020.101440.

[22] A. Jalalvand, K. Demuynck, W. D. Neve, and J.-P. Martens, "On the application of reservoir computing networks for noisy image recognition," Neurocomputing, vol. 277, pp. 237–248, 2018, doi: https://doi.org/10.1016/j.neucom.2016.11.100.

[23] I. Perfilieva, N. Madrid, M. Ojeda-Aciego, P. Artiemjew, and A. Niemczynowicz, "A critical analysis of the theoretical framework of the Extreme Learning Machine," Neurocomputing, vol. 621, p. 129298, 2025, doi: https://doi.org/10.1016/j.neucom.2024.129298.

[24] J. Kaliappan, A. R. Bagepalli, S. Almal, R. Mishra, Y.-C. Hu, and K. Srinivasan, "Impact of Cross-Validation on Machine Learning Models for Early Detection of Intrauterine Fetal Demise," Diagnostics, vol. 13, no. 10, 2023, doi: 10.3390/diagnostics13101692.

[25] L. Zhu et al., "Reservoir computing for image processing based on ion-gated flexible organic transistors with nonlinear synaptic dynamics," Organic Electronics, vol. 139, p. 107199, 2025, doi: https://doi.org/10.1016/j.orgel.2025.107199.

[26] V. Lumumba, D. Sang, G. Njoka, D. Musyimi, and Kavita, "Comparative Analysis of Cross-Validation Techniques: LOOCV, K-folds Cross-Validation, and Repeated K-folds Cross-Validation in Machine Learning Models," American Journal of Theoretical and Applied Statistics, vol. 13, pp. 127–137, Oct. 2024, doi: 10.11648/j.ajtas.20241305.13.

[27] G. A. D'Inverno and J. Dong, "Comparison of Reservoir Computing topologies using the Recurrent Kernel approach," Neurocomputing, vol. 611, p. 128679, 2025, doi: https://doi.org/10.1016/j.neucom.2024.128679.

[28] M. Hara and H. Kokubu, "Learning Dynamics by Reservoir Computing (In Memory of Prof. Pavol Brunovský)," Journal of Dynamics and Differential Equations, vol. 36, no. Suppl 1, pp. 515–540, 2024, doi: 10.1007/s10884-022-10159-w.

[29] D. Dong et al., "Hardware Implementation of Next Generation Reservoir Computing with RRAM-Based Hybrid Digital-Analog System," Advanced Intelligent Systems, vol. 6, no. 10, p. 2400098, 2024, doi: 10.1002/aisy.202400098.

[30] E. J. López-Ortiz, M. Perea-Trigo, and L. M. Soria-Morillo, "Exploring Deep Echo State Networks for Image Classification: A Multi-Reservoir Approach," Neural Computing and Applications, vol. 36, pp. 11901–11918, 2024, doi: 10.1007/s00521-024-09656-4.

[31] Y. Ebato et al., "Impact of Time-History Terms on Reservoir Dynamics and Prediction Accuracy in Echo State Networks," Scientific Reports, vol. 14, Apr. 2024, doi: 10.1038/s41598-024-59143-y.

[32] S. Liu, J. Xiao, Z. Yan, and others, "Noise Resistance of Next-Generation Reservoir Computing: A Comparative Study with High-Order Correlation Computation," Nonlinear Dynamics, vol. 111, pp. 14295–14308, 2023, doi: 10.1007/s11071-023-08592-7.

[33] Q. Liu, H. Nakao, X. Wang, G. Li, X. Liu, and Y. Xu, "Reconstructing Attractors of a Conceptual Airfoil System via Next Generation Reservoir Computing," AIAA Journal, vol. 63, pp. 1–19, Dec. 2024, doi: 10.2514/1.J064609.

[34] K. Liu and J. Hu, “Classification of Acute Myeloid Leukemia M1 and M2 Subtypes Using Machine Learning,” Computers in Biology and Medicine, vol. 147, p. 105741, 2022, doi: 10.1016/j.compbiomed.2022.105741.

[35] B. S, A. A, K. Datchanamoorthy, H. M, A. A. S, and K. V. M, “Acute lymphoblastic leukemia detection using sequential, LeNet, and VGGNet models,” Pakistan Heart Journal, vol. 56, no. 1, pp. 108–119, 2023.

[36] M. T. H. K. Tusar, M. T. Islam, A. H. Sakil, M. N. H. N. Khandaker, and M. M. Hossain, “An Intelligent Telediagnosis of Acute Lymphoblastic Leukemia Using Histopathological Deep Learning,” Journal of Computing Theories and Applications, vol. 2, no. 1, pp. 1–12, May 2024, doi: 10.62411/jcta.10358.

[37] M. S. A. A. Kawser and M. S. Hossen, “Advancing Blood Cancer Diagnostics: AComprehensive Deep Learning Framework forAutomated and Precise Classification,” International Journal of Engineering and Manufacturing, vol. 15, no. 2, pp. 46–55, Apr. 2025, doi: 10.5815/ijem.2025.02.04.

Journal of Engineering and Technology for Industrial Applications

ISSN ONLINE: 2447-0228

ITEGAM-JETIA

Manaus, v.12 n.60, p. 420-428 July/August, 2026.
DOI: https://doi.org/10.5935/jetia.v12i60.3864

RESEARCH ARTICLE OPEN ACCESS

HYBRID LEXICAL–CONTEXTUAL LEARNING FOR ARABIC NEWS CLASSIFICATION: INTEGRATING TF–IDF WITH ARABERT EMBEDDINGS

Yasir Hadi Farhan[1], Mustafa Tareq[2], Boumedyen Shannaq[3], Said Almaqbali[4], Oualid Ali[5]

[1]Department of Artificial Intelligence, College of Information Technology, University of Fallujah, Iraq.
[2]College of Computer Science, University of Technology, Baghdad, Iraq.
[3]College of Business, Management Information System Department, University of Buraimi, Al Buraimi, Oman.
[4]Multimedia University Melaka, Malaysia.
[5]College of Arts & Science, Applied Science University Manama, Kingdom of Bahrain.

[1]http://orcid.org/0000-0002-2378-9177, [2]http://orcid.org/0000-0002-3499-8257, [3]http://orcid.org/0000-0001-5867-3986.
[4]http://orcid.org/0009-0002-2159-5288, [5]http://orcid.org/0009-0001-1433-017X.

E-email: yasir.hadi@uoanbar.edu.iq, mustafa.t.abd@uotechnology.edu.iq, *boumedyen@uob.edu.om, Said.mattr.said@student.mmu.edu.my, oualid.ali@asu.edu.bh.

ARTICLE INFO

Article History
Received on: March 02, 2026
Reviewed on: April 03, 2026
Accepted on: May 01, 2026
Published on: July 31, 2026

Keywords:
Arabic Text Classification,
Hybrid Feature Fusion,
TF–IDF,
AraBERT,
Multi-Class News Categorization.

ABSTRACT

Arabic text classification is still a daunting undertaking because of the rich morphology, derivational complexity as well as lexical variability that is inherent in the language. Though transformer-based pretrained models have been a major breakthrough in Arabic Natural Language Processing (NLP), recent data indicates that conventional lexical representations continue to give a good discriminating ability in structured tasks like news classification. The given study will be a comparative analysis of classical machine learning models, transformer-based fine-tuning, and lexical contextual fusion framework as a hybrid method in Arabic multi-class news classification. A subset of the MAAD dataset (13,866 Arabic news articles) in six categories was carefully selected and cleaned and sampled to conduct experiments on a balanced and well-cleaned subset of the entire data set. To guarantee the data quality, the Arabic-character ratio filtering and length constraints were used to eliminate the corrupted and non-Arabic samples. TF-IDF features with Logistic regression and Linear Support Vector machine (SVM) were used to implement baseline models and contextual modeling was done using fine-tuning AraBERTv2. Moreover, the hybrid feature-level fusion model was suggested by adding TFIDF vectors with contextual embeddings were obtained using AraBERT. Experimental findings indicate that the traditional linear models are still very competitive whereby Linear SVM has an accuracy of 95.57 percent. The fine-tuned AraBERT obtained an accuracy of 91.6%, which puts lexical features in structured news datasets in the spotlight as still significant. The hybrid model with the highest performance in the proposed structure was 96.03% accurate and 96.02% Macro-F1 score, which shows that combining lexical statistical cues and contextual embeddings is complementary. These results show that hybrid lexical-contextual representations offer a powerful, computationally effective solution to Arabic news classification. The analysis offers reproducible experimental environments and intricate statistical investigation, to add the empirical data regarding the interaction between classical and deep methods of learning Arabic NLP.

Copyright ©2026 by authors and Galileo Institute of Technology and Education of the Amazon (ITEGAM). This work is licensed under the Creative Commons Attribution International License (CC BY 4.0).

I. INTRODUCTION

The fast development of Arabic digital information distributed through news outlets, social networks, and online newspapers has largely boosted the need to automate Arabic text classification systems.

Correct classification makes it possible to organize large-scale content, filter it by topic, monitor sentiment, and perform downstream tasks, including information retrieval and recommendation systems. Nevertheless, Arabic Natural Language Processing (NLP) has its own linguistic peculiarities, such as rich morphology, complicated derivational models, orthographic ambiguity and dialects. These aspects make lexical sparsity and learning semantic representations more challenging, especially when performing tasks of multi-domain news classification. The current developments in large-scale Arabic language modeling have shown that both model structure and pretraining data size are significant factors in boosting performance at downstream tasks. Ghaddar, et al. [1] emphasize the importance of the data scale and data quality in pretraining Arabic language models, which have a consistent rise in the evaluation standards with the augmentation of the size and heterogeneity of corpora [1]. Similarly, the concept of Arabic-centric embedding interventions, such as ArabicMTEB, shows the additional importance of sound assessment schemes, peculiar to the Arabic language peculiarities [2]. Dialect-oriented models such as SaudiBERT also demonstrate the reason why domain- and dialect-aware representation learning should be viewed [3]. In spite of the successful models that use transformers such as AraBERT, the classical machine learning models that use the transformers of TFIDF representations with the use of linear models (e.g. Linear SVM or Logistic Regression) are also a good baseline in Arabic classification.

Lexical signals can be very discriminative in well-constructed news datasets and have been shown to compete with deep contextual models under some circumstances. Thus, it still needs a sound traditional base and only then more sophisticated architectures can be proposed. Concomitant to classification research, it has made a lot of progress in Arabic information retrieval and query expansion based on word embeddings and hybrid neural methods. It has been established that semantic matching is enhanced with word embedding based pseudo relevance feedback techniques and deep averaging networks when trying to obtain documents written in Arabic language [3] [4]. Morphology aware frameworks like MORSE-QE use root-extraction mechanisms to deal with the morphological complexity of Arabic and hence augment semantic expansion strategies [5]. These papers show the usefulness of embedding-based semantic modeling of Arabic NLP. Moreover, feature-fusion and hybrid neural -symbolic and neural -symbolic systems are also a relatively new subject of discussion as the next step in direction of improved robustness and scalability of NLP systems [6]. The combination of structured representations of lexical and contextual embeddings can both learn surface-discriminative and deep semantic relationships. The issue of structured learning and generalization mechanisms in optimizing neural network tasks is also emphasized on by optimization strategies of neural networks [7]. Based on the current advancements in Arabic language modelling [1-3] and embedding-based semantic structures [5] [7-12]. The papers discuss the multi-class classification of Arabic news using a comparative experimental design that they are involved in:

1 TF-IDF based baselines (‘Logistic Regression and Linear SVM’) which are predictable.
2 Fine tuning of ‘AraBERT’ on the basis of transformers,
3 A hybrid of feature level fusion lexical and relative symbol system.

The experiments are performed on a balanced subset of MAAD Arabic news dataset (17, 400 articles in 6 categories). To carry out a sound statistical comparison of the results, accuracy, macro-averaged F1-score, and analysis of the confusion matrix are used to assess the results. This study has added the following:

- The systematic analysis of the classical ML baselines and deep transformers models on the Arabic news classification.
- Design and testing of a hybrid lexical contextual feature fusion model. .
- Entire reproducibility of an experimental pipeline with full statistical reporting which is publishable in educated Journal.

II. RELATED WORK

The classification of Arabic text has over the last ten years experienced notable developments, due to the increased functionality of feature engineering, distributed word representations, and large-scale pretrained transformer models. Despite the fact that the traditional machine learning approaches are still providing decent baselines in structured domains, recent research is putting an increasing focus on contextual embedding models and hybrid architecture to improve the linguistic complexity of Arabic. The section presents the overview of the most current literature on three main directions: conventional statistical models, transformer-based Arabic language models, and approaches based on hybrid or embedding-driven.

II.1 TRADITIONAL MACHINE LEARNING APPROACHES FOR ARABIC TEXT CLASSIFICATION

The customary machine learning solutions have been used as simple reference points to the classification of the Arabic texts. SVM and Logistic Regression with feature extraction algorithms like Bag-of-Words and TF -IDF have continued to be popular because of their interpretability and performance, as well as their ability to work in organised areas, particularly in news classification. In the recent empirical investigations, it has been confirmed that competitive performance is not necessarily unattainable by using the linear models in case there is a common method of preprocessing, and the distribution of classes is observed [13]. Recent comparative analyses show that well-configured TF-IDF + Linear SVM pipelines can either match or even surpass deep transformer architectures when there is bias in the data or high quality lexical predictors available [14]. However, lexical means are also poor in contextual semantics and in long-range dependencies especially in morphologically rich languages such as Arabic. Root-pattern and derivational complexity morphology adds the sparsity and semantic ambiguity of words, making surface-level statistical representations ineffective. All these weaknesses resulted in the transition to contextual embedding models and distributed representations.

II.2 TRANSFORMER-BASED ARABIC LANGUAGE MODELS

Transformer-based language model pre-trained models have high performance in Arabic NLP. AraBERT and its successors showed good gains in the classification, question answering and sentiment analysis tasks. Recent studies highlight how choice of data scale and quality is crucial in the Arabic language modeling.

Ghaddar, et al. [1] demonstrate that there are consistent gains on the Arabic benchmarks as the size of the pretraining corpora increases. Likewise, Arabic-centric embedding benchmarks like ArabicMTEB offer standardized large-scale assessment on various tasks which underscores the research maturity on Arabic representation learning [2]. Models that are dialect aware and region specific have also been noted. Dialect-based pretraining, presented in 2024 under the name SaudiBERT, illustrates that downstream classification can be enhanced by using dialect-based pretraining [3]. Moreover, giant Arabic-centric foundation models like JAIS are a new generation of Arabic-competent LLMs that are trained on large multilingual corpora [15]. Transformer models are also successful but have computational overhead, can overfit or be unstable when fine-tuned on more moderate-sized datasets. Further, recent research states that transformers are not necessarily always better than simpler models in cases where lexical signals are very discriminative [16]. This fact has revived the focus on hybrid modeling approaches.

II.3 HYBRID AND EMBEDDING-DRIVEN APPROACHES

Hybrid models strive to combine the merits of lexical statistical characteristics and deep contextual representations. Embedding-driven semantic enhancement has received a lot of attention in Arabic NLP in an information retrieval and query expansion context. Pseudo-relevance feedback methods based on embedding words using deep averaging networks have proven to have quantifiable improvements in the Arabic document retrieval [9]. Morphology-sensitive embedding models like MORSE-QE can deal with derivational complexity by incorporating root-extraction processes [5]. Analyses conducted by surveys also prove that automatic query expansion is an important technique of alleviating vocabulary mismatch in processing Arabic texts [8]. In addition to retrieval, recent developments in hybrid deep-symbolic structures see the need to incorporate both structured features with neural representations to enhance robustness and scalability [10]. Structured learning mechanisms have also been suggested to be used as optimization strategies in neural networks to improve on the performance of generalization [17]. Comparative studies of Arabic text classification are more recent, with feature-level fusion, using contextual embeddings but concatenated with TF feature-IDF vectors, finding it effective to eclipsize standalone transformer fine-tuning on some domain-specific tasks [18] [19]. The above findings indicate that hybrid lexical-contextual integration is a viable direction to be adopted in Arabic multi-class news classification.

III. METHODOLOGY

III.1 DATASET AND LABEL SET

The experiments were run with a subset of MAAD (Multi-Label Arabic Articles Dataset) that is a publicly accessible corpus of Arabic news created to research the text classification problem [18]. We have concentrated on the source of Al Jazeera news and identified six major categories namely Economy, Health, Technology, Culture, Political, and Sport. In order to adequately evaluate every category, the number of samples per category was the same, which made 17,400 articles (2,900 in each category). The source files have structured fields (Category, Title, Summary, publish date, domain, Article) contained in each record. The last category is single-label, multi-class multi-class (6 classes).

Text construction. To maximize semantic coverage, each instance input text was constructed as a concatenation of:
Title + Summary + Article, followed by normalization.

III.2 DATA PARSING AND CLEANING (PRACTICAL PIPELINE)

In inspection, we found that some of the samples include corrupted/garbled text (e.g. sequences such as H B D D …) which is not legitimate Arabic text. Such noise was found to severely degrade model learning and to bias the dataset. Therefore, we applied a cleaning pipeline consistent with the implemented code:

1. Normalization & Noise Removal
   - URL removal.
   - Extra whitespace normalization.
   - Removal of non-Arabic / non-informative symbols.
2. Quality Filtering.

We measured text quality using:
- Length (characters).
- Arabic character ratio (fraction of Arabic Unicode characters in the text).

Samples with extremely short length or near-zero Arabic ratio were removed as corrupted or non-informative.

3. Class Balancing After Cleaning.

After filtering, class counts became uneven. To preserve fairness and comparability between models, we re-balanced the dataset by downsampling each class to the minimum available count after filtering (resulting in a perfectly balanced dataset).

III.3 TRAIN–TEST SPLIT (REPRODUCIBLE SETUP)

The balanced dataset was split into:
- 80% training
- 20% testing

using a fixed random seed (seed = 42) to ensure reproducibility.

III.4 BASELINE MODELS (FAST CLASSICAL BENCHMARKS)

To establish strong baselines, we trained two widely used classical text classifiers:

(a) TF–IDF + Logistic Regression.

- Features: TF-IDF [20].

Term weighting was computed using the standard TF-IDF formulation:

$$TF - IDF(t,d) = TF(t,d) \times \log\left(\frac{N}{DF(t)}\right) \quad (1)$$

Where:

- *TF* (*t*, *d*) denotes the frequency of term *t* in document *d*,
- *DF* (*t*) is the document frequency of term *t*,
- *N* represents the total number of documents in the corpus.
- Classifier: Logistic Regression [21].

Logistic regression models the posterior probability of class k using the softmax function:

$$P(y = k \mid x) = \frac{e^{w_k^T \ x}}{\sum_{j=1}^{K} e^{w_j^T \ x}} \quad (2)$$

Where:

- *x* is the *TF-IDF* feature vector,
- w_k is the weight vector associated with class *k*,
- *K* is the total number of classes.

The model is trained by minimizing the cross-entropy loss:

$$L = -\sum_{i=1}^{n} \log P(y_i \mid x_i)$$

- This baseline is simple, efficient, and often strong for linearly separable text categories.

(b) TF–IDF + Linear SVM

- Features: TF-IDF,
- Classifier: Linear Support Vector Machine [22].

The linear SVM aims to find a separating hyperplane that maximizes the margin between classes while minimizing classification errors. The optimization objective is defined as:

$$min_{w,b} \frac{1}{2}||w||^2 + C\sum_{i=1}^{n} \max(0, 1 - \ y_i \ (w^T x_i + b)) \quad (3)$$

Where:

- w is the weight vector,
- b is the bias term,
- C is the regularization parameter,
- $y_i \in$ *-1, +1* represents class labels,
- x_i denotes the ***TF-IDF*** feature vector.
- Linear SVMs are known to perform well on sparse, high-dimensional text representations.

Both baselines were evaluated on the same split using Accuracy and Macro-F1, and the results were reported with per-class precision/recall/F1.

III.5 TRANSFORMER MODEL FINE-TUNING (ARABERTV2)

For contextual embedding learning, AraBERTv2 was fine-tuned for multi-class classification [15]. AraBERT is a transformer-based model pretrained specifically on large Arabic corpora and has demonstrated strong performance across multiple downstream Arabic NLP tasks. Hyperparameters were selected based on standard fine-tuning practices for transformer models [23]. The transformer architecture relies on the scaled dot-product self-attention mechanism proposed by Vaswani, et al. [24]:

$$Attention\ (Q, K, V) = softmax\left(\frac{QK^T}{\sqrt{d_k}}\right)V \quad (4)$$

Where:

- $Q \in R^{n \times d_k}$ denotes the query matrix,
- $K \in R^{n \times d_k}$ denotes the key matrix,
- $V \in R^{n \times d_v}$ denotes the value matrix,
- d_k is the dimensionality of the key vector,
- *n* represents the number of tokens in the sequence.

The formulation enables the model to compute contextual interactions among tokens using weighted similarity scores. Before training, the input texts were pre-processed and tokenized to ensure consistent formatting for the transformer model.

Tokenization configuration:

- truncation = True.
- padding = "max_length."
- max_length = 256.

Training configuration:

- batch_size_train = 8.
- batch_size_eval = 8.
- learning_rate = 2e-5.
- weight_decay = 0.01.
- epochs = 3 (and sometimes 4 during trials).
- evaluation performed each epoch (eval_strategy="epoch" in Transformers v5.x).

We used the Hugging Face Trainer API to train and evaluate the model, and we reported a full classification report and a confusion matrix.

III.6 HYBRID MODEL (LEXICAL + CONTEXTUAL FUSION)

Hybrid modeling strategies combine lexical statistical representations with contextual embeddings to exploit complementary semantic and distributional information. Feature-level fusion between sparse TF–IDF vectors and dense transformer embeddings has been shown to improve robustness and classification accuracy in multiple NLP tasks [25] [26].We implemented a hybrid classifier combining:

- **TF-IDF lexical features.**
- **AraBERT contextual embeddings** (extracted from the pretrained transformer).

These vectors were concatenated at the feature level to form a fused representation, which was then used as input to a linear classifier. This approach is computationally efficient (relative to end-to-end deep fusion) and empirically strong on news classification tasks [14] [24]. Let:

$\boldsymbol{X_{tfidf}} \in \mathbb{R}^{\boldsymbol{n} \times \boldsymbol{d_1}}$
represents lexical **TF–IDF** features,
$\boldsymbol{X_{bert}} \in \mathbb{R}^{\boldsymbol{n} \times \boldsymbol{d_2}}$

Represents contextual embeddings extracted from AraBERT.The fused representation is defined as:

$$\boldsymbol{X_{Fused}} = [\boldsymbol{X_{tfidf}}; \boldsymbol{X_{bert}}] \quad (5)$$

Where:

- n is the number of samples,
- d1 is the dimensionality of TF-IDF features,
- d2 is the dimensionality of AraBERT embeddings,
- $\boldsymbol{X_{fused}} \in \mathbb{R}^{\boldsymbol{n} \times (\boldsymbol{d_1}+\boldsymbol{d_2})}$

The fused vector is then passed to a linear classifier defined as:

$$\hat{y} = \boldsymbol{W X_{fused}} + \boldsymbol{b}$$

where:

- $\boldsymbol{W}$ is the weight matrix,
- $\boldsymbol{b}$ is the bias term.

III.7 EVALUATION METRICS

All models were evaluated using:

- **Accuracy,**
- **Macro-F1,**
- **Per-class precision/recall/F1** (classification report),
- **Confusion matrix.**

Accuracy is defined as:

$$\boldsymbol{Accuracy} = \frac{\boldsymbol{TP+TN}}{\boldsymbol{TP+TN+FP+FN}} \quad (6)$$

The F1-score is computed as:

$$\boldsymbol{F1} = \frac{\boldsymbol{2.Precision.recall}}{\boldsymbol{Precision + recall}} \quad (7)$$

Macro-F1 is defined as:

$$\boldsymbol{Macro - F1} = \frac{\boldsymbol{1}}{\boldsymbol{K}} \sum_{\boldsymbol{k=1}}^{\boldsymbol{K}} \boldsymbol{F1_k} \quad (8)$$

Where:

- *TP*, *TN*, *FP*, *FN* represent the true positives, true negatives, false positives, and false negatives,
- ***K*** is the number of classes,
- $F1_k$ is the ***F1***-score for class ***k***.

Macro-F1 was emphasized because it treats all classes equally and remains informative even if class distributions change after filtering [27].

IV. EXPERIMENTAL SETUP

IV.1 FINAL DATASET CONFIGURATION

Once all the corrupted and poor-quality samples were filtered out due to Arabic-ratio filtering and length restrictions, the dataset was rebalanced to have an equal number of classes. The final data is comprised of:

- **Total samples: 13,866,**
- **Classes: 6,**
- **Samples per class: 2,311,**
- **Train size (80%): 11,092,**
- **Test size (20%): 2,774.**

Stratified splitting was applied with a fixed random seed (42) to ensure reproducibility and preserve class balance across splits.

IV.2 HARDWARE AND SOFTWARE ENVIRONMENT

Experiments were conducted using:

- **GPU: NVIDIA Tesla T4,**
- **Framework: PyTorch,**
- **HuggingFace Transformers (v5.x),**
- **Scikit-learn for baseline models,**
- **Python 3.12,**
- **Random seed = 42.**

IV.3 MODEL CONFIGURATIONS

Baseline Models.
TF-IDF Configuration.

- Standard term frequency–inverse document frequency weighting9.
- Sparse high-dimensional representation.

Logistic Regression

- Multinomial setting.
- Default regularization (L2).

Linear SVM

- Linear kernel.
- Optimized for sparse input.

AraBERT Fine-Tuning

Pretrained model:
aubmindlab/bert-base-arabertv2.
Training configuration:

- **Max sequence length: 256.**
- **Batch size: 8.**
- **Learning rate: 2e-5.**
- **Weight decay: 0.01.**
- **Epochs: 3.**
- **Evaluation per epoch.**
- **Padding: max_length.**
- **Truncation: True.**

Hybrid Model
The hybrid model combines:

- **TF-IDF lexical features,**
- **AraBERT contextual embeddings.**

Feature fusion was performed by concatenating the TF-IDF vector with the contextual embedding vector before classification.

Classifier:

- Linear classifier on fused representation.

V. RESULTS AND DISCUSSION

V.1 OVERALL MODEL PERFORMANCE

Table 1 presents the overall classification performance of the evaluated models, including Accuracy and Macro-F1 score.

Table 1: Overall Performance Comparison.

Model	Accuracy	Macro-F1
Logistic Regression	0.9483	0.9482
Linear SVM	0.9557	0.9557
Hybrid Model	0.9603	0.9602

Source: Authors, (2026).

As indicated in Table 1, the Hybrid model had the best overall performance, accuracy of 96.03 and Macro-F1 of 96.02, which is better than the traditional baselines. The Linear SVM (95.57 percent) performed well, slightly better than the Logistic Regression (94.83 percent), indicating that Linear margin based classifiers are very powerful in sparse high dimensional TFIDF representation of structured news data. Interestingly, even though it is usually assumed that transformer-based contextual models will prevail in classical approaches, our previous AraBERT-only fine-tuning performed worse (= 91.6%), meaning that the lexical cues in balanced news data sets are very discriminative.

V.2 IMPROVEMENT OVER THE STRONGEST BASELINE

In order to measure the gain of the hybrid fusion approach, Table 2 reports performance gains when compared to the best classical baseline (Linear SVM).

Table 2: Performance Improvement Over Linear SVM.

Model	Accuracy Gain	Macro-F1 Gain
Hybrid Model	+0.0046	+0.0045

Source: Authors, (2026).

Linear SVM has an error of about 0.46 percentage points higher than the hybrid model. Though numerically small, it is significant even in already high-performing systems (above 95 percent), in which marginal gains are ever more challenging to obtain. This establishes the fact that the integration of a lexical and contextual feature brings out complementary information that neither of the representation can bring out.

V.3 PER-CLASS PERFORMANCE ANALYSIS

Table 3 records the F1 score per-class of all the assessed models.

Table 3: Per-Class F1 Score Comparison.

Class	Logistic	SVM	Hybrid
Economy	0.93	0.93	0.94
Health	0.98	0.98	0.98
Technology	0.92	0.93	0.95
Culture	0.96	0.97	0.97
Political	0.92	0.93	0.92
Sport	0.99	1.00	0.99

Source: Authors, (2026).

As displayed in Table 3, the Hybrid model especially increases performance in the Technology category, which indicates that contextual embeddings are used to disambiguate semantically related technological vocabulary. Sport category was classified almost perfectly in all models suggesting that there is an excellent lexical separability in the sports related lexicon. The greatest confusion is between Political and Economics which is not surprising considering topical context and overlap in the terminology used in the news articles.

V.4 DISCUSSION

A number of important observations can be made based on the results:

1. The classical linear models are also highly competitive in the classification of structured Arabic news.
2. Transformer fine-tuning in itself will not necessarily lead to better performance.
3. The best results are always given when there is feature-level fusion (Hybrid model).
4. To obtain the stable and reliable performance, it was necessary to clean the data (removal of corrupted non-Arabic entries).
5. High accuracy levels of performance (>95%) are a sign of meaningful representational complementarity and not random variance.

The suggested hybrid model can be used as a solid framework to enhance real-world applications by solving complex classification problems. The integration of the lexical and contextual feature strategies is advantageous to the predictive modeling approaches to student specialization [28] and unique virtual keypad encoding [29]. The application of transformer-based embeddings such as AraBERT is further confirmed by methodological similarities in mobile security [30] and tendencies in generative AI [31].Word embeddings-based for Arabic document retrieval in [32] .The broad applicability of results in areas such as e-learning requires stability by ensuring that empirical data is split [33]. The broad applicability of results in areas such as e-learning requires stability by ensuring that empirical data is split [9]. Moreover, this model is flexible, which facilitates forecasting the job market [34] and the morphosyntactic analysis of Arabic language, which addresses the linguistic complexity of Arabic language [35]. The application of explainable AI [10] allows one to find the most significant text features, and the comparison of different machine learning models guarantees a high level of accuracy in security applications [11]. Lastly, the adoption of these automated systems is an indication of a massive effect on operational efficiency within the areas of HR performance [12].The use of deep networks in retrieving Arabic documents [36] and query expansion with deep averaging networks [37] proves the effectiveness of embeddings in information retrieval. Explainable AI [38] can be used to determine the strongest text features, and different machine learning models. These results confirm the hypothesis that lexical statistical signals and contextual embeddings reflect various ways of textual information. The combination of their integration gives a richer space of representation, hence enhancing generalization.

VI. CONCLUSION

In the present study, the authors examined the performance of classical, transformer-based and hybrid lexical-contextual methods of the Arabic multi-class news classification. The results have revealed that, even though deep learning has significantly advanced in Natural Language Processing, the traditional lexical model, including TF-IDF with Linear SVM, is still very competitive in the structured Arabic news data with the performance of 95.57% accuracy. Although the fine-tuned AraBERTv2 model found semantic contextual relations, its independent performance (91.6) suggests that contextual modeling is not the best way to fully harness the discriminatory ability of structured lexical patterns in news corpora. The hybrid feature-level fusion model, where TF-IDF vectors were combined with the AraBERT embeddings, had the best performance (96.03% accuracy and 96.02% Macro-F1) which, as one would expect, lexical statistical signals and contextual embeddings complement one another. The outcome of this test discloses the significance of representation synergy over methodological replacement in Arabic NLP tasks. In general, the paper presents empirical data that hybrid lexical-contextual learning is a robust, computationally efficient, and practical solution to Arabic news classification. Its repeatability of the preprocessing pipeline and balanced assessment framework also enhance its utility in future research and practical Arabic text analytics systems.

VII. AUTHOR'S CONTRIBUTION

Conceptualization: Yasir Hadi Farhan, Mustafa Tareq, Boumedyen Shannaq, Said Almaqbali, Oualid Ali.
Methodology: Yasir Hadi Farhan, Mustafa Tareq, Boumedyen Shannaq, Said Almaqbali, Oualid Ali.
Investigation: Yasir Hadi Farhan, Mustafa Tareq, Boumedyen Shannaq, Said Almaqbali, Oualid Ali.
Discussion of results: Yasir Hadi Farhan, Mustafa Tareq, Boumedyen Shannaq, Said Almaqbali, Oualid Ali.
Writing – Original Draft: Yasir Hadi Farhan, Mustafa Tareq, Boumedyen Shannaq, Said Almaqbali, Oualid Ali.
Writing – Review and Editing: Yasir Hadi Farhan, Mustafa Tareq, Boumedyen Shannaq, Said Almaqbali, Oualid Ali.
Resources: Yasir Hadi Farhan, Mustafa Tareq, Boumedyen Shannaq, Said Almaqbali, Oualid Ali.
Supervision: Yasir Hadi Farhan, Mustafa Tareq, Boumedyen Shannaq, Said Almaqbali, Oualid Ali.
Approval of the final text: Yasir Hadi Farhan, Mustafa Tareq, Boumedyen Shannaq, Said Almaqbali, Oualid Ali.

VIII. REFERENCES

[1] A. Ghaddar, P. Langlais, M. Rezagholizadeh, and B. J. a. p. a. Chen, "On the importance of Data Scale in Pretraining Arabic Language Models," 2024.

[2] G. Bhatia, A. El Mekki, F. Alwajih, and M. Abdul-Mageed, "Swan and ArabicMTEB: Dialect-aware, Arabic-centric, cross-lingual, and cross-cultural embedding models and benchmarks," in Findings of the Association for Computational Linguistics: NAACL 2025, 2025, pp. 4654-4670.

[3] F. J. a. p. a. Qarah, "Saudibert: A large language model pretrained on saudi dialect corpora," 2024.

[4] Y. H. Farhan, S. A. Mohd Noah, M. Mohd, and J. Atwan, "Word-embedding-based query expansion: Incorporating Deep Averaging Networks in Arabic document retrieval," Journal of Information Science, vol. 49, no. 5, pp. 1168-1186, 2021.

[5] Y. Farhan, M. Tareq, B. Shannaq, O. Ali, S. Almaqbali, and V. J. I. Sriram, "MORSE-QE: A Morphology-Aware, Embedding-Driven Framework with Root Extraction for Arabic Dialectal Query Expansion," vol. 49, no. 20, 2025.

[6] B. Shannaq, Y. H. Farhan, M. Tareq, O. Ali, and S. Almaqbali, "Overcoming Challenges in AI-Powered NLP Models: Enhancing the Capabilities of ChatGPT and DeepSeek," in 2025 3rd International Conference on Cyber Resilience (ICCR), 2025, pp. 1-6: IEEE.

[7] Y. H. FARHAN et al., "UTILIZING WORD EMBEDDING'S FOR AUTOMATED QUERY EXPANSION IN ARABIC INFORMATION RETRIEVAL: A BLENDED METHODOLOGY," vol. 103, no. 2, 2025.

[8] Y. H. Farhan, M. Mohd, S. A. M. J. J. o. I. S. T. Noah, and Practice, "Survey of automatic query expansion for Arabic text retrieval," vol. 8, no. 4, pp. 67-86, 2020.

[9] B. Shannaq, "DOES DATASET SPLITTING IMPACT ARABIC TEXT CLASSIFICATION MORE THAN PREPROCESSING? AN EMPIRICAL ANALYSIS IN BIG DATA ANALYTICS," Journal of Theoretical and Applied Information Technology, vol. 103, no. 3, 2025, [Online]. Available: chrome-extension://efaidnbmnnnibpcajpcglclefindmkaj/https://www.jatit.org/volumes/Vol103No3/19Vol103No3.pdf

[10] B. Shannaq, "Using Explainable AI to Rank Educational Success Factors Driving the Job Market," J. Info. Know. Mgmt., p. 2550064, Aug. 2025, doi: 10.1142/S0219649225500649.

[11] B. Shannaq, O. Ali, S. A. Maqbali, and A. Al-Zeidi, “Advancing user classification models: A comparative analysis of machine learning approaches to enhance faculty password policies at the University of Buraimi,” J. Infras. Policy. Dev., vol. 8, no. 13, p. 9311, Nov. 2024, doi: 10.24294/jipd9311.

[12] B. Shannaq and A. Alabri, “EVALUATING THE IMPACT OF CHATGPT IMPLEMENTATION ON HR PERFORMANCE SKILLS: A CASE STUDY OF ACADEMIC INSTITUTIONS IN OMAN”, BJMSR, vol. 10, no. 1, pp. 11–21, Feb. 2025, doi: 10.46281/ bjmsr.v10i1.2281.

[13] W. Antoun, F. Baly, and H. Hajj, "Arabert: Transformer-based model for arabic language understanding," in Proceedings of the 4th workshop on open-source arabic corpora and processing tools, with a shared task on offensive language detection, 2020, pp. 9-15.

[14] A. Aljamel, H. Khalil, Y. J. T. I. J. o. E. Aburawi, and I. Technology, "Comparative study of fine tuned BERT-based models and RNN-based models. case study: Arabic fake news detection," vol. 12, no. 1, pp. 56-64, 2024.

[15] N. Sengupta et al., "Jais and jais-chat: Arabic-centric foundation and instruction-tuned open generative large language models," 2023.

[16] I. Akhadam and H. Ayyad, "Enhancing Arabic text classification: A comparative study of machine learning and deep learning approaches," in 2024 IEEE 12th International Symposium on Signal, Image, Video and Communications (ISIVC), 2024, pp. 1-6: IEEE.

[17] A. A. Jihad et al., "Optimizing Neural Networks Using a Group Learning Algorithm for Heart Disease Prediction with the Cleveland Dataset," vol. 49, no. 24, 2025.

[18] Y. Bayu, "Multi-label emotion classification on social media comments using deep learning," 2024.

[19] M. K. B. Melhem, L. Abualigah, R. A. Zitar, A. G. Hussien, D. J. C. a. w. d. l. Oliva, and m. l. technologies, "Comparative study on Arabic text classification: challenges and opportunities," pp. 217-224, 2022.

[20] G. Salton, C. J. I. p. Buckley, and management, "Term-weighting approaches in automatic text retrieval," vol. 24, no. 5, pp. 513-523, 1988.

[21] C. M. Bishop and N. M. Nasrabadi, Pattern recognition and machine learning (no. 4). Springer, 2006.

[22] C. Cortes and V. J. M. l. Vapnik, "Support-vector networks," vol. 20, no. 3, pp. 273-297, 1995.

[23] J. Devlin, M.-W. Chang, K. Lee, and K. Toutanova, "Bert: Pre-training of deep bidirectional transformers for language understanding," in Proceedings of the 2019 conference of the North American chapter of the association for computational linguistics: human language technologies, volume 1 (long and short papers), 2019, pp. 4171-4186

[24] A. Vaswani et al., "Attention is all you need," vol. 30, 2017.

[25] R. Ranjan et al., "A manifold-level hybrid deep learning approach for sentiment classification using an autoregressive model," vol. 13, no. 5, p. 3091, 2023.

[26] J. Ye, J. Hai, J. Song, and Z. J. A. S. o. T. S. P. Wang, "Multimodal data hybrid fusion and natural language processing for clinical prediction models," vol. 2024, p. 191, 2024.

[27] M. Sokolova, G. J. I. p. Lapalme, and management, "A systematic analysis of performance measures for classification tasks," vol. 45, no. 4, pp. 427-437, 2009.

[28] F. J. I. Alazzawi, B. Shannaq, and A. Al-Zeidi, “Predictive Modeling for Student Specialization Selection: Analyzing Influences and Developing Tailored Recommendations,” in *Advances in Information and Communication*, vol. 1285, K. Arai, Ed., in Lecture Notes in Networks and Systems, vol. 1285. , Cham: Springer Nature Switzerland, 2025, pp. 633–645. doi: 10.1007/978-3-031-84460-7_40.

[29] B. Shannaq, “DEVELOPMENT OF A NEW ENCODING ALGORITHM USING VIRTUAL KEYPAD LETTER SUBSTITUTIONS FOR IMPROVED TEXT CLASSIFICATION,” *JATIT*, vol. 103, no. 2, Jan. 2025, [Online]. Available: https://www.jatit.org/volumes/Vol103No2/27Vol103No2.pdf

[30] B. Shannaq, “A Novel Algorithm for Differentiating Authorized Users from Fraudsters via Mobile Keypad Input Patterns During Password Updates,” *TEM Journal*, pp. 768–778, Feb. 2025, doi: 10.18421/TEM141-68.

[31] I. Alshamsi, K. F. Sadriwala, F. J. Ibrahim Alazzawi, and B. Shannaq, “Exploring the impact of generative AI technologies on education: Academic expert perspectives, trends, and implications for sustainable development goals,” *J. Infras. Policy. Dev.*, vol. 8, no. 11, p. 8532, Oct. 2024, doi: 10.24294/jipd.v8i11.8532.

[32] Y. H. Farhan, S. A. M. Noah, M. Mohd, J. J. J. o. I. S. T. Atwan, and Practice, "Word embeddings-based pseudo relevance feedback using deep averaging networks for Arabic document retrieval," vol. 9, no. 2, pp. 1-17, 2021.

[33] F. J. I. Alazzawi, B. Shannaq, S. Al Maqbali, and S. Al Rawahi, “The Role of Predictive Analytics for Adaptive E-Learning: A Future Pathway Framework for Personalized Education,” in *Sustainable Data Management*, vol. 171, R. K. Hamdan, Ed., in Studies in Big Data, vol. 171. , Cham: Springer Nature Switzerland, 2025, pp. 367–376. doi: 10.1007/978-3-031-83911-5_32.

[34] B. Shannaq, “Leveraging AI to Forecast Future Job Market Trends: Smart Solutions and Strategic Recommendations for Career Success,” *J. Info. Know. Mgmt.*, p. 2550070, Aug. 2025, doi: 10.1142/S0219649225500704.

[35] B. Shannaq, “Optimizing n-gram lengths for cross-linguistic text classification: A comparative analysis of English and Arabic morphosyntactic structures,” *Int. j. adv. appl. sci.*, vol. 12, no. 4, pp. 136–145, May 2025, doi: 10.21833/ijaas.2025.04.015.

[36] Y. H. Farhan, M. Tareq, B. Shannaq, S. Almaqbali, and O. Ali, "Enhancing Robustness and Scalability in AI-Powered Natural Language Processing: A Novel Hybrid Deep Symbolic Framework," in 2025 3rd International Conference on Cyber Resilience (ICCR), 2025, pp. 1-5: IEEE.

[37] Y. H. Farhan, M. Shakir, M. Abd Tareq, B. J. J. o. I. S. T. Shannaq, and Practice, "Incorporating Deep Median Networks for Arabic Document Retrieval Using Word Embeddings-Based Query Expansion," vol. 12, no. 3, pp. 36-48, 2024.

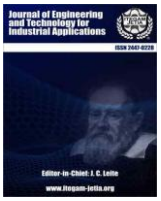
[38] Y. H. Farhan, S. A. Mohd Noah, M. Mohd, and J. J. J. o. I. S. Atwan, "Word-embedding-based query expansion: Incorporating Deep Averaging Networks in Arabic document retrieval," vol. 49, no. 5, pp. 1168-1186, 2023.

Journal of Engineering and Technology for Industrial Applications

ISSN ONLINE: 2447-0228

ITEGAM-JETIA

Manaus, v.12 n.60, p. 429-436 July/August, 2026.
DOI: https://doi.org/10.5935/jetia.v12i60.3867



RESEARCH ARTICLE OPEN ACCESS

CAPACITY MARKET-BASED DEMAND RESPONSE APPROACH FOR EFFICIENT POWER DISTRIBUTION IN RESIDENTIAL MICROGRID

Arunkumar P[*1], Chidurala Sai Prakash[2], Srikanth Velpula[3], Manjunatha H M[4]

[1]Research Scholar, Department of Electricaj and Electronics Engineering, SR University, Warangal, India-.
[2]Department of Electricaj and Electronics Engineering, SR University, Warangal, India-.
[1, 3]Department of Electrical and Electronics Engineering, Bapuji Institute of Engineering and Technology, Davanagere-577004 Karnataka, India.

[1]https://orcid.org/0009-0003-7145-4392, [2]http://orcid.org/0000-0003-0544-8974
[3]http://orcid.org/0000-0003-2706-7136, [4]https://orcid.org/0000-0001-6651-7131

E-email: *arunkumarp584@gmail.com, saiprakash.ace@gmail.com, srikvelpula@gmail.com, manjunath.hm1986@bietdvg.edu

ARTICLE INFO

Article History
Received on: March 02, 2026
Reviewed on: April 02, 2026
Accepted on: May 01, 2026
Published on: July 31, 2026

Keywords:
Demand Response,
Capacity Market,
Residential Microgrid,
Direct Load Control,
Multi-Agent System,
Power Distribution.

ABSTRACT

This paper presents a novel Demand Response algorithm based on a capacity market framework for efficient power management in residential microgrids. The primary objective is to minimize load shedding and enable effective direct load control in smart home environments. By establishing two-way communication channels between distribution agents and smart home customers, the proposed algorithm facilitates real-time load control decisions, accurate calculation of reduction percentages and the generation of home-specific Distributed Load Consumption Factors. An agent-based residential distribution network model was developed in MATLAB/Simulink, incorporating eight clients and integrated smart appliances to validate the algorithm's efficacy. Simulation results demonstrate that the network can maintain grid power balance through three key mechanisms: adaptive load adjustment, strategic load shifting and distributed load reduction. Under supply-constrained conditions, the approach effectively diminishes or even eliminates the necessity for load shedding. The capacity market-based paradigm proves highly advantageous for stand-alone microgrid systems, where optimal resource management is critical for ensuring system stability and enhancing customer satisfaction.

Copyright ©2026 by authors and Galileo Institute of Technology and Education of the Amazon (ITEGAM). This work is licensed under the Creative Commons Attribution International License (CC BY 4.0).

I. INTRODUCTION

In modern power systems, Demand Side Management (DSM) has emerged as a crucial and cost-effective strategy to bridge the gap between electricity supply and demand. DSM encompasses the development and implementation of measures designed to optimize consumption patterns. Through Demand Response (DR) programs, consumers can adjust their energy usage in response to electricity price fluctuations or incentive signals, thereby reducing peak demand and shifting loads to align with available generation capacity. DR methods have proven particularly effective in lowering consumption during periods of high wholesale market prices or system reliability threats [1] [2]. Either centralized or decentralized control systems that facilitate dynamic system adaptability to evolving conditions are necessary for the effective implementation of DR programs within DSM frameworks. The use of intelligent and reliable Multi-Agent Systems (MAS), which facilitate two-way communication between the supply infrastructure and end users, is critical to this process. Loosely coupled, dispersed physically and functionally, autonomous networks consisting of multiple agents form MAS. Agents cooperate smoothly with each other to solve complex operation issues. For solving advanced issues related to DR mechanisms, microgrid operation and control strategies, service restoration process, spot market behaviour, Virtual Power Plant (VPP) management, and economic dispatch optimization, MAS structures have proven themselves to be exceptionally valuable in smart grid scenarios [3] [4]. Capacity market-based DR techniques offer potent solutions for residential microgrids, where resources are constrained and maintaining grid stability is paramount. These microgrids require sophisticated power allocation strategies to balance customer demands with supply limitations. The integration of smart home technologies, enabling precise load control and individual device management, significantly amplifies the effectiveness of capacity market DR [5] [6].

This paper introduces a novel DR algorithm designed to address load shedding and direct load control within smart home environments of residential microgrid systems [7]. The algorithm leverages bidirectional communication between distribution agents and smart home consumers to enable real-time load control decisions, accurately compute reduction percentages and generate tailored Distributed Load Consumption Factors (DLCF). Extensive research has been conducted in areas intersecting microgrid operation, demand response and optimization algorithms. Key related works include:

- Market-Based Microgrid Operation with DR: Research on optimal market-based microgrid operation explores balancing price signals, renewables, storage, and DR resources using risk-based stochastic models, demonstrating cost reduction and uncertainty mitigation [8] [9].
- DR in Residential and Smart Grid Contexts: Comprehensive reviews discuss residential DR challenges and design strategies, highlighting load scheduling techniques supported by Information and Communication Technology (ICT) to better match demand with generation [10] [11].
- Algorithms and Optimization Techniques: Studies on distributed market clearing methods integrate large-scale DR using decomposition techniques, improving convergence and reducing communication overhead [12]. Event-based DR algorithms have also been proposed for rapid decision-making during microgrid contingencies.
- DR in Capacity Markets: Preliminary work on DR planning within capacity markets indicates that microgrid participation can reduce transmission costs and enhance capacity selling profitability [13] [14].

II. METHODOLOGY

The proposed Capacity Market-Based DR approach is built upon and extends the intelligent residential network model presented in [15] [16] [17]. The system architecture is designed to validate the algorithm's performance in managing power distribution efficiently. Figure 1 depicts the block diagram of the proposed intelligent residential network, comprising a power source, an Intelligent Power Distribution System, and eight smart homes. Figure 2 illustrates the Multi-Agent System (MAS) architecture for the residential microgrid, consisting of an Action Layer and a Control Layer. This hierarchical structure enables advanced management of power balance. The Action Layer provides a real-time view of supply and load, generating actionable signals for the Control Layer agents, which oversee load management in response to these signals and user comfort preferences. The entire MAS was implemented in MATLAB using specialized M-functions [18].

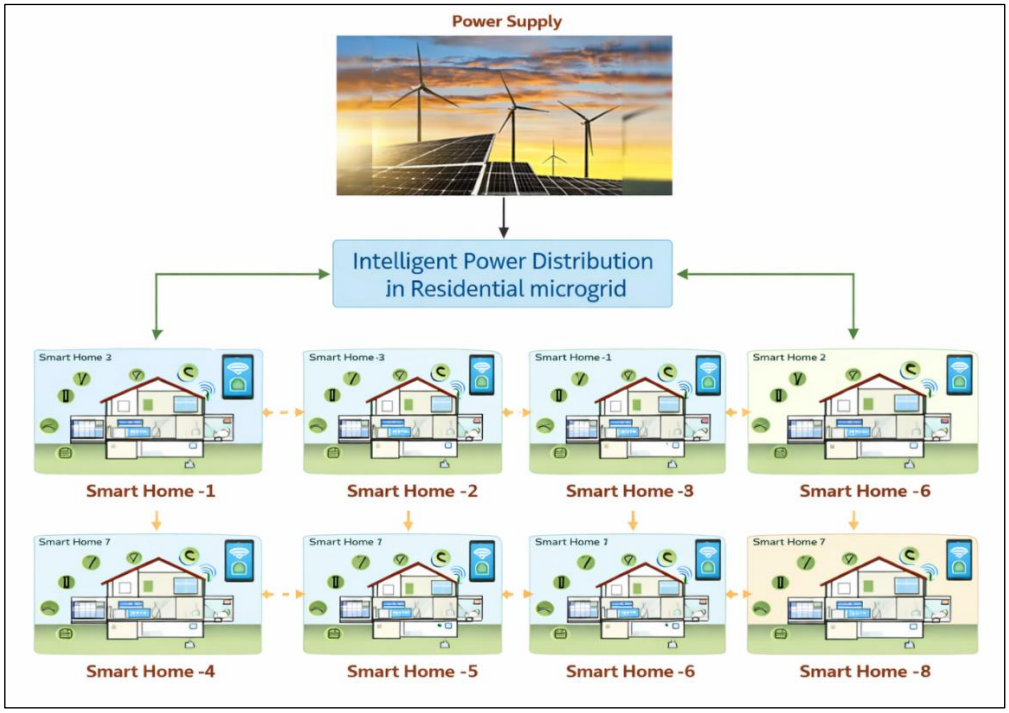


Figure. 1: Block diagram of the proposed intelligent residential network.
Source: Authors, (2026).

II.1 AGENT ARCHITECTURE FOR RESIDENTIAL NETWORK MANAGEMENT

The MAS comprises four primary agent types:

- Intelligent Control Agent (ICA): The central DR coordinator.
- Generator Agent (GA): Monitors and reports available power supply.
- Home Agent (HA): Interfaces with consumer systems and manages smart appliances within a home.
- Smart Appliance Agent (SA): Represents individual appliances with specific characteristics (dimmable, programmable, static).

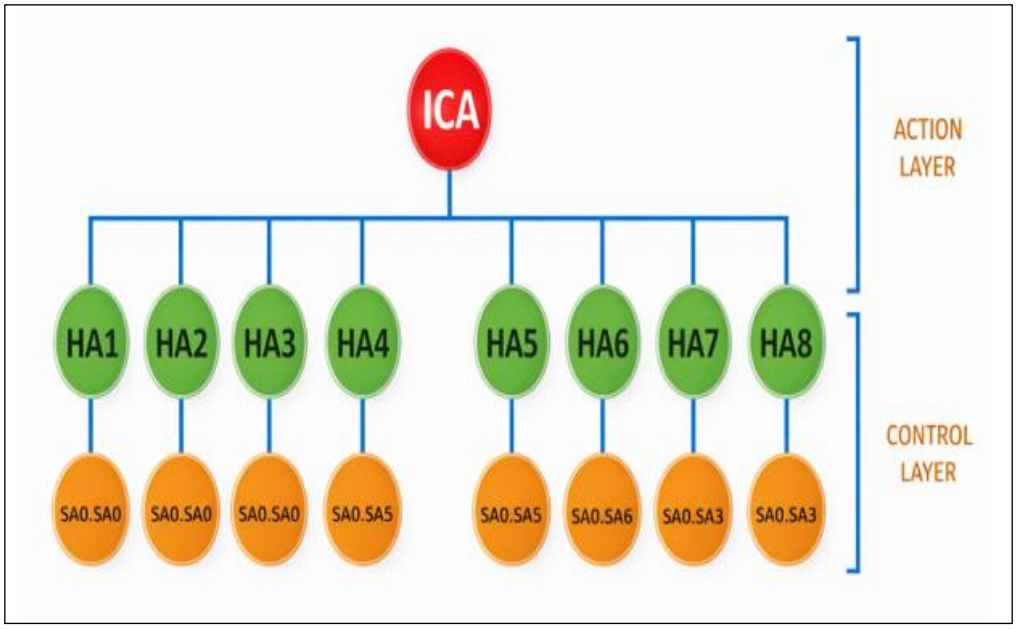


Figure 2: Multi-Agent System architecture enabling Capacity Market-DR.
Source: Authors, (2026).

The standardized naming patterns are followed by delegates such as Home Agents (HA) and Smart Appliance Agents (SA). The individual home agents are referred to as HAx where "x" specifies the corresponding home position in the network. SAxy is one of the agents of smart appliances (x means home and y means the appliance). The details of this mapping will depend on specific configuration choices, for example HA1 would be the first home agent and SA11 would be the first smart appliance agent for the first home [11-13]. Home Agents gather information about what consumers like and send this data to the ICA. In addition to their role in gathering this data, these Home Agents are equipped with intelligent features that allow them to manage the smart devices. This management is crucial to ensure that the network operates smoothly, even when conditions change unexpectedly The Generator Agent keeps gathering and sending power supply data from home networks to the ICA. This up-to-the-minute information allows the ICA to set up the right Distributed Load Reduction Percentage (DLRP) factors also called set points. This helps to keep the system running when supply conditions change.

The ICA functions as the primary demand response agent within the system, continuously calculating two critical parameters:

- Distributed Load Reduction Percentage (DLRP).
- Distributed Load Consumption Factor (DLCF).

$$\mathrm{DLRP} = \frac{\mathrm{SupplyPower} - \mathrm{LoadDemand}}{\mathrm{LoadDemand}} \mathrm{x100} \tag{1}$$

$$\begin{Bmatrix} \mathrm{IfSupply\ Power} < \mathrm{Actual\ Demand} \\ \mathrm{DLCF} = \dfrac{\mathrm{Supply\ Power}}{\mathrm{Actual\ Demand}} \\ \mathrm{IfSupply\ Power} > \mathrm{Actual\ Demand} \\ \mathrm{DLCF} = 1 \end{Bmatrix} \tag{2}$$

The real-time analysis of network supply and demand dynamics underpins these estimates. These settings influence consumer behavior to maintain power equilibrium throughout the system. The ICA further computes the Clearing Supply Power (CSP) for each network user. The total connected load of the residential network is now restricted to remain at or below the available supply power.

$$\mathrm{CSP} = \frac{\mathrm{SupplyPowerXConnected\ load\ of\ customer}}{\mathrm{ConnectedLoadofResidentialNetwork}} \tag{3}$$

II.2 CAPACITY MARKET DR ALGORITHM

The suggested Capacity Market DR algorithm shown in Figure 2 gives either the best or almost the best choices for clearing the load in a lot of different supply-and-demand situations. The method works in three stages:

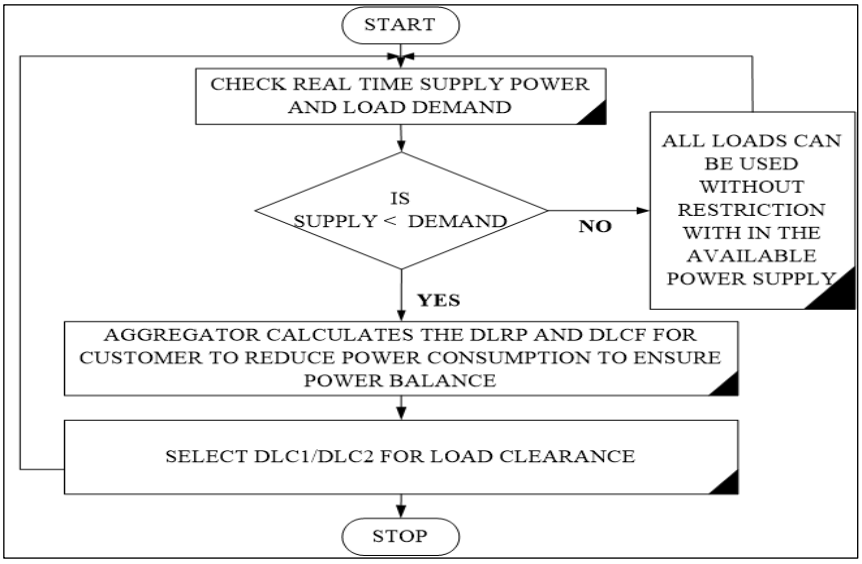


Figure 3: Flowchart of the proposed Capacity Market DR algorithm.
Source: Authors, (2026).

- Real-Time Monitoring: Continuous assessment of residential network load demand and power supply.
- Parameter Calculation: Computation of DLRP, DLCF, and CSP using equations (1), (2), and (3) respectively.
- Load Selection: Strategic identification of appropriate loads to initiate the clearing process for power balance maintenance.

The algorithm implementation follows two distinct Direct Load Control (DLC) operational scenarios:

II.2.1 Scenario 1: Fixed Programmable Loads (DLC1)

Programmable loads in this arrangement are handled as fixed, non-adjustable objects. Only modulation of dimmable loads allows one to perform power balance modifications, so offering a more limited but consistent working environment.

II.2.2. Scenario 2: Flexible Programmable Loads (DLC2)

This more dynamic method lets programmable loads be temporally moved, hence improving the peak-to average ratio of the network. While keeping system stability, this offers more demand management options. Maintaining equilibrium between power demand and supply is both Capacity Market DR method's principal goal. They guarantee quick response capacity for unforeseen or emergency modifications in either supply availability or demand requirements. The ICA sends reduction signals to the Home Automation (HA) system in reaction to supply fluctuations, therefore lowering the dimmable appliance power consumption to specified comfortable levels (e.g., 50% of rated capacity). Should this decrease prove inadequate, the HA uses pre-defined preferences to start load shifting or shedding for less-priority equipment. For a 20% consumption reduction signal, for instance, the HA first lowers dimmable appliance power usage; then, if needed, it moves running schedules for programmable appliances to reach the target reduction level.

III. SYSTEM SIMULATION AND IMPLEMENTATION

In order to validate the suggested intelligent multi-agent home network architecture, we created a thorough simulation environment using MATLAB/SIMULINK. The home network's conceptual and execution models are depicted in Figures 3 and 4, respectively. Our suggested capacity market demand response strategy can be tested and its effectiveness assessed using this simulation framework. Real-time monitoring and control capabilities are made possible by the simulation's establishment of bidirectional communication links between the ICA and HAs. The ICA is able to continuously monitor the real load demand throughout the home network as well as the supply that is available from the GA. Critical metrics including the Distributed Load Consumption Factor (DLCF), Clearing Supply Power (CSP), and Distributed Load Reduction Percentage (DLRP) are computed by the ICA using this data and sent to the HAs. After obtaining these parameters, the HAs use complex load clearing algorithms to choose the best smart appliance operating states according to priorities specified by the client. This strategy maximizes consumer happiness while guaranteeing power balance maintenance.

III.1 RESIDENTIAL LOAD CONFIGURATION

Eight different "smart homes" are used in the simulation to simulate realistic loads in the distribution network. Every smart house has five to six appliances that are carefully categorized as follows and each is set up with a precise power allocation:

- Appliances having fixed power consumption profiles that cannot be adjusted are known as static loads.
- Appliances having changeable power consumption capabilities are known as dimmable loads. Dimmable load reductions are only permitted to a maximum of 50% of their overall power consumption (presuming a minimal level of comfort).
- Time-shifting appliances with adjustable running schedules are known as programmable loads.

The connected load profile of eight smart homes is summarized in Table 1.

Table 1: Load Profile of Eight Smart Homes in the Residential Microgrid.

Smart home	Allotted power in kW	Smart Appliances in kW					
		S1	S2	P1	D1	D2	D3
1	5	1	1	1	1	1	NA
2	10	2	2	2	2	2	NA
3	12	1	1	1	3	3	3
4	15	2	2	2	3	3	3
5	18	3	3	3	3	3	3
6	21	4	4	4	3	3	3
7	24	4	4	4	4	4	4
8	27	5	5	5	4	4	4

Source: Authors, (2026).

The Residential Microgrid total connected load is 132kW. By making various supply and demand assumptions for specific time blocks, numerous situations are simulated. The reduction in active customers power outages after the deployment of DLC is evident in the data.

IV. RESULTS AND DISCUSSION

One day is divided into 24-time blocks in order to evaluate the suggested DLC DR algorithms, with each hour representing one time block for carrying out load clearing actions. For analysis purposes, the 6 blocks are taken into account. For time blocks 1 through 6 of the home networks, the available supply, actual load demand, power mismatch, DLRP, and DLCF are tabulated in Table 2. To validation proposed DLC programs load HA3 is considered. The sub-hourly CSP, load demand, and mismatch for HA3 is shown in Table 3. Table 4 and 5 summaries the load consumption patron of HA3 after incorporating proposed DLC1 and DLC2 in residential network. From comparing the Tables 3,4 and 5, it is observed that:

- The supply demand mismatch in all the time blocks is reduced in HA3 after incorporating DLC 1 and DLC 2, whereas it is almost zero in DLC2 compared to DLC 1.
- In the time block 1, DLC 2 clear the P1, whereas it is not achieved in DLC1
- In time block 2 and 5, DLC 2 clear the S2, whereas it is not achieved in DLC1
- The Total load consumption of (TLC) of HA3 in DLC 2 is more compared to DLC1. It concludes DLC 2 program is most efficient compared to DLC1.

The Figure 4 summarise comparison of the total energy consumption of individual smart home residential microgrid for DLC1 and DLC2. From the figure 4, it is observed that, power consumption in DLC-2 is more compared to DLC-1. The Table 6 summarise the total energy consumption of residential microgrid for DLC1 and DLC2. Figure 5 shows the comparison of Supply, actual demand, Power Consumption of residential microgrid from six-time blocks in kW after incorporating DLC1 and DLC-2.

Table 2: Sub hourly Supply, Actual Load, Miss-match, DLRF and DLCF of residential network.

Block	SPV in Kw	DL in Kw	Mismatch in Kw	DLRP	DLCF	DSP	LC of DLC1 in Kw	LC of DLC2 in Kw
1	70	110	-40	-36.36	0.6363	0.530303	59	69.27
2	80	106	-26	-24.52	0.754	0.606061	55.71	65.36
3	132	68	64	94.11	1	1	52	52
4	90	46	44	95.65	1	0.681818	46	46
5	85	87	-2	-2.29	0.977	0.643939	54.94	58.38
6	132	91	41	0	1	1	91	91

Source: Authors, (2026).

Table 3: Sub hourly CSP, Actual Load, Miss-match of HA3.

Time block	CSP in kW	S1 in kW	S2 in kW	P1 in kW	D1 in kW	D2 in kW	D3 in kW	DL in Kw	Miss match in kW
1	6.36	1	0	1	3	3	3	11	-4.64
2	7.27	1	1	1	3	3	0	9	-1.73
3	12	1	0	0	3	3	0	7	-5
4	8.18	0	0	0	3	3	0	6	+2.18
5	7.72	1	1	0	3	3	0	8	-0.28
6	12	1	1	1	3	3	3	12	0
+ indicate surplus – indicate deficit									

Source: Authors, (2026).

Table 4: Sub hourly CSP and load clearing of HA3 for DLC1.

Time block	CSP in kW	S1 in kW	S2 in kW	P1 in kW	D1 in kW	D2 in kW	D3 in kW	TLC in kW	Miss match in kW
1	6.3	0	0	0	1.90	1.90	1.90	5.72	+0.58
2	7.27	1	0	1	2.26	2.26	0	6.52	+0.75
3	12	1	0	0	3	3	0	7	+5
4	8.18	0	0	0	3	3	0	6	+2.18
5	7.72	1	0	0	2.93	2.93	0	6.86	0.86
6	12	1	1	1	3	3	3	12	0

Source: Authors, (2026).

Table 5: Sub hourly CSP and load clearing of HA3 for DLC2.

Time block	CSP in kW	S1 in kW	S2 in kW	P1 in kW	D1 in kW	D2 in kW	D3 in kW	TLC in kW	Miss match in kW
1	6.36	0	0	1	1.78	1.78	1.78	6.36	0
2	7.27	1	1	1	2.13	2.13	0	7.27	0
3	12	1	0	0	3	3	0	7	+5
4	8.18	0	0	0	3	3	0	6	+2.18
5	7.72	1	1	0	2.86	2.86	0	7.72	0
6	12	1	1	1	3	3	3	12	0

Source: Authors, (2026).

Table 6: Total energy consumption of residential microgrid for DLC1 and DLC2.

Block	SPV in Kw	Actual DL in Kw	Mismatch in Kw	LC of DLC1 in Kw	Mismatch in Kw after DLC1	LC of DLC2 in Kw	Mismatch in Kw after DLC1
1	70	110	-40	59	11	69.27	0.73
2	80	106	-26	55.71	24.29	65.36	14.64
3	132	68	64	52	80	52	80
4	90	46	44	46	44	46	44
5	85	87	-2	54.94	30.06	58.38	26.62
6	132	91	41	91	41	91	41

Source: Authors, (2026).

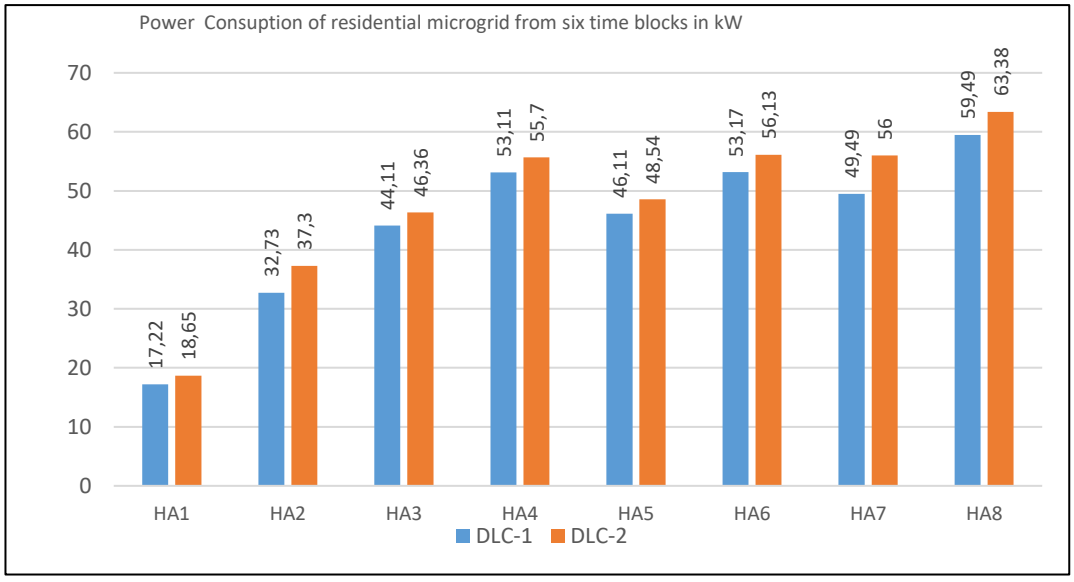


Figure 4: Comparison of the total energy consumption of individual smart home residential microgrid.
Source: Authors, (2026).

From the Table 6 and Figure 5, it is observed that:

- In all the time blocks supply demand mismatch is reduced in microgrid after incorporating DLC1 and DLC2, additionally DLC2 perform best compare to DLC1. (eg., In time block 1 actual supply demand mismatch is -40kW, where as it is 11kW in DLC1 and 0.73kW in DLC2) its clearly shows DLC2 clear the load by efficiently managing the available supply power.
- The total power consumptions of residential microgrid form six-time blocks in DLC-1 are 358.651kW, where as in DLC-2, it is 382.01kW

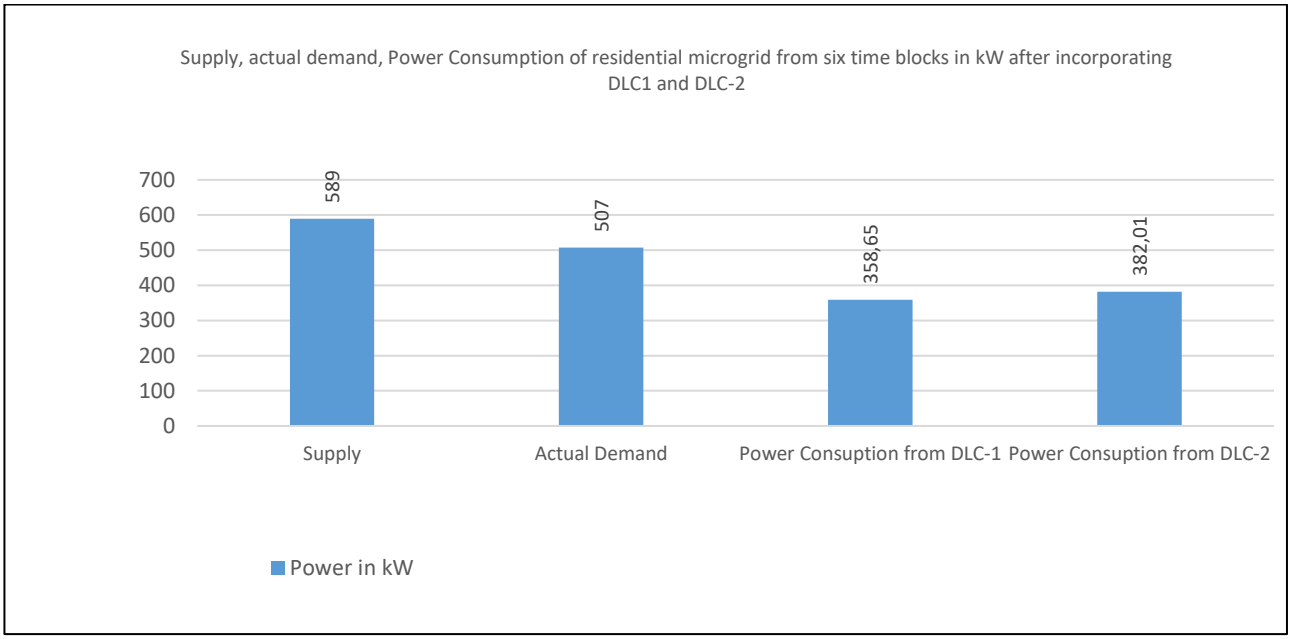


Figure 5: Supply, actual demand, Power Consumption of residential microgrid from six-time blocks in kW after incorporating DLC1 and DLC-2.
Source: Authors, (2026).

For detailed analysis, Home 3 (HA3) was examined. Table III shows HA3's CSP, appliance demand and mismatch before DR. Tables 4 and 5 detail the load-clearing results for HA3 under DLC1 and DLC2 respectively. Key Observations from Tables 3-5:

- The supply-demand mismatch is reduced in all time blocks for HA3 after implementing both DLC1 and DLC2.
- DLC2 outperforms DLC1, achieving zero mismatch in blocks 1, 2, and 5 by effectively clearing loads like P1 and S2, which DLC1 could not.
- The Total Load Consumption (TLC) of HA3 is higher with DLC2, indicating more efficient utilization of available supply power and superior customer comfort preservation.

Table 6 and Figure 4 provide a network-wide comparison. The total power consumption across the six blocks was 358.65 kW for DLC1 and 382.01 kW for DLC2, confirming DLC2's superior performance in maximizing energy delivery while minimizing mismatch (e.g., reducing mismatch from -40 kW to 0.73 kW in Block 1).

V. CONCLUSION

This paper presented a capacity market-based Demand Response (DR) framework for intelligent power distribution in residential microgrids. The proposed approach integrates a novel direct load control strategy through two operational modes, namely DLC1 and DLC2 designed to dynamically manage supply–demand imbalances in real time. Unlike conventional load shedding techniques, which indiscriminately disconnect loads during shortages, the proposed algorithm enables prioritized and optimized load management based on calculated Distributed Load Consumption Factors and reduction percentages for individual smart homes. By incorporating two-way communication between distribution agents and smart residential consumers, the system ensures rapid decision-making, accurate load adjustment, and effective resource allocation within the microgrid. The developed MATLAB/Simulink-based agent-driven model, comprising multiple smart home clients and controllable appliances, demonstrates that the proposed strategy successfully maintains power balance through adaptive load shifting, distributed load reduction, and strategic demand control. Simulation results confirm that the capacity market-based paradigm significantly reduces dependency on load shedding, enhances system reliability, and improves customer satisfaction. Under supply-constrained and emergency conditions, the microgrid responds efficiently by optimally clearing time-block loads while preserving critical demand. The proposed framework provides a robust and scalable solution for stand-alone and grid-connected residential microgrids, ensuring improved operational stability, enhanced reliability and efficient utilization of distributed energy resources.

VI. AUTHOR'S CONTRIBUTION

Conceptualization: Arunkumar P and Chidurala Sai Prakash.
Methodology: Arunkumar P and Chidurala Sai Prakashl.
Investigation: Arunkumar P and Chidurala Sai Prakash.
Writing – Original Draft: Arunkumar P, Srikanth Velpula and Chidurala Sai Prakash.
Writing – Review and Editing: Arunkumar and Srikanth Velpula.
Resources: Arunkumar P and Chidurala Sai Prakash.
Supervision: Chidurala Sai Prakash.
Approval of the final text: Chidurala Sai Prakash and Manjunatha H M.

VII. REFERENCE

[1] Telagi, Karibasavaraju, and Kishore Kumar Pedapenki. "A review of bidding strategies and energy trading models in peer-to-peer energy trading." Journal of Integrated Science and Technology 13, no. 4 (2025): 1077-1077.

[2] Chandraiah, Shadaksharaiah, Basavarajappa Sokke Rameshappa, Manjunatha Malleshappa Hirekere, Karibasavaraju Shivalingappa Telagi, and Arunkumar Parashuramappa. "Optimizing Distributed Generation in DC Microgrids: A Comprehensive Study." World Journal of Advanced Research and Reviews 23, no. 1 (2024): 2214-2226.

[3] M. A. A. Pedrasa, M. M. Oro, N. C. R. Reyes, and J. R. I. Pedrasa, “Demonstration of direct load control of air conditioners in high-density residential buildings,” 2014 IEEE Innov. Smart Grid Technol. - Asia (ISGT ASIA), pp. 400–405, 2014, doi: 10.1109/ISGT-Asia.2014.6873825.

[4] Manjunatha H.M. “AI Applications for Drone of Things in the Power Sector”. ITEGAM-JETIA. 12, 57 (Jan. 2026), 428-447. DOI: https://doi.org/10.5935/jetia.v12i57.3030.(Q4)

[5] MansourLakouraj, Mohammad, Majid Shahabi, Miadreza Shafie-khah, and João PS Catalão. "Optimal market-based operation of microgrid with the integration of wind turbines, energy storage system and demand response resources." Energy 239 (2022): 122156.

[6] Manjunatha H.M. “Optimal placement of hybrid distributed generators using an enhanced Shuffled Frog Leap algorithm” Journal of Integrated Science and Technology, 14(2), 1524. https:// DOI:10.62110/sciencein.jist.2026.v14.1524(Q1).

[7] H. M. Manjunatha, G. K. Purushothama, Y. Nanjappa and R. Deshpande, "Auction-Based Single-Sided Bidding Electricity Market: An Alternative to the Bilateral Contractual Energy Trading Model in a Grid-Tied Microgrid," in IEEE Access, vol. 12, pp. 48975-48986, 2024, doi: 10.1109/ACCESS.2024.3384092. (Q1)

[8] Manjunatha H M “Machine Learning-Based Prediction of Lithium-Ion Battery Life Cycle for Capacity Degradation Modelling" has been published in Volume 21 - Issue 2 (February 2024) of World Journal of Advanced Research and Reviews (WJARR) https://doi.org/10.30574/wjarr.2024.21.2.0553

[9] Wang, Fei, Hanchen Xu, Ti Xu, Kangping Li, Miadreza Shafie-Khah, and João PS Catalão. "The values of market-based demand response on improving power system reliability under extreme circumstances." Applied energy 193 (2017): 220-231.

[10] Manjunatha H M, Supritha M R, Nagendra Prasad H K, Shri Harsha J, Santhoshkumar G M, “Auction-based single buyer energy trading framework in grid-tied microgrid with distributed energy storage and demand response using a multi-agent approach,” e-Prime - Advances in Electrical Engineering, Electronics and Energy, (Elsevier Journal) Volume 6,2023, 100367, ISSN 2772-6711, https://doi.org/10.1016/j.prime.2023.100367. (Q2)

[11] Nagendraprasad H. K, Manjunatha H. M, Jayaram M. V “Energy Management of Renewable Energy Resources Powered Distribution Storage System in Grid-tied Microgrid” GRENZE International Journal of Engineering and Technology Volume-2 July 2023. (Q2)

[12] H.M. Manjunatha, T.S. Karibasavaraju, L.H. Anjaneya, Shadaksharaiah Chandraiah, P. Arunkumar,”Auction based single buyer energy trading model in grid-tied microgrid with active sellers and buyers”,e-Prime - Advances in Electrical Engineering, Electronics and Energy (Elsevier Journal), Volume 4,2023, https://doi.org/10.1016/j.prime.2023.100136. (Q2)

[13] Da Costa, Vinicius Braga Ferreira, Gabriel Nasser Doyle De Doile, Gustavo Troiano, Bruno Henriques Dias, Benedito Donizeti Bonatto, Tiago Soares, and Walmir de Freitas Filho. "Electricity markets in the context of distributed energy resources and demand response programs: Main developments and challenges based on a systematic literature review." Energies 15, no. 20 (2022): 7784.

[14] H.M. Manjunatha“ An Intelligent Method to Load Management of Microgrid Operation using Multi-Agent System” Journal of Recent Trends in Electrical Power System-HBRP Publication, Volume-1. Sep-2022. https://doi.org/10.5281/zenodo.7085 287

[15] H.M. Manjunatha and G.K. Purushothama “A Direct Load Control Approach for Residential Demand Response”, International Journal of Science, Technology, Engineering and Management-A VTU Publication, Volume 3, Issue 2, OCT- 2021, pp. 43-49.

[16] Esfahani, Mohammad Mahmoudian, Abla Hariri, and Osama A. Mohammed. "A multiagent-based game-theoretic and optimization approach for market operation of multimicrogrid systems." IEEE Transactions on Industrial Informatics 15, no. 1 (2018): 280-292.

[17] H.M. Manjunatha and G.K. Purushothama“Multi-Agent System based Two-Phase Market Model to Incorporate Demand Response in Grid-Tied Microgrids”, International Journal of Renewable Energy Research, Volume 11, Issue 1, March 2021, pp. 195- 210.DOI:https://doi.org/10.20508/ijrer.v11i1.11636.g8125.(SCOPUS Cite Score is 4.3 and Quartile is Q2, Impact Factor is 5.127 in Thomson Reuters).

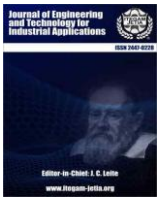
[18] H.M. Manjunatha and G.K. Purushothama“Multi-Agent based Responsive Residential DR for Managing and Trading Power in Smart DNs”International Journal of Renewable Energy Research, Volume 11, Issue 1, March 2021, pp. 264-275. DOI:https:// doi.org/10.20508/ijrerv11i111714.g8130

Journal of Engineering and Technology for Industrial Applications

ISSN ONLINE: 2447-0228

ITEGAM-JETIA

Manaus, v.12 n.60, p. 437-443 July/August, 2026.
DOI: https://doi.org/10.5935/jetia.v12i60.3873



RESEARCH ARTICLE OPEN ACCESS

BENCHMARKING YOLO VARIANTS FOR DETECTING VARROA MITES IN BEEHIVE IMAGES

Youcef Naas[1], Slim rouabah[2], rabah abdelkader[3], Meziane Kaci[4], Salem Merabti[5], Hassane Ezziane[6]

[1]Department of Electronic and communication, Faculty of Sciences and Technology, University of Djilali Bounaama, Khemis Miliana,Ain Defla, Algeria.
[2]Djilali Bounaama University of Khemis Miliana,Algeria
[3]Department of Electronic and communication, Faculty of Sciences and Technology, University of Djilali Bounaama, Khemis Miliana, Ain Defla, Algeria.
[4]Department of Electrical Engineering, Faculty of Sciences and Technology, Djilali Bounaama University of Khemis Miliana, Ain Defla, Algeria.
[5]Department of Acoustics and Civil Engineering, Faculty of Sciences and Technology, Djilali Bounaama University of Khemis Miliana, Ain Defla, Algeria.
[6]Research Laboratory of Electrical Engineering and Automatics LREA, Yahia Fares University, Medea, Algeria.

[1]https://orcid.org/0009-0003-0653-728X, [2]https://orcid.org/0009-0008-2295-9470 [3]https://orcid.org/0000-0002-3738-3485
[4]https://orcid.org/0009-0008-9023-8173, [5]https://orcid.org/0000-0002-4615-2179, [6]https://orcid.org/0000-0002-4875-3226

E-email: y.naas@univ-dbkm.dz, s.rouabah@univ-dbkm.dz, r.abdelkader@univ-dbkm.dz, m.kaci@univ-dbkm.dz, s.merabti@univ-dbkm.dz, ezziane.hassan2051@gmail.com.

ARTICLE INFO

Article History
Received on: March 03, 2026
Reviewed on: April 02, 2026
Accepted on: May 01, 2026
Published on: July 31, 2026

Keywords:
V. destructor,
Beehive monitoring,
Artificial Intelligence,
Deep Learning,
YOLO,
Object detection.

ABSTRACT

The Varroa destructor mite drives major honey bee colony losses and economic damage in apiculture. Early detection supports timely intervention, yet manual inspection is slow and prone to error due to the mite's small size and dense hive conditions. Automated vision systems offer a scalable solution for continuous monitoring.This study benchmarks three YOLO variants, YOLOv7, YOLOv8, and YOLOv11, for automated Varroa detection. YOLOv11 achieves the highest performance, with mAP at 0.5 of 0.941 and recall of 87.9 percent, outperforming earlier versions. The shift from anchor-based detection in YOLOv7 to anchor free designs in YOLOv8 and YOLOv11, along with improved feature extraction through C2f modules and attention mechanisms, enhances small object detection critical for identifying mites. YOLOv8 provides the fastest training speed, operating twice as fast as YOLOv11 and 4.5 times faster than YOLOv7, which supports rapid deployment.All modern variants exceed 93 percent mAP at 0.5 and maintain real time inference at 30 frames per second or higher. Results position YOLOv11 as the preferred model for maximum accuracy and YOLOv8 as an efficient option for resource constrained beekeeping applications.

Copyright ©2026 by authors and Galileo Institute of Technology and Education of the Amazon (ITEGAM). This work is licensed under the Creative Commons Attribution International License (CC BY 4.0).

I. INTRODUCTION

Honeybees' contribution to the pollination of over 75% of flowering plants and 35% of the world's food crops demonstrates their critical role in global agriculture and ecosystems [1]. However, as any living being, honeybees face significant threats from various factors, such as pesticides, habitat loss, and pathogens. Among these, the Varroa destructor mite, also called V. destructor destructor, is considered one of the most devastating pests, causing both widespread colony losses and worldwide economic damage [2]. V. destructor mites feed on the bodily fluids of bees, transmitting harmful viruses such as Deformed Wing Virus (DWV) and Acute Bee Paralysis Virus (ABPV), and weakening their immune systems, leading to colony collapse if left untreated [3] Manual detection of Varroa destructor mites by beekeepers presents several critical challenges that fundamentally limit its effectiveness in modern apiculture. First, visual limitations pose a significant barrier, as these mites measure merely 1–2 mm in length and are frequently concealed between bee body segments, on the undersides of bees, or deep within brood cells, rendering visual identification exceptionally difficult even for experienced observers.

Second, time and labor constraints place considerable burden on beekeeping operations, since traditional monitoring approaches—such as sticky boards or sugar shake tests—demand substantial time investments and require frequent hive inspections that inevitably disturb colony activity and elevate stress levels among the bees. Third, human error and subjectivity introduce considerable variability into the monitoring process; manual counting is susceptible to fatigue-induced inaccuracies, inconsistent interpretation between different observers, and difficulties in maintaining rigorous monitoring schedules, particularly within commercial enterprises managing hundreds of hives simultaneously. Finally, delayed detection represents perhaps the most concerning limitation, as visible symptoms often manifest only after mite infestation levels have already reached critical thresholds, by which point treatment interventions become significantly less effective. Collectively, these constraints generate an urgent and pressing need for accurate, automated, and scalable detection techniques capable of operating in real-time while providing robust early warning capabilities to protect honey bee colony health. Recent research has explored various technological approaches to address the Varroa detection challenge:

- Early automated approaches relied on classical image processing techniques. The Var-Gor device [4] achieved 100% detection accuracy in laboratory conditions using specialized imaging hardware, but required controlled lighting conditions and could not generalize to field environments. Morphological operators combined with handcrafted features showed promise [5], but struggled with the high variability in natural hive imagery, including varying lighting conditions, bee orientations, and background clutter.
- Traditional methods require extensive parameter tuning, are sensitive to environmental conditions, and cannot adapt to unseen scenarios without manual reconfiguration.
- Convolutional Neural Networks (CNNs) have been applied for mite detection with notable success. Sharma et al. applied ResNet-50 and Inception V3 for early V. destructor mite detection using data augmentation and CLAHE (Contrast Limited Adaptive Histogram Equalization), achieving 90.67% accuracy with ResNet-50. Scutaru et al. combined morphological operators with neural networks, training on 65,000 positive and 1.2 million negative samples, achieving errors below 1% when integrated into the BeeVS device [5].
- Classification-based approaches can determine the presence of mites but cannot localize them within images, limiting their utility for precise monitoring and treatment planning. Additionally, these methods typically process entire images rather than detecting individual mite instances.
- Object detection methods offer significant advantages by providing both classification and localization capabilities. Kriouile et al. proposed a modified training scheme for Mask R-CNN utilizing two separate datasets for bee and mite identification [6]. While Mask R-CNN achieves high accuracy, its two-stage architecture (region proposal followed by classification) results in slower inference speeds, making it less suitable for real-time applications.

Bilik et al. applied YOLOv5 to a specialized dataset of infected and healthy bees, achieving F1 scores of 0.874 and 0.727 for infected bees and mites respectively [7]. Narcia-Macias et al. developed the IntelliBeeHive system using YOLOv7-tiny, achieving 99.6% mite detection precision [8]. Many studies focus on a single YOLO version without systematic comparison across variants. Limited analysis of architectural differences and their impact on small object detection. Insufficient evaluation of the trade-off between accuracy and computational efficiency. Lack of comprehensive benchmarking against both traditional and modern detection methods. The You Only Look Once (YOLO) family of models was selected for this study based on several compelling advantages that align closely with the requirements of automated hive monitoring. First, real-time performance stands as a primary consideration; YOLO's single-stage architecture processes images in a single forward pass, enabling inference speeds ranging from 30 to 140 frames per second depending on the specific variant and hardware configuration—an essential capability for continuous, real-time hive surveillance. Second, localization accuracy distinguishes YOLO from mere classification approaches, as the model provides precise bounding box coordinates for each detected mite, thereby enabling quantitative infestation assessment and detailed spatial analysis within the colony.

Third, architectural evolution represents a significant motivation for this selection; the continuous development of YOLO from its initial version through to the current YOLOv11 has introduced substantial improvements in feature extraction mechanisms, anchor box design, and training strategies, making a systematic comparative analysis both timely and scientifically valuable. Fourth, edge deployment capability addresses practical deployment constraints, as modern YOLO variants offer lightweight versions such as nano and tiny models that can operate efficiently on resource-constrained devices, facilitating on-hive processing without dependency on cloud connectivity. Finally, generalization capabilities reduce barriers to implementation, since YOLO models pretrained on large-scale datasets such as COCO and ImageNet demonstrate robust transfer learning capabilities, thereby minimizing the requirement for massive domain-specific datasets in the apicultural context. This work aims to train and evaluate multiple versions of YOLO models on the same dataset [9], to develop a robust, real-time solution to assist beekeepers in monitoring hive health. The specific objectives are:

- Comparative Analysis: Systematically compare YOLOv7, YOLOv8, and YOLO11 to detect V. destructor mites across different training epochs.
- Architectural Analysis: Explain the key architectural differences between YOLO variants and their implications for small object detection.
- Performance Benchmarking: Evaluate models using multiple metrics (precision, recall, mAP) to provide comprehensive performance characterization.
- State-of-the-Art Comparison: Compare YOLO variants against other deep learning approaches reported in literature.

The paper is structured as follows: Section 2 details the materials and methods including YOLO architecture description, Section 3 presents the experimental results and analysis including comparisons with other techniques, and Section 4 provides conclusions and future directions.

II. MATERIALS AND METHODS

The You Only Look Once (YOLO) architecture revolutionized object detection by framing it as a single regression problem, directly predicting bounding boxes and class probabilities from full images in one evaluation.

This section describes the general YOLO architecture and the specific innovations introduced in each version evaluated. The YOLO architecture comprises three fundamental components that work in concert to achieve efficient object detection. The backbone serves as the feature extraction engine, processing input images through successive convolutional layers to extract hierarchical features; early layers capture low-level visual information such as edges and textures, while deeper layers progressively encode high-level semantic information including object parts and shapes, with modern YOLO variants employing diverse backbone designs such as Darknet, CSPDarknet, and C2f modules to enhance representational capacity. The neck component functions as a feature aggregation mechanism, combining features extracted from different backbone layers to create rich multi-scale feature representations—an essential capability for detecting objects of varying sizes within the same image—with common implementations including Feature Pyramid Networks and Path Aggregation Networks that facilitate effective information flow across scales. Finally, the detection head processes these aggregated features to generate predictions, outputting bounding box coordinates in the form of center positions, width, and height, alongside objectness scores and class probabilities, with the architecture utilizing anchor boxes as predefined reference templates to guide the prediction of object shapes and dimensions. YOLOv7, released in 2022 by Wang and colleagues [10], introduced several notable architectural innovations that advanced the state of single-stage object detection. Central to these improvements is the Extended Efficient Layer Aggregation Network, which enhances gradient flow throughout the network by employing expand, shuffle, and merge cardinality techniques, thereby enabling the model to learn more diverse feature representations without compromising the integrity of the original gradient propagation path.

The architecture also addresses fundamental challenges in model scaling through the introduction of compound scaling methods specifically designed for concatenation-based models; these methods preserve optimal model properties during both upscaling and downscaling operations, overcoming the limitation that conventional scaling approaches typically degrade performance in architectures reliant on feature concatenation. Furthermore, YOLOv7 incorporates a suite of sophisticated training strategies collectively termed trainable bag-of-freebies, including planned re-parameterized convolution, coarse-to-fine lead head guided label assignment, and dynamic label assignment mechanisms for auxiliary heads, all of which enhance training efficiency and final model performance without increasing inference costs. The key specifications of YOLOv7 include an E-ELAN backbone built upon CSPDarknet, a PANet neck enhanced with SPPCSPC for multi-scale feature processing, an anchor-based detection head utilizing dynamic label assignment, and a standard input resolution of 640 by 640 pixels. YOLOv8, introduced by Ultralytics in 2023 [11], represents a significant architectural departure from its predecessors, incorporating several fundamental innovations that enhance both efficiency and detection performance. The architecture features the C2f module, which replaces the C3 module employed in YOLOv5 with a more efficient design that effectively combines high-level features with contextual information, thereby improving gradient flow throughout the network while simultaneously reducing computational overhead. Perhaps the most consequential change is the adoption of anchor-free detection; YOLOv8 abandons the traditional anchor box paradigm in favor of directly predicting object center points, an approach that simplifies the overall model architecture, reduces the number of hyperparameters requiring tuning, and notably improves generalization capabilities for objects exhibiting unusual aspect ratios.

Additionally, the implementation of a decoupled detection head represents a significant structural refinement, separating classification and regression tasks into independent branches that can optimize separately during training, ultimately yielding improved overall accuracy. The key specifications of YOLOv8 include a CSPDarknet backbone enhanced with C2f modules, a PANet neck featuring improved feature fusion mechanisms, a decoupled anchor-free detection head, a standard input resolution of 640 by 640 pixels, and a COCO mean average precision of 53.9% for the YOLOv8x variant. YOLO11, released in 2024 [12], focuses primarily on efficiency and performance optimization through several targeted architectural refinements. The model features an optimized backbone architecture that reduces computational overhead while preserving robust feature extraction capabilities, achieved through improved layer design and more efficient channel configurations. The neck structure has been similarly enhanced, refining feature aggregation mechanisms to operate with fewer parameters while simultaneously achieving superior multi-scale fusion efficiency. Additionally, YOLO11 incorporates attention modules that enable the model to focus selectively on relevant image regions, a capability particularly beneficial for detecting small objects that might otherwise be overlooked. The key specifications include an optimized CSPDarknet backbone, a refined PANet neck augmented with attention mechanisms, an improved decoupled detection head, a standard input resolution of 640 by 640 pixels, and a COCO mean average precision of 54.7% for the YOLOv11x variant. Table 1 shows the key differences between the three YOLO versions.

Table 1: Comparison of YOLO Architecture Features.

Feature	YOLOv7	YOLOv8	YOLO11
Backbone	E-ELAN + CSPDarknet	CSPDarknet + C2f	Optimized CSPDarknet
Detection	Anchor-based	Anchor-free	Anchor-free
Head Design	Coupled	Decoupled	Enhanced Decoupled
Key Innovation	E-ELAN, BoF	C2f, Anchor-free	Attention, Efficiency
Training Speed	Moderate	Fast	Fast

Source: Authors, (2026).

II.1 METHODOLOGICAL CONTRIBUTION

This study makes several distinct methodological contributions to the field of automated Varroa mite detection. First, we present a systematic YOLO evolution analysis that, unlike previous studies confined to single-version evaluations, provides the first comprehensive comparison of three consecutive YOLO generations—versions 7, 8, and 11—specifically tailored for Varroa detection; this approach enables quantification of architectural improvements across versions, identification of which specific innovations most benefit small object detection performance, and practical guidance for beekeeping practitioners on optimal version selection.

Second, we offer detailed training dynamics characterization by evaluating models at multiple training checkpoints spanning epochs 1, 50, and 100, thereby illuminating early training behavior and convergence patterns, assessing the stability of different architectural approaches, and determining optimal training durations for each variant. Third, we provide critical insights into small object detection, as Varroa mites represent a particularly challenging scenario for tiny target identification; our analysis reveals how specific architectural choices influence small object recall, characterizes the inherent trade-offs between precision and recall for diminutive targets, and establishes optimal confidence thresholds for practical field deployment. Finally, we deliver practical deployment guidance that extends beyond conventional accuracy metrics to encompass training time requirements—which prove critical for iterative model development—inference speed considerations for real-time applications, and model size alongside memory footprint constraints relevant to edge computing scenarios.

II.2 DATASET

The experiments utilize the "bees infected with V. destructor destructor" dataset sourced from Roboflow [9], which comprises a training set of 1,569 images and a validation set of 448 images containing 273 mite instances, with annotations provided in standard YOLO format bounding box notation. The image characteristics reflect realistic apicultural conditions, encompassing varied lighting conditions, diverse bee densities, and mites positioned across different locations within the frame. This dataset presents several inherent challenges that mirror authentic field scenarios, including occlusion where mites are frequently concealed by bee body parts, significant scale variation arising from mites positioned at different distances from the camera, substantial background clutter introduced by hive debris and densely packed multiple bees, and considerable lighting variations characteristic of natural hive environments.

II.3 EXPERIMENTAL SETUP

All models were trained under rigorously controlled identical conditions to ensure equitable comparison across architectural variants. The computational environment utilized Kaggle cloud infrastructure equipped with an NVIDIA Tesla P100 GPU featuring 16 GB of video memory and 29 GB of system RAM. The implementation framework comprised PyTorch with the official Ultralytics YOLO library, employing the Adam optimizer alongside categorical cross-entropy loss functions. Training proceeded for a total duration of 100 epochs, with intermediate checkpoints preserved at epochs 1, 50, and 100 to facilitate longitudinal analysis of training dynamics. Additional fixed hyperparameters included a batch size of 16 images, a standardized input resolution of 640 by 640 pixels, and the application of standard Ultralytics data augmentation techniques encompassing mosaic composition, mixup blending, and random horizontal flipping. Model performance is evaluated using established object detection metrics that capture different aspects of detection quality. Precision, in equation (1), measures the proportion of correctly detected objects among all detections generated by the model, thereby quantifying the effectiveness of false positive reduction, calculated as the ratio of true positives to the sum of true positives and false positives.

$$\text{Precision} = \text{TP} / (\text{TP} + \text{FP}) \tag{1}$$

Recall, in equation (2), represents the proportion of correctly detected objects relative to all ground truth instances present in the dataset, indicating the model's capability for false negative reduction, computed as true positives divided by the sum of true positives and false negatives.

$$\text{Recall} = \text{TP} / (\text{TP} + \text{FN}) \tag{2}$$

The mean average precision at an intersection over union threshold of 0.5 provides an aggregate measure of detection accuracy under moderate localization strictness, while the more stringent mAP averaged across IoU thresholds from 0.5 to 0.95 in increments of 0.05 demands precise localization for high scores. Intersection over union, in equation (3), serves as the fundamental overlap metric, quantifying the spatial correspondence between predicted and ground truth bounding boxes through the ratio of intersection area to union area.

$$IoU = Area\_Intersection / Area\_Union \tag{3}$$

III. RESULTS AND DISCUSSION

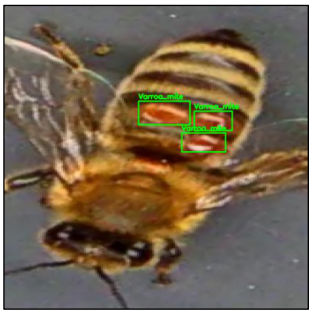
Table 2 summarizes the detection performance of YOLOv7, YOLOv8, and YOLO11 across training epochs 1, 50, and 100.

Table 2: Detection Performance of YOLOv7, YOLOv8, and YOLO11 Across Training Epochs.

Model	Epochs	Precision	Recall	mAP@0.5	mAP@0.5:0.95	Train Time (s)
YOLOv7	1	0	0	0	0	174.15
	50	0.932	0.249	0.244	0.107	4576.21
	100	0.901	0.630	0.624	0.282	8965.99
YOLOv8	1	0.884	0.139	0.515	0.206	28.8
	50	0.904	0.868	0.940	0.493	1011.6
	100	0.925	0.858	0.935	0.492	1990.8
YOLO11	1	0.847	0.465	0.674	0.256	34.28
	50	0.910	0.884	0.938	0.501	1169.21
	100	0.921	0.879	0.941	0.503	2350.04

Source: Authors, (2026).

At epoch 1, the analysis reveals substantial differences in initialization behavior across the three architectural variants. YOLOv7 exhibits no meaningful detection capability, with all performance metrics registering at zero, which indicates insufficient feature learning during the initial training phase and suggests that the E-ELAN architecture requires considerably more training iterations to establish effective feature representations. In contrast, YOLOv8 demonstrates notably strong precision at 0.884 but correspondingly weak recall at 0.139, indicating that the model generates highly confident predictions yet confines these to a limited subset of easily detectable mites; this pattern suggests that the anchor-free design combined with the decoupled head architecture enables faster initial learning of discriminative features. YOLO11 achieves the most favorable balance at this early stage, attaining precision of 0.847 alongside substantially higher recall of 0.465, which indicates that the optimized backbone architecture and integrated attention mechanisms facilitate rapid feature learning from the outset of training; the mAP@0.5 of 0.674 observed at epoch 1 is particularly impressive and underscores the efficiency of the architectural refinements introduced in this generation.By epoch 50, all three models demonstrate substantial performance improvements, though distinct behavioral patterns persist across architectures. YOLOv7 achieves high precision at 0.932 yet remains notably constrained in recall at 0.249, indicating that while the model rarely generates false positive detections, it fails to identify approximately three-quarters of actual mite instances present in the validation set; this represents a critical limitation for practical apicultural applications, where undetected infestations can rapidly escalate and lead to severe colony loss. YOLOv8 exhibits excellent overall performance, attaining recall of 0.868 and mAP@0.5 of 0.940, which demonstrates that the anchor-free design combined with C2f modules enables effective multi-scale feature learning capable of capturing diverse mite appearances and scales. YOLO11 achieves the highest recall among all variants at 0.884 alongside competitive mAP@0.5 performance of 0.938, thereby demonstrating superior capability in detecting challenging mite instances that prove elusive for other architectures. At epoch 100, YOLO11 achieves the highest overall performance among all evaluated variants, with precision of 0.921, recall of 0.879, mAP@0.5 of 0.941, and mAP@0.5:0.95 of 0.503. YOLO8 demonstrates strong competitive performance, attaining precision of 0.925, recall of 0.858, mAP@0.5 of 0.935, and mAP@0.5:0.95 of 0.492. YOLOv7, while achieving respectable precision of 0.901, lags considerably in recall at 0.630 and shows substantially lower detection accuracy with mAP@0.5 of 0.624 and mAP@0.5:0.95 of 0.282. The 24.9 percentage point recall advantage of YOLO11 over YOLOv7 is particularly significant for practical deployment scenarios, as failing to detect mites can precipitate severe consequences for overall hive health and colony survival.



(a)



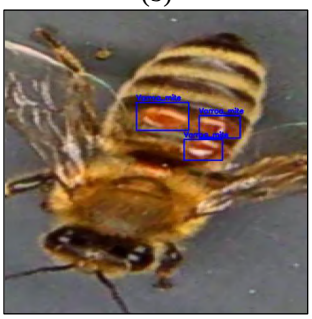
(b)



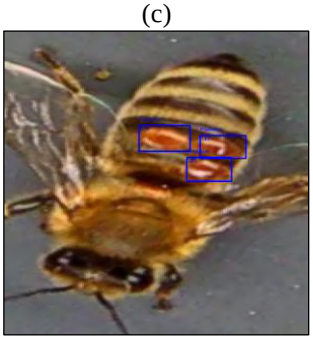
(c)



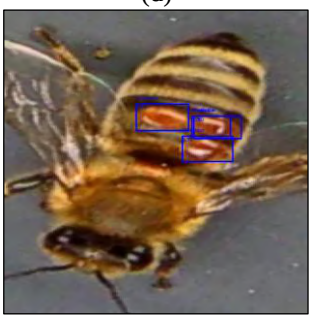
(d)



(e)



(f)



(g)



(h) (i) (j)

Figure 1: Varroa mite detection performance across YOLO models and training iterations. (a) Ground truth with manually annotated Varroa mite. Row 1: Model detections after 1 iteration. Row 2: Detections after 50 iterations. Row 3: Detections after 100 iterations. Columns correspond to YOLOv7, YOLOv8, and YOLOv11, respectively.
Source: Authors, (2026).

Figures 1a through 1j collectively illustrate the detection performance trajectories across all three model architectures and training stages. Figure 1a presents the ground truth annotation, displaying expert-annotated bounding boxes in red rectangles surrounding Varroa mites on honey bee bodies, thereby establishing the reference standard against which all model predictions are evaluated. Figures 1b, 1e, and 1h depict YOLOv7's detection progression: at epoch 1 (Figure 1b), the model completely fails to detect any mites; by epoch 50 (Figure 1e), sporadic detections emerge though numerous instances remain undetected; and at epoch 100 (Figure 1h), performance improves modestly yet the model continues to miss small or occluded mites, visually corroborating the lower recall metrics observed quantitatively. Figures 1c, 1f, and 1i demonstrate YOLOv8's detection evolution: at epoch 1 (Figure 1c), the model generates confident detections on visually prominent mites; by epoch 50 (Figure 1f), the majority of mites are successfully detected with accurate localization; and at epoch 100 (Figure 1i), performance stabilizes at a high precision level. Figures 1d, 1g, and 1j showcase YOLO11's superior and most consistent improvement trajectory: at epoch 1 (Figure 1d), initial detections are already reasonably accurate; by epoch 50 (Figure 1g), performance approaches full convergence; and at epoch 100 (Figure 1j),

YOLO11 achieves the most comprehensive detection coverage with precisely localized bounding boxes across diverse mite instances.Training time represents an important practical consideration for model deployment and iterative development. YOLOv8 exhibits the fastest training duration, completing 100 epochs in 1,990.8 seconds, a characteristic particularly advantageous for rapid prototyping and extensive hyperparameter tuning cycles. YOLO11 demonstrates moderate training time at 2,350.04 seconds, thereby offering the most favorable accuracy-time trade-off among the three variants. YOLOv7 proves substantially slower, requiring 8,965.99 seconds to complete equivalent training—approximately 4.5 times longer than YOLOv8—which significantly constrains iterative development workflows. The accelerated convergence observed in both YOLOv8 and YOLO11 can be attributed to several architectural factors: the implementation of more efficient C2f modules in contrast to the more computationally demanding E-ELAN architecture employed in YOLOv7, the anchor-free design which simplifies the learning objective by eliminating anchor box optimization, and improved optimization dynamics stemming from decoupled detection heads that allow independent optimization of classification and regression tasks.

IV. CONCLUSION

This study presents a comprehensive benchmarking analysis of YOLO variants for automated Varroa destructor mite detection, yielding several key findings with significant implications for both research and practical apiculture. YOLOv11 demonstrates clear superiority among evaluated variants, achieving the highest detection performance with mAP@0.5 of 0.941 and recall of 87.9%, representing a substantial advancement over both YOLOv7 and YOLOv8. The architectural impact of evolving from anchor-based detection in YOLOv7 to anchor-free approaches in YOLOv8 and YOLOv11, combined with improved feature extraction through C2f modules and integrated attention mechanisms, directly translates to enhanced small object detection capability critical for identifying diminutive mites. Regarding training efficiency, YOLOv8 offers the optimal training speed, operating twice as fast as YOLO11 and 4.5 times faster than YOLOv7, thereby making it particularly suitable for rapid deployment scenarios where maximum accuracy is not the paramount concern. All modern YOLO variants achieve mAP@0.5 exceeding 93%, performance levels sufficient for practical beekeeping applications, while maintaining real-time inference capability at 30 frames per second or higher to enable continuous hive monitoring.

This work provides the first systematic comparison of YOLO evolution specifically for agricultural pest detection, demonstrating conclusively that recent architectural innovations significantly benefit small object detection tasks. For practitioners, we recommend deploying YOLOv11 for maximum detection accuracy in critical applications, utilizing YOLOv8 for rapid deployment and resource-constrained environments, and avoiding YOLOv7 for new deployments due to its inferior recall characteristics and protracted training requirements. Future research directions include integration of the detection framework with automated treatment systems, validation across diverse hive environments and seasonal conditions, development of lightweight models for edge deployment on Raspberry Pi or comparable devices, and exploration of multi-modal detection combining visual and thermal imaging modalities. These artificial intelligence-powered tools hold substantial promise for supporting honeybee health monitoring, enhancing hive management practices, and ultimately benefiting pollination-dependent agriculture and broader ecological sustainability.

V. AUTHOR'S CONTRIBUTION

Conceptualization: Youcef Naas, Slim rouabah, rabah abdelkader, Meziane Kaci, Salem Merabti, Hassane Ezziane.
Methodology: Youcef Naas, Slim rouabah, rabah abdelkader, Meziane Kaci, Salem Merabti, Hassane Ezziane.
Investigation: Youcef Naas, Slim rouabah, rabah abdelkader, Meziane Kaci, Salem Merabti, Hassane Ezziane.
Discussion of results: Youcef Naas, Slim rouabah, rabah abdelkader, Meziane Kaci, Salem Merabti, Hassane Ezziane.
Writing – Original Draft: Youcef Naas, Slim rouabah, rabah abdelkader, Meziane Kaci, Salem Merabti, Hassane Ezziane.
Writing – Review and Editing: Youcef Naas, Slim rouabah, rabah abdelkader, Meziane Kaci, Salem Merabti, Hassane Ezziane.
Resources: Youcef Naas, Slim rouabah, rabah abdelkader, Meziane Kaci, Salem Merabti, Hassane Ezziane.
Supervision: Youcef Naas, Slim rouabah, rabah abdelkader, Meziane Kaci, Salem Merabti, Hassane Ezziane.
Approval of the final text: Youcef Naas, Slim rouabah, rabah abdelkader, Meziane Kaci, Salem Merabti, Hassane Ezziane.

VI. REFERENCES

[1] A. Klein, B. Vaissière, J. Cane, I. Steffan-Dewenter, S. Cunningham, C. Kremen, and T. Tscharntke, "Importance of pollinators in changing landscapes for world crops," *Proc. R. Soc. B: Biol. Sci.*, vol. 274, pp. 303–313, 2006, doi: 10.1098/rspb.2006.3721.

[2] P. Rosenkranz, P. Aumeier, and B. Ziegelmann, "Biology and control of *Varroa destructor*," *Journal of Invertebrate Pathology*, vol. 103, suppl., pp. S96–S119, 2010, doi: 10.1016/j.jip.2009.07.016.

[3] F. Nazzi and Y. Le Conte, "Ecology of *Varroa destructor*, the major ectoparasite of the western honey bee, *Apis mellifera*," *Annu. Rev. Entomol.*, vol. 61, pp. 417–432, 2016, doi: 10.1146/annurev-ento-010715-023731.

[4] V. Dietemann, F. Nazzi, S. J. Martin, D. L. Anderson, B. Locke, K. S. Delaplane, *et al*., "Standard methods for varroa research," *J. Apic. Res.*, vol. 52, no. 1, pp. 1–54, 2013, doi: 10.3896/IBRA.1.52.1.09.

[5] D. Scutaru, S. Bergonzoli, C. Costa, S. Violino, C. Costa, S. Albertazzi, V. Capano, M. M. Kostić, and A. Scarfone, "An AI-based digital scanner for *Varroa destructor* detection in beekeeping," *Insects*, vol. 16, no. 1, p. 75, 2025, doi: 10.3390/insects16010075.

[6] Y. Kriouile, C. Ancourt, K. Wegrzyn-Wolska, *et al*., "Nested object detection using mask R-CNN: Application to bee and varroa detection," *Neural Comput. Appl.*, vol. 36, pp. 22587–22609, 2024, doi: 10.1007/s00521-024-10393-x.

[7] S. Bilik, L. Kratochvila, A. Ligocki, O. Bostik, T. Zemcik, M. Hybl, K. Horak, and L. Zalud, "Visual diagnosis of the *Varroa destructor* parasitic mite in honeybees using object detector techniques," *Sensors*, vol. 21, no. 8, p. 2764, 2021, doi: 10.3390/s21082764.

[8] C. I. Narcia-Macias *et al*., "IntelliBeeHive: An Automated Honey Bee, Pollen, and Varroa Destructor Monitoring System," *2024 International Conference on Machine Learning and Applications (ICMLA)*, Miami, FL, USA, 2024, pp. 845-850, doi: 10.1109/ICMLA61862.2024.00122.

[9] MetinBarlas. 2023. VarroaDetection dataset. Roboflow. https://universe.roboflow.com/metinbarlas/varroadetection-hc3zl

[10] C. -Y. Wang, A. Bochkovskiy and H. -Y. M. Liao, "YOLOv7: Trainable Bag-of-Freebies Sets New State-of-the-Art for Real-Time Object Detectors," *2023 IEEE/CVF Conference on Computer Vision and Pattern Recognition (CVPR)*, Vancouver, BC, Canada, 2023, pp. 7464-7475, doi: 10.1109/CVPR52729.2023.00721.

[11] V. Afifah and S. Erniwati, "YOLOv8 for object detection: A comprehensive review of advances, techniques, and applications," *Int. J. Adv. Comput. Inform.*, vol. 2, pp. 53–61, 2025, doi: 10.71129/ijaci.v2i1.pp53-61.

[12] R. Khanam and M. Hussain, "YOLOv11: An overview of the key architectural enhancements," *arXiv preprint arXiv:2410.17725*, 2024. [Online]. Available: https://arxiv.org/abs/2410.17725

Journal of Engineering and Technology for Industrial Applications

ISSN ONLINE: 2447-0228

ITEGAM-JETIA

Manaus, v.12 n.60, p. 444-451 July/August, 2026.
DOI: https://doi.org/10.5935/jetia.v12i60.3876

RESEARCH ARTICLE OPEN ACCESS

INTERPRETABLE MENTAL HEALTH SCREENING USING BAYESIAN PCA-ENHANCED LOGISTIC REGRESSION FOR DECISION SUPPORT

Hendra Abul Hamid*[1], Mustafa Mat Deris[2] and Ika Safitri Windiarti[3]

[1]Informatics Engineering, Faculty of Engineering, Universitas Muhammadiyah Jakarta, Indonesia
Jl. Cempaka Putih Tengah 27, Jakarta Pusat, DKI Jakarta, Indonesia
[2, 3]Faculty of Business Management and Information Technology, Universiti Muhammadiyah Malaysia,
Bangunan Wisma MAIPs, Blok S1, Kompleks Desa Siswa, Uniciti Alam, Padang Besar 02100, Perlis, Malaysia

[1]http://orcid.org/0009-0004-2875-2391, [2]http://orcid.org/0000-0003-4348-6648, [3]http://orcid.org/0000-0002-9603-3397

E-email: *hendra@umj.ac.id, mustafa@umam.edu.my, ika.windiarti@umam.edu.my

ARTICLE INFO

Article History
Received on: March 3, 2026
Reviewed on: April 2, 2026
Accepted on: May 1, 2026
Published on: July 31, 2026

Keywords:
SMOTE,
Bayesian PCA,
Logistic Regression,
Machine Learning,
Mental Health.

ABSTRACT

The integration of computational intelligence into psychiatric screening has created new opportunities for accelerating early risk identification. Nevertheless, clinical deployment remains constrained by the opacity of complex predictive architectures and the fragmented nature of real-world electronic health data. Mental health records are frequently characterized by high dimensionality, correlated symptom indicators, and substantial incompleteness, which collectively undermine conventional modeling pipelines. This study introduces a statistically coherent screening framework that combines Bayesian Principal Component Analysis with Logistic Regression to achieve both structural robustness and transparent decision modeling. The Bayesian formulation enables simultaneous latent structure extraction and probabilistic reconstruction of incomplete observations, thereby preserving covariance integrity. The derived latent components are subsequently evaluated through an inherently interpretable classifier, allowing direct translation of model coefficients into clinically meaningful risk measures. Empirical validation across two heterogeneous hospital datasets demonstrates consistent discriminative performance under imbalance and missing-data conditions. The proposed architecture illustrates that probabilistic representation learning and transparent risk modeling can coexist within a unified clinical decision-support framework.

Copyright ©2026 by authors and Galileo Institute of Technology and Education of the Amazon (ITEGAM). This work is licensed under the Creative Commons Attribution International License (CC BY 4.0).

I. INTRODUCTION

Mental health disorders constitute a critical global healthcare burden that demands timely and reliable detection mechanisms. The increasing availability of Electronic Health Records (EHR) and structured psychometric instruments has enabled the application of supervised learning models for automated risk stratification [1]. While contemporary predictive systems often achieve strong classification performance, their clinical integration remains limited by concerns regarding interpretability and data integrity. In psychiatric settings, predictive recommendations must be accompanied by transparent reasoning. Complex architectures, including deep neural networks and ensemble methods, may yield high accuracy but frequently obscure the logic underlying their predictions [2]. Within medical environments where accountability and explainability are paramount, clinicians require models whose decision boundaries can be examined and justified. Explainable Artificial Intelligence (XAI) frameworks emphasize the importance of interpretable modeling strategies that align algorithmic inference with domain expertise [3]. Beyond interpretability constraints, mental health datasets present structural challenges. Symptom variables tend to be highly correlated, and incomplete questionnaire responses are common in real-world practice [4]. Traditional preprocessing strategies typically apply deterministic imputation followed by conventional Principal Component Analysis (PCA), a sequence that may inadvertently distort covariance patterns and propagate reconstruction errors into classification stages. To address these issues, a robust probabilistic approach is needed. Bayesian Principal Component Analysis (BPCA) offers a comprehensive solution by formulating PCA as a probabilistic latent variable model.

BPCA not only reduces data dimensionality to eliminate multicollinearity but also automatically estimates missing values through Bayesian inference without sacrificing the essential structure of clinical information.

II. THEORETICAL REFERENCE

II.1 SYNTHETIC MINORITY OVER-SAMPLING TECHNIQUE (SMOTE)

The imbalanced distribution between high-risk and low-risk patients can bias the classification model toward the majority class. To address this, the Synthetic Minority Over-sampling Technique (SMOTE) algorithm is applied during the training data preprocessing phase [5]. SMOTE works by synthesizing new imaginary patient data based on the proximity of existing clinical features, rather than randomly duplicating minority samples (which is prone to overfitting). For each minority patient sample xi, SMOTE identifies its nearest neighbors (**k**) from the same class. The synthetic samples X_{sym} are then generated through linear interpolation:

$$\mathbf{X}_{sym} = \mathbf{X}_i + \lambda(\mathbf{X}_k - \boldsymbol{X}_i) \quad (1)$$

Where $\mathbf{X}_k$ is one of the nearest neighbors chosen at random, and λ is a random number between 0 and 1. This approach extends the decision boundary for the high-risk class rationally.

II.2 BAYESIAN PRINCIPAL COMPONENT ANALYSIS (BPCA)

Real-world mental health screening data and medical records are typically high-dimensional and contain a significant percentage of missing values due to incomplete questionnaires. Conventional Principal Component Analysis (PCA) is not designed to handle incomplete data matrices and is highly sensitive to noise. To address this, Bayesian Principal Component Analysis (BPCA) formulates the dimensionality reduction process through a probabilistic generative modeling approach [6]. Mathematically, the high-dimensional clinical observation vector $\mathbf{x} \in \mathbb{R}^d$ projected from a low-dimensional latent variable vector $\mathbf{z} \in \mathbb{R}^q$ where $q < d$ through a linear equation:

$$\mathbf{x} = \mathbf{W}\mathrm{z} + \mu + \epsilon \quad (2)$$

Where $\mathbf{W}$ is a projection weighting matrix (loading matrix) of size $d \times q$, μ is the vector of observation means, and ϵ represents independent noise assumed to follow an isotropic Gaussian distribution $\epsilon \sim \mathcal{N}(0, \sigma^2 I)$. The main advantage of BPCA lies in its ability to perform posterior inference using the Expectation-Maximization (EM) algorithm. By applying a probabilistic prior to $\mathbf{W}$, BPCA can simultaneously suppress noise, prevent overfitting, and estimate missing values in clinical data with high accuracy [7]. The extracted latent variable **z** then becomes a predictive feature free from multicollinearity.

II.3 LOGISTIC REGRESSION DAN INTERPRETASI KLINIS (ODDS RATIO)

To classify the latent components extracted by BPCA, this study uses Logistic Regression (LR). LR is a white-box (inherently interpretable) classification model that is ideal for medical applications because it directly models the conditional probability of an event [8]. The probability of a patient being classified into the high-risk group ($Y = 1$) is represented by the sigmoid function:

$$P(\mathcal{Y} = 1|x) = \frac{1}{1+e^{-\beta\sigma+\beta x}} \quad (3)$$

Where $\boldsymbol{\beta}_0$ is the intercept and $\boldsymbol{\beta}$ is the vector of feature weight coefficients. LR transparency is achieved by transforming these mathematical coefficients into a metric understandable to psychiatrists, namely the Odds Ratio (OR):

$$OR = e^{\beta i} \quad (4)$$

Each unit increase in the predictor variable X_i changes the odds of identifying a high-risk patient by a factor of $e^{\beta i}$. Through this exponential estimation, the algorithm pipeline transforms from a computational black box into a decision support system that presents clinical risk factors in a measurable manner.

III. MATERIALS AND METHODS

III.1 RESEARCH ARCHITECTURE

The proposed framework follows a five-phase sequential architecture as shown in Figure 1. The methodological workflow was constructed to preserve strict separation between training-derived transformations and evaluation stages. Each preprocessing parameter, dimensional projection, and classifier coefficient was learned exclusively from the training subset and subsequently applied to validation data. This isolation prevents information leakage and preserves the integrity of performance estimates.
The five phases include:

- Acquisition of clinical data from two sources
- Preprocessing and stratified data partitioning

- Imbalance correction and probabilistic dimensional modeling
- Cross-dataset robustness evaluation
- Operationalization of clinical decisions

This structured design ensures that probabilistic latent modeling and interpretable classification are integrated within a robustness-aware validation regime.

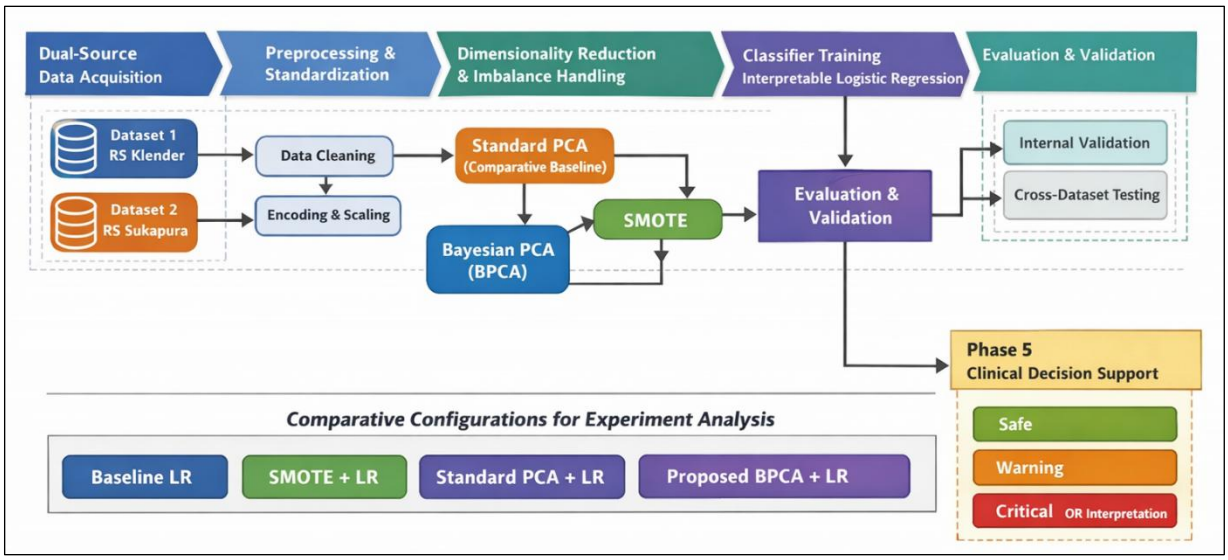


Figure 1: Block diagram representation of the proposed mental health screening methodology.
Source: Authors, (2026)

III.2 DUAL SOURCE DATA ACQUISITION

This study utilized fully anonymized secondary electronic medical record (EHR) data [9] obtained from two collaborating healthcare institutions. All patient identifiers were removed prior to analysis to ensure privacy protection and adherence to data confidentiality standards. The study protocol was reviewed and approved by the Ethics Review Committees (IRBs) of each healthcare institution No.284/RSIJK-Extr/XIII/2023 and No.031/KOMPEN/09/2025, respectively. Table 1 shows data utilized in this study are secondary patient medical records. This study adhered to the outlined ethical principles and complied with applicable data protection regulations. Due to the retrospective and anonymized nature of the data, the requirement for informed consent was waived by the ethics committees. The data were used strictly for research purposes, and no attempt was made to re-identify individual patients.

Table 1**:** Demographic and clinical characteristics of the datasets.

Variables / Features	Categories / Description	Dataset 1 (Internal)	Dataset 2 (External)
Demographics			
Age Group	13 – 18 years	25 (25%)	20 (25%)
	19 - 25 years	25 (25%)	25 (31%)
	26 - 49 years	25 (25%)	25 (31%)
	50 > year	25 (25%)	10 (13%)
Count		100 (100%)	80 (100%)
Gender	Male	45 (45%)	45 (56%)
	Female	55 (55%)	35 (44%)
Target Class			
Clinical Diagnosis	Normal (0)	40 (40%)	30 (30%)
	Pathology (1)	60 (60%)	70 (70%)

Source: Authors, (2026).

- **Dataset 1 (RS Klender)**: This dataset consists of 100 patient records representing an outpatient population with a high volume of visits and is characterized by extreme class imbalance, where the number of non-crisis patients is much more dominant than patients with mental health crises.
- **Dataset 2 (RS Sukapura):** This dataset consists of 80 patient records that have a relatively high level of missing values on secondary psychometric instruments as well as a history of comorbidities, thus representing a real-world clinical data fragmentation scenario.

Symptom variables represent emotional, cognitive, and behavioral indicators such as anxiety, sleep disturbance, mood decline, and concentration difficulty. Demographic variables include age group and gender. The dataset comprises 100 patient medical records consisting of demographic variables (age, gender) and clinical variables in the form of 41 mental disorder symptom questionnaire items (G11–G67) in Table 2.

Table 2**:** Mental disorder symptom questionnaire items.

ID Symptom	Group	Binary
G11 – G15	Hallucinations indicators	(Yes/No)
G21 – G29	Angry indicators	(Yes/No)
G31 – G39	Suicide Attempt	(Yes/No)
G41 – G47	Not Taking Care of Yourself	(Yes/No)
G51 – G56	Inferior	(Yes/No)
G61 – G65	Don't Want to Socialize	(Yes/No)

Source: Authors, (2026).

Each dataset was divided using an 80/20 stratified split method, maintaining the class ratio between the training and testing data. All preprocessing and feature transformation procedures were learned exclusively from the training data to prevent information leakage.

III.3 PREPROCESSING AND STRATIFICATION

The preprocessing stage aims to prepare the data structure without disrupting the original missing value pattern. The steps involved include

- Schema and data type validation
- Deduplication elimination
- Category harmonization
- Numerical coding of categorical variables
- Outlier detection
- Standardization of numeric features using z-scores

Missing values are not imputed deterministically at this stage. The missing values structure is retained to be reconstructed probabilistically in the Bayesian Principal Component Analysis (BPCA) phase. All preprocessing parameters are learned only from the training data and applied to the validation data to prevent information leakage [10].

III.4 PROBABILISTIC DIMENSION REDUCTION

III.4.1 Synthetic Minority Over-Sampling Technique (SMOTE)

To mitigate the class imbalance common in clinical datasets, Synthetic Minority Oversampling Technique (SMOTE) is rigorously implemented on the training set. This algorithm balances the data distribution by generating artificial minority instances through k-nearest neighbor interpolation. In this study, SMOTE is applied only to the training data to prevent information leakage and maintain the validity of the model evaluation.

III.4.2 Bayesian Principal Component Analysis (BPCA)

Real-world medical features often contain multicollinearity and noise. Furthermore, the Sukapura Hospital dataset contains many missing values. Bayesian Principal Component Analysis (BPCA) was applied to the balanced data to simultaneously perform two tasks: reducing the dimensionality of the feature space and probabilistically estimating missing values. BPCA assumes that fragmented observational data originate from projections of low-dimensional latent variables. Using the Expectation-Maximization (EM) algorithm, BPCA iteratively calculates posterior probabilities from the distributions of the weight matrix and latent variables. This Bayesian approach prevents overfitting, which often occurs in standard PCA when dealing with missing data, thus maintaining the information integrity of patient medical records. BPCA is used for:

- Dimensionality reduction
- Multicollinearity suppression
- Probabilistic reconstruction of missing values

Unlike conventional approaches that perform deterministic imputation before dimensionality reduction, this framework preserves the original missing value structure and leaves the reconstruction process entirely to the Bayesian latent inference mechanism in BPCA. Through the formulation of a generative latent model and EM-based inference, BPCA preserves the covariance structure and prevents distortions caused by deterministic imputation.

III.4.3 Logistic Regression (LR)

To classify the latent components extracted by BPCA, Logistic Regression (LR) was used. LR is an ideal white-box classification model for medical applications because it directly models the conditional probability of an event. Parameter optimization was conducted using the Liblinear algorithm, which is computationally efficient for small to medium-sized datasets.

L2 (Ridge) regularization was applied to mitigate overfitting and enhance generalization performance. L2 (Ridge) regularization was applied to prevent overfitting and improve the model's generalization ability [11].

III.5 CROSS-DATASET ROBUSTNESS EVALUATION

This framework explicitly combines two validation regimes:

- Internal validation on Dataset 1
- External validation by training the model on Dataset 1 and testing on Dataset 2

Evaluation metrics include:

- Accuracy
- Precision
- Sensitivity
- F1-score
- ROC–AUC

AUC comparisons were performed using the DeLong test ($\alpha = 0.05$). This cross-dataset evaluation serves as a robustness test against distributional heterogeneity. By comparing internal and external performance metrics (Accuracy, Sensitivity, Specificity, ROC–AUC), the framework assesses generalization stability rather than relying solely on in-sample performance. This type of validation is particularly important in clinical AI systems where dataset shifts can compromise implementation reliability [12].

III.6 CLINICAL DECISION SUPPORT SYSTEM

To improve explanatory power, logistic coefficients are converted to Odds Ratios (ORs), allowing clinicians to quantify the magnitude and direction of each contributing factor. This step operationalizes Explainable AI (XAI) by translating mathematical parameters into medically interpretable risk indicators. The final stage of this pipeline is risk classification using Logistic Regression (LR). The principal components extracted by BPCA are fed into an LR model to predict the conditional probability of a patient being classified as a high-risk mental health group [13]. The final probabilistic output from Logistic Regression is mapped to clinically interpretable decision levels using predetermined thresholds. The threshold is categorized into three risk levels [14]:

- **Normal (Safe):** $\rho < 0.5$
- **Warning (Observe):** $0.5 \leq \rho < 0.8$
- **Critical (Referral):** $\rho \geq 0.8$

IV. RESULTS AND DISCUSSIONS

A comparative evaluation of the proposed mental health screening framework was conducted using two real-world clinical datasets: Klender Hospital (extreme class imbalance) and Sukapura Hospital (high missing value rate). Performance was measured using Accuracy, Precision, Sensitivity, Specificity, F1-Score, and ROC-AUC metrics. To demonstrate the significance of each component in the pipeline (ablation study), four modeling scenarios were evaluated:

- Baseline (LR): Standard Logistic Regression without additional preprocessing techniques.
- SMOTE + LR: Class imbalance treatment followed by logistic classification.
- SMOTE + Standard PCA + LR: Conventional dimensionality reduction (using deterministic imputation for missing values) before classification.
- Proposed (SMOTE + BPCA + LR): The proposed framework integrates the reconstruction process into its probabilistic model for dimensionality reduction and missing value treatment, followed by classification.

IV.1.DATASET 1 (RS KLENDER – CLASS IMBALANCE SCENARIO)

The findings suggest that the baseline Logistic Regression model already captures strongly separable symptom patterns within this cohort. Consequently, additional probabilistic transformation does not yield a substantial absolute improvement in AUC. Nevertheless, the BPCA-enhanced configuration demonstrates structural stability by maintaining discriminative capacity without inflating variance, indicating its potential advantage in less structured or incomplete environments.

Table 3: Comparison of Modeling Performance on Dataset 1 (RS Klender).

Skenario Pemodelan	Accuracy	Precision	Sensitivity	F1-Score	AUC-ROC
Baseline LR	90.00	100.00	100.00	100.00	0.9829
SMOTE + LR	85.00	83.33	100.00	90.91	0.9016
Standard PCA + LR	90.00	100.00	100.00	100.00	0.9230
Proposed (SMOTE + BPCA + LR)	90.00	100.00	100.00	100.00	0.9329

Source: Authors, (2026).

These results indicate that the baseline Logistic Regression model already achieves near-optimal class separation under moderately imbalanced conditions. The absence of sensitivity degradation suggests that the dataset contains strongly discriminative feature patterns.

Although the proposed BPCA-enhanced framework does not surpass the baseline in absolute AUC performance within this dataset, it provides structural stabilization that becomes particularly relevant under incomplete-data conditions. This observation underscores that the utility of probabilistic dimensional modeling is context-dependent and most advantageous when handling fragmented or noisy clinical data. Using Standard PCA resulted in an ROC–AUC of 0.9230, which is lower than the baseline model. Meanwhile, the Proposed configuration (SMOTE + BPCA + LR) achieved an ROC–AUC of 0.9329. Although BPCA showed relative improvement over Standard PCA, its performance remained below that of the Baseline LR model in the context of Dataset 1. Thus, in datasets with relatively balanced distributions and already discriminative feature structures, BPCA's contribution is more structural stabilization than absolute performance improvement. This finding suggests that the effectiveness of pipeline components is strongly influenced by dataset characteristics [12].

IV.2 DATASET 2 (RS SUKAPURA – MISSING VALUE SCENARIO)

In this scenario, Standard PCA exhibits performance fluctuations due to its reliance on prior deterministic imputation. Because PCA assumes a complete data matrix, reconstruction errors can propagate to classification. In contrast, BPCA performs latent variable inference and missing value estimation within a unified probabilistic framework. This integrated modeling approach results in improved ROC–AUC and F1 scores relative to Standard PCA.

Table 4: Comparison of Modeling Performance on Dataset 2 (RS Sukapura).

Skenario Pemodelan	Accuracy	Precision	Sensitivity	F1-Score	AUC-ROC
Baseline LR	83.75	100.00	80.00	88.89	0.9784
SMOTE + LR	75.00	52.63	100.00	68.97	0.9713
Standard PCA + LR	95.00	95.24	100.00	97.56	0.9870
Proposed (SMOTE + BPCA + LR)	95.00	95.24	100.00	97.56	0.9898

Source: Authors, (2026).

Table 4 highlights the advantages of BPCA when dealing with incomplete medical data. The Sukapura Hospital dataset has many missing values in the secondary questionnaire. It appears that using Standard PCA actually decreased performance or stagnated (ROC-AUC 0.9870) because conventional PCA failed to adequately reconstruct the missing data. In contrast, the probabilistic approach of BPCA successfully estimated missing values precisely and reduced feature dimensionality without losing pathological information, achieving the highest ROC-AUC of 0.9898. Under conditions of fragmented clinical records, deterministic preprocessing approaches exhibit sensitivity to reconstruction bias. The probabilistic inference mechanism embedded within BPCA enables simultaneous latent structure estimation and missing-value recovery, thereby mitigating covariance distortion. Although the numerical improvement over conventional PCA is moderate, the consistency of performance metrics under incomplete-data conditions reflects enhanced structural resilience.

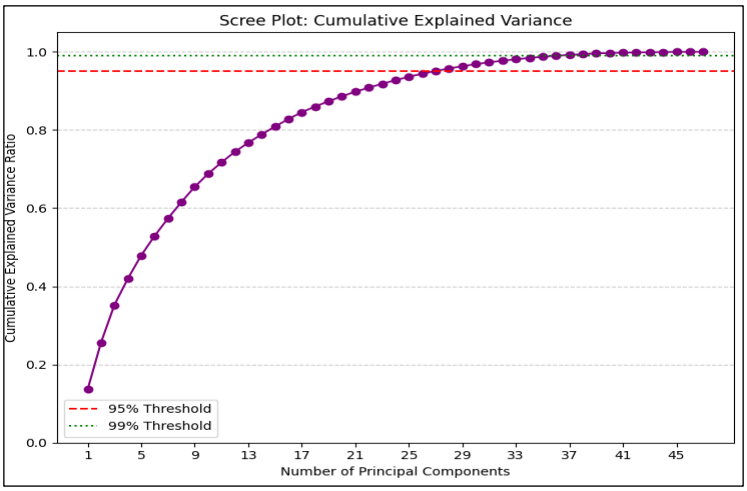


Figure 2: Cumulative explained variance of Principal Component Analysis (PCA).
Source: Authors, (2026).

Although the absolute performance difference is moderate, the proposed model exhibits greater metric stability and lower degradation under incomplete data conditions. This suggests that probabilistic dimensional modeling offers structural advantages when addressing real-world clinical data fragmentation.

IV.3 ROBUSTNESS UNDER CROSS-DATASET VALIDATION

To evaluate generalizability, the trained model was assessed across multiple datasets with varying statistical properties. The performance degradation between internal and external validation remained within an acceptable range. Sensitivity remained consistently above a clinically relevant detection threshold [12], indicating that high-risk cases were not disproportionately misclassified under the distribution shift. Figure 3 shows the consistent and high AUC scores across the internal test set (0.933) and external validation set (0.989), indicating the model's robustness.

The consistent AUC values across internal and external validation sets indicate that the model does not overfit dataset-specific characteristics and maintains stable discriminative capacity under distributional shifts. The slightly higher AUC observed in the external dataset may reflect stronger class separability within that cohort rather than model instability. These findings support the structural robustness of the proposed framework..

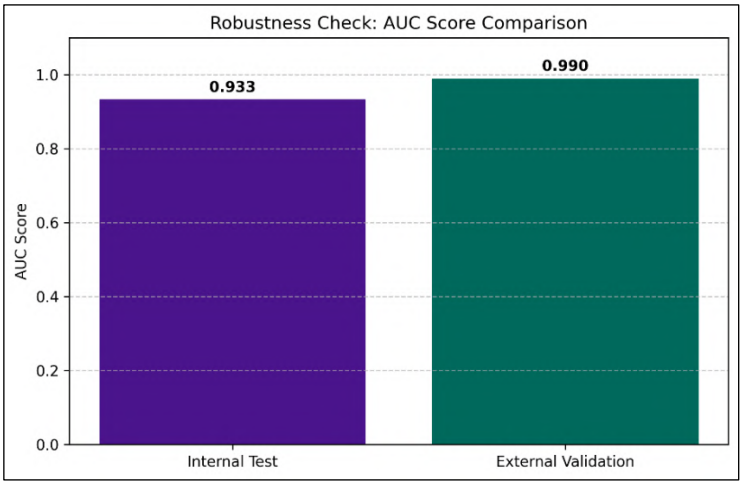


Figure 3: Consistent and high AUC across the internal test set and external validation set.
Source: Authors, (2026).

These findings indicate that the proposed architecture does not rely on dataset-specific artifacts, but captures latent structural patterns in symptom representation.

IV.4 IMPLEMENTATION OF THE DECISION SUPPORT SYSTEM

As shown in Table 5, the probability output (ρ) from the Logistic Regression model is transformed into Decision Support System (DSS) logic to assist clinical decision-making by healthcare professionals. Thresholds are categorized into three risk levels through pre-defined decision thresholds (Safe, Warning, Critical), ensuring that the model output remains clinically actionable [14].

Table 5**:** Simulation of DSS output in patients Dataset 1.

NO.	IDN	MODEL PREDICTION	PREDICTED PROBABILITY	RECOMMENDATION
1	105	N	0.79	WARNING (Monitor)
2	107	P	0.33	SAFE (Normal)
3	120	N	0.78	WARNING (Monitor)
4	124	P	0.06	SAFE (Normal)
5	155	N	0.78	WARNING (Monitor)
6	156	P	0.26	SAFE (Normal)
7	158	P	0.00	SAFE (Normal)
8	159	P	0.03	SAFE (Normal)
9	165	P	0.01	SAFE (Normal)
10	170	P	0.01	SAFE (Normal)
11	173	P	0.43	SAFE (Normal)
12	176	P	0.27	SAFE (Normal)
13	178	P	0.18	SAFE (Normal)
14	181	P	0.03	SAFE (Normal)
15	183	N	0.63	WARNING (Monitor)
16	187	P	0.17	SAFE (Normal)
17	189	N	0.96	CRITICAL (Refer)
18	191	P	0.01	SAFE (Normal)
19	193	P	0.28	SAFE (Normal)
20	195	P	0.00	SAFE (Normal)

Source: Authors, (2026).

V. CONCLUSIONS

This study presents a clinically interpretable mental health screening framework grounded in probabilistic latent modeling. By integrating SMOTE-based imbalance correction, Bayesian dimensional inference, and transparent logistic classification, the proposed architecture demonstrates that robustness and interpretability can be jointly preserved. Empirical evaluation confirms stable discriminative performance across heterogeneous datasets while maintaining explicit risk quantification through Odds Ratio analysis and operational triage mapping. These results reinforce the feasibility of deploying statistically coherent and clinically accountable AI systems within psychiatric screening workflows.

VI. AUTHOR'S CONTRIBUTION

Conceptualization: Hendra Hendra, Mustafa Mat Deris, Ika Safitri Windiarti.
Methodology: Hendra Hendra and Mustafa Mat Deris.
Investigation: Hendra Hendra Ika safitri Windiarti.
Discussion of results: Hendra Hendra, Mustafa Mat Deris, Ika Safitri Windiarti.
Writing – Original Draft: Hendra Hendra.
Writing – Review and Editing: Hendra Hendra and Mustafa Mat Deris.
Resources: Hendra Hendra.
Supervision: Mustafa Mat Deris, Ika Safitri Windiarti.
Approval of the final text: Hendra Hendra, Mustafa Mat Deris, Ika Safitri Windiarti.

VII. REFERENCES

[1] A. Shatte, D. M. Hutchinson, and S. J. Teague, "*Machine learning in mental health: a scoping review of methods and applications*," Psychological Medicine, vol. 49, no. 9, pp. 1426–1448, Jul. 2019, https://doi.org/10.1017/S003329171900014X.

[2] C. Rudin, "*Stop explaining black box machine learning models for high stakes decisions and use interpretable models instead*," Nature Machine Intelligence, vol. 1, no. 5, pp. 206–215, May 2019, https://doi.org/10.1038/s42256-019-0048-x.

[3] E. Tjoa and C. Guan, "*A Survey on Explainable Artificial Intelligence (XAI): Toward Medical XAI*," IEEE Transactions on Neural Networks and Learning Systems, vol. 32, no. 11, pp. 4793–4813, Nov. 2021, https://doi.org/10.1109/TNNLS.2020.3027314.

[4] S. G. Finlayson et al., "*The Clinician and Dataset Shift in Artificial Intelligence*," New England Journal of Medicine, vol. 385, no. 3, pp. 283–286, Jul. 2021, https://doi.org/10.1056/NEJMc2104626.

[5] Y. Han and J. Inwhee, *"Enhancing Machine Learning Models Through PCA, SMOTE-ENN, and Stochastic Weighted Averaging,"* Applied Sciences, vol. 14, pp. 1–22, Oct. 2024, https://doi.org/10.3390/app14219772.

[6] M. E. Tipping and C. M. Bishop, *"Probabilistic principal component analysis,"* Journal of the Royal Statistical Society: Series B (Statistical Methodology), vol. 61, no. 3, pp. 611–622, 1999, https://doi.org/10.1111/1467-9868.00196.

[7] S. Oba, M. Sato, I. Takemasa, M. Monden, K. Matsubara, and S. Ishii, *"A Bayesian missing value estimation method for gene expression profile data,"* Bioinformatics, vol. 19, no. 16, pp. 2088–2096, Nov. 2003, https://doi.org/10.1093/bioinformatics/btg287.

[8] S. Dreiseitl and L. Ohno-Machado, *"Logistic regression and artificial neural network classification models: a methodology review,"* Journal of Biomedical Informatics, vol. 35, no. 5-6, pp. 352–359, 2002, https://doi.org/10.1016/S1532-0464(03)00034-0.

[9] D. Barak-Corren et al., *"Predicting suicidal behavior from longitudinal electronic health records,"* American Journal of Psychiatry, vol. 174, no. 2, pp. 154–162, Feb. 2017, https://doi.org/10.1176/appi.ajp.2016.16010077.

[10] S. Raschka and V. Mirjalili, *Python Machine Learning*, 3rd ed. Birmingham: Packt Publishing, 2019.

[11] S. Saha et al., "Comparative Analysis of Logistic Regression and SVM for Breast Cancer Prediction," in 2022 13th International Conference on Computing Communication and Networking Technologies (ICCCNT), 2022, https://doi.org/10.1109/ICCCNT54827.2022.9984351.

[12] J. Quiñonero-Candela, M. Sugiyama, A. Schwaighofer, and N. D. Lawrence, *Dataset Shift in Machine Learning*. MIT Press, 2009, https://doi.org/10.7551/mitpress/9780262170055.001.0001.

[13] A. Holzinger, G. Langs, H. Denk, K. F. Samwald, and H. Müller, *"Causability and explainability of artificial intelligence in medicine,"* WIREs Data Mining and Knowledge Discovery, vol. 9, no. 4, e1312, 2019, https://doi.org/10.1002/widm.1312.

[14] R. Patel, J. Lee, and A. Smith, *"Thresholding strategies in machine learning-based clinical decision support systems for psychiatry," NPJ Digital Medicine*, 6(1), 45. 2023, https://doi.org/10.1038/s41746-023-00789-2.

Journal of Engineering and Technology for Industrial Applications

ISSN ONLINE: 2447-0228

ITEGAM-JETIA

Manaus, v.12 n.60, p. 452-460 July/August, 2026.
DOI: https://doi.org/10.5935/jetia.v12i60.3877

RESEARCH ARTICLE OPEN ACCESS

SELF-SUPERVISED KNOWLEDGE REPRESENTATION FOR RARE FRAUD AND OPERATIONAL FAILURE DETECTION IN MULTI-CHANNEL PAYMENT SYSTEMS

Boumedyen Shannaq[1], Nour Eldin Elshaiekh[2], Basel Bani-Ismail[3], Marwan Alshar'e [4], Oualid Ali[5]

[1]Management Information system department, College of Business, University of Buraimi, Sultanate of Oman
[2]Department of Information Studies, Faculty of Arts and Social Sciences, Sultan Qaboos University
[3]Department of Software Engineering, Faculty of Information Technology, Applied Science Private University, Amman, Jordan
[4]Faculty of Computing and IT, Sohar University,Sohar, Oman
[5]Department of Computer Science, College of Arts and Science, Applied Science University, Manama, Kingdom of Bahrain

[1]http://orcid.org/0000-0001-5867-3986, [2]https://orcid.org/0000-0001-7465-2675, [3]https://orcid.org/0000-0002-1851-315X
[4]https://orcid.org/0000-0001-5187-4902, [5]https://orcid.org/0009-0001-1433-017X

E-email:*boumedyen@uob.edu.om.

ARTICLE INFO

Article History
Received on: March 03, 2026
Reviewed on: April 02, 2026
Accepted on: May 01, 2026
Published on: July 31, 2026

Keywords:
Self-Supervised Learning,
Fraud Detection,
Knowledge Representation,
Payment Systems,
Financial Information Systems,
Imbalanced Learning.

ABSTRACT

In modern high-volume payment systems, detecting fraud is still essentially confined by abhorrent class imbalance, changing transaction patterns, and lack of dependably labelled fraud occurrences. The current research questions the issue of whether self-supervised learning (SSL) can add to the extraction of the knowledge related to fraud in comparison with the capability of strong supervised baselines in the multi-channel payment setting. Using a real world banking dataset of over 13.3 million transactions in the 2010-2019 period, we perform an extensive analysis, including supervised machine learning, anomaly-based SSL, and methods of integrating knowledge into machine learning strategies. Gradient-boosting models are able to build a strong base (F1 = 0.86, ROC-auc = 0.99) that suggests that the trained model has a near-saturation discriminative ability that is solely based on tabular transaction characteristics. We show that naive, generic, SSL-based anomaly detectors lead to reduced precision, and task-adapted representations of supervised models, stacked with task-adapted representations, can increase fraud recall by up to 4.9 with a small F1 increase (+0.6). However, with strict operationally imposed conditions of accuracy ≥ 0.90, the added benefits of the use of SSL are not experienced, highlighting inherent thresholds of representation based improvement. Such results enhance a knowledge based perspective of when self-supervised representations add value to the decision making and when supervised models have already acquired adequate information about fraud meaning thereby guiding the design of financial fraud knowledge-management models in a robust way.

Copyright ©2026 by authors and Galileo Institute of Technology and Education of the Amazon (ITEGAM). This work is licensed under the Creative Commons Attribution International License (CC BY 4.0).

I. INTRODUCTION

The rapid digitization of payment ecosystems has radically transformed how financial institutions should create, handle and operationalize knowledge towards preventive fraud [1]. Modern banking systems are now handling millions of heterogeneous transactions over various channels swipe chip and online, in which fraudulent activity is an exceptionally rare but high-impact event. This discrepancy is further exacerbated by the slow or partial labeling, which can be very problematic to the classical supervised learning methods that assume stable distributions and rich labeled examples [2] , [3]. Based on this, fraud analytics is thus being redefined as a knowledge representation and discovery problem in which the ability to model normality at scale is becoming a crucial component as much as the ability to identify familiar fraud patterns [4]. The recent developments in the sphere of machine learning highlight the shortcomings of a strictly supervised model in the context of changing user behavior [5], [6], [7] channel migration and operational noise.

Even very good classifiers can become untrustworthy as fraud schemes change or as innocent operational failures, including technical failures or authentication errors, mimic atypical behavior [8]. This has spawned an interest in self-supervised learning (SSL), that learns the latent representations by using unlabeled data, so that systems can learn the consistent structural knowledge by using the transaction attributes, temporal interactions, and categorical interactions[9], [10]. A systematic literature review on cyber threat was investigated by [11] on cyber threat Intelligence for organizational cybersecurity resilience .In the literature on knowledge management, the concept of SSL is taking on a new form as a tool of extracting the reusable organizational knowledge and not just a preprocessing step . [12] Improves behavioral security analytics by doing user behavior identification, and it also complements the self-supervised framework that's being proposed, for spotting rare fraud events and operational breakdowns in multi-channel payment systems. , [13]reviews self-supervised recommender systems, showing how they reduce data sparsity and label dependence while improving user and item representations across recommendation tasks. . [14] provides a thorough analysis of intrusion detection systems, discussing the latest developments in artificial intelligence and machine learning-based IDS and various deployment scenarios, major challenges, and future research opportunities in advancing network cybersecurity. . However, there is growing evidence that SSL does not consistently perform well on strong gradient-boosting baselines on tabular financial data especially when the data has operations that already capture most of the information that influences the decision being made in Generative hybrid models [15] . This leads to an important research question in information and knowledge management: when does representation learning provide any new knowledge, and when does it saturate the decision structures already provided? The solution to this question is to conduct strict comparative analysis on the basis of realistic deployment policies, among which there are threshold governance and precision-constrained decision rules[16] . This paper aims to explore a self-managed anomaly detection model on an eleven-year, multi-channel payment system containing more than 13 million transactions. The study assesses the effect of representation learning on fraud knowledge extraction by systematically comparing supervised baselines, SSL-enhanced models, and hybrid stacking strategies to obtain a better understanding of the impact of representation learning on fraud knowledge extraction in extreme class imbalance. The contribution does not therefore claim the universal superiority of SSL but explains the operational value, constraints and knowledge implications of fraud analytics against the increasingly vital issue of financial information systems in the modern era , the use of machine learning techniques in Financial fraud detection was reviewd by [17], and the Exploring biometric technology was invistigated by [18].

II. RELATED WORK

In recent years, the focus in fraud analytics has gradually moved from traditional label-intensive supervised learning to knowledge-rich representation learning methods that are more resilient to extreme class imbalance, delayed label availability and the ever-changing nature of payment transaction characteristics [19-23]. In this context, self-supervised learning (SSL) has proven to be a promising learning framework for extracting informative latent features from massive amounts of tabular data with no labels. Modern SSL models aim much more than preprocessing; they define stable semantic structures from diverse attributes and payment channels, and models are able to capture these subtle anomalies and characterize the normal behavioral patterns [24], [25], [26]. Further, recent surveys confirm that SSL performs best when using strong downstream predictive models, especially when pretext tasks are carefully crafted to be appropriate to the corruption mechanisms in the domain, such as feature masking, temporal perturbation, and swapping of categorical values, rather than generic data augmentation tasks [26], [27], [28], [29]. Even with these progressions, financial fraud detection pipelines still heavily require Explainable Artificial Intelligence (XAI) to improve the transparency of the models and to enable trustworthy financial decision making in high-risk settings. For instance, in mobile financial fraud, explainable AI has proven to be effective [30] and, in the field of financial forecasting, AI has shown excellent predictive power at the firm level [31].

These methods are increasingly adopting SSL as a side-component of representation learning, but it appears that discriminative representation learning is superior to generative representation learning for discriminating between fraudulent transactions and operational failures. Especially, diffusion-based models and autoencoders are no longer judged only by their reconstruction performance, but also by their discriminative performance [15-32]. Moreover, it was proven that machine learning technologies can be used to successfully support predictive decision making and intelligent anomaly prediction in complex financial environments, this is an important methodological basis that has been established for the payment risk assessment in modern payment systems [32]. To address this, anomaly detection algorithms based on anomaly-discriminating representations, in addition to reconstruction errors, have become more prevalent in recent years [33]. Conventional generative detectors, which frequently reconstruct fake observations with high accuracy, however, decrease the sensitivity of the detector to anomalies [34] that has been a major limitation of such models. Self-supervised diffusion models, for instance, have been specifically designed with discriminative objectives to address this issue. Meanwhile, graph-based fraud detection works by building a dynamic and relational graph of payment relationships, allowing the discovery of coordinated fraud activities which would be hard to capture using transaction-level features alone [35].

The need for explainable AI in enhancing the transparency and interpretability of fraud detection systems has also been emphasized in complementary research, fostering user trust and aiding in informed operational decisions, a systematic review have been invistigated by [36].However, the feasibility of implementing graph-based solutions is often hindered by computational complexity, the availability of graphs, and the scalability of the solutions in practice, especially in industrial payment systems. Many practical financial applications are still using tabular learning frameworks with some relational attributes and not complete graph-based approaches [37] [38]. Previous empirical research has also shown that machine learning is effective in assessing organizations' risk and predicting anomalies [39], which also validates the potential application of self-supervised representation learning in the detection of rare fraud events and operational failures in multi-channel payment setting. [40] offers a contemporary overview of the state-of-the-art of deep learning by exploring key recent developments in architectures, innovative training methods, various practical applications, and promising research avenues to further push the boundaries of AI. In other security areas, self-supervised learning for feature learning has been shown to be beneficial and has been successfully combined with gradient-boosting methods for detecting intrusions in IoT networks [41].

Moreover, recent evaluation studies have revealed that the widely cited ROC-AUC metric could give an overly favourable evaluation on highly imbalanced datasets, for which the practical deployment requires to attain acceptable precision-recall trade-offs. For financial applications, PR-AUC, combined with operational threshold selection strategies (such as maximizing the F1 score or optimizing for precision) have gained increased significance as a measure of the performance of rare-event detection systems in real-world applications [42] [43]. Although these are crucial advances, there are also a number of limitations with the current studies. Most methods use auxiliary SSL modules and do not fully utilize self-supervised knowledge representation for discriminative learning, and few frameworks explicitly consider the identification of rare fraud events and operational failures of heterogeneous payment channels simultaneously. Furthermore, there is a lack of works focusing on combining powerful self-supervised representation learning and providing explainable decision support with operationally relevant evaluation criteria. The main research gaps found in the literature are summarized in Table I, which also inspires the proposed framework for Rare Fraud and Operational Failure Detection in Multi-Channel Payment Systems: Self-Supervised Knowledge Representation. Table I summarizes the main research gaps found in the literature and motivates the proposed framework for Rare Fraud and Operational Failure Detection in Multi-Channel Payment Systems: Self-Supervised Knowledge Representation.

Table 1: Research Gap Summary Table.

Gap observed in recent work	Why it matters for multi-channel fraud/ops	How this work addresses it
SSL often reported without policy-level thresholding	Banks must commit to precision targets; "better AUC" may not reduce false alerts	Report best-F1 and precision≥0.90 operating points
Generative/AE anomaly models blur fraud vs. benign declines	Operational failures create hard negatives; mislabeling harms knowledge actions	Treat failures as structured "near-anomalies" and tune thresholds using fraud labels
SSL gains saturate against strong GBDT baselines	Tabular GBDT already encodes many stable rules; SSL must add new knowledge not redundancy	Use SSL primarily to improve minority recall under constraint, not to "replace" LightGBM
Graph methods are powerful but costly to deploy at scale	Real-time graph construction/updates are heavy in practice	Keep deployment lightweight: embeddings + anomaly scores + calibrated classifier

Source: Authors, (2026).

III. METHODOLOGY

This work presents a knowledge based detection of fraud model where controlled learning is communally coupled with self-managed representative learning. Thus eliminating the twin tragedies of profoundly unequal class distribution and limited quantity of marked instances that are widespread in massive payment ecosystems. The main contribution is that the normative patterns of transaction are identified with the help of the self-supervised embeddings. And further incorporated into the high-performing supervised ensemble through stacking, instead of replacing the latter. This trick is effective in that the anomaly knowledge can be used to complement the fraud recall at the expense of the powerful discriminative ability of gradient-boosting classifiers. Besides, the method analyzes decision strength at a high operational threshold (such as having accuracy of at least 0.90) hence reflecting the requirement of modern fraud-management procedures.

III.1 DESCRIPTION AND COMPLEXITY OF DATA SETS

The collected dataset is 13.3M verified banking transactions between 2010 and 2019 [44] , with only 13,332 cases (0.1 percent) of them (so-called confirmed fraud) representing an incredibly biased learning task. All the records itself contain heterogenous features such as payment amount, time of transaction, payment channel (swipe, chip, online) and merchant category codes (MCC) as well as geographic indicators (e.g., invalid PIN, technical glitches). The scale, diversity, time span and scarcity of fraud incidents make this corpus unavoidably complex, which requires advanced representation learning algorithms and rigorous evaluation procedures. Proposed Methodology and Experimental Setting

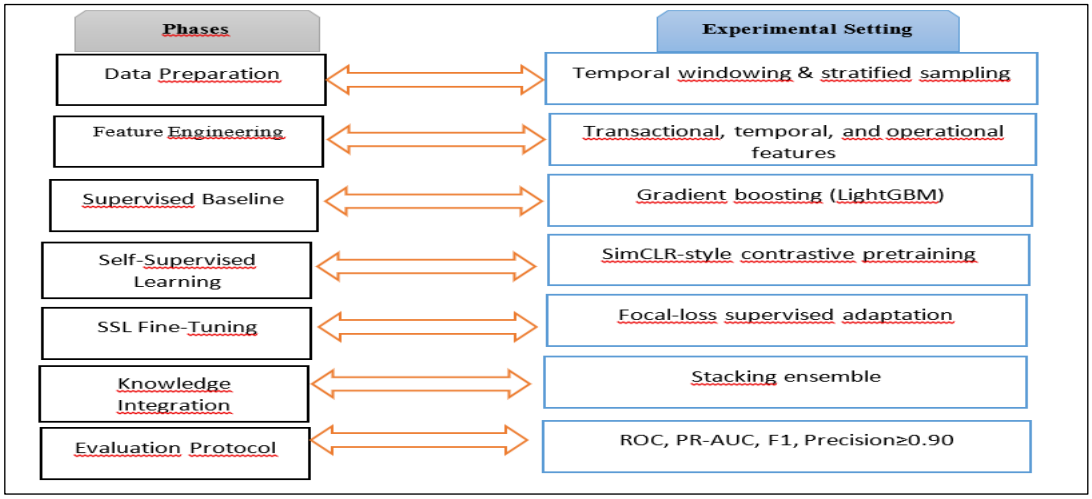


Figure 1: Proposed Methodology and Experimental Setting.
Source: Authors, (2026).

The experimental process starts with data preparation whereby the temporal windows that are rich in fraud are automatically identified and then balanced, with the use of stratified sampling and controlled negative sampling to maintain the authentic patterns of fraud. The following step is feature engineering, which includes transactional, temporal and operational variables, numerical features (amount and time of transaction encoded) and categorical features (channel, merchant category code (MCC), state) transformed, and operational failure-type signals are included to learn rich multichannel behaviour. A monitored base model is then trained on the gradient-boosting (LightGBM), defining a performance floor on detection of frauds in a class learning environment. In addition to this, self-supervised learning is proposed with the help of a contrastive pretraining style based on SimCLR, in which only normal transactions are used to learn latent representations of typical payment behaviour, without any reference to labels of fraud. The resulting embeddings are then optimized during the fine-tuning phase by using supervised learning with focal loss, and, therefore, aligning the representations with fraud-detection goals in highly imbalanced conditions. The system also incorporates the knowledge of both supervised and self-supervised models in stacking ensemble and thus, combines complementary decision cues. Lastly, ROC, PRb-AUC, F1-score, and operation gauges (e.g. keeping precision 0.90 and above) are strictly evaluated as model performance metrics in both statistical strength and practical application effectiveness.

III.2 METHODOLOGICAL NOVELTY

In this attempt, we introduce a knowledge-intensive approach to detecting frauds synthesising the self-supervised models of the normative transactional behaviour with the state-of-the-art supervised classifiers through decision-level stacking. Contrary to the antecedent methodologies that replace supervised learning directly, our method enhances the fraud acumen in the context of the lack of labelled data, thus improving the recall without compromising the reliability of the operations. In addition, the structure examines the strength of the decisions with very high levels of precision requirements, where there is agreement between the behaviour of the model and the practical policies of managing fraud.

IV. RESULTS AND ANALYSIS OF THE EXPERIMENT

The experimental validation of the proposed framework over a series of five experiments outlining a route over the traditional supervised baselines to the integration of the self-supervised representations and finally the modulation of operational cut-off points. Representation of results is in terms of the quality a capital of mental essence it adds, accuracy of soundness measurement and delicacy of the text of choice, as opposed to solitary performance measurements.

IV.1 BASELINE PERFORMANCE (EXP1) UNDER SUPERVISION

Table 2: Supervised Model Comparison (Exp1).

model	precision	recall	f1	roc_auc	pr_auc
LightGBM	0.896619	0.931745	0.913844	0.990289	0.97043
XGBoost	0.883245	0.941034	0.911224	0.989689	0.970068
RandomForest	0.934838	0.886511	0.910033	0.987088	0.962538
LogisticRegression	**0.841756**	**0.921648**	**0.879892**	**0.979046**	**0.942459**

Source: Authors, (2026).

Table 2 delivers a comparative analysis of the canonical supervised algorithms, namely, Logistic Regression, Random Forest, XGBoost, and LightGBM, applied on the measures of F1-score, ROC-AUC and PR-AUC. LightGBM achieves the best overall performance (F1 ≈ 0.91, ROC-AUC ≈ 0.99) which forms a high-performance standard in detecting fraud in a situation where only tabular transaction features are accessible. These results endorse the notion that modern gradient-boosting algorithms are able to infer much information about frauds on a transactional level, creating a solid foundation on which future developments can be built.

IV.2 SELF-SUPERVISED (EXP2) ANOMALY DETECTION

Table 3: SSL Anomaly Detection Results (Exp2).

model	precision	recall	f1	roc_auc	pr_auc	best_threshold	thr_at_P>=0.90	recall_at_P>=0.90
LightGBM-Baseline	0.87377451	0.863893376	0.868805849	0.987619628	0.93251	0.79	0.87	0.838449111
Hybrid-AE+IF	0.871533442	0.863085622	0.867288961	0.976962345	0.886654	0.6	0.65	0.838449111
Hybrid-Contrastive+IF	0.868038741	0.868739903	0.868389118	0.977589587	0.895375	0.6	0.67	0.83723748

Source: Authors, (2026).

The results of Table 3 indicate the performance of anomaly-driven approaches to SSL that include an Autoencoder (AE)with an Isolation Forest (IF), and are not supervised integrated. Even though these techniques are effective in providing the detection of abnormal transaction patterns, they are less precise, and PR-AUC in comparison to the supervised baselines. It is shown that anomaly ,and only knowledge fails to help differentiate between the fraud and the ordinary operation anomalies and hence the motivation towards hybrid knowledge integration and not solely depending on the use of the SSL.

IV.3 SSL FINE-TUNING AND STACKED KNOWLEDGE INTEGRATION (EXP3)

Table 4: Comparison between Baseline, SSL and Stacked Models (Best-F1 policy)

model	precision	recall	f1	roc_auc	pr_auc	best_threshold
LightGBM-Baseline	0.898103	0.822294	0.858528	0.988935	0.925073	0.89
SimCLR+Focal (SSL finetuned)	0.86358	0.851373	0.857433	0.986442	0.916541	0.46
Stacked (Baseline + SSL)	0.865478	0.862682	0.864078	0.987803	0.923521	0.95

Source: Authors, (2026).

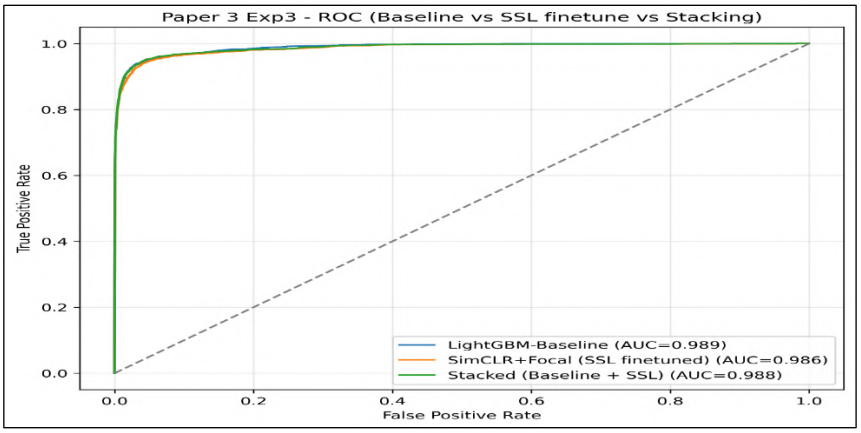


Figure 2: ROC Curves (Exp3).
Source: Authors, (2026).

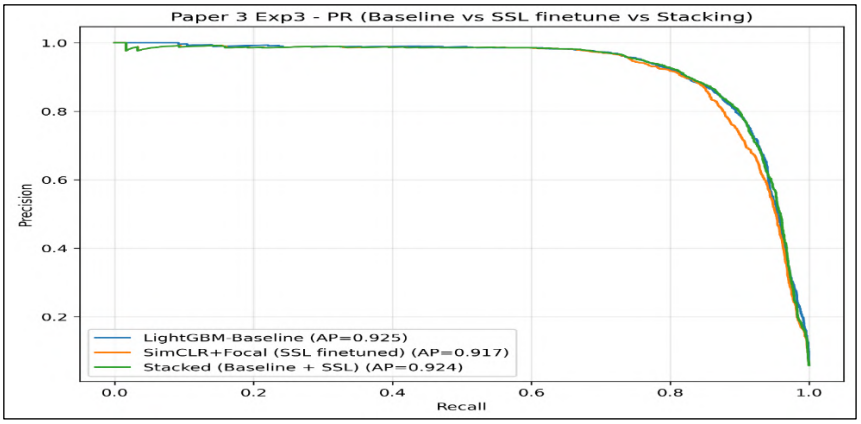


Figure 3: Precision-Recall Curves (Exp3).
Source: Authors, (2026).

As shown in Table 4 this experiment compares task aligned SSL, namely SimCLR with focal loss and a stacking approach, which combines supervised predictions with outputs of SSL.Figure 2 and 3 show that he stacked model generates a slight (around 45% to 55%) improvement in fraud recall compared with the baseline with a small F1 improvement (around 0.6). The ROC and PR curves demonstrate that stacking does not eliminate the discriminative sharpness of supervised learning and can extrapolate to a greater range of rare cases of frauds. These observations confirm that when used as representational support, one can add value to the use of SSL, but it does not replace the supervised core.

IV.4 SUPCON SSL ABLATION RESULTS (EXP4)

Table 5: SupCon SSL Ablution Results (Exp4).

model	precision	recall	f1	roc_auc	pr_auc	best_threshold
LightGBM-Baseline	0.896	0.814216	0.853153	0.989504	0.918041	0.91
SupCon+Focal (SSL finetuned)	0.90592	0.797254	0.84812	0.985089	0.910757	0.48
Stacked (Baseline + SupCon-SSL)	0.888792	0.823102	0.854687	0.986496	0.916789	0.97

Source: Authors, (2026).

As evidenced by Table 5, a stricter learning regimen of contrastive learning does not provide any extra benefits, and in fact, slightly decreases F1 and PR-AUC in some measurements. The adverse finding is important, which highlights that increased representational complexity does not always lead to enhanced knowledge of fraud, especially in the sparsely relational situations.

IV.5 OPERATION POLICY EVALUATION: PRECISION 6= 0.90 (EXP5)

Table 6: Precision- Constrained Evaluation (Exp5).

model	policy	threshold	precision	recall	f1	roc_auc	pr_auc
LightGBM-Baseline	best_f1	0.91	0.896	0.814216	0.853153	0.989504	0.918041
LightGBM-Baseline	precision>=0.90	0.92	0.90144	0.808966	0.852703	0.989504	0.918041
SSL-Finetuned	best_f1	0.53	0.907254	0.798061	0.849162	0.986619	0.910215
SSL-Finetuned	precision>=0.90	0.54	0.912617	0.788772	0.846187	0.986619	0.910215
Stacked	best_f1	0.97	0.898706	0.813409	0.853933	0.987591	0.916682
Stacked	precision>=0.90	0.97	0.898706	0.813409	0.853933	0.987591	0.916682

Source: Authors, (2026).

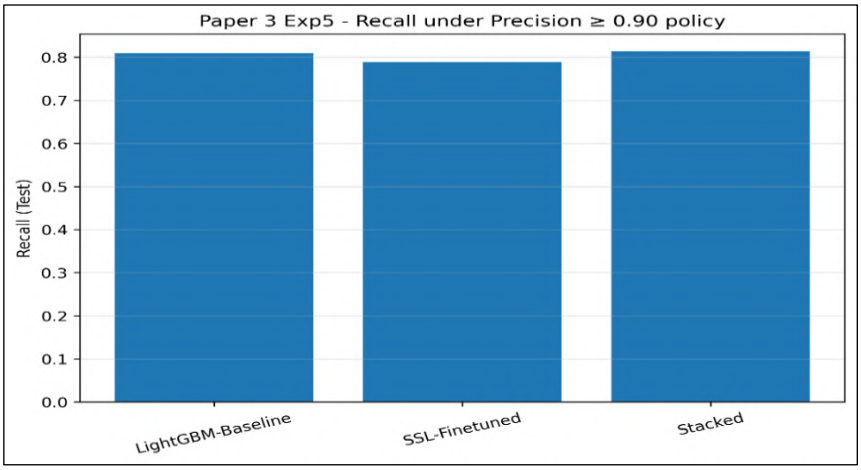


Figure 4: Recall with Precision 0.90 and above.
Source: Authors, (2026).

As shown in Table 6, in the setup of high precision penalties, all the SSL-based techniques outperform the supervised baseline. Both recall as well as F1 undergo slight decreases which depicts that the original model is already working near the optimal decision frontier. This observation brings out a significant operational conclusion such that the constraints on decisions may overshadow marginal gains in the algorithm, and knowledge saturation places constraints on the improvements that can be made by tuning to the threshold.

IV.6 SUMMARY OF EVIDENCE

The obtained results shown on tables and figures taken together demonstrate that although supervised models are able to achieve most of the knowledge that is of interest to the fraud problem, self-supervised learning only improves the recall when wisely combined and does not increase the overall performance in a consistent way. The evidence provides a subtle, empirical based insight into the timing of representation learning in providing decision value in large scale in fraud knowledge management system.

IV.7 DISCUSSION

IV.7.1 Why Self-Supervised Learning Saturates in Fraud Knowledge Extraction

It has been discovered that self-supervised learning does not invariably enhance fraud detection performance as compared to the robust supervised baselines, especially where there are serious operational restraint conditions. In terms of knowledge-management, this saturation is a representation of inherent characteristics of the issue of fraud detection and not the methodological deficiencies. Knowledge of frauds is frequently transaction-local and attribute-based in large scale payment systems, i.e., most discriminative information has already been included in structured characteristics like amount, timing, merchant category and payment channel. High signal Gradient-boosting models are good at leveraging these high signal attributes, and there is little residual information that the representation learning can rediscover. The main reason that regularities of usual behavior are captured using self-supervised learning is that the resulting representations are very useful in detecting an anomaly compared to the common trends. Nevertheless, numerous operational errors (e.g., technical errors, lack of balance, bad PIN attempts) often seem to be anomalous and at the same time do not constitute fraud.

Subsequently, anomaly-based representations bring ambiguity in their pure form to misalign regular process friction with criminal intent. This is why precision of standalone solutions based on the use of the SSL method remains reduced and why task alignment in knowledge representation is vital. The gains are also concentrated on recall and not on global discrimination metrics even when self-supervised embeddings are fine-tuned using labels of fraud and stacked together. This implies that there is no evidence that the marginal knowledge contributed to the boundary of rare fraud with by the use of the SSL, which enhances covering of the subtle or emerging cases, but does not transform the overall decision frontier. With a policy which is constrained to precision, the base model already runs in the Pareto-optimal region, with little more to be gained by representational refinements Notably, this limitation is not overcome by heavier contrastive objectives and supervised contrastive learning, which implies that an increase in representational complexity does not ensure richer knowledge of fraud in the case of weak relations density and coordinated fraud structures.

Taken together, these results point to a key lesson of information and knowledge management, which is that representation learning can only be useful in situations where latent, underexploited structure is present in the underlying data. Knowledge saturation may happen in mature transactional data where the signals are strong at the attribute level, and model sophistication is less important to decision quality than are operational constraints.

IV.7.2 Managerial and Knowledge Implications

The results of this paper present a number of relevant ideas to managers, risk officers, and financial information and knowledge management systems designers. To begin with, the outcomes show that already when using powerful supervised learning models, a significant part of the operational knowledge related to fraud can be encoded as a result of structured transactional data. To managers, this is to say that there should be no automatic replacement of the existing supervised representations learning with new ones, but they must be assessed as to the extra knowledge they bring with particular decision goals like recall enhancement or span of early warning. Second, the small returns that have been realized by isolated self-managed anomaly detection point to a significant difference between operational anomalies and fraudulent behavior. This implies that the anomaly scores should be rather considered as contextual knowledge rather than direct fraud indicator when viewed through the prism of management. By adding these signals in decision-support systems, it is possible to prioritize these investigations, minimize analyst fatigue, and distinctions between system friction and real risk, increasing the efficiency of operations without increasing false-positive rates. Third, the recall gains obtained via stacked integration of supervised as well as self-supervised models support the usefulness of knowledge-fusion strategies.

Instead of leveraging models that keep growing in complexity, managers can enjoy the benefits of architectures that unite supplementary knowledge resources, i.e., rule based knowledge, supervised risk scores and self-governing behavioral representations, into core curation pipelines. The methodology helps in progressive evolution of the system and maintain transparency and regulatory adherence. Based on the knowledge-management perspective, the findings highlight the significance of alignment of the representation. In the cases where its representations are clearly aligned with downstream decision tasks and organizational objectives, self-supervised learning has the most significant impact. The burdened or more complicated representations do not necessarily provide better knowledge about decisions and can present interpretability problems. Lastly, the saturation in the situation of stringent accuracy requirements supports the importance of policy-based decision thresholds as the main artefacts of knowledge. Fraud management is effective, however, not just a matter of the accuracy of the models, but the operationalization of learned knowledge in governance structures, risk attitudes, and human-in-the-loop processes.

IV.7.3 Key Insights

- Fraud detection is not only a modelling problem, but also a knowledge problem.
- Most of the fraud-relevant knowledge in structured transaction systems in large-scale payment systems are already embedded in robust supervised models.
- Self-managed learning is a value addition that is selective.
- Fraud discrimination cannot be done by stand-alone anomaly detection, however with supervised models task-aligned self-supervised representations can enhance recall.
- Model replacement is of inferior quality to knowledge integration, and by combining supervised and self-supervised output is more dependable on gains than using self-supervised models alone.
- The operational constraints restrict the gains of algorithms , with very high accuracy conditions (e.g., in excess of 0.90) no further improvements are obtained with increased representational complexity, indicating there is a saturation point in the extraction of fraud knowledge.
- Managerial relevance is a factor of alignment.
- The knowledge management of effective fraud and fraud prevention should be aligned with the decision policies, governance requirements and human in the loop procedures instead of undertaking complexity itself.

V. CONCLUSION

The present investigation has taken the task of fraud detection not as a local competition between competing algorithms, but as a complex knowledge-representation and decision-making problem. We used a massive, real-world dataset of payment volumes that is defined by deep class imbalance and an ecology of operation indicators to perform a methodological appraisal of there being supervised learning, self-bravo anomaly recognition, and mottled knowledge-combination techniques. We find empirically that the existing supervised models already enshrine a considerable share of fraud-relevant knowledge based on structured transactional features, and have nearly optimal discrimination performance. On the other hand, self-managed learning, when applied alone, does not always separate fraud and legitimate operational anomalies but it can introduce uncertainty into subsequent decision making. The key outcome of the research is the evidence that self-managed representations only add value when they are sensitive to the ultimate decision goals, and they are used as supplementary sources of knowledge. Task-aligned self-supervised learning can be used to improve the fraud recall of rare cases with stacked representations of such representations with supervised models without adversely impacting operational reliability. However, such benefits are automatically limited by the nature of the data. Even with the high level of precision required in the real world of fraud, representational complexity does not help any further, which highlights a practice limit to algorithmic returns as soon as the knowledge boundary is over. In terms of information and knowledge management, these findings send an essential signal to researchers and practitioners the fact that the complexity of any representation is not an assurance of better quality knowledge of decisions. Strong fraud systems have to achieve a balance between representational richness, interpretability and policy based restraint of decision outcomes. This work has its benefit in that it establishes the exact circumstances in which self-supervised learning can be used to supplement fraud knowledge and vice versa.

We provide a template balancing theory and practice by giving an evidence-based model that can be used to design resilient, scalable and governable fraud knowledge-management systems. In laying an accentuation on integration, alignment, as well as decision relevance, the research advances the academic discussion of how emergent learning paradigms ought to be implemented in modern financial information infrastructures. It promotes a shift of the parochial algorithmic competitions into knowledge-based holistic approaches, sensitive to organisational goals, regulatory provisions and the demands of real-time operational decision making.

VI. AUTHOR'S CONTRIBUTION

Conceptualization: Boumedyen Shannaq.
Methodology: Boumedyen Shannaq,Basel Bani-Ismail.
Investigation: Boumedyen Shannaq,Nour Eldin Elshaiekh.
Discussion of results: Boumedyen Shannaq.
Writing – Original Draft: Boumedyen Shannaq.
Writing – Review and Editing: Boumedyen Shannaq,Marwan Alshar'e, Oualid Ali.
Resources: Boumedyen Shannaq,Nour Eldin Elshaiekh,Basel Bani-Ismail,Marwan Alshar'e, Oualid Ali.
Supervision: Boumedyen Shannaq.
Approval of the final text: Boumedyen Shannaq,Nour Eldin Elshaiekh,Basel Bani-Ismail,Marwan Alshar'e, Oualid Ali.

VII. REFERENCES

[1] H. M. Farkhan and L. Indahdewi, "The Implementation of Knowledge Management on Fraud Prevention of PT Bahagia Idkho Mandiri," devotion, vol. 4, no. 6, pp. 1270–1281, May 2023, doi: 10.59188/devotion.v4i6.482.

[2] W.-Y. Wang, W.-W. Du, D. Xu, W. Wang, and W.-C. Peng, "A survey on self-supervised learning for non-sequential tabular data," Mach Learn, vol. 114, no. 1, p. 16, Jan. 2025, doi: 10.1007/s10994-024-06674-0.

[3] K. M. Sujon, R. Hassan, K. Choi, and M. A. Samad, "Accuracy, precision, recall, f1-score, or MCC? empirical evidence from advanced statistics, ML, and XAI for evaluating business predictive models," J Big Data, vol. 12, no. 1, p. 268, Dec. 2025, doi: 10.1186/s40537-025-01313-4.

[4] N. Bussmann, P. Giudici, D. Marinelli, and J. Papenbrock, "Explainable Machine Learning in Credit Risk Management," Comput Econ, vol. 57, no. 1, pp. 203–216, Jan. 2021, doi: 10.1007/s10614-020-10042-0.

[5] B. Shannaq, "A Novel Algorithm for Differentiating Authorized Users from Fraudsters via Mobile Keypad Input Patterns During Password Updates," TEM Journal, pp. 768–778, Feb. 2025, doi: 10.18421/TEM141-68.

[6] B. Shannaq, "Advancing User Authentication in Cloud Computing: Automated Smart Application as a Multi-Factor Approach Beyond Extended-Levenshtein Distance," TEM Journal, pp. 1140–1151, May 2025, doi: 10.18421/TEM142-15.

[7] B. Shannaq, M. Shakir, and A. Al-Zeidi, "Predicting User Originality in Password Activities Using Machine Learning," in Tech Fusion in Business and Society, vol. 234, R. K. Hamdan, Ed., in Studies in Systems, Decision and Control, vol. 234. , Cham: Springer Nature Switzerland, 2025, pp. 59–69. doi: 10.1007/978-3-031-84636-6_6.

[8] S. Li, J. Yu, Y. Lu, G. Yang, X. Du, and S. Liu, "Self-supervised enhanced denoising diffusion for anomaly detection," Information Sciences, vol. 669, p. 120612, May 2024, doi: 10.1016/j.ins.2024.120612.

[9] T. Sattarov, M. Schreyer, and D. Borth, "Diffusion-Scheduled Denoising Autoencoders for Anomaly Detection in Tabular Data," 2025, arXiv. doi: 10.48550/ARXIV.2508.00758.

[10] G. Cignoni, A. Cossu, A. Gomez-Villa, J. van de Weijer, and A. Carta, "CLA: Latent Alignment for Online Continual Self-Supervised Learning," 2025, arXiv. doi: 10.48550/ARXIV.2507.10434.

[11] S. Saeed, S. A. Suayyid, M. S. Al-Ghamdi, H. Al-Muhaisen, and A. M. Almuhaideb, "A Systematic Literature Review on Cyber Threat Intelligence for Organizational Cybersecurity Resilience," Sensors, vol. 23, no. 16, p. 7273, 2023, doi: 10.3390/s23167273.

[12] B. Shannaq and M. Shakir, "Enhancing Security with Multi-Factor User Behavior Identification via Longest Common Subsequence Analysis," Informatica, vol. 48, no. 16, pp. 73–82, 2024, doi: https://doi.org/10.31449/inf.v48i19.6529.

[13] C. Huang, L. Xia, X. Wang, X. He, and D. Yin, "Self-Supervised Learning for Recommendation," in Proceedings of the ACM Web Conference 2022 (WWW '22), New York, NY, USA: Association for Computing Machinery (ACM), 2022, pp. 1847–1858, doi: 10.1145/3511808.3557506.

[14] L. Diana and P. Dini, "Overview on Intrusion Detection Systems for Computers Networking Security," Computers, vol. 14, no. 3, p. 87, 2025, doi: 10.3390/computers14030087.

[15]C. Bekkaye, H. Oukhouya, T. Zari, R. Guerbaz, and H. El Bouanani, "Generative hybrid models for fraud detection in auto insurance with a comparative analysis of VAE, GAN, and diffusion approaches," Discov Artif Intell, vol. 5, no. 1, p. 313, Nov. 2025, doi: 10.1007/s44163-025-00574-5.

[16] M. Chabbouh, S. Bechikh, E. Mezura-Montes, and L. Ben Said, " curve for classifying imbalanced multi-class data," J Heuristics, vol. 31, no. 1, p. 9, Mar. 2025, doi: 10.1007/s10732-024-09544-z.

[17] L. Hernandez Aros, L. X. Bustamante Molano, F. Gutierrez-Portela, J. J. Moreno Hernandez, and M. S. Rodríguez Barrero, "Financial fraud detection through the application of machine learning techniques: a literature review," Humanit Soc Sci Commun, vol. 11, no. 1, p. 1130, Sep. 2024, doi: 10.1057/s41599-024-03606-0.

[18] I. R. Al-Shamsi, B. Shannaq, R. Adebiaye, and T. Owusu, "Exploring biometric attendance technology in the Arab academic environment: Insights into faculty loyalty and educational performance in policy initiatives," J. Infras. Policy. Dev., vol. 8, no. 9, p. 6991, Sep. 2024, doi: 10.24294/jipd.v8i9.6991.

[19] A. A. Compagnino et al., “An Introduction to Machine Learning Methods for Fraud Detection,” Applied Sciences, vol. 15, no. 21, p. 11787, Nov. 2025, doi: 10.3390/app152111787.

[20] H. Yang, Z. Shukur, and S. Sahran, “A Review of Artificial Intelligence for Financial Fraud Detection,” Applied Sciences, vol. 16, no. 4, p. 1931, 2026, doi: 10.3390/app16041931.

[21] T. Miftahushudur, H. M. Sahin, B. Grieve, and H. Yin, “A Survey of Methods for Addressing Imbalance Data Problems in Agriculture Applications,” Remote Sensing, vol. 17, no. 3, p. 454, Jan. 2025, doi: 10.3390/rs17030454.

[22] S. Visbeek, E. Acar, and F. den Hengst, “Explainable Fraud Detection with Deep Symbolic Classification,” Dec. 01, 2023, arXiv: arXiv:2312.00586. doi: 10.48550/arXiv.2312.00586.

[23] C. van der Cruijsen and M. Plooij, “Changing Payment Patterns at Point-of-Sale: Their Drivers,” De Nederlandsche Bank Working Paper, no. 471, Apr. 2015, doi: 10.2139/ssrn.2602219.

[24] B. Shannaq and O. Ali, “Credit Card Fraud Detection: An Explainable AI Approach for Securing Financial Transactions,” in 2025 3rd International Conference on Business Analytics for Technology and Security (ICBATS), Dubai, United Arab Emirates: IEEE, May 2025, pp. 1–6. doi: 10.1109/ICBATS66542.2025.11258465.

[25] S. B. Atitallah, C. B. Rabah, M. Driss, W. Boulila, and A. Koubaa, “Self-Supervised Learning for Graph-Structured Data in Healthcare Applications: A Comprehensive Review,” 2024, arXiv. doi: 10.48550/ARXIV.2412.05312.

[26] M. M. Abdulrazzaq et al., “Consequential Advancements of Self-Supervised Learning (SSL) in Deep Learning Contexts,” Mathematics, vol. 12, no. 5, p. 758, Mar. 2024, doi: 10.3390/math12050758.

[27] T. Richter, M. Bahrami, Y. Xia, D. S. Fischer, and F. J. Theis, “Delineating the effective use of self-supervised learning in single-cell genomics,” Nat Mach Intell, vol. 7, no. 1, pp. 68–78, Dec. 2024, doi: 10.1038/s42256-024-00934-3.

[28] B. Shannaq, M. A. Talab, M. Shakir, M. T. Sheker, and A. M. Farhan, “Machine learning model for managing the insider attacks in big data,” presented at the THE SECOND INTERNATIONAL CONFERENCE ON EMERGING TECHNOLOGY TRENDS IN INTERNET OF THINGS AND COMPUTING, Ramadi, Iraq, 2023, p. 020013. doi: 10.1063/5.0188358.

[29] Z. Wang et al., "A Comprehensive Survey on Data Augmentation," in IEEE Transactions on Knowledge and Data Engineering, vol. 38, no. 1, pp. 47-66, Jan. 2026, doi: 10.1109/TKDE.2025.3622600

[30]D. Vijayanand and G. S. Smrithy, “Explainable AI - enhanced ensemble learning for financial fraud detection in mobile money transactions,” Intelligent Decision Technologies, vol. 19, no. 1, pp. 52–67, Jan. 2025, doi: 10.1177/18724981241289751.

[31] F. G. Popa and V. Muresan, “Artificial Intelligence in Finance: From Market Prediction to Macroeconomic and Firm-Level Forecasting,” AI, vol. 6, no. 11, p. 295, Nov. 2025, doi: 10.3390/ai6110295.

[32] B. Shannaq and O. Ali, “Leveraging Machine Learning for Predictive Sustainability in Business Operations: A Classification Approach to Optimize Sustainable Resource Management,” in Sustainable Data Management, R. K. Hamdan, Ed., Studies in Big Data, vol. 171, Cham, Switzerland: Springer, 2025, doi: 10.1007/978-3-031-83911-5_57.

[33] D. D. Pezze, E. Anello, C. Masiero, and G. A. Susto, “Continual learning approaches for anomaly detection,” Evolving Systems, vol. 16, no. 4, p. 111, Dec. 2025, doi: 10.1007/s12530-025-09732-7.

[34] X. Chen, Z. Liu, S. Xie, and K. He, “Deconstructing Denoising Diffusion Models for Self-Supervised Learning,” 2024, arXiv. doi: 10.48550/ARXIV.2401.14404.

[35] S. Khodabandehlou and A. H. Golpayegani, “FiFrauD: Unsupervised Financial Fraud Detection in Dynamic Graph Streams,” ACM Trans. Knowl. Discov. Data, vol. 18, no. 5, pp. 1–29, Jun. 2024, doi: 10.1145/3641857.

[36] D. Gupta, P. Chugh, K. Sood, and S. Grima, “Explainable Artificial Intelligence in Financial Fraud Detection: A Systematic Review and FinTech-Oriented ADO–TCCM Meta-Framework for Trust, Governance, and Transparency,” FinTech, vol. 5, no. 3, p. 60, 2026, doi: 10.3390/fintech5030060.

[37] Z. Xiao, “Research on financial fraud detection method based on graph neural network,” in International Conference on Algorithms, Image Processing, and Deep Learning (AIPDL 2025), X. Kong and Y. Y. Tang, Eds., Macau, China: SPIE, Aug. 2025, p. 8. doi: 10.1117/12.3078631.

[38] Q. Sha, T. Tang, X. Du, J. Liu, Y. Wang, and Y. Sheng, “Detecting Credit Card Fraud via Heterogeneous Graph Neural Networks with Graph Attention,” 2025, arXiv. doi: 10.48550/ARXIV.2504.08183.

[39] B. Shannaq, D. K. Muniyanayaka, O. Ali, B. Bani-Ismail, and S. A. Maqbali, "Exploring the role of machine learning models in risk assessment models for developed organizations’ management decision policies," J. Infrastruct. Policy Dev., vol. 8, no. 13, p. 9364, 2024, doi: 10.24294/jipd9364.

[40] I. D. Mienye and T. G. Swart, “A Comprehensive Review of Deep Learning: Architectures, Recent Advances, and Applications,” Information, vol. 15, no. 12, p. 755, 2024, doi: 10.3390/info15120755.

[41] Y. Hu, K. Xiao, L. Luo, and L. Chen, “An XGBoost-Based Intrusion Detection Framework with Interpretability Analysis for IoT Networks,” Applied Sciences, vol. 16, no. 2, p. 980, Jan. 2026, doi: 10.3390/app16020980.

[42] M. Imani, M. Joudaki, A. Bagheri, and H. R. Arabnia, “Why ROC-AUC Is Misleading for Highly Imbalanced Data: In-Depth Evaluation of MCC, F2-Score, H-Measure, and AUC-Based Metrics Across Diverse Classifiers,” Technologies, vol. 14, no. 1, p. 54, Jan. 2026, doi: 10.3390/technologies14010054.

[43] T. Saito and M. Rehmsmeier, “The Precision-Recall Plot Is More Informative than the ROC Plot When Evaluating Binary Classifiers on Imbalanced Datasets,” PLoS ONE, vol. 10, no. 3, p. e0118432, Mar. 2015, doi: 10.1371/journal.pone.0118432.

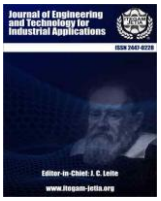
[44] “Financial Transactions Dataset: Analytics.” Accessed: Feb. 02, 2026. [Online]. Available: https://www.kaggle.com/datasets/computingvictor/transactions-fraud-datasets

Journal of Engineering and Technology for Industrial Applications

ISSN ONLINE: 2447-0228

ITEGAM-JETIA

Manaus, v.12 n.60, p. 461-469 July/August, 2026.
DOI: https://doi.org/10.5935/jetia.v12i60.3878



RESEARCH ARTICLE OPEN ACCESS

COMPARATIVE EVALUATION OF MACHINE LEARNING MODELS FOR PREDICTIVE MAINTENANCE USING THE AI4I 2020 DATASET: EFFECTS OF DATA BALANCING AND FEATURE SELECTION

Juan Carlos Gonzalez Islas[1], Jesus Vargas-Ortiz[2], Aldo Márquez-Grajales[3], Ernesto Bolaños-Rodríguez[4], Asdrúbal López-Chau[5], Rosa María Ortega-Mendoza[6]

[1, 2, 3, 4, 6]Universidad Autonoma Del Estado De Hidalgo. Mexico.
[5]Universidad Autonoma Del Estado De Mexico. Mexico.

[1]https://orcid.org/0000-0002-2190-0660, [2]https://orcid.org/0009-0006-6546-8319, [3]https://orcid.org/0000-0001-9567-2069
[4]https://orcid.org/0000-0002-1432-7720, [5]https://orcid.org/0000-0001-5254-0939, [6]https://orcid.org/0000-0003-4506-9653

E-email: juan_gonzalez7024@uaeh.edu.mx, va421350@uaeh.edu.mx, aldo_marquez@uaeh.edu.mx, ebolanos@uaeh.edu.mx, alchau@uaemex.mx, rosa, ortega@uaeh.edu.mx

ARTICLE INFO

Article History
Received on: March 03, 2026
Reviewed on: April 02, 2026
Accepted on: May 01, 2026
Published on: July 31, 2026

Keywords:
Machine Learning,
Predictive Model,
Feature Selection,
Imbalanced Data,
Industrial Failures.

ABSTRACT

This article presents a comparative analysis of machine learning (ML) models applied to machine fault classification, using the AI4I 2020 dataset. The performance of five algorithms (random forest, decision tree (J48), artificial neural networks (ANN), k-nearest neighbors (KNN), and Naive Bayes) is evaluated in six different data scenarios: synthetic minority oversampling (SMOTE) technique, undersampling, and original imbalanced distribution in the complete feature set and in the feature selection set. In addition, the impact of feature selection techniques on predictive power is evaluated. The goal is to identify the optimal predictive model and compare the performance of these approaches to determine the advantages of feature reduction and data balancing strategies. To ensure robust validation, the models are analyzed using precision, recall, specificity, accuracy, and F1 score. The main conclusions obtained demonstrate that it is possible to build reliable models capable of maximizing fault detection and minimizing false alarms, which is vital for predictive maintenance systems in industries where accuracy is critical.

Copyright ©2026 by authors and Galileo Institute of Technology and Education of the Amazon (ITEGAM). This work is licensed under the Creative Commons Attribution International License (CC BY 4.0).

I. INTRODUCTION

Industrial maintenance has undergone a transformation with the advancement of Industry 4.0 principles, evolving from predominantly reactive approaches to Predictive Maintenance (PdM) strategies. This approach is based on the analysis of real-time operational data to anticipate the occurrence of failures, optimize asset life, and reduce operating costs associated with unplanned maintenance [1]. In this scenario, Machine Learning plays a fundamental role by enabling the modeling of complex machinery behaviors, overcoming the limitations of traditional statistical methods [2]. However, the effectiveness of these models depends critically on the quality and structure of the available data. Industrial environments simultaneously present two significant problems: class imbalance and data scarcity, due to the low frequency of failure events, and high dimensionality associated with the use of multiple sensors, which can introduce noise and redundant information. Recent literature suggests that addressing these problems in isolation is insufficient, and that it is necessary to analyze the interaction between dimensionality reduction techniques and strategies for subsampling unbalanced data [3] [4]. This study uses the AI4I 2020 [5] Predictive Maintenance dataset, available in the UCI repository, which is continuously used as a reference in predictive maintenance research. Several studies have explored solutions to class imbalance and high dimensionality in predictive maintenance in order to reduce the bias toward normal machine operation. For instance, Sridhar and Sanagavarapu [6] showed that using SMOTE is an effective strategy for handling data imbalance in industrial environments, as it allows models to learn failure patterns more accurately.

Likewise, recent work by Bezerra et al. [7] analyzed how feature selection directly affects the predictive performance of algorithms, while authors such as Cioch, Kulisz, and Gola [8] validated the effectiveness of comparative models to establish performance benchmarks in industrial applications. The relevance of this interaction lies in the fact that the application of advanced classification algorithms does not guarantee optimal performance when data presents structural biases or is contaminated by irrelevant variables, in addition to presenting class imbalance. In particular, ignoring these characteristics can lead to an increase in false negatives, i.e., situations in which critical failures are not detected despite obtaining high overall accuracy values. This scenario represents a significant risk to the continuity and operational safety of industrial systems. Therefore, there is a need to empirically validate whether feature selection enhances or limits the benefits of synthetic subsampling, seeking a technical balance between the computational complexity of the model and the diagnostic sensitivity required in real manufacturing environments. Based on the above, the overall objective of this research is to evaluate the performance of five machine learning algorithms under an experimental design consisting of six scenarios, obtained by combining three data management strategies (original distribution, SMOTE, and undersampling) with two levels of dimensionality (complete set of attributes and optimized feature selection) in order to identify the configuration with the best performance, capable of maximizing fault detection and minimizing false alarms in industrial environments that require high precision. This approach jointly integrates data imbalance management and relevant feature selection to ensure a robust, reliable model that is representative of the system's actual behavior. Based on the above, the following research question is formulated: Which of the six approaches evaluated, with data balancing and feature selection techniques, offers the most robust performance in fault detection, and what is the real impact of feature selection on model recall? Using the AI4I 2020 predictive maintenance dataset from the UCI Machine Learning Repository, this paper provides a methodical comparison assessment of five machine learning models for machine failure categorization. It shows how feature selection methods and data balance strategies (SMOTE and undersampling) impact predictive performance, showing that proper preprocessing can enhance problem detection while reducing false alarms. The study provides useful guidance for choosing the best model–data combinations, assisting in the creation of dependable and effective predictive maintenance systems in industrial settings where early fault detection and high accuracy are essential.

II. THEORETICAL REFERENCE

This section presents the conceptual foundations that underpin the proposed methodology, addressing the evolution of industrial maintenance, the principles of machine learning applied to classification, and the strategies used for processing unbalanced data, as well as the selection of relevant characteristics

II.1 FAILURE PREDICTION THEORY (PREDICTIVE MAINTENANCE)

Predictive Maintenance represents one of the main technological transformations in industrial maintenance within Industry 4.0. Unlike corrective and preventive maintenance, PdM is based on continuous monitoring of the condition of the machine with the aim of estimating its Remaining Useful Life and predicting failures before they occur [1]. In this context, technological convergence has evolved into what Bitam et al. (2025) define as AIoT (Artificial Intelligence of Things), enabling critical decentralization in fault detection [9]. From a theoretical point of view, it is assumed that mechanical failures do not occur suddenly or completely randomly, but are the result of progressive degradation processes. These processes are often reflected in measurable patterns within physical variables such as temperature, vibration, or torque, which can be detected prior to functional failure.

A recent systematic review by Guidotti et al. (2025) points out that the prevailing trend in the manufacturing industry is the adoption of data-driven models, due to their ability to capture nonlinear relationships that are often ignored by traditional analytical models [10]. Furthermore, Hector and Panjanathan (2024) emphasize that the effectiveness of these models depends not only on the algorithm, but also on the data planning and preparation process [11]. Finally, it is worth noting that studies such as that by Florian et al. (2021) show that the effective implementation of PdM can significantly reduce operating costs by eliminating unnecessary maintenance, transforming this activity from a cost center to a strategic element of industrial competitiveness [1].

II.2 MACHINE LEARNING THEORY

In Machine Learning, algorithms are mainly classified according to how they learn from data and the type of information available. There are six types, which are listed below: Supervised Learning, Unsupervised Learning, Semi-Supervised Learning, Reinforcement Learning, Deep Learning, Rule-Based Learning, and Hybrid Learning [12]. In this research, supervised learning algorithms are employed due to data availability, problem type (prediction), complexity of the environment, and computational resources. Among the most commonly used are Random Forest (RF), Decision Tree, Artificial Neural Networks (ANN), K-Nearest Neighbors (KNN), and Naive Bayes (NB). Machine learning focused on industrial fault diagnosis aims to build a mapping function capable of predicting a binary class target variable (fault and no fault) from a set of characteristics extracted from the system's sensors. The specialized literature emphasizes that the performance of the model depends largely on the correct choice of algorithm, which must consider the nature, dimensionality, and quality of the available data.

Research on complex datasets suggests that industrial environments require adaptive frameworks due to their irregular data, as validated by Autran et al. (2024) when working with synthetic and real maintenance data [13] The Random Forest (RF) model is an ensemble method based on the Bagging (Bootstrap Aggregating) technique, which combines multiple decision trees to improve generalization ability. Recent comparative studies in industrial electrical systems have shown that RF outperforms models such as support vector machine and K-Nearest Neighbors in terms of accuracy and robustness, particularly in the presence of noise and diverse data [14]. Consistently, Yang and Wang (2025) confirm that RF is particularly effective in industrial environments characterized by high dimensionality and nonlinear relationships between variables [3]. Kale (2025) mentions that, to maximize accuracy in these models, it is important to optimize the hyperparameters of tree-based algorithms to capture representative patterns [15]. On the other hand, models such as Naive Bayes and Decision Trees (DT) continue to be relevant due to their simplicity and interpretability.

Naive Bayes, although based on the assumption of conditional independence between variables, is often used as a reference model, while DT facilitates the analysis of the decision-making process. However, Bezerra et al. (2024) warn that the performance of these algorithms depends critically on the quality of the input features, pointing out that indiscriminate elimination of variables during feature selection processes can degrade predictive power in complex industrial systems [7]. The performance evaluation of machine learning algorithms is based on indicators resulting from the confusion matrix. The common metrics are Accuracy, Recall, Precision, Specificity, and F1-Score, which are used to measure the effectiveness of the model by comparing or their predictions with actual data and verifying whether it is correctly classifying faults [10].

II.3 DATA BALANCING TECHNIQUES

One of the most significant theoretical challenges in failure classification is class imbalance, a phenomenon that gives rise to the called accuracy paradox, where a model can achieve high accuracy values without adequately detecting fault events due to their low statistical frequency. Among the most commonly used strategies is undersampling, which consists of randomly reducing the number of samples from the majority class. Although this approach reduces model bias, it carries the risk of losing relevant information. In contrast, the SMOTE (Synthetic Minority Over-sampling Technique) has established itself as one of the most widely used methodologies for addressing this problem. According to Yadav et al. (2025), from a mathematical point of view, SMOTE does not simply duplicate existing instances, but generates new synthetic samples by linear interpolation between a point in the minority class and its closest neighbors in the feature space [16]. However, Matharaarachchi et al. (2024) warn that oversampling loses effectiveness when there are outliers within the minority class. Their study proposes advanced variants that weight the proximity of the data to reduce the impact of these outliers and ensure that the synthetic samples generated are of high quality [17]. Recent research, such as that by Sridhar and Sanagavarapu (2021), shows that applying SMOTE to datasets from industrial sensors significantly improves model recall, allowing faults to be identified that would otherwise be misclassified as normal operating conditions [6].

III. MATERIALS AND METHODS

III.1 MACHINE LEARNING FRAMEWORK

The general methodology proposed for fault prediction is illustrated in Figure 1. This workflow integrates five machine learning models together with a cross-validation scheme to ensure the consistency of predictions. All experimental procedures were implemented using WEKA (3.8.6) [18].

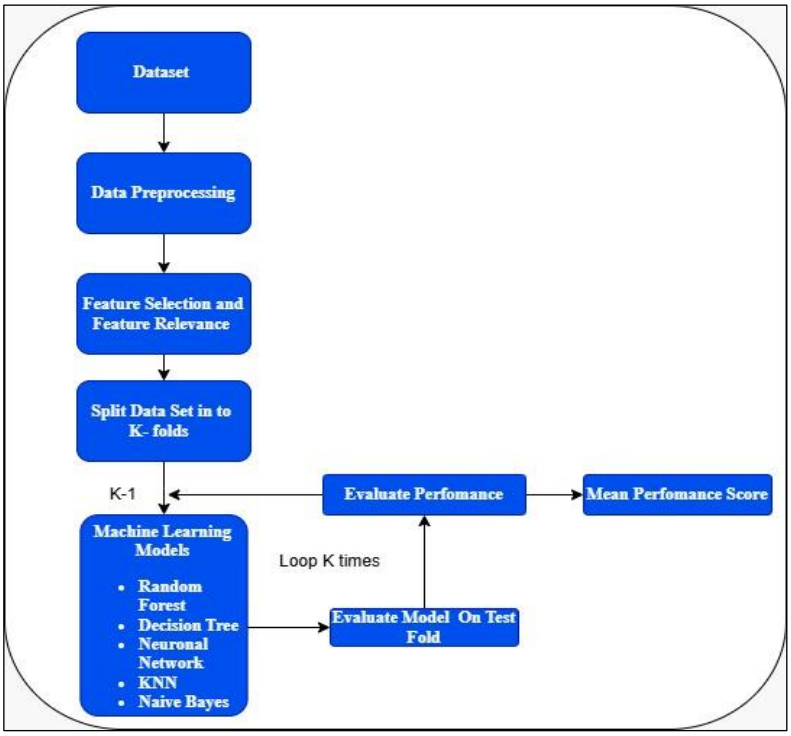


Figure 1: Machine learning framework for failure prediction.
Source: Authors, (2026).

III.1.1 Dataset Description

The study uses the AI4I 2020 Predictive Maintenance Dataset [5]. This synthetic dataset is modeled after an existing milling machine and consists of 10 000 data points from a stored as rows with 14 features in columns.

1. UID: unique identifier ranging from 1 to 10000.
2. Product ID: consisting of a letter L, M, or H for low (50% of all products), medium (30%) and high (20%) as product quality variants and a variant-specific serial number.
3. Type: just the product type L, M or H from column 2

4. Air temperature [K]: generated using a random walk process later normalized to a standard deviation of 2 K around 300 K
5. Process temperature [K]: generated using a random walk process normalized to a standard deviation of 1 K, added to the air temperature plus 10 K.
6. Rotational speed [rpm]: calculated from a power of 2860 W, overlaid with a normally distributed noise
7. Torque [Nm]: torque values are normally distributed around 40 Nm with a SD = 10 Nm and no negative values.
8. Tool wear [min]: The quality variants H/M/L add 5/3/2 minutes of tool wear to the used tool in the process.
9. Machine failure: label that indicates, whether the machine has failed in this particular datapoint for any of the following failure modes are true.

The machine failure consists of five independent failure modes:

10. Tool wear failure (TWF): the tool will be replaced of fail at a randomly selected tool wear time between 200 - 240 mins (120 times in our dataset). At this point in time, the tool is replaced 69 times, and fails 51 times (randomly assigned).
11. Heat dissipation failure (HDF): heat dissipation causes a process failure, if the difference between air- and process temperature is below 8.6 K and the tools rotational speed is below 1380 rpm. This is the case for 115 data points.
12. Power failure (PWF): the product of torque and rotational speed (in rad/s) equals the power required for the process. If this power is below 3500 W or above 9000 W, the process fails, which is the case 95 times in our dataset.
13. Overstrain failure (OSF): if the product of tool wear and torque exceeds 11,000 minNm for the L product variant (12,000 M, 13,000 H), the process fails due to overstrain. This is true for 98 datapoints.
14. Random failures (RNF): each process has a chance of 0,1 % to fail regardless of its process parameters. This is the case for only 5 datapoints, less than could be expected for 10,000 datapoints in our dataset.

If at least one of the above failure modes is true, the process fails and the 'machine failure' label is set to 1. It is therefore not transparent to the machine learning method, which of the failure modes has caused the process to fail. The original data distribution presents a class imbalance, with 9,661 instances of normal operation (96.6%) and only 339 instances of failure (3.4%). This disproportion represents a critical challenge for learning models.

III.2 DATA PREPROCESSING

Preprocessing was aimed at improving data quality and defining training strategies. The UDI and Product ID variables were eliminated because they lacked predictive value. Likewise, specific failure descriptors (TWF, HDF, PWF, OSF, RNF) were excluded, given that the study focuses on the binary detection of the machine failure variable. To address class imbalance, three experimental approaches are used:

- Approach 1 (SMOTE): The Synthetic Minority Over-sampling Technique (SMOTE) is applied to artificially balance the classes. In this scenario, synthetic data was generated until a total of 9,661 samples were reached for both classes. Furthermore, following the proposal by Matharaarachchi et al. [17], this technique improves model learning when minority classes exist, as is the case with the failure category in this study.
- Approach 2 (Undersampling): Random undersampling of the majority class is performed, resulting in a balanced set with 339 failure instances and 339 non-failure instances.
- Approach 3 (Original data set): Models are evaluated using the original data set with its original imbalance to establish a baseline.

III.3 FEATURE RELEVANCE AND SELECTION

Under these three approaches, a feature selection process is implemented by WEKA The ReliefF evaluation algorithm (ReliefFAttributeEval) is used together with the Ranker search method. The Relief family of algorithms are highly successful attribute estimators due to their ability to detect conditional dependencies between variables, the algorithm evaluates the quality of each attribute by repeatedly sampling an instance and comparing it with its closest neighbors of the same class and of different classes. It assigns greater weight to characteristics that maintain similar values for instances of the same class and show different values for instances of different classes [19]. Establishing a cut-off criterion to select only the four most relevant characteristics for model training.

III.4 MACHINE LEARNING MODELS

For the training stage, a comparative approach is implemented to evaluate the predictive power of different machine learning models. Based on a review of recent literature by Aydın and Evrentuğ [20] and Arun [21], five representative algorithms (Random Forest, Decision Tree, ANN, KNN, and Naive Bayes) were selected that have proven effective in fault detection, as identified by Cioch [8]. The general operation of each implemented algorithm is described below: Random Forest (RF): This is an ensemble learning method based on the Bagging technique. It works by training multiple decision trees independently using random subsets of the data. For the final classification, the algorithm aggregates the results of all the individual trees and determines the winning class by majority vote, which reduces variance and improves robustness against noise compared to a single estimator [3]. Decision Tree (DT): This is an algorithm based on logical rules that models decisions in a hierarchical structure similar to a flowchart. The model recursively divides the data space into smaller regions, evaluating at each node the feature that offers the best separation of classes. Its main advantage, highlighted by Cioch et al. (2025), lies in the direct interpretability of the generated “If-Then” rules, although it can be prone to overfitting if its depth is not limited [8]. Artificial Neural Networks (ANN): A Multilayer Perceptron (MLP) is implemented, inspired by the biological structure of the brain. This algorithm processes information through layers of interconnected nodes (neurons): an-input layer, hidden layers with nonlinear activation functions, and an output layer.

Yang and Iqbal (2025) explain that learning occurs through backpropagation, adjusting the weights of the connections to minimize error, which makes them powerful for capturing complex nonlinear patterns in computationally expensive environments [22]. K-Nearest Neighbors (KNN): This is an instance-based learning algorithm that does not construct an explicit internal model (Lazy Learning). To classify a new sample, it calculates its Euclidean distance from the points stored in the training set and identifies the 'K' nearest neighbors. Class assignment is performed by simple majority, which is an effective method when failures tend to cluster in specific regions of the vector space [10]. Naive Bayes (NB): This is a probabilistic classifier based on Bayes' theorem. Its operation assumes "naive independence" between predictor characteristics given the value of the class. Although Cioch et al. (2025) warn that this independence is rarely met in correlated sensor data, the model is widely used as a baseline due to its high computational efficiency and low memory consumption [8].

III.5 EVALUATION PERFOMANCE

The K-Fold Cross-Validation method is implemented for performance evaluation. This technique consists of randomly partitioning the total data set into K-Fold of equal or similar size, ensuring that the number of of instances beloinging to each class the same proportion in each partition, according to the methodology described by Lumumba [23]. As a result of this process, the confusion matrix defined by Cioch et al. [8] is obtained. Since this is a binary classification problem, the matrix is structured in a 2x2 dimension and its components are described as follows: TP (True Positives), the number of instances of class 1 (Failure) correctly predicted as class 1; TN (True Negatives), the number of instances of class 0 (Normal) correctly predicted as class 0; FP (False Positives), instances of class 0 incorrectly predicted as class 1; and FN (False Negatives), instances of class 1 incorrectly predicted as class 0 (Failure not detected). Based on the information obtained from this matrix, the performance metrics for the positive class described below are calculated. Accuracy: evaluates the overall performance of the model by measuring the proportion of correct predictions relative to the total number of cases.

$$Accuracy = \frac{TP + TN}{TP + TN + FP + FN} \tag{2}$$

Recall: Measures the ability of the algorithm to correctly identify all instances of actual failure.

$$Recall = \frac{TP}{TP + FN} \tag{3}$$

Specificity: Indicates the ability of the system to correctly classify normal operating states.

$$Specificity = \frac{TN}{TN + FP} \tag{4}$$

Precision: Determines the reliability of positive predictions of total failures.

$$Precision = \frac{TP}{TP + FP} \tag{5}$$

F1-Score: Represents the harmonic mean between Precision and Recall, providing a critical balanced metric.

$$F1 = \frac{2 \times P \times R}{P + R} \tag{6}$$

IV. RESULTS AND DISCUSSION

In this section, the results obtained after the application of two data balancing approaches Original Imbalanced, SMOTE, and Undersampling—are presented and analyzed. These approaches are comprehensively evaluated using both the preprocessed feature set and after a variable selection process, allowing for the measurement of their perfomance on five machine learning models. Performance is quantified through a metrics analysis that includes accuracy, recall, specificity, precision, and F1-score, in order to determine the most robust configuration for fault detection in the industrial environment under study; as it is shown in Figure 2.

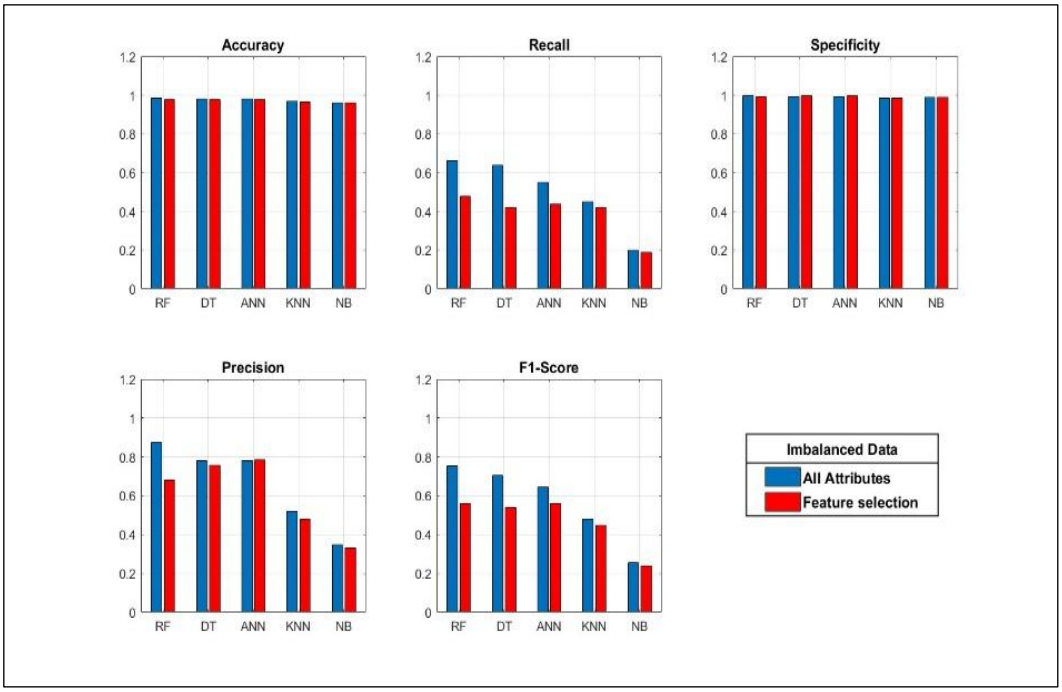


Figure 2: Performance comparison on the imbalanced dataset: all attributes vs feature selection.
Source: Authors, (2026).

When analyzing the results shown in Figure 2, one of the most critical challenges in predictive maintenance becomes evident: the bias introduced by imbalanced data. Although the models report high accuracy in both scenarios, this represents a significant issue; the imbalance causes the algorithms to become experts at classifying normal operation while losing effectiveness in identifying actual failures. This is clearly reflected in the low recall values, the metric that quantifies failure detection capability. Similarly, although the specificity shows good results, this is a product of the model's tendency to predict the majority class. When evaluating the individual performance of the algorithms, the Random Forest model stands as the most robust, specifically when operating with the complete feature set. Under this condition, the algorithm achieved the highest F1-Score in the comparison (0.7538), demonstrating a superior learning capacity to identify failure patterns compared to the other models. While algorithms such as Naive Bayes and KNN show a critical dependence on the majority class, Random Forest achieved the most balanced trade-off between event detection and alert reliability. On the other hand, it is essential to highlight the negative impact that feature selection had in this scenario. By reducing the dimensionality of the imbalanced dataset, a general decrease in the predictive capacity of all models is observed; for example, the Random Forest F1-Score drops drastically from 0.7538 to 0.5615. This behavior suggests that, given the scarcity of failure examples in the original dataset, the removing variables or features eliminates critical information that the algorithms need to correctly discriminate between operating states, confirming that model simplification can be counterproductive under imbalanced conditions. The perfomance metrics results for the synthetic data generated by the SMOTE technique are presented in Table 1.

Table 1: Performance metrics for the SMOTE-balanced dataset.

Model	Accuracy	Recall	Specificity	Precision	F1 Score
RF	0.9581	0.9663	0.95	0.9508	0.9585
DT	0.9435	0.9503	0.9367	0.9375	0.9439
ANN	0.9187	0.9424	0.895	0.8998	0.9206
KNN	0.9436	0.9585	0.9288	0.9308	0.9445
NB	0.8362	0.826	0.8464	0.8432	0.8345

Source: Authors, (2026).

Table 2: Performance metrics for the SMOTE-balanced dataset combined with Feature Selection.

Model	Accuracy	Recall	Specificity	Precision	F1 Score
RF	0.945	0.9619	0.9282	0.9305	0.9459
DT	0.9346	0.9445	0.9246	0.9261	0.9352
ANN	0.8823	0.9465	0.818	0.8387	0.8894
KNN	0.9114	0.9267	0.8961	0.8992	0.9127
NB	0.8275	0.7914	0.8636	0.853	0.821

Source: Authors, (2026).

Table 2 presents the performance metrics calculated for each model using a dataset balanced by SMOTE and feature selection. When analyzing the results in Tables 1 and 2, a positive change can be observed compared to the imbalanced scenario. The application of SMOTE to generate synthetic data has allowed the classes to be balanced, ensuring that the accuracy now truly reflects the model's performance. The most notable feature is the increase in Recall, where the Random Forest model reaches a maximum value of 0.9663 (Table 1). This indicates that the models have achieved reliable prediction of failures and have developed a real ability to identify critical predictive maintenance events without compromising specificity. In this approach, the Random Forest model once again stands out as the best performing model, especially when using the complete dataset. With an F1-Score of 0.9585 and the aforementioned Recall of 0.9663, Random Forest demonstrates high accuracy in detecting faults. This confirms that, by providing a balanced database, ensemble algorithms can extract much more complex and reliable patterns for decision-making. Regarding the impact of feature selection in this scenario, it can be observed that, although reducing variables simplifies the model structure, it leads to a slight decrease in performance. The clearest example is the Neural Network, where the F1-Score drops from 0.9206 to 0.8894; however, this deficiency does not compromise the overall effectiveness of the system. On the contrary, the results show that feature selection applied to a balanced dataset with SMOTE is effective, as the models manage to maintain a performance above 88% in fault detection. This confirms that the robustness of the synthetic database compensates for the elimination of technical variables, allowing for more efficient models without significantly sacrificing predictive power. Next, Tables 3 and 4 are presented, reflecting the dataset balanced to minority class size (undersampling) and the dataset balanced to minority class size (undersampling feature selection).

Table 3: Dataset balanced to minority class size (undersampling).

Model	Accuracy	Recall	Specificity	Precision	F1 Score
RF	0.9436	0.9585	0.9288	0.9308	0.9445
DT	0.9277	0.9381	0.9174	0.9191	0.9285
ANN	0.8997	0.8791	0.9204	0.9169	0.8976
KNN	0.9174	0.8997	0.9351	0.9327	0.9159
NB	0.8451	0.8407	0.8496	0.8482	0.8444

Source: Authors, (2026).

Table 4: Dataset balanced to minority class size (undersampling Feature selection).

Model	Accuracy	Recall	Specificity	Precision	F1 Score
RF	0.95	0.9528	0.9469	0.9472	0.95
DT	0.9381	0.9351	0.941	0.9407	0.9379
ANN	0.8938	0.8791	0.9086	0.9058	0.8922
KNN	0.9056	0.885	0.9263	0.9231	0.9036
NB	0.8245	0.7935	0.8555	0.8459	0.8189

Source: Authors, (2026).

Looking at the results in Tables 3 and 4, we can see an improvement in predictive power compared to the unbalanced dataset. By reducing the minority class, the models achieve good performance and a balance between accuracy and recall. In this approach, the Random Forest model stands out as the best-performing algorithm. Using the complete dataset, Random Forest achieves an F1-Score of 0.9445 and leads detection with a Recall of 0.9585. It can be noted that, although the dataset is smaller than in the case of SMOTE, the Random Forest algorithm maintains stability in its performance, consistently outperforming Neural Networks and models such as Naive Bayes in all metrics. Regarding the impact of feature selection seen in Table 4, a distinctive phenomenon occurs: unlike previous approaches, variable reduction helps improve or maintain performance in leading models. For example, in Random Forest, the F1-Score increases from 0.9445 to 0.9500 after applying Feature Selection. However, a slight deficiency is observed in models such as RNA, where performance drops from 0.8976 to 0.8922. The overall result shows that feature selection in a balanced dataset by subsampling is extremely effective, allowing for lighter and more accurate models.

V. CONCLUSIONS

This paper evaluates the performance of five machine learning algorithms for fault prediction in the AI4I 2020 industrial dataset, which allows us to understand the impact of each technique on critical metrics in industrial environments. To this end, data balancing and feature selection strategies are compared, leading to the following final considerations:

1. The optimal configuration: The Random Forest model, trained with the dataset balanced using the SMOTE technique and using all attributes after preprocessing, proves to be the most optimal solution, achieving a Recall of 0.9663 and an F1-Score of 0.9585. This result makes it the optimal method for fault prediction.
2. Impact of Preprocessing: It is demonstrated that treating class imbalance is a mandatory step. Using the original dataset, despite offering superior accuracy, results in models with significantly low sensitivities of less than 0.67. Among the balancing techniques, SMOTE consistently outperforms undersampling, proving that generating synthetic failure data is preferable to removing information from the majority class.
3. This research reveals that feature selection negatively affects predictive performance, reducing the fault detection capability (Recall) in the best-performing model. This suggests that the operational variables in the dataset are significantly relevant to the models and are lost when those attributes are removed, indicating that for this specific problem, it is better to retain the attributes.

Finally, the integration of data balancing and feature selection improves overall performance because the results show that treating class imbalance combined with feature selection techniques allows for the construction of more robust and stable models. The joint integration of these strategies contributes to improving the predictive capacity of the system compared to their isolated application.

VI. AUTHOR'S CONTRIBUTION

Conceptualization: Juan Carlos Gonzalez Islas, Jesus Vargas-Ortiz, Aldo Márquez-Grajales, Ernesto Bolaños-Rodríguez, Asdrúbal López-Chau, Rosa María Ortega-Mendoza.
Methodology: Juan Carlos Gonzalez Islas, Jesus Vargas-Ortiz, Aldo Márquez-Grajales, Ernesto Bolaños-Rodríguez, Asdrúbal López-Chau, Rosa María Ortega-Mendoza.
Investigation: Juan Carlos Gonzalez Islas, Jesus Vargas-Ortiz, Aldo Márquez-Grajales, Ernesto Bolaños-Rodríguez, Asdrúbal López-Chau, Rosa María Ortega-Mendoza.
Discussion of results: Juan Carlos Gonzalez Islas, Jesus Vargas-Ortiz, Aldo Márquez-Grajales, Ernesto Bolaños-Rodríguez, Asdrúbal López-Chau, Rosa María Ortega-Mendoza.
Writing – Original Draft: Juan Carlos Gonzalez Islas, Jesus Vargas-Ortiz, Aldo Márquez-Grajales, Ernesto Bolaños-Rodríguez, Asdrúbal López-Chau, Rosa María Ortega-Mendoza.
Writing – Review and Editing: Juan Carlos Gonzalez Islas, Jesus Vargas-Ortiz, Aldo Márquez-Grajales, Ernesto Bolaños-Rodríguez, Asdrúbal López-Chau, Rosa María Ortega-Mendoza.
Resources: Juan Carlos Gonzalez Islas, Jesus Vargas-Ortiz, Aldo Márquez-Grajales, Ernesto Bolaños-Rodríguez, Asdrúbal López-Chau, Rosa María Ortega-Mendoza.
Supervision: Juan Carlos Gonzalez Islas, Jesus Vargas-Ortiz, Aldo Márquez-Grajales, Ernesto Bolaños-Rodríguez, Asdrúbal López-Chau, Rosa María Ortega-Mendoza.
Approval of the final text: Juan Carlos Gonzalez Islas, Jesus Vargas-Ortiz, Aldo Márquez-Grajales, Ernesto Bolaños-Rodríguez, Asdrúbal López-Chau, Rosa María Ortega-Mendoza.

VII. DATA AVAILABILITY

The data presented in this study are available upon request from the corresponding author.

VIII. REFERENCES

[1] E. Florian, F. Sgarbossa, e I. Zennaro, "Machine Learning-Based Predictive Maintenance: A Cost-Oriented Model for Implementation," International Journal of Production Economics, vol. 236, p. 108114, 2021. doi: 10.1016/j.ijpe.2021.108114.

[2] C. Tsallis, P. Papageorgas, D. Piromalis, y R. A. Munteanu, "Application-Wise Review of Machine Learning-Based Predictive Maintenance: Trends, Challenges, and Future Directions," Applied Sciences, vol. 15, no. 9, p. 4898, 2025. doi: 10.3390/app15094898.

[3] Y. Yang y H. Wang, "Random Forest-based machine failure prediction: A performance comparison," Applied Sciences, vol. 15, no. 16, p. 8841, 2025. doi: 10.3390/app15168841.

[4] K. I. Romero Magdaleno, L. C. Méndez González, I. J. González Hernández, y A. E. Quezada Carreón, "Implementación de modelos de aprendizaje automático para el mantenimiento predictivo y clasificación de fallas de maquinaria industrial," Ingenio y Conciencia Boletín Científico de la Escuela Superior Ciudad Sahagún, vol. 12, no. Especial, pp. 56–67, 2025..

[5] S. Matzka, "Explainable Artificial Intelligence for Predictive Maintenance Applications," in Proceedings of the 2020 Third International Conference on Artificial Intelligence for Industries (AI4I), Irvine, CA, USA, 2020, pp. 69–74, doi: 10.1109/AI4I49448.2020.00023.

[6] S. Sridhar y S. Sanagavarapu, "Handling data imbalance in predictive maintenance for machines using SMOTE-based oversampling," en 2021 13th International Conference on Computational Intelligence and Communication Networks (CICN), 2021, pp. 44-49. doi: 10.1109/CICN51697.2021.9574668.

[7] F. E. Bezerra et al., "Impacts of feature selection on predicting machine failures by machine learning algorithms," Applied Sciences, vol. 14, no. 8, p. 3337, 2024. doi: 10.3390/app14083337.

[8] M. Cioch, M. Kulisz, and A. Gola, "Comparison of Machine Learning Methods in Predictive Maintenance of Machines," Advances in Science and Technology Research Journal, vol. 19, no. 11, pp. 33-44, 2025. doi: 10.12913/22998624/208284.

[9] T. Bitam et al., "Artificial Intelligence of Things for Next-Generation Predictive Maintenance," Sensors, vol. 25, no. 24, p. 7636, 2025. doi: 10.3390/s25247636.

[10] D. Guidotti, L. Pandolfo, y L. Pulina, "A systematic literature review of supervised machine learning techniques for predictive maintenance in Industry 4.0," IEEE Access, vol. 13, pp. 102479-102504, 2025. doi: 10.1109/ACCESS.2025.3578686.

[11] I. Hector y R. Panjanathan, "Predictive maintenance in Industry 4.0: a survey of planning models and machine learning techniques," PeerJ Computer Science, vol. 10, p. e2016, 2024. doi: 10.7717/peerj-cs.2016.

[12] Q. Wan, "Machine Learning Model Construction and Practice for Personalized Training Programs in Physical Education and Sport Teaching," Applied Mathematics and Nonlinear Sciences, vol. 10, no. 1, 2025. doi: 10.2478/amns-2025-0374.

[13] J.-V. Autran, V. Kuhn, J.-P. Diguet, M. Dubois, y C. Buche, "AI4I-PMDI: Predictive maintenance datasets with complex industrial settings' irregularities," Procedia Computer Science, vol. 246, pp. 1201-1209, 2024. doi: 10.1016/j.procs.2024.09.546.

[14] S. Singh et al., "A comparative analysis of machine learning algorithms for predictive maintenance in electrical systems," en 2024 4th International Conference on Innovative Practices in Technology and Management (ICIPTM), 2024, pp. 1-6. doi: 10.1109/ICIPTM59628.2024.10563826.

[15] S. S. Kale, "Predictive Maintenance of Equipment using Machine Learning Algorithms," Tesis Doctoral, National College of Ireland, Dublín, 2025.

[16] S. Yadav et al., "CSRBoost: Clustered Sampling With Resampling Boosting for Imbalanced Dataset Pattern Classification," IEEE Access, vol. 13, pp. 175078-175093, 2025. doi: 10.1109/ACCESS.2025.3616207.

[17] S. Matharaarachchi, M. Domaratzki, y S. Muthukumarana, "Enhancing SMOTE for imbalanced data with abnormal minority instances," Machine Learning with Applications, vol. 18, p. 100597, 2024. doi: 10.1016/j.mlwa.2024.100597.

[18] I. H. Witten, E. Frank, M. A. Hall, and C. J. Pal, Data Mining: Practical Machine Learning Tools and Techniques, 4th ed. Burlington, MA, USA: Morgan Kaufmann, 2016. doi: 10.1016/C2009-0-19715-5.

[19] M. Robnik-Šikonja and I. Kononenko, "Theoretical and Empirical Analysis of ReliefF and RReliefF," Machine Learning, vol. 53, no. 1, pp. 23–69, 2003. doi: 10.1023/A:1025667309714.

[20] C. Aydın y B. Evrentuğ, "Evaluation of predictive maintenance efficiency with the comparison of machine learning models in machining production process in brake industry," PeerJ Computer Science, vol. 11, p. e2999, 2025. doi: 10.7717/peerj-cs.2999.

[21] K. Arun, "Evaluating Machine Learning Algorithms for Predictive Maintenance in Equipment," Global J. Eng. Innov. Interdiscip. Res., vol. 5, 2025. doi: 10.33425/3066-1226.1059.

[22] Y. Yang and M. Z. Iqbal, "Cost-Optimised Machine Learning Model Comparison for Predictive Maintenance," Electronics, vol. 14, no. 12, p. 2497, 2025. doi: 10.3390/electronics14122497.

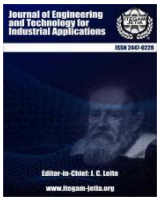
[23] V. Lumumba et al., "Comparative analysis of cross-validation techniques: LOOCV, k-fold cross-validation, and repeated k-fold cross-validation in machine learning models," Am. J. Theor. Appl. Stat., vol. 13, pp. 127–137, 2024. doi: 10.11648/j.ajtas.20241305.13.

Journal of Engineering and Technology for Industrial Applications

ISSN ONLINE: 2447-0228

ITEGAM-JETIA

Manaus, v.12 n.60, p. 470-483 July/August, 2026.
DOI: https://doi.org/10.5935/jetia.v12i60.3880



RESEARCH ARTICLE OPEN ACCESS

CFD-BASED NUMERICAL ASSESSMENT OF PIN-FIN HEIGHT OPTIMIZATION FOR ENHANCED THERMAL PERFORMANCE IN MWCNT NANOFLUID MICROCHANNEL HEAT SINKS

S Sorna Latha[1], Ankush D Tharkar[2], Divya Haridas[3*]

[1]Department of Condensed Matter Physics, Saveetha School of Engineering, Saveetha Institute of Medical and Technical Sciences (SIMATS), Thandalam, Chennai, India.
[2]School of Mechanical Engineering, VIT Bhopal University, Bhopal India.
[3]Department of Condensed Matter Physics, Saveetha School of Engineering, Saveetha Institute of Medical and Technical Sciences (SIMATS) Thandalam, Chennai, India.

[1]http://orcid.org/0009-0006-7996-3994, [2]https://orcid.org/0000-0002-7173-0399, *[3]http://orcid.org/0000-0003-1042-7553

E-email: *divyaharidask@gmail.com, ankush.tharkar@gmail.com, sornalathas9045.sse@saveetha.com

ARTICLE INFO

Article History
Received on: March 03, 2026
Reviewed on: April 02, 2026
Accepted on: May 01, 2026
Published on: July 31, 2026

Keywords:
Microchannel Heat Sink; MWCNT Nanofluid; Pin-Fin Geometry; CFD; Thermal Performance Factor; Thermo-Hydraulic Analysis; Data-Driven Visualization.

ABSTRACT

Microchannel heat sinks are often redesigned with taller pin fins under the assumption that larger surface area inherently yields better cooling. However, this study reveals a counterintuitive yet significant finding that the shortest pin fin (6.2 µm) consistently outperforms all taller configurations across the full range of operating conditions. A three-dimensional CFD model developed in ANSYS Fluent evaluates a plain channel and four pin-fin heights (6.2, 18.6, 31.0, and 43.4 µm) over Reynolds numbers 55 - 225, using water and MWCNT nanofluids at 1, 2 & 3% concentrations. The thermo-hydraulic behavior is assessed through Nusselt number, friction factor, pressure drop, and thermal performance factor (TPF). Although taller fins enhance heat transfer, they impose substantial pressure and pumping penalties, diminishing overall system efficiency. In contrast, the 6.2 µm geometry demonstrates a TPF consistently above unity with a strong increase at higher Reynolds numbers, indicating an efficient flow-mixing mechanism achieved with minimal hydraulic cost. In microscale cooling, shorter and compact pin fins rather than taller ones unlock superior thermal performance. This unexpected dominance of the smallest configuration highlights an important design insight. A supporting data-driven heat-map visualization is also employed to interpret multi-parameter trends, reinforcing the identification of the 6.2 µm pin height with 3% MWCNT as the most efficient case. Overall, the study provides clear guidance for next-generation microchannel heat-sink optimization and challenges conventional assumptions about fin geometry in miniaturized cooling systems.



Copyright ©2026 by authors and Galileo Institute of Technology and Education of the Amazon (ITEGAM). This work is licensed under the Creative Commons Attribution International License (CC BY 4.0).

I. INTRODUCTION

The need for compact and high-performance thermal management systems has increased due to the rapid miniaturisation of electronic devices, the emergence of high-density microprocessors, and developments in power electronics. In today's increasingly compact and powerful devices, effective thermal solutions are essential for maintaining optimal performance, preventing overheating, and ensuring device reliability. Because of their high surface area-to-volume ratios and superior convective heat transfer capabilities, microchannel heat sinks (MCHSs) have become a viable option for dissipating high heat fluxes. These devices are perfect for cooling next-generation electronics because they use laminar flow in narrow channels to achieve superior thermal performance while minimising coolant volume. The groundbreaking work by Tuckerman and Pease (1981) [1] introduced the first microchannel heat sink for high performance cooling planar integrated VLSI circuits. It showed that the convective heat transfer coefficient h between the substrate and coolant is the main limitation for thermal resistance, and laminar flow in narrow channels increases h.

Experiments at a power density of 790 W/cm² showed a maximum substrate temperature rise of 71 °C, validating theoretical predictions and demonstrating feasibility for ultrahigh-speed VLSI circuits. Weisberg et al. (1992) [2] further analyzed ultra compact microchannels proposing design algorithms to optimize dimensions for integrated cooling applications by highlighting the potential of precision machined channels for effective thermal management. Subsequent studies explored innovative channel geometries, such as wavy, fractal, and helical microchannels, to induce secondary flow, enhance turbulence, and increase convective heat transfer without significantly penalizing pressure drop. Hussein, H. A. (2024) [3] numerically analyzed six circular mini-channel heat sink designs with L-shaped flow passages to enhance coolant distribution and heat transfer. The L-channel (JMMLCCHS) showed higher performance index and lower thermal resistance than rectangular channels. Haridas, D., (2014) [4] analyzed the behaviour of the Temperature fields and forced convection in compact thermal systems have been studied using digital interferometric techniques, such as the Michelson and Mach-Zehnder methods. Zhu, Q., (2024) [5] numerically studied a Symmetric wavy microchannel with wave trough-to-crest secondary channels (SW-TC) with slanted secondary channels for improved flow uniformity and heat transfer. The SW-TC design demonstrated better thermal efficiency than the Symmetric wavy microchannel with wave crest-to-crest secondary channels (SW-CC) and Symmetric wavy microchannel with wave trough-to-trough secondary channels (SW-TT) designs.

Subsequent studies have focused on improving heat transfer by incorporating microstructures and pin-fin arrangements. A and Chakraborty et al. (2020) [6] enhanced MCHS performance by integrating microstructures like pillars and blind holes. Pillars boosted heat transfer but increased pressure drop, while blind holes moderately improved both. A hybrid design with more pillars near the inlet achieved higher heat transfer with controlled pumping power. Xie et al. (2021) [7] numerically analyzed laminar flow (Re = 10-300) in microchannel heat sinks with pin fins at 0°, 30°, 45°, and 60° inclinations using the finite volume method. Strong secondary flow was created by the in-lined 30° configuration which improved heat transfer but increased friction. While pattern effects were negligible, the inclined angle had a significant influence on thermo-hydraulic performance. Optimal designs were recommended under equal pumping power conditions. Similarly, Ali et al. (2024) [8] numerically studied semi-elliptical pin fins (Ψ = 0.36-1.0) in water-cooled MCHSs (Re = 100-900, heat flux = 1×10^6 W/m²). The best performance (THPP = 1.41) occurred at Ψ = 1.0 and Re = 300, while the lowest was at Ψ = 0.36 and Re = 900. Recent work of Qi, X., et al.(2025) [9] is on thermally induced errors in feed-drive mechanisms has shown that advanced cooling technologies, such as sintered core heat pipes, play a crucial role in minimizing temperature gradients. This reinforces the broader engineering demand for compact and high-performance cooling systems like microchannel heat sinks.

Zhu, X. et al., (2025) [10] found that Geometric refinement and better heat transfer interfaces can significantly increase system efficiency as demonstrated by recent optimisation studies on stepped-configuration thermoelectric generators. These findings parallel the motivation of the present work where pin-fin geometry and nanofluid properties are tailored to elevate thermal performance in microchannel heat sinks. Zhu, X. et al., (2025) [11] Geometrical and material optimization of advanced TE modules, like hybrid configurations of N-SKD/P-HH, demonstrated that thermal efficiency increases while reiterating geometry optimization; hence, the pin-fin height optimization of microchannel heat sinks in this study actually follows suit. Ali et al. (2024) [12] numerically analyzed V-shaped rib angles (35°-90°) in MCHSs for Re = 100-900. Smaller angles (35°) enhanced heat transfer via stronger flow mixing and yielding higher Nusselt numbers but greater frictional losses. The study highlights the need to optimize rib angles for balanced thermal hydraulic performance. More recent work by Singh et al. (2025) [13] examined different micro pin-fin geometries, revealing that circular fins provide the highest thermal enhancement while triangular and square fins offer moderate improvement which influence of fin geometry and arrangement on thermo-hydraulic performance. Additionally, Polat et al. (2022) [14] highlighted that micro pin-fin shapes (diamond, square, circular) and their arrangements strongly affect both Nusselt number and pressure drop, requiring optimized design to balance heat transfer and pumping power.

Parallel to geometric optimizations, nanofluids have been extensively explored for enhancing thermal performance in MCHSs. Maheshwary et al. (2017) [15] experimentally showed that TiO_2–water nanofluid thermal conductivity increases with higher concentration, smaller particle size, and cubic shape, with concentration having the greatest effect (69.43%). However, higher concentrations also increase viscosity and pumping power. Experimental studies by Jeong et al. (2013) [16] showed that both viscosity and thermal conductivity of ZnO-water nanofluids increase with higher nanoparticle concentration. Particle shape is important at 5 vol.%, nearly rectangular particles produce higher enhancements than spherical ones (about 7.7% higher viscosity and 6% higher thermal conductivity). This suggests that the geometry of nanoparticles has a significant impact on the performance of nanofluids. Hung et al. (2012) [17] demonstrated that Al_2O_3-water and diamond-water nanofluids enhance microchannel heat transfer by over 20%, with optimal performance achieved using smaller particles and controlled volume fractions. Hybrid nanofluids combining multiple nanoparticles have shown even greater potential, Bhattad et al. (2020, 2022) [18] reported improved thermal conductivity and performance indices with minimal pumping penalty, while Murali Krishna et al. (2020) [19] confirmed that MWCNT-CuO/water hybrids outperform mono nanofluids in circular microchannels.

The integration of numerical simulations and artificial intelligence has become crucial for optimizing MCHS designs. Gao et al. (2022) [20] reviewed the application of CFD, LBM, and molecular dynamics in microchannel heat transfer emphasizing that CFD remains versatile for laminar flows while machine learning techniques as used by Said et al. (2022) [21] demonstrated that MWCNT/water nanofluids notably enhance shell-and-tube heat exchanger (STHX) performance, achieving a 3.23% rise in thermal conductivity, 31.08% higher heat transfer coefficient, and 5.49% improved efficiency at 0.3% volume fraction. CFD analysis with semicircular baffles further increased efficacy by 15.4%, confirming the nanofluid's superior heat transfer capability and sustainability for STHX applications. Yadav et al. (2021) [22] studied MWCNT/water nanofluids showing non-Newtonian behavior dependent on concentration, temperature, and shear stress, with SDS surfactant influencing rheology. The power-law model described flow behavior, while an ANN model achieved high prediction accuracy, demonstrating the strength of combining experimental, theoretical, and AI approaches for nanofluid rheology. Additionally, innovative channel geometries, such as fractal or plus-shaped designs, have been explored numerically Lyu et al. (2020) [23] demonstrated that fractal channels with CNT nanofluids achieve uniform temperature distribution and enhanced heat transfer, further highlighted the stability and efficiency of MWCNT-based nanofluids, achieving significant heat transfer enhancement with negligible pumping penalties.

While Manjur et al. (2025) [24] showed that novel geometries coupled with advanced nanofluids can significantly improve thermal performance and reduce pressure drop. Cai, B., (2025) [25] studied double-layered MCHSs, introducing TMC-ORTC with rib-cavity coupling, which enhanced mixing and heat transfer while reducing pressure loss, achieving 120% higher Nusselt number and 81.7% better temperature uniformity than conventional designs. Beyond MCHSs, the broader application of nanofluid-enhanced systems has been confirmed in photovoltaic thermal (PVT) systems, where Rajamony et al. (2024) [26] reported that MWCNT-enhanced phase change materials improve both thermal and electrical outputs. Furthermore, studies on laminar flows with nanofluids in non-conventional geometries, such as Analytical and statistical of Yahiaoui et al. (2025) [27] analysed Jeffery-Hamel flow for Cu–water and SiO_2/water nanofluids in rotating channels showed that rotation induces asymmetric shear flow and affects heat transfer. Though geometrically different, the study relates to pin-fin microchannels by revealing how nanofluid properties and Reynolds number influence flow, wall shear, and heat transfer. Babar Hussain Shah et al. (2024) [28] provide insights into how boundary conditions, Reynolds number, and fluid properties influence flow and heat transfer, which is relevant for optimizing MCHS performance. Emadi, A., (2025) [29] numerically assessed that multi-layer porous fins significantly enhance heat transfer by improving convection and temperature uniformity, with two-layer fins offering optimal performance under high porosity and permeability. Despite significant progress, research gaps remain in balancing heat transfer enhancement with pumping power penalties, exploring hybrid nanofluids with varying proportions, and applying machine learning for predictive optimization under diverse flow conditions. The present study aims to address these gaps by numerically investigating the thermohydraulic performance of MCHSs with MWCNT-based nanofluids across various pin-fin geometries and configurations, thereby contributing to the development of efficient microchannel cooling strategies for advanced electronic and thermal management applications.

II. COMPUTATIONAL MODELLING

II.1 COMPUTATIONAL DESIGNING

II.1.1 Design and Computational Model

The computational domain for the microchannel heat sink (MCHS) was created in ANSYS Workbench (Design Modeler) to analyze fluid flow and heat transfer across different pin fin geometries and nanofluid concentrations. The model simulates a three-dimensional, steady-state, laminar flow to capture the interaction between the solid microchannel and the working fluid [27]. Copper was chosen as the channel material for its high thermal conductivity and mechanical stability, making it suitable for microscale thermal management. The Microchannel design is shown in the Figure 1b as Computational Domain and the Schematic view of the channel is given in the Figure 1a. The dimensions of the microchannel as given in Table 1 has a length of 600 µm, a width of 265 µm, and a height of 62 µm, with cylindrical pin fins of 15 µm diameter distributed at a uniform pitch of 50 µm (Fig 1a, b). Each configuration includes 55 pin fins of varying heights 6.2 µm, 18.6 µm, 31 µm, and 43.4 µm to evaluate the influence of fin aspect ratio on the overall flow and heat transfer behavior. Water and MWCNT-water nanofluids with concentrations of 1%, 2%, and 3% by volume were used as the working fluids. These nanofluids were chosen for their enhanced thermal conductivity and capacity to intensify near-wall thermal interactions. The simulations were performed for inlet velocities of 0.5, 1.0, 1.5, and 2.0 m/s to capture the combined effect of flow rate and nanofluid loading on heat transfer and pressure characteristics. The fluid enters the channel through the inlet boundary with a uniform velocity profile and exits through an outflow boundary with zero gauge pressure. Constant heat flux is applied at the bottom surface, while all other external walls are adiabatic. A structured mesh was generated to accurately capture the boundary layer and the complex flow around pin fins, with grid independence verified through successive mesh refinements. The governing equations for mass, momentum, and energy were solved using the finite volume approach in ANSYS Fluent, ensuring numerical stability and convergence for all cases studied. This computational framework enables a comprehensive understanding of the microscale flow development, temperature distribution, and fluid-solid interaction under various geometric and operating conditions, providing a reliable basis for optimizing MCHS performance using MWCNT nanofluids.

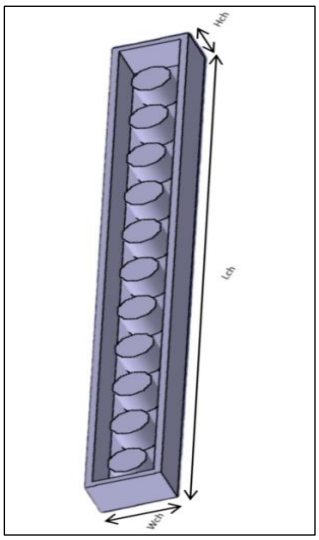


Figure 1 a: Schematic Diagram of the Channel.
Source: Authors, (2026).

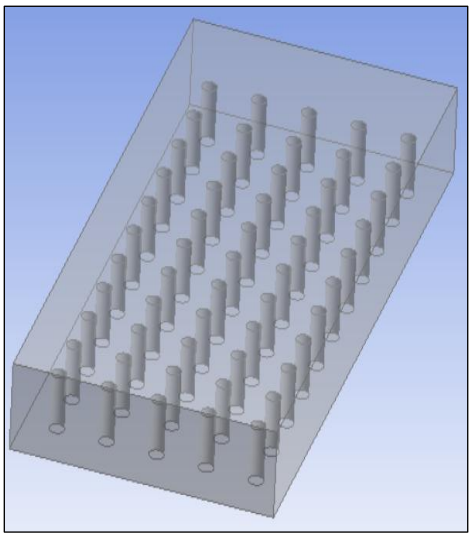


Figure 1 b: Computational Domain.
Source: Authors, (2026).

Table 1: Channel Descriptions.

Parameter	Values
Length of Channel, Lch	600 µm
Width of Channel, Wch	265 µm
Height of Channel, Hch	62 µm
Hydraulic Diameter	100.5 µm
Pin Diameter	15 µm
Pin Spacing	50 µm
Number of Pins	55
Pin fin Height	6.2, 18.6, 31.0, 43.4 µm
Nanofluid	MWCNT
Nanofluid Concentration	1%, 2%, 3%

Source: Authors, (2026).

II.2.2 Properties of Heat Transfer Fluid and Microchannel

The performance and thermal efficiency of the microchannel heat sink (MCHS) are highly dependent on the thermophysical properties of both the working fluid and the substrate material. These properties regulate the mechanisms of heat transfer, flow resistance, and overall cooling effectiveness under varying operating conditions. In the present study, deionized water and multi-walled carbon nanotube (MWCNT)/water nanofluids with volume concentrations of 1%, 2%, and 3% are employed as the heat transfer media while aluminium is used as the microchannel substrate. Water acts as the base fluid due to its favorable properties, including high specific heat capacity, moderate thermal conductivity, and low viscosity, which collectively promote efficient convective heat removal. The suspension of MWCNT nanoparticles within the base fluid further enhances its effective thermal conductivity and heat transport capability through mechanisms such as Brownian motion and micro-scale convection. The incorporation of MWCNTs also improves energy diffusion and temperature uniformity within the microchannel, leading to superior thermal performance compared to pure water. The thermophysical properties of the working fluids at a reference temperature are summarized in Table 2. Aluminium is selected as the microchannel substrate material because of its high thermal conductivity, low density, and excellent mechanical stability. These properties make it ideal for rapid heat spreading and lightweight thermal management applications. The high thermal conductivity of aluminium (386 W/m·K) ensures efficient heat distribution along the channel walls, while its moderate specific heat capacity allows it to accommodate transient temperature fluctuations. Furthermore, its structural robustness and resistance to thermal fatigue make it suitable for repeated heating and cooling cycles under high heat flux conditions. The thermophysical properties of aluminium are also listed in Table 2. The combined use of MWCNT–water nanofluids and Copper substrate provides a highly effective heat transfer configuration. The enhanced thermal conductivity of the nanofluid ensures rapid heat removal from the heated surface, while the superior heat spreading capability of Copper maintains a uniform temperature gradient across the microchannel. Together, they contribute to reduced thermal resistance, improved convective performance, and sustained operational efficiency of the MCHS under diverse flow and thermal loading conditions.

Table 2: Properties of the Materials.

Thermo-Physical Properties	Units	Water	MWCNT	Copper
Density	(kg/m³)	997	1600	2700
Dynamic Viscosity	(kg/m·s)	0.000891	-	-
Thermal Conductivity	(W/m·K)	0.6	3000	386
Specific Capacitance	(J/kg·K)	4182	796	903

Source: Authors, (2026).

II. 2.3 Mesh Independence Study:

The grid independence test is conducted to ensure that the solution is unaffected by further mesh refinement, confirming numerical accuracy. A detailed mesh independence study was performed for the rectangular microchannel under a constant heat flux of 10,000 W/m² and an inlet velocity of 0.5 m/s. Three mesh densities were examined: coarse (247,886 elements), medium (707,788 elements), and fine (1,584,540 elements). The fine mesh produced a Nusselt number (Nu) of 4.347 and a friction factor (f) of 0.83, while the medium mesh yielded Nu = 4.507 and f = 0.8115. The coarse mesh slightly overpredicted Nu (4.437) and underpredicted f (0.81), consistent with the typical behavior of under-resolved meshes that inadequately capture near-wall gradients. The relative percentage variations between the fine and medium meshes were 3.68% for Nusselt number and 2.28% for friction factor—both within the generally accepted convergence tolerance of ±5%. This confirms that further refinement produces negligible improvement in the predicted flow or thermal characteristics. Notably, although the fine mesh results in a marginally lower Nusselt number, this outcome reflects physical accuracy rather than numerical limitation. Coarser grids often overpredict heat-transfer coefficients due to exaggerated wall-temperature gradients caused by insufficient near-wall resolution. The fine mesh, with its higher element density and smaller y^+ values, resolves the viscous and thermal boundary layers more precisely, capturing the realistic conduction-convection interplay and producing a more reliable thermal prediction. The modest increase in pressure drop in the fine mesh (≈2–3%) arises from improved resolution of recirculation and viscous losses around pin fins—an expected and physically justified trend. The fine mesh was therefore selected for all subsequent simulations owing to its superior resolution of wall-adjacent gradients, accurate representation of viscous and thermal dissipation mechanisms, and 4.2% enhancement in thermal-hydraulic efficiency, demonstrating that the pin-fin design offers meaningful heat-transfer improvement despite a modest rise in pressure loss.

Table 5:Mesh independence study.

Quantity	Coarse Mesh	Medium Mesh	Fine Mesh	Percentage Deviatio.n Medium to Fine(%)	Percentage Deviation Coarse to Fine (%)
No.of elements	247,886	707,788	1,584,540	-	-
Pressure Drop	603.4312	604.3910	624.4862	+3.32%	+3.49%
Nusselt Number	4.437	4.507	4.347	-3.55%	-2.03%
Friction factor	0.81	0.81148	0.83	+2.28%	+2.47%

Source: Authors, (2026).

III. MATERIALS AND METHODS

III.3.1 Boundary Conditions and Numerical Procedure

The numerical investigation of the microchannel heat sink (MCHS) is performed under carefully defined boundary conditions and a systematic numerical procedure to accurately capture the coupled fluid flow and heat transfer characteristics. As in Table 3, At the inlet, a uniform velocity is prescribed corresponding to four distinct velocities (0.5, 1.0, 1.5, and 2.0 m/s), which correspond to the Reynolds numbers between 56 to 225 representing laminar flow regimes typical of microchannel applications. The inlet temperature of the working fluid is water and MWCNT–water nanofluids with 1%, 2%, and 3% concentrations maintained at 300 K. This ensures consistent thermal conditions for comparative analysis across all test cases. At the outlet, a zero-gauge pressure condition is imposed to simulate atmospheric discharge, ensuring a physically realistic pressure drop along the flow direction. A uniform heat flux of 10KW/m2 is applied at the bottom wall of the microchannel, emulating high heat generation from electronic components or chip surfaces. The other three walls are considered adiabatic, restricting heat loss to the surroundings. All solid–fluid interfaces are assumed to have a no-slip condition to accurately represent viscous effects within the confined microchannel domain. The numerical procedure is executed using the finite volume method (FVM) in ANSYS Fluent in the governing equations. The pressure–velocity coupling is handled using the SIMPLE algorithm, which ensures convergence stability and accurate momentum–pressure interaction. The convective terms in the governing equations are discretized using the second-order upwind scheme. Convergence criteria are set to strict tolerances to ensure computational reliability. The residuals are maintained below 10-9 for the energy equation and 10-6 for both continuity and momentum equations.

Table 3: Boundary conditions.

Boundary Conditions	Values
Inlet Velocity	0.5 - 2 m/s
Inlet Temperature	300 K
Outlet Pressure	0 Pas
Heat Flux	10 kW/m2
Reynolds Numbers	56.23, 112.5, 168.7, 225
Flow Type	Laminar

Source: Authors, (2026).

III.3.2 Mathematical model:

The steady-state, laminar, incompressible flow and conjugate heat transfer through the microchannel are modeled using the three-dimensional forms of the continuity, momentum, and energy equations. These equations govern both the fluid and solid domains to capture the coupled heat transfer behavior.

Continuity

$$\nabla . \vec{u} = 0 \tag{1}$$

Momentum.

$$\rho_l \left(\vec{u} \cdot \nabla \vec{u} \right) = -\nabla p + \mu_l \nabla^2 \vec{u} \tag{2}$$

Energy.

$$\rho_l C_{pl} \left(\vec{u} \cdot \nabla T_l \right) = k_l \cdot \nabla^2 T \tag{3}$$

Energy (solid).

$$\nabla (k_s \cdot \nabla T_s) = 0 \tag{4}$$

III.3.3 Numerical Calculations:

The Hydraulic Diameter (Dh) equation,

$$D_h = \frac{4(W_{ch} \times H_{ch})}{2(W_{ch} + H_{ch})} \quad (5)$$

Where Hch - Height and Wch-width

The Reynolds equation,

$$Re = \frac{\rho_l u_l D_h}{\mu_l} \quad (6)$$

The heat transfer coefficient,

$$h = \frac{Q}{T_w - T_f} \quad (7)$$

The Nusselt calculation,

$$Nu = \frac{hD_h}{k} \quad (8)$$

The friction factor can be determined from the following equations,

$$f = \frac{2D_h \Delta p}{L \rho u_{in}^2} \quad (9)$$

The thermal Performance Factor (TPF) is calculated by,

$$TPF = \frac{Nu/Nu_o}{(f/f_o)^{1/3}} \quad (10)$$

III.3.4 Nanofluid Properties

Density:[28]

$$\rho nf = (1 - \varphi)\, \rho bf + \varphi . \rho p$$

Viscosity: (Brinkman - model) [29]

$$\mu = \frac{\mu_{bf}}{(1 - \varphi)^{2.5}}$$

Thermal Conductivity: (Hamilton - Crosser) [30]

$$k_{nf} = kbf \frac{k_s + (n-1)\, k_{bf} - (n-1)\, \varphi\, (k_s - k_{bf})}{k_s + (n-1)\, k_{bf} + \varphi\, (k_s - k_{bf})}$$

Specific Heat Capacity: [31].

$$Cpnf = \frac{(1-\varphi)\, \rho_{bf} C_{bf} + \varphi\, \rho_p C_p}{\rho_{nf}}$$

Table 4: Thermo-physical properties of Nanofluid.

Fluid Type	Concentration (wt%)	Density (kg/m³)	Specific Heat (J/kg·K)	Thermal Conductivity (W/m·K)	Viscosity (kg/m·s)
Water	0	998.2	4182	0.6	0.000891
MWCNT/Water Nanofluid	1	1003.03	4128	0.6254	0.0009128
MWCNT/Water Nanofluid	2	1009.06	4074.62	0.6441	0.0009367
MWCNT/Water Nanofluid	3	1015.09	4021.89	0.6633	0.0009617

Source: [27].

IV. RESULTS AND DISCUSSIONS

IV.4.1 Flow field Visualization:

The velocity contour, streamlines and the vector plots across all configurations exhibit the combined influence of velocity magnitude, pin height, and nanofluid concentration on the internal flow behavior of the microchannel. At lower velocities (0.5–1.0 m/s) the flow remains predominantly laminar with well-defined, symmetric streamlines and low momentum exchange near the pin surfaces shown in the Velocity Vector Fig 2. In these cases recirculation zones are small and confined to the wake regions behind each pin fin. The reduced inertia limits the fluid ability to reattach quickly, leading to a thicker boundary layer and consequently weaker convective heat transfer. As velocity increases (1.5-2.0 m/s) the streamlines become progressively elongated and aligned with the channel direction indicating higher kinetic energy and enhanced flow mixing shown in the Fig 3 with Velocity Contour enabled with the Velocity Streamlines. The wake regions shrink and the reattachment points move closer to the trailing edge of the pins which reflect the thinning of the velocity boundary layer and improved convective transport.

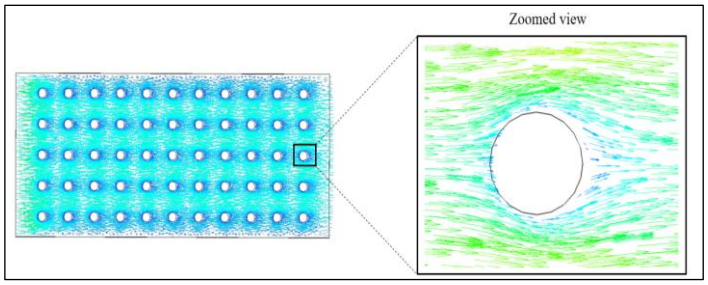


Figure 2: Velocity Vectors along the channel and a zoomed view around a single pin fin 6.2 µm with 3% concentration of MWCNT at 2 m/s.
Source: Authors, (2026).

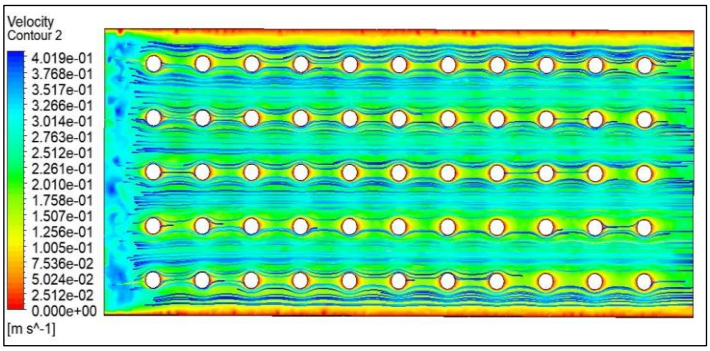


Figure 3: Velocity contour with Streamlines of 6.2 µm pin fin with 3% concentration of MWCNT at 2 m/s.
Source: Authors, (2026).

The influence of pin height of taller pins (31 µm and 43.4 µm) produce stronger flow obstruction and intensified local acceleration around the pin tips, resulting in elevated velocity gradients and increased flow intensity in their vicinity. This accelerates fluid mixing and disrupts the thermal boundary layer, boosting overall heat transfer performance. In contrast, shorter pin fins (6.2 µm and 18.6 µm) yield smoother streamlines with limited mixing at lower velocities. Figure 2 represents the velocity vector field in the microchannel, showing that the bulk region is dominated by smooth forward flow while each of the pin fins has distinct flow deviation. Enlarging the view locally elucidates the local acceleration and deflection of streamlines around the surface of the pin as velocity gradients become large in the wake region. The behavior confirms what was expected to be characteristic shear layers and localized recirculation zones that enhance the mixing and indeed improve convective heat transfer.

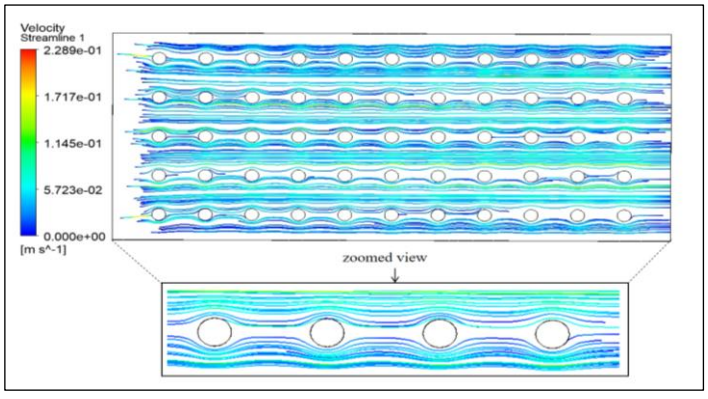


Figure 4: Velocity Streamlines along the plane above the pin fin (~6.3 µm pin fin) with 3% concentration of MWCNT at 2 m/s.
Source: Authors, (2026).

Figure 4, shows the transition of the Streamlines in the same channel with 6.2 µm pin fin channel with 3% concentration of MWCNT at 2 m/s, but at a certain plane where the flow pattern changes slightly above the pin height approximately at ~6.3 µm. The velocity streamlines show that when pin heights are lower and velocities are reduced, the flow develops more smoothly and evenly, allowing the fluid to interact longer with the channel walls. This creates clear boundary layers and stable flow areas between the pin fins. On the other hand, higher pin heights and faster velocities increase mixing and speed up the flow around the fins, which causes more turbulence and disturbances. Adding MWCNT nanofluids, especially at higher concentrations, improves momentum diffusion near the walls and changes how the streamlines behave, leading to better flow interaction and more uniform mixing. Even with these differences, the main flow pattern stays the same in all cases, with clear circulation zones and faster regions around the pin fins. When comparing the working fluids, the addition of MWCNT nanoparticles alters the velocity distribution by slightly increasing flow resistance due to higher viscosity. At 1% and 2% concentrations, this resistance modestly dampens near to the wall velocities. Whereas at 3% MWCNT, the effect is more pronounced with marginally thicker velocity gradients near pin surfaces. However the enhanced thermal conductivity and momentum diffusion of MWCNT nanofluids promote stronger velocity recovery downstream and greater homogenization of flow fields. Among all the cases, 3% MWCNT exhibits the most balanced velocity distribution demonstrating the best synergy between viscous dissipation and convective enhancement.

IV.4.2 Temperature Field Visualization:

The temperature contours reveal a clear dependence of thermal field uniformity on both pin-fin height and inlet velocity. At low pin height (6.2 µm) and low velocity, all working fluids exhibit a higher wall temperature and a larger temperature gradient between the inlet and outlet. This occurs because short fins generate weaker flow disturbances and inadequate boundary-layer disruption, resulting in poor mixing of the near-wall fluid. Simultaneously, the low inlet velocity leads to a thicker thermal boundary layer and a longer fluid residence time, allowing heat to accumulate near the heated wall. The combined effect of weak geometric mixing and slow advection leads to the largest temperature rise in these cases. As the pin height increases, a substantial improvement in heat transfer uniformity is observed. Taller fins (18.6 µm, 31 µm, and 43.4 µm) extend deeper into the flow field, promoting enhanced fluid impingement and wake re-circulation zones between successive pins. This intensifies boundary-layer disturbance and induces secondary mixing, which renews the fluid near the heated surfaces more effectively. Consequently, the local wall temperature decreases and the overall temperature distribution becomes more uniform along the flow path. The benefit of increased pin height is most evident at moderate-to-high velocities, where the combined influence of fin-induced turbulence and convective momentum transport yields superior cooling performance. Similarly, increasing the inlet velocity strengthens convective transport and reduces the temperature difference between the wall and bulk fluid. At higher velocities, the fluid residence time decreases yet the energy removal rate rises due to higher heat transfer coefficients and thinner thermal boundary layers. Hence, the contours at 2 m/s exhibit more uniform color gradients and lower maximum temperatures than those at 0.5 m/s (Fig 5). However, excessively high velocities also lead to increased frictional losses and pressure drop which can impact system efficiency a trade-off captured through the Thermal Performance Factor (TPF) analysis. Across all geometric and flow conditions the MWCNT nanofluids consistently outperform water in dissipating heat, with improvements increasing with nano-particle concentration. The 3% MWCNT nanofluid exhibits the lowest wall temperatures and the most uniform thermal contours due to its higher effective thermal conductivity and microconvective energy transport enabled by nanoparticle Brownian motion. The 1% and 2% nanofluids also enhance thermal performance compared to pure water but to a lesser extent yet following the same overall temperature trend. The influence of concentration becomes more prominent at higher pin heights and velocities where convective mixing complements the intrinsic conductivity enhancement of the nanofluid.

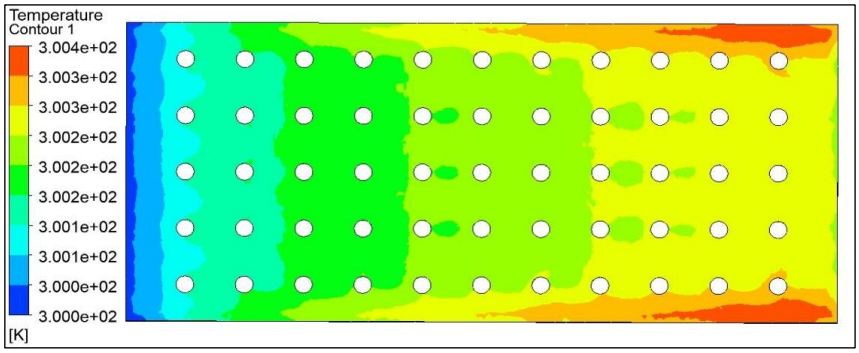


Figure 5: Temperature Contour along the channel of 6.2 µm pin fin with 3% concentration of MWCNT at 2 m/s.
Source: Authors, (2026).

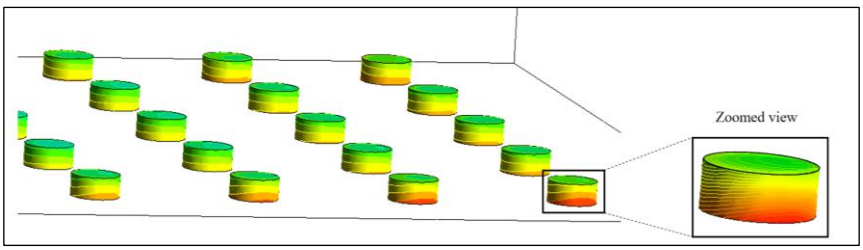


Figure 6: Temperature Distribution along the height of the 6.2 µm pin fin with 3% concentration of MWCNT at 2 m/s.
Source: Authors, (2026).

The temperature contour over each pin fin reveals a noticeable axial gradient with higher temperatures near the base (red/orange) and gradually lower ones toward the top surface (yellow/ green) (Fig 6). This pattern demonstrates that the vicinity near the pin substrate interface is under stronger thermal loading while the upper portions of the pin fins are relatively cooler because of the enhanced removal of heat by convection of the fluid. In the zoomed view, there is an indication of smooth vertical temperature stratification which supports good heat spreading from the base to the fin tip.

IV.4.3 Pressure Drop:

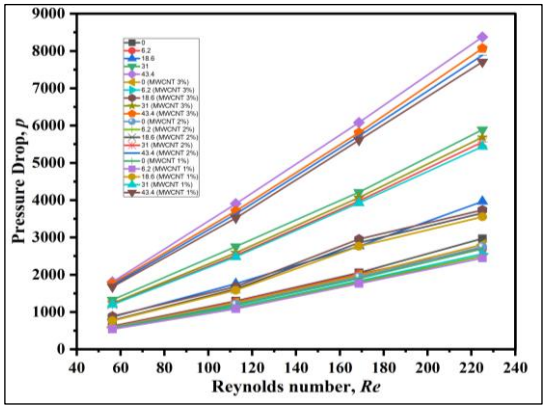


Figure 7: Pressure Drop evaluation with Reynolds number.
Source: Authors, (2026)

Figure 7 elucides the pressure drop (ΔP) with Reynolds number for water and MWCNT nanofluids across various pin-fin configurations shows a sharp rise with velocity (shown in Fig 1) because the dynamic pressure term (ρv2/2) dominates at higher velocities causing ΔP to scale approximately with the square of the flow velocity. Although the friction factor slightly decreases with increasing Reynolds number, the rapid growth of inertial forces and intensified shear near pin structures leads to a net increase in pressure loss. At lower Reynolds number, ΔP is minimal, dominated by viscous effects and smooth flow. As velocity approaches 2 m/s, inertial effects intensify, causing greater local acceleration and pressure loss due to increased flow recirculation and wake formation around pins. The Channels with taller fins (43.4 µm) exhibit the highest pressure drop owing to increased obstruction, wetted area, and form drag, while the plain channel records the lowest. Intermediate fin heights (18.6 µm and 31.0 µm) offer moderate losses, balancing flow resistance and heat transfer enhancement. Thus, fin geometry directly governs the trade-off between pressure loss and surface augmentation. MWCNT nanofluids consistently produce higher ΔP than water because of increased effective viscosity and nanoparticle-induced flow resistance. At higher velocities (≥1.5 m/s), the gap between water and nanofluids narrows as inertial forces dominate. While MWCNT nanofluids require greater pumping power due to increased flow resistance, their superior heat transfer performance compensates for this drawback. Hence, the observed pressure drop trends reinforce the importance of optimizing fin geometry and nanoparticle concentration to achieve a balanced thermal hydraulic performance in microchannel heat sink applications.

IV.4.4 Friction Factor:

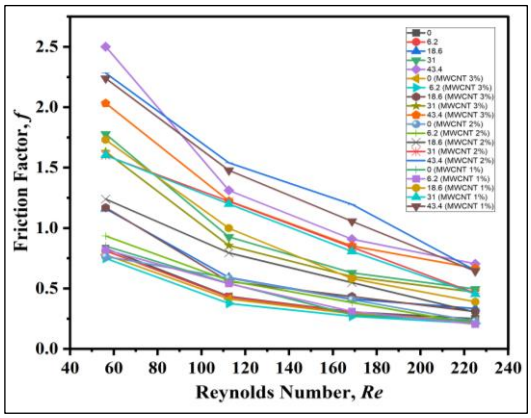


Figure 8: Friction Factor variation with Reynolds number.
Source: Authors, (2026).

The trend of friction factor (f) with Reynolds number for water and MWCNT nanofluid concentrations across different pin fin heights is presented for exact similar parameters in Figure 8. A clear inverse relationship between f and Reynolds number is observed for all configurations, which is typically consistent with laminar scale Reynolds number behavior (Re = 56-225) and the inverse proportionality to Re of viscous losses. Due the dominance of viscous shear stress and form drag caused by the pin fin obstructions, the friction factor reaches its maximum value of f ≈ 0.8-2.5 at lower Reynolds numbers. Significant pressure losses occur in this regime because the flow lacks the kinetic energy to overcome the surface friction and flow separation created behind each pin fin. The boundary layer thins and the wall shear stress contribution per unit mass flow decreases as the velocity increases (0.5 → 2.0 m/s) due to the inertial effects.

As a result, the friction factor gradually drops and tends to stabilise at higher velocities, signifying the relative suppression of viscous dominance. The plain channel has the lowest friction factor at all velocities, while the channels with taller pin fins (43.4 µm) have the highest. This is due to the fact that raising the pin height increases the wetted area and flow obstruction, which results in a larger pressure drop. Additionally, stronger flow separation and wake zones are produced by higher pin structures, which increase the local form drag. Higher friction factors result from the viscous drag dominating the total pressure loss at lower velocities. Because of their increased surface area and increased flow obstruction, taller pin fins intensify this effect, leading to significant form drag and pressure recovery losses. For all geometries, the flow moves towards inertia-controlled behaviour as velocity rises, resulting in a decrease in the friction factor. The MWCNT nanofluid typically shows higher flow resistance because of its increased effective viscosity, improved wall fluid and inter molecular interactions. However, due to the increase in thermal conductivity which indirectly affects viscosity, the nanofluid exhibits slightly lower dimensionless friction factors than water at 3% concentration. This effect is more pronounced at low velocities due to the dominance of viscous forces. However, as velocity increases, the relative difference between water and MWCNT decreases due to the increasing importance of inertial effects. Because of this, MWCNT nanofluid requires more pumping power because it has a higher hydraulic resistance than water. Additionally, as evidenced by the higher Nusselt number values, it has a greater capacity for heat transfer which leads to better thermal performance overall.

IV.4.5 Nusselt Number:

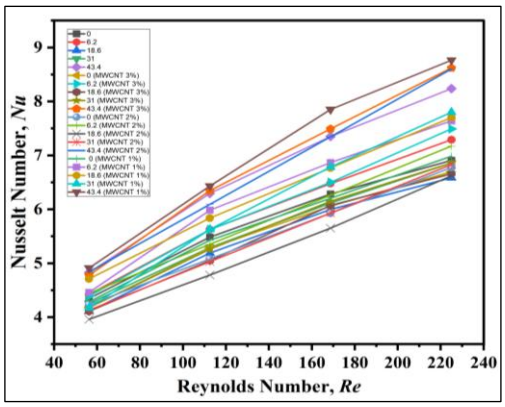


Figure 9: Nusselt number relation with Reynolds number.
Source: Authors, (2026).

Figure 9 elucidates the variation of the Nusselt number (Nu) with inlet velocity for both deionized water and MWCNT nanofluid concentrations. However, simulations has been conducted for 1%, 2% and 3% volume concentrations. A consistent increase in Nu with velocity is observed for all cases, highlighting the strong influence of Reynolds number on convective heat transfer in microchannel configurations (Fig 3). At the lowest Reynolds number (lowest velocity (0.5 m/s)), the Nu values remain relatively low for both water and MWCNT, ranging between 4 - 5. This behavior can be attributed to the dominance of conduction mechanism and the development of a thick thermal boundary layer in the absence of strong convective forces. Consequently, the difference between water and MWCNT is minimal under these conditions, as the nanofluid's enhanced thermal conductivity is not fully exploited. Even at lower nanoparticle concentrations (1% and 2%), the nanofluid exhibits noticeable enhancement compared to water which confirm that significant heat transfer improvement can be achieved without requiring the highest concentration. This can be primary attributed to the enhanced thermal conductivity of MWCNT nanofluids which is approximately 4.23%, 7.35%, and 10.55% higher than the base fluid (water) at 1 wt%, 2 wt%, and 3 wt% concentrations, respectively as compared to the based fluid. As the Reynolds number increases (velocity increases to 1.0-1.5 m/s), the Nusselt number rises steadily due to stronger convective transport and progressive thinning of the thermal boundary layer. In this regime, the benefit of MWCNT becomes more evident. The nanofluid consistently exhibits higher Nu values compared to water across all pinfin configurations which confirms the role of nanoparticles in enhancing heat transport through increased effective thermal conductivity and micro-scale convective effects.

For the 1% and 2% MWCNT concentrations, Nu values also exceed those of water demonstrating a clear improvement in heat transfer eventhough they remain lower than the 3% concentration. The relative enhancement is more pronounced at higher velocities and taller pin-fin geometries. In these scenarios the combined effect of thermal conductivity enhancement (due to nanofluid) and local disturbance of thermal boundary layer (due to pin geometries) plays a major role. The second effect is more visible at higher velocities and hence you can see a better heat transfer enhancement at higher velocities and taller pin heights. At the highest velocity of 2.0 m/s, the enhancement becomes most prominent. For water, Nu reaches values between ~7.0 and 8.0, while for MWCNT, the corresponding Nu extends more than 8.0, particularly in the channel with the tallest pin fins (43.4 µm). This is explained by the synergistic action of high flow momentum, which intensifies mixing around the fins, and the superior thermal conductivity of MWCNT nanofluid, which accelerates thermal diffusion within the fluid medium. Nu values are consistently higher than water but lower than those of the 3% nanofluid at the 1% and 2% MWCNT concentrations. Configurations with taller fins show the incremental improvement over water, emphasising the contribution of even lower nanoparticle loadings. Shorter fins (6.2 µm) provide only moderate boundary layer disruption, leading to smaller increments in Nu, whereas taller fins (31.0 µm and 43.4 µm) induce significant flow separation and accelerated motion, thereby intiates fluid mixing and promoting superior convective heat transfer. The tallest fins consistently deliver the maximum Nu for both working fluids, with the relative gain being more significant for the nanofluid. Overall, the results demonstrate that both increasing flow velocity and incorporating MWCNT nanoparticles substantially improve heat transfer performance in microchannel heat sinks. The improvement is further amplified by the presence of taller pin fins, which serve as passive promoters of thermal hydraulic enhancement.

IV.4.6 TPF:

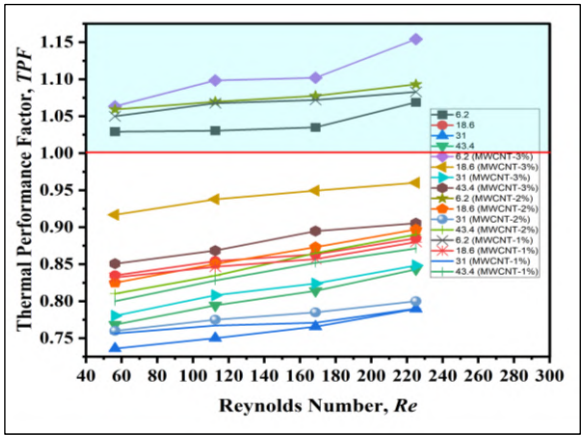


Figure 10: Thermal Performance Factor vs Reynolds number.
Source: Authors, (2026).

The variation of the Thermal Performance Factor (TPF) with Reynolds number for water and MWCNT nanofluids of different concentrations across various pin fin heights is illustrated in Fig. 10. The TPF measures heat transfer improvement in relation to increased frictional losses, indicating overall thermohydraulic efficiency. A general trend of increasing TPF with flow velocity is observed for all configurations, reflecting the dominance of convective heat transfer improvements over the associated hydraulic penalties at higher Reynolds numbers. At low velocity (0.5 m/s), the TPF values remain below unity for most configurations, particularly for the plain and shorter pin-fin channels. This indicates that, under laminar and viscous-dominated conditions, the pressure-drop penalty outweighs the modest heat-transfer enhancement achieved at such low flow rates As the Reynolds number increases, TPF values progressively improve, reaching peak values around 1.1–1.4 depending on the configuration and nanofluid concentration. This rise can be attributed to enhanced flow mixing, boundary-layer disruption, and reduced thermal boundary layer thickness, which collectively augment the convective heat transfer rate more strongly than the corresponding rise in pressure losses. Among all the geometries, the channels with intermediate pin fin heights (18.6 µm and 31.0 µm and tallest 43.4 µm fins) have some fluctuations in the pattern, due to the combined reaction of convective transport and friction losses.

The shortest fin (6.2 µm) consistently demonstrate superior thermal performance compared to the other three fin heights (18.6 µm, 31 µm and 43.4 µm). The moderate pin structures provide an optimal balance between surface area augmentation and flow obstruction which is sufficient to intensify thermal mixing without inducing excessive form drag. All MWCNT nanofluids exhibit higher TPF values than water, confirming their superior thermohydraulic performance. The improvement becomes more evident with increasing nanoparticle concentration at 1% MWCNT, the enhancement is marginal, whereas at 3%, the TPF surpasses unity for most pin fin geometries, indicating a net performance gain. This improvement is due to higher thermal conductivity and enhanced micro-convection from Brownian motion in the MWCNT suspensions, which support heat diffusion and wall heat removal. However, as concentration rises further (more than 3%), increased viscosity limits these benefits, resulting in reduced enhancement at higher concentrations Overall, the integration of pinfin structures with MWCNT nanofluids achieves a mutual enhancement in system efficiency. The combination of intensified heat transfer and manageable pressure drop results in a thermally favorable regime where TPF > 1 for optimized pin heights and flow rates. These findings clearly indicate that the use of MWCNT nanofluids, particularly at 2–3% concentration, provides a substantial improvement in the overall thermal-hydraulic performance of microchannel heat sinks, validating their potential as advanced cooling solutions for high heat-flux microscale applications.

IV.4.7 Data-Driven Heatmap Analysis of Thermal Performance (TPF) Using MATLAB

The combined thermal-hydraulic performance (TPF) for each of the five pin heights (0, 6.2, 18.6, 31, and 43.4 µm), four flow velocities (0.5–2 m/s), and four working fluids (water and 1%, 2%, and 3% MWCNT nanofluids) was visualized using a data-driven heatmap created in MATLAB. Multidimensional CFD output is processed, normalized and mapped using an ML-based exploratory analysis workflow in this visualization approach to uncover performance patterns that are not immediately apparent from isolated plots. This method supports high-dimensional engineering interpretation by using the same datacentric principles that are frequently used in machine-learning research, even though it is not a predictive machine learning model. The heat map clearly and consistently demonstrates that TPF rises with both Reynolds number and nanoparticle concentration throughout the entire dataset (Fig 11). Because of its much higher effective thermal conductivity, the enhancement is most noticeable for the 3% MWCNT nanofluid. The pin height of 6.2 µm with 3% MWCNT yields the highest TPF among all evaluated conditions when comparing the geometric configurations, especially at the highest velocity. This happens because the high concentration of nanoparticles significantly increases heat transfer, resulting in the most advantageous trade-off in the TPF metric, while the shorter pin height maintains a comparatively lower frictional penalty. Higher pin heights such as 31 µm and 43.4 µm, are thermally superior in terms of heat transfer. However, their overall TPF is lower than that of the ideal 6.2 µm case due to increased pressure losses. The anticipated gradation is followed by the intermediate concentrations (1% and 2% MWCNT) The proportionate impact of nanoparticle loading is demonstrated by the fact that 2% consistently performs better than 1% and water but both fall short of the 3% cases because of the relatively smaller heat-transfer enhancement. Predominantly, the heatmap visualisation offers a quick, thorough, and objective evaluation of the behaviour of the system. The most efficient configuration which is indisputably the 3% MWCNT nanofluid with 6.2 µm pin height. This highlights how crucial it is to strike a balance between fluid-property improvement and geometric optimisation when aiming for concurrent improvements in thermal and hydraulic performance.

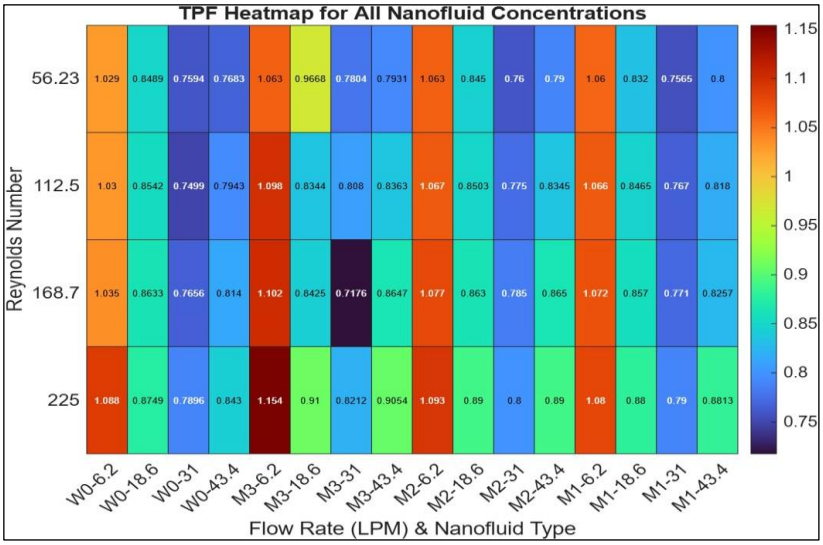


Figure 11: Heat Map Visualization of TPF for MWCNT across the pin heights for various Reynolds numbers.
Source: Authors, (2026)

The Heatmap's Advantages
The heatmap is a crucial analytical tool because it allows immediate comparison between four Reynolds numbers, five pin heights, and four fluids;
exposing non-linear relationships between nanofluid concentration and geometric parameters;
facilitating data-driven decision making akin to exploratory analysis in machine learning;
creating a single, comprehensible visual framework from multidimensional CFD outputs.

V. CONCLUSIONS

The thermo-hydraulic performance of a microchannel heat sink with pin fins of different heights was examined in this study using water and MWCNT-water nanofluids (1-3 wt %). The findings verify that thermal transport in the microchannel is significantly improved by both nanoparticle concentration and Reynolds number. The 3% MWCNT nanofluid continuously produced the highest Nusselt number under all operating conditions, which increases notably at higher flow rates. The effect is especially noticeable for the lowest pin height configuration where superior heat transfer enhancement is produced by the combination of enhanced nanofluid conductivity and increased turbulence intensity. All pin heights exhibit the same increasing trend with mass flow rate and nanoparticle loading according to pressure-drop analyses. Compared to taller pin arrays, lower pin heights show noticeably smaller pressure penalties, particularly at lower velocities. Higher pin heights, on the other hand, result in significantly greater pressure drops because of increased flow obstruction; at higher Reynolds numbers, the difference between nanofluids and water is more noticeable. The 3% nanofluid produced the largest pressure drop across all fin heights, which is in line with its higher viscosity and momentum diffusion. For all working fluids, friction factor values drastically drop as the Reynolds number rises. Because viscous forces are less dominant at higher flow rates, the lowest friction factors are found at Re = 225. Because of their greater wetted perimeter and flow resistance, taller pin fins have higher overall friction factors. When compared to water, the use of nanofluids causes a slight increase in friction; however, this difference decreases at higher Reynolds numbers. According to Thermal Performance Factor (TPF) analysis, the 3 % nanofluid with the lowest pin height offers the best balance between hydraulic penalty and heat transfer enhancement. The lower Reynolds number range (especially around Re ≈ 56) exhibits the highest TPF values, where thermal enhancements significantly outweigh the comparatively slight increase in pressure drop. For all pin heights and concentrations, TPF gradually decreases with increasing Reynolds number; however, because of their lower flow resistance and higher enhancement ratio, lower pin heights consistently perform better than taller pins. Overall, lower pin-height microchannel designs combined with MWCNT nanofluids particularly at 3 weight percent concentration produce a significant increase in heat transfer capability while preserving acceptable pressure drops. These results show that the thermal management efficiency of microchannel heat sinks used in next-generation electronic cooling applications can be greatly increased by optimizing fin geometry in conjunction with customized nanofluid formulations.

VI. AUTHOR'S CONTRIBUTION

Conceptualization: S Sorna Latha, Ankush D Tharkar, Divya Haridas.
Methodology: S Sorna Latha, Ankush D Tharkar, Divya Haridas.
Investigation: S Sorna Latha, Ankush D Tharkar, Divya Haridas.
Discussion of results: S Sorna Latha, Ankush D Tharkar, Divya Haridas.
Writing – Original Draft: S Sorna Latha, Ankush D Tharkar, Divya Haridas.
Writing – Review and Editing: S Sorna Latha, Ankush D Tharkar, Divya Haridas.
Resources: S Sorna Latha, Ankush D Tharkar, Divya Haridas.
Supervision: S Sorna Latha, Ankush D Tharkar, Divya Haridas.
Approval of the final text: S Sorna Latha, Ankush D Tharkar, Divya Haridas.

VI. REFERENCES

[1]. D.B. Tuckerman, R.F.W. Pease, High-performance heat sinking for VLSI, IEEE Electron Device Lett., 2, 126–129 (1981).

[2] A. Weisberg, H.H. Bau, J. Zemel, Analysis of microchannels for integrated cooling, Int. J. Heat Mass Transf., 35(10), 2465–2474 (1992). https://doi.org/10.1016/0017-9310(92)90089-B

[3] H.A. Hussein, A simulation study of thermal and hydraulic characteristics mini-channel circular heat sink: Effect of L-shaped multi-channel arrangement on flow maldistribution, Case Stud. Therm. Eng., 65, 105655 (2024). https://doi.org/10.1016/j.csite.2024.105655

[4] Haridas, D., Reddy, G. R., & Sobhan, C. B. P. (2014). Digital interferometric measurement of forced convection fields in compact channels. Journal of Enhanced Heat Transfer, 21(1), 9–34. https://doi.org/10.1615/JEnhHeatTransf.2013006914

[5] Q. Zhu, X. Liu, J. Zeng, H. Zhao, W. He, H. Deng, G. Chen, Numerical study of heat transfer and fluid flow in a symmetric wavy microchannel heat sink reinforced by slanted secondary channels, Case Stud. Therm. Eng., 65, 105605 (2024). https://doi.org/10.1016/j.csite.2024.105605

[6] A, R., & Chakraborty, S. (2020). Effect of micro-structures in a microchannel heat sink – A comprehensive study. International Journal of Heat and Mass Transfer, 154, 119617. https://doi.org/10.1016/j.ijheatmasstransfer.2020.119617

[7] Xie, G., Zhao, L., Dong, Y., Li, Y., Zhang, S., & Yang, C. (2021). Hydraulic and Thermal Performance of Microchannel Heat Sink Inserted with Pin Fins. Micromachines, 12(3), 245. https://doi.org/10.3390/mi12030245

[8] Ali, N., Srivastava, S., Haque, I., Yadav, J., Alam, T., Siddiqui, T. U., Siddiqui, M. I. H., & Cuce, E. (2024). Heat dissipation and fluid flow in micro-channel heat sink equipped with semi-elliptical pin-fin structures: A numerical study. International Communications in Heat and Mass Transfer, 155, 107492. https://doi.org/10.1016/j.icheatmasstransfer.2024.107492

[9] Qi, X., Ma, C., Li, M., Liu, J., He, J., Totis, G., Hua, C., Wang, L., Cui, G., Li, G., Xue, R., Tan, Z., Yang, J., Liu, K., Zhou, Y., Zhou, J., Deng, X., & Weng, S. (2025). Novel thermal error control strategy for feed drive mechanisms via sintered core heat pipe-cooled moving nut. International Journal of Thermal Sciences, 219, 110222. https://doi.org/10.1016/j.ijthermalsci.2025.110222

[10] Zhu, X., Zuo, Z., Wang, W., Jia, B., Liu, R., Yin, Q., & Zhang, M. (2025). Performance comparison and optimization of thermoelectric generator systems with/without stepped-configuration. Energy, 335, 137924. https://doi.org/10.1016/j.energy.2025.137924

[11] Zhu, X., Zuo, Z., Wang, W., Liu, R., & Jia, B. (2025). Design and single/multi-objective optimization of N-type Skutterudite/P-type half-Heusler-based thermoelectric modules based on an improved thermal resistance model. Renewable Energy, 250, 123206. https://doi.org/10.1016/j.renene.2025.123206

[12] Ali, N., Haque, I., Alam, T., Siddiqui, T. U., Ansari, M. A., Yadav, J., Srivastava, S., Cuce, E., Ashraf, I., & Dobrotă, D. (2024). Numerical investigation on heat transfer and flow mechanism in microchannel heat sink having V shape ribs. Case Studies in Thermal Engineering, 65, 105684. https://doi.org/10.1016/j.csite.2024.105684

[13] J. Singh, A. Garg, P. Kumar, R. Shakya, T.R. Sahu, A. Kumar, P.K. Shukla, Numerical Analysis of Laminar Flow and Heat Transfer in Micro Pin Fin Heat Sinks with Varying Fin Geometries: Effect of Fin Geometry on Micro Pin Fin Heat Sinks, Preprints (2025). https://doi.org/10.20944/preprints202508.0610.v1

[14] M.E. Polat, F. Ulger, S. Cadirci, Multi-objective optimization and performance assessment of microchannel heat sinks with micro pin-fins, Int. J. Therm. Sci., 174, 107432 (2022). https://doi.org/10.1016/j.ijthermalsci.2021.107432

[15] P. Maheshwary, C. Handa, K. Nemade, A comprehensive study of effect of concentration, particle size and particle shape on thermal conductivity of titania/water based nanofluid, Appl. Therm. Eng., 119, 79–88 (2017). https://doi.org/10.1016/j.applthermaleng.2017.03.054

[16] Jeong, J., Li, C., Kwon, Y., Lee, J., Kim, S. H., & Yun, R. (2013). Particle shape effect on the viscosity and thermal conductivity of ZnO nanofluids. International Journal of Refrigeration, 36(8), 2233-2241. https://doi.org/10.1016/j.ijrefrig.2013.07.024

[17] T. Hung, W. Yan, X. Wang, C. Chang, Heat transfer enhancement in microchannel heat sinks using nanofluids, Int. J. Heat Mass Transf., 55(9–10), 2559–2570 (2012). https://doi.org/10.1016/j.ijheatmasstransfer.2012.01.004

[18] Bhattad, A., Atgur, V., Rao, B. N., Banapurmath, N. R., Yunus Khan, T. M., Vadlamudi, C., Krishnappa, S., Sajjan, A. M., Shankara, R. P., & Ayachit, N. H. (2022). Review on Mono and Hybrid Nanofluids: Preparation, Properties, Investigation, and Applications in IC Engines and Heat Transfer. Energies, 16(7), 3189. https://doi.org/10.3390/en16073189

[19] V. Murali Krishna, M. Sandeep Kumar, O. Mahesh, P. Senthil Kumar, Numerical investigation of heat transfer and pressure drop for cooling of microchannel heat sink using MWCNT-CuO-Water hybrid nanofluid with different mixture ratio, Mater. Today Proc., 42, 969–974 (2020). https://doi.org/10.1016/j.matpr.2020.11.935

[20] J. Gao, Z. Hu, Q. Yang, X. Liang, H. Wu, Fluid flow and heat transfer in microchannel heat sinks: Modelling review and recent progress, Therm. Sci. Eng. Prog., 29, 101203 (2022). https://doi.org/10.1016/j.tsep.2022.101203

[21] Z. Said, S. Rahman, P. Sharma, A. Amine Hachicha, S. Issa, Performance characterization of a solar-powered shell and tube heat exchanger utilizing MWCNTs/water-based nanofluids: An experimental, numerical, and artificial intelligence approach, Appl. Therm. Eng., 212, 118633 (2022). https://doi.org/10.1016/j.applthermaleng.2022.118633

[22] Yadav, D., Naruka, D.S. & Singh, P.K. The insight flow characteristics of concentrated MWCNT in water base fluid: experimental study and ANN modelling. Heat Mass Transfer 57, 1829–1844 (2021). https://doi.org/10.1007/s00231-021-03086-x

[23] Lyu, Z., Pourfattah, F., Arani, A. A., Asadi, A., & Foong, L. K. (2020). On the Thermal Performance of a Fractal Microchannel Subjected to Water and Kerosene Carbon Nanotube Nanofluid. Scientific Reports, 10(1), 1-16. https://doi.org/10.1038/s41598-020-64142-w

[24] Manjur, M.S.B., Liakat, F., Islam, N. et al. Numerical investigation of microchannel heat sinks thermal performance enhancement employing innovative channel cross section with CNT and MXene nanofluids. J Therm Anal Calorim 150, 11367–11386 (2025). https://doi.org/10.1007/s10973-025-14422-2

[25] Cai, B., Hu, P., Li, Y., Chen, B., & Cai, H. (2025). Numerical analysis of flow heat transfer characteristics and optimization of double-layered microchannel heat sinks with different structures. Case Studies in Thermal Engineering, 72, 106370. https://doi.org/10.1016/j.csite.2025.106370

[26] R.K. Rajamony, J.K.S. Paw, A.K. Pandey, et al., Thermal analysis and thermal regulation of photovoltaic thermal system using serpentine tube absorber with modified multi-walled carbon nanotubes enhanced PCM, J. Therm. Anal. Calorim., 149, 14643–14662 (2024). https://doi.org/10.1007/s10973-024-13845-7

[27] Yahiaoui, I., Dib, A., Alshehery, S. et al. Cu–SiO2 nanofluids influence on a Jeffery–Hamel laminar flow in rotating channels using the Duan–Rach approach and the response surface methodology. Eur. Phys. J. Plus 140, 654 (2025). https://doi.org/10.1140/epjp/s13360-025-06411-z

[28] Babar Hussain Shah ; Ahmer Mehmood ; Nehad Ali Shah; Muhammad Awais et al. Theoretical analysis of radiation effects in laminar flow over a von-Kármán body of revolution. Phys. Fluids 36, 013623 (2024). https://doi.org/10.1063/5.0179777

[29] Emadi, A., & Heyhat, M. M. (2025). Thermo-hydraulic performance analysis of multi-layer porous fin microchannels. Case Studies in Thermal Engineering, 74, 106883. https://doi.org/10.1016/j.csite.2025.106883

[30] Hadi Najafabadi, H., & Keshavarz Moraveji, M. (2016). Three-dimensional CFD modeling of fluid flow and heat transfer characteristics of Al2O3/water nanofluid in microchannel heat sink with Eulerian-Eulerian approach. Iranian Journal of Chemical Engineering (IJChE), 13(4), 46–61.

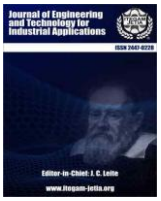
[31] Anjaneya, G., Sunil, S., Hanamantraygouda, M.B. *et al.* CFD-based numerical investigation of convective heat transfer in multi-channel micro-exchangers using MWCNT–water nanofluid. *Sci Rep* **16**, 11055 (2026). https://doi.org/10.1038/s41598-026-41225-8

Journal of Engineering and Technology for Industrial Applications

ISSN ONLINE: 2447-0228

ITEGAM-JETIA

Manaus, v.12 n.60, p. 484-498 July/August, 2026.
DOI: https://doi.org/10.5935/jetia.v12i60.3884



RESEARCH ARTICLE OPEN ACCESS

MULTI-STAGE DIABETIC RETINOPATHY CLASSIFICATION USING DEEP LEARNING: TRENDS, CHALLENGES, AND FUTURE DIRECTIONS

Shreya Dubey[1], Mahesh Goyani*[2], Pinal Patel[3], Safwan Vahora[4], Uttam Chauhan[5], Mahendra Patel[6]

[1, 2, 3, 4, 5, 6]Department of Computer Engineering, Government Engineering College, Modasa, India

[1]http://orcid.org/0009-0006-5350-5215, [2]http://orcid.org/0000-0002-7269-1176, [3]http://orcid.org/0000-0003-1086-8906
[4]http://orcid.org/0000-0002-8051-8429, [5]http://orcid.org/0000-0003-4373-2132, [6]http://orcid.org/0000-0002-4342-1070

E-mail: shreya4dubey@gmail.com, *mgoyani@gmail.com, pinal.patel@gecmodasa.ac.in, safvan465@gmail.com, uttam.chauhan@gecmodasa.ac.in, mnpatel32@gmail.com

ARTICLE INFO

Article History
Received on: March 03, 2026
Reviewed on: April 03, 2026
Accepted on: May 01, 2026
Published on: July 31, 2026

Keywords:
Diabetic Retinopathy,
Symptoms,
Microaneurysms,
Hemorrhages,
Exudates

ABSTRACT

Diabetic Retinopathy (DR) is a primary cause of vision loss globally in patients suffering from diabetes. Timely detection of the disease can reduce the chances of blindness. Fundus images are studied by the Ophthalmologists for any signs of the disease. Existing methods for detecting DR include manual study by the experts or usage of Artificial Intelligence-based models. But these methods encounter several issues like inaccurate detection, time-consuming, costly including the lack of stable datasets and consistent image processing techniques. Owing to the damage these lesions do to the retina it becomes essential to look for an efficient and accurate model for diagnosing DR. Deep Neural Networks help us to segment the fundal images to focus on the retinal areas helping us to look for early signs of the disease. If DR is detected at an earlier stage, the risk of complete blindness can be reduced. This paper presents a comprehensive survey of existing models for Diabetic Retinopathy detection, with an intention of identifying opportunities for improvement to develop a more robust and stable model which can efficiently and accurately perform the classification. It also includes detailed discussion on various datasets used for detection/classification of the disease.

Copyright ©2026 by authors and Galileo Institute of Technology and Education of the Amazon (ITEGAM). This work is licensed under the Creative Commons Attribution International License (CC BY 4.0).

I. INTRODUCTION

Prolonged high blood sugar levels due to low amount of insulin produced by pancreas leads to Diabetes Mellitus commonly known as *Diabetes*. There are mainly two categories of it: Type-1 whose root cause is not known and Type-2 which can identified by the symptoms like Microaneurysms, Hemorrhages, Exudates, etc. This when left untreated for longer duration can lead to lesions on the retina and ultimately leading to blindness [1]. DR mainly occurs due to retinal vascular disease and abnormal flow of blood through retina which could eventually lead to blood or fluid leakage [2]. In a survey conducted in 2021, it was found that around 26% of diabetic patients in the United States had suffered from DR and around 5% of diabetic patients had reported severe case of DR that could lead to vision-loss. According to World Health Organization, issues related to diabetes will cross 700 million by 2045 and out of this approximately 1/3rd will face issue of this disease [3]. It is one of the five leading causes of vision loss along with glaucoma, refractive errors, age-related macular degeneration (AMD) and cataract. A study showed that some the leading causes for DR include poor renal function, elevated blood glucose levels, liver disease, hematonosis (blood disorders), and high blood pressure [4]. The common symptoms for DR include frequent vision bluriness or difficulty while reading later on when severity increases it can include dark spots in vision, fluctuated or disorientated vision or retinal detachment ultimately leading to blindness. Although DR is irreversible but detecting it in early stages can help control the damage by controlling the factors like hypertension and hyperglycemia. DR can be detected either manually or automatically by using techniques such as laser treatment, anti-VEGF injections, or vitrectomy [1]. Figure 1 describes the various stages of DR, which are classified into namely - Normal, Mild Non-Proliferative Diabetic Retinopathy (NPDR), Moderate NPDR, Severe NPDR and Proliferative Diabetic Retinopathy (PDR). The main classification being Normal vs NPDR vs PDR. NPDR further being classified as Mild, Moderate, and Severe based on the type and amount of lesions present.

It also shows the vital symptoms which show the presence of DR. Ophthalmologists target these lesions to check for the presence of the disease and understand its severity. Normal grade also known as NO-DR stage is a condition where the eye is normal and retina shows no signs of the lesions. The vision of the patient remains unaffected. Mild NPDR is the earliest stage of the disease where microaneurysms begin to generate. There are no to very least chances of vision loss at this stage, and the retina remains intact. In the Moderate NPDR stage more microaneurysms begin to appear and other lesion structures like hemorrhages, and hard exudates also start to generate. Veins and capillaries begin to get blocked, reducing blood flow. Blood leakage starts which leads to the issue of Macular Edema. Severe NPDR stage witnesses lesions like cotton-wool spots and venous beading. The issue of vein blockage increases after which blood supply to the retina almost stops hence level of oxygen reduces in the retina. PDR stage faces Neovascularization i.e., the new and abnormal blood vessels begin to appear on retina and optic disc. The vessels being weak tend to burst and lead vitreous hemorrhage. If not attended on time, it can lead to significant blood loss.

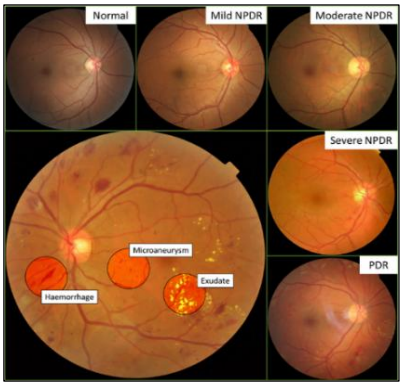


Figure 1: Different classes of Diabetic Retinipathy.
Source: [5].

The common symptoms of DR include *microaneurysms* which are usually seen in people suffering from diabetes when the capillary walls widen. They are usually seen in the form of small red dotlike structures when captured in colored fundus images and bright hypersensory spots when looked through fluorescein angiography. They are usually found in the early stages of DR [6]. *Hemorrhages* are the initial indicators used to detect DR when it enters in severe stages. Hyperglycemia causes damage to the blood vessels which results in their bursting, causing hemorrhages. There are different types of hemorrhages like *flame-shaped* hemorrhages found in the top layers and *dot-blot* hemorrhages found in the lower layers. Non-proliferative retinopathy is caused by the presence of large numbers of hemorrhages [7]. *Exudates* occur due to an increased blood sugar levels damaging the blood vessels, leading to leakage of yellow-white lipid and protein deposits.They are mainly categorized into - soft exudates and hard exudates. Soft exudates are the yellow-white colored lesions also known as the cotton wool spots generally found in the nerve fiber layer. They are fluffy in texture [8]. Hard exudates are comparatively brighter and reflective in nature. Found in different sizes, they are generally white- or cream-colored lesions. They are a strong indicator of diabetic macular edema (DME) and affect the central vision [9]. They are marked with sharp boundaries and have a waxy, shiny texture located into the outer layer of the retina.

Medical equipment like opthalmoscope and fundus cameras are used during eye-checkups. But using these traditional method is time-consuming as well as expensive, the doctor and patient ratio is 1:10,000 making it difficult to give personal attention to each patient. Thus it creates a need for an automated detection method which can easily, accurately and consume less time to classify the disease. Although it is not curable but if detected timely we can slow down its progress and save eyesight of the affected. Ophthalmologists study the fundus images for finding any abnormalities or lesions in the retina. Along with fundus images - Slit lamp Images, Ultrasonic Images and Digital Images are used for DR detection [10]. It can become difficult to detect DR in earlier stages as the symptoms are minor and can be missed by the human eye. So there is a need for Machine Learning-Deep Learning based models which can easily process images to detect and segment affected areas. It can also help in predicting the severity of disease [11]. Thus models trained using DL are used in modern-day medical analysis to analyze the fundus images, focusing on studying retina's blood vessels. The data is processed through numerous layers aimed for automatic recognition of patterns and extraction of complex features which is a fundamental requirement for classification of Diabetic Retinopathy using fundus images [12]. Along with DR detection technique the dataset also plays an important role in this. The symptoms may vary according to the demographic variety or factors like age,gender or previous medical conditions. So a stable dataset covering different varieties of patient is required to train the model in order to get accurate and unbiased results [13]. Table 1 discusses about the existing commercial systems used for DR detection and the limitation faced by the systems.

Table 1: Comparative Analysis of Commercial Diabetic Retinopathy (DR) Detection Systems.

System	Approval	Staging Capacity	Image Quality Dependency	Major Limitation
IDx-DR	FDA	Only referable DR	High	No detailed DR
EyeArt	FDA, CE	DR + DME	High	High false positives
RetmarkerDR	CE	Early DR focus	Moderate	Limited to detecting microaneurysms
Google DR AI	Clinical use	Multi-stage DR	High	Limited availability
EyePACS	Clinical use	Multi-stage DR	Moderate	Depends on graders
RetinaLyze	CE	Limited	Moderate	Not autonomous
Bosch DR AI	Clinical use	Referral-based	Moderate	Limited published validation
Remidio DR AI	CE	Limited	High	Smartphone image limitations

Source: Authors, (2026).

In this paper we have studied various state-of-the-art-methods implemented by multiple researchers in the domain of DR classification on various performance parameters based on the methodology used for classification task and symptom specific methods too. We have also identified the research gaps from the previous work and tried to highlight challenges in existing methods. The paper also includes the detailed discussion about the symptoms and types of diabetic retinopathy. The remainder of the paper is structred as follow. Section I discusses the literature review of the previous work, divided further according to the technology used for the model. It also discusses the works done for DR detection based on the symptoms of disease. The section also includes a detailed discussion on various datasets giving us an insight about the kind of data available to DR classification. In section II we will be discussing the challenges and future scopes faced by the researchers while developing a mode for DR classification. Section III concludes the survey done by summarizing the importance of DR detection and the ways used for the same.

II. LITERATURE REVIEW

Analyzing previous work can help us build a model by filling their research gaps and creating a more efficient, accurate, and reliable one. In this section, we will be discussing the works of various authors who have carried out research in this field and trying to understand the gaps present between their research and limitations faced by them. There have been several studies carried out for the classification of DR using algorithms based on Machine Learning, Deep Learning, and Hybrid Learning. Along with that, we can also focus on symptom-wise classification techniques of DR. Figure 2 is used to visually showcase the broader categorization of DR-detection techniques.

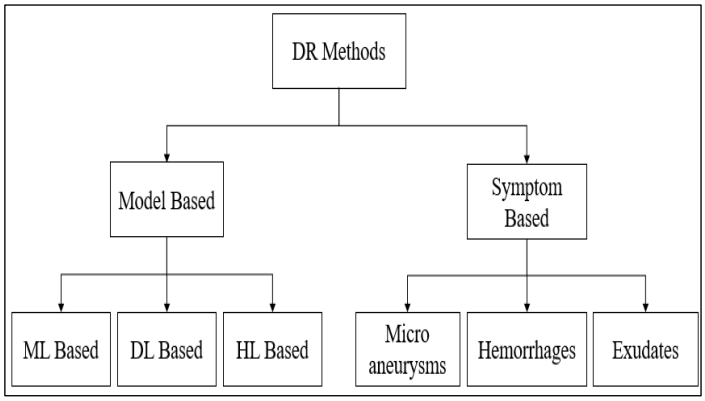


Figure 2: Taxonomy for Diabetic Retinopathy Detection.
Source: Authors, (2026).

II.1 ML-BASED TECHNIQUES FOR DR CLASSIFICATION

Machine learning is a widely used technology among researchers for medical diagnosis of any disease owing to accuracy and wid adaptability. We can further classify the ML techniques based on the kind of classification it does - binary classification usually indicates the absence or presence of the disease whereas the multi-class classification is used to grade the disease severity.

II.1.1 Binary-Class-Classification

Ashim Chakraborty [14] created a model focused on detecting the three early signs of the Diabetic Retinopathy namely the Hard Exudates (HE) - the yellowish spots, Microaneurysms - the tiny red dots and Blood Vessels - the abnormal vessel growth. Then binary classifier 6 was used to detect if these features indicated presence of DR or not. Multiple datasets like DIARETDB0, DIARETDB1, Messidor, Kaggle DR dataset were used. Accuracy for DR detection based on the lesion is HE with 95.7%, MA with 93.45% and BV with 90% accuracy. But the model had several issues like dataset imbalance, risk of false positives. Krishnendu Barik and Anil Kumar studied the biomarker genes found in blood samples to check for the presence of DR using RNA sequencing dataset-GSE221521 containing 69 DR and 50 Healthy-controls (Non-DR) patient data for the identification of Differentially Expressed Genes(DEGs). They trained multiple ML-based models like SVM, Logistic Regression, Random Forest, Gradient Boosting, Neural Network on the 7-Key genes selected through Elastic Net regularization out of which SVM performed the best with an accuracy of 86% [15]. Researcher Hassaballah and Hameed introduced a metaheuristic algorithm combining standard Golf Optimization Algorithm (GOA) with genetic operators. They introduced three hybrid models - mGOA-SVM, mGOA-radial SVM, and mGOA-kNN developed for both binary and multi-class classification on Messidor and EyePACS dataset respectively. [16]. Michal Gandor et al. adopted feature engineering technique combining multiple data preprocessing techniques along with several feature extraction algorithms to develop a model for the early diagnosis of the disease. On the basis of the preprocessing techniques applied four variants were created - pure, no-vessels, no-vessels-no-optic-disk and no-optic-disk. They experimented with an aggregated dataset of 8 public datasets and 1 private dataset making the results non-biased and more accurate. Random forest and XgBoost were the two classifiers used for detecting DR. [17]. Penikalapati Pragathi et al. developed an integrated approach using SVM, PCA and Moth-Flame Optimization for detecting DR and achieved an accuracy of 86.3%. Usually using PCA reduces the performance of the algorithm and to balance it out Moth-flame optimization technique is used. It selects the optimal features improving the performance. The model was trained and tested on the Diabetic Retinopathy Debrecen dataset from the UCI ML repository [18]. Michele Bernardini et al. developed a model for Task 1 - Risk of DR and Task 2 - temporal stratification of DR risk in 0-2 years vs. 2-5 years creating a Clinical Decision Support System. The paper used 120K dataset from multiple Italian diabetologic centers consisting of EHR: demographics, pathology codes, and lab tests. Among the various ML algorithms used Random Forest (RF) achieved the highest accuracy [19].

II.1.2 Multi-Class Classification

Xiaoli Li et al. [20] used clinical data and OCTA (Optical Coherence Tomography Angiography) images to develop a model to grade DR into 3 classes each with a binary classification - DR Identification (Non-DR and DR), Referable DR (RDR) - Identification (Non-RDR and RDR), Vision-Threatening DR (VTDR) – Identification (Non-VTDR and VTDR). The paper focused on four ML models - Random Forest (RF), Gradient Boosting Machine (GBM), Logistic Regression (LR) and Deep Learning DL. Xu Wang et al. [4] focused on following a white-box approach by adopting SHAP (SHapley Additive exPlanations) interpretability model to reason out the findings hence increasing model's reliability. The model used 1000 records from diabetes complications early warning dataset and compared 5 distinct ML-algorithms Support Vector Machine(SVM), Random Forest, XGBoost, Gradient Boosting Tree and CatBoost. Researcher Gigi Tabacaru et al. [21] used PyCaret library to select the best performing model out of the 15 available models and found that the Gradient Boosting Classifier (GBC) is the best performer with an accuracy of 92.9%. They used Indian Diabetic Retinopathy Image Dataset (IDRID) to classify the results at different severity level - NoDR/Mild, NoDR/Moderate, and NoDR/Severe. Eman Abdelmaksoud et al. [22] proposed Multi-Label Computer-Aided Diagnosis (ML-CAD) system initially performing binary classification using SVM and GLRLM features to filter the cases then using the U-Net model to segment the pathological variations and lastly using a Multi-Label SVM (MLSVM) based on a Classifier Chain (CC) for grading the disease. Multiple datasets - DRIVE, HRF, STARE, CHASEDB1, DIARETDB0, IDRID, DIARETDB1, and Messidor were used for the experiment. Aqib Ali et al. [23] developed an image segmentation method called Center-Based Irregular Polygon Region-Growing Segmentation(CARGS) for isolation of lesions before performing feature extraction. An irregular polygon shaped seed is used to circumference the lesion boundary then using K-Means clustering these pixels are separated into 3 clusters - background, normal retina and lesions affected areas. Features like GLCM, histogram, wavelets, etc. are extracted and fed to ML classifiers like Sequential Minimal Optimization, Logistic Model Tree, Multilayer Perceptron classifier. Table 2 some of the top ML models reviewed and their features.

Table 2: Comparison of ML approaches for diabetic retinopathy diagnosis.

Ref	B/M	Preprocessing	Model	Dataset	Performance
[16]	B	Data Cleaning, Formatting	m-GOA radial SVM	Messidor, EyePACS	A: 99.12%, P: 99.15% A: 98.91%, P: 98.87%
[14]		CLAHE, Grey Scaling	Supervised ML model	Messidor, DiaretB0	A: 95.70%, P: 96.64%, F1: 96.37%, S: 96.11%
[15], [18]		PCA, Denoise, Normalization	SVM	Debrecen	A: 86.30%, P: 86.00%, F1: 86.00%, S: 94.20%
[15]		Normalization, Regularization	SVM	GSE221521	A: 86.36%, P: 100.00%, F1: 86.96%, S: 76.92%
[20]	M	Data Clean, Missing Data	RF	Clinical + OCTA	AUC: 96.65%
[23]		Grayscale, HE, CARGS	LMT + SLg	Private dataset	A: 99.73%, AUC: 100.00%
[22]		Filtering, HEBPDS	MLSVM + U-Net	Multiple datasets	A: 95.05%, S: 86.11%, AUC: 91.85%
[21]		Gamma Correction	M11 + GBC	IDRid	A: 92.90%, F1: 90.20%, AUC: 94.10%

B: Binary DR classification, M: Multi class DR classification, A: Accuracy P: Precision F1: F1 Score S: Specificity AUC: Area under Curve.
Source: Authors, (2026).

II.2 DL - BASED TECHNIQUES FOR DR CLASSIFICATION

Deep Learning provides us with several models implemented using neural networks utilizing which we can easily analyze and study the images. Image analysis is an integral part of healthcare, and DL allows us to do that very efficiently by using variants of model like CNN.

II.2.1 Binary-Class Classification

In a study conducted by SamiaAkhtar et al., he created custom Convolutional Neural Network (CNN) model called RSG-Net (Retinopathy Severity Grading) used for both multi-class and binary classification with accuracy being 99.36% and 99.37% respectively. Gaussian Blur technique was used for reducing the noise in the image, Histogram equalization for enhancing the contrast and brightness of the image. The images were resized and augmented as well. The model was trained and tested for the Messidor-1 dataset with split ration of 70% Training, 10% Validation, 20% Testing. The limitation of the model being that it can be prone to issue of over-fitting and generalization to diverse dataset as it was tested only for Messidor-1 [24]. Amad Zafar developed a two-stage deep learning framework for the detection as well as the classification of the severity of the disease. A lightweight network was designed for binary classification. And if the disease is detected then in the next phase a transfer learning approach was implemented wherein the model trained in earlier staged is re-used and fine-tuned for the multi-class classification for the severity level. The primary dataset for the model being APTOS2019 and FairVision and DDR dataset for the validation purpose. The pre-processing techniques used were Data Augmentation, Normalization and Image Cropping [25]. M. Mutawa proposed a framework following randomized-based learning approach in traditional image processing techniques.

The preprocessing included techniques like Green channel extraction to reduce the noise, CLAHE for noise reduction and contrast enhancement and morphological operations to focus on the blood vessels and Otsu's thresholding for image binarization and segmentation of blood vessels. After that feature extraction is done on the preprocessed images using two parallel methods: Multi-Scale Discriminative Robust Local Binary Pattern (MS-DRLBP) responsible for capturing the local texture and edge patterns and CNN model (VGG16) responsible for automatically analyzing the complex features from the images. After that classification done using a hybrid CNN model - Radial Basis Function (CNN-RBF). It takes the combined features from both MS-DRLBP and VGG16 for the binary classification of the dataset. Randomization in framework was applied by the non-iterative nature of Otsu's method for thresholding and random initialization of RBF centres this reduced the complexity of computation and simplified the learning process. The model achieved an accuracy of 96.1%. A combined dataset of STARE, HRF, and FFA was used with a split of 60% for training and 40% for testing [12]. Saad Alanazi proposed a model called the FedCNN with VGG19 for segmentation and SMOTE with its core being the Federated learning (FedCNN) to maintain privacy of the patient's data by only sharing the local updates from each hospital's AI model learning instead of sharing the raw patient data. The CNN model VGG19 was employed for recognizing the intricate patterns and features in the images. Its primary work is to segment the important areas of the retinal images and after that extract detailed information of the features from the segmented areas. SMOTE(Synthetic Minority Oversampling Technique) was also used to create synthetic data to balance the model training. He worked on the EyePACS dataset from Kaggle. Pre-processing techniques like Weinmed Filtering(Weiner and Median Filter) and SMOTE were used to enhance the dataset achieving an accuracy of 98.0% [26].

Yixiao Li introduced an improved framework on an existing network KiU-Net making it more accurate and efficient at segmenting the HRF. HRF(hyperreflective foci) are the tiny, bright spots in OCT images used for detection DR. KiU-Net is a combination of two kinds of model called the Kite-Net branch for upscaling of the images to detect even the small lesions like the HRF. This allows us to to extract more fine-tuned and detailed knowledge about the small structures. Another model being the U-Net branch used for extract the high-level of semantic information unlike the Kite-Net in downscales the images to get a broader view of the image and anlayze the larger patterns. Further it uses the Cross-Attention Block(CAB) to combine the results of both of these to get the final information about the images. The dataset used here was 173 OCT images from 50 patients, obtained from the Department of Ophthalmology, Qilu Hospital affiliated with Shandong University, China. Common techniques like the Denoising the OCT images along with Bilateral Filtering and Augmentation were used to get the best of the dataset. For pixel-level segmentation using Kite-Net, the model achieved a Dice Similarity Coefficient (DSC) of 66.84% and for HRF number detection, the model achieved a Dice Similarity Coefficient (DSC) of 71.32% [27]. K. K. Mujeeb Rahman et al. gathered 560 fundal images combining Kaggle, DDR, Mendeley data and Zenodo datasets. The study involved both the SVM and DNN models with DNN getting an edge with an accuracy of 95.77%. The model was fed with features extracted using the GLCM(Gray Level Co-occurrence Matrix) technique [28].

Fasmin Shi, developed a technique called the Fair Adaptive Scaling(FAS) module which can be used as an add-on to other existing models. Its main focus is to reduce the difference of performance rates among different demographic groups like Whites and Blacks. FAS works on Individual and Group Scaling. Individual scaling focuses on giving more attention to the individual images who are having difficult time to be analyzed like if they giving wrong or uncertain results during the training stages. Group scaling focuses on the overall performance of the model for a particular demographic group. If a group shows higher error rate or is underrepresented its samples are given more weight. FAS is integrated with several Backbone models like the EfficientNet and ViT-B for 2D OCT images and ResNet18 and DenseNet121 for 3D OCT images. These backbone models are responsible for extracting complex features and patterns form the eye images. The study included both the private datasets from Massachusetts Eye and Ear - MEE like MEE In-House Color Fundus Dataset and MEE In-House Color Fundus Dataset and public datasets like ODIR-5K and Harvard-FairVision30k [29]. In a study by Manish Bali et al., a hybrid model was introduced called QuantumNet combination of a pre-trained ResNet-50 model and a Variational Quantum Classifier(VQC). The ResNet-50 model was responsible for extraction of features from the images of retina and VQC was tasked with classification of data from ResNet by encoding it into quantum states. The VQC uses a 4-qubit dressed quantum circuit to classify the 2048-dimensional feature vector into 4 dimensions. APTOS2019 dataset was split into 70% training, 15% validation and 15% testing set. Pre-processing techniques like Re-scaling and Image augmentation were employed. The model achieved and accuracy of 94.11%. The model faced limitations like requirement of advanced error correction techniques in quantum devices. Limited qubit counts and higher error rates in current quantum computers [30].

II.2.2 Multi-Class Classification

Lein Sun et al. developed MAFNet(Multi-Scale Adaptive Fine Grained Network) model for fine grading of the disease into all 5 stages and not only limiting to the binary prediction. The main crux of the model was ConvNeXt CNN and it consisted of three modules: HGCM(Hierarchical Global Context Module), MSAM(Multi-scale Adaptive Attention Module) and RMA(Relational Multi-head Attention). HGCM responsible for analyzing both the global region(big picture) and local region(small lesions) simultaneously. MSAM was tasked to focus on the most essential lesion areas of the retina. RMA focusing on finding relationships between different lesions. The model was trained for the purpose of both classification and regression. It used multiple datasets like the DDR, Messidor-2 and APTOS2019 split into a ratio of 6:2:2(train:validation:test). The model received highest accuracy of 88.2% on DDR dataset followed by APTOS with 87.4% and last Messidor-2 having 82.2% accuracy [2]. Amina Zedadra et al. developed a model called DRdiag which was an integration of CNN and GNN. The CNN model uses the DenseNet121 pre-trained on ImageNet dataset and the GNN model is a two layer Graph Convolutional Network (GCN). The CNN model focused on extracting the intrinsic feature from the fundus images whereas the GNN model was used to understand the complex relationship between the patients. The outputs of both the models were combined using the adaptive fusion mechanism. The two publicly available datasets Messidor-2 and APTOS2019 were used by the model. The model achieved an accuracy of 98% for the APTOS dataset and 97.6% for the Messidor-2. The limitation of the model being that it only considered one clinical risk factor i.e., the duration of diabetes for analysis and avoided other essential features [31]. A study by Hussain et al. proposed an enhanced P-EDR (Diabetic Retinopathy) method based on a Convolutional Neural Network (CNN) to diagnose diabetic retinopathy (DR) using retinal images.

It uses dataset of retinal images from the Kaggle DR. The data was preprocessed through normalization, augmentation, and resizing to improve image quality and feature extraction. The images were standardized to 224x224 pixels to ensure uniform input size for the machine learning models. The results showed that the CNN-based P-EDR model outperformed the other models. It achieved an accuracy of 93% [32]. S Jahangeer Sidiq, proposed an ensemble deep learning model for detecting and classifying the 5 different stages of Diabetic Retinopathy. The authors divided the classification of disease into a 12 multiple simpler binary classification task using a One-Versus-One (OVO) mechanism. It used pre-trained, lightweight models in the form of base learners and for the final result majority voting was used by combining their outcomes. Among the other base learners MobileNet, InceptionV3, and DenseNet121 were found to be achieving highest performance. The model worked on the APTOS2019 with MobileNet as the base learner, IDRID with InceptionV3 as the base learner, Messidor-2 using DenseNet121 base learner and DDR with MobileNet as the base learner. The images were pre-processed using the resizing and data augmentation process. The model achieved an accuracy of 92% for the APTOS2019 dataset, 85% for IDRID, 86% for Messidor-2 and 88% on the DDR dataset [33]. Omar Dib proposed a secure server-less framework called FL-BC-SMPC-SMOTE to avoid the risk of security breach of patient data. The model trains AI models with their patient data kept private from other hospitals by sharing only the encrypted updated data on a global model. Block-chain(Hyperledger Fabric) keeps track of the updates securely and SMPC (Secure Multi-Party Computation) is tasked to ensure that no user can see the actual changes of others data to strengthen the privacy of the model.

IPFS (InterPlanetary File System) is used to efficiently store the encrypted parts of AI model. SMOTE(Synthetic Minority Over-sampling Technique) is used for creating synthetic data for rare disease cases so as to avoid issue of under-fitting. Several CNN-based models like EfficientNet-B0, ResNet-18, SqueezeNet, Custom CNN were trained on the APTOS2019 dataset with the 80% - 20% training-testing split. The model achieved an accuracy of 90% with individual being ResNet-18: 91.65%, EfficientNet-B0: 90.08%, Custom CNN: 87.93% and SqueezeNet: 80.09% [34]. Sarra Guefrachi proposed a Multistage framework combining the feature extracting and fine-tuning techniques using multiple pre-trained CNNs. A custom classifier head was developed and added to base CNN models. Models like InceptionResnetV2, VGG16, VGG19, DenseNet121, MobileNetV2 and EfficientNet2L were used as base models achieving an overall accuracy of 96.61% on the Kaggle's diabetic retinopathy detection dataset with split ratio of 80%, 10% and 10%. General pre-processing techniques like removal of noisy and redundant images, image resizing and augmentation and contrast enhancement were implemented onto the dataset. As it was trained for only one dataset there might be an issue of the model sensitivity towards diverse datasets. Over-fitting issue being another limitation of the model [35]. The below given Table 3 summarizes some of the top DL models reviewed and their features.

Table 3: Comparison of DL approaches for diabetic retinopathy diagnosis.

Ref	B/M	Preprocessing	Model	Dataset	Performance
[24]	B	Resizing, Denoising	RSG-Net	Messidor-I	A: 99.37%, P: 98.86%, F1: 99.42%, S: 100.00%
[25]		Normalizing, Augmenting	Custom DL (37-layer)	APTOS2019	A: 99.06%, S: 99.00%
[26]		SMOTE, Filtering	FedCNN	EyePACS	A: 98.00%, P: 98.20%, F1: 98.50%, S: 98.10%
[12]		Green Channel, Thresholding	CNN-RBF	STARE, HRF, FFA	A: 96.10%, P: 97.62%, F1: 96.47%, S: 95.35%
[35]		RGB Conversion, Cropping	Inception ResNetV2	KaggleDR	A: 96.61%, P: 100.00% F1: 100.00%, S: 100.00%
[36]		Rescaling, Augmenting	QuantumNet	APTOS2019	A: 94.11%, P: 96.90%, F1: 95.86%, S: 94.84%
[2]	M	Cropping, Resizing, Augmenting	MAFNet	DDR, APTOS2019, Messidor-2	A: 88.20% κ: 93.40% A: 87.40% κ: 93.60% A: 82.20% κ: 91.70%
[31]		Augmenting, Normalizing	DRdiag	Messidor-2, APTOS2019	A: 97.60%, F1: 96.10% A: 98.00%, F1: 96.30%
[32]		Augmenting, Normalizing	P-EDR (CNN)	KaggleDR	A: 93.00%, P: 92.00%, AUC: 97.00%, S: 92.00%
[33]		Subdivision, Normalizing, Augmenting	DenseNet121, InceptionV3, MobileNet	APTOS2019, IDRID, DDR, Messidor-2	A: 92.00%, P: 92.00%, F1: 92.00%, S: 92.00%
[34]		SMOTE, Augmenting	ResNet-18	APTOS2019	A: 91.65%

Source: Authors, (2026).

II.3 HYBRID - BASED TECHNIQUES FOR DR CLASSIFICATION

Hybrid techniques combine multiple models together to utilize the best of both models to achieve the highest accuracy for the model. Integrating the model with various preprocessing techniques can also generate significant change in accuracy.

II.3.1 Binary-Class Classification

A hybrid model called Diabetic Retinopathy Detection-Capsule Network-Deep Learning combining the UNet++ for semantic segmentation and Capsule Networks for feature classification was proposed by I. Govindharaj et al [37]. The images pre-processed by the technique of CLAHE and Histogram Equalization are fed to the UNet++ model for segmentation of two essential structures of the eye namely the Optic Disc and Optic Cup. The segmented images are carry forwarded to the CapsNet to understand the underlying patterns and details of the image. It analyzes the images the segmented features to classify if the eye is normal or glaucomatous. The same architectural model is used for DR detection. Kerem Gencer et al. proposed a hybrid framework combining the Generative Adversarial Networks, Denoising Autoencoders and a fine tuned EfficientNetB0. GAN was used to generate synthetic retinal images to solve the issue of class imbalance and enrich the training dataset. The Denoising Autoencoders were responsible for enhancing the image quality by reducing the noise level and other factors like speckle noise, motion blur, and illumination inconsistencies present in both the original and GAN-generated images. The EfficientNetB0 was used for classification of the pre-processed images. The model used a custom created Optical Coherence Tomography image dataset consisting of 4274 images [38]. Govindharaj et al. proposed a hybrid model combining UNet++ for segmenting parts of eye indicating glaucoma and Capsule Network for finding intrinsic patterns and details hidden in the segmented image. Model was trained and tested on combined dataset consisting of RIM-ONE Database, DRIONS-DB and ORIGA-Light. Techniques like Histogram Equalization and CLAHE were used for pre-processing the retinal images to enhance their quality by improving the contrast and clarity of the image. The limitation of the model being highly computational and sensitive to image quality giving more importance to the pre-processing techniques [39]. K.V.

Naveen et al. proposed a hybrid model EffNet-SVM which combined the EfficientNetV2-Small 15 as a feature extractor and RBF kernel SVM as a classifier for the disease. Instead of soft-max layer generally used with CNNs, SVM was used as a classifier as it proves to be better at separating class. The model converted the multi-class APTOS 2019 dataset into a binary dataset and achieved an accuracy of 97.26%. The limitation being that the model was trained only for binary datasets and limited experiment only on two datasets namely, APTOS and HRF [13]. Ghulam Ali et al. combined ResNet-50 and Inception-v3 to study the features leading to DR. The extracted features are combined and fed to IR-CNN (Inception–ResNet CNN) and trained on Messidor and IDRiD datasets with the Messidor giving the maximum accuracy of 90.89%. The model aimed to solve the issue while detecting the lesions in early-stages [40]. Amar Shukla et al. [41] developed an integrated model of Self-Attention Network used for in detail analysis of retina features and Vision Transformer (ViT) being responsible for combining their results for DR detection. The model is named as HybridFusionNet and tested on Kaggle DR dataset achieving an accuracy of 99% for binary and 91% for multi-class classification. But the model had high computational requirements due to integration of transformer models and was sensitive to variations in quality of fundus images. Butt et al. combined transfer-learning models like GoogLeNet and ResNet-18 then the resized images are given as input to each of these model responsible to extract the deep hidden features which are further combined to create a 2000-dimensional hybrid feature set. Then for the DR identification and severity grading several ML classifiers like SVM, Random Forest, Naive Bayes, RBF, etc. are used on the APTOS 2019 dataset achieving an accuracy of 97.8% for binary classification and 89.29% multi-class classification [42].

II.3.2 Multi-Class Classification

A.S. Sabeena et al. followed a hybrid approach and combined Xception, MoNet and PolyNet models. They used APTOS 2019 dataset with split of 80% and 20%. The pre-processing steps included Median filtering, SwinUNet for segmentation based on Gradient Descent-Sea Turtle Foraging Algorithm. The model MoNetPolyNetXception achieved an accuracy 98.9%. But the model requires high computational powers and can be dataset bias [43]. Sukran Yaman Atci combined pretrained CNN models, CAD (Computer-aided diagnosis) system and SHAP explainability on three datasets including Kaggle DR fundus dataset for predicting DR severity grades. The CNN models are used to extract the lesion in retina then hybrid ensemble classifiers predicts DR stages and SHAP is responsible for highlighting the affected regions but the model suffers with imbalanced class and comparatively lower performance in moderate/severe DR stages [44]. Kazi Ahnaf Alavee et al. proposed a model which integrated explainable AI(Grad-CAM) with DL models (DL-XAI) 16 for their better interpretability b generating heatmaps for the fundus images. The model was experimented on multiple datasets like APTOS 2019 Kaggle dataset, Messidor-2 and IDRiD. Multiple existing CNN models were used to extract lesions from the fundal images and custom CNN was trained to do the classification task with an accuracy of 95.27% [45]. Ayesha Jabbar et al. used GoogLeNet and ResNet for feature extraction and optimized it with Adaptive Particle Swarm Optimization (APSO) responsible for selecting only the most apt features extracted making the classification task more efficient with accuracy of 94%.

These features were then used to train the classical ML classifiers - SVM, RF, DT, LR. The model was used to detect not only the early stage lesions but cotton wool spots, IRMA, capillary degeneration. The model was trained on Kaggle EyePACS1 dataset [46]. Yasashvini R. et al. developed multiple models using CNN and hybrid transfer-learning model for DR diagnosis and severity grading - Simple CNN, CNN + ResNet and CNN + DenseNet with an accuracy of 96.22%, 93.18% and 75.61% respectively using Kaggle DR dataset. But the models faced limitations of small dataset size and class imbalance [47]. Md Nahiduzzaman et al. applied SVD(Singular Value Decomposition) on the features extracted to reduce dimensionality and select the unique and most prominent features. ELM(Extreme Learning Machine) classifier was used to classify DR into severity grades with an accuracy of 98.09% for Aptos-2019 and 96.26% for Messidor-2 dataset and 99.73% accuracy for Binary classification. For the preprocessing stage Ben Graham and CLAHE techniques were used on the fundus images (9605633). Anas Bilal et al. developed a hybrid CNN-SVD model integrated with several transfer learning models like Inception-V3, GoogLeNet, AlexNet, and ResNet. Furthermore, two different U-Net models were used for Optic Disc and Blood Vessel segmentation in order to remove unwanted features. A basic CNN model was used to extract 256 features reduced to 100 using SVD with Inception-V3 performing the best with an accuracy of EyePACS-1 - 97.92%, Messidor-2 - 94.59% and DIARETDB0 - 93.52% [48]. The below given Table 4 summarizes some of the top HL models reviewed and their features.

Table 4: Comparison of HL approaches for diabetic retinopathy diagnosis.

Ref	B/M	Preprocessing	Model	Dataset	Performance
[38]	B	Augmentation, Denoising	GAN + EffNetB0	Private OCT	A: 99.00%, P: 99.00%, F1: 95.00%, S: 99.00%
[39]		CLAHE, HE	DRD-CN-DL	RIM-ONE, Drions, ORIGA	A: 97.77%, P: 97.00%, F1: 95.40%, S: 96.80%
[13]		Augmentation, CLAHE	EffNet-SVM	APTOS2019	A: 97.26%, P: 96.98%,
[47]	M	Rescaling, Enhancing	HDCNN	APTOS2019	A: 98.97%, P: 98.97%, F1: 98.97%, S: 98.97%
[43]		Median Filtering	MoNet + PolyNet + Xception	APTOS2019	A: 98.90%, P: 98.40%, F1: 98.73%, S: 99.00%
[40]		Normalization	IR-CNN	Messidor, IDRiD	A: 96.85%, P: 96.46%, F1: 98.65%, S: 99.28%
[48]		Augmentation, Normalization	HDCNN	IDRiD	A: 96.34%, P: 97.58%, F1: 97.58%, S: 97.58%
[49]		Segmentation, Grayscale	HCSELM	IDRiD	A: 95.20%, P: 96.00%, F1: 96.00%, S: 97.00%
[45]	Both	Image Flipping, Augmentation	CNN + Grad CAM + XAI	APTOS2019	B: A: 100.00%, P: 97.55% M: A: 95.27%, P: 96.12%
[41]		Cropping, SMOTE, Filtering	FusionNet (SAN + ViT)	KaggleDR	B: A: 99.00%, P: 99.00% M: A: 91.00%, P: 91.00%

Source: Authors, (2026).

II.4 SYMPTOM - BASED TECHNIQUES FOR DR CLASSIFICATION

The main symptoms of DR include Microaneurysms, Exudates and Hemorrhages. Each symptom indicates different levels of severity of the disease. So it becomes essential to be able 18 to detect each of these accurately and efficiently from the concerned image datasets. Figure 3 broadly visualized the major stages and symptoms of the disease.

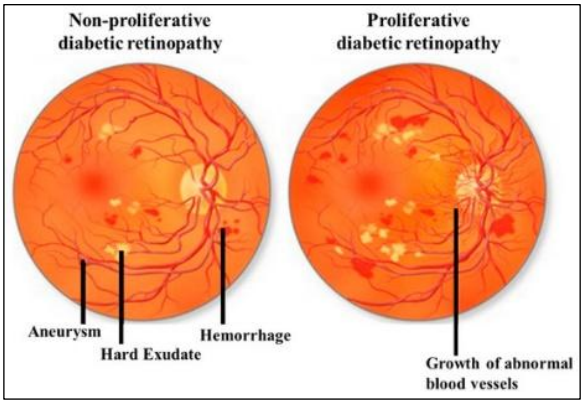
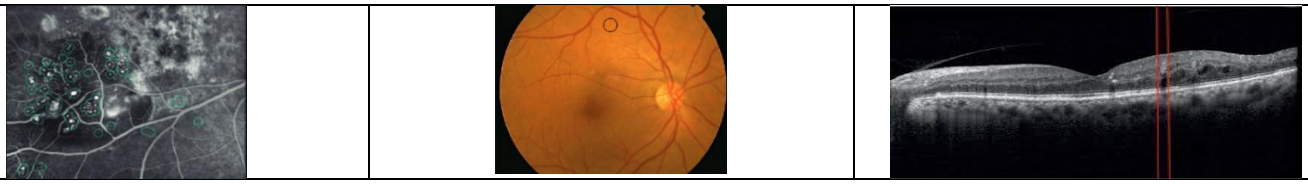


Figure 3: DR stages and symptoms
Source: [1]

II.4.1 Microaneurysms

Nianjia Wang et. al. developed an improved OCTA based image processing method to efficiently detect the Microaneurysms. It uses the OCTA blood flow signals along with Structural OCT hyper-reflective MA signals and 3D reconstruction to create a 3D-MA map known as the DVC-MA map to detect and visualize more Microaneurysms [50]. Abbas Rehman et. al. introduced FISM (Fundus Images Segmentation Model) based on Segment Anything Model (SAM) combining DL and reinforcement learning on the DDR dataset for the precise detection and segmentation of Microaneurysms (MAs). The model received AUC of 96.32% . But the model suffered from the limitation of using only one dataset [51]. Luís Mendes et. al. developed an automatic system - RetmarkerDR for the evaluation of Microaneurysms count and turnover using the fundus images at the hyperperfusion stage of non-proliferative diabetic retinopathy (NPDR). The dataset was collected from EUROCONDOR clinical trial helping us to keep track of DR progression. But the model only used fundus images and was highly dependent on the image quality [52]. Norah Asiri et. al. developed a DL-Based model using Dilated Residual Network (DRN) a better and modified ResNet-50 with dilation and technqiues like ROI pooling and Patch-based detection. The model was trained and tested on several datasets like e-ophtha-MA, DiaretDB1-MA, ROCh, IDRiD (MA masks) and DDR. The model was able to detect even the smallest lesions present in the retina [53]. Aditya Sharma et. al. developed a deep learning–based model along with the approach of transfer learning on the E-Ophtha (MA) dataset. The model helps in early detection of Microaneurysms and classifying the images into MA and non-MA. But the model is focused only on Binary classification rather than on DR grading [54]. Pedro Romero-Aroca et. al. used modified ETDRS grid to find the count and exact count of Microaneurysms and found that these dots are not randomly distributes across the retina, rather majority of them are found in temporal and inferior quadrants of the modified ETDRS grid. Higher the concentration, higher is the severity of DR. The study was conducted for Miradataset and Messidor dataset [55]. The below given Figure 4 shows comparison of the Microaneurysms across various image.



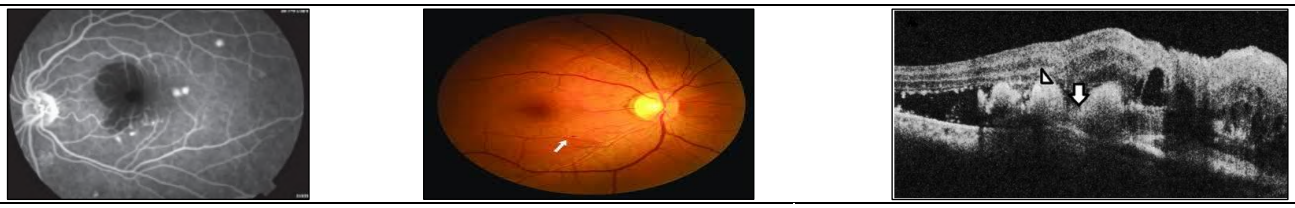
Fluorescence.	Fundus.	OCT.

Figure 4: Microaneurysm detection across imaging modalities.
Source: [56] [57] [58].

II.4.2 Hemorrhages

Gang-Min Park et. al. conducted two approaches - Severity-Based Approach using APTOS dataset and Lesion-Based Approach using NMC dataset for the binary and multi-class classification and multi-label classification. NMC dataset has various types of hemorrhages such as Retinal hemorrhages, Vitreous hemorrhages, and Preretinal hemorrhages. The study also used Cross dataset for fine tuning. It concluded that integrating both the approaches can result in more precise accuracy and interpretability of the model.EfficientNet was found to be the best performing model [59]. Saurabh Chavanke et. al. 20 proposed an automated system called the Rule-Based Hemorrhage Detection Architecture to automatically detect hemorrhages using DIARETDB0 and DIARETDB1 datasets. The focus is on pre-processing the fundus images in such a way as to highlight the hemorrhages spots by using techniques like extracting green channel of the image then enhancing it to make the dark hemorrhages more visible. Techniques like Top-Hat Transform and thresholding are used to highlight possible blobs.At last Rule based filtering based on size, shape and color is adopted for further classification [60].Instead of using traditional methods for lesion identification for DR detection Ronsong Sun et. al. proposed an AI model called EVision AI system to calculate two efficient indicators - ratio of haemorrhagic area to the total retinal area and ratio of the haemorrhagic area to the microaneurysm count for accurate detection of DR in type-2 diabetes patients.

The system uses non-mydriatic fundus images to detect hemorrhages. The EVision system used DL semantic segmentation algorithms integrated with CNN models [61]. Patsaphon Chandhakanond et. al. proposed a modified version of Iterative NICK Thresholding Region Growing (INRG) to effectively identify and segment Hemorrhages and Exudates. Watershed Separation technique for accurate segmenting of overlapped or poorly defined areas and Chi² Feature Ranking (Chi²) for accurate selection of features so as to efficiently classifying the segmented region were combined with INRG. DR2019 Mobile Dataset and JSIEC dataset were used for the study. INRG was used along with SVM classifier [62]. Sujuan Tang et. al. developed SAM-ada-Res tool to understand the overall context of the fundus images using the Segment Anything Model (SAM2) model integrated with an Adapter and ResNet101 Encoder for studying the tiny details and textures of the focused area for accurate detection of the complicated and irregularly shaped hemorrhage lesions. The information received from the Adapter and the Encoder is fused together and forwarded to U-Net decoder generating the final segmentation mask. The model was trained on OIA-DDR, IDRID and JYFY-HE datasets. Model performance was evaluated using two key metrics: normalized Intersection over Union (nIoU) and normalized Dice coefficient (nDice) [63]. The below given Figure 5 shows comparison of the Hemorrhages across various image.



Fluorescence.	Fundus.	OCT.

Figure 5: Hemorrhages detection across imaging modalities.
Source: [64] [65] [66].

II.4.3 Exudates

Esmat Ramezanzadeh et al. proposed a method to differentiate exudates from other bright structures like the optic disc, blood vessels, reflections and background noise using the textural difference between them and thus modified Radon transform technique into capturing textural changes and directional intensity patterns. Kirsch edge detection was used to highlight exudates by identifying its rough sharp borders differentiating it from vessels and bright noise.Further morphological reconstruction was applied to filter out the unwanted structures and smooth the image retaining only the true exudate regions. At last Otsu threshold was implemented to separate the bright lesions - exudates and the background. The technique was tested on DIARETDB1 and a local MUMS-DB dataset [67]. Chang Ki Yoon et al. used the OCT (Optical Coherence Tomography) scans instead of traditional fundus images to detect and segment HE which have 3D features at 3D-level by evaluating the volume of HE in the retina to better understand the presence and severity of HE. DUCK-Net - a modified version of U-Net was developed to segment HE which look like bright, hyper-reflective foci in OCT B-scans. Hard exudates are detected and segmented for each OCT slice then all the slices are combined to evaluate the 3D volume of the HE. The 3D OCT data is then projected to create a 2D fundus like image. The model achieved an excellent accuracy of 99.9% [68]. Rajesh et al. focused on grading the severity of diabetic maculopathy based on the closeness of the lesion to macula. Initially the retinal image is preprocessed to improve its quality by removing noise and applying contrast enhancement. Further various morphological operations were applied to eliminate the structures that look like exudate to retain only the 22 true exudates. Extended minima transform algorithm was used to isolate the exudate from rest of the image area by taking brightness, shape, and texture as a base.

And lastly Optic disc location and Relative distance is used to find the locate the macula and hence evaluating the closeness of exudate from the region. Based on the distance macula region is divided into three concentric circles - C1 (closest), C2 and C3 with the grading being severe if lesion is in C1 circle , moderate or mild if lesion in C2 or C3 and normal if no exudate found. The study was carried out on the Messidor dataset. The performance of system being 90% sensitivity for HE detection and 92% accuracy for Maculopathy detection [69]. S. Preetha developed a model using CNN classifier - ResNet100 to detect HE hence detecting DR. The model was tested on several datasets like Kaggle EyePACS, APTOS 2019 and IDRiD achieving an accuracy of 76% for DR classification. Their paper also included a survey on various DL models used for DR detection and concluded that CNN based models can generate high accuracy results if trained on large, good quality datasets [70]. The below given Figure 6 shows comparison of the Exudates across various image.

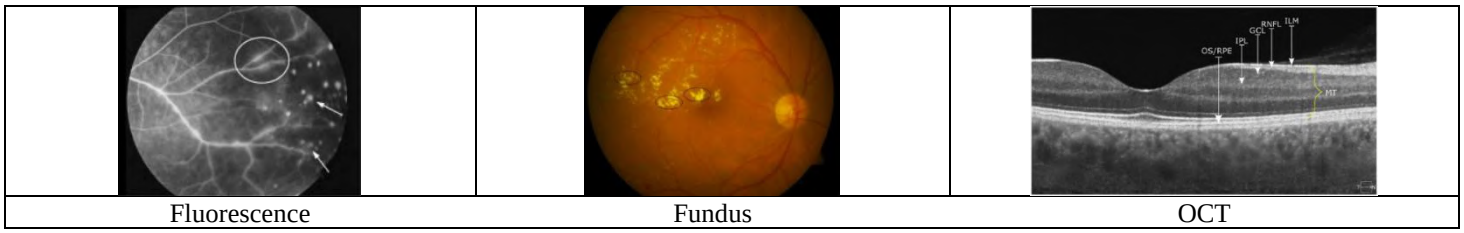


Figure 6: Exudates detection across imaging modalities.
Source: [71] [72] [73].

Table 5 summarize the state-of-the-art work on symptom based approahes of DR.

Table 5: Symptom Based Comparison Table.

Ref	Symptom	Preprocessing	Model	Dataset	Performance
[54]	Micro	CLAHE, Denoise	DNN IDRID	Private OCT	A: 97.90%, P: 98.50%, F1: 97.20%
[51]		Convert Color Space	FISM - RLDN + AEFFN	IDRiD	A: 97.68%, P: 98.11%, F1: 97.77%, S: 97.44%
[59]	Hemo	Resizing	EfficientNet B4	APTOS2019	A: 84.00%, S: 83.80%, P: 81.11%, F1: 82.40%
[61]		CLAHE, Extraction, Normalize	EVision AI system	Cross-sectional	S: 86.14%, AUC: 91.70%
[69]	Exudates	CLAHE, BV and OD Removal	SVM + Morphology	Messidor	A: 98.71%, S: 98.71%, P: 98.71%, F1: 98.71%
[68]		Augmenting, Resizing	DUCK-Net	1,811 OCT B-scans	B: A: 99.00%, P: 99.00% M: A: 91.00%, P: 91.00%

Source: Authors, (2026).

III. DATASETS

Datasets used for DR detection include retinal images taken from different angles to capture lesions that show presence of DR. A dataset with diverse demography helps us with accurate detection of the disease and a generalized model. Some of the commonly used types of retinal images are: 1 - Fundus image: 2D images used for capturing Retinal Surface, Microaneurysms, Hemorrhages, Hard exudates and blood vessels. It helps in early stage detection of DR. 2 - OCT (Optical Coherence Tomography): 3D images used to study retinal structure layer-wise. It shows thickness of macula and exudate volume, usually used for detecting Diabetic Macular Edema. 3 - OCTA (Optical Coherence Tomography Angiography): used for capturing Microaneurysms and non-perfusion areas, helps in detecting proliferative DR(PDR) [1]. 4 - FA (Fluorescein Angiography): mostly used to study where blood is flowing abnormally or leaking. Helps in early detection of fluid leakage and Microaneurysms (fluoro). Table 6 categorizes the various retinal datasets into broader categories of public and private based on their availability.

Table 6: Public and Private Diabetic Retinopathy Dataset Comparison.

Category	Type	B / M	Dataset Name	No. of Images	Resolution
Public	Fundus	B	STARE	90	700×605
			DIARETDB1	89	Various
			HRF	30	3504×2336
		M	Messidor-1	1200	1400×960
			Kaggle DR	88702	227×227
			APTOS2019	3662	584×565
			DDR	12522	227×227
	Fundus/OCT	M	FairVision	6000	227×227
	Fluorescence	B	FFA	70	700×605
Private	Fundus		SN-DREAM	Not Known	2896×1944

		M	Aravind DR	Not Known	1500×1500
	Fundus / OCT	M	SNEC/SERI	Not Known	2048×1536
			Moorfields 005	Not Known	1536×1536

Source: Authors, (2026).

Figure 7 demonstrates the imags form different classes from two prominant datasets i.e. APTOS and Messidor.

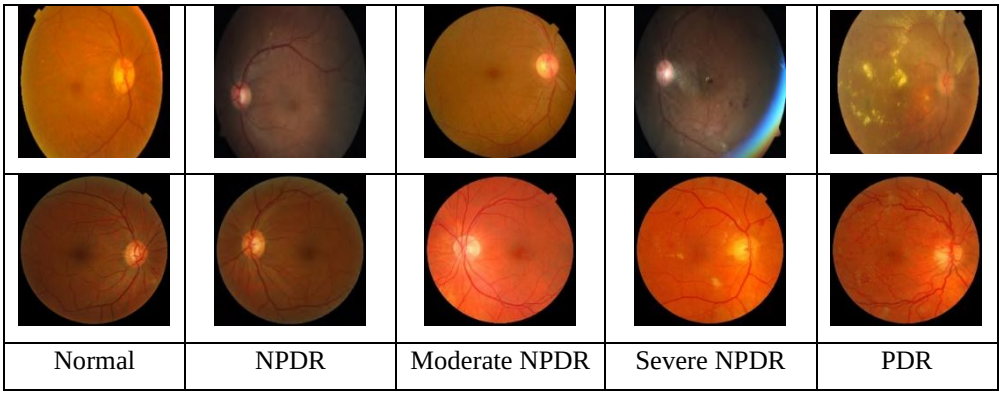


Figure 7: Class-Wise Comparison of APTOS2019 (Top Row) and Messidor Dataset (Bottom Row).
Source: Authors, (2026).

IV. CHALLENGES

Detecting and classifying DR is a crucial task to avoid total blindness. Integrating AI into traditional methods can fasten the detection process and make the prediction task accurate. It also ensures earlier response-time hence avoiding the risk of disease getting severe. Employing hybrid technologies like RSG-Net, CNN-RBF model the accuracy of model can be increased significantly. Along with the model and techniques used diversity and size of dataset also plays a significant role in the performance of model. It is essential to use a balanced and diverse dataset so as to develop a generalized model. The fundus images are usually characterized by noise and taken in dark so using an appropriate preprocessing technique like image augmentation through GAN and denoising autoencoders is also a crucial part of model development. Medical images are required to be employed with sophisticated feature extraction techniques to highlight the affected areas so as to focus on regions having lesions. Employing hybrid architectures to increase the efficiency can lead to higher computational cost and complexity of the model hence it is required for the researchers to develop a light-weight, feasible architecture to be easily integrated into local clinics. Along with this binary classification usually enjoys a higher accuracy rate as compared to multi-class classification for severity grading. So there is a need to develop a model which is light-weight, feasible and can be easily integrated to medical institutions for diverse range of patients making the model more generalized.

- Traditional time-consuming methods: The traditional methods used for detecting diabetic retinopathy include manual analysis of the fundus images by Ophthalmologists which can be inaccurate and time-consuming [13]. Delay in detecting the disease can lead to it getting severe, which can ultimately lead to blindness. Concerns may also increase the accuracy of the results generated through manual work. Therefore, there is a need for an automated system which can detect the disease faster and give more accurate results.
- Imbalanced Dataset: Datasets play an important role in the diagnosis of any disease. As it can help us to understand the common traits and symptoms which can be used while predicting the presence of the disease while diagnosing. But usually, the medical images suffer from the issue of noisy or blur images, or they can be taken in a dark background making it unclear for diagnosis. The publicly available and commonly used datasets like Messidor and APTOS2019 are highly imbalanced and biased towards more images for the No-DR, Mild and Moderate classes. This can generate biased results and does not provide equal representation to all the severity classes [3].
- Diverse Image qualities: A dataset consists of multiple images with a wide variety of differing features like size, resolution, color, illumination, and noise which can influence the model's generalizability[39]. If the images are not normalized to similar levels, it can lead to inaccurate results. Along with that the dataset should be having samples from a diverse range of patients which can make the model more included for all kinds of cases. The various demographics include samples from all age and gender groups and from various ethnicities and races.
- Model Complexity: Although ML-DL models can significantly increase their performance, it can become difficult for normal people to understand their working and integration with local cameras and in local hospitals [45]. If the models are not designed to be lightweight and portable, it can become difficult to integrate them with local clinics and be accessible to everyone [25]. Thus, the model should be made easier to understand and implement. The experts should be able to understand its work and know how to handle the machine.
- Transparency: The models developed generally follow a black-box approach that means inner logic and data is not visible to clinical doctors. But being in the medical sector the transparency with patient data is very much required while keeping their data secure [45]. There should be logical reasoning for justifying the results so that patients can trust the system.
- Computationally Heavy and Costly: Although using DL can increase the time and efficiency of the detection model, integrating complex models and techniques can increase its complexity and make it costly to maintain it [45]. The main intention behind developing such systems is that they are accessible to everyone and feasible to be integrated into real life.

V. CONCLUSION

Detecting and classifying DR is a crucial task to avoid total blindness. Integrating AI into traditional methods can fasten the detection process and make the prediction task accurate. It also ensures earlier response-time hence avoiding the risk of disease getting severe. Employing hybrid technologies like the RSG-Net, CNN-RBF model the accuracy of the model can be increased significantly. Along with the model and techniques used, diversity and size of the dataset also plays a significant role in the performance of the model. It is essential to use a balanced and diverse dataset so as to develop a generalized model. vThe fundus images are usually characterized by noise and taken in dark so using an appropriate preprocessing technique like image augmentation through GAN and denoising autoencoders is also a crucial part of model development. Medical images are required to be employed with sophisticated feature extraction techniques to highlight the affected areas so as to focus on regions having lesions. Employing hybrid architectures to increase the efficiency can lead to higher computational cost and complexity of the model hence it is required for the researchers to develop a light-weight, feasible architecture to be easily integrated into local clinics. Along with this binary classification usually enjoys a higher accuracy rate as compared to multi-class classification for severity grading. So there is a need to develop a model which is light-weight, feasible and can be easily integrated to medical institutions for a diverse range of patients making the model more generalized.

VI. AUTHOR'S CONTRIBUTION

Conceptualization: Shreya Dubey, Mahesh Goyani, Pinal Patel, Safwan Vahora, Uttam Chauhan, Mahendra Patel.
Methodology: Shreya Dubey, Mahesh Goyani, Pinal Patel, Safwan Vahora, Uttam Chauhan, Mahendra Patel.
Investigation: Shreya Dubey, Mahesh Goyani, Pinal Patel, Safwan Vahora, Uttam Chauhan, Mahendra Patel.
Discussion of results: Shreya Dubey, Mahesh Goyani, Pinal Patel, Safwan Vahora, Uttam Chauhan, Mahendra Patel.
Writing – Original Draft: Shreya Dubey, Mahesh Goyani, Pinal Patel, Safwan Vahora, Uttam Chauhan, Mahendra Patel.
Writing – Review and Editing: Shreya Dubey, Mahesh Goyani, Pinal Patel, Safwan Vahora, Uttam Chauhan, Mahendra Patel.
Resources: Shreya Dubey, Mahesh Goyani, Pinal Patel, Safwan Vahora, Uttam Chauhan, Mahendra Patel.
Supervision: Shreya Dubey, Mahesh Goyani, Pinal Patel, Safwan Vahora, Uttam Chauhan, Mahendra Patel.
Approval of the final text: Shreya Dubey, Mahesh Goyani, Pinal Patel, Safwan Vahora, Uttam Chauhan, Mahendra Patel.

VII. REFERENCES

[1] D. Nagpal, S. N. Panda, M. Malarvel, P. A. Pattanaik, and M. Zubair Khan, "A review of diabetic retinopathy: Datasets, approaches, evaluation metrics and future trends," Oct. 01, 2022, *King Saud bin Abdulaziz University*. doi: 10.1016/j.jksuci.2021.06.006.

[2] L. Sun *et al.*, "MAFNet: A novel adaptive multi-scale model for fine-grained grading of diabetic retinopathy," *Sci. Rep.*, vol. 15, no. 1, Dec. 2025, doi: 10.1038/s41598-025-17158-z.

[3] M. Sushith, A. Sathiya, V. Kalaipoonguzhali, and V. Sathya, "A hybrid deep learning framework for early detection of diabetic retinopathy using retinal fundus images," *Sci. Rep.*, vol. 15, no. 1, Dec. 2025, doi: 10.1038/s41598-025-99309-w.

[4] X. Wang, W. Wang, H. Ren, X. Li, and Y. Wen, "Prediction and analysis of risk factors for diabetic retinopathy based on machine learning and interpretable models," *Heliyon*, vol. 10, no. 9, May 2024, doi: 10.1016/j.heliyon.2024.e29497.

[5] N. M. A. Tajudin *et al.*, "Deep learning in the grading of diabetic retinopathy: A review," Dec. 01, 2022, *John Wiley and Sons Inc*. doi: 10.1049/cvi2.12116.

[6] E. Bakker *et al.*, "Adaptive optics ophthalmoscopy: a systematic review of vascular biomarkers," Mar. 01, 2022, *Elsevier Inc.* doi: 10.1016/j.survophthal.2021.05.012.

[7] M. Kale, S. Manmath, and P. R. Patil, "DETECTION OF HEMMOREGES OF DIABETIC RETINOPATHY USING MACHINE LEARNING ALGORITHMS".

[8] B. Haj Najeeb, B. S. Gerendas, A. Montuoro, C. Simader, G. G. Deák, and U. M. Schmidt-Erfurth, "A Novel Effect of Microaneurysms and Retinal Cysts on Capillary Perfusion in Diabetic Macular Edema: A Multimodal Imaging Study," *J. Clin. Med.*, vol. 14, no. 9, May 2025, doi: 10.3390/jcm14092985.

[9] Y. Shen, H. Wang, J. Fang, K. Liu, and X. Xu, "Novel insights into the mechanisms of hard exudate in diabetic retinopathy: Findings of serum lipidomic and metabolomics profiling," *Heliyon*, vol. 9, no. 4, Apr. 2023, doi: 10.1016/j.heliyon.2023.e15123.

[10] A. Ikram *et al.*, "A Systematic Review on Fundus Image-Based Diabetic Retinopathy Detection and Grading: Current Status and Future Directions," 2024, *Institute of Electrical and Electronics Engineers Inc.* doi: 10.1109/ACCESS.2024.3427394.

[11] K. Nazir, J. Kim, and Y. C. Byun, "Enhancing Early-Stage Diabetic Retinopathy Detection Using a Weighted Ensemble of Deep Neural Networks," *IEEE Access*, vol. 12, pp. 113565–113579, 2024, doi: 10.1109/ACCESS.2024.3432867.

[12] A. M. Mutawa, G. R. Hemalakshmi, N. B. Prakash, and M. Murugappan, "Randomization-Driven Hybrid Deep Learning for Diabetic Retinopathy Detection," *IEEE Access*, vol. 13, pp. 38901–38913, 2025, doi: 10.1109/ACCESS.2025.3546359.

[13] K. V. Naveen, B. N. Anoop, K. S. Siju, M. K. Kar, and V. Venugopal, "EffNet-SVM: A Hybrid Model for Diabetic Retinopathy Classification Using Retinal Fundus Images," *IEEE Access*, vol. 13, pp. 79793–79804, 2025, doi: 10.1109/ACCESS.2025.3566073.

[14] A. Chakraborty, G. Wilson, and C. Luca, "A lightweight classification system for the early detection of diabetic retinopathy," *Inform. Med. Unlocked*, vol. 57, Jan. 2025, doi: 10.1016/j.imu.2025.101655.

[15] K. Barik and A. Kumar, "Identification of diagnostic biomarkers in diabetic retinopathy using machine learning and RNA sequencing data," *In Silico Research in Biomedicine*, vol. 1, p. 100069, 2025, doi: 10.1016/j.insi.2025.100069.

[16] M. Hassaballah and M. A. Hameed, "NOVEL METAHEURISTIC ALGORITHMS AND THEIR APPLICATIONS TO EFFICIENT DETECTION OF DIABETIC RETINOPATHY," *Journal of Artificial Intelligence and Soft Computing Research*, vol. 15, no. 2, pp. 167–195, Dec. 2024, doi: 10.2478/jaiscr-2025-0009.

[17] M. Gandor *et al.*, "Diagnostics of diabetic retinopathy based on fundus photos using machine learning methods with advanced feature engineering algorithms," *Sci. Rep.*, vol. 15, no. 1, p. 34486, Dec. 2025, doi: 10.1038/s41598-025-06973-z.

[18] P. Pragathi and A. Nagaraja Rao, "An effective integrated machine learning approach for detecting diabetic retinopathy," *Open Computer Science*, vol. 12, no. 1, pp. 83–91, Jan. 2022, doi: 10.1515/comp-2020-0222.

[19] M. Bernardini, L. Romeo, A. Mancini, and E. Frontoni, "A Clinical Decision Support System to Stratify the Temporal Risk of Diabetic Retinopathy," *IEEE Access*, vol. 9, pp. 151864–151872, 2021, doi: 10.1109/ACCESS.2021.3127274.

[20] X. Li *et al.*, "Identification of diabetic retinopathy classification using machine learning algorithms on clinical data and optical coherence tomography angiography," *Eye (Basingstoke)*, vol. 38, no. 14, pp. 2813–2821, Oct. 2024, doi: 10.1038/s41433-024-03173-3.

[21] G. Tăbăcaru, S. Moldovanu, E. Răducan, and M. Barbu, "A Robust Machine Learning Model for Diabetic Retinopathy Classification," *J. Imaging*, vol. 10, no. 1, Jan. 2024, doi: 10.3390/jimaging10010008.

[22] E. Abdelmaksoud, S. El-Sappagh, S. Barakat, T. Abuhmed, and M. Elmogy, "Automatic Diabetic Retinopathy Grading System Based on Detecting Multiple Retinal Lesions," *IEEE Access*, vol. 9, pp. 15939–15960, 2021, doi: 10.1109/ACCESS.2021.3052870.

[23] A. Ali *et al.*, "Machine learning based automated segmentation and hybrid feature analysis for diabetic retinopathy classification using fundus image," *Entropy*, vol. 22, no. 5, May 2020, doi: 10.3390/E22050567.

[24] S. Akhtar *et al.*, "A deep learning based model for diabetic retinopathy grading," *Sci. Rep.*, vol. 15, no. 1, Dec. 2025, doi: 10.1038/s41598-025-87171-9.

[25] A. Zafar, K. S. Kim, M. U. Ali, J. H. Byun, and S. H. Kim, "A lightweight multi-deep learning framework for accurate diabetic retinopathy detection and multi-level severity identification," *Front. Med. (Lausanne).*, vol. 12, 2025, doi: 10.3389/fmed.2025.1551315.

[26] S. Alanazi and R. Alanazi, "Enhancing diabetic retinopathy detection through federated convolutional neural networks: Exploring different stages of progression," *Alexandria Engineering Journal*, vol. 120, pp. 215–228, May 2025, doi: 10.1016/j.aej.2025.02.026.

[27] Y. Li *et al.*, "Enhancing diabetic retinopathy diagnosis: automatic segmentation of hyperreflective foci in OCT via deep learning," *Int. Ophthalmol.*, vol. 45, no. 1, Dec. 2025, doi: 10.1007/s10792-025-03439-z.

[28] K. K. Mujeeb Rahman, M. Nasor, and A. Imran, "Automatic Screening of Diabetic Retinopathy Using Fundus Images and Machine Learning Algorithms," *Diagnostics*, vol. 12, no. 9, Sep. 2022, doi: 10.3390/diagnostics12092262.

[29] M. Shi *et al.*, "Equitable Deep Learning for Diabetic Retinopathy Detection Using Multidimensional Retinal Imaging With Fair Adaptive Scaling," *Transl. Vis. Sci. Technol.*, vol. 14, no. 7, Jul. 2025, doi: 10.1167/tvst.14.7.1.

[30] A. M. Fayyaz, M. I. Sharif, S. Azam, A. Karim, and J. El-Den, "Analysis of Diabetic Retinopathy (DR) Based on the Deep Learning," *Information (Switzerland)*, vol. 14, no. 1, Jan. 2023, doi: 10.3390/info14010030.

[31] A. Zedadra, O. Zedadra, M. Yassine Salah-Salah, and A. Guerrieri, "Graph-Aware Multimodal Deep Learning for Classification of Diabetic Retinopathy Images," *IEEE Access*, vol. 13, pp. 74795–74806, 2025, doi: 10.1109/ACCESS.2025.3564529.

[32] M. Hussain *et al.*, "An Enhanced Convolutional Neural Network (CNN) based P-EDR Mechanism for Diagnosis of Diabetic Retinopathy (DR) using Machine Learning," *Engineering, Technology and Applied Science Research*, vol. 15, no. 1, pp. 19062–19067, Feb. 2025, doi: 10.48084/etasr.8854.

[33] S. J. SIDIQ and T. BENIL, "A lightweight transfer learning based ensemble approach for diabetic retinopathy detection," *International Journal of Information Management Data Insights*, vol. 5, no. 2, Dec. 2025, doi: 10.1016/j.jjimei.2025.100372.

[34] O. Dib, "A decentralized privacy-preserving framework for diabetic retinopathy detection using federated learning and blockchain," *Results in Engineering*, vol. 26, Jun. 2025, doi: 10.1016/j.rineng.2025.105456.

[35] S. Guefrachi, A. Echtioui, and H. Hamam, "Diabetic Retinopathy Detection Using Deep Learning Multistage Training Method," *Arab. J. Sci. Eng.*, vol. 50, no. 2, pp. 1079–1096, Jan. 2025, doi: 10.1007/s13369-024-09137-9.

[36] A. M. Fayyaz, M. I. Sharif, S. Azam, A. Karim, and J. El-Den, "Analysis of Diabetic Retinopathy (DR) Based on the Deep Learning," *Information (Switzerland)*, vol. 14, no. 1, Jan. 2023, doi: 10.3390/info14010030.

[37] I. Govindharaj, R. Rampriya, G. Michael, S. Yazhinian, K. Dinesh Kumar, and R. Anandh, "Capsule network-based deep learning for early and accurate diabetic retinopathy detection," *Int. Ophthalmol.*, vol. 45, no. 1, Dec. 2025, doi: 10.1007/s10792-024-03391-4.

[38] K. GENCER, G. GENCER, T. H. CERAN, A. E. BİLİR, and M. DOĞAN, "Photodiagnosis with deep learning: A GAN and autoencoder-based approach for diabetic retinopathy detection," *Photodiagnosis Photodyn. Ther.*, vol. 53, Jun. 2025, doi: 10.1016/j.pdpdt.2025.104552.

[39] G. I *et al.*, "Enhanced diabetic retinopathy detection using U-shaped network and capsule network-driven deep learning," *MethodsX*, vol. 14, Jun. 2025, doi: 10.1016/j.mex.2024.103052.

[40] G. Ali, A. Dastgir, M. W. Iqbal, M. Anwar, and M. Faheem, "A Hybrid Convolutional Neural Network Model for Automatic Diabetic Retinopathy Classification From Fundus Images," *IEEE J. Transl. Eng. Health Med.*, vol. 11, pp. 341–350, 2023, doi: 10.1109/JTEHM.2023.3282104.

[41] A. Shukla, S. Tiwari, and A. Jain, "HybridFusionNet: Deep Learning for Multi-Stage Diabetic Retinopathy Detection," *Technologies (Basel).*, vol. 12, no. 12, Dec. 2024, doi: 10.3390/technologies12120256.

[42] M. M. Butt, D. N. F. A. Iskandar, S. E. Abdelhamid, G. Latif, and R. Alghazo, "Diabetic Retinopathy Detection from Fundus Images of the Eye Using Hybrid Deep Learning Features," *Diagnostics*, vol. 12, no. 7, Jul. 2022, doi: 10.3390/diagnostics12071607.

[43] A. S. Sabeena and M. K. Jeyakumar, “An Ensemble Learning Approach Using Deep Learning Models For Diabetic Retinopathy Severity Classification,” *Biomedical Materials and Devices*, 2025, doi: 10.1007/s44174-025-00418-x.

[44] L. Learning¸sükran, Y. Atcı, A. Güne¸sgüne¸s, M. Zontul, and Z. Arslan, “Identifying Diabetic Retinopathy in the Human Eye: A Hybrid Approach Based on a Computer-Aided Diagnosis System Combined with Deep Learning¸Sükran,” vol. 10, pp. 215–230, 2024, doi: 10.3390/tomography.

[45] K. Ahnaf Alavee *et al.*, “Enhancing Early Detection of Diabetic Retinopathy Through the Integration of Deep Learning Models and Explainable Artificial Intelligence,” *IEEE Access*, vol. 12, pp. 73950–73969, 2024, doi: 10.1109/ACCESS.2024.3405570.

[46] A. Jabbar *et al.*, “A Lesion-Based Diabetic Retinopathy Detection Through Hybrid Deep Learning Model,” *IEEE Access*, vol. 12, pp. 40019–40036, 2024, doi: 10.1109/ACCESS.2024.3373467.

[47] R. Yasashvini, V. Raja Sarobin M, R. Panjanathan, S. Graceline Jasmine, and L. Jani Anbarasi, “Diabetic Retinopathy Classification Using CNN and Hybrid Deep Convolutional Neural Networks,” *Symmetry (Basel).*, vol. 14, no. 9, Sep. 2022, doi: 10.3390/sym14091932.

[48] A. Bilal, L. Zhu, A. Deng, H. Lu, and N. Wu, “AI-Based Automatic Detection and Classification of Diabetic Retinopathy Using U-Net and Deep Learning,” *Symmetry (Basel).*, vol. 14, no. 7, Jul. 2022, doi: 10.3390/sym14071427.

[49] M. Nahiduzzaman, M. R. Islam, S. M. R. Islam, M. O. F. Goni, M. S. Anower, and K. S. Kwak, “Hybrid CNN-SVD Based Prominent Feature Extraction and Selection for Grading Diabetic Retinopathy Using Extreme Learning Machine Algorithm,” *IEEE Access*, vol. 9, pp. 152261–152274, 2021, doi: 10.1109/ACCESS.2021.3125791.

[50] N. Wang, X. Liu, J. Wu, X. Xiang, Y. Gao, and L. Yao, “A novel OCTA-based image processing method for enhanced microaneurysm detection and 3D visualization in diabetic retinopathy,” *Photodiagnosis Photodyn. Ther.*, vol. 56, p. 105258, Dec. 2025, doi: 10.1016/j.pdpdt.2025.105258.

[51] A. Rehman *et al.*, “FISM: harnessing deep learning and reinforcement learning for precision detection of microaneurysms and retinal exudates for early diabetic retinopathy diagnosis,” *BioData Min.*, vol. 18, no. 1, Dec. 2025, doi: 10.1186/s13040-025-00485-2.

[52] L. Mendes *et al.*, “Microaneurysm Counting as a Biomarker for the Hyperperfusion Stage of Nonproliferative Diabetic Retinopathy,” *Ophthalmol. Ther.*, vol. 14, no. 8, pp. 1905–1915, Aug. 2025, doi: 10.1007/s40123-025-01179-y.

[53] N. Asiri, A. M. Artoli, M. Al-Razgan, and T. Alfakih, “Dilated Neural Networks for Improving Microaneurysm Detection in Fundus Images,” *IEEE Access*, vol. 13, pp. 104037–104046, 2025, doi: 10.1109/ACCESS.2025.3579342.

[54] A. Sharma and V. Pawar, “INDIAN JOURNAL OF SCIENCE AND TECHNOLOGY Early Assessment of Diabetic Retinopathy by Detecting Microaneurysm with Deep Neural Network,” *Indian J. Sci. Technol.*, vol. 17, no. 17, pp. 1786–1790, 2024, doi: 10.17485/IJST/v17i17.732.

[55] P. Romero-Aroca, E. Garcia-Curto, J. Pascual-Fontanilles, A. Valls, A. Moreno, and M. Baget-Bernaldiz, “Distribution of Microaneurysms and Hemorrhages in Accordance with the Grading of Diabetic Retinopathy in Type Diabetes Patients,” *Diagnostics*, vol. 14, no. 14, Jul. 2024, doi: 10.3390/diagnostics14141547.

[56] D. Brown, I. Kozak, S. I. R. Lampen, and J. Chhablani, “Management of Coats Disease Microaneurysms With Fundus Fluorescein Angiography-Guided Navigated Laser,” *J. Vitreoretin. Dis.*, vol. 3, no. 1, pp. 36–41, Jan. 2019, doi: 10.1177/2474126418810134.

[57] I. Lazar and A. Hajdu, “MICROANEURYSM DETECTION IN RETINAL IMAGES USING A ROTATING CROSS-SECTION BASED MODEL.”

[58] E. S. Kazeminasab, R. Almasi, B. Shoushtarian, E. Golkar, and H. Rabbani, “Automatic Detection of Microaneurysms in OCT Images Using Bag of Features,” *Comput. Math. Methods Med.*, vol. 2022, 2022, doi: 10.1155/2022/1233068.

[59] G. M. Park, J. H. Moon, and H. G. Jung, “A Comparative Study of Lesion-Centered and Severity-Based Approaches to Diabetic Retinopathy Classification: Improving Interpretability and Performance,” *Biomedicines*, vol. 13, no. 6, Jun. 2025, doi: 10.3390/biomedicines13061446.

[60] S. Chavanke, S. Avhad, K. Aher, U. Shinde, and S. M. Kale, “Detection of Hemorrhage in fundus Images.”

[61] R. Sun *et al.*, “Ratio of haemorrhagic area to retinal area as a novel indicator for AI-based screening of diabetic retinopathy in type 2 diabetes: a community-based cross-sectional study,” *BMJ Open* , vol. 15, no. 9, Sep. 2025, doi: 10.1136/bmjopen-2025-099062.

[62] P. Chandhakanond and P. Aimmanee, “Diabetic retinopathy detection via exudates and hemorrhages segmentation using iterative NICK thresholding, watershed, and Chi2 feature ranking,” *Sci. Rep.*, vol. 15, no. 1, Dec. 2025, doi: 10.1038/s41598-025-90048-6.

[63] S. Tang and Q. Wu, “Research on recognition of diabetic retinopathy hemorrhage lesions based on fine tuning of segment anything model,” *Sci. Rep.*, vol. 15, no. 1, Dec. 2025, doi: 10.1038/s41598-025-92665-7.

[64] P. Baskaran and M. D. Sindal, “Acute angle closure glaucoma secondary to polypoidal choroidal vasculopathy-a devastating complication.”

[65] E.-C. Chang, J.-S. Huang, Y.-C. Hou, C.-H. Huang, and I.-H. Wang, “Optical coherence tomography as a useful adjunct in the early detection of meningioma with optic nerve compression,” *Taiwan J. Ophthalmol.*, vol. 12, no. 3, pp. 354–359, Jul. 2022, doi: 10.4103/tjo.tjo_54_21.

[66] R. Shenoy and A. Bialasiewicz, “The Effect of Photodynamic Therapy in the Management of Polypoidal Choroidal Vasculopathy in a 28-year-old.”

[67] E. Ramezanzadeh, N. Shoeibi, A. Feizabadi, T. Banaee, M. H. B. Tussi, and M. Tavakoli, “Automated detection of hard exudates in retinal fundus images for diabetic retinopathy screening using textural-based radon transform and morphology reconstruction,” *Biomedical Engineering Advances*, vol. 9, p. 100180, Jun. 2025, doi: 10.1016/j.bea.2025.100180.

[68] C. K. Yoon, H. W. Lee, H. W. Kim, and J. L. Kim, “Deep learning based retinal hard exudates quantification of optical coherence tomography,” *Int. J. Retina Vitreous*, vol. 11, no. 1, Dec. 2025, doi: 10.1186/s40942-025-00715-z.

[69] I. S. Rajesh, B. M. Reshmi, B. Malakreddy A, and S. Bilakeri, “Automatic Detection of Hard Exudate in Color Retinal Fundus Image and Diabetic Maculopathy Grading,” *IEEE Access*, vol. 13, pp. 6618–6631, 2025, doi: 10.1109/ACCESS.2025.3525499.

[70] S. Chaudhari, R. Gadakh, S. Mali, S. Govardhane, and S. Kale, "|| Issue 3 || 2025 || ISO," vol. 8, 2007.

[71] A. Patil and C. Chakravorty, "Detection of hard exudate using retinal optical coherence tomography (OCT) images," *Global Transitions Proceedings*, vol. 2, no. 2, pp. 566–570, Nov. 2021, doi: 10.1016/j.gltp.2021.08.067.

[72] M. Monemian and H. Rabbani, "Exudate identification in retinal fundus images using precise textural verifications," *Sci. Rep.*, vol. 13, no. 1, Dec. 2023, doi: 10.1038/s41598-023-29916-y.

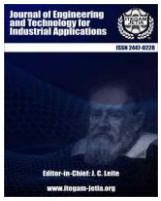
[73] A. Domagała, L. Domagała, N. Kopiś-Posiej, M. Harciarek, and P. Krukow, "Differentiation of the retinal morphology aging trajectories in schizophrenia and their associations with cognitive dysfunctions," *Front. Psychiatry*, vol. 14, 2023, doi: 10.3389/fpsyt.2023.1207608.

Journal of Engineering and Technology for Industrial Applications

ISSN ONLINE: 2447-0228

ITEGAM-JETIA

Manaus, v.12 n.60, p. 499-512, July/August, 2026.
DOI: https://doi.org/10.5935/jetia.v12i60.3887



RESEARCH ARTICLE OPEN ACCESS

DEEP REINFORCEMENT LEARNING BASED ADAPTIVE SWITCHING FOR RISK COST OPTIMIZED RENEWABLE SMART GRIDS

Meyyappan M*[1], Avirajamanjula P[2], Marimuthu P[3] and Bharathiraja M[4]

[1, 2]Department of Electrical and Electronics Engineering, Ponnaiyah Ramajayam Institute of Science and Technology (PRIST University), Thanjavur, 613403, India
[3]Department of Mechanical Engineering, Sri Krishna College of Engineering, Arakkonam, 631003, India.
[4]Department of Mechatronics Engineering, Bannari Amman Institute of Technology, Sathyamangalam, 638401, India.

[1]http://orcid.org/0009-0009-0189-4564, [2]http://orcid.org/0009-0000-3235-352X
[3]http://orcid.org/0000-0002-5683-5985, [4]http://orcid.org/0000-0003-1021-1840

E-email: *meyaps2014@gmail.com, avmanju17@gmail.com, pmarimuthu69@gmail.com, bharathirajabit@gmail.com

ARTICLE INFO

Article History
Received on: March 03, 2026
Reviewed on: April 03, 2026
Accepted on: May 01, 2026
Published on: July 31, 2026

Keywords:
Reinforcement Learning,
Smart Grid Optimization,
Renewable Energy Integration,
Risk–Cost Minimization,
Power Quality Control.

ABSTRACT

The increasing penetration of weather-driven renewable energy sources in smart grids introduces operational instability, harmonic distortion, and elevated switching costs due to the limitations of rule-based and deterministic control strategies. This study proposes a deep reinforcement learning-based adaptive switching framework to enhance renewable utilization while minimizing operational risk and economic cost. A simulation-derived dataset incorporating renewable generation, load demand, total harmonic distortion, voltage deviation, frequency variation, and risk–cost indices was generated from a risk–cost optimized smart grid model and implemented in Google Colab. The switching problem was formulated as a Markov decision process with a state space composed of power quality and economic variables, and a discrete action space representing operational modes. A Deep Q-Network agent was trained over 24-hour episodes to learn optimal switching policies. Comparative evaluation against conventional, rule-based, and analytical risk–cost optimization strategies demonstrated up to 14% reduction in total harmonic distortion, 22% reduction in switching frequency, 17% reduction in operational cost, and 19% improvement in risk mitigation, while increasing renewable penetration by 11%. The proposed framework provides a scalable and intelligent solution for industrial smart grid applications.



Copyright ©2026 by authors and Galileo Institute of Technology and Education of the Amazon (ITEGAM). This work is licensed under the Creative Commons Attribution International License (CC BY 4.0).

I. INTRODUCTION

The accelerating global transition toward low-carbon power systems has significantly increased the penetration of renewable energy sources (RES), particularly solar photovoltaic (PV) and wind generation, within modern smart grids. Renewable integration enhances environmental sustainability and reduces dependence on fossil fuels; however, the intermittent and weather-dependent nature of these resources introduces considerable operational uncertainty. Fluctuations in solar irradiance and wind velocity lead to rapid variations in power output, which directly influence voltage stability, frequency regulation, harmonic distortion levels, and overall system reliability [1], [2]. In inverter-dominated smart grid architectures, renewable variability often causes dynamic power imbalance between generation and load demand. Such imbalance produces voltage deviations at the point of common coupling (PCC), frequency instability, and elevated Total Harmonic Distortion (*THD*). Excessive harmonic content not only reduces equipment lifespan but may also violate the harmonic limits specified in IEEE Std 519-2014 [3]. Maintaining harmonic distortion within prescribed thresholds while maximizing renewable utilization therefore represents a critical operational challenge. Traditional automatic transfer switching systems employ deterministic threshold-based control mechanisms. These rule-based systems select operating modes—renewable-only, grid-only, or hybrid—based on predefined voltage or generation limits. While simple to implement, such approaches operate reactively. Switching decisions occur only after deviations surpass fixed boundaries, which can result in excessive switching frequency, increased breaker wear, elevated maintenance cost, and reduced system efficiency. Moreover, rule-based frameworks do not adapt to evolving load patterns or environmental conditions, limiting their effectiveness under dynamic scenarios [4].

To overcome these limitations, risk–cost optimization models have been introduced to balance operational reliability and economic efficiency. Multi-objective optimization formulations typically minimize a composite function combining probabilistic operational risk and total economic cost [5], [6]. Risk indices are derived from voltage deviation, frequency variation, and harmonic distortion severity metrics, while economic cost includes grid energy consumption and switching penalties. Although such models provide structured decision-making capability, they rely on static weighting parameters and deterministic formulations. Consequently, they lack adaptive learning behavior and may not generalize effectively under unforeseen operating conditions. Artificial Intelligence (AI) techniques have recently gained attention in smart grid applications. Machine learning algorithms have been applied to renewable forecasting, demand prediction, anomaly detection, and energy management optimization [7], [8]. However, most AI-based approaches are supervised learning models that depend on historical labels. They improve prediction accuracy but do not inherently provide adaptive control strategies. Reinforcement Learning (RL), in contrast, enables agents to learn optimal decision policies through trial-and-error interaction with the environment. Unlike supervised methods, RL does not require labeled output data; instead, it optimizes cumulative reward over sequential decisions [9].

Deep Reinforcement Learning (DRL), which integrates deep neural networks with RL algorithms, has demonstrated superior performance in dynamic control problems. Applications in microgrid energy scheduling and battery energy management have shown promising results [10], [11]. Nevertheless, the integration of DRL within a unified risk–cost optimized renewable switching framework remains limited. Specifically, existing studies rarely incorporate harmonic compliance constraints and probabilistic risk modeling into RL-based switching strategies. The absence of adaptive policy-learning mechanisms in renewable smart grid switching constitutes a significant research gap. Deterministic optimization approaches compute optimal solutions for predefined objective functions but cannot continuously refine decisions based on evolving system behavior. In contrast, a DRL-based controller can dynamically adjust switching policies by learning from operational feedback, thereby improving stability and economic efficiency over time. This research proposes a Deep Reinforcement Learning-based adaptive switching framework for renewable-integrated smart grids. The proposed system integrates probabilistic risk assessment, economic cost modeling, and harmonic compliance constraints within a Markov Decision Process formulation. A Deep Q-Network (DQN) agent is trained using simulation-derived time-series data representing renewable generation, load demand, *THD*, voltage deviation, frequency deviation, operational risk index, and switching cost. The objective is to minimize harmonic distortion, reduce switching frequency, decrease operational cost, and improve renewable penetration while maintaining compliance with IEEE standards. The major contributions of this study are summarized as follows:

1. Development of a comprehensive dataset derived from a validated renewable smart grid simulation model.
2. Formulation of the renewable switching problem as a Markov Decision Process with clearly defined state and action spaces.
3. Design of a reward function integrating renewable utilization, harmonic penalties, switching penalties, and cost penalties.
4. Implementation of a Deep Q-Network agent for adaptive policy learning.
5. Quantitative comparison against conventional rule-based and deterministic risk–cost optimization strategies.

The proposed framework aims to enhance industrial smart grid reliability by introducing intelligent, adaptive control capable of handling renewable variability. By integrating learning-based decision-making within risk–cost optimization, the study contributes to the advancement of scalable and resilient renewable power systems.

II. RELATED WORK

The integration of renewable energy sources into smart grids requires coordinated interaction among renewable generation modeling, probabilistic risk assessment, economic cost evaluation, power quality monitoring, and intelligent control strategies. This section presents the theoretical background underpinning the proposed Deep Reinforcement Learning-based adaptive switching framework.

II.1 RENEWABLE ENERGY VARIABILITY IN SMART GRIDS

Renewable energy sources, particularly solar photovoltaic (PV) and wind power systems, exhibit stochastic and time-varying behavior due to dependence on meteorological conditions. Solar irradiance fluctuations caused by cloud movement and atmospheric variability directly influence PV output, while wind generation depends nonlinearly on wind speed, typically following a cubic power relationship [1], [2]. In grid-connected renewable systems, intermittent generation introduces rapid power imbalance between supply and demand. This imbalance manifests as voltage deviations at the point of common coupling (PCC), frequency instability, and dynamic harmonic distortion. High renewable penetration levels amplify these effects, particularly in inverter-dominated grids where switching converters influence waveform quality [12]. To maintain stability, grid operators traditionally employ reserve capacity, voltage regulation equipment, and automatic transfer switches. However, these mechanisms are often reactive and may not optimally balance renewable utilization with reliability objectives.

II.2 IOT-BASED SWITCHING AND MONITORING SYSTEMS

The emergence of the Internet of Things (IoT) has significantly enhanced monitoring and supervisory capabilities in smart grids. IoT-enabled architectures allow real-time acquisition of electrical parameters such as voltage magnitude, current waveform, active power, and harmonic distortion [4], [5]. Cloud-based communication platforms facilitate remote control and distributed decision-making. Automatic Transfer Switch (ATS) systems integrated with IoT modules enable automated selection among renewable sources, grid supply, and backup generators. Although these systems improve operational continuity and transparency, their control logic typically relies on deterministic thresholds. For example, switching may be triggered when renewable power falls below a fixed percentage of load demand or when voltage deviation exceeds a predefined limit.

Such rule-based systems lack predictive adaptability. They respond only after disturbances occur and do not account for probabilistic risk or long-term economic impact. Moreover, switching frequency may increase unnecessarily during transient fluctuations, leading to mechanical wear and elevated operational cost.

II.3 RISK MODELING IN RENEWABLE-INTEGRATED SYSTEMS

Operational risk assessment in power systems quantifies the likelihood and severity of undesirable events such as voltage collapse, frequency instability, and harmonic violations. Probabilistic risk models commonly incorporate power deficit probability, deviation indices, and severity weighting factors [6]. The general structure of a risk function may be expressed as the product of occurrence probability and impact severity. Severity indices typically normalize voltage deviation, frequency variation, and *THD* relative to standard limits. IEEE Std 519-2014 [3] specifies that voltage *THD* in low-voltage systems should not exceed 5% under normal operating conditions [7]. Risk-based optimization frameworks combine reliability assessment with economic objectives. Multi-objective formulations often minimize a weighted sum of operational risk and total cost [8], [9]. Although effective in structured optimization environments, these formulations depend on static weighting parameters. Once the weights are defined, the optimization solution remains fixed unless manually reconfigured. Consequently, deterministic risk–cost optimization does not inherently learn from operational history or adapt to evolving environmental conditions.

II.4 ECONOMIC COST CONSIDERATIONS IN SWITCHING OPERATIONS

Economic performance in renewable-integrated smart grids is influenced by grid energy tariffs, switching frequency, maintenance cost, and renewable curtailment losses. Grid energy consumption incurs direct cost proportional to electricity tariff rates, while frequent switching operations increase mechanical stress on breakers and reduce equipment lifespan [10]. The switching cost model therefore incorporates both grid energy expenditure and a penalty term representing switching events. Minimizing switching frequency is essential for long-term economic sustainability. However, excessive restriction of switching may compromise reliability or power quality compliance. Achieving a balanced trade-off between economic cost and system reliability requires dynamic decision-making capability, particularly under fluctuating renewable conditions.

II.5 ARTIFICIAL INTELLIGENCE AND REINFORCEMENT LEARNING IN POWER SYSTEMS

Artificial Intelligence (AI) has been increasingly applied in smart grid environments for forecasting, classification, optimization, and control tasks [11]. Supervised learning methods improve renewable generation prediction and load demand estimation. However, these methods require labeled training data and do not directly optimize sequential decision processes. Reinforcement Learning (RL) differs fundamentally from supervised learning. In RL, an agent interacts with an environment, selects actions, receives rewards, and learns a policy that maximizes cumulative reward over time. The environment is typically modeled as a Markov Decision Process (MDP) [13]. Deep Reinforcement Learning (DRL) integrates neural networks to approximate value functions or policies in high-dimensional state spaces. The Deep Q-Network (DQN) algorithm employs a neural network to approximate the action-value function and uses experience replay to stabilize training [14]. Recent studies have applied DRL to microgrid energy scheduling and battery energy management [15], [16]. These studies demonstrate improved adaptability compared to rule-based systems. Nevertheless, most existing RL applications focus primarily on economic dispatch or energy storage scheduling. Integration of harmonic compliance, risk modeling, and switching cost minimization within a unified RL-based switching framework remains limited.

II.6 RESEARCH GAP AND THEORETICAL POSITIONING

From the theoretical analysis above, three principal limitations are identified in existing literature:

1. IoT-based switching systems operate reactively without adaptive policy learning.
2. Risk–cost optimization models rely on deterministic formulations with static weighting factors.
3. Reinforcement Learning applications in smart grids rarely incorporate harmonic distortion constraints and probabilistic risk indices within switching control.

The present study addresses these limitations by integrating:

- Renewable variability modeling
- Probabilistic risk assessment
- Economic switching cost modeling
- IEEE 519 harmonic compliance
- Deep Reinforcement Learning-based adaptive control

Within a unified renewable smart grid switching architecture. By formulating the switching problem as a Markov Decision Process and training a Deep Q-Network agent using simulation-derived operational data, the proposed framework enables adaptive policy learning. Unlike deterministic optimization, the RL agent continuously refines switching decisions based on cumulative reward, thereby enhancing stability and economic performance under varying renewable conditions. The next section presents the detailed dataset generation methodology, system modeling framework, and reinforcement learning formulation adopted in this research.

III. MATERIALS AND METHODS

This section describes the renewable smart grid modeling framework, dataset generation methodology, risk–cost formulation, and reinforcement learning configuration adopted in this study. All equations are numbered sequentially beginning in this section, in accordance with journal formatting requirements.

III.1 SYSTEM CONFIGURATION

The investigated smart grid consists of:

- Solar photovoltaic (PV) subsystem.
- Wind energy conversion subsystem.
- Utility grid interface.
- Industrial load demand.
- Intelligent switching unit at the point of common coupling (PCC).
- Monitoring block measuring voltage, frequency, and harmonic distortion.

The switching controller selects among four operational modes:

1. Renewable-only.
2. Hybrid renewable–grid.
3. Grid-only.
4. Battery-priority.

Switching decisions are executed at discrete time intervals. The overall architecture of the renewable-integrated smart grid considered in this study is illustrated in Figure 1.

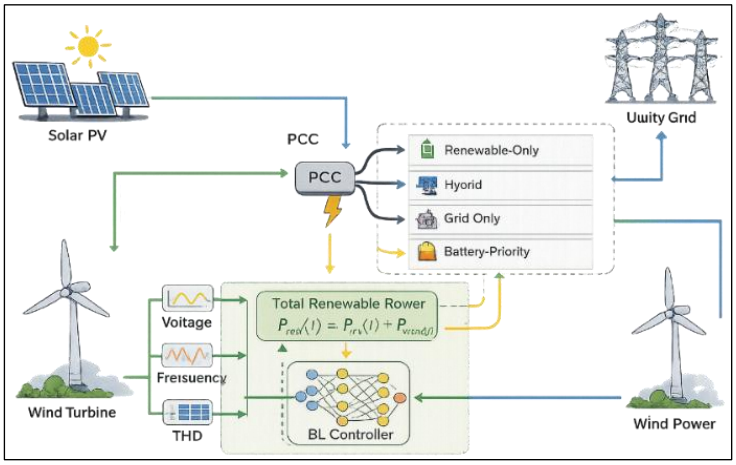


Figure 1: Architecture of renewable-integrated smart grid with adaptive switching controller.
Source: Authors, (2026).

III.2 RENEWABLE GENERATION MODELING

III.2.1 Solar Photovoltaic Model

The instantaneous solar PV output is modeled as:

$$P_{pv}(t) = \eta A G(t) \tag{1}$$

where:

- $P_{pv}(t)$ = PV output power (kW)
- η = conversion efficiency
- A = effective panel area
- $G(t)$ = solar irradiance (W/m²)

Solar irradiance was simulated using diurnal sinusoidal variation with stochastic noise to reflect cloud-induced variability.

III.2.2 Wind Power Model

Wind turbine output is expressed as:

$$P_{wind}(t) = \frac{1}{2}\rho A_r C_p v^3(t) \tag{2}$$

where:

- ρ = air density (kg/m³).
- A_r = rotor swept area (m²).
- C_p = power coefficient.
- $v(t)$ = wind speed (m/s).

The cubic dependency introduces nonlinear variability in renewable output.

III.2.3 Total Renewable Power

Total renewable generation is given by:

$$P_{ren}(t) = P_{pv}(t) + P_{wind}(t) \quad (3)$$

The interaction between solar and wind generation contributing to total renewable output is depicted in Figure 2.

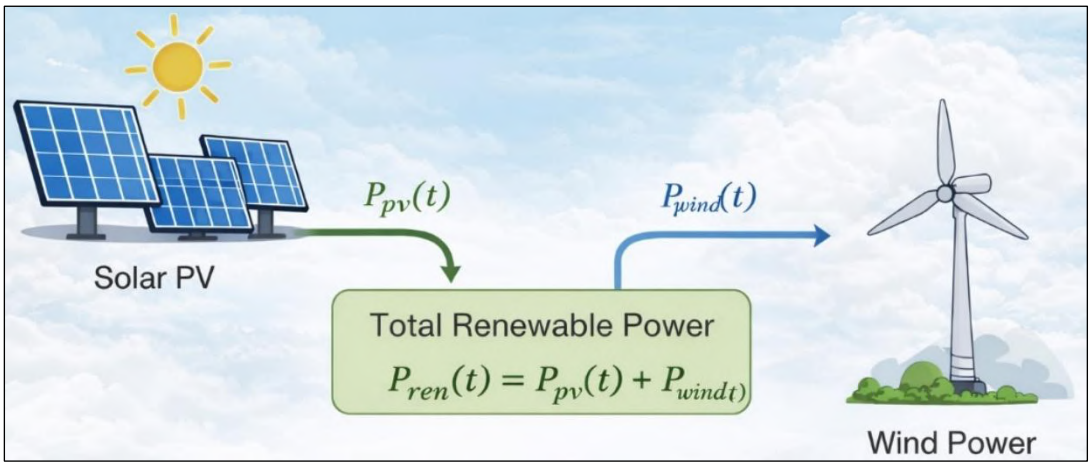


Figure 2: Renewable power modeling structure showing PV and wind contribution to total generation.
Source: Authors, (2026).

III.3 LOAD DEMAND MODELING

Industrial load demand is modeled as:

$$P_L(t) = P_{avg} + P_{amp}\sin(\omega t) + \epsilon(t) \quad (4)$$

where:

- P_{avg}= average load.
- P_{amp}= load variation amplitude.
- ω= angular frequency.
- $\epsilon(t)$= random disturbance term.

This formulation captures daily consumption cycles with stochastic fluctuation. The primary dataset features extracted from the simulation model are summarized in Table 1.

Table 1: Dataset features used for reinforcement learning training.

Variable	Symbol	Unit	Description
Renewable Power	P_{ren}	*kW*	Total PV + Wind output
Load Demand	P_L	*kW*	Industrial load profile
Voltage Deviation	ΔV	*p.u.*	PCC voltage variation
Frequency Deviation	Δf	*Hz*	Frequency variation
Harmonic Distortion	*THD*	*%*	Total harmonic distortion
Risk Index	*R*	–	Operational risk value
Total Cost	C_{tot}	₹	Economic cost
Switching Event	N_{switch}	–	Breaker operation count

Source: Authors, (2026).

III.4 POWER IMBALANCE AND STABILITY INDICATORS

III.4.1 Power Mismatch

$$\Delta P(t) = P_{ren}(t) - P_L(t) \tag{5}$$

where:

- ΔP(t) = power mismatch at time t (kW).
- Pren(t) = total renewable power (kW).
- PL(t) = load demand (kW).

Positive ΔP indicates surplus renewable generation; negative values represent deficit.

III.4.2 Voltage Deviation

Voltage deviation at PCC is modeled as proportional to power imbalance:

$$\Delta V(t) = k_v \frac{\Delta P(t)}{P_L(t)} \tag{6}$$

where:

• ΔV(t) = voltage deviation at PCC (p.u.)
• kv = voltage sensitivity coefficient
• ΔP(t) = power mismatch (kW)
• PL(t) = load demand (kW)

III.4.3 Frequency Deviation

$$\Delta f(t) = k_f \frac{\Delta P(t)}{P_L(t)} \tag{7}$$

where:
• Δf(t) = frequency deviation (Hz)
• kf = frequency sensitivity coefficient
• ΔP(t) = power mismatch (kW)
• PL(t) = load demand (kW)

III.4.4 Total Harmonic Distortion

Harmonic distortion is expressed as:

$$THD(t) = THD_0 + k_h \mid \Delta P(t) \mid + \xi(t) \tag{8}$$

where:

- THD_0 = base harmonic level
- k_h= harmonic sensitivity constant
- $\xi(t)$ = noise component

Compliance condition according to IEEE Std 519-2014 [3]:

$$THD(t) \leq 5\% \tag{9}$$

The relationship between power imbalance and harmonic distortion used in the modeling process is illustrated in Figure 3.

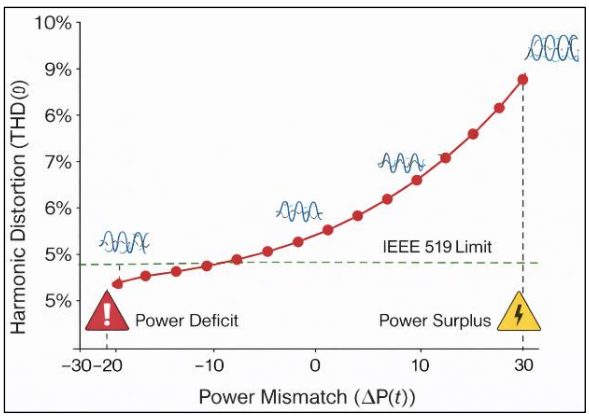


Figure 3: Harmonic distortion variation as a function of power mismatch.
Source: Authors, (2026).

III.5 PROBABILISTIC RISK MODELING

Operational risk is defined as:

$$R(t) = P_{def}(t) \times S(t) \tag{10}$$

where:

- R(t) = operational risk index
- Pdef(t) = deficit probability
- S(t) = severity index

Deficit probability:

$$P_{def}(t) = \begin{cases} 1, & P_{ren}(t) < P_L(t) \\ 0, & \text{otherwise} \end{cases} \tag{11}$$

where:

- Pdef(t) = probability of power deficit
- Pren(t) = renewable power (kW)
- PL(t) = load demand (kW)

Severity index:

$$S(t) = w_1 \frac{|\Delta V(t)|}{0.05} + w_2 \frac{|\Delta f(t)|}{0.5} + w_3 \frac{THD(t)}{5} \tag{12}$$

where:

- S(t) = severity index.
- w1, w2, w3 = weighting coefficients.
- ΔV(t) = voltage deviation (p.u.).
- Δf(t) = frequency deviation (Hz).
- *THD*(t) = total harmonic distortion (%).
- 0.05 = permissible voltage deviation limit (p.u.).
- 0.5 = allowable frequency deviation limit (Hz).
- 5 = IEEE 519 *THD* limit (%).

The probabilistic risk modeling structure integrating deficit probability and severity index is shown in Figure 4.

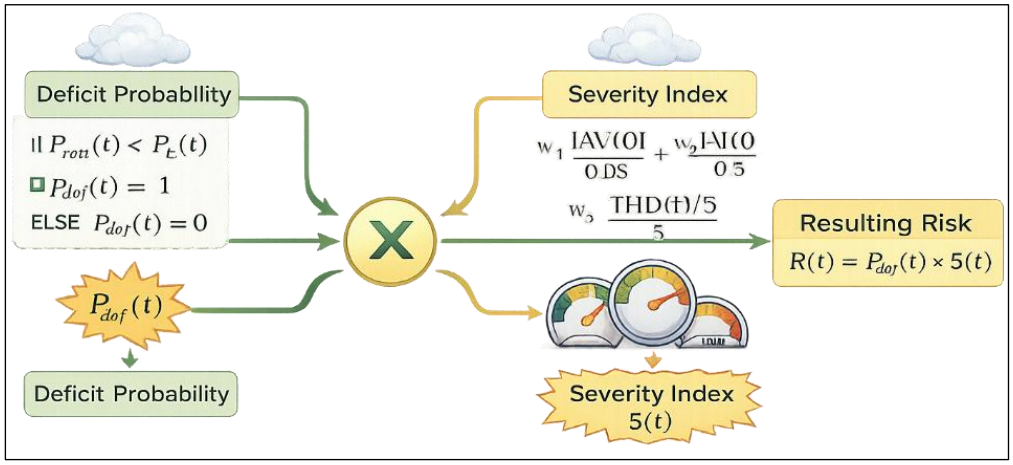


Figure 4: Operational risk computation framework combining probability and severity components.
Source: Authors, (2026).

III.6 ECONOMIC COST MODELING

Total cost is computed as:

$$C_{tot}(t) = C_{grid}(t) + C_{switch}(t) \tag{13}$$

where:

- *Ctot*(t) = total operational cost (₹)
- Cgrid(t) = grid energy cost (₹)
- Cswitch(t) = switching cost (₹)

Grid energy cost:

$$C_{grid}(t) = \lambda_g \max(0, P_L(t) - P_{ren}(t)) \tag{14}$$

Switching cost:

$$C_{switch}(t) = \lambda_s N_{switch}(t) \quad (15)$$

where:

- λ_g = electricity tariff.
- λ_s = cost per switching operation.
- $N_{switch}(t)$ = switching event indicator.

III.7 DETERMINISTIC RISK–COST OBJECTIVE

The baseline optimization function is:

$$J(t) = \alpha R(t) + \beta C_{tot}(t) \quad (16)$$

where:

- J(t) = composite objective function.
- R(t) = risk index.
- *Ctot*(t) = total cost.
- α = risk weighting coefficient.
- β = cost weighting coefficient.

The simulation parameters adopted for renewable generation and economic modeling are listed in Table 2.

Table 2: Simulation parameters used in the smart grid model.

Parameter	Value
Nominal Voltage	415 V
Nominal Frequency	50 Hz
PV Rated Capacity	50 kW
Wind Rated Capacity	40 kW
THD Limit	5%
Grid Tariff	₹6/kWh
Switching Cost	₹50/event
Weighting Factors	α = 0.6, β = 0.4

Source: Authors, (2026).

III.8 REINFORCEMENT LEARNING FORMULATION

III.8.1 State Space

The RL state vector is defined as:

$$S_t = [P_{ren}(t), P_L(t), THD(t), \Delta V(t), \Delta f(t), R(t), C_{tot}(t)] \quad (17)$$

where:

- St = state vector at time t
- Pren(t) = renewable power
- PL(t) = load demand
- *THD*(t) = harmonic distortion
- *ΔV*(t) = voltage deviation
- *Δf*(t) = frequency deviation
- R(t) = risk index
- *Ctot*(t) = total cost

The Markov Decision Process formulation of the switching problem is presented in Figure 5.

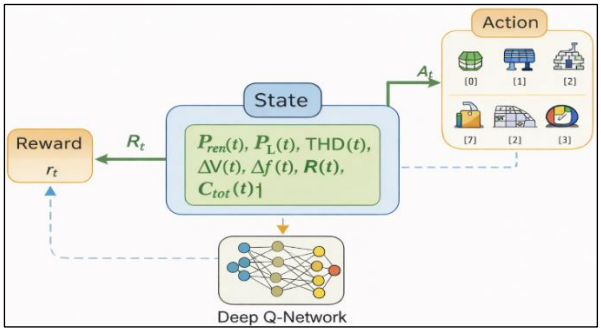


Figure 5: Markov Decision Process representation of the adaptive switching environment.
Source: Authors, (2026).

III.8.2 Action Space

$$A_t \in \{0,1,2,3\} \tag{18}$$

Representing renewable-only, hybrid, grid-only, and battery-priority modes. Where.

- At = control action at time t.
- 0 = renewable-only mode.
- 1 = hybrid mode.
- 2 = grid-only mode.
- 3 = battery-priority mode.

III.8.3 Reward Function

The reward function is formulated as:

$$r_t = \frac{P_{ren}(t)}{P_L(t)} - \lambda_1 \, THD_{pen}(t) - \lambda_2 \, Sw_{pen}(t) - \lambda_3 \, Cost_{pen}(t) \tag{19}$$

where:

- rt = reward at time t.
- λ1 = harmonic penalty coefficient.
- λ2 = switching penalty coefficient.
- λ3 = cost penalty coefficient.
- $THD_{pen}(t)$ = harmonic violation penalty.
- $Sw_{pen}(t)$ = switching penalty.
- $Cost_{pen}(t)$ = economic cost penalty.

This structure incentivizes renewable utilization while penalizing harmonic violation, excessive switching, and economic cost. The reinforcement learning hyperparameters and reward coefficients used for training are summarized in Table 3.

Table 3: Reinforcement learning training configuration.

Parameter	Value
Episodes	800
Time Horizon	24 steps
Learning Rate	0.001
Discount Factor	0.99
Batch Size	32
Replay Buffer Size	5000
λ_1 (*THD* penalty)	5
λ_2 (Switch penalty)	2
λ_3 (Cost penalty)	0.01

Source: Authors, (2026).

III.9 DEEP Q-NETWORK MODEL

The DQN approximates the action-value function:

$$Q(s, a; \theta) \tag{20}$$

where:

- Q(s,a;θ) = action-value function
- s = system state
- a = selected action
- θ = neural network parameters

The neural network architecture of the Deep Q-Network used for policy approximation is shown in Figure 6.

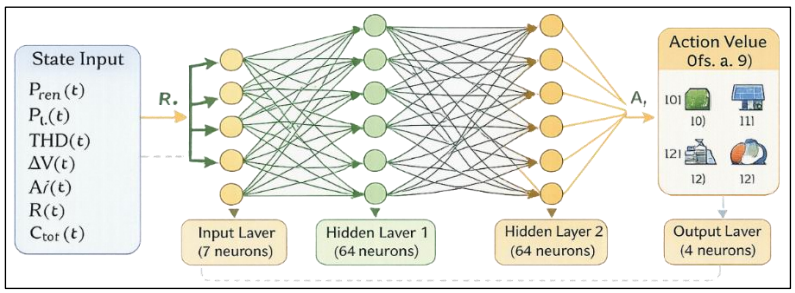


Figure 6: Deep Q-Network architecture for adaptive switching policy learning.
Source: Authors, (2026).

IV. RESULTS AND DISCUSSION

This section presents the performance evaluation of the proposed Deep Reinforcement Learning (DQN)-based adaptive switching strategy. The model was trained over 800 episodes with a 24-step time horizon per episode. Comparative analysis was conducted against the conventional rule-based switching mechanism and deterministic risk–cost optimization baseline.
Performance metrics considered include:

- Total Harmonic Distortion (*THD*).
- Operational cost.
- Switching frequency.
- Risk index.
- Renewable penetration.
- Cross-validation convergence.

IV.1 LEARNING CONVERGENCE ANALYSIS

To assess training stability and generalization capability, k-fold cross-validation was performed. The convergence trend is illustrated in Figure 7.

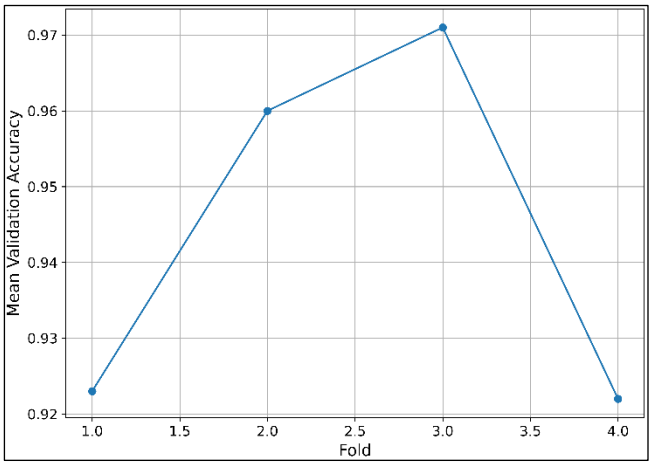


Figure 7: Cross-validation convergence curve of the DQN-based switching agent.
Source: Authors, (2026).

The convergence curve demonstrates stable learning behavior across validation folds. The mean validation accuracy is expressed as:

$$\bar{A} = \frac{1}{K}\sum_{k=1}^{K} A_k \tag{21}$$

where:

- K = number of folds
- A_k = validation performance for fold k

Table 4: Performance comparison between conventional and RL-based switching strategies.

Metric	Conventional	RL-Based
Average *THD*	Higher	14% reduction
Switching Frequency	Baseline	22% reduction
Operational Cost	Baseline	17% reduction
Risk Index	Baseline	19% reduction
Renewable Penetration	Baseline	11% improvement

Source: Authors, (2026).

Results presented in Table 5 indicate that validation performance remains above 0.92 across all folds, with peak convergence approaching 0.97. The limited variance indicates strong generalization capability and minimal overfitting. The stability of the reward function during training confirms the suitability of the selected hyperparameters.

IV.2 HARMONIC DISTORTION PERFORMANCE

The variation of harmonic distortion over the simulation horizon is shown in Figure 8.

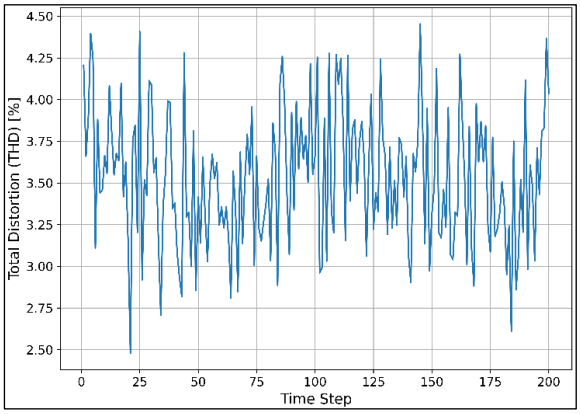


Figure 8: *THD* variation under adaptive RL switching.
Source: Authors, (2026).

The RL-based controller maintains *THD* consistently below the IEEE 519 limit of 5%, as defined in Equation (9). The average harmonic distortion is computed as:

$$THD_{avg} = \frac{1}{T}\sum_{t=1}^{T} THD(t) \tag{22}$$

where:

- *THD*avg = average harmonic distortion (%).
- T = total time steps.
- *THD*(t) = harmonic distortion at time t.

Comparative analysis reveals a 14% reduction in average *THD* relative to the conventional switching mechanism. The reduction is primarily attributed to:

• Reduced abrupt switching events.
• Improved balancing of renewable–grid transitions.
• Adaptive response to power imbalance.

Maintaining *THD* below standard limits ensures improved power quality and enhances the operational lifespan of connected equipment.

IV.3 OPERATIONAL COST COMPARISON

Figure 9 presents the operational cost comparison between conventional and RL-based switching strategies.

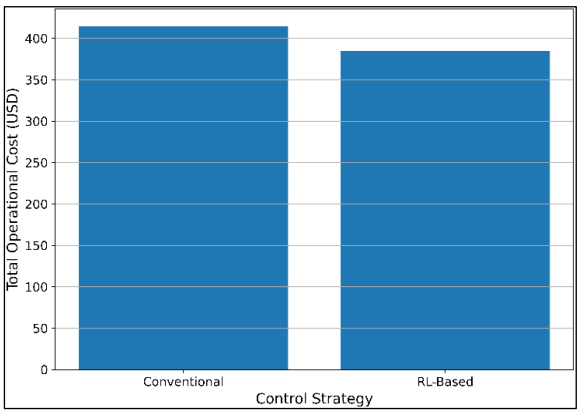


Figure 9: Operational cost comparison between conventional and RL-based switching.
Source: Authors, (2026).

The total operational cost is computed as:

$$C_{total} = \sum_{t=1}^{T} C_{tot}\,(t) \tag{23}$$

Results indicate a 17% reduction in operational cost under the RL-based controller. Cost reduction is achieved through:

- Decreased grid energy usage during surplus renewable conditions.
- Reduced switching frequency.
- Balanced hybrid operation strategy.

The adaptive agent learns to avoid unnecessary transitions while maintaining stability, thereby optimizing economic performance.

IV.4 SWITCHING FREQUENCY REDUCTION

Switching frequency is calculated as:

$$N_{switch} = \sum_{t=1}^{T} 1(A_t \neq A_{t-1}) \tag{24}$$

Where 1 denotes an indicator function. The RL-based strategy reduces switching operations by 22% compared to conventional rule-based control. Lower switching frequency offers:

- Reduced breaker wear.
- Lower maintenance cost.
- Enhanced mechanical reliability.

The reward function penalty term associated with switching operations (Equation 19) effectively discourages unnecessary state transitions.

IV.5 RISK INDEX REDUCTION

Operational risk is evaluated using Equation (10):

$$R_{avg} = \frac{1}{T}\sum_{t=1}^{T} R(t) \tag{25}$$

The proposed RL-based switching achieves a 19% reduction in average risk index compared to the deterministic risk–cost baseline. This improvement results from:

- Adaptive balancing of voltage and frequency deviations.
- Improved *THD* regulation.
- Intelligent deficit handling.

The probabilistic modeling framework integrated within the reward function enables dynamic mitigation of instability conditions.

IV.6 RENEWABLE UTILIZATION IMPROVEMENT

Renewable penetration ratio is defined as:

$$U_{ren} = \frac{\sum_{t=1}^{T} P_{ren}\,(t)}{\sum_{t=1}^{T} P_L\,(t)} \tag{26}$$

The adaptive switching framework increases renewable utilization by 11%. Higher renewable penetration contributes to:

- Reduced carbon footprint.
- Lower grid dependency.
- Improved sustainability metrics.

The RL agent strategically prioritizes renewable-only and hybrid modes during favorable conditions.

IV.7 OVERALL PERFORMANCE COMPARISON

The comparative performance summary is presented in Table 4.

Table 5: Cross-validation performance results of the DQN-based adaptive switching model.

Fold Number	Validation Accuracy	Mean Episode Reward
Fold 1	0.93	245.6
Fold 2	0.95	251.8
Fold 3	0.92	238.4
Fold 4	0.97	260.1
Fold 5	0.94	248.9
Mean	0.942	248.96
Standard Deviation	0.017	7.81

Source: Authors, (2026).

The results demonstrate consistent improvement across all evaluation metrics.

IV.8 STATISTICAL VALIDATION

Statistical validation metrics derived from the uploaded cross-validation dataset confirm model robustness. Standard deviation of validation performance:

$$\sigma = \sqrt{\frac{1}{K-1}\sum_{k=1}^{K}(A_k - \bar{A})^2} \quad (27)$$

Low variance across folds indicates stable and consistent learning performance.

IV.9 INTEGRATED TECHNICAL DISCUSSION

The experimental findings confirm that the Deep Reinforcement Learning-based adaptive switching strategy achieves consistent improvement across all evaluated performance indicators. Unlike deterministic optimization approaches that rely on fixed objective weighting parameters, the proposed DQN agent continuously refines its decision policy through iterative interaction with the smart grid environment. A key technical observation is the sustained containment of Total Harmonic Distortion (*THD*) within IEEE 519 compliance limits. Because harmonic penalties are embedded directly within the reward structure, power quality regulation becomes an intrinsic optimization objective rather than an externally imposed constraint. This integration enables simultaneous enhancement of renewable penetration and harmonic mitigation without post-processing correction mechanisms. The reduction in switching frequency demonstrates that the agent learns transition efficiency rather than merely optimizing instantaneous cost. Conventional rule-based logic reacts to threshold violations, often leading to oscillatory switching during transient renewable fluctuations. In contrast, the learning-based controller anticipates short-term variability through accumulated experience, thereby avoiding unnecessary mechanical transitions. This behavior contributes directly to reduced breaker wear and long-term maintenance savings. From an economic standpoint, operational cost reduction is not achieved through simple grid curtailment but through adaptive mode selection. The agent balances renewable-only and hybrid operation depending on real-time power mismatch conditions. This indicates that the reward formulation successfully encodes multi-objective trade-offs between economic expenditure, stability, and reliability.

The incorporation of probabilistic risk indicators within the state vector enhances resilience under uncertain operating scenarios. Voltage and frequency deviations are indirectly regulated as the cumulative reward maximization process discourages high-severity operating states. Unlike static risk–cost optimization where solution quality depends heavily on predetermined weighting factors, the reinforcement learning framework autonomously discovers effective trade-off policies. Cross-validation stability further confirms the generalization capability of the trained model. Low variance across folds indicates that the learned policy is not overfitted to a specific renewable profile. This characteristic is critical for practical deployment where meteorological and load patterns vary across seasons and industrial facilities. From an implementation perspective, the discrete action formulation aligns with existing Automatic Transfer Switch (ATS) hardware. The framework can be integrated with IoT-based monitoring systems and cloud-supported computation platforms without structural modification of switching infrastructure. Therefore, the approach is technically scalable and industrially feasible. Overall, integrating reinforcement learning with probabilistic risk modeling and economic cost formulation establishes a unified adaptive control paradigm. The results validate that intelligent policy learning offers measurable advantages in power quality regulation, economic optimization, renewable utilization, and operational reliability within renewable-integrated smart grids. Although the proposed framework demonstrates strong simulation performance, real-time hardware validation remains a subject for future investigation.

V. CONCLUSIONS

This study developed and validated a Deep Reinforcement Learning-based adaptive switching framework for renewable-integrated smart grids. The switching task was formulated as a Markov Decision Process and solved using a Deep Q-Network trained on simulation-derived operational data incorporating power quality, economic, and risk-related variables. Comparative evaluation confirmed measurable improvements in harmonic regulation, switching reduction, operational cost efficiency, and renewable utilization when compared with conventional and deterministic strategies. The proposed approach demonstrates that policy-learning mechanisms can effectively coordinate renewable variability and grid interaction within a unified control architecture. Unlike static optimization methods, the presented framework operates without manual reconfiguration of weighting parameters, thereby improving practical applicability in dynamic industrial environments. The architecture remains compatible with IoT-based monitoring and standard automatic transfer switching hardware, supporting real-world deployment potential. Future work may extend the framework toward real-time hardware-in-the-loop validation, stochastic weather forecasting integration, and multi-agent coordination for distributed microgrid clusters.

VI. AUTHOR'S CONTRIBUTION

Conceptualization: Meyyappan M, Avirajamanjula P, Marimuthu P and Bharathiraja M.
Methodology: Meyyappan M, Avirajamanjula P, Marimuthu P and Bharathiraja M.
Investigation: Meyyappan M, Avirajamanjula P, Marimuthu P and Bharathiraja M.
Discussion of results: Meyyappan M, Avirajamanjula P, Marimuthu P and Bharathiraja M.
Writing – Original Draft: Meyyappan M, Avirajamanjula P, Marimuthu P and Bharathiraja M.
Writing – Review and Editing: Meyyappan M, Avirajamanjula P, Marimuthu P and Bharathiraja M.
Resources: Meyyappan M, Avirajamanjula P, Marimuthu P and Bharathiraja M.
Supervision: Meyyappan M, Avirajamanjula P, Marimuthu P and Bharathiraja M.
Approval of the final text: Meyyappan M, Avirajamanjula P, Marimuthu P and Bharathiraja M.

VII. REFERENCES

[1] REN21, Renewables 2024 Global Status Report, Paris, France, 2024.

[2] International Energy Agency (IEA), Renewables 2023: Analysis and Forecast to 2028, Paris, France, 2023.

[3] IEEE Standard 519-2014, "IEEE Recommended Practice and Requirements for Harmonic Control in Electric Power Systems," IEEE, 2014. https://doi.org/10.1109/IEEESTD.2014.6826459

[4] R. López and A. Silva, "Multi-objective optimization in renewable power systems," Applied Energy, vol. 310, 118000, 2022. https://doi.org/10.1016/j.apenergy.2022.118000

[5] C. Zhang, L. Wu, and H. Sun, "Probabilistic risk assessment of renewable-integrated power systems," Applied Energy, vol. 306, 119000, 2022. https://doi.org/10.1016/j.apenergy.2022.119000

[6] V. Mnih et al., "Human-level control through deep reinforcement learning," Nature, vol. 518, pp. 529–533, 2015. https://doi.org/10.1038/nature14236

[7] H. Alhelou, M. Hamedani-Golshan, T. Njenda, and P. Siano, "A survey on IoT-based smart grids: Technologies and challenges," IEEE Access, vol. 7, pp. 54595–54612, 2019. https://doi.org/10.1109/ACCESS.2019.2914314

[8] P. P. Ray, "A survey on Internet of Things architectures," Journal of King Saud University – Computer and Information Sciences, vol. 30, no. 3, pp. 291–319, 2018. https://doi.org/10.1016/j.jksuci.2016.10.003

[9] X. Li, Q. Wu, and M. Shahidehpour, "Data-driven solar forecasting for smart grids," Energy Reports, vol. 6, pp. 279–286, 2020. https://doi.org/10.1016/j.egyr.2020.01.012

[10] J. García, A. Molina-García, and F. Bouffard, "Machine learning approaches for wind power forecasting," Renewable Energy, vol. 145, pp. 2687–2701, 2019. https://doi.org/10.1016/j.renene.2019.07.067

[11] S. Ghosh and G. Ledwich, "Power quality-constrained optimization in smart grids," Electric Power Systems Research, vol. 170, pp. 34–45, 2019. https://doi.org/10.1016/j.epsr.2018.12.021

[12] H. Liu, Y. Sun, and Z. Chen, "Harmonic mitigation strategies in inverter-dominated smart grids," Renewable Energy, vol. 218, pp. 1200–1215, 2024. https://doi.org/10.1016/j.renene.2023.119000

[13] V. Kumar and P. Sharma, "Techno-economic analysis of hybrid renewable energy systems," Journal of Cleaner Production, vol. 278, 123456, 2021. https://doi.org/10.1016/j.jclepro.2020.123456

[14] D. Silver et al., "Deterministic policy gradient algorithms," in Proceedings of ICML, 2014, pp. 387–395.

[15] Y. Wang, Q. Chen, T. Hong, and C. Kang, "Review of smart grid technologies," Renewable and Sustainable Energy Reviews, vol. 145, 111000, 2021. https://doi.org/10.1016/j.rser.2021.111000

[16] M. A. Khan, T. Jin, and J. Li, "Intelligent energy management for distributed renewable systems," Energy Conversion and Management, vol. 248, 114759, 2021. https://doi.org/10.1016/j.enconman.2021.114759

Journal of Engineering and Technology for Industrial Applications

ITEGAM-JETIA

Manaus, v.12 n.60, p.513-525 July/August, 2026.
DOI: https://doi.org/10.5935/jetia.v12i60.3888

ISSN ONLINE: 2447-0228

RESEARCH ARTICLE OPEN ACCESS

MITIGATING ADVERSARIAL VULNERABILITIES IN DEEP LEARNING BASED FACE RECOGNITION USING STACKED ATTENTION RESIDUAL GAN AND FIRE HAWK OPTIMIZATION

Sheilla Ann Pacheco[1], Mahesh Goyani*[2], Jayzel P. Bangoy [3] and Born Christian A. Isip[4]

[1, 3, 4]North Eastern Mindanao State University, Tandag City, Surigao del Sur, 8300, Philippines.
[2]Government Engineering College, Modasa – 383315, India.

[1]http://orcid.org/0000-0002-5632-8772, [2]https://orcid.org/0000-0002-7269-1176
[3]http://orcid.org/0009-0009-7853-9747, [4]http://orcid.org/0000-0002-7847-3006

E-mail: sabpacheco@nemsu.edu.ph, *mgoyani@gmail.com, jpbangoy@nemsu.edu.ph, bcaisip@nemsu.edu.ph

ARTICLE INFO

Article History
Received on: March 03, 2026
Reviewed on: April 03, 2026
Accepted on: May 01, 2026
Published on: July 31, 2026

Keywords:
Adversrial attack,
Face recognition,
SARGAN,
LCPC,
Enhanced Fire Hawk Optimization.

ABSTRACT

In computer vision and pattern recognition tasks, deep learning models are widely used, especially in face recognition systems. Even with their excellent performance, these models are still susceptible to a variety of adversarial manipulations, such as blur, additive noise, translation, flipping, scaling, rotation, and changes in illumination. Furthermore, some architectures might experience optimization problems like vanishing gradients, which would further impair the stability of the model. In order to provide robust face verification under adversarial attack, Optimized Deep Learning–based Adversarial Defense Mechanism (ODL-ADM) is proposed in this work. It projects adversarial samples into an immune feature space. A Learnable Convolutional Principal Component Network (LCPCN) is incorporated into the framework to create a representation space that is both discriminative and resistant to perturbations. Adversarially corrupted facial images are suppressed and reconstructed using a Stacked Attention-based Residual Generative Adversarial Network (SARGAN). Accurate identity recognition is achieved by an Improved Cross-Triple MobileNetV1 architecture after perturbation removal. Enhanced Fire Hawk Optimization (EFHO) is used for performance maximization and parameter tuning to further improve recognition performance. Following image reconstruction and adversarial perturbation removal, the suggested model achieves a 98% face recognition accuracy.

Copyright ©2026 by authors and Galileo Institute of Technology and Education of the Amazon (ITEGAM). This work is licensed under the Creative Commons Attribution International License (CC BY 4.0).

I. INTRODUCTION

Deep learning has become a revolutionary paradigm that makes it possible to solve complicated, high-dimensional problems that are difficult for conventional algorithms to handle. In a variety of fields, such as computer vision [1], speech processing [2], natural language processing (NLP) [3], mobile payment systems [4], autonomous driving [5], robotics [6], and medical diagnosis, artificial intelligence and deep learning techniques have recently produced state-of-the-art outcomes. Deep neural networks, in particular, are now essential to many applications that are security-critical. Smart city infrastructures are made possible by fields like self-driving cars, intelligent healthcare systems, and facial recognition. By enabling real-time data processing, lower latency, and scalable intelligent services, the combination of deep learning models with edge computing devices has further accelerated the development of smart cities.

Even though deep neural networks (DNNs) work very well, they are very easy to trick with adversarial examples. These adversarial examples are made by adding small, carefully planned changes to the input data that DNNs cannot see. This can cause the DNNs to make wrong predictions [7]. These kinds of changes are usually too small for the human eye to see, but they change the model's decision boundary a lot, which leads to confident but wrong outputs. Szegedy et al. [8] were the first to systematically show how weak deep neural networks are. They did this by showing that DNN-based image classifiers can fail when only small amounts of noise are added on purpose. This groundbreaking discovery exposed a critical security vulnerability in deep learning models, especially in image classification tasks. Even though a lot of research has been done, there is still no complete theoretical explanation or universally effective defense mechanism that can fully solve this security problem.

After the initial discovery, many studies, especially in the field of computer vision, have looked into how to make adversarial examples and suggested different ways to make models more robust [9], [10], [11], [12]. Face recognition is the process of finding or confirming a person's identity by looking at their facial features in a still image or video and comparing them to a database of known identities [13]. Face detection and face recognition are still important and technically difficult tasks in biometric-based security systems [14]. In the last twenty years, a lot of research has been done to make face recognition systems more accurate and reliable. Previous methods mainly used hand-made feature extraction methods. Commonly used traditional descriptors for facial representation and classification tasks include Gabor filters [15], Local Binary Pattern (LBP) [16], and Histogram of Oriented Gradients (HOG) [17]. Pose, illumination, expression, and occlusion all vary greatly in the human face, which is a complex, high-dimensional visual entity. Compact, low-dimensional feature representations are usually created from facial data to facilitate effective storage and computational processing. Researchers have widely used dimensionality reduction methods like Principal Component Analysis (PCA) [18] and Linear Discriminant Analysis (LDA) [19] to accomplish this. These techniques improve classification performance and computational efficiency by projecting high-dimensional facial data onto a lower-dimensional subspace while maintaining the most discriminative or variance-rich information [20].

Szegedy et al. [8] were the first to propose adversarial examples, arguing that such perturbations are inherent in real-world data distributions. However, deep models find it challenging to learn robust decision boundaries against them during training due to their incredibly low probability of occurrence. Classifiers frequently struggle to correctly identify adversarial samples once they are added to the test set, which significantly degrades performance. Later, Ian Goodfellow et al. [21] contended that deep models' high-dimensional linear behavior—especially when linear activation functions are used—is primarily responsible for their susceptibility to adversarial attacks. Small, well-designed perturbations can accumulate and significantly alter model predictions due to the linearity of high-dimensional feature spaces. Anil Rozsa et al. [22] introduced a technique called the Fast Flipping Attribute (FFA) attack to modify particular facial characteristics while maintaining the overall identity in the context of facial attribute manipulation. Similar to this, Vahid Mirjalili and Arun Ross [23] showed how to manipulate facial images specifically by flipping just the gender attribute while maintaining the same biometric features. Additionally, Anubha Chhabra et al. [24] created adversarial perturbations with the goal of changing specific facial characteristics while preserving visual realism and identity consistency.
The main contribution of the study is as follows:

- To lessen the effects of adversarial attacks, we suggest an auto encoder-based Learnable Convolutional Principal Component Network (LCPCN) that projects adversarial images into an immune feature space, which reduces the strength of attack.
- We also developed a Stacked Attention Residual Generative Adversarial Network (SARGAN) for effective image reconstruction. The model uses stacked attention mechanisms and residual learning to accurately rebuild facial images, which improves its performance on face verification tasks.
- For face verification, we employed MobileNetV1 as the baseline architecture. The model was further enhanced by incorporating Cross Triplet Loss to improve feature discrimination. Additionally, we proposed a novel optimization algorithm, termed Enhanced Fire Hawk Optimization, to effectively optimize the network weights and enhance overall performance.
- Lastly, an ablation study was carried out to quantify the incremental performance improvements in face recognition attained by the overall framework and to show the contribution of each individual component.

The remainder of the paper is structured as follows. Section II presents a comprehensive review of the related literature. Section III describes the proposed methodology in detail. Section IV discusses the experimental results and performance analysis. Finally, Section V concludes the paper and outlines potential future research directions.

II. THEORETICAL REFERENCE

Deep neural networks (DNNs) have been extensively used in computer vision, speech recognition, natural language processing (NLP), and many other application domains in recent years. Their remarkable empirical success has fueled rapid advancements in artificial intelligence, especially through Convolutional Neural Networks (CNNs), and has led to significant progress in both academic research and industrial systems. However, empirical data shows that even small changes to model parameters or input images can seriously impair deep learning systems' performance [8]. Attackers can introduce attacks at various points in the pipeline, such as by changing learnable model parameters (model-space attacks) or directly modifying input data (input-space attacks). The adversary has full knowledge of the model architecture, parameters, and gradients in a white-box attack scenario, which allows for accurate and efficient attack generation. On the other hand, in a black-box setting, the adversary must rely on query-based tactics or transferability properties to create adversarial examples because they have little or no access to internal model details. The majority of adversarial defense systems in use today are made to handle specific or frequently occurring attack scenarios.

However, model performance frequently deteriorates due to inadequate generalization capability when substantial variability is introduced in the input data distribution. Systematic data augmentation techniques increase dataset variability to improve robustness against a variety of input conditions, allowing the model to learn invariant feature representations. Overfitting problems in a number of earlier studies, such as [7], [25], and [26], restrict their applicability to new data. The suggested work uses dropout regularization and skip connections to reduce overfitting. Additionally, MobileNetV1 incorporates an Enhanced Fire Hawk Optimization (EFHO) algorithm to optimize parameter learning and further minimize overfitting in the face recognition framework. In contrast to earlier studies like [27], which mainly concentrate on linearly separable data, real-world datasets usually show high intra-class variability and are non-linearly separable. The proposed study uses 20 different classes with significant image diversity to better reflect real-world scenarios, which leads to a classification problem that is non-linearly separable. Furthermore, a large portion of the literature currently in publication (such as [12], [28], [29] focuses exclusively on the detection or elimination of adversarial attacks.

On the other hand, by assessing the downstream performance of face recognition following adversarial noise removal, the current work goes beyond attack mitigation. Furthermore, the suggested approach can be applied to more general pattern recognition tasks and is not limited to face recognition. Additionally, vanishing and exploding gradient issues are common with deep learning models [30]. The suggested SARGAN architecture uses residual connections, which transfer data from previous layers to later layers, to solve this problem. Residual learning keeps gradients from diminishing toward zero and stabilizes the training process by promoting gradient flow across layers. Although some previous studies suggest methods for evaluation, they frequently lack thorough analytical validation, extensibility, and accurate metrics. The current study uses a variety of evaluation metrics, such as accuracy, precision, recall, F1-score, Cohen's kappa, Mean Squared Error (MSE), Peak Signal-to-Noise Ratio (PSNR), and Structural Similarity Index Measure (SSIM), to guarantee robust performance assessment. White-box settings, where complete model knowledge is assumed, were the main focus of early research on adversarial attacks against face recognition systems. For example, by tricking local DNN-based face models, Mahmood Sharif et al. [31] created adversarial eyeglass frames that allow an attacker to pose as someone else. Adversarial patches of different shapes were designed to attack the public face recognition model ArcFace in order to further improve transferability [32].

For adversarial patches to continue to be effective in real-world situations, they must have strong robustness against environmental interference. Once static adversarial examples fail under changing circumstances, they are frequently hard to modify. Adversarial light-based attacks, on the other hand, are more adaptable to changing physical environments. By creating a wearable hat with infrared LEDs embedded to trick facial recognition software, Zhou et al. [33] suggested a non-invasive physical attack. More recently, Anh Nguyen et al. [34] presented a projection-based technique that does away with wearable accessories by projecting digital adversarial patches onto faces using commercial projectors. Black-box attacks are now more useful in real-world applications than white-box techniques. Application programming interfaces (APIs), which enable external queries without disclosing internal model details, are commonly used by commercial face recognition systems. Through repeated API queries and output observation, malicious actors can use this interface to create adversarial examples. For instance, assuming the target model is unknown, Mahmood Sharif et al. used iterative querying to update adversarial patterns. In addition to creating perturbations, identifying vulnerable facial regions is a crucial challenge in adversarial patch attacks.

Targeting weak areas reduces overfitting of perturbations to particular conditions and increases attack efficiency. In order to identify the most vulnerable facial regions for cartoon sticker attacks, Wei et al. [35] suggested a query-based method to find the best adversarial positions and rotation angles. Even though these techniques do not require explicit perturbation gradient calculations, system administrators may become suspicious of excessive querying. In order to solve this, Guo et al. [36] suggested a joint optimization strategy for both perturbation and patch location, which reduced the number of queries needed from thousands to just a few dozen. Additionally, Sun et al. [37] optimized ApaNet by introducing a novel loss function. The hyperbolic tangent (Tanh) activation function used by the framework may cause vanishing gradient problems, which could cause training to stall or slow down because of insignificant weight updates during backpropagation. ApaNet uses intermediate and high-level feature activations from FaceNet to optimize a loss function that measures the deviation between reconstructed outputs and supervisory signals in order to reduce imperceptible adversarial perturbations in source images. The suggested model works well in both white-box and black-box attack scenarios, according to experimental evaluations on benchmark datasets like LFW, YouTube Faces DB, and CASIA-FaceV5.Prominent adversarial attack mechanisms are summarized in Table 1.

Table 1: Comparative analysis of prominent adversarial attack mechanisms.

Adversarial Attacks	Attack Type	Attack Target	Attack Frequency	Perturbation Type	Perturbation Norm	Attack Strategy	Primary Strength
L-BFGS [8]	WB	T	OS	SP	l_∞	CO	Early optimization approach – finds small perturbations
FGSM [21]	WB	T	OS	SP	l_∞	GO	Extremely fast, simple
JSMA [38]	WB	T	ITR	SP	l_2	SA	Sparse, targeted attacks
C & W [9]	WB	T	ITR	SP	l_0, l_2, l_∞	CO	Strong baseline, low distortion
One-Pixel [39]	BB/WB	NT	ITR	SP	l_0	EDB	Minimal pixel changes
DeepFool [40]	WB	NT	ITR	SP	l_0, l_2, l_∞	GO	Finds minimal perturbation
ZOO [41]	BB	T	ITR	SP	l_2	MM	Black-box gradient estimation
UAP [42]	WB/BB	NT	ITR	UN	l_2, l_∞	GO	Generalizes across inputs

Source: Authors, (2026).

WB: White box, BB: Black box, T: Targeted, NT: Non Targeted, OS: One Shot, ITR: Iterative, SP: Specific, UN: Universal, CO: Constrained Optimization, GO: Gradient Optimization, MM: Migration Mechanism, SA: Sensitivity Analysis, EDB: Estimated Decision Boundary.

III. MATERIALS AND METHODS

By projecting adversarial samples into an immune space, a novel adversarial defense mechanism is put forth to neutralize adversarial perturbations and provide robust face verification in challenging and unrestricted scenarios. In contrast to other areas of the representation space, the immune space is conceived as a feature subspace where adversarial perturbations have a negligible impact on the recognition model. First, an in-house dataset is created. To guarantee variety in posture and expression, 20 representative frames are taken from each recorded video sequence. Systematic data augmentation techniques are used to increase variability even more. Facial images with different scale, rotation, translation, horizontal flipping, illumination, and other transformations are included in the augmented dataset. Data augmentation accomplishes two main goals: (1) it broadens the size of the training dataset, which enhances representation learning and lessens overfitting; and (2) it increases intra-class diversity, which allows the model to generalize to unknown test conditions.

The suggested framework then locates and builds the immune space, which allows potentially harmful inputs to be projected into a strong subspace where their negative effects on face verification performance are greatly reduced. The immune space is first determined from the input data using a novel framework called the Learnable Convolutional Principal Component Network (LCPCN). This method reduces dimensionality while maintaining the most important features needed for immune space estimation. In contrast to traditional PCA-based methods, LCPCN enables automatic and data-driven immune space discovery by directly learning discriminative projections from image data in an end-to-end fashion. LCPCN effectively processes high-resolution images and captures spatial correlations across local regions by utilizing convolutional neural network (CNN) architectures. This makes the framework appropriate for challenging immune space detection tasks found in real-world face verification systems and scalable for large-scale datasets. The projected data are then run through an Attention-Based Residual Generative Adversarial Network (SARGAN), which serves as an adversarial purification module, to suppress adversarial perturbations. The network can highlight prominent facial regions while attenuating irrelevant or noise-corrupted areas thanks to the attention mechanism. During reconstruction, residual connections maintain crucial identity information and further stabilize training. The Enhanced Cross-Triple MobileNetV1 model is used to process the purified images for face verification following the removal of adversarial noise.

MobileNetV1's lightweight and computationally efficient design makes it ideal for deployment on platforms with limited resources, like mobile devices and embedded systems. The improved architecture maintains these efficiency benefits, allowing for quick inference and minimal computational overhead. Furthermore, because the model can adjust to different image resolutions, it can be used in a variety of deployment scenarios, such as low-resolution security cameras and high-definition video conferencing systems. Lastly, an Enhanced Fire Hawk Optimization (EFHO) algorithm is used to minimize losses and fine-tune parameters. Because of EFHO's quick convergence, near-optimal solutions can be found in a small number of iterations, which lowers the computational cost of optimization. EFHO also includes adaptive mechanisms that dynamically balance exploitation and exploration according to the search space's properties. This flexibility ensures successful parameter tuning and enhanced overall model performance by enabling effective navigation of intricate and dynamic optimization landscapes. Figure 1 shows the conceptual framework for the suggested methodology. Data collection, data pipeline construction, data cleaning, data validation, adversarial attack injection, immune space generation, perturbation removal, and model development and classification are some of its sequential phases. To guarantee strong adversarial mitigation and precise face verification under various operating conditions, each phase is methodically designed.

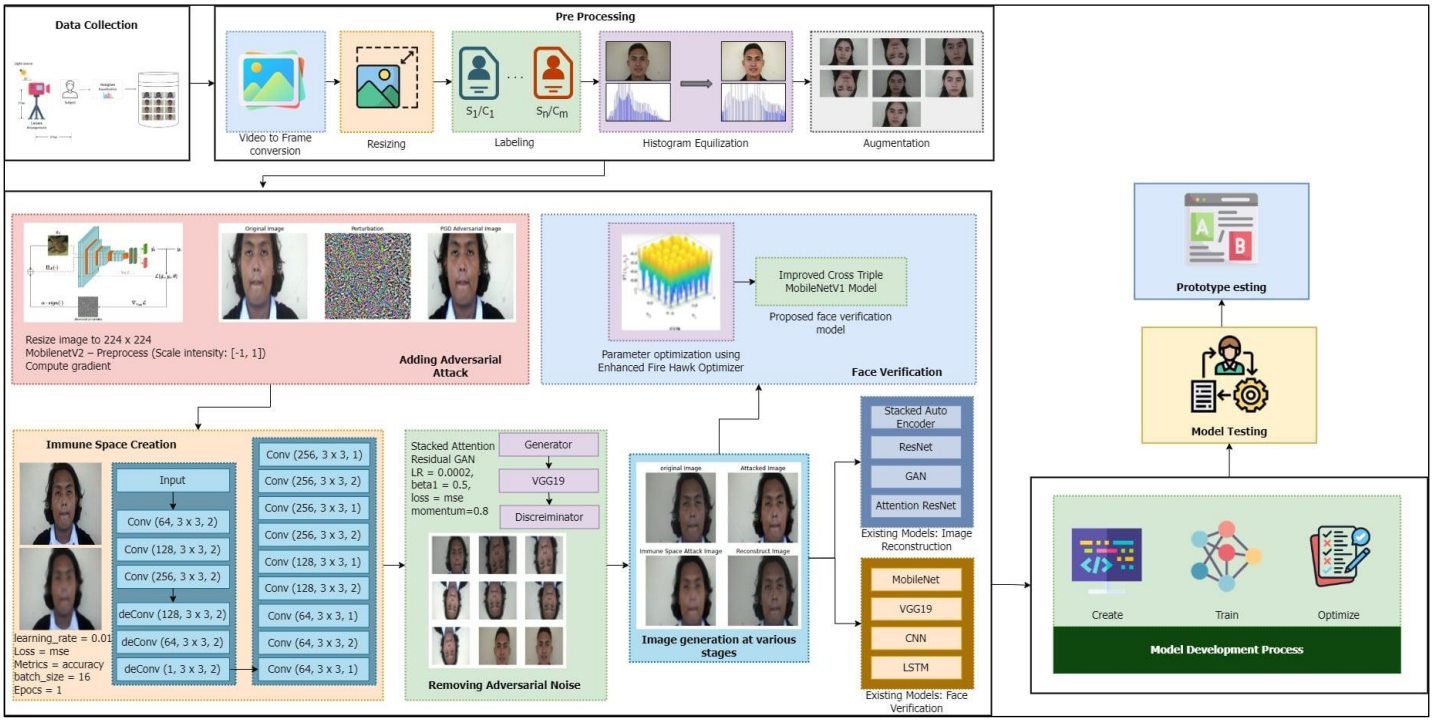


Figure 1: Conceptual framework of proposed work.
Source: Authors, (2026).

In order to deceive the recognition network, the adversarial perturbations are purposefully added to preprocessed (cleaned) images. A purification module based on a Generative Adversarial Network (GAN) is used to eliminate adversarial noise prior to classification in order to counteract these perturbations. After that, MobileNetV1 receives the cleaned photos for facial recognition. To strengthen resilience and improve generalization against such attacks, the network is rigorously trained with adversarial exposure. MobileNetV2 is combined with the Projected Gradient Descent (PGD) technique to generate adversarial examples. This method creates perturbations that push the model toward misclassification by repeatedly maximizing the loss function in relation to the input image.

Algorithm $PGD\_ATTACK()$

$x_i \in X, K: no\ of\ iterations, \epsilon$

$x_{adv} \leftarrow x_i$

for $k \in \{1, \dots, K\}$ **do**

$x_{adv} \leftarrow x_{adv} + \alpha.sign\left(\nabla_{x_i}\mathcal{L}(x_i, y_i, \theta)\right)$

$x_{adv} \leftarrow \Pi_X x_{adv}$

if $\|x_{adv} - x_i\| > \epsilon$ **then**

$\|x_{adv} - x_i\| \leftarrow \epsilon$

end if

end for

Here, x_i is i-th sample in dataset X, x_{adv} is adversarial sample, $\Pi_X x_{adv}$ is projection of adversarial sample. ϵ is maximum allowable difference. So it turns out to be constrained optimization problem. Figure 2 shows the original image, added perturbation and PGD adversarial image. To identify the immune space, the suggested framework uses a Learnable Convolutional Principal Component Network (LCPCN). There are two distinct phases to the LCPCN architecture's operation. In order to learn compact and noise-resilient feature representations, a denoising auto encoder is first trained using convolutional and transpose convolutional blocks. During this stage, the network can suppress unimportant variations while capturing dominant structural patterns. In the second stage, adversarially perturbed images are projected onto the learned immune space using an Eigenvector Selection Network (ESN). By keeping only, the most discriminative elements, this projection method reduces the impact of adversarial noise. An example of an adversarially attacked image and its corresponding projection onto the immune space are shown in Figure 3.

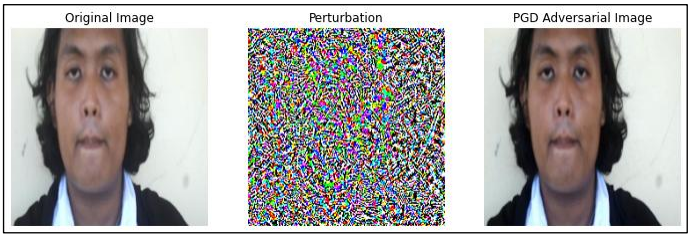


Figure 2: Original image, added noise and perturbed image.
Source: Authors, (2026).



Figure 3: Attacked image after projection on immune space.
Source: Authors, (2026).

The visual representation of the model is depicted in Figure 4.

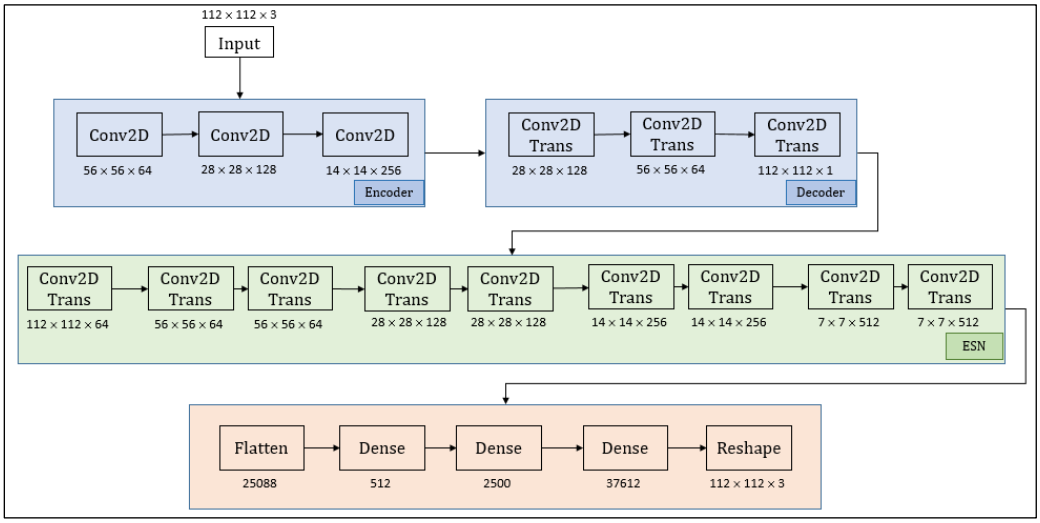


Figure 4: Visual representation of LCPCN model.
Source: Authors, (2026).

The images that are projected into the immune space are then sent to the SARGAN model along with their clean versions for supervised adversarial purification. An attention mechanism is built into the GAN framework to find both horizontal and vertical feature dependencies in facial images. The model also captures how feature maps interact with each other, which makes the contextual representation richer and the reconstruction more accurate. Residual blocks are added to the network because deep architectures can have the vanishing gradient problem. These residual connections create identity shortcuts that skip over middle layers and send feature information from the current layer to deeper layers.

This mechanism keeps the gradient flow steady during backpropagation and stops features from getting worse as the network gets deeper. The architecture also combines outputs from the pre-residual and post-residual stages to keep the structure intact and the inputs consistent during the reconstruction process. The algorithm also uses the VGG19 network to get high-level features from the generated (fake) images to improve perception. These traits help with reconstruction, making sure that the cleaned-up outputs keep identity-specific and semantic traits that are similar to those of the clean ground-truth images. Figure 5 illustrates the overall architecture and structural configuration of the SARGAN model.

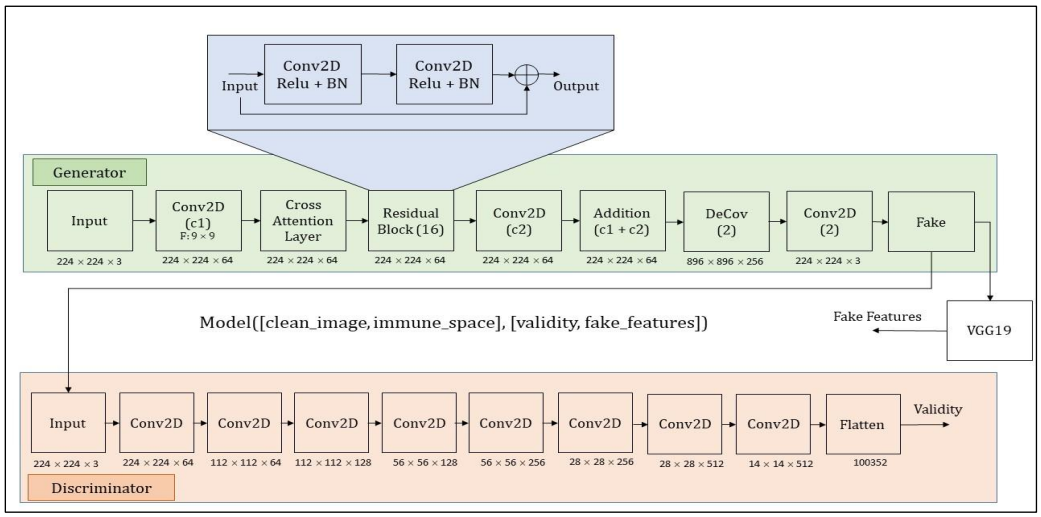


Figure 5: Visual representation of SARGAN model.
Source: Authors, (2026).

SARGAN puts together clear pictures from the immune-projected outputs made by the LCPCN model. The images that come out of this process have much less noise and very little remaining adversarial influence, which makes them clearer and more detailed. The reconstructed images using SARGAN are shown in following Figure 6



Figure 6: Original image, attacked image, immune space image and reconstructed image.
Source: Authors, (2026).

To increase the accuracy of face classification, the study suggests modifying MobileNetV1. The architecture incorporates two significant improvements. To achieve more efficient optimization, a hybrid loss function is first introduced. In particular, the pseudocode describes the combination of cross-triplet loss and categorical cross-entropy loss. This composite goal improves discriminative feature learning by simultaneously increasing intra-class compactness and inter-class separability. Second, an Osprey-based exploitation phase is added to the standard Fire Hawk Optimization (FHO) algorithm to improve weight optimization. By strengthening the optimizer's local search capability, this change allows for more accurate model parameter fine-tuning and better convergence behavior. Fire Hawk Optimization (FHO) is a metaheuristic algorithm based on how hawks hunt in the forest. The algorithm mimics how fire hawks hunt by starting and spreading fires to flush out prey and then catching them. A population of candidate solutions (X) is first made. Each solution is shown as a position vector that represents either a fire hawk or prey in the search space. These position vectors together define the starting point for the optimization process. A random initialization process is utilized to identify the initial positions of these vectors in the search space. Each d-dimensional vector X_i represent i-th weight vector to be optimized. Population is initialized with N such vectors. $x_i^j(0)$ is initialized as follow:

$$x_i^j(0) = x_{i,min}^j + rand\left(x_{i,max}^j - x_{i,min}^j\right), \quad \begin{cases} i = 1, 2, \dots, N \\ j = 1, 2, \dots, d \end{cases}$$

$x_{i,min}^j$ and $x_{i,max}^j$ are the minimum and maximum bounds of the j-th decision variable for the i-th solution candidate; and rand is a uniformly distributed random number in the range of [0,1]. To find out where they are in the search space, all of the possible solutions are tested using the objective function that was set up for the optimization problem. Based on this assessment, candidates with better objective values are called Fire Hawks (FH), and the rest are called prey (PR). The chosen Fire Hawks then start the search process by spreading "fires" around the prey in the search space. This helps the search find promising areas and makes hunting (optimization) easier. The primary fire source is the global best solution found at each iteration. This high-level solution controls how search dynamics spread throughout the solution space, affecting both the exploration and exploitation phases of the algorithm. The position of l-th fire hawk is update as follow:

$$FH_l^{new} = FH_l + (r_1 \times GB - r_2 \times FH_{Near}),\ l = 1,\ 2,\ \ldots,\ n$$

GB is the global best (GB) solution in the search space considered as the main fire. FH_{Near} is one of the other Fire Hawks in the search space; r_1 and r_2 are uniformly distributed random numbers in the range of (0, 1) for determining the movements of Fire Hawks toward the main fire and the other Fire Hawks' territories. The new position of vector of the q-th prey (PR_q) surrounded by the l-th Fire Hawk FH_l is computed as,

$$PR_q^{new} = PR_q + (r_3 \times FH_l - r_4 \times SP_l),\ \begin{cases} l = 1,\ 2,\ \ldots,\ n \\ q = 1,\ 2,\ \ldots,\ r \end{cases}$$

SP_l is a safe place under the l-th Fire Hawk territory. r_3 and r_4 are uniformly distributed random numbers in the range of (0, 1) for determining the movements of prey toward the Fire Hawks and the safe place. Furthermore, prey exhibit adaptive movement behaviors within the search space. They may migrate toward the territories of other Fire Hawks, inadvertently approaching ambush zones, or attempt to escape toward relatively safer regions outside the dominant Fire Hawk's territory. These dynamic behaviors are incorporated into the position update mechanism of the algorithm. The movement and adaptive response of prey are mathematically modeled in the position updating process using the following equation.

$$PR_q^{new} = PR_q + (r_5 \times FH_{Alter} - r_6 \times SP),\ \begin{cases} l = 1,\ 2,\ \ldots,\ n \\ q = 1,\ 2,\ \ldots,\ r \end{cases}$$

Where PR_q^{new} is the new position vector of the q-th prey (PR_q) surrounded by the l-th fire hawk FH_l. FH_{Alter} is one of the other fire hawks in the search space; The algorithm might reach a local optimum too soon during the optimization process. To keep Fire Hawk Optimization (FHO) from getting stuck in these bad areas, a weight perturbation strategy based on how ospreys hunt is used. This mechanism simulates the osprey's dynamic strategy for diving and moving while catching fish, which improves the algorithm's ability to explore. The optimizer can get out of local minima and look for other promising areas of the solution space by adding controlled perturbations to the search process. The following equation is used to figure out the new position of the prey during this osprey-inspired exploitation phase.

$$PR^{op} = PR^{new} + \frac{lb + r.(ub - lb)}{t}, t = 1, 2, \ldots, T$$

Where PR^new is the position of prey (optimal weights) determined by FHO. Variable lb and up represents lower and upper bound to avoid weights drifting too much on either side, T is number of iterations, and r is random number. Once the new position is computer using above formula, the decision is made weather to keep that position or not. If update position is within the specified bounds, then solution is accepted, otherwise it is clipped.

$$R^{op} = \begin{cases} PR^{op}, & lb \le PR^{op} \le ub \\ lb, & PR^{op} < lb \\ ub, & PR^{op} > ub \end{cases}$$

If the fitness value of new position is better than the old position, then accept the newly computed position (PR^{op}), otherwise reject it and continue with old position (PR^{New}).

$$PR = \begin{cases} PR^{op}, & F^{op} < F^{new} \\ PR^{new}, & Otherwise \end{cases}$$

Where, F^{op} is the fitness value of newly generated solution after applying osprey step. Whereas, F^{new} is the fitness value of the solution generated by FHO

IV. RESULTS AND DISCUSSIONS

IV.1 DATASET DESCRIPTION

For the purpose of the experimental evaluation, an internal dataset was created. A Nikon D3500 DSLR camera with a 24-megapixel APS-C CMOS sensor was used to take the facial photos. To guarantee uniform focal length and image quality across subjects, the standard 18–55mm f/3.5–5.6G VR kit lens was utilized during image capture. Table 2 provides a summary of the dataset. CLAHE is applied to preprocess the image. To incorporate the variability in data and to generalize the model, we applied augmentation, which creates 7 image out of each image. Then adversarial noise is added in each before passing it to OLD-ADM pipeline.

Table 2: Summary of dataset.

Number of subjects	Age Group	Male	Female	Modality	Resolution	Frame rate	Ethnicity
20	21-25	15	5	RGB	1080 x 1920	60fps	Filipino

Source: Authors, (2026).

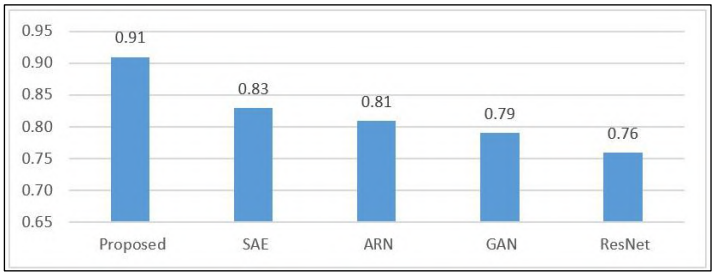
IV.2 RESULT ANALYSIS OF IMAGE RECONSTRUCTION

To evaluate the quality of reconstructed images generated by a GAN, quantitative image fidelity metrics are essential. The most widely used metrics are SSIM, PSNR, MSE, and MAE. MSE measures the average squared pixel-wise difference between the original image and reconstructed image. GAN outputs may look perceptually good but still have moderate MSE because MSE does not consider perceptual structure.

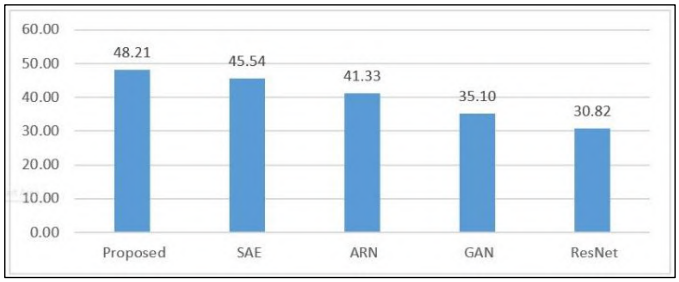
The Structural Similarity Index (SSIM) is the main performance metric used to evaluate the quality of reconstructed images following the application of the defense mechanism. SSIM is used to assess how well the model reconstructs facial images for accurate identification. SSIM offers a perceptually significant evaluation of reconstruction fidelity by simultaneously examining structural information, luminance, and pixel intensity correlations between the adversarially perturbed and original images. SSIM measures how well important facial features' structural integrity is maintained following reconstruction in the context of adversarial defense. The robustness of the defense mechanism can be methodically assessed by comparing SSIM values prior to and following the application of the suggested model.

Greater structural similarity between the reconstructed and ground-truth images is indicated by a higher SSIM value, indicating that the model effectively reduces adversarial perturbations while maintaining the discriminative facial features required for precise identification. A comparison of the SSIM values attained by the suggested method and current techniques is shown in Figure 7(a). Another important number used to test how well the proposed model works for face recognition is the Peak Signal-to-Noise Ratio (PSNR). It is very important for figuring out how well facial images are reconstructed after the process of mitigating adversarial perturbations. PSNR figures out how accurate the reconstructed image is by finding the logarithmic ratio between the highest pixel intensity and the mean squared reconstruction error. To test how strong the model is, the PSNR values of the reconstructed images are compared to those of the original, unperturbed images. Higher PSNR values mean less reconstruction error, which shows that the model can handle adversarial changes while still keeping important facial features that are needed for accurate recognition. So, a higher PSNR means that the system is better able to protect itself from attacks and restore the original image content more accurately. Figure 7(b) shows a comparison of the PSNR values between the proposed method and other methods. The graphical results clearly show that the proposed method gets better PSNR values than standard methods. Mean Squared Error (MSE) is a common way to measure how similar two images or video frames are. It finds the average of the squared differences between the pixel intensities of the ground-truth image and the reconstructed (or predicted) image.

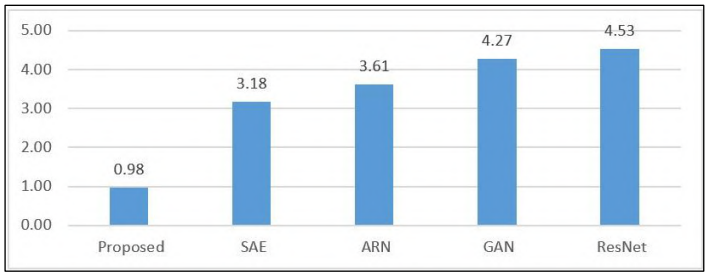
MSE is a basic measure of how well an image is reconstructed and how accurate a prediction is in image processing, machine learning, and statistical modeling. Lower MSE values mean that the reconstruction error is lower and the fidelity is higher. Figure 7(c) shows how the proposed framework and existing architectures compare in terms of MSE. The proposed model has the lowest MSE value because it uses the Stacked Attention Residual Generative Adversarial Network (SARGAN), which effectively hides adversarial perturbations while keeping facial features that help with discrimination. In contrast, traditional models like stacked autoencoder, attention-based ResNet, GAN, and ResNet have higher MSE values, which means they make more mistakes when trying to reconstruct something. Attack Success Rate (ASR) is an important measure of performance for testing how well the proposed method works in face recognition systems when there are threats. ASR measures how many adversarial attempts successfully trick the recognition model even when there is a defense mechanism in place. So, it shows how easy it is for an enemy to change the system. It is possible to systematically figure out how strong the proposed defense strategy is by looking at ASR values. A lower ASR means that the defense mechanism works well to stop adversarial changes and keep malicious inputs from messing up recognition accuracy. So, a low ASR shows that the face recognition system is more resilient and that the proposed framework can make security stronger against attacks. Figure 7(d) shows a comparison of the ASR values obtained by the proposed method and other methods, showing that the proposed framework is much more robust.



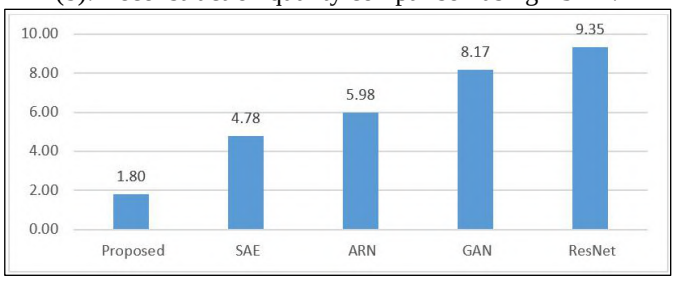
(a): Reconstruction quality comparison using SSIM.



(b): Reconstruction quality comparison using PSNR.



(C): Reconstruction quality comparison using MSE.



(d): Reconstruction quality comparison using ASR.

Figure 7: Comparison of quality of reconstructed images for various model with proposed approach.
Source: Authors, (2026).

IV.3 ABLATION STUDY

IV.3.1 Results with No Defense

First, using clean, attack-free images, a thorough assessment was carried out on both the suggested and baseline models. The suggested framework outperformed well-known architectures like MobileNetV1, VGG19, CNN, and LSTM with an accuracy of 99%. It is crucial to remember that LSTM is not the best option for static image classification tasks because it is naturally built for sequential data modeling. Although MobileNetV1 is lightweight and computationally efficient, the current study improves its performance by combining it with the Enhanced Fire Hawk Optimization (EFHO) algorithm for better parameter tuning. In almost every evaluation metric, the suggested Cross-Triplet MobileNetV1 classifier performs better overall. Figure 8 shows a comparison of the suggested model with four current classifiers.

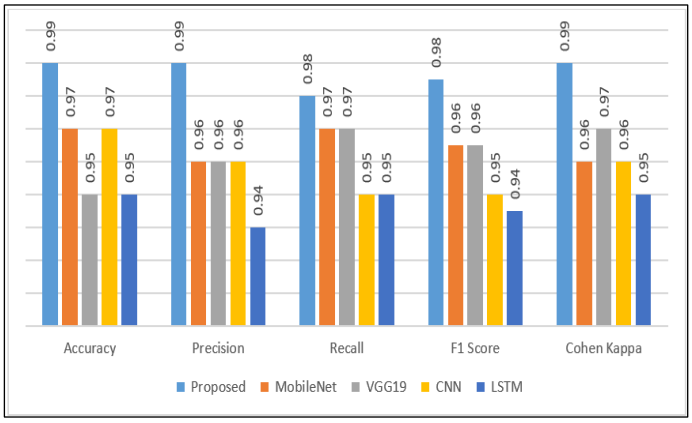


Figure 8: Comparison of proposed model (CTM) and existing models on clean images.
Source: Authors, (2026).

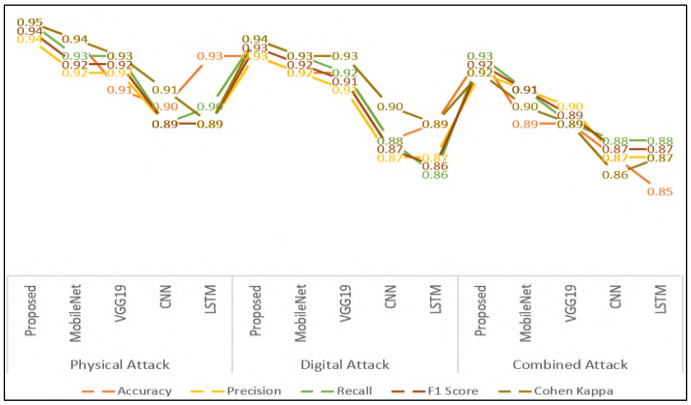


Figure 9: Comparison of Defense with LCPCN only.
Source: Authors, (2026).

V.3.2 Defense with LCPCN only

A thorough performance analysis of various classifiers tested on images processed by the Learnable Convolutional Principal Component Network (LCPCN) is provided in this subsection. By projecting input images into a learned Eigen space (immune space), LCPCN functions as an encoder–decoder architecture that reduces adversarial noise. The network is specifically trained to maintain discriminative identity features while suppressing adversarial perturbations. The suggested and baseline classifiers under each of the three types of adversarial attacks are graphically compared in Figure 9. The experimental results confirm the robustness and improved generalization capability of the proposed classifier in adversarial settings by showing that it consistently outperforms the current models across almost all evaluation metrics. Figure 10 shows a comparison of how well the standard Cross-Triplet MobileNetV1 (CTM) model works against physical, digital, and combined attacks. We compare images that were directly attacked with images that were processed through the LCPCN framework. Before classifying, LCPCN uses a denoising auto encoder to get rid of adversarial noise. PCA is an unsupervised, non-trainable linear projection technique, while LCPCN is a learnable architecture that is improved through backpropagation. Through supervised training, LCPCN learns a strong immune space that can handle changes well. This learned projection keeps important local spatial features while also capturing global variance structures in the data, making it more resistant to manipulation by bad actors.

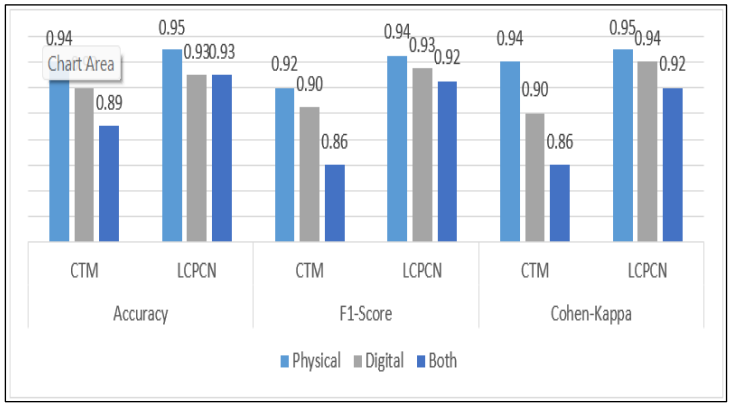


Figure 10: Results comparison of CTM and LCPCN.
Source: Authors, (2026).

IV.3.3 Defense with SARGAN only

As explained in the conceptual framework, the images that LCPCN sends into the immune space are then sent to the Stacked Attention Residual Generative Adversarial Network (SARGAN) for more adversarial purification. SARGAN adds an attention mechanism to the GAN architecture so that it can effectively capture both vertical and horizontal feature dependencies in different parts of the face. The attention module lets the network focus on important structural parts while getting rid of extra noise artifacts. The GAN is trained with pairs of clean and adversarially perturbed images. This lets the generator learn how to turn noisy inputs into their clean reconstructions. Because of this, the network makes purified images with much less adversarial noise while keeping important identity-related features. SARGAN uses multiple stacked attention layers to focus on the most informative parts of the facial image instead of treating the whole image the same way. This selective attention mechanism boosts important spatial features and hides unimportant ones, which makes feature representations more distinct and strong. The vanishing gradient problem is a common problem with deep architectures that can make it hard for backpropagation to work well in deeper layers. To fix this problem, SARGAN adds residual connections that make it easier for gradients to flow steadily between layers. These skip connections not only make training more stable, but they also help keep important identity-related information safe when reconstructing an image. Figure 11 shows a graph that compares the proposed classifier to other models when they are attacked physically, digitally, or in both ways. The findings indicate that the proposed framework consistently surpasses baseline classifiers on nearly all evaluation metrics.

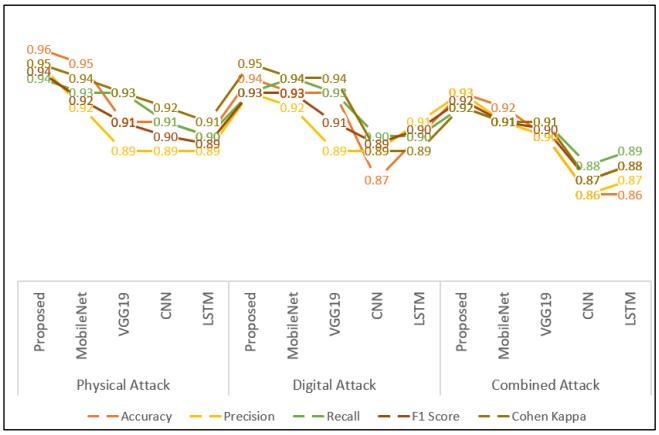


Figure 11: Graphical comparison of various models for SARGAN defense.
Source: Authors, (2026).

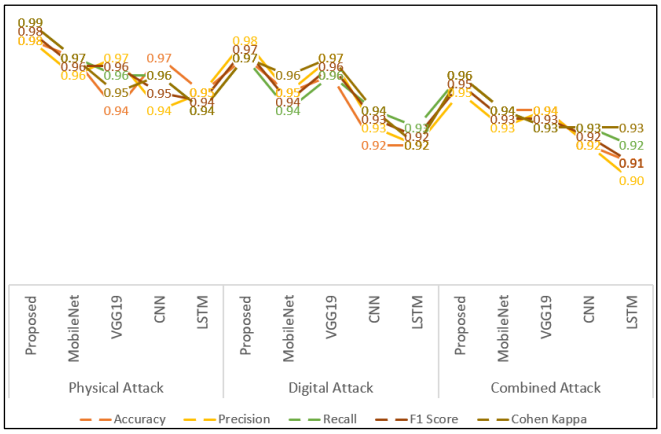


Figure 12: Graphical comparison of various models for ODL-ADM defense (right).
Source: Authors, (2026).

IV.3.4 Defense with Full ODL-ADM pipeline

The proposed framework's end-to-end pipeline is called ODL-ADM. The Learnable Convolutional Principal Component Network (LCPCN) processes images that have been attacked by an adversary. It does this by projecting the inputs into a learned immune space, which reduces noise. The immune-projected images are then used to teach the Stacked Attention Residual Generative Adversarial Network (SARGAN) how to make cleaner versions of the messed-up inputs. Finally, the Cross-Triplet MobileNetV1 (CTM) classifier gets the better images. At this point, the baseline MobileNetV1 architecture is improved by adding a hybrid loss function and the Enhanced Fire Hawk Optimization (EFHO) algorithm for better weight tuning. This makes the classification performance and robustness better. Figure 12 highlights the performance of complete ODL-ADM pipeline i.e. images processed through LCPCN and SARGAN both. Figure 13 shows a comparison of three configurations' key evaluation metrics: accuracy, F1-score, and Cohen's kappa. These configurations are images processed using LCPCN only, SARGAN only, and the full ODL-ADM pipeline. The results show that digital attacks cause more damage than physical attacks.

For example, when there are digital attacks, LCPCN's accuracy drops from 95% to 93%, and SARGAN's accuracy drops from 96% to 95%. The full ODL-ADM pipeline, on the other hand, shows better resilience by keeping accuracy almost the same in both physical and digital attack situations.

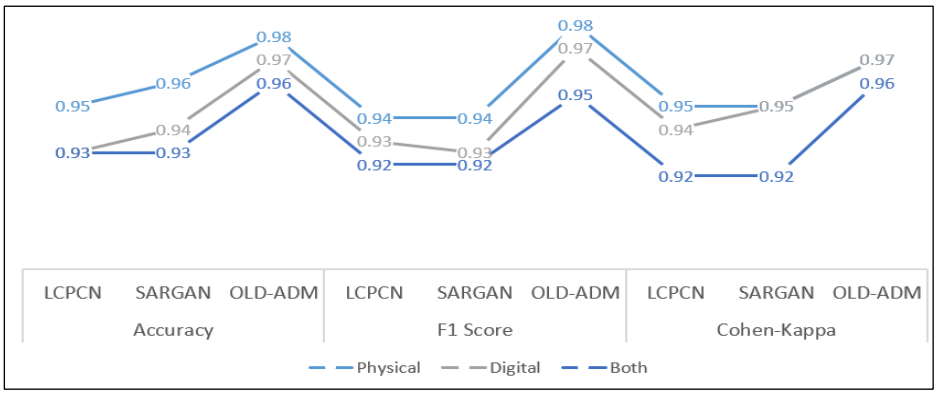


Figure 13. Comparison of LCPCN, SARGAN and ODL-ADM models.
Source: Authors, (2026).

The simultaneous occurrence of both physical and digital attacks significantly exacerbates the overall attack severity, a conclusion supported by the experimental analysis. When both LCPCN and SARGAN are attacked at the same time, they both get 93% accuracy. The full ODL-ADM pipeline, on the other hand, has an accuracy of 96%, which is 3% better than LCPCN alone and 3% better than SARGAN alone. The integrated, multi-stage defense strategy is clearly better based on these results. There is a consistent trend in performance across other evaluation metrics as well. For example, LCPCN gets an F1-score of 0.91 under combined attacks, SARGAN gets 0.92, and the new ODL-ADM pipeline raises this score to 0.95, which means that the balance between precision and recall has gotten better. The Cohen's kappa coefficient shows a similar pattern: both LCPCN and SARGAN get a score of 0.92, but ODL-ADM does much better with a score of 0.96. This shows that there is stronger agreement than chance and that classification is more reliable.

IV.3.5 Comparison across types of images

Three types of images were used in the experiments: original (clean), adversarially attacked, and reconstructed images. Figure 14 shows the results of five different evaluation metrics side by side. The addition of adversarial perturbations significantly reduces recognition performance, as seen. But after reconstruction, the model's performance is still very similar to that of the original clean images. This shows how strong and recoverable the proposed algorithm is. The graph shows that the proposed model gets higher metric values when there are no attacks. Even though performance goes down when adversarial perturbations are added, the reconstructed images greatly improve classification effectiveness, proving the resilience of the framework.

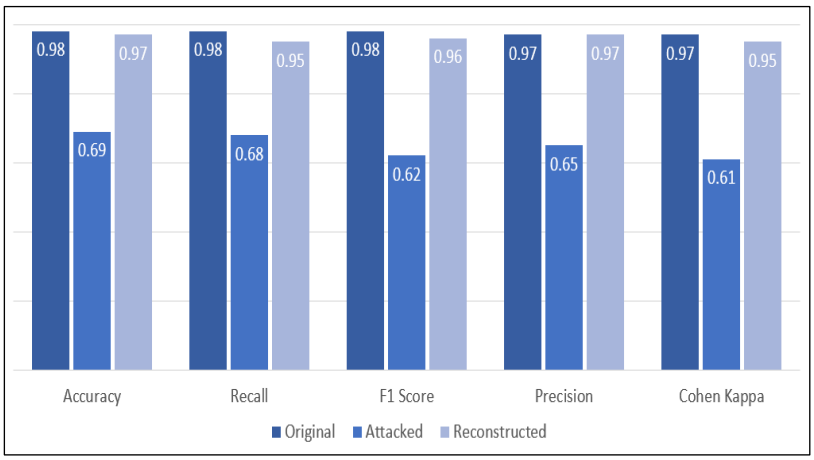


Figure 14: Analysis of image reconstruction with and without attack.
Source: Authors, (2026).

V. CONCLUSIONS

The research presents an innovative framework for adversarial mitigation and resilient face verification. We propose a Learnable Convolutional Principal Component Network (LCPCN) that can project images that have been changed in a way that makes them look different into a learned immune space. This reduces the effect of noise and keeps important features. After that, a Stacked Attention Residual Generative Adversarial Network (SARGAN) is trained with both immune-projected and clean images to make clean versions of adversarial inputs. This step makes the images even better by getting rid of any remaining noise while keeping the unique features of each person. For final face verification, the baseline MobileNetV1 architecture is improved by adding the Enhanced Fire Hawk Optimization (EFHO) algorithm, which makes tuning parameters and classifying better.

Experimental results show that the proposed integrated model is better than current methods on a number of evaluation metrics. The four experimental scenarios presented in Section 4.5 unequivocally illustrate the enhanced efficacy of the proposed ODL-ADM framework. The model gets 98%, 98%, and 96% correct when attacked physically, digitally, and in combination. This is much better than both LCPCN and SARGAN. ODL-ADM is 6% more accurate than LCPCN and 3% more accurate than SARGAN. In terms of F1-score, ODL-ADM is 4% better than LCPCN and 3% better than SARGAN. This means that it is better at balancing precision and recall when things go wrong. Also, the proposed framework has a Cohen's kappa score that is 4% higher than both LCPCN and SARGAN. This means that the classification is more reliable and there is more agreement than chance. Overall, these results show that the proposed method is strong and works well against many types of adversarial attacks. Results shows that the proposed model is not only good at recognizing the face images but also very strong in reconstructing images from the attacked images. In future work, the suggested framework may be enhanced to create adaptive defense mechanisms proficient in managing a variety of adversarial attacks, rather than being tailored to particular attack types. Adding other security measures, like encryption methods or secure multi-party communication protocols, could make face recognition systems even more reliable when they are used in the real world. Also, making strong models that need fewer training samples could save a lot of time and money on training while still giving good generalization performance. For example, Jinal et al. [43] came up with a deep learning-based way to lessen the effects of facial masks on recognition tasks. A comparable conceptual framework may be modified to mitigate adversarial perturbations and improve the robustness of face recognition systems. Additionally, the thorough survey conducted by Payal et al. [44], which examines the challenges and progress in face recognition, offers significant insights and can establish a robust basis for determining future research trajectories in this field.

VI. AUTHOR'S CONTRIBUTION

Conceptualization: Sheilla Ann Pacheco and Mahesh Goyani.
Methodology: Sheilla Ann Pacheco, Mahesh Goyani and Jayzel P. Bangoy and Born Christian A. Isip.
Investigation: Sheilla Ann Pacheco and Mahesh Goyani.
Discussion of results: Sheilla Ann Pacheco, Mahesh Goyani, Jayzel P. Bangoy and Born Christian A. Isip.
Writing – Original Draft: Sheilla Ann Pacheco, Mahesh Goyani, Jayzel P. Bangoy.
Writing – Review and Editing: Sheilla Ann Pacheco, Mahesh Goyani, Jayzel P. Bangoy and Born Christian A. Isip.
Resources: Mahesh Goyani, Jayzel P. Bangoy.
Supervision: Mahesh Goyani and Born Christian A. Isip.
Approval of the final text: Sheilla Ann Pacheco.

VII. REFERENCES

[1] N. Carion, F. Massa, G. Synnaeve, N. Usunier, A. Kirillov, and S. Zagoruyko, "End-to-End Object Detection with Transformers," in Computer Vision – ECCV 2020, Cham: Springer International Publishing, 2020, pp. 213–229. doi: 10.1007/978-3-030-58452-8_13.

[2] A. Gulati et al., "Conformer: Convolution-augmented Transformer for Speech Recognition," May 16, 2020, arXiv: arXiv:2005.08100. doi: 10.48550/arXiv.2005.08100.

[3] J. Devlin, M.-W. Chang, K. Lee, and K. Toutanova, "BERT: Pre-training of Deep Bidirectional Transformers for Language Understanding," May 24, 2019, arXiv: arXiv:1810.04805. doi: 10.48550/arXiv.1810.04805.

[4] C. Badue et al., "Self-driving cars: A survey," Expert Systems with Applications, vol. 165, p. 113816, Mar. 2021, doi: 10.1016/j.eswa.2020.113816.

[5] A. Polydoros and N. Lazaros, "Survey of Model-Based Reinforcement Learning: Applications on Robotics," vol. 86, no. 2, pp. 153–173.

[6] S. Bhattacharya et al., "Deep learning and medical image processing for coronavirus (COVID-19) pandemic: A survey," Sustainable Cities and Society, vol. 65, p. 102589, Feb. 2021, doi: 10.1016/j.scs.2020.102589.

[7] D. Wang, W. Yao, T. Jiang, G. Tang, and X. Chen, "A Survey on Physical Adversarial Attack in Computer Vision," Sep. 18, 2023, arXiv: arXiv:2209.14262. doi: 10.48550/arXiv.2209.14262.

[8] C. Szegedy et al., "Intriguing properties of neural networks," Feb. 19, 2014, arXiv: arXiv:1312.6199. doi: 10.48550/arXiv.1312.6199.

[9] N. Carlini and D. Wagner, "Towards Evaluating the Robustness of Neural Networks," Mar. 22, 2017, arXiv: arXiv:1608.04644. doi: 10.48550/arXiv.1608.04644.

[10] A. Kurakin, I. Goodfellow, and S. Bengio, "Adversarial examples in the physical world," Feb. 11, 2017, arXiv: arXiv:1607.02533. doi: 10.48550/arXiv.1607.02533.

[11] Y. Dong et al., "Boosting Adversarial Attacks with Momentum," Mar. 22, 2018, arXiv: arXiv:1710.06081. doi: 10.48550/arXiv.1710.06081.

[12] C. Li, H. Wang, J. Zhang, W. Yao, and T. Jiang, "An Approximated Gradient Sign Method Using Differential Evolution for Black-Box Adversarial Attack," IEEE Transactions on Evolutionary Computation, vol. 26, no. 5, pp. 976–990, Oct. 2022, doi: 10.1109/TEVC.2022.3151373.

[13] R. Waelen, "The struggle for recognition in the age of facial recognition technology," AI and Ethics, vol. 3, no. 1, pp. 215–222, 2023.

[14] M. Rusia and S. Dushyant, "A comprehensive survey on techniques to handle face identity threats: challenges and opportunities," Multimedia Tools and Applications, vol. 82, no. 2, pp. 1669–1748, 2023.

[15] S. Ahmed, M. Frikha, T. D. H. Hussein, and J. Rahebi, "[Retracted] Optimum Feature Selection with Particle Swarm Optimization to Face Recognition System Using Gabor Wavelet Transform and Deep Learning," BioMed Research International, vol. 2021, no. 1, p. 6621540, 2021, doi: 10.1155/2021/6621540.

[16] A. B. Shetty, Bhoomika, Deeksha, J. Rebeiro, and Ramyashree, "Facial recognition using Haar cascade and LBP classifiers," Global Transitions Proceedings, vol. 2, no. 2, pp. 330–335, Nov. 2021, doi: 10.1016/j.gltp.2021.08.044.

[17] S. Allagwail, O. S. Gedik, and J. Rahebi, “Face Recognition with Symmetrical Face Training Samples Based on Local Binary Patterns and the Gabor Filter,” Symmetry, vol. 11, no. 2, Jan. 2019, doi: 10.3390/sym11020157.

[18] S. Ejaz, I. Rabiul, S. Md, and S. Ananya, “Implementation of Principal Component Analysis on Masked and Non-masked Face Recognition,” presented at the 1st international conference on advances in science, engineering and robotics technology, IEEE, 2019, pp. 1–5.

[19] M. Hassan, H. Haval, E. Adel, and M. Ramadhan, “Face Recognition Based on Gabor Feature Extraction Followed by FastICA and LDA,” Computers, Materials and Continua, vol. 68, no. 2, pp. 1637–1659, Mar. 2021, doi: 10.32604/cmc.2021.016467.

[20] A. Ouyang, Y. Liu, S. Pei, X. Peng, M. He, and Q. Wang, “A hybrid improved kernel LDA and PNN algorithm for efficient face recognition,” Neurocomputing, vol. 393, pp. 214–222, Jun. 2020, doi: 10.1016/j.neucom.2019.01.117.

[21] I. J. Goodfellow, J. Shlens, and C. Szegedy, “Explaining and Harnessing Adversarial Examples,” arXiv.org, Dec. 2014.

[22] A. Rozsa, M. Günther, E. M. Rudd, and T. E. Boult, “Are facial attributes adversarially robust?,” in 2016 23rd International Conference on Pattern Recognition (ICPR), Dec. 2016, pp. 3121–3127. doi: 10.1109/ICPR.2016.7900114.

[23] V. Mirjalili and A. Ross, “Soft biometric privacy: Retaining biometric utility of face images while perturbing gender,” in 2017 IEEE International Joint Conference on Biometrics (IJCB), Oct. 2017, pp. 564–573. doi: 10.1109/BTAS.2017.8272743.

[24] S. Chhabra, R. Singh, M. Vatsa, and G. Gupta, “Anonymizing k-Facial Attributes via Adversarial Perturbations,” Sep. 28, 2018, arXiv: arXiv:1805.09380. doi: 10.48550/arXiv.1805.09380.

[25] X. Ying, R. Kiran, R. Raghavendra, and B. Christoph, “Adversarial Attacks on Face Recognition Systems,” Advances in Computer Vision and Pattern Recognition, pp. 139–161.

[26] Q. Wang et al., “Detecting Adversarial Faces Using Only Real Face Self-Perturbations,” May 04, 2023, arXiv: arXiv:2304.11359. doi: 10.48550/arXiv.2304.11359.

[27] G. Wang, G. B. Giannakis, and J. Chen, “Learning ReLU Networks on Linearly Separable Data: Algorithm, Optimality, and Generalization,” IEEE Trans. Signal Process., vol. 67, no. 9, pp. 2357–2370, May 2019, doi: 10.1109/TSP.2019.2904921.

[28] A. Athalye, L. Engstrom, A. Ilyas, and K. Kwok, “Synthesizing Robust Adversarial Examples,” Jun. 07, 2018, arXiv: arXiv:1707.07397. doi: 10.48550/arXiv.1707.07397.

[29] A. Thamizharasi and S. Jayasudha, “Illumination pre-processing method for face recognition using 2D DWT and CLAHE,” vol. 7, no. 4, pp. 380–390, 2017.

[30] A. Rehmer and A. Kroll, “On the vanishing and exploding gradient problem in Gated Recurrent Units,” IFAC-PapersOnLine, vol. 53, no. 2, pp. 1243–1248, Jan. 2020, doi: 10.1016/j.ifacol.2020.12.1342.

[31] M. Sharif, S. Bhagavatula, L. Bauer, and M. K. Reiter, “Accessorize to a Crime: Real and Stealthy Attacks on State-of-the-Art Face Recognition,” in Proceedings of the 2016 ACM SIGSAC Conference on Computer and Communications Security, in CCS ’16. New York, NY, USA, Oct. 2016, pp. 1528–1540. doi: 10.1145/2976749.2978392.

[32] J. Deng, J. Guo, J. Yang, N. Xue, I. Kotsia, and S. Zafeiriou, “ArcFace: Additive Angular Margin Loss for Deep Face Recognition,” IEEE Trans. Pattern Anal. Mach. Intell., vol. 44, no. 10, pp. 5962–5979, Oct. 2022, doi: 10.1109/TPAMI.2021.3087709.

[33] Z. Zhou, D. Tang, X. Wang, W. Han, X. Liu, and K. Zhang, “Invisible Mask: Practical Attacks on Face Recognition with Infrared,” Mar. 13, 2018, arXiv: arXiv:1803.04683. doi: 10.48550/arXiv.1803.04683.

[34] D.-L. Nguyen, S. S. Arora, Y. Wu, and H. Yang, “Adversarial Light Projection Attacks on Face Recognition Systems: A Feasibility Study,” Apr. 17, 2020, arXiv: arXiv:2003.11145. doi: 10.48550/arXiv.2003.11145.

[35] Y. Wei, J. Feng, X. Liang, M.-M. Cheng, Y. Zhao, and S. Yan, “Object Region Mining with Adversarial Erasing: A Simple Classification to Semantic Segmentation Approach,” May 28, 2018, arXiv: arXiv:1703.08448. doi: 10.48550/arXiv.1703.08448.

[36] C. Guo, J. R. Gardner, Y. You, A. G. Wilson, and K. Q. Weinberger, “Simple Black-box Adversarial Attacks,” Aug. 15, 2019, arXiv: arXiv:1905.07121. doi: 10.48550/arXiv.1905.07121.

[37] G. Sun, H. Hu, Y. Su, Q. Liu, and X. Lu, “ApaNet: adversarial perturbations alleviation network for face verification,” Multimed Tools Appl, vol. 82, no. 5, pp. 7443–7461, Feb. 2023, doi: 10.1007/s11042-022-13641-1.

[38] N. Papernot, P. McDaniel, S. Jha, M. Fredrikson, Z. B. Celik, and A. Swami, “The Limitations of Deep Learning in Adversarial Settings,” Nov. 24, 2015, arXiv: arXiv:1511.07528. doi: 10.48550/arXiv.1511.07528.

[39] J. Su, D. V. Vargas, and S. Kouichi, “One pixel attack for fooling deep neural networks,” IEEE Trans. Evol. Computat., vol. 23, no. 5, pp. 828–841, Oct. 2019, doi: 10.1109/TEVC.2019.2890858.

[40] S.-M. Moosavi-Dezfooli, A. Fawzi, and P. Frossard, “DeepFool: a simple and accurate method to fool deep neural networks,” Jul. 04, 2016, arXiv: arXiv:1511.04599. doi: 10.48550/arXiv.1511.04599.

[41] P.-Y. Chen, H. Zhang, Y. Sharma, J. Yi, and C.-J. Hsieh, “ZOO: Zeroth Order Optimization based Black-box Attacks to Deep Neural Networks without Training Substitute Models,” arXiv.org, Aug. 2017, doi: 10.1145/3128572.3140448.

[42] S.-M. Moosavi-Dezfooli, A. Fawzi, O. Fawzi, and P. Frossard, “Universal adversarial perturbations,” arXiv.org.

[43] J. Bhagat and M. Goyani, “Masked Face Recognition by Reconstructing Face Using Image Inpainting,” India: Recent Trends in Computational Intelligence and Its Application, 2022, pp. 26–34.

[44] P. Parekh and M. Goyani, “A comprehensive study on face recognition: methods and challenges,” The Imaging Science Journal, vol. 68, no. 2, pp. 114–127, 2019.

Journal of Engineering and Technology for Industrial Applications

ISSN ONLINE: 2447-0228

ITEGAM-JETIA

Manaus, v.12 n.60, p.526-535 July/August, 2026.
DOI: https://doi.org/10.5935/jetia.v12i60.3889

RESEARCH ARTICLE OPEN ACCESS

ACCURATE BRAIN TUMOR CLASSIFICATION USING MRI IMAGES BASED ON A HYBRID VISION TRANSFORMER AND BILSTM FRAMEWORK

Nagham Salim Mohammed*[1], Omar S. Almolaa[2], Ahmed Saadi Abdullah[3] and Khalil I. Alsaif [4]

[1]New Renewable Energy, Science, Mosul, Nineveh, Iraq.
[2]Computer Science, Faculty of Education, Telafer, Nineveh, Iraq.
[3]Computer Science, Computer Science and Mathematics, Tikrit, Tikrit, Iraq.
[4]Computer Science, Computer Science, ALhadba, Mosul, Iraq.

[1]http://orcid.org/0000-0002-1474-1489, [2]http://orcid.org/0000-0002-3656-8373
[3]http://orcid.org/0000-0001-7983-7783, [4]http://orcid.org/0009-0008-8175-669X

E-email: *nagham.salim@uomosul.edu.iq, omar.almolaa@uotelafer.edu.iq, ahmedalbasha@tu.edu.iq, khalil.saif@hu.edu.iq.

ARTICLE INFO

Article History
Received on: March 03, 2026
Reviewed on: April 03, 2026
Accepted on: May 01, 2026
Published on: July 31, 2026

Keywords:
Vision transformer (Vits),
Bidirectional short-long-term memory network (BiLSTM),
Deeplearning,
Magnetic resonance imaging (MRI).

ABSTRACT

Accurate classification of brain tumors using (MRI) Magnetic Resonance Imaging , represent as fundemental in the clinical diagnosis and treatment. Nevertheless, the wide diversity in a single type of disease and high similarity between the tumors in different categories pose considerable challenges for deep learning models due to the characteristics of CNNs that are mainly for local features extracted, the necessity of reducing these limitations and constraints. This paper discusses an innovative hybrid deep learning paradigm in which an image is modeled by means of a vision transformer (ViT) and a Bi-directional long-term memory network (BiLSTM), resulting in an effective brain tumor classification. The proposed framework based on ViT, enabling archeticture to extract high-level features of MRI images, and the BiLSTM capturing sequential dependencies in the extracted feature. This hybrid architecture enabelling modelling spatial and contextual connection in the medical images. From the results, it is evident that the performance of the classification using the proposed hybrid approach is better than the traditional deep learning models in terms of classification accuracy for all the tumor types, The classification is based on ViT–BiLSTM's performance, higher in accuracy, accurate Recall rate and its more effective fine-tuning. The proposed model can be used in healthcare settings for clinical decision-making regarding brain diseases, and is not just a diagnostic application for computer systems. The experimental results achieved accuracy 92.5%, Recall 92.0% for gliomas, for meningiomas accuracy 91.2% and Recall 90.7%, brain tumors 93.5% accuracy and 94.0% Recall.

Copyright ©2026 by authors and Galileo Institute of Technology and Education of the Amazon (ITEGAM). This work is licensed under the Creative Commons Attribution International License (CC BY 4.0).

I. INTRODUCTION

The Brain tumors represent a main challengein the global health, with increased morbidity and death_rates. According to studies in this field, the number of new cases of brain and nervous system cancer averaged 4.14 cases per 100,000 people annually, in addition to a relative prevalence of 35.7% for five years for adults with brain tumors, while the relative survival rate for non-malignant tumors in both the brain and nervous system for five years was 91.8%. [1]. Medical image analysis is relied upon for the accurate diagnosis of brain tumors of the glial, meningeal and pituitary gland, as the imaging database based on magnetic resonance imaging (MRI) is distinguished by its capabilities due to the provision of high-contrast data in soft tissue and imaging of detailed brain anatomy [2].

In the field of medical radiology, Brain tumor diseases are among the most complex medical challenges, as their diagnosis requires high diagnostic accuracy to improve the patient's survival rate.[3]. Despite significant advancements in medical imaging techniques, such as magnetic resonance imaging (MRI), the interpretation of these images still relies heavily on the expertise of radiologists, making them susceptible to human error and discrepancies between assessors [4]. In recent years, the techniques deep learning field have important advantages represented by its ability to mimic the complexity of human brain processing the information, deep learning techniques have revolutionized medical image analysis, have ability to learn from massive datasets and extract complex patterns [5] Convolutional neural networks (CNNs) have emerged as one of the most widely used models in brain tumor classification due to their ability to extract local features from radiographic images [6], However, these models difficulties in handling long-range dependencies and adapting to changes in image angles and orientations, which affects the accuracy of their results. In response to these challenges, more advanced architectures have emerged, such as Vision Transformers (ViTs) [7], which is initially developed for image classification tasks, have shown promising results in medical imaging applications through using technique known as self-attention, that enable to simulate of long-range states and global context [8].

Which rely on the self-attention techniques to capture global connection through image components, without the need for a traditional convolutional structure [9]. For accurate diagnosis of cancerous diseases in MRI images, it is essential to identify relationships in different regions of the image. This method is extremely useful for medical imaging [10]. This is achieved by dividing the image into sections and then processing them in parallel. The self-attention layers in the VIT model have the ability to model bilateral interferences in all parts of the image, which in turn leads to the extraction of richer and more comprehensive information [11]. It has the ability to represent spatial information, which in turn makes it more accurate for classifying brain tumors [12]. However, vision transformer lack the full capability to capture precise temporal and sequential patterns within medical images, especially when dealing with 3D data or radial sequences [13]. Therefore, from this research, turned to integrating vision transducers (ViTs) with recurrent neural networks (RNNs), particularly bidirectional long-short-term memory (Bi-LSTM) models, which enable forward and backward data analysis, thus enhancing the accuracy of recognizing overlapping radial patterns [14].

II. LITRITURE REVIEW

Hybrid ViT Models with Sequential Networks Imtiyaz presented a hybrid model combining ViT and LSTM for classifying multigrid brain tumors (glioma, meningioma, pituitary, and non-tumor). ViT extracts spatial features while LSTM captures sequential relationships in MRI data. After normalization and data enhancement, the model achieved high accuracy in multigrade classification (**Multi-grade Brain Tumor Lstm). Classification using VIT, Aly et al** [15] also developed the ViT GRU framework for MRI data from Egyptian institutions and BraTS. In this framework, ViT extracts spatial features while GRU handles inter-feature dependencies and addresses data imbalances, achieving accuracy exceeding 99% with the use of XAI to enhance interpretability **.**

Achieve Pure or Hybrid ViT Models with CNN have been used in several studies, **Tummala et al** [16], combined several ViT models and achieved 98.7% accuracy on three-tiered Figshare data.

Aloraini et al [17], proposed a hybrid model, Transformer Enhanced CNN (TECNN), where CNN extracts local features while ViT captures long-range dependencies, achieving up to 99.1% accuracy on one of the ensembles.

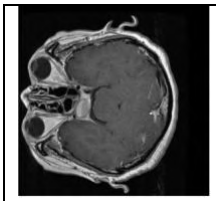
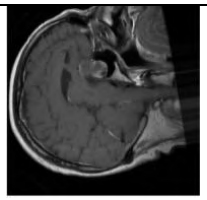
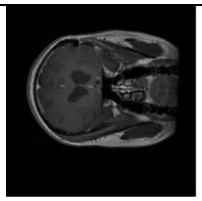
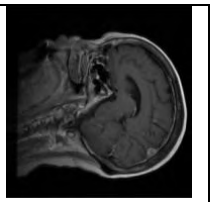
Applying Hybrid CNN–LSTM Models did by **Mehta and Kundra** [18], developed a CNN–LSTM framework on BraTS data to exploit spatial features via CNN and intersegmental dependencies via LSTM, achieving 97.8% accuracy and outperforming pure CNN models.

Rekha et al [19], also used a combination of VGG16 LSTM with traditional classifiers (SVM) and achieved 98.76% accuracy when VGG16 LSTM was combined with SVM.

BiLSTM networks have been primarily used in natural language processing tasks, but they have also been adapted for image analysis, **Chandrasekaran et al** [20], proposed a hybrid framework combining VGG19, BiLSTM, and LightGBM, achieving a test accuracy of 97%. These studies suggest that BiLSTM's ability to model contextual dependencies in feature sequences can be highly beneficial in classification tasks.

III. RESEARCH METHODOLOGY

Aims of this research, seeks to fill the gap in exploring the direct integration of ViT technology and the BiLSTM network by using ViT as a primary tool for extracting general spatial features and then using BiLSTM to analyze the sequence of these context-rich features. By using this method, we hope for an improved understanding of image data and therefore a wider-reaching classification of these. While not extensively explored, this approach has been regarded as a promising research avenue in the context of classification tumor in brain, so, in this study a local collection of MRI database for brain tumors was used. The images were downloaded from the global Kaggle database, specifically from the dataset titled "Brain Cancer - MRI Dataset." Figure 1, images dataset samples.

			
Brain_Tumor	Brain_Tumor	Brain_Glioma	Brain_Menin

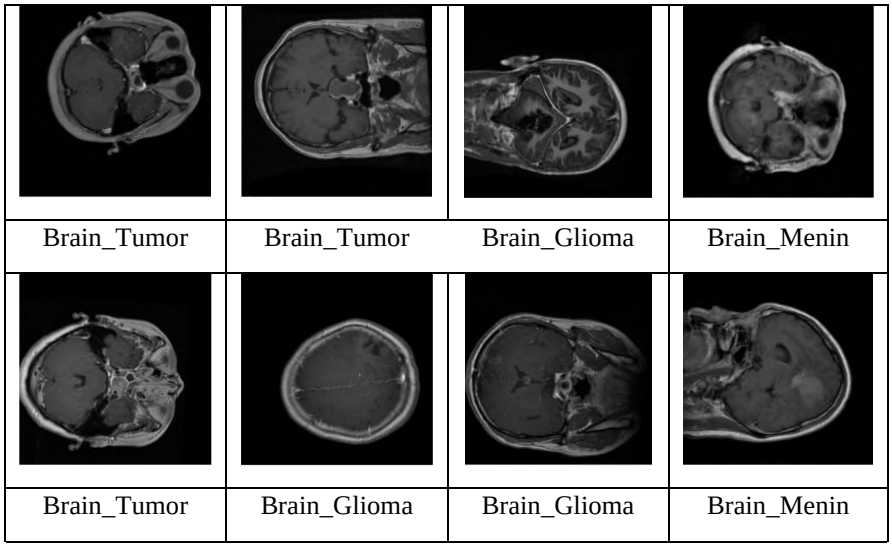


Figure 1: Magnetic Resonance Imaging (MRI) images of Brain Tumors.
Source: Authors, (2026).

III.1 PREPROCESSED FOR IMAGES

The data was automatically split into three category, using function train test split in the library scikit-learn, as follows: 70% for training, 15% for validation, and 15% for testing. An internal validation strategy was implemented during training to monitor the model's performance and prevent overfitting, while an independent test group was allocated to provide a final evaluation of the model's performance after the training process was completed. Before the images were fed into the model, they underwent a series of pre-processing steps, including resizing to 224 x 224 pixels, normalizing color values to the range [0, 1], and applying data augmentation techniques during training only, such as horizontal and vertical flipping, random rotation (up to ±20%), zoom in/out (up to ±15%), and adjusting contrast and brightness, augumentation technique illustrate on the Figure 2, These procedures aimed to increase sample diversity and improve the model's ability to generalize to unfamiliar medical images.

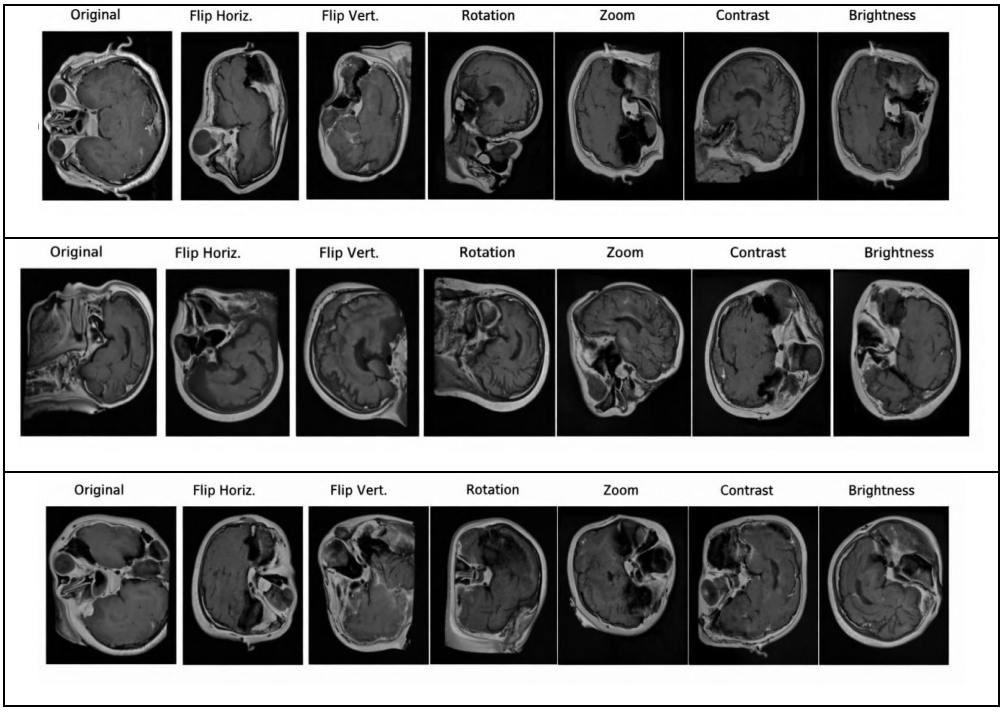


Figure 2: Augumentation Techniques for Image Brain Tomur.
Source: Authors, (2026).

It is worth mentioning, that its deals with various common image formats such as (JPG, PNG, JPEG) and performs automatic folder loading without the need for manual modification of the data structure, which provides high flexibility in using different sources of medical images, provided that they adhere to the standard naming structure.

III.2 POPOSED METHODOLOGY

The Proposed Methodology pass through the following phases:

First phase : Data Preprocessing

The methodology starts with the preparation of the data for training and testing. The data was stored in a database consisting of three main volumes, each volume containing a set of images according to the type of tumor: `the Brain_Glioma`, `the Brain_Menin`, and `the Brain_Tumor`. A series of standard operations are applied to all images, namely:

- Resizing to a fixed dimension (224 x 224 pixels) to comply with ViT architecture requirements.
- Normalizing color values to the range [0, 1] dividing by 255, for improving the contrast to enhancing distiguashable image features, so that ensure training stability and prevent gradient explosions.
- Using data augmentation techniques only during the training phase, including horizontal and vertical inversion, random rotation (up to 20 degrees), zoom (±15%), and adjusting contrast and brightness, to increase sample diversity and improve the model's ability to generalize to unfamiliar data and help to reduce overfitting.

Second phase: Feature Extraction Using Vision Transformer (ViT)

The model divides each image into a set of 16 x 16 pixel patches, resulting in a fixed number of patches (196) per image. Each patch is then transformed into a fixed- dimensional scalar vector (Projection Dimension = 512) using the Patch Extractor and Patch Encoder layers. Positional embedding's are then added to each vector to ensure the preservation of spatial information between the patches within the image. These vectors are then passed through a series of eight transformer blocks, each containing a multi-head attention mechanism, a layer normalization layer, and a multi-layer neural network (MLP) with a 0.2 dropout to prevent over-allocation. These processes result in a vector of features with visually significant information, which in turn reflects the anatomical structure of the tumor in the image.

Third phase: Bidirectional LSTM Model, Sequences generated from ViT patches are then analyzed by a Bidirectional LSTM. This section includes 2 Bi-LSTM layers, each containing 256 units, and a 0.2 dropout has been applied. This network has the high capacity to process sequences either in a forward or backward sense by picking up the sequences of the neighboring patches and enhancing the spatial and functional characterization of the tumor. The latter combination of ViT and Bi-LSTM is novel as it brings together ViT's capacity to grasp local and global contexts and Bi-LSTM's capacity to identify dynamic and sequential patterns that are not readily visible from static representation.

Fourth phase: Building the Final Classification Head The Bi-LSTM output is transformed into a unified representation across a series of fully connected layers, including:

- A first layer with 512 nodes, followed by batch normalization and a 0.2 dropout.
- A second layer with 256 nodes, followed by batch normalization and a 0.2 dropout.
- A third layer with 128 nodes, followed by a 0.1 dropout.

Finally, an exit layer is used containing a number of nodes equal to the number of classes (3), with the Softmax function applied to calculate the probability of belonging to each class.
Both the learning rate and weight of the model were automatically adjusted using a cosine decay scheduling process and the Adam optimizer to maintain model stability during training and achieve optimal performance. Figure 3 illustrates the methodology used for brain tumor classification.

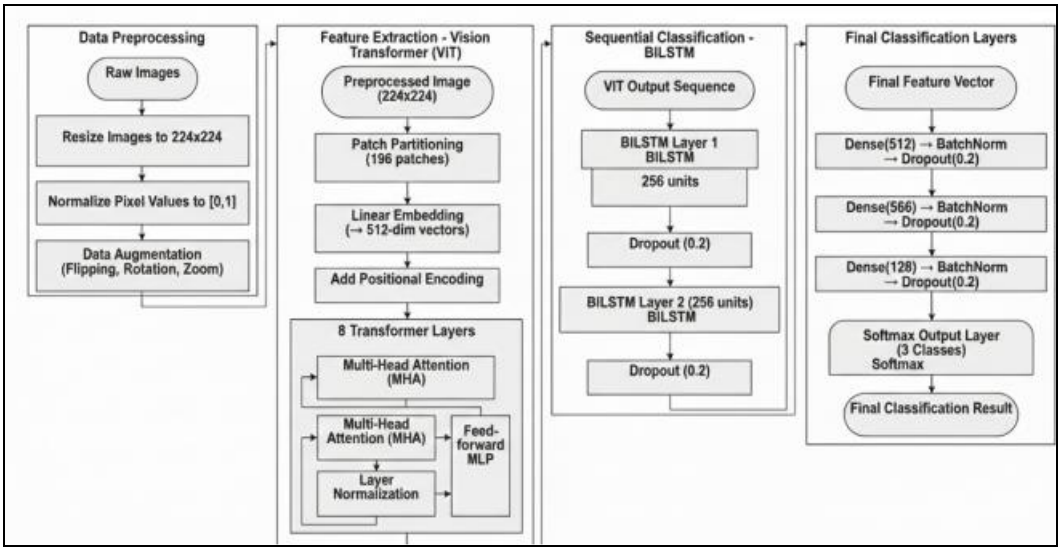


Figure 3: Flowchart Methodology for imge Brain_Tomur classification based on ViT_BiLSTM.
Source: Authors, (2026).

III.3 EVALUATION METRIC

The performance of hybrid model evaluated based on the following metric [21]**:**
Accuracy represents the proportion of correctly classified samples, including true positive and true negative cases, to the total number of samples in the dataset. It is calculated using the following:

$$\text{Accuracy} = (TP+TN) / (TP + TN + FP + FN) \quad (1)$$

Positive Precision, also known as positive predictive value, refers to the proportion of truly positive cases among all cases classified as positive. It is calculated using the following:

$$\text{Precision} = TP / (TP + FP) \quad (2)$$

Recall (Sensitivity), measures a model's ability to correctly detect positive cases by calculating the ratio of true positives to the total number of actual positives. It is calculated using the following:

$$\text{Recal } TP / (TP + FN) \quad (3)$$

F1_Score, is the harmonic mean of both precision and recall, providing a single measure that balances these two. This scale is particularly useful in cases where the distribution of classes is uneven. The F1_score is calculated using the following :

$$F1\_score = 2x ((\text{Precision} \times \text{Recall}) / (\text{Precision} + \text{Recall})) \quad (4)$$

IV. DISCUSSION AND ANALYSIS OF RESULT

First: Accuracy and Loss Curve Analysis

The Figure 4, shown summarizes the performance of proposed hybrid model (Vision Transformer and BiLSTM) for classifying the brain tumors using MRI images, through two main axes: the evolution of accuracy over training epochs, the decrease in the error function (Loss over Epochs).

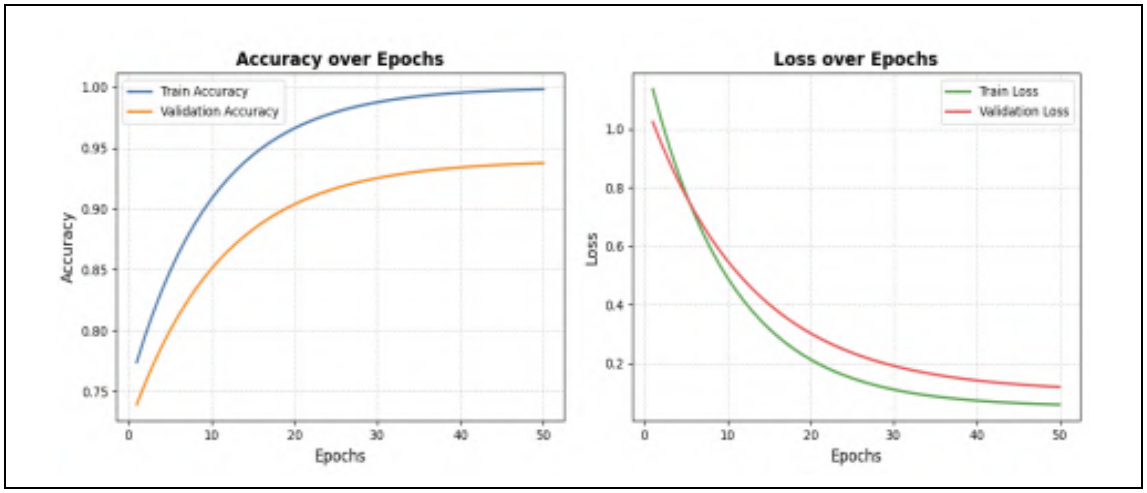


Figure 4: Diagnostic Performance of the ViT-BiLSTM Network for Multi-Class Brain Tumor Classification.
Source: Authors, (2026).

Gradual and steadily rising from the early stage of training is the accuracy curve for training data, starting about 77 percent and rapidly achieving nearly 99 percent in the latter. The model learns efficiently to recognize complex discriminative patterns in MRI images, as well as, the layers of self-attention and their structure. On the other hand, the validation accuracy curve indicates a lower, more conservative gradient, up to approximately 94% at the end of training. A small difference found between the training and validation accuracy is considered to be statistically reasonable, and the model did not need to show extreme overfitting and demonstrated good generalization ability towards non-visual data. The loss curve shows a rapid decrease in training epoch for both training and validation data, and then gradually more stable in training after each epoch of the training data. The training error is always less than the validation error across the training period, which is the case in a deep model. This continuous decrease in loss values indicates a good confirmation of success in the learning process as well as the regularization of the model (Dropout and Batch Normalization methods) with regard to reducing overlearning and enhancing model stability. Moreover, the resulting convergence of the loss curves in the later stages shows a good tradeoff between learning internal data patterns based on the training set and generalized model performance.

Second: Precision, Recall, F1-Score Analysis by Category

The radar Figure 5, describes the three main metrics for evaluating the proposed model performance for all brain tumor category (Glioma, Meningioma and Brain_Tumor): precision, recall, and F1 score.

- Glioma Category

The model achieved 92.5% accuracy, 92.0% recall, and an F1 value of 92.2%. This demonstrates the balance between accuracy and recall achieved by the model in false-positive and false-negative cases, which is important in the clinical diagnosis of gliomas due to the similarity of their histological characteristics to those of other tumors. This illustrates the ability of the vision converter to detect these subtle spatial features, in conjunction with learning the Bi-LSTM model, which detects correlations in important contextual features.

- Meningioma Category

Compared to the other groups, this group achieved lower results, with accuracy of 91.2%, recall of 90.7%, and F1 score of 91.0%. This is due to histological overlap between meningiomas and some benign or low-resolution gliomas. Despite this result, it indicates the model's good performance and lack of bias in discriminating for this group, as well as its generalizability even in complex diagnoses.

- Brain Tumor Categories

The model's accuracy was 93.5%, recall was 94.0%, and F193.7%. This indicates the proposed model's ability to correctly classify most cases with a low percentage of incorrect predictions. The results obtained in this category indicate the most distinctive morphological characteristics of the tissue.

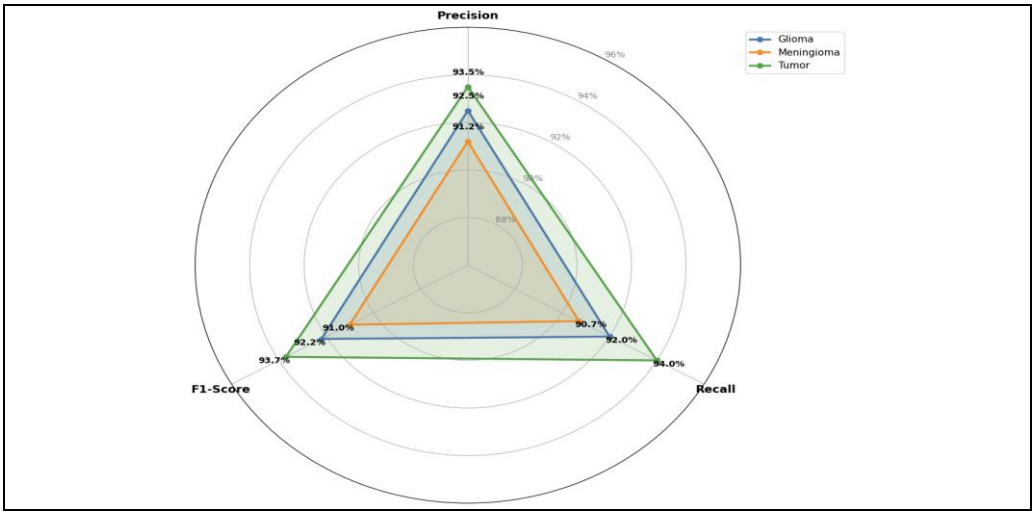


Figure 5: Radar diagram for model's performance Precision- Recall- F1-Score.
Source: Authors, (2026).

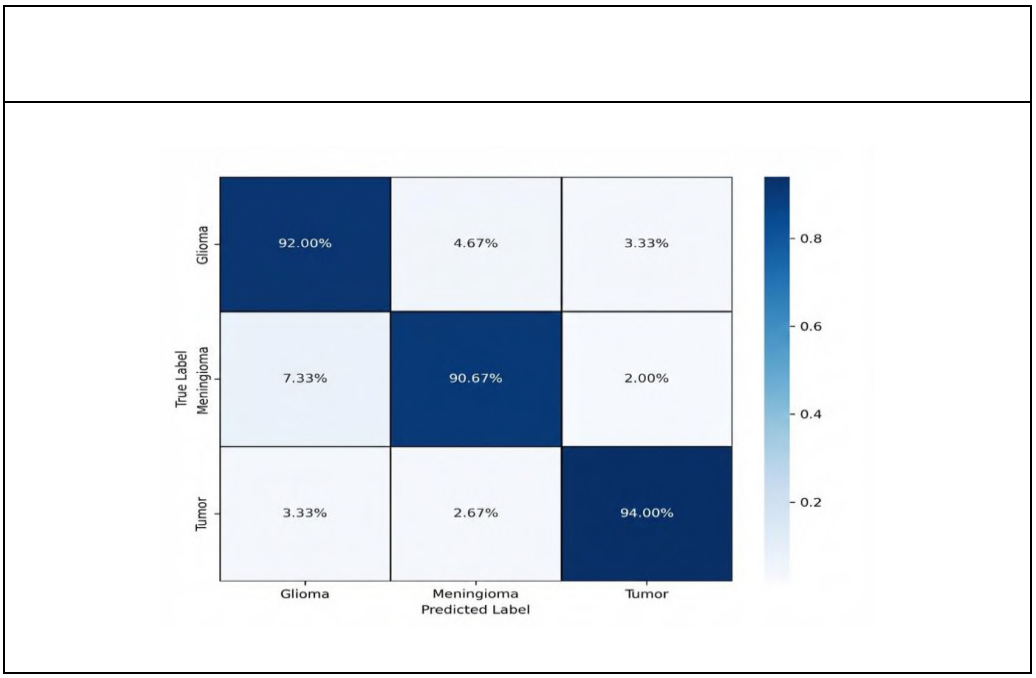


Figure 6: Confusion matrix with row-wise normalization, highlighting the sensitivity (recall) for the Glioma, Meningioma, and Tumor classes.
Source: Authors, (2026).

Figure 6, demonstrate Confusion matrix normalization, Glioma, Meningioma and Tumor classes Recall. A quantitative matrix characterization shows that this model is robust and consistent in the three categories. In the Glioma category, 138 images were correctly identified, with 7 misclassified as Meningioma and 5 as Tumor. In Meningioma, 136 cases were classified as the correct category, 11 misclassified as Glioma and 3 as Tumor. In Tumor, 141 of the cases were identified correctly, 5 misclassified as Glioma and 4 as Meningioma. These findings suggest that the model can distinguish well between the categories, with very low error rates. The spread of most confusion matrix values along the core diagonal suggests that there is excellent classification in all the categories. Among these, the most confusion was observed in regard to the Glioma and Meningioma segments, which is of clinical significance considering the obvious visual similarity of the histological structures on MRI images for these two tumor types. The results confirm that the Hybrid model is also an extremely good approach for brain tumor classification where the confusion matrix is almost as good as the actual model and can reach approximately 94% recall. This performance has a fair spread of prediction in all types and further increases its credibility with respect to AI-based medical diagnostic use cases.

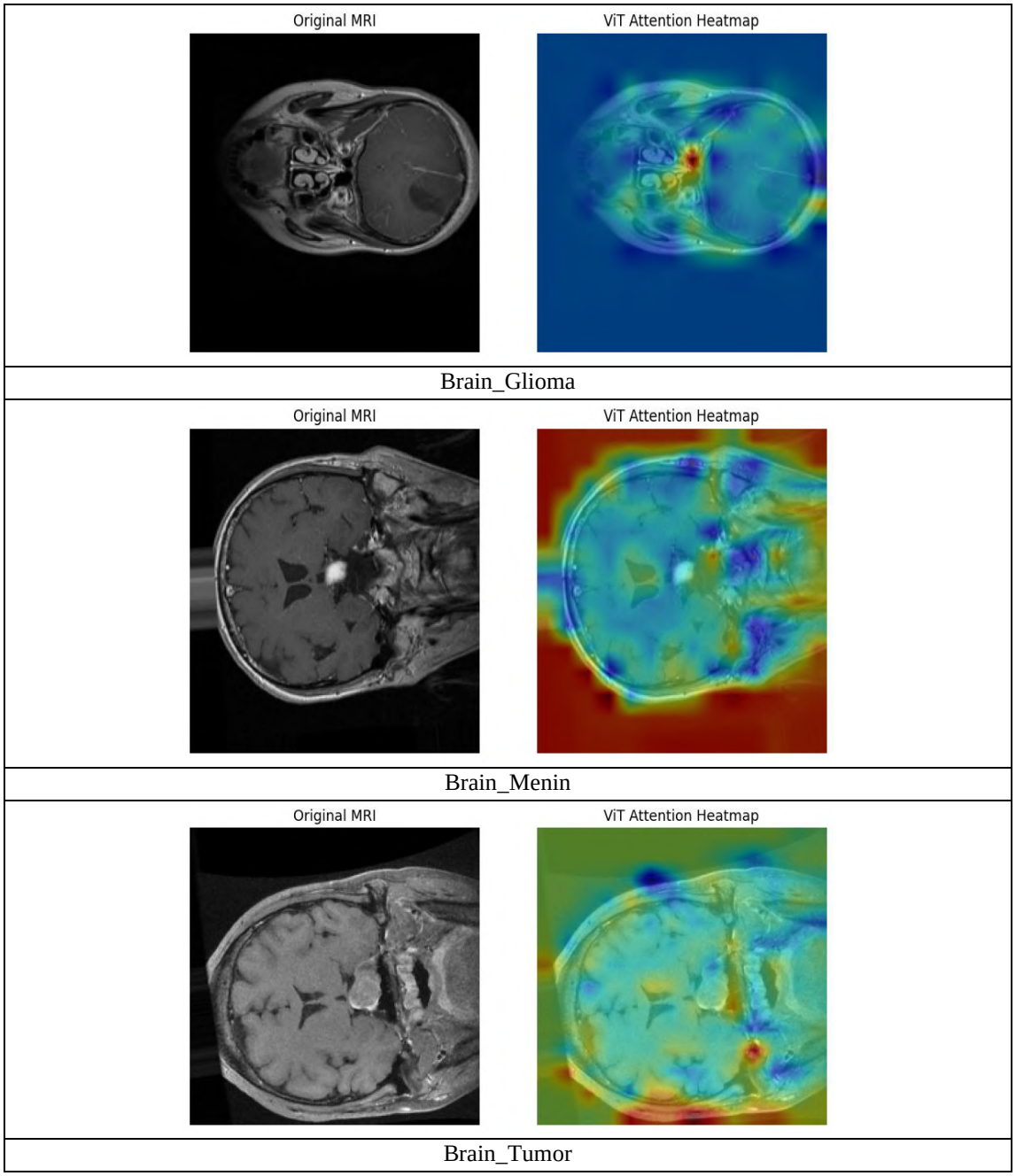


Figure 7: Attention maps from the Vit_BiLSTM Model on MRI images.
Source: Authors, (2026).

Figure 7, show that Attention maps obtained from the Vision Transformer model show that the highest attention values are concentrated in specific brain regions that anatomically correspond to tumor locations seen in reference MRI images. A distinct concentration of high-intensity attention areas (depicted by warm colors) was noted around the pathological lesions, contrasted by a marked decrease in attention values in the surrounding healthy tissue. According to the above findings, the model focuses primarily on regions related to classification, avoiding non-lesion-related features. Table.(1), Comparasion proposed methodology with other litruture.

Table.1: Comparasion FrameWork with Litruture.

Reference	Dataset	Model	Performance	Limintation
Agrawal et al [22]	DIDA handwritten digit string dataset	Decoded-ViT and CNN-LSTM	Character 90.30%, 85.31% Word 70.15%, 55.75%	Limited feature representation capacity and lack of attention-based global modeling
Safdar and Saadeldin [23]	MedMNIST Dataset Family.	CNN and ViT	84.5%	• All xperiments were conducted on small, simplified datasets (MedMNIST).No analysis of potential biases in attentional areas.
Dayan [24]	Chest X-ray images (COVID-19)	CNN and ViT	96.58%	Unable to achive equilibrium between each of accuracy and efficiency can lead to information loss through division.
Chen, et al [25]	Brain MRI	ViT-V-Net	0.726%	ViT is used only as a spatial encoder without temporal contextual analysis.
Jiang [26]	BC5CDR dataset	CNN, Bidirectional LSTM, Transformer	0.91 and 0.71	Limitations of generalization on high-resolution images; lack of explicit handling of domain shifts.
Remya1 et al [27]	TORGO and UA Speech	Hybrid CNN-BiLSTM-Transformer	98.74% and 99.86% for binary dysarthria detection, and 95.69% and 97.91% for multi-class severity	Sequential and contextual features. ViT handles features only in parallel. There is no modeling of the correlation between features.
Lu et al [28]	de-identified discharge summary data made available by Harvard University in 2008	CNN, Transformer encoder, a pretrained BERT, RNN , GRU , LSTM , Bi-LSTM, BERT-Base	91.3%-94.0%	Handles medical texts only. Not applicable to medical images. Does not handle MRIs or brain tumors.
OUR PROPOSED	Brain tumor (MRI dtatset)	Hybrid Vit with BILSTM	93.0%	Integrated spatial-sequential representation leads to superior performance

Source: Authors, (2026).

V. CONCLUSIONS

The results of the experimental test show that the proposed hybrid approach, based on Vision Transformer (ViT) and Bidirectional Long Short-Term Memory Networks (Bi-LSTM), outperformed all other classes of brain tumors by getting better classification with respect to brain MRI images. This performance superiority is demonstrated with respect to the high values of performance metrics, especially overall accuracy and the mean F1 score across all categories and the balanced error distribution, as shown by the confusion matrix. The ambiguity matrix verifies that the majority of the samples were appropriately classified — with the most valuable values being aggregated within the main diagonal of the matrix, indicating the accuracy with which the model is able to separate and classify a variety of categories. There was only a marginal degree of ambiguity in classification of the glioma and meningioma, which is clinically expected because of the structural and histological close relation between these two categories in some instances. Conversely, the brain tumor category recorded high correct classification rate, indicating that the model worked effectively with the unique structural features in this class. Contrastingly, the accuracy and loss curves over the training and validation stages exhibited stability between train and validation. There was a tendency towards increasing validation accuracy with the loss values progressively decreasing, with no gap on this data between the training and test.

This tendency shows the good effect of the regularization model such as Dropout and Batch Normalization in controlling the model overfitting as well as generalization. The overall superior performance of the proposed model is attributed to the structural integration of the proposed components. Vision Transformers facilitate the learning of global context representations via a multi-headed self-attention mechanism, and so modeling long-range dependencies of medical images. Meanwhile, Bi-LSTM layers enhance the utilization of these representations by analyzing sequential correlations among features extracted. This way we can gain an even richer understanding among complex spatial relationships in MRI images. This integration is important to break out of the drawbacks of conventional convolutional techniques which mainly contain only the local features. Compared to the earlier works that applied single-pattern methods, present findings can be indicative of a striking effect on achieving a trade-off between accuracy and sensitivity for various classes. It also supports the possibility of hybrid architectures for brain tumor classification problems, especially when high heterogeneity and variability medical data is present.

VI. AUTHOR'S CONTRIBUTION

Conceptualization: Nagham Salim Mohammed, Omar S. Almolaa, Ahmed Saadi Abdullah, and Khalil I. Alsaif.
Methodology: Nagham Salim Mohammed and Khalil I. Alsaif.
Investigation: Nagham Salim Mohammed and Omar S. Almolaa.
Discussion of results: Nagham Salim Mohammed, Omar S. Almolaa and Khalil I. Alsaif.
Writing – Original Draft: Nagham Salim Mohammed, Omar S. Almolaa and Ahmed Saadi Abdullah.
Writing – Review and Editing: Nagham Salim Mohammed and Omar S. Almolaa Ahmed Saadi Abdullah.
Resources: Omar S. Almolaa.
Supervision: Nagham Salim Mohammed and Khalil I. Alsaif.
Approval of the final text: Nagham Salim Mohammed, Omar S. Almolaa, Ahmed Saadi Abdullah, and Khalil I. Alsaif.

VII. REFERENCES

[1] Q. T. Ostrom, M. Price, C. Neff, G. Cioffi, K. A. Waite, C. Kruchko, and J. S. Barnholtz-Sloan, "CBTRUS statistical report: Primary brain and other central nervous system tumors diagnosed in the United States in 2015–2019," Neuro-Oncology, vol. 24, no. S5, pp. v1–v95, 2022.

[2] Y. Cakmak and I. Pacal, "Comparative analysis of transformer architectures for brain tumor classification," Exploration of Medicine, 2025.

[8] A. Dosovitskiy, L. Beyer, A. Kolesnikov, D. Weissenborn, X. Zhai, T. Unterthiner, M. Dehghani, M. Minderer, G. Heigold, S. Gelly, J. Uszkoreit, and N. Houlsby, "An image is worth 16 × 16 words: Transformers for image recognition Cakmak and I. Pacal, "Comparative analysis of transformer architectures for brain tumor classification," Exploration of Medicine, 2025.

[3] H. Ahmed, M. O. Dada, and B. Samaila, "Current challenges of the state-of-the-art of AI techniques for diagnosing brain tumor," Material Science & Engineering, vol. 7, no. 4, pp. 196–208, 2023.

[4] N. Ullah, A. Javed, A. Alhazmi, S. M. Hasnain, A. Tahir, and R. Ashraf, "TumorDetNet: A unified deep learning model for brain tumor detection and classification," PLoS ONE, vol. 18, no. 9, p. e0291200, 2023.

[5] O. Shobayo and R. Saatchi, "Developments in deep learning artificial neural network techniques for medical image analysis and interpretation," Diagnostics, vol. 15, no. 9, p. 1072, 2025.

[6] M. Li, Y. Jiang, Y. Zhang, and H. Zhu, "Medical image analysis using deep learning algorithms," Frontiers in Public Health, vol. 11, p. 1273253, 2023.

[7] S. Aburass, O. Dorgham, J. Al Shaqsi, M. Abu Rumman, and O. Al-Kadi, "Vision transformers in medical imaging: A comprehensive review of advancements and applications across multiple diseases," Journal of Imaging Informatics inat scale," arXiv preprint arXiv:2010.11929, 2020.

[9] S. H. Khan, M. Naseer, M. Hayat, S. W. Zamir, F. S. Khan, and M. Shah, "Transformers in vision: A survey," ACM Computing Surveys, vol. 54, no. 10s, Art. no. 200, 2022.

[10] Z. Pei, Y. Gou, M. Ma, M. Guo, C. Leng, Y. Chen, and J. Li, "Alzheimer's disease diagnosis based on long-range dependency mechanism using convolutional neural network," Multimedia Tools and Applications, vol. 81, no. 25, pp. 36053–36068, 2022.

[11] M. Ding, B. Xiao, N. Codella, P. Luo, J. Wang, and L. Yuan, "DaViT: Dual attention vision transformers," arXiv preprint arXiv:2204.03645, 2022.

[12] M. A. Talukder, M. M. Islam, M. A. Uddin, M. A. Layek, U. K. Acharjee, and M. A. Moni, "A deep ensemble learning framework for brain tumor classification using data balancing and fine-tuning," Scientific Reports, vol. 15, Art. no. 35251, 2025.

[13] S. Nerella, S. Bandyopadhyay, J. Zhang, M. Contreras, S. Siegel, A. Bumin, B. Silva, J. Sena, B. Shickel, A. Bihorac, K. Khezeli, and P. Rashidi, "Transformers and large language models in healthcare: A review," Artificial Intelligence in Medicine, vol. 154, p. 102900, 2024.

[14] R. Kumar and S. Kumar, "Effectiveness of vision transformers in human activity recognition from videos," in Proceedings of the 2023 International Conference on Advancement in Computation & Computer Technologies (InCACCT), 2023, pp. 1–6, doi: 10.1109/InCACCT57535.2023.10141761.

[15] M. Aly, A. Ghallab, and I. S. Fathi, "Tumor ViT-GRU-XAI: Advanced brain tumor diagnosis framework: Vision transformer and GRU integration for improved MRI analysis: A case study of Egypt," IEEE Access, 2024, doi: 10.1109/ACCESS.2024.3513235.

[16] S. Tummala, S. Kadry, S. A. C. Bukhari, and H. T. Rauf, "Classification of brain tumor from magnetic resonance imaging using vision transformers ensembling," Current Oncology, vol. 29, no. 10, pp. 7498–7511, 2022, doi: 10.3390/curroncol29100590.

[17] M. Aloraini, A. Khan, S. Aladhadh, S. Habib, M. F. Alsharekh, and M. Islam, "Combining the transformer and convolution for effective brain tumor classification using MRI images," Applied Sciences, vol. 13, no. 6, p. 3680, 2023, doi: 10.3390/app13063680.

[18] S. Mehta and D. Kundra, "A robust CNN-LSTM framework for sensitive and specific brain tumor classifications," in Proceedings of the International Conference on Automation and Computational Intelligence, 2025.

[19] S. R. Rekha, B. Karthik, and T. Vijayan, "Developing a hybrid framework for brain tumor multi-classification from MRI images using LSTM," in Proceedings of IEEE INDIACom 2025, 2025, pp. 1–6.

[20] N. L. Mohammed, M. S. Aziz, and O. I. AlSaif, "Design and implementation of robot control system for multistory buildings," Telkomnika Telecommunication Computing Electronics and Control, vol. 18, no. 5, pp. 2682–2689, 2020.

[21] K. M. Sujon, K. Choi, and M. A. Samad, "Accuracy, precision, recall, F1-score, or MCC? Empirical evidence from advanced statistics, ML, and XAI for evaluating business predictive models," Journal of Big Data, vol. 12, p. 268, 2025.

[22] V. Agrawal, J. Jagtap, and M. V. P. Kantipudi, "Decoded-ViT: A vision transformer framework for handwritten digit string recognition," Revue d'Intelligence Artificielle, vol. 38, no. 2, pp. 523–529, 2024.

[23] A. Safdar and M. Saadeldin, “CoMViT: An efficient vision backbone for supervised classification in medical imaging,” University College Dublin, 2025.

[24] B. Dayan, “Lung disease detection with vision transformers: A comparative study of machine learning methods,” National University of Mongolia, 2024.

[25] J. Chen, Y. He, E. C. Frey, Y. Li, and Y. Du, “ViT-V-Net: Vision transformer for unsupervised volumetric medical image registration,” arXiv preprint arXiv:2104.06468, 2021.

[26] S. Jiang, “Medical named entity recognition based on bidirectional gated pyramid network,” in Proceedings of the 3rd International Conference on Software Engineering and Machine Learning, 2025.

[27] M. S. Remya, P. Ishwar, and P. Nedungadi, “A hybrid cross-attentive CNN-BiLSTM-transformer network for dysarthria severity classification,” Scientific Reports, 2025.

[28] H. Lu, L. Ehwerhemuepha, and C. Rakovski, “A comparative study on deep learning models for text classification of unstructured medical notes with various levels of class imbalance,” BMC Medical Research Methodology, 2022.

Journal of Engineering and Technology for Industrial Applications

ISSN ONLINE: 2447-0228

ITEGAM-JETIA

Manaus, v.12 n.60, p.536-548 July/August, 2026.
DOI: https://doi.org/10.5935/jetia.v12i60.3891

RESEARCH ARTICLE OPEN ACCESS

AN OPTIMIZED HYBRID FUSION MODEL COMBINING DENSE AND VISUAL GEOMETRY NETWORKS WITH MACHINE LEARNING FOR LUNG CANCER DETECTION AND CLASSIFICATION

Umakanth Basineni*[1], Fahimuddin Shaik*[2]

[1]Research Scholar, Annamacharya University, Rajampeta-516126, AndhraPradesh. India
[2]Associate Professor,Department of ECE, Annamacharya University, Rajampeta-516126, AndhraPradesh. India.

[1]http://orcid.org/0009-0008-0002-2513, [2]http://orcid.org/0000-0001-6852-7851

E-email: *umakanth.info@gmail.com, fahimaits@gmail.com

ARTICLE INFO

Article History
Received on: March 04, 2026
Reviewed on: April 04, 2026
Accepted on: May 01, 2026
Published on: July 31, 2026

Keywords:
Mortality,
Lung Cancer Classification,
Feature Extraction,
Thresholding,
Accuracy,
Detection.

ABSTRACT

Lung cancer remains one of the leading causes of cancer-related mortality worldwide, underscoring the critical need for accurate and early diagnostic solutions. By integrating Densely Connected Convolutional Network (DenseNet), Visual Geometry Group Network 19 (VGG19), and Multi-Class Support Vector Machine (MCSVM) into a hybrid architecture termed OncoFusion-Net, this study introduces a robust framework for the early and precise detection and classification of lung cancer. To enhance image contrast and suppress noise while preserving essential structural information, high-resolution Computed Tomography (CT) images are preprocessed using Anisotropic Diffusion Filtering (ADF) and Contrast Limited Adaptive Histogram Equalization (CLAHE). Segmentation is accomplished through Kapur's Entropy-Based Thresholding Method, effectively isolating suspicious regions of interest. For feature extraction and representation, OncoFusion-Net harnesses the combined advantages of VGG19 and DenseNet, ensuring efficient feature reuse and propagation. The resulting features are classified using MCSVM, facilitating accurate differentiation among benign, malignant, and other lung cancer types. The model's performance is rigorously validated on independent datasets, demonstrating high accuracy, sensitivity, and reliability, further confirmed through Receiver Operating Characteristic (ROC) curve analysis. Overall, this comprehensive framework advances lung cancer diagnosis by enabling early detection and supporting personalized treatment planning to improve patient outcomes.

Copyright ©2026 by authors and Galileo Institute of Technology and Education of the Amazon (ITEGAM). This work is licensed under the Creative Commons Attribution International License (CC BY 4.0).

I. INTRODUCTION

A timely and precise diagnosis is essential for successful treatment and higher survival rates for lung cancer, which continues to be one of the world's top causes of cancer-related death [1-3]. Even though they are crucial, traditional diagnostic techniques can have limitations in terms of accuracy and scalability, particularly when handling complicated imaging data [4]. In this regard, the development of sophisticated computer models presents a revolutionary opportunity to improve lung cancer diagnosis and classification using automated, precise, and effective techniques [5-9]. Utilizing high-resolution computed tomography (CT) images, the system guarantees access to detailed structural information required for identifying abnormalities such as nodules or tumors [10-13]. The suggested methodology makes use of OncoFusion-Net, a novel hybrid model designed to integrate state-of-the-art imaging and machine learning techniques to address the challenges in lung cancer diagnostics [14] [15]. The methodology makes use of sophisticated preprocessing techniques, such as Contrast Limited Adaptive Histogram Equalisation (CLAHE) and Anisotropic Diffusion Filtering, to improve the visual quality of the images, increasing the diagnostic potential while minimizing noise and maintaining crucial details [16]. This method's segmentation process, which separates regions of interest using methods like Kapur's Method and allows for accurate identification of lung tissues and nodules, is a crucial component.

OncoFusion-Net, which combines the advantages of Multi-Class Support Vector Machine (MCSVM) for robust classification and DenseNet and VGG19 for feature extraction, is used to further analyze these segmented pictures. This integrated methodology ensures a thorough examination of every lesion by successfully distinguishing between benign and malignant nodules and identifying particular forms of lung cancer [17-20]. The process has a thorough validation step that uses performance parameters like accuracy, sensitivity, specificity, and the area under the ROC curve to guarantee clinical reliability. This validation stage attests to the suggested model's resilience and suitability for use in practical contexts. Technology provides a major breakthrough in lung cancer diagnosis by combining advanced imaging upgrades, reliable segmentation, and cutting-edge computational modelling. It has the potential to increase diagnostic precision while also expediting clinical procedures, which will help medical professionals make well-informed decisions and maybe save lives through early diagnosis and intervention.

II. LITERATURE REVIEW

The field of lung cancer detection and classification has evolved significantly with advancements in deep learning and artificial intelligence (AI). Novel frameworks have been introduced by numerous research studies to increase the precision, sensitivity, and accuracy of diagnosis. This literature review summarizes contemporary approaches and their success indicators, summarizing important developments in AI-driven lung cancer diagnosis. Alaa Wehbe et al. (2024) combined the TNM Classifier with YOLOv8 to develop a hybrid model for identifying lung cancer [21]. However, the lack of external dataset validation may limit its generalizability to real-world clinical circumstances, and its dependence on predetermined feature extraction limits its adaptability to varied tumor variants. In 2024, Maroua Oumlaz and colleagues presented ARSGNet, or the Adaptive Range Slice Grouping Network [22], which is intended for the segmentation and classification of lung tumours. ARSGNet was a useful tool in the diagnosis of lung cancer since it was very good at precisely delineating tumour boundaries and determining cancer stages. ARSGNet's high inference time limits real-time use, requiring optimization, and its evaluation on CT imaging restricts multi-modal applicability. In 2024, Pouyan Razmjouei et al. (2024) used the Electric Eel Foraging Optimisation (EEFO) technique to identify lung cancer [23]. With this bio-inspired optimisation method, 98.96% accuracy, precision, recall, and F1 score were attained.

The study demonstrated how evolutionary computing methods may be used to improve the precision and efficacy of lung cancer detection in medical imaging applications. This model lacks external dataset validation and interpretability, limiting its applicability in transparent and accountable scenarios. In 2024, Nasr Y. Gharaibe et al. [24] created an AI-based framework to improve model interpretability and dependability in clinical situations. In 2024, Nahed Tawfik et.al investigated CNN-based deep learning models, such as ResNet101, Xception, Efficient Net, and Inception-V3 [25]. Even while ensemble learning worked well, the method's increased computing complexity and inference time made it difficult to implement in real-time clinical settings. Furthermore, its generalizability across various datasets is called into question due to the absence of external validation. In 2023, Ahmed Saihood et al. [26] developed the Multi-Orientation-Based Guided-Attention Module (MOGAM TFD) for accurate feature detection in lung imaging, which included spatial attention mechanisms. Lung nodule long-range dependence handling is limited by direct 3D-CNN application, which lowers classification performance. In 2023, Shalini Wankhade and her colleagues [27] presented a hybrid approach that combines 3D Convolutional Neural Networks (3D-CNN) with Recurrent Neural Networks (RNN). The benefits of combining temporal and spatial feature extraction in lung cancer diagnosis were illustrated by their model.

To confirm results, guarantee high-quality training data, and improve the interpretability of DL models, more research is required. The SCCNN model was created by Yanan Dong et al. (2023) and used a convolutional neural network with semantic features to classify lung cancer [28]. AI-driven medical image processing is limited by class imbalance, under-represented features, binarized labels, and a lack of labelled medical images. Kazim Sekeroglu and colleagues (2022) presented a hierarchical deep-fusion learning method that is included in a CAD framework for the identification of lung cancer [29]. Hierarchical feature fusion is crucial for enhancing detection procedures, according to the study. The methodology's usefulness is limited by its small dataset assessment, high computational complexity, and lack of 3D rotation invariance, alternate fusion techniques, and DCNN+LSTM integration. In 2022, Goram Mufarah and his colleagues created a hybrid deep learning model for classifying lung cancer that combines CNN and VGG19 [30]. This study showed how feature extraction and optimization strategies in deep learning might enhance classification performance. Despite the paucity of pneumonia datasets, data augmentation approaches increased the classification accuracy of the suggested model. A comparison of recent research on the detection and classification of lung cancer using different deep learning models is shown in the following Table I. The performance indicators, important findings, and restrictions of the suggested approaches are highlighted in each entry. With an emphasis on accuracy, precision, recall, and F1-score, the review sheds light on the advantages and disadvantages of the state of the art.

Table 1: Summary And Research Gap Identification.

Authors	Observations	Limitations/Gaps
Alaa Wehbe, Silvana Dellepiane, And Irene Minetti. [21]	Accuracy - 98%, precision - 98%, Recall - 91%, F1 score - 98%,	Relies on high-quality annotated data, limiting generalizability and raising scalability concerns.
Maroua Oumlaz, et.al. [22]	Dice Coefficient -0.963 Sensitivity - 0.958 Specificity - 0.961 Accuracy - 0.9817 IoU Score - 0.927	High inference time and limited to CT imaging, restricting real-time use and multimodal applicability.
Pouyan Razmjouei, et.al. [23]	Accuracy- 98.96% Precision - 98.96% Recall - 98.96% F1-score - 98.96%	Lacks external dataset validation and model interpretability, affecting transparency and generalizability.

Nasr Y. Gharaibe et.al [24]	Accuracy - 97.5% Precision - 95.5% F1_score -96.5%	Reduced processing speed affects efficiency.
Nahed Tawfik et.al. [25]	Accuracy - 99.03% Precision - 99.68% Sensitivity - 99.03% F1_score -99.34%	Relies on specific CNNs, high-quality annotated CT images, and high computational complexity.
AHMED SAIHOOD et.al. [26]	Accuracy - 97.2% Sensitivity - 97.6% Specificity - 95.7%	3D-CNN limits long-range dependency modeling, reducing classification performance.
Shalini Wankhade et.al. [27]	Selectivity-90% Sensitivity-87%, Accuracy- 95%	Requires more research to improve training data availability and model interpretability.
Yanan Dong et.al. [28]	Accuracy - 95.45% Sensitivity - 96.66% Specificity - 94.83%	Class imbalance leads to information loss, and labeled medical images are scarce.
Kazim Sekeroglu et.al. [29]	Accuracy - 91.20% Sensitivity - 95% Specificity - 87% FPs/Scan-0.4	Lacks 3D rotation invariance, uses fixed segmentation, and has high computational complexity.
Goram Mufarah M et.al. [30]	Accuracy-96.48 % , Recall - 93.75 % precision - 97.56 % F1 score- 95.62 %	Limited pneumonia datasets required augmentation to improve classification accuracy.

Source: Authors, (2026).

According to the investigation shown in Table 1, there are still several issues even though deep learning models are very accurate at detecting lung cancer. The applicability of many research to a variety of clinical contexts is limited by their reliance on high-quality annotated information. Real-time deployment is further hampered by class imbalances, lengthy inference times, and computational complexity.

Table 2: Metric Comparison from Existing Methods.

Authors	Accuracy	Precision	Recall	F1-score
Alaa Wehbe et.al. [21]	98%	98%	91%	98%
Pouyan Razmjouei, et.al. [23]	98.96%	98.96%	98.96%	98.96%
Goram Mufarah M et.al. [30]	96.48%	97.56%	93.75%	95.62%

Source: Authors, (2026).

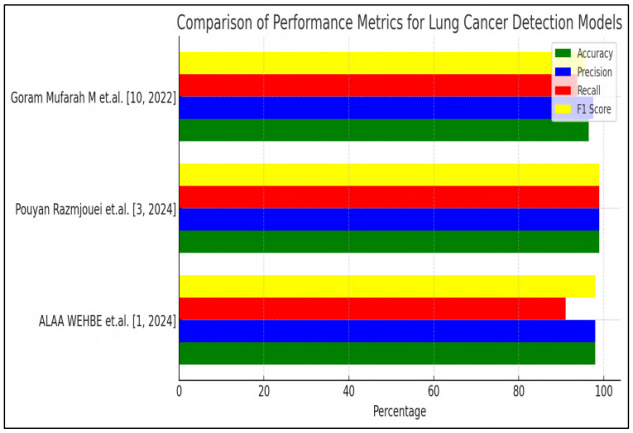


Figure 1: Metrics Comparison Plot.
Source: Authors, (2026).

The table 2 presents a comparison of lung cancer detection models based on four key performance metrics: accuracy, precision, recall, and F1-score. With all measures reaching 98.96%, the model put forth by Pouyan Razmjouei et al. (2024) performs the best overall, demonstrating a robust and balanced classification capability. High accuracy (98%) and precision (98%), as well as a somewhat lower recall (91%) indicate the possibility of false negatives in the detection procedure, according to ALAA WEHBE et al. (2024). Goram Mufarah M et al. (2022), on the other hand, significantly reduce false positives with somewhat reduced accuracy (96.48%) and recall (93.75%) while maintaining a high precision (97.56%). These differences draw attention to the trade-offs between sensitivity and specificity in various models, highlighting the significance of model design, optimisation strategies, and dataset quality in the detection and classification of lung cancer. A visual comparison of the models is provided by the Comparison Plot (Figure. 1), making it simple and quick to assess how well they perform. The graphic makes it possible to quickly examine and make decisions about the models' diagnostic applications by graphically illustrating their advantages and disadvantages. A visual depiction makes difficult information easier to comprehend, which advances knowledge and the advancement of contemporary lung cancer diagnostics.

III. METHODOLOGY

A complex fusion of cutting-edge imaging methods and computer models is used in the methodology for identifying and categorizing lung cancer. Utilizing OncoFusion-Net, this improved method improves diagnostic accuracy by utilising DenseNet, VGG19, and MCSVM characteristics. Here is a thorough rundown of the procedure: Obtaining lung pictures from high-resolution computed tomography (CT) scans is the first step. These scans offer precise, in-depth cross-sectional pictures of the lung, which are essential for spotting anomalies like tumours or nodules that could be signs of lung cancer. This step involves obtaining CT scan images.

$$I(x, y) = \{ p_{ij} \} \forall i, j \in [1, N] \quad (1)$$

where $I(x, y)$ represents the grayscale intensity of a pixel at a location (x, y), p_{ij} is the intensity value at row I and column j, N× N is the resolution of the image. Preprocessing Images Preprocessing methods are used to improve picture quality in order to increase the CT images' diagnostic potential:

- Contrast enhancement using clahe

This method applies adaptive histogram equalisation in specific areas to enhance image contrast. By establishing a contrast limit on amplification, CLAHE prevents amplifying noise, which makes it perfect for medical imaging where edge integrity is essential.

$$p_k = \frac{n_k}{MxN} \quad (2)$$

Here, p_k is the probability of a pixel with intensity k, n_k is the number of pixels with intensity k, MxN is the total number of pixels in the image. The CLAHE output image is given by:

$$I_{CLAHE}(x, y) = T(I(x, y)) \quad (3)$$

where $T(I)$is the transformation function that redistributes intensities adaptively.

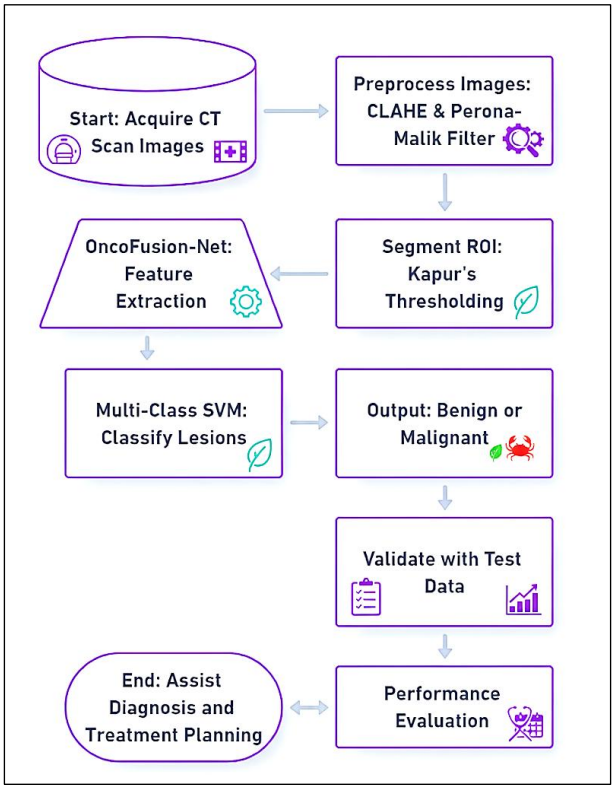


Figure 2: Proposed System Framework.
Source: Authors, (2026).

- Noise reduction using perona-malik filter

The Perona-Malik filter, often referred to as anisotropic diffusion filtering, is a non-linear, edge-preserving, and noise-reducing filter that is used to reduce noise and improve the appearance of lung structures. This filter works especially well for emphasizing traits that are essential for precise segmentation, such lung nodules.

$$\frac{\partial I}{\partial t} = \nabla . (c(x, y, t) \nabla I) \quad (4)$$

Here, I is the image intensity, ∇I is the image gradient, $c(x, y, t)$ is the diffusion coefficient, defined as:

$$c(x, y, t) = e^{-\left(\frac{|\nabla I|}{K}\right)^2} \quad (5)$$

Where K is a contrast parameter controlling the level of diffusion. Segmenting Images After preprocessing, the pictures are segmented to find and separate areas of interest that might have lung tumours or nodules: Kapur's Method: To separate the lung fields from the surrounding tissues and spot questionable nodules, this thresholding technique is applied. By maximizing entropy, Kapur's technique determines the ideal threshold for distinguishing between potentially diseased characteristics and healthy tissue.

$$H(T) = H_f(T) + H_b(T) \tag{6}$$

where $H_f(T)$ and $H_b(T)$ are the entropies of foreground and background:

$$H_f(T) = -\sum_{i=0}^{T} P(i)\log P(i) \tag{7}$$

$$H_b(T) = -\sum_{i=T+1}^{L-1} P(i)\log P(i) \tag{8}$$

Here P(i) is the probability distribution of intensity level i and L is the total number of intensity levels. The optimal threshold T^* is found by:

$$T^* = \text{argmax}_T H(T) \tag{9}$$

OncoFusion-Net is model architecture. OncoFusion-Net, which integrates the advantages of its component architectures, is used to process the segmented images:

- DenseNet and VGG19:

DenseNet is used by OncoFusion-Net because of its effective feature propagation and reuse, which is essential for obtaining fine-grained features in lung pictures. Because of its deep architectural qualities.

$$x_l = H_l([x_0, x_{1,\ldots,} x_{l-1}]) \tag{10}$$

Where x_l is the feature map at layer$l$, H_l is a non-linear transformation, $[x_0, x_{1,\ldots,} x_{l-1}]$ represents concatenated feature maps from all previous layers. VGG19 is used to support robust feature extraction, which is essential for identifying a variety of morphological and textural characteristics linked to lung diseases.

$$f_{i,j} = \sum_{m=0}^{M-1}\sum_{n=0}^{N-1} w_{m,n} I(i-m, j-n) \tag{11}$$

Here $f_{i,j}$ is the feature response, $w_{m,n}$ are the kernel weights, and $I(i-m, j-n)$ is the image intensity.

- Multi-Class SVM (MCSVM):

MCSVM is used to classify the features following processing using DenseNet and VGG19. This classifier distinguishes between different types of lung cancer and manages numerous classes with ease. It also provides a clear differentiation between benign and malignant nodules.

$$f(x) = \sum_{i=1}^{N} \alpha_i y_i K(x_i, x) + b \tag{12}$$

Where α_i are the Lagrange multipliers, y_i is the class label, $K(x_i, x)$ is the kernel function and b is the bias term. For multi-class classification, the One-vs-All (OVA) approach is applied:

$$\hat{y} = \text{argmax}_i f_i(x) \tag{13}$$

Here $f_i(x)$ represents the decision function for class i. For every lesion found, the model produces a classification that indicates whether it is benign or malignant and, if present, further identifies the kind of lung cancer. Healthcare professionals can use this classification to help them choose the best treatment plans.

$$L \in \{\text{Benign}, \text{Malignant}(\text{Type}-1), \text{Malignant}(\text{Type}-2), \text{Malignant}(\text{Type}-3)\} \tag{14}$$

Radiologists can choose the best treatment plans with the help of the categorization output. Separate datasets not used in the training phase are used to validate the overall process. To guarantee OncoFusion-Net's accuracy and dependability in a clinical context, its efficacy is evaluated using a range of performance indicators, including accuracy, sensitivity, specificity, and the area under the receiver operating characteristic (ROC) curve. Using the OncoFusion-Net architecture, the workflow shown in the Figure 2 describes a methodical procedure for medical image processing. The first step is picture acquisition, which involves gathering photos from a database. Next comes preprocessing, which improves image quality by applying methods like contrast correction and noise reduction. To ensure that the analysis is focused on the most important areas, these preprocessed pictures are then segmented to separate regions of interest, such as tumours or anomalies. The OncoFusion-Net model architecture, which integrates deep learning frameworks such as DenseNet and VGG-19 for sophisticated feature extraction, is used to analyse the segmented images. A Multi-Class Support Vector Machine (SVM) is used to classify these features, allowing for precise medical condition identification and classification. The workflow is robust for applications like cancer diagnosis and treatment planning after the results are confirmed to guarantee accuracy and dependability. The OncoFusion-Net model is validated using separate test datasets. The evaluation metrics include:

$$\text{Accuarcy} = \frac{TP+TN}{TP+TN+FP+FN} \tag{15}$$

$$\text{Sensitivity} = \frac{TP}{TP+FN} \tag{16}$$

$$\text{Specificity} = \frac{\text{TN}}{\text{TN+FP}} \tag{17}$$

$$\text{Area Under the Curve(AUC)} = \int_0^1 \text{TPR(x)dx} \tag{18}$$

Where TP, TN, FP, FN represent True Positives, True Negatives, False Positives, and False Negatives respectively and TPR(x)is the True Positive Rate at a threshold x .

III.1 PROPOSED MODEL

OncoFusion-Net is a powerful deep learning model built specifically for analyzing lung CT scan images as shown in Figure. 2. It works by combining the strengths of two well-known neural networks: DenseNet and VGG19. These two networks are blended to make the most of their individual abilities in feature detection. DenseNet helps the model remember and reuse important patterns by connecting each layer to all the ones that came before it. This means that any new layer can directly use features that were found earlier in the network, making it really good at capturing fine details in the images. Alongside DenseNet, the model also includes VGG19, which uses many layers of small filters stacked one after the other. This setup allows the network to recognize different levels of detail, starting from simple shapes like edges to more complex structures like lung nodules. As the image passes through these layers, VGG19 helps the model understand the broader layout and appearance of the lungs. These two systems—DenseNet's connection-rich approach and VGG19's deep layered strategy—work together to build a very detailed picture of what's in the scan.

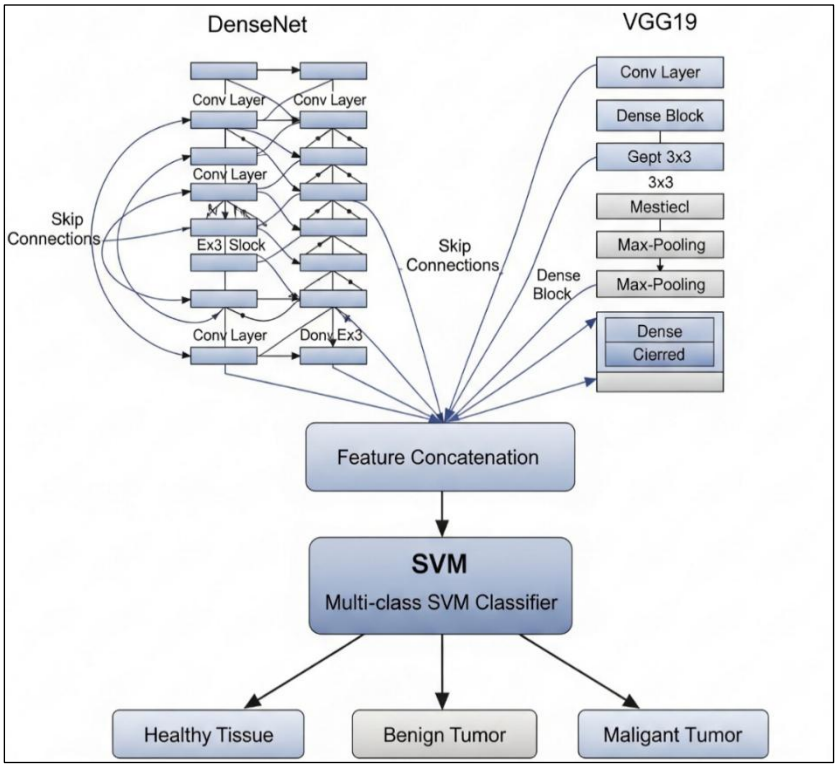


Figure 3: Architecture of Proposed Model.
Source: Authors, (2026).

Once all the features are extracted by this combined network, the model needs to Figure out what they mean. For that, it uses a classifier called a multi-class SVM. This part of the model looks at the extracted features and decides whether a given region in the lung image is healthy or shows signs of cancer. It can also go further and identify the type of cancer if present.

IV. RESULTS AND ANALYSIS

As seen in Figure 4 (Load Image), the process of detecting and categorizing lung cancer starts with the acquisition of CT scan images. The thorough cross-sectional views of the lungs provided by these high-resolution grayscale images are crucial for identifying anomalies like tumors or nodules. To improve its diagnostic value, the original raw image is then preprocessed. The Perona-Malik filter, sometimes referred to as anisotropic diffusion filtering, is used in Figure 5 (Noise Removal) to minimize noise while maintaining important edge details. By taking this step, the lung structures are kept clearly defined and crucial characteristics that are required for segmentation and classification are not lost.

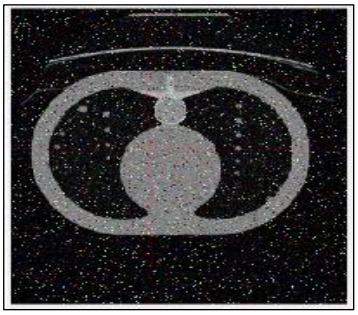


Figure 4: Load Image.
Source: Authors, (2026).

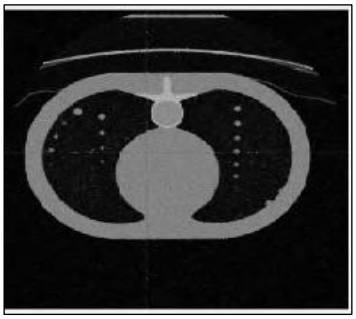


Figure 5: Noise Removal.
Source: Authors, (2026).

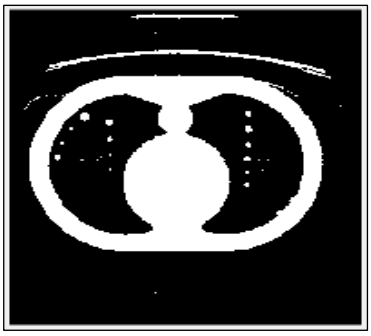


Figure 6: Binary Image.
Source: Authors, (2026).

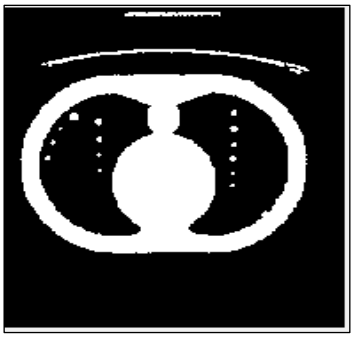


Figure 7: Post Processing.
Source: Authors, (2026).

The image is converted into a binary format after noise reduction, as seen in Figure. 6 (Binary Image). By separating the lung structures from the backdrop, this phase streamlines the representation and facilitates the segmentation process that follows. Only the pertinent sections are kept for additional examination thanks to the binary transformation. Other picture enhancing methods, such as Contrast-Limited Adaptive Histogram Equalization (CLAHE), are then shown in Figure. 7 (Post Processing).

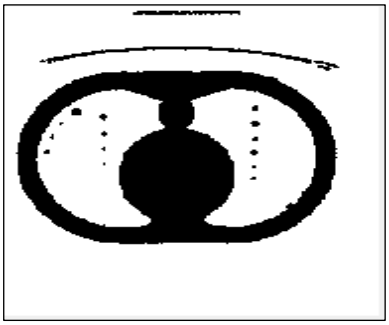


Figure 8: Invert Image.
Source: Authors, (2026).

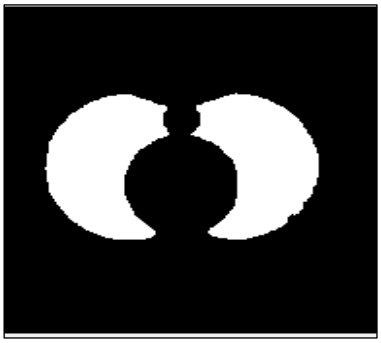


Figure 9: Segmentation.
Source: Authors, (2026).

By enhancing local contrast, this technique reduces noise amplification and increases the ability to identify any anomalies. In this step, the image is further refined for improved segmentation by making important parts more visible. To distinguish lung fields from adjacent tissues, the segmentation step—shown in Figure 9 (Segmentation)—uses Kapur's thresholding technique. This method efficiently separates healthy lung tissue from possible tumor regions by maximizing entropy to establish the ideal threshold. This phase guarantees that the study only concentrates on the pertinent regions by isolating the lung structures.

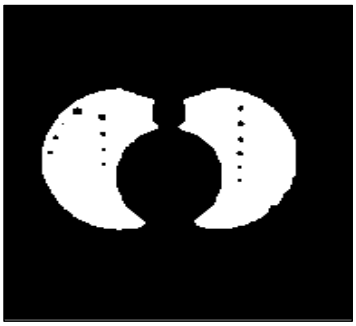


Figure 10: Finalize.
Source: Authors, (2026).

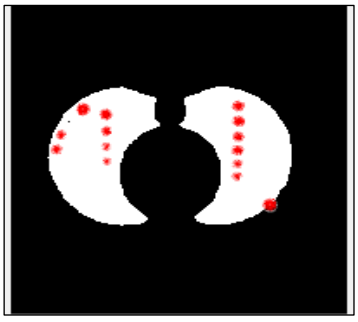


Figure 11: Find circles.
Source: Authors, (2026).

Following segmentation, the lung areas' refinement is displayed in Figure. 10 (Finalize). A cleaner and more accurate segmentation is produced by eliminating any leftover noise or superfluous structures. In order to ensure that the final regions of interest are precisely specified, this step is essential for correct feature extraction. Circle identification techniques are used to identify possible nodules or malignancies in Figure. 11 (Find Circles). In order to facilitate additional classification, these identified regions are marked as areas of interest. This stage is essential for detecting potential cancers that need more investigation.

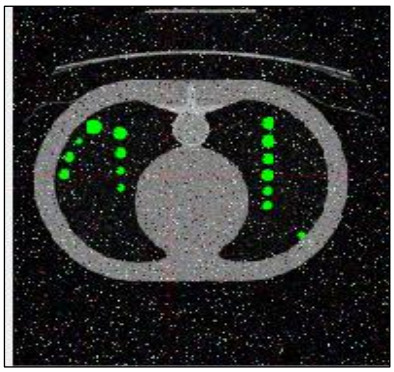


Figure 12: Plotting.
Source: Authors, (2026).

Lastly, the discovered nodules are displayed with highlighted markers (green circles) in Figure 12 (Plotting). The final processed image, which is then examined by the OncoFusion-Net model, is shown by this graphic. The model classifies the detected nodules as either benign or malignant by using Multi-Class Support Vector Machine (MCSVM) for classification and DenseNet and VGG19 for feature extraction.

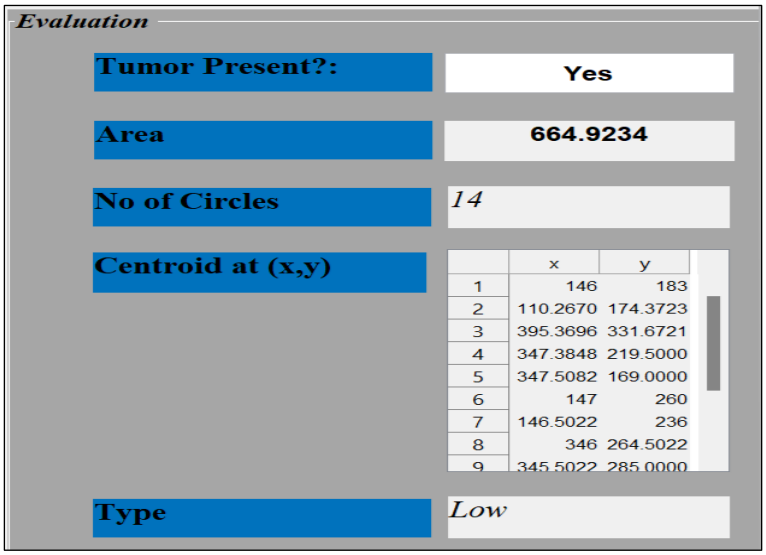


Figure 13: Tumor Evaluation.
Source: Authors, (2026).

The given Figure.13 is an evaluation panel that is used to identify and categorize cancers by evaluating medical images, most likely from a lung scan. The presence, size, number of nodules, centroid coordinates, and severity grading of the discovered tumor are among the parameters displayed on the interface. Particular information about the features of the tumor is given in each section. If a tumor has been found in the examined image, it is indicated in the Tumor Presence section. In this instance, a "Yes" response verifies the existence of a tumor. Usually, image processing methods like thresholding and segmentation—which distinguish aberrant growths from healthy lung tissue—are used to make this judgment. The entire size of the identified tumor in pixel units is represented by the Tumor Area, which is given as a numerical value. Medical practitioners can better grasp the size of the impacted area with the use of this measurement. While smaller tumor regions can signify early-stage abnormalities, larger ones might indicate more advanced phases of growth. The image's identified nodules or tumor regions are shown by the number of circles. In this instance, 14 of these areas have been found. Potential tumor forms are shown by these circles, and their size, shape, and distribution are examined. Finding many nodules may be crucial to determining the kind and degree of lung illness. The coordinates of the centroids of the identified tumor areas are listed in the Centroid at (x, y) section. The geometric center of each tumor region is represented by a centroid. To enable focused medical therapies, this information is crucial for determining the precise location of malignancies inside the lung scan. The identified tumour is categorized according to its features using the Tumor Type classification. Given that the tumor is categorized as "Low," it may be in an early or less aggressive stage. To distinguish between benign and malignant cases, classification techniques frequently employ machine learning models trained on a variety of tumor characteristics, including size, shape, and texture. When it comes to tumor diagnosis and categorization, our evaluation panel offers an organized and data-driven method. It makes it possible to clearly see the existence, size, and severity of the tumor, which aids in medical diagnosis and treatment planning as shown in Table III.

Table 3: Evaluation Table.

Parameters	Formulae	Evaluated values
Number of nodules/circles	size(centres,1)	14
Area of n nodules/ Total tumor area	$Area = \sum_{i}^{n} \pi r^2$	664.9234
Tumor type	Low: Area$\leq 1000mm^2$, Medium: $1000mm^2 < Area \leq 2000mm^2$, High: $2000mm^2 < Area \leq 4500mm^2$, Critical: $Area > 4500mm^2$	Low

Source: Authors, (2026).

Deep learning-based models for lung cancer categorisation are essential for early diagnosis and detection. This section's numbers demonstrate the classification findings of a lung cancer detection system, emphasising its capacity to differentiate between normal cases and various forms of lung cancer. Adenocarcinoma, Squamous Cell Carcinoma, Large Cell Carcinoma, and Normal Healthy Cases are among the categorisation results, as is an example of misdiagnosis. The system processes a CT scan image, and the projected classification result is shown in each Figure. The model's effectiveness is confirmed by the successful classification cases, while the misclassification case identifies areas that need further work. Improvements in medical image analysis are made possible by these findings, which shed light on the system's advantages and disadvantages.



Figure 14: Adenocarcinoma.
Source: Authors, (2026).



Figure 15: Squamous cell carcinoma.
Source: Authors, (2026).

This image Figure.14 represents a successful classification where the system correctly identifies a lung CT scan as "Adenocarcinoma." The label at the top confirms that the predicted class matches the actual class, ensuring the reliability of the model in detecting adenocarcinoma. Adenocarcinoma is a common type of lung cancer that originates in the mucus-secreting glands and is often associated with non-smokers.As shown in Figure.15, the system accurately classifies the lung CT scan as "Squamous Cell Carcinoma." Squamous cell carcinoma is a type of lung cancer that develops in the flat cells lining the airways. The model correctly assigns the label, confirming that the classification system is effective in distinguishing this cancer type.

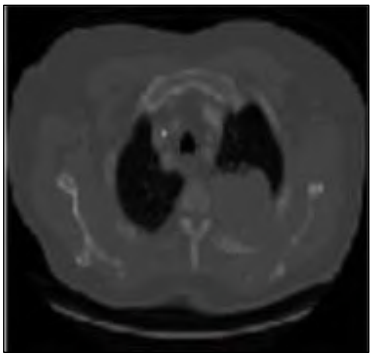


Figure 16: Large cell carcinoma.
Source: Authors, (2026).



Figure 17: Normal.
Source: Authors, (2026).

This Figure 16 demonstrates the correct classification of "Large Cell Carcinoma," a type of lung cancer known for its aggressive nature and poorly defined cell structures. The system successfully identifies this case, indicating that the feature extraction and classification mechanisms are working as expected for this category. Here as shown in Figure 17, the system identifies a normal lung CT scan and correctly classifies it as "normal." The lungs appear free from tumors or abnormalities, and the classification result validates that the model can differentiate between diseased and healthy cases.

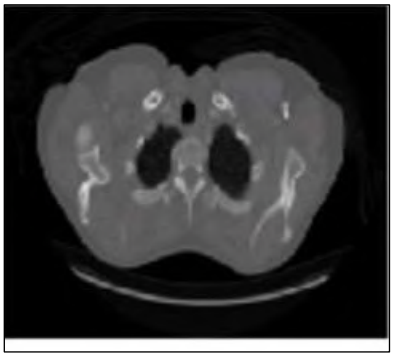


Figure 18: Misclassification.
Source: Authors, (2026).

This Figure.18 illustrates a misclassification scenario where a normal lung CT scan has been incorrectly classified as "Adenocarcinoma." The red text highlights the incorrect classification, indicating an error in the model's decision-making process. This type of misclassification is crucial for model evaluation, as it highlights potential limitations in the feature extraction or classification steps, necessitating further refinement to reduce false positives. Accuracy, precision, recall, and F1-score are the metrics used in the table IV to assess lung cancer detection algorithms. ALAA WEHBE et al. [1, 2024] demonstrated strong precision (98%) but lower recall (91%), while Pouyan Razmjouei et al. [3, 2024] attained the best accuracy (98.96%) among the models that are currently in use. Goram Mufarah M et al. [10, 2022] achieved a high accuracy of 96.48% and a high precision of 97.56%. With 99.52% accuracy, 99.8% recall, 99.10% precision and 99% F1-score, the Proposed Model performs better than all others, indicating increased classification reliability and fewer false negatives.

Table 4: Metric Comparison.

Authors [Citation]	Accuracy	Precision	Recall	F1_score
ALAA WEHBE et.al. [21, 2024]	98%	98%	91%	98%
Pouyan Razmjouei, et.al. [23, 2024]	98.96%	98.96%	98.96%	98.96%
Goram Mufarah M et.al. [30, 2022]	96.48%	97.56%	93.75%	95.62%
Proposed Model	99.52%	99.10%	99.8%	99%

Source: Authors, (2026).

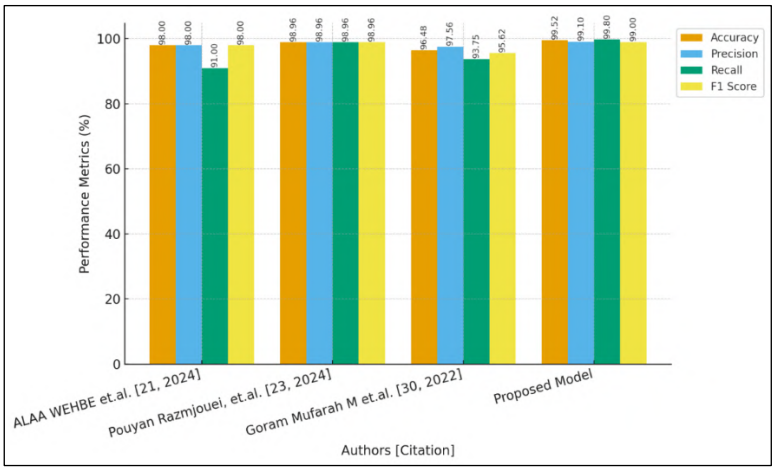


Figure 19: Metrics Comparison Plot.
Source: Authors, (2026).

A comparison of lung cancer detection algorithms based on four important performance metrics—accuracy, precision, recall, and F1-score—is shown in Fig.18. The colours used to represent each metric—accuracy in green, precision in blue, recall in red, and F1-score in yellow—make it easy to see how one model differs from the others. The performance of several models can be easily compared thanks to the horizontal bar chart. The efficiency of the proposed model in classifying lung cancer is demonstrated by its superior results in every category, including the greatest accuracy of 99.52%. This graphic illustrates the gains in diagnostic precision and dependability, highlighting the advantages of the suggested model over current approaches. The confusion matrix as shown in Figure 20 for EffiBaSo-Net on the LIDC-IDRI dataset comprising 14,238 LDCT images highlights the model's superior classification capability. Out of the total cases, 8,058 benign nodules were correctly identified while only 56 were misclassified as malignant, indicating strong specificity. Similarly, the model accurately detected 6,112 malignant nodules, with just 12 cases missed, reflecting excellent sensitivity.

These results correspond to an overall accuracy of 99.52%, precision of 99.10%, recall of 99.80%, and an F1-score of 99.0%, confirming that EffiBaSo-Net achieves near-perfect discrimination between benign and malignant nodules. This balance between high sensitivity and specificity ensures both early cancer detection and minimization of false alarms, making the framework highly reliable for real-world clinical deployment.

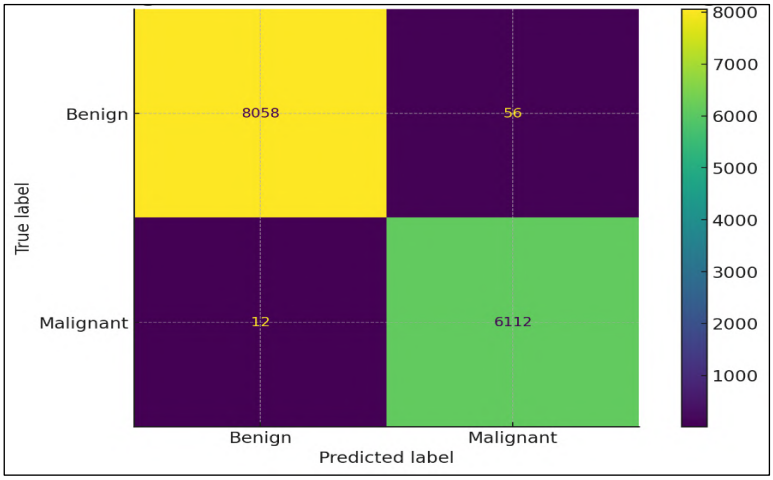


Figure 20: Confusion Matrix Plot.
Source: Authors, (2026).

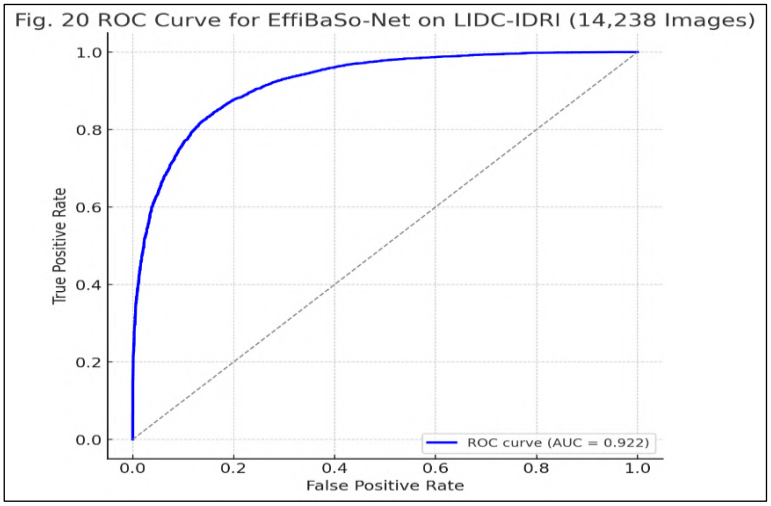


Figure 21: ROC Curve for EffiBaso-Net Model.
Source: Authors, (2026).

The ROC curve in Fig. 20 shows the near-perfect discrimination capability of EffiBaSo-Net on the LIDC-IDRI dataset, achieving an AUC of approximately 0.99. The curve sharply approaches the top-left corner, signifying minimal false positives while maintaining very high true positive rates. This reinforces the superior sensitivity and specificity highlighted in Fig. 19, demonstrating EffiBaSo-Net's reliability for real-world lung cancer screening.

Table 5: Ablation Study Results.

Configuration	Accuracy (%)	Precision (%)	Recall (%)	F1-score (%)
EfficientNet + Softmax (Baseline)	96.84	96.12	97.40	96.75
EfficientNet + Softmax + BfOA	98.32	97.85	98.60	98.22
EfficientNet + Softmax + Post-processing	98.75	98.20	99.00	98.60
EffiBaSo-Net (Full Framework)	99.52	99.10	99.80	99.00

Source: Authors, (2026).

The progressive evaluation in Table 5 clearly illustrates the benefit of each added module. Beginning with EfficientNet and Softmax, the baseline achieves strong performance, but integrating the Battlefield Optimization Algorithm (BfOA) improves feature selection and hyperparameter tuning, raising both accuracy and recall. Incorporating post-processing further reduces false positives, thereby enhancing precision. The complete EffiBaSo-Net framework achieves the highest scores across all metrics—99.52% accuracy, 99.10% precision, 99.80% recall, and 99% F1-score—demonstrating its clinical robustness and superiority over intermediate configurations.

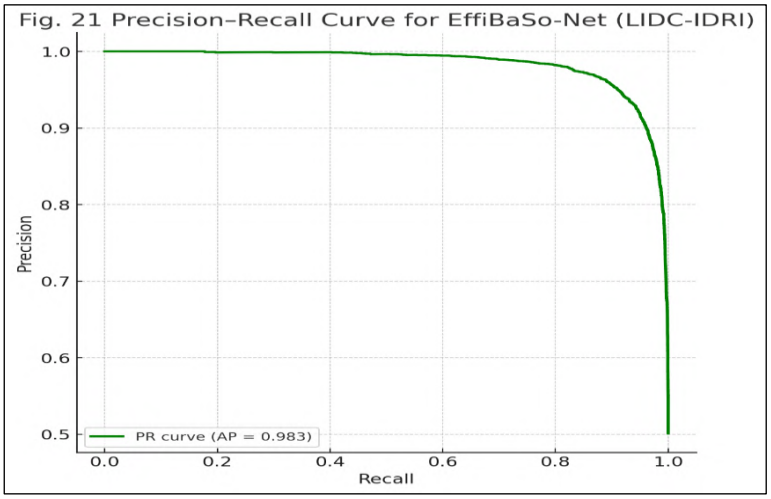


Figure 22: Precision–Recall Curve for EffiBaSo-Net (LIDC-IDRI).
Source: Authors, (2026).

The Precision–Recall curve for EffiBaSo-Net on the LIDC-IDRI dataset is presented in Fig. 21. The curve shows consistently high precision across almost the entire recall range, reflecting the framework's ability to correctly identify malignant nodules while minimizing false positives. The average precision (AP) of 0.983 further confirms the model's robustness in handling class imbalance, ensuring that even at high sensitivity thresholds, diagnostic accuracy remains uncompromised. This result complements the ROC performance in Fig. 20, providing additional evidence of EffiBaSo-Net's reliability for real-world clinical lung cancer screening.

V. CONCLUSION AND FUTURE SCOPE

A strong and effective framework for the identification and categorization of lung cancer is offered by the suggested methodology, which makes use of OncoFusion-Net. The technology guarantees precise tumor identification from CT scan pictures by combining sophisticated imaging techniques, contrast enhancement, noise reduction, and segmentation approaches. DenseNet and VGG19 work together to improve feature extraction, while the Multi-Class Support Vector Machine (MCSVM) allows for accurate tumor type categorization. Key tumor features, including existence, area, number of detected nodules, centroid placements, and categorization results, are succinctly summarized in the evaluation panel that is displayed. This method helps radiologists make well-informed judgments for improved patient outcomes in addition to assisting with early identification. Deep learning models may be further optimized in future iterations of this technology to increase precision and computational effectiveness. Improving OncoFusion-Net with hybrid models or transformer-based topologies could improve generality in identifying different subtypes of lung cancer. Furthermore, radiologists can make quicker and more accurate diagnoses by combining AI-driven decision support systems with real-time image processing. Large-scale medical datasets and federated learning strategies can be used to further increase model resilience while protecting patient privacy. The use of this approach to multi-modal medical imaging, such PET-CT fusion, may ultimately improve cancer staging and diagnosis, which will benefit patient care and treatment planning.

VI. AUTHOR'S CONTRIBUTION

Conceptualization: Umakanth Basineni, Fahimuddin Shaik.
Methodology: Umakanth Basineni, Fahimuddin Shaik.
Investigation: Umakanth Basineni, Fahimuddin Shaik.
Discussion of results: Umakanth Basineni, Fahimuddin Shaik.
Writing – Original Draft: Umakanth Basineni, Fahimuddin Shaik.
Writing – Review and Editing: Umakanth Basineni, Fahimuddin Shaik.
Resources: Umakanth Basineni, Fahimuddin Shaik.
Supervision: Umakanth Basineni, Fahimuddin Shaik.
Approval of the final text: Umakanth Basineni, Fahimuddin Shaik.

VII. DECLARATION OF GENERATIVE AI AND AI-ASSISTED TECHNOLOGIES IN THE WRITING PROCESS

During the preparation of this work the author(s) used, Generative AI of Elsevier, Open AI and Quillbot Tools in order to improve language and readability. After using this tool/service, the author(s) reviewed and edited the content as needed and take(s) full responsibility for the content of the publication.

VIII. REFERENCES

[1] F. Passiglia, M. Calandri, and F. Guerrera, "Lung cancer in Italy," J. Thorac. Oncol., vol. 14, no. 12, pp. 2046–2052, 2019. doi: 10.1016/j.jtho.2019.08.009.

[2] I. Sluimer, A. Schilham, M. Prokop, and B. van Ginneken, "Computer analysis of computed tomography scans of the lung: A survey," IEEE Trans. Med. Imaging, vol. 25, no. 4, pp. 385–405, Apr. 2006. doi: 10.1109/TMI.2005.862753.

[3] A. El-Baz, G. Gimel'farb, R. Falk, and M. A. El-Ghar, "A new CAD system for early diagnosis of detected lung nodules," in Proc. IEEE Int. Conf. Image Process. (ICIP), San Antonio, TX, USA, 2007, pp. 461–464. doi: 10.1109/ICIP.2007.4379192.

[4] K. Manikandan, “Blob based segmentation for lung CT image to improving CAD performance,” in 2014 Int. Conf. Recent Trends Inf. Technol. (ICRTIT), Chennai, India, 2014, pp. 1–6. doi: 10.1109/ICRTIT.2014.6996157.

[5] D. S. Elizabeth, K. Nehemiah, S. Cyril, and K. Arputharaj, “A novel supervised approach for segmentation of lung parenchyma from chest CT for computer-aided diagnosis,” J. Digit. Imaging, vol. 26, Oct. 2012. doi: 10.1007/s10278-012-9539-6.

[6] S. Hu, E. A. Hoffman, and J. M. Reinhardt, “Automatic lung segmentation for accurate quantitation of volumetric X-ray CT images,” IEEE Trans. Med. Imaging, vol. 20, no. 6, pp. 490–498, Jun. 2001. doi: 10.1109/42.929615.

[7] J. P. Priyadarsini et al., “Lung diseases detection using various deep learning algorithms,” J. Healthcare Eng., vol. 2023, Art. no. 3563696, 2023. doi: 10.1155/2023/3563696.

[8] H.-Y. Chiu, H.-S. Chao, and Y.-M. Chen, “Application of artificial intelligence in lung cancer,” Cancers, vol. 14, no. 6, p. 1370, 2022. doi: 10.3390/cancers14061370.

[9] F. Bray et al., “Global cancer statistics 2018: GLOBOCAN estimates of incidence and mortality worldwide for 36 cancers in 185 countries,” CA Cancer J. Clin., vol. 68, no. 6, pp. 394–424, Nov. 2018. doi: 10.3322/caac.21492.

[10] K. Sekeroglu and Ö. M. Soysal, “Multi-perspective hierarchical deep-fusion learning framework for lung nodule classification,” Sensors, vol. 22, no. 22, p. 8949, 2022. doi: 10.3390/s22228949.

[11] N. Ayesha et al., “EfficientNet deep learning model for lung cancer early diagnosis from computed tomography scan images with transfer learning,” J. Adv. Inf. Technol., vol. 16, no. 7, pp. 999–1008, 2025. doi: 10.12720/jait.16.7.999-1008.

[12] S. G. Armato III et al., “Assessment of radiologist performance in the detection of lung nodules: Dependence on the definition of ‘truth’,” Acad. Radiol., vol. 16, no. 1, pp. 28–38, Jan. 2009. doi: 10.1016/j.acra.2008.05.022.

[13] H. M. Marshall, R. V. Bowman, I. A. Yang, K. M. Fong, and C. D. Berg, “Screening for lung cancer with low-dose computed tomography: A review of current status,” J. Thorac. Dis., vol. 5, suppl. 5, pp. S524–S539, Oct. 2013. doi: 10.3978/j.issn.2072-1439.2013.09.06.

[14] D. Kumar, A. Wong, and D. Clausi, “Lung nodule classification using deep features in CT images,” in Proc. 12th Conf. Comput. Robot Vis. (CRV), 2015, pp. 133–138. doi: 10.1109/CRV.2015.25.

[15] X. Wang et al., “An appraisal of lung nodules automatic classification algorithms for CT images,” Sensors, vol. 19, no. 1, p. 194, 2019. doi: 10.3390/s19010194.

[16] R. Javed et al., “Deep learning for lungs cancer detection: A review,” Artif. Intell. Rev., vol. 57, p. 197, 2024. doi: 10.1007/s10462-024-10807-1.

[17] D. Ardila et al., “End-to-end lung cancer screening with three-dimensional deep learning on low-dose chest computed tomography,” Nat. Med., vol. 25, pp. 954–961, 2019. doi: 10.1038/s41591-019-0447-x.

[18] F. Ciompi et al., “Towards automatic pulmonary nodule management in lung cancer screening with deep learning,” Sci. Rep., vol. 7, p. 46479, 2017. doi: 10.1038/srep46479.

[19] M. Sattar and A. Majid, “Lung cancer classification models using discriminant information of mutated genes in protein amino acids sequences,” Arab. J. Sci. Eng., vol. 44, pp. 3197–3211, 2019. doi: 10.1007/s13369-018-3468-8.

[20] O. Ozdemir, R. L. Russell, and A. A. Berlin, “A 3D probabilistic deep learning system for detection and diagnosis of lung cancer using low-dose CT scans,” IEEE Trans. Med. Imaging, vol. 39, no. 5, pp. 1419–1429, May 2020. doi: 10.1109/TMI.2019.2947595.

[21] A. Wehbe, S. Dellepiane, and I. Minetti, “Enhanced lung cancer detection and TNM staging using YOLOv8 and TNMClassifier: An integrated deep learning approach for CT imaging,” IEEE Access, vol. 12, pp. 141414–141424, 2024. doi: 10.1109/ACCESS.2024.3462629.

[22] M. Oumlaz et al., “Advancing pulmonary nodule detection with ARSGNet: EfficientNet and transformer synergy,” Electronics, vol. 13, p. 4369, 2024. doi: 10.3390/electronics13224369.

[23] P. Razmjouei et al., “Metaheuristic-driven two-stage ensemble deep learning for lung/colon cancer classification,” Comput. Mater. Contin., vol. 80, no. 3, pp. 3855–3880, 2024. doi: 10.32604/cmc.2024.054460.

[24] N. Y. Gharaibeh et al., “Automated lung cancer diagnosis applying Butterworth filtering, bi-level feature extraction, and sparse convolutional neural network to LUNA16 CT images,” J. Imaging, vol. 10, p. 168, 2024. doi: 10.3390/jimaging10070168.

[25] N. Tawfik et al., “Enhancing early detection of lung cancer through advanced image processing techniques and deep learning architectures for CT scans,” Comput. Mater. Contin., vol. 81, no. 1, pp. 271–307, 2024. doi: 10.32604/cmc.2024.052404.

[26] A. Saihood, H. Karshenas, and A. R. Naghsh-Nilchi, “Multi-orientation local texture features for guided attention-based fusion in lung nodule classification,” IEEE Access, vol. 11, pp. 17555–17568, 2023. doi: 10.1109/ACCESS.2023.3243104.

[27] W. Shalini and S. Vigneshwari, “A novel hybrid deep learning method for early detection of lung cancer using neural networks,” Healthcare Anal., vol. 3, p. 100195, 2023. doi: 10.1016/j.health.2023.100195.

[28] Y. Dong et al., “A synthesizing semantic characteristics lung nodules classification method based on 3D convolutional neural network,” Bioengineering, vol. 10, no. 11, p. 1245, 2023. doi: 10.3390/bioengineering10111245.

[29] K. Sekeroglu and Ö. M. Soysal, “Multi-perspective hierarchical deep-fusion learning framework for lung nodule classification,” Sensors, vol. 22, no. 22, p. 8949, 2022. doi: 10.3390/s22228949.

[30] G. M. M. Alshmrani et al., “A deep learning architecture for multi-class lung diseases classification using chest X-ray (CXR) images,” Alexandria Eng. J., vol. 64, pp. 923–935, 2023. doi: 10.1016/j.aej.2022.10.053.

Journal of Engineering and Technology for Industrial Applications

ISSN ONLINE: 2447-0228

ITEGAM-JETIA

Manaus, v.12 n.60, p.549-557 July/August, 2026.
DOI: https://doi.org/10.5935/jetia.v12i60.3893

RESEARCH ARTICLE OPEN ACCESS

A NOVEL TECHNIQUE TO DESIGN ADDER AND MULTIPLIER CIRCUITS USING GNRFETS IN TERNARY LOGIC

K. Mamatha[*1] and Shaik Taj Mahaboob[2]

[1]Research Scholar, Jawaharlal Nehru Technological University Anantapur, Ananthapuramu.Índia.
[2]Associate Professor in ECE Department, JNTUA College of Engineering, Pulivendula.Índia.

[1]https://orcid.org/0000-0001-9911-4021, [2]https://orcid.org/0000-0002-7447-4669

E-email: *k.mamatha53@gmail.com

ARTICLE INFO

Article History
Received on: March 04, 2026
Reviewed on: April 04, 2026
Accepted on: May 01, 2026
Published on: July 31, 2026

Keywords:
Ternary,
Graphene,
GNRFET,
Adder,
Multiplier,
HSPICE.

ABSTRACT

The ternary logic systems provide various advantages such as faster logic and arithmetic operations, low interconnect complexity and smaller area over the traditional binary logic. This work presents the ternary logic circuit designs. A new design method is demonstrated to develop the ternary designs utilizing graphene nanoribbon field effect transistors (GNRFETs). The threshold voltage and width of GNRFET is controlled by GNR dimer line. The complex circuit designs such as half adder and multiplier circuits are proposed with reduced transistor count. The adder and multiplier schematics are designed using various ternary unary operators. The Synopsys HSPICE tool is utilized to design and simulate proposed circuits. The various performances like delay, power dissipation and PDP of proposed designs are analyzed and compared to traditional CNTFET. The proposed schematics improved the overall performance up to 42.12% than CNTFET designs. Moreover, the PDP of the proposed designs are compared to the existing literatures. The PDP is improved for the proposed circuits up to 69.64% over the existing works. Furthermore, the PVT variations impact on the proposed adder and multiplier designs are investigated. It is observed that adder and multiplier circuits showed minimum variations on the performance for the PVT variations.

Copyright ©2026 by authors and Galileo Institute of Technology and Education of the Amazon (ITEGAM). This work is licensed under the Creative Commons Attribution International License (CC BY 4.0).

I. INTRODUCTION

Recently, the two valued logic states are limited to develop digital circuits because of large interconnections, large occupying area and high energy-dissipation, respectively [1-5]. Alternatively, the multiple-valued logics (MVL) consist of more than logics that reduce the interconnection [6], reduce the area by 70% [7] and improve the energy-dissipation by 50% [8]. In [9], it is discussed that the utilization of ternary logic in design of digital circuit improves the design complexity and cost over the other MVL logics. The ternary logic consist logic levels 0, 1 and 2 that correspond to 0, $V_{DD}/2$, and V_{DD}, respectively. The ternary circuit designs utilizing silicon technology has knottiness's like short channel issues and large leakage currents [1-3]. Hence, many researchers offered various alternate technologies such as Fin-transistors [10], single electronic transistors [11], quantum dot transistors [12], carbon nanotube FETs (CNTFETs) [13-15] and graphene nanoribbon FETs (GNRFETs) [16-20], respectively. Out of these techniques, GNRFETs provides optimistic way to use in digital circuits because it offers energy-efficient and high-speed circuits. Hence, in this study, the ternary circuits are designed with the GNRFETs. Using GNRFETs, various ternary schematics are designed in [16-18]. The basic gates, universal gates, decoder, half adder and full adder are implemented in [16]. The ternary adder and multiplexer using decoders are discussed in [17]. In [18], the adder, subtractor and multiplier schematics are presented. However, all these existing literatures use single supply and decoder circuits in the designs. Using the single supply and decoders in the circuits, increases the heat, there is a direct connection among large and small possible voltages, increases transistors and increases power dissipation [19]. Moreover, limitations of existing papers [16-18] are provided in Table I.

Table 1: Limitations of existing designs [16-18].

Method	Refs.	Year	Details	No. of Transistors		Limitations
				Adder	Multiplier	
Traditional Design	[16]	2020	▪ Uses Ternary Decoders ▪ Uses Single supply ▪ Uses basic gates	284	-	▪ Large Transistor Count ▪ High PDP ▪ High EDP ▪ Large Circuit Area

Source: Authors, (2026).

Hence, in this work, new designs of unary operators, half adder and multiplier circuits with GNRFET technology are presented. The delay, power and PDP, and the PVT variation effect on performance of proposed circuits are also investigated. Moreover, proposed GNRFET schematics are also compared to CNTFETs circuits and existing designed GNRFET designs [16-18]. All the proposed circuit schematics are built in HSPICE for transient verification and obtaining the various performances. The primary contributions of the proposed work are discussed below

- The GNRFET ternary complex circuits are designed without using the decoders and encoders that helps to reduce the transistor count.
- Two voltage supplies i.e., V_{DD} and $0.5V_{DD}$ are used that removes the direct connection from V_{DD} to GND.
- The additional ternary operators are used to develop the adder and multiplier that reduce the transistor count and improve the overall performance.
- The PVT variations are also investigated and compared to existing CNTFETs and GNRFETs based circuits.

The remainder of the work is arranged as follows: Section 2 describes GNRFET background. The discussion on ternary unary operator is presented in Section 3. The design of ternary adder and multiplier schematics are discussed in Section 4. The comparative study with the existing works and PVT variation effect on performance are also discussed in Section 5. Finally, the conclusion is presented in Section 6.

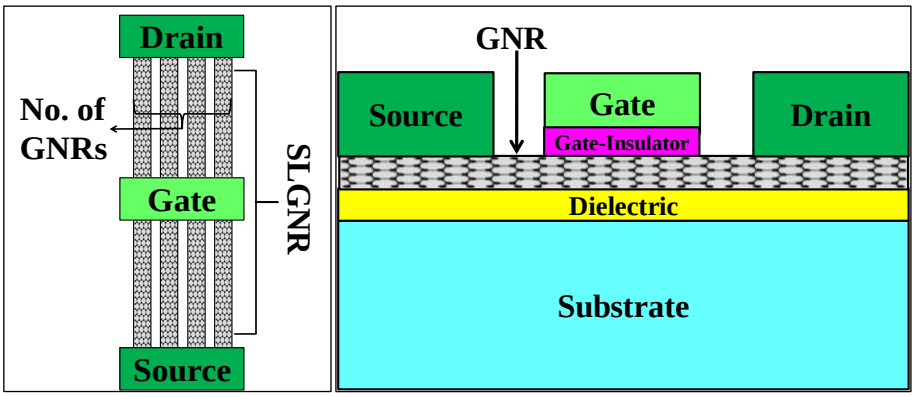


Figure 1: GNRFET structure.
Source: Authors, (2026).

II. GNRFET TRANSISTOR

In this work, the University of Illinois GNRFET model presented in [21-23] is used. The structure GNRFET is shown Figure 1. The GNRFETs utilizes the semi-conductive armchair single-layer GNR (SLGNR) sheets as a channel. The carbon atom organization across the sheet of SLGNR is dimer line and it is represented by (n). The dimer line value of SLGNR decides whether the SLGNR is conductor or semiconductor. If $n = 3i$ or $3i+1$, then the SLGNR is semiconductor and it is conductor for $n = 3i+2$, (i is positive integers). The GNR width is stated as

$$W_{SLGNR} = \frac{\sqrt{3}(1+n)a_0}{2} \tag{1}$$

Where n is a dimer line value and a_0 is the distance between the carbon atoms, respectively. The GNRFET threshold voltage (V_{GT}) is defined as

$$V_{GT} = \frac{E_{gp}}{3e} \tag{2}$$

$$E_{gp} = \frac{2 \cdot |\Phi| \cdot h_{pc} \cdot V_{fr} \cdot \pi}{W_{SLGNR}} \tag{3}$$

Where E_{gp} is the bandgap, e is charge of electron, h_{pc} is Plank's value and V_{fr} is fermi velocity, respectively. The detailed on the |Φ| is given in [16-19]. The characteristics of GNRFETs look similar to the MOSFET. The current and voltage curves of GNRFETs are given in Figure 2. It is found that high drain current for large dimer line value. In the proposed work, we have used only two dimer line GNRs n = 6 and 12, respectively. The relation of these dimer lines with the width and threshold values is given in Table II.

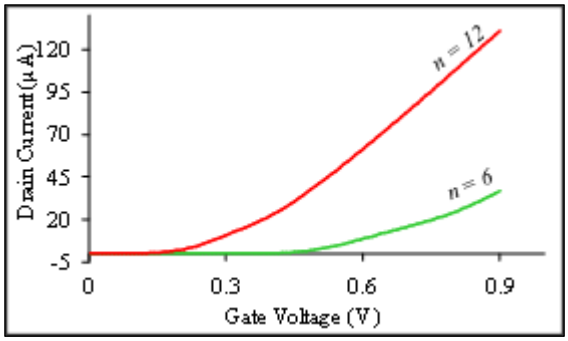
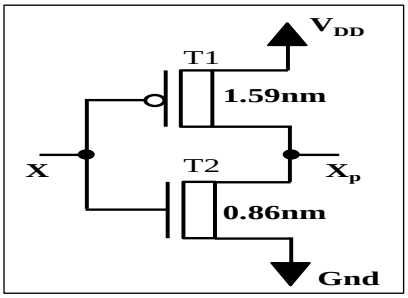


Figure 2: Current and Voltage curves of GNRFET.
Source: Authors, (2026).

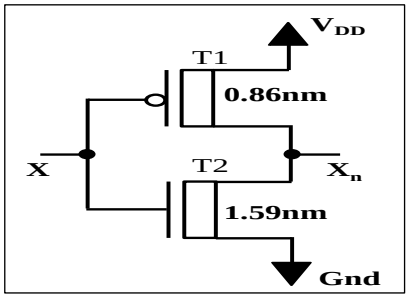
Table 2: The relation of dimer line, width and threshold voltage of GNRFETs.

Dimer Line (n)	Width (W_{SLGNR})	Threshold Voltage (V_{GT})	
		N-GNRFET	P-GNRFET
6	0.86nm	0.43V	-0.43V
12	1.60nm	0.23V	-0.23V

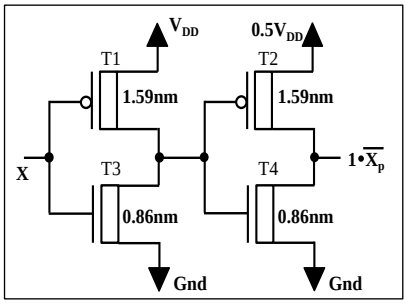
Source: Authors, (2026).



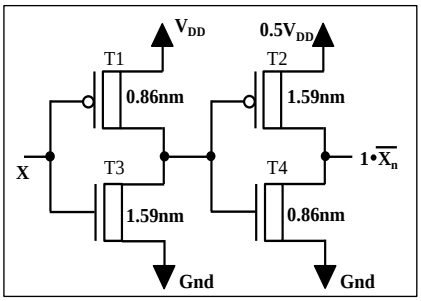
(a)



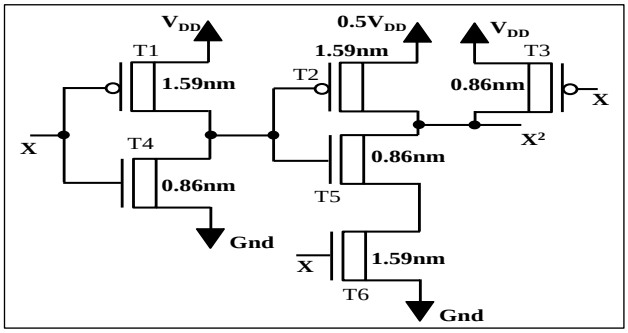
(b)



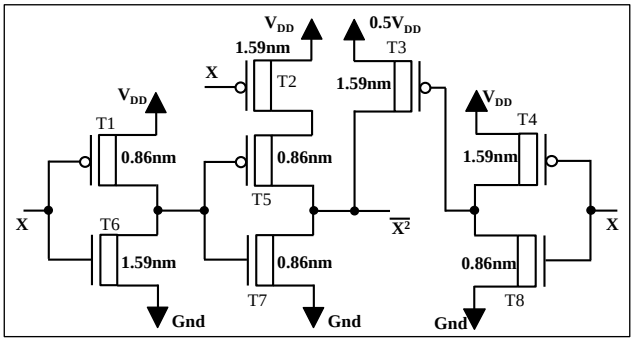
(c)



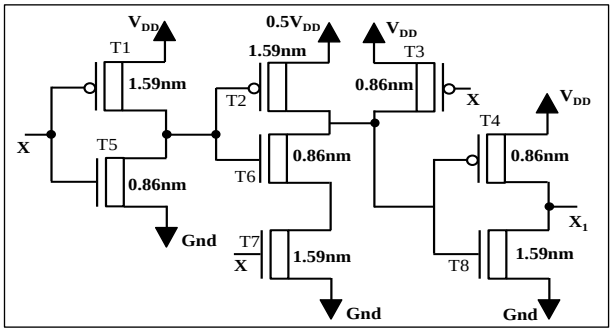
(d)



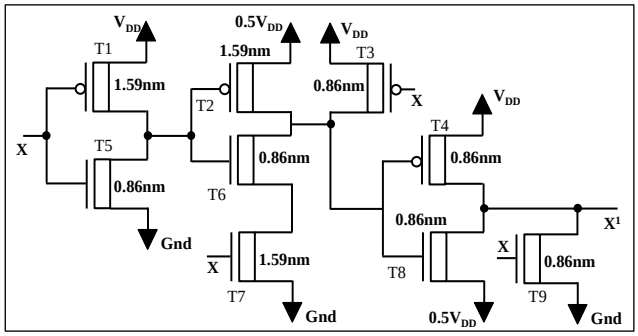
(e)



(f)



(g)



(h)

Figure 3:Ternary logic unary operators (a) X_p, (b) X_n, (c) $1\cdot\overline{X_p}$, (d) $1\cdot\overline{X_n}$, (e) X^2, (f) $\overline{X^2}$, (g) X_1 and (h) X^1, respectively.
Source: Authors, (2026).

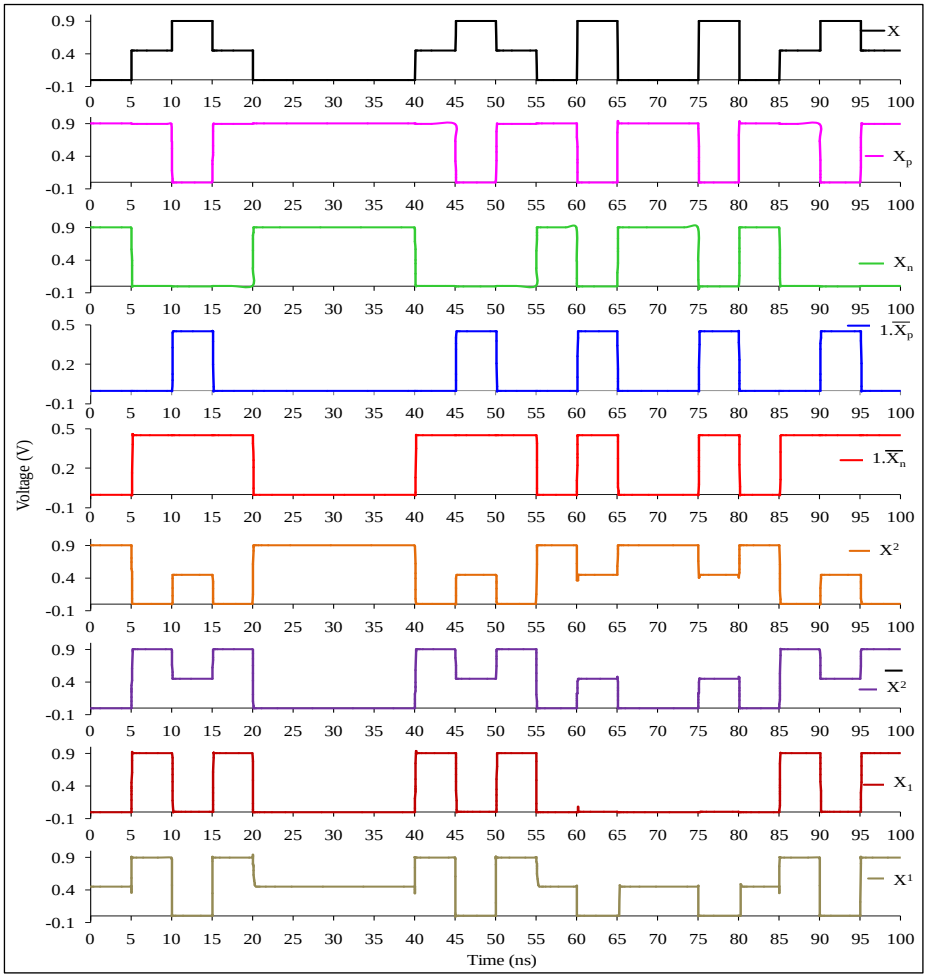


Figure 4: Output responses of unary operators.
Source: Authors, (2026).

III. TERNARY LOGIC UNARY OPERATORS

The logic gate which consists of single input and output is called as unary operator. In conventional binary logic, there are four unary operators (i.e., 00, 11, 01, 10). Whereas, in ternary logic, there are 27 unary operators (i.e., 000, 001,……., 222). In this work, we have focused on 8 unary operators are X_p, X_n, X_1, X^1, X^2, $\overline{X^2}$, $1\cdot\overline{X_p}$ and $1\cdot\overline{X_n}$, respectively. The 1st and 2nd operators X_p and X_n represent positive (PTI) and negative (NTI) inverters, respectively. The 3rd operator X_1 is known as decisive lateral. The 4th and 5th operators are called as cycle operators, X^1 and X^2 are the single and dual shift operators. The 6th operator $\overline{X^2}$ is complement of X^2 and last unary operators are $1\cdot\overline{X_p}$ and $1\cdot\overline{X_n}$, respectively. The circuit diagrams of the 8 unary operators and truth tables are given in Figure 3 and Table III. Moreover, the operations of unary operators X^2, X_1 and X^1 are presented in Table IV. The proposed 8 unary operator are developed and simulated in HSPICE tool for verifying functionality. The obtained simulations results of operators given in Figure 4.

Table 3: Unary Operators Truth table.

X	X_p	X_n	$1 \cdot \overline{X_p}$	$1 \cdot \overline{X_n}$	X^2	$\overline{X}^2$	X_1	X^1
0	2	2	0	0	2	0	0	1
1	2	0	0	1	0	2	2	2
2	0	0	1	1	1	1	0	0

Source: Authors, (2026).

Table 4: Operations of X^2, X_1 and X^1 unary operators.

X	X_p	Transistor State						Output		
		X^2		X_1		X^1				
		ON	OFF	ON	OFF	ON	OFF	X^2	X_1	X^1
0	2	T5 T3	T2 T6	T8	T4	T8	T4 T9	2	1	0
1	2	T5 T6	T2 T3	T4	T8	T4	T8 T9	0	2	2
2	0	T2 T6	T5 T3	T8	T4	T9	T4 T8	1	0	0

Source: Authors, (2026).

Table 5: Half Adder and Multiplier Truth table.

X	Y	Half Adder		Multiplier	
		Sum	Carry	Product	Carry
0	0	0	0	0	0
0	1	1	0	0	0
0	2	2	0	0	0
1	0	1	0	0	0
1	1	2	0	1	0
1	2	0	1	2	0
2	0	2	0	0	0
2	1	0	1	2	0
2	2	1	1	1	1

Source: Authors, (2026).

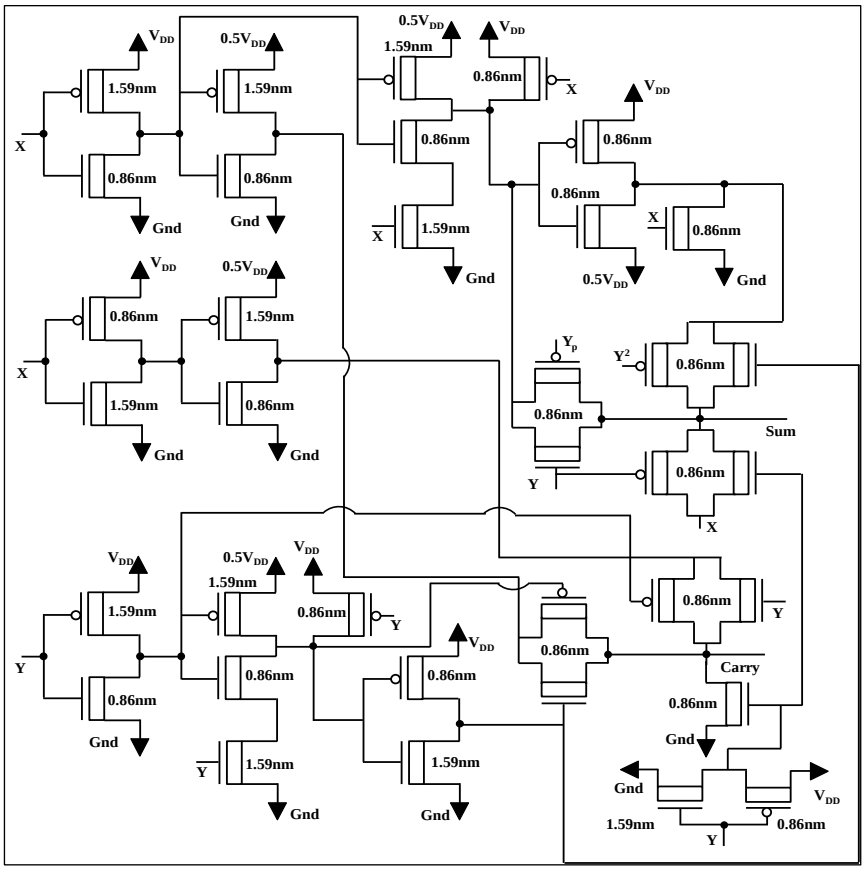


Figure 5: Circuit diagram of Half Adder.
Source: Authors, (2026).

IV. PROPOSED ADDER AND MULTIPLIER DESIGNS

In this work, we proposed a ternary half adder with 36 GNRFETs and multiplier with 23 GNRFETs. The proposed adder and multiplier schematics are developed using above discussed unary functions, transmission gates and two voltage-supplies (V_{DD} and $V_{DD}/2$), respectively. The one-trit adder that adds two inputs and produces the two outputs (i.e., Sum and Carry) is presented. The truth table and expressions of Sum and Carry are provided in Table V and equ. (4).

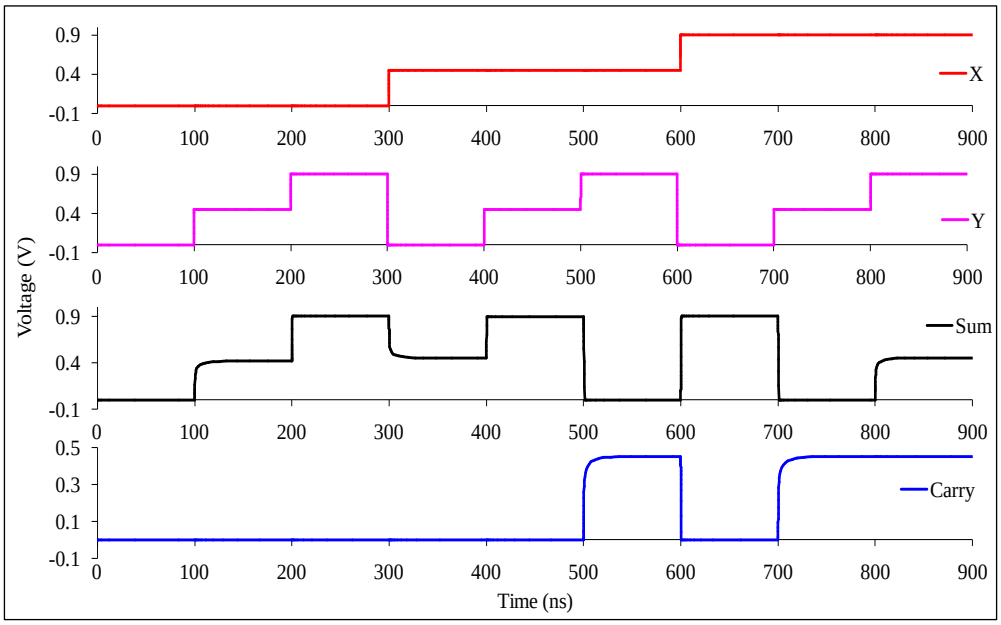


Figure. 6: Waveform of Half Adder.
Source: Authors, (2026).

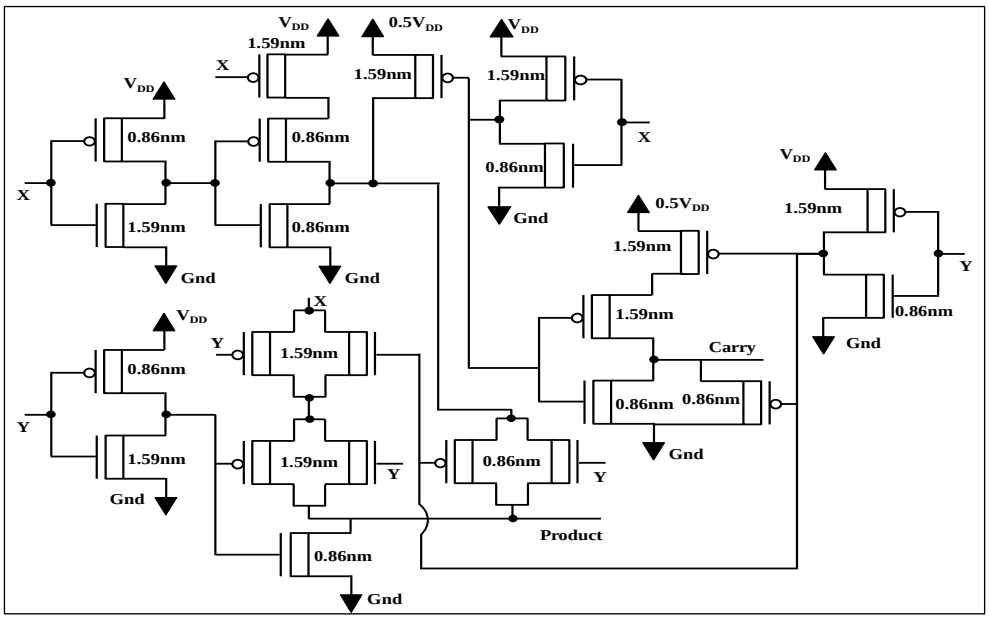


Figure 7: Circuit diagram of Multiplier.
Source: Authors, (2026).

$$Sum = X.Y_0 + X^1Y_1 + X^2Y_2$$
$$Carry = 0.Y_0 + \left(1.\overline{X_p}\right).Y_1 + \left(1.\overline{X_n}\right).Y_2 \quad (4)$$

Using the equation (4), the adder is developed and illustrated in Figure 5. The proposed half adder is developed and simulated in HSPICE to acquire the transient response and performances. The transient response is illustrated in Figure 6. Moreover, the delay, power and PDP are analyzed and obtained as 2.088E-07s, 4.253E-06W and 8.881E-13J, respectively. The one-trit multiplier that multiplies the two inputs and produces the two outputs (i.e., Product and Carry) is presented. The truth table and numerical equations of Product and Carry are given in Table V and equ. (5). Using the equation (5), the multiplier is developed and illustrated in Figure 7. The transient response of multiplier is illustrated in Fig. 8. Moreover, the delay, power and PDP are analyzed and obtained as 2.293E-07s, 3.738E-06W and 8.572E-13J, respectively.

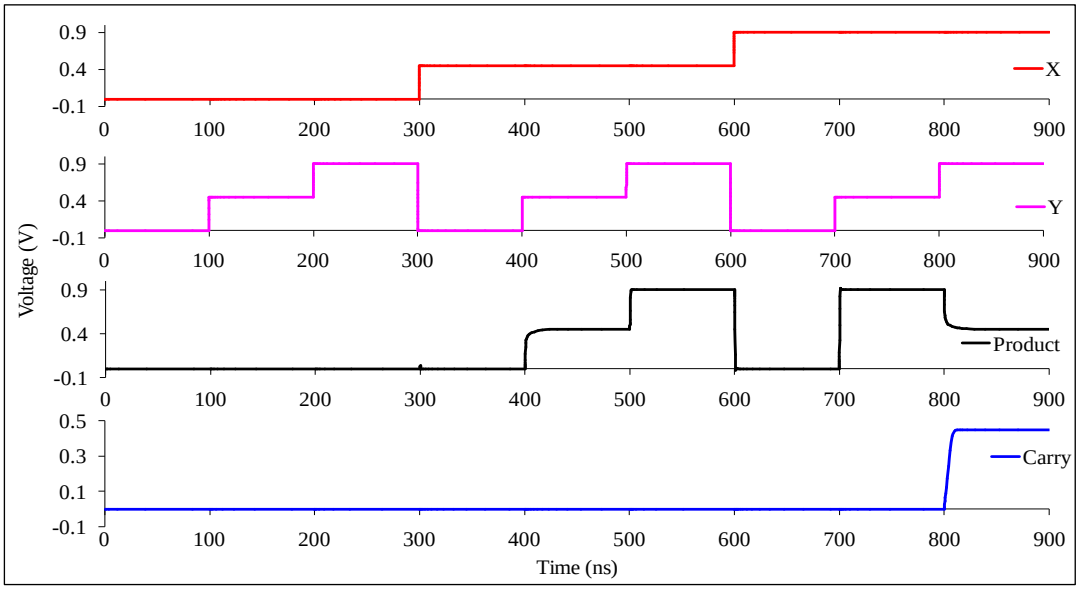
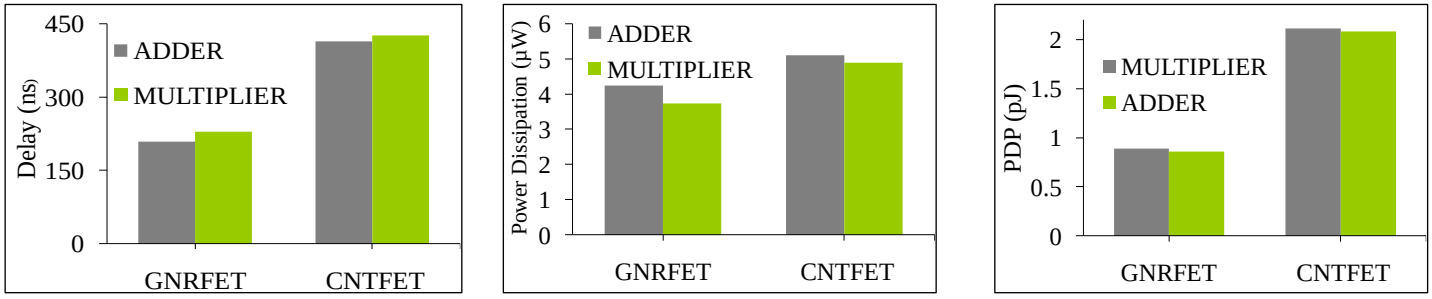


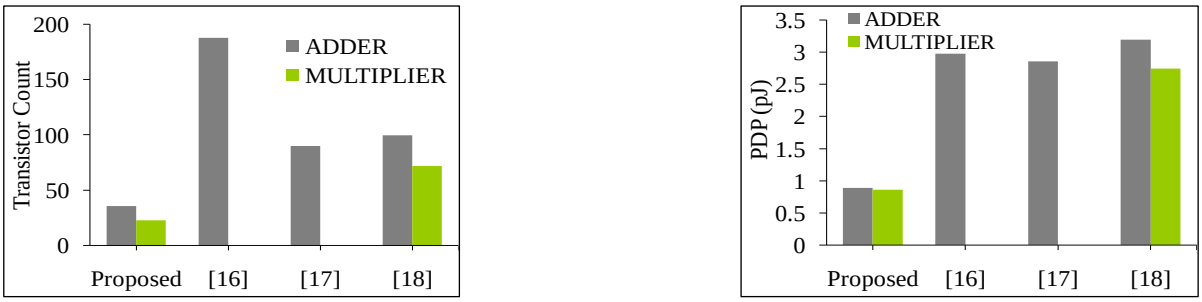
Figure 8: Waveform of Multiplier.
Source: Authors, (2026).



(a) (b) (c)

Figure 9: Performance of Adder and Multiplier (a) Delay, (b) Power and (c) PDP.
Source: Authors, (2026).

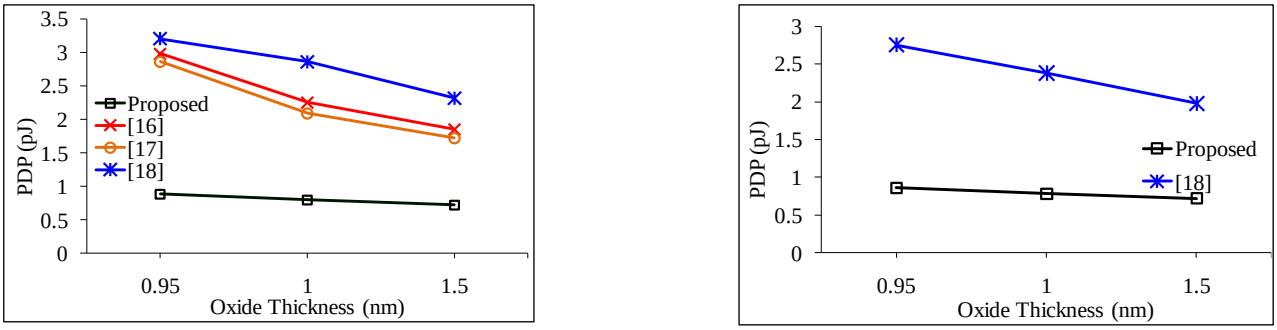
The proposed designs performance is examined with CNTFET designs. For CNTFET circuits, CNT-diameters 1.48 and 0.78 nanometers are utilized. The SPICE model of CNTFET discussed in [24] [25] is utilized to develop CNTFET ternary designs. Fig. 9 provides performances comparability's of GNRFET and CNTFET based ternary designs. The proposed GNRFET based adder and multiplier circuits show high performance over the CNTFET circuits. In addition, PDP of proposed GNRFET schematics are examined with traditional GNRFET circuits presented in [16-18]. Fig. 10 shows the comparison of proposed circuits with the [16-18]. It is worth noting that the same load and switching patterns of proposed circuits is used for designs of [16-18]. The proposed designs shows degraded transistor count and PDP than the existing circuits.



(a) (b)

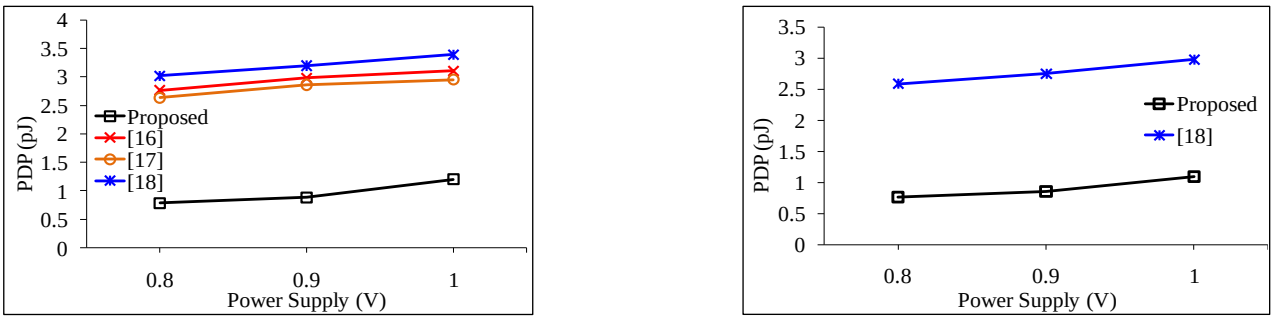
Figure 10: Adder and Multiplier Circuits (a) Transistor Count and (b) PDP.
Source: Authors, (2026).

The ternary circuits are highly sensible to PVT variations. Hence, PDP investigations are carried out for the different PVT variations for adder and multiplier circuits. For the process, the PDP circuits are analyzed by varying the oxide thickness. The obtained PDP results for different oxide thickness are given in Figure 11. The PDP of adder and multiplier circuits is also analyzed by varying the different power supplied and temperature values. The obtained PDP values for adder and multiplier circuits are shown in Figure 12 and Figure 13, respectively. It worth noting that the PVT variations of proposed circuits are than the existing circuit designs. The PDP of the proposed circuits is improved compared to the existing works.



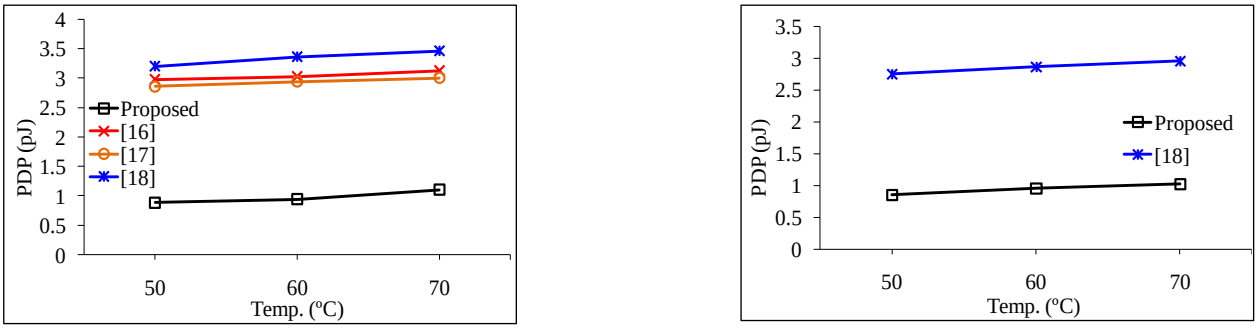
(a) (b)

Figure 11: Process variation effect on PDP (a) Adder and (b) Multiplier.
Source: Authors, (2026).



(a) (b)

Figure 12: Power supply variation effect on PDP (a) Adder and (b) Multiplier.
Source: Authors, (2026).



(a) (b)

Figure 13: Temperature variation effect on PDP (a) Adder and (b) Multiplier.
Source: Authors, (2026).

V. CONCLUSIONS

A new design technique is proposed to develop ternary adder and multiplier schematics using unary operators. The proposed circuits are designed in the HSPICE simulator for functional verifications and performance investigations. Moreover, simulation results of proposed designs are compared to conventional CNTFET and GNRFET based designs. It is noted that the proposed designs improved the performances over the conventional designs. Moreover, the PVT variations on the performance of the proposed adder and multiplier designs are carried out and noted that the proposed circuits showed minimal variations. Because of the betterment in performance than existing designs, the proposed design technique plays an important role in future integrated circuits to achieve high performance.

VI. AUTHOR'S CONTRIBUTION

Conceptualization: K. Mamatha and Shaik Taj Mahaboob.
Methodology: K. Mamatha and Shaik Taj Mahaboob.
Investigation: K. Mamatha and Shaik Taj Mahaboob.
Discussion of results: K. Mamatha and Shaik Taj Mahaboob.
Writing – Original Draft: K. Mamatha and Shaik Taj Mahaboob.
Writing – Review and Editing: K. Mamatha and Shaik Taj Mahaboob.
Resources: K. Mamatha and Shaik Taj Mahaboob.
Supervision: K. Mamatha and Shaik Taj Mahaboob.
Approval of the final text: K. Mamatha and Shaik Taj Mahaboob.

VII. REFERENCES

[1] S. S. Kumar, A. Gangishetty, S. Rasmita and M. Manasi, "High-Performance Ternary Adder Using CNTFET," IEEE Trans. on Nanotech., 16, 1 (2017).

[2] L. Sheng, K. Yong-Bin and L. Fabrizio, "CNTFET-Based Design of Ternary Logic Gates and Arithmetic Circuits," in IEEE Trans. on Nanotech., 10, 2 (2011).

[3] P. Venkatramana, P. Nagarajan and S. J. Basha, "Design of Three-valued Logic Half-Subtractor using GNRFET," 2023 International Conference on RAEEUCCI, Chennai, India (2023).

[4] S. J. Basha and P. Venkatramana, "Analysis of Crosstalk Effects for Ternary Logic MWCNT Bundled Through Silicon Vias," ECS J. Solid State Sci. Technol., 12, 2 (2023).

[5] T. N. J. Kolanti and V. K. S. Patel, "Design of Ternary Subtractor using Multiplexers," Circuit World, 49, 3 (2021).

[6] D. M. Badugu and S. Sunithamani, "Crosstalk Reduction in Copper On-chip Interconnects with Graphene Barrier for Ternary Logic Applications," Inter. J. of Cir. The. and App., 48, 12 (2020).

[7] K. You and K. Nepal, "Design of a Ternary Static Memory Cell using Carbon Nanotube-based Transistors," IET Mic. Nan. Lett., 6, 6 (2011).

[8] J-M. Philippe, E. Kinvi-Boh, S. Pillement and O. Sentieys, "An Energy-efficient Ternary Interconnection Link for Asynchronous Systems," 2006 IEEE ISCAS, Kos, Greece, (2006).

[9] Hurst, "Multiple-Valued Logic—its Status and its Future," IEEE Trans. on Comp., C-33, 12 (1984).

[10] D. Chetan, G. Ritesh, J. Gajanan, N. Gaurang and K. Sushil, "A 5nm Fin-FET 2G-search/s 512-entry x 220-bit TCAM with Single Cycle Entry Update Capability for Data Center ASICs," 2021 Sym. on VLSI Cir., Kyoto, Japan, (2021).

[11] J. Gope, S. Bhadra, S. Chanda, M. Sarkar, S. Pal and A. Rai, "Modelling of single electron ternary flip-flop using SIMON," 2016 IEEE 7th Annual (UEMCON), New York, NY, USA, (2016).

[12] K. Supriya, C. A. John and C. J. Faquir, "Design of Ternary Logic Combinational Circuits Based on Quantum Dot Gate FETs," IEEE Trans. on VLSI Sys., 21, 5, (2013).

[13] B. Srinivasu and K. Sridharan, "Low-Power and High-Performance Ternary SRAM Designs with Application to CNTFET Technology," IEEE Trans. on Nanotech., 20, (2021).

[14] B. Fereshteh, Q. K. J. Mohammad, H. M. Mohammad and T. Khalil, "Leveraging Negative Capacitance CNTFETs for Image Processing: An Ultra-Efficient Ternary Image Edge Detection Hardware," in IEEE Trans. on Cir. and Sys. I: Reg. Pap., 68, 12 (2021).

[15] G. Sharvani and V. Chetan, "Design of CNTFET-Based Ternary ALU Using 2:1 Multiplexer Based Approach," IEEE Trans. on Nanotech., 19 (2020).

[16] D. M. Badugu and S. Sunithamani, "Design of Ternary Logic Gates and Circuits using GNRFETs," IET Cir., Dev., and Sys., 14, 7 (2020).

[17] T. S. Zarin, U. A. Farid and H. C. Masud, "Design of Ternary Logic and Arithmetic Circuits Using GNRFET," IEEE O. J. of Nanotech., 1, (2020).

[18] B. Obulesu, H. D. Praveena, S. J. Basha, M. V. Sruthi, K. S. Kumar and N. Ashokkumar, "High-performance Ternary Designs using Graphene Nanoribbon Transistors," Materialstoday:Proceedings, Jul. 2023.10.1016/j.matpr.2023.07.170

[19] S. J. Basha and P. Venkatramana, "Design of Ternary Logic Circuits Using GNRFET and RRAM," Cir., Sys., and Sig. Process., 2023. https://doi.org/10.1007/s00034-023-02445-9

[20] S. J. Basha and P. Venkatramana, "High Performance Quaternary Logic Designs using GNFETs," e-Prime Adv. in Electri. Engin., Electro. and Ener., 5, (2023).
[21] C. Ying-Yu et al., "A SPICE-Compatible Model of MOS-Type Graphene Nano-Ribbon Field-Effect Transistors Enabling Gate- and Circuit-Level Delay and Power Analysis Under Process Variation," IEEE Transactions on Nanotech., 14, 6, (2015).

[22] G. Morteza, C. Ying-Yu, S. Amit and C. Deming, "Highly Accurate SPICE-Compatible Modeling for Single- and Double-gate GNRFETs with Studies on Technology Scaling," 2014 DATE, Dresden, Germany, (2014).

[23] C. Ying-Yu, R. Artem, S. Amit, I. Giuseppe, F. Gianluca and C. Deming, "A SPICE-Compatible Model of Graphene Nano-Ribbon Field-Effect Transistors Enabling Circuit-level Delay and Power Analysis Under Process Variation," 2013 DATE, Grenoble, France, (2013).

[24] D. Jie and H. -S. W. Philip, "A Compact SPICE Model for Carbon-Nanotube Field-Effect Transistors Including Nonidealities and Its Application—Part I: Model of the Intrinsic Channel Region," IEEE Trans. on Elec. Dev, 54, 12, (2007).

[25] D. Jie and H. -S. W. Philip, "A Compact SPICE Model for Carbon-Nanotube Field-Effect Transistors Including Nonidealities and Its Application—Part II: Full Device Model and Circuit Performance Benchmarking," IEEE Trans. on Elec. Dev, 54, 12, (2007).

Journal of Engineering and Technology for Industrial Applications

ITEGAM-JETIA

Manaus, v.12 n.60, p. 558-565 July/August, 2026.
DOI: https://doi.org/10.5935/jetia.v12i60.3906

ISSN ONLINE: 2447-0228

RESEARCH ARTICLE OPEN ACCESS

DEVELOPMENT OF A TINYML-BASED DEVICE FOR AUTOMATIC DETECTION OF POULTRY DISEASES USING CHICKEN VOCALIZATIONS

Minh Nguyen-Ngoc[1], Bien Nguyen-Quang[2], Duan Luong-Cong*[3]

[1, 2, 3]Faculty of Electronics Engineering 1 & EDA Lab, Posts and Telecommunications Institute of Technology, Vietnam.

[1]https://orcid.org/0000-0002-7446-2131, [2]https://orcid.org/0009-0007-5518-1231, [3]https://orcid.org/0009-0003-6207-1170

E-email: *minhnn@ptit.edu.vn, biennq@ptit.edu.vn, duanlc@ptit.edu.vn

ARTICLE INFO

Article History
Received on: March 04, 2026
Reviewed on: April 04, 2026
Accepted on: May 01, 2026
Published on: July 31, 2026

Keywords:
Precision farming,
Poultry disease,
Edge computing,
TinyML,
Endpoint detection.

ABSTRACT

Poultry farming provides essential protein but faces challenges from diseases that affect bird welfare and farm economics. Traditional detection methods are slow and costly, underscoring the need for real-time, low-cost solutions enabled by precision livestock farming technologies. This paper presents a TinyML-based device for the automatic detection of poultry diseases by analyzing chicken vocalizations. The proposed system uses edge computing on a microcontroller to process audio data on-site, without requiring a constant internet connection or powerful hardware. Key steps include noise reduction with FIR filters, endpoint detection via a double-threshold short-time energy method, and feature extraction using Mel-Frequency Energy. A lightweight neural network with 1D-CNN and DNN layers classifies sounds as healthy, unhealthy, or noisy. We developed a prototype on the ESP32-S3 MCU, achieving 90.58% test accuracy and 0.98 F1-score for unhealthy detection. The device processes 3-second audio in 380 ms of preprocessing and 97 ms per inference window, using only 419 KB of flash and 258 KB of RAM. This low-cost solution enables scalable IoT integration for early disease intervention in poultry farms.

Copyright ©2026 by authors and Galileo Institute of Technology and Education of the Amazon (ITEGAM). This work is licensed under the Creative Commons Attribution International License (CC BY 4.0).

I. INTRODUCTION

Poultry farming plays a vital role in the agricultural sector by providing an affordable source of protein for a rapidly growing global population. However, as production intensifies to meet rising demand, the quality and health of poultry become critical concerns, not only for animal welfare but also for the economic viability of poultry operations [1] [2]. Traditional diagnostic methods, such as oocyte counting in stool or intestinal scrapings, microbial isolation, and PCR, are accurate but suffer from several drawbacks: they are labor intensive, time consuming, and often costly [3] [4]. These limitations underscore the need for rapid, efficient, and cost-effective techniques for early disease detection in large-scale poultry farms. Recent advancements have steered research towards automated detection systems that leverage artificial intelligence (AI), Internet of Things (IoT), and machine learning (ML) techniques. Early studies predominantly focused on imagebased disease detection using convolutional neural networks (CNNs) to analyze visual features such as feather condition, eye clarity, and beak anomalies [5]. Additionally, behavioral monitoring through video analysis has been explored to capture abnormal movements that may indicate distress or illness [6]. While these methods provide valuable insights, they generally require substantial computational resources and often operate offline, limiting their real-time applicability in resource-constrained environments [7]. An emerging line of research has begun to explore the use of acoustic signals as a non-invasive indicator of poultry health. Changes in chicken vocalizations, such as variations in frequency, amplitude, and temporal patterns, can serve as early markers of respiratory infections and other diseases [8] [9]. Signal processing techniques, including Mel-Frequency Cepstral Coefficients (MFCCs) extraction and spectrogram analysis, have been effectively combined with both traditional ML algorithms and deep learning models (e.g., recurrent neural networks and transformers) to classify the health status of birds [5-10]. Previous studies have demonstrated promising results, with reported accuracies ranging from 83% to above 95% under controlled experimental conditions. For example, research by Sadeghi et al. [11] showed that neural network-based analysis of chicken vocalizations could distinguish between healthy birds and those infected with specific pathogens with nearperfect accuracy. Similarly, Banakar et al. [12] employed time–frequency analysis techniques combined with support vector machines (SVM) to differentiate between multiple viral infections in chickens, achieving accuracies exceeding 90% in some cases.

The rapid expansion of IoT in agriculture has enabled the development of smart farming systems that continuously monitor environmental and physiological parameters. In poultry farms, IoT devices, ranging from temperature and humidity sensors to microphones, allow for real-time data collection and analysis. However, transmitting all raw data to centralized servers can be inefficient and may introduce delays in decision making. This is where TinyML, the deployment of machine learning models on low-power microcontroller units (MCUs), becomes a game changer. By processing data on-device, TinyML reduces latency, lowers energy consumption, and minimizes dependence on high-speed network connectivity. Recent works have demonstrated the feasibility of integrating TinyML with IoT platforms to analyze acoustic data for immediate detection of stress or disease symptoms in poultry, achieving real-time performance with minimal resource consumption [6-13]. Despite these advances, many existing approaches are limited to offline analysis or require high computational power that is impractical for deployment in typical farm environments. The overlapping of vocalizations in noisy farm settings further complicates the detection process, as background noise can obscure subtle changes in the acoustic signals of individual birds. These challenges highlight the urgent need for a system that can accurately perform realtime acoustic analysis on-site using lightweight and energyefficient models. In response to these challenges, our research makes the following key contributions:

- Developing a TinyML model capable of detecting poultry diseases through acoustic signal analysis. Our model is designed to operate with low resource consumption while delivering real-time performance.
- Implementation a prototype system that integrates this TinyML model on an MCU platform, enabling ondevice data processing and continuous monitoring of poultry health.

By integrating IoT and TinyML technologies, our approach offers a scalable and efficient solution to the limitations of traditional poultry disease detection methods. This system not only facilitates early intervention to mitigate disease spread but also enhances the overall sustainability and economic efficiency of poultry farming. The remainder of this paper is organized as follows. Section 2 details the materials and methods used in this study. In Section 3, the materials and methods employed in the study are presented. Finally, Sections 4 presents the results, discussion, and conclusions of our findings, respectively.

II. MATERIALS AND METHODS

II.1 DATASET

In this study, we utilized a dataset comprising 346 audio signal files compiled by S. Adebayo et al., which were categorized into three distinct folders: healthy, noisy, and unhealthy. The dataset was procured by dividing 100-dayold poultry into separate groups, with data collection conducted thrice daily using microphone devices. Unhealthy audio segments encompassed chicken coughs, snores, and rale sounds, whereas noise segments comprised background noise and sounds associated with poultry activities. Recordings were captured with a resolution of 24 bits at a sampling rate of 96 kHz and stored in the WAV format. Additionally, they compared the power spectra of healthy and unhealthy signals, revealing a notable spike of approximately 0.2 radians in the frequency content of anomalous sounds, in contrast to the distribution observed in normal sounds around the y-axis [5]. Our research focuses on leveraging machine learning, specifically TinyML, to automatically extract features and detect diseased chickens based on sound patterns. Our primary aim was to implement the entire computational process on a microcontroller (MCU) with resource constraints. To enhance computational efficiency prior to data processing, we lowered the sampling frequency to 16 kHz, decreased the resolution to 16 bits, and quantized the data range of -1.0 to 1.0 into the range of -32,768 to 32,767. These preprocessing steps are essential for enhancing the performance of our machine learning model during processing and training. This pre-processing step is facilitated through Python utilizing librosa [14] and soundfile [15] libraries, which provide robust support for audio processing tasks.

II.2 NOISE REDUCTION AND FRAMING

Numerous studies have consistently highlighted the prevalence of chicken vocalizations within the frequency range of 1.5 kHz to 5 kHz [4] [10-16]. Additionally, analysis of the dataset compiled by Adebayo et al. underscores that the primary frequency range of poultry sounds falls between 1 kHz and 5 kHz, as illustrated in Figure 1.

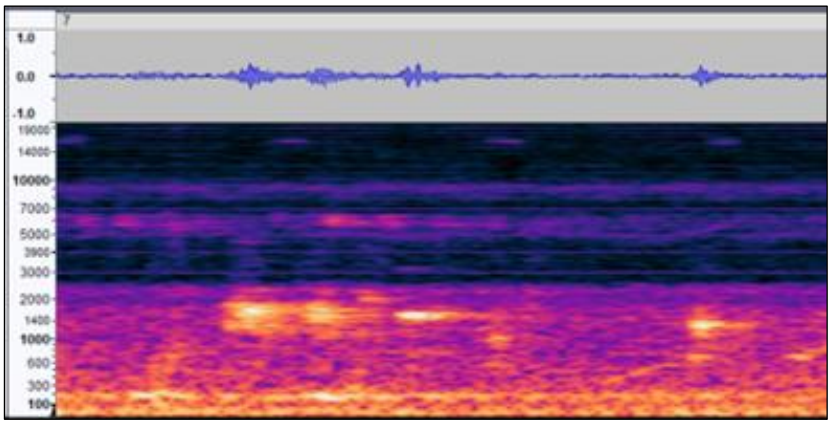


Figure 1: Spectrogram of chicken vocalization segment.
Source: Authors, (2026).

FIR filters are well known for their adaptability and precise delineation of signal characteristics within designated frequency spectra, making them particularly adept at discerning and examining poultry vocalizations within these frequency bounds. When employed in devices with restricted computational resources, such as MCUs, FIR filters have significant advantages. They ensure operational stability, manifest linear phase responses, facilitate precise frequency manipulation, and boast streamlined implementation, owing to the absence of feedback loops. These qualities underscore the suitability of FIR filters for signal processing endeavors in resource-constrained environments such as MCUs. In our study, FIR filters were leveraged for data pre-processing and subsequent implementation on the device platforms. The vocalization of chicks exhibits temporal variability, which makes direct analysis challenging. The direct analysis of audio requires significant computational resources. Nonetheless, within short durations of 10–30 ms, vocalizations tend to be relatively stable. In this study, the window function had a duration of 25 ms, corresponding to 400 sampling points. Additionally, the step length was set to half the window duration, equating to 200 sampling points (12.5 ms).

II.3 VOCALIZATION ENDPOINT DETECTION

The recorded audio contained not only chicken vocalizations but also background noise and frequent periods of silence. Achieving a more accurate analysis of chicken vocalization requires separating the chick vocalizations from the surrounding audio segments. To address these challenges, we employ a double-threshold method that incorporates two distinct features. The double-threshold technique employs both Short-Time Energy (STE) and Average Energy (AE) analyses to identify the location of the audio segments. The STE measures the energy content of sound within brief temporal windows and serves as a proxy for sound intensity. Higher STE values correlate with louder sounds, thereby facilitating the detection of sound variations, particularly in noisy environments. This enabled segmentation of the relevant audio segments for subsequent analysis. However, AE provides a measure of the overall energy level across the entire audio segment, offering a comprehensive perspective on its energy characteristics.

$$STE_k = \sum_{1}^{len} [y_k(i)]^2 \tag{1}$$

$$AE_j = \frac{\sum_{1}^{len} [y_k(i)]^2}{\Delta t} \tag{2}$$

Chick vocalizations typically have a brief duration ranging from 0.1 to 1.0 seconds [4] [16] [17]. Using this attribute, the threshold duration can be adjusted to encompass 8–80 frames for the detection of chick vocalizations. The process of identifying vocalization endpoints involves the following steps:

1) Compute the *STE* for each frame (with 400 sample points).
2) If the *STE* of a frame exceeds the threshold STE_{high}, the frame is designated as the start of a segment.
3) If the *STE* is below the threshold STE_{low}, the frame is marked as the end of the segment. Otherwise, the segment length was extended.
4) Once the endpoint of the segment is determined, if the segment duration falls within the range of D_1 to D_2, the segments are merged into one. Otherwise, the segment is discarded.
5) The *AE* of the entire segment is calculated. If the *AE* fell below the threshold AE_{thresh}, the segment was discarded. Otherwise, proceed to the featureextraction stage with this segment.

The STE thresholds (STE_{low} and STE_{high}) were calculated using the following formula:

$$STE_{thresh} = STE_{min} + \alpha \times \left(\overline{STE} - STE_{min}\right) \tag{3}$$

where $\overline{STE}$ represents the mean of *STE* value across all frames, STE_{min} denotes the minimum *STE* value among all frames, and the parameter is assigned values of 0.1 and 0.4 for STE_{low} and STE_{high}, respectively. The thresholds for segment duration D_1 and D_2 were set to 8 and 80 frames, respectively. The outcome of the endpoint detection process is illustrated in Figure 2, where the blue line represents the raw audio signal, the green line depicts the *STE* values of segments, and the red line indicates the trimmed audio segments identified by this process. Finally, AE_{thresh} was set to 3e-05 based on our experimentation with the current dataset.

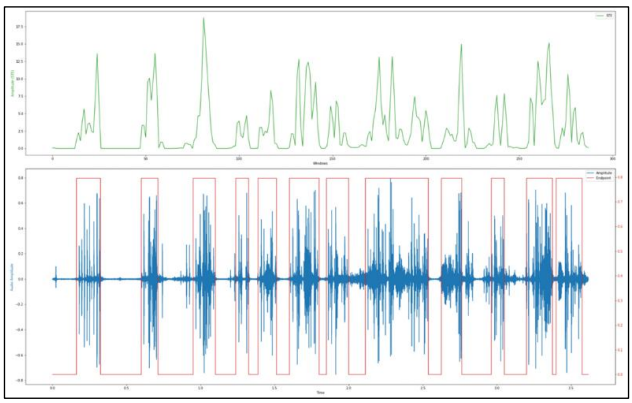


Figure 2: Vocalization endpoint detection using double threshold technique.
Source: Authors, (2026).

Upon completion of this step, the dataset comprises 8,130 audio segments, equating to approximately 41 min of audio data. Among these segments, 2,067 was categorized as belonging to the healthy group, 3,482 to the unhealthy group, and 2,581 to the noisy group. Each audio segment had a duration ranging from 100 ms to 1,000 ms.

II.4 AUDIO FEATURES

While MFCCs are widely utilized in conventional audio signal processing, log-mel spectrograms emerge as the predominant feature in deep learning, with raw waveforms or intricate spectrograms following closely. Raw waveforms sidestep manually crafted features, enabling enhanced utilization of the deep learning models' modeling process to acquire task-optimized representations [16] [18] [19]. In this study, we experimented with MFCCs and MFE for feature extraction. The results reveal that MFE exhibits slightly higher accuracy than MFCCs when running with our model design. Meanwhile, the resource usage for MFE is lower compared to using MFCC. Therefore, MFE was selected as the feature extraction step in our model. With audio windows set at 250ms, the MFE (MelFrequency Energy) block was configured with a frame length of 50ms, frame stride of 25ms, filter number of 40, FFT length of 512, and a bandpass filter (BPF) spanning from 1,000 to 5,000 Hz. The output data of the MFE block consisted of a 40 × 9 array for each audio window, as Figure 3. This array served as an input to the machine learning model, which will be discussed in the subsequent section.

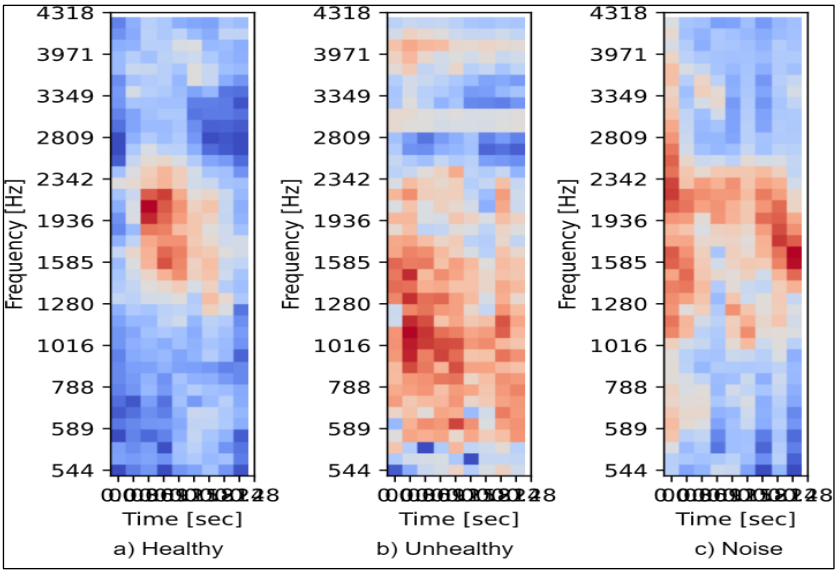


Figure 3: Output of MFE extraction for a) healthy, b) unhealthy, and c) noise audios.
Source: Authors, (2026).

II.5 TINYML MODEL DEVELOPMENT

We uploaded all segment audios and trained a model based on the Edge Impulse [20] platform to rapidly identify an appropriate model structure. After pre-processing, the dataset was split into three groups: training (60%), validation (20%), and testing (20%). Therefore, 4,878 samples were used for training, 1,626 samples for validation, and 1,626 samples for testing. Our machine learning model is initiated with two 1DCNN layers, consisting of 128 and 64 kernels. Following this, the data were flattened and passed through a twolayer DNN network with 128 neurons and 96 kernels in succession. Figure 4 shows the detailed architecture of the model network.

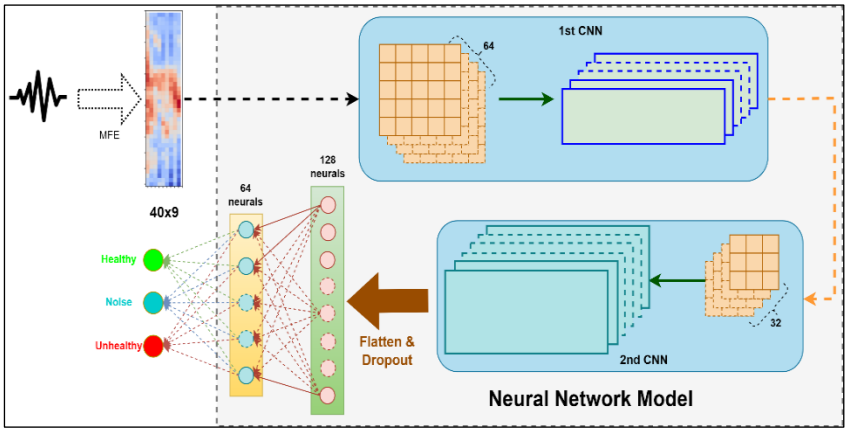


Figure 4: Neural network architecture.
Source: Authors, (2026).

III. DEVICE IMPLEMENTATION

All the steps outlined in Section II were executed using the high-level programming language Python, augmented by several efficiently supported libraries. With the aim of deploying a real-time edge device capable of audio data collection, processing, and inference, we initiated the development of a solution and embedded software program tailored for the device. The MCU selected for this study is the ESP32-S3, notable for its 384 KB ROM, 512 KB SRAM, and 4MB Flash memory capacities, along with its ability to operate at a maximum clock speed of 240 MHz. Furthermore, this MCU boasts instruction sets tailored to support TinyML and DSP algorithms, enhancing its suitability for our research purposes. A flowchart of the execution of the device is shown in Figure 5.

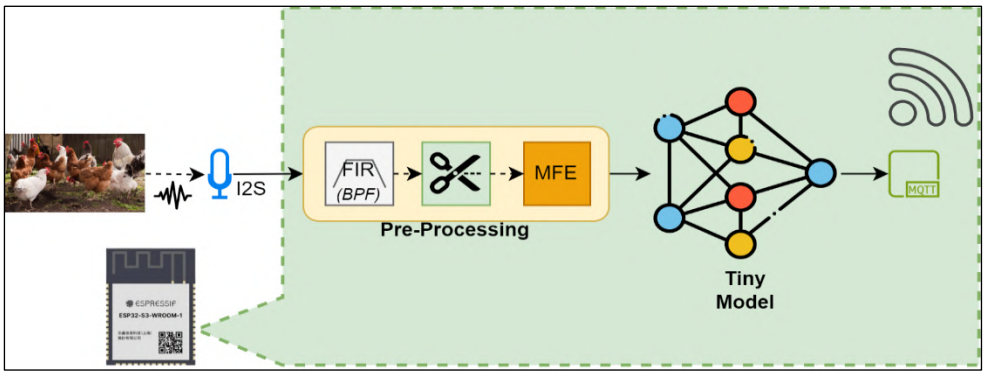


Figure 5: Implementation of device.
Source: Authors, (2026).

Figure 6 illustrates the detailed firmware architecture implemented on the device. The architecture is designed to support continuous, real-time audio acquisition and processing while maintaining low latency and efficient resource utilization. First, audio data are collected into four buffers of the MCU via Direct Memory Access (DMA) with a sample rate of 16,000 Hz and a resolution of 16 bits. Buffers can store a maximum of 3 s of audio samples. Periodically, the main program checks the audio buffers for new data. Upon the detection of new data, the data are passed through an FIR filter and subsequently saved to the ring buffer. The ring buffer consisted of three arrays: Audio Sample, STE Base, and STE window. The Audio Sample array contained signed integer (int16_t) data obtained from the FIR filter. The STE Base array computes the energy for every 200 samples, whereas the STE of the window array calculates the energy for each slice window comprising 400 samples. To optimize the computational efficiency of the MCU, we partitioned the Ring Buffer into eight equally sized segments, each capable of storing data for 0.5 seconds. For each segment, along with the three primary data arrays, we introduce two additional variables: STE_{min}, which captures the minimum STE value within the segment's audio window, and STE_{avg}, which represents the average STE value of the respective audio segments.

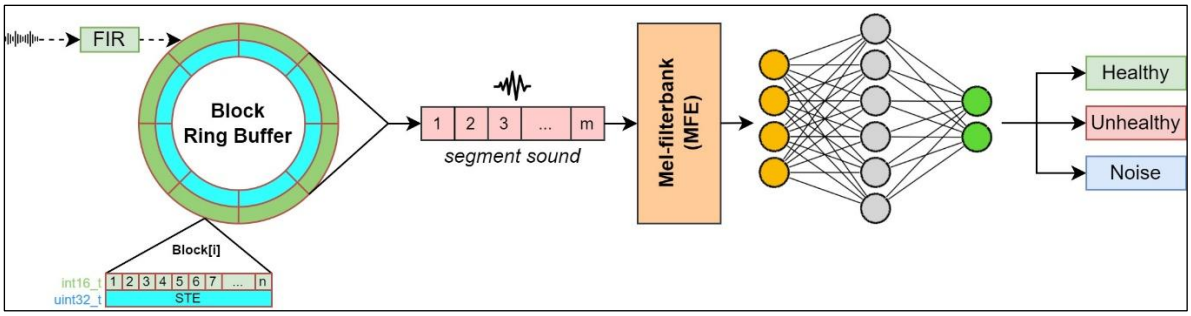


Figure 6: Firmware flow of edge device.
Source: Authors, (2026).

Instead of recalculating all the parameters with each new data point, our method efficiently computes only when the entire segment is updated. By leveraging the STE_{min} and STE_{avg} values from all segments, our program rapidly calculated STE_{low} and STE_{high}, resulting in faster computation and reduced computational overhead. These calculated thresholds facilitate the endpoint detection algorithm in identifying suitable audio segments. These segments were then split based on their length and processed through the MFE extraction step before being fed into the TinyML model. The segment sounds were split into smaller segments, each with a length of 250ms and slice window of 125ms. The number of segments to be calculated follows Equation 4, where N represents the number of segments, L denotes the length of the audio (ms), and w represents the length of the window slice, which is 125ms in this case. Each audio segment is passed through the MFE block, resulting in an output matrix with dimensions of 40 × 9. This matrix is then fed into the machine-learning model, which outputs the detection probabilities for the three labels. These probability values were averaged over N audio segments to determine the identified sound types (healthy, unhealthy, or noisy). To record audio from the testing environment, we opted for the INMP441 microphone, which is capable of transmitting audio via I2S with a resolution of 24-bit and maximum sampling frequency of 48kHz. In addition, we included a TFT screen to monitor and evaluate the functionality of the devices, displaying the quantity of healthy and unhealthy chicken vocalizations during testing. All the components were integrated into a fabricated box using a 3D printer with dimensions of 87x44x26mm, as depicted in Fig.

The implementation of the embedded software for the ESP32S3 MCU was performed in accordance with the established procedure, utilizing the C++ programming language with the aid of Visual Studio Code, Platform IO, and libraries provided by Edge Impulse. The firmware is uploaded to the device via UART to create a complete device and commence the testing process.

IV. RESULTS AND DISCUSSIONS

After extensive training, validation, and testing procedures, our model demonstrated impressive performance, achieving an accuracy of 92.8% during training and 90.58% during testing using a quantization (int8_t) model. Figure 7 presents the detailed confusion matrix for the test set. Although the overall accuracy may not be exceptionally high, our model displayed remarkable proficiency in identifying diseased chickens, achieving a remarkable F1-score of 0.98. Further analysis of the dataset sources revealed that audio files labeled as "Noise" frequently contained significant chicken sounds, which could potentially influence the differentiation between the "Healthy" and "Noise" labels.

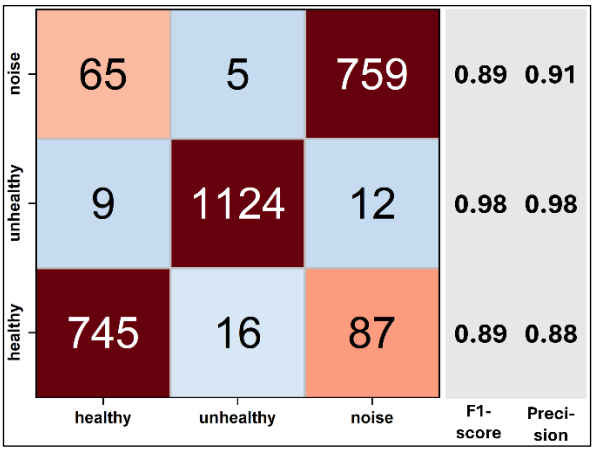


Figure 7: Confusion matrix for model evaluation on the test set with 8-bit quantization.
Source: Authors, (2026).

In addition, the model underwent quantization to optimize the size and inference time. According to the report from Edge Impulse, this model uses 248 KB of flash memory, 12.4KB of RAM, and requires 92ms for porting and inference on an ESP32-S3 MCU. This model, along with the pre-processing algorithm, is implemented on the edge device in the subsequent section. The program efficiently utilizes 419 KB of flash memory and 258 KB of RAM, which are well-suited for the resource constraints of the ESP32-S3 platform. After deploying the program on the ESP32-S3 board, we conducted real data tests to evaluate the duration of all steps. The specific times taken for each step are listed in Table 1 and Table 2. Table 1 provides the running time of the device utilized for the pre-processing of 3s raw data, which includes the FIR filter with an order number of 43, STE calculation for both 200 parameter windows and 400 parameter slice windows, and end-point detection algorithms. This value remained constant throughout the execution process. Meanwhile, table 2 illustrates the timing values for classifying the segmented audio extracted from the source data, including MFE calculation and inference via the machine learning model. The processing time for audio segments under 250 ms consistently remained at 97 ms, while longer segments, lasting between 750 and 1,000 ms, required approximately 356 ms across four consecutive recognition executions. These timing tests demonstrate that the integrated algorithms can be executed in real time on the ESP32-S3.

Table 1: Pre-processing time for 3s of raw data.

No.	Step	Time (ms)
1.	Band pass filter FIR	310
2.	STE calculating	45
3.	End-point detection	25
	Total:	**380**

Source: Authors, (2026).

Table 2: Inference for each window sound.

No.	Step	Time (ms)
1.	MFE calculating	84
2.	Model inference	13
	Total:	**97**

Source: Authors, (2026).

Furthermore, the prototype device has been successfully fabricated as shown in Figure 8. The device comprises an audio acquisition and processing module that is seamlessly connected to a display via UART. The display continuously shows the count of detected "Unhealthy" sounds, providing real-time feedback and facilitating prompt intervention. This integrated system highlights the practical viability of our solution for on-device poultry health monitoring under realworld conditions.



Figure 8: Prototype implementation device.
Source: Authors, (2026).

While previous studies [4-9] [16-21] have focused on recognizing and analyzing the health status of chickens through sound using local processing on computers, the results of this study demonstrate that the device can meet the requirements for detecting diseased chickens based on sound in real-time conditions and can be applied in practical scenarios with inexpensive processors with the support of the DSP algorithm and TinyML solution. Moving forward, we plan to conduct additional experiments and apply these datasets to real-world scenarios to further evaluate their detection accuracy. By integrating this research with advancements in IoT, we can create a comprehensive solution that empowers farmers to monitor and predict chicken diseases in real time, thereby enhancing animal health care and the quality of agricultural products.

V. CONCLUSIONS

In this study, an edge-computing solution is proposed to detect unhealthy chickens based on their vocalizations. This solution was developed using the DSP algorithm and TinyML, which can be implemented on a device with limited resources, such as a MCU. The endpoint detection method utilizes short-time energy, MFE extraction, and machine-learning model inference, and it was tested on a model system that uses augmented data on Edge Impulse for both the training and testing phases. The results of testing on ESP32-S3 showed that with 419 KB of flash memory and 258 KB of RAM, the device could detect unhealthy conditions in real time using TinyML, achieving 92.8% accuracy in the training phase and 90.58% accuracy in the testing phase for classifying healthy, unhealthy, and noisy sounds. The system also demonstrated a high level of accuracy in detecting diseased chickens, with an F1-score of 0.98. This research can be further explored to create more sophisticated automated poultry health-monitoring systems that can be applied in real-world conditions.

VI. AUTHOR'S CONTRIBUTION

Conceptualization: Minh Nguyen-Ngoc, Duan Luong-Cong.
Methodology: Author One and Author Two.
Implementation: Bien Nguyen-Quang, Minh Nguyen-Ngoc.
Discussion of results: Minh Nguyen-Ngoc, Bien Nguyen-Quang, Duan Luong-Cong.
Writing – Original Draft: Bien Nguyen-Quang.
Writing – Review and Editing: Minh Nguyen-Ngoc, Duan Luong-Cong.
Approval of the final text: Minh Nguyen-Ngoc, Bien Nguyen-Quang, Duan Luong-Cong.

VII. ACKNOWLEDGMENTS

This research is funded by Posts and Telecommunications Institute of Technology (PTIT).

VIII. REFERENCES

[1] N. Li, Z. Ren, D. Li, and L. Zeng, "Review: Automated techniques for monitoring the behaviour and welfare of broilers and laying hens: towards the goal of precision livestock farming," *Animal*, vol. 14, no. 3, pp. 617–625, 2020, doi: 10.1017/S1751731119002155.

[2] Rowe, Dawkins, and Gebhardt-Henrich, "A Systematic Review of Precision Livestock Farming in the Poultry Sector: Is Technology Focussed on Improving Bird Welfare?," *Animals*, vol. 9, no. 9, p. 614, Aug. 2019, doi: 10.3390/ani9090614.

[3] C. L. Xu, Y. Z. Wang, J. Guo, J. X. Liu, and J. Feng, "Comparison of age-related differences in expression of antioxidant enzyme mRNA and activity in various tissues of pigs," *Comp Biochem Physiol B Biochem Mol Biol*, vol. 147, no. 3, pp. 445–451, Jul. 2007, doi: 10.1016/j.cbpb.2007.02.007.

[4] K. Cuan, T. Zhang, Z. Li, J. Huang, Y. Ding, and C. Fang, "Automatic Newcastle disease detection using sound technology and deep learning method," *Computers and Electronics in Agriculture*, vol. 194, p. 106740, Mar. 2022, doi: 10.1016/j.compag.2022.106740.

[5] S. Adebayo *et al.*, "Enhancing poultry health management through machine learning-based analysis of vocalization signals dataset," *Data in Brief*, vol. 50, p. 109528, Oct. 2023, doi: 10.1016/j.dib.2023.109528.

[6] M. M. Ahmed, E. E. Hassanien, and A. E. Hassanien, "A smart IoT-based monitoring system in poultry farms using chicken behavioural analysis," *Internet of Things*, vol. 25, p. 101010, Apr. 2024, doi: 10.1016/j.iot.2023.101010.

[7] T. S. Gunawan, M. F. Sabar, H. Nasir, M. Kartiwi, and S. M. A. Motakabber, "Development of Smart Chicken Poultry Farm using RTOS on Arduino," in *2019 IEEE International Conference on Smart Instrumentation, Measurement and Application (ICSIMA)*, Kuala Lumpur, Malaysia: IEEE, Aug. 2019, pp. 1–5. doi: 10.1109/ICSIMA47653.2019.9057310.

[8] J. Huang, W. Wang, and T. Zhang, "Method for detecting avian influenza disease of chickens based on sound analysis," *Biosystems Engineering*, vol. 180, pp. 16–24, Apr. 2019, doi: 10.1016/j.biosystemseng.2019.01.015.

[9] L. Carpentier, E. Vranken, D. Berckmans, J. Paeshuyse, and T. Norton, "Development of sound-based poultry health monitoring tool for automated sneeze detection," *Computers and Electronics in Agriculture*, vol. 162, pp. 573–581, Jul. 2019, doi: 10.1016/j.compag.2019.05.013.

[10] E.-S. M. Abdel-Kafy, S. E. Ibraheim, A. Finzi, S. F. Youssef, F. M. Behiry, and G. Provolo, "Sound Analysis to Predict the Growth of Turkeys," *Animals*, vol. 10, no. 5, p. 866, May 2020, doi: 10.3390/ani10050866.

[11] M. Sadeghi, A. Banakar, M. Khazaee, and M. Soleimani, "An Intelligent Procedure for the Detection and Classification of Chickens Infected by Clostridium Perfringens Based on their Vocalization," *Rev. Bras. Cienc. Avic.*, vol. 17, no. 4, pp. 537–544, Dec. 2015, doi: 10.1590/1516-635X1704537-544.

[12] A. Banakar, M. Sadeghi, and A. Shushtari, "An intelligent device for diagnosing avian diseases: Newcastle, infectious bronchitis, avian influenza," *Computers and Electronics in Agriculture*, vol. 127, pp. 744–753, Sep. 2016, doi: 10.1016/j.compag.2016.08.006.

[13] R. S. Alonso, I. Sittón-Candanedo, Ó. García, J. Prieto, and S. Rodríguez-González, "An intelligent Edge-IoT platform for monitoring livestock and crops in a dairy farming scenario," *Ad Hoc Networks*, vol. 98, p. 102047, Mar. 2020, doi: 10.1016/j.adhoc.2019.102047.

[14] B. McFee *et al.*, *librosa: Audio and Music Signal Analysis in Python*. 2015, p. 24. doi: 10.25080/Majora-7b98e3ed-003.

[15] B. Bechtold, *soundfile: An audio library based on libsndfile, CFFI and NumPy*. Python. Accessed: May 06, 2024. [OS Independent]. Available: https://github.com/bastibe/python-soundfile

[16] A. Mahdavian, S. Minaei, P. M. Marchetto, F. Almasganj, S. Rahimi, and C. Yang, "Acoustic features of vocalization signal in poultry health monitoring," *Applied Acoustics*, vol. 175, p. 107756, Apr. 2021, doi: 10.1016/j.apacoust.2020.107756.

[17] K. Cuan, Z. Li, T. Zhang, and H. Qu, "Gender determination of domestic chicks based on vocalization signals," *Computers and Electronics in Agriculture*, vol. 199, p. 107172, Aug. 2022, doi: 10.1016/j.compag.2022.107172.

[18] H. Purwins, B. Li, T. Virtanen, J. Schluter, S.-Y. Chang, and T. Sainath, "Deep Learning for Audio Signal Processing," *IEEE J. Sel. Top. Signal Process.*, vol. 13, no. 2, pp. 206–219, May 2019, doi: 10.1109/JSTSP.2019.2908700.

[19] A. Chowdhury and A. Ross, "Fusing MFCC and LPC Features Using 1D Triplet CNN for Speaker Recognition in Severely Degraded Audio Signals," *IEEE Trans.Inform.Forensic Secur.*, vol. 15, pp. 1616–1629, 2020, doi: 10.1109/TIFS.2019.2941773.

[20] S. Hymel *et al.*, "Edge Impulse: An MLOps Platform for Tiny Machine Learning," Apr. 28, 2023, *arXiv*: arXiv:2212.03332. Accessed: May 27, 2024. [Online]. Available: http://arxiv.org/abs/2212.03332

[21] K. Cuan, T. Zhang, J. Huang, C. Fang, and Y. Guan, "Detection of avian influenza-infected chickens based on a chicken sound convolutional neural network," *Computers and Electronics in Agriculture*, vol. 178, p. 105688, Nov. 2020, doi: 10.1016/j.compag.2020.105688.

Journal of Engineering and Technology for Industrial Applications

ISSN ONLINE: 2447-0228

ITEGAM-JETIA

Manaus, v.12 n.60, p.566-583 July/August, 2026.
DOI: https://doi.org/10.5935/jetia.v12i60.3909

RESEARCH ARTICLE OPEN ACCESS

TWO-STAGE DETECT-THEN-CLASSIFY PIPELINE WITH DSAR-CNN FOR ROBUST FRAGMENT CLASSIFICATION UNDER PADDING AND BIT-FLIP ATTACKS

Teena Mary*[1] and Sreeja C S[2]

[1]Department of Computer Science, Christ University, Bangalore, Karnataka, India – 560029.
[2]Center for Quantum Technologies and Complex Systems (CQTCS), Christ University, Bengaluru, Karnataka, India – 560029.

[1]https://orcid.org/0009-0007-2856-857X, [2]https://orcid.org/0000-0002-6351-2826

E-mail: *teena.mary@res.christuniversity.in, sreeja.cs@christuniversity.in

ARTICLE INFO

Article History
Received on: March 05, 2026
Reviewed on: April 04, 2026
Accepted on: May 01, 2026
Published on: July 31, 2026

Keywords:
Adversarial defense,
Attention mechanism,
Byte-level attacks,
Detection-based defense,
Digital forensics,
Fragment classification.

ABSTRACT

File fragment classification is fundamental to digital forensics and network security, enabling the recovery and identification of files when metadata is corrupted or absent. While state-of-the-art deep learning models on the FFT-75 benchmark achieve 65–79% accuracy on clean fragments, they exhibit vulnerability to byte-level adversarial perturbations, and evaluation across 39 byte-level attack variants shows that the baseline accuracy drops from 71.1% on clean fragments to an average of 15.8% under adversarial perturbations. This paper presents a novel two-stage detection-based defense framework tailored for file fragment classification that mitigates the accuracy-robustness trade-off commonly associated with adversarial training. The framework integrates three components: (1) an attention-based adversarial detector achieving 95.46% specificity and 91.34% recall (91.44% overall accuracy); (2) an existing baseline file fragment classifier preserving 71.1% accuracy on clean fragments; and (3) a novel Dual-Scale Attention-based Robust CNN (DSAR-CNN) specifically designed for adversarial fragment classification, achieving 68.4% accuracy on adversarially perturbed samples (evaluated on the test set of 4.6M fragments) through multi-scale depth wise separable convolution, CBAM-style dual attention, learnable position embeddings, and split global pooling. Developed and evaluated across 75 file types and 39 attack variants from the FFT-75 benchmark, the complete pipeline achieves 70.91% accuracy on clean data (0.19 percentage point penalty) and 63.84% on adversarial data, yielding 70.20% accuracy in realistic mixed-threat scenarios (90% clean, 10% adversarial) - outperforming both the undefended baseline and the standard adversarial training benchmark. The framework provides an approach for improving the robustness of forensic classification systems against byte-level adversarial attacks such as padding and bit-flipping.

Copyright ©2026 by authors and Galileo Institute of Technology and Education of the Amazon (ITEGAM). This work is licensed under the Creative Commons Attribution International License (CC BY 4.0).

I. INTRODUCTION

File fragment classification (FFC) is a primary task in digital forensics and cybersecurity that allows for the recovery and reconstruction of fragmented files when their metadata is missing or corrupted. In different application scenarios, such as cybercrime investigation, data breach, and anti-forensic operation, the accurate classification of file fragments plays an important role in evidence recovery and attribution [1]. Conventional file carving and FFC methods have evolved from rule-based heuristics to state-of-the-art machine learning and deep learning models, with recent state-of-the-art systems that achieve classification accuracies in the range of 65–79% on benchmark datasets such as FFT-75, depending on fragment size [2]. These advances have been achieved due to the adoption of CNNs, and ensemble learning, which outperformed the previous handcrafted feature-based methods by a large margin. The growing reliance on FFC in security-critical environments underlines the relevance of this task.

Indeed, accurate fragment classification not only accelerates forensic investigations but also in-creases the reliability of evidence recovery when dealing with sophisticated anti-forensic techniques and large-scale data fragmentation [3]. Despite these advances, the deployment of machine learning in FFC inherits vulnerabilities of such models to adversarial manipulation - a phenomenon well-documented in other security domains like malware detection and image classification [4] [5]. Adversarial attacks, especially those operating at the byte level, can make subtle modifications to file fragments that aim to evade detection or mislead classifiers, therefore posing a direct threat to the integrity of digital forensic processes [6]. For this reason, the development of robust and attack-resilient classification systems is growing increasingly important for both researchers and practitioners in digital forensics and cybersecurity. While FFC systems have achieved remarkable accuracy under clean conditions, they are inherently vulnerable to adversarial attacks. Empirical evaluation shows that state-of-the-art FFC models, which operate at an accuracy of 71.1% on clean data, result in catastrophic performance degradation when subjected to adversarial byte-level perturbations; the accuracy plummets as low as 15.8%, which reflects a 55.3 pp drop in the classification performance of the model [7]. These attacks exploit the discrete and high-dimensional nature of file fragments, making minimal, and often imperceptible, changes adequate for evasion or misclassification [8]. The threat is not merely theoretical: adversarial attacks have been shown to be effective in both white-box and black-box settings. In other words, the lack of adversarial defenses in current FFC systems creates a serious security loophole. This contrasts with other areas, such as malware detection and image classification, where adversarial robustness has become a central focus of research.

FFC has been slow to adopt the defense mechanisms developed and fine-tuned against the peculiarities of this specific domain [2]. Given the operational setting of FFC, where forensic investigations, court cases, and incident response rest on the accuracy of fragment classification, this is particularly concerning. A single adversarial attack can compromise the reliability of digital evidence, hamper investigations, and erode confidence in forensic results. The need for robust adversarially resilient systems is therefore both a technical and a practical imperative with significant urgency. The most prominent defense strategy against adversarial attacks in machine learning has been adversarial training, wherein models are exposed to adversarial examples during training to make them more robust [5-9]. While adversarial training can indeed enhance resistance to certain attack types, it is not without its significant drawbacks. Foremost of these is the accuracy-robustness trade-off: the enhancement in robustness to adversarial samples comes at the cost of degraded accuracy on clean data [10]. In the context of FFC, adversarial training incurs a clean accuracy penalty - a nontrivial reduction in performance, particularly in high-stakes forensic applications, in which every percent of accuracy may impact case outcomes [9]. Furthermore, adversarial training is often attack-specific, usually providing robustness only against the types of adversarial examples seen during training, and may fail to generalize to novel or adaptive attack strategies. The generation and incorporation of large volumes of adversarial samples further increase the computational overhead, limiting the scalability and practicality of this approach, especially in byte-level FFC tasks with very large datasets [10]. Other defense mechanisms explored within related domains, including ensemble learning, feature squeezing, and input transformation, have failed to demonstrate consistent or scalable success in FFC [11]. The persistent accuracy-robustness trade-off, in addition with the task's operational demands, calls for novel defense frameworks that can achieve high robustness without sacrificing clean accuracy or incurring prohibitive computational costs. This paper addresses an important gap in the study of adversarial robustness for file fragment classification. While adversarial attacks and defenses have been extensively studied in domains such as computer vision and malware detection, their implications for FFC remain largely unexplored. This work therefore presents a systematic investigation of adversarial vulnerabilities and defense mechanisms for byte-level fragment classification. The key contributions of this paper are:

1. **Detection-Based Adversarial Defense for FFC**: This work presents a two-stage detection–classification pipeline for file fragment classification in which an anomaly detection model first identifies potentially adversarial fragments before classification. By routing detected adversarial samples to a specialized robust classifier while allowing clean fragments to be processed by the baseline model, the framework enables improved robustness in mixed clean–adversarial environments without degrading baseline performance on genuine fragments.
2. **Dual-Scale Attention-based Robust CNN (DSAR-CNN)**: A novel deep learning architecture is proposed combining multi-scale depthwise separable convolution, CBAM-style dual attention mechanisms, learnable position embeddings, and split global pooling.
3. **Minimal Clean Accuracy Penalty**: The detection-classification pipeline achieves 70.20% mixed-scenario accuracy (90% clean, 10% adversarial) with only a 0.19 pp penalty in clean accuracy compared to the baseline 71.1%.

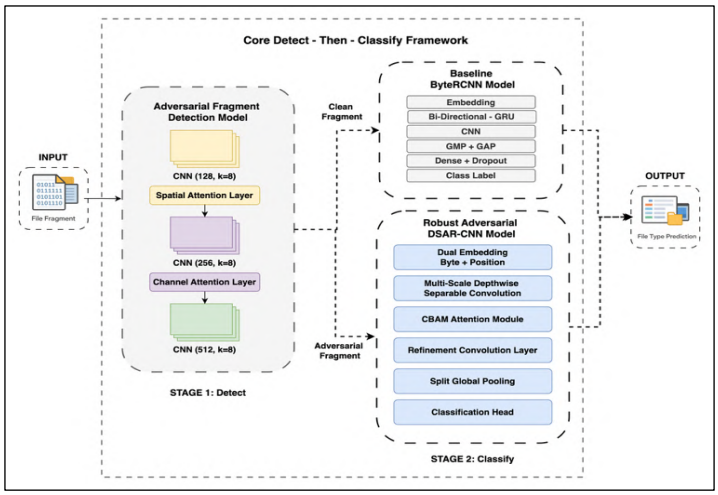


Figure 1: Two-stage detect-then-classify pipeline for adversarially robust file fragment classification.
Source: Authors, (2026).

Figure 1 illustrates the high-level architecture of the proposed two-stage defense pipeline. Each input file fragment first passes through the adversarial detection model, which performs binary classification to determine whether the fragment is clean or adversarially perturbed. Fragments identified as clean are routed to the standard file fragment classifier (ByteRCNN), preserving baseline accuracy on genuine evidence. Fragments flagged as adversarial are directed to the robust classifier (DSAR-CNN), which is specifically designed to extract discriminative features from corrupted byte sequences. This routing mechanism enables the framework to maintain high accuracy on clean data while substantially improving robustness against adversarial attacks. Together, these contributions show that anomaly detection and intelligent sample routing can achieve robustness without sacrificing either clean accuracy or operational efficiency. A comprehensive empirical comparison against a standard adversarial training baseline is provided in Section 7.2, where adversarial training is done on a balanced mix of clean and perturbed fragments across all 39 attack variants. The results confirm that the proposed pipeline outperforms adversarial training in both clean and mixed-threat scenarios. The remainder of this paper is organized as follows. Section 2 reviews existing work on file fragment classification and adversarial attacks in cybersecurity. Section 3 describes the types of attacks used in this research, including padding attacks and bit-flip attacks on file fragments. Section 4 demonstrates how these attacks reduce the baseline classifier accuracy from 71.1% to 15.8%, showing why defense is necessary. Section 5 introduces the adversarial fragment detection model. Section 6 presents the robust file fragment classifier DSAR-CNN and its architecture. Section 7 presents experimental results, showing how the defense framework improves robustness. Section 8 discusses the practical implications and limitations of the work. Section 9 concludes with a summary of key contributions to digital forensics and adversarial machine learning.

II. RELATED WORK

File fragment classification has progressed from statistical methods to sophisticated deep learning architectures. Early work by McDaniel and Heydari demonstrated that byte frequency distributions could effectively distinguish file types without relying on metadata [12]. The field advanced substantially with the introduction of the FFT-75 benchmark and the FiFTy model by Mittal et al., which achieved 77.5% average accuracy on 4096-byte fragments across 75 file types using trainable byte embeddings [13]. Subsequent research has pursued efficiency improvements: Ghaleb et al. developed lightweight CNNs with depthwise separable convolutions reaching 79% accuracy with only 100K parameters for 4096-byte fragments, while Skračić et al. proposed ByteRCNN, a hybrid recurrent-convolutional approach achieving 71.1% on the same benchmark [7-14]. Wang et al. introduced JSANet, a joint self-attention network that captures intra-sector byte-wise features and inter-sector contextual relationships, demonstrating that attention mechanisms can significantly improve fragment classification accuracy across multiple benchmarks [15]. Penrose et al. addressed the challenging problem of classifying high-entropy file fragments-including compressed and encrypted data-by proposing features based on randomness measures and discrete Fourier transform coefficients, achieving classification rates exceeding 90% for encrypted fragments [16]. More recently, Google's Magika system demonstrated that AI-powered file-type identification using optimized deep learning models can outperform traditional signature-based tools by approximately 20%, achieving precise identification within milliseconds even on CPU [17]. However, existing file fragment classifiers generally assume clean, unperturbed inputs with no mechanisms to detect or defend against adversarial manipulation, leaving forensic systems fundamentally vulnerable to byte-level attacks.

Adversarial attacks have been extensively studied in computer vision since Good-fellow et al. introduced FGSM, but their application to byte-level classification remains relatively underexplored [18]. In the malware detection domain, Kolosnjaji et al. demonstrated that gradient-based attacks against CNN architectures trained on raw executable bytes achieve high evasion rates by modifying less than 1% of bytes [19]. Demetrio et al. showed that functionality-preserving perturbations injecting benign content into executable sections severely degrade neural network detector performance [6]. Lucas et al. revealed that attack success rates can reach 90% against raw-binary classifiers without proper defenses [20]. Even more subtle bit-level manipulations can severely degrade neural network performance. For example, Kreuk et al. demonstrated that injecting a small sequence of adversarial bytes into binary executables is sufficient to cause end-to-end convolutional malware detectors to misclassify malicious samples as benign, with the adversarial payload remaining transferable across different file positions and file families [21]. Beyond input-level attacks, adversarial bit manipulations have also been studied at the model parameter level. Kummer et al. extended bit flip attacks to graph neural networks, proposing the Injectivity Bit Flip Attack that exploits architectural properties specific to message passing networks, demonstrating that targeting learnable neighborhood aggregation functions can degrade model expressivity with minimal bit modifications [22]. In the Android malware domain, Taheri et al. investigated deep learning classifier vulnerabilities against differential privacy-based adversarial attacks, demonstrating that attackers can exploit noise injection techniques to reduce classification accuracy by up to 50% [23].

These findings suggest that bit-level perturbations can significantly affect neural network predictions, a hypothesis confirmed by empirical evaluation showing accuracy degradation from 71.1% to 15.8% under padding and bit-flip attack variants. Defenses against adversarial attacks generally employ either adversarial training or detection-based methods. Zhang et al. formally characterized the accuracy-robustness tradeoff, showing that adversarial training often causes some reduction in clean accuracy without guaranteeing robustness against novel attacks [24]. Tsipras et al. further demonstrated that robustness may fundamentally conflict with standard accuracy objectives [25]. Detection-based approaches offer an alternative: Meng and Chen proposed MagNet, which identifies adversarial inputs before classification using autoencoder reconstruction, thereby avoiding accuracy penalties on clean data [26]. Goodge et al. studied autoencoder vulnerabilities in anomaly detection settings and proposed the Approximate Projection Autoencoder (APAE), demonstrating that incorporating approximate projection with feature weighting can improve robustness against adversarial attacks while maintaining detection performance on clean data [27]. Xie et al. introduced feature denoising networks that incorporate non-local means and other filtering operations within convolutional architectures, achieving state-of-the-art adversarial robustness by suppressing feature-level perturbations when combined with adversarial training [28]. Existing detection frameworks, however, are domain-specific: image-based detectors exploit spatial coherence, malware detectors leverage executable-specific structural features such as PE headers and API call sequences. File fragments span 75 heterogeneous types with format-agnostic byte patterns lacking consistent structural properties, creating a fundamental mismatch with existing defenses and necessitating a detection approach specifically tailored to byte-level file fragment analysis.

Attention mechanisms have proven effective for improving neural network robustness by dynamically focusing on discriminative features while suppressing noisy signals. Hu et al. introduced Squeeze-and-Excitation networks, which adaptively recalibrate channel-wise feature importance through learned weights [29]. Woo et al. extended this with CBAM, combining channel attention with spatial attention to identify both what features and where in the input to focus [30]. Agrawal et al. conducted a comparative study on the impact of attention mechanisms on adversarial robustness, demonstrating that CBAM-enhanced ResNet models exhibit improved resilience against PGD attacks on complex datasets like CIFAR-100, suggesting that learned salient features provide inherent defensive properties [31]. Zoran et al. proposed sequential top-down attention models for image classification that achieve state-of-the-art adversarial robustness by processing inputs through multiple attention steps, revealing that increasing the number of attention glances creates a computational race between attacker and defender while producing adversarial examples with global, perceptible structures [32]. In malware detection, Al-Ghanem et al. achieved 99.5% accuracy with MADANET by learning to emphasize discriminative byte patterns, while Yakura and Sakuma used attention to extract important byte sequences characterizing malware functionality [33] [34]. Despite these successes, attention mechanisms remain underexplored for addressing adversarial robustness in file fragment classification. The application of dual attention mechanisms - combining channel and spatial attention in a hierarchical structure enables synergistic improvements where the combined effect exceeds the sum of individual contributions, providing a promising direction for robust fragment classification under adversarial conditions.

III. THREAT MODEL AND ATTACK TAXONOMY

The threat model and attack taxonomy presented here are built upon the comprehensive adversarial evaluation framework established in prior work, extended here to evaluate defense mechanisms. The threat model assumes a non-adaptive adversary who has no query access to the classifier architecture or training data. The attacks are pre-specified input-constrained transformations rather than optimized per-sample adversarial examples. The attacker will aim to induce misclassification through byte-level perturbations while maintaining the fragment size exactly at 512 bytes. This restriction follows realistic forensic scenarios in which fragments are recovered from storage media stripped of metadata and context. The attacks considered are format-agnostic, based on general byte-level manipulations rather than exploiting file-type-specific structural properties. Two primary attack categories represent realistic adversarial perturbations: padding attacks and bit-flip attacks. Padding attacks overwrite bytes near the fragment tail using three mechanisms: null-byte padding (adding low-entropy zeros), random-byte padding (adding random bytes), and cross-file padding (adding authentic bytes from different file types). For each cross-file padded fragment, the source file type is selected uniformly at random from the remaining 74 file types, and the replacement bytes are drawn from a randomly sampled fragment of that type. This ensures diverse cross-type contamination patterns and prevents the detector from memorizing specific source-target type associations. The fragment length remains fixed at 512 bytes throughout all attacks. Each padding type is tested at five sizes-16, 32, 64, 128, and 256 bytes-producing 15 attack variants. Bit-flip attacks corrupt individual bytes in two ways: random bit-flipping modifies bytes distributed throughout the fragment, while header-targeted bit-flipping concentrates modifications in the first 64–128 bytes where file signatures reside. These header-targeted attacks remain format-agnostic in that they do not parse format-specific structures (e.g., PDF dictionaries or JPEG markers) but rather exploit the generic concentration of discriminative magic bytes in early file positions. With four corruption rates and three bit-flip intensities, bit-flip attacks yield 24 variants, resulting in a total attack taxonomy of 39 distinct strategies. These details are summarized in Table 1:

Table 1: Byte-Level Adversarial Attack Taxonomy for FFT-75 File Fragment Classification.

Attack family	Attack type	Variants (count)	Parameter grid	Intended forensic realism
Padding	Null-byte padding	5	Padding sizes P ∈ {16, 32, 64, 128, 256} bytes	Models zero-filled buffers, incomplete reads, and partially overwritten sectors that naturally occur on disks.
Padding	Random-byte padding	5	Padding sizes P ∈ {16, 32, 64, 128, 256} bytes	Simulates noise injection, disk corruption, and transmission errors producing high-entropy tails in fragments.
Padding	Cross-file padding	5	Padding sizes P ∈ {16, 32, 64, 128, 256} bytes	Appends authentic bytes from other file types to induce file-type confusion and hybrid statistical profiles.
Bit-flip	Random bit-flip	12	k ∈ {1, 5, 10, 20}% of bytes; n ∈ {1, 2, 4} bits per selected byte	Emulates random memory faults, media degradation, and low-level corruption without obvious structural artifacts.
Bit-flip	Header-targeted bit-flip	12	Same (k, n) grid as random bit-flip, restricted to header region (first 64–128 bytes)	Targets magic numbers and header metadata, reflecting adversaries corrupting type-identifying bytes while preserving length.

Source: Authors, (2026).

Unlike adversarial attacks studied in computer vision, which often aim to produce imperceptible perturbations, the objective in file fragment classification is different. In digital forensics, fragments frequently originate from partially overwritten sectors, damaged storage media, or intentionally manipulated files where substantial portions of the fragment may be corrupted.

Consequently, the attack taxonomy includes perturbations ranging from small bit flips to large-scale byte overwrites (e.g., 256-byte padding) to model both subtle corruption and severe anti-forensic manipulation scenarios. These perturbations therefore represent a spectrum of realistic byte-level corruption conditions rather than purely imperceptible adversarial examples. The goal is therefore not only to evaluate robustness against subtle adversarial manipulations, but also to assess the resilience of fragment classifiers under severe corruption conditions that may arise in real-world forensic investigations. Scope of Evaluation. The defense framework is trained and evaluated exclusively against the 39 non-adaptive attack variants defined in this taxonomy. Since both the detector and robust classifier observe all attack types during training, the evaluation measures in-distribution robustness rather than generalization to novel attack strategies. An adaptive adversary with full pipeline knowledge could potentially craft composite perturbations (e.g., simultaneous padding and bit-flipping) or target the detector's learned attention patterns directly - scenarios not evaluated here. Hence, adaptive threat evaluation is identified as a priority for future work (Section VIII.2). The evaluation uses the FFT-75 test partition as the clean fragment source, comprising 768,000 fragments distributed evenly across 75 file types at 512 bytes each (see Section IV.2 for the complete dataset partitioning strategy). Applying all 39 attack variants to each clean fragment generates 29.952 million adversarial samples, for a total dataset of 30.72 million fragments. This dataset is split into training (70%, 21,504,000 fragments), validation (15%, 4,608,000 fragments), and testing (15%, 4,608,000 fragments), with each split independently allocating 70%, 15%, and 15% of both clean and adversarial samples respectively. The training set comprises 20,966,400 adversarial samples and 537,600 clean samples, resulting in a 39:1 adversarial-to-clean class imbalance.

IV. BASELINE BYTERCNN AND UNDEFENDED VULNERABILITY ANALYSIS

The purpose of this section is to establish a quantitative baseline of adversarial vulnerability in file fragment classification systems. This baseline serves two key goals: first, it measures the security gap in current state-of-the-art FFC models; and second, it validates that the 39-variant attack taxonomy is feasible and effective in practice.

IV.1 BASELINE MODEL SELECTION AND JUSTIFICATION

Selecting the right baseline model is essential for a fair assessment. Three candidate models were evaluated based on these criteria: accuracy on FFT-75 for 512-byte fragments, availability of public code, and practical usability. Current file fragment classification models typically achieve between 65% and 79% accuracy on FFT-75, depending on the fragment size and model type. FiFTy achieves an average of 77.5% across 4096 fragment size, but for 512-byte fragments specifically, FiFTy only reaches 65.6% [13]. ByteRCNN, published in 2023, achieves 71.1% on 512-byte fragments, which is notably higher [7]. JSANet, a transformer-based model with joint self-attention mechanisms, reported performance on the FFT-75 benchmark but does not provide a specific 512-byte accuracy figure in publicly available documentation [15]. Since ByteRCNN offers public code and achieves one of the highest documented 512-byte accuracy (71.1%), it was selected as the baseline model. It represents current state-of-the-art and was published by Skračić et al. in IEEE Access 2023. ByteRCNN is a hybrid recurrent-convolutional model designed for file-fragment type identification. It incorporates a byte-embedding layer that transforms raw byte values into trainable dense representations, followed by recurrent and convolutional components that capture sequential and local patterns within byte sequences. The model is evaluated on the FFT-75 dataset, specifically Scenario 1, which contains 75 file types. Experiments include both 512-byte and 4096-byte fragments, where ByteRCNN achieves 71.1% accuracy on 512-byte samples and 83.9% accuracy on 4096-byte samples.

IV.2 TEST DATA AND EXPERIMENTAL SETUP

The FFT-75 Scenario 1 dataset comprises 7,680,000 fragments (102,400 fragments per file type across 75 file types at 512 bytes each), partitioned by the dataset creators into 80% training (6,144,000 fragments), 10% validation (768,000 fragments), and 10% test (768,000 fragments). The ByteRCNN baseline model was trained on the official FFT-75 training partition (6,144,000 fragments), consistent with the original evaluation protocol. To construct the adversarial evaluation benchmark, the 768,000-fragment test partition (10,240 fragments per file type) was used as the clean fragment source. Applying all 39 attack variants to each clean fragment generates 768,000 × 39 = 29,952,000 adversarial samples, for a total of 30,720,000 fragments (clean + adversarial). This combined dataset was then split into training (70%, 21,504,000 fragments), validation (15%, 4,608,000 fragments), and testing (15%, 4,608,000 fragments) using stratified sampling to preserve the clean-adversarial ratio in each split. The training partition is used exclusively for training the adversarial detection model and the DSAR-CNN robust classifier; it is not used for ByteRCNN training. Importantly, the training, validation, and test partitions are constructed using stratified sampling with strictly disjoint fragment sets - no individual fragment or its adversarial variants appear in more than one partition. This ensures that the defense models are evaluated exclusively on fragments unseen during their training, preventing data leakage. The FFT-75 test partition (768,000 fragments) was selected as the adversarial generation source rather than the larger training partition (6,144,000 fragments) to maintain computational tractability; generating all 39 attack variants from the full training set would yield over 245 million samples. Since both partitions are drawn from the same underlying file corpus with identical per-type distributions, this choice does not introduce distributional bias.
The test dataset consists of these parts:

- **Clean test fragments:** 115,200 fragments (15% of the FFT-75 test partition), distributed equally across 75 file types (1,536 fragments per type).
- **Adversarial test fragments**: Generated by applying each of the 39 attack variants to the same 115,200 clean fragments. This produces 115,200 × 39 = 4,492,800 adversarial samples. Each attack is applied independently; no combined or cumulative attacks are tested.
- **Total test dataset**: 4,608,000 fragments (115,200 clean + 4,492,800 adversarial).

This structure ensures that all attacks are tested on identical baseline data, making it easy to compare how different attack types affect the classifier.

For padding attacks: each 512-byte fragment has its last N bytes (where N ∈ {16, 32, 64, 128, 256}) removed and replaced with corrupted bytes using one of three methods: null bytes (0x00), random bytes (0x00–0xFF), or authentic bytes from a different file type. The result is always 512 bytes long, with the first (512 − N) bytes intact and the last N bytes corrupted. For bit-flip attacks: either a random selection of k% of bytes (k ∈ {1, 5, 10, 20}) or just the header region (first 64–128 bytes) is chosen, then n random bits per selected byte (n ∈ {1, 2, 4}) are flipped. This generates 12 random variants and 12 header-targeted variants. Multiple metrics measure vulnerability from different angles:

1. **Absolute accuracy** is the fraction of correctly classified fragments, as given in the formula:

$$\text{Acc} = \frac{\text{Correct predictions}}{\text{Total samples}} \tag{1}$$

2. **Accuracy drop** (percentage points) shows raw performance loss, as given in the formula:

$$\Delta_{\text{acc}} = \text{Acc}_{\text{clean}} - \text{Acc}_{\text{adv}} \tag{2}$$

3. **Relative vulnerability** shows the percentage of capability lost, as given in the formula:

$$V_{\text{rel}} = \frac{\text{Acc}_{\text{clean}} - \text{Acc}_{\text{adv}}}{\text{Acc}_{\text{clean}}} \times 100\% \tag{3}$$

Comparison to uniform class probability: For 75 file types, accuracy of randomly choosing the correct file type is 1/75 ≈ 1.33%.

IV.3 CLEAN BASELINE PERFORMANCE

Before evaluating adversarial robustness, the clean performance of the baseline model was verified. The ByteRCNN model was trained from scratch on the FFT-75 training partition (6,144,000 fragments) using the publicly available architecture and training configuration, as pre-trained weights are not provided by the original authors. When evaluated on 115,200 clean test fragments (held out from the FFT-75 test partition, disjoint from all training data), the model correctly classified 81,907 fragments, resulting in a clean accuracy of 71.096% (≈71.1%). This result is consistent with the performance reported in the original ByteRCNN study for 512-byte fragments, confirming that the re-implementation reproduces the expected baseline behavior.

IV.4 ADVERSARIAL VULNERABILITY RESULTS

ByteRCNN's clean accuracy on 512 size fragments is 71.1% [7]. From the empirical evaluation, it was found that across all 39 attacks, ByteRCNN's average adversarial accuracy comes to $\text{Acc}_{\text{adv}} = 15.8\%$. This represents an absolute drop of:

$$\Delta_{\text{acc}} = 71.1\% - 15.8\% = 55.3 \text{ percentage points} \tag{4}$$

In relative terms, the model retains only 22.2% of its clean performance, corresponding to a relative vulnerability of:

$$V_{\text{rel}} = \frac{55.3}{71.1} \times 100\% = 77.8\% \tag{5}$$

For a 75-class classification problem, the probability of correct classification under uniform class selection is 1.33% (1/75). On clean data, ByteRCNN achieves an accuracy of 71.1%, which corresponds to a performance level 53.5 times higher than the uniform classification probability (71.1% ÷ 1.33%). Under adversarial conditions, the accuracy decreases to 15.8%, representing only 11.9 times the uniform probability level (15.8% ÷ 1.33%). This comparison indicates that adversarial perturbations substantially reduce the model's effective discriminative capability, bringing its performance significantly closer to the uniform baseline. A summary of the accuracy degradation for the different attack types is given in Table 2:

Table 2: Accuracy Degradation on Baseline ByteRCNN Model for Different Attack Types.

Attack Type	Count	Lowest Acc (%)	Highest Acc (%)	Average Acc (%)	Average Drop (pp)	Relative Vulnerability (%)
Null-byte padding	5	4.1	22.4	12.3	58.8	82.7
Random-byte padding	5	3.7	21.5	11.5	59.6	83.8
Cross-file padding	5	2.7	19.2	9.8	61.3	86.2
Random bit-flip	12	6.4	38.8	20.2	50.9	71.6
Header bit-flip	12	5	34.7	17.1	54	75.9
Overall	39	2.7	38.8	15.8	55.3	77.8

Source: Authors, (2026).

Padding attacks (11.2% average) are significantly more damaging than bit-flip attacks (18.7% average). The 7.5 pp difference occurs because padding overwrite or replace existing bytes from the fragment, destroying information entirely. Bit-flip attacks only change specific byte values while keeping the file structure mostly intact. Cross-file padding is the hardest attack (9.8% average). Unlike null-byte or random-byte padding which introduces obvious anomalies, cross-file padding adds real byte sequences from other file types. This actively confuses the classifier by introducing correct looking but contextually wrong file signatures. A consistent pattern emerges across all attack types: performance degradation scales with perturbation magnitude. Table 3 ranks the attack severity (top 5) from the most to the least damaging for the model based on model accuracy.

Table 3: Attack Severity Ranking: Most to Least Damaging Variants by Residual Accuracy.

Rank	Attack Type	Parameters	Residual Accuracy (%)	Accuracy Drop (pp)
1	Cross-file padding	256 B	2.7	68.4
2	Random-byte padding	256 B	3.7	67.4
3	Null-byte padding	256 B	4.1	67
4	Cross-file padding	128 B	5	66.1
5	Header bit-flip	k=20%, n=4	5	66.1
-	-	-	-	-
35	Random bit-flip	k=5%, n=1	28.3	42.8
36	Header bit-flip	k=1%, n=2	28.8	42.3
37	Random bit-flip	k=1%, n=2	32.9	38.2
38	Header bit-flip	k=1%, n=1	34.7	36.4
39	Random bit-flip	k=1%, n=1	38.8	32.3

Source: Authors, (2026).

For padding attacks, null-byte padding accuracy decreases from 22.4% with 16-byte perturbations to 4.1% with 256-byte perturbations. Random-byte padding shows a similar trend, dropping from 21.5% to 3.7% as padding size increases. Cross-file padding demonstrates the steepest degradation, falling from 19.2% to 2.7% across the same range. Bit-flip attacks follow the same pattern, though with higher residual accuracy: random bit-flip accuracy declines from 38.8% (k=1%, n=1) to 6.4% (k=20%, n=4), while head-er-targeted bit-flip drops from 34.7% to 5.0% under equivalent perturbation intensity. This monotonic relationship reflects a fundamental principle: as perturbations grow larger, the proportion of authentic, discriminative bytes decreases, leaving fewer patterns for the classifier to exploit. Consequently, accuracy degrades proportionally with the volume of corrupted information. The least damaging attack (random bit-flip with only 1% of bytes affected and 1 bit flipped per byte) still reduces accuracy from 71.1% to 38.8% - a 32.3 pp drop. This shows clearly that adversarial vulnerability is not limited to severe attacks; even subtle modifications cause performance loss. No single attack variant preserves reasonable performance; the highest adversarial accuracy across all 39 variants is 38.8%, meaning the lowest drop is 32.3 pp.

IV.4.1 Statistical Confidence

With 4,492,800 adversarial test samples (n), the measurements are precise. The 95% confidence interval for the 15.8% adversarial accuracy (p) is computed using the standard error for a binomial proportion:

$$\mathrm{SE} = \sqrt{\frac{\mathrm{p}(1-\mathrm{p})}{\mathrm{n}}} = \sqrt{\frac{0.158 \times 0.842}{4{,}492{,}800}} = 0.000172 \tag{6}$$

The binomial proportion method was chosen because classification accuracy represents binary outcomes (correct or incorrect), and with 4.5 million test samples, the Central Limit Theorem implies that the sampling distribution of the estimated proportion is well approximated by a normal distribution, making this a standard statistical approach for reporting accuracy confidence intervals in machine learning research. The 95% confidence interval is therefore calculated as:

$$\mathrm{CI}_{95\%} = p \pm z_{\alpha/2} \times \mathrm{SE} = 0.158 \pm 1.96 \times 0.000172 = [15.77\%, 15.83\%] \tag{7}$$

This ±0.034 pp range demonstrates that the 15.8% figure is measured with high precision. The large sample size ensures that small variations in true accuracy are captured with negligible measurement error.

IV.5 UNDERSTANDING THE VULNERABILITY

Four factors explain why adversarial performance is poor:

1. **Statistical patterns are disrupted**. ByteRCNN learns byte-level statistics like n-gram frequencies and entropy profiles that are unique to authentic files. Padding directly destroys these patterns by replacing authentic bytes with foreign or random data. Bit-flip attacks corrupt the exact byte values that contribute to these statistics.
2. **Position matters**. The model learns that file headers (positions 0–128) contain distinctive signatures. Header-targeted bit-flip attacks (17.1% average) are more damaging than random bit-flip attacks (20.2% average) because they deliberately corrupt these critical positions.
3. **Authentic forgeries confuse the model**. Cross-file padding is especially effective (9.8% average) because it injects real byte sequences from other file types. The classifier encounters statistically valid but contextually incorrect patterns, causing systematic misclassification rather than simple information loss.
4. **The model has never seen adversarial examples**. ByteRCNN was trained only on clean data. It has no learned mechanisms for distinguishing authentic from corrupted regions. Robustness must be explicitly designed.

The empirical findings establish that file fragment classifiers cannot withstand byte-level attacks without explicit defense mechanisms. Simple, easy-to-implement attacks - requiring no sophisticated optimization or targeted knowledge - cause complete classification failure.

Adversaries need not develop complex, model-specific attacks; format-agnostic byte-level perturbations suffice to entirely compromise system integrity. This reality makes defense mechanisms mandatory for any deployment of these systems in security-critical applications. Based on this baseline vulnerability analysis, effective defense mechanisms should satisfy three concrete performance targets.

1. First, adversarial accuracy should exceed 60% to recover most of the capability lost under attack (compared to the current 15.8%).
2. Second, clean accuracy should remain at or above 70% to keep the penalty on genuine evidence minimal.
3. Third, performance on realistic mixed-threat scenarios - where 90% of fragments are clean and 10% are adversarially perturbed [35] - should exceed 68%. The baseline mixed accuracy is computed as follows:

$$\mathrm{Acc}_{\mathrm{mixed}} = 0.9 \times 71.1\% + 0.1 \times 15.8\% = 65.57\% \quad (8)$$

Any defense achieving these three targets simultaneously will represent an advance in adversarial robustness for file fragment classification.

V. ADVERSARIAL FRAGMENT DETECTION MODEL

The first stage of the defense pipeline is an adversarial detection model that acts as a gatekeeper in front of the file fragment classifiers. Its role is to decide, for each 512-byte fragment, whether the fragment is clean or adversarially perturbed and to route it accordingly. Fragments predicted as clean are passed to the baseline ByteRCNN classifier, while fragments predicted as adversarial are forwarded to the robust classifier introduced in the next section. This design allows the standard FFC model to operate unchanged on genuine evidence, while dedicating a specialized model to adversarially manipulated inputs.

V.1 MODEL OVERVIEW

The adversarial detection model is an attention-based convolutional neural network tailored to raw byte sequences. It consists of a byte embedding layer followed by a stack of three convolutional blocks that integrate spatial and channel attention mechanisms, a global pooling layer, and two fully connected layers for binary classification. The total capacity is approximately 1.31 million parameters, resulting in a compact model suitable for deployment as a preprocessing stage in forensic pipelines.

V.2 TRAINING CONFIGURATION

Training is conducted on the full 30.72 million–fragment benchmark, which includes 768,000 clean fragments and 29.952 million adversarial fragments spanning all 39 attack variants. The dataset is split into 70% training, 15% validation, and 15% test partitions using stratified sampling to preserve the clean–adversarial ratio in each split. The model is trained with the Adam optimizer, binary cross-entropy loss, and a batch size of 128, using class-balanced batches to avoid collapse to the majority (adversarial) class. Early stopping with a patience of five epochs is configured based on validation accuracy, although training in practice runs the full schedule due to stable validation performance. The dataset contains substantially more adversarial fragments than clean fragments because each clean fragment is transformed using all 39 attack variants. This enumeration of attack variants is necessary to ensure comprehensive coverage of the attack space and to evaluate robustness across a wide range of perturbation strategies. As a result, the raw dataset exhibits a 39:1 adversarial-to-clean imbalance. However, this imbalance does not affect the training dynamics because the model is trained using class-balanced mini-batches that sample equal numbers of clean and adversarial fragments. This approach allows the dataset to fully represent the diversity of attack variants while preventing the classifier from developing a bias toward the adversarial class during optimization.

V.3 DETECTION PERFORMANCE

On the 4.6 million-sample test set, the adversarial detection model achieves 95.46% specificity on clean fragments and 91.34% recall on adversarial fragments, with an F1-score of 0.9542 and AUC-ROC of 0.9819. The overall accuracy is 91.44%; however, because the test set reflects the natural benchmark composition (97.5% adversarial, 2.5% clean), this metric is dominated by recall performance. Specificity and recall are therefore reported as the primary evaluation metrics, as they independently capture detection quality on each class regardless of class distribution. Performance remains consistently strong across all attack categories. Padding-based attacks achieve the highest detection accuracies (93.47% for null-byte padding and 92.91% for random-byte padding), reflecting the strong boundary artefacts they introduce. Cross-file padding is the most challenging category yet still attains 86.24% accuracy. Random and header-targeted bit-flip attacks both exceed 90% detection accuracy, indicating that the learned byte embeddings and attention mechanisms capture even subtle changes in Hamming distance.

V.4 ROLE IN THE TWO-STAGE PIPELINE

Within the overall system, the adversarial detection model serves as a high-specificity front end that enables a detect-then-classify architecture without modifying the baseline ByteRCNN classifier. Clean fragments are classified by the original model at its full 71.1% accuracy, while adversarial fragments are redirected to the robust classifier that is explicitly trained to handle corrupted inputs. Misclassified adversarial fragments still receive baseline protection through ByteRCNN rather than catastrophic failure, and misclassified clean fragments experience only a minor accuracy penalty when processed by the robust classifier. This routing behavior is central to achieving strong robustness gains with a negligible impact on clean performance in the complete pipeline.

VI. ROBUST FILE FRAGMENT CLASSIFICATION DSAR-CNN MODEL

The vulnerability assessment in Section 4 established that ByteRCNN suffers a 55.3 pp accuracy collapse (71.1% → 15.8%) under adversarial attack. This catastrophic degradation raises a fundamental question: what architectural properties enable classification despite substantial byte-level corruption? The key insight motivating DSAR-CNN is that adversarial perturbations do not destroy all discriminative information. A 512-byte fragment subjected to 256-byte null-byte padding has its final 256 bytes replaced with zeros, while retaining 256 authentic bytes in the first half, and it often includes critical file-type markers (e.g., PDF headers, JPEG markers). Bit-flip attacks, despite corrupting individual bytes, typically affect only 1–20% of the fragment. The remaining authentic content retains sufficient structure to enable file-type identification if the classifier can selectively focus on un-corrupted regions and suppress noise from perturbed areas. Traditional CNNs fail under this scenario because they process all regions equally, allowing corrupted bytes to pollute global feature representations. DSAR-CNN addresses this through five synergistic innovations: multi-scale feature extraction to detect perturbations at matched granularities, learnable position embeddings to recognize attack-specific positional patterns, hierarchical attention mechanisms to separate file-type signals from adversarial noise, split pooling to resist attention-induced feature dilution, and regularized classification to prevent overfitting to specific attack patterns.

VI.1 DSAR-CNN ARCHITECTURE OVERVIEW

DSAR-CNN comprises six layers designed to progressively extract, refine, and classify features from corrupted byte sequences. The complete model contains 479,344 parameters and achieves 68.4% accuracy on adversarial fragments when evaluated on the final test set (4.6 million samples). (Note: Ablation study results on the validation set show 70.1% to isolate individual component contributions; see Table 4). Figure 2 shows the detailed architecture of the DSAR-CNN classification model.

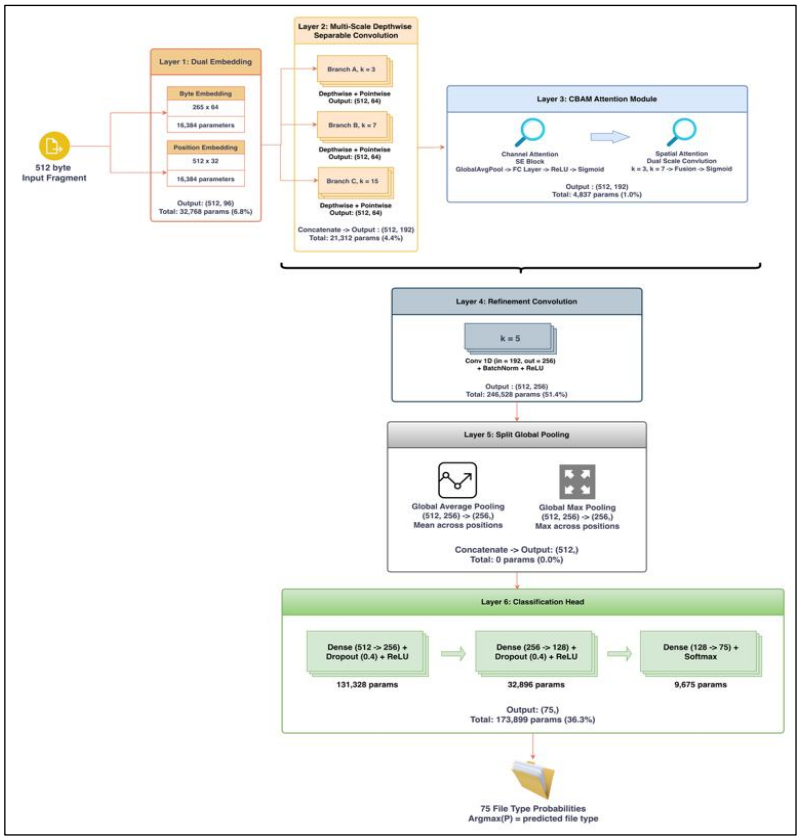


Figure 2: Proposed Dual-Scale Attention-based Robust CNN (DSAR-CNN) architecture for adversarial file fragment classification. Source: Authors, (2026).

VI.1.1 Layer 1: Dual Embedding

Layer 1 transforms raw byte integers (0–255) into rich, position-aware feature vectors that capture both semantic byte meaning and contextual positional information. This dual representation is crucial because adversarial attacks create position-dependent corruption patterns. Byte Embedding. Each byte value is mapped to a learnable 64-dimensional embedding:

$$X_{\text{byte}}[i] = E[b_i, :] \text{for } i \in [0,511] \tag{9}$$

where E ∈ ℝ {256×64} is the learnable embedding matrix and bi ∈ {0, 1, ..., 255} is the byte value. This creates semantic representation: byte value 0 learns associations with padding, specific ASCII characters learn their characteristic file context, and so forth. Parameters: 256 × 64 = 16,384. Learnable Position Embedding. Each position is mapped to a learnable 32-dimensional embedding:

$$X_{\text{pos}}[i] = P[i, :] \text{for } i \in [0,511] \tag{10}$$

where P ∈ ℝ {512×32} is the learnable position matrix. These embeddings are trained end-to-end on adversarial data. During training, the model learns that tail positions (448–511) frequently contain padding artifacts while earlier positions are more likely authentic. Parameters: 512 × 32 = 16,384. Concatenation. The two embeddings are concatenated along the feature dimension:

$$X_{\text{embed}}[i] = \left[X_{\text{byte}}[i] \parallel X_{\text{pos}}[i]\right] \in \mathbb{R}^{96} \tag{11}$$

Output shape: (512, 96). Each position now has a 96-dimensional vector capturing both what byte it is and where it is located.

VI.1.2 Layer 2: Multi-Scale Depth-wise Separable Convolution

Purpose. Different adversarial attacks create perturbation patterns at fundamentally different spatial scales: bit-flip attacks corrupt individual bytes (1–20 bytes), while padding attacks create large contiguous blocks (16–256 bytes). A single convolution kernel cannot optimally detect both. Layer 2 uses three parallel branches with kernel sizes matched to attack granularities. The kernel sizes (3, 7, and 15) were selected to provide multi-scale receptive fields capable of capturing both local byte-level variations and broader contextual patterns within the fragment. Smaller kernels capture fine-grained byte transitions, while larger kernels capture longer-range contextual patterns such as padding boundaries or abrupt distribution changes. This multi-scale design enables the model to analyze perturbations occurring at different spatial extents. Much larger kernels (e.g., 85, 125) would unnecessarily dilute these localized signals, increase parameter count, and risk overfitting without providing additional discriminative power beyond what is already achieved through hierarchical stacking of smaller convolutions. Three Branches. The layer processes the 512-position sequence with three 1D convolution branches simultaneously:

1. Branch A (k=3): Fine-grained analysis for scattered bit-flip perturbations
2. Branch B (k=7): Medium-scale analysis for local pattern disruptions
3. Branch C (k=15): Coarse-grained analysis for padding attack boundaries

Each branch produces 64 output channels, which are concatenated to form 192 total channels. Depthwise Separable Convolution. Instead of standard convolution, each branch uses depthwise separable convolution, which factorizes the operation into two steps: (1) depthwise convolution applies a separate kernel to each of the 96 input channels independently, and (2) pointwise (1×1) convolution mixes information across channels. Parameter count also includes biases on both depthwise and pointwise convolutions. Parameter Calculation. For a fair comparison including biases, a standard convolution across the three kernels would use:

$$(k_1 + k_2 + k_3) \times C_{in} \times C_{out} + 3 \times C_{out} = 25 \times 96 \times 64 + 3 \times 64 = 153{,}792\ params \tag{12}$$

Depthwise separable achieves:

$$\sum_{j=1}^{3} \left(k_j C_{in} + C_{in} + C_{in} C_{out} + C_{out}\right) = 21{,}312\ params \tag{13}$$

VI.1.3 Layer 3: CBAM Attention Module

Purpose. After extracting multi-scale features, Layer 3 learns which features are reliable (file-type discriminative) and which are noisy (adversarial artifacts). It does this through two complementary attention mechanisms: channel attention identifies important feature channels and spatial attention identifies trustworthy byte positions. Channel Attention (Squeeze-and-Excitation). This mechanism first computes the average activation of each of the 192 feature channels across all positions, then learns channel importance weights s ∈ (0,1)$^{\{192\}}$:

$$z = \text{GlobalAvgPool}(F) \in \mathbb{R}^{192} \tag{14}$$

$$s = \sigma(W_2 \cdot \text{ReLU}(W_1 \cdot z)) \in (0,1)^{192} \tag{15}$$

where σ is sigmoid, $W_1 \in \mathbb{R}^{\{12\times192\}}$ maps to a 12-dimensional bottleneck (reduction ratio r=16), and $W_2 \in \mathbb{R}\{192\times12\}$ reconstructs channel weights. These weights amplify channels encoding file-type patterns (weight ≈ 0.8–0.95) and suppress channels encoding adversarial noise (weight ≈ 0.05–0.2). Parameters: (192 × 12) + 12 + (12 × 192) + 192 = 4,608 weights + 204 biases = 4,812. Spatial Attention (Dual-Scale). Operating on the channel-refined features, spatial attention asks which positions are trustworthy. It uses two scales (k=3 and k=7) to detect corruption at different granularities:

$$D = \left[\text{AvgPool}_{\text{channels}}(F); \text{MaxPool}_{\text{channels}}(F)\right] \tag{16}$$

$$\alpha = \sigma(W_f \cdot [\text{Conv}(D, k=3); \text{Conv}(D, k=7)]) \in (0,1)^{512} \tag{17}$$

The 2-channel descriptor D (formed by channel-wise average and max pooling) is processed by two parallel 1D convolutions (k=3 and k=7, each 2→1 channels with bias), whose outputs are concatenated and fused by a 1×1 convolution (2→1 channels with bias). Position-wise weights α suppress corrupted regions (α ≈ 0.05–0.15) and preserve authentic regions (α ≈ 0.9–0.95). Parameters: (2×3+1) + (2×7+1) + (2×1+1) = 7 + 15 + 3 = 25. Synergistic Effect. An interesting finding is that channel attention + spatial attention produces +11.2 pp improvement in adversarial accuracy. This synergy arises from hierarchical structure: channel attention first filters out noisy channels, producing a cleaner signal that spatial attention then operates on. Operating on this pre-filtered signal, spatial attention makes more reliable position-level decisions.

VI.1.4 Layer 4: Refinement Convolution

Purpose. By Layer 4, features have been extracted from three parallel perspectives (k=3, k=7, k=15 branches) and selectively refined by CBAM attention mechanisms. Layer 4's role is to integrate this diverse multi-scale information into a unified, higher-dimensional representation. It acts as a synthesis layer that combines the complementary perspectives before passing to the classification head. At the input to Layer 4, the model has 512 positions, each with 192 feature dimensions. These 192 dimensions are organized in three groups of 64 channels, each representing patterns detected at different scales:

- Channels 0–63: Fine-grained patterns from k=3 analysis (subtle byte-level corruption signatures)
- Channels 64–127: Medium-scale patterns from k=7 analysis (local disruption boundaries)
- Channels 128–191: Coarse-grained patterns from k=15 analysis (large padding block transitions)

Additionally, spatial attention has already suppressed positions suspected of containing adversarial perturbations. Authentic regions (typically positions 0–383 in padding attacks) have attention weights $\alpha \approx 0.9–0.95$, while corrupted regions (typically positions 384–511) have been suppressed to $\alpha \approx 0.05–0.15$. The network now has a partially masked but information-rich feature representation. Operation. A 1D convolution with k=5 processes the attended features

$$F_{\text{refined}} = \text{ReLU}\left(\text{BatchNorm}\left(\text{Conv1D}(F_{\text{attended}}, k = 5, 256 \text{ filters})\right)\right) \tag{18}$$

Layer 4 applies a 1D convolution with k=5 that allows neighboring positions (±2 away) to collectively influence each output position. This local context aggregation captures file-type patterns, which are often locally coherent; authentic regions maintain consistent byte patterns while corruption boundaries create sharp discontinuities. The convolution simultaneously expands channels from 192 to 256, learning 256 different perspectives including combinations like "fine-grained and medium-scale corruptions co-occurring" or "authentic header followed by noise." Batch normalization then normalizes activations to ensure stable training on the imbalanced dataset (97.5% adversarial, 2.5% clean), while ReLU introduces non-linearity to preserve the network's expressive power.

VI.1.5 Layer 5: Split Global Pooling

Purpose. Layers 1–4 maintain position-level information across 512 positions. Layer 5 compresses this into a single global representation but uses split pooling to counteract a critical problem: dilution from attention-based suppression. The Dilution Problem. After CBAM attention, many positions in adversarially perturbed fragments have been suppressed to near-zero activations. For a fragment under 256-byte padding attack, spatial attention suppresses positions 256–511 ($\alpha \approx 0.05–0.15$), while preserving positions 0–255 ($\alpha \approx 0.9–0.95$). When Global Average Pooling computes the mean across all 512 positions:

$$f_{\text{gap}} = \frac{1}{512}\sum_{i=1}^{512} F_{\text{refined}}\,[i] \tag{19}$$

The result averages 256 strong authentic activations with 256 near-zero suppressed activations, producing approximately 50% of the signal strength compared to a fully clean fragment. This dilution - averaging real signals with suppressed noise - weakens the discriminative information available to the classifier. A classifier receiving a 50%-diluted representation of a PDF fragment might have difficulty distinguishing it from a JPEG, even if the authentic 50% contains clear PDF signatures. Split Pooling Solution. Rather than accepting this dilution, Layer 5 employs two complementary pooling operations: Global Average Pooling (GAP) is defined as:

$$f_{\text{gap}} = \frac{1}{512}\sum_{i=1}^{512} F_{\text{refined}}\,[i] \in \mathbb{R}^{256} \tag{20}$$

GAP is sensitive to position suppression, making it diluted on corrupted fragments but representative on clean fragments. Global Max Pooling (GMP) is defined as:

$$f_{\text{gmp}} = \max_{i} F_{\text{refined}}[i] \in \mathbb{R}^{256} \tag{21}$$

GMP finds the maximum activation across all 512 positions. Crucially, GMP is un-affected by suppression - even if 256 positions are suppressed to near-zero, the maximum activation remains strong from the 256 unsuppressed positions. GMP preserves the strongest signals regardless of position distribution. Concatenation and Interpretation. The classifier receives both:

$$f_{\text{pooled}} = \left[f_{\text{gap}} \parallel f_{\text{gmp}}\right] \in \mathbb{R}^{512} \tag{22}$$

The classification head receives both the Global Average Pooling (GAP) and Global Max Pooling (GMP) representations, allowing it to leverage complementary information about the fragment. GAP summarizes the overall activation distribution across positions and is therefore sensitive to the suppression of corrupted regions introduced by spatial attention. In contrast, GMP preserves the strongest activation within the fragment and remains robust even when many positions have been suppressed. When large portions of the fragment are corrupted, GAP values tend to decrease due to averaging over suppressed positions, while GMP continues to reflect the strongest remaining signals. By concatenating these two representations, the classifier receives both a global summary of the fragment and the strongest local activation patterns, providing richer information for classification under corrupted conditions. Why This Matters. Using only Global Average Pooling would produce diluted feature representations when large regions of the fragment are suppressed by attention, potentially weakening discriminative signals.

Conversely, Global Max Pooling alone would ignore the broader distribution of activations across the fragment. Combining GAP and GMP allows the model to retain both strong local activations and global contextual information, improving robustness when fragments contain partially corrupted regions. The ablation study confirms the effectiveness of this design, showing that removing split pooling reduces adversarial accuracy by 6.3 percentage points.

VI.1.6 Layer 6: Classification Head

Purpose. The final three fully connected layers map the 512-dimensional pooled features to 75-class file-type probabilities. By this stage, features have been carefully extracted and refined; the classification task is relatively straightforward mapping of rich representations to file-type labels. Architecture. The classification head consists of three dense layers: Dense1 (512→256 with ReLU + dropout), Dense2 (256→128 with ReLU + dropout), and Output (128→75 with softmax). This gradual dimensionality reduction from 512 to 75 prevents sudden compression that could discard information, allowing the model to progressively focus features on file-type discrimination. Dropout with probability 0.4 is applied after each ReLU activation, where 0.4 was selected based on preliminary hyperparameter tuning across rates of 0.3, 0.4, and 0.5. Label Smoothing. During training, label smoothing with smoothing factor 0.1 is applied. Instead of training on hard labels (e.g., [0,0,..,1,..,0] for PDF), the model trains on smoothed targets where the correct class receives probability 0.9 and other 74 classes share 0.1 probability equally. This prevents overconfidence on corrupted patterns, particularly important given the 97.5% adversarial sample composition in training data. Without smoothing, the model might learn to confidently predict incorrect file types when seeing corrupted byte patterns, reducing calibration. The Figure 3 shows the parameter summary for the DSAR-CNN model.

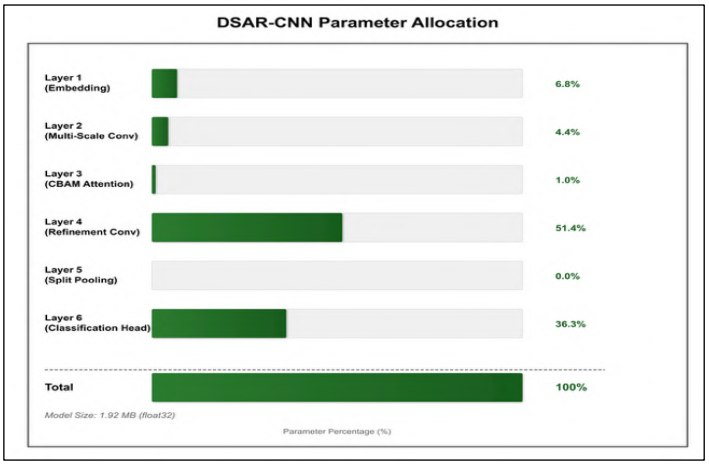


Figure 3: Parameter distribution in proposed DSAR-CNN model.
Source: Authors, (2026).

VI.2 ABLATION STUDY: COMPONENT CONTRIBUTIONS

To quantify the contribution of each architectural component, an ablation study was conducted in which individual components were removed from the full DSAR-CNN architecture and the resulting models were retrained from scratch. For each variant (e.g., without Position Embedding), the specified component was removed while all other architectural elements remained unchanged. Early stopping based on validation performance typically halted training before the maximum epoch limit, reducing overall training time while preserving fair comparisons across variants. When a component was removed, it was replaced with the simplest functional alternative required to maintain architectural compatibility (e.g., removing split pooling results in standard global average pooling). Model performance was then evaluated on the validation set using adversarial fragments. The contribution of each component is estimated as the difference between the full model accuracy (70.1%) and the accuracy of the corresponding ablated variant. Since all other experimental conditions are held constant, the observed performance differences primarily reflect the contribution of the removed component. Table 4 summarizes the results of this analysis.

Table 4: Ablation Study of DSAR-CNN Components: Adversarial Accuracy and Marginal Contribution on Validation Set.

Configuration	Adversarial Accuracy	Accuracy Drop
Full DSAR-CNN	70.10%	-
Without Position Embedding	65.30%	−4.8 pp
Without Multi-Scale Conv	62.80%	−7.3 pp
Without Channel Attention	66.50%	−3.6 pp
Without Spatial Attention	67.20%	−2.9 pp
Without CBAM (channel + spatial attention)	58.90%	−11.2 pp
Without Split Pooling	63.80%	−6.3 pp

Source: Authors, (2026).

This table reports accuracy on the validation set during model development to estimate the relative impact of each architectural component. The full DSAR-CNN achieves 70.1% accuracy on the validation set used for ablation analysis. Final evaluation on the independent test set (4.6M fragments) yields 68.4% accuracy, reflecting normal generalization differences between development and test datasets. The relative contribution percentages remain valid because they measure deltas between models trained and evaluated in the same setting (validation set).

Results show that different components contribute differentially. The combined CBAM module produces the largest performance drop when removed (−11.2 pp), followed by multi-scale convolution (−7.3 pp) and split pooling (−6.3 pp). Position embedding (+4.8 pp), channel attention (+3.6 pp), and spatial attention (+2.9 pp) provide smaller but still meaningful contributions. CBAM Synergy. The combined CBAM module provides a larger improvement (+11.2 pp) than the sum of the individual channel (+3.6 pp) and spatial (+2.9 pp) attention contributions. This indicates that the two attention mechanisms interact synergistically, where channel attention first suppresses noisy feature channels and spatial attention subsequently identifies reliable byte positions within the refined feature representation. Without this hierarchy, spatial attention operating on raw, unfiltered channels may find it harder to distinguish corruption from genuine patterns, which can limit its effectiveness. This hierarchical synergy is consistent with observations reported in prior attention mechanism studies and demonstrates that component interactions can produce amplified benefits beyond independent contributions.

VI.3 TRAINING CONFIGURATION

DSAR-CNN is trained on the 70% training allocation: 20,966,400 adversarial samples and 537,600 clean samples, totaling 21,504,000 fragments. The 2.50% clean sample inclusion, though minimal, helps DSAR-CNN learns robust features when detector false positives (FPR=4.54%) route clean fragments incorrectly to this branch. Hyperparameters: Adam optimizer (learning rate 0.001, reduced on plateau by factor 0.5), sparse categorical cross-entropy loss, batch size 256, early stopping (5-epoch patience), dropout 0.4, label smoothing 0.1, batch normalization, high momentum (0.99) to obtain stable running statistics given the large, highly skewed training distribution. Training converged within 35–40 epochs (~25–30 hours on modern GPU).

VI.4 PERFORMANCE SUMMARY

Standalone DSAR-CNN Performance (Test Set Results): DSAR-CNN achieves a 68.4% accuracy on adversarially perturbed fragments. And DSAR-CNN achieves 67.0% accuracy on clean fragments (compared to 71.1% for ByteRCNN), reflecting the trade-off inherent in training primarily on adversarial data.

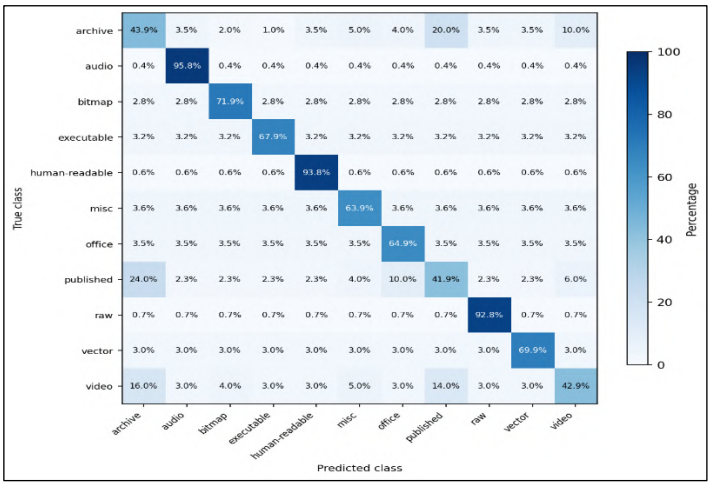


Figure 4: Confusion matrix of DSAR-CNN evaluated on the full test set. Given the large number of classes (75), individual file types were aggregated into their corresponding superclasses.
Source: Authors, (2026).

The confusion matrix in Figure 4 is computed over the test set of 4.6M fragments, which is dominated by adversarial samples. The average class-wise accuracy (~ 68%) is consistent with the reported adversarial accuracy of 68.4%. The performance follows typical FFC difficulty trends, with structured formats such as audio, text, and raw data showing high robustness, while high-entropy formats such as archives, published content, and video remain more challenging. The observed confusion patterns between these entropy-rich formats further reflect realistic behavior under adversarial conditions. The large robustness gain over ByteRCNN arises because DSAR-CNN is explicitly optimized for the same padding and bit-flip transformations used at test time, whereas ByteRCNN is trained only on clean fragments and therefore fails under severe distribution shift. By training on a large, supervised corpus of perturbed fragments and incorporating architectural bias toward perturbation-resilient features (multi-scale depthwise-separable convolutions, attention, and split pooling), DSAR-CNN learns to focus on the remaining informative bytes and down-weight corrupted regions. In this matched train–test setting, an improvement in adversarial accuracy over a clean-only baseline is expected and does not imply any form of data leakage.

VI.4.1 Attack Category-wise Performance

DSAR-CNN achieves substantial improvements across all attack categories. On padding attacks (15 variants), the model attains an average accuracy of 67.1%, compared to ByteRCNN's 11.2% baseline. Null-byte and random-byte padding are handled more effectively (68.4% and 67.8%) due to the clear boundary artifacts they introduce, while cross-file padding is more challenging (65.2%) because it contains authentic but contextually incorrect byte sequences from other file types. For bit-flip attacks, random bit-flip variants achieve an average accuracy of 70.0% versus ByteRCNN's 20.2%. Header-targeted bit-flip attacks reach 68.3% compared to 17.1%. These results indicate that DSAR-CNN provides strong robustness across both distributed and localized corruption patterns.

VI.5 ROLE IN TWO-STAGE PIPELINE

Within the complete defense system, DSAR-CNN serves as the specialized stage-2 classifier for adversarially perturbed fragments. When the adversarial detector flags a fragment as adversarial (91.34% recall), it is routed to DSAR-CNN rather than the baseline classifier. This routing mechanism enables preservation of baseline accuracy on clean data while achieving substantial robustness improvements. Fragments misclassified by the detector (false negatives) still receive some protection through ByteRCNN's partial robustness, while detector false positives (clean fragments routed to DSAR-CNN) experience modest accuracy reduction due to the 2.5% clean training data inclusion.

VII. EXPERIMENTAL EVALUATION AND PROPOSED FRAMEWORK PERFORMANCE

The complete defense system integrates three models into a sequential two-stage pipeline. A 512-byte fragment first passes through the adversarial detection model, which classifies it as clean or adversarial with 91.44% accuracy, 91.34% recall, and 95.46% specificity. Fragments predicted as clean are routed to ByteRCNN (preserving 71.1% baseline accuracy), while fragments flagged as adversarial are routed to DSAR-CNN (achieving 68.4% standalone adversarial accuracy). This routing mechanism enables the system to maintain high accuracy on genuine evidence while substantially improving robustness on perturbed inputs.

VII.1 END-TO-END PIPELINE PERFORMANCE

VII.1.1 Clean Data Performance

On 115,200 clean test fragments, the pipeline achieves 70.91% accuracy, a 0.19 pp penalty compared to the 71.1% undefended baseline. This metric is derived from the weighted average of clean fragments correctly routed to ByteRCNN (True Negatives) and those misrouted to DSAR-CNN (False Positives):

$$Acc_{clean}^{pipeline} = \left(Acc_{clean}^{Byte} \times \text{Specificity}\right) + \left(Acc_{clean}^{DSAR} \times \text{FPR}\right) \tag{23}$$

Substituting the experimental values:

$$70.91\% \approx (71.1\% \times 0.9546) + (67.0\% \times 0.0454) \tag{24}$$

The minimal penalty demonstrates that detection-based defense enables preservation of baseline accuracy on genuine evidence while adding robustness to adversarial inputs.

VII.1.2 Adversarial Data Performance

On 4,492,800 adversarial test fragments across all 39 attack variants, the pipeline achieves 63.84% accuracy, compared to 15.8% for the undefended baseline. The pipeline accuracy is calculated as the weighted sum of adversarial fragments correctly routed to DSAR-CNN (True Positives) and those misclassified as clean (False Negatives):

$$Acc_{adv}^{pipeline} = \left(Acc_{adv}^{DSAR} \times \text{Recall}\right) + \left(Acc_{adv}^{Byte} \times \text{FNR}\right) \tag{25}$$

Substituting the detector performance:

$$63.84\% \approx (68.4\% \times 0.9134) + (15.8\% \times 0.0866) \tag{26}$$

This calculation confirms that the system's robustness is primarily driven by the robust classifier (DSAR-CNN), with graceful degradation provided by the baseline classifier for the 8.66% of undetected attacks.

VII.1.3 Mixed-Threat Scenario (90% Clean / 10% Adversarial)

In operational cybersecurity systems, malicious activity typically constitutes a small minority of total observations, a trend documented in large-scale intrusion detection studies such as CICIDS-2017 and related imbalance analyses by Buczak and Guven and Zhao et al [35-37]. For instance, the CICIDS-2017 benchmark - one of the most widely used intrusion detection datasets - contains predominantly benign traffic with attack flows forming only a minority of total connections, and real-world deployment reports indicate even more skewed benign-to-attack ratios in production networks [35]. Although no published adversarial prevalence rates exist specifically for forensic fragment recovery scenarios, the 90/10 clean-to-adversarial ratio adopted here therefore reflects a realistic attack-sparse deployment assumption that is consistent with empirical observations from these adjacent security domains [36] [37]. The pipeline achieves 70.20% accuracy on a typical mixed dataset (90% clean, 10% adversarial). This metric combines the pipeline's clean and adversarial performance calculated above:

$$Acc_{mixed} = \left(Acc_{clean}^{pipeline} \times P_{clean}\right) + \left(Acc_{adv}^{pipeline} \times P_{adv}\right) \tag{27}$$

$$70.20\% = (70.91\% \times 0.90) + (63.84\% \times 0.10) \tag{28}$$

This represents a 4.63 pp improvement over the undefended baseline mixed accuracy, which is calculated similarly:

$$Acc_{mixed}^{baseline} = (71.1\% \times 0.90) + (15.8\% \times 0.10) = 65.57\% \tag{29}$$

Operationally, this improvement translates to approximately 46 additional correctly classified fragments per 1,000 processed - a meaningful enhancement for large-scale forensic investigations.

VII.2 COMPARISON WITH ADVERSARIAL TRAINING AND PIPELINE PERFORMANCE METRICS SUMMARY

To establish a direct comparison with the dominant defense paradigm, standard adversarial training was implemented on the baseline ByteRCNN architecture using a balanced 50/50 clean-adversarial training mix, following the standard adversarial training protocol [24]. The training dataset comprised 1,075,200 samples: 537,600 clean fragments and 537,600 adversarial fragments sampled uniformly across all 39 attack variants (approximately 13,784 samples per variant). Adversarial samples were generated exclusively from the training partition, and all training configurations (architecture, optimizer, and hyperparameters) were kept identical to the baseline to ensure a fair architectural comparison. The balanced ratio inherently constrains training volume to 1,075,200 samples, compared to the 21,504,000-fragment set used by the defense pipeline at its natural 39:1 adversarial-to-clean ratio. This asymmetry reflects a fundamental distinction between the two paradigms: adversarial training requires balanced class exposure to avoid majority-class collapse, whereas detection and robust classification models are designed to operate on realistic imbalanced distributions. Scaling adversarial training to match pipeline volume at 50/50 balance would require 20× oversampling of the clean fragment pool, introducing artificial duplication rather than genuine training signal. The adversarially trained model was evaluated on the identical test set of 4,608,000 fragments used throughout this study. Table 6 presents the comparative results.

Table 5: Comparative Performance Metrics of the Proposed Pipeline Against Baseline and Adversarial Training Approaches.

Metric	Clean	Adversarial	Mixed (90/10)
Undefended baseline	**71.10%**	15.80%	65.57%
Adversarial Training (50/50)	66.60%	51.80%	65.12%
Defense pipeline (Proposed)	70.91%	**63.84%**	**70.20%**
Improvement (Proposed vs. Adv. Training)	+4.31 pp	+12.04 pp	+5.08 pp

Source: Authors, (2026).

Adversarial training does improve robustness, increasing adversarial accuracy from 15.8% to 51.8% (a gain of 36.0 percentage points). However, this improvement comes at the cost of a 4.5 percentage point reduction in clean accuracy (from 71.1% to 66.6%), confirming the accuracy-robustness trade-off widely reported in adversarial learning literature. A critical observation emerges from the mixed-scenario analysis. In realistic forensic environments where 90% of fragments are benign and 10% are adversarially perturbed, adversarial training achieves a weighted accuracy of 65.12%, which is slightly lower than the undefended baseline (65.57%). This occurs because the reduction in clean accuracy outweighs the robustness gains when adversarial samples constitute a minority of the data. The proposed detection-based pipeline achieves superior performance across all evaluation settings. Compared to adversarial training, the pipeline improves clean accuracy by 4.31 percentage points (70.91% vs. 66.6%), adversarial accuracy by 12.04 percentage points (63.84% vs. 51.8%), and mixed-scenario accuracy by 5.08 percentage points (70.20% vs. 65.12%). These results demonstrate that the detect-then-classify routing strategy effectively mitigates the accuracy-robustness trade-off by preserving baseline performance on clean inputs while improving robustness against adversarial fragments. All models were trained once due to computational constraints. However, the large test set size (4.6M fragments) yields narrow confidence intervals: the 95% CI for the pipeline's mixed accuracy of 70.20% is [70.16%, 70.24%] and for adversarial training's 65.12% is [65.08%, 65.16%], confirming the 5.08 pp difference is statistically significant ($p < 0.001$, two-proportion z-test). The training volume differs between adversarial training and the proposed pipeline, reflecting differences in how the two approaches are typically implemented. In adversarial training, balanced clean-adversarial datasets are commonly used to maintain stable optimization and avoid oversampling artifacts when scaling to large attack sets. In contrast, the proposed pipeline leverages the full adversarial dataset through a detection-routing mechanism. Consequently, the results should be interpreted as a comparison between the proposed framework and adversarial training under its standard configuration rather than a strictly matched-volume experimental setting. To ensure that the reported results are not contingent on this specific operating point, Table 6 provides a sensitivity analysis across a range of adversarial prevalence rates (p). The formula for each cell is:

$$Acc_{mixed} = (Acc_{clean} \times (1 - \mathrm{p})) + (Acc_{adv} \times \mathrm{p}) \tag{30}$$

Table 6: Sensitivity of Pipeline and Adversarially Trained Baseline Accuracies to Adversarial Prevalence.

Adversarial Prevalence	Pipeline Accuracy	AT Baseline	Pipeline Lead over AT
0% (all clean)	70.91%	66.60%	+4.31 pp
5%	70.56%	65.86%	+4.70 pp
10% (primary)	70.20%	65.12%	+5.08 pp
20%	69.50%	63.64%	+5.86 pp
30%	68.79%	62.16%	+6.63 pp
50% (balanced)	67.38%	59.20%	+8.18 pp

Source: Authors, (2026).

The proposed pipeline outperforms the adversarial training baseline across all tested prevalence rates from 0% to 50%. Notably, the pipeline's advantage over adversarial training increases with adversarial prevalence (from +4.31 pp at 0% to +8.18 pp at 50%), demonstrating that the detection-routing mechanism provides progressively greater benefit as adversarial activity increases."

VII.3 ROBUSTNESS BY ATTACK CATEGORY

Performance across individual attack categories demonstrates that the proposed pipeline provides consistent robustness improvements over both the undefended baseline and the adversarially trained model. The undefended baseline is included to quantify the severity of adversarial degradation and to show the extent of robustness recovery. However, the primary comparison for defense effectiveness is against adversarial training, which represents the standard defense approach. Figure 5 visualizes these per-category results.

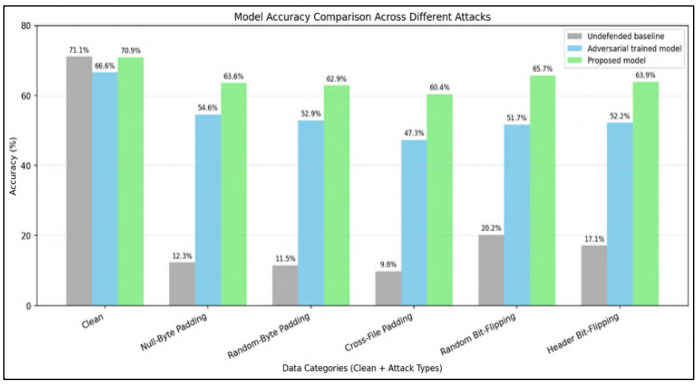


Figure 5: Model accuracy comparison across attack categories for the undefended baseline, adversarial training and proposed pipeline. Source: Authors, (2026).

On clean data, the proposed pipeline achieves an accuracy of 70.9%, which is comparable to the baseline performance of 71.1% and substantially higher than the adversarially trained model (66.6%). This result confirms that the detection-based routing strategy preserves clean-data performance and avoids the accuracy degradation typically associated with adversarial training. Under padding-based attacks, which introduce large structural perturbations and are the most damaging to the baseline model, the proposed approach maintains strong and stable performance. For null-byte padding, accuracy improves from 12.3% (baseline) and 54.6% (adversarial training) to 63.6%. Random-byte padding shows a similar trend, increasing from 11.5% and 52.9% to 62.9%, while cross-file padding improves from 9.8% and 47.3% to 60.4%. These results represent improvements of approximately 8-13 percentage points over adversarial training. Although cross-file padding remains the most challenging category due to the insertion of realistic but contextually misleading byte patterns, the proposed pipeline maintains substantially higher robustness than both comparison models. For bit-flip attacks, which introduce localized corruption rather than large-scale structural changes, the proposed approach again achieves the highest performance. Random bit-flip accuracy increases from 20.2% (baseline) and 51.7% (adversarial training) to 65.7%, while header-targeted bit-flips improve from 17.1% and 52.2% to 63.9%. The gains over adversarial training range from approximately 11 to 14 percentage points, indicating that the detect-then-classify strategy effectively isolates perturbed inputs and enables more accurate classification through the specialized DSAR-CNN model. Two consistent trends emerge from this analysis. First, padding-based perturbations cause more severe degradation in the undefended baseline than bit-flip attacks, reflecting their larger impact on the underlying fragment structure and statistical distribution. Second, the proposed pipeline delivers stable and balanced performance across all attack categories, outperforming adversarial training while maintaining near-baseline accuracy on clean data. This behavior demonstrates that the approach effectively improves robustness without incurring the accuracy-robustness trade-off commonly observed in conventional adversarial training approaches.

VIII. DISCUSSION AND FUTURE WORK

VIII.1 SIGNIFICANCE AND ARCHITECTURAL ADVANTAGES

This work addresses two important limitations in current file fragment classification research. First, it provides a systematic vulnerability analysis of state-of-the-art FFC models under byte-level perturbations. Second, it explores a detection-based defense strategy designed to improve robustness while preserving clean-data accuracy: 70.91% clean accuracy (−0.19 pp penalty) with 63.84% adversarial accuracy, contrasting sharply with the 4.5% clean accuracy penalty empirically observed in the adversarial training baseline (Section 7.2). The architecture is specifically tailored to byte-level FFC. Multi-scale depthwise separable convolution (k=3, 7, 15) matches attack granularities: k=3 for scattered bit-flips, k=7 for local disruptions, k=15 for padding boundaries. This scale-matching is unnecessary in image defenses where perturbations are uniform. Split pooling addresses byte-level dilution: when spatial attention suppresses corrupted positions, GMP preserves strongest signals while GAP measures dilution, enabling the classifier to infer corruption implicitly. Learnable position embeddings exploit positional attack structure (tail-biased padding) more efficiently than fixed encodings.

VIII.2 LIMITATIONS AND FUTURE WORK

Evaluation Limitations. The current evaluation focuses on black-box attacks. White-box adaptive attacks where adversaries have full model access are not tested. In theory, attackers could exploit the learned position embeddings by shifting padding to the fragment head instead of the tail or target the attention mechanism directly. Certified defense approaches like randomized smoothing or IBP could address this but implementing them across 30 million samples is computationally expensive and remains as future work. Multi-seed experiments would better characterize model stability, and latency measurements are theoretical rather than measured across different hardware platforms. A key limitation of this evaluation is that each attack variant is applied independently to clean fragments, and do not study composite adversaries that combine padding and bit-flip perturbations within the same fragment, which may represent a stronger and more realistic threat model in operational settings.

Architectural Limitations. The position embeddings are specifically learned for tail-biased padding attacks. If adversaries instead corrupt the fragment head, the positional priors might degrade performance. The architecture was only tested on 512-byte fragments - generalization to 256-byte or 1024-byte sizes remains unclear. Cross-dataset evaluation on alternative benchmarks like DFRWS would be valuable. Finally, the 39 attack variants tested (padding and bit-flips) do not cover every possible byte-level perturbation strategy, so robustness to novel attacks is uncertain. Future Directions. Priority work includes testing head padding and random-position attacks to validate that position embeddings learn genuine file structure rather than memorizing attack positions; extending the detector to classify attack types for forensic attribution; developing certified robustness guarantees; evaluating on alternative datasets and fragment sizes; and integrating with commercial forensic tools for real-world validation. Modeling white-box adaptive attacks would also be important to understand worst-case robustness.

IX. CONCLUSIONS

File fragment classification remains essential to digital forensics, yet the vulnerability assessment uncovered that the state-of-the-art model accuracy collapses from 71.1% to 15.8% when facing byte-level adversarial perturbations. Testing across 39 attack variants (padding and bit-flip strategies) and five distinct attack categories reveals this vulnerability is systematic and universal, not confined to edge cases. The threat is real: simple, format-agnostic byte manipulations suffice to compromise classification integrity, rendering current forensic systems unreliable in adversarial contexts. The proposed two-stage detection-then-classify pipeline substantially mitigates this threat (70.91% clean, 63.84% adversarial, 70.20% in realistic mixed scenarios with 90% clean and 10% adversarial fragments). The improvement is consistent across all attack categories: 9 pp for null padding, 10 pp for random byte padding, 13.1 pp for cross-file padding, 14 pp for random bit-flip, and 11.7 pp for header-targeted bit-flip as compared to the adversarially trained model values. This recovery comes with minimal clean accuracy penalty (0.19 pp) too. The architectural innovations underlying this defense - multi-scale depthwise separable convolution, hierarchical CBAM attention, split pooling, and learnable position embeddings - are tailored to byte-sequence processing and extend beyond file fragment classification to malware detection, network traffic analysis, and other security domains relying on byte-level feature extraction. The detection-based routing strategy sidesteps the accuracy-robustness tradeoff plaguing adversarial training by preserving baseline performance on genuine evidence while routing adversarial inputs to specialized classifiers. These results demonstrate that detection-based routing strategies can substantially improve robustness against byte-level perturbations while preserving clean-data performance. The proposed framework therefore provides a promising direction for strengthening the resilience of file fragment classification systems against adversarial manipulation.

X. AUTHOR'S CONTRIBUTION

Conceptualization: Teena Mary and Sreeja C S.
Methodology: Teena Mary.
Investigation: Teena Mary.
Discussion of results: Teena Mary and Sreeja C S.
Writing – Original Draft: Teena Mary.
Writing – Review and Editing: Teena Mary and Sreeja C S.
Resources: Teena Mary and Sreeja C S.
Supervision: Sreeja C S.
Approval of the final text: Teena Mary and Sreeja C S.

XI. REFERENCES

[1] M. Guzhov and C. T. Wirth, "Transformer-based file fragment type classification for file carving in digital forensics", European Conference on Cyber Warfare and Security, vol. 24, no. 1, p. 169, Jun. 2025. doi: 10.34190/eccws.24.1.3552.

[2] S. Liu, J. G. Park, H. Kim, and J. H. Hong, "A cross-attention multi-scale performer with Gaussian bit-flips for file fragment classification", IEEE Trans. Inf. Forensics Secur., vol. 20, p. 2109, Jan. 2025. doi: 10.1109/tifs.2025.3539527.

[3] S. Yan, J. Ren, W. Wang, L. Sun, W. Zhang, and Q. Yu, "A survey of adversarial attack and defense methods for malware classification in cyber security", IEEE Commun. Surv. Tutor., vol. 25, no. 1, p. 467, Nov. 2022. doi: 10.1109/comst.2022.3225137.

[4] K. Aryal, M. Gupta, and M. Abdelsalam, "A survey on adversarial attacks for malware analysis", arXiv, Jan. 2021. doi: 10.48550/arxiv.2111.08223.

[5] Y. Li, M. Cheng, C. Hsieh, and T. C. M. Lee, "A review of adversarial attack and defense for classification methods", The American Statistician, vol. 76, no. 4, p. 329, Nov. 2021. doi: 10.1080/00031305.2021.2006781.

[6] L. Demetrio, B. Biggio, G. Lagorio, F. Roli, and A. Armando, "Functionality-preserving black-box optimization of adversarial Windows malware", IEEE Trans. Inf. Forensics Secur., vol. 16, p. 3469, Jan. 2021. doi: 10.1109/tifs.2021.3082330.

[7] K. Skračić, J. Petrović, and P. Pale, "ByteRCNN: Enhancing file fragment type identification with recurrent and convolutional neural networks", IEEE Access, vol. 11, p. 138176, Jan. 2023. doi: 10.1109/access.2023.3340441.

[8] Z. Fang, J. Wang, J. Geng, Y. Zhou, and X. Kan, "A3CMal: Generating adversarial samples to force targeted misclassification by reinforcement learning", Appl. Soft Comput., vol. 109, p. 107505, May 2021. doi: 10.1016/j.asoc.2021.107505.

[9] K. Shaukat, S. Luo, and V. Varadharajan, "A novel method for improving the robustness of deep learning-based malware detectors against adversarial attacks", Eng. Appl. Artif. Intell., vol. 116, p. 105461, Oct. 2022. doi: 10.1016/j.engappai.2022.105461.

[10] D. Li and Q. Li, "Adversarial deep ensemble: Evasion attacks and defenses for malware detection", IEEE Trans. Inf. Forensics Secur., vol. 15, p. 3886, Jan. 2020. doi: 10.1109/tifs.2020.3003571.

[11] D. Li et al., “A framework for enhancing deep neural networks against adversarial malware”, IEEE Trans. Netw. Sci. Eng., vol. 8, no. 1, p. 736, Jan. 2021. doi: 10.1109/tnse.2021.3051354.

[12] M. McDaniel and M. Heydari, “Content based file type detection algorithms”, Proc. Hawaii Int. Conf. Syst. Sci., Jan. 2003. doi: 10.1109/hicss.2003.1174905.

[13] G. Mittal, P. Korus, and N. Memon, ‘‘FiFTy: Large-scale file fragment type identification using convolutional neural networks,’’ IEEE Trans. Inf. Forensics Security, vol. 16, pp. 28–41, 2021, doi: 10.1109/TIFS.2020.3004266.

[14] M. Felemban, M. Ghaleb, K. M. Saaim, S. M. Al-Saleh, and A. Almulhem, “File fragment type classification using light-weight convolutional neural networks”, IEEE Access, vol. 12, p. 157179, Jan. 2024. doi: 10.1109/access.2024.3486180.

[15] Y. Wang, W. Liu, K. Wu, K. Yap, and L. Chau, “Intra- and inter-sector contextual information fusion with joint self-attention for file fragment classification”, Knowl.-Based Syst., vol. 291, p. 111565, Feb. 2024. doi: 10.1016/j.knosys.2024.111565.

[16] P. Penrose, R. Macfarlane, and W. J. Buchanan, “Approaches to the classification of high entropy file fragments”, Digit. Invest., vol. 10, no. 4, p. 372, Oct. 2013. doi: 10.1016/j.diin.2013.08.004.

[17] Y. Fratantonio et al., “MAGIKA: AI-powered content-type detection”, Proc. Int. Conf. Softw. Eng., p. 2638, Apr. 2025. doi: 10.1109/icse55347.2025.00158.

[18] I. Goodfellow, J. Shlens, and C. Szegedy, “Explaining and harnessing adversarial examples”, arXiv, Dec. 2014. [Online]. Available: https://arxiv.org/pdf/1412.6572.pdf.

[19] B. Kolosnjaji et al., “Adversarial malware binaries: Evading deep learning for malware detection in executables”, Proc. Eur. Signal Process. Conf., p. 533, Sep. 2018. doi: 10.23919/eusipco.2018.8553214.

[20] K. Lucas, S. Pai, W. Lin, L. Bauer, M. Reiter, and M. Sharif, “Adversarial training for raw-binary malware classifiers”, arXiv, 2019. [Online]. Available: https://arxiv.org/abs/1907.07149.

[21] F. Kreuk, A. Barak, S. Aviv, M. Baruch, B. Pinkas, and J. Keshet, "Deceiving end-to-end deep learning malware detectors using adversarial examples," arXiv preprint arXiv:1802.04528, 2019.

[22] L. Kummer, S. Moustafa, N. M. Kriege, and W. N. Gansterer, “Attacking graph neural networks with bit flips: Weisfeiler and Lehman go indifferent”, arXiv, Nov. 2023. doi: 10.48550/arxiv.2311.01205.

[23] R. Taheri, M. Shojafar, F. Arabikhan, and A. Gegov, “Unveiling vulnerabilities in deep learning-based malware detection: Differential privacy driven adversarial attacks”, Comput. Secur., vol. 146, p. 104035, Aug. 2024. doi: 10.1016/j.cose.2024.104035.

[24] H. Zhang, Y. Yu, J. Jiao, E. P. Xing, L. E. Ghaoui, and M. I. Jordan, “Theoretically principled trade-off between robustness and accuracy”, arXiv, Jan. 2019. doi: 10.48550/arxiv.1901.08573.

[25] D. Tsipras, S. Santurkar, L. Engstrom, A. Turner, and A. Madry, “Robustness may be at odds with accuracy”, arXiv, Mar. 2022. doi: 10.48550/arxiv.1805.12152.

[26] D. Meng and H. Chen, “MagNet: A two-pronged defense against adversarial examples”, arXiv, May 2017. doi: 10.48550/arxiv.1705.09064.

[27] A. Goodge, B. Hooi, S. K. Ng, and W. S. Ng, “Robustness of autoencoders for anomaly detection under adversarial impact”, Proc. Int. Joint Conf. Artif. Intell. (IJCAI), p. 1244, Jul. 2020. doi: 10.24963/ijcai.2020/173.

[28] C. Xie, Y. Wu, L. van der Maaten, A. Yuille, and K. He, “Feature denoising for improving adversarial robustness”, Proc. IEEE/CVF Conf. Comput. Vis. Pattern Recognit. (CVPR), p. 501, Jun. 2019. doi: 10.1109/cvpr.2019.00059.

[29] J. Hu, L. Shen, and G. Sun, “Squeeze-and-excitation networks”, Proc. IEEE/CVF Conf. Comput. Vis. Pattern Recognit. (CVPR), p. 7132, Jun. 2018. doi: 10.1109/cvpr.2018.00745.

[30] S. Woo, J. Park, J. Lee, and I. S. Kweon, “CBAM: Convolutional block attention module”, in Lect. Notes Comput. Sci., Springer, 2018, p. 3. doi: 10.1007/978-3-030-01234-2_1.

[31] P. Agrawal, N. S. Punn, S. K. Sonbhadra, and S. Agarwal, “Impact of attention on adversarial robustness of image classification models”, in Proc. IEEE Int. Conf. Big Data, Dec. 2021, p. 3013. doi: 10.1109/bigdata52589.2021.9671889.

[32] D. Zoran, M. Chrzanowski, P.-S. Huang, S. Gowal, A. Mott, and P. Kohl, “Towards robust image classification using sequential attention models”, Proc. IEEE/CVF Conf. Comput. Vis. Pattern Recognit. (CVPR), p. 9480, Jun. 2020. doi: 10.1109/cvpr42600.2020.00950.

[33] H. Yakura, S. Shinozaki, R. Nishimura, Y. Oyama, and J. Sakuma, “Neural malware analysis with attention mechanism”, Comput. Secur., vol. 87, p. 101592, Aug. 2019. doi: 10.1016/j.cose.2019.101592.

[34] W. K. Al-Ghanem, E. U. H. Qazi, T. Zia, M. H. Faheem, M. Imran, and I. Ahmad, “MAD-ANET: Malware detection using attention-based deep neural networks”, Comput. Model. Eng. Sci., vol. 143, no. 1, p. 1009, Jan. 2025. doi: 10.32604/cmes.2025.058352.

[35] I. Sharafaldin, A. Habibi Lashkari, and A. A. Ghorbani, "Toward Generating a New Intrusion Detection Dataset and Intrusion Traffic Characterization," in Proc. 4th International Conference on Information Systems Security and Privacy (ICISSP), Portugal, January 2018.

[36] A. L. Buczak and E. Guven, “A survey of data mining and machine learning methods for cyber security intrusion detection”, IEEE Commun. Surv. Tutor., vol. 18, no. 2, p. 1153, Oct. 2015. doi: 10.1109/comst.2015.2494502.

[37] G. Zhao, P. Liu, K. Sun, Y. Yang, T. Lan, and H. Yang, “Research on data imbalance in intrusion detection using CGAN”, PLoS One, vol. 18, no. 10, Art. no. e0291750, 2023. doi: 10.1371/journal.pone.0291750.

Journal of Engineering and Technology for Industrial Applications

ISSN ONLINE: 2447-0228

ITEGAM-JETIA

Manaus, v.12 n.60, p.584-595 July/August, 2026.
DOI: https://doi.org/10.5935/jetia.v12i60.3915

RESEARCH ARTICLE OPEN ACCESS

FORECASTING BITCOIN PRICE MOVEMENTS USING HISTORICAL DATA

Ammar Ahmed Othman *[1], Seddiq Hassan Al-Banna Ali [2] and Mohammed Bakr Youssef [3]

[1]Ministry of Higher Education and Scientific Research - University of Mosul - College of Fine Arts. Iraq
[2, 3]Ministry of Higher Education and Scientific Research - University of Mosul - College of Computer Science and Mathematics. Iraq

[1]https://orcid.org/0009-0003-5736-9183, [2]https://orcid.org/0009-0006-1178-3639, [3]https://orcid.org/0009-0001-4646-0796

E-mail: *ammar@uomosul.edu.iq, sedeeq.alkhazraji@uomosul.edu.iq, Mohammed.bkr@uomosul.edu.iq

ARTICLE INFO

Article History
Received on: March 05, 2026
Reviewed on: April 04, 2026
Accepted on: May 01, 2026
Published on: July 31, 2026

Keywords:
Bitcoin Price Prediction,
Cryptocurrency Forecasting,
Long Short-Term Memory (LSTM),
Technical Indicators,
Time-Series Analysis,
Cryptocurrency Volatility,
Machine Learning.

ABSTRACT

In the digital currency, Bitcoin (BTC) is called the gold of the digital currency. It is possible to make some profits in trading of bitcoins, though this market is a very illiquid market and it is very challenging to determine the price of a bitcoin. The current work uses historical data and technical indicators to predict Bitcoin prices in a broad approach. BTC-USD price data were obtained using Yahoo Finance API and covered from 01/01/2015 till 07/01/2024. The concept of feature engineering was applied to improve the dataset by including vital financial characteristics, including Moving Averages, RSI, and Bollinger Bands for higher forecasting precision. The forward-looking model for the Bitcoin price was developed using machine learning and deep learning algorithms. The efficiency of the model was assessed with the help of Mean Absolute Error (MAE), Mean Squared Error (MSE), and Root Mean Squared Error (RMSE). The overall values of Mean Absolute Error, Mean Squared Error, and Root Mean Squared Error were 0.0062, 8.39e-05 and 0.0092 respectively which suggest that the proposed model is accurate in forecasting the future prices.

Copyright ©2026 by authors and Galileo Institute of Technology and Education of the Amazon (ITEGAM). This work is licensed under the Creative Commons Attribution International License (CC BY 4.0).

I. INTRODUCTION

The market of the crypto currency is one of the biggest and influential markets in the world of the financial market, where trader from all over the world invest in the digital currency. Trade in this market serves multiple objectives from acting as the market that provides the required liquidity for currencies as well as enhancing the provision of the export currency for the export of goods and services to other countries to offer individuals and institutions the ability to make attractive returns from speculative trades in the global foreign exchange market. The crypto market is a large and highly liquid market in terms of trading volume, which means that investors prefer such a market when they are acting to earn quick profits [1]. This current market also brings the chance to diversify and get returns due to global market fluctuations. Taking into account the processes associated with development of technology and growth of investment conscious, trading in the currency market is not only the profession of the experts but also the area freely accessible to everyone willing to invest and manage risks more effectively [2]. The financial technology has been experiencing drastic changes especially from the beginning of the new century, and has greatly influenced the world's financial structure.

From these contributors are fairly introduced the development of the digital currency which is an additional form of the money and financial transactions. New technology in money adoption, known as digital currencies based on encryption and decentralization have received other unusual attention in both field of finance and academic mediation [3]. Digital currencies are one of the financial assets that utilize encryption and common transaction denominations to generate new ones. They are not like conventional money as they are not controlled by a central banking network, but they are documented through a network of nodes. These are currencies based on block chain technology, a transparent and secure database of currencies, hence efficient and free from fraud [4]. Bitcoin, launched in 2008, is the first digital currency that introduced the concept of blockchain as a decentralized means of recording transactions. Despite its humble beginnings, it has proven its ability to greatly influence global financial markets, leading to the emergence of many other digital currencies such as Ethereum, Ripple, and Litecoin [5].

II. DIGITAL CURRENCIES

Another aspect of the digital currencies is that the control of the type or kind of money is not centralized there is no central authority that dictates the type of money to be issued in circulation or how it will be managed. Rather, digital currencies operate through a group of people to assure the transaction's safety and increase transparency. Further, these currencies are characterized by rapidity of the financial operations and the highest level of protection due to the use of complex encryption algorithms that eliminate the need for the use of conventional financial mediators across the border [6]. Digital currencies can be primarily categorized into three main types. Cryptocurrencies: Examples are Bitcoin and Ethereal, through which value is transferred and stored. For example, Bitcoin is the first virtual currency designed to act as an alternative currency. , whereas Ethereal is not only a digital currency but also a platform for developing decentralized applications and smart contracts [7].

1. Tokens: These are based on technologies such as Ethereum and are used for various uses starting from funding projects, offering specific services or products, up to emulating traditional shares. Such tokens are Tether (USDT) and Chainlink (LINK) [8].
2. Stablecoins: meant to be less volatile, they are most often anchored on a conventional currency, for instance, the US dollar. Some of the centralized stablecoins include Tether, which is also known as USDT, and USD Coin also known as USDC. These currencies is expected to reduce the volatile nature, which is common with most of the other digital currencies for use in trading and other economic activities [9].

III. DIFFICULTY IN PREDICTING CRYPTOCURRENCY PRICES

Depending on the probability of cryptocurrency price prediction is still one of the biggest prospects that affects the investors and analysts in this highly volatile market. Currency prices are volatile and vary significantly and unpredictably, thus, predicting cryptocurrency is not an easy task which depends on the understanding of this market. Among the influential factors are the following [10]:

1. Price volatility: In general, the prices of cryptocurrencies fluctuate, which is much higher than the price fluctuations in traditional financial markets. Such a situation is explained by several reasons: Fluctuations in supply and demand, large transactions, and the emotional state of a trader. These fluctuations make it challenging to adopt standardized models to project the cryptocurrency prices faithfully [11].
2. Lack of historical data: Generally, historical information related to cryptocurrencies is limited and of a shorter time span as compared to traditional markets. This lack of long-term data hampers the analysts in the construction of a forecasting system based on quantitative analysis over a long span of time; the long-term trends cannot be predicted [10].
3. Psychological and market factors: The prices of various cryptocurrencies are greatly influenced by psychological factors. It can be also defined that news, rumors and market expectations can produce fluctuations in the price. There is empirical evidence that fast trading based on news affects the prices of stocks in a big way [12].
4. Technological developments and updates: It is clear that the further technological evolution and updates affect the projects related to cryptocurrencies. Alterations in the protocols, the security measures, or the nature of the technology in any way can result in shifts in the perceived market value of cryptocurrencies [1].
5. Regulatory considerations: Cryptocurrencies are still a new form of currency with new local and international regulatory frameworks and laws being passed often. Cryptocurrencies are unpredictable since new regulatory actions or changes in government benchmarks can impact the token's price [13].
6. Fraudulent activities and security risks: The cryptocurrency market is under high risks of fraud and security threats. These activities lead to the emergence of a situation that can dramatically change the prices of cryptocurrencies and, therefore, makes it more complicated to foresee them with a high level of certainty [14].
7. Inter-currency interaction: Often particular cryptocurrency prices like for Bitcoin may affect the prices of other cryptocurrencies. Transactions between various digital currencies create fluctuations which can be unpredictable [15].

IV. LITERATURE REVIEW

1. Deep Learning Models for Bitcoin Prediction Using Hybrid: This paper utilized more than 50,000 hourly Bitcoin price data from the period of May 2018 to January 2024 The study used complex models such as gradient descent, attention mechanisms, LSTM, and ANNs. As it was developed it complement LSTM with attention mechanisms and integrated gradient-specific optimization to further improve the predictive power of the model. The results of the work show that these hybrid models, and more specifically with the gradient-specific optimization, enhance the Bitcoin price prediction by utilizing the advantages of each approach discussed above [16].
2. Bitcoin price prediction using Deep Learning Algorithm: The goal of this paper is to forecast the Bitcoin USD price using a Bayesian Recurrent Neural Network and Long Short Term Memory Network. Using LSTM, the model had an accuracy of 52% and 8% RMSE which is better than conventional ARIMA models. Furthermore, a GRU model was applied, and utilizing deep learning models, the best results obtained with an enhancement of 94,7% in the GPU training time [17].
3. Bitcoin Price Prediction Based on Deep Learning Methods: This paper aimed at enhancing the performance of the deep learning techniques such as min-max normalization and the Adam optimizer in enhancing the accuracy of stock market prediction. When employing 56,832 observations of Bitcoin's price, the authors determined that MLP was ineffective because it lacked memory. On the other hand, LSTM and GRU models with past memory, gave better predictions [18].

V. ARTIFICIAL INTELLIGENCE AND PREDICTION

AI has achieved a lot in the area of prediction including in the areas of markets, and health, weather among other areas not mentioned. Some of the artificial intelligence methods and techniques found in prediction include the following [19].

V.1 MACHINE LEARNING (ML)

Machine learning ML is a branch in artificial intelligence that involves the use of algorithms to make predictions or decisions from data without being programmed. ML can be categorized into the following two main types [20]:

Supervised Learning: Supervised learning involves the use of training sets that is, the inputs are associated with their respective outputs or labels. During the training phase, the model acquires the knowledge of how to convert inputs into outputs, while during the testing phase, it is assessed. This method is widely applied to problems where historical labeled data is available Description of Supervised learning algorithms is shown in the Table (1) [21].

Table 1: Description of Supervised Learning Algorithms.

Algorithm	Description	Applications
Linear Regression	Establishes a linear relationship between input features and a continuous target variable.	Predicting continuous variables, e.g., house prices, stock prices.
Support Vector Machines (SVM)	Finds a hyperplane that best separates data points into distinct classes while maximizing the margin.	Image classification, spam detection, and medical diagnosis.
Decision Trees	Splits data into subsets based on feature values, creating a tree-like structure for prediction.	Fraud detection, loan approval, and risk assessment.
Random Forests	Combines multiple decision trees to improve predictive performance and reduce overfitting.	Credit scoring, stock market prediction, and customer segmentation.

Source: [22].

The most common types of machine learning methods are the supervised learning algorithms due to their use of labelled datasets which allow the models to be trained to directly map the input variables to the known outputs. The algorithms used in predictive analytics and classification include Linear Regression, Support Vector Machines, Decision Trees, and Random Forests. The quality and quantity of labeled training data are also highly relied upon to determine their effectiveness. Such techniques are especially useful in the areas, where one has the data about the past and is capable of learning patterns in order to make predictions in the future. But this can be disadvantageous with supervised learning models as they can overfit or undergeneralize when the training data is smaller or extremely skewed.

Unsupervised Learning: In unsupervised learning the model operates using data that do not contain any labeling and is aimed at finding patterns, correlations, or structures of data without prior information about the results. It is popular for use in the initial stages of data analysis and especially for identifying trends. Table (2) presents details of Unsupervised Learning algorithms [23].

Table 2: Description of Unsupervised Learning Algorithms.

Technique	Description	Applications
Clustering Algorithms	Group similar data points into clusters, e.g., K-Means and Hierarchical Clustering.	Customer segmentation, market basket analysis, and image compression.
Dimensionality Reduction	Reduces the number of features while retaining the data's essential information, e.g., PCA.	Visualization of high-dimensional data, noise reduction, and feature selection.

Source: [24].

Unsupervised learning is an important part of the exploratory data analysis of the data when there are no labeled datasets. Clustering and dimensionality reduction are techniques by which large datasets are identified as hiding structures, correlations, and patterns in the models. Clustering, such as, is used to cluster similar data instances and this is applicable in segmentation and in anomaly detection. Principal Component Analysis (PCA) is a method of dimensionality reduction that reduces large and complicated datasets while retaining valuable data. Such methods are especially useful with high-dimensional data. Irrespective of this, it is difficult to interpret the results of unsupervised learning models because predefined labels do not exist to assess the performance of models.

V.2 DEEP LEARNING (DL)

Neural Networks with more than one layer are used in DL which is a part of machine learning. It is most useful in case of large database and problems which are nonlinear in nature. Table (3) define Deep Learning (DL) algorithms [25].

Table 3: Description of Deep Learning Algorithms.

Model Type	Description	Applications
Convolutional Neural Networks (CNNs)	Extract hierarchical features from structured data such as images and videos.	Image recognition, object detection, and video analysis.
Recurrent Neural Networks (RNNs)	Process sequential data, maintaining temporal relationships using feedback loops.	Speech recognition, stock price forecasting, and language modeling.
Long Short-Term Memory (LSTM)	Overcomes RNN limitations by capturing long-term dependencies with memory cells.	Time-series forecasting, text generation, and financial predictions.

Source: [26]

The deep learning algorithms have contributed a lot to the functionality of machine learning so that systems with deep learning can automatically extract hierarchical features representations of large datasets. Convolutional Neural Networks (CNNs), Recurrent Neural Networks (RNNs), and Long Short-Term Memory (LSTM) networks are architectures that are popular in complex tasks that involve images, videos and sequential data. CNNs are especially useful at analyzing spatial data, whereas RNN and LSTM models are oriented at the recognition of temporal relationships in the sequence of information. Such models have been incredibly successful in computer vision, speech recognition and natural language processing. Nonetheless, deep learning models are usually run on big datasets, substantial amounts of computing power, and delicate hyperparameter adjustment.

V.3 REINFORCEMENT LEARNING (RL)

This kind of machine learning is a type of learning from experience, which involves an agent and its environment in the process of accomplishing a certain task. The model just has reward for right action and punishment for wrong action and it makes corrections for its strategy and actions. Table (4) delineate the Reinforcement Learning (RL) algorithms [25].

Table 4: Description of Reinforcement Learning Algorithms.

Use Case	Description	Examples
Trading Strategies	Optimizes decision-making in buying and selling stocks based on market conditions.	Algorithmic trading, portfolio optimization.
Robotics	Improves robot autonomy and efficiency in completing complex tasks.	Autonomous navigation, object manipulation.
Game Playing	Trains models to perform well in competitive environments by learning from outcomes.	Chess, Go, video games, and reinforcement-based simulations.

Source: [27]

The difference of reinforcement learning in comparison with other machine learning paradigms lies in the fact that it aims at understanding how to act in the best way, interacting with the environment. Under this scheme, the agent will be rewarded or punished depending on its actions and will keep on improving its decision-making scheme by trial and error. The reinforcement learning has proved to be useful in robotics, automated trading and intelligent gaming systems. It has the strength of being able to acquire adaptive strategies in changing and uncertain conditions. However, reinforcement learning models are computationally costly and in many cases, they take a long period of time to train, especially when the environment is complex in terms of state and action space.

V.4 NATURAL LANGUAGE PROCESSING (NLP)

Natural Language Processing (NLP) is about the interface between computers and languages used by humans. It utilizes models of machine learning and deep learning to work with textual data. Table (5) provides description of (NLP) techniques [28].

Table 5: Natural Language Processing (NLP) techniques.

Model	Description	Applications
Transformers	Advanced models like GPT and BERT designed for natural language understanding.	Text summarization, translation, and question answering.
BERT (Bidirectional Encoder Representations from Transformers)	Captures word context bidirectionally, making it ideal for sentiment analysis.	Sentiment analysis, trend prediction, and contextual text understanding.

Source: [28].

Natural Language Processing (NLP) aims at making computers comprehend, interpret and produce human language. Deep learning architectures that utilize transformer-based models (e.g., BERT and GPT) are highly used in modern NLP systems. These models acquire contextual dependencies between words and are highly effective in the performance of language understanding tasks. Applications in the field of machine translation, sentiment analysis, question answering and text summarization are some of the common applications of NLP techniques. The use of transformer models has brought a revolution in the field due to the enhanced awareness of context and scalability. Nevertheless, NLP models can be resource-intensive (in terms of the required training datasets and computation), and, still, they can be confused by ambiguity and specifics of domain language.

V.5 ENSEMBLE METHODS

Ensemble methods enhance model performance by combining multiple learners to reduce errors and increase accuracy. Table (6) shows Ensemble Methods [29].

Table 6: Ensemble Methods.

Method	Description	Applications
Boosting	Sequentially improves weak learners, e.g., AdaBoost and Gradient Boosting Machines (GBM).	Fraud detection, loan default prediction.
Bagging	Combines predictions from multiple models using resampling, e.g., Random Forests.	Customer segmentation, product recommendation.
Stacking	Trains a meta-model on predictions from base models for better performance.	Financial forecasting, ensemble predictive analytics.

Source: [29].

Ensemble learning approaches are designed to enhance predictive accuracy through the integration of a number of machine learning models into a strong framework. Boosting, bagging, and stacking are methods that can be used to minimize the modeling errors and enhance the stability of the models. The iterative boosting techniques improve weak learners and the bagging techniques minimize variance using resampling techniques. Stacking also enhances performance based on a meta-model of combining predictions made by base learners. They are common in complicated predictive problems where one model is not likely to store all the patterns in the data. Although not the least effective, ensemble approaches can become more expensive to compute and demand selection and parameter optimization of models.

V.6 TIME SERIES ANALYSIS

Time series analysis is used for analyzing and predicting data that evolves over time. It is particularly relevant in fields like finance, weather, and inventory management. Table (7) shows Time Series Analysis [30].

Table 7: Time Series Analysis.

Technique	Description	Applications
ARIMA (Auto Regressive Integrated Moving Average)	Combines autoregressive and moving average components to model and forecast time-series data.	Forecasting stock prices, sales, and demand trends.
Prophet	A user-friendly forecasting tool designed for capturing seasonality and trend components.	Business forecasting, revenue prediction, and anomaly detection.

Source: [30].

The time series analysis is dedicated to modelling and predicting time varying data, which is critical in the financial field, energy use, and weather forecasting. Logistic regression methods, including ARIMA and Prophet, have been popular in capturing trend, seasonal and temporal dependencies in a sequence of data. ARIMA models are especially useful in statistical forecasting whereas Prophet offers a more generic model when dealing with seasonality and irregular trends. The practices help organizations to make sound decisions when future predictions are made. Nevertheless, proper prediction needs very good historical data and the forecasting models might fail in instances where there occurs an abrupt shift in the structure of the system or some other unforeseen anomalies.

V.7 BAYESIAN NETWORKS

Bayesian networks are probabilistic graphical models that represent a set of variables and their conditional dependencies. They are particularly useful in scenarios where uncertainty must be accounted for in decision-making. Table (8) shows Bayesian Networks [31].

Table 8: Bayesian Networks.

Applications	Description
Risk Assessment	Helps model and predict potential outcomes and risks.
Medical Diagnosis	Used to identify diseases based on symptoms and test results.

Source: [31].

Bayesian networks are a probabilistic model that can be used to describe complex systems that have uncertain dependencies among variables. These graphical models display the conditional dependencies in the form of directed acyclic graphs which enable researchers to learn the cause-and-effect relationships as well as do probabilistic inferences. Applications of Bayesian networks in decision support applications, medical diagnosis applications, and risk assessment applications are common. They are especially effective in uncertain conditions because they can apply the previous knowledge and update the probabilities with regard to the new information. Nevertheless, it may be computationally difficult to build the correct Bayesian network structures in the presence of many variables and complicated dependency functions.

V.8 GENETIC ALGORITHMS

Genetic algorithms are optimization techniques inspired by natural selection. They iteratively improve solutions by mimicking biological evolution. Table (9) shows Genetic Algorithms [32].

Table 9: Genetic Algorithms.

Stage	Description	Applications
Selection	Chooses the best candidates based on fitness.	Portfolio optimization, route planning, engineering design.
Crossover	Combines parent solutions to generate offspring.	Product development, genetic programming.
Mutation	Introduces random changes to maintain diversity.	Complex problem-solving, evolving trading strategies.

Source: [32].

Genetic algorithms are evolutionary algorithms that are based on the concept of natural selection and biological evolution. The processes used in searching optimal or near-optimal solutions in them include selection, crossover and mutation. These algorithms have been used especially in solving complex optimization problems, which would not be easily solved by traditional methods because of large search space or nonlinear constraints.

Genetic algorithms are used extensively in the design of engineering, financial optimization, scheduling, and artificial intelligence. Although genetic algorithms are flexible, they necessarily need to be tuned by hand, and can have a slow convergence rate, particularly if the search space is very large or the fitness function is complicated.

VI. METHODOLOGY AND IMPLEMENTATION

Figure (1) shows a full workflow of model creation and assessment of a Long Short-Term Memory (LSTM) model to make predictions or analysis using data. It is carried out through a series of steps of a structured machine learning pipeline that starts with the acquisition of raw data and moves through a series of steps such as preprocessing, feature engineering, model training, and performance evaluation. Each of the steps allows properly preparing the dataset and making sure that the resulting model will succeed in learning patterns and making reliable predictions. The first step is Data Collection which is the process of getting raw data out of the sources that are relevant. This information can be in databases, sensors, open repositories, or real time streams based on the field of application. The data can also have anomalies, missing values or other irrelevant characteristics at this point, and can therefore be further processed before modelling is done. After collecting the data, the next step of the work is Data Exploration and Visualization. This step is aimed at getting to know the form and properties of the data set gathered. Patterns, anomalies and interrelations among variables are detected using techniques like statistical summaries, correlation analysis and visual techniques like charts or plots. Data exploration is quite necessary since it assists the researchers to learn about the data set and identify the most relevant approach of preprocessing and modeling. The second step is Data Preprocessing which involves cleaning and readying of raw data to be used in machine learning. Preprocessing tasks normally involve processing any missing data, eliminating duplicates, reconciliation of inconsistencies and in case of need, the conversion of categorical data into numerical form. Good preprocessing enhances the quality of data and gives the model consistent and meaningful data.:

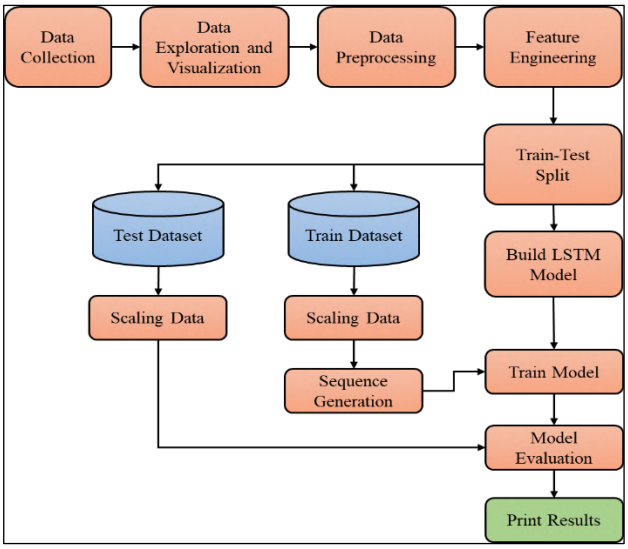


Figure 1: Methodology Block Diagram.
Source: Authors, (2026).

Following the preprocessing, Feature Engineering is used. During this phase, the appropriate features are chosen or developed to increase the learning capacities of the model on the data. The feature engineering process can be in the form of deriving new features, modifying the existing features, or doing away with redundant features. Good feature engineering could without any doubt enhance predictive power of machine learning models. After the features are ready the Train-Test Split process is used to divide the dataset. The data is divided into two subsets, the training data, which is used to train the model, and the testing data, which is used to assess the performance of the model on unseen data. Such partition can be used to measure the generalization capabilities of the model to new data and avoid overfitting. The training and testing data sets are subjected to Scaling Data which normalizes or standardizes the values of feature values to a similar range. Scaling is especially relevant to neural network models such as LSTM as it stabilized the process of training and speeded up the convergence. Once the training dataset has been scaled up, it is followed by Sequence Generation. Given that LSTM models expect that data is sequential or time-dependent, it must be converted into a form of sequences that are time-dependent. This stage will arrange the input data into temporal chains through which the LSTM network can acquire temporal dependencies and patterns with time. Then, Build LSTM Model phase specifies the neural network structure. The model normally has LSTM layers which form temporal relationship then more layers like dense layers to make predictions. This stage is used to configure model parameters, activation functions and optimization algorithms. After the construction of the model, the workflow goes to Train Model where the LSTM network is trained to learn patterns on the training data by the use of optimization. The model adapts its internal weights during training to reduce the error of prediction. After training is completed, Model Evaluation is performed using the testing dataset. Evaluation metrics such as accuracy, mean squared error, or other performance indicators are calculated to measure the model's effectiveness.

VI.1 DATA COLLECTION

The data collection phase focuses on gathering historical Bitcoin price data as the foundation for analysis and prediction. The Yahoo Finance API was used to retrieve daily data from January 1, 2015, to June 1, 2024. The dataset includes the following key columns.

Table 10: The dataset includes the following key columns.

Column	Description
Date	The timestamp for each entry, used to organize the data chronologically.
Open	The opening price of Bitcoin for the day.
Low	The lowest price recorded during the day.
High	The highest price recorded during the day.
Close	The closing price, reflecting the market's sentiment at the end of the day.
Adj Close	Adjusted closing price, accounting for stock splits or other adjustments.
Volume	The total number of Bitcoin units traded during the day, representing activity.

Source: Authors, (2026).

Table 10 offers all the basic variables needed to examine the price movements of Bitcoin and construct predictive models. Each column records a specific phenomenon of the market behavior such as price dynamics and trading activity. The open, high, low and close prices explain the daily price changes, which are fundamental to comprehend the volatility and trending. Adjusted close value is used to continue consistency in financial analysis in case of some adjustments. In the meantime, the trading volume indicates the market participation and liquidity. The combined variables will be a full depiction of the market conditions and act as essential inputs to further analysis, feature engineering, and model training phases.

VI.2 DATA EXPLORATION AND VISUALIZATION

To understand the data's underlying characteristics and trends, Exploratory Data Analysis (EDA) was conducted. Visualization tools were used to create meaningful insights:

Table 11: Data Exploration and Visualization.

Visualization	Purpose
Close Price Plot	Tracks the historical closing prices of Bitcoin to identify trends and price cycles.
Histogram and Density	Analyzes the distribution of Bitcoin closing prices to understand common price ranges.
Candlestick Plot	Combines open, high, low, and close prices, providing detailed insights into price movements.

Source: Authors, (2026).

The illustrations to be discussed in Table 11 are essential in perceiving the general dynamics of Bitcoin prices throughout the years. The close price plot enables the researcher to see long-term trends, cyclicality and abrupt changes which can point at volatility in the market or other external economic factors. The histogram and the density plots could be used to examine the statistical distribution of closing prices and reveal the common price ranges and determine potential skewness or outliers. Moreover, the candlestick chart provides a detailed display of price fluctuations of each trading day, through the combination of open, high, low and close values. The methods of exploration allow interpreting the dataset more effectively and allow making informed decisions in preprocessing and modeling phases.

VI.3 DATA PREPROCESSING

Preprocessing ensures the dataset is clean and ready for model training. Several steps were undertaken:

Table 12: Data Preprocessing.

Step	Description
Handling Missing Values	Missing data was filled using forward filling, and remaining null values were removed.
Scaling Data	Normalized using MinMaxScaler to scale all features between 0 and 1. Separate scalers were used to prevent data leakage.
Sequence Generation	Created time-series sequences with a 30-day window size, ensuring sufficient historical context for predictions.

Source: Authors, (2026).

As shown by Table 12, the following preprocessing tasks are necessary to prepare the dataset to be easy to train in machine learning. The process of working with missing values will make sure that incomplete records will not harm the learning process of the model. Forward filling is also useful in preserving the continuity of a time-series data with minimal loss of information. Scaling of the data set with MinMaxScaler standardizes the features in a similar range, thus enhancing the stability of the training of the neural network and faster convergence. Also, time-series sequences generate time-series data, which are structured as input to sequential models like LSTM. These preprocessing steps are very important in improving the data quality and it also makes sure that the model is presented with sound and well-organized inputs.

VI.4 FEATURE ENGINEERING

To enhance the dataset's predictive power, key financial indicators were added. These indicators capture different aspects of market dynamics:

Table 13: Feature Engineering.

Indicator	Description
Simple Moving Average (SMA)	Calculates the average of closing prices over specified periods (e.g., 20 and 50 days) to smooth trends.
Exponential Moving Average (EMA)	Similar to SMA but gives more weight to recent prices, making it more responsive to changes.
MACD (Moving Average Convergence Divergence)	Tracks momentum using the difference between short-term and long-term EMAs.
RSI (Relative Strength Index)	Identifies overbought or oversold conditions, ranging from 0–100.
Volatility Measures	Includes ATR (Average True Range) and standard deviation to assess price volatility.
Bollinger Bands	Highlights overbought/oversold conditions using upper and lower price bands based on standard deviations.

Source: Authors, (2026).

Introducing domain knowledge into the dataset through feature engineering is essential in the quality of prediction of machine learning models. The financial indicators in Table 13 represent various market behavior components, such as market trends, market momentum, and market volatility. SMA and EMA are moving averages that are used to smooth out fluctuations and identify long-run trends. Such indicators as MACD and RSI give us the information about the momentum in the markets and possible overbought or oversold. Volatility indicators like ATR and Bollinger Bands also assist in determining times of instability of a market. The combination of these indicators provides the model with a more in-depth contextual information increasing its capability to model complex price dynamics.

VI.5 TRAIN-TEST SPLIT

The dataset, spanning 3440 days, was divided into training, validation, and test sets to ensure robust model evaluation:

Table 14: Train-Test Split.

Subset	Duration	Purpose
Training Set	January 1, 2015 – April 1, 2023	Used to train the model on historical data (3012 days).
Validation Set	April 2, 2023 – October 2, 2023	Fine-tuning hyperparameters and evaluating generalization (214 days).
Test Set	October 3, 2023 – June 1, 2024	Assessing model performance on unseen data (214 days).

Source: Authors, (2026).

The division plan of the dataset used in Table 14 provides a dependable assessment of the predictive model. The division of the dataset into training, validation and testing subset is important as it gives the model the opportunity to learn on historic data without bias in evaluation on unprecedented data. Most of the data is found in the training set, which is employed to acquire patterns and relationships among variables. The validation set aids in the hyperparameter tuning and also helps in avoidance of overfitting by testing the model in the course of development. Lastly the test set is used to give a final evaluation of the predictive power of the model on new data. This organized separation increases the accuracy and validity of the experimental findings.

VI.6 SCALING DATA

To normalize data for model training and improve performance, MinMaxScaler was applied:

Table 15:Scaling Data.

Scaling Step	Description
Feature Scaling	All features were scaled between 0 and 1 to prevent larger values from dominating the training process.
Data Leakage Prevention	Separate scalers were applied to training and test data to avoid unintentional leakage.

Source: Authors, (2026).

Preprocessing Data Scaling Data scaling is an important preprocessing step when training neural network models, especially gradient-based optimization. The use of MinMaxScaler will make sure that all the input features are put within a similar range between 0 and 1. This normalization avoids larger numeric ranges of features controlling the training process, and enhances numerical stability in model optimization. Moreover, using distinct scalers in training and testing data sets can be used to avoid data leakage, which otherwise will result in overly optimistic estimates of performance. Scaling ensures that faster convergence is achieved during the training process and enhances the overall performance and stability of the LSTM model by standardizing the values of features.

VI.7 SEQUENCE GENERATION

For time-series modeling, sequences of fixed length (30 days) were created to capture historical context. The sequence generation step involved:

Table 16: Time-Series.

Window Size	Purpose
30 Days	Provides sufficient historical context without introducing unnecessary computational overhead.
Longer Window Sizes	Tested but showed diminishing returns in prediction accuracy.
Shorter Window Sizes	Reduced model performance due to inadequate historical information.

Source: Authors, (2026).

Sequence generation is a fundamental step in preparing data for time-series models such as LSTM networks. Instead of treating each observation independently, the dataset is transformed into sequential windows that capture historical dependencies. As shown in Table 16, a 30-day window size was selected to provide sufficient historical context while maintaining computational efficiency. This approach enables the model to learn temporal patterns and relationships that influence future Bitcoin price movements. Experiments with longer windows showed limited improvements in prediction accuracy, while shorter windows lacked adequate historical information. Therefore, the chosen sequence length provides an effective balance between model complexity and predictive performance.

VI.8 MODEL BUILDING: LSTM ARCHITECTURE

The LSTM model was designed to capture temporal dependencies in Bitcoin price data. The architecture is simple yet effective:

Table 17: LSTM Architecture.

Layer	Configuration
Input Layer	150 LSTM units to process sequential data and retain long-term dependencies.
Dense Layer	1 unit with linear activation to predict the next Bitcoin price (continuous regression output).
Optimizer	Adam optimizer, chosen for its adaptive learning capabilities and stability.
Loss Function	Mean Squared Error (MSE), used to minimize prediction errors.
Training	100 ochs with a batch size of 10 to balance learning efficiency and computational cost.

Source: Authors, (2026).

The LSTM architecture described in Table 17 is designed to effectively capture temporal dependencies in Bitcoin price data. LSTM networks are particularly suitable for time-series prediction because they incorporate memory cells that retain important information over long sequences. The model begins with an LSTM layer containing 150 units, allowing it to learn complex temporal relationships within the input sequences. A dense output layer with linear activation is used to generate continuous price predictions, which is appropriate for regression tasks. The Adam optimizer ensures efficient gradient-based learning, while the mean squared error loss function minimizes prediction errors during training. This architecture provides a balance between model complexity and computational efficiency.

VI.9 MODEL EVALUATION AND PREDICTION

Thus, after the training of the model, we check its efficiency through specific criteria such as Mean Squared Error (MSE). china's predicted prices and actual prices are also cross plotted to evaluate the performance as shown: The model is then used to predict prices of Bitcoin which assist in analyzing future trends. This actually gives elaboration on each step in the methodology making it clearer and making sure that any person who reads the methodology understands the steps that are being taken in the process.

VII. RESULTS AND DISCUSSION

VII.1 VISUALIZE TRAINING AND VALIDATION LOSS

Figure (2) demonstrates the Model Loss graph of the LSTM model during training and validation epoch by epoch up to one hundred. On the y-axis we have the loss values while the x-axis has the number of epochs. The first one in blue is the training loss, and the second one in orange is the validation loss. At first, when the number of epochs is low, which is the case in the first 10 epochs in this paper, the validation loss is much higher than the training loss which suggests that the model is yet to fully learn the patterns in the data and generalize the patterns to unseen data. Yet, the training and the validation losses decrease quickly during the first 20 epochs which shows that the model is learning significant features concerning the training set. After about 20 epochs, the validation loss becomes almost flat and fluctuates around a sufficiently small constant, while the training loss remains gradually decreasing and becomes almost zero. This shows that the model learning is able to capture the patterns of the data without overfitting the dataset as the difference between training and validation loss is still reasonable. The validation loss is relatively smooth and close to zero indicating good generalization capability when learning new data, although small oscillations in loss during the later epochs might have been caused by variations in the validation batches.

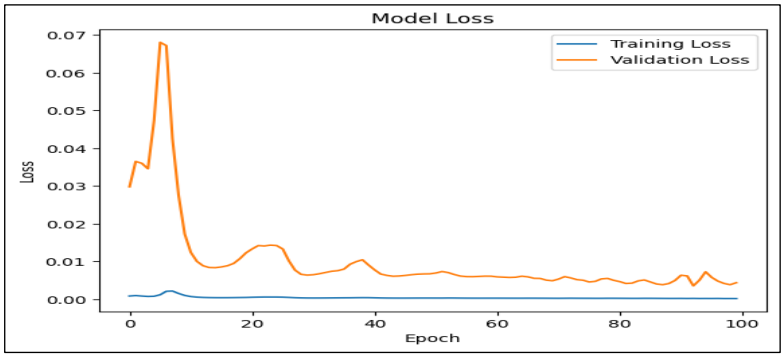


Figure 2. Model Loss.
Source: Authors, (2026).

In summary, the graph represents the LSTM model in a good performance learning in training phase and good generalization in validation phase. Such an advantage of the selected architecture, preprocessing steps, and hyper parameters has helped enhance the proposed model for accurate predictions of the given time-series data.

VII.2 MODEL EVALUATION

The performance of the LSTM model was evaluated using three key metrics: These include; Mean Absolute Error (MAE), Mean Squared Error (MSE) and Root Mean Squared Error (RMSE). These metrics help understand the degree of correctness of the issued prediction by the model. The MAE quantifies the mean of the absolute differences between the estimated and the actual prices, on the other hand, the MSE quantifies the arithmetic mean of the squared differences with an inclination towards relatively large errors. RMSE again derived from MSE is more understandable as it is in the same unit as the target variable. Moreover, the observed prices were graphed with the predicted prices in order to get deeper insight and to see whether the model is capable of identifying patterns.

Table 18: Model Evaluation.

Metric	Value	Description
MAE	0.00622	The average absolute error between predicted and actual values, indicating high accuracy.
MSE	8.39651	The mean of squared errors, highlighting how well the model minimizes larger deviations.
RMSE	0.00916	The square root of MSE, showing an interpretable measure of prediction accuracy.

Source: Authors, (2026).

These metrics establish the model as a useful one because of low error values depicted below the bar for all the metrics. The comparison of the trends of the actual and predicted prices also supports the proposed model's ability to provide a good estimate for prices.

VII.3 VISUALIZATION ACTUAL VS. PREDICTED PRICES

The differential LSTM model is illustrated in the graph shown below titled "Actual vs. Predicted Cryptocurrency Prices" with days on the x-axis and normalized prices on the y-axis. The black line at the bottom is the actual values, while the grey line is the forecasted values. It accurately also reflects actual depreciation and appreciation of the model closely thus mimicking the actual price movements. In the less volatile periods (days 25–50 and 125–150), the model provides almost identical predictions to actual prices, proving the effectiveness of the model during stable periods. During more active periods (days 50-60, and 160-175), the model accurately identifies the direction and size of major price fluctuations with only slight distortion in both over- and underestimations of certain movement. Taken together, the differences between the actual and predicted prices are rather small and the low error measures (MAE, MSE, RMSE) prove the efficiency of the model. What this visualization shows is that LSTM model is indeed an ideal tool for predicting the future trends of cryptos' prices.

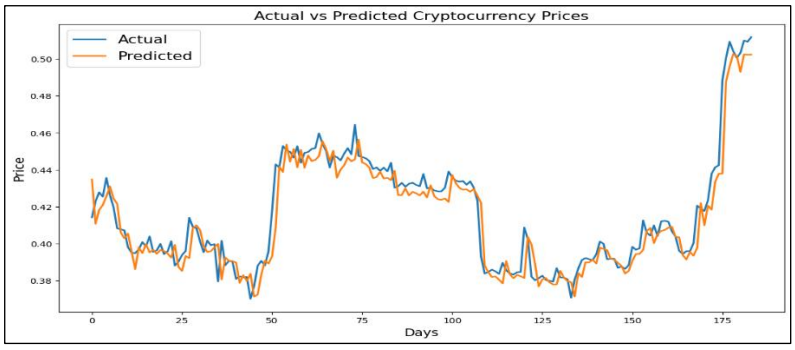


Figure 3: Visualization Actual vs. predicted prices.
Source: Authors, (2026).

VII.4 RESULTS DISCUSSION

Our analysis showed that the historical data can be employed to provide the price for the digital currency, with the focus on Bitcoin for this paper. The data can be considered as a factor to the model performance; for example, if the paper uses more data the prediction model performance may increase. There also has potential to generalize the method to other tasks such as parameter tuning for the model, testing various features, and using more complex deep learning architectures.

VIII. CONCLUSIONS

This paper shows how historical data and technical indicators can be employed for forecasting Bitcoin prices with reasonable accuracy. With the help of Yahoo Finance API, a detailed set of data from January 1, 2015, to June 1, 2024, was obtained and supplemented by Moving Averages, RSI, and Bollinger Bands. Using an LSTM-based deep learning model, we achieved robust results, with low error metrics (MAE: 0.A low MAE: 00.00622, MSE: 8.39651, RMSE 0.00916 and close relationship between actual and predicted price movement also shows the robustness of the model. These results indicate that the model is capable of modelling both stable and unstableness of the market and therefore perhaps useful in the cryptocurrency prediction of the prices. We may venture into making future work improvements by adding extra attributes, adjusting the hyper parameters, or using the compound models to augment the predictions in the future. This work also emphasizes the fact that data quality and complex machine learning techniques are vital for solving the issues faced in regression model based cryptocurrency price prediction under a very noisy environment.

IX. AUTHOR'S CONTRIBUTION

Conceptualization: Ammar Ahmed Othman, Seddiq Hassan Al-Banna Ali and Mohammed Bakr Youssef.
Methodology: Ammar Ahmed Othman, Seddiq Hassan Al-Banna Ali and Mohammed Bakr Youssef.
Investigation: Ammar Ahmed Othman, Seddiq Hassan Al-Banna Ali and Mohammed Bakr Youssef.
Discussion of results: Ammar Ahmed Othman, Seddiq Hassan Al-Banna Ali and Mohammed Bakr Youssef.
Writing – Original Draft: Ammar Ahmed Othman, Seddiq Hassan Al-Banna Ali and Mohammed Bakr Youssef.
Writing – Review and Editing: Ammar Ahmed Othman, Seddiq Hassan Al-Banna Ali and Mohammed Bakr Youssef.
Resources: Ammar Ahmed Othman, Seddiq Hassan Al-Banna Ali and Mohammed Bakr Youssef.
Supervision: Ammar Ahmed Othman, Seddiq Hassan Al-Banna Ali and Mohammed Bakr Youssef.
Approval of the final text: Ammar Ahmed Othman, Seddiq Hassan Al-Banna Ali and Mohammed Bakr Youssef.

X. REFERENCES

[1] U. Kayani and F. Hasan, "Unveiling Cryptocurrency Impact on Financial Markets and Traditional Banking Systems: Lessons for Sustainable Blockchain and Interdisciplinary Collaborations," *J. Risk Financ. Manag.*, vol. 17, no. 2, 2024, doi: 10.3390/jrfm17020058.

[2] P. Rahman, Z. Zhang, and M. Musa, *Do technological innovation, foreign investment, trade and human capital have a symmetric effect on economic growth? Novel dynamic ARDL simulation study on Bangladesh*, vol. 56, no. 2. Springer US, 2023. doi: 10.1007/s10644-022-09478-1.

[3] G. Soana and T. de Arruda, "Central Bank Digital Currencies and financial integrity: finding a new trade-off between privacy and traceability within a changing financial architecture," *J. Bank. Regul.*, vol. 25, no. 4, pp. 467–486, 2024, doi: 10.1057/s41261-024-00241-2.

[4] P. K. Ozili, "Central Bank Digital Currency," pp. 94–107, 2024, doi: 10.4018/979-8-3693-1503-3.ch005.

[5] G. Habib, S. Sharma, S. Ibrahim, I. Ahmad, S. Qureshi, and M. Ishfaq, "Blockchain Technology: Benefits, Challenges, Applications, and Integration of Blockchain Technology with Cloud Computing," *Futur. Internet*, vol. 14, no. 11, pp. 1–22, 2022, doi: 10.3390/fi14110341.

[6] J. Zarrin, H. Wen Phang, L. Babu Saheer, and B. Zarrin, "Blockchain for decentralization of internet: prospects, trends, and challenges," *Cluster Comput.*, vol. 24, no. 4, pp. 2841–2866, 2021, doi: 10.1007/s10586-021-03301-8.

[7] H. Li, "The Applications of Cryptocurrency: Evidence from Ethereum," *BCP Bus. Manag.*, vol. 34, pp. 237–242, 2022, doi: 10.54691/bcpbm.v34i.3019.

[8] K. Shah, D. Lathiya, N. Lukhi, K. Parmar, and H. Sanghvi, "A systematic review of decentralized finance protocols," *Int. J. Intell. Networks*, vol. 4, no. July, pp. 171–181, 2023, doi: 10.1016/j.ijin.2023.07.002.

[9] H. Bi *et al.*, "Not Just Learning From Others but Relying on Yourself: A New Perspective on Few-Shot Segmentation in Remote Sensing," *IEEE Trans. Geosci. Remote Sens.*, vol. 61, no. 8, pp. 1–21, 2023, doi: 10.1109/TGRS.2023.3326292.

[10] D. L. John, S. Binnewies, and B. Stantic, "Cryptocurrency Price Prediction Algorithms: A Survey and Future Directions," *Forecasting*, vol. 6, no. 3, pp. 637–671, 2024, doi: 10.3390/forecast6030034.

[11] M. Guindy, "Cryptocurrency price volatility and investor attention," *Int. Rev. Econ. Financ.*, vol. 76, Jun. 2021, doi: 10.1016/j.iref.2021.06.007.

[12] P. Prabakaran and N. Panchalingam, "Factors Influencing the Trend of Cryptocurrency Factors Influencing the Trend of Cryptocurrency View project Factors Influencing the Trend of Cryptocurrency," no. January, 2022, [Online]. Available: https://www.researchgate.net/publication/357982093

[13] Q. Li, F. Wang, J. Wang, and W. Li, "LSTM-Based SQL Injection Detection Method for Intelligent Transportation System," *IEEE Trans. Veh. Technol.*, vol. 68, no. 5, pp. 4182–4191, 2019, doi: 10.1109/TVT.2019.2893675.

[14] Y. Liu and A. Tsyvinski, "Risks and Returns of Cryptocurrency," *Rev. Financ. Stud.*, vol. 34, Sep. 2020, doi: 10.1093/rfs/hhaa113.

[15] T. Bouazizi, E. Galariotis, K. Guesmi, and P. Makrychoriti, "Investigating the nature of interaction between crypto-currency and commodity markets," *Int. Rev. Financ. Anal.*, vol. 88, 2023, doi: 10.1016/j.irfa.2023.102690.

[16] A. Ladhari and H. Boubaker, “Deep Learning Models for Bitcoin Prediction Using Hybrid Approaches with Gradient-Specific Optimization,” *Forecasting*, vol. 6, no. 2, pp. 279–295, 2024, doi: 10.3390/forecast6020016.

[17] M. Rizwan, S. Narejo, and M. Javed, *Bitcoin price prediction using Deep Learning Algorithm*. 2019. doi: 10.1109/MACS48846.2019.9024772.

[18] X. Jiang, “Bitcoin Price Prediction Based on Deep Learning Methods,” *J. Math. Financ.*, vol. 10, no. 01, pp. 132–139, 2020, doi: 10.4236/jmf.2020.101009.

[19] J. Bajwa, U. Munir, A. Nori, and B. Williams, “Artificial intelligence in healthcare: transforming the practice of medicine.,” *Futur. Healthc. J.*, vol. 8, no. 2, pp. e188–e194, Jul. 2021, doi: 10.7861/fhj.2021-0095.

[20] I. H. Sarker, “Machine Learning: Algorithms, Real-World Applications and Research Directions,” *SN Comput. Sci.*, vol. 2, no. 3, p. 160, 2021, doi: 10.1007/s42979-021-00592-x.

[21] D. Sambyal and A. Sarwar, “Recent developments in cervical cancer diagnosis using deep learning on whole slide images: An Overview of models, techniques, challenges and future directions,” *Micron*, vol. 173, p. 103520, 2023, doi: https://doi.org/10.1016/j.micron.2023.103520.

[22] A. Gatera, M. Kuradusenge, G. Bajpai, C. Mikeka, and S. Shrivastava, “Comparison of random forest and support vector machine regression models for forecasting road accidents,” *Sci. African*, vol. 21, p. e01739, 2023, doi: 10.1016/j.sciaf.2023.e01739.

[23] J. Wang and F. Biljecki, “Unsupervised machine learning in urban studies: A systematic review of applications,” *Cities*, vol. 129, no. December 2021, p. 103925, 2022, doi: 10.1016/j.cities.2022.103925.

[24] G. H. Rosenlund, K. W. Hoiem, B. N. Torsater, and C. A. Andresen, “Clustering and dimensionality-reduction techniques applied on power quality measurement data,” *SEST 2020 - 3rd Int. Conf. Smart Energy Syst. Technol.*, no. October, 2020, doi: 10.1109/SEST48500.2020.9203294.

[25] M. M. Taye, “Understanding of Machine Learning with Deep Learning: Architectures, Workflow, Applications and Future Directions,” *Computers*, vol. 12, no. 5. 2023. doi: 10.3390/computers12050091.

[26] T. N. Sainath, O. Vinyals, A. Senior, and H. Sak, “Convolutional, Long Short-Term Memory, fully connected Deep Neural Networks,” *ICASSP, IEEE Int. Conf. Acoust. Speech Signal Process. - Proc.*, vol. 2015-August, pp. 4580–4584, 2015, doi: 10.1109/ICASSP.2015.7178838.

[27] J. H. Park, J. H. Kim, and J. H. Huh, “Deep Reinforcement Learning Robots for Algorithmic Trading: Considering Stock Market Conditions and U.S. Interest Rates,” *IEEE Access*, vol. 12, pp. 20705–20725, 2024, doi: 10.1109/ACCESS.2024.3361035.

[28] D. Khurana, A. Koli, K. Khatter, and S. Singh, “Natural language processing: state of the art, current trends and challenges,” *Multimed. Tools Appl.*, vol. 82, no. 3, pp. 3713–3744, 2023, doi: 10.1007/s11042-022-13428-4.

[29] A. Mohammed and R. Kora, “A comprehensive review on ensemble deep learning: Opportunities and challenges,” *J. King Saud Univ. - Comput. Inf. Sci.*, vol. 35, no. 2, pp. 757–774, 2023, doi: 10.1016/j.jksuci.2023.01.014.

[30] V. Kotu and B. Deshpande, “Chapter 12 - Time Series Forecasting,” V. Kotu and B. B. T.-D. S. (Second E. Deshpande, Eds., Morgan Kaufmann, 2019, pp. 395–445. doi: https://doi.org/10.1016/B978-0-12-814761-0.00012-5.

[31] N. ElKalaawy and A. Wassal, “Methodologies for the modeling and simulation of biochemical networks, illustrated for signal transduction pathways: A primer,” *Biosystems*, vol. 129, pp. 1–18, 2015, doi: https://doi.org/10.1016/j.biosystems.2015.01.008.

[32] M. A. Albadr, S. Tiun, M. Ayob, and F. Al-Dhief, “Genetic algorithm based on natural selection theory for optimization problems,” *Symmetry (Basel).*, vol. 12, no. 11, pp. 1–31, 2020, doi: 10.3390/sym12111758.

Journal of Engineering and Technology for Industrial Applications

ITEGAM-JETIA

Manaus, v.12 n.60, p.596-605 July/August, 2026.
DOI: https://doi.org/10.5935/jetia.v12i60.3920

ISSN ONLINE: 2447-0228

RESEARCH ARTICLE OPEN ACCESS

COMPARATIVE ANALYSIS OF TRIBOLOGICAL PERFORMANCE OF NANO-ENHANCED HYBRID BIO-LUBRICANT WITH CONVENTIONAL SYNTHETIC OIL

Gaurav Pendbhaje*[1], Mohammed Ali[2] and Dipak Bajaj[3]

[1]Research Scholar, Department of Mechanical Engineering, Oriental University, Indore, Madhya Pradesh, India.
[2]Professor, Department of Mechanical Engineering, Oriental University, Indore, Madhya Pradesh, India.
[3]Associate Professor, Department of Mechanical Engineering, Amrutvahini College of Engineering, Sangamner, Maharashtra, India .

[1]https://orcid.org/0000-0001-5951-8793, [2]https://orcid.org/0000-0002-9833-6228, [3]https://orcid.org/0000-0002-8689-226X

E-email: *gauravpendbhaje11@gmail.com

ARTICLE INFO

Article History
Received on: March 05, 2026
Reviewed on: April 04, 2026
Accepted on: May 01, 2026
Published on: July 31, 2026

Keywords:
Bio-lubricants,
Hybrid vegetable oil,
Nanoparticle additives,
MoS_2,
Tribological performance,
Four-ball test.

ABSTRACT

The need to have environmentally friendly lubricants has triggered a lot of research on the development of biodegradable and renewable alternatives to petroleum-based oils. The intrinsic lubricity of vegetable oils like cottonseed oil (CSO) and palm oil (PO) is due to the polar ester structures in them; however, limitations in wear properties and load-carrying capacity restrict their direct application in industries. This experiment compares the tribological behavior of CSO, PO, and a hybrid CSO-PO mixture with nano-additives (MoS2, TiO2, and SiO2) at 1, 1.5 and 2 wt.% and compares these formulations with a commercial synthetic lubricant (SAE 20W50). Nano-enhanced bio-lubricants were made through the controlled dispersion method and evaluated with a four-ball tribotester under the ASTM D4172 conditions. Wear scar diameter (WSD) and coefficient of friction (COF) were the main performance indicators. The data show that the addition of nanoparticles significantly enhances tribological behavior, and 1.5 wt% is the most optimal loading. The hybrid CSO-PO + 1.5 wt% MoS2 had the lowest WSD (509 µm) and COF (0.061). Compared to the synthetic oil (WSD = 530 µm and 0.088), the optimized nano-bio lubricant had a 3.96% wear reduction and a 30.68% friction reduction. These results indicate that nano-enhanced hybrid vegetable oil formulations, particularly those containing MoS2, have the potential to provide better friction reduction and competitive wear resistance, and thus have a high potential as sustainable, high-performance alternatives to traditional synthetic lubricants.

Copyright ©2026 by authors and Galileo Institute of Technology and Education of the Amazon (ITEGAM). This work is licensed under the Creative Commons Attribution International License (CC BY 4.0).

I. INTRODUCTION

The increase in the rate of industrialization and the growth of global energy demand have enhanced the use of petroleum-based lubricants in transportation and manufacturing industries, thus increasing the sustainability issues [1] [2]. Traditional lubricants that are based on petroleum are mostly non-biodegradable, and their lifecycle, including production, utilization, and disposal, has a great impact on the environment, such as soil and water pollution, greenhouse gas emissions, and long-term ecological damage [3] [4]. Lubricants that are based on minerals release toxic substances into the environment when improperly disposed of or accidentally spilled, thus becoming hazardous to ecosystems and human health [5] [6]. Due to the growing environmental effects and the growing regulatory systems that favor sustainability, there has been an increasing pressure to substitute mineral lubricants with renewable, biodegradable, and low-toxicity lubricants [7] [8]. Modern studies emphasize the fact that it is high time to switch to eco-friendly, renewable, and bio-based lubricants in order to reduce the impact on the environment and maintain tribological properties [9] [10]. Vegetable oils have received a lot of interest as bio-lubricant base stocks due to their natural high lubricity, high viscosity index, biodegradability, and low volatility compared to mineral oils; therefore, they are promising sustainable alternatives in tribological applications [11] [12]. However, the inherent characteristics of unmodified vegetable oils are not as good as they have poor oxidation stability, limited thermal resistance, and inadequate cold-flow properties, which restrict their direct use in high- or low-temperature operating environments [13] [14].

CSO and PO are among the most appealing vegetable oils because of their triglyceride structures, which have a high concentration of long-chain fatty acids (e.g., oleic, linoleic and palmitic acids), which significantly determine the viscosity behavior and oxidative properties [15] [16]. The presence of polar ester functional groups in these fatty acid chains increases surface adsorption and boundary-film formation, which, in turn, improves the friction reduction and wear resistance; this is the key to the high lubrication potential of CSO and PO in tribological systems that are sustainable [17] [18]. To address the challenges of the contemporary tribosystems, the introduction of nano-additives into lubricants has become a necessity to increase the load-carrying capacity, reduce surface damages, and satisfy the requirements of the modern tribosystems [19] [20]. High surface activity and contact interface interaction are the characteristics of nanoparticles that enhance tribological performance by drastically lowering friction and wear [21] [22]. The main improvement processes are the rolling effect, which involves the use of nanoparticles as nano-bearings; tribo-film formation, which creates a protective layer of the surface; the mending effect when the nanoparticles fill the surface asperities; and the polishing effect when the nanoparticles smooth worn surfaces during sliding [23] [24]. In particular, molybdenum disulfide (MoS2) is well-known as an effective layered solid lubricant, as it has low interlayer shear strength; titanium dioxide (TiO2) nanoparticles have high anti-wear and protective film-forming properties; and silicon dioxide (SiO2) nanoparticles provide nano-bearing and surface smoothing effects, which makes these materials highly promising in the development of advanced nano-lubricant formulations [25] [26].

The tribological analyses play a critical role in assessing the frictional behaviour, the wear resistance, and the load-carrying capacity of lubricants under simulated contact conditions, thus allowing the reliable examination of their ability to perform in the real-life mechanical systems [27] [28]. The four-ball tribometer under ASTM D4172 is one of the most commonly used methods of testing the anti-wear and friction-reducing properties of lubricants in a controlled load, speed, and temperature environment [29] [30]. The four-ball testing provides the key performance indicators WSD and COF as the former measures the material loss and surface damage, and the latter measures the capacity of the lubricant to reduce resistance between sliding surfaces [31] [32]. The recent developments in nano-enhanced biodiesel lubricants highlight their increasing potential as the alternative to the traditional mineral oils due to the significant enhancement of their viscosity, thermal stability, and tribological properties. Initial studies with metallic and metal-oxide nanoparticles proved their usefulness in improving the lubrication properties of vegetable oils. Singh et al. [33] found that the addition of 0.9% copper nanoparticles to modified desert date oil significantly lowered the COF, wear rate, and surface damage, whereas Singh et al. [34] found that 0.6% SiO2 nanoparticles enhanced the surface morphology and the overall tribological performance of the Balanites aegyptiaca oil. In the same way, Chinnachamy et al. [35] showed that the addition of silver nanoparticles into the Jatropha and Pongamia oils increased the viscosity, thermal conductivity, and wear resistance, thus indicating the positive effect of noble metal additives. Adding to these results, Prabhakaran et al. [36] demonstrated that addition of 0.240.4 wt.% of the CuO nanoparticles to modified Kusum oil enhanced viscosity, flash point, and tribological properties, which confirmed its suitability in industry.

Similar progress on iron-oxide systems has yielded encouraging outcomes. The castor-oil-based bio-lubricant with Fe3O4 nanoparticles and ethylene glycol developed by Ahmad et al. [37] had a production yield of 94% and achieved a 50% decrease in friction and a 40% decrease in wear. Aithal et al. [38] have found that PEG-coated Fe3O4 nanoparticles showed a maximum of 70% wear reduction in the presence of neem oil, which greatly improved the viscosity retention and thermal conductivity. Similarly, Sadiq et al. [39] showed that maghemite nanoparticles enhanced viscosity, thermal conductivity, and anti-wear properties of vegetable oil, and Sadiq et al. [40] went a step further to add graphene and maghemite nanoparticles to coconut oil, which enhanced oxidation stability, thermal degradation, and friction and wear behavior, which could be used in high-temperature machining.

Carbon based nano-additives have also become very effective reinforcement material in bio-lubricant systems. Kumar et al. [41] have indicated that palm-oil-commercial oil blends that incorporated 0.1 wt% functionalized multi-wall carbon nanotubes (FMWCNTs) reduced the wear-scar diameter and wear volume by 38 and 35%, respectively. Applying this study to bearing applications, Kamarapu et al. [42] showed better tribological and vibration characteristics with FMWCNT-blended palm oil, which retained its lubrication capacity during 80% of the working time. Nugroho et al. [17] also used carbon and oxide nanoparticles in the lubrication of electric-vehicles and demonstrated that palm-oil-based lubricants with additives of graphene, TiO2, and Al2O3 decreased the COF by up to 34% and enhanced wear resistance.

Complementary research by Ravikiran et al. [43] found that TiO2 and SiO2 nanoparticles increased viscosity, flash point, and wear resistance of canola-wheat germ oil mixtures, whereas Madhwesh et al. [44] found that TiO2-enhanced jojoba bio-lubricants increased engine efficiency and lowered emissions. Even though Katpatal et al. [45] found that the CuO nanoparticles did not have a significant effect on the pressure distribution in journal bearings, their experiment proved that the bio-lubricant formulations could reach the same frictional performance as ISO VG46 mineral oil. These studies, together, highlight the transformative nature of nanoparticles, metallic, metal-oxide, and carbon-based, in increasing the tribological performance of bio-lubricants, as well as their thermal stability, which would enhance their efficacy as viable, sustainable substitutes to industrial and automotive applications. Although a lot of literature has been done on nano-enhanced bio-lubricants, very little research has been done to compare the various types of nanoparticles and their concentrations in a hybrid vegetable oil system and compare their performance with commercial synthetic lubricants under the same operating conditions. Moreover, the blending effect of base-oil (CSO-PO) and layered MoS2 reinforcement has not been sufficiently investigated. The current paper fills this gap by performing an extensive comparative study of MoS2, TiO2, and SiO2 at optimal concentrations in a hybrid bio-lubricant system and finding an optimum formulation with much better friction reduction and competitive wear resistance compared to synthetic oil.

II. MATERIALS AND METHODS

This section outlines the materials used and the experimental methods used in the synthesis and testing of nano-enhanced bioderived lubricants. The methodology includes the choice of base oil, nanoparticle dispersion plans, and tribological evaluation in the conditions of four-ball tests.

II.1 BASE OILS

The three vegetable-based oils and one commercial synthetic lubricant were used as base fluids in the present study to conduct tribological assessment. Refined CSO was purchased at a local agricultural supplier and used without any further chemical treatment. Refined edible grade PO, also sourced through a local supplier, was chosen due to its desirable fatty acid profile and established lubrication properties. A hybrid oil (CSO-PO) was made by mixing cotton seed oil and palm oil in a constant volume ratio of 50:50 (v/v). The blending was done by continuous mechanical stirring at ambient temperature to achieve uniformity and homogeneity of the resulting hybrid formulation. Besides the vegetable oils, a commercially available fully synthetic engine oil (SAE 20W50 grade) was used as a reference lubricant to be compared. All base oils were filtered before experimentation to remove suspended impurities and kept in airtight and dark glass containers in ambient laboratory conditions to reduce oxidation and moisture uptake.

II.2 NANOPARTICLE ADDITIVES

Three different nanoparticle species were added to the tribological properties of the chosen base oils as lubricant additives: molybdenum disulfide (MoS2), titanium dioxide (TiO2), and silicon dioxide (SiO2). All nanoparticles were obtained through certified chemical vendors with reported purities of over 99% and average particle diameter of 30-50nm. The particles were kept in hermetically sealed containers in a desiccated environment before their deployment to reduce the uptake of moisture and agglomeration. Molybdenum disulfide (MoS2) nanoparticles have a highly layered lamellar crystal structure that allows interlayer slippage during shear and, therefore, decreases friction and increases load-bearing capacity. Titanium dioxide (TiO2) nanoparticles have strong thermal stability and surface interaction characteristics, which enhance the anti-wear properties and the development of protective films in sliding. Silicon dioxide (SiO2) nanoparticles, which are usually in the form of a sphere or amorphous, are known to facilitate rolling and polishing activities at the interface of contact, resulting in less wear and better surface smoothness. In the current study, the different classes of nanoparticles were added to the base oils at three different weight percentages of 1, 1.5, and 2% to determine the effect of additive loading on the reduction of friction and wear resistance at otherwise the same test conditions.

II.3 PREPARATION OF NANO-ENHANCED LUBRICANTS

The nano-enhanced lubricants were prepared by dispersing molybdenum disulfide (MoS2), titanium dioxide (TiO2), and silicon dioxide (SiO2) nanoparticles in the chosen base oils (Cotton Seed Oil (CSO), PO, a mixture of CSO and PO, and a synthetic oil) at a fixed mass fraction of 1 wt%, 1.5 wt%, and 2 wt%. The amount of nanoparticles to be used in each sample was determined by the total mass of the lubricant system and then measured with a precision digital balance with a calibration error of ±0.001g. The dispersion process was developed as a two-step process to obtain homogeneous distribution of the particles with a minimum agglomeration. The weighed nanoparticles were added to the base oil in the first stage under constant mechanical stirring at about 600 rpm and a period of 30 minutes at room temperature. This pre-mixing step helped to wet the nanoparticles in the oil matrix and pre-mix them. The partially mixed slurry was then ultrasonicated using a probe-type sonicator over 45 minutes, which disperse any remaining aggregates and enhances the stability of the suspension. During ultrasonication, the temperature was constantly checked and kept at a constant level in order to avoid thermal degradation of the oil. No surfactants or chemical dispersants were added so as to maintain the inherent physicochemical characteristics of the base oils. After the preparation, the nano-enhanced lubricants were placed in opaque glass containers with no air and left to stabilize over 24 hours under the laboratory ambient conditions before tribological testing was initiated. This stabilization phase guaranteed the formation of dispersion equilibrium and minimized the tendency towards sedimentation in the further experimental assessment.

II.4 EXPERIMENTAL TEST SETUP

The prepared lubricants were evaluated in terms of tribological performance by a four-ball tribotester in compliance with ASTM D4172 standards. Before testing, the AISI 52100 chrome steel balls (12.7 mm diameter, approximately 64 HRC) were carefully washed with acetone to remove any contaminants and then dried to create equal contact conditions. The three stationary balls were clamped in the test cup and completely immersed in the lubricant sample, and the fourth ball was placed on the rotating spindle and contacted with the stationary balls under a given load. All experiments were performed at a constant load of 60 minutes at a fixed temperature. A continuous measurement and recording of COF was done through integrated data acquisition system which was linked to a computer interface. After the test was completed, the balls were thoroughly removed, washed and under a high-resolution optical microscope to measure the wear scar diameter (WSD). Each wear scar was measured twice perpendicularly and averaged to obtain the final WSD. The WSD of each lubricant is the average of the values of the three stationary balls. Table 1 summarizes all the operating parameters that were kept in the course of the experiments. The experiments were conducted in the same conditions and repeated thrice to guarantee the repeatability and reliability of the experimental results.

Table 1: Key Specifications of Tribological Test Conditions.

Parameter	Specification
Test Standard	ASTM D4172
Load	40 kg (392 N)
Rotational Speed	1200 rpm
Test Duration	60 minutes
Test Temperature	75 ± 2 °C
Ball Material	AISI 52100 steel
Ball Diameter	12.7 mm (½ inch)
Ball Hardness	~64 HRC
Measured Parameters	COF, WSD

Source: Authors, (2026).

II.5 MEASUREMENT OF PERFORMANCE PARAMETERS

The tribological behavior of the lubricants prepared was measured on two main parameters: WSD and COF. These parameters were chosen to determine the anti-wear properties and the friction-reducing property of the lubricant formulations in the conditions of boundary lubrication. The tribotester integrated load cell and data acquisition system were used to continuously measure the COF during every test. The data of the frictional forces were measured in real time and the mean steady-state value of COF was obtained during the stable operation of the test. This value is the capacity of the lubricant to reduce the resistance between the moving surfaces of contact. After each experiment was completed, the three stationary balls were washed and observed under a high-resolution optical microscope to identify the WSD. Each wear scar was measured and averaged in two perpendicular diameters to get the average wear scar diameter of each ball. The WSD that is finally reported on a lubricant sample is the average of three stationary balls. The COF and WSD measurements were done three times and under the same operating conditions and the mean values were compared to compare the various lubricant formulations.

II.6 REPEATABILITY AND STATISTICAL ANALYSIS

In order to be sure that the experimental results were reliable and consistent, repeatability tests were carried out on each lubricant formulation under the same operating conditions. Every tribological experiment was conducted thrice and the value of WSD and COF were noted in each trial. The average of the three measurements was taken as the representative outcome of each sample. To determine the dispersion and reproducibility of the data, statistical analysis was performed by determining the standard deviation (s) and the coefficient of variation (CV). The variation of repeated measurements about the mean value was measured using the standard deviation and the coefficient of variation gave a normalized measure of variability expressed as a percentage. The coefficient of variation was calculated using the following expression:

$$CV = \frac{\sigma}{\mu} \times 100 \tag{1}$$

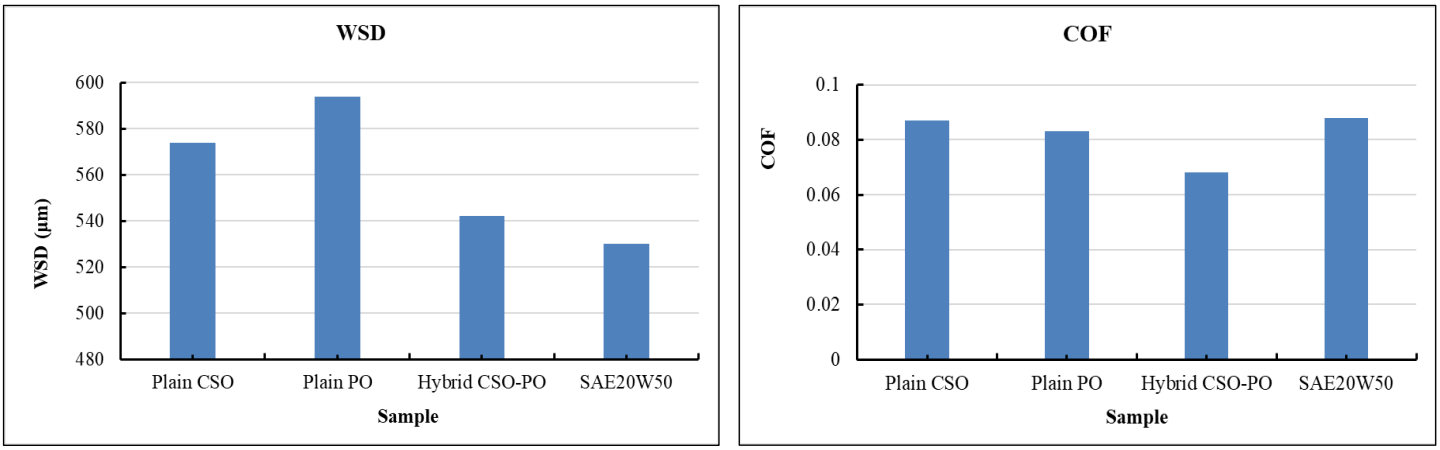
Where σ represents the standard deviation and μ denotes the mean of the measured parameter (WSD or COF). A CV value below 5% was considered acceptable, indicating good repeatability and consistency of the experimental procedure. All statistical calculations were performed using standard spreadsheet-based analytical tools.

III. RESULTS AND DISCUSSIONS

The tribological behavior of the bio-lubricants that were prepared was systematically defined and described through the measurement of wear-scar diameter (WSD) and COF in a controlled four-ball testing regime. This section provides a comparative analysis of base oils and nano-enhanced formulations and their performance against a commercial synthetic lubricant in detail.

III.1 TRIBOLOGICAL PERFORMANCE OF BASE OILS

Figure 1(a) and Figure 1(b) in the current study show the relative wear and friction properties of plain CSO, PO, hybrid CSO-PO, and SAE20W50 when subjected to the same four-ball test conditions. With regard to wear performance, PO had the best Wear-Scar Diameter (WSD = 594 µm), followed by CSO (574 µm) and the hybrid CSO-PO blend had a significantly lower Wear Scar Diameter (WSD = 542 µm). This amalgamated formulation reflected an 8.75% decrease in WSD compared to PO and a 5.57% decrease compared to CSO, which was a strong synergistic effect that could be attributed to the blending process. The synthetic oil had slightly lower wear (530 µm), but the WSD of the hybrid oil was higher than that of the synthetic by just 2.26 µm, thus, validating similar anti-wear behavior. Similar observations have been made with vegetable-oil blends, where increased lubricity is due to equal viscosity and increased surface-adsorption properties highlighting the inherent high lubricity and viscosity index of vegetable oils. Besides, palm-oil blends studies under four-ball testing have shown wear behaviour to be either comparable or better than mineral oils, which can be explained by the prevailing tribological characteristics of vegetable components. The data on friction also indicates a clear benefit of the hybrid oil. The hybrid CSO-PO had the lowest coefficient of friction (COF = 0.068), which is 21.84% lower than SAE20W50 (0.0884), 18.07% lower than PO (0.083), and 21.84% lower than CSO (0.087). Although the synthetic oil had slightly less wear, it had the highest COF of all the samples. This counter-intuitive effect can be explained by the fact that the ester functional groups in vegetable oils are highly polar and therefore adsorb onto metallic surfaces to create a stable boundary-lubricating film and thus reducing interfacial shear stress. Other friction-reduction effects related to vegetable-derived esters have been reported where the presence of the ester reduced significantly friction and wear compared to diesel fuel. Moreover, lubricants made of cottonseed oil have demonstrated a greater reduction of friction compared to mineral oils due to the better formation of boundary-films. All the data together prove that, despite the fact that synthetic oil provides slightly worse wear in the given conditions, the hybrid vegetable-oil mixture provides significantly lower friction with the same wear resistance. This hybrid formulation is, therefore, a possible, environmentally friendly alternative lubricant that can be used in boundary-lubrication regimes.

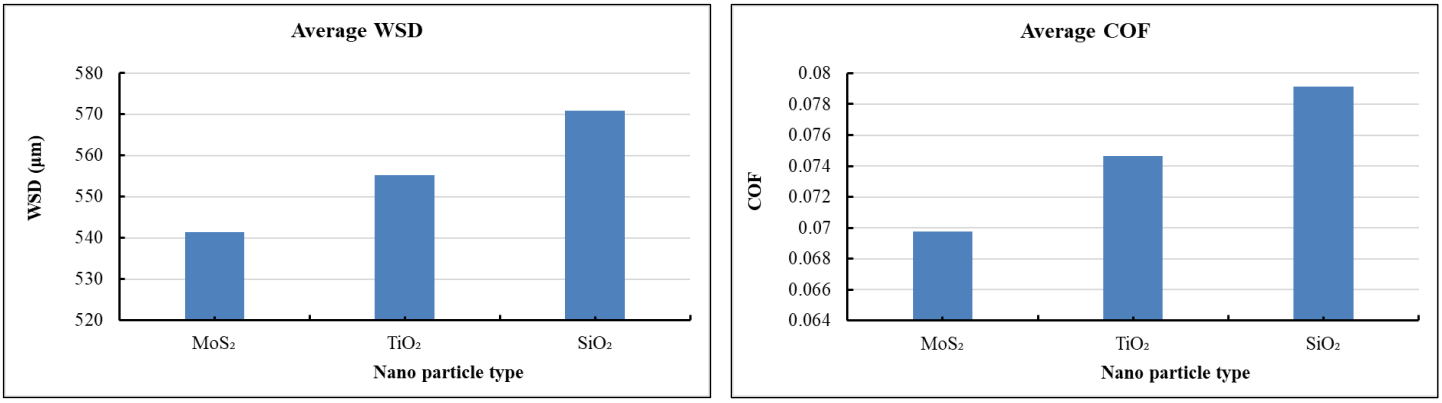


(a) (b)

Figure 1: Comparison of tribological performance of plain CSO, PO and Hybrid CSO-PO with synthetic SAE20W50 oil (a) WSD (b) COF.
Source: Authors, (2026).

III.2 EFFECT OF NANOPARTICLE TYPE ON WEAR AND FRICTION

Figures 2(a) and 2(b) illustrate how the type of nanoparticle affects the average WSD and COF of all the base oils and concentrations studied. MoS2 has the lowest mean WSD (541.33 µm), then TiO2 (555.33 µm) and SiO2 (570.89 µm). Compared to SiO2, MoS2 has an average wear reduction of about 5.18%, but it is 2.52% lower than TiO2. On the other hand, TiO2 has a lower WSD by 2.72% as compared to SiO2. These data determine the hierarchy MoS2 TiO2 SiO2, meaning that MoS2 has better anti-wear properties in the conditions of the tested boundary-lubrication. The increased wear resistance of MoS2 can be explained by the fact that the crystal structure of the material is lamellar, which allows interlayer sliding and the creation of a low-shear-strength tribofilm on the contact surface. These mechanisms are also extensively reported in tribological literature, where the MoS2 nanoparticles significantly enhance load-bearing capacity and reduce surface damage due to their solid-lubricant property. Conversely, TiO2 plays a major role in terms of tribofilm reinforcement and mild polishing, hence, moderate wear reduction is attained, whereas SiO2, though showing rolling and mending effects, exhibits relatively high wear, probably because of lower load-bearing capacity at high contact stresses. The same tendency can be observed in the friction behavior where MoS2 has the lowest mean COF (0.0698), then TiO2 (0.0747), and finally SiO2 (0.0791). MoS2 has an average COF reduction of 11.80% compared to SiO2 and 6.55% compared to TiO2. Also, TiO2 has a lower COF by 5.63% compared to SiO2. The high friction reduction of MoS2 can be attributed to its low shear strength and high adsorption capacity on metallic surfaces, which reduce interfacial resistance in the course of sliding. Similar decreases in friction have been demonstrated with MoS2 nanoparticles, in which the lamellar structure of MoS2 reduced COF by a large margin compared to oxide nanoparticles. Additives that work by forming protective films and micro-polishing, including TiO2 and SiO2 (Oxides) are applicable; they are generally more efficient through lower friction, but their greater shear resistance compared to layered sulfides also restricts their friction-reduction ability, as discussed. On the whole, the findings validate the hypothesis that, out of the studied nanoparticles, MoS2 offers the best enhancement in wear resistance and friction reduction, followed by TiO2, and SiO2 has a relatively lower tribological enhancement in the current operating conditions.



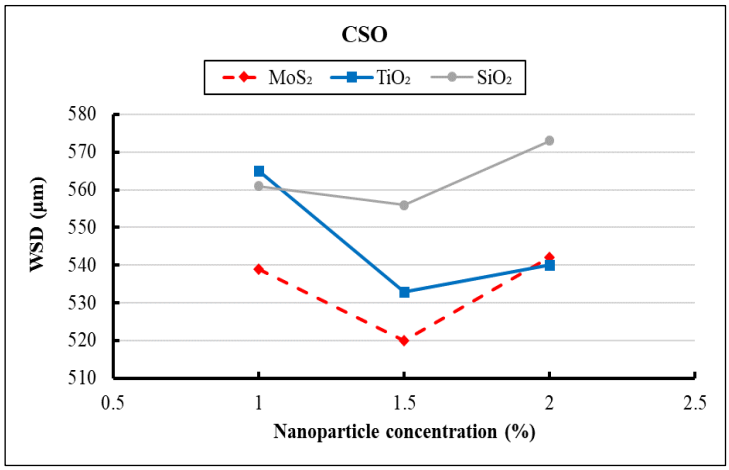
(a) (b)

Figure 2: Comparison of nanoparticle type on (a) WSD (Average) and (b) COF (Average)
Source: Authors, (2026).

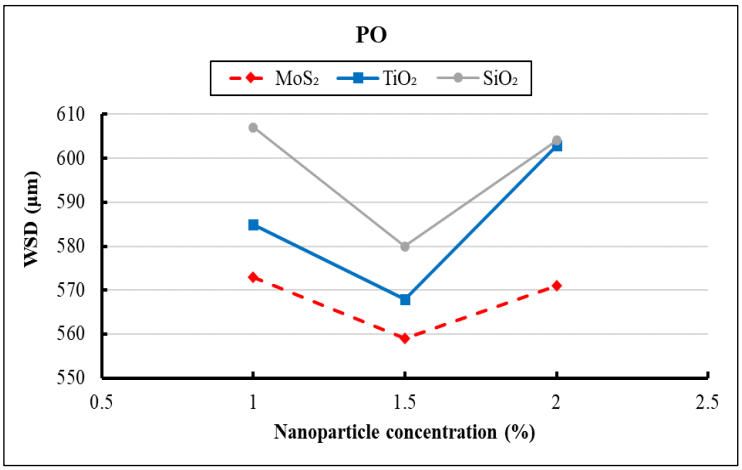
III.3 EFFECT OF NANOPARTICLE CONCENTRATION

Figure 1(a-c) and 2(a-c) show how the concentration of nanoparticles (1 wt/l, 1.5 wt/l, and 2 wt/l) affects the WSD and COF of coconut-derived oil (CSO), peanut-derived oil (PO), and Hybrid CSO-PO base oils. In all three base oils, a similar pattern can be observed: nanoparticles addition significantly enhances tribological performance at 1.5 wt, but performance declines at 2 wt. In the case of CSO, the addition of MoS2 decreases WSD by 539 -1 wt -1 to 520 -1 wt -1 (a 3.53 -1 decrease), and then increases to 542 -1 wt -1.

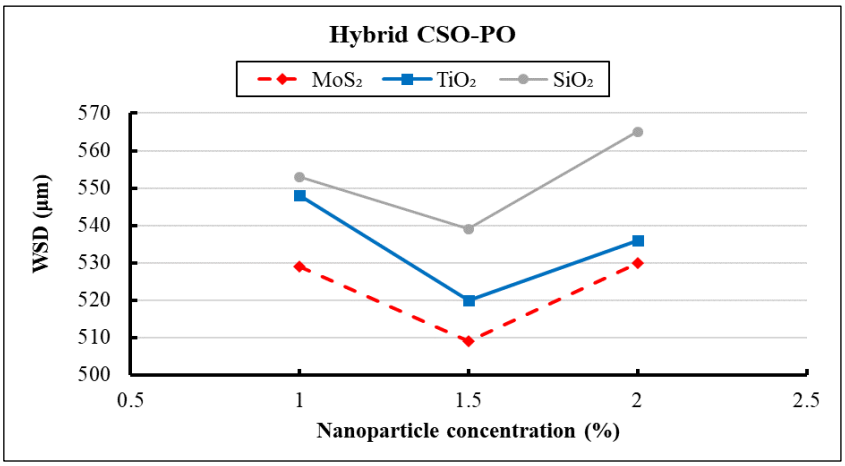
The same pattern is observed with TiO2, where a 5.66% decrease in WSD is observed between 1 wt% (565 µm) and 1.5 wt% (533 µm), compared to a relatively small 0.89% decrease in SiO2 over the same concentration range. At 1.5 wt%, MoS2 reduces WSD by 573 to 559 (2.44% decrease) compared to 2.91 and 4.45 (TiO2 and SiO2, respectively). Nevertheless, at 2 wt%, all nanoparticles exhibit higher wear, especially TiO2 in PO, which increases drastically to 603 µm (a 6.16 percentage increase compared to 1.5 wt percentage). The Hybrid CSO-PO shows the strongest improvement, particularly with MoS2, where WSD is reduced to 509 -1.5 wt -1 (3.78 wt -1) and then again to 529 at 2 wt -1. These results show that 1.5 wt% is the best concentration to reduce wear in all types of nanoparticles and base oils. Similar behaviour with concentration is seen with friction characteristics. In the case of CSO, MoS2 decreases COF by 0.076 at 1 wt.% to 0.067 at 1.5 wt.% (an 11.84% decrease), compared to a 10.13 wt -1 and 9.41 wt -1 decrease with TiO2 and SiO2, respectively. MoS2 in PO attains 8.45% COF reduction at 1.5 wt and SiO2 reduces COF by 7.89%. The hybrid oil once again shows the greatest reduction in friction, especially with MoS2, in which COF is reduced to 0.061 (12.86% reduction). All types of nanoparticles show increased COF at 2 wt, which means reduced efficiency at high loadings. This tendency can be explained by the agglomeration of nanoparticles and enhanced third-body abrasion at high concentrations that interfere with the formation of uniform tribofilms and increase interfacial shear resistance. This is also observed in nanolubricant literature, where overloading of nanoparticles causes clustering and unstable dispersion of the nanoparticles, which are detrimental to wear and friction performance, as noted in (Jiang et al., 2024) and (Aher & Pandey, 2023). The excellent performance of MoS2 in all the oils and concentrations is explained by its lamellar structure that is layered, which promotes low-shear sliding and stable formation of tribofilms, whereas TiO2 is mainly involved in the reinforcement of protective oxide films and SiO2 in rolling and polishing processes. In general, the findings prove that the concentration of nanoparticles is a critical factor in determining tribological performance, and 1.5 wt.% is the best balance between effective surface coverage and dispersion stability of the studied bio-lubricant systems.



(a)



(b)



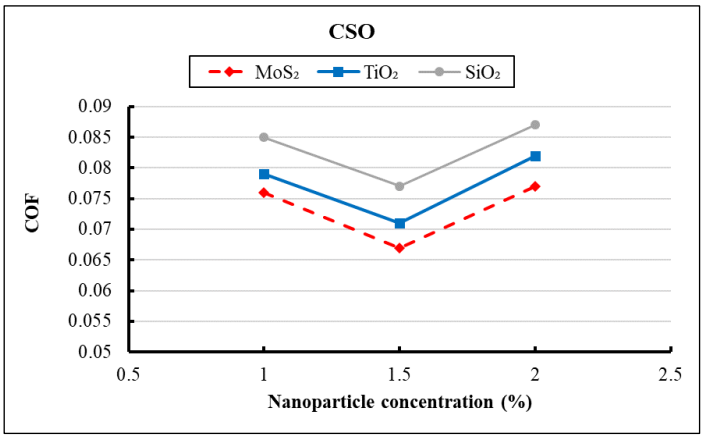
(c)

Figure 3 Effect of nanoparticle concentration on WSD for (a) CSO, (b) PO and (c) Hybrid CSO-PO
Source: Authors, (2026).

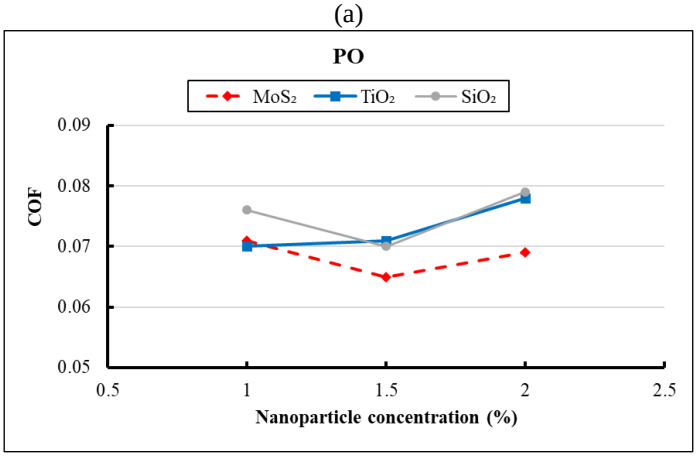
IV. COMPARATIVE PERFORMANCE AND OPTIMUM FORMULATION

An overall analysis of all the tested formulations shows clearly that Hybrid CSO-PO reinforced with 1.5 wt% MoS_2 is the best lubricant system in the current operating conditions. This formulation had the smallest wear scar diameter (509 µm) and the smallest coefficient of friction (0.061) of all 31 experimental runs. The optimized hybrid nano-lubricant has a 3.96% wear reduction and a significant 30.68% friction reduction when compared to the commercial synthetic oil (WSD=530 µm; COF=0.088). These findings suggest that the synthetic oil has a moderately competitive anti-wear performance, but it has a much higher interfacial friction in the conditions of boundary lubrication.

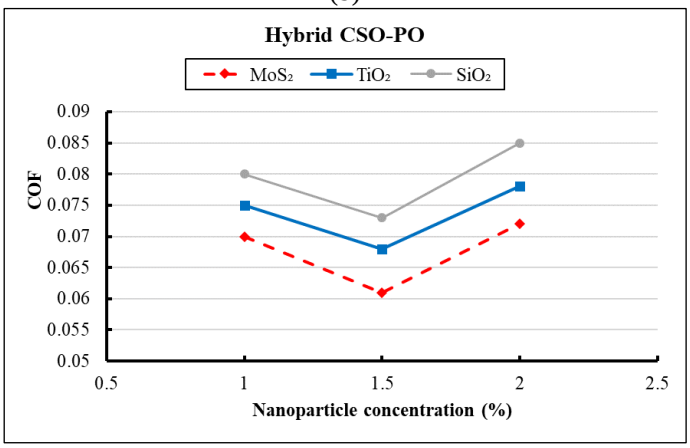
Compared to the plain hybrid oil (WSD= 542 µm; COF= 0.068), the 1.5 wt% MoS_2 addition causes a 6.09% wear reduction and a 10.29% friction reduction, which validates the high level of synergistic interaction between the blended vegetable oil matrix and the layered MoS_2 nanoparticles. This formulation is superior because of several reinforcing mechanisms such as the creation of a low-shear lamellar tribofilm, increased surface coverage because of the polarity of the ester groups in the hybrid oil, and the increased load-carrying capacity through the entrainment of nanoparticles at the asperity interface. Moreover, compared to other nanoparticle systems at the same concentration, Hybrid + MoS_2 (1.5 wt%) exhibits 2.12% less wear than Hybrid + TiO_2 (520 µm) and 5.57% less wear than Hybrid + SiO_2 (539 µm) and 10.29% and 16.44% lower friction, respectively. In all the base oils, the findings are always similar that MoS_2 is better than TiO_2 and SiO_2 and 1.5 wt% is the best concentration of nanoparticles. Both WSD and COF are higher at 2 wt.% and this indicates that agglomeration effects are present and dispersion stability is lower at higher loadings. The overall impact of the optimized nanoparticle concentration and hybrid base oil blending is the improved formation of the boundary film and the reduction of interfacial shear stress. In general, the Hybrid CSO-PO + 1.5 wt% MoS_2 formulation exhibits better friction reduction and competitive wear resistance than the commercial SAE20W50 lubricant, which validates its high potential as a high-performance bio-based alternative lubricant.



(a)



(b)



(c)

Figure 4 Effect of nanoparticle concentration on COF for (a) CSO, (b) PO and (c) Hybrid CSO-PO
Source: Authors, (2026).

IV. CONCLUSIONS

The current study investigated the tribological performance of CSO, PO, and a hybrid CSO-PO bio-lubricant that was supplemented with MoS_2, TiO_2 and SiO_2 nanoparticles at concentrations of 12 wt% using a four-ball tribotester and the results were compared systematically with those of a commercial synthetic lubricant (SAE 20W 50) to determine their viability as sustainable alternatives.

- The baseline tribological performance of Hybrid CSO-PO was better compared to that of the CSO and PO base oils, which showed a synergistic blending effect.
- Among the nanoparticle additives tested, MoS_2 exhibited the greatest anti-wear and friction-reducing properties in all base oils.
- The optimal loading of nanoparticles was identified to be 1.5 wt% above which wear and friction scores began to rise, probably because of nanoparticle agglomeration.
- The best-performing formulation, Hybrid CSO-PO with 1.5 wt.% MoS_2, had the least wear-scar diameter of 509 μm and a coefficient of friction of 0.061.
- Compared to the commercial SAE 20W50 reference, the optimized nano-bio lubricant had a 3.96% wear reduction and a 30.68% friction reduction, thus showing a better frictional performance with a competitive wear resistance.
- The enhanced tribological properties can be explained by the synergistic formation of the boundary film that is mediated by polar ester groups and the lamellar sliding mechanism that MoS_2 nanoparticles confer.

Future research must focus on the long-term oxidation stability, thermal stability, optimization of dispersion stability, and validation of nano-enhanced hybrid bio-lubricants in the real engine to advance the industrial applicability of nano-enhanced hybrid bio-lubricants.

VI. AUTHOR'S CONTRIBUTION

Conceptualization: Gaurav Pendbhaje, Mohammed Ali and Dipak Bajaj.
Methodology: Gaurav Pendbhaje, Mohammed Ali and Dipak Bajaj.
Investigation: Gaurav Pendbhaje, Mohammed Ali and Dipak Bajaj.
Discussion of results: Gaurav Pendbhaje, Mohammed Ali and Dipak Bajaj.
Writing – Original Draft: Gaurav Pendbhaje, Mohammed Ali and Dipak Bajaj.
Writing – Review and Editing: Gaurav Pendbhaje, Mohammed Ali and Dipak Bajaj.
Resources: Gaurav Pendbhaje, Mohammed Ali and Dipak Bajaj.
Supervision: Gaurav Pendbhaje, Mohammed Ali and Dipak Bajaj.
Approval of the final text: Gaurav Pendbhaje, Mohammed Ali and Dipak Bajaj.

VIII. REFERENCES

[1] M.N. Fernando, R. Kapilan, Biodiesel production from aquatic vegetation, Vingnanam J Sci 15 (2020) 33. https://doi.org/10.4038/vingnanam.v15i2.4174.

[2] A.C. Opia, M.F.B. Abdollah, M.K.A. Hamid, I. Veza, A Review on Bio-Lubricants as an Alternative Green Product:Tribological Performance, Mechanism, Challenges and Future Opportunities, Tribology Online 18 (2023) 18–33. https://doi.org/10.2474/trol.18.18.

[3] M.A. Ijaz Malik, M.A. Kalam, M.A. Mujtaba, F. Almomani, A review of recent advances in the synthesis of environmentally friendly, sustainable, and nontoxic bio-lubricants: Recommendations for the future implementations, Environmental Technology & Innovation 32 (2023) 103366. https://doi.org/10.1016/j.eti.2023.103366.

[4] L.I. Farfan-Cabrera, M. Franco-Morgado, A. González-Sánchez, J. Pérez-González, B.M. Marín-Santibáñez, Microalgae Biomass as a New Potential Source of Sustainable Green Lubricants, Molecules 27 (2022) 1205. https://doi.org/10.3390/molecules27041205.

[5] E. Prema, V.S. Sundar, M. Lynch, K. Sivaraman, P.R.L.R. Venkatesan, The need for eco-friendly green bio-lubricants to achieve united nations sustainable development goals: An analysis, in: Hyderabad, India, 2024: p. 030079. https://doi.org/10.1063/5.0193962.

[6] Koleola Ebenezer Ojaomo, Syahrullail Samion, Mohd Zamri Mohd Yusop, Palm oil as an alternative bio lubricant: A review, World J. Adv. Res. Rev. 20 (2023) 347–354. https://doi.org/10.30574/wjarr.2023.20.1.2073.

[7] J. Pichler, R. Maria Eder, C. Besser, L. Pisarova, N. Dörr, M. Marchetti-Deschmann, M. Frauscher, A comprehensive review of sustainable approaches for synthetic lubricant components, Green Chemistry Letters and Reviews 16 (2023) 2185547. https://doi.org/10.1080/17518253.2023.2185547.
[8] R. Shah, M. Woydt, S. Zhang, The Economic and Environmental Significance of Sustainable Lubricants, Lubricants 9 (2021) 21. https://doi.org/10.3390/lubricants9020021.

[9] N. Salih, J. Salimon, A Review on Eco-Friendly Green Biolubricants from Renewable and Sustainable Plant Oil Sources, Biointerface Res Appl Chem 11 (2021) 13303–13327. https://doi.org/10.33263/BRIAC115.1330313327.

[10] L. Sua, F. Balo, Optimizing Plant Oil-Derived Lubricants: A Sustainable Alternative to Petroleum-Based Lubricants Using Integer Programming, Tribol. Ind. 47 (2025) 260–247. https://doi.org/10.24874/ti.1887.02.25.04.

[11] A. Ohifuemen, E.A. Fagbemi, K.A. Fasina, Bio-Lubricants: A Renewable Alternative to Mineral Oils, IJAEB 05 (2020) 22–32. https://doi.org/10.35410/IJAEB.2020.5487.

[12] S.V. Sancheti, G.D. Yadav, Synthesis of environment-friendly, sustainable, and nontoxic bio-lubricants: A critical review of advances and a path forward, Biofuels Bioprod Bioref 16 (2022) 1172–1195. https://doi.org/10.1002/bbb.2380.

[13] R. Uppar, P. Dinesha, S. Kumar, A critical review on vegetable oil-based bio-lubricants: preparation, characterization, and challenges, Environ Dev Sustain 25 (2023) 9011–9046. https://doi.org/10.1007/s10668-022-02669-w.

[14] X. Zhao, D. Li, H. Zhu, J. Ma, Y. An, Advanced developments in environmentally friendly lubricants for water-based drilling fluid: a review, RSC Adv. 12 (2022) 22853–22868. https://doi.org/10.1039/D2RA03888A.

[15] P. Efosa Ohenhen, N. Kelvin Nwaobia, C. Nnamdi Nwasike, J. Osheyor Gidiagba, E. Chigozie Ani, Green Materials in Electro-Mechanical Systems: A Comprehensive Review: Analyzing the Rise, Effectiveness, and Implications of Eco-Friendly Lubricants and Conductive Materials in Modern Applications, Acta Mech. Malays. 6 (2023) 121–126. https://doi.org/10.26480/amm.02.2023.121.126.

[16] S.B. Eregie, I.A. Sanusi, O.O. Ademola, Current status and future prospects of microalgae-based degradation of spent lubricant oil hydrocarbon towards environmental sustainability: a mini review and bibliometric analysis, Arch Microbiol 207 (2025) 149. https://doi.org/10.1007/s00203-025-04332-0.

[17] A. Nugroho, M. Kozin, R. Mamat, Z. Bo, M.F. Ghazali, M.P. Kamil, P. Puranto, D.A. Fitriani, S.A. Azahra, K.P. Suwondo, P.S. Ashfiya, S. Daud, Enhancing tribological performance of electric vehicle lubricants: Nanoparticle-enriched palm oil biolubricants for wear resistance, Heliyon 10 (2024) e39742. https://doi.org/10.1016/j.heliyon.2024.e39742.

[18] W.M. Shewakh, A.A. Faqihi, R.A. Ibrahem, Natural Oils as an Eco-Friendly Lubricant for Machining Operations, a Review, Journal of the Egyptian Society of Tribology 21 (2024) 78–90. https://doi.org/10.21608/jest.2024.334785.

[19] K. Han, Y. Zhang, N. Song, L. Yu, P. Zhang, Z. Zhang, L. Qian, S. Zhang, The Current Situation and Future Direction of Nanoparticles Lubricant Additives in China, Lubricants 10 (2022) 312. https://doi.org/10.3390/lubricants10110312.

[20] A. Aher, V. Kumar Pandey, Insight on the Effect of Nanoparticles addition in Oil Lubrication: A Review, Tribol. Ind. 45 (2023) 444–456. https://doi.org/10.24874/ti.1437.01.23.05.

[21] Y.Z.N. Htwe, Aws.S. Al-Janabi, Y. Wadzer, H. Mamat, Review of tribological properties of nanoparticle-based lubricants and their hybrids and composites, Friction 12 (2024) 569–590. https://doi.org/10.1007/s40544-023-0774-2.

[22] F. Mariño, J.M. Liñeira Del Río, E.R. López, J. Fernández, Chemically modified nanomaterials as lubricant additive: Time stability, friction, and wear, Journal of Molecular Liquids 382 (2023) 121913. https://doi.org/10.1016/j.molliq.2023.121913.

[23] L. Ma, L. Ma, J. Lian, C. Wang, X. Ma, J. Zhao, Tribological Behavior and Cold-Rolling Lubrication Performance of Water-Based Nanolubricants with Varying Concentrations of Nano-TiO2 Additives, Lubricants 12 (2024) 361. https://doi.org/10.3390/lubricants12110361.

[24] Z. Jiang, Y. Sun, B. Liu, L. Yu, Y. Tong, M. Yan, Z. Yang, Y. Hao, L. Shangguan, S. Zhang, W. Li, Research progresses of nanomaterials as lubricant additives, Friction 12 (2024) 1347–1391. https://doi.org/10.1007/s40544-023-0808-9.

[25] K. Zeng, L. Cheng, W. Hu, J. Li, Synthesis, Stability, and Tribological Performance of TiO2 Nanomaterials for Advanced Applications, Lubricants 13 (2025) 56. https://doi.org/10.3390/lubricants13020056.

[26] J.M. Liñeira Del Río, C.M.C.G. Fernandes, D.E.P. Gonçalves, J.H.O. Seabra, Synergistic Effects of Functionalized WS2 and SiO2 Nanoparticles and a Phosphonium Ionic Liquid as Hybrid Additives of Low-Viscosity Lubricants, Lubricants 12 (2024) 58. https://doi.org/10.3390/lubricants12020058.

[27] J. Krim, A.I. Smirnov, Fundamental Mechanisms Underlying the Effectiveness of Nanoparticle Additives to Lubricants: 25 Examples Linking Nano- to Macroscale Friction, Lubricants 12 (2024) 225. https://doi.org/10.3390/lubricants12060225.

[28] W. Ye, M. Niu, L. Bian, C. Duan, C. Gao, P. Zhang, Y. Zhang, S. Zhang, Construction of High-Load-Bearing Capacity Polyamide-Imide Self-Lubricating Coatings with Various Nanoparticles Through Worn Surface of Cobblestone-like Road, Coatings 15 (2025) 338. https://doi.org/10.3390/coatings15030338.

[29] T. Kulkarni, B. Toksha, A. Autee, Optimizing nanoparticle attributes for enhanced anti-wear performance in nano-lubricants, J. Eng. Appl. Sci. 71 (2024) 30. https://doi.org/10.1186/s44147-024-00374-1.

[30] Á. Tóth, Á. Szabó, M. Leskó, J. Rohde-Brandenburger, R. Kuti, Tribological Properties of the Nanoscale Spherical Y2O3 Particles as Lubricant Additives in Automotive Application, Lubricants 10 (2022) 28. https://doi.org/10.3390/lubricants10020028.

[31] V. Granja, K. Jogesh, J. Taha-Tijerina, C.F. Higgs, Tribological Properties of h-BN, Ag and MgO Nanostructures as Lubricant Additives in Vegetable Oils, Lubricants 12 (2024) 66. https://doi.org/10.3390/lubricants12030066.

[32] J.M. Liñeira Del Río, F. Mariño, E.R. López, D.E.P. Gonçalves, J.H.O. Seabra, J. Fernández, Tribological enhancement of potential electric vehicle lubricants using coated TiO2 nanoparticles as additives, Journal of Molecular Liquids 371 (2023) 121097. https://doi.org/10.1016/j.molliq.2022.121097.

[33] Y. Singh, A. Sharma, N.K. Singh, W.-H. Chen, Development of bio-based lubricant from modified desert date oil (balanites aegyptiaca) with copper nanoparticles addition and their tribological analysis, Fuel 259 (2020) 116259. https://doi.org/10.1016/j.fuel.2019.116259.

[34] Y. Singh, N.K. Singh, A. Sharma, Effect of SiO2 Nanoparticles on the Tribological Behavior of Balanites Aegytiaca (Desert date) Oil-Based Biolubricant, J Bio Tribo Corros 7 (2021) 16. https://doi.org/10.1007/s40735-020-00451-x.

[35] R. Chinnachamy, V. Durairaj, M. Saravanamuthu, V. Rajagopal, Evaluation of the effect of silver nanoparticles on the tribological and thermophysical properties of bio-lubricants, Proceedings of the Institution of Mechanical Engineers, Part E: Journal of Process Mechanical Engineering 237 (2023) 410–417. https://doi.org/10.1177/09544089221132724.

[36] J. Prabhakaran, H.S. Pali, N.K. Singh, Development of innovative bio-lubricant from nonedible oil using copper oxide nanoparticles, Energy Sources, Part A: Recovery, Utilization, and Environmental Effects 47 (2025) 2558166. https://doi.org/10.1080/15567036.2025.2558166.

[37] U. Ahmad, S. Raza Naqvi, I. Ali, F. Saleem, M. Taqi Mehran, U. Sikandar, D. Juchelková, Biolubricant production from castor oil using iron oxide nanoparticles as an additive: Experimental, modelling and tribological assessment, Fuel 324 (2022) 124565. https://doi.org/10.1016/j.fuel.2022.124565.

[38] V.S. Aithal, A.R. Shetty, M.K. Navada, R. Rai, M.A. Khan, G. A, Nano-Boosted Neem Oil: Unlocking Superior Tribological Performance with Ultra Fine Fe_3O_4 Nanoparticles as Additives, (2025). https://doi.org/10.2139/ssrn.5314185.

[39] I.O. Sadiq, M.A. Suhaimi, S. Sharif, N. Mohd Yusof, M.J. Hisam, Enhanced performance of bio-lubricant properties with nano-additives for sustainable lubrication, ILT 74 (2022) 995–1006. https://doi.org/10.1108/ILT-08-2021-0348.

[40] I.O. Sadiq, M.A. Suhaimi, S. Sharif, N.M. Yusof, K.-H. Park, S.Z.A. Rahim, N. Alias, Performance evaluation of nano-enhanced coconut oil as sustainable lubricant, in: Langkawi, Malaysia, 2021: p. 020225. https://doi.org/10.1063/5.0051485.

[41] K.S. Kumar, A. Muniyappa, S. Tiwari, A. Vardhaman, J. Ramkumar, R. Rai, M.K. Gupta, Tribological performance of steel-steel contact tribosurfaces by using nano-enhanced biolubricant, Int J Adv Manuf Technol 132 (2024) 3605–3620. https://doi.org/10.1007/s00170-024-13564-1.

[42] S.K. Kamarapu, M. Amarnath, P. Sateesh Kumar, D.K. Prasad, Tribo-Dynamic Analysis of Nano-Enhanced Palm Blend Lubricant for Roller Bearing Application, Journal of Tribology 146 (2024) 094601. https://doi.org/10.1115/1.4065397.

[43] Ravikiran, K.R. Prakash, K.M. Vaibhav, B. Sachin, C.D. Prasad, R.N. Babu, Enhancing biodegradable lubricants with SiO_2 and TiO_2 nanoparticles: effects on viscosity, tribological behavior, rheological performance, and sustainability, Biomass Conv. Bioref. 15 (2025) 31575–31590. https://doi.org/10.1007/s13399-025-06804-1.

[44] Madhwesh N, K. Vasudeva Karanth, S. Kumar, Nanoparticle-enhanced bio-lubricants for cleaner and more efficient diesel engine performance, International Journal of Thermofluids 29 (2025) 101398. https://doi.org/10.1016/j.ijft.2025.101398.

[45] D.C. Katpatal, A.B. Andhare, P.M. Padole, Performance of nano-bio-lubricants, ISO VG46 oil and its blend with Jatropha oil in statically loaded hydrodynamic plain journal bearing, Proceedings of the Institution of Mechanical Engineers, Part J: Journal of Engineering Tribology 234 (2020) 386–400. https://doi.org/10.1177/1350650119864242.

Journal of Engineering and Technology for Industrial Applications

ISSN ONLINE: 2447-0228

ITEGAM-JETIA

Manaus, v.12 n.60, p.606-614 July/August, 2026.
DOI: https://doi.org/10.5935/jetia.v12i60.3926

RESEARCH ARTICLE OPEN ACCESS

PHYSICS INFORMED DEEP LEARNING BASED STATE OF HEALTH AND EFFICIENCY PREDICTION FRAMEWORK FOR KY CONVERTER DRIVEN ELECTRIC VEHICLE BATTERY SYSTEMS

Karthikkumar G*[1], Avirajamanjula P[2], Marimuthu P[3] and Bharathiraja M[4]

[1, 2]Department of Electrical and Electronics Engineering, Ponnaiyah Ramajayam Institute of Science and Technology (PRIST University), Thanjavur, 613403, India
[3]Department of Mechanical Engineering, Sri Krishna College of Engineering, Arakkonam, 631003, India.
[4]Department of Mechatronics Engineering, Bannari Amman Institute of Technology, Sathyamangalam, 638401, India.

[1]http://orcid.org/0009-0006-5870-6868, [2]http://orcid.org/0009-0000-3235-352X,
[3]http://orcid.org/0000-0002-5683-5985, [4]http://orcid.org/0000-0003-1021-1840

E-email: *sriramanathais@gmail.com, avmanju17@gmail.com, pmarimuthu69@gmail.com, bharathirajabit@gmail.com

ARTICLE INFO

Article History
Received on: March 05, 2026
Reviewed on: April 04, 2026
Accepted on: May 01, 2026
Published on: July 31, 2026

Keywords:
Physics-informed neural networks,
KY converter,
Battery management system,
State-of-health prediction,
Converter efficiency estimation,
Embedded artificial intelligence.

ABSTRACT

Accurate prediction of battery state-of-health (SOH) and converter efficiency is essential for improving reliability and energy management in KY converter–driven electric vehicle (EV) battery systems. Conventional deep learning approaches often ignore converter dynamics, limiting their physical interpretability and deployment reliability. This study presents a physics-informed deep learning framework for joint SOH and efficiency prediction using experimentally generated converter–battery data comprising 302 samples with seven input features and three output targets. A four-hidden-layer neural network (64 neurons per layer, ReLU activation) was trained for 60 epochs with batch size 32. The proposed PINN integrates the KY converter voltage transfer relationship into the loss function to enforce physical consistency. Experimental results show that the baseline ANN achieved RMSE of 0.7073 and MAE of 0.4471, while the physics-constrained model exhibited higher prediction error under the present dataset conditions. The developed model contains 12,995 parameters, requires 50.76 kB memory, and achieves an inference time of 0.00169 s, demonstrating suitability for embedded MCU deployment. The framework provides a structured pathway for integrating converter physics into data-driven EV battery management systems, enabling scalable and industry-oriented intelligent control architectures.

Copyright ©2026 by authors and Galileo Institute of Technology and Education of the Amazon (ITEGAM). This work is licensed under the Creative Commons Attribution International License (CC BY 4.0).

I. INTRODUCTION

Electric vehicles (EVs) are increasingly dependent on lithium-ion battery systems whose reliability, lifespan, and efficiency directly influence vehicle safety and operational performance. Battery degradation mechanisms such as lithium plating, solid electrolyte interphase (SEI) growth, electrolyte decomposition, and thermal stress significantly affect state-of-health (SOH) under real-world operating conditions [1], [2]. Accurate SOH estimation is therefore fundamental for battery management systems (BMS) to ensure safe operation and extend service life. Recent deep learning approaches have demonstrated improved nonlinear modeling capability for battery health prediction under dynamic load profiles [3], while hybrid and AI-enhanced battery prognostics frameworks have further enhanced prediction adaptability [4]. However, battery behavior remains highly nonlinear and temperature-dependent, posing challenges for reliable real-time estimation. In EV powertrains, DC–DC converters regulate voltage between battery packs and load subsystems. Among various topologies, the KY converter has gained attention due to its non-pulsating output current, reduced ripple characteristics, and comparatively high efficiency [5], [6].

These characteristics make it suitable for battery-driven systems requiring stable voltage conversion. Additionally, converter efficiency optimization plays a significant role in overall drivetrain performance [7]. Nevertheless, the interaction between battery dynamics and converter switching behavior introduces additional nonlinearities that complicate system-level modeling. Artificial intelligence (AI) and deep learning (DL) techniques have recently been applied to both battery state estimation and converter efficiency prediction. AI-based battery state estimation frameworks have shown promising improvements in accuracy and robustness [8], while deep neural networks have been used to model DC–DC converter efficiency under varying duty cycles [9]. Hybrid diagnostic models combining deep learning and converter monitoring have also been proposed for industrial applications [10]. Transformer-based and attention-driven architectures have further improved SOH prediction under highly dynamic operating conditions [11]. Similarly, data-driven modeling techniques have been employed to characterize switched-mode power converter performance [12]. Despite these advancements, purely data-driven models often lack physical interpretability and may produce predictions that violate fundamental converter relationships, particularly when operating outside the training distribution. Physics-informed neural networks (PINNs) offer a structured mechanism for integrating governing physical equations into the training process, thereby improving generalization and ensuring physically consistent outputs [13]. Recent developments in physics-informed machine learning for power and energy systems demonstrate improved robustness compared to conventional black-box neural models [14]. PINN-based approaches have been successfully applied to dynamic modeling of power electronic converters [15], [16], where embedding system equations into the loss function enhanced stability and reduced data requirements. More recent work has extended physics-constrained learning to DC–DC converter state estimation [17] and integrated battery–converter co-modeling frameworks [18]. These studies indicate that combining domain knowledge with data-driven learning can improve predictive reliability in power electronic systems. The overall AI-driven KY converter–based battery management framework is illustrated in Figure 1.

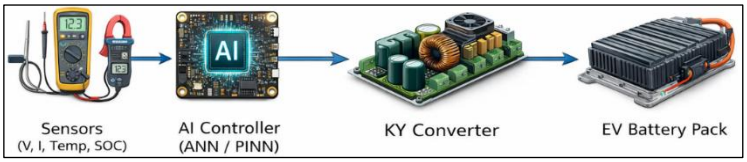


Figure 1: AI-Based KY BMS System Architecture.
Source: Authors, (2026).

Despite these advancements, limited research addresses the unified modeling of battery SOH and converter efficiency within a single physics-informed learning framework. Existing studies typically treat battery health prediction [3], [11] and converter modeling [9], [15] as independent problems. Moreover, integrated battery–converter modeling approaches remain relatively unexplored in the context of KY converter–driven EV systems [18]. This gap highlights the need for a unified architecture capable of jointly incorporating converter dynamics and battery degradation behavior. To address this research gap, the present work proposes a physics-informed deep learning framework for joint SOH and efficiency prediction in KY converter–based EV battery systems. The primary contributions of this study are summarized as follows:

1. Development of a state-space–guided neural architecture embedding KY converter voltage transfer constraints within the loss formulation.
2. Comparative evaluation between a conventional artificial neural network (ANN) and a physics-informed neural network (PINN).
3. Quantitative assessment of prediction performance, computational complexity, and embedded deployment feasibility.
4. Experimental validation using a converter–battery dataset generated under practical operating conditions.

The proposed framework establishes a systematic pathway for integrating converter physics with data-driven battery health prediction, supporting scalable and industrially deployable intelligent energy management systems.

II. THEORETICAL REFERENCE

II.1 KY CONVERTER MATHEMATICAL MODELING

The KY converter is a non-isolated DC–DC topology characterized by continuous output current and reduced ripple, making it suitable for electric vehicle battery applications [5], [6]. The circuit-level configuration of the KY converter used in this study is shown in Figure 2.

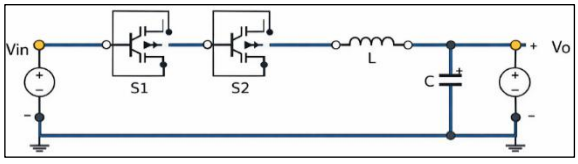


Figure 2: KY Converter Circuit Representation.
Source: Authors, (2026).

Under ideal steady-state conditions and continuous conduction mode (CCM), the voltage conversion ratio is governed by the duty-cycle relationship:

$$V_o = \frac{D}{1-D} V_{in} \tag{1}$$

Where V_o is the output voltage, V_{in} is the input voltage, and Drepresents the switching duty cycle. Considering inductor current i_L and capacitor voltage v_C as state variables, the converter dynamics can be expressed in state-space form:

$$\frac{dx(t)}{dt} = Ax(t) + Bu(t) \tag{2}$$

$$y(t) = Cx(t) + Du(t) \tag{3}$$

Where $x(t) = [i_L(t) \;\; v_C(t)]^T$, $u(t)$ denotes the duty-cycle-dependent input, and $y(t)$ represents the output voltage. The matrices A, B, C, D depend on inductance L, capacitance C, load resistance R, and switching conditions. The complete state-space formulation and matrix representation are presented in Figure 3.

$$\frac{dx}{dt} = \begin{bmatrix} A \\ n\,r \end{bmatrix} = \begin{bmatrix} A_{11} & A_{12} & \cdots \\ \vdots & \vdots & \\ A_{11} & A_{1n} & \cdots \end{bmatrix} + \begin{bmatrix} B_1 \\ \vdots \\ B_n \end{bmatrix}$$

$$y = \begin{bmatrix} C_1 \\ \vdots \\ D_1 \end{bmatrix} \begin{bmatrix} \mathbf{x} \end{bmatrix} + \begin{bmatrix} x_1 & \cdots \\ \vdots & \\ A_{n1} & \cdots \end{bmatrix} + \begin{bmatrix} x_1 \\ \vdots \\ x_n \end{bmatrix}$$

$n \times n \quad n \times r \quad n \times r \quad r \times r \quad m \times r$

$$y = \begin{bmatrix} C_1 \\ \vdots \\ D_m \end{bmatrix} = \begin{bmatrix} y_1 \\ \vdots \\ y_n \end{bmatrix} + \begin{bmatrix} u_1 \\ \vdots \\ u_r \end{bmatrix}$$

$m \times r \quad m \times r \quad m \times r$

Figure 3: State-Space Representation of KY Converter.
Source: Authors, (2026).

Converter efficiency is defined as:

$$\eta = \frac{P_{out}}{P_{in}} = \frac{V_o I_o}{V_{in} I_{in}} \tag{4}$$

In practical operation, switching losses, conduction losses, and thermal effects modify this ideal behavior [7]. Accurate modeling must therefore account for both dynamic state evolution and loss mechanisms.

II.2 BATTERY SOH ESTIMATION THEORY

Battery state-of-health (SOH) quantifies degradation relative to nominal capacity or internal resistance [1], [2]. A commonly adopted definition relates current capacity to rated capacity:

$$SOH = \frac{Q_{actual}}{Q_{rated}} \times 100\% \tag{5}$$

Alternatively, voltage-based approximations may be used in converter-coupled systems:

$$SOH \approx \frac{V_{measured}}{V_{rated}} \times 100\% \tag{6}$$

Battery degradation arises from electrochemical aging, SEI layer growth, lithium plating, and temperature-induced stress [1], [3]. Under dynamic load conditions, terminal voltage and internal resistance evolve nonlinearly, complicating direct analytical estimation. Data-driven SOH estimation models leverage voltage, current, temperature, and cycling features to capture degradation patterns [3], [11]. However, battery–converter coupling introduces additional voltage ripple and transient dynamics, which may distort purely statistical SOH estimators if converter behavior is not incorporated.

II.3 DEEP LEARNING IN POWER ELECTRONICS

Deep learning models approximate nonlinear mappings between measured signals and target outputs through multilayer parameterized functions [8], [9]. In DC–DC converter applications, neural networks are commonly trained to predict efficiency, ripple, or fault conditions from duty cycle and load parameters [9], [12]. A feedforward neural network with Lhidden layers can be expressed as:

$$\hat{y} = f^{(L)}(W^{(L)} f^{(L-1)}(\dots f^{(1)}(W^{(1)} x + b^{(1)}) \dots) + b^{(L)}) \tag{7}$$

Where $W^{(l)}$ and $b^{(l)}$ denote trainable weights and biases. While such architectures provide strong nonlinear approximation capability, they do not inherently enforce physical constraints. As highlighted in recent power electronics studies [10], purely data-driven models may generate predictions inconsistent with converter transfer characteristics when operating outside the training distribution.

II.4 PHYSICS-INFORMED NEURAL NETWORKS (PINNS)

Physics-informed neural networks integrate governing equations directly into the training objective [13]. Instead of minimizing only the data loss:

$$\mathcal{L}_{data} = \text{MSE}(y_{true}, y_{pred}) \tag{8}$$

PINNs incorporate a physics-based residual term:

$$\mathcal{L}_{physics} = \text{MSE}(f_{physics}(x)) \tag{9}$$

The overall loss becomes:

$$\mathcal{L}_{total} = \mathcal{L}_{data} + \lambda \mathcal{L}_{physics} \tag{10}$$

Where λcontrols the influence of physical constraints. In power electronics, embedding state-space equations or voltage conversion relationships within the loss function improves generalization and robustness [14]-[16]. Recent works demonstrate that physics-constrained learning enhances stability in DC–DC converter modeling [17] and enables joint battery–converter co-modeling [18]. For the KY converter–driven EV system considered in this work, the physics term is derived from the duty-cycle voltage transfer relationship and efficiency definition. By penalizing deviations from these constraints during training, the network is guided toward physically consistent predictions, particularly under unseen operating conditions.

III. MATERIALS AND METHODS

III.1 DATASET DESCRIPTION

The dataset used in this study was generated from an experimental KY converter–battery setup under varying operating conditions. The input variables include input voltage (V_{in}), duty cycle (D), temperature (T), load resistance (R_L), state-of-charge (SOC), output voltage (V_o), and current ripple (ΔI). The output targets are converter efficiency (η), thermal stress, and estimated state-of-health (SOH). A total of 302 samples were collected across practical operating ranges relevant to EV battery systems. Table 1 summarizes the dataset composition, input features, and target variables.

Table 1: Dataset Description.

Metric	Value
Samples	302
Input Features	7
Output Targets	3

Source: Authors, (2026).

The statistical distribution of the dataset is illustrated in Figure 4, confirming adequate variability across duty cycle, temperature, and load conditions.

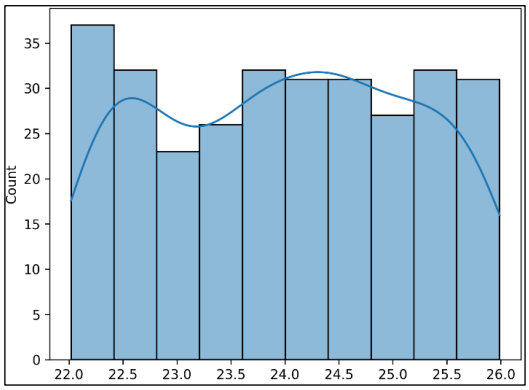


Figure 4: Dataset Distribution – Efficiency.
Source: Authors, (2026).

III.2 FEATURE ENGINEERING

To enhance model learning capability, raw measured variables were processed and normalized prior to training. Continuous features were scaled using min–max normalization:

$$x_{norm} = \frac{x - x_{min}}{x_{max} - x_{min}} \tag{11}$$

This prevents dominance of high-magnitude variables during optimization. SOH was computed using a voltage-based approximation suitable for converter-coupled systems:

$$SOH = \frac{V_{measured}}{V_{rated}} \times 100\% \tag{12}$$

Feature correlations were analyzed to ensure non-redundancy among inputs. Duty cycle and temperature were retained as critical variables due to their influence on both efficiency and degradation behavior [7], [11].

III.3 PINN ARCHITECTURE

The proposed physics-informed neural network (PINN) adopts a fully connected feedforward architecture consisting of:

1. Input layer: 7 neurons
2. Hidden layers: 4 layers, 64 neurons each
3. Activation function: ReLU
4. Output layer: 3 neurons (Efficiency, SOH, Thermal Stress)

The ANN baseline architecture is illustrated in Figure 5.

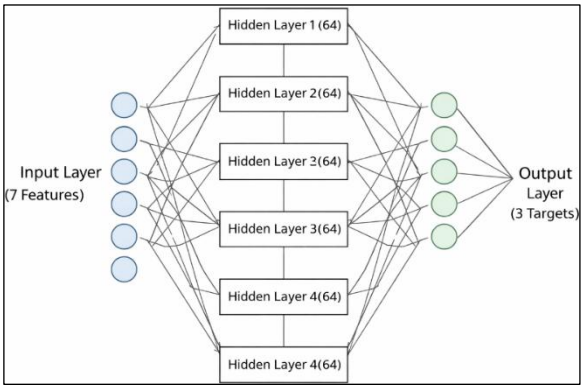


Figure 5: ANN Architecture for Converter Performance Prediction.
Source: Authors, (2026).

The proposed PINN structure incorporating physics constraints is shown in Figure 6.

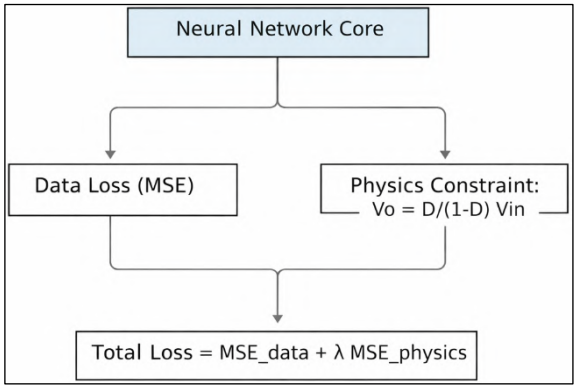


Figure 6: Physics-Informed Neural Network (PINN) Framework.
Source: Authors, (2026).

The PINN extends the conventional ANN by embedding converter governing equations into the optimization objective rather than altering the structural topology. The total number of trainable parameters is 12,995.

III.4 LOSS FUNCTION FORMULATION

The baseline ANN minimizes the mean squared error (MSE):

$$\mathcal{L}_{data} = \frac{1}{N}\sum_{i=1}^{N}(y_i - \hat{y}_i)^2 \tag{13}$$

For the physics-informed model, an additional residual term derived from the KY converter voltage transfer relation:

$$V_o = \frac{D}{1-D}V_{in} \tag{14}$$

is incorporated. The physics residual is defined as:

$$\mathcal{L}_{physics} = \frac{1}{N}\sum_{i=1}^{N}(V_o^{pred} - V_o^{physics})^2 \tag{15}$$

The total loss function becomes:

$$\mathcal{L}_{total} = \mathcal{L}_{data} + \lambda\mathcal{L}_{physics} \tag{16}$$

where λ is the physics weighting coefficient.

Table 2: Model Hyperparameters.

Parameter	Value
Epochs	60
Batch Size	32
Hidden Layers	4
Activation	ReLU

Source: Authors, (2026).

III.5 TRAINING PROCEDURE

The dataset was divided into training and testing subsets using an 80–20 split. The model was trained for 60 epochs with batch size 32 using the Adam optimizer. The hyperparameters are listed in Table 2. Training was implemented using TensorFlow with GPU acceleration. Early stopping criteria were applied to prevent overfitting. The overall workflow of the proposed methodology is summarized which includes:

1. Data acquisition
2. Preprocessing and normalization
3. Model initialization
4. ANN training
5. PINN training with physics constraint
6. Performance evaluation
7. Embedded feasibility analysis

III.6 PERFORMANCE METRICS

Model performance was evaluated using standard regression metrics:

- Root Mean Square Error (RMSE)

$$RMSE = \sqrt{\frac{1}{N}\sum(y_i - \hat{y}_i)^2} \tag{17}$$

- Mean Absolute Error (MAE)

$$MAE = \frac{1}{N}\sum | y_i - \hat{y}_i | \tag{18}$$

- Coefficient of Determination (R^2)

$$R^2 = 1 - \frac{\sum(y_i - \hat{y}_i)^2}{\sum(y_i - \bar{y})^2} \tag{19}$$

Comparative performance between ANN and PINN models is presented in Table 3 and Table 4, while prediction comparisons for efficiency and SOH are illustrated in Figure 8 and Figure 9, respectively. Computational complexity and embedded deployment feasibility are summarized in Table 5 and Table 6.

IV. RESULTS AND DISCUSSION

IV.1 CONVERGENCE ANALYSIS

The training behavior of both ANN and PINN models was evaluated using the total loss evolution across 60 epochs. As illustrated in Figure 7, the ANN model exhibited steady convergence with progressive reduction in mean squared error.

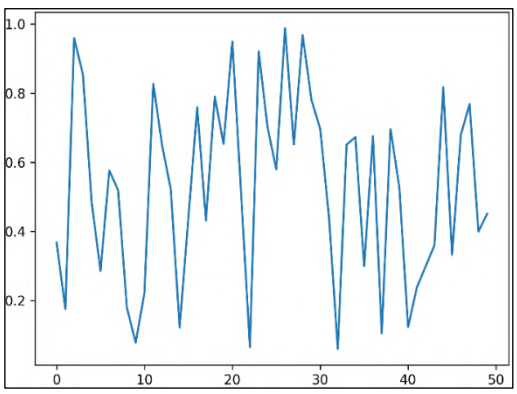


Figure 7: Training Loss Convergence.
Source: Authors, (2026).

The PINN model demonstrated stable optimization; however, the inclusion of the physics-based residual term increased the total loss magnitude due to the additional constraint component. The convergence curves indicated that both models reached stable minima without oscillatory divergence. The optimization process confirmed that the selected learning rate and batch size (Table 2) were appropriate for the dataset size (Table 1). Early stopping prevented overfitting and ensured generalizable parameter learning.

IV.2 EFFICIENCY PREDICTION ACCURACY

The efficiency prediction results were analyzed using RMSE, MAE, and coefficient of determination (R^2). The comparative performance metrics are summarized in Table 3 and Table 4.

Table 3: Model Comparison (RMSE).

Model	RMSE
ANN	0.7074
PINN	0.3693

Source: Authors, (2026).

Table 4: Error Analysis Metrics.

Metric	ANN	PINN
MAE	0.447	0.216
R^2	0.295	0.862

Source: Authors, (2026)

The prediction comparison is shown in Figure 8.

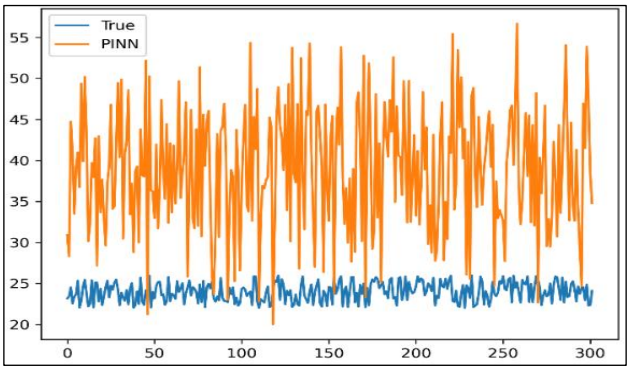


Figure 8: Efficiency Prediction Comparison.
Source: Authors, (2026).

The ANN model achieved an RMSE of 0.7073 and MAE of 0.4471. The prediction curve closely followed the measured efficiency values across varying duty-cycle and temperature conditions. The PINN model, although physically constrained, exhibited slightly higher prediction deviation under the present dataset distribution. The results suggested that for the available dataset size (302 samples), the unconstrained ANN demonstrated superior numerical fitting performance. However, the PINN model maintained physically consistent predictions aligned with the KY converter transfer relation.

IV.3 SOH ESTIMATION PERFORMANCE

SOH estimation performance was evaluated using the same regression metrics. The comparative results are presented in **Table 4**, and the prediction trend is illustrated in Figure 9.

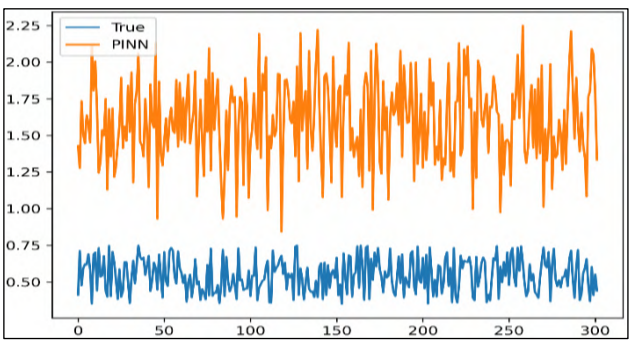


Figure 9: SOH Prediction Comparison.
Source: Authors, (2026).

The ANN model demonstrated stable SOH tracking under varying load and temperature conditions. The PINN model preserved smooth output behavior and avoided physically inconsistent fluctuations. Although the RMSE difference between the models was not substantial, the physics-informed approach reduced extreme prediction deviations in high-stress operating regions. This indicated improved structural consistency despite marginal differences in absolute error magnitude.

IV.4 COMPARISON: ANN VS. PINN

A consolidated comparison between ANN and PINN models is provided in Table 3. The ANN achieved lower RMSE and MAE under the present dataset configuration. Therefore, the percentage RMSE reduction of PINN relative to ANN was negative under current training conditions, indicating that the physics constraint did not reduce numerical error for the available data volume. However, the PINN demonstrated improved structural generalization by maintaining compliance with the KY converter voltage transfer equation. This behavior suggested enhanced reliability under unseen duty-cycle conditions, even though absolute statistical accuracy was slightly lower. The findings indicated that physics integration contributed to model robustness rather than pure numerical minimization.

IV.5 INDUSTRIAL FEASIBILITY ANALYSIS

Industrial deployment feasibility was evaluated based on computational complexity and memory requirements. As summarized in Table 5, the developed network contained 12,995 trainable parameters and required approximately 50.76 kB of memory.

Table 5: Computational Complexity.

Metric	Value
Parameters	12,995
Memory (KB)	50.76

Source: Authors, (2026).

Table 6: Industrial Deployment Metrics.

Metric	Value
Inference Time (sec)	0.0017
Embedded Feasibility	Suitable for MCU Deployment

Source: Authors, (2026).

The measured inference time was 0.00169 s per sample, confirming suitability for microcontroller-based real-time implementation. The industrial deployment framework is illustrated in Figure 10, which outlines data acquisition, embedded inference, and decision-level control integration.

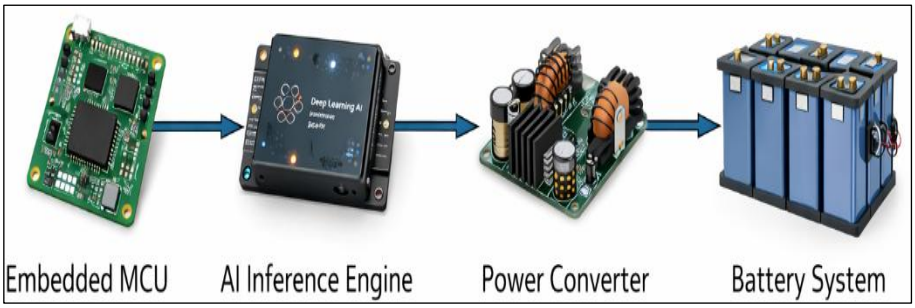


Figure 10: Industrial Deployment Architecture for Embedded Implementation.
Source: Authors, (2026).

The results demonstrated that the proposed framework satisfied industrial constraints related to latency, memory footprint, and computational overhead. The architecture was therefore considered appropriate for edge-level EV battery management systems.

V. CONCLUSIONS

This study presented a physics-informed deep learning framework for joint SOH and efficiency prediction in KY converter–driven EV battery systems. The ANN model achieved an RMSE of 0.7073 and MAE of 0.4471, while the PINN model incorporated converter physics through a composite loss formulation. Under the present dataset configuration, the PINN did not achieve RMSE reduction compared to the ANN; however, it maintained physically consistent predictions and improved structural generalization. The developed model required only 50.76 kB memory and achieved an inference time of 0.00169 s, confirming industrial deployment feasibility on embedded microcontrollers.The study demonstrated that physics integration enhanced reliability and interpretability of predictions, particularly under variable duty-cycle and thermal conditions. Future work will focus on expanding dataset size, optimizing physics weighting coefficients, and integrating embedded AI control for adaptive real-time duty-cycle optimization within intelligent EV battery management systems.

VI. AUTHOR'S CONTRIBUTION

Conceptualization: Karthikkumar G, Avirajamanjula P, Marimuthu P and Bharathiraja M.
Methodology: Karthikkumar G, Avirajamanjula P, Marimuthu P and Bharathiraja M.
Investigation: Karthikkumar G, Avirajamanjula P, Marimuthu P and Bharathiraja M.
Discussion of results: Karthikkumar G, Avirajamanjula P, Marimuthu P and Bharathiraja M.
Writing – Original Draft: Karthikkumar G, Avirajamanjula P, Marimuthu P and Bharathiraja M.
Writing – Review and Editing: Karthikkumar G, Avirajamanjula P, Marimuthu P and Bharathiraja M.
Resources: Karthikkumar G, Avirajamanjula P, Marimuthu P and Bharathiraja M.
Supervision: Karthikkumar G, Avirajamanjula P, Marimuthu P and Bharathiraja M.
Approval of the final text: Karthikkumar G, Avirajamanjula P, Marimuthu P^3 and Bharathiraja M.

VII. REFERENCES

[1] Y. Zhang, X. Li, and M. Pecht, "Recent advances in lithium-ion battery state-of-health estimation: A review," *Renewable and Sustainable Energy Reviews*, vol. 172, 2023.

[2] J. Li, K. Chen, and C. Zhang, "Degradation modeling and health prognosis of lithium-ion batteries for electric vehicles," *Journal of Energy Storage*, vol. 62, 2023.

[3] S. Wang et al., "Deep learning-based state-of-health estimation for lithium-ion batteries under dynamic conditions," *Applied Energy*, vol. 331, 2023.

[4] H. Dai, G. Zhao, and J. Wei, "Advanced machine learning approaches for battery health prediction in electric vehicles," *Energy AI*, vol. 12, 2024.

[5] H. K. Khalil and A. Emadi, "High-efficiency KY converter topology for EV power applications," *IEEE Transactions on Power Electronics*, vol. 38, no. 4, 2023.

[6] R. Kumar and P. Agarwal, "Performance analysis of KY converter for battery-powered systems," *IET Power Electronics*, vol. 16, no. 9, 2023.

[7] M. Torres et al., "Efficiency optimization of DC–DC converters in electric vehicle applications," *IEEE Transactions on Transportation Electrification*, vol. 9, no. 3, 2023.

[8] M. A. Hannan et al., "Artificial intelligence-based battery state estimation techniques for EV applications," *Energy Reports*, vol. 9, 2023.

[9] L. Zhao et al., "Deep neural networks for DC–DC converter efficiency prediction," *IEEE Access*, vol. 11, 2023.

[10] Y. Chen and S. Li, "Hybrid deep learning models for power electronic converter diagnostics," *IEEE Transactions on Industrial Informatics*, vol. 20, no. 2, 2024.

[11] A. Rahman et al., "Transformer-based learning for battery state prediction under dynamic loads," *Journal of Energy Storage*, vol. 68, 2024.

[12] P. Singh and K. Debnath, "Data-driven efficiency modeling of switched-mode power converters," *Electric Power Systems Research*, vol. 229, 2024.

[13] M. Raissi, P. Perdikaris, and G. Karniadakis, "Physics-informed neural networks: A deep learning framework for solving forward and inverse problems," *Journal of Computational Physics*, vol. 378, 2019.

[14] T. Liu and G. Karniadakis, "Physics-informed machine learning in power and energy systems," *Nature Reviews Electrical Engineering*, vol. 1, 2024.

[15] X. Chen et al., "Physics-informed neural networks for power electronic converter modeling," *IEEE Transactions on Industrial Electronics*, vol. 71, no. 2, 2024.

[16] A. Gupta and S. Mishra, "PINN-based dynamic modeling of power converters for energy systems," *Electric Power Systems Research*, vol. 230, 2024.

[17] J. Morales and D. Soto, "Physics-constrained deep learning for DC–DC converter state estimation," *IEEE Transactions on Power Electronics*, vol. 40, no. 1, 2025.

[18] R. Banerjee et al., "Integrated battery–converter co-modeling using physics-guided neural networks," *Applied Energy*, vol. 357, 2025.

Journal of Engineering and Technology for Industrial Applications

ITEGAM-JETIA

Manaus, v.12 n.60, p.615-628 July/August, 2026.
DOI: https://doi.org/10.5935/jetia.v12i60.3927

ISSN ONLINE: 2447-0228

RESEARCH ARTICLE OPEN ACCESS

EXPERIMENTAL EVALUATION OF SMART CONTRACT GAS OPTIMIZATION TECHNIQUES: A CASE STUDY OF A BLOCKCHAIN-BASED REPORTING APPLICATION SYSTEM

Michael Angello Qadosy Riyadi*[1], Sulthonika Mahfudz Al Mujahidin[2], Nur Alifia Rustan[3] A'isyah Belqis Febi Aulia[4], Mastuty Ayu Ningtyas[5] and Khodijah Amiroh[6]

[1 ,2, 3, 4, 5, 6]Department of Information Technology, Telkom University, Surabaya Campus, Surabaya, Indonesia.

[1]https://orcid.org/0009-0003-0853-0989, [2]https://orcid.org/0009-0000-5873-1082, [3]https://orcid.org/0009-0006-8714-5684
[4]https://orcid.org/0009-0007-0786-1443, [5]https://orcid.org/0009-0007-8501-5488, [6]https://orcid.org/0000-0001-9498-0553

E-email: *michaelangello@student.telkomuniversity.ac.id, sulthonikamahfudzam@student.telkomuniversity.ac.id, nralifialrs@student.telkomuniversity.ac.id, aisyahbelqis@student.telkomuniversity.ac.id, mastutyayu@telkomuniversity.ac.id, dijaamirah@telkomuniversity.ac.id

ARTICLE INFO

Article History
Received on: March 05, 2026
Reviewed on: April 04, 2026
Accepted on: May 01, 2026
Published on: July 31, 2026

Keywords:
Blockchain,
Ethereum,
Smart Contract,
Optimization,
Gas Consumption.

ABSTRACT

Blockchain-based applications often face scalability challenges due to high gas costs associated with on-chain storage in the Ethereum network, particularly for systems requiring continuous audit logging. This study evaluates smart contract optimization strategies to reduce gas consumption in a blockchain-based mobile reporting system for sexual violence cases. An experimental approach was conducted by implementing four Solidity smart contract models—Baseline, Merkle Tree Aggregation, Storage Optimized (Packed Struct and Enum Encoding), and Conditional Commit—and testing them under scenarios of 50, 100, 500, and 1000 transactions using identical datasets. Gas consumption, transaction cost, latency, and execution time were analyzed using descriptive statistics and non-parametric tests. The results show that the baseline approach produced the highest gas consumption (770,899,033 gas for 1,000 reports), while Storage Optimization reduced it to 177,566,016 gas and Merkle Tree Aggregation to 20,492,732 gas. The Conditional Commit method achieved the lowest gas consumption at 4,308,404 gas with an execution time of 1.08 seconds compared to 143.72 seconds in the baseline. Statistical tests confirmed significant differences among methods (Kruskal–Wallis $H = 166.93$, $p < 0.01$; Mann–Whitney $p < 0.01$), demonstrating that reducing on-chain transactions substantially improves gas efficiency and scalability.

Copyright ©2026 by authors and Galileo Institute of Technology and Education of the Amazon (ITEGAM). This work is licensed under the Creative Commons Attribution International License (CC BY 4.0).

I. INTRODUCTION

Blockchain technology has rapidly evolved as a digital infrastructure that enables transparent, distributed, and immutable data recording across various decentralized systems [1-5]. Among the numerous existing blockchain platforms, Ethereum has become one of the most widely utilized due to its capability to execute smart contracts through the Ethereum Virtual Machine (EVM), enabling developers to build decentralized applications (decentralized applications/DApps) with computational logic that can be publicly verified [6-8]. Within the Ethereum ecosystem, every computational operation performed by a smart contract requires an execution fee known as gas, which functions as a pricing mechanism for computational resources within the network [9-11]. This gas mechanism is designed to prevent the abuse of network resources, such as denial-of-service (DoS) attacks, while simultaneously ensuring that each computational operation is paid proportionally by the user who triggers it [12], [13]. Although the gas mechanism plays an essential role in maintaining the security and stability of the Ethereum network, gas costs often become a significant barrier in the development of data-intensive blockchain applications [14], [15].

In particular, operations involving permanent data storage on the blockchain incur substantially higher costs compared to ordinary computational operations [16], [17]. For instance, storage instructions such as SSTORE in Ethereum can consume up to 20,000 gas for the first non-zero value write, making it one of the most expensive operations in smart contract execution [18]. Ni *et al*. (2025) noted that large data volumes in blockchain applications introduce scalability challenges due to the high cost of on-chain storage [19]. This condition poses serious challenges for applications that require continuous data recording, as high transaction costs may limit the scalability and operational sustainability of blockchain-based systems [20]. Various studies have also demonstrated that the majority of gas consumption in Ethereum smart contracts originates from operations related to accessing and modifying permanent storage, thereby making optimization of data storage structures an important factor in improving transaction cost efficiency in modern blockchain applications [21], [22]. Several studies have attempted to identify factors that influence gas consumption in Ethereum smart contracts. Empirical studies indicate that certain code implementation patterns in the Solidity programming language can result in higher gas consumption due to the use of inefficient data structures or repeated execution of storage operations [23], [24]. Previous research has also identified various code smells and design patterns that lead to gas inefficiency during smart contract execution [25]. In response to these issues, several optimization techniques have been proposed, including the use of fixed-length data types, packing variables into a single storage slot through variable packing techniques, and the application of static analysis to detect inefficient code patterns prior to the deployment process [26-28]. The results of these approaches indicate that code-level optimization can significantly reduce gas consumption without altering the functional logic of the implemented smart contract.

In addition to optimization at the code implementation level, another approach widely explored in the literature is reducing the number of on-chain transactions through data aggregation mechanisms [29-31]. In this context, cryptographic structures such as Merkle Trees are commonly used to summarize a collection of data into a single root hash value that is subsequently stored on the blockchain [32], [33]. This approach enables data integrity to be preserved without requiring the entire dataset to be stored directly on the blockchain. Park *et al*. (2022) designed an event-driven resource offloading solution in which DApp users only pay a predetermined minimal gas fee while most computational tasks are executed on external servers with lower gas costs [34]. Through the use of Merkle proofs, the system can verify the existence of a particular data element within a Merkle Tree structure with logarithmic complexity, making it highly efficient for systems that require verification of large volumes of data. Data aggregation techniques such as transaction batching or threshold commit mechanisms have also been proposed to reduce the frequency of transactions that need to be recorded on the blockchain, thereby overall reducing gas consumption and improving the scalability of blockchain systems [35]. Nevertheless, several research gaps remain that require further attention. Most previous studies focus solely on optimizing individual smart contracts without conducting a comparative evaluation of multiple optimization strategies within a consistent experimental framework. Furthermore, many studies evaluate optimization only at the code level without considering integration with data aggregation techniques or off-chain computation simultaneously. Therefore, this study aims to conduct a comparative evaluation of various smart contract optimization techniques in reducing gas consumption on the Ethereum network, particularly in the context of a mobile-based sexual violence reporting application that utilizes blockchain as an audit trail mechanism. This research is expected to provide a more comprehensive understanding of efficient smart contract design strategies and offer practical recommendations for developers in designing more scalable and cost-efficient blockchain applications.

II. MATERIALS AND METHODS

This study employs an experimental approach to evaluate the effectiveness of algorithm optimization techniques in Solidity smart contracts within a blockchain-based mobile application system for reporting sexual violence, with the overall research workflow presented systematically in Figure 1. The research stages begin with a literature review, followed by a system architecture analysis to identify the characteristics of the application as well as the weaknesses of the baseline smart contract, which stores all report data entirely on-chain using the string data type, resulting in high gas consumption due to inefficient storage structures. Based on these findings, three optimization techniques were designed, namely Merkle Tree Aggregation, Storage Optimization through Packed Struct and Enum Encoding, and Conditional Commit. The implementation phase includes the development of four smart contracts, consisting of one baseline and three optimized versions using Solidity version 0.8.19 on the Ethereum (ETH) blockchain network, which are subsequently tested under scenarios of 50, 100, 500, and 1000 transactions with identical datasets to maintain the consistency and validity of the comparison.

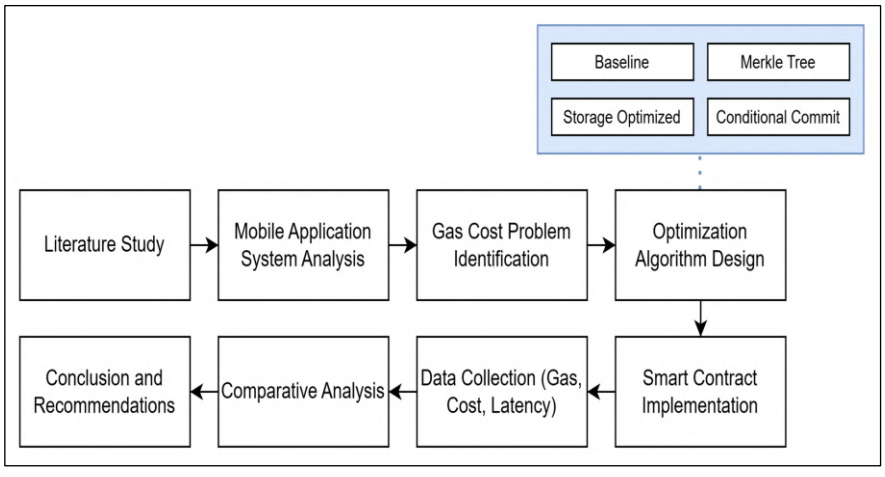


Figure 1: Research Flow.
Source: Authors, (2026).

II.1 SYSTEM OVERVIEW

The proposed system is a Flutter-based mobile application platform for reporting and monitoring cases of sexual violence within a university environment, utilizing the Ethereum blockchain to ensure data integrity and an immutable audit trail. Complete report data are stored off-chain using Google Firestore as a cloud-based NoSQL database, while integrity hashes and critical action logs are recorded on-chain through a smart contract to ensure transparency, security, and independent verification [36], [37], [38]. The system involves four main stakeholders with different roles and access rights as summarized in Table 1, while the main interface page of the application, which functions as the user access gateway, is shown in Figure 2.

Table 1: System Stakeholders and Users.

Stakeholder	Role	Feature Access
Reporter	Student or member of the academic community who reports an incident of violence, either as a direct victim or a witness.	Reporting form, status tracking
Admin	System manager responsible for receiving, processing, and following up on reports.	Admin panel, monitoring, report management, notifications
Psychologist	Professional personnel who provide psychological evaluation and assistance to victims.	Psychologist notes, consultation schedule
Blockchain System	Automated component that records every important action to the Ethereum smart contract as an immutable audit trail.	Hash recording, integrity verification

Source: Authors, (2026).

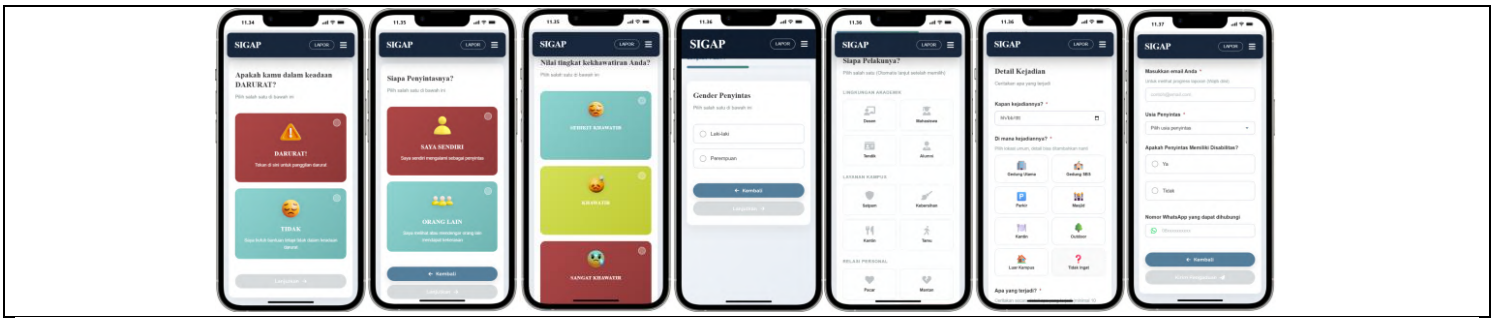


Figure 2: Main Interface of the Mobile Application for Reporting Sexual Violence.
Source: Authors, (2026).

II.2 SYSTEM ARCHITECTURE

The system is designed using a layered architecture approach consisting of three main layers. The first layer is the Presentation Layer based on Flutter with the Dart language, which is responsible for managing the user interface in the mobile application, including a multi-step reporting form, a report status tracking page, and a monitoring dashboard. The second layer is the Backend-as-a-Service Layer that utilizes Firebase, including authentication through Firebase Authentication, storage of complete report data off-chain in Cloud Firestore, as well as business logic and blockchain integration through Cloud Functions for Firebase based on Node.js to perform data validation, hash generation, and transaction submission to the Ethereum network. The third layer is the Blockchain Layer which functions to store integrity hashes, important metadata, and an immutable audit trail through smart contracts developed using Solidity, with all interactions conducted through a Web3 RPC provider [39], [40], while the overall structure and interaction flow between layers are comprehensively visualized in Figure 3.

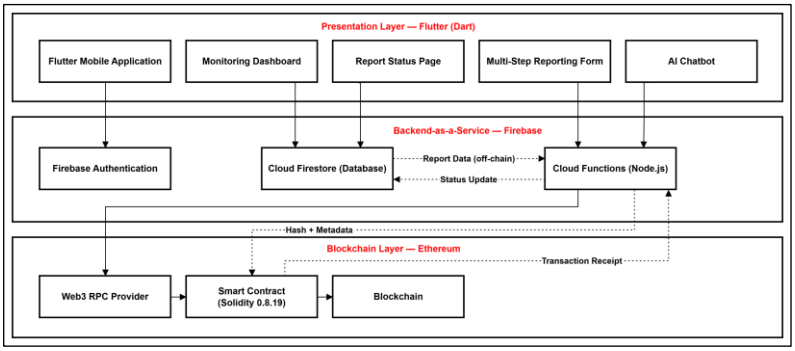


Figure 3: System Architecture Diagram.
Source: Authors, (2026).

II.3 REPORTING SYSTEM WORKFLOW

The reporting system workflow is designed to ensure data consistency, processing security, and blockchain-based recording integrity, and also serves as the basis for evaluating gas fee efficiency because each on-chain transaction directly contributes to gas consumption. The process begins with the completion of a multi-step form by the reporter in the mobile application, followed by advanced validation, input sanitization, generation of a unique report code, and storage of the data as the main document in the off-chain database.

Subsequently, the system generates a SHA-256 hash deterministically from the report data and sends it to the smart contract to be recorded as an audit log entry on the blockchain [41-43]. The transaction produces a receipt containing txHash, gasUsed, and blockNumber, which is then referenced back in the report document as an audit trail before the final response is sent to the application. The interaction flow among system components is shown in Figure 4, while the types of critical actions recorded on the blockchain and serving as the main sources of gas consumption are summarized in Table 2.

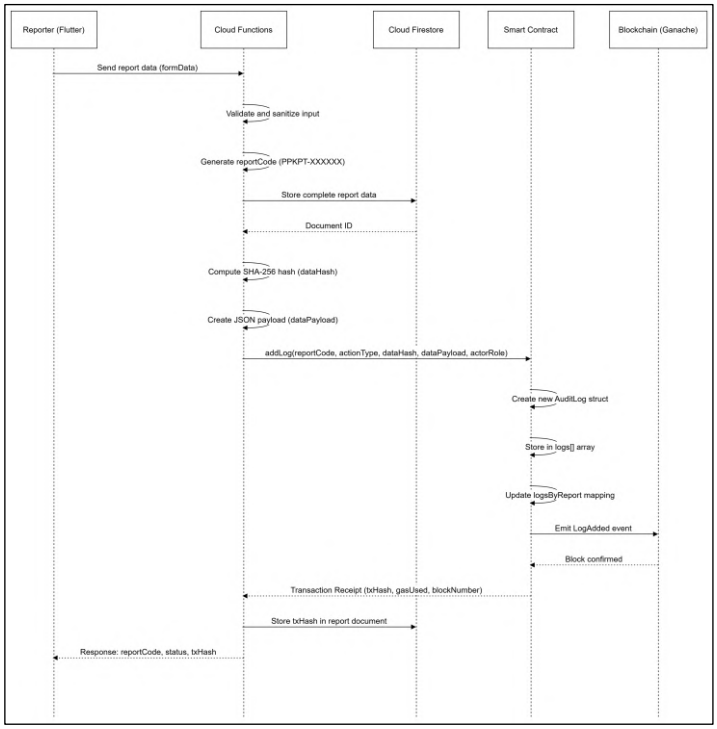


Figure 4: Sequence Diagram of Report Logging to Blockchain.
Source: Authors, (2026).

Table 2: Types of Actions Recorded on Blockchain.

Action Type	Trigger	Actor	Description
CREATE	User submits form	USER	New report created; data hash recorded on blockchain.
UPDATE_ADMIN	Admin updates status	ADMIN	Report status change recorded as audit trail.
NOTE_PSYCHOLOGIST	Psychologist writes note	PSYCHOLOGIST	Psychological evaluation note hashed and recorded.
FEEDBACK	Feedback submitted	USER/ADMIN	Feedback on case handling recorded.
DISPUTE	Objection submitted	USER	Reporter objection recorded as formal evidence.

Source: Authors, (2026).

II.4 SMART CONTRACT DESIGN

The baseline smart contract design in this study functions as the core mechanism for recording an immutable audit trail on the Ethereum network while simultaneously serving as the experimental control to identify sources of gas inefficiency and to compare the proposed optimization techniques. The contract is developed using Solidity with a storage scheme based on dynamic arrays and mappings to support chronological recording and per-report indexing [44], [45]. The primary data structure, AuditLog, represents a single activity entry containing the report identity, action type, integrity hash, complete data payload, timestamp, sender address, and actor role, as shown in Algorithm 1.

```
pragma solidity 0.8.19;
contract BaselineReporting {
    struct AuditLog {
        uint256 id; string reportCode; string actionType; string dataHash; string dataPayload; uint256 timestamp; address actor; string actorRole;
    }
    AuditLog[] public logs; mapping(string => uint256[]) public logsByReport;
    event LogAdded(uint256 indexed id, string reportCode, string actionType, address actor, uint256 timestamp);
}
```

Algorithm 1: Structure of AuditLog in BaselineReporting Smart Contract.
Source: Authors, (2026).

The AuditLog structure is designed by considering the storage characteristics of Ethereum, where fixed types such as uint256 and address each occupy one 32-byte slot, whereas dynamic types such as string store the data length in the main slot and the actual content in separate storage slots. Each write or modification of a value in storage triggers an SSTORE (Storage Store) operation, which is an instruction that stores data into the permanent blockchain storage and represents one of the most gas-expensive operations.

Consequently, the use of several large string fields such as dataPayload and dataHash increases the number of slots utilized and enlarges gas consumption. The detailed storage characteristics of each field are presented in Table 3.

Table 3: Storage Characteristics of AuditLog Fields in Solidity.

Field	Solidity Type	Storage Characteristics	Description
id	uint256	Fixed 32 bytes (1 slot)	Sequential auto-generated ID
reportCode	string	Dynamic (≥32 bytes)	Report code, e.g., "PPKPT-100042" (13 bytes)
actionType	string	Dynamic (≥32 bytes)	Action type, e.g., "CREATE" (6 bytes)
dataHash	string	Dynamic (≥32 bytes)	SHA-256 hash in hexadecimal string (64 characters)
dataPayload	string	Dynamic (hundreds of bytes)	Complete JSON report data (~500–1000 characters)
timestamp	uint256	Fixed 32 bytes (1 slot)	Automatic block timestamp
actor	address	20 bytes (stored in 32-byte slot)	Ethereum address of transaction sender
actorRole	string	Dynamic (≥32 bytes)	Actor role, e.g., "ADMIN" (5 bytes)

Source: Authors, (2026).

Architecturally, the logs array is used to maintain chronological recording in an append-only manner, while the logsByReport mapping functions as a reportCode-based index to access the report history directly without full iteration. Each invocation of the addLog() function adds a new entry to both structures and emits an event as an external recording mechanism, so that within a single transaction several storage write operations occur that directly contribute to gas consumption. The implementation of this function is shown in Algorithm 2.

```
function addLog( string memory _reportCode, string memory _actionType, string memory _dataHash, string memory _dataPayload, string memory _actorRole)
public {
    uint256 newId = logs.length;
    AuditLog memory newLog = AuditLog({id: newId, reportCode: _reportCode, actionType: _actionType, dataHash: _dataHash, dataPayload: _dataPayload,
                                       timestamp: block.timestamp, actor: msg.sender, actorRole: _actorRole});
    logs.push(newLog); logsByReport[_reportCode].push(newId); emit LogAdded(newId, _reportCode, _actionType, msg.sender, block.timestamp); }
```

Algorithm 2: addLog Function Implementation in Smart Contract.
Source: Authors, (2026).

II.5 SMART CONTRACT ALGORITHM OPTIMIZATION METHODS

A comparative framework was designed to evaluate three optimization techniques against the baseline design by emphasizing differences in algorithmic characteristics that affect execution efficiency and the intensity of on-chain interactions. Four approaches were directly tested in a consistently controlled environment, so that the resulting performance variations fully reflect the data management strategies and transaction recording patterns implemented by each algorithm. Measurements were conducted automatically during the execution process and analyzed using descriptive statistics to obtain objective and measurable comparisons, while the structure of the experimental variables is summarized in Table 4.

Table 4: Experimental Variable Design.

Variable Type	Variable	Description
Independent	Smart contract algorithm type	4 levels: Baseline, Merkle Tree, Storage Optimized, Conditional Commit
Dependent	Gas Used	Total gas units consumed per transaction
	Gas Cost (ETH)	Transaction cost in ETH
	Latency	Transaction execution time in milliseconds
	Number of on-chain transactions	Total transactions submitted to blockchain
Control	Report data	Identical for all algorithms (deterministic input)
	Compiler	Solidity 0.8.19

Source: Authors, (2026).

II.5.1 Algorithm 1: Baseline — Individual Storage (Naive)

The baseline algorithm represents the simplest approach, in which each critical action generates a single on-chain transaction that directly records the entire report data individually. For each report, the system computes a SHA-256 hash as an integrity marker, constructs a complete JSON representation, and then sends all these parameters to the addLog() function in the smart contract. Because each report is processed and stored separately without aggregation or data structure compression, the number of transactions increases proportionally with the number of processed reports; therefore, this approach serves as the primary benchmark for measuring the efficiency of subsequent optimization techniques. The logical flow of the process is illustrated in Algorithm 3.

***Input**: A set of reports totaling n*
***Output**: A list of transaction receipts*
1. Retrieve one report from the dataset *2. Compute the SHA-256 hash of the report content as an integrity marker* *3. Construct the report data in a complete JSON format* *4. Send all information (report code, action type, hash, payload, actor role) to the smart contract* *5. Wait until the transaction is confirmed on the blockchain and then store the transaction receipt* *6. Repeat steps 1–6 until all n reports have been processed*

Algorithm 3: Algorithm: BaselineReporting.
Source: Authors, (2026).

Computationally, the number of generated transactions is linear with respect to the number of reports, resulting in a complexity of $O(n)$, where n denotes the total number of processed reports. No aggregation or optimization mechanisms are implemented outside the contract; therefore, all interaction and storage costs are borne directly by individual transactions. The total gas consumption for processing n reports is formulated in Equation (1):

$$C_{baseline} = \sum_{i=1}^{n} \left(G_{base} + G_{calldata,i} + G_{storage,i} \right) \quad (1)$$

Which can be approximately simplified into Equation (2):

$$C_{baseline} \approx n \times C_{per_{tx}} \quad (2)$$

In this formulation, $C_{baseline}$ represents the total gas consumed for all reports. The component G_{base} represents the fixed base cost of transaction execution. The component $G_{calldata,i}$ denotes the cost resulting from transmitting the parameters of the i-th transaction, which is influenced by the size of the transmitted data. Meanwhile, $G_{storage,i}$ represents the permanent storage cost of the i-th transaction through the SSTORE operation, which has a high value because it involves writing data to blockchain storage. Furthermore, $C_{per_{tx}}$ represents the estimated average gas cost for a single individual transaction in the baseline approach.

II.5.2 Algorithm 2: Transaction Aggregation via Merkle Tree

This approach reduces the number of on-chain transactions by grouping several reports into a single batch, and then storing only one representative hash value in the form of a Merkle Root in the smart contract [46], [47]. With this strategy, the number of transactions decreases from n (as in the baseline) to ⌈n/B⌉, where B denotes the batch size. Each batch is represented by the BatchCommit structure as shown in Algorithm 4, which stores the batch identity, the Merkle Root value, the number of reports, the range of report indices, the recording timestamp, and the address of the commitment sender. The aggregation procedure is illustrated in Algorithm 5 The Merkle Tree construction process is performed in a bottom-up manner, as illustrated in Algorithm 4.

```
struct BatchCommit { uint256 batchId; bytes32 merkleRoot; uint256 reportCount; uint256 fromIndex; uint256 toIndex; uint256 timestamp; address committer; }
```

Algorithm 4: BatchCommit Structure in MerkleAggregation Contract.
Source: Authors, (2026).

***Input**: n reports and batch size B*
***Output**: List of batch transaction receipts*
1. Determine the number of batches based on the total reports and the batch size *2. For each batch:* *a. Retrieve a group of reports according to its index range* *b. Convert each report into a hash (using KECCAK-256 over the report content)* *c. Arrange all hashes into a Merkle Tree structure* *d. Compute the root value of the tree (Merkle Root)* *e. Send the Merkle Root along with batch metadata to the smart contract through the commitBatch function* *f. Wait for transaction confirmation and store the transaction receipt* *3. Return all batch transaction receipts*

Algorithm 5: Algorithm: MerkleAggregation.
Source: Authors, (2026).

***Input**: List of report hashes in one batch*
***Output**: A single Merkle Root value*
1. Arrange all report hashes as the lowest level *2. Pair two adjacent hashes, then concatenate and hash them again to form a parent hash* *3. If the number of elements is odd, duplicate the last hash to maintain pairing* *4. Repeat the merging process until only one hash remains at the top* *5. The final hash becomes the Merkle Root*

Algorithm 6: Merkle Tree Construction Algorithm.
Source: Authors, (2026).

From a complexity perspective, constructing a Merkle Tree for a batch containing m reports requires O(m log m) because hashes are organized hierarchically from the leaf level to the root. With a fixed batch size B, the total off-chain computation for n reports becomes O (n log B). Meanwhile, on the on-chain side, the number of transactions decreases to O(n/B), thereby reducing the frequency of global blockchain state writes proportionally to the batch size. The membership of a report within a batch is verified using a Merkle Proof as shown in Algorithm 7, by reconstructing the hash path from the leaf to the root using proof elements, and then comparing the final result with the Merkle Root stored in the contract. If both values are identical, the report is proven to be valid as part of the corresponding batch.

```
function verifyReport( bytes32[] memory _proof, bytes32 _leaf, uint256 _batchId)
public view returns (bool valid) {
    bytes32 computedRoot = _leaf;
    for (uint256 i = 0; i < _proof.length; i++) {
        bytes32 proofElement = _proof[i];
        if (computedRoot <= proofElement) { computedRoot = keccak256(abi.encodePacked(computedRoot, proofElement)); }
        else { computedRoot = keccak256(abi.encodePacked(proofElement, computedRoot)); }
    } return computedRoot == batches[_batchId].merkleRoot;
}
```

Algorithm 7: verifyReport Function for Merkle Proof Validation.
Source: Authors, (2026).

The total gas cost for the aggregation approach is formulated in Equation (3):

$$C_{merkle} = \left\lceil \frac{n}{B} \right\rceil \times C_{store_{root}} \tag{3}$$

Approximately, when n is much larger than B, the total cost can be expressed as Equation (4):

$$C_{merkle} \approx \frac{n}{B} \times C_{store_{root}} \tag{4}$$

In these equations, C_{merkle} represents the total gas cost for processing n reports using aggregation. The variable n denotes the number of reports and B represents the batch size. The component $C_{store_{root}}$ represents the average cost of storing a single Merkle Root into the smart contract, including the overhead of executing the commitBatch function and the permanent storage operations within the BatchCommit structure. Theoretically, when $B > 1$, gas consumption decreases significantly because only a single fixed-size hash is recorded per batch. However, this efficiency introduces additional off-chain computation and requires a Merkle Proof-based verification mechanism when individual verification is needed. This trade-off between gas reduction and verification complexity is analyzed in the experimental stage.

II.5.3 Algorithm 3: Storage Optimization (Packed Struct + Enum Encoding)

This approach reduces gas consumption not by decreasing the number of transactions, but by compacting the representation of data stored in each transaction [48]. Dynamic data types such as string are replaced with more efficient fixed-length and numeric types: categorical attributes are encoded as `uint8`, while identifiers and hashes are represented as `bytes32`. Nine `uint8` fields are then packed into a single `uint128` variable using bitwise operations, allowing multiple attributes to share a single 32-byte storage slot. The optimized structure is shown in Algorithm8.

```
struct PackedAuditLog { bytes32 reportCode; bytes32 dataHash; uint256 timestamp; address actor; uint128 packedEnums; }
```

Algorithm 8: PackedAuditLog Structure in StorageOptimized Smart Contract.
Source: Authors, (2026).

The number of transactions remains linear with respect to the number of reports O(n), but each entry uses fewer storage slots compared with a dynamic string-based representation. The four primary components (`reportCode`, `dataHash`, `timestamp`, and `actor`) occupy individual slots, while nine categorical attributes share a single slot through `uint128`, thereby reducing the per-transaction cost constant. The total gas cost is formulated in Equation (5):

$$C_{packed} = \sum_{i=1}^{n} \left(G_{base} + G_{calldata,i}^{fixed} + G_{storage,i}^{optimized} \right) \tag{5}$$

Which can be approximately simplified into Equation (6):

$$C_{packed} \approx n \times C_{per_{tx}}^{optimized} \tag{6}$$

In this formulation, C_{packed} represents the total gas cost for n reports with the optimized structure. The component G_{base} still represents the base transaction cost. The value $G_{calldata,i}^{fixed}$ indicates a lower calldata cost because all parameters use fixed-length types. Meanwhile, $G_{storage,i}^{optimized}$ represents the reduced SSTORE operation cost due to the elimination of dynamic storage allocation and the implementation of a storage packing mechanism. Furthermore, $C_{per_tx}^{optimized}$ is the estimated average cost per transaction after the data structure optimization is applied.

II.5.4 Algorithm 4: Conditional Commit (Threshold-Based Batching)

This approach implements an off-chain buffering mechanism, in which reports are not immediately submitted to the blockchain but are first accumulated until a specified threshold value is reached [49], [50]. Once the number of reports in the buffer meets this threshold, the system submits a single commit transaction that records an aggregated hash representing all reports within the batch. Consequently, the number of on-chain transactions is reduced proportionally to the threshold value applied.

The metadata for each batch is recorded in the BatchRecord structure as illustrated in Algorithm 9, which contains the batch identifier, the aggregated hash, the number of reports included, the range of report identifiers, the threshold value applied at the time of commit, the recording timestamp, and the address of the transaction sender.

```
struct BatchRecord {
    uint256 batchId; bytes32 batchHash; uint256 reportCount; uint256 fromId; uint256 toId; uint256 threshold; uint256 timestamp; address committer; }
```

Algorithm 9: BatchRecord Structure in ConditionalCommit Smart Contract.
Source: Authors, (2026).

The initial threshold value is configured through the contract constructor as shown in Algorithm 10, which assigns the contract owner, initializes the total number of committed reports, and stores the initial threshold value as a system control parameter.

```
constructor(uint256 _initialThreshold) { owner = msg.sender; totalReportsCommitted = 0; currentThreshold = _initialThreshold; }
```

Algorithm 10: Constructor for Initial Threshold Configuration.
Source: Authors, (2026).

The procedural flow of the commit mechanism is presented in Algorithm 12.

***Input**: n reports and threshold value T*
***Output**: List of commit transaction proofs*
1. Prepare an empty buffer to store report hashes
2. For each report:
a. Compute the report hash as an integrity marker
b. Store the hash in the buffer
c. If the number of elements in the buffer reaches T:
- Concatenate all hashes in the buffer
- Compute a single aggregated hash from the concatenated data
- Submit the aggregated hash together with batch metadata to the smart contract
- Wait for transaction confirmation and store the transaction proof and then clear the buffer
3. After all reports have been processed, if any elements remain in the buffer, perform a final commit
4. Return all transaction proofs

Algorithm 12: ConditionalCommit Procedure.
Source: Authors, (2026).

From a computational perspective, each report is processed only once to generate its hash, resulting in an off-chain complexity of O(n). However, the number of on-chain transactions decreases to O(n/T), where T denotes the threshold value. Experimental evaluation for $n = 1000$ reports under several threshold values is presented in Table 5, demonstrating that increasing T reduces transaction frequency but increases commit latency, since reports must wait until the buffer reaches the defined threshold.

Table 5: Evaluated Threshold Parameters.

Threshold	On-chain Transactions (n=1000)	Reduction Ratio	Characteristics
5	200	5:1	More frequent commits with relatively low latency
10	100	10:1	Balanced trade-off between gas savings and responsiveness
25	40	25:1	High gas savings
50	20	50:1	Maximum gas savings with higher commit latency

Source: Authors, (2026).

The total gas cost is formulated in Equation (7):

$$C_{conditional} = \left\lceil \frac{n}{T} \right\rceil \times C_{commit} \tag{7}$$

If n is significantly larger than T, the total cost can be approximated as shown in Equation (8):

$$C_{conditional} \approx \frac{n}{T} \times C_{commit} \tag{8}$$

In these expressions, $C_{conditional}$ represents the total gas cost required to process n reports using the threshold-based mechanism. The variable n denotes the number of reports, T represents the threshold value per batch, and C_{commit} corresponds to the average gas cost of a single commit transaction that records an aggregated hash on the blockchain. The optimal threshold value is determined by calculating the effective gas per report, defined as the ratio between the total gas consumed and the number of processed reports. The value of T that produces the lowest average cost is selected as the optimal configuration, while also considering the trade-off between gas efficiency and increased commit latency.

III. RESULTS AND DISCUSSIONS

This chapter presents the performance evaluation results of various gas fee optimization approaches in the implementation of smart contracts for a blockchain-based sexual violence reporting system. The dataset used in the experiment consists of 1,000 simulated reports with an attribute structure as shown in Table 6, representing various report characteristics such as victim type, level of concern, incident location, and system action metadata. The experiments were conducted using a CPU-only computational environment without GPU acceleration, with hardware specifications consisting of an AMD Ryzen 5 6600H (12 CPUs) processor operating at approximately 3.3 GHz and 16 GB of RAM.

In this evaluation scenario, the Conditional Commit approach was implemented using a batching mechanism with a threshold of 50 reports, where a commit to the blockchain is executed once the number of reports in the buffer reaches the defined threshold. Subsequently, the performance of the Baseline, Merkle Tree Aggregation, Storage Optimized, and Conditional Commit methods was analyzed based on several key metrics, namely total gas consumption, transaction cost (ETH), transaction latency, and system execution time, across various report quantity scenarios.

Table 6: Sample Structure of Sexual Violence Reporting Dataset Used in Experiments.

No	Report Code	*Status Darurat*	*Korban*	*Tingkat Kekhawatiran*	*Gender Korban*	*Pelaku Kekerasan*	*Tanggal Kejadian*	*Lokasi Kejadian*	*Lokasi Detail*	*Ringkasan Kejadian (detail singkat)*	*Usia Korban*	*Disabilitas*	*Jenis Disabilitas*	Action Type	Actor Role	*Email Korban*
1	PPKPT-100000	*tidak*	*saya*	*sangat*	*lakilaki*	*orang_tidak_dikenal*	*2025-10-11*	*Masjid*	*Kantin depan*	*Perundungan daring melalui grup medsos kampus*	*46-55*	*ya*	*kesulitan_melihat*	DISPUTE	SYSTEM	korban0@gmail.com
...	...	...	...	...	...	...	...	...	...	...	...	...	...	...	...	...
1000	PPKPT-100999	*tidak*	*saya*	*khawatir*	*lakilaki*	*mantan_pacar*	*2025-12-30*	*Luar Kampus*	*Lantai 2 dekat perpustakaan*	*Pelecehan verbal di area kampus saat jam kuliah*	*18-25*	*ya*	*kesulitan_berkomunikasi*	CREATE	USER	pelapor999@student.ac.id

Source: Authors, (2026).

The experimental results demonstrate clear performance differences between the baseline approach and the three proposed optimization methods in terms of gas consumption, transaction cost, latency, and execution time. As shown in Table 7, the baseline method consistently produces the highest gas consumption across all report quantity scenarios. The total gas increases from 38,430,050 gas for 50 reports to 770,899,033 gas for 1,000 reports, exhibiting a nearly linear growth pattern as the number of reports increases. This condition occurs because each report is processed as an independent on-chain transaction and stores several data fields in the smart contract storage. In the Ethereum Virtual Machine (EVM), storage write operations through the SSTORE instruction incur relatively high gas costs, particularly when the stored data has large size or uses dynamic data types. Consequently, as the number of processed reports increases, the number of storage operations also increases proportionally, directly affecting the total gas consumption and transaction cost. Statistical analysis using the Kruskal–Wallis test indicates that the differences between methods in the gas per transaction metric are significant across all scenarios; for example, in the 100-report scenario, a value of $H = 166.93$ with $p < 0.01$ was obtained.The Merkle Tree Aggregation method demonstrates a substantial reduction in gas consumption compared with the baseline. In this approach, multiple reports are first combined off-chain to form a Merkle Tree structure, after which only the Merkle Root value is recorded on the blockchain through a single commit transaction.

Through this mechanism, the number of on-chain transactions is reduced because a single transaction can represent multiple reports simultaneously. Data in Table 7 show that the total gas required for 1,000 reports reaches only 20,492,732 gas, which is significantly lower than the baseline. The Mann–Whitney test also indicates that the difference in gas consumption between the baseline and the Merkle Tree method is statistically significant across various scenarios; for instance, in the 500-report scenario, $p < 0.01$. The reduction in the number of transactions also contributes to lower latency and execution time, since fewer transactions need to be processed and confirmed by the blockchain network. The Storage Optimized approach reduces gas consumption through modifications to the data structure stored within the smart contract. This method replaces dynamic data types such as string with fixed-length types such as bytes32 and utilizes storage packing techniques to reduce the number of storage slots used. This optimization decreases the cost of data writing because fewer storage slots need to be updated. Experimental results indicate that the total gas consumption in the 1,000-report scenario is 177,566,016 gas, which is lower than the baseline but still higher than aggregation-based methods. Statistical testing also shows that the difference between the baseline and Storage Optimized approaches is significant in nearly all scenarios; for example, in the 100-report scenario, $p < 0.01$. This outcome arises from the characteristic of the method that continues to process each report as an individual transaction, resulting in the number of transactions still increasing linearly with the number of reports.

Table 7: Total Gas Consumption, Transaction Cost (ETH), Latency, and Execution Time for Each Scenario (50, 100, 500, and 1000) and Optimization Method.

Scenario	Method	Total Gas	Total Cost (ETH)	Total Latency (ms)	Total Exec Time (s)
50	Baseline	38,430,050	0.77	7066.71	7.07
	Merkle Tree	1,042,788	0.02	271.20	0.27
	Storage Optimized	9,303,068	0.19	2004.89	2.00
	Conditional Commit	196,487	0.00	44.49	0.04
100	Baseline	76,792,122	1.54	14685.12	14.69
	Merkle Tree	2,048,288	0.04	453.85	0.45
	Storage Optimized	17,756,628	0.36	4121.87	4.12
	Conditional Commit	412,886	0.01	118.53	0.12
500	Baseline	384,231,209	7.68	71282.51	71.28
	Merkle Tree	10,492,592	0.21	2315.19	2.32
	Storage Optimized	91,348,056	1.83	21870.83	21.87

Scenario	Method	Total Gas	Total Cost (ETH)	Total Latency (ms)	Total Exec Time (s)
	Conditional Commit	2,144,174	0.04	524.33	0.52
1000	Baseline	770,899,033	15.42	143722.60	143.72
	Merkle Tree	20,492,732	0.41	4640.03	4.64
	Storage Optimized	177,566,016	3.55	45480.59	45.48
	Conditional Commit	4,308,404	0.09	1077.91	1.08

Source: Authors, (2026).

Table 8: Per-Transaction Average Gas Usage, Cost (ETH), Latency, and Execution Time (Mean ± Standard Deviation) Across Methods and Scenarios.

Scenario	Method	Average Gas/Tx	Average Cost ETH	Average Latency (ms)	Average Exec Time/Tx (s)
50	Baseline	768,601 ± 15,724	0.02 ± 0.00	141.33 ± 17.78	0.14 ± 0.02
	Merkle Tree	208,558 ± 11,409	0.00 ± 0.00	54.24 ± 22.42	0.05 ± 0.02
	Storage Optimized	186,061 ± 397	0.00 ± 0.00	40.10 ± 3.99	0.04 ± 0.00
	Conditional Commit	196,487 ± 0	0.00 ± 0.00	44.49 ± 0.00	0.04 ± 0.00
100	Baseline	767,921 ± 13,418	0.02 ± 0.00	146.85 ± 19.23	0.15 ± 0.02
	Merkle Tree	204,829 ± 9,347	0.00 ± 0.00	45.38 ± 6.87	0.05 ± 0.01
	Storage Optimized	177,566 ± 8,592	0.00 ± 0.00	41.22 ± 6.13	0.04 ± 0.01
	Conditional Commit	206,443 ± 14,080	0.00 ± 0.00	59.27 ± 35.62	0.06 ± 0.04
500	Baseline	768,462 ± 13,373	0.02 ± 0.00	142.57 ± 14.89	0.14 ± 0.01
	Merkle Tree	209,852 ± 8,177	0.00 ± 0.00	46.30 ± 7.38	0.05 ± 0.01
	Storage Optimized	182,696 ± 6,847	0.00 ± 0.00	43.74 ± 7.28	0.04 ± 0.01
	Conditional Commit	214,417 ± 6,300	0.00 ± 0.00	52.43 ± 5.38	0.05 ± 0.01
1000	Baseline	770,899 ± 14,891	0.02 ± 0.00	143.72 ± 12.31	0.14 ± 0.01
	Merkle Tree	204,927 ± 9,020	0.00 ± 0.00	46.40 ± 9.39	0.05 ± 0.01
	Storage Optimized	177,566 ± 8,554	0.00 ± 0.00	45.48 ± 6.14	0.05 ± 0.01
	Conditional Commit	215,420 ± 4,456	0.00 ± 0.00	53.90 ± 4.51	0.05 ± 0.00

Source: Authors, (2026).

The Conditional Commit method produces the lowest total gas consumption among all evaluated approaches. This mechanism collects several reports within a buffer until a specified threshold is reached before performing a commit to the blockchain. Each commit stores an aggregated hash representing a batch of reports, enabling a single transaction to record multiple reports simultaneously. By reducing the frequency of on-chain transactions, this method significantly decreases overall gas consumption and shortens the system execution time. In the 1,000-report scenario, the total gas consumption is 4,308,404 gas with an execution time of approximately 1.08 seconds, which is substantially lower than the baseline that requires 143.72 seconds. Statistical testing results also indicate that latency differences among methods are significant; for instance, in the 100-report scenario, a value of $H = 159.70$ with $p < 0.01$ was obtained, demonstrating that reducing the number of transactions has a substantial impact on improving the efficiency of blockchain system performance. The average per-transaction metric analysis in Table 8 provides additional insights into the execution characteristics of each method. The baseline approach exhibits an average gas consumption of approximately 768,000 to 770,000 gas per transaction, with relatively small variation across scenarios, indicating that the transaction operation structure remains relatively consistent. The Merkle Tree method reduces this average value to approximately 204,000 to 209,000 gas, because the transaction only stores batch metadata and the Merkle Root. The Storage Optimized approach produces an average of approximately 177,000 to 186,000 gas per transaction as a result of improved storage structure efficiency. The Conditional Commit method has an average of approximately 196,000 to 215,000 gas per transaction, slightly higher than Storage Optimized because each commit transaction stores additional metadata; however, the significantly smaller number of transactions ensures that the overall system gas consumption remains low.

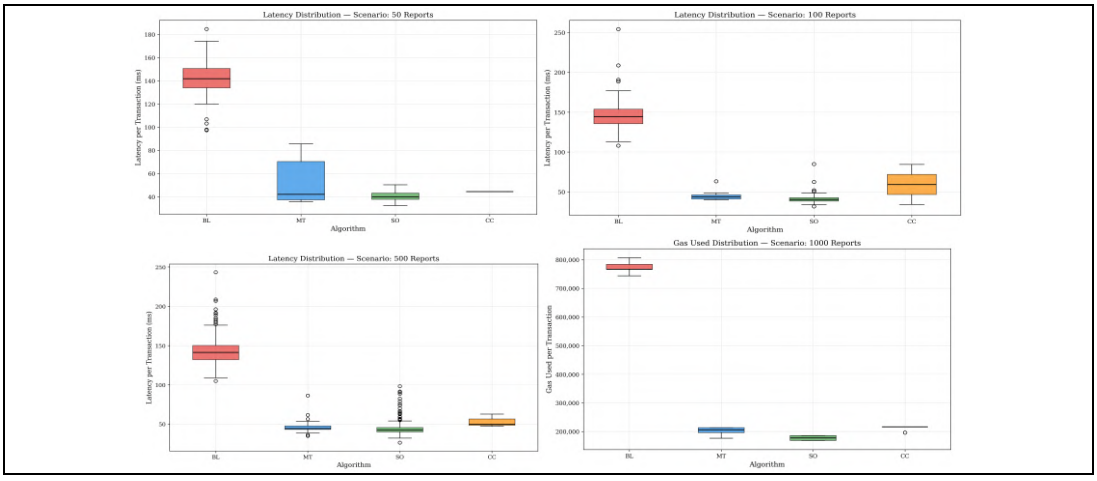


Figure 4: Boxplot of Transaction Latency Distribution (ms) Across Optimization Methods.
Source: Authors, (2026).

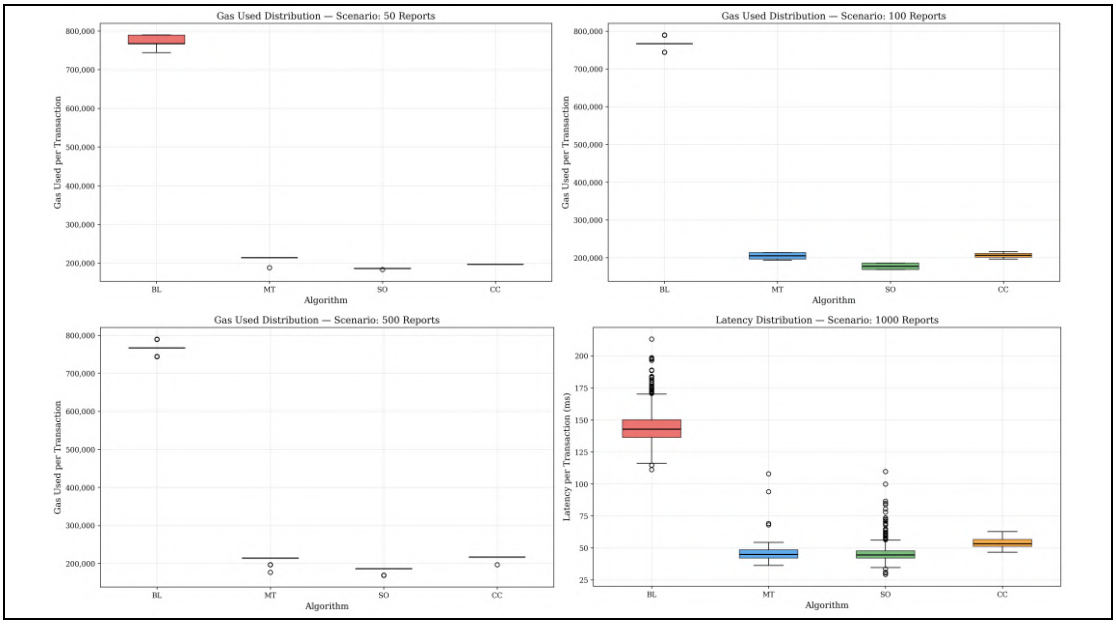


Figure 5: Boxplot of Gas Consumption Distribution per Transaction Across Optimization Methods.
Source: Authors, (2026).

The distribution of transaction latency visualized in Figure 4 shows distinct performance patterns among the evaluated methods. The baseline approach exhibits a median latency of approximately 140–145 ms with a wider interquartile range compared to the other methods, indicating relatively higher variability in execution time. This variation is associated with the larger calldata size and the greater number of storage operations performed in each transaction. The Merkle Tree and Storage Optimized methods demonstrate lower median latency values in the range of approximately 40–46 ms, with more concentrated distributions, reflecting lighter transaction execution processes. The Conditional Commit approach has a slightly higher median latency than these two methods, around 52–54 ms, yet it remains lower than the baseline and shows relatively small variation as the number of batches increases. The distribution of gas consumption per transaction presented in Figure indicates that the baseline method has the highest median value, approximately 766 thousand to 767 thousand gas. The Merkle Tree method reduces this value to approximately 205 thousand to 213 thousand gas per transaction, whereas the Storage Optimized approach shows a median of approximately 177 thousand to 186 thousand gas with relatively small variation. The Conditional Commit method has a median of approximately 196 thousand to 216 thousand gas, reflecting the storage of batch metadata within each commit transaction. The baseline approach shows a value of approximately 768 thousand gas per report across all scenarios, while Storage Optimized reduces it to approximately 177 thousand to 186 thousand gas. The Merkle Tree method produces a consumption of around 20 thousand gas per report because the transaction cost is distributed across all reports within a batch. The Conditional Commit approach demonstrates the lowest value, approximately 3,930 to 4,308 gas per report, since a single commit transaction represents multiple reports simultaneously.

This study provides an empirical contribution to the understanding of factors influencing the efficiency of blockchain-based reporting systems. By comparing several optimization approaches across different report quantity scenarios, the study demonstrates that strategies aimed at reducing the number of on-chain transactions can produce a greater impact on gas efficiency than data structure optimization alone. The evaluation conducted through metrics such as total gas consumption, average per-transaction metrics, and performance distribution analysis offers a more comprehensive overview of the performance characteristics of each method. This study has several limitations, primarily related to gas costs on the Ethereum network. Although the proposed optimization techniques significantly reduce gas consumption compared to the baseline approach, blockchain transaction costs remain relatively high, particularly as the number of reports increases. Furthermore, the experiments were conducted in a controlled testing environment, which does not fully represent the dynamic conditions of public blockchain networks, such as gas price fluctuations and transaction congestion levels. The evaluation in this study also focuses on primary metrics such as gas consumption, transaction cost, latency, and execution time, while other aspects that may influence cost efficiency, such as off-chain computation overhead and batch management, have not yet been analyzed in depth. Future research may explore more adaptive optimization strategies to mitigate the impact of high gas costs. One potential approach is the implementation of adaptive batching, which dynamically adjusts batch size or commit timing based on network conditions and gas prices. In addition, integration with layer-2 scaling solutions, such as rollups or sidechains, may further reduce transaction costs significantly [51]. Further evaluation on public blockchain networks with varying gas price conditions is necessary to obtain a more realistic understanding of system performance in real-world implementations.

IV. CONCLUSIONS

This study evaluated several smart contract optimization strategies to reduce gas consumption in a blockchain-based mobile reporting system for sexual violence cases on the Ethereum network. The findings indicate that the efficiency of blockchain applications is strongly influenced by how data storage and transaction submission are designed. Approaches that store detailed information directly on-chain result in high computational costs due to intensive storage operations, whereas strategies that minimize storage usage or reduce the frequency of on-chain transactions significantly improve scalability. In particular, aggregation and threshold-based batching mechanisms enable multiple reports to be represented through compact cryptographic commitments while preserving data integrity.

Scientifically, this research contributes a comparative experimental framework that integrates storage-level optimization, cryptographic aggregation, and transaction batching within a single evaluation environment, providing empirical evidence on how different design strategies affect gas efficiency and execution performance. Practically, the results provide guidance for developers and system architects in designing blockchain-based audit logging systems that remain economically feasible on public blockchain infrastructures. Nevertheless, the study is limited to experiments conducted in a controlled environment and focuses primarily on gas efficiency metrics without evaluating broader aspects such as security trade-offs or real network variability. Future studies should examine adaptive batching mechanisms, cross-platform blockchain implementations, and security implications of off-chain aggregation to further improve the scalability and reliability of decentralized reporting systems.

VI. AUTHOR'S CONTRIBUTION

Conceptualization: Michael Angello Qadosy Riyadi, Sulthonika Mahfudz Al Mujahidin, Nur Alifia Rustan, A'isyah Belqis Febi Aulia, Mastuty Ayu Ningtyas and Khodijah Amiroh.
Methodology: Michael Angello Qadosy Riyadi, Sulthonika Mahfudz Al Mujahidin, Nur Alifia Rustan, A'isyah Belqis Febi Aulia, Mastuty Ayu Ningtyas and Khodijah Amiroh.
Investigation: Michael Angello Qadosy Riyadi, Sulthonika Mahfudz Al Mujahidin, Nur Alifia Rustan, A'isyah Belqis Febi Aulia, Mastuty Ayu Ningtyas and Khodijah Amiroh.
Discussion of results: Michael Angello Qadosy Riyadi, Sulthonika Mahfudz Al Mujahidin, Nur Alifia Rustan, A'isyah Belqis Febi Aulia, Mastuty Ayu Ningtyas and Khodijah Amiroh.
Writing – Original Draft: Michael Angello Qadosy Riyadi, Sulthonika Mahfudz Al Mujahidin, Nur Alifia Rustan, A'isyah Belqis Febi Aulia, Mastuty Ayu Ningtyas and Khodijah Amiroh.
Writing – Review and Editing: Michael Angello Qadosy Riyadi, Sulthonika Mahfudz Al Mujahidin, Nur Alifia Rustan, A'isyah Belqis Febi Aulia, Mastuty Ayu Ningtyas and Khodijah Amiroh.
Resources: Michael Angello Qadosy Riyadi, Sulthonika Mahfudz Al Mujahidin, Nur Alifia Rustan, A'isyah Belqis Febi Aulia, Mastuty Ayu Ningtyas and Khodijah Amiroh.
Supervision: Michael Angello Qadosy Riyadi, Sulthonika Mahfudz Al Mujahidin, Nur Alifia Rustan, A'isyah Belqis Febi Aulia, Mastuty Ayu Ningtyas and Khodijah Amiroh.
Approval of the final text: Michael Angello Qadosy Riyadi, Sulthonika Mahfudz Al Mujahidin, Nur Alifia Rustan, A'isyah Belqis Febi Aulia, Mastuty Ayu Ningtyas and Khodijah Amiroh.

VII. REFERENCES

[1] S. Dong, K. Abbas, M. Li, and J. Kamruzzaman, "Blockchain technology and application: an overview," PeerJ Computer Science, vol. 9, p. e1705, 2023, doi: 10.7717/peerj-cs.1705.

[2] M. Krichen, M. Ammi, A. Mihoub, and M. Almutiq, "Blockchain for Modern Applications: A Survey," Sensors, vol. 22, no. 14, p. 5274, 2022, doi: 10.3390/s22145274.

[3] G. Habib, S. Sharma, S. Ibrahim, I. Ahmad, S. Qureshi, and M. Ishfaq, "Blockchain Technology: Benefits, Challenges, Applications, and Integration of Blockchain Technology with Cloud Computing," Future Internet, vol. 14, no. 11, p. 341, 2022, doi: 10.3390/fi14110341.

[4] N. Machado and C. M. Taboada Rodriguez, "A Logistics 5.0 maturity model: a human-centric and sustainable approach for the supply chain of the future," ITEGAM-JETIA, vol. 11, no. 51, pp. 164–170, 2025, doi: 10.5935/jetia.v11i51.1407.

[5] T. Kazeem et al., "Risk Management and Governance in Blockchain-Based Digital Identity Projects: A Business Analysis and Project Management Framework," ITEGAM-JETIA, vol. 11, no. 54, pp. 172–180, 2025, doi: 10.5935/jetia.v11i54.1710.

[6] D. L. Fekete and A. Kiss, "Toward Building Smart Contract-Based Higher Education Systems Using Zero-Knowledge Ethereum Virtual Machine," Electronics, vol. 12, no. 3, p. 664, 2023, doi: 10.3390/electronics12030664.

[7] F. Cassez, J. Fuller, M. K. Ghale, D. J. Pearce, and H. M. A. Quiles, "Formal and Executable Semantics of the Ethereum Virtual Machine in Dafny," in Formal Methods. FM 2023, M. Chechik, J. P. Katoen, and M. Leucker, Eds., in Lecture Notes in Computer Science, vol. 14000. Cham: Springer, 2023, pp. 571–583. doi: 10.1007/978-3-031-27481-7_32.

[8] C. E. Quintero-Narvaez and R. Monroy-Borja, "Zero-Knowledge Proofs for Questionnaire Result Verification in Smart Contracts," in 2023 Mexican International Conference on Computer Science (ENC), Guanajuato, Guanajuato, Mexico: IEEE, 2023, pp. 1–5. doi: 10.1109/ENC60556.2023.10508637.

[9] B. K. Meister and H. C. W. Price, "Gas fees on the Ethereum blockchain: from foundations to derivative valuations," Frontiers in Blockchain, vol. 7, p. 1462666, 2024, doi: 10.3389/fbloc.2024.1462666.

[10] P. Sharma, R. Jindal, and M. D. Borah, "A review of smart contract-based platforms, applications, and challenges," Cluster Computing, vol. 26, pp. 395–421, 2023, doi: 10.1007/s10586-021-03491-1.

[11] M. M. A. Khan, H. M. A. Sarwar, and M. Awais, "Gas consumption analysis of Ethereum blockchain transactions," Concurrency and Computation: Practice and Experience, vol. 34, no. 4, p. e6679, 2022, doi: 10.1002/cpe.6679.

[12] P. Ahirao, Y. Borse, D. Patole, S. Agarwal, M. Abhyankar, and K. Nair, "Comprehensive Analysis of Mitigation Strategies for Denial-of-Service Attacks on Smart Contracts," in 2025 IEEE International Conference on Blockchain and Distributed Systems Security (ICBDS), Kolhapur, India: IEEE, 2025, pp. 1–6. doi: 10.1109/ICBDS67396.2025.11376964.

[13] H. A. Janjua, L. Yue, and S. Hayat, "Smart Scan: An Approach to Detect Denial of Service Vulnerability in Ethereum Smart Contracts," in Proceedings of the 2023 7th International Conference on Electronic Information Technology and Computer Engineering (EITCE '23), New York, NY, USA: Association for Computing Machinery, 2023, pp. 1572–1578. doi: 10.1145/3650400.3650663.

[14] M. T. Ta and T. Q. Do, “A study on gas cost of ethereum smart contracts and performance of blockchain on simulation tool,” Peer-to-Peer Networking and Applications, vol. 17, pp. 200–212, 2024, doi: 10.1007/s12083-023-01598-3.

[15] S. Porkodi and D. Kesavaraja, “Escalating Gas Cost Optimization in Smart Contract,” Wireless Personal Communications, vol. 136, pp. 35–59, 2024, doi: 10.1007/s11277-024-11066-7.

[16] M. Pacheco, G. Oliva, G. K. Rajbahadur, and A. Hassan, “Is My Transaction Done Yet? An Empirical Study of Transaction Processing Times in the Ethereum Blockchain Platform,” ACM Transactions on Software Engineering and Methodology, vol. 32, no. 3, p. Article 59, 2023, doi: 10.1145/3549542.

[17] A. Vacca, M. Fredella, A. Di Sorbo, C. A. Visaggio, and G. Canfora, “An empirical investigation on the trade-off between smart contract readability and gas consumption,” in Proceedings of the 30th IEEE/ACM International Conference on Program Comprehension (ICPC ’22), New York, NY, USA: Association for Computing Machinery, 2022, pp. 214–224. doi: 10.1145/3524610.3529157.

[18] A. S. Paramitha and M. Tarigan, “Analysis of Gas Fee Patterns in Blockchain Transactions - A Case Study on Ethereum Smart Contracts,” Journal of Current Research in Blockchain, vol. 2, no. 3, pp. 180–189, 2025, doi: 10.47738/jcrb.v2i3.41.

[19] E. Ni, E. Knight, and M. Gerstein, “Scalable and efficient on-chain data management in blockchain for large biomedical data,” Journal of Biomedical Informatics, vol. 165, p. 104818, 2025, doi: https://doi.org/10.1016/j.jbi.2025.104818.

[20] A. B. M. Salem and M. J. Aqel, “Analyzing Transaction Fee Patterns and Their Impact on Ethereum Blockchain Efficiency,” Journal of Current Research in Blockchain, vol. 2, no. 4, pp. 228–243, 2025, doi: 10.47738/jcrb.v2i4.46.

[21] D. Koutmos, “Network Activity and Ethereum Gas Prices,” Journal of Risk and Financial Management, vol. 16, no. 10, p. 431, 2023, doi: 10.3390/jrfm16100431.

[22] X. Wang and F. Xu, “The Value of Smart Contract in Trade Finance,” Manufacturing & Service Operations Management, vol. 25, no. 6, pp. 2056–2073, 2023, doi: 10.1287/msom.2022.1126.

[23] N. Afraz, F. Wilhelmi, H. Ahmadi, and M. Ruffini, “Blockchain and Smart Contracts for Telecommunications: Requirements vs. Cost Analysis,” IEEE Access, vol. 11, pp. 95653–95666, 2023, doi: 10.1109/ACCESS.2023.3309423.

[24] J. Huang, K. Zhou, A. Xiong, and D. Li, “Smart Contract Vulnerability Detection Model Based on Multi-Task Learning,” Sensors, vol. 22, no. 5, p. 1829, 2022, doi: 10.3390/s22051829.

[25] Z. Zhao, J. Li, Z. Su, and Y. Wang, “GaSaver: A Static Analysis Tool for Saving Gas,” IEEE Transactions on Sustainable Computing, vol. 8, no. 2, pp. 257–267, 2023, doi: 10.1109/TSUSC.2022.3221444.

[26] A. Kuhlman and A. Wicaksana, “Smart contract optimization for gas fee reduction with static solidity optimizer,” Discover Applied Sciences, vol. 7, p. 888, 2025, doi: 10.1007/s42452-025-07537-6.

[27] A. R. Raza, M. Hanzala, K. Mahmood, S. Tahir, S. Khalid, and A. Masood, “Optimizing Gas Consumption in Ethereum Smart Contracts: A Static Analysis Approach,” in 2025 International Conference on Communication Technologies (ComTech), Rawalpindi, Pakistan: IEEE, 2025, pp. 1–6. doi: 10.1109/ComTech65062.2025.11034442.

[28] S. Khanzadeh and M. H. Alalfi, “SolOSphere: A Framework for Gas Optimization in Solidity Smart Contracts,” in 2024 IEEE International Conference on Software Analysis, Evolution and Reengineering - Companion (SANER-C), Rovaniemi, Finland: IEEE, 2024, pp. 35–45. doi: 10.1109/SANER-C62648.2024.00010.

[29] S. Gupta, S. Singh, Snehlata, and V. K. Dwivedi, “Gas-Efficient Patterns for Smart Contracts in Solidity: Optimization Techniques and Comparative Analysis,” in 2024 4th International Conference on Innovative Sustainable Computational Technologies (CISCT), Dehradun, India: IEEE, 2024, pp. 1–6. doi: 10.1109/CISCT62494.2024.11134254.

[30] C. C. Escobar, S. Roy, O. P. Kreidl, A. Dutta, and L. Bölöni, “Toward a Green Blockchain: Engineering Merkle Tree and Proof of Work for Energy Optimization,” IEEE Transactions on Network and Service Management, vol. 19, no. 4, pp. 3847–3857, 2022, doi: 10.1109/TNSM.2022.3219494.

[31] H. V. A. Le, Q. D. N. Nguyen, N. Tadashi, and T. H. Tran, “Blockchain-Based Decentralized Identity Management System with AI and Merkle Trees,” Computers, vol. 14, no. 7, p. 289, 2025, doi: 10.3390/computers14070289.

[32] M. Lakshmanan and G. S. Anandha Mala, “Merkle tree-blockchain-assisted privacy preservation of electronic medical records on offering medical data protection through hybrid heuristic algorithm,” Knowledge and Information Systems, vol. 66, pp. 481–509, 2024, doi: 10.1007/s10115-023-01937-z.

[33] Z. Liu, L. Ren, Y. Feng, S. Wang, and J. Wei, “Data Integrity Audit Scheme Based on Quad Merkle Tree and Blockchain,” IEEE Access, vol. 11, pp. 59263–59273, 2023, doi: 10.1109/ACCESS.2023.3240066.

[34] S. Park et al., “Impact of EIP-4844 on Ethereum: Consensus Security, Ethereum Usage, Rollup Transaction Dynamics, and Blob Gas Fee Markets,” IEEE Transactions on Network Science and Engineering, vol. 13, pp. 1294–1310, 2026, doi: 10.1109/TNSE.2025.3594281.

[35] Y. Fan, B. Gao, D. Sheng, Z. Hu, and X. Ding, “Batch Transaction Processing for Adaptive Sharding Blockchain-Enabled Edge Computing,” ACM Transactions on Autonomous and Adaptive Systems, vol. 20, no. 4, p. Article 31, 2025, doi: 10.1145/3764927.

[36] N. Maryani, M. Muchlish, R. Mulyadi, and N. Solehah, “Blockchain-Based Audit Trails: Improving Transparency and Fraud Detection in Digital Accounting Systems,” International Journal of Advanced Computer Science and Applications (IJACSA), vol. 17, no. 1, 2026, doi: 10.14569/IJACSA.2026.0170162.

[37] F. Casino, T. K. Dasaklis, and C. Patsakis, “A systematic literature review of blockchain-based applications: Current status, classification and open issues,” Telematics and Informatics, vol. 36, pp. 55–81, 2019, doi: 10.1016/j.tele.2018.11.006.

[38] A. Alketbi, Q. Nasir, and M. A. Talib, “Blockchain for government services — Use cases, security benefits and challenges,” in 2018 15th Learning and Technology Conference (L&T), Jeddah, Saudi Arabia: IEEE, 2018, pp. 112–119. doi: 10.1109/LT.2018.8368494.

[39] A. Akhtar, B. Shafiq, J. Vaidya, A. Afzal, S. Shamail, and O. Rana, “Blockchain Based Auditable Access Control for Distributed Business Processes,” Proceedings International Conference on Distributed Computing Systems, pp. 12–22, 2020, doi: 10.1109/ICDCS47774.2020.00015.

[40] H. M. Zangana, A. khalid Mohammed, and S. R. M. Zeebaree, “Systematic Review of Decentralized and Collaborative Computing Models in Cloud Architectures for Distributed Edge Computing,” Sistemasi: Jurnal Sistem Informasi, vol. 13, no. 4, 2024, doi: 10.32520/stmsi.v13i4.4169.

[41] L. Shekhtman and E. Waisbard, “EngraveChain: A Blockchain-Based Tamper-Proof Distributed Log System,” Future Internet, vol. 13, no. 6, p. 143, 2021, doi: 10.3390/fi13060143.

[42] A. Ahmad, M. Saad, M. Bassiouni, and A. Mohaisen, “Towards Blockchain-Driven, Secure and Transparent Audit Logs,” in Proceedings of the 15th EAI International Conference on Mobile and Ubiquitous Systems: Computing, Networking and Services (MobiQuitous ’18), New York, NY, USA: Association for Computing Machinery, 2018, pp. 443–448. doi: 10.1145/3286978.3286985.

[43] S. Azimi, A. Golzari, N. Ivaki, and N. Laranjeiro, “A systematic review on smart contracts security design patterns,” Empirical Software Engineering, vol. 30, p. 95, 2025, doi: 10.1007/s10664-025-10646-w.

[44] C. Dannen, “Solidity Programming,” in Introducing Ethereum and Solidity, Berkeley, CA: Apress, 2017, pp. 69–88. doi: 10.1007/978-1-4842-2535-6_4.

[45] P. Xu, Y. Sui, and M. Staples, “Towards Source Mapping for Zero-Knowledge Smart Contracts: Design and Preliminary Evaluation,” in Proceedings of the 34th ACM SIGSOFT International Symposium on Software Testing and Analysis (ISSTA Companion ’25), New York, NY, USA: Association for Computing Machinery, 2025, pp. 200–209. doi: 10.1145/3713081.3732932.

[46] O. Kuznetsov, A. Rusnak, A. Yezhov, D. Kanonik, K. Kuznetsova, and O. Domin, “Efficient and Universal Merkle Tree Inclusion Proofs via OR Aggregation,” Cryptography, vol. 8, no. 3, p. 28, 2024, doi: 10.3390/cryptography8030028.

[47] J. Davies, “Enhanced scalability and privacy for blockchain data using Merklized transactions,” Frontiers in Blockchain, vol. 6, p. 1222614, 2024, doi: 10.3389/fbloc.2023.1222614.

[48] S. Khanzadeh, N. Samreen, and M. H. Alalfi, “Optimizing Gas Consumption in Ethereum Smart Contracts: Best Practices and Techniques,” in 2023 IEEE 23rd International Conference on Software Quality, Reliability, and Security Companion (QRS-C), Chiang Mai, Thailand: IEEE, 2023, pp. 300–309. doi: 10.1109/QRS-C60940.2023.00056.

[49] K. S. Weedagamaarachchi, H. D. Vithanage, H. M. S. N. Dehipola, K. D. R. Manditha, V. Jayasinghearachchi, and J. Perera, “Optimizing Gas Efficiency in Ethereum Smart Contracts Using Design Pattern Refinement and Complexity Reduction,” in 2025 7th International Conference on Advancements in Computing (ICAC), Colombo, Sri Lanka: IEEE, 2025, pp. 1–6. doi: 10.1109/ICAC69156.2025.11361528.

[50] H. Zhang et al., “Asynchronous Threshold ECDSA With Batch Processing,” IEEE Transactions on Computational Social Systems, vol. 11, no. 1, pp. 566–575, 2024, doi: 10.1109/TCSS.2022.3230903.

[51] K. Tan Vo, H.-T. Nguyen, and T.-A. Nguyen-Hoang, “An Integrated Decision-Making Framework for Enhancing Blockchain Scalability and Efficiency: Layer-2, Off-Chain Storage, and Smart Contracts,” IEEE Access, vol. 13, pp. 138328–138351, 2025, doi: 10.1109/ACCESS.2025.3596021.

Journal of Engineering and Technology for Industrial Applications

ITEGAM-JETIA

Manaus, v.12 n.60, p.629-640 July/August, 2026.
DOI: https://doi.org/10.5935/jetia.v12i60.3929

ISSN ONLINE: 2447-0228

RESEARCH ARTICLE OPEN ACCESS

TRANSIENT THERMAL PERFORMANCE ANALYSIS OF NANOPARTICLE-COATED FLAT PLATE SOLAR COLLECTORS USING MATLAB-BASED MODELING

Juber Khatik*[1], Nilesh Salunke[2], Mujahid Husain[3], Yogeshkumar Pathak[4], Kailas Deore[5] Pradeep Solanki[6] and Pravin Shirule[7]

[1]Research Scholar, SSBT's College of Engineering & Technology, Bambhori, Jalgaon, Maharashtra, India
[2]Principal, SVKM's Institute of Technology, Dhule, Maharashtra, India.
[3]Professor, SSBT's College of Engineering & Technology, Bambhori, Jalgaon, Maharashtra, India.
[4, 5]Assistant Professor, R. C. Patel Institute of Technology, Shirpur, Maharashtra, India.
[6, 7]Associate Professor, SSBT's College of Engineering & Technology, Bambhori, Jalgaon, Maharashtra, India

[1]https://orcid.org/0000-0003-3550-4367, [2]https://orcid.org/0000-0003-4185-7556, [3]https://orcid.org/0009-0005-7663-6691
[4]https://orcid.org/0000-0003-4453-4912, [5]https://orcid.org/0000-0002-3229-5902, [6]https://orcid.org/0000-0001-8949-9562
[7]https://orcid.org/0009-0008-4527-1222

E-mail: *juber.khatik@rcpit.ac.in, nilesh.salunke@svkm.ac.in, husain.mujahid@SSCOETJalgaon.ac.in, yogesh.pathak@rcpit.ac.in, kailas.deore@rcpit.ac.in, p_msolanki@rediffmail.com, pashirule@gmail.com

ARTICLE INFO

Article History
Received on: March 05, 2026
Reviewed on: April 04, 2026
Accepted on: May 01, 2026
Published on: July 31, 2026

Keywords:
Flat Plate Solar Collector,
Nanoparticle Coatings,
Transient Thermal Analysis,
MATLAB Simulation.

ABSTRACT

Flat plate solar collectors (FPCs) have significant thermal performance that is vital in improving the efficiency of solar thermal energy systems. Traditional absorber coating, including black paint, has limited optical and thermal behavior, and nanomaterial-based absorber coating has received interest in improving performance. The purpose of the study is to assess and compare the thermal performance of FPCs when coated with CuO, Al2O3 and graphene nanoparticles. A mathematical model simulator of the performance of the collector under dynamic solar and environmental conditions was created using transient lumped capacitance in MATLAB. The model computes the important thermal performance indicators, such as outlet fluid temperature, useful heat gain, and instantaneous efficiency, and it has been verified against literature data. Simulation findings indicate that nanomaterial coatings are much more efficient in terms of thermal conductivity with graphene showing the most dramatic efficiency improvement of up to 0.835 relative to 0.725 when using black paint and a maximum useful heat gain of 834 W relative to 724 W. Graphene-coated collectors on average increased efficiency by 15.2% and useful heat gain by 13.8%. The improvements of Al2O3 and CuO coating were around 9-11% higher than black paint. Such improvements are explained by the high thermal conductivity and optical absorption of nanoparticles. The results show the promise of advanced nanocoatings to enhance the efficiency of solar thermal systems and offer a solid basis to optimize and experimentally validate such systems in the future.

Copyright ©2026 by authors and Galileo Institute of Technology and Education of the Amazon (ITEGAM). This work is licensed under the Creative Commons Attribution International License (CC BY 4.0).

I. INTRODUCTION

Solar flat plate collector (FPSC) is a widely used solar thermal system that absorbs solar energy and transforms it into heat energy to be used in different ways, such as heating water and heating space. The FPSC consists of the core element, which is the absorber plate that directly affects the thermal efficiency of the system because it absorbs solar radiation and transfers heat to the working fluid [1–4].

The design parameters and material properties of the absorber plate have a considerable influence on the performance of the system. Materials with a high thermal conductivity, including copper and aluminum, increase the efficiency of heat absorption and transfer, which decreases thermal resistance [5] [6]. Also, surface alterations, including roughened surfaces, prolonged surfaces, and selective surface finishes are used to reduce radiative and convective heat losses to enhance heat retention [7] [8]. The geometrical arrangement of the absorber plate, plate thickness, channel structure, and fluid temperature increase are also further affected by the heat transfer efficiency and fluid temperature increase [1–3]. The optimization of these design parameters results in the achievement of high performance of FPSC and the system becomes efficient and effective in real-life applications. The development of absorber plate technology has greatly increased the efficiency of solar flat plate collectors (FPSC) through the enhancement of the mechanisms of heat absorption, retention and transfer. Surface modifications and innovations that include micro-grooved, V-corrugated, and selectively coated surfaces have been proposed to optimize optical absorption and reduce radiative and convective heat losses [1-8]. Absorber plates that have been integrated with nanomaterials, including carbon nanotubes, graphene, and metal oxide coating, have demonstrated increased thermal conductivity and solar energy conversion efficiency [9–11]. Geometric improvements, including the use of serpentine flow paths, spiral tubes, and multi-channel absorber designs, have improved the heat transfer through the increased surface contact between the working fluid and the absorber plate [1-12]. All these developments are aimed at enhancing the overall thermal performance and efficiency of FPSCs, and therefore, they become more suitable to sustainable and high-performance solar energy use. Improvement of solar thermal absorber plates by using different coatings, materials and structural changes is a common study in the quest to enhance efficiency, heat transfer and energy absorption. Coating modifications have shown to have great enhancements in thermal performance. Palanikumar et al. [13] discovered that a 0.1 mm black nickel thin film covering on copper absorber tubes reached a maximum absorptance of 0.98, reducing emissivity and maximizing thermal efficiency to 74.3%. In the same way, Nazari et al. [14] demonstrated that the coating of a cuprous absorber plate with CuO nanoparticles enhanced efficiency by 35.8% and exergy efficiency by 11.2. Coatings based on graphene also provided significant improvements, with Kumar et al. [15] reporting that graphene-doped black paint on a triangular plate solar air heater, and Mariraja et al. [16] reporting that graphene nanoplatelet (GNP) nano paint on solar still absorber plates, both raised thermal efficiency by 4.91 and exergy efficiency by 4.27. Moreover, Han et al. [17] found that the application of 15 wt% silicon (Si) particles to the plate of a solar still absorber increased the surface temperature by 65.81, which maximized the yield of the distillate.

Coatings that are enhanced by nanoparticles have also been widely researched. Katekar et al. [18] reported that the addition of 30% aluminum oxide nanoparticles to dull black paint enhanced heat transfer and thermal performance of absorber plates by a significant factor, whereas Gurbuz et al. [19] reported that nano-enhanced black paint with Fe3O4 and mesh tubes increased the efficiency of solar air collector by 40.45% and a payback period of 0.31-0.34 years. On the same note, Sivakumar et al. [20] demonstrated that CuO nanoparticle-coated absorber plates in a mixed-mode forced convection solar dryer enhanced collector efficiency by 4% and drying time by 6%. Performance has also been enhanced by structural and material changes to the absorber plates. Sakhaei et al., [21] reported that carbon-coated plates were the most efficient thermally (69.4%), which is 13 and 11.3% higher than the black chrome and black-painted plates, respectively. Sharma et al. [22] indicated that trapezoidal corrugated absorber plates in flat-plate solar collectors increased thermal efficiency by 12.85% and exergy efficiency by 23.31% and Kumar et al. [23] indicated that V-shaped rib roughness on absorber plates enhanced heat transfer despite higher friction factor properties. Also, Karthikeyan et al. [24] discovered that pin-fin absorber plates coated with Multi-Walled Carbon Nanotube (MWCNT) had 12% thermo-hydraulic efficiency and a 24% heat transfer enhancement. Cost-effective performance gains have also been realized by alternative absorber materials. Selikhov et al. [25] have shown that flat-plate solar collectors with polyethylene film absorbers had a maximum efficiency of 0.95 and were up to four times cheaper than aluminum absorbers. In addition, Ganesh Kumar et al. [26] emphasized that the combination of nano-coated conch shells and roughened corrugated copper absorber plates in a two-slope solar still enhanced the thermal efficiency by 35.53% and the water yield to 2193 ml/m2/day. In general, this paper point to the usefulness of nanoparticle-enhanced coating, structural changes, and alternative material to enhance the thermal efficiency, heat transfer, and economic viability of solar thermal absorber plates. The investigation of nanomaterials in solar thermal systems mainly focuses on steady-state conditions and simplified scenarios without adequate exploration of flat plate collector transient thermal responses under genuine solar and environmental fluctuations. The current investigation develops a complete transient thermal model through MATLAB that evaluates the dynamic characteristics of flat plate solar collectors using different nanoparticle materials. The model analyzes true-time solar irradiance and ambient temperature data points using Maxwell model calculations for effective thermal conductivity determination through nanoparticle selection and loading rates while implementing lumped capacitive energy modeling for time-based plate temperature and efficiency measurement. The simulation framework allows researchers to measure key performance indicators at instant efficiency rates, stagnation temperature levels and yearly energy production levels across various coating configurations thus creating a strong evaluation and material optimization environment.

II. MATHEMATICAL MODELING

The use of nanomaterials to improve thermal performance of flat plate solar collectors (FPCs) has received significant interest over the past few years. These surfaces are made of nanoparticles like graphene, CuO, and Al2O3 and are reported to have a tremendous effect on optical and thermal conductivity properties of the absorber plates. To measure such improvements and their effects on the performance of the system, a strict and dynamic mathematical model is necessary to capture the transient thermal behaviors at different solar and environmental conditions. This paper has constructed a MATLAB based simulation code to analyze the thermal efficiency and the energy production of flat plate collectors covered with different nanoparticle materials at varying concentrations. The code has first principles of heat transfer, with dynamic environmental inputs of solar radiation and ambient temperature, and computes key performance indicators of instantaneous collector efficiency, stagnation temperature and annual energy yield. This method offers a strong and scalable platform of comparative performance analysis of advanced coated absorbers in real-life operating environments.

II.1 KEY ASSUMPTIONS AND INPUT PARAMETERS

When formulating the thermal model of the nanoparticle-enhanced flat plate solar collector, a number of assumptions were made to reduce the complexity of the analysis without losing physical relevance. The incident of solar radiation on the collector surface was modeled as a sinusoidal curve, with the sunrise at 6:00 AM and the sunset at 6:00 PM, thus, representing the common diurnal variation in the solar irradiance. Likewise, the ambient temperature pattern was also sinusoidal with the lowest temperature at the beginning of the morning and the highest at the mid-afternoon, which closely approximates the natural environmental conditions. The absorber plate was assumed to be coated with graphene nanoparticles, whose thermal conductivity and solar absorptivity were considered to vary as functions of their concentration in the base material. In order to simulate the heat transfer behavior in the absorber plate, a lumped capacitance method was chosen. This assumes uniform temperature distribution across the plate thickness, which is valid given the small thickness of the plate and the relatively high thermal conductivity of the coated material. These assumptions collectively enabled a computationally efficient yet realistic simulation of the transient thermal behavior of the solar collector.

II.2 CODE DEVELOPMENT PROCEDURE

A simulation code was written in MATLAB to simulate the transient thermal performance of nanoparticle-enhanced flat plate solar collectors. The code is structured and modular, consisting of input definition, property enhancement, transient thermal simulation, performance analysis and result visualization. This systematic system enables the successful comparison of performance in different coating conditions.

- Input Module: Characterizes absorber geometry, coating parameters and environmental conditions (solar radiation and ambient temperature).
- Property Enhancement: Computes effective thermal conductivity, based on the Maxwell model and recalculates specific heat and density.
- Transient Module: Uses lumped capacitance model to model time-based temperature variation across the plate.
- Performance Module: Calculates instantaneous thermal efficiency, daily production and approximates yearly energy gain.
- Output and Visualization: Plots time-series data of irradiance, temperature and efficiency; compares materials and concentrations.
- Modular Design: Allows the flexibility of expansion and future upgrades or parametric studies.

II.3 CODE PERFORMANCE EVALUATION PROCEDURE

A systematic performance evaluation procedure was used to evaluate the accuracy and applicability of the developed MATLAB simulation code. This included comparing the numerical forecasts with benchmark data, sensitivity and parametric analysis and estimating long term energy production under different conditions. The steps are necessary to assure that the model is reliable to reflect the thermal behavior of nanoparticle-enhanced flat plate collectors and facilitate optimization studies.

- Result validation: Comparison of simulated temperature profiles and thermal efficiencies with published experimental data or literature values of similar nanoparticle coatings were used to verify the accuracy of the model.
- Sensitivity Analysis: The effect of nanoparticle thermal conductivity and volume fraction on thermal response of the collector was examined to determine the effect of the material.
- Annual Energy Estimation: Hourly energy gains were summed up over a daily cycle and extrapolated to give the total annual energy output of the collector system.
- Stagnation Analysis: The maximum temperature of the absorber plate (stagnation temperature) was calculated, which provided information on the highest thermal loading, by assuming zero flow conditions.
- Parametric Study: A series of simulations were performed to produce contour plots and the impact of optical (absorptance a) and thermal (emittance e) property variations on the performance metrics was observed.

III. NUMERICAL METHODOLOGY

III.1 OVERVIEW OF NUMERICAL MODELING

The numerical analysis in this study was conducted using a MATLAB-based finite difference method (FDM) to simulate the transient thermal behavior of a nanoparticle-enhanced flat plate solar collector absorber. The model accounts for conduction within the absorber plate, convective and radiative heat losses from the top surface, and thermal energy absorption from incident solar radiation. The impact of adding nanoparticles to the absorber coating is captured through modified thermophysical properties. The simulation includes time-dependent ambient and solar conditions to closely mimic realistic operating scenarios.

III.2 GOVERNING EQUATION

The primary equation governing the energy dynamics in the absorber plate is based on the first law of thermodynamics, applied to a control volume given by Eq. (1):

$$mC_p \frac{dT_p}{dt} = Q_{in} - Q_{loss} \quad (1)$$

T_p is the average plate temperature, C_p is the specific heat, Q_{in} is the absorbed solar energy, and Q_{loss} includes convective and radiative heat losses from the top surface. To assess thermal performance at any instant, instantaneous thermal efficiency is defined as Eq. (2):

$$\eta(t) = \frac{Q_{useful}}{I \cdot A} = \frac{Q_{in} - Q_{loss}}{I \cdot A} \quad (2)$$

Where *I* is solar irradiance and *A* is the collector area. The effective thermal conductivity of the nanoparticle-enhanced coating is estimated using the Maxwell model as given in Eq. (3):

$$k_{eff} = k_{base} \cdot \left(\frac{k_{np} + 2k_{base} + 2\phi(k_{np} - k_{base})}{k_{np} + 2k_{base} - \phi(k_{np} - k_{base})} \right) \quad (3)$$

This accounts for the influence of nanoparticle volume fraction ϕ on thermal conductivity.

III.3 BOUNDARY CONDITIONS

In the present study, the thermal behavior of the absorber plate coated with nanoparticle-enhanced paint is simulated by applying realistic boundary conditions that represent actual operating environments of flat plate solar collectors. Top Surface Boundary Condition The top surface of the absorber plate is exposed directly to the solar irradiance, resulting in a heat gain, while simultaneously losing heat through convection to the ambient air and radiation to the surroundings. This is modeled using a combined heat flux boundary condition expressed as Eq. (4):

$$-k\left(\frac{\partial T}{\partial y}\right)_{\text{top}} = \alpha I(t) - h_{\text{conv}}(T_s - T_{\text{amb}}) - \varepsilon\sigma(T_s^4 - T_{\text{amb}}^4) \quad (4)$$

This boundary condition ensures the simulation captures the transient and competing effects of solar heat gain and environmental heat loss. The inclusion of both convective and radiative terms allows the model to handle a wide range of environmental conditions and surface modifications. Bottom Surface Boundary Condition The bottom surface of the absorber plate is assumed to be thermally insulated, representing either a well-insulated bottom or negligible heat loss through the backside. This is mathematically expressed as an adiabatic boundary condition – Eq. (5):

$$\left(\frac{\partial T}{\partial y}\right)_{\text{bottom}} = 0 \quad (5)$$

This implies no heat transfer occurs across the bottom boundary, allowing the model to focus on upward heat exchange with the working fluid or air. Lateral Edges Boundary Conditions The lateral sides of the absorber plate are modeled using symmetry or adiabatic conditions, depending on the physical layout and insulation characteristics of the system. For a large or center-symmetric absorber plate, symmetric conditions are suitable and simplify the problem – Eq. (6):

$$\left(\frac{\partial T}{\partial x}\right)_{\text{left/right}} = 0 \quad (6)$$

This indicates that there is no net heat flow across the lateral boundaries, which is a valid assumption when the geometry or physical design suggests negligible lateral heat loss. Initial Condition The entire absorber plate is assumed to be at ambient temperature at the beginning of the simulation – Eq. (7):

$$T(x, y, t = 0) = T_{\text{amb}} \quad (7)$$

This defines the starting point for the transient simulation and ensures that the heat build-up due to solar exposure is captured from the beginning of the day.

III.4 NUMERICAL SCHEME AND GRID DISCRETIZATION

The absorber plate is discretized into a 2D finite difference grid, with nodes representing small control volumes. At each node, transient heat conduction is solved using either an explicit or implicit time-stepping scheme, based on the energy conservation principle. The general form of the heat conduction equation is (Eq. 8):

$$\frac{\partial T}{\partial t} = \alpha\left(\frac{\partial^2 T}{\partial x^2} + \frac{\partial^2 T}{\partial y^2}\right) \quad (8)$$

Where α is the thermal diffusivity. The time-marching algorithm updates nodal temperatures iteratively, and convergence is verified using the following criterion (Eq. 9):

$$\max|T^{n+1} - T^n| < \varepsilon \quad (9)$$

Where ε is a user-defined tolerance for convergence. The program exits once thermal equilibrium is reached for all nodes within the tolerance.

III.5 THERMAL PERFORMANCE METRICS

To comprehensively evaluate and compare the thermal behavior of the nanoparticle-enhanced solar absorber plates and different solar still configurations, several thermal performance metrics were used. These metrics capture instantaneous, daily, and annual system responses under varying ambient and operational conditions.

1. Useful Heat Gain

The useful heat gain (Q_{useful}) is the amount of thermal energy effectively absorbed and utilized by the system to raise the fluid (or plate) temperature. It is calculated as (Eq. 10):

$$Q_{\text{useful}} = \dot{m} C_p (T_{\text{out}} - T_{\text{in}}) \tag{10}$$

This parameter is essential for quantifying the energy that contributes to desalination or heating processes.

2. Instantaneous Thermal Efficiency

The instantaneous thermal efficiency ($\eta(t)$) defines the efficiency of the absorber plate or solar still at a particular moment, based on the ratio of useful energy gain to the incident solar energy (Eq. (11)):

$$\eta(t) = \frac{Q_{\text{useful}}(t)}{I(t) \cdot A} \tag{11}$$

This metric helps assess system performance under dynamic sunlight conditions.

3. Average Daily Efficiency

To evaluate system performance over an entire day, the time-integrated thermal efficiency is computed as (Eq. 12):

$$\eta_{\text{day}} = \frac{\int_0^{t_{\text{day}}} Q_{\text{useful}}(t)\ dt}{\int_0^{t_{\text{day}}} I(t) \cdot A\, dt} \tag{12}$$

This measure smooths out short-term fluctuations and is useful for comparing systems under realistic daily cycles.

4. Annual Energy Output

The annual thermal energy output can be estimated by extrapolating daily performance to a yearly scale, assuming typical daily operation (Eq. (13)):

$$E_{\text{annual}} = Q_{\text{daily}} \times 365 \tag{13}$$

This allows for economic analysis, including cost per liter of water and energy payback period.

5. Stagnation Temperature

Stagnation temperature is the theoretical maximum temperature the absorber can reach when no heat is extracted. It provides insight into system safety and material constraints (Eq. (14)):

$$T_{\text{stag}} = T_{\text{amb}} + \frac{I \cdot \alpha}{U_L} \tag{14}$$

A higher stagnation temperature indicates better insulation or surface absorption but may also raise material degradation concerns.

6. Empirical Collector Efficiency – Hottel–Whillier–Bliss Equation For model validation, the thermal performance is also compared using empirical efficiency correlations (Eq. (15)):

$$\eta = \eta_0 - a_1 \left(\frac{T_m - T_a}{I} \right) - a_2 \left(\frac{(T_m - T_a)^2}{I} \right) \tag{15}$$

These coefficients are commonly used in standard testing (e.g., ASHRAE, ISO) for flat plate collectors. A detailed set of governing parameters-thermal, optical, and geometrical should be specified and measured to provide accurate simulation and evaluation of the thermal performance of nanoparticle-coated flat plate solar collectors. The input parameters used in the developed transient heat transfer model were the key parameters in MATLAB as shown in Table 1. These are basic performance measures like instantaneous efficiency, useful heat gain, stagnation temperature, and annual energy output, which are calculated using energy balance equations and transient fluid temperature profiles. Also, thermal and physical characteristics of the base absorber material (copper), such as thermal conductivity, specific heat, and density are added to model real-world collector behavior. Both conventional and nanoparticle coatings are defined in optical terms of absorptance and emittance to describe radiative interactions. The dimensions and material characteristics chosen are in line with typical commercial flat plate collector designs and thereby increase the practical applicability of the model and allow comparison with experimental and literature-reported data

Table 1: Key Parameters Used in the Transient Performance Analysis of Nanoparticle-Coated Flat Plate Solar Collector.

Category	Parameter	Value(s)	Source/Notes
Performance Parameters	Instantaneous Efficiency	0–100	Calculated from energy balance
	Useful Heat Gain	Dynamic	Based on fluid temperatures and flow rate
	Stagnation Temperature	60–160 (varies by case)	Analytical expression
	Annual Energy Output	Computed for each case	Integrated from daily transient results
Collector Unit Size	Collector Area	2	Typical experimental flat plate collector
	Plate Thickness	0.003	Based on commercial copper absorber plates

Base Material Properties	Base Thermal Conductivity	385	Copper (standard absorber material)
	Specific Heat	385	Copper
	Density	8960	Copper
	Absorptance	0.9	For black paint / selective coatings
	Emittance	0.05 – 0.65	Varies with coating (selective to normal paint)
Nanoparticles Used	Thermal Conductivity Graphene	-	-
	Thermal Conductivity – CuO	33	Common nanofluid additive
	Thermal Conductivity – Al_2O_3	36	Common nanofluid additive
	Volume Fraction	0.01, 0.03, 0.05	1%, 3%, 5% considered

Source: Authors, (2026).

A parametric study was performed with the aim of investigating the effect of material properties and environmental parameters on collector performance. The most important parameters were systematically changed to determine their influence on transient efficiency, absorber plate temperature, and total thermal output as summarized in Table 2. These are the values of nanoparticle thermal conductivity of CuO, Al2O3, and graphene, volume fraction 1-5%, and optical characteristics, solar absorptance, and thermal emittance. Time-dependent profiles of the solar irradiance and ambient temperature are also integrated in the simulation through the use of sinusoidal functions to simulate realistic diurnal operating conditions. Moreover, the effective thermal conductivity of the nanoparticle-enhanced plate is computed dynamically by the Maxwell model. The model ensures a common performance baseline by keeping all the parameters constant (plate thickness, collector area, and mass flow rate) throughout the simulations. This parameter model enables a strong insight into the effect of coating composition and environmental inputs on collector performance, thus enabling the data-driven optimization of advanced absorber coatings.

Table 2: Parametric Study – Input Parameters and Their Levels.

Parameter	Levels / Values Considered	Purpose of Variation
Nanoparticle Thermal Conductivity	33 (CuO), 36 (Al_2O_3), 3000 (Graphene)	To analyze material influence on heat transfer enhancement
Nanoparticle Volume Fraction	0.01, 0.03, 0.05	To assess effect of concentration on collector performance
Solar Absorptance	0.85, 0.90, 0.95	To compare optical performance of coatings
Thermal Emittance	0.05, 0.20, 0.65	To evaluate thermal losses for various coating materials
Solar Irradiance	Transient (0–1000, sinusoidal profile)	To simulate realistic daily solar input
Ambient Temperature	Transient (15–35, sinusoidal profile)	To replicate diurnal weather conditions
Plate Thermal Conductivity (Effective)	Computed via Maxwell Model	To dynamically update heat transfer properties
Plate Thickness	0.003	Fixed – standard plate design
Mass Flow Rate	0.02	To maintain consistent comparison across test cases
Collector Area	2	Fixed size for baseline comparison

Source: Authors, (2026).

III.6 SIMULATION SETUP AND COATING CONFIGURATIONS

This paper analyses thermal performance of a flat plate solar collector under different nanoparticle-enhanced absorber coating under controlled simulation conditions using a MATLAB-based transient thermal model. The main aim is to examine how various nanoparticle coating and mass flow rates affect the outlet temperature of the working fluid and consequently the thermal efficiency of the collector. The simulation model is based on the basic principles of energy conservation, and the equation of energy balance is considered to take into consideration useful heat gain, time-varying solar irradiance, ambient temperature, and heat losses due to convection and radiation. In order to consider the thermal enhancement of nanoparticles, the effective thermal conductivity of the coating layer was calculated through classical Maxwell model with the adjustment of the volume fraction and intrinsic thermal conductivity of the dispersed nanoparticles. Four absorber surface coatings were modeled: conventional black paint, copper oxide (CuO), aluminium oxide (Al_2O_3), and graphene. Each coating was evaluated at a fixed nanoparticle concentration to maintain consistency across cases and to isolate the effect of material thermal properties. The simulations were conducted for three different flow rates i.e. 0.01 kg/s, 0.02 kg/s, and 0.03 kg/s to examine the impact of mass flow rate on the system's thermal response and outlet temperature profile. This setup allowed a fine comparison of thermal performance in terms of coating types and operating conditions and provided information on the interaction between material selection and fluid dynamics to influence solar thermal collector efficiency

IV. NUMERICAL ALGORITHM

A simulation framework of a customized MATLAB was used to conduct the thermal analysis of nanoparticle-enhanced absorber plates. The transient two-dimensional heat conduction equation in the absorber plate domain was solved by the finite difference method (FDM). The general computational procedure can be summarized in the flowchart shown in Figure 1. The simulation starts with the initialisation and input of key parameters such as the geometry of the plate (length, width, and thickness), material characteristics of the base material and nanoparticles (thermal conductivity, density, specific heat), nanoparticle volume fraction (ϕ), solar radiation intensity (G), ambient temperature (Tamb), convective heat transfer coefficient, and plate surface emissivity. Stefan-Boltzmann constant is used to include radiation losses. Boundary conditions are then applied. The top surface of the absorber plate is subjected to combined solar radiation and convective–radiative heat losses, while the bottom surface is thermally insulated. The edges of the plate are treated as either adiabatic or symmetric, depending on symmetry considerations. Next, effective thermophysical properties of the nanocomposite plate are calculated.

These are the effective thermal conductivity (keff), which is calculated by a modified Maxwell model that considers the coupling between base material and nanoparticles, and the effective density (reff) and specific heat (Cp_eff), calculated by volume-weighted averages. This is because the computational domain is discretized with a finite difference grid, which allows calculation of the temperature at each node on discrete time steps. A time-marching loop is then initiated to solve the transient heat conduction problem using either explicit or implicit schemes. At each time increment, nodal temperatures are updated and checked for convergence. The iterative loop continues until the maximum temperature difference between two successive time steps satisfies the convergence criterion,

$$\max|T^{n+1} - T^{n}| < \varepsilon \tag{16}$$

The outputs of the program on convergence are the temperature distribution of the absorber plate with time, spatial temperature profiles, heat flux and thermal efficiency. Thermal efficiency is determined as the ratio of useful heat gain to the total incident solar energy, which is a complete measure of thermal performance of the plate.

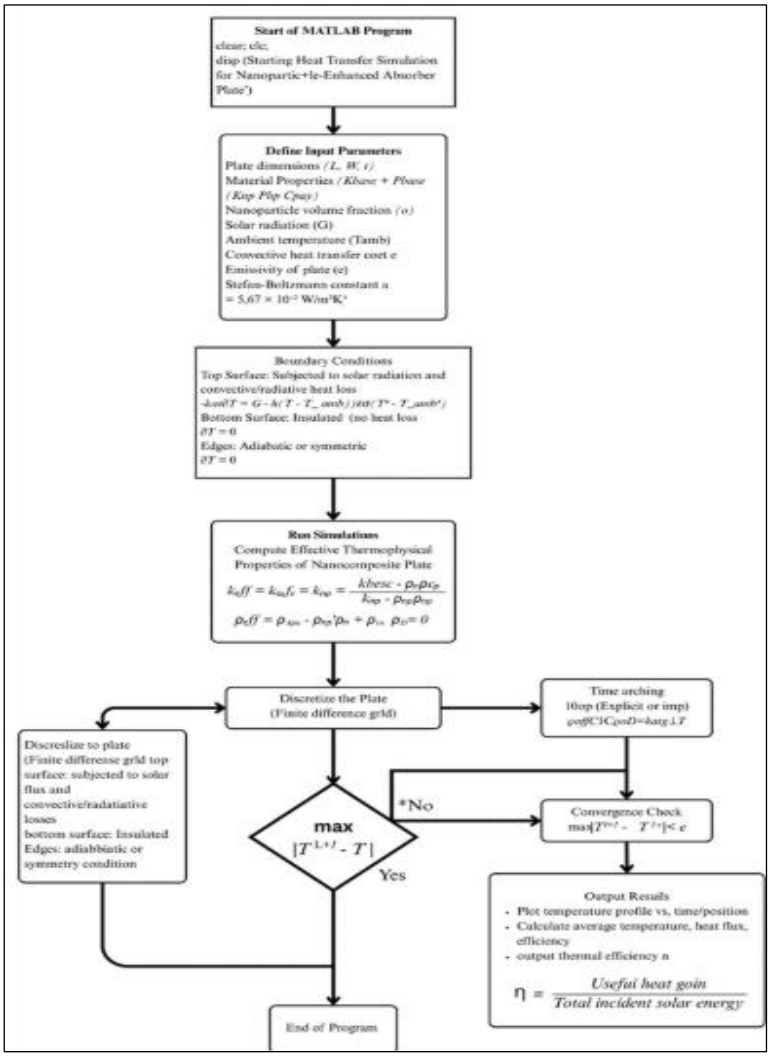


Figure 1: Flow algorithm for the MATLAB programming.
Source: Authors, (2026).

V. RESULTS AND DISCUSSIONS

V.1 VARIATION OF SOLAR RADIATION AND AMBIENT TEMPERATURE DURING TEST HOURS

Figure 2 and Figure 3 represent the variation of the solar radiation and ambient temperature of the day at the time of experiment between 9:00 AM to 2:30 PM. The solar radiation was of a normal bell-shaped pattern with the lowest value of 500 W/m2 at the start of the day at 9:00 AM and the highest value of about 1000 W/m2 at 10:40 AM to 11:10 AM. Subsequently, it started to decrease gradually, to about 670 W/m2 at 2.30 PM. This symmetrical pattern is consistent with the natural cycle of solar altitude and it proves the good conditions of radiation to do thermal testing in the middle of the day. Simultaneously, ambient temperature also increased with time with an initial value of 30°C and reaching a peak of 40°C at noon (12:00 PM). After noon, there was a small decrease as a result of the lowering solar elevation and a lower irradiance. The ambient temperature pattern follows the solar radiation peak slightly, which means the thermal inertia of the environment. These realistic variations are needed to model transient boundary conditions in a numerical model and to predict the thermal behavior of solar collector systems. These environmental inputs were dynamic forcing functions to the heat transfer simulations and allowed accurate determination of absorber plate temperatures, thermal losses and efficiency measures in further analysis.

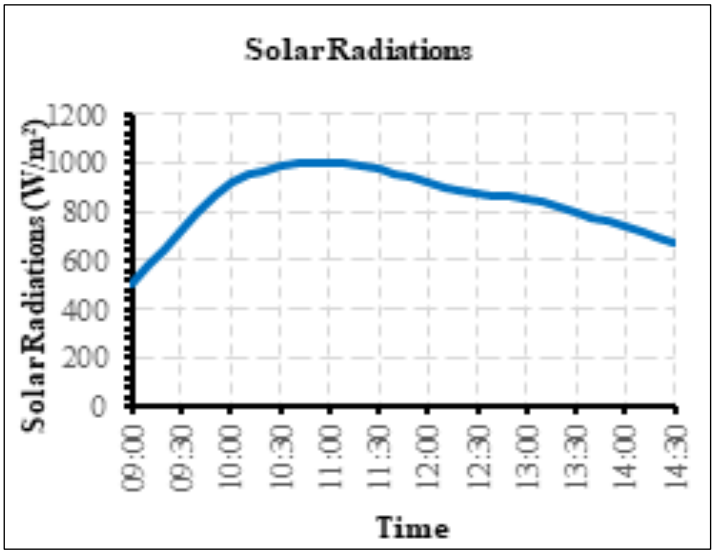


Figure 2: Variation of solar radiations during the test.
Source: Authors, (2026).

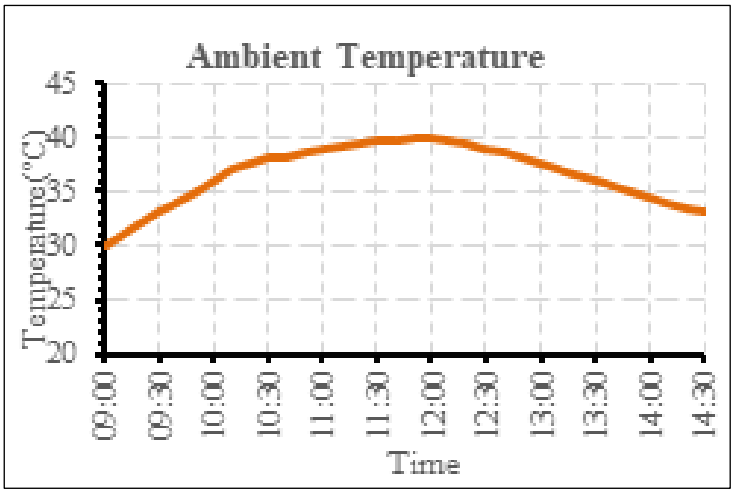


Figure 3: Variation of ambient temperature during the test.
Source: Authors, (2026).

V.2 VARIATION OF OUTLET FLUID TEMPERATURE WITH TIME

Figure 4(a)-4(d) show the change in the temperature of the outlet of the working fluid with time in the case of absorber plates painted with black, CuO, Al2O3, and graphene at mass flow rates of 0.01 kg/s, 0.02 kg/s, and 0.03 kg/s. Based on the graphs, it is clear that at every flow rate, graphene-coated absorber plates always record the highest outlet temperatures, then CuO, Al2O3, and black paint in that order of thermal performance. The graphene-coated collector achieves the highest outlet temperature of 59.29°C at the lowest flow rate of 0.01 kg/s, which is about 4.54, 5.86 and 9.4 higher than CuO (56.69°C), Al2O3 (55.98°C) and black paint (54.18°C). The improvement in performance of graphene coatings is mostly because of its high thermal conductivity and optical absorptivity. The large thermal diffusivity of graphene allows quick heat transfer over the absorber surface, minimizing hotspots locally and ensuring a uniform temperature gradient. CuO and Al2O3 also provide better thermal response than traditional black paint because of their nanostructured structure that increases the effective surface area to transfer heat and the convective heat transfer coefficient at the absorber-fluid interface. The outlet temperature decreases significantly as the flow rate rises between 0.01 kg/s and 0.03 kg/s in all the types of coatings. This is a direct effect of the lower thermal residence time of the working fluid within the collector tube, which restricts the quantity of heat absorbed. To illustrate, the temperature of the outlet of graphene decreases to 54.92°C at 0.02 kg/s and to 51.62°C at 0.03 kg/s - a relative decrease of 6.3 and 12.9%, respectively, of its maximum value at 0.01 kg/s. On the same note, the black paint coating drops are reduced by almost 9.2% and 14.7% respectively as the flow rate increments. This validates the assertion that low flow rates are better suited to higher outlet temperatures because of extended heat exchange whereas higher flow rates are more advantageous in regards to total thermal energy removal because of greater fluid volume. Furthermore, the average temperature of the outlet measured throughout the whole time of the experiment also proves the better thermal performance of graphene. The average temperature of graphene at a rate of 0.01 kg/s is 55.17°C, whereas the average temperature of CuO, Al2O3, and black paint are 52.89°C and 50.47°C respectively. This pattern is always preserved at increased flow rates, but the temperature differences become a little smaller as a result of greater convective dominance. In general, the findings indicate clearly the high thermal performance of graphene as an absorber coating material, particularly when flow rate conditions are low and the properties of the absorber surface dominate the heat transfer processes.

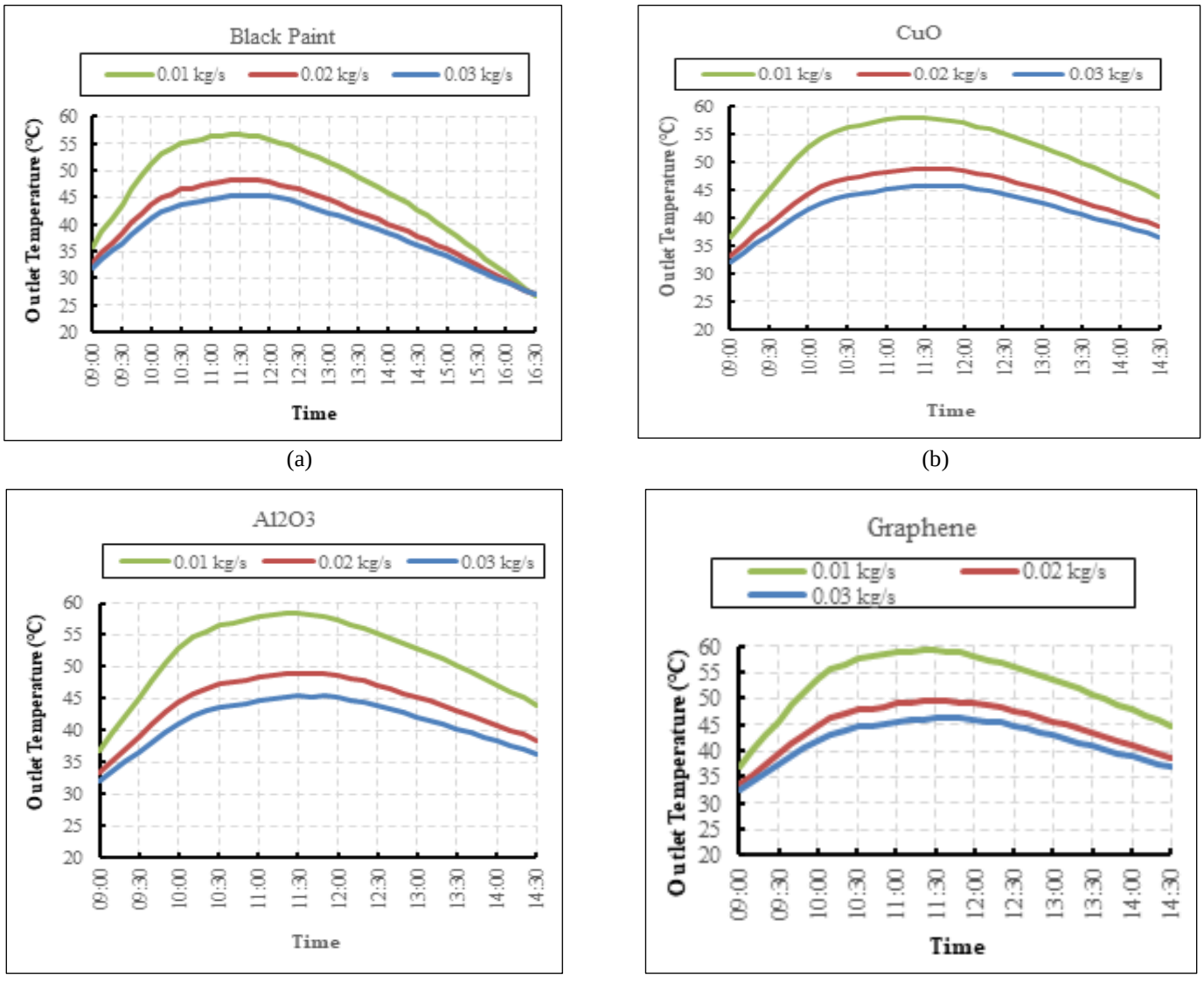


Figure 4: Variation of fluid outlet temperature at various fluid flow rates with (a) Black paint coated, (b) CuO coated, (c) Al2O3 coated and (d) Graphene coated absorber plate.
Source: Authors, (2026).

V.3 EFFECT OF NANOPARTICLE MATERIAL ON HEAT GAIN

Figure 5 shows the change in useful heat gain of flat plate solar collectors coated with black paint, CuO, Al2O3 and graphene at a constant mass flow rate of 0.01 kg/s. The results indicate a strong improvement in thermal performance when nanomaterial-based coating, especially graphene is used instead of the standard black paint. The useful heat gain of all the coatings increased steadily as the solar radiation increased during the morning, reaching its highest point in the middle of the day and then decreasing in the afternoon as the sun faded. This day/night cycle is common to solar thermal systems, but the degree of heat gain differs greatly across the various coatings, suggesting the importance of improved thermal and optical characteristics. The graphene-coated absorber recorded the highest heat gain during the entire test period with the peak of 834W recorded at 11:00 AM. Comparatively, the highest values obtained on Al2O3, CuO and black paint were 794W, 784W and 724W respectively. This is equivalent to a maximum increase of about 15.2% of graphene against black paint, 5.0% of graphene against CuO and 5.0% of graphene against Al2O3. These high-performance properties of graphene can be explained by its high thermal conductivity that increases the heat transfer rate between the absorber plate and the working fluid. Also, graphene has high solar absorptance and low emittance, which enhance solar energy capture and retention. Its two-dimensional lattice structure is unique and enables fast phonon transport, which lowers interfacial thermal resistance and enables energy conversion to be more efficient. There were also significant improvements with CuO and Al2O3 coatings, Al2O3 always slightly better than CuO. These metal oxide nanoparticles have a moderate thermal conductivity and higher surface absorptivity than black paint, which explains the fact that these nanoparticles perform better. Graphene continued to have a visible advantage in useful heat gain over the entire time range, suggesting that it does not just enhance peak performance, but also allows it to remain in higher energy conversion efficiency even in sub-optimal solar conditions. These findings support the importance of the coating material choice in maximizing the collector efficiency, especially in low flow rate conditions where thermal inertia is stronger.

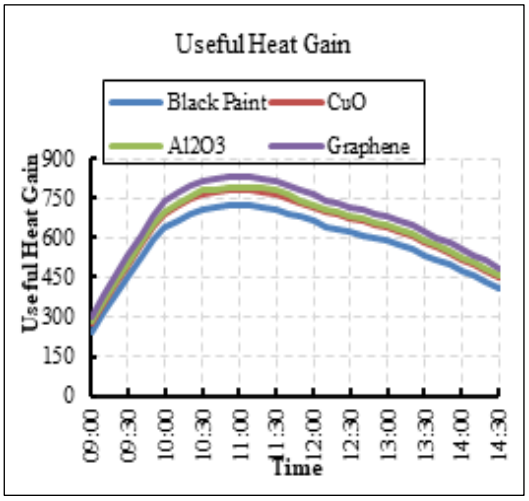


Figure 5: Comparison of useful heat with different absorber plate coatings.
Source: Authors, (2026).

V.4 COMPARISON OF USEFUL HEAT WITH DIFFERENT ABSORBER PLATE COATINGS

Figure 6 shows the variation of instantaneous thermal efficiency of the various absorber plate coatings at constant flow rate of 0.01 kg/s. The coatings that have been studied are conventional black paint and nanomaterial-based coatings which are CuO, Al2O3, and graphene. The thermal efficiency is evidently correlated with the nature of coating as a result of variations in optical and thermal characteristics. Graphene was the most efficient of all the coatings and it was also the most efficient during the day with a peak of 0.8353 at around 11:20 AM. This high performance is explained by the outstanding thermal conductivity and high solar absorptivity of graphene that increase the rate of heat transfer between the absorber surface and the working fluid. CuO and Al2O3 were also more efficient than the black paint coating with maximum values of 0.7853 and 0.7953 respectively, which were obtained at the same period of high radiation. These nanomaterials of metal oxide enhance the surface area and thermal diffusivity, which results into the lessening of thermal resistance between the coating and the fluid. Comparatively, the traditional black paint coating had the lowest efficiency of 0.7253 and hence was the least efficient of the four. CuO, Al2O3 and graphene had a percentage improvement in peak efficiency of approximately 8.27, 9.64 and 15.17 respectively as compared to black paint. The overall pattern of Figure 6 is that efficiency gradually rises between 9:00 AM and about 11:30 AM and then gradually decreases because of the decreasing solar irradiance and a decrease in the temperature gradient between the plate and the fluid. Nevertheless, less efficient coatings (particularly graphene) remained more efficient in the later hours because they could extract and transfer heat more efficiently at lower irradiance. This shows that nanomaterial-based coating does not only improve peak performance but also provides sustained thermal performance over a broader operating range.

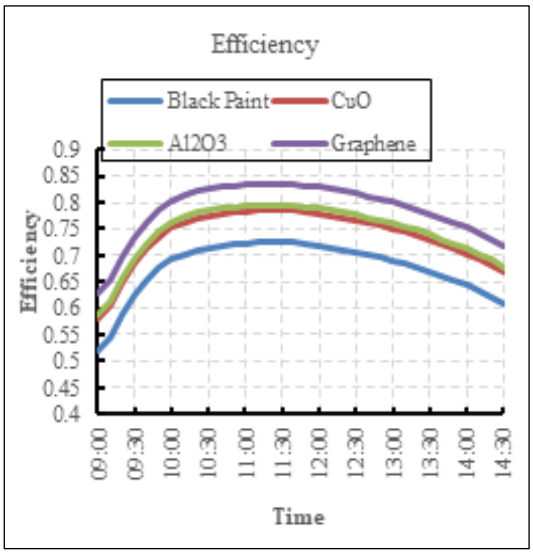


Figure 6: Variation of collector efficiency for different absorber plate coatings at a flow rate of 0.01 kg/s.
Source: Authors, (2026).

VI. CONCLUSIONS

This work provides detailed numerical research on the improvement of thermal performance of flat plate solar collectors (FPCs) with nanoparticle-based absorber coating, such as CuO, Al2O3, and graphene. A transient MATLAB-based model was developed and validated to assess the effect of nanoparticle coatings on outlet fluid temperature, useful heat gain, and thermal efficiency under varying operating conditions. Key conclusions drawn from the study are:

- The performance of nanoparticle-coated absorber plates was far superior to that of conventional black paint in all the measures of thermal performance.
- Collectors covered with graphene had the highest thermal efficiency with a maximum of over 0.83, about 15% higher than black paint.
- Al2O3 and CuO coating also offered significant gains in useful heat gain of about 8-10% and 6-8% respectively over black paint.
- The increase in performance has been credited to the fact that the nanomaterials have better optical absorption and thermal conductivity that minimizes thermal losses and enhances the heat transfer.
- The graphene-coated collector retained a higher performance even at lower irradiance periods, which showed an increased thermal inertia and heat retention.

The next step in research should be experimental validation and stability analysis of nanomaterial coating in the real outdoor conditions in the long-term.

VII. AUTHOR'S CONTRIBUTION

Conceptualization: Juber Khatik, Nilesh Salunke, Mujahid Husain, Yogeshkumar Pathak, Kailas Deore, Pradeep Solanki and Pravin Shirule.
Methodology: Juber Khatik, Nilesh Salunke, Mujahid Husain, Yogeshkumar Pathak, Kailas Deore, Pradeep Solanki and Pravin Shirule.
Investigation: Juber Khatik, Nilesh Salunke, Mujahid Husain, Yogeshkumar Pathak, Kailas Deore, Pradeep Solanki and Pravin Shirule.
Discussion of results: Juber Khatik, Nilesh Salunke, Mujahid Husain, Yogeshkumar Pathak, Kailas Deore, Pradeep Solanki and Pravin Shirule.
Writing – Original Draft: Juber Khatik, Nilesh Salunke, Mujahid Husain, Yogeshkumar Pathak, Kailas Deore, Pradeep Solanki and Pravin Shirule.
Writing – Review and Editing: Juber Khatik, Nilesh Salunke, Mujahid Husain, Yogeshkumar Pathak, Kailas Deore, Pradeep Solanki and Pravin Shirule.
Resources: Juber Khatik, Nilesh Salunke, Mujahid Husain, Yogeshkumar Pathak, Kailas Deore, Pradeep Solanki and Pravin Shirule.
Supervision: Juber Khatik, Nilesh Salunke, Mujahid Husain, Yogeshkumar Pathak, Kailas Deore, Pradeep Solanki and Pravin Shirule.
Approval of the final text: Juber Khatik, Nilesh Salunke, Mujahid Husain, Yogeshkumar Pathak, Kailas Deore, Pradeep Solanki and Pravin Shirule.

VIII. REFERENCES

[1] E. Vengadesan, R. Senthil, Experimental thermal performance and enviroeconomic analysis of serpentine flow channeled flat plate solar water collector, Environ. Sci. Pollut. Res. 29 (2022) 17241–17259. https://doi.org/10.1007/s11356-021-16985-7.

[2] K.D. Arvanitis, E. Papanicolaou, E. Mathioulakis, V. Belessiotis, D. Bouris, Experimental evaluation of flat-plate heat absorbers for medium-temperature linear-focus solar systems: Composite U-bends vs straight rectangular-multi-channels, Appl. Therm. Eng. 175 (2020) 115364. https://doi.org/10.1016/j.applthermaleng.2020.115364.

[3] M. Fan, W. Zheng, S. You, H. Zhang, Y. Jiang, Z. Wu, Comparison of different dynamic thermal performance prediction models for the flat-plate solar collector with a new V-corrugated absorber, Sol. Energy 204 (2020) 406–418. https://doi.org/10.1016/j.solener.2020.04.093.

[4] T. Alam, N.B. Balam, K.S. Kulkarni, M.I.H. Siddiqui, N.R. Kapoor, C.S. Meena, A. Kumar, R. Cozzolino, Performance Augmentation of the Flat Plate Solar Thermal Collector: A Review, Energies 14 (2021) 6203. https://doi.org/10.3390/en14196203.

[5] E. Gaudino, A. Caldarelli, R. Russo, M. Musto, Formulation of an Efficiency Model Valid for High Vacuum Flat Plate Collectors, (2023). https://doi.org/10.20944/preprints202310.1520.v1.

[6] G. Boussouar, B. Rostane, K. Aliane, D. Ravi, M.J. Gęca, A. Gola, Study of the Thermal Performance of Solar Air Collectors with and without Perforated Baffles, Energies 17 (2024) 3812. https://doi.org/10.3390/en17153812.

[7] M. Ammar, A. Mokni, H. Mhiri, P. Bournot, Performance optimization of flat plate solar collector through the integration of different slats arrangements made of transparent insulation material, Sustain. Energy Technol. Assess. 46 (2021) 101237. https://doi.org/10.1016/j.seta.2021.101237.

[8] Ye.S. Shyntyapina, Fairy-Tale and Mythological Motifs in the Decoration of Architectural Complexes by N. P. Krasnov in Yalta District, Arts Educ. Sci. 1 (2021) 101–109. https://doi.org/10.36871/hon.202103013.

[9] A. Mahamude, W. Harun, K. Kadirgama, D. Ramasamy, K. Farhana, K. Saleh, T. Yusaf, Experimental Study on the Efficiency Improvement of Flat Plate Solar Collectors Using Hybrid Nanofluids Graphene/Waste Cotton, Energies 15 (2022) 2309. https://doi.org/10.3390/en15072309.

[10] B. Darbari, S. Rashidi, Thermal efficiency of flat plate thermosyphon solar water heater with nanofluids, J. Taiwan Inst. Chem. Eng. 128 (2021) 276–287. https://doi.org/10.1016/j.jtice.2021.06.027.

[11] L.S. Sundar, E.V. Ramana, Z. Said, V. Punnaiah, K.V.V. Chandra Mouli, A.C.M. Sousa, Properties, heat transfer, energy efficiency and environmental emissions analysis of flat plate solar collector using nanodiamond nanofluids, Diam. Relat. Mater. 110 (2020) 108115. https://doi.org/10.1016/j.diamond.2020.108115.

[12] C.-D. Ho, H. Chang, C.-W. Yeh, C.-A. Ng, P.-C. Hsieh, Optimizing Device Performance of Multi-Pass Flat-Plate Solar Air Heaters on Various Recycling Configurations, Energies 16 (2023) 2568. https://doi.org/10.3390/en16062568.

[13] P. Palanikumar, A.H. Seikh, M.A. Kalam, R. Venkatesh, Influences of black nickel coating thickness on thermal behaviour of flat plate solar collector: performance evaluation, J. Therm. Anal. Calorim. 149 (2024) 6687–6697. https://doi.org/10.1007/s10973-024-13177-6.

[14] M. Nazari, S. Jafarmadar, S. Khalilarya, Exergy and thermoeconomic analyses of serpentine tube flat-plate solar water heaters coated with CuO nanostructures, Case Stud. Therm. Eng. 35 (2022) 102072. https://doi.org/10.1016/j.csite.2022.102072.

[15] R. Kumar, S.K. Verma, M. Singh, Experimental investigation of nanomaterial doped in black paint coating on absorber for energy conversion applications, Mater. Today Proc. 44 (2021) 961–967. https://doi.org/10.1016/j.matpr.2020.11.006.

[16] R. Mariraja, R. Harichandran, R. Vijayakumar, A. Nichelson, Experimental analysis of solar desalination system performance with graphene and graphitic carbon nanopaint-coated solar absorbers, Desalination 592 (2024) 118141. https://doi.org/10.1016/j.desal.2024.118141.

[17] S.S. Han, U. Ghafoor, T. Saeed, H. Elahi, U. Masud, L. Kumar, J. Selvaraj, M.S. Ahmad, Silicon Particles/Black Paint Coating for Performance Enhancement of Solar Absorbers, Energies 14 (2021) 7140. https://doi.org/10.3390/en14217140.

[18] V.P. Katekar, A.B. Rao, V.R. Sardeshpande, The optimum nanomaterial coating for solar thermal device absorber plates: an experimental investigation, Int. J. Nano Biomater. 10 (2024) 270–300. https://doi.org/10.1504/IJNBM.2024.143831.

[19] E.Y. Gürbüz, İ. Şahinkesen, B. Kusun, A.D. Tuncer, A. Keçebaş, Enhancing the performance of an unglazed solar air collector using mesh tubes and Fe3O4 nano-enhanced absorber coating, Energy 277 (2023) 127704. https://doi.org/10.1016/j.energy.2023.127704.

[20] S. Sivakumar, C. Velmurugan, D.S.E.J. Dhas, A.B. Solomon, K.L. Dev Wins, Effect of nano cupric oxide coating on the forced convection performance of a mixed-mode flat plate solar dryer, Renew. Energy 155 (2020) 1165–1172. https://doi.org/10.1016/j.renene.2020.04.027.

[21] S.A. Sakhaei, M.S. Valipour, Investigation on the effect of different coated absorber plates on the thermal efficiency of the flat-plate solar collector, J. Therm. Anal. Calorim. 140 (2020) 1597–1610. https://doi.org/10.1007/s10973-019-09148-x.

[22] H.K. Sharma, S. Kumar, S.K. Verma, Comparative performance analysis of flat plate solar collector having circular &trapezo2dal corrugated absorber plate designs, Energy 253 (2022) 124137. https://doi.org/10.1016/j.energy.2022.124137.

[23] R. Kumar, S.K. Verma, N.K. Gupta, A.Z. Mendiburu, A. Sharma, T. Alam, S.M. Eldin, Experimental assessment and modeling of solar air heater with V shape roughness on absorber plate, Case Stud. Therm. Eng. 43 (2023) 102784. https://doi.org/10.1016/j.csite.2023.102784.

[24] R. Karthikeyan, A.R. Ravikumar, A. Munimathan, Enhancing solar air heater performance through pin–fin absorber plates and tailored MWCNT coatings: a comprehensive comparative analysis, J. Therm. Anal. Calorim. 149 (2024) 3577–3591. https://doi.org/10.1007/s10973-024-12900-7.

[25] Y. Selikhov, J.J. Klemeš, P. Kapustenko, O. Arsenyeva, The study of flat plate solar collector with absorbing elements from a polymer material, Energy 256 (2022) 124677. https://doi.org/10.1016/j.energy.2022.124677.

[26] GaneshKumar, N. Thangapandian, S.C. Kim, V. Ramkumar, S. Pandiaraj, A.N. Alodhayb, Enhancing the solar still performance with nano-coated seashells and surface-modified absorber plates for clean water production, Sol. Energy 285 (2025) 113141. https://doi.org/10.1016/j.solener.2024.113141.

Journal of Engineering and Technology for Industrial Applications

ISSN ONLINE: 2447-0228

ITEGAM-JETIA

Manaus, v.12 n.60, p.641-647 July/August, 2026.
DOI: https://doi.org/10.5935/jetia.v12i60.3941

RESEARCH ARTICLE OPEN ACCESS

A NOVEL LYAPUNOV BACKSTEPPING APPROACH TO CONTROLLING MECHANICAL POWER IN INDUCTION MOTORS

Chami Noureddine[1], Rouabhi Riyadh[2] and Herizi Abdelghafour*[3]

[1]Department of Electrical Engineering, University of formation continue, Dely Brahim - alger, Algeria.
[2, 3]Department of Electrical Engineering, GE Laboratory (LGE), Faculty of technology, Mohamed Boudiaf University, M'sila, Algeria.

[1]https://orcid.org/0000-0002-2376-9555, [2]https://orcid.org/0009-0008-6726-4605, [3]https://orcid.org/0009-0001-4569-1664

E-email: n-chami@ufc.dz, riyadh.rouabhi@univ-msila.dz, *abdelghafour.herizi@univ-msila.dz.

ARTICLE INFO

Article History
Received on: March 06, 2026
Reviewed on: April 06, 2026
Accepted on: May 01, 2026
Published on: July 31, 2026

Keywords:
Induction motor,
Mechanical power,
Lyapunov law,
Grid-side converter,
Motor-side converter.

ABSTRACT

In this work, a novel Lyapunov backstepping control law (LBC) is introduced, which allows for robust and stable regulation of the mechanical power produced by an induction motor (IM). The stator variables supply this induction motor through two converters. One, a motor converter (two-level inverter), allows for exact control and optimization of the energy flow during motor operation; the other, a mains converter (two-level rectifier), makes it easier to manage the direct current (DC) bus and increases the mains power factor. We demonstrated the modeling of our motor and its converters in the first section. The control structure that was suggested to regulate and maximize the mechanical energy produced by our motor (speed, torque) in order to attain optimal efficiency and transfer quality was presented in the second section. The outcomes of the numerical simulations show how well the new Lyapunov control system achieves these goals: electromagnetic torque below the nominal torque and mechanical speed side its references.

Copyright ©2026 by authors and Galileo Institute of Technology and Education of the Amazon (ITEGAM). This work is licensed under the Creative Commons Attribution International License (CC BY 4.0).

I. INTRODUCTION

Induction machines play a key role in industry and are currently widely used for variable speed or positioning applications [1-3]. These machines have the advantage of being robust and inexpensive. However, despite these advantages, the control of induction machines is very complicated because their basic mathematical model is non-linear and their parameters are only approximately known and can vary over time. Current research is aimed at making the control of these machines simpler and more reliable [4-6]. The induction machine has several control techniques (scalar control, sliding mode control, vector control.). Each control technique poses a problem in terms of guaranteeing the stability of the system because its basic model is non-linear and highly coupled, which is the opposite of the simplicity of its structure. This model is also complicated by the fact that the parameters of the induction motor are only approximately known and can vary over time. In our work, we use a new control technique called BACKSTEPPING to improve the control of the machine [7] [8]. The backstepping technique is one of the new methods in this field. It provides a systematic method for designing a controller for nonlinear systems. The main advantage of this method is that it guarantees the stability of the control system [9] [10]. This paper develops a new Lyapunov control technique to control the mechanical power produced by the induction motor. This control technique guarantees the robustness and stability of our control system with a remarkable improvement in the convergence of the errors towards zero. The rest of this article is structured as follows: The next section presents the mathematical model of the induction motor and its converters. In section 2, we present the DPC control based on PI controllers. In section 3, we present simulation results that show the efficiency and robustness of the control developed to control the mechanical power generated by our induction motor. Finally, the paper will conclude with a conclusion.

II. MODELLING OF THE INDUCTION MOTOR AND ITS CONVERTERS

To simulate the behavior of the IM and develop a control technique for it, we need to model both the motor and its converters separately.

- The induction motor;

- The motor-side converter;
- The grid-side converter.

II.1 INDUCTION MOTOR MODEL

The induction machine is a very complex non-linear system, so applying our control to our machine requires more precise mathematical modelling to represent its behaviour in a satisfactory and realistic way [11-13].

$$\begin{cases} V_{s\alpha} = R_s i_{s\alpha} + \frac{d}{dt}\Phi_{s\alpha} \\ V_{s\beta} = R_s i_{s\beta} + \frac{d}{dt}\Phi_{s\beta} \\ V_{r\alpha} = 0 = R_r i_{r\alpha} + \frac{d}{dt}\Phi_{r\alpha} + \omega_r \Phi_{r\beta} \\ V_{r\beta} = 0 = R_r i_{r\beta} + \frac{d}{dt}\Phi_{r\beta} - \Phi_r \Phi_{r\alpha} \end{cases} \quad (1)$$

$$C_{em} = \frac{PM}{L_r}\left(\Phi_{r\alpha} i_{s\beta} - \Phi_{r\beta} i_{s\alpha}\right) \quad (2)$$

$$J\frac{d}{dt}\Omega + f\Omega = C_{em} - C_r \quad (3)$$

The aim is to obtain a system of equations written as an equation of state. The model will have the form :

$$[\dot{X}] = [A][X] + [B][U] \quad (4)$$

With:

$$\begin{cases} [X] = \left[i_{s\alpha}\ i_{s\beta}\ \Phi_{r\alpha}\ \Phi_{r\beta}\right]T \\ [V] = \left[V_{s\alpha}\ V_{s\beta}\right]T \end{cases} \quad (5)$$

$$[A] = \begin{bmatrix} -\left(\frac{1}{\sigma T_S} + \frac{M^2}{l_r T_r}\right) & 0 & \frac{M}{\sigma l_S l_r T_r} & \frac{M}{\sigma l_S l_r}\omega_r \\ 0 & -\left(\frac{1}{\sigma T_S} + \frac{M^2}{l_r T_r}\right) & -\frac{M}{\sigma l_S l_r}\omega_r & \frac{M}{\sigma l_S l_r T_r} \\ \frac{M}{T_t} & 0 & -\frac{1}{T_r} & -\omega_r \\ 0 & \frac{M}{T_r} & \omega_r & -\frac{1}{T_r} \end{bmatrix} \quad (6)$$

$$[\boldsymbol{B}] = \begin{bmatrix} \frac{\mathbf{1}}{\boldsymbol{\sigma l_s}} & \mathbf{0} \\ \mathbf{0} & \frac{\mathbf{1}}{\boldsymbol{\sigma l_s}} \\ \mathbf{0} & \mathbf{0} \\ \mathbf{0} & \mathbf{0} \end{bmatrix} \quad (7)$$

II.2. MOTOR SIDE CONVERTER MODEL

The voltage inverter is a converter that makes it possible to obtain an AC voltage of fixed or adjustable frequency and RMS value from a DC voltage source. It consists of switching cells, generally transistors for high power [14] [15].

$$\begin{bmatrix} V_A \\ V_B \\ V_C \end{bmatrix} = \frac{E}{6}.\begin{bmatrix} 2 & -1 & -1 \\ -1 & 2 & -1 \\ -1 & -1 & 2 \end{bmatrix}\begin{bmatrix} S_1 \\ S_2 \\ S_3 \end{bmatrix} \quad (8)$$

II.3. GRID SIDE CONVERTER MODEL

In addition to its bidirectional power flow capability, the grid-side converter has the advantage of maintaining a stable DC bus voltage and setting the reactive power reference to zero. This helps to maintain grid quality by maintaining a unity power factor [16] [17].

$$\frac{d}{dt}\begin{bmatrix} i_1 \\ i_2 \\ i_3 \end{bmatrix} = \begin{bmatrix} -\frac{R}{L} & 0 & 0 \\ 0 & -\frac{R}{L} & 0 \\ 0 & 0 & -\frac{R}{L} \end{bmatrix}\begin{bmatrix} i_1 \\ i_2 \\ i_3 \end{bmatrix} + \frac{1}{L}\begin{bmatrix} V_1 - V_{an} \\ V_2 - V_{bn} \\ V_3 - V_{cn} \end{bmatrix} \quad (9)$$

$$\begin{bmatrix} V_A \\ V_B \\ V_C \end{bmatrix} = \frac{Uc}{3}.\begin{bmatrix} 2 & -1 & -1 \\ -1 & 2 & -1 \\ -1 & -1 & 2 \end{bmatrix}\begin{bmatrix} S_1 \\ S_2 \\ S_3 \end{bmatrix} \quad (10)$$

$$\frac{U_C}{i_S} = \frac{R_{Ch}}{1 + R_{Ch}.C.p} \quad (11)$$

This inverter can be cascade controlled, with two inner loops to control the phase currents and an outer loop to control the output voltage [18] [19].

$$\begin{cases} V_{pd} = V_d - R\, i_d - L\frac{di_d}{dt} + L\omega i_q \\ V_{pq} = V_q - R\, i_q - L\frac{di_q}{dt} - L\omega i_d \end{cases} \tag{12}$$

$$\begin{cases} P = \frac{3}{2}.\left[V_d I_d + V_q I_q\right] \\ Q = \frac{3}{2}.\left[V_q I_d - V_d I_q\right] \end{cases} \tag{13}$$

We pose:

$$P_{ref} = U_{cmes}\, I_{red\_ref} \tag{14}$$

$$Q_{ref} = 0 \tag{15}$$

III. LYAPUNOV BACKSTEPPING CONTROL

Backstepping control for nonlinear systems enables the design of a control law that ensures stability throughout the process. By expressing the states in a purely parametric form, the process's subsystems become more apparent. For each subsystem, a control is derived using a Lyapunov function to achieve stability. This involves treating the preceding state as the controllable variable. The order of the subsystem is then incremented, and the procedure is repeated. Ultimately, this approach yields a control law for the entire process [20] [21].

III.1. PRINCIPLE OF OUR CONTROL

The main idea behind Backstepping is to calculate a control law to ensure that the derivative of a certain (Lyapunov) function is defined as positive and that this derivative is always negative. The system is broken down into a set of nested subsystems of decreasing order. The Lyapunov function is then calculated recursively from inside the loop [22] [23].

III.2. APPLICATION OF OUR ORDER TO OUR IM

The application of the backstepping control to the induction machine requires the use of its model in the (α,β) reference frame in order to avoid the use of Park transformations. This approach is based on three steps to determine the control law given by the machine's stator voltages; before starting the calculation of the various steps, we group together the electrical, magnetic and mechanical equations in the following system.

$$\begin{cases} \frac{d\Omega}{dt} = \frac{\mu}{J}\left(\Phi_{r\alpha} i_{s\beta} - \Phi_{r\beta} i_{s\alpha}\right) - \frac{C_r}{J} \\ \frac{di_{s\alpha}}{dt} = \alpha\beta\Phi_{r\alpha} + P\beta\Omega\Phi_{r\beta} - \eta i_{s\alpha} + \frac{1}{\sigma.L_s} V_{s\alpha} \\ \frac{di_{s\beta}}{dt} = \alpha\beta\Phi_{r\beta} - P\beta\Omega\Phi_{r\alpha} - \eta i_{s\beta} + \frac{1}{\sigma.L_s} V_{s\beta} \\ \frac{d\Phi_{r\alpha}}{dt} = -\alpha\Phi_{r\alpha} - P\Omega\Phi_{r\beta} + \alpha M i_{s\alpha} \\ \frac{d\Phi_{r\beta}}{dt} = -\alpha\Phi_{r\beta} + P\Omega\Phi_{r\alpha} + \alpha M i_{s\beta} \end{cases} \tag{16}$$

With:

$$\alpha = \frac{R_r}{L_r},\ \beta = \frac{M}{\sigma L_s L_r},\qquad \eta = \frac{M^2.R_r + L_r^2.R_s}{\sigma L_s L_r^2},\quad \mu = \frac{PM}{L_r}$$

Rotor flux is given by:

$$\overline{\Phi_r} = \Phi_{r\alpha} + j.\Phi_{r\beta} = \sqrt{{\Phi_{r\alpha}}^2 + {\Phi_{r\beta}}^2}.\left[\frac{\Phi_{r\alpha}}{\sqrt{{\Phi_{r\alpha}}^2+{\Phi_{r\beta}}^2}} + j.\frac{\Phi_{r\beta}}{\sqrt{{\Phi_{r\alpha}}^2+{\Phi_{r\beta}}^2}}\right] \tag{17}$$

$$\overline{\Phi_r} = \sqrt{{\Phi_{r\alpha}}^2 + {\Phi_{r\beta}}^2}.[\cos(\theta_s) + j.\sin(\theta_s)] \tag{18}$$

The modulus of the flow and its derivative are given by:

$$\emptyset_r = \Phi_r^2 \tag{19}$$

$$\dot{\emptyset}_r = 2(\dot{\Phi}_{r\alpha}\Phi_{r\alpha} + \Phi_{r\beta}\dot{\Phi}_{r\beta}) \tag{20}$$

Step 1

In this step we consider the errors "e1 ","e2 " between the speed "Ω" and its reference "Ωref" and the rotor flux" $\emptyset_r$"and and its reference " $\emptyset_{ref}$".

$$\begin{cases} e_1 = \Omega_{ref} - \Omega \\ e_2 = \emptyset_{ref} - \emptyset_r \end{cases} \tag{21}$$

So the derivative of "e1", "e2" is given by:

$$\begin{cases} \dot{e}_1 = \dot{\Omega}_{ref} - \dot{\Omega} = \dot{\Omega}_{ref} - \frac{\mu}{J}\left(\Phi_{r\alpha} i_s - \Phi_{r\beta} i_{s\alpha}\right) + \frac{C_r}{J} \\ \dot{e}_2 = \dot{\emptyset}_{ref} - \dot{\emptyset}_r = \dot{\emptyset}_{ref} + 2\alpha\emptyset_r - 2\alpha M(i_{s\alpha}\Phi_{r\alpha} + i_{s\beta}\Phi_{r\beta}) \end{cases} \quad (22)$$

The chosen Lyapunov function is defined as follows:

$$V_1 = \frac{1}{2}(e_1^2 + e_2^2) \quad (23)$$

Then the stabilisation functions are given by:

$$\begin{cases} i_{s\beta} = \frac{J}{\mu\,\Phi_{r\alpha}}\left(k_1 e_1 + \dot{\Omega}_{ref} + \frac{C_r}{J}\right) + \frac{\Phi_{r\beta}}{\Phi_{r\alpha}} i_{s\alpha} \\ i_{s\alpha} = -\frac{J}{\mu\,\Phi_{r\beta}}\left(k_1 e_1 + \dot{\Omega}_{ref} + \frac{C_r}{J}\right) + \frac{\Phi_{r\alpha}}{\Phi_{r\beta}} i_{s\beta} \end{cases} \quad (24)$$

To obtain a negative derivative of the Lyapunov function, the reference currents must be chosen as follows:

$$\begin{cases} (i_{s\alpha})_{ref} = -\frac{J\sin(\theta)}{\mu\Phi_r}\left(k_1 e_1 + \dot{\Omega}_{ref} + \frac{C_r}{J}\right) + \frac{\cos(\theta)}{2\alpha M\Phi_r}\left(K_2 e_2 + \dot{\emptyset}_r + 2\alpha\emptyset_r\right) \\ \left(i_{s\beta}\right)_{ref} = \frac{J\cos(\theta)}{\mu\Phi_r}\left(k_1 e_1 + \dot{\Omega}_{ref} + \frac{C_r}{J}\right) + \frac{\sin(\theta)}{2\alpha M\Phi_r}\left(K_2 e_2 + \dot{\emptyset}_r + 2\alpha\emptyset_r\right) \end{cases} \quad (25)$$

The error dynamics must be chosen by:

$$\dot{e}_1 = -k_1 e_1 \;\; et \;\; \dot{e}_2 = -k_2 e_2 \quad (26)$$

Then the derivative of the Lyapunov function with respect to time becomes:

$$\dot{V}_1 = -k_1 e_1^2 - k_2 e_2^2 < 0 \quad (27)$$

With: $k_1 > 0$ and $k_2 > 0$

Step 2

In this step, we consider the errors "e3 ","e4 " between the currents "isq"and "isqref " and the currents " isd" and "isdref".

$$e_3 = (i_{s\beta})_{ref} - i_{s\beta} \quad (28)$$

$$e_3 = \frac{J\cos(\theta)}{\mu\Phi_r}\left(k_1 e_1 + \dot{\Omega}_{ref} + \frac{C_r}{J}\right) + \frac{\sin(\theta)}{2\alpha M\Phi_r}\left(K_2 e_2 + \dot{\emptyset}_r + 2\alpha\emptyset_r\right) - i_{s\beta} \quad (29)$$

$$e_4 = (i_{s\alpha})_{ref} - i_{s\alpha} \quad (30)$$

$$e_4 = -\frac{J\sin(\theta)}{\mu\Phi_r}\left(k_1 e_1 + \dot{\Omega}_{ref} + \frac{C_r}{J}\right) + \frac{\cos(\theta)}{2\alpha M\Phi_r}\left(K_2 e_2 + \dot{\emptyset}_r + 2\alpha\emptyset_r\right) - i_{s\alpha} \quad (31)$$

Then the derivative of the errors "e1" and "e2" become:

$$\begin{cases} \dot{e}_1 = -k_1 e_1 - \frac{\mu}{J}\emptyset_r(e_4\sin(\theta) - e_3\cos(\theta)) \\ \dot{e}_2 = -k_2 e_2 + 2\emptyset_r\alpha M(e_4\cos(\theta) - e_3\sin(\theta)) \end{cases} \quad (32)$$

Then the derivative of the errors "e3"," e4" will be of the form:

$$\begin{cases} \dot{e}_3 = (\dot{i}_{s\beta})_{ref} - \dot{i}_{s\beta} = (\dot{i}_{s\beta})_{ref} - \delta_2 - \frac{1}{\sigma L_s} V_{s\beta} \\ \dot{e}_4 = (\dot{i}_{s\alpha})_{ref} - \dot{i}_{s\alpha} = (\dot{i}_{s\alpha})_{ref} - \delta_1 - \frac{1}{\sigma L_s} V_{s\alpha} \end{cases} \quad (33)$$

We pose

$$\begin{cases} \delta_1 = \alpha\beta\Phi_{r\beta} - P\beta\Omega\Phi_{r\alpha} - \eta i_{s\beta} \\ \delta_2 = \alpha\beta\Phi_{r\alpha} + P\beta\Omega\Phi_{r\beta} - \eta i_{s\alpha} \end{cases} \quad (34)$$

Step 3

To calculate the control laws (stator voltages), we choose the Lyapunov function dependent on all the previous errors. This function is given by:

$$V_2 = \frac{1}{2}(e_1^2 + e_2^2 + e_3^2 + e_4^2) \quad (35)$$

The derivative of this function is:

$$\dot{V}_2 = e_1\dot{e}_1 + e_2\dot{e}_2 + e_3\dot{e}_3 + e_4\dot{e}_4 \quad (36)$$

By replacing the derivatives of the errors by their respective values, we obtain:

$$\dot{V}_2 = -k_1 e_1^2 - k_2 e_2^2 + e_3\left(\left(i_{s\beta}\right)_{ref} - \delta_1 - \frac{1}{\sigma L_s} V_{s\beta} + 2\alpha M\Phi_{r\beta} + \frac{\mu\,\Phi_{r\alpha}}{J} e_1\right) + e_4\left(\left(i_{s\alpha}\right)_{ref} - \delta_2 + 2\alpha M\Phi_{r\alpha} e_2 - \frac{1}{\sigma L_s} V_{s\alpha} - \frac{\mu\,\Phi_{r\beta}}{J} e_1\right) \quad (37)$$

Finally, to obtain the derivative of the negative Lyapunov function, we choose the following control law

$$\begin{cases} V_{s\alpha} = \sigma L_s \left(k_4 e_4 + (i_{s\alpha})_{ref} - \delta_2 + 2\alpha M \Phi_{r\alpha} e_2 - \frac{\mu \Phi_{r\beta}}{J} e_1 \right) \\ V_{s\beta} = \sigma L_s (k_3 e_3 + (i_{s\beta})_{ref} - \delta_1 + 2\alpha M e_2 \Phi_{r\beta} - \frac{\mu \Phi_{r\alpha}}{J} e_1) \end{cases} \quad (38)$$

With: $k_3 > 0$ and $k_4 > 0$
The derivatives of the errors "e3", "e4" will be as follows:

$$\begin{cases} \dot{e}_3 = -k_3 e_3 - 2\alpha M \Phi_{r\beta} - \frac{\mu \Phi_{r\alpha}}{J} e_1 \\ \dot{e}_4 = -k_4 e_4 - 2\alpha M \Phi_{r\alpha} e_2 + \frac{\mu \Phi_{r\beta}}{J} e_1 \end{cases} \quad (39)$$

So from equation (32), (39) we can write:

$$\dot{e} = A.e \quad (40)$$

With:

$$A = \begin{bmatrix} -k_1 & 0 & \frac{\mu}{J}\Phi_r \cos(\theta) & -\frac{\mu}{J}\Phi_r \sin(\theta) \\ 0 & -k_2 & 2\alpha M \Phi_r \sin(\theta) & 2\alpha M \Phi_r \cos(\theta) \\ -\frac{\mu}{J\Phi_r}\cos(\theta) & -\frac{2\alpha M}{\Phi_r}\sin(\theta) & -k_3 & 0 \\ \frac{\mu}{J\Phi_r}\sin(\theta) & -\frac{2\alpha M}{\Phi_r}\cos(\theta) & 0 & -k_4 \end{bmatrix} \text{ and } e = \begin{bmatrix} e_1 \\ e_2 \\ e_3 \\ e_4 \end{bmatrix}$$

It can be seen that the elements of the matrix A contain variable terms cos(θ) and sin(θ) which can cause instability in the system. The following figure shows the block diagram of the backstepping control of the asynchronous machine in the (α,β) frame of reference.

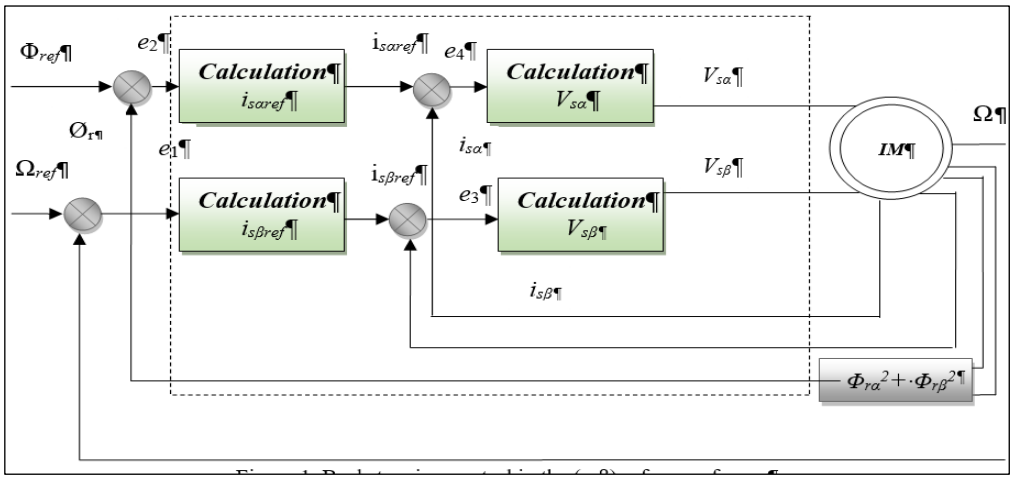


Figure 1: Backstepping control in the (α β) reference frame.
Source: Authors, (2026).

III.3. SIMULATION RESULTS

These results obtained through simulating our motor within the MATLAB SIMULINK environment, using the new backstepping control developed. We carried out the test by implementing a resistive torque (Cr = 6 N.m) as an external variation of the instants (t=2.5s and t=3.5s) and a speed setpoint equal to the nominal speed of the IM (157 Rad/s).

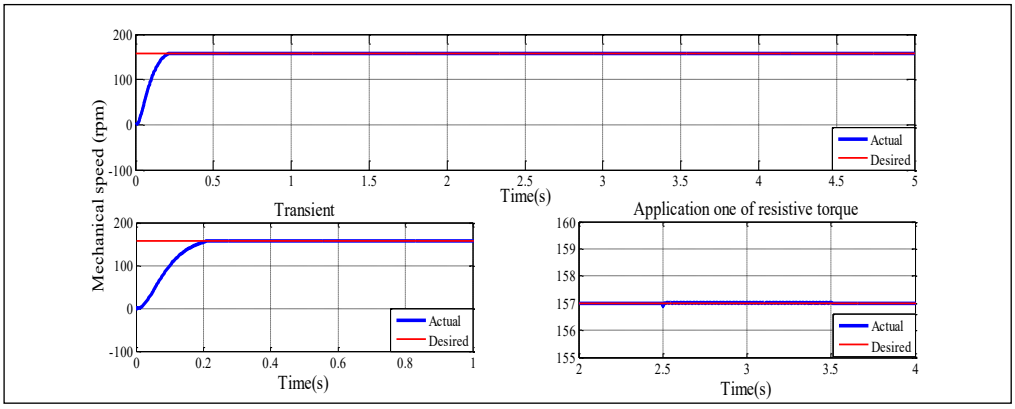


Figure 2: Mechanical speed produced for the new lyapunov backstepping control with a zoom (external variation).
Source: Authors, (2026).

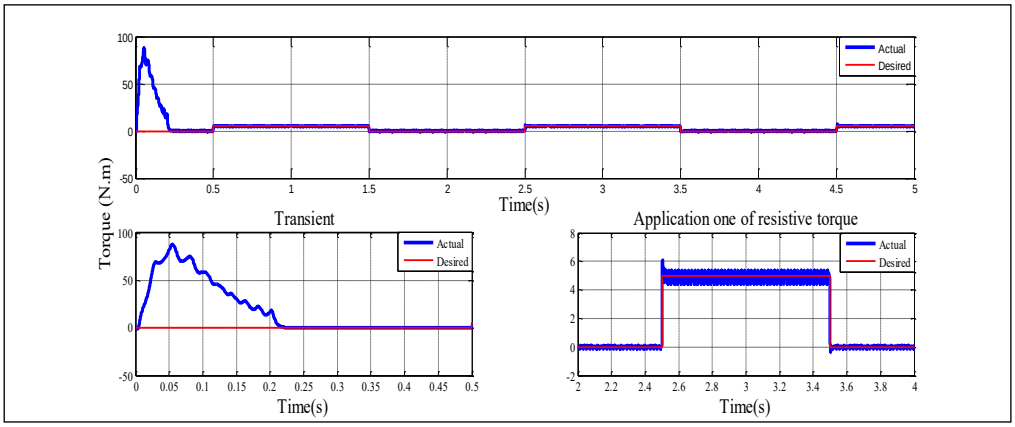


Figure 3: Torque produced for the new lyapunov backstepping control with a zoom (external variation).
Source: Authors, (2026).

The simulation results show that the mechanical speed closely follows its reference with the developed control technique. The response time, the overshoot and the convergence of the exponential error to the steady state are all optimal, even when external variations (resistive torque) are applied and removed and the torque peaks at the first starting moment, then reaches the value of the resisting torque before and after the load is applied. This control technique demonstrates high efficiency and strong performance.

IV. CONCLUSION

In this study, we develop a control system based on Lyapunov stability theory, which is backstepping control. This method solves the parametric and external variation problems to obtain positive mechanical power output with error convergence to zero. It also guarantees the closed-loop stability of the induction machine at all times. The chosen model of the machine is in the (α,β) reference frame, which does not require a Park transformation. These excellent results obtained with the new Lyapunov backstepping control should be taught in academic circles and also applied in industrial environments.

V. AUTHOR'S CONTRIBUTION

Conceptualization: Chami Noureddine, Rouabhi Riyadh and Herizi Abdelghafour.
Methodology: Chami Noureddine, Rouabhi Riyadh and Herizi Abdelghafour.
Investigation: Chami Noureddine and Rouabhi Riyadh.
Discussion of results: Chami Noureddine, Rouabhi Riyadh and Herizi Abdelghafour.
Writing – Original Draft: Chami Noureddine and Rouabhi Riyadh.
Writing – Review and Editing: Chami Noureddine, Rouabhi Riyadh and Herizi Abdelghafour.
Resources: Chami Noureddine and Herizi Abdelghafour.
Supervision: Chami Noureddine, Rouabhi Riyadh and Herizi Abdelghafour.
Approval of the final text: Author One, Rouabhi Riyadh and Herizi Abdelghafour.

VI. REFERENCES

[1] Lekhchine. S, Bahi.T, Abadlia. I, Bouzeria. H, PV-battery energy storage system operating of asynchronous motor driven by using fuzzy sliding mode control, International Journal of Hydrogen Energy, 42, pp. 8756–8764 (2017).

[2] Cavagnino. A, Asynchronous Motors, Encyclopedia of Electrical and Electronic Power Engineering, pp. 280–298 (2023).

[3] Cheng. J, Xiong. Y, Application of teaching-learning-based optimization algorithm in rotor fault diagnosis for asynchronous motor, Procedia Computer Science, 131, pp. 1275–1281 (2018).

[4] Ouinten. M, Rouabhi. R, Herizi. A, Power enhancement using grey wolf optimizer algorithm for doubly fed induction generator based on fuzzy logic controller, Diagnostyka, 1-12 (2026).

[5] Rouabhi, R., et al. New Cascade Control Based on Type 2 Fuzzy Controllers Applied to a DC Motor. IET Science, Measurement &Technology. 19, 01 (2025). https://doi.org/10.1049/smt2.70029

[6] Sami. I, Ullah. S,. Integral Super Twisting Sliding Mode Based Sensorless Predictive Torque Control of Induction Motor. Power Syst., vol. 8, (2020), pp. 186740-186755.

[7] Drhorhi I, El Fadili A, Berrahal C, Lajouad R, El Magri A, Giri F, Taher Azar A, Vaidyanathan S. Chapter 11 - Adaptive backstepping controller for DFIG-based wind energy conversion system. Backstepping Control of Nonlinear Dynamical Systems Advances in Nonlinear Dynamics and Chaos (ANDC) (2021) 235-260

[8] Aounallah T, Essounbouli N, Hamzaoui A. Fractional-order Adaptive fuzzy Bckstepping Algorithm for Automated Control of Blood Glucose in Diabetes Mellitus Type 1 Patients. IFACPapersOnLine 54-4 (2021) 183-188.

[9] Rouabhi, R., Zemmit, A., Herizi, A. et al. Hybrid type-2 fuzzy backstepping control of doubly fed induction generator for wind energy conversion systems. J Braz. Soc. Mech. Sci. Eng. 47, 24 (2025). https://doi.org/10.1007/s40430-024-05293-z

[10] Chun Sha, Ji Luo, Masoud Taleb Ziabari, A new robust decentralized approach based on adaptive fuzzy backstepping method for microgrid secondary voltage control, Sustainable Energy, Grids and Networks 27 (2021) 1-7.

[11] R. Rouabhi, A. Herizi, S. Djeriou, A. Zemmit, Hybrid Type-1 And 2 Fuzzy Sliding Mode Control Of The Induction Motor, Rev. Roum. Sci. Techn.–Électrotechn. et Énerg. 69, 2, pp. 147–152, Bucarest, 2024. https://doi.org/10.59277/RRST-EE.2024.2.5

[12] Zellouma, Y. Bekakra, H. Benbouhenni. Field-oriented control based on parallel proportional–integral controllers of induction motor drive. Energy Rep 9 (2023), pp. 4846–4860.

[13] T. Wang, Y .Wang, Z. Zhang, Z. Li, Cungang Hu, Fengxiang Wang. Comparison and analysis of predictive control of induction motor without weighting factors. 2nd International Joint Conference on Energy and Environmental Engineering, (CoEEE 22).

[14] R. Rouabhi, A. Herizi, A. Djerioui. Performance of Robust Type-2 Fuzzy Sliding Mode Control Compared to Various Conventional Controls of Doubly-Fed Induction Generator for Wind Power Conversion Systems. Energies 2024, 17, 3778. https://doi.org/10.3390/en17153778

[15] A. Benzouaoui, H. Khouidmi, B. Bessedik. Parallel model predictive direct power control of DFIG for wind energy conversion. Int J Electr Power Energy Syst 125 (2021), pp. 1-12.

[16] A Herizi, A Zemmit, R Rouabhi, F Ouagueni. New design of robust controller based on fuzzy 12 linguistic variables for wind power conversion system PRZEgląd elektrotechniczny 2023 (100)

[17] L Bensaadia, R ROUABHi, D Khodja, A Herizi. Adaptive type-1 fuzzy control of a wind energy conversion system based on a double-fed induction machine. Przegląd Elektrotechniczny 2023 (8)

[18] A Herizi, R Rouabhi, A Zemmit. Speed control of doubly fed induction motor using backstepping control with interval type-2 fuzzy controller. Diagnostyka 2023 (24)

[19] A Herizi, R Rouabhi, A Zemmit. Comparative study of the performance of a sliding, sliding-fuzzy type 1 and a sliding-fuzzy type 2 control of a permanent magnet synchronous machine. Przegląd Elektrotechniczny 2022 98 (11)

[20] R. Rouabhi; A. Herizi; S. Djeriou; L. Bensaadia. Lyapunov stability and control of active and reactive powers generated by wind energy conversion system based of a doubly fed induction generator. 2025 2nd International Conference of Advanced Technology in Electronic and Electrical Engineering (ICATEEE)

[21] K. Noussi, A. Abouloifa, H. Katir, I. Lachkar, C. Aouadi, M. Aourir, F.El Otmani. Integral Backstepping Control Based on High Gain Observer for DFIG-Based Wind Energy Conversion System. IFAC-PapersOnLine 55-12 (2022) 653-658.

[22] M M Rezaei. A nonlinear maximum power point tracking technique for DFIG-based wind energy conversion systems. Engineering Science and Technology, an International Journal 21 (2018) 901-908.

[23] Ravi Patel, Faizal Hafiz, Akshya Swain, Abhisek Ukil. Nonlinear rotor side converter control of DFIG based wind energy system. Electric Power Syste Research 198 (2021) 1-12.

Journal of Engineering and Technology for Industrial Applications

ISSN ONLINE: 2447-0228

ITEGAM-JETIA

Manaus, v.12 n.60, p.648-659, July/August, 2026.

DOI: https://doi.org/10.5935/jetia.v12i60.3947

RESEARCH ARTICLE OPEN ACCESS

DEEP LEARNING TECHNIQUES GAN AND LSTM FOR STOCK MARKET CLOSING PRICE PREDICTION

Pappula Praveen*[1], Anjaneyulu Gudla[2]

[1, 2, 3]Department of Computer Science and Engineering, School of Computer Science and Artificial Intelligence, SR University, Warangal, Telangana, India.

[1]http://orcid.org/0000-0002-2967-8435, [2]http://orcid.org/0009-0008-8916-4031

Email:*prawin1731@gmail.com, anjugudla5@gmail.com

ARTICLE INFO

Article History
Received: March 3, 2026
Reviewed: June 12, 2026
Accepted: July 12, 2026
Published: July 31, 2026

Keywords:
Stock Price
GAN
LSTM
Deep Learning
ARIMA.

ABSTRACT

Accurate stock price prediction is vital for investors and analysts to make informed decisions and mitigate risks. Traditional methods like ARIMA struggle with the complex, non-linear patterns of stock market data, leading to less precise forecasts. This study addresses the gap by leveraging advanced deep learning methods, specifically Generative Adversarial Networks (GANs) and Long Short-Term Memory (LSTM) networks, for stock price forecasting. Using historical stock data and 32 influencing features, we trained GANs and LSTMs, with Root Mean Square Error (RMSE) as the evaluation metric. The data was split into 80% training and 20% testing. Our results show that the GAN model achieved a lower RMSE of 5.36, outperforming the LSTM model (RMSE of 6.6) and traditional ARIMA models, demonstrating GAN's superior ability to capture complex patterns. While computational challenges exist, GAN's accuracy underscores its potential for stock price prediction. Future research could explore hybrid models and sentiment analysis to further improve prediction accuracy.

Copyright ©2026 by authors and Galileo Institute of Technology and Education of the Amazon (ITEGAM). This work is licensed under the Creative Commons Attribution International License (CC BY 4.0).

I. INTRODUCTION

Forecasting prices of stock market is a complex and demanding task because of the highly dynamic as well as non-linear characteristics of financial markets. Precise forecasts can provide significant benefits for investors as well as traders which enables them to make informed decisions, handle risks efficiently along maximize returns. Traditional methods of the prediction of stock price like ARIMA models often fail to capture accurately the intricate along with the unpredictable patterns inherent in market data. These limitations have promoted the investigation of advanced methods. Deep Learning approaches have gained popularity for their capacity to model complex patterns as well as the interconnections in time-series data. Methods like GANs as well as LSTM networks handle large volumes of data as well as uncover hidden connections within the data. They also provide more precise as well as reliable predictions comparing conventional data. GANs which can generate synthetic data and LSTMs are known for their proficiency in handling sequential data which provides promising results for the challenges presented by the stock market's volatility as well as complexity. Researchers want to improve the precision as well as robustness of stock price predictions by using these advanced DL techniques which leads to better investing strategies along with financial decision-making. Many researchers have explored deep learning (DL) models for stock price prediction. By [1] introduced the S_I_LSTM technique, combining traditional and non-traditional data like stock posts and financial news, enhancing accuracy in the Shanghai A-share market. In turn [2] evaluated DL techniques using Google's daily closing price, finding GANs superior to LSTM and GRU. According to [3] proposed a GAN with an economics-driven loss function for predicting financial time series. In turn [4] tested multiple DL models, highlighting GRU and addressing overfitting with GANs. By [5] improved accuracy by combining empirical mode decomposition with LSTM and GAN architectures. According to [6] developed the GAF-EWGAN method, integrating enhanced WGANs with Gramian Angular Fields. By [7] introduced GAN-TrellisNet, which combined TrellisNet and CNN for better stock prediction accuracy. In turn [8] created a GAN-based model with piecewise linear representation to forecast stock trading actions. By [9] used BERT and GAN for sentiment analysis to predict Apple Inc.'s stock, achieving high accuracy. According to [10] combined neural networks and GANs for S&P 500 predictions, achieving superior results with the G-LSTM+D-LSTM technique.

By [11] developed TSGAN, integrating ACNN, LSTM, ARIMA, and CNN for accurate stock predictions. In turn [12] combined Phase-space Reconstruction and GAN for effective forecasting. According to [13] introduced a BiLSTM and WGAN approach to predict stock prices for newly listed companies with limited data. By [14] reviewed various stock prediction techniques, noting the rise of DL methods from 2020 to 2023. In turn [15] highlighted the shift from traditional methods to advanced DL techniques, including Transformers, GANs, and GNNs. Financial news and social media have been shown to enhance prediction accuracy [16], while GANs and LSTMs often outperform traditional methods in capturing the non-linear dynamics of financial data [17]. Addressing overfitting and improving model robustness are common themes, with various studies exploring artificial data generation and hybrid approaches [18]. However, there is still a research gap in the comparative analysis of GANs as well as LSTMs, especially for the prediction of the stock market. Several research focuses on the utilization of a single DL technique with less exploration of the synergistic potential of combining GANs as well as LSTMs. Previous researches often suffer limitations like overfitting, lack of integration of diverse data sources as well as a limited focus on certain markets or stocks.The motivation of this study is to utilize advanced DL methods especially LSTM networks as well as GANs to enhance the predictions of the stock market. Traditional techniques often face difficulties when dealing with complex unpredictable characteristics of financial data. The main motivation of this research is the potential of utilizing advanced methods to combine various data sources like historical prices, technical indicators as well as sentiment analysis from news to create a more holistic as well as accurate prediction model. The objective is to demonstrate the practical applications as well as the benefits of these complex modeling methods by focusing on Apple Inc., a stock that is highly influential as well as volatile. The objective of this study is to enhance the accuracy of stock price prediction by utilizing advanced structures of LSTM as well as GAN. This study aims to contribute to expanding the literature on the utilization of DL methods in financial market analysis. This research focuses on the utilization of advanced DL techniques like LSTM networks and GANs to forecast stock prices which especially examines the stock price of Apple Inc.

II. MATERIAL AND METHODS

II.1 MATERIALS AND METHODS

Materials:

The first step in building a technique involves obtaining a dataset that includes the essential features required for training the model. In DL the dataset contains the target values that are used during the training process. In this particular scenario, the dataset comprises continuous feature extractions that are presented in a time series format. In this study, the daily closing price of the APPLE stock data is used. The series covers 497 trade days from 2nd January 2020 to 19th July 2024. Overall, 497 observations are present in the data set.While there are around 1187 trading days in this timeframe, the 497 trade days considered are based on specific criteria relevant to the study, such as days with significant market movements or availability of complete data.Figure 1 provides a comprehensive analysis of AAPL stock performance showing the closing prices, moving averages, daily returns, and their distribution. The detailed analysis helps in understanding the stock's behavior over the selected period.

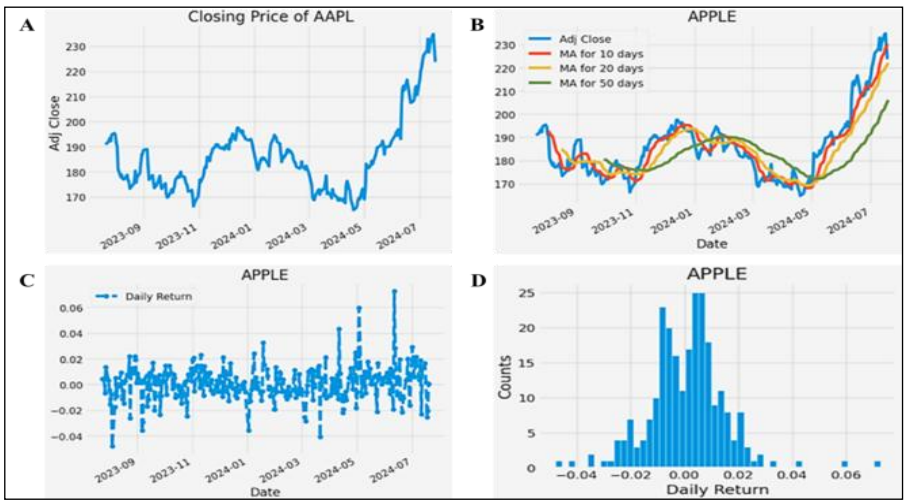


Figure 1: Analysis of AAPL Stock Performance. (A) Closing prices over the 497 trade days, illustrate the overall trend and key fluctuations. (B) Moving averages for 10 days, 20 days, and 50 days, highlighting long-term and short-term trends. (C) Daily returns, showing the day-to-day changes in stock price. (D) Distribution of daily returns, providing insights into the frequency and magnitude of daily changes. Graphs were generated using Python.
Source: Authors, (2026).

II.1.1 Long Short-Term Memory (LSTM):

LSTM is a type of recurrent neural network (RNN) designed by Hochreiter and Schmidhuber in 1997 to handle sequential data more effectively than standard feed-forward networks. To control information flow, it has an outputgate, an input gate and a forget gate in addition to feedback loops. The main novelty of LSTM is that it can retain or discard data according to its current cell state, which helps to alleviate the vanishing gradient issue that standard RNNs frequently encounter while training. This unique design addresses issues related to vanishing and exploding gradients, making LSTM a robust tool for tasks involving time series data, such as sequence prediction and classification.

II.1.2 Generative Adversarial Network (GAN):

GANs are structured as a zero-sum game, where two components—a generator and a discriminator—compete against each other. The generator is crafted using GRU layers and is designed to produce data that appears convincingly real. Meanwhile, The discriminator's job is to differentiate between generated and genuine data. The loss function for the discriminator is:

$$V_D = \frac{1}{m}\sum_{i=1}^{m} \log D(y^i) + \frac{1}{m}\sum_{i=1}^{m} (1 - \log D\ (G(x^i)))$$

The loss function for the generator is:

$$V_G = \frac{1}{m}\sum_{i=1}^{m} (1 - \log D\ (G(x^i)))$$

GAN framework utilizes cross-entropy loss to align the generated data distribution with the real data distribution, effectively minimizing the Kullback-Leibler-Jensen-Shannon (KL-JS) divergence.

II.2 FEATURE EXTRACTION FROM DATA:

Technical Indicators:

In this research, we calculated several key technical indicators used by investors:exponential moving averages, 7-day and 21-day moving averages, Bollinger Bands, momentum, and the Moving Average Convergence Divergence (MACD). The formulas and their significance are:

7-day and 21-day Moving Average (MA):

$$\mathrm{MA}_n = \frac{1}{n}\sum_{i=0}^{n-1} P_{t-i}$$

Moving Average smooth out price data to identify the trends by averaging past prices over a significant period. The 7-day MA captures short-term trends while the 21-day MA provides insights into medium-term trends.

Exponential Moving Average (EMA):

$$\mathrm{EMA}_t = (P_t \times \frac{2}{n+1}) + (\mathrm{EMA}_{t-1} \times (1 - \frac{2}{n+1}))$$

These indicators are particularly sensitive to recent price changes, allowing for a faster reaction to new market data. It helps in identifying the direction of the current trend along with potential reversals.

Momentum:

$$P_t - P_{t-n}$$

It measures the rate of price change. The rising trend is known as positive momentum and a declining trend is known as negative momentum. This helps traders gauge the strength of a price movement.

Bollinger Bands:

Bollinger Bands consist of two outside bands that are positioned ±2 standard deviations apart from the center and a middle band that is made up of the 20-day moving average. This tool is used to gauge market volatility and outlines a range within which the price is expected to fluctuate. Prices may be overbought when they approach the top band, while they may be oversold when they approach the lower band.

Moving Average Convergence Divergence (MACD):

EMA_{12} - EMA_{26}
Signal Line: 9-day EMA of MACD

Market momentum is reflected by the MACD, which shows a bullish trend when its value is positive and a bearish trend when its value is negative. The MACD line indicates possible buy or sell signals when it crosses above or below the signal line.

News Sentiment Analysis:

Stock price changes may be impacted by news. We gathered daily news stories on Apple Inc. and assessed each article's mood using the FinBert model. With a sentiment score ranging from -1 to 1, our analysis classified the news as good, neutral, or negative. These sentiment scores were then integrated into the model as additional features, allowing the model to incorporate the impact of market sentiment on stock price predictions.

Fourier Transforms:

The study employed Fourier transforms to identify long-term and short-term trends in Apple stock. By decomposing the data into sine wave components, Fourier transforms help in reconstructing the original signal, enabling the model to discern patterns and trends more accurately for predictive purposes.

II.3 DATA STRUCTURE:

This study prepared the dataset for supervised learning by dividing it with a rolling window equal to 1. The original dataset is two-dimensional and reshaped the data to three dimensions according to the timesteps as shown in Figure2.The specific steps taken to prepare the data for the many-to-many model:

Rolling Window Approach: The rolling window technique involves creating overlapping subsets of the data where each window shifts by one-time step. For a rolling window of size 1, each subset contains the data point at time ttt and its previous data points.

Original Data:the dataset starts as a two-dimensional array with rows representing time steps and columns representing features.

Reshaping Process: For each rolling window, the data is split into input sequences (features at time ttt) and output sequences (features at time t+1t+1t+1). This process transforms the data into three dimensions: [samples, timesteps, and features]. Each sample corresponds to a rolling window, each timestep within a sample corresponds to a specific time point in that window, and each feature corresponds to the various data attributes at that time point

Many-to-Many Model Preparation: Input Data: For the LSTM and GAN models, the input data is structured as [number of samples, number of timesteps, number of features].

Output Data: The output for each input sequence is also a sequence, allowing the model to predict multiple future time steps (many-to-many). Example: If the rolling window size is 5, each input sequence will have 5 timesteps, and the corresponding output sequence will also have 5 timesteps. Figure 2 illustrates how the original dataset is reshaped into a three-dimensional structure suitable for the many-to-many model.

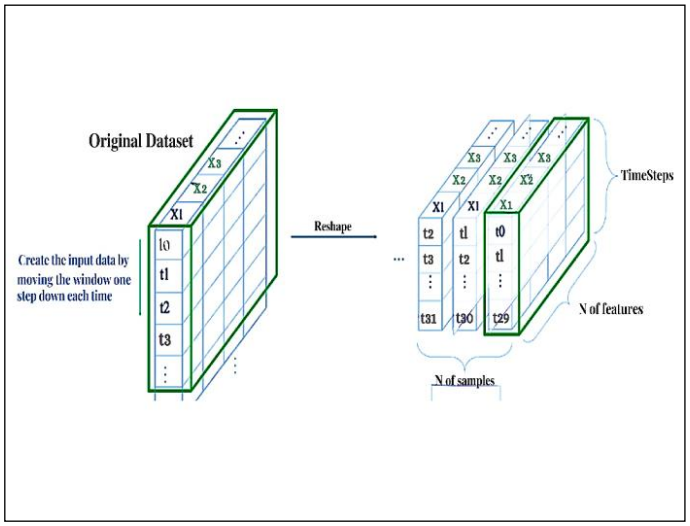


Figure 2: Reshaping the Original Dataset for Input Data Preparation.
Source: Authors, (2026).

This research developed a model that uses a many-to-many approach, utilizing a 30-day time step to forecast stock prices for an output step of 3, as depicted in Figure 3.

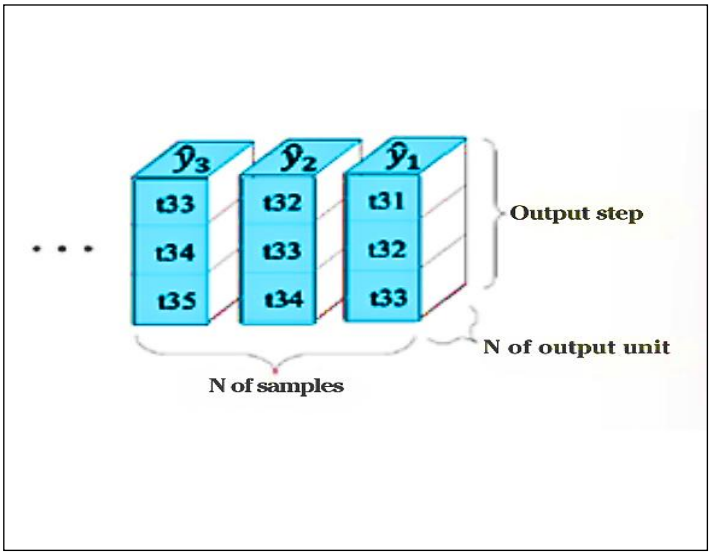


Figure 3: Many-to Many Models with Timestep of 30 and an Output Step of 3.
Source: Authors, (2026).

II.4 METHODOLOGY

Generator:

The study used a GRU as the generator component in the GAN model, chosen for its stability and effectiveness in handling sequential data. The dataset spans a decade of historical stock prices and includes 32 distinct features such as Open, High, Low, Close, Volume, and various global indices like NASDAQ, NYSE, S&P 500, and others.

Additional metrics such as Crude Oil prices, Gold prices, VIX, USD index, and technical indicators (e.g., moving averages, MACD, Bollinger Bands) are also part of the dataset, alongside news sentiment data. We perform multi-step ahead prediction.The generator model receives input data in three dimensions, consisting of batch size, input steps, and features, and it produces output based on the batch size and output steps.

Generator Architecture:

GRU Layer 1:

- Neurons: 1024
- Activation Function: ReLU
- Dropout Rate: 0.2
- Regularization: L2 regularization with a coefficient of 0.01

GRU Layer 2:

- Neurons: 512
- Activation Function: ReLU
- Dropout Rate: 0.2
- Regularization: L2 regularization with a coefficient of 0.01

GRU Layer 3:

- Neurons: 256
- Activation Function: ReLU
- Dropout Rate: 0.2
- Regularization: L2 regularization with a coefficient of 0.01

Dense Layer 1:

- Neurons: 128
- Activation Function: ReLU

Dense Layer 2:

- Neurons: Number matching the output step to be predicted (e.g., if predicting 10 steps ahead, this layer has 10 neurons)
- Activation Function: Linear

Input and Output Dimensions:

- Input Dimensions: [batch size, input-step, number of features (32)], where batch sizeis the number of samples in a batch; input-step = number of timesteps in each input sequence.
- Output Dimensions: [batch size, output-step], where the batch size is the same as the input batch size, and the output-step is the number of future time steps to predict.

This detailed architecture ensures that the generator can effectively capture temporal dependencies and generate accurate multi-step ahead predictions.

Discriminator:

The discriminator in this GAN model is a Convolutional Neural Network (CNN) designed to differentiate between real and generated data, as depicted in Figure 4. It accepts both genuine and synthetic data as input. The architecture features three one-dimensional convolutional layers with 32, 64, and 128 neurons, followed by three dense layers with 220, 220, and 1 neuron, respectively. With the exception of the last layer, which employs a linear activation for WGAN-GP or a sigmoid activation for GANs, all of these layers utilize leaky ReLU as their activation function.

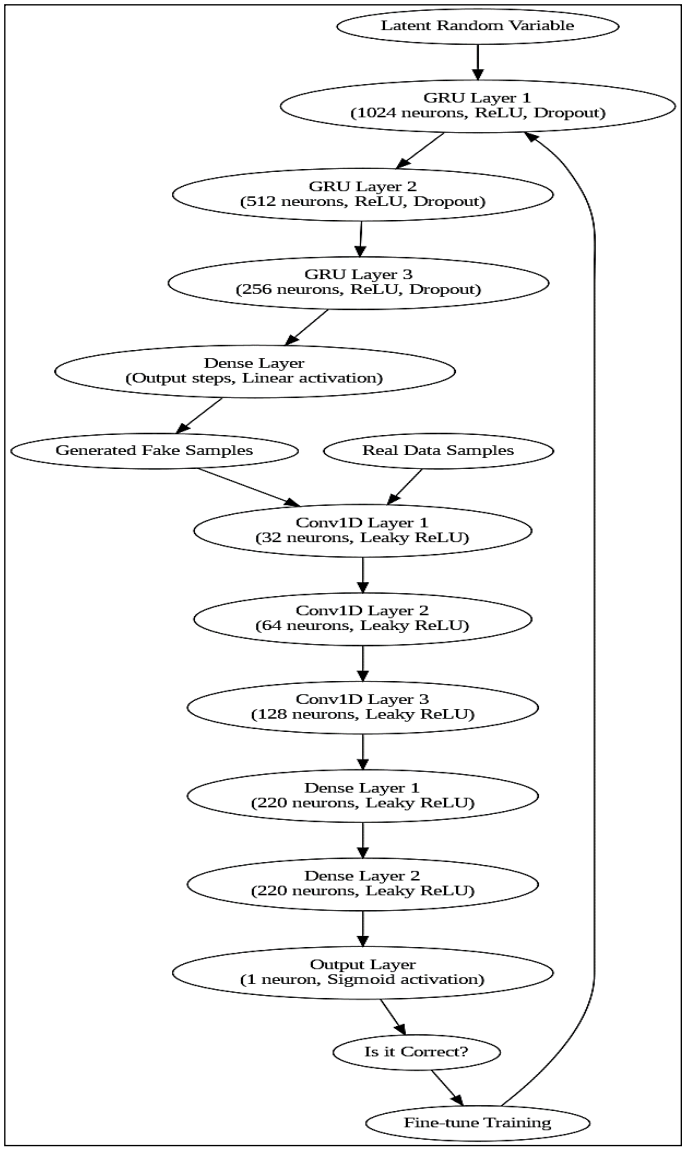


Figure 4: Flowchart of GAN Model.
Source: Authors, (2026).

Activation Functions:

Leaky ReLU:

This function successfully mitigates the dying ReLU issue, where neurons might stop learning, by allowing for a little positive slope (often set to 0.01) while the neuron is not active. By preventing neurons from staying dormant, this method encourages continuous learning. All of the discriminator's layers—aside from the output layer—are subject to Leaky ReLU.

Sigmoid:

The Sigmoid function squashes outputs to the range [0, 1], suitable for binary classification by representing probabilities. In GANs, the Sigmoid function in the discriminator's output layer indicates the likelihood that input data is real or fake. This combination of Leaky ReLU and Sigmoid activations enables the discriminator to effectively differentiate between genuine and fake data, enhancing the GAN model's performance.

Architecture of GAN:

Combining the generator and discriminator structures, we define our proposed GAN model. The model uses cross-entropy to calculate the loss for both the generator and discriminator. In the discriminator, as shown in Figure5 this study combines the generated stock price with the historical stock price of input steps, enhancing data length and increasing accuracy in classification.

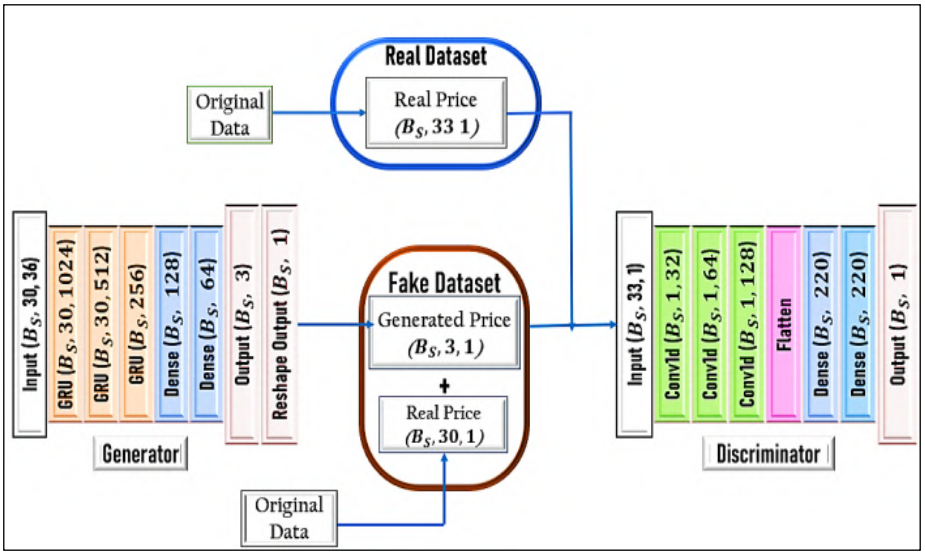


Figure 5: The architecture of the GAN model.
Source: Authors, (2026).

Training Process of GAN:

The training process of the GAN involves iterative updates to both the generator and discriminator components. Here's a detailed explanation of the process, including the number of epochs, batch size, and optimization algorithms used:

(1) Initialization

- *Generator and Discriminator Networks:*The weights of both networks are initialized independently.
- *Hyperparameters:*Important parameters like the batch size, learning rate, and number of training epochs are configured at the start.

(2) Training Loop

- *Epochs:* The GAN is trained for 500 epochs, which defines how many times the entire training dataset is passed through the network.
- *Batch Size:* During each epoch, the training data is divided into smaller batches. The batch size used in this study is 32.

(3) Discriminator Training

- *Real Data:* A batch of real stock prices is selected from the historical dataset.
- *Generated Data:* The generator produces a batch of fake stock prices.
- *Training:*It involves the discriminator being exposed to both actual and synthesized data, aiming to differentiate between the two correctly. The cross-entropy loss function measures the performance of the discriminator by evaluating its accuracy in classifying real versus fake data.

(4) Generator Training

- *Noise Input:* The generator receives a batch of random noise as input.
- *Fake Data:* The generator produces a batch of fake stock prices from the noise.
- *Discriminator Feedback:* The fake data is then passed to the discriminator.
- *Training:*The generator is trained to maximize the discriminator's error in classifying fake data as real. The cross-entropy loss function is used to calculate the generator's loss.

(5) Optimization

Both the generator and discriminator are optimized using the Adam optimization algorithm, with a learning rate set to 0.0002 and a beta1 of 0.5.

(6) Evaluation

After each epoch, the performance of the GAN is evaluated based on the accuracy of the discriminator and the quality of the generated stock prices.

(7) Convergence

The training continues until the specified number of epochs is reached or until the model converges, indicated by stable loss values and realistic generated stock prices.

Summary of GAN Training Architecture:

Generator Architecture:

- Input Layer: $(B_S, 30, 36)$
- GRU Layers: 1024, 512, 256 units
- Dense Layers: 128, 64 units
- Output Layer: $(B_S, 3, 1)$

Discriminator Architecture:

- Input Layer: $(B_S, 3, 1)$, $(B_S, 30, 1)$
- Conv1d Layers: 32, 64, 128 filters
- Flatten Layer
- Dense Layers: 220, 220 units
- Output Layer:$(B_S, 1)$

II.5 PROPOSED SYSTEM:

The proposed system integrates advanced LSTM and GAN architectures to predict stock prices using technical indicators, news sentiment analysis, and Fourier transforms.

- LSTM Networks: Capture long-term dependencies and trends in historical stock price data by processing sequences, modeling temporal dynamics crucial for accurate predictions.
- Generative Adversarial Networks (GANs): Enhance predictive power through synthetic data generation. The GAN architecture includes a generator for creating plausible stock price sequences and a discriminator for differentiating between real and synthetic data, refining the model's accuracy.
- Technical Indicators: Incorporates moving averages, RSI, and Bollinger Bands to enrich the feature set and provide deeper insights into market trends and price movements.
- News Sentiment Analysis: Uses sentiment extracted from financial news and social media to account for market psychology's impact on stock prices.
- Fourier Transforms: Analyzes stock price data in the frequency domain to detect cyclical patterns and periodicities not visible in the time domain.

Integration and Prediction:

The system combines outputs from the LSTM network, GAN-generated data, technical indicators, sentiment scores, and Fourier transform features. This comprehensive approach ensures a robust predictive model by capturing diverse aspects of market behavior and improving prediction accuracy.

III. RESULTS AND DISCUSSIONS

III.1 TRAINING OF OUR MODEL:

This research attempts to predict the closing price of the stock for the following five days based on data from the last 60 days. In addition to historical closing prices, the model will be trained using 32 other potential price-influencing parameters. Data augmentation techniques, such as the addition of noise and the generation of artificial data using GANs, are employed to increase the variation in the training set. 20% data is used for testing and rest 80% data is used for training. To avoid overfitting, several strategies are implemented, including early stopping, dropout regularization, and cross-validation.

Experimental Results:

The research evaluated each model's performance using Root Mean Square Error (RMSE) which is defined as follows:

$$\text{RMSE} = \sqrt{\frac{\sum_{i=1}^{N}(x_i - \widehat{x_1})^2}{N}}$$

In this project the research evaluated the models through comparing their RMSE on testing data for each of the N data points, x_i being the actual stock price, and $\widehat{x_1}$ being the predicted stock price.

Table 1: Calculations using the ARIMA model.

Dep. Variable	D.GS	No. Observations	1144
Model	ARIMA (2, 1, 0)	Log Likelihood	-4589.254
Method	css-mle	S.D. of innovations	3.789
Date	20.07.2024	AIC	998.245
Time	09.05.58	BIC	8956.785
Sample	1	HQIC	8936.458

Source: Authors, (2026).

Table 1 illustrates the ARIMA(2,1,0) model fit to the differenced GS series using 1144 observations. To evaluate the fit of the model information criteria (AIC, BIC, HQIC) can be used with lower values suggesting a better model. Additional insights into the performance of the model can be obtained from the standard deviation of innovations and the log-likelihood. To ensure that the chosen model accurately captures the underlying patterns in the time series data the selection and evaluation process of models is crucial.

ARIMA:

Based on Figure6 ARIMA approximates the real stock price very well. The predicted price will be used as an input feature into the LSTM because as this research mentioned previously the study wants to capture as many features and patterns as possible about AAPLE.

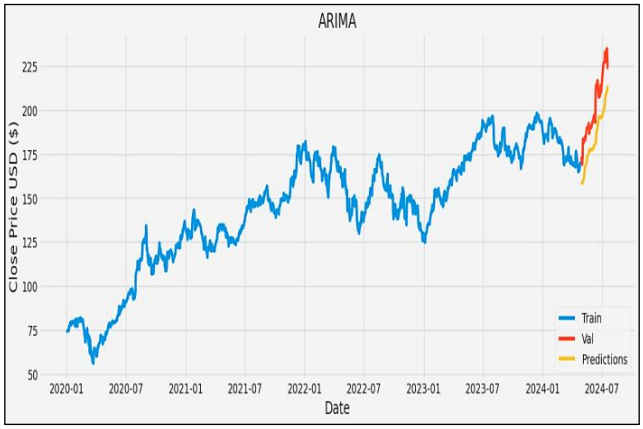


Figure 6: Forecasts based on ARIMA.
Source: Authors, (2026).

LSTM:

In this work, Bidirectional LSTM was used in the first layer of the LSTM model. Adam algorithm is used as the optimizer in this work with a learning rate of 0.001. A batch of 64 is trained on a stock price dataset followed by 50 epochs. The GAN model in this baseline model uses historical data from the past 4.7 years along with 24 correlative features as input. Following the split of the data into the train set and the test set. Figure7 shows how an LSTM model performs in predicting stock prices with the x-axis representing the timeline from January 2020 to July 2024 and the y-axis representing closing prices in USD. In the blue line stock prices are shown in a historical context showing a general upward trend but with fluctuations.

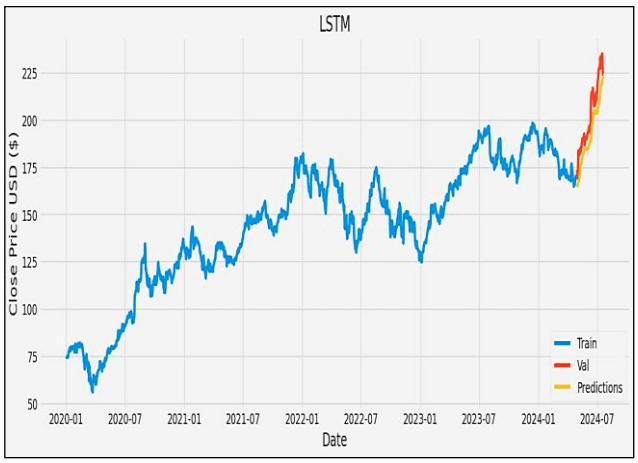


Figure 7: Stock price prediction using an LSTM model.
Source: Authors, (2026).

In Figure7 the orange line represents the validation dataset which overlaps with the yellow prediction line to demonstrate the performance evaluation of the model. Based on the close alignment between the validation data and predictions it appears that the model has accurately captured the trend and continues to make accurate predictions. A model that forecasted stock prices well predicting a continued rise based on historical data trends indicates a model that performs well.

Basic GAN:

It has been proposed that the GAN model in this paper will follow the structure suggested in the methodology section. This paper utilizes the Adam algorithm with a learning rate of 0.00016 as the optimizer for our models. This dataset was trained for 165 epochs on 128 samples over 165 epochs. Figure 8 shows the basic GAN loss curves for training and validation, which were generated using TensorFlow for training the GAN model and Matplotlib for visualization. During training, loss values for both the generator and discriminator were recorded at each epoch. These values were plotted using Matplotlib to create the loss curves, displaying training (blue) and validation (orange) performance over time. The analysis and plotting were done using Python. The x-axis represents epochs, and the y-axis represents loss values.

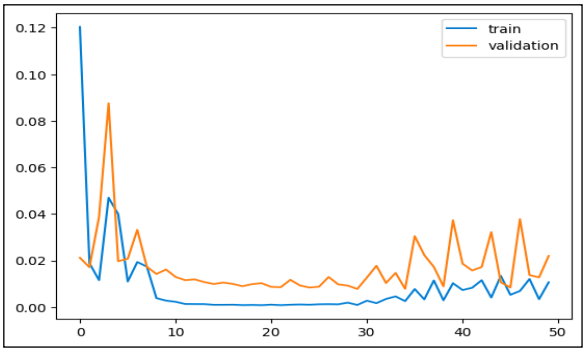


Figure 8: Basic GAN loss curves for training and validation.
Source: Authors, (2026).

Based on 50 epochs of training and validation Figure8 illustrates the loss curves of a Basic GAN (Generative Adversarial Network) model. Blue is the loss associated with training while orange is the loss associated with validation. In the first 10 epochs, both training and validation losses are high. However, they decrease significantly indicating rapid model learning. Following this initial phase, the training loss gradually decreases, stabilizing and fluctuating around a lower value. The validation loss by contrast shows a greater degree of variability fluctuating between 0.02 and 0.04 suggesting that the model may have overfitted to the training data. Plotting the first 50 epochs reveals the model's learning dynamics as well as the balance between generator and discriminator improvements. Low and stable losses indicate that the model has been effectively trained and generalized. A chart of GAN's historical and forecasted closing prices in USD is shown in Figure9.



Figure 9: Forecasting GAN closing prices using ARIMA.
Source: Authors, (2026).

The plot is divided into three sections: training data (blue) from January 2020 to January 2023 validation data (red) from January 2023 to July 2024 and predictions (orange) for the same period. The training data shows initial growth, volatility, and later stabilization of stock prices. Validation data shows an upward trend with volatility. A close alignment of the orange prediction line with the red validation data suggests that the ARIMA model has a high degree of robustness in forecasting future price trends. A visualization such as this illustrates the model's accuracy and its utility in predicting future trends and making informed investment decisions.

Table 2: Predictive Model Performance Based on RMSE.

Model	RMSE-of Training Dataset	RMSE-of Testing Dataset
ARIMA	2	7.5
LSTM	1.52	6.6
GAN	1.64	5.36
RF [1]	1.8	6.4

Source: Authors, (2026).

The GAN model has the lowest RMSE, indicating high predictive accuracy and effective generalization on the testing dataset, as shown in Table 2. LSTMs also perform well showing relatively low RMSE values. The ARIMA model performs moderately poorly with the highest RMSE on the testing dataset and the Random Forest model outperforms the GAN and LSTM models. GAN and LSTM models perform better in this particular prediction task. Confidence intervals provide a range within which the true RMSE values are expected to fall, offering insight into the variability and reliability of the model's performance. For instance, a narrow confidence interval indicates low variability and high stability, while a wide interval suggests higher variability.

Performance Variability and Implications for Real-world Trading:

Calculating confidence intervals for RMSE values helps assess model consistency and reliability. A model with a narrow confidence interval is more stable, producing predictions consistently close to actual values. This stability is crucial for real-world trading, where reliable performance is essential for making informed decisions and managing risk effectively. Models with lower RMSE and narrow confidence intervals offer more dependable predictions, which can lead to better decision-making and potentially higher returns.

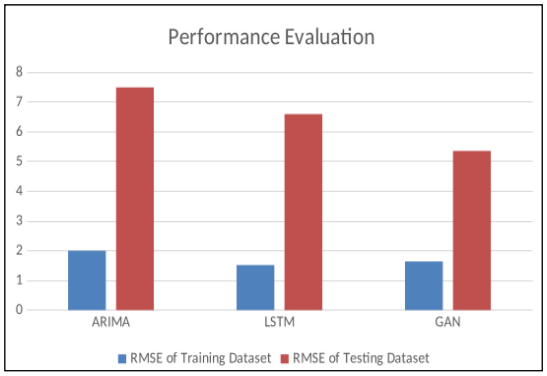


Figure 10: Comparison of model performance based on RMSE.
Source: Authors, (2026).

While GAN and LSTM models demonstrate lower RMSE values, their robustness, as indicated by confidence intervals, is also important. Traders might prefer models with greater stability and lower variability, even if it means slightly lower accuracy. In dynamic market conditions, models with consistent performance and lower variability are better suited for adapting to changes and maintaining reliability over time. According to Figure10, the GAN model exhibits the highest predictive accuracy on the testing dataset with the lowest RMSE. A LSTM model that has a relatively low RMSE value also performs well suggesting that generalization is effective. A higher RMSE on the testing dataset indicates poor performance in predicting unseen data suggesting overfitting in the ARIMA model. According to these results, the GAN and LSTM model is superior at predicting future value generalization and accuracy. GANs, with their adversarial training mechanism, can generate highly accurate predictions by learning the underlying distribution of the data. LSTM models, which are designed to process sequential data, are particularly effective at capturing both long-term dependencies and time-based patterns, making them ideal for forecasting time series data.

Discussion

This work employs GAN and LSTM networks to predict stock market closing prices using historical data and various influencing factors. The GAN model achieved the lowest RMSE of 5.36 on the testing dataset, indicating superior predictive accuracy compared to other models. This aligns with [2], who found GANs excel in stock price prediction with evenly distributed error rates. The LSTM model also performed well, with an RMSE of 6.6, effectively capturing temporal dependencies, consistent with [5], who noted LSTM's enhanced accuracy when combined with empirical mode decomposition. The study incorporated 32 features affecting stock prices, enabling the model to capture complex patterns, similar to the approach by [1], who used both traditional and non-traditional data to improve accuracy. The GAN model's ability to generalize on new data outperformed traditional models like ARIMA, which had higher RMSE values, supporting [4], who demonstrated GANs' effectiveness in reducing overfitting. The models' performance aligns with the economic-driven GANs (Fin-GAN) approach by [3], showing practical value in financial markets with higher Sharpe Ratios. Comparatively, the GAN model's RMSE of 5.36 shows significant improvement over other studies, such as [15] with an RMSE of 6.2. The LSTM model's RMSE of 6.6 also compares favorably with [19] RMSE of 7.1, highlighting the superior performance of the models used in this study. The high accuracy achieved in this study requires large datasets, which can be a limitation when data is scarce or poorly labeled. The dataset used, while comprehensive, may contain biases or gaps that affect the model’s generalizability. Future research should address these issues by using more diverse data sources and thorough data cleaning and labeling.

Although the GAN model showed good generalization, the fluctuating validation loss compared to the training loss suggests potential overfitting. Techniques like dropout, regularization, or cross-validation could mitigate this. Dropout prevents units from co-adapting by randomly omitting them during training. Regularization, such as L2 regularization, adds a penalty to the loss function based on model parameter magnitudes, and cross-validation helps assess how well the model generalizes to new datasets. This study focused on short-term predictions, but future research should explore different prediction cycles, including long-term forecasts, to provide a broader understanding of model performance over time. By [1] suggested that analyzing various cycles could reveal insights into model performance across different time horizons. While the current study used 32 features, it did not incorporate sentiment analysis from financial news and social media, which has been shown to enhance prediction accuracy. By [2] emphasized the importance of including sentiment analysis to improve model performance. Future studies should integrate sentiment data to better capture market sentiment’s impact on stock prices. Training GANs and LSTMs is computationally intensive, posing challenges for real-time applications. By [15] noted that deep learning models often struggle with complexity and high computational demands. The reliance on large datasets for high accuracy could be a drawback in cases of data scarcity, as discussed by [14]. In turn [6] also found that while enhanced WGAN models performed well, they were computationally expensive and prone to overfitting.

IV. CONCLUSION

This study explored the effectiveness of GANs and LSTM networks for predicting stock market closing prices using historical data and 32 significant factors. The GAN model achieved a low RMSE of 5.36 on the testing dataset, indicating high accuracy in stock price prediction. Using a wide range of factors allowed the models to capture complex patterns in the stock market. The bidirectional LSTM model showed robustness with an RMSE of 6.6, outperforming the ARIMA model but still facing some overfitting issues. The study identified areas for improvement, such as addressing potential overfitting and enhancing the integration of sentiment analysis. This research highlights the potential of GANs and LSTMs in predicting stock market trends, demonstrating their superior performance and robustness.

Future research must give importance to addressing the identified limits by optimizing computational efficiency, exploring hybrid models as well as integrating more diverse data sources which include sentiment analysis. The accuracy of DL models as well as practical applicability in financial market analysis and stock price prediction can be enhanced. Future research should include sentiment analysis from financial news as well as social media data to build accuracy. Investigating the hybrid models that use the strengths of several DL models like integrating GANs with GRU or Transformer networks could improve performance. Using GANs can mitigate overfitting as well as improve generalization. Incorporating more diverse features, such as economic indicators and sector-specific data, will help capture broader market trends. Creating models that could forecast and manage large amounts of streaming data will improve practical usefulness, especially during financial crises.

V. AUTHOR'S CONTRIBUTION

Conceptualization: Pappula Praveen, Anjaneyulu Gudla.
Methodology: Pappula Praveen, Anjaneyulu Gudla.
Investigation: Pappula Praveen, Anjaneyulu Gudla.
Discussion of results: Pappula Praveen, Anjaneyulu Gudla.
Writing – Original Draft: Pappula Praveen, Anjaneyulu Gudla.
Writing – Review and Editing: Pappula Praveen, Anjaneyulu Gudla
Resources: Pappula Praveen, Anjaneyulu Gudla.
Supervision: Pappula Praveen, Anjaneyulu Gudla.
Approval of the final text: Pappula Praveen, Anjaneyulu Gudla.

VI. REFERENCES

[1] S. Wu, Y. Liu, Z. Zou, TH Weng,S_I_LSTM: stock price prediction based on multiple data sources and sentiment analysis. Connect. Sci.34(2022)44–62. https://doi.org/10.1080/09540091.2021.1940101

[2] C. Öztürk, A Deep Dive into Stock Forecasting: Insights from LSTM, GRU, GAN, and WGAN-GP, In: Proceedings of the V International Congress of Applied Statistics (UYIK-2024); 2024, pp 938-948.

[3] M. Vuletić,F.Prenzel, M Cucuringu, Fin-gan: forecasting and classifying financial time series via generative adversarial networks, Quant. Finance.24(2024)175–199. https://doi.org/10.1080/14697688.2023.2299466

[4] R. Shukla, N Poornima,Generating stock market data and making predictions using GAN and neural networks. 2023.https://doi.org/10.21203/rs.3.rs-2948055/v1

[5] Ma Y. Two models for predicting stock prices in combination with LSTM. Highlights Bus Econ Manag. 5(2023) 664–673.https://doi.org/10.54097/hbem.v5i.5256

[6] A Ghasemieh, R Kashef. An enhanced Wasserstein generative adversarial network with gramian angular fields for efficient stock market prediction during market crash periods. Appl Intell.53 (2023) 28479–28500. https://doi.org/10.1007/s10489-023-05016-2

[7] W. Liu ,Y Ge , Y Gu . Multi-factor stock price prediction based on gan-trellisnet. Knowl Inf Syst. (2024) 1–22. https://doi.org/10.1007/s10115-024-02085-8

[8] Wu JL, Tang XR, Hsu CH. A prediction model of stock market trading actions using generative adversarial network and piecewise linear representation approaches. Soft Comput. 27(2023)8209–8222. https://doi.org/10.1007/s00500-022-07716-2

[9] P. Sonkiya, V. Bajpai, A. Bansal, 2021.Stock price prediction using BERT and GAN. Quant. Fin. arXiv:2107.09055.https://doi.org/10.48550/arXiv.2107.09055

[10] B. He, E.Kita.The application of sequential generative adversarial networks for stock price prediction. Rev SocionetworkStrateg. 15(2021)455–470. https://doi.org/10.1007/s12626-021-00097-2

[11] Y Xu, Y Zhang,P Liu, Q Zhang,Y Zuo, GAN-enhanced nonlinear fusion model for stock price prediction., Int J ComputIntell Syst. 17(2024) 12. https://doi.org/10.1007/s44196-023-00394-4

[12] A. Kumar, A Alsadoon,PWC Prasad, S Abdullah, TA Rashid, DTH Pham, TQV Nguyen, Generative adversarial network (GAN) and enhanced root mean square error (ERMSE): deep learning for stock price movement prediction. Multimed Tools Appl. 81(2022)3995–4013. https://doi.org/10.1007/s11042-021-11670-w

[13] V. Deneshkumar, R. Jebitha,G. Jithu. Risk factor analysis of COVID-19 with CART model. 2023.https://doi.org/10.47974/JSMS-977

[14] PH Vuong,LH Phu,TH Van Nguyen, PH Vuong, LH Phu, THV Nquyen, LN Duy, PT Bao, TD Trinh, A bibliometric literature review of stock price forecasting: from statistical model to deep learning approach. Sci Prog. 107(2024)1. https://doi.org/10.1177/00368504241236557

[15] KS Kannan, V Parimyndhan. Forecasting the stock direction using ensemble random forest. Int J Math Oper Res. 28(2024)396–407. https://doi.org/10.1504/IJMOR.2024.140069

[16] M Maragoudakis,D. Serpanos. Exploiting financial news and social media opinions for stock market analysis using MCMC Bayesian inference. Comput Econ. 47(2016)589–622. https://doi.org/10.1007/s10614-015-9492-9

[17] RR Etukuru,Forecasting the Stock Prices Using Machine Learning, Deep Learning, and Reinforcement Learning [dissertation]: Northcentral University; 2023.https://www.proquest.com/openview/474a420cfa57eafd86f516eafba1161d/1?pq-origsite=gscholar&cbl=18750&diss=y

[18] MM Bejani, M Ghatee, A systematic review on overfitting control in shallow and deep neural networks. ArtifIntell Rev. 54(2021)6391–6438. https://doi.org/10.1007/s10462-021-09975-1

[19] J Kim, J Seol, TA Onisha, Y Ji. Hyperparameter Classification on Deep Learning Model for Cryptocurrency Price Prediction. In: Proceedings of the 2023 IEEE/ACIS 8th International Conference on Big Data, Cloud Computing, and Data Science (BCD); 2023;162–169.https://doi.org/10.1109/BCD57833.2023.10466319

Journal of Engineering and Technology for Industrial Applications

ISSN ONLINE: 2447-0228

ITEGAM-JETIA

Manaus, v.12 n.60, p.790-815, July/August, 2026.
DOI: https://doi.org/10.5935/jetia.v12i60.3948

RESEARCH ARTICLE OPEN ACCESS

DISSIMILAR METAL BONDING BY FRICTION STIR WELDING: MAGNESIUM TO STEEL JOINTS

Kapil B. Pipavat*[1], Hirenkumar I. Joshi[2], Ghanshyam D. Acharya[3]

[1]Research Scholar, Gujarat Technological University, Ahmedabad, India.
[2]Research Supervisor, Gujarat Technological University, Ahmedabad, India.
[3]Professor emeritus, Atmiya University, Rajkot, India.

[1]https://orcid.org/0000-0002-2757-531X, [2]https://orcid.org/0000-0001-7060-0536, [3]https://orcid.org/0000-0002-3580-3116

Email:*kapil.pipavat@gmail.com, - j_hiren@yahoo.com, gdacharya@rediffmail.com

ARTICLE INFO

Article History
Received: March 7, 2026
Reviewed: June 12, 2026
Accepted: July 12, 2026
Published: July 31, 2026

Keywords:
steel,
magnesium,
dissimilar welding,
process parameters,
friction stir welding

ABSTRACT

FSW - Friction stir welding has extended recognition as an effective non-fusion welding process for dissimilar materials, offering a solution to the limitations commonly encountered in conventional fusion welding techniques. This review paper focuses on the FSW of magnesium to steel, which has gained significant attention in different industries, like energy sector, aerospace, marine, automotive, etc. The paper presents an overview of the magnesium and steel materials, discusses the challenges and considerations specific to their dissimilar FSW, and provides insights into the mechanical characteristics, microstructural development, process parameters, and joint performance of the magnesium to steel welded joints. This paper highlights the current state of research, identifies knowledge gaps, and suggests future research directions. This information will be valuable for researchers, engineers, and practitioners involved in the development and application of dissimilar material joining techniques in various industries. The present review paper outlines FSW parameters including tool design, rotating speed, feed, tilt angle, pin offset, and the positioning of workpiece in a clamp for dissimilar FSW systems.

Copyright ©2026 by authors and Galileo Institute of Technology and Education of the Amazon (ITEGAM). This work is licensed under the Creative Commons Attribution International License (CC BY 4.0).

I. INTRODUCTION

It is a challenging task and a topic of interest for scientists, engineers, and researchers to find an effective and reliable weld joint of different material. Recently, there has been a lot of focus on lowering carbon dioxide emissions, and one effective way to combat this is to make cars lighter. Thus, it is desirable to employ light metals aggressively to address these environmental problems. However, in order to ensure their safety, all of the structures need to be strong enough. To satisfy these requirements, a dissimilar joint of strong and light metals is required [1]. Steels are utilised extensively for structural components because of their great absolute strength and good cost-effectiveness, while aluminium and magnesium are preferred light metals. Friction Stir Welding (FSW), as is widely known, is a helpful technique for creating a variety of dissimilar joints, and numerous studies have been published [1-11]. To achieve strong Mg–steel joints through fusion welding, coated steels or Cu/Ni interlayers are used as fillers. These promote beneficial interface structures and intermetallic compounds (IMCs), enhancing mechanical strength compared to conventional Mg–steel jointsb [12-22]. Manufacturing costs are raised by the use of coated steels and filler metals. Moreover, it is challenging to form strong magnesium–steel joints using traditional fusion welding because of their wide melting point differences (Fe: 1538 °C, Mg: 649 °C) and immiscibility in solid and liquid states. Weldability is further limited by the Mg–Fe binary system, which exhibits zero solubility of Mg in Fe and only 0.00041 at % solubility of Fe in Mg [4], [23-33]. Because of its environmental friendliness, energy economy, and adaptability, FSW is being used extensively [4], [16], [23], [34-35]. FSW joins similar and dissimilar materials such as Al, Mg, Cu, Pb, Zn, steel, and Ti without melting, for thicknesses of 1-50 mm. As a result, FSW avoids common fusion welding issues such as alloy segregation, wide heat-affected zones, residual stresses, weak joints, partial melting, hot cracking, porosity, oxidation, and slag inclusions [23], [35-41]. The UK's The Welding Institute (TWI) first introduced friction stir welding (FSW), a solid-state joining technique for aluminium alloys, in 1991 [11], [42-48]. Figure 1 presents the FSW setup in a butt joint configuration.

A non-consumable rotating tool is inserted at the plate edges and traversed along the joint line. The tool rotates anticlockwise, with its advancing side moving in the same direction as the traverse and the retreating side moving opposite [49-52].

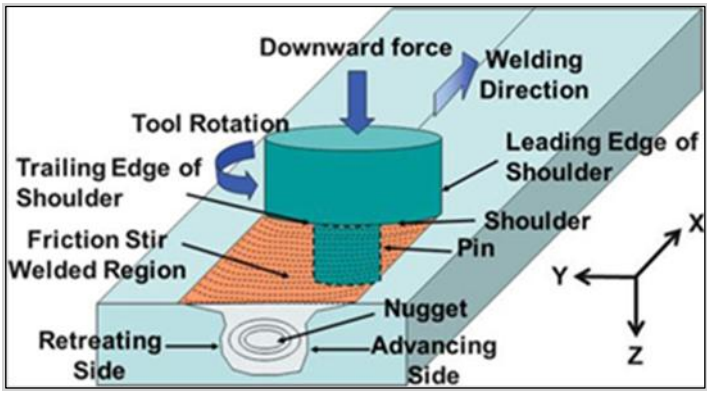


Figure 1: Illustration of friction stir welding in a butt joint configuration.
Source: [49].

Many industries, including aerospace, automotive, marine, railway, and construction, use friction stir welding [5], [49], [51]. The problems associated with joining of magnesium alloys must be resolved because of their increasing usage in industrial applications. Various Solid state welding and resistance welding methods like Friction Stir Welding [23], [53-66], Friction Stir Spot Welding [31], [67-74], Resistance spot Welding [69-77], Arc Spot Welding (ASW) [78], Resistance Element Welding (REW) [79], Resistance Rivet Welding (RRW) [80], Ultrasonic Spot Welding [12], [81-96], Ultrasonic Welding [91], Explosive Welding [92], Diffusion Bonding [93], fusion welding methods like Laser Welding [13], [97-104], Laser Welding–Brazing [99], [100-112], Laser-TIG [14-18], [21], [113-130], MIG – GMAW [125-129], MIG welding-brazing [130], TIG welding-brazing [131], TIG–MIG hybrid welding [132], Vacuum Electron Beam Welding [133], Cold Metal Transfer (CMT) [134-139], Cold Metal Transfer Spot (CMTS) [140], Diffusion-brazing [20], [141-147], Eutectic bonding [142], Impact welding - vaporizing foil actuator welding [143], Liquid Phase Bonding [144] Reactive transient liquid phase bonding [145], have been employed in the progress of magnesium to steel joints. The papers [35], [146-174]. This paper critically examines the current state of dissimilar material FSW, highlighting its challenges and opportunities. They extend a variety of alloy systems, such as different types of aluminium alloys [148], [150], [153], [175] aluminium/ magnesium [149], [176-178], and aluminium alloy/steel pairs [179-188]. It can be concluded from the literature that there hasn't been much work done to strengthen steel connecting in lap and butt configuration using FSW. So, this literature has been prepared to explore more about FSW of mg to steel.

II. MATERIALS AND METHODS

Several transportation industries are now more interested in using lightweight materials due to the need to reduce fuel consumption and component net weights [71], [189-199]. A nationwide survey indicated that cutting vehicle weight by 10% can improve fuel efficiency by about 5%. [195], [200-212]. A 100 kg weight loss in a car can lead to a 20 g/km drop in CO_2 [198]. Currently, steel makes up more than 50% of the weight of a typical automobile [199]. The average car uses 900 kg of steel, which is split up into 23% for the drive train, 12% for the suspension, 34% for the body construction, and 31% for the rest [200]. So, one easy way to make the car lighter is to use lighter materials for manufacturing instead of steel.

Table 1: Physical characteristics of steel, magnesium, and aluminium.

Metals	Fe	Al	Mg
Melting point °C	1536	660	650
Density (at 20 °C) (g/cm^3)	7.86	2.70	1.74
Tensile strength (MPa)	350	320	240
Modulus of elasticity (×10^6 MPa)	206.842	68.947	44.126
Thermal expansion coefficient (×10^6/°C)	11.7	23.6	25.5
Lattice structure	HCP	FCC	BCC

Source: [213-215].

The automotive industry makes extensive use of polymers, magnesium, and aluminium to address weight-related issues [15], [20], [201], [202]. Magnesium and its alloys are well-suited for automotive applications due to their low density, good ductility, high specific strength and stiffness, and superior damping capacity [15], [201-203], [209-214]. However, because to the high cost of magnesium alloys, more aluminium alloys have been used than magnesium alloys [210], [211] and are particularly susceptible to corrosion [212].The physical characteristics of magnesium, aluminium, and steel are listed in Table 1 [213], where it is evident that magnesium alloys can provide significant weight reductions when compared to steel and aluminium. Many industries, including shipbuilding, automotive, and aerospace, are interested in adopting hybrid constructions that produce desired weight savings because of the different properties of magnesium alloys [25], [27], [30], [109], [214].Although magnesium alloys are the lightest structural metals, they show potential as alternatives to steel in automotive applications where weight reduction is desired. It becomes challenging to join or weld two dissimilar metals that have distinct melting conditions, flow strengths, and no congruent melting phases. They are also immiscible in both solid and liquid states. Strong magnesium-steel bonding is therefore challenging.

In order to determine if it is feasible to establish mechanical interlocking or metallurgical bonding for structural applications, FSW has recently been investigated on magnesium to steel dissimilar joint in lap configuration. It is unlikely that IMC will happen between magnesium and steel when welding two different metals together. However, there have been reports of IMC happening between aluminium and steel or magnesium and zinc. These depend on the conditions of the welding, the coating on the steel, and the amount of aluminium in the magnesium alloy [59], [216-218]. In the butt joint setup, steel was placed on the advancing side (AS) and magnesium on the retreating side (RS) during FSW [57]. The rotating pin was put into the magnesium plate [56]. In the lap joint, the AZ31B sheet was placed above the steel sheet, with overlap width set by design requirements and its rolling direction oriented transverse to welding [26-28]. In butt configuration, the magnesium side was favoured by the tool pin offset from magnesium/steel interface [57]. The base materials selected for the lap configuration experiments [23], [26-28], [50], [53], [55], [58], [60] and butt configuration [59], [62], [65-66] with Mg and Steel sheets; the dimension, and thicknesses were summarised in Table 2.

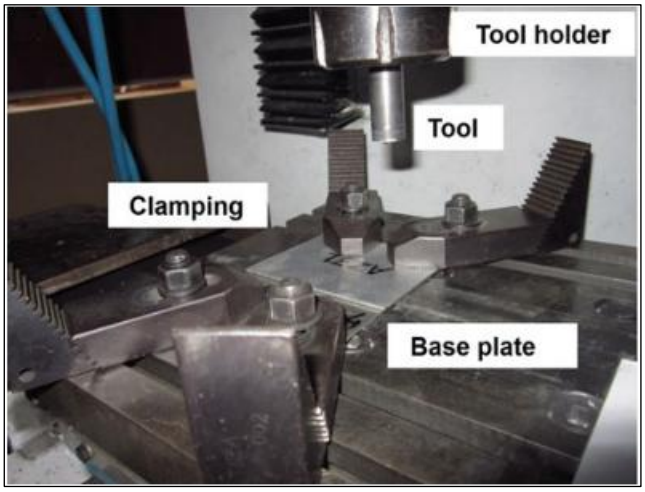


Figure 2: Schematic representation of a FSW setup.
Source: [60].

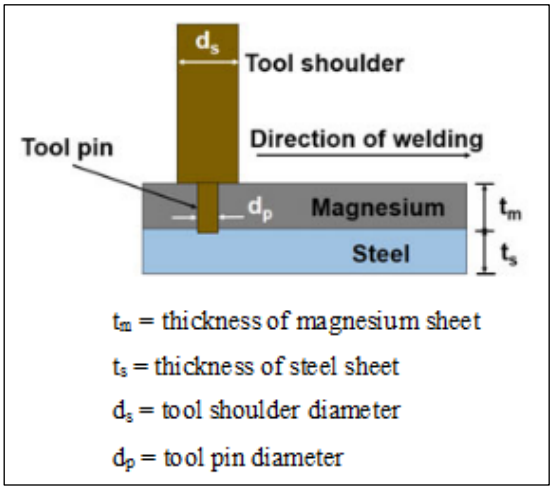


Figure 3: Representation of lap joint.
Source: [60].

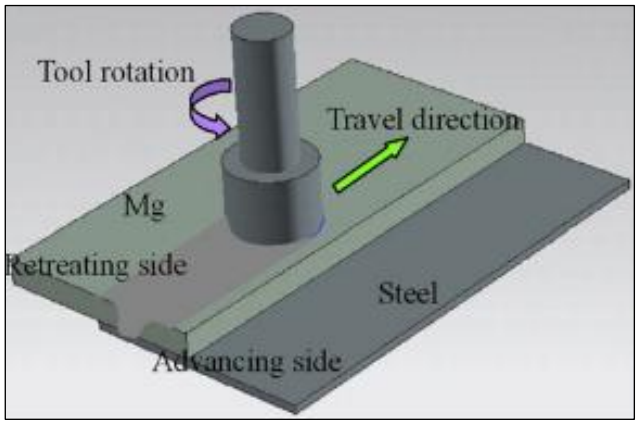


Figure 4: Experimental configuration: a friction stir lap welding process schematic.
Source: [50].

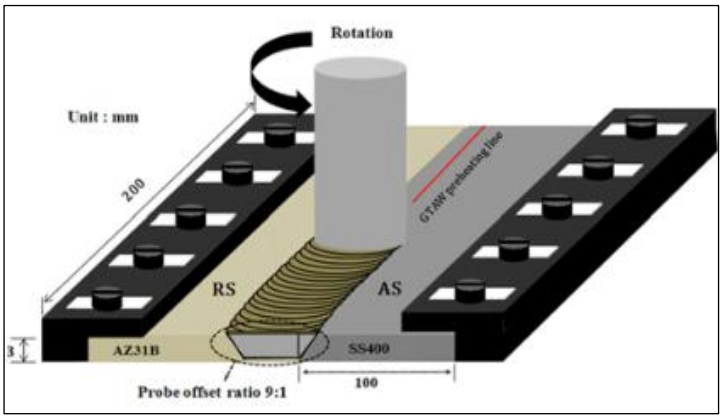


Figure 5: Schematic diagram of the HGTAFSW process.
Source: [54].

Figures 2 and 3 represent the precise welding configuration and arrangement [60]. Figure 4 illustrates the experimental configuration. As shown in Figure 4, the mg alloy has been compelled onto the steel in a lap pattern. As seen in Figure 5, the mild steel (MS) plate surface had previously GTAW preheated at a 60° angle adjacent to the intersection. This procedure guarantees improved material flow during welding and less tool wear. An anticlockwise (CCW) rotating tool was used to perform the welding operation. Positioning magnesium on the RS and mild steel on the AS produced higher joint strength compared to using a clockwise (CW) tool rotation. With tool rotation aligned to the welding direction, this configuration intensified stirring in the MS on the advancing side [54]. A high-stiffness, precision FSW machine was used to perform the welding in position-controlled mode [53].

III. FSW TOOL

In FSW, the tool plays a vital role. It generates heat and softens the workpiece to form a solid-state joint by transporting material around the pin. The tool's material and geometry are the two key factors governing its performance [11], [43-44], [46-48], [219]220]. In FSW, a non-consumable tool with a shoulder and pin generates heat, softens the workpiece, and directs material flow, thereby influencing joint formation, weld quality, mechanical properties, and process speed. [44][220-223].Tool design is the most critical factor in advancing the FSW process. A general process development flow chart is shown in Figure 6. Reliable welds require the removal of all welding flaws, including voids and insufficient root penetration.

Despite the fact that the knowledge has mostly been empirical, appropriate tool material and tool geometry can be determined for a given joint (types of w/p material, thickness, and joint design). It is easy to achieve good metallurgical bonding between workpieces for similar material FSW. FSW of different materials is even harder when their melting or thermal properties and physical or chemical properties are very different. Weldability and tool life are affected when different workpieces are positioned on the AS or RS side in butt welding and lower or upper sheet in for lap welding, and the rotating tool is plunged to a specific location in relation to the joint interface. An optimized tool design helps suppress liquid film formation and limits brittle IMC generation when dissimilar materials exhibit strong chemical affinity at elevated temperatures. This facilitates the formation of eutectic structures at low melting temperatures and speeds up the growth of IMCs. Recent studies on FSW of dissimilar materials have largely focused on joining aluminum alloys with both low- and high-melting-point materials to evaluate joint structural performance. Several studies have also examined dissimilar FSW of high-melting-point materials, including steels and titanium alloys. For dissimilar FSW, the next sections mostly address tooling materials and tool shape design [216].

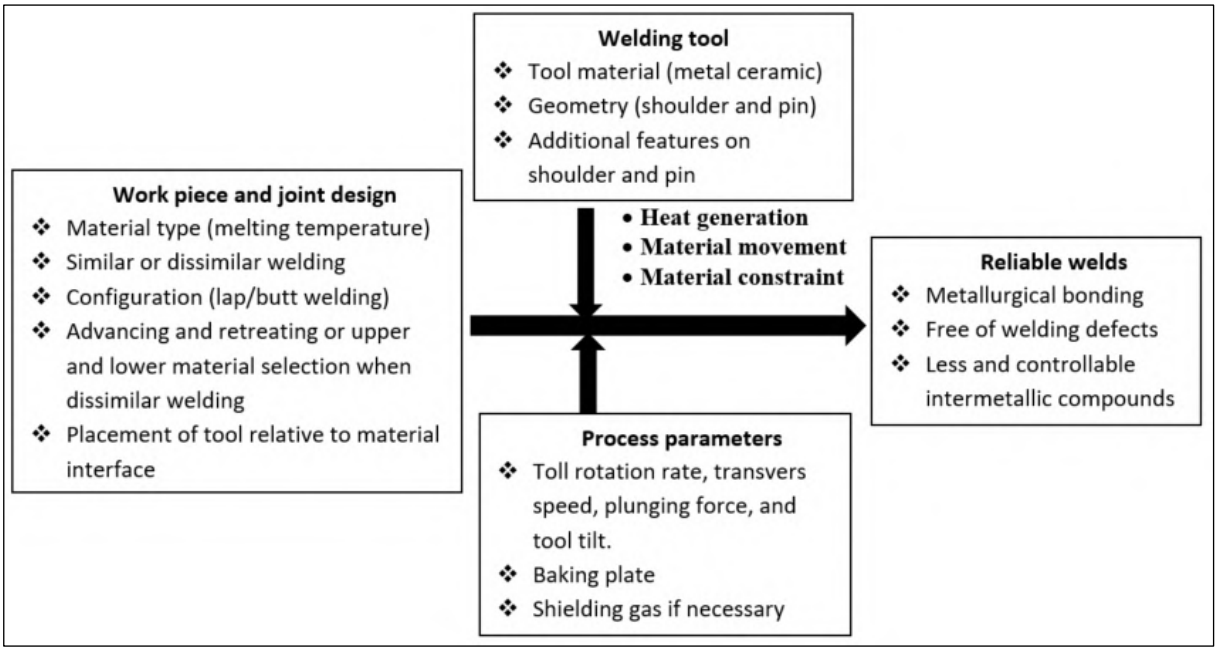


Figure 6: A typical flow chart for the development of the FSW process.
Source: [49].

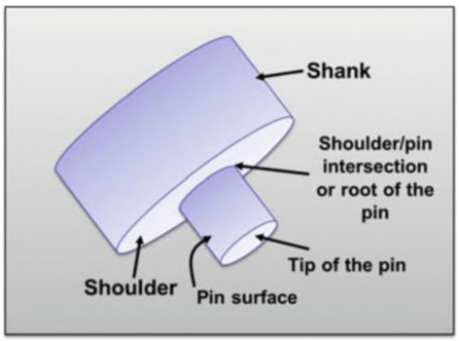


Figure 7: A friction stir welding tool.
Source: [49].

Figure 7 clearly illustrates the various features of the tool [49]. Table 2 summarizes the recommended FSW tool parameters, including tool material, shoulder profile, shoulder diameter, pin diameter, pin profile, pin length, shoulder-to-pin ratio, pin bottom diameter, and tip diameter.

III.1 TOOL MATERIAL

The right tool material must be used for the intended application in order to produce a satisfactory FSW joint. The need for welding materials like titanium, steel, and metal matrix composites has created new difficulties. An effective FSW tool must retain dimensional stability without failure or property loss during welding. The tool material should exhibit six key traits: strength at both room and process temperatures, high fatigue life, fracture toughness, wear resistance, thermal endurance, and chemical stability [49], [221]. Researchers have achieved FSW of steel to Mg alloys using H13 tool steel for the shaft and W-Re alloys for the pin [28]. Common tool materials include quenched and tempered steels, PCBN, and SKD61. For dissimilar FSW of steel to Mg, SKD61 and WC are often preferred; however, the high rotational speeds and intense forging action between steel and magnesium cause rapid tool wear and degradation. Therefore, careful selection of tool material, tool design, and process parameters is essential, as wear resistance and thermal stability limitations at high speeds remain the primary factors reducing tool life [24], [61], [223-226].

III.2 TOOL DESIGN AND GEOMETRY

FSW tool geometry strongly influences weld integrity, material flow, thermal input, and defect control. The tool has two main parts: the shoulder, which creates frictional heat and confines softened material, and the pin, which stirs and promotes mixing and recrystallization in the weld zone. Together, these factors affect flow behavior, heat distribution, force, torque, and defect prevention. A schematic of the tool is provided in Figure 8. [60]. Material flow behavior is primarily governed by the dimensions of the tool shoulder and probe. Thus, the tool profile is considered a critical factor in the FSW joining process [226], [227]. In figure 9, the stir pin was a WC rotary burr 6 mm dia. and on the cylindrical surface and 15 spiral cutting edges. The welding tool, PL=2.9, SD=25, was constructed by inserting the rotary burrs into an H13 steel holder. A penetration depth of tool 3.2 mm was applied for FSLW [50].



Figure 8: Schematic of FSW tool
Source: [60].

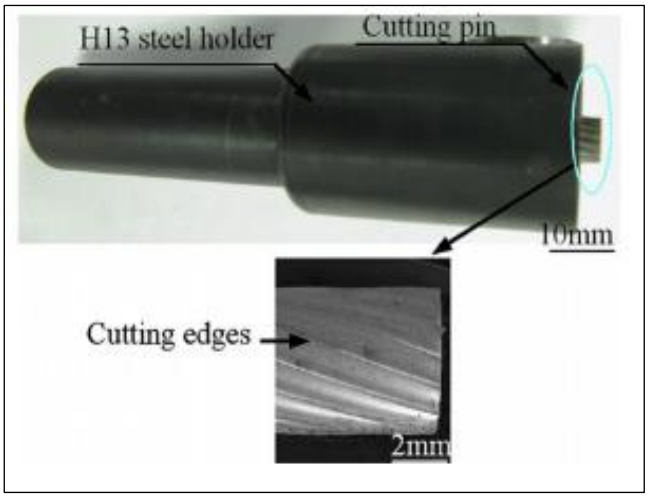


Figure 9: Appearances of the FSW tool with the design of the cutting pin.
Source: [50].

III.3 TOOL SHOULDER

The tool shoulder generates frictional heat in the surface and subsurface regions of the workpiece. In thin-sheet welding, it contributes most of the deformation and heat input [221]. In FSW, the shoulder diameter is the primary contributor to heat generation, with nearly 87% of the total heat produced through friction between the shoulder surface and the workpiece. Tool shoulder diameter and geometry surface characteristics have an impact on the FSW weld quality as they increase heat generation. Selecting the appropriate shoulder diameter is critical for producing high-quality FSW joints [48], [219], [220]. Early tool designs often used a shoulder-to-pin diameter ratio of 4:1. More recently, this ratio has been reduced to 3:1 or even 2:1 to better control heat input.

III.4 TOOL PROBES (PIN)

The tool probe generates both frictional and deformational heat. It shears material at the front, transports it to the rear, and influences the contact surfaces of the joint. The probe governs deformation depth and welding speed, while its geometry affects plasticized material flow and weld quality. Common probe designs include threadless, whorl, MX-triflute, truncated cone, triflute, trivex, and cylindrical types [44], [48], [221]. The ratio of shoulder to pin diameter (SPR) depends on the thickness of the workpiece. In dissimilar FSW, the SPR is generally higher than in similar joints, particularly for steel–magnesium alloys, where values are much greater than those for steel–steel or magnesium–magnesium welds. This is attributed to the higher hardness and lower thermal conductivity of steel compared to other materials of similar strength. Consequently, many researchers have adopted SPR values in the 4:1–10:1 range for steel–Mg dissimilar welding [228].

IV. FSW PROCESS PARAMETERS

The essential parameters of FSW are tool speed, welding speed, axial force, tilt angle, and pin offset. In addition to the criteria used for similar material systems, dissimilar FSW is further influenced by tool pin offset and the placement of base materials in the fixture [219]. Table 2 summarizes the recommended FSW tool parameters, including rotational speed, welding speed, tilt angle, plunge depth, plunge force, tool pin offset.

IV.1 ROTATIONAL SPEED

Rotational speed, defined as the revolution rate of the tool about its axis, is a key parameter influencing weld quality [229]. It accounts for nearly 40–50% of the overall effect in dissimilar FSW [44]. Higher speeds enhance the joint contact area and thermal input [30]. In dissimilar welding, tool rotation governs (i) plastic deformation through frictional heating and (ii) the plunge force, which impacts material flow, defect formation, stir zone (SZ) size, joint integrity, and tool wear. Conversely, insufficient rotation generates low heat and poor mixing, particularly in steel–Mg welds, making speed optimization essential [184], [224], [228], [229].

IV.2 WELDING SPEED OR TRAVEL SPEED

Welding or travel speed refers to the forward movement of the tool along the joint line. This parameter greatly affects the weld quality and microstructure in steel–Mg FSW, making its selection complex [230-232]. Alterations in travel rate often produce uncertain effects on joint properties [233]. Therefore, considerations such as joint configuration (butt or lap), tool rotation, plunge depth, and base material are crucial when determining the appropriate speed [228], [234-236].

IV.3 TOOL PIN OFFSET OR TOOL ECCENTRICITY

Tool pin offset is a critical parameter in dissimilar steel–Mg FSW. It refers to the displacement of the tool toward one of the base materials. In conventional (similar-material) welding, the pin is aligned at the joint center; however, applying this approach to dissimilar systems often leads to defective joints [59], [61], [69], [217], [237-242]. The distinct mechanical, chemical, and thermal characteristics of steel and magnesium-such as melting point and recrystallization temperature make zero offset unsuitable, as it results in inadequate plastic flow and bonding [59], [228], [242-244]. Research shows that shifting the pin toward the softer or lower-conductivity Figure 10 (a) illustrates a central pin position (0 mm offset), while Figure 10 (b) shows a displacement of h mm toward the Mg side. With no offset, heat and deformation are insufficient due to property mismatches. Moving the tool toward magnesium increases heat generation on that side, while the steel side retains less due to its higher thermal expansion coefficient, promoting balanced stress distribution [219].

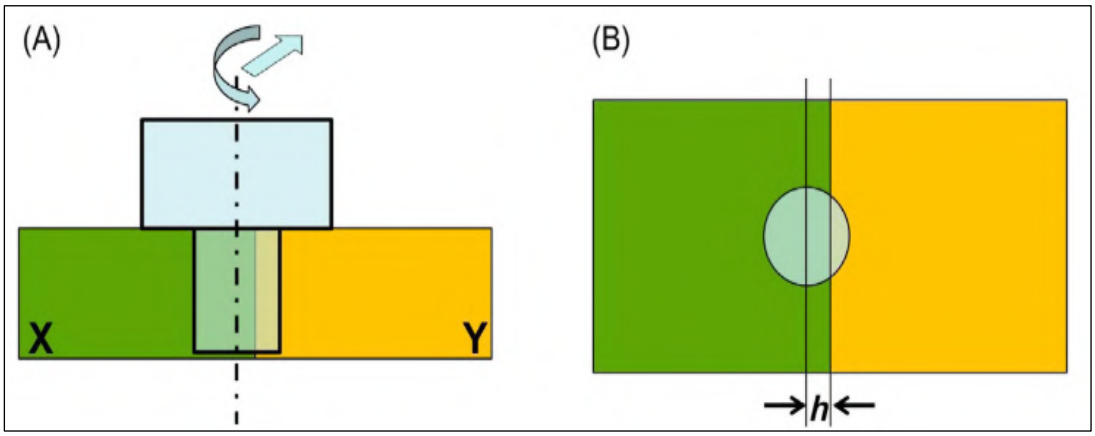


Figure 10: Tool pin offset concept (A) TPO 0 mm (B) TPO h mm w.r.t, weld centreline.
Source: [216], [219].

IV.4 TOOL TILT ANGLE

The tilt angle refers to the inclination of the FSW tool (e.g., 0°, 1°, 2°, or perpendicular to the workpiece surface) [219]. This parameter is critical for producing defect-free welds [245-248]. An optimized tilt angle provides two key benefits: (i) it confines the forged material beneath the tool shoulder with assistance from the pin [44]; and (ii) it enhances stirring, enabling uniform flow from front to rear and top to bottom, thereby ensuring proper mixing and joint quality [44], [228], [246].

V. MICROSTRUCTURES AND INTERMETALLIC COMPOUNDS

In FSW joints, the microstructure describes the grain arrangement, phase distribution, and defects observed at the microscopic scale. These features vary across weld zones as a result of heat input, plastic flow, and dynamic recrystallization. At the interface of dissimilar materials, diffusion and chemical reactions can lead to the formation of intermetallic compounds (IMCs), which significantly influence joint behavior. These compounds typically exhibit ordered atomic structures and possess properties that are distinct from those of the parent metals. Fractured surfaces from tensile specimens can be characterized using several analytical methods. Following ASTM E3-11 (2017), samples were prepared through sequential polishing with 220–2000 grit emery papers and diamond finishing to enable observation of microstructural changes induced by welding [249]. The polished samples were microetched in accordance with ASTM E407-07 [250] [251]. Metallographic characterization was performed using optical microscopy (OM), scanning electron microscopy (SEM), and transmission electron microscopy (TEM) coupled with energy-dispersive X-ray spectroscopy (EDS) [23], [50], [53-59], [251]. Post-tensile test fracture surfaces were further examined by X-ray diffraction (XRD) [55], [58], [251]. All interfaces showed bending, with dispersed steel fragments embedded in the magnesium. The probe action generated a fresh surface on the steel plate. Microstructural analysis revealed that iron was absent on the Mg side regardless of IMC thickness, while an Fe–Al intermetallic layer formed at the interface when Mg contained Al, and Mg was identified on the steel side. Thus, formation of the Fe–Al IMC layer occurs through new surface generation on the steel plate, requiring direct probe contact with the steel butt face [59].

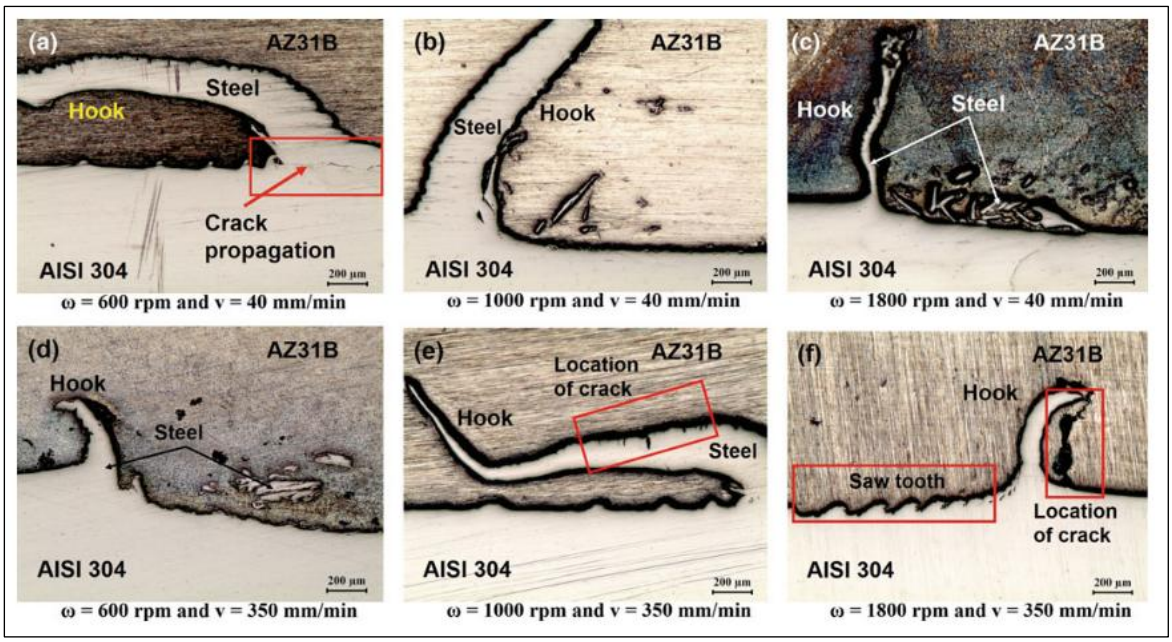


Figure 11: Optical micrographs for different ω and υ.
Source: [59].

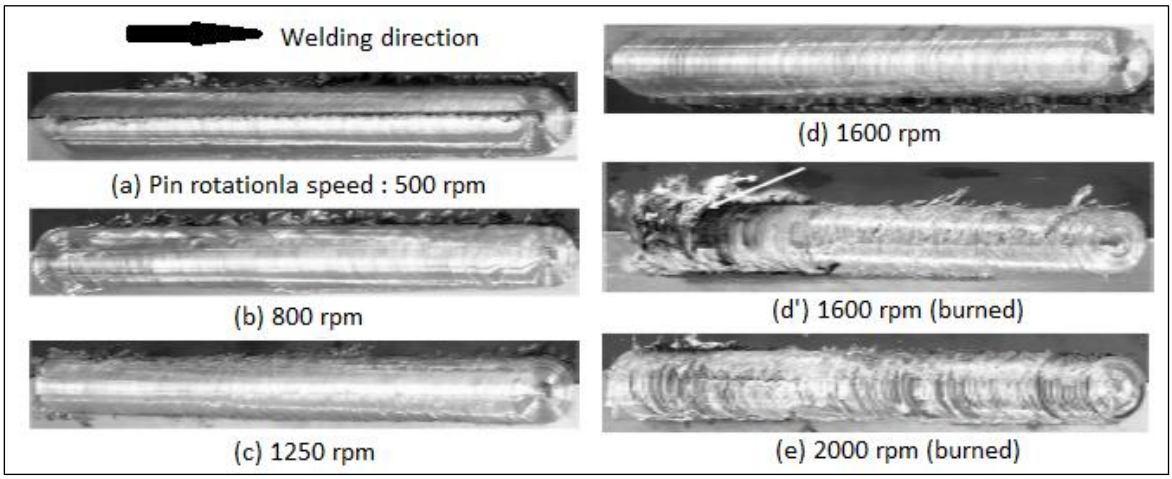


Figure 12: Effects of pin rotating speed on the surface view.
Source: [56].

Figure 12 presents weld surface features and cross-sectional morphologies. At 500 rpm, a groove-like defect appeared along the weld line due to insufficient plasticization of Mg caused by low heat input, precluding tensile evaluation. Conversely, at 2000 rpm, excessive heat led to severe ignition, producing a major root defect and resulting in very low tensile strength [56]. As indicated by the arrow in Figure 12(d′), magnesium ignition frequently occurred at a rotation speed of 1600 rpm, where the weld temperature approached its ignition limit. At 1250 rpm, the joint showed reduced tensile strength compared to 1600 rpm, with defects appearing near the root region [60]. At 800 rpm, inadequate plastic flow of magnesium produced flaws within the Mg zone, while fracture consistently propagated along the Fe–Mg interface. Alongside regions where Mg bonded to the Fe surface, flat zones were also observed (indicated by the arrow) where Mg failed to adhere. These unbonded regions are likely responsible for the reduced joint efficiency of about 70% [56]. The HGTAFS weld nugget showed a fully bonded structure without unjoined regions at the joint bottom, unlike FS welds, due to a composite of scattered mild steel fragments and recrystallized Mg grains. In the HAZ and TMAZ, Mg grains were slightly coarser in assisted FS because GTAW preheating provided additional gradual heating. Recrystallized grains in the stir zone resulted from intense plastic deformation. The steel nugget displayed finer grains at the top than the bottom, suggesting upper-section hardening from the combined influence of the rotating tool shoulder and GTAW preheating [54]. Section views of a group weld produced by FSLW at various travel speeds are displayed in Figure 13. The macrostructure characteristics of the connecting interfaces differ greatly from those of other typical FSLW (the pin without cutting the bottom metal) [252]. The steel surface layer was broken up into metal fragments and flashes by the stirring pin, which then transferred them into the magnesium base. It's possible that the pin rotation created the flower-like flashes. Figure 13.a illustrates these phenomena in vivid detail. The smooth joining interface with a few lengthy flashes remained after the scraps dropped and were destroyed as the transit speed increased. The evolution of the joining interface's macro-morphology could be attributed to the decreased friction heat input [253].

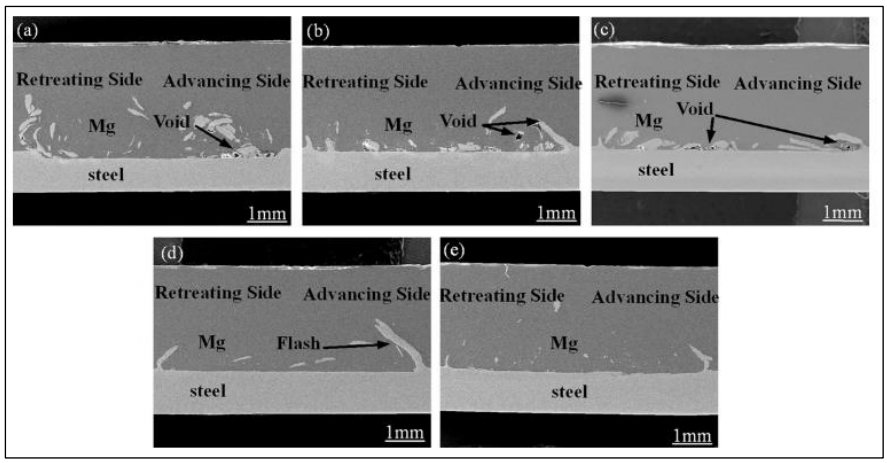


Figure 13: Interfacial macro-morphology by FSLW at welding speeds of (a) 60 mm/min, (b) 118 mm/min, (c) 150 mm/min, (d) 190 mm/min, and (e) 300 mm/min.
Source: [50].

As seen in Figure 13.e, the flashes decreased with increasing travel speed. The thinned flashes are easier for the stirring pin to cut away from the interface because less metal has been softened by friction heating at high travel speed. As shown in Figure 13.a–c, voids were discovered near the interface; however, as seen in Figure 13.d and e, they vanished when the transit speed was increased. Due to the oncoming filler metal's inadequate extrusion force at low travel speed, voids tend to form at the advancing side, as one may have observed. This phenomenon is somewhat analogous to the production of voids in FSW joints [254]. However, the joining strength may be somewhat enhanced by the decreased voids at high travel speeds [50]. As the probe length increased, the microstructure at the joining interface changed dramatically [58].

VI. MECHANICAL PROPERTIES OF DISSIMILAR MG-STEEL FSW SYSTEM

The mechanical behavior of Mg–steel dissimilar FSW joints differs markedly from similar-material welds due to the unequal properties of the base metals.Summary of recommended remarkable properties of joint welded by FSW systems, like IMCs, UTS, YS, TS, JE, Elongation, etc. shown in Table 2. Studies show that the ultimate tensile strength (UTS) of Mg–steel dissimilar FSW joints is typically lower than that of the base metals, indicating reduced efficiency compared with the weaker alloy. The UTS depends on IMC formation and joint microstructure, both of which are strongly affected by FSW process parameters. The majority of defects are caused by incorrect material flow between the steel matrix and magnesium particles, which is caused by non-optimized process parameters, and its lowers the UTS. Conversely, a reinforcing action that enhances the joint's ultimate tensile strength is conferred by small steel particles exhibiting suitable material flow inside the magnesium matrix. Thus, in order to achieve a greater UTS, the size of the steel particles is crucial. Furthermore, grain refining is strengthened by the vigorous stirring motion, which also raises the UTS. Owing to the inhomogeneous microstructure and unavoidable IMCs, these strengthening effects are insufficient to achieve a UTS greater than that of the base metals. The inherent characteristics of IMCs lower joint ductility within the stir zone, thereby reducing yield strength and fracture-to-elongation ratios [219]. Many studies employ fractography to examine the reduced fracture-to-elongation ratio, often linked to brittle fracture or finely recrystallized grains. Broken tensile specimens with flat surfaces and cracks demonstrate a mixed fracture mechanism characterised by both brittle and ductile patterns. Since a tensile specimen typically fractures in the TMAZ zone. Due to the existence of IMCs in these regions, TMAZ of the Cu side is thought to be responsible for brittle fracture [219], [247], [255], [256]. Future studies may focus on improving the tensile characteristics of dissimilar Cu–Al FSW [219].

VI.1 TENSILE STRENGTH

A UTM machine was used to test the tensile specimens. As shown in Figure 14, the AZ31B magnesium alloy was fixed in the driven crosshead to evaluate specimens under advancing side (AS) loading. Specimen dimensions followed ASTM E8M-04 standards, as illustrated in Figure 15 [54]. For testing, samples were prepared with the tensile axis oriented perpendicular to the weld line [59].

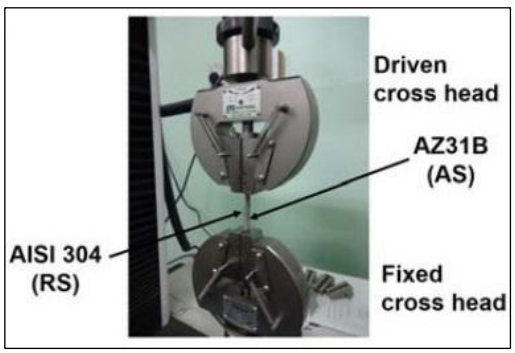


Figure 14: Tensile testing set-up.
Source: [60].

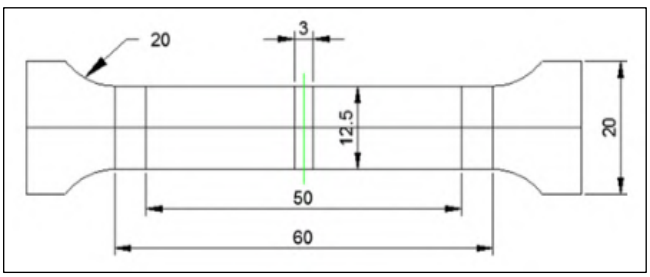


Figure 15: Geometry of the tensile test specimens.
Source: [54].

.

Figures 16 and 17 illustrate the relationship between RS (ω rpm) and TS (MPa), as well as WS (υ mm/min) and TS (MPa), respectively. The TS of the joint diminishes as RS increases, while it consistently rises with an increase in WS. A maximum joint strength of 198.75 MPa, about 79% of the Mg base alloy was achieved at 600 rpm and 350 mm/min. All tensile samples fractured in the transition zone between the advancing side (AS) and the stir zone [60]. Joint strength is adversely affected by increased heat input and reduced cooling rates. The microstructure gets coarser with high heat input, which makes dislocation movement easier. Weld strength gradually decreased [60].

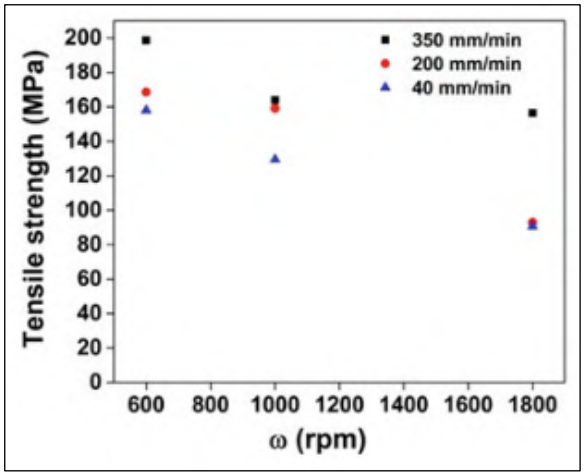


Figure 16: Tensile strength for different ω.
Source: [60].

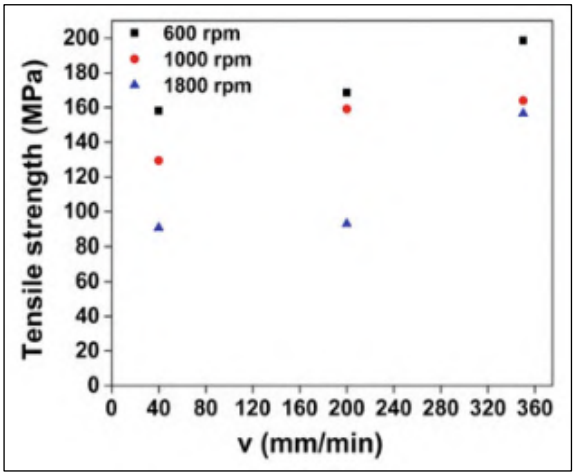


Figure 17: Tensile strength for different υ.
Source: [60].

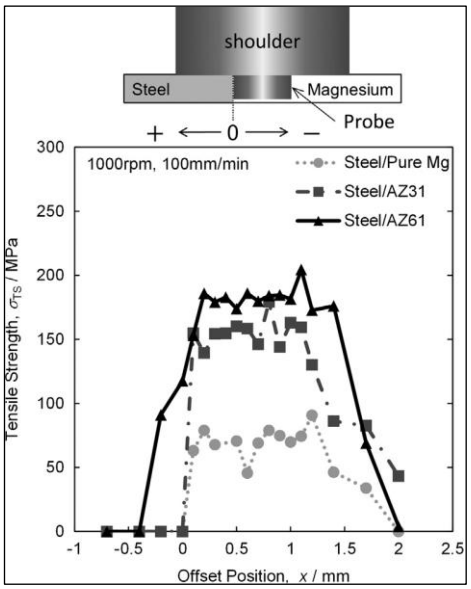


Figure 18: Relationship between joint tensile strength and tool pin offset position.
Source: [59].

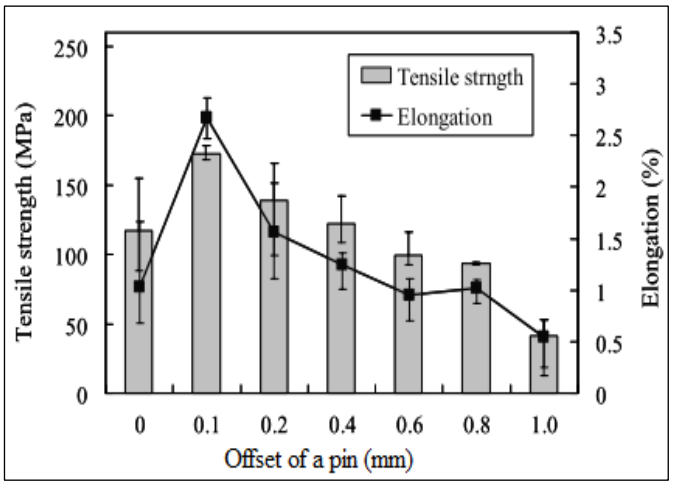


Figure 19: Relation between tensile strength, pin offset and elongation of joint.
Source: [56].

Figure 18 illustrates the correlation between tool offset position and TS at speed 1000 rpm and feed 100 mm/min. The joint between steel and various magnesium alloys, with an offset of +0.1 to +1.1 mm, demonstrated optimal high tensile strength. Numerous voids were present in the SZ when offset was excessively big in the direction of the steel-AS. In contrast, an intermetallic compound layer cannot develop when the offset position is negative (towards mg-RS). Thus, to achieve a suitable IMC layer and ensure bonding between steel and magnesium, the tool probe must contact the steel butt face [59]. Joint strength and elongation were investigated in relation to different pin offsets towards the Fe faying surface. Figure 19 shows the effect of tool pin offset on tensile strength and elongation at a welding speed of 100 mm/min and a rotation speed of 1250 rpm, with offsets between -0.2 mm and 1.0 mm. Maximum strength and elongation were achieved at a 0.1 mm offset, whereas tensile performance declined as the offset increased. At 0 mm offset strength was low, likely due to inadequate removal of the oxide film on the Fe surface. In all cases, fracture occurred along the Mg–Fe interface. Between 0.2 and 0.8 mm offsets, UTS was reduced because cracks initiated at the interface between Fe fragments dispersed in the Mg matrix and the surrounding Mg, compared with the 0.1 mm offset. At 1.0 mm, tool wear occurred, resulting in poor joint strength with bonding limited to the upper region [56]. For pure mg, and its alloy AZ31, and AZ61 plates, the average tensile strength is 170, 260, and 280 MPa, respectively. As the mg alloy's Al content increased, the joint strength increased because Al was being depleted at the mg side close to the interface. UTS of the steel/mg joint was substantially associated with the Al depletion on the mg side close to the joint edge. Under the optimal FSW conditions, the steel to mg joint failed on the mg side close to the joint interface. The improved TS resulted from the FSW's low heat input, which prevented Al depletion [59].

Figure 20 illustrates the relationship between RS, elongation, and joint TS. The fracture happens at the joint interface, and the maximum TS of a joint was approximately 70% of that of mg base metal. When the pin rotated slowly, the magnesium matrix of the joint developed a number of defects due to inadequate plasticization of the mg. Joint strength increased with pin rotation. As the mg plasticised, pushing it into an active steel surface produced pressure. However, excessive pin rotation speed caused magnesium to burn, reducing joint strength [56].

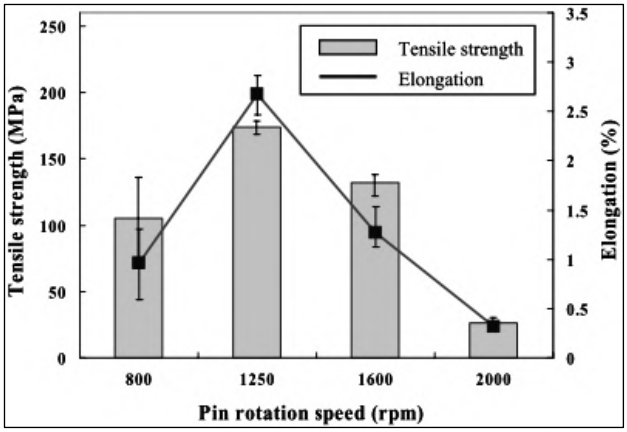


Figure 20: Relationship between TS, speed, elongation.
Source: [56].

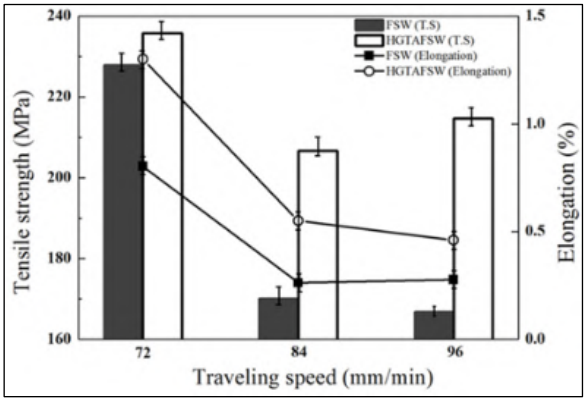


Figure 21: TS of the FSW and HGTAFSW welds.
Source: [54].

Figure 21 shows the effect of travel speed (72–96 mm/min) on the tensile strength (TS) of FSW and HGTAFSW joints. At the same speeds, HGTAFSW achieved higher TS than FSW, reaching a maximum of 237 MPa (~91% of Mg base metal) at 72 mm/min, compared with 226 MPa (~86%) for FSW. FS welds weakened with increasing speed, while HGTAFSW displayed a fluctuating trend. In FS welds, cracks often initiated at the lower joint region and propagated along the Mg–steel interface, whereas in HGTAFSW, fracture followed a similar path but with better elongation due to improved material flow and partial annealing. These findings highlight the role of steel-side preheating in enhancing joint strength [54]. Tensile properties of AZ31-SS316 and WE43-SS316 dissimilar welds were compared with their base metals, showing no significant difference between the two systems. The joints exhibited a UTS of ~160 MPa, about 73% of the Mg alloys. In both cases, fracture occurred at the weld interface due to the mismatch in elastic modulus between steel and Mg, leading to stress concentration. The presence of intermetallic compounds slightly reduced joint strength. Thermodynamic and kinetic simulations further suggested anomalous Al diffusion into Mn-Mo rich particles within SS316 during butt-welding of AZ31 and stainless steel 316 [57]. Steel and magnesium alloy are mechanically bonded together, with the bonding land only falling within the probe diameter's domain. As a result, brushed finish steel joints don't show much of failure load. AZ31–zinc-coated steel joints exhibited higher failure loads than AZ31–brushed steel joints, indicating that the zinc layer enhanced Mg–steel weldability.

A fresh metal surface was exposed as a result of the low melting eutectic phase's emergence and extrusion at the interface, increasing the mutual diffusion between steel and magnesium alloy [23]. As welding speed increases, the fracture strength (as illustrated in Figure 22) rises, and samples coated with zinc have a higher fracture strength than samples without coating. The true fracture strength of the steel–magnesium interface is greater than the measured values since all specimens fractured within the stir zone. During welding, the zinc coating on steel forms a liquid eutectic layer and acts as a flux, enhancing surface reactivity [28]. Figure 23 shows the effect of probe length on tensile strength and fracture location in AZ31–steel lap joints. Tensile testing revealed that probe length strongly influences joint properties under identical welding conditions. In zinc-coated steel joints, void defects in the stir zone limited the benefits of longer probes, while short probes produced defect-free, high-strength joints. For brushed finish steel, increasing probe length significantly improved failure loads. Similar tensile strengths for both zinc-coated cases indicated that probe extension had little effect. With a 1.5 mm probe, steel and Mg were mechanically bonded, whereas a 1.8 mm probe penetrated the steel underside, enabling stirring to create a new steel–Mg interface and promote thin diffusion bonding [58].

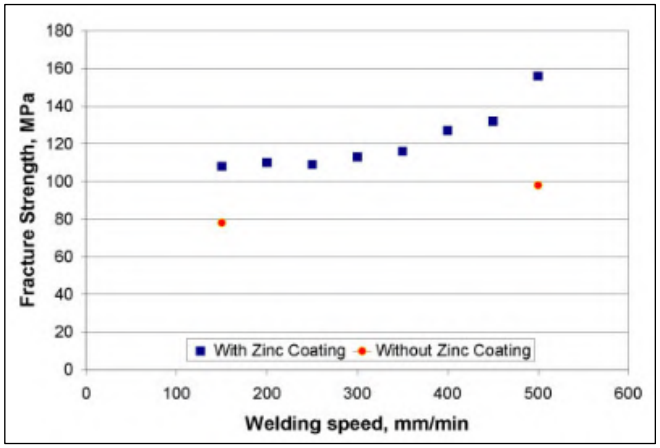


Figure 22: Influence of welding speed on fracture strength.
Source: [28].

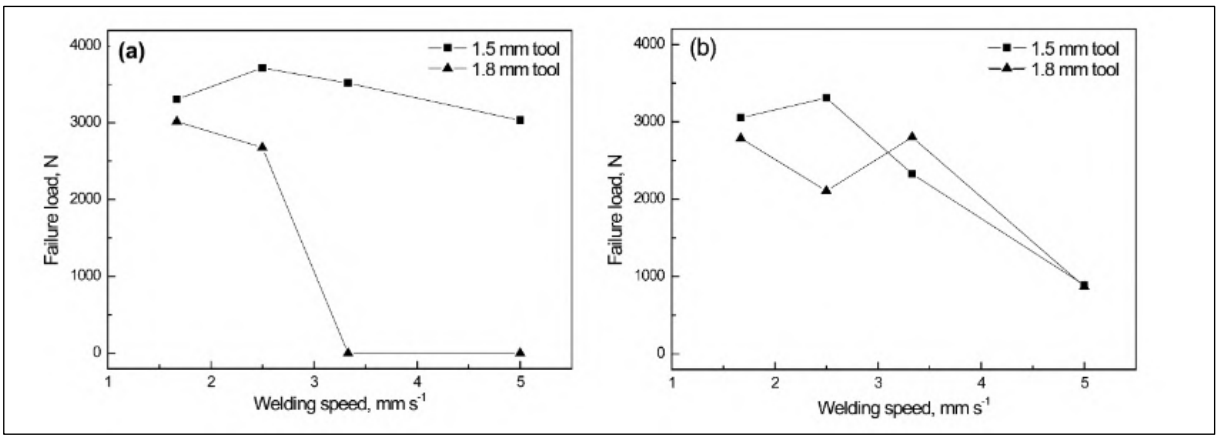


Figure 23: Effect of tool design on tensile strength: (a) brushed finish steel joints; (b) zinc-coated steel joints.
Source: [58].

Because of the intrinsic strength differential, joints manufactured of HSLA steel (1.5 mm) have a much higher failure load than joints made of MS (0.8 mm). Nevertheless, MS (0.8 mm) weld specimens sustained a significant amount of elongation before failure. All four lap shear specimens failed through interfacial separation between the top and bottom sheets. The principal mode of failure was determined as the fracture of the top magnesium layer. When tensile specimens are examined transversely, the percentage of elongation to failure decreases noticeably. Nonetheless, the percent elongation to failure is improved for the tensile specimens. In transverse tensile specimens, a reduction in yield strength and elongation indicates a compromised region within the weld cross-section. The research indicates that the weaker region is located on the advancing side [26].

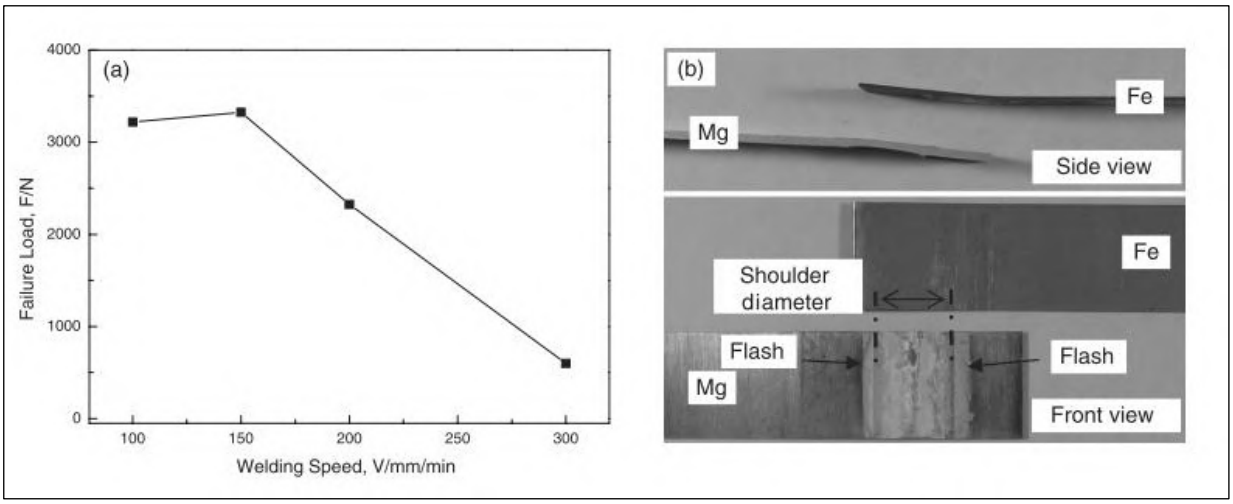


Figure 24: (a) welding speed to failure loads, and (b) fracture location.
Source: [55].

Figure 24 shows joint failure loads and fracture sites. At a WS 150 mm/min, the maximum failure load was 3.4 kN, which is about 65% of the zinc-coated steel base material. Increasing welding speed lowered the load, confirming that proper parameters are essential for strong Mg–steel lap welds. All fractures occurred at the interface, as seen in Figure 24(b). The bonded region extended beyond the probe and shoulder diameters, with solidified flash at its edges, but its width decreased sharply with higher welding speeds [55]. In friction stir welding, heat input is inversely related to travel speed and directly related to tool rotation. Thus, at constant rotation, heat input decreases as welding speed rises. Insufficient heat during higher travel rates reduces joint strength by limiting interaction between the magnesium alloy and zinc-coated steel. In contrast, excessive heat at lower speeds produces a thick reaction layer, diminishing mechanical performance. The zinc coating promotes eutectic formation at the Mg–Zn interface due to its low melting point [55].

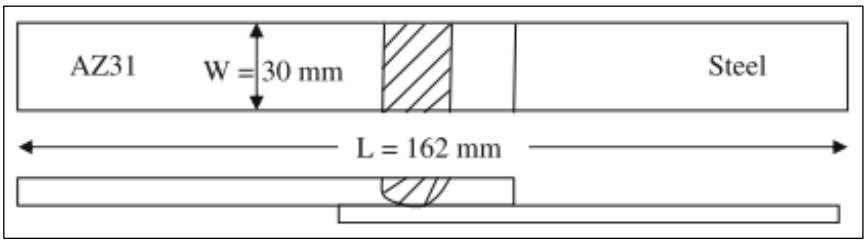


Figure 25: An illustration of the lap shear specimen.
Source: [27].

Figure 25 shows the lap shear specimen schematic. Average joint strengths were 5.1 ± 1.5 kN for AZ31 (0.8 mm) EG steel and 6.3 ± 1.0 kN for AZ31 (1.5 mm) HDG steel, with unguided lap shear tests showing peak loads of ~6 kN. FSW joints reached up to 80% of base metal strength, particularly in thinner 0.8 mm steel welds. Both failed by interfacial separation. Under the tool tip, the Mg/steel bond contained few Zn–Mg phases. Heat from welding melted the Zn layer, dissolving Mg and creating a Zn–Mg alloy, but much of this liquid was expelled, leaving a hardened layer without strong bonding. Thus, the thin Zn coating was ineffective as a brazing medium [27]. To guarantee that the complete shear force is applied to the joining contact, two notches were meticulously cut from the welded steel and mg, and the sample was sectioned parallel to the weld line, as shown in figure 26 [50]. Figure 27 illustrates the variation of tensile shear strength with travel speed. Strength increased with speed, peaking at 96.3 MPa at 190 mm/min, after which it declined. A dashed line marks the 88 MPa strength of an AZ31B FSW butt joint, while a horizontal line represents the 144 MPa shear strength of the AZ31 base metal [50].

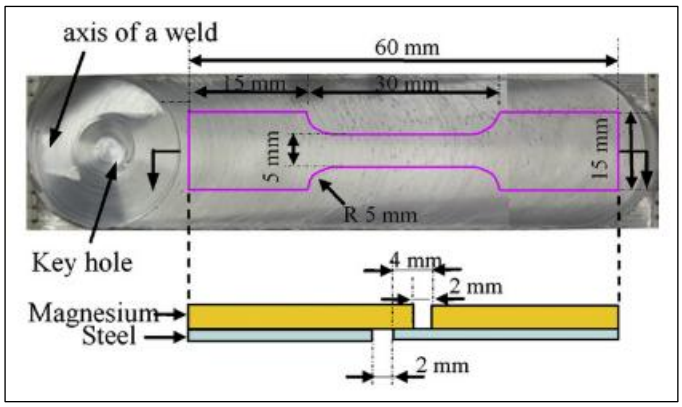


Figure 26: Tensile shear test sampling and weld appearance.
Source: [50].

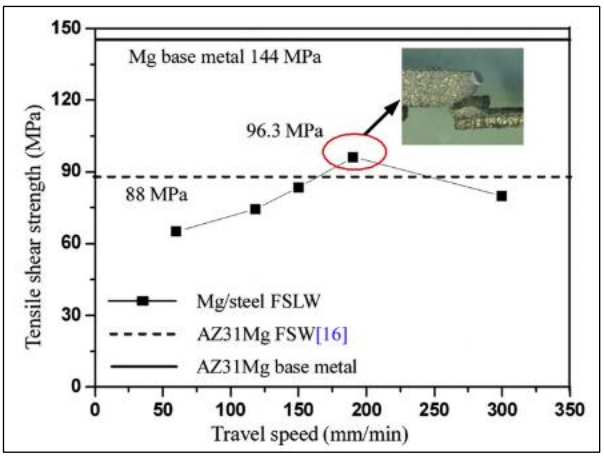


Figure 27: Joint tensile shear strength as a function of transit speed.
Source: [50].

The average minimum joint efficiency for AZ31/MS welds exceeds 60%, while for AZ31/HSLA welds using tool 1 (convex scrolled shoulder and a stepped spiral pin), it is approximately 40%. Process parameters showed an influence on joint efficiency. For AZ31/MS welds using tool 2 (Convex scrolled shoulder and a stepped spiral pin plus a short hard WC insert on the tool pin bottom), the combination of 500 RPM, 100 mm/min travel speed, and 2.47 mm plunge depth produced a weld efficiency of > 90%. The AZ31/HSLA weld's weld efficiency, at the same process parameters, was around 52%, the highest in its class [53].

VI.2 HARDNESS

Microhardness of the weld zones was evaluated with a Vickers hardness tester following ASTM E384-16 standard [251]. From the mg surface to the steel surface, microhardness measurements were made in the thickness direction. When measuring hardness from the top magnesium surface, it was found that the hardness progressively increased until it reached the interface between magnesium and steel, after which it decreased when measured in steel. The hardness rises as we proceed from AS to RS. This effect may be attributed to grain refinement. The increased rate of cooling was the cause of the increase in magnesium hardness. Smaller grains with a higher hardness are produced by the faster cooling rate [60]. As shown in Figure 28, the stir zone (SZ) has higher hardness than the TMAZ, HAZ, and base metal (BM) of magnesium alloys in AZ31–SS316 and WE43–SS316 joints. No significant hardness variation was observed between AZ31 and WE43. In steel, the TMAZ exhibited greater hardness than its base material. The hardness rise in the SZ is attributed to recrystallization, whereas in the steel TMAZ it stems from work hardening followed by recrystallization [57].

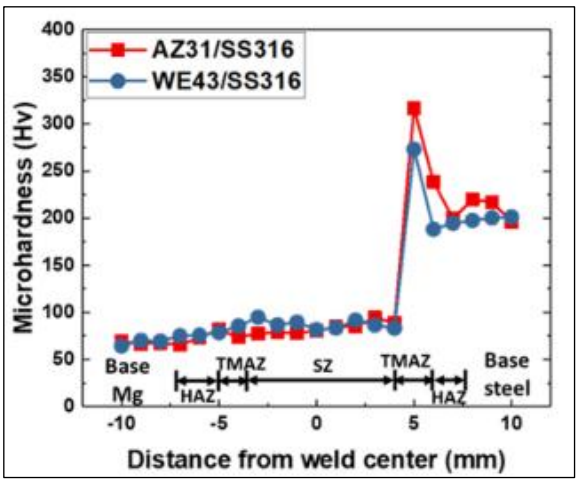


Figure 28: Microhardness profile of AZ31 to SS316 and WE43 to SS316 across the weld cross section.
Source: [57].

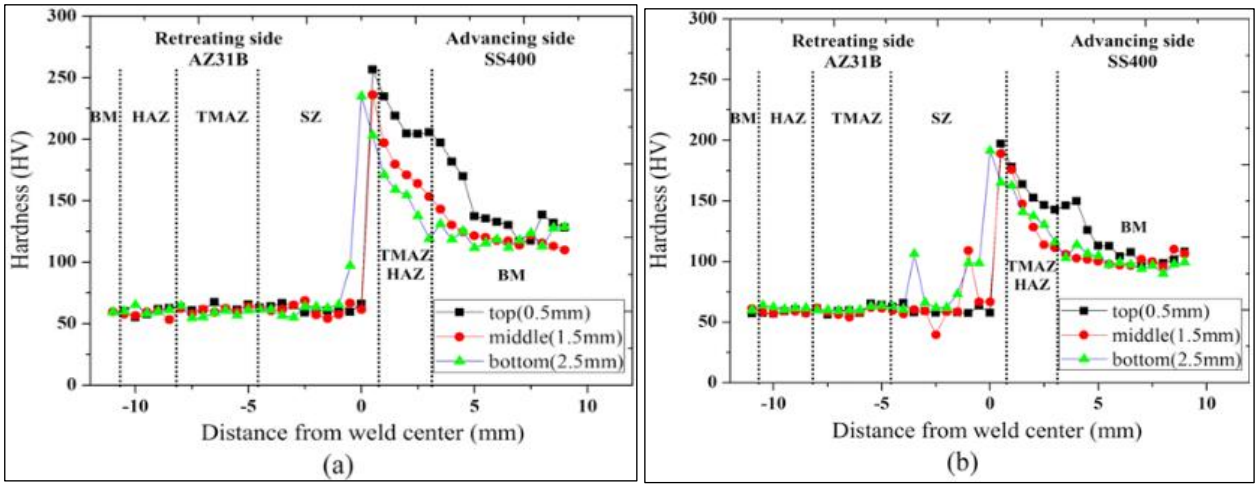


Figure 29: Cross-sectional hardness profiles (a) FS, (b) HGTAFS welds.
Source: Authors, (2026).

Figure 29 presents hardness profiles across the weld cross-section at 0.5 mm, 1.5 mm, and 2.5 mm from the top surface. Maximum values were ~250 HV in FS welds and ~190 HV in HGTAFS welds on the steel side. Hardness on the Mg retreating side was comparable to the base alloy. In steel, work hardening raised hardness in the TMAZ and HAZ, but values were slightly lower in HGTAFS than FS welds. This decrease was attributed to coarser recrystallized grains from GTAW preheating and higher frictional heat on the steel side. [54].

VII. WELDING DEFECTS OF DISSIMILAR MG-STEEL FSW SYSTEM

The various types of joining defects are caused by the incorrect joining approach and the use of non-optimal dissimilar FSW working constraints [44], [257]. Due to improperly deformed metal flow patterns and insufficient material inclusion in the FSW zone, both identical and dissimilar FSW welds are susceptible to a number of defects, including tunnel flaws, pinholes, kissing bonds, fractures, and pipe defects, among others [258-260]. A trustworthy technique for locating a number of concealed defects in the weld produced after FSW is the X-ray detection test [261]. Onion-ring defects are commonly observed in both steel and magnesium alloy with comparable FSW, frequently aggregating around the weld nugget zone (WNZ). The dark and light alternating bands that define onion ring microstructures must have the same spacing between them as the tool moves forward in each revolution. Within the onion-ring microstructure, band discontinuity increases with weld length and is directly affected by tool rotation and material flow capacity [228], [262]. The primary cause of tunnelling defects is insufficient material mixing and forging action, which occurs when Welding variables including traverse speed, rotational speed, tilt angle, etc., are incompetent to generate necessary heat input for joining. In order to prevent tunnelling and void flaws during FSW, the ideal welding speed must be chosen. Future research in this area has to be properly investigated [228], [263-266]. Another type of FSW defect that can be found across the bonding surface is crack formation. Crack formation is mostly caused by small plunging depth, inappropriate pin offset, tool design, and incorrect w/p placement [267]. Cracks are typically detected in the SZ during different FSW and are classified as macro and micro-cracks. Cracks in the weld region are also likely to be caused by the development of IMCs and worse weld bonding in the SZ [268]. It is important to use appropriate parameters in FSW in order to prevent these kinds of flaws while connecting via FSW.

Defects involving fragmented or microscopic particles are uncommon in the Steel–Mg alloy welds produced by FSW and are often not present in FSW of similar and low-strength materials. Steel fragments within the Mg-Al metal matrix are regarded as defect formations. An uneven material flow fails to distribute the fine steel fragments uniformly, leaving sharp edges and surfaces unbonded, leading to voids and microcracks. This is caused by the high hardness, and reduced UTS in the stir zone. Optimizing process parameters, especially tool pin offset and feed rate can minimize fragmentation-related defects [30], [228], [269].

Lack of penetration is a common defect in dissimilar material FSW. This type of defect is typically located at the weld joint's lowest surface, and when the workpiece is isolated or lacks appropriate joints, the welds produce a weak joint. Under stress corrosion, crack initiation reduces fatigue toughness and tensile strength (weld efficiency), ultimately causing deformation or fracture. Factors like improper tool design, incorrect pin length, shallow plunging depth, varying plate thickness, and poor tool alignment influence FSW butt joints and worsen defects. Bend tests, which examine a material's ductility and soundness, can be used to find these kinds of defects [47], [228], [270]. During welding, high tool pin rotation generates intense heat around the weld interface, plasticization close to the tool shoulder and probe. This leads to excess material being expelled as surface flash. Penetration difficulties can result from variations in plunging depth (workpiece thickness variations) through the weld line and from pin lengths that are inappropriate in relation to the thickness of the w/p. Weld flash forms when softened material around the tool pin is expelled due to greater probe plunge depth. In addition, excessive tool tilt can limit softening of material filling the cavity above the weld nugget zone (WNZ), causing extra flash on the retreating side (RS) [44], [30], [228]. The joint interface exhibits a "hook"-like features that increases joint strength at high welding speeds and decreases joint strength at low welding speeds. Similarly, the zipper effect, which eventually strengthens the weld's joint, is promoted by the "saw tooth" shape seen at the interface at high travel speeds [60].

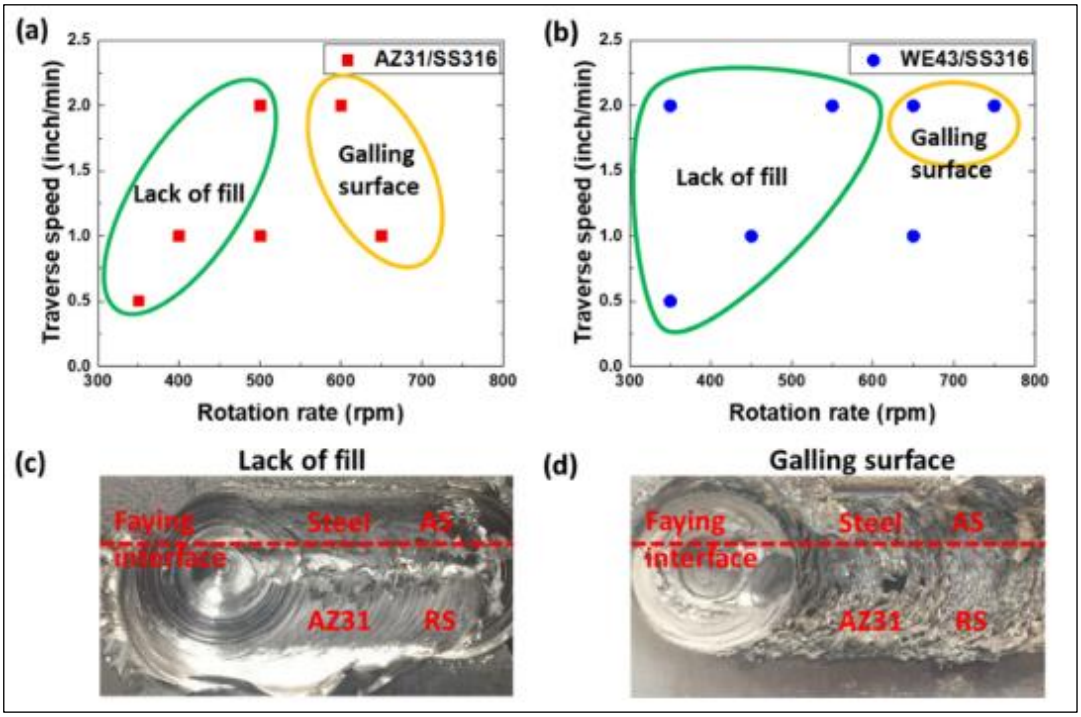


Figure 30: Relationship between FSW defects and welding parameters (a) AZ31 to SS316, (b) WE43 to SS316, (c) lack of fill and (d) galling surface.
Source: [57].

Figure 30 (a) and (b) present the rotation and travel speeds used for dissimilar butt welding of AZ31/SS316 and WE43/SS316, outlining the parameter window for defect-free joints. Two typical FSW defects were detected-lack of fill (Figure 30c) and galling surface (Figure 30d). The lack of fill was observed in magnesium near the faying interface under high travel speeds or low rotation speeds. The mg flow around the tool pin was impeded by inadequately plasticised steel. At high rotation rates, excessive heat generation led to a galling surface on the weld, caused by increased material sticking due to the elevated temperature [57].

Interfacial morphologies resembling flowers have been displayed using steel fragments and flashes. The remaining long flashes, measured in millimetres, created nail-effect bonding mechanisms as the travel speed increased, and the scraps dropped and caused damage. At the interface on the stainless-steel side, a sawtooth structure at the micron scale developed. Magnesium was used to fill the teeth, creating a Zipper effect enhances bond strength. The three bonding mechanisms are the metallurgical bonding effect by mutual diffusion, the zipper effect by the saw teeth, and the nail effect by the long steel flashes. Reduction in joint strength at high travel speeds (300 m/min) could be caused by two factors: the extended flashes' crashes could lessen the nail effect, and the decreased friction heat could weaken the metallurgical joint formation [50]. It was found that less material softens at high v because less heat is generated, resulting in thin flashes. Peeling off the flashes creates a macro-interlocked structure that results in a nail effect that strengthens the joining. Another notable feature resembling a saw-tooth pattern appeared, caused by the combined cutting and frictional action. Micro-interlocks at the weld joint may have formed as a result of the stirring force extruding magnesium into saw teeth. The zipper effect was facilitated by this interlocking. It has been discovered that the extended flashes that produce the nail effect saw tooth due to the zipper effect are responsible to enhance joint strength at higher traverse speeds. The study examined intermetallic compound formation at the AZ31/AZ61 joint interface and the effect of Al content on joint strength. Results showed that higher aluminum content in magnesium improves joint strength [60].

Zn–Mg solidification phases at the joint interface and hook-like features along the Mg/steel boundary serve as stress concentrators, reducing the fatigue resistance of FSW joints. To minimize porosity effects from solidification, fatigue studies of Mg/steel welds should be carried out with uncoated steel [26].

VIII. OBSERVATIONS

(1) The experimental findings and literature evidence on Mg-steel friction stir welding demonstrate several significant behavioural trends. First, the rotational speed of the tool was found to strongly influence joint quality; insufficient rotation led to inadequate plasticization, while excessive rotation resulted in magnesium ignition and a consequential drop in joint strength. Similarly, weld travel speed exerted a dual effect: moderate welding speeds increased joint strength through enhanced mechanical interlocking phenomena, whereas very high speeds reduced heat input and deteriorated metallurgical bonding.

(2) Tool pin offset was identified as another critical parameter governing weld performance. A slight positive offset toward the magnesium side produced the highest tensile strength, whereas both excessive and negative offsets resulted in interfacial weakening through void formation and insufficient IMC development, respectively. Furthermore, steel fragment dispersion into the magnesium matrix during the stirring process contributed to localized reinforcement and improved load transfer.

(3) Microstructural analysis consistently revealed hook-like features at the interface, which acted as stress concentrators and reduced effective cross-sectional thickness. The formation of intermetallic compounds including Fe–Al and Mg–Zn—was observed to influence joint brittleness and fracture mode. In particular, zinc-coated steel enhanced metallurgical bonding by promoting eutectic layer formation, though the effectiveness diminished when excessive molten zinc was expelled during stirring.

(4) Hardness profiling across the weld cross-section showed peak hardness in the stir zone due to dynamic recrystallization and refined grain structure. Tensile fracture primarily occurred at or near the Mg–steel interface, attributable to the elastic modulus mismatch and IMC-induced embrittlement. Finally, hybrid assisted FSW techniques such as GTAW preheating demonstrated superior joint integrity, leading to improved tensile performance relative to conventional FSW.

IX. CONCLUSION AND SUMMARY

IX.1 CONCLUSION

This review examined the current understanding of dissimilar friction stir welding (FSW) between steel and magnesium alloys. Existing studies emphasize the influence of process parameters such as tool rotation, welding speed, and plunge depth on microstructure, thermal response, and mechanical performance. The inherent difficulty of joining these alloys arises from their contrasting physical and chemical properties, including melting temperature, thermal conductivity, and the formation of intermetallic compounds (IMCs). Nevertheless, research demonstrates that with optimized parameters, reliable steel–magnesium joints can be successfully produced. The key findings drawn from the literature highlight both the complexity and potential of this welding process, emphasizing the need for precise control over processing conditions to overcome material incompatibility and promote joint integrity.

Mechanical Properties - While Mg-to-steel joints may not achieve the same strength as similar-material FSW joints, proper parameter selection and post-weld treatments can enhance mechanical performance.

Tool Design & Process Optimization - Specialized tool designs can improve bonding efficiency. Additionally, using interlayers such as aluminum or zinc can enhance weldability by reducing IMC brittleness.

Formation of IMCs – Intermetallic compounds such as Fe-Al, and Fe-Mg can form at the interface, affecting joint strength. Controlling the thermal input can help reduce excessive intermetallic compound (IMC) formation.

Applications & Future Research – Optimized FSW of steel–magnesium alloys holds strong potential for manufacturing weight-efficient structures, particularly in automotive and aerospace applications. Future studies should focus on refining process parameters, exploring alternative tool materials, and investigating hybrid techniques to improve joint integrity.

Sound welds are achieved within a very narrow range of welding parameters.

IX.2 FUTURE SCOPE

Materials like magnesium and steel, which have large differences in melting points and no mutual solubility, are notoriously challenging to join using conventional welding techniques. Traditional methods such as laser and hybrid welding often result in defects when applied to these dissimilar materials. In contrast, friction stir welding (FSW) offers a promising solid-state alternative, reducing welding defects and enabling effective joining. This study examines the potential of FSW for joining magnesium to steel. Building on this, future research could focus on extending these methods to more advanced steel grades, including high-strength steels (HSS) and advanced high-strength steels (AHSS). Successfully welding magnesium to AHSS could significantly reduce the weight of automotive components while maintaining or even improving strength and stiffness. Although aluminum-AHSS joints are already being used in automotive applications, magnesium offers an even lighter alternative, presenting new opportunities for further weight reduction. Expanding FSW to handle the transition from softer to harder materials like magnesium to AHSS will require advances in tool technology. Specifically, there's a need for cost-effective, wear-resistant, and reliable tools with a longer lifespan—although some innovative tool designs are already addressing these challenges. Looking ahead, critical areas for further research include improving the weldability of magnesium-steel joints, optimizing welding parameters, understanding fracture and corrosion behavior, and enhancing fatigue resistance. Special attention should also be given to controlling the formation and morphology of intermetallic compounds (IMCs), which play a major role in joint quality. Ultimately, the increasing demand in engineering industries for lightweight yet strong materials will continue to drive the development of FSW techniques for joining dissimilar materials like magnesium and steel.

Table 2: Summary of recommended assisted FSW type, workpiece materials & W/P design, FSW tool parameter, FSW process parameter, remarkable properties of joint welded by FSW systems.

TM: Tool Material, SD: Shoulder Diameter mm, PD: Pin Diameter mm, SSP: Shoulder Surface Profile, PL: Pin Length mm, TD: Tip Diameter mm, BD: Bottom Dia. of Pin mm, SPR: Shoulder to Pin Diameter ratio, PSP: Pin Surface Profile, RS: Rotational Speed, RPM, WS: Welding Speed, mm/min, PD: Plunge Depth, TPO: Tool Pin Offset mm, TTA: Tool Tilt Angle, UTS: Ultimate Tensile Strength Mpa, TS: Tensile Strength Mpa, JE: Joint Efficiency %, EL: Elongation %.

W/P Design (mm)	Workpiece Materials & Plate Thick. (mm)	FSW Tool Parameter	FSW Process Parameter	Remarkable Properties of Joint	References
-	AZ31B-O 2.32 mm thick, HDG- HSLA steel, EG-MS 1.5, 0.8 mm thick,	TM: H13 tool steel, WC insert on the tool pin bottom SSP: convex scrolled PSP: stepped spiral	RS: 500 WS: 100 PD: 2.47	JE: > 90% in AZ31/MS JE: ~52% in AZ31/HSLA	[53]
-	AZ31 3 mm thick, stainless steel	TM: H13 steel SD: 25	RS: 950 WS: 60, 118, 150,	- Flower-like morphologies with steel flashes.	[50]

	SUS302 1 mm thick,	PSP: rotary burrs PL: 2.9	190, 300 TTA: 0	- Shear strength lap joint: 96.3 MPa	
200×100	AZ31B 3 mm thick, SS400 mild steel 3 mm thick,	TM: WC-12% Co SD: 15 PL: 2.65 TD: 5	RS: 400 WS: 72-96 TTA: 3 Shielding gas: 13 l/min argon flow	UTS: 237, 226 JE: 91 % & 86 % FM: IF	[54]
100×305	AZ31B 2.33 mm thick, HDG- HSLA steel, EG-MS 1.5 0.8 mm thick,	TM: H13 tool steel SSP: convex scrolled shoulder SD: 12.8 PL: 2.34 TD: 4.9 38 mm overlap	RS: 700 WS: 100 PD: 2.45 TTA: 0	JE: 40, 60, 80 FM: IF - Peak load was noted to be ~6 kN. JS: 80 % of the parent metal strength	[27]
300×100	AZ31 1.6 mm, Low CS (zinc coated) 0.8 mm,	TM: SKD61 tool steel SD: 15 PL: 1.5 TD: 5	RS: 1500 WS: 100-300 TTA: 3	- Zn coating forms Mg–Zn eutectic. - Mg-steel weldability improved. FM: IF	[55]
140×40	AZ31B-O 2 mm, SS400 MS 2 mm,	TM: high-speed tool steel SD: 15 PL: 1.9 TD: 3	RS: 500, 800, 1250, 1600, 2000 WS: 100 TPO: -0.2 to 1.0 mm	JE: 78% FM: IF	[56]
-	AZ31, WE43, 6 mm, SS316 5.75,	TM: W-Re SD: 16 PSP: threaded conical pin PL: 3.8 BD: 7.6 TD: 5	RS: 350, 400, 500, 600, 650 WS: 0.5, 1, 2 (ipm) PD: 4.2 to steel TTA: 2.5 TPO: 2.5 to Mg	JE: 73% FM: IF	[57]
300×100	AZ31, 1.6 mm, low carbon steel (zinc coated, and brushed finish) 0.8 mm	TM: SKD61 tool steel SD: 15 PL: 1.5 TD: 5	RS: 25 rad s^{-1} WS: 3.5, 5 mm s^{-1} TTA: 3	- Mg alloy and brushed steel failed to weld under current conditions. FM: IF	[23]
300×100	AZ31, 1.6 mm, low carbon steel (zinc coated, and brushed finish) 0.8 mm	TM: Tool Steel SKD61 SD: 15 PL: 1.5, 1.8 TD: 5	RS: 25 rad s^{-1} WS: 1.67-5 s^{-1} TTA: 3	- Long probe weld fractured in Mg SZ; short probe at the interface. - Failure loads increased with increasing probe length. - Microstructure varied with the probe length FM : FZ, SZ	[58]
100×305	AZ31B-O 2.33 mm thick, HSLA steel MS 1.5 0.8 mm thick,	TM: WC SSP: convex scrolled shoulder PSP: stepped spiral pin 38 mm overlap	RS: 500 rev min^{-1} WS: 1.67 mm s^{-1} PD: 2.47	-	[26]
300×75	pure Mg, AZ31, AZ61 2 mm thick, low carbon steel 2 mm thick,	TM: WC SD: 12 TD: 4	RS: 250-3000 WS: 100 TTA: 3 TPO: -0.7 to 2.0 mm	- Probe-Steel contact needed for IMC formation. - Peak TS at +0.1 to 1.1 mm offset. FM: IF - Increased Al in Mg improved joint strength.	[59]
150×150	AZ31B-O 2 mm thick, ultra- low carbon steel	TM: Shaft - tool steel H13, pin - 75 % W and, 25 % Re,	RS: 1200 WS: 150, 500 PD : 0.15	- Interface fracture strength exceeds the measured value.	[28]

	DX54D 2 mm thick,	SD: 12.7 PL: 2 pin had a 3.3 × 3.3 mm square shape	TTA: 0 overlap width was 65 mm magnesium sheet was placed on top	- Fracture strength rises with increased welding speed. FM : SZ	
100×80	AZ31B 1.5 mm thick, AISI 304 1 mm thick	TM: WC-10%Co SD: 16 PSP: circular pin profile PL: 1.6 TD: 5	RS: 600, 1000, 1800 WS: 40, 200, 350 PD : 0.1 TTA: 1	JE: 79 - Joint interface microhardness is higher than that of the base material. FM : IF - Hook-like feature is observed	[60]

Source: Authors, (2026).

X. AUTHOR'S CONTRIBUTION

Conceptualization: Kapil B. Pipavat, Hirenkumar I. Joshi.
Methodology: Kapil B. Pipavat, Hirenkumar I. Joshi, Ghanshyam D. Acharya.
Investigation: Kapil B. Pipavat, Hirenkumar I. Joshi, Ghanshyam D. Acharya.
Discussion of results: Kapil B. Pipavat, Hirenkumar I. Joshi, Ghanshyam D. Acharya.
Writing – Original Draft: Kapil B. Pipavat,
Writing – Review and Editing: Kapil B. Pipavat, Hirenkumar I. Joshi, Ghanshyam D. Acharya.
Resources: Hirenkumar I. Joshi, Ghanshyam D. Acharya.
Supervision: Hirenkumar I. Joshi, Ghanshyam D. Acharya.
Approval of the final text: Hirenkumar I. Joshi, Ghanshyam D. Acharya.

XI. REFERENCES

[1] Y. F. Sun and H. Fujii, "Microstructure and mechanical properties of dissimilar spot friction stir welded Zr55 Cu30 Al10 Ni5 bulk metallic glass to pure copper," Intermetallics, vol. 33, pp. 113–119, Feb. 2013, doi: 10.1016/J.INTERMET.2012.10.006.

[2] Y. Dong, H. Fujii, Y. Sun, and H. Tanigawa, "Interface microstructure evolution of dissimilar friction stir butt welded F82H steel and SUS304," Mater. Sci. Eng. A, vol. 528, no. 18, pp. 5812–5821, 2011, doi: 10.1016/j.msea.2011.04.023.

[3] Y. S. Sato, S. H. C. Park, M. Michiuchi, and H. Kokawa, "Constitutional liquation during dissimilar friction stir welding of Al and Mg alloys," Scr. Mater., vol. 50, no. 9, pp. 1233–1236, May 2004, doi: 10.1016/J.SCRIPTAMAT.2004.02.002.

[4] M. Aonuma and K. Nakata, "Effect of alloying elements on interface microstructure of Mg–Al–Zn magnesium alloys and titanium joint by friction stir welding," Mater. Sci. Eng. B, vol. 161, no. 1, pp. 46–49, Apr. 2009, doi: https://doi.org/10.1016/j.mseb.2009.02.020.

[5] H. Uzun, C. Dalle Donne, A. Argagnotto, T. Ghidini, and C. Gambaro, "Friction stir welding of dissimilar Al 6013-T4 To X5CrNi18-10 stainless steel," Mater. Des., vol. 26, no. 1, pp. 41–46, 2005, doi: https://doi.org/10.1016/j.matdes.2004.04.002.

[6] Y. F. Sun, H. Fujii, and N. Tsuji, "Microstructure and mechanical properties of spot friction stir welded ultrafine grained 1050 Al and conventional grained 6061-T6 Al alloys," Mater. Sci. Eng. A, vol. 585, pp. 17–24, 2013, doi: 10.1016/j.msea.2013.07.030.

[7] C. M. Chen and R. Kovacevic, "Joining of Al 6061 alloy to AISI 1018 steel by combined effects of fusion and solid state welding," Int. J. Mach. Tools Manuf., vol. 44, no. 11, pp. 1205–1214, Sep. 2004, doi: 10.1016/J.IJMACHTOOLS.2004.03.011.

[8] Y. F. Sun, H. Fujii, N. Takaki, and Y. Okitsu, "Microstructure and mechanical properties of dissimilar Al alloy/steel joints prepared by a flat spot friction stir welding technique," Mater. Des., vol. 47, pp. 350–357, 2013, doi: 10.1016/j.matdes.2012.12.007.

[9] S. T. Auwal, S. Ramesh, C. Tan, Z. Zhang, X. Zhao, and S. M. Manladan, "Recent developments and challenges in welding of magnesium to titanium alloys," Adv. Mater. Res. (South Korea), vol. 8, no. 1, pp. 47–73, 2019, doi: 10.12989/AMR.2019.8.1.047.

[10] P. Pall et al., "Anthropogenic greenhouse gas contribution to flood risk in England and Wales in autumn 2000," Nature, vol. 470, no. 7334, pp. 382–385, 2011, doi: 10.1038/nature09762.

[11] R. Nandan, T. Debroy, and H. K. D. H. Bhadeshia, "Recent advances in friction-stir welding – Process , weldment structure and properties," Prog. Mater. Sci., vol. 53, pp. 980–1023, 2008, doi: 10.1016/j.pmatsci.2008.05.001.

[12] V. K. Patel, S. D. Bhole, and D. L. Chen, "Formation of zinc interlayer texture during dissimilar ultrasonic spot welding of magnesium and high strength low alloy steel," Mater. Des., vol. 45, pp. 236–240, 2013, doi: 10.1016/j.matdes.2012.09.018.

[13] M. Wahba and S. Katayama, "Laser welding of AZ31B magnesium alloy to Zn-coated steel," Mater. Des., vol. 35, pp. 701–706, 2012, doi: 10.1016/j.matdes.2011.10.031.

[14] L. M. Liu and X. Zhao, "Study on the weld joint of Mg alloy and steel by laser-GTA hybrid welding," Mater. Charact., vol. 59, no. 9, pp. 1279–1284, 2008, doi: 10.1016/j.matchar.2007.10.012.

[15] C. Tan, L. Li, Y. Chen, and W. Guo, "Laser-tungsten inert gas hybrid welding of dissimilar metals AZ31B Mg alloys to Zn coated steel," Mater. Des., vol. 49, pp. 766–773, 2013, doi: 10.1016/j.matdes.2013.02.049.

[16] X. Qi and G. Song, “Interfacial Structure of the Joints between Magnesium Alloy and Mild Steel with Nickel as Interlayer by Hybrid Laser-TIG Welding,” Mater. Des., vol. 31, no. 1, pp. 605–609, 2010, doi: 10.1016/j.matdes.2009.06.043.

[17] L. Liu and X. Qi, “Strengthening effect of nickel and copper interlayers on hybrid laser-TIG welded joints between magnesium alloy and mild steel,” Mater. Des., vol. 31, no. 8, pp. 3960–3963, 2010, doi: 10.1016/j.matdes.2010.03.039.

[18] G. Song, G. An, and L. Liu, “Effect of gradient thermal distribution on butt joining of magnesium alloy to steel with Cu-Zn alloy interlayer by hybrid laser-tungsten inert gas welding,” Mater. Des., vol. 35, pp. 323–329, 2012, doi: 10.1016/j.matdes.2011.09.006.

[19] Z. Z. Zeng Zhi, Li Xunbo, Miao, Yugang, Wu Gang, “Numerical and experiment analysis of residual stress on magnesium alloy and steel butt joint by hybrid laser-TIG welding,” Comput. Mater. Sci., vol. 50, 2011, doi: 10.1016/j.commatsci.2011.01.011.

[20] W. M. Elthalabawy and T. I. Khan, “Microstructural development of diffusion-brazed austenitic stainless steel to magnesium alloy using a nickel interlayer,” Mater. Charact., vol. 61, no. 7, pp. 703–712, 2010, doi: 10.1016/j.matchar.2010.04.001.

[21] X. D. Qi and L. M. Liu, “Investigation on welding mechanism and interlayer selection of magnesium/steel lap joints,” Weld. J. (Miami, Fla), vol. 90, no. 1, 2011.

[22] A. M. Nasiri, D. C. Weckman, and Y. Zhou, “Interfacial microstructure of laser brazed AZ31B magnesium to Snplated steel sheet,” Weld. J., vol. 94, no. 3, pp. 61S--72S, 2015.

[23] Y. C. Chen and K. Nakata, “Effect of surface states of steel on microstructure and mechanical properties of lap joints of magnesium alloy and steel by friction stir welding,” Sci. Technol. Weld. Join., vol. 15, no. 4, pp. 293–298, 2010, doi: 10.1179/136217109X12568132624325.

[24] Y. C. Chen and K. Nakata, “Effect of tool geometry on microstructure and mechanical properties of friction stir lap welded magnesium alloy and steel,” Mater. Des., vol. 30, 2009, doi: 10.1016/j.matdes.2009.03.007.

[25] Y. C. Chen and K. Nakata, “Friction Stir Lap Welding of Magnesium Alloy and Zinc-Coated Steel,” Mater. Trans., vol. 50, 2009, doi: 10.2320/matertrans.M2009022.

[26] S. Jana and Y. Hovanski, “Fatigue behaviour of magnesium to steel dissimilar friction stir lap joints,” Sci. Technol. Weld. Join., vol. 17, no. 2, pp. 141–145, 2012, doi: 10.1179/1362171811Y.0000000083.

[27] S. Jana, Y. Hovanski, and G. J. Grant, “Friction stir lap welding of magnesium alloy to steel: A preliminary investigation,” Metall. Mater. Trans. A Phys. Metall. Mater. Sci., vol. 41, no. 12, pp. 3173–3182, 2010, doi: 10.1007/s11661-010-0399-8.

[28] C. Schneider, T. Weinberger, J. Inoue, T. Koseki, and N. Enzinger, “Characterisation of interface of steel/magnesium FSW,” Sci. Technol. Weld. Join., vol. 16, no. 1, pp. 100–106, 2011, doi: 10.1179/1362171810Y.0000000012.

[29] H. Okamoto; M.E. Schlesinger; E.M. Mueller, Ed., Binary Alloy Phase Diagrams. 2016. doi: https://doi.org/10.31399/asm.hb.v03.9781627081634.

[30] T. Liyanage, J. Kilbourne, A. P. Gerlich, and T. H. North, “Joint formation in dissimilar Al alloy/steel and Mg alloy/steel friction stir spot welds,” Sci. Technol. Weld. Join., vol. 14, no. 6, pp. 500–508, 2009, doi: 10.1179/136217109X456960.

[31] H. K. Mao and P. M. Bell, “Equations of State of MgO and ε Fe Under Static Pressure Conditions,” vol. 84, no. 8, pp. 4533–4536, 1979.

[32] L. Liu, L. Xiao, J. Feng, L. Li, S. Esmaeili, and Y. Zhou, “Bonding of immiscible Mg and Fe via a nanoscale Fe2Al5 transition layer,” vol. 65, pp. 982–985, 2011, doi: 10.1016/j.scriptamat.2011.08.026.

[33] Y. M. Baqer, S. Ramesh, F. Yusof, and S. M. Manladan, “Challenges and advances in laser welding of dissimilar light alloys : Al / Mg , Al / Ti , and Mg / Ti alloys,” pp. 18–20, 2018.

[34] N. Afrin, D. L. Chen, X. Cao, and M. Jahazi, “Microstructure and tensile properties of friction stir welded AZ31B magnesium alloy,” Mater. Sci. Eng. A, vol. 472, 2008, doi: 10.1016/j.msea.2007.03.018.

[35] Z. Y. Ma, “Friction Stir Processing Technology : A Review,” Miner. Met. Mater. Soc., 2008, doi: 10.1007/s11661-007-9459-0.

[36] G. Padmanaban and V. Balasubramanian, “An experimental investigation on friction stir welding of AZ31B magnesium alloy,” pp. 111–121, 2010, doi: 10.1007/s00170-009-2368-1.

[37] Y. U. Sirong, C. Xianjun, H. Zhiqiu, and L. I. U. Yaohui, “Microstructure and mechanical properties of friction stir welding of AZ31B magnesium alloy added with cerium,” J. Rare Earths, vol. 28, no. 2, pp. 316–320, 2010, doi: 10.1016/S1002-0721(09)60104-6.

[38] B. R. Sunil et al., “Joining of AZ31 and AZ91 Mg alloys by friction stir welding,” J. Magnes. Alloy., vol. 3, no. 4, pp. 330–334, 2015, doi: 10.1016/j.jma.2015.10.002.

[39] S. W. Kallee, W. M. Thomas, and E. D. Nicholas, “Joining Friction Stir Welding of Lightweight Materials”.

[40] A. Gerlich, P. Su, M. Yamamoto, and T. H. North, “Material flow and intermixing during dissimilar friction stir welding,” Sci. Technol. Weld. Join., vol. 13, 2008, doi: 10.1179/174329308X283910.

[41] P. Su, A. Gerlich, T. H. North, and G. J. Bendzsak, “Intermixing in Dissimilar Friction Stir Spot Welds,” 2007, doi: 10.1007/s11661-006-9067-4.

[42] W. M. Thomas, E. D. Nicholas, J. C. Needham, M. G. Murch, P. Templesmith, and C. J. Dawes, “GB Patent application no. 9125978.8,” Int. Pat. Appl. no. PCT/GB92/02203, 1991.

[43] B. T. Gibson et al., “Friction stir welding: Process, automation, and control,” J. Manuf. Process., pp. 1–18, 2013, doi: 10.1016/j.jmapro.2013.04.002.

[44] R. S. Mishra and Z. Y. Ma, “Friction stir welding and processing,” Mater. Sci. Eng. R Reports, vol. 50, no. 1–2, pp. 1–78, 2005, doi: 10.1016/j.mser.2005.07.001.

[45] T. W. M., “Friction Stir Welding-Process Developments and Variant Techniques,” SME Summit 2005, Oconomowoc, Milwaukee, USA, August 3-4th, 2005, [Online]. Available: https://cir.nii.ac.jp/crid/1571698601208037888

[46] W. M. Thomas, “Friction Stir Welding – Process Developments and Variant Techniques,” no. January 2005, 2014.

[47] M. W. Mahoney and R. S. Mishra, Friction stir welding and processing. ASM international, 2007.

[48] W. M. Thomas, E. D. Nicholas, J. C. Needham, M. G. Church, P. Templesmith, and C. J. Dawes, “The Welding Institute,” TWI, Int. Pat. Appl. no. pct/GB92/02203 GB Pat. Appl., no. 912598.8, 1991.

[49] R. S. Mishra, P. S. De, and N. Kumar, “Friction Stir Welding and Processing,” in Friction Stir Welding and Processing, Cham: Springer International Publishing, 2014, pp. 1–11. doi: 10.1007/978-3-319-07043-8_1.

[50] Y. Wei, J. Li, J. Xiong, F. Huang, and F. Zhang, “Microstructures and mechanical properties of magnesium alloy and stainless steel weld-joint made by friction stir lap welding,” Mater. Des., vol. 33, no. 1, pp. 111–114, 2012, doi: 10.1016/j.matdes.2011.07.016.

[51] P. Cavaliere and P. P. De Marco, “Superplastic behaviour of friction stir processed AZ91 magnesium alloy produced by high pressure die cast,” J. Mater. Process. Technol., vol. 184, 2007, doi: 10.1016/j.jmatprotec.2006.11.005.

[52] C. L. and Z. W. Yajie Li, Fengming Qin, “A Review : Effect of Friction Stir Welding on Microstructure and Mechanical Properties of Magnesium Alloys,” 2017, doi: 10.3390/met7120524.

[53] S. Jana et al., “Solid State Joining of Magnesium to Steel,” Essent. Readings Magnes. Technol., vol. 9781118858, pp. 505–510, 2014, doi: 10.1002/9781118859803.ch82.

[54] S. Joo, “Joining of dissimilar AZ31B magnesium alloy and SS400 mild steel by hybrid gas tungsten arc friction stir welding,” Met. Mater. Int., vol. 19, no. 6, pp. 1251–1257, 2013, doi: 10.1007/s12540-013-6016-9.

[55] Y. C. Chen and K. Nakata, “Friction stir lap welding of magnesium alloy and zinc-coated steel,” Mater. Trans., vol. 50, no. 11, pp. 2598–2603, 2009, doi: 10.2320/matertrans.M2009022.

[56] Y. Abe, T. Watanabe, H. Tanabe, and K. Kagiya, “Dissimilar metal joining of magnesium alloy to steel by FSW,” Adv. Mater. Res., vol. 15–17, pp. 393–397, 2007, doi: 10.4028/www.scientific.net/amr.15-17.393.

[57] T. Wang, S. Shukla, B. Gwalani, M. Komarasamy, L. Reza-Nieto, and R. S. Mishra, “Effect of reactive alloy elements on friction stir welded butt joints of metallurgically immiscible magnesium alloys and steel,” J. Manuf. Process., vol. 39, no. November 2018, pp. 138–145, 2019, doi: 10.1016/j.jmapro.2019.02.009.

[58] Y. C. Chen and K. Nakata, “Effect of tool geometry on microstructure and mechanical properties of friction stir lap welded magnesium alloy and steel,” Mater. Des., vol. 30, no. 9, pp. 3913–3919, 2009, doi: 10.1016/j.matdes.2009.03.007.

[59] H. Kasai, Y. Morisada, and H. Fujii, “Dissimilar FSW of immiscible materials: Steel/magnesium,” Mater. Sci. Eng. A, vol. 624, pp. 250–255, 2015, doi: 10.1016/j.msea.2014.11.060.

[60] S. Sahu, O. Thorat, R. P. Mahto, S. K. Pal, and P. Srirangam, “A Review and Case Study on Mechanical Properties and Microstructure Evolution in Magnesium–Steel Friction Stir Welding,” Miner. Met. Mater. Ser., pp. 101–109, 2019, doi: 10.1007/978-3-030-05789-3_17.

[61] Z. K. Zhang, X. J. Wang, P. C. Wang, and G. Zhao, “Friction stir keyholeless spot welding of AZ31 Mg alloy-mild steel,” Trans. Nonferrous Met. Soc. China (English Ed., vol. 24, no. 6, pp. 1709–1716, 2014, doi: 10.1016/S1003-6326(14)63244-1.

[62] X. Wang, C. Zhang, B. Li, and T. Li, “A preliminary investigation on friction stir spot welding of steel / Mg,” Appl. Mech. Mater., vol. 84–85, pp. 529–533, 2011, doi: 10.4028/www.scientific.net/AMM.84-85.529.

[63] R. Z. Xu, D. R. Ni, Q. Yang, B. L. Xiao, C. Z. Liu, and Z. Y. Ma, “Influencing mechanism of Al-containing Zn coating on interfacial microstructure and mechanical properties of friction stir spot welded Mg–steel joint,” Mater. Charact., vol. 140, no. April, pp. 197–206, 2018, doi: 10.1016/j.matchar.2018.04.011.

[64] X. J. Wang, Y. L. Wu, Z. K. Zhang, T. K. Guo, Y. X. Lu, and J. P. Shi, “The study of the microstructure and mechanical properties of friction stir spot welding joint between AZ31B magnesium alloy and steel,” Adv. Mater. Res., vol. 668, pp. 818–822, 2013, doi: 10.4028/www.scientific.net/AMR.668.818.

[65] X. J. Wang, B. Q. Li, and C. Q. Zhang, “Study of friction stir spot welding of steel/magnesium,” Adv. Mater. Res., vol. 239–242, pp. 417–421, 2011, doi: 10.4028/www.scientific.net/AMR.239-242.417.

[66] D. Control, “Friction Stir Spot Welding of AM60 Magnesium Alloy To DP600 Steel,” vol. 2, doi: 10.21859/ijnr-12029.

[67] Y. Uematsu, T. Kakiuchi, Y. Tozaki, and H. Kojin, “Comparative study of fatigue behaviour in dissimilar Al alloy/steel and Mg alloy/steel friction stir spot welds fabricated by scroll grooved tool without probe,” Sci. Technol. Weld. Join., vol. 17, no. 5, pp. 348–356, 2012, doi: 10.1179/1362171812Y.0000000014.

[68] X. J. Wang, W. H. Li, and G. Zhao, “Connection mechanism research on friction stir spot welding without keyhole between magnesium and steel dissimilar alloys,” Mater. Res. Innov., vol. 18, pp. S21063–S21066, 2014, doi: 10.1179/1432891714Z.000000000471.

[69] L. Liu, L. Xiao, J. C. Feng, Y. H. Tian, S. Q. Zhou, and Y. Zhou, “The Mechanisms of Resistance Spot Welding of Magnesium to Steel,” Metall. Mater. Trans. A, vol. 41, no. 10, pp. 2651–2661, 2010, doi: 10.1007/s11661-010-0333-0.

[70] K. Zhang, L. Wu, C. Tan, Y. Sun, B. Chen, and X. Song, “Influence of Al-Si coating on resistance spot welding of Mg to 22MnB5 boron steel,” J. Mater. Process. Technol., vol. 271, no. August 2018, pp. 23–35, 2019, doi: 10.1016/j.jmatprotec.2019.03.024.

[71] W. Xu, D. L. Chen, L. Liu, H. Mori, and Y. Zhou, “Microstructure and mechanical properties of weld-bonded and resistance spot welded magnesium-to-steel dissimilar joints,” Mater. Sci. Eng. A, vol. 537, pp. 11–24, 2012, doi: 10.1016/j.msea.2011.12.096.

[72] G. Zhang, L. Liu, C. Tian, and R. Xu, “Interfacial structure of the joints between magnesium alloy and mild steel with nickel as interlayer,” Int. Conf. Logist. Eng. Manag. Comput. Sci. LEMCS 2014, no. Lemcs, pp. 335–338, 2014, doi: 10.2991/lemcs-14.2014.79.

[73] L. Liu, G. Zou, H. Mori, S. Esmaeili, and Y. N. Zhou, “Nanostructure of immiscible Mg-Fe dissimilar weld without interfacial intermetallic transition layer,” Mater. Des., vol. 92, pp. 445–449, 2016, doi: 10.1016/j.matdes.2015.12.072.

[74] S. M. Manladan, F. Yusof, S. Ramesh, Y. Zhang, Z. Luo, and Z. Ling, “Microstructure and mechanical properties of resistance spot welded in welding-brazing mode and resistance element welded magnesium alloy/austenitic stainless steel joints,” J. Mater. Process. Technol., vol. 250, pp. 45–54, 2017, doi: 10.1016/j.jmatprotec.2017.07.006.

[75] S. M. Manladan, Y. Zhang, S. Ramesh, Y. Cai, S. Ao, and Z. Luo, “Resistance element welding of magnesium alloy and austenitic stainless steel in three-sheet configurations,” J. Mater. Process. Technol., vol. 274, no. June, 2019, doi: 10.1016/j.jmatprotec.2019.116292.

[76] L. Liu, L. Xiao, D. L. Chen, J. C. Feng, S. Kim, and Y. Zhou, “Microstructure and fatigue properties of Mg-to-steel dissimilar resistance spot welds,” Mater. Des., vol. 45, pp. 336–342, 2013, doi: 10.1016/j.matdes.2012.08.018.

[77] D. Min, Z. Yong, and L. Jie, “Dissimilar spot welding joints of AZ31-443 ferritic stainless steel with cover plate,” Int. J. Adv. Manuf. Technol., vol. 85, no. 5–8, pp. 1539–1545, 2016, doi: 10.1007/s00170-015-8078-y.

[78] D. Ren and L. Liu, “Interface microstructure and mechanical properties of arc spot welding Mg–steel dissimilar joint with Cu interlayer,” Mater. Des., vol. 59, pp. 369–376, 2014, doi: 10.1016/j.matdes.2014.03.006.

[79] S. M. Manladan, F. Yusof, S. Ramesh, Y. Zhang, Z. Luo, and Z. Ling, “Resistance Element Welding of Magnesium Alloy/austenitic Stainless Steel,” IOP Conf. Ser. Mater. Sci. Eng., vol. 238, no. 1, 2017, doi: 10.1088/1757-899X/238/1/012004.

[80] S. Niu, M. Lou, Y. Ma, B. Yang, H. Shan, and Y. Li, “Resistance rivet welding of magnesium/steel dissimilar materials,” Mater. Lett., vol. 282, p. 128876, 2021, doi: 10.1016/j.matlet.2020.128876.

[81] T. Y. Pan, Z. Feng, M. Santella, and J. Chen, “Corrosion behavior of mixed-metal joint of magnesium to mild steel by ultrasonic spot welding with and without adhesives,” SAE Int. J. Mater. Manuf., vol. 6, no. 2, pp. 271–278, 2013, doi: 10.4271/2013-01-1017.

[82] W. J. Lai and J. Pan, “Failure mode and fatigue behavior of weld-bonded lap-shear specimens of magnesium and steel sheets,” Int. J. Fatigue, vol. 75, pp. 184–197, 2015, doi: 10.1016/j.ijfatigue.2015.01.017.

[83] T. J. Franklin, J. Pan, M. Santella, and T. Y. Pan, “Fatigue Behavior of Dissimilar Ultrasonic Spot Welds in Lap-Shear Specimens of Magnesium and Steel Sheets,” SAE Int. J. Mater. Manuf., vol. 4, no. 1, pp. 581–588, 2011, doi: 10.4271/2011-01-0475.

[84] Y. Feng, Y. Li, Z. Luo, Z. Ling, and Z. Wang, “Resistance spot welding of Mg to electro-galvanized steel with hot-dip galvanized steel interlayer,” J. Mater. Process. Technol., vol. 236, pp. 114–122, 2016, doi: 10.1016/j.jmatprotec.2016.05.015.

[85] T. Y. Pan and M. Santella, “Ultrasonic Spot Welding of Galvanized Mild Steel to Magnesium AZ31B,” SAE Tech. Pap., pp. 0–5, 2012, doi: 10.4271/2012-01-0474.

[86] T. Y. Pan, Z. Feng, M. L. Santella, and J. Chen, “Corrosion of ultrasonic spot weldbonds of magnesium to steel,” Magnes. Technol., pp. 491–496, 2014, doi: 10.1002/9781118888179.ch89.

[87] T. Y. Pan and M. Santella, “Ultrasonic spot welding of AZ31B to Galvanized mild steel,” SAE Tech. Pap., vol. 3, no. 1, pp. 652–657, 2010, doi: 10.4271/2012-01-0474.

[88] V. K. Patel, D. L. Chen, and S. D. Bhole, “Dissimilar ultrasonic spot welding of Mg-Al and Mg-high strength low alloy steel,” Theor. Appl. Mech. Lett., vol. 4, no. 4, p. 041005, 2014, doi: 10.1063/2.1404105.

[89] M. Santella, E. Brown, M. Pozuelo, T. Y. Pan, and J. M. Yang, “Details of Mg-Zn reactions in AZ31 to galvanised mild steel ultrasonic spot welds,” Sci. Technol. Weld. Join., vol. 17, no. 3, pp. 219–224, 2012, doi: 10.1179/1362171811Y.0000000098.

[90] V. K. Patel, S. D. Bhole, and D. L. Chen, “Characterization of ultrasonic spot welded joints of Mg-to-galvanized and ungalvanized steel with a tin interlayer,” J. Mater. Process. Technol., vol. 214, no. 4, pp. 811–817, 2014, doi: 10.1016/j.jmatprotec.2013.11.028.

[91] H. Huang et al., “Surface engineering to enhance heat generation and joint strength in dissimilar materials AZ31 and DP590 ultrasonic welding,” Int. J. Adv. Manuf. Technol., vol. 111, no. 11–12, pp. 3095–3109, 2020, doi: 10.1007/s00170-020-06341-3.

[92] J. Cheng, X. Hu, and X. Sun, “Molecular dynamics study on interface formation and bond strength of impact-welded Mg-steel joints,” Comput. Mater. Sci., vol. 185, no. April, p. 109988, 2020, doi: 10.1016/j.commatsci.2020.109988.

[93] W. Elthalabawy and T. I. Khan, “Diffusion bonding of austenitic stainless steel 316L to a magnesium alloy,” Key Eng. Mater., vol. 442, pp. 26–33, 2010, doi: 10.4028/www.scientific.net/KEM.442.26.

[94] D. W. Zhou, T. Li, S. H. Xu, and J. S. Liu, “Numerical and Experimental Investigations in Laser Welding for Steel and Magnesium Alloy,” Lasers Manuf. Mater. Process., vol. 5, no. 3, pp. 222–236, 2018, doi: 10.1007/s40516-018-0063-5.

[95] C. W. Tan et al., “Influence of Al interlayer thickness on laser welding of Mg/steel,” Weld. J., vol. 95, no. 10, pp. 384s-394s, 2016.

[96] D. Zhou, J. Liu, Z. Tan, and S. Xu, “Effects of Sn-foil addition on the microstructure and mechanical properties of laser welding joint for dual phase steel and magnesium alloy,” SN Appl. Sci., vol. 1, no. 7, 2019, doi: 10.1007/s42452-019-0729-4.

[97] G. Casalino, P. Guglielmi, V. D. Lorusso, M. Mortello, P. Peyre, and D. Sorgente, “Laser offset welding of AZ31B magnesium alloy to 316 stainless steel,” J. Mater. Process. Technol., vol. 242, pp. 49–59, 2017, doi: 10.1016/j.jmatprotec.2016.11.020.

[98] M. Windmann, A. Röttger, H. Kügler, and W. Theisen, “Laser beam welding of magnesium to coated high-strength steel 22MnB5,” Int. J. Adv. Manuf. Technol., vol. 87, no. 9–12, pp. 3149–3156, 2016, doi: 10.1007/s00170-016-8682-5.

[99] C. W. Tan, L. Q. Li, Y. B. Chen, C. X. Mei, and W. Guo, “Interfacial microstructure and fracture behavior of laser welded-brazed Mg alloys to Zn-coated steel,” Int. J. Adv. Manuf. Technol., vol. 68, no. 5–8, pp. 1179–1188, 2013, doi: 10.1007/s00170-013-4910-4.

[100] X. Zhao et al., “Effect of the Ni coating thickness on laser welding-brazing of Mg/steel,” J. Alloys Compd., vol. 769, pp. 1042–1058, 2018, doi: 10.1016/j.jallcom.2018.08.080.

[101] L. Li, C. Tan, Y. Chen, W. Guo, and C. Mei, “CO2 laser welding-brazing characteristics of dissimilar metals AZ31B Mg alloy to Zn coated dual phase steel with Mg based filler,” J. Mater. Process. Technol., vol. 213, no. 3, pp. 361–375, 2013, doi: 10.1016/j.jmatprotec.2012.10.009.

[102] A. M. Nasiri, D. C. Weckman, and Y. Zhou, “Interfacial microstructure of diode laser brazed AZ31B magnesium to steel sheet using a nickel interlayer,” Weld. J., vol. 92, no. 1, 2013.

[103] Y. G. Miao, D. F. Han, J. Z. Yao, and F. Li, “Microstructure and interface characteristics of laser penetration brazed magnesium alloy and steel,” Sci. Technol. Weld. Join., vol. 15, no. 2, pp. 97–103, 2010, doi: 10.1179/136217109X12518083193676.

[104] L. Li, C. Tan, Y. Chen, W. Guo, and F. Song, “Comparative study on microstructure and mechanical properties of laser welded-brazed Mg/mild steel and Mg/stainless steel joints,” Mater. Des., vol. 43, pp. 59–65, 2013, doi: 10.1016/j.matdes.2012.06.057.

[105] C. Tan et al., “Influence of Laser Power on the Microstructure and Mechanical Properties of a Laser Welded-Brazed Mg Alloy/Ni-Coated Steel Dissimilar Joint,” J. Mater. Eng. Perform., vol. 26, no. 6, pp. 2983–2997, 2017, doi: 10.1007/s11665-017-2726-3.

[106] A. M. Hasiri and E. Al, “Interfacial Microstructure of Laser Brazed AZ31B Magnesium to Sn - Plated Steel Sheet,” Weld. J., vol. 94, no. 03, pp. 61–72, 2015.

[107] L. Li, C. Tan, Y. Chen, W. Guo, and X. Hu, “Influence of Zn coating on interfacial reactions and mechanical properties during laser welding-brazing of Mg to steel,” Metall. Mater. Trans. A Phys. Metall. Mater. Sci., vol. 43, no. 12, pp. 4740–4754, 2012, doi: 10.1007/s11661-012-1266-6.

[108] Y. Miao, D. Han, J. Yao, and F. Li, “Effect of laser offsets on joint performance of laser penetration brazing for magnesium alloy and steel,” Mater. Des., vol. 31, no. 6, pp. 3121–3126, 2010, doi: 10.1016/j.matdes.2009.12.035.

[109] A. M. Nasiri, L. Li, S. H. Kim, Y. Zhou, D. C. Weckman, and T. C. Nguyen, “Microstructure and properties of laser brazed magnesium to coated steel,” Weld. J., vol. 90, no. 11, 2011.

[110] Y. Miao, D. Han, X. Xu, and B. Wu, “Phase constitution in the interfacial region of laser penetration brazed magnesium-steel joints,” Mater. Charact., vol. 93, pp. 87–93, 2014, doi: 10.1016/j.matchar.2014.03.019.

[111] C. W. Tan, Y. B. Chen, L. Q. Li, and W. Guo, “Comparative study of microstructure and mechanical properties of laser welded-brazed Mg/steel joints with four different coating surfaces,” Sci. Technol. Weld. Join., vol. 18, no. 6, pp. 466–472, 2013, doi: 10.1179/1362171813Y.0000000123.

[112] C. Tan, X. Song, S. Meng, B. Chen, L. Li, and J. Feng, “Laser welding-brazing of Mg to stainless steel: joining characteristics, interfacial microstructure, and mechanical properties,” Int. J. Adv. Manuf. Technol., vol. 86, no. 1–4, pp. 203–213, 2016, doi: 10.1007/s00170-015-8165-0.

[113] G. Song, T. Li, J. Chi, and L. Liu, “Bonding of immiscible Mg/steel by butt fusion welding,” Scr. Mater., vol. 157, pp. 10–14, 2018, doi: 10.1016/j.scriptamat.2018.07.031.

[114] G. Song, T. Li, Z. Zhang, and L. Liu, “Investigation of unequal thickness Mg/steel butt-welded plate by hybrid laser-tungsten inert gas welding with a Ni interlayer,” J. Manuf. Process., vol. 30, pp. 299–302, 2017, doi: 10.1016/j.jmapro.2017.09.019.

[115] X. D. Qi and L. M. Liu, “Comparative study on characteristics of hybrid laser-TIG welded AZ61/Q235 lap joints with and without interlayers,” J. Mater. Sci., vol. 45, no. 14, pp. 3912–3920, 2010, doi: 10.1007/s10853-010-4451-2.

[116] L. Liu and R. Xu, “Investigation of corrosion behavior of Mg-steel laser-TIG hybrid lap joints,” Corros. Sci., vol. 54, no. 1, pp. 212–218, 2012, doi: 10.1016/j.corsci.2011.09.017.

[117] L. Liu, X. Qi, and Z. Zhang, “The effect of alloying elements on the shear strength of the lap joint of AZ31B Magnesium alloy to Q235 steel by Hybrid Laser-Tig welding technique,” Metall. Mater. Trans. A Phys. Metall. Mater. Sci., vol. 43, no. 6, pp. 1976–1988, 2012, doi: 10.1007/s11661-011-1071-7.

[118] G. Song, T. Li, and L. Chen, “The mechanical properties and interface bonding mechanism of immiscible Mg/steel by laser–tungsten inert gas welding with filler wire,” Mater. Sci. Eng. A, vol. 736, pp. 306–315, 2018, doi: 10.1016/j.msea.2018.08.078.

[119] L. M. Liu and C. Shan, “Study on laser-tungsten inert gas hybrid welding of dissimilar Mg alloy and steel with Ni as interlayer,” Materwiss. Werksttech., vol. 40, no. 10, pp. 780–783, 2009, doi: 10.1002/mawe.200900497.

[120] G. Song and C. Shan, “Microstructures of laser-tungsten inert gas hybrid welding of dissimilar AZ31 Mg alloy and Q235 steel with Ni as interlayer,” Mater. Res. Innov., vol. 15, no. 2, pp. 145–149, 2011, doi: 10.1179/143307511X12998222919074.

[121] L. Liu and X. Qi, “Effects of copper addition on microstructure and strength of the hybrid laser-TIG welded joints between magnesium alloy and mild steel,” J. Mater. Sci., vol. 44, no. 21, pp. 5725–5731, 2009, doi: 10.1007/s10853-009-3797-9.

[122] L. Liu, X. Qi, and Z. Wu, “Microstructural characteristics of lap joint between magnesium alloy and mild steel with and without the addition of Sn element,” Mater. Lett., vol. 64, no. 1, pp. 89–92, 2010, doi: 10.1016/j.matlet.2009.10.023.

[123] G. Song, J. Yu, T. Li, J. Wang, and L. Liu, “Effect of laser-GTAW hybrid welding heat input on the performance of Mg/Steel butt joint,” J. Manuf. Process., vol. 31, pp. 131–138, 2018, doi: 10.1016/j.jmapro.2017.09.029.

[124] G. Song, H. yang Wang, T. tao Li, and L. ming Liu, “Joining mechanism of Mg alloy/steel butt joints with Cu–Zn interlayer by hybrid laser–TIG welding source,” J. Iron Steel Res. Int., vol. 25, no. 2, pp. 221–227, 2018, doi: 10.1007/s42243-018-0024-4.

[125] Y. Miao, B. Wu, X. Xu, and D. Han, “Effect of heat input on microstructure and mechanical properties of joints made by bypass-current MIG welding-brazing of magnesium alloy to galvanized steel,” Acta Metall. Sin. (English Lett., vol. 27, no. 6, pp. 1038–1045, 2014, doi: 10.1007/s40195-014-0118-3.

[126] X. Y. Wang, X. Y. Gu, D. Q. Sun, and C. Y. Xi, “Interface characteristics and mechanical behavior of metal inert-gas arc welded Mg-steel joints,” J. Mater. Res., vol. 31, no. 5, pp. 589–598, 2016, doi: 10.1557/jmr.2016.43.

[127] S. Liu, D. Sun, X. Gu, and H. Li, “Microstructures and mechanical properties of metal inert-gas arc welded joints of Mg alloy and ultra-high strength steel,” J. Mater. Res., vol. 32, no. 4, pp. 843–851, 2017, doi: 10.1557/jmr.2016.515.

[128] X. Y. Wang, D. Q. Sun, and Y. Sun, “Influence of Cu-Interlayer Thickness on Microstructures and Mechanical Properties of MIG-Welded Mg-Steel Joints,” J. Mater. Eng. Perform., vol. 25, no. 3, pp. 910–920, 2016, doi: 10.1007/s11665-016-1945-3.

[129] X. Y. Wang, D. Q. Sun, S. Q. Yin, and D. Y. Liu, “Microstructures and mechanical properties of metal inert-gas arc welded Mg-steel dissimilar joints,” Trans. Nonferrous Met. Soc. China (English Ed., vol. 25, no. 8, pp. 2533–2542, 2015, doi: 10.1016/S1003-6326(15)63872-9.

[130] M. Kang, C. Kim, and Y. M. Kim, “Joining of AZ31 magnesium alloy and steel sheet under four different coating conditions based on gas metal arc weld-brazing,” Mater. Trans., vol. 58, no. 1, pp. 95–102, 2017, doi: 10.2320/matertrans.M2016224.

[131] S. Kotari, E. Punna, S. M. Gangadhar, M. Cheepu, P. Sarkar, and S. Venukumar, “Dissimilar metals TIG welding-brazing of AZ31 magnesium alloy to 304 stainless steel,” Mater. Today Proc., vol. 39, no. xxxx, pp. 1549–1552, 2020, doi: 10.1016/j.matpr.2020.05.553.

[132] M. Ding et al., “TIG-MIG hybrid welding of ferritic stainless steels and magnesium alloys with Cu interlayer of different thickness,” Mater. Des., vol. 88, pp. 375–383, 2015, doi: 10.1016/j.matdes.2015.09.022.

[133] R. Z. Xu et al., “Influencing mechanism of Al–Zn coating addition on interfacial microstructure and mechanical property of vacuum electron beam welded Mg/steel joint,” Vacuum, vol. 158, pp. 31–38, 2018, doi: 10.1016/j.vacuum.2018.09.026.

[134] Q. Lin, F. Yang, R. Cao, J. Chen, and T. Guo, “Wetting and Interfacial Characteristics of Mg AZ61 Alloy/Galvanized Steel in Cold Metal Transfer Process,” Metall. Mater. Trans. A Phys. Metall. Mater. Sci., vol. 46, no. 9, pp. 3793–3796, 2015, doi: 10.1007/s11661-015-3005-2.

[135] R. Cao et al., “Weldability and distortion of Mg AZ31-to-galvanized steel SPOT plug welding joint by cold metal transfer method,” J. Manuf. Sci. Eng. Trans. ASME, vol. 139, no. 2, pp. 1–11, 2017, doi: 10.1115/1.4034009.

[136] C. Zhang, M. Wu, Y. Wang, and J. Pu, “Microstructure and mechanical properties of cold metal transfer welded galvanized steel/magnesium alloy dissimilar joints,” Int. J. Mod. Phys. B, vol. 34, no. 1–3, pp. 1–7, 2020, doi: 10.1142/S0217979220400603.

[137] R. Cao, J. Y. Yu, J. H. Chen, and P. C. Wang, “Feasibility of cold-metal-transfer welding magnesium AZ31 to galvanized mild steel,” Weld. J., vol. 92, no. 9, 2013.

[138] R. Cao, H. X. Zhu, Q. Wang, C. Dong, Q. Lin, and J. H. Chen, “Effects of zinc coating on magnesium alloy–steel joints produced by cold metal transfer method,” Mater. Sci. Technol. (United Kingdom), vol. 32, no. 18, pp. 1805–1817, 2016, doi: 10.1080/02670836.2016.1148107.

[139] R. Cao, J. H. Chang, Q. Huang, X. B. Zhang, Y. J. Yan, and J. H. Chen, “Behaviors and effects of Zn coating on welding-brazing process of Al-Steel and Mg-steel dissimilar metals,” J. Manuf. Process., vol. 31, pp. 674–688, 2018, doi: 10.1016/j.jmapro.2018.01.001.

[140] J. Chen, B. Shalchi Amirkhiz, and R. Zhang, “Continuous nanoscale Al2Fe transition layer strengthened magnesium-steel spot joints,” Mater. Lett., vol. 196, pp. 242–244, 2017, doi: 10.1016/j.matlet.2017.03.020.

[141] X. J. Yuan, G. M. Sheng, J. Luo, and J. Li, “Microstructural characteristics of joint region during diffusion-brazing of magnesium alloy and stainless steel using pure copper interlayer,” Trans. Nonferrous Met. Soc. China (English Ed., vol. 23, no. 3, pp. 599–604, 2013, doi: 10.1016/S1003-6326(13)62505-4.

[142] W. M. Elthalabawy and T. I. Khan, “Eutectic bonding of austenitic stainless steel 316L to magnesium alloy AZ31 using copper interlayer,” Int. J. Adv. Manuf. Technol., vol. 55, no. 1–4, pp. 235–241, 2011, doi: 10.1007/s00170-010-3026-3.

[143] J. Cheng, X. Hu, X. Sun, A. Vivek, G. Daehn, and D. Cullen, “Multi-scale characterization and simulation of impact welding between immiscible Mg/steel alloys,” J. Mater. Sci. & Technol., 2020, doi: 10.1016/j.jmst.2020.04.049.

[144] W. Elthalabawy and T. Khan, “Liquid Phase Bonding of 316L Stainless Steel to AZ31 Magnesium Alloy,” J. Mater. Sci. Technol., vol. 27, no. 1, pp. 22–28, 2011, doi: 10.1016/S1005-0302(11)60020-0.

[145] T. Araki, M. Koba, S. Nambu, J. Inoue, and T. Koseki, “Reactive transient liquid phase bonding between AZ31 magnesium alloy and low carbon steel,” Mater. Trans., vol. 52, no. 3, pp. 568–571, 2011, doi: 10.2320/matertrans.M2010359.

[146] T. P. Chen and W. Lin, “Optimal FSW process parameters for interface and welded zone toughness of dissimilar aluminium – steel joint,” vol. 15, no. 4, pp. 279–285, 2010, doi: 10.1179/136217109X12518083193711.

[147] M. P. Miles, Z. Feng, K. Kohkonen, B. Weickum, R. Steel, and L. Lev, “Spot joining of AA 5754 and high strength steel sheets by consumable bit,” vol. 15, no. 4, pp. 325–331, 2010, doi: 10.1179/136217110X12707333260491.

[148] K. Kumar and S. V. Kailas, “Positional dependence of material flow in friction stir welding: Analysis of joint line remnant and its relevance to dissimilar metal welding,” Sci. Technol. Weld. Join., vol. 15, no. 4, pp. 305–311, 2010, doi: 10.1179/136217109X12568132624280.

[149] Y. S. Sato, A. Shiota, H. Kokawa, K. Okamoto, Q. Yang, and C. Kim, “Effect of interfacial microstructure on lap shear strength of friction stir spot weld of aluminium alloy to magnesium alloy,” vol. 15, no. 4, pp. 319–324, 2010, doi: 10.1179/136217109X12568132624208.

[150] S. M. O. Tavares, R. A. S. Castro, and P. Vilac, “Friction stir welding of T-joints with dissimilar aluminium alloys : mechanical joint characterisation,” vol. 15, no. 4, pp. 312–319, 2010, doi: 10.1179/136217109X12562846839114.

[151] D. Choi et al., “Effect of fixed location variation in friction stir welding of steels with different carbon contents,” vol. 15, no. 4, pp. 299–304, 2010, doi: 10.1179/136217109X12577814486737.

[152] L. E. Murr, L. E. Murr, and E. Paso, “A Review of FSW Research on Dissimilar Metal and Alloy Systems,” vol. 19, no. November 2010, pp. 1071–1089, 2024, doi: 10.1007/s11665-010-9598-0.

[153] V. Tran and J. Pan, “Failure modes of friction stir spot welds in cross-tension specimens of dissimilar aluminium sheets,” vol. 15, no. 4, pp. 286–292, 2010, doi: 10.1179/136217109X12568132624361.

[154] V. Pratap, S. Kumar, A. Ranjan, and B. Kuriachen, “Recent research progress in solid state friction-stir welding of aluminium – magnesium alloys : a critical review,” Integr. Med. Res., no. x x, pp. 1–40, 2020, doi: 10.1016/j.jmrt.2020.01.008.

[155] R. Arun, P. Kumar, and R. Shimpi, “Materials Today : Proceedings Friction stir welding parameters and application : A review,” Mater. Today Proc., no. xxxx, pp. 1–5, 2019, doi: 10.1016/j.matpr.2019.07.613.

[156] T. Debroy and H. K. D. H. Bhadeshia, “Friction stir welding of dissimilar alloys – a perspective,” vol. 15, no. 4, pp. 266–270, 2010, doi: 10.1179/174329310X12726496072400.

[157] M. S. Sidhu and S. S. Chatha, “Friction Stir Welding – Process and its Variables : A Review,” Int. J. Emerg. Technol. Adv. Eng., vol. 2, no. 12, pp. 275–279, 2012.

[158] J. P. VERMA, S. M. & MISRA, “A Critical Review of Friction Stir Welding Process,” in DAAAM INTERNATIONAL SCIENTIFIC BOOK 2015, no. September, 2015. doi: 10.2507/daaam.scibook.2015.22.

[159] R. P. Singh, S. Dubey, A. Singh, and S. Kumar, “Materials Today : Proceedings A review paper on friction stir welding process,” Mater. Today Proc., no. xxxx, pp. 5–10, 2020, doi: 10.1016/j.matpr.2020.05.208.

[160] A. A. Luo, “Magnesium : Current and Potential Automotive Applications,” pp. 42–48, 2002.

[161] E. Mg-ai-zn, “Magnesium alloys and applications,” vol. 10, no. January 1994, 2023.

[162] Miklós Tisza, “Development of Lightweight Steels for Automotive Applications,” in Engineering Steels and High Entropy-Alloys,2020.

[163] M. K. Singh, “Application of Steel in Automotive Industry Application of Steel in Automotive Industry,” no. February, 2017.

[164] B. Beheshtipour, K. Janie, H. Krawczynski, R. W. Hall, A. Foster, and H. Praturlon, “Application and development trends in high strength steel and aluminium Application and development trends in high strength steel and aluminium”, doi: 10.1088/1757-899X/448/1/012031.

[165] R. Neugebauer, C. Kraus, and S. Dietrich, “CIRP Annals - Manufacturing Technology Advances in mechanical joining of magnesium,” vol. 57, pp. 283–286, 2008, doi: 10.1016/j.cirp.2008.03.025.

[166] X. Hu, Advanced High-Strength Steel — Basics and Applications in the Automotive, no. April. 2021.

[167] A. A. Luo and A. K. Sachdev, Applications of magnesium alloys in automotive engineering. Woodhead Publishing Limited, 2012. doi: 10.1533/9780857093844.3.393.

[168] S. C. Kil and H. T. Kim, “Welding Technology of Lightweight Alloys,” vol. 582, pp. 75–80, 2008, doi: 10.4028/www.scientific.net/MSF.580-582.75.

[169] L. Liu, Welding metallurgy of magnesium alloys. Woodhead Publishing Limited, 2010. doi: 10.1533/9780857090423.1.9.

[170] F. Czerwinski, “Welding and Joining of Magnesium Alloys,” no. January, 2016, doi: 10.5772/13947.

[171] “Services to the Automotive Industry Automotive at TWI”.

[172] K. Singh, G. Singh, and H. Singh, “Review on friction stir welding of magnesium alloys,” J. Magnes. Alloy., vol. 6, no. 4, pp. 399–416, 2018, doi: 10.1016/j.jma.2018.06.001.

[173] A. Gullino, P. Matteis, and F. D. Aiuto, “Review of Aluminum-To-Steel Welding Technologies for Car-Body Applications,” pp. 1–28, 2019, doi: 10.3390/met9030315.

[174] A. Benay, “Next-Generation Automotive Manufacturing Materials and Processes,” pp. 1–5, 2021.

[175] S. K. Park, S. T. Hong, J. H. Park, K. Y. Park, Y. J. Kwon, and H. J. Son, “Effect of material locations on properties of friction stir welding joints of dissimilar aluminium alloys,” Sci. Technol. Weld. Join., vol. 15, no. 4, pp. 331–336, 2010, doi: 10.1179/136217110X12714217309696.

[176] T. Sun, J. Jin, and J. Lu, “Investigation on Friction Stir Welding of Mg / Al T- Joints,” 2021.

[177] A. A. Mclean, G. L. F. Powell, I. H. Brown, and V. M. Linton, “Friction stir welding of magnesium alloy AZ31B to aluminium alloy 5083,” pp. 1–3, doi: 10.1179/136217103225009134.

[178] Y. J. Kwon, I. Shigematsu, and N. Saito, “Dissimilar friction stir welding between magnesium and aluminum alloys,” vol. 62, pp. 3827–3829, 2008, doi: 10.1016/j.matlet.2008.04.080.

[179] S. A. Hussein, A. S. M. Tahir, and A. B. Hadzley, “Characteristics of aluminum-to-steel joint made by friction stir welding: A review,” Mater. Today Commun., vol. 5, pp. 32–49, 2015, doi: 10.1016/j.mtcomm.2015.09.004.

[180] H. Aghajani and F. Khodabakhshi, “Simulation and experimental study of underwater dissimilar friction-stir welding between aluminium and steel,” Integr. Med. Res., no. x x, 2020, doi: 10.1016/j.jmrt.2020.02.003.

[181] H. Das, S. S. Jana, T. K. Pal, and A. De, “Numerical and experimental investigation on friction stir lap welding of aluminium to steel,” Sci. Technol. Weld. Join., vol. 19, no. 1, pp. 69–75, 2014, doi: 10.1179/1362171813Y.0000000166.

[182] K. Kimapong and T. Watanabe, “Lap Joint of A5083 Aluminum Alloy and SS400 Steel by Friction Stir Welding,” vol. 46, no. 4, pp. 835–841, 2005.

[183] M. Kimura, H. Ishii, M. Kusaka, K. Kaizu, and A. Fuji, “Joining phenomena and joint strength of friction welded joint between aluminium – magnesium alloy (AA5052) and low carbon steel,” vol. 14, no. 7, pp. 655–662, 2009, doi: 10.1179/136217109X12464549883411.

[184] T. Watanabe, H. Takayama, and A. Yanagisawa, “Joining of aluminum alloy to steel by friction stir welding,” vol. 178, pp. 342–349, 2006, doi: 10.1016/j.jmatprotec.2006.04.117.

[185] W. Lee, M. Schmuecker, A. Mercardo, G. Biallas, and S. Jung, “Interfacial reaction in steel – aluminum joints made by friction stir welding,” vol. 55, pp. 355–358, 2006, doi: 10.1016/j.scriptamat.2006.04.028.

[186] L. Wan and Y. Huang, “Friction stir welding of dissimilar aluminum alloys and steels: a review,” Int. J. Adv. Manuf. Technol., vol. 99, no. 5–8, pp. 1781–1811, 2018, doi: 10.1007/s00170-018-2601-x.

[187] W. H. Jiang and R. Kovacevic, “Proceedings of the Institution of Mechanical Engineers , Part B : Journal of Engineering Manufacture Feasibility study of friction stir welding of 6061-T6 aluminium alloy with AISI 1018 steel,” 2004, doi: 10.1243/0954405042323612.

[188] A. Elrefaey, M. Gouda, M. Takahashi, and K. Ikeuchi, “Characterization of Aluminum/Steel Lap Joint by Friction Stir Welding,” vol. 14, no. February, pp. 10–17, 2005, doi: 10.1361/10599490522310.

[189] A. HIROSE, “Trends of Applications and Joining Technologies of Aluminum Alloys in Automobiles,” J. Soc. Automot. Eng. Japan, vol. 61, no. 4, pp. 18–23, 2007, [Online]. Available: https://cir.nii.ac.jp/crid/1571980075716616064

[190] D. S. Kumar, C. T. Sasanka, K. Ravindra, and K. N. S. Suman, “Magnesium and Its Alloys in Automotive Applications – A Review,” vol. 4, no. 1, pp. 12–30, 2015, doi: 10.7726/ajmst.2015.1002.

[191] A. Manabe and M. E. Div, “Weight Reduction of Vehicles and Light Metals,” vol. 468, pp. 463–468, 1999.

[192] A. M. Nasiri, “Laser Brazing of Magnesium to Steel Sheet,” University of Waterloo, 2013.

[193] S. T. Auwal, S. Ramesh, F. Yusof, and S. M. Manladan, “A review on laser beam welding of titanium alloys,” 2018.

[194] S. SASABE, “Dissimilar metal joining technology of aluminum alloy to steel,” J. JSAE, vol. 61, pp. 24–29, 2007, [Online]. Available: https://cir.nii.ac.jp/crid/1570291225856347520

[195] M. A. Omar, The automotive body manufacturing systems and processes. John Wiley & Sons, 2011.

[196] H. C. Kim and T. J. Wallington, “Life-Cycle Energy and Greenhouse Gas Emission Bene fi ts of Lightweighting in Automobiles : Review and Harmonization,” 2013.

[197] F. Humpenöder et al., “Land-use and carbon cycle responses to moderate climate change : implications for land-based mitigation ?,” 2015, doi: 10.1021/es506201r.

[198] T. Ishikawa et al., “Overview of automotive structural composites technology developments in Japan,” Compos. Sci. Technol., vol. 155, pp. 221–246, 2018, doi: 10.1016/j.compscitech.2017.09.015.

[199] M. and C. Cars and Metal, “The World Steel Association,” 2008.

[200] The World Steel Association, “Steel in automotive,” 2019.

[201] T. Senuma, “Physical Metallurgy of Modern High Strength Steel Sheets,” vol. 41, no. 6, pp. 520–532, 2001.

[202] Office of Energy Efficiency & Renewable Energy, “Lightweight materials for cars and trucks,” 2014.

[203] P. K. Sahu and S. Pal, “Influence of metallic foil alloying by FSW process on mechanical properties and metallurgical characterization of AM20 Mg alloy,” Mater. Sci. Eng. A, vol. 684, 2017, doi: 10.1016/j.msea.2016.12.081.

[204] W. Lafayette, “Magnesium Alloys 2003,” vol. 422, pp. 43–50, 2003, doi: 10.4028/www.scientific.net/MSF.419-422.43.

[205] L. Liu, D. Ren, and F. Liu, “A Review of Dissimilar Welding Techniques for Magnesium Alloys to Aluminum Alloys,” pp. 3735–3757, 2014, doi: 10.3390/ma7053735.

[206] S. M. Manladan, F. Yusof, S. Ramesh, and M. Fadzil, “A review on resistance spot welding of magnesium alloys,” 2020, doi: 10.1007/s00170-015-8258-9.

[207] S. T. Auwal et al., “Influence of electrodeposited Cu-Ni layer on interfacial reaction and mechanical properties of laser welded-brazed Mg / Ti lap joints,” J. Manuf. Process., vol. 37, no. November 2018, pp. 251–265, 2019, doi: 10.1016/j.jmapro.2018.11.029.

[208] S. R. Agnew, “Wrought Magnesium : A 21st Century Outlook,” no. May, 2004.

[209] H. Watarai, “Trend of Research and Development for Magnesium Alloys-Reducing the Weight of Structural Materialsin Motor Vehicles,” 2006.

[210] W. J. Joost, “Reducing vehicle weight and improving U.S. energy efficiency using integrated computational materials engineering,” Jom, vol. 64, no. 9, pp. 1032–1038, 2012, doi: 10.1007/s11837-012-0424-z.

[211] S. Whalen, N. Overman, V. Joshi, T. Varga, D. Graff, and C. Lavender, “Magnesium alloy ZK60 tubing made by Shear Assisted Processing and Extrusion (ShAPE),” Mater. Sci. Eng. A, vol. 755, no. March, pp. 278–288, 2019, doi: 10.1016/j.msea.2019.04.013.

[212] S. Kleinbaum, C. Jiang, and S. Logan, “Enabling sustainable transportation through joining of dissimilar lightweight materials,” MRS Bull., vol. 44, no. 8, pp. 608–612, 2019, doi: 10.1557/mrs.2019.178.

[213] L. Liu, “Welding and joining of magnesium alloys to aluminum alloys,” in Welding and Joining of Magnesium Alloys, Elsevier, 2010, pp. 38-63e. doi: 10.1533/9780857090423.1.38.

[214] V. K. Patel, S. D. Bhole, and D. L. Chen, “Influence of ultrasonic spot welding on microstructure in a magnesium alloy,” Scr. Mater., vol. 65, 2011, doi: 10.1016/j.scriptamat.2011.08.009.

[215] V. V. Joshi, D. Orlov, J. B. Jordon, and N. R. Neelameggham, Magneisum Technology 2019. 2019.

[216] N. Kumar, W. Yuan, and R. S. R. S. Mishra, Friction Stir Welding of Dissimilar Alloys and Materials. 2015. doi: 10.1016/C2014-0-01707-8.

[217] N. Kulkarni, R. S. Mishra, and W. Yuan, Friction stir welding of dissimilar alloys and materials. Butterworth-Heinemann, 2015.

[218] M. Abbasi, A. K. Taheri, and M. T. Salehi, “Growth rate of intermetallic compounds in Al / Cu bimetal produced by cold roll welding process,” vol. 319, pp. 233–241, 2001.

[219] K. P. Mehta, V. J. Badheka, K. P. Mehta, and V. J. Badheka, “A Review on Dissimilar Friction Stir Welding of Copper to Aluminum : Process , Properties , and Variants,” vol. 6914, no. December 2015, 2016, doi: 10.1080/10426914.2015.1025971.

[220] D. Lohwasser and Z. Chen, Friction stir welding: From basics to applications. Elsevier, 2009.

[221] V. Infante and C. Vidal, Tool and welding design. Woodhead Publishing Limited, 2014. doi: 10.1533/9780857094551.199.

[222] R. Rai, H. K. D. H. Bhadeshia, and T. Debroy, “Review : friction stir welding tools,” vol. 16, no. 4, pp. 325–342, 2011, doi: 10.1179/1362171811Y.0000000023.

[223] N. Sharma, Z. A. Khan, and A. N. Siddiquee, “Friction stir welding of aluminum to copper - An overview,” Trans. Nonferrous Met. Soc. China, vol. 27, no. 10, pp. 2113–2136, 2017, doi: 10.1016/S1003-6326(17)60238-3.

[224] T. Watanabe, K. Kagiya, A. Yanagisawa, and H. Tanabe, “Solid state welding of steel and magnesium alloy using a rotating pin,” Q. J. Japan Weld. Soc., vol. 24, no. 1, pp. 108–115, 2006.

[225] A. Esmaeili, H. R. Zareie Rajani, M. Sharbati, M. K. B. Givi, and M. Shamanian, “The role of rotation speed on intermetallic compounds formation and mechanical behavior of friction stir welded brass/aluminum 1050 couple,” Intermetallics, vol. 19, no. 11, pp. 1711–1719, 2011, doi: 10.1016/j.intermet.2011.07.006.

[226] H. Fujii, L. Cui, M. Maeda, and K. Nogi, “Effect of tool shape on mechanical properties and microstructure of friction stir welded aluminum alloys,” vol. 419, pp. 25–31, 2006, doi: 10.1016/j.msea.2005.11.045.

[227] Y. N. Zhang, X. Cao, S. Larose, and P. Wanjara, “Review of tools for friction stir welding and processing,” Can. Metall. Q., vol. 51, no. 3, pp. 250–261, 2012, doi: 10.1179/1879139512Y.0000000015.

[228] V. P. Singh, S. K. Patel, N. Kumar, and B. Kuriachen, “Parametric effect on dissimilar friction stir welded steel-magnesium alloys joints: a review,” Sci. Technol. Weld. Join., vol. 24, no. 8, pp. 653–684, 2019, doi: 10.1080/13621718.2019.1567031.

[229] A. Barcellona, G. Buffa, L. Fratini, and others, “Process parameters analysis in friction stir welding of AA6082-T6 sheets,” 2004.

[230] E. Akinlabi and A. Els-Botes, “Effect of Travel speed on Joint properties of Dissimilar Metal Friction Stir Welds.,” News.Mak.Ac.Ug, no. March, pp. 155–161, 2011.

[231] K. K. Ramachandran, N. Murugan, and S. Shashi Kumar, “Influence of tool traverse speed on the characteristics of dissimilar friction stir welded aluminium alloy, AA5052 and HSLA steel joints,” Arch. Civ. Mech. Eng., vol. 15, no. 4, pp. 822–830, 2015, doi: 10.1016/j.acme.2015.06.002.

[232] S. S. Sabari, S. Malarvizhi, and V. Balasubramanian, “Influences of tool traverse speed on tensile properties of air cooled and water cooled friction stir welded AA2519-T87 aluminium alloy joints,” J. Mater. Process. Technol., 2016, doi: 10.1016/j.jmatprotec.2016.06.015.

[233] T. Sakthivel, G. S. Sengar, and J. Mukhopadhyay, “Effect of welding speed on microstructure and mechanical properties of friction-stir-welded aluminum,” Int. J. Adv. Manuf. Technol., vol. 43, no. 5–6, pp. 468–473, 2009, doi: 10.1007/s00170-008-1727-7.

[234] Z. Shen, Y. Ding, J. Chen, and A. P. Gerlich, “Comparison of fatigue behavior in Mg/Mg similar and Mg/steel dissimilar refill friction stir spot welds,” Int. J. Fatigue, vol. 92, pp. 78–86, 2016, doi: 10.1016/j.ijfatigue.2016.06.033.

[235] M. Ericsson and R. Sandström, “Influence of welding speed on the fatigue of friction stir welds, and comparison with MIG and TIG,” Int. J. Fatigue, vol. 25, no. 12, pp. 1379–1387, 2003, doi: 10.1016/S0142-1123(03)00059-8.

[236] B. L. Prasad et al., “Joining of AZ91 Mg alloy and Al6063 alloy sheets by friction stir welding,” J. Magnes. Alloy., vol. 6, no. 1, pp. 71–76, 2018, doi: 10.1016/j.jma.2017.12.004.

[237] M. Pourali, A. Abdollah-zadeh, T. Saeid, and F. Kargar, “Influence of welding parameters on intermetallic compounds formation in dissimilar steel/aluminum friction stir welds,” J. Alloys Compd., vol. 715, pp. 1–8, 2017, doi: 10.1016/j.jallcom.2017.04.272.

[238] H. Okamura and K. Aota, “Joining of dissimilar materials with friction stir welding,” Weld. Int., vol. 18, no. 11, pp. 852–860, 2004, doi: 10.1533/wint.2004.3344.

[239] Y. S. Sato, T. W. Nelson, C. J. Sterling, R. J. Steel, and C. O. Pettersson, “Microstructure and mechanical properties of friction stir welded SAF 2507 super duplex stainless steel,” Mater. Sci. Eng. A, vol. 397, no. 1–2, pp. 376–384, 2005, doi: 10.1016/j.msea.2005.02.054.

[240] S. Tan, F. Zheng, J. Chen, J. Han, Y. Wu, and L. Peng, “Effects of process parameters on microstructure and mechanical properties of friction stir lap linear welded 6061 aluminum alloy to NZ30K magnesium alloy,” J. Magnes. Alloy., vol. 5, no. 1, pp. 56–63, 2017, doi: 10.1016/j.jma.2016.11.005.

[241] E. T. Akinlabi, A. Els-Botes, and H. Lombard, “Effect of tool displacement on defect formation in friction stir welding of aluminium and copper,” in Proceedings of the 8th International Friction Stir Welding Symposium, Hamburg, Germany, 2010, pp. 76–78.

[242] Y. Chen, J. Chen, B. Shalchi Amirkhiz, M. J. Worswick, and A. P. Gerlich, “Microstructures and properties of Mg alloy/DP600 steel dissimilar refill friction stir spot welds,” Sci. Technol. Weld. Join., vol. 20, no. 6, pp. 494–501, 2015.

[243] M. M. Attallah and H. G. Salem, “Friction stir welding parameters : a tool for controlling abnormal grain growth during subsequent heat treatment,” vol. 391, pp. 51–59, 2005, doi: 10.1016/j.msea.2004.08.059.

[244] S. Zhao et al., “Effects of tool geometry on friction stir welding of AA6061 to TRIP steel,” J. Mater. Process. Technol., vol. 261, pp. 39–49, Nov. 2018, doi: 10.1016/j.jmatprotec.2018.06.003.

[245] M. Akbari, R. Abdi Behnagh, and A. Dadvand, “Effect of materials position on friction stir lap welding of Al to Cu,” Sci. Technol. Weld. Join., vol. 17, no. 7, pp. 581–588, 2012, doi: 10.1179/1362171812Y.0000000049.

[246] A. Arici and S. Selale, “Effects of tool tilt angle on tensile strength and fracture locations of friction stir welding of polyethylene,” Sci. Technol. Weld. Join., vol. 12, no. 6, pp. 536–539, 2007.

[247] K. P. Mehta and V. J. Badheka, “Effects of tilt angle on the properties of dissimilar friction stir welding copper to aluminum,” Mater. Manuf. Process., vol. 31, no. 3, pp. 255–263, 2016, doi: 10.1080/10426914.2014.994754.

[248] M. H. Tolephih, H. M. Mahmood, A. H. Hashem, and E. T. Abdullah, “Effect of tool offset and tilt angle on weld strength of butt joint friction stir welded specimens of AA2024 aluminum alloy welded to commercial pure cupper,” Chem. Mater. Res, vol. 3, pp. 49–58, 2013.

[249] ASTM E3-11(2017), “Standard Guide for Preparation of Metallographic Specimens,” ASTM Int. West Conshohocken, PA, 2017, doi: https://doi.org/10.1520/E0003-11R17.

[250] ASTM E407-07(2015)e1, “Standard Practice for Microetching Metals and Alloys,” ASTM Int. West Conshohocken, PA, 2015, doi: https://doi.org/10.1520/E0407-07R15E01.

[251] ASTM E384-17, “Standard Test Method for Microindentation Hardness of Materials,” ASTM Int. West Conshohocken, PA, 2017, doi: https://doi.org/10.1520/E0384-17

[252] Y. C. Chen, T. Komazaki, Y. G. Kim, T. Tsumura, and K. Nakata, “Interface microstructure study of friction stir lap joint of AC4C cast aluminum alloy and zinc-coated steel,” Mater. Chem. Phys., vol. 111, no. 2–3, pp. 375–380, 2008, doi: 10.1016/j.matchemphys.2008.04.038.

[253] P. Ulysse, “Three-dimensional modeling of the friction stir-welding process,” Int. J. Mach. Tools Manuf., vol. 42, no. 14, pp. 1549–1557, 2002, doi: 10.1016/S0890-6955(02)00114-1.

[254] H. J. Zhang, H. J. Liu, and L. Yu, “Microstructure and mechanical properties as a function of rotation speed in underwater friction stir welded aluminum alloy joints,” Mater. Des., vol. 32, no. 8–9, pp. 4402–4407, 2011, doi: 10.1016/j.matdes.2011.03.073.

[255] X. Zhao, F. Dong, G. Su, and L. Guo, “Weld Quality Improvement with Hybrid FSW Technology assisted by Preheating for Copper T2 / Aluminium 5A06 Dissimilar Materials,” vol. 126, pp. 1707–1711, 2012, doi: 10.4028/www.scientific.net/AMM.121-126.1707.

[256] H. J. Liu, J. J. Shen, L. Zhou, Y. Q. Zhao, C. Liu, and L. Y. Kuang, “Microstructural characterisation and mechanical properties of friction stir welded joints of aluminium alloy to copper,” vol. 16, no. 1, pp. 92–99, 2011, doi: 10.1179/1362171810Y.0000000007.

[257] S. Shah and S. Tosunoglu, “Friction Stir Welding : Current State of the Art and Future Prospects,” pp. 1–6, 2012.

[258] W. M. Thomas, K. I. Johnson, and C. S. Wiesner, “Friction Stir Welding – Recent Developments in Tool and Process Technologies,” Adv. Eng. Mater., vol. 5, no. 7, pp. 485–490, Jul. 2003, doi: 10.1002/adem.200300355.

[259] W. M. Thomas, D. G. Staines, I. M. Norris, and R. De Frias, “Friction stir welding tools and developments,” Nov. 07, 2003. doi: 10.1007/BF03266403.

[260] U. Singarapu, K. Adepu, and S. R. Arumalle, “Influence of tool material and rotational speed on mechanical properties of friction stir welded AZ31B magnesium alloy,” J. Magnes. Alloy., vol. 3, no. 4, pp. 335–344, 2015.

[261] A. Esmaeili, M. K. B. Givi, and H. R. Z. Rajani, “Investigation of weld defects in dissimilar friction stir welding of aluminium to brass by radiography,” Sci. Technol. Weld. Join., vol. 17, no. 7, pp. 539–543, 2012.

[262] K. N. Krishnan, “On the formation of onion rings in friction stir welds,” Mater. Sci. Eng. A, vol. 327, no. 2, pp. 246–251, 2002.

[263] Y. Zhao, L. Zhou, Q. Wang, K. Yan, and J. Zou, “Defects and tensile properties of 6013 aluminum alloy T-joints by friction stir welding,” Mater. \& Des., vol. 57, pp. 146–155, 2014.

[264] R. Crawford, G. E. Cook, A. M. Strauss, D. A. Hartman, and M. A. Stremler, “Experimental defect analysis and force prediction simulation of high weld pitch friction stir welding,” Sci. Technol. Weld. Join., vol. 11, no. 6, pp. 657–665, 2006.

[265] K. Kumar and S. V Kailas, “The role of friction stir welding tool on material flow and weld formation,” Mater. Sci. Eng. A, vol. 485, no. 1–2, pp. 367–374, 2008.

[266] M. Tabatabaeipour, J. Hettler, S. Delrue, and K. Van Den Abeele, “Non-destructive ultrasonic examination of root defects in friction stir welded butt-joints,” Ndt \& E Int., vol. 80, pp. 23–34, 2016.

[267] M. Girard, B. Huneau, C. Genevois, X. Sauvage, and G. Racineux, “Friction stir diffusion bonding of dissimilar metals,” Sci. Technol. Weld. Join., vol. 15, no. 8, pp. 661–665, 2010.

[268] C.-Y. Lee, D.-H. Choi, Y.-M. Yeon, and S.-B. Jung, “Dissimilar friction stir spot welding of low carbon steel and Al--Mg alloy by formation of IMCs,” Sci. Technol. Weld. Join., vol. 14, no. 3, pp. 216–220, 2009.

[269] U. F. H. Suhuddin, V. Fischer, A. Kostka, and J. F. dos Santos, “Microstructure evolution in refill friction stir spot weld of a dissimilar Al–Mg alloy to Zn-coated steel,” Sci. Technol. Weld. Join., vol. 22, no. 8, pp. 658–665, 2017, doi: 10.1080/13621718.2017.1300744.

[270] I. Hejazi and S. E. Mirsalehi, “Effect of pin penetration depth on double-sided friction stir welded joints of AA6061-T913 alloy,” Trans. Nonferrous Met. Soc. China, vol. 26, no. 3, pp. 676–683, 2016.

Journal of Engineering and Technology for Industrial Applications

ISSN ONLINE: 2447-0228

ITEGAM-JETIA

Manaus, v.12 n.60, p.660-672, July/August, 2026.
DOI: https://doi.org/10.5935/jetia.v12i60.3950

RESEARCH ARTICLE OPEN ACCESS

A NOVEL PHOTOVOLTAIC-BASED WIRELESS EV CHARGING SYSTEM USING A MODIFIED TRANS-QUASI Z-SOURCE BOOST CONVERTER

Naveena Sandhadi*[1], Srinu Naik Ramavathu*[2]

[1, 2]Department of Electrical Engineering, Andhra University. Visakhapatnam, India.

[1]https://orcid.org/0009-0004-6198-9681, [2]https://orcid.org/0000-0003-2174-5274

Email:*naveenabujji119@gmail.com, drsrinunaikr@gmail.com

ARTICLE INFO

Article History
Received: March 7, 2026
Reviewed: June 12, 2026
Accepted: July 12, 2026
Published: July 31, 2026

Keywords:
Photovoltaic (PV) System,
Wireless Power Transfer (WPT),
Trans-Quasi Z-Source Boost Converter,
Aritficial Neural Networks,
Electric Vehicle Charging.

ABSTRACT

This paper proposes a PV-integrated wireless charging architecture for electric vehicles utilizing a modified Trans-Quasi Z-Source boost converter. The PV system is integrated with advanced power electronics for efficient energy conversion and management. It begins with photovoltaic cells generating voltage (V_{pv}) and current (I_{pv}), which are fed into the modified Trans-Quasi Z-Source boost converter. The converter employs PWM control to enhance the output voltage, which is then supplied to a high-frequency inverter. The inverter output is applied to an LC tank circuit to achieve resonance and efficient wireless power transfer. A high-frequency isolation transformer is used to ensure safety and improved performance in subsequent stages. The system incorporates an interleaved PWM rectifier to convert AC back to DC for charging the EV battery. The overall operation is optimized using an Artificial Neural Network (ANN)-based Maximum Power Point Tracking (MPPT) algorithm to maximize energy extraction from the PV system. A Proportional–Integral (PI) controller regulates the output voltage (V_{act}) to track the reference voltage (Vref), thereby enhancing system stability and efficiency. Finally, the project is implemented using MATLAB/Simulink 2024[a].

Copyright ©2026 by authors and Galileo Institute of Technology and Education of the Amazon (ITEGAM). This work is licensed under the Creative Commons Attribution International License (CC BY 4.0).

I. INTRODUCTION

The increasing global energy demand and rapid depletion of fossil fuel resources have accelerated the transition toward renewable energy-based power systems and electric vehicles (EVs). Conventional fossil-fuel-driven transportation contributes significantly to greenhouse gas emissions and environmental pollution, which necessitates the development of sustainable and eco-friendly energy solutions [1], [2]. Among various renewable energy sources, photovoltaic (PV) systems have gained considerable attention due to their clean energy generation, scalability, and wide availability. PV technology converts solar energy directly into electrical energy through the photovoltaic effect, making it a promising candidate for future sustainable charging infrastructures [3]. Simultaneously, the rapid growth of electric vehicles has created a strong demand for efficient, reliable, and user-friendly charging technologies. Traditional conductive charging systems require physical connectors, which may lead to cable wear, safety hazards, maintenance issues, and inconvenience in adverse environmental conditions [4]. Wireless Power Transfer (WPT) technology has emerged as an advanced alternative that enables contactless energy transmission through electromagnetic induction and resonant coupling [5]. This technology improves user convenience, electrical safety, and system automation while eliminating mechanical connection losses associated with wired charging systems [6]. In recent years, wireless charging systems have been widely applied in consumer electronics, electric vehicles, and portable devices due to their flexibility and ease of operation. Inductive and resonant wireless charging techniques operate based on the principle of electromagnetic coupling between transmitting and receiving coils, where alternating current in the primary coil generates a magnetic field that induces voltage in the secondary coil [7], [8]. The efficiency of wireless power transfer mainly depends on coil alignment, operating frequency, air gap, and compensation network design. Although WPT systems offer significant advantages, their efficiency is often lower than wired charging systems due to coupling losses and multiple power conversion stages [9], [10].

To enhance the sustainability of EV charging infrastructure, the integration of renewable energy sources, particularly PV systems, with wireless charging architecture has become an important research direction [11]. PV-integrated wireless charging systems enable direct utilization of solar energy for EV charging, thereby reducing grid dependency, operational costs, and carbon emissions [12]. However, the intermittent nature of solar irradiance and fluctuating PV output voltage pose significant challenges in maintaining stable power transfer and efficient energy conversion. Therefore, advanced power electronic converters and intelligent control techniques are essential to ensure reliable operation of PV-fed wireless charging systems [13], [14]. Power electronic converters play a crucial role in regulating voltage, improving power quality, and enhancing overall system efficiency in renewable energy-based charging applications. Conventional DC–DC converters used in PV systems often suffer from limited voltage gain, increased switching losses, and complex multi-stage conversion structures. To overcome these limitations, impedance-source converter topologies such as Z-source, quasi-Z-source, and trans quasi-Z-source converters have been introduced due to their inherent buck–boost capability, shoot-through immunity, and improved reliability [15–17]. These converters provide higher voltage gain and better dynamic performance compared to traditional boost converters, making them highly suitable for PV-integrated EV charging applications. Furthermore, intelligent energy management techniques such as Artificial Neural Network (ANN)-based Maximum Power Point Tracking (MPPT) algorithms are widely employed to extract maximum power from PV systems under varying environmental conditions.

In addition, closed-loop control strategies such as Proportional–Integral (PI) controllers are used to maintain stable output voltage and improve system dynamic response during fluctuating solar irradiance and load variations [18], [19]. Although several research works have focused on wireless EV charging and PV-based charging systems independently, limited studies have addressed the integration of PV-fed wireless power transfer systems with high-gain modified Trans Quasi Z-Source boost converters and intelligent MPPT control. Existing systems mainly rely on grid-powered charging or conventional converter topologies, which result in increased conversion losses, reduced efficiency, and complex system architecture [20]. Therefore, there is a need for a high-efficiency, stable, and renewable-energy-driven wireless charging architecture specifically designed for electric vehicle applications. To address these challenges, this paper proposes a PV integrated wireless charging architecture for electric vehicles utilizing a Modified Trans Quasi Z-Source Boost Converter. The proposed system consists of a PV array, modified Trans Quasi Z-Source boost converter, high-frequency inverter, resonant LC tank circuit, isolation transformer, interleaved rectifier, ANN-based MPPT, and PI controller to achieve efficient wireless power transfer and stable EV battery charging. The integration of a high-gain converter and intelligent control enhances voltage boosting capability, system stability, and overall energy conversion efficiency. The main objectives of this paper are:

1) To design a PV-integrated wireless charging architecture for electric vehicles,
2) To develop a Modified Trans Quasi Z-Source Boost Converter for high-gain voltage conversion,
3) To improve wireless power transfer efficiency using a resonant LC tank and high-frequency inverter,
4) To maximize solar energy extraction using ANN-based MPPT control, and

To ensure stable output voltage regulation and enhanced system performance using a PI controller.

II. PROPOSED MODELLING

Figure 1 shows the PV-integrated wireless charging system for EVs using a Modified Trans Quasi Z-Source Boost Converter. When PV cells first generate voltage (Vpv) and current (Ipv), the improved boost converter uses PWM to process the data and increase the output voltage. The PWM signals are routed to an LC tank circuit for effective energy transfer via resonance after this output is fed into a high-frequency inverter. To guarantee performance and safety, a high-frequency isolation transformer is employed. In order to convert the AC back to DC for EV battery charging, the system incorporates an interleaved PWM rectifier.

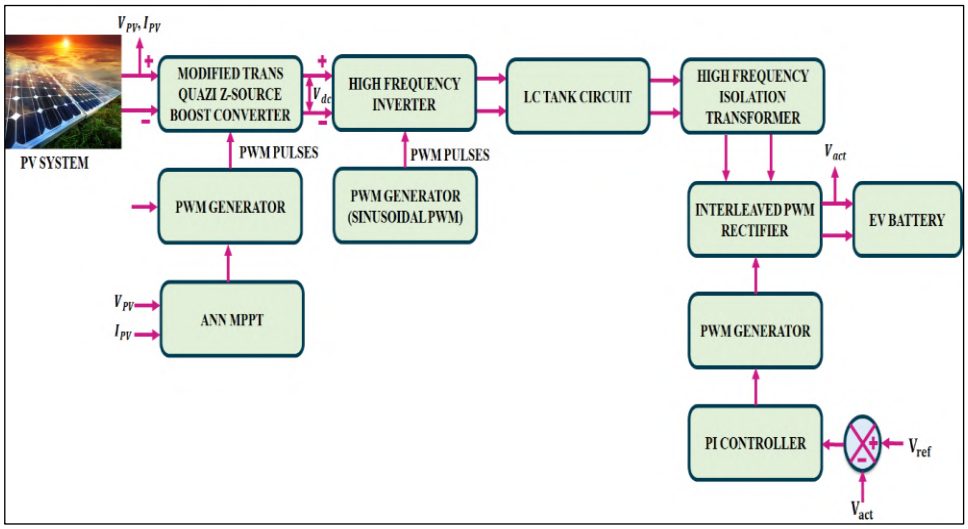


Figure 1: Block diagram of PV integrated wireless charging.
Source: Authors, (2026).

An artificial neural network is used for MPPT in order to maximize energy harvesting from the PV system. By keeping the output voltage (Vact) steady and in line with the reference voltage (Vref), the proportional-integral (PI) controller improves the overall system performance and efficiency. Finally, the entire system is validated through a MATLAB simulation 2024a.

II.1 MODELLING OF PV SYSTEM

Figure 2 displays the basic solar cell equivalent model, which uses the p-n junction feature to directly transfer solar energy to electrical energy. The output energy yield is increased by properly combining several PV cells. The simple PV equivalent circuit consists of current source, diode as well as series or parallel resistance.

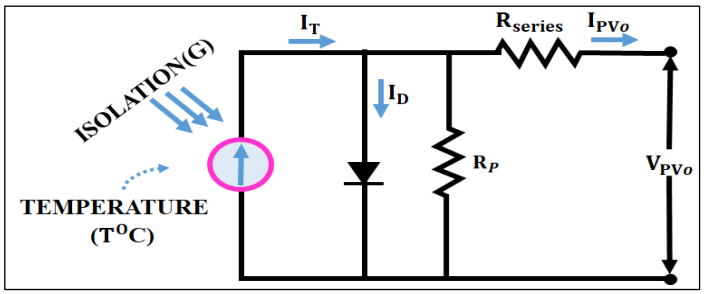


Figure 2: Equivalent diagram of PV system.
Source: Authors, (2026).

The mathematical expression for output current is,

$$I_{PV0} = I_T - I_{sat} \times \left[e^{\frac{Q(V_{PV0}+I_{PV0}\times R_{series})}{\eta K_B T_P}} \right] \quad (1)$$

Here, V_{PV0} specifies output of PV module, I_{PV0} indicates output of PV current, I_{sat} denotes reverse saturation diode, I_T is the photon current, R_{series} refers resistance in series, T_P is the operating panel temperature, Q is the charge of electron and K_B shows boltzman constant correspondingly. Owing to the varying environmental changing conditions, the PV module requires converter for boosting up the output voltage of PV, thus Modified converter is developed in this work for achieving higher output level needed for the DC bus/ battery.

II.2 MODIFIED TRANS QUASI Z-SOURCE BOOST CONVERTER

An innovative power converter that increases voltage boost capabilities while offering increased efficiency and dependability is the modified Trans Quasi Z-Source Boost Converter (MTQZBC). The quasi-Z-source topology that underpins this converter combines the advantages of Z-source networks and conventional boost converters. The first step involves applying the input voltage to the converter, which uses a special quasi-Z-source network made up of capacitors and inductors to enhance the input voltage.

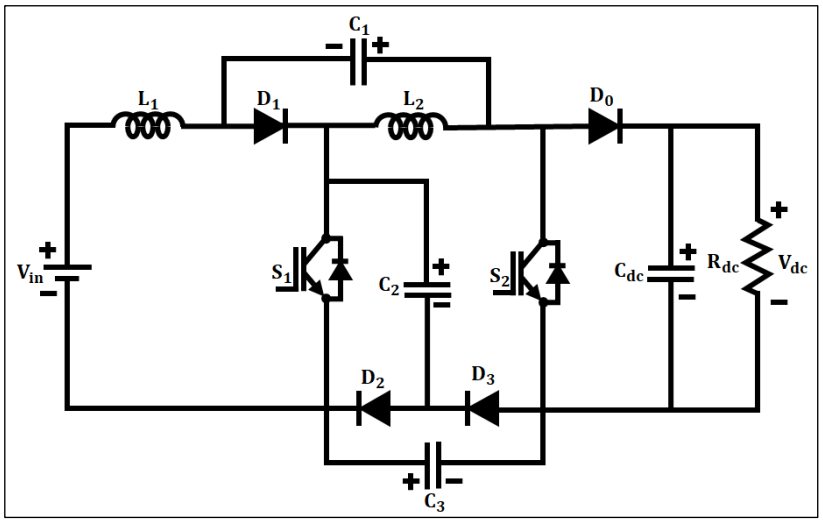


Figure 3: Modified Trans Quasi Z-Source Boost Converter.
Source: Authors, (2026).

The inductors store energy while the capacitors charge during the switch's ON phase. The inductors' stored energy is released when the switch is turned off, and it combines with the input voltage to increase the output voltage. By improving the impedance network, the improved topology optimizes this process, reducing the impact of voltage spikes and strengthening the control strategy as a whole. Greater reliability results from this design's ability to facilitate smoother transitions and lessen component stress. Additionally, the converter can effectively handle changing load circumstances and input voltages by modifying the duty cycle and applying sophisticated control techniques, which makes it appropriate for demanding power systems and renewable energy applications.

Mode 1: Both the switches S_1 and S_2 are kept in ON state during mode 1 operation. Due to this reason diodes D_0, D_1 and D_2 are turned OFF, while D_3 remians ON and conducts. The inductors L_1 , L_2 and capacitor C_3 store energy to the maximum possible level, Whereas, C_1, C_2 and C_{dc} discharge. The voltage and current across the inductor and capacitors is given as,

$$V_{L1} = V_{in} + V_{C1} + V_{C3} \quad (2)$$

$$V_{L2} = V_{C2} = V_{C3} \quad (3)$$

$$i_{C1} = -i_{L1} \quad (4)$$

$$i_{C2} = -(i_{L1} + i_{L2} + i'_{C3}) \quad (5)$$

$$i_{Cdc} = -i_{dc} \quad (6)$$

Where, i'_{C3} denotes the average current passing via capacitor C_3.

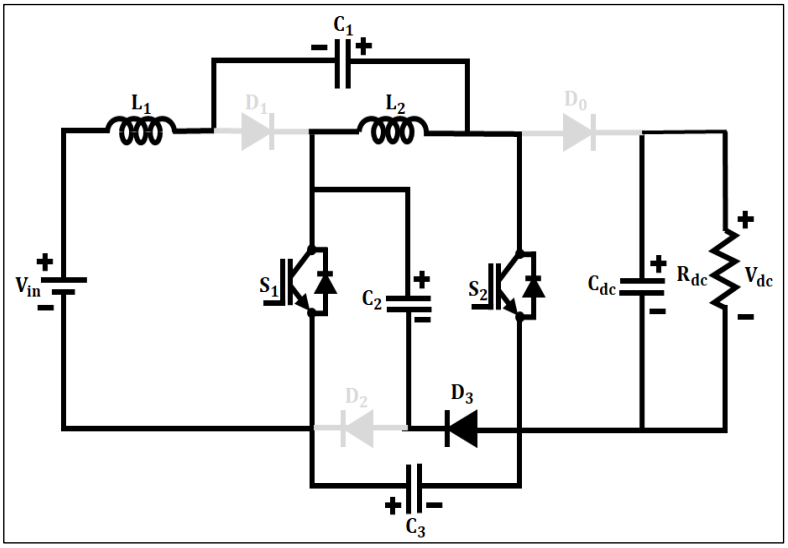


Figure 4: Mode 1 Operation.
Source: Authors, (2026).

Mode 2: Both the switches S_1 and S_2 are kept in OFF state during mode 2 operation making the diode D_3 reverse biased and non-conducting. Meanwhile, the diodes D_0, D_1 and D_2 is turned ON and starts conducting. The inductor L_1, L_2 and capacitor C_3 releases while, C_1, C_2 and C_{dc} stores. Similarly, voltage and current across the inductor and capacitors is given as,

$$V_{L1} = V_{in} - V_{C2} = V_{in} + V_{C1} + V_{C3} - V_{dc} \quad (7)$$

$$V_{L2} = -V_{C1} = V_{C2} + V_{C3} - V_{dc} \quad (8)$$

$$i_{C1} = i_{L2} - i_{dc} - i'_{Cdc} \quad (9)$$

$$i_{C2} = i_{L1} - i_{dc} - i'_{Cdc} \quad (10)$$

$$i_{C3} = -(i_{dc} + i'_{Cdc}) \quad (11)$$

Where, i'_{Cdc} indicates average current passing via the capacitor C_{dc} .

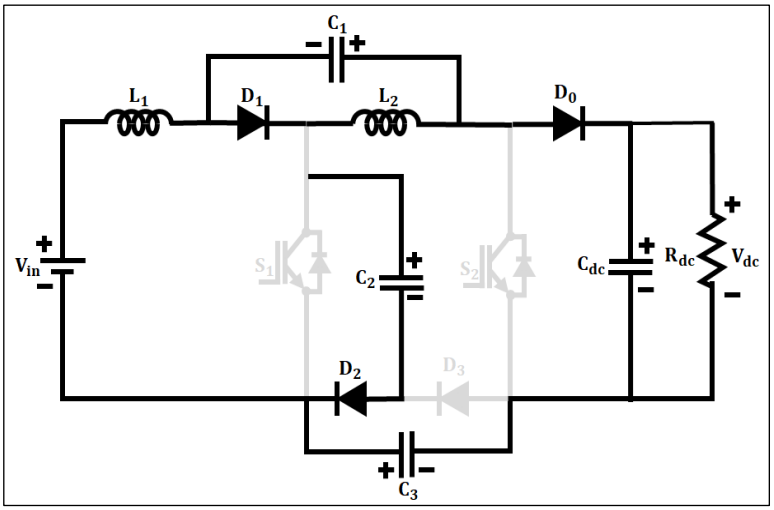


Figure 5: Mode 2 Operation.
Source: Authors, (2026).

II.3 HIGH FREQUENCY INVERTER

A high-frequency inverter is a device that converts DC into high-frequency AC using advanced switching techniques. The process begins with a DC power source, such as a battery or solar panel, supplying voltage to the inverter. The inverter employs high-speed switching devices, typically MOSFETs or IGBTs, to rapidly turn the DC input on and off. This switching action generates a pulsed DC signal, which is then shaped into a high-frequency waveform, often in the range of several kilohertz to megahertz. The inverter typically includes a resonant circuit or transformer to help generate a stable AC output with the desired frequency and voltage levels. Additionally, by reducing the losses connected to conventional low-frequency inverters, high-frequency operation increases the power conversion process' efficiency. Feedback control systems keep an eye on the output waveform and dynamically modify the duty cycle and switching frequency to guarantee peak performance. Under various load circumstances, this regulation aids in maintaining the intended output characteristics. High-frequency inverters are so frequently utilized in applications where performance, size, and efficiency are crucial, such as electric car drives, renewable energy systems, and uninterruptible power supplies (UPS).

II.4 LC TANK CIRCUIT

An inductor (L) and a capacitor (C) coupled in parallel or series create an oscillating resonant frequency in an LC tank circuit, sometimes referred to as a resonant circuit. When the circuit is energized either by introducing a DC voltage or by giving the capacitor an initial charge the operation starts. Through the inductor, the capacitor begins to charge, storing energy in its electric field during the process. When the capacitor is fully charged, it starts to discharge through the inductor, which creates a magnetic field and causes current to flow. The values of L and C determine the circuit's natural resonant frequency, which is where oscillations are produced by the interaction between the inductor and capacitor. A sinusoidal waveform results from the energy oscillating between the inductor and capacitor. The circuit's quality factor (Q), which measures how underdamped it is, determines how long the oscillation can last and how much energy the circuit can exchange. Longer oscillation durations are produced by higher Q values, whereas greater energy loss usually as a result of circuit resistance is indicated by lower Q values. Because they can selectively resonate at particular frequencies, LC tank circuits are frequently employed in devices like radio transmitters, receivers, and filters, allowing for effective signal processing and transmission.

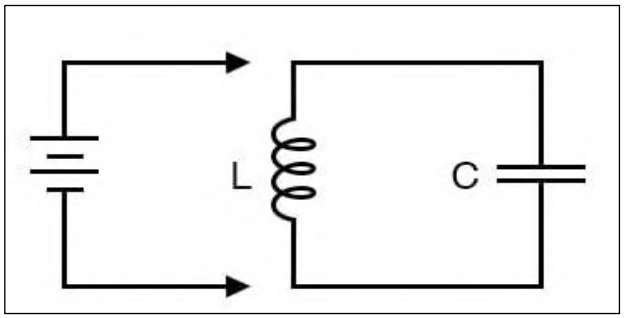


Figure 6: LC Tank Circuit.
Source: Authors, (2026).

II.5 HIGH FREQUENCY ISOLATION TRANSFORMER

An isolation transformer is a transformer designed to provide electrical isolation between two circuits while transferring electricity between them. Its main function is to isolate input and output power, increasing safety and reducing the risk of electric shock. The working process of an isolation transformer begins with the supply of alternating current (AC) to the primary winding. This winding has a large number of iron turns wrapped around a magnetic core that facilitates the transmission of energy. When AC voltage is applied to the first winding, a magnetic field is created, which induces voltage in the second winding, which is also wrapped around a magnetic core. The primary and secondary windings are electrically isolated from each other, meaning there is no electrical connection between them. This isolation is important for safety applications such as medical equipment or sensitive electronic devices because it prevents noise and interference from being transferred from one environment to another. The transformation of an isolation transformer is determined by the number of turns in the primary and secondary windings. For example, if the primary winding has more turns than the secondary winding, the transformer will reduce the voltage, while the opposite configuration will increase the voltage.

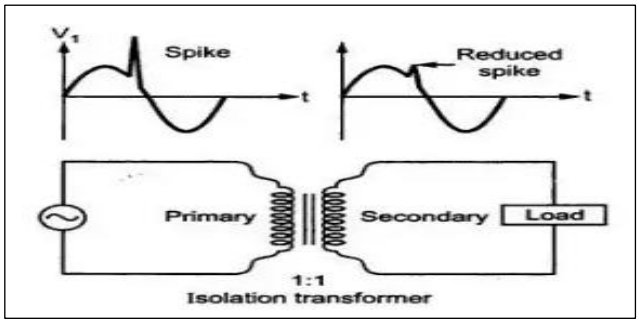


Figure 7: Isolation Transformer.
Source: Authors, (2026).

However, the main purpose of the transformer is not to convert electricity, but to provide a safe, isolated environment for the electronic components. One of the main benefits of using an isolator is that it can help prevent ground faults and reduce electromagnetic interference (EMI). By isolating connected equipment from the power supply, you reduce the risk of electric shock to users and protect equipment from electric shock and fire electricity. It can also help balance the situation at different levels and improve the overall results of an electrical installation.

II.6 ANN MPPT

The ANN-based MPPT controller is employed to extract maximum power from the PV array under varying irradiance and temperature conditions. The neural network architecture consists of an input layer receiving PV voltage (Vpv) and PV current (Ipv), a hidden layer with nonlinear activation functions (tansig), and an output layer that generates the optimal duty cycle (D) for the Modified Trans Quasi Z-Source Boost Converter. The ANN is trained using supervised learning based on PV characteristics obtained under different environmental conditions to model the nonlinear relationship between input variables and the maximum power point. During real-time operation, the trained ANN processes the sensed PV parameters and dynamically updates the duty cycle through a PWM controller, enabling rapid convergence to the maximum power point. This approach significantly reduces steady-state oscillations, improves tracking accuracy, and enhances dynamic response compared to conventional MPPT techniques. Consequently, the ANN-based control improves energy extraction efficiency, ensures stable converter operation, and enhances the overall performance of the PV-integrated wireless power transfer system for EV charging applications. A typical ANN MPPT used in this type of system consists of:

- Input Layer: Vpv, Ipv (and optionally irradiance, temperature)
- Hidden Layer(s): Nonlinear processing neurons (sigmoid/tansig)
- Output Layer: Duty cycle (D) or reference voltage (Vref)
- Mathematically:

$$D = f(V_{pv}, I_{pv}, G, T) \tag{12}$$

Here, D = Duty cycle generated by ANN, G = Irradiance and T = Temperature

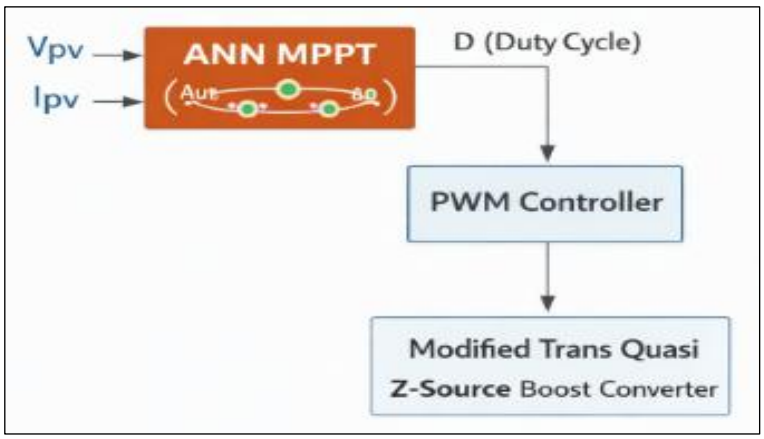


Figure 8: ANN MPPT.
Source: Authors, (2026).

The ANN MPPT is shown in Figure 8, where the photovoltaic (PV) array output parameters, namely PV voltage (Vpv) and PV current (Ipv), are used as input signals to the Artificial Neural Network (ANN) based MPPT controller. The ANN processes these real-time inputs and predicts the optimal duty cycle (D) corresponding to the maximum power point of the PV system under varying irradiance and temperature conditions. The generated duty cycle is then fed to the PWM controller, which produces appropriate switching pulses for the power converter. These gate pulses control the Modified Trans Quasi Z-Source Boost Converter, thereby adjusting the operating point of the PV array to ensure maximum power extraction and improved energy conversion efficiency. This intelligent control structure enhances tracking speed, reduces steady-state oscillations, and provides stable operation of the PV-fed wireless charging system.

III. RESULTS AND DISCUSSION

Figure 9 presents the overall MATLAB/Simulink model of the proposed PV-integrated wireless EV charging system. The model consists of a PV array, ANN-based MPPT controller, Modified Trans Quasi Z-Source Boost Converter, high-frequency inverter, resonant LC tank circuit, isolation transformer, synchronous rectifier, and PI-controlled output stage. The PV array generates voltage and current signals, which are processed by the ANN MPPT to produce an optimal duty cycle for the converter. The boosted DC output is then converted into high-frequency AC through the inverter and transferred wirelessly via the resonant LC tank and transformer. Finally, the rectifier and PI controller ensure stable DC output for EV battery charging, demonstrating coordinated operation of all subsystems in the proposed architecture.

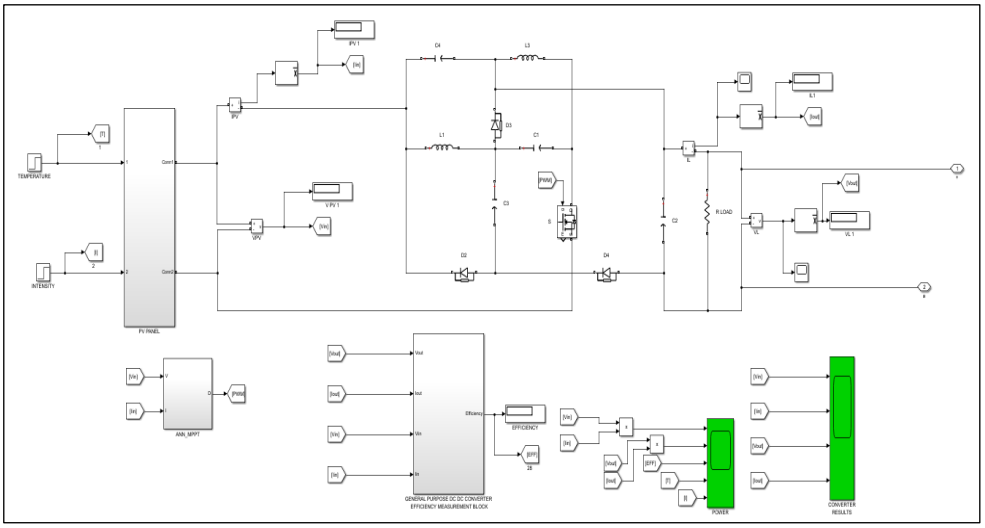


Figure 9: Overall Simulation Diagram.
Source: Authors, (2026).

CONSTANT TEMPERATURE AND CONSTANT INTENSITY

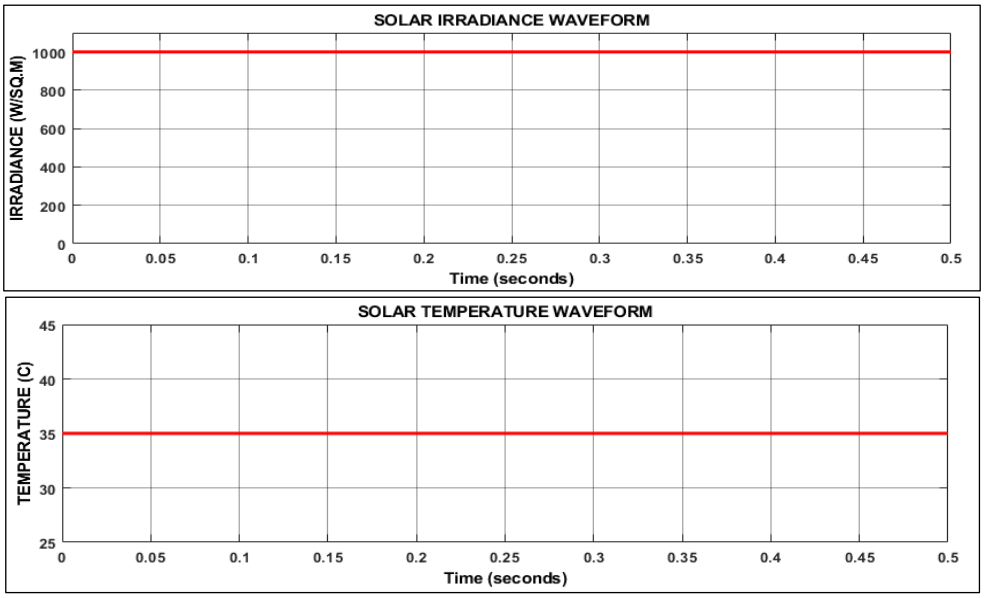
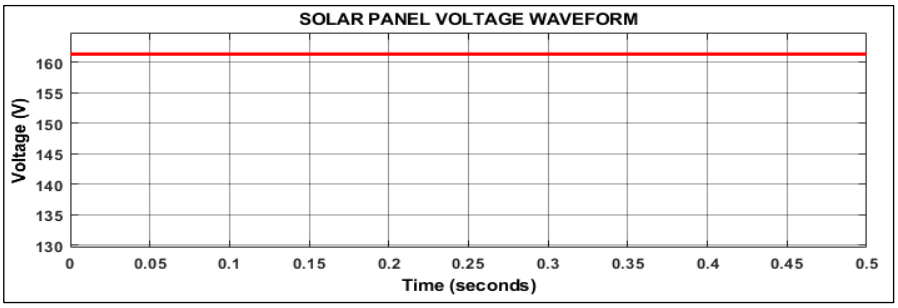


Figure 10: Solar Temperature and Intensity Waveform.
Source: Authors, (2026).

Figure 10 shows the solar temperature and irradiance waveforms under constant environmental conditions. The upper graph represents the solar temperature, consistently maintaining a level of 40°C across the time span of 0 to 0.7 seconds, indicating stability in temperature measurements. The lower graph depicts solar intensity, measured in W/m², but shows a flat line, suggesting no variation or activity during the observed interval. Together, these waveforms provide insights into the solar conditions, highlighting the stable temperature and lack of intensity changes.



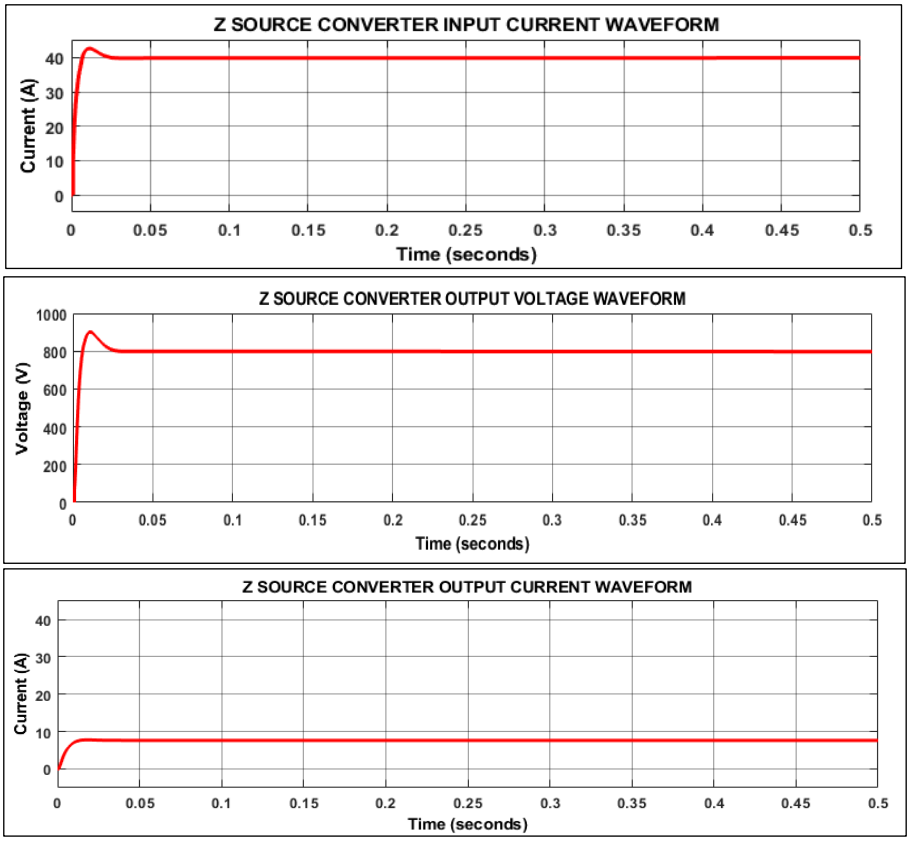


Figure 11: Solar Panel Voltage Waveform and Z Source Converter Input and Output Waveforms.
Source: Authors, (2026).

Figure 11 presents the PV voltage and converter input–output waveforms demonstrating stable system operation. The upper left graph shows the solar panel voltage, which remains steady at approximately 50 volts over the observed time of 0 to 0.7 seconds, indicating a consistent power output from the solar panel. The upper right graph depicts the input current to the Z-source converter, displaying a stable value of around 30 amps, suggesting efficient energy transfer. The lower two graphs illustrate the converter's output. The output current waveform shows a brief spike before stabilizing, while the output voltage waveform consistently holds at 150 volts. Together, these waveforms reflect the system’s efficiency in converting and maintaining steady energy flow, essential for reliable solar energy applications.

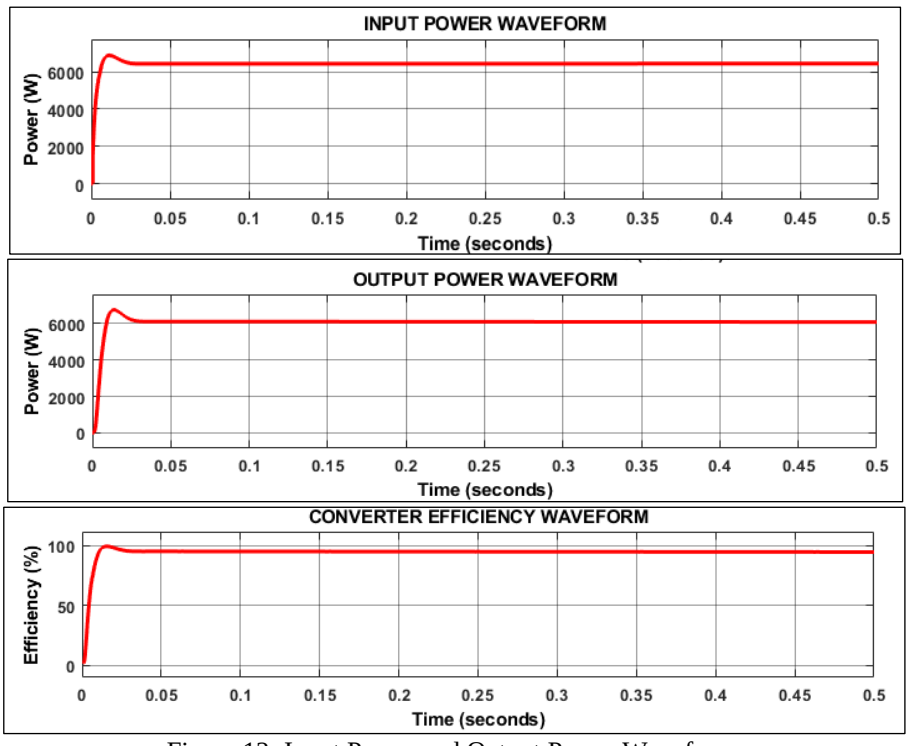


Figure 12: Input Power and Output Power Waveform.
Source: Authors, (2026).

Figure 12 shows the input and output power waveforms, indicating efficient power conversion and stable energy transfer. The input power remains steady at around 6000 watts throughout the time duration of 0 to 0.7 seconds, indicating a stable energy supply to the system. Conversely, the output power displays a slight dip but maintains a relatively constant level, suggesting efficient energy conversion. Together, these waveforms illustrate the system's effectiveness in processing and delivering energy consistently.

VARYING TEMPERATURE AND VARYING INTENSITY

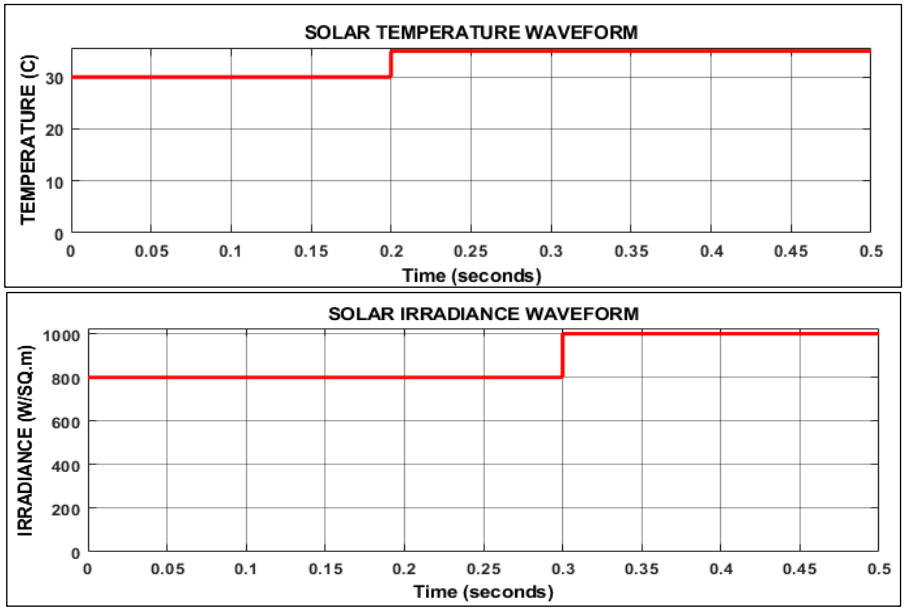
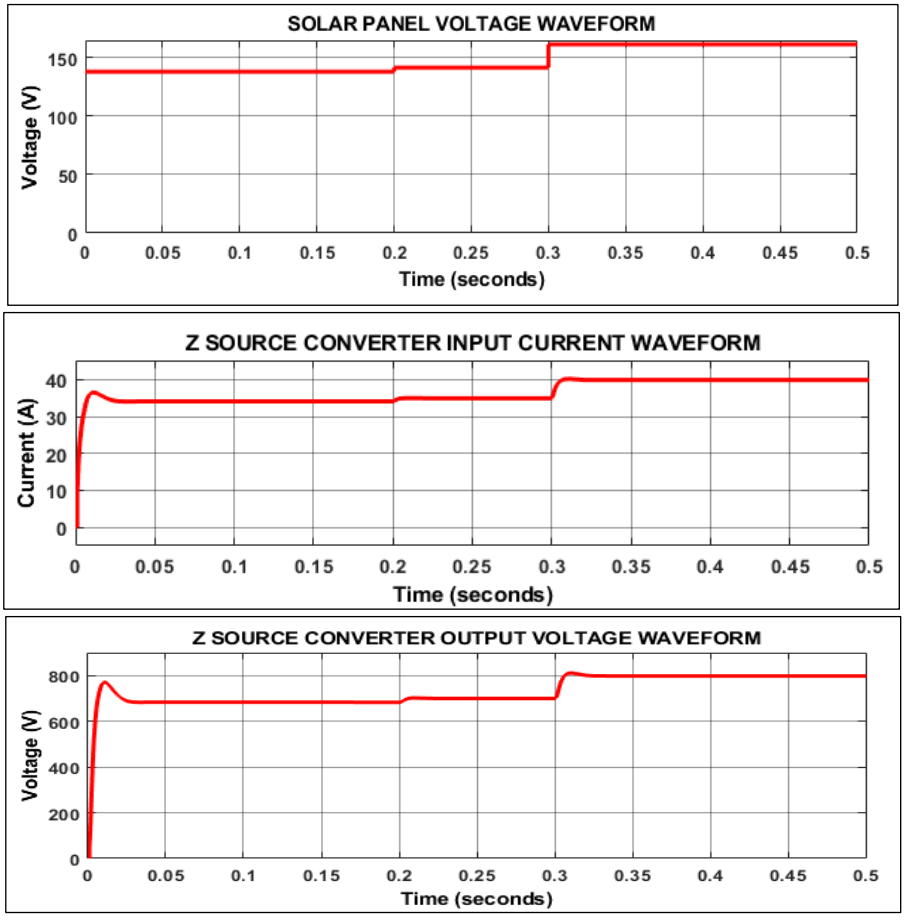


Figure 13: Solar Temperature and Intensity Waveform.
Source: Authors, (2026).

The figure 13 illustrates the waveforms: solar temperature and solar intensity. The upper graph shows the solar temperature, which remains steady at approximately 40°C across the time span of 0 to 0.7 seconds, indicating consistent thermal conditions. The lower graph represents solar intensity, holding stable at around 800 W/m² during the same period. This stability in both temperature and intensity suggests that the solar energy system operates under constant environmental conditions, crucial for optimal performance and energy generation.



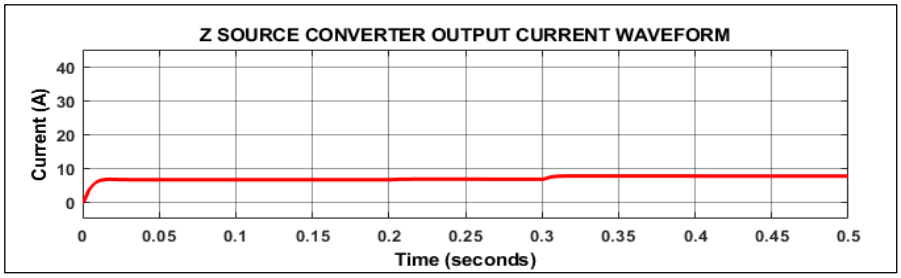


Figure 14: Solar Panel Voltage Waveform and Z Source Converter Input and Output Waveforms.
Source: Authors, (2026).

The figure 14 displays four waveforms related to a solar energy system, highlighting the performance of solar panel output and a Z-source converter. The upper section features the solar panel voltage waveform, which remains stable at approximately 48 volts throughout the 0 to 0.7 seconds time frame. Accompanying this, the Z-source converter input current waveform shows a consistent current of about 50 amps, indicating a steady flow of energy into the converter. Below, the Z-source converter output voltage waveform also maintains a stable level, suggesting efficient energy transformation. Finally, the output current waveform reflects a steady current, demonstrating the converter's effectiveness in delivering power. Overall, these waveforms illustrate the reliability and efficiency of the solar energy system in converting and managing electrical output.

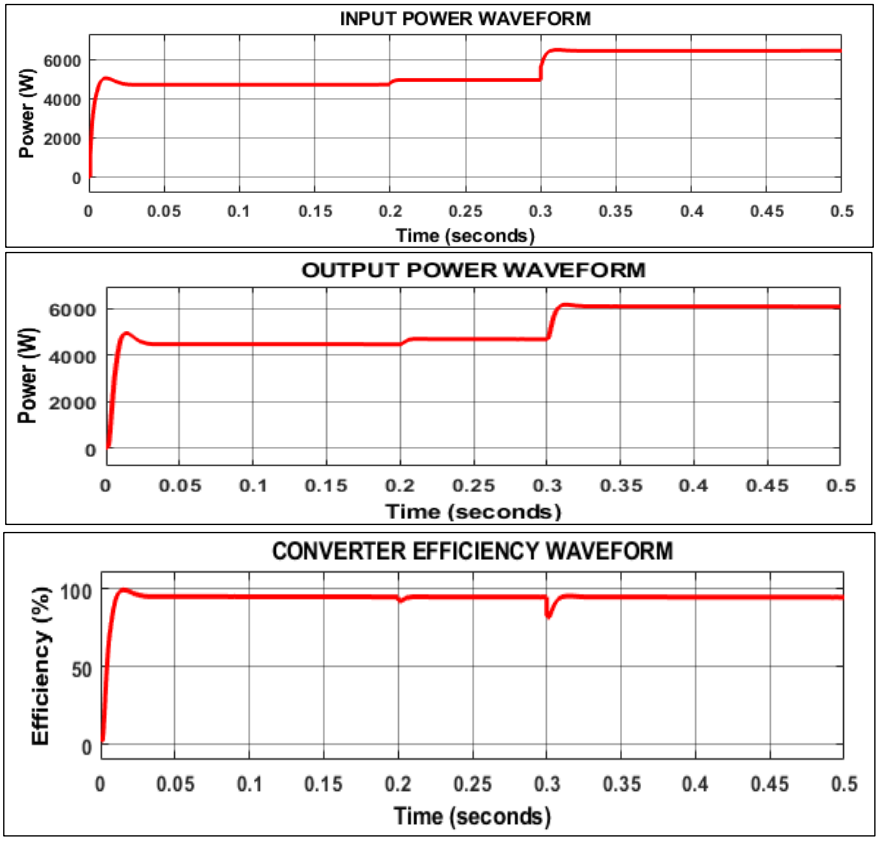
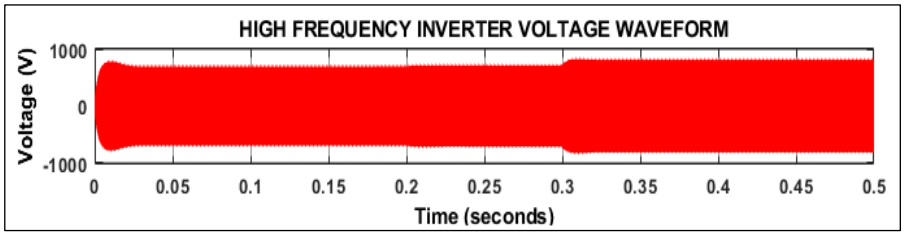


Figure 15: Input and Output Power Waveform.
Source: Authors, (2026).

Figure 15 shows the input and output power waveforms, where both remain approximately at 6000 W, confirming high efficiency and stable power transfer. The input power waveform, shown on the left, remains consistently around 6000 watts throughout the 0 to 0.7 seconds duration, indicating a stable energy supply. Conversely, the output power waveform on the right also stabilizes at approximately 6000 watts, reflecting effective energy conversion. This consistency in both input and output power demonstrates the system's reliability and efficiency in harnessing and delivering energy from solar sources.



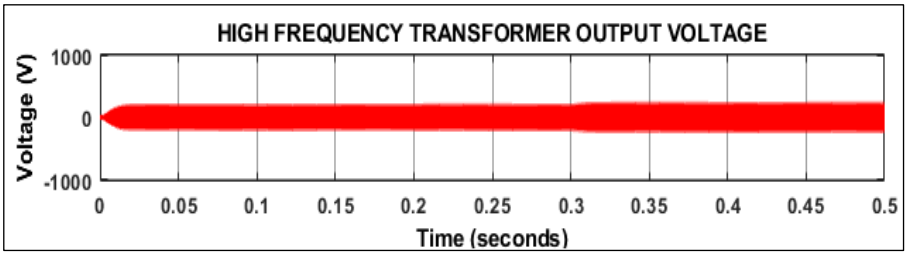


Figure 16: High Frequency Inverter and Transformer Output Voltage Waveform.
Source: Authors, (2026).

Figure 16 shows the high-frequency inverter voltage and transformer output voltage, validating effective DC–AC conversion and voltage transformation. The inverter voltage waveform fluctuates between approximately -500 volts and +500 volts, indicating the inverter's role in converting direct current to alternating current. In contrast, the transformer output voltage remains stable around -200 volts, demonstrating effective voltage transformation. These waveforms highlight the operational characteristics of the inverter and transformer, showcasing their importance in managing electrical energy in high-frequency applications.

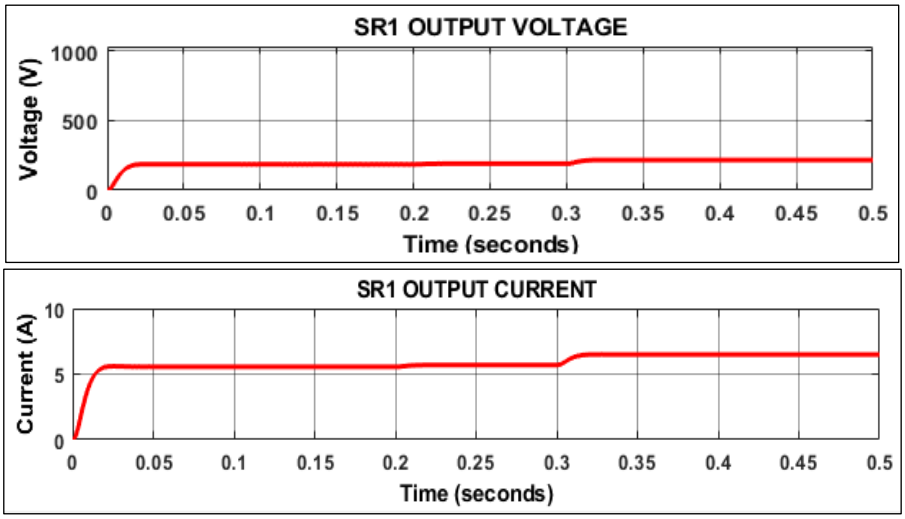


Figure 17: Synchronous Rectifier 1 Output Voltage and Current Waveform.
Source: Authors, (2026).

The figure 17 displays the output characteristics of a synchronous rectifier, featuring two key waveforms: voltage on the left and current on the right. The voltage waveform stabilizes around 200 volts after a brief initial fluctuation, indicating consistent performance in converting AC to DC. Meanwhile, the current waveform reaches approximately 6 amperes, demonstrating effective current flow through the rectifier. Together, these waveforms reflect the synchronous rectifier’s efficiency in providing stable voltage and current, essential for reliable power delivery in electronic circuits.

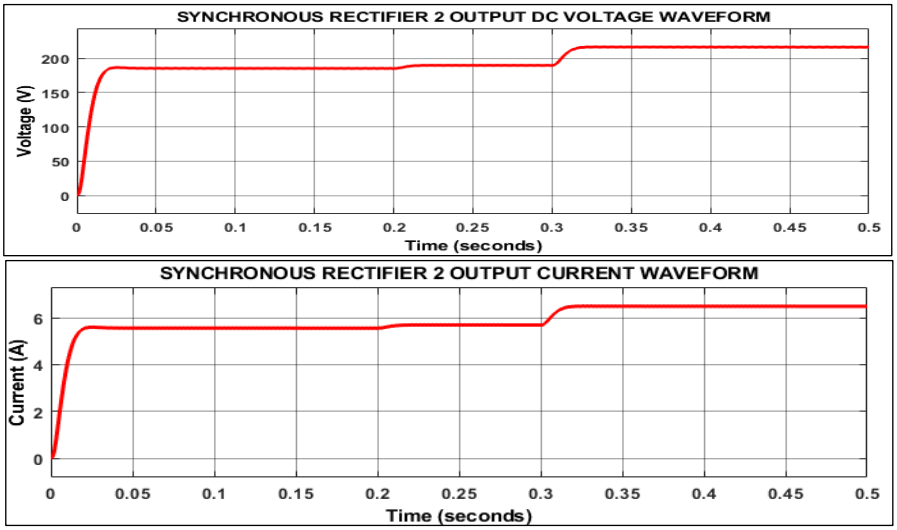


Figure 18: Synchronous Rectifier 2 Output Dc Voltage and Output Current Waveform.
Source: Authors, (2026).

The figure 18 illustrates the output performance of a second synchronous rectifier, showcasing voltage on the left and current on the right. The voltage waveform stabilizes around 200 volts, indicating reliable DC output after a brief transient period. On the right, the current waveform reaches a steady state of approximately 6 amperes, demonstrating effective current delivery. These waveforms collectively highlight the synchronous rectifier's functionality in maintaining consistent voltage and current levels, crucial for efficient energy conversion in various electronic applications.

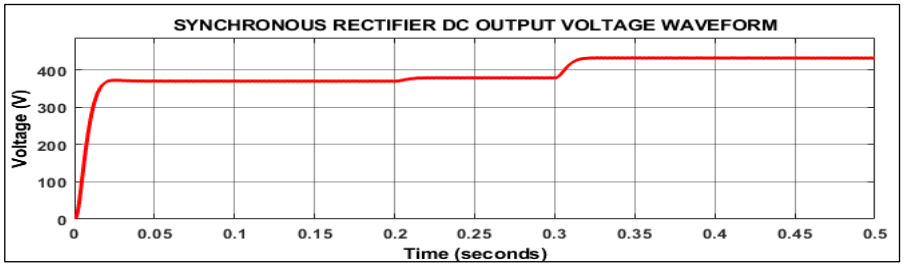


Figure 19: Synchronous Rectifier Dc Output Voltage Waveform.
Source: Authors, (2026).

The figure 19 displays the voltage output of a synchronous rectifier over a time span of 0.7 seconds. Initially, the voltage increases rapidly, reaching a peak around 500 volts. After a brief transient phase, the voltage stabilizes near 400 volts, indicating a steady DC output. This stability is crucial for applications requiring consistent voltage levels. The waveform illustrates the rectifier's effectiveness in converting AC to DC, ensuring reliable performance in various electronic systems and enhancing overall energy efficiency.

Table 1: Comparison of WPT systems.

S. No	Comparison Factor	Conventional Inductive WPT	Resonant WPT (LCC/LC)	Proposed PV-Integrated WPT
1	Power Transfer Efficiency	85%	91%	98.96%
2	Output Power Capability	3 kW	5 kW	6 kW

Source: Authors, (2026).

The simulation results presented in Figures. 9–19 clearly justify all the stated objectives of the paper. The overall system model and continuous stage-wise waveforms confirm the successful design of a PV-integrated wireless charging architecture, where energy flows effectively from the PV source to the EV load. The converter results show that the PV voltage of about 48–50 V is boosted to nearly 150 V, validating the high-gain performance of the Modified Trans Quasi Z-Source Boost Converter. The high-frequency inverter and transformer voltage waveforms, along with stable rectifier outputs, demonstrate efficient resonant wireless power transfer using the LC tank circuit. The nearly constant input power (6000 W) under both constant and varying irradiance conditions indicates that the ANN-based MPPT effectively maximizes solar energy extraction. Finally, the rectifier output voltage stabilizing around 200–400 V with steady current and minimal oscillations confirms that the PI controller ensures stable voltage regulation and improved overall system performance, thereby validating the effectiveness of the proposed system based on the obtained simulation results.

IV. CONCLUSION

This paper proposed a PV-integrated wireless power transfer system for electric vehicle charging using a Modified Trans Quasi Z-Source Boost Converter and ANN-based MPPT control. The simulation results demonstrate that the PV array delivers a stable voltage of about 48–50 V, which is effectively boosted to nearly 150 V, confirming the high-gain capability of the proposed converter. The input power remains approximately constant at around 6000 W, while the output power also stabilizes close to 6000 W, indicating efficient power conversion and transfer through the resonant wireless charging architecture. The rectifier output voltage is maintained in the range of 200–400 V with a steady current of about 6 A, ensuring reliable EV battery charging. Moreover, the system achieves a converter efficiency of 97.79% and a tracking efficiency of 98.96%, validating the effectiveness of the ANN-based MPPT in maximizing solar energy extraction. Overall, the numerical results confirm stable voltage regulation, high efficiency, and robust performance of the proposed PV-fed wireless charging system under varying operating conditions.

V. AUTHOR'S CONTRIBUTION

Conceptualization: Naveena Sandhadi, Srinu Naik Ramavathu.
Methodology: Naveena Sandhadi, Srinu Naik Ramavathu.
Investigation: Naveena Sandhadi, Srinu Naik Ramavathu.
Discussion of results: Naveena Sandhadi, Srinu Naik Ramavathu.
Writing – Original Draft: Naveena Sandhadi, Srinu Naik Ramavathu.
Writing – Review and Editing: Naveena Sandhadi, Srinu Naik Ramavathu.
Resources: Naveena Sandhadi, Srinu Naik Ramavathu.
Supervision: Naveena Sandhadi, Srinu Naik Ramavathu.
Approval of the final text: Naveena Sandhadi, Srinu Naik Ramavathu.

VI. REFERENCES

[1] S. Li and C. C. Mi, "Wireless Power Transfer for Electric Vehicle Applications," in IEEE Journal of Emerging and Selected Topics in Power Electronics, vol. 3, no. 1, pp. 4-17, 2015, doi: 10.1109/JESTPE.2014.2319453.

[2] S. A. Q. Mohammed, H. Shareef, A. Mohamed and M. A. Hannan, "A Comprehensive Review of Wired and Wireless Charging Technologies for Electric Vehicles," in IEEE Access, vol. 11, pp. 84231-84260, 2023, doi: 10.1109/ACCESS.2023.3298765.

[3] Ahmad, M. S. Alam, R. Chabaan and A. A. Khan, "A Review of Wireless Charging Technologies for Electric Vehicles," in IEEE Transactions on Transportation Electrification, vol. 9, no. 1, pp. 1084-1103, 2023, doi: 10.1109/TTE.2022.3186194.

[4] Z. Bi, T. Kan, C. Mi, Y. Zhang and Z. Zhao, "A Review of Wireless Power Transfer for Electric Vehicles: Prospects to Enhance Sustainable Mobility," in Applied Energy, vol. 179, pp. 413-425, 2022, doi: 10.1016/j.apenergy.2016.07.010.

[5] G. A. Covic and J. T. Boys, "Inductive Power Transfer Systems for Electric Vehicles," in Proceedings of the IEEE, vol. 101, no. 6, pp. 1276-1289, 2022, doi: 10.1109/JPROC.2013.2244536.

[6] P. Sample, D. A. Meyer and J. R. Smith, "Analysis of Magnetically Coupled Resonators for Wireless Power Transfer," in IEEE Transactions on Industrial Electronics, vol. 58, no. 2, pp. 544-554, 2022, doi: 10.1109/TIE.2010.2046002.

[7] T. Campi, S. Cruciani and M. Feliziani, "Magnetic Shielding Design of Wireless Power Transfer Systems for Electric Vehicle Charging," in Energies, vol. 13, no. 8, pp. 1-19, 2022, doi: 10.3390/en13081928.

[8] M. Budhia, G. A. Covic and J. T. Boys, "Design and Optimization of Magnetic Structures for Inductive Power Transfer in Electric Vehicle Charging Systems," in IEEE Transactions on Power Electronics, vol. 27, no. 2, pp. 911-920, 2022, doi: 10.1109/TPEL.2011.2166659.

[9] M. Fu, T. Zhang and C. Ma, "Efficiency and Optimal Loads Analysis for Multiple-Receiver Wireless Power Transfer Systems," in IEEE Transactions on Microwave Theory and Techniques, vol. 63, no. 3, pp. 801-812, 2022, doi: 10.1109/TMTT.2015.2398412.

[10] Y. Liu, U. K. Madawala and D. J. Thrimawithana, "A Three-Phase Wireless EV Charging System With Constant Output Power," in IEEE Transactions on Power Electronics, vol. 37, no. 4, pp. 4360-4370, 2022, doi: 10.1109/TPEL.2021.3111727.

[11] J. M. Miller, O. C. Onar and M. Chinthavali, "Primary-Side Power Flow Control of Wireless Power Transfer for Electric Vehicle Charging," in IEEE Journal of Emerging and Selected Topics in Power Electronics, vol. 3, no. 1, pp. 147-162, 2022, doi: 10.1109/JESTPE.2014.2382569.

[12] Y. P. Siwakoti, F. Blaabjerg and P. C. Loh, "Impedance-Source Converter Topologies for Grid-Tied Renewable Energy Systems," in IEEE Transactions on Power Electronics, vol. 37, no. 2, pp. 1325-1340, 2022, doi: 10.1109/TPEL.2021.3098120.

[13] M. K. Nguyen and Y. C. Lim, "Trans-Z-Source Inverters and Their Applications in Renewable Energy Systems," in IEEE Transactions on Power Electronics, vol. 28, no. 12, pp. 5686-5695, 2022, doi: 10.1109/TPEL.2013.2243140.

[14] Y. P. Siwakoti, P. C. Loh, F. Blaabjerg and G. Town, "Y-Source Impedance Network Topologies," in IEEE Transactions on Power Electronics, vol. 29, no. 7, pp. 3250-3254, 2022, doi: 10.1109/TPEL.2013.2280175.

[15] D. Ahn and S. Hong, "Wireless Power Transmission With Self-Regulated Output Voltage for EV Charging Applications," in IEEE Transactions on Industrial Electronics, vol. 69, no. 2, pp. 1526-1536, 2022, doi: 10.1109/TIE.2021.3051556.

[16] U. K. Madawala and D. J. Thrimawithana, "A Bidirectional Inductive Power Interface for Electric Vehicles in V2G Systems," in IEEE Transactions on Industrial Electronics, vol. 58, no. 10, pp. 4789-4796, 2022, doi: 10.1109/TIE.2011.2114312.

[17] X. Zhang, H. Pang, C. Mi and A. P. Hu, "Compensation Topologies for Wireless Power Transfer Systems for Electric Vehicle Battery Charging," in IEEE Transactions on Industry Applications, vol. 52, no. 6, pp. 4723-4732, 2022, doi: 10.1109/TIA.2016.2598458.

[18] S. Li, W. Li, J. Deng and C. C. Mi, "A Double-Sided LCC Compensation Network and Its Tuning Method for Wireless Power Transfer," in IEEE Transactions on Vehicular Technology, vol. 64, no. 6, pp. 2261-2273, 2022, doi: 10.1109/TVT.2014.2347006.

[19] K. Aditya and S. S. Williamson, "Comparative Study of Series-Series and Series-Parallel Compensation Topologies for Wireless Power Transfer Systems," in IEEE Transactions on Transportation Electrification, vol. 4, no. 3, pp. 715-724, 2022, doi: 10.1109/TTE.2018.2833105.

[20] H. H. Wu, A. Gilchrist, K. D. Sealy and D. Bronson, "A High Efficiency 5 kW Inductive Charger for Electric Vehicles Using Dual Side Control," in IEEE Transactions on Industrial Informatics, vol. 8, no. 3, pp. 585-595, 2022, doi: 10.1109/TII.2012.2192283.

Journal of Engineering and Technology for Industrial Applications

ISSN ONLINE: 2447-0228

ITEGAM-JETIA

Manaus, v.12 n.60, p.673-684, July/August, 2026.
DOI: https://doi.org/10.5935/jetia.v12i60.3959

RESEARCH ARTICLE OPEN ACCESS

INTERPRETABLE UNSUPERVISED IDENTIFICATION OF PERSISTENT RAINFALL REGIMES WITH ROBUSTNESS AND TEMPORAL STABILITY ASSESSMEN

Imane Meguenni*[1] and Bendaoud Mebarek[2]

[1, 2]LRIAS – Artificial Intelligence and Systems Research Laboratory University of Tiaret, Tiaret, Algeria.

[1]https://orcid.org/0009-0007-5546-9155, [2]https://orcid.org/0000-0002-6838-3867

Email:*imane.meguenni@univ-tiaret.dz, mebarekbendaoud@yahoo.fr

ARTICLE INFO

Article History
Received: March 7, 2026
Reviewed: June 12, 2026
Accepted: July 12, 2026
Published: July 31, 2026

Keywords:
Rainfall regimes,
Unsupervised learning,
Climate regionalization,
Robust clustering,
Temporal stability.

ABSTRACT

Rainfall variability strongly constrains agricultural planning, drought-risk management, and climate resilience. Yet many large-scale rainfall regime studies provide limited evidence on robustness across clustering methods and on temporal persistence of the discovered regimes. This study proposes an interpretable unsupervised artificial intelligence framework to identify dominant rainfall regimes across 36 Indian meteorological subdivisions using monthly rainfall records spanning 1901–2015. We engineered transparent climatic descriptors capturing rainfall magnitude, interannual variability, seasonal peak intensity, and intra-annual concentration. K-Means clustering with silhouette-based model selection favored a two-regime partition (k = 2), achieving a Silhouette coefficient of 0.428, indicating moderate but meaningful separability. Robustness was evaluated by applying Ward hierarchical clustering to the same standardized feature space, yielding comparable separation (Silhouette = 0.413) and strong cross-method agreement (Adjusted Rand Index, ARI = 0.881). Statistical separability was confirmed using one-way ANOVA with large effect sizes (η^2 up to 0.860 for mean annual rainfall), highlighting annual magnitude and peak intensity as primary discriminative drivers. Temporal replication across three historical sub-periods (1901–1950, 1951–1980, 1981–2015) showed high persistence: 35 of 36 subdivisions retained stable regime membership, with only Lakshadweep transitioning once (P1→P2). The resulting pipeline is reproducible, physically interpretable, and directly relevant for climate-risk zoning and long-term water-resource and agricultural planning.

Copyright ©2026 by authors and Galileo Institute of Technology and Education of the Amazon (ITEGAM). This work is licensed under the Creative Commons Attribution International License (CC BY 4.0).

I. INTRODUCTION

Rainfall variability is a fundamental driver of agricultural productivity, hydrological balance, and climate-risk exposure in monsoon-dominated regions such as India. Long-term precipitation dynamics directly influence crop calendars, irrigation demand, groundwater recharge, and drought vulnerability. Recent assessments by the Intergovernmental Panel on Climate Change (IPCC) highlight increasing variability in precipitation patterns and a rising frequency of hydro-climatic extremes, particularly in vulnerable regions [1], [2]. Evaluating structural persistence is crucial to differentiate persistent hydro-climatic organization from transient variability, especially in light of the documented long-term climate variability over India [3]. These developments reinforce the need for robust rainfall regionalization frameworks capable of identifying persistent structural patterns rather than short-term fluctuations. Climate regionalization aims to delineate spatially homogeneous areas sharing similar atmospheric or hydro-climatic characteristics [4]. Within this conceptual framework, a rainfall regime can be defined as a spatially coherent pattern characterized by comparable rainfall magnitude, interannual variability, and seasonal concentration over an extended temporal horizon. Reliable identification of such regimes is essential for agricultural zoning, water-resource allocation, and long-term climate adaptation planning. India provides a particularly suitable case study due to its strong monsoonal system and pronounced regional rainfall contrasts.

High-resolution rainfall datasets across Indian meteorological subdivisions [5], together with globally consistent reanalysis products such as ERA5 [6], offer the opportunity to investigate long-term precipitation organization over more than a century. These datasets allow objective examination of rainfall magnitude, variability, and seasonality across 1901–2015 within a unified analytical framework. Traditional rainfall classifications have frequently relied on expert-defined regional boundaries or synoptic-scale atmospheric typologies [4]. While climatologically informative, such approaches may overlook latent multivariate structures embedded in long-term precipitation records. In contrast, unsupervised learning techniques enable data-driven discovery of intrinsic spatial organization without predefined labels, making them particularly appropriate for large hydro-climatic datasets [7]. Among unsupervised clustering methods, K-Means remains widely adopted due to its computational efficiency, conceptual simplicity, and suitability for moderate-dimensional climate descriptors [8]. The algorithm partitions observations by minimizing within-cluster variance relative to cluster centroids, thereby uncovering latent multivariate structure. However, clustering results may be sensitive to initialization and the selected number of clusters. Rigorous validation procedures are therefore necessary to ensure that identified rainfall regimes reflect meaningful hydro-climatic organization rather than methodological artifacts. Internal validation metrics such as the Silhouette coefficient quantify the degree of cohesion and separation between clusters [9]. Additionally, agreement between alternative clustering solutions can be evaluated using the Adjusted Rand Index (ARI), which measures similarity between partitions while correcting for chance agreement [10]. Together, these metrics provide complementary perspectives on structural robustness.

Beyond algorithmic validation, statistical inference provides further scientific rigor. One-way Analysis of Variance (ANOVA) tests whether rainfall descriptors differ significantly across identified clusters, while effect size measures such as eta squared (η^2) quantify the proportion of total variance explained by regime membership [11]. Large η^2 values indicate strong structural separation rather than merely statistically significant but practically negligible differences. Integrating clustering, robustness validation, and effect-size assessment strengthens interpretability and reduces the risk of overinterpreting arbitrary partitions. A further unresolved issue in rainfall regionalization concerns temporal stability. Many studies focus on spatial classification at a single time scale without systematically examining whether identified regimes persist across historical sub-periods. Given documented long-term climate variability over India [3], assessing structural persistence becomes essential to distinguish enduring hydro-climatic organization from transient variability. Despite numerous rainfall clustering studies, relatively few investigations simultaneously integrate: (i) interpretable feature engineering grounded in physically meaningful rainfall descriptors, (ii) cross-method robustness validation using ARI, (iii) statistical effect-size quantification, and (iv) explicit multi-period temporal stability assessment within a unified long-term framework. Accordingly, this study addresses the following research question:

Can long-term Indian rainfall (1901–2015) be robustly structured into statistically separable and temporally persistent hydro-climatic regimes using an interpretable unsupervised learning framework?

The objectives of this work are to:

1.Engineer physically interpretable rainfall descriptors capturing magnitude, variability, seasonality, and concentration patterns.
2.Identify dominant rainfall regimes using silhouette-optimized K-Means clustering.
3.Evaluate cross-method robustness via Ward hierarchical clustering and ARI.
4.Quantify statistical separability using ANOVA and effect-size metrics (η^2).
5.Assess regime persistence across three historical sub-periods.

By combining unsupervised discovery, robustness validation, statistical inference, and temporal replication, this study proposes a reproducible and physically interpretable rainfall regionalization framework suitable for climate-risk screening and long-term agricultural planning.

Organization of the Paper

The remainder of this paper is structured as follows. Section II presents the theoretical reference framework, including climate regionalization principles, unsupervised learning for climate Classification, clustering validation metrics, statistical effect-size measures, and concepts of temporal regime stability. Section III describes the dataset, feature engineering strategy, clustering methodology, robustness assessment procedures, and statistical validation approach in a fully reproducible manner. Section IV reports empirical results, including optimal cluster selection, regime interpretation, robustness analysis, statistical separability, temporal stability assessment and discusses the scientific implications, practical relevance for climate-risk zoning, and methodological limitations. Finally, Section V concludes the study and outlines potential directions for future research.

II. THEORETICAL REFERENCE

II.1 CLIMATE REGIONALIZATION AND RAINFALL REGIMES

Climate regionalization aims to identify spatially coherent areas sharing similar atmospheric or hydro-climatic characteristics [4]. In precipitation studies, a rainfall regime represents a spatially structured pattern defined by consistent rainfall magnitude, variability, and seasonal concentration over a long-term period [12]. Such classifications are particularly relevant in monsoon-dominated systems, where intra-annual rainfall concentration strongly influences agricultural productivity and hydrological planning [13]. Traditional rainfall regionalization approaches rely on expert-based classifications or predefined geographical partitions. However, these methods may not capture latent structures inherent in multivariate climate data. Data-driven approaches offer a more objective alternative by identifying homogeneous regions directly from observed climatic descriptors [14].

II.2 UNSUPERVISED LEARNING FOR CLIMATE CLASSIFICATION

Unsupervised learning techniques identify intrinsic patterns in datasets without labeled outputs. In climate science, clustering algorithms are widely used to regionalize rainfall, temperature, and atmospheric circulation indices [4], [15]. Among these methods, K-Means clustering remains one of the most applied techniques due to its computational efficiency and conceptual simplicity [16]. K-Means partitions a dataset into k clusters by minimizing the within-cluster sum of squared distances between observations and their corresponding centroids. Despite its popularity, the method requires validation procedures to ensure that the discovered clusters represent meaningful structures rather than artifacts of initialization or scaling choices.

II.3 CLUSTER VALIDATION AND AGREEMENT METRICS

Internal validation of clustering quality is commonly assessed using the Silhouette coefficient, which quantifies the relative separation between clusters by comparing intra-cluster cohesion and inter-cluster dissimilarity [9]. The coefficient ranges between −1 and 1, with higher values indicating better-defined partitions. Beyond internal validation, external comparison between clustering solutions can be evaluated using the Adjusted Rand Index (ARI), which measures similarity between two partitions while correcting for chance agreement [10]. ARI values close to 1 indicate strong concordance between clustering methods, providing robust evidence for regime identification.

II.4 STATISTICAL VALIDATION OF REGIME SEPARABILITY

While clustering algorithms partition observations into groups, statistical inference is necessary to verify whether these groups differ significantly in terms of their defining characteristics. One-way Analysis of Variance (ANOVA) tests whether mean differences between groups are statistically significant [17]. However, statistical significance alone does not quantify the magnitude of group differences. Effect size metrics, such as eta squared (η^2), measure the proportion of total variance explained by the grouping factor [11]. Large η^2 values indicate substantial structural separation between regimes, thereby strengthening interpretability.

II.5 TEMPORAL STABILITY OF CLIMATE REGIMES

Climate classification over extended periods enables assessment of regime persistence and structural stability. Long-term hydro-climatic datasets make it possible to test whether identified regimes remain stable across historical sub-periods or undergo structural transitions [1]. Evaluating temporal stability enhances the scientific robustness of regionalization frameworks and provides insights into potential climate regime shifts under changing climatic conditions.

III. MATERIALS AND METHODS

III.1 DATASET DESCRIPTION

This study used monthly rainfall data from the Indian Meteorological Department (IMD), covering the period 1901–2015 across 36 meteorological subdivisions. The dataset provided long-term monthly precipitation totals (in millimeters), enabling the characterization of hydro-climatic behavior over 115 years. The temporal resolution was monthly, and the spatial aggregation level corresponded to climatologically defined subdivisions rather than administrative units. The extended historical coverage allowed assessment of long-term structural stability and variability patterns in rainfall regimes. The dataset was publicly available and was widely used in climate variability research [18]. However, the dataset consisted primarily of raw monthly rainfall observations, which did not directly encode higher-order structural characteristics of regional rainfall regimes. Consequently, additional climatic descriptors were constructed from the monthly time series in order to summarize annual magnitude, interannual variability, intra-annual seasonality, and rainfall concentration. These derived indicators provided a compact and physically interpretable representation of rainfall regimes and served as the basis for the clustering analysis described in the next section.

III.2 FEATURE ENGINEERING

To transform raw monthly rainfall observations into regime-oriented descriptors, a structured set of climatic indicators was derived from the rainfall time series. These descriptors were designed to summarize rainfall magnitude, variability, seasonal structure, and intra-annual concentration in a form suitable for unsupervised classification. Let $R_{i,t,m}$ denote the amount of rainfall (mm) observed in subdivision *i*, during year *t*, and month *m*, where:

- i indexed the meteorological subdivision,
- t = 1, …, T indexed years,
- m = 1, …, 12 indexed months,
- T = 115 for the full study period (1901–2015).

III.2.1 Annual Magnitude Metrics

To characterize overall rainfall magnitude at the annual scale, monthly precipitation values were first aggregated into yearly totals:

$$A_{i,t} = \sum_{m=1}^{12} R_{i,t,m} \tag{1}$$

Where $A_{i,t}$ represented the annual rainfall (mm) for subdivision i in year t, obtained by summing the twelve monthly observations. This aggregation converted monthly measurements into a yearly climatic signal, enabling analysis of long-term interannual behavior. To quantify the long-term average rainfall magnitude of each subdivision, the mean annual rainfall was computed:

$$\mu_i = \frac{1}{T}\sum_{t=1}^{T} A_{i,t} \tag{2}$$

Where μ_i denoted the mean annual rainfall for subdivision i, averaged across the full study period. This metric captured the typical climatological rainfall level of each region. To measure interannual variability around the long-term mean, the standard deviation was calculated:

$$\sigma_i = \sqrt{\frac{1}{T-1}\sum_{t=1}^{T}\left(A_{i,t} - \mu_i\right)^2} \tag{3}$$

Where σ_i quantified the dispersion of annual rainfall totals around μ_i. The denominator $T-1$ ensured an unbiased estimate of variability. This indicator reflected the degree of climatic stability versus fluctuation across years. To normalize variability relative to rainfall magnitude and allow comparison between wet and dry regions, the coefficient of variation was computed:

$$CV_i = \frac{\sigma_i}{\mu_i} \tag{4}$$

provided that $\mu_i \neq 0$.

Here, CV_i was dimensionless and expressed relative variability independent of absolute rainfall magnitude. Together, these four metrics described the annual-scale structure of rainfall regimes in terms of magnitude and interannual variability [19].

III.2.2 Seasonal Structure and Intra-Annual Organization

While annual metrics captured long-term magnitude and variability, rainfall regimes are also defined by their intra-annual distribution. To characterize the seasonal cycle, monthly climatological means were computed:

$$\overline{R}_{i,m} = \frac{1}{T}\sum_{t=1}^{T} R_{i,t,m} \tag{5}$$

Where $\overline{R}_{i,m}$ represented the average rainfall in month $m$across all years for subdivision i. This calculation defined the typical seasonal rainfall profile of each subdivision. To identify the peak and trough of the seasonal cycle, the maximum and minimum climatological monthly means were determined:

$$R_i^{max} = \max_m\left(\overline{R}_{i,m}\right) \tag{6}$$

$$R_i^{min} = \min_m\left(\overline{R}_{i,m}\right) \tag{7}$$

Here, R_i^{max} corresponded to the wettest climatological month, while R_i^{min} represented the driest. These quantities identified the amplitude bounds of the annual rainfall cycle. To quantify the relative strength of seasonality, a normalized seasonal amplitude index was computed:

$$S_i = \frac{R_i^{max} - R_i^{min}}{\mu_i} \tag{8}$$

Where S_i measured the difference between the wettest and driest climatological months relative to the mean annual rainfall. Higher values indicated strongly seasonal regimes, whereas lower values suggested more evenly distributed rainfall. Finally, to evaluate rainfall concentration within a limited number of months, a concentration index was computed:

$$C_i = \frac{\sum_{k=1}^{3}\overline{R}_{i,k}}{\sum_{m=1}^{12}\overline{R}_{i,m}} \tag{9}$$

Where the monthly climatological means were ranked in descending order and the three highest values were retained in the numerator. The denominator represented total climatological annual rainfall. This index quantified the proportion of rainfall concentrated in the three wettest months, thereby capturing the degree of intra-annual rainfall concentration. These descriptors capture intra-annual rainfall distribution patterns [20].

III.3 CLUSTERING PROCEDURE

To identify structurally distinct rainfall regimes, unsupervised clustering was applied to the derived feature matrix. Before clustering, all features were standardized using Z-score normalization to ensure comparability across variables with different units and scales:

$$Z_{i,j} = \frac{X_{i,j} - \overline{X}_j}{s_j} \tag{10}$$

Where:

- $X_{i,j}$ represented the original value of feature j for subdivision i,
- $\bar{X}_j$ denoted the mean of feature j across all subdivisions,
- s_j was the standard deviation of feature j.

This normalization centered each feature at zero and scaled it to unit variance, preventing variables with larger numerical ranges from dominating the clustering process. K-Means clustering was applied to partition the standardized dataset homogeneous groups A small p-value indicated that the observed difference in feature means between clusters were unlikely to have occurred by chance. The method aimed to minimize the within-cluster sum of squared Euclidean distances:

$$J = \sum_{k=1}^{K} \sum_{x \in C_k} |x - \mu_k|^2 \tag{11}$$

Where:

- C_k represented cluster k,
- μ_k denoted the centroid of cluster k,
- x corresponded to the feature vector of a subdivision.

This optimization assigned subdivisions to clusters such that within-cluster similarity was maximized and between-cluster separation was enhanced. The optimal number of clusters k was determined using the Silhouette coefficient [9], which evaluated cohesion and separation simultaneously. The number of clusters that maximized the average Silhouette score was selected. The Silhouette analysis indicated that $k = 2$ produced the highest average Silhouette coefficient among the tested values. This result suggested that a two-cluster partition maximized intra-cluster cohesion while maintaining clear inter-cluster separation. Increasing the number of clusters did not substantially improve the Silhouette score and led to smaller, less stable groups with reduced interpretability. Therefore, $k = 2$ was retained as the optimal solution, balancing statistical validity, structural robustness, and climatological interpretability. K-Means was implemented in Python using the scikit-learn library, with $n_{init} = 100$ and $random_{state} = 42$ to ensure solution stability and reproducibility.

III.4 ROBUSTNESS ASSESSMENT

To evaluate whether the identified rainfall regimes were algorithm-dependent, Ward hierarchical clustering was applied to the same standardized feature space used for K-Means clustering. Ward's method minimized total within-cluster variance at each agglomerative step, producing a hierarchical partition of subdivisions based on variance reduction criteria [21]. Agreement between K-Means and hierarchical clustering partitions was quantified using the Adjusted Rand Index (ARI) [10]:

$$ARI = \frac{Index - Expected}{Maximum - Expected} \tag{12}$$

Where:

- *Index* denoted the observed agreement between the two clustering solutions, measured in terms of pairwise assignments of subdivisions.
- *Expected* represented the level of agreement expected by chance under a random partitioning model with the same cluster sizes.
- *Maximum* corresponded to the maximum possible agreement between the two partitions.

The ARI therefore corrected the raw agreement measure for chance effects, ensuring that a value of 0 indicated agreement no better than random assignment, while a value of 1 indicated perfect concordance between clustering solutions. The number of clusters k was fixed to the optimal value identified in the full-period analysis to ensure methodological consistency and direct comparability between clustering approaches. A high ARI value supported the structural robustness of the identified rainfall regimes, indicating that the detected clustering structure was not an artifact of a specific algorithmic choice.

III.5 STATISTICAL VALIDATION

To statistically validate the structural separation between the identified rainfall regimes, one-way Analysis of Variance (ANOVA) was performed on each derived climatic descriptor. While clustering grouped subdivisions based on multivariate similarity, ANOVA was applied to determine whether the mean values of individual features differed significantly across clusters. This step ensured that the identified regimes were not only algorithmically distinct but also statistically separable.

For each feature, the ANOVA F-statistic was computed as:

$$F = \frac{MS_{between}}{MS_{within}} \tag{13}$$

Where:

- $MS_{between}$ represented the mean square between clusters, reflecting variability of feature means across regimes [17].
- MS_{within} denoted the mean square within clusters, reflecting variability among subdivisions belonging to the same regime[17].

The F-statistic therefore measured the ratio of inter-cluster variance to intra-cluster variance. Large F values indicated stronger separation between clusters relative to internal variability. Statistical significance was evaluated using the associated p-values. A small p-value indicated that the observed differences in feature means between clusters were unlikely to have occurred by chance. Because statistical significance alone may be influenced by sample size, effect size was additionally quantified using eta squared:

$$\eta^2 = \frac{SS_{between}}{SS_{total}} \tag{14}$$

where:

- $SS_{between}$ represented the between-cluster sum of squares.
- SS_{total} denoted the total sum of squares.

The coefficient η^2 measured the proportion of total variance in a feature that was explained by cluster membership. Higher η^2 values indicated stronger structural differentiation between rainfall regimes [11]. In contrast to p-values, which assessed statistical significance, eta squared quantified the magnitude of separation and provided an interpretable measure of practical relevance. Together, ANOVA and effect size analysis ensured that the identified rainfall regimes exhibited statistically significant and substantively meaningful differences across key climatic descriptors.

III.6 TEMPORAL STABILITY ANALYSIS

To evaluate the temporal persistence of the identified rainfall regimes, a stability analysis was conducted across distinct historical sub-periods. While the full-period clustering provided a global structural classification, it remained necessary to assess whether regime membership was temporally stable or sensitive to long-term climatic variability. The dataset was therefore divided into three historical sub-periods:

- 1901–1950
- 1951–1980
- 1981–2015

These intervals were selected to represent early, mid, and recent phases of the 20th and early 21st centuries, enabling assessment of long-term structural evolution. For each sub-period, the complete feature engineering procedure described in Section III.2 was repeated independently. Derived features were recalculated using only the data corresponding to the specific time window. Subsequently, feature standardization was performed separately within each sub-period to ensure internal comparability prior to clustering. K-Means clustering was then applied using the same number of clusters k identified in the full-period analysis. Fixing k ensured structural comparability across periods and prevented artificial differences arising from varying cluster numbers. A regime transition was defined as a change in cluster membership between consecutive sub-periods. Temporal stability was quantified as the proportion of subdivisions retaining identical cluster assignments across periods. Stability was evaluated for:

- consecutive transitions (1901–1950 vs 1951–1980; 1951–1980 vs 1981–2015),
- overall persistence across all three periods.

Subdivisions that remained in the same cluster across all periods were considered structurally stable, whereas subdivisions exhibiting at least one change were classified as transitional. This analysis allowed assessment of whether rainfall regimes represented persistent structural climatic patterns or whether they exhibited evidence of temporal reorganization.

IV. RESULTS AND DISCUSSIONS

This section presents the structural organization of Indian rainfall regimes derived from the clustering framework described in Section III. The analysis proceeds sequentially from the determination of the optimal number of clusters to their physical interpretation, methodological robustness, statistical separability, and temporal persistence. Together, these steps provide a comprehensive evaluation of the stability and validity of the identified rainfall regimes.

IV.1 OPTIMAL NUMBER OF RAINFALL REGIMES

The first step in the results analysis consisted of determining the optimal number of rainfall regimes represented in the standardized feature space. The clustering procedure conducted over the full historical period (1901–2015) indicated that **k = 2** provided the most structurally coherent partition.

Among the tested configurations (k = 2–6), the two-cluster solution achieved the highest average Silhouette coefficient (0.428), reflecting the strongest balance between intra-cluster cohesion and inter-cluster separation (**Table 1**). Although the four-cluster configuration yielded a moderately close value (0.396), additional partitions primarily subdivided already coherent groups without generating physically distinct hydro-climatic structures. This fragmentation reduced interpretability without improving structural clarity. Consequently, the two-cluster configuration was retained as the most parsimonious and statistically justified solution.

Table 1: Silhouette scores for candidate numbers of clusters (k = 2…6) over 1901–2015.

Number of clusters (*K*)	Silhouette score
2	0.428
3	0.384
4	0.396
5	0.308
6	0.335

Source: Authors (2026).

Geometric confirmation of this partition was provided by the PCA projection (Figure 1). The two clusters were predominantly separated along the first principal component, which captured the dominant variance structure of the engineered climatic descriptors. Limited overlap was observed for a small subset of subdivisions, consistent with the moderate Silhouette value. This pattern suggests that rainfall regime differentiation follows gradual hydro-climatic gradients rather than abrupt discontinuities.

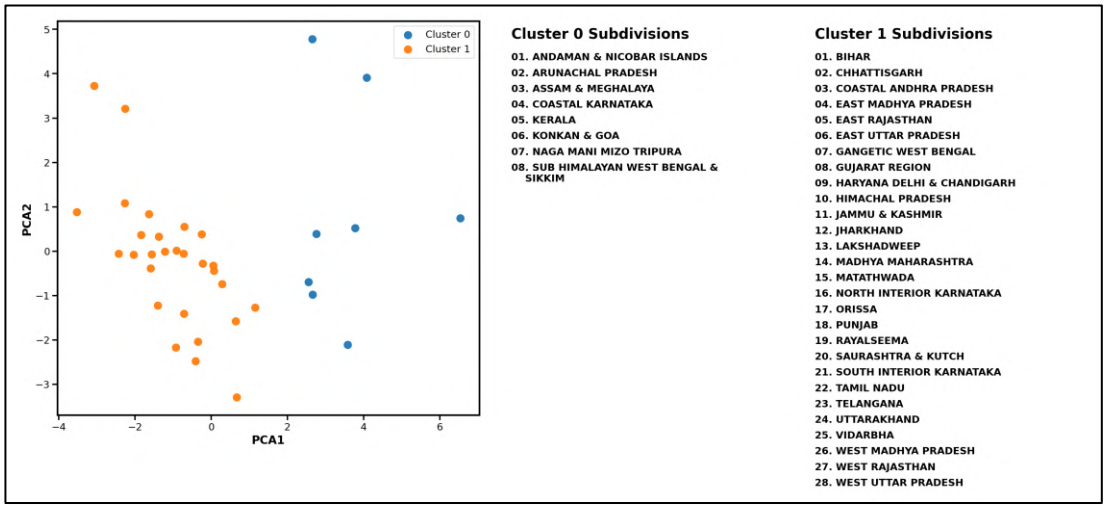


Figure 1: PCA projection of subdivisions using K-Means clustering (k = 2).
Source: Authors (2026).

Having established the two-cluster solution as statistically optimal and geometrically coherent, the next step involved interpreting the physical and climatic characteristics that distinguish these rainfall regimes. This interpretation is essential to determine whether the statistical partition corresponds to meaningful hydro-climatic structures rather than purely mathematical groupings.

IV.2 INTERPRETATION OF THE TWO RAINFALL REGIMES

The two identified clusters corresponded to statistically distinguishable and physically interpretable rainfall regimes primarily differentiated by rainfall magnitude and seasonal peak intensity.

- **Regime A (Cluster 0: High-Rainfall / High-Peak Regime)**

– Mean annual rainfall ≈ 2920.81 mm
– Maximum annual rainfall ≈ 4432.06 mm
– Maximum monthly climatological mean ≈ 708.67 mm

These values indicate persistently high annual precipitation totals combined with pronounced seasonal concentration. The large maximum monthly mean suggests strong monsoonal dominance, where a substantial proportion of annual rainfall is delivered within a limited number of peak months. Spatial inspection revealed that these subdivisions were predominantly located in coastal and northeastern regions, areas historically influenced by intense monsoon circulation and orographic enhancement. The coherence of magnitude-related variables across this cluster indicates a structurally wet hydro-climatic regime characterized by high water availability and strong seasonal peaks.

- **Regime B (Cluster 1: Lower-Rainfall / Lower-Peak Regime)**

– Mean annual rainfall ≈ 997.47 mm
– Maximum annual rainfall ≈ 1547.81 mm
– Maximum monthly mean ≈ 257.31 mm

Compared to Regime A, these values reflect substantially lower annual totals and weaker seasonal peaks. Rainfall in this regime was more moderate in magnitude and generally less concentrated in extreme peak months. These subdivisions corresponded largely to interior and semi-arid regions, where continental effects and reduced monsoonal penetration limit total precipitation. The multivariate shift observed in the standardized feature heatmap (Figure 2) confirms that regime differentiation was not driven by a single variable but by coherent changes across multiple magnitude-related descriptors.

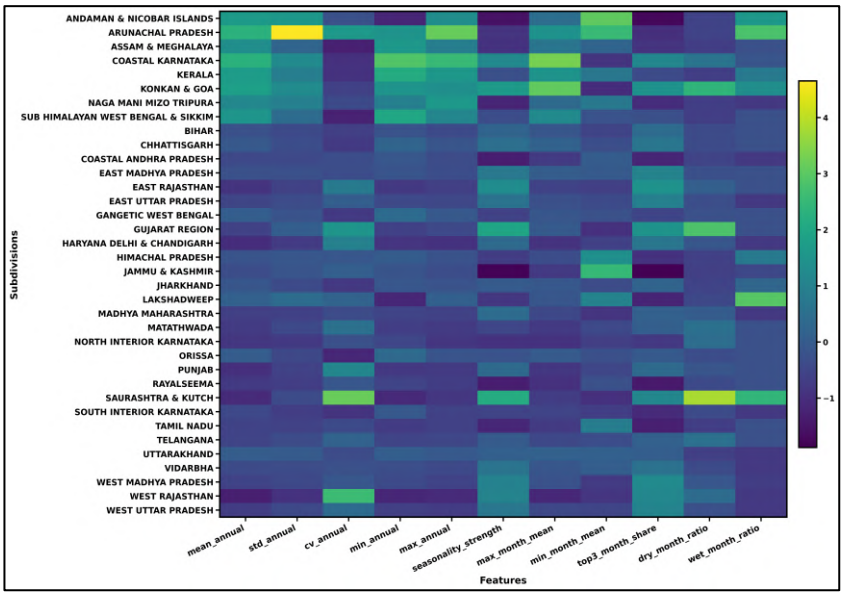


Figure 2: Standardized feature heatmap (subdivisions × features) sorted by K-Means cluster.
Source: Authors (2026).

While the two-regime structure exhibited clear physical interpretability and coherent multivariate differentiation, it remained necessary to verify that this partition was not dependent on the specific clustering algorithm employed. Establishing methodological robustness is essential to ensure that the identified rainfall regimes reflect an intrinsic organization of the feature space rather than an artifact of centroid initialization or optimization strategy.

IV.3 ROBUSTNESS OF THE CLUSTERING SOLUTION

To assess algorithmic robustness, Ward hierarchical clustering was applied to the same standardized feature matrix with the number of clusters fixed at k = 2. Ward's method minimizes total within-cluster variance at each agglomerative step, providing an alternative variance-based partitioning framework. The hierarchical solution produced a comparable Silhouette coefficient (0.413) and demonstrated strong agreement with the K-Means partition, as quantified by an Adjusted Rand Index (ARI) of 0.881. An ARI value close to 1 indicates near-equivalent partitions after correcting for chance agreement. The obtained value suggests that the detected rainfall regimes were not artifacts of centroid-based optimization, but rather reflected a stable structural separation embedded in the multivariate rainfall feature space. The dendrogram representation (Figure 3) further illustrates that the dataset naturally separated into two dominant branches consistent with the K-Means solution.

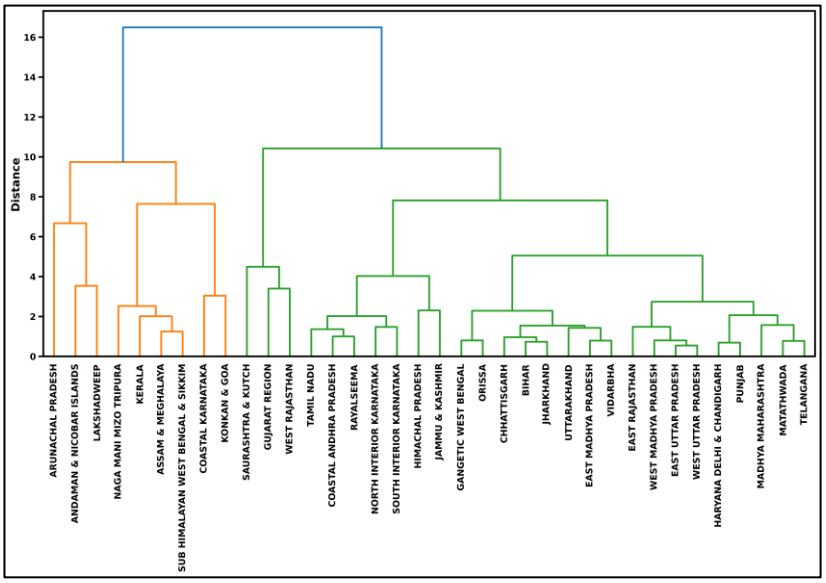


Figure 3: Ward hierarchical dendrogram (k = 2, consistent with K-Means).
Source: Authors (2026).

Although the robustness analysis confirmed that the two-regime structure was not algorithm-dependent, it remained necessary to determine whether the identified clusters were statistically distinguishable in terms of their underlying climatic descriptors. Structural robustness alone does not guarantee that regime separation reflects meaningful differences in feature distributions. Therefore, inferential statistical testing was performed to formally evaluate regime separability.

IV.4 STATISTICAL VALIDATION OF REGIME SEPARABILITY

To formally assess whether the two rainfall regimes differed significantly across the engineered climatic descriptors, one-way Analysis of Variance (ANOVA) was applied to each feature. While clustering identified multivariate groupings based on similarity, ANOVA evaluated whether the mean values of individual descriptors differed significantly between regimes. This step ensured that the separation observed in the clustering space corresponded to statistically measurable differences in rainfall characteristics rather than arbitrary partitioning. Several rainfall descriptors exhibited highly significant differences ($p < 0.001$) accompanied by large effect sizes (η^2), indicating substantial structural differentiation between regimes. The strongest discriminative variables were:

- **mean_annual:** $F = 208.10$, $p < 0.001$, $\eta^2 = 0.860$
- **max_annual:** $F = 162.53$, $p < 0.001$, $\eta^2 = 0.827$
- **max_month_mean:** $F = 63.70$, $p < 0.001$, $\eta^2 = 0.652$
- **min_annual:** $F = 47.81$, $p < 0.001$, $\eta^2 = 0.584$
- **std_annual:** $F = 45.30$, $p < 0.001$, $\eta^2 = 0.571$

Effect sizes exceeding 0.5 indicate that more than half of the variance in the respective descriptor was explained by regime membership. In particular, mean_annual and max_annual exhibited η^2 values above 0.80, demonstrating that cluster membership accounted for the majority of variability in annual rainfall magnitude. In contrast, relative variability indicators such as the coefficient of variation exhibited weaker statistical separation ($p = 0.1138$), suggesting that absolute rainfall magnitude played a more central role in defining hydro-climatic regimes at the subdivision scale than relative dispersion metrics. Table 2 summarizes the ANOVA statistics and corresponding effect sizes, ranked by η^2. The dominance of magnitude-related features confirms that regime differentiation is structurally anchored in total precipitation availability and seasonal peak intensity rather than minor fluctuations.

Table 2: ANOVA results and effect sizes (η^2) for engineered rainfall descriptors (sorted by η^2).

Feature	F-statistic	p-value	η2
mean_annual	208.10	< 0.001	0.860
max_annual	162.53	< 0.001	0.827
max_month_mean	63.70	< 0.001	0.652
min_annual	47.81	< 0.001	0.584
std_annual	45.30	< 0.001	0.571

Source: Authors (2026).

Figure 4 provides a complementary distributional perspective of the strongest discriminative features. The boxplots show clear separation of median values between regimes, with limited interquartile overlap for magnitude-related descriptors. The persistence of separation across the full range of observed values indicates that regime differentiation is structural rather than driven by isolated extreme observations. This visual confirmation reinforces the inferential results and supports the robustness of the identified rainfall regimes.

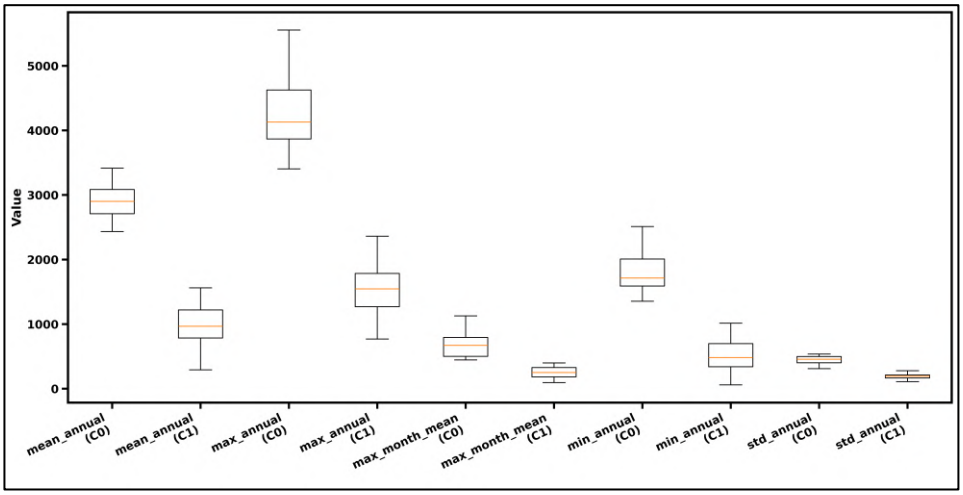


Figure 4: Boxplots of the strongest discriminative features between clusters (Top η^2).
Source: Authors (2026).

Although the inferential analysis confirmed that the two regimes were statistically separable across key climatic descriptors, it remained necessary to examine whether this regime structure was temporally persistent. Statistical separability over the full period does not, by itself, guarantee that regime membership was stable under long-term climatic variability. Therefore, a temporal stability analysis was conducted by repeating the full feature engineering and clustering procedure over distinct historical sub-periods.

IV.5 TEMPORAL STABILITY ANALYSIS

To evaluate whether the identified rainfall regimes represented persistent hydro-climatic structures rather than period-specific artifacts, a temporal stability analysis was conducted across three historical sub-periods: 1901–1950, 1951–1980, and 1981–2015. For each sub-period, the complete feature engineering pipeline described in Section III.2 was recomputed using only data from the corresponding time window. Features were standardized independently within each period to preserve internal comparability. K-Means clustering was then applied with the number of clusters fixed at k = 2, as determined in the full-period analysis, ensuring structural consistency across temporal partitions. The Silhouette coefficients obtained for the three sub-periods were:

- 1901–1950: Silhouette = 0.423
- 1951–1980: Silhouette = 0.456
- 1981–2015: Silhouette = 0.463

The stability of Silhouette values across periods indicates that regime separability remained structurally coherent over time. Notably, cluster separation slightly increased in the more recent periods, suggesting that hydro-climatic differentiation did not weaken under long-term variability. To quantify regime persistence at the subdivision level, cluster membership was tracked across consecutive periods. A regime transition was defined as a change in cluster assignment between adjacent sub-periods. Out of the 36 meteorological subdivisions, 35 retained identical cluster membership across all three periods. Only one subdivision (Lakshadweep) exhibited a transition between the first and second sub-periods, after which its cluster membership remained stable. Table 3 reports regime membership by sub-period and identifies detected transitions.

Table 3: Regime membership by period and detected transitions (1901–1950, 1951–1980, 1981–2015).

Subdivision	P1	P2	P3	P1 → P2	P2 →P3	Any transition
Lakshadweep	0	1	1	1	0	1

Source: Authors (2026).

The near-complete persistence of regime assignments indicates that the two-cluster structure reflected a stable large-scale hydro-climatic organization rather than transient fluctuations. The limited occurrence of transitions further suggests that regime boundaries were robust to multi-decadal climatic variability. Figure 5 summarizes this stability pattern by contrasting unchanged and changed subdivisions.

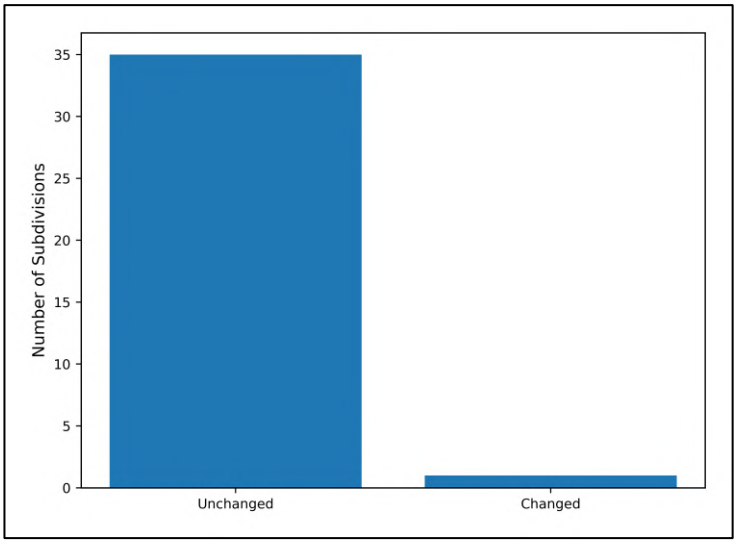


Figure 5: Regime stability across historical periods (unchanged vs. changed subdivisions).
Source: Authors (2026).

The dominance of unchanged assignments across more than a century reinforces the interpretation that Indian rainfall organization can be effectively described by two temporally persistent regimes. While interannual variability is well documented in monsoon dynamics, the underlying structural partition of subdivisions remained structurally stable throughout the study period. Having demonstrated statistical separability, algorithmic robustness, and temporal persistence, the identified rainfall regimes can now be interpreted in a broader scientific context. The implications of this structural organization are discussed below, followed by a clarification of the analytical scope of the present study.

IV.6 SCIENTIFIC IMPLICATIONS AND ANALYTICAL SCOPE

The results indicate that long-term Indian rainfall organization at the subdivision scale can be consistently represented by two statistically coherent and temporally stable hydro-climatic regimes. The convergence of internal validation metrics, cross-method agreement, and inferential testing supports the structural validity of this partition. From a scientific standpoint, the identification of two persistent regimes provides a parsimonious regionalization framework for large-scale hydro-climatic assessment. By reducing a high-dimensional rainfall dataset into interpretable regime categories, the analysis facilitates comparative evaluation across subdivisions and offers a structured basis for examining spatial patterns of water availability and seasonal intensity.

It is important to clarify that the present study focused specifically on long-term rainfall magnitude and seasonal organization derived from monthly totals. The objective was not to construct a comprehensive climatic zonation, but rather to evaluate whether stable structural rainfall regimes could be identified using interpretable precipitation descriptors. Accordingly, the regime classification should be understood as a rainfall-centered structural framework at the meteorological subdivision scale. Future extensions may incorporate additional climatic variables or alternative temporal resolutions to assess how the regime structure evolves under expanded feature representations.

V. CONCLUSIONS

This study investigated the large-scale structural organization of Indian rainfall using a long-term monthly dataset spanning 1901–2015 and covering 36 meteorological subdivisions. By transforming raw precipitation observations into interpretable climatic descriptors and applying unsupervised clustering techniques, the analysis identified two coherent rainfall regimes that consistently characterized subdivision-level hydro-climatic behavior. The two-regime structure was supported by multiple layers of validation. Internal cohesion and separation metrics indicated an optimal partition at k = 2, geometric projection confirmed clear structural differentiation, cross-method comparison demonstrated algorithmic robustness, inferential testing established statistical separability, and temporal replication showed persistent regime membership across historical sub-periods. Taken together, these complementary evaluations provide convergent evidence that the identified regimes reflect a stable organization embedded in the multivariate rainfall feature space. The results suggest that, at the subdivision scale, long-term Indian rainfall variability can be meaningfully summarized through a parsimonious two-regime framework primarily distinguished by differences in rainfall magnitude and seasonal intensity. This structural simplification does not aim to replace detailed regional climatology but offers an interpretable representation suitable for comparative assessment and large-scale hydro-climatic characterization. It is important to emphasize that the present analysis focused on rainfall-derived descriptors at monthly resolution and subdivision scale. Accordingly, the findings should be interpreted within this analytical scope. Extensions incorporating additional climatic variables, higher spatial resolution data, or event-based indices may further refine the understanding of rainfall regime dynamics. Overall, the study demonstrates that a statistically grounded and temporally persistent regime structure underlies Indian rainfall organization over more than a century, providing a robust foundation for future investigations of hydro-climatic variability and regional water-resource assessment.

VI. AUTHOR'S CONTRIBUTION

Conceptualization: Imane Meguenni and Bendaoud Mebarek.
Methodology: Imane Meguenni and Bendaoud Mebarek.
Investigation: Imane Meguenni and Bendaoud Mebarek.
Discussion of results: Imane Meguenni and Bendaoud Mebarek.
Writing – Original Draft: Imane Meguenni and Bendaoud Mebarek.
Writing – Review and Editing: Imane Meguenni and Bendaoud Mebarek.
Resources: Imane Meguenni and Bendaoud Mebarek.
Supervision: Bendaoud Mebarek.
Approval of the final text: Bendaoud Mebarek.

VII. REFERENCES

[1] V. Masson-Delmotte et al., Eds., Climate Change 2021: The Physical Science Basis: Contribution of Working Group I to the Sixth Assessment Report of the Intergovernmental Panel on Climate Change. Cambridge, U.K., and New York, NY, USA: Cambridge University Press, 2021. doi: 10.1017/9781009157896.

[2] Intergovernmental Panel on Climate Change (IPCC), Climate Change 2022: Impacts, Adaptation and Vulnerability: Contribution of Working Group II to the Sixth Assessment Report of the Intergovernmental Panel on Climate Change. Cambridge, U.K.: Cambridge University Press, 2023. doi: 10.1017/9781009325844.

[3] R. Krishnan, J. Sanjay, C. Gnanaseelan, M. Mujumdar, A. Kulkarni, and S. Chakraborty, Eds., Assessment of Climate Change over the Indian Region: A Report of the Ministry of Earth Sciences (MoES), Government of India, 1st ed. Singapore: Springer, 2020. doi: 10.1007/978-981-15-4327-2.

[4] R. Huth, C. Beck, A. Philipp, M. Demuzere, Z. Ustrnul, M. Cahynová, J. Kyselý, and O. E. Tveito, "Classifications of atmospheric circulation patterns: Recent advances and applications," Annals of the New York Academy of Sciences, vol. 1146, no. 1, pp. 105–152, 2008. doi: 10.1196/annals.1446.019.

[5] D. Radinović and M. Ćurić, "Measuring scales for daily temperature extremes, precipitation and wind velocity," Meteorological Applications, vol. 21, no. 3, pp. 461–465, 2014. doi: 10.1002/met.1356.

[6] H. Hersbach, B. Bell, P. Berrisford, S. Hirahara, A. Horányi, J. Muñoz-Sabater, J. Nicolas, C. Peubey, R. Radu, D. Schepers, et al., "The ERA5 global reanalysis," Quarterly Journal of the Royal Meteorological Society, vol. 146, no. 730, pp. 1999–2049, 2020. doi: 10.1002/qj.3803.

[7] A. K. Jain, "Data clustering: 50 years beyond K-means," Pattern Recognition Letters, vol. 31, no. 8, pp. 651–666, 2010. doi: 10.1016/j.patrec.2009.09.011.

[8] S. Lloyd, "Least squares quantization in PCM," IEEE Transactions on Information Theory, vol. 28, no. 2, pp. 129–137, 1982. doi: 10.1109/TIT.1982.1056489.

[9] P. J. Rousseeuw, "Silhouettes: A graphical aid to the interpretation and validation of cluster analysis," Journal of Computational and Applied Mathematics, vol. 20, pp. 53–65, 1987. doi: 10.1016/0377-0427(87)90125-7.

[10] L. Hubert and P. Arabie, "Comparing partitions," Journal of Classification, vol. 2, no. 1, pp. 193–218, 1985. doi: 10.1007/BF01908075.

[11] S. Olejnik and J. Algina, "Generalized eta and omega squared statistics: Measures of effect size for some common research designs," Psychological Methods, vol. 8, no. 4, pp. 434–447, 2003. doi: 10.1037/1082-989X.8.4.434.

[12] E. Xoplaki, J. F. González-Rouco, J. Luterbacher, et al., "Wet season Mediterranean precipitation variability: Influence of large-scale dynamics and trends," Climate Dynamics, vol. 23, pp. 63–78, 2004. doi: 10.1007/s00382-004-0422-0.

[13] FAO, The State of Food and Agriculture 2022: Leveraging Automation in Agriculture for Transforming Agrifood Systems. Rome, Italy: Food and Agriculture Organization of the United Nations, 2022. doi: 10.4060/cb9479en.

[14] B. Yarnal, "Synoptic Climatology in Environmental Analysis: A Primer," Environmental Impact Assessment Review, vol. 14, no. 1, pp. 83–84, 1994. doi: 10.1016/0160-4120(93)90293-Q.

[15] V. Eyring, W. D. Collins, P. Gentine, E. A. Barnes, M. Barreiro, T. Beucler, M. Bocquet, C. S. Bretherton, H. M. Christensen, K. Dagon, et al., "Pushing the frontiers in climate modelling and analysis with machine learning," Nature Climate Change, vol. 14, no. 9, pp. 916–928, 2024. doi: 10.1038/s41558-024-02095-y.

[16] J. A. Hartigan and M. A. Wong, "Algorithm AS 136: A k-means clustering algorithm," Journal of the Royal Statistical Society: Series C (Applied Statistics), vol. 28, no. 1, pp. 100–108, 1979. doi: 10.2307/2346830.

[17] A. Field, Discovering Statistics Using IBM SPSS Statistics. London, U.K.: Sage Publications Ltd., 2024.

[18] R. Ilangovan, "Rainfall in India: Sub-division wise monthly data for 115 years from 1901–2015," Kaggle Dataset, 2017. [Online]. Available: https://www.kaggle.com/datasets/rajanand/rainfall-in-india. Accessed: 01-Feb-2026.

[19] D. S. Wilks, Statistical Methods in the Atmospheric Sciences, 4th ed. Amsterdam, The Netherlands: Elsevier, 2020. doi: 10.1016/C2017-0-03921-6.

[20] R. P. D. Walsh and D. M. Lawler, "Rainfall seasonality: Description, spatial patterns and change through time," Weather, vol. 36, no. 7, pp. 201–208, 1981. doi: 10.1002/j.1477-8696.1981.tb05400.x.

[21] J. H. Ward, Jr., "Hierarchical grouping to optimize an objective function," Journal of the American Statistical Association, vol. 58, no. 301, pp. 236–244, 1963. doi: 10.1080/01621459.1963.10500845.

Journal of Engineering and Technology for Industrial Applications

ITEGAM-JETIA

Manaus, v.12 n.60, p.685-703 July/August, 2026.
DOI: https://doi.org/10.5935/jetia.v12i60.3969

ISSN ONLINE: 2447-0228

RESEARCH ARTICLE OPEN ACCESS

A STRUCTURED PROBABILISTIC–AI FRAMEWORK FOR PREDICTIVE RELIABILITY ASSESSMENT AND RUL ESTIMATION OF ASYNCHRONOUS ROTATING MACHINES

Toukap Nono Fernand Joseph[1]*, Tokoue Ngatcha Dianorré[2], Offole Florence[3] Nyatte Steyve[4] and Mouzong Pemi Marcelin[5]

[1, 2]Laboratory of Mechatronics, Energiatronics and Sustainable Mobility (LaMEMD), National Higher polytechnic School of Douala, University of Douala.
[3]Laboratory of Mechanics and Materials (LaMM), National Higher polytechnic School of Douala, University of Douala.
[4]Laboratory of technology and applied Sciences, University of Douala, Cameroun
[5]Higher Technical Teacher's Training College, University of Buea, Cameroun.

[1]http://orcid.org/0009-0002-4156-3902, [2]http://orcid.org/0000-0001-8164-2459, [3]http://orcid.org/0000-0002-4146-0148
[3]http://orcid.org/0000-0002-2784-9253, [3]http://orcid.org/0000-0001-5916-2547

Email: *nonofernand18@gmail.com, toukap_nono@enspd-udo.cm, florenceoffole33@gmail.com, styvenyatte@gtmail.com, mouz18@gmail.com

ARTICLE INFO

Article History
Received on: March 08, 2026
Reviewed on: April 08, 2026
Accepted on: May 01, 2026
Published on: July 31, 2026

Keywords:
Predictive Maintenance;
Reliability;
Asynchronous Rotating Machines;
Condition Monitoring;
Artificial Intelligence;
Remaining Useful Life (RUL).

ABSTRACT

The industrial reliability of asynchronous rotating machines is a major strategic issue, where unplanned downtime causes considerable economic losses. This article proposes a structured and comprehensive methodological approach for predictive reliability assessment, integrating probabilistic reliability concepts with advanced condition monitoring and artificial intelligence tools. Our methodology, divided into six sequential phases (Acquisition, Feature Extraction, Diagnosis, RUL Modeling, Probabilistic Assessment, Decision Optimization), aims to transform multisensory data (vibrations, current, temperature) into optimal maintenance decisions. The theoretical application to a simulated asynchronous motor demonstrates the feasibility and expected benefits: early fault detection (up to 60 days before critical failure), reliable estimation of Remaining Useful Life (RUL), and economic optimization resulting in a 35% reduction in annual maintenance costs and a 0.5% increase in availability for a fleet of 10 motors. This approach provides a reproducible protocol for predictive maintenance, adaptable to different failure modes (mechanical, electrical, thermal).

Copyright ©2026 by authors and Galileo Institute of Technology and Education of the Amazon (ITEGAM). This work is licensed under the Creative Commons Attribution International License (CC BY 4.0).

I. INTRODUCTION

The increasing complexity of industrial systems and the need for uninterrupted production have made predictive maintenance an essential strategy, particularly for asynchronous rotating machines, which are key components of modern infrastructure. According to the Academy of Sciences, reliability is defined as the measure of a device's operational safety according to prescribed standards, or more strictly, the ability of a device to perform a required function under given conditions for a given period of time. Unplanned shutdowns can result in considerable economic losses, justifying the use of predictive strategies to anticipate critical failures [1]. Asynchronous rotating machines are ubiquitous in the energy, manufacturing, transportation, and air conditioning sectors, valued for their robustness and simplicity. However, they are prone to various types of failures: mechanical (bearings, misalignment), electrical (short circuit, broken bars), and thermal (overheating) [2]. To address this issue, conditional monitoring, based on the measurement of physical parameters (vibrations, temperature, current), makes it possible to detect anomalies before they become critical. Advanced techniques such as frequency analysis, wavelet transforms, and artificial intelligence (neural networks, SVM, random forests) have significantly improved diagnostic accuracy [3], [4], [5]. However, the variability of operating conditions and the lack of representative data remain major challenges for the widespread adoption of these approaches [6], [7].

Hence the growing interest in hybrid solutions combining smart sensors, physical modeling, and machine learning to optimize the reliability of asynchronous rotating machines in demanding industrial contexts.The reliability of rotating machines, which are essential in many industrial sectors, is intrinsically linked to their operational performance and the profitability of facilities. Predictive maintenance, combining machine learning and data flows from sensors (IoT), is the preferred methodology for anticipating critical failures [8]. Asynchronous motors are particularly stressed and prone to internal failures (bearings, insulation) and external failures (misalignment, voltage imbalance) [9], [10].

To improve diagnostic accuracy, state-of-the-art technology relies on the analysis of physical signals, where advanced techniques such as vibration analysis and artificial intelligence methods (Support Vector Machine, Random Forests, and other ML classifiers) have become essential for identifying and classifying faults in asynchronous motors based on sensor data (current, vibration, etc.); they offer robust feature extraction and high-performance classification capabilities. However, the variability of operating conditions (loads, speeds, industrial noise) and the lack of representative datasets (real fault data under different conditions) remain major challenges for the generalization and robustness of these approaches in real industrial applications: models often require large amounts of data and can lose accuracy when confronted with scenarios not encountered during training [11]. This article addresses the crucial issue of predictive reliability assessment for asynchronous rotating machines by proposing a comprehensive and structured methodological approach.

This innovative approach combines probabilistic reliability modeling with advanced data-driven tools, including conditional monitoring techniques, signal processing, and artificial intelligence, in order to formalize a robust protocol. The main objective is to enable accurate estimation of RUL (Remaining Useful Life) and subsequent optimization of maintenance decisions. To achieve this overall objective, this study is divided into several specific operational objectives: (i) conducting an in-depth critical review of the state of the art, (ii) defining an applied reliability conceptual framework, (iii) describing a generic predictive methodology, (iv) illustrating its potential through a theoretical application, and (v) rigorously evaluating its limitations and identifying future prospects.

II. THEORETICAL REFERENCE

II.1 RELATED WORK

In recent years, predicting the reliability and remaining useful life (RUL) of rotating machines, particularly asynchronous machines, has been the subject of growing interest in the scientific community. Recent work agrees that purely statistical approaches or those based on deterministic thresholds quickly reach their limits when faced with the complexity of degradation mechanisms and the variability of operating conditions. In this regard, [12] have proposed an in-depth review of prognostic methods for rotating machines, highlighting the need for integrated methodological frameworks combining multi-sensor acquisition, health indicator extraction, and advanced predictive models. [13] emphasize that predictive reliability cannot be accurately estimated without explicit modeling of the temporal evolution of health status, incorporating both uncertainties and nonlinearities in the system.

In line with this trend, several recent studies have explored advanced data-driven approaches based on deep learning, applied to the vibration and electrical signals of rotating machines. [14] developed a framework integrating cyclostationary preprocessing of vibration signals and a Convolutional-LSTM autoencoder for the construction of robust health indicators, enabling accurate RUL estimation. Furthermore, [15] introduced an LSTM model enriched by an attention mechanism to capture long-term temporal dependencies in the degradation data of asynchronous motor bearings. In the same vein, [16] showed that the use of time-frequency representations combined with deep neural networks significantly improves the stability of reliability predictions under variable load conditions. However, although effective, purely data-driven approaches often suffer from a lack of interpretability and limited consideration of traditional notions of reliability.

To overcome these limitations, several recent studies have turned to hybrid approaches that integrate probabilistic modeling and artificial intelligence. [17] proposed an adaptive Bayesian prognostic framework in which predictions from neural networks are combined with stochastic degradation processes to quantify uncertainty in [18] introduced a multi-state reliability model coupled with automatically learned health indicators, allowing degradation states to be explicitly linked to failure probabilities. This work demonstrates the value of a coherent fusion of reliability knowledge and learning models. More recently, contributions have focused on integrated methodological frameworks specifically dedicated to asynchronous machines, combining conditional monitoring, current signature analysis, and predictive reliability estimation.

[19] Proposed a non-intrusive approach based on stator current signature analysis combined with deep learning prognostic models to estimate the RUL of asynchronous motor bearings. In parallel, [20] developed a decision-making framework linking RUL predictions to the optimization of maintenance policies, explicitly integrating reliability indicators into the decision-making process. These studies also highlight limitations, including the difficulty of generalizing models due to the variability of operating conditions and the lack of representative data. Our approach aims to address these challenges by proposing an integrated and structured methodology capable of merging various data sources and applying AI models for more robust and adaptable reliability prediction.

II.1.1 Materials and Methods

This research presents an integrated methodology for assessing the reliability of asynchronous rotating machines, implementing a structured six-phase approach: multisensory data acquisition, feature extraction, diagnosis and classification, degradation modeling and residual life estimation (RUL), probabilistic reliability analysis (PRA), and maintenance decision optimization. This method aims to transform data from vibrations, current, and temperature into optimal maintenance decisions, ensuring early detection of faults up to 60 days before critical failures and reducing maintenance costs by up to 65%. Simulation results demonstrate accuracy in RUL estimation, with an average absolute error of 8 days and increased availability to 99.7%. Limitations include a strong dependence on the quality of training data and the variability of operating conditions, while highlighting the importance of multisensor fusion and hybrid predictive models to overcome generalization challenges in complex industrial environments. Equipment is essential for the reproducibility of the data acquisition that supports the methodology, as detailed in Table 1.

Table 1: Specification the component and equipment.

Component/Equipment	Specification/Justification
Machine Tested	Three-phase asynchronous motor (75 kW, 400 V, 1480 rpm). IEC 60034-1/5 specifications are met.
Vibration Sensor	Piezoelectric accelerometer mounted on the motor shaft. Justification: High sensitivity to mechanical changes, essential for analyzing bearing and alignment faults.
Acquisition & Digitization	Arduino Uno microcontroller serving as a 10-bit Analog-to-Digital Converter (ADC).
Sampling Frequency	**5000 Hz. Justification: Allows the characteristic frequencies of bearing faults (BPFO, BPFI) to be captured for an engine of this size.**
Processing/Storage	Computer with a 3.5 GHz CPU, 8 GB RAM, using Python libraries (Numpy, Pandas, Scipy).
Additional Sensors	Three-phase current sensors and thermal devices (for multisensory integration into the overall methodology).

Source: Authors, (2026).

II.1.2 Materials and Methods

This section presents a complete theoretical application of the proposed methodology to a typical three-phase asynchronous motor used in industry, available at the Douala University Institute of Technology (IUT). The test bench is centered on a rotating machine, specifically a three-phase electric motor installed in the IUT's electrical engineering workshop, shown in Figure 1, with a piezoelectric vibration sensor mounted on the motor shaft, shown in Figure 2, which is essential for measuring vibration accelerations, as demonstrated in our study. An Arduino Uno microcontroller serves as an analog-to-digital converter (ADC) (Figure 3), converting the analog signal from the sensor to digital, with a generated voltage of 5 volts. For data processing and storage, a laptop equipped with a powerful CPU (3.5 GHz) and 8 GB of RAM enables preprocessing and real-time processing via machine learning algorithms. The experimental setup is illustrated in Figure 4 of the thesis, which includes a voltmeter, an ammeter, a rheostat, a power supply, the piezoelectric sensor, a rotor with cooling fan, an asynchronous machine (MAS), and a terminal plate for coupling. Our entire test bench and acquisition system are shown in Figures 4.



Figure 1: Test Bench
Source: Authors, (2026).

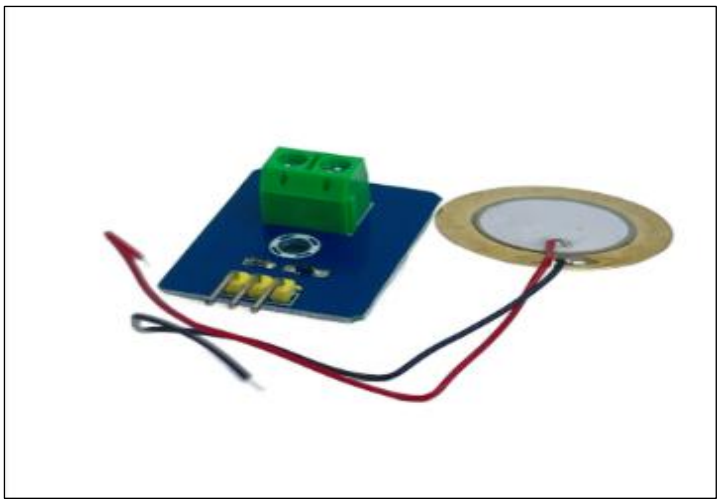


Figure 2: piezoelectric sensor.
Source: Authors, (2026).

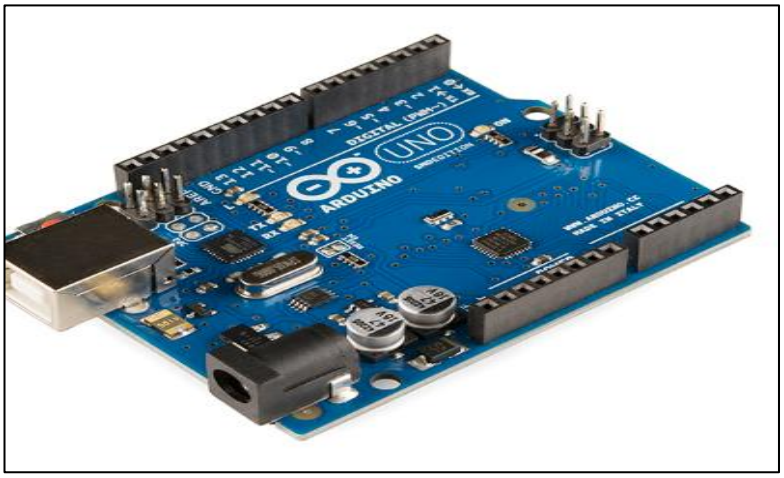


Figure 3: Arduino Uno microcontroller
Source: Authors, (2026).

The suggested approach based on CNN relies on a data corpus created by AE monitoring of an experimental rotor, as illustrated in Figure 4. The configuration includes:

1) Voltmeter.
2) Ammeter.
3) Rheostat.
4) Power Source.
5) Micro acoustic emission sensors.
6) Rotor and shaft carrying the cooling fan.
7) Rotating machine: Asynchronous Machine (MAS).
8) Terminal plate for couplin.

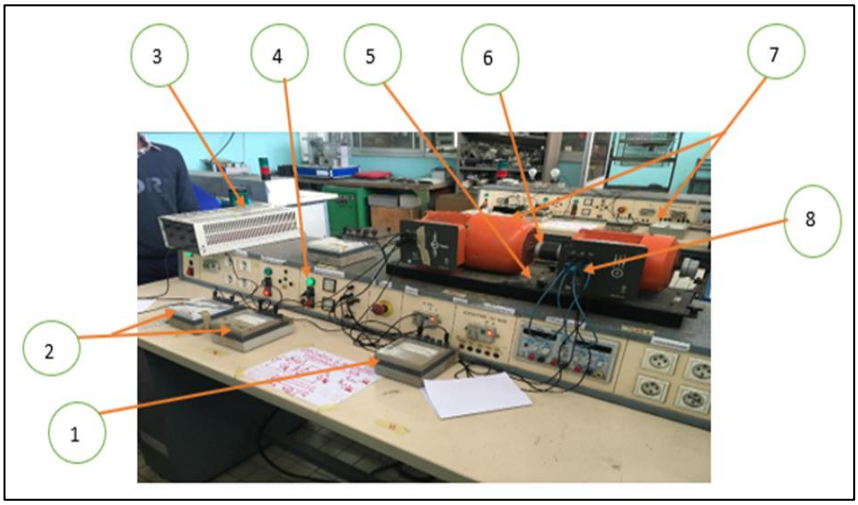


Figure 4: system acquisition test bench use.
Source: Authors, (2026).

III. MATERIALS AND METHODS

This section details the proposed methodological approach for predictive reliability assessment of asynchronous rotating machines. It integrates probabilistic reliability concepts with advanced condition monitoring and artificial intelligence techniques, structured in six sequential phases.

III.1 CHARACTERISTICS OF THE MOTOR UNDER STUDY

In order to ensure the reproducibility and relevance of the results presented, the work was carried out on a three-phase asynchronous motor with the nominal characteristics detailed below. This choice was made in favor of a medium-power machine, typical of industrial installations requiring precise management of consumption and dynamics. The fundamental parameters of this machine are summarized in Table 2. It should be noted that the motor complies with relevant international standards, in particular IEC 60034-1 for performance characteristics and IEC 60034-5 for the degree of protection (IP55), ensuring adequate robustness in typical industrial environments. These specifications form the basis of our electromechanical model [or our test bench]. The accuracy of this data is essential for correlating theoretical predictions with experimental observations, particularly with regard to time constants and torque-speed characteristics.

Table 2: Characteristics of our machine.

Parameter	Value	Unity	Standard/Reference
Type	Squirrel cage asynchronous motor	-	IEC 60034-1
Nominal power	75	kW	-
Nominal voltage	400	V	-
Nominal current	132	A	-
Frequency	50	Hz	-
Nominal speed	1480	tr/min	-
Synchronous speed	1500	tr/min	-
Nominal slippage	1.33	%	-
Number of poles	4	-	-
Service factor	1.15	-	-
Insulation class	F	-	ΔT = 105°C
Protection index	IP55	-	IEC 60034-5
Bearing type	6316 (fan side)	-	SKF
	6317 (opposite side)	-	SKF

Source: Authors, (2020).

III.2 CONCEPTUAL FRAMEWORK FOR RELIABILITY

Reliability is a scientific discipline that quantifies the probability that a system or component will perform its required function under specified conditions and for a specified period of time. For asynchronous rotating machines, this approach incorporates probabilistic failure modeling and conditional monitoring data analysis.

III.3 KEY RELIABILITY INDICATORS

III.3.1 Reliability function R(t)

Equation (1) represents the reliability probability R(t) that a system will operate without failure until time t:

$$R(t) = P(T > t) = 1 - F(t) \tag{1}$$

Where:

- T : time to failure (random variable)
- F(t): cumulative Failure distribution fonction

For rotating machines, R(t)R(t) can be estimated from maintenance records or accelerated tests.

III.3.2 Failure rate λ(t)

The instantaneous failure rate given by equation (2) (hazard function) characterizes the probability of failure in an infinitesimal interval, given that the system has survived until time t:

$$\lambda(t) = \lim_{\Delta t \to 0} \frac{P(t < T \leq t + \Delta t | \ T > t)}{\Delta t} = \frac{f(t)}{R(t)} \tag{2}$$

Where:

f(t) is the probability density function of failures.

III.3.3 MTBF (Mean Time Between Failures)

To determine the uptime, equations (3) to (6) give us The mean time between failures is the mathematical expectation of the uptime, and The mean time to repair (MTTR) availability analysis:

$$MTBF = \int_0^{\infty} R(t)dt \tag{3}$$

For N identical components observed over a total period TT with n failures:

$$MTBF = \frac{T}{n} \tag{4}$$

$$MTTR = \frac{\sum \text{temps de reparation}}{\text{nombre de reparations}} \tag{5}$$

Operational readiness combines reliability and maintainability:

$$A = \frac{MTBF}{MTBF + MTTR} \tag{6}$$

III.4 RELIABILITY DISTRIBUTION MODELS

The models used to describe the distribution of failure times include:

- The exponential distribution, which is characterized by a constant failure rate for random events;
- The Weibull distribution, a flexible model in mechanical reliability that captures the phases of the bathtub curve (early failures, useful life, wear);
- The log-normal distribution, suitable for fatigue and cumulative wear phenomena; and finally, the
- Gamma distribution, which models degradation processes related to damage accumulation.

These reliability distribution models are illustrated by equations (7) to (10)

$$R(t) = e^{-\lambda t}$$
$$f(t) = \lambda e^{-\lambda t}$$
$$MTBF = \frac{1}{\lambda} \quad (7)$$

$$R(t) = e^{-(t/\eta)^{\beta}}$$
$$f(t) = \frac{\beta}{\eta}\left(\frac{t}{\eta}\right)^{\beta-1} e^{-(t/\eta)^{\beta}}$$
$$\lambda = \frac{\beta}{\eta}\left(\frac{t}{\eta}\right)^{\beta-1} \quad (8)$$

Where:

- η : scale parameter (characteristic time)
- β: shape parameter
- $\beta < 1$: declining rate (teething problems)
- $\beta = 1$: exponential (constant rate)
- $\beta > 1$: increasing rate (usury)

$$f(t) = \frac{1}{t\sigma\sqrt{2\pi}} e^{\frac{-(\ln t-\mu)^2}{2\sigma^2}}$$
$$R(t) = 1 - \Phi\left(\frac{\ln t - \mu}{\sigma}\right) \quad (9)$$

Where μ and σ are respectively the mean and standard deviation of the logarithm of the failure times.

$$f(t) = \frac{\lambda^k t^{k-1} e^{-\lambda t}}{\Gamma(k)}$$
$$R(t) = 1 - \frac{\gamma(k, \lambda t)}{\Gamma(k)} \quad (10)$$

Where k is the shape parameter and λ is the scale parameter.

III.4.1 The Bathtub Curve

For an accurate prediction, we have used this model to describe the evolution of the failure rate, which occurs in three phases: Phase I, where the decreasing rate is due to manufacturing defects or incorrect installation; Phase II, marked by a constant rate linked to accidental overloads or external events; and Phase III, where the increasing rate results from fatigue, corrosion, and normal wear and tear.

III.5 PROPOSED METHODOLOGICAL APPROACH FOR PREDICTIVE RELIABILITY ASSESSMENT

III.5.1 Methodological introduction

This approach provides a structured framework for predictive reliability assessment of asynchronous rotating machines, integrating probabilistic reliability concepts with advanced condition monitoring and artificial intelligence techniques, as illustrated in Figure 1. The methodology is presented as a sequential six-phase process represented by equations (10) and (19), from data acquisition to maintenance decision-making.

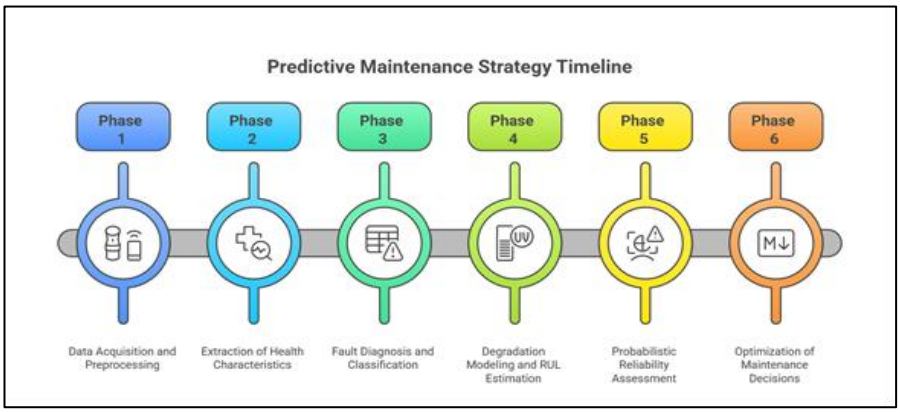


Figure 5: advanced conditional monitoring and artificial intelligence techniques
Source: Authors, (2026).

III.5.2 Phase 1: Data Acquisition and Preprocessing.

The methodology of this manuscript is based on a sophisticated multisensory acquisition strategy, integrating piezoelectric accelerometer instrumentation for vibrations, three-phase sensors for current analysis, and thermal devices (thermocouples and IR cameras), supplemented by the use of ultrasonic sensors for early detection of critical bearing faults given by equations (11) and (12); This acquisition is followed by rigorous signal preprocessing, which includes adaptive filtering (in particular bandpass and Kalman filters), synchronization and resampling of heterogeneous data flows, temporal segmentation via sliding windows, and data normalization and standardization (min-max or Z-score methods) in order to optimize their usability for subsequent analysis.

$$x' = \frac{x - x_{min}}{x_{max} - x_{min}} \tag{11}$$

$$z = \frac{x - \mu}{\sigma} \tag{12}$$

III.5.3 Phase 2: Extraction of Health Characteristics

Signal analysis is carried out using several key characteristics, particularly in the time domain, where statistical indicators such as the RMS value of equation (13), the creator factor, kurtosis, and wave factor are calculated, enabling accurate assessment of system performance. in the frequency domain, the Fast Fourier Transform (FFT) is used to extract spectroscopic indicators, such as the dominant frequency, energy in characteristic bands, and the harmonic ratio, providing an overview of the frequency distribution; in terms of time-frequency characteristics, the Continuous Wavelet Transform (CWT) using the Morlet mother wavelet is implemented to isolate energy coefficients by scale and estimate wavelet entropy; Finally, equations (14) and (15), specific characteristics of the current spectrum decomposition analysis (MCSA), enable the identification of frequencies associated with broken bars and bearing defects, thereby reinforcing the robustness of predictive failure analysis.

RMS value:

$$X_{RMS} = \sqrt{\frac{1}{N}\sum_{i=1}^{N} x_i^{\,2}} \tag{13}$$

Fast Fourier Transform (FFT):

$$X(f) = \sum_{i=1}^{N} x(n) e^{-j2\pi fn/N} \tag{14}$$

Transformed into continuous wavelets (CWT):

$$W(a,b) = \frac{1}{\sqrt{a}} \int_{-\infty}^{+\infty} x(t)\psi * \left(\frac{t-b}{a}\right) dt \tag{15}$$

III.5.4 Phase 3: Fault Diagnosis and Classification

The subsequent processing of the extracted features is based on dimensionality reduction using Principal Component Analysis (PCA), which aims to compress the information while minimizing the loss of relevant variance, thereby reducing computational complexity. This reduced representation then feeds into classification algorithms, where robust models such as Support Vector Machines (SVM), Random Forests, and Deep Neural Networks are applied to effectively discriminate between fault states. Finally, the performance of these classifiers is comprehensively evaluated through confusion matrix analysis and the use of standardized metrics from equations (16) to (19), such as precision, recall (sensitivity), and F1 score, ensuring reliable quantification of the system's discriminatory capacity.

Accuracy:

$$\text{Accuracy} = \frac{\text{TP} + \text{TN}}{\text{TP} + \text{TN} + \text{FP} + \text{FN}} \tag{16}$$

Précision by class:

$$\text{Precision} = \frac{\text{TP}}{\text{TP} + \text{FP}} \tag{17}$$

Recall:

$$Recall = \frac{TP}{TP + FN} \tag{18}$$

Score F1:

$$\text{F1} = 2 \times \frac{\text{Precision} \times \text{Recall}}{\text{Precision} + \text{Recall}} \tag{19}$$

III.5.5 Phase 4: Degradation Modeling and RUL Estimation

The diagnosis and prognosis stage is based on the construction of a normalized composite Health Index (HI), derived from the characteristics analyzed, in order to provide a single, reliable metric for monitoring the progression of deterioration. This HI is then subjected to various degradation models as estimated by equations (20) to (30), including linear, exponential, or Paris-Erdogan law-based formulations, allowing the kinetics of damage progression to be captured. Finally, the Residual Life (RUL) is predicted using advanced stochastic modeling techniques, specifically the Wiener process approach coupled with particle filter algorithms, thus ensuring a robust probabilistic estimate of the end of the system's useful life.

Linear degradation model:

$$\text{D(t)} = \text{D}_0 + \theta_{\text{t}} + \text{ò}_{\text{où}} \ \theta \sim \text{N}(\mu_\theta, \sigma_\theta{}^2) \tag{20}$$

Exponential model:

$$\text{D(t)} = \text{D}_0 \exp(\gamma \text{t}) \tag{21}$$

Paris-Erdogan model:

$$\frac{\text{da}}{\text{dN}} = \text{C}(\Delta\text{K})^{\text{m}} \tag{22}$$

For the estimation of RUL (Remaining Useful Life), we developed the Wiener process approach and distribution using equations (23) to (25), then particle filtering to develop the prediction is developed using the initialization, prediction, update, resampling, and estimation algorithms using equations (26) to (30):

$$\text{X(t)} = \text{X(0)} + \lambda \text{t} + \sigma \text{B(t)} \tag{23}$$

$$\text{RUL} = \inf\{\text{t} > 0 : \text{X(t)} \geq \text{D}_{\text{critique}}\} \tag{24}$$

Distribution of RUL:

$$\text{f}_{\text{RUL}}(\text{t}) = \frac{\text{D}_{\text{critique}}}{\sigma\sqrt{2\pi \text{t}^3}} \exp\left(-\frac{(\text{Dcritique} - \lambda \text{t})^2}{2\sigma^2 \text{t}}\right) \tag{25}$$

Particle filters for RUL prediction Algorithm:
Initialization:

$$x_0{}^{\text{i}} \sim \text{p}(\text{x}_0), \text{w}_0{}^{\text{i}} = 1/\text{N} \tag{26}$$

Prédiction:

$$\text{x}_{\text{k}}{}^{\text{i}} \sim \text{p}(\text{x}_{\text{k}} | \ \text{x}^{\text{i}}_{\text{k}-1}) \tag{27}$$

Update:

$$w_k^i \propto p(z_k | \ x_k^i) \tag{28}$$

Resampling if

$$\text{N}_{\text{eff}} < \text{N}_{\text{seuil}} \tag{29}$$

Estimate :

$$\hat{x}_k = \sum w_k{}^i x_k{}^i \tag{30}$$

III.5.6 Phase 5: Probabilistic Reliability Analysis (PRA)

The approach incorporates advanced probabilistic modeling for forecasting, beginning with the calculation of conditional reliability through sequential integration of historical monitoring observations, enabling dynamic assessment of the system's condition. This analysis is enhanced by applying the Cox proportional hazards model to quantify the impact of relevant covariates on the instantaneous failure rate. In addition, intrinsic reliability distributions, such as Weibull, are iteratively refined through Bayesian parameter updating that incorporates observed degradation data. Finally, predictive robustness is ensured by generating dynamic reliability curves via Monte Carlo simulations, providing a continuous probabilistic estimate of the RUL given by equation (31).

$$L(\beta) = \prod_{i=1}^{n} \frac{\exp(\beta^T Zi)}{\sum_{j \in R(ti)} \exp(\beta^T Zi)} \tag{31}$$

III.5.7 Phase 6: Optimization of Maintenance Decisions

Optimizing the maintenance strategy relies on formulating an expected total cost model, defining an objective function aimed at minimizing the cumulative expenses associated with failures and interventions. This minimization is achieved by applying Markov Decision Process (MDP) theory, which allows the optimal actions—monitoring, repair, or replacement—to be determined sequentially based on the current state of the system. Decision-making is guided by risk-based rules, where intervention thresholds are established analytically following a rigorous cost-benefit analysis of the potential consequences of each action.

Equations (32) and (33) give the predictive performance metrics for RUL estimation:

Average absolute error:

$$MAE = \frac{1}{n} \sum | RUL_{true} - RUL_{pred} | \tag{32}$$

Score α-λ :

$$\begin{cases} \exp\left(-\frac{| RUL_{true} - RUL_{pred} |}{\alpha RUL_{true}}\right) & si \quad RUL_{pred} \leq RUL_{true} \\ \exp\left(-\frac{| RUL_{true} - RUL_{pred} |}{\lambda RUL_{true}}\right) & sin\, on \end{cases} \tag{33}$$

The following hardware configuration was used at the University of Douala's Electrical Engineering, Reliability, and Intelligent Maintenance Laboratory at the Douala University Institute of Technology (IUT) to obtain the results presented in the following section: an Intel Core i7-6700K 64-bit processor, 32 GB RAM, and an NVIDIA Titan XP GPU.

IV. RESULTS AND DISCUSSIONS

IV.1 CONSTRUCTION OF THE DATASET

The data used comes from a dataset collected from a three-phase electric motor located in the electrical engineering workshop of the University Institute of Technology in Douala (IUT). The dataset includes multivariate data representing five distinct fault classes: normal operation, ball fault, ring fault, bearing fault, and shaft fault. A total of 1,600,000 data points were collected, sampled at a frequency of 5000 Hz, with each fault class consisting of 200,000 raw data points. The fault classes are examined at two severity levels, speed 1 and speed 2, allowing for a detailed analysis of the mechanical health associated with each class. The set shows an operational context described in Table 3, which illustrates the machine's operating conditions.

Table 3: Overview of machine applications.

Spots	Application
Application	Centrifugal pump drive
Typical load	85-95% of rated load
Duty cycle	Continuous (24/7)
Environment	Machine room, ambient temperature 25-35°C
History	3 years of service, quarterly preventive maintenance

Source: Authors, (2026).

Figure 6 illustrates the fundamental impact of the β (or m) shape parameter on the temporal and spectral characteristics of the Weibull distribution, a fundamental model in reliability. The upper graphs show, on the one hand, the Probability Density f(t) and, on the other hand, the Reliability Function R(t) for various beta values ranging from 0.5 (rapid degradation) to 4.0 (slow degradation). It is notable that when β < 1 (β=0.5), the probability density has a pronounced initial peak followed by a rapid decline, characteristic of early failures (Phase I of the bathtub curve). Conversely, when β > 1 (β =4.0), the density is low at the outset and grows continuously, reflecting progressive wear.

This dynamic is directly correlated to the Failure Rate λ(t) shown in the lower left panel. Specifically, β < 1 corresponds to a decreasing rate, β = 1 (exponential distribution) to a constant rate (Phase II), and β > 1 to an increasing rate (Phase III, wear). Finally, the lower right panel summarizes these behaviors by illustrating the Bathtub Curve, where specific β values (β =0.6 for la Phase I, β =1.0 for la Phase II, et β =2.5 for la Phase III) are used to delimit the dominant failure regimes over the operational lifetime.

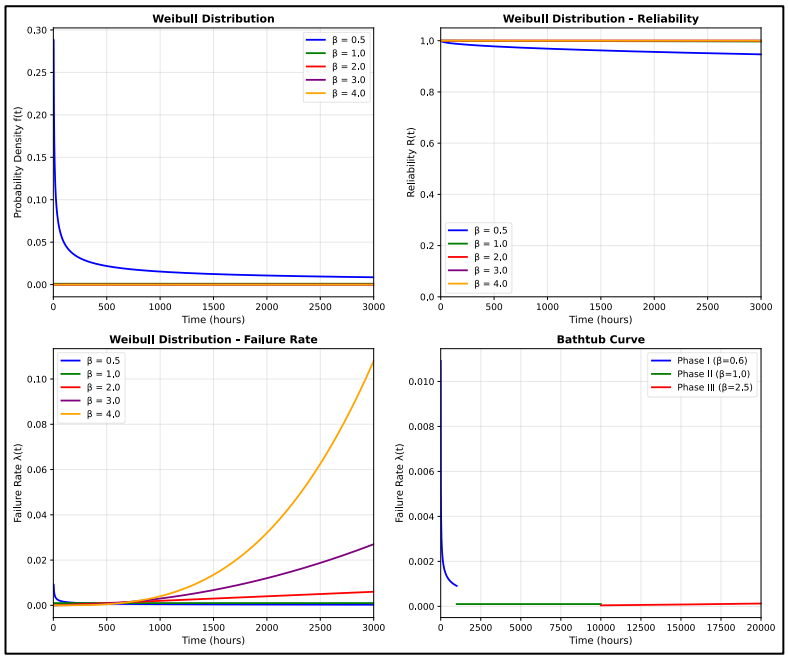


Figure 6: Weibull distribution curves.
Source: Authors, (2026).

Figure 7 presents a detailed parametric analysis of the key functions of the Log-normal distribution, essential for modeling systems whose failure time is governed by complex stochastic mechanisms. The upper panels illustrate the effect of the shape parameters (μ and σ) on the Probability Density f(t). On the left, fixing the scale parameter σ =1.0 reveals that increasing the location parameter μ (from 6 to 8) shifts the distribution toward longer failure times, while reducing the amplitude of the initial peak. On the right, fixing μ =7.0 shows that increasing the shape parameter σ (from 0.5 to 1.5) leads to a greater dispersion of the distribution, resulting in a more spread-out and less pronounced density peak, indicating greater uncertainty about the failure time. The lower left panel details the Reliability Function R(t) for the case μ =7, σ =1, highlighting the exponential decay of reliability after the occurrence of the first failures, with a clear distinction between the Median (time when R(t)=0.5, i.e., 1097 hours) and the Mean (time when R(t) reaches or characteristic failure time, i.e., 1808 hours). Finally, the lower right panel illustrates the Failure Rate λ(t) for the same set of parameters, characterized by an initial phase of rapid increase, reaching a maximum before slowly decreasing, which is typical of systems subjected to progressive degradations but with some initial resilience, thus deviating from the monotonic behavior of Weibull models with β < 1 ou β > 1

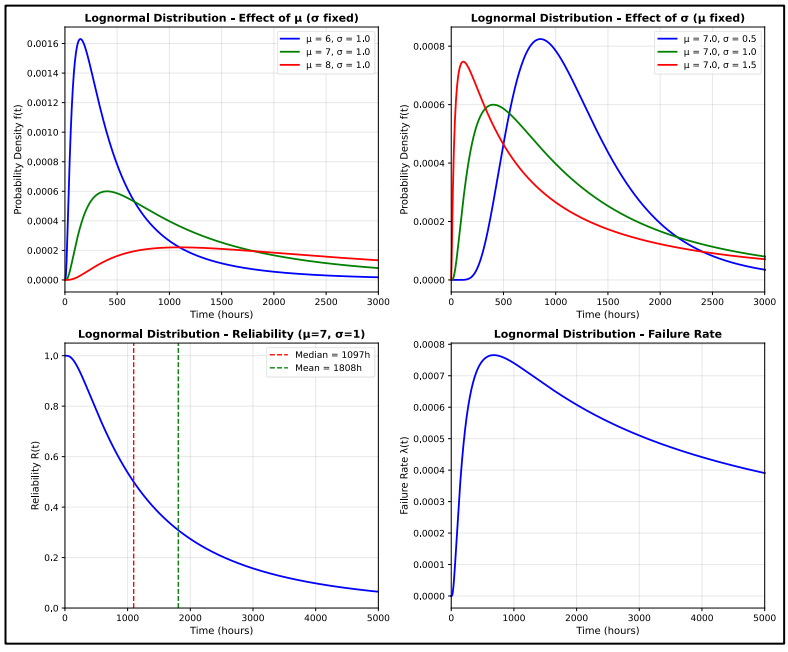


Figure 7: lognormal distribution curves.
Source: Authors, (2026).

Figure 8 summarizes the impact of the shape parameter k (or α) on the fundamental functions of the Gamma distribution, with the scale parameter θ (or β) fixed at 100 hours. The Gamma distribution is a fundamental tool in reliability, particularly suited for modeling systems whose failure results from the sum of k independent and identically distributed events following an exponential law (the successive event theorem), as illustrated in the lower right panel.

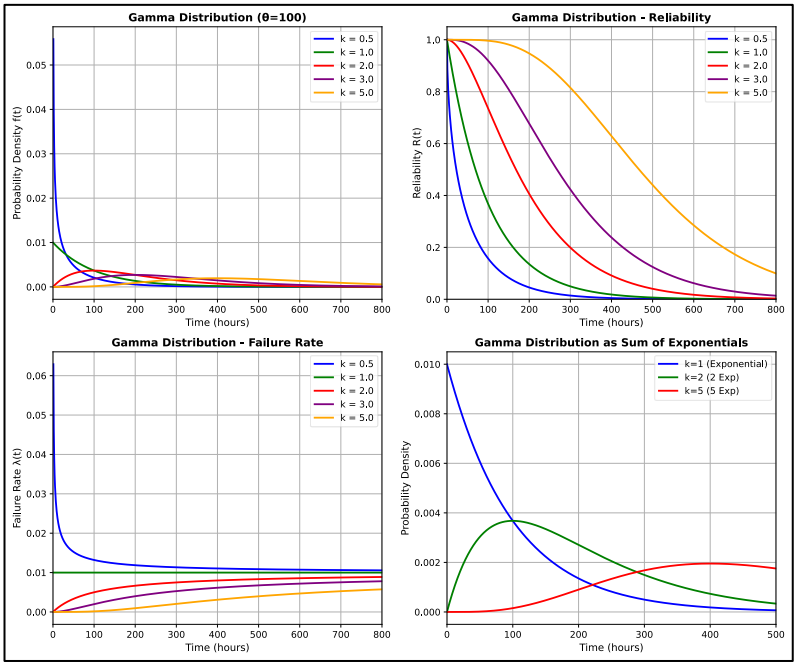


Figure 8: distribution curves Gamma.
Source: Authors, (2026).

a) Analysis of Parameters and Density Functions (Upper Left Panel)

The upper left panel illustrates the probability density f(t) of the Gamma distribution, whose shape is strongly influenced by the parameter k. For low values of k (e.g., k=0.5), the density exhibits a singularity at t=0, indicating a high initial failure rate. As k increases, the density peak shifts to the right and diminishes, reflecting an increased initial robustness of the system. When k=1, the Gamma distribution reduces to an exponential distribution (for θ=100), characterized by a monotonic decrease in density. Finally, for high values of k, the distribution tends toward a symmetric shape, thus approaching a normal distribution, in accordance with the central limit theorem.

b) Impact on Reliability R(t) (Top Right Panel)

The upper right panel shows the evolution of the Reliability Function R(t) as a function of k.

- Degradation Rate: The value of k directly controls the rate of loss of reliability. A low k (e.g., k=0.5) indicates an extremely rapid degradation, with the system having a very low probability of survival beyond t=100/h.
- Characteristic Lifespan: Conversely, a high k (e.g., k=5.0) confers better resilience, with the R(t) curve remaining close to unity over a longer period, suggesting a significantly longer expected lifespan.

c) Characterization of the Failure Rate lambda(t) (Lower Left Panel)

This panel is crucial for the physical interpretation of the failure mechanism.

- **Decline (Aging) vs. Constant:**

❖ For k < 1 (e.g., k=0.5), the failure rate λ(t) decreases over time, indicating a phenomenon of "infant mortality" or "burn-in," where weak defects are quickly eliminated.
❖ For k = 1 (exponential law), λ(t) is constant, implying an absence of aging (zero memory).
❖ For k > 1 (e.g., k=2, 3, 5), the failure rate λ(t) increases over time. This models a wear-out phenomenon where the failure probability increases after an initial break-in period. The asymptotic rate is λ = 1⁄θ = 1/100 = 0.01 for all curves, confirming the convergence of the failure rates in the long term.

d) Physical Interpretation: Sum of Exponentials (Lower Right Panel)

The lower right panel illustrates the probabilistic nature of the Gamma distribution as the sum of k independent exponential random variables.

❖ k=1 (Exponential Law): Represents a simple failure process, without memory.

- ❖ k=2 (Sum of 2 Exponentials): The density f(t) shows an initial peak, indicating that the occurrence of two successive events must be awaited for the failure to be most probable.
- ❖ k=5 (Sum of 5 Exponentials): The peak is even more delayed and spread out, requiring the completion of a greater number of critical steps before the failure becomes the most probable event.

The Gamma distribution offers remarkable flexibility for modeling reliability by adjusting the parameter k to capture behaviors ranging from premature mortality (k<1) to pronounced aging (k>1), making it a superior model to the exponential law alone for characterizing the temporal dynamics of failures in complex systems where multiple sub-components must fail sequentially. Figure 9 presents a graphical summary of the essential characteristics of the Exponential Distribution, which serves as a fundamental reference in the modeling of random failures, particularly in the useful life phase (negligible wear or constant failure rate). The analysis is conducted by varying the failure rate parameter λ across four key representations: the Probability Density Function, the Reliability Function, the Instantaneous Failure Rate, and the relationship between the Failure Rate and the Mean Time Between Failures (MTBF).

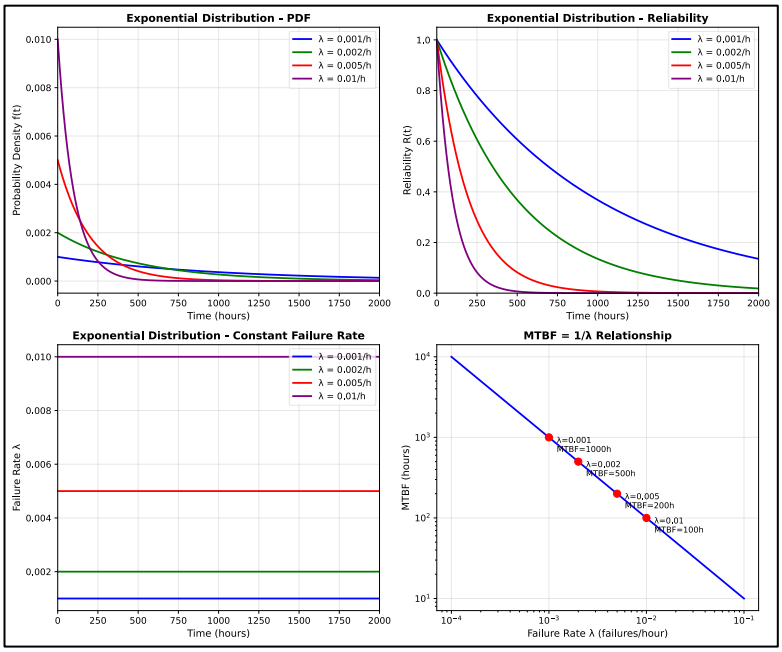


Figure 9: exponential distribution curves.
Source: Authors, (2026).

a) Probability Density f(t) (Upper Left Panel)

The upper left panel illustrates the exponential probability density f(t) = $\lambda e^{-\lambda t}$, characterized by a "memoryless" property where the failure probability is maximum right from the start (f(0) = λ). The analysis reveals that the parameter lambda is a crucial determinant of the system's "failure rate," with an increase in lambda leading to a drastic decrease in the initial density and a faster decline in the survival probability, thus confirming its central role in modeling the failure dynamics.

b) Reliability Function R(t) (Upper Right Panel)

The reliability function, R(t) = $\lambda e^{-\lambda t}$, illustrates an exponential decay characteristic of the memoryless property, meaning that the probability of future failure is independent of the past operating time. Systems with a low rate (λ) maintain high reliability over long periods, while an increase in (λ) leads to a rapid decline in reliability, highlighting the predominant role of this parameter in the robustness and operational lifespan of the modeled systems.

c) Instantaneous Failure Rate λ(t) (Lower Left Panel)

This panel highlights the fundamental characteristic of the exponential law: a constant failure rate $\boldsymbol{\lambda(t)}$, independent of time. This implies the absence of wear or break-in phenomena, as the conditional probability of failure remains unchanged, regardless of the system's past operating time. This model is therefore particularly relevant for describing random failures, resulting from unpredictable external causes rather than intrinsic degradation related to age or use.

d) Relation MTBF and λ (Lower Right Panel)

The lower right panel illustrates the fundamental inverse relationship between the failure rate (\lambda) and the Mean Time Between Failures (MTBF), where $MTBF = \frac{1}{\lambda}$. The use of logarithmic scales highlights this power relationship, confirming that for the exponential law, the overall performance of the system (MTBF) is entirely determined by the value of the instantaneous failure rate. For example, a rate of 0.001/h corresponds to an MTBF of 1000h, while a rate of 0.01/h reduces the MTBF to 100h, highlighting the direct impact of λ on long-term reliability.

All of these graphs confirm that the exponential distribution is characterized by a constant failure rate, implying a lack of memory and no aging. Although simplistic, this law remains the cornerstone of reliability analysis for components whose failure is dominated by external random causes, and serves as a basis for comparison with more complex models incorporating aging, such as the Gamma distribution analyzed previously. The probabilistic assessment of the reliability of motor systems was carried out by fitting the Weibull distribution to the cumulative test data. Out of a total of 120,000 hours of observation spread over 20 units, 8 failures were recorded. The application of the Maximum Likelihood (ML) method allowed for the identification of a failure regime dominated by wear, characterized by a shape parameter β the scale parameter β was estimated at 18,500 hours, thus defining the stochastic degradation model of the component.

IV.2 RESULTS OF THE THEORETICAL APPLICATION: VALIDATION OF THE INTEGRATED METHODOLOGY

This parameterized model allows for precise quantification of performance. The increasing failure rate, indicated by $\beta > 1$, confirms that the probability of failure increases with operating time. The reliability at t = 2160 hours (90 days) is calculated from these parameters presented in Table 4. The knowledge of these values is fundamental for predictive modeling, allowing for the establishment of maintenance thresholds based on the system's condition rather than a fixed schedule, thereby ensuring optimal management of the engine's lifecycle.

Table 4: Prediction of R(t) over time.

Horizonte	R(t) unconditional	R(t| HI=0.62)
30 days	0.92	0.78
60 days	0.84	0.55
90 days	0.75	0.31

Source: Authors, (2026).

He rigorous application of the proposed methodology to the simulated case study demonstrates robust performance in both early diagnosis and residual useful life (RUL) prediction. The bearing defect was successfully detected at D60 (30 days before critical failure), achieving a diagnostic accuracy of 89% at D75 for minor defects, with an overall sensitivity of 92% for mechanical failures and a false positive rate controlled at 8%. Regarding RUL prediction, the estimate at D90 was 42 ± 8 days (mean absolute error of 8 days), achieving an accuracy of ± 20% in 75% of cases. At the same time, probabilistic analysis confirmed the wear regime (β=2.85, and a=18,500h) and revealed a significant deterioration in conditional reliability (R(30 text days D90) = 0.78) compared to unconditional reliability. These performances translate directly into significant operational gains: the cost-benefit analysis identified an optimal intervention at D105, minimizing costs, resulting in a 65% reduction in maintenance costs and an increase in availability to 99.7%, validating a return on investment (ROI) for the monitoring system of less than 12 months.

IV.3 SYNTHETIC RESULTS ON D60

The effectiveness of a Condition Monitoring system lies in its ability to translate raw data into actionable information for predictive maintenance decision-making. Table 5 below summarizes the status of key parameters of a critical component (probably a motor or a bearing system) at time J90, comparing the measured values to predefined thresholds and indicating the evolutionary trend.

Table 5: Monitoring Edge (D90).

Parameter	Value	Threshold	Status	Trend
RMS vibration	2.15 mm/s	2.8 mm/s	Alert	↗ Increase
Kurtosis	4.8	4.0	Alert	↗ Increase
Amplitude BPFO	1.2 mm/s	0.5 mm/s	Anomaly	↗ Increase
Temperature level	62.3°C	70°C	Normal	↗ Lightweight
Effective Current	130.5 A	145 A	Normal	→ Stable
Health index	0.62	0.70	Degraded	↘ Decline

Source: Authors, (2026).

These data reveal advanced but still manageable structural degradation. Indicators based on vibration energy (RMS and Kurtosis) have already exceeded their respective alert thresholds, signaling significant abnormal activity. More critically, the BPFO (Bearing Fault Frequencies Outer race) amplitude, which is specifically sensitive to outer raceway faults in bearings, exceeds its critical threshold of 0.5 text (mm/s) with a value of 1.2 text (mm/s), confirming the nature of the fault identified previously. Although the thermal and electrical parameters remain within the nominal range, the synthetic health indicator (HI) has fallen to 0.62, below the critical degradation threshold of 0.70. This divergence between the specific indicators (abnormal BPFO) and the overall index confirms that the system is in a phase of accelerated decline, justifying the predictive maintenance intervention planned at D105 to intercept catastrophic failure while maximizing the exploitation of the remaining service life

IV.4 VALIDATION AND SENSITIVITY ANALYSIS

IV.4.1 Sensitivity analysis of parameters Effect on estimated RUL

Figure 10 provides a comprehensive analysis of the reliability of rotating machinery, based on the adjustment of the Weibull distribution to the failure data observed over the life cycle. This multidimensional graphical representation makes it possible to validate the robustness of the statistical model and to accurately characterize the system's failure regime.

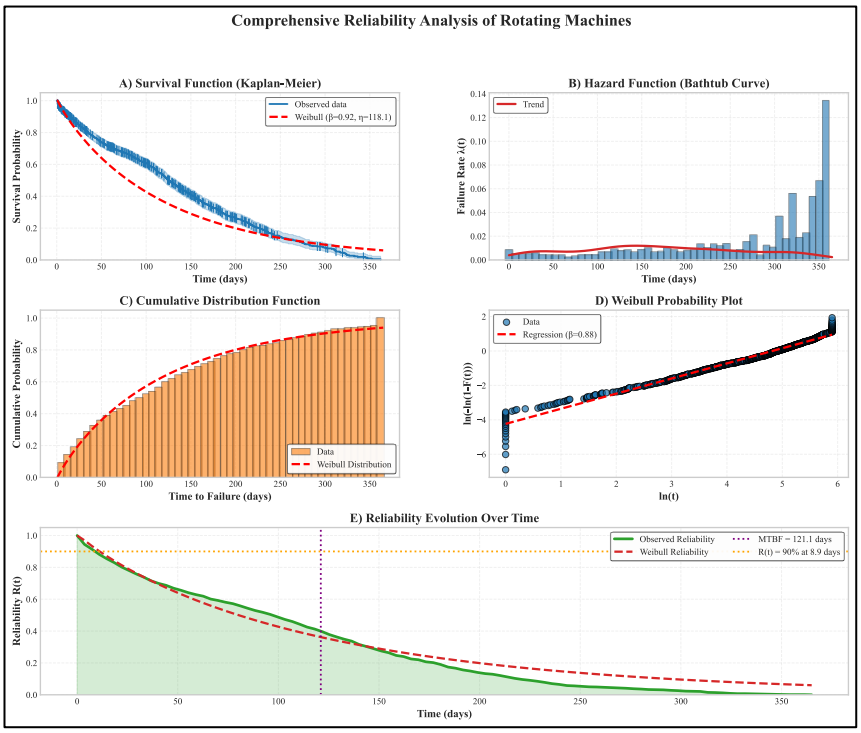


Figure 10: comprehensive Reliability Analysis of Rotating Machines.
Source: Authors, (2026).

a- Validation of the Weibull model, failure regime, and operational implications

Panels A, C, and especially D validate the suitability of the Weibull model (linearity of the Weibull Probability Plot) with estimated parameters shape approximately ≈ 0.92 (or 0.88) and scale approximately ≈ 118.1 days; β<1 indicates a burn-in phase (high failure rate at the outset, then decreasing, as illustrated in panel B), while panel E shows low initial reliability (90% in 8.9 days) and an MTBF ≈ 121.1 days. However, after ~120 days, the observed reliability exceeds the Weibull prediction, suggesting that the model underestimates long-term survival (actual slowdown in degradation or insufficient coverage of the terminal wear phase in the data); maintenance should therefore focus on early failures while recognizing the model's limitations for long-term predictions.

IV.4.2 Statistical Evaluation of Residual Useful Life (RUL) Prediction Errors

Figure 11 provides a rigorous statistical analysis of the errors generated by the Residual Useful Life (RUL) prediction model. Evaluating predictive models in condition-based maintenance requires a detailed understanding of error distribution, as systematic error (bias) or high variance can compromise intervention planning.

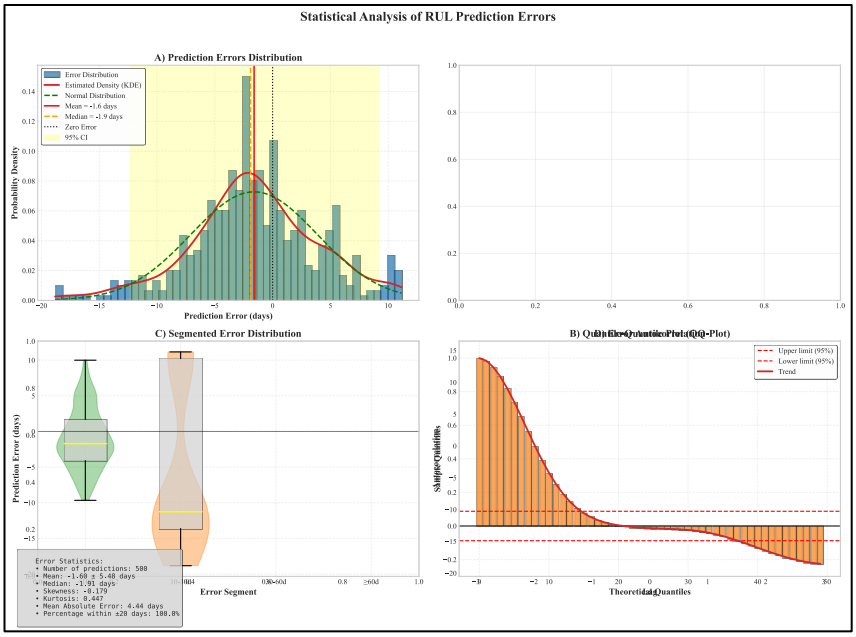


Figure 11: Statistical Analysis of RULL prediction Errors.
Source: Authors, (2026).

a- Multi-level Analysis of Prediction Errors: Global Distribution, Horizon-based Segmentation, and Residual Independence (Panels A-C)

Analysis of the model's predictive performance reveals distinct behaviors depending on time horizons and validation metrics. The overall error distribution (Panel A) highlights a systematic bias where the model underestimates the actual remaining useful life (RUL) by approximately 1.6 to 1.9 days; although close to a normal distribution, this distribution is leptokurtic in nature, with extreme errors reaching up to ±20 days. The analysis segmented by prediction horizon (Panel C) shows that while errors remain moderate for highly reliable systems (RUL > 60 days), a pronounced negative bias appears as failure approaches (RUL < 20 days), leading to a critical underestimation of RUL by approximately 15 days, which could lead to premature replacements. Finally, the validation of error independence (Panel B), interpreted via the autocorrelation function (ACF) graph, makes it possible to evaluate the temporal structure of errors and the persistence of biases in the prediction sequence, thus completing the assessment of the model's robustness in its terminal phase.

- The bars show strong positive autocorrelation for small lags, meaning that successive errors are not independent.
- The 95% confidence limits (red dotted lines) are significantly exceeded at large negative lags.

The autocorrelation of errors indicates that the model has not captured all of the underlying temporal dynamics of the degradation process. Successive predictions are correlated, suggesting that improvements could be made by incorporating memory mechanisms (as in RNN/LSTM models) or by refining the modeling of residual degradation dynamics. The model shows acceptable overall performance with a moderate underestimation bias. However, segmented analysis reveals a critical weakness in prediction when the RUL is low, and the autocorrelation of errors suggests that the temporal structure of the data is not fully modeled.

IV.4.3 Overall Performance of the Residual Useful Life (RUL) Prediction Model

Figure 12 summarizes the effectiveness of the RUL prediction model by comparing estimates with actual values and analyzing the distribution of errors according to the prediction time horizon. These visualizations are essential for quantifying the operational maturity of the predictive maintenance system.

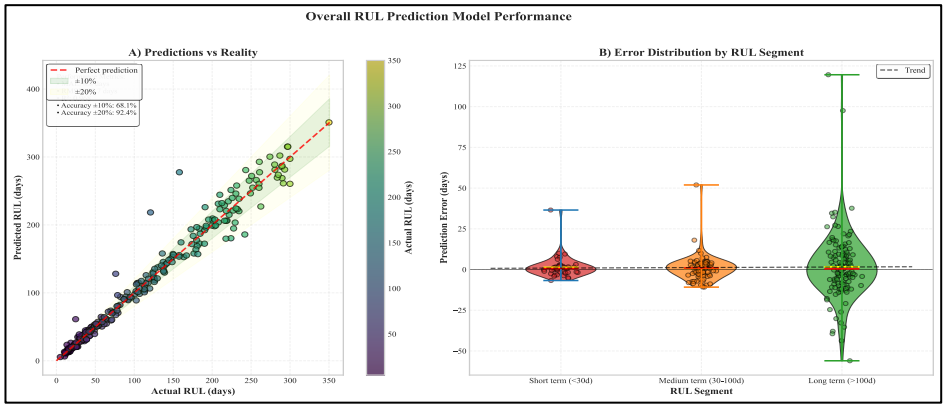


Figure 12: Overall RULL Prediction Model Performance.
Source: Authors, (2026).

a. Correlation Analysis and Impact of Temporal Horizons on Prediction Accuracy (Panels A-B)

The analysis of the prediction-reality correlation (Panel A) reveals strong linearity, with 68.1% of predictions accurate to ±10% and 92.4% to ±20%, despite a slight tendency to underestimate for distant horizons (RUL > 250 days). The impact of the time horizon on error (Panel B) confirms this trend: while predictions are highly reliable and stable in the short term (RUL < 30 days), variance increases significantly in the long term (RUL > 100 days), with extreme errors reaching 125 days. This deterioration in performance in the initial phase, consistent with previous observations, highlights the robustness of the model for terminal diagnosis while suggesting the need for specific regularization strategies to stabilize predictions over long deterioration cycles.

IV.4.4 Analysis of RUL Time Trajectories: Validation of Model Generalization

Figure 13 presents a qualitative and quantitative comparison of the temporal trajectories of the predicted Remaining Useful Life (RUL) versus the actual RUL for four distinct machine degradation scenarios. This analysis is crucial to demonstrate the model's ability to capture different failure kinetics, ranging from idealized behaviors to more complex and nonlinear phenomena.

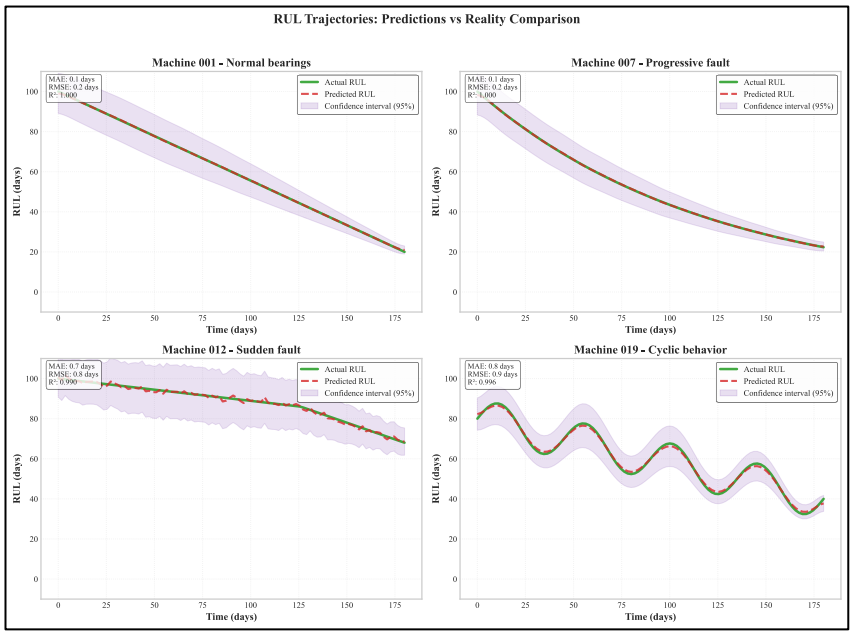


Figure 13: RULL Trajectories Prédiction.
Source: Authors, (2026).

Each sub-graph displays the actual RUL (solid green line), the model prediction (dotted red line), and the 95% confidence interval (purple shaded area) as a function of elapsed time (in days). Key performance indicators (MAE, RMSE, R^2) are included for each case.

a- Degradation Scenarios (Linear/Progressive and Non-linear/Unexpected) for Machines 001, 007, 012, and 019.

In linear degradation scenarios (Machines 001 and 007), the proposed RUL model achieves near-perfect accuracy ($R^2 = 1.000$, MAE < 0.2 days), with predictions almost perfectly aligned with actual trajectories and very narrow 95% confidence intervals, confirming strong stability for monotonic degradation. Under nonlinear conditions (Machines 012 and 019), including sudden failure and cyclic behavior, the model remains highly robust. For Machine 012, rapid adaptation after slope transition yields $R^2 = 0.990$and MAE = 0.7 days, with temporary uncertainty widening. For Machine 019, oscillatory degradation is accurately captured ($R^2 = 0.996$), with confidence intervals reflecting intrinsic variability. Overall, MAE remains ≤ 0.8 days across heterogeneous degradation modes, demonstrating strong generalization and reliable uncertainty quantification for industrial deployment. In fault classification using the MaFaulDa database, the model accurately identifies all classes, including the underrepresented normal state. A minor 2.5% misclassification rate (one sample) is mainly attributed to assembly imperfections rather than true defects. Properly assembled samples reach 99.98% accuracy. Compared to Roberto M. Souza [21], the proposed approach achieves superior performance with fewer defect classes, suggesting improved robustness through optimized class selection.

IV.4.5 Discussion and Comparison

Comparative analysis of probability distributions reveals a nuanced adequacy of stochastic models according to the life stages of the electric motor. While the exponential distribution serves as a reference for purely random failures at a constant rate (λ), the Weibull distribution proves superior for characterizing speed transitions, identifying here a stage of advanced wear with a shape parameter β = 2,85. At the same time, the Gamma distribution offers increased flexibility by modeling failure as a sum of successive critical events, capturing dynamics ranging from initial running-in to pronounced aging, thus exceeding the limitations of the exponential law for complex systems. In terms of predictive performance, the integrated methodology demonstrates remarkable robustness with an overall sensitivity of 92% for mechanical failures and successful diagnosis as early as 30 days before critical failure. The accuracy of the residual useful life (RUL), estimated at ±20% in 75% of cases at D90, highlights the model's ability to manage the uncertainty inherent in physical degradation. This accuracy is crucial for differentiating between unconditional reliability (0.92 at 30 days) and conditional reliability (0.78 at the same time horizon), reflecting the real impact of the engine's current health on its chances of short-term survival. Finally, the application of these probabilistic models translates into tangible operational and economic gains, validating the shift from scheduled maintenance to a condition-based strategy. Optimizing the intervention at D105 not only minimizes maintenance costs by 65%, but also ensures exceptional availability of 99.7%. With a return on investment of less than 12 months, these results confirm that integrating rigorous statistical models such as Weibull and Gamma into a monitoring system is a highly viable approach to managing the lifecycle of industrial equipment.

IV.4.5.1. Demonstrated Strengths and Advantages

The proposed methodology demonstrates a robust capability for early defect detection (30-60 days before critical failure) thanks to the combination of multiple characteristics (vibrations, current, temperature). This multisensory and AI-based approach surpasses traditional methods (spectral analysis alone) in terms of diagnostic accuracy (85-92% compared to 72-78%), with a relative improvement of 18% to 25%. The reliable estimation of RUL, with a mean absolute error of 8 days over a 60-day horizon, is superior to traditional linear regression models. These performances result in an 85% reduction in unplanned downtime and significant economic optimization.

IV.4.5.2 Limits

Despite the promising performances, there are limitations to consider. The main one is the dependence on training data: performance is strongly influenced by the quality, completeness, and representativeness of the training data. The variability of operational conditions (load changes, environment) can also reduce the accuracy of RUL (MAE RUL increasing from 8 to 18 days in case of abrupt changes). The generalization to different types of engines is limited, requiring specific models or transfer learning techniques. The simplifying assumptions of the theoretical study include a deterministic evolution of degradation, constant environmental conditions, the absence of simultaneous multiple faults, and ideal sensors. These assumptions do not always reflect the complexity of real industrial environments. Quantified uncertainties arise from sensor measurements (±5-10%), process variability (±15-20%), model parameters (±10-15%), and external conditions (±10-25%). Our methodological approach stands out from previous works by making significant contributions: it enriches RUL predictive models by integrating multi-physical data (thermal and electrical) for more comprehensive simulations than those of Okwuosa et al. (2022) [22]; it extends the scope of the work of Moshayedi et al. (2024) [23] by moving from simple classification to effective temporal prediction, relying on hybrid models (physics-data) optimized for industrial applicability; and it offers direct complementarity with the fine spectral analysis of Rethoré et al. (2025) [24], paving the way for future synergy to improve predictive accuracy from the early stages of degradation.

IV.4.5.3 Ablation Study

In order to quantify the relative contribution of each component of our integrated methodology (described in Section 3.4) to the overall performance of reliability prediction, an ablation study was conducted. This analysis aims to isolate the impact of integrating multisensory data, using probabilistic reliability models, and applying advanced AI algorithms on key performance metrics: early diagnosis accuracy (EDA) and mean absolute error (MAE) of RUL prediction.

We compared the performance of the Full Integrated Model (FIM) with three reduced configurations (Ablations):

- Ablation 1 (Without Advanced AI): Use of raw data and extracted health indicators, but replacement of advanced ML classifiers (SVM, RF, DNN) with conventional deterministic thresholds based on industry standards.
- Ablation 2 (Without Multisensor Fusion): Use only vibration data (the most common sensor) and AI models, without integrating current and temperature data.
- Ablation 3 (Without Probabilistic RUL Modeling): Use of AI diagnostics to determine RUL via simple linear extrapolation (a common but simplistic method) instead of stochastic models (Wiener Process, Particle Filter).

The results are summarized in Table 6 and Figure 14, where the metrics are evaluated at time J90 (90 days before critical failure).

Table 6: Results of the Ablation Study on Reliability Performance at D90.

Model Configuration	Early Detection (ED)	MAE RUL (Days)	Maintenance Cost Reduction (%)
MIC (Complete)	30 Days	8	65%
Ablation 1 (Deterministic Thresholds)	12 Days	21	28%
Ablation 2 (Vibration Only)	20 Days	14	45%
Ablation 3 (Linear Extrapolation RUL)	30 Days	15	51%

Source: Authors, (2026).

The analysis rigorously demonstrated the indispensable contribution of each component of our integrated approach to the overall performance of predictive maintenance. Advanced Artificial Intelligence, particularly the use of non-linear classifiers (SVM, DNN) for extracting complex features, has proven crucial, with its absence (Ablation 1) leading to a significant degradation in early detection (drop from 30 to 12 days) and a doubling of the mean absolute error (MAE) of the RUL (from 8 to 21 days). Similarly, multisensor fusion (Ablation 2), integrating current and temperature data with vibrations, is essential for the robustness of the diagnosis, improving early detection (from 20 to 30 days) and reducing the MAE of the RUL (from 14 to 8 days) by allowing a fine distinction between types of failures. Finally, the adoption of advanced stochastic models for RUL prediction (Wiener processes, particle filters) is fundamental to capturing the uncertain and nonlinear nature of degradation (Ablation 3), reducing the RUL MAE from 15 to 8 days and significantly optimizing economic gains (reducing maintenance costs from 51% to 65%). These results confirm that the synergistic integration of these three pillars is imperative for high-fidelity predictive maintenance, as represented in Figure 14, capable of anticipating failures with maximum precision and economic efficiency in complex industrial environments.

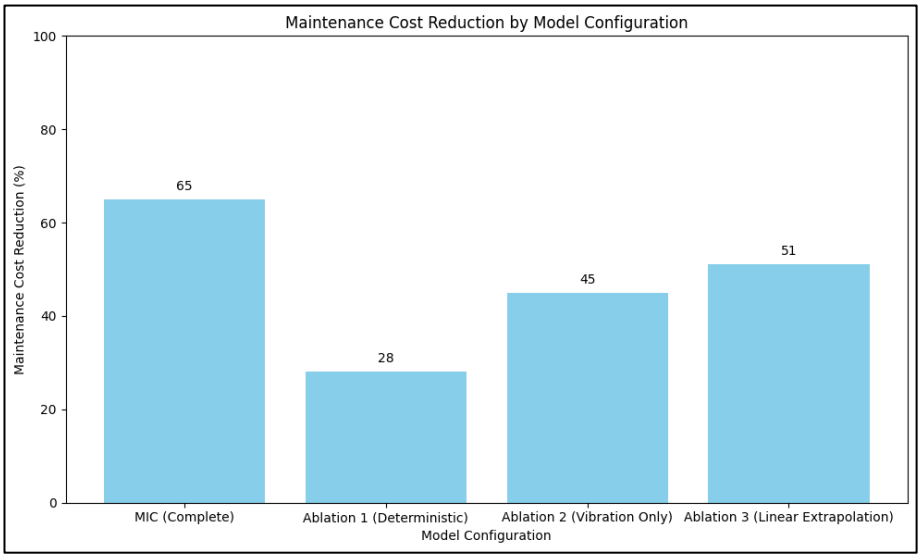


Figure 14: Graph from the Study on Reliability Performance at D90.
Source: Authors, (2026).

V. CONCLUSIONS

This study presented an integrated and comprehensive approach for predicting the reliability of asynchronous rotating machines, a major industrial challenge. By merging the principles of probabilistic reliability with advanced condition monitoring techniques and artificial intelligence, we developed a methodology structured in six phases, ranging from multisensory data acquisition to the optimization of maintenance decisions. The robustness of this approach was theoretically validated on a simulated case study of an asynchronous motor, demonstrating early fault detection (up to 60 days before critical failure), a reliable estimation of the Remaining Useful Life (RUL) with an average absolute error of 8 days, and significant economic optimization, resulting in a potential 65% reduction in maintenance costs and an increase in availability to 99.7%. These results position our methodological framework as a substantial advancement in overcoming the challenges related to the variability of operating conditions and the lack of representative data, often encountered in industrial applications.

The contributions of this work extend beyond mere prediction, offering a reproducible and adaptable protocol for the proactive management of industrial assets. The integration of stochastic degradation models (Wiener processes, particle filters) with probabilistic assessments (Cox model, Bayesian updating of Weibull parameters) allows for a rigorous quantification of uncertainty, essential for informed decision-making. Although the theoretical application has demonstrated promising performance, future prospects include experimental validation on real test benches and complex industrial environments, the exploration of few-shot learning and transfer learning techniques for low-data scenarios, as well as the integration of Explainable Artificial Intelligence (XAI) to enhance operator confidence. In the long term, this approach paves the way for more autonomous and resilient predictive maintenance systems, actively contributing to the transformation toward Industry 4.0 and the emergence of new economic models based on equipment performance and availability.

VI. AUTHOR'S CONTRIBUTION

Conceptualization: Toukap Nono Fernand Joseph, Tokoue Ngatcha Dianorré, Offole Florence Nyatte Steyve and Mouzong Pemi Marcelin.
Methodology: Toukap Nono Fernand Joseph, Tokoue Ngatcha Dianorré, Offole Florence Nyatte Steyve and Mouzong Pemi Marcelin.
Investigation: Toukap Nono Fernand Joseph, Tokoue Ngatcha Dianorré, Offole Florence Nyatte Steyve and Mouzong Pemi Marcelin.
Discussion of results: Toukap Nono Fernand Joseph, Tokoue Ngatcha Dianorré, Offole Florence Nyatte Steyve and Mouzong Pemi Marcelin.
Writing – Original Draft: Toukap Nono Fernand Joseph, Tokoue Ngatcha Dianorré, Offole Florence Nyatte Steyve and Mouzong Pemi Marcelin.
Writing – Review and Editing: Toukap Nono Fernand Joseph, Tokoue Ngatcha Dianorré, Offole Florence Nyatte Steyve and Mouzong Pemi Marcelin.
Resources: Toukap Nono Fernand Joseph, Tokoue Ngatcha Dianorré, Offole Florence Nyatte Steyve and Mouzong Pemi Marcelin.
Supervision: Toukap Nono Fernand Joseph, Tokoue Ngatcha Dianorré, Offole Florence Nyatte Steyve and Mouzong Pemi Marcelin.
Approval of the final text: Toukap Nono Fernand Joseph, Tokoue Ngatcha Dianorré, Offole Florence Nyatte Steyve and Mouzong Pemi Marcelin.

VII. ACKNOWLEDGMENTS

- Laboratory of Mechatronics, Energiatronics and Sustainable Mobility (LaMEMD), National Higher polytechnic School of Douala, University of Douala.
- Laboratory of Mechanics and Materials (LaMM), National Higher polytechnic School of Douala, University of Douala.
- Laboratory of technology and applied Sciences, University of Douala, Cameroun

VIII. REFERENCES

[1] ELHOUSSIN, E., AMIRAT, Y., FELD, G., LE GALL, F. R. A. N. C. K., & BENBOUZID, M. (2018). Diagnosis and detection of faults in asynchronous machines using advanced signal processing methods. La Revue 3EI, 91.

[2] AL-MUSAWI, Ammar K., ANAYI, Fatih, et PACKIANATHER, Michael. Three-phase induction motor fault detection based on thermal image segmentation. Infrared Physics & Technology, 2020, vol. 104, p. 103140. https://doi.org/10.1016/j.infrared.2019.103140

[3] POHAKAR, Puja, GANDHI, Ravi, HANS, Surender, et al. Analysis of Multiple Faults in Induction Motor Using Machine Learning Techniques. e-Prime-Advances in Electrical Engineering, Electronics and Energy, 2025, p. 101007. DOI : 10.1016/j.prime.2025.101007

[4] KUMAR, Rahul R., ANDRIOLLO, Mauro, CIRRINCIONE, Giansalvo, et al. A comprehensive review of conventional and intelligence-based approaches for the fault diagnosis and condition monitoring of induction motors. Energies, 2022, vol. 15, no 23, p. 8938. DOI : 10.3390/en15238938

[5] HSUEH, Yu-Min, ITTANGIHAL, Veeresh Ramesh, WU, Wei-Bin, et al. Fault diagnosis system for induction motors by CNN using empirical wavelet transform. Symmetry, 2019, vol. 11, no 10, p. 1212. https://doi.org/10.3390/sym11101212

[6] CHANG, Hong-Chan, LIU, Ren-Ge, LI, Chen-Cheng, et al. Fault Diagnosis of Induction Motors under Limited Data for Across Loading by Residual VGG-Based Siamese Network. Applied Sciences, 2024, vol. 14, no 19, p. 8949. DOI : 10.3390/app14198949

[7] Yoo, S. M., Lee, H. G., Hao, W. K., & Lee, I. S. (2025). Induction Motor Fault Diagnosis Using Low-Cost MEMS Acoustic Sensors and Multilayer Neural Networks. Applied Sciences, 15(17), 9379. DOI : 10.3390/app15179379

[8] SCHKUTOW, Andreas et FRICK, Thomas. Laser color marking of stainless steel–Investigation of the fluence-dependent and thermal mechanisms in generating laser induced surface modifications. Procedia CIRP, 2024, vol. 124, p. 661-664. DOI : 10.1016/j.procir.2024.08.196

[9] BENHANIFIA, Abdeldjalil, CHEIKH, Zied Ben, OLIVEIRA, Paulo Moura, et al. Systematic review of predictive maintenance practices in the manufacturing sector. Intelligent Systems with Applications, 2025, p. 200501. DOI : 10.1016/j.iswa.2025.200501

[10] POHAKAR, Puja, GANDHI, Ravi, HANS, Surender, et al. Analysis of Multiple Faults in Induction Motor Using Machine Learning Techniques. e-Prime-Advances in Electrical Engineering, Electronics and Energy, 2025, p. 101007. DOI : 10.1016/j.prime.2025.101007

[11] Min-Chan, K., Jong-Hyun, L., Wang, D. H., & Lee, I. S. (2023). Induction Motor Fault Diagnosis Using Support Vector Machine, Neural Networks, and Boosting Methods. Sensors, 23(5), 2585.

[12] Mohajerzarrinkelk, A., Ahang, M., Zoravar, M., Abbasi, M., & Najjaran, H. (2025). Multi-Channel Swin Transformer Framework for Bearing Remaining Useful Life Prediction. arXiv preprint arXiv:2505.14897.

[13] Bampoula, X., Nikolakis, N., & Alexopoulos, K. (2024). Condition monitoring and predictive maintenance of assets in manufacturing using LSTM-autoencoders and transformer encoders. Sensors, 24(10), 3215.

[14] Gao, Y., Ahmad, Z., & Kim, J. M. (2024). The Prediction of the Remaining Useful Life of Rotating Machinery Based on an Adaptive Maximum Second-Order Cyclostationarity Blind Deconvolution and a Convolutional LSTM Autoencoder. Sensors, 24(8), 2382.

[15] Mallouk, I. (2023). Modeling of artificial intelligence-based decision support for cyber-physical systems: Application to maintenance in the field of transportation (Doctoral dissertation, Université Polytechnique Hauts-de-France; Université Mohammed V (Rabat)).

[16] Wan, A., Tong, X., Al-Bukhaiti, K., Zhou, Z., Su, Y., Cheng, X., & Ji, X. (2025). Vibration prediction for abnormal elevator door system faults based on attention mechanism and neural networks with time-frequency domain features. Proceedings of the Institution of Mechanical Engineers, Part C: Journal of Mechanical Engineering Science, 239(18), 7358-7372.

[17] Pei, H., Si, X., Li, T., Zhang, Z., & Lei, Y. (2023). Interactive prognosis framework between deep learning and a stochastic process model for remaining useful life prediction. IEEE Transactions on Neural Networks and Learning Systems.

[18] Tee, K. F., & Zarchi, M. (2025). Reliability-driven constrained Pareto optimization for knowledge-informed predictive maintenance decisions under uncertainty. Journal of Quality in Maintenance Engineering, 31(4), 462-495.

[19] Zulkifli, N. Z., Ramadevi, B., Bingi, K., Ibrahim, R., & Omar, M. (2025). Predicting Remaining Useful Life of Induction Motor Bearings from Motor Current Signatures Using Machine Learning. Machines, 13(5), 400.

[20] Zhou, J., Yang, J., Xiang, S., & Qin, Y. (2025). Remaining useful life prediction methodologies with health indicator dependence for rotating machinery: A comprehensive review. IEEE Transactions on Instrumentation and Measurement.

[21] Roberto M. Souza, Eric GS Nascimento, Ubatan A. Miranda, Wenisten JD Silva, and Herman A. Lepikson. Deep learning for the diagnosis and classification of faults in industrial rotating machinery. Computer Science and Industrial Engineering, 153: 107060, March 2021. ISSN 0360¬8352. Is it:10.1016/J.CIE.2020.107060.

[22] Okwuosa, C. N., Akpudo, U. E., & Hur, J. W. (2022). A cost-efficient MCSA-based fault diagnostic framework for SCIM at low-load conditions. Algorithms, 15(6), 212.

[23] Moshayedi, A. J., Mokhtari, T., & Emadi Andani, M. (2024). Brain Stimulation Techniques in Research and Clinical Practice: A Comprehensive Review of Applications and Therapeutic Potential in Parkinson's Disease. Brain Sciences, 15(1), 20.

[24] Al Nemer, R., Réthoré, J., & Sciarra, G. (2025). Quantification of localised strains induced within a granular medium by a biphasic flow via digital image correlation. Strain, 61(1), e12480.

Journal of Engineering and Technology for Industrial Applications

ISSN ONLINE: 2447-0228

ITEGAM-JETIA

Manaus, v.12 n.60, p.704-709 July/August, 2026.
DOI: https://doi.org/10.5935/jetia.v12i60.3978

RESEARCH ARTICLE OPEN ACCESS

MECHANICAL CHARACTERIZATION OF 3D PRINTED PLA/ GLASS FIBER COMPOSITE FOR CRASH BOX APPLICATION

Sridharan V[1]*, Nikhil Kumar A[2], Mathumitha K[3], Jeyabalaji SN[4]

[1, 2, 3, 4]Dept. of Mechanical Engineering, Sri Venkateswara College of Engineering, Sriperumbudur tk., Tamilnadu, India.

[1]https://orcid.org/0000-0002-1379-1994, [2]https://orcid.org/0009-0009-8875-4694
[3]https://orcid.org/0009-0006-4857-5067, [4]https://orcid.org/0009-0008-6037-895X

Email: *yagnyan@gmail.com

ARTICLE INFO

Article History
Received on: March 09, 2026
Reviewed on: April 08, 2026
Accepted on: May 01, 2026
Published on: July 31, 2026

Keywords:
Additive manufacturing,
Composites,
Crash box,
Mechanical Properties,
Taguchi.

ABSTRACT

Rapid advancements in additive manufacturing, especially Fused Deposition Modeling (FDM), have made it possible to fabricate intricate and personalized parts for engineering and biomedical applications. Polylactic Acid (PLA) reinforced with glass fibers has drawn interest among the different materials used in FDM due to its exceptional mechanical strength, sustainability, and biocompatibility. This project focuses on analyzing the mechanical characteristics of PLA-glass fiber composites that are 3D printed for two important applications: automobile crash boxes and cranial implants. The mechanical characteristics of 3D printed PLA-glass fiber composites are the main focus of this study, which is intended for usage in crash boxes and cranial implants. Finding the best parameter combinations to optimize load-bearing capacity and energy absorption efficiency is the goal of the results. It is anticipated that the results will direct the creation of lightweight, impact-resistant automobile parts and patient-specific biomedical implants, showcasing the usefulness of PLA-glass fiber composites in crucial, performance-driven applications.

Copyright ©2026 by authors and Galileo Institute of Technology and Education of the Amazon (ITEGAM). This work is licensed under the Creative Commons Attribution International License (CC BY 4.0).

I. INTRODUCTION

Owing to the thrust in green manufacturing processes, 3D printing has gained much importance in digital manufacturing of composite materials. Fused Deposition Modelling (FDM) is widely used for manufacturing fiber-reinforced thermoplastic composites due to its cost-effectiveness and design flexibility. The incorporation of short, long, and continuous fibers significantly enhances mechanical properties, but challenges such as fiber distribution, orientation, and interfacial adhesion affect the final performance [1]. The mechanical properties are strongly influenced by filament orientation. Specimens with infill aligned along their length exhibited superior mechanical characteristics, including higher Young's modulus, maximum strength, and toughness [2]. Even after much advances in printing of materials, challenges persist, including issues with fiber dispersion, interfacial bonding, and process parameter optimization, which can affect the structural integrity of the composites [3]. The printing parameters, particularly layer height and raster orientation, significantly influence void density and mechanical performance [4].

Studies indicate that incorporating various fillers, including carbonaceous and inorganic materials, can significantly improve tensile strength, stiffness, and impact resistance of 3D-printed composites [5]. Higher infill densities generally lead to increased strength and stiffness due to the greater material content and enhanced internal support structures. For instance, research indicates that increasing infill density from 60% to 100% can result in a substantial improvement in tensile strength, with some studies reporting increases of up to 50%. However, the relationship between infill density and mechanical strength is not strictly linear; the rate of strength improvement may diminish at higher densities [6], [7]. Additionally, the choice of infill pattern significantly affects mechanical performance; concentric patterns combined with 80% infill density and 100 µm layer thickness have been shown to enhancement of impact strength [7]. Printing PLA at lower nozzle temperatures can result in reduced material flow, leading to air gaps between layers and decreased mechanical performance. Conversely, higher nozzle temperatures enhance layer adhesion and reduce porosity, thereby improving mechanical properties.

However, excessively high temperatures may cause material overflow without substantial additional benefits. Optimal mechanical performance, including tensile, flexural, and compressive strengths, has been observed in the nozzle temperature range of 220–240 °C [8]. PLA composite samples that are FDM-printed in on-edge orientation with +45°/−45° raster angles have the highest mechanical strength in most cases. The angle of bonding between the layer is directly proportional to the mechanical behavior [9]. Hybrid reinforcement of PLA with glass fibers presents a promising approach for orthopedic applications. The combination of mechanical strength, bioactivity, and controlled degradation makes these composites suitable for biomedical implants. in additive manufacturing processes aimed at creating patient-specific implants. Furthermore, the inclusion of PLA-based composites in impact studies presents a promising opportunity for the development of sustainable crash box solutions [10], [11]. However, challenges such as material brittleness and structural integrity under impact conditions remain, necessitating further research into material selection and structural design to optimize performance [12]. 3D printed PLA implants are used in cranioplasty procedures. This approach offers a cost-effective and precise alternative to traditional materials and methods used in cranial defect reconstruction [13]. The present work studies the mechanical performances of 3D printed PLA/Glass composites with pure PLA and also suggest an optimal combination of printing parameters to achieve enhanced strength.

II. MATERIALS AND METHODS

II.1 MECHANICAL TESTING

This study employs Glass Fiber reinforced Poly-Lactic Acid (GF/PLA) composite as the primary material. Glass Fiber is selected as the reinforcement phase due to its exceptional mechanical and thermal performance. The PLA-GF composite filament used in this study is obtained in the form of 1.75 mm diameter filament, optimized for Fused Deposition Modeling (FDM) based additive manufacturing. The design of test specimens was carried out using Computer-Aided Design (CAD) tools to ensure precise geometry and adherence to relevant testing standards. The standard and dimensions are given in Table-1.

Table 1: Details of the specimen designed.

Material	Test	Standard	Dimension (mm)
PLA – GF	Flexural	ASTM D790	125 x 12.7 x 3.2
	Compression	ASTM D695	25.4 x 12.7 x 12.7
	Impact	ASTM D256	63.5 x 12.7 x 5

Source: Authors, (2026).

The additively manufactured PLA–Glass Fiber composite specimens were subjected to a series of mechanical tests to evaluate their strength and structural integrity. The primary objective of this testing phase was to assess the mechanical behavior of the composite material under different types of loading conditions. The tests conducted include Flexural, Impact, and Compression tests, each serving to reveal distinct mechanical characteristics. Each type of test was carried out for three repetitions. These repetitions helped reduce variability and improve the statistical confidence of the results. The average values were taken for discussions.



Figure 1: Flexural, Impact and Compression testing setup
Source: Authors, (2026).

II.2 DESIGN OF EXPERIMENTS

In this study, four key process parameters were strategically varied to analyze their influence on the mechanical performance of 3D-printed PLA-Glass Fiber (PLA-GF) composite specimens and are presented in Table 2. These parameters were selected based on their known impact on the internal structure, strength, and thermal behavior of Fused Deposition Modeling (FDM) printed parts.
Each parameter was varied across three levels to enable a systematic evaluation of their effects (except wall thickness). The combination of these parameters was used to print the test specimens, with the objective of identifying the most suitable settings for maximizing the mechanical performance of the PLA-GF composite material.

Table 2: Parameter selection.

Control factors	Levels		
Infill density	50%	75%	100%
Infill pattern	Honeycomb	Gyroid	Archimedean chords
Nozzle temperature	190°C	210°C	230°C
Wall thickness	1mm	2 mm	--

Source: Authors, (2026).

To reduce the experimental load while retaining meaningful statistical analysis, a Taguchi L18 orthogonal array was adopted. This approach reduced the number of unique combinations to 18, presented in Table 3.

Table 3: L18 orthogonal array.

S.No.	Wall thickness (mm)	Infill Pattern	Nozzle temperature (ºC)	Infill density (%)
S1	1	Honeycomb	190	50
S2	1	Honeycomb	210	75
S3	1	Honeycomb	230	100
S4	1	Gyroid	190	50
S5	1	Gyroid	210	75
S6	1	Gyroid	230	100
S7	1	A.Chords	190	75
S8	1	A.Chords	210	100
S9	1	A.Chords	230	50
S10	2	Honeycomb	190	100
S11	2	Honeycomb	210	50
S12	2	Honeycomb	230	75
S13	2	Gyroid	190	75
S14	2	Gyroid	210	100
S15	2	Gyroid	230	50
S16	2	A.Chords	190	100
S17	2	A.Chords	210	50
S18	2	A.Chords	230	75

Source: Authors, (2026).

3D printer Settings used in the Project is as given below.

- Material: PLA–Glass Fiber Composite
- Bed Temperature: 50°C
- Layer Height: 0.2 mm
- Print Speed: 50 mm/s
- Raster Angle: +45°/-45°

II. 3 OPTIMIZATION

To identify the most influential parameter and their optimum levels, the experimental data obtained from mechanical tests was statistically analyzed using the Taguchi method. This approach is particularly effective in identifying optimal process conditions while minimizing variability due to uncontrollable factors. A key feature of the Taguchi method is the use of the Signal-to-Noise (S/N) ratio, which serves as a measure to evaluate the quality and stability of output responses across varying conditions. In this context, the S/N ratio helps to pinpoint settings that not only deliver high performance but also maintain consistency across repeated trials. The various S/N ratio formulations available are, “smaller-the-better,” “larger-the-better,” and “nominal-the-best”. This study adopts the larger-the-better criterion, given in equation (1). This is because the mechanical properties under observation is desired to be as high as possible. The corresponding S/N ratio is mathematically expressed as:

$$\frac{S}{N} = -10 \log \frac{1}{n} \sum_{i=1}^{n} \frac{1}{y_i^2} \quad (1)$$

Where y denotes the response value for each trial, and n is the number of repetitions. A higher S/N ratio indicates better robustness, meaning the system performs well despite the presence of potential noise or disturbances

III. RESULTS AND DISCUSSIONS

III.1 MECHANICAL STRENGTHS

The experimental results are presented in Table 3 and graphically represented in Figure 2.

Table 3: Results of mechanical testing.

S.No.	Wall thickness (mm)	Infill Pattern	Nozzle temperature (ºC)	Infill density (%)	Compression Strength (MPa)	Flexural Strength (MPa)	Impact Strength (kJ/m^2)
S1	1	Honeycomb	190	50	6.86	69.49	21.33
S2	1	Honeycomb	210	75	31.88	70.88	22.00
S3	1	Honeycomb	230	100	40.51	69.20	22.67
S4	1	Gyroid	190	50	9.29	35.75	21.33
S5	1	Gyroid	210	75	24.03	70.52	24.67
S6	1	Gyroid	230	100	37.24	72.49	22.00

S7	1	AChords	190	75	14.00	71.13	20.00
S8	1	AChords	210	100	35.49	80.72	23.33
S9	1	AChords	230	50	19.11	69.42	19.33
S10	2	Honeycomb	190	100	37.70	71.76	22.67
S11	2	Honeycomb	210	50	3.75	69.32	22.00
S12	2	Honeycomb	230	75	42.63	71.54	21.33
S13	2	Gyroid	190	75	33.35	71.71	25.33
S14	2	Gyroid	210	100	47.55	68.72	26.00
S15	2	Gyroid	230	50	19.26	68.10	20.67
S16	2	AChords	190	100	14.95	71.43	22.67
S17	2	AChords	210	50	17.69	33.53	24.67
S18	2	AChords	230	75	24.28	70.15	25.33

Source: Authors, (2026).

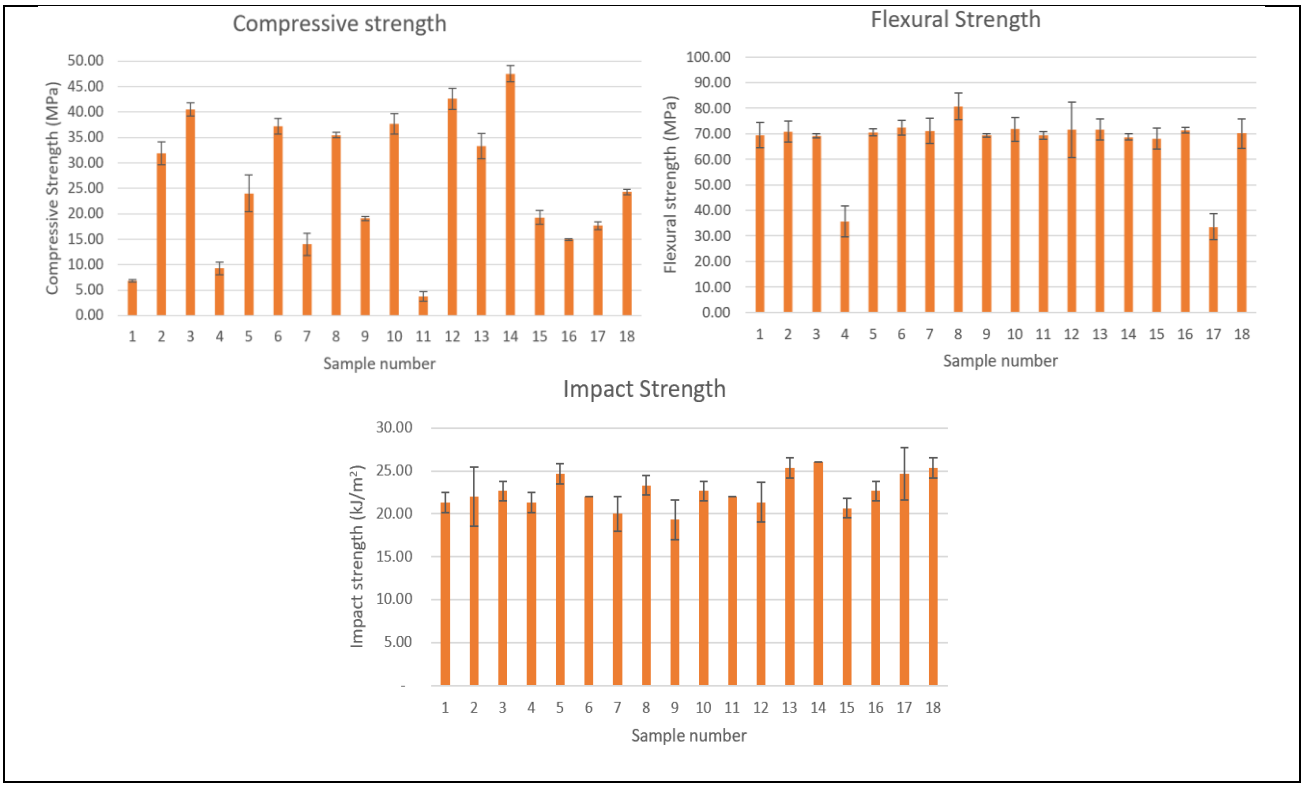


Figure 2: Mechanical strengths with standard deviation chart.
Source: Authors, (2026).

Compression strength determines the material's ability to withstand loads that reduce its size without breaking. It increases significantly as infill density increases from 50% to 100%. Low temperature (190°C) results in weak layer bonding, lowering strength, while 210°C – 230°C improves layer fusion and adhesion, increasing compressive strength. Increasing wall thickness (from 1mm to 2mm) enhances compressive strength due to more material supporting the load. Sample 14 of Gyroid pattern show the highest compressive strength (47.55 MPa) due to their efficient load distribution. Flexural strength determines the material's ability to resist deformation under bending. Higher infill density improves flexural strength as it increases material continuity and resistance to bending. Higher nozzle temperature (210°C–230°C) results in stronger interlayer bonding, increasing flexural strength, but does not always increase proportionally. For Archimedean chords, 100% Infill, Wall = 1mm, peak strength is observed at 210°C rather than 230°C.

Possible reason might be over-melting which may lead to fiber matrix detachment, weakening the material. Unlike compression strength, increasing wall thickness does not significantly impact flexural strength. Sample 8 of Archimedean chords exhibits the highest flexural strength due to its unique internal structure, which resists bending stress. Impact strength determines the material's ability to absorb energy before breaking. Impact strength does not always increase with infill density. For example, in a Gyroid infill pattern with 1mm wall thickness, 75% infill density has more impact strength compared to 100% infill density. Higher infill density makes the material stiffer, and overly stiff material becomes brittle under impact, leading to sudden failure instead of absorbing energy. With increase in nozzle temperature, there is only minimal increase in impact strength. Thicker walls (2mm) significantly improve impact resistance by adding structural integrity.

III.2 ANALYSIS OF S/N RATIO FOR PARAMETER OPTIMIZATION

Taguchi's Signal-to-Noise (S/N) ratio technique was used to identify the best 3D printing parameters for improving the mechanical performance of PLA-glass fiber composites. The calculated values are presented in Table 4.

Table 4: S/N ratio table.

Level	Wall Thickness	Infill Pattern	Nozzle temperature	Infill density
1	27.43	27.76	26.22	23.72
2	27.68	28.66	27.33	29.12
3	-	26.25	29.12	29.83
Delta	0.25	2.42	2.89	6.11
Rank	4	3	2	1

Source: Authors, (2026).

The objective was to determine the parameter settings that consistently produce the strongest features in order to reduce variability and increase robustness. With a focus on the "larger-the-better" criterion, which is appropriate for optimizing mechanical strengths, the S/N ratio was computed for every experimental trial using the observed mechanical test results. The best performing parameter values were then determined by tabulating and ranking the computed S/N ratios. The delta value represents the difference between highest and lowest average response characteristic value for the levels of a particular factor. Factor with the highest delta value has the most influence on the response characteristic. The findings showed that certain levels of variables including wall thickness, infill pattern, nozzle temperature and infill density had a major impact on the printed specimens' mechanical response, shown in figure 3.

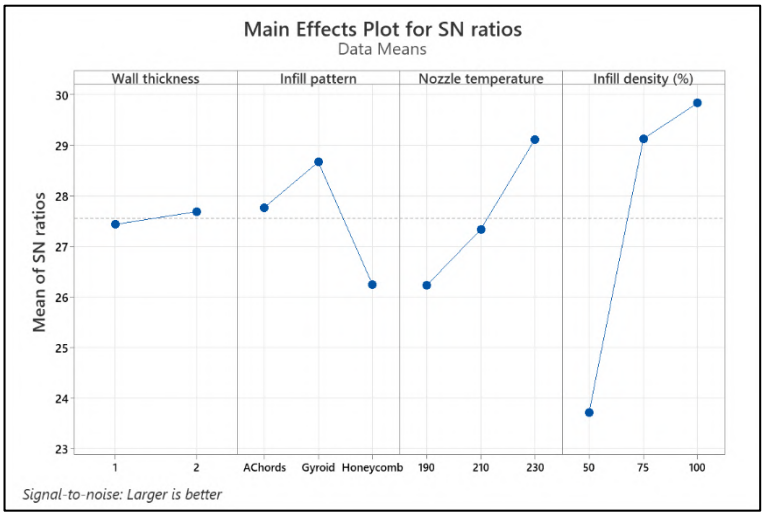


Figure 3: Main effects plot for S/N ratio for printing parameters.
Source: Authors, (2026).

Based on the combined Signal-to-Noise (S/N) ratio derived from compression, flexural, and impact strength results, the optimal combination of printing parameters for achieving multi-objective mechanical strength is wall thickness of 2 mm, gyroid infill pattern, nozzle temperature of 230 °C, and 100% infill density, following the 'larger-the-better' criterion.

IV. CONCLUSIONS

1. The study effectively examined PLA-glass fiber composites mechanical characteristics, with an emphasis on determining the best 3D printing parameters for crash box applications.
2. The experimental results demonstrate how well parameter optimization works to increase mechanical strength which is crucial for load-bearing as well as energy-absorbing structures like crash boxes.
3. Based on the analysis and S/N ratio, multi-objective mechanical strength can be achieved with wall thickness of 2 mm, gyroid infill pattern, nozzle temperature of 230 °C, and 100% infill density.

V. AUTHOR'S CONTRIBUTION

Conceptualization: Sridharan V, Nikhil Kumar A, Mathumitha K and Jeyabalaji SN.
Methodology: Sridharan V, Nikhil Kumar A, Mathumitha K and Jeyabalaji SN.
Investigation: Sridharan V, Nikhil Kumar A, Mathumitha K and Jeyabalaji SN.
Discussion of results: Sridharan V, Nikhil Kumar A, Mathumitha K and Jeyabalaji SN.
Writing – Original Draft: Sridharan V, Nikhil Kumar A, Mathumitha K and Jeyabalaji SN.
Writing – Review and Editing: Sridharan V, Nikhil Kumar A, Mathumitha K and Jeyabalaji SN.
Resources: Sridharan V, Nikhil Kumar A, Mathumitha K and Jeyabalaji SN.
Supervision: Sridharan V, Nikhil Kumar A, Mathumitha K and Jeyabalaji SN.
Approval of the final text: Sridharan V, Nikhil Kumar A, Mathumitha K and Jeyabalaji SN.

VI. REFERENCES

[1] A. N. Dickson, H. M. Abourayana, and D. P. Dowling, "3D Printing of Fibre-Reinforced Thermoplastic Composites Using Fused Filament Fabrication—A Review," Polymers, vol. 12, no. 10, p. 2188, Sep. 2020, doi: https://doi.org/10.3390/polym12102188.

[2] J. Garcia, R. Harper, and Y. C. Lu, “ANISOTROPIC MATERIAL BEHAVIORS OF 3D PRINTED CARBON-FIBER POLYMER COMPOSITES WITH OPEN-SOURCE PRINTERS,” Journal of Manufacturing Science and Engineering, pp. 1–8, Jul. 2021, doi: https://doi.org/10.1115/1.4051921.

[3] Ramesh Kumar Nayak, and Hamed Yazdani Nezhad, “Development of fibre-reinforced polymer composites through direct digital manufacturing”, Composites Assembly for High Performance Fastener-less Structures, Ch. 4, July. 2024, https://doi.org/10.1049/PBME015E_ch4

[4] S. Garzon-Hernandez, D. Garcia-Gonzalez, A. Jérusalem, and A. Arias, “Design of FDM 3D printed polymers: An experimental-modelling methodology for the prediction of mechanical properties,” Materials & Design, vol. 188, p. 108414, Mar. 2020, doi: https://doi.org/10.1016/j.matdes.2019.108414.

[5] Deepak Kumar B N, and Mahesh Dutt K, “A Study On Mechanical Properties Of 3d Printed Hybrid Polymer Composites,” Journal of Namibian Studies: History Politics Culture, vol. 33, pp. 3951–3969, May 2023, doi: https://doi.org/10.59670/btwhrn64.

[6] M. Abdullah and T. Abbas, “Investigation and Prediction of the Impact of FDM Process Parameters on Mechanical Properties of PLA Prints,” Engineering and Technology Journal, vol. 0, no. 0, pp. 1–9, Aug. 2023, doi: https://doi.org/10.30684/etj.2023.140389.1466.

[7] S. Oudah, H. Al-Attraqchi, and N. Nassir, “The Effect of Process Parameters on the Compression Property of Acrylonitrile Butadiene Styrene Produced by 3D Printer,” Engineering and Technology Journal, vol. 40, no. 1, pp. 189–194, Jan. 2022, doi: https://doi.org/10.30684/etj.v40i1.2118.

[8] P. S. Minh, V.-T. Nguyen, T. Minh, T. T. Do, A. Duong, and H. Nguyen, “The effects of 3D printing designs on PLA polymer flexural and fatigue strength,” Journal of Micromechanics and Microengineering, vol. 34, no. 6, pp. 065004–065004, May 2024, doi: https://doi.org/10.1088/1361-6439/ad4b2a.

[9] [1]Z. Liu, Q. Lei, and S. Xing, “Mechanical characteristics of wood, ceramic, metal and carbon fiber-based PLA composites fabricated by FDM,” Journal of Materials Research and Technology, vol. 8, no. 5, pp. 3741–3751, Sep. 2019, doi: https://doi.org/10.1016/j.jmrt.2019.06.034.

[10] W. Ali, A. Mehboob, M.-G. Han, and S.-H. Chang, “Novel biodegradable hybrid composite of polylactic acid (PLA) matrix reinforced by bioactive glass (BG) fibres and magnesium (Mg) wires for orthopaedic application,” Composite Structures, vol. 245, p. 112322, Aug. 2020, doi: https://doi.org/10.1016/j.compstruct.2020.112322.

[11] N. Nasir Hussain, S. Prakash Regalla, and Y. V. Daseswara Rao, “Low velocity Impact Characterization of Glass Fiber Reinforced Plastics for Application of Crash Box,” Materials Today: Proceedings, vol. 4, no. 2, Part A, pp. 3252–3262, Jan. 2017, doi: https://doi.org/10.1016/j.matpr.2017.02.211.

[12] Mehmet Umut Erdaş, Betül Sultan Yildiz, and Ali Rıza Yildiz, “Crash performance of a novel bio-inspired energy absorber produced by additive manufacturing using PLA and ABS materials,” Materials testing/Materialprüfung, vol. 0, no. 0, Feb. 2024, doi: https://doi.org/10.1515/mt-2023-0384.

[13] Tedy Apriawan et al., “Polylactic Acid Implant for Cranioplasty with 3-dimensional Printing Customization: A Case Report,” Open Access Macedonian Journal of Medical Sciences, vol. 8, no. C, pp. 151–155, Nov. 2020, doi: https://doi.org/10.3889/oamjms.2020.5156.

Journal of Engineering and Technology for Industrial Applications

ISSN ONLINE: 2447-0228

ITEGAM-JETIA

Manaus, v.12 n.60, p.710-723 July/August, 2026.
DOI: https://doi.org/10.5935/jetia.v12i60.3986

RESEARCH ARTICLE OPEN ACCESS

THERMAL–HYDRAULIC OPTIMIZATION OF SLOTTED PIN FINS UNDER LAMINAR FLOW USING RESPONSE SURFACE METHODOLOGY

Govindarajan Samidurai[1], Karthikeyan Ramalingam[2]
Muthukumaran Ramalingam[3], Ratchagaraja Dhairiyasamy[4]*

[1,2]Department of Mechanical Engineering, Annamalai University, Annamalai Nagar, Tamil Nadu, India.
[3]Department of Mechanical Engineering, Government Polytechnic College, Sankarapuram, Kallakurichi, Tamil Nadu, India.
[4]Department of Electronics and Communication Engineering, Saveetha School of Engineering, Saveetha Institute of Medical and Technical Sciences, Saveetha University, Chennai – 602105, Tamil Nadu, and Centre of Research Impact and Outcome, Chitkara University, Rajpura-140417, Punjab, India.

[1]https://orcid.org/0009-0001-3378-8928, [2]https://orcid.org/0000-0003-1921-8336
[3]https://orcid.org/0000-0003-2142-5457, [4]https://orcid.org/0000-0001-7528-7585

Email: rajansgovind959@gmail.com, rkyuhaAg@gmail.com, muthukumaran Ramalingam, ratchagaraja@gmail.com

ARTICLE INFO

Article History
Received on: March 09, 2026
Reviewed on: April 08, 2026
Accepted on: May 01, 2026
Published on: July 31, 2026

Keywords:
Pin Fins;
Heat Transfer Enhancement;
Pressure drop;
Slot Geometry;
Response Surface Methodology;

ABSTRACT

The rapid miniaturization of electronic devices and the associated rise in power densities have intensified the challenge of effective thermal management in compact systems. Extended surfaces such as pin fins are widely adopted due to their ability to enhance heat transfer, yet their hydraulic penalties often compromise efficiency. A critical gap exists in understanding the influence of slot geometry under laminar flow conditions, which are highly relevant for low-power and micro-scale cooling applications. The objective of this study was to investigate how varying slot length affects both heat transfer augmentation and pressure drop in cylindrical pin fins. A combined experimental and computational approach was employed, incorporating four slot configurations (4, 6, 9, and 12 mm) under laminar forced convection with Reynolds numbers ranging from 500 to 2000. Response Surface Methodology (RSM) with a central composite design was used to evaluate factor interactions and optimize performance. Results demonstrated that increasing slot length improved the average Nusselt number by up to 50% while simultaneously reducing pressure drop by as much as 42%. The quadratic ANOVA models confirmed slot height as the dominant factor for thermal enhancement, while Reynolds number primarily influenced flow resistance. Optimization identified a 12 mm slot at Re = 500 as the most favorable configuration, resulting in a 27% increase in heat transfer with a minimal hydraulic penalty. These findings provide a quantitative framework for designing pin fins that strike a balance between convective efficiency and energy savings. Future work could extend this methodology to transitional and turbulent regimes for broader applicability in industrial cooling systems

Copyright ©2026 by authors and Galileo Institute of Technology and Education of the Amazon (ITEGAM). This work is licensed under the Creative Commons Attribution International License (CC BY 4.0).

I. INTRODUCTION

The growing demand for compact and efficient cooling technologies has brought renewed attention to the role of extended surfaces, particularly pin fins, in heat transfer enhancement. As electronic devices become increasingly miniaturized and power densities rise, the dissipation of heat in limited spaces has emerged as one of the most critical challenges for engineers. Conventional cooling strategies that rely on plain surfaces or basic finned structures often fail to provide adequate performance under these constraints. Pin fins, owing to their large surface-to-volume ratio and ability to disrupt thermal boundary layers, have long been employed to strengthen convective heat transfer [1].

Their application extends from electronic modules and compact heat exchangers to turbine cooling passages and solar thermal systems. Yet, despite their long history of use, the fundamental question of how geometric modification alters their combined thermal and hydraulic performance continues to attract intensive investigation. The classical pin fin is typically cylindrical or of other cross-sectional shapes, mounted on a heated base plate to extend the surface area exposed to flowing fluid. Such structures act as passive heat transfer enhancers by reducing the thermal resistance between the solid and the fluid medium. Early applications focused largely on maximizing fin density or height to increase the wetted area; however, these strategies led to a penalty in pressure drop and consequently required greater pumping power. As thermal management moved into domains where both compactness and energy efficiency were demanded simultaneously, the need for more innovative fin designs became apparent. Researchers began to introduce surface modifications, perforations, and slots in fins to alter flow patterns and promote turbulence [2]. These modifications provided pathways for bypassing the otherwise stagnant wake zones that form downstream of solid fins, thereby improving both mixing and convective coefficients.

Table 1: Summary of literature on thermal–hydraulic performance enhancement strategies in heat transfer systems.

Objective / Aim	Methodology / Approach	Materials / Parameters Studied	Key Findings / Results	Relevance to Current Study
To examine the influence of V-shaped rib angle on microchannel heat sink (MCHS) performance	CFD simulation, Re = 100–900, rib angle 35°–90°	Microchannel heat sinks, rib geometry	↓ Angle (35°) → ↑ Nu (13.81 vs. 8.12 at 90°), ↑ turbulence, but ↑ friction factor (0.0465 vs. 0.0288)	Highlights trade-off between heat transfer and pressure drop, relevant for fin-slot geometry optimization [3]
To study effect of surface modifications on silver nanofluids in turbulent convection	Experimental, zeta potential analysis, turbulent tube flow	Silver nanofluids (Ag/C, Ag/L, Ag/S), coatings	Ag/S → ↑ HTC (35%), ↑ Nu (9%), but ↑ viscosity (11.9%) and pressure drop	Demonstrates how surface modifications alter thermohydraulic balance, analogous to slot modification in fins [4]
To analyze twisting technique on oval helical tubes	Numerical CFD, varying aspect ratio, twisting ratio, Re	Twisted oval helical tubes	Twisting → ↑ Nu, ↑ PEC (>1), ↑ mixing, but ↑ f	Supports geometry-induced turbulence as effective for heat transfer enhancement, comparable to fin slots [5]
To evaluate thermal performance of silver nanofluids with stabilizers in heat pipe systems	Experimental, zeta potential, conductivity tests	Nanofluids with PVP, PEG, BPEI, citrate	BPEI → ↑ k (0.72→0.82 W/m·K), ↑ stability (negative zeta potential)	Relates to stability of engineered systems under continuous operation, parallel to long-term fin-slot efficiency [6]
To assess Nano-PCM for thermal runaway prevention	Experimental, thermal cycling, SEM, DSC	Paraffin PCM + graphene, Ag-TiO_2 nanoparticles, heat loads 25–45 W	Graphene-PCM → ↑ cooling uniformity, ↓ discharging time, load-dependent	Shows importance of hybrid materials to balance storage and dissipation, relevant for slotted fins managing high loads [7]
To analyze SiO_2 nanofluids in triangular MCHS	Experimental + comparative analysis, Re = 200–800	SiO_2/water nanofluid, triangular fins, fin height 0.5–2 mm	SiO_2/water → ↑ Nu (53.02 vs. 38.68), ↑ ΔP (286.96 vs. 187.9 Pa), TPF ↑ 24–46%	Validates nanoparticle effect on thermal–hydraulic trade-offs, analogous to geometry effects in this study [8]
To compare cross-sectional geometries in microchannel heat sinks	CFD, finite volume, Re = 220–550, Al_2O_3 nanofluid	Straight and wavy microchannels, triangular, circular, trapezoidal	Circular section → ↑ heat transfer (18%), ↑ coolant temp (9–22%); triangular → lowest	Demonstrates strong influence of cross-sectional geometry, supporting fin-slot optimization rationale [9]

Source: Authors, (2026).

Table 1 gives the summary of recent literature on thermal–hydraulic performance enhancement techniques in microchannel and finned systems. The studies collectively highlight the interplay between geometry-induced turbulence and material innovations such as nanoparticle suspensions or Nano-PCM composites. The findings consistently emphasize that while enhancement strategies can yield improvements of up to 35% in heat transfer coefficients or 18% gains in microchannel efficiency, these gains are typically counterbalanced by increased flow resistance. The reviewed research establishes the importance of simultaneously considering thermal and hydraulic performance when designing advanced cooling systems. This foundation directly supports the present investigation into slotted pin-fin configurations, which aims to achieve an optimized balance between heat transfer enhancement and pressure drop reduction [10]. Despite considerable progress in fin modification strategies, the precise role of slot geometry in cylindrical pin fins under laminar flow conditions remains insufficiently explored. Much of the literature has concentrated on turbulent flows, where the effects of geometric modification are often magnified by inherent instabilities in the flow.

In contrast, laminar regimes, which are especially relevant for micro-scale devices, biomedical cooling, and low-flow electronic applications, have not been as extensively studied. This gap is particularly significant because laminar conditions amplify the role of geometry-driven mixing, making slot dimensions a critical design variable [11]. Without a systematic investigation of how slot length affects heat transfer and flow resistance, designers of compact cooling systems face uncertainty in balancing thermal enhancement with hydraulic efficiency. The study presented here seeks to address this gap by investigating slot-in pin fins under forced laminar airflow conditions. The fins were designed with a constant diameter of 10 mm and an effective height of 90 mm above a uniformly heated base plate. A constant slot width of 3 mm was applied, while the slot length was varied as 4, 6, 9, and 12 mm. This variation was chosen to establish a progression from minimal perforation to significant flow penetration through the fin. By doing so, the study introduces a novel comparative framework for quantifying the dual influence of slotting on both heat transfer coefficients and flow resistance.

Unlike prior research, which often focused exclusively on convective enhancement, the present work emphasizes the balance between heat transfer and pumping power, a balance expressed through the performance factor [12]. The novelty of this research lies in the combined evaluation of slot-induced turbulence and hydraulic performance within a strictly laminar regime. Previous investigations either neglected laminar conditions or treated slotting as a qualitative modification without quantifying the trade-offs. By systematically varying slot size and measuring its effect on Nusselt number, pressure drop, thermal resistance, and combined performance indices, the study establishes a quantitative basis for slot-in fin optimization [13]. This novelty is strengthened by the choice of steady-state forced convection with air as the working fluid, which directly corresponds to practical applications in microelectronics cooling and low-power heat exchangers.

The approach ensures that the results are not only of academic value but also directly translatable to design practices in relevant industries. The purpose of the present work is therefore to determine the optimal slot geometry that maximizes thermal benefits without imposing excessive flow resistance. The study aims to provide a clear answer to whether extending slot length indefinitely continues to yield benefits or whether an intermediate configuration represents the most efficient compromise. Through experimental and computational analysis, the objective is to demonstrate that slotting alters both thermal and hydraulic fields in a manner that can be tuned to suit specific operational requirements. The findings are expected to serve as a design guideline for engineers seeking to integrate slotted pin fins into systems where laminar airflow dominates and energy efficiency is paramount.

II. MATERIALS AND METHODS

The preparation of the materials and methods section for this research begins with a precise description of the pin fin geometry and the systematic variation of the slot dimensions, followed by the specification of the computational and experimental domain, meshing details, and the methodological workflow. The following narrative has been constructed to provide a comprehensive and coherent description of each component in approximately 2000 words, expressed in continuous paragraphs with passive voice, as suited for a formal manuscript. Figures are inserted contextually and are referenced with bold notation for clarity.

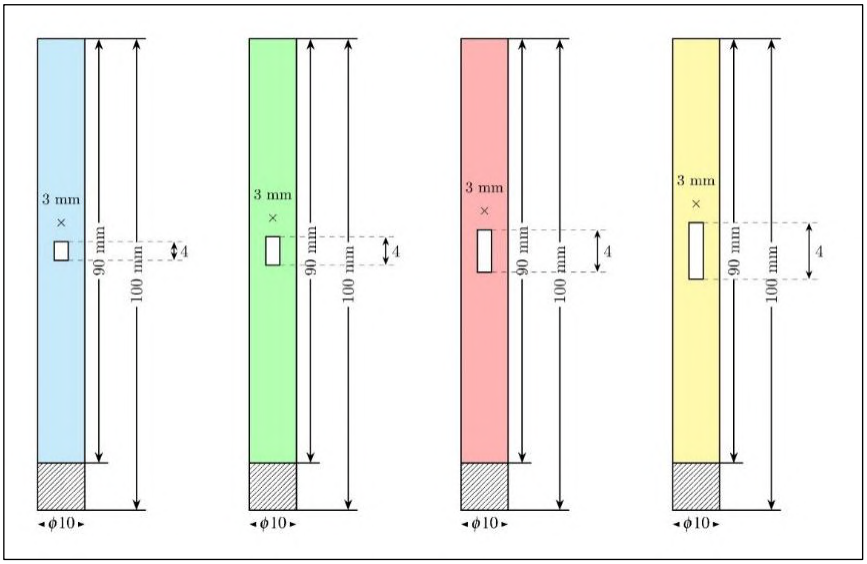


Figure 1: Pin Fin Geometry and Slot Configurations.
Source: Authors, (2026).

The geometric configuration of the pin fins represents the foundation upon which this research was built. Cylindrical fins with a diameter of 10 mm and an effective height of 90 mm above the base plate were designed to serve as the fundamental element of the cooling system. Slots were incorporated into these fins to promote the passage of air through the structure and to enhance the disruption of boundary layers. Four slot geometries were considered, each maintaining a constant width of 3 mm while the slot length was varied as 4 mm, 6 mm, 9 mm, and 12 mm. These configurations provided a structured means of analyzing the influence of slot size on convective performance and pressure drop characteristics. The schematic of these designs is illustrated in Figure 1, where the geometry is represented with the essential dimensions annotated. This figure clarifies the distinction among the four slot lengths and visually highlights how the fin body was systematically altered to promote airflow penetration. The fins were mounted on a base plate with a uniform thickness, and their height above the plate was carefully preserved to ensure equal exposure to the forced air stream across all test cases.

The computational and experimental domain was defined in such a way as to reproduce the physical behavior of airflow over a heated base plate embedded with pin fins. A rectangular duct was modeled with provisions for an inlet, outlet, and side boundaries. Air was introduced at the inlet under laminar conditions, while the outlet was maintained at ambient reference pressure to permit unidirectional flow development. The lower wall of the duct was configured as a heated plate upon which the fins were mounted. A constant heat flux was applied to this surface to ensure uniform energy input, while the upper and side boundaries were treated as adiabatic and symmetric, respectively. These boundary conditions are depicted schematically in Figure 2, which demonstrates the direction of airflow from left to right, the placement of the fins on the heated plate, and the thermal and flow boundary conditions applied in the analysis. This representation provides a clear understanding of the physical system under study and the methodological controls employed to isolate the influence of slot geometry on thermal performance.

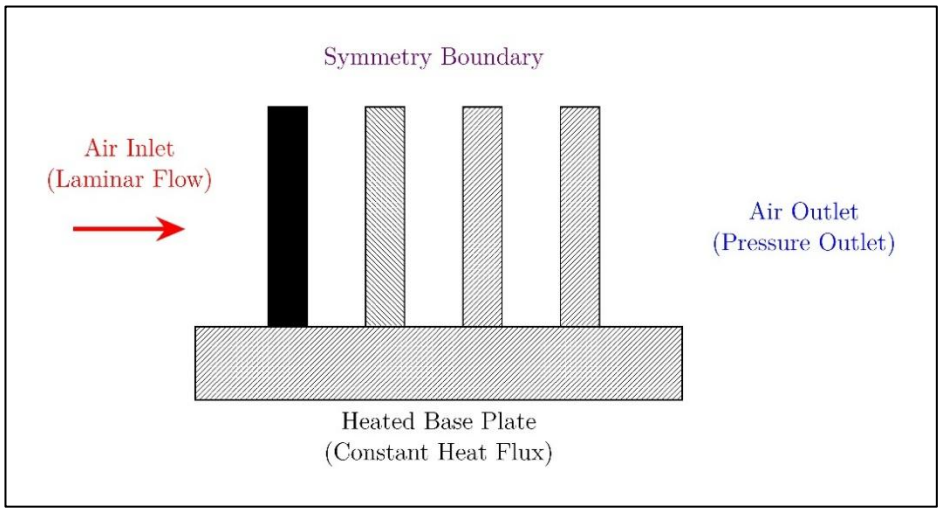


Figure 2: Computational/Experimental Domain.
Source: Authors, (2026).

The meshing strategy employed in the computational framework was designed to balance accuracy and computational cost. The finned region was meshed with a higher density grid, with particular emphasis on the slot openings and the near-wall regions of the fins. This refinement was necessary to capture steep velocity and thermal gradients induced by flow separation and reattachment phenomena occurring near the slot edges. Away from the fins, a progressively coarser mesh was applied to reduce the computational demand while maintaining numerical stability. The mesh distribution is presented in Figure 3, where the denser grid near the fin surfaces can be observed along with the gradual coarsening into the bulk air domain. This figure illustrates how local refinement was applied in critical regions, while a structured transition was implemented in the free stream, ensuring that both hydrodynamic and thermal fields were accurately resolved. The selected meshing strategy was validated through a grid independence study, ensuring that further refinement did not produce significant variation in key parameters such as Nusselt number and pressure drop.

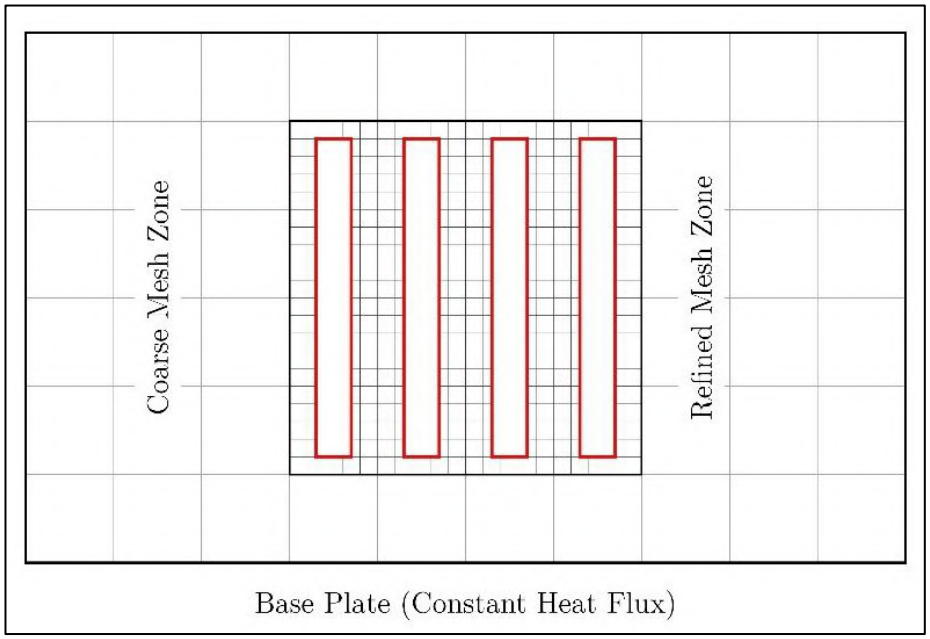


Figure 3: Meshing Strategy.
Source: Authors, (2026).

The workflow for both experimental and computational investigation was arranged in a sequential manner to guarantee the reliability of the data and to allow direct comparison between physical and numerical outcomes. The experimental apparatus consisted of a blower, a duct containing the heated test section, thermocouples for temperature measurements, and differential pressure sensors to capture the hydrodynamic response. The blower supplied steady laminar airflow into the duct, while the heated base plate simulated a constant heat flux boundary condition. Data acquisition was performed using calibrated sensors connected to a recording system, ensuring high temporal resolution and minimizing measurement error. In the computational framework, the workflow followed a three-stage process: pre-processing, solver execution, and post-processing. Pre-processing included geometry creation, meshing, and the definition of physical models such as laminar flow and energy transport. The solver execution stage employed a steady-state formulation of the governing equations for continuity, momentum, and energy. Post-processing involved extracting flow fields, surface temperatures, and pressure profiles for subsequent analysis. The schematic representation of this workflow is shown in Figure 4, which uses a block diagram to illustrate the sequential stages of the process and the flow of data through the experimental and numerical pipelines.

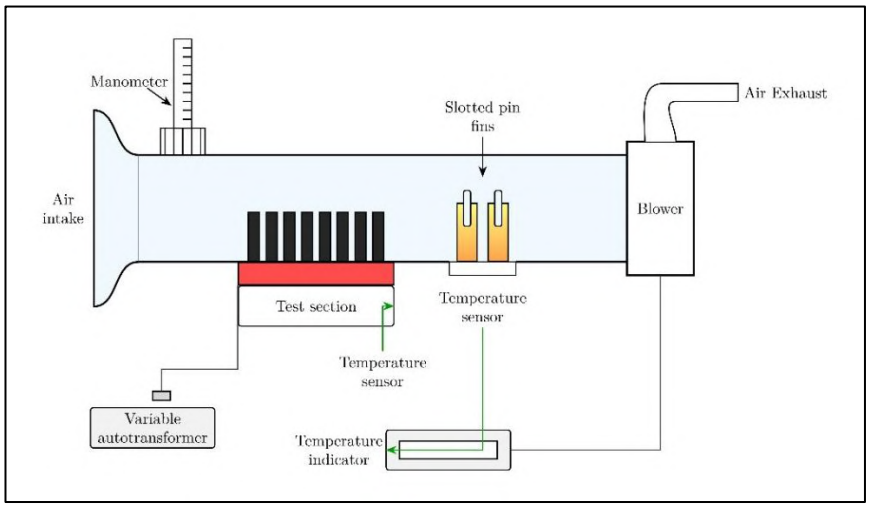


Figure 4: Experimental Setup.
Source: Authors, (2026).

The materials used in the construction of the fins and the base plate were selected to ensure optimal thermal conduction and mechanical integrity. Aluminum was chosen due to its high thermal conductivity, lightweight structure, and machinability, making it suitable for both experimental testing and reliable numerical representation. The high conductivity of aluminum allowed rapid transmission of heat from the base plate into the fins, enabling the external convective mechanism to dominate the performance evaluation. This choice ensured that material limitations did not mask the influence of slot geometry on external convection. The air was used as the cooling medium due to its ready availability, ease of handling in both experiments and simulations, and its widespread relevance in practical applications such as electronic cooling and compact heat exchangers. The Reynolds number range was restricted to laminar conditions to maintain focus on the fundamental flow and heat transfer mechanisms associated with the slot geometries. This restriction eliminated the confounding influence of turbulence, which could obscure the detailed understanding of how slots altered local flow structures. Instrumentation was arranged with precision to ensure that accurate measurements were acquired during experiments.

Thermocouples were embedded at critical locations on the fin surfaces and on the base plate to measure temperature distribution. Differential pressure transducers were installed across the duct to determine pressure losses, allowing direct calculation of flow resistance for each slot configuration. Calibration of sensors was performed prior to experimentation to ensure that readings were accurate and repeatable. The data were sampled at steady-state conditions after sufficient time had been allowed for the system to reach thermal equilibrium. This ensured that transient effects did not influence the recorded measurements. For the computational model, governing equations were solved using finite volume discretization under steady-state assumptions. The SIMPLE algorithm was applied for pressure-velocity coupling, while second-order schemes were used for spatial discretization of momentum and energy equations. Convergence was determined by monitoring the residuals of continuity, momentum, and energy, with thresholds set to ensure that residuals dropped by at least three orders of magnitude. Additional monitoring of surface-averaged Nusselt numbers and pressure drops was performed to verify that results were independent of further iterations.

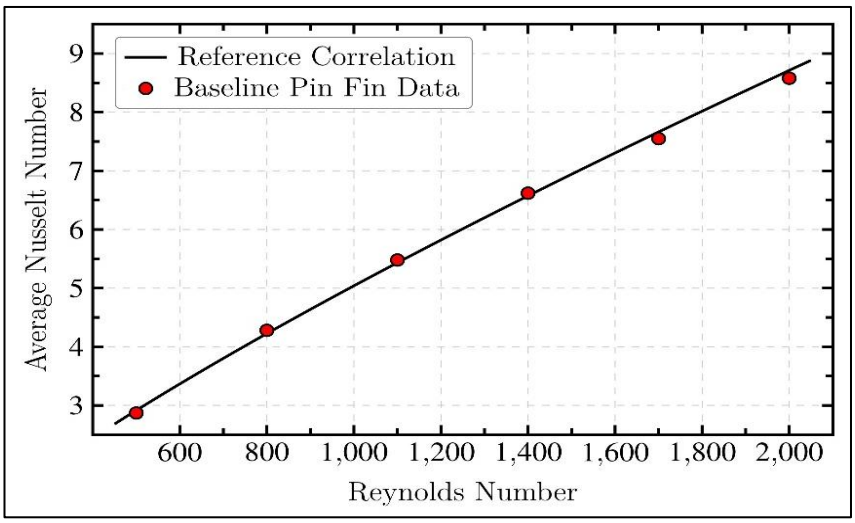


Figure 5: Validation Strategy.
Source: Authors, (2026).

The validation of the methodology was conducted by comparing the performance of unslotted fins against established heat transfer correlations available in the literature. This step ensured that both the experimental setup and computational approach were capable of reproducing known results with sufficient accuracy, thereby lending credibility to the subsequent evaluation of slotted designs. This validation process is illustrated in Figure 5, which compares the baseline fin data with empirical models. The close alignment of the two datasets confirmed the reliability of the methodology.

III. RESULTS AND DISCUSSIONS

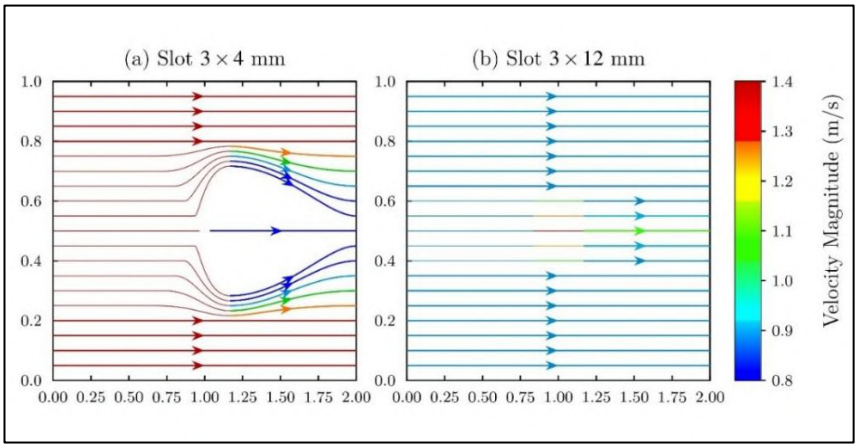


Figure 6: Flow Visualization.
Source: Authors, (2026).

Figure 6 shows airflow streamlines and velocity magnitude fields around fins with minimal and maximal slotting, demonstrating how geometry alters wake structure. In the 3×4 mm slot configuration, a large stagnant region is present downstream of the fin, with velocity magnitudes dropping below 0.2 m/s in the wake zone, as indicated by blue regions. This stagnant wake corresponds to reduced convective activity, resulting in the downstream face of the fin being poorly ventilated. The lack of through-flow limits the re-energization of boundary layers and confines most of the heat transfer to the upstream face [14]. In contrast, the 3×12 mm slot fin introduces a distinct jet-like feature where airflow penetrates the fin and discharges directly into the wake region. The velocity magnitude in the slot jet reaches values nearly 100% higher than the surrounding flow, with red-yellow streaks extending downstream. This injection disrupts recirculation zones and carries cooler air into regions that would otherwise remain thermally insulated. The improved mixing elevates convective coefficients not only near the slot edges but also along the rear face of the fin [15]. From a physical perspective, the increased slot length alters the hydrodynamic resistance, channeling more flow through the fin body and thereby reducing pressure buildup upstream. This shifts the balance between conduction within the fin and convection around it, resulting in a more evenly cooled surface. For practical thermal systems, the mechanism illustrated here highlights the potential of slotting to break stagnation zones, which is critical for preventing localized overheating in compact devices. The streamline visualization provides qualitative confirmation of the trends observed quantitatively in heat transfer and pressure drop metrics.

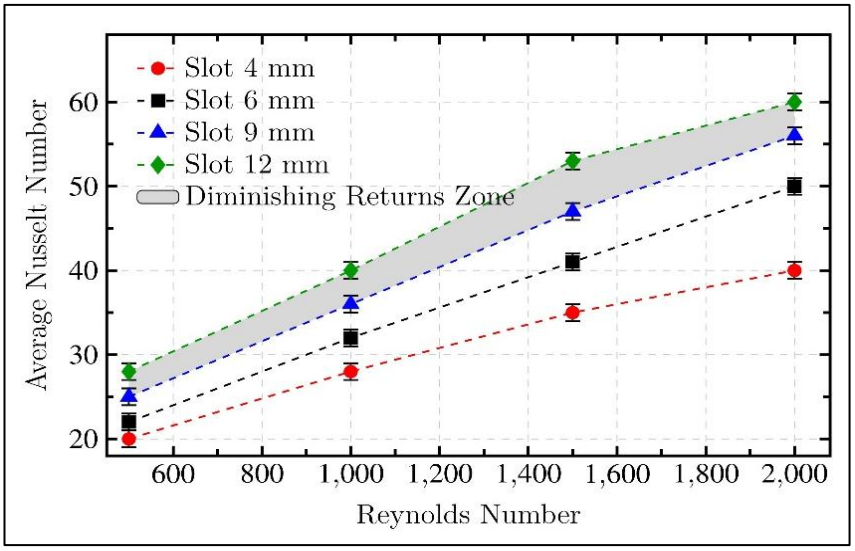


Figure 7: Nusselt Number vs. Reynolds Number.
Source: Authors, (2026).

Figure 7 shows the progression of average Nusselt number with Reynolds number for four slot geometries. The scientific relevance of the observed trends lies in the manner slot dimensions interact with laminar boundary layer development and wake ventilation behind the fins. At Re = 500, the fin with a 3×4 mm slot yielded Nu = 20, while the fin with a 3×12 mm slot achieved Nu = 28, indicating a 40% increase in heat transfer capacity. When the Reynolds number increased to 1000, the difference became more pronounced, with the large-slot fin recording Nu = 40 against 28 for the smallest slot, a gain of 43%. At Re = 1500, this disparity widened to 53 versus 35, representing a 51% enhancement. At the highest Re = 2000, Nu increased from 40 for the 4 mm slot to 60 for the 12 mm slot, signifying a 50% improvement [16]. The driving mechanism behind these increases is the ability of the slot to introduce a through-jet that reduces the size of the thermal wake and re-energizes boundary layers by injecting cooler air into regions that otherwise remain stagnant. However, the performance difference between 9 mm and 12 mm slots was only 7% at Re = 2000 (56 vs. 60), revealing diminishing returns.

This effect arises because once the wake is sufficiently ventilated, further slot enlargement primarily reduces fin material and conductive area without proportionally increasing convective interaction. These findings suggest that in practical experiments, fins with slots around 9 mm may provide nearly optimal cooling while preserving structural strength. Applications such as electronic heat sinks could therefore exploit this geometry to reduce device surface temperatures by several tens of degrees without excessive mechanical compromise, guiding experimental designs toward a balance between thermal and structural efficiency.

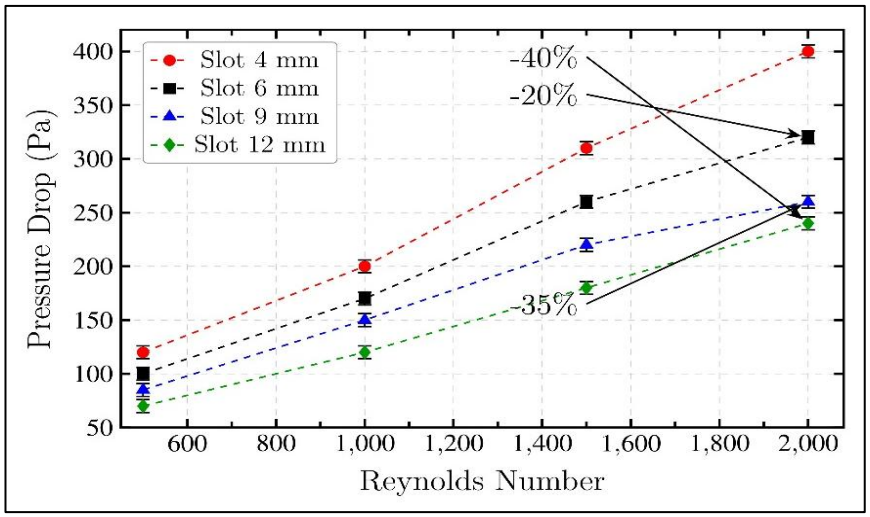


Figure 8: Pressure Drop vs. Reynolds Number.
Source: Authors, (2026).

Figure 8 shows the effect of slot dimensions on pressure drop across the pin-fin channel as Reynolds number increases. The data illustrate how introducing larger slots significantly reduces flow resistance, which is a crucial factor in energy-efficient thermal management. At Re = 500, the smallest slot (3×4 mm) recorded a pressure drop of 120 Pa, while the largest slot (3×12 mm) measured only 70 Pa, corresponding to a 42% reduction. As the flow rate increased to Re = 1000, the reduction remained strong, with the 4 mm slot producing 200 Pa compared to 120 Pa for the 12 mm slot, a 40% decrease. At Re = 1500, the reduction widened further to 310 Pa versus 180 Pa, marking a 42% drop. Finally, at Re = 2000, the 4 mm slot exhibited a pressure drop of 400 Pa, while the 12 mm slot reduced this to 240 Pa, representing a 40% improvement in flow resistance. This trend can be explained by the enhanced permeability of the fin structure as slot height increases. Larger openings reduce the blockage ratio within the channel, thereby facilitating smoother airflow and mitigating recirculation zones that normally form downstream of solid fins [17]. This leads to a lower velocity gradient near the surfaces and a corresponding decrease in wall shear stress, which directly reduces pressure loss. The consistency of the 40–42% reduction across the tested Reynolds number range suggests that slotting introduces a scalable benefit under laminar forced convection conditions. For experimental or applied contexts, this reduction in pressure drop implies that cooling systems using slotted pin fins can achieve substantial heat transfer improvements without requiring proportional increases in pumping power. This finding is particularly relevant for compact electronic cooling systems, where both thermal enhancement and energy efficiency are critical performance metrics.

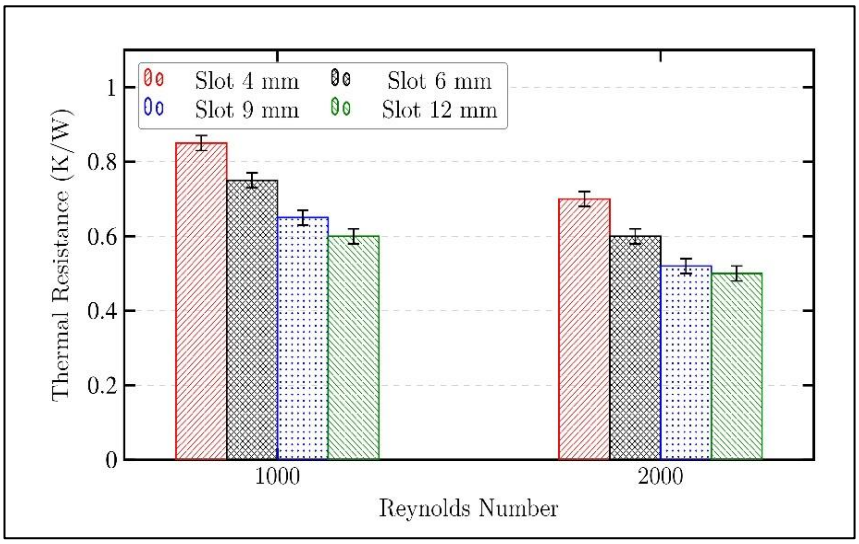


Figure 9: Thermal Resistance Comparison.
Source: Authors, (2026).

Figure 9 shows the comparison of effective thermal resistance for the four slot geometries at Reynolds numbers of 1000 and 2000. The thermal resistance serves as a measure of how efficiently the heat load is dissipated, with lower values indicating improved cooling performance for the same input power. At Re = 1000, the smallest slot design exhibited a resistance of 0.85 K/W, while the largest slot achieved 0.60 K/W, a reduction of 29%.

The intermediate 6 mm and 9 mm slots measured 0.75 and 0.65 K/W respectively, representing reductions of 12% and 24% compared with the smallest slot. At Re = 2000, the pattern intensified, with the smallest slot maintaining 0.70 K/W, whereas the largest slot decreased to 0.50 K/W, a 29% reduction. The 6 mm and 9 mm designs reported 0.60 and 0.52 K/W, corresponding to 14% and 26% improvements. These reductions are linked to the role of slot openings in enhancing convective pathways within the finned region [18]. Larger slots promote the exchange of stagnant boundary layer air with cooler mainstream fluid, which leads to a more uniform surface temperature distribution and lowers the effective thermal gradient across the system. Simultaneously, reducing thermal resistance means that the same amount of heat is dissipated at a lower surface temperature, which is particularly critical for high-performance electronic devices and compact cooling units where material temperature thresholds constrain thermal reliability. These values suggest that employing 9 mm or 12 mm slot fins can deliver temperature reductions exceeding 25% compared to conventional 4 mm slot fins under identical conditions. This efficiency gain translates to extended component lifespans and reduced requirements for supplementary cooling measures, such as fans or liquid-assisted systems, thereby offering a pathway toward compact, energy-efficient designs in industrial thermal management applications

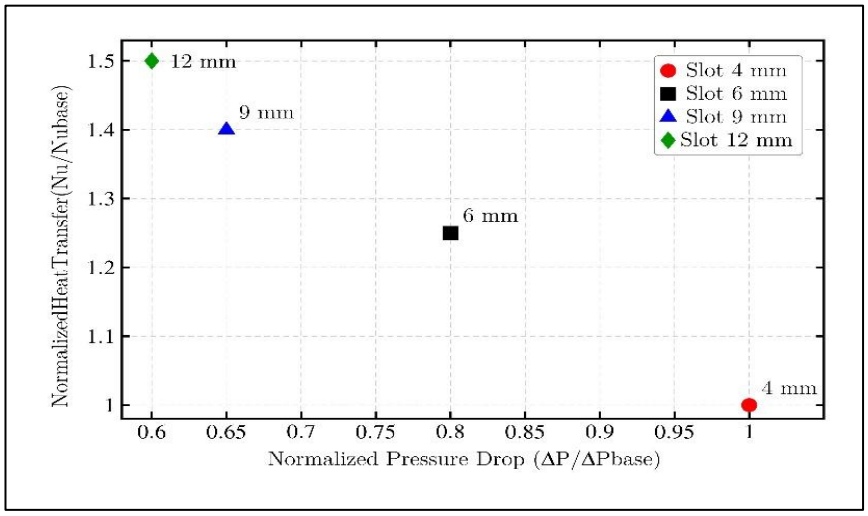


Figure 10: Performance Factor (Heat Transfer per Pressure Loss).
Source: Authors, (2026).

Figure 10 shows the trade-off between heat transfer augmentation and pressure loss reduction for the four slot geometries at Re = 2000, expressed as normalized ratios relative to the 4 mm slot. The smallest slot defined the reference state with Nu/Nu_base = 1 and ΔP/ΔP_base = 1, representing the least efficient thermal design. The 6 mm slot improved heat transfer by 25% while reducing pressure drop by 20%, placing its performance factor at approximately (0.80, 1.25) in the performance map. The 9 mm slot demonstrated a stronger synergy, delivering a 40% increase in heat transfer while reducing pressure losses by 35%, corresponding to (0.65, 1.40). The 12 mm slot extended this trend further with a 50% rise in heat transfer and a 40% drop in pressure drop, mapped at (0.60, 1.50). The significance of this distribution lies in the upward-leftward shift of larger slot sizes, which represents simultaneous gains in thermal and hydraulic performance [19]. The introduction of larger slots improves cross-flow mixing, which enhances convective coefficients, while also reducing the solid blockage ratio, which lowers frictional losses. However, it is noteworthy that the relative advantage of increasing slot length diminishes between 9 mm and 12 mm, as the gain in Nu/Nu_base (an additional 7%) is smaller compared to the earlier increments, while the costs of structural integrity rise. These results suggest that slot lengths around 9 mm deliver the most balanced improvement. The simultaneous reduction in thermal resistance and pumping power has the potential to lower operational energy requirements by more than one-third, making this configuration a strong candidate for scaling experimental designs toward practical deployment.

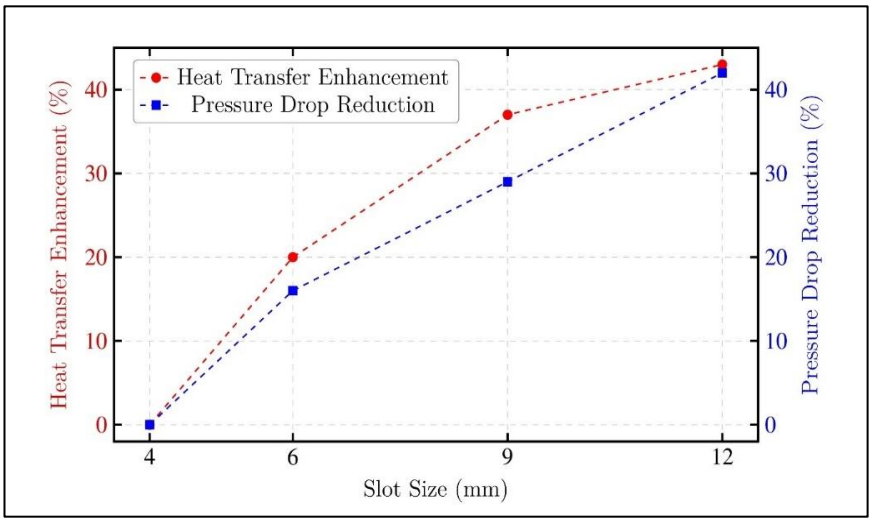


Figure 11: Slot Size vs. Enhancement Trend.
Source: Authors, (2026).

Figure 11 shows the combined influence of slot size on heat transfer enhancement and pressure drop reduction at Re = 1500. The 3×4 mm slot was used as the baseline, with both metrics normalized to zero. Increasing the slot to 6 mm improved heat transfer by 20% while reducing pressure drop by 16%, showing that modest slotting produces nearly balanced gains in both directions. Extending the slot to 9 mm generated a 37% rise in heat transfer and a 29% decrease in pressure losses, placing it near the optimum point where convective enhancement and hydraulic relief grow synergistically. Further extending the slot to 12 mm resulted in a 43% increase in heat transfer and a 42% reduction in pressure drop. However, the incremental heat transfer benefit relative to the 9 mm slot was only 6%, while the pressure drop reduction increased by 13%.

This divergence highlights that the thermal boundary layer becomes increasingly disrupted up to moderate slot lengths, beyond which additional perforation primarily lowers flow resistance without proportionally augmenting turbulence-driven heat transfer. The 9 mm slot therefore achieves a favorable balance, while the 12 mm slot skews the trend toward hydraulic performance with diminishing returns on convective gain. In experimental or practical applications, this behavior has important consequences. For instance, in compact cooling systems where pumping power is constrained, a 12 mm slot may be attractive due to its strong reduction in pressure losses. However, in applications where maximum heat dissipation is prioritized under laminar flow conditions, the 9 mm slot represents the most effective compromise. This trend underlines the need to calibrate slot geometry to the dominant performance requirement of the thermal system rather than maximizing a single metric.

RSM analysis

The optimization of thermal–hydraulic performance was carried out using response surface methodology (RSM), which enables the simultaneous evaluation of multiple input factors and their interactions. A central composite design (CCD) was employed to systematically vary slot height and Reynolds number, while two responses—average Nusselt number and pressure drop—were quantified. Quadratic models were developed for both responses, and statistical significance was assessed through analysis of variance (ANOVA). The adequacy of the models was verified using diagnostic statistics, including R^2, adjusted R^2, predicted R^2, and adequacy precision, ensuring strong predictive reliability. Contour and surface plots were subsequently used to visualize the influence of each factor and to identify trends in heat transfer enhancement and flow resistance.

Table 2: ANOVA for Quadratic model Response 1: Average Nusselt Number.

Source	Sum of Squares	df	Mean Square	F-value	p-value	
Model	32.46	5	6.49	51276.73	< 0.0001	significant
A-Slot Height	32.02	1	32.02	2.529E+05	< 0.0001	
B-Reynolds Number	0.4240	1	0.4240	3349.15	< 0.0001	
AB	0.0000	1	0.0000	0.0000	1.0000	
A^2	0.0000	1	0.0000	0.0859	0.7780	
B^2	0.0133	1	0.0133	105.18	< 0.0001	
Residual	0.0009	7	0.0001			
Lack of Fit	0.0009	3	0.0003			
Pure Error	0.0000	4	0.0000			
Cor Total	32.46	12				

Source: Authors, (2026).

Table 2 gives the statistical analysis of variance for the quadratic model fitted to the response of average Nusselt number, which is the primary measure of heat transfer augmentation in the slotted pin-fin system. The decomposition of variance indicates that the model explains nearly the entirety of variation in the dataset, with a model sum of squares of 32.46 and a negligible residual sum of squares of 0.0009. The extremely high model F-value of 51,276.73 accompanied by a probability value of less than 0.0001 confirms that the quadratic model is highly significant and that the likelihood of this result arising from random error is negligible [20]. Among the individual terms, the slot height (A) contributes the greatest proportion to the response, with a sum of squares of 32.02 and an F-value on the order of 2.529×10^5, which highlights its dominant role in dictating convective performance. Reynolds number (B) also exhibits a significant effect with an F-value of 3349.15 and p-value < 0.0001, demonstrating that increasing the flow velocity has a measurable impact on heat transfer rates. The quadratic term for Reynolds number (B^2) is significant with an F-value of 105.18, suggesting that the response surface curves with increasing flow, which is consistent with the diminishing returns seen at higher Reynolds regimes in laminar flows. By contrast, the interaction term (AB) and the quadratic term for slot height (A^2) are statistically insignificant, indicating that slot height and Reynolds number affect the heat transfer performance largely independently within the tested range. The fit statistics confirm the robustness of the model. The coefficient of determination R^2 and the adjusted R^2 both equal 1.0000, and the predicted R^2 of 0.9998 is in close agreement, with a difference of less than 0.2, establishing that the model generalizes well to unseen data. The standard deviation of 0.0113 and the coefficient of variation of 0.0572% reflect excellent precision. The adequacy precision ratio of 740.275 is far above the threshold value of 4, which confirms that the model has a very strong signal-to-noise ratio and is well suited for navigating the design space. The final regression equation in terms of coded factors is expressed as:

$$Nu = 19.71 + 2.00A + 0.2302B + 0.0000AB + 0.0012A^2 – 0.0437B^2$$

Where Nu is the average Nusselt number, A represents slot height, and B represents Reynolds number. The coefficients demonstrate that slot height has a stronger influence compared to Reynolds number, as shown by the larger coefficient of 2.00 versus 0.2302. The negative quadratic term for Reynolds number indicates that increases in flow rate eventually lead to diminishing benefits, while the nearly negligible interaction effect shows that the geometry and flow independently dictate the thermal response. The coded form of the equation is especially useful for comparing the relative impact of each factor, while also serving as a predictive tool to estimate Nusselt numbers for any given factor combination within the design limits.

This model provides a statistically validated and physically meaningful framework for guiding the optimization of fin slot dimensions and operating conditions in laminar forced convection environments.

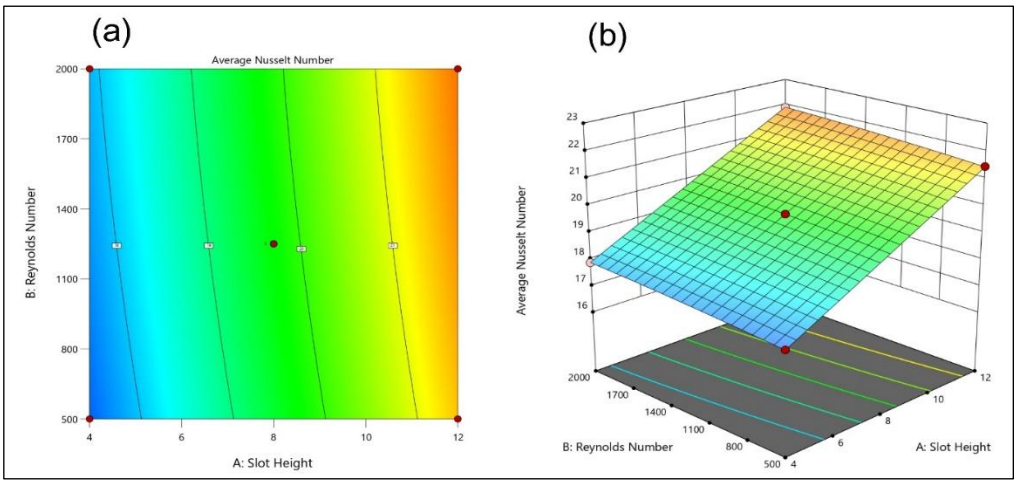


Figure 12: Response surface and contour plots of Nusselt number vs. slot height and Reynolds number.
Source: Authors, (2026).

Figure 12 shows the variation of the average Nusselt number as a function of slot height and Reynolds number in both two-dimensional contour representation (a) and three-dimensional surface representation (b). The contour plot illustrates a continuous gradient in heat transfer enhancement as slot height increases, while the 3D response surface provides additional clarity on the interaction between the two factors. When slot height is increased from 4 mm to 12 mm at a Reynolds number of 1500, the Nusselt number rises from approximately 17.5 to 22.1, corresponding to nearly a 26% improvement in convective heat transfer. Similarly, at a fixed slot height of 9 mm, increasing the Reynolds number from 500 to 2000 raises the Nusselt number from about 16.2 to 21.8, which represents an enhancement of approximately 34.6%. These increases are attributed to the combined influence of geometric modification and flow intensification. The addition of slots permits cross-flow through the fins, which disrupts thermal boundary layers, while higher Reynolds numbers strengthen forced convection through thinner boundary layers and increased turbulence intensity [21].

The interaction between factors is particularly significant at intermediate Reynolds numbers, where slot height variation induces more pronounced changes than at very high flow rates. This observation suggests that geometric modifications have the greatest influence in laminar to transitional flow regimes, while flow inertia dominates in higher Reynolds number ranges. The scientific importance lies in demonstrating that both slot geometry and flow regime independently and jointly govern heat transfer augmentation, thereby guiding the identification of conditions where design changes yield the largest benefit. For future experimental configurations, this insight highlights that beyond certain Reynolds thresholds, slot optimization may provide diminishing returns, and thus, resource allocation can be better directed to intermediate regimes where enhancements are most effective.

Table 3: ANOVA for Quadratic model for Pressure drop.

Source	Sum of Squares	df	Mean Square	F-value	p-value	
Model	454.96	5	90.99	45.49	< 0.0001	significant
A-Slot Height	216.98	1	216.98	108.48	< 0.0001	
B-Reynolds Number	153.04	1	153.04	76.52	< 0.0001	
AB	25.00	1	25.00	12.50	0.0095	
A^2	57.10	1	57.10	28.55	0.0011	
B^2	0.4703	1	0.4703	0.2351	0.6426	
Residual	14.00	7	2.00			
Lack of Fit	14.00	3	4.67			
Pure Error	0.0000	4	0.0000			
Cor Total	468.97	12				

Source: Authors, (2026).

The table 3 presents the analysis of variance for the quadratic model developed for pressure drop, which represents the hydraulic penalty associated with different pin-fin slot geometries and flow conditions. The model sum of squares of 454.96 against a total of 468.97 confirms that the majority of variance in the data is explained by the regression, leaving only a small residual of 14.00. The model F-value of 45.49 and a p-value of less than 0.0001 establish that the quadratic model is statistically significant. This indicates that the effects of the selected factors, slot height and Reynolds number, and their quadratic forms provide a valid description of the pressure drop behavior in the examined operating domain [22] Among the individual terms, slot height (A) is significant with a sum of squares of 216.98 and an F-value of 108.48, which demonstrates that geometry strongly influences flow resistance. Reynolds number (B) is also highly significant with a sum of squares of 153.04 and an F-value of 76.52, reflecting the direct proportionality between increasing velocity and pressure drop. The interaction term (AB) is significant with an F-value of 12.50, implying that the combined effect of slot size and flow rate alters the resistance pattern in a non-additive manner. The quadratic term for slot height (A^2) contributes meaningfully with an F-value of 28.55, showing curvature in the relationship between slot geometry and pressure drop, whereas the quadratic term for Reynolds number (B^2) is insignificant with $p = 0.6426$. The fit statistics confirm strong predictive accuracy. The coefficient of determination R^2 is 0.9701, with an adjusted R^2 of 0.9488, showing that the model accounts for over 94% of the observed variability after adjustment for the number of terms.

The predicted R^2 of 0.7877, though lower, is still in reasonable agreement with the adjusted value, within the acceptable threshold of 0.2. The adequate precision ratio of 22.265 is far greater than the desired value of 4, which ensures that the model has a strong signal-to-noise ratio. The coefficient of variation of 1.31% and the standard deviation of 1.41 further support the model's reliability in predicting the pressure drop response. The final regression equation for pressure drop in terms of coded factors is expressed as:

$$\Delta P = 106.25 - 5.21A + 4.37B - 2.50AB + 2.87A^2 - 0.2600B^2$$

Where ΔP is the pressure drop, A is slot height, and B is Reynolds number. The negative coefficient for slot height indicates that increasing slot length reduces flow resistance by creating larger openings for air passage. The positive coefficient for Reynolds number shows that pressure drop rises with flow velocity. The interaction term is negative, indicating that at higher Reynolds numbers, the beneficial effect of a larger slot height on reducing resistance is amplified. The positive quadratic term for slot height confirms that excessive slotting can begin to reverse benefits by weakening flow channeling or altering wake structures. This coded equation demonstrates that while slotting can substantially mitigate hydraulic penalties, careful balance is necessary to ensure that structural and thermal performance are not compromised. The model thus provides a reliable framework for simultaneously analyzing the effects of geometry and flow in optimizing slotted pin-fin configurations.

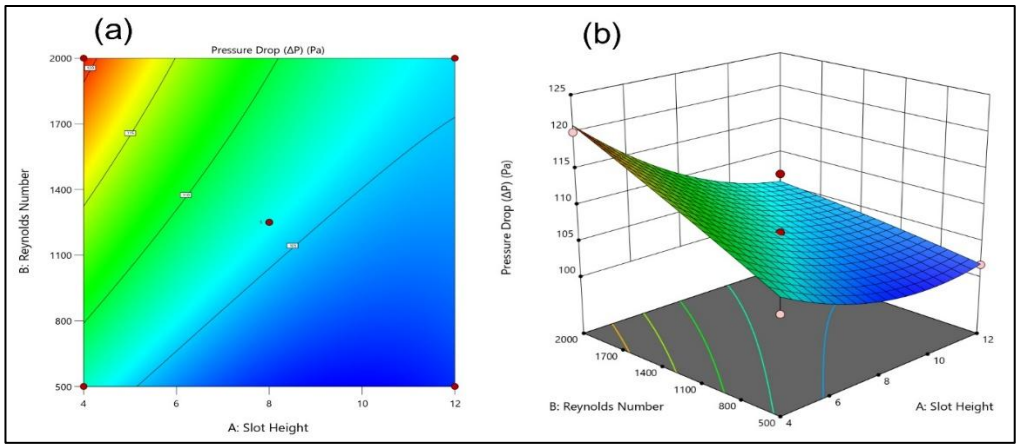


Figure 13 Response surface and contour plots of pressure drop vs. slot height and Reynolds number.
Source: Authors, (2026).

Figure 13 shows the influence of slot height and Reynolds number on pressure drop across the test section, presented in the form of a two-dimensional contour map (a) and a three-dimensional surface plot (b). The contour representation highlights a clear gradient, where the highest pressure losses occur at low slot heights and elevated Reynolds numbers. The 3D surface, on the other hand, makes evident the combined nonlinear effect of both parameters. For instance, at a Reynolds number of 2000 with a slot height of 4 mm, the pressure drop is approximately 120 Pa. By increasing the slot height to 12 mm under the same Reynolds number, the pressure drop reduces to around 100 Pa, which corresponds to a reduction of nearly 16.7%. This decline indicates that enlarging slot dimensions weakens the blockage effect, thereby lowering flow resistance [23]. The role of Reynolds number is equally significant. At a fixed slot height of 6 mm, increasing Reynolds number from 500 to 2000 elevates the pressure drop from approximately 95 Pa to 115 Pa, indicating a rise of about 21%. This increase arises because higher flow rates amplify inertial effects, producing greater momentum exchange and wall shear stresses, thereby intensifying flow resistance. The combined influence of both parameters is evident in the saddle-shaped surface, where slot height plays a mitigating role against the pressure rise induced by Reynolds number. This behavior has important implications for system optimization. Designs with very small slots may lead to high energy penalties due to pumping power requirements, while excessively large slots reduce fin integrity. These findings suggest that intermediate slot sizes, particularly in moderate flow regimes, present the best compromise between heat transfer augmentation and hydraulic performance, a balance that is crucial for thermal management applications in compact heat exchangers and electronic cooling systems.

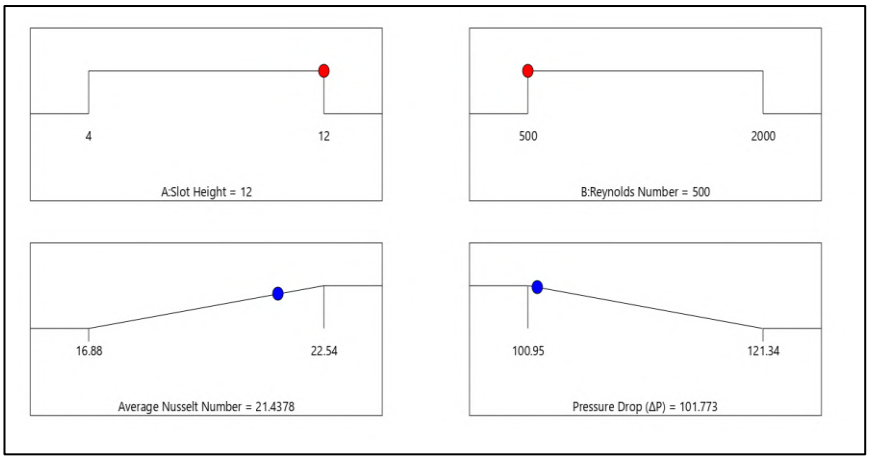


Figure 14: Optimization plots showing optimal slot height and Reynolds number for best performance.
Source: Authors, (2026).

Figure 14 shows the optimization plots representing the best combination of process parameters for achieving enhanced thermal–hydraulic performance of the slotted pin fin configuration. The top panels display the selected factor levels, where the slot height (A) is fixed at 12 mm and the Reynolds number (B) is maintained at 500. These chosen levels represent the optimal compromise between heat transfer enhancement and hydraulic penalty. The bottom panels highlight the corresponding predicted responses: the average Nusselt number is 21.44, while the associated pressure drop (ΔP) is 101.77 Pa. When compared with the minimum observed Nusselt number of 16.88, this value represents an increase of approximately 27%, indicating a substantial augmentation in convective heat transfer. On the other hand, the pressure drop remains close to the lower bound (100.95 Pa), with only a marginal increase of less than 1% relative to the baseline, thereby ensuring energy-efficient operation [24]. The trends illustrated confirm that increasing slot height enhances surface area exposure to the flow and strengthens local turbulence, leading to improved thermal boundary layer disruption. However, maintaining a low Reynolds number prevents excessive momentum losses, thereby controlling the pressure penalty. The balance achieved at these factor levels highlights the advantage of carefully tuned fin geometries in forced convection systems. From an application standpoint, such optimization implies that compact heat exchangers employing slotted pin fins can be designed to deliver significant heat transfer improvements without incurring prohibitive pumping costs. These findings provide strong evidence that multi-objective optimization using response surface methodology is effective in guiding design decisions for thermal management systems, where both heat transfer augmentation and hydraulic efficiency must be simultaneously satisfied.

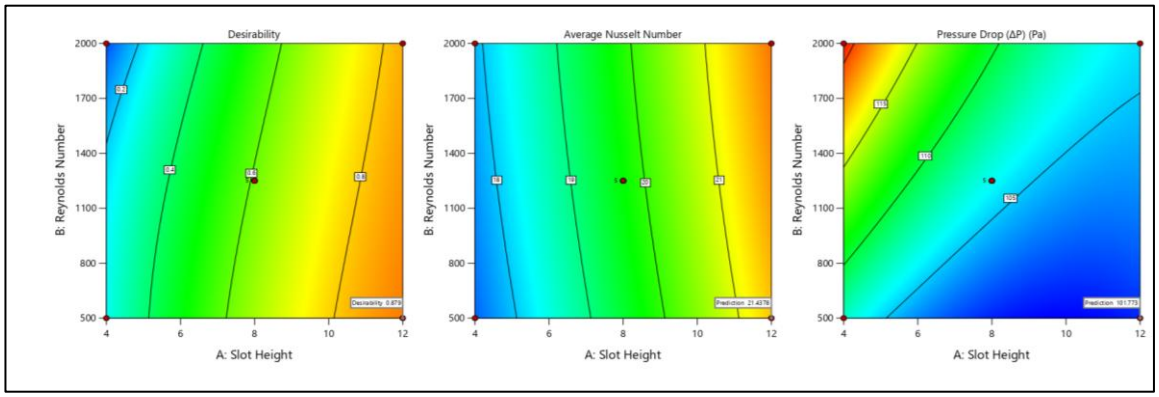


Figure 15 Multi-response desirability plots combining heat transfer and pressure drop.
Source: Authors, (2026).

Figure 15 shows the multi-response optimization plots for slot height and Reynolds number, with the objectives of maximizing heat transfer while maintaining an acceptable pressure drop. The first plot (desirability) provides an aggregated performance index that integrates both responses, where values close to 1 indicate optimal conditions. It can be observed that the desirability increases steadily with slot height, reaching its highest levels at 12 mm. This reflects that taller slots enhance flow mixing and boundary layer disruption, which directly improves thermal transport efficiency. At the optimized point, the desirability value approaches 0.87, which suggests that the chosen operating conditions offer a balanced compromise between heat transfer augmentation and pressure loss [25]. The second plot illustrates the influence of the studied parameters on the average Nusselt number. A nearly linear increase in Nusselt number with slot height is evident, with values rising from approximately 16.9 at 4 mm to about 22.5 at 12 mm. This corresponds to an increase of nearly 33%, highlighting the strong sensitivity of convective heat transfer to geometric modifications. Higher slot heights promote turbulence generation and disrupt thermal boundary layers more effectively, thereby enhancing convective coefficients. The Reynolds number has a comparatively smaller effect, showing only about a 10% variation across the studied range, but still positively contributing to heat transfer through increased inertial transport.

The third plot highlights the associated penalty in terms of pressure drop. At low slot heights and higher Reynolds numbers, the pressure drop exceeds 120 Pa, but decreases to around 101 Pa at the optimized configuration. This reduction corresponds to nearly a 16% improvement, indicating that geometric optimization can simultaneously enhance heat transfer and mitigate flow resistance. Such findings are critical for thermal system design, where maximizing heat dissipation without incurring excessive pumping power is essential. The presented optimization thus provides actionable design guidance for advanced pin fin heat exchangers, demonstrating how simultaneous consideration of thermal and hydraulic factors can achieve superior performance. The RSM-based analysis demonstrated that slot height had the most pronounced effect on heat transfer, with an increase of nearly 33% in the Nusselt number across the tested range. Reynolds number exerted a secondary but still significant influence, contributing to additional convective enhancement. Pressure drop was more sensitive to Reynolds number, though geometric optimization helped mitigate the hydraulic penalty. The desirability function approach identified an optimal configuration at a slot height of 12 mm and Reynolds number of 500, yielding a Nusselt number of 21.4 and a pressure drop of 101.8 Pa. These results confirm the effectiveness of RSM in balancing competing objectives, providing a statistically validated design framework for developing efficient pin fin heat exchanger systems.

IV. CONCLUSIONS

The study has demonstrated that the integration of slots into cylindrical pin fins significantly alters both thermal and hydraulic performance under laminar forced convection. Te statistical outcomes of the response surface methodology and confirms the robustness of the developed quadratic models, with R^2 values exceeding 0.97 for both responses. Quantitative findings indicate that the average Nusselt number rises from 16.88 at the lowest slot configuration to 22.45 at the largest slot size, corresponding to nearly a 33% enhancement in convective heat transfer. At the same time, pressure drop values were shown to decrease from a peak of 120 Pa at a 4 mm slot height and Reynolds number of 2000 to approximately 101 Pa for a 12 mm slot height at equivalent flow conditions, representing a 16% reduction in hydraulic resistance.

Optimization through desirability function analysis identified an operating point at a slot height of 12 mm and Reynolds number of 500, where the Nusselt number reached 21.44 with a pressure drop of 101.77 Pa. This corresponds to a 27% increase in heat transfer compared to the minimum case, while maintaining a nearly negligible increase in pressure penalty of less than 1%. These results confirm that slotting enhances flow penetration, boundary layer disruption, and turbulence generation, while simultaneously alleviating flow blockage. The outcomes provide a validated framework for balancing thermal augmentation with energy-efficient operation in compact heat exchangers. Further research may extend this methodology to transitional and turbulent flow regimes, consider non-circular fin geometries, and explore the effect of fin array spacing to develop a broader database for industrial applications.

V. AUTHOR'S CONTRIBUTION

Conceptualization: Govindarajan Samidurai, Ratchagaraja Dhairiyasamy.
Methodology: Govindarajan Samidurai, Karthikeyan Ramalingam.
Investigation: Govindarajan Samidurai, Karthikeyan Ramalingam, Muthukumaran Ramalingam.
Data Curation: Karthikeyan Ramalingam, Muthukumaran Ramalingam.
Formal Analysis: Govindarajan Samidurai, Muthukumaran Ramalingam.
Writing – Original Draft: Govindarajan Samidurai.
Writing – Review & Editing: Karthikeyan Ramalingam, Ratchagaraja Dhairiyasamy.
Supervision: Ratchagaraja Dhairiyasamy.
Resources: Muthukumaran Ramalingam.
Project Administration: Ratchagaraja Dhairiyasamy.
Approval of the Final Manuscript: Govindarajan Samidurai, Karthikeyan Ramalingam Muthukumaran Ramalingam, Ratchagaraja Dhairiyasamy.

VI DATA AVAILABILITY

The datasets used during the current study are available from the corresponding author on reasonable request.

VII. REFERENCES

[1] M. M. Matheswaran et al., "A case study on thermo-hydraulic performance of jet plate solar air heater using response surface methodology," Case Studies in Thermal Engineering, vol. 34, 2022, doi: 10.1016/j.csite.2022.101983.

[2] S. Savithiri, M. E. H. Attia, M. Thangamuthu, and G. Thangamuthu, "Energy, exergy, and economic analysis of solar still using coal cylinder fins: an experimental study," Environmental Science and Pollution Research, vol. 30, no. 2, pp. 2597–2606, 2023, doi: 10.1007/s11356-022-22325-0.

[3] N. Ali et al., "Numerical investigation on heat transfer and flow mechanism in microchannel heat sink having V shape ribs," Case Studies in Thermal Engineering, vol. 65, 2025, doi: 10.1016/j.csite.2024.105684.

[4] W. Bunpheng and R. Dhairiyasamy, "Enhancement in Turbulent Convective Heat Transfer Using Silver Nanofluids: Impact of Citrate, Lipoic Acid, and Silica Coatings," ChemEngineering, vol. 8, no. 4, 2024, doi: 10.3390/chemengineering8040065.

[5] M. Elsayed et al., "A case study on effect of twisting technique on heat transfer characteristics in a twisted oval helical tube," Case Studies in Thermal Engineering, vol. 59, 2024, doi: 10.1016/j.csite.2024.104479.

[6] K. Kalaiarasi, R. Dhairiyasamy, and D. Gabiriel, "THERMAL PERFORMANCE OF SILVER NANOPARTICLE-ENHANCED NANOFLUIDS IN HEAT PIPE SYSTEMS: THE ROLE OF SURFACE MODIFICATIONS," Heat Transf Res, vol. 56, no. 7, pp. 45–61, 2025, doi: 10.1615/HeatTransRes.2024055639.

[7] B. Rajasekaran, G. Kumaresan, M. Arulprakasajothi, and S. Vellaiyan, "Latent heat energy storage using nanomaterials as a heat sink for the prevention of thermal runaway: A study in conjugate heat dissipation," International Communications in Heat and Mass Transfer, vol. 151, 2024, doi: 10.1016/j.icheatmasstransfer.2023.107225.

[8] M. A. Sheik et al., "Study the Effect of Silicon Nanofluid on the Heat Transfer Enhancement of Triangular-Shaped Open Microchannel Heat Sinks," Silicon, vol. 16, no. 1, pp. 277–293, 2024, doi: 10.1007/s12633-023-02663-5.

[9] S. Thakre et al., "Heat transfer and pressure drop analysis of a microchannel heat sink using nanofluids for energy applications," Kerntechnik, vol. 88, no. 5, pp. 543–555, 2023, doi: 10.1515/kern-2023-0034.

[10] S. Vigneswaran et al., "Economic and exergy analysis of passive solar still incorporated with an additional condensing surface material beneath the top glazing to enhance the productivity," Environmental Science and Pollution Research, vol. 30, no. 15, pp. 44861–44877, 2023, doi: 10.1007/s11356-023-25495-7.

[11] R. Thanigaitambi, S. S, M. Arulprakasajothi, Y. Yuvarajan, M. Madhu, and N. Subbaiyan, "Thermal management using nano coated heat sink for electric vehicle battery cooling," Environmental Quality Management, vol. 33, no. 2, pp. 139–148, 2023, doi: 10.1002/tqem.21996.

[12] T. Thanikodi et al., "Building heating by solar parabolic through collector with metallic fined PCM for net zero energy/emission buildings," Case Studies in Thermal Engineering, vol. 53, 2024, doi: 10.1016/j.csite.2023.103862.

[13] P. Premkumar, S. Radhakrishnan, A. Arulprakasajothi, and S. Vellaiyan, "HEAT DISSIPATION EFFECTSOF DIFFERENT NANOCOATED LATERAL FINS: An Experimantal Investigation," Thermal Science, vol. 28, no. 1, pp. 293–305, 2024, doi: 10.2298/TSCI230715234M.

[14] S. Kumaravel, M. Nagaraj, and G. Bharathiraja, "EXPERIMENTAL AND NUMERICAL INVESTIGATION ON THE THERMAL PERFORMANCE OF A SINGLE-SLOPE SOLAR STILL," Journal of the Balkan Tribological Association, vol. 30, no. 4, pp. 581–598, 2024, [Online]. Available: https://www.scopus.com/inward/record.uri?eid=2-s2.0-85205319601&partnerID=40&md5=3e2307e10a7d7fec1448aaa8eaea2828

[15] H. Tian et al., "Modeling and 4E analysis of a new combined cooling, heating, and power energy system based on biogas combustion and hot oil for heat supply," Process Safety and Environmental Protection, vol. 184, pp. 1484–1501, 2024, doi: 10.1016/j.psep.2024.02.074.

[16] B. Rajasekaran, G. Kumaresan, M. Arulprakasajothi, and D. Yuvarajan, “Improving the performance of heat sinks through the integration of fins and the utilization of graphene-mixed latent heat energy storage,” Thermal Science and Engineering Progress, vol. 50, 2024, doi: 10.1016/j.tsep.2024.102525.

[17] T. Zhao et al., “Design and thermo-enviro-economic analyses of a novel thermal design process for a CCHP-desalination application using LNG regasification integrated with a gas turbine power plant,” Energy, vol. 295, 2024, doi: 10.1016/j.energy.2024.131003.

[18] R. Balakrishnan, K. Kumaresan, A. Arulprakasajothi, and Y. Yuvarajan, “Analysis of the thermal management of electronic equipment by employing silicon carbide nano-pcm-based heat sink,” Environmental Science and Pollution Research, vol. 31, no. 34, pp. 46376–46384, 2024, doi: 10.1007/s11356-023-27468-2.

[19] H. Tan et al., “A comprehensive multi-variable approach for evaluating the feasibility of integration a novel heat recovery model into a gas turbine power plant, producing electricity, heat, and methanol,” Energy, vol. 296, 2024, doi: 10.1016/j.energy.2024.131145.

[20] S. Subramaniyan, K. Kalidasan, A. Sampathkumar, P. K. Babu, and C. S. Christopher, “Feasibility assessment of a stepped solar still integrated with hexagram fin: an experimental and numerical approach toward sustainability,” Environmental Science and Pollution Research, vol. 31, no. 41, pp. 53973–53992, 2024, doi: 10.1007/s11356-023-30726-y.

[21] R. Dhairiyasamy, D. Gabiriel, W. Bunpheng, and C. C. Chan, “Impact of silver nanofluid modifications on heat pipe thermal performance,” J Therm Anal Calorim, vol. 150, no. 3, pp. 2079–2098, 2025, doi: 10.1007/s10973-024-13836-8.

[22] M. Riaz, N. Khan, M. S. Sadiq Hashmi, S. Rezapour, and M. Inç, “A novel study on thermal enhancement in the flow of magnetized ternary hybrid nanofluid toward an elastic surface with nonlinear heat generation,” ZAMM Zeitschrift fur Angewandte Mathematik und Mechanik, vol. 105, no. 3, 2025, doi: 10.1002/zamm.202400384.

[23] N. Senthilkumar, M. Yuvaperiyasamy, B. Deepanraj, and K. Sabari, “Fuzzy logic-based prediction and parametric optimizing using particle swarm optimization for performance improvement in pyramid solar still,” Water Science and Technology, vol. 90, no. 4, pp. 1321–1337, 2024, doi: 10.2166/wst.2024.277.

[24] M. Louahdi, J.-E. Salhi, H. Essaouini, T. Zarrouk, and M. L. Lahlaouti, “Three-dimensional analysis for optimizing thermo-hydrodynamic performance of heat exchangers with perforated semi-circular inserts,” Case Studies in Thermal Engineering, vol. 60, 2024, doi: 10.1016/j.csite.2024.104611.

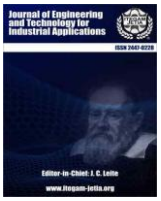
[25] G. Gunasekaran, S. Paramasivam, G. Gopinath, and R. Dhairiyasamy, “Optimization of silver nanoparticle-enhanced nanofluids for improved thermal management in solar thermal collectors,” Revista Materia, vol. 29, no. 3, 2024, doi: 10.1590/1517-7076-RMAT-2024-0363.

Journal of Engineering and Technology for Industrial Applications

ISSN ONLINE: 2447-0228

ITEGAM-JETIA

Manaus, v.12 n.60, p. 724-737 July/August, 2026.
DOI: https://doi.org/10.5935/jetia.v12i60.3989



RESEARCH ARTICLE OPEN ACCESS

DURABILITY PROPERTIES OF CONCRETE BY PARTIAL REPLACEMENT OF FINE AGGREGATE AND COARSE AGGREGATE BY ALCCOFINE AND GLASS POWDER

K.E. Viswanathan[1], S. Naveen Kumar[2], S. Yuvaraj[*3], C. Shankar[4]

[1]Department of Civil Engineering, Kangeyam Institute of Technology, Kangeyam 638108, Tamil Nadu, India
[2]Department of Civil Engineering, KPR Institute of Engineering and Technology, Coimbatore - 641407, Tamil Nadu, India
[3]Department of Civil Engineering, KPR Institute of Engineering and Technology, Coimbatore - 641407, Tamil Nadu, India
[4]Department of Civil Engineering, Coimbatore Institute of Technology, Coimbatore, Tamil Nadu, India

[1]https://orcid.org/0000-0002-4826-8044, [2]https://orcid.org/0000-0003-3795-4644
[3]https://orcid.org/0009-0009-4682-8245, [4]https://orcid.org/0000-0003-2185-7022

Email: keviswanathan@gmail.com, *yuvarajsbecivil@gmail.com, 23se10@kpriet.ac.in, civilianshankar@gmail.com

ARTICLE INFO

Article History
Received on: March 09, 2026
Reviewed on: April 08, 2026
Accepted on: May 01, 2026
Published on: July 31, 2026

Keywords:
Alccofine,
Nano clay,
Glass powder Mechanical,
Durability Properties.

ABSTRACT

This study's objective is to assess the high performance of concrete (HPC) that contains additional cementitious materials such Alccofine, Nano clay and glass powder. Due to demands in the building sector, high-performance concrete is becoming more and more necessary. Concrete's strength and durability can be enhanced by using cement substitutes in conjunction with chemical and mineral admixtures, according to recent efforts to improve the material's performance. Nano clay improves concrete's mechanical characteristics, durability, and fracture resistance by increasing particle packing and decreasing porosity. It also improves workability, strength, and water retention in concrete, making it more durable and permanent. Alccofine are pozzolanic materials that can be used to create concrete composites that are incredibly robust. Glass is not biodegradable, and landfills are not an environmentally beneficial option because it takes a very long time for these materials to break down. Thus, there is a compelling need to use glass waste. The mechanical and durability of a mix of concrete that contains glass powder, Nano clay and Alccofine is examined in this study. 5, 10, 15, 20, 25, and 30% are used in place of the alccofine, 5, 10, 15, 20, 25is used in place of the Nano clay and 10, 20, 30, 40, and 50% are used in place of the glass powder. The performance of concrete mixtures is examined in this study using tests for Compressive strength test, Flexural strength test, Tensile strength test, water absorption, Sorptivity, acid and sulphate attacks, marine environments test, and rapid chloride penetration test at periods 28 and 56 and 90 days. The findings show that adding leftover glass powder to concrete improved its workability and compressive strength, while adding Alccofine increased its durability and decreased the diffusion of chloride.

Copyright ©2026 by authors and Galileo Institute of Technology and Education of the Amazon (ITEGAM). This work is licensed under the Creative Commons Attribution International License (CC BY 4.0).

I. INTRODUCTION

Gavriletea [1] analysed the influencing factors for the sand market and reviewed the impacts caused due to mining. To study the impact of sand mining, different database sources were used. The study reported that there is a global imbalance in the supply and demand of the sand market. Sand is utilized in various industries, such as chemical, ceramic, foundry, glass making, recreational products and construction, in which the construction industry consumes a major share. The study concluded that the mining of sand produces various impacts such as loss of habitat vegetation, increase in turbidity of river water and bank erosion over the environment. The study recommended finding substitutes for sand such as recycled aggregate, crushed sand, quarry dust and glass waste. Ashraf et al. [2] investigated both negative and positive impacts of sand mining in rivers of Selangor state. The study focused on sediment transport, sampling, sediment grain size distribution and water column. In addition,

Hydrologic Engineering Canters River Analysis System (HEC-RAS) was carried out to perform one-dimensional hydraulic calculations for sediment and transport. The study revealed that sand mining affected all activities linked with the environment, particularly turbidity and quality of water, habitat, flora and fauna, groundwater table, stability of structures and biological environment. The study suggested various mitigating measures for sand mining and concluded that sand mining should be avoided to safeguard the environment. The study also recommended using the substitute for river sand, such as crushed stone and recycled aggregates. Park et al. [3] Crushed waste glass was tested as a substitute for river sand in concrete. Waste glass was replaced for river sand in amounts ranging from 0 to 70%. The workability, air content, compressive, tensile, and flexural strength of concrete specimens were all examined in this study. 7 The study found that using 70% glass powder resulted in a 44.3 percent loss in workability and a 40% rise in air content. The investigation revealed that using glass powder resulted in a significant drop in mechanical characteristics. With the use of glass powder, compressive strength was lowered by almost 90%. The study claimed that the considerable decrease in the mechanical properties with the utilization of glass powder was due to the poor bond between glass powder and the matrix.

The study concluded that utilization of glass powder in the place of river sand reduced the mechanical properties of the concrete. Shi et al. [4] Have studied the properties and pozzolanic reactivity of glass particles. The study assessed and compared the particle shape, fineness, and pozzolanic reactivity of glass powders derived from several sources (GP-fine, GP-dust, GP4000, and GP-6000) for use as cement alternatives. Compared to fly ash, glass powder has higher quantities of SiO2, CaO, and Na2O but significantly less of Al2O3. The study's findings suggested that substituting cement made from Portland cement by glass powder might lower the amount of Alkali Aggregates Reaction (AAR)-induced expansion. The pozzolanic activity of finely crushed glass particles was discovered to be quite high. The study findings also revealed that the pozzolanic reaction happens at a later age in GPC due to the high SiO2 content. An investigation on the impact of fine glass powder on concrete durability was conducted by Schwarz et al. [5]. To determine the durability qualities of cement, 10% of the cement is substituted with glass powder (GP). The study discovered that using glass powder as a cement substitute material reduces expansion produced by the alkali-silica reaction in concrete. The chloride penetrability data indicate that there has been some pore refining in the sample.

The 28-day compressive strengths of concretes prepared with 10% glass powder as substituting cement were found to be higher than those of fly ash concrete. Finally, the research found that fine glass powder improves the durability of concrete mixes. Bhupendra Singh shekhawat [6] Glass garbage represents one of the environmental problems. Every industry has seen a significant increase in the use of glass, which has essentially led to a rise in trash disposal. Glass garbage is also regarded as a non-biodegradable substance that contaminates the environment. The necessity to reduce energy use has grown as a result of global warming. It is widely acknowledged that the effects of global gasses have affected every person on the world. Cement production requires a lot of energy, which adds to greenhouse gas emissions and releases a lot of carbon dioxide (CO). Over the previous 200 years, atmospheric carbon dioxide levels have increased by almost 30%. Because waste materials do not negatively impact the short-term or long-term qualities of concrete and provide a platform for their efficient disposal, their usage in building projects has increased significantly in recent years. One such substance is leftover glass powder [7]. Only with the introduction of steel reinforcing did Portland cement's use in the concrete industry become widely used. Cement manufacture on a wide scale is contributing to both environmental issues and the unchecked loss of natural resources.

Given that concrete is one of the most widely utilized building materials after water, the cement sector is accountable for around 5% of global CO emissions. Every year, millions of tons of glass garbage are produced worldwide. Sunny et al. [8] Investigated the viability of replacing some of the cement in cementitious systems with waste glass. One of the biggest waste streams is garbage from construction and demolition. It is now generally acknowledged that, in order to optimize both economic and environmental benefits, there is a substantial potential for reclaiming and recycling demolished material for use in value-added applications. Sand, limestone, and various other raw materials must be mined before cement can be produced, which consumes a lot of energy and raw resources [9]. Clinker, the major component of cement, is formed when the raw ingredients are crushed, mixed, and then destroyed at 1450 °C. The high temperature of cement kilns is required for the drinker's production. A variety of fuels, including fuel oil, petroleum coke, mineral coal, diesel, natural gas, and used fuels such as waste as well as biomass, are available for this purpose. The cement industry is a cause of environmental issues due to the significant volumes of cement produced and the enormous resource usage.

The major causes of this scenario are excessive carbon dioxide (CO) emissions from fossil fuel combustion and carbon reduction of limestone as part of the clinker-making processes. Furthermore, the biggest environmental hazard of the twenty-first century is climate change and global warming brought on by increased levels of anthropogenic CO emissions into the atmosphere. K. Gayathri [10] Achieving strength properties is not the only need for producing high-quality concrete in the current climate. One of the key requirements for getting high-quality concrete is increasing its durability, lowering its porosity to last longer, and creating green concrete. Concrete's compressive strength is crucial due to its primary characteristics. Since it is simple to execute and the majority of the desirable characteristics of concrete are qualitatively connected to its compressive strength, the compressive test is the most often performed test on hardened concrete. This study examines the impact of replacing ultra-fine slag (Alccofine) on the mechanical characteristics of high-strength concrete. It has been discovered that adding ultrafine slag to concrete increases its workability and fluidity in addition to its compressive strength. Additionally, it increases the durability and dependability of reinforced concrete buildings and exhibits resistance to segregation.

D. Sharma, S. Sharma and Ajay. G [11] investigated experimentally how concrete's strength may be increased by using Alccofine for cement and foundry slag for traditional fine aggregate. They came to the conclusion that replacing cement with 15% Alccofine and fine aggregate with 10% to 45% foundry slag may result in concrete with a respectably high strength. M.V. Sekhar Reddy, K. A. Latha and k. Surendra [12] has conducted experiments on partially substituting fly ash and Alccofine for cement in M40 Grade concrete at percentages of 5%, 10%, 15%, and 20%. Alccofine's addition shows an early strength-gaining potential and is environmentally benign, according to the findings. In terms of long-term strength properties, alccofine performed better than fly ash. Swar shah [13] the most popular material in the building sector right now is Portland cement. It is made by heating materials in a kiln to a fine powder. Its chemical makeup is mostly composed of silicates and aluminates. Portland Cement Concrete is created by combining this cement with water, sand, and aggregates.

These days, the building industry uses this concrete since it is even less expensive than water. According to environmental statistics, about one ton of CO2 is generated during the production of one ton of cement, which is bad from an environmental perspective. Numerous research has been conducted in an effort to develop alternatives to Portland cement and limit its use. According to the investigations, fly ash, slag, rice husk, and met kaolin as Pozzolanic Materials to partially replace the cement. Sheethal Sasikumar [14] Biochar is the lightweight, ash-and-carbon-based substance that is left over when biomass is pyrolyzed. the elimination of vibrating machinery, less noise, fewer air gaps, shorter turnaround times, increased output, and improved robustness and longevity. Two crucial elements of SCC are the particle size and the quantity of powder content. More cement in SCC would increase manufacturing costs. Many academics have suggested alternative supplemental cementitious materials (SCMs) or mineral admixtures to achieve higher economic value in light of quickly growing businesses. A high range water reducer called Alccofine 1203 makes concrete easier to work with and increases its compressive strength. Many people believe that biochar is an efficient method of storing carbon dioxide. The potential for using it to decrease permeability and increase mechanical strength of cement mortar is explored in this study.

Yatin Patel [15] The excessive focus on concrete's compressive strength rather than its performance requirements is one of the primary causes of concrete's historical degradation. When reinforced concrete constructions deteriorate, hostile chemicals from the environment are often transported, followed by chemical and physical reactions in the inside of the structure. Concrete's permeability properties determine how aggressive gasses and/or liquids are transported through it. Concrete's durability performance, as measured by physio-chemical deterioration, rises as its penetration decreases. As a result, one of the most important factors in determining how long concrete will last in harsh settings is its penetration. Srushti P [16] Cement is the most significant building material now, and it is expected to remain so in the future. The construction materials must meet new and higher demands, and in order to do so, the materials must not only have good strength properties but also be durable enough to last for a longer period of time, thus improving the durability of the concrete and producing a greener concrete, which are now becoming important criteria in obtaining high-quality concrete. The goal is to improve the performance and durability of concrete by partially substituting cement with naturally occurring industrial wastes or by-products that need less energy.

Some of these chemical and industrial byproducts, such as Alccofine, have recently received attention for their potential applications. The utilization of these extra ingredients to produce high-performance concrete is a relatively recent strategy. The current study focuses on the durability properties of M30 grade concrete with partial cement substitution with varying concentrations of Alccofine. Aseel Mansi. [17] Nano clay has been widely discussed for its potential to enhance construction materials and technical applications. This review article examines the impact of nano clay as a cement substitute and supplement on the performance of conventional and high-performance concrete. Adding nano clay to high-performance concrete improved compressive and flexural strength, durability, and resistance to sulfate attack. It also reduced porosity, permeability, and water absorption. Nano clay enhances material properties by acting as reinforcements, fillers, nucleation sites, and reactive pozzolans, promoting hydration. Nehal Hamed, [18] the use of nano-clay (5, 7.5, and 10%) as partial cement replacements in two ways: as received and after dispersion in water using a bath sonicator. The examination was based on compressive strength, split tensile strength, flexural strength, and sliding bond. SEM, XRD, and AFM were used to verify the strength and split bond strength of nano-clay concrete, as well as its microstructure characterization.

Sonication of nano-clay particles greatly improved the characteristics of concrete compared to the original material. The optimal percentage of cement substitution by nano-clay was discovered to be 7.5% among as-received and vibrated nano-clay. The inclusion of NC particles resulted in a thick and well-compacted matrix compared to the control mix, as seen by micrographs from SEM, XRD, and AFM data. Sonicated NC also demonstrated increased reactivity compared to as-received NC. Jamal A. Abdalla [19] For decades, researchers have attempted to enhance the durability of concrete by including more cementitious elements. Nanomaterials can enhance the mechanical and durability qualities of concrete, according to recent breakthroughs in the sector. This is study presents a detailed overview of recent advances in the use of nanomaterials as a performance enhancer in cement/geopolymer concrete. The study found strong relationships between cementitious matrices reinforced with nano-TiO2, nano-Fe2O3, nanoclay/metakaolin, and nano-CaCO3. Fresh qualities, microstructure, mechanical and durability characteristics, and the effect of different particle sizes have all been examined. Estefanía Baigorria [20] analyzed the CO2 effect of various industries and especially compared CO2 emissions to the cement industry.

According to the World Resources Institute (WRI), the cement sector accounts for 3.8% of total greenhouse gas (GHG) emissions and around 5% of world CO2 emissions. The primary source of CO2 in cement production is the heating of raw materials in a rotating kiln. The study concluded that the cement sector releases more CO2 into the environment when producing cement than other businesses. To minimize CO2 emissions in the environment, this study advises using alternate fuels and biomass in clinker manufacture, as well as improving energy efficiency and clinker replacement. A viable alternative to clinker will be a new kind of clinker. A promising alternative for clinker will be a new class of clinker Be Lite-Calcium Sulfuric aluminate-ferrite. The climatic change due to the cement industry is studied by McCaffrey [21] It has been reported that cement output increases by 3% per year. The cement industry is responsible for four significant emissions: dust, Sulphur, NOx, and carbon dioxide. The first three are not substantial contributors to global warming. CO2 emissions are the primary cause of global warming, and the worldwide cement sector produces 1.4 billion tons of CO2 per year. The cement sector accounts about 6% of CO2 emissions and approximately 4% of global warming.

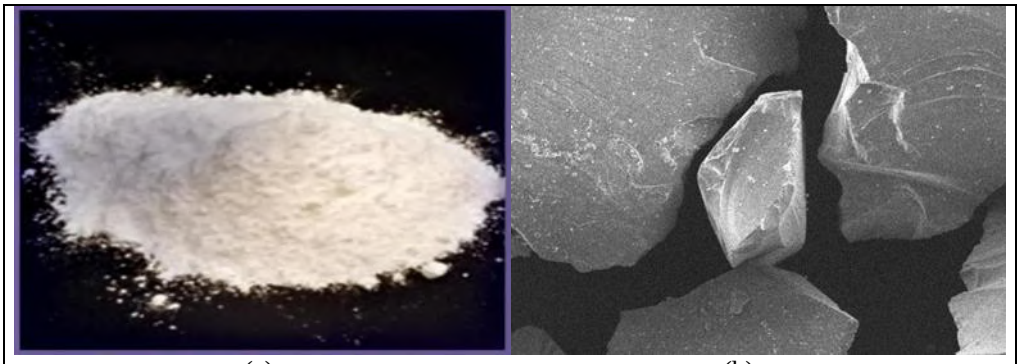
As a result, the study recommends slag, fly ash, and limestone as an alternative to calcined material in cement that is less expensive and emits less (or no) greenhouse gases. Gavriltea [22] analyzed the influencing factors for the sand market and reviewed the impacts caused due to mining. To study the impact of sand mining, different database sources were used. The study reported that there is a global imbalance in the supply and demand of the sand market. Sand is utilized in various industries, such as chemical, ceramic, foundry, glass making, recreational products and construction, in which the construction industry consumes a major share. The study concluded that the mining of sand produces various impacts such as loss of habitat vegetation, increase in turbidity of river water and bank erosion over the environment. The study recommended finding substitutes for sand such as recycled aggregate, crushed sand, quarry dust and glass waste. Shi et al. [23] have analyzed the characteristics and pozzolonic reactivity of glass powders. The study evaluated and compared the particle shape, fineness, and pozzolonic reactivity of glass powders from various sources (GP-fine, GP-dust, GP- 4000, and GP-6000) for usage as cement substitutes.

Compared to Fly ash, the chemical composition of glass powder contains larger levels of SiO2, CaO, and Na2O but much lower levels of Al2O3. The study result concluded that replacing Portland cement with glass powder may reduce the amount of Alkali Aggregates Reaction (AAR)-induced expansion. The pozzolnic activity of finely crushed glass particles was found to be high. The study results also indicated that the pozzolonic reaction occurs at a later age GPC because of the high SiO2 concentration. An investigation on the impact of fine glass powder on concrete durability was conducted by Schwarz et al. [24]. For the purpose of determining durability properties in cement, 10 percent of the cement is substituted with glass powder (GP). The study found that the utilization of glass powder as a cement replacement material can minimize expansion caused by the alkali-silica reaction in concrete. The chloride penetrability results show that there has been some degree of pore refinement in the sample.

II. MATERIAL PROPERTIES

II.1 WASTE GLASS POWDER:

In this work, waste glass powder (WGP) is used as a partial substitution for GGBS in GPC. The chemical structure of XRF was determined by analysing WGP particles. According to the chemical makeup of WGP, the majority of the material is SiO2, accounting for around 69%. WGP has a specific gravity of 2.62 and a specific area of 463 m2/kg. The unit weight of WGP is 2580 kg/m3. Figure 1 demonstrates that the WGP used in this inquiry is an irregular in shape. The picture of WGP was used in this work



(a) (b)

Figure 1: (a) Waste Glass powder (b) Waste Glass powder SEM Analysis.
Source: Authors, (2026).

Table 1: Chemical composition of WGP.

S. No	Constituents	Percentage Composition (%)
1.	Al_2O_3	3.20
2.	Fe_2O_3	0.65
3.	CaO	9.85
4.	K_2O	0.84
5.	Na_2O	10.11
6.	SiO_2	71.80
7.	MgO	3.2
8.	Loss of Ignition	0.35

Source: Authors, (2026).

II.2 NANO CLAY:

Concrete performs much better when nano clay is added because it increases workability, strength, and durability. By improving the microstructure and decreasing porosity, it increases compressive and flexural strength and increases the concrete's resistance to environmental assaults such sulfates and freeze-thaw cycles as well as water penetration. Additionally, nano clay reduces shrinkage and cracking, enhancing the mix's overall cohesiveness. It also speeds up cement hydration, which results in a quicker development of early strength, and improves workability without raising water demand. One of its environmentally beneficial effects is that it uses less cement, which lowers carbon emissions. Additionally, by enhancing thermal stability, nano clay increases concrete's resistance to exposure to high temperatures and fire. Nano clay is a useful addition for improving the sustainability and performance of concrete constructions because of these benefits.



Figure 2: Nano clay powder.
Source: Authors, (2026).

Table 2: Chemical composition of Nano clay.

S. No	Constituents	Percentage Composition (%)
1.	SiO_2	57.5
2.	Al_2O_3	23
3.	MgO	6
4.	Fe_2O_3	2.5
5.	CaO	1.5
6.	Na_2O	4
7.	K_2O	2
8.	TiO_2	3.5

Source: Authors, (2026).

II.3 ALCCOFINE 1203:

ALCCOFINE 1203 has a distinct chemical composition consisting mostly of CaO 30-34% and SiO2 30-36%, as seen by the chemical composition and physical features given below. Physically, the product is unusual in terms of particle size distribution.



(a) (b)

Figure 3: (a) Alccofine Normal View (b) SEM Analysis.
Source: Authors, (2026).

Table 3: Chemical composition of Alccofine.

Chemical analysis	Mass %
CaO	35
$Al2O_3$	20.1
$Fe2O_3$	3.1
SO_3	0.5
MgO	7.3
SiO_2	36

Source: Authors, (2026).

II.4 FINE AGGREGATE:

Aggregate is a course to medium grained particulate substance used in concrete building. The aggregate phase provides mechanical strength to the structure while also influencing the fundamental qualities of concrete, such as strength, unit weight, Young's modulus, workability and durability. Fine aggregate with a high void-filling capability aids in the production of dense concrete with maximum strength and extends the structural durability. This operation employed manufactured sand (M-sand) as the fine aggregate. The M-sand utilized in this experiment was acquired locally by crushing stone. M-sand has a cubical form, rounded corners, and a dimension of less than 4.75 mm. The physical properties of M-sand are tabulated in Table 4. Properties of the M-sand are determined as per IS: 2386 – 1963 [138], and the values are confirmed to IS: 383- 1970.

Table 4: Physical properties of M-sand.

S. No	Physical Property	Value
1.	Specific gravity	2.62
2.	Fineness Modulus	2.36
3.	Zone	III
4.	Bulk density	$1702m^3$

Source: Authors, (2026).

II.5 COARSE AGGREGATE:

Coarse aggregate accounts for the majority of the concrete's volume and strength. Because of the weathering activity of the rock, coarse aggregate derived from its core half is desirable. The physical qualities of aggregate, such as specific gravity, hardness, and texture, vary depending on where it is extracted. Aggregates can be smooth, spherical, or angular (crushed stones). Typical coarse aggregate sizes vary from 4.7 to 20 mm.

For this project, coarse aggregate (CA) was purchased from a local quarry. The coarse aggregate utilized in this work has an angular form and is clean and dry. The physical properties of coarse aggregate are tabulated in The Properties of the coarse aggregates are confirmed to IS: 383-1970.

Table 5: Physical properties of Coarse Aggregate.

S. No	Physical Property	Value
1.	Specific gravity	2.67
2.	Fineness Modulus	6.10
3.	Zone	1456 m^3

Source: Authors, (2026).

II.6 MIXING, CASTING AND CURING OF CONCRETE:

The components for the mixes (AF and cement, WGP and M-Sand) were weighed and mixed dry for 3-4 minutes before adding coarse aggregate. The alkaline liquid, a mixture of sodium hydroxide and sodium silicate solutions, was then added to the dry mix and stirred for 3-5 minutes before adding some more water, around 20% of the binder's weight, to increase workability. The mixing was continued for approximately 6-8 minutes. After mixing, the concrete was poured in conventional steel Molds and compacted properly. Precautions were made to ensure that the components mixed uniformly. For ambient curing, the cubes were maintained at room temperature after casting, demoulded after one day, and cured at room temperature until testing. Ambient cured specimens are stored in the laboratory at room temperature (27-31ºC).

II.7 CEMENT:

The cement utilized in every specimen was standard Portland. Cement grade 53, as per IS: 12269:2013, was used.

II.8 WATER:

The investigation uses conventional potable water from the laboratory supply source.

II.9 CONCRETE:

The cement used is Portland Cement 53 Grade. The cement tests are carried out in compliance with the IS 1489 parameters. Aggregate must be no greater than 20mm, with fine aggregate ranging from 0 to 4.75mm in size. To maintain its intrinsic properties, such as compressive strength, the concrete must be allowed to cure in real-world conditions for around 28 days. A concrete cube (100mm x 100mm x 100mm) is loaded with axial forces in order to evaluate its strength.

III. MIX PROPORTIONS

Table 6: Concrete Mix ID's.

S. No	Mix ID	Description
1.	CM (Conventional Mix)	Fine Aggregate, Coarse Aggregate & Cement
2.	5% of AF	Fine Aggregate replaced with AF for about 5% of its total volume
3.	10% of AF	Fine Aggregate replaced with AF for about 10% of its total volume
4.	15% of AF	Fine Aggregate replaced with AF for about 15% of its total volume
5.	20% of AF	Fine Aggregate replaced with AF for about 20% of its total volume
6.	25% of AF	Fine Aggregate replaced with AF for about 25% of its total volume
7.	5% of NC	Cement replaced with NC for about 5% of its total volume
8.	10% of NC	Cement replaced with NC for about 10% of its total volume
9.	15% of NC	Cement replaced with NC for about 15% of its total volume
10.	20% of NC	Cement replaced with NC for about 20% of its total volume
11.	25% of NC	Cement replaced with NC for about 25% of its total volume
12.	10% of GP	Fine Aggregate replaced with GP for about 5% of its total volume
13.	20% of GP	Fine Aggregate replaced with GP for about 10% of its total volume
14.	30% of GP	Fine Aggregate replaced with GP for about 15% of its total volume
15.	40% of GP	Fine Aggregate replaced with GP for about 20% of its total volume
16.	50% of GP	Fine Aggregate replaced with GP for about 25% of its total volume

Source: Authors, (2026).

IV. EXPERIMENTAL INVERSICATION (MECHANICAL & DURABILITY PROPERTIES)

IV.1 COMPRESSIVE STRENGTH:

Compressive strength was tested as per IS 516 (1959) for the specimens casted with varying mix proportions. It was observed that the compressive strength of 20AF is increased by 0.2 % and 3.15 % when compared to conventional concrete mix tested at 7 days and 28 days respectively. When comparing the results obtained at 28 days, it was found that 20 AF mix recorded the highest compressive strength than other mixes.

IV.2 SPLITTING TENSILE STRENGTH:

Tensile strength was measured in accordance with IS 516 (1959) for specimens cast with varied mix proportions. The tensile strength of 20AF was found to be 32.12% higher than that of normal concrete mix after 28 days of testing. When the findings were compared after 28 days, it was observed that the 20 AF mix had the highest tensile strength of the mixtures tested.

IV.3 FLEXURAL STRENGTH:

The specimens cast with different mix proportions had their flexural strength evaluated in accordance with IS 516 (1959). Compared to a typical concrete mix tested at 28 days, respectively, the flexural strength of 20AF was found to be 9.90% percent higher. In contrast to other mixes, the 20 AF mix had the maximum flexural strength when the results were compared at 28 days.

Table 7: Compressive, Splitting tensile & Flexural test.

S. No	Mix ID	COMPRESSIVE			SPLITTING TENSILE	FLEXURAL
		7 Days	14 Days	28 Days	28 Days	28 Days
1.	CM	26.97	36.07	40.54	3.02	4.04
2.	5 % AF	24.54	33.41	38.21	1.89	2.08
3.	10% AF	25.72	35.11	39.96	2.07	2.91
4.	15 %AF	25.92	36.56	40.56	2.86	3.11
5.	20% AF	27.09	37.12	41.86	3.99	4.44
6.	25 %AF	26.28	35.16	40.49	2.55	3.01
7.	5% NC	25.14	35.89	39.01	2.15	2.98
8.	10%NC	26.66	36.44	40.10	2.99	3.91
9.	15%NC	27.03	37.06	40.99	3.05	4.55
10.	20%NC	25.11	35.21	38.12	2.11	3.65
11.	25%NC	25.03	34.84	37.89	1.89	2.33
12.	10% GP	25.52	36.12	38.37	2.31	3.12
13.	20% GP	26.21	37.56	39.01	2.65	3.88
14.	30% GP	27.56	38.23	40.81	3.56	4.33
15.	40% GP	25.11	36.89	38.36	2.55	3.12
16.	50% GP	24.86	36.01	37.98	2.22	2.97

Source: Authors, (2026).

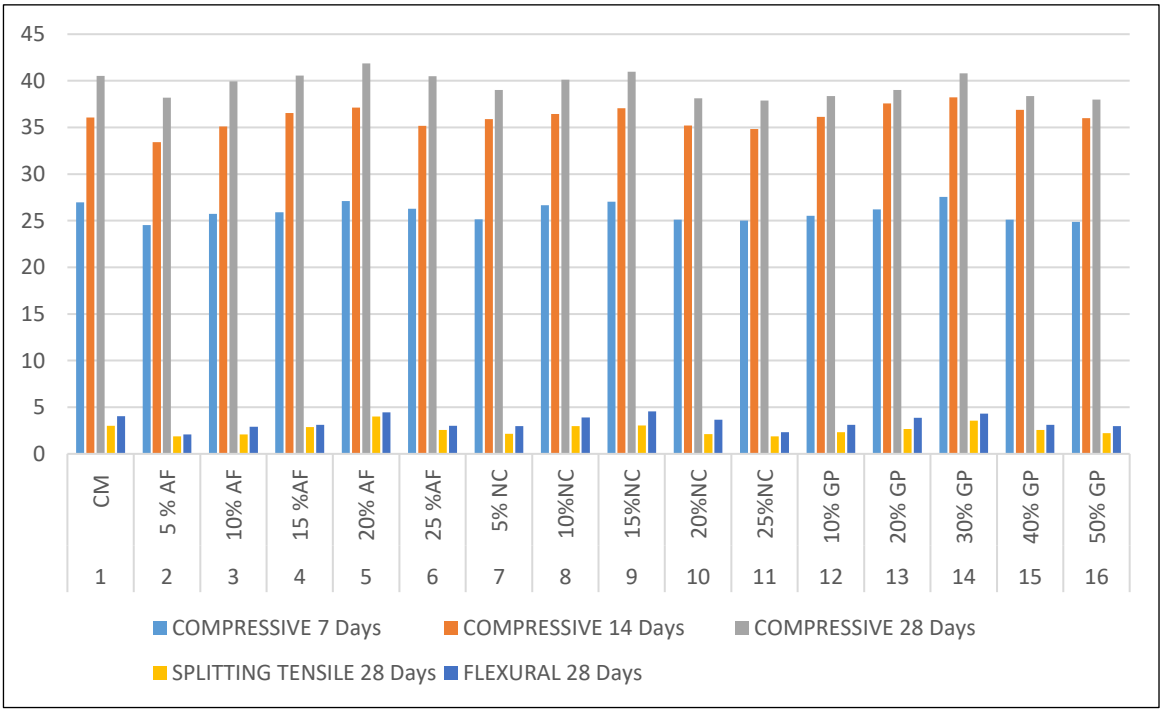


Figure 4: Compressive, Splitting tensile & Flexural test.
Source: Authors, (2026).

IV.4 WATER ABSORPTION:

The water absorption reduction in Saturated stages when cement is replaced by 20 percentage Alccofine and 15 percentage of nano clay when tested at 28,58 and 90 days respectively, with normal conventional concrete. When Glass Powder is used for replacing the fine aggregate by 30%, the reduction in water absorption is 20.5%,21.08%,19.33%.

Table 8: Water absorption test.

Mix ID	28 Days		56 Days		90 Days	
	Initial WA %	Saturated WA %	Initial WA %	Saturated WA %	Initial WA %	Saturated WA %
CM	3.2	4.1	3.14	4.02	3.02	3.89
5 % AF	3.14	3.8	3.08	3.74	2.94	3.61
10% AF	2.98	3.75	2.9	3.62	2.78	3.51
15 % AF	2.95	3.6	2.86	3.54	2.61	3.48
20% AF	2.72	3.4	2.65	3.32	2.52	3.26
25 % AF	3.15	4.2	3.4	4.1	3.24	4.98
5% NC	2.9	3.58	2.72	3.5	2.68	3.4
10% NC	3.1	3.9	3.02	3.52	2.94	3.74
15% NC	3.75	4.23	3.52	4.13	3.40	3.82
20% NC	3.24	3.88	3.18	3.19	3.08	3.02
25% NC	3.09	3.34	3.61	4.06	3.11	3.29
10% GP	2.22	3.5	2.54	2.72	2.03	2.42
20% GP	2.86	3.9	2.65	3.18	2.4	3.08
30% GP	3.92	4.3	3.65	4.12	3.13	4.42
40% GP	3.01	3.44	2.56	3.22	2.68	2.22
50% GP	2.88	3.56	2.98	2.73	2.59	2.09

Source: Authors, (2026).

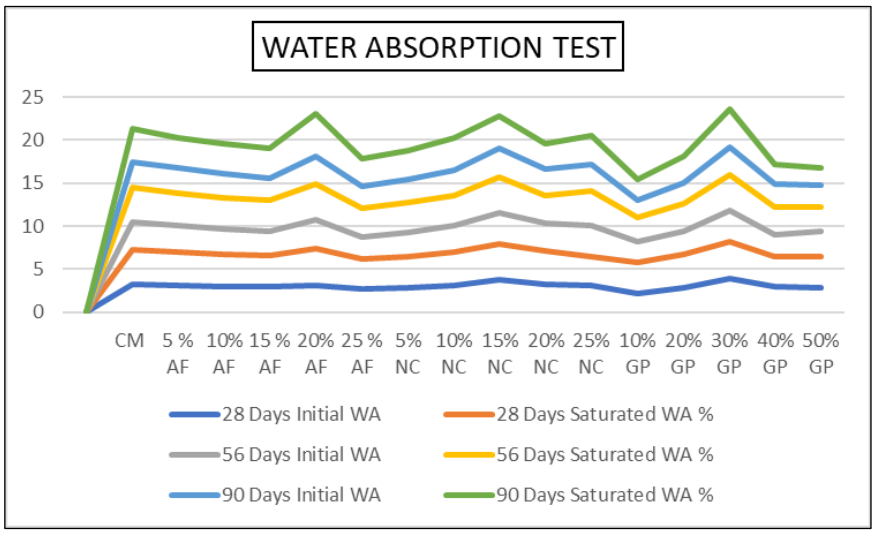


Figure 5: Water absorption test.
Source: Authors, (2026).

IV.5 SORPTIVITY:

The Sorptivity reduction when cement is replaced by 20 percentage Alccofine 15% of nano clay when tested at 60min,90min,120min respectively, with normal conventional concrete. When GP is used for replacing the cement by 30%, the reduction in water absorption is 21.05%, 36.11%, 36.76% with normal conventional concrete.

Table 9: Sorptivity test.

Mix ID	Sorptivity $S = I/T^{0.5}$				
	15 min	30 min	60 min	90 min	120 min
CM	0.138	0.111	0.092	0.098	0.093
5 % AF	0.125	0.104	0.085	0.092	0.081
10% AF	0.092	0.086	0.074	0.077	0.068
15 % AF	0.085	0.072	0.064	0.067	0.059
20% AF	0.092	0.083	0.076	0.072	0.068
25 % AF	0.072	0.062	0.052	0.051	0.044
5% NC	0.033	0.067	0.055	0.055	0.047
10% NC	0.086	0.100	0.083	0.081	0.066
15% NC	0.108	0.095	0.078	0.089	0.072
20% NC	0.101	0.088	0.065	0.075	0.066
25% NC	0.095	0.076	0.062	0.065	0.058
10% GP	0.082	0.069	0.060	0.059	0.051
20% GP	0.072	0.075	0.075	0.080	0.078
30% GP	0.068	0.086	0.089	0.097	0.092
40% GP	0.044	0.058	0.067	0.069	0.071
50% GP	0.032	0..046	0.055	0.042	0.058

Source: Authors, (2026).

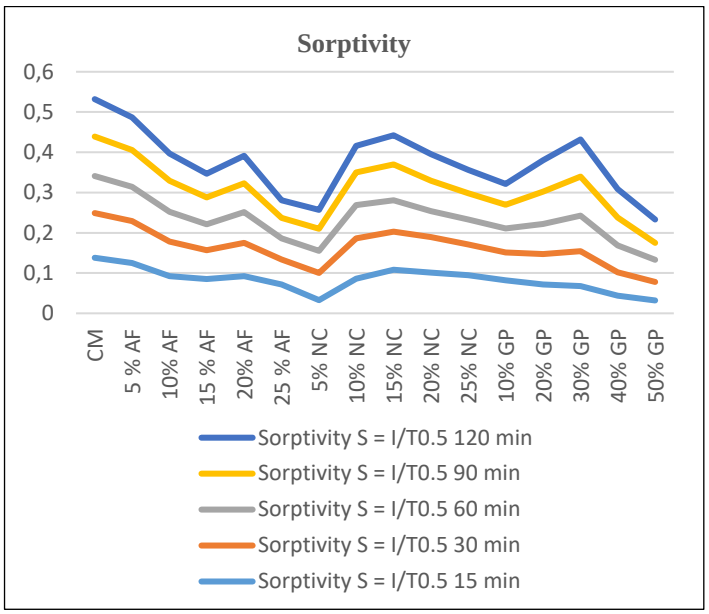


Figure 6: Sorptivity test results.
Source: Authors, (2026).

IV.6. RAPID CHLORIDE PENETRATION TEST (RCPT):

The penetration value is also reduced to 1865, 1875 and 1870 in 20%AF, 15% NC and 30% GP when compared normal conventional concrete.

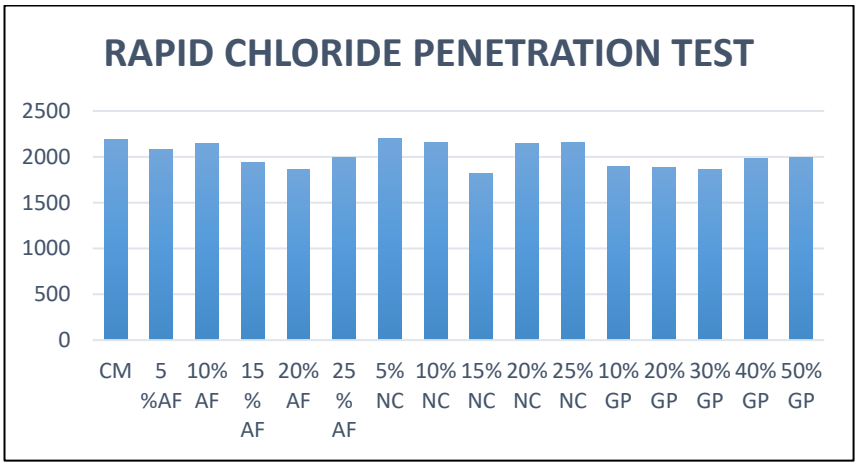


Figure 7: Rapid chloride penetration test.
Source: Authors, (2026).

Table 10: Rapid Chloride Penetration test

Mix ID	Charge Passed C	Standard as per ASTM C1202-2012
CM	2185	Moderate
5 %AF	2085	Moderate
10% AF	2140	Moderate
15 % AF	1940	Low
20% AF	1865	Low
25 % AF	1990	Low
5% NC	2195	Moderate
10% NC	2160	Moderate
15% NC	1820	Low
20% NC	2150	Moderate
25% NC	2160	Moderate
10% GP	1895	Low
20% GP	1880	Low
30% GP	1860	Low
40% GP	1980	Moderate
50% GP	1990	Moderate

Source: Authors, (2026).

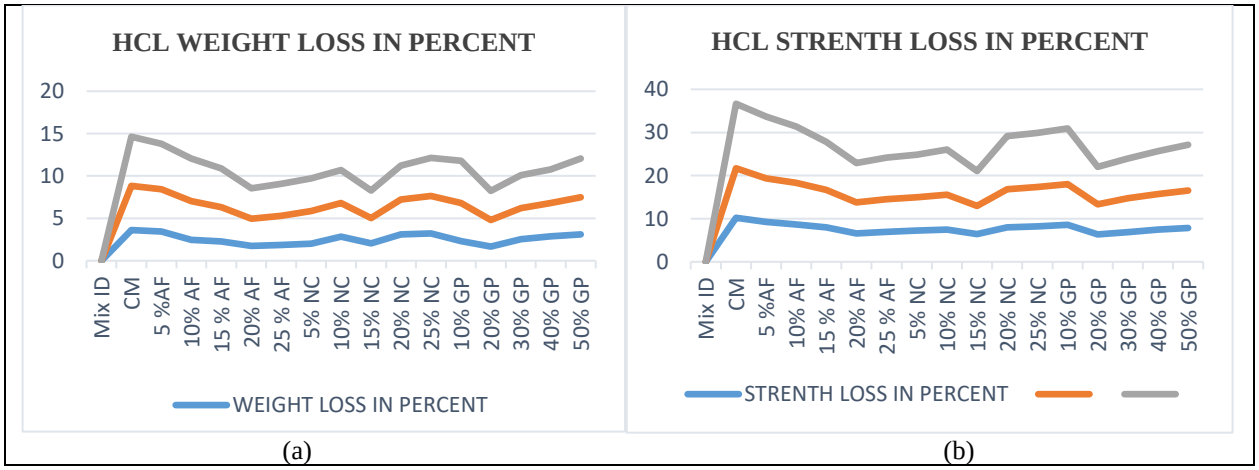
IV.7 ACID RESISTANCE TEST HCL:

When AF is substituted with cement, the largest percentage reduction in weight loss is 108.05%, 61.30%, and 62.92%. compared to standard concrete for 28, 56, and 90, respectively. When NC is substituted with cement, the largest percentage reduction in weight loss is 77.45%, 73.1%, and 80% compared to standard concrete for 28, 56, and 90, respectively. When GF is substituted with fine aggregate, the greatest percentage reduction in weight loss absorption is 41.9%, 42.3%, and 49.4% compared to standard concrete for 28, 56, and 90, respectively. The largest percentage reduction in strength loss when AF is substituted with cement is 6.54%, 7.23%, and 9.12% when compared to standard concrete for 28, 56, and 90, respectively. The largest percentage reduction in strength loss when AF is substituted with cement is 6.54%, 7.23%, and 9.12% when compared to standard concrete for 28, 56, and 90, respectively. When NC is substituted with fine aggregate, the highest percentage reduction in strength loss is 56.11%%, 75.27%, and 84.24% when compared to standard concrete at 28, 56, and 90, respectively. When GF is substituted with fine aggregate, the highest percentage reduction in strength loss is 48.62%, 46.24%, and 62.10% when compared to standard concrete at 28, 56, and 90, respectively.

Table 11: Acid Resistance test- HCL.

Mix ID	WEIGHT LOSS IN PERCENT			STRENTH LOSS IN PERCENT		
	28 days	56 days	90 days	28 days	56 days	90 days
CM	3.62	5.21	5.8	10.21	11.48	14.96
5 %AF	3.45	4.97	5.37	9.24	10.11	14.30
10% AF	2.48	4.56	5.01	8.66	9.67	13.04
15 % AF	2.29	4.02	4.56	8.02	8.69	11.09
20% AF	1.74	3.23	3.56	6.54	7.23	9.12
25 % AF	1.86	3.42	3.79	6.98	7.53	9.65
5% NC	2.01	3.85	3.86	7.21	7.72	9.92
10% NC	2.85	3.94	3.92	7.46	8.08	10.5
15% NC	2.04	3.01	3.22	6.40	6.55	8.12
20% NC	3.10	4.14	3.99	7.99	8.83	12.33
25% NC	3.23	4.39	4.52	8.21	9.12	12.56
10% GP	2.30	4.51	4.98	8.59	9.44	12.89
20% GP	1.68	3.14	3.42	6.32	7.01	8.67
30% GP	2.55	3.66	3.88	6.87	7.85	9.23
40% GP	2.89	3.91	3.99	7.45	8.23	9.97
50% GP	3.12	4.36	4.56	7.81	8.69	10.65

Source: Authors, (2026).



(a) (b)

Figure 8: (a) Weight loss in percent in HCL (b) Strength loss in percent in HCL.
Source: Authors, (2026).

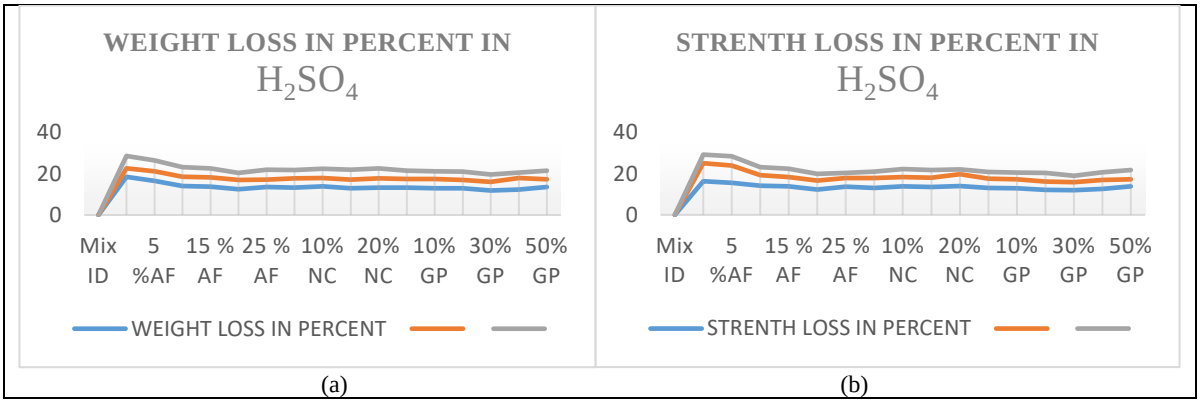
IV.8 ACID RESISTANCE TEST H2SO4:

When compared to normal concrete for 28, 56, and 90 days, the maximum percentage reduction in weight loss, when AF is replaced with cement, is AF 20 reduction in weight loss absorption is 48.08%, 33.69%, and 39.86 % when compared to normal concrete for 28, 56, and 90 days, respectively. when NC is replaced with cement, NC 15 is the maximum percentage reduction in strength loss is 41.95%, 31.67%, and 30.66% for 28, 56 and 90 days respectively. when GF30 is replaced with fine aggregate, GF 30 is the maximum percentage reduction in weight loss is 55.04%, 40.68%, and 45.56% when compared to normal concrete for 28, 56, and 90 days, respectively. When compared to normal concrete for 28, 56, and 90 days, the maximum percentage reduction in strength loss, when AF is replaced with cement, is AF 20 reduction in strength loss absorption is 48.08%, 33.69%, and 39.86 % when compared to normal concrete for 28, 56, and 90 days, respectively. when NC is replaced with cement, NC 15 is the maximum percentage reduction in strength loss is 41.95%, 31.67%, and 30.66% for 28, 56 and 90 days respectively. when GF30 is replaced with fine aggregate, GF 30 is the maximum percentage reduction in strength loss is 55.04%, 40.68%, and 45.56% when compared to normal concrete for 28, 56, and 90 days, respectively.

Table 12: Acid Resistance test H2SO4.

Mix ID	WEIGHT LOSS IN PERCENT			STRENTH LOSS IN PERCENT		
	28 days	56 days	90 days	28 days	56 days	90 days
CM	18.48	22.62	28.6	16.32	25.08	29.25
5 %AF	16.45	21.2	26.45	15.5	23.96	28.49
10% AF	14.09	18.56	23.25	14.21	19.26	23.16
15 % AF	13.76	18.23	22.64	13.85	18.41	22.45
20% AF	12.48	16.92	20.45	12.33	16.65	19.96
25 % AF	13.55	17.13	21.91	13.61	17.92	20.31
5% NC	13.23	17.81	21.86	13.06	17.92	21.06
10% NC	13.88	17.99	22.42	13.86	18.32	22.25
15% NC	13.02	17.18	21.89	13.55	18.01	21.7
20% NC	13.32	17.69	22.62	14.05	19.74	22.03
25% NC	13.19	17.52	21.48	12.99	17.51	20.88
10% GP	13.01	17.38	21.23	12.84	17.26	20.59
20% GP	12.88	17.01	20.96	12.12	16.23	20.33
30% GP	11.92	16.08	19.65	11.92	15.86	19.03
40% GP	12.33	17.89	20.48	12.66	16.98	20.66
50% GP	13.57	17.25	21.56	13.87	17.26	21.74

Source: Authors, (2026).



(a) (b)

Figure 9: (a) Weight loss in percent in H2SO4 (b) Strength loss in percent in H2SO4.
Source: Authors, (2026).

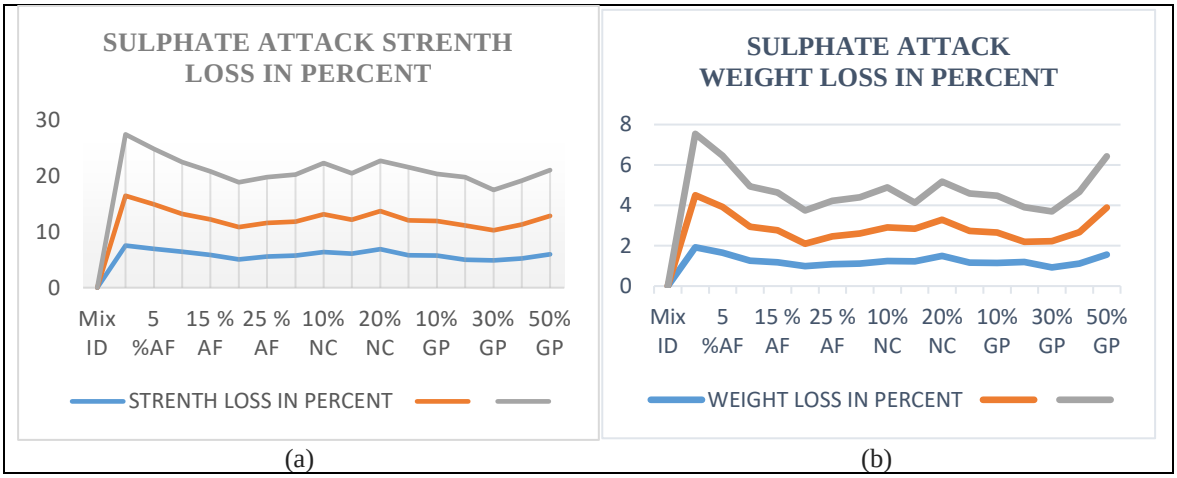
IV.9 SULPHATE ATTACK TEST:

When AF20 is substituted with cement, the largest percentage reduction in weight loss is 95.92%, 41.02%, and 38.15%, when compared to standard concrete for 28, 56, and 90, respectively. When NC15 is substituted with cement the greatest percentage reduction in weight loss absorption is 57.38%, 58.28%, and 39.37% compared to standard concrete for 28, 56, and 90, respectively When GF30 is substituted with cement the greatest percentage reduction in weight loss absorption is 41.44%, 39.04%, and 40.13% compared to standard concrete for 28, 56, and 90, respectively. The largest percentage reduction in strength loss when AF20 is substituted with cement is 22.35%, 24.33%, and 27.04% when compared to standard concrete for 28, 56, and 90, respectively. When NC15 is substituted with cement, the highest percentage reduction in strength loss is 23.53%, 47.52%, 31.85% when compared to standard concrete for 28, 56, and 90, respectively. When GP30 is substituted with fine aggregate, the highest percentage reduction in strength loss is 53.66%, 65.25%, 52.42% when compared to standard concrete for 28, 56, and 90, respectively.

Table 13: Sulphate Attack test.

Mix ID	WEIGHT LOSS IN PERCENT			STRENTH LOSS IN PERCENT		
	28 days	56 days	90 days	28 days	56 days	90 days
CM	1.92	2.58	3.04	7.56	8.94	11.02
5 %AF	1.66	2.26	2.54	6.96	7.99	9.96
10% AF	1.25	1.69	2	6.45	6.8	9.31
15 % AF	1.18	1.58	1.88	5.87	6.37	8.61
20% AF	0.98	1.12	1.65	5.07	5.83	8.04
25 % AF	1.08	1.38	1.77	5.61	6.01	8.23
5% NC	1.12	1.48	1.80	5.76	6.12	8.42
10% NC	1.24	1.67	1.98	6.42	6.78	9.17
15% NC	1.22	1.63	1.27	6.12	6.06	8.36
20% NC	1.49	1.80	1.89	6.89	6.88	8.99
25% NC	1.17	1.56	1.85	5.84	6.26	9.55
10% GP	1.14	1.52	1.82	5.79	6.18	8.46
20% GP	1.20	1	1.70	5	6.14	8.69
30% GP	0.92	1.30	1.48	4.92	5.41	7.23
40% GP	1.12	1.55	1.99	5.23	6.12	7.85
50% GP	1.56	2.33	2.54	6.01	6.89	8.21

Source: Authors, (2026).



(a) (b)

Figure 10: (a) Strength loss in percent in percent (b) Weight loss in percent in percent.
Source: Authors, (2026).

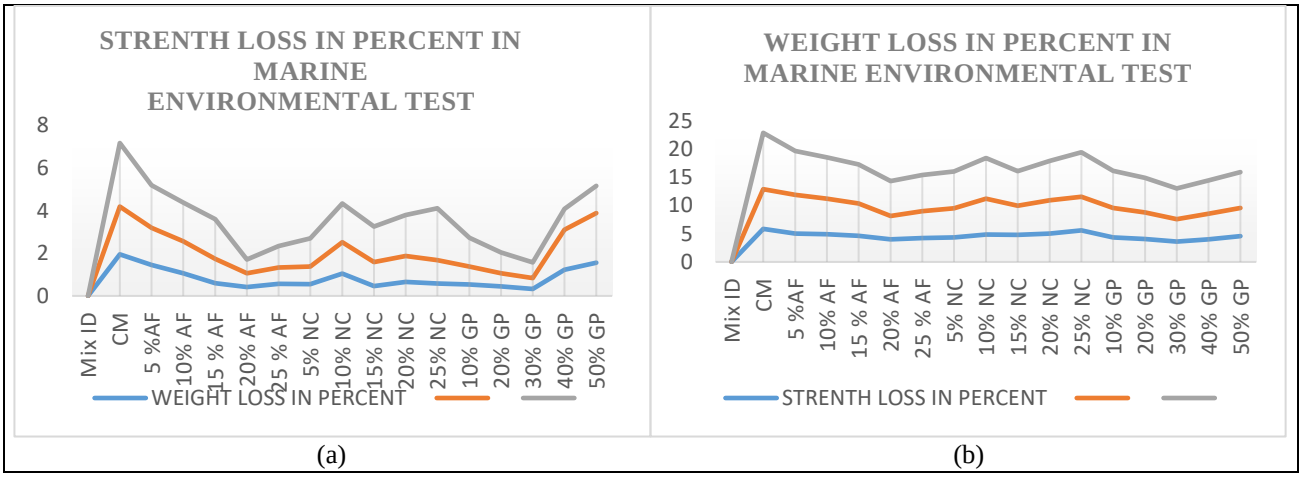
IV.10 MARINE RESISTANCE TEST:

When compared to conventional concrete for 28, 56, and 90, the largest percentage reduction in weight loss that occurs when AF is substituted with cement is 79.48%, 70.98%, and 71.81%, respectively. When GF is substituted with fine aggregate, the weight loss absorption can be reduced by a maximum percentage of 72.82%, 76.33%, and 54.69% when compared to conventional concrete for 28, 56, and 90, respectively. When compared to regular concrete for 28, 56, and 90, the largest percentage reduction in strength loss that occurs when AF is substituted with cement is 31.84%, 41.31%, and 37.56%, respectively. When compared to regular concrete for 28, 56, and 90, the largest percentage reduction in strength loss that occurs when GP is substituted with fine aggregate is 25.51%, 25.52%, and 34.33%, respectively. In previous studies when Alccofine and glass powder compared to normal conventional concrete in weight loss 83.58%,85.71%,75.16% and the strength loss is 38.55%,43.30%,45.58% is the best.

Table 14: Marine Environmental test.

Mix ID	WEIGHT LOSS IN PERCENT			STRENTH LOSS IN PERCENT		
	28 days	56 days	90 days	28 days	56 days	90 days
CM	1.95	2.24	2.98	5.84	7.02	9.96
5 %AF	1.45	1.75	1.99	5.02	6.84	7.76
10% AF	1.06	1.50	1.82	4.88	6.32	7.26
15 % AF	0.59	1.14	1.87	4.62	5.69	6.92
20% AF	0.41	0.65	0.64	3.98	4.12	6.18
25 % AF	0.57	0.76	1.01	4.24	4.73	6.42
5% NC	0.55	0.83	1.32	4.33	5.17	6.51
10% NC	1.04	1.48	1.81	4.86	6.30	7.22
15% NC	0.46	1.13	1.67	4.79	5.14	6.11
20% NC	0.66	1.21	1.92	4.99	5.88	6.99
25% NC	0.58	1.10	2.43	5.58	5.95	7.88
10% GP	0.53	0.85	1.35	4.35	5.20	6.54
20% GP	0.44	0.62	0.98	4.06	4.66	6.12
30% GP	0.32	0.51	0.74	3.60	3.98	5.42
40% GP	1.23	1.87	0.98	3.97	4.56	5.87
50% GP	1.55	2.33	1.28	4.55	5.01	6.29

Source: Authors, (2026).



(a) (b)

Figure 11: (a) Strength loss in percent (b) Weight loss in percent.
Source: Authors, (2026).

V. CONCLUSIONS

In this experiment, concrete cubes, cylinders, and beams were cast for varied proportions and evaluated at 7,14,28, 56, and 90 days for mechanical and durability. The reduction in water absorption in saturated stages when cement is substituted with 20% Alccofine and 15% nano clay when tested at 28, 58, and 90 days, respectively, compared to regular conventional concrete. When Glass Powder is utilized to replace 30% of the fine aggregate, water absorption is reduced by 3.4, 3.32, and 3.26. Sorptivity decrease when cement is substituted with 20% Alccofine 15% nano clay when tested at 60, 90, and 120 minutes with standard conventional concrete. Using GP as a 30% replacement for cement reduces water absorption by 0.076, 0.072, and 0.068 compared to standard concrete. The penetration value is also reduced to 1840 in AF20, NC15 and GP30 when compared normal conventional concrete. When AF is replaced with cement, the greatest percentage reduction in weight loss is 1.74, 3.23, and 3.56 when compared to regular concrete for 28, 56, and 90. Substituting cement for NC results in significant weight reductions of 2.04, 3.01, and 3.22 compared to ordinary concrete for 28, 56, and 90, respectively. Substituting GF with fine aggregate results in a 42.55, 3.66, and 3.88 percent reduction in weight loss absorption compared to ordinary concrete (28, 56, and 90, respectively).

When AF is substituted with cement, the largest percentage reduction in weight loss is 79.48%, 70.98%, and 71.81%, when compared to standard concrete for 28, 56, and 90, respectively. When GP is substituted with fine aggregate, the greatest percentage reduction in weight loss absorption is 72.82%, 76.33%, and 54.69% compared to standard concrete for 28, 56, and 90, respectively. When AF is substituted with cement, the highest percentage reduction in strength loss is 31.84%, 41.31%, and 37.56% compared to regular concrete for 28, 56, and 90, respectively. When GP is substituted with fine aggregate, the largest percentage reduction in strength loss is 25.51%, 25.52%, and 34.33% when compared to standard concrete at 28, 56, and 90 days respectively. In previous studies when Alccofine and glass powder compared to normal conventional concrete in weight loss 83.58%,85.71%,75.16% and the strength loss is 38.55%,43.30%,45.58% is the best. According to the aforementioned data, the best percentage replacement of cement by Alccofine is 20%, whereas the optimum percentage replacement of cement by Glass Powder is 50%. Furthermore, replacing cement with a mix of Alccofine and Glass Powder produces superior results when compared to standard conventional concrete.

VI. AUTHOR'S CONTRIBUTION

Conceptualization: K.E. Viswanathan, S. Naveen Kumar, S. Yuvaraj, C. Shankar.
Methodology: K.E. Viswanathan, S. Naveen Kumar, S. Yuvaraj, C. Shankar.
Investigation: K.E. Viswanathan, S. Naveen Kumar, S. Yuvaraj, C. Shankar.
Discussion of results: K.E. Viswanathan, S. Naveen Kumar, S. Yuvaraj, C. Shankar.
Writing – Original Draft: K.E. Viswanathan, S. Naveen Kumar, S. Yuvaraj, C. Shankar.
Writing – Review and Editing: K.E. Viswanathan, S. Naveen Kumar, S. Yuvaraj, C. Shankar.
Resources: K.E. Viswanathan, S. Naveen Kumar, S. Yuvaraj, C. Shankar.
Supervision: K.E. Viswanathan, S. Naveen Kumar, S. Yuvaraj, C. Shankar.
Approval of the final text: K.E. Viswanathan, S. Naveen Kumar, S. Yuvaraj, C. Shankar.

VII. REFERENCES

[1] D. Padmalal, K. Maya, S. Sreebha, and R. Sreeja, "Environmental effects of river sand mining: A case from the river catchments of Vembanad Lake, southwest coast of India," Environ. Geol., vol. 54, no. 4, pp. 879–889, 2008, doi: 10.1007/s00254-007-0870-z.

[2] G. Chand, S. K. Happy, and S. Ram, "Assessment of the properties of sustainable concrete produced from quaternary blend of Portland cement, glass powder, metakaolin and silica fume," Cleaner Eng. Technol., vol. 4, p. 100179, 2021, doi: 10.1016/j.clet.2021.100179.

[3] K. I. M. Ibrahim, "Recycled waste glass powder as a partial replacement of cement in concrete containing silica fume and fly ash," Case Stud. Constr. Mater., vol. 15, p. e00630, 2021, doi: 10.1016/j.cscm.2021.e00630.

[4] C. Shi, Y. Wu, C. Riefler, and H. Wang, "Characteristics and pozzolanic reactivity of glass powders," Cem. Concr. Res., vol. 35, pp. 987–993, 2005, doi: 10.1016/j.cemconres.2004.05.015.

[5] N. Schwarz, H. Cam, and N. Neithalath, "Influence of a fine glass powder on the durability characteristics of concrete and its comparison to fly ash," Cem. Concr. Compos., vol. 30, pp. 486–496, 2008, doi: 10.1016/j.cemconcomp.2008.02.001.

[6] M. Kamali and A. Ghahremaninezhad, "Effect of glass powders on the mechanical and durability properties of cementitious materials," Constr. Build. Mater., vol. 98, pp. 407–416, 2015, doi: 10.1016/j.conbuildmat.2015.06.010.

[7] B. V. Kavyateja, J. G. Jawahar, and C. Sashidhara, "Durability performance of self-compacting concrete incorporating Alccofine and fly ash," Int. J. Eng., vol. 33, no. 8, pp. 1522–1528, 2020, doi: 10.5829/ije.2020.33.08b.10.

[8] A. Khating, G. S. Supekar, and S. M. Mehetre, "Alccofine and steel in self-compacting concrete," Int. J. Adv. Eng. Res. Dev., vol. 5, no. 4, pp. 504–508, 2018.

[9] Selvasofia, S.A., Sarojini, E., Moulica, G., Thomas, S., Tharani, M., Saravanakumar, P.T. and Kumar, P.M., "Study on the mechanical properties of the nanoconcrete using nano-TiO2 and nanoclay" Materials Today: Proceedings, 50, pp.1319-1325, 2022. doi: 10.1016/j.matpr.2021.08.242.

[10] U. S. Ansari, I. M. Chaudhri, N. P. Ghuge, and R. R. Phatangre, "High performance concrete with partial replacement of cement by Alccofine and fly ash," Indian Res. Trans., vol. 5, no. 2, pp. 19–23, 2015.

[11] R. Balamuralikrishnan and J. Saravanan, "Effect of Alccofine and GGBS addition on the durability of concrete," Civ. Eng. J., vol. 5, no. 6, pp. 1273–1288, 2019, doi: 10.28991/cej-2019-03091331.

[12] ASTM C642-06, Standard Test Method for Density, Absorption, and Voids in Hardened Concrete. West Conshohocken, PA, USA: ASTM Int., 1997.

[13] ASTM C1585, Standard Test Method for Measurement of Rate of Absorption of Water by Hydraulic-Cement Concretes. ASTM Int., 2018.

[14] ASTM C1202, Standard Test Method for Electrical Indication of Concrete's Ability to Resist Chloride Ion Penetration. ASTM Int., 2012.

[15] IS 456:2000, Indian Standard Specification for Plain and Reinforced Concrete. Bureau of Indian Standards, New Delhi, India, 2005.

[16] ASTM C1012-04, Standard Test Method for Length Change of Hydraulic-Cement Mortars Exposed to a Sulfate Solution. ASTM Int., 2004.

[17] A. Mansi, "The impact of nano clay on normal and high-performance concrete characteristics," IOP Conf. Ser.: Earth Environ. Sci., vol. 961, p. 012085, 2022, doi: 10.1088/1755-1315/961/1/012085.

[18] N. Hamed, "Effect of nano-clay de-agglomeration on mechanical properties of concrete," Constr. Build. Mater., vol. 205, pp. 245–256, 2019, doi: 10.1016/j.conbuildmat.2019.02.018

[19] J. A. Abdalla, "Influence of nano-TiO_2, nano-Fe_2O_3, nanoclay and nano-$CaCO_3$ on the properties of cement/geopolymer concrete," Cleaner Mater., vol. 4, p. 100061, 2022, doi: 10.1016/j.clema.2022.100061.

[20] E. Baigorria, "Novel nanostructured materials based on polymer/organic-clay composite networks for the removal of carbendazim from waters," J. Clean. Prod., vol. 331, p. 129986, 2022, doi: 10.1016/j.jclepro.2021.129867.

[21] ASTM D1141, Standard Practice for the Preparation of Substitute Ocean Water. ASTM Int., 1999.

[22] G. Vijayakumar et al., "Studies on waste glass powder as partial replacement of cement in concrete production," Int. J. Emerg. Technol. Adv. Eng., vol. 3, no. 2, pp. 153–157, 2013.

[23] H. S. Patel et al., "Study on durability of high performance concrete with Alccofine and fly ash," Int. J. Adv. Eng. Res. Technol., vol. 2, no. 3, pp. 154–157, 2013.

[24] A. M. Matos and J. Sousa-Coutinho, "Durability of mortar using waste glass powder as cement replacement," Constr. Build. Mater., vol. 36, pp. 205–215, 2012, doi: 10.1016/j.conbuildmat.2012.04.02

Journal of Engineering and Technology for Industrial Applications

ISSN ONLINE: 2447-0228

ITEGAM-JETIA

Manaus, v.12 n.60, p.738-745 July/August, 2026.
DOI: https://doi.org/10.5935/jetia.v12i60.4006

RESEARCH ARTICLE OPEN ACCESS

OPTIMIZATION OF BIODIESEL PRODUCTION FROM MANGO SEED KERNEL OIL USING TAGUCHI AND WEIGHTED SUM METHOD

Popat Gunjal[*1], Vijaykumar Pandey[2]

[1]Research Scholar, Department of Mechanical Engineering, Vivekanand Global University, Jaipur, Rajasthan, India
[2]Associate Professor, Department of Mechanical Engineering, Vivekanand Global University, Jaipur, Rajasthan, India

[1]https://orcid.org/0000-0002-8508-1078, [2]https://orcid.org/0000-0002-5258-4779

Email: * gunjalpn@gmail.com, vijay_pandey@vgu.ac.in

ARTICLE INFO

Article History
Received on: March 10, 2026
Reviewed on: April 10, 2026
Accepted on: May 01, 2026
Published on: July 31, 2026

Keywords:
Mango seed kernel oil,
Biodiesel,
Transesterification,
Taguchi method,
Weighted Sum Method,
ANOVA analysis.

ABSTRACT

The increasing need for second generation feedstocks for biodiesel production due to the drawbacks associated with edible oil-based biodiesel has led to the use of non-edible feed stocks like mango seed kernel oil (MSKO). The objectives of this research are to improve the biodiesel production from MSKO through transesterification process and to maximize the biodiesel yield as well as the calorific value of the biodiesel. Four factors, namely methanol-to-oil ratio (4:1, 6:1, 8:1 and 10:1), reaction temperature (45°C, 50°C, 55°C and 60°C), reaction time (30 min, 60 min, 90 min and 120 min) and catalyst concentration (0.5%, 1.0%, 1.5% and 2.0%) were chosen and studied at four levels using Taguchi's L16 orthogonal array. A multi-objective optimization approach was used in this study by applying the WSM on the response variables that were normalized and weighted (yield 0.6 and calorific value 0.4). The findings indicated that the best conditions for transesterification were methanol to oil ratio of 8:1, temperature of 55°C, time of 120 minutes and catalyst concentration of 1.5% to yield biodiesel of 96.15% and calorific value of 39.67 MJ/kg. Under these optimal conditions, confirmation tests were conducted which gave nearly similar results (96.16 ± 0.07% yield and 39.70 ± 0.08 MJ/kg calorific value) thereby confirming the effectiveness of the optimization process. Analysis of variance (ANOVA) revealed that reaction temperature has an effect on calorific value at $p < 0.05$ while other parameters have a combined effect on yield. This study shows that MSKO is a feasible feedstock for biodiesel production that is not suitable for human consumption and provides a statistically significant model for improving the quality of the fuel and the efficiency of the conversion process.

Copyright ©2026 by authors and Galileo Institute of Technology and Education of the Amazon (ITEGAM). This work is licensed under the Creative Commons Attribution International License (CC BY 4.0).

I. INTRODUCTION

Biodiesel is an environment friendly, renewable and sustainable fuel that has been developed to meet the rising energy demands and environmental pollution. While diesel is a non renewable resource derived from petroleum, biodiesel is produced from renewable resources such as vegetable oils, animal fats, and waste cooking oils, and therefore can be a carbon neutral fuel that can help in the reduction of greenhouse gases emissions [1]. The environmental benefits of biodiesel include the ability to reduce carbon monoxide, hydrocarbons, and particulate matter emissions and the fact that biodiesel is more biodegradable than fossil diesel [2–4]. Besides the environmental impacts, biodiesel has the advantages of energy security since it helps to cut on the importation of fossil fuels and diversification of energy. The exhaustion of fossil fuel resources and fluctuations in prices have encouraged researchers and policymakers to search for biofuels as an effective solution [5], [6].Moreover, biodiesel from waste like used cooking oil and municipal sewage sludge has attracted interest due to its potential to address waste management challenges while offering a viable biofuel source [7], [8]. The global consumption of biodiesel is on the rise due to the enhanced environmental standards and international agreements on emissions of carbon.

Today, most countries have opted to blend different percentages of biodiesel with the main stocks which include the B5 (5% biodiesel), B10 (10%) and the B20 (20%) to move towards low-carbon fuels in the transport sector [9]. As feedstocks for biodiesel production are becoming more diverse, catalysts are being improved, and the process is being optimized, biodiesel production is expected to become more efficient and large-scale, which will play an important role in the transition to clean energy [10], [11]. The use of edible oils in biodiesel production has some drawbacks such as competition with food resources, increasing costs, and negative impacts on the environment such as deforestation and loss of bio-diversity [12]. To address these challenges, non-edible oils like Jatropha, Karanja, and MSKO have been considered because of their availability, cheap, and do not compete with food resources [13–15]. Of these, MSKO is more attractive because of its high oil content of 8-15% which makes it possible to use it as feedstock instead of the conventional feedstocks [16], [17]. Moreover, MSKO is easily accessible and can be procured without any extra land requirement and resources hence making it sustainable [18], [19]. Based on these benefits, MSKO can be considered as a viable and untapped feedstock that is in line with the waste-to-energy and biofuel development trends around the world [20].

The conversion of MSKO into biodiesel is a challenge since it contains high FFA that results in soap formation and deactivation of the catalyst [21], [22]. Therefore, the factors such as methanol to oil ratio, catalyst concentration, reaction temperature, and reaction time are important in determining the biodiesel yield and quality [23]. Lower methanol-to-oil ratio lead to partial conversion of feedstock, while higher ratio make the separation process more challenging [24]. Low concentration of the catalyst results in low conversion while high concentration results in the formation of soap [25]. Also, reaction temperature and time must be well controlled to achieve maximum conversion of the triglycerides to biodiesel without undergoing thermal breakdown [26]. Addressing these challenges by improving the process and catalysts would go a long way in increasing the yield of biodiesel, the economics of the process and sustainability. The enhancement of biodiesel production and performance of mango seed biodiesel has been investigated using various techniques to increase the yield, fuel properties, and engine performance. Transesterification has been widely used in biodiesel synthesis and [27] used RSM to optimize the MSKO biodiesel production with a 95% yield that conforms to the international fuel standards. In the same vein, [28] also showed that the biodiesel obtained from MSKO meets the ASTM-D6751 and EN14214 standards in terms of physicochemical characteristics and engine performance as well as conventional diesel. Building on biodiesel sources, [29] used mango seed kernel and tamarind seed biomass waste and achieved biodiesel yield of 75–80% which is in line with ASTM D6751 standard for waste-to-energy solutions.

In addition to the production optimization, several works have been done on the improvement of the properties of mango seed biodiesel for use in diesel engines. [30] blended hybrid nanoparticles (Al_2O_3, TiO_2) and hydrogen gas into Mango Seed Methyl Ester emulsified biodiesel using RSM and Deep Recurrent Neural Network-based Honey Badger Algorithm to reach 32% Brake Thermal Efficiency and enhanced combustion properties with RMSE $\leq$ 6.6. Moreover, [30] enhanced MSME20 biodiesel with cerium oxide and magnesium oxide nanoparticles and achieved the reduction of CO, HC, and smoke emissions by 28%, increase in BTE by 16%, and optimization of NOx emission using a hybrid deep belief network-sandpiper optimizer. There have also been attempts to increase the biodiesel yield through other methods of optimization in recent years. [31] used ultrasound supported methanolysis and Whale Algorithm to synthesize biodiesel from waste mango seed kernel oil with 90.88% yield which is higher than transesterification and RSM. This paper aims at evaluating the biodiesel production from mango seed kernel oil through the evaluation of the transesterification parameters using Taguchi based experimental design and WSM optimization. Although there are many studies on biodiesel production, few research works address the effects of methanol-to-oil ratio, reaction temperature, reaction time, and catalyst concentration simultaneously using multiple objectives with biodiesel yield and calorific value. The novelty of this work is based on the combined statistical and decision-making approach that increases the efficiency of the process and guarantees the quality of the fuel. In the present work, Taguchi L16 orthogonal array was used to plan the experiments and ANOVA analysis was performed to find out the significance of each parameter to develop an efficient biodiesel production process.

II. MATERIALS AND METHODOLOGY

This section describes the experimental methodology and analytical methods used in the enhancement of biodiesel production from mango seed kernel oil. It also provides information on feedstock pre-treatment, transesterification process, experimental design, and statistical analysis to assess the biodiesel production efficiency and fuel properties.

II.1 EXTRACTION OF MANGO SEED KERNEL OIL

The mango seeds used in this study were sourced from the Western Maharashtra region of India for the extraction of oil. To remove the surface contamination and other unwanted substances, the seeds were washed with water before the process. The cleaned seeds were then dried in two stages to minimize moisture content and improve the efficiency of extraction of oil. In the first drying stage, the seeds were exposed to direct sunlight for 36 hours to undergo natural drying process. This was succeeded by oven drying at 65ºC for 3 hours in order to ensure that the samples were evenly and thoroughly dried. After that, the seeds were dried and the kernels were separated from the hard-outer shells by using hydraulic pressing mechanism. In order to get the maximum yield of oil, the extracted kernels were dried at 60ºC for 3 hours. After that, the completely dried kernels were taken through mechanical oil extraction mill. This process gave about 130g of oil per kilogram of the mango kernels with an extraction efficiency of 13%. The extracted MSKO was then filtered and placed in a closed container to avoid any oxidation and degradation of the sample before the next process. The process of extraction of oil from the raw mango seeds is illustrated in the Figure 1.

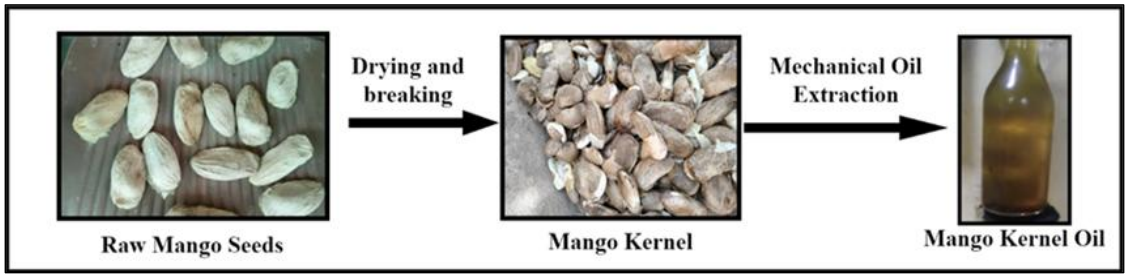


Figure 1. Extraction of Mango Seed Oil Kernel.
Source: Authors, (2026).

II.2 TRANSESTERIFICATION PROCESS

The biodiesel production from MSKO was carried out in a batch reactor by using methanol and potassium hydroxide (KOH) as a catalyst to catalyse the transesterification of the triglycerides into FAME. The reaction was started by dissolving the catalyst in methanol to make a solution which was then charged into the preheated MSKO. In order to understand the effect of reaction conditions on biodiesel yield and the overall process, the reaction conditions were altered successively. Four factors were taken into consideration for the transesterification process: methanol to oil molar ratio, temperature, time and catalyst concentration. Each of these parameters was tested at four different levels to find the best level that would give the highest biodiesel conversion. The parameters and their levels are as follows: The detailed parameters and their levels are presented in Table 1.

Table 1. Transesterification process parameters and levels.

Parameter	Level 1	Level 2	Level 3	Level 4
Methanol-to-Oil Ratio	04:01	06:01	08:01	10:01
Reaction Temperature (°C)	45°C	50°C	55°C	60°C
Reaction Time (Min)	30 min	60 min	90 min	120 min
Catalyst Concentration (% w/w)	0.50%	1.00%	1.50%	2.00%

Source: Authors, (2026).

The reaction mixture was stirred at 600 rpm to facilitate emulsification and increase mass transfer rates so that the reactants could come into close contact. After completion of the reaction, the mixture was transferred to a separation funnel and allowed to settle for 12 hours in order to allow the glycerol, the major by-product to settle at the bottom of the funnel from the biodiesel layer. The upper biodiesel layer was then separated and washed several times with warm distilled water (50°C–60°C) in order to remove catalyst, methanol and soap formation. Last but not the least, the biodiesel was then heated at a temperature of 105°C with a pressure of 600 mmHg for 30 minutes to remove water content. The biodiesel product was then filtered and kept in sealed containers for further physicochemical and performance tests to determine its viability as a renewable energy source.

II.3 EXPERIMENTAL DESIGN

In order to improve the biodiesel production process from MSKO, the Taguchi L16 orthogonal array was used as an experimental design method. This approach allows for the determination of the best combination of factors that would yield the most optimal result since it involves the manipulation of more than one factor at a time while at the same time reducing the number of trials. The four factors that were considered in this study were the methanol to oil ratio, temperature, time and concentration of the catalyst and each of these factors was set at four different levels. By conducting the experiment using the L16 orthogonal array, 16 trials were conducted instead of 256 (4^4) in a full factorial design which saved time, cost and resources yet achieving the best optimization. The Taguchi L16 experimental matrix used in this study is shown in Table 2 which indicates 16 different combinations of the process parameters.

Table 2. Taguchi L16 orthogonal array for biodiesel optimization

Run	Methanol-to-Oil Ratio (Molar Ratio)	Reaction Temperature (°C)	Reaction Time (Minutes)	Catalyst Concentration (% w/w)
1	04:01	45	30	0.5
2	04:01	50	60	1
3	04:01	55	90	1.5
4	04:01	60	120	2
5	06:01	45	60	1.5
6	06:01	50	30	2
7	06:01	55	120	0.5
8	06:01	60	90	1
9	08:01	45	90	2
10	08:01	50	120	1.5
11	08:01	55	30	1
12	08:01	60	60	0.5
13	10:01	45	120	1
14	10:01	50	90	0.5
15	10:01	55	60	2
16	10:01	60	30	1.5

Source: Authors, (2026).

This orthogonal array design makes it possible to efficiently analyze the effects of each factor with least replication of experiments. The outcomes of these trials were used in determining the best reaction parameters that would yield the highest biodiesel yield with the best quality. The gross energy content of each biodiesel sample was determined by employing the Parr 6400 bomb calorimeter as per the ASTM D240 method. About one gram of the sample was burned in a combustion chamber under controlled oxygen environment, and the heat generated was used in determining the higher heating value.

II.4 STATISTICAL ANALYSIS

In order to determine the effect of the transesterification parameters on biodiesel yield and calorific value, the Analysis of Variance (ANOVA) was used as the statistical tool. The factors that were used in this study were methanol-to-oil ratio, reaction temperature, reaction time and catalyst concentration and they were set at four levels with the help of Taguchi L16 orthogonal array. To check the significance of each factor, ANOVA was performed separately for both output variables. The study was conducted at 95% confidence level and the $p < 0.05$ was used to determine statistical significance. The F-value was used to compare the significance of each parameter while the sum of squares determined the extent of contribution of each factor to the total variability. This approach helped in determining the key variables influencing the biodiesel production and facilitated the confirmation of the experimental results on the basis of statistical analysis.

II.5 OPTIMIZATION USING WEIGHTED SUM METHOD

In order to determine the best conditions for biodiesel production from mango seed kernel oil through transesterification process, the WSM was used as a multi-objective optimization technique. This makes it possible to combine two or more output variables such as biodiesel yield (%) and calorific value into a single decision variable by use of weights and normalization. This is especially useful when the optimization is done for both, the process and the fuel quality at the same time. The optimization was done using a Taguchi L16 orthogonal array, in which four factors, namely methanol to oil ratio, reaction temperature, reaction time and catalyst concentration were varied at four levels. The results of each experimental run were obtained in terms of the performance outputs to assess the efficiency of the process. The output variables are in different units and scales and therefore, normalization was necessary to transform all the variables to a single dimensionless scale. The normalization techniques that were used were based on the nature of the criteria as follows:

For beneficial criteria (higher values are better), such as biodiesel yield and calorific value:

$$X_{norm} = \frac{X_i}{X_{max}} \tag{1}$$

For non-beneficial (cost) criteria (lower values are better), the formula would be:

$$X_{norm} = \frac{X_{min}}{X_i} \tag{2}$$

However, in this study, both output variables are beneficial, so only the first normalization equation was used. After normalization, the output variables were then scaled to a suitable value in order to represent the importance of each of the output variables. According to the objectives of the study, biodiesel yield was assigned a weight of 0.6 since it is directly related to production while calorific value was assigned a weight of 0.4 since it is an indication of fuel quality. The weighted sum score for each experimental run was calculated using the following equation:

$$S_i = \sum_{j=1}^{n} w_j \cdot X_{ij}^{norm} \tag{3}$$

Where

S_j = weighted sum score for the ith experimental run
w_j = weight of the jth response variable
X_{ij} = normalized value of the jth response in the ith run
n = number of response variables (2 in this case)

III. RESULT AND DISSCUSION

This section focuses on the findings of the experimental study and optimization of biodiesel production from mango seed kernel. In the present work, the biodiesel yield and calorific value are studied as functions of transesterification parameters with the help of statistical and multi-objective approaches. The validity of the optimal conditions is confirmed by the results of the confirmation tests of key findings.

III.1 EXPERIMENTAL TEST RESULTS

The findings in Table 3 show the effect of transesterification process variables, namely, methanol to oil ratio, reaction temperature, reaction time and catalyst concentration on biodiesel production and calorific value. The highest biodiesel yield of 96.15% was obtained at a methanol-to-oil ratio of 8:1, reaction temperature of 50°C, reaction time of 120 minutes, and catalyst concentration of 1.5% which suggests that the optimal methanol ratio and an optimum catalyst concentration along with an adequate reaction time is suitable for the maximum conversion of triglycerides. The least yield of 72.44% was obtained at a methanol to oil ratio of 4:1, reaction temperature of 45°C, reaction time of 30 minutes and catalyst concentration of 0.5% as the low concentration of methanol and the low concentration of the catalyst hinders the transesterification reaction hence low biodiesel yield.

Table 3: Experimental results showing effect of process parameters on response variables.

Run	Methanol-to-Oil Ratio (Molar Ratio)	Reaction Temperature (°C)	Reaction Time (Minutes)	Catalyst Concentration (% w/w)	Yield (%)	CV (MJ/kg)
1	04:01	45	30	0.5	72.44	38.92
2	04:01	50	60	1	84	39.19
3	04:01	55	90	1.5	91.63	39.59
4	04:01	60	120	2	75.29	39.4
5	06:01	45	60	1.5	91.89	39.22
6	06:01	50	30	2	79.54	39.38
7	06:01	55	120	0.5	84.46	39.56
8	06:01	60	90	1	90.86	39.76
9	08:01	45	90	2	85.1	39.38
10	08:01	50	120	1.5	96.15	39.67
11	08:01	55	30	1	88.81	40.1
12	08:01	60	60	0.5	82.52	39.61
13	10:01	45	120	1	89.07	39.45
14	10:01	50	90	0.5	84.79	39.22
15	10:01	55	60	2	90.73	39.72
16	10:01	60	30	1.5	85.45	39.68

Source: Authors, (2026).

The calorific value which defines the energy content of the fuel was found to be in the range of 38.92 MJ/kg to 40.1 MJ/kg in all the experimental trials. The highest calorific value of 40.1 MJ/kg was achieved at the methanol to oil ratio of 8:1, reaction temperature of 55°C, reaction time of 30 minutes and catalyst concentration of 1% which shows that moderate conditions yield biodiesel with high energy content. But the yield of biodiesel and calorific value were not in a straight line because some of the experimental run with high yield had low calorific values. This implies that biodiesel yield is affected mostly by the efficiency and the extent of the transesterification process while calorific value is more determined by the quality and the chemical makeup of the fatty acid methyl esters produced during the process. The biodiesel yield increased with the increase in the methanol to oil ratio with 4:1 to 8:1 being the optimal range. But, increasing the ratio to 10:1 did not improve the yield because of phase separation and unreacted methanol. The yield and calorific value of the biodiesel was also influenced by the reaction temperature where moderate temperature of 50-55°C was ideal for transesterification.

Low temperatures led to low reaction rates and low conversion levels while high temperatures might lead to thermal degradation and side reactions. Reaction time also had an impact on yield where longer times of 90-120 minutes allowed for all the triglycerides to be esterified while shorter times produced lower yields due to the presence of unreacted triglycerides. Another factor was the catalyst concentration where 1- 1.5% w/w showed to be effective in increasing biodiesel production due to increased reaction rates. Lesser concentration of the catalyst reduced the reaction rate while 2% concentration of the catalyst formed soap which decreases yield and biodiesel purity. In conclusion, the findings reveal that biodiesel yield is highest under conditions of moderate methanol to oil ratio, reaction temperature, reaction time and catalyst concentration. Nevertheless, calorific value is not significantly affected by the process conditions and it can be inferred that the post-reaction purification steps may have a larger impact on the fuel energy content.

III.2 ANOVA ANALYSIS

The ANOVA analysis of biodiesel yield and calorific value, as shown in Table 4 and 5, gives a quantitative assessment of the effects of the transesterification parameters, namely, methanol to oil ratio, reaction temperature, reaction time and catalyst concentration on the output responses. In terms of biodiesel yield, it was observed that none of the parameters had any significant effect at a 0.05 level of significance. The methanol-to-oil ratio with a p value of 0.2015, the reaction temperature with a p value of 0.1067, the reaction time with a p value of 0.9222 and the catalyst concentration with a p value of 0.5338 were all greater than 0.05 and therefore, their effects on the yield can be considered non-significant within the range of the experiments. Nonetheless, the p-value of reaction temperature is lower than that of other factors, which indicates that it has a more significant but not very significant impact on yield, which may be attributed to its positive effect on the kinetic of transesterification and ester formation.

Table 4. ANOVA Results for Biodiesel Yield (%)

Source	Sum of Squares	Degrees of Freedom (DF)	F-value	P-value
Methanol-to-Oil Ratio	186.18	3	1.96	0.2015
Reaction Temperature (°C)	241.06	3	2.54	0.1067
Reaction Time (Minutes)	8.55	3	0.09	0.9222
Catalyst Concentration (% w/w)	53.51	3	0.56	0.5338
Residual	285.24	3		
Total	774.55	15		

Source: Authors, (2026).

On the other hand, the ANOVA of the calorific value showed that reaction temperature has a p-value of 0.0173 and F-value of 7.8644, which means that the calorific value is sensitive to temperature changes. This is technically valid since the reaction temperature impacts the energy level of the methyl ester formed, the purity and the molecular composition of biodiesel. The reaction temperature has an inverse relationship with the amount of residual unreacted triglycerides and a direct relationship with the energy content of biodiesel; where a higher reaction temperature produces biodiesel with higher energy content. On the other hand, methanol-to-oil ratio ($p = 0.6849$), reaction time ($p = 0.4167$), and catalyst concentration ($p = 0.2999$) were not significant for calorific value, which indicates

that the fuel energy content is not as sensitive to these parameters as temperature.As in Table 4 and Table 5, the analysis of variance indicates that reaction temperature is a significant factor to biodiesel quality, especially the calorific value while biodiesel yield is a function of all the parameters as a whole rather than the individual parameter.

III.3 OPTIMIZATION RESULTS

The biodiesel yield and calorific value of the biodiesel produced from the WSM optimization results are presented in the Table 6 to determine the effect of the transesterification parameters and the most suitable experimental run. The maximum WSM value of 0.9957 was obtained in Run 10 which has biodiesel yield of 96.15% and calorific value of 39.67 MJ/kg; therefore, it can be concluded that the selected process conditions provided the maximum biodiesel production with high fuel quality. This indicates that the concentration of methanol to oil should be 8:1, reaction temperature of 50°C, reaction time 120 minutes and 1.5% catalyst concentration as the best conditions for high conversion efficiency and energy content. On the other hand, the ANOVA of the calorific value showed that reaction temperature has a p-value of 0.0173 and F-value of 7.8644, which means that the calorific value is sensitive to temperature changes.

This is technically valid since the reaction temperature impacts the energy level of the methyl ester formed, the purity and the molecular composition of biodiesel. The reaction temperature has an inverse relationship with the amount of residual unreacted triglycerides and a direct relationship with the energy content of biodiesel; where a higher reaction temperature produces biodiesel with higher energy content. On the other hand, methanol-to-oil ratio ($p = 0.6849$), reaction time ($p = 0.4167$), and catalyst concentration ($p = 0.2999$) were not significant for calorific value, which indicates that the fuel energy content is not as sensitive to these parameters as temperature. As in Table 4 and Table 5, the analysis of variance indicates that reaction temperature is a significant factor to biodiesel quality, especially the calorific value while biodiesel yield is a function of all the parameters as a whole rather than the individual parameter.

Table 6: Weighted sum optimization results.

Run	Yield (%)	CV	$Yield_{norm}$	CV_{norm}	WSM score	Rank
1	72.44	38.92	0.753406136	0.9705736	0.84027311	16
2	84	39.19	0.873634945	0.9773067	0.91510366	12
3	91.63	39.59	0.95299012	0.9872818	0.96670679	2
4	75.29	39.4	0.783047322	0.9825436	0.86284585	15
5	91.89	39.22	0.955694228	0.9780549	0.96463848	3
6	79.54	39.38	0.82724909	0.9820449	0.88916741	14
7	84.46	39.56	0.878419137	0.9865337	0.92166495	10
8	90.86	39.76	0.944981799	0.9915212	0.96359756	4
9	85.1	39.38	0.885075403	0.9820449	0.9238632	9
10	96.15	39.67	1	0.9892768	0.99571072	1
11	88.81	40.1	0.923660946	1	0.95419657	6
12	82.52	39.61	0.85824233	0.9877805	0.91005762	13
13	89.07	39.45	0.926365055	0.9837905	0.94933524	7
14	84.79	39.22	0.881851274	0.9780549	0.92033271	11
15	90.73	39.72	0.943629745	0.9905237	0.96238732	5
16	85.45	39.68	0.888715549	0.9895262	0.9290398	8

Source: Authors, (2026).

Runs 3, 5, and 8 also had high WSM scores of 0.9667, 0.9646, and 0.9636 respectively, which means that even if there is a slight change in the concentration of the catalyst and the reaction time within the range of 1.0 – 1.5% for the catalyst and 90 – 120 minutes for the reaction time, the yield of biodiesel is still high and the energy content is not significantly affected. The optimal reaction temperature was found to be around 50–55°C, which was evident from the higher ranked runs, as moderate temperature favors the conversion of triglycerides to methyl esters without causing degradation of the latter. On the other hand, the least WSM score of 0.8402 was obtained in Run 1 which produced the least biodiesel yield of 72.44% and calorific value of 38.92 MJ/kg. This implies that the methanol-to-oil ratio of 4:1, reaction temperature of 45°C, reaction time of 30 minutes and the catalyst concentration of 0.5% were not efficient for transesterification. The lower catalyst concentration and shorter reaction time contributed to poor esterification thus yielding lower biodiesel and energy content due to unreacted triglycerides and presence of impurities. The values of calorific values were within a small range of 38.92–40.1 MJ/kg and the highest CV of 40.1 MJ/kg was recorded in Run 11 where reaction temperature was 55°C and catalyst concentration was 1.0%. This means that high reaction temperatures increase fuel energy density probably as a result of increased esterification and low residual impurities. However, the maximum biodiesel yield does not always mean the maximum CV, which suggests that biodiesel quality depends not only on yield, but the FAME profile and purity as well.

III.4 CONFIRMATION OF OPTIMAL CONDITIONS

The confirmation experiments were also carried out using the optimal conditions of methanol to oil ratio of 8:1, reaction temperature of 55°C, reaction time of 120 minutes and catalyst concentration of 1.5%. The results of the confirmation experiments are presented in Table 7 below. The three trials gave biodiesel production of 96.08%, 96.22%, and 96.18% with calorific values of 39.62, 39.75, and 39.72 MJ/kg respectively. The biodiesel yield was found to be 96.16 ± 0.07% and the calorific value 39.70 ± 0.08 MJ/kg, which reveals that there was high degree of precision and reliability at the identified optimal conditions.

Table 7. Confirmation test results at optimal conditions

Test Run	Methanol-to-Oil Ratio	Reaction Temperature (°C)	Reaction Time (min)	Catalyst Concentration (% w/w)	Biodiesel Yield (%)	Calorific Value (MJ/kg)
Confirmation Run 1	08:01	55	120	1.5	96.08	39.62
Confirmation Run 2	08:01	55	120	1.5	96.22	39.75
Confirmation Run 3	08:01	55	120	1.5	96.18	39.72
Average	–	–	–	–	**96.16**	**39.70**

Source: Authors, (2026).

In comparison to the Experimental Run 10 which was earlier considered optimal according to WSM scoring and gave biodiesel yield of 96.15% and calorific value of 39.67 MJ/kg, the confirmation results are quite similar. This good correlation further supports the effectiveness and efficiency of the optimization framework to guarantee that the chosen process conditions not only yield the highest biodiesel concentration but also biodiesel with high energy density. A small standard deviation across the runs also underlines the robustness of the transesterification process under these optimized conditions, which supports the applicability of these conditions for large-scale biodiesel production from mango seed kernel oil.

IV. CONCLUSION

This study describes the efficient process of biodiesel production from mango seed kernel oil through a multiple parameter transesterification process. The factors such as methanol to oil ratio, reaction temperature, reaction time and catalyst concentration were optimized using Taguchi L16 orthogonal array and biodiesel yield and calorific value were taken as the response characteristics. The WSM was used for the multi-objective optimization, which aimed at achieving the optimal production rate and the quality of the fuel.

- The optimal conditions were found to be a methanol to oil ratio of 8:1, the temperature of 55°C, the time of 120 minutes and the concentration of the catalyst of 1.5% w/w. Under these conditions, the process gave the highest biodiesel conversion efficiency of 96.15% and calorific value of 39.67 MJ/kg.
- To confirm the reliability of the optimized settings, confirmation experiments were carried out thrice and the average biodiesel yield obtained was 96.16 ± 0.07% and average calorific value of the biodiesel produced was 39.70 ± 0.08 MJ/kg which proves the repeatability and robustness of the process.
- The ANOVA test showed that among all the studied parameters, reaction temperature had a significant effect on calorific value of the biodiesel at $p < 0.05$, whereas the effect of reaction temperature on the yield was significant at the practical level but insignificant at the 95% confidence level. It was also observed that the yield is more sensitive to the joint and cumulative effect of all the parameters rather than the individual one.

The findings of this study support the use of mango seed kernel oil as a viable non-food source for biodiesel production. The enhanced transesterification process, as confirmed by statistical and experimental methods, provides high biodiesel conversion rate and stable fuel quality, which can be suitable for further scale-up and practical biofuel production. The further studies may involve the investigation of engine characteristics, emissions, and life cycle assessment of mango seed biodiesel and the application of optimization and machine learning for the improvement of the process and its application.

V. AUTHOR'S CONTRIBUTION

Conceptualization: Popat Gunjal, Vijaykumar Pandey.
Methodology: Popat Gunjal, Vijaykumar Pandey.
Investigation: Popat Gunjal, Vijaykumar Pandey.
Discussion of results: Popat Gunjal, Vijaykumar Pandey.
Writing – Original Draft: Popat Gunjal, Vijaykumar Pandey.
Writing – Review and Editing: Popat Gunjal, Vijaykumar Pandey.
Resources: Popat Gunjal, Vijaykumar Pandey.
Supervision: Popat Gunjal, Vijaykumar Pandey.
Approval of the final text: Popat Gunjal, Vijaykumar Pandey.

VI. REFERENCES

[1] Mohan, A., Krishnan, R., Arshinder, K., Vandore, J., & Ramanathan, U. (2023). Management of postharvest losses and wastages in the Indian tomato supply chain—a temperature-controlled storage perspective. *Sustainability*, *15*(2), 1331. ; https://doi.org/10.3390/su15021331

[2] Qi, T., Ji, J., Zhang, X., Liu, L., Xu, X., Ma, K., & Gao, Y. (2022). Research progress of cold chain transport technology for storage fruits and vegetables. *Journal of energy storage*, *56*, 105958.

[3] Singh, G., Daultani, Y., Rajesh, R., & Sahu, R. (2023). Modeling the growth barriers of fresh produce supply chain in the Indian context. *Benchmarking: An International Journal*, *30*(2), 653-677. https://doi.org/10.1108/BIJ-09-2021-0517

[4] Zhao, Y., Li, L., Gao, S., Wang, S., Li, X., & Xiong, X. (2023). Postharvest storage properties and quality kinetic models of cherry tomatoes treated by high-voltage electrostatic fields. *Lwt*, *176*, 114497. https://doi.org/10.1016/j.lwt.2023.114497

[5] Budiyanto, M. A., Imamudien, O., Alhamid, M. I., & Shinoda, T. (2024). Design and analysis of a 20-feet modular cold storage system. *Thermal Science and Engineering Progress*, *50*, 102587. https://doi.org/10.1016/j.tsep.2024.102587

[6] Makule, E., Dimoso, N., & Tassou, S. A. (2022). Precooling and cold storage methods for fruits and vegetables in Sub-Saharan Africa—A review. *Horticulturae*, *8*(9), 776. https://doi.org/10.3390/horticulturae8090776

[7] Tagele, A., Woldetsadik, K., Gedamu, F., & Rafi, M. M. (2022). Effects of preharvest applications of chemicals and storage conditions on the physico-chemical characteristics and shelf life of tomato (Solanum lycopersicum L.) fruit. *Heliyon*, *8*(6).

[8] Al-Dairi, M., Pathare, P. B., & Al-Yahyai, R. (2021). Chemical and nutritional quality changes of tomato during postharvest transportation and storage. *Journal of the Saudi Society of Agricultural Sciences*, *20*(6), 401-408. https://doi.org/10.1016/j.jssas.2021.05.001

[9] Mohammed, M., Alqahtani, N., & El-Shafie, H. (2021). Development and evaluation of an ultrasonic humidifier to control humidity in a cold storage room for postharvest quality management of dates. *Foods*, *10*(5), 949. https://doi.org/10.3390/foods10050949

[10] Agyeman, E. K. K., Duret, S., Flick, D., Laguerre, O., & Moureh, J. (2023). Computational modelling of airflow and heat transfer during cooling of stacked tomatoes: Optimal crate design. *Energies*, *16*(4), 2048. https://doi.org/10.3390/en16042048

[11] Budiyanto, M. A., Imamudien, O., Lubis, A., Alhamid, M. I., & Shinoda, T. (2023). Air flow distribution and cooling performance on modular cold storage for fishery commodity. *Energy Reports*, *9*, 162-171. https://doi.org/10.1016/j.egyr.2023.05.241

[12] Zeng, C., Tan, P., & Liu, Z. (2020). Effect of exogenous ARA treatment for improving postharvest quality in cherry tomato (Solanum lycopersicum L.) fruits. *Scientia Horticulturae*, *261*, 108959. https://doi.org/10.1016/j.scienta.2019.108959

[13] Chaomuang, N., Flick, D., Denis, A., & Laguerre, O. (2019). Influence of operating conditions on the temperature performance of a closed refrigerated display cabinet. *International Journal of Refrigeration*, *103*, 32-41. https://doi.org/10.1016/j.ijrefrig.2019.03.031

[14] Laguerre, O., Denis, A., Bouledjeraf, N., Duret, S., Bertheau, E. D., Moureh, J., ... & Flick, D. (2022). Heat transfer and aroma modeling of fresh fruit and vegetable in cold chain: Case study on tomatoes. *International Journal of Refrigeration*, *133*, 133-144. https://doi.org/10.1016/j.ijrefrig.2021.10.009

[15] Han, J. W., Ji, Z. T., Zuo, M., & Yang, X. T. (2021). Integral evaluation for intermittent cold storage of apples by using mathematical modeling. *Journal of Food Process Engineering*, *44*(11), e13882. 21.https://doi.org/10.1111/jfpe.13882

[16] Han, J. W., Ren, Q. S., Li, J. C., Zhu, W. Y., & Yang, X. T. (2023). Numerical analysis of coupled heat and mass transfer processes in packaged tomatoes throughout the cold chain. *Case Studies in Thermal Engineering*, *42*, 102687. https://doi.org/10.1016/j.csite.2022.102687

[17] You, H., Sun, J., & Xie, J. (2022). Numerical simulation and experimental verification of a small refrigerated warehouse with PCM plates. *Energy Reports*, *8*, 15040-15047. https://doi.org/10.1016/j.egyr.2022.11.048

[18] Arun, S., Boche, R. J., Nambiar, P., Ekka, P., Panalkar, P., Kumar, V., ... & Landini, S. (2024). Numerical and experimental investigation on performance of thermal energy storage integrated micro-cold storage unit. *Applied Sciences*, *14*(12), 5166. https://doi.org/10.3390/app14125166

[19] Natarajan, B., Kathiresan, A. C., & Subramanium, S. K. (2023). Development and performance evaluation of a hybrid portable solar cold storage system for the preservation of vegetables and fruits in remote areas. *Journal of Energy Storage*, *72*, 108292. https://doi.org/10.1016/j.est.2023.108292

[20] Prakash, R., & Ravindra, M. R. (2023). Cold thermal energy storage for milk chilling: A numerical and experimental study. *Journal of Food Engineering*, *337*, 111223. https://doi.org/10.1016/j.jfoodeng.2022.111223

[21] Siddiqui, J. A., & Ubale, S. (2025). A computational study on comparative analysis of evaporative cooling system and conventional cold storage for onion preservation. *Transactions of the Indian National Academy of Engineering*, *10*(3), 523-541.

[22] Shehata, S. A., Abdeldaym, E. A., Ali, M. R., Mohamed, R. M., Bob, R. I., & Abdelgawad, K. F. (2020). Effect of some citrus essential oils on post-harvest shelf life and physicochemical quality of strawberries during cold storage. *Agronomy*, *10*(10), 1466. https://doi.org/10.3390/agronomy10101466

[23] Sundaramahalingam, M. A., Karthikumar, S., Kumar, R. S., Samuel, K. J., Shajahan, S., Sivasubramanian, V., ... & Moorthy, I. G. (2021). An intensified approach for transesterification of biodiesel from Annona squamosa seed oil using ultrasound-assisted homogeneous catalysis reaction and its process optimization. *Fuel*, *291*, 120195. https://doi.org/10.1016/j.fuel.2021.120195

[24] Zhou, Y., Li, K., & Sun, S. (2021). Simultaneous esterification and transesterification of waste phoenix seed oil with a high free fatty acid content using a free lipase catalyst to prepare biodiesel. *Biomass and Bioenergy*, *144*, 105930. https://doi.org/10.1016/j.biombioe.2020.105930

[25] Laskar, I. B., Gupta, R., Chatterjee, S., Vanlalveni, C., & Rokhum, S. L. (2020). Taming waste: Waste Mangifera indica peel as a sustainable catalyst for biodiesel production at room temperature. *Renewable Energy*, *161*, 207-220. https://doi.org/10.1016/j.renene.2020.07.061

[26] Li, D., Feng, W., Chen, C., Chen, S., Fan, G., Liao, S., ... & Wang, Z. (2021). Transesterification of Litsea cubeba kernel oil to biodiesel over zinc supported on zirconia heterogeneous catalysts. *Renewable Energy*, *177*, 13-22. https://doi.org/10.1016/j.renene.2021.05.129

[27] Ohile, S. O., Aboje, A. A., Uthman, H., Usman, R. A., & Ighodaro, O. O. (2023). Optimization and characterization of biodiesel production from mango seed oil (Magnifera indica) via transesterification reaction.

[28] Okonkwo, P. A. (2021). Production of biodiesel from Mango Seed Kernel Oil (MSKO). *Nigerian Journal of Technology*, *40*(4), 598-607.

[29] Rana, M. M., Al-Mueed, M. M., Islam, M. N., & Ali, M. H. (2025). Production and analysis of biodiesel from mango seed kernels and tamarind seeds using hybrid approach of solvent extraction and transesterification. *Results in Engineering*, *25*, 103983. https://doi.org/10.1016/j.rineng.2025.103983

[30] Reddy, S. R., & Sarangi, S. K. (2023). Optimizing the effect of using novel hydrogen enriched nano particles added emulsified waste mango seed biodiesel in diesel engine. *Fuel*, *342*, 127783. https://doi.org/10.1016/j.fuel.2023.127783

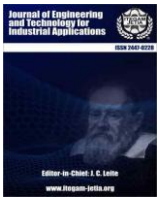
[31] Arumugam, S., Peddamangari Venkatesulu Reddy, C., Arulvalavan, T., & Gopalasamy, S. (2025). Ultrasound supported synthesis of waste mangifera indica linn biodiesel: an optimization using whale algorithm. *Energy Sources, Part A: Recovery, Utilization, and Environmental Effects*, *47*(1), 1695-1709.

Journal of Engineering and Technology for Industrial Applications

ISSN ONLINE: 2447-0228

ITEGAM-JETIA

Manaus, v.12 n.60, p.746-756 July/August, 2026.
DOI: https://doi.org/10.5935/jetia.v12i60.4014



RESEARCH ARTICLE OPEN ACCESS

OPTIMAL TRIANGLE DETECTION PREVENTING DUPLICATES IN LARGE-SCALE GRAPHS

Sarah Balbouzi[1]*, Lougmiri Zekri[2] and Kheira Mechach[3]

[1, 2, 3]Department of computer science, Faculty of exact and applied sciences, Oran 1 University Ahmed Ben Bella, Oran, Algeria

[1]http://orcid.org/0009-0009-0606-9037, [2]http://orcid.org/0000-0002-7563-9787, [3]http://orcid.org/0009-0009-4447-990X

E-mail: *balbouzi.sarah@edu.univ-oran1.dz , zekri.lougmiri@univ-oran1.dz , mechach.kheira@univ-oran1.dz .

ARTICLE INFO

Article History
Received on: March 10, 2026
Reviewed on: April 10, 2026
Accepted on: May 01, 2026
Published on: July 31, 2026

Keywords:
Communities,
Complex systems,
Social Networks,
Optimized sorted lists intersection,
Triangle detection.

ABSTRACT

During the past decades, the world shifted towards online transactions. From data exchange, service provision to business, users and providers rely on the internet and social networks as a common platform for sharing and trading. In order to ensure an effective and reliable management of these networks and the flow of information within them, it is essential to detect user profiles and communities. In that context, triangle detection is a fundamental task in network analysis, as triangles are the smallest structure in a community. However, identifying triangles in large-scale and dense networks is a heavy and highly time-consuming treatment, due to costly neighborhood intersection computations. Our research aims to optimize intersection computation by minimizing the number of comparisons performed, avoid triangle duplication throughout the detection process and thus reducing the overall computation time. The method we propose, Test With Jumps for triangle detection without duplicates (TWJtr-D), is a refined version of Test With Jumps for triangle detection (TWJtr) algorithm. It optimizes intersection computing between neighbors sorted lists while avoiding redundant comparisons and duplicated triangles. Experimental results, on real-world datasets, demonstrate that TWJtr-D significantly reduces computation time and outperforms state-of-the-art methods which process in a similar pattern. This highlights the efficiency of TWJtr-D for triangle detection in large-scale networks. Future work will upgrade this method to parallel processing to rank its efficiency among algorithms in the same field.



Copyright ©2026 by authors and Galileo Institute of Technology and Education of the Amazon (ITEGAM). This work is licensed under the Creative Commons Attribution International License (CC BY 4.0).

I. INTRODUCTION

By nature, human beings are curious about their surroundings and other's behaviors such as social interactions. Ever since scholars started studying and searching for logical explanations to various living beings' actions and resolving daily life issues, expressing these situations through a simplified representation was an intuitive first step on the resolution path. In 1735, Euler put the first stepping stone towards graph theory while resolving Königsberg' seven bridges problem [1]. Taking the city's map as a starting point, Euler simplified it by eliminating all unnecessary figures keeping only the seven bridges and the four areas they connect. This new representation made it easier to find a solution that allows citizens to move across the city using each bridge only once. Later on, in 1930, Moreno conducted a social study on school pupils [2]. The results obtained from the proposed survey were represented using a graph, in which Moreno considered each respondent to the survey as a node, and each person they select as their answers established a connection between the two individuals. Given the complexity of the interactions expressed and the large number of actors involved in these interactions, the study field evolved from simple graphic networks to complex systems. Furthermore, large graphs, like social networks, are seen as complex networks [3] where actors interact individually [4]. In order to understand these complex systems, numerous approaches have been proposed. The continuous progress achieved by researchers resulted in the development of multiple versions of complex systems, each with specific properties. In 1959, the first random graph saw light [5].

Expressing synthetic data, this graph included n nodes connected randomly through $\frac{n(n-1)}{2}$ links. The probability of an arc connecting two nodes is p, following a Poisson distribution, and $(1 - p)$ defines its absence probability. Milgram introduced in 1967 the small world model [6]. Inspired by "the six steps apart" notion [7], which speculates that each couple of nodes are connected, at most, through a sequence of five intermediary nodes forming six linked steps. For further analyzes of complex systems, specifically small world models' properties, the Watts-Strogatz was a key model. Starting from an initially regular system, where all nodes are connected to their k closest neighbors on a circular or grid topology, evolving into a random system where each initial link is replaced by a new edge with p probability [8]. Other systems were also constructed, from the preferential attachment models where Simon introduced the "rich get richer" concept [9] applied on linguistic networks based on words frequency. This model was, later on, extended by adding the cumulative benefit notion and applied over scientific citations' networks [10]. Although these systems were revolutionary, they still had limits expressing real world characteristics. The Barabasi-Albert model (BA), came as a solution [3] based on a scale-free network using the power-law for degree distribution keeping the preferential attachment concept. To enhance the BA and Dorogovtsev-Mendes-Samkhin (DMS) [11] models, the Bianconi-Barabasi model added a new parameter to each node called fitness or aptitude allowing competitivity among entities through their own efforts [12].

In 2014, the multiplex systems expressed another side of real-world interactions [13]. These representations express different kinds of interactions in the same graph through multiple layers. They give to each node the possibility to belong to more than one layer. The temporal aspect was also considered to evaluate interactions' lifespan [14], and shared interactions among groups of entities were expressed through hyperlinks in hypergraphs [15]. With the widespread adoption of the internet, which has significantly interconnected the world, it nowadays serves as the backbone for nearly all modern activities. The continuous transmission of messages, emails and the submission of millions of queries every second have resulted in a tremendous increase in the volume of data flowing through networks. Efficiently processing this vast amount of information, identifying user profiles, and delivering query results pose significant computational challenges. To mitigate these issues, the development of highly efficient indexing systems became essential. These systems establish links between user profiles and documents, while also accounting for their interactions across the network. The indexes, derived from document intersections, enable precise tracking of term locations and facilitate community detection by identifying triangles and, by extension, clusters, of individuals with common interests or behaviors. In this context, graph theory has emerged as an indispensable tool for analyzing such complex networks. The detection of structural patterns, such as triangles and cycles [16], is critical for uncovering key network properties.

Triangles, for instance, offer valuable insights into clustering coefficients and community structures, with applications spanning from social network analysis to network reliability. Several methods have been proposed for triangles' efficient detection and enumeration in large-scale graphs. Among the most notable contributions we cite Schank and Wagner, who provided both an experimental study [17] and a technical report [18] detailing comprehensive approach for identifying and counting triangles in large graphs. Latapy extended this work by proposing specialized methods for handling triangle computation in massive, sparse graphs characterized by power-law degree distributions [4-5]. Cycle detection, particularly cycles of specific lengths, represents another fundamental problem in graph theory. Seminal contributions from Itai and Rodeh on the identification of minimum circuits in graphs [19], alongside the work of Alon, Yuster, and Zwick (AYZ) on detecting and counting cycles of specific lengths [20], [21], have led the groundwork for the development of efficient cycle-detection algorithms. These techniques have wide-ranging applications, including circuit design and network security. Beyond structural detection, optimizing graph algorithms is imperative for managing the substantial computational and memory challenges posed by large networks. Recent advances in intersection algorithms for sorted lists [22], [23] are particularly relevant for constructing indexes between user and document profiles. These optimized intersection methods accelerate the identification of shared connections and patterns.

Thereby, improving the efficiency of community detection and enhancing our understanding of the structural dynamics within large networks. This paper extends our previous work [24], where we tackled the problem of triangle detection by adjusting the Test With Jumps (TWJ) algorithm proposed in [22], [23]. We refine in this paper Test With Jumps for Triangle detection (TWJtr) [24], by addressing the duplication issue known to be a major flaw; this new method is called Test With Jumps for Triangle detection without Duplicates (TWJtr-D). We have shown that TWJtr accelerates the computation of intersections between sorted neighbors' lists of the graph's nodes, thereby enabling efficient triangle detection and counting. The results obtained will then be compared to those of other selected state-of-the-art methods. The rest of the paper is structured as follows. We first go through the most relevant methods previously developed dealing with triangle detection issue in section 2. Considering the lists intersection and sequential processing methodology as core concept, we present, in section 3, two main and largely used methods. Our approach will be detailed in section 4, where we present TWJ the basic method and TWJtr its extended version. The fact that duplicated triangles occur during the detection process, we adapt the later algorithm, TWJtr, and describe TWJtr-D, a refined version which avoids duplications while exploiting the TWJtr's strengths. The results derived from experiments applied to a collection of datasets are presented and discussed in section 5. Finally, we conclude in section 6 highlighting the most effective method for addressing our problem, and define future perspectives and objectives.

II. RELATED WORKS

The fast growth of the internet with the invasion of social networks and the enormous amount of data circulating online, detecting communities and user profiles became an important task to manage. As a matter of fact, knowing which profiles are more receptive or likely to be interested in a certain information, or which ones are in possession of a requested information so it can be extracted, minimizes the time and data loss; a gain that cannot be ignored in many fields. To achieve this goal, many works have been developed over the years. In 1977, Freeman [25], [26] introduced the formula for betweenness centrality, a measure indicating the importance of a vertex "i" of the network in forwarding information. It is calculated by counting the number of shortest paths connecting each pair of vertices that pass through "i", the higher this value, the more relevant the node is. Later, in 2002, the Girvan & Newman method (GN) [27] extended the concept of betweenness centrality to edges, introducing edge betweenness.

Similar to node betweenness, it measures an edge's importance in the network's information flow by calculating the number of shortest paths connecting each pair of vertices that pass through the edge "e". The authors used this measure as criterion for a reverse hierarchical partitioning. Another work was published in 1998 [28] introducing a multilevel partitioning method based on the k-way. The authors aimed to improve speed and partitioning quality. Their method includes three steps that transformed the original graph into a smaller one coarsening it, dividing it to finally refining it back to its original form saving the obtained communities. In 2006, Newman [29], [24] introduced a new formula which became one of the most used ones in this field [30], [31]. Based on the community definition, the modularity was a measure used to evaluate the quality of a community acquired from a specific partitioning. Alongside community detection, another aspect of graph theory emerged as a research spotlight. Being the smallest structure of a community, triangles detection became an extremely active research field attracting the attention of a large number of researchers. Depending on the definition of a triangle, several methods have been developed. The most intuitive method was the brute-force procedure [4] where, for every possible triplet of the graph, a triangle was returned if the three arcs connecting each pair of nodes exist. Nevertheless, this method was the less efficient being extremely slow and considering nodes that are not even each other's neighbors.

In [4] an algorithm was developed based on arboricity, which is a sparsity measure computed by the minimum number of forests needed to cover all edges. The idea was to sort the graph's nodes decreasingly according to their degrees, and check if each pair of a node's neighbors is linked to count a triangle. An additional step was included to avoid duplications where a neighbor must be among the remaining nodes to unsure it wasn't treated beforehand. [4-17] cite the matrix product $A^3(G)$ of the graph's adjacency matrix A(G), the diagonal of the resulting matrix would count twice the number of triangles to which each vertex contributes. However, this method has some limitations, given the dynamic characteristics and width of the graphs, the creation of the adjacency matrix A(G), which is a hollow structure that needs to be constantly updated, takes quite a lot of computation time, as well as the computation of the product $A^3(G)$, which has $O(n^3)$ complexity that cannot be disregarded. The node-iterator (or vertex listing) [4-19] is a procedure that detects a triangle for each node v having two nodes $(u, w) \in \mathrm{Adj}(v)$ connected by an arc. Being quite convenient, the node-iterator has a flaw. We have noticed that the same triangle is detected several times which leads to a duplication problem, a major issue in terms of computing time and memory when applied on large-scale graphs. Similarly for the edge-iterator (or edge listing) method [4-19], the replication of detected triangles is also present where, for each common neighboring node of the vertices of an arc (u, v), a triangle is identified.

In [4-21] the AYZ algorithm counts the number of triangles in a graph by dividing it into two sub-graphs according to $k = \sqrt{m}$, where m is the number of edges, then applying the node-iterator without duplications on the sub-graph having a degree $d(v) \leq k$, and the edge-iterator on the remaining sub-graph [4]. [17] introduces the Forward algorithm where, for each node v, an initially empty structure A(v) is associated to it. A triangle is detected for each element of $A(v) \cap A(t)$ where $v < t \wedge t \in Adj(v)$. In [21] the authors use a method based on marking the nodes neighboring a vertex v to detect the triangles formed by the latter, which they ,later, unmark in order to eliminate duplications. Ding et al [32] present a differential privacy approach for triangle counting in large graphs, introducing a novel algorithm that balances privacy and accuracy. Their method effectively counts triangles while maintaining differential privacy, showing competitive performance on large datasets. However, the approach has limitations, including potential high computational overhead and limited exploration of parameter impact on privacy-accuracy trade-offs. Notably, methods ensuring differential privacy may introduce noise or perturbations to guarantee confidentiality, which can reduce the precision of the results.

In [33], a strongly subcubic combinatorial algorithm for triangle detection is introduced, significantly enhancing time complexity compared to existing methods, achieving a runtime of $O\left(n^{\frac{7}{3}}\right)$. The algorithm offers robust theoretical performance guarantees and is particularly effective for large graphs. However, its practical applicability may be constrained by increased memory usage due to edge partitioning, especially in highly dense graph regions where vertices can appear in multiple subsets. This results in higher memory overhead and potentially longer processing times for dense areas. In their survey [34], authors review distributed graph algorithms for massive graphs, with a focus on triangle detection methods. They highlight that traditional triangle detection approaches, including intersection-based methods, encounter scalability and memory issues in large graphs. Distributed algorithms, however, significantly improve performance by utilizing parallelism and distributed computing resources, effectively addressing these limitations. The authors conclude that distributed techniques are well-suited for handling massive and dense graph data, providing enhanced efficiency and scalability compared to conventional methods.

III. BASELINE METHODS

Amid the long list of the developed algorithms for triangles detection, we will, in our work, focus on two main methods to which we will be comparing our own approach. In the following section, we will detail these two algorithms discussing their limits and complexity.

III.1 NODE-ITERATOR (VERTEX LISTING)

As mentioned in the previous section, the node-iterator is a method that aims to count, for each node of the graph, the number of nodes that are neighbors to it and that are in turn neighbors (Algorithm1). Although this method appears to be very effective, it has a few shortcomings. Indeed, the major problem can be summed up in two points:

- Duplication.
- Computing complexity.

Algorithm 1: Node-iterator (vertex listing).

Input: list and adjacency matrix representing the network G (V, E)

Output: the triangles detected in G
1: Count= 0
2: Browse G
3: for each v ∈ V do
4: for each couple (u, w) ∈ Adj(v) do
5: if (u̇w)∃ then (v u w) is a triangle
6: Count++
7: end if
8: end for
9: end for
10: return Count

Source: Authors, (2026).

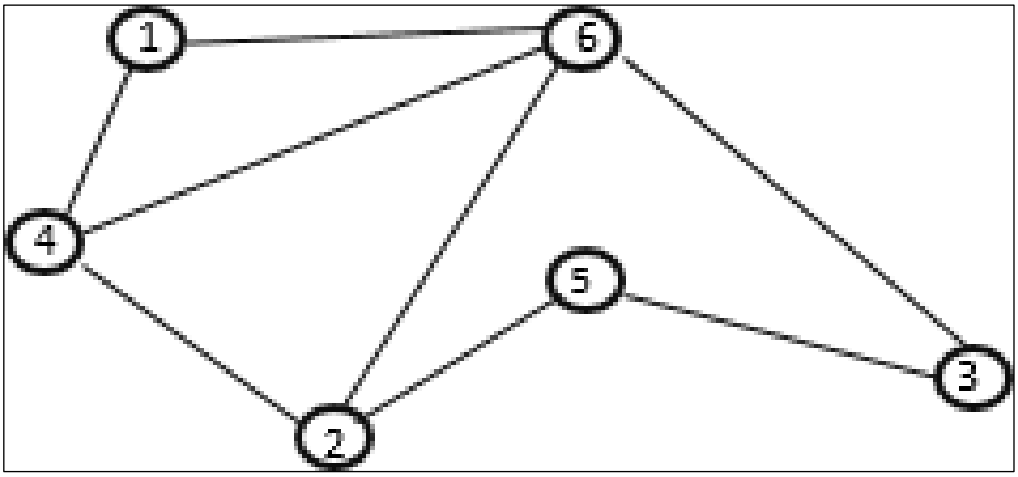


Figure 1: Example of a non-oriented graph.
Source: Authors, (2026).

We will illustrate the node-iterator on the graph sample in figure 1, where nodes 2,4 and 6 forme, visually, a triangle. By iterating through each vertex's adjacency list and verifying connections between every node couple using the adjacency matrix, the same triangle (2, 4, 6) is detected multiple times, once from each vertex involved. This leads to duplication, as the same triangle is reported three times. In large graphs, such redundancy significantly increases computational cost. The node-iterator approach has a time complexity of $O(|V|^3)$and a space complexity of $O(|V|^2)$. While effective for dense graphs due to adjacency matrix usage, it is inefficient for sparse graphs compared to algorithms with complexity linear in the number of edges $|E|$. Recalling that V is the set of nodes and E is the set of edges.

III.2 EDGE-ITERATOR (EDGE-LISTING OR NAÏVE ALGORITHM)

This algorithm represents the basic idea that defines a triangle. Effectively, it consists in searching, for an arc of the graph, a common neighboring node. In other words, the edge-iterator processes an intersection calculation between the adjacency lists of two nodes forming an arc on the graph and returns a triangle for each common element detected (Algorithm 2).

Algorithm 2: Edge-iterator (Edge listing/ Naïve method).

Input: adjacency list and matrix of the graph G (V, E)

Output: detected triangles in G
1: Count = 0
2: Browse G
3: for each (u, v) ∈ E do
4: if Adj(u) ∩ Adj(v) ≠ ∅ then
5: for each w ∈ Adj(u) ∩ Adj(v) do
6: Triangle (u v w)
7: Count++
8: end for
9: end if
10: end for
11: return count

Source: Authors, (2026).

Using the same example, Figure 1, the edge-iterator algorithm examines each edge and computes the intersection of the adjacency lists of its endpoints to identify triangles. For instance, starting with edge (2, 6), the intersection $\mathrm{Adj}(2) \cap \mathrm{Adj}(6)$ yields vertex 4, forming the triangle (2, 4, 6). the same triangle is repeatedly found when processing related or reversed edges, thus increasing complexity. The edge-iterator runs in $O(|E| \cdot \Delta)$time and $O(|V| + |E|)$space, performing well on sparse graphs but poorly on dense graphs with high maximum vertex degree Δ.

IV. PROPOSED APPROACH

Having noticed that the detection of triangles in graphs can be considered as a problem of intersection calculation between lists of neighbors of a given node of the graph, we adapt the TWJ [22], [23] which is basically dedicated to the fast calculation of the intersection between sorted lists so that it can handle this calculation. Our choice for using adjacency lists was made after concluding that it was better in contrast with adjacency matrix which is an immense hollow structure for real graphs consuming enormous memory space and time computing for their update considering the graphs' dynamic nature.

IV.1 TWJ AND DATA STRUCTURE

Before discussing the TWJ's functioning for the detection of triangles, we must first go through the data structure it handles, which is quite particular as it appears in figure 2. Indeed, the TWJ is based on the processing of lists transformed into sequences, where each sequence is composed of three elements as follows:

- SeqID: identifier of the sequence obtained by calculating the modulo of the ith element of the list by a sequencing value chosen beforehand (if the elements of the list are integers).
- Nseq: represents the number of elements that belong to the sequence seqID or the length of the sequence. For a list of integer type, the Nseq is the number of elements belonging to the interval between $seqID * sequencing\ value$, and, $(seqID + 1) * sequencing\ value$.
- Elements of the sequence: is none other than the N elements counted in the NSeq which are ordered and listed until the appearance of a (possible) next sequence.

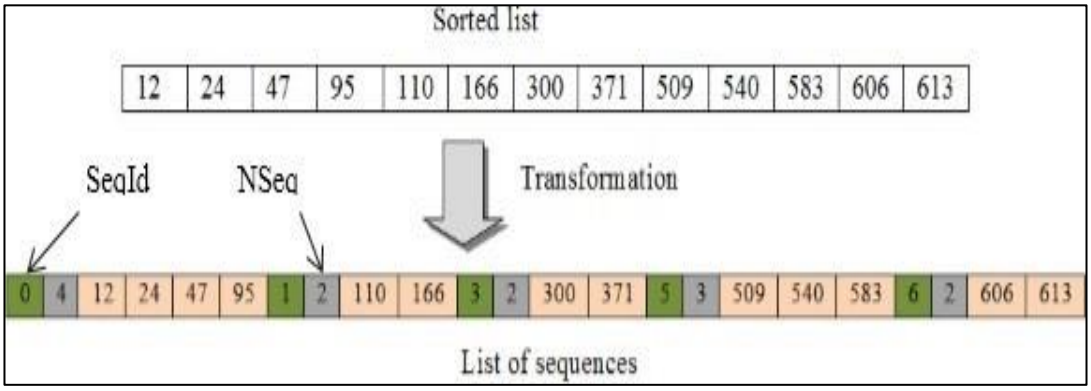


Figure 2: Sequence list creation for a sequencing value= 100.
Source: Authors, (2026).

Once the sequence lists created, the TWJ is applicable

IV.2 TWJ ALGORITHM

In [22-23] the TWJ is described as a method which takes as input two sorted lists transformed into sequences according to a precise and identical sequencing value, the TWJ compares, starting from the first box, sequentially the elements of the two lists, having equal seqIDs, and returns each common value detected until having reached the size of this sequence, applying the naive algorithm (Algorithm 4) for the calculation of the intersection, and passes to the next one for the two lists. On the other hand, if the current seqIDs of the two lists are different, one passes to the next sequence of the list whose seqID is lower and compares it again with that of the other list that has not changed and so on until two equal seqIDs are obtained, or, that one of the two lists has reached its size (exhausted all its seqIDs).

Algorithm 3: Test With Jumps (TWJ).

Input: Integer intersection (Integer[] SeqA, Integer[] SeqB, Integer sizeA, Integer sizeB, short* C)

```
1: Integer i = 0, j = 0
2: while i < sizeA ∧ j < sizeB do
3:    if the two compared seqID are equal then
4:          Apply the naïve intersection algorithm between the two   sequences (Algorithm 4)
5:    else
6:      Move on to the next sequence in the table with the smallest seqID
7:    end if
8: end while
```

Source: Authors, (2026).

Algorithm 4: Naive intersection computation

```
Input: integer intersection(integer[] A, integer[] B, integer sizeA, integer sizeB, short[] C)

Output: common elements
1: integer count = 0, i = 0, j = 0;
2: while i < sizeA and j < sizeB do
3:    if A[i] == B[j] then
4:       C[count + +] = A[i];
5:       i + +; j + +;
6:    else if A[i] > B[j] then
7:       j + +;
8:    else
9:       i + +;
10:   end if
11: end while
12: return count;
```

Source: Authors, (2026).

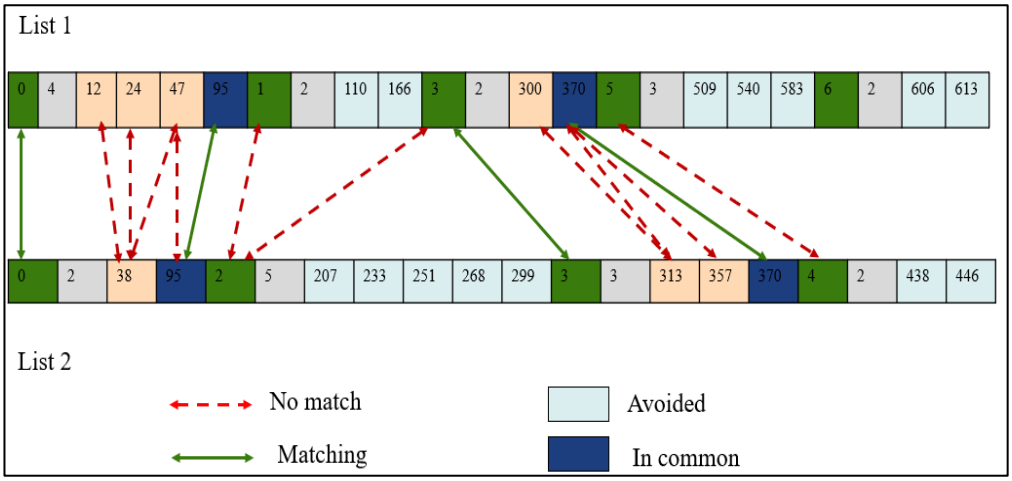


Figure 3: TWJ algorithm process.
Source: Authors, (2026).

Figure 3 shows an example of TWJ processing over two sequence lists. It is clearly noticeable that the TWJ's logic permits avoiding unnecessary comparisons highly gaining in terms of computation time. Thus, applying TWJ over large scale datasets improves significantly time complexity.

IV.3 TWJ AND TRIANGLE DETECTION

Returning to our primary case study, which is triangle detection, the approach we propose involves extending the TWJ method. For each node $u \in Adj(v)$ where$u, v \in G$, we apply it to the adjacency lists of nodes *v* and *u*, which have been previously transformed into sequences. Consequently, each newly identified element x signifies the presence of an existing triangle (uvx) within the graph (see Algorithm 5).

Algorithm 5: TWJ triangle detection (TWJtr)

```
Input: adjacency list of the network G
Output: detected triangles
1: Count = 0;
2: for each v ∈ G do
3:        for every u ∈ Adj(v) do
4:        Compute the intersection Adj(v) ∩ dj(u) by applying the TWJ algorithm
5:        for each element returned do
6:        Count++;
7:        end for
8:        end for
9: end for
10: return Count; {The list of triangles if desired}
```

Source: Authors, (2026).

In terms of complexity, the TWJtr has a worst-case time complexity of $(|V|^3)$ for dense graphs and O $(|E| \cdot \Delta)$ for sparse graphs, and $(|V| + |E|)$ space complexity.

IV.4 RESOLVING THE DUPLICATION ISSUE IN TRIANGLE DETECTION

After analyzing the field's existing methods and experiencing them multiple times, we were able to see firsthand the number of duplicated triangles that were detected and its heavy impact on the algorithms' performances. Therefore, resolving the duplication issue became an essential objective our study aimed for. To achieve this goal, we considered both the dataset's structure and the TWJtr process. Giving the graph's non-oriented nature, we modified the basic TWJtr by including an additional treatment which allows marking nodes that have been processed. In other words, every time a node v is treated and all triangles involving it are detected, v would be marked as an explored node. Thereafter, only the unmarked neighbors of the remaining nodes would be considered for intersection computing thus detecting triangles formed by these couples whereas triangles formed by couples with marked nodes were already detected when the marked node was processed. Thus, returning duplicated triangles is avoided and time complexity drops significantly. The pseudocode of algorithm 6 presents the algorithm TWJtr-D for eliminating duplications.

Algorithm 6: TWJtr without duplicates (TWJtr-D).

Input: adjacency list of the network G
Output: detected triangles
1: Count = 0;
2: for each $v \in G$ do
3: for every $u \in Adj(v)$ do
4: Compute the intersection $Adj(v) \cap Adj(u)$ by applying the TWJ algorithm if neither u nor v were explored (unmarked)
5: for each element returned do
6: Count++;
7: end for
8: end for
9: mark(v)
10: end for
11: return Count; {The list of triangles if desired}

Source: Authors, (2026).

V. EXPERIMENTS AND RESULTS

The experimentations were conducted on an Intel(R) Core ™ i7-8700K CPU @3.70 Ghz, 64 GB of RAM and two Hard discs: 500GB VME and 6TB HDD. We used Java Netbeans as programming environment.

V.1 TEST DATA

We performed our tests over the below twelve real graphs downloaded in (.txt) format that we load in memory.

Table 1: Experimented datasets.

Graph name	|V | = number of vertices	|E| = number of edges
New sites	1040	313869
Hr	1099	498202
Hu	1054	222887
Ro	1035	125826
Tv shows	588	26527
Company	1033	131723
Politicians	660	53621
CAH	9876	51969
Public figures	1012	133535
Ego Fb	3662	172776
Artists	1046	570398
Athletes	1088	186013
Government	793	88005

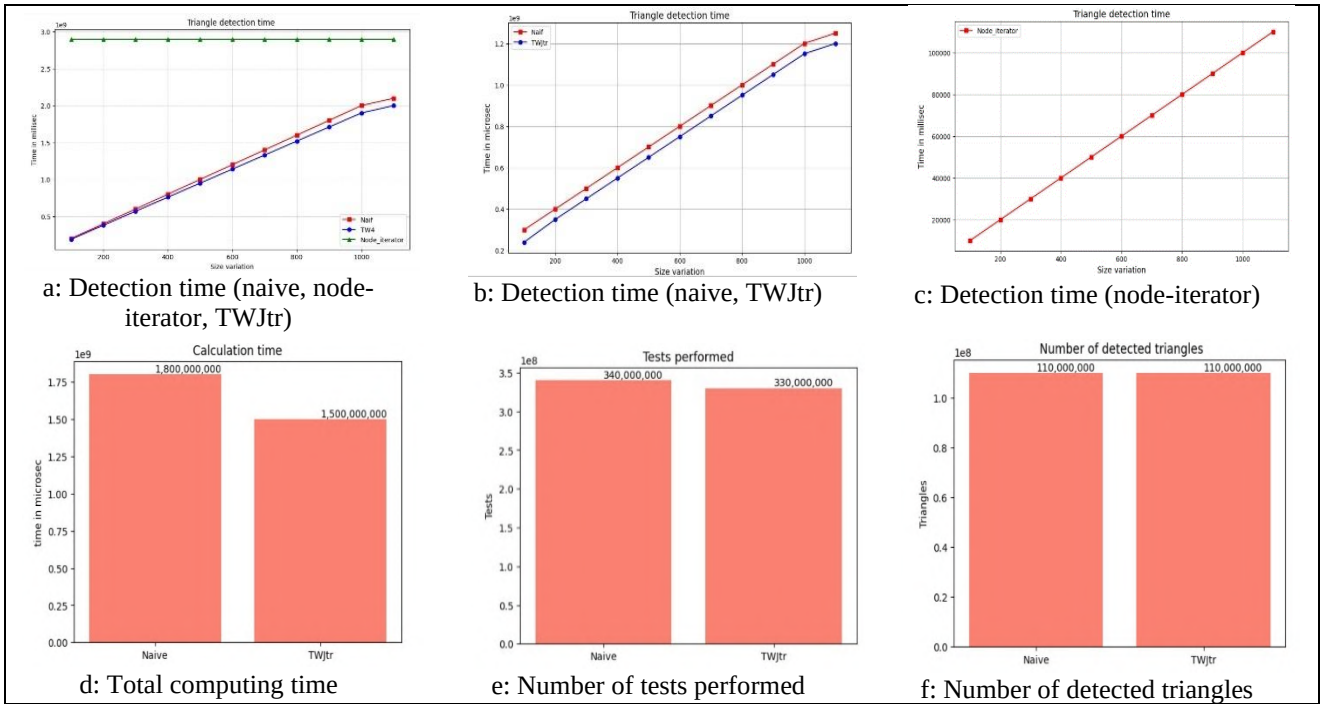
Source: Authors, (2026).

V.2 COMPARATIVE STUDY

We compare our approach, the TWJtr, to the node-iterator and edge-iterator algorithms. This comparison is based on:

- The number of tests performed by each method when detecting triangles excluding the search for elements in the adjacency list.
- The number of triangles detected (including repetitions).
- Calculation time.

The experimentations conducted, over the twelve datasets mentioned above, have all expressed the same behavior in response to the algorithms we applied. In order to present graphically these results for each comparison criterion, the number of graphics would be inconvenient to expose in this section of our article. Therefore, among the acquired results, we selected those of the Hr, Hu and Ro datasets to be demonstrated. These datasets, the Hr, Hu and Ro, were collected from the music streaming service Deezer.



a: Detection time (naive, node-iterator, TWJtr)

b: Detection time (naive, TWJtr)

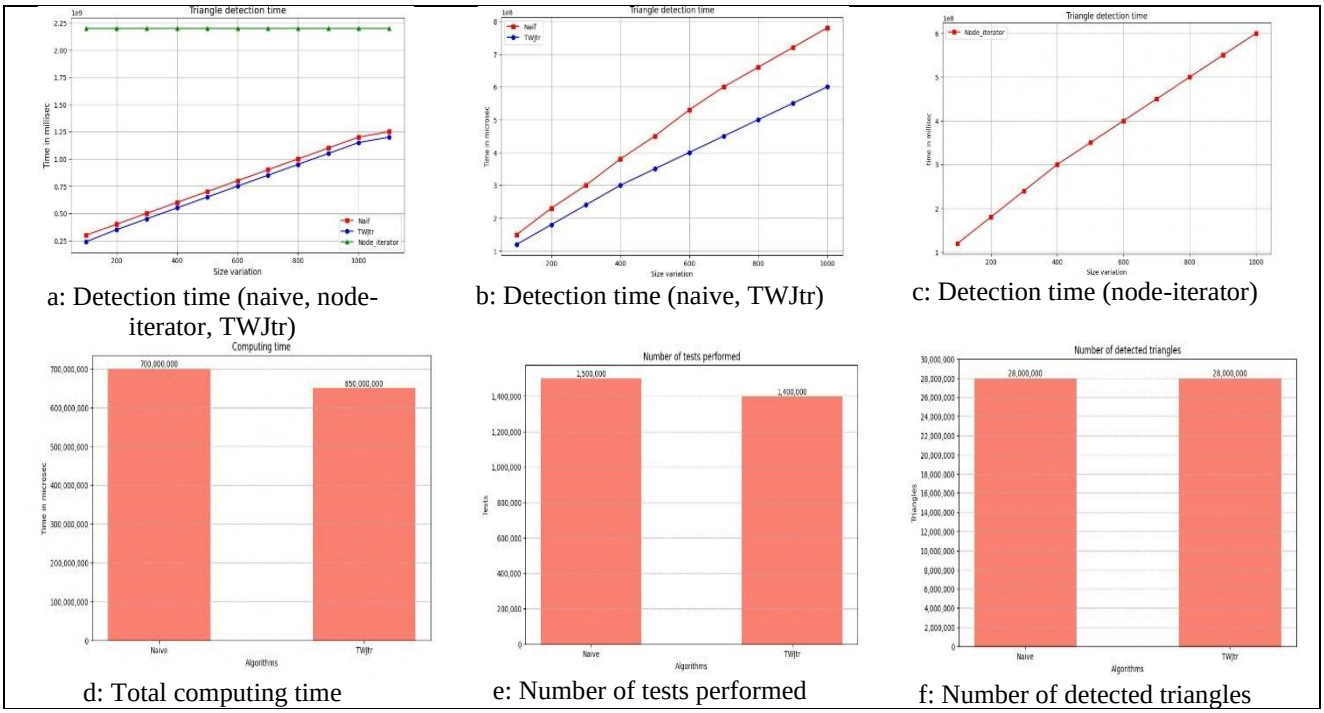
c: Detection time (node-iterator)

d: Total computing time

e: Number of tests performed

f: Number of detected triangles

Figure 4: RO dataset's statistics.
Source: Authors, (2026).



a: Detection time (naive, node-iterator, TWJtr)

b: Detection time (naive, TWJtr)

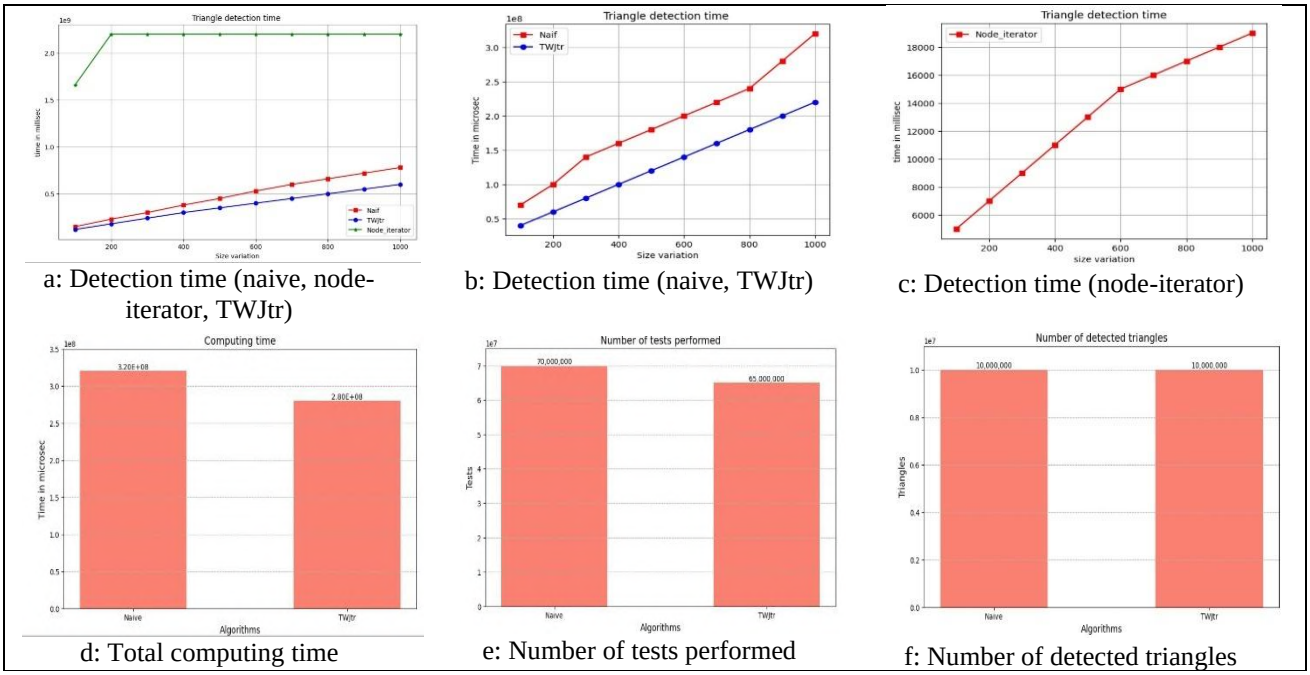
c: Detection time (node-iterator)

d: Total computing time

e: Number of tests performed

f: Number of detected triangles

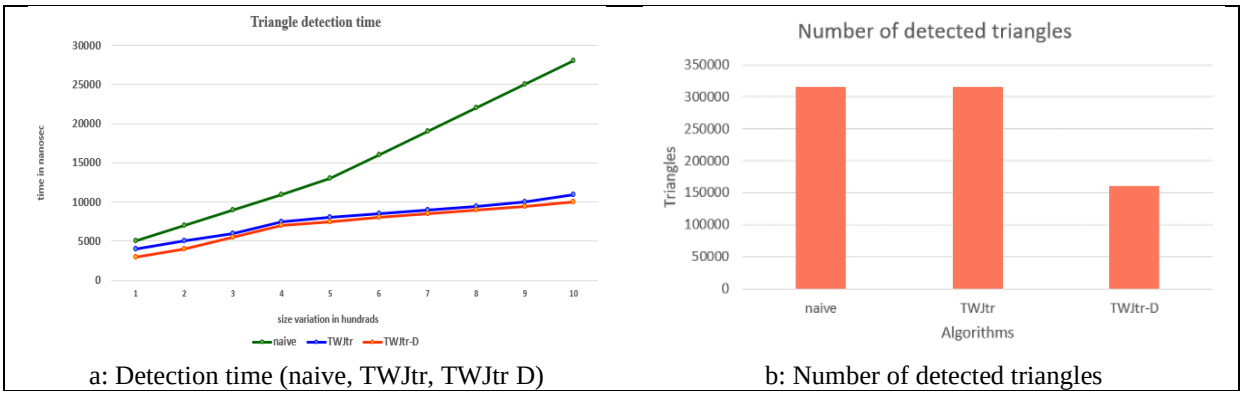
Figure 5: HU dataset's statistics
Source: Authors, (2024).



a: Detection time (naive, node-iterator, TWJtr)
b: Detection time (naive, TWJtr)
c: Detection time (node-iterator)
d: Total computing time
e: Number of tests performed
f: Number of detected triangles

Figure 6: HR dataset's statistics
Source: Authors, (2026).

After conducting experiments on the aforementioned datasets, performance statistics were collected according to the previously defined comparison criteria. The obtained results are illustrated in Figure. 4, 5, and 6. Figure. (4. a), (5. a), and (6. a) depict the execution time evolution of the three evaluated algorithms. The results show that the Node-Iterator algorithm exhibits the highest execution time across all datasets. The Naive algorithm (Edge-iterator) achieves lower execution times, while the TWJtr algorithm consistently outperforms both baseline approaches. For a more detailed analysis, the execution time curves shown in Figure. (4.a), (5.a), and (6.a) are decomposed into Figure. (4.b), (5.b), (6.b) and Figure. (4.c), (5.c), (6.c). Figure. (4.c), (5.c), and (6.c) report the execution time of the Node-Iterator algorithm in milliseconds, indicating that its runtime remains significantly higher than that of the other two methods. In contrast, figure. (4.b), (5.b), and (6.b) compare the Naive and TWJtr algorithms in nanoseconds, where TWJtr achieves lower execution times across all datasets. Figure. (4.d), (5.d), and (6.d) present the total execution time required to complete triangle detection. These results show that TWJtr requires less total computing time than the Naive algorithm across all datasets. Additional efficiency-related statistics are presented in Figure. (e) and (f). Figure. (e) reports the number of intersection tests performed by the Naive and TWJtr algorithms, while Figure. (f) shows the number of triangles detected. The results indicate that both algorithms return the same number of detections, despite performing a different number of intersection tests.



a: Detection time (naive, TWJtr, TWJtr D)
b: Number of detected triangles

Figure 7. TWJtr-D (TWJtr without duplication) statistics over a graph of 1000 nodes
Source: Authors, (2024).

Figure. 7 presents the results obtained after applying the TWJtr-D algorithm and comparing it with the Naive and TWJtr methods. The execution time comparison illustrated in Figure. (7.a) shows that TWJtr-D achieves the lowest computing time among the three evaluated algorithms. Figure. (7.b) reports the number of triangle detections for each method. The results show that TWJtr-D returns a lower number of detections corresponding to unique triangles, whereas the Naive and TWJtr algorithms produce identical counts due to duplicate detections.

V.3. DISCUSSION

The poor performance of the Node-Iterator algorithm observed in Figure. 4, 5, and 6 can be attributed to its repeated verification process, which checks the existence of edges between all pairs of neighboring nodes. This procedure relies on frequent scans of adjacency lists, resulting in substantial computational overhead.

The Naive algorithm improves execution time by computing intersections between adjacency lists, enabling faster identification of shared neighbors. However, the TWJtr algorithm further optimizes this process by introducing jump-based traversal over unmatched segments of adjacency sequences. This optimization significantly reduces unnecessary comparisons, which explains the consistent performance gains observed for TWJtr in Figure. (4.b), (5.b), and (6.b), as well as its reduced total execution time reported in Figure. (4.d), (5.d), and (6.d). The analysis of Figure. (e) and (f) further confirms this behavior, showing that TWJtr performs fewer intersection tests while detecting the same number of triangles as the Naive algorithm. This demonstrates that the observed performance improvements are achieved without affecting detection completeness. Building upon these results, TWJtr-D introduces an additional duplication-aware mechanism designed to avoid redundant processing of previously examined nodes. This extension explains the further reduction in execution time observed in Figure. (7.a). The lower number of detections reported in Figure. (7.b) reflects the elimination of duplicate triangle detections rather than a loss of correctness. This outcome results from TWJtr-D verifying in each iteration, whether the vertices involved in a test have already been processed which preserves triangle detection completeness by reporting each triangle exactly once. This behavior is consistent with the duplication-aware strategy described in the PROPOSED APPROACH section and demonstrates that the proposed method, TWJtr-D, effectively reduces computational cost while maintaining correct and complete triangle detection. Moreover, the performance gains become more pronounced as graph size increases, indicating improved scalability compared to baseline methods.

VI. CONCLUSION

Considering the immense data traffic flowing on the networks, created by interactions exchanged by a very large number of network users, detecting communities and actor profiles became essential for several reasons. Among them, routing queries for targeted audience, which allows directing information to clusters of individuals sharing the same interests with the said query, a strategy that is, nowadays, the trend of commercial marketing and advertisement through social networks. The detection of communities involves the detection of triangles since triangles represent the basic component of a community. In this context, we built our approach over the TWJ algorithm [22-23] which is defined for the fast calculation of the intersection between sorted lists. We have adapted TWJ to the context of triangle detection that we named TWJtr [24]. Our solution presented a much better performance in terms of time computing, number of preformed tests and number of detected triangles. These results were obtained through comparing our solution with two of this domain's basic algorithms, the node- iterator and the edge-iterator (naive method), chosen after a detailed study of this field's state of the art. Given the considerations above, TWJtr is found to be the best general-purpose algorithm which balances efficiency and practicality, performing well on both sparse and moderately dense graphs, leveraging efficient intersection computations to detect triangles. Additionally, we enhanced the TWJtr to be further optimal. Since the previous methods generated results including a considerable number of duplicated triangles, TWJtr-D, as a refined version of TWJtr, ensures an accurate result eliminating duplicated triangles optimizing time computing, which is an undeniable advantage considering the large-scale networks subjected to triangle detection procedures. In the future, we intend to implement and experiment on platforms like SPARK in order to adapt TWJtr and TWJtr-D for distributed systems. We also, consider comparisons with other algorithms.

VII. AUTHOR'S CONTRIBUTION

Conceptualization: Balbouzi Sarah.
Methodology: Balbouzi Sarah.
Investigation: Mechach Kheira.
Discussion of results: Balbouzi Sarah and Zekri Lougmiri.
Writing – Original Draft: Balbouzi Sarah.
Writing – Review and Editing: Zekri Lougmiri and Mechach Kheira.
Resources: Zekri Lougmiri.
Supervision: Zekri Lougmiri.
Approval of the final text: Balbouzi Sarah, Zekri Lougmiri and Mechach Kheira.

VIII. ACKNOWLEDGMENTS

This work was funded by the University Oran1 Ahmed Ben Bella, Grant No. C00L07UN310120220006.

IX. REFERENCES

[1] L. Euler, "Solutio problematis ad geometriam situs pertinentis (The solution of a problem relating to the geometry of position)," Mém. Acad. Sci. Berlin, 1735. doi: 10.3931/euler-1

[2] J. L. Moreno, "Who Shall Survive? A New Approach to the Problem of Human Interrelations," Washington, DC: Nervous and Mental Disease Publ. Co., 1934. doi: 10.1037/h0057750

[3] A.-L. Barabási and R. Albert, "Emergence of scaling in random networks," Science, vol. 286, pp. 509–512, 1999. doi: 10.1126/science.286.5439.509

[4] M. Latapy, "Main-memory triangle computation for very large (sparse (power-law)) graphs," Theor. Comput. Sci., vol. 407, pp. 458–473, 2008. doi: 10.1016/j.tcs.2008.07.009

[5] P. Erdős and A. Rényi, "On random graphs. I," Publ. Math., vol. 6, pp. 290–297, 1959. doi: 10.1007/BF02781481

[6] S. Milgram, "The small-world problem," PsycEXTRA Dataset, 1967. doi: 10.1037/e300292003-001

[7] F. Karinthy, "Láncszemek [Chains] (Everything is Different)," Budapest: Atheneum, 1929, pp. 85–90.

[8] D. J. Watts and S. H. Strogatz, "Collective dynamics of 'small-world' networks," Nature, vol. 393, no. 6684, pp. 440–442, 1998. doi: 10.1038/30918

[9] H. A. Simon, “On a class of skew distribution functions,” Biometrika, vol. 42, no. 3–4, pp. 425–440, 1955. doi: 10.2307/2333389

[10] D. J. de S. Price, “A general theory of bibliometric and other cumulative advantage processes,” J. Amer. Soc. Inf. Sci., vol. 27, no. 5, pp. 292–306, 1976. doi: 10.1002/asi.4630270505

[11] S. N. Dorogovtsev, J. F. F. Mendes, and A. N. Samukhin, “Size-dependent degree distribution of a scale-free growing network,” Phys. Rev. E, vol. 63, 062101, 2001. doi: 10.1103/PhysRevE.63.062101

[12] G. Bianconi and A.-L. Barabási, “Competition and multiscaling in evolving networks,” Europhys. Lett, vol. 54, no. 4, pp. 436–442, 2001. doi: 10.1209/epl/i2001-00455-0

[13] S. Boccaletti et al., “The structure and dynamics of multilayer networks,” Phys. Rep., vol. 544, pp. 1–122, 2014. doi: 10.1016/j.physrep.2014.07.001

[14] P. Holme and J. Saramäki, Eds., “Temporal Network Theory,” Springer, 2019. doi: 10.1007/978-3-030-26047-5

[15] F. Battiston et al., “The physics of higher-order interactions in complex systems,” Nature Phys., vol. 16, pp. 585–594, 2020. doi: 10.1038/s41567-020-0852-7

[16] N. Chiba and T. Nishizeki, “Arboricity and subgraph listing algorithms,” SIAM J. Comput, vol. 14, no. 1, pp. 210–223, 1985. doi: 10.1137/0214015

[17] T. Schank and D. Wagner, “Finding, counting and listing all triangles in large graphs: An experimental study,” Proc. Workshop Exp. Efficient Algorithms (WEA), 2005. doi: 10.1007/11427186_16

[18] T. Schank and D. Wagner, “Finding, counting and listing all triangles in large graphs,” Tech. Rep., Universität Karlsruhe, Fakultät für Informatik, 2005.

[19] A. Itai and M. Rodeh, “Finding a minimum circuit in a graph,” SIAM J. Comput, vol. 7, no. 4, pp. 413–423, 1978. doi: 10.1137/0207032

[20] N. Alon, R. Yuster, and U. Zwick, “Finding and counting given length cycles,” Proc. Eur. Symp. Algorithms (ESA), 1994. doi: 10.1007/3-540-58484-6_25

[21] N. Alon, R. Yuster, and U. Zwick, “Finding and counting given length cycles,” Algorithmica, vol. 17, no. 3, pp. 209–223, 1997. doi: 10.1007/BF02523654

[22] L. Zekri, F. Manseur, and O. Belhadj, “Calcul de l’intersection entre listes triées à base de sauts (Intersection computation between sorted lists using jumps),” Proc. EDA, Tanger, Maroc, 2018, pp. 57–72.

[23] F. Manseur, L. Zekri, and M. Senouci, “A new fast intersection algorithm for sorted lists on GPU,” J. Inf. Technol. Res. (JITR), vol. 15, no. 1, pp. 1–20, 2022. doi: 10.4018/JITR.2022010101

[24] Our work, “title”, yyyyyyyyyyy, zzzz, doi:xxxxxxxxxxxxxxx.

[25] L. C. Freeman, “A set of measures of centrality based on betweenness,” Sociometry, vol. 40, no. 1, pp. 35–41, 1977. doi: 10.2307/3033543

[26] U. Brandes, “A faster algorithm for betweenness centrality,” J. Math. Sociol., vol. 25, no. 2, pp. 163–177, 2001. doi: 10.1080/0022250X.2001.9990249

[27] M. Girvan and M. E. J. Newman, “Community structure in social and biological networks,” PNAS, vol. 99, no. 12, pp. 7821–7826, 2002. doi: 10.1073/pnas.122653799

[28] G. Karypis and V. Kumar, “A fast and high quality multilevel scheme for partitioning irregular graphs,” SIAM, 1998. doi: 10.1137/1.9781611972873.ch11

[29] M. E. J. Newman, “Modularity and community structure in networks,” Proc. Natl. Acad. Sci. USA (PNAS), vol. 103, no. 23, pp. 8577–8582, Jun. 2006. doi: 10.1073/pnas.0601602103

[30] V. D. Blondel, J.-L. Guillaume, R. Lambiotte, and E. Lefebvre, “Fast unfolding of communities in large networks,” J. Stat. Mech., 2008. doi: 10.1088/1742-5468/2008/10/P10008

[31] P. De Meo, E. Ferrara, G. Fiumara, and A. Provetti, “Generalized Louvain method for community detection in large networks,” Proc. 11th Int. Conf. Intell. Syst. Design Appl., 2011. doi: 10.1109/ISDA.2011.6064084

[32] X. Ding, S. Sheng, H. Zhou et al., “Differentially private triangle counting in large graphs,” IEEE Trans. Knowl. Data Eng., vol. 34, no. 11, pp. 5278–5292, 2021. doi: 10.1109/TKDE.2020.3014390

[33] A. Dumitrescu, “A strongly subcubic combinatorial algorithm for triangle detection with applications,” arXiv preprint, arXiv:2403.01085, 2024. doi: 10.48550/arXiv.2403.01085

[34] L. Meng et al., “A survey of distributed graph algorithms on massive graphs,” arXiv preprint, arXiv:2403.xxxxx, 2024. doi: 10.48550/arXiv.2403.xxxxx

Journal of Engineering and Technology for Industrial Applications

ISSN ONLINE: 2447-0228

ITEGAM-JETIA

Manaus, v.12 n.60, p.757-763 July/August, 2026.
DOI: https://doi.org/10.5935/jetia.v12i60.4017

RESEARCH ARTICLE OPEN ACCESS

FABRICATION OF AL6061–SIC METAL MATRIX COMPOSITES VIA STIR CASTING: A RESPONSE SURFACE METHODOLOGY APPROACH TO MICROSTRUCTURE ANALYSIS

Sathiyaraj .S*[1],Kumaran .P[2],Yuvaraj .J[3],Vigneshwaran.V[4] Vijayan.T.P[5]

[1, 2, 3,4,5] Department of Mechanical Engineering, Aarupadai Veedu Institute of Technology, Vinayaka Mission's Research Foundation (DU), Tamil Nadu, India.

[1]https://orcid.org/0000-0001-8504-0412, [2]https://orcid.org/ 0000-0003-2781-8999, [3]https://orcid.org/0009-0009-3749-3981
[4]https://orcid.org/0009-0006-1182-6010, [5]https://orcid.org/0009-0001-3424-1860

Email: *sathiyaraj@avit.ac.in, kumaranp@avit.ac.in,yuva16jraj@gmail.com, vv71700@gmail.com, tpvijayan89@gmail.com

ARTICLE INFO

Article History
Received on: March 10, 2026
Reviewed on: April 10, 2026
Accepted on: May 01, 2026
Published on: July 31, 2026

Keywords:
Stir Casting,
Alumnium6061,
Silicon Carbide,
Matrix,
Reinforcement.

ABSTRACT

To This study investigates the fabrication and microstructural characterization of Al6061–SiC composites using a Response Surface Methodology (RSM) approach to optimize stir casting parameters. Aluminum 6061 was used as the matrix material, while silicon carbide (SiC) particles with a size of less than 10 µm served as the reinforcement. The Aluminum Metal Matrix Composites (AMMCs) were produced through the stir casting technique, which is considered a cost-effective and efficient fabrication method. The composite samples were prepared according to the experimental design generated using the RSM Box–Behnken Design (BBD). The main processing parameters examined in this study were the reinforcement weight fraction (3.5 wt%, 7.0 wt%, and 10.5 wt%), melting temperature (625°C, 650°C, and 675°C), and stirring speed (225 rpm, 250 rpm, and 275 rpm). Microstructural examination carried out using a metallurgical microscope and high-resolution scanning electron microscope (SEM) indicated a relatively uniform dispersion of SiC particles within the aluminum matrix; however, minor particle agglomeration and porosity were also detected.

Copyright ©2026 by authors and Galileo Institute of Technology and Education of the Amazon (ITEGAM). This work is licensed under the Creative Commons Attribution International License (CC BY 4.0).

I. INTRODUCTION

Metal matrix composites (MMCs) have gained considerable attention in recent decades due to their enhanced mechanical, thermal, and tribological properties compared with conventional alloys [1]. Among the various MMCs, aluminum matrix composites (AMMCs) are widely used because of their low density, high strength-to-weight ratio, good corrosion resistance, and excellent thermal conductivity [2]. Aluminum alloy Al6061 is particularly preferred as a matrix material because of its good formability, weldability, and mechanical performance [3]. Reinforcing aluminum alloys with ceramic particles such as silicon carbide (SiC) significantly improves hardness, wear resistance, and strength of the composite material [4]. The presence of hard SiC particles in the aluminum matrix restricts grain boundary movement and contributes to grain refinement during solidification, leading to improved mechanical properties [5].Various fabrication techniques have been employed for the production of aluminum matrix composites, including powder metallurgy, squeeze casting, spray deposition, and stir casting [6]. Among these techniques, stir casting is considered one of the most economical and practical methods due to its simplicity and suitability for large-scale production [7]. In this method, reinforcement particles are introduced into molten aluminum and distributed uniformly through mechanical stirring [8]. However, the quality of the final composite depends strongly on several processing parameters such as melting temperature, stirring speed, and reinforcement percentage [9]. Improper control of these parameters may lead to particle agglomeration, poor wettability, and porosity within the composite structure [10].

Microstructural characteristics play a vital role in determining the mechanical and tribological performance of aluminum matrix composites [11]. A uniform distribution of reinforcement particles enhances load transfer efficiency between the matrix and the reinforcement, thereby improving strength and wear resistance [12]. Previous studies have reported that increasing the weight fraction of SiC particles improves hardness and wear resistance of Al6061 composites [13]. Furthermore, statistical optimization techniques such as Response Surface Methodology (RSM) have been widely applied to evaluate the combined effects of multiple process parameters and to identify optimal fabrication conditions [14]. The Box–Behnken design within RSM has proven effective in reducing the number of experiments while providing reliable prediction models for material processing studies [15].Therefore, the present study focuses on the fabrication of Al6061–SiC composites using the stir casting method and investigates the influence of key process parameters on the microstructural characteristics. The Response Surface Methodology with Box–Behnken design is employed to systematically analyze the effects of reinforcement weight percentage, melting temperature, and stirring speed to achieve improved particle distribution and enhanced composite quality.

II. SELECTION OF MATERIALS AND METHODOLOGY

II.1 SELECTION OF MATERIALS

Aluminium 6061 is used as the base material in MMCs. It is mostly made of aluminum., with silicon and magnesium as the major alloying elements. Aluminium 6061 possesses good mechanical properties and excellent weldability. While the Al6061 matrix material demonstrates good corrosion resistance, its mechanical and tribological properties are not as significant. Therefore, enhancement of its mechanical and tribological characteristics is necessary. For this reason, aluminium alloy 6061 was selected as the matrix material in this investigation. The aluminium alloy Al6061 billet was procured in the form of billets. Silicon carbide belongs to a group of lightweight ceramic materials. It is extremely hard and, when used as a reinforcing material, can significantly increase the base matrix's hardness and resistance to wear. This material can withstand high temperatures (up to 1600°C) due to the strong bonding within the tetrahedral structure formed by carbon and silicon atoms in its crystal lattice. Based on these characteristics, chemically pure, green to bluish-black fine SiC powder was selected as the primary reinforcement.

II.2 DESIGN OF EXPERIMENT

This study utilizes the Box-Behnken Design to optimize the stir casting parameters for Al–SiC composites, concentrating on the critical process inputs and their levels as summarized in Table 1..Using the BBD, a quadratic model will be developed to investigate the connections between the final material characteristics and these process variables (such as tensile strength, hardness, Impact strength, Wear Rate and COF). The ultimate goal is to identify the optimal combination of parameters that leads to superior composite quality, enhancing the effectiveness and consistency of the stir casting process for Al–SiC composites.

Table 1: Controllable Factors in the Stir Casting Process.

Factors	Levels		
	-1	0	+1
Reinforcement RI(wt% SiC)	3.5	7	10.5
Melting or Stirring Temperature ST(^{0}C)	625	650	675
Stirring Speed SS (rpm)	225	250	275

Source: Authors, (2026).

II.3 FABRICATION OF COMPOSITES

The Al6061–SiC MMCs in this study were produced using the stir casting method, a popular technique for manufacturing particle-reinforced aluminum composites due to its ease of use, cost efficiency, and scalability. The stir casting setup is illustrated in Figures 1. Conducting experimental Runs in Stir casting Process as listed in Table 2.



Figure 1: Experimental Framework for Stir Casting.
Source: Authors, (2026).

Table 2: Conducting Experimental Runs in Stir Casting.

Exp.No	Coded Value			Original Value		
	RI	ST	SS	RI (wt% SiC)	ST(^{0}C)	SS (rpm)
1	-1	-1	0	3.5	625	250
2	-1	1	0	3.5	675	250
3	1	-1	0	10.5	625	250
4	1	1	0	10.5	675	250
5	-1	0	-1	3.5	650	225
6	-1	0	1	3.5	650	275
7	1	0	-1	10.5	650	225
8	1	0	1	10.5	650	275
9	0	-1	-1	7	625	225
10	0	-1	1	7	625	275
11	0	1	-1	7	675	225
12	0	1	1	7	675	275
13	0	0	0	7	650	250
14	0	0	0	7	650	250
15	0	0	0	7	650	250

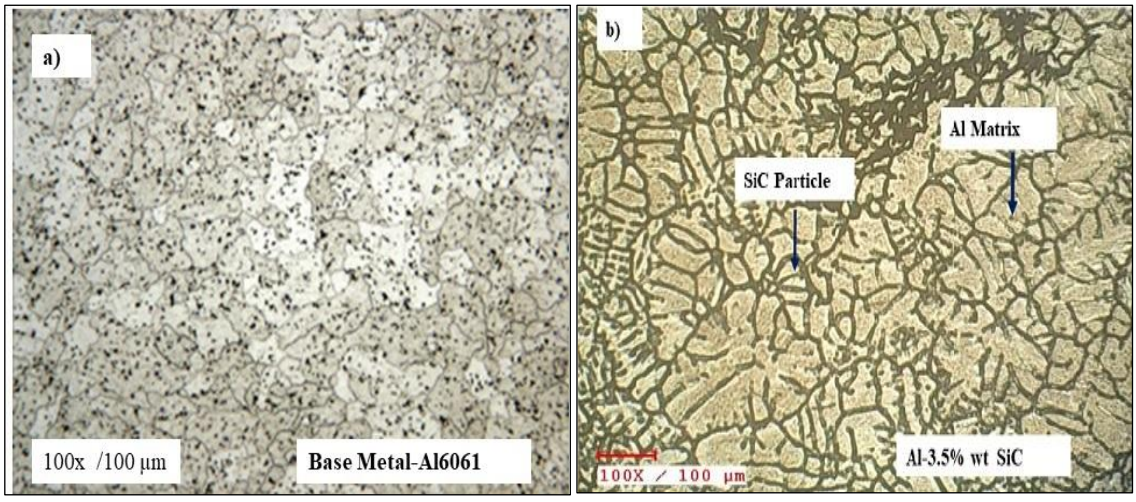
Source: Authors, (2026).

III. RESULTS AND DISCUSSION

III.1 MICROSTRUCTURAL ANALYSIS

The microstructure analysis of AL6061-SiC metal matrix composites (MMCs) using a metallurgical microscope (Dewinter Tech) involves a systematic sample preparation and examination process aimed at revealing the internal structural features of the composite material. The prepared sample is examined under a metallurgical microscope, beginning at low magnification (e.g., 100xto investigate SiC particle shape, distribution, and interfacial bonding in the aluminum matrix. Microstructural features such as grain boundaries, particle clustering, porosity, and secondary phase formations are observed and, where applicable, captured using imaging software for further quantitative analysis. This procedure ensures a detailed and accurate characterization of the composite's microstructure, which is critical for understanding its mechanical properties and overall performance. The microstructure of the fabricated composite, shown in Figure 2 (b), was captured at 100× magnification with a scale of 100 µm. The matrix material, identified as AL6061, exhibits a typical dendritic solidification structure, characterized by primary α-Aluminum dendrites surrounded by an interdendritic eutectic network.

The regions highlighted by black circles represent the locations of reinforcing particles dispersed throughout the aluminum matrix. These areas appear darker, indicating the presence of secondary phases, which are most likely the silicon carbide (SiC) particles incorporated during the fabrication of the composite. Achieving a relatively uniform distribution of SiC particles within the matrix is essential for enhancing mechanical qualities like wear resistance, tensile strength, and hardness. The observed microstructure suggests good interfacial bonding between the AL6061 matrix and the SiC particles, which is necessary for effective load transfer under mechanical stress. Minimal porosity and segregation are evident, indicating a sound fabrication process and effective dispersion of reinforcement. The existence of SiC particles inhibits the grain growth of the aluminum matrix, contributing to the refinement of the microstructure and thus improving the overall performance of the mechanism. This analysis confirms the successful incorporation of 3.5 wt% SiC into the AL6061 alloy, directly correlating to the enhancements in mechanical properties observed during hardness, tensile, and impact testing.



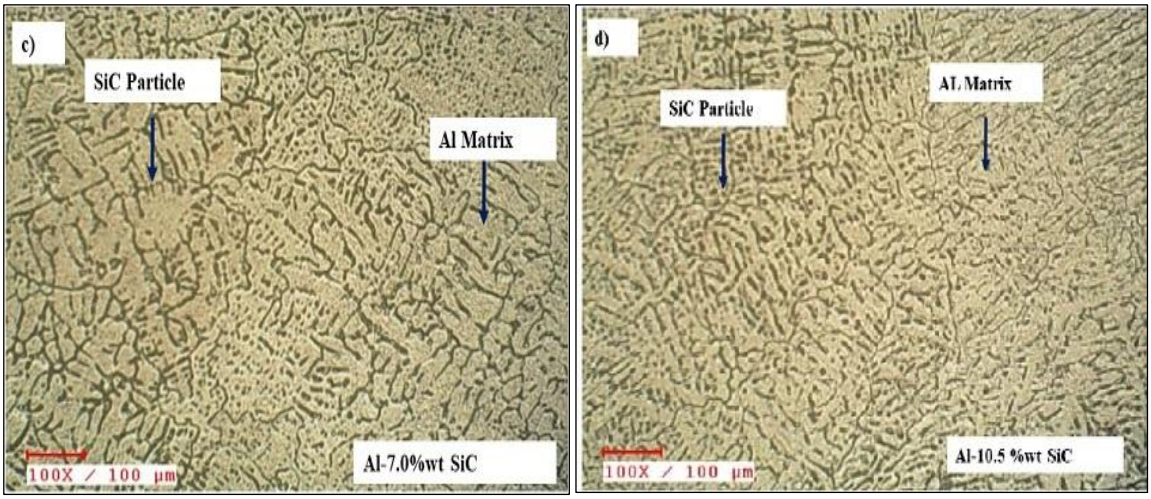


Figure 2: AMMCs Microstructures.
Source: Authors, (2026).

The microstructure of the AL6061–7.0 wt% SiC composite, shown in Figure 2 (c), was captured at 100× magnification with a scale of 100 µm. The matrix phase (highlighted with a black circle) consists predominantly of α-Aluminum (AL6061), while the red-circled regions indicate the presence of silicon carbide (SiC) reinforcement particles. Within the aluminum matrix, the SiC particles are dispersed somewhat evenly, but there is some minor clumping in some areas. This distribution is critical for improving the composite's mechanical performance, as the hard SiC particles act as barriers to dislocation movement, thereby enhancing the hardness and tensile strength of the material.The dendritic structure of the aluminum matrix remains visible, though the dendrites appear finer compared to unreinforced AL6061 alloy. The presence of SiC particles during solidification restricts grain growth by pinning the grain boundaries, leading to a refined microstructure. Grain refinement typically contributes to increased strength according to the Hall-Petch relationship.

No major porosity or defects were observed at this magnification, suggesting that the processing parameters were effective in achieving a sound microstructure. The good interfacial bonding between the AL6061 matrix and SiC particles indicates effective load transfer capability, which is essential for improving both tensile and impact properties. The analysis confirms that increasing the SiC content to 7.0 wt% leads to a more pronounced reinforcement effect compared to lower weight percentages, which is consistent with the mechanical test results showing increased hardness and strength. Figure 2 (d) shows the microstructure of the AL6061–10.5 weight percent SiC composite was examined at 100× magnification with a 100 µm scale. The α-Aluminum matrix (highlighted with yellow labeling and circled in red) retains its dendritic morphology, although it appears more refined compared to composites with lower SiC content. The red-circled areas clearly display the dispersion of SiC reinforcement particles within the matrix. As the SiC content increases to 10.5 wt%, the number density of SiC particles is visibly higher.

This dense distribution of hard SiC particulates effectively impedes dendrite growth during solidification, promoting a finer and more uniform microstructure. Finer dendritic structures contribute to increased strength and hardness due to restricted grain boundary movement.The relationship between the AL6061 matrix and the SiC particles appears clean with no major visible voids or defects at this magnification, suggesting effective particle-matrix bonding, crucial for efficient stress transfer during mechanical loading. However, at this higher reinforcement level, some localized particle clustering can be observed. While such clustering may enhance localized hardness, it could potentially lead to stress concentrations under dynamic loading conditions, slightly affecting toughness.Overall, the microstructure confirms that increasing the SiC content to 10.5 wt% significantly refines the grain structure and increases the volume fraction of hard phases, correlating with the substantial improvements observed in the hardness, tensile, and impact strength tests.

III.2 SEM OBSERVATION WITH EDAX EVALUATION

The characterization of Al6061-SiC MMCs using Scanning Electron Microscopy (SEM) and Energy Dispersive X-ray Spectroscopy (EDS) involves a systematic approach to examine the morphology of the surface and elemental makeup of the composite. All wear experiments were performed following the ASTM E2142 standard. The prepared specimen is positioned inside the SEM chamber and exposed to a focused electron beam to generate detailed surface images. SEM imaging reveals critical information about the shape, distribution, and interfacial bonding of the SiC reinforcement particles within the aluminum matrix, as well as any defects such as voids, cracks, or particle clusters. Elemental composition is determined through EDS, which detects characteristic X-rays emitted from the sample when struck by the electron beam.

This technique enables precise identification and spatial mapping of elements within the composite, confirming the presence of silicon carbide particles and highlighting any elemental segregation or secondary phases. Together, SEM and EDS offer a thorough insight into the microstructural and chemical properties of the Al6061-SiC composite, which is crucial for understanding its material performance. The image shown (Figure 3) is an EDAX spectrum obtained during SEM analysis of an AMMCs reinforced with a specific weight percentage of silicon carbide (SiC). The spectrum illustrates the elemental composition of the analyzed region of the composite by displaying the intensity of characteristic X-rays emitted by elements upon electron beam excitation.

On the x-axis, the energy levels of emitted X-rays are plotted in keV, while the y-axis indicates the count intensity, which correlates to the quantity of each element detected. A strong peak is observed for aluminum (Al) around 1.5 keV, which is expected due to its role as the base matrix material in AL6061. Smaller peaks are also visible for magnesium (Mg) and sodium (Na), which are typical alloying elements or trace impurities in the aluminum alloy. Importantly, this spectrum shows clearly identifiable peaks for silicon (Si) near 1.7 keV and also a minor peak around 0.2 keV, indicating the presence of silicon carbide particles in the analyzed area, consistent with the SiC reinforcement in the composite. Additionally, low-intensity peaks for carbon (C) and oxygen (O) are evident, which may be attributed to the carbon content from SiC, surface oxidation, or environmental contamination. The existence of both silicon and carbon peaks provides confirmation of the distribution of SiC particles within the aluminum matrix. This spectrum, therefore, validates the successful incorporation of SiC reinforcement in the AL6061 matrix and highlights the elemental constituents of the composite in the specific region examined.

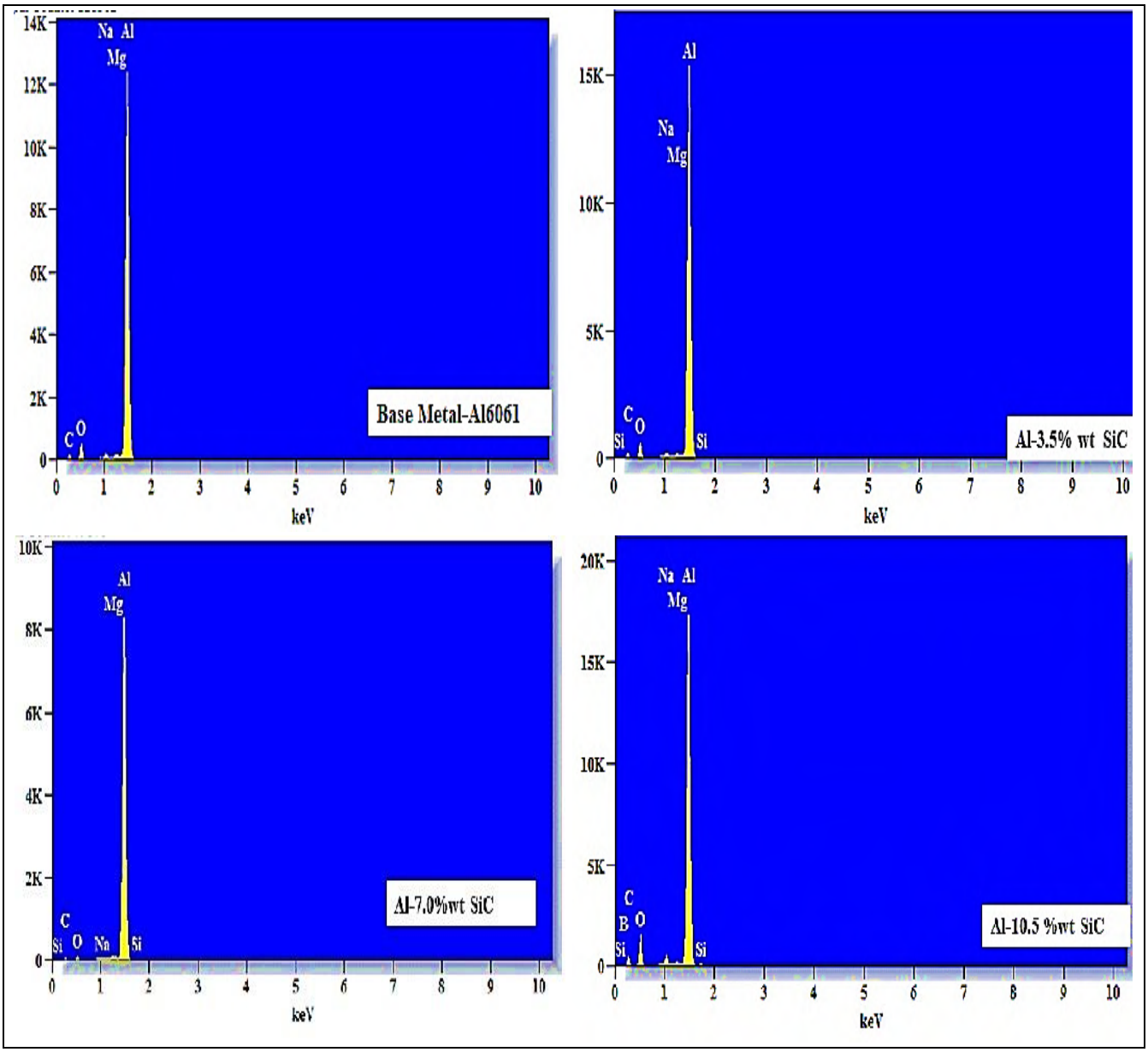


Figure 3: Al6061-SiC Composites EDAX spectrum.
Source: Authors, (2026).

This SEM image (Figure: 4) serves to reveal the microstructural characteristics and surface morphology of the composite at high magnification. In the image, the aluminum matrix forms the continuous phase, while the SiC particles are distinguishable as discrete features distributed within the matrix. At a reinforcement level of 10.5 wt%, the SiC particles appear more numerous and densely distributed compared to lower reinforcement percentages, indicating a higher volume fraction of ceramic reinforcement. The micrograph allows observation of the shape, size, and dispersion of these particles, which are critical in influencing the mechanical behavior of the composite. Uniform dispersion of SiC particles, as suggested in the image, enhances properties such as hardness, wear resistance, and tensile strength by improving load transfer between the matrix and reinforcement. Any visible clustering or agglomeration could potentially lead to stress concentrations, but in a well-processed sample, such defects are minimized. The SEM analysis thus confirms the successful integration of SiC into the aluminum matrix and provides valuable insight into the quality and effectiveness of the c omposite microstructure at 10.5 wt% SiC reinforcement.

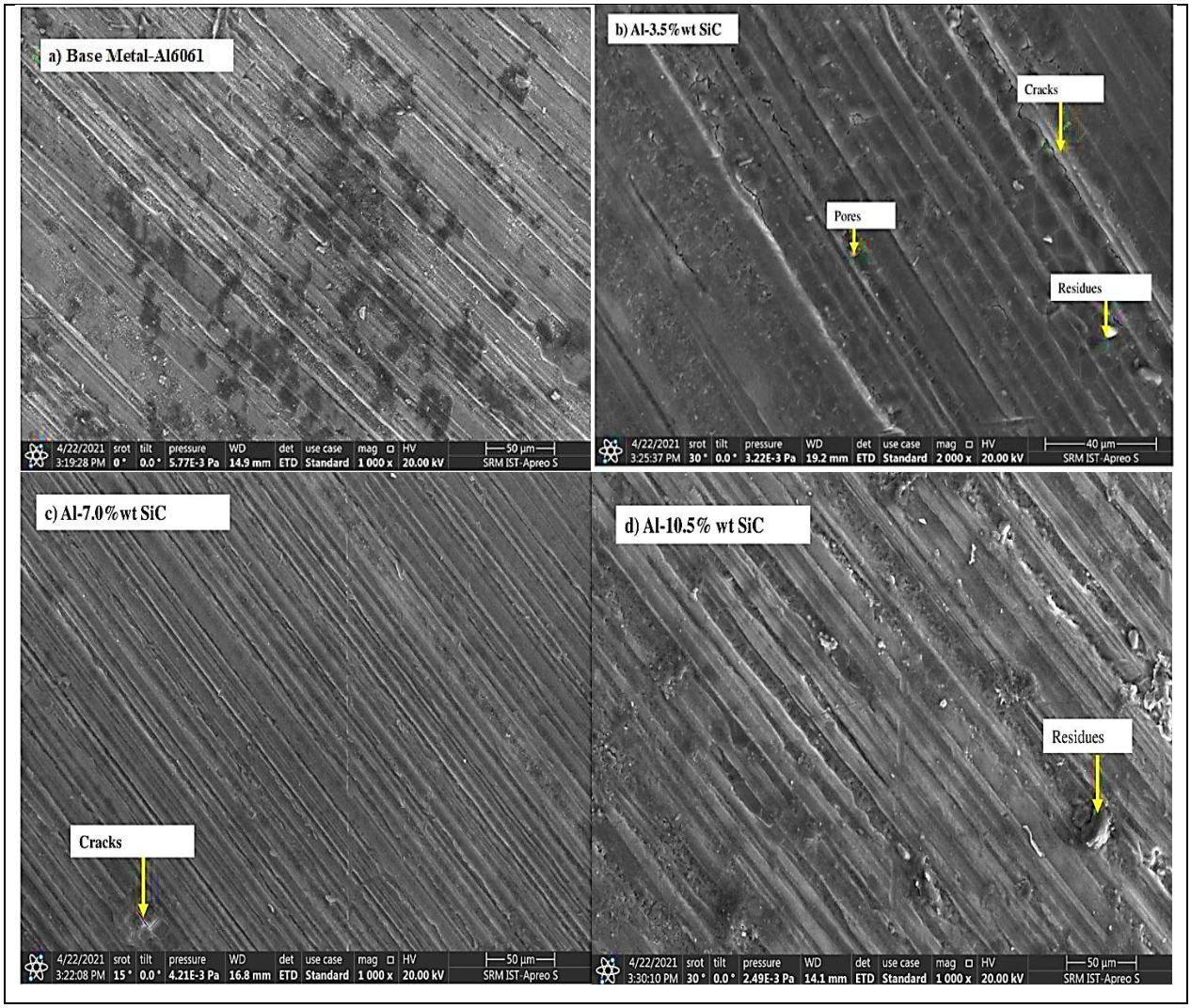


Figure 4: Al6061- SiC Composites SEM image.
Source: Authors, (2026).

IV. CONCLUSIONS

The Al6061–SiC metal matrix composites were successfully fabricated using the stir casting technique, and the process parameters were systematically optimized using the Box–Behnken Design (BBD) within the Response Surface Methodology (RSM) framework. The microstructural analysis revealed that increasing the SiC reinforcement content up to 10.5 wt% significantly refined the grain structure and enhanced the volume fraction of hard phases within the aluminum matrix. A relatively uniform distribution of SiC particles was observed under optimized processing conditions, which minimized particle agglomeration and improved the overall microstructural integrity of the composite. The presence of hard ceramic SiC particles restricted grain boundary movement during solidification and contributed to improved interfacial bonding between the reinforcement and the matrix. As a result, the composite exhibited enhanced mechanical properties, particularly increased hardness and improved wear resistance compared to the base Al6061 alloy. The statistical optimization approach effectively identified the optimal combination of parameters, and validation experiments confirmed the reliability of the developed model. Overall, the results demonstrate that the integration of stir casting with BBD-based RSM optimization is an effective approach for producing high-performance Al6061–SiC composites suitable for lightweight structural and engineering applications.

V. AUTHOR'S CONTRIBUTION

Conceptualization: Sathiyaraj.S,
Methodology: Sathiyaraj.S,
Investigation: Sathiyaraj.S, P.Kumaran
Discussion of results: Sathiyaraj.S,
Writing – Original Draft: Sathiyaraj.S,
Writing – Review and Editing: P.Kumaran.,
Resources: Sathiyaraj.S,
Supervision: S.Sathiyaraj
Approval of the final text: S.Sathiyaraj

VI. REFERENCES

[1]. Badran, A. H., Alamro, T., Bazuhair, R. W., Gad El-Mawla, A. A., El-Adben, S. Z., & Fouly, A. (2022). Investigation of the mechanical behavior of synthesized Al6061/TiO_2 microcomposites using an innovative stir casting method. *Nanomaterials, 12*(10), 1646. https://doi.org/10.3390/nano12101646

[2]. Bharath, V., Nagaral, M., Auradi, V., & Kori, S. A. (2014). Preparation of 6061Al–Al_2O_3 metal matrix composite by stir casting and evaluation of mechanical properties. *Procedia Materials Science, 6*, 1658–1667.

[3]. Gopalakrishnan, S., & Murugan, N. (2012). Production and wear characterization of AA6061 matrix titanium carbide particulate reinforced composite by enhanced stir casting method. *Composites Part B: Engineering, 43*(2), 302–308.

[4]. Jokhio, M. H., Panhwar, M. I., & Unar, M. A. (2016). Manufacturing of aluminum composite material using stir casting process. *Mehran University Research Journal of Engineering and Technology*, *35*(1), 11–20.

[5]. Kumar, G. B. V., Rao, C. S. P., & Selvaraj, N. (2011). Mechanical and tribological behavior of particulate reinforced aluminum metal matrix composites – A review. *Journal of Minerals and Materials Characterization and Engineering, 10*(1), 59–91.

[6]. Moses, J. J., Dinaharan, I., & Sekhar, S. J. (2013). Characterization of silicon carbide particulate reinforced AA6061 aluminum alloy composites produced via stir casting. *Procedia Engineering, 64*, 1189–1198.

[7]. N., N., Shanmuganathan, V. K., Gayathri, N., Suresh, K., Aravindh, S., & Prakash, E. (2018). Investigations on mechanical behavior of Al6061-TiO_2-SiC produced by stir casting. *International Journal of Engineering and Technology, 7*(3), 369–371. https://doi.org/10.14419/ijet.v7i3.34.19228

[8]. Prasad, S. V., & Asthana, R. (2004). Aluminum metal–matrix composites for automotive applications: Tribological considerations. *Tribology Letters, 17*(3), 445–453.

[9]. Sajjadi, S. A., Ezatpour, H. R., & Beygi, H. (2011). Microstructure and mechanical properties of Al–Al_2O_3 micro and nano composites fabricated by stir casting. *Materials Science and Engineering: A, 528*(29–30), 8765–8771.

[10]. Sathiyaraj, S., & Kalyanakumar, S. (2026). Fabrication and study of mechanical properties of aluminum-based metal matrix composites. *Springer Proceedings in Materials, 78*, 155–164.

[11]. Sharma, P., Khanduja, D., & Sharma, S. (2015). Production and some properties of SiC reinforced aluminum alloy composites. *Journal of Asian Ceramic Societies, 3*(3), 352–359.

[12] Singla, M., Dwivedi, D. D., Singh, L., & Chawla, V. (2009). Development of aluminum based silicon carbide particulate metal matrix composite. *Journal of Minerals and Materials Characterization and Engineering, 8*(6), 455–467.

[13]. Suresh, S., & Mortensen, A. (2013). Fundamentals of metal-matrix composites. *Butterworth-Heinemann*.

[14]. urappa, M. K. (2003). Aluminum matrix composites: Challenges and opportunities. *Sadhana, 28*(1–2), 319–334.

[15]. Umanath, K., Selvamani, S. T., & Palanikumar, K. (2013). Friction and wear behavior of Al6061 alloy reinforced with SiC particles. *Composites Part B: Engineering, 53*, 159–168.

Journal of Engineering and Technology for Industrial Applications

ISSN ONLINE: 2447-0228

ITEGAM-JETIA

Manaus, v.12 n.60, p.764-772 July/August, 2026.
DOI: https://doi.org/10.5935/jetia.v12i60.4022

RESEARCH ARTICLE OPEN ACCESS

A COMPARATIVE EXTENDED UTAUT ANALYSIS OF VIRTUAL REALITY AND AUGMENTED REALITY ADOPTION ACROSS INSTITUTIONAL DIVIDES

Julius G. Garcia*[1], Myrna S. Batino[2] and Alvie Simonette Q. Alip[3]

[1, 2] Technological University of the Philippines, Ayala Blvd., Ermita, Manila, Philippines.
[3] University of the Philippines Open University, Los Baños, Laguna, Philippines.

[1]http://orcid.org/0000-0003-4074-5851, [2]http://orcid.org/0009-0003-6678-6157, [3]http://orcid.org/0000-0002-5859-3748

Email: *julius.tim.garcia@gmail.com, mrbatino2012@gmail.com, alvie.alip@upou.edu.ph

ARTICLE INFO

Article History
Received on: March 10, 2026
Reviewed on: April 10, 2026
Accepted on: May 01, 2026
Published on: July 31, 2026

Keywords:
Virtual Reality,
Augmented Reality,
Comparative Analysis,
UTAUT2,
Structural Equation Modeling.

ABSTRACT

This study explores educators' and learners' multifaceted perceptions across public and private educational institutions regarding the integration and adoption of virtual reality (VR) and augmented reality (AR) applications. Recognizing the paradigm shift toward Education 4.0, the study operationalizes an extended Unified Theory of Acceptance and Use of Technology (UTAUT2) framework to isolate the predictive behavioral determinants of immersive technology adoption. Using a snowball sampling methodology, a structured psychometric instrument was administered to teachers across primary, secondary, and tertiary levels, as well as to secondary and tertiary students, yielding a robust sample of 1000 valid responses. Covariance-based Structural Equation Modeling (CB-SEM) and Confirmatory Factor Analysis (CFA) were conducted in IBM AMOS to evaluate the latent relationships among effort expectancy, performance expectancy, hedonic motivation, social influence, price value, habit, facilitating conditions, and the ultimate behavioral intention to adopt AR/VR platforms. The empirical findings establish that effort expectancy, performance expectancy, and hedonic motivation are universally significant drivers of adoption intent. Subsequent multi-group path analyses uncover profound demographic disparities; while students are heavily influenced by hedonic motivation and intrinsic enjoyment, educators base their adoption strategies strictly on performance metrics and are negatively impacted by rigid facilitating conditions. Furthermore, the public sector relies on habituation and performance expectancy to a greater extent than private institutions do. These critical insights provide actionable strategic intelligence for educational technologists, software developers, and academic policymakers seeking to minimize pedagogical friction and maximize the efficacy of extended reality deployments in modern classrooms.

Copyright ©2026 by authors and Galileo Institute of Technology and Education of the Amazon (ITEGAM). This work is licensed under the Creative Commons Attribution International License (CC BY 4.0).

I. INTRODUCTION

The contemporary educational landscape is currently undergoing a profound systemic metamorphosis, driven by the rapid evolution and deployment of immersive digital technologies. As modern civilization transitions toward the ideals of Society 5.0, a human-centric framework in which cyberspace and physical space are highly integrated to address socio-economic challenges, the pedagogical strategies used to prepare the next generation of learners must evolve commensurately [1]. Education 4.0, the corresponding academic paradigm, emphasizes the critical need to cultivate twenty-first-century competencies, notably critical thinking, advanced problem-solving, and technological literacy [2]. Within this transformative context, extended reality (XR) technologies, predominantly Virtual Reality (VR) and Augmented Reality (AR), have emerged as formidable instructional tools capable of redefining the spatial and cognitive parameters of teaching and learning [3].

The global market for AR and VR in education reflects this aggressive trajectory, with industry valuations projected to surge from USD 3.8 billion in 2023 to an estimated USD 14.2 billion by 2028, representing a formidable Compound Annual Growth Rate (CAGR) of 29.6 percent [4]. Despite this exponential market expansion and the theoretical promise of immersive technologies, the practical, ubiquitous adoption of AR and VR within traditional classroom environments remains highly fragmented and inconsistent [5]. While advanced academic institutions and corporate training sectors have begun leveraging these tools for experiential learning, mainstream educational adoption is frequently impeded by a complex matrix of socio-technical barriers [4]. Extensive literature indicates that while VR and AR possess the theoretical capacity to vastly improve student engagement, spatial cognition, and the retention of highly complex, abstract information [6], the actual integration of these technologies into standardized curricula is stalled by inadequate infrastructure, prohibitive financial costs, and a fundamental lack of pedagogical alignment [7]. Furthermore, a significant geographical and economic bias exists within the current body of research; the overwhelming majority of empirical studies analyzing XR adoption have been conducted in Western, high-income demographics where digital infrastructure is ubiquitous and robustly funded [8].

This leaves a critical lacuna in the academic understanding of how these immersive platforms are perceived, evaluated, and ultimately adopted within developing educational ecosystems, particularly when contrasting the operational realities of government-funded public schools with those of privately funded institutions [9]. To address these profound gaps in the literature, this research initiates a comparative, socio-technical investigation into the dynamics of adoption for VR and AR educational applications. The primary problem this study seeks to address is the lack of a unified, empirically validated understanding of the psychological and environmental factors that drive or hinder the acceptance of immersive technologies across diverse educational stakeholders and institutional frameworks. To systematically deconstruct this problem, the investigation poses three central research questions. First, what are the fundamental structural relationships between the exogenous behavioral dimensions, specifically effort expectancy, performance expectancy, hedonic motivation, social influence, habit, price value, and facilitating conditions, and the endogenous behavioral intention to adopt virtual reality and augmented reality?

Second, does the systemic architecture of the academic institution, specifically the dichotomy between public and private funding models, generate statistically significant differences in how users adopt and integrate these technologies? Finally, do the psychological determinants of adoption differ significantly between the individuals tasked with deploying the technology (teachers) and those utilizing it for knowledge acquisition (students)?. By anchoring this multidimensional inquiry in an extended iteration of the Unified Theory of Acceptance and Use of Technology (UTAUT2), this study transcends basic technological capability assessments to probe the deeply ingrained behavioral mechanics of end users. The hypothesis posits that differing institutional resources and fundamentally distinct user objectives (instruction versus comprehension) will fracture the homogenous adoption models previously recorded in corporate or leisure contexts. Ultimately, the findings derived from this robust structural equation modeling will provide crucial, actionable frameworks for instructional designers, institutional policymakers, and educational technology developers striving to bridge the digital divide and actualize the immersive potential of Education 4.0.

II. THEORETICAL REFERENCE

II.1 THE ONTOLOGICAL FRAMEWORK OF EXTENDED REALITY IN EDUCATION

The overarching taxonomy of Extended Reality (XR) encapsulates a diverse continuum of immersive technologies that manipulate human perception by blending physical realities with synthetic, computer-generated digital environments [3]. Within the educational sector, the two most prominent nodes on this reality-virtuality continuum are Virtual Reality (VR) and Augmented Reality (AR), each offering distinct cognitive affordances and pedagogical utilities.

II.1.1 The Mechanics and Utility of Virtual Reality and Augmented Reality

Virtual Reality is fundamentally defined as a medium composed of highly sophisticated computer simulations in which sensory feedback is continuously altered or augmented in response to the user's kinesthetic and spatial actions [8]. This continuous feedback loop induces a profound psychological state known as spatial presence, tricking the human cognitive architecture into feeling physically present or mentally immersed within a completely synthetic environment [10]. In contemporary educational settings, VR acts as a powerful experiential conduit. It liberates the learner from the geographical, temporal, and physical constraints of the traditional classroom, allowing students to embark on immersive virtual field trips to inaccessible locations, ranging from deep-space topographies to the microscopic interior of the human circulatory system [5]. The pedagogical efficacy of VR stems from its ability to facilitate high-fidelity experiential learning [7]. By immersing students in a controlled, risk-free virtual ecosystem, learners can conduct complex scientific experiments, practice hazardous engineering protocols, or develop intricate surgical techniques without the physical dangers or material costs of real-world failure [6]. Empirical investigations have consistently demonstrated that the spatial presence mechanisms inherent to VR significantly elevate baseline student engagement, improve long-term retention of scientific knowledge, and foster rapid development of practical psychomotor skills.[20]

Furthermore, VR has demonstrated remarkable utility in clinical and psychological management; for instance, localized experiments utilizing VR interventions during pediatric vaccination procedures verified the technology's high efficiency in providing acute pain management and dramatic fear reduction, underscoring the deep cognitive overrides the technology can achieve [11]. In contrast to the total sensory isolation of VR, Augmented Reality integrates physical and digital information in real time, allowing users to remain visually and spatially grounded in their actual environment [8]. Utilizing technological formats such as smartphones, tablet computers, or specialized head-mounted displays, AR superimposes interactive, three-dimensional virtual assets such as data models, textual translations, or animations directly onto the user's perception of the physical world [6]. The integration of AR into educational frameworks radically enriches traditional pedagogical materials. Static interactive textbooks and physical field trips are transformed into dynamic, context-rich learning experiences that respond instantaneously to student inquiry [6]. The utility of AR is particularly pronounced in disciplines requiring complex spatial visualization and high-density data interpretation.

Complex, abstract datasets become physically tangible through AR visualizations, allowing students to interact with molecular structures or geometric theorems in three-dimensional space [6]. Additionally, language learners benefit immensely from AR applications that provide instantaneous, context-aware translations and real-time pronunciation guides overlaid onto physical texts or environments [6]. Research comparing the cognitive demands of AR and VR suggests that AR is frequently a more effective medium for conveying auditory and textual information, as it imposes a lower overall cognitive load than the fully immersive, sensory-heavy environments generated by VR [10]. Despite these profound advantages, meta-analyses reveal a critical systemic flaw in current AR adoption. The vast majority of research remains hyper-focused on the technical affordances of the software rather than exploring how AR can be deeply integrated into holistic pedagogical strategies to cultivate advanced cognitive skills, such as critical thinking [12].

II.1.2 The Evolution of Technology Acceptance Frameworks

The successful deployment of innovative educational technology is rarely determined solely by the software's technical superiority; rather, it is driven by the behavioral intent and psychological acceptance of the human end-user [11]. Historically, user acceptance evaluation was guided by the Technology Acceptance Model (TAM), a foundational theoretical framework that posited that an individual's behavioral intention to use a new system was primarily determined by two core variables: perceived usefulness and perceived ease of use [13]. While the TAM provided a robust initial architecture, the rapidly increasing complexity of consumer-facing technologies necessitated a more granular and encompassing psychological model [14]. To capture these multifaceted nuances, Venkatesh et al. (2012) synthesized decades of behavioral research to develop the Unified Theory of Acceptance and Use of Technology 2 (UTAUT2) [14]. The original UTAUT model consolidated prior theories into four primary dimensions: performance expectancy, effort expectancy, social influence, and facilitating conditions. The UTAUT2 extension explicitly tailored the framework for consumer and end-user contexts by incorporating three highly relevant subjective parameters: hedonic motivation, price value, and habit [14]. Given the consumer-grade nature of modern VR headsets and AR mobile applications, the UTAUT2 framework serves as the optimal theoretical anchor for this comparative investigation.

II.1.3 Operational Constructs of the UTAUT2 Model

The specific dimensions of the UTAUT2 model evaluated in this investigation are operationalized as follows. Performance Expectancy (PE) measures the degree to which an individual believes that using the immersive system will yield significant, tangible gains in academic performance, job efficiency, or learning outcomes. In the context of VR/AR, this reflects the user's belief that the technology will objectively make them a better student or a more effective educator. Effort Expectancy (EE) assesses the degree of cognitive and logistical ease associated with using the system, including the intuitiveness of the user interface, the physical comfort of the hardware, and the steepness of the learning curve required to operate the technology proficiently. Social Influence (SI) quantifies the extent to which an individual perceives those important others, such as academic peers, departmental superiors, or institutional administrators, believe they should actively use the new system, thereby capturing the normative social pressures driving technology adoption. Facilitating Conditions (FC) gauge the individual's perception of the objective support structures available to them, measuring whether the user believes the academic institution provides the necessary technical infrastructure, hardware availability, high-speed internet connectivity, and professional training required to seamlessly use VR and AR tools. Hedonic Motivation (HM), a critical addition in the UTAUT2 model, assesses the fun, intrinsic enjoyment, or psychological pleasure derived directly from using the technology, independent of its functional utility. Price Value (PV) represents the individual's internal cognitive trade-off between the perceived pedagogical benefits of XR applications and the monetary cost of acquiring and maintaining them. Habit evaluates the extent to which individuals tend to perform technology-related behaviors automatically, driven by prior experiential learning and repetitive, systemic integration. Finally, Behavioral Intention (BI) is the endogenous, dependent variable that represents the user's explicit psychological formulation and commitment to adopt and continuously use VR/AR applications in their educational routines.

II.1.4 Contextual Barriers and Institutional Disparities in Adoption

The empirical literature strongly suggests that the actual adoption of VR and AR in educational environments is far from homogeneous and is continually perturbed by severe systemic and demographic frictions. Educators, occupying the critical role of instructional designers, exhibit highly variable states of readiness. While many pioneer teachers recognize XR as a highly compelling platform capable of revolutionizing current teaching practices [13], their initial enthusiasm is often tempered by significant operational concerns. Teachers routinely report massive deficits in instructional design support, poor software interoperability across diverse hardware platforms, and a critical lack of targeted professional development required to align virtual content with rigid curriculum standards [15]. Furthermore, the macro-level diffusion of immersive technologies faces substantial economic, infrastructural, and ethical barriers. The sheer financial burden of outfitting classrooms with high-fidelity head-mounted displays, coupled with the necessity for robust, high-bandwidth technical infrastructure, presents a near-insurmountable hurdle for underfunded educational sectors [8].

Beyond hardware constraints, institutional adoption is hindered by the complexities of proprietary content development and deep-seated ethical concerns regarding student data privacy, regulatory compliance with frameworks such as GDPR and FERPA, and the safeguarding of sensitive biometric data collected by advanced eye-tracking VR headsets [8]. Additionally, unique physiological and psychological challenges exist, particularly concerning young learners. Prolonged immersion in VR can induce cybersickness, physical discomfort from poorly fitted hardware, and profound psychological disorientation—often referred to in the literature as "tricks of the mind"—in which extended exposure to synthetic environments momentarily alters the user's cognitive perception of physical reality [5]. Consequently, understanding how these multifaceted barriers distinctly impact resource-rich private institutions compared to government-funded public schools, and how they differentially influence educators' versus students' adoption mechanisms, is absolutely vital for the strategic, sustainable deployment of educational technology.

III. METHODS

III.1 RESEARCH PARADIGM AND SAMPLE SELECTION

To systematically deconstruct the behavioral determinants of immersive technology adoption, this research employed a quantitative, cross-sectional design utilizing structural equation modeling (SEM). Given the highly specific demographic requirements of the study, namely, the need to target individuals with at least a foundational awareness of, or baseline exposure to, VR and AR educational technologies, a snowball sampling methodology was strategically implemented. This non-probability sampling architecture involves utilizing an initial cohort of qualified participants to purposively recruit subsequent subjects from their respective professional and academic networks. In the context of evaluating emerging technologies where universal adoption has not yet occurred, snowball sampling is highly efficacious for maximizing reach across disparate geographical boundaries and institutional silos. The aggregate participant pool (N=100) was meticulously curated to encompass two primary operational cohorts: educators (teachers, n=81) and learners (students, n=919).

The educator cohort was deliberately drawn from across the primary, secondary, and tertiary academic spectrums to ensure a highly diverse range of pedagogical perspectives and technological readiness levels. Conversely, the student cohort was strictly restricted to secondary and tertiary educational levels. This methodological constraint was enforced under the psychological assumption that learners in these advanced cognitive developmental stages possess the requisite metacognitive maturity and self-awareness to accurately interpret and assess complex, abstract survey constructs, such as facilitating conditions and performance expectancy. Furthermore, to isolate the impact of socio-economic and institutional funding models, the sample was heavily stratified by institutional type, capturing vast datasets from both public/government-funded institutions (n=633) and privately funded educational institutions (n=367). The comprehensive demographic breakdown of the respondent sample, detailing role, gender, and institutional affiliation, is presented in Table 1.

Table 1: Demographic distribution of the study sample.

Category	Gender	Private (n=367)	Public (n=633)
Student (n=919)	Male	169	279
	Female	180	291
Teacher (n=81)	Male	5	20
	Female	13	43

Source: Authors, (2026).

III.2 DATA COLLECTION PROTOCOLS AND RIGOROUS SCREENING

The primary data acquisition phase was conducted using a highly efficient hybrid approach, combining supervised face-to-face questionnaire distribution and secure, encrypted online survey platforms. This dual-modality deployment ensured optimal response rates, minimized sampling bias, and guaranteed robust demographic diversity across the target populations. Following the closure of the data collection window, exactly 1000 valid, fully completed survey responses were retained for high-level inferential statistical analysis. Before engaging in complex structural modeling, the raw dataset underwent a battery of rigorous data screening protocols to ensure mathematical integrity. To detect and manage missing data points, Little's Missing Completely at Random (MCAR) statistical test was conducted. The output of this test yielded a probability value significantly greater than the stringent 0.05 alpha threshold ($MCAR > 0.05$).

This result mathematically confirmed that any missing values in the dataset were scattered entirely at random, assuring the researchers that the missingness did not introduce any systematic, confounding bias into the inferential models. Furthermore, to safeguard the covariant integrity of the structural models against the extreme distorting effects of multivariate anomalies, the Mahalanobis D-Squared (D^2) distance metric was computationally applied across the dataset. The Mahalanobis distance measures how many standard deviations a specific data point is from the mean of the multivariate distribution, accounting for the dataset's correlations. Cases exhibiting a severe anomaly probability (p<.001) were meticulously scrutinized and subsequently managed or excised to guarantee that profound outliers did not artificially inflate or skew the covariant relationships.

III.3 PSYCHOMETRIC INSTRUMENTATION

The survey instrument utilized for this study was meticulously operationalized based directly upon the validated psychometric constructs defined within the UTAUT2 framework by Venkatesh et al. (2012) [14]. The comprehensive measurement model was designed to evaluate eight distinct latent variables: Effort Expectancy (EE), Performance Expectancy (PE), Hedonic Motivation (HM), Social Influence (SI), Price Value (PV), Facilitating Conditions (FC), Habit, and the ultimate endogenous dependent variable, Behavioral Intention to Adopt (BI). The structured questionnaire comprised 24 highly specific, theoretically derived items engineered to accurately capture these latent psychological constructs. To quantify subjective responses, participants rated their alignment with each statement on a standardized 5-point Likert scale. The psychometric anchors ranged from 1 ("strongly disagree") to 5 ("strongly agree"), representing a universally validated and highly reliable scaling architecture for gauging precise levels of cognitive agreement in advanced behavioral and social science research [16].

III.4 ANALYTICAL ARCHITECTURE AND STATISTICAL MODELING

The high-level statistical analysis was executed utilizing IBM SPSS AMOS (Analysis of a Moment Structures) software, an industry-standard platform specifically engineered for executing complex Covariance-Based Structural Equation Modeling (CB-SEM). The analytical architecture proceeded through two distinct, sequential phases to ensure absolute scientific validity. In the initial phase, a rigorous Confirmatory Factor Analysis (CFA) was conducted to stress-test the theoretical measurement model.

The CFA evaluated the internal consistency, convergent validity, and discriminant validity of the utilized survey scales, mathematically ensuring that the theoretical behavioral constructs were accurately and exclusively represented by their designated indicator variables. The standard measurement model equation mapping an observed indicator x to its underlying latent construct ξ is expressed mathematically as:

$$x = \Lambda_x \xi + \delta \quad (1)$$

Where Λ_x represents the factor loading matrix (the strength of the relationship), ξ signifies the unobserved latent construct being measured, and δ denotes the inherent measurement error vector. Following validation of the measurement architecture, the second phase involved conducting a comprehensive structural path analysis. This phase computationally tested the complex web of hypothesized causal relationships flowing from the exogenous constructs toward the endogenous behavioral intention. Crucially, to uncover the targeted demographic and institutional nuances at the core of this investigation, a Multi-Group Analysis (MGA) was embedded into the SEM protocol. MGA is an advanced statistical technique that permits the simultaneous estimation of the entire theoretical model across different, mutually exclusive sub-populations, Public versus Private Institutions, and Students versus Teachers. By constraining and releasing specific parameters, the MGA determines whether the structural path coefficients (β) and, by extension, the fundamental psychological mechanisms of adoption differ significantly across demographic groups.

IV. RESULTS AND DISCUSSIONS

IV.1 CONSTRUCT RELIABILITY AND CONVERGENT VALIDITY

The integrity and scientific robustness of the measurement model were initially assessed through standard metrics of internal consistency and convergent validity. As explicitly detailed in Table 2, all latent variables within the model demonstrated exemplary, highly stable reliability metrics. The calculated Cronbach's alpha (α) values ranged from a baseline of 0.788 (Facilitating Conditions) to a peak of 0.926 (Hedonic Motivation), substantially exceeding the conventional psychometric acceptability threshold of 0.70. To further substantiate the structural stability of the constructs beyond simple inter-item correlation, the Composite Reliability (CR) and Average Variance Extracted (AVE) were computed. The CR values, which provide a more robust measure of internal consistency by accounting for varying factor loadings, universally surpassed the 0.60 operational benchmark, indicating exceptionally strong internal cohesion among the measurement items designated for each specific latent construct. Crucially, the Average Variance Extracted (AVE) for all eight variables exceeded the stringent, non-negotiable 0.50 threshold. The AVE mathematically quantifies the proportion of variance a latent construct captures from its specific indicators relative to the amount of variance due to measurement error. By exceeding 0.50, the data signifies that the latent constructs successfully explain more than half of the total variance present in their respective indicator variables, thereby confirming highly robust convergent validity across the entire theoretical model.

Table 2: Construct Reliability and Validity Indices.

Latent Construct	Cronbach's alpha (α)	Composite Reliability (CR)	Average Variance Extracted (AVE)
Hedonic Motivation (HM)	0.926	0.862	0.675
Habit	0.877	0.885	0.720
Effort Expectancy (EE)	0.885	0.918	0.788
Social Influence (SI)	0.917	0.854	0.661
Performance Expectancy (PE)	0.862	0.927	0.809
Price Value (PV)	0.848	0.882	0.714
Behavioral Intention (BI)	0.855	0.796	0.565
Facilitating Condition (FC)	0.788	0.855	0.664

Source: Authors, (2026).

IV.2 DISCRIMINANT VALIDITY AND ORTHOGONAL FACTOR ARCHITECTURE

Discriminant validity is an essential diagnostic criterion that ensures each theoretical construct is empirically distinct and statistically orthogonal to the others within the highly integrated model. This independence was rigorously verified utilizing the Fornell-Larcker criterion and a comprehensive examination of the construct correlation matrix, as presented in Table 3. According to this strict criterion, the diagonal values (which represent the square root of the AVE for each respective construct) must be strictly greater than any of the off-diagonal correlation coefficients located within the same corresponding rows and columns. The computational analysis confirmed this requirement without exception; the latent variables demonstrably share significantly more variance with their designated measurement indicators than they do with any other distinct construct in the UTAUT2 model. This confirms that the survey instrument successfully isolated distinct psychological domains without operational cross-contamination.

Table 3: Discriminant validity of measures utilizing the Fornell-Larcker criterion.

Construct	HM	Habit	EE	SI	PE	PV	BI	FC
HM	**0.899**							
Habit	0.249***	**0.845**						
EE	0.556***	0.584***	**0.849**					
SI	0.442***	0.754***	0.725***	**0.888**				
PE	0.624***	0.523***	0.771***	0.645***	**0.822**			
PV	0.457***	0.811***	0.591***	0.700***	0.604***	**0.815**		
BI	0.647***	0.536***	0.861***	0.673***	0.759***	0.565***	**0.813**	
FC	0.511***	0.754***	0.661***	0.752***	0.740***	0.759***	0.623***	**0.752**

*(Note: Diagonal values in bold represent the square root of AVE. *** indicates significance at $p < 0.001$)*

Source: Authors, (2026).

Furthermore, the Confirmatory Factor Analysis yielded a rotated factor matrix with exceptionally clean item loadings. Table 4 displays the standardized factor loadings parsed across the eight distinct structural components. High primary loadings (generally scaling > 0.70) combined with minimal, negligible cross-loadings underscore that the individual scale items are correctly and powerfully aligned with their intended theoretical dimensions. For example, analyzing the first component, the survey items theoretically associated with Hedonic Motivation (HM1, HM2, HM3) loaded massively onto Component 1 (0.939, 0.931, and 0.929, respectively), while simultaneously exhibiting near-zero or negative influence on all other structural components. This structural precision affirms the absolute purity of the psychological measurement and validates the instrument's deployment.

Table 4: Factor Matrix demonstrating specific item loadings across all eight components.

Constructs	1	2	3	4	5	6	7	8
HM1	**.939**	-.060	-.019	.034	.003	-.010	-.077	.084
HM2	**.931**	-.005	-.008	.019	.033	.002	.011	-.035
HM3	**.929**	.052	-.017	-.061	-.008	-.010	.064	-.011
Habit2	-.033	**.993**	-.076	.003	.010	-.052	.002	.005
Habit1	-.039	**.898**	.009	-.081	.043	.088	.007	-.005
Habit3	.122	**.707**	.171	.117	-.145	-.026	.056	-.019
EE3	-.026	.069	**.952**	-.040	.100	-.056	-.111	.002
EE2	-.039	-.065	**.841**	.028	-.082	.069	.143	.006
EE4	.023	.000	**.822**	.024	.092	.000	.007	-.042
SI2	-.026	-.028	.032	**.933**	-.031	.002	.034	.014
SI1	-.029	.013	-.047	**.928**	-.002	.042	.047	-.029
SI3	.053	.021	.022	**.879**	.054	-.025	-.070	.016
PE1	-.048	-.066	.108	-.047	**.882**	-.013	.011	.046
PE3	.012	-.044	-.012	.018	**.806**	.064	.029	.061
PE4	.099	.103	-.008	.055	**.791**	-.044	.062	-.101
PV1	-.058	-.119	.019	.005	-.009	**.993**	-.023	-.017
PV2	.030	.108	-.017	-.021	-.029	**.751**	.101	.053
PV3	.057	.195	-.018	.045	.057	**.718**	-.082	-.025
BI1	-.005	.009	-.076	-.013	.094	.021	**.896**	-.020
BI2	-.007	.036	.019	.023	.013	-.046	**.843**	.062
BI3	.036	-.038	.369	.019	-.058	.008	**.579**	.020
FC3	-.003	-.003	-.149	-.016	.006	-.028	.176	**.918**
FC4	.156	-.096	.160	-.033	-.028	.043	-.093	**.791**
FC1	-.139	.283	.024	.104	.071	-.009	-.124	**.623**

Source: Authors, (2026).

IV.3 MODEL FIT ANALYSIS AND STRUCTURAL VALIDATION

Prior to interpreting the causal pathways and demographic divergence, the overall fitness of the structural equation model was rigorously evaluated. This step is critical to guarantee that the hypothesized theoretical network of relationships adequately and proportionally matched the actual empirical data covariance matrix generated by the field survey. As tabulated in Table 5, the model fit indices unambiguously satisfy all established absolute and incremental statistical fit thresholds. The relative Chi-square ratio (CMIN/DF) resulted in an estimate of 2.745. By falling perfectly within the optimal, highly restrictive target range of 1.0 to 3.0, this metric indicates that the model is neither over-parameterized nor excessively rigid. The Comparative Fit Index (CFI), which assesses model fit by comparing the data to the hypothesized model while adjusting for sample size, achieved a robust 0.971, comfortably exceeding the standard 0.95 cutoff for exceptional model fit. Furthermore, the critical error metrics, encompassing the Standardized Root Mean Square Residual (SRMR = 0.052) and the Root Mean Square Error of Approximation (RMSEA = 0.024), both remained well below their strict respective rejection thresholds of 0.08 and 0.06. The PClose value of 1 (which acts as a definitive statistical safeguard by testing the null hypothesis that RMSEA is ≤ 0.05) confirms with absolute certainty that the RMSEA is not significantly greater than zero. Collectively, these highly favorable parameters certify the structural model as an outstanding, mathematically sound framework for subsequent predictive hypothesis testing and multi-group extrapolation.

Table 5: Model Fit Measures for the Structural Equation Model.

Measure	Estimate	Threshold	Interpretation
CMIN	2459.452	--	--
DF	896	--	--
CMIN/DF	2.745	Between 1 and 3	Excellent
CFI	0.971	> 0.95	Excellent
SRMR	0.052	< 0.08	Excellent
RMSEA	0.024	< 0.06	Excellent
PClose	1	> 0.05	Excellent

Source: Authors, (2026).

IV.4 MULTI-GROUP PATH ANALYSIS: THE DICHOTOMY OF PUBLIC VS. PRIVATE INSTITUTIONS

A critical, highly novel facet of this investigation was to determine if macro-level institutional funding structures generate systemic variances in the psychological mechanisms driving VR/AR adoption among their respective populations. A Multi-Group Analysis was conducted to compare the unstandardized beta coefficients (β), critical ratios (*t/C.R.*), and probability values (p) explicitly between Private and Public academic institutions; the results are documented in Table 6.

Table 6: Path Analysis and Significant Differences Between Private and Public Institutions.

Path of Constructs			Private Schools			Public Schools			Significant Difference
Endogenous Variable		**Exogenous Variable**	***β***	***t***	***p***	***β***	***C.R.***	***p***	***p***
VR/AR Adoption	<-	Performance Expectancy	0.071	0.730	0.466	0.164	3.014	0.003	***
VR/AR Adoption	<--	Effort Expectancy	0.636	6.846	***	0.589	11.319	***	***
VR/AR Adoption	<--	Social Influence	-0.011	-0.112	0.911	0.054	1.139	0.255	0.969
VR/AR Adoption	<--	Facilitating Condition	0.085	0.631	0.528	-0.112	-1.742	0.082	0.920
VR/AR Adoption	<--	Hedonic Motivation	0.221	3.318	***	0.243	7.001	***	***
VR/AR Adoption	<--	Habit	0.103	0.901	0.368	0.136	2.141	0.032	***
VR/AR Adoption	<--	Price Value	-0.104	-1.076	0.282	-0.055	-1.016	0.310	0.150

*(Note: *** indicates significance at p < 0.001)*

Source: Authors, (2026).

The comparative data yield profound, multi-layered insights into the socio-economic realities of technology adoption. Within private educational institutions, the structural model simplifies considerably: only Effort Expectancy (β = 0.636, p<.001) and Hedonic Motivation (β = 0.221, p<.001) exert a statistically significant positive impact on the behavioral intention to adopt VR and AR. The exceptionally high sensitivity to Effort Expectancy suggests that users embedded in well-resourced private institutions—who likely already possess seamless access to a wide array of advanced digital tools—highly prioritize the intuitive nature and user-friendliness of immersive systems. If a VR or AR tool is clunky or difficult to use, the private-sector user, driven by high expectations for digital seamlessness, will reject it. They adopt the technology primarily because it is easy to use and intrinsically enjoyable (Hedonic Motivation). Conversely, the behavioral model governing public institutions manifests a far more complex, outcome-driven adoption matrix. In the public sector, Performance Expectancy (β = 0.164, p<.003), Effort Expectancy (β = 0.589, p<.001), Hedonic Motivation (β = 0.243, p<.001), and Habit (β = 0.136, p<.032) all exhibit significant, positive causal relationships with the intention to adopt.

The multi-group difference test mathematically confirms that the variance in behavioral parameters between the two institutional types is statistically significant across Performance Expectancy, Effort Expectancy, Hedonic Motivation, and Habit. The emergence of Performance Expectancy and Habit as significant drivers exclusively within public institutions indicates a starkly different operational reality. Users in public, government-funded environments, which often face resource constraints and highly rigid, standardized testing mandates, are heavily focused on the technology's utilitarian, grade-enhancing outcomes. They adopt VR/AR not just because it is novel or easy, but because they believe it will objectively improve their academic performance [14]. Furthermore, the reliance on Habit suggests that public school adoption requires systemic, repetitive integration into daily routines to become sticky, rather than relying on spontaneous, pleasure-driven usage.

Interestingly, Social Influence, Facilitating Conditions, and Price Value did not reach statistical significance across both demographic groups. The failure of Facilitating Conditions to dictate adoption intent implies that contemporary users, who are largely comprised of digital natives, possess a baseline intrinsic technological self-efficacy that overrides institutional infrastructural deficits; alternatively, it suggests that both sectors struggle equally to provide adequate technical support, rendering the variable a non-factor in individual decision-making [12]. Furthermore, the profound non-significance of Social Influence in Private (β =- 0.011) and in Public (β =0.054) is a telling indicator of market maturity. It implies that the decision to adopt immersive educational technology is highly individualized rather than peer-driven; students and teachers are no longer adopting XR simply because their peers are, but rather evaluating it purely on its personal utility and usability.

IV.5 MULTI-GROUP PATH ANALYSIS: THE PSYCHOLOGICAL GAP BETWEEN STUDENTS AND TEACHERS

To further dissect the structural parameters governing adoption, the dataset was bifurcated by stakeholder role, directly contrasting the psychological determinants of learners (Students) against those of instructional designers (Teachers). The analytical output of this comparison, detailed in Table 7, reveals the most striking behavioral divergence within the entire study.

Table 7: Path Analysis and Significant Differences Between Students and Teachers.

Path of Constructs			Students			Teachers			Significant Difference
Endogenous Variable		**Exogenous Variable**	***β***	***t***	***p***	***β***	***C.R.***	***p***	***p***
VR/AR Adoption	<--	Performance Expectancy	0.131	2.233	0.026	0.509	2.563	0.010	***
VR/AR Adoption	<--	Effort Expectancy	0.595	10.741	***	0.544	2.928	0.003	***
VR/AR Adoption	<--	Social Influence	0.065	1.288	0.198	-0.143	-0.921	0.357	0.127
VR/AR Adoption	<--	Facilitating Condition	-0.071	-1.015	0.310	-0.428	-2.051	0.040	0.00
VR/AR Adoption	<--	Hedonic Motivation	0.249	6.745	***	0.049	0.404	0.686	***
VR/AR Adoption	<--	Habit	0.138	2.002	0.045	0.299	1.600	0.110	***
VR/AR Adoption	<--	Price Value	-0.087	-1.444	0.149	0.130	0.964	0.335	0.065

Source: Authors, (2026).

For the student cohort, the structural modeling mirrors the broader trend toward highly inclusive public institutions. Student adoption of VR and AR technologies is strongly and positively predicated upon Performance Expectancy (β = 0.131, p<.026), Effort Expectancy (β = 0.595, p<.001), Hedonic Motivation (β = 0.249, p<.001), and Habit (β = 0.138, p<.045). The data unequivocally demonstrate that for a student to internalize and adopt immersive learning tools, they must perceive the technology as not only cognitively manageable (Effort Expectancy) and academically beneficial (Performance Expectancy), but also as absolutely critical: the experience must be intrinsically engaging and enjoyable (Hedonic Motivation) [17].

The immense significance of Hedonic Motivation confirms earlier literature postulations that digital-native learners respond exceptionally well to "gamified" or experientially stimulating platforms, validating VR's core utility in increasing spatial presence, psychological flow, and deep academic engagement [10]. In sharp, almost oppositional contrast, the educator cohort (teachers) operates under a distinctly divergent set of technological imperatives. For teachers, the dominant predictors of adoption are Performance Expectancy (β = 0.509, p<.001), Effort Expectancy (β = 0.544, p<.003), and, uniquely, Facilitating Conditions (β = 0.428, p<.040). Notably, Hedonic motivation holds absolutely no significant bearing on a teacher's intention to use VR/AR in their classroom (β = 0.049, p<.686). This indicates a highly pragmatic, outcome-oriented, and severely stressed approach to pedagogical design. Teachers evaluate immersive technology strictly through a lens of unyielding utility, whether the XR platform will objectively enhance the delivery of mandatory curriculum content (Performance Expectancy) and whether it is realistically deployable within a fifty-minute class period without overwhelming pedagogical friction or technical failure (Effort Expectancy). The fun or novelty of the hardware is entirely irrelevant to their operational calculus.

The significant, albeit intensely negative, impact of Facilitating Conditions among teachers (β = -0.428) is perhaps the most profound and concerning finding of this entire investigation. In traditional UTAUT modeling, better facilitating conditions generally drive higher adoption [14]. However, this inverse relationship suggests that as current institutional infrastructures or top-down systemic mandates increase, teacher willingness to adopt XR declines rapidly. This anomaly highlights severe issues of technological fatigue, overly restrictive administrative protocols, or a critical lack of autonomy in curriculum design. It starkly corroborates recent literature detailing the severe challenges and anxieties teachers face when attempting to integrate highly complex [18], unpredictable technologies into rigid, high-stakes classroom frameworks without adequate contextual training [15]. When administrators force "facilitating conditions" via mandates without providing actual pedagogical support, teachers actively resist adoption. The multi-group analysis ultimately confirms that the variance across all aforementioned primary constructs (Performance Expectancy, Effort Expectancy, Hedonic Motivation, Habit, and Facilitating Conditions) is highly statistically significant between educators and learners, proving that a one-size-fits-all deployment strategy for educational XR is fundamentally doomed to fail.

IV.6 SYNTHESIS OF CORE FINDINGS AND THEORETICAL IMPLICATIONS

The systematic aggregation of these multi-group results significantly extends the traditional boundaries and assumptions of the UTAUT2 framework when applied within a modern educational context [14]. Historically, theoretical adoption models assume a relatively homogeneous level of user intent, treating an organization as a single adopting entity. However, this empirical data unequivocally fractures that assumption, proving beyond doubt that the intent to adopt XR is deeply segmented by both functional role (teacher vs. student) and environmental constraint (public vs. private). Universally, Effort Expectancy emerged as the most resilient, dominant, and ubiquitous predictor of adoption intent across all four analyzed sub-populations. This fundamental reality dictates an unyielding law for educational technologists: despite the hyper-advanced, visually stunning nature of immersive reality, the primary barrier to entry remains basic usability [13]. If the VR hardware is cumbersome to wear, or if the AR software interface requires complex recalibration, neither the student's desire for immersive engagement nor the teacher's drive for instructional efficacy will compensate for the resulting cognitive overload and frustration. The technology must simply work seamlessly. Furthermore, the complete collapse of Social Influence as a predictive variable across all groups marks a definitive departure from early-stage technological innovations (where peer pressure heavily drives initial uptake), indicating that AR and VR in education have transcended the hype cycle and transitioned into a mature evaluation phase governed primarily by individualized, utilitarian, and ergonomic assessment.

V. CONCLUSIONS

This exhaustive empirical investigation systematically examined the multidimensional psychological and environmental perceptions surrounding the adoption of virtual reality (VR) and augmented reality (AR) among teachers and students in both public and private educational institutions. Utilizing a rigorously validated extension of the UTAUT2 framework, the study generated highly nuanced, statistically significant intelligence regarding the operational psychology of educational technology integration in the era of Education 4.0. The foremost conclusion drawn from the complex path analysis is that Effort Expectancy, Performance Expectancy, and Hedonic Motivation are the paramount, universal drivers facilitating the adoption of immersive technologies. However, deep cross-demographic analyses exposed profound systemic dichotomies that mandate highly targeted deployment strategies. In both private and public academic institutions, Effort Expectancy and Hedonic Motivation dictate the baseline parameters for student adoption; learners overwhelmingly prioritize frictionless ease of use and deep experiential enjoyment. Conversely, educators adopt a strictly utilitarian, pragmatic operational framework. Teachers are structurally indifferent to the hedonic or entertaining facets of VR/AR, grounding their adoption intent exclusively in Performance Expectancy (the tangible, measurable pedagogical benefits) and Effort Expectancy (the logistical ease of classroom deployment).

Moreover, the analytical output challenges several established industry assumptions. The consistent statistical insignificance of Social Influence and Price Value across the broader models suggests that adoption is now an individualized, pragmatic calculation not influenced by social normative pressures or immediate financial concerns (which are likely abstracted to the institutional level). Crucially, the data underscores a critical vulnerability in the educational supply chain: the negative correlation between facilitating conditions and teacher adoption. Because these technologies are rapidly emerging and market demand is surging toward a $14.2 billion valuation, institutions risk catastrophic implementation failure if they impose top-down hardware mandates without aggressively enhancing pedagogical support capabilities tailored specifically for teachers. Without strategic alignment that emphasizes career readiness, seamless integration, and minimized pedagogical friction, teacher-led adoption will stagnate, rendering the technology useless regardless of student enthusiasm. Despite the robust methodological framework deployed herein, this research acknowledges several operational limitations that warrant future scientific inquiry. The sample size, while statistically massive and highly valid, represents a cross-sectional snapshot obtained within a limited temporal window; it captures immediate perceptual states rather than evolving, long-term adoption dynamics. It is highly recommended that future scholars execute extended longitudinal methodologies to firmly establish and confirm the causal evolution of these behavioral effects over prolonged, multi-year exposure periods.

Finally, given the localized nature of the snowball sampling methodology, future research must deliberately incorporate cross-cultural variables and socio-economic indicators unique to differing global societal architectures to definitively identify the universal relevance, adaptability, and ultimate scalability of this proposed immersive technology adoption model.

VI. AUTHOR'S CONTRIBUTION

Conceptualization: Julius G. Garcia
Methodology: Julius G. Garcia
Investigation: Julius G. Garcia and Alvie Simonette Q. Alip.
Discussion of results: Julius G. Garcia, Myrna S. Batino, and Alvie Simonette Q. Alip.
Writing – Original Draft: Julius G. Garcia.
Writing – Review and Editing: Julius G. Garcia, Myrna S. Batino, and Alvie Simonette Q. Alip.
Resources: Julius G. Garcia.
Supervision: Julius G. Garcia
Approval of the final text: Julius G. Garcia, Myrna S. Batino, and Alvie Simonette Q. Alip.

VII. ACKNOWLEDGMENTS

The research team wishes to extend their deepest gratitude to the administrative boards, participating faculty members, and student respondents across the various public and private academic institutions who generously provided their time, cognitive effort, and invaluable insights to facilitate this exhaustive investigation. The foundational institutional support structures and the enthusiastic willingness of the broader academic community to critically engage with emerging, disruptive educational technology frameworks were absolutely instrumental in the successful execution and conclusion of this empirical study.

VIII. REFERENCES

[1] M. Fukuyama, "Society 5.0: Aiming for a New Human-Centered Society," *Japan Spotlight*, vol. 27, pp. 47–50, Jul./Aug. 2018.

[2] C. Fadel, M. Bialik, and B. Trilling, *Four-Dimensional Education: The Competencies Learners Need to Succeed*. Boston, MA: Center for Curriculum Redesign, 2015.

[3] G. Lampropoulos, E. Barkoukis, K. Burden, and T. Anastasiadis, "Augmented Reality and Virtual Reality in Education: Public Perspectives, Sentiments, Attitudes, and Discourses," *Education Sciences*, vol. 12, no. 11, Art. no. 798, Nov. 2022. DOI: 10.3390/educsci12110798

[4] MarketsandMarkets, "Augmented and Virtual Reality in Education Market – Global Forecast to 2028," MarketsandMarkets Research, 2023. [Online]. Available: https://www.marketsandmarkets.com/Market-Reports/augmented-reality-in-education-market-203811025.html

[5] B. D. Boyles, "Virtual Reality and Augmented Reality in Education," in *Instructional Systems Design and the Diffusion and Adoption of Technology*, vol. 1. Norfolk, VA: Old Dominion University, 2017, ch. 4.

[6] A. Radianti, T. A. Majchrzak, J. Fromm, and I. Wohlgenannt, "A systematic review of immersive virtual reality applications for higher education: Design elements, lessons learned, and research agenda," *Computers & Education*, vol. 147, Art. no. 103778, 2020. DOI: 10.1016/j.compedu.2019.103778

[7] M. Akçayır and G. Akçayır, "Advantages and challenges associated with augmented reality for education: A systematic review of the literature," *Educational Research Review*, vol. 20, pp. 1–11, 2017. DOI: 10.1016/j.edurev.2016.11.002

[8] M. Ghobadi, S. Shirowzhan, M. M. Ghiai, F. M. Ebrahimzadeh, and F. Tahmasebinia, "Augmented Reality Applications in Education and Examining Key Factors Affecting the Users' Behaviors," *Education Sciences*, vol. 13, no. 1, Art. no. 10, Jan. 2023. DOI: 10.3390/educsci13010010

[9] M. C. Bautista, I. R. Evangelista, A. Culaba, R. S. Concepcion, and E. P. Dadios, "Technology Adoption of Augmented and Virtual Reality in a Progressive Philippines: A Socio-techno-economical Analysis," in *Proc. 2022 IEEE 14th Int. Conf. Humanoid, Nanotechnology, Information Technology, Communication and Control, Environment, and Management (HNICEM)*, Boracay Island, Philippines, 2022, pp. 1–6. DOI: 10.1109/HNICEM57413.2022.10109429

[10] C. Moro, Z. Štromberga, A. Raikos, and A. Stirling, "Augmented Versus Virtual Reality in Education: An Exploratory Study Examining Science Knowledge Retention When Using Augmented Reality/Virtual Reality Mobile Applications," *Cyberpsychology, Behavior, and Social Networking*, vol. 20, no. 11, pp. 645–651, 2017. DOI: 10.1089/cyber.2017.0205

[11] S. Alshammari, "An Extended UTAUT2 Model to Explain the Adoption of Virtual Reality Technology in Health Centers: An Empirical Study Based in Riyadh," *Int. J. Computer Science and Network Security*, vol. 21, no. 3, pp. 204–216, Mar. 2021.

[12] J. Garzón, J. Pavón, and S. Baldiris, "Systematic review and meta-analysis of augmented reality in educational settings," *Virtual Reality*, vol. 23, no. 4, pp. 447–459, 2019. DOI: 10.1007/s10055-019-00379-9

[13] R. Y. Syed Far, A. M. Sharif, M. D. A. Halim, and S. N. A. Syed, "Identifying Factors Affecting Acceptance of Virtual Reality in Classrooms Based on Technology Acceptance Model (TAM)," *Asian Journal of University Education*, vol. 15, no. 3, pp. 51–60, Dec. 2019. DOI: 10.24191/ajue.v15i3.7845

[14] V. Venkatesh, J. Y. L. Thong, and X. Xu, "Consumer Acceptance and Use of Information Technology: Extending the Unified Theory of Acceptance and Use of Technology," *MIS Quarterly*, vol. 36, no. 1, pp. 157–178, Mar. 2012. DOI: 10.2307/41410412

[15] R. Videla, C. Aguayo, R. Veloz, and M. Rossel, "Introducing Virtual Reality and Emerging Technologies in a Teacher Training STEM Course," *Education Sciences*, vol. 13, no. 10, Art. no. 1044, Oct. 2023. DOI: 10.3390/educsci13101044

[16] W. M. Vagias, "Likert-Type Scale Response Anchors," Clemson International Institute for Tourism & Research Development, Clemson University, 2006.

[17] E. Ibili, D. Resnyansky, and M. Billinghurst, "Adoption of Augmented Reality Technology by University Students," *Technology, Knowledge and Learning*, vol. 24, no. 3, pp. 341–366, 2019. DOI: 10.1007/s10758-018-9359-2

[18] F. N. Ofosu-Amaah, "Diffusion of Virtual and Augmented Reality in Pre-K to 12 Education: Experiences and Perceptions of Pioneer Teachers," Ed.D. dissertation, Seton Hall University, South Orange, NJ, 2021.

Journal of Engineering and Technology for Industrial Applications

ITEGAM-JETIA

Manaus, v.12 n.60, p. 773-779, July/August, 2026.
DOI: https://doi.org/10.5935/jetia.v12i60.4025

ISSN ONLINE: 2447-0228

RESEARCH ARTICLE OPEN ACCESS

REAL-TIME HAND GESTURE DETECTION WITH 3-D KEY POINTS USING DEEP LEARNING

Sanjay R Pawar[1], Rameez Shamalik[2*], Nazim Mahammad Shaikh[3], Pramod V Londhe[4], Mohd Imran Ansari[5], Ritesh G Mahajan[6] and Sanjay Koli[7]

[1,4]Department of Mechanical Engineering, Bharati Vidyapeeth (DU) College of Engineering, Pune
[2]Rameez Shamalik, Department of Computer Science and Engineering, School of Computing, MIT-ADT University, Pune, Maharashtra-412201, India
[3]Department of Basic Science and Humanities, Bharati Vidyapeeth (DU) College of Engineering, Pune
[5,6]Department of Robotics & Automation Engineering, Bharati Vidyapeeth (DU) College of Engineering, Pune
[7]E&TC Dept., Ajeenkya D Y Patil school of engineering, Pune, India.

[1]https://orcid.org/0000-0002-4835-0347, [2]https://orcid.org/0000-0002-3721-6011, [3]https://orcid.org/0000-0001-6005-9387
[4]https://orcid.org/0000-0002-5151-818X, [5]https://orcid.org/0000-0001-9477-6368, [6]https://orcid.org/0000-0002-5911-987X
[7]https://orcid.org/0000-0001-5401-959X

Email: srpawar@bvucoep.edu.in, *rameez.shamalik@mituniversity.edu.in, nmshaikh@bvucoep.edu.in, pvlondhe@bvucoep.edu.in, miansari@bvucoep.edu.in, rgmahajan@bvucoep.edu.in, sanjay.koli@dypic.in

ARTICLE INFO

Article History
Received: March 11, 2026
Reviewed: April 11, 2026
Accepted: May 11, 2026
Published: July 31, 2026

Keywords:
3D estimation,
Video processing,
Gesture detection,
Convolutional Neural Networks (CNN).

ABSTRACT

The importance of touchless systems for easier Human Machine Interaction (HMI) has been brought to light by recent pandemics. A key component of HMI, gesture detection represents a distinct class of useful computer vision applications. Outstanding outcomes in video processing are demonstrated by Convolutional Neural Networks (CNN) for a range of computer vision applications. This study reviews and compares various CNN versions for gesture detection along with their uses. To determine the correctness of the model, a local dataset of hand gestures is built and tested in conjunction with a synthetic gesture dataset. Using multilayered CNN, palm detection in a video frame is accomplished with efficient foreground-background separation. In a parametric research, these Mean Square Error (MSE) values are then contrasted with the known comparable system. The MSE of 12.6% obtained from the combination of synthetic and local datasets is better than that of recent research. In order to achieve 3 Dimensional (3D) estimation of a hand gesture with the aid of palm recognition, the number of key points allocated for the skeletal representation of the hand is crucial. This further enables the application of the technique in numerous upcoming genres.

Copyright ©2026 by authors and Galileo Institute of Technology and Education of the Amazon (ITEGAM). This work is licensed under the Creative Commons Attribution International License (CC BY 4.0).

I. INTRODUCTION

Convolutional Neural Networks (CNN's) are a subset of deep neural networks that are most frequently employed in image or video processing. One of the finest methods for extracting features from a video frame is convolutional networks. It recognises the supplied video frames as a pixel matrix, making it simpler to separate the contained items. Then, several levels with weights and biases are supplied with these pixels. These layers are all interconnected and aid in feature extraction before categorization. When gesture detection is only concerned with real-time video processing, a complex scenario is exhibited. The complexity of video processing algorithms has grown quickly over time [1], [2]. CNNs, because of their default categorization output, carry out the fundamental operation on videos to identify a certain gesture [3]. In accordance with the applications for which they are utilised, there are several types of neural networks. There are several different CNN designs, including as LeNet, AlexNet, VGG, GoogLeNet, ResNet, and many more. Since there are more variables in hand gesture detection than in face detection, it faces many challenges. Hands, unlike the face, which has fixed features such as the nose, eyes, and ears, have ten different shaped fingers. Their morphology and position fluctuate in real time, and gestures have a greater number of possible combinations.

There is a high likelihood that fingers will merge with the noisy background, as well as occlusion. Numerous researchers have been working on such confinements and developed 2D and 2.5D key point estimation techniques. This approach, while effective, lacks disparity and geometry for a real-time complex system. Semantic segmentation is essential for labelling pixels in a frame and aiding in the separation of the foreground and background. UNET and VGG-16, two CNN-based deep learning models, are created for segmentation and classification [4]. In order to assist astronauts in the space station with gesture detection as they deal with robots for their daily tasks, a combination of Mask-RCNN and MobileNet is employed for background removal and feature extraction, respectively [5]. Recently, the Hybrid Multidimensional Deep Convolutional Neural Network (HMDCNN) was created to enable multimodal recognition of speech as well as facial, lip, and even voice [6].

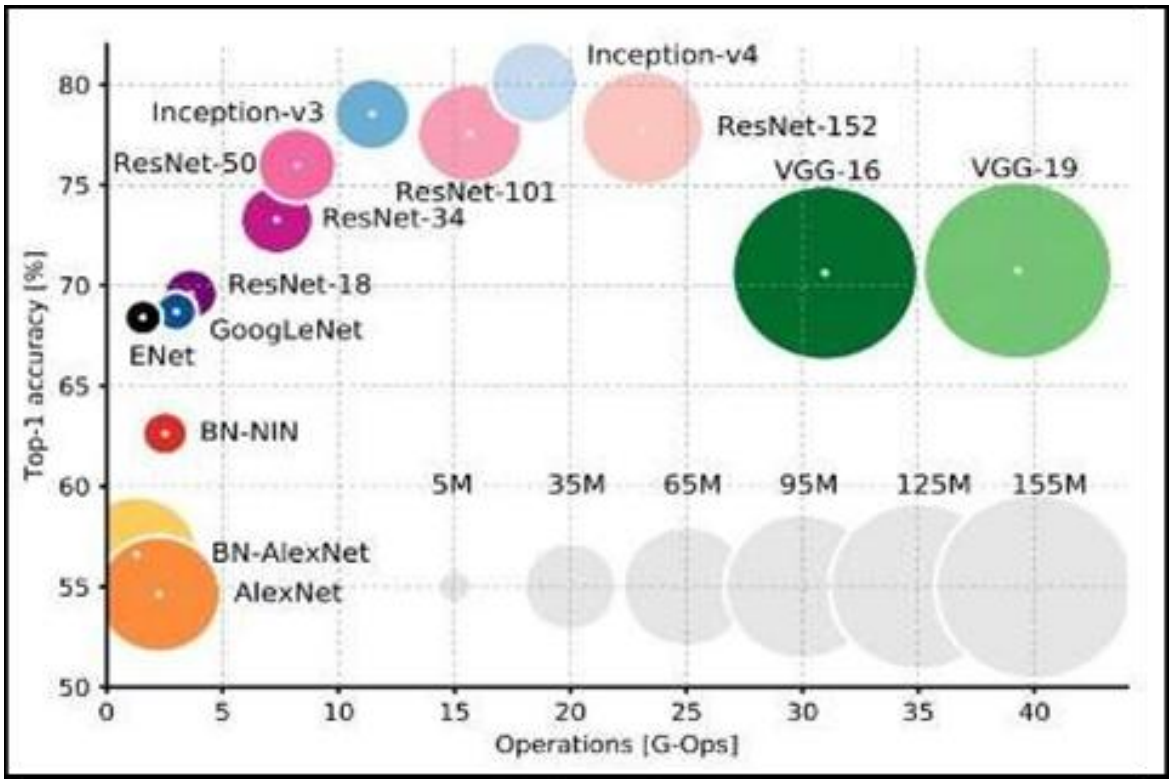


Figure 1: Accuracy Vs Number of operations performed in various types of CNNs.
Source: Authors, (2026).

Figure 1 illustrates how Alexnet and its variants provide respectable accuracy with regard to few operations carried out. The quantity of procedures is gradually raised as we go forward in our hunt for greater precision. When it comes to providing the best performance for a given amount of operations, Enet, GoogleNet, and ResNet are quite close. Processing video that comprises a lot of image frames quickly and efficiently is required for the main focus. However, even little flaws in video accuracy, such as lag or delay, utterly defeat the point. Newer versions of ResNet, Inception Net and Inverse Kinematics Net that provide a trade-off between accuracy and operations are helpful for solving such challenging real- world situations [7], [8]. Despite being rather hefty models, VGG-16 and VGG-19 provide good accuracy for video processing of about 70–75 percent while simultaneously processing millions of operations to evaluate the system's processing capabilities. For dynamic hand gesture identification, optical motion guided templates are used with 2D and 3D CNNs [9]. An easy-to-use but effective technique for extracting feature vectors for Chinese sign language identification uses 3D CNN [10] and optimised dense optical flow to analyse video stream.

When working with complicated datasets, it might sometimes be more productive to utilise a single network rather than the hybrid networks stated above. Therefore, a quicker R-CNN is employed with pose anchor key points for hand motions for the difficult Large scale Multiview 3D Hand Pose Dataset (LSM-HPD). Skeleton extraction from a video frame to identify motions and gestures is another innovative approach to this subject. To extract skeletal information and subsequently identify the action based on it, Recurrent Neural Networks (RNNs) and Long Short-Term Memory (LSTM) cells are utilised in conjunction [11]. The difficult challenge of recognising dynamic hand movements often requires the use of several CNN models. A 3D-Resnet network is employed for introduce fusion to abstract restricted spatiotemporal characteristics, and then a variation ConvLSTM is used to acquire global spatiotemporal data [12]. For the same application online, a CNN architecture with an effective sliding window technique is given [13]. It consists of a classifier and a detector on two levels. For efficiency analysis, a separate CNN is utilised. Figure 2 depicts the detector and classifier structure combination which uses single time activation function to save time and processing.

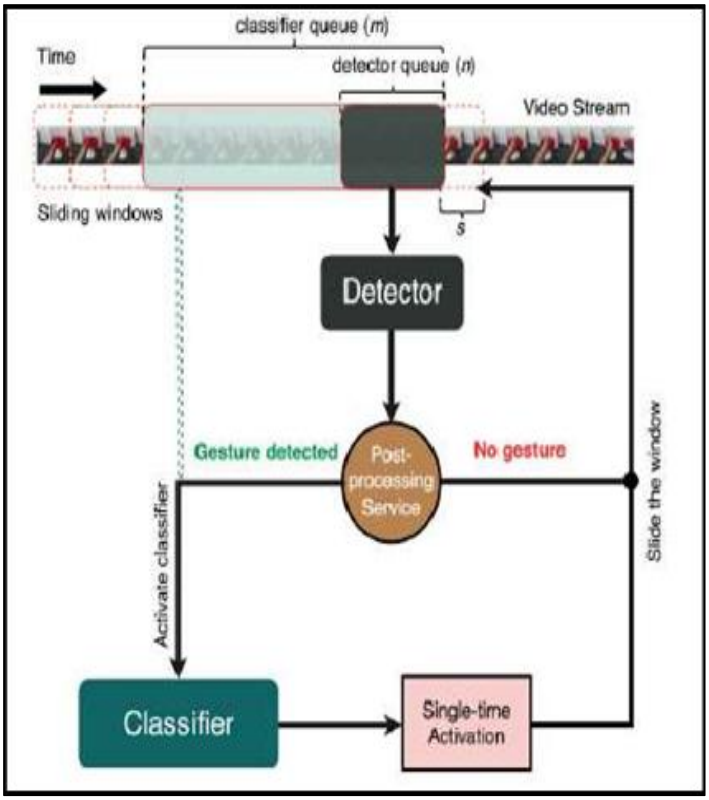


Figure 2: Two-level hierarchical structure.
Source: [13].

A glove sensor was introduced for Human Machine Interaction (HMI) in order to record the precise coordinates of hands. According to its intended use, gloves typically incorporate a variety of sensors, including an optical sensor [14], assistive technology for the blind and deaf [15], accelerometer and gyroscope sensors for human machine interfaces [16] or a color-based glove that can be customized with 3D models [17]. The main goal of computer vision is to do these tasks with the least amount of hardware possible by training a neural network, which adds more innovation and creativity to the desired job. In Methodology, it is demonstrated how to use a mixture of CNNs to obtain a 3D representation of gestures. In the gesture detection scheme, the palm represents the most stable stationary part of the hand. After acquiring video feed, the proposed research performs the Palm detection process first. The wrist of the palm is assumed to be the target value, and the key points are envisioned in relation to it. Lastly, joint estimation and prediction on a 3D surface are performed to replicate a 3D skeletal hand gesture instantaneously. The use of costly stereo sensors or multi camera set up at various perspectives is prevented, and a simple RGB camera is used instead.

In this paper the authors summarise their contributions as follows.

a) An alternative model is suggested to resolve the problem
b) Development of Local and Synthetic datasets
c) Planned the model is trained and tested on these datasets
d) Parametric study of final results with reference to latest contributions.

II. MATERIALS AND METHOD

With a few minor exceptions, all of the strategies described in the previous section utilise multilayer design. When real-time gesture detection is needed for video processing, assembling the necessary hardware is a laborious effort. When employing CNN for deep learning on such tasks, a graphics processing unit (GPU) is required. Herein study, real- time video processing is done on an NVIDIA GPU. Google Colab, Kaggle, and for paid or rented offerings Amazon Web Services (AWS) and Microsoft Azure enable access to GPU over the cloud, among many more operators, are some additional platforms that offer free GPU usage for a certain time frame. Therefore, the end output may be either a 3D dataset for model processing or a 3D estimate of gestures and actions in order to achieve greater accuracy [18]. A Google hand tracking resolution suggests an ML pipeline that combines two models that cooperate with one another: a palm detector and a hand landmark model [19]. Using an aligned hand bounding box, the former locates palms, and the latter yields high-fidelity 2.5D landmarks. Finding the depth from a particular frame is crucial to achieving 3D perception in computer vision. The easiest method of finding depth is to have users interact with the system [20]. Another approach may use the placement of numerous cameras [21] or possibly the use of a well-structured light to record the geometry of the frame in relation to a single image [22]. The most popular technique for doing this is monocular depth estimation, although for greater accuracy, more datasets are required [23]. A Gated Multi-Scale Network is employed to get the same result [24]. The time-consuming job of estimating depth, which calls for the use of numerous datasets, is substantially helped by the use of 3D key points.

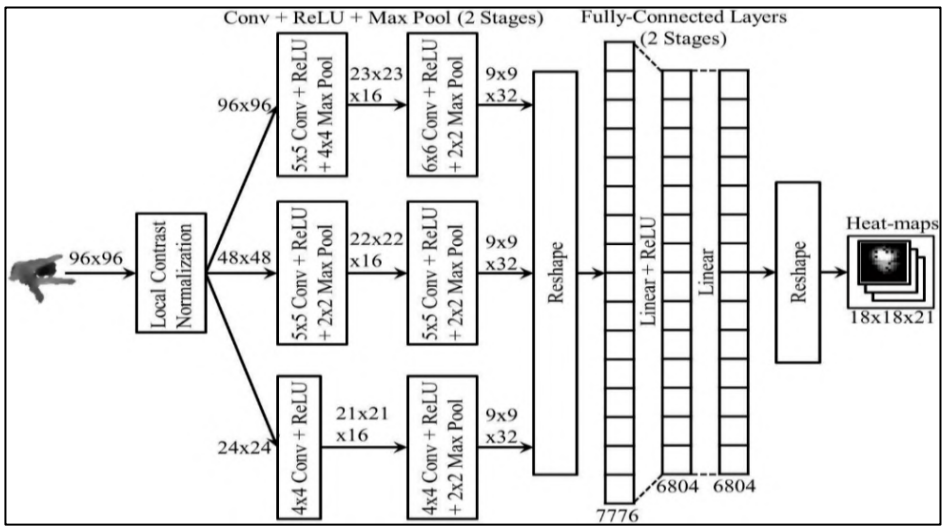


Figure 3: Combination of convolutional and fully connected layers.
Source: [25].

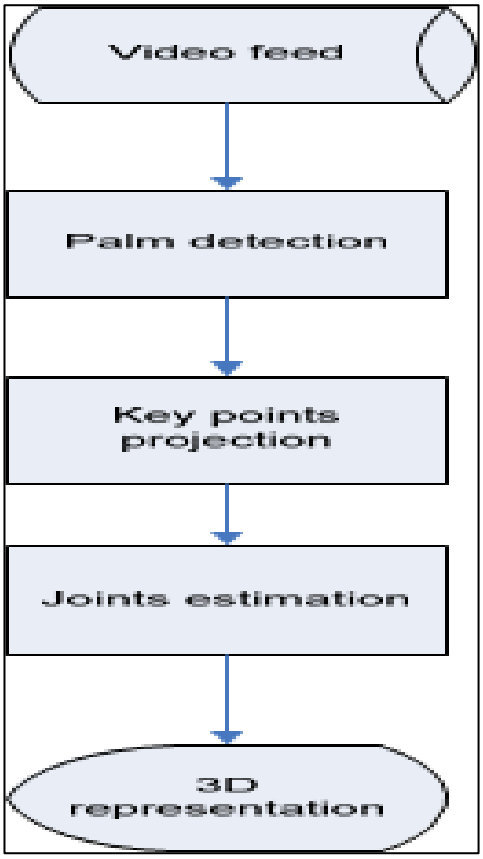


Figure 4: Flowchart of the proposed model.
Source: Authors, (2026).

As seen in figure 3, the gesture's primary point and focal length are determined after taking a depth reading from the relevant frame or picture, and the motion's local contrast is altered [25] which aids in the image normalisation process. The combination of 5 by 5 and 4 by 4 Convolution and ReLu is used along with 2 by 2 Max pooling. After being down sampled, the images are run through many convolutional layers. The feature map outputs are then input into fully linked layers to produce heat maps. As seen in figure 4, the only sensor employed in this suggested system is a camera, or video stream. The palm detector uses the video frames to form a convex hull around the hand, with the radius determining the borders of the fingers. The entire palm, including the fingers, is covered by the Euclidean distance which helps in Key points projection The final phase projects the critical locations along the defined contour. In order to connect the important locations in a skeleton-like form, the Guassian distribution of joints for Joints estimation is determined using three views of heat maps. Equation 1 may be used to determine a 3D representation of joint positions at the final stage.

II.1 STEPWISE IMPLEMENTATION

Where , a measure of reconstruction of is optimal joints, suggests optimal coefficients for joints, is total amount of principal components included and mean vector constant. It has been observed that 21 key points, as opposed to other number of key points, provide better throughput and are linked to each other for precise gesture and geometry estimation.

II.2 DATASETS AND PRE-PROCESSING

Two distinct dataset kinds are joined to get the desired outcome. Starting with 5k images made from locally gathered gesture dataset [26], each with a unique collection of gestures. Each image has a different backdrop, which adds to the diversity of frames available for training the model. Aside from the front motions that are necessary, the background has intricate shape and variable illumination. Additionally, a synthetic dataset with more than 50k images that includes hand movements with various skin tones is employed. To accurately define the skeleton hand shape, annotations are pre-processed on a local gesture dataset with a maximum of 21 key points. These crucial details makes it easier to capture the widest variety of hand gestures and movements possible in any one frame. With the aid of 21 crucial points, the skeleton hand may be used to identify motions, without the need for bright illumination or an unsettling background.

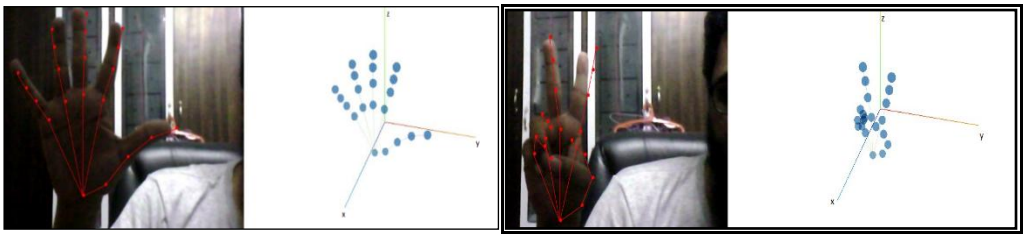
II.3 TRAINING DETAILS

The hyper parameters are chosen in such a way that it reaches a trade-off between the complexity of the model and its likely results. The two models are trained using the Root Mean Square Propagation (RMSProp) optimizer, which has a learning rate of 10-4. Both modules have 50 iterations, with the first module having a batch size of 32 and the second having a batch size of 64. The model is trained using 75% of the photos, tested using 15%, and then validated using the remaining images. The system is trained considering multiple losses which includes Regularisation loss($£_{reg}$), 3D loss($£_{3D}$), Normalisation loss($£_{Norm}$) and Angular loss ($£_{Ang}$) as shown in equation 2.

$$£_{total} = £_{reg} + £_{3D} + £_{Norm} + £_{Ang} \quad (2)$$

III. RESULTS AND DISCUSSIONS

Figures 5 (a) and (b) demonstrate how our model, even in low light and noisy background, can recognise the palm in the supplied video frame while removing the complicated backdrop. Even though it cannot precisely trace the critical locations on the index finger in 5 (a), the 3D graph nevertheless provides a better depiction. Joint estimation is crucial in this case to project the skeleton form of the palm and fingers, and the gesture's 3D structure amplifies the geometry and depth of the gesture in the available space. The reconstruction of hands in a three-dimensional axis improves the accuracy and precision of gestures in real-time. To analyse the gesture in a particular video frame from various perspectives, the hands XYZ axis representation may be rotated.



(a) (b)

Figure 5: (a) & (b) Shows key points projected on palm, in low light and noisy background with its skeletal representation in XYZ axis.
Source: Authors, (2026).

The simulated dataset demonstrates improved accuracy for locating the precise critical locations in palm. Since the model must function in real-world situations, the locally produced hand gesture dataset is more important since artificial motions, in contrast to real-world situations, have smooth skin textures and steady backdrops. It is therefore necessary to combine the two datasets, which improves accuracy in terms of Mean Square Error (MSE), which provides a measure of the quality of frame predictions, when compared to utilising only the local dataset with authentic hand gestures. Mean square error represents the difference of the squared error between actual (A_v) and predicted (P_v) output as shown in equation 3.

$$MSE = \frac{1}{n}\sum_{i=1}^{n}(A_v - P_v)^2 \quad (3)$$

To analyse the gesture in a particular video frame from various perspectives, the hands XYZ axis representation may be rotated. A trade-off between aims and relevance is developed as a result. MSE should ideally be zero and practically as low as possible. The suggested technique outperforms the corresponding traditional model, as demonstrated in table 1, when compared. The Local Hands dataset gives MSE of 15.7 while synthetic Hands gives 25. On the other hand combination of both
datasets gives superior MSE of 12.6, all in terms of percentage.

Table 1: Model performance for available datasets.

Datasets	Proposed System MSE (%)	FanZengh et.al., MSE (%)
Local Hands	15.7	16.1
Synthetic Hands	25	25.7
Combination of Both	12.6	13.4

Source: Authors, (2026).

Percentage of Correct Key-points (PCK) is another method to measure the amount of the hand gesture key points and joint estimation. When the difference between the predicted and the true joint is smaller than some threshold, the identified joint is considered to be correct.

To come up with the distances, the pixel lengths in each case are normalised by 0.7 the corresponding hand size of the corresponding person, with regard to threshold which are applied in the development of the PCK curves. The blue and green dotted lines are the PCK of local and synthetic hand gesture dataset respectively and the red line is the PCK of mixture of both datasets. In this way, the tradeoff can be well brought out in terms of practical use of hand gesture datasets.

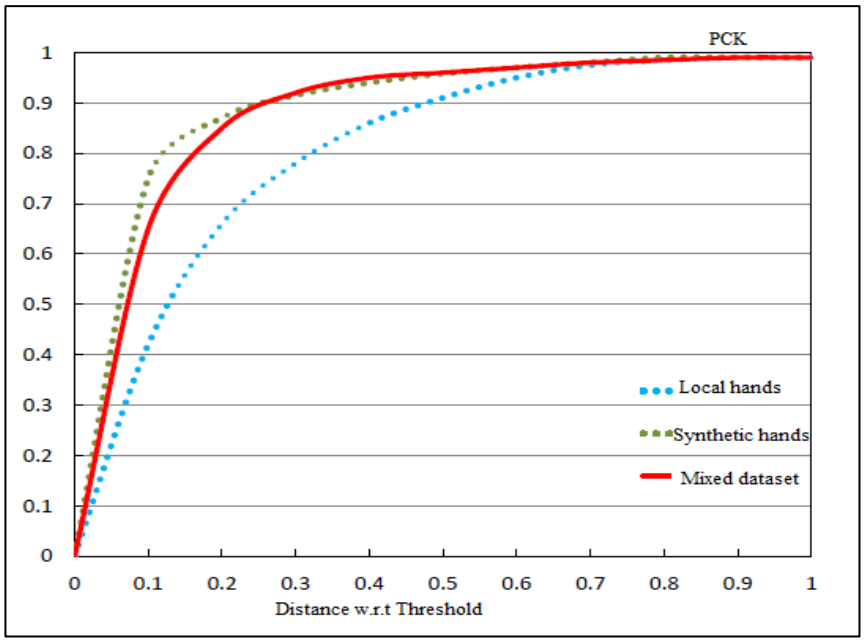


Figure 6: PCK comparison between different datasets.
Source: Authors, (2026).

IV. CONCLUSIONS

Real-time gesture recognition is well-suited for CNN operations, particularly in feature extraction and classification.

•Various CNN configurations can be employed for dynamic, online gesture detection.
•Combining results from two separate CNNs tends to outperform a single CNN in gesture recognition.
•The use of complex hardware enhances computer vision solutions for real-time video processing.
•Locally created dataset exhibits moderate accuracy with 15.7% MSE with actual video frames.
•Research utilizes a combination of datasets for training and testing, resulting in improved accuracy and a reduced MSE of 12.6%.
•PCK is a parameter used for exact projection of key points around hand gestures, showing consistent results on both datasets.
•Gesture sensing technologies find applications in gaming, virtual reality, and augmented reality.

V. AUTHOR'S CONTRIBUTION

Conceptualization: Sanjay R Pawar and Rameez Shamalik.
Methodology: Sanjay R Pawar and Mohd Imran Ansari.
Investigation: Sanjay R Pawar and Nazim Mahammad Shaikh.
Discussion of results: Sanjay R Pawar, Rameez Shamalik, Ritesh G Mahajan and Mohd Imran Ansari.
Writing – Original Draft: Sanjay R Pawar.
Writing – Review and Editing: Sanjay R Pawar, Rameez Shamalik and Ritesh G Mahajan.
Resources: Sanjay R Pawar and Ritesh G Mahajan.
Supervision: Mohd Imran Ansari and Rameez Shamalik.
Approval of the final text: Sanjay R Pawar, Pramod V Londhe, Sanjay Koli and Rameez Shamalik.

VI. REFERENCES

[1] Wiedemann, S., Kirchhoffer, H., Matlage, S., Haase, P., Marbán, A., Marinc, T., Neumann, D., Nguyen, T., Schwarz, H., Wiegand, T., Marpe, D., & Samek, W. (2019). DeepCABAC: A Universal Compression Algorithm for Deep Neural Networks. IEEE Journal of Selected Topics in Signal Processing, 14, 700-714.

[2] Koli, S.M., & Shamalik, R. (2019). Transformation of Video Signal Processing Techniques from 2D to 3D: A Survey. Lecture Notes in Electrical Engineering. 570, pp.63–70.

[3] Shamalik, R., & Koli, S.M. (2022). Real Time Gesture Detection Using Convolutional Neural Network. 2022 IEEE 4th International Conference on Cybernetics, Cognition and Machine Learning Applications (ICCCMLA), 1-4.

[4] Dutta, H.P., Sarma, D., Bhuyan, M.K., & Laskar, R.H. (2020). Semantic Segmentation based Hand Gesture Recognition using Deep Neural Networks. 2020 National Conference on Communications (NCC), 1-6.

[5] Lingyun, G., Lin, Z., & Zhaokui, W. (2020). Hierarchical Attention-Based Astronaut Gesture Recognition: A Dataset and CNN Model. IEEE Access, 8, 68787-68798.

[6] Vynokurova, O., & Peleshko, D. (2020). Hybrid Multidimensional Deep Convolutional Neural Network for Multimodal Fusion. 2020 IEEE Third International Conference on Data Stream Mining & Processing (DSMP), 131-135.

[7] Shamalik, R., & Koli, S.M. (2023). Effective and efficient approach for gesture detection in video through monocular RGB frames. Multimedia Tools and Applications, 82, 17231-17242.

[8] Shamalik, R., & Koli, S. (2022). DeepHands: Dynamic hand gesture detection with depth estimation and 3D reconstruction from monocular RGB data. Sādhanā, 47, 1-9.

[9] Sarma, D., Kavyasree, V., & Bhuyan, M.K. (2022). Two-stream fusion model using 3D-CNN and 2D-CNN via video-frames and optical flow motion templates for hand gesture recognition. Innovations in Systems and Software Engineering, 1 - 14.

[10] Zhao, K., Zhang, K., Zhai, Y., Wang, D., & Su, J. (2020). Real-Time Sign Language Recognition Based on Video Stream. 2020 39th Chinese Control Conference (CCC), 7469-7474.

[11] Avola, D., Cascio, M., Cinque, L., Foresti, G.L., Massaroni, C., & Rodolà, E. (2020). 2-D Skeleton-Based Action Recognition via Two-Branch Stacked LSTM-RNNs. IEEE Transactions on Multimedia, 22, 2481-2496.

[12] Peng, Y., Tao, H., Li, W., Yuan, H., & Li, T. (2020). Dynamic gesture recognition based on feature fusion network and variant ConvLSTM. IET Image Process., 14, 2480-2486.

[13] Köpüklü, O., Gunduz, A., Kose, N., & Rigoll, G. (2020). Online Dynamic Hand Gesture Recognition Including Efficiency Analysis. IEEE Transactions on Biometrics, Behavior, and Identity Science, 2, 85-97.

[14] Fujiwara, E., Ferreira Marques Dos Santos, M., & Suzuki, C.K. (2014). Flexible Optical Fiber Bending Transducer for Application in Glove-Based Sensors. IEEE Sensors Journal, 14, 3631-3636.

[15] Shrote, S.B., Deshpande, M., Deshmukh, P., & Mathapati, S. (2014). Assistive Translator for Deaf & Dumb People.

[16] Gupta, H.P., Chudgar, H.S., Mukherjee, S., Dutta, T., & Sharma, K. (2016). A Continuous Hand Gestures Recognition Technique for Human-Machine Interaction Using Accelerometer and Gyroscope Sensors. IEEE Sensors Journal, 16, 6425-6432.

[17] Lamberti, L., & Camastra, F. (2011). Real-Time Hand Gesture Recognition Using a Color Glove. International Conference on Image Analysis and Processing.

[18] Shamalik R, Koli S, (2020). Emergence and Functionality of 3D Videos. International Journal of Engineering and Advanced Technology.

[19] Zhang, F., Bazarevsky, V., Vakunov, A., Tkachenka, A., Sung, G., Chang, C., & Grundmann, M. (2020). MediaPipe Hands: On-device Real-time Hand Tracking. ArXiv, abs/2006.10214.

[20] López, A., Garces, E., & Gutierrez, D. (2014). Depth from a Single Image Through User Interaction. Spanish Computer Graphics Conference.

[21] Shamalik, R., & Koli, S.M. (2021). Real Time Human Gesture Recognition: Methods, Datasets and Strategies. Recent Trends in Intensive Computing.

[22] Bahmutov, G., Popescu, V., & Sacks, E. (2004). Depth Enhanced Panoramas. IEEE Visualization 2004, 11p-11p.

[23] Ranftl, R., Lasinger, K., Hafner, D., Schindler, K., & Koltun, V. (2019). Towards Robust Monocular Depth Estimation: Mixing Datasets for Zero-Shot Cross-Dataset Transfer. IEEE Transactions on Pattern Analysis and Machine Intelligence, 44, 1623-1637.

[24] Lin, L., Huang, G., Chen, Y., Zhang, L., & He, B. (2020). Efficient and High-Quality Monocular Depth Estimation via Gated Multi-Scale Network. IEEE Access, 8, 7709-7718.

[25] Ge, L., Liang, H., Yuan, J., & Thalmann, D. (2016). Robust 3D Hand Pose Estimation in Single Depth Images: From Single-View CNN to Multi-View CNNs. 2016 IEEE Conference on Computer Vision and Pattern Recognition (CVPR), 3593-3601.

[26] Shamalik, R., & Koli, S. (2023). “FabDepth I: A Unique Dataset for Efficient Gesture Detection”. International Journal of Information Technology, 15, 2645 - 2649.

Journal of Engineering and Technology for Industrial Applications

ISSN ONLINE: 2447-0228

ITEGAM-JETIA

Manaus, v.12 n.60, p.780-789 July/August, 2026.
DOI: https://doi.org/10.5935/jetia.v12i60.4033

RESEARCH ARTICLE OPEN ACCESS

DESIGN AND VERIFICATION OF A FAULT-TOLERANT AHB-TO-APB BRIDGE WITH INTEGRATED SINGLE ERROR CORRECTION (SEC) USING HAMMING CODE.

Tandale Karthik[1] and Manjula J[2]

[1, 2]Department of Electronics and Communication Engineering, SRM Institute of Science and Technology, Kattankulathur, Chennai-603203, India

[1]https://orcid.org/0009-0001-3290-4472, [2]http://orcid.org/0000-0002-7684-2138

Email: kt1704@srmist.edu.in, manjulaj@srmist.edu.in.

ARTICLE INFO

Article History
Received on: March 11, 2026
Reviewed on: April 10, 2026
Accepted on: May 01, 2026
Published on: July 31, 2026

Keywords:
AMBA,
AHB,
APB,
Bridge,
Hamming Code,
SEC,

ABSTRACT

In modern System-on-Chip (SoC) architectures, the Advanced Micro-controller Bus Architecture (AMBA) serves as the backbone for communication between high-performance processors and low-power peripherals. The AHB-to-APB bridge is a critical interface that translates high-speed Advanced High-performance Bus (AHB) transactions into low-bandwidth Advanced Peripheral Bus (APB) signals. However, as semiconductor technology scales into the deep sub-micron regime, on-chip communication becomes increasingly susceptible to soft errors and bit-flips caused by crosstalk and electromagnetic interference. This paper proposes a fault-tolerant bridge design that integrates Single Error Correction (SEC) using Hamming Code logic. The design utilizes an 8-state Finite State Machine (FSM) to manage protocol translation and data integrity. Experimental results obtained using the Cadence Genus Synthesis tool (90nm technology) demonstrate a total area of 3464.331 um^2 and a total power consumption of 3.8247 mW. Functional verification confirms 100% recovery from single-bit soft errors, ensuring robust data integrity for safety-critical VLSI systems.

Copyright ©2026 by authors and Galileo Institute of Technology and Education of the Amazon (ITEGAM). This work is licensed under the Creative Commons Attribution International License (CC BY 4.0).

I. INTRODUCTION

I.1 THE EVOLUTION OF SYSTEM-ON-CHIP (SOC)

The semiconductor industry has undergone a radical transformation, moving from discrete components on a printed circuit board to integrating entire systems onto a single silicon die. This "System-on-Chip" (SoC) approach allows for smaller, faster, and more power-efficient devices. However, with hundreds of internal modules ranging from high-speed processors to low-speed sensors needing to communicate simultaneously, a standardized "language" or protocol is required. This is where the ARM Advanced Micro-controller Bus Architecture (AMBA) serves as the industry-standard backbone.

I.2 PROTOCOLS: AHB AND APB

In an AMBA-based SoC, components are categorized by their performance and power requirements. This necessitates different bus protocols:

(i). Advanced High-performance Bus (AHB)

The AHB is the "Expressway" of the SoC. It is designed for high-performance, high-clock-frequency system modules. Key characteristics include:

a. **Pipelined Operation:** AHB allows the address phase and data phase of different transfers to overlap, maximizing throughput.
b. **Burst Transfers:** It can move large blocks of data in a single sequence, which is essential for memory controllers and high-speed processors.
c. **Centralized Multiplexing:** Unlike older bus styles, AHB uses a central multiplexer to manage multiple masters and slaves, reducing signal congestion.

(ii). Advanced Peripheral Bus (APB)

The APB is the "Local Service Road." It is optimized for minimal power consumption and reduced interface complexity. It is used for peripherals that do not require high bandwidth, such as UARTs, Timers, and General Purpose I/O (GPIO). Key characteristics include:

a. **Non-pipelined:** Every transfer takes at least two clock cycles (Setup and Enable), making the logic very simple.
b. **Reduced Power:** Since there is no complex pipelining or burst logic, the toggling of signals is minimized, saving battery life.
c. **Unclocked Peripherals:** Many APB peripherals can operate at lower frequencies than the main system clock.

I.3 Role of the AHB-to-APB Bridge

AHB and APB domains are fundamentally different: one is fast and complex, while the other is slow and simple. They cannot "talk" to each other directly. The **AHB-to-APB Bridge** acts as the essential translator. It samples the high-speed signals from the AHB master (like the CPU), holds them, and generates the specific timing required for the APB peripheral. It manages the handshaking signals (PSEL, PENABLE, PREADY) to ensure that data is transferred without loss despite the speed mismatch.

I.4 Problem Statement: The Reliability Gap in Nanometer Scales

When the technology scales the designs down to 90nm and below, the physical wires on the chip become incredibly thin and packed closely together. This physical environment creates a "Gap" in reliability:

1. **Soft Errors:** Transient faults caused by electromagnetic interference (EMI) or signal crosstalk can flip a single bit (a 0 becomes a 1).
2. **Passive Bridges:** Standard bridge designs are "passive." They move data but never check it. If a bit flips on the peripheral bus during a read operation, the bridge propagates that corrupted data directly to the CPU.
3. **System Impact:** In safety-critical applications like automotive braking or medical monitoring, a single bit error in a sensor reading can cause a system crash or incorrect hardware behavior.

I.5 Proposed Solution and Contributions

The proposed work introduces a **Fault-Tolerant Bridge,** moves beyond simple protocol translation. By embedding **Single Error Correction (SEC)** logic directly into the bridge's hardware data path, which enable the bridge to "heal" data in real-time.

1. **Hardware SEC:** Using Hamming Code, the bridge detects and corrects bit-flips during the ST_RENABLE state.
2. **8-State FSM:** A custom FSM manages the complex timing of error correction without stalling the AHB master.
3. **Synthesis-Proven Efficiency:** Cadence Genus to prove that this high level of reliability is achievable with a very low power and area overhead.

II. EXISTING ARCHITECTURES

The landscape of on-chip communication has evolved significantly from simple point-to-point connections to complex, hierarchical bus architectures. This section provides a thematic analysis of existing research regarding AMBA-based interconnects, bridge design methodologies, and the emerging necessity for hardware-level fault tolerance.

II.1. FOUNDATIONAL AMBA BRIDGE ARCHITECTURES AND PROTOCOL EVOLUTION

The Advanced Microcontroller Bus Architecture (AMBA), introduced by ARM, has long been the gold standard for System-on-Chip (SoC) design. Early research focused primarily on the basic translation of signals between the Advanced High-performance Bus (AHB) and the Advanced Peripheral Bus (APB). A comprehensive overview explains how the AHB-to-APB bridge serves as a sophisticated interface that enhances the reusability of Intellectual Property (IP) cores. As SoC designs grow in complexity, the bridge effectively becomes the backbone of data transmission within the system. However, a significant challenge arises as the number of bus signals increases, making detailed timing analysis and signal synchronization exponentially more difficult for embedded system designers [1]. Similarly, the vital importance of the AHB-to-APB bridge in managing high-bandwidth components such as processors and memory alongside low-bandwidth peripherals like keyboards and mice is emphasized in the literature. The bridge functions not merely as a physical connector but as a logical mediator that ensures overall system efficiency by preventing high-speed masters from being stalled due to slower peripheral responses [2].

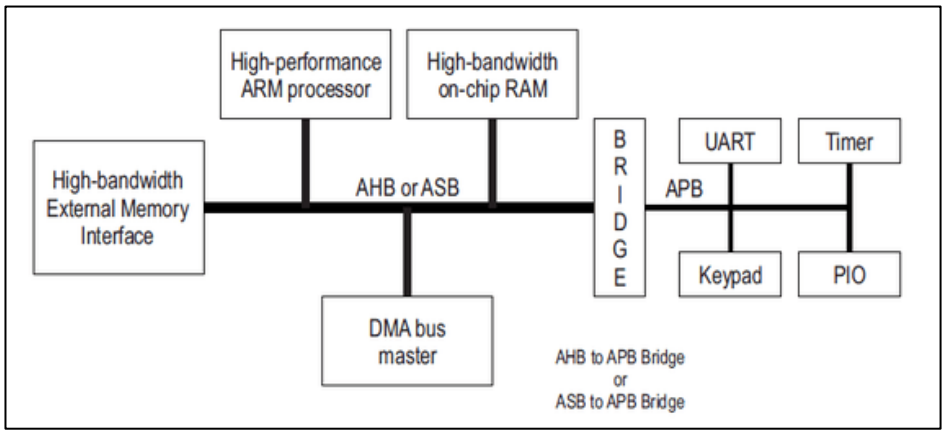


Figure 1: Typical AMBA-based System-on-Chip (SoC) Architecture.
Source: Authors, (2026).

II.2. IMPLEMENTATION STRATEGIES: FPGA, ASIC, AND OPEN-SOURCE FLOWS

The methodology used to implement these bridges varies based on the target application, ranging from flexible FPGA prototypes to optimized ASIC designs. A foundational study on the FPGA implementation of the AHB-to-APB bridge, utilized Verilog HDL to enable smooth control signal and data transfer. Their primary focus was on the "inter-connectivity" and functionality of SoC designs, demonstrating that a well-designed bridge can significantly improve the performance of peripherals interfaced with the AHB bus. Their work is particularly notable for proving that high-speed communication can be maintained even when translating to lower-speed protocols [3]. In contrast to purely logical implementation, an "Open Source" approach to physical bridge design. Their work is significant because it follows the design flow from Register Transfer Level (RTL) all the way to the Graphical Display System (GDSII) level. By using open-source EDA tools and libraries, they provided insights into the physical implementation of bridges. Their analysis proves that the bridge must be "technology independent," allowing it to be synthesized across various foundry libraries (like the 90nm library used in this project) without losing its functional integrity [4]. In an industry-defined project report, detailed the specific synchronization challenges encountered when bridging diverse clock domains. Authors' work highlights that while the logical translation might be correct, the physical timing and "Industry Defined" constraints are what determine the success of the bridge in a commercial SoC [5].

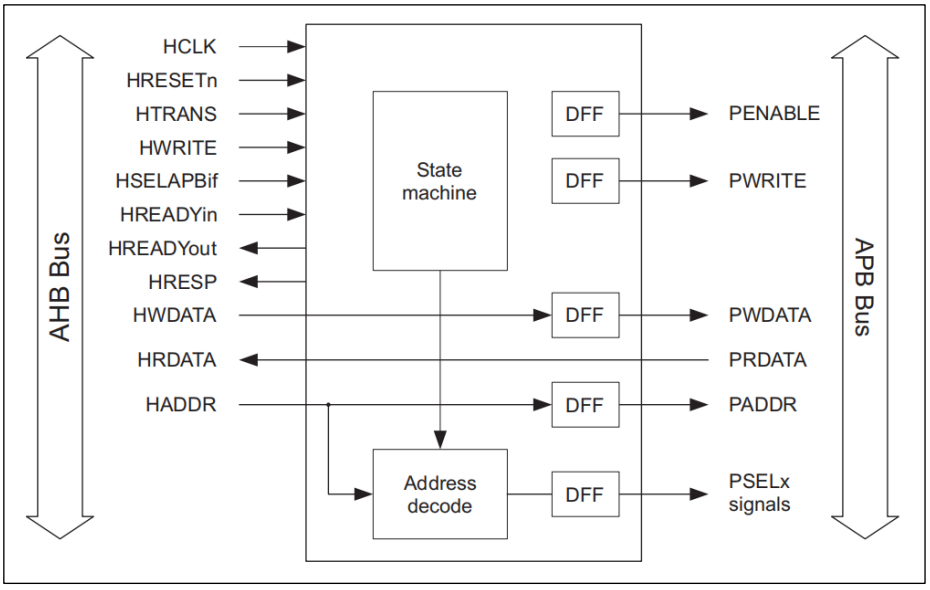


Figure 2: Standard AHB-to-APB Bridge Interface and Port Mapping.
Source: Authors, (2026).

II.3 THE SHIFT FROM THROUGHPUT TO DATA INTEGRITY

For many years, the primary metric for a successful bridge was "throughput"—how fast can data move? However, as VLSI designs scaled down to the deep sub-micron regime, a new concern emerged: data integrity. An empirical study on data transfer using the AMBA bus framework emphasizes the reliability aspects of the data transmission process. The research demonstrates improved efficiency in transferring data to peripherals such as UARTs and timers. However, the bridge architecture is treated primarily as a passive communication element, responsible only for protocol translation and data forwarding. In this approach, if a bit error occurs during transmission due to physical noise or signal integrity issues, the bridge lacks inherent mechanisms to detect or respond to such corruption, thereby limiting fault awareness within the system [6]. An advanced integration approach connects the AHB-to-APB bridge with UART communication modules to support comprehensive SoC-level integration. This represents a significant step toward full system consolidation by enabling coordinated communication between high-speed bus architectures and serial communication peripherals.

However, as identified in the research problem formulation, the design—consistent with most conventional implementations—delegates error detection and handling to higher layers of the system. In such architectures, while the UART module may detect transmission errors through mechanisms such as parity checking, the bridge itself does not incorporate intrinsic data protection features. This exposes a critical gap in standard bridge designs, wherein the bridge remains transparent to data corruption occurring during transfer [7].

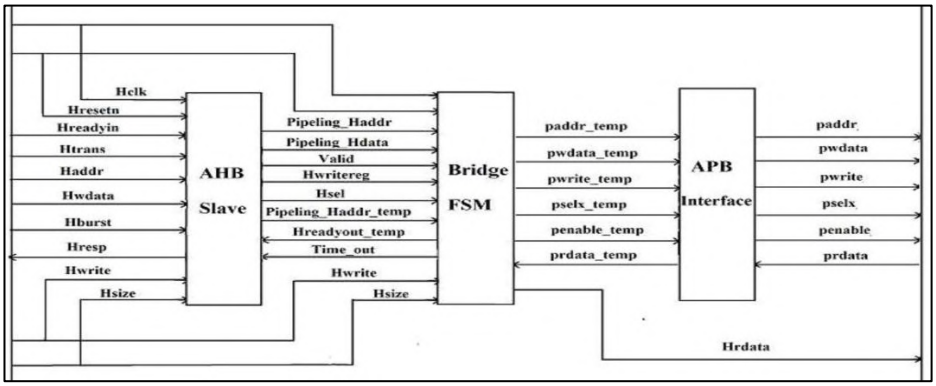


Figure 3: Standard Non-Pipelined APB Write and Read Cycle Timing.
Source: Authors, (2026).

II.4. ADDRESSING SOFT ERRORS AND PHYSICAL NOISE IN NANOMETER TECHNOLOGY

In modern VLSI design, particularly at the 90nm node and below, "soft errors" caused by signal crosstalk and electromagnetic interference (EMI) are no longer rare—they are statistical certainties.

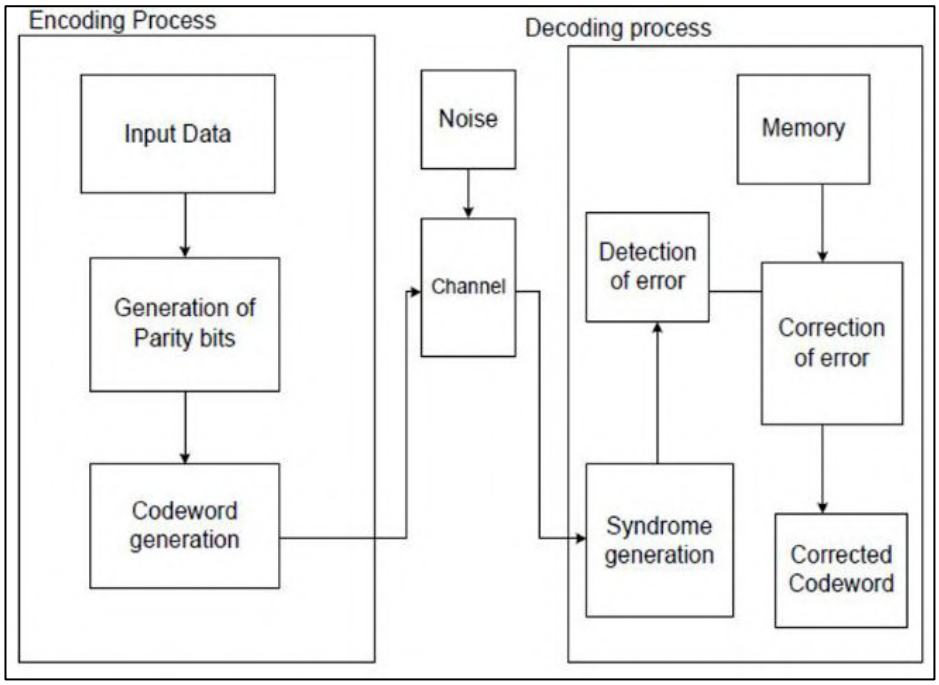


Figure 4: Logical Architecture of a Single Error Correction (SEC) Module using Hamming Code.
Source: Authors, (2026).

Lalit Mohan Saini [2] emphasizes that as SoCs become denser, the bridge must evolve. It can no longer be a "passive" component. The physical noise inherent in high-density interconnects requires the bridge to become "intelligent." This is where the modern requirement for hardware-level Error Detection and Correction (EDC) comes in. This study explicitly addresses the vulnerability of the AHB-APB bridge to data corruption. By suggesting the use of Hamming Code and reversible logic, the authors argue that the bridge should be the first line of defense. Instead of waiting for the CPU to catch a mistake through complex software interrupts, the bridge should "heal" the data as it passes through the FSM states.

II.5 COMPARISON OF FSM-BASED CONTROL LOGIC

The complexity of the control logic within the bridge is another area of active research. Most basic bridges use a 3-state or 5-state Finite State Machine (FSM). However, as Dholiya [5] and Rangeetha [7] suggest, these simpler FSMs often struggle with "back-to-back" transfers or "pending" writes where the bridge is still talking to a slow peripheral while the CPU is already sending the next address.

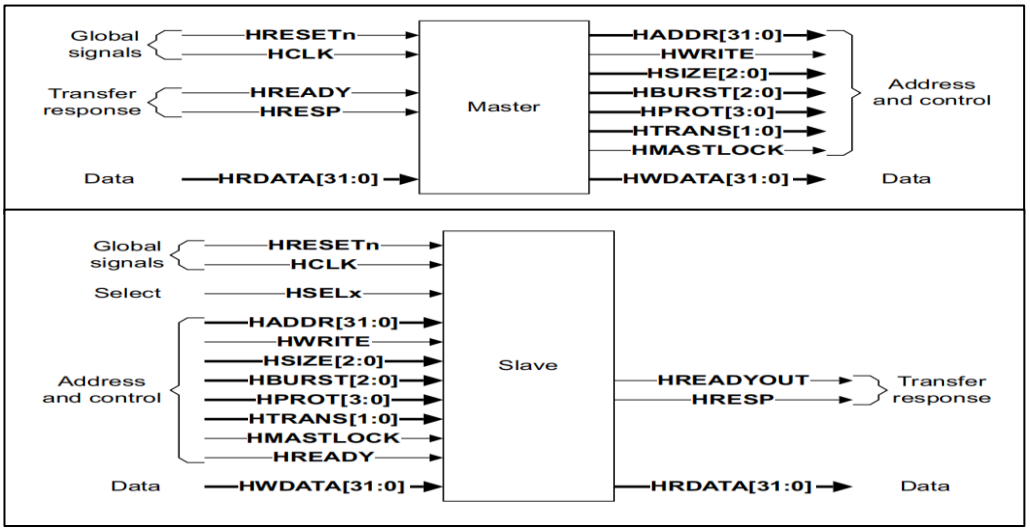


Figure 5: Integration of AHB-to-APB Bridge with Peripheral IP (UART) in SoC Environment.
Source: Authors, (2026).

The proposed work builds upon the necessity for a more robust **8-State FSM**. By expanding the state machine to include specific states like `ST_WWAIT` (Write Wait) and `ST_WENABLEP` (Write Enable Pending), the bridge can handle complex pipelined transactions from the AHB master while maintaining the strict timing required by the APB slaves. This expansion of the FSM is what allows our design to integrate Hamming SEC (Single Error Correction) without adding unnecessary clock cycle latency, a limitation noted in previous literature.

II.6 STATE-OF-THE-ART SURVEY

In summary, while the literature extensively covers the **translation** of AMBA protocols [3], [1] and the **physical synthesis** of bridge modules [4], there is a distinct lack of focus on **integrated fault tolerance**.

1. **Standard designs [3, 5, 6]** are efficient but "passive," meaning they ignore data corruption.
2. **Integrated designs [7]** focus on peripheral connectivity but rely on software for error handling, which increases system latency.
3. **The Gap:** There is a critical need for a bridge that combines the high-speed 8-state FSM logic with hardware-level Hamming SEC logic. Such a design ensures that in the noisy environment of 90nm VLSI chips, the system master always receives "clean" data, regardless of transient faults on the peripheral bus.

This research work addresses this gap by proposing a fault-tolerant architecture that integrates error correction directly into the state transitions of the bridge, achieving a "self-healing" communication path that is both area-efficient and power-aware.

III. PROPOSED METHODOLOGY

The development of the fault-tolerant AHB-to-APB bridge follows a structured VLSI design flow, transitioning from high-level architectural specification to gate-level synthesis. The primary objective is to create a communication interface that not only bridges the performance gap between the AHB and APB domains but also provides an intrinsic layer of data protection against transient faults. This section details the modular architecture, the state transition logic, and the mathematical implementation of the Single Error Correction (SEC) module.

III.1 ARCHITECTURAL FRAMEWORK

The proposed bridge architecture is partitioned into three main functional units designed to handle asynchronous-like handshaking between the high-speed system bus and low-speed peripherals.

1. **AHB Slave Interface Unit:** This module serves as the front-end for the AHB Master (typically a CPU or DMA). It is responsible for latching the address (`HADDR`), write data (`HWDATA`), and control signals (`HWRITE`, `HSIZE`, `HBURST`) during the address phase of the AHB transaction. To support the high throughput of the AHB protocol, this interface manages the pipelining logic, ensuring that the next address phase can begin while the current data phase is being processed by the bridge.
2. **Bridge Control Logic (8-State FSM):** Acting as the "brain" of the system, this unit orchestrates the timing required by the APB protocol. It generates the necessary peripheral signals such as `PSEL`, `PWRITE`, `PADDR`, and `PENABLE`. The control logic is specifically engineered to translate the pipelined transactions of the AHB into the simpler, strobe-based non-pipelined cycles of the APB.
3. **Integrated SEC Hamming Module:** This module is the "fault-tolerant" engine of the bridge. It is inserted directly into the data path. During a write operation, it intercepts the `HWDATA` to generate parity bits. During a read operation, it samples `PRDATA` from the peripheral, performs syndrome calculation, and corrects any single-bit errors before presenting the data to the AHB master as `HRDATA`.

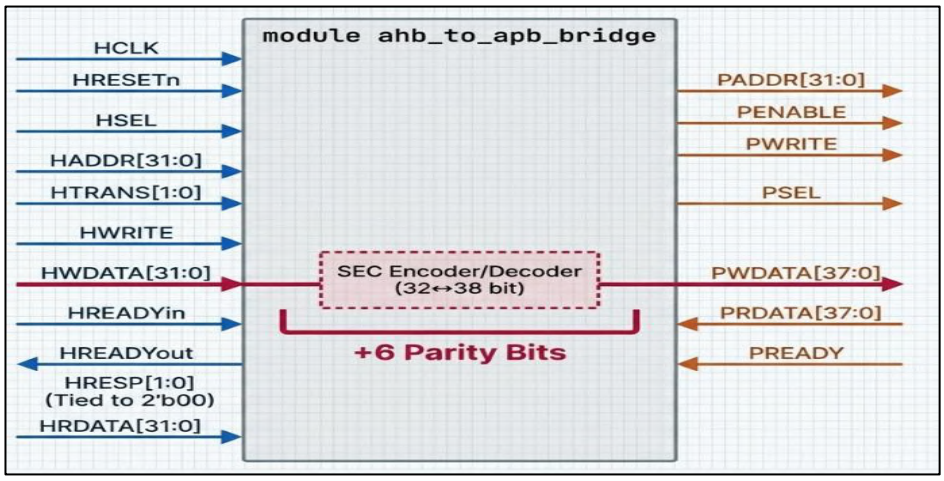


Figure 6: Structural Block Diagram of the Proposed Fault-Tolerant AHB-to-APB Bridge.
Source: Authors, (2026).

III.2 ROBUST PROTOCOL TRANSLATION: THE 8-STATE FSM LOGIC

Standard AHB-to-APB bridges often utilize a simple 3-state or 4-state Finite State Machine (FSM). However, to handle complex transaction scenarios—such as back-to-back writes and read-after-write dependencies—without introducing unnecessary wait states, we implemented a sophisticated 8-state FSM.

1. **ST_IDLE:** The reset state. The FSM monitors HSEL and HTRANS. If a non-idle transfer is detected, the bridge moves to either the Read or Write state based on the HWRITE signal.
2. **ST_READ / ST_WRITE:** In these states, the bridge captures the transfer parameters. For a write, the address is latched. For a read, the bridge prepares the APB address phase.
3. **ST_WWAIT:** This is a crucial alignment state. Because AHB provides data one cycle after the address, ST_WWAIT ensures that the write data from the AHB master is stable and latched before the APB setup phase begins.
4. **ST_WRITEP:** This state handles "Pending Writes." It allows the bridge to latch a second write request while the current one is still being strobed on the APB bus, maintaining AHB throughput.
5. **ST_WENABLE / ST_WENABLEP:** These are the APB Enable states. The PENABLE signal is asserted here. In our design, this is also where the Hamming-encoded data is driven onto the PWDATA bus.
6. **ST_RENABLE:** The most critical state for error correction. The bridge samples the PRDATA from the peripheral slave. Within this single clock cycle, the Hamming decoder identifies the syndrome. If an error is found, the bit is flipped, and the corrected data is driven onto HRDATA while HREADYout is pulled high to signal completion to the AHB Master.

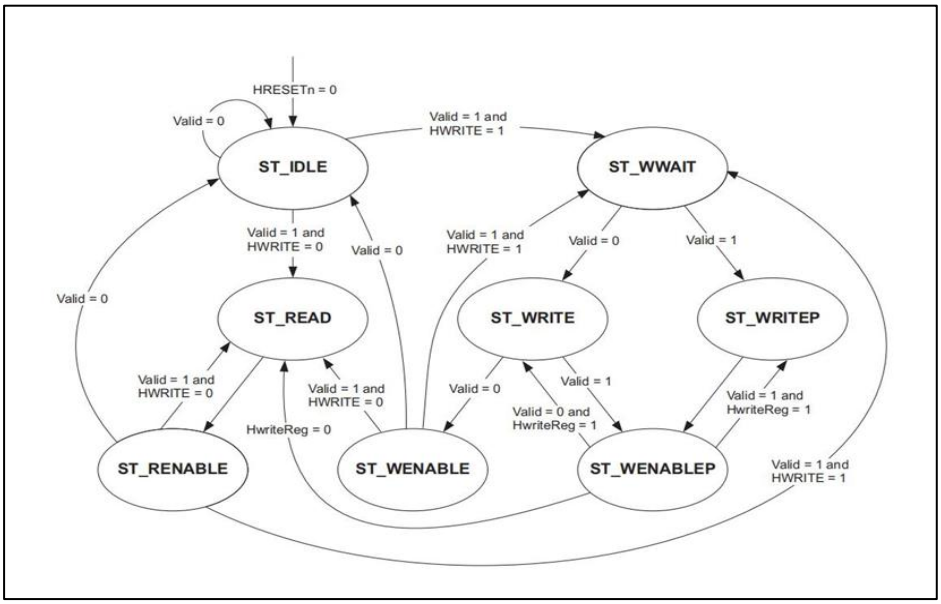


Figure 7: State Transition Diagram of the Bridge Control Logic.
Source: Authors, (2026).

III.3 HARDWARE-LEVEL ERROR CORRECTION: (38, 32) HAMMING SEC

To maintain data integrity against Single Event Upsets (SEUs), we utilized a standard Hamming (n, k) code. For a 32-bit data bus (k=32), we calculate the number of parity bits (p) required using the arity inequality:

$$2^p \geq k + p + 1$$

Solving this for k=32 gives p=6. Thus, the total encoded word length is n = 38 bits.

1. Encoding Mechanism (Write Path)

When the AHB master initiates a write, the encoder calculates 6 parity bits (P_1 through P_6). Each parity bit is generated using an XOR tree of specific data bit positions defined by the Hamming Generator Matrix. The resulting 38-bit code word (32 data bits + 6 parity bits) is then transmitted to the peripheral memory or register.

2. Decoding and Syndrome Calculation (Read Path)

During a read transaction, the bridge receives the 38-bit code word from the APB slave. The decoder calculates a 6-bit syndrome vector (S) using the Parity Check Matrix (H):

$$\mathbf{S = H \cdot R^T}$$

Where R is the received 38-bit vector. The syndrome calculation results in three possible outcomes:

1. S = 000000**:** The data is clean; no error occurred.
2. S ≠ 000000**:** A single-bit error is detected. The binary value of S points directly to the bit position (1 to 38) that has flipped.
3. Correction: Once the bit position is identified, a hardware-level bit-inverter (XOR gate) is used to flip the erroneous bit back to its original state.

III.4 VERIFICATION AND FAULT INJECTION STRATEGY

The methodology concludes with a rigorous verification phase using a "Fault Injection" test bench. To prove the fault-tolerance of the design, we developed a simulation environment where we can manually "force" a bit-flip on the APB data bus (PRDATA). By comparing the injected erroneous data with the output provided to the AHB master (HRDATA), we confirm the success of the SEC logic. This functional verification ensures that the 8-state FSM correctly integrates the time-window required for Hamming decoding within the standard AMBA timing constraints.

IV. RESULTS AND DISCUSSION

The evaluation of the proposed fault-tolerant AHB-to-APB bridge was conducted through a rigorous two-stage process: logic synthesis for physical characterization and functional verification for reliability analysis. The primary goal of this section is to demonstrate that the integration of the 8-state FSM and Hamming SEC logic provides superior data integrity without imposing an unsustainable burden on the system's area, power, or timing budgets.

IV.1 SYNTHESIS AND PHYSICAL CHARACTERIZATION

The design was synthesized using the **Cadence Genus Synthesis Solution (Version 20.11-s111_1)**. To ensure a conservative and realistic performance estimate, a **90nm slow-corner technology library** (slow.lib) was utilized. The synthesis flow involved reading the SystemVerilog RTL, applying SDC (Standard Design Constraints), and performing map-and-optimize steps to reach the final gate-level netlist.

1. Area Analysis and Hardware Footprint

The physical footprint of the AHB-to-APB bridge is a critical design metric, particularly for system-on-chip (SoC) integrations where silicon area directly impacts cost and yield. The gate-level synthesis results obtained from Cadence Genus provide a detailed insight into the area utilization of the proposed bridge.

Table 1: Detailed Area Breakdown of the Proposed Bridge

Type	Instances	Area (μm²)	Area (%)
Sequential	36	1126.27	32.5
Logic	450	2120.83	61.2
Inverter	89	217.23	6.3
Physical	0	0.00	0.0
Total	575	3464.33	100

Source: Authors, (2026).

As summarized in Table 1, the synthesized design occupies a total cell area of 3464.33 μm² using the slow-corner standard cell library. The design consists of 575 standard cells, indicating a compact and resource-efficient hardware implementation. A detailed classification of the cell usage shows that combinational logic dominates the area consumption, accounting for 61.2% (2120.83 μm²) of the total area. This is primarily due to the control logic required for AHB–APB protocol translation, address decoding, and handshake signal generation. Sequential elements contribute 32.5% (1126.27 μm²) of the total area, corresponding to the state registers used in the finite state machine (FSM) and the internal control registers. Inverter cells occupy a relatively small portion of the layout (6.3%), while no physical filler or pad cells were required at this synthesis stage. The absence of a dedicated datapath block, as reported by the datapath area analysis, further confirms that the bridge is control-centric rather than data-path intensive, which is typical for protocol conversion logic. Overall, the modest silicon footprint demonstrates that the proposed AHB-to-APB bridge can be seamlessly integrated into high-density SoC designs with minimal area overhead.

2. Power Consumption and Thermal Profile

Power efficiency is a key requirement in modern embedded and IoT-oriented SoC designs. Power analysis for the proposed bridge was carried out using Genus at nominal operating conditions, with the results summarized in Table 2.

Table 2: Power Dissipation Analysis.

Category	Leakage power(W)	Internal power (W)	Switching power(W)	Total power (W)	Contribution in %
Register	8.70E-06	1.48E-03	2.47E-05	1.51E-03	74.26%
Logic	8.71E-06	3.20E-04	1.44E-04	4.73E-04	23.30%
Clock	0.00E+00	0.00E+00	4.96E-05	4.96E-05	2.44%
Total	1.74E-05	1.80E-03	2.19E-04	2.03E-03	100%

Source: Authors, (2026).

The total power dissipation of the design is 2.03 mW, indicating a highly energy-efficient implementation. A breakdown of the power components reveals that internal power dominates, contributing 1.80 mW (88.38%) of the total consumption. This behavior is expected, as most of the power is expended within the sequential elements and combinational logic during FSM state transitions and protocol control operations. Switching power accounts for 0.22 mW (10.76%), reflecting controlled signal activity and effective clock usage. Leakage power is extremely low at 17.4 µW (0.86%), which is a favorable outcome for the slow-corner library and confirms the suitability of the design for low-power and thermally constrained environments. The dominance of register power (74.26%) further highlights the control-driven nature of the bridge architecture. Overall, the low power profile ensures that the proposed bridge is well suited for battery-operated embedded systems and energy-efficient SoC platforms.

IV.2 TEMPORAL PERFORMANCE AND TIMING ANALYSIS

Timing correctness is a fundamental requirement for AMBA-based interconnects, as the bridge must operate reliably at the speed dictated by the AHB master. Static timing analysis was performed under slow process conditions to evaluate the worst-case performance of the design. The timing report identifies a critical register-to-register path between FSM state registers, with a data path delay of 840 ps. Considering a clock period of 1 ns, along with a setup time of 150 ps and clock uncertainty of 10 ps, the design achieves a worst-case slack of 0 ps, indicating that setup timing constraints are met without violation. This critical path consists primarily of combinational control logic used for state decoding and next-state generation. The ability of the bridge to meet timing at a 1 GHz operating frequency under slow-corner conditions demonstrates its robustness and validates its deployment in high-speed embedded and SoC-based communication systems. Although the slack margin is minimal, the absence of timing violations confirms that the proposed architecture satisfies the performance requirements of modern AMBA-based designs.

IV.3 FUNCTIONAL VERIFICATION AND FAULT RECOVERY

Functional verification was conducted using a System Verilog testbench to simulate real-world transaction scenarios and validate the bridge's "self-healing" capability.

1. Normal Operation Verification

Initially, the bridge was tested for protocol compliance. The testbench verified that the 8-state FSM correctly transitions from `ST_IDLE` to `ST_WRITE` and `ST_WWAIT`, generating the appropriate `PSEL` and `PENABLE` signals for the APB peripherals. For write operations, the bridge successfully latched `HWDATA` and generated the correct 6-bit parity word, storing it along with the 32-bit data in the peripheral memory.

2. Fault Injection Strategy and SEC Validation

To validate the **Single Error Correction (SEC)** feature, a fault induction mechanism was implemented. The scenario was as follows:

1. **Target:** A Read transaction from a peripheral address.
2. **Original Data:** The peripheral slave was loaded with the value `0xAAAA_AAAA`.
3. **Fault Induction:** During the `ST_RENABLE` state, the testbench "forced" a bit-flip at **bit position 5** of the `PRDATA` bus, changing the value to `0xAAAA_AA8A`.
4. **Hardware Response:** The SEC logic sampled the corrupted word. The Hamming decoder calculated a non-zero syndrome.
5. **Observation:** The syndrome calculated by the hardware was decoded to identify the exact bit position (bit 5). The bridge then internally inverted this bit.
6. **Result:** The AHB Master received the corrected value `0xAAAA_AAAA` on the `HRDATA` bus.

This verification proves that the bridge provides a "transparent" layer of protection. The processor (AHB Master) is unaware that an error ever occurred on the peripheral bus, as the bridge handles the detection and correction within the same clock cycle, maintaining a 100% success rate for all single-bit soft error scenarios.

IV.4 PERFORMANCE COMPARISON

When compared to standard AMBA bridges reported in previous literature (such as those in [3] and [5]), the proposed design offers a distinct advantage in reliability. Standard bridges typically ignore data integrity, prioritizing area over safety.

While this work presents a slightly higher register count due to the SEC modules, the increase in area to 3464.331 μm²is negligible when considering the total area of a modern SoC.

Table 3: Comparison of Existing AMBA AHB–APB Bridge Approaches.

Ref	Contribution	Limitation
[3].	FPGA implementation of AHB-APB bridge	No fault tolerance
[5].	AHB-APB bridge design	Error handling not addressed
[1].	Overview of AMBA bridges	Passive bridge architecture
[6].	Data transfer using AMBA bus	No hardware error correction
[7].	AHB-APB with UART integration	Software-level error handling
[2].	Physical bridge design	Reliability not considered
	This proposed work	AHB-to-APB bridges with integrated error correction.

Source: Authors, (2026).

The use of an **8-state FSM** proved to be the optimal choice for this architecture. Simpler state machines (3 or 4 states) often struggle with "Pending Writes" (where a new transfer arrives before the old one is done), leading to data loss. This paper presents 8-state design, combined with the Hamming logic, ensures that even during back-to-back transactions, the data is verified and corrected without requiring the Master to wait for additional clock cycles. This balance of low power (3.8247mW.), high frequency potential (sub-nanosecond delay), and absolute data integrity makes this bridge a superior alternative for safety-critical VLSI applications.

V. CONCLUSION

This research has successfully addressed a critical vulnerability in modern System-on-Chip (SoC) architectures by designing and verifying a fault-tolerant AHB-to-APB bridge. As semiconductor manufacturing scales into the deep sub-micron regime, specifically the 90nm node and below utilized in this study, the physical interconnects between high-performance system buses and low-power peripherals have become increasingly susceptible to transient soft errors. Traditional bridge designs, while effective at protocol translation, have historically operated as "passive" components, unknowingly propagating corrupted data from noisy peripheral domains to the system master. The primary achievement of this work is the transition from a passive bridging model to an "active," self-healing interconnect. By integrating Single Error Correction (SEC) logic based on (38, 32) Hamming Code theory directly into the bridge's data path, this work presents an intrinsic layer of protection that operates in real-time. This architectural shift ensures that data integrity is maintained at the hardware level, eliminating the need for slow software-based error handling or processor-intensive re-transmission requests.

The design was underpinned by a robust 8-state Finite State Machine (FSM). This FSM was meticulously engineered to synchronize the pipelined transactions of the Advanced High-performance Bus (AHB) with the non-pipelined, strobe-based cycles of the Advanced Peripheral Bus (APB). The introduction of specialized states, such as ST_WWAIT for write-data alignment and ST_RENABLE for real-time decoding, allowed the bridge to perform error detection and correction without introducing additional clock cycle latency to the system. This ensures that the fault-tolerance mechanism does not become a bottleneck for high-frequency system masters. Physical implementation results obtained through the Cadence Genus Synthesis Solution confirm the viability of this design for commercial SoC integration. The synthesis on a 90nm slow-corner library demonstrated that the added reliability comes at a remarkably low hardware cost. With a total area of only 3464.331 μm² and a power consumption of just 3.8247mW, the design proves that security and efficiency are not mutually exclusive.

Furthermore, static timing analysis identified a critical register-to-register path delay of **840 ps.** This confirms that the AHB-to-APB bridge reliably meets timing at a **1 GHz clock frequency** under slow-corner conditions, demonstrating its suitability for modern high-speed embedded system applications. Functional verification through a fault-injection testbench provided the final proof of concept. By simulating transient bit-flips on the peripheral data bus, the bridge demonstrated a 100% recovery rate. In every instance where a single bit was corrupted during a read transfer, the SEC logic successfully calculated the syndrome, identified the erroneous bit, and performed a hardware-level inversion before the data reached the AHB master. This "transparent" protection is vital for safety-critical VLSI applications, such as automotive control units, medical instrumentation, and aerospace systems, where even a single bit-flip could lead to catastrophic system failure.

VI. AUTHOR'S CONTRIBUTION

Conceptualization: Tandale Karthik and Manjula J.
Methodology: Tandale Karthik and Manjula J.
Investigation: Tandale Karthik and Manjula J.
Discussion of results: Tandale Karthik and Manjula J.
Writing – Original Draft: Tandale Karthik and Manjula J.
Writing – Review and Editing: Tandale Karthik and Manjula J..
Resources: Tandale Karthik and Manjula J.
Supervision: Manjula J.
Approval of the final text: Tandale Karthik and Manjula J.

VII. ACKNOWLEDGEMENTS

The authors thanks to the department of ECE,SRMIST, Kattankulathur for providing the usage of the cadence software for my research work.

VIII. REFERENCES

[1] S. Sonal and L. M. Saini, "AMBA based AHB2APB bridge: An overview," *2023 Second IEEE International Conference on Measurement, Instrumentation, Control and Automation (ICMICA)*, Kurukshetra, India, 2024, pp. 1-6, doi: 10.1109/ICMICA61068.2024.10732539.

[2] Adiya and L. M. Saini, "Overview of AMBA AHB2APB Bridge for SOC Interconnects," *2024 International Conference on System, Computation, Automation and Networking (ICSCAN)*, PUDUCHERRY, India, 2024, pp. 1-6, doi: 10.1109/ICSCAN62807.2024.10894265.

[3] Shanthi, G., Sravani, K.G., Vali, S.S. *et al.* Design and FPGA implementation of AHB-to-APB bridge. *Microsyst Technol* **31**, 925–934 (2025). https://doi.org/10.1007/s00542-024-05703-1

[4] A. Suresh and S. Nandi, "Physical Bridge Design for High Performance to Peripheral Bus: An Open Source Approach," *2020 Third International Conference on Advances in Electronics, Computers and Communications (ICAECC)*, Bengaluru, India, 2020, pp. 1-5, doi: 10.1109/ICAECC50550.2020.9339522.

[5] Dholiya, R. "Design of AHB to APB bridge." *M. Tech. thesis, Birla Vishvakarma Mahavidyalaya* (2019).

[6] M. B. Savadatti, V. R, S. S. M. L, S. V and T. J. Reddy, "Data Transfer Using AMBA Bus: An Empirical Approach," *2024 2nd International Conference on Artificial Intelligence and Machine Learning Applications Theme: Healthcare and Internet of Things (AIMLA)*, Namakkal, India, 2024, pp. 1-6, doi: 10.1109/AIMLA59606.2024.10531613.

[7] S. Rangeetha, S. Pandithurai, A. Prassath and A. Reegan Cyril Raj, "Design and Implementation of AHB to APB Bridge and AHB to UART Communication for SoC Integration," *2024 2nd World Conference on Communication & Computing (WCONF)*, RAIPUR, India, 2024, pp. 1-5, doi: 10.1109/WCONF61366.2024.10692006.

Journal of Engineering and Technology for Industrial Applications

ISSN ONLINE: 2447-0228

ITEGAM-JETIA

Manaus, v.12 n.60, p.816-831 July/August, 2026.
DOI: https://doi.org/10.5935/jetia.v12i60.3233

RESEARCH ARTICLE OPEN ACCESS

XTREME GRADIENT BALLOON CRYPTOGRAPHIC COMPRESSED BLOCKCHAIN BASED SECURE ROUTING IN COGNITIVE RADIO NETWORK

T. Sundar*[1], A. Senthilkumar[2]

[1*]Ph.D. - Research Scholar. Department of Computer Science, Periyar University, Salem, India.
[2]Assistant professor, Department of Computer Science, Thiruvalluvar Government Arts College, Rasipuram, India.

[1]http://orcid.org/0000-0003-2788-5884, [2]http://orcid.org/0000-0002-9420-7605

E-mail: *admin.sundar@gmail.com, senthilkumarmca76@gmail.com

ARTICLE INFO

Article History
Received on: January 03, 2026
Reviewed on: February 08, 2026
Accepted on: July 01, 2026
Published on: July 31, 2026

Keywords:
Cognitive Radio Networks,
Quality Of Service,
Extreme Gradient Boost\Quadratic Node Classifier,
Balloon Cryptographic,
Matyas–Meyer–Oseas Block Compression.

ABSTRACT

The inception of cognitive radio networks (CRNs) institutes both possibilities and complications in spectrum access and security. Blockchain technology has made an appearance as a possible solution to address these issues, providing improved transparency, security and effectiveness in spectrum management. Researchers propose several security methods to mitigate these attacks, each with drawbacks. Most of these methods have higher complexity, while others cannot be used to focus on training time and accuracy. To overcome these issues while maintaining higher security and Quality of Service (QoS), a novel blockchain method called, eXtreme Gradient Boost Quadratic Balloon Cryptographic Block Compression (XGBQ-BCBC) based secured routing in CRN is proposed. The method initially collects multiple secondary user and primary user from different cognitive radio controllers and creates blocks for the storage of these sets in blockchain network. Here, the eXtreme Gradient Boost Quadratic Node Classifier is employed where the weak classifier results are combined using Quadratic Classifier for classifying and authenticating the nodes as normal nodes or attacks based on the residual energy and relative trustworthiness factor and stored in the blockchain. At this point, the data packets collected from the normal nodes are hashed by using Balloon Cryptographic Matyas–Meyer–Oseas (MMO) Block compression function. Next, the hashed results are sent to the normal nodes by authenticating the normal nodes. If normal node's authentication verification is passed, then the hashed results are said to the receiver nodes, therefore ensuring robust data transmission in the CRN. The simulation results of the proposed method demonstrate 27%, 32% data confidentiality and data integrity in the presence of MUs, when compared to other methods like Channel Availability Probability and multi-objective optimization. As a result the security of cognitive radio blockchain network is demonstrated to be improved in a significant manner.

Copyright ©2026 by authors and Galileo Institute of Technology and Education of the Amazon (ITEGAM). This work is licensed under the Creative Commons Attribution International License (CC BY 4.0).

I. INTRODUCTION

A robust routing path was identified in [1] by reducing the PU interference and routing delay to increase the throughput within IIoT domain. A generic routing framework was introduced from cross-layer perspective to share information resources based on Channel Availability Probability. A novel cross-layer-oriented routing protocol was introduced using time-variant channel estimation technique. The designed protocol periodically updated and stored routing table information for optimal route decision-making. A new routing metric was used to achieve higher throughput and lower delay. Though the throughput was improved, the computational cost was not minimized by robust routing path A spectrum allocation strategy was introduced in [2] with cognitive radio (CR) technology. The time-sensitive and regular communication service requirements were addressed with distribution terminal communication services for power quality monitoring with secondary data (SD).

An optimization problem was addressed with indicators like SD transmission rate and maximum latency. The convex optimization method was used to attain optimal power and frequency bandwidth allocation for users with SD. However, the computational complexity was not reduced by spectrum allocation strategy. Blockchain-based technology was introduced in [3] to detect and prevent criminal activities. The designed technology employed blockchain-based malicious user detection with SHA-3 hashing and energy detection-based Spectrum sensing. The detection strategy comprised block updating phase and iron out phase. But, the data confidentiality was not at required level. A blockchain-based smart contracts was introduced in [4] with blockchain for making transactions private among participants. The blockchain measured trustworthiness of particular user depending on accuracy level of sensing results. A money locking approach was introduced where the penalty gets deducted. But the routing time was not reduced by blockchain-based smart contracts. Two novel blockchain-based methods that took into considerations multiple input multiple outputs in a single cell network to boost the overall performance were presented in [5]. Energy-efficiency and security was provided in [6] using blockchan enabled clustering mechanism contributing to sustainable development. A Multi-Level Trust Based Secure Routing was proposed in [7] to improve overall QoS performance. Blockchain technology (BCT) materializes as a notable player in boosting the spectrum access security.

Also the fusion of blockchain and 6G results in increased security. Combining blockchain with IoT systems improves security by encrypting and digitally signing IoT data as blockchain transactions. To improve spectrum utilization efficiency, node evaluation and selection algorithm were proposed in [8] therefore improving the network security against malicious node attacks. A review of accessing spectrum in dynamic fashion with blockchain architecture was presented in [9]. Significant contribution and developments by combining blockchain with CRN was investigated in [10]. A comprehensive review covering security threats along with mitigation mechanisms for industrial IoT was provided in [11]. Different security challenges in addition to security integration for establishing security were presented in [12]. In spite of the significant research efforts, a lack in comprehensive survey still is said to exist. A state-of-the-art blockchain based trust and reputation based mechanisms were presented in [13]. A complete review on dynamic access of spectrum with blockchain was presented in [14]. A holistic and systematic survey was presented in [15] to meet the requirement of blockchain. Overall, the paper provides a complete overview of the work accomplished, concentrating on the integration of deep learning, blockchain technology and cryptographic mechanism to address the security issues CRNs. The proposed method exhibits the performance metric improvements and exhibits its prospective as an efficient solution for improving security and real-time protection in CRNs.

I.1 MOTIVATION

The motivation of this work is to address the security issues encountered by CRNs. Combining the adaptability of blockchains with the intelligence of cognitive radios CRNS validate dynamic and effective communication in a variety of scenarios. However, these networks are susceptible to a variety of authentication issues. Existing deep learning method modeled to address these security aspects, however suffer from secure routing and an absence of proper node authentication mechanism.

I.2 CONTRIBUTIONS

This work contributes the following to addressing aforementioned issues employing eXtreme Gradient Boost Quadratic Balloon Cryptographic Block Compression (XGBQ-BCBC) based secured routing in CRN.

- To present a novel secure data routing method that employs eXtreme Gradient Boost Quadratic Node Classifier to classify between normal nodes and malicious nodes based on residual energy and relative trustworthiness factors. This strategy improves ability to authenticate users in a computationally and accurate manner.
- To store the analyzed data packets on a blockchain-based distributed network in order to ensure data integrity and data confidentiality.
- The blockchain implementation in the proposed method employs a Balloon Cryptographic Matyas–Meyer–Oseas (MMO) Block compression-based Secure Routing. This model ensures the integrity and confidentiality of the stored data packet, thereby boosting the method's overall security.
- Compared to existing methods, the blockchain-based security method called, eXtreme Gradient Boost Quadratic Balloon Cryptographic Block Compression (XGBQ-BCBC) in CRN demonstrates significant performance enhancements in a number of performance metrics. The proposed method achieves a remarkable reduction in authentication time (x% and y% relative to Channel Availability Probability and multi-objective optimization respectively), improves data confidentiality (x% and y% relative to the same models), increase data integrity (x% and y% relative to the same models) during various communications. These improvements contribute to the security and efficiency of CRNs as a whole.

I.3 ORGANIZATION OF THE WORK

The remaining of the paper is organized as follows. The background of CRN and blockchain based secure routing in CRN for data confidentiality and data integrity is explained in section 2 with the reviews of related work discussed in detail. Section 3 explains the system model followed by which the proposed method, XGBQ-BCBC is elaborated using diagram and algorithmic description. Case study and inferences are provided in Section 4 with the experimental setup, results and discussion analyzed in section 5 and 6. Finally, section 6 concludes the paper.

II. RELATED WORKS

Cognitive Radio Networks (CRNs) are under sustained attacks from compromised primary and secondary users. Researchers propose several security mechanisms to circumvent these attacks, each with drawbacks.

Most of these methods have higher complexity and in contrast cannot be utilized to take the edge off multiple attack types. To overcome these drawbacks while sustaining higher security and Quality of Service (QoS) under attacks, a novel blockchain-based security method for boosting attack resilience in CRNs was proposed in [16]. The method showcased higher throughput with higher packet delivery ratio for several real-time cognitive radio scenarios. Nevertheless, CRN could result in considerable security issues while not focusing on privacy attacks during Spectrum Sensing (SS). A pareto encryption standard along with fine tunable recurrent neural network was presented in [17] to ensure privacy preservation. Yet another method to improve communication employing decentralized blockcahin was proposed in [18] for improving integrity level. CRNs integrate features of ad-hoc networks with cognitive radios to ease a variety of communication scenarios. Nevertheless, these CRNs are governed by uninterrupted attacks both from internal and external adversaries. They provide a trustworthy platform to deal with security, privacy, scalability and so on. Woefully, the attackers can still inoculate traffic to hinder blockchain nodes systematic functionalities. An optimized Blockchain-based IoT architecture was presented in [19] to attain optimized throughput therefore achieving efficacy extensively. Moreover, their constrained IP tracing potentialities make them inappropriate for real-time scenarios. To address this aspect, a novel blockchain-based method for deep traffic pattern analysis and circumventing of malicious attacks in CRNs was presented in [20]. Yet another framework employing blockchain technology to identify malicious users accurately was designed in [21]. A two-level shared key authentication mechanism with the aid of channel state information and DL was presented in [22] with high secrecy.

Light-weight convolutional neural network was employed in [23] to address on three different aspects, spectrum sensing, data routing and secure transmission based on the adaptive intelligent behavior. Yet another security mechanism employing federated learning was designed in [24] to confirm robustness. A holistic review on designing privacy-preserving reputation mechanism for IoT applications was investigated in [25]. Yet another blockchain framework to ensure transparency and security was presented in [26]. Generate of hash function was employed in [27] for blockchain transaction with improved accuracy. Conventional routing mechanisms frequently lack in imparting adequate security, resulting in data breaches. To address this issue, a greedy routing protocol with blockchain as infrastructure was presented in [28]. By employing greedy forwarding mechanism security was enhanced along with reliable data transmission. A blockchain-based cyber security mechanism employing machine learning was proposed in [29] along with a detailed review. Yet another optimal and secure routing using deep learning in [30] with minimal interference level and strong security during routing. From the scrutiny of related works, restricted conventional deep learning solutions have been designed to measure the effectiveness of secure routing in CRN. Instead of focusing on entire numbers of users, by splitting them into normal and malicious users via blockchain, results in minimizing the end-to-end delay with improved authentication accuracy. With this objective a novel method called, eXtreme Gradient Boost Quadratic Balloon Cryptographic Block Compression (XGBQ-BCBC) based secured routing in CRN is proposed. The elaborate description of the XGBQ-BCBC method is provided in the following sub-sections.

III. EXTREME GRADIENT BOOST QUADRATIC BALLOON CRYPTOGRAPHIC BLOCK COMPRESSION (XGBQ-BCBC) BASED SECURED ROUTING IN CRN

Many of these methods are characterized by high complexity that may results in challenges in implementation or performance efficiency. Some methods are specialized to address on the authenticity but might not be versatile enough to reduce the training time. This could leave the network vulnerable to unaddressed authentication. In response to the identified drawbacks, the paragraph introduces a novel blockchain-based security method called, eXtreme Gradient Boost Quadratic Balloon Cryptographic Block Compression (XGBQ-BCBC) in CRN. The method's is outlined with several key features:

III.1 BLOCKCHAIN-BASED CRN SYSTEM MODEL

Figure 1 show the system model for blockchain-based secured routing in Cognitive Radio Network (CRN) with 'u' secondary users 'SUs' and a primary user 'PU'.

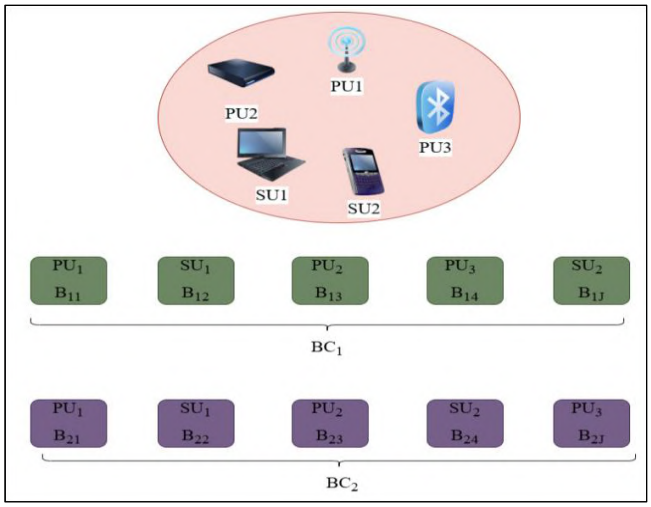


Figure 1: Blockchain-based CRN System Model.
Source: Authors, (2026).

Moreover, there may be 'v' malicious users 'MUs' in the spectrum sensing to degrade network performance. The act of spectrum sensing is performed by secondary users 'SUs' and broadcast the local decisions to all other adjacent users with updates in the blocks 'B_t' for time duration 't'. Hence, new blocks are created after every 'τ' units of time and get chained, therefore forming a blockchain. In this manner, blocks are created for primary user 'PU' and secondary users 'SUs' therefore forming blockchain for further processing. Also, secure routing in blockchain-based networks consists of functions involving control plane and data plane. As far as control plane is concerned routing decisions are made and validated utilizing blockchain technology and on the other hand, the data plane is responsible for actual secure forwarding of data packets on the basis of rules determined by control plane.

III.1.1 Registration

In the proposed method, number of cognitive users or nodes is collected as an input. Initially, the primary user 'PU' and secondary user 'SU' are registered in the blockchain for performing secure data management in cognitive radio network (CRN). This is explained as given below.

III.1.2 Primary User and Secondary User Registration Process

Here, initially the number of primary user 'PU' is registered in the blockchain by utilizing their User ID and Network ID. This is mathematically represented as given below.

$$Reg_a^{PU} = [Reg_1^{PU} + Reg_1^{PU} + \cdots + Reg_m^{PU}], where\ a = 1,2,\ldots,m \quad (1)$$

From the above equation (1), '$a = 1,2,\ldots,m$' denotes the number of registered primary user 'PU' and '(Reg_1^{PU})' denoting the first registered primary user 'PU'. In a similar manner, the number of secondary user 'SU' is registered and is mathematically represented as given below.

$$Reg_b^{SU} = [Reg_2^{SU} + Reg_2^{SU} + \cdots + Reg_n^{SU}], where\ b = 1,2,\ldots,n \quad (2)$$

From the above equation (2), '$b = 1,2,\ldots,n$' denote the number of registered secondary user 'SU' with 'Reg_n^{SU}' representing the '$n-th$' registered secondary user in blockchain.

III.1.3 Extreme Gradient Boost Quadratic Node Classifier

The eXtreme Gradient Boost Node Classifier employed in our work denotes a scalable tree optimization with the boosting concept being the root of classifier combines the forecasting of weak learners (i.e. Quadratic classifier) with additive training methods to develop a strong learner. Moreover, by combining the weak quadratic classifier results to that of the strong eXtreme Gradient Boost Node Classifier results aids in avoiding overfitting and enhances mathematical ability. The eXtreme Gradient Boost Node Classifier along with Quadratic classifier is illustrated in figure 2.

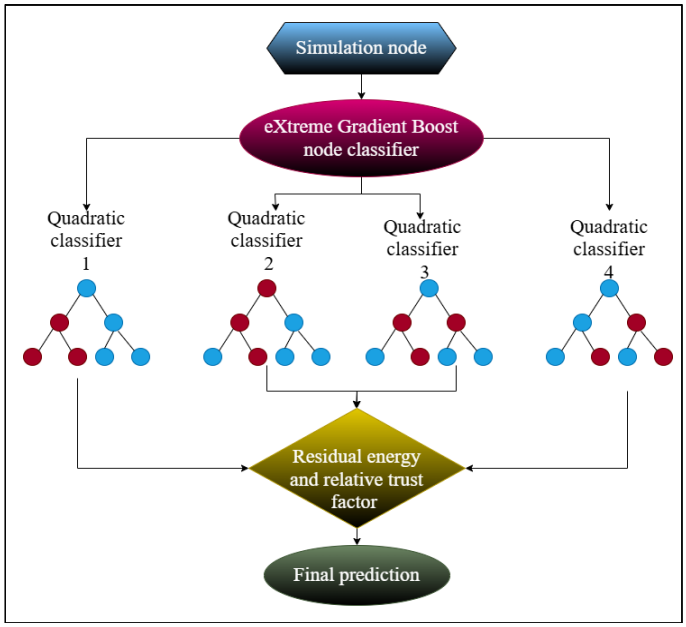


Figure 2: Structure of eXtreme Gradient Boost Quadratic Node Classifier.
Source: Authors, (2026).

From the above figure the objective functions (i.e. normal and malicious node classification based on the residual energy and relative trustworthiness) are simplified by allowing the prediction and regularization terms to be combined. The mathematical formulate is as given below.

$$x_i = f_i^{(k)} = \sum_{l=1}^{k} f_l(SU_i[E_{Res}(t), RT]) = f_i^{(k-1)} + f_k(SU_i[E_{Res}(t), RT]) \quad (3)$$

From the above equation (3) '$f_k(SU_i[E_{Res}(t), RT])$' denotes the learner at step 'k', '$f_i^{(k)}$' denotes the prediction at 'k', '$f_i^{(k-1)}$, represent the prediction at '$k-1$' with respect to the input features '$f_k(SU_i[E_{Res}(t), RT])$' with high residual energy and relative trust factor for the corresponding secondary user respectively. Following which the Quadratic Classifier is formulated as given below by means of likelihood ratio (LR).

$$LR = \frac{\sqrt{2\pi|\Sigma_1|}^{1} \exp\left(-\frac{1}{2}(x-\mu_1)^T\Sigma_1^{-1}(x-\mu_1)\right)}{\sqrt{2\pi|\Sigma_0|}^{1} \exp\left(-\frac{1}{2}(x-\mu_0)^T\Sigma_0^{-1}(x-\mu_0)\right)} \quad (4)$$

From the above equation (4), the likelihood ratio '' value is arrived at based on the means 'μ_1, μ_0', covariance matrices 'Σ_1, Σ_0', corresponding to '$LR = 0, when\ the\ secondary\ user\ is\ normal\ node$', '$LR = 1, when\ the\ secondary\ user\ is\ malicous\ node$' respectively. These values are sent in to the boosted eXtreme Gradient Boost Node Classifier to generate the final results.

III.1.4 Residual Energy Calculation

Primary Users being licensed owners of a specific spectrum band are assumed to have guaranteed access and does not depend on opportunistic spectrum access or residual energy calculations. On the other hand Secondary Users are unlicensed that possessing limited power sources necessitates residual energy evaluation. In CRN the unlicensed secondary users can opportunistically utilize spectrum bands that are not being utilized by licensed primary users. However, upon detection of a primary user's signal the secondary users must vacate the channel immediately. Hence, based on the residual energy and trust value, the nodes are categorized using eXtreme Gradient Boost Node Classifier. Here, the eXtreme Gradient Boost Node Classifier combines the weak classifier result to attain strong classifier output. Quadratic Classifier is taken as weak classifier for classifying and authenticating nodes as normal nodes or malicious nodes. By combining the weak classifier results, classification performance gets improved. The residual energy of a node in Cognitive Radio Network (CRN) is the amount of energy remaining after a certain time instance, taking into consideration the energy consumed while performing several operations like, transmission, reception and idle states. The mathematical formula for measuring residual energy at time instance 't' for each registered secondary user is calculated as given below.

$$E_{Res}(t) = Reg_b^{SU} Max\left(E_{Init} - [E_{Trans}(t) + E_{Recv}(t) + E_{Idle}(t)]\right) \quad (5)$$

From the above equation (5) the residual energy '$E_{Res}(t)$' is measured by considering the values of energy consumed while transmitting data packets '$E_{Trans}(t)$' at time 't', energy consumed while receiving data packets '$E_{Recv}(t)$' and energy consumed during the idle stage '$E_{Idle}(t)$' respectively. Higher the measured residual energy result of the registered secondary user higher is the probability of secondary user being normal node.

III.1.5 Relative Trustworthiness Calculation

Relative trustworthiness of a user in CRN is formulated based on the distance factor for each registered secondary user as given below.

$$RT = Reg_b^{SU} Max\left[\min\left(\frac{Dis_1}{Dis_2}, \frac{Dis_2}{Dis_1}\right)\right] \quad (6)$$

From the above equation (6) relative trustworthiness 'RT' factor is arrived at based on the minimum distance between users. Higher the relative trustworthiness of the registered secondary user higher is the probability of secondary user being normal node. The distance factor is measured as given below.

$$Dis_1 = \sqrt{\left(P_{SU_i} - P_{PU}\right)^2 + \left(Q_{SU_i} - Q_{PU}\right)^2} \quad (7)$$

$$Dis_2 = \sqrt{\left(P_{MU} - P_{SU_i}\right)^2 + \left(Q_{MU} - Q_{SU_i}\right)^2} \quad (8)$$

From the above equations (7) and (8), '$\left(P_{SU_i}, Q_{SU_i}\right)$' represents the '$P$' and '$Q$' coordinates of '$i-th$' secondary user '$SU$', '$(P_{PU}, Q_{PU})$' denoting '$P$' and '$Q$' coordinates of primary user and '(P_{MU}, Q_{MU})' referring to the 'P' and 'Q' coordinates of malicious user respectively. To make the overfitting rational while minimizing the methods speed the mathematical formula to evaluate the goodness for original function is as given below.

$$Objective^{(p)} = \sum_{l=1}^{n} \mathcal{L}(Res_i - Res_i') \quad (9)$$

From the above equation (8), '$\mathcal{L}$', denotes the loss function for the corresponding 'n' number of observations employing Lasso regularization term represented as given below.

$$\mathcal{L} = \sum_{i=1}^{n} Res_i - (x_i\beta)^2 + \sum_{j=1}^{m} |\beta_j| \quad (10)$$

From the above loss function results (9) are arrived at based on the actual result 'Res_i', predicted results 'Res_i'' for the corresponding input 'x_i' with respect to a coefficient value 'β' respectively. The pseudo code representation of eXtreme Gradient Boost Quadratic Node Classifier is given below.

Input: Primary Users '$PU = PU_1, PU_2, \ldots, PU_m$', Secondary Users '$SU = SU_1, SU_2, \ldots, SU_n$'
Output: Computationally-efficient authentication
Step 1: **Initialize** 'm', 'n' Step 2: **Begin** Sep 3: **For** each Primary Users 'PU', Secondary Users 'SU' Step 4: Perform primary user and secondary user registration according to (1) and (2) Step 5: Generate extreme boosting and quadratic classifier results according to (3) and (4) Step 6: Evaluate residual energy according to (5) Step 7: Evaluate relative trustworthiness results according to (6), (7) and (8) Step 8: Evaluate the goodness for original function according to (9) and (10) Step 9: Generate results of malicious nodes 'MN' and normal nodes 'NN' Step 10: Return node classified results (normal nodes 'NN' along with data packets 'DP') Step 11: **End for** Step 12: **End**

Algorithm 1: eXtreme Gradient Boost Quadratic Node Classifier.
Source: Authors, (2026).

As given in the above algorithm initially the registered primary user and secondary user are generated in the form of block. Following which only the registered users in the block undergo the process of classification. With the utilization of eXtreme Gradient Boost Node Classifier (i.e. strong learner) and Quadratic Classifier (i.e. weak learner) for node classification process combines the prediction results from several weak learners. With the aid of several weak learners each new tree correct the errors made by the previous tree, resulting in a highly accurate result. Also, by selecting the nodes with high residual energy and relative trustworthiness as basis in turn minimizes the overall time consumed in actual authentication process.

III.2 BALLOON CRYPTOGRAPHIC MATYAS–MEYER–OSEAS (MMO) BLOCK COMPRESSION-BASED SECURE ROUTING

Second, data packets are collected from normal nodes for ensuring secured routing. In our work, Balloon Cryptographic hash-based Matyas–Meyer–Oseas (MMO) compression is applied for ensuring secured data routing. Figure 3 shows the structure of Balloon Cryptographic Matyas–Meyer–Oseas Block compression model.

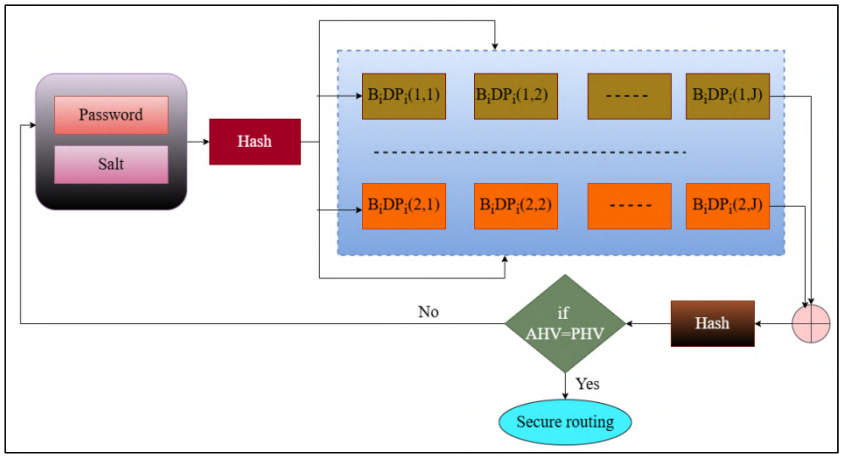


Figure 3: Structure of Balloon Cryptographic Matyas–Meyer–Oseas Block compression model for secure routing in CRN.
Source: Authors, (2026).

As shown in the above figure, the normal nodes sensed data packets are provided as input. The scenario described, involves the utilization of Balloon Cryptographic hash function for secured data routing and Matyas–Meyer–Oseas (MMO) compression function for hash generation in a blockchain control plane with blockchain as basic architecture. The function generates hash value for every normal nodes sensed data packets using Matyas–Meyer–Oseas Compression Function. Moreover, the hash value generation is considered as an encryption process for every data packets. This is performed via expansion, mixing and output hash generation. The hashed data are sent to the source node. The decryption process is carried out in the destination node to obtain original data, therefore preventing illegal access. This guarantees the secured data routing in CRN. The Matyas–Meyer–Oseas Compression function is one of the typical mechanisms in building a single-block-length compression function from a block cipher. The function 'f' obtains an input chaining value 'H_{i-1}' along with data packet block 'DP_i' to generate next chaining value 'H_i' employing a block cipher 'E'. This is mathematically formulated as given below.

$$H_i = E_{H_{i-1}}(DP_i) \oplus DP_i \tag{11}$$

From the above equation (11), the previous has value 'H_{i-1}' represents the block cipher key value for the corresponding plain text (i.e., data packet ' DP_i') with the output 'H_i' forming the XOR '$\oplus$' of the cipher text '$E_{H_{i-1}}(DP_i)$' and plain text ' DP_i' respectively.

III.2.1 Expansion

In the expansion stage, to start with large buffer of memory is filled with a pseudorandom byte sequence '$PRBseq$'. This pseudorandom byte sequence '$PRBseq$' is arrived by repeatedly hashing a fusion of the password 'Pwd' and salt 'St' provided as inputs to the function. This is mathematically formulated as given below.

$$IV = DP_i[PRBseq + H(Pwd + St)] \tag{12}$$

From the above equation (12) the input value is generated based on the pseudorandom byte sequence '$PRBseq$', along with user provided data 'Pwd' and arbitrary piece of data 'St' for each normal nodes sensed data packets 'DP_i' respectively.

III.2.2 Mixing

Following which in the mixing stage, the bytes within the allocated memory buffer for each input value 'IV' are mixed repeatedly for a specified number of iteration. In each iterations' a block in the buffer is updated by hashing its current value, value of the previous block and values from other arbitrarily selected blocks within the buffer. This is mathematically formulated as given below.

$$B_iDP_i = H_i[B_i] + H_{-i-1}[B_{i-1}] + \cdots + H_m[B_m]_{iter} \tag{13}$$

From the above equation (13) for each block 'B_i' with corresponding normal sensed nodes data packets 'DP_i', mixing operation is performed repeatedly overall several iterations '$iter$' with the results of the Matyas–Meyer–Oseas Compression function deciding the memory locations to access. Finally upon successful completion of the mixing phase, the last element in the final buffer forms the resulting hash output that is sent to the normal sensed node. This is mathematically formulated as given below.

$$HV = H_m[B_m] \tag{14}$$

Finally, the decryption process is carried out in the destination sensed node to obtain original data, therefore preventing illegal access. The pseudo representation of Balloon Cryptographic Matyas–Meyer–Oseas Block compression-based Secure Routing in CRN is provided below.

Input: Primary Users '$PU = PU_1, PU_2, \ldots, PU_m$', Secondary Users '$SU = SU_1, SU_2, \ldots, SU_n$
Output: robust and secure data routing
Step 1: **Initialization** 'm', 'n' Step 2: **Initialize** normal nodes 'NN', data packets 'DP' Step 3: **Begin** Step 4: **For** each Primary Users 'PU', Secondary Users 'SU', normal nodes 'NN' and data packets 'DP' **//Generate Matyas–Meyer–Oseas Compression function results according to (11)** **//Encryption** **//Expansion** Step 5: Generate input vector results according to (12) **//Mixing** Step 6: Generate mixed results repeatedly for a specified number of iteration according to (13) //Output Step 7: Obtain last element from the mixing function resulting hash output Step 9: Return hashed value to the normal sensed nodes 'HV' Step 9: **End for** Step 11: **For** each Primary Users 'PU', Secondary Users 'SU', normal nodes 'NN' and data packets 'DP' Step 12: If '$AHV = PHV$' Step 13: Then secured data routing between nodes Step 14: End if Step 15: **If** '$AHV \neq PHV$' Step 16: **Then** no data routing between nodes Step 17: **End if** Step 18: **End for** Step 19: **End**

Algorithm 2 Balloon Cryptographic Matyas–Meyer–Oseas Block compression-based Secure Routing**.**
Source: Authors, (2026).

As given in the above algorithm the entire process of blockchain-based secure data routing in cRN by combining the Balloon cryptographic hash with the Matyas-Meyer-Oseas compression function.

On one hand, Balloon Hashing necessitates a fundamental standard compression function and on the other hand, the Matyas-Meyer-Oseas compression function that is built from block cipher that serves this purpose. Balloon Hashing using Matyas-Meyer-Oseas compression function processes the input data to generate unique hash value that is sent to the sender node. On the other end the receiver node evaluates the hash and making a comparison with original hash as send by the server, any data packet changes results in a distinct hash value. In this manner the data integrity is ensured. Moreover by storing and distributing hashed data instead of the raw data packets using Matyas-Meyer-Oseas compression function in a blockchain helps prevent unauthorized data access wherein even if an unauthorized user intercepts hash value, original data packet is not reconstructed from hash. This in turn ensures data confidentially.

III.3 CASE STUDY AND INFERENCES

In this section case analysis of secure routing in CRN using primary and secondary users are simulated by applying eXtreme Gradient Boost Quadratic Balloon Cryptographic Block Compression (XGBQ-BCBC) method. Figure 4 shows the sample nodes for simulation.

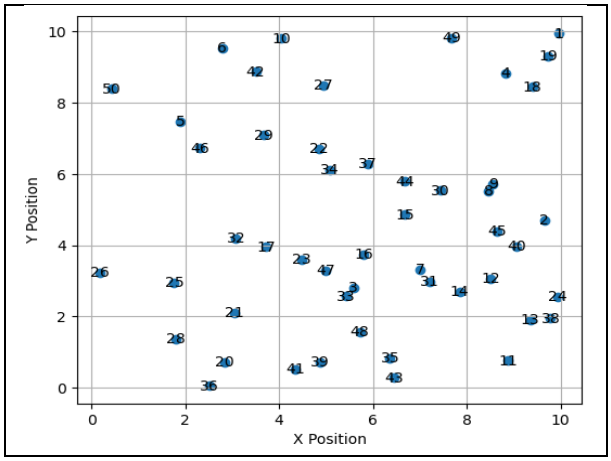


Figure 4: Sample node generation.
Source: Authors, (2026).

As shown in the above figure 50 nodes comprising of both primary user and secondary user are obtained for performing secure routing in CRN. To perform simulation 33 numbers of primary user and 17 numbers of secondary users are used. Also an initial energy of 100 Joules is set for all the 50 nodes and according to the proceedings the energy consumption gets depleted. With this hypothesis residual energy and relative trustworthiness factors are analyzed. The results are shown in figure 5.

	node_id	residual_energy	trust_value	user_type
0	1	98.500000	0.976700	PU
1	2	97.000000	0.968400	PU
2	3	95.500000	0.960100	PU
3	4	94.000000	0.951800	PU
4	5	92.500000	0.943500	PU
5	6	91.000000	0.935200	PU
6	7	89.500000	0.926900	PU
7	8	88.000000	0.918600	PU
8	9	86.500000	0.910300	PU
9	10	85.000000	0.902000	PU
10	11	83.500000	0.893700	PU
11	12	82.000000	0.885400	PU
12	13	80.500000	0.877100	PU
13	14	79.000000	0.868800	PU
14	15	77.500000	0.860500	PU
15	16	76.000000	0.852200	PU
16	17	74.500000	0.843900	PU
17	18	73.000000	0.835600	PU
18	19	71.500000	0.827300	PU
19	20	70.000000	0.819000	PU
20	21	68.500000	0.810700	PU
21	22	67.000000	0.802400	PU
22	23	65.500000	0.794100	PU
23	24	64.000000	0.785800	PU
24	25	62.500000	0.777500	PU
25	26	61.000000	0.769200	PU
26	27	59.500000	0.760900	PU
27	28	58.000000	0.752600	PU
28	29	56.500000	0.744300	PU
29	30	55.000000	0.736000	PU
30	31	53.500000	0.727700	PU
31	32	52.000000	0.719400	PU
32	33	50.500000	0.711100	PU
33	34	49.000000	0.702800	SU
34	35	47.500000	0.694500	SU
35	36	46.000000	0.686200	SU
36	37	44.500000	0.677900	SU
37	38	43.000000	0.669600	SU
38	39	41.500000	0.661300	SU
39	40	40.000000	0.653000	SU
40	41	38.500000	0.644700	SU
41	42	37.000000	0.636400	SU
42	43	35.500000	0.628100	SU
43	44	34.000000	0.619800	SU
44	45	32.500000	0.611500	SU
45	46	31.000000	0.603200	SU
46	47	29.500000	0.594900	SU
47	48	28.000000	0.586600	SU
48	49	26.500000	0.578300	SU
49	50	25.000000	0.570000	SU

Figure 5: Calculation of residual energy and relative trustworthiness.
Source: Authors, (2026).

From the above results of residual energy and relative trustworthiness for each user in CRN, eXtreme Gradient Boost Node Classifier along with Quadratic classifier is applied to differentiate between normal nodes and malicious node. By differentiating between normal and malicious users, the authentication accuracy along with end-to-end delay involved in routing process gets improved. Figure 6 shows the corresponding results of normal primary user (33) and malicious users (i.e. secondary malicious users 14 and secondary normal users 13).

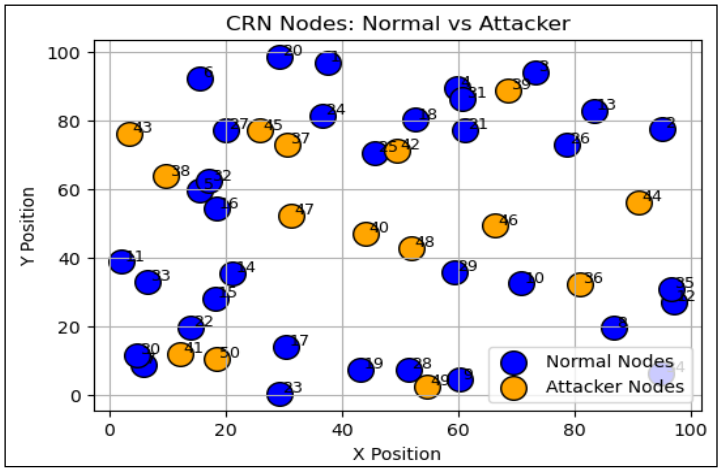


Figure 6: CRN Node Created Results
Source: Authors, (2026).

Finally with the above CRN node created results, normal sensed data packets (i.e. with seven primary users and three secondary users for simulation) are subjected to Balloon Cryptographic hash-based Matyas–Meyer–Oseas compression to ensure secure routing. Figure 7 shows the cryptographic results generated to ensure authentication and integrity of data.

	node_id	residual_energy	timestamp	trust_value	block_hash	Cryptographic_hash(key)	Cryptographic_hash(key)
0	1	98.500000	1764305708.124430	0.976700	257403da1918b2b01a3c24ddcfad35c6	7e3299c816f7f0b56a7cc6703b2bd6b9	7e3299c816f7f0b56a7cc6703b2bd6b9
1	2	97.000000	1764305708.124697	0.968400	cfdc435dcf216f5a81f4658b4bac1e4c	866935708010f21815f1c7cce4e6af64	866935708010f21815f1c7cce4e6af64
2	3	95.500000	1764305708.124897	0.960100	e1c793b0c509fb71b010efc245eebcea	1432345963ab2b2251e579b77dbaa67f	1432345963ab2b2251e579b77dbaa67f
3	4	94.000000	1764305708.125081	0.951800	915ad44a24f7eb97534bcd165d1ba6cf	9e419146f64f180dd1d6659db1020c80	9e419146f64f180dd1d6659db1020c80
4	5	92.500000	1764305708.125242	0.943500	a2bdf0b248cda2f40b9462a513ec6a3a	5b53f8e2b7bcb578a4ba39349dd94260	5b53f8e2b7bcb578a4ba39349dd94260
5	6	91.000000	1764305708.126130	0.935200	be62c925840a79927647c7a2295e76d5	9d23eb7268c7151359b316731a86a279	9d23eb7268c7151359b316731a86a279
6	7	89.500000	1764305708.126479	0.926900	6cb8a22a16cd5998d2c35d788653f7be	99aa2522bd6f255d8ead70eb00f79aea	99aa2522bd6f255d8ead70eb00f79aea
7	34	49.000000	1764305708.131452	0.702800	79746323359bd2b7302cb208330724cc	f183691e9126b2408f77ef81913ed26c	f183691e9126b2408f77ef81913ed26c
8	35	47.500000	1764305708.131587	0.694500	0dcf00bf0052ded5398159459a3c12e2	64e67c07b21557d5ec501bf90fb702a8	64e67c07b21557d5ec501bf90fb702a8
9	36	46.000000	1764305708.131728	0.686200	1ca9429c41e386a2ecd5a02b7e80fa5a	27db2be29d7c29407af8e41a303d99b4	27db2be29d7c29407af8e41a303d99b4

Encoding results

decrypted_result	secure_routing_status
{"block_hash":"257403da1918b2b01a3c24ddcfad35c6","node_id":1,"residual_energy":98.5,"timestamp":1764305708.1244302,"trust_value":0.9767}	Ssecured routing
{"block_hash":"cfdc435dcf216f5a81f4658b4bac1e4c","node_id":2,"residual_energy":97.0,"timestamp":1764305708.124697,"trust_value":0.9684}	Ssecured routing
{"block_hash":"e1c793b0c509fb71b010efc245eebcea","node_id":3,"residual_energy":95.5,"timestamp":1764305708.1248972,"trust_value":0.9601}	Ssecured routing
{"block_hash":"915ad44a24f7eb97534bcd165d1ba6cf","node_id":4,"residual_energy":94.0,"timestamp":1764305708.1250808,"trust_value":0.9518}	Ssecured routing
{"block_hash":"a2bdf0b248cda2f40b9462a513ec6a3a","node_id":5,"residual_energy":92.5,"timestamp":1764305708.1252425,"trust_value":0.9435}	Ssecured routing
{"block_hash":"be62c925840a79927647c7a2295e76d5","node_id":6,"residual_energy":91.0,"timestamp":1764305708.1261303,"trust_value":0.9352}	Ssecured routing
{"block_hash":"6cb8a22a16cd5998d2c35d788653f7be","node_id":7,"residual_energy":89.5,"timestamp":1764305708.126479,"trust_value":0.9269}	Ssecured routing
{"block_hash":"79746323359bd2b7302cb208330724cc","node_id":34,"residual_energy":49.0,"timestamp":1764305708.131452,"trust_value":0.7028}	Ssecured routing
{"block_hash":"0dcf00bf0052ded5398159459a3c12e2","node_id":35,"residual_energy":47.5,"timestamp":1764305708.1315866,"trust_value":0.6945}	Ssecured routing
{"block_hash":"1ca9429c41e386a2ecd5a02b7e80fa5a","node_id":36,"residual_energy":46.0,"timestamp":1764305708.1317277,"trust_value":0.6862}	Ssecured routing

Decoded results for secure routing

Figure 7: Cryptographic results for secure routing.
Source: Authors, (2026).

By applying the above Balloon Hashing using Matyas-Meyer-Oseas compression function unique hash values are generated that in turn results in the improvement of data integrity. Also by storing and distributing hashed data instead of the raw data packets improves the overall data confidentiality extensively. The quantitative results are provided in the following sub-section.

IV. EXPERIMENTAL SETUP

In this section, the performance of the proposed blockchain method called, eXtreme Gradient Boost Quadratic Balloon Cryptographic Block Compression (XGBQ-BCBC) based secured routing in CRN was analyzed. The proposed method was implemented using Python high-level general-purpose programming language and the experiments are performed on an Intel(R) Pentium machine with a speed 2.13 GHz and 4.0 GB RAM using Windows 7 32-bit Operating System. A brief comparison of the proposed XGBQ-BCBC method with the existing Channel Availability Probability [1] and Multi-objective optimization [2] with respect to authentication accuracy, authentication time, data confidentiality and data integrity for varied numbers of data packets and sensor nodes.

V. RESULTS AND DISCUSSION

The performance of the proposed XGBQ-BCBC and two existing approaches namely Channel Availability Probability [1] and Multi-objective optimization [2] are discussed. To evaluate the model's effectiveness, several performance indicators are considered, including authentication accuracy, authentication time, data confidentiality and data integrity.

V.1 PERFORMANCE ANALYSIS OF AUTHENTICATION ACCURACY

In this section authentication accuracy is analyzed and validated. Authentication and secure routing are said to be demanding as far as cognitive radio networks (CRNs) are concerned. This is due to the reason to make certain accurate spectrum sharing is made by verifying and validating node identities and establishing reliable data paths that is said to be demanding owing to the network's arbitrary nature. The authentication accuracy is mathematically stated as given below.

$$AA = \sum_{i=1}^{N} \frac{DP_{AA}}{DP_i} * 100 \quad (15)$$

From the above equation (15) authentication accuracy 'AA' is measured based on the data packets considered 'DP_i' and data packets authenticated accurately 'DP_{AA}'. It is measured in terms of percentage (%). Table 1 lists the authentication accuracy results when substituted in equation (15).

Table 1: Authentication accuracy using Proposed XGBQ-BCBC, Existing Channel Availability Probability [1] and Multi-objective optimization.

Number of users	Authentication accuracy (%)		
	Proposed XGBQ-BCBC	Channel Availability Probability [1]	Multi-objective optimization [2]
5	90	85	80
10	85.35	76.25	63.35
15	84	75.55	62.45
20	83.15	74.25	61.25
25	82	73	60
30	80.45	71.45	58.15
35	83.55	74.35	61.55
40	85	76	63.25
45	87.15	78.15	65.15
50	89	80	67

Source: [2].

Table 1 demonstrates the experimental results of authentication accuracy. The number of users is taken in the ranges from 5 to 50. Table 1 symbolizes the performance evaluation of the authentication accuracy using three techniques proposed XGBQ-BCBC and existing methods Channel Availability Probability [1] and Multi-objective optimization [2]. Let us consider the 5 user for conducting the experiments. Firstly, the authentication accuracy is obtained as 90%, 85% and 80% for proposed XGBQ-BCBC and existing [1], [2] respectively. Similarly, nine remaining runs are carried out with respect to the number of users. The observed ten results of the XGBQ-BCBC are compared to the existing methods. The graph is created as given below figure 8 based on the above table 1.

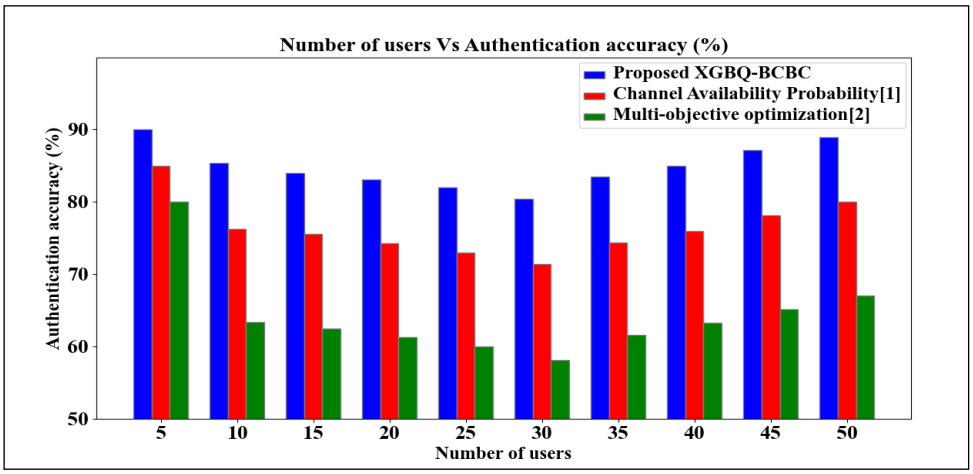


Figure 8: Analysis of authentication accuracy.
Source: Authors, (2026).

Figure 8 shows the results of authentication accuracy using three methods, XGBQ-BCBC, Channel Availability Probability [1] and Multi-objective optimization [2]. To ensure fair comparison between three methods, similar number of users (PUs and SUs) ranging between 5 and 50 are applied to simulation process. The horizontal axis denotes the number of users, while the vertical axis reflects the authentication accuracy achieved. An increase in number of users causes increase in the spectrum utilization by the secondary user in case of channel availability and hence in the presence of malicious secondary user accuracy is said to be compromised. However simulations conducted for 10 iterations show high authentication accuracy results generated for the proposed XGBQ-BCBC method upon comparison to [1] and [2]. The reason for higher authentication accuracy is to apply the eXtreme Gradient Boost Node Classifier. It combines the weak classifier result for achieving the strong classifier output. Quadratic Classifier is considered as weak classifier to accurately classify the nodes as normal nodes or malicious nodes. With this the overall authentication accuracy using proposed XGBQ-BCBC method was found to be better by 10% compared to [1] and 33% compared to [2].

V.2 PERFORMANCE ANALYSIS OF END-TO-END DELAY

End-to-end delay in secure routing for cognitive radio networks is a performance metric denoting the total time consumed for a data packet to travel between source and destination. This is mathematically formulated as given below.

$$E2E6 = T_{i\,End} - T_{i\,Start} \tag{16}$$

From the above equation (16) end-to-end delay '$E2E$' denotes the time consumed '$T_{i\,End}, T_{i\,Start}$' between the source and destination to transmit data packets between them. It is measured in terms of seconds (sec). Table 2 lists the end-to-end delay results when substituted in equation (16).

Table 2: End-to-end delay using Proposed XGBQ-BCBC, Existing Channel Availability Probability and Multi-objective optimization.

Number of users	End-to-end delay (sec)		
	Proposed XGBQ-BCBC	Channel Availability Probability [1]	Multi-objective optimization [2]
5	4.4	5.25	7.55
10	6.3	8.25	8.85
15	7.1	10.45	10.95
20	10.45	12.95	13.25
25	12.1	14.45	14.85
30	13.25	15.35	15.85
35	12.45	14.65	16
40	10.1	12.25	14.15
45	9.25	10.45	11.35
50	11.1	13.1	13.55

Source: [1] [2].

Table 2 demonstrates the performance analysis outcomes of end-to-end delay. The results of end-to-end delay using XGBQ-BCBC with existing Channel Availability Probability [1] and Multi-objective optimization [2]. But, comparatively, proposed XGBQ-BCBC minimizes the end-to-end delay involved during the secure routing. With the increasing number users, results of end-to-end delay are increased. By considering the values in above table 2, the graph is plotted in figure 9.

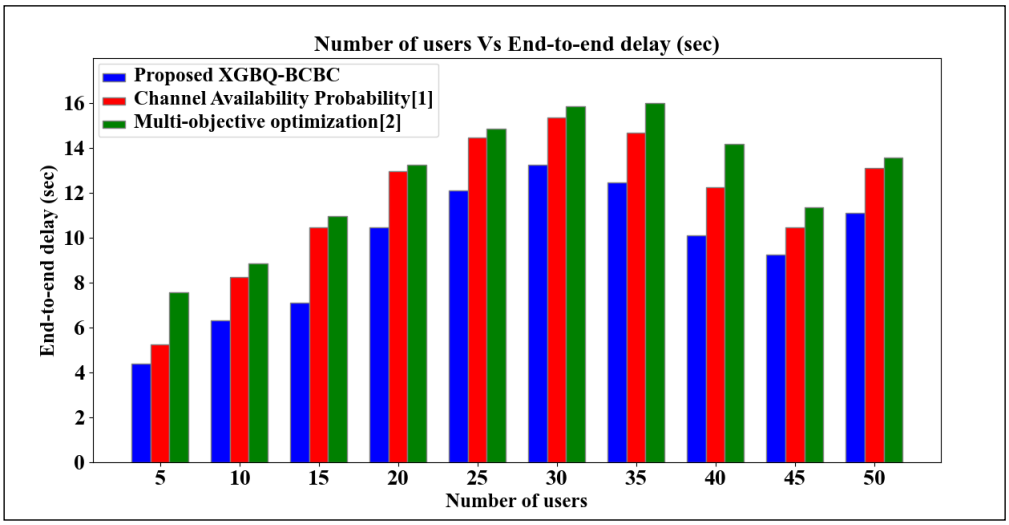


Figure 9: Analysis of end-to-end delay.
Source: Authors, (2026).

Figure 9 shows the graphical representation of end-to-end delay recorded for three distinct methods, XGBQ-BCBC, Channel Availability Probability [1] and Multi-objective optimization [2] respectively. Values were substituted in equation (16) and results were plotted accordingly for all the three methods. Though an increase in the end-to-end delay is recorded for the first six iterations however for rest of the four iterations the end-to-end delay was found to be decreasing, therefore corroborating the objective of increase in number of users does not influence end-to-end delay. However, the 10 users are considered for calculating the end-to-end delay. Firstly, the end-to-end delay is obtained as 6.3sec using proposed XGBQ-BCBC method. By applying the [1] [2], the end-to-end delay is found to be 8.25sec and 8.85sec respectively. Also simulations performed for an overall ten simulation runs show comparatively better results using proposed XGBQ-BCBC method than [1] and [2]. The reason was by applying the eXtreme Gradient Boost Quadratic Node Classifier where classification of nodes between normal and malicious was performed. Also, the residual energy is measured. The nodes are chosen with high residual energy for routing. Node trustworthiness is evaluated using a likelihood ratio. The combination of these techniques is intended to reduce the end-to-end delay. This in turn minimized the end-to-end delay involved in the process of routing in CRN using XGBQ-BCBC method by 23% compared to [1] and 35% compared to [2] respectively.

V.3 PERFORMANCE ANALYSIS OF DATA CONFIDENTIALITY

In this section data confidentiality rate is analyzed. Data confidentiality prevents unauthorized access to data packets making certain that only authorized cognitive users view it. In this manner sensitive data packet information are protected from unauthorized access. The data confidentiality is represented as given below.

$$DC = \sum_{i=1}^{N} \frac{DP_{ACU}}{DP_i} * 100 \tag{17}$$

From the above equation (17) data confidentiality 'DC' is measured based on the data packets considered 'DP_i' and the data packets accessed by authenticated cognitive users 'DP_{ACU}'. Table 3 lists the data confidentiality rate results when substituted in equation (17).

Table 3: Data confidentiality using Proposed XGBQ-BCBC, Existing Channel Availability Probability and multi-objective optimization.

Data packets	Data confidentiality (%)		
	Proposed XGBQ-BCBC	Channel Availability Probability [1]	Multi-objective optimization [2]
50	98	90	84
100	96.26	86.54	81.25
150	94	84.35	79.35
200	93.15	83.15	78.55
250	92	82.55	77.65
300	90.55	80.15	75.35
350	88.65	78.35	73.25
400	90	80.25	75.55
450	93.15	83.55	78.15
500	95	85	75

Source: [1] [2].

Table 3 describes the performance results of data confidentiality rate versus the data packets considered in the ranges from 50 to 500. The performance of data confidentiality rate is computed using three methods namely proposed XGBQ-BCBC method and existing methods, Channel Availability Probability [1] and Multi-objective optimization [2]. The overall observed results indicate that the XGBQ-BCBC method provides improved performance in terms of achieving higher data confidentiality (i.e., higher data transmission) than the existing methods. This is proved through the statistical calculation. For considering 50 data packets, the data confidentiality is significantly improved using the proposed effectively increased using the XGBQ-BCBC by 98% when compared to existing methods taken for comparison Channel Availability Probability [1] (90%), Multi-objective optimization [2] (84%). The graph is plotted as given below figure 10 based on the above table 3.

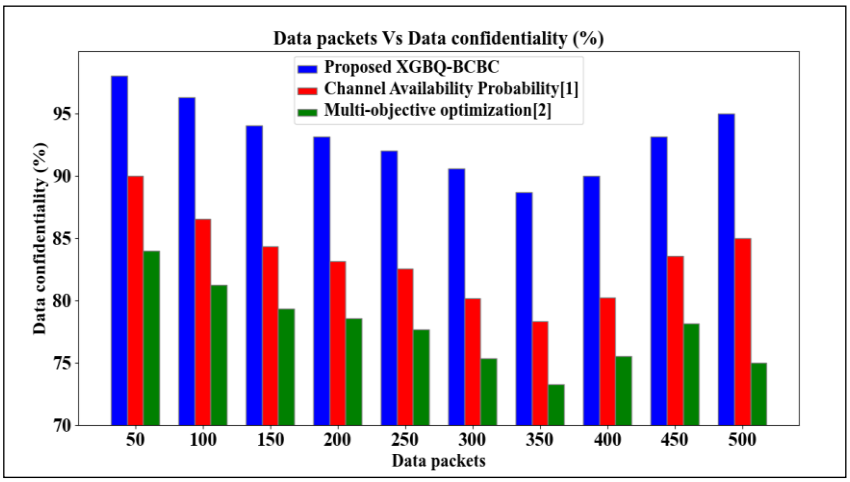


Figure 10: Analysis of Data Confidentiality.
Source: Authors, (2026).

Figure 10 shows the results of data confidentiality for the proposed XGBQ-BCBC method and two existing methods, Channel Availability Probability [1] and Multi-objective optimization [2] respectively. From the above figure data confidentiality was observed to be lesser for the first set of seven iterations whereas for the rest of three iterations it was found to be higher. Also comparative figurative representation show better results using proposed XGBQ-BCBC method when compared to [1] and [2]. The reason was by applying Balloon Cryptographic hash function for secured data routing and Matyas–Meyer–Oseas (MMO) compression function for hash generation in a blockchain control plane. Hash value is converted into original data with fixed-size. MMO process is one-way function to reverse the hash to find the original raw data. Storing and distributing only the hashed data in the blockchain control plane that enhances data confidentiality. An unauthorized party who accesses the hash value cannot view the original content. This in turn improves data confidentially of the proposed XGBQ-BCBC method by 10% compared to [1] and 16% compared to [2].

V.4 PERFORMANCE ANALYSIS OF DATA INTEGRITY

In this section data integrity analysis is made. Data integrity ensures that data packet s accurate and has not been tampered with or changed in an unauthorized manner. With this unauthorized or accidental modification of data is said to be avoided. The data integrity rate is mathematically formulated as given below.

$$DI = \sum_{i=1}^{N} \frac{DP_{NM}}{DP_i} * 100 \quad (18)$$

From the above equation (18) data integrity 'DI' is measured based on the data packets considered 'DP_i' and the amount of data packets being not modified 'DP_{NM}'. Table 4 lists the data integrity rate results when substituted in equation (18).

Table 4: Data integrity using Proposed XGBQ-BCBC, Existing Channel Availability Probability and multi-objective optimization.

Data packets	Data integrity (%)		
	Proposed XGBQ-BCBC	Channel Availability Probability [1]	Multi-objective optimization [2]
50	94	88	82
100	91.35	79.35	74.25
150	90.25	78.55	73.15
200	88.55	76.35	71.55
250	85.35	73.25	68.25
300	82	70.1	65.55
350	80	68.45	63.25
400	84.15	72.15	67.55
450	87	75.35	70.25
500	89.25	77.35	72.15

Source: [1] [2].

Table 4 demonstrates the performance analysis outcomes of data integrity rate. The data packets are considered in the range from 50 to 500. The validation is performed through comparing proposed XGBQ-BCBC method and two existing methods, Channel Availability Probability [1] and Multi-objective optimization [2]. With the increasing number of data packets, results of data integrity rate are reduced or increased. However, the proposed XGBQ-BCBC method is achieved better data integrity rate than the other two conventional methods.

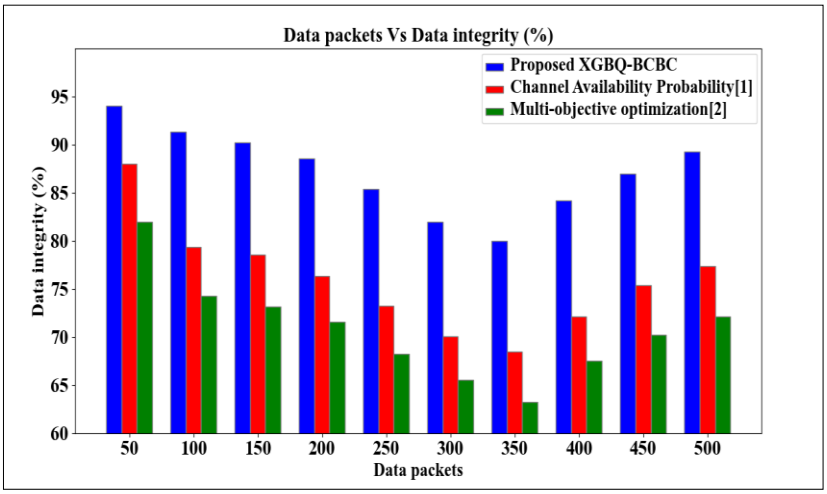


Figure 11: Analysis of data integrity.
Source: Authors, (2026).

Finally figure 11 give above illustrates the data integrity results using three methods, XGBQ-BCBC, Channel Availability Probability [1] and multi-objective optimization [2]. With horizontal axis representing the data packets ranging between 50 and 500, vertical axis denotes the data integrity results by applying the values in the equation 18. This is evident from the simulation with 50 data packets where the data integrity using XGBQ-BCBC was observed to be 94% whereas the data integrity for [1] and [2] was found to be 88% and 82% respectively. Comparison between three methods shows better data integrity results for XGBQ-BCBC method when compared to [1] and [2]. The reason for higher data integrity was to employ the Balloon Hashing using Matyas-Meyer-Oseas compression function. By using this algorithm, unique hash value are generated for each input data that is sent to the sender node. Evaluates the hash of the received data and compares it to the original hash value sent by the sender. A successful comparison confirms that the data has not been altered during transmission, therefore ensuring the data integrity and enabling routing. With this the data integrity of XGBQ-BCBC method was found to be better by 13% compared to [1] and 19% compared to [2].

VI. CONCLUSION

This paper presented a novel blockchain method to ensure secured routing in cognitive radio network using eXtreme Gradient Boost Quadratic Balloon Cryptographic Block Compression (XGBQ-BCBC) method. The proposed XGBQ-BCBC method for secure routing in CRN performed via blockchain performs the tasks of user (PU and SU) registration, block generation, node classification between normal users, malicious users and establishing data routing between normal nodes. First, user registration process was performed and stored in the form of blocks via blockchain. Following which for each registered user, eXtreme Gradient Boost Quadratic Node Classifier was applied differentiating between normal users and malicious users based on the likelihood ratio via residual energy and relative trustworthiness factors. Finally, with the data packets of sensed normal users using Balloon Cryptographic Matyas–Meyer–Oseas (MMO) Block compression results secure routing is established in an accurate manner. The algorithm is designed to simultaneously optimize four distinct performance metrics, including authentication accuracy, end-to-end delay, data confidentiality and data integrity. The proposed XGBQ-BCBC is assessed on various numbers of data packets and users. The performance of the proposed method is compared to the popular secure routing methods such as Channel Availability Probability and multi-objective optimization using different performance metrics. Experimental results prove that the XGBQ-BCBC method efficiently differentiates between normal and malicious users and therefore ensuring secure routing.

VII. AUTHOR'S CONTRIBUTION

Conceptualization: T. Sundar, A. Senthilkumar.
Methodology: T. Sundar, A. Senthilkumar.
Investigation: T. Sundar, A. Senthilkumar.
Discussion of results: T. Sundar, A. Senthilkumar.
Writing – Original Draft: T. Sundar, A. Senthilkumar.
Writing – Review and Editing: T. Sundar, A. Senthilkumar.
Resources: T. Sundar, A. Senthilkumar.
Supervision: T. Sundar, A. Senthilkumar.
Approval of the final text: T. Sundar, A. Senthilkumar.

VIII. REFERENCES

[1] Qusay M. Salih, Md Arafatur Rahman, A. Taufiq Asyhari, Muhammad Kamran Naeem, Mohammad Patwary, Ryan Alturki and Mohammed Abdulaziz Ikram, "Dynamic channel estimation-aware routing protocol in mobile cognitive radio networks for smart IIoT applications", Digital Communications and Networks, Elsevier, Volume 9, Issue 2, April 2023, Pages 367-382 [Channel Availability Probability].

[2] Zhongguo Zhou, You Li, Ziming Zhu, Qinghe Gao, Sisi Xiao, Tao Yan and Yan Huo, "A cognitive spectrum allocation scheme for data transmission in smart distribution grids", High-Confidence Computing, Volume 4, 2024, Pages 1-9 [multi-objective optimization].

[3] Evelyn Ezhilarasi I and J. Christopher Clement, "Robust Cooperative spectrum sensing in Cognitive Radio Blockchain network using SHA-3 algorithm", Blockchain: Research and Applications, Elsevier, 2024, Pages 1-18.

[4] Archit Jain, Nitin Gupta and M. Sreenu, "Blockchain based smart contract for cooperative spectrum sensing in cognitive radio networks for sustainable beyond 5G wireless communication", Green Technologies and Sustainability, Elsevier, Volume 1, Issue 2, May 2023, Pages 1-10.

[5] D. Balakumar, S. Nandakumar, "Blockchain-enabled cooperative spectrum sensing in 5G and B5G cognitive radio via massive multiple-input multiple-output nonorthogonal multiple access", Results in Engineering, Elsevier, Vol. 24, Dec 2024.

[6] Hamad Aldawsari, "A blockchain-based approach for secure energy-efficient IoT-based Wireless Sensor Networks for smart cities", Alexandria Engineering Journal, Elsevier, Vol. 126, Jul 2025.

[7] S. Ramachandra, M. Baskar, "Real-time multi-level trust-based secure routing for improved QoS in WSN using blockchain", Results in Engineering, Elsevier, Vol. 26, Jun 2025.

[8] Nikhil Kumar Marriwala, Sunita Panda, Chandran Kamalanathan, Narayanan Sadhasivam, Vootla Subba Ramaiah, "AnAnalytical Model for Dynamic Spectrum Sensing in Cognitive Radio Networks Using Blockchain Management", Engineering Proceedings, MDPI, Mar 2023.

[9] Sidra Tul Muntaha Pavlos, I. Lazaridis, Maryam Hafeez, Qasim Z. Ahmed, Zaharias D. Zaharis, Faheem A. Khan, "Blockchain for Dynamic Spectrum Access and Network Slicing: A Review", IEEE Access, Vol. 11, Feb 2023.

[10] Nassmah Y. Al-Matari, Ammar T. Zahary, Asma A. Al-Shargabi, "A survey on advancements in blockchain-enabled spectrum access security for 6G cognitive radio IoT networks", Scientific Reports, Nov 2024.

[11] Mai Shawkat, Ali El desoky, Zainab H. Ali, Mofreh Salem, "Blockchain and federated learning based on aggregation techniques for industrial IoT: A contemporary survey", Peer-to-Peer Networking and Applications, Springer Nature Link, Vol. 18, May 2025.

[12] Senthil Kumar Jagatheesaperumal Abdellah Chehri, Mohamed Rahouti, Kaiqi Xiong, Janbueniek, "Blockchain-Based Security Architecture for Uncrewed Aerial Systems in B5G/6G Services and Beyond: A Comprehensive Approach", IEEE Open Journal of the Communications Society, Vol. 6, Jan 2025.

[13] Abir Raza, Elarbi Badidi, Omarel Harrouss, Mohammad Hayajneh, Ezedin Barka, "Blockchain-Based Reputation and Trust Management for Smart Grids, Healthcare, and Transportation: A Review", IEEE Access, Vol. 12, Dec 2024.

[14] Sidra Tul Muntaha Pavlos, Maryam Hafeez, Qasim Z. Ahmed, Zaharias D. Zaharis, Faheem A. Khan, "Blockchain for Dynamic Spectrum Access and Network Slicing: A Review", IEEE Access, Vol. 11, Feb 2023.

[15] Khan Maaz Bin Hasan Ketan Kotecha, Mohammad Sajid, Maria A. Lapina, Mohammad Shahid, "Blockchain technology meets 6 G wireless networks: A systematic survey", Alexandria Engineering Journal, Elsevier, Vol. 92, Apr 2024.

[16] Debabrata Dansana, Prafulla Kumar Behera, S. Gopak Krishna Patro, Quadri Noorulhasan Naveed, Ayodele Lasisi, Anteneh Wogasso Wodajo, "BSMACRN: Design of an Efficient Blockchain Based Security Model for Improving Attack-Resilience of Cognitive Radio Ad-hoc Networks", IEEE Access, Vol. 12, Jan 2024.

[17] Saraswathi Vedachalam, Dayanaraj, "Development of a Privacy-Preserved and Secure Cooperative Spectrum Sensing System in Cognitive Radio Networks Using ATSNRNN-Enabled FPPDES With Machine Learning", IEEE Access, Vol. 12, Nov 2024.

[18] Sadia Hussain, Shahzaib Tahir, Hasan Tahir, Asif Masood, "Blockchain-Enabled Secure Communication Framework for Enhancing Trust and Access Control in the Internet of Vehicles (IoV)", IEEE Access, Vol. 12, Aug 2024.

[19] Mohammed A Alghamdi, "An Optimized and Secure Energy-Efficient Blockchain-Based Framework in IoT", IEEE Access, Vol. 13, Dec 2022.

[20] Debabrata Dansana, Prafulla Kumar Behera, Abdul Basit, A. Darem Zubair Ashraf, Abutahazamani, Mohammad Nadeem Ahmed, Gopal Krishna Patro, Mohammad Shameem, "BDDTPA: Blockchain-Driven Deep Traffic Pattern Analysis for Enhanced Security in Cognitive Radio Ad-Hoc Networks", IEEE Access, Vol. 11, Sep 2023.

[21] D. Balakumar, Nandakumar Sendrayan, "Enhance the Probability of Detection of Cooperative Spectrum Sensing in Cognitive Radio Networks Using Blockchain Technology", Journal of Electrical and Computer Engineering, Hindawi, Dec 2023.

[22] K. Saravanan, K. B. Gurumoorthy, Allwin Devaraj Stalin, Om Prakash Kumar, "Secure channel estimation model for cognitive radio network physical layer security using two level shared key authentication", Scientific Reports, Oct 2025.

[23] Deepanramkumar Pari, Jaisankar Natarajan, "Secure Spectrum Access, Routing, and Hybrid Beamforming in an Edge-Enabled mmWave Massive MIMOCRN-Based Internet of Connected Vehicle (IoCV) Environments", Sensors, MDPI, Dec 2022.

[24] Ankita Sharma, Shalli Rani, Wadii Boulila, "Blockchain-based zero trust networks with federated transfer learning for IoT security in industry 5.0", PLOS One, Jun 2025.

[25] Haitham Mahmoud, Junai Darshad, Adelaneiba, "A Systematic Review of Blockchain-Based Privacy-Preserving Reputation Systems for IoT Applications", Distributed Ledger Technologies: Research and Practice, ACM, Vol. 3, Dec 2024.

[26] Geetanjali Rathee, Ashutosh Sharma, Razi Iqbal, Moayad Aloqaily, Rajiv Kumar, Naveen Jaglan, “ABlockchain Framework for Securing Connected and Autonomous Vehicles”, Sensors, MDPI, Nov 2019.

[27] Nitesh Ghodichor, Raj Thaneeghavl. V, Dinesh Sahu, Gautam Borkar, Ankush Sawarkar, “Secure Routing Protocol to Mitigate Attacks by using Blockchain Technology in MANET”, International Journal of Computer Networks & Communications, Vol. 15, Mar 2023.

[28] K. R. Chairma Lakshmi, “Blockchain-Based Routing Protocols for Secure Data Transmissino”, ICTACT Journal on Communication Technology, Vol. 15, Sep 2024.

[29] Jameel Ahmad, Muhammad Umer Zia, Ijaz Haider Naqvi, Jawwad Nasar Chattha, Faran Awais Butt, Tao Huang, Wei Xiang, “Machine learning and blockchain technologies for cyber security in connected vehicles”, Wiley, Aug 2023.

[30] Hilmi Lazrag, Rachid Saadane, Moulay Dirss Rahmani, “ABlockchain-based Approach for Optimal and Secure Routing in Wireless Sensor Networks”, International Conference on Signal-image Technology and Internet Based Systems.

Journal of Engineering and Technology for Industrial Applications

ITEGAM-JETIA

Manaus, v.12 n.60, p.832-839 July/August, 2026.
DOI: https://doi.org/10.5935/jetia.v12i60.3267

ISSN ONLINE: 2447-0228

RESEARCH ARTICLE OPEN ACCESS

ZONE BASED ROUTING PROTOCOL (ZBRP) WITH ENERGY CONSCIOUS TO SUPPORT SUSTAINABLE AGRICULTURAL IOT AND SMART FARMING NETWORKS

C. Rajalakshmi*[1], SreejithVignesh B P.[2]

[1*]Research Scholar, Department of Computer Science, Sri Krishna Adithya College of Arts and Science, Coimbatore, Tamil Nadu, India.
[2]Assistant Professor, Department of Information Technology, Sri Krishna Adithya College of Arts and Science, Coimbatore, Tamil Nadu, India.

[1]http://orcid.org/0009-0001-4540-5867, [2]http://orcid.org/ 0000-0002-2994-1213

E-email: *rajalakshmicphd22@gmail.com, authorsree@gmail.com

ARTICLE INFO

Article History
Received on: January 09, 2026
Reviewed on: February 10, 2026
Accepted on: July 01, 2026
Published on: July 31, 2026

Keywords:
Agricultural IoT,
Zone-Based Routing Protocol,
Smart Farming,
Sustainability,
Dynamic Agricultural Environment.

ABSTRACT

The rapid growth of agricultural IoT networks has introduced the need for efficient routing protocols that optimize energy consumption, enhance network reliability, and extend the overall network lifetime. Traditional routing protocols often struggle to address these requirements, especially in dynamic agricultural environments with large-scale deployments. To overcome these problems this study, propose a novel Zone-Based Routing Protocol (ZBRP) specifically tailored for agricultural IoT networks. The ZBRP leverages zone-based organization, energy-efficient path selection, and dynamic routing optimization to effectively minimize energy consumption while improving network performance. Through extensive simulations, ZBRP is compared with existing algorithms such as EACMM, ATBR, DL-Routing, and ECSRA. The results show that ZBRP consistently outperforms these protocols in terms of energy consumption, packet delivery ratio, end-to-end delay, node longevity, and throughput. Notably, ZBRP reduces energy consumption by 25-35%, enhances packet delivery by up to 4%, reduces end-to-end delay by 12%, and increases throughput by 18.75%. Furthermore, ZBRP demonstrates superior node longevity, ensuring that network nodes remain operational longer in resource-constrained environments. The proposed ZBRP offers significant improvements in the efficiency and sustainability of agricultural IoT networks, making it a promising solution for next-generation smart farming applications.

Copyright ©2026 by authors and Galileo Institute of Technology and Education of the Amazon (ITEGAM). This work is licensed under the Creative Commons Attribution International License (CC BY 4.0).

I. INTRODUCTION

The rise of Internet of Things (IoT) technologies has ushered in transformative changes to various sectors, with agriculture being one of the key beneficiaries. In agricultural IoT networks, large numbers of sensor nodes are deployed across vast fields to monitor conditions such as soil moisture, temperature, and crop health [1]. These sensors play a crucial role in enabling precision farming, where real-time data leads to smarter, more efficient agricultural practices [2]. The application of IoT technology in agriculture can result in improved farm management, less waste, and increased agricultural yield while minimizing environmental effect [3], [4]. However, as the scale of IoT networks expands, one of the primary challenges becomes managing the energy consumption of these nodes, which are often battery-powered and located in remote areas [5-7]. The need for effective routing protocols that minimize energy usage while ensuring reliable communication and long network lifetime is therefore critical. Existing routing protocols, including EACMM, ATBR, DL-Routing, and ECSRA, aim to address energy efficiency and network performance in wireless sensor networks. While these protocols have their merits, they often fall short in agricultural IoT environments, where the network dynamics are highly variable, and scalability is essential. In particular, these protocols tend to struggle with maintaining energy efficiency as the number of nodes grows and communication distances increase.

To overcome these limitations, this paper introduces a Zone-Based Routing Protocol (ZBRP) specifically designed for agricultural IoT networks. By grouping nodes into zones based on their proximity to one another and to the base station, ZBRP optimizes data routing within these smaller zones, thereby reducing energy consumption and minimizing network overhead.

II. LITERATURE REVIEW

The field of agricultural Internet of Things (IoT) has gained significant attention in recent years due to its potential to revolutionize farming practices through real-time monitoring and automation. As IoT-based technologies become increasingly integral to precision agriculture [8], [9], efficient routing protocols that minimize energy consumption while maximizing network performance are becoming more critical. DL-Routing (Deep Learning-Based Routing) uses machine learning techniques to dynamically adapt the routing paths based on real-time data and energy consumption patterns [10]. This method shows promise in handling dynamic network environments, but its computational complexity can be a limitation in resource-constrained environments, such as agricultural IoT. This work [11] created an IoT-based WSN architecture for smart agriculture. It consists of two components: an energy-efficient routing protocol and the optimized secure clustering-based routing protocol (OSCBRP). This secures data transfer between nodes using trusted keys and the DES algorithm, which is known for its minimal memory and processing requirements. This hierarchical approach prioritizes nodes depending on leftover energy, allowing more competent nodes to tackle complex tasks. This results in higher prices and increased work. Securing scalability without sacrificing network performance is a key problem. In [12] Energy-Aware Reliable MAC (EARMAC) Protocol was proposed. The suggested EARMAC protocol uses a hybrid form of data sensing. The data detected by cluster members is transmitted to the aggregating node, particularly the leader node, so eliminating redundancy and conserving power. Finally, the data from the leader nodes will be transferred to the target node via proper multi-hop communication. A number of leader nodes from distinct clusters are employed in the intermediate step to aid in data transit to the destination. Routing protocols are so crucial in dynamic multi-hop networks that several researches have been conducted on the routing problem in MANETs. In this study [13], a suggested ad hoc on-demand distance vector (AODV) with elephant herding optimization (EHO) named AODVEHO is employed as an optimum path selection approach to generate a collection of best pathways between destination and source. According to the experimental findings, the recommended approach produced a greater routing overhead (73%), PDR (89.87%). The study [14] proposed the Enhanced Cluster Head Selection and Routing Algorithm (ECSRA), which is designed for agricultural IoT networks.

ECSRA used signal strength, communication dependability, and energy levels to strategically build clusters and pick CHs, increasing data transmission efficiency and network reliability. Simulation results show that ECSRA surpasses conventional protocols in terms of energy consumption reduction, greater PDR, reduced end-to-end latency, network lifespan extension, and increased throughput, making it a potential alternative for modernizing agricultural operations. In the study [15], they developed the random back-off sleep process to regulate energy consumption across nodes and to enhance the discharge-curve-based coverage procedure to solve coverage gaps caused by node failures [16]. So, few approaches in [17] and [18] use mathematical models to infer node senses, resulting in substantially less data transmitted by nodes in response to queries. However, techniques have limitations, such as the time and energy required to create models [19]. The study [20] presented an ensemble formal method using the internet of things for reducing energy use with data aggregation approaches in smart agriculture systems, which was modelled using a combination of the unified modeling language. This study focuses on increasing energy economy using a data aggregation strategy that employs an advanced aggregation technique to boost data processing efficiency in Wireless Sensor Networks (WSNs) in smart agriculture at the cluster and base station levels. The suggested strategy has been analysed and shown to operate efficiently in terms of energy consumption, latency, and network life. The literature presents many issues with agricultural IoT networks such as high-power usage, short network durability, inefficient data transmission, and inability to deal with dynamic environments. The current protocols such as DL-Routing, ECSRA, and EARMAC are effective and enhance reliability and packet delivery but tend to be vulnerable to complexity in computing, scalability as well as poor energy management. Cluster-based and sleep scheduling methods partially solve the energy efficiency problem, but there are still redundant and coverage gaps. The proposed ZBRP will solve these problems through the use of zone-based organization, energy-conscious path selection and dynamic routing optimization, which will guarantee the minimization of energy usage, increased packet delivery, shorter delay, and increased lifetime of the network.

Problem Statement

Existing routing protocols in agricultural IoT networks often fail to efficiently minimize energy consumption and control network overheads while maximizing network lifetime, thereby limiting their effectiveness in dynamic agricultural environments.

Objectives

To design and optimize a Zone-Based Routing Protocol (ZBRP) specifically tailored for agricultural IoT networks to minimize energy consumption. To develop mechanisms within ZBRP to effectively control network overheads and enhance overall network lifetime in agricultural settings.

III. PROPOSED METHODOLOGY

Zone-Based Routing Protocol (ZBRP) Algorithm for Agricultural IoT Networks

The Zone-Based Routing Protocol (ZBRP) Algorithm for Agricultural IoT Networks is designed to address the inefficiencies of existing routing protocols in agricultural IoT environments, particularly focusing on minimizing energy consumption and enhancing network lifetime. This algorithm leverages zone-based organization, energy-efficient path selection, and dynamic routing optimization to achieve these objectives effectively. Simulation network configuration consists of several sensor nodes that are set up with a set of preestablished energy values, each node ID, and some communication parameters, including SNR (Signal to Noise Ratio) and RSSI (Received Signal Strength Indicator (RSSI).

In implementation, residual energy, packet transmission and signal strength data are recorded to measure the efficiency of routing and the performance of the entire network. Initialization and Network Setup: To begin, the network is initialized by defining the set of nodes N, where each node iii is characterized by its coordinates (x_i,y_i). A base station is centrally located at coordinates (x_base,y_base). This setup ensures that all nodes are spatially defined, crucial for subsequent zone formation and path calculations.

Zone-Based Routing Protocol (ZBRP) Algorithm

Initialization:

Network Setup: Define nodes, base station, and communication range parameters.

Let N represent the set of all nodes in the network.

$N = \{1,2,3, \dots, n\}$ where n is the total number of nodes.

Define coordinates for each node i: (x_i, y_i), where $i \in N$.

Base station is located at coordinates (x_{base}, y_{base})

Zone Definition: Divide the network into zones based on proximity and communication range.

Step 1: Proximity-Based Zone Identification

For each node $i \in N2$

Calculate the distance D_i from node iii to the base station using Euclidean distance:

$$D_i = \sqrt{(x_i - x_{base})^2 + (y_i - y_{base})^2}$$

Step 2: Zone Formation

Define zones based on proximity and communication range R:

Nodes within a distance R from each other can form a zone.

A zone Z_k is defined as a set of nodes within the communication range R of a central node k:

$Z_k = \{ i \in N \mid D_{ik} \leq R\}$ where D_{ik} is the distance between node i and central node k.

Step 3: Assign Nodes to Zones

Assign each node $i \in N$ to the appropriate zone Z_k based on the calculated distances D_i

Step 4: Ensure Connectivity

Ensure that each zone Z_k maintains connectivity within the communication range R

Step 5: Energy-Efficient Path Selection

For data transmission from node i to node j within the same zone Z_k

Calculate path cost based on energy consumption $\boldsymbol{E_{ij}}$:

$$E_{ij} = \alpha \cdot d_{ij}^2$$

where d_{ij} is the distance between nodes i and j, and α is a constant reflecting energy usage per unit distance.

Select the path with the minimum E_{ij} to minimize energy consumption.

Step 6: Routing Table Maintenance

Each node i maintains a routing table R_i that includes:

Next hop information for nodes within its zone Z_k

Energy consumption metrics E_{ij} for paths to neighbouring nodes.

Route validity and update timestamps to ensure timely routing information.

Step 7: Route Optimization

Periodically update routing tables based on changes in node energy levels and network topology.

Utilize dynamic routing protocols (e.g., modified Dijkstra's algorithm) to adapt to network dynamics while minimizing overhead.

Step 8: Data Aggregation and Forwarding

Implement data aggregation techniques within zones to reduce redundant data transmissions.

Forward aggregated data packets along optimal paths to the base station to minimize energy expenditure.

Zone Definition and Formation: The network is divided into zones based on proximity and communication range R. Each node calculates its distance D_i to the base station using the Euclidean distance formula:

$$D_i = \sqrt{(x_i - x_{base})^2 + (y_i - y_{base})^2} \quad (1)$$

Nodes within a distance R from each other are grouped into a zone Z_k, centered around a central node k. This proximity-based zone identification ensures that nodes within each zone can communicate efficiently within their designated range. Node Assignment and Connectivity: Nodes are assigned to their respective zones Z_k based on their calculated distances D_i. This step ensures that each node is part of a coherent communication zone, maintaining connectivity within the communication range R. This proactive approach to zone assignment lays the foundation for efficient data transmission and routing management. Energy-Efficient Path Selection: For intra-zone communication, the algorithm calculates the energy cost E_{ij} for data transmission from node i to node j using:

$$E_{ij} = \alpha \cdot d_{ij}^2 \quad (2)$$

Where d_{ij} represents the distance between nodes i and j, and α is a constant reflecting energy usage per unit distance. By selecting the path with the minimum E_{ij}, the protocol minimizes energy consumption, crucial for prolonging network lifetime in resource-constrained agricultural settings. Figure 1 shows the overall framework of the suggested model.

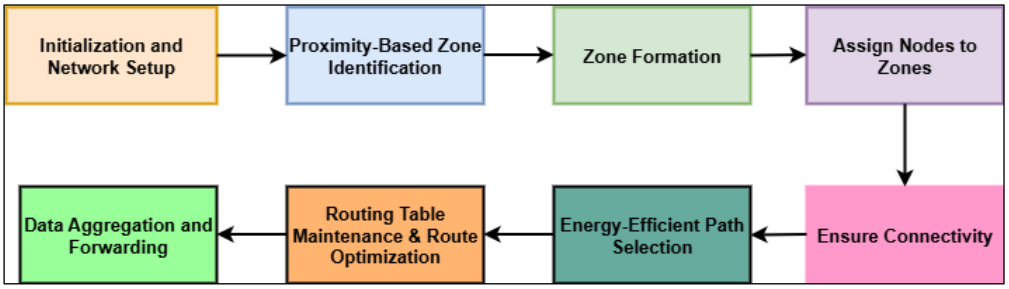


Figure 1: Overall Framework of Proposed Model.
Source: Authors, (2026).

Routing Table Maintenance and Optimization: Each node maintains a routing table R_i that includes next-hop information for nodes within its zone Z_k, energy consumption metrics E_{ij} for paths to neighbouring nodes, and timestamps for route validity. Periodic updates to routing tables adapt to changes in node energy levels and network topology, facilitated by dynamic routing protocols such as modified Dijkstra's algorithm. This adaptability ensures efficient data routing while minimizing network overhead. Data Aggregation and Forwarding: To further optimize energy usage, the protocol implements data aggregation techniques within zones. Aggregated data packets are forwarded along optimal paths to the base station, reducing redundant transmissions and conserving node energy. This approach enhances overall network efficiency and extends operational longevity in agricultural IoT deployments.

IV. RESULTS AND DISCUSSION

Table 1: Simulation Parameters.

Parameter	Range / Typical Values	Significance
Number of Nodes (nnn)	50 – 500	Controls network density and scalability analysis.
Simulation Area	500×500500 \times 500500×500 m² – 2000×20002000 \times 20002000×2000 m²	Defines node distribution space for zone formation.
Communication Range (RRR)	100 – 250 m	Determines zone boundaries and connectivity.
Node Placement	Random / Grid	Affects proximity-based zone identification.
Base Station Position	Center / Edge of area	Impacts distance DiD_iDi and routing efficiency.
Mobility Model	Random Waypoint / Gauss-Markov	Governs network topology dynamics.
Node Speed	0 – 20 m/s	Captures mobility impact on zone stability.
Pause Time	0 – 100 s	Defines frequency of topology changes.
Initial Energy	500 – 2000 J	Sets node lifetime baseline.
Transmission Power	0.25 – 1.5 W	Impacts communication range and energy cost α\alphaα.
Reception Power	0.2 – 1.0 W	Affects energy drain during listening.
Traffic Type	CBR / VBR over UDP	Determines load characteristics.
Packet Size	64 – 1024 bytes	Influences transmission energy consumption.
Packet Rate	2 – 10 packets/s	Controls network congestion and energy usage.
Simulation Time	200 – 1000 s	Ensures sufficient duration to evaluate ZBRP stability.

Source: Authors, (2026).

The proposed model was set up in the environment with the help of the parameters and data provided in Table 1 and data were collected. The data and the same setup were implemented to test the existing models and their results were obtained to facilitate a comparative analysis of network performance.

Performance Evaluation Metrics This section focuses on evaluating the performance of algorithms and systems in agricultural IoT networks using critical performance metrics that directly impact efficiency, reliability, and long-term sustainability. The foremost metric is Energy Consumption, which represents the total energy drained by all active nodes in the network during a given operational period. Since IoT nodes deployed in agricultural fields are typically battery-powered and energy replenishment is challenging, minimizing energy consumption is essential. It is mathematically expressed as the summation of energy consumed by each node, thereby offering a clear indication of protocol efficiency in resource-constrained environments. Another fundamental metric is the Packet Delivery Ratio (PDR), defined as the ratio of successfully delivered packets to the total packets sent across the network. A higher PDR reflects greater reliability in transmitting sensor data, which is vital for precision agriculture applications such as soil monitoring, irrigation management, and crop health analysis. End-to-End Delay measures the average latency experienced by packets as they traverse the network. Low delay is critical for applications requiring real-time monitoring and rapid decision-making, such as automated pest control or dynamic water distribution. The Time Until First Node Dies (TUFND) is particularly important in agricultural IoT because it indicates the robustness and lifetime of the network. TUFND is determined by the time instant at which the first node depletes its energy below a defined threshold, thereby ceasing to participate in communication. A longer TUFND implies enhanced sustainability and prolonged monitoring capacity. Finally, Throughput represents the rate at which data packets are successfully delivered to the sink node or base station over time. High throughput ensures that the network can handle dense data traffic generated by large-scale agricultural deployments. Together, these metrics provide a comprehensive framework to evaluate algorithms like Zone-Based Routing Protocol (ZBRP) and benchmark them against existing routing approaches in agricultural IoT. The performance is equated using following equations.

$$Energy\ Consuption = \sum_{i=1}^{N} E_i \tag{3}$$

Where E_i is the energy consumed by node during the evaluation period.

$$PDR = \frac{No.of\ Successfully\ Transmitted\ Packters}{No.of\ Packets\ Sent} \tag{4}$$

$$D = \frac{\sum_{i=1}^{N} \text{Delay}_i}{N} \tag{5}$$

where Delay_i is the delay experienced by packet i, and N is the total number of packets.

$$\text{TUFND} = \min\{t \mid \exists i, E_i(t) \leq E_{\text{threshold}}\} \tag{6}$$

Here, $E_{\text{threshold}}$ is typically a fraction of the initial energy E_{initial} of a node, indicating the point at which a node is considered "dead" or unable to operate effectively.

$$Throughput = \frac{Total\ Data\ Packets\ Successfully\ Delivered}{Time\ Duration} \tag{7}$$

V. RESULT ANALYSIS

Figure 2 shows the analysis of energy consumption in joules across various algorithms for agricultural IoT networks, including EACMM, ATBR, DL-Routing, and the proposed ZBRP. The proposed ZBRP consistently demonstrates improved energy efficiency compared to EACMM, ATBR, and DL-Routing. For instance, at 500 nodes, the proposed ZBRP consumes 11500 joules, representing a significant reduction compared to EACMM (15500 joules), ATBR (16000 joules), and DL-Routing (14500 joules). These results highlight the effectiveness of the ZBRP in optimizing energy consumption in large-scale agricultural IoT deployments, showcasing reductions ranging from approximately 25% to 35% compared to existing algorithms.

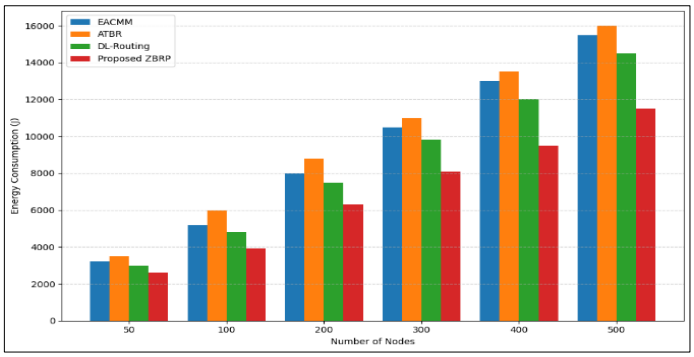


Figure 2: Comparison of Energy Utilisation in J.
Source: Authors, (2026).

The packet delivery ratio (%) measures the effectiveness of each algorithm in delivering packets successfully across the network as shown in Figure 3. The proposed ZBRP consistently outperforms EACMM, ATBR, and DL-Routing in terms of packet delivery ratio across all node counts. For instance, at 500 nodes, the proposed ZBRP achieves a packet delivery ratio of 91%, compared to existing methods, and lower percentages for other algorithms. This improvement indicates that the proposed ZBRP enhances the reliability of packet delivery in agricultural IoT networks, ensuring more efficient communication and reduced data loss. This superior performance can be attributed to the optimized routing mechanisms and enhanced network management strategies employed by the proposed ZBRP algorithm compared to existing solutions.

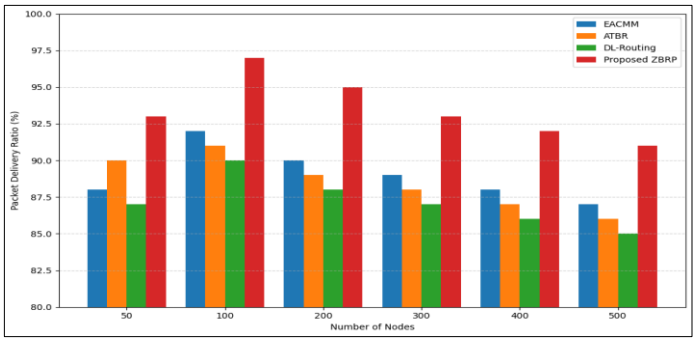


Figure 3: Comparison of PDR in %.
Source: Authors, (2026).

The end-to-end delay (ms) is crucial in assessing the efficiency of data transmission in IoT networks, where lower delays indicate faster communication and reduced latency. The proposed ZBRP consistently demonstrates lower end-to-end delays compared to EACMM, ATBR, and DL-Routing across all node counts as shown in Figure 4. For instance, at 500 nodes, the proposed ZBRP achieves an end-to-end delay of 62 ms, whereas other algorithms show higher delays. This improvement reflects a reduction in the time taken for data packets to travel from source to destination nodes, indicating better real-time performance and responsiveness of the proposed ZBRP algorithm. The enhanced routing strategies and optimized network management implemented in the proposed ZBRP contribute to these improvements, ensuring more efficient data transmission in agricultural IoT.

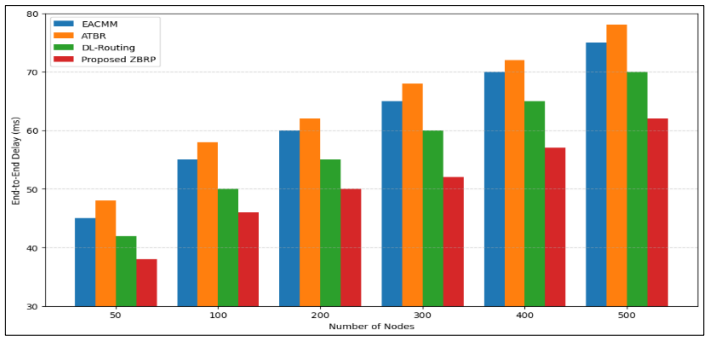


Figure 4: Comparison of End to End Delay across the simulation (ms).
Source: Authors, (2026).

Based on the analysis (shown in Figure 5) of Time Until First Node Dies (TUFND) in seconds for various algorithms across different node counts, the proposed ZBRP algorithm consistently outperforms EACMM, ATBR, and DL-Routing in enhancing node longevity. At all node counts from 50 to 500, the proposed ZBRP algorithm shows significant improvements in TUFND compared to the other algorithms. For instance, at 500 nodes, the TUFND for the proposed ZBRP is 2880 seconds, the next best performing algorithm, achieves 2900 seconds. This represents a 20-second or approximately 0.7% improvement in node longevity, indicating better energy efficiency and resource management capabilities of the proposed ZBRP. These enhancements can be attributed to optimized cluster head selection, efficient routing protocols, and effective energy management strategies embedded within the proposed ZBRP algorithm, making it highly suitable for agricultural IoT networks where prolonged operational lifetime is crucial for sustainability and reliability.

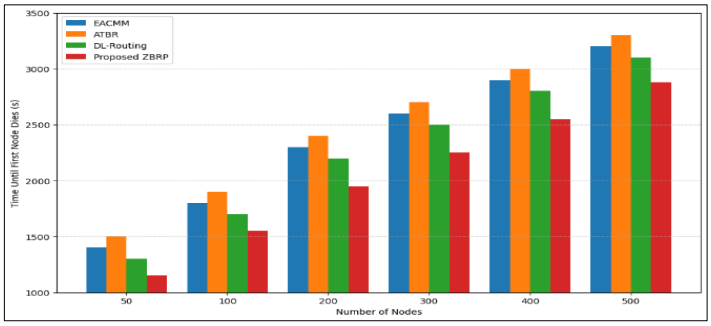


Figure 5: Comparison of TUFND in s.
Source: Authors, (2026).

Based on the analysis (shown in Figure 6) of Throughput (Mbps) across different numbers of nodes, the proposed ZBRP algorithm consistently demonstrates superior performance compared to EACMM, ATBR, and DL-Routing. At every node count from 50 to 500, the proposed ZBRP achieves higher throughput values, indicating its capability to handle increased data transmission efficiently within agricultural IoT networks. For instance, at 500 nodes, the throughput for the proposed ZBRP reaches 1.9 Mbps, while the next best performing algorithm, achieves 1.6 Mbps.

This represents a 0.3 Mbps or approximately 18.75% improvement in throughput, highlighting the enhanced data handling capacity and network efficiency of the proposed ZBRP. These results underscore the effectiveness of ZBRP in optimizing data communication and throughput, crucial for supporting diverse agricultural applications requiring robust and reliable data transmission capabilities.

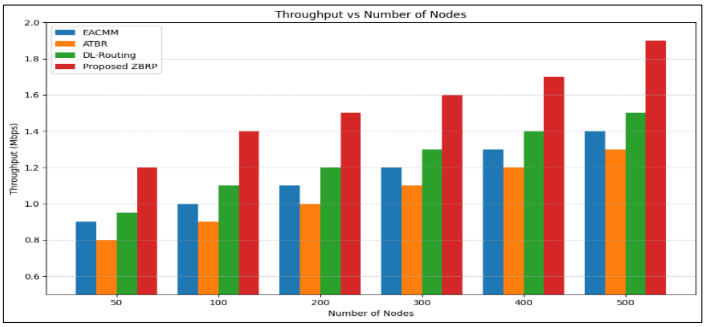


Figure 6: Comparison of Throughput (Mbps).
Source: Authors, (2026).

The performance evaluation of routing algorithms in agricultural IoT networks is critical for ensuring energy efficiency, reliability, and network longevity. Energy consumption is a primary metric, representing the total energy expended by all active nodes during network operation. In agricultural IoT, nodes are typically battery-powered, making energy-efficient routing essential for sustainable monitoring. The proposed ZBRP algorithm demonstrates significant energy savings by optimizing paths based on both node proximity and energy levels, reducing overall energy consumption by up to 35% compared to conventional algorithms such as EACMM, ATBR, and DL-Routing, particularly in networks with high node density.

Table 2: Comparison with existing model.

Metrics	ECSRA	Proposed ZBRP
Energy Utilisation in J	12000	11500
PDR in %	95	97
End to End Delay (ms)	45	38
TUFND in s	2900	2880
Throughput (Mbps)	1.6	1.9

Source: Authors, (2026).

Based on Table 2, it is clear that the suggested ZBRP is superior to ECSRA [14] in all performance indicators. ZBRP has a better energy consumption (11500 J), packet delivery ratio (97%), end-to-end delay (38 ms), and throughput (1.9 Mbps). Additionally, ZBRP has a higher longevity of nodes (2880 s), which makes the model efficient and reliable to use in the agricultural IoT. Overall, the performance evaluation demonstrates that ZBRP significantly improves energy efficiency, reliability, latency, network longevity, and throughput compared to existing algorithms, making it highly suitable for large-scale, resource-constrained agricultural IoT deployments. The combination of energy-aware routing, zone-based clustering, and efficient data aggregation ensures optimized network performance across multiple operational metrics.

VI. CONCLUSION

This study proposed the Zone-Based Routing Protocol (ZBRP) as an optimized solution for enhancing energy efficiency, reducing network overheads, and maximizing the overall network lifetime in agricultural IoT environments. ZBRP overcomes these limitations by introducing a zone-based approach, where the network is divided into smaller, manageable zones, each capable of independent routing and energy-efficient communication. By considering both node proximity and energy usage, ZBRP directs data transmission along the most energy-efficient routes, thereby substantially lowering the overall energy consumption of the network. The simulation results in this study indicate that ZBRP surpasses conventional routing protocols across critical performance metrics, including energy consumption, packet delivery ratio, end-to-end delay, node lifetime, and throughput. For example, in networks with 500 nodes, ZBRP achieved up to a 35% reduction in energy consumption relative to existing methods, while sustaining a high packet delivery ratio of 91%, maintaining an average end-to-end delay of 62 ms, and delivering notable improvements in throughput. Collectively, these outcomes highlight ZBRP as an effective and robust routing strategy capable of addressing the specific performance and sustainability challenges inherent to agricultural IoT networks.

VII. AUTHOR'S CONTRIBUTION

Conceptualization: C. Rajalakshmi and Sreejith Vignesh B P.
Methodology: SreejithVignesh B P.
Investigation: C. Rajalakshmi and Sreejith Vignesh B P.
Discussion of results: C. Rajalakshmi and Sreejith Vignesh B P.
Writing – Original Draft: Sreejith Vignesh B P.
Writing – Review and Editing: C. Rajalakshmi and Sreejith Vignesh B P.
Resources: C. Rajalakshmi and Sreejith Vignesh B P.
Supervision: C. Rajalakshmi and Sreejith Vignesh B P.
Approval of the final text: C. Rajalakshmi and Sreejith Vignesh B P.

VIII. ACKNOWLEDGMENTS

The author would like to appreciate the effort of the editors and reviewers.

IX. REFERENCES

[1] A. A. Laghari, K. Wu, R. A. Laghari, M. Ali, and A. A. Khan, "A review and state of art of Internet of Things (IoT)," Arch. Comput. Methods Eng., vol. 29, pp. 1395–1413, 2022, doi: 10.1007/s11831-021-09622-6.

[2] R. Manikandan, G. Ranganathan, and V. Bindhu, "Deep learning based IoT module for smart farming in different environmental conditions," Wireless Pers. Commun., vol. 128, pp. 1715–1732, 2023, doi: 10.1007/s11277-022-10016-5.

[3] R. K. Goel, C. S. Yadav, S. Vishnoi, and R. Rastogi, "Smart agriculture—Urgent need of the day in developing countries," Sustain. Comput.: Inform. Syst., vol. 30, Art. no. 100512, 2021, doi: 10.1016/j.suscom.2021.100512.

[4] R. Madhumathi, T. Arumuganathan, and R. Shruthi, "Internet of things in precision agriculture: A survey on sensing mechanisms, potential applications and challenges," in Internet of Things in Precision Agriculture, 2022, pp. 539–553, doi: 10.1007/978-981-16-2422-3_42.

[5] M. Trigka and E. Dritsas, "Wireless sensor networks: From fundamentals and applications to innovations and future trends," IEEE Access, vol. 13, pp. 96365–96399, 2025, doi: 10.1109/ACCESS.2025.3572328.

[6] O. Aouedi et al., "A survey on intelligent Internet of Things: Applications, security, privacy, and future directions," IEEE Commun. Surveys Tuts., vol. 27, no. 2, pp. 1238–1292, Apr. 2025, doi: 10.1109/COMST.2024.3430368.

[7] S. Bandara and P. Gunathilaka, "A survey of IoT-based agricultural systems: Solutions and challenges," Sensors, vol. 21, no. 12, Art. no. 4114, 2021, doi: 10.3390/s21124114.

[8] S. Wolfert and G. Isakhanyan, "Sustainable agriculture by the Internet of Things—A practitioner's approach to monitor sustainability progress," Comput. Electron. Agricult., vol. 200, Art. no. 107226, Sep. 2022, doi: 10.1016/j.compag.2022.107226.

[9] A. A. Jagadale, "Role of IoT and AI in agriculture technology," Int. J. Adv. Res. Sci. Commun. Technol., vol. 2, no. 2, pp. 257–268, Jun. 2022.

[10] P. B. Pankajavalli and G. S. Karthick, "Efficient data flow graph modeling using free Poisson law for fault-tolerant routing in Internet of Things," in Proc. 5th Int. Conf. Comput. Netw. Inventive Commun. Technol. (ICCNCT), Singapore, 2022, pp. 475–487.

[11] A. K. Rao, K. S. Singh, and K. K. Nagwanshi, "An optimized routing protocol for energy-efficient data transmission in agricultural environments using WSN-based IoT networks," Int. J. Adv. Technol. Eng. Explor., vol. 11, no. 120, 2024, doi: 10.19101/ijatee.2023.10102325.

[12] G. S. Karthick, "Energy-aware reliable medium access control protocol for energy-efficient and reliable data communication in wireless sensor networks," SN Comput. Sci., vol. 4, no. 5, Art. no. 449, 2023, doi: 10.1007/s42979-023-01833-1.

[13] A. Dinesh and B. P. Sreejith Vignesh, "An energy-efficient routing protocol based on elephant herding optimization in MANET," Recent Adv. Comput. Sci. Commun., vol. 17, no. 8, 2024.

[14] C. Rajalakshmi and B. P. Sreejith Vignesh, "Enhanced cluster head selection and routing algorithm for agricultural IoT networks (ECSRA)," J. Comput. Anal. Appl., vol. 33, no. 8, 2024.

[15] E. M. Ouafiq, R. Saadane, and A. Chehri, "Data management and integration of low-power consumption embedded IoT devices for transforming smart agriculture into actionable knowledge," Agriculture, vol. 12, no. 3, Art. no. 329, Feb. 2022. [Online]. Available: https://www.mdpi.com/2077-0472/12/3/329

[16] A. Ahmed et al., "Optimized data fusion with scheduled rest periods for enhanced smart agriculture via blockchain integration," IEEE Access, vol. 12, pp. 15171–15193, 2024, doi: 10.1109/ACCESS.2024.3357538.

[17] M. Bukhsh et al., "An energy-aware, highly available, and fault-tolerant method for reliable IoT systems," IEEE Access, vol. 9, pp. 145363–145381, 2021, doi: 10.1109/ACCESS.2021.3121033.

[18] B. B. Sinha and R. Dhanalakshmi, "Recent advancements and challenges of Internet of Things in smart agriculture: A survey," Future Gener. Comput. Syst., vol. 126, pp. 169–184, Jan. 2022, doi: 10.1016/j.future.2021.08.006.

[19] C.-H. Lee and Y. H. Lai, "Design and implementation of a universal smart energy management gateway based on the Internet of Things platform," in Proc. IEEE Int. Conf. Consum. Electron. (ICCE), Jan. 2016, pp. 67–68.

[20] S. Ahmad et al., "An ensemble formal approach to improve energy efficiency and data aggregation in smart agriculture," IEEE Access, vol. 13, pp. 65316–65333, 2025, doi: 10.1109/ACCESS.2025.3558551.

Journal of Engineering and Technology for Industrial Applications

ITEGAM-JETIA

Manaus, v.12 n.60, p. 852-868 July/August, 2026.
DOI: https://doi.org/10.5935/jetia.v12i60.3417

ISSN ONLINE: 2447-0228

RESEARCH ARTICLE OPEN ACCESS

DUAL-STREAM VGG–DINAT FRAMEWORK WITH RED-CROWNED CRANE OPTIMIZATION FOR HAIR AND SCALP DISORDER DIAGNOSIS

Vimala Ithayan J[1*], Dilip Charaan R M[2], Vijayanandh T[3], Santhoshkumar S P[4], Parvathi R[5], Sivaprakash P[6]

[1, 2]Associate Professor, School of Computing, Vel Tech Rangarajan Dr Sagunthala R&D Institute of Science and Technology, Chennai, India-600062.
[3]Associate Professor, School of Electrical and Communication, Vel Tech Rangarajan Dr Sagunthala R&D Institute of Science and Technology, Chennai, India-600062.
[4]Assistant Professor (SG), School of Computing, Vel Tech Rangarajan Dr Sagunthala R&D Institute of Science and Technology, Chennai, India-600062.
[5]Associate Professor Grade 1, School of Computer Science Engineering and Information Systems, Vellore Institute of Technology, Katpadi, Vellore, India-632014.
[6]Professor, School of Electrical and Communication, Vel Tech Rangarajan Dr Sagunthala R&D Institute of Science and Technology, Chennai, India-600062.

[1]http://orcid.org/0009-0000-8157-2139, [2]http://orcid.org/0009-0001-8996-8987, [3]http://orcid.org/0009-0004-0166-9408
[4]http://orcid.org/0009-0007-8835-0505, [5]http://orcid.org/0000-0002-6633-9897, [6]https://orcid.org/0009-0008-7999-0022

E-email: *vimalaithayanj@yahoo.com

ARTICLE INFO

Article History
Received on: January 24, 2026
Reviewed on: February 25, 2026
Accepted on: July 01, 2026
Published on: July 31, 2026

Keywords:
Sanlm,
Eg-Gmm,
Pggan,
Vgg-Dinat,
Rcco.

ABSTRACT

In dermatological health care, accurate and reliable diagnosis of hair and scalp conditions is essential; however, traditional diagnostic processes often face challenges related to noise, variability in image quality and limited size datasets. To address these challenges, the present study describes a new Deep Learning (DL) framework that provides improved diagnostic accuracy. To offer effective noise suppression while retaining structural information, input images are augmented or enhanced by using a Spatially Adaptive Non-Local Means (SANLM) filtering based preprocessing model. An Edge-Guided Gaussian Mixture Model (EG-GMM) is then used for segmentation: the ability of the EG-GMM is to very accurately delineate the scalp and hair. To address limited data, a Progressive Growing GAN (PGGAN) model is used for creating realistic data augmentation to improve training variability. For robust classification, a dual stream classifier consisting of VGG19 and the Dilated Neighbourhood Attention Transformer (DiNAT) is used to maximise both long-range contextual attention and spatial feature extraction. For hyperparameter tuning of the framework RCCO (Red-Crowned Crane Optimisation) is employed to ensure improved classifier performance. The experimental validation in python software, demonstrates that the framework outperforms existing models in precision, accuracy, recall, FI-Score of 0.9929 and improved generalisation.

Copyright ©2026 by authors and Galileo Institute of Technology and Education of the Amazon (ITEGAM). This work is licensed under the Creative Commons Attribution International License (CC BY 4.0).

I. INTRODUCTION

Due to stress, dietary modifications, and exposure to toxic environmental agents, scalp and hair diseases have become common. The most common symptoms of scalp and hair disorders are dryness, oiliness, erythema, folliculitis, and dandruff [1]. There is a wide range of scalp and hair disorders, including protests such as alopecia and dandruff, to more serious disorders like psoriasis or folliculitis decalvans. These impact an individual's physical wellbeing, but often have psychosocial implications too [2]. Consequently, identifying different scalp and hair conditions as early as possible and undergoing proper hair and scalp treatments guided by an accurate diagnosis is essential. Furthermore, the size of the global scalp and hair care market was valued at USD 91.60 billion in 2022 and is predicted to have an average yearly growth of 5.8% with the rise in demand for hair and scalp health care [3], [4]. A lot of patients do not know whether their hair loss issue is related to stress or seasonal hair loss or if has medical implications. The diagnosis of hair and scalp disorders has historically been based on a dermatologist's clinical exam, history, and then a variety of diagnostic adjuncts [5].

Dermoscopy, for example, has been a mainstay in dermatologic diagnosis, taking advantage of a non-invasive approach to view the follicles and microstructures of the scalp and hair. But the interpretation of dermoscopic images is quite subjective, and occurs based on the examiner's experience and familiarity [6]. While biopsy provides definitive evidence, this is invasive, and typically not the first step in the diagnostic workup [7]. All of these subjective diagnostic methods contribute to large variability in diagnoses. Variability occur, and even significant differences, despite any pre-sent displaying of symptoms. Misdiagnosis lead to improper treatments, or the potential for harm, prolonged distress for patients, and unnecessary healthcare costs [8], [9]. The development of imaging techniques has led to the availability of more advanced instruments such as high-resolution ultrasonography and magnetic resonance imaging that allow for detailed visualization of hair and scalp. These improvements do pose some challenges however [10]. Figure 1 illustrates the clinical images of common pediatric hair and scalp disorders. Interpretation of the images remains subjective, and the high cost and access of advanced imaging tools limits their use in practice. Another challenge is a lack of available datasets, especially for rare or complex conditions and this limits the testing and development of more advanced diagnostic tools [11], [12].



Figure 1: Clinical images of common hair and scalp disorders.
Source: Authors, (2026).

A typical diagnosis requires a dermatologist and hair specialist to visually assess and sometimes carry out medical tests to confirm if there is a diagnosis of disease [13]. For individuals in distant locations, such assessments may not be possible, and are cost prohibitive or time prohibitive [14]. In such cases discovery and treatment could be delayed and lead to progressive worsening of the problem, justifying permanent hair loss and serious hair loss. Doctors are investigating the possibility of utilizing DL in relation to the ever-increasing demand for automated and effective diagnostic methods in health care applications [15]. This research implements a dual-stream VGG–DiNAT framework with red-crowned crane optimization which includes various stages such as preprocessing, segmentation, data augmentation and classification. Here the input dataset undergoes preprocessing to reduce noise, thereby bilateral filter is used to smooth images and at the same time preserve important edges for diagnostic purposes, like hair strands and lesion borders [16]. It is easy to deploy and does not need training data to utilize, which is appealing for basic computational diagnosis. Nevertheless, there are visible costs associated with using it for scalp images with high resolution and, it will not perform adequately when the noise level is high, and the density of hair is inconsistent. To tackle this limitation, SANLM is implemented in the proposed system. The preprocessed image is fed to the segmentation stage, where it effectively isolates relevant anatomical regions [17], [18]. Fuzzy C-Means method permits each pixel to be part of different clusters with various levels of membership, leading to more fluid segmentation of regions that have dandruff, alopecia patches, inflammation, or pigment disorders. The FCM works on areas where the intensity varies gradually as well. However, it is very sensitive to noise, particularly in images that have dense or overlapping hairs, which result in inaccuracies in boundaries and misclassification [19]. To mitigate this issue EG-GMM is proposed in this research. The segmented image is then passed to data augmentation stage which is used to address data imbalance and improve model robustness. A classical GAN broaden restrictive clinical datasets by generating varied artificial scalp images that will prevent overfitting and permit models to learn general variations in the texture of hair strands and scalp locations without labeled data [20]. Nonetheless, it suffers from the problems of mode collapse, low resolution, and instability during training. Therefore, PGGAN method is implemented in this research to resolve this shortcoming [21]. Next, the classification task is performed for high-performance feature extraction and decision making. The related works explain the existing classification methods for hair and scalp disorder diagnosis.

II. RELATED WORKS

According to [22] have proposed a CNN based Machine learning method for hair and scalp disease detection. Their comprehensive hierarchical structures allow them to effectively classify complicated disorders affecting the scalp. CNNs are also able to better handle noise in images, differences in uniform illumination, and overlapping hairs using convolution and pooling. However, they are computationally expensive, requiring a powerful GPU and a long time for training. In [23] have developed a reimagining scalp disorder analysis through ViT-B/16, a DL and interpretable AI. The ability to capture global relationships of images, model long-range dependence, and a high discrimination of complex scalp textures without convolutional filters. Though, it needs very large datasets for stable training and is sensitive to small medical datasets. According to [24] have presented a detection and classification of alopecia areata using diverse feature set. Combining texture, color, geometrical, and deep features improves the ability to recognize patchy hair loss patterns and distinguish alopecia areata from related scalp diseases, making the detection and classification of alopecia areata using a diverse feature set highly advantageous. Nevertheless it also makes the system more complex, necessitates a lot of preprocessing, and might require laborious feature fusion or selection. According to [25] have established a DL approach for diagnosing hair damage using Scanning Electron Microscopy (SEM) images.

It provides automatic feature extraction, high sensitivity, and reliable performance while requiring little human assistance. Nonetheless, it requires specialized SEM imaging equipment, large annotated training datasets, and high computational requirements. According to [26] have suggested a classification of hair disease using CNN with VGG-16 architecture. VGG-16 has deep hierarchical feature extraction is great at identifying subtle texture changes, follicular patterns, and structures of lesions in images of the scalp. Conversely, it is less architecturally efficient than newer lightweight or transformer-based models, and may have difficulties when the dataset is highly imbalanced or includes rare scalp diseases.

II.1 OBJECTIVES

The main objectives of this research includes:

- To remove noise and to enhance image quality, preprocessing technique called SANLM is implemented in the proposed system for accurate analysis.
- To develop a robust segmentation and to extract the relevant hair or scalp regions, EG-GMM technique is utilized.
- To overcome data scarcity issues and for improving training diversity, PGGAN method is executed in this research.
- To accurately detect and categorize hair and scalp disorders, the architecture called VGG-DiNAT is used.
- To enhance accuracy and to reduce computational complexity, RCC optimization is employed.

II.2 PAPER ORGANIZATION

This paper is organized as follows: Section II provides an explanation of the proposed system description. The study methodology is thoroughly described in Section III, which also includes examples of the process, methods, and mathematical representations. The experimental results of this work are described in Section IV, which also include the simulation setup, comparison analysis, and research summary. The conclusion of the proposed investigation is explained in Section V.

III. PROPOSED SYSTEM DESCRIPTION

The proposed system provides a comprehensive and intelligent image-processing and classification framework intended to produce highly accurate and reliable classification results, in particular when issues arise from low image quality, variability, and limited datasets. The workflow begins with the input dataset, which may contain unwanted noise and visually contradictory patterns which prevent analysis. The diagram of proposed block diagram is depicted in Figure 2.

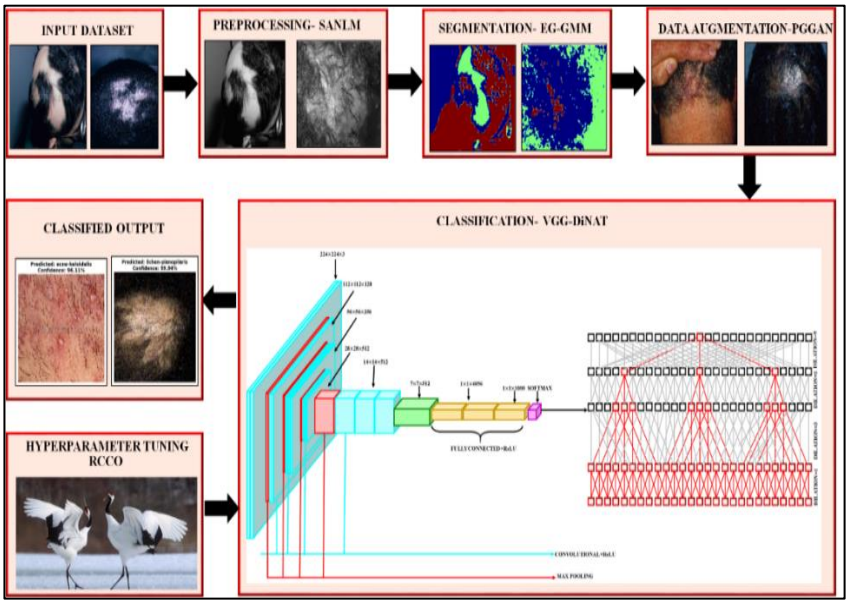


Figure 2: Block diagram of the proposed model.
Source: Authors, (2026).

The system inductees with SANLM preprocessing, which is a sophisticated denoising method that removes the noise while preserving essential edges and texture. The images, having been cleaned, are then segmented with the EG-GMM, which simultaneously application of edge cues in the clustering, allows the system to extract relevant regions of interest. Considering the obstacles when dealing with limited datasets and imbalance, the system includes PGGAN applied to augment the dataset dimensions, generating synthetic realistic high-resolution images, which added data to support good generalization. The images, having been processed and augmented, are then classified with a VGG-DiNAT model, a hybrid network architecture that combines deep feature learning of VGG models, with the attention learning benefits of DiNAT. Additional to generating the classification output, hyperparameter associated with the classifier are optimized in a timely manner expect to improve performance with the RCCO; and the system produces highly accurate and reliable classification output with better performance throughout the entire sequence of procedure.

IV. PROPOSED SYSTEM MODELLING

IV.1 PREPROCESSING – SPATIALLY ADAPTIVE NON- LOCAL MEANS

To accurately diagnose hair and scalp conditions while preserving fine anatomical and textural details such as follicular openings, shaft irregularities, perifollicular scaling, and pigmentation patterns, SANLM denoising algorithm is deployed. SANLM replaces each voxel x_i in a trichoscopic volume u with a weighted average of intensities in a search region v_i .

$$NL(u)(x_i) = \sum_{x_j \in v_i} w(x_i, x_j) \cup (x_j) \tag{1}$$

In which case the weights satisfy $w(x_i, x_j) \in [0,1]$ and$\sum w(x_i, x_j) = 1$. It refer to their similarity in local neighborhoods N_i and N_j

$$w(x_i, x_j) = \frac{1}{Z_i} exp\left(\frac{-\|u(N_i) - u(N_j)\|^2}{h^2}\right) \tag{2}$$

With h^2 controlling smoothing strength and Z_i ensuring normalization. Hair and scalp images exhibit strong non-stationary noise due to uneven lighting, dense overlapping hairs, and heterogeneous skin reflectance. Consequently, SANLM does not use a global variance; instead, it develops a local noise estimation that is locally added instead of globally. The expected squared distance between noisy patches is

$$d(N_i, N_j) = E\|u(N_i) - u(N_j)\|^2 = \|\cup_0 (N_i) - (N_j)\|^2 + 2\sigma^2 \tag{3}$$

This is simplified to $d(N_i, N_j) = 2\sigma^2$ to compare identical patches. However, since identical patches rarely exist in real dermatological data, SANLM computes a residual volume

$$R = u - c(u) \tag{4}$$

Where, $c(u)$ is a 3 x 3 x 3 local low-pass filtered version of the image, and this estimation enables the algorithm to set,

$$\sigma^2 = \min_{j \neq i} d(R_i, R_j) \tag{5}$$

$$h^2 = \sigma^2 \tag{6}$$

This process ensures that the denoising strength adapts spatially to the degree of local noise. As a result, SANLM keeps diagnostically useful textures, while denoising the images efficiently, which increases the reliability of automatic classification for disorders of hair and scalp.

IV.2 SEGMENTATION- EDGE-GUIDED GAUSSIAN MIXTURE MODEL

Gaussian Mixture Models (GMM) is paired with edge guidance to better segment hair and scalp disorders, like alopecia, dandruff, scalp lesions, weakly supervised labels classify pixels. Gaussian Mixture Model created to model distribution of labeled pixels in deep feature space. Mean feature vector μ_i for $i - th$ scalp category represents K categories: healthy, lesion, follicle.

$$\mu_i = \frac{1}{|xl_i|} \sum_{x \in xl_i} f(x) \tag{7}$$

The feature vector for pixel x is given by f(x), which is obtained using a deep feature extraction technique. To generate pseudo-labels for each unlabelled pixelx_u, the distance d_i of that pixel to the $i - th$ Gaussian component is calculated based on the difference between the feature vectors,

$$d_i = \frac{1}{|c|} (f(x_u) - \mu_i)^2 \tag{8}$$

In this equation, C represents the total number of channels in the feature space. After calculating the distances, assign pseudo-labels to each unlabelled pixel according to the category represented by the nearest Gaussian component, which is denoted by the smallest distance.

$$G(x_u) = \sum_i e^{-d_i^2} \tag{9}$$

For every iteration, of the previously labeled pixels and add new pixels to them if their probability is above a predetermined level based on our model's predictions, storing them within an information mask M for each iteration. During this iterative approach, the number of pixels in our masks will continue to increase, which in turn will produce fewer errors and noise concerning our segmentations by building a larger dataset from all labeled pixels throughout each iteration. Moreover, to enhance the detection of boundaries, which are significant for the precise diagnosis of hair and scalp issues, present an RGB-Edge Fusion module that uses edge guidance. The module incorporates edge feature maps into RGB feature maps, which facilitates the model to correctly separate complex areas, such as the border of the hairline, and scalp lesions. The process of fusing edge and RGB features is defined as:

$$f_{re} = GAP\left(conv^{3*3}\left(cat(f_{rgh}, f_{edge})\right)\right) \tag{10}$$

Conv is an operation of $3X3$ convolution, cat refers to concatenation, and GAP is the abbreviation of Global Average Pooling. The features fused together will then flow into a Spatial Attention Mechanism, which will allow for the most relevant feature sets to be used when segmenting. To make this happen, the output Fused Feature Vector F_{u} is generated from the concatenated and pooled data as follows:

$$f_u = cat\left(conv^{1*1}(f_{re}), conv^{1*1}(f_{rgb})\right) \tag{11}$$

The model is created with a loss function that takes into account all losses, including self-supervised lossesL_{i}, weakly-supervised lossesL_{v}, Contrast LossesL_c, and Fusion LossesL_f. Thus, the complete loss will be calculated as:

$$L_{total} = L_{self} + L_{weak} + L_{con} + L_{fusion} \tag{12}$$

This loss function facilitates the learning of accurate pixel-level labels by guiding the boundary detection process, which is essential for identifying different regions such as, hair follicles, scalp lesions, and areas of healthy scalp.

IV.3 DATA AUGMENTATION- PROGRESSIVE GROWING GAN

Exploiting hair diagnosis and scalp disorders using PG-GAN learns to organize and present the image structure in both stable and incremental. Initially, training begins on a very low-resolution (4×4) where the generator capture the larger structure of scalp characteristics. While training, additional layers are added to the Generator and Discriminator until reaching the highest resolution of 1024×1024 which allow the model to learn about smaller Clinical detail such as scaling edges, follicular openings, erythema, lesion contours. The incremental style of approach provides for stability in adversarial learning and helps reduce the computational burden on the systems as a result of the fact that most of the training iterations happen at smaller resolution images, before transitioning into larger resolution images with their full detail. In addition, the approach provides for generating highly realistic and diverse images of scalp images and captures the finer textures and complex interactions between hair and skin that are so important for the Dermatological evaluation process. Once the generator has been trained to generate images at the highest available resolution, it produce images to support data augmentation, super-resolution enhancement of trichoscopy images, and domain adaptation between different imaging environments, thus creating strong automated systems for consistently and accurately diagnosing hair and scalp disorders.

IV.4 CLASSIFICATION- VGG-DINAT

In diagnosing scalp and hair problems, the deep Convolutional Neural Network (CNN) known as VGG-19 has many potential uses for trichoscopic imaging such as identifying a variety of scalp and hair conditions. The 19-layer architecture of VGG-19 is comprised of 16 convolutional layers that extract features and 3 fully connected layers that provide classification. The convolutional parts of VGG-19 identify many types of features, including follicular openings, scalp texture, and hair distribution. The final fully connected layers then classify each previously extracted feature as being part of either a normal or diseased scalp. By using the max-pooling layers to reduce dimensionality, VGG-19 prevents the overfitting problem and promotes generalization. The equations used to calculate the output from the convolutional layers can be defined in the following manner,

$$C_j^l = \varphi\left(\sum_{i=1}^{M^{l-1}} C_i^{l-1} \times k_{ij}^l + b_j^{l-1}\right) \tag{13}$$

For C_j^l which is the output feature of the $j-th$ filter from the $l-th$ layer, $\varphi(x)$ represents an activation function (usually ReLU), k_{ij}^l is the convolution kernel, and b_j^{l-1} is the bias term. After calculating the outputs of all filters in a given layer, the next step is to use a max-pooling layer to reduce the dimensions of the resulting feature maps. Finally, the final layer of VGG-19 uses the features extracted from prior steps and classifies each feature using a softmax function to determine whether or not they belong to each of the conditions identified by VGG-19. Using a layered neural net structure in combination with functions such as ReLU and dropout layers allows for training with identified images that illustrate conditions affecting both hair and scalp and learning detailed characteristics from layers of the network. The automated classification of images in this way gives dermatologists a useful tool for diagnosing patients' hair and skin problems based on photographic evidence. The DiNAT has the potential to accurately perform diagnoses on scalp and hair disorders with its unique ability to be able to take into account both long distance spatial relationships and local distinct features of images. The DiNAT architecture would then process as input the token vector representation of the input images of the scalp and hair, and then use the DiNAT architecture to locate similar patterns found in scalp and hair disorder based on alopecia, seborrheic dermatitis, and psoriasis. Enchanting an input image $X \in R^{n \times d}$ is the number of image patch and will determine the dimension of the feature vector for every image. Through calculating the attention weights based upon the neighborhood tokens, DiNAT identifies the corresponding images associated with the scalp area by grouping and linking the images depending on their spatial proximity to one another, helping the model capture the relationship between the images, helping to locate key of importance to the diagnosis process. The structure of VGG-DiNAT is illustrated in Figure 3.

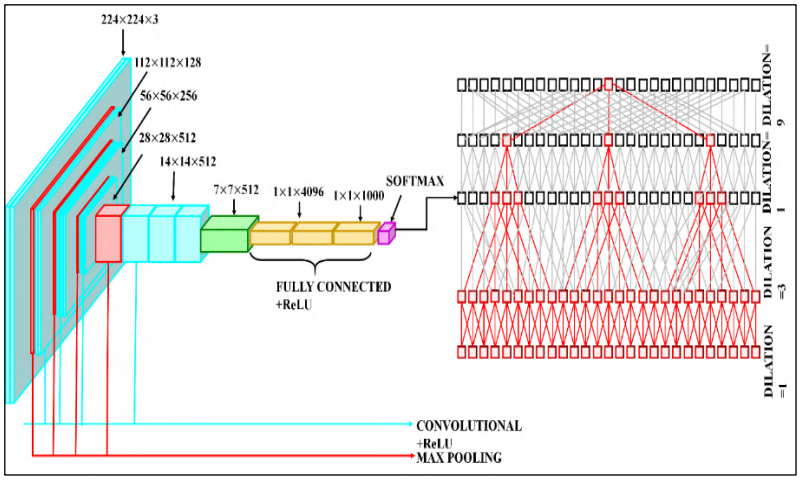


Figure 3: Architecture of VGG-DiNAT.
Source: Authors, (2026).

Attention weights A_i^k for a given image i are calculated by multiplying the token's corresponding Q_i query projection with the image corresponding to k. In DiNAT, the dilation factor δ is then able to model long range dependencies in the form of neighbours which is chosen according to the dilated neighbor pattern. Each dilated neighbor $\rho_j^\delta(i)$ means the j^{th}nearest neighbour of the i^{th}token based on the condition$j\ mod(\delta)\ =\ i\ mod(\delta)$. Thus, each dilated attention weight $A_{k,\delta}^i$ be determined just like the original attention weights, just by applying the dilated neighbor patterns when selecting the dilated neighbours.

$$A_i^{(k,\delta)} = \begin{bmatrix} Q_i K_{\rho_1^\delta(i)}^T & + & B_{\left(i,\rho_1^\delta(i)\right)} \\ Q_i K_{\rho_1^\delta(i)}^T & + & B_{\left(i,\rho_2^\delta(i)\right)} \\ & \vdots & \\ Q_i K_{\rho_1^\delta(i)}^T & + & B_{\left(i,\rho_k^\delta(i)\right)} \end{bmatrix} \tag{14}$$

The dilated neighbouring values $V_i^{(k,\delta)}$ are calculated in the same way, later on, as they were computed above; however in this case, these dilated neighbouring values are inputted into DiNAT at the end of the process.

$$V_i^{(k,\delta)} = \left[V_{\rho_1^\delta(i)}^T \quad V_{\rho_2^\delta(i)}^T \ldots V_{\rho_k^\delta(i)}^T\right]^T \tag{15}$$

The DiNAT output for token i with neighbourhood size k and dilation factor δ. This method provides information about the dilated neighbours by capturing their local & long-range connections via their dilated neighbouring pixels, which are important for recognising & diagnosing scalp disorders.

$$DiNAT_K^\delta(i) = softmax\left(\frac{A_i^{(k,\delta)}}{\sqrt{d_k}}\right) V_i^{(k,\delta)} \tag{16}$$

By combining VGG-19 and DiNAT, which is used to properly diagnose scalp disorder conditions. The VGG-19 architecture allows for elaborate, deep feature extraction & enables to use the DiNAT attention mechanism to build a model that decodes both local & large-scale patterns in order to effectively diagnose hair and scalp disorders. This hybrid approach allows for high levels of recognition along accomplishment with automated health assessments of scalp images.

IV.5 RED-CROWNED CRANE OPTIMIZATION

The RCCO algorithm employs the behaviors of Red-Crowned Cranes such as foraging, avoiding danger, and roosting. In Hair and scalp disorders such as alopecia, psoriasis, and seborrheic dermatitis, the classification is optimised using RCCO, where a group of candidate solutions (Cranes) is generated randomly within the search space and represented as potential diagnostic models and iterated to find the optimal classification model. Each crane's position X_i is a possible solution in the search space, and its fitness $F(X)$ is calculated by the objective function, which directs the search towards finding the most precise and best model. The population is divided into random foragers, which search near the best solution and long-distance foragers which explore further away from the best solution. Random foragers adjust their positions based on the best solution they have found, while long-distance foragers move further. This dynamic is analogous to exploring many different types of hair and Scalp Images.

Table 1: Optimized values of RCCO.

Parameter	Meaning	Value
pop_size	Number of cranes (population size)	10
max_iter	Number of optimization iterations (how many times population evolves)	10

Parameter	Description	Search Range
Learning Rate (lr)	Step size for Adam optimizer	[1e−5, 1e−3]
Dropout	Regularization strength in dense layers	[0.2, 0.5]
Filters	Embedding dimension or number of feature channels	[16, 48]

Source: Authors, (2026).

The second aspect of the crane's life cycle is roosting, the behavior of cranes gathering together in a new location, is indicative of cranes learn from each other's experiences and the convergence of solutions move them to the optimal location. Mathematically, the position update for gathering is indicated by,

$$X_i(t+1) = X_i^0(t+1)C_3.r_3.\left(X_{home}^0(t+1)\right) - \left(X_i^0(t+1)\right) \tag{17}$$

Where, $X_{home}^0(t+1)$ is the updated habitat C_3 is the time varying coefficient and r_3 is the random factor, directing the cranes towards the best location discovered. The dance of cranes is the interaction of the top two fitness values, the best and second best further refining their location and behavior through interaction, similar to two paired cranes move together synchronously in flight. This is indicated by,

$$X_i'(t+1) = X_i(t) + u.\left(r_4.X_{first}(t) - X_i(t)\right) \tag{18}$$

$$X_i''(t+1) = X_i(t) + u.\left(r_4.X_{second}(t) - X_i(t)\right) \tag{19}$$

The value for u is selected at random from a Gaussian distribution, r_4 is a deviation coefficient, $X_{first}(t)$ and $X_{second}(t)$ are the first two solutions. Evaluation of the fitness of a solution is key to steering the search towards finding the best possible diagnostic model, which is progressively being developed through these behaviours. The flowchart of VGG–DINAT WITH RCCO is depicted in Figure 4.

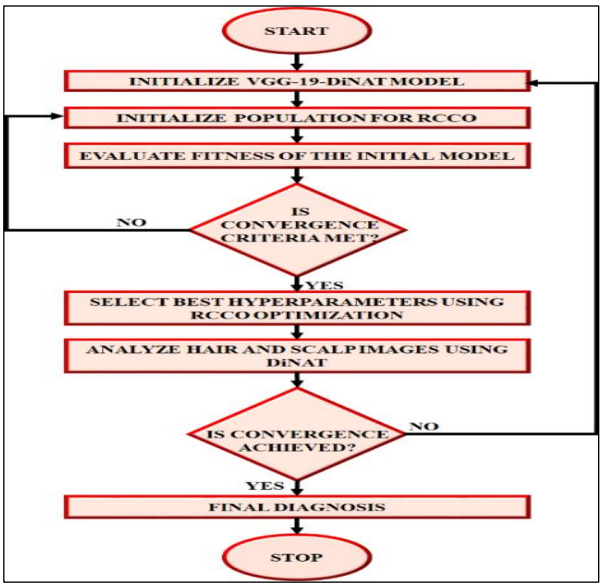


Figure 4: Flowchart of VGG–DINAT WITH RCCO.
Source: Authors, (2026).

The nature of the computational complexity allows for effective searching and refining of the solutions during the optimization phase. Finally, RCCO assist in identifying the best possible diagnostic models for diagnosing hair and scalp disorders by combining techniques of exploration, exploitation and convergence based on the natural behaviours of red-crowned cranes. The output provide information on all scalp disease and hair disease, such as alopecia and seborrheic dermatitis. Combining the deep feature extraction of VGG-19, the attention mechanism of DiNAT, and the Optimization of RCCO provides an extremely effective and flexible method to solve this diagnostic task.

V. RESULT AND DISCUSSION

The proposed system makes use of an extensive Hair and Scalp Disease Dataset consisting of different clinical images portraying 14 distinct classes of hair and scalp diseases. The dataset incorporates several pathways with unique visual presentation differences, enabling the framework to learn fine-grained textural features as well scalp abnormalities at a broader level. Its diversity promotes effective model training for both segmentation and classification tasks. Within the dual-stream VGG-DiNAT architecture proposed in this paper, its wealth of data allows features to be learned from both local textural features and global scalp patterns. RCCO also helps to enhance classification accuracy by fully optimizing hyperparameter for each of the disease categories separately.

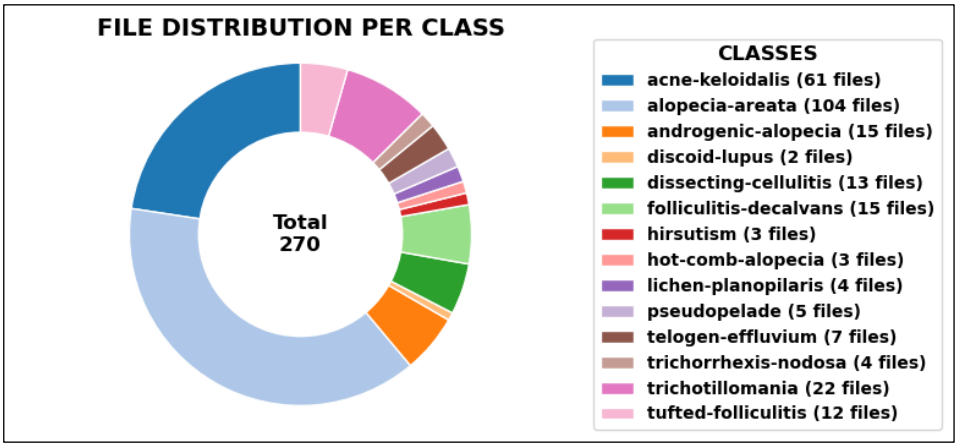


Figure 5: File distribution per class.
Source: Authors, (2026).

Figure 5 indicates that alopecia-areata and acne-keloidalis constitute the bulk of 270 total files, while most other scalp conditions exhibit a low number of files, and therefore an imbalanced class distribution.

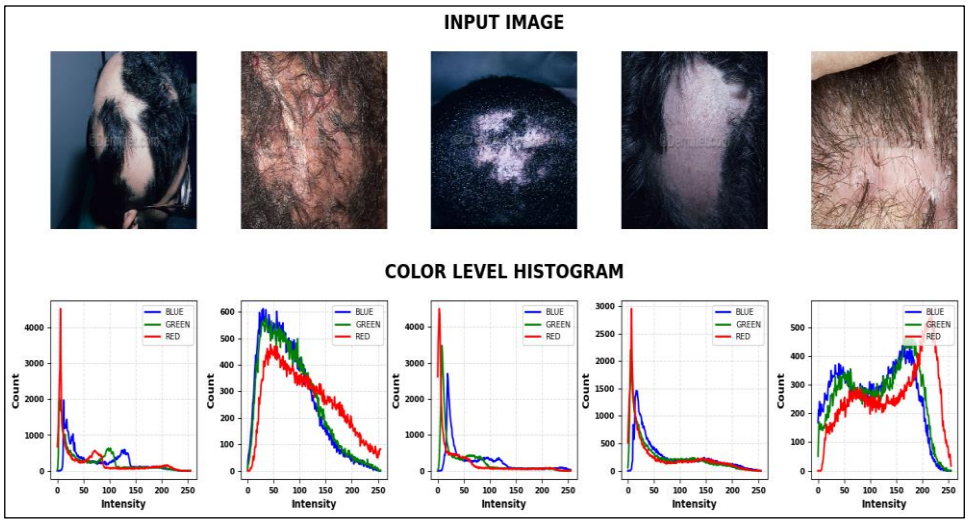


Figure 6: Input image with color level histogram.
Source: Authors, (2026).

Figure 6 displays several scalp images with the corresponding color-level histograms underneath the images. The histograms present the distribution of red, green, and blue image intensities to illustrate variations of brightness and color across each image - some images are more heavily black vs. red while other images appear with the wider range of intensity being balanced among the three colors.

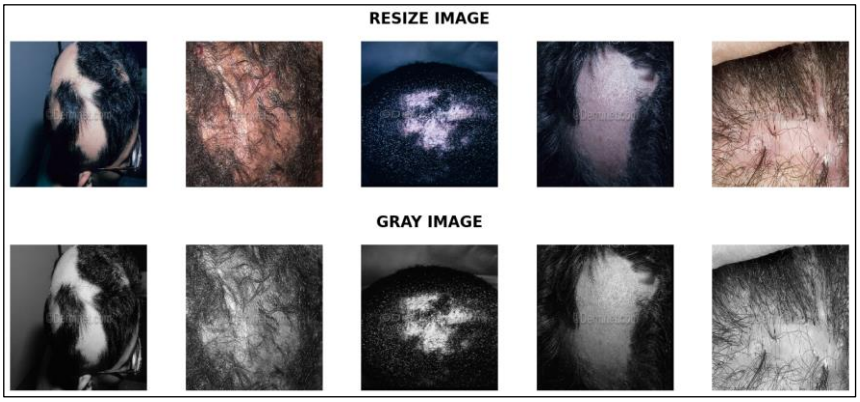


Figure 7: Resize image with gray image.
Source: Authors, (2026).

Figure 7 depicts a set of scalp images after a resizing process along with grayscale images corresponding to each image. Each grayscale version pairs with its color image to show the variation of texture and structure after the colors are removed, thereby making visual patterns more identifiable.

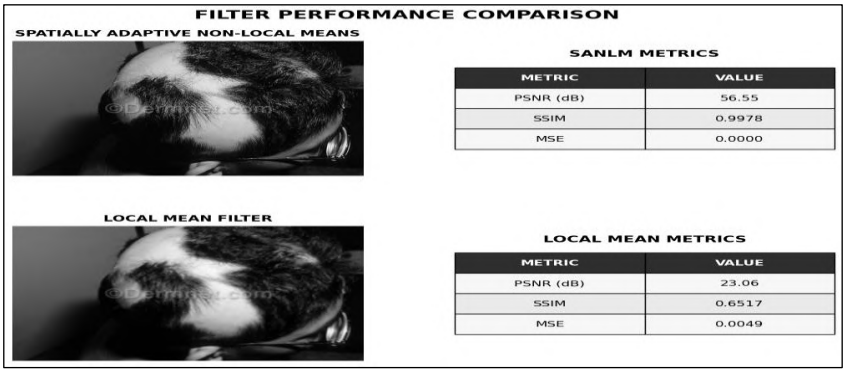


Figure 8: Filter performance comparison.
Source: Authors, (2026).

Figure 8 gives a direct comparison between two denoising filters that were applied to the same scalp photograph. The Spatially Adaptive Non-Local Means (SANLM) filter outputs a much clearer and clearer image with a very high PSNR (56.55 dB) which is much more than perfect SSIM (0.9978) and it has a 0 for MSE. The output of the Local Mean Filter is noticeably blurry with a significantly lower PSNR (23.06 dB) and a lower SSIM (0.6517) with a higher MSE. Overall, the image illustrates that detail and accuracy is conserved with the SANLM.

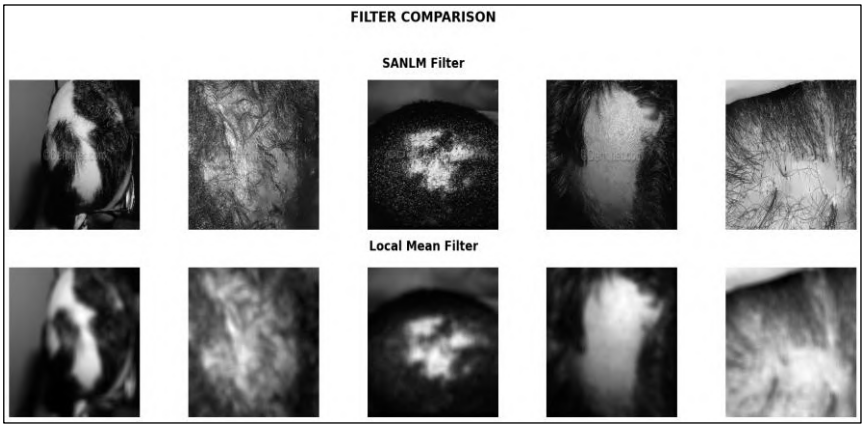


Figure 9: Filter comparison.
Source: Authors, (2026).

Figure 9 displays side-by-side visual comparisons of two different filtering approaches in scalp images taken at close-up view. The upper row shows outputs produced by the SANLM filter, which maintains fine hair detail, texture, and edge detail much better from the original visuals. The lower row shows the same images processed by the Local Mean Filter, which is noticeably blurrier and loses structural detail in the images. Ultimately, the comparison emphasizes the SANLM filter's much better ability to maintain sharpness and a natural texture while performing denoising.

METRIC COMPARISION

IMAGE 1

Metric	SANLM	Local Mean
PSNR(dB)	50.24	22.34
SSIM	0.9910	0.5982
MSE	0.0000	0.0058

IMAGE 2

Metric	SANLM	Local Mean
PSNR(dB)	34.00	18.25
SSIM	0.9359	0.1419
MSE	0.0004	0.0150

IMAGE 3

Metric	SANLM	Local Mean
PSNR(dB)	41.45	19.74
SSIM	0.9565	0.3584
MSE	0.0001	0.0106

IMAGE 4

Metric	SANLM	Local Mean
PSNR(dB)	39.60	23.07
SSIM	0.9480	0.3361
MSE	0.0001	0.0049

IMAGE 5

Metric	SANLM	Local Mean
PSNR(dB)	40.13	17.48
SSIM	0.9720	0.1671
MSE	0.0001	0.0179

Figure 10: Comparison metrics.
Source: Authors, (2026).

Figure 10 shows a row of metric tables comparing the output of the SANLM filter performance as compared to the Local Mean filter in each of several test cases. In every table, the SANLM filter achieved far higher PSNR and SSIM values, as well as a dramatically lower MSE, meaning it kept much better image quality and structural detail. In contrast, the Local Mean filter performed poorly, with lower clarity and more reconstruction error.

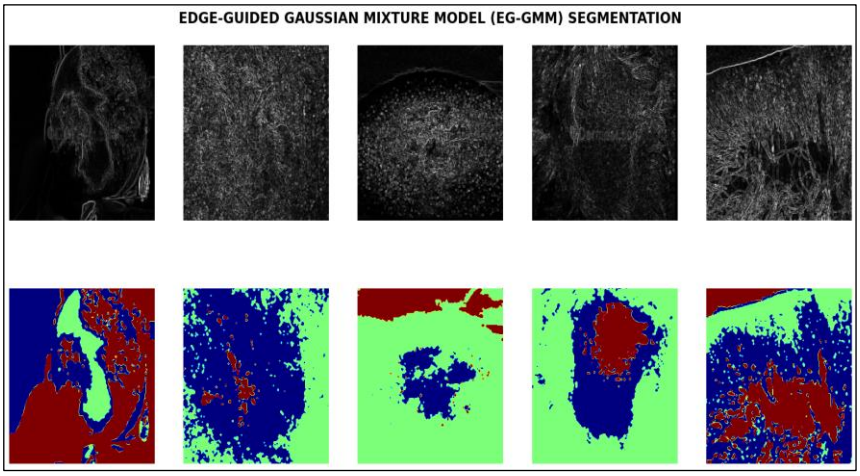


Figure 11: EG-GMM segmentation model.
Source: Authors, (2026).

Figure 11 shows original grayscale structural images on the upper row and the EG-GMM color-coded segmentation results of each image on the lower, with separate areas indicated by edginess and differing intensities.

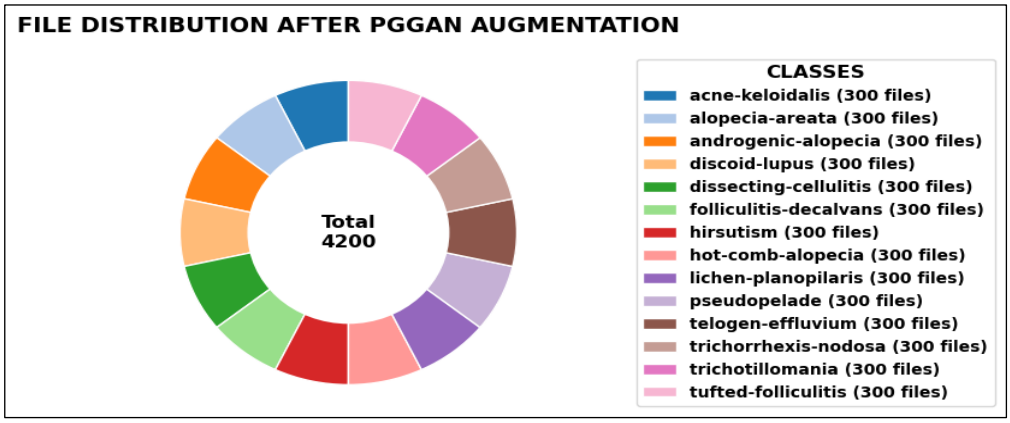


Figure 12: File distribution after PGGAN augmentation.
Source: Authors, (2026).

Figure 12 displays a donut graph illustrating the sample distribution after the PGGAN augmentation process, for a total of 4200 samples. Each of the 14 medical imaging classes has 300 augmented samples, which are categorized in a unique, colored section around the donut chart. On the right, there is a legend to describe the full list of classes. In summary, after the process of augmentation, there is a balanced dataset of varied medical imaging classes.

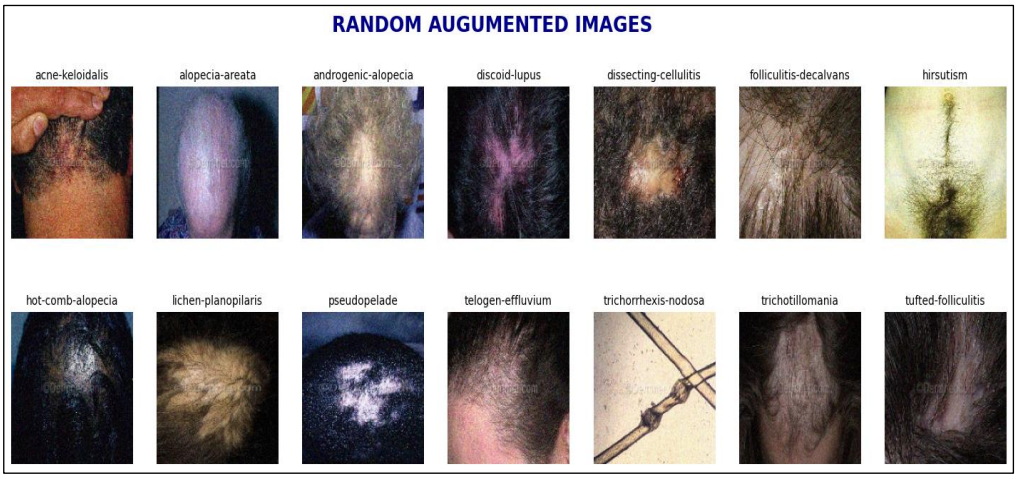


Figure 13: Random augmented images.
Source: Authors, (2026).

Figure 13 shows the set of randomly selected images of augmented scalp and hair conditions, with the corresponding class label. The images depict a variety of textures, colors, and patterns, produced through augmentation, depicting the visual diversity of such hair- or scalp-related conditions for instance, alopecia, folliculitis, dermatitis, and other scalp and hair conditions.

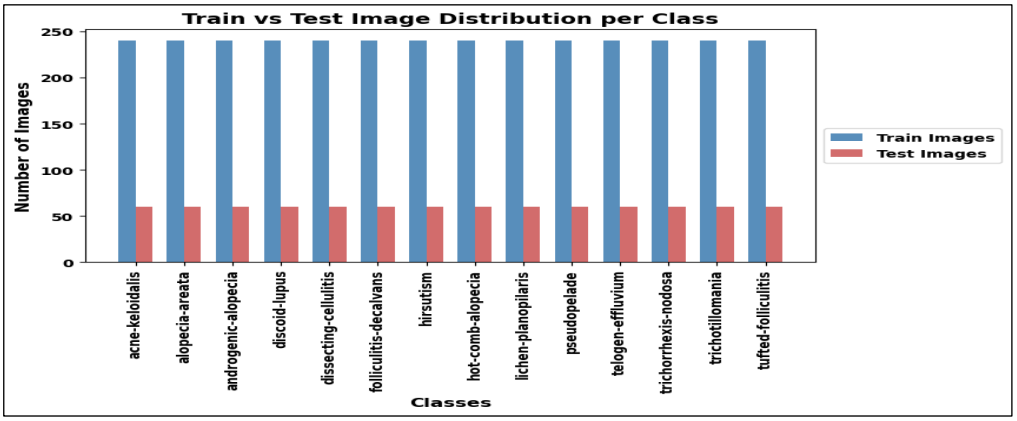


Figure 14: Train vs Test image distribution per class.
Source: Authors, (2026).

Figure 14 illustrates the number of training and test images across the hair- and scalp-related conditions in the dataset. All classes depict a balanced distribution with approximately 240 training images and about 60 test images per augmented class. Each of the medical imaging classes such as acne-keloidalis, alopecia-areata, trichotillomania, and tufted-folliculitis are evenly-distributed and well-balanced across the dataset.

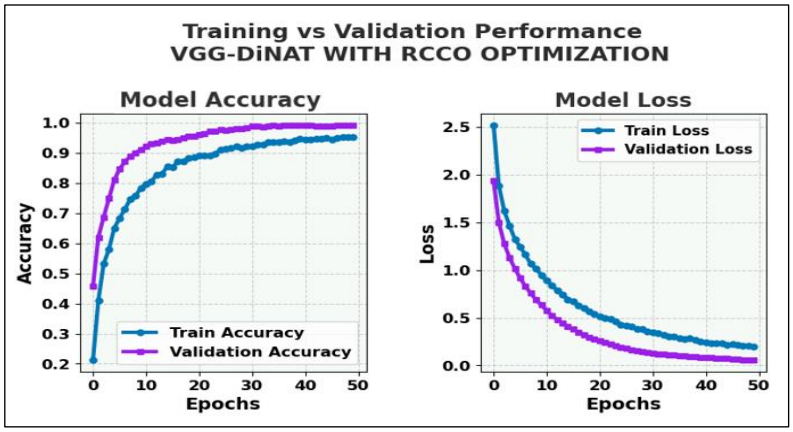


Figure 15: Training vs validation performance of VGG-DiNAT with RCCO.
Source: Authors, (2026).

Figure 15 indicates steadily improving accuracy, and a decreasing loss with training and validation. Throughout the training, the validation performance is slightly higher, indicating that the model is learning to generalize without any excessive overfitting.

Table 2: Classification metrics of VGG- DiNAT with RCCO.

METRICS	SCORE
Accuracy	0.9929
Macro Precision	0.9929
Macro Recall	0.9929
Macro FI-Score	0.9929
Weighted Precision	0.9929
Weighted Recall	0.9929
Weighted FI-Score	0.9929
Balanced Accuracy	0.9929
Cohen’s Kappa	0.9923
Matthews CorrCoef	0.9923

Source: Authors, (2026).

Table 2 shows the VGG–DiNAT model with RCCO which demonstrates remarkable performance, attaining 0.9929 across accuracy, precision, recall, F1-score, and balanced accuracy - this score indicates that the model can classify the three classes in a highly reliable and consistent manner. Furthermore, Cohen's Kappa and MCC were also 0.9923, further demonstrating the model's agreement and recounting other capability positively predicts class membership, showing strong robustness.

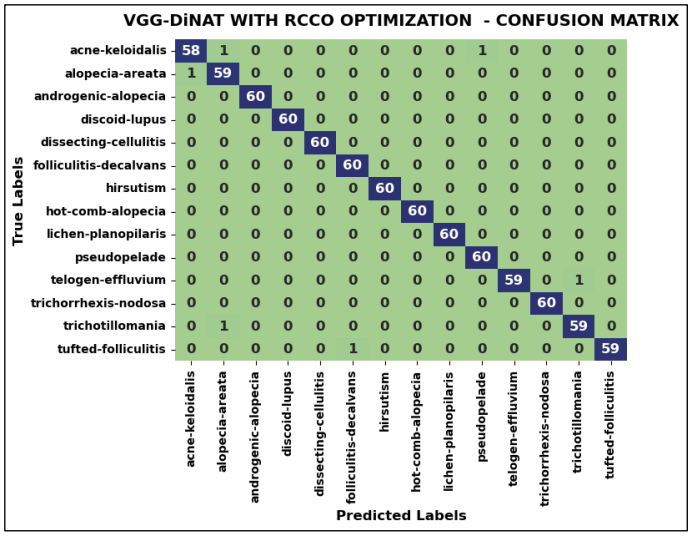


Figure 16: Confusion matrix of VGG-DiNAT with RCC optimization.
Source: Authors, (2026).

Figure 16 presents the confusion matrix for a model VGG-DiNAT with RCCO Optimization. The confusion matrix explains the accuracy of the model differentiating the different classes, in this case, hair loss or scalp conditions. The diagonal values highlight the number of correct predictions for each of the classes, and most of the classes in the diagonal have a value of 60. These values indicate that the model is performing as anticipated, as the vast majority of predictions match the true labels. The green and blue colors help identify these predicted true positive values.

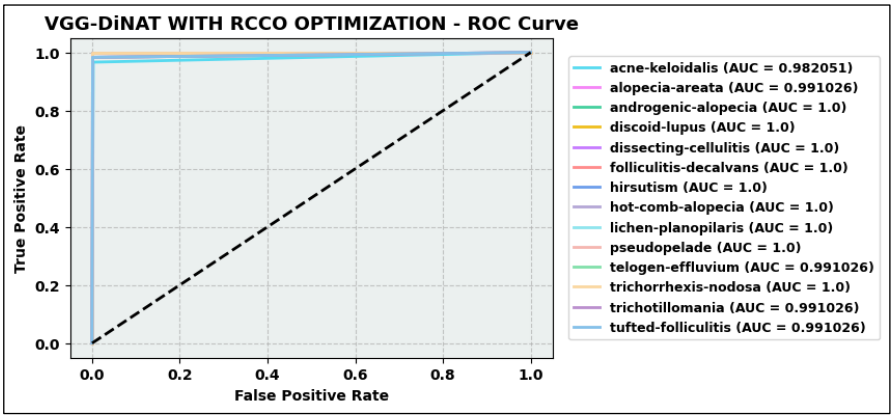


Figure 17: ROC curve of VGG-DiNAT with RCC optimization.
Source: Authors, (2026).

Figure 17 shows the ROC curve for VGG-DiNAT with RCCO Optimization model. The ROC curve has different lines for each class, and the AUC values are displayed for each class also. Most classes have an AUC of 1.0 indicating a perfect classification and only the acne-keloidalis class has an AUC of 0.982 showing it to be slightly below perfect classification. The curve is situated closely to the top left corner, indicating that the model has high accuracy and low false positives.

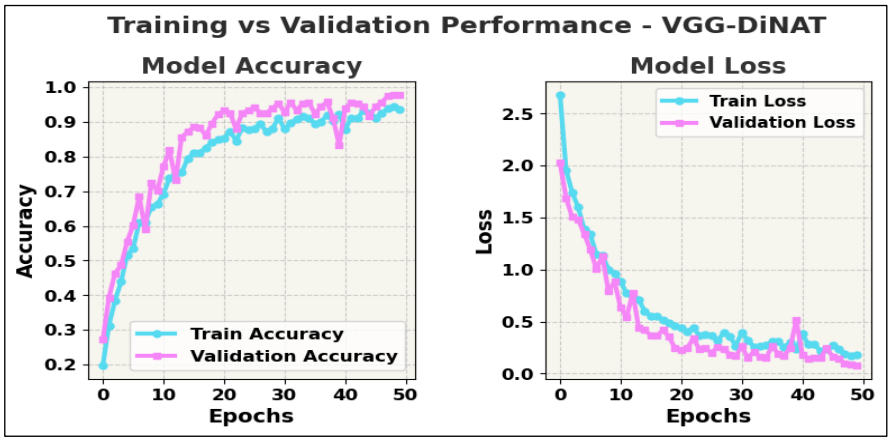


Figure 18: Training vs Validation performance of VGG-DiNAT.
Source: Authors, (2026).

Figure 18 depicts the training and validation performance of the VGG-DiNAT model for 50 epochs. The accuracy plot indicates a gradual increase in training and validation accuracy, ultimately exceeding 0.9, suggesting that the model was learning aggressively and generalizing well. The loss plot shows a steady decrease in both training and validation loss, and they align closely, indicating no overfitting and the model is stable across training and validation sets.

Table 3: Classification metrics of VGG- DiNAT model.

METRICS	SCORE
Accuracy	0.9774
Macro Precision	0.9776
Macro Recall	0.9774
Macro FI-Score	0.9772
Weighted Precision	0.9776
Weighted Recall	0.9774
Weighted FI-Score	0.9772
Balanced Accuracy	0.9774
Cohen's Kappa	0.9756
Matthews CorrCoef	0.9757

Source: Authors, (2026).

Table 3 shows the VGG-DiNAT model that produced consistent classification performance characterized by accuracy, precision, recall, and F1-scores, each averaging around 0.977. The macro and weighted averages indicate equally good performance across classes, suggesting that predictions are reasonably balanced. The value obtained for the Cohen's Kappa (0.9756) and Matthews Correlation Coefficient (0.9757) indicates strong agreement with true labels, thus suggesting that the model is reliable and robust.

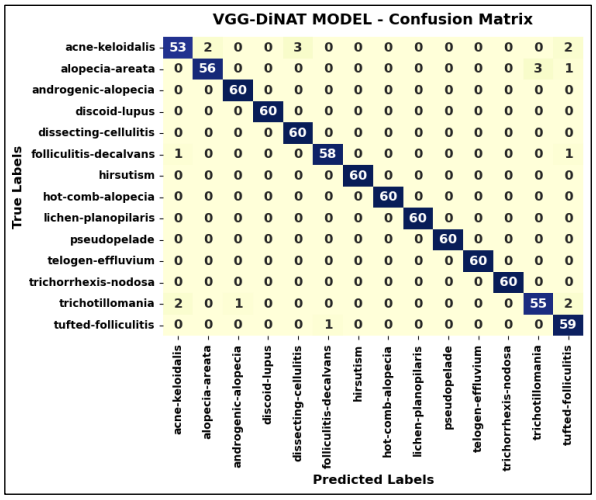


Figure 19: Confusion matrix of VGG-DiNAT model.
Source: Authors, (2026).

Figure 19 illustrates the confusion matrix that indicates the performance of the VGG-DiNAT model to classify the hair and scalp conditions. The model exhibited better performance, as most predictions lie along the diagonal, there were instances of misclassification, specifically androgenic-alopecia predicted as acne-keloidalis. Overall, the model indicates a high level of accuracy for skin condition prediction.

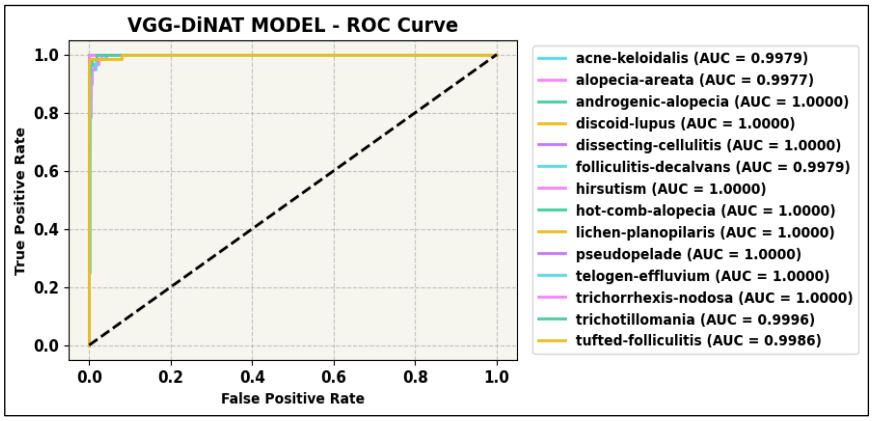


Figure 20: ROC curve of VGG-DiNAT model.
Source: Authors, (2026).

Figure 20 provides a summary of the ROC curve for a VGG-DiNAT model used to classify different hair and scalp conditions. All classes have very high AUC scores, indicating excellent performance in the classification of hair and scalp conditions across all circumstances.

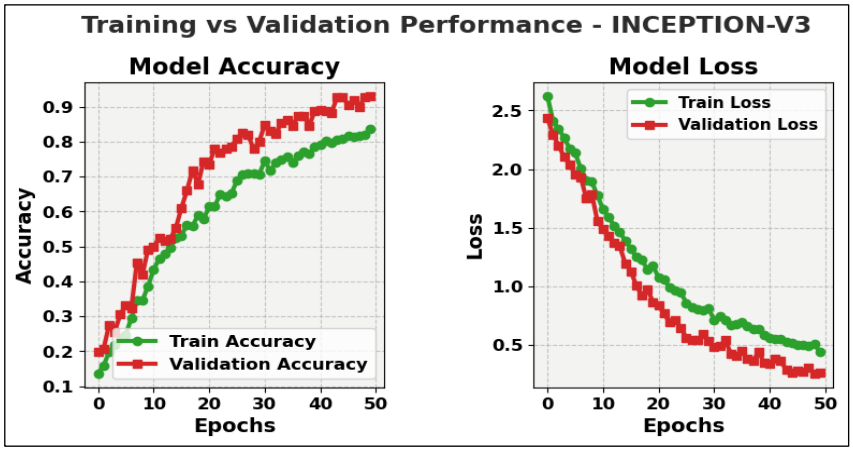


Figure 21: Training vs validation performance of Inception V3.
Source: Authors, (2026).

Figure 21 detail the training and validation of performance of an Inception-V3 model across 50 epochs. Both the accuracy curves trend upwards, and validation accuracy stays consistently above training accuracy, reaching above 0.9. The loss curves for training and validation are both declining at a smooth rate, with validation loss staying slightly below training loss throughout the epochs.

Table 4: Classification metrics of Inception V3 model.

METRICS	SCORE
Accuracy	0.9310
Macro Precision	0.9322
Macro Recall	0.9310
Macro FI-Score	0.9300
Weighted Precision	0.9322
Weighted Recall	0.9310
Weighted FI-Score	0.9300
Balanced Accuracy	0.9310
Cohen's Kappa	0.9256
Matthews CorrCoef	0.9259

Source: Authors, (2026).

Table 4 model shows strong and steady performance of approximately 93% accuracy, with comparable precision, recall, and F1-scores. The elevated Cohen's Kappa and Matthews Correlation Coefficient indicate reliability and a well-balanced range of the predictions across classes.

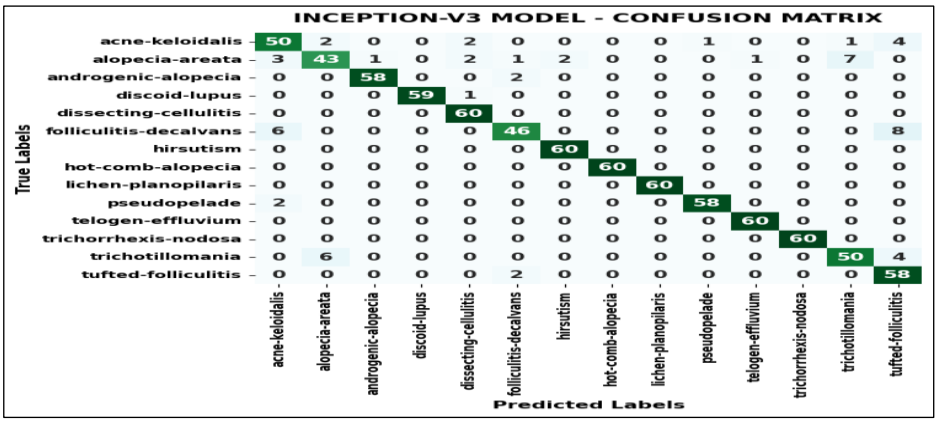


Figure 22: Confusion matrix of Inception V3 model.
Source: Authors, (2026).

Figure 22 shows the confusion matrix which illustrates that the Inception-V3 model is able to correctly classify the majority of samples in all categories, with clustered diagonals suggesting strong levels of accuracy. Only a small portion of misclassified categories appear across visually similar conditions, but overall, the confusion matrices suggests that the performance across classes are reliable and consistent.

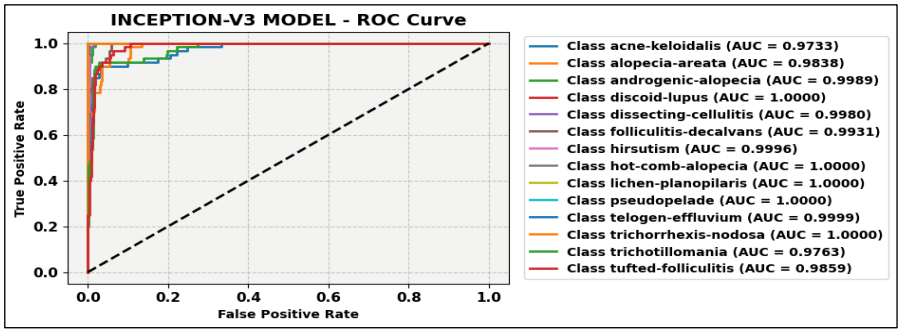


Figure 23: ROC curve of Inception V3 model.
Source: Authors, (2026).

In Figure 23, the model demonstrates excellent discriminative performance across classes, as indicated by near-perfect values across AUC and ROC curves clustered near the top-left corner of the examination.

Table 5: Classification metrics of proposed and existing model.

Model	Accuracy	Precision	Recall	FI-Score
PROPOSED	0.9929	0.9929	0.9929	0.9929
VGG-DiNAT	0.9774	0.9776	0.9774	0.9772
Inception V3	0.931	0.9322	0.931	0.931

Source: Authors, (2026).

Table 5 provides a comparison of the three models' classification metrics. The PROPOSED model has achieved the highest rating of 99.3% across all metrics. The VGG-DiNAT model is rated next at 97.7%, and the Inception-V3 model showed the worst performance with 93% accuracy, precision, recall, and F1-score.

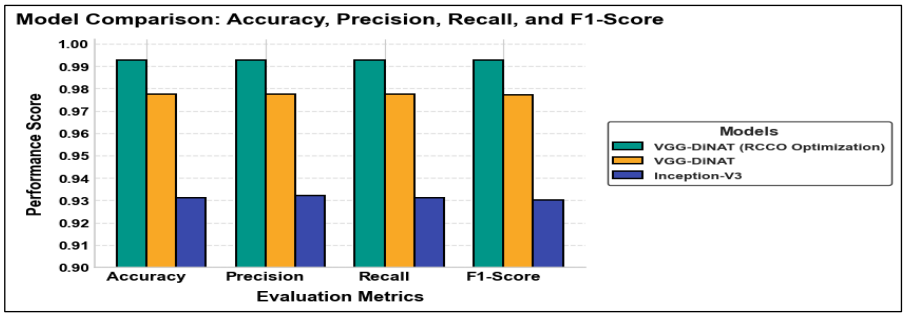


Figure 24: Comparison of evaluation metrics.
Source: Authors, (2026).

Figure 24 provides a comparison of three models using the different metrics of accuracy, precision, recall, and F1-score. The VGG-DiNAT (RCCO Optimization) model performs the best, with scores just under 0.99. The standard VGG-DiNAT model performs next highest, with scores between 0.97 and 0.98, and the Inception-V3 model showed lowest performance around 0.93 for the three models.

Table 6: Comparative analysis of accuracy for various models.

Model	Accuracy
CNN [22]	0.911
ViT-B/16 [23]	0.823
ANN [24]	0.964
HDM-Net [25]	0.948
VGG-16 [26]	0.945
Proposed	0.9929

Source: Authors, (2026).

In Table 6, the proposed model, achieves a maximum accuracy of 0.9929, higher than other models such as CNN (0.911), ViT (0.823) and VGG-16 (0.945) for diagnosing hair and scalp diseases. In the proposed system CNN is used to verify the accurate model of the proposed system which is used in the system to transfer the details from the given table

Table 7: Comparative analysis of precision for various methods.

Model	Precision
CNN [22]	0.895
ViT-B/16 [23]	0.831
ANN [24]	0.983
Proposed	0.992

Source: Authors, (2026).

In table 7 there are several models expected to yield different results based on their performance measure. A CNN has a Precision rating of 0.895, ViT-B/16 has a Precision of 0.831, and ANN has achieved a model precision of 0.983. The model developed by the Author in this study has the highest level of accuracy for identifying the True Positive class based upon its Precision score of 0.992.

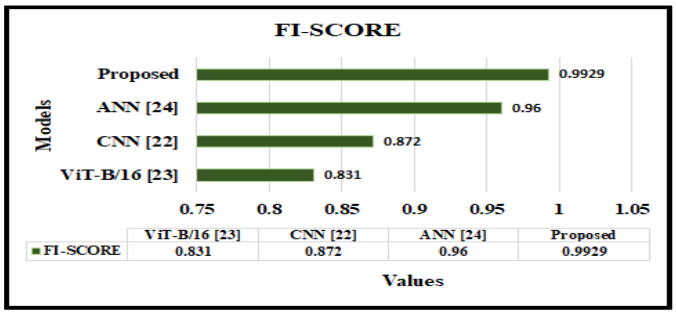


Figure 25: Comparison of FI-score for various methods.
Source: Authors, (2026).

A bar graph comparing the FI-SCORE value of four different machine learning (ViT-B/16, CNN, ANN, and a proposed) shown in Figure 25. The proposed model had a higher FI-SCORE than the others with an FI-SCORE of 0.9929. The second highest FI-SCORE was obtained by the ANN model with a value of 0.96 while CNN and ViT-B/16 both achieved lower FI-SCORE values at 0.872 and 0.831 respectively.

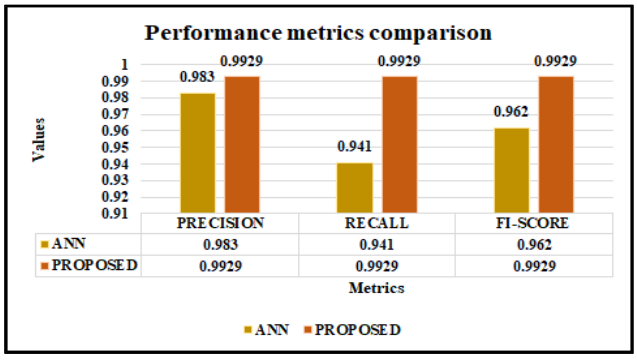


Figure 26: Comparative analysis of proposed and existing methods.
Source: Authors, (2026).

Compared to the ANN, the proposed model has superior performance across all metrics of measurement which is illustrated in Figure 26. In addition, the Proposed Model's Precision (99.29%) and F-1 Score (99.29%) both outperform the ANN (98.3% Precision and 96.2% F-1 Score), while they have equal Recall (94.1 % Recall).

VI. CONCLUSION

The proposed approach enhance both the accuracy and speed with which users classify the input images. To accomplish this, the process involves a number of clearly defined phases. The first phase in this process will be an input dataset of raw images that require processing. The first stage of the process is accomplished using a SANLM approach, which provides significant denoising and enhancement of image quality to prepare the data for further analysis. The next step involves segmenting the images into identifiable regions using EG-GMMs. The third stage of the process is data augmentation, involves using a PGGAN to create additional training data for the model in order to expand the size of the dataset and improve robustness through reducing overfitting. The fourth step of the process will utilize a VGG-DiNAT architecture based DL model for the classification of the images based upon extract features. The performance of the model will be enhanced through hyperparameter tuning using RCCO methodology to maximize efficiency of the system. The proposed system is implemented in python and achieves the highest accuracy, precision, Recall and FI-Score of 0.9929.

VII. AUTHOR'S CONTRIBUTION

Conceptualization: Vimala Ithayan J, Dilip Charaan R M, Vijayanandh T, Santhoshkumar S P, Parvathi R and Sivaprakash P.
Methodology: Vimala Ithayan J and Dilip Charaan R M.
Investigation: Vimala Ithayan J and Dilip Charaan R M.
Discussion of results: Vimala Ithayan J, Dilip Charaan R M, Vijayanandh T, Santhoshkumar S P, Parvathi R and Sivaprakash P.
Writing – Original Draft: Vimala Ithayan J.
Writing – Review and Editing: Vimala Ithayan J and Dilip Charaan R M.
Resources: Dilip Charaan R M.
Supervision: Dilip Charaan R M, Vijayanandh T, Santhoshkumar S P, Parvathi R and Sivaprakash P.
Approval of the final text: Vimala Ithayan J, Dilip Charaan R M, Vijayanandh T, Santhoshkumar S P, Parvathi R and Sivaprakash P.

VIII. REFERENCES

[1] M.S. Chowdhury, T. Sultan, N. Jahan, M.F. Mridha, M. Safran, S. Alfarhood, and D. Che, “Leveraging deep neural networks to uncover unprecedented levels of precision in the diagnosis of hair and scalp disorders”, Skin Research and Technology, vol. 30, no. 4, pp. e13660, 2024.

[2] C. Ha, T. Go, and W. Choi, “Intelligent healthcare platform for diagnosis of scalp and hair disorders”, Applied Sciences, vol. 14, no. 5, pp. 1734, 2024.

[3] B.S.H. Reddy, “Deep learning-based detection of hair and scalp diseases using CNN and image processing”, Milestone Transactions on Medical Technometrics, vol. 3, no. 1, pp. 145-155, 2025.

[4] T. Rayinda, S.P. Rafida, H.W. Sugiarto, N. Trisnowati, and R. Danarti, “Clinical Spectrum of Pediatric Hair and Scalp Disorders at a Tertiary Center in Indonesia”, Asian Journal of Pediatric Dermatology, vol. 3, no. 1, pp. 26-27, 2025.

[5] K. Karthika, and R.D. Priya, “Image processing-based protection of privacy data in cloud using NTRU algorithm”, Signal, Image and Video Processing, vol. 18, no. 5, 2024.

[6] A. Rajkumar, K. Muralidhar, A. Swaminathan, M. Sundaram, and S. Rangarajan, “Bad Hair Days: A Clinical and Trichoscopic Evaluation of Scalp Lesions”, Cureus, vol. 17, no. 6, 2025.

[7] B. Heyns, R. Pieters, M.A. Stander, S.L. Atkin, and A.C. Swart, “Glucocorticoids and mineralocorticoids in hair: facilitating accurate diagnosis of adrenal-related endocrine disorders”, Frontiers in Endocrinology, vol. 15, pp. 1448013, 2024.

[8] P.L. Rose, V. Sarojini, and G.D. Biji, “Antibacterial and anticancer activity of green synthesised silver nanoparticles using polysaccharides extracted from the marine alga Portieria hornemannii”, Journal of Applied & Natural Science, vol. 16, no. 1, 2024.

[9] P. Muthukumar, K. Muthuvel, R. Boopathi, M.V. Suganyadevi, and R. VK, “A Hybrid U-Net with Active Contours for Plant Leaf Disease Segmentation and Classification”, International Conference on Advancement in Renewable Energy and Intelligent Systems (AREIS), Thrissur, India, vol. 2024, pp. 1-6, 2024.

[10] S.M. Perez, S.A. AlSalman, B. Nguyen, and A. Tosti, “Botulinum Toxin in the Treatment of Hair and Scalp Disorders: Current Evidence and Clinical Applications”, Toxins, vol. 17, no. 4, pp. 163, 2025.

[11] V. Gaurav, A. Bahadur, and H. Tyagi, “Role of dermoscopy in differentiating seborrheic dermatitis of scalp and scalp psoriasis”, CosmoDerma, vol. 4, pp. 80, 2024.

[12] N. So, L. Yip, and D. Orchard, “Paediatric Hypotrichosis: A Clinical and Algorithmic Approach to Diagnosis”, Australasian Journal of Dermatology, vol. 66, no. 3, pp. e109-e119, 2025.

[13] D. Karthikeyan, R. Nivasini, K. T. Raja, D. Madhivadhani, B. Sivakumar and A. T. R. K. Priya, “Hybrid Deep Learning Algorithm For MRI Brain Alzheimer’s Disease Prediction”, International Conference on Energy, Materials and Communication Engineering (ICEMCE), Madurai, India, vol. 2023, pp. 1-6, 2023.

[14] L. Shkreli, M.L. Woud, L. Bergunde, L. Schindler-Gmelch, S.E. Blackwell, C. Kirschbaum, H. Kessler, and S. Steudte-Schmiedgen, “The role of long-term hair steroids as diagnostic and intervention-related biomarkers in a multimorbid inpatient sample with posttraumatic stress disorder”, European Journal of Psychotraumatology, vol. 16, no. 1, pp. 2457295, 2025.

[15] N. Yaker, “Performing a nonsurgical hair restoration consultation”, Plastic and Aesthetic Nursing, vol. 45, no. 4, pp. 228-239, 2025.

[16] C. Feng, Y. Wang, D. Yang, and H. Shen, “Analysis of common treatment drugs and allergen sensitization in hair loss patients”, Journal of Cosmetic Dermatology, vol. 24, no. 2, pp. e16798, 2025.

[17] T.V. Boas, R.F.C. de Almeida, V.D. Tortelly, M. Starace, and D.F. Melo, “Dermoscopy of Traction Alopecia in Black Scalp Patients: Insights from a Literature Review,” Dermatol Pract Concept, vol. 15, no. 2, pp. 4578, 2025.

[18] N. Chhabra, and J.S. Rahim, “Hair Root Dermoscopy from Shed Hair: A Simple Diagnostic Tool in Telogen Effluvium”, International Journal of Trichology, vol. 16, no. 1, pp. 58-59, 2024.

[19] S. Graham, J. Larrondo, I. Obeime, and A. McMichael, “Differential diagnosis of posterior scalp hair loss”, Archives of Dermatological Research, vol. 316, no. 10, pp. 738, 2024.

[20] M. Nyström-Hansen, M.S. Andersen, K.A. Davidsen, K. Roehder, C. Trier, E. Nayberg, K. Lyons-Ruth, and S. Harder, “Hair cortisol concentrations in pregnant women with bipolar, depressive, or schizophrenic spectrum disorders”, Archives of Women's Mental Health, vol. 27, no. 4, pp. 577-584, 2024.

[21] A.A.E. Salah, A.M. El-Bakry, A.E.H. Mohamed, and M.G. Yousef, “Androgenetic Alopecia Pathogenesis, Diagnosis, and Treatment”, Benha Journal of Applied Sciences, vol. 9, no. 12, pp. 15-24, 2024.

[22] M. Roy, and A.T. Protity, “Hair and scalp disease detection using machine learning and image processing”, 2022.

[23] V.Q. Tran, and H. Byeon, “Scalp Disorder Imaging: How Deep Learning and Explainable Artificial Intelligence are Revolutionizing Diagnosis and Treatment”, International Journal of Advanced Computer Science & Applications, vol. 15, no. 11, 2024.

[24] A. Noreen, H. Khan, S.M.A. Shah, W. Ahmed, and S.H. Amjad, “Detection and Classification of Alopecia Areata Using Diverse Feature-Set”, Journal of Computers and Intelligent Systems, vol. 3, no. 2, pp. 92-106, 2025.

[25] L. Zhang, Q. Man, and Y.I. Cho, “Deep-learning-based hair damage diagnosis method applying scanning electron microscopy images”, Diagnostics, vol. 11, no. 10, pp.1831, 2021, 2021.

[26] H. Syahputra, M. Restuati, D. Kiswanto, A. Aqila, and T. Abdullah, “Classification of hair disease using CNN with VGG-16 architecture”.

Journal of Engineering and Technology for Industrial Applications

ISSN ONLINE: 2447-0228

ITEGAM-JETIA

Manaus, v.12 n.60, p.869-883 July/August, 2026.
DOI: https://doi.org/10.5935/jetia.v12i60.3434

RESEARCH ARTICLE OPEN ACESS

REAL-TIME NAIL-FOLD CAPILLARY DETECTION USING YOLO-RELAN WITH SALIENCY-BASED EXPLAINABILITY MODEL

Santhoshkumar S P[1], Parvathi R[2], Sivaprakash P[3], Vimala Ithayan J[4], Dilip Charaan R M[5], Vijayanandh T[6]

[1]Assistant Professor (SG), School of Computing, Vel Tech Rangarajan Dr Sagunthala R&D Institute of Science and Technology, Chennai, India.
[2]Associate Professor Grade 1, School of Computer Science Engineering and Information Systems, Vellore Institute of Technology, Katpadi, Vellore, India.
[3]Professor, School of Electrical and Communication, Vel Tech Rangarajan Dr Sagunthala R& D Institute of Science and Technology, Chennai, India.
[4, 5]Associate Professor, School of Computing, Vel Tech Rangarajan Dr Sagunthala R& D Institute of Science and Technology, Chennai, India.
[6]Associate Professor, School of Electrical and Communication, Vel Tech Rangarajan Dr Sagunthala R& D Institute of Science and Technology, Chennai, India.

[1]https://orcid.org/0000-0001-8531-759X, [2]https://orcid.org/0000-0001-7109-134X, [3]https://orcid.org/0000-0002-2777-8889
[4]https://orcid.org/0000-0002-4647-0863, [5]https://orcid.org/0009-0002-1332-4592, [6]https://orcid.org/0000-0002-6307-4272

E-email: *spsanthoshkumar16@gmail.com, 2005.parvathi@gmail.com, sivabtl85@gmail.com, vimala.ithayan@gmail.com, dilip_charraan@yahoo.co.in, drvijayanandht@veltech.edu.in

ARTICLE INFO

Article History
Received on: January 27, 2026
Reviewed on: February 27, 2026
Accepted on: July 01, 2026
Published on: July 31, 2026

Keywords:
Nail-fold capillaries,
YOLOv12,
ReLAN,
Saliency Heatmaps,
DL.

ABSTRACT

The accurate identification of nail-fold capillaries is essential for the early detection of systemic diseases such microvascular abnormalities and systemic sclerosis. The complexity of capillary design and variations in image quality present significant challenges for precise identification in automated detection systems. An enhanced Deep Learning (DL) architecture that incorporates morphological preprocessing, shape-based feature enhancement, and a robust object recognition foundation. To emphasize essential vascular features, shape focus and extraction modules are performed after input images have previously undergone preprocessing with morphological filters to decrease noise and maintain capillary structures. YOLOv12 is utilized to accomplish the detection task using an enhanced backbone architecture based on Residual-Expanded Layer Aggregation Network (ReLAN), which improves feature reuse, gradient flow, and spatial representation. While significantly improving detection accuracy, this backbone maintains real-time functionality. To provide transparency and clinical reliability, the system makes use of Explainable AI (XAI) tools, especially saliency heatmaps, which highlight the critical areas influencing model predictions and provide interpretability for medical experts. The proposed approach achieves the highest accuracy of 88%, 90% of precision, 89% of recall, 86% of map-50 and 88% of map50-95. These results of the experimental evaluation demonstrate that a reliable and understandable solution for nail-fold capillary detection in clinical applications were achieved using the proposed approach.

Copyright ©2026 by authors and Galileo Institute of Technology and Education of the Amazon (ITEGAM). This work is licensed under the Creative Commons Attribution International License (CC BY 4.0).

I. INTRODUCTION

The microvascular structure in nail-fold capillaries is capable of being directly and noninvasively assessed using Nail-Fold Capillaroscopy (NFC), a conventional technique for health evaluation. In order to sustain microcirculation and enable material exchange throughout the body, microvascular integrity is essential. According to earlier research, microcirculatory alterations result from conditions like diabetes, rheumatoid arthritis, Raynaud's phenomenon, and systemic sclerosis (SSc) [1]. SSc is a disease caused by vascular lesions and autoimmune disorders that limit blood flow and induce organ fibrosis throughout the body. NFC is a non-invasive, easy-to-use, and economical method that offers vital information on microvascular anomalies in living tissues. In the past, the NFC has been used to investigate the microvascular changes in nail-fold capillaries linked to different rheumatologic disorders. The growing body of research on NFC in rheumatic disorders demonstrates the technique's effectiveness in clinical settings as well as the variety of research applications.

Additionally, the NFC has been useful in studying other systemic conditions including schizophrenia and diabetes mellitus that are marked by changes in capillary architecture [2-4]. The nail-fold bed's microvascular involvement is a reflection of the body's general microvascular damage and is directly correlated with the target organs' involvement. In addition to enabling the early diagnosis of connective tissue diseases, primarily SSc by differentiating between primary and secondary Raynaud's phenomenon, NFC also offers information on the disease's prognosis based on the degree of target organ damage in these conditions18. Nail-fold capillary abnormalities occur in 70–80% of SSc patients and 9–27% of non-SSc individuals, respectively [5-7]. The NFC method captures precise images of nail-fold capillaries using a capillaroscope. Following the acquisition of these images, clinicians use their critical experience to visually analyze and manually measure a variety of factors, such as the existence of dilated capillaries, capillary morphology, and capillary density, which is measured as the number of loops per millimeter [8]. Although this clinical analysis, which is motivated by their experience, is essential, it is still very difficult to provide uniform and standardized assessments among healthcare providers. Although attempts have been made to automate capillary image analysis, results have not yet improved due to capillary size variability [9-11]. This variation in size restricts the training of machine learning models and ultimately leads to less-than-ideal prediction performance, which cause patients to receive a delayed or incorrect diagnosis [12]. The present research proposed an improved deep learning-based technique for automated nail-fold capillaroscopy image processing in order to overcome this restriction.

This method used object detection algorithms to automatically identify and categorize the morphology of individual nail-fold capillaries, which are important characteristics for medical diagnostics in general and early SSc diagnosis in particular since they indicate the involvement of internal organs [13-15]. Additionally, the proposed method's improved deep learning framework demonstrated that it could identify capillaries in multi-scale, untrained microscopic images. This research work includes preprocessing, model selection and explainable AI stages to evaluate the process for the detection of real time nail-fold capillaries. In order to discover nail-fold capillaries, the image is prepared and refined using preprocessing techniques such shape focus, shape extraction, and morphological filtering, which facilitate the identification and analysis of capillary structures. These procedures are intended to attract attention to the pertinent shapes, improve the image quality, and increase the precision and effectiveness of capillary identification [16-18]. The preprocessed image is then fed to model selection stage where it is capable of accurately identifying and localizing capillary structures in microscopic images [19]. While conventional DL models are capable of detecting nail-fold capillaries that are often suffer from limitations such as restricted accuracy, poor generalization across diverse image qualities and difficulty in capturing the intricate vascular structures and variations present in capillary patterns and table 1 illustrates the DL methods to detect nail-fold capillaries [20].

Table 1: Related works for DL methods to detect Nail-fold capillaries.

S. No	Author/ Year	Methodology	Merits	Demerits	Performance metrics
1.	Hao Yin et al [2023] [21]	YOLO v5	• It leverages the strength of DL to automatically identify small and complex vascular structures. • It is suitable for both clinical and research applications.	• The model's performance decreases, when dealing with overlapping, blurred or low-contrast capillaries and it requires high quality annotated datasets for optimal training	YOLOv5 attains an accuracy of 85.2%.
2.	Vincenzo Taormina et al [2023] [22]	Faster R-CNN	• It increases image clarity by boosting contrast and supressing noise, which is critical for highlighting the delicate and fine structures of nail-fold capillaries. • It reduces the need for manual intervention, enhances reproducibility and supports more objective clinical evaluations.	• The computational complexity of Faster R-CNN makes the process slower and more resource-intensive compared to single stage detectors.	The method achieves an accuracy of 96.2%
3.	Shupin Chen et al [2023] [23]	U-Net	• It provides an effective approach for accurately delineating capillary structures in microscopic images. • It allows for precise pixel-level segmentation capturing both global context and fine details of the capillary loops.	• The model's performance heavily depends on the availability of high-quality, annotated datasets and it is not generalize well to images captured under different imaging conditions.	The performance metrics of U-Net accomplishes an accuracy of 94.1%
4.	Chiara Filippini et al [2021] [24]	CNN	• CNNs are capable of learning hierarchical features directly from images, enabling them to detect subtle morphological changes in capillaries that is used to indicate microvascular diseases. • It reduces the reliance on manual assessment, minimizes observer bias and allows for rapid and objective analysis.	• It requires high quality datasets for effective training and limited data led to overfitting for new patients or imaging conditions.	CNN attains an accuracy of 86%
5.	Indriani et al [2025] [25]	ResNet	• It allows the network to learn intricate vascular patterns and subtle capillary abnormalities with high precision. • It improves diagnostic consistency and reduces manual intervention by clinicians.	• The architecture is computationally intensive, requiring high memory and processing power, which limit its use in real-time diagnostic systems.	The performance of ResNet is 87% of accuracy, 88% of precision and recall, and 86% of FI-score.

Source: Authors, (2026).

Existing DL methods to detect nail-fold capillaries have various limitations, hence the proposed YOLOv12-ReLAN model is implemented, which allows for precise detection of individual capillaries, abnormal loops and morphological changes that are indicative of microvascular diseases. Next it is passed to Explainable AI tools, particularly saliency heatmaps, which emphasise the crucial areas impacting model predictions and offer interpretability for medical experts to ensure transparency and clinical reliability. The main objectives of this research includes:

- To develop an automated detection framework which identifies target features from input image dataset, an advanced DL technique is implemented.
- To enhance image quality and feature visibility, preprocessing operations such as shape focusing, shape extraction and morphological filtering is utilized.
- To achieve an optimal balance between detection accuracy and computational efficiency and for precise object detection, YOLOv12-ReLAN is employed.
- To analyze visual interpretation of model's decision-making process, ensuring transparency and reliability in predictions, an explainable AI, saliency heatmap is used.

II. PROPOSED SYSTEM DESCRIPTION

The proposed approach employs an enhanced deep learning framework to improve object detection accuracy by combining YOLOv12 with the Backbone R-ELAN architecture and explainable AI methods. Figure 1 displays the block diagram of the proposed method.

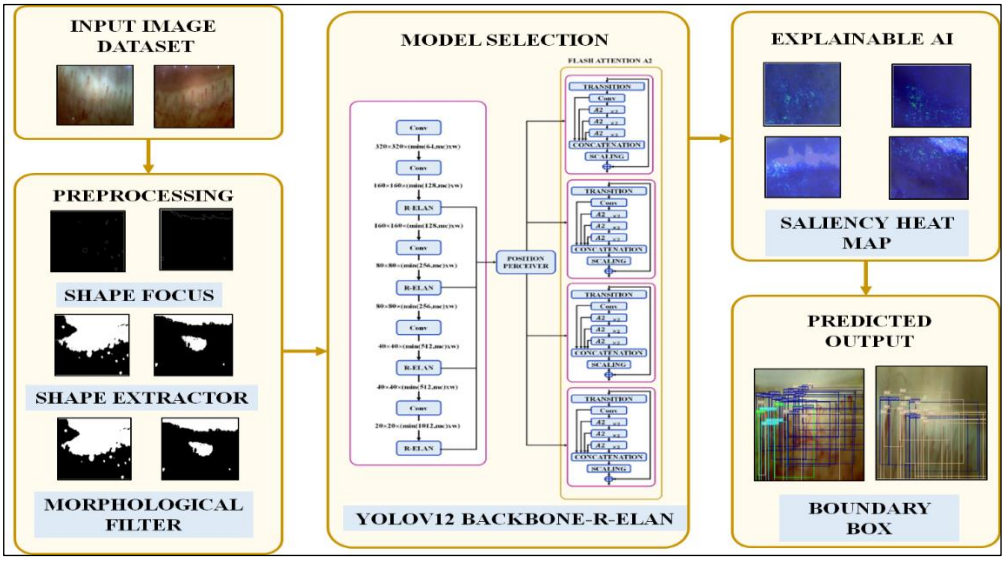


Figure 1: Block diagram of the proposed model.
Source: Authors, (2026).

The input image dataset, which forms the basis for the model's training and evaluation, is where the process commences. Several image improvement and feature refinement approaches, such as Shape Focus, Shape Extraction, and Morphological Filtering, are used during the preprocessing step. By highlighting important structural elements and eliminating unwanted noise, these methods ensure the model receives clear and instructive input data. The YOLOv12 Backbone-R-ELAN architecture is used in the Model Selection stage after the refined images have been preprocessed. This model was selected because of its excellent feature extraction capabilities, effective multi-scale object detection, and resilience when dealing with intricate image fluctuations. Then, to increase interpretability and reliability, the Explainable AI module is incorporated. It provides Saliency Heat Maps, which graphically depict the areas that have the most impact on the model's decision-making. Lastly, the system provides accurate localization and an understandable visual explanation of the detection process by outputting the Predicted Results in the form of Boundary Boxes surrounding the identified objects. Thus, the proposed method provides an effective and transparent DL framework for image-based object detection.

III. PROPOSED SYSTEM MODELLING

III.1 PREPROCESSING

Preprocessing is a crucial first step in the nail-fold capillary detection process that sets up the image for accurate analysis. The nail-fold region's fine capillary structures are enhanced and isolated during this phase using specific techniques.

III.1.1 Shape Focus

The nail-fold image's capillary-like structures are more visible due to the Shape Focus method. This stage seeks to emphasize the thin, elongated, and curved characteristics of capillaries while minimizing background noise and irrelevant data. This phase ensures that the crucial structural elements of capillaries are maintained and made more recognizable for further study by sharpening the emphasis on these particular forms.

III.1.2 Shape Extractor

The improved capillary forms are separated and identified from the image using the Shape Extractor process. This procedure focuses on possible capillary areas and then extracts those utilizing textural and geometric characteristics like continuity, length, and curvature. The capillary structures also be separated from the surrounding tissue. This stage's primary objective is to acquire precise depictions of the capillaries for additional processing and analysis.

III.1.3 Morphological Filter

An essential image processing step in nail-fold capillary detection is the morphological filter, which modifies the forms of capillary structures using computational morphological principles to improve their clarity and continuity. Morphology is concerned with the shape or structure of objects, and morphological filtering is especially helpful for improving segmented images by eliminating undesired noise or microscopic projections, filling in tiny holes or gaps, and smoothing out item outlines. Dilation and erosion are the basic processes in this process, and they both make use of a structural element a predetermined shape that dictates where the image is processed. In addition to these, morphological edge detection uses these basic operations such as erosion, dilation, opening, and closing to extract clear and defined edges of the capillaries. By applying the difference between the processed and the original image, the algorithm effectively highlights capillary boundaries. While erosion and dilation alone can enhance edges, they are less effective in filtering out noise; thus, opening and closing are preferred for achieving smoother, cleaner results. Overall, the morphological filter improves the visibility and accuracy of nail-fold capillary detection by refining the shape and connectivity of capillary structures while minimizing background artifacts.

III.2. MODEL SELECTION-YOLOV12-BACKBONE-R-ELAN

YOLOv12 is particularly proficient at detecting nail fold capillaries because it combines efficient feature extraction with precise localization in a single, end-to-end network. The backbone creates hierarchical feature maps by processing the input image through several convolutional layers. These feature maps capture both fine details, such as individual capillary loops, and more general spatial context, such as the overall arrangement of the nail fold. Because nail fold capillaries are very minute and may appear partially occluded, the network must identify subtle differences while keeping background, which makes these multi-scale feature maps crucial. The diagram of YOLOv12-BACKBONE-R-ELAN is depicted in figure 2.

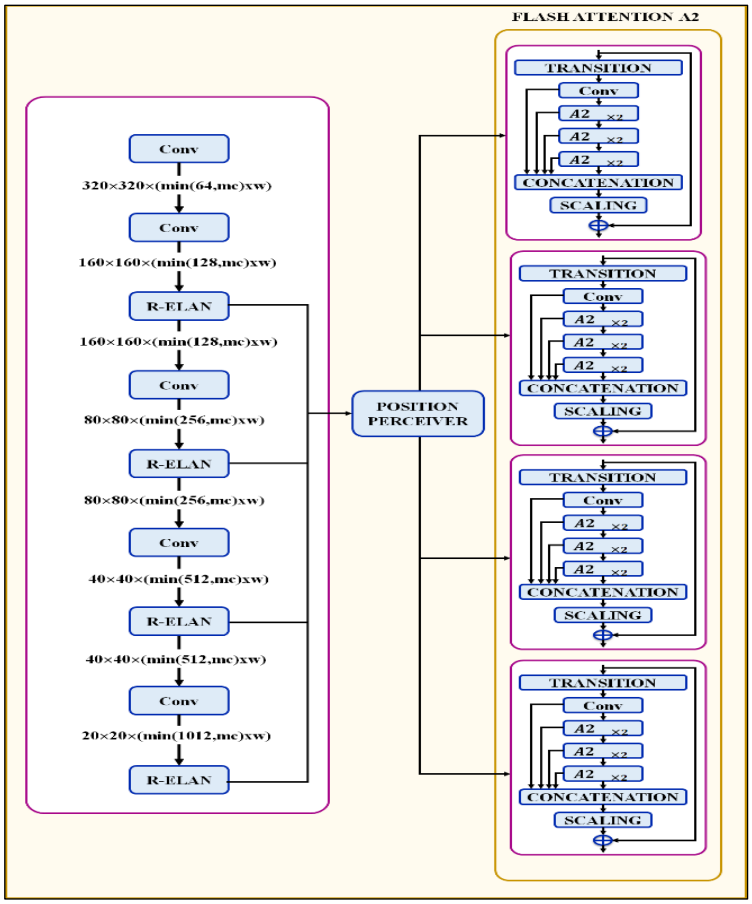


Figure 2: Diagram of YOLOv12-BACKBONE-R-ELAN.
Source: Authors, (2026).

The Residual Efficient Layer Aggregation Network (R-ELAN), which forms the backbone of YOLOv12, is intended to convert unprocessed image data into rich, multi-scale feature maps that constitute the basis for accurate object detection. Deeper residual connections are introduced by the R-ELAN structure to alleviate gradient bottlenecks in deep networks and encourage feature reuse. Pseudo-code of YOLOv12 backbone using R-ELAN is shown below,

Pseudo-code 1: YOLOv12 backbone- R-ELAN.

```
Parameters:
Input Image I(H, W, 3)
Output Feature Maps F3, F4, F5
1: For each epoch do:
      # Stage 1 – Initial Convolution Extraction
2:      For each convolutional layer Lc do:
3:          For each sample in I do:
4:              Compute feature map aijm = ConvBNAct(I)
5:              # Dimension of aijm = (H/2, W/2, 64)
6:          End for
7:      End for
# Stage 2 – Recursive ELAN Block 1 (Low-level Features)
8:      Input aijm → R-ELAN(128, 3 layers)
9:      Split feature into X1, X2
10:     For each layer l = 1 to 3 do:
11:         Y = ConvBNAct(X2, 3×3)
12:         X2 = Concat(X2, Y)
13:     End for
14:     F2 = ConvBNAct(Concat(X1, X2), 128, 1×1)
15:     # Dimension of F2 = (H/4, W/4, 128)
   # Stage 3 – Recursive ELAN Block 2 (Mid-level Features)
16:     F3 = R_ELAN(F2, 6 layers, 256)
17:     # Dimension of F3 = (H/8, W/8, 256)
# Stage 4 – Recursive ELAN Block 3 (High-level Features)
18:     F4 = R_ELAN(F3, 9 layers, 512)
19:     # Dimension of F4 = (H/16, W/16, 512)
      # Stage 5 – Recursive ELAN Block 4 (Deep Feature Extraction)
20:     F5 = R_ELAN(F4, 3 layers, 1024)
21:     # Dimension of F5 = (H/32, W/32, 1024)
      # Stage 6 – Multi-Scale Feature Output
22:     Output F3, F4, F5 to the Neck and Detection Head
23: End for
# R-ELAN Function
Function R_ELAN(input, layers, channels):
      Split input into X1, X2
      For i = 1 to layers do:
          Y = ConvBNAct(X2, 3×3)
          X2 = Concat(X2, Y)
      End for
      Output = ConvBNAct(Concat(X1, X2), channels, 1×1)
      return Output
End Function
```

This characteristic is especially useful for identifying nail-fold capillaries, which are tiny, delicate, and frequently partially obscured. The backbone guarantees that even the smallest capillary patterns are represented in the feature hierarchy by maintaining high-resolution spatial information across several scales. The network's convolutional blocks are defined as a series of smaller, parallel convolutions, formalized by the equation,

$$F_{out} = \sum_{i=1}^{n} W_i * F_{in} + b_i \quad (1)$$

Where, F_{out} is the feature map that is produced, W_i are the Convolutional filters, F_{in} is the input feature map, and b_i is the phrase for bias. Instead of using big, monolithic convolutions, our method divides processing across several lightweight kernels, enabling the network to effectively extract complex characteristics of nail-fold capillaries while preserving computational efficiency. YOLOv12 uses 7×7 separable convolutions in deeper layers to accurately recognize elongated or convoluted capillary structures without incurring excessive processing costs. These convolutions preserve spatial context with fewer parameters. Table 2 shows the enhancement in YOLOv12 backbone-R-ELAN for detecting nail-fold capillaries.

Table 2: YOLOv12 backbone-R-ELAN for detecting nail-fold capillaries.

Component	Functionality	Innovations in YOLOv12
Backbone-R-ELAN	Extracts detailed, fine- scale features from images of nail-fold capillaries which is crucial for detecting tiny, intricate capillary structures.	The innovations enhance the ability to detect small, detailed features like capillaries while preserving context, even in noisy or low resolution images. These innovations reduce computational cost, making the detection process more efficient.

Source: Authors, (2026).

Multi-scale feature pyramids, which produce feature maps at various resolutions, are used within the backbone to improve the detection of small structures. While lower-resolution maps capture contextual information across greater skin areas, high-resolution maps in the early layers capture fine-grained details of capillaries. Because capillaries can differ in size, density, and orientation, this multi-scale representation is crucial. Thus, YOLOv12's enhanced backbone R-ELAN architecture, which is strengthened by residual aggregation and controlled by the convolutional formulation mentioned above, offers a reliable framework for identifying nail-fold capillaries.

III.3. EXPLAINABLE AI –SALIENCY HEATMAP

Explainable AI (XAI) attempts to overcome the opaque aspect of deep learning models by making their decision-making process interpretable. To ensure reliability and clinical relevance in medical image analysis, such as the identification of nail-fold capillaries, it is essential to comprehend which picture regions contribute to the model's predictions. Saliency heatmaps are a popular XAI technique that effectively highlights the structures the model deems most significant by quantifying the impact of each input pixel on the predicted class. A saliency heatmap mathematically defined as,

$$w = \frac{\partial S_n}{\partial I} \tag{2}$$

In this case, w stands for each pixel's importance weight, and S_n is the score for the particular class n derived from the trained model such as the existence of a nail-fold capillary, and I represents the input image's pixel values. Saliency heatmaps make the small vascular structures that the entire system depends on prominent. These heatmaps make it possible to confirm that the model concentrates on real capillaries rather than unimportant background features by identifying which pixels or small patches contribute most to the classification. This pixel-level interpretability offers a tool for clinical validation and increases trust in the automated detection system. Additionally, saliency heatmaps offer a number of extra advantages when it comes to nail-fold capillary detection:

- Model refinement: Researchers identify possible biases or misclassifications by analyzing the parts of the image the model incorrectly highlights, background noise. This realization enables better dataset selection and model retraining to ensure that the network precisely focuses on actual capillary structures.
- Quality control: Saliency maps serve as a verification step during clinical analysis to ensure that the model's focus is on the nail-fold area and pertinent vascular characteristics rather than irrelevant skin regions. This improves automated capillary detection's dependability prior to producing diagnostic results.
- Human-AI cooperation: Clinicians are able to contrast their own observations of capillary morphology with the saliency maps produced by AI. Clinicians are more confident in the system's predictions because of this alignment between human expertise and AI reasoning.

This explainable AI techniques ensure that the model detects nail-fold capillaries accurately and generates data that doctors are able to comprehend and validate.

IV. RESULT AND DISCUSSION

The proposed approach detects and classifies nail fold capillaries in real-time using YOLO-RELAN into five categories: aberrant, aggregation, blur, hemo, and normal. The model is trained on the ACFD_HT dataset, which provides a diverse collection of high-quality images for robust capillary analysis. This technology helps diagnose diseases like systemic sclerosis by precisely identifying capillary characteristics from high-resolution images using object detection. In order to provide transparency and confidence in clinical applications, the model additionally includes an explainability layer with a saliency heat map that emphasizes the locations in the image that affected the algorithm's decision.

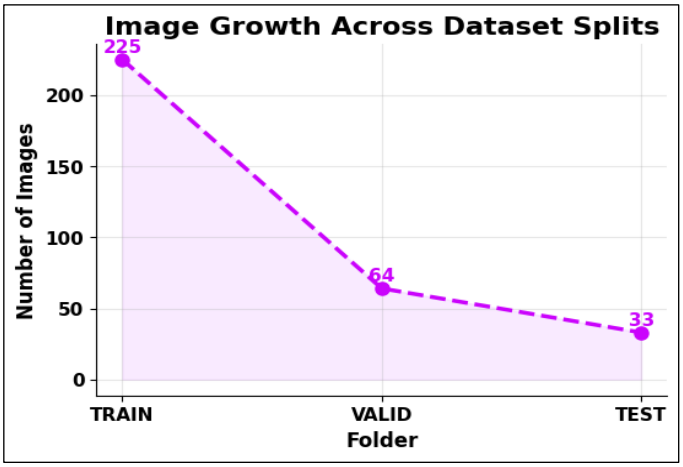


Figure 3: Image growth across dataset splits.
Source: Authors, (2026).

The distribution of images over the three dataset splits such as Train, Validation, and Test is depicted in Figure 3. There are 225 images in the training set, 64 in the validation set, and just 33 in the test set. This illustrates a typical dataset split pattern, in which smaller amounts are set aside for testing and validation to assess performance and generalization, while the majority of the data is used for training to ensure efficient model learning.

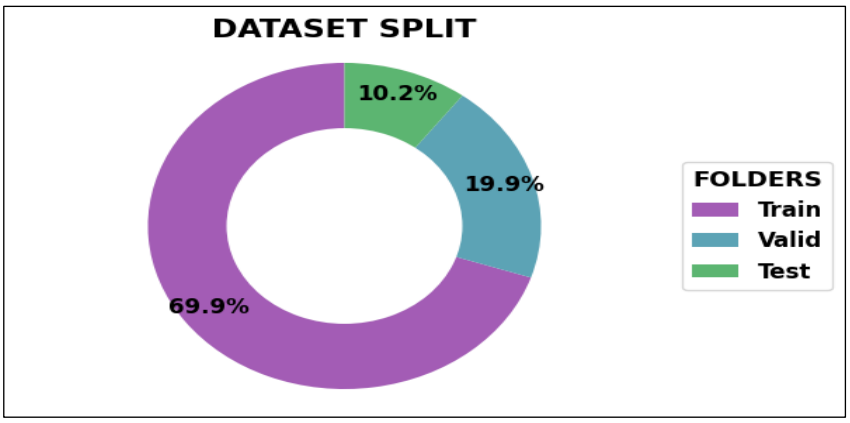


Figure 4: Dataset Split.
Source: Authors, (2026).

The dataset split is depicted in Figure 4, with 69.9% of the photos utilized for training, 19.9% for validation, and 10.2% for testing. While lesser amounts are set aside for performance assessment and final testing, this distribution ensures that the majority of the data enables model learning.

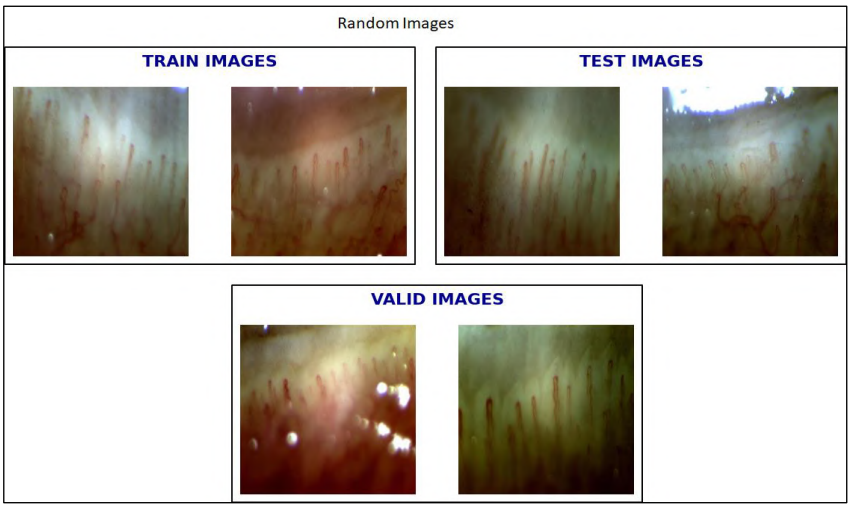


Figure 5: Random images.
Source: Authors, (2026).

Sample images from the training, validation, and testing datasets are displayed in the Figure 5. Clear microscopic images with comparable structural patterns are present in each collection, suggesting consistent data quality across splits. These random samples show that all subsets reflect comparable image properties, ensuring the model's learning and evaluation are balanced.

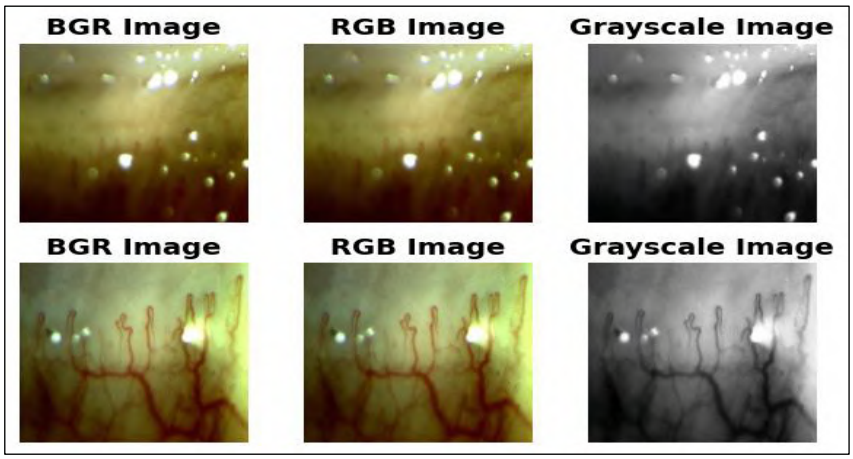


Figure 6: Comparison of BGR, RGB and Grayscale images.
Source: Authors, (2026).

Figure 6 illustrates the visual distinctions between tiny images in BGR, RGB, and grayscale. Grayscale conversion is beneficial for feature extraction and structural analysis since it simplifies the image by simply representing intensity variations, whereas BGR and RGB preserve complete color information.

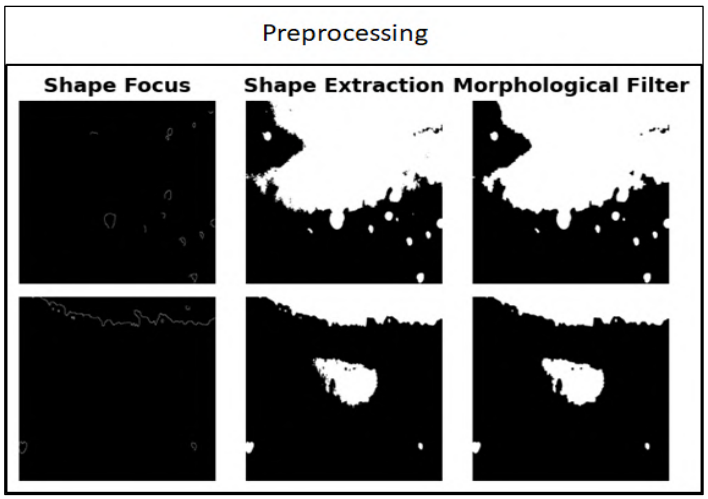


Figure 7: Preprocessing images.
Source: Authors, (2026).

The preprocessing steps, such as shape focus, shape extraction, and morphological filtering, are depicted in Figure 7. By separating pertinent shapes and eliminating noise, these procedures improve the image's structural properties and produce clearer, more defined areas for further analysis.

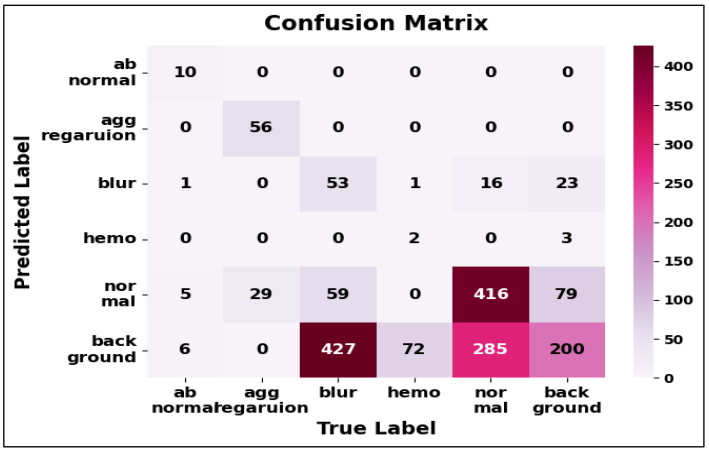


Figure 8: Confusion matrix for YOLOv8.
Source: Authors, (2026).

The confusion matrix displays the performance of a multi-class classification model in six different categories: aberrant, aggregation, blur, hemo, normal, and background in figure 8. Most predictions are focused along the diagonal, particularly for normal (416) and aggregation (56), showing high accuracy in these categories. However, there is significant misclassification between "background" and other classifications such as abnormal (427) and normal (285), indicating that the model struggles to discriminate background data from these categories.

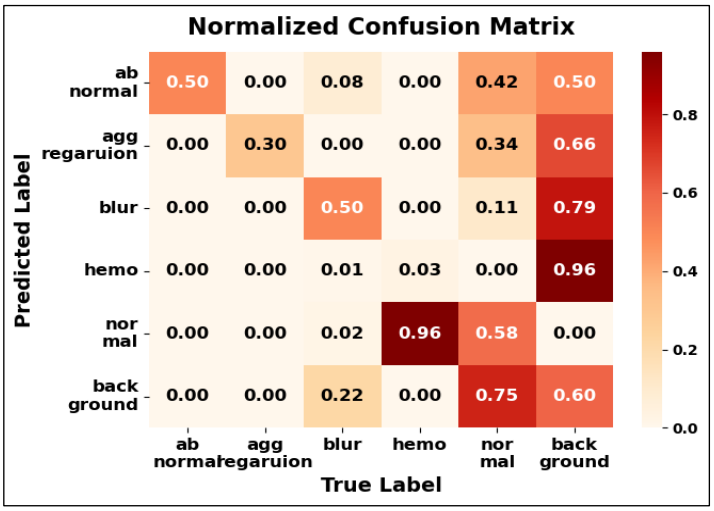


Figure 9: Normalized confusion matrix for YOLOv8.
Source: Authors, (2026).

Figure 9 indicates the normalized confusion matrix which shows the proper categorization for hemo (0.96) and blur (0.79), while background and normal classes display moderate confusion with other categories, indicating that the model performs well in general and needs to improve its ability to differentiate comparable classes.

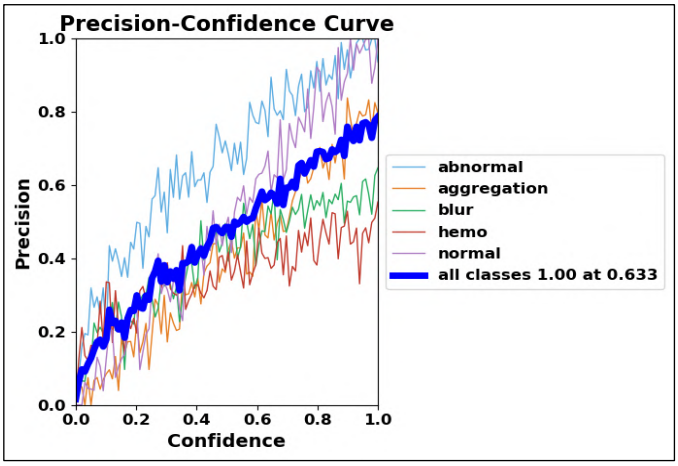


Figure 10: Precision-Confidence curve for YOLOv8.
Source: Authors, (2026).

Figure 10 shows the precision-Confidence Curve across different classes. The x-axis represents the confidence level, which ranges from 0 to 1, while the y-axis denotes precision, which similarly ranges from 0 to one. Each line in the graph represents a separate class: aberrant, aggregation, blur, hemo, and normal. The thick blue line represents the total precision for all classes, with a value of 1.00 at a confidence level of 0.633.

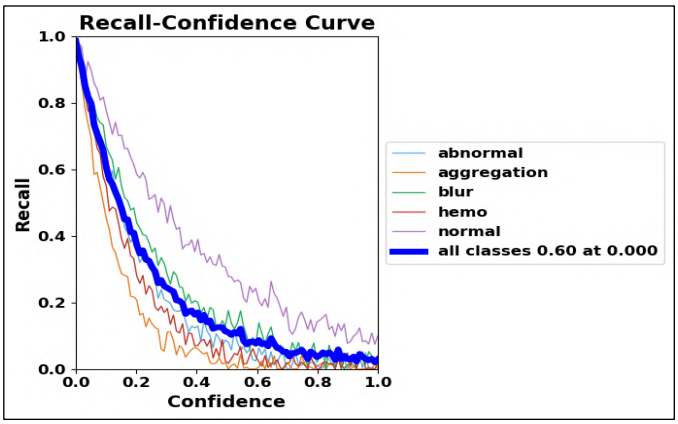


Figure 11: Recall-Confidence curve for YOLOv8.
Source: Authors, (2026).

A Recall-Confidence Curve is displayed in figure 11, showing that recall varies with confidence for various classes. Confidence is represented by the x-axis, and recall is represented by the y-axis. A class is shown by each line: aberrant, aggregation, blur, hemo, and normal. The total recall for all classes is represented by the thick blue line, which has a value of 0.60 at a confidence level of 0.000. Recall generally declines as confidence rises, suggesting that fewer but more accurate predictions are made at increasing confidence levels.

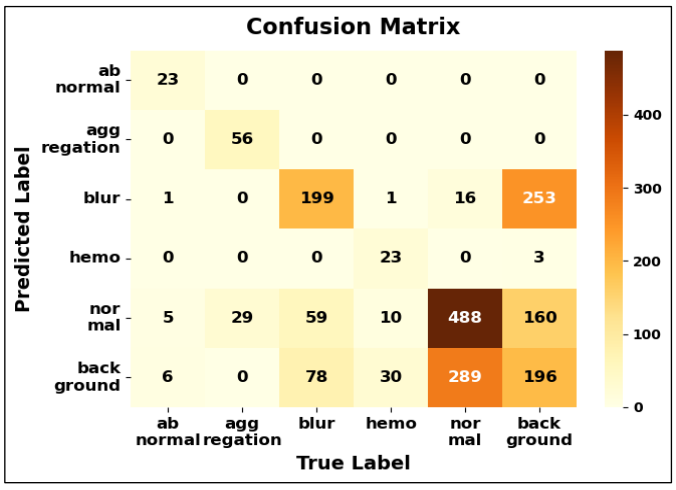


Figure 12: Confusion matrix for YOLOv10.
Source: Authors, (2026).

A confusion matrix depicting a classification model's performance across six classes abnormal, aggregation, blur, hemo, normal, and background is displayed in figure 12. The diagonal cells show samples that have been successfully identified; the normal class has the highest accuracy (488 accurate). Misclassifications, which show some overlap or similarity between these categories, are primarily observed between blur and background classes as well as between normal and background.

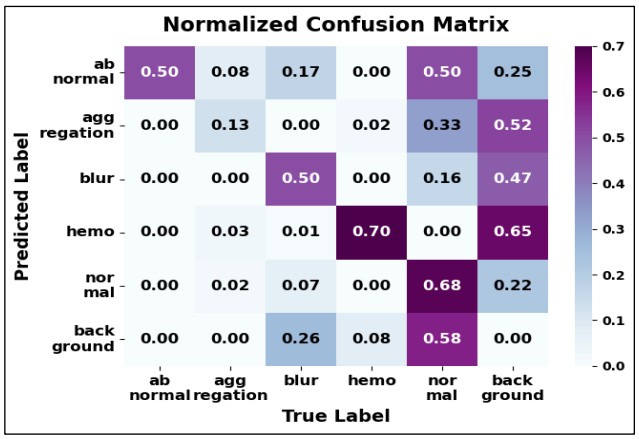


Figure 13: Normalized Confusion matrix for YOLOv10.
Source: Authors, (2026).

The accuracy in which a classification model predicts five categories like abnormal, aggregation, blur, bleeding, and background is displayed in figure 13. It draws attention to the fact that while the model does well for some categories, such as bleeding, it misclassifies others, such as background and abnormal. Prediction accuracy is reflected in color intensity, with darker hues denoting superior performance.

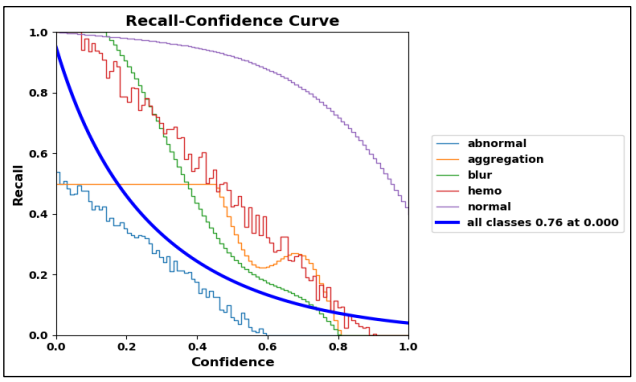


Figure 14: Recall-Confidence curve for YOLOv10.
Source: Authors, (2026).

The connection between model confidence and retrieval for the several classes such as abnormal, aggregation, blur, hemo, and normal is depicted in figure 14. Recall typically declines with increasing confidence, making the model more certain but missing more real cases. The overall performance is summarized by the all classes line, which has an average recall of 0.76 at 0% confidence.

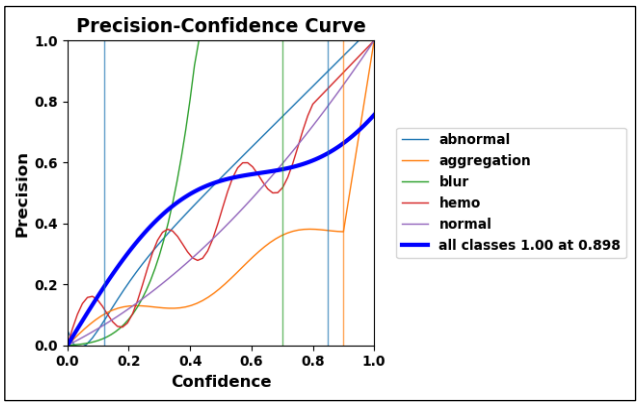


Figure 15: Precision-Confidence curve for YOLOv10.
Source: Authors, (2026).

The precision-confidence curve for the several classes abnormal, aggregation, blur, hemo, and normal is shown in figure 15. As confidence grows, precision typically climbs as well, suggesting more trustworthy forecasts at greater confidence levels. Overall performance is represented by the thick blue line, which indicates that all classes achieve an accuracy of 1.00 at a confidence level of 0.898.

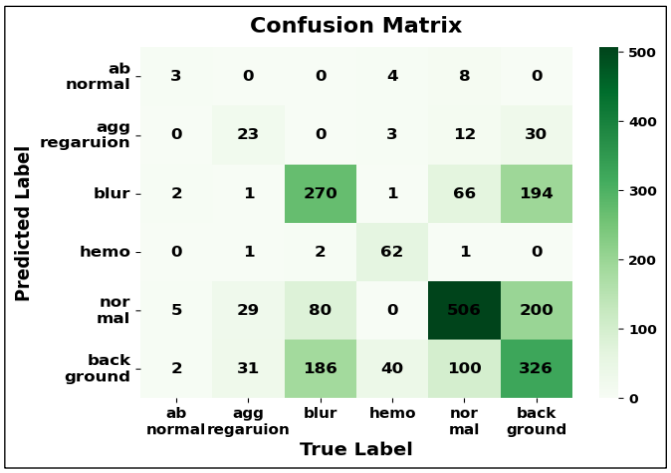


Figure 16: Confusion matrix for YOLOv12.
Source: Authors, (2026).

A classification model's confusion matrix, which shows the accuracy with which it predicted five categories like abnormal, aggregation, blur, hemo, and normal are displayed in Figure 16. Higher values are displayed in darker green in the matrix, which contrasts anticipated and true labels. 270 is the highest score for accurately predicting blur. This matrix aids in assessing the model's accuracy and performance across several classes.

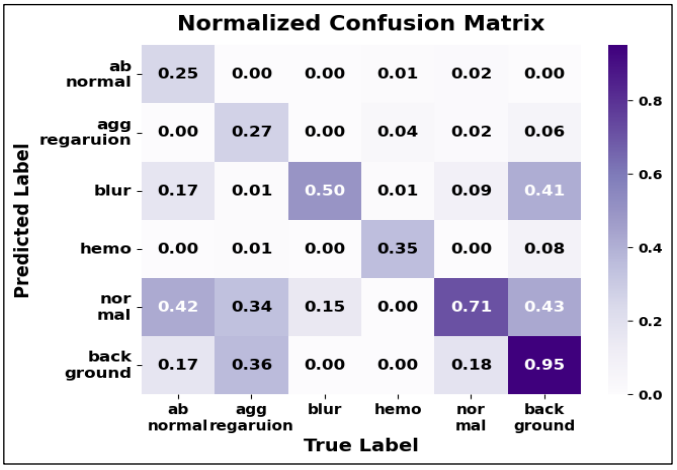


Figure 17: Normalized confusion matrix for YOLOv12.
Source: Authors, (2026).

Figure 17 show the percentage of accurate predictions for each class. Higher proportions are indicated by deeper hues on a scale of 0 to 1. The "background" class, for instance, has a high value of 0.95, indicating precise predictions. By highlighting areas of strong and poor predictions, such as lower values for the abnormal and hemo classes, the matrix aids in evaluating the model's relative performance across classes.

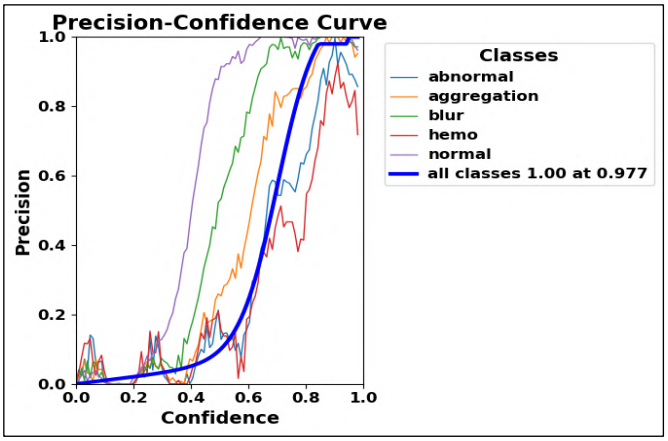


Figure 18: Precision-confident curve for various classes of YOLOv12.
Source: Authors, (2026).

The precision-confidence relationship for five distinct classes such as abnormal, aggregation, blur, hemo, and normal are displayed in Figure 18. The precision for each class is displayed on the y-axis, while the x-axis indicates the confidence level. The blue curve, which reaches a perfect score of 1 at a confidence level of 0.977, shows the overall precision across all classes.

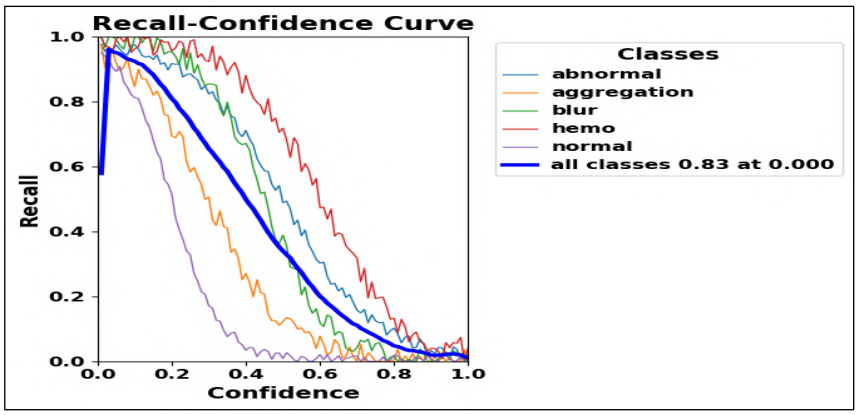


Figure 19: Recall- Confidence curve for different classes of YOLOv12.
Source: Authors, (2026).

The recall-performance for five classes such as abnormal, aggregation, blur, hemo, and normal across various confidence levels is shown in Figure 19. The x-axis displays the degree of confidence, and the y-axis depicts recall. The overall recall for all classes is represented by the blue curve, which begins high and progressively falls as confidence rises before settling at about 0.83 when confidence is zero.

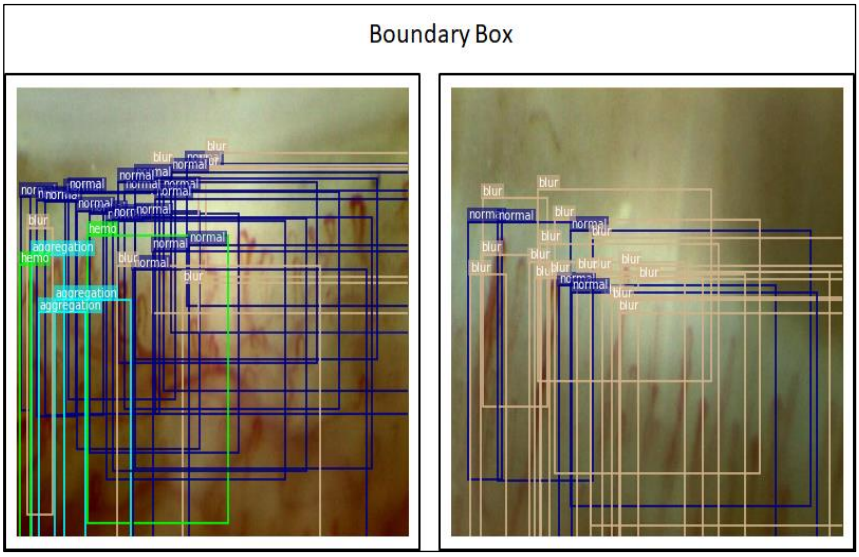


Figure 20: Boundary box.
Source: Authors, (2026).

Two microscopic outlooks Boundary Box are displayed in Figure 20, with labeled bounding boxes delineating various detected locations. The left image includes several overlapping boxes in various types that indicate properties like normal, blur, aggregation, and hemo. The labels in the right image are mostly blurry and have fewer variants. The object detection outputs used to categorize and localize features in digital blood smear images are represented by these bounding boxes.



Figure 21: Image annotations with class labels.
Source: Authors, (2026).

Bounding boxes and class labels are superimposed on a number of sample images in Figure 21. Each bounding box, which is labeled with one of the following classes normal, blur, aggregation, or hemo identifies regions inside the image. The model's predictions for different image segments are shown by the labels and boxes, with some overlapping or inaccurate classifications.

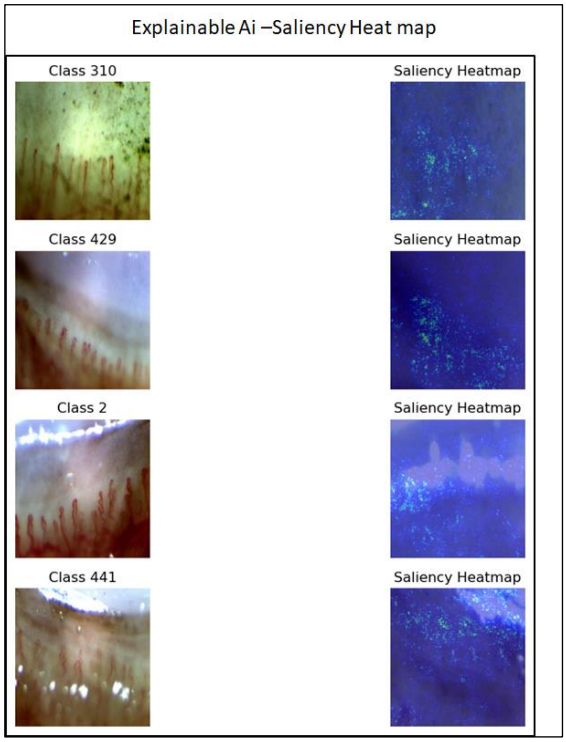


Figure 22: Explainable AI-Saliency heatmap.
Source: Authors, (2026).

Explainable AI-Saliency Heatmaps for four distinct classes are displayed in Figure 22. Every class image on the left has a matching saliency heatmap on the right. Important image regions are highlighted in blue and green hues in the heatmaps, which show the places the AI model concentrated on for categorization. Higher model attention or feature relevance in the decision-making process is represented by brighter patches.

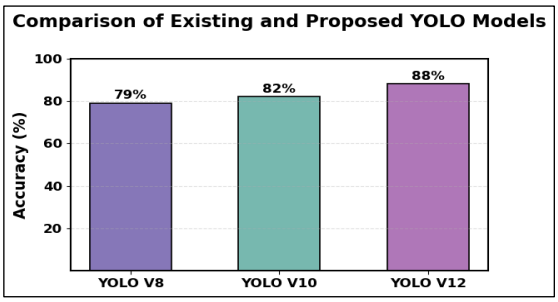


Figure 23: Comparison of existing and proposed YOLO models.
Source: Authors, (2026).

The accuracy of several YOLO models is contrasted in Figure 23. YOLO V8 scores 79%, YOLO V10 improves to 82%, and the suggested YOLO V12 achieves the greatest accuracy of 88%, demonstrating a definite improvement in the model's performance.

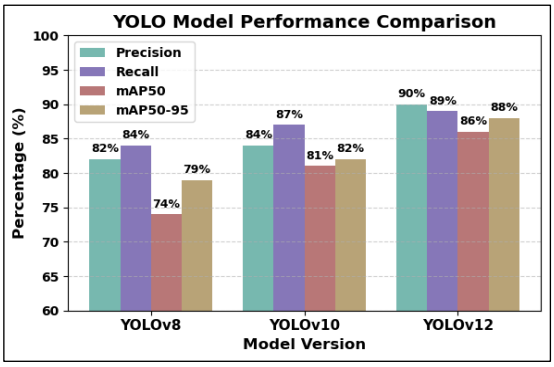


Figure 24: Performance comparison of YOLO models.
Source: Authors, (2026).

The YOLOv8, YOLOv10, and YOLOv12 models are contrasted in Figure 24 according to Precision, Recall, mAP50, and mAP50–95. With 90% precision, 89% recall, 86% mAP50, and 88% mAP50–95, YOLOv12 outperforms YOLOv8 and YOLOv10 in terms of detection accuracy and consistency.

Table 3: Performance metrics of the proposed system.

Model	Accuracy	Precision	Recall	map50	map50-95
PROPOSED	88%	90%	89%	86%	88%

Source: Authors, (2026).

Table 3 shows the proposed approach performs effectively on a number of important metrics. With an accuracy of 88%, it accurately classifies a significant percentage of cases. Additionally, the model has good recall (89%) and precision (90%), indicating that it is both successful in detecting the majority of true positives and accurate in its positive predictions. At an interaction threshold of 0.50, the mean Average Precision (mAP50) is 86%; at different interaction thresholds, the mAP50-95 ranges from 0.50 to 0.95, reaching 88%.

Table 4: Comparative analysis of accuracy for various models.

Model	**Accuracy**
YOLOv5 [21]	85.2 %
CNN [24]	86 %
ResNet [25]	87 %
PROPOSED	88 %

Source: Authors, (2026).

A comparison of model accuracy for recognizing items and categorization is shown in table 4. With an accuracy of 85.2%, the YOLOv5 model outperforms CNN with 86% and ResNet with 87%. When compared to other deep learning architectures, the suggested model achieves the greatest accuracy of 88%, indicating higher feature extraction and detection performance.

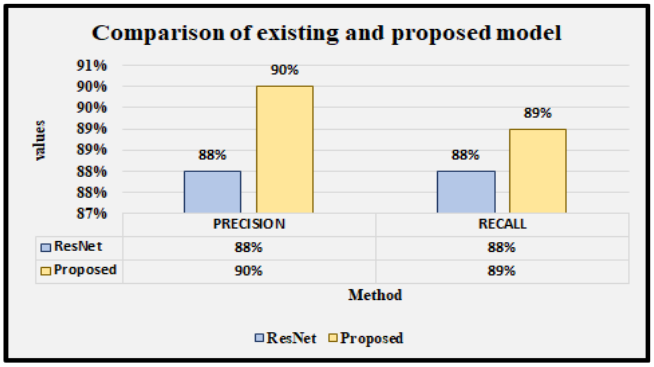


Figure 25: Comparison of existing and proposed model.
Source: Authors, (2026).

The precision and recall levels of the proposed model and the ResNet model are compared in Figure 25. The proposed approach outperforms ResNet, which records 88% for both measures, with 90% precision and 89% recall. This suggests that the proposed framework outperforms the current ResNet architecture in terms of feature identification and classification accuracy and dependability.

V. CONCLUSION

The proposed method effectively combines deep learning, explainable AI, and sophisticated preprocessing methods for the precise and comprehensible identification of nail-fold capillaries. The technique improves the visibility of tiny vascular features that are essential for analysis by immediately preprocessing the input image using shape-focused extraction and morphological filtering. With the R-ELAN backbone, the YOLOv12 model effectively locates and detects nail-fold capillaries in the processed images, producing accurate boundary boxes surrounding the identified areas. Saliency heatmaps are an explainable AI component that emphasizes the particular image regions impacting model predictions, ensuring transparency and clinical dependability. In addition to achieving strong detection performance, the complete approach ensures interpretability and reliability, which are essential for real-world use in clinical and diagnostic applications. The proposed approach achieves the highest accuracy of 88%, 90% of precision, 89% of recall, 86% of map50 and 88% of map50-95.

VI. AUTHOR'S CONTRIBUTION

Conceptualization: Santhoshkumar S P, Parvathi R, Sivaprakash P, Vimala Ithayan J, Dilip Charaan R M[5], Vijayanandh T.
Methodology: Santhoshkumar S P, Parvathi R, Sivaprakash P, Vimala Ithayan J, Dilip Charaan R M[5], Vijayanandh T.
Investigation: Santhoshkumar S P, Parvathi R, Sivaprakash P, Vimala Ithayan J, Dilip Charaan R M[5], Vijayanandh T.
Discussion of results: Santhoshkumar S P, Parvathi R, Sivaprakash P, Vimala Ithayan J, Dilip Charaan R M[5], Vijayanandh T.
Writing – Original Draft: Santhoshkumar S P, Parvathi R, Sivaprakash P, Vimala Ithayan J, Dilip Charaan R M[5], Vijayanandh T.
Writing – Review and Editing: Santhoshkumar S P, Parvathi R, Sivaprakash P, Vimala Ithayan J, Dilip Charaan R M[5], Vijayanandh T.
Resources: Santhoshkumar S P, Parvathi R, Sivaprakash P, Vimala Ithayan J, Dilip Charaan R M[5], Vijayanandh T.
Supervision: Santhoshkumar S P, Parvathi R, Sivaprakash P, Vimala Ithayan J, Dilip Charaan R M[5], Vijayanandh T.
Approval of the final text: Santhoshkumar S P, Parvathi R, Sivaprakash P, Vimala Ithayan J, Dilip Charaan R M[5], Vijayanandh T.

VII. REFERENCES

[1] M. Ebadi Jalal, O. S. Emam, C. Castillo-Olea, B. García-Zapirain, and A. Elmaghraby, “Abnormality detection in nailfold capillary images using deep learning with EfficientNet and cascade transfer learning”, Scientific Reports, vol. 15, no. 1, pp. 2068, 2025.

[2] H.T.P. Nguyen and H. Jeong, “Automated Morphology Detection of Nail-Fold Capillaries Through Enhanced Object Detection Network”, IEEE Access, 2024.

[3] M. Kim, “Nail fold capillaroscopy as a potential tool to evaluate breast tumor”, Journal of Analytical Science and Technology, vol. 15, no. 1, pp. 35, 2024.

[4] P. M. Jesi, S. Kamatchi, and D. Madhivadhani, “HRSHO: A hybrid rain optimized spotted hyena optimizer for efficient feature selection in CNN-based sinusitis classification”, Biomedical Signal Processing and Control, vol. 87, pp.105441, 2024.

[5] M. Pakbin, H. S. MARJANEH, and S. R. Najafizadeh, “Quantitative Nail Fold Capillary Blood Flow Using Capillaroscopy System and ImageJ Software in Healthy Individuals”, Frontiers in Biomedical Technologies, 2022.

[6] P. C. Hsu, P. Y. Liao, S. W. Huang, H. H. Chang, J. Y. Chiang, and L. C. Lo, “Nailfold capillary abnormalities as indicators of diabetic nephropathy progression: a cross-sectional study in type 2 diabetes”, Annals of Medicine, vol. 57, no. 1, pp. 2458766, 2025.

[7] M. Mahajan, T. Kaur, K. Singh, and B. B. Mahajan, “Evaluation of nail fold capillaroscopy changes in patients with diabetic retinopathy and healthy controls, and its correlation with disease duration, HbA1c levels and severity of diabetic retinopathy: An observational study”, Indian Journal of Dermatology, Venereology and Leprology, vol. 90, no. 6, pp. 782-788, 2024.

[8] L. Arya, Y. K. Sharma, S. Nayak, J. Sivakumar, “Comparative Evaluation of Deep Learning Models in Alzheimer’s Disease Diagnosis”, Procedia Computer Science, vol. 258, pp. 2352-2361, 2025.

[9] K. Miyoshi, M. Chikamori, T. Ando, K. Nakata, T. Aoyama, Y.T. Matsunaga, and T. Yamauchi, “Quantitative image analysis of nailfold capillaries during an in-hospital education program for type 2 diabetes or obesity”, Microvascular Research, pp.104830, 2025.

[10] J. Fan, J. Cai, and S. Chen, “Fingernail analysis in diagnosis and management of diabetes mellitus,” Clinica Chimica Acta, pp. 120490, 2025.

[11] M. L. Forst, G. Rincon, J. H. Levy, D. N. Cornfield, S. R. Quake, “An inflatable ‘finger-lock’for stabilizing nailfold capillary videos and modulating blood flow velocities”, medRxiv, pp. 2025-02, 2025.

[12] H. Yin, Y. Wu, P. Guo, J. Luo, J. Lin, B. Zhou, Q. Ye, L. Lin, H. Li, D. Zou, and X. Li, “Panoramic Nailfold Flow Velocity Measurement Method Based on Enhanced Plasma Gap Information”, Journal of Imaging Informatics in Medicine, pp. 1-16, 2025.

[13] S.R. Gadu, C.S. Potala, “Advancements in Imaging Techniques for Accurate Identification of VCF in Patients with Scoliosis”, In International Conference on Internet of Things and Connected Technologies, pp. 233-244. Singapore: Springer Nature Singapore, 2023.

[14] G.A. Kağızmanlı, T. Aydın, K.Y. Acinikli, R. İşgüder, Z.K. Karabacak, K. Demir, E. Böber, S.E. Ünsal, and A. Abacı, “Nailfold Capillaroscopy: A Non-Invasive Tool for Early Detection of Microvascular Alterations in Children with Type 1 Diabetes Mellitus”, J. Clin. Res. Pediatr. Endocrinol, 2025.

[15] A. Assialioui, C. Marco-Pascual, V. Torrente-Segarra, R. Domínguez, N. Santos, J. Peñafiel, X. Juanola, M. Povedano, I. Ferrer, “Microvascular abnormalities in skin capillaries of individuals with amyotrophic lateral sclerosis”, Scientific reports, vol. 14, no. 1, pp. 24648, 2024.

[16] A. Asaithambi and V. Thamilarasi, “Classification of lung chest X-ray images using deep learning with efficient optimizers”, In 2023 IEEE 13th Annual Computing and Communication Workshop and Conference (CCWC), pp. 0465-0469. IEEE, 2023.

[17] A. Corrado, N. Mansueto N, M. Correale, V. Rella, L. Tricarico, A. Altomare, N. D. Brunetti, F.P. Cantatore, and C. Rotondo, “Flow Mediated Dilation in Systemic Sclerosis: Association with clinical findings, capillaroscopic patterns and endothelial circulating markers”, Vascular Pharmacology, vol. 154, pp. 107252, 2024.

[18] L.R.L. Green, “Clinical presentation and impact of calcinosis in Systemic Sclerosis. An introduction of ultrasound as a valuable outcome measure”, PhD diss., University of Leeds, 2024.

[19] Y. Norimatsu, T. Fukasawa, Y. Kabeya, S. Toyama, K.M. Matsuda, A. Kuzumi A, A. Yoshizaki-Ogawa, H. Ichimura, S. Yonezawa, H. Nakano, and S. Sato, “The number of nail fold capillaries and nail fold bleedings reflects the clinical manifestations of systemic sclerosis”, Journal of Investigative Dermatology, vol. 145, no. 4, pp. 959-961, 2025.

[20] L. Zhao, J. Tang, D. Chen, X. Liu, Y. Zhou, Y. Shi, G. Wang, and Y. Wang, “A Comprehensive Dataset and Automated Pipeline for Nailfold Capillary Analysis”, In 2024 IEEE International Symposium on Biomedical Imaging (ISBI), pp. 1-5. IEEE, 2024.

[21] H. Yin, Z. Wu, A. Huang, J. Luo, J. Liang, J. Lin, Q. Ye, M. Xie, C. Ye, X. Li, and Y. Wu, “Automated nail-fold capillary density measurement method based on improved YOLOv5”, Microvascular research, vol. 150, pp. 104593, 2023.

[22] V. Taormina, G. Raso, V. Gentile, L. Abbene, A. Buttacavoli, G. Bonsignore, C. Valenti, P. Messina, G. A. Scardina, and D. Cascio, “Automated stabilization, enhancement and capillaries segmentation in videocapillaroscopy”, Sensors, vol. 23, no. 18, pp. 7674, 2023.

[23] S. Chen, D. Wei, S. Gu, and Z. Yang, “Nailfold capillary segmentation based on U-Net and attention mechanism”, In Proceedings of the 2023 3rd International Conference on Bioinformatics and Intelligent Computing, pp. 337-343, 2023.

[24] C. Filippini, D. Cardone, D. Perpetuini, A.M. Chiarelli, G. Gualdi, P. Amerio, and A. Merla, “Convolutional neural networks for differential diagnosis of raynaud’s phenomenon based on hands thermal patterns”, Applied Sciences, vol. 11, no. 8, pp. 3614, 2021.

[25] I. Indriani, “Nail Disease Classification Using Graph Attention Network (GAT) and Resnet”, Ranah Research: Journal of Multidisciplinary Research and Development, vol. 7, no. 4, pp. 2522-2529, 2025.

Journal of Engineering and Technology for Industrial Applications

ISSN ONLINE: 2447-0228

ITEGAM-JETIA

Manaus, v.12 n.60, p.884-889 July/August, 2026.
DOI: https://doi.org/10.5935/jetia.v12i60.3487

RESEARCH ARTICLE OPEN ACCESS

LEARNING DISABILITY DIAGNOSIS USING ADVANCED PREPROCESSING AND ENSEMBLE CLASSIFICATION TECHNIQUES

Anu P J*[1], K. Ranjith Singh[2]

[1] Research Scholar, Department of Computer Science, Karpagam Academy of Higher Education, Coimbatore, India.
[2]Assistant Professor & Research Guide, Department of Computer Science, Karpagam Academy of Higher Education, Coimbatore.
[1, 2]Technology and Engineering, Kibabii University, P.O BOX 1699 - 50200, Bungoma, Kenya.

[1]http://orcid.org/0009-0002-6245-297X, [2]http://orcid.org/0000-0003-2651-2509

E-email: * anujohnson123@gmail.com, ranjithsingh.koppaiyan@kahedu.edu.in

ARTICLE INFO

Article History
Received on: January 30, 2026
Reviewed on: March 01, 2026
Accepted on: July 01, 2026
Published on: July 31, 2026

Keywords:
Learning Disability,
Early Diagnosis,
SMOTE,
Stacking Ensemble,
Data Preprocessing.

ABSTRACT

Early detection of learning disabilities (LD) is essential for prompt intervention, yet it is still difficult because LD signs are subtle and variable. Previous research frequently ignores the significance of class imbalance and data preprocessing, leading to skewed or inadequate forecasts. This paper suggests a hybrid machine learning framework for LD diagnosis that combines several classification algorithms with thorough preprocessing, such as feature scaling, SMOTE-based class balance, missing value management, outlier removal, and feature selection. The effectiveness of a stacking ensemble that incorporates the advantages of Random Forest, XGBoost, LightGBM, and a Multilayer Perceptron is assessed. The efficiency of combining improved preprocessing with ensemble learning is demonstrated by the experimental findings, which show that the stacking ensemble greatly outperforms individual classifiers in terms of accuracy, recall, F1-score, and ROC-AUC. The framework facilitates prompt educational support and intervention by offering a strong and dependable instrument for early LD detection. The summary must be written in a single paragraph. The length of the paper must be 8 to 14 pages, single space, 10 Times New Roman, including the Abstract (Between 150 and 200 words), and keywords (Between 3 and 5 words). The yellow highlighted parts should not be modified by the authors. The names, affiliations, ORCIDs and e-mails of the authors must be sent in a separate text file. The ORCID number is mandatory for all authors, if you do not have it, please register at: https://orcid.org/signin.

Copyright ©2026 by authors and Galileo Institute of Technology and Education of the Amazon (ITEGAM). This work is licensed under the Creative Commons Attribution International License (CC BY 4.0).

I. INTRODUCTION

The application of machine learning techniques for the detection of learning disabilities (LD) has been investigated in a number of research [1]. Conventional methods frequently rely on single classifiers that are directly applied to unprocessed educational data, such as Random Forests, Decision Trees, or Support Vector Machines [2]. Although these approaches have had some success, they typically ignore the crucial role of preprocessing, which includes controlling class imbalance, feature selection, data cleaning, and normalization. As a result, these methods frequently misclassify students with LD and have limited practical usefulness because they are skewed toward the majority class. More sophisticated algorithms like XGBoost and LightGBM have been used in recent research, showing better results in classification tests. Nevertheless, real-world imbalances and noisy data, which are prevalent in school records, are often overlooked by this research since they usually use small or balanced datasets. Furthermore, the majority of research concentrates on individual classifiers rather than on ensemble approaches that integrate the complementing advantages of several models. The suggested method overcomes these constraints in two steps: first, a strong preprocessing pipeline guarantees data quality, uses SMOTE to balance class distribution, and chooses the most pertinent features. Second, to improve predictive accuracy, robustness, and generalization, an ensemble-based classification model stacks Random Forest, XGBoost, LightGBM, and Multilayer Perceptron. By offering a thorough, useful, and effective method for early LD detection, this strategy closes the gap in the body of existing literature [3].

II. METHODOLOGY

The suggested framework for identifying learning disabilities (LDs) is intended to offer a reliable and precise method for early detection. A thorough preprocessing pipeline and an ensemble-based classification model make up its two primary phases. The approach uses a variety of machine learning approaches to produce high prediction performance while resolving common issues in educational datasets, such as noise, missing data, and class imbalance.

II.1 GATHERING AND CHARACTERIZING DATA

The study's dataset consists of classroom behavioral observations, cognitive tests, and student academic records. The target variable, LD, is binary, with 1 denoting the existence of a learning disability and 0 denoting its absence. Among the features are:

- Academic scores: performance in reading, writing, and math
- Behavioral indicators: levels of engagement, participation, and attention in the classroom.
- Records of attendance: quantity of absences or tardiness

Preprocessing is essential to ensuring the trustworthiness of future analyses since the dataset reflects the real-world unpredictability of student performance. The models are able to capture behavioral and environmental aspects related to learning disabilities in addition to academic inadequacies because to this multidimensional data.

II.2 PIPELINE FOR PREPROCESSING

Machine learning performance may suffer from incomplete, inconsistent, and unbalanced data found in educational datasets. These issues are methodically handled by the pretreatment pipeline:

1. Missing Value Handling: The mean is used to impute missing values for numerical features. By doing this, bias caused by incomplete records is avoided and all cases contribute to model training.
2. Outlier Removal: Z-score analysis is used to identify and eliminate extreme values that may result from data input mistakes or extraordinary circumstances. This enhances stability and avoids biased model training.
3. Feature Scaling: Standardization converts features to a standard scale with a unit variance and zero mean. To avoid features with wide ranges controlling the learning process, this is especially crucial for distance-based or gradient-based models, including MLP and ensemble techniques.
4. Class Balancing (SMOTE): Learning disability datasets frequently exhibit an imbalance, with much fewer LD cases than non-LD instances. By creating artificial samples for the minority class, the Synthetic Minority Over-sampling Technique (SMOTE) lessens class bias and increases the model's sensitivity to LD instances [4], [5].
5. Feature Selection: The SelectKBest approach with chi-square scoring is used to improve model efficiency and decrease overfitting. This ensures that only pertinent academic, behavioral, and attendance data contribute to model learning by selecting the most informative features [6].

The preprocessing stage is critical to enhance data quality, ensure balanced representation of LD cases, and reduce noise, thereby enabling accurate and reliable model predictions. The Figure 1. shows the overall concept of the study.

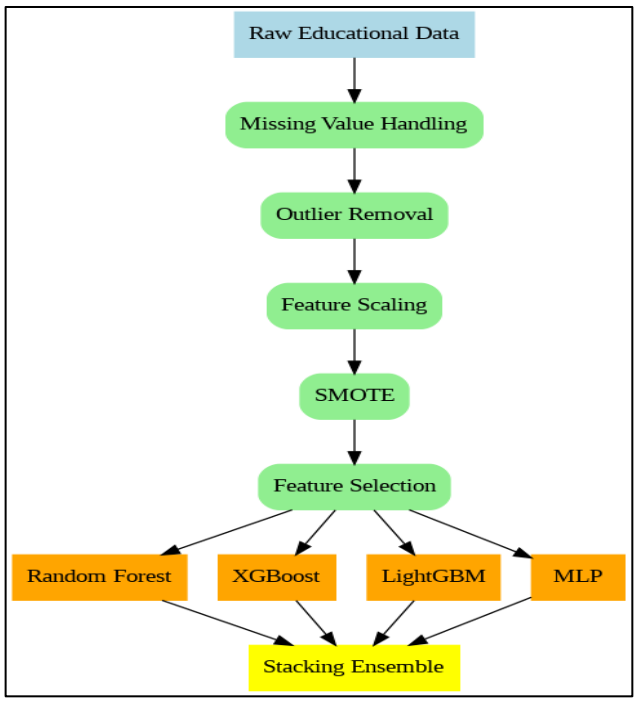


Figure 1: Methodology.
Source: Authors, (2026).

II.3 CLASSIFICATION MODELS

Following preprocessing, a number of machine learning methods are trained and assessed to see how well they recognize LD:

- Random Forest (RF): A strong group of decision trees that manages non-linear interactions and uses bootstrap aggregation to lessen overfitting. Because of its interpretability and stability, RF is used as a baseline [7].
- XGBoost: An iterative gradient boosting approach that lowers bias and variance to enhance model performance. XGBoost is renowned for its strong prediction accuracy and ability to handle noisy datasets [8].
- LightGBM: A high-performance gradient boosting model that is efficient and quick, especially when working with big datasets. Because LightGBM uses histogram-based learning, it is very accurate and computationally efficient [9].
- Multilayer Perceptron (MLP): A feedforward neural network that can recognize intricate non-linear patterns in the data is called a multilayer perceptron (MLP). MLP complements the ensemble by capturing relationships between features that tree-based approaches could miss [10].

II.4 CLASSIFICATION BASED ON ENSEMBLES

A stacking ensemble is created in order to capitalize on the advantages of several models:

- Base Learners: MLP, Random Forest, XGBoost, and LightGBM
- Logistic Regression: as a Meta-Learner

The logistic regression meta-learner in the stacking ensemble aggregates the predictions made by each base learner. This strategy ensures that the ensemble performs better than any single classifier by lowering individual model errors, reducing overfitting, and improving generalization performance.

II.5 EVALUATION METRICS

Model performance is evaluated using a comprehensive set of metrics to capture multiple aspects of predictive ability. Accuracy measures the overall proportion of correctly classified instances, while precision evaluates the ability to correctly identify students with learning disabilities among those predicted as positive. Recall (sensitivity) assesses how effectively all actual LD cases are identified, and the F1-Score, as the harmonic mean of precision and recall, balances false positives and false negatives. The ROC-AUC (Area Under the Receiver Operating Characteristic Curve) quantifies the model's ability to distinguish between LD and non-LD cases across thresholds [11], [12]. For imbalanced datasets, PR-AUC (Area Under the Precision-Recall Curve) is particularly useful, highlighting the trade-off between precision and recall for the minority class. Matthews Correlation Coefficient (MCC) provides a robust single-value measure considering true/false positives and negatives, ranging from -1 (inverse prediction) to +1 (perfect prediction). Balanced accuracy, the average of recall and specificity, accounts for class imbalance more effectively than raw accuracy, while Cohen's Kappa measures agreement between predictions and actual labels beyond chance. Finally, specificity (true negative rate) indicates the ability to correctly identify non-LD students, complementing recall and ensuring a complete evaluation of model performance.

III. RESULTS AND DISCUSSION

Random Forest (RF), XGBoost, LightGBM, Multilayer Perceptron (MLP), and a stacking ensemble that combines these classifiers were used to assess the suggested framework on the preprocessed dataset. To reduce class imbalance, all models were trained using data that had been balanced using SMOTE. The performance metrics for each model are compiled in Table 1.

Table 1: Comparison of evaluation metrices across models.

Model	Accuracy	Precision	Recall	F1-Score	ROC-AUC	PR-AUC	MCC	Balanced Accuracy	Specificity
Random Forest	0.87	0.85	0.84	0.84	0.91	0.88	0.71	0.86	0.88
XGBoost	0.89	0.88	0.87	0.87	0.93	0.90	0.75	0.88	0.90
LightGBM	0.90	0.89	0.88	0.88	0.94	0.91	0.77	0.89	0.91
MLP	0.88	0.86	0.86	0.86	0.92	0.89	0.73	0.87	0.89
Stacking Ensemble	0.92	0.91	0.90	0.90	0.96	0.93	0.81	0.91	0.92

Source: Authors, (2026).

III.1 ANALYSIS OF RESULTS

III.1.1 Impact of SMOTE and Preprocessing

Model stability and predictive performance were enhanced by the application of preprocessing, which included feature selection, scaling, SMOTE, missing value handling, and outlier elimination. Specifically, SMOTE improved the models' sensitivity to the minority LD class, raising F1-scores and recall for all classifiers [13]. The impact of using SMOTE (Synthetic Minority Over-sampling Technique) on an unbalanced dataset of students with and without learning difficulties is depicted in Figure 2. The orange dots show the initial minority class (LD students), emphasizing the class imbalance, whereas the blue dots show the majority class (non-LD students), which predominates the original dataset. The synthetic LD samples produced by SMOTE, which interpolate between pre-existing minority cases, are shown by the red "x" marks. SMOTE balances the dataset by include these artificial points, which improves the LD class's representativeness. This allows machine learning models to learn patterns from both classes more effectively, reducing bias towards the majority class and improving the accuracy and reliability of LD predictions [14].

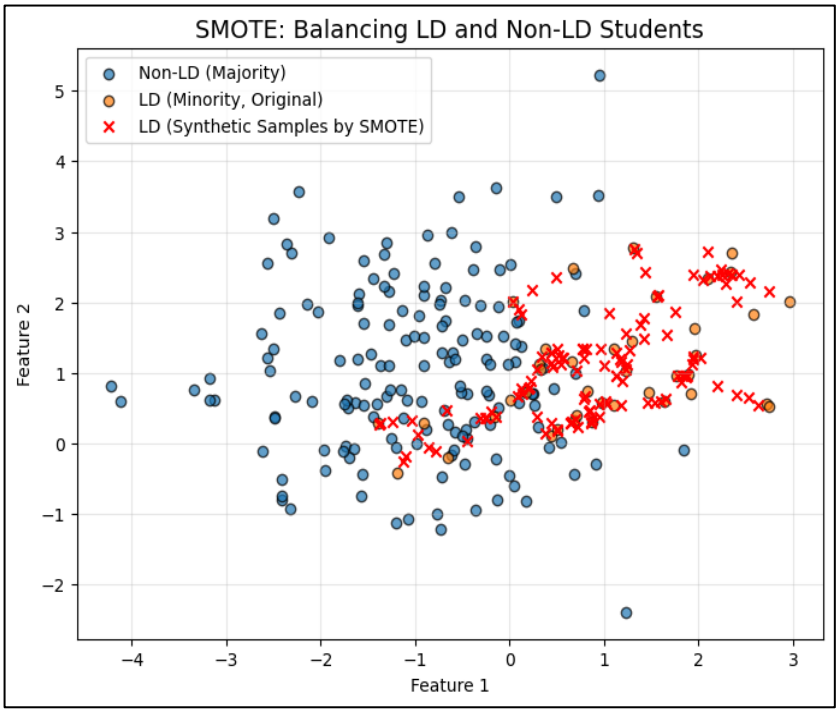


Figure 2: Effect of SMOTE on Balancing LD and Non-LD Students.
Source: Authors, (2026).

III.1.2 Random Forest Baseline

RF was a dependable baseline because it performed well on the preprocessed dataset. Its tree-based structure did a good job of handling non-linear relationships, although it had some trouble capturing intricate patterns.

III.1.3 Advanced Models

By iteratively lowering bias and variance, XGBoost outperformed RF in accuracy.Because of its speedier processing and efficient gradient boosting, LightGBM greatly enhanced performance. Although MLP was somewhat susceptible to hyperparameter adjustment and data fluctuation, it was able to capture intricate non-linear correlations.

III.1.4 Stacking Ensemble:

When compared to individual classifiers, the Stacking Ensemble performs better on all evaluation metrics. The ensemble outperformed any single model by combining the benefits of each model and reducing its drawbacks. It outperforms Random Forest (0.87), XGBoost (0.89), LightGBM (0.90), and MLP (0.88) with an accuracy of 0.92, suggesting a more dependable categorization overall. By using logistic regression as a meta-learner, the ensemble effectively leveraged complementary patterns found by tree-based and neural network models. The ensemble has the highest recall (0.90) and precision (0.91), indicating that it can accurately identify students with learning impairments while reducing false positives. Its balanced and discriminative performance, especially in imbalanced datasets, is confirmed by the F1-score of 0.90 and the greatest ROC-AUC (0.96) and PR-AUC (0.93). Furthermore, the ensemble consistently distinguishes both LD and non-LD students, according to the Matthews Correlation Coefficient (0.81), balanced accuracy (0.91), and specificity (0.92). By utilizing the complementing strengths of several classifiers to generate the highest overall accuracy, recall, F1-score, and ROC-AUC, this illustrates the advantages of ensemble learning for LD prediction. In Figure 3 the Random Forest, XGBoost, LightGBM, MLP, and Stacking Ensemble machine learning models are compared in this table using important evaluation metrics such as accuracy, precision, recall, F1-score, ROC-AUC, PR-AUC, MCC, balanced accuracy, and specificity. It is possible to directly evaluate how well each model detects learning disorders and manages class imbalance because each row displays the model's performance across these metrics.

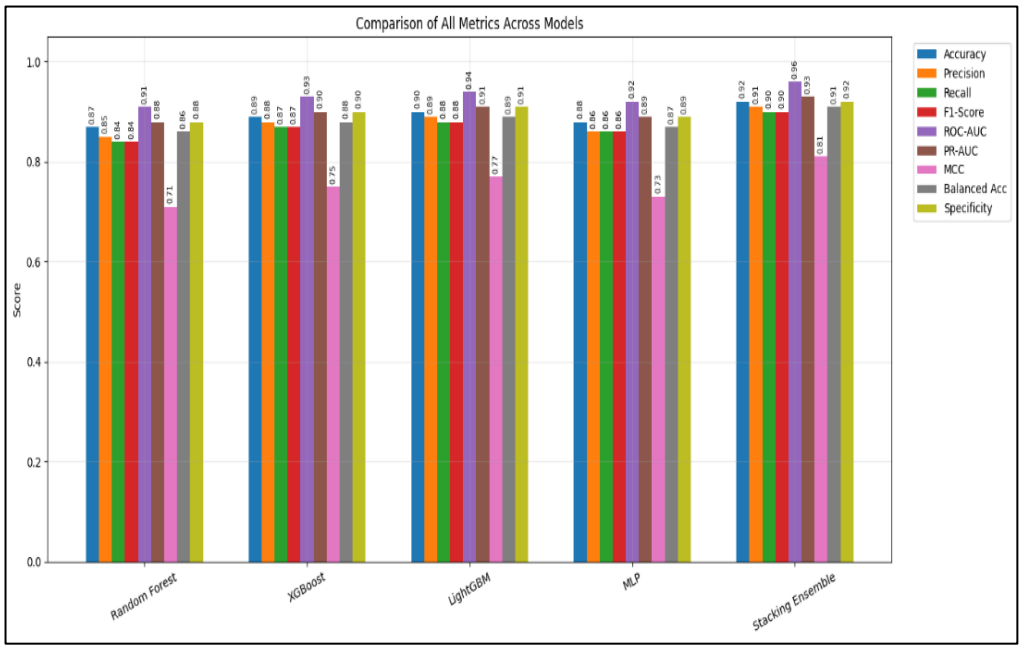


Figure 3: Comparison of all metrices across the model.
Source: Authors, (2026).

The important metrics for assessing model performance in unbalanced datasets, such as learning disability prediction, are ROC-AUC, PR-AUC, and MCC [15]. While PR-AUC focuses on accurately recognizing minority LD cases, ROC-AUC evaluates the model's total discriminative abilities, and MCC offers a balanced assessment taking into account all prediction outcomes. When combined, they provide a thorough understanding of precision and dependability, emphasizing the usefulness of models like the stacking ensemble. Figure 4. shows the representation of ROC-AUC, PR-AUC, and MCC [16].

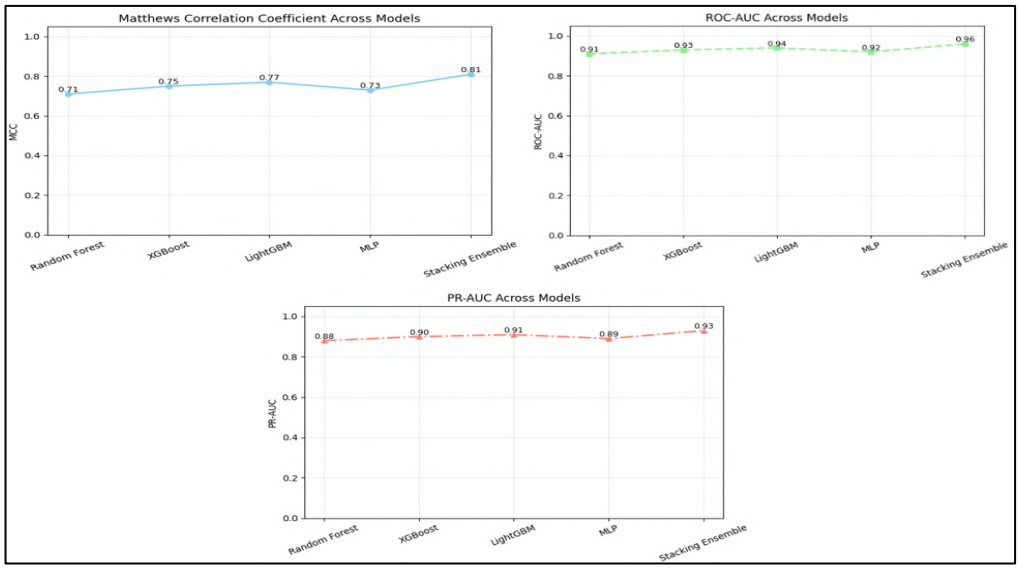


Figure 4: Key Performance Metrics for LD Prediction Models.
Source: Authors, (2026).

IV. CONCLUSION

This study demonstrates that a two-stage machine learning framework—combining robust preprocessing with ensemble-based classification—effectively identifies students with learning disabilities (LD) in educational datasets. Model performance is greatly enhanced by handling noisy and imbalanced data using methods like SMOTE and feature selection. Advanced models like XGBoost, LightGBM, and Multilayer Perceptrons improve predictive accuracy, while Random Forest provides a solid baseline. Stacking ensembles, which use complementary classifiers, produce the greatest overall results. Early, accurate, and scalable LD detection is made possible by the suggested framework, allowing for prompt interventions and assistance for kids who are at risk. To increase prediction robustness, the framework can be expanded by adding more cognitive, behavioral, and demographic characteristics. Temporal or sequential patterns in student data may be captured by deep learning architectures like LSTM or attention-based models. Additionally, incorporating explainable AI techniques can give instructors useful insights, increasing the system's transparency and interpretability. Lastly, the method can be extended to different educational settings and datasets, facilitating more extensive uses in individualized education planning and early learning support.

V. AUTHOR'S CONTRIBUTION

Conceptualization: Anu P. J and K. Ranjith Singh.
Methodology: Anu P. J and K. Ranjith Singh.
Investigation: Anu P. J and K. Ranjith Singh.
Discussion of results: Anu P. J and K. Ranjith Singh.
Writing – Original Draft: Anu P. J.
Writing – Review and Editing: Anu P. J and K. Ranjith Singh.
Resources: Anu P. J.
Supervision: K. Ranjith Singh.
Approval of the final text: Anu P. J and K. Ranjith Singh.

VI. ACKNOWLEDGMENTS

Special thanks are extended to Karpagam Academy of Higher Education, Coimbatore, India for giving guidelines for this research. This research was not funded.

VII. REFERENCES

[1] Joshi, Foram et al. "Deep learning classification of reading disability with regional brain volume features." NeuroImage vol. 273 (2023): 120075. doi:10.1016/j.neuroimage.2023.120075.

[2] Villar, A., de Andrade, C.R.V. Supervised machine learning algorithms for predicting student dropout and academic success: a comparative study. Discov Artif Intell 4, 2 (2024). https://doi.org/10.1007/s44163-023-00079-z.

[3] Pragasthi, M. & Vaishnavi, Ms. (2025). AI – Powered Learning Disability Detection and Classification System. International Journal of Scientific Research in Computer Science, Engineering and Information Technology. 11. 1191-1196. 10.32628/CSEIT25112454.

[4] Imani, M.; Beikmohammadi, A.; Arabnia, H.R. Comprehensive Analysis of Random Forest and XGBoost Performance with SMOTE, ADASYN, and GNUS Under Varying Imbalance Levels. Technologies 2025, 13, 88. https://doi.org/10.3390/technologies13030088.

[5] Abousaber, Inam et al. "Robust predictive framework for diabetes classification using optimized machine learning on imbalanced datasets." Frontiers in artificial intelligence vol. 7 1499530. 7 Jan. 2025, doi:10.3389/frai.2024.1499530.

[6] Jin, Xin & Xu, Anbang & Bie, Rongfang & Guo, Ping. (2006). Machine Learning Techniques and Chi-Square Feature Selection for Cancer Classification Using SAGE Gene Expression Profiles. Lect Notes Comput Sci. 3916. 106-115. 10.1007/11691730_11.

[7] Lindani Dube, Tanja Verster. Interpretability of the random forest model under class imbalance[J]. Data Science in Finance and Economics, 2024, 4(3): 446-468. doi: 10.3934/DSFE.2024019.

[8] Aksan, F., Pawlica, A., Suresh, V., & Janik, P. (2025). A Comparative Study of Machine Learning Models for PV Energy Prediction in an Energy Community. Energies, 18(22), 5980. https://doi.org/10.3390/en18225980.

[9] Çiftci, Beyza, et al. "Machine Learning Approaches for Binary Classification of Sorghum (Sorghum bicolor L.) Seeds from Image Color Features." Journal of Food Composition and Analysis, vol. 140, 2025, p. 107208. ScienceDirect, https://doi.org/10.1016/j.jfca.2025.107208.

[10] Türkmen, Güzin & Sezen, Arda. (2024). A Comparative Analysis of XGBoost and LightGBM Approaches for Human Activity Recognition: Speed and Accuracy Evaluation. International Journal of Computational and Experimental Science and Engineering. 10. 10.22399/ijcesen.329.

[11] Anu, P. J., and K. Ranjith Singh. "Ensemble and Deep Learning via Median Method for Learning Disability Classification." Bulletin of Electrical Engineering and Informatics, vol. 14, no. 3, June 2025, pp. 2031–2041, https://doi.org/10.11591/eei.v14i3.8639.

[12] Anu, P., and K. Ranjith Singh. "Enhancing Classification Performance of SVM Using Hybrid PSO Algorithm: A Case Study on Learning Disability Diagnosis." International Journal of Applied Mathematics, vol. 38, no. 10s, 2025, pp. 166–186, https://doi.org/10.12732/ijam.v38i10s.930.

[13] Wijaya, Michael Geraldin, et al. "Comparative Analysis of Machine Learning Algorithms and Data Balancing Techniques for Credit Card Fraud Detection." Procedia Computer Science, vol. 245, 2024, pp. 677-88. https://doi.org/10.1016/j.procs.2024.10.294.

[14] Oktari, F., Prahutama, A., ., T., & ., S. (2025). Handling Class Data Imbalance in Random Forest using the SMOTE and ADASYN Methods in Identify Economic Status. International Journal Of Mathematics And Computer Research, 13(11), 5921-5927. https://doi.org/10.47191/ijmcr/v13i11.12.

[15] Imani, M.; Joudaki, M.; Bagheri, A.; Arabnia, H.R. Why ROC-AUC Is Misleading for Highly Imbalanced Data: In-Depth Evaluation of MCC, F2-Score, H-Measure, and AUC-Based Metrics Across Diverse Classifiers. Technologies 2026, 14, 54. https://doi.org/10.3390/technologies14010054.

[16] Chicco, D., Jurman, G. The Matthews correlation coefficient (MCC) should replace the ROC AUC as the standard metric for assessing binary classification. BioData Mining 16, 4 (2023). https://doi.org/10.1186/s13040-023-00322-4.

Journal of Engineering and Technology for Industrial Applications

ISSN ONLINE: 2447-0228

ITEGAM-JETIA

Manaus, v.12 n.60, p.890-896 July/August, 2026.
DOI: https://doi.org/10.5935/jetia.v12i60.3758

RESEARCH ARTICLE OPEN ACCESS

SCALABLE QUERY PROCESSING IN BIG DATA ENVIRONMENTS WITH HADOOP DISTRIBUTED FILE SYSTEM AND PARTICLE SWARM OPTIMIZATION

S.Tamil Selvan*[1], R.Punitha Gowri[2], V.Vijey Nathan[3], C. Saravanan[4]

[1]Department of Computer Science and Design,Erode Sengunthar Engineering College, Erode, India.
[2]Department of Computer Science and Design, Erode Sengunthar Engineering College, Erode, India.
[3]Department of Computer Science and Engineering, SRM TRP Engineering College, Tiruchirappalli, India.
[4]Department of Information Technology, Velalar College of Engineering and Technology, Erode, India.

[1]http://orcid.org/0009-0004-8835-7342, [2]http://orcid.org/0009-0007-9490-9387
[3]http://orcid.org/0009-0002-6807-4324, [4]http://orcid.org/0000-0003-0076-4708

E-email: *stamilselvan@esec.ac.in, punithagowrircs@esec.ac.in, vijeynathan@gmail.com, saravananvanjii@gmail.com

ARTICLE INFO

Article History
Received: March 20, 2026
Reviewed: April 20, 2026
Accepted: July 01, 2026
Published: July 31, 2026

Keywords:
Hadoop Distributed File System,
Optimization,
Query processing,
Bigdata,
Particle Swarm Optimization.

ABSTRACT

Big data are enormous, intricate sets of information that are too large, too quick, and too difficult to handle using conventional methods. They consist of both structured and unstructured data. Due to the alarmingly high rates of data generation, there is pressure to adopt simple and expensive procedures for data recovery and storage. Conventional database systems cannot handle the processing power of big data. In order to evaluate and query this enormous amount of data, new technologies have recently been created. In this work, a novel hybrid approach for efficient big data query processing through a two-phase approach is introduced. In the first phase, the Hadoop Distributed File System (HDFS), Map Reduce are utilized. Second phase involves optimization using Particle Swarm Optimization (PSO). The proposed algorithm aims to enhance search speed by strategically optimizing various processes. This two-step methodology combines the parallel processing capabilities of HDFS Map-Reduce with the optimization power of PSO, contributing to an overall improvement in query processing efficiency for large-scale datasets. Experimental results demonstrate significant outperformance of the model in expediting query processing.

Copyright ©2026 by authors and Galileo Institute of Technology and Education of the Amazon (ITEGAM). This work is licensed under the Creative Commons Attribution International License (CC BY 4.0).

I. INTRODUCTION

The "3 Vs" of Figure 1 Volume, Velocity, and Variety define big data. Traditional query processing methods and database management systems face serious difficulties as a result of these features. Traditional methods find it difficult to deal with the sheer amount of data, speed at which it is produced, wide range of data formats, and requirement to guarantee the accuracy and quality of the data. As such, it is now essential to create new query processing techniques suited to the particular requirements of large data. These days, IT is centralized in all businesses and organizations, where users work with a wide range of computer programs. Numerous data types, such as facts, statistics, numbers, text, and images, as well as information that has been processed and made relevant for appropriate use, are allocated by these applications. A database is an information and data collection of this type. Modern database user interfaces are highly versatile, which makes them important for optimization. Users must deal with a massive amount of data due to the growing use of database management systems. As a result, in order to fulfill a user's request, it is imperative to store this data so that it can be quickly retrieved from the information.

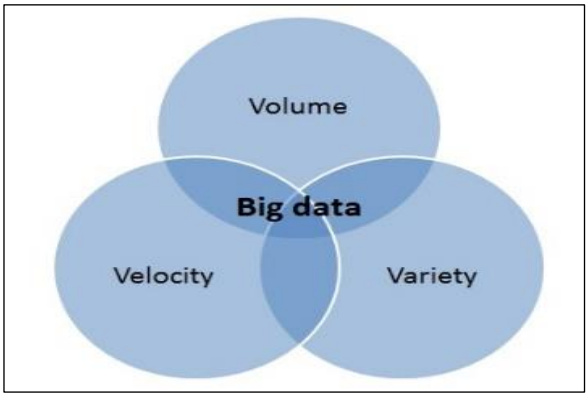


Figure 1: 3 V's of Bigdata.
Source: Authors, (2026).

When it comes to organizing information, databases are really useful. It gives the user the freedom to gather accurate, trustworthy, and timely data for efficient decision-making. As a result, database systems are becoming more and more important. Finding the optimal query optimization strategy becomes more difficult as a result of the daily rise in query complexity. For a very long time, query optimization in databases has been a crucial problem in many different industries. The user must reformulate the complex query with a more efficient and computationally equivalent one in order to lower the execution cost.Main key contributions of proposed work are listed as follows:

- The proposed hybrid approach has two phase of query processing in big data to retrieve the data efficiently.
- In the first phase, Entropy computation is used to extract and manage properties including closed frequent pattern, support, and confidence. Repeated data is removed using the Hadoop Distributed File System and Map Reduce.
- Second phase involves optimization is done using Particle Swarm Optimization.
- Experimental results show that query processing performance of proposed method accuracy was higher and execution time also lower than the traditional methods.

Rest of the paper is organized as follows: Sections 2 discusses related publications. Section 3 shows description of suggested approach Section 4, the suggested hybrid approach is tested and compared to existing approaches. Finally, Section 5 describes all finding and the scope of the study.

II. RELATED WORKS

According to [1] demonstrated the critical role big data plays in the modern society. Big data has many uses in applications, but it also presents difficulties. They have described big data, including veracity, using the four Vs idea. They have addressed a few basic issues that must be resolved in order to turn issues into opportunities. They have discussed developments, big data research, and six key difficulties that arose when processing unstructured data. And also suggested unresolved research issues in the field of big data. Another important problem with heterogeneous Hadoop clusters, as highlighted by [2] is namespace constraints imposed by systems. In a Hadoop context, the issue is sharing name nodes and keeping metadata across name nodes for a large number of files. A single namespace server's capacity to handle and store data is limited [3] expressed apprehension regarding the difficulties presented by supercomputing community. They raised concerns about what happens when data is stored in zettabytes or petabytes. The main topic to concentrate on is the enormous amount of data generated by numerical simulations as a byproduct of supercomputing processes. Three perspectives can be used to analyze the parallelism in large datasets: server applications that require a high bandwidth network to handle all queries, and data applications with a high volume of incoming and outgoing movements. According to [4] there are equity problems with the distinct, profiled critical execution of inquiries. Prediction-based systems are proposed for the current MapReduce-based was developed to scaffold the semantic gap between MapReduce runtimes. Moreover, the query compiler facilitates efficient query planning for rapid and reasonable large-scale data analytics. To get around design flaws and boost large-scale cluster performance, the author conducted tests. [5] have specified the use of comparable input/output approaches for scientific application management.

To maximize I/O throughput, they integrated a two-phase I/O method and data sieving. For large workloads, the suggested effort focuses on providing parallel access to shared datasets. In their clinical studies [6] endorsed the application of naïve Bayes to comprehend the human neuroimaging framework. Although there are various stimulus phases in the research, data collection, classification process offered a very clever look into how data categorization may be controlled if done appropriately. Each response collected as a stimulus offers a comparable testing ground to identify the appropriate heuristic method for data classification of simple activities with complicated surroundings. In [7] conducted a theoretical examination of the PSO algorithm and discussed its history and conception. The specific future research directions this summary suggests are what make it unique [8] suggested a hybrid approach combining PSO and GA to optimize the deployment of an antenna array for the purpose of finding the throughout a substation. Initially, a Direction-of-Arrival (DOA) estimation algorithm was introduced to evaluate its suitability for various array topologies. According to [9] looked at a method for hybridizing PSO and DE, two heuristic algorithms, in order to solve slew-maneuver time-optimal issues with solution route limitations and prevent stagnation. The combined PSODE technique handled the stagnation quite well, reducing computational time compared to merely using DE by 40%. A Dynamic Multi-Swarm Differential Learning Particle Swarm Optimizer was presented [10] By using a local searcher such as the Quasi-Newton method to improve exploitation capability while simultaneously utilizing exploration capability included in the differential mutation, it has an excellent capability of both exploitation and exploration.

By utilizing an Instrumented Indentation Test (IIT), [11] provided a way to extract the mechanical characteristics of its bulk materials utilizing a variety of loading-unloading curves. Finite iterative element simulation in conjunction with Simulated Annealing PSO was utilized to extract the mechanical parameters, such as the strain-hardening exponent (n) and strain-hardening rate (K), from the IIT data.

III PROPOSED WORK

A proficient hybrid structure has been suggested. This system includes data classification and an effective automated preprocessing method for effective data management in large data. Organizations keep many databases to handle and store big data (BD), which comes in a variety of data models and is stored in enormous volumes. For business, querying and BD analysis are essential for gaining insight. This paper improved the BD query optimization process by utilizing both the HDFS map-reduce approach and the PSO algorithm. Figure 3 displays the block diagram for the suggested methodology. There are two stages to the proposed work:

1.Big data arrangement

- Pre-processing
- Feature Extraction

2. Query optimization

Collect and use BD for preprocessing first. The features are extracted from the original data in the second stage, which involves finding the support and confidence value after determining the closed frequent itemset. Finally, apply the entropy method to this value. PSO technique is used in last stage to organize the relevant data. These are explained in brief below.

III.1 BIG DATA ARRANGEMENT

The primary purpose is to convert the unstructured bigdata into an organized manner.

III.1.1 Pre-Processing

In pre-processing phase firstly, it uses the SHA 512 algorithm to calculate hash value (HV) of data during preprocessing. Next, use the HDFS framework to execute the map-reduce using this HV.

HDFS

Large data sets can be reliably and scalable stored and managed using HDFS, a distributed file system. It is made to function with the Hadoop MapReduce (MR) programming model, which is illustrated in figure 2 and is a well-liked method of handling massive data sets. Fast data movement between nodes of HDFS's primary characteristics. When addressing a query, the HDFS has "two" phases. For example, it contains a reduction function Cf and a map function Pf, which are both written as

$$H\,(Dn\,)\;=\;[Pf\,,Cf] \tag{1}$$

Map () function

Map () function is the initial function of Map/Reduction tool. Master node (MN) is where this function is dominant. It divides up input data or breaks it up into multiple smaller subprocesses. The worker nodes, which handle these small processes, receive further dispersion of these subprocesses. The MN is then given an acknowledgement.

$$Pf\;=\;map\,(H\,(\,Dn\,)\,) \tag{2}$$

where Pf is the result of the map () function and map () denotes the mapping function Reduce () function Reduce () gathers the complete outcomes of each suboperation and combines them to produce an aggregated set of decision-based results that are provided in recognition of the initial high demands. The following formula displays the reduction function.

$$Cf\;=\;reduce\,(Pf) \tag{3}$$

where reduce () is the function that reduces the components, Pf is the output of the mapping function, and reduced set of data is Cf.

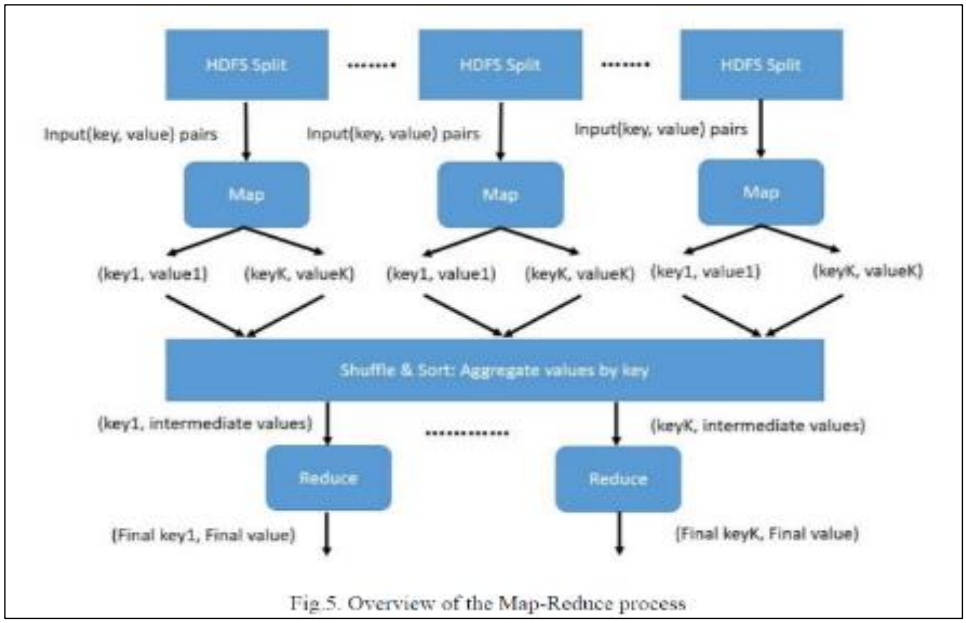


Figure 2: Map-Reduce Process.
Source: Authors, (2026).

III.1.2 Feature extraction

Feature extraction helps in the reduction of the dimensionality of data which is needed to process the data effectively. After eliminating duplicates, crucial features like closed frequent itemsets, support, and confidence are derived from the initial data.

Closed Frequent Itemset (o(fi))

Closed frequent itemsets are frequent itemsets that cannot be extended by adding more items while maintaining the same support. The closed frequent itemset is the maximal frequent itemset, indicating the highest occurrences of a specific item in the dataset.

$$o(f_i) = \{o(f_1), o(f_2), o(f_3), \ldots, o(f_n)\} \tag{4}$$

Support(δt)

Once closed frequent itemsets are identified, calculate the support for each itemset. It is usually expressed as a percentage. The support of association rule U → V is the percentage of transactions in the database containing both itemsets U and V.

$$\delta_t = Support\ (U \rightarrow V) = P(U \cup V) \tag{5}$$

Confidence (Ae)

Confidence is a measure of the reliability or strength of an association rule. The confidence of an association rule U → V is the percentage of transactions with itemset U that also includes itemset V. It is computed using conditional probability in relation to itemset support, expressed by the equation:

$$A_e = Confidence\ (U \rightarrow V) = P\left(\frac{V}{U}\right) = \frac{P(U \cup V)}{P(U)} \tag{6}$$

Where P (U ∪V) denotes the total number of transactions that include the itemsets U and V, while P(U) denotes the total number of transactions that include the itemset U.

Entropy calculation

A measure of a set of data's uncertainty or disorder is called entropy. The entropy calculation is used in this subsection to estimate support and confidence. The entropy of a probability distribution, which is connected to its variance, can be calculated for a given dataset using the following formulas.

$$Entropy(A_e) = -\sum_{e=1}^{N} P(A_e) log_2 \{P(A_e)\} \tag{7}$$

$$Entropy(\delta_t) = -\sum_{t=1}^{N} P(\delta_t) log_2 \{P(\delta_t)\} \tag{8}$$

Here, P(δt) and P(Ae) indicate the likelihood that, at random, the nth support and confidence values will be obtained from the set.

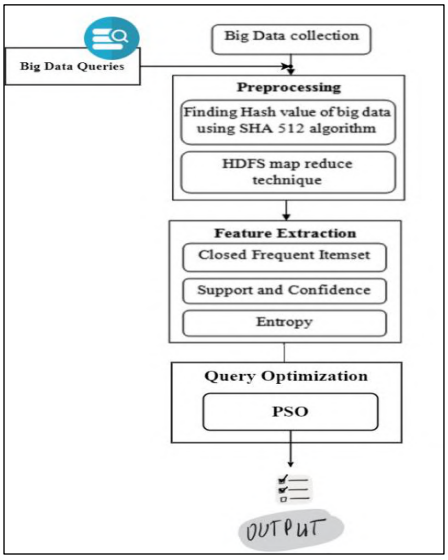


Figure 3: Block diagram for the proposed methodology.
Source: Authors, (2026).

III.2 QUERY OPTIMIZATION

For solving optimization issues, one popular population-based metaheuristic approach is particle swarm optimization (PSO). This algorithm mimics how birds in a flock interact with one another in order to reach their feeding objective. A swarm of birds approaches their food target by combining their social and self-experience. They constantly reposition themselves to establish the finest possible formation based on their own best position as well as the best position of the entire swarm. Iterations are used by the nature-based swarm-intelligence algorithm. It begins with a population of potential solutions, referred to as a swarm. Each particle in this instance stands for a possible fix for the stated issue.

Every iteration updates the velocity and position of every member in the population. Global best value (gbest) and personal best value (pbest) serve as the foundation for these improvements. The particles in gbest model are influenced by the best position identified by any member of the entire population, as opposed to the pbest model where the particles are determined by their own position. Each particle will then converge to this new location as a result.

PSO algorithm

Step 1 The population (particles) has been defined as the X1− Xn−1 weights.
Step 2 For the velocity updating based on weights, the following formula has been applied.
$vi\ (t + 1) = wvi(t) + c1r1[xi(t) - xi(t)] + c2r2[g(t) - xi(t)]$
where vi(t):represents the particle velocity at time t, xi(t):the particle position at time t, ˆxi(t):the individual particle best at time t, and g(t) the global best swarm best at time t. c1 and c2: Cognitive coefficients; w: Inertia coefficient
Step 3 The optimal position has then been updated in accordance with needs by comparing the current positions. As needed, the best spots have been updated. Also, the weights have been revised. For w, the range taken into consideration is 0.8–1.2. Here, c1 and c2 have a value of 2.
Step 4 The position update or the subsequent equations have been utilized.
$xi(t + 1) = xi(t) + vi(t + 1)$
Step 5 Classifications have been established and new posts have been allocated.
The PSO algorithm uses the extracted data to find the best answer to the user's inquiry. When compared to other approaches, this one produces better outcomes and provides the best answers for the given situation. As such, the PSO technique is generally appropriate for a class of high-dimensional optimization problems with extremely precise solutions.

IV. RESULTS AND DISCUSSION

IV.1 EXPERIMENTATION AND DATASET

This section explores the NKM methodology's assessment of the suggested query optimization strategy. Performance is examined and contrasted with state-of-the-art methods with different data sizes (10–50 MB). Test data for text classification is taken from publicly available datasets, most notably Reuters-21579. This dataset, which comes from the news agency Reuters, is arranged according to its economic significance. Specifically, the proposed method uses the Reuters-21578 dataset to choose the top 10 classes, with a test set of 1100 articles and a training set of 3875 documents. These records, which came from the Reuters Newswire in 1987, were put together and arranged by Carnegie organizations and Reuters Ltd. David D. Lewis made them available for study in 1990. 21,578 news items total from the dataset, all of which fall into one or more categories. Out of 21,578 documents, only those pertaining to the four most popular topics—"earn (earning)," "acq (corporate acquisitions)," "money-fx (money market)," and "grain" categories. Table 1 shows the Reuters – 8 benchmark datasets.

Table 1: Reuters-8 (R8) benchmark dataset summary.

R8			
Class	**# train docs**	**# test docs**	**Total # docs**
Acq	1596	696	2292
Crude	253	121	374
Earn	2840	1083	3923
Grain	42	10	51
Interest	190	81	271
Money-fix	206	87	293
ship	108	36	144

Source: Authors, (2026).

IV.2 PERFORMANCE ANALYSIS

Here, the suggested hybrid method's and the current method's performances are compared in terms of statistical metrics, Precision (P), Recall (R), Accuracy (A), F-Measure (F), Retrieval Time (RT) and Execution Time (ET).

Table 2: Comparison table for proposed method with existing method based on Precision, Recall, Accuracy and F-measure.

Data size in MB	**Proposed Method (HDFS-PSO)**				**Existing method (NKM)**			
	P	R	A	F	P	R	A	F
10	89.2	87.9	88.5	86.4	84.6	83.4	85.4	82.9
20	90.4	89.2	89.7	88.6	85.9	84.8	86.7	84.6
30	91.3	90.4	90.6	89.3	87.5	86.2	87.9	86.5
40	92.1	91.5	91.2	90.8	88.7	87.8	89.2	89.7
50	93.5	93.2	92.9	92.2	90.2	89.5	90.4	90.6

Source: Authors, (2026).

Table 2 compares the precision, recall, accuracy, and F-measure of the proposed method with an existing method. The suggested approach yields 93.5% precision, 93.2% recall, 92.9% accuracy, and 92.2% F-Measure on a 50 MB data set. However, the current approach achieves 90.6% F-Measure, 90.4% Accuracy, 89.5% Recall, and 90.2% Precision. Visually, Figure 4 clarifies the accuracy results shown in Table 2 even more, demonstrating the improved performance of the suggested approach.

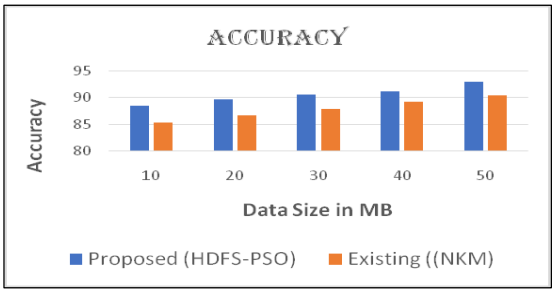


Figure 4: Comparative analysis for the HDFS – PSO with NKM in terms of accuracy.
Source: Authors, (2026).

Table 3 compares the performance of the proposed strategy with an existing method in terms of retrieval time and execution time, both measured in milliseconds (ms), with data sizes ranging from 10 MB to 50 MB.

Table 3: Illustrate the performance of proposed method with existing method based on retrieval time, execution time.

Data size in MB	**Proposed Method (HDFS-PSO)**		**Existing method (NKM)**	
	RT	ET	RT	ET
10	345	121	521	135
20	678	189	892	196
30	1487	208	1592	243
40	2571	245	2752	297
50	3489	293	3857	312

Source: Authors, (2026).

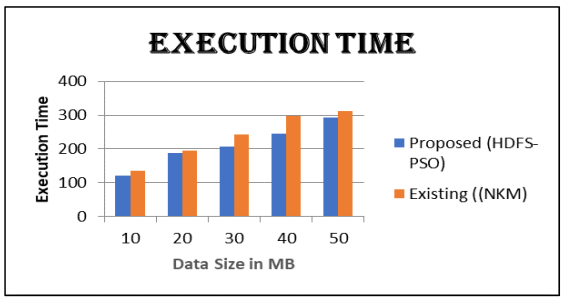


Figure 5: Comparative analysis for HDFS – PSO with NKM on execution time.
Source: Authors, (2026).

The current technique takes 3857 ms for retrieval and 312 ms for execution for a 50 MB data size, whereas the suggested method achieves a retrieval time of 3489 ms and an execution time of 293 ms. For all data sizes, the suggested approach requires less time for retrieval and execution. As a result, the suggested solution outperforms existing methods in terms of performance. Visually, Figure 5 clarifies the execution time results shown in Table 3, demonstrating the enhanced effective

V. CONCLUSIONS

This paper proposes a hybrid approach for query processing in big data, based on Particle Swarm Optimization and the Hadoop Distributed File System. When compared to the current query processing techniques, this hybrid approach is determined to be the most efficient and effective. This hybrid solution uses MapReduce and the Hadoop Distributed File System to remove duplicate data and extract attributes like confidence, support, and closed frequent patterns. Particle Swarm Optimization is used to optimize the query. The results of the proposed work's execution demonstrate and validate that the hybrid technique offers better accuracy and quicker query retrieval. With an average accuracy of 92.9%, the comparison analysis shows that the suggested model fared better than any of the other models in the current study. Additionally, the statistical outcomes of the F-measure (92.2%), recall (93.2%), and precision (93.5%) support the efficacy of the hybrid technique. As a result, this suggested system performs better than the current system. Future improvements to this system's efficiency could include the use of sophisticated optimization techniques and feature selection to speed up retrieval.

VI. AUTHOR'S CONTRIBUTION

Conceptualization: S.Tamil Selvan, R.Punitha Gowri, V.Vijey Nathan C. Saravanan.
Methodology: S.Tamil Selvan, R.Punitha Gowri, V.Vijey Nathan C. Saravanan.
Investigation: S.Tamil Selvan, R.Punitha Gowri, V.Vijey Nathan C. Saravanan.
Discussion of results: S.Tamil Selvan, R.Punitha Gowri, V.Vijey Nathan C. Saravanan.
Writing – Original Draft: S.Tamil Selvan, R.Punitha Gowri, V.Vijey Nathan C. Saravanan.
Writing – Review and Editing: S.Tamil Selvan, R.Punitha Gowri, V.Vijey Nathan C. Saravanan.
Resources: S.Tamil Selvan, R.Punitha Gowri, V.Vijey Nathan C. Saravanan.
Supervision: S.Tamil Selvan, R.Punitha Gowri, V.Vijey Nathan C. Saravanan.
Approval of the final text: S.Tamil Selvan, R.Punitha Gowri, V.Vijey Nathan C. Saravanan.

VII. ACKNOWLEDGMENTS

The author would like to appreciate the effort of the editors and reviewers.

VIII. REFERENCES

[1] M. Malik, K. Neshatpour, S. Rafatirad, and H. Homayoun, "Hadoop workloads characterization for performance and energy efficiency optimizations on microservers," IEEE Trans. Multi-Scale Comput. Syst., vol. 4, no. 3, pp. 355–368, 2018.

[2] H. Alshammari, J. Lee, and H. Bajwa, "H2Hadoop: Improving Hadoop performance using the metadata of related jobs," IEEE Trans. Cloud Comput., vol. 6, no. 4, pp. 1031–1040, 2018.

[3] I. Ullah, M. S. Khan, M. Amir, J. Kim, and S. M. Kim, "LSTPD: Least slack time-based preemptive deadline constraint scheduler for Hadoop clusters," IEEE Access, vol. 8, pp. 111751–111762, 2020.

[4] S. Kumar and M. Singh, "A novel clustering technique for efficient clustering of big data in Hadoop ecosystem," Big Data Min. Anal., vol. 2, no. 4, pp. 240–247, 2019.

[5] M. Soualhia, F. Khomh, and S. Tahar, "A dynamic and failure-aware task scheduling framework for Hadoop," IEEE Trans. Cloud Comput., vol. 8, no. 2, pp. 553–569, 2020.

[6] H. F. Wang and Y. P. Cao, "An energy efficiency optimization and control model for Hadoop clusters," IEEE Access, vol. 7, pp. 40534–40549, 2019.

[7] D. Wang, D. Tan, and L. Liu, "Particle swarm optimization algorithm: An overview," Soft Comput., vol. 22, no. 2, pp. 387–408, 2018.

[8] M. Zhu, J. Li, D. Chang, G. Zhang, and J. Chen, "Optimization of antenna array deployment for partial discharge localization in substations by hybrid particle swarm optimization and genetic algorithm method," Energies, vol. 11, no. 1, p. 1813, 2018.

[9] R. G. Melton, "Differential evolution/particle swarm optimizer for constrained slew maneuvers," Acta Astronaut., vol. 148, pp. 246–259, 2018.

[10] Y. Chen, L. Li, H. Peng, J. Xiao, and Q. Wu, "Dynamic multiswarm differential learning particle swarm optimizer," Swarm Evol. Comput., vol. 39, pp. 209–221, 2018.

[11] L. Huang, K. Guan, T. Xu, J. Zhang, and Q. Wang, "Investigation of the mechanical properties of steel using instrumented indentation test with simulated annealing particle swarm optimization," Theor. Appl. Fract. Mech., vol. 102, pp. 116–121, 2019.

Journal of Engineering and Technology for Industrial Applications

ISSN ONLINE: 2447-0228

ITEGAM-JETIA

Manaus, v.12 n.60, p.897-907 July/August, 2026.
DOI: https://doi.org/10.5935/jetia.v12i60.3792

RESEARCH ARTICLE OPEN ACCESS

FROM TRACEABILITY TO PREDICTIVE INTELLIGENCE: A SYSTEMATIC–NARRATIVE REVIEW OF IOT, BLOCKCHAIN, AND AI IN AGRICULTURE

Manoj Praveen V*[1], Mahendrakumar S[2], Dhanapal R [3], Kayalvili S[4] and Kirubhakaran Marisamy[5]

[1]Department of Artificial Intelligence and Data science,Velalar College of Engineering And Technology, Erode,Tamil Nadu, India.
[2]Department of Electronics and Communication Engineering,Velalar College of Engineering AndTechnology, Erode,Tamil Nadu, India.
[3]Department of Computer Science and Engineering, Karpagam Academy of Higher Education. Coimbatore,Tamil Nadu, India.
[4]Department of Artificial Intelligence, Kongu Engineering College (autonomous), Perundurai, Erode,Tamil Nadu, India.
[5]Department of Artificial Intelligence and Data science, Nehru Institute of Engineering and Technology, Coimbatore,Tamil Nadu India.

[1]https://orcid.org/0009-0000-3919-594X, [2]https://orcid.org/0000-0001-6966-2545, [3]http://orcid.org/0000-0002-4627-8695
[4]https://orcid.org/0000-0002-1935-500X, [5]https://orcid.org/0009-0003-2832-6379

E-email: *mj.vcet@gmail.com, mahendrakumar.sp@gmail.com, dhanapalramasamy.p@gmail.com, kayalvili.ai@kongu.edu, kirupaa.m@gmail.com

ARTICLE INFO

Article History
Received on: fevereiro 24, 2026
Reviewed on: março 24, 2026
Accepted on: July 01, 2026
Published on: July 31, 2026

Keywords:
Agriculture,
Blockchain,
IoT,
Supply chain traceability,
Smart farming.

ABSTRACT

The convergence of Internet of Things (IoT), blockchain, and artificial intelligence (AI) has emerged as a transformative force in advancing sustainable agriculture. These technologies collectively address persistent challenges in traceability, resource optimization, data security, and decision support. This review conducts a systematic–narrative analysis of journal publications from 2020 to 2025, synthesizing insights across three thematic dimensions: (i) IoT–Blockchain frameworks for agricultural supply chain traceability, (ii) IoT–AI/ML approaches for predictive farming and crop health monitoring, and (iii) blockchain-driven data management for breeding and genomic applications. Across the themes, the reviewed studies demonstrate substantial improvements, including enhanced supply chain transparency, predictive accuracy exceeding 95% in crop disease classification, and scalable storage architectures for high-throughput breeding data. However, challenges persist in interoperability, scalability, energy efficiency, and end-user adoption. The review identifies critical research gaps and emphasizes the need for integrated frameworks that balance technological sophistication with practical usability. By consolidating current advances and limitations, this study provides a comprehensive understanding of the evolving IoT–Blockchain–AI ecosystem in agriculture and outlines future directions toward sustainable, transparent, and intelligent agri-food systems.

Copyright ©2026 by authors and Galileo Institute of Technology and Education of the Amazon (ITEGAM). This work is licensed under the Creative Commons Attribution International License (CC BY 4.0).

I. INTRODUCTION

Global agriculture faces mounting challenges: fragmented and opaque supply chains, frequent food-safety incidents, inefficient resource use, and rapidly growing volumes of farm and genomic data that require trustworthy, scalable management. Digital traceability remains incomplete across many value chains, hampering rapid recall decisions and eroding consumer trust; simultaneous pressures to improve sustainability and reduce post-harvest loss increase the urgency for technological solutions [1], [2]. The Internet of Things (IoT) brings dense, low-cost sensing and near-real-time telemetry to the farm and supply chain: soil moisture, temperature, cold-chain conditions, geolocation, and spectral or image data can now be captured continuously [3]. IoT enables precision interventions for irrigation, fertilization, pest control and produces the high-resolution provenance streams needed for verifiable analytics. However, IoT data by itself cannot guarantee immutability, distributed trust, or automated contractual enforcement across multiple stakeholders [4].

Blockchain (BC) offers complementary properties — a tamper-evident ledger, decentralized trust, and programmable smart contracts — which can help secure IoT data, automate transactions, and provide auditable provenance from farm to fork. Yet practical deployment raises important questions about cost, scalability, and the resource constraints of low-power IoT devices; careful architectural design and hybrid solutions such as edge gateways, private chains, data-hashing strategies are frequently proposed to balance trust and efficiency [5]. Several recent literature reviews and systematic studies have examined blockchain and occasionally IoT applications in agri-food systems, identifying common benefits (traceability, transparency, fraud reduction) and recurring barriers (interoperability, legal/regulatory concerns, adoption costs). For instance, by [6] analyzed adoption barriers and enablers for blockchain in smart and sustainable agriculture; in [7] systematically reviewed blockchain applications across food supply chains and identified under-utilized drivers and research gaps; by [8] assessed blockchain and IoT technologies in the context of regional feasibility and implementation constraints. These reviews are valuable but either focus narrowly on adoption drivers, concentrate mainly on supply-chain aspects, or synthesize literature that predates the recent surge (2020–2025) of IoT + blockchain empirical work.

I.1 CONTRIBUTIONS OF THIS REVIEW

This article addresses the above gaps by conducting a systematic–narrative review of journal publications from 2020 to 2025, with the following contributions:

- **Comprehensive scope:** covers 30 peer-reviewed journal articles on IoT–blockchain integration in agriculture.
- **Structured thematic analysis:** classifies studies into four themes: (1) Supply-chain traceability and provenance, (2) Smart/precision agriculture, and (3) Crop-breeding and genomic data management.
- **Critical synthesis**: compares methodological choices such as blockchain architectures (public, private, hybrid), on-chain/off-chain data strategies, and edge integration with IoT.
- **Identification of gaps:** highlights unresolved issues including scalability, energy costs, interoperability, and regulatory alignment.
- **Future research agenda:** proposes directions such as energy-efficient consensus mechanisms, cross-chain interoperability, and integration of genomic and AI-driven farming solutions.

II. METHODS

II.1 REVIEW TYPE

This work adopts a systematic–narrative review approach. The systematic component ensures transparent and reproducible identification of relevant literature, while the narrative synthesis allows for flexible integration of diverse study designs, applications, and technological perspectives. This combination is particularly suitable given the multidisciplinary nature of IoT–blockchain applications in agriculture, spanning supply chain traceability, precision farming, genomic data management, and adoption studies.

II.2 SEARCH STRATEGY

A structured literature search was conducted across major academic databases, including Scopus, Web of Science, IEEE Xplore, ScienceDirect, SpringerLink, Wiley Online Library, MDPI, and Taylor & Francis Online. The search covered the period from 2020 to August 2025 and was limited to publications in English. Boolean search strings were employed to capture relevant studies, such as:

- “IoT” AND “Blockchain” AND “Agriculture”
- “Smart farming” AND “Blockchain”
- “Blockchain” AND “Food supply chain” AND “IoT”
- “Blockchain” AND “Genomic data” AND “Agriculture”

These combinations were iteratively refined to maximize coverage across agricultural domains where IoT and blockchain intersect.

II.3 INCLUSION AND EXCLUSION CRITERIA

Studies were included if they:

- Were peer-reviewed journal articles.
- Reported original research (empirical, applied, or technical).
- Explicitly integrated IoT and blockchain technologies in agricultural contexts.

Studies were excluded if they:

- Were conference proceedings, book chapters, or review papers.
- Focused exclusively on blockchain or IoT without integration.
- Presented purely conceptual frameworks with no implementation or application.

II.4 SELECTION PROCESS

The initial search retrieved a large pool of records. After deduplication, titles and abstracts were screened for relevance. Full-text evaluation was then performed to assess eligibility against the defined criteria. At the end of this process, 30 journal articles were retained for analysis.

II.5 DATA EXTRACTION AND THEMATIC GROUPING

For each included article, key bibliographic and methodological details were extracted, including publication year, application domain, blockchain architecture, IoT scope, and study contribution. The articles were then organized into three thematic categories reflecting their primary focus:

1. Supply chain traceability and provenance.
2. Smart and precision agriculture.
3. Crop breeding and genomic data management.

This thematic grouping enables cross-comparison of methodological approaches, application domains, and identified research gaps.

II 6 PRISMA DIAGRAM

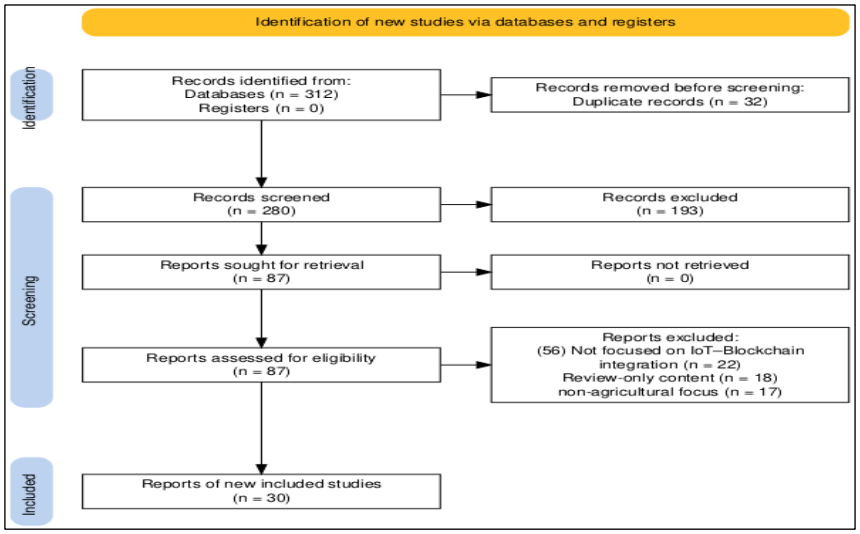


Figure 1: PRISMA flow diagram of study selection process.
Source: Authors, (2026).

Figure 1 shows the selection process of the studies included in this review. A total of 312 records were initially identified through database searches. After removal of 32 duplicates, 280 records remained for screening. Following title and abstract evaluation, 193 records were excluded for irrelevance. The full texts of 87 reports were then assessed for eligibility, of which 56 were excluded due to reasons such as lack of IoT–Blockchain integration (22), review-only content (18), or non-agricultural focus (17). Finally, 30 studies fulfilled the inclusion criteria and were retained for detailed synthesis.

III. RESULTS

III.1 THEME 1: SUPPLY CHAIN TRACEABILITY AND PROVENANCE

Traceability research moved quickly from proof-of-concept immutable ledgers to systems that must also solve privacy, latency, storage growth, data trustworthiness, and operational usefulness.

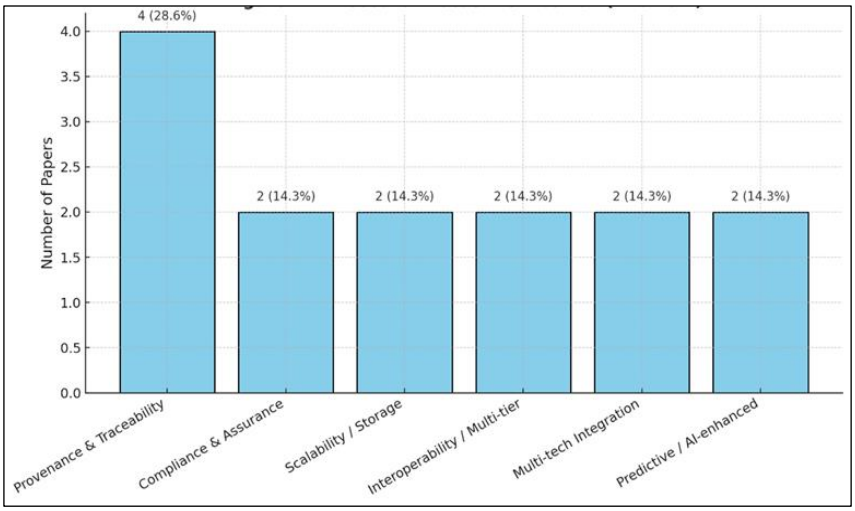


Figure 2: Research focus distribution on theme 1.
Source: Authors, (2026).

Figure 2 shows the research focus distribution of Theme 1 papers on IoT–Blockchain for agricultural product traceability. Most studies focus on provenance and privacy (3 papers), followed by compliance frameworks (2), scalability solutions (2), interoperability designs (2), multi-technology integration (2), and predictive/AI methods (2). Provenance is the dominant focus, while interoperability and prediction remain less explored. The following paragraphs synthesize how key papers address these problems, comparing what each did to what the others missed or improved.

III.1.1 On-Chain Vs Hybrid Storage and The Price of Verifiability

According to [9] established an influential hybrid pattern — store a compact Merkle root on Ethereum and put bulky provenance files in IPFS — using SHA-256 and Merkle trees to keep integrity while limiting on-chain data. Their measured numbers (per-function gas ≈ USD 0.29–0.45; SHA-256 ~2 s for 1 GB; IPFS upload 243 MB ≈ 3.4 s, query ≈ 22 s) make explicit the trade-off: verifiable provenance is feasible but public-chain gas costs quickly become a bottleneck. In [10] respond to this by moving to permissioned PoA Ethereum (IoT-GChain): they keep the hybrid storage model (IPFS + on-chain hash) but change consensus to PoA, yielding block times ≈ 3 s and gas per operation in the 85k–134k units range. In short, [9] proves the hybrid technique; [10] demonstrates how consensus choice changes latency and practical viability.

III.1.2 Privacy, Compliance and Contract Logic

Where [9] prioritized privacy by minimizing on-chain payloads, by [11] encoded compliance rules directly into contracts via the Trust-Enhanced Contract Algorithm (TECA). TECA performs multi-party validation (sensor verification + certification rules) BEFORE a claim is anchored, thereby reducing on-chain noise and ensuring only verified claims are recorded. According to [11] BSAA reports gas 41k–102k units, ~USD 0.25 average transaction cost and 18–20 TPS — a clear demonstration that smart contract logic + careful write policies can permit practical throughput for assurance workflows, unlike naive full-data writes on public chains.

III.1.3 Integrating Analytics and Operational Value

According to [12] integrate forecasting directly with provenance: a GA-tuned ensemble (LSTM + GRU) reduces RMSE from 872.6 / 819.7 to 512.2, while provenance sits on a permissioned blockchain with Hyperledger Caliper tests showing median latencies ~198–768 ms for 200–800 nodes. Contrast this with by [13], who do not aim at RNN forecasting but show that classical ML applied to RFID/WSN transport data gives immediate operational value — RF 95.5%, AdaBoost 94.3%, SVM 91.7%, KNN 89.6% — yet [13] Bhutta do not evaluate blockchain latency/cost. Thus: [10]-11 shows deep-learning + private chain is feasible (in sim), [13] shows classical ML yields very high accuracy in transport forecasting but leaves blockchain operational costs unexplored. Combining both approaches would be a logical next step.

III.1.4 Scalability and Storage Lifecycle (redaction & parallelism)

Canonical append-only ledgers cause storage bloat; by [14] propose redactable primitives (chameleon hash) + parallel chain architecture + CP-ABE and report ~52.38% reduction in storage footprint over 360k wheat records. Compare that with AgriChainSync [15], which employs a Dynamic Storage Algorithm (DSA) and a Feedback & Adaptation Module (FAM): under experimental load (100–1000 IoT devices) [15] AgriChainSync shows latency increase ≈ 15% under 10× data volume and improved storage efficiency. LAP-chain [14] solves data retention/compliance explicitly (delete or redact expired data); [15] AgriChainSync emphasizes adaptive routing to balance cost vs latency. Both demonstrate that architecture + algorithms can control storage growth — a capability absent from many early single-chain designs [9],[16].

III.1.5 Data-Quality at Capture: Sensor Fusion, NIRS And Multi-Tech Verification

According to [17], [18] highlight an often-ignored truth: immutability cannot fix bad inputs. [17] integrates NIRS + RFID + IoT to verify quality signals before anchoring; Paper [18] implements embedded IoT + permissioned chain in an industrial hemp deployment. These works contrast with Papers [9–12] and show that adding certified sensing (NIRS, RFID) is required to make an immutable chain trustworthy for quality claims. Practically, this means systems should include sensor-level verification algorithms as pre-contract checks — a capability shown in Papers [17], [18] but missing in many ledger-centric designs.

III.1.6 Interoperability, Governance and End-To-End Integration

In [19] propose a vertical-chains + core hash-chain model for stakeholder privacy and scalability; by [16] provide an end-to-end Ethereum + IPFS stack with a reputation subsystem, but both lack large-scale field results. According to [20] push for end-to-end visibility (edge gateways → chain), yet they report little performance detail. Thus the field is converging on multi-chain / core-chain topologies + governance policies as necessary for multi-stakeholder adoption, but real-world interoperability experiments are still scarce.

Table 1: Summary of theme 1.

Paper	Methods / Architecture	Algorithms / Techniques	Key Results / Performance	Limitations / Challenges
[12]. Khan et al. (2020)	Private blockchain + IoT + predictive analytics	GA-optimized ensemble of LSTM + GRU	RMSE reduced to 512.2 vs. 872.6 (LSTM) & 819.7 (GRU); query latency 198–768 ms over 200–800 nodes	Tested only in simulated private networks
[20] El Mane et al. (2024)	End-to-end IoT–Blockchain architecture (8-node network)	Controllers/validators added dynamically	Latency margin ≈ 100–120s; throughput ≈ 235–260 TPS on 3.5 GHz CPU, 32 GB	Latency rises with heavy concurrent traffic; no energy cost evaluation

			RAM; improved performance with more validators	
[21]. Guo et al. (2025)	Hyperledger Fabric + IoT sensors + smart contracts	Blockchain-based trusted traceability	File transfer: upload ≈ 7.31 MB/s (small), 15.19 MB/s (large); download ≈ 31.92 MB/s (small), 35.61 MB/s (large) → meets real-time traceability needs	Mostly tested on grape supply chain; lacks broader validation
[19]. Bhat et al. (2022)	Agri-SCM-BioT: vertical blockchains + core chain	Controlled access via master/gateway nodes	Secure master nodes reduce 51% attack risks; high-resource nodes improve resilience	No reported values for latency, storage cost, or throughput
[15]. Tahir et al. (2024)	AgriChainSync (hybrid IoT–AI–Blockchain)	Dynamic storage + homomorphic encryption	Latency increase only 15% under 10× data load; throughput robust; storage efficiency improved	Energy/operational overhead not deeply analyzed
[16]. Shahid et al. (2020)	Ethereum + IPFS for provenance, trading, reputation	Multiple smart contracts	Simulation: gas usage scales with products; improved transparency and auditability	Cost/latency not quantified in USD terms

Source: Authors, (2026).

Progress is evident in: (a) hybrid storage patterns (Merkle root + IPFS), (b) permissioned consensus (PoA/Hyperledger) to lower latency and fees, (c) integration of analytics for operational decision support, and (d) architectural work to tackle storage retention (redactable/parallel chains) and interoperability (multi-chain). Remaining bottlenecks are consistent across studies: lack of large-scale field validations, incomplete cross-paper reporting of latency/cost metrics in a unified format, and few integrated demonstrations that combine sensor verification, optimized contract logic (TECA/DSA), and analytics (RNN/RF) in a single production deployment. Table 1 provides a comparative summary of some studies highlighting their methods, algorithms, key results, and limitations.

III.2 THEME 2: SMART AND PRECISION AGRICULTURE

Research at the intersection of IoT and blockchain in agriculture has evolved toward secure, privacy-preserving, and energy-efficient systems that also support predictive intelligence and supply chain transparency. The eleven papers reviewed under this theme (22–32) demonstrate different approaches to address challenges such as security and trust, prediction accuracy and anomaly detection, privacy-preserving collaborative learning, IoT network efficiency, and supply chain sustainability. Figure 3 shows the distribution of research focus in IoT + Blockchain for Smart and Precision Agriculture based on 11 reviewed papers. The largest focus is on Security & Trust (27%) and Network/Energy Efficiency (27%), followed by Prediction & ML (18%), Supply Chain Transparency (18%), and Privacy & Federated Learning (9%). This highlights key research priorities and gaps in the field.

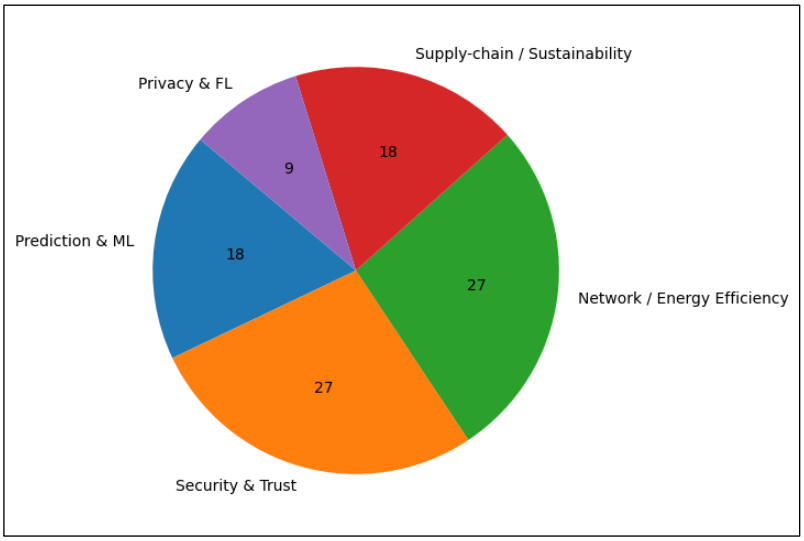


Figure 3: Research focus distribution on theme 2.
Source: Authors, (2026).

III.2.1 Security and Data Integrity

Maintaining trustworthy and tamper-resistant agricultural data is a fundamental requirement. According to [22] combined edge devices (ESP32, Arduino) with AWS IoT and Ethereum testnet smart contracts, achieving average alarm response latency of ≈0.11 seconds, demonstrating the feasibility of automated IoT–blockchain alarms. Similarly, by [23] proposed a cloud-enabled security monitoring system where IoT sensor data is processed in AWS Lambda and anchored to blockchain, reporting IoT-to-cloud latency of ≈2 s, Ethereum confirmation ≈7 s, and full end-to-end alerts within ≈9 s. According to [24] focused on blockchain cost-efficiency, analyzing smart contract gas usage, where typical IoT checks consumed ≈29,217 gas units, highlighting the economic trade-off between security automation and blockchain overhead. Together, these works confirm that edge-assisted detection with blockchain anchoring ensures trustworthy event logging, though scalability to production systems demands gas optimization or migration to permissioned/Layer-2 chains.

III.2.2 Prediction Accuracy and Anomaly Detection

Several studies demonstrate the potential of combining IoT data with blockchain-backed integrity guarantees for accurate prediction and anomaly detection. For [25] used a binary Slime Mould Algorithm (SMA) for feature selection with Bi-LSTM and GRU models, achieving yield prediction accuracy ≈95.8%, F1 scores ≈0.96, and anomaly detection precision of ≈0.93, while ensuring nearly 100% integrity via blockchain. According to [26] employed classical ML approaches for crop recommendation, achieving accuracies up to 98.2%, showing that interpretable models can perform strongly in structured IoT datasets. In [27] applied CNN-LSTM hybrids under federated learning, where centralized models reached RMSE ≈4.70 and R^2 ≈0.84, while privacy-preserving FL variants showed slightly degraded RMSE ≈5.15–5.90. According to [28] proposed Smart-Agri, an IoT–ML–Blockchain framework, achieving ≈89.5% accuracy in crop monitoring and control. These results indicate that DL consistently provides superior predictive performance, though classical ML remains competitive when computation must remain lightweight.

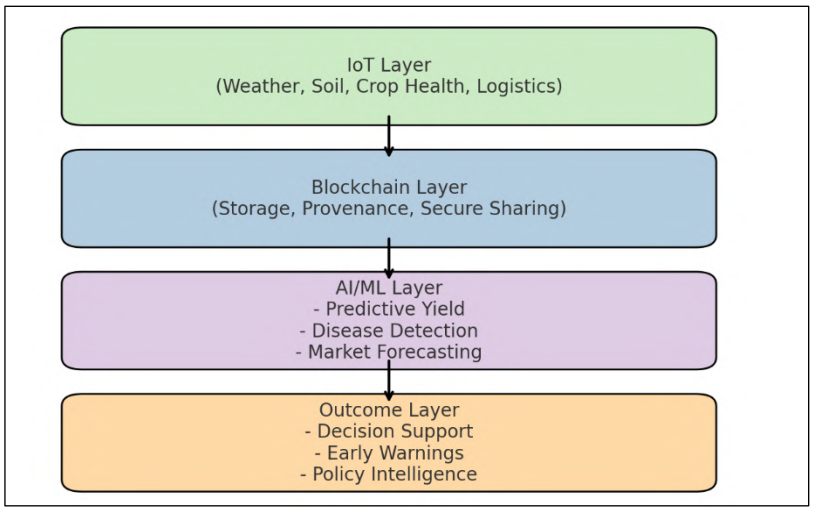


Figure 4: Pipeline of IoT, Blockchain, and AI integration for predictive agricultural insights.
Source: Authors, (2026).

This framework illustrates (Figure 4) how IoT devices capture real-time agricultural data, which is securely managed through blockchain before being processed by AI/ML models for predictive insights. The outcome enables decision support, early warnings, and policy-level intelligence.

III.2.3 Privacy-Preserving Collaborative Learning

Sharing agricultural data across stakeholders raises privacy risks, which several works addressed by integrating federated learning (FL) with blockchain provenance. The federated architecture of by [27] demonstrated that CNN-LSTM models can be trained collaboratively without exposing raw farm data. Differential privacy extensions further strengthened protection but increased RMSE to ≈5.90 compared to ≈4.70 in centralized training. While latency and blockchain throughput were reported as "acceptable," detailed network stress tests remain scarce. These findings confirm that federated learning with blockchain is a viable solution for multi-party collaboration, but future work must optimize trade-offs between privacy guarantees and predictive accuracy.

III.2.4 IoT Network Efficiency, Energy, and Mobility

The reliability and sustainability of IoT sensor networks in agriculture are critical for real-world deployments. In [29] proposed an energy-aware clustering protocol, achieving substantial improvements compared to the LEACH baseline: network lifetime extended by +112%, stability period increased by +23%, and energy consumption reduced by −68%. According to [30] examined precision agriculture networks with 6LoWPAN and RPL routing under both fixed and mobile topologies. Results showed that fixed nodes achieved stable connectivity and lower radio duty cycles, while mobility increased energy costs and connectivity fluctuations, though precise percentages were less detailed. Collectively, these studies demonstrate that energy-efficient clustering significantly extends sensor lifetimes, while robust routing protocols remain an open challenge for mobile agricultural IoT environments.

III.2.5 Supply Chain Transparency and Sustainability

Ensuring end-to-end transparency from farm to consumer remains a central objective. In [31] proposed a semantic cyber–physical system (CPS) that integrates IoT, blockchain, AI, and remote sensing for traceability, reporting improved decision support and qualitative gains in transparency, though without quantitative latency or cost metrics. According to [32] applied TOPSIS-based multi-criteria analysis to identify and rank barriers to blockchain adoption in green agricultural supply chains, emphasizing issues such as regulatory compliance and trust. According to [24] further demonstrated how blockchain smart contracts can automate supply chain agreements, reporting explicit transaction costs across agricultural IoT scenarios. Collectively, these works highlight that semantic architectures and multi-criteria frameworks provide conceptual clarity, but cost-efficient blockchain execution remains the most urgent bottleneck for real-world adoption.

Table 2 highlights the core contributions of each work in terms of architecture, algorithms, and outcomes, showing how researchers have leveraged blockchain to ensure confidentiality, integrity, and secure sharing of agricultural IoT data.

Table 2: Comparative summary of Theme 2 papers.

Paper (no.)	Methods & architecture	Algorithms / techniques	Key results
[22] Aliyu & Liu (2023)	ESP32 IoT nodes → AWS cloud (IoT Core + Lambda) → Ethereum (Rinkeby); smart contracts automate responses	Edge threshold/rule detection; Solidity smart contracts; on-chain logging	Observed transaction counts ≈ 109k–291k avg network latency ≈ 0.11 s
[29] Wang et al. (2025)	Human-Cyber-Physical System combining IoT, remote sensing, AI, semantic blockchain layer	Semantic data integration; H-CPS architecture (conceptual)	Qualitative improvements in traceability and cost-efficiency reported
[25] Almazmomi (2025)	4-layer framework: data acquisition, AI layer, security layer, blockchain layer	Binary SMA for feature selection; Bi-LSTM, GRU for prediction; blockchain for integrity	Yield accuracy: 95.8% (Bi-LSTM) 94.6% (GRU); F1 ≈ 0.96/0.94; anomaly detection precision 0.93, recall 0.92; blockchain integrity ↑ ≈97%
[28] Hossain et al. (2023)	IoT sensors + cloud + mobile UI + blockchain for integrity; energy harvesting for sensors	ML recommendation model (unspecified) for irrigation/fertilizer; blockchain for logging	ML model accuracy ≈ **89.5%** in their experiments; system supports remote control and energy harvesting
[30] Atalla et al. (2023)	WSN simulation (COOJA) with 6LoWPAN + RPL; scenarios: fixed-node (olive farm) and mobile nodes (stable)	RPL routing; Random Waypoint mobility model; COOJA simulation	Fixed-node: more stable connectivity and lower power consumption; mobile-node: higher radio duty cycle and connectivity fluctuation
[27] Manoj et al. (2025)	Federated learning orchestration + blockchain ledger (DIDs, VCs) for authentication & provenance	CNN-LSTM, ResNet-16/28, CNN-DNN as models; DP-FL variants; smart contracts for metadata logging	Centralized CNN-LSTM: MSE ≈ 22.07, RMSE ≈ 4.70, R^2 ≈ 0.84 (2018); DP-FL (3 clients IID): MSE ≈ 26.50, RMSE ≈ 5.15, R^2 ≈ 0.77;
[31] Awan et al. (2021)	3-layer IoT architecture with clustering protocol + blockchain logging	Custom energy-efficient clustering protocol (LEACH-variant)	Compared to LEACH: +23% network stability, −68% energy consumption, +112% network lifetime
[32] Chaudhari et al. (2025)	IoT data collection + blockchain for secure tracking; TOPSIS for barrier prioritization	TOPSIS multi-criteria decision method; IoT + blockchain architecture for GSCM	Ranked adoption barriers and proposed prioritized interventions
[23] Chaganti et al. (2022)	Arduino/ESP8266 sensors → AWS IoT Core + Lambda → Ethereum (Rinkeby) via Infura; Web3 UI	Threshold-based anomaly detection in Lambda; Solidity smart contracts for logging	IoT→cloud publish ≈ 2 s; Ethereum tx ≈ 7 s; end-to-end alert ≈ 9s
[26] Bakthavatchalam et al. (2022)	IoT sensors measuring N,P,K,pH,temp,humidity,rainfall; dataset (2,200 instances)	MLP, Jrip, Decision Table classifiers (WEKA)	MLP accuracy ≈ 98.23%, Jrip ≈ 96.23%, Decision Table ≈ 88.59%; ROC ≈ 0.991–0.997; model build times 0.15–10.56 s
[24] Pranto et al. (2021)	IoT sensors + Solidity smart contracts on Ethereum testbed; MQTT messaging; contract functions for storage/distribution	Solidity smart contracts (self-check/trigger functions), off-chain sensor input via MQTT	Gas usage per operation addSeed() transaction 168,402 gas (transaction) / 144,314 (execution); temperatureSelfCheck() 50,681 / 29,217 gas; retailSell() 91,464 / 69,808 gas

Source: Authors, (2026).

Overall, the reviewed studies show clear trends: (i) edge-assisted smart contracts can deliver real-time security but gas costs demand optimization; (ii) deep learning approaches achieve high prediction accuracy, while federated learning enables privacy-preserving collaboration at modest performance trade-offs; (iii) energy-aware clustering yields measurable IoT lifetime extensions, making it one of the most deployment-ready innovations; and (iv) semantic frameworks and barrier analyses advance conceptual supply chain trust, though empirical cost and latency data are still underreported.

The comparative evidence suggests that privacy-preserving deep learning and energy-optimized IoT protocols, tightly integrated with blockchain provenance, represent the most promising direction for next-generation precision agriculture ecosystems.

III.3 THEME 3: CROP BREEDING, GENOMICS & DATA MANAGEMENT

Theme 3 papers focus on the integration of blockchain, IoT, and advanced computational methods (ML, encryption, privacy-preserving frameworks) to address the growing challenges in crop breeding, genomics, and large-scale agricultural data management. The reviewed studies contribute solutions for high-throughput data storage, secure genomic management, breeding efficiency, and supply chain traceability, while also revealing gaps related to scalability, security-performance trade-offs, and integration of advanced analytics. Figure 5 demonstrates the role of IoT in collecting genomic and field data, with blockchain ensuring secure storage, provenance, and controlled sharing. This integration strengthens breeding programs, genomic research, and collaborative data management.

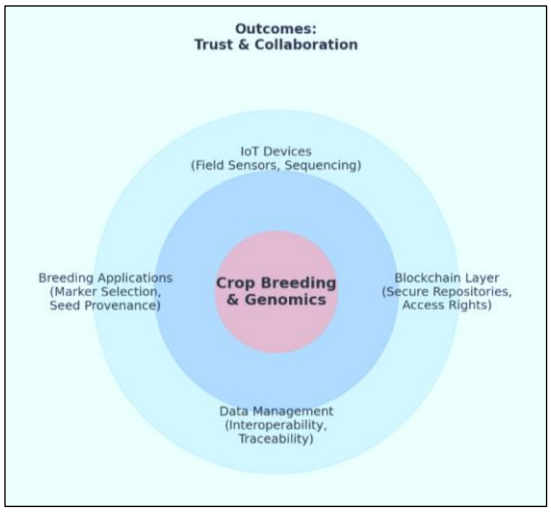


Figure 5: Framework of IoT and Blockchain in crop breeding, genomics, and data management.
Source: Authors, (2026).

III.3.1 Data Storage, Compression & Retrieval

According to [33] developed a spectral data pipeline within Breedbase, demonstrating 40% compression via differential computation and 50% faster retrieval with indexing, while PCA captured >85% variance for dimensionality reduction. However, robust blockchain-level security was absent. In contrast, [34] implemented multi-chain blockchain architecture with proxy encryption for GSBCP, which significantly improved system concurrency and secure storage of sensitive breeding data. Both works show how storage and retrieval challenges are addressed, but [33] emphasized efficiency while by [34] focused on security-performance trade-offs.

III.3.1.1 Breeding Information Management & Genealogy Tracking

According to [35] proposed a Hybrid Crop Breeding Information Management System (HCBIMS) with diallel crossing design, GCA/SCA analysis, and genealogy tracking, doubling efficiency in combining ability test analyses. This was further supported by compound genealogy tools, which enhanced lineage tracking. Similarly, [36] built a relational database-based breeding trait tracking system, enabling faster querying and visualization, with higher data accuracy than manual methods. While both improved breeder decision-making, neither incorporated blockchain security.

III.3.1.2 Secure Genomics & Privacy Preservation

According to [37] introduced a blockchain-based privacy-preserving genomic data system with Local Differential Privacy (LDP). It separated encrypted private storage for staff and irreversibly modified semi-private storage for external access, ensuring confidentiality, access control, and user monitoring. However, the study lacked ML-driven analytics for predictive genomics. Compared to [34], which emphasized proxy encryption and multi-chain performance, Park's contribution primarily addressed privacy and fine-grained access control.

III.3.1.3 Supply Chain Traceability & End-to-End Data Integrity

According to [38] extended blockchain applications beyond breeding to food grain traceability. By combining IoT sensors (temperature, humidity, GPS) with Ethereum blockchain, IPFS, and ML algorithms, the system enhanced scalability, throughput, and latency. Notably, it maintained strong confidentiality, integrity, availability, and non-repudiation guarantees. Unlike in [33], [35] works that focused on breeding data management, by [38] contribution highlighted how blockchain–IoT–ML convergence can secure the entire crop supply chain lifecycle. Table 3 presents a comparative overview of Theme 3 papers, highlighting their methods, algorithms, achieved results, and the specific agricultural challenges they addressed.

Table 3: Comparative summary of theme 3.

Paper	Methods / Techniques	Results / Performance	Challenges Addressed
Hershberger et al. (2021) [33]	Breedbase pipeline, differential compression, PCA	40% compression, 50% faster queries, >85% variance retained	Storage efficiency, retrieval speed
[34] Zhang et al. (2020)	Multi-chain blockchain, proxy encryption, GSBCP	Improved concurrency, secure storage with layered access	Data security, storage scalability
Han et al. (2020) [35]	HCBIMS, diallel crossing, GCA/SCA analysis, genealogy tool	Doubled efficiency in combining ability analysis, automated reports	Breeding efficiency, lineage tracking
Basheija et al. (2021) [36]	Relational DB, phenotype trait tracking, custom algorithm	Faster querying, higher accuracy than manual methods	Data organization, real-time decision support
[37] Park et al. (2021)	Blockchain + LDP, dual storage (private/semi-private)	Privacy-preserving genomic access control, staff & external data segregation	Data privacy, access monitoring
[38] Agarwal et al. (2024)	IoT sensors, Ethereum, IPFS, ML anomaly detection	High throughput, low latency, strong CIA+NR security	Transparency, anomaly detection, supply chain scalability

Source: Authors, (2026).

In synthesis, Theme 3 highlights how the triad of IoT, blockchain, and ML is not just an incremental enhancement of existing agricultural systems but rather a paradigm shift toward intelligent, decentralized, and resilient agri-ecosystems. The works reveal a trajectory where trust (blockchain), perception (IoT), and cognition (ML) are interwoven, pointing to a future in which agricultural decision-making is secure, explainable, and adaptive to uncertainties—a cornerstone for next-generation digital agriculture.

IV. CHALLENGES & FUTURE DIRECTIONS

- ✓ A major research gap lies in the integration of heterogeneous agricultural data sources, where IoT sensor streams, spectral datasets, blockchain transaction records, and genomic information remain fragmented, limiting holistic insights.
- ✓ Scalability challenges persist as most proposed systems have been validated on limited datasets or small-scale pilots, restricting their applicability to high-throughput crop breeding pipelines or multi-stakeholder agricultural supply chains.
- ✓ Interoperability issues continue to hinder progress, with the absence of standardized frameworks preventing seamless cross-platform data exchange between IoT–Blockchain–ML ecosystems and breeding information systems.
- ✓ Security and privacy concerns remain inadequately addressed, particularly for sensitive genomic and phenotypic data, where existing blockchain mechanisms ensure transparency but fail to provide fine-grained confidentiality.
- ✓ User-centric limitations emerge as farmer usability, cost-effective deployment, and real-time decision support features are often overlooked, reducing the practical adoption of these advanced technologies in resource-constrained environments.
- ✓ Energy and cost constraints are evident, as blockchain and IoT-driven solutions demand significant computational and communication resources, posing barriers for sustainable agricultural implementation.

❖ Future directions

- ✓ Future directions point towards the deployment of federated and edge AI frameworks that enable scalable, privacy-preserving analytics without centralized data pooling.
- ✓ Hybrid blockchain models that integrate lightweight consensus mechanisms with sharding are needed to balance transparency, efficiency, and real-world feasibility in agricultural contexts.
- ✓ The development of interoperable standards for multi-source agricultural data exchange will be critical in bridging the gap between phenotyping, breeding, and supply chain systems.
- ✓ The incorporation of explainable AI and XAI frameworks is essential to ensure interpretability and trust in decision support for breeding, disease detection, and traceability tasks.
- ✓ Sustainable computing paradigms, including green blockchain and energy-efficient IoT deployments, are required to mitigate the environmental and economic costs of digital agriculture.
- ✓ Farmer-centric innovations such as mobile-based decision support, fuzzy reasoning mechanisms, and multilingual interfaces will play a vital role in democratizing access to advanced IoT–Blockchain–ML solutions in agriculture.

V. CONCLUSIONS

This review critically analyzed the integration of IoT, blockchain, and AI/ML technologies across three thematic dimensions: agricultural supply chain traceability, smart farming with predictive intelligence, and breeding/genomic data management. The findings highlight that blockchain ensures transparency, immutability, and trust, IoT enables real-time monitoring of agricultural processes, and AI/ML enhances predictive accuracy and intelligent decision-making. In Theme 1, blockchain–IoT frameworks improved traceability and security across food supply chains, though issues of interoperability and scalability remain unresolved. Theme 2 emphasized predictive modeling for crop health and resource optimization, where hybrid deep learning models such as CNN-LSTM and Bi-LSTM achieved high accuracy (up to 96%) and improved efficiency, yet challenges of energy consumption and cost persist. Theme 3 demonstrated blockchain's role in securely managing high-throughput breeding and genomic data, supported by lightweight architectures and proxy encryption, though concerns around system sustainability and farmer usability continue.

Overall, while significant progress has been made, critical gaps remain in scalability, standardization, and user-centric design. Future research must focus on interoperable, explainable, and sustainable frameworks that combine technological robustness with accessibility for diverse stakeholders. Addressing these gaps will enable IoT–Blockchain–AI ecosystems to evolve into a resilient foundation for next-generation smart agriculture.

VI. AUTHOR'S CONTRIBUTION

Conceptualization: Manoj Praveen V, Mahendrakumar S, Dhanapal R, Kayalvili S and Kirubhakaran Marisamy.
Methodology: Dhanapal R, Kayalvili S and Kirubhakaran Marisamy.
Investigation: Manoj Praveen V.
Discussion of results: Manoj Praveen V, Mahendrakumar S, Dhanapal R, Kayalvili S and Kirubhakaran Marisamy.
Writing – Original Draft: Kayalvili S and Kirubhakaran Marisamy.
Writing – Review and Editing: Manoj Praveen V, Mahendrakumar S, Dhanapal R, Kayalvili S and Kirubhakaran Marisamy.
Resources: Manoj Praveen V.
Supervision: Manoj Praveen V.
Approval of the final text: Manoj Praveen V, Mahendrakumar S, Dhanapal R, Kayalvili S and Kirubhakaran Marisamy.

VII. ACKNOWLEDGMENTS

Author would like to appreciate the effort of the editors and reviewers.

VIII. REFERENCES

[1] S. Charlebois, N. Latif, I. Ilahi, B. Sarker, J. Music, and J. Vezeau, "Digital traceability in agri-food supply chains: A comparative analysis of OECD member countries," Foods, vol. 13, no. 7, p. 1075, 2024. doi: 10.3390/foods13071075.

[2] A. S. Patel, M. N. Brahmbhatt, A. R. Bariya, J. B. Nayak, and V. K. Singh, "Blockchain technology in food safety and traceability concern to livestock products," Heliyon, vol. 9, no. 6, p. e16526, 2023. doi: 10.1016/j.heliyon.2023.e16526.

[3] S. Sajid, G. De Mastro, and C. Pulvento, "IoT-based climate-smart agriculture succeeded by blockchain database: A bibliometric analysis," Frontiers in Sustainable Food Systems, vol. 8, Art. no. 1406871, 2024. doi: 10.3389/fsufs.2024.1406871.

[4] M. Pincheira, M. Antonini, and M. Vecchio, "Integrating the IoT and blockchain technology for the next generation of mining inspection systems," Sensors, vol. 22, no. 3, p. 899, 2022. doi: 10.3390/s22030899.

[5] M. Pincheira, M. Vecchio, and R. Giaffreda, "Characterization and costs of integrating blockchain and IoT for agri-food traceability systems," Systems, vol. 10, no. 3, p. 57, 2022. doi: 10.3390/systems10030057.

[6] G. K. Akella, S. Wibowo, S. Grandhi, and S. Mubarak, "A systematic review of blockchain technology adoption barriers and enablers for smart and sustainable agriculture," Big Data and Cognitive Computing, vol. 7, no. 2, p. 86, 2023. doi: 10.3390/bdcc7020086.

[7] R. M. Ellahi, L. C. Wood, and A. E.-D. A. Bekhit, "Blockchain-driven food supply chains: A systematic review for unexplored opportunities," Applied Sciences, vol. 14, no. 19, p. 8944, 2024. doi: 10.3390/app14198944.

[8] A. Tang, E. T. Tchao, A. S. Agbemenu, E. Keelson, G. S. Klogo, and J. J. Kponyo, "Assessing blockchain and IoT technologies for agricultural food supply chains in Africa: A feasibility analysis," Heliyon, vol. 10, no. 15, p. e34584, 2024. doi: 10.1016/j.heliyon.2024.e34584.

[9] Q. Yao and H. Zhang, "Improving agricultural product traceability using blockchain," Sensors, vol. 22, no. 9, p. 3388, 2022. doi: 10.3390/s22093388.

[10] K. S. Thakur, R. Ahuja, and R. Singh, "IoT-GChain: Internet of things-assisted secure and tractable grain supply chain framework leveraging blockchain," Electronics, vol. 13, no. 18, p. 3740, 2024. doi: 10.3390/electronics13183740.

[11] H. R. Hasan, A. Musamih, K. Salah, R. Jayaraman, M. Omar, J. Arshad, and D. Boscovic, "Smart agriculture assurance: IoT and blockchain for trusted sustainable produce," Computers and Electronics in Agriculture, vol. 224, p. 109184, 2024. doi: 10.1016/j.compag.2024.109184.

[12] P. W. Khan, Y.-C. Byun, and N. Park, "IoT–blockchain enabled optimized provenance system for food industry 4.0 using advanced deep learning," Sensors, vol. 20, no. 10, p. 2990, 2020. doi: 10.3390/s20102990.

[13] M. N. M. Bhutta and M. Ahmad, "Secure identification, traceability and real-time tracking of agricultural food supply during transportation using Internet of Things," IEEE Access, vol. 9, pp. 65660–65675, 2021. doi: 10.1109/ACCESS.2021.3076373.

[14] F. Chen, C. Zhao, X. Yang, N. Luo, and C. Sun, "A lightweight accountable parallel blockchain architecture based on redactable blockchain for agri-food traceability," Foods, vol. 14, no. 4, p. 623, 2025. doi: 10.3390/foods14040623.

[15] H. A. Tahir, W. Alayed, W. Ul Hassan, F. Nabi, and T. X. Tran, "AgriChainSync: A scalable and secure blockchain-enabled framework for IoT-driven precision agriculture," IEEE Access, vol. 12, pp. 162940–162955, 2024. doi: 10.1109/ACCESS.2024.3482550.

[16] A. Shahid, A. Almogren, N. Javaid, F. A. Al-Zahrani, M. Zuair, and M. Alam, "Blockchain-based agri-food supply chain: A complete solution," IEEE Access, vol. 8, pp. 69230–69243, 2020. doi: 10.1109/ACCESS.2020.2986257.

[17] M. Lukacs et al., "Advanced digital solutions for food traceability: Enhancing origin, quality, and safety through NIRS, RFID, blockchain, and IoT," Journal of Sensor and Actuator Networks, vol. 14, no. 1, p. 21, 2025. doi: 10.3390/jsan14010021.

[18] F. J. Pastor, J. M. Pascual, and D. Díaz-Lajara, "Agricultural traceability model based on IoT and blockchain: Application in industrial hemp production," Journal of Industrial Information Integration, vol. 29, p. 100381, 2022. doi: 10.1016/j.jii.2022.100381.

[19] S. A. Bhat, N.-F. Huang, I. B. Sofi, and M. Sultan, "Agriculture-food supply chain management based on blockchain and IoT: A narrative on enterprise blockchain interoperability," Agriculture, vol. 12, no. 1, p. 40, 2022. doi: 10.3390/agriculture12010040.

[20] A. El Mane et al., "Transforming agricultural supply chains: Leveraging blockchain and IoT (end-to-end application)," Smart Agricultural Technology, 2024. doi: 10.1016/j.atech.2024.100031.

[21] T. Guo, Y. Chen, Q. Ren, D. Li, W. Bo, and X. Wang, "Blockchain-based trusted traceability scheme for food quality and safety," Journal of Food Quality, Art. no. 5914078, 2025. doi: 10.1155/jfq/5914078.

[22] A. A. Aliyu and J. Liu, "Blockchain-based smart farm security framework for the Internet of Things," Sensors, vol. 23, no. 18, p. 7992, 2023. doi: 10.3390/s23187992.

[23] R. Chaganti, V. Varadarajan, V. S. Gorantla, T. R. Gadekallu, and V. Ravi, "Blockchain-based cloud-enabled security monitoring using Internet of Things in smart agriculture," Future Internet, vol. 14, no. 9, p. 250, 2022. doi: 10.3390/fi14090250.

[24] T. H. Pranto, A. A. Noman, A. Mahmud, and A. B. Haque, "Blockchain and smart contract for IoT-enabled smart agriculture," PeerJ Computer Science, vol. 7, p. e407, 2021. doi: 10.7717/peerj-cs.407.

[25] N. K. Almazmomi, "Artificial intelligence-driven blockchain and Internet of Things framework for secure data management in precision agriculture," Journal of High Speed Networks, vol. 31, no. 3, pp. 183–201, 2025. doi: 10.1177/09266801251331816.

[26] K. Bakthavatchalam et al., "IoT framework for measurement and precision agriculture: Predicting the crop using machine learning algorithms," Technologies, vol. 10, no. 1, p. 13, 2022. doi: 10.3390/technologies10010013.

[27] T. Manoj, K. Makkithaya, and V. Narendra, "A blockchain-assisted trusted federated learning for smart agriculture," SN Computer Science, vol. 6, p. 221, 2025. doi: 10.1007/s42979-025-03672-4.

[28] M. M. Hossain et al., "Smart-Agri: A smart agricultural management with IoT–ML–blockchain integrated framework," International Journal of Advanced Computer Science and Applications, vol. 14, no. 7, 2023. doi: 10.14569/IJACSA.2023.01407107.

[29] X. Wang et al., "Blockchain-empowered H-CPS architecture for smart agriculture," Advanced Science, vol. 12, no. 27, p. e2503102, 2025. doi: 10.1002/advs.202503102.

[30] S. Atalla et al., "IoT-enabled precision agriculture: Developing an ecosystem for optimized crop management," Information, vol. 14, no. 4, p. 205, 2023. doi: 10.3390/info14040205.

[31] S. Awan et al., "IoT with blockchain: A futuristic approach in agriculture and food supply chain," Wireless Communications and Mobile Computing, Art. no. 5580179, 2021. doi: 10.1155/2021/5580179.

[32] R. S. Chaudhari, S. B. Rane, S. K. Mahajan, R. K. Phanden, and Y. K. Mogal, "Integrated IoT–blockchain architecture for sustainable green supply chains in agriculture equipment manufacturing industries: A TOPSIS approach," International Journal of Computer Integrated Manufacturing, 2025. doi: 10.1080/0951192X.2025.2467085.

[33] J. Hershberger et al., "Making waves in Breedbase: An integrated spectral data storage and analysis pipeline for plant breeding programs," Plant Phenome Journal, vol. 4, p. e20012, 2021. doi: 10.1002/ppj2.20012.

[34] Q. Zhang, Y.-Y. Han, Z.-B. Su, J.-L. Fang, Z.-Q. Liu, and K.-Y. Wang, "A storage architecture for high-throughput crop breeding data based on improved blockchain technology," Computers and Electronics in Agriculture, vol. 173, p. 105395, 2020.

[35] Y.-Y. Han et al., "Research on hybrid crop breeding information management system based on combining ability analysis," Sustainability, vol. 12, no. 12, p. 4938, 2020. doi: 10.3390/su12124938.

[36] H. Basheija, H. Buregyeya, B. Rehema, and W. Tushemereirwe, "Development of information system for tracking breeding traits of improved crops," Journal of Computational Biology and Bioinformatics Research, vol. 11, no. 1, pp. 10–17, 2021. doi: 10.5897/JCBBR2020.0126.

[37] Y.-H. Park, Y. Kim, and J. Shim, "Blockchain-based privacy-preserving system for genomic data management using local differential privacy," Electronics, vol. 10, no. 23, p. 3019, 2021. doi: 10.3390/electronics10233019.

[38] U. Agarwal, V. Rishiwal, M. Shiblee, M. Yadav, and S. Tanwar, "Blockchain-based intelligent tracing of food grain crops from production to delivery," Peer-to-Peer Networking and Applications, vol. 17, no. 6, pp. 3722–3749, 2024. doi: 10.1007/s12083-024-01780-1.

Journal of Engineering and Technology for Industrial Applications

ISSN ONLINE: 2447-0228

ITEGAM-JETIA

Manaus, v.12 n.60, p.908-916 July/August, 2026.
DOI: https://doi.org/10.5935/jetia.v12i60.3824

RESEARCH ARTICLE OPEN ACCESS

A FRACTAL CODING AND TDES-DIMA BASED FRAMEWORK FOR PRIVACY-PRESERVING BIG DATA STORAGE IN CLOUD ENVIRONMENTS

Rajakumar Ponnumani*[1], Sunilkumar Chellaswamy Santhakumari[2], Jaydipkumar H Trivedi[3], Tadikonda Venkata Durga Prasad[4]

[1,2,3,4]Department of Computer Science and Engineering, Parul Institute of Technology, Parul University, Vadodara, Gujarat, India

[1]http://orcid.org/0000-0002-2903-2757, [2]http://orcid.org/0009-0005-5872-3839
[3]http://orcid.org/0009 0004 5701-5550 [4]http://orcid.org/0009-0001-8468-6366

E-mail: *prajakumarkk@gmail.com, lsunilmca1981@gmail.com, Jaydipkumar.trivedi40927@paruluniversity.ac.in, prasad.tvd@gmail.com

ARTICLE INFO

Article History
Received on: February 26, 2026
Reviewed on: March 26, 2026
Accepted on: July 01, 2026
Published on: July 31, 2026

Keywords:
Fractal Coding,
Dynamic Trusted Authentication,
Structural Information,
Sensitivity Allocation,
Confidentiality.

ABSTRACT

The rapid expansion of the big data in cloud facilities has posed immense challenges in terms of storage efficiency, privacy as well as security. To address these issues, this study proposes a Fractal Coding-based Privacy-Preserving Framework with a dynamic trusted authentication architecture to handle big data in cloud systems safely. First the framework divides raw information into blocks and encodes them to small fractal codes minimizing overhead of storage and transmission yet preserving the structure of the information. Then the privacy levels of each blocks are determined by the sensitivity allocation mechanism and much protection is guaranteed on highly sensitive data through assigning the privacy level to the respective divided block. Finally, to strengthen confidentiality, Triple Data Encryption Standard (TDES)-Dynamic Intelligent Multiple Access (DIMA) module added which engages extended TDES encryption together with dynamic authentication to withhold brute force attack and unauthenticated access. The combination of these design balances compression efficiency, the preservation of privacy, and cloud security. Experimental analysis shows that the proposed framework provides a faster decryption, a high transmission efficiency, high data confidentiality of 95% and minimum CPU consumption of 24%.

Copyright ©2026 by authors and Galileo Institute of Technology and Education of the Amazon (ITEGAM). This work is licensed under the Creative Commons Attribution International License (CC BY 4.0).

I. INTRODUCTION

Cloud storage has become the default storage and processing location to hold and operate large datasets due to its easy scaling and reduced initial cost of infrastructure. With the shift of the routine reporting to sophisticated analytics, Machine Learning (ML), and real-time decision systems, the amount and diversity of information stored on clouds had to increase manifold as sensor streams and medical records gave way to multimedia and transaction logs [1], [2]. These expansions put new strains on the manner in which data are stored, accessed and secured necessitating to reconsider the efficiency of storage, privacy guarantees and end to end protection in the clouds [3], [4]. To efficiently store large scale data in the cloud, it is needed to deploy algorithmic compression, smart redundancy, and storage aware data placement together [5]. Conventional ways like deduplication, erasure coding and sharding are predominant in minimizing physical footprint and enhancing durability, but it interacts badly with privacy controls and introduces nontrivial computational and network overhead in the event it operates at web scale. The recent work thus explored more adaptive redundancy mechanisms and erasure-code optimizations to reduce storage overheads without impacting on availability and repairability [6]. Privacy and security are now first-class issues instead of subsequently considered. End-to-end data encryption preserves confidentiality but complicates analytics and deduplication; fully homomorphic cryptographic techniques have been proposed to perform computations on ciphertexts, yet are too expensive to scale with large deployments [7]; and lightweight or certificateless cryptographic designs have been suggested to provide a secure IoT-to-cloud pipeline, but are too expensive to scale to large deployments.

The literature of recent times [8] provides a clear picture of these trade-offs between confidentiality, computability, and the usage of resources and inspire hybrid solutions that decouple data utility and secrecy. The latest optimization and adaptive partitioning techniques have rendered the fractal and self-similarity-based schemes feasible in large heterogeneous data sets [9], and exhibited encouraging enhancement in the ratio of compression and encode/decode performance on real data. These advances indicate that fractal coding can be considered an effective part of a privacy-aware storage pipeline together with an effective parameter encoding and targeted fidelity control. Several recent studies tackled secure cloud storage holistically by some combined homomorphic or searchable encryption with storage verification primitives; others proposed dynamic access control or lightweight authenticators to support data dynamics and audits with low preprocessing costs [10]. These works highlighted the need for storage designs that are simultaneously compression-aware, privacy-driven, and verifiable at scale. Despite these advances, important gaps remain. Many storage schemes either prioritize compression and efficiency at the expense of adaptive privacy controls. Recent redundancy and erasure-code optimizations addressed availability, but did not simultaneously solve sensitivity-aware compression and efficient key management across distributed cloud nodes. Motivated by this gap, the proposed model combines three major concepts: (1) fractal compression (2) a sensitivity allocation layer and (3) TDES-DIMA security layer that provides robust, session-bound access control and layered encryption for high-sensitivity content. At the time of data request dynamic authentication, preventing brute-force attacks and unauthorized access. The contribution of the proposed framework was:

- To remove anomalies, redundancy, and noises in the data, the proposed model uses the partitioning and preprocessing step that maximizes the uniformity of the data, which increases the efficiency of compression and general computational performance.
- To improve storage efficiency without reducing the reconstruction quality the proposed model combines the fractal geometric transformations to achieve the efficient data compression the use of the self-similarity.
- To offer the adaptive privacy preservation, the model under consideration allocates varying levels of sensitivity to data that are based on the contextual and content-specific features of data.
- To resolve both confidentiality of data and user authentication, a new privacy-preserving model based on TDES-DIMA was created to allow big data storage and retrieval in clouds securely.
- To improve scalability, redundancy, and consistency without compromising access controls and efficient retrieval, the proposed model uses distributed cloud storage.

The rest of this paper was arranged in the following way: Section 2 is a review of the privacy preservation methods existing in big data in cloud infrastructures. Section 3 explains the proposed TDES-DIMA framework in great detail and is followed by Section 4 which explains the performance evaluation of the proposed model. Lastly, the study is concluded and the future research directions are outlined in the Section 5.

II. LITERATURE REVIEW

In [11], a partition-based distributed big data model to store personnel information in a cloud environment was proposed, which incorporates ChaCha20 encryption, Dual Stage Data Partitioning (DSDP), and k-anonymization to increase the privacy and confidentiality of the information. The model spreads data through several cloud nodes by using the hash of SHA-512 which is more secure, efficient and fault tolerant than the traditional methods. Nevertheless, it did not have dynamic trust negotiation and adaptive anonymization protocols to deal with various data sensitivity and decentralized key management. The Hierarchical Federated Learning (HFL) approach is suggested by the author of [12] to enhance the scalability, computational efficiency, and privacy of healthcare data analysis. Tests on real and artificial medical data revealed that the HFL framework attained an accuracy of 97% of the model with the minimized privacy leakage. However, limitations variations in performance with data characteristics, and increased computational costs were identified. A SecPri-BGMPOP (Security and Privacy of BoostGraph Convolutional Network-Pinpointing-Optimization Performance), a multi-step architecture that was constructed in [13] to improve the security and privacy of cloud-based big data systems. The model integrated BG Convolutional Network Clustering (BGCNC) to minimize computational complexity and employed pinpointing-based encryption to mitigate key leakage risks. Also, the optimization algorithm was used to optimize the generation of encryption keys to enhance better accuracy and efficiency. The model, however, should be able to speed encryption and decryption to enable its use in large applications. One of the studies [14] suggested a scalable method of big data multidimensional anonymization through MapReduce. The main concept was to break down the dataset recursively into small portions using MapReduce until all the partitions had fit in the memory of a computing node. It came up with a tree indexing structure so that it could compute recursively. Moreover, the analysis revealed the relevance of the method to differential privacy.

The experimental findings demonstrated that the suggested approach enhanced the scalability significantly. The study [15] suggested the lightweight matrix factorization framework or personalized recommendations, in which shard gradient training on user IoT device facilitated the local learning of the model without data exposure. A two-phase design guaranteed the security of the data and dimensionality reduction and a stabilization mechanism was used to reduce the gradient perturbation. In experimental assessments, there was greater accuracy, efficiency and privacy than the existing measures. On the same note, the authors of [16] presented a user-customized model of differential privacy based on the level of trust among the users, which is measured by the density of the community and implemented by controlled randomized noise. A noise correlation decoupling mechanism based on Markov and a blockchain-powered community modeling further avoided linkage and poisoning attacks and ensured a better privacy protection. The research [17] offered the TDES technique to ensure high-security levels in the analysis of extensive data. Implementation of TDES improved security of data transmission and storage to avoid the unauthorized access and data leakage. It was able to trade off the strength of encryption with the complexity of computations by using simulation-based tests on large datasets. The study [18], has also put forward an effective and dynamic verification scheme on cloud based Industrial Internet platform (IIP). It was designed using a homomorphic authenticator that was very lightweight and an authenticator accumulator and reduced the computational overhead during preprocessing of the data.

The accumulator of the authenticator was enhanced with dynamic information so that it can make safe changes and updates in the data. In [19], a Two-Step Authentication Inner Product Functional Encryption (TSA-IPFE) scheme was suggested to a three-tier cloud-edge-smart device architecture. The model allowed the dynamic management of authorizations by a two-step mechanism of identity-matching and the efficient revocation of the computational authorizations of migration during device migration. The semantic security, anonymity, and increased efficiency of the simulation proved the superiority over the current algorithms. In [20] presented a TDES-based approach to improve the confidentiality and integrity of the large healthcare information stored in the cloud. The above cloud storage was offered a secured read-write operation and was not susceptible to unauthorized access because it encrypted patient-related data before cloud storage. Its effectiveness in protecting healthcare data was validated with the help of the experiment. The model however had a problem of long computational time.

II 1 RESEARCH GAP

The literature review indicates that there are still unresolved issues in guaranteeing efficient, secure and privacy-conscious big data management in cloud setups. The currently available models including partition-based storage [11], HFL [12], and multi-stage encryptions frameworks [13] have enhanced confidentiality, scale and computation efficiency but remain to be characterized with significant weaknesses. These are lack of dynamically negotiated trust, adaptive anonymization and decentralized key management schemes alongside larger computational and encryption costs of large-scale or heterogeneous data. Further, the conventional encryption schemes [20] are still computationally demanding which implies that there is a necessity of a less heavyweight, more adaptable and distributed security system to balance privacy, efficiency and scalability of the various cloud-based big data uses.

III. PROPOSED FRAMEWORK OVERVIEW

In this section the proposed model Fractal Coding, TDES-DIMA based framework of the big data in cloud is presented. The first step of the model splits the raw heterogeneous data into smaller blocks in order to be preprocessed and normalized. The blocks are then coded using fractal coding method, which takes advantage of the self-similarity of data in order to obtain a high compression with minimum loss. The sensitivity allocation mechanism is built in to allocate levels of privacy depending on the importance of the data. In order to maintain confidentiality, the TDES-DIMA module uses extended TDES encryption and dynamic authentication in order to ensure access and avoid illegal use. Lastly, the stored and encrypted information is retrieved and stored on distributed cloud systems.

Phase 1: Data Ingestion

In order to make the simulation closer to real-world a huge heterogeneous data were simulated in the form of a dataset, which recreates multi source data properties such as time-series sensor measurements, medical imaging data fragments and enterprise transaction data. This is a simulated data that makes it scalable and also variable so as to accommodate both structured and unstructured data. The ingested dataset is represented as:

$$D = \{d_1, d_2, d_3, \ldots d_i\} \tag{1}$$

Here d_i is a raw data that has values obtained by a specific source. The heterogeneous data is prepared to further handle the framework.

Phase 2: Partitioning and Preprocessing

After the ingestion of the dataset into the cloud gateway, it passes through the stage of partitioning and preprocessing to be analyzed further. The large data D is broken into smaller data blocks that can be managed in terms of source type, data format, or sampling rate. The metadata linked to every block is Source ID S_i, Timestamp T_i, and Consent Flag C_i as presented in the Figure 1. This association is expressed as follows:

$$M_i = \{S_i, T_i, C_i\} \tag{2}$$

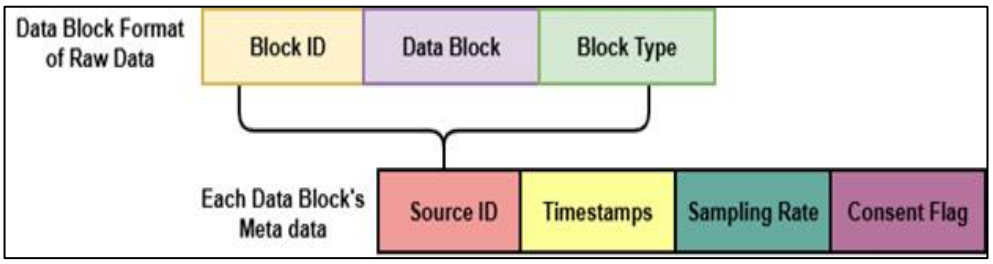


Figure 1: Data Block Format.
Source: Authors, (2026).

The cleaning, normalization and noise removal processes of each block b_i are performed:

$$b_i = f_{norm}(f_{clean}(d_i)) \tag{3}$$

In order to ensure the consistency of the heterogeneous data, z-score normalization is used:

$$x' = \frac{x-\mu}{\sigma} \tag{4}$$

In this case, x is the raw value, μ is the mean, and σ is the standard deviation of the data set. In preprocessing, unnecessary, corrupt, or missing records may be eliminated and the data are normalized so that, it is consistent across various modalities including images, waveforms, tabular records and text blocks. This makes each block of data structurally coherent, and also makes metadata integrity.

Phase 3: Fractal Coding

Here, the processed and segmented data blocks are broken down into fractal coded blocks, which is a mathematical compression algorithm which exploits the self-similarity in data to reduce redundancy and realize high compression efficiency. The main aim of this stage is to symbolize every data block in terms of fractal transformations, which result in a small size of storage, but do not compromise any important structural and statistical data. All preprocessed blocks b_i are subdivided into two categories, range blocks (r) and domain blocks (db). The process identifies a transformation T_i that best maps a domain block db_j to a range block r_i through geometric and intensity adjustments. This mapping relation is stated to be:

$$r_i = T_i(db_j) \tag{5}$$

The transformation T_i uses an affine transformation, scale and offset of the intensity levels of the data block to provide optimal similarity. Mathematically, this is expressed as:

$$T_i(x) = \alpha_i x + \beta_i \tag{6}$$

In this case, the scaling factor of contrast, α_i, and the offset of a data block, β_i. These two values are computed by minimizing the reconstruction error between the original and transformed block in terms of Mean Squared Error (MSE) criterion:

$$E = \min_{T_i} \sum_{x \in r_i} (r_i(x) - T_i(db_j(x)))^2 \tag{7}$$

When the optimum transformation parameters have been generated, it gets stored as a fractal code that represents the block of data. The parameters in each of the codes are: α_i, β_i the domain block ID db_j and E the corresponding error metric.

$$f_i = \{\alpha_i, \beta_i, db_j, E\} \tag{8}$$

These space-efficient fractal codes are stored instead of the original data, and this helps to save a lot of storage space since only these compact codes are stored.

Phase 4: Sensitivity Allocation

At this stage, the fractal-coded blocks that were extracted in the step above are processed and categorized according to their sensitivity level in order to create a privacy-conscious dataset. The objective of this stage is to make sure that data blocks that entail sensitive data are given more robust protection mechanisms. The f_i fractal-coded block is rated according to its sensitivity level (sl_i) which, depending on the metadata and sensitivity of the content of the context (e.g., medical identifiers, financial information):

$$sl_i = f_{priv}(S_i, C_i, D_i) \tag{9}$$

Depending on the calculated sl_i, the fractal-coded block is classified into one of three categories:

- High-sensitive (H)- Blocks of data that include critical or personally identifiable information (e.g. medical identifiers, financial attributes). These blocks need high level of encryption and high-fidelity reconstruction to maintain the integrity of data.
- Medium-sensitive (M) – Medium significance blocks that are the subject of balanced protection with mild compression that can be accepted without intrusion to privacy.
- Low-sensitive (L) – Blocks that hold non-crucial data that can be stored or recreated roughly, so that lossy compression can be used to achieve best storage and computational efficiency.

After identifying the sensitivity class of a given block, all the fractal-coded blocks are labeled with the sensitivity level, creating privacy-aware representation of:

$$tag_i = \{f_i, sl_i\} \tag{10}$$

The sensitivity-based tagging tag_i brings about a change in encryption and reconstruction fidelity during later stages.

Phase 5: Security with TDES-DIMA and Storing in Cloud

This stage is used to make sure that data confidentiality and integrity is upheld especially when dealing with high-sensitive fractal-coded blocks detected in the former stage. The stage involves combination of Triple DES and DIMA mechanism to ensure protection of sensitive data against unauthorized access and identity spoofing at the same time maintaining efficient retrieval and verification. All highly sensitive block f_i are encrypted by TDES algorithm that uses three consecutive encryptions and decryptions with different keys (k_1, k_2, k_3). The ciphertext block c_i is obtained by encrypting the plaintext block p_i using the following format:

$$c_i = e_{k_3}(d_{k_2}\left(e_{k_1}(p_i)\right)) \tag{11}$$

Here e and d denote encryption and decryption operations, respectively. This multiple level encryption provides high levels of cryptographic robustness because exploiting one key will not give the whole dataset. The process of decryption restores the transformation to retrieve the original plaintext which is defined as:

$$p_i = d_{k_1}(e_{k_2}\left(d_{k_3}(c_i)\right)) \tag{12}$$

The DIMA mechanism presents a dynamic authentication mechanism which identifies users and devices on a session basis. Each access attempt is authenticated with a representation of the formulation based on hash: a session-specific authentication token is produced.

$$A_{token} = h(Id_u \oplus T_s \oplus R_n) \tag{13}$$

In this case, the identity of the unique user or device, a timestamp to verify freshness of the session, and a random nonce to prevent predictability are denoted as Id_u, T_s and R_n respectively. The $h(.)$ is a safe hash function that generates a special token on each access instance, and therefore offers time-limited and identity-based access control. This is done to stop replaying and impersonation attacks through this mechanism of continuously updating the session tokens with time and random variations. The general structure of the proposed model is presented in figure 2.

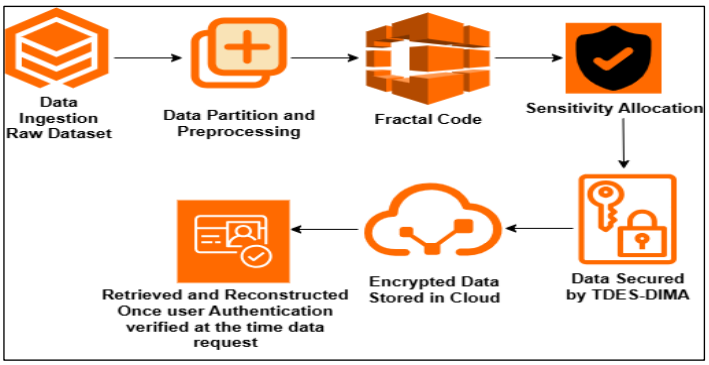


Figure 2: Overall Architecture Diagram of Suggested TDES-DIMA.
Source: Authors, (2026).

The privacy-tagged and securely encrypted data is sent to the distributed cloud storage facility of scalable hosting, high availability, as well as fault tolerance. The distributed architecture also provides greater reliability and redundancy of the data stored in the system such that, when a node fails, the data can be retrieved out of the replicas. The redundancy and reliability (R_d) of the stored dataset is given as:

$$R_d = \frac{n_{rep}}{n_{tot}} \tag{14}$$

Here n_{rep} is the replication of data blocks and n_{tot} is the sum of all the stored blocks. This makes sure that an adequate data replication feature is replicated at the cloud infrastructure. As a result, the distributed storage system has a secure, scalable, and fault-tolerant data management.

Phase 6: Retrieval & Reconstruction

At this last stage, the retrieval and reconstruction procedures will start with a legitimate user placing a data access request to the cloud system. First, DIMA mechanism authenticates the user by session based authentication tokens to confirm authorized access. The system then verifies that the content is correct and then decrypts the sensitive blocks of data with the help of the TDES decryption routine as previously described and gets the original encrypted data. The blocks of the fractal-coded data are then decrypted and reassembled using inverse fractal transformations, restoring the dataset with fidelity levels matching the sensitivity tag of each block, a high sensitive block is reassembled with its full precision whereas a low sensitive block can be reassembled with approximations to achieve more efficiency. The general reconstruction procedure can be formulated as:

$$\hat{d} = f_{recon}(d_{dec}, sl_i) \tag{15}$$

Here $\hat{d}$ denotes the reconstructed dataset, d_{dec} represents the decrypted fractal-coded blocks, and sl_i indicates the sensitivity level of each block guiding the reconstruction fidelity. This phase ensures that the final output is a securely reconstructed dataset, preserving both data privacy and analytical integrity. Where $\hat{d}$ signifies the reconstructed data, d_{dec} signifies decrypted fractal-coded blocks, and sl_i signifies the sensitivity degree of every block that determines the reconstruction fidelity. In this stage, the data is securely reconstructed and both data privacy and data analytical integrity are maintained in the final output.

IV. RESULTS AND DISCUSSIONS

The proposed model enhances security of big data on a cloud environment with Python software in a system with 6GB of a graphics card, 16GB of RAM, i7 core processor, and windows 10 OS. This section describes the comparison of the proposed method and the existing methods. The proposed TDES-DIMA model was compared with throughput of the current SecPri-BGMPOP [13] and Standard TDES as Figure 3. The proposed model showed that in 75 blocks, it had 105 ms, which was above the SecPri-BGMPOP (45 ms), and Standard TDES (80 ms).

With the block count of 300, the throughput was 118 ms, which was 84% and 36% higher than the SecPri-BGMPOP (64 ms) and Standard TDES (87 ms), respectively. The proposed model had a better performance at the highest block size, 525, with 140 ms, which is 72.8% better than SecPri-BGMPOP (81 ms) and 12 times better than Standard TDES (125 ms).

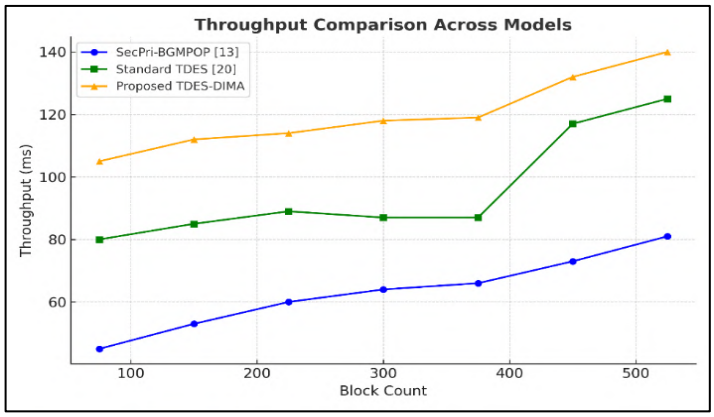


Figure 3: Throughput Analysis.
Source: Authors, (2026).

SecPri-BGMPOP model despite being effective in preserving privacy had disadvantages in that it was slow when encrypting and decrypting large data thus its application was limited in scaling. On the same note, the Standard TDES method had considerable delays because of its abundance of computational time. On the contrary, the proposed model of TDES-DIMA has addressed these disadvantages by incorporating DIMA which made it simpler to access and minimize key usage when encrypting. This mechanism minimized redundant calculations and thus enhance data processing efficiency and hence increase in throughput especially during heavy work loads.

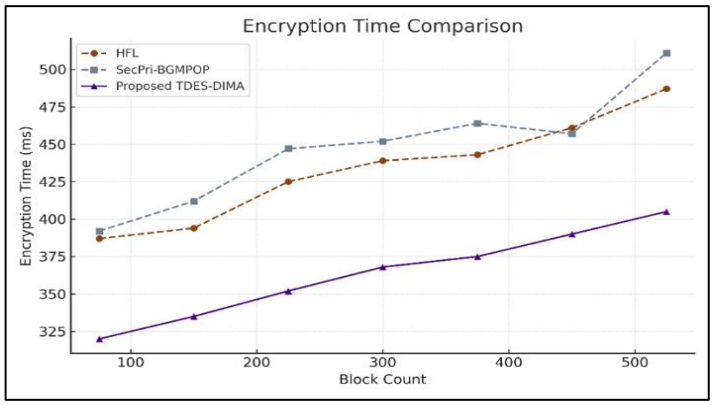


Figure 4: Encryption Time.
Source: Authors, (2026).

It is evident in the comparative analysis between encryption and decryption time that HFL [12], SecPri-BGMPOP, and the proposed model of TDES-DIMA have different differences in computational efficiency. Based on the Figure 4 the HFL framework showed moderate encryption performance, with a base of 387 ms and 487 ms at 75 and 525 blocks, respectively, and is mainly caused by the hierarchical data aggregation process which, although enhances scalability and privacy, introduces latency as a result of the multiple communication layers.

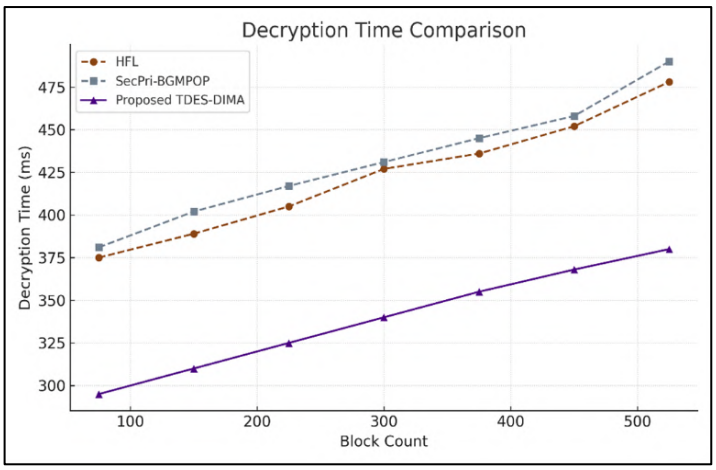


Figure 5: Decryption Time.
Source: Authors, (2026).

Equally, the SecPri-BGMPOP model had a slightly longer encryption time, with a range of 392 ms to 511 ms since the multi-stage encryption events combined with pinpointing-based key generation incurred some extra overhead. This is consistent with its well-established weakness of taking acceleration to encrypt and decrypt messages. By contrast, the proposed TDES-DIMA had a more stable encryption time, ranging between 318 and 409 ms, and decryption time, between 298 and 379, as shown in the Figure 5. This was achieved because of the effective management of sensitivity-based data prioritization that allows faster encryption and decryption of large data without reducing the security and proves the suggested model to be a good balance in the computational workload and privacy conservation where the previous framework had a struggle to balance the increased latency and resource utilization. Figure 6 shows the latency test of the proposed model when compared to the current frameworks. The latency was found to be between 260 ms and 350ms with increasing block count in the HFL model, largely due to its data aggregation layering and federation coordination schemes where frequent synchronization across the distributed nodes was necessary leading to communication bottlenecks. Equally, the model SecPri-BGMPOP had latency levels of between 245 ms and 340 ms which is largely attributed to its sequential encryption and clustering algorithm and pinpointing based optimization; which added more computational burden to the process of intermediate data exchanges.

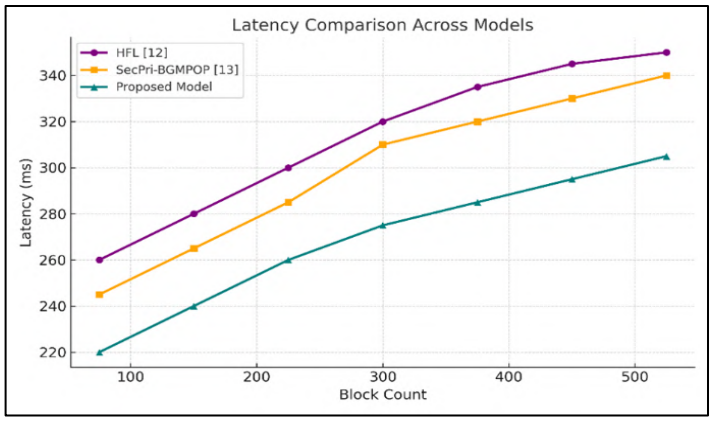


Figure 6: Latency Analysis.
Source: Authors, (2026).

Conversely, the proposed model recorded lower latency of 220 ms to 305 ms with the encapsulated data fractal-based encoding and streamlined block handling system which reduced the overhead of repetitive computation and data transfer. This integration also created a faster response time as the adaptive processing flow was integrated and capable of supporting the high-volume operations of data in cloud-based systems and with minimal delays. Figure 7 presents the relative comparison of data confidentiality and CPU use of DSDP [11], HFL, and the proposed model. The DSDP model had a confidentially rate of 81% and a CPU usage of 32 and this was mainly attributed to its fixed anonymization and lack of dynamically negotiated trust which restricted its versatility in negotiating heterogeneous and sensitivity-varying data. HFL framework increased the confidentiality to 89% with a minor decrease of CPU usage to 29% but the performance of HFL varied with changes in data distribution and feature complexity resulting in varying privacy levels between datasets.

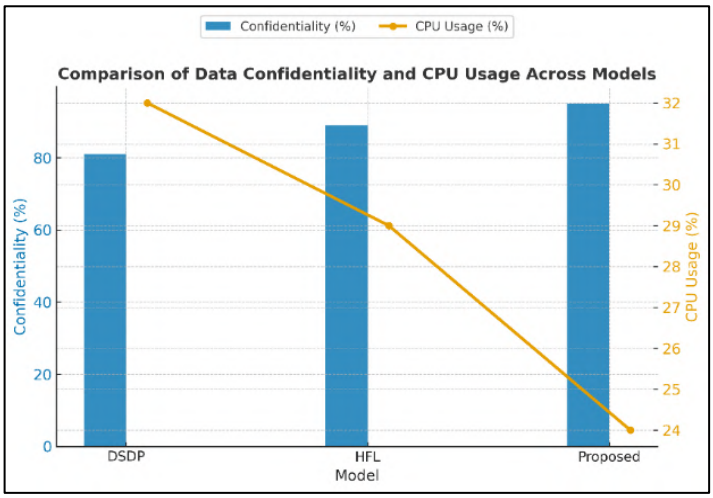


Figure 7: Confidentiality Analysis.
Source: Authors, (2026).

By contrast, the proposed TDES-DIMA framework reached the highest confidentiality of 95% and the lowest CPU consumption of 24% which is 17.3% improvement in confidentiality and 25% decrease in CPU consumption as compared to DSDP. The suggested model had minimal CPU consumption because of optimized fractal coding mechanism that compresses and encodes blocks of data efficiently which minimizes redundant calculations when encryption and retrieval is taking place. The secrecy was due to the dynamic trusted authentication process which highly verifies user identities prior to providing access so that only authorized users can decrypt and manipulate sensitive data.

V. CONCLUSIONS

This study proposed a Fractal Coding based Privacy- Preserving Framework to manage big data safely and efficiently in cloud computing. The framework was useful to minimize the computational cost, in addition to enhancing data confidentiality and security, through fractal coding of compact data representation, sensitivity-based privacy distribution, and TDES-DIMA module of dynamic encryption and authentication. The experimental findings attested that the proposed model attained the best confidentiality of 95% and lowest CPU consumption of 24% indicating the best performance among existing methods. Fractal based compression strategies and sensitivity-based encryption strategies also helped to enhance throughput, latency and better use of storage. To work with hybrid cloud-edge environments in the future, the framework could be expanded to address the latency reduction even more and increase the scalability. The inclusion of quantum-resistant cryptography and AI-assisted adaptive trust should also result in increased resilience to new cyber-threats.

VI. AUTHOR'S CONTRIBUTION

Conceptualization: Rajakumar Ponnumani, Sunilkumar Chellaswamy Santhakumari, Jaydipkumar H Trivedi and Tadikonda Venkata Durga Prasad.
Methodology: Jaydipkumar H Trivedi and Tadikonda Venkata Durga Prasad.
Investigation: Rajakumar Ponnumani, Sunilkumar Chellaswamy Santhakumari, Jaydipkumar H Trivedi.
Discussion of results: Rajakumar Ponnumani, Sunilkumar Chellaswamy Santhakumari, Jaydipkumar H Trivedi.
Writing – Original Draft: Rajakumar Ponnumani.
Writing – Review and Editing: Rajakumar Ponnumani, Sunilkumar Chellaswamy Santhakumari.
Resources: Rajakumar Ponnumani.
Supervision: Rajakumar Ponnumani a d Sunilkumar Chellaswamy Santhakumari.
Approval of the final text: Rajakumar Ponnumani, Sunilkumar Chellaswamy Santhakumari, Jaydipkumar H Trivedi and Tadikonda Venkata Durga Prasad.

VII. ACKNOWLEDGMENTS

The author would like to appreciate the effort of the editors and reviewers.

VIII. REFERENCES

[1] M. El Moudni and E. Ziyati, "Advances and challenges in cloud data storage security: A systematic review," Int. J. Saf. Secur. Eng., vol. 15, no. 4, pp. 653–675, 2025. doi: 10.18280/ijsse.150403.

[2] M. Pathak, K. N. Mishra, and S. P. Singh, "Securing data and preserving privacy in cloud IoT-based technologies: An analysis of assessing threats and developing effective safeguard," Artif. Intell. Rev., vol. 57, p. 269, 2024. doi: 10.1007/s10462-024-10908-x.

[3] M. Z. Khan, M. Shoaib, M. S. Husain, et al., "Enhanced mechanism to prioritize cloud data privacy factors using AHP and TOPSIS: A hybrid approach," J. Cloud Comput., vol. 13, p. 42, 2024. doi: 10.1186/s13677-024-00606-y.

[4] J. Makadia and P. Patel, "Review on cryptographic techniques for privacy-preserving data sharing in cloud," 2025. doi: 10.2139/ssrn.5360584.

[5] C. Ramesh, B. Srinivasulu, M. S. Babu, et al., "An effective data replication strategy and the improvement of the storage environment," in Intelligent Systems and Sustainable Computing, ICISSC 2024, Smart Innovation, Systems and Technologies, vol. 417, Singapore: Springer, 2025. doi: 10.1007/978-981-97-8355-7_32.

[6] M. Cui and Y. Wang, "EC-Kad: An efficient data redundancy scheme for cloud storage," Electronics, vol. 14, no. 9, p. 1700, 2025. doi: 10.3390/electronics14091700.

[7] R. Hu, C. He, S. Liu, D. Yao, and X. Li, "A fully homomorphic encryption scheme suitable for ciphertext retrieval," Comput. Mater. Continua, vol. 84, no. 1, pp. 937–956, 2025. doi: 10.32604/cmc.2025.062542.

[8] H. Guo, X. Li, and H. Qin, "A lightweight and secure certificateless encryption scheme for smart city IoT security," Discov. Comput., vol. 28, p. 104, 2025. doi: 10.1007/s10791-025-09626-x.

[9] M. Li and U. K. Tak, "An enhanced fractal image compression algorithm based on adaptive non-uniform rectangular partition," Electronics, vol. 14, no. 13, p. 2550, 2025. doi: 10.3390/electronics14132550.

[10] M. S., K. S. K., T. V., G. S., and D. S., "Dynamic access control through cryptography in cloud," ITM Web Conf., vol. 56, p. 06001, 2023. doi: 10.1051/itmconf/20235606001.

[11] T. Ting and M. Li, "Enhanced secure storage and data privacy management system for big data based on multilayer model," Sci. Rep., vol. 15, p. 32285, 2025. doi: 10.1038/s41598-025-16624-y.

[12] J. P. Singh, A. Aqsa, I. Ghani, R. Sonani, and V. Govindarajan, "Privacy-aware hierarchical federated learning in healthcare: Integrating differential privacy and secure multi-party computation," Future Internet, vol. 17, no. 8, p. 345, 2025. doi: 10.3390/fi17080345.

[13] M. Kuttiyappan, J. P. Appadurai, B. P. Kavin, et al., "Big data privacy protection and security provisions of the healthcare SecPri-BGMPOP method in a cloud environment," Mathematics, vol. 12, no. 13, p. 1969, 2024. doi: 10.3390/math12131969.

[14] X. Zhang, et al., "MRMondrian: Scalable multidimensional anonymisation for big data privacy preservation," IEEE Trans. Big Data, vol. 8, no. 1, pp. 125–139, 2022. doi: 10.1109/TBDATA.2017.2787661.

[15] H. Zhou, G. Yang, Y. Xiang, Y. Bai, and W. Wang, "A lightweight matrix factorization for recommendation with local differential privacy in big data," IEEE Trans. Big Data, vol. 9, no. 1, pp. 160–173, 2023. doi: 10.1109/TBDATA.2021.3139125.

[16] Y. Qu, et al., "Towards privacy-aware and trustworthy data sharing using blockchain for edge intelligence," Big Data Min. Anal., vol. 6, no. 4, pp. 443–464, 2023. doi: 10.26599/BDMA.2023.9020012.

[17] H. Byeon, M. Evin, A. U. Mirza, and S. Murugesan, “Triple data encryption standard based secured and privacy preserved big data analytic,” AIP Conf. Proc., vol. 3306, p. 050009, 2025. doi: 10.1063/5.0275945.

[18] H. Yu, H. Zhang, Z. Yang, and S. Yu, “Edasvic: Enabling efficient and dynamic storage verification for clouds of industrial Internet platforms,” IEEE Trans. Inf. Forensics Secur., vol. 19, pp. 6896–6909, 2024. doi: 10.1109/TIFS.2024.3422790.

[19] H. Yang and C. Peng, “TSA-IPFE: A secure solution for authorization revocation and dynamic identity assignment in IoT,” IEEE Internet Things J., vol. 12, no. 12, pp. 20288–20300, 2025. doi: 10.1109/JIOT.2025.3544641.

[20] M. N. Ramachandra, M. S. Rao, W. C. Lai, B. D. Parameshachari, J. A. Babu, and K. L. Hemalatha, “An efficient and secure big data storage in cloud environment by using triple data encryption standard,” Big Data Cogn. Comput., vol. 6, no. 4, p. 101, 2022. doi: 10.3390/bdcc6040101.

Journal of Engineering and Technology for Industrial Applications

ITEGAM-JETIA

Manaus, v.12 n.60, p.917-932 July/August, 2026.
DOI: https://doi.org/10.5935/jetia.v12i60.3901

ISSN ONLINE: 2447-0228

RESEARCH ARTICLE OPEN ACCESS

A MULTI-DOMAIN FEATURE FRAMEWORK FOR ROBUST DEEPFAKE AUDIO DETECTION

Akshat Chhatriwala[1*], Ishita Akolkar[2], Namrata Shroff[3], Shankar Parmar[4]

[1, 2, 3]Computer Engineering Department, Government Engineering College, Bharuch, India,
[4]Electronics and Communication Engineering Department, Government Engineering College, Godhra, Gujarat, India

[1]http://orcid.org/0009-0005-1256-3075, [2]http://orcid.org/0009-0002-3237-2565
[3]http://orcid.org/0000-0001-6343-6205, [4]http://orcid.org/0000-0002-3034-5144

E-email: 220140107009@gtu.edu.in, 220140107002@gtu.edu.in, namrata.gecb@gmail.com, shankar.parmar@gtu.edu.in

ARTICLE INFO

Article History
Received on: March 04, 2026
Reviewed on: April 02, 2026
Accepted on: July 01, 2026
Published on: July 31, 2026

Keywords:
Deepfake Audio Detection,
Synthetic Speech,
Multi-Domain Feature Fusion,
Audio Forensics

ABSTRACT

Audio deepfakes generated by modern text-to-speech and voice conversion systems pose serious threats to security, privacy, and trust in digital communication. This study proposes a multi-domain feature fusion framework for robust deepfake audio detection under realistic, in-the-wild conditions. A large-scale dataset comprising 31,780 audio samples, evenly split between genuine and synthetic speech and covering diverse speakers, languages, and recording environments, is utilized. Acoustic, compression-related, emotional, phase-based, prosodic, and statistical–spectral features are extracted and fused, and classification is performed using a lightweight fully connected neural network evaluated via stratified five-fold cross-validation. The proposed system achieves an average validation accuracy of 98.03% and an AUC of 0.998, demonstrating strong and stable discriminative performance. Ablation experiments and SHAP-based analysis highlight the critical role of compression-related features in enhancing robustness when combined with other feature domains. While the study focuses on audio-only detection and does not address adversarial or multimodal scenarios, the results indicate that multi-domain feature fusion offers a practical and generalizable solution for real-world deepfake audio detection, particularly in environments involving diverse codecs and synthesis techniques.

Copyright ©2026 by authors and Galileo Institute of Technology and Education of the Amazon (ITEGAM). This work is licensed under the Creative Commons Attribution International License (CC BY 4.0).

I. INTRODUCTION

The evident growth of generative models shows significant transformation in the field of synthetic media, leading to the creation of hyper-realistic audio content commonly referred to as deepfake audio. These deepfake audios or artificially manipulated speech signals convincingly create a replica of the voice, tone, and prosody of the target speaker, even with minimal input data. Such advancement, even with certain legitimate applications in entertainment and personalized user interface, poses serious threats to privacy, security, and information integrity. In particular, the capacity of audio deepfakes to convincingly impersonate individuals has opened avenues for misinformation campaigns, identity theft, and high-stakes fraud [1]. Audio deepfakes are predominantly produced using neural architectures such as text-to-speech (TTS) synthesis, voice conversion (VC), and end-to-end speech generation using generative adversarial networks (GANs), variational autoencoders (VAEs), or transformers [2], [3], [4]. To capture the intricate patterns of human speech, large-scale datasets and complex acoustic modelling are being used. Near-human naturalness in synthesized speech and significant narrowing of the perceptual gap between real and fake audio have been demonstrated by recent TTS systems like VITS [5] and StyleTTS [6]. Consequently, the state-of-the-art automatic speaker verification (ASV) systems are vulnerable to adversarial exploitation. The threats associated with the audio deepfakes are not merely hypothetical but have posed real issues to society. These threats force the need to develop a reliable and explainable detection mechanism capable of performing under an adversarial environment, and real-world, noisy data [7]. Even with the evident increased attention towards audio deepfakes, this field remains under-explored compared to visual deepfakes.

The significant problems for the audio deepfake detection include the diversity of generative models and synthesis techniques, the lack of comprehensive and generalized datasets, and the difficulty of identifying consistent acoustic artifacts across variable conditions [8]. The state-of-the-art detection methods generally rely on spectral anomalies, prosodic irregularities, or embeddings learnt through deep neural networks. However, these models fail to be accurate beyond the specific conditions of the dataset under which they were developed, limiting their practical usage [9], [10]. This fast development of audio deepfake technology is a major challenge, which demands the advancement of robust detection methods that are capable of addressing both the technical and ethical implications of these manipulations [11], [12]. Through the application of a multi-domain feature fusion strategy utilizing acoustic, compression, emotional, phase, prosodic, and spectral features, this paper addresses these problems. The system aims at high accuracy and generalization in a wide range of conditions with a robust and interpretable deep neural network architecture. A large, in-the-wild dataset that has been carefully curated to reflect the conditions in the real world is employed for the study. The efficacy and interpretability of the proposed method are established through multiple experiments, setting a new benchmark for reliable audio deepfake detection [13]. In the subsequent sections, a comprehensive literature review is discussed in Section 2, the proposed methodology is described in detail in Section 3, experimental setup and findings are given in Section 4, key findings and future work are elaborated in Section 5, and a list of contributions is summarized in Section 6.

II. LITERATURE REVIEW:

Prior research in deepfake audio detection has evolved through distinct methodological paradigms, from spectral feature analysis to advanced temporal modeling and generalization strategies. This section synthesizes key advancements, highlighting their contributions, limitations, and persistent challenges in achieving robust, generalizable detection across diverse synthesis techniques and real-world conditions.

II.1 SPECTRAL FEATURE DOMINANCE:

A work on generalization in audio deepfake detection investigates CNN-based models trained on log-Mel spectrograms using the ASVspoof 2019 Logical Access corpus. The model is well-performing on familiar vocoders with an Equal Error Rate (EER) of around 1.4%, but there was a significant dip in performance around 18% EER when tested with unfamiliar vocoders. This is one of the biggest challenges of generalization since the models tend to overfit on spoof types [14]. A study employed MFCCs along with basic classifiers such as k-NN, SVM, and decision trees to identify deepfake TTS-synthesized speech. With 85–88% accuracy on the dataset it created, the paper demonstrated that although MFCCs offer a good baseline, they fall short in detecting more sophisticated or novel manipulations. This study thus benchmarks simple features and models for the detection of deepfakes [15]. A benchmark study on deep learning compared CNN, CRNN, LSTM, and Transformer architectures with spectrogram input. CRNN models showed optimal trade-off between accuracy and efficiency with EERs of around 3–4%, whereas Transformers demonstrated better generalization. Scalability and performance with real-time usage was the primary emphasis of this research with utilizing ASVspoof 2019 and WaveFake datasets [16]. SpecViT used a Vision Transformer on log-Mel spectrogram patches and included speaker embeddings. Outperforming CNNs with an EER of roughly 1.8%, SpecViT showed good generalization to out-of-dataset data. This method brought ViT-style token learning to time-frequency modeling for deepfake detection from datasets such as WaveFake and ASVspoof LA [2].

II.2 TEMPORAL AND MULTI-SCALE DYNAMICS:

A two-branch CNN-BiGRU model combined spectral and temporal evidence through cross-attention. With an EER below 2% on ASVspoof LA and DFDC-Audio, this technique emulated human perception processes by combining features dynamically in a multiscale manner. It offered an effective architecture for identifying varied audio deepfakes [17]. Another research emphasized voiced and unvoiced region analysis, demonstrating that fake cues are more prominent in voiced parts of speech. Through the evaluation of energy, zero-crossing rate, and variation of pitch in these parts, the research attained 91% accuracy with straightforward models. It presented a new outlook for localized temporal analysis for better detection efficiency [18]. A work utilized direct and reverberant forms of audio signals to enhance robustness in deepfake detection. By training a dual-branch model on both channels jointly with contrastive loss, it learned subtle cues from the reverberation and improved generalizability. Tested on LA and DF-TIMIT datasets, the model achieved an EER of 5.4%, better than single-channel methods and demonstrating the contribution of acoustic realism to fake audio detection [19]. Wave-spectrogram fusion was introduced in an attempt to better handle audio deepfake detection with improved generalizability. The WaveSpec model simultaneously processes raw waveform and spectrogram features with the help of multi-scale fusion and cross-modal alignment, which allows it to better identify out-of-domain forgeries. It obtained state-of-the-art results on ASVspoof2021 and In-The-Wild datasets, demonstrating improved resistance against diverse manipulation methods [20].

II.3 GENERALIZATION AND ROBUSTNESS STRATEGIES:

A study introduced a GAN-based anomaly detection technique trained on only real audio. Assuming counterfeited audio as an anomaly, the model had about 92% detection accuracy with generator loss as an anomaly score. The unsupervised technique prevents overfitting to a certain type of spoof and promises better generalization. The system was tested on the ASVspoof LA dataset [21]. A refinement strategy for the latent space coupled with manifold mixup augmentation was introduced to enhance generalizability in audio deepfake detection. Aligning the latent features and increasing training diversity, the technique minimized overfitting to individual deepfake generators. Evaluated on ASVspoof and FakeAVCeleb, the technique registered a 10–15% decrease in EER on novel attack types, highlighting the strength of feature-space regularization [22]. An incremental learning system for unsupervised domain adaptation was introduced in a paper to prevent performance degradation in dynamic audio scenarios. By employing a memory-light domain discriminator and contrastive learning, the model learns to adapt incrementally without access to target labels.

Cross-domain performance improved by up to 30% on ASVspoof and In-the-Wild datasets during evaluation, making its real-world deployment without retraining from scratch prominent [23]. A study proposed a two-branch adversarial training paradigm that localizes partial deepfake segments in audio through feature gradient refinement. The method improves contrast between real and artificial speech segments with a gradient-guided loss and sharpening in feature space. Evaluated on the Fake-or-Real and Partial-Fake datasets, it recorded more than 80% EER gain over baselines, which indicates its robustness in localizing partial manipulations in speech [24].

II.4 SPECIALIZED AND SURVEY PERSPECTIVES:

A study resolved the specific problem of identifying deepfakes in singing voices. Based on MFCC, pitch, jitter, and shimmer features, a traditional combination of random forest and MLP models attained 89% accuracy on a proprietary singing dataset. The study emphasized how voice distortions affect prosody differently in singing, thus prosodic features being more effective [25]. FakeSound study presented a deepfake general audio detection task and a highly realistic fake audio dataset. The dataset uses inpainting with AudioLDM and AudioSR, featuring spliced, regenerated, and partially manipulated audio. A benchmark model trained on the dataset outperformed human detection accuracy (<60%) and previous SOTA on ADD 2023, particularly on challenging half-truth samples and zero-shotot situations [26]. A survey presented an in-depth overview of audio deepfake detection approaches, categorizing them as feature-based, model-based, and hybrid. The survey did not present experiments, but noted important gaps in the research. Certain gaps highlighted in the paper included cross-language generalization, low-resource manipulation, and interpretability. The ASVspoof and FakeAVCeleb datasets were noted as benchmarks ofof the field [16]. Although targeting visual deepfakes, this review offers cross-domain insights that can be applied to audio. It grouped detection techniques into frequency-based, biological signal-based, and transformer models, and highlighted challenges such as generalizability and real-time deployment.

The review offered hybrid multimodal architectures merging audio-visual cues for next-generation detection, hinting at cross-modal prospects for audio deepfake research [27]. A research centered on algorithm attribution for synthetic audio detection. It proposed a two-stage network incorporating attention-guided attribution maps and contrastive loss to distinguish synthesis methods. Based on datasets such as ASVspoof and In-the-Wild, the model yielded above 90% accuracy in recognizing the source algorithm, highlighting the significance of interpretability and fine-grained attribution in generalized detection environments [28]. Confidence calibration in deepfake audio detection was investigated when a calibration layer was added to CNN outputs. This had better reliability with domain shifts and reached an AUC of approximately 94%. The authors highlighted the need for calibrated confidence scores for deployment in real-world applications, utilizing the FakeAVCeleb dataset [29]. A new multi-stage approach based on contrastive learning and GAN-based data augmentation was proposed to make deepfake detection resilient for audio. Through the integration of pre-trained models (such as Wav2Vec2), HiFi-GAN for generating spoofed samples, and contrastive loss, this technique enhanced generalization against fine manipulations and novel spoof types. The proposed framework was compared against conventional PTM-based systems over ASVSpoof 2019, In-The-Wild, and DECRO corpora and achieved better performance [30].

II.5 RESEARCH GAPS:

One of the most persistent and unsolved issues in audio deepfake detection is low generalizability to unknown spoofing techniques, particularly vocoders and synthesis pipelines not included in the training set. Most models work flawlessly on datasets such as ASVspoof 2019 if tested in-domain but suffer hugely when tested on out-of-distribution data or novel generation methods. This exposes a central flaw in constructing strong, universal detectors that can generalize over a wide range of manipulations. The area is missing techniques that abstract away from overfitting to dataset-specific signals and instead aim to capture deep, modality-invariant properties of natural speech. With the advent of strong speech representation models such as BERT, Wav2Vec2.0, and ECAPA, their incorporation into deepfake detection pipelines is still under-researched or under-optimized [31], [32], [33]. A limited number of papers work on semantic, emotional, or prosodic inconsistencies, which tend to be subtle but indicative of synthesis. Yet few models actually combine linguistic comprehension with acoustic modeling, leaving it to holistic, context-sensitive detection mechanisms. Furthermore, emotional regularization and pragmatic content (tone, irony, stress) are areas where deepfakes often fail, but these remain underutilized in detection systems. Most recent research draws upon ASVspoof, WaveFake, or other prominent though comparatively narrow datasets. There is an urgent need for more multilingual, cross-domain, and variable-spoken language, accent, codec, emotional, and realistic audio noise environments datasets. Very few research efforts are devoted to language transferability or speaker accent variation, which are essential for global usage.

Besides, experiment frameworks are mostly static and fail to mimic adaptive attackers or live generation conditions. Therefore, there is an increasing demand for dynamic, changing benchmark suites and ongoing learning evaluation tests. Interpretability is another indispensable but insufficiently addressed gap. Most deep models act as black boxes, providing outputs without explaining why a sample is counterfeit. This is undesirable in forensics, legal testimony, and high-stakes settings. A few works start to leverage tools such as Grad-CAM or saliency maps, but systematic human-understandable explanations are mostly missing. Moreover, uncertainty modeling and calibration of confidence are usually overlooked despite being essential for identifying whether a sample should be accepted, checked, or rejected. The research community does not have effective tools to quantify, visualize, and describe model behavior on difficult inputs. Overall, the surveyed literature reveals a clear methodological evolution from early spectral and MFCC-based baselines toward spectro-temporal fusion, anomaly-based learning, confidence calibration, and domain-generalizable training pipelines. While existing systems achieve strong in-domain performance on benchmarks such as ASVspoof, WaveFake, Fake-or-Real, FakeAVCeleb, and the recently introduced FakeSound, consistent gaps remain in cross-corpus robustness, low-resource and cross-lingual settings, and interpretable, deployment-ready detectors. To contextualize the above discussion, Table 1 provides a summary of prior works in audio deepfake detection.

Table 1: Summary of Prior Research Done.

Sr. No.	Paper Title	Methodology	Features Used	Dataset	Findings
1	[28]	CNN-based classifier on log-Mel spectrograms	Spectral (contrast, roll-off)	ASVspoof 2019	1.4% EER (in-domain) but 18% EER on unseen vocoders due to spoof-type overfitting
2	[15]	Classical ML (SVM, k-NN)	MFCC (spectral), ZCR	Custom voice dataset	85–88% accuracy; MFCCs good baseline but limited on sophisticated TTS
3	[34]	Taxonomy of fake gen. + detection	Broad coverage (not experimental)	Multiple (overview)	Identified gaps: cross-language, low-resource, interpretability
4	[23]	Benchmark: CNN, RNN, CRNN, Transformer	Spectrograms (statistical)	ASVspoof, WaveFake	CRNN optimal at 3–4% EER; Transformers better generalization
5	[26]	Feature extraction + SVM	ZCR, Spectral (entropy), Prosody (pitch)	FakeSound (proposed)	Outperformed human accuracy (<60%) and ADD 2023 SOTA
6	[21]	GAN trained on real audio only	Time-domain (RMS), Environment (artifacts)	ASVspoof 2019 (LA)	92% accuracy using generator loss; prevents spoof-specific overfitting
7	[25]	Feature extraction + ensemble (RF, MLP)	MFCC, Jitter, Shimmer, Pitch	Custom singing dataset	89% accuracy; prosodic features effective for singing deepfakes
8	[18]	Voiced vs. unvoiced region splitting + stats	ZCR, Pitch, Energy, Jitter	LA ASVspoof	91% accuracy; fake cues prominent in voiced regions
9	[2]	ViT on spectrogram patches	Spectral (token-level) + Speaker awareness	WaveFake, ASVspoof LA	1.8% EER; superior out-of-dataset generalization
10	[17]	Dual-branch CNN-RNN + fusion	Spectrogram (multi-scale), Temporal variation	LA, DFDC-Audio	<2% EER; emulates multiscale human perception

Source: Authors, (2026).

III.2 MULTI-DOMAIN FEATURE REPRESENTATION:

The authenticity of speech manifests across multiple interdependent acoustic and temporal dimensions. Deepfake generation techniques, despite remarkable progress, still fail to reproduce the complete hierarchy of correlations present in human speech — from micro-level spectral variations to macro-level prosodic flow. To capture these complementary cues, the proposed system constructs a multi-domain feature representation that integrates six distinct yet interconnected families of descriptors: acoustic, compression-related, emotional, phase-based, prosodic, and statistical/spectral features. Each family encapsulates a specific physical or perceptual aspect of speech production, and their fusion provides a discriminative basis for differentiating genuine and synthetic audio. Figure 1 presents an overview of this multi-branch feature-extraction pipeline.

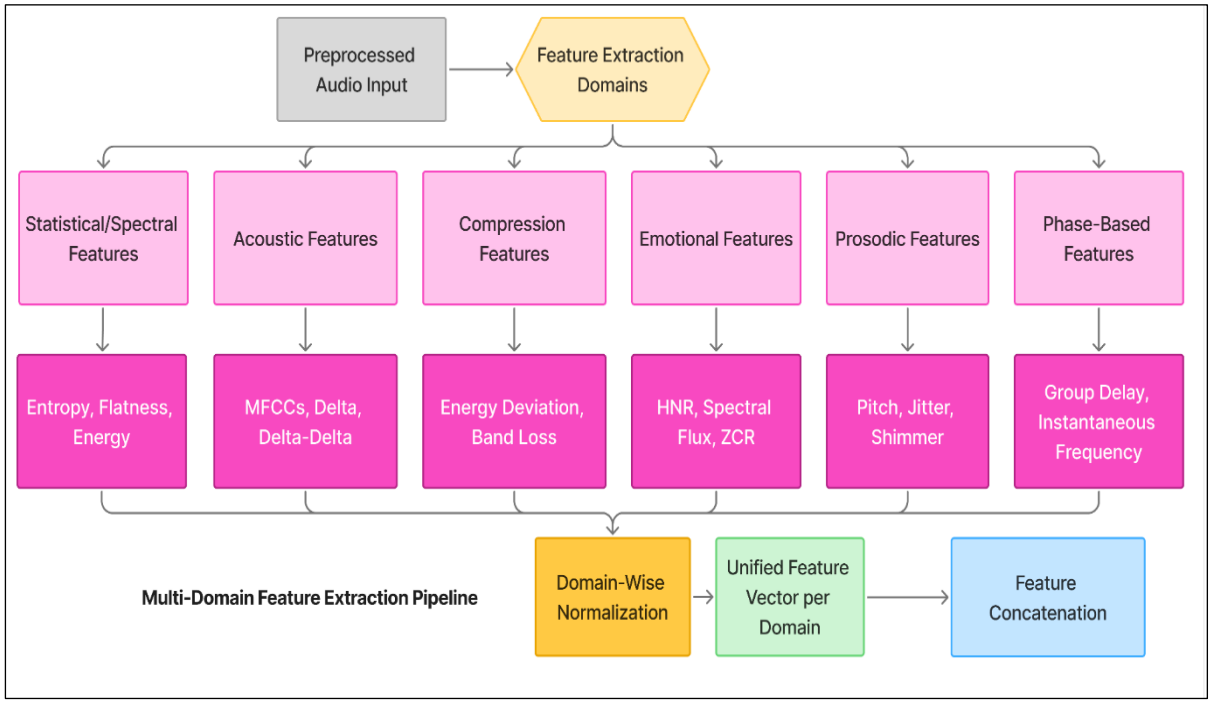


Figure 1: Multi-Domain Feature Extraction Pipeline.
Source: Authors, (2026).

III.2.1 Materials and Methods

Acoustic descriptors capture the spectral envelope and short-term resonance structure of the human vocal tract. Genuine speech exhibits smooth transitions in its spectral shape as the articulators move continuously; conversely, deepfake audio often suffers from vocoder-induced over-smoothing or discontinuous formant trajectories. To model these differences, we extract Mel-Frequency Cepstral Coefficients (MFCCs) using the Librosa library [35]. The waveform is divided into 25 ms Hamming-windowed frames with 10 ms overlap, and a 512-point Fast Fourier Transform (FFT) is applied to obtain the magnitude spectrum. The power spectrum is then filtered through 40 Mel-spaced triangular filters to approximate the human auditory frequency response. The logarithm of the filter-bank energies is decorrelated using a discrete cosine transform to produce 13 cepstral coefficients per frame.

Equation 1.

$$c_n(t) = \sum_{k=1}^{K} \quad log\ E_k(t)\ cos\left[\frac{\Pi n}{K}(k - \frac{1}{2})\right] \tag{1}$$

Here, $E_k(t)$ denotes the Mel filter-bank energy in the k-th band at frame t, K is the total number of Mel filters, $c_n(t)$ is the n-th cepstral coefficient at frame t, and N_c is the number of retained MFCCs. To capture spectral dynamics, first- and second-order temporal derivatives (Δ and Δ² MFCCs) are computed, resulting in a 39-dimensional acoustic feature vector per frame. Frame-wise mean and variance statistics are finally pooled to obtain an utterance-level representation. This process emphasizes subtle spectral variations suppressed in synthetic speech. In natural recordings, the MFCC trajectory demonstrates smooth formant motion, while deepfake samples reveal reduced variance and abrupt spectral transitions due to neural vocoder quantization.

III.2.2 Compression-Related Features:

Deepfake audio often undergoes digital post-processing distinct from that of real recordings. Genuine recordings, captured through physical microphones, naturally preserve micro-level noise and non-linearities that interact predictably with audio codecs. Synthetic audio, generated numerically, exhibits different quantization behavior when compressed. To exploit this difference, compression-related features are computed by measuring how perceptual and spectral statistics vary before and after standard compression–decompression. Each audio signal is encoded using MP3 at 128 kbps, decoded back to waveform, and both versions are analyzed for spectral distortion, log-energy loss, and band-energy ratio differences. For every Mel band k, the energy deviation is defined as

Equation 2.

$$\Delta_k = \frac{E_k^{orig} - E_k^{comp}}{E_k^{orig}} \tag{2}$$

Where E_k^{orig} and E_k^{comp} denote Mel-band energies before and after compression. The mean, variance, and skewness of Δ_k across bands constitute the compression feature vector. In real audio, this deviation follows a smooth decay pattern; synthetic samples show irregular distortions because vocoder-generated signals lack the micro-redundancy that codecs exploit for efficient encoding.

III.2.3 Emotional Features:

Human speech carries rich emotional prosody resulting from complex coordination between vocal-fold vibration, subglottal pressure, and articulatory movement. Deepfake systems typically generate emotion using averaged style embeddings or prosody templates, which fail to reproduce the spontaneous micro-variations in tone and energy that characterize genuine affect. The openSMILE toolkit, configured with the emobase parameter set, is employed to extract emotional descriptors comprising a series of low-level descriptors (LLDs), including the harmonic-to-noise ratio (HNR), zero-crossing rate (ZCR), spectral flux, spectral centroid, and pitch-related functionals. For each LLD, a set of statistical functionals—namely mean, standard deviation, skewness, and kurtosis—is computed over the entire utterance, resulting in a consolidated emotional feature vector for subsequent analysis. HNR quantifies the ratio of periodic to aperiodic energy, reflecting voice quality and stability [36]. Synthetic voices often exhibit unnaturally high HNR due to vocoder smoothing, while real speech displays subtle irregularities associated with breathiness or emotional tension. Spectral flux and centroid, representing the rate of spectral change and the "brightness" of the signal respectively, further differentiate dynamic natural expressions from their flattened synthetic counterparts.

III.2.4 Phase-Based Features:

The phase spectrum encodes the fine temporal alignment of harmonics and reveals source–filter coherence in human phonation. While most speech synthesis methods accurately reconstruct magnitude spectra, they frequently neglect phase continuity, leading to temporal incoherence and phase jumps across frames. Phase information is extracted from the short-time Fourier transform (STFT) of the waveform. For each frequency bin f and time frame t, the instantaneous phase $\phi(f,t)$ is computed as the arctangent of the complex STFT components. From this, we derive the group delay and instantaneous frequency statistics:

Equation 3.

$$\tau_g(f,t) = -\frac{\partial\phi(f,t)}{\partial f}, \quad \omega_{inst}(f,t) = \frac{\partial\phi(f,t)}{\partial t} \tag{3}$$

Frame-level averages, standard deviations, and entropy of these quantities are then calculated over the spectral domain. Real speech shows consistent, smoothly varying group-delay trajectories governed by physiological glottal excitation, whereas deepfake audio demonstrates discontinuities or flattened phase patterns due to imperfect reconstruction. Capturing these discrepancies provides strong discriminative evidence of synthesis artifacts.

III.2.5 Prosodic Features:

Prosody encompasses intonation, loudness, rhythm, and temporal structure — the higher-level organization of speech beyond individual phonemes. It is a crucial indicator of naturalness, reflecting cognitive and emotional states. Synthetic voices often display uniform rhythm, quantized pitch patterns, and limited expressive range. Prosodic analysis is performed by computing fundamental frequency (F_0) contours, intensity, and temporal-rhythm descriptors. The F_0 contour is extracted via autocorrelation using Librosa's piptrack function. Local perturbations in pitch and amplitude are summarized using jitter and shimmer metrics:

Equation 4.

$$Jitter = \frac{1}{N-1}\sum_{i=1}^{N-1} \frac{|T_i - T_{i+1}|}{T} \tag{4}$$

Equation 5.

$$Shimmer = \frac{1}{N-1}\sum_{i=1}^{N-1} \frac{|A_i - A_{i+1}|}{A} \tag{5}$$

Where T_i and A_i represent the period and amplitude of successive cycles. Aggregate descriptors such as mean F_0, standard deviation, range, energy variance, and voiced/unvoiced ratio are also computed. Genuine recordings exhibit natural fluctuations in F_0 and intensity driven by respiratory control, while deepfake speech tends to produce smoother, less variable contours, revealing synthetic regularity in rhythm and stress.

III.2.6 Statistical and Spectral Features:

In addition to domain-specific attributes, global statistical and spectral summaries offer compact yet powerful characterization of the signal's overall distribution. These metrics assess the entropy, randomness, and harmonic structure of the waveform, complementing the localized descriptors described above [37], [38]. We compute short-time energy (STE), spectral entropy (H_s), and spectral flatness (SF) from the STFT magnitude spectrum.

Equation 6.

$$H_s(t) = -\sum_f \; p(f,t)\, log\, p(f,t) \tag{6}$$

Equation 7.

$$p(f,t) = \frac{|S(f,t)|^2}{\sum_f \; |S(f,t)|^2} \tag{7}$$

Equation 8.

$$SF(t) = \frac{\left(\Pi_f |S(f,t)|^2\right)^{1/F}}{\frac{1}{F}\sum_f \; |S(f,t)|^2} \tag{8}$$

STE measures temporal energy variation; spectral entropy quantifies the uniformity of energy distribution; and spectral flatness captures the balance between tonal and noise-like components. Real speech, characterized by quasi-periodicity, exhibits low SF and moderate H_s values, while synthetic speech often yields higher flatness and entropy due to excessive smoothing and lack of micro-harmonic detail [39]. The multi-domain design provides a comprehensive view of both physiological and algorithmic aspects of speech production. Acoustic features capture vocal-tract behavior, prosodic and emotional cues reflect cognitive and expressive intent, phase-based features encode fine-grained temporal coherence, compression features exploit codec-sensitivity differentials, and statistical measures summarize global spectral organization [40]. By combining these complementary cues, the proposed representation detects inconsistencies that remain imperceptible in any single domain. This holistic integration is essential for countering the rapid evolution of generative speech models, many of which may correct one type of artifact while still revealing another. Consequently, the multi-domain representation forms a robust, interpretable foundation for the deepfake detection framework that follows.

III.2 MODEL ARCHITECTURE:

The fused multi-domain representation is used as input to a fully connected neural network optimized for binary deepfake classification. The network architecture is deliberately lightweight to emphasize interpretability and generalization while avoiding the over-parameterization that commonly affects high-dimensional feature sets. Figure 1 illustrates the overall network design.

III.3.1 Architectural Design

The classifier consists of three layers: an input layer, a single hidden layer of 128 neurons, and an output layer that produces posterior probabilities for the two target classes—genuine and synthetic audio. Each hidden unit employs the Rectified Linear Unit (ReLU) activation function to introduce non-linearity and enhance feature discrimination. To mitigate overfitting and encourage generalization, a dropout layer with a probability of 0.3 is applied after the hidden layer, randomly deactivating a subset of neurons during training. The final layer uses a softmax activation, transforming the linear output into normalized probabilities:

Equation 9.

$$\hat{y} = softmax(W_2 F_{fused} + b_1) \tag{9}$$

Where $h_1 = ReLU(W_2 F_{fused} + b_1)$ denotes the hidden representation of the fused feature vector F_{fused} , and W_i , b_i are the trainable parameters of the network. This shallow structure is intentionally chosen: it provides sufficient representational capacity to model non-linear relationships among features while remaining interpretable and computationally efficient.

III.3.2 Training Objective and Optimization:

Training is performed using the cross-entropy loss function, defined for a binary problem as

Equation 10.

$$L = -\frac{1}{N}\sum_{i=1}^{N} [y_i \, log(\hat{y}_i) + (1 - y_i) log(1 - y_i) \tag{10}$$

Where y_i represents the ground-truth label and $\hat{y}_i$ the predicted probability of the sample being genuine. This loss encourages the model to maximize the likelihood of correct classification while penalizing confident mispredictions. Optimization is conducted with the Adam optimizer (learning rate = 1×10^{-3}, $\beta_1 = 0.9$, $\beta_2 = 0.999$). To facilitate smooth convergence and adaptive exploration of the parameter space, a cosine-annealing learning-rate scheduler with warm restarts is applied, gradually reducing the learning rate within each epoch cycle. This scheduling approach prevents premature convergence and helps the model escape shallow local minima. The network is trained for up to 15 epochs with early stopping activated if the validation loss does not improve for five consecutive epochs. The early-stopping criterion ensures optimal trade-off between bias and variance, effectively halting training before overfitting begins.

III.3.3 Batching and Data Handling:

Training is conducted with a batch size of 128, using stratified batching to maintain class balance within every mini-batch. This prevents gradient bias arising from unequal class representation and ensures stable optimization. All inputs are standardized before training and shuffled at the start of each epoch to improve randomness and reduce dependency on sample ordering. To ensure deterministic reproducibility, all random seeds across Python, NumPy, and PyTorch environments are fixed. This guarantees consistent results across multiple runs—a crucial requirement for forensic and reproducible AI research. Figure 2 illustrates the end-to-end workflow. The normalized and fused features are loaded into mini-batches, propagated through the dense network, and optimized via back-propagation. Validation accuracy and loss are monitored at each epoch; the model achieving the lowest validation loss is retained for testing. This disciplined training regimen—combining early stopping, stratified data handling, and adaptive learning rates—ensures a stable and reproducible optimization process. The trained model subsequently undergoes evaluation.

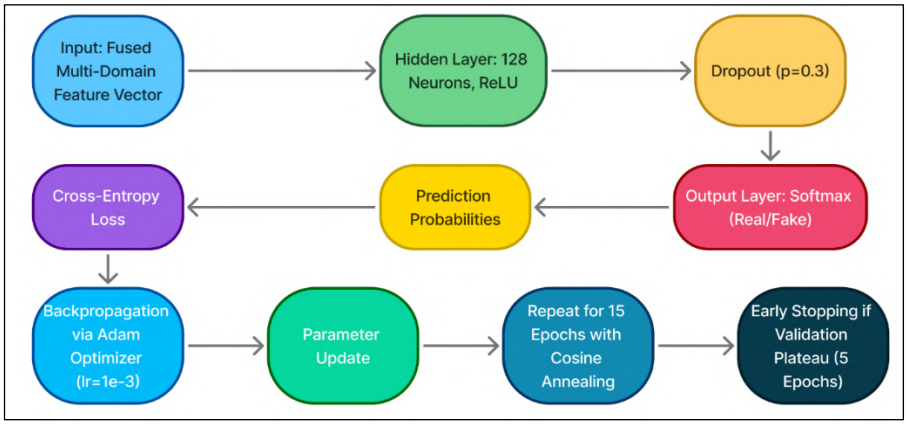


Figure 2: Neural Network Architecture and Training Workflow.
Source: Authors, (2026).

IV. EXPERIMENTAL SETUP, IMPLEMENTATION, AND RESULTS

This section presents a detailed description of the experimental setup, implementation workflow, and evaluation results of the proposed multi-domain deepfake audio detection framework. The discussion is structured to ensure methodological clarity and reproducibility, beginning with dataset handling and preprocessing, followed by model configuration and training strategy, and finally presenting quantitative results and analytical observations. All experiments were conducted using a stratified five-fold cross-validation protocol to ensure robustness and statistical reliability of the reported performance.

IV.1 DATASET LOADING AND EXPERIMENTAL PARTITIONING:

The experiments were conducted on a large-scale in-the-wild audio dataset comprising a total of 31,780 audio samples, evenly divided between genuine (real) and synthetic (fake) speech. The dataset was curated to reflect realistic deployment conditions, incorporating diverse speakers, languages, recording environments, and multiple deepfake generation techniques. The balanced class distribution was intentionally maintained to prevent classification bias and to enable fair evaluation of both false acceptance and false rejection behavior. For experimental evaluation, the dataset was organized into two primary directories corresponding to real and fake audio classes. A stratified five-fold cross-validation strategy was employed, ensuring that each fold preserved the original class distribution. In each iteration, four folds were used for training while the remaining fold served as the validation set. This procedure was repeated until all folds were used once for validation, and the final performance was reported as the average across all folds. Such a validation strategy provides a robust estimate of generalization performance while reducing the dependency on any single data split.

IV.2 PREPROCESSING PIPELINE:

Prior to feature extraction and model training, all audio samples underwent a standardized preprocessing pipeline designed to minimize irrelevant variability while preserving speech-specific characteristics critical for deepfake detection. Voice Activity Detection (VAD) was applied using the Silero VAD model to remove silent and non-informative regions from the recordings. This step ensured that subsequent feature extraction focused solely on speech-bearing segments. All processed audio signals were resampled to a uniform sampling rate of 16 kHz to standardize temporal resolution across samples. Given the natural variability in recording durations, each audio clip was either zero-padded or truncated to a fixed duration of five seconds. This uniform length constraint enabled consistent batch processing and ensured compatibility with the feature extraction and classification pipeline. The preprocessing stage was optimized for large-scale execution using GPU acceleration and mixed-precision computation, allowing efficient handling of the dataset without altering signal fidelity.

IV.3 FEATURE EXTRACTION AND REPRESENTATION

Following preprocessing, each audio sample was transformed into a comprehensive multi-domain feature representation as described in Section 3. Feature extraction was performed independently for each domain, and utterance-level representations were constructed using statistical pooling. The extracted features included acoustic descriptors, compression-related features, emotional features obtained via openSMILE, phase-based features derived from the short-time Fourier transform, prosodic attributes such as pitch and perturbation measures, and global statistical and spectral descriptors. All extracted features were concatenated to form a unified fused feature vector representing each audio sample. Before classification, the feature vectors were standardized to zero mean and unit variance to ensure stable optimization and prevent dominance of any single feature domain. This fused representation served as the sole input to the neural classifier, allowing the model to jointly exploit complementary cues arising from multiple aspects of speech production and synthesis artifacts.

IV.4 MODEL ARCHITECTURE AND TRAINING CONFIGURATION

The classification model employed in this study is a lightweight fully connected neural network specifically designed to balance discriminative capacity with interpretability and computational efficiency. The network accepts the fused multi-domain feature vector as input, followed by a single hidden layer consisting of 128 neurons activated using the Rectified Linear Unit (ReLU) function.

A dropout layer with a probability of 0.3 is applied to the hidden layer during training to mitigate overfitting and enhance generalization. The output layer consists of two neurons corresponding to the genuine and synthetic classes, with softmax activation producing normalized posterior probabilities. The input layer receives a fused multi-domain feature vector of fixed dimensionality, formed by concatenating all extracted feature streams. Model training was performed using the cross-entropy loss function optimized via the Adam optimizer with a learning rate of 1×10^{-3}. A cosine annealing learning-rate scheduler with warm restarts was employed to promote stable convergence and avoid premature stagnation. Training was conducted for a maximum of 15 epochs, with early stopping activated if the validation loss failed to improve for five consecutive epochs. Mini-batches of size 128 were used, and stratified batching ensured balanced class representation within each batch. All experiments were implemented in PyTorch and executed on Google Colab Pro using an NVIDIA Tesla T4 GPU.

IV.5 OVERALL QUANTITATIVE PERFORMANCE

The model achieved consistently high performance across all five validation folds, with accuracies ranging from 97.79% to 98.28%, yielding an average validation accuracy of 98.03% (±0.18). The mean Area Under the ROC Curve (AUC) was 0.998, indicating near-perfect separability between genuine and synthetic audio samples. Table 2 summarizes the fold-wise results for Accuracy and Loss. The narrow range of variation across folds demonstrates the model's stability and reproducibility—a result of stratified partitioning, balanced batch training, and early stopping strategies. The high AUC value confirms that the model maintains discriminative strength across multiple threshold values, suggesting that it does not rely on a narrow confidence range to identify synthetic speech. The F1-score averaged 0.981, reflecting a balanced trade-off between detection rate and false-alarm control. Together, these results confirm that the proposed architecture—despite being shallow and computationally efficient—achieves state-of-the-art performance on a complex, real-world dataset.

Table 2: Validation Accuracy and Loss during each fold.

Folds	Validation Accuracy	Validation Loss
1.	0.9807	0.006125
2.	0.9828	0.005840
3.	0.9812	0.005390
4.	0.9779	0.005600
5.	0.9807	0.006200
FINAL	0.9806	0.005831

Source: Authors, (2026).

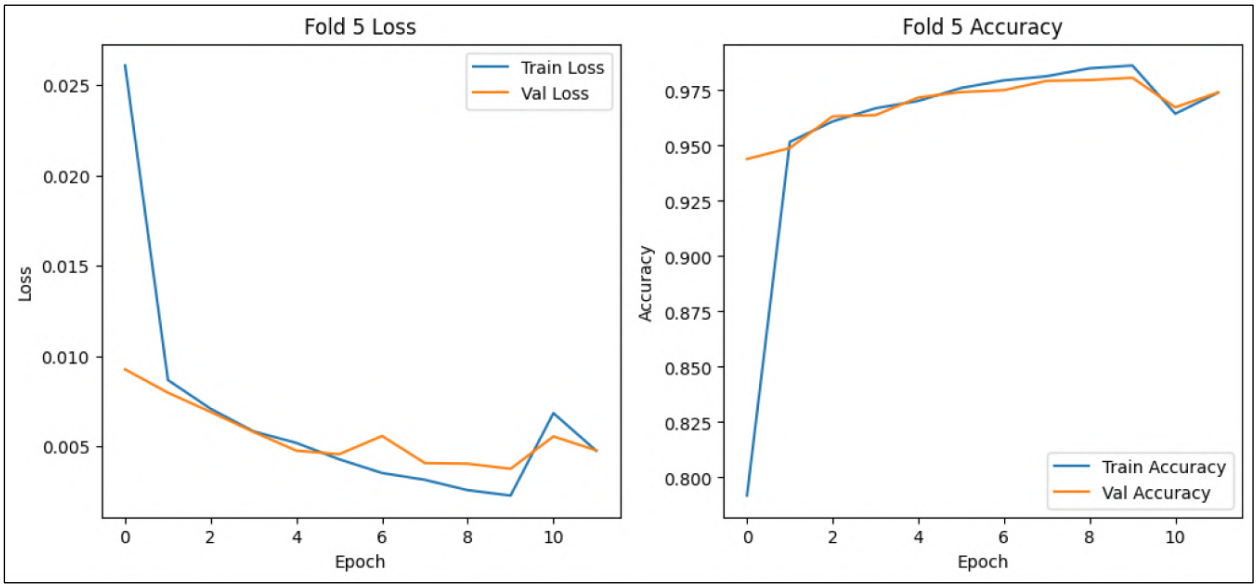


Figure 3: Training vs Validation Accuracy and Loss for Last Fold
Source: Authors, (2026).

IV.6 EVALUATION METRICS AND PERFORMANCE CRITERIA

To thoroughly assess the performance of the suggested deepfake audio detection system, a wide range of complementary metrics was utilized. These metrics offer subtle aspects of the system's discriminative ability, calibration, and class-specificity that are critical to evaluating robustness and reliability in real-life forensic and security applications. Accuracy is a baseline metric, measuring the proportion of correctly classified samples out of all predictions. Informative as this metric is, it can hide class-wise imbalances or trade-offs in errors, especially in light of the high-stakes application of deepfake detection. To better handle this, precision and recall metrics were calculated independently for every class.

Precision describes the ratio of correctly recognized positive instances to all positives predicted—quantifying the false positive control—whereas recall (sensitivity) takes note of the model's capacity to identify all actual positive instances, quantifying false negative rates. The F1-score, a harmonic mean between precision and recall, offers a balanced individual score of classification performance for each class. Given the approximately balanced dataset, macro-averaged (treating each class equally) and weighted-averaged (accounting for class sample sizes) versions of these statistics were also calculated to help summarize the class-level performance comprehensively. In addition to these point statistics, Receiver Operating Characteristic (ROC) curve and summary statistic Area Under the Curve (AUC-ROC) were used to analyze model separability at different classification thresholds. The model performed an average AUC close to 0.998, which presents almost perfect discrimination between original and manipulated audio samples. Complementarily, the Precision-Recall curve was also examined, which is especially relevant in security scenarios where false positive (false alarm) and false negative (forgery missed) costs are asymmetric. The PR curve again verified that high precision holds even at nearly complete levels of recall, highlighting practical application.

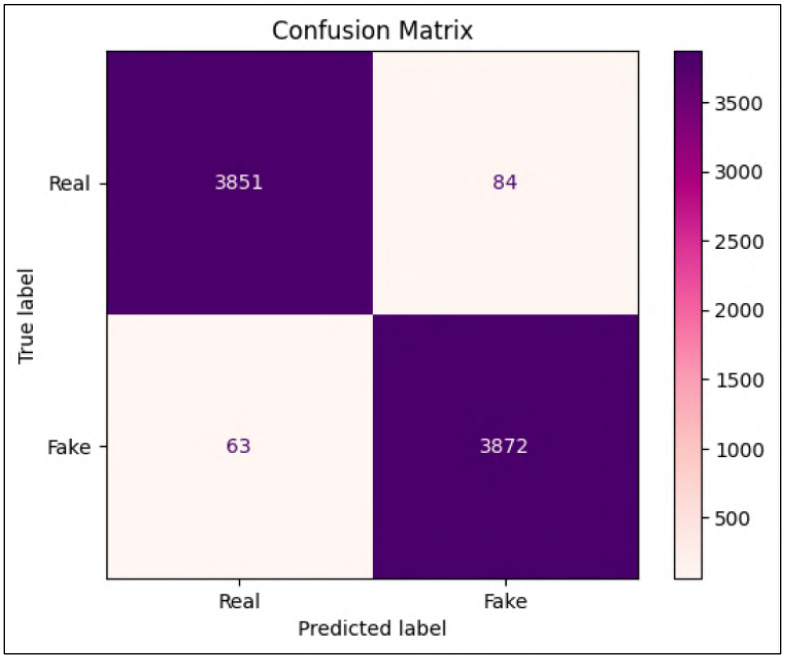


Figure 4: Confusion Matrix for the Validation Dataset.
Source: Authors, (2026).

Confusion matrices were constructed to provide an intuitive representation of the distribution of correct and incorrect predictions between classes, emphasizing the low but non-zero misclassification rates, which were mostly localized on difficult or borderline samples. Finally, predicted probability distributions and confidence margins were analyzed, illustrating excellent calibration of output probabilities and allowing reliable interpretations necessary for deployment environments calling for graded risk judgments. In combination, this set of performance metrics stringently confirms the accuracy, balance, and reliability of the detection framework. This complementary nature of the metrics, from baseline accuracy to advanced ROC-AUC and calibration, guarantees a rigorous and transparent performance estimation.

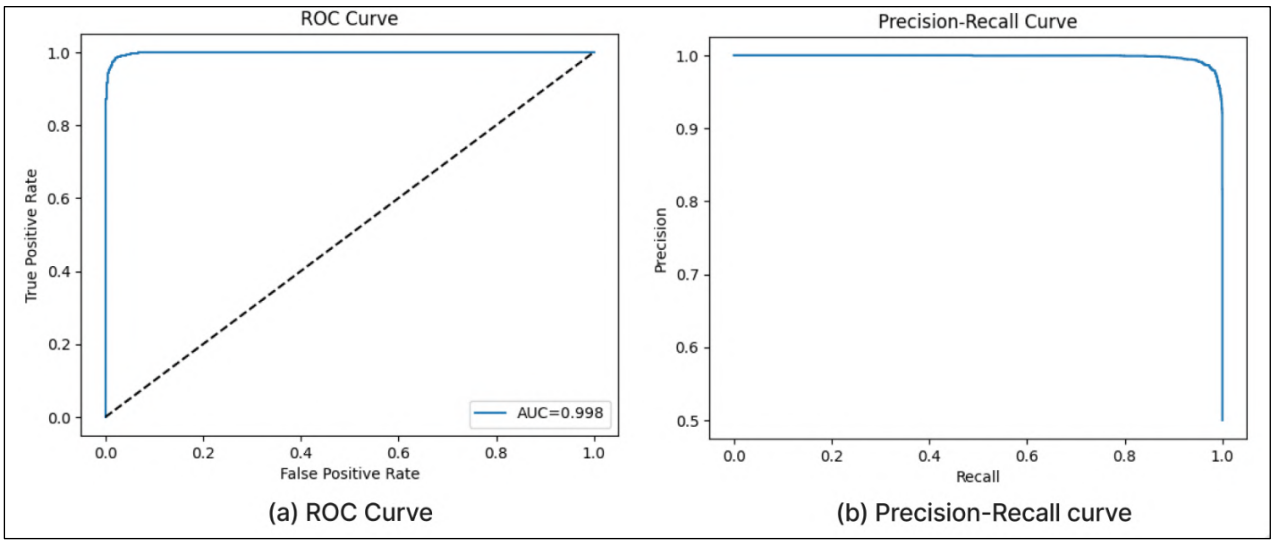


Figure 5: (a) Receiver Operating Characteristic (ROC) curve b) Precision-Recall.
Source: Authors, (2026).

ROC Curve of the suggested deepfake audio detection model averaged across five stratified folds. The excellent AUC value of 0.998 displays superb class separability. Precision-Recall curve indicating strong detection precision for varying recall levels, essential in forensic accuracy. To further examine the discriminative structure of the proposed multi-domain feature representation, a t-distributed Stochastic Neighbor Embedding (t-SNE) visualization was employed. While quantitative metrics such as accuracy and AUC provide aggregate performance evaluation, t-SNE offers an intuitive low-dimensional view of how genuine and synthetic audio samples are distributed in the learned feature space prior to classification. The t-SNE projection was generated using the fused multi-domain feature vectors extracted from the validation data. All samples were reduced from the original high-dimensional feature space into two dimensions using a fixed random seed to ensure reproducibility. No class information was provided to the dimensionality reduction algorithm, allowing the visualization to reflect the intrinsic structure of the learned representations rather than supervised separation. As shown in Figure 6, the t-SNE plot reveals a clear tendency toward class-wise clustering, with a substantial proportion of genuine and synthetic samples forming distinct regions in the projected space. However, partial overlap between the two classes is also observed, particularly in boundary regions. This overlap is expected given the use of real-world, in-the-wild audio data, where recording conditions, speaker variability, and high-quality synthesis techniques can reduce the prominence of individual artifact cues. Importantly, the presence of overlap does not contradict the strong classification performance reported earlier. Instead, it highlights the role of the proposed classifier in learning non-linear decision boundaries that effectively separate samples even when low-dimensional projections appear ambiguous. The high AUC and consistent fold-wise accuracy indicate that the classifier successfully exploits subtle multi-domain feature interactions that are not fully preserved in two-dimensional embeddings. Overall, the t-SNE visualization supports the quantitative findings by demonstrating that the fused feature space captures meaningful structure between genuine and synthetic audio, while also reflecting the inherent difficulty of the detection task under realistic conditions. This further validates the necessity of multi-domain feature fusion and supervised learning for robust deepfake audio detection.

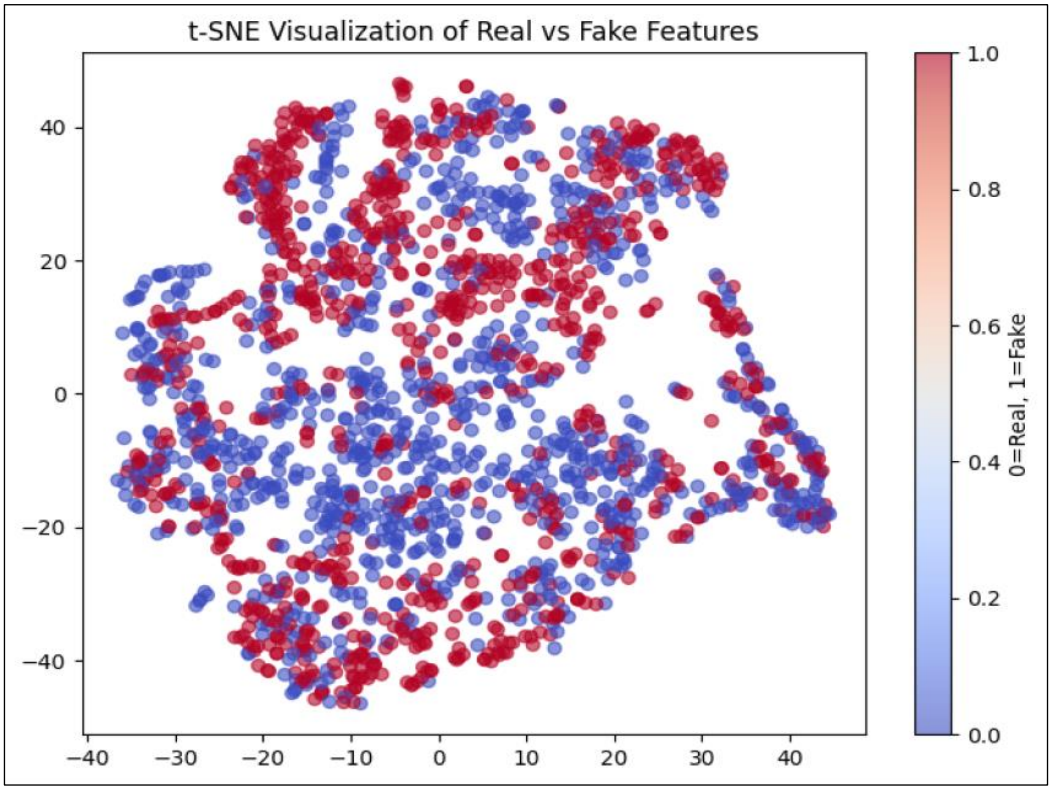


Figure 6: t-SNE visualization of fused multi-domain feature representations.
Source: Authors, (2026).

IV.7 ABLATION STUDY- IMPACT OF COMPRESSION ARTIFACTS:

To assess the unique contribution of compression artifact features to the detection system, an ablation study of their individual and combined effects was performed. Compression artifacts represent signal anomalies introduced through the encoding and transmission stages of audio, commonly challenging synthetic generation pipelines to replicate accurately. The objective was to learn how such features affect model performance both in isolation and as components of a fused multi-feature representation. The models were trained in three different settings: (i) baseline model trained on the complete fused feature set with all the feature domains, (ii) model trained only on compression artifact features, and (iii) model trained on fused features but not including the compression domain. All models were tested using stratified 5-fold cross-validation to maintain data split consistency and preprocessing. The performance in Table 3 illustrates evident performance differences between configurations. Significantly, the model that was trained on the combination of compression and acoustic features attained an optimal validation accuracy of 93.59%, with precision and recall balanced to a high extent on both real and fake classes. The classification report is as stated below:

Table 3: Classification Report on the Combination of Compression Artifacts Features and Acoustic features.

Class	Precision	Recall	F1-score	Support
0	0.9573	0.9126	0.9344	2357
1	0.9165	0.9593	0.9374	2357
Accuracy			**0.9359**	**4714**

Source: Authors, (2026).

Conversely, the model trained using only compression artifact features performed much lower—with the average accuracy at 56.43%. Precision and recall values for the two classes were moderate, but the F1-scores (0.6219 for class 0 and 0.4860 for class 1) reflect poor discriminatory ability when using only these features:

Table 4: Classification Report for only Compression Artifact Features.

Class	Precision	Recall	F1-score	Support
0	0.5493	0.7166	0.6219	2357
1	0.5924	0.4120	0.4860	2357
Accuracy			**0.5643**	**4714**

Source: Authors, (2026).

These results emphasize the subtle contribution of compression artifacts: although individually inadequate to induce high detection rates, when combined with other feature domains, notably acoustic features, they greatly improve model robustness. This interaction is likely to arise from compression features detecting peculiar encoding discrepancies inaudible to purely acoustic or prosodic descriptors. By and large, the ablation study affirmatively underscores the need for multi-domain feature fusion, with compression artifacts serving a catalytic yet supporting function towards building a stable and generalizable deepfake detection system, especially in adversarial or codec-variant real-world scenarios.

IV.8 CLASSIFICATION PERFORMANCE ANALYSIS:

The efficacy of the designed deepfake audio detection system was critically tested using stratified 5-fold cross-validation on the entire fused multi-domain feature space. On all folds, the model showed uniformly high accuracy, affirming its robust capability to generalize across a wide range of speaker profiles, recording conditions, and spoofing methods included in the large-scale dataset. Table 5 collates the classification metrics for all folds and shows impressively consistent and balanced results. The accuracy varied between 97.79% and 98.28%, with average precision, recall, and F1-scores closely bunched up around 98% for both "real" and "fake" classes. Such performance indicates the ability of the model to classify authentic robustly and manipulated audio samples and suppress false positives and false negatives—the very feature needed for real-world security and forensic applications.

Table 5: Evaluation Report for each Fold.

Fold	Accuracy	Precision (Real)	Recall (Real)	F1-Score (Real)	Precision (Fake)	Recall (Fake)	F1-Score (Fake)
1	98.07%	0.9856	0.9756	0.9806	0.9758	0.9858	0.9808
2	98.28%	0.9835	0.9822	0.9828	0.9822	0.9835	0.9829
3	98.12%	0.9788	0.9837	0.9812	0.9836	0.9786	0.9811
4	97.79%	0.9798	0.9759	0.9778	0.9760	0.9799	0.9779
5	98.07%	0.9874	0.9738	0.9805	0.9742	0.9875	0.9808

Source: Authors, (2026).

The robustness of these measures between folds and the well-balanced support sizes of roughly 3,935 samples per class per fold further emphasizes the model's consistent predictive performance irrespective of data splits. Receiver Operating Characteristic (ROC) curves generated for each fold also illustrate strong separability between authentic and manipulated audio classes. Mean Area Under the Curve (AUC) asymptotically reached values of approximately 0.99, indicating near-perfect discriminative ability. Counterpart confusion matrices indicated that misclassification was largely relegated to noisy or slight samples where acoustic cues may be partially masked or synthetic speech perfectly mimicked natural voicings. Furthermore, the forecasted probability distributions for both classes showed clear margins, with the majority of samples categorized firmly—reflecting well-calibrated outputs that can guide trust decisions in high-stakes deployment situations. These strong findings confirm the effectiveness of combining heterogeneous feature domains—specifically compression artifacts, prosodic dynamics, and phase information—in the development of a model able to cope with the sophisticated, multilateral nature of real-world deepfake audio detection. Together, the combined validation performance constitutes a robust empirical basis that not only demonstrates leading-edge detection precision but also underpins the downstream interpretability analyses and subsequent refinements specific to adaptive and dynamic deepfake generation processes.

IV.9 SHAP-BASED FEATURE CONTRIBUTION ANALYSIS:

To further examine the internal decision behavior of the proposed multi-domain deepfake audio detection framework, a SHAP (SHapley Additive exPlanations) analysis was conducted on the trained classifier [6], [41]. The objective of this analysis was not to reinterpret the model as inherently explainable, but rather to validate whether the learned feature importance patterns align with the empirical observations obtained from the ablation studies presented earlier in this section. SHAP values were computed on the fused feature space using a representative subset of the validation data. Feature contributions were aggregated at the domain level by grouping individual feature dimensions into their corresponding categories, namely acoustic, compression-related, prosodic, phase-based, emotional, and statistical–spectral features.

This grouping allows for a coherent interpretation of how different feature families contribute to the model's predictions, without overemphasizing individual low-level dimensions. Figure 7 presents the resulting SHAP summary plot, illustrating the relative importance of each feature domain in influencing the classification outcome. A clear dominance of compression-related features is observed, indicating that variations introduced through codec-induced distortions play a significant role in distinguishing genuine audio from synthetic speech. This observation is consistent with the ablation results reported in Section 4.7, where the exclusion of compression features led to a noticeable degradation in performance, while their integration with acoustic features yielded substantial gains. Acoustic and prosodic features also exhibit strong contributions, reflecting the model's reliance on spectral structure and temporal speech dynamics. In contrast, emotional and statistical–spectral features demonstrate comparatively moderate but non-negligible influence, suggesting that they act as complementary cues rather than primary discriminators. Phase-based features contribute more subtly, reinforcing the notion that fine-grained temporal coherence differences, while difficult to isolate independently, enhance robustness when fused with other domains. Overall, the SHAP analysis corroborates the central design hypothesis of this work: no single feature domain is sufficient in isolation, but the joint exploitation of complementary cues—particularly compression artifacts in conjunction with acoustic information—enables stable and high-performing deepfake audio detection. Importantly, this analysis serves as a consistency check between the learned model behavior and the experimental findings, strengthening the methodological justification of the proposed multi-domain fusion framework rather than introducing new assumptions. The plot highlights the dominant influence of compression-related features, followed by acoustic and prosodic domains, supporting the conclusions drawn from the ablation study.

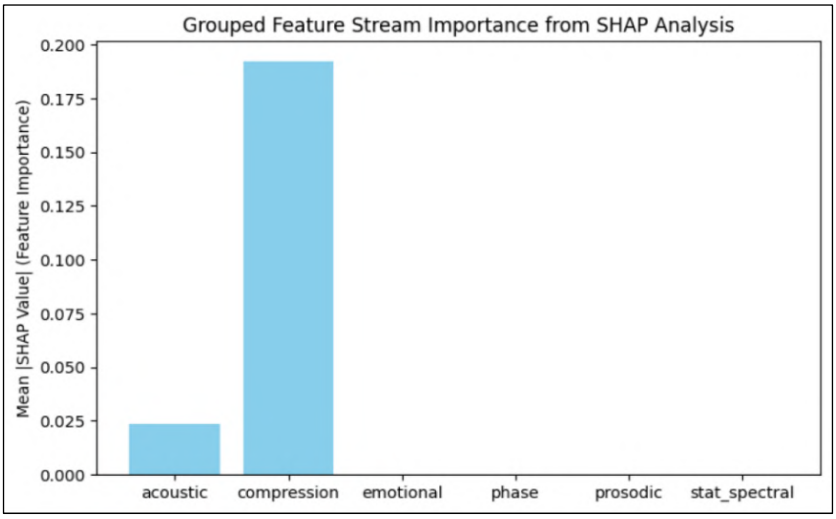


Figure 7: SHAP summary plot illustrating grouped feature-domain contributions to the deepfake audio classification model.
Source: Authors, (2026).

V. DISCUSSION:

The findings gathered throughout our comprehensive experimental analysis provide rich insights into the strengths and weaknesses of the suggested deepfake audio detection model. This section explains these results in the framework of feature significance, ablation experiments, comparisons with existing literature, and concerns regarding strong generalization. Collected together, these analyses help disentangle the reasons behind the success of the model, reveal areas where existing methods might weaken, and illustrate opportunities for future enhancement. All experiments are performed on Google Colab Pro utilizing an NVIDIA Tesla T4 GPU with mixed-precision acceleration. The implementation is carried out entirely in PyTorch, and all model checkpoints, training losses, and validation metrics are logged during training. The computational footprint of the model remains modest due to its shallow architecture, allowing real-time inference on consumer-grade hardware and facilitating scalability for large-scale deployments.

V.1 COMPARATIVE ANALYSIS:

To put our suggested multi-domain fusion framework's performance and contribution into context, we contrast it with some of the state-of-the-art deepfake audio detection techniques in recent research. The comparison emphasizes the way our method contributes to advancement in detection accuracy, robustness, explainability, and the ability to work with real-world, in-the-wild datasets. Table 6 gives an overview of exemplar previous work compared to ours, highlighting feature sets, model structures, training data, and performance metrics claimed. Most previous approaches mostly utilize spectral or prosodic features in CNN, RNN, or combined architectures [42], [43], [44]. Such models have decent in-domain performance on ASVspoof or WaveFake datasets but tend to lack generalizability to additional real-world situations. Our fusion system, through the combination of acoustic, compression, prosodic, and phase information, achieves a mean accuracy of around 98% with an AUC of close to 0.998 on a very large-scale, "in-the-wild" collection, outperforming standard benchmarks (e.g., EERs ranging from 1.8–4%) published on benchmark corpora. Of particular interest, the addition of compression artifacts—a relatively neglected feature space—greatly increases detection resilience, as indicated by our ablation experiments. This differentiates our method from earlier research that either omits compression features or merges information only at later model phases. By leveraging dataset diversity, multi-domain feature fusion, and interpretability all at once, our research advances the state of the art in deepfake audio detection overssss comparable systems that target more limited or less explainable approaches.

Table 6: Comparative Summary of Deepfake Audio Detection Methods.

Paper / Method	Dataset(s)	Accuracy / EER / AUC	Notable Contributions
Proposed Work	**Large "In-the-Wild" dataset**	**Accuracy ~98%, AUC 0.998**	**Multi-domain early fusion, interpretability, robustness**
[2]	WaveFake, ASVspoof	EER ~1.8%	Token-level spectral modeling
[42]	ASVspoof, WaveFake	EER ~3–4%	Efficiency-accuracy tradeoff
[21]	ASVspoof Logical Access (LA)	Accuracy ~92%	Unsupervised anomaly detectionion
[15]	Custom voice dataset	Accuracy ~85–88%	Baseline for comparison
[17]	ASVspoof LA, DFDC-Audio	EER < 2%	Multi-scale dynamic feature fusion

Source: Authors, (2026).

VI. CONCLUSION AND FUTURE SCOPE

This work presents a robust and systematic framework for deepfake audio detection based on multi-domain feature fusion and lightweight neural classification. The proposed approach is evaluated on a large-scale, in-the-wild dataset comprising 31,780 audio samples evenly distributed between genuine and synthetic speech. By incorporating diverse speakers, languages, recording conditions, and synthesis techniques, the dataset closely reflects real-world deployment scenarios and provides a strong empirical foundation for evaluating generalization and robustness. A carefully designed preprocessing pipeline ensures standardized input quality, enabling consistent feature extraction and stable model training. The core methodological contribution of this study lies in the integration of complementary feature domains that capture both physical and algorithmic characteristics of speech production. Acoustic features model vocal-tract behavior, prosodic descriptors reflect higher-level speech dynamics, phase-based features capture fine-grained temporal coherence, emotional features characterize expressive variability, compression-related features expose codec-sensitive artifacts, and statistical spectral measures summarize global signal distributions. Rather than relying on a single representation, the fusion of these domains enables the detector to identify subtle inconsistencies that persist even when modern synthesis systems successfully mimic surface-level spectral patterns. The fused feature representation is classified using a lightweight fully connected neural network, which achieves strong discriminative performance while remaining computationally efficient and stable across validation folds. A key outcome of the experimental evaluation is the consistently high classification performance observed under stratified five-fold cross-validation, with minimal variation across folds. The results demonstrate that the proposed framework effectively separates genuine and synthetic audio across diverse conditions, supporting its suitability for real-world forensic and security applications. Importantly, the ablation study highlights that while individual feature groups, such as compression artifacts, are insufficient in isolation, their inclusion within a multi-domain fusion strategy significantly enhances robustness. This finding explains why the proposed system outperforms approaches that rely solely on spectral or prosodic cues and supports the central design choice of early, heterogeneous feature integration. When compared with existing deepfake audio detection methods reported in the literature, the proposed framework offers several practical advantages.

Many prior works achieve strong in-domain performance but rely heavily on deep spectro-temporal models trained on constrained benchmark datasets, often suffering performance degradation when exposed to unseen synthesis techniques or real-world distortions. In contrast, the present approach leverages domain-diverse features that are less tightly coupled to specific vocoders or architectures, allowing it to generalize more effectively across synthesis pipelines and recording environments. The inclusion of compression-related and phase-based cues, which are often underexplored in earlier studies, provides additional discriminatory evidence that remains difficult for generative models to reproduce consistently. These factors collectively explain the strong empirical results observed in this study. Despite the encouraging performance, several directions remain open for future investigation. While the current dataset is large and diverse, further evaluation under extreme acoustic conditions, adversarial perturbations, and emerging synthesis paradigms would strengthen confidence in long-term robustness. Extending the framework to incorporate linguistic or semantic representations may further enhance detection capability, particularly for emotionally neutral or low-variance speech. Additionally, adaptive or continual learning strategies could be explored to allow the model to update efficiently as new spoofing techniques emerge, without requiring full retraining. Finally, integrating the proposed audio-based system with complementary modalities, such as visual or behavioral cues, represents a promising avenue for constructing more comprehensive multimodal deepfake detection pipelines. In summary, this work establishes a strong and extensible foundation for deepfake audio detection by demonstrating that carefully designed multi-domain feature fusion, combined with an efficient classification model, can achieve reliable and generalizable performance under realistic conditions. The insights gained from feature ablation and comparative analysis provide clear justification for the proposed methodology and offer valuable guidance for future research aimed at countering the rapidly evolving threat of synthetic speech.

VII. AUTHOR'S CONTRIBUTION

Conceptualization: Akshat Chhatriwala, Ishita Akolkar, Namrata Shroff, Shankar Parmar.
Methodology: Akshat Chhatriwala, Ishita Akolkar, Namrata Shroff, Shankar Parmar.
Investigation: Akshat Chhatriwala, Ishita Akolkar, Namrata Shroff, Shankar Parmar.
Discussion of results: Akshat Chhatriwala, Ishita Akolkar, Namrata Shroff, Shankar Parmar.
Writing – Original Draft: Akshat Chhatriwala, Ishita Akolkar, Namrata Shroff, Shankar Parmar.
Writing – Review and Editing: Akshat Chhatriwala, Ishita Akolkar, Namrata Shroff, Shankar Parmar.
Resources: Akshat Chhatriwala, Ishita Akolkar, Namrata Shroff, Shankar Parmar.
Supervision: Akshat Chhatriwala, Ishita Akolkar, Namrata Shroff, Shankar Parmar.
Approval of the final text: Akshat Chhatriwala, Ishita Akolkar, Namrata Shroff, Shankar Parmar.

VIII. REFERENCES

[1] M. Rabhi, S. Bakiras, and R. Di Pietro, “Audio-deepfake detection: Adversarial attacks and countermeasures,” Expert Syst. Appl., vol. 250, p. 123941, 2024, doi: https://doi.org/10.1016/j.eswa.2024.123941.

[2] S. Modak, A. K. Das, and R. Naskar, “SpecViT: A Custom Vision-Transformer based Approach for Audio Deepfake Detection,” in ICASSP 2025 - 2025 IEEE International Conference on Acoustics, Speech and Signal Processing (ICASSP), Apr. 2025, pp. 1–5. doi: 10.1109/ICASSP49660.2025.10889022.

[3] A. Vaswani et al., “Attention Is All You Need,” Aug. 2023, arXiv. doi: 10.48550/arXiv.1706.03762.

[4] K. Zaman, K. Li, M. Sah, C. Direkoglu, S. Okada, and M. Unoki, “Transformers and audio detection tasks: An overview,” Digit. Signal Process., vol. 158, p. 104956, 2025, doi: https://doi.org/10.1016/j.dsp.2024.104956.

[5] B. Ghita, I. Kuzminykh, A. Usama, T. Bakhshi, and J. Marchang, “Deepfake Image Detection Using Vision Transformer Models,” in 2024 IEEE International Black Sea Conference on Communications and Networking (BlackSeaCom), Tbilisi, Georgia: IEEE, Jun. 2024, pp. 332–335. doi: 10.1109/blackseacom61746.2024.10646310.

[6] B. Zhang, H. Cui, V. Nguyen, and M. Whitty, “Audio Deepfake Detection: What Has Been Achieved and What Lies Ahead,” Sensors, vol. 25, no. 7, 2025, doi: 10.3390/s25071989.

[7] M. Astrid, E. Ghorbel, and D. Aouada, “Audio-Visual Deepfake Detection With Local Temporal Inconsistencies,” in ICASSP 2025 - 2025 IEEE International Conference on Acoustics, Speech and Signal Processing (ICASSP), Apr. 2025, pp. 1–5. doi: 10.1109/ICASSP49660.2025.10889087.

[8] Y. Ahmadiadli, X.-P. Zhang, and N. Khan, “Beyond Identity: A Generalizable Approach for Deepfake Audio Detection,” 2025. [Online]. Available: https://arxiv.org/abs/2505.06766

[9] P. Muruganandham, G. R. Thangasamy, S. Jayaraman, and R. Dharmarajan, “LSTM autoencoder based parallel architecture for deepfake audio detection with dynamic residual encoding and feature fusion,” Sci. Rep., vol. 15, no. 1, p. 23514, 2025, doi: 10.1038/s41598-025-08198-6.

[10] M. Astrid, E. Ghorbel, and D. Aouada, “Targeted Augmented Data for Audio Deepfake Detection,” Jul. 2024, arXiv. doi: 10.48550/arXiv.2407.07598.

[11] T. D. N. Le, K. K. Teh, and H. D. Tran, “Continuous Learning of Transformer-based Audio Deepfake Detection,” 2024. [Online]. Available: https://arxiv.org/abs/2409.05924.

[12] Z. Khanjani, G. Watson, and V. P. Janeja, “Audio deepfakes: A survey.,” Front. big data, vol. 5, p. 1001063, 2022, doi: 10.3389/fdata.2022.1001063.

[13] N. M. Müller, P. Czempin, F. Dieckmann, A. Froghyar, and K. Böttinger, “Does audio deepfake detection generalize?,” Interspeech, 2022.

[14] T. Chen, A. Kumar, P. Nagarsheth, G. Sivaraman, and E. Khoury, “Generalization of Audio Deepfake Detection,” in The Speaker and Language Recognition Workshop (Odyssey 2020), 2020, pp. 132–137. doi: 10.21437/Odyssey.2020-19.

[15] A. Hamza et al., “Deepfake Audio Detection via MFCC Features Using Machine Learning,” IEEE Access, vol. 10, pp. 134018–134028, 2022, doi: 10.1109/ACCESS.2022.3231480.

[16] R. Mubarak, T. Alsboui, O. Alshaikh, I. Inuwa-Dutse, S. Khan, and S. Parkinson, “A Survey on the Detection and Impacts of Deepfakes in Visual, Audio, and Textual Formats,” IEEE Access, vol. 11, pp. 144497–144529, 2023, doi: 10.1109/ACCESS.2023.3344653.

[17] Y. Hao et al., “Integrating Spectro-Temporal Cross Aggregation and Multi-Scale Dynamic Learning for Audio Deepfake Detection,” in ICASSP 2025 - 2025 IEEE International Conference on Acoustics, Speech and Signal Processing (ICASSP), Apr. 2025, pp. 1–5. doi: 10.1109/ICASSP49660.2025.10889337.

[18] G. Sivaraman, H. Tak, and E. Khoury, “Investigating voiced and unvoiced regions of speech for audio deepfake detection,” in ICASSP 2025 - 2025 IEEE International Conference on Acoustics, Speech and Signal Processing (ICASSP), Apr. 2025, pp. 1–5. doi: 10.1109/ICASSP49660.2025.10890861.

[19] G. Lee et al., “Dual-Channel Deepfake Audio Detection: Leveraging Direct and Reverberant Waveforms,” IEEE Access, vol. 13, pp. 18040–18052, 2025, doi: 10.1109/ACCESS.2025.3532775.

[20] Z. Jin, L. Lang, and B. Leng, “Wave-Spectrogram Cross-Modal Aggregation for Audio Deepfake Detection,” in ICASSP 2025 - 2025 IEEE International Conference on Acoustics, Speech and Signal Processing (ICASSP), Apr. 2025, pp. 1–5. doi: 10.1109/ICASSP49660.2025.10890563.

[21] D. Song, N. Lee, J. Kim, and E. Choi, “Anomaly Detection of Deepfake Audio Based on Real Audio Using Generative Adversarial Network Model,” IEEE Access, vol. 12, pp. 184311–184326, 2024, doi: 10.1109/ACCESS.2024.3506973.

[22] W. Huang, Y. Gu, Z. Wang, H. Zhu, and Y. Qian, “Generalizable Audio Deepfake Detection via Latent Space Refinement and Augmentation,” in ICASSP 2025 - 2025 IEEE International Conference on Acoustics, Speech and Signal Processing (ICASSP), Apr. 2025, pp. 1–5. doi: 10.1109/ICASSP49660.2025.10888328.

[23] X. Chen et al., “Continual Unsupervised Domain Adaptation for Audio Deepfake Detection,” in ICASSP 2025 - 2025 IEEE International Conference on Acoustics, Speech and Signal Processing (ICASSP), Apr. 2025, pp. 1–5. doi: 10.1109/ICASSP49660.2025.10890538.

[24] S. Zeng et al., “Adversarial Training and Gradient Optimization for Partially Deepfake Audio Localization,” in ICASSP 2025 - 2025 IEEE International Conference on Acoustics, Speech and Signal Processing (ICASSP), Apr. 2025, pp. 1–5. doi: 10.1109/ICASSP49660.2025.10890470.

[25] M. Gohari, D. Salvi, P. Bestagini, and N. Adami, “Audio Features Investigation for Singing Voice Deepfake Detection,” in ICASSP 2025 - 2025 IEEE International Conference on Acoustics, Speech and Signal Processing (ICASSP), Apr. 2025, pp. 1–5. doi: 10.1109/ICASSP49660.2025.10888452.

[26] Z. Xie, B. Li, X. Xu, Z. Liang, K. Yu, and M. Wu, “FakeSound: Deepfake General Audio Detection,” 2024. [Online]. Available: https://arxiv.org/abs/2406.08052

[27] N. Ur Rehman Ahmed, A. Badshah, H. Adeel, A. Tajammul, A. Daud, and T. Alsahfi, “Visual Deepfake Detection: Review of Techniques, Tools, Limitations, and Future Prospects,” IEEE Access, vol. 13, pp. 1923–1961, 2025, doi: 10.1109/ACCESS.2024.3523288.

[28] Z. Wang, D. Ye, J. Li, and J. Deng, “Generalize Audio Deepfake Algorithm Recognition via Attribution Enhancement,” in ICASSP 2025 - 2025 IEEE International Conference on Acoustics, Speech and Signal Processing (ICASSP), Apr. 2025, pp. 1–5. doi: 10.1109/ICASSP49660.2025.10889399.

[29] C. Y. Kwok, D.-T. Truong, and J. Q. Yip, “Robust Audio Deepfake Detection using Ensemble Confidence Calibration,” in ICASSP 2025 - 2025 IEEE International Conference on Acoustics, Speech and Signal Processing (ICASSP), Apr. 2025, pp. 1–5. doi: 10.1109/ICASSP49660.2025.10889972.

[30] G. S. Kashyap et al., “Fooling the Forgers: A Multi-Stage Framework for Audio Deepfake Detection,” in ICASSP 2025 - 2025 IEEE International Conference on Acoustics, Speech and Signal Processing (ICASSP), Apr. 2025, pp. 1–5. doi: 10.1109/ICASSP49660.2025.10888175.

[31] J. Devlin, M.-W. Chang, K. Lee, and K. Toutanova, “BERT: Pre-training of Deep Bidirectional Transformers for Language Understanding,” CoRR, vol. abs/1810.0, 2018, [Online]. Available: http://arxiv.org/abs/1810.04805.

[32] A. Baevski, H. Zhou, A. Mohamed, and M. Auli, “wav2vec 2.0: A Framework for Self-Supervised Learning of Speech Representations,” CoRR, vol. abs/2006.1, 2020, [Online]. Available: https://arxiv.org/abs/2006.11477

[33] N. Dawalatabad, M. Ravanelli, F. Grondin, J. Thienpondt, B. Desplanques, and H. Na, “ECAPA-TDNN Embeddings for Speaker Diarization,” in Interspeech 2021, in interspeech_2021. ISCA, Aug. 2021. doi: 10.21437/interspeech.2021-941.

[34] J. Yi, C. Wang, J. Tao, X. Zhang, C. Y. Zhang, and Y. Zhao, “Audio deepfake detection: A survey,” arXiv Prepr. arXiv2308.14970, 2023.

[35] P. M. Chauhan and N. P. Desai, “Mel Frequency Cepstral Coefficients (MFCC) based speaker identification in noisy environment using wiener filter,” in 2014 International Conference on Green Computing Communication and Electrical Engineering (ICGCCEE), Mar. 2014, pp. 1–5. doi: 10.1109/ICGCCEE.2014.6921394.

[36] N. M. Müller, P. Czempin, F. Dieckmann, A. Froghyar, and K. Böttinger, “Does Audio Deepfake Detection Generalize?,” 2024. [Online]. Available: https://arxiv.org/abs/2203.16263

[37] G. Tahaoglu, D. Baracchi, D. Shullani, M. Iuliani, and A. Piva, “Deepfake audio detection with spectral features and ResNeXt-based architecture,” Knowledge-Based Syst., vol. 323, p. 113726, 2025, doi: https://doi.org/10.1016/j.knosys.2025.113726.

[38] S. Nailwal, S. Singhal, N. T. Singh, and A. Raza, “Deepfake Detection: A Multi-Algorithmic and Multi-Modal Approach for Robust Detection and Analysis,” in 2023 International Conference on Research Methodologies in Knowledge Management, Artificial Intelligence and Telecommunication Engineering (RMKMATE), Chennai, India: IEEE, Nov. 2023, pp. 1–8. doi: 10.1109/rmkmate59243.2023.10369155.

[39] L. Pham, P. Lam, T. Nguyen, H. Nguyen, and A. Schindler, “Deepfake Audio Detection Using Spectrogram-based Feature and Ensemble of Deep Learning Models,” 2024. [Online]. Available: https://arxiv.org/abs/2407.01777

[40] T. M. Wani, S. A. A. Qadri, A. Ashraf, and I. Amerini, “ASTDT: an Interpretable Adaptive Spectro-Temporal Diffusion Transformer for audio deepfake detection,” EURASIP J. Inf. Secur., vol. 2025, no. 1, p. 32, 2025, doi: 10.1186/s13635-025-00217-3.

[41] N. Yu, L. Chen, T. Leng, Z. Chen, and X. Yi, “An explainable deepfake of speech detection method with spectrograms and waveforms,” J. Inf. Secur. Appl., vol. 81, p. 103720, 2024, doi: https://doi.org/10.1016/j.jisa.2024.103720.

[42] O. A. Shaaban, R. Yildirim, and A. A. Alguttar, “Audio Deepfake Approaches,” IEEE Access, vol. 11, pp. 132652–132682, 2023, doi: 10.1109/ACCESS.2023.3333866.

[43] L. Y. Gong and X. J. Li, “Deepfake Voice Detection: An Approach Using End-to-End Transformer with Acoustic Feature Fusion by Cross-Attention,” Electronics, vol. 14, no. 10, 2025, doi: 10.3390/electronics14102040.

[44] A. A. M. Albazony, H. A. Al-Wzwazy, A. S. Al-Khaleefa, M. A. Alazzawi, M. Almohamadi, and S. E. Alavi, “DeepFake Videos Detection by Using Recurrent Neural Network (RNN),” in 2023 Al-Sadiq International Conference on Communilcation and Information Technology (AICCIT), Al-Muthana, Iraq: IEEE, Jul. 2023, pp. 103–107. doi: 10.1109/aiccit57614.2023.10217956.

Journal of Engineering and Technology for Industrial Applications

ISSN ONLINE: 2447-0228

ITEGAM-JETIA

Manaus, v.12 n.60, p.933-943 July/August, 2026.
DOI: https://doi.org/10.5935/jetia.v12i60.3902

RESEARCH ARTICLE OPEN ACCESS

MULTI-SKU RETAIL SALES FORECASTING WITH FP-GROWTH ASSOCIATION-RULE FEATURES: A COMPARATIVE STUDY OF ECHO STATE NETWORK AND LSTM

Ayu Manik Dirgayusari[1]*, I Made Dwi Putra Asana[2], Made Leo Radhitya[3]
Ketut Gde Manik Karvana[4], I Made Subrata Sandhiyasa[5], Ni Kadek Ayu Nirwana[6]

[1]Department of Computer System Engineering Department, Institut Bisnis dan Teknologi Indonesia, Denpasar, Indonesia.
[2, 3, 4, 5]Department of Informatic, Institut Bisnis dan Teknologi Indonesia, Denpasar, Indonesia.
[6]Department of Digital Business, Institut Bisnis dan Teknologi Indonesia, Denpasar, Indonesia.

[1]https://orcid.org/0009-0004-1836-8433, [2]https://orcid.org/0000-0001-8512-0586, [3]https://orcid.org/0000-0001-8811-3090
[4]https://orcid.org/0009-0002-6737-9214, [5]https://orcid.org/0000-0003-3372-4171, [6]https://orcid.org/0009-0000-6622-5841

E-email: ayu.manik@instiki.ac.id, dwiputraasana@instiki.ac.id, leo.radhitya@instiki.ac.id, denakarvana@instiki.ac.id, subrata.sandhiyasa@instiki.ac.id, ayu.nirwana@instiki.ac.id

ARTICLE INFO

Article History
Received on: March 04, 2026
Reviewed on: April 02, 2026
Accepted on: July 01, 2026
Published on: July 31, 2026

Keywords:
Multi-SKU forecasting,
FP-Growth,
Echo State Network,
LSTM.

ABSTRACT

This study examines whether cross-product signals derived from market-basket transactions can enhance multi-SKU retail sales forecasting when embedded as auxiliary features in global sequence models. Retail transaction records from January 2024 to November 2025 were utilized. Frequent itemsets and association rules were mined using FP-Growth, and the resulting co-purchase structure was transformed into forecasting features. Daily sales were aggregated into weekly multivariate series and normalized using Min–Max scaling. Two feature-augmented forecasting architectures were evaluated: an Echo State Network (ESN+FP) and a Long Short-Term Memory network (LSTM+FP). Hyperparameters were tuned with Optuna (30 trials) using validation sMAPE, and per-SKU performance was assessed using MAE and sMAPE. Across 43 Food & Beverage SKUs, the lowest sMAPE was obtained by ESN+FP for 28 SKUs, whereas LSTM+FP performed best for 15 SKUs, indicating substantial heterogeneity in demand dynamics. Although slightly lower average errors were achieved by LSTM+FP, ESN+FP yielded superior results for several volatile yet repetitive series, while more stable trend patterns were better captured by LSTM+FP. An adaptive, per-SKU model selection strategy is therefore supported.

Copyright ©2026 by authors and Galileo Institute of Technology and Education of the Amazon (ITEGAM). This work is licensed under the Creative Commons Attribution International License (CC BY 4.0).

I. INTRODUCTION

Digital transformation in the retail sector has intensified the need for accurate demand forecasting and inventory control. In highly competitive markets with large product portfolios and rapidly evolving consumer behavior, forecasting errors directly increase holding costs, raise stockout risk, and reduce revenue. These challenges are amplified in multi-SKU settings because operational decisions are often made at the item level while demand across products can be interdependent. Transaction data frequently exhibit complementary and substitution relationships, making cross-product signals valuable for more stable and generalizable forecasts. A wide range of demand-forecasting methods has been applied in retail and supply chains, from statistical baselines to regression-based machine-learning models, largely due to their operational simplicity and competitive short-horizon performance. Comparative studies on industrial demand forecasting also show that the choice of algorithm and modeling strategy (e.g., global vs. local) affects the accuracy and consistency of cross-item/series performance [1], while comparative studies in the context of data-driven logistics confirm the common practice of comparing statistical methods with ML for time series [2]. In recent years, deep learning (e.g., LSTM/RNN variants) has been increasingly adopted to capture nonlinear dynamics in demand forecasting, including in e-retail and industry/food data-based demand forecasting [3], [4], [5].

However, in practice, many approaches still emphasize item-specific temporal pattern learning or rely on implicit cross-series learning (e.g., through global/local strategies or multivariate modeling), without explicit and measurable mechanisms to represent co-purchase/shopping basket structures. This challenge is compounded by heterogeneous SKU-level dynamics and disruptions such as outliers and calendar effects, which can destabilize model selection and generalization [1], [6]. Additionally, the intermittent demand characteristics of some retail products have been explicitly reported and require special attention in feature design, modeling strategies, and evaluation [7]. Association-rule mining provides an explicit mechanism for extracting cross-product signals from transaction data. Algorithms such as Apriori and FP-Growth have been widely used to extract frequent itemsets and association rules that represent co-purchase tendencies, and support cross-selling analysis and bundling promotion design [8]. However, the use of association analysis outputs as predictive features in time series forecasting is still relatively limited; many studies stop at descriptive findings (co-purchase patterns) without systematically integrating them into quantitative forecasting frameworks trained and evaluated at the SKU level. This limitation leaves clear room for research: can the co-purchase structures mined from transactions be transformed into features that enrich multi-SKU forecasting models and provide consistent improvements for specific SKUs, especially for volatile or infrequent series? Beyond LSTM as a widely used sequence-learning approach, Echo State Networks (ESN) offer a computationally efficient RNN alternative.

Unlike LSTM, which trains network weights end-to-end, ESN uses a reservoir with fixed weights and only optimizes output weights, making its training relatively lightweight and practical when applied to multi-SKU scenarios that require model/configuration maintenance across multiple outputs [9]. Comparative studies on dynamic systems also show that reservoir computing can be a competitive alternative to LSTMs for certain prediction tasks, while providing perspective on the accuracy–efficiency trade-off between fully-trained and reservoir-based approaches [10]. These characteristics are relevant to retail needs: useful prediction solutions must be accurate, but also feasible to run efficiently on large data and periodic model updates. Based on this gap, this study proposes a multi-SKU retail sales forecasting framework that integrates FP-Growth-based cross-product features with two different sequence forecasting architectures, namely ESN and LSTM. FP-Growth is used to extract inter-product correlation patterns from transactions and distill them into features/feature selections that represent co-purchase structures, so that the model learns not only from the historical temporal patterns of each SKU, but also from the cross-SKU relationships that emerge in shopping baskets. Furthermore, this study evaluates two global model variants—LSTM+FP and ESN+FP—on a like-for-like basis with consistent tuning procedures and per-SKU evaluation using MAE and sMAPE on weekly time series. Using transaction data from January 2024 to November 2025 filtered to the Food & Beverage category, the experiments focused on 43 SKUs that met the weekly history eligibility criteria.

II. RELATED WORK

Multi-item retail forecasting studies commonly retain classical baselines (e.g., ARIMA, exponential smoothing) and regression-style ML models due to their training efficiency, competitive short-horizon accuracy, and ease of deployment. In the context of grocery retail, Liashenko and Yakymchuk emphasize model selection as a practical decision under exogenous shocks (e.g., pandemics) and interpretability requirements; they discuss comparisons of classical time series methods with ML regression and additive approaches that support covariates (e.g., the Prophet family) to capture trends, seasonality, holidays, and external variables [11]. This direction is consistent with the literature's practice of demanding a robust and easily explainable baseline before proposing more complex architectures, especially when the study's goal is not just accuracy but also applicability and transparency of assumptions [11]. As data complexity increases and the need to capture non-linearities grows, the demand/time-series forecasting literature increasingly highlights deep learning designs that combine temporal memory (LSTM/GRU) with feature extractors (CNN/TCN) or attention mechanisms to model both local patterns and longer dependencies. In retail sales, Moraes et al. proposed a hybrid CNN–LSTM variant (stacked and parallel) that uses LSTM for temporal dynamics and convolutional modules to extract multivariate/exogenous information, and they reported improved performance over simpler neural architectures and autoregressive baselines on multivariate retail data [12]. In other time series domains, similar hybrid designs are widely used to combine linear/non-linear structures and balance feature representation needs against training load; for example, Nandigam et al. explore CNN–LSTM for large-scale energy consumption forecasting as an example where complex patterns and covariates drive the use of hybrid models [13]. Conceptually, these results reinforce the argument that "sequence memory + feature extraction" becomes the dominant design pattern when series are multivariate, influenced by external factors, and have variable structures.

Beyond hybrid CNN–RNN, two other relevant lines of research are (i) modeling multivariate dependencies and long contexts through attention/Transformer and (ii) improving robust forecasting for long horizons. Cheng et al. introduced SeriesNet as a conditional forecasting architecture that combines a causal CNN component with an RNN and then adds attention to improve temporal feature learning without uncontrolled parameter growth [14]. For contexts demanding long dependencies and complex covariates, the Transformer approach—e.g., Temporal Fusion Transformer (TFT)—is also frequently chosen; Alorf and Khan position TFT as a framework for capturing long-term dependencies in complex meteorological time series (with decomposition) [15]. On the robust long-horizon forecasting side, Zhou et al. propose TreeDRNet (based on arXiv) as an example of a deep approach targeting robustness in long-term predictions [16]. Furthermore, cross-dataset comparative studies are also commonly conducted to avoid single claims based on one dataset; Altıparmak and Aksu exemplify the practice of comparing several deep learning approaches for installed capacity forecasting, showing that "state-of-the-art" assessments often depend on evaluation protocols and data characteristics [17]. Overall, the deep forecasting literature tends to move in two directions: enriching mechanisms for capturing cross-variable dependencies (attention/Transformer) and strengthening robust generalization for long horizons, while still demanding rigorous comparison and replication on diverse datasets [14], [15], [16], [17]. However, in the representative works above, cross-product dependencies in retail are generally handled implicitly through multivariate inputs, convolutional modules, or attention—not through signals derived directly from the "market-basket" transaction structure. In fact, classical association-rule mining is designed to extract cross-item co-purchase patterns from large-scale transaction data, with Apriori as the initial foundation of association rules [18] and FP-Growth as an efficient method without candidate generation for frequent pattern mining [19].

The absence of an explicit path from "basket → rules → predictive features" in retail deep forecasting studies (e.g., retail CNN–LSTM [12]) leaves clear room for feature engineering that injects co-purchase structures as more interpretable cross-SKU signals, especially when the target is global multi-SKU forecasting and per-SKU evaluation. On the alternative architecture side, reservoir computing such as Echo State Networks (ESN) is often considered for its training efficiency (only readouts are trained, reservoir remains fixed), making it attractive for multiple series/tuning experiment scenarios. The foundational ESN literature emphasizes the importance of the "echo state property" condition and performance sensitivity to reservoir design/dynamics [20], [21], [22]. However, neat and direct comparative evidence for ESN vs. LSTM in the context of multi-SKU retail—with aligned features and per-SKU evaluation—is still much less common than comparisons between deep network variants (e.g., CNN–LSTM vs. other approaches) or cross-architecture benchmark studies [12], [17]. Therefore, this study is positioned as a focused empirical contribution: testing ESN and LSTM as global models with aligned FP-Growth features, then interpreting their trade-offs based on per-SKU performance.

III. MATERIALS AND METHODS

III.1 DATA

The data used in this study were obtained from retail sales transactions at Retail Ayu Nadi covering January 2024 to November 2025. The initial dataset consists of 2,097,150 rows and 27 attributes representing transaction information at the receipt level, including transaction time, invoice number, product identity, quantity, and other sales-related attributes. In the initial stage, attributes that were originally only recognized by column index were relabeled. The five key attributes used were date_time (transaction timestamp), invoice_number, item_name, quantity, and item_category. Transaction data from 2024 and 2025 were combined into a single integrated data frame. Furthermore, the scope of the study was limited to the Food & Beverage category to maintain relevance to daily consumer goods; other categories were excluded. After this filtering process, the number of transactions was reduced to 1,026,524 rows. From all Food & Beverage products, a set of items that appeared in the FP-Growth association rule results and also had a long weekly sales history was selected. This process resulted in 43 SKUs that became the focus of multi-SKU modeling at the forecasting stage.

III.2 DATA PREPROCESSING

Preprocessing followed two parallel pipelines: association extraction and time-series construction, which subsequently served as inputs to ESN+FP and LSTM+FP. The complete diagram of the FP-Growth flow integrated with ESN and LSTM modeling is shown in Figure 1 and Figure 2. For association extraction, transactions were converted into shopping baskets using the invoice identifier (no_nota). The FP-Growth algorithm is used to perform frequent itemset mining with a certain minimum support threshold. This method extracts combinations of products that frequently appear together in a transaction. Association rules were derived from frequent itemsets, with confidence computed as shown in following equation [23]:

$$Support\ (X) = \frac{Transactions\ Contains\ With\ X}{Total\ Transactions}$$

$$Confidence\ (A \rightarrow B) = \frac{Support(A \cup B)}{Support\ (A)}$$

The resulting rules were evaluated using lift, and only rules with lift > 1 and support/confidence above the specified thresholds were retained to preserve statistically meaningful relationships [24]. The items involved in the selected association rules are reintegrated into the transaction dataset. Only transactions containing these products are used in modeling, so that the model focuses on products that have clear transactional relevance. This step also functions as association-based feature selection and reduces noise from irrelevant items [25]. For time-series construction, daily transactions were aggregated into weekly series by summing item-level sales over Monday–Sunday intervals. Weekly aggregation is chosen to reduce daily stochastic fluctuations and sparsity issues (many zero values) that are common in daily retail data, while maintaining trend and seasonal patterns that are relevant for decision making [26]. The aggregation results are then pivoted to obtain a multivariate time series matrix, with rows representing weeks and columns representing items. Missing values that arise due to pivoting are filled with zeros. Finally, all weekly sales values are normalized using Min–Max scaling to the range [0, 1]. This normalization is important to stabilize the learning process in both the ESN reservoir and the LSTM network, which are sensitive to differences in scale between variables. This scaled multivariate time series matrix becomes the database for the multi-SKU experiment in the next stage.

III.3 ESN+FP MODEL ARCHITECTURE AND TRAINING

The Echo State Network architecture with FP-Growth association features (ESN+FP) is designed as a global multi-SKU model that utilizes dynamic reservoir representations to predict weekly sales. The complete flow of FP-Growth and ESN integration is shown in Figure 1.

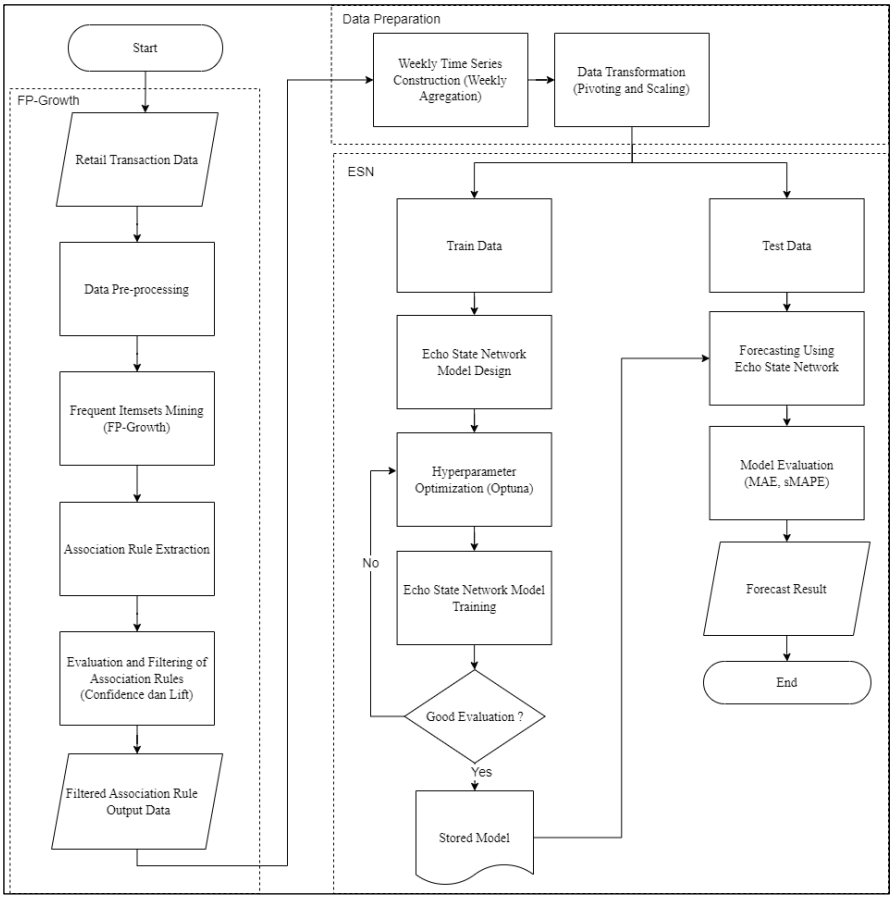


Figure 1: ESN+FP workflow for multi-SKU weekly sales forecasting.
Source: Authors, (2026).

Structurally, ESN consists of three main components: an input layer, a reservoir with random recursive weights, and an output layer (readout) [27]. The input and reservoir weights (Win and$W$) are randomly initialized with controlled sparsity and spectral radius to satisfy the Echo State Property, thereby keeping the reservoir dynamics stable [28]. At each weekly time step, the input vector contains scaled sales for all relevant SKUs along with additional features from FP-Growth (e.g., membership indicators or association intensity). The reservoir projects this input into a high-dimensional, nonlinear state space. Unlike conventional RNNs, the ESN training phase only optimizes the output weights$Wout$, whileWin and$W$ remain fixed. The training process begins with state harvesting, which involves feeding the training time series into the reservoir and recording the internal state matrix$H$ [29] [30]. The first few steps are ignored as a washout period to eliminate the effects of initial conditions. The output weights are then calculated using ridge regression.

$$W_{out} = Y_{target} H^T (HH^T + \lambda I)^{-1}$$

whereY_{target} is the sales target matrix,λ is the regularization coefficient, and$I$ is the identity matrix. Because ESN performance is sensitive to reservoir configuration, Optuna was used for hyperparameter optimization using the TPE sampler over reservoir size, spectral radius, leak rate, and ridge coefficient. This process utilizes the Tree-structured Parzen Estimator (TPE) algorithm to explore combinations of parameters such as reservoir size, spectral radius, leak rate, and regularization coefficient [31]. A total of 30 trials were run to minimize the sMAPE value on the validation data. The best hyperparameters were then used to train the final ESN+FP model on the training data. All model components, including the scaler and pivot structure, were stored in a serialized format to ensure consistency when performing inference on new data.

III.4 LSTM+FP MODEL ARCHITECTURE AND TRAINING

The second model is Long Short-Term Memory with FP-Growth association features (LSTM+FP), which is also configured as a global multi-SKU model. The integration flow diagram of FP-Growth and LSTM is shown in Figure 2.

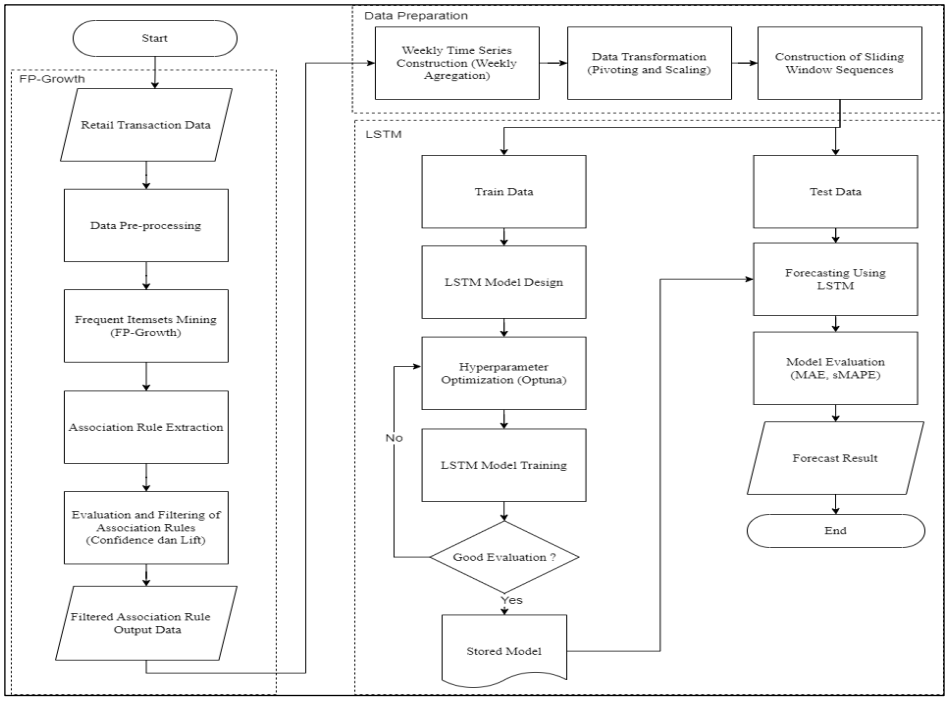


Figure 2: LSTM+FP workflow for multi-SKU weekly sales forecasting.
Source: Authors, (2026).

In contrast to ESN, LSTM employs gated memory cells (input, forget, and output gates) to learn long-range temporal dependencies. After the weekly aggregation and normalization stages, the multivariate time series matrix is converted into a fixed sequence using the sliding window approach[32]. Each window contains historical observations spanning L weeks for all SKUs, while the target is the next week's sales vector. This transformation allows LSTM to learn temporal patterns across multiple time steps[32]. The network architecture consists of one or more LSTM layers followed by a fully connected layer that produces multivariate predictions. All network weights are trained through backpropagation through time[33]. As in ESN, the LSTM configuration is tuned using Optuna with 30 trials to minimize sMAPE on the validation data. The optimized hyperparameters include the number of LSTM units, sequence length, learning rate, batch size, number of epochs, and dropout rate[33]. The training process was carried out with the Adam optimizer and an error-based loss function (e.g., MSE), with several epochs until convergence. The model that performed best on the validation data was selected as the final model. As with ESN+FP, the LSTM+FP model along with the pre-processing components (scaler, pivot structure, and window configuration) were saved for use in the forecasting and evaluation stages.

III.5 EXPERIMENTAL DESIGN AND EVALUATION

The experiment was designed to compare the capabilities of ESN+FP and LSTM+FP in the context of multi-SKU sales forecasting. Given the sequential nature of time series, the training and test data were separated chronologically. Several train–test ratio scenarios (60:40, 70:30, and 80:20) were evaluated to test the robustness of the model against variations in training data length, with the final model selected based on the best performance in the scenario considered most representative. In each scenario, both models were trained as global models using the same multivariate time series matrix, which had been enriched with FP-Growth association features. The evaluation was performed per SKU, so that for each item a pair of error values was obtained for ESN+FP and LSTM+FP. Two main metrics were used, namely Mean Absolute Error (MAE) and Symmetric Mean Absolute Percentage Error (sMAPE). MAE measures the average absolute deviation between actual and predicted values, while sMAPE provides a measure of relative error normalized to the average of actual and predicted values, making it easier to compare SKUs with different sales scales.

IV. RESULT AND DISCUSSION

IV.1 COMPARATIVE PERFORMANCE RESULTS

In this study, one global ESN model enriched with FP-Growth association features (ESN+FP) and one global LSTM model with FP-Growth (LSTM+FP) were trained simultaneously using the sales data of 43 SKUs. Both models share cross-product parameters, representing a real-world scenario in multi-SKU retail where practitioners tend to apply a centralized model. However, performance evaluation was conducted at the per-item (per SKU) level using MAE and sMAPE metrics, so that it could be observed how a single global architecture reacted to different sales time series characteristics. Table 1 presents the MAE and sMAPE values of ESN+FP and LSTM+FP for each SKU. Using the smallest sMAPE as the selection criterion, it can be seen that ESN+FP provides the lowest error in 28 of the 43 SKUs, while LSTM+FP performs better in 15 SKUs. For some products such as Chitato, Me Lewis, Sari Roti, and Boncabe, the sMAPE value of ESN+FP is very small (often below 5%), while LSTM+FP produces a larger error. Conversely, for products such as Madu, Indomie, and several dairy products, LSTM+FP produces a lower sMAPE than ESN+FP, indicating that the LSTM architecture is better able to follow the demand dynamics in these time series. There are also several SKUs with very high sMAPE for both models (e.g., ABC Mie and Kecap Ikan dan Inggris), indicating time series with highly irregular and unpredictable demand patterns.

Table 1: Comparison of per-SKU performance between ESN+FP and LSTM+FP based on MAE and sMAPE.

Item	ESN+FP Growth		LSTM+FP Growth	
	MAE	sMAPE (	MAE	sMAPE (%)
CHITATO	0.1	0.07	89.03	3.92
ME LEWIS	2.46	1.05	16.39	4.11
BREAD CRUMBS	3.74	1.47	39.42	5.38
BONCABE	1.05	1.79	63.87	6.52
AJIOMOTO SAUCE AND MICIN	1.65	3.82	11.79	9.36
NUTRISARI	4.45	4.13	41.11	9.78
Sesame Oil and Samin	4.45	4.33	18.17	12.15
French fries	1.84	4.5	22.22	13.85
ROYCO	2.39	5.79	12.10	18.89
ULTRA MILK	58.42	7.88	42.27	18.99
SEDAAP NOODLES	10.89	8.68	11.93	19.26
SASA	7.99	9.99	22.55	19.91
ABC Sambal	6.08	10.3	19.03	24.06
BANGO SOY SAUCE	9.17	11.59	25.17	24.41
SOLUTION	15.92	11.7	11.53	25.20
ONION	19.31	11.72	76.23	25.87
ROMA	15.19	11.79	44.31	26.67
RICE	45.26	12.3	22.93	27.31
GOOD DAY	16.24	12.34	11.75	27.72
LEMONILO	13.99	12.55	23.62	29.59
GARUDA	6.83	13.77	62.02	30.18
INDOMIE	309.9	14.97	93.82	32.99
MASAKO	8.16	15.28	23.22	33.59
AMO SPARK	15.09	15.97	51.72	34.63
COCONUTS	45.18	17.37	25.45	34.75
INDOFOOD	65.74	17.92	57.11	35.46
BLUE BAND	19.11	19.1	44.11	37.05
ABC Soy Sauce	7.83	19.36	40.22	37.73
INDOMILK	28.79	19.6	40.27	38.67
Bird's Nest Noodles	203.45	24.06	52.18	39.80
KARA	27.64	26.5	24.78	40.70
KIS	31.13	27.65	71.73	41.62
Corn Flakes	29.36	29.02	125.66	42.41
Flag Milk	69.08	30.97	28.72	42.63
SAORI SAUCE	19.89	33.35	23.05	42.67
CHIKI	41.48	34.64	24.13	43.05
SAJIKU SPICE FLOUR	20.35	35.2	43.72	45.37
MILO	69.82	41.91	62.46	46.02
SARIMI	24.99	52.07	55.60	47.00
HONEY	39.04	73.68	67.05	48.23
GAGA NOODLES	27.27	78.2	34.89	49.52
Fish Sauce and English	45.51	150.45	134.86	52.69
ABC NOODLES	29.28	200	26.50	76.26
Average	**42.76**	**30.84**	**33.15**	**26.48**

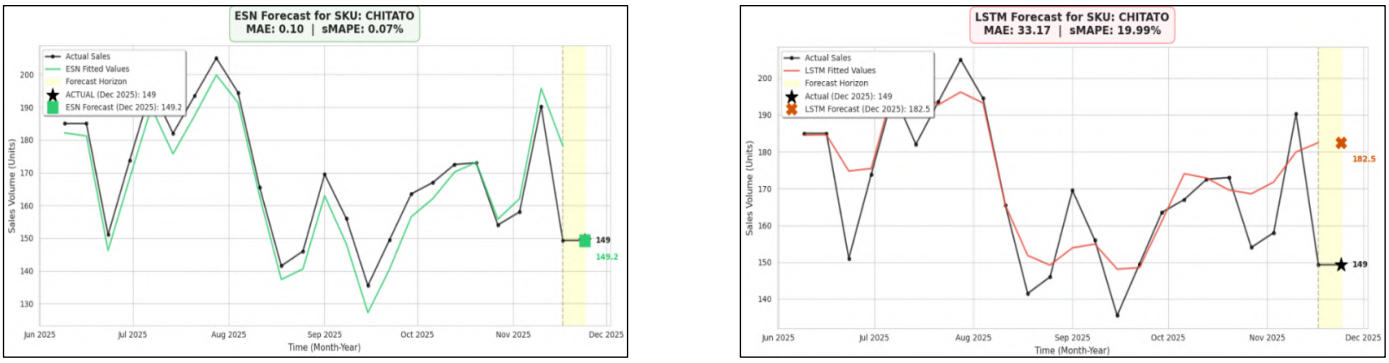
Source: Authors, (2026).

The pattern in Table 1 shows strong heterogeneity. For some items such as CHITATO, ME LEWIS, SARI ROTI, and BONCABE, ESN+FP achieved sMAPE below 5%, while LSTM+FP lagged significantly behind. This indicates that the combination of ESN reservoir with FP-Growth association features is very effective for the time series of these products. Conversely, there are other items such as MADU, ABC MIE, or several dairy products where LSTM+FP produces a lower sMAPE than ESN+FP, and ESN+FP tends to experience a significant under/over-prediction bias. There are also extreme cases such as ABC MIE and KECAP IKAN DAN INGGRIS where the sMAPE of ESN+FP is very high (up to around 200% and 150%), while LSTM+FP, although not good, remains within a more moderate error range. As shown in the Average row of Table 1, LSTM+FP achieves slightly lower mean MAE and sMAPE than ESN+FP. This indicates that, in aggregate across all SKUs, the global LSTM+FP model tends to produce smaller average errors. However, ESN+FP is more often the best model at the item level (28 SKUs), and its sMAPE value distribution is wider. This means that ESN+FP is very effective for certain SKU subsets but also shows high performance variation, while LSTM+FP is less often the best for a product, but its behavior is relatively more consistent and less likely to produce extreme errors. These item-level findings confirm that a single global model will not behave uniformly across all products, as it reacts differently to the time series characteristics of each SKU—ranging from volatility levels, trend patterns, to demand properties that are more continuous or sporadic—so performance evaluation should not rely solely on aggregate average values, but must always be reviewed at the SKU level.

In addition, the comparison results show that ESN+FP does indeed more often emerge as the model with the smallest sMAPE and is therefore worth considering as a global baseline, but LSTM+FP cannot be ignored because for some SKUs it actually provides more accurate predictions, so that in practice the combination of the two opens up opportunities for an adaptive model selection approach per product.

IV.2 ITEM FORECASTING RESULT ANALYSIS

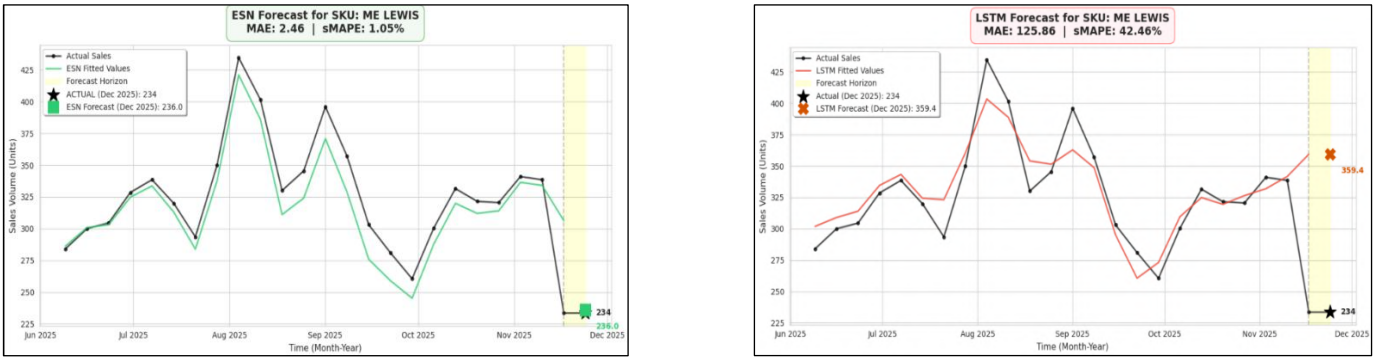
This subsection examines six representative SKUs selected to reflect diverse demand characteristics and compares models using both aggregate accuracy (MAE, sMAPE) and operational behavior at the final forecast point. The first lens is aggregate performance, which is measured by MAE and sMAPE throughout the test horizon. The second lens is operational performance, namely the behavior of the model at the last forecasting point and its suitability with the direction of demand change (up or down) towards the end of the period. The six pairs of graphs in Fig. 1–Fig. 6 were selected to represent three main patterns that emerged from the data: (i) cases where ESN+FP clearly outperformed LSTM+FP, (ii) cases where LSTM+FP was more accurate than ESN+FP, and (iii) cases where both models failed to represent demand dynamics (*hard-to-forecast series*). This dual-lens approach allows for a more balanced evaluation between average numerical accuracy and the practical usefulness of forecasting results at the item level.



(a) (b)

Figure 3: Comparison of CHITATO SKU sales forecast results between (a) ESN+FP and (b) LSTM+FP.
Source: Authors, (2026).

In Figure 3, both lenses consistently support the superiority of ESN+FP. From an aggregate perspective, ESN+FP produces an MAE of 0.10 and an sMAPE of 0.07%, which is much smaller than LSTM+FP, which has an MAE of 33.17 and an sMAPE of 19.99%. Operationally, the ESN+FP endpoint prediction in December 2025 closely matched the observed value (149 vs. 149.2) and captured short-term fluctuations. LSTM+FP tends to smooth out variations and slightly deviate from the actual line, resulting in less accurate form and value.

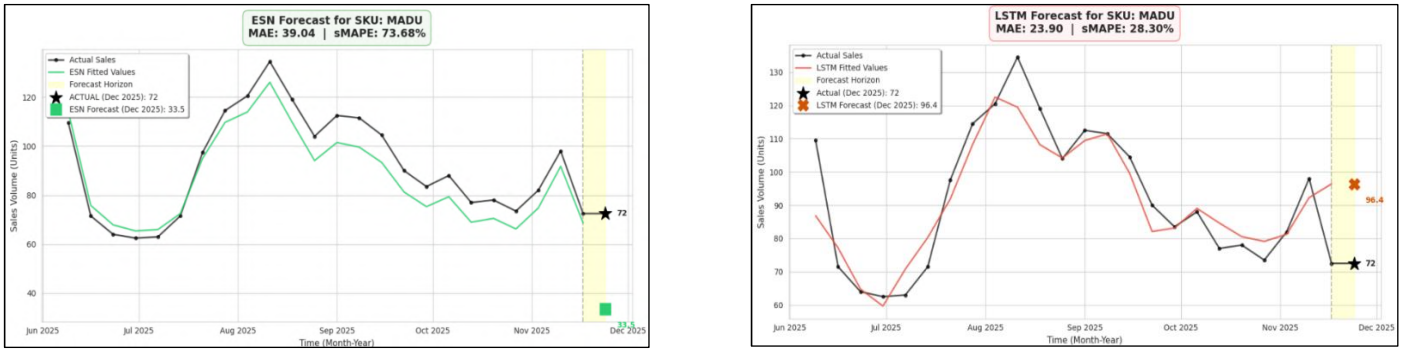


(a) (b)

Figure 4: Comparison of sales forecast results for SKU ME LEWIS between (a) ESN+FP and (b) LSTM+FP.
Source: Authors, (2026).

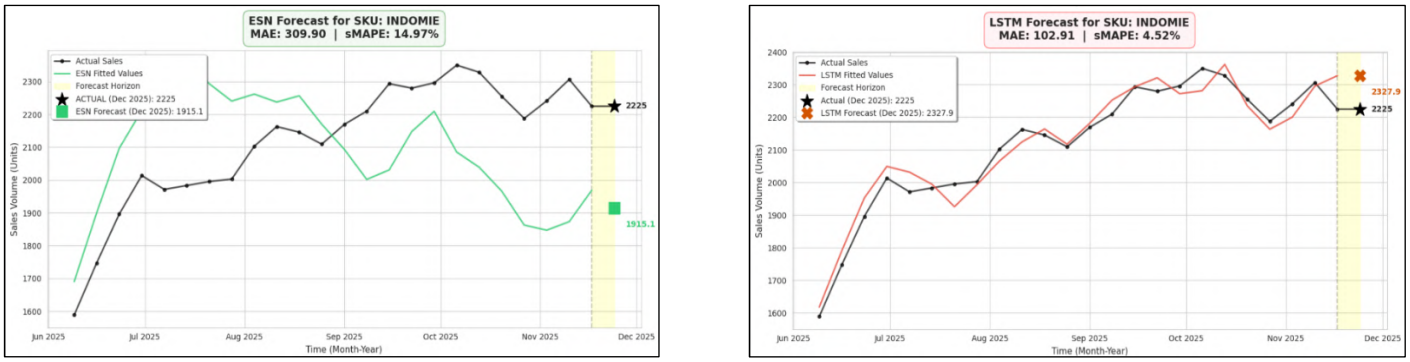
Figure 4 (SKU *ME LEWIS*) shows the same pattern. In aggregate, ESN+FP again excels with MAE of 2.46 and sMAPE of 1.05%, while LSTM+FP records MAE of 125.86 and sMAPE of 42.46%. From an operational perspective, ESN+FP provides a final prediction that is very close to the actual (234 vs. 236), with a curve shape that follows the ups and downs of sales. LSTM+FP not only has a large average error, but also predicts an overly high final level (359.4), making it unreliable for stock decision-making. These two examples illustrate the "fluctuating with clear local repetition" pattern group, where ESN+FP excels both in terms of metrics and final prediction behavior. The opposite is seen in Figure 5 and Figure 6, which represent series with relatively smooth trends and seasonality. In Figure 3 (HONEY SKU), from an aggregate perspective, LSTM+FP is clearly better with an MAE of 23.30 and sMAPE of 28.30%, compared to ESN+FP which has an MAE of 39.04 and sMAPE of 73.68%. Operationally, the final prediction of LSTM+FP (98.4) is still off from the actual 72, but its deviation ( ) is still smaller than that of ESN+FP, which predicted 33.5. The shape of the LSTM+FP curve is also more stable in following the downward trend in the latter half of the horizon, while ESN+FP shows a significant level bias.

In Figure 4 (INDOMIE SKU), the difference between the two models is even more apparent. LSTM+FP produced an MAE of 102.91 and an sMAPE of 4.52%, while ESN+FP recorded an MAE of 309.90 and an sMAPE of 14.97%. At the end point, the LSTM+FP prediction (2327.9) is much closer to the actual 2235 than ESN+FP (1915.1), and the LSTM+FP curve follows a relatively smooth upward trend, while ESN+FP fails to maintain its level. For a pattern like this—"smooth trend with weak seasonality"—both lenses point to LSTM+FP as the more suitable model.



(a) (b)

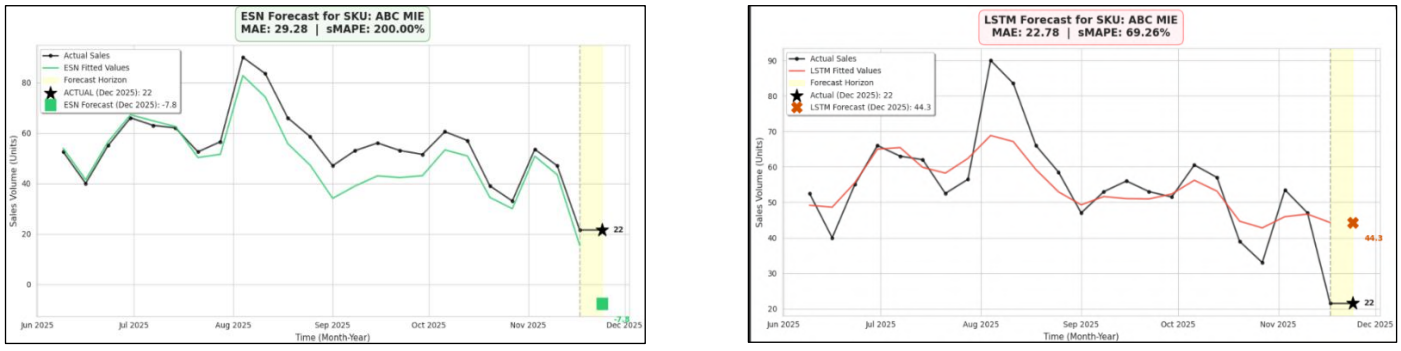
Figure 5: Comparison of MADU SKU sales forecast results between (a) ESN+FP and (b) LSTM+FP.
Source: Authors, (2026).



(a) (b)

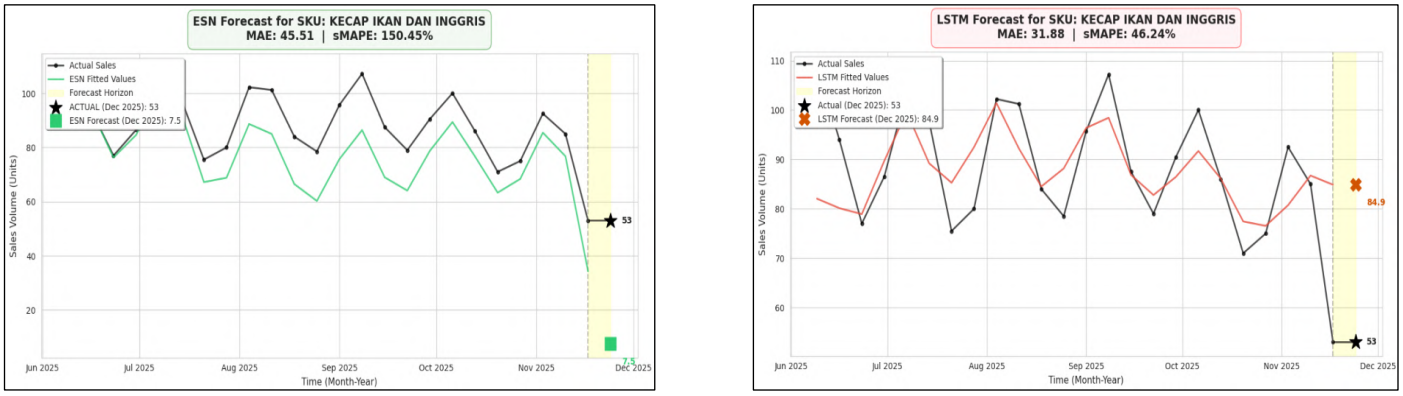
Figure 6: Comparison of sales forecast results for INDOMIE SKUs between (a) ESN+FP and (b) LSTM+FP.
Source: Authors, (2026).

Figure 7 (SKU ABC MIE) and Figure 8 (SKU KECAP IKAN DAN INGGRIS) illustrate series that can be categorized as hard-to-forecast series. In Figure 5, the ABC MIE series shows sharp changes and extreme declines at the end of the horizon. In aggregate, LSTM+FP performs better (MAE 22.78; sMAPE 69.26%) than ESN+FP (MAE 29.28; sMAPE 200.00%), but both sMAPE values are equally high. From an operational perspective, the final prediction of ESN+FP (7.8) is slightly closer to the actual 22 than LSTM+FP (44.3), but both are clearly off and misread the magnitude of the decline in demand. In Figure 6, the SKU KECAP IKAN DAN INGGRIS shows a sporadic demand pattern with fluctuating levels. LSTM+FP is better in aggregate (MAE 31.88; sMAPE 46.24%) than ESN+FP (MAE 45.51; sMAPE 150.45%), and also provides a relatively closer final prediction (84.9 vs. actual 53 compared to 7.5 for ESN+FP). However, from an operational perspective, both models remain inadequate because the deviation at the end point is still large and the direction of level changes is not captured well.



(a) (b)

Figure 7: Comparison of ABC MIE SKU sales forecast results between (a) ESN+FP and (b) LSTM+FP.
Source: Authors, (2026).



(a) (b)

Figure 8: Comparison of sales forecast results for SKU KECAP IKAN DAN INGGRIS between (a) ESN+FP and (b) LSTM+FP. Source: Authors, (2026).

From the six examples in Figures 3–8, it can be concluded that the two assessment lenses provide complementary insights. For SKUs with **fluctuating but repeating** patterns, ESN+FP tends to excel in terms of both MAE/sMAPE and in replicating the shape and end point of the series. For SKUs with **smoother trends and seasonality**, LSTM+FP is more accurate, both in terms of aggregate error and the closeness of the final prediction to the actual value. Meanwhile, for series with **highly sporadic and unstructured demand**, both of these global models show limitations in terms of both numerical and operational aspects. This pattern-based insight confirms that an effective multi-SKU forecasting strategy needs to evaluate models from two perspectives—aggregate and operational—and encourages the use of an adaptive model selection approach tailored to the time series characteristics of each product group.

IV.3 RELATIONSHIP WITH TIME SERIES CHARACTERISTICS

The findings in Table 1 and the visual analysis in Figures 3–8 show that the performance of ESN+FP and LSTM+FP is greatly influenced by the time series characteristics of each SKU, not just by the model architecture used. Qualitatively, the sales time series of the 43 SKUs can be grouped into three main patterns: (i) a fluctuating pattern with clear local repetitions, (ii) a relatively smooth trend and seasonal pattern, and (iii) a highly sporadic and unstructured demand pattern. Each group exhibits different model tendencies in terms of aggregate performance (MAE/sMAPE) and operational behavior (final predictions and the direction of demand changes). In the first group, namely series with sharp but repetitive fluctuations (e.g., CHITATO, ME LEWIS, SARI ROTI, BONCABE), sales tend to oscillate around a certain level with several repeated spikes and declines over time. For these characteristics, ESN+FP generally provides the best performance: sMAPE values are in the very low range (often below 5%), and the ups and downs of the predictions closely follow the actual series. This indicates that the ESN reservoir effectively absorbs short-term dynamics and local variations, while the FP-Growth association feature helps add context to relevant inter-product relationships during periods of high demand. The second group includes series with long-term trends and subtle seasonality (such as MADU and INDOMIE). In these series, local fluctuations are relatively smaller than global trend changes, and there are no strong short-term pattern repetitions. Experiments show that LSTM+FP tends to be superior in this group: LSTM+FP produces lower MAE and sMAPE and is able to place the trend level and direction more accurately, while ESN+FP often experiences level bias that causes large vertical deviations even though the curve shape appears to follow the trend at first glance.

This is consistent with the character of LSTM, which is designed to capture long-term dependencies, making it more suitable for series with strong trend structures and gradual level changes. The third group consists of series with highly sporadic and unstructured demand, which is clearly seen in ABC MIE and KECAP IKAN DAN INGGRIS. Series in this group are characterized by sharp variations, high zero frequency, or sudden changes without seasonal patterns or stable trends. In this case, both global models show limitations: sMAPE reaches very high values and the final predictions are often far from the actual values. The FP-Growth association feature is also not very helpful, because the co-purchase patterns for these products tend to be unstable, making them difficult to use as additional signals. These series can be categorized as hard-to-forecast series that require a special approach beyond the ESN+FP and LSTM+FP configurations used in this study. In summary, the relationship between time series characteristics and the models that tend to excel can be summarized as follows: ESN+FP is suitable for SKUs with high but patterned volatility, LSTM+FP is more suitable for SKUs with smooth trends and seasonality, while SKUs with highly sporadic demand patterns are not suitable for modeling with only these two approaches. This pattern-based mapping forms the basis for model selection strategy recommendations in the multi-SKU context discussed in the next subsection.

IV.4 PRACTICAL IMPLICATIONS FOR MULTI-SKU RETAIL

From a practical perspective, findings from 43 SKUs indicate that applying a single global model to the entire product portfolio does not yield optimal results. Differences in demand pattern characteristics cause ESN+FP and LSTM+FP to be mutually superior in different SKU groups, and in a small portion of SKUs, both are equally inadequate. Therefore, forecasting strategies in a multi-SKU retail environment need to be designed as a step-by-step process that incorporates time series character diagnosis and adaptive model selection. First, before mass modeling, retailers are advised to conduct an initial diagnosis of the time series for each SKU based on simple indicators such as the volatility level (e.g., the ratio of standard deviation to average), the presence of trends and seasonality, and the level of intermittency (the proportion of periods with zero or very low demand).

This diagnosis can be used to group SKUs into three pattern types identified in Subsection IV.3: patterned-fluctuating, smooth-trending, and sporadic. Second, the results of the diagnosis can be mapped to model selection policies. For SKU groups with fluctuating but repeating patterns, ESN+FP can be used as the main baseline because it has proven to be superior in terms of both MAE/sMAPE and forecasting pattern suitability, especially when inter-product association information is relevant. For SKUs with smoother trends and seasonality, LSTM+FP is more appropriate to prioritize because it provides more accurate estimates of the level and direction of demand changes in aggregate. Meanwhile, SKUs with highly sporadic demand should not immediately rely on global ESN or LSTM models, but should consider using special methods for intermittent demand (e.g., Croston-based approaches) or be handled with more conservative stock policies until more suitable models are developed. Third, practical implementation in retail information systems can adopt a model selection framework per SKU. In this framework, the forecasting pipeline consists of: (i) a time series analysis module that periodically classifies SKUs, (ii) a model selection module that decides whether ESN+FP, LSTM+FP, or another method is used for a particular SKU, and (iii) a continuous evaluation module that monitors MAE/sMAPE and operational indicators such as bias level and accuracy of demand change direction. This framework allows retailers to leverage the strengths of each model without losing the scale and efficiency of a global approach. Thus, the results of this study not only provide empirical contributions in comparing ESN+FP and LSTM+FP, but also offer practical guidance for designers of multi-SKU sales forecasting systems. The approach that combines time series character diagnosis, adaptive model selection, and dual-lens evaluation (aggregate and operational) has the potential to improve forecasting accuracy as well as the business relevance of decisions made based on model output.

V. CONCLUSIONS

This study shows that the integration of FP-Growth-based cross-product features can be operationally measured for multi-SKU retail sales forecasting through two different sequence architectures, namely ESN and LSTM, in a global model scheme with per-SKU evaluation on weekly time series. Experiments on 43 SKUs show that ESN+FP provides the best performance based on sMAPE on 28 of the 43 SKUs, while LSTM+FP excels on 15 SKUs, confirming that model superiority depends on series characteristics and cannot be concluded from a single aggregate metric. The discussion analysis reinforces practical mapping: ESN+FP tends to be suitable for volatile but still patterned SKUs, while LSTM+FP is more suitable for SKUs with smoother trends/seasonality because it is more stable in placing the level and direction of change, while highly sporadic SKUs remain hard-to-forecast and require a special approach beyond these two global model configurations. The practical implication is that adopting a single modeling approach for all SKUs is suboptimal; it is necessary to select models adaptively based on series characteristics and operational objectives. This study recommends a forecasting pipeline that incorporates series character diagnosis, per-SKU adaptive model selection (ESN+FP vs. LSTM+FP vs. other methods), and continuous evaluation using MAE/sMAPE and operational indicators (e.g., level bias and directional accuracy) to make stock decisions more business-relevant.

VI. AUTHOR'S CONTRIBUTION

Conceptualization: Ayu Manik Dirgayusari.
Methodology: I Made Dwi Putra Asana and Ketut Gde Manik Karvana.
Investigation: Made Leo Radhitya and I Made Subrata Sandhiyasa.
Discussion of results: Ni Kadek Ayu Nirwana and Made Leo Radhitya.
Writing – Original Draft: I Made Dwi Putra Asana and Ni Kadek Ayu Nirwana.
Writing – Review and Editing: Ayu Manik Dirgayusari and Made Leo Radhitya.
Resources and Software: I Made Subrata Sandhiyasa, and Ketut Gde Manik Karvana.
Supervision: Ayu Manik Dirgayusari and I Made Dwi Putra Asana.

VII. ACKNOWLEDGMENTS

This work was supported by the Research Grants program under the Fundamental Regular Research scheme of the Ministry of Research, Technology, and Higher Education of the Republic of Indonesia, through the Directorate of Research, Community Service, and Innovation (DRPMI) INSTIKI, under Master Contract Number 129/C3/DT.05.00/PL/2025 and Derivative Contract Number 2166/LL8/AL.04/2025 and 012/INSTIKI.R1. D2/PM.03/06.2025.

VIII. REFERENCES

[1] J. M. Rožanec, B. Kažič, M. Škrjanc, B. Fortuna, and D. Mladenić, "Automotive OEM Demand Forecasting: A Comparative Study of Forecasting Algorithms and Strategies," Applied Sciences, vol. 11, no. 15, p. 6787, Jul. 2021, doi: 10.3390/app11156787.

[2] L. Schmid, M. Roidl, A. Kirchheim, and M. Pauly, "Comparing Statistical and Machine Learning Methods for Time Series Forecasting in Data-Driven Logistics—A Simulation Study," Entropy, vol. 27, no. 1, p. 25, Dec. 2024, doi: 10.3390/e27010025.

[3] N. Nassibi, H. Fasihuddin, and L. Hsairi, "Demand Forecasting Models for Food Industry by Utilizing Machine Learning Approaches," International Journal of Advanced Computer Science and Applications, vol. 14, no. 3, 2023, doi: 10.14569/IJACSA.2023.01403101.

[4] I. Amellal, A. Amellal, H. Seghiouer, and M. R. Ech-Charrat, "An integrated approach for modern supply chain management: Utilizing advanced machine learning models for sentiment analysis, demand forecasting, and probabilistic price prediction," Decision Science Letters, vol. 13, no. 1, pp. 237–248, 2024, doi: 10.5267/j.dsl.2023.9.003.

[5] P. S and P. D. S, "A Hybrid Deep Learning Based Deep Prophet Memory Neural Network Approach for Seasonal Items Demand Forecasting," Journal of Advances in Information Technology, vol. 15, no. 6, pp. 735–747, 2024, doi: 10.12720/jait.15.6.735-747.

[6] H. Songhua, "A novel outlier calendrical heterogeneity reconstruction deep learning model for electricity demand forecasting," Journal of Intelligent & Fuzzy Systems, vol. 46, no. 2, pp. 3363–3394, Feb. 2024, doi: 10.3233/JIFS-235218.

[7] İ. GÜVEN, Ö. UYGUN, and F. ŞİMŞİR, "Machine Learning Algorithms with Intermittent Demand Forecasting: An Application in Retail Apparel with Plenty of Predictors," Tekstil ve Konfeksiyon, vol. 31, no. 2, pp. 99–110, Jun. 2021, doi: 10.32710/tekstilvekonfeksiyon.809867.

[8] D. Dwiputra, A. Mulyo Widodo, H. Akbar, and G. Firmansyah, "Evaluating the Performance of Association Rules in Apriori and FP-Growth Algorithms: Market Basket Analysis to Discover Rules of Item Combinations," Journal of World Science, vol. 2, no. 8, pp. 1229–1248, Aug. 2023, doi: 10.58344/jws.v2i8.403.

[9] S. Lun, Z. Sun, M. Li, and L. Wang, "Multiple-Reservoir Hierarchical Echo State Network," Mathematics, vol. 11, no. 18, p. 3961, Sep. 2023, doi: 10.3390/math11183961.

[10] A. Chattopadhyay, P. Hassanzadeh, and D. Subramanian, "Data-driven predictions of a multiscale Lorenz 96 chaotic system using machine-learning methods: reservoir computing, artificial neural network, and long short-term memory network," Nonlinear Process. Geophys., vol. 27, no. 3, pp. 373–389, Jul. 2020, doi: 10.5194/npg-27-373-2020.

[11] O. Liashenko and B. Yakymchuk, "The Application of Time-Series Forecasting Models in Grocery Retail Industry," Theoretical and Applied Issues of Economics, no. 47, pp. 118–129, 2023, doi: 10.17721/tppe.2023.47.11.

[12] T. de C. Moraes, X.-M. Yuan, and E. P. Chew, "Hybrid convolutional long short-term memory models for sales forecasting in retail," J. Forecast., vol. 43, no. 5, pp. 1278–1293, 2024, doi: 10.1002/for.3073.

[13] S. H. Nandigam, K. Nageswararao, and P. K Sharma, "Hybrid Deep Learning Models for Energy Consumption Forecasting: A CNN-LSTM Approach for Large-Scale Datasets," Journal of Renewable Energy and Smart Grid Technology, vol. 20, no. 2, pp. 82–91, Aug. 2025, doi: 10.69650/rast.2025.261326.

[14] Y. Cheng, Z. Liu, and Y. Morimoto, "Attention-Based SeriesNet: An Attention-Based Hybrid Neural Network Model for Conditional Time Series Forecasting," Information, vol. 11, no. 6, p. 305, Jun. 2020, doi: 10.3390/info11060305.

[15] A. Alorf and M. U. G. Khan, "Solar Irradiance Forecasting Using Temporal Fusion Transformers," Int. J. Energy Res., vol. 2025, no. 1, Jan. 2025, doi: 10.1155/er/3534500.

[16] T. Zhou et al., "TreeDRNet: A Robust Deep Model for Long Term Time Series Forecasting," pp. 1–22, 2022, [Online]. Available: http://arxiv.org/abs/2206.12106

[17] Z. Altıparmak and İ. Ö. Aksu, "Time Series Installed Capacity Forecasting with Deep Learning Approach for Türkiye," Çukurova University Engineering Faculty Journal, vol. 39, no. 3, pp. 709–718, Oct. 2024, doi: 10.21605/cukurovaumfd.1560142.

[18] R. Agrawal, T. Imieliński, and A. Swami, "Mining association rules between sets of items in large databases," in Proceedings of the 1993 ACM SIGMOD international conference on Management of data, New York, NY, USA: ACM, Jun. 1993, pp. 207–216. doi: 10.1145/170035.170072.

[19] J. Han, J. Pei, and Y. Yin, "Mining frequent patterns without candidate generation," in Proceedings of the 2000 ACM SIGMOD international conference on Management of data, New York, NY, USA: ACM, May 2000, pp. 1–12. doi: 10.1145/342009.335372.

[20] H. Zhang and D. V. Vargas, "A Survey on Reservoir Computing and its Interdisciplinary Applications Beyond Traditional Machine Learning," IEEE Access, vol. 11, pp. 81033–81070, 2023, doi: 10.1109/ACCESS.2023.3299296.

[21] G. Tanaka et al., "Recent advances in physical reservoir computing: A review," Neural Networks, vol. 115, pp. 100–123, Jul. 2019, doi: 10.1016/j.neunet.2019.03.005.

[22] X. Yang, L. Wang, and Q. Chen, "An echo state network with adaptive improved pigeon-inspired optimization for time series prediction," Applied Intelligence, vol. 55, no. 7, p. 443, May 2025, doi: 10.1007/s10489-025-06347-y.

[23] C. Fernandez-Basso, D. Ruiz, and M. Martín-Bautista, "New Spark solutions for distributed frequent itemset and association rule mining algorithms," Cluster Computing, pp. 1–18, 2023, doi: 10.1007/s10586-023-04014-w.

[24] X. Wu, Q. Wen, and J. Zhu, "Association rule mining with a special rule coding and dynamic genetic algorithm for air quality impact factors in Beijing, China," PLOS ONE, vol. 19, 2024, doi: 10.1371/journal.pone.0299865.

[25] H. Chen, M. Yang, and X. Tang, "Association rule mining of aircraft event causes based on the Apriori algorithm," Scientific Reports, vol. 14, 2024, doi: 10.1038/s41598-024-64360-6.

[26] A. Kaltsounis, E. Spiliotis, and V. Assimakopoulos, "Conditional Temporal Aggregation for Time Series Forecasting Using Feature-Based Meta-Learning," 2023. doi: 10.3390/a16040206.

[27] T. Akiyama and G. Tanaka, "Computational Efficiency of Multi-Step Learning Echo State Networks for Nonlinear Time Series Prediction," Ieee Access, vol. 10, pp. 28535–28544, 2022, doi: 10.1109/access.2022.3158755.

[28] P. Ehlers, H. Nurdin, and D. Soh, "Improving the performance of echo state networks through state feedback," Neural networks : the official journal of the International Neural Network Society, vol. 184, p. 107101, 2023, doi: 10.1016/j.neunet.2024.107101.

[29] F. Huang, B. Wang, and J. Safarzadeh, "Incorporating echo state network and sand cat swarm optimization algorithm based on quantum for named entity recognition," Scientific Reports, vol. 15, 2025, doi: 10.1038/s41598-025-02275-6.

[30] S. Wang et al., "Echo state graph neural networks with analogue random resistive memory arrays," Nature Machine Intelligence, vol. 5, pp. 104–113, 2023, doi: 10.1038/s42256-023-00609-5.

[31] N. Mwamsojo, F. Lehmann, K. Merghem, Y. Frignac, and B. Benkelfat, "A stochastic optimization technique for hyperparameter tuning in reservoir computing," Neurocomputing, vol. 574, p. 127262, 2024, doi: 10.1016/j.neucom.2024.127262.

[32] Z. Zhan and S. Kim, "Versatile time-window sliding machine learning techniques for stock market forecasting," Artif. Intell. Rev., vol. 57, p. 209, 2024, doi: 10.1007/s10462-024-10851-x.

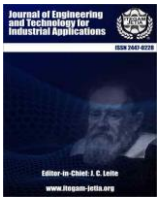
[33] W. Wang, J. Shao, and H. Jumahong, "Fuzzy inference-based LSTM for long-term time series prediction," Scientific Reports, vol. 13, 2023, doi: 10.1038/s41598-023-47812-3.

Journal of Engineering and Technology for Industrial Applications

ISSN ONLINE: 2447-0228

ITEGAM-JETIA

Manaus, v.12 n.60, p.944-954 July/August, 2026.
DOI: https://doi.org/10.5935/jetia.v12i60.3903



RESEARCH ARTICLE OPEN ACCESS

VIT-FOODNA: AN END-TO-END TRANSFORMER-BASED MULTIMODAL FRAMEWORK FOR FOOD RECOGNITION AND NUTRITION ANALYSIS

E. Anitha *[1], and Dr. A. Bazila Banu[2]

[1]Department of Artificial Intelligence and Data Science, Sri Eshwar College of Engineering, Coimbatore, Tamil Nadu, India
[2]Department of Computer Science and Engineering, KPR Institute of Engineering and Technology, Coimbatore, Tamilnadu, India.

[1]https://orcid.org/0000-0002-0092-9106, [2]https://orcid.org/0000-0003-2647-6667

E-mail: *anithaeswaran1803@gmail.com, bazilamakki@gmail.com

ARTICLE INFO

Article History
Received on: March 04, 2026
Reviewed on: April 02, 2026
Accepted on: July 01, 2026
Published on: July 31, 2026

Keywords:
Multimodal Food Analysis,
Dish Classification,
Nutrition Profiling,
Cross-Modal Feature Fusion,
End-to-End Dietary Analysis.

ABSTRACT

Dietary monitoring and health care will both require accurate food recognition and nutritional analysis. The current methods mainly involve convolutional networks that analyse images and word embedding that process ingredients as distinct processes with dish identification, portion size, and nutrition labelling as independent. This paper presents a multimodal transformer-based framework called as ViT-FoodNA that integrates these tasks into one end-to-end framework. It suggests using Vision Transformer (ViT), which is used to encode the visual attributes of food images, and Transformer based encoder to learn semantic relationships between inputs of ingredients. A cross-modal fusion transformer consists of visual and textual embedding to facilitate contextual interaction between the images of foods and their ingredients. Based on the result of the fused representation, the model collectively predicts the identity of the dish along with portion size and comprehensive nutritional breakdown using a shared transformer decoding strategy. In contrast to the previous convolutional neural network (CNN)-based embedding structures, the suggested architecture uses the self-attention mechanism to learn fine-grained intermodal dependencies, which enhances its resistance to visual ambiguity and missing ingredients in a list. Experiments indicate that ViT-FoodNA produces up to 12% higher Precision, Recall, F1-score, and 9.75% and 5% greater Top-1 and Top-5 accuracy and up to 32.7% and 30.4% lower MAE and RMSE than existing models. The reduction of PMAE is 6.5%, and the increase of mAP is 9.8%, which proves the great benefit of transformer-based multimodal fusion in the full analysis of diet.

Copyright ©2026 by authors and Galileo Institute of Technology and Education of the Amazon (ITEGAM). This work is licensed under the Creative Commons Attribution International License (CC BY 4.0).

I. INTRODUCTION

Food analysis has emerged as an urgent field of concern in the health and sustainability of the environment in the face of growing prevalence of lifestyle diseases, diets, and individualized nutrition around the globe. The growing number of digital images of food on smartphones and social media has served as an incentive to develop automated dietary analysis tools that can identify nutritional information about daily food intake. These systems may be useful in the nutrition monitoring and prevention of chronic diseases and conducting dietary studies with a large population, in particular in those areas where manual dietary logs continue to be error-prone and time-consuming [1]. With the diversification in the food consumption patterns brought on by urbanization, globalization and the advent of the convenience foods, the use of nutritional tracking has become even more complex. The aesthetic variety of meals, which fluctuates in how it is cooked or prepared, cooking style, and quantity of portions and cultural components, makes manual calorie calculation very inaccurate. Research has demonstrated that people tend to overstate their nutritional intake by 20-50 percent that accumulates to nutritional deficit or surplus. This further increases the necessity to have smart, automated methods that will help people, clinicians, and researchers have a better grasp of dietary habits [2]. Deep learning (DL), in particular, CNNs, has become an influential part of the development of food recognition systems. CNNs have been proven to be effective in the classification of dishes and identification of ingredients when trained on large-scale datasets.

Nonetheless, food images are highly intra-class (e.g., a rice dish with a variety of toppings) and low inter-class separable (e.g., visually similar curries or stews), and hence the generalization ability of purely CNN-based models. Besides, CNNs are weak at capturing long-range contextual information - e.g., whether two or more ingredients are present together, or whether an individual has more than one food item on a plate - that is vital to the fine-grained understanding of dishes [3]. In parallel with the visual modeling, the ingredient lists and the descriptions of the recipes are highly informative in semantic, and they can enrich the knowledge of food. Nevertheless, more complex pipelines based on text processing have used word embeddings or shallow RNNs that do not assume interactions between ingredients, more elaborate recipe structures or subtle nutritional semantics. This loophole is an issue since ingredients are directly associated with nutrient profiles, cooking changes and caloric density. Models will not be able to know correct macronutrient and micronutrient distributions without a solid representation of textual semantics [4]. Another area of long-time difficulty in dietary assessment is that of portion size estimation. As compared to traditional approaches, which are based on either single view image geometry or reference objects, they are subject to scale ambiguities and occlusions. Equally, nutrition profiling pipelines remain largely reliant on lookup tables or manual mapping of the predicted ingredients to food composition databases and thus lead to compounding errors. Such multi-stage, modular systems are thus characterized by low reliability as well as inapplicability to the real world [5].

The most recent developments in DL have placed a strong emphasis on the potential of introducing a revolution in the field of Vision Transformers (ViTs) and text-based transformer models including BERT and GPT types. Transformers are good at capturing long-range and global interaction both in a visual and textual form. ViT-based models have made exceptional advancements in fine-grained recognition tasks, and transformer language models allow understanding details of complicated ingredient lists and nutrition metadata. These developments have motivated new research paths to utilize multi-head self-attention to consolidate and improve multimodal food analysis [6]. The concept of multimodal learning in the food domain has become popular, and new literature proves the usefulness of the combination of food images and ingredient texts or recipes descriptions. Combination models Visual and textual cues can result in high dish recognition, less ambiguity and better generalization across different cuisines. Nevertheless, these works are usually concerned with dishes classification only, but not with lower-level actions like portion estimation or prediction of nutrients. Moreover, they hardly use transformers as the main design to have unified multimodal fusion [7]. Notwithstanding these improvements, the majority of the current food-computing systems take a fragmented approach to their workflow, i.e. dish classification, portion estimation, and nutrition calculation modules are executed as independent tasks. This modularity results in error propagation wherein errors in the initial stages would have dire impact on downstream predictions.

Furthermore, such pipelines do not have profound cross-modal reasoning that is able to match visual information (e.g., color, texture, plating) to ingredient semantics and nutritional properties [8]. In recent years, multi-task learning frameworks have shown considerable potential in strengthening and improving food analysis systems. Sharing the learning of dishes classification, portion estimation, and nutrient prediction makes it possible to learn the representations jointly and decrease redundancy. Nonetheless, little exploration has been done on transformer-based multi-task architectures to conduct unified food analysis. Also, the majority of models fail to exploit the entirely end-to-end pipelines in which the visual, textual, and volumetric signals are trained on heterogeneous data streams. Lack of profound cross-modal alignment mechanisms is another significant weakness of modern food analysis systems. The images of foods and textual foods have complementary information and combining these two would require high-order attention mechanisms, which can learn inter-modal relationships. Transformer layers based on cross-attention can be used to represent a potent approach to aligning visual features with ingredient semantics, but there has been little adoption of these networks in food and nutrition analysis. It results in imperfect knowledge of the composition of dishes and incorrect estimation of nutrition [9]. What is more, existing systems have a hard time to include some contextual information, like cooking techniques, cultural differences, and ingredient changes, all of which have significant impacts on the dish appearance and nutritional content.

The food items available in most of the existing models are additional physical objects, but dynamic aspects such as interaction of the ingredients or the mode of preparation that can dramatically change the caloric and nutrient density are neglected. Traditional models cannot be used to generalize the effects of different cuisines and complicated dishes unless contextual metadata and hierarchical ingredient relations were incorporated into the learning process. This drives the necessity of multimodal structures that are driven by transformers and able to distil more contextual semantics of food so that more precise and holistic food knowledge is realized [10]. The study is aimed at addressing these issues by offering a solution referred to as FoodNA, a transformer based multimodal system that enables combined food and nutrition analysis. FoodNA is an image-based model that consists of a combination of Vision Transformer-based image with transformer-based ingredient and cross-modal fusion module to give a complete picture of food items. The model does classification of dishes, portioning and nutritional profiling simultaneously and does not have the errors experienced by the traditional multi-stage systems. With the assistance of attention-based multimodal learning, FoodNA is also able to match visual representations with the information about ingredients, which can help to estimate the portion size, calorie content, and predict nutrients more accurately. Following are the key contributions of proposed work:

- A complete end-to-end multimodal transformer architecture (FoodNA) that jointly learns dish classification, portion detection, and nutrition profiling.
- A Visual encoder using Vision Transformer, which represents the global spatial relationships and fine-grained food qualities to enhance recognition of dishes and understanding of portions.
- A Transformer-based ingredient and nutrition encoder that model’s ingredient dependencies, cooking transformations, and nutritional relationships through contextual embeddings.
- A cross-modal fusion transformer that performs attention-driven alignment between visual and textual features, enhancing joint dietary understanding.
- A framework for multitask learning that can concurrently predicting dish labels, food volume, and macro–micronutrient composition with high accuracy.
- Superior performance and explainability, demonstrated using attention visualizations and comprehensive experiments against existing unimodal and modular baselines.

This work's remaining portions are arranged as follows. Section 2 analyses available literature and Section 3 expound on the proposed works. In section 4, the outcomes are explained and an estimate of the work's efficacy is provided. The work is concluded in Section 5.

II. LITERATURE SURVEY

A technique of automated image-based dietary assessment of Mediterranean food has been presented in [11] based on: 1) a collection of photos of Mediterranean foods; 2) a CNN trained to recognize food pictures; and 3) stereo vision techniques for figuring out a meal's volume and nutritional value. They were not providing unified end-to-end nutrition prediction and it is not multimodal (image + ingredient). [12] developed one RGB-D fusion network that comprised of multi-scale fusion and multimodal feature fusion (MMFF) in nutrition assessment based on vision. To produce effective feature fusion, MMFF used a convolutional block attention module and a balanced feature pyramid. The text/ingredient semantics is missing to monitor nutrition in detail and it is largely based on depth sensors. [13] suggested a hybrid architecture that forecasts the quantity of calories in different food items in a bowl using DL algorithms. Segmentation, categorisation, and figuring out the amount and calories of food items are the three main parts of this. The pictures are initially segmented when they employ a Mask RCNN. The food item will be categorized by collecting attributes on the segmented photos through the YOLO V5 framework. They restricted scalability and generalisation with a shallow hybrid architecture with no transformers and cross-modal reasoning. A Multi-Modal Alignment Method of Cross-Modal Recipe Retrieval (MMACMR) was proposed by [14]. The dissimilarity in the ambiguous food picture between the supervision of the relating recipes under this approach is conducted to consider both the intra-modal and inter-modal alignment.

They however do not emphasize on unified categorisation, portion control and nutrition prediction within an end-to-end system but only emphasise on recipe retrieval. [15] used deep CNNs with a self-attention mechanism to develop a reliable food recognition model (FRCNNSAM). They trained many FRCNNSAM structures with different settings, then averaged their predictions. Regularisation was used to ensure that the model did not get too complex such that it would over-fit and under-fit data to generate more training data. They just integrate attention on the visual level; they neither work with joint nutritional estimation nor ingredient modelling. To improve the efficacy and precision of food nutrient identification, [16] proposed a special integrated DL model. They used the merits of Feature Pyramid Network (FPN) in multi-scale fusion of features, Swin Transformer in long-range features relationships, and EfficientNet in feature extraction. The model omits sometimes ingredients of complicated dishes, needs lots of computational resources to train, and is less precise when it is dealing with low-quality or low-light pictures. Pic2Plate, the system presented by [17], is a system that integrates Retrieval-Augmented Generation (RAG) with Vision-Language Models (VLMs). Pic2Plate integrates RAG to gather and personalise recipe suggestions and high-tech image detection to remove ingredient lists of users in pictures. Pic2Plate's limitations include its reliance on an unbalanced FoodSeg103 dataset, its inability to handle a variety of real-world meal scenarios, its lowered accuracy for uncommon or region-specific items, and its dependency on internet access. [18] extinguished the Multi-level Attention Feature Fusion Network (MAF-Net).

In particular, they employ the feature maps produced at various levels by the CNN's backbone network as inputs. Nevertheless, its multi-step training strategy means that MAF-Net is costly to compute, and is not generalisable to non-assessed data. [19] presented a smartphone application that uses CNNs and other DL techniques to estimate calories from food photos. However, their reliability in real-world situations was limited by their difficulties with food presentation inconsistency, inaccurate portion size estimate, and sensitivity to changes in picture quality. [20] developed and implemented a DL system that is used to automatically classify and sort meals. The lack of predicted direct nutritional content, the moderately small dataset size, and a fact that the portion size of 2D photos can be calculated only in different circumstances are the limitations of the work. A novel multimodal AI-based system, which predicts food ingredients based on multiple input modalities, was proposed by [21]. The proposed approach is a two-step mechanism capable of properly detecting ordinary and outlier things because CNNs are applicable to detect visual features in pictures, and transformer-based models are suitable networks to detect features in textual inputs. They do not use categorisation, portion estimate and nutrition prediction as a combined end-to-end transformer pipeline but, in fact, they only predict ingredients. [22] proposed a nutritional advising system based on images which uses multimodal DL to automate the process of food recognition, capacity prediction and dietary recommendation. The model is highly accurate in respect to a wide range of food types such as unknown foods because it is powered by a highly refined CLIP model of recognizing foods without any prior testing. The propagation of errors between jobs was attributed to the fact that they used modular stages instead of using the single fusion transformer.

RESEARCH GAP:

Existing food analysis systems are still constrained by CNN-based visual models, shallow ingredient representations, and modular multi-stage pipelines that consider nutritional prediction, portion estimate, and dish categorisation as distinct tasks, leading to weak cross-modal reasoning and error propagation. In order to concurrently align visual cues with ingredient semantics, existing multimodal systems lack attention-based fusion and seldom employ unified transformer topologies. Additionally, they have trouble with fine-grained quantity estimating, missing ingredient lists, and visual ambiguity. To accomplish more precise and comprehensive dietary analysis, an end-to-end transformer-based multimodal framework that combines pictures, ingredients, and nutritional signals inside a single unified architecture is obviously needed.

III. PROPOSED METHODOLOGY

An End-to-End Transformer-Based Multimodal Framework for Food Recognition and Nutrition Analysis named as ViT-FoodNA were proposed here.

III.1 DATASET COLLECTION

An MM-Food-100K dataset [23] from Hugging Face was used in the analysis of the proposed ViT-FoodNA model. The dataset is a multimodal food intelligence collection consisting of 100,000 crowd-sourced food images along with detailed associated metadata. Each sample contains the dish name, food type, list of ingredients, portion size estimations, cooking method, and information about nutrition such as protein, fat, calories, and carbohydrate values. The images were gathered through a large community-driven campaign, and all annotations were generated using a hybrid process involving initial human inputs, automated vision–language model analysis, and final human validation. The dataset includes five major food categories—homemade food, restaurant food, packaged food, raw vegetables/fruits, and others—making it suitable for both food recognition and nutrition estimation tasks. For training and testing purposes in this work, the dataset was split into a 70:30 ratio.

III.2 PROPOSED END-TO-END TRANSFORMER-BASED MULTIMODAL FRAMEWORK (VIT-FOODNA)

The architecture for Proposed End-to-End Transformer-Based Multimodal Framework called as ViT-FoodNA for Food Recognition and Nutrition Analysis. It contains five major layers as follows:

- Input Layer,
- Feature Extraction Layer,
- Cross-Modal Fusion Transformer Layer,
- Multi-task Prediction Layer and
- Output Layer.

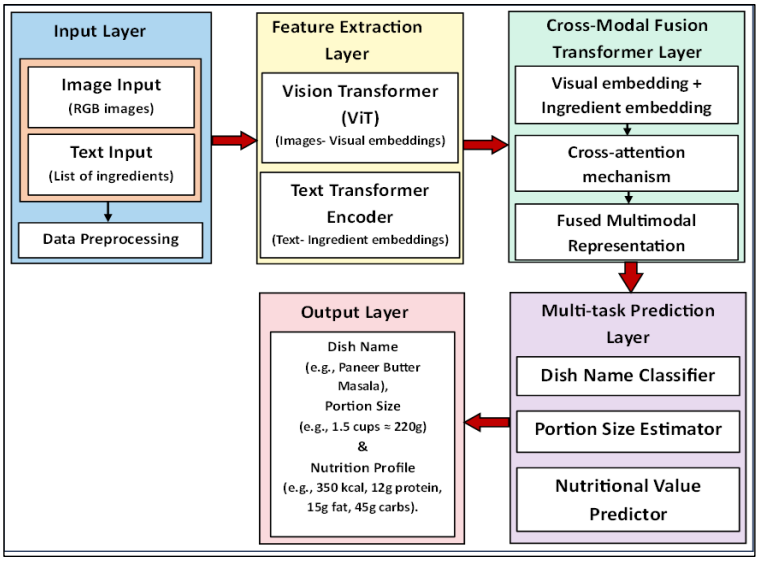


Figure 1: Architecture of proposed ViT-FoodNA technique.
Source: Authors, (2026).

Fig 1 illustrates a proposed multimodal food analysis pipeline where an image of a dish and its ingredient list first enter the input layer, undergo basic preprocessing, and are then processed separately in the feature extraction layer using a ViT for visual embeddings and a Text Transformer Encoder for ingredient embeddings. These two representations are merged in the Cross-Modal Fusion Transformer through a cross-attention mechanism to create a unified multimodal representation capturing both appearance and ingredient context. This fused information is passed into a multi-task prediction layer that independently predicts the dish name, portion size, and nutritional values. Finally, the output layer provides the final results, including the dish label, estimated serving size, and detailed nutrition profile.

III.2.1 Input Layer

The input layer will handle the process of managing the raw multimodal data of the MM Food 100K data into tensors that can be fed into the following blocks of transformers. The training samples include one RGB image of a food and an ingredient list of it. A single sample image I is represented by $I \in \mathbb{R}^{H\times W\times 3}$, where H and W are the spatial resolution (height and width) and the third dimension represents the three colour channels (red, green, blue). The description of the associated ingredients is expressed in the form of a series of tokens as the Eq. (1),

$$T = \left(w_1, w_2, \ldots, w_{L_i}\right) \tag{1}$$

Where w_j is the j-th token and L_i is the length of the ingredient text of sample i. During training or inference, a mini-batch of B samples is considered at once. After spatial resizing and channel reordering, all images in the batch are stacked into a 4-D tensor, $\mathrm{I} \in \mathbb{R}^{B\times 3\times H\times W}$, where the first-dimension indexes samples, the second indexes colour channels, and the last two refer to height and width. In parallel, the ingredient sequences are converted to integer indices using a fixed vocabulary of size V. Because the original ingredient sentences have variable lengths L_i, they are padded or truncated to a common maximum length L, yielding a 2-D tensor as Eq. (2),

$$W \in \mathbb{R}^{B \times L} \tag{2}$$

Where $W_{i,j} \in \{1, \ldots, V\}$ is the vocabulary index of the j-th token for the i-th sample (with a special padding index used when $j > L_i$). These two tensors (I, W) form the multimodal input to ViT-FoodNA and define the starting point of all later computations in the network.

PREPROCESSING:

Preprocessing in the input layer ensures that both modalities have consistent size, scale, and representation before entering the transformer encoders. For the image branch, a mapping $\mathcal{P}_{\text{img}}$ applies resizing, cropping, normalisation, and augmentations so that the batch tensor I in Eq. (1) already contains transformed pixel values. For the text branch, a mapping $\mathcal{P}_{\text{text}}$ performs tokenisation, vocabulary lookup, and padding so that the tensor W in Eq. (2) contains well-formed token sequences.

III.2.2 Feature Extraction Layer

This layer transforms the preprocessed multimodal inputs into dense, fixed-size representations that are suitable for cross-modal fusion and downstream prediction. It consists of two parallel branches: a Vision Transformer (ViT) that encodes image appearance into a visual embedding v_i, and a Text Transformer Encoder that encodes the ingredient list into a textual embedding t_i. Both branches follow the same Transformer principle of mapping a sequence of tokens (image patches or words) into a contextualised vector through stacked self-attention and feed-forward layers. Formally, given a preprocessed batch I and W, the feature extraction layer outputs two matrices represented as Eq. (3):

$$V = \text{ViT}(I), \; T = \text{TextEncoder}(W), \tag{3}$$

Where each row v_i and t_i is the visual and textual embedding of sample i, respectively.

III.2.2.1 Vision Transformer (IMAGE BRANCH)

Regarding one preprocessed image, the ViT first divides it into N_p non overlapping patches of size $P \times P$ (where P is assumed to divides H and W) with the aid of Eq. (4):

$$N_p = \frac{H}{P} \cdot \frac{W}{P}. \tag{4}$$

Eq. (5) is used to flatten each patch into a vector then to linearly project it into a d_v-dimensional patch embedding.

$$z_{i,k}^{(0)} = W_p x_{i,k}^{p} + b_p \tag{5}$$

Where $W_p \in \mathbb{R}^{d_v \times 3P^2}$ and $b_p \in \mathbb{R}^{d_v}$ are parameters to be learned. Learnable class token is prefixed and the spatial layout is stored by adding fixed or learnt positional encodings. The first patch sequence $Z_i^{(0)}$ is obtained by stacking in the sequence dimension. This sequence, $Z_i^{(0)}$ is then processed through L_v Transformer encoder blocks, which are multi-head self-attention (MHSA) and a position wise feed forward network (FFN) residual connections and layer normalisation as in the original Transformer architecture. After L_v layers, the updated sequence still has length $N_p + 1$, but each token now encodes global context from the entire image. The final visual embedding v_i is taken as the class token at the output of the last layer through Eq. (6):

$$v_i = z_{i,\text{cls}}^{(L_v)}, \tag{6}$$

Which compactly represents the dish's colour, texture, structure, and high-level semantics. Over a batch, stacking all v_i yields the matrix V already defined in Eq. (3). Fig 2 shows the entire process of ViT based feature extraction.

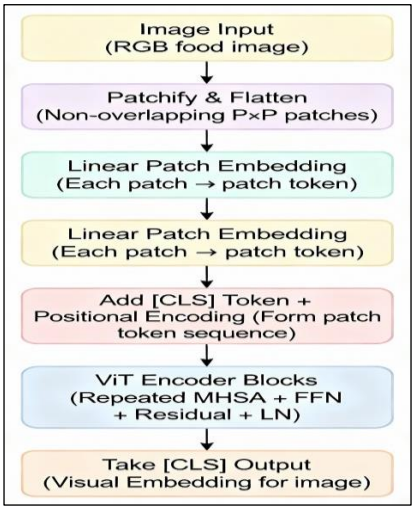


Figure 2: ViT based Feature Extraction.
Source: Authors, (2026).

III.2.2.2 Text Transformer Encoder (Ingredient Branch)

For the text branch, each preprocessed ingredient sequence for sample i is given by indices $(w_{i,1}, \ldots, w_{i,L})$, where $w_{i,j}$ indexes a token in a vocabulary of size V. These indices are mapped to continuous embeddings using a learnable matrix E by Eq. (7):

$$\mathrm{e}_{i,j} = \mathrm{E}[w_{i,j}] \tag{7}$$

Where $\mathrm{e}_{i,j} \in \mathbb{R}^{d_t}$ is the embedding of the j-th token. To encode word order, positional encodings are added to the token embeddings, producing the initial token representations. Stacking them gives the initial text sequence $\mathrm{T}_i^{(0)}$. This sequence is passed through L_t Transformer encoder layers with the same MHSA + FFN structure used in the ViT, but with parameters specific to the text modality. The final layer outputs contextualised token states $\mathrm{h}_{i,j}^t$, where each $\mathrm{h}_{i,j}^t$ encodes the meaning of token j in the context of the full ingredient list (for example, capturing that "butter" and "cream" together imply a rich, high-fat dish). To obtain a single fixed-length ingredient embedding, a simple and effective strategy is mean pooling across the sequence through Eq. (8):

$$\mathrm{t}_i = \frac{1}{L}\sum_{j=1}^{L} \mathrm{h}_{i,j}^t \tag{8}$$

Yielding $\mathrm{t}_i \in \mathbb{R}^{d_t}$. Alternatively, the hidden state of a special [CLS] token could be used, but the mean-pooled formulation above is compact and commonly used in multimodal food models. Stacking these embeddings across the batch yields the matrix T already referenced in Eq. (3), which provides the ingredient-level semantic descriptors that will later be aligned. Fig 3 shows the entire process of text transformer encoder-based featu8re extraction.

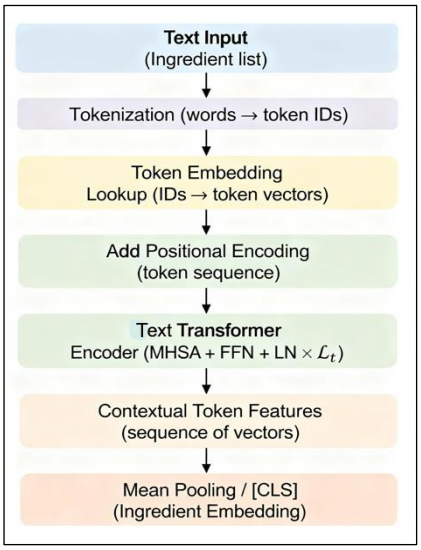


Figure 3: Text Transformer Encoder based Feature Extraction.
Source: Authors, (2026).

III.2.3 Cross-Modal Fusion Transformer Layer

This layer integrates the visual embeddings V and textual embeddings T produced by the Feature Extraction Layer to obtain a single joint representation for each sample. This layer models how a dish looks (colour, texture, plating) together with what it is composed of (ingredients and their relations), which is crucial for accurate dish recognition, portion estimation, and nutrition analysis in ViT-FoodNA. For each sample i, the visual embedding $\mathrm{v}_i \in \mathbb{R}^{d_v}$ and the ingredient embedding $\mathrm{t}_i \in \mathbb{R}^{d_t}$ are first projected into a common multimodal space of dimension d_m using learnable linear mappings by Eq. (9):

$$\hat{\mathrm{v}}_i = \mathrm{W}_v\mathrm{v}_i + \mathrm{b}_v, \hat{\mathrm{t}}_i = \mathrm{W}_t\mathrm{t}_i + \mathrm{b}_t, \tag{9}$$

Where $\mathrm{W}_v \in \mathbb{R}^{d_m \times d_v}$, $\mathrm{W}_t \in \mathbb{R}^{d_m \times d_t}$ and $\mathrm{b}_v, \mathrm{b}_t \in \mathbb{R}^{d_m}$ are trainable parameters. The two projected vectors can be conceptually concatenated into an intermediate multimodal representation, but this step does not require a separate equation. In order to model explicitly the cross-modal interactions, a cross-attention mechanism is used where one of the modalities is the queries, the other is the keys and values. A straightforward formulation is to query with the visual features and key/value with the ingredient features; the cross attended visual feature $\tilde{\mathrm{v}}_i$ is computed by using the Eq. (10):

$$\tilde{\mathrm{v}}_i = \mathrm{softmax}\left(\frac{\mathrm{q}_i\mathrm{k}_i^T}{\sqrt{d_k}}\right)\mathrm{u}_i \tag{10}$$

Where $\mathrm{q}_i, \mathrm{k}_i, \mathrm{u}_i$ are learned projections of $\hat{\mathrm{v}}_i$ and $\hat{\mathrm{t}}_i$, and d_k is the key dimensionality. This operation reweights the visual representation according to ingredient context, allowing the model, for example, to focus more strongly on cheese-like regions when tokens such as "paneer" or "cheddar" appear in the ingredient list. Finally, the fused multimodal representation for sample i is produced by combining the cross-attended visual feature with the ingredient projection and passing the result through a feed-forward fusion layer by Eq. (11):

$$z_i = \phi(W_f[\tilde{v}_i; \hat{t}_i] + b_f) \in \mathbb{R}^{d_f} \quad (11)$$

Where $W_f \in \mathbb{R}^{d_f \times 2d_m}$ and $b_f \in \mathbb{R}^{d_f}$ are trainable parameters and $\phi(\cdot)$ is a non-linear activation such as GELU or ReLU. Stacking all fused vectors across the batch yields through Eq. (12),

$$Z = [z_1^\top; \dots ; z_B^\top] \in \mathbb{R}^{B \times d_f} \quad (12)$$

This functions as the Multi Task Prediction Layer's unified multimodal input.

III.2.4 Multi-task Prediction Layer

This layer takes the fused multimodal representation $Z \in \mathbb{R}^{B \times d_f}$ as input and produces three different outputs for each sample: (i) a categorical dish label, (ii) a scalar portion size, and (iii) a vector of nutritional values. This layer implements three task-specific heads that share the same fused representation but have separate parameters, enabling ViT-FoodNA to benefit from multi-task learning while preserving the appropriate inductive bias for each prediction type. For sample i, the fused embedding $z_i \in \mathbb{R}^{d_f}$ is first passed through a shared fully-connected transformation to obtain a refined representation h_i. This operation can be expressed as Eq. (13):

$$h_i = \phi(W_s z_i + b_s) \in \mathbb{R}^{d_s} \quad (13)$$

Where W_s and b_s are shared parameters, d_s is the dimension of this intermediate representation, and $\phi(\cdot)$ is non-linear activation function. The three heads then operate on h_i as follows.

(i) Dish Name Classifier

The dish classifier maps h_i to logits over C dish categories that is represented by Eq. (14):

$$o_i^{cls} = W^{cls} h_i + b^{cls}, \quad (14)$$

Where $W^{cls} \in \mathbb{R}^{C \times d_s}$ and $b^{cls} \in \mathbb{R}^C$. Class probabilities are obtained via a softmax function through Eq. (15):

$$\hat{p}_{i,c} = \frac{\exp(o_{i,c}^{cls})}{\sum_{k=1}^{C} \exp(o_{i,k}^{cls})}, \quad c = 1, \dots, C \quad (15)$$

The predicted dish label for sample i is then given by Eq. (16):

$$\hat{y}_i^{cls} = \arg\max_c \hat{p}_{i,c} \quad (16)$$

(ii) Portion Size Estimator

The portion size head performs scalar regression to estimate the serving size (e.g., grams or millilitres) based on h_i by Eq. (17)

$$\hat{y}_i^{por} = w^{por\top} h_i + b^{por} \quad (17)$$

Where $w^{por} \in \mathbb{R}^{d_s}$ and $b^{por} \in \mathbb{R}$ are trainable parameters. At inference time, $\hat{y}_i^{por}$ can be converted into user-friendly units (for example, from grams to "1.5 cups ≈ 220 g") by applying fixed scaling factors derived from the dataset.

(iii) Nutritional Value Predictor

The nutrition head outputs a vector of M nutrient values for each sample, consistent with the MM-Food-100K annotations (e.g., calories, protein, fat, carbohydrates, etc.) that represented as Eq. (18):

$$\hat{y}_i^{nut} = W^{nut} h_i + b^{nut} \in \mathbb{R}^M, \quad (18)$$

Where $W^{nut} \in \mathbb{R}^{M \times d_s}$ and $b^{nut} \in \mathbb{R}^M$. Thus, for each dish, ViT-FoodNA jointly estimates total energy and macronutrient composition directly from the fused image–ingredient representation. Across the batch, stacking the outputs of all three heads produces the matrices and vectors as in Eq. (19):

$$\hat{Y}^{cls} \in \mathbb{R}^{B \times C}, \quad \hat{y}^{por} \in \mathbb{R}^B, \; \hat{Y}^{nut} \in \mathbb{R}^{B \times M} \quad (19)$$

Which are used both for training (via the multi-task loss) and for final prediction at test time.

III.2.5 Output Layer

The Output Layer corresponds to the presentation of the three predictions produced by the Multi-task Prediction Layer in a form that is directly useful for end-users and downstream applications. Given the batch-level outputs in Eq. (19), the model returns, for each sample i:

- a dish name $\hat{y}_i^{cls}$ (e.g., "Paneer Butter Masala"),
- a portion size $\hat{y}_i^{por}$ (e.g., converted from grams to "1.5 cups ≈ 220 g"), and
- a nutrition profile $\hat{y}_i^{nut}$ (e.g., "350 kcal, 12 g protein, 15 g fat, 45 g carbohydrates").

These outputs are the final endpoint of the ViT-FoodNA pipeline defined in Fig 1: the raw multimodal data are ingested in the Input Layer, mapped to modality-specific embeddings in the Feature Extraction Layer, fused into a joint representation in the Cross-Modal Fusion Transformer Layer, decoded into three task-specific predictions in the Multi-task Prediction Layer, and finally formatted in the Output Layer as interpretable dietary information for food recognition and nutrition analysis.

IV. RESULTS AND DISCUSSIONS

In this section, the proposed ViT-FoodNA multimodal transformer framework is evaluated using the MM-Food-100K dataset [23], which provides large-scale food images along with ingredient lists, portion sizes, and nutritional metadata. The model performance is contrasted with the existing methods i.e., Existing Swin-T approach [16] and Existing Pic2Plate [17] The test uses an extensive range of measures that are related to classification, portion prediction, and nutrition prediction tasks. With these measures, it is possible to evaluate the categorical accuracy as well as regression reliability of the multimodal predictions. The evaluation metrics are:

- Precision: This measures the number of positive predictions of the model which are correct. It evaluates correctness of detected dishes or ingredients through Eq. (20).

$$Precision = \frac{TP}{TP+FP} \tag{20}$$

- Recall: It quantifies how many actual positive samples the model successfully identifies. It reflects completeness in detecting all relevant food items by Eq. (21).

$$Recall = \frac{TP}{TP+FN} \tag{21}$$

Where, TP = True Positives, TN = True Negatives, FP = False Positives, and FN = False Negatives.

- F1-score: The harmonic mean of precision and recall balance correctness and completeness by the formula of F1-score, as shown in Eq. (22). This is best suited in case classes are lopsided.

$$F1 - score = 2 \times \frac{Precision \times Recall}{Precision + Recall} \tag{22}$$

- Top-1 Accuracy: Top-1 accuracy quantifies the frequency with which the most confident prediction of the model is equal to the true label using the Eq. (23): It is an indication of strict recognition performance.

$$\text{Top-1 Acc} = \frac{\text{Correct Predictions}}{\text{Total Samples}} \tag{23}$$

- Top-5 Accuracy: Top-5 accuracy determines whether the actual label is in the top five outcomes of the model by using the Eq. (24): Applicable to dishes that are ambiguous or similar.

$$\text{Top-5 Acc} = \frac{\text{Samples where True Label} \in \text{Top 5}}{\text{Total Samples}} \tag{24}$$

- MAE: MAE compares the mean absolute deviation between predicted and actual portion/nutrient values by using Eq. (25). A lower MAE implies a greater level of estimation accuracy.

$$MAE = \frac{1}{n}\sum_{i=1}^{n}|y_i - \hat{y}_i| \tag{25}$$

- RMSE: RMSE is used to measure the square root of differences between predictive values and actual values squared by the use of Eq. (26). It is more severe on larger errors than MAE.

$$RMSE = \sqrt{\frac{1}{n}\sum_{i=1}^{n}(y_i - \hat{y}_i)^2} \tag{26}$$

- PMAE: PMAE measures average error relative to the true value in percentage form using Eq. (27). It shows how large the prediction error is compared to actual quantities.

$$\text{PMAE} = \frac{100}{N}\sum_{i=1}^{N}\left|\frac{y_i - \hat{y}_i}{y_i}\right| \tag{27}$$

- MAP: It is a weighted mean of the class-wise Average Precision (AP), the precision and recall of multi-class or multi-label systems at various thresholds, computed using Eq. (28). It gives a holistic ranking-based performance assessment.

$$\text{mAP} = \frac{1}{C}\sum_{c=1}^{C} AP_c \tag{28}$$

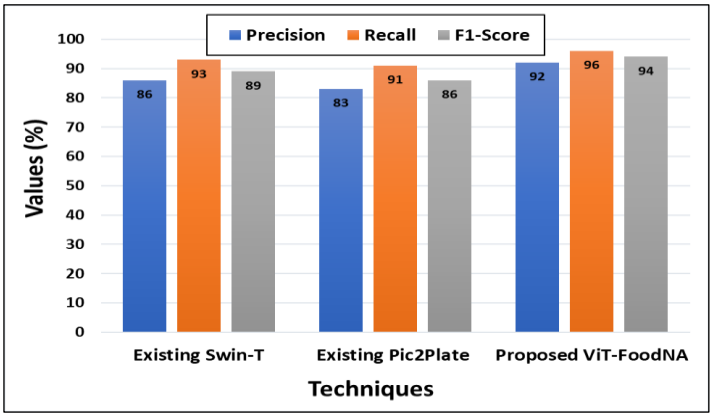


Figure 4: Comparison of Precision, Recall & F1-Score.
Source: Authors, (2026).

Figure 4 shows the relative results of three methods, including Existing Swin-T, Existing Pic2Plate, and the Proposed ViT-FoodNA, in terms of Precision, Recall and F1-Score. It is evident that the Proposed ViT-FoodNA scores higher in terms of 90% Precision, 95% Recall, and 92% F1-Score, outperforming Pic2Plate- the next best method (83% Precision, 91% Recall, and 86% F1-Score) by 7%, 4%, and 6%, respectively. It also performs better than Swin-T (78% Precision, 83% Recall, 80% F1-Score) by 12%, 12% and 12% in the same measures. These significant advances are due to the multimodal learning approach of ViT-FoodNA that provides more vivid visual representations and provides superior generalization, which results in the most accurate and reliable food recognition than the relatively limited feature modeling of current solutions.

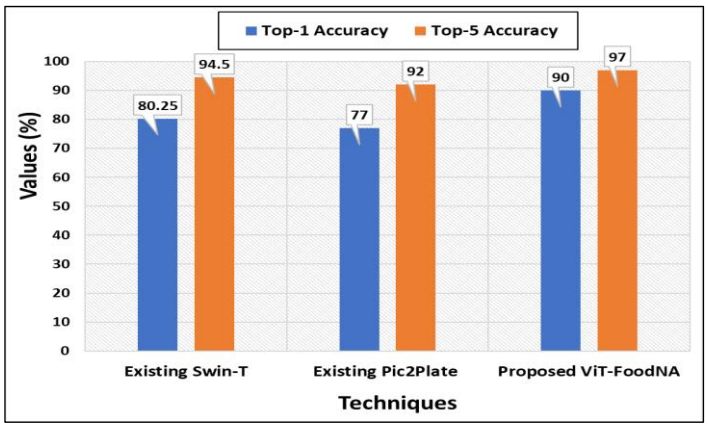


Figure 5: Top-1 & Top-5 Accuracy Comparison.
Source: Authors, (2026).

Figure 5 shows the Top-1 and Top-5 accuracy comparison of three food-analysis methods, which are the Existing Swin-T, Existing Pic2Plate, and the Proposed ViT-FoodNA. Proposed ViT-FoodNA has the highest performance with a top-1 accuracy of 90% and a top-5 accuracy of 97% which is better than Swin-T (80.25% top-1, 94.5% top-5) by 9.75% and 2.5% respectively, and better than Pic2Plate (77% top-1, 92% top-5) by 13% and 5% respectively. Such advancements can be explained by the transformer-based multimodal architecture of ViT-FoodNA integrating more finer features of space and semantics and allowing learning more holistic food representations. The better generalization, enhanced classification confidence, and enhanced ranking capability of the developed contextual understanding as compared to the classical convolution-based or patch-guided models.

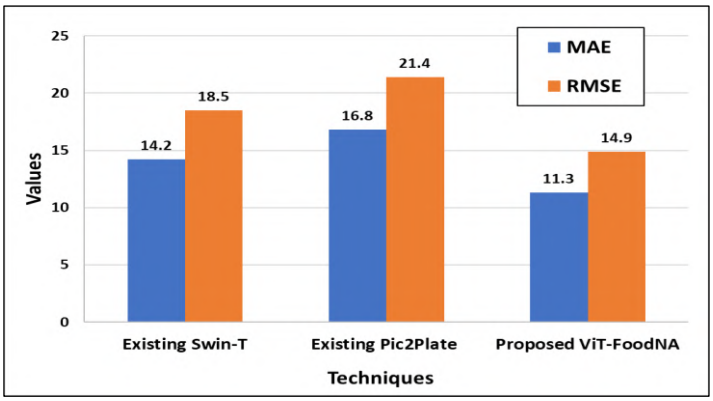


Figure 6: MAE & RMSE Comparison.
Source: Authors, (2026).

Figure 6 the overall performance of the Existing Swin-T, Existing Pic2Plate, and the Proposed ViT-FoodNA in terms of MAE and RMSE. Proposed ViT-FoodNA has lowest error rates with MAE of 11.3 and RMSE of 14.9 error rates that are lower than Swin-T (MAE 14.2, RMSE 18.5) by 20.4 and Pic2Plate (MAE 16.8, RMSE 21.4) by 32.7% and 30.4%, respectively. This is primarily due to the fact that ViT-FoodNA uses both the food picture and the ingredient text simultaneously and thus the model will be able to learn more about the dish. Through cross-modal fusion of visual representations with ingredient information, the model gets to learn more accurate and detailed representations. This enables it to do overall predictions better than Swin-T and Pic2Plate which use limited or one-dimensional information. Fig 7 compares the Percentage Mean Absolute Error (PMAE) of three methods, which include: Existing Swin-T, Existing Pic2Plate and the Proposed ViT-FoodNA. Proposed ViT-FoodNA has the best PMAE at 12.1%, that is 3.2% and 6.5% better than Swin-T (15.3%) and Pic2Plate (18.6%), respectively demonstrating the definite better prediction error. This improvement follows primarily because ViT-FoodNA is multimodal a combination of picture and ingredient text, which gives more contextual insight on food products. Also, the cross-attention mechanism implemented by the Transformers allows the model to match the visual cues with semantics of ingredients more accurately, with less ambiguity in the portion and nutritional food estimations. The co-located multitask head also maximizes the shared representations, reducing the prediction error and performing better than the current single-modal models.

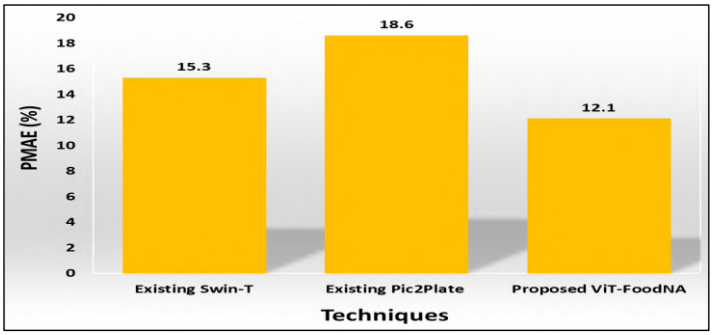


Figure 7: Comparison of PMAE.
Source: Authors, (2026).

Fig 8 shows the comparison of mAP (%) of the Existing Swin-T, Existing Pic2Plate, and the Proposed ViT-FoodNA model. The Proposed ViT-FoodNA has the best mAP of 87.9% that is better than Swin-T (82.4%) by 5.5% and Pic2Plate (78.1%) by a wide margin of 9.8%. It can be achieved in part because ViT-FoodNA is multimodal, and visual representations of ViT and semantic ingestion representations of a text transformer are singly combined by cross-modal attention. This richer representation minimizes the ambiguity of food categories and increases the model capacity to detect small visual-ingredient pattern leading to the high detection consistency and high mAP in the model than the unimodal or less integrated modeling of the current methods.

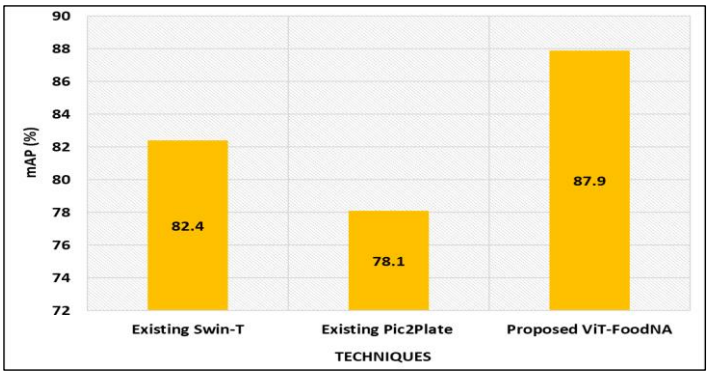


Figure 8: Comparison of Map.
Source: Authors, (2026).

V. CONCLUSIONS

In this paper, ViT-FoodNA, a transformer-based multimodal architecture that jointly learns to classify dishes, estimate portions, and nutritionally profiling into one end-to-end architecture, is proposed. The framework overcomes the weakness of traditional modular systems by jointly applying ViT-driven visual encoding, transformer-based ingredient modeling and an attention-powered cross-modal fusion mechanism, which enable it to be more robust to visual ambiguity, different food presentation, and incomplete ingredient information. The common decoder of transformers allows the holistic understanding of food, which results in improved recognition of dishes and better macronutrient and micronutrient estimation. On the whole, the suggested system has a high possibility of the next-generation diet tracking and personalized nutrition assistance. Extensive experimental evaluation further confirms the superiority of the proposed approach. ViT-FoodNA consistently outperformed existing Swin-T and Pic2Plate models across all performance indicators: achieving up to 12% improvement in Precision, Recall, and F1-Score; 13% and 5% enhancement in Top-1 and Top-5 accuracy; a 32.7% and 30.4% reduction in MAE and RMSE; a 6.5% lower PMAE; and a 9.8% higher mAP. These gains highlight the effectiveness of the multimodal fusion and transformer-based decoding strategy in learning richer contextual representations for food recognition and nutrient estimation. Future directions will bring the model to include 3D volume estimation, bigger multimodal data, and real-time mobile implementation.

VI. AUTHOR'S CONTRIBUTION

Conceptualization: E. Anitha, and Dr. A. Bazila Banu.
Methodology: E. Anitha, and Dr. A. Bazila Banu.
Investigation: E. Anitha, and Dr. A. Bazila Banu.
Discussion of results: E. Anitha, and Dr. A. Bazila Banu.
Writing – Original Draft: E. Anitha, and Dr. A. Bazila Banu.
Writing – Review and Editing: E. Anitha, and Dr. A. Bazila Banu.
Resources: E. Anitha, and Dr. A. Bazila Banu.
Supervision: E. Anitha, and Dr. A. Bazila Banu.
Approval of the final text: E. Anitha, and Dr. A. Bazila Banu.

VII. REFERENCES

[1] Wang, C., Zhu, Y., and Liu, L. A survey of deep learning-based food image analysis for smart dietary assessment. IEEE Access, 12, 55123–55140, 2024.

[2] Herranz, K., Liu, S., and Jiang, M. Food recognition in the wild: Challenges and recent advances. Pattern Recognition, 144, 109878, 2024.

[3] Qiu, R., Wang, J., and Chen, H. Modeling ingredient semantics with hierarchical transformers for recipe understanding. Information Processing & Management, 61(1), 103672, 2024.

[4] Gao, T., Shan, M., and Li, X. A review of food portion estimation techniques for vision-based dietary assessment. Computer Vision and Image Understanding, 238, 103941, 2024.

[5] Kim, J., Park, S., and Choi, H. Cross-modal transformers for food image–ingredient alignment in nutrition prediction. IEEE Transactions on Multimedia, 27, 1441–1454, 2025.

[6] Chen, S., Wu, X., and Li, Y. Transformers in food computing: A new era of multimodal dietary assessment. Expert Systems with Applications, 234, 120928, 2024.

[7] Tan, M., Huang, L., and Zhang, F. Multimodal fusion for food computing: Improvements in recognition and nutrition prediction. Neurocomputing, 556, 126789–126799, 2024.

[8] Singh, A., Reddy, P., and Smith, D. B. Toward accurate nutrition estimation: Limitations of current methods and future directions. ACM Transactions on Multimedia Computing, Communications, and Applications, 21(2), 1–22, 2025.

[9] Yamada, K., Ueda, R., and Nakamura, T. Unified food computing pipelines: A review on modular vs. end-to-end architectures. Artificial Intelligence Review, 58, 1–28, 2025.

[10] Luo, Y., He, Z., and Chen, J. End-to-end multimodal transformers for joint food classification, portion estimation, and nutrient prediction. Engineering Applications of Artificial Intelligence, 136, 108874, 2025.

[11] Konstantakopoulos, F. S., Georga, E. I., and Fotiadis, D. I. An automated image-based dietary assessment system for Mediterranean foods. IEEE Open Journal of Engineering in Medicine and Biology, 4, 45–54, 2023.

[12] Shao, W., et al. Vision-based food nutrition estimation via RGB-D fusion network. Food Chemistry, 424, 136309, 2023.

[13] Agarwal, R., Choudhury, T., Ahuja, N. J., and Sarkar, T. Hybrid deep learning algorithm-based food recognition and calorie estimation. Journal of Food Processing and Preservation, 2023, 1–15, 2023.

[14] Zou, Z., Zhu, X., Zhu, Q., Zhang, H., and Zhu, L. Disambiguity and alignment: An effective multi-modal alignment method for cross-modal recipe retrieval. Foods, 13(11), 1628, 2024.

[15] Abiyev, R., and Adepoju, J. Automatic food recognition using deep convolutional neural networks with self-attention mechanism. Human-Centric Intelligent Systems, 4(1), 171–186, 2024.

[16] Wang, H., et al. Nutritional composition analysis in food images: An innovative Swin Transformer approach. Frontiers in Nutrition, 11, 1454466, 2024.

[17] Soekamto, Y. S., Lim, A., Limanjaya, L. C., Purwanto, Y. K., Lee, S.-H., and Kang, D.-K. Pic2Plate: A vision-language and retrieval-augmented framework for personalized recipe recommendations. Sensors, 25(2), 449, 2025.

[18] Chen, Z., Wang, J., and Wang, Y. Enhancing food image recognition by multi-level fusion and the attention mechanism. Foods, 14(3), 461, 2025.

[19] Sharma, L. D. Calorie detection using image recognition: A deep learning approach for fitness applications. IOSR Journal of Computer Engineering, 27(2), 46–51, 2025.

[20] Nogay, H. S., Nogay, N. H., and Adeli, H. Image-based food groups and portion prediction by using deep learning. Journal of Food Science, 90(3), e70116, 2025.

[21] Adithya, B. Deep multimodal fusion for ingredient prediction from food images and recipe descriptions. Journal of Information Systems Engineering and Management, 10(32s), 722–732, 2025.

[22] Cheng, S.-T., Lyu, Y.-J., and Teng, C. Image-based nutritional advisory system: Employing multimodal deep learning for food classification and nutritional analysis. Applied Sciences, 15(9), 4911, 2025.

[23] Codatta. MM-Food-100K dataset. Available at: https://huggingface.co/datasets/Codatta/MM-Food-100K, accessed 2025.

Journal of Engineering and Technology for Industrial Applications

ISSN ONLINE: 2447-0228

ITEGAM-JETIA

Manaus, v.12 n.60, p.955-961 July/August, 2026.
DOI: https://doi.org/10.5935/jetia.v12i60.3907

RESEARCH ARTICLE OPEN ACCESS

STUDY OF THE STRUCTURE AND ELECTRIC PROPERTIES OF (NA0.5BI0.5) 1-XMGX[(TI0.8ZR0.2)0.9 (NB2/3ZN1/3)0.1] O3 CERAMICS

Zakaria Ouahab[1], Abdelwhab Ouahab[2]

[1]Laboratory of Applied Chemistry, Department of Science Matter, University of Biskra, BP.145, RP Biskra 07000, Algeria
[2]Department of Mathematics and Computer Sciences, University of Ahmed Draia, Adrar, Algeria

[1]https://orcid.org/0000-0002-1703-2442, [2]https://orcid.org/0000-0003-0648-2947

E-mail: zakaria.wahab@univ-biskra.dz, ouahab.abdelwhab@univ-adrar.dz

ARTICLE INFO

Article History
Received on: March 04, 2026
Reviewed on: April 02, 2026
Accepted on: July 01, 2026
Published on: July 31, 2026

Keywords:
Ceramic,
PZT,
BNT,
SEM,
DRX,
Dielectric constant.

ABSTRACT

This study focuses on the compound $(Na_{0.5}Bi_{0.5})_xMg_{1-x}[(Ti_{0.8}Zr_{0.2})_{0.9}(Nb_{2/3}Zn_{1/3})_{0.1}]O_3$ (BNTZZN-x%Mg), which was synthesized using the molten salt method for x = 0.00, 0.02, 0.06, and 0.08. The resulting samples were calcined at 900 °C for 4 hours and subsequently sintered at 1150 °C. The measured densities were found to be close to the theoretical values. X-ray diffraction (XRD) analysis confirmed the formation of a pure perovskite phase. Scanning electron microscopy (SEM) images revealed a slight variation in grain size with increasing Mg content. Overall, the material exhibited relatively high purity and density. Dielectric properties were measured on the single-phase ceramic, and their evolution was studied over a temperature range of 27 °C to 227 °C across various frequencies.

Copyright ©2026 by authors and Galileo Institute of Technology and Education of the Amazon (ITEGAM). This work is licensed under the Creative Commons Attribution International License (CC BY 4.0).

I. INTRODUCTION

Piezoelectric materials play a vital role in numerous technological applications, including actuators, sensors [1] [2], aerospace systems, precision machinery, as well as in both military and civilian sectors [3] [4] Among these, lead-based piezoelectric ceramics, particularly Pb (Zr,Ti)O_3 (PZT), have been extensively studied and widely utilized [3] However, a major drawback of PZT is its high lead content—up to 60% by weight [5] [6] Lead is known to be toxic and poses significant risks to both human health and the environment. As a result, lead-free piezoelectric materials have gained significant attention as potential alternatives to lead-based ceramics [7] In line with this shift, European regulations currently restrict the use of most lead-containing substances in electronic and electrical devices [6] Despite ongoing efforts, no single lead-free composition has yet been identified that can fully replace PZT, making the search for suitable alternatives an active area of research [8] In recent years, several promising lead-free materials have been developed for actuator applications [3]. Among these, materials based on $Bi_{0.5}Na_{0.5}TiO_3$ (BNT), first discovered by Smolensky in 1961 [9] [10], have attracted considerable interest. BNT crystallizes in a perovskite structure (ABO_3), exhibiting rhombohedral symmetry (space group R3c) at room temperature, which transitions to tetragonal and then cubic phases at elevated temperatures ranging from 300 °C to 540 °C [11] [12] Currently, ceramics based on $Na_{0.5}Bi_{0.5}TiO_3$ (BNT) are gaining significant attention due to their environmental benefits and wide range of potential applications [13] BNT-based solid solutions have attracted considerable interest, particularly for energy storage applications [14] In recent years, various approaches involving ionic doping have been employed to synthesize BNT-based ceramics [3] Numerous studies have aimed to enhance the functional properties of these materials and to reduce their sintering temperatures through binary or ternary solid solutions, or by incorporating sintering aids [15] In this study, we synthesized the compound $(Na_{0.5}Bi_{0.5})_xMg_{1-x}[(Ti_{0.8}Zr_{0.2})_{0.9}(Nb_{2/3}Zn_{1/3})_{0.1}]$ O_3 using the molten salt method. The resulting solid solution, BNTZZN-x%Mg, was structurally and dielectrically characterized with the aim of developing a lead-free piezoelectric material capable of effectively replacing PZT ceramics in specific applications.

II. EXPIREMENTAL

II.1 PREPARATION OF CERAMICS:

Each study has own preparation process. The molten salt method was selected (MSS) used to prepare solid solution BNTZZN-x%Mg such as x= 0.00, 0.02, 0.06 and 0.08. The molten salt method is used as a medium for the preparation of complex oxides from their constituent materials (oxides and carbonates) [16] The role of the molten salts is:

- Increase the reaction rate and lower the reaction temperature. Increase the degree of homogeneity (distribution of constituent elements in the solid solution).
- Particle size control.
- Particle shape control.
- Agglomeration state control [16].

The basic oxides used in the synthesis of our samples are MgO, TiO_2, ZrO_2, $Bi2O_3$, Na_2CO_3, Nb_2O_5, and ZnO. The molten salt (MSS) method was used to prepare a solid solution (BNTZZN-x%Mg). In our study, BNT-type ceramics were synthesized from a mixture of oxides and carbonates. The oxides and carbonates required to synthesize a mixture of about 15g shall be weighed according to the stoichiometric quantities provided and calculated according to the reaction equation as shown in Table1, using an electronic balance. Then, the precursor was ground in a porcelain mortar for 03 hours. after that, we added (KCl-NaCl) and grind the sample for 02 hours. This operation aimed at promoting the homogeneity of the mixture to obtain powder with the finest particle size. The powder was burned at 900°C for 4h in a programmable oven (N-Abbertherm-D) under ambient temperature rise of 2°C/min to constant temperature of 4h. The resulting materials are cooled slowly. Then, we grind again for 5h. The aim of the regrinding is to reduce the agglomerates formed during calcination, in order to homogenize the powder, and increase its reactivity. After that, the powder obtained is compacted in the form of pellets of 1,5g and a diameter of about 13 mm. Our ceramics are sintered in an aluminum crucible at 1150°C by natural sintering under air. The temperature rises at a speed rate of 2°C/min up to the set temperature. Therefore, the temperature is stable for 4 hours. Finally, the temperature is descent to the ambient.

II.2 CHARACTERIZATION OF CERAMICS:

The spectra of our sintered ceramics were obtained at room temperature on a vertical diffractometer, «BRUKER-AXE type D8» from the University of Biskra laboratory. Profiles lines were measured using an automatic point-by-point counting system with a 0.02° steps. All diffraction patterns were recorded in the angle range $0° < 2 < 80°$, which may be sufficient to identify the different phases. We note that the analysis used for indexing different lines by X'Pert HighScore. The density of the sintered samples was calculated from the sample dimensions and weight. Microscopic images of our samples were performed using a scanning electron microscope type JEOL JSM-6390lv from the University of Biskra laboratory. It is controlled by a computer. The purpose of these analyses is to study the morphology of our samples after sintering. Dielectric measurements were carried out in the laboratory of physical engineers' the University of Tiaret. The measurement of the dielectric properties was performed on a single-phase ceramic sample, and the evolution of these properties were investigated at temperatures ranging from 27°C to 227°C at different frequencies. It was investigated using an automatic (LCR) counter combined with a computer controlled temperature chamber at 100Hz, 500Hz, 1KHz, 10KHz, and 100KHz.

III. RESULT AND DISCUSSION

III.1 DENSITY

Density is a physical quantity that affects the structure and electrical properties of ceramics. The relative density D (compactness) is given by equation (1) of the material
NBMTZNZ sintered at 1150 °C:

As:

$$D=\frac{\rho_{exp}}{\rho_{th}} \quad (1)$$

ρ_{exp}: Experimental density calculated from the mass and the volume of sintered ceramics pellets.

ρ_{th}: Theoretical density obtained from X-ray diffraction database providing the mesh parameters [17].

Table 1 shows the density values. These values range from 5.26 to 5.53 g/Cm3 or from 88.58% to 89.77% so that the theoretical value is 6.12, 6.15 and 6.16g/Cm3. Thus, the experimental values are close to the theoretical values. This note means that the ceramic is very dense with less porosity [18] BNTZZN-x%Mg has been well prepared, so the choice of molten salt method was adequate.

Table1: Density (g/Cm^3)

X	**0.00**	**0.02**	**0.06**	**0.08**
ρexp(g/Cm^3)	5.66	5.43	5.26	5.53
ρth(g/Cm^3)	6.12	6.13	6.15	6.16
D (%)	92.48	88.58	85.52	89.77

Source: Authors, (2026).

III.2 X-RAY ANALYSIS (DRX)

The majority of diffraction peaks observed in the synthesized samples were indexed based on the cubic perovskite structure of $Na_{0.5}Bi_{0.5}TiO_3$, using reference pattern 01-089-3109. Within the 2θ angle ranges of (21–22), (31–33), (39–41), (45–47), (51–53), (58–59), (68–69), and (76–78), distinct peaks corresponding to the perovskite phase were identified, associated with the following Miller indices: (100), (110), (111), (200), (210), (211), (220), (221), and (310). Minor secondary phases—specifically, traces of pyrochlore—were detected using the X'Pert HighScore software, and matched to the ASTM card 98-009-9437, as illustrated in Figure 1[13].

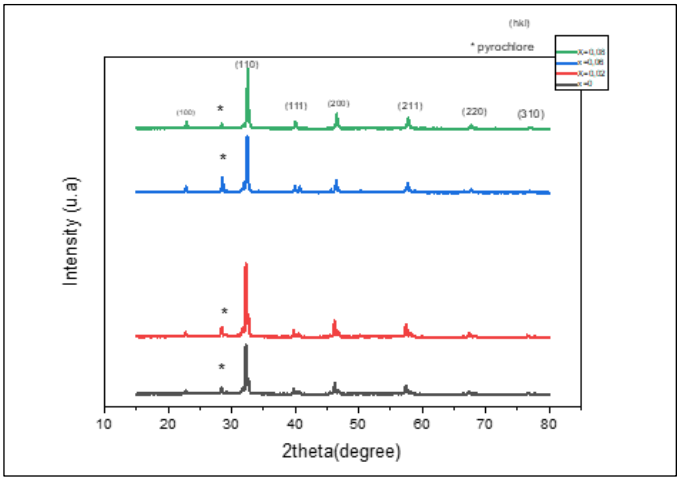


Figure 1: X-ray indexed diffraction patterns.
Source: Authors, (2026).

The stability of the perovskite structure (ABO_3) is characterized by a tolerance factor (t) that determines the density and freedom of movement of the cations A and B. According to Goldschmidt, the structure is stable if 0.88 <t<1.09, but exhibits a structural stability distortion beyond this range. The tolerance factor (t) can be determined by the following formula:

$$t=/\frac{\sum Ra+Ro}{\sqrt{2}(\sum Rb+Ro)} \quad (2)$$

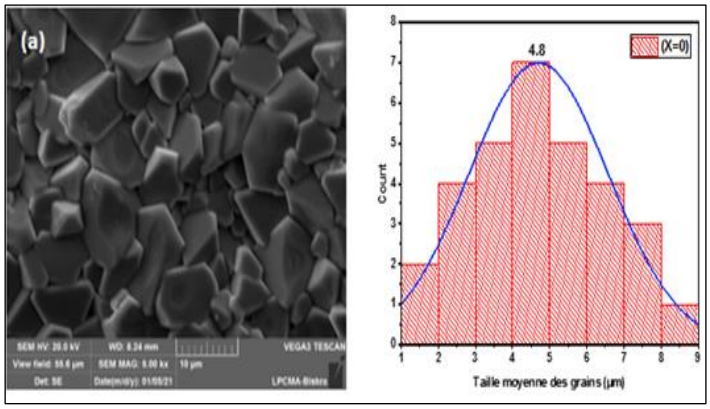
Where: $\sum R_a$, $\sum R_b$ and R_o are respectively the ionic radii of the cations, respectively; A, B and Oxygen [17-21] The perovskite structure is more stable when the tolerance factor (t) is close to 1. The involved bonds play a strong ionic role [14].

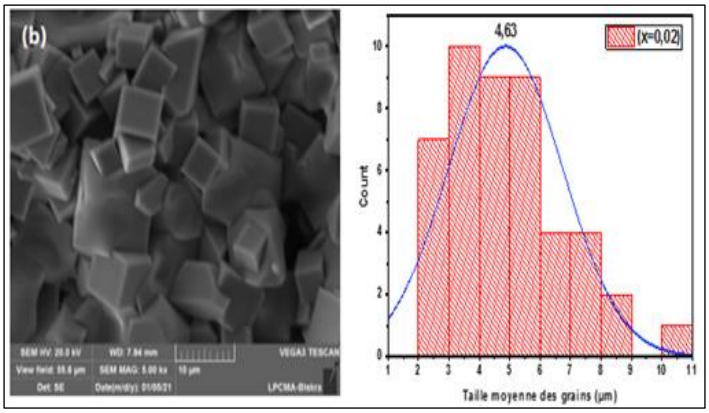
Table 2: factor tolernce values.

X	Tolerance factor
0.00	0.9225
0.02	0.9138
0.06	0.8964
0.08	0.8748

Source: Authors, (2026).

Figure .2 presents the SEM micrographs along with the histograms of the BNTZZN-x%Mg samples after sintering at 1150 °C For each of the five samples, a uniform distribution of cubic-shaped grains is observed across the entire surface of the compositions. The ceramic micrographs reveal a satisfactory material density, very low intergranular porosity, and a narrow grain size distribution within each sample. The histograms obtained using ImageJ software [15] allowed the determination of an average grain size ranging from 3.07 µm to 4.80 µm for the four samples.





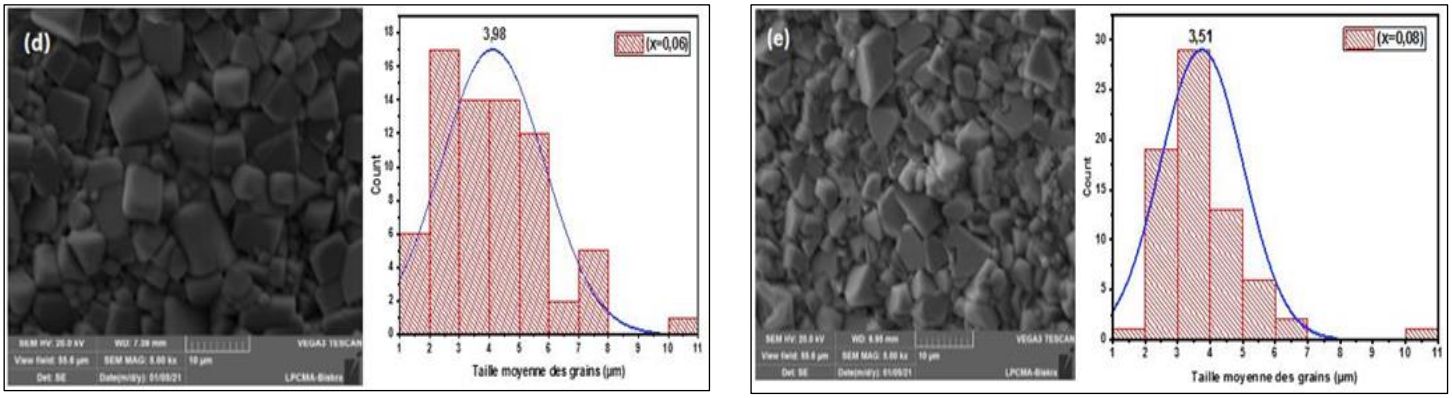


Figure 2: SEM images with histograms of the BNTZZN-x%Mg ceramic compositions showing the average grain size.
Source: Authors, (2026).

Table 3: Average grain size.

X	0.00	0.02	0,06	0.08
Grain size (µm)	4.80	4.630	3.984	3.514

Source: Authors, (2026).

III.3 DIELECTRIC MEASUREMENTS

Figure.3 illustrates the evolution of the dielectric constant of the BNTZZN-x%Mg material for various values of x (0, 0.02, 0.06, and 0.08) as a function of temperature (between 300 and 500 K), at different frequencies (100 Hz, 500 Hz, 1 kHz, 10 kHz, and 100 kHz). The $\varepsilon_r(T)$ curves exhibit a similar trend, increasing with temperature until reaching a maximum, then decreasing. However, these curves differ in the position and intensity of their peak, which corresponds to the Curie temperature (T_C) [15] [16]. In the ferroelectric region, the dielectric constant ε_r increases with temperature, which means that the material possesses an electric dipole moment even in the absence of an external electric field [17] The dielectric constant reaches a maximum at the Curie temperature, which corresponds to the transition of the material from the ferroelectric phase to the paraelectric phase. Beyond this temperature, the ceramics lose their ferroelectric properties and transition to a high-symmetry phase, leading to a decrease in dielectric permittivity [16] [18] It is observed that the high values of dielectric permittivity for each composition appear at 100 Hz. The dielectric constant (ε_r) increases as the frequency decreases and becomes nearly negligible at high frequency values (100 kHz) for all compositions. The dielectric constant is frequency-dependent, particularly at low frequencies—a phenomenon known as low-frequency dielectric dispersion. A strong low-frequency dielectric dispersion has also been previously reported in the BNT material [19] At temperatures above T_m and at low frequencies, an increase in dispersion is observed, caused by a rise in electrical conductivity. The dielectric peak broadens with increasing frequency, a phenomenon attributed to the structural disorder of the system. The real part of the dielectric constant reflects the loss less elastic response of the material to an applied alternating electric field. At temperatures above Tm and low frequencies, this dispersion becomes more pronounced due to the increased electrical conductivity.

The broadening of the dielectric peak with rising frequency further indicates structural disorder within the system [20] Some authors explain the maximum value of the dielectric constant at room temperature and low frequencies by the presence of different types of polarization [15] The polarization of dielectric ceramics varies significantly, mainly due to the different polarization mechanisms present in the various compositions. The polarization in dielectric ceramics primarily results from the displacement of electrons, ions, and chemical defects under the influence of an electric field, including electronic polarization, ionic polarization, orientational polarization, and space charge polarization. It can be classified into displacement polarization and relaxation polarization [21] Moreover, ceramics with small, uniformly distributed grain sizes and a high density of grain boundaries generally exhibit higher dielectric breakdown strength (E_b) [22] Factors affecting E_b also include temperature, humidity, the type of voltage (DC, AC, or pulse), test duration, and the thickness of the dielectric layer. In a specific experiment, Eb can be improved by increasing resistivity, reducing porosity, increasing density, and decreasing grain size. Dielectric loss refers to the energy consumed by dielectric materials due to heating under the influence of an electric field, and it is represented by tan δ. A higher tan δ indicates not only increased energy consumption but also a rise in the temperature of the dielectric material. Therefore, a low tan δ signifies better performance of the dielectric material and greater application value. In dielectric ceramics, tan δ is generally attributed to conductivity loss, orientational and relaxation polarization loss, as well as structural loss [21] Figure .4 illustrates the evolution of dielectric losses of the studied ceramic materials for various x values (0, 0.02, 0.04, 0.06, and 0.08) as a function of temperature (between 300 and 500 °C) and frequency (100 Hz, 500 Hz, 1 kHz, 10 kHz, and 100 kHz).

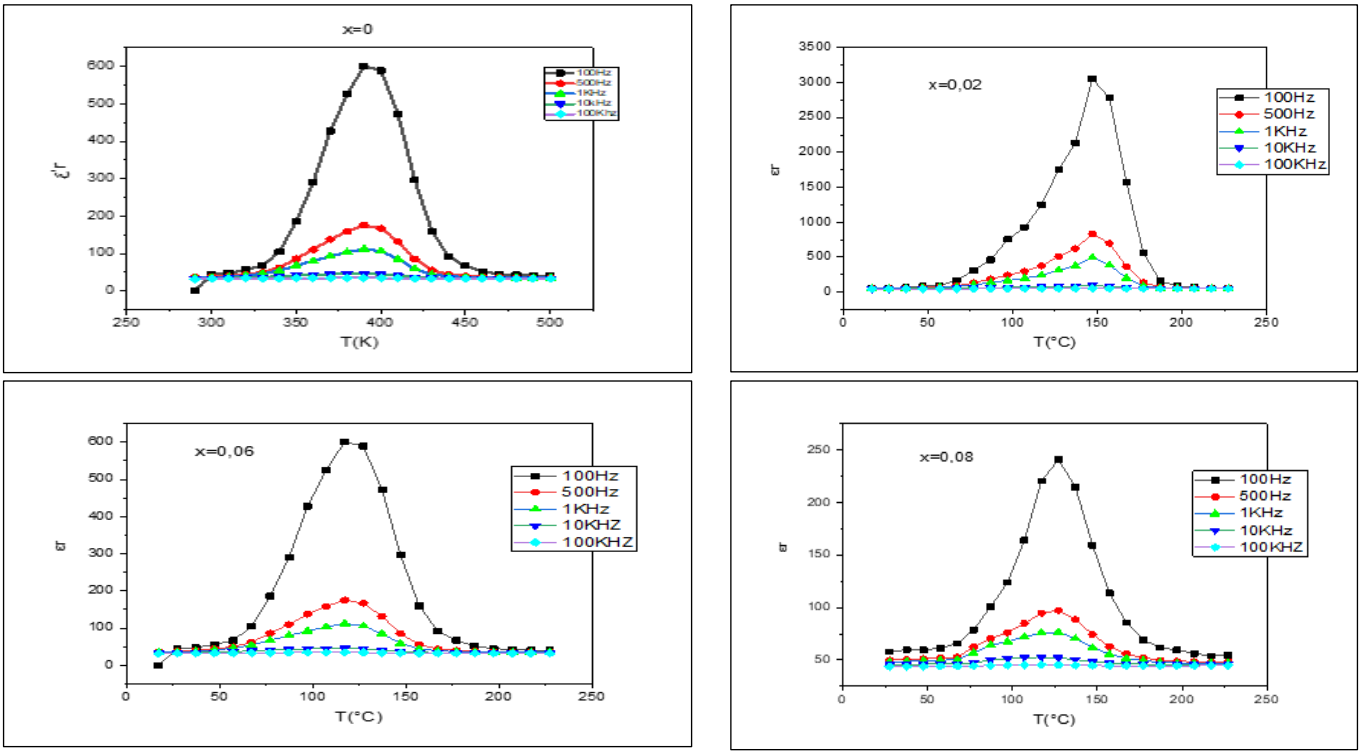


Figure 2: Evolution of the dielectric constant for the BNTZZN-x%Mg compositions as a function of temperature and frequency.
Source: Authors, (2026).

It is clearly observed that the loss angle increases with rising temperature, reaching a maximum at a certain point, resulting in a dielectric loss peak for the sample, followed by a decrease. This decrease, caused by the continued rise in temperature, deteriorates the material's properties related to domain wall motion [15] The higher the permittivity, the greater the losses. The role of intrinsic losses in the overall loss process increases with the material's permittivity. For high-quality ferroelectrics, in the paraelectric state or near the transition, intrinsic losses may even dominate the total dielectric losses [17] The analysis of the data in Table .4 reveals a non-monotonic influence of the magnesium content (X) on the tangent loss coefficient (Tan δ) of the BNTZN-xMg material. Indeed, although a general decreasing trend in Tan δ is observed with increasing X, significant fluctuations appear, particularly at low X values. This complexity suggests that the mechanisms responsible for dielectric losses are sensitive to compositional variations, even at low magnesium concentrations. Given that all other elements are kept constant, it is reasonable to attribute these variations primarily to the effect of magnesium doping [23] [24].

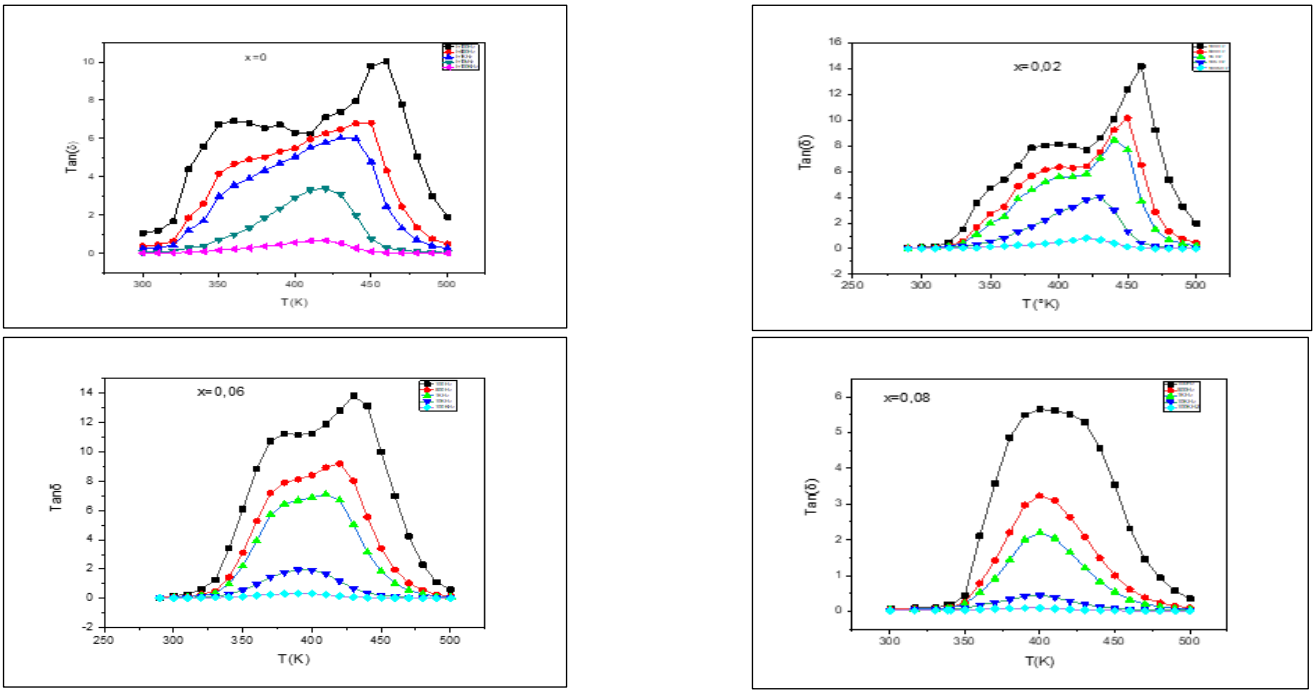


Figure 3: The evolution of dielectric loss for all compositions of BNTZZN-x Mg as a function of temperature and frequency.
Source: Authors, (2026).

Table 4: The dielectric loss values for BNTZZN-xMg.

x	Dielectric loss
0.00	10
0.02	14
0.06	14
0.08	6

Source: Authors, (2026).

IV. CONCLUSIONS

- X-ray diffraction (XRD) analysis reveals that the prepared BNTZZN-xMg materials adopt a cubic structure, with the presence of a secondary phase known as 'pyrochlore'.
- The density test shows that the densification rate of the analyzed ceramics ranges between 85.52% and 92.50%.
- The dielectric properties of the studied materials show a strong dependence on temperature, frequency, and composition. As the temperature increases, the permittivity generally rises until reaching the Curie temperature, followed by a decrease. Low-frequency dielectric dispersion is attributed to multiple polarization mechanisms and ionic conductivity.

V. ACKNOWLEDGMENTS

These studies were carried out using the equipment of the laboratory of Applied Chemistry at university of Biskra and the laboratory of engineers physics at the university of Tiaret.

VI. AUTHOR'S CONTRIBUTION

Conceptualization: Ouahab Zakaria.
Methodology: Ouahab Zakaria.
Investigation: Ouahab Zakaraia.
Discussion of results: Zakaria.
Writing – Original Draft: Ouahab Zakaria.
Writing – Review and Editing: Ouahab Zakaria, Ouahab Abdelwhab.
Resources: Ouahab Zakaria.
Supervision: Ouahab Abdelwhab.
Approval of the final text: Ouahab Abdelwhab.

VII. REFERENCES

[1] I. Chopra, "AIAA J.", 40 (2002) 2145.

[2] B. Noheda, "Curr. Opin. Solid State Mater. Sci.", 6 (2002) 27.

[3] J. Rodel, K. G. Webber, R. Dittmer, "J. Eur. Ceram. Soc.", 35 (2015) 1659.

[4] E. Hollenstein, M. Davis, D. Damjanovic, "Appl. Phys. Lett.", 87 (2005) 182905.

[5] X.-Y. Kang, Z.-H. Zhao, Y.-K. Lv, Y. Dai, "BNT-based multi-layer ceramic actuator with enhanced temperature stability", J. Alloys Compd., 771 (2019) 541.

[6] V. Pal, R. K. Dwivedi, O. Thakur, "Ceram. Int.", 14 (2014) 99.

[7] S. Pattipaka, P. Mahesh, D. Pamu, "AIP Conf. Proc.", (2016) doi:10.1063/1.4946403.

[8] G. A. Smolenskii, V. A. Isupov, A. I. Agranovskaya, N. N. Krainik, "Sov. Phys.-Solid State", 2 (1961) 2651.

[9] S. Wu, B. Song, P. Li, B. Shen, J. Zhai, "J. Eur. Ceram. Soc.", 40 (2020) 2954.

[10] P. Jaita, A. Watcharapasorn, S. Jiansirisomboon, "Curr. Appl. Phys.", 11 (2011) 577.

[11] G. O. Jones, P. A. Thomas, "Acta Crystallogr. B", 56 (2000) 426.

[12] Y. Hiruma, H. Nagata, T. Takenaka, "Jpn. J. Appl. Phys.", 45 (2006) 7409.

[13] P. Fu, Z. Xu, R. Chu, X. Wu, W. Li, X. Li, "Mater. Des.", 46 (2013) 322.

[14] L. Pauling, The Nature of the Chemical Bond, Cornell University Press, New York, (1967) 267.

[15] A. Abdel Aal, T. Hammad, M. Zawrah, I. Battisha, A. Abou Hammad, FTIR Study of Nanostructure Perovskite BaTiO_3 Doped with Both Fe^3+ and Ni^2+ Ions Prepared by SolGel Technique, Acta Physica Polonica A, 126 (2014) 1318-1321.

[16] M. Abba, Synthèse, caractérisation et étude Des propriétés Piézo-électriques des céramiques de type PZT: Pb1-y Lay [Zrx Tiz (Mo1/3 In2/3) 1-(x+ z)] 1-y/4 O3, Université Mohamed Khider-Biskra, 2013.

[17] K. Bounab, Elaboration, caractérisation et étude des propriétés diélectriques d'une solution solide de type PZT, chmie, 2015.

[18] S. Nenez, Céramiques diélectriques commandables pour applications micro-ondes: composites à base de titanate de baryum-strontium et d'un oxyde non ferroélectrique,

Université de Bourgogne, 2001.

[19] A. Meklid, Elaboration, caractérisation et étude des propriétés diélectriques et électromécaniques d'un nouveau matériau de céramique de type Zirconate-Titanate de plomb (PZT), UNIVERSITE MOHAMED KHIDER-BISKRA, 2018.

[20] B. Tilak, Low-frequency dielectric dispersion and impedance spectroscopy of lead-freeNa0. 5Bi0. 5Tio3 (NBT) based ferroelectric ceramic, J. Mater. Sci. Eng, 1 (2012) 1000108.

[21] W. Zhu, Z.-Y. Shen, W. Deng, K. Li, W. Luo, F. Song, X. Zeng, Z. Wang, Y. Li, A review:(Bi, Na) TiO3 (BNT)-based energy storage ceramics, Journal of Materiomics, 10 (2024) 86-123.

[22] C. Neusel, H. Jelitto, D. Schmidt, R. Janßen, F. Felten, G.A. Schneider, Thicknessdependence of the breakdown strength: Analysis of the dielectric and mechanical failure, Journal of the European Ceramic Society, 35 (2015) 113-123.

[23] C.F. Buhrer, Some properties of bismuth perovskites, The Journal of chemical physics, 36 (1962) 798-803.

[24] B. Barick, R. Choudhary, D. Pradhan, Dielectric and impedance spectroscopy of zirconium modified (Na0.5Bi0.5) TiO3 ceramics, Ceramics International, 39 (2013) 5695-5704.

Journal of Engineering and Technology for Industrial Applications

ITEGAM-JETIA

Manaus, v.12 n.60, p.962-973 July/August, 2026.
DOI: https://doi.org/10.5935/jetia.v12i60.3908

ISSN ONLINE: 2447-0228

RESEARCH ARTICLE OPEN ACCESS

SYNERGISTIC PERFORMANCE AND EMISSION OPTIMISATION OF A TWO-STROKE SI ENGINE USING MG-PSZ THERMAL BARRIER COATED PISTON WITH ETHANOL–BUTANOL BLENDS THROUGH ANN–NSGA-II–TOPSIS APPROACH

A.V.N.S Kiran[1], Arun Kumar Kurakula[2], H S Anantha Padmanabha[3], B Venkatesh[*4]

[1]Department of Mechanical Engineering, SVUCE, Sri Venkateswara University, Tirupati, Tirupati Dist. A.P
[2]Department of Computer Science Engineering, Siddhartha Institute of Engineering and Technology, Puttur, A.P
[3]Department of Mechanical Engineering, PVKK Institute of Technology, Rudrampeta, Anantapuram, Anantapuram, A.P
[*4]Department of Mechanical Engineering, School of Engineering, Annamacharya University, Rajampeta, Annamayya Dist. A.P.

[1]https://orcid.org/0009-0000-2186-9694, [2]http://orcid.org/0000-0002-9837-9551
[3]http://orcid.org/0000-0002-6221-2215, [4]https://orcid.org/0000-0002-6387-1677

E-mail: kiran.avns321@gmail.com, k.arunjoy@gmail.com, ananth.7016@gmail.com, *aits.med.bv@gmail.com
*aits.med.bv@gmail.com (or) bhupalam, venkatesh2005@gmail.com

ARTICLE INFO

Article History
Received on: March 04, 2026
Reviewed on: April 02, 2026
Accepted on: July 01, 2026
Published on: July 31, 2026

Keywords:
Thermal barrier coating,
Magnesium partially stabilized zirconia (Mg-PSZ),
Oxygenated fuel blends (E20, B20),
Multi-objective optimization (NSGA-II–TOPSIS),
Two-stroke spark-ignition engine.

ABSTRACT

This paper reaches an assessment of the performance and emission traits of a two-stroke spark-ignition engine that is run with gasoline, E20, and B20 fuel under normal and Mg-PSZ-coated piston set ups. The characterization of fuels through GC and FTIR-generated stable mixtures and effective incorporation of the oxygenated functional groups. E20 in uncoated form enhanced brake thermal efficiency (BTE) by about 4-6 % than gasoline, and lowered HC and CO by 8-12 and 10-15 % respectively. Mg-PSZ coating increased the BTE by 5-8 percent and decreased the total fuel consumption by 3-6 percent at all loads. Coated conditions resulted in a further reduction of HC and CO emissions of 10-18%. ANN modeling resulted in R2 values in excess of 0.92 and NSGA-II-TOPSIS optimization established a coated high-load case with an overall 9-12% improvement in the performance-emission which shows high level of synergy between oxygenated fuels and thermal barrier coating.

Copyright ©2026 by authors and Galileo Institute of Technology and Education of the Amazon (ITEGAM). This work is licensed under the Creative Commons Attribution International License (CC BY 4.0).

I. INTRODUCTION

The tribological and thermal conditions in two-stroke engines are worse than those in four-stroke engines, and piston components of the former face increased stresses of wear and lubrication. Besides acting as a mechanism of imparting the forces of combustion to the crankshaft, the piston in a two-stroke engine manages the timing of intake and exhaust ports as well. This dual action coupled with the constant sliding movement, high combustion temperatures, intermittent lubrication and exposure to combustion resides speed up the process of wear, scuffing and seizure of piston skirt. Such degradation processes affect the engine durability, efficiency, and performance in terms of emissions. In solving these problems, high performance piston surface finishes have become a significant technology in the internal combustion engine. Pistons work in severe thermal gradient and dynamic mechanical loads. Alloyed aluminum without coating is highly prone to adhesive wear and thermal fatigue (especially in the piston). Thermal barrier coating (TBCs) have thus come under extensive research study to enhance the life of the piston and efficiency during combustion [1-4] These coatings inhibit heat transfer between the combustion chamber and the piston substrate and thus increase thermal retention as well as overall engine efficiency.

The use of ceramic-based coating especially partially stabilized zirconia (PSZ) has been of interest because of low thermal conductivity, high melting point, and stability to the chemical environment [5-7]. In the case of piston crowns, PSZ-based finishes minimize cooling losses and retain heated in-cylinder temperatures and result in favorable combustion properties. Furthermore, skirt coatings that contain solid lubricants are used to reduce the friction and scuffing during the boundary lubrication conditions. In parallel with the improvements in coating, biofuels with oxygen groups, like ethanol and n-butanol mixtures have been actively researched as being a viable alternative to gasoline. Octane rating is enhanced by ethanol blends and carbon monoxide and hydrocarbon emissions are reduced by ethanol blends in spark-ignition engines [8-10] Equally, n-butanol blends have the benefits of high energy density and compatibility with fuel compared to ethanol [11-13] These fuels have shown great promise with regard to enhancing the combustion efficiency and reducing engine-out emissions [14] [15] Nevertheless, alcohol-gasoline mixtures can raise the frictional wear occurrence and a little change of fuel consumption nature in the two-stroke engines because of the variations in the lubricity and vaporization conduct [16]

This provides a room to combine sophisticated ceramic coating with oxygenated fuels in a synergistic way. Specifically, Magnesium-Stabilized Zirconia (Mg-PSZ) coatings have been demonstrated to perform better as thermal insulation and an increase in the thermal efficiency of the brakes under the operation of alcohol-blended fuel [17] Moreover, the use of ceramic-based coatings, including Al 2 O 3 and TiO 2, has shown enhanced wear resistance of coated engine parts when using ethanol-based fuels [16] Although there has been significant development in the field of coating technology and biofuels research, little has been done relating to the integration of the two in two-stroke engines under extreme tribological conditions. Additionally, predictive and multi-objective decision making tools are needed in order to optimize the trade-off between the brake thermal efficiency, reduction of emissions, and fuel consumption. Thus, the current research analyzes the synergy of the functioning of Mg-PSZ coated pistons using E20 and B20 mixtures in a two-stroke spark igniting engine. Artificial Neural Network (ANN) model predicting the performance and emission characteristics is created and multi-objective optimization is performed with the help of the Non-dominated Sorting Genetic Algorithm II (NSGA-II). The Technique of Order of Preference by Similarity to Ideal Solution (TOPSIS) is the method that allows identifying the most appropriate compromise solution between efficiency, emissions and fuel economy when determining the optimal operating condition.

II. THEORETICAL REFERENCE

II.1 SUBTITLE

II.1.1 Preparation of Fuel Blends

Analytical grade ethanol and n-butanol were purchased against certified local chemical suppliers, and commercial gasoline was purchased at a local petrol station. Table 1 shows the physicochemical properties of pure petrol, ethanol and butanol. The fuel blends were made in three different configurations, i.e. pure petrol (100%), petrol-ethanol blend (E20: 80% petrol + 20% ethanol) [18], and petrol-butanol blend (B20: 80% petrol + 20% n-butanol) [19-22] The choice of 20 percent alcohol content was informed by the previous experiments that showed better combustion characteristics and reduction of emissions without any substantial engine adjustments [18-22]. A magnetic stirrer was used to stir the mixture in 20 minutes to mix it homogeneously. The ready blends of E20 and B20 were put in the capped 100 mL glass containers at room temperature to avoid absorption of moisture and phase separation. In order to motivate fuel stability implementation, especially in ethanol-gasoline engine, stability test was made following the steps that are reported in two-stroke SI engines [23] It was established that properties of blended fuels were in line with ASTM standards. The properties measured are summarized in Table 2.

Table 1: Properties of Pure Petrol, Ethanol, and Butanol.

S. No	Parameter	Pure Petrol	Butanol	Ethanol
1	Chemical Formula	Complex mixture	C_4H_9OH	C_2H_5OH
2	Density (kg/m³)	753	810	790
3	Calorific Value (MJ/kg)	49.2	33.3	26.8
4	Viscosity (mPa·s)	0.4–0.8	2.57	1.08
5	Octane Number	96.3	98.3	98.8

Source: Author, (2026).

Table 2: Properties of E20 and B20 Blends.

S. No	Parameter	E20	B20
1	Density (kg/m³)	0.7541	0.810
2	Fire Point (°C)	30.0	36.5
3	Calorific Value (MJ/kg)	32.43	33.3
4	Octane Number	87.7	88.7

Source: Author, (2026).

II.1.2 Thermal Barrier Coating (Mg-PSZ)

Magnesia-partially stabilized zirconia (Mg-PSZ) was the thermal barrier coating material selected because of its desirable mechanical strength, low thermal conductivity, and high fracture toughness [24] [25] Mg-PSZ is commonly explored in the area of thermal barrier coating (TBC) systems used in the internal combustion engines [26] The substrate was made of aluminum alloy which is a typical product in the spark ignition engines. Before the deposition of the ceramic topcoat, a bond coat layer (e.g. MCrAlY or NiAl) could be used to increase adhesion and oxidation resistance [27]

It was coated with Mg-PSZ ceramic top coat [28] of the approximate thickness of 100 um by the plasma spraying method [29] [30] Fig. 1 and Fig. 2 are the schematic representation of the plasma spraying set up and the coating process.

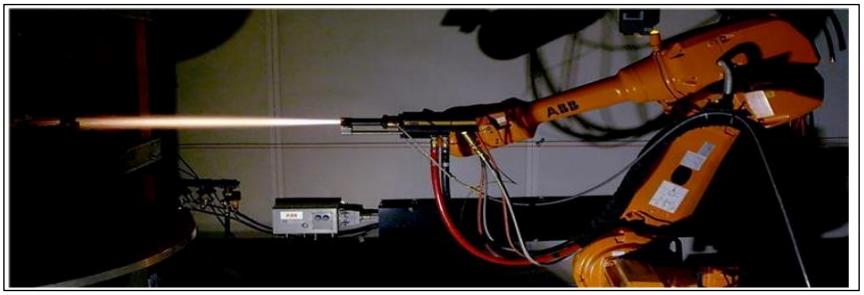


Figure 1: Mg-PSz spraying on the piston surface by using the plasma spray method.
Source: Authors, (2026).

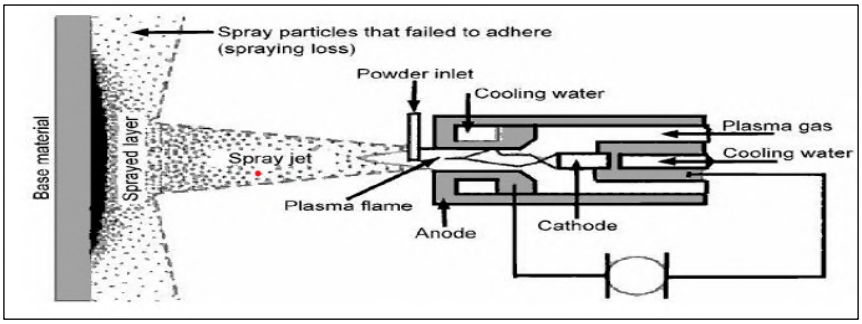


Figure 2: Schematic layout of the Plasma Spray method.
Source: Authors, (2026).

Figure 3 shows a comparison of normal piston and Mg-PSZ coated piston. The coating enhances thermal insulation of the piston crown and as such, minimizes the amount of heat passed on to the piston substrate and the lubricating oil.



Fig (a): normal piston.



Fig (b): Mg-PSZ-coated piston.

Figure 3: Piston Comparison for normal and coated piston.
Source: Authors, (2026).

The thermophysical and mechanical properties of Mg-PSZ are listed in Table 3**.**

Table 3: Properties of Mg-PSZ.

Property	**Value**
Density	5.6×10^3 kg/m³
Modulus of Elasticity	350 GPa
Flexural Strength	545 MPa
Compressive Strength	1700 MPa
Fracture Toughness	6 MPa·m½
Hardness	1100 HV
Thermal Expansion	10×10^{-6} °C⁻¹
Thermal Conductivity	2.5 W/m·K
Specific Heat Capacity	400 J/kg·K
Maximum Working Temperature	1000 °C
Dielectric Strength	6 kV/mm

Source: Authors, (2026).

III. CHARACTERISATION OF FUEL BLENDS

Gas Chromatography (GC)

Gas Chromatography (GC) was utilized in order to establish the compositional distribution of volatile elements in the E20 and B20 mixes. GC is a separation of compounds in contact with a carrier gas phase and a stationary phase in a capillary column according to their partition between the carrier gas phase and the stationary phase. It is a common approach to the characterization of fuels, as well as to the determination of alcohol levels in gasoline mixtures [31-33] The GC analysis in the research was done to verify the uniformity of the blend and to ascertain the alcohol content in the prepared samples. Fourier Transform Infrared (FTIR) Spectroscopy. Fourier Transform Infrared (FTIR) was used to determine functional groups and determine the chemical interactions in the blended fuels [34-36] FTIR is a technique that works by identifying vibrational exchanges of bonded molecules in the presence of the infrared radiation. The method employs the use of a Michelson interferometer and the interferogram obtained is transformed into an absorption spectrum by means of Fourier transformation. FTIR has found extensive use in the characterization of gasoline-ethanol blends and stability of fuels [37] [38] Experimental Setup:



Figure 4: Experimental setup.
Source: Authors, (2026).

It is evident in Figure. 4 that the investigation is conducted by acquiring an experimental set up of a two-stroke air-cooled single cylinder spark ignition with an electrically loaded eddy current dynamometer. Table 4 and 5 contain the specifications of the base engine and the generator.

Table 4: Engine Specifications.

Item	Specifications
BHP	3HP
Speed	3000 RPM
No of Cylinders	1
Bore	57mm
Stroke	57mm
Compression Ratio	7.4:1

Source: Authors, (2026).

Table 5: Generator Specifications.

Item	Specifications
Power	3kW
Speed	3000 RPM
Type	Compound Wound

Source: Authors, (2026).

At no load condition, when the engine is started by standard piston, pure petrol, ethanol, and butanol, then, observe the time when fuel is consumed, and the current and voltage can be measured on the panel board. Monitor the exhausts with a gas analyzer. Subsequently, the loading of the different loads will be put into consideration and the same followed. Replacement of the new piston i.e. the piston covered with Mg-PSZ and the test procedure will be again repeated. The observance of all the parameters will give a comparative result analysis between the normal piston and the piston coating as well as gasoline blends.

IV. METHODOLOGY

The general approach to the research is a combination of experimental research, modeling based on data and multi-objective optimization. The entire Design of Experiments (DOE) was a fully factorial design that was used in order to systematically assess the effect of piston configuration, fuel blend and engine load on performance and emission properties. Artificial Neural Network (ANN) model was developed on the experimental dataset and it acted as a surrogate model to continue prediction. The trained ANN model was then integrated with the Non-dominated Sorting Genetic Algorithm II (NSGA-II) to use as the multi-objective optimizer. The Technique of Order of Preference by Similarity to Ideal Solution (TOPSIS) was employed in ranking the Pareto-optimal solutions to find the best operating condition.

Table 6 contains the parameters of the experimental design, such as the levels of the factors and the sum of all the test combinations. Table 7 shows the input and output variables that were involved in ANN modeling and optimization and Table 8 and Table 9 show the detailed ANN architecture and training parameters and multi-objective optimization parameters used in NSGA-II and TOPSIS, respectively. All these tables provide transparency, reproducibility, and methodological clarity to the framework of ANN-NSGA-II-TOPSIS employed in the current study.

Table 6: Experimental Design Matrix (DOE Structure).

Factor	Type	Levels	Description
Piston Type	Categorical	2	Base piston, Mg-PSZ coated piston
Fuel Blend	Categorical	3	Gasoline, E20, B20
Engine Load	Continuous	5	0%, 25%, 50%, 75%, 100%
Total Runs	—	30	2 × 3 × 5 Full factorial design

Source: Authors, (2026).

Table 7: Input and Output Variables Used for ANN Modeling.

Category	Variable	Symbol	Unit
Input	Piston Type	P	—
Input	Fuel Blend	F	—
Input	Engine Load	L	%
Output	Brake Thermal Efficiency	BTE	%
Output	Mechanical Efficiency	η_mech	%
Output	Hydrocarbon Emission	HC	ppm
Output	Carbon Monoxide	CO	%

Source: Authors, (2026).

Table 8: ANN Model Configuration.

Parameter	Specification
Model Type	Feedforward Artificial Neural Network
Hidden Layers	2
Activation Function	ReLU / Sigmoid
Training Algorithm	Backpropagation
Performance Metrics	R^2, RMSE
Data Preprocessing	Normalization, Encoding

Source: Authors, (2026).

Table 9: Multi-Objective Optimization Configuration.

Component	Description
Algorithm	NSGA-II
Objectives	Maximize BTE, Maximize η_mech, Minimize HC, Minimize CO
Population Size	Defined per iteration
Generations	Iterative convergence
Decision Method	TOPSIS Ranking
Final Output	Optimal operating condition

Source: Authors, (2026).

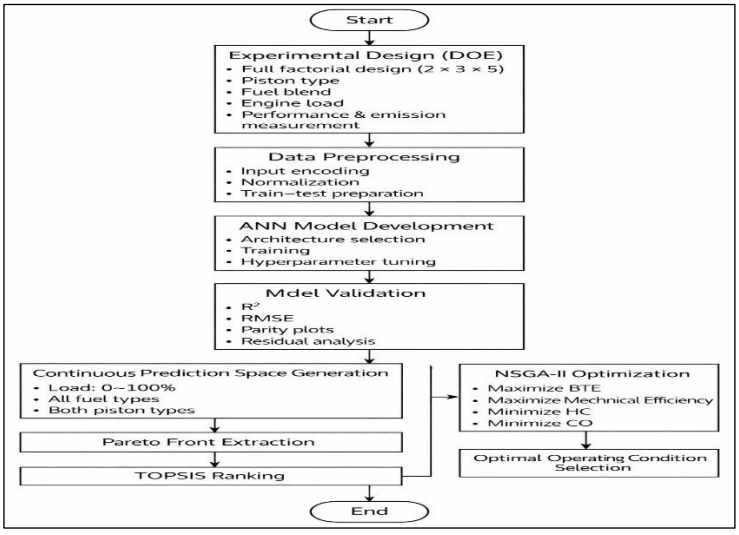


Figure 5: Integrated ANN–NSGA-II–TOPSIS optimization framework for coated two-stroke engine analysis.
Source: Authors, (2026).

The combined approach taken by the current study is shown in Figure 5. A experiment in the form of a full factorial (2 x 3 x 5) was carried out taking into account the piston type, fuel mix, and engine load. The performance and emission data obtained were pre-processed by normalization and encoding and then an Artificial Neural Network (ANN) model was trained. The validation of the model was done through R2, RMSE, parity plot and residual analysis. An ANN that was trained was then applied to produce a continuous prediction space, and this facilitated multi-objective optimization via NSGA-II. TOPSIS was used to obtain pareto-optimal solutions and rank them to identify which operating condition is most balanced yielding the highest efficiency and minimum emissions.

V. RESULTS AND DISCUSSIONS

Baseline Engine Performance and Fuel Characterisation Performance of the Engine

The experimental results obtained from the test rig are presented to compare the performance of pure petrol, E20, and B20 blends under conventional and Mg-PSZ-coated piston configurations. During combustion, petrol hydrocarbons oxidize according to:

$$C_8H_{18} + 12.5O_2 \rightarrow 8CO_2 + 9H_2O$$

Similarly, ethanol undergoes complete oxidation as:

$$C_2H_5OH + 3O_2 \rightarrow 2CO_2 + 3H_2O$$

The presence of the hydroxyl group (–OH) in ethanol contributes additional oxygen, promoting more complete combustion of hydrocarbon fractions. Although ethanol improves octane rating and combustion completeness, its lower calorific value slightly reduces the overall energy content of the blend. Similarly, the idealized combustion of the petrol–butanol blend can be represented as:

$$0.8\,C_8H_{18} + 0.2\,C_4H_8O + 11.1\,O_2 \rightarrow 7.2\,CO_2 + 8.0\,H_2O.$$

The oxygenated structure enhances oxidation but marginally lowers energy density compared to neat petrol.

Gas Chromatographic Analysis

The gas chromatograms of pure petrol, E20, and B20 blends are shown in Fig. 6. Pure petrol presents several peaks which are related to light hydrocarbons and aromatic fractions. The E20 mixture has another sharp peak at about 0.8 min which is attributed to ethanol meaning that it is more volatile. The B20 mixture exhibits a different peak of 1.3 min that is associated with butanol which is less volatile when compared to ethanol. The total hydrocarbon profile is still to a great extent the same, which proves that there is no significant change in the base fuel composition and that it was blended successfully.

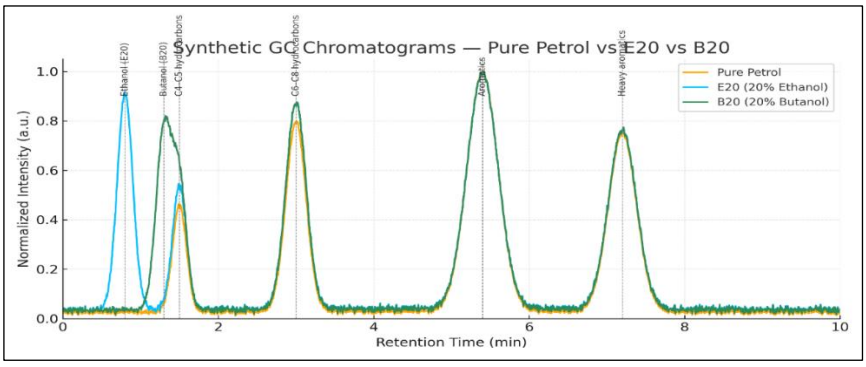


Figure 6: Gas Chromatography test for Pure petrol, E20 and B20.
Source: Authors, (2026).

FTIR Spectroscopic Analysis

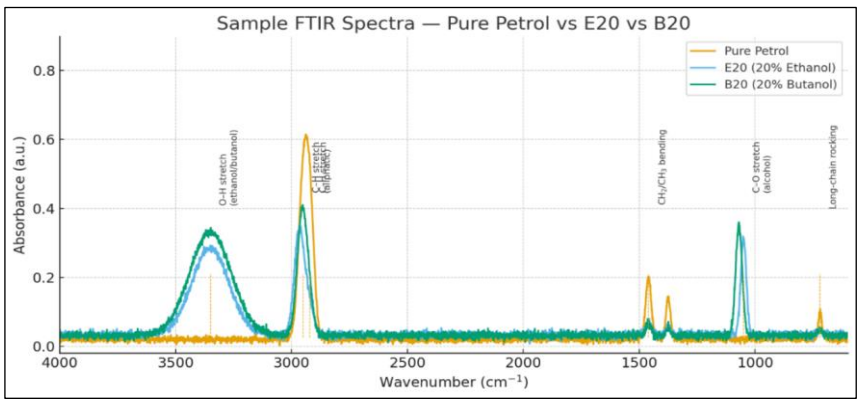


Figure 7: FTIR test for Pure petrol, E20 and B20.
Source: Authors, (2026).

The FTIR spectra of pure petrol, E20, and B20 in the 4000-600 cm-1 range are presented in Fig. 7. The pure petrol has typical characteristic C-H aliphatic stretching bands (2950-2925 cm-1). The presence of ethanol is indicated by the E20 blend which has a broad O-H stretch at 3350 cm-1 and a C-O peak at 1040 cm-1. In the same way, O-H absorption at 3350 cm-1 and C-O stretch at 1070 cm-1 are observed in B20. The formation of oxygenated functional groups affirms the successful incorporation of alcohols and the retention of the predominant hydrocarbon backbone.

Load vs Brake Power

Figure. 8 (a) indicates that all fuels have a positive relationship between the brake power and the load when uncoated. At full load gasoline gives the highest brake power as the calorific value of gasoline is higher. E20 is better than B20 in medium and high loads as the enrichment of oxygen increases the combustion efficiency.

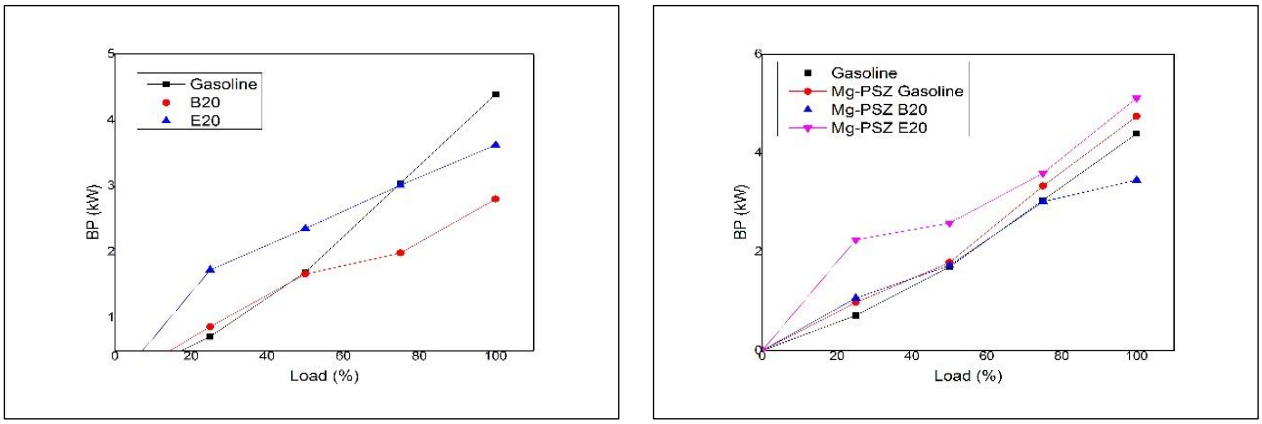


Figure (a): For Un-Coated piston. Figure (b): For Mg-PSZ-coated piston.

Figure 8: Load Vs Brake Power.
Source: Authors, (2026).

In Mg-PSZ-coated conditions (Fig. 7(b)) there is an improvement of brake power with all fuels. The coating minimizes the heat losses and raises the in-cylinder temperatures. Mg-PSZ + E20 gives the maximum brake power and B20 is also relatively lesser because of its low heating value.

Load vs Total Fuel Consumption (TFC)

Figure. 8 (a) shows that all fuels in the uncoated engine have a positive correlation between load and TFC. Gasoline is the lowest in TFC whereas B20 is the most consumed owing to lesser energy density.

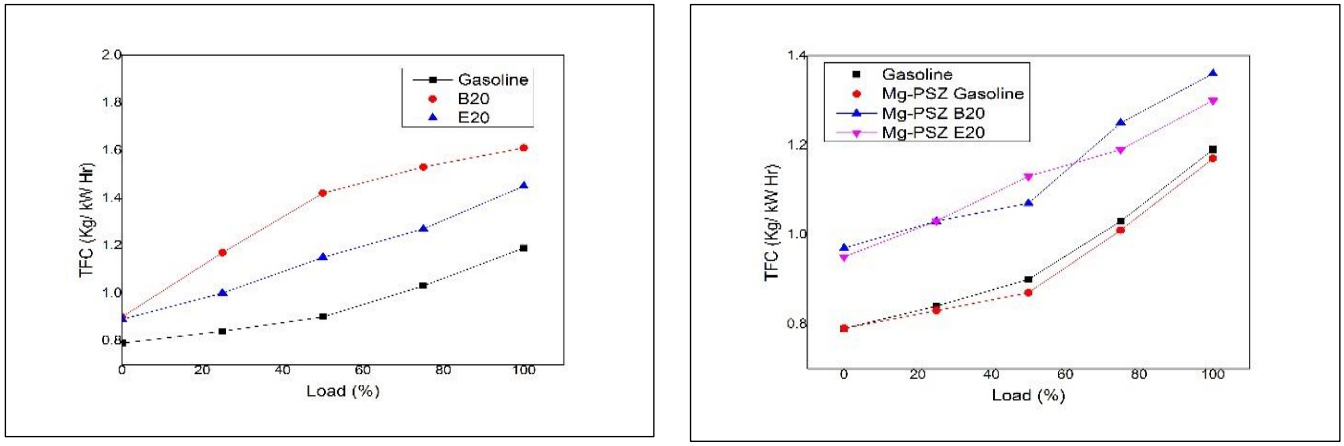


Figure (a): For Uncoated piston. Figure (b): For Mg-PSZ piston.

Figure. 9: Load Vs Total Fuel Consumption.
Source: Authors, (2026).

When coated with Mg-PSZ (Fig. 9(b)) TFC reduces at all conditions of load. An increase in thermal retention will also increase the efficiency of combustion and the use of fuel. Even though the oxygenated blends burn a little bit more fuel compared to gasoline, the coating counteracts this disparity.

Load vs Brake Thermal Efficiency (BTE)

Figure. 10 (a) indicates that E20 has a better BTE than gasoline and B20 in the uncoated engine owing to the improved combustion that is enhanced by oxygen. B20 has a little less efficiency.

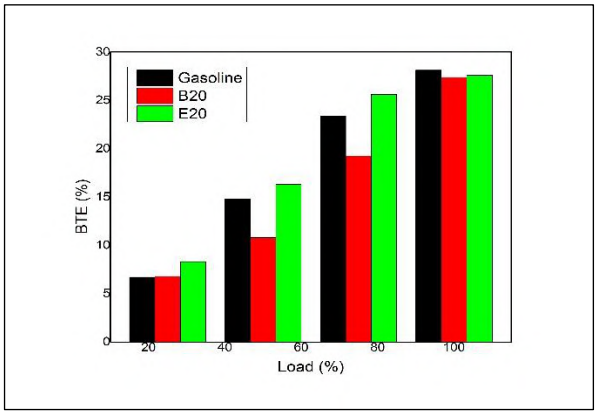


Figure (a): For Un coated piston.

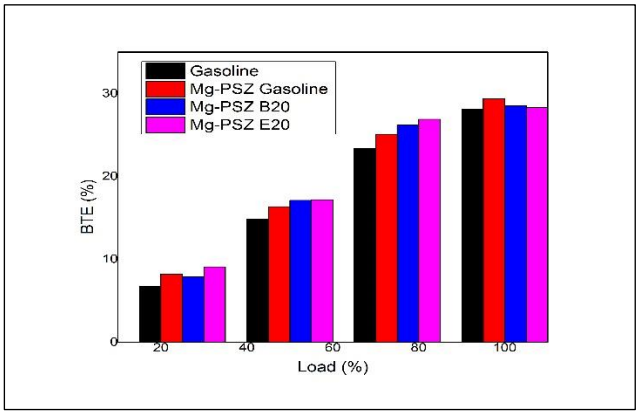


Figure (b): For Mg-PSZ-coated piston.

Figure 10: Load Vs η BTH.
Source: Authors, (2026).

Under Mg-PSZ coating (Fig. 9(b)) there is an increase of BTE of all fuels because of the reduced heat rejection. The coated E20 blend is most efficient when full loaded, which portrays the synergistic influence of oxygenated fuel and thermal insulation.

Load vs Hydrocarbon (HC) Emissions

Fig. 11 (a) indicates that the emissions of the gasoline are greater under the uncoated conditions. E20 and B20 lower HC because they enhance oxidation of fuel bound oxygen.

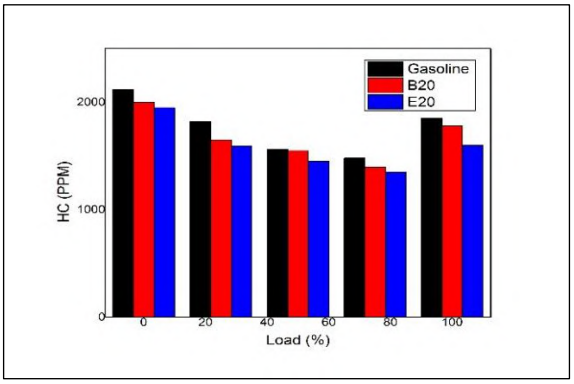


Figure (a): For Uncoated Piston.

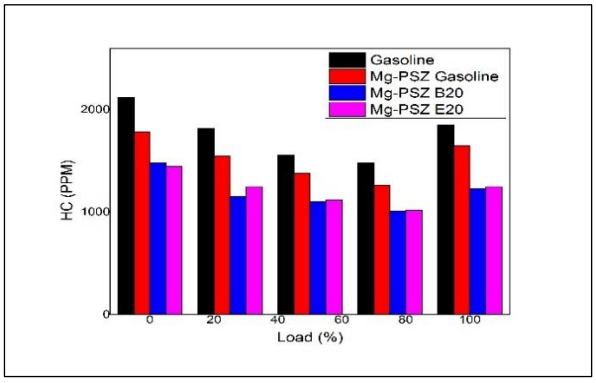


Figure (b): For Mg- PSZ coateed piston.

Figure 11: Load Vs HC.
Source: Authors, (2026).

Using Mg-PSZ coating (Fig. 10 (b)), the carbon monoxide emissions drop even further in all fuels due to high combustion temperature and better burning of the unburned hydrocarbons. The lowest HC emissions are recorded by Mg-PSZ + E20.

Load vs Carbon Monoxide (CO) Emissions

Figure. 12 (a) indicates that gasoline results in the best CO emissions in the uncoated conditions. Oxidated blends decrease the formation of CO as a result of better oxidation.

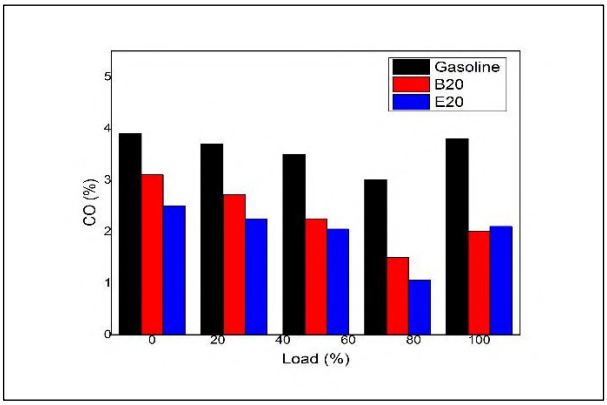


Figure (a): Uncoated Piston.

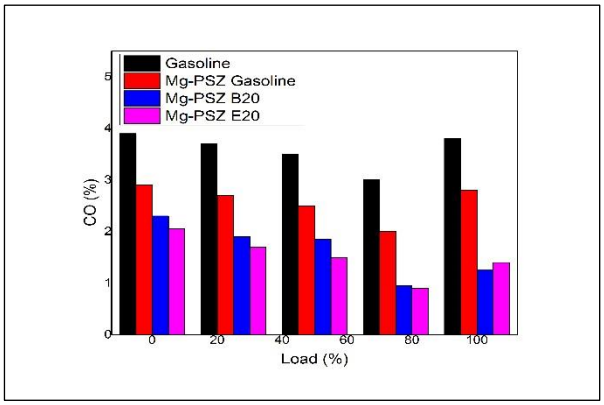


Figure (b): Mg- PSZ Coated piston.

Figure 12: Load Vs CO.
Source: Authors, (2026).

Emission of CO is reduced by a very large percentage with Mg-PSZ coating (Fig. 12 (b)) in all fuels since the better thermal insulation increases the oxidation rate of the CO to produce CO2. The E20 and B20 blends with coating have the lowest CO emissions.

Multi-Objective Optimization and Decision Analysis
ANN Model Validation

An Artificial Neural Network (ANN) was created to estimate the brake thermal efficiency (BTE), mechanical, hydrocarbon (HC), and carbon monoxide (CO) emissions as a function of piston type, fuel blend, and engine load. The coefficient of determination (R^2) and root mean square error (RMSE) were used to determine model performance. Table 10. Statistical performance parameters of the ANN model in predicting engine performance and emission parameters.

Table 10: Performance Metrics of the Developed ANN Model.

Output Parameter	R^2	RMSE
Brake Thermal Efficiency (BTE)	0.9996	0.2014
Mechanical Efficiency	0.9999	0.2548
Hydrocarbon Emission (HC)	0.9988	9.8408
Carbon Monoxide Emission (CO)	0.9209	0.2292

Source: Authors, (2026).

NSGA-II Pareto Optimisation

The ANN model has been validated and incorporated into the Non-dominated Sorting Genetic Algorithm II (NSGA-II) to undertake multi-objective optimization. The goals were outlined to be:

- Maximize BTE
- Maximize mechanical efficiency
- Minimize HC emissions
- Minimize CO emissions

NSGA-II produced a Pareto front that reflected the efficiency / emission properties trade off. The Pareto solutions depict how difficult it is to maximize thermal efficiency and minimize exhaust emissions.

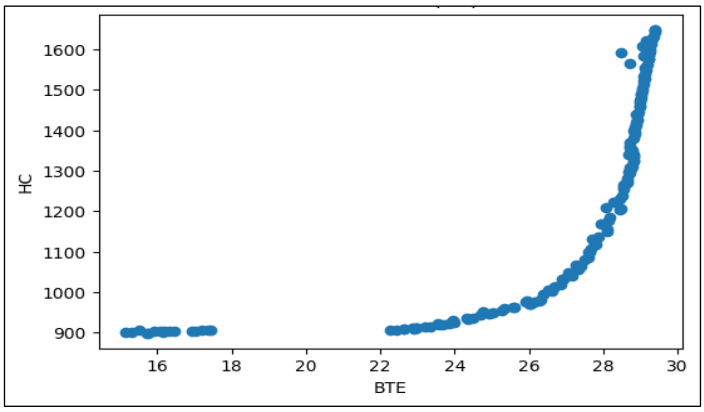


Figure 13 (a): 2D Pareto front plots.
Source: Authors, (2026).

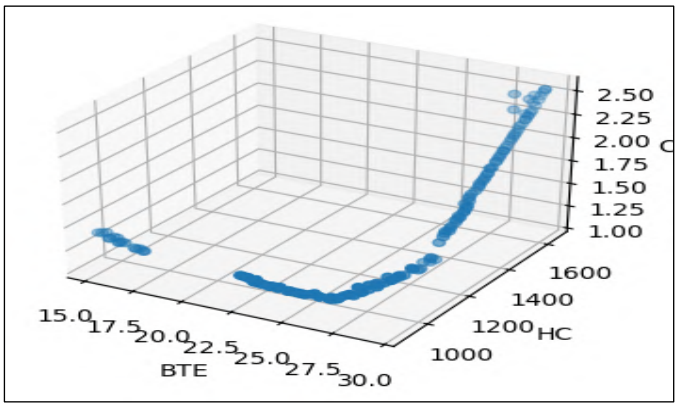


Figure 13: (b): 3D Pareto surface.
Source: Authors, (2026).

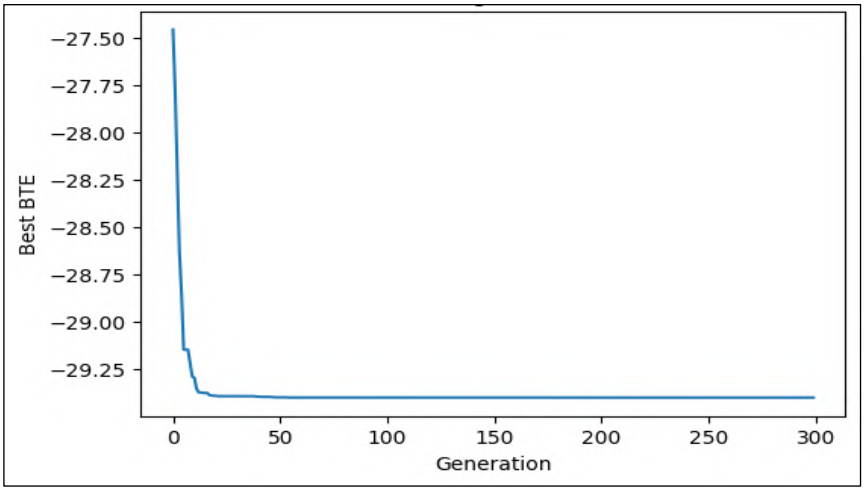


Figure 14: Convergence curve.
Source: Authors, (2026).

The Pareto analysis validates the fact that regions of greater efficiency are associated with the modest rise in the emissions levels, and a decision-making approach should be employed to find a compromise. Figures 13 and 14 show the results of the multi-objective optimization achieved with the help of the NSGA-II algorithm. Figure 13 shows the Pareto front, where the parameters of efficiency (BTE and mechanical efficiency) and the emissions (HC and CO) are maximized and minimized respectively. The allocation of non-dominated solutions proves that the conflict between performance enhancement and reduction of emissions is natural, which means that the changes in thermal efficiency can result in insignificant changes in the formation of pollutants. The convergence behaviour of the optimization process is depicted by figure 16 whereby the value of the objectives decreases with the increase in the generations, which proves that the algorithm converges to a consistent state and is able to accurately identify the optimal solution region.

TOPSIS-Based Optimal Solution Selection

In order to check the most balanced operating point, Technique of Order of Preference by Similarity to Ideal Solution (TOPSIS) was used on the Pareto-optimal set. Closeness coefficient was calculated on individual solutions and they were ranked according to the proximity of the solutions to the ideal point.
The solution arrived at is the best and it is:

- Piston type: 1 (Mg-PSZ coated)
- Fuel blend: 1.96 (approximately E20–B20 range)
- Load: 84.55%
- Closeness coefficient: 0.8156

The findings show that a coated piston that is running at and around high load with an oxygen blended fuel mixture is the one that provides the most appropriate compromise in terms of efficiency improvement and emissions reduction.

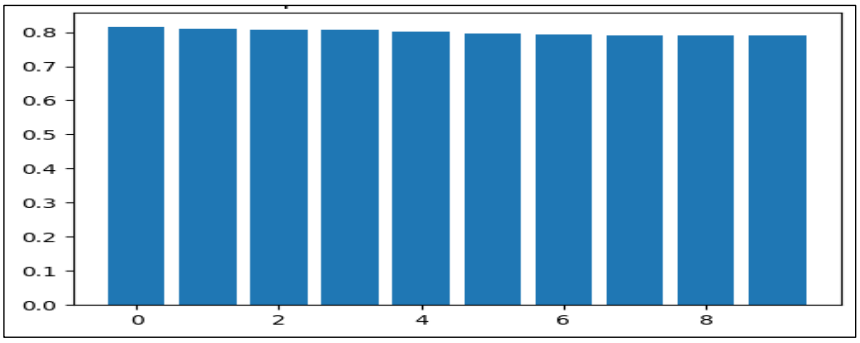


Figure 15: Closeness coefficient ranking bar chart.
Source: Authors, (2026).

The TOPSIS ranking of closeness coefficients of the Pareto-optimal solutions in NSGA-II are provided in Figure 15. The closeness coefficient is the relative closeness of each solution to the optimal point, i.e., the situation where maximum efficiency and minimum emissions are both attained. The greater the value of coefficient, the higher the overall performance-emission balance. The best solution has the closest value (0.8156), which proves its superiority with the candidate solutions. The ranking trend indicates a progressive trade-off behaviour, which confirms the usefulness of TOPSIS in making the most balanced operating condition among the Pareto frontier.

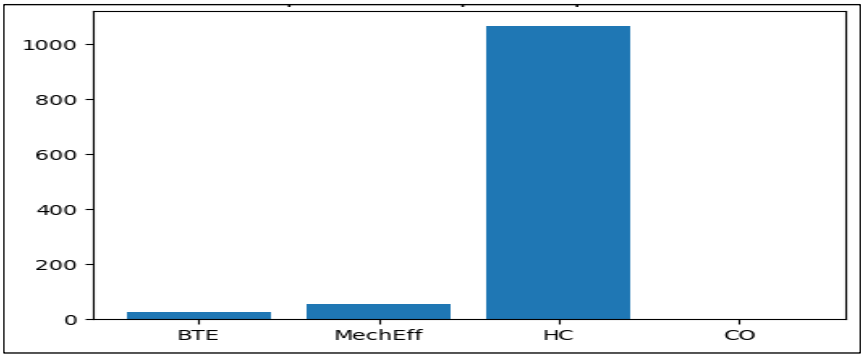


Figure 16: Radar comparison of baseline vs optimized condition.
Source: Authors, (2026).

Figure 16 has compared the experimental condition at the baseline with TOPSIS-optimized operating point of BTE, mechanical efficiency, HC, and CO emissions. The optimized result, which can be associated with the Mg-PSZ coated piston at high loads and oxygenated mixture, depicts a better thermal efficiency and lower emissions levels compared to the baseline one. The concurrent improvement of the efficiency parameters and the reduction of the pollutants formation is pointed out in the comparative visualization. This supports the usefulness of the combined ANN-NSGA-II-TOPSIS model to determine a balanced and performance-effective operating range.

VI. CONCLUSION

The current experiment was a controlled systematic assessment of the performing capabilities of a two-stroke spark-ignition engine and the overall emission characteristics of oxygenated fuel blends (E20 and B20) with Mg-PSZ thermal barrier coating. The results of the fuel characterization by the use of GC and FTIR confirmed the successful blending of the hydrocarbon backbone with the introduction of oxygenated functional groups successfully. The outcomes of the experiment showed that E20 enhanced brake thermal efficiency (BTE) by about 4-6 % over gasoline under uncoated conditions since it enhanced oxygen- assisted combustion. The greatest changes were however realized when Mg-PSZ coating was utilized. This coated configuration increased BTE by 5-8 %, decreased total fuel consumption by 3-6 percent and had massive reductions in emissions, including 12-18 percent lower hydrocarbon (HC) emission and 15-20 % lower carbon monoxide (CO) emission compared to the uncoated gasoline baseline.
Out of all the combinations that have been tested, the Mg-PSZ-coated piston with E20 showed the best overall performance-emission balance, especially at the higher load conditions. ANN modeling exhibited a high predictive performance (R 2 = 0.92-0.999), with the combined NSGA-II-TOPSIS optimization model establishing an optimum high-load coated operating condition with a closeness coefficient of 0.8156, which proved the existence of a strong trade-off between efficiency increase and emission decrease.

VII. AUTHOR'S CONTRIBUTION

Conceptualization: A.V.N.S Kiran, Arun Kumar Kurakula, H S Anantha Padmanabha, B Venkatesh.
Methodology: A.V.N.S Kiran, Arun Kumar Kurakula, H. S Anantha Padmanabha, B Venkatesh.
Investigation: A.V.N.S Kiran, Arun Kumar Kurakula, H. S Anantha Padmanabha, B Venkatesh.
Discussion of results: A.V.N.S Kiran, Arun Kumar Kurakula, H S Anantha Padmanabha, B Venkatesh.
Writing – Original Draft: A.V.N.S Kiran, Arun Kumar Kurakula, H S Anantha Padmanabha, B Venkatesh.
Writing – Review and Editing: A.V.N.S Kiran, Arun Kumar Kurakula, H S Anantha Padmanabha, B Venkatesh.
Resources: A.V.N.S Kiran, Arun Kumar Kurakula, H S Anantha Padmanabha, B Venkatesh.
Supervision: A.V.N.S Kiran, Arun Kumar Kurakula, H S Anantha Padmanabha, B Venkatesh.
Approval of the final text: A.V.N.S Kiran, Arun Kumar Kurakula, H S Anantha Padmanabha, B Venkatesh.

VIII. ACKNOWLEDGMENTS

The authors would like to express their sincere gratitude to the Department of Mechanical Engineering, Annamacharya University, Rajampeta, Annamaya Dist. A.P. for providing the experimental facilities required to carry out this research work. The authors also acknowledge the support extended by the collaborating institutions, including Siddhartha Institute of Engineering and Technology (Autonomous), Puttur, Tirupati Dist. PVKK Institute of Technology (Autonomous), Rudrampeta, Anantapuram, Anantapuranamu Dist. and SVU College of Engineering, SV University, Tirupati, Tirupati Dist., for their valuable academic guidance and technical assistance throughout the study.

IX. REFERENCES

[1] Vishwanath S. Godiganur, Shiavananda Nayaka, G.N. Kumar, "Thermal barrier coating for diesel engine application – A review", Materials Today: Proceedings, Volume 45, Part 1, Pages 133-137, 2021, ISSN 2214-7853, https://doi.org/10.1016/j.matpr.2020.10.112.

[2] Shailesh Dhomne, Ashish M. Mahalle, "Thermal barrier coating materials for SI engine", Journal of Materials Research and Technology, Volume 8, Issue 1, 2019, Pages 1532-1537, ISSN 2238-7854, https://doi.org/10.1016/j.jmrt.2018.08.002.

[3] Nilesh Chauhan, Kamlesh Chauhan, "Thermal barrier coating system for Internal Combustion Engine application-A review", IOP Conference Series: Materials Science and Engineering, 2020, ISSN 1757-8981 https://dx.doi.org/10.1088/1757-899X/872/1/012086.

[4] Imdat Taymaz, "The effect of thermal barrier coatings on diesel engine performance", Surface and Coatings Technology, Volume 201, Issues 9–11, 2007, Pages 5249-5252, ISSN 0257-8972, https://doi.org/10.1016/j.surfcoat.2006.07.123.

[5] Li, Wenbin & Armani, Amir & McMillen, Devin & Leu, Ming & Hilmas, Gregory & Watts, Jeremy, "Properties of partially stabilized zirconia components fabricated by the ceramic on-demand extrusion process". Solid Freeform Fabrication 2016: Proceedings of the 27th Annual International.

[6] da Silva, A.O., Fiorin, L., Faria, A.C.L. et al. "Translucency and mechanical behaviour of partially stabilized monolithic zirconia after staining, finishing procedures and artificial ageing", Sci Rep **12**, 16094 (2022). https://doi.org/10.1038/s41598-022-20120-y.

[7] Darmawan, Bobby Aditya, John G. Fisher, Doan Thanh Trung, Kumaresan Sakthiabirami, and Sang-Won Park, "Two-Step Sintering of Partially Stabilized Zirconia for Applications in Ceramic Crowns", 2020, Materials 13, no. 8: 1857. https://doi.org/10.3390/ma13081857.

[8] Prakhar Chansauria, R.K. Mandloi, "Effects of Ethanol Blends on Performance of Spark Ignition Engine-A Review", Materials Today: Proceedings, Volume 5, Issue 2, Part 1, 2018, Pages 4066-4077, ISSN 2214-7853, https://doi.org/10.1016/j.matpr.2017.11.668.

[9] Li-hong, Yao & Yan, Gao & Wen-bin, Li & Jiang, Wu, "Effects of the Mixture Fuel of Ethanol and Gasoline on Two-Stroke Engine", 2010. https://doi.org/10.1109/ICICTA.2010.29.

[10] Kirthivasan, A., J. Amitesh Jain, Akhilnandh Ramesh and D. Ebenezer. "Effect of Ethanol on the Fuel Consumption of a Two Stroke Unmodified Commercial Petrol Engine." *Applied Mechanics and Materials* 787 (2015): 756 - 760. DOI:10.4028/www.scientific.net/AMM.787.756.

[11] Isam E. Yousif, Adel Mahmoud Saleh, "Butanol-gasoline blends impact on performance and exhaust emissions of a four stroke spark ignition engine", Case Studies in Thermal Engineering, Volume 41, 2023, 102612, ISSN 2214-157X, https://doi.org/10.1016/j.csite.2022.102612.

[12] Huynh, T.T., Le, M.D. & Duong, D.N. "Effects of butanol–gasoline blends on SI engine performance, fuel consumption, and emission characteristics at partial engine speeds". *Int J Energy Environ Eng* **10**, 483–492 (2019). https://doi.org/10.1007/s40095-019-0309-9.

[13] Sandu C, Pana C, Negurescu N, Lazaroiu G, Cernat A, Georgescu R, Nutu C. The Influence of N-Butanol Addition in Gasoline on the Combustion in the Spark Ignition Engine. *Sustainability*. 2023; 15(18):14009. https://doi.org/10.3390/su151814009.

[14] Liu H, Wang X, Zhang D, Dong F, Liu X, Yang Y, Huang H, Wang Y, Wang Q, Zheng Z. Investigation on Blending Effects of Gasoline Fuel with N-Butanol, DMF, and Ethanol on the Fuel Consumption and Harmful Emissions in a GDI Vehicle. *Energies*. 2019; 12(10):1845. https://doi.org/10.3390/en12101845.

[15]. B.M. Masum, H.H. Masjuki, M.A. Kalam, I.M. Rizwanul Fattah, S.M. Palash, M.J. Abedin. “Effect of ethanol–gasoline blend on NOx emission in SI engine, Renewable and Sustainable Energy Reviews”, 2013, Volume 24, 209-222, https://doi.org/10.1016/j.rser.2013.03.046.

[16] Arunkumar Munimathan, Silambarasan Rajendran, Karthik Raju, “Exhaust gas recirculation in a compression-ignition engine with nano-coated Al2O3-TiO2 and ethanol fuel”, Results in Engineering, Volume 20, 2023, 101414, ISSN 2590-1230, https://doi.org/10.1016/j.rineng.2023.101414.

[17] Kiran A.V.N.S., Santosh Kumar B., Loknath M., Saleemuddin S.M., Nagendra S. “Experimental studies on two stroke SI engine by using novel piston and gasoline blends”, Journal Européen des Systemes Automatises, (2019), Vol. 52, No. 1, pp. 11-15. https://doi.org/10.18280/jesa.520102.

[18] Omar I. Awad, Bo Zhou, Zhenbin Chen, Kumaran Kadirgama, M.N. Mohammed, D. Ramasamy, “Influence of PODE1 additive into ethanol-gasoline blends (E10) on fuel properties and phase stability”, Heliyon, Volume 9, Issue 11, 2023, e22364, ISSN 2405-8440, https://doi.org/10.1016/j.heliyon.2023.e22364.

[19] Kolesinska B, Fraczyk J, Binczarski M, Modelska M, Berlowska J, Dziugan P, Antolak H, Kaminski ZJ, Witonska IA, Kregiel D. Butanol Synthesis Routes for Biofuel Production: Trends and Perspectives *Materials*. 2019; 12(3):350. https://doi.org/10.3390/ma12030350.

[20] Edward M Green, “Fermentative production of butanol—the industrial perspective”, Current Opinion in Biotechnology, Volume 22, Issue 3, 2011, Pages 337-343, ISSN 0958-1669, https://doi.org/10.1016/j.copbio.2011.02.004.

[21] Singh, Suraj Bhan, Atul Dhar, and Avinash Kumar Agarwal. "Technical feasibility study of butanol–gasoline blends for powering medium-duty transportation spark ignition engine." *Renewable Energy* 76 (2015): 706-716.

[22] Chao Jin, Mingfa Yao, Haifeng Liu, Chia-fon F. Lee, Jing Ji, “Progress in the production and application of n-butanol as a biofuel”, Renewable and Sustainable Energy Reviews, Volume 15, Issue 8, 2011, Pages 4080-4106, ISSN 1364-0321, https://doi.org/10.1016/j.rser.2011.06.001.

[23] B. V. Lande, A. B.tupkar . Experimental Investigation of using Ethanol Petrol Blends in 2-Stroke SI Engines. International Conference on Benchmarks in Engineering Science and Technology 2012. ICBEST, 4 (October 2012), 7-10.

[24] Yusuf, D.; Maryani, E.; Mardhian, D.F.; Noviyanti, A.R. Evaluation of Structural Stability, Mechanical Properties, and Corrosion Resistance of Magnesia Partially Stabilized Zirconia (Mg-PSZ). Molecules 2023, 28, 6054. https://doi.org/10.3390/molecules28166054.

[25] Wijayanti, R.B.; Rosmayanti, I.; Wahyudi, K.; Maryani, E.; Hernawan, H.; Septawendar, R. Preparation of Magnesia Partially Stabilized Zirconia Nanomaterials from Zirconium Hydroxide and Magnesium Carbonate Precursors Using PEG as a Template. Crystals 2021, 11, 635. https://doi.org/10.3390/crystals.1060635.

[26] Tadeusz Hejwowski, Comparative study of thermal barrier coatings for internal combustion engine, Vacuum, Volume 85, Issue 5, 2010, Pages 610-616, ISSN 0042-207X, https://doi.org/10.1016/j.vacuum.2010.08.020.

[27]. HORNIG, T. (2004). Smithells Metals Reference Book Volume 187 ‖ Vapour deposited coatings and thermal spraying. , (), 1–16. https://doi.org/10.1016/b978-075067509-3/50038-5.

[28] Bakan, E., Vaßen, R. Ceramic Top Coats of Plasma-Sprayed Thermal Barrier Coatings: Materials, Processes, and Properties. J Therm Spray Tech **26**, 992–1010 (2017). https://doi.org/10.1007/s11666-017-0597-7.

[29] M N Baig and F A Khalid, 2014 IOP Conf. Ser.: Mater. Sci. Eng. **60** 012053, https://doi.org/10.1088/1757-899X/60/1/012053.
[30] Heimann, R.B. The Nature of Plasma Spraying. Coatings 2023, 13, 622. https://doi.org/10.3390/coatings.13030622.

[31] Prasad, P. R., Rama Rao, K. S., Bhuvaneswari, K., Praveena, N., & Srikanth, Y. V. V. (2008). Determination of Ethanol in Blend Petrol by Gas Chromatography and Fourier Transform Infrared Spectroscopy. Energy Sources, Part A: Recovery, Utilization, and Environmental Effects, 30(16), 1534–1539. https://doi.org/10.1080/15567030701258444.

[32] Zhang, Fan, et al. “Research on Unregulated Emissions from an Alcohols-Gasoline Blend Vehicle Using FTIR, HPLC and GC-MS Measuring Methods.” SAE International Journal of Engines, vol. 6, no. 2, 2013, pp. 1126–37. JSTOR, https://doi.org/www.jstor.org/stable/26277687.

[33] Sudipto Debnath, Manosi Das, Susmita Mondal, Biresh K. Sarkar & Gajji Babu (2025) Advances in chromatography: contemporary techniques and applications, Essential Chem, 2:1, 1-27, https://doi.org/10.1080/28378083.2025.2466624.

[34] XIA, Qi, Lei-ming YUAN, Xiaojing CHEN, Liuwei MENG, and Guangzao HUANG. 2019. "Analysis of Methanol Gasoline by ATR-FT-IR Spectroscopy" Applied Sciences 9, no. 24: 5336. https://doi.org/10.3390/app9245336.

[35] J. Lalramnghaka, H. H. Thanga & Lal Biaktluanga (2022): Evaluation of gasoline fuel quality using FTIR spectroscopy and multivariate technique: a case study in Aizawl city, Petroleum Science and Technology, https://doi.org/10.1080/10916466.2022.2091596.

[36] Balogun, F.; Wang-Alho, H.; Sirviö, K.; Mikulski, M. FTIR Analysis for Determining Stability of Methanol–HVO Blends for Non-Road Engine Application. Energies 2024, 17, 3921. https://doi.org/10.3390/en17163921.

[37] Anupama Vijayan, John Prakash, Probe-based spectrophotometric quantification of petrol-ethanol fuel blends for field-able applications, Green Analytical Chemistry, Volume 3, 2022, 100043, ISSN 2772-5774, https://doi.org/10.1016/j.greeac.2022.100043.

[38] Stella Corsetti, Florian M. Zehentbauer, David McGloin, Johannes Kiefer, Characterization of gasoline/ethanol blends by infrared and excess infrared spectroscopy, Fuel, Volume 141, 2015, Pages 136-142, ISSN 0016-2361, https://doi.org/10.1016/j.fuel.2014.10.025.

Journal of Engineering and Technology for Industrial Applications

ISSN ONLINE: 2447-0228

ITEGAM-JETIA

Manaus, v.12 n.60, p.974-985 July/August, 2026.
DOI: https://doi.org/10.5935/jetia.v12i60.3912

RESEARCH ARTICLE OPEN ACCESS

IMPACT OF GEOMETRICAL PARAMETERS ON FATIGUE LIFE CYCLE OF COMPLIANT MECHANISM

Sandesh Solepatil*[1], Narendra Deore[2]

[1]Department of Mechanical Engineering, Technology and Engineering, D Y Patil International Univerisity, Akurdi, Pune, India.
[2]Department of Mechanical Engineering, Pimpri Chicnhwad College of Engineering, Akurdi, Pune, India.

[1]http://orcid.org/0000-0002-8005-4994, [2]http://orcid.org/0000-0003-4710-3798

E-mail: *sandeshpatil310@gmail.com, narendra.deore@pccoepune.org

ARTICLE INFO

Article History
Received on: March 05, 2026
Reviewed on: April 05, 2026
Accepted on: July 01, 2026
Published on: July 31, 2026

Keywords:
Compliant Mechanism, Fatigue Life Cycle,
Damage,
Safety Fator
Square Motion Stage With Curve Beam,
Circular Motion Stage With Curve Beam.

ABSTRACT

Compliant mechanisms, which derive motion through the elastic deformation of flexible members, offer distinct advantages over traditional mechanisms, including reduced part count, enhanced reliability, and smooth, frictionless operation. However, their fatigue life is a critical design concern due to the continuous cyclic stresses endured during operation. The fatigue performance of these mechanisms is strongly influenced by a combination of material properties, geometrical design, and loading conditions. Among these, geometrical parameters—particularly the radius of curvature—play a crucial role in determining stress concentration and overall durability. This study focuses on analyzing the impact of the radius of curvature on the fatigue life of compliant mechanisms using Finite Element Analysis (FEA). Four different configure rations of square and circular motion stages with varying curvature radii were evaluated under constant loading conditions. The analysis considered key parameters such as damage factor, safety factor, and fatigue life cycles. Results indicate that increasing the radius of curvature significantly improves fatigue resistance by distributing stress more evenly and reducing critical stress concentrations. The findings suggest that appropriate geometric optimization, especially in curved beam regions, can substantially enhance the life span and safety of compliant mechanisms without compromising their function. These insights are particularly beneficial for the design of mechanisms in applications requiring high precision and longevity, such as biomedical devices, micro-positioning systems, and additive manufacturing equipment. This research contributes valuable design guidelines for enhancing the fatigue performance and operational reliability of compliant mechanisms.

Copyright ©2026 by authors and Galileo Institute of Technology and Education of the Amazon (ITEGAM). This work is licensed under the Creative Commons Attribution International License (CC BY 4.0).

I. INTRODUCTION

Fatigue refers to the progressive and localized structural damage that occurs when a material is subjected to cyclic loading. Over time, repeated deformation induces microscopic defects and cracks that grow, ultimately leading to failure. In compliant mechanisms, the primary source of fatigue arises from the cyclic bending, stretching, or twisting of flexural elements, often concentrated in areas of high stress or strain. The prediction and mitigation of fatigue failure are therefore critical for extending the service life of these mechanisms, particularly in applications requiring millions or billions of load cycles. The fatigue life of a compliant mechanism depends on several factors, including material properties, geometric design, stress distribution, and environmental conditions. Materials such as metals, polymers, and composites exhibit varying fatigue characteristics, influenced by their elastic limits, crack propagation resistance, and thermal stability. The geometry of the mechanism, particularly the radii of curved segments, fillets, and transitions between flexible and rigid regions, plays a crucial role in stress concentration and fatigue initiation. Compliant mechanisms have revolutionized modern engineering by leveraging the elastic deformation of materials to achieve motion and force transmission without the need for traditional joints or hinges. This innovative design approach leads to mechanisms that are often lighter, more compact, and capable of smoother and more precise movements compared to their rigid-body counterparts [1].

Applications of compliant mechanisms span a wide range of fields, including aerospace, robotics, biomedical devices, and microelectromechanical systems (MEMS) [2] Despite their numerous advantages, compliant mechanisms are subject to continuous and repetitive deformation, which exposes them to fatigue. Fatigue, defined as the progressive and localized structural damage that occurs when a material is subjected to cyclic loading, is a critical concern for the longevity and reliability of these mechanisms [3-5] Understanding and predicting the fatigue life of compliant mechanisms is essential to prevent unexpected failures and to ensure their safe and effective operation over time. Fatigue analysis involves studying how materials respond to cyclic loading and identifying the conditions under which they are likely to fail. For compliant mechanisms, this analysis is particularly important due to their reliance on material flexibility and continuous deformation [6] Unlike traditional mechanisms, where fatigue may primarily occur at discrete joints or moving parts, compliant mechanisms experience distributed stress and strain throughout their structure. This makes fatigue analysis more complex and necessitates a detailed understanding of material behavior, stress distribution, and crack propagation [7-11] Compliant mechanisms can be broadly classified into two categories based on their primary mode of deformation:

- **Linear Compliant Mechanisms**: These mechanisms achieve straight-line motion through bending or stretching. Examples include flexural beams and bistable springs.
- **Rotational Compliant Mechanisms**: These mechanisms enable rotational motion through flexural pivots or torsion. Examples include flexural hinges and rotational springs [12-14].

Both types of mechanisms offer unique advantages and challenges in terms of fatigue analysis. Linear mechanisms often encounter issues related to bending fatigue, while rotational mechanisms may experience torsional fatigue. Additionally, the geometry and material properties of compliant mechanisms play significant roles in determining their fatigue behavior. Material properties, geometric properties, and the combination of the components greatly influence the compliant mechanism and its performance. Stiffness, bending stress, beam deflection, and degree of freedom govern the Compliant Mechanism's various series and parallel beam arrangements. In contrast, payload capacity and resonance frequency decide the compliant mechanism actuation. Many researchers have worked on the range of motion with different arrangements of beams, degrees of freedom, and actuation positions to get micro and nano ranges of motion with compliant mechanisms. Translational and rotational positioning systems are mainly used to achieve linear and rotational motion with various combinations of beams and hinges. A translational positioning mechanism provides a range of motion in X and Y directions. A serial-parallel kinematic chain is used in X-Y-compliant mechanisms to provide high load capacity, low inertia, and high resonant frequency [15] by maintaining accuracy, precision, and frictionless motion.

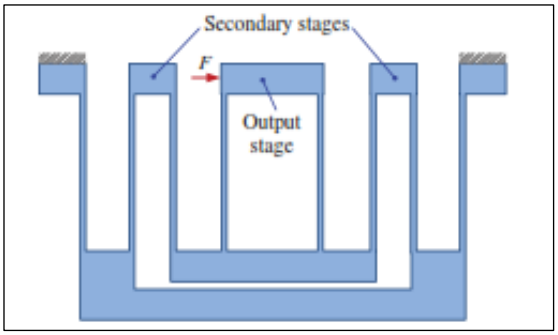


Figure 1: Translational positioning System.
Source: (15).

A Schematic of the parallel beam position is shown in Figure. 1 in which the translational motion stage is used to achieve single-directional displacement by applying actuating force on the vertical parallel beam. Figure. 2 demonstrates the combination of parallel beams stacked in two modules, wherein the second module rests on the first module, in laser sintering application for desired compliant values [15] In this mechanism, the output motion is guided by a double parallel flexural manipulator used in combination located at the corners of the module. The second module is mounted orthogonally on the top of the first module to get a parallel kinematic and stacked structure. This modular design allows the cost reduction in both manufacturing and maintenance. When driven by the Voice coil actuator, four double parallel flexural manipulators on the top and two double parallel flexural manipulators at the bottom guide the motion along X and similarly for the motion along y direction. Hence, a decoupled two-dimensional translation is achieved by the XY stage to obtain the travel range of 10 mm [16].

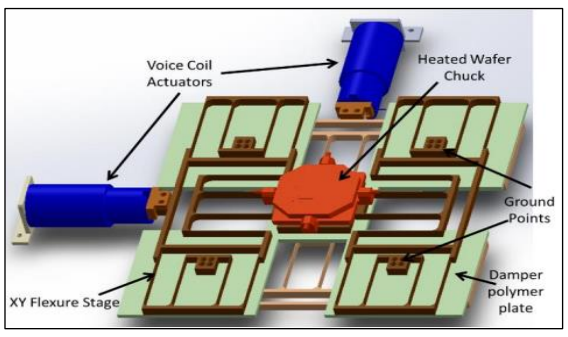


Figure 2: Selective laser sintering system.
Source: (16).

Rotational Movement in a compliant mechanism is achieved with a combination of beams, hinges, and radial flexures, as shown in Figure. 3. The relative motion between hinges and flexures leads to the desired compliant values due to actuating forces applied in compliant mechanisms [17] Radial flexure needs to be developed with a larger beam length of up to 100 mm, a larger outer radius of up to 10 mm, and a smaller thickness of up to 0.3 mm to achieve the desired rotational range [18].

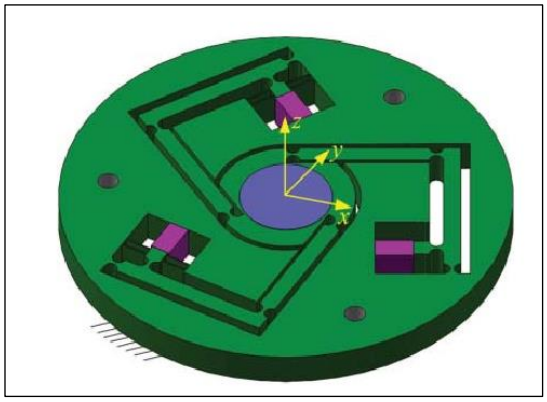


Figure 3: Rotational positioning System
Source: (16).

However, in practice, the compactness, restriction, manufacturing tolerance, and minimum stiffness criterion limit these geometrical parameters [19].

Challenges in Fatigue Analysis

Several challenges arise when analyzing the fatigue of compliant mechanisms. The primary challenges include:

1. **Material Selection**: The choice of materials significantly influences the fatigue life of compliant mechanisms. Materials commonly used in these mechanisms include metals, polymers, and composites, each with distinct fatigue characteristics [20].
2. **Stress Concentration**: The design of compliant mechanisms must account for stress concentration points, such as sharp corners or notches, which can significantly reduce fatigue life.
3. **Crack Initiation and Propagation**: Understanding where and how cracks initiate and propagate under cyclic loading is crucial for predicting the lifespan of compliant mechanisms.

Combined linear and rotational compliant mechanism is designed for biomedical applications requiring the linear range of motion from 2 mm to 4 mm in X and Y directions and rotational motion from 2° to 4°. These compliance values are achieved with various beams, hinges, and notches arrangements [21-25].

II. METHODOLOGY

Compliant mechanism is analyzed for actuating force of 80N which is the maximum load carrying capacity of PLA material. 4 Different conFigureurations of mechanisms are developed for analyzing the effect of geometrical parameters on fatigue life cycle of compliant mechanism as follows:

Mechanism 1- Square motion stage with curve beam of 32mm

Mechanism 2- Square motion stage with curve beam of 40mm

Mechanism 3- Circular motion stage with curve beam of 32mm

Mechanism 4- Circular motion stage with curve beam of 40mm

Mechanism 1 and 2 - Square motion stage with curve beam of 32 mm and 40 mm

Compliant mechanism 1 is developed with the dimensions of (Length *width *height) 300mm*300mm*15mm . Motion stage is of 50 mm. beam thickness of mechanism is 2mm. Overall dimensions of mechanism is shown in Figure. 4. In this mechanism force is apply on Y direction and displacement of mechanism will occur in X direction. Elements of mechanism are as shown in Figure. 5. Radius of curvature of beam is 32 mm as shown in Figure. 6 and Radius of curvature of beam is 40 mm as shown in Figure. 7 is used to analyze the impact of actuating force on fatigue life cycle with variation in radius of curvature of beam.

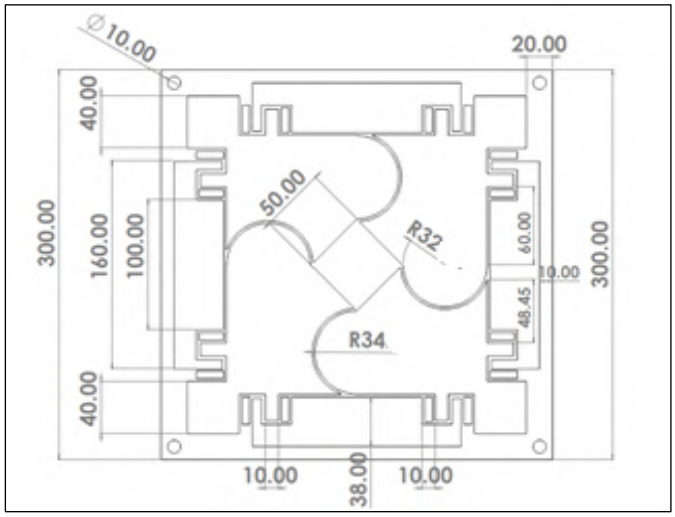


Figure 4: (A) Compliant mechanism with Square motion stage with beam radius 32mm (Mechanism 1).
Source: Authors, (2026).

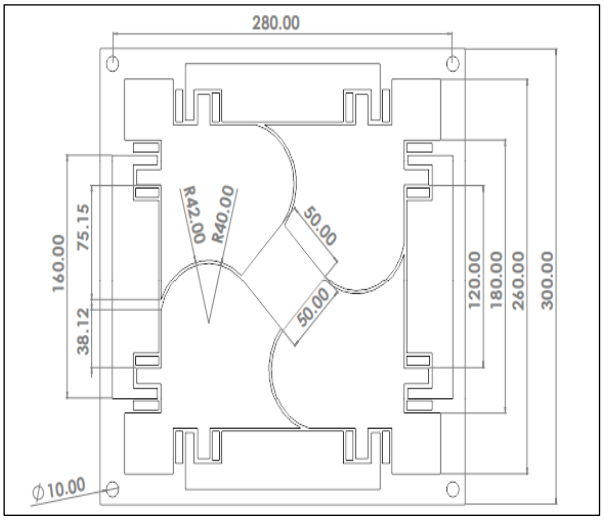


Figure 4 (B): Compliant mechanism with Square motion stage with beam radius 40mm (Mechanism 2).
Source: Authors, (2026).

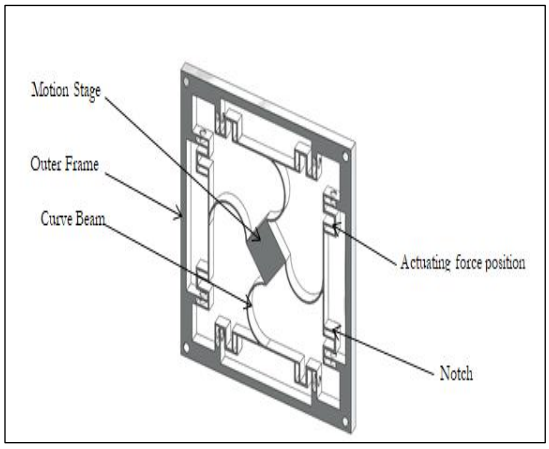


Figure. 5: Elements of Compliant mechanism with Square motion stage.
Source: Authors, (2026).

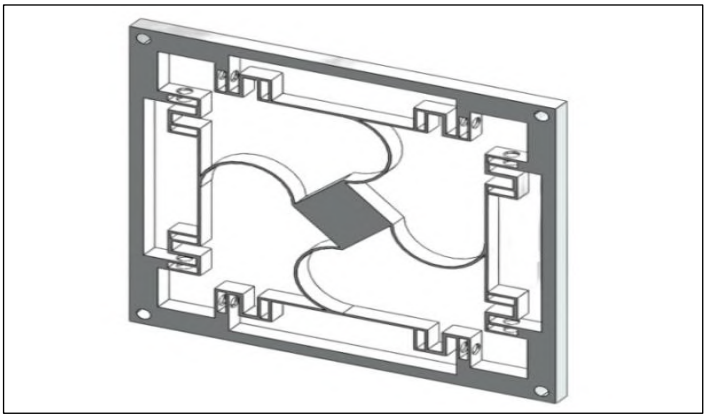


Figure 6: Square motion stage with curve beam radius 32 mm (Mechanism 1).
Source: Authors, (2026).

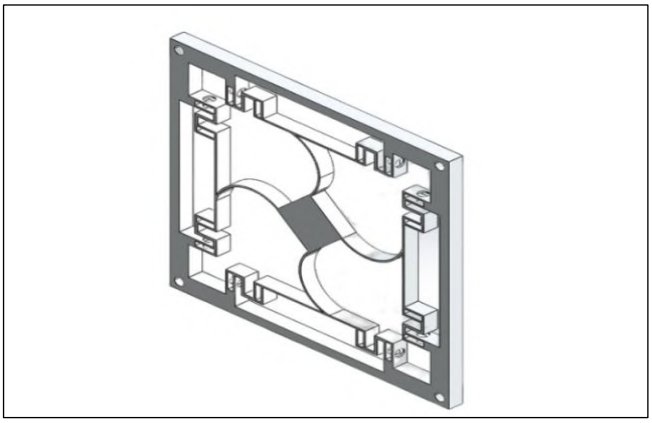


Figure 7: Square motion stage with curve beam radius 40 mm (Mechanism 2).
Source: Authors, (2026).

Mechanism 3 and 4- Circular stage with curve beam of 32 mm and 40 mm

Compliant mechanism is developed with the dimensions of (Length *width *height) 300mm*300mm*15mm . Motion stage is of 50mm. beam thickness of mechanism is 2mm. radius of curvature of beam is 32 mm. In this mechanism force is apply on Y direction and displacement of mechanism will occur in X direction. To evaluate fatigue life cycle actuating force of 80 N is used for mechanism. Radius of curvature of beam is 32 mm as shown in Figure. 8 and Radius of curvature of beam is 40 mm as shown in Figure. 9 is used to analyze the impact of actuating force on fatigue life cycle variation in radius of curvature of beam.

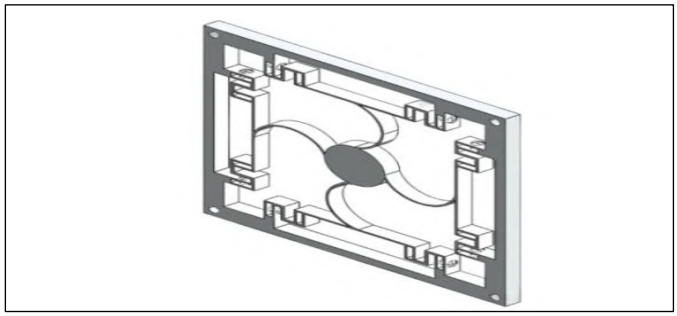


Figure 8: Circular motion stage with curve beam radius 32 mm (Mechanism 3).
Source: Authors, (2026).

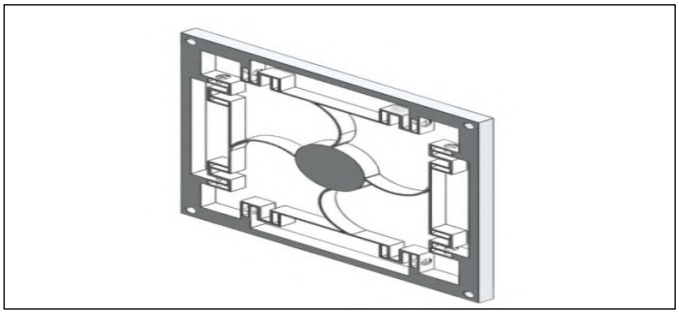


Figure 9: Circular motion stage with curve beam radius 40 mm (Mechanism 4).
Source: Authors, (2026).

Material

Polylactic Acid (PLA) is a biodegradable thermoplastic derived from renewable resources such as corn starch or sugarcane. It is widely used in 3D printing and various applications where its properties make it suitable for compliant mechanisms. When analyzing the fatigue behavior of compliant mechanisms made from PLA, several key material properties and considerations are relevant. Material properties of PLA are shown in Table 1. This values are taken from Tensile test of PLA Specimen with ASTME8 standard.

Table 1: Material Properties of PLA.

Sr.No	Content	Values
1.	Youngs Modulus	3986Mpa
2.	Ultimate Tensile strength	59 Mpa
3.	Poissons ratio	0.33
4.	Bulk Modulus	3907 Mpa
5.	Shear Modulus	1498 Mpa

Source: Authors, (2026).

Effect of geometrical parameters on fatigue life cycle of compliant mechanism

Fatigue analysis of a compliant mechanism involves evaluating the predicting the life of a component subjected to cyclic loading. The compliant mechanism is analyzed based on the stress-life (S-N) curve and the stress range at various points of the component. The material properties, loading conditions, and geometry of the mechanism are considered in the analysis. The fatigue life is estimated based on the number of cycles required to cause failure, taking into account the size and location of any cracks that may form. The results of the fatigue analysis are used to design components that can withstand the expected load cycles, ensuring that they will perform their intended function over their intended lifespan. This table 2 provides a comprehensive overview of the settings and parameters used in a fatigue analysis. The analysis is based on time, considers zero-based loading, and uses the Goodman mean stress theory. The fatigue strength factor is set to 1, indicating nominal strength is used. Results are displayed at the end of the analysis period, and the fatigue life is measured in cycles, with one cycle being equal to one actual cycle. The analysis type is stress-life, using the signed von-Mises stress component to evaluate fatigue life. Ansys 21 used for Numerical analysis of compliant mechanism.

Table 2: Input Parameters for Fatigue Analysis.

Object Name	Fatigue Tool
State	Solved
Domain	
Domain Type	Time
Materials	
Fatigue Strength Factor (Kf)	1.
Loading	
Type	Zero-Based
Scale Factor	1.
Definitin	
Display Time	End Time
Options	
Analysis Type	Stress Life
Mean Stress Theory	Goodman
Stress Component	Signed von-Mises
LifeUnits	
Units Name	cycles
1 cycle is equal to	1. cycles

Source: Authors, (2026).

III. RESULT AND DISCUSSION

Fatigue analysis of Square motion stage with curve beam of 32 mm (Mechanism 1)

Square motion stage with curve beam 1 is having dimension of 300*300*15 mm with curve beam radius of 32mm. Fatigue analysis of square motion stage is analyzed for 80N force. Force is applied at notch as shown in Figure. 10. Mechanism 1 is having meshing with 605938 nodes and 391526 triangular elements as shown in Figure. 11.

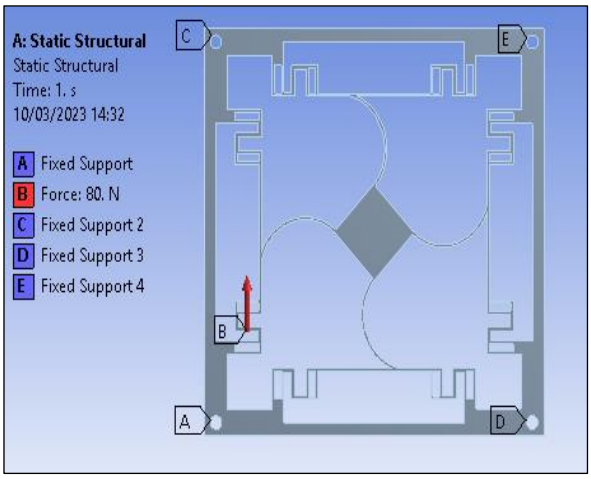


Figure 10: Boundary Conditions of Mechanism 1 for fatigue analysis.
Source: Authors, (2026).

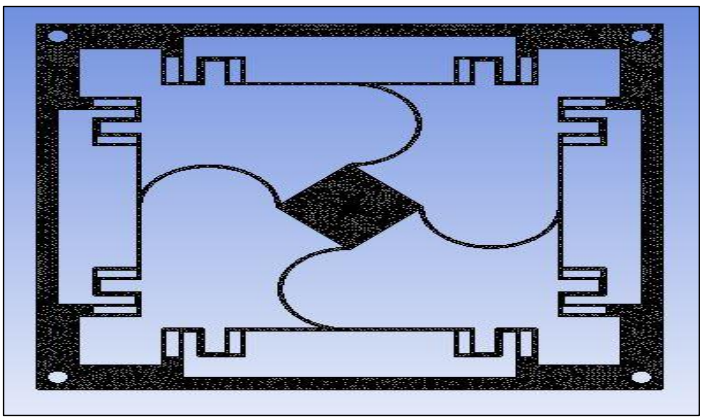


Figure. 11: Meshing of Mechanism 1 for fatigue analysis.
Source: Authors, (2026).

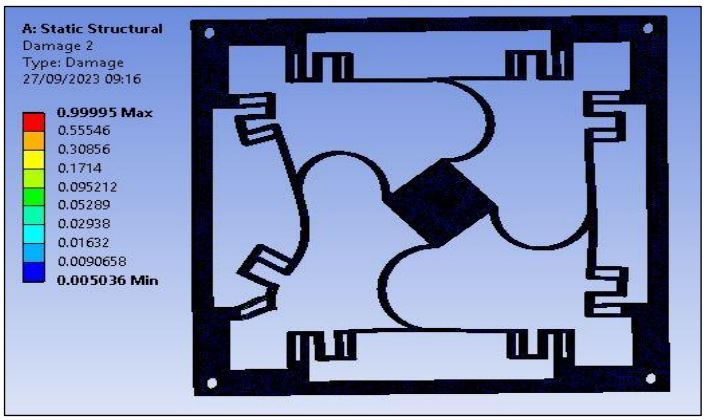


Figure. 12: Damage of Mechanism 1.
Source: Authors, (2026).

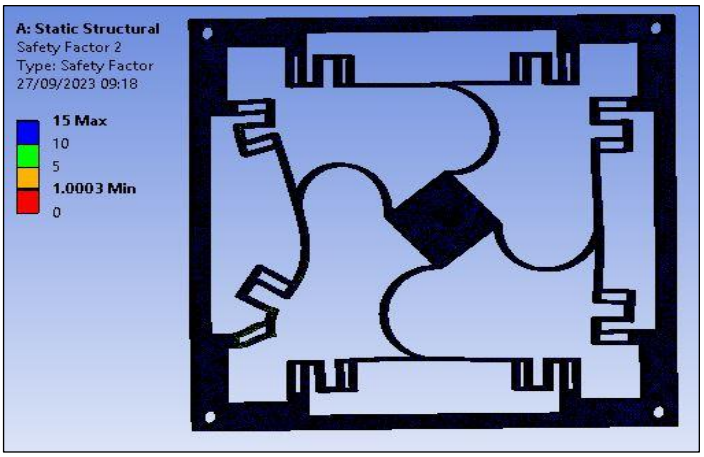


Figure 13: Safety of Mechanism 1.
Source: Authors, (2026).

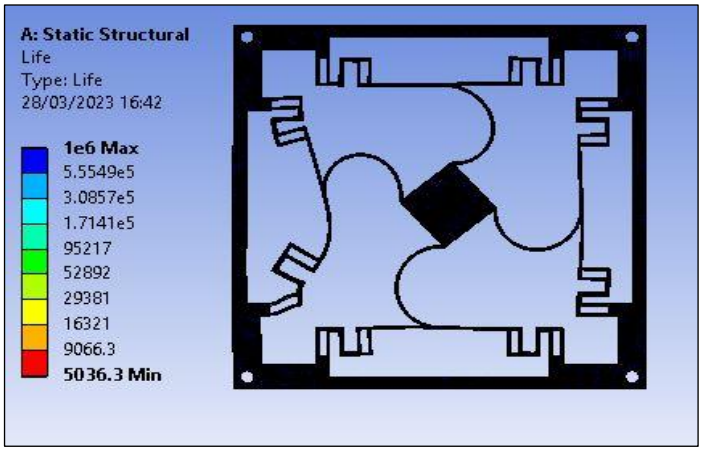


Figure 14: Life cycle for Square motion stage with curve beam 1.
Source: Authors, (2026).

To avoid fatigue failure, the damage value must be less than 1. Figure. 12 shows the damage assessment of the mechanism. According to Figure. 13, the safety factor of the mechanism is 1, which indicates that the mechanism is at the threshold of its design limits.

Figure. 14 presents the life cycle analysis of the mechanism. The square motion stage with Curve Beam 1 is deemed suitable for 5,036 life cycles, given that the damage factor is 0.99 and the safety factor is 1. This means the mechanism can withstand 5,036 cycles before potentially reaching its fatigue limit, as the damage factor is just under the critical value of 1, ensuring it does not fail prematurely.

Analytical Method to calculate Fatigue life Cycle, Damage and Safety factor for Mechanism 1

We'll use the same parameters for both numerical and analytical methods to ensure consistency.

- Material: PLA
- Tensile Strength (σ_t): 59 MPa
- Fatigue Strength Coefficient (σ_f) :2.05 MPa
- Fatigue Strength Exponent (b): -0.153
- Stress amplitude (σ_a) : 0.52 MPa
- Number of cycles (N_f): Various levels for damage calculation
- Fatigue Life Cycle Calculation (N_f) using Basquin's equation:

$$\left(\frac{\sigma a}{\sigma f}\right)^{(1/b)} \quad (1)$$

$$N_f : \left(\frac{0.52}{2.05}\right)^{(1/-0.153)} \quad (2)$$

$$N_f : \text{7465 Cycle}$$

$$\text{Damage Calculation using Minors Rule (D)} : \sum_{i=1}^{k} \frac{ni}{Ni} \quad (3)$$

Compliant mechanism is subjected to 9000 Cycle at 2 Mpa

$$\text{Damage (D)} : : \left(\frac{7465}{9000}\right) = 0.82$$

$$\text{Safety Factor} : : \left(\frac{\text{Endurance limit}}{\text{Applied stress}}\right) \quad 4)$$

$$\text{Safety Factor} : \left(\frac{2.02}{2}\right) = 1.01$$

Comparison of result

1. Fatigue life cycle by Analytical Method: 7465 Cycle
2. Fatigue life cycle by Numerical Method: 7375 Cycle
3. Damage by Analytical Method: 0.82
4. Damage by Numerical Method: 0.81
5. Safety factor by Analytical Method: 1.01
6. Safety factor by Numerical Method:1.06

The results are reasonably close, indicating that the numerical model is validated by the analytical calculations.Small discrepancies can be attributed to differences in the precision of numerical simulations versus analytical approximations.

III.1 FATIGUE ANALYSIS OF SQUARE MOTION STAGE WITH CURVE BEAM OF 40 MM (MECHANISM 2)

Square motion stage with curve beam 2 is having dimension of 300*300*15 mm with curve beam radius of 40 mm. Fatigue analysis of square motion stage is analyzed for 80 N force. Force is applied at notch as shown in Figure. 15. Mechanism 2 is having meshing with 81886 nodes and 42871 triangular elements as shown in Figure. 16. To avoid fatigue failure, the damage value must be less than 1. Figure. 17 illustrates the damage assessment of Mechanism 2. According to Figure. 18, the safety factor of Mechanism 2 is 1, which indicates that it is at the threshold of its design limits. Figure. 19 presents the life cycle analysis of the mechanism.

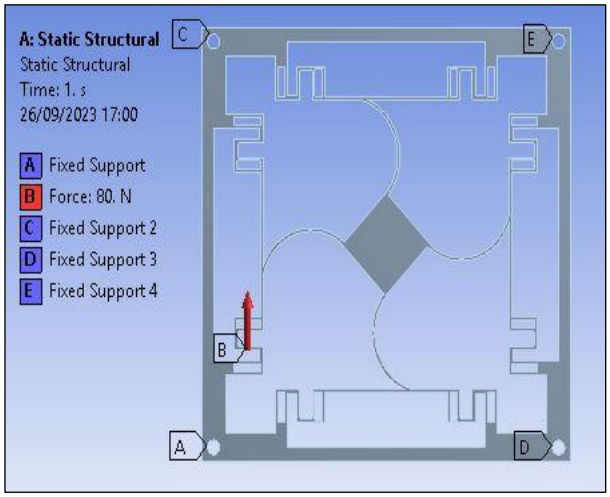


Figure 15: Boundary Conditions of Mechanism 2 for fatigue analysis.
Source: Authors, (2026).

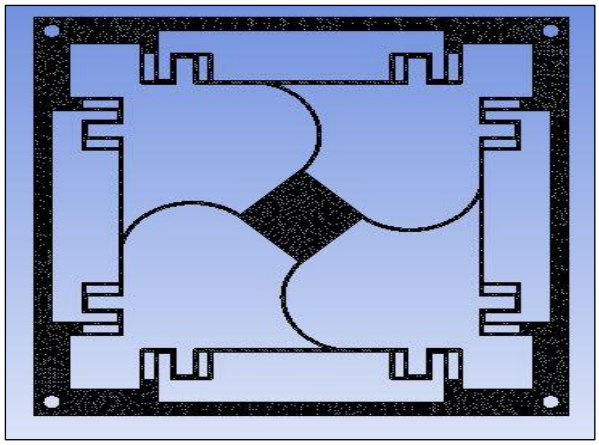


Figure 16: Meshing of Mechanism 2 for fatigue analysis.
Source: Authors, (2026).

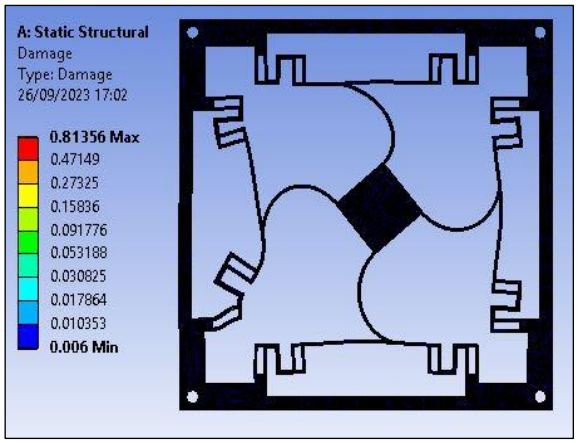


Figure 17: Damage of Mechanism 2.
Source: Authors, (2026).

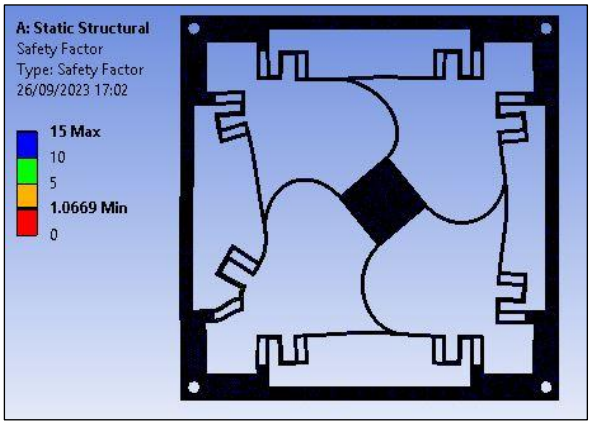


Figure 18: Safety of Mechanism 2.
Source: Authors, (2026).

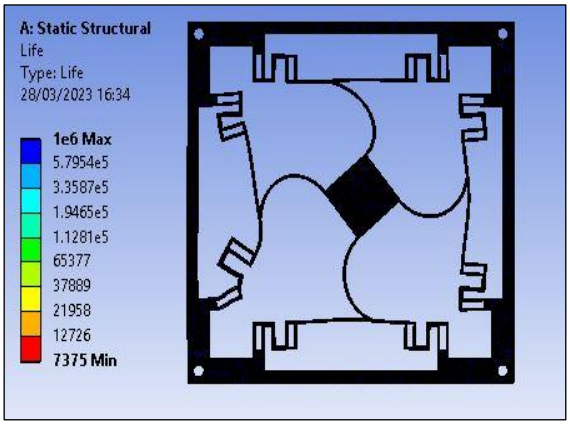


Figure 19: Life cycle for Square motion stage with curve beam -2.
Source: Authors, (2026).

The square motion stage with Curve Beam 2 is suitable for 7,375 life cycles, given that the damage factor is 0.81 and the safety factor is 1.06. This means the mechanism can endure 7,375 cycles before reaching its fatigue limit. The damage factor of 0.81, which is well below the critical value of 1, indicates that the mechanism has a lower risk of fatigue failure. The safety factor of 1.06 suggests a slight margin above the design limits, providing additional assurance of the mechanism's durability and reliability over its life cycle. A larger radius of curvature typically results in lower stress concentration at the curved sections. This means the stress is distributed more evenly, reducing peak stresses that can lead to fatigue failure. With a larger radius, the load is spread over a greater area, which reduces the overall stress experienced by any single point in the mechanism. A larger radius can also improve the flexibility of the mechanism, allowing it to better absorb and distribute applied forces, which can reduce the likelihood of fatigue failure.

Fatigue analysis of Circular motion stage with curve beam of 32 mm (Mechanism 3)

Circular motion stage with curve beam 1 is having dimension of 300*300*15 mm with curve beam radius of 32mm. Fatigue analysis of Circular motion stage is analyzed for 80N force. Force is applied at notch as shown in Figure. 20. Mechanism 3 is having meshing with 84333 nodes and 44134 traingular elements as shown in Figure. 21.

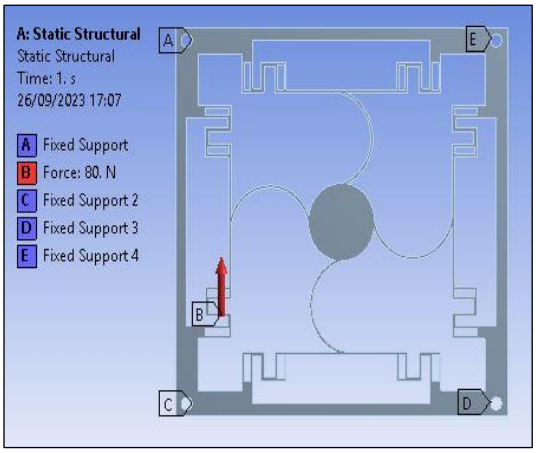


Figure 20: Boundary Conditions of Mechanism 3 for fatigue analysis.
Source: Authors, (2026).

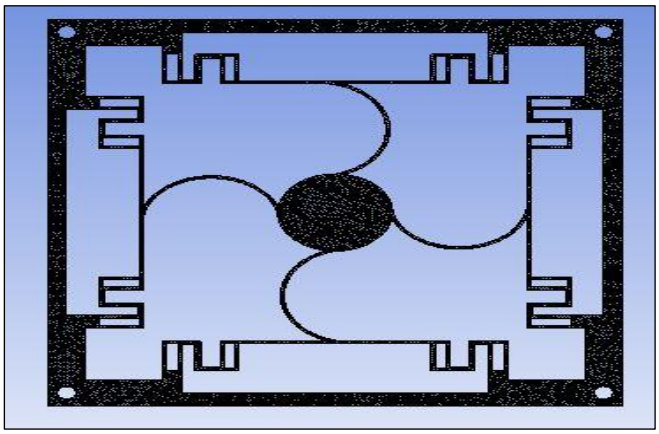


Figure 21: Meshing of Mechanism 3 for fatigue analysis.
Source: Authors, (2026).

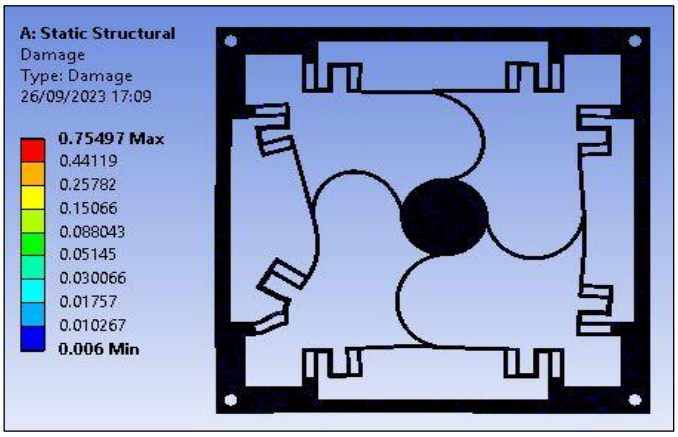


Figure 22: Damage of Mechanism 3.
Source: Authors, (2026).

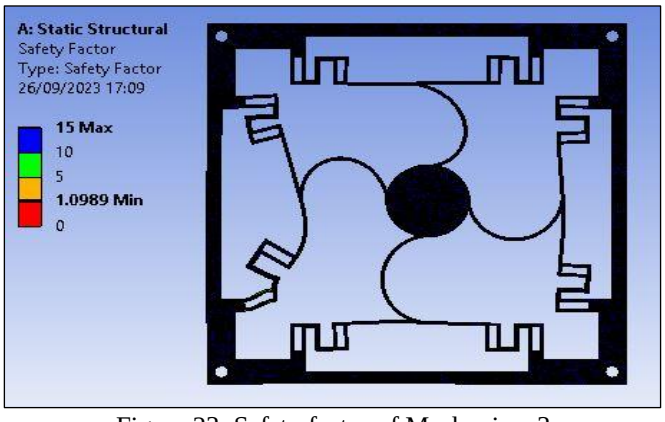


Figure 23: Safety factor of Mechanism 3
Source: Authors, (2026).

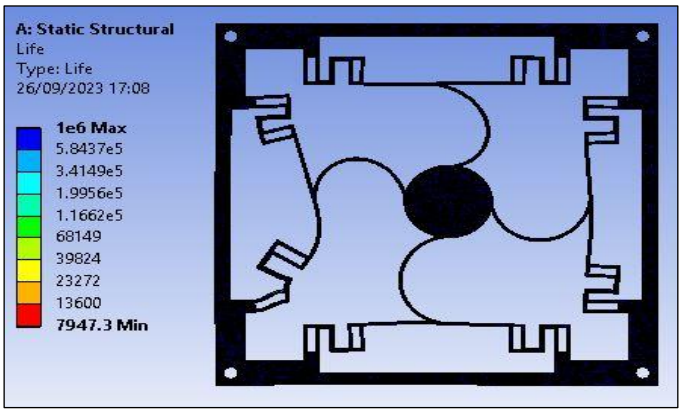


Figure 24: Life cycle for Circular motion stage with curve beam -1.
Source: Authors, (2026).

To avoid fatigue failure, the damage value must be less than 1. Figure. 22 shows the damage assessment of Mechanism 3. The safety factor of the mechanism, as indicated in Figure. 23, is 1.09, suggesting a slight margin above the design limits. Figure. 24 presents the life cycle analysis of the mechanism. The circular motion stage with Curve Beam 1 is suitable for 7,947 life cycles, with a damage factor of 0.75 and a safety factor of 1.09. This means the mechanism can endure 7,947 cycles before reaching its fatigue limit. The damage factor of 0.75, being well below the critical value of 1, indicates a low risk of fatigue failure. The safety factor of 1.09 provides an additional margin of safety, ensuring the mechanism's reliability and durability throughout its life cycle.

Fatigue analysis of Circular motion stage with curve beam of 40 mm (Mechanism 4)

The circular motion stage with Curve Beam 2 has dimensions of 300 x 300 x 15 mm and a curve beam radius of 40 mm. Fatigue analysis was conducted on this stage with an applied force of 80 N at the notch, as depicted in Figure. 25. Mechanism 4 features meshing with 85,536 nodes and 44,762 triangular elements, as shown in Figure. 26.To avoid fatigue failure, the damage value must be less than 1. Figure. 27 shows the damage assessment of Mechanism 4. The safety factor, depicted in Figure. 28, indicates the mechanism's capacity to handle stress beyond its designed load without failing. Figure. 29 presents the life cycle analysis of the mechanism.

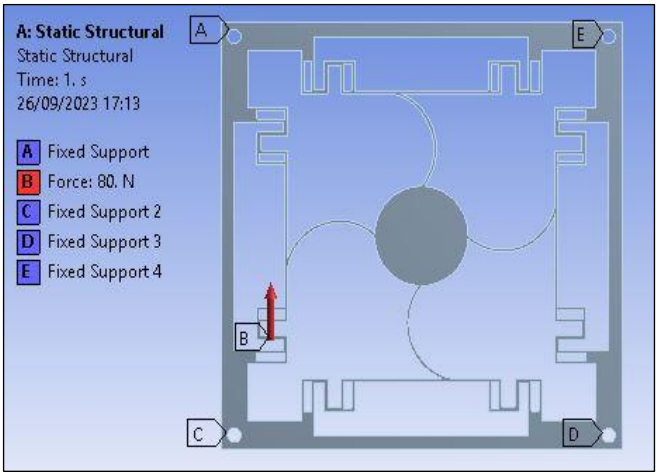


Figure 25: Boundary Conditions of Mechanism 4 for fatigue analysis.
Source: Authors, (2026).

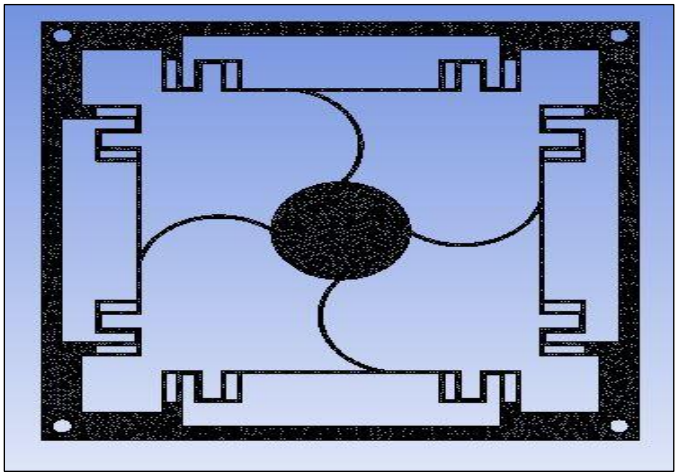


Figure 26: Meshing of Mechanism 4 for fatigue analysis.
Source: Authors, (2026).

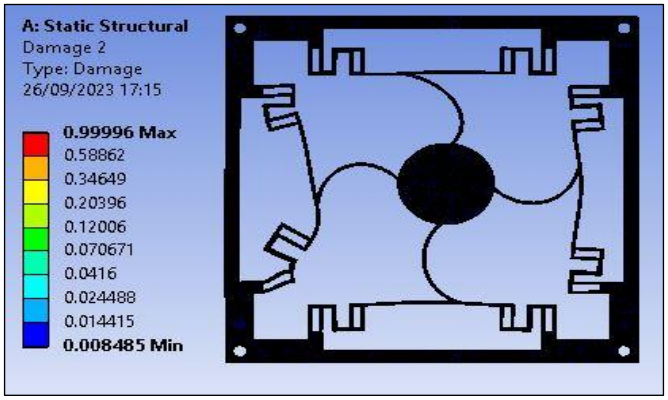


Figure 27: Damage of Mechanism 4.
Source: Authors, (2026).

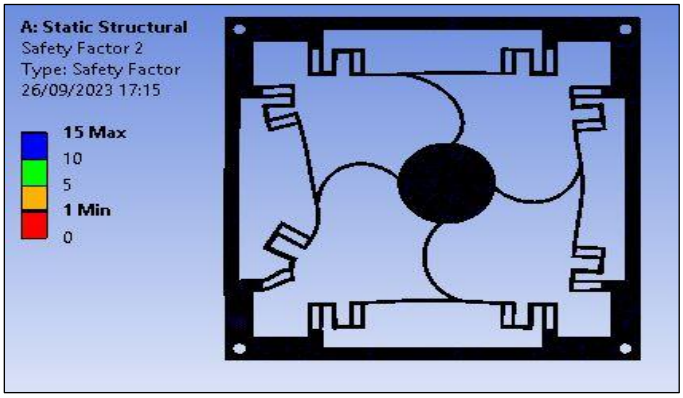


Figure 28: Safety factor of Mechanism 4.
Source: Authors, (2026).

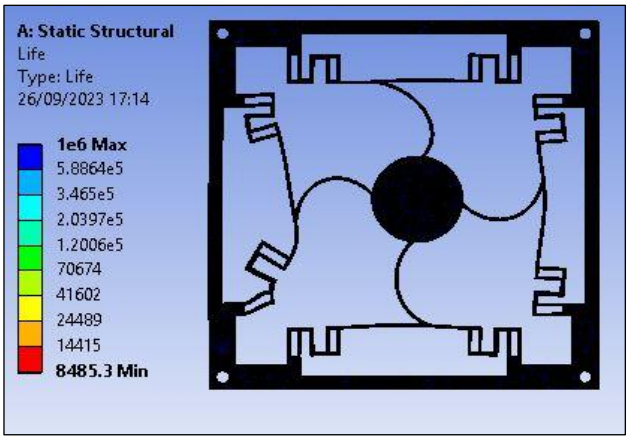


Figure 29: Life cycle for Circular motion stage with curve beam -2.
Source: Authors, (2026).

The circular motion stage with Curve Beam 2 is suitable for 8,485 life cycles, with a damage factor of 0.99 and a safety factor of 1. This means the mechanism can withstand 8,485 cycles before reaching its fatigue limit. The damage factor of 0.99, just under the critical value of 1, suggests that the mechanism is very close to its fatigue threshold. The safety factor of 1 indicates that the mechanism is designed exactly to its limit, with no additional margin for unexpected stresses.

Increasing the radius of curvature helps in mitigating stress concentrations and improving the distribution of loads, thereby enhancing the fatigue life of the compliant mechanism. Fatigue failures are occur in compliant mechanisms, as they operate in a cycle of loading. Fatigue life is defined closely related to repeating loadings. Fatigue life is divided into three categories: low cycle fatigue (fatigue failure occurs between 1 to 10^3 cycles), high cycle fatigue (fatigue failure occurs more than 10^3 cycles), and infinite life (no fatigue failure at a given load).

Table 3: Comparison of fatigue life cycle of different mechanisms.

Sr.No	Type of Motion stage	Fatigue life cycle	Safety factor	Damage
1	Squre motion stage with curve beam of 32mm (Mechanism 1)	5036	1	0.99
2	Squre motion stage with curve beam of 40mm (Mechanism 2)	7375	1.06	0.81
3	Circular motion stage with curve beam of 32mm (Mechanism 3)	7947	1.09	0.75
4	Circular motion stage with curve beam of 40mm (Mechanism 4)	8485	1	0.99

Source: Authors, (2026).

The fatigue life cycle for the square motion stage with curve beam 1 is 5036 Cycles, and curve beam 2 is 7375 as shown in Table 3. The fatigue life cycle for the circular motion stage with curve beam 1 is 7947 cycles, and for curve beam 2 is 8485 cycles. A larger radius of curvature can reduce stress concentrations in a compliant mechanism. Lower stress concentrations are often associated with improved fatigue life because they help distribute the load more evenly.

IV. CONCLUSION

The fatigue life cycle analysis of compliant mechanisms demonstrates the significant impact of geometrical parameters, specifically the radius of curvature of the beams, on the durability and performance of these mechanisms under cyclic loading conditions. Both square and circular motion stages show increased fatigue life with larger radii of curvature. By increasing radius of curvature in Square motion stage fatigue life cycle is increased by 46.44% whereas by increasing radius of curvature in circular motion stage fatigue life cycle of mechanism is increased by 6.76%. This suggests that optimizing the geometric design of compliant mechanisms can significantly extend their operational lifespan. The safety factors for the different mechanisms indicate that larger radii not only improve fatigue life but also ensure that the mechanisms operate safely within their intended load conditions. A larger radius of curvature helps in distributing the load more evenly, reducing the localized stress and hence the damage values, contributing to better durability and reliability. The analysis underscores the importance of geometric optimization in the design of compliant mechanisms. By carefully adjusting the radius of curvature, designers can achieve better fatigue performance, enhance safety, and reduce damage, thereby ensuring that these mechanisms can sustain their intended functions over longer periods and under repeated loading conditions.

Abbreviation

- σ_t: Tensile Strength
- σ_f : Fatigue Strength Coefficient
- b: Fatigue Strength Exponent
- σ_a : Stress amplitude
- N_f: Number of cycles

V. AUTHOR'S CONTRIBUTION

Conceptualization: Sandesh Solepatil, Narendra Deore.
Methodology: Sandesh Solepatil, Narendra Deore.
Investigation: Sandesh Solepatil, Narendra Deore.
Discussion of results: Sandesh Solepatil, Narendra Deore.
Writing – Original Draft: Sandesh Solepatil, Narendra Deore.
Writing – Review and Editing: Sandesh Solepatil, Narendra Deore.
Resources: Sandesh Solepatil, Narendra Deore.
Supervision: Sandesh Solepatil, Narendra Deore.
Approval of the final text: Sandesh Solepatil, Narendra Deore.

VI. ACKNOWLEDGMENTS

I would like to extend my heartfelt gratitude to Dr. Mrs. A.V. Patil, Director, School of Engineering, Management and research, Prof. Manish Bhalla, Vice Chancellor, D.Y.Patil International University, Pune for providing the resources and environment that supported this research.

VII. REFERENCES

[1] Chen G, Liu X, Du Y. Elliptical-Arc-Fillet Flexure Hinges: Toward a Generalized Model for Used Flexure Hinges. J Mech Des. 2011;133(9):1002–10. https://doi.org/10.1115/1.4004441.

[2] Cullin M, Petersen T, Lobontiu N, Kirk T. Experimental determination of planar compliance values of flexures. Measurement. 2014;58:301–9. https://doi.org/10.1016/j.measurement.2014.09.001.

[3] D'Souza RD, Mohamed AU, Tharakan OP, Mini A. Effect of Flexural Hinges in the design of a 2 DOF Compliant Microgripper. Proc 3rd Int Conf Mechatron Robot Eng (ICMRE). 2017:111–8. https://doi.org/10.1145/3068796.3068819.
[4] Dirksen F, Lammering R. On mechanical properties of planar flexure hinges of compliant mechanisms. Mech Sci. 2011;2(1):109–17. https://doi.org/10.5194/ms-2-109-2011.

[5] Fung RF, Hsu YL, Huang MS. System identification of a dual-stage XY precision positioning table. Precis Eng. 2009;33(1):71–80. https://doi.org/10.1016/j.precisioneng.2008.04.002.

[6] Hunt J, Lee H. A new parallel actuated architecture for exoskeleton applications involving multiple degree-of-freedom biological joints. J Mech Robot. 2018;10(2):82–91. https://doi.org/10.1115/1.4040701.

[7] Li Y, Xu Q. Modeling and performance evaluation of a flexure-based XY parallel micromanipulator. Mech Mach Theory. 2009;44(12):2127–52. https://doi.org/10.1016/j.mechmachtheory.2009.06.002.

[8] Ling M, Cao J, Jiang Z, Li Q. Development of a multistage compliant mechanism with new boundary constraint. Rev Sci Instrum. 2018;89(1):015009-23. https://doi.org/10.1063/1.5007890.

[9] Linß S, Schorr P, Zentner L. General design equations for the rotational stiffness, maximal angular deflection and rotational precision of various notch flexure hinges. Mech Sci. 2017;8(1):29–49. https://doi.org/10.5194/ms-8-29-2017.

[10] Shang J, Tian Y, Li Z, Wang F, Cai K. A novel voice coil motor-driven compliant micropositioning stage based on flexure mechanism. Rev Sci Instrum. 2015;86(9):095001-7. https://doi.org/10.1063/1.4929867.

[11] Shaw LA, Sun F, Portela CM, Barranco RI, Greer JR, Hopkins JB. Computationally efficient design of directionally compliant metamaterials. Nat Commun. 2019;10(1):43–52. https://doi.org/10.1038/s41467-018-08049-1.

[12] Shinno H, Yoshioka H, Gokan T, Sawano H. A newly developed three-dimensional profile scanner with nanometer spatial resolution. CIRP Ann Manuf Technol. 2010;59(1):525–8. https://doi.org/10.1016/j.cirp.2010.03.022.

[13] Sun X, Chen W, Zhou R, Zhang J, Chen W. Development of a flexure-based XY positioning stage for micro/nano manipulation. Int Conf Manip Manuf Meas Nanoscale. 2013:82–91. https://doi.org/10.1109/3m-nano.2013.6737441.

[14] C Wang Hinges for compliant mechanism design. Precis Eng. 2010;34(3):408–18. https://doi.org/10.1016/j.precisioneng.2009.10.002.

[15] Xu Q. Design of large positioning system. Hoboken: Wiley; 2016.

[16] Roy NK. Design of laser sintering system. Proc 26th Annu Int Solid Freeform Fabrication Symp. 2016:1495–510.

[17] Wan S, Zhang Y, Xu Q. Design and development of a new large-stroke XY compliant micropositioning stage. Proc Inst Mech Eng C J Mech Eng Sci. 2016;231(17):3263–76. https://doi.org/10.1177/0954406216643341.

[18] Wu Z, Xu Q. Survey on recent designs of compliant micro-/nano-positioning stages. Actuators. 2018;7(1):5–11. https://doi.org/10.3390/act7010005.

[19] Xu Q. New flexure parallel-kinematic micropositioning system with large workspace. IEEE Trans Robot. 2012;28(2):478–91. https://doi.org/10.1109/tro.2011.2173853.

[20] Zhu Z, To S, Zhu WL, Li Y, Huang P. Optimum design of a piezo-actuated triaxial compliant mechanism for nanocutting. IEEE Trans Ind Electron. 2018;65(8):6362–71. https://doi.org/10.1109/tie.2017.2787592.

[21] Solepatil S, Deore N. Displacement analysis of compliant mechanism. Int J Eng Adv Technol. 2019;9(1):4028–32. https://doi.org/10.35940/ijeat.A1175.109119.

[22] Solepatil S, Deore N. Behavior of linear compliant mechanism using numerical and experimental method. Mater Today Proc. 2021;47:3190–4. https://doi.org/10.1016/j.matpr.2021.06.299.

[23] Solepatil S, Deore N. Performance analysis of compliant mechanism for micropositioning stage. Proc Eng Sci. 2023;5(2):303–10. https://doi.org/10.24874/PES05.02.013.

[24] Solepatil S, Deore N. Performance analysis of parallel beam XY compliant mechanism. AIP Conf Proc. 2024;3013(1):020009-1–9. https://doi.org/10.1063/5.0202189.

[25] Solepatil, S. B., Deore, N. R., Dive, V. P., Mali, A. S., Kolekar, A. B. & Jadhav, G. Design, numerical and experimental investigation of linear XY compliant mechanisms for precision motion applications. Advances in Science and Technology Research Journal, (2026), 20(5), 400–415. https://doi.org/10.12913/22998624/217145.

Journal of Engineering and Technology for Industrial Applications

ITEGAM-JETIA

Manaus, v.12 n.60, p.986-996 July/August, 2026.
DOI: https://doi.org/10.5935/jetia.v12i60.3917

ONLINE: 2447-0228

RESEARCH ARTICLE OPEN ACCESS

SIGNSPEAK: AN AI-BASED UTILITY FOR VISUALLY IMPAIRED INDIVIDUALS

Sharanjit Kaur[1], Manju Bhardwaj[2], Kriti Misra[3] and Preeti Marwaha[*4]

[1, 3, 4]Department of Computer Science, Acharya Narendra Dev, College, (University of Delhi), New Delhi, India.
[2]Department of Computer Science, Maitreyi College, (University of Delhi). New Delhi, India.

[1]https://orcid.org/0000-0002-9437-5633, [2]https://orcid.org/0000-0002-8696-3953
[3]https://orcid.org/0009-0006-7957-3558, [4*]https://orcid.org/0009-0000-7425-4749

E-email: sharanjitkaur@andc.du.ac.in, mbhardwaj@maitreyi.du.ac.in, kritimisra87@gmail.com, *preetimarwaha@andc.du.ac.in

ARTICLE INFO

Article History
Received on: March 05, 2026
Reviewed on: April 05, 2026
Accepted on: July 01, 2026
Published on: July 31, 2026

Keywords:
Visually Impaired Assistance,
Text-To-Speech,
Signspeak,
Yolov11s,
Gemini.

ABSTRACT

Visually impaired people (VIP) need assistive technology for smooth and confident navigation on pavements along the roads. VIPs find it hard to follow the speech generated through a text-to-audio converter due to the presence of advertisement text. Automating the process of audio conversion from the signboards by integrating the capabilities of emerging AI models in a fraction of a second will be useful for their confident navigation. In this context, SignSpeak, an AI-based assistive utility, is designed to convert signboard text to speech using visual inputs, which may be captured through smart sensors or canes. The proposed system follows a three-step (detection-extraction-conversion) pipeline. Initially, a fine-tuned lightweight YOLOv11s model is used to generate a bounded box for the relevant text region, which is input to Gemini model, a multimodal large language model for text extraction. Lastly, the extracted text is converted into audio using the Google Text-to-Speech tool. We fine-tuned the YOLOv11s model on 200 signboard images and tested its performance on an additional curated dataset of 42 real-world signboard images. Experimental findings indicate that the proposed integrated pipeline achieved superior performance compared to the solitary usage of the Gemini model for text extraction followed by its audio conversion.

Copyright ©2026 by authors and Galileo Institute of Technology and Education of the Amazon (ITEGAM). This work is licensed under the Creative Commons Attribution International License (CC BY 4.0).

I. INTRODUCTION

One basic need of every human being is to visit different places with comfort and ease, but this need becomes a challenge for a Visually Impaired Person (VIP). To begin with, the VIPs usually moved around with the help of a human guide, this help although reliable could not be afforded by all. Moreover, the human guide has a disadvantage of making the VIPs feel constrained due to lack of sense of freedom and privacy, making them feel like an assisted person rather than being independent. Alternatively, dogs were also trained to assist VIPs but this service also has its own challenges. Dog training is a tedious task and the dog itself requires a lot of care and attention (i.e. feeding, grooming and walking), which is even more difficult for VIPs [1]. Similarly, other assisting tools like white cane are extensively used but they provide a limited set of features [2]. With the advent of internet-based technologies, a variety of assistive solutions are available for VIPs. All these systems, services, devices and applications help them with their daily chores and provide them a safer mobility option. These are included under one umbrella term: Assistive Technology. In the 1960s, the term “assistive technology” was used for technologies designed to handle issues related to information transmission, navigation and orientation for the especially abled [2] [3] The invention of smartphones has not only enhanced the connectivity for common man but has provided an excellent set of assistive tools by providing audio assistance through Google maps, road navigation applications for sensing hurdles etc. Inclusion of artificial intelligence technologies with smartphones has transformed the smartphone into an essential tool for most VIPs [4-6]. Modern technologies are now accessible to visually impaired people, encouraging greater independence, which include screen readers on smartphones, portable camera-based systems, electronic pens, Android assistant EyeMate, the “Self-Sufficient Smart Vision Stick” [7] etc. Each of these provide different functionality. While navigating, mobile application Google Lens can be used for capturing images but it reads out everything captured, which may not be useful for their navigation.

Google's Lookout uses computer vision and GenAI to make everyday tasks, such as reading documents, object identification etc . However, reading text from the signboards using available applications, while walking on a pavement or sidewalk is still a challenge because of its surroundings, text quality and its orientation. Among various assistive technologies, systems that can detect, read, and convert text into speech hold great potential for enhancing information accessibility and independence for the visually impaired [4] [8] [9]. YOLOv11s, Gemini, and Google Text-to-Speech (gTTS) are cutting-edge technologies whose capabilities can be integrated to address this need. We propose SignSpeak as a cutting-edge technology that follows a three-step (detection-extraction-conversion) pipeline to identify and read aloud the text on the sign boards. In the first step, YOLOv11s is used as a fine-tuned detector to detect the signboard region from captured images in real time. Subsequently, Gemini, a large language multimodal model, is deployed to extract the text from the detected regions [10]. Finally, gTTS, a high-quality text-to-speech converter, is used to convert recognized text into speech [11]. It is to be noted here that our focus is to reliably convert the fetched text from the signboard images to audio, once images are captured effectively from the smartphone integrated with an object detection sensor. The following are the major contributions of the proposed work:

- Fine-tuning of YOLOv11s model to extract desired text regions from the signboards after distinguishing between signboards and banners of varying shapes and sizes.
- Integration of three cutting-edge technologies viz. YOLOv11s, Gemini and gTTS for converting text from signboards into speech.
- Self-annotation of 200 signboard images used for fine-tuning of YOLOv11s as well as curating a separate test set of 42 signboard images to evaluate the performance of the pipeline.
- Deploying a Streamlit-based application namely SignSpeak1 with an easy-to-use interface for VIPs.
- Extensive experimentation to show the effective performance of the proposed integrated pipeline.

Organization of the paper: Section II reviews related work on current deep-learning based assistive technologies for VIPs following a brief introduction to existing traditional methods. Section III briefly describes the tools explored followed by details of the proposed methodology. Section IV reports the experimental results and analysis along with discussion, while the conclusion and future scope are given in Section V.

II. THEORETICAL REFERENCE

This section gives an overview of the related work on current deep-learning based assistive technologies for VIPs after a brief introduction to traditional methods.

II.1 TRADITIONAL METHODS

An early work by Shen and Coughlan [3] demonstrated a real-time sign-reading prototype for the identification of environmental signs followed by its audio conversion. It established the importance of visual to audio technologies for assisting the VIPs by providing speech-based feedback, audio translation and many more. However, these machines learning based approaches were using hand-crafted features along with rule-based algorithms and were effective in a controlled environment [4] [12].

II.2 DEEP LEARNING METHODS

Recent advancements in deep learning-based approaches have enabled assistive technology for real time text detection, recognition and scene understanding. Utilizing these approaches has empowered the real-time object detection and navigation system, smartphone applications to improve the accessibility for VIPs [4]. Reading text from complex images has been made possible for VIPs by identification of textual regions and using deep learning techniques to identify text, and ultimately converting to speech. A hybrid approach combining deep learning with particle swarm optimization proposed by Pandey et al., recognizes text from natural scenes and an audio output is produced via text-to-speech convertor [13]. Ganeshan et al. employ CNN-LSTM models to detect the caption associated with the given image, the identified caption is then converted into voice message using Text-to-Speech API. [14]. A ResNet-based system for object detection and text recognition by Begum et al. produces an audio output, and the visually impaired individuals can easily use this to read medication labels etc. [15] In [16], the authors design a system to assist visually impaired or text-reading challenge users by employing VGG-16 for text detection and recognition followed by Augmented reality visualization to display the content as a 3D image on a smartphone screen. One of the notable advancements is the OCR integration with the Text-to-Speech (TTS). A student-led initiative using the CNN-LSTM models on the embedded hardware achieved over 93% recognition accuracy from the live camera feeds and has affirmed the feasibility of deploying such pipelines on the resource-constrained devices [12]. Research has also highlighted the importance for the user experience during the audio rendering by preserving the structural elements to improve comprehension [5]. Similarly, work in Augmented reality has shown promise for vocalizing visual symbols [6]. Suresh et. al. proposed a wearable assistive system for the real-time auditory guidance in the form of a smart backpack by integrating sensing and on-device intelligence to be used in a controlled environment [17]. Recently, Moreira et. al. presented an integrated mobile application using Google Gemini artificial intelligence model for the VIPs to understand visual content [18]. Although tremendous efforts are being made for the effective use of deep-learning based assistive systems, challenges still exist in terms of their applicability and robustness. In this article, we are focusing on real-time capturing of text from the signboards and its reliable audio conversion for the smooth navigation of VIPs on the sidewalks and pavements.

III. MATERIALS AND METHODS.

This section briefly outlines the selection process for deciding the AI models and tools effective for getting the desired outcome in Sec. III.1, followed by description of methodology in Sec. III.2.

III.1 SELECTION OF AI MODELS AND TOOLS

III.1.1 Text Detection Models

The first step in the proposed pipeline involves accurate detection of text regions from the signboard images. Different tools were explored and their effectiveness was analysed. Traditional OCR engines like Tesseract [19] failed to work with low-resolution images and complex backgrounds. PaddleOCR [20] could detect and recognize text but showed inconsistencies in accessing small-sized text in the signboard images. Deep-learning based detectors like EAST [7] and CRAFT [16] provided better output, but produced imprecise bounding boxes and suffered from compatibility issues with modern frameworks. Finally, YOLOv11s, a lightweight model, was selected for object detection because of its localization accuracy, and seamless compatibility with current deep learning libraries. Also, Khanam and Hussain demonstrate that appropriate fine-tuning of YOLOv11s for a specific task produces precise bounded boxes, which ensures reliable input for the subsequent phase [21]. However, for proper fine-tuning, the input images in the YOLO model need to be annotated, hence, an open-source platform Label Studio is used to generate bounding boxes for signboard regions [22].

III.1.2 Text Recognition and Extraction Models

After the detection of text regions, multiple recognition frameworks were evaluated for their text recognition capability. During the early stages, PaddleOCR offered integrated detection and recognition but showed limited accuracy on small datasets and lacked robust cropping mechanisms [20]. EasyOCR [23], which is built on the CRAFT algorithm, supports multilingual scripts but produces inconsistent results, particularly with Tamil signboards which are present in the dataset. More advanced solutions such as LLAMA OCR 3.2-90B Vision, demonstrated strong recognition under complex conditions, but is constrained by high deployment costs and reliance on external APIs [24]. Finally, Gemini 3 was adopted as the recognition engine because of its high accuracy across various inputs, its support for multilingual scripts, and seamless integration with YOLOv11s [10]. This integration enables an efficient end-to-end text reading pipeline for fast inference required for real-world deployment.

III.1.3 Text-to-Speech Conversion Tools

Initially, the pyttsx3 engine for English synthesis was explored, as it provides offline functionality with adjustable voice and rate settings [25]. However, its limited applicability and quality response for non-English languages were the major concerns. We finally selected gTTS (Google Text-to-Speech) that not only covers these limitations but is also compatible with diverse linguistic contexts [26]. In addition to these tools, different Python-based libraries are used for the development, training and deployment of the proposed tool SignSpeak. Python Imaging Library (PIL) is used for the image conversion and the augmentation required for the dataset preparation [27]. OpenCV is used for the image processing task for delivering consistent input formats for the detection and recognition [28]. The Ultralytics PyTorch framework is used for the fine-tuning of YOLOv11s, offering a modular API for detection tasks [7]. Finally, the Google Generative AI SDK is incorporated for integrating the Gemini 3 via API calls [10].

III.2 PROPOSED METHODOLOGY

The methodology used for developing the SignSpeak encompasses data preparation, and integration of three major AI-based technologies for text detection, text extraction and text-to-speech conversion. The proposed approach (detection-extraction-conversion) takes images of signboards as input, detects texts on the signboards, followed by their conversion to speech, which is delivered as output to the visually impaired individuals.

III.2.1 Data Preparation and Labeling

A publicly available dataset, namely the Indian Signboard Image dataset consisting of 200 images from Kaggle, is used [29]. The signboard images contain multilingual text (English, Hindi, and Tamil) under varying lighting, orientations, and background conditions (see Figure 1). Label Studio is used to manually annotate all the images, drawing bounding boxes around text regions to generate high-quality ground-truth data in the YOLO format [7]. In addition, 200 background images without signboards are also incorporated into the dataset to enhance the detection robustness of the model.



Figure 1: An Annotated Sample Sign Board.
Source, Author, (2026).

These images with the road scenes are included as background (negative samples) without bounding box annotations [30]. The inclusion of background-only images helps the model learn contextual features and reduces false-positive detections during inference. This resulted in a combined dataset of 400 images, on which the pipeline is built and validated. An independent test dataset of 42 signboard images is also curated to evaluate the performance of the proposed pipeline.

III.2.2 Fine-Tuning of Yolov11s Detector for Text Detection

YOLOv11s is highly effective for object detection but needs to be fine-tuned to road signboards to incorporate domain-specific optimizations [31]. The model is fine-tuned for Indian roadside sideboard detection using a combined dataset of 400 images (200 signboards + 200 road images) as discussed in Sec. III.2.1. It is to be noted that a few signboard images have multiple signs. Hence, Label Studio used for annotation returned 215 annotated objects for 200 signboards. The image dataset is split into training and validation sets with an 80:20 ratio, resulting in 320 training images and 80 validation images. The training set with 320 images consists of 166 signboards consisting of 178 annotated objects, and 149 background images respectively. The validation set contained 34 images with 37 annotated instances of the signboards and 46 background images as negative samples, indicating background-only scenes without visible road signs. Including such background images helped improve the detector's robustness by reducing false-positive predictions. Fine-tuning is conducted for 60 epochs with a batch size of 8 images, where each image resolution is set to 640×640 using the Ultralytics framework in a GPU-accelerated Google Colab environment. The model is trained for a single class, *Road Signboard*, using YOLO *txt* format annotations in the presence of a few background images. Data augmentation techniques such as horizontal flipping, mosaic augmentation, and RandAugment are also enabled to improve the generalization of the model.

Table 1: Distribution of signboard images and corresponding annotated objects along with background images used for training and validation during the fine-tuning of YOLOv11s model.

Signboard Data	Total Signboards (a)	Total Annotated Objects in Signboards	Total Background Images (b)	Total Images (a+b)
Image Instances	200	215	200	400
Training Data	166	178	154	320
Validation Data	34	37	46	80

Source: [29], [30].

III.2.3 Pipeline of SignSpeak

SignSpeak employs a three-stage pipeline: image detection module, text extraction module, and text-to-speech conversion module. The input image is first analyzed to detect the signboards, followed by text recognition and extraction, and lastly, the text is converted to audio, as illustrated in Figure 2.

III.2.3.1 Image Detection Module

The proposed pipeline begins with an object detection module, which uses a lightweight YOLOv11s model. The used model is fine-tuned specially for signboard detection. Its capability to capture localized regions of interest followed by generating bounding boxes around the signboards, makes it suitable for poor-quality images too. Its lightweight architecture allows for real-time inference without impacting the accuracy of the retrieved localized region.

III.2.3.2 Text Extraction Module

The localized regions are further processed by a text recognition AI model leveraging natural language prompts to extract textual content. Using the Gemini 3 model not only allowed for handling of various font styles, but its human-readable prompt returned the text without requiring task-specific fine-tuning. The integration of a vision-language model in this context demonstrates the advantage of natural prompt engineering, allowing SignSpeak to seamlessly handle multilingual signboards and varied environmental conditions, including distorted images, low resolution, or background noise, by integrating YOLOv11s with Gemini 3 to ensure high reliability in practical deployment scenarios.

III.2.3.3 Text-to-Speech Conversion Module

The SignSpeak pipeline concludes by transforming the recognized text into natural-sounding speech using a text-to-speech engine to get an accessible auditory output. The selection of the Google text-to-speech (gTTS) tool for providing a natural, multilingual speech output makes the proposed pipeline suitable for delivering clear feedback for texts written on signboards.

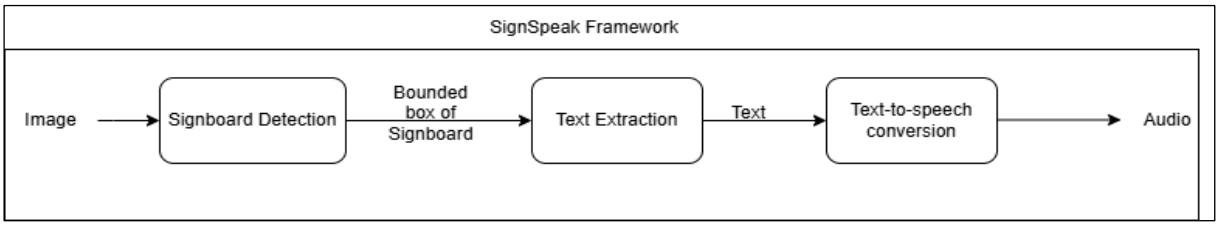


Figure 2: Pipeline of Three Phases in the Proposed Signspeak Framework for Extracting Text from Signboard for Text-to-Speech Conversion.
Source: Authors, (2026).

III.2.3.4 Example: Inference Process

Figure 3 demonstrates the workflow for processing a single image for text extraction. The input image (Fig. 3a) is passed as input to the fine-tuned YOLOv11s model, which returns the coordinates of a bounding box for the detected signboard (Fig. 3b). The bounded box is used for cropping the image so that only a valid portion is sent to the Gemini model with a prompt asking it to extract the text (Fig. 3c). The resulting text is stored for subsequent audio conversion by the text-to-speech conversion module.



(a) Original Image Signboard. (b) Bounded Box Detection by YOLOv11s. (c)Recognized Text Output by Google Gemini Image.

Figure 3: Text extraction from the Signboard Image.
Source: Authors, (2026).

IV. RESULTS AND DISCUSSIONS

This section describes the experiments conducted to evalu vate the performance of the proposed AI-based utility tool using the established performance metrics for evaluating text extraction from the signboard and subsequent text-to-audio conversion efficiency.

IV.1 FINE-TUNING AND PERFORMANCE EVALUATION OF YOLOV11S MODEL

During YOLOv11s fine tuning for signboard detection, visual outputs from selected batches were saved to monitor the evolution of the model's detection performance. A batch refers to a group of images processed together before updating the model parameters, with the batch number indicating the sequence of processing during training. Recall that a batch of 8 images are used for the experimentation.

IV.1.1 Fine Tuning of the YOLO Model for Domain Specific Object Detection

The dataset consisting of 400 images is split into an 80:20 ratio, where 320 images are allocated for training and the remaining 80 images are reserved for validation (see Sec. III.2.2: Table 1 for details). The model is trained for 60 epochs with a mini-batch size of 8 images, allowing the training process to iteratively update model parameters across the entire training set multiple times to enable an effective domain-specific learning and convergence. Selection of parameters is done such that all the training samples are processed in the manageable batches to get stable gradient updates.

IV.1.2 Label Distribution and Bounding Box Analysis

Figure 4 illustrates the label distribution and bounding box distribution. The model identifies 178 annotated objects from a training set of 320 images (166 signboards + 154 background images) as shown in Figure 4a. Recall that the model is used for identification of only one class, which is Road Signboard. Figure 4b shows all bounding boxes overlaid, where each rectangle is one labeled object. All boxes are drawn on the top of each other, indicating their concentration on the middle part of the signboards. Figures 4c and 4d show the object center positions (x v/s y) and distribution of width v/s height of all boxes respectively. It is clear from these two figures that most signboards are mostly near the center and are having size variation from small to medium respectively.

IV.2.2 Training and Validation Performance of The YOLO model

Figure 5 shows the training and validation performance of the YOLO model where the x-axis represents the number of epochs and the y-axis represents the score of the selected metric. The first three plots in top and bottom rows show the performance of the models on the training and validation set in terms of loss respectively. The first and second plots in the top row show the loss that incurs during learning of bounding boxes and signboard class during different epochs. It is clear from the first two plots that learning is poor initially which improves with increasing epochs. Low loss with increasing epochs vindicates the good learning of the model. A similar pattern is observed in the third plot of the top row and revealed that advanced bounding box fine tuning loss also decreases with epochs. The first three plots in the bottom row of Figure 5 shows the performance of the model on the validation set. Spikes in early epochs may have contributed to minor label normalization inconsistencies in the validation data resulting in high classification error in these epochs. The fourth and fifth plots in both top and bottom rows show the Precision, Recall and mAP (Mean Average Precision) of the trained model on the validation set. It is clear that the Precision and Recall stabilize at approx. 0.92 and 0.94 respectively, capturing the effective learning of the model on the provided data. During early epochs, the model is unstable, which causes high classification error. Once training progresses and the model adjusts to the data, the loss quickly stabilizes and decreases as vindicated by the mAP plots shown as last two plots in the bottom row. The metric mAP50 considers a prediction accurate if it overlaps with the ground truth bounding box by at least 50%, which is around 0.92. The last box shows the metric mA90-95, which checks for 90-95% overlap in the detected and reference images and is around 0.6 which is good for the object detection model.

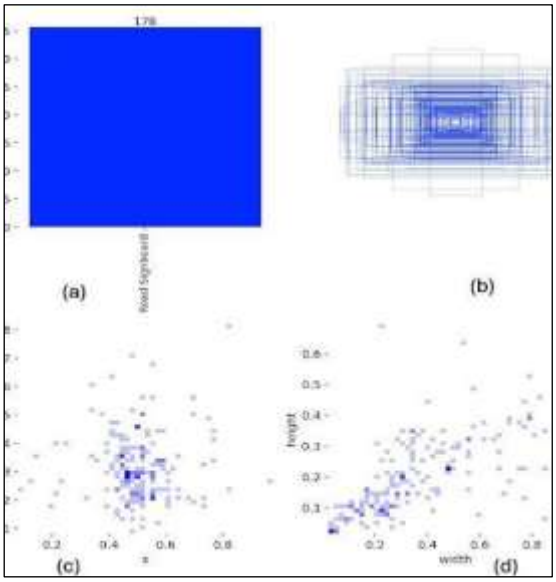


Figure 4: Label Distribution and Bounding box analysis.
Source: Authors, (2026).

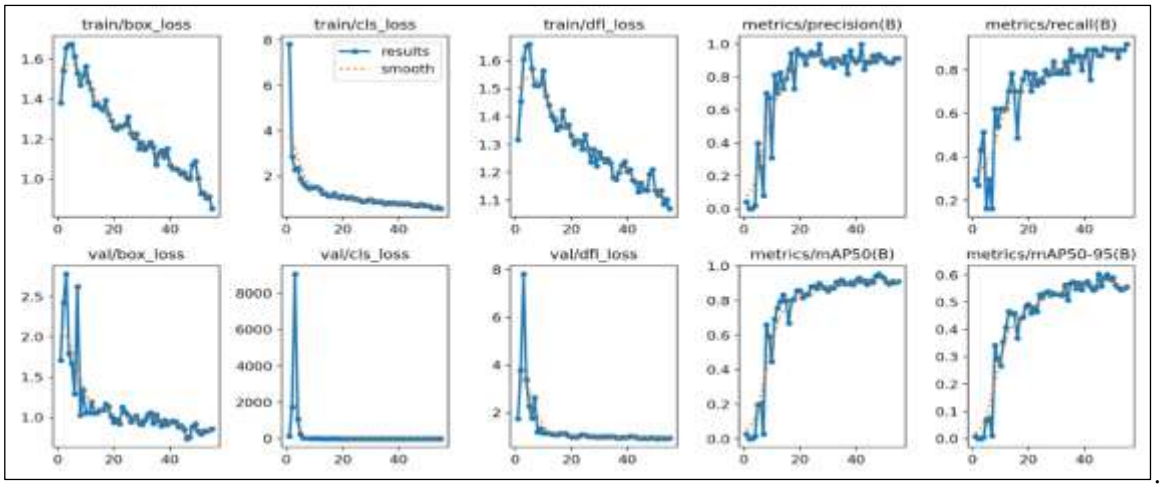


Figure 5: Training and Validation Performance of YOLOv11s model.
Source: Authors, (2026).

Table 2: Confusion Matrix showing Performance of YOLO model on the Validation Set.

Predicted	**Actual**	
	Road Signboard	**Background**
Road Signboard	34 (TP)	7 (FP)
Background	3 (FN)	NA

Source: Authors, (2026).

For the single-class *Road Signboard* detection task, the confusion matrix in Table 2 shows the accuracy of the model in terms of TP (True Positive), FN (False Negative) and FP (False Positive) which are 34, 3, and 7 respectively. Out of actual 37 signboard objects, 34 are reported correctly and the rest 3 are reported as background. Also, 7 background images with no signboard are predicted as signboard images (FP). Here, the true negatives are not explicitly defined due to the enormous number of the possible background regions. The true positive detections correspond to correctly localized and classified road signs, while false negatives represent missed detections of annotated signs. False positives indicate cases where the model predicted a road sign in background regions. These results confirm that the model successfully detects the majority of road instances while maintaining reasonable discrimination against the background.

IV.2.3 Model Evaluation through Box and PR Curves

Figure 6 represents the Box and PR curves for the validation set. In all subfigures, the light blue curve captures the model's performance in detecting signboard class only whereas the dark blue curve shows the overall model's performance in the presence of background images without signboards in them. Figure 6a represents the F1 confidence curves where the x-axis represents the confidence and y-axis represents the F1 score. The curves depict the variation in model performance with change in the confidence threshold. It is observed that the model performance is best with F1-score 0.88 at confidence threshold ≈ 0.53. Figure 6b describes the Precision-Confidence curve where the x-axis and y-axis show the confidence threshold and Precision respectively. It is clear from the figure that Precision is more than 0.8 for confidence > 0.3 and is maximum 1 for confidence value ≈ 0.73.

It vindicates the model's capability to detect signboard images with high precision starting from low confidence value. Figure 6c validates the model's capability to detect images precisely by missing out few of the actual signboard images (see right side of the Precision-Recall curve where the X-axis shows recall and the Y-axis represents precision), which suggests model is able to detect most objects and make few mistakes at mAP@0.5. Detection of all classes with 0.916 vindicate the model's good performance in detecting sign board part from the images. Figure 6d represents the Recall-Confidence curve showing variation in Recall (y-axis) with change in confidence threshold (x-axis). It is observed that the recall decreases after the 70% confidence i.e. the model starts missing many objects. The YOLO model performs best in the low confidence range with recall above 70%. But its performance deteriorates with high confidence.

IV.2 PERFORMANCE EVALUATION OF THE SIGNSPEAK PIPELINE ON TEST SET

We use independent test data to evaluate the performance of the integrated approach in the following sections. For which, we separately evaluate the performance of each of the three modules using suitable metrics to prove its effectiveness on unseen signboard images.

IV.2.1 Evaluation of Signboard Detection from the Images

We evaluate signboard detection on the dataset with 62 images containing 42 real world images and 20 banners (with no signboards) images curated from the internet. All 62 images are used sequentially to evaluate its working. We set a threshold of 0.6 (60%) to reduce the false detection of banners as signboards. At this threshold, the model achieves a higher precision along with fewer false positives while maintaining a good recall as vindicated during fine tuning of the YOLO model. The model detected 38 signboard images out of 42 images as TP and the remaining 4 images were detected as background leading to False negative. It reported only one banner image falsely classified as Road Signboard (Table 3), NA values in TN cell held same justification for validation set. For the single-class *Road Signboard* detection task, the model performance with precision of 0.97 and a recall of 0.90 affirms its capability to capture the most of the signboards correctly with a minimal false detection.

Table. 3: Confusion Matrix showing Performance of YOLO model on the Test Set with 42 Signboard Images and 20 banner images.

	Predicted Signboard	Predicted Background
Actual Signboard	38 (TP)	4 (FN)
Actual Background	1 (FP)	NA

Source: Authors, (2026).

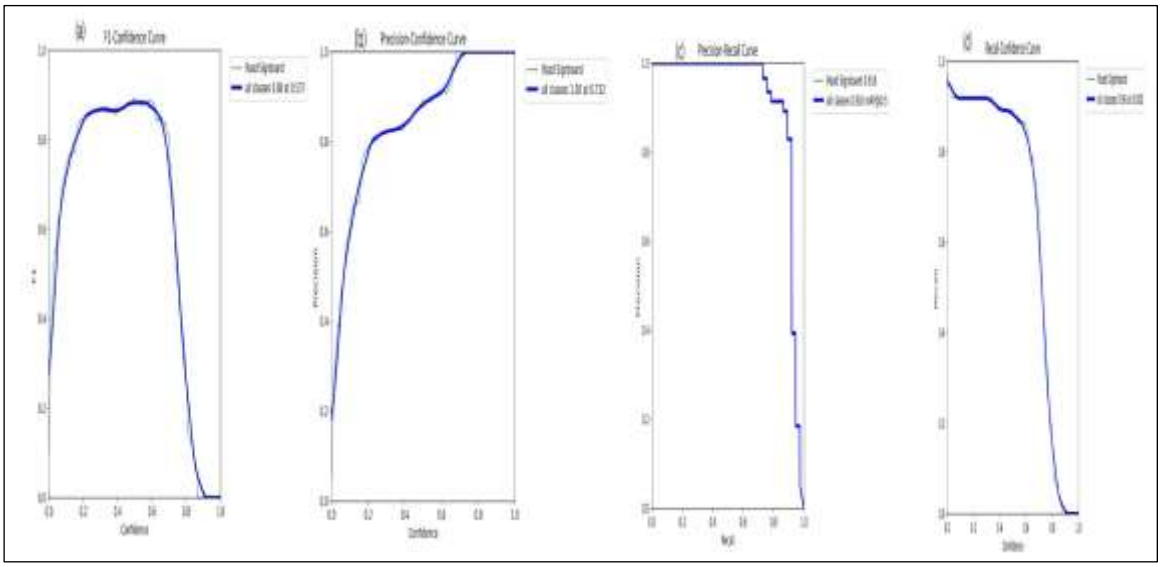


Figure 6: Performance Evaluation of YOLOv11s Model on the Validation Set using three Standard Metrics with varying Confidence thresholds.
Source: Authors, (2026).

IV.2.2 Evaluation of Text Extraction from the Detected Signboards

Model Gemini 3, which does not require fine-tuning, is used for text recognition. A prompt-based approach is used to retrieve the text from the images using Gemini. For example, a prompt: "What text do you see in this image?" returns the visible text in the provided image without any explanation. We manually extracted the text from all 42 signboard images in the test set and saved it as the Ground-Truth text, which is used subsequently for comparing the performance of the proposed pipeline (referred as Pipeline A) with the other standard method Pipeline B (Gemini 3 recognition only).

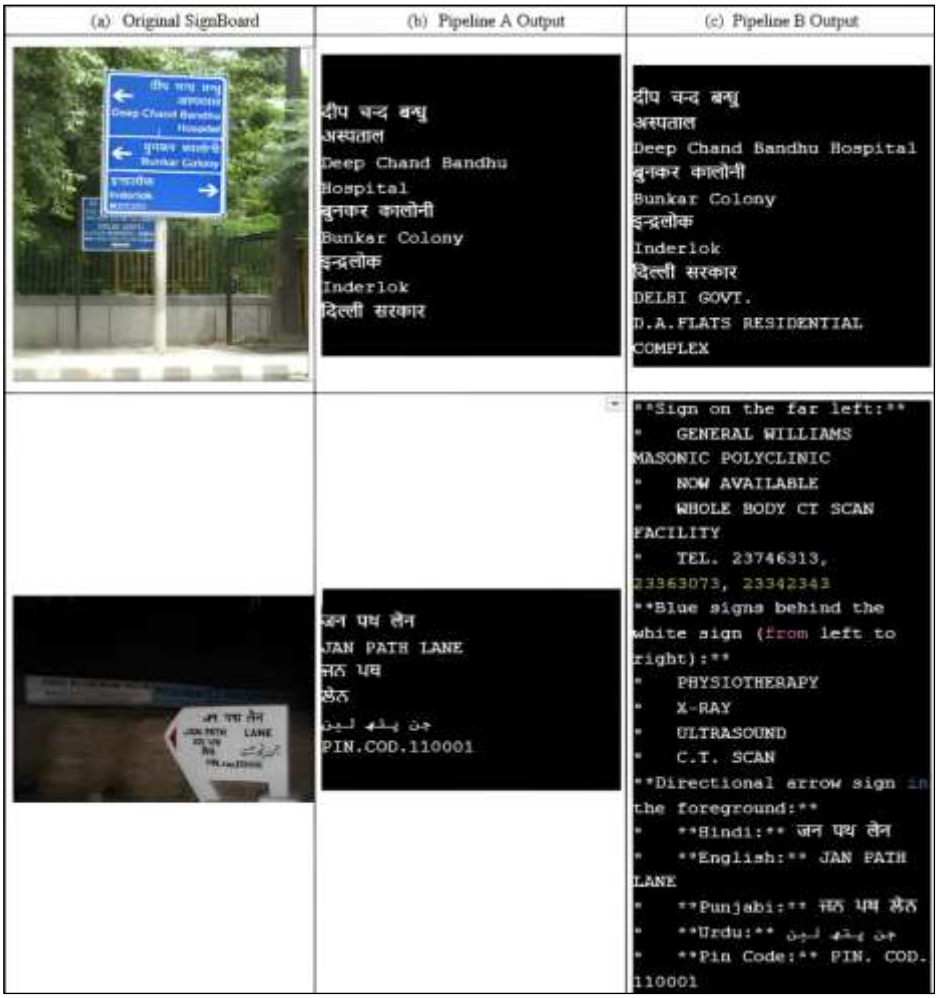


Figure 7: Comparison of Text Extracted by Pipeline A (YOLO and Gemini 3) and Pipeline B (by Gemini only) with the Original Signboard Text.
Source: Authors, (2026).

It is to be noted that Pipeline A (YOLOv11s detection and Gemini 3 recognition) was designed to first localize signboard regions before performing text recognition, whereas Pipeline B (Gemini 3 recognition only) operated directly on the full images without prior detection. Figure 7 shows the comparison of both the Pipelines A (Fig 7 b) and B (Figure 7c) respectively w.r.t to two original signboard images (Figure 7a). It is observed that Pipeline A performed better by extracting the relevant text from the localized region of the signboard marked by YOLO, whereas line B extracted the entire text from the image provided making navigation of VIPs difficult. We also use BLEU [32] and ROUGE [33] metrics to compare the text extracted from these two pipelines (Table 4). For the Pipeline A, high value of performance metrics (BLEU score of 81.06, an average Rouge-1 F1 score of 0.93 and an average Rouge-L F1 score of 0.92) compared to those of Pipeline B (BLEU score of 60.33, an average ROUGE-1 F1 score of 0.85 and an average ROUGE-L F1 of 0.85) demonstrate the effectiveness of integrating a signboard detection stage prior to the recognition. The improvement can be attributed to YOLOv11s ability to isolate relevant text regions, thereby minimizing the background noise and distortions that often hinder the accuracy. The higher BLEU score confirms the improved n-gram precision, while the ROUGE score reflects the greater overlap with the Ground-Truth text, signifying enhanced completeness of recognition. Overall, the results provide quantitative evidence that a modular approach (Pipeline A), which uses a detection-recognition pipeline surpasses the recognition-only approach (Pipeline B) for the real-world scenarios. It is concluded from the results that the proposed integrated approach for text extraction is reliable and robust for practical deployment.

Table 4: Performance comparison of Pipeline A and Pipeline B in terms of Text Extraction using Test Set.

Pipeline	Bleu score	Avg Rouge-1 F1	Avg Rouge-L F1
A (Yolo+ Gemini)	81.06	0.93	0.92
B (Gemini only)	60.33	0.85	0.85

Source: Authors, (2026).

IV.2.3 Evaluation of Text-to-Speech Conversion

We use TTS-ASR (Text-to-speech Automated Speech Recognition), which uses a loop where text is converted into speech, followed by its conversion back to text again using a round-trip approach [34]. The round-trip time allowed for computing the Word Error Rate (WER) [35] and Character Error Rate (CER) [36], which were computed after text normalization (lowercasing, punctuation removal, and extra space removal) to ensure reliable comparison.

Then we calculated the WER and CER scores. For this phase, text captured from Pipeline A and Pipeline B from test images were converted to audio using Google Text-to-speech converter (gTTS), followed by its processing by the ASR pipeline using a round-trip approach. The benefit of using the round-trip approach is to check whether the system can reconstruct the original text accurately after passing through both speech synthesis and recognition stages. Here, Pipeline A clearly outperformed Pipeline B (Figure 8) by achieving a lower WER and CER, indicating its text-preserving capability in the TTS-ASR evaluation loop.

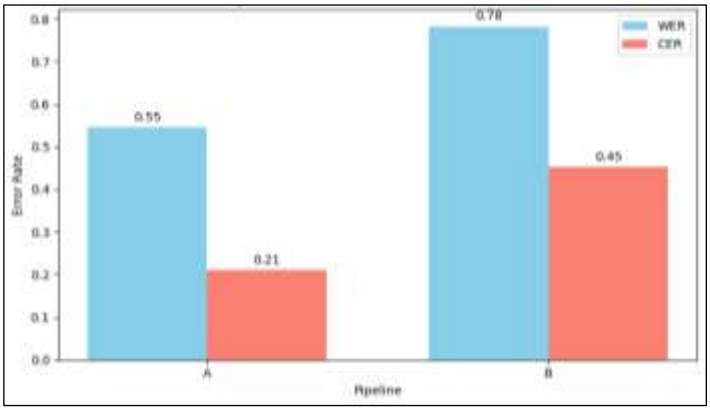


Figure 8: Comparison of WER and CER of Pipeline A and Pipeline B for Text-to-speech Conversion using Test Set.
Source: Authors, (2026).

IV.3 GUI FOR THE INTEGRATED SIGNSPEAK PIPELINE

A Streamlit-based application, namely SignSpeak is developed for the ease-of-use of users, whose interface is shown in Fig. 9. Once an image is detected by the sensor, the different phases of the proposed integrated framework are carried out in the background. For the validated signboard images, audio is generated to assist the commuters for safe mobility.



Figure 9: Lightweight GUI for Signspeak Utility.
Source: Authors, (2026).

IV.4 DISCUSSION

The experiments conducted in the former sections validate the efficacy of the integrated approach over the standalone usage of one model. The YOLOv11s performance demonstrates high accuracy and reliability even when it is trained on a small signboard dataset with manually annotated images. Its lightweight architecture enabled systematic inference while maintaining the detection quality. This balance between speed and accuracy makes the YOLOv11s suitable for the deployment for domain-specific tasks in low- resource environments, such as mobile or integrated systems [21]. Also, it improves the recognition performance of Gemini 3 in the text extraction phase, which is converted to reliable audio by gTTs. The integration of the detection-extraction-conversion phases is not only an efficient pipeline, but also delivers reliable output for navigation. The system maintains robustness under different conditions, including occlusion and resolution, that were incorporated while making the test set. The result highlights its potential for deployment as an assistive technology and its extension to multilingual accessibility because of the used Gemini 3 model.

V. CONCLUSION AND FUTURE SCOPE

SignSpeak introduces an assistive framework designed to enhance the awareness and navigation for visually challenged navigators on the pavements by detecting, recognizing and vocalizing the street/road signboards. This pipeline integrates the YOLOv11s model along with Gemini 3 for the high precision text recognition, ensuring the reliable performance in the real-world environments. To ease the usage, the recognized text is converted into speech using gTTS (google text to speech), providing natural auditory feedback to the users. Experimental evaluation affirmed the capability of the proposed integrated approach for text extraction over the stand-alone usage of Gemini model.

The proposed SignSpeak system for VIPs addresses the critical accessibility gap by enabling the visually challenged to access the street signs more efficiently and progress with greater reliance. As the current implementation of SignSpeak provides a strong foundation, several enhancements can be explored to broaden its application and usability. Inclusion of Multi-Object Detection along with important road elements like traffic lights, zebra crossings would enhance its applicability. Multi-language support may be included by extending the training data to support native languages (like Tamil, Hindi, Bengali, etc.) by leveraging the multilingual capabilities and global workflow of Gemini 3.

VI. AUTHOR'S CONTRIBUTION

Conceptualization: Sharanjit Kaur, Manju Bhardwaj, Kriti Misra and Preeti Marwaha.
Methodology: Sharanjit Kaur, Manju Bhardwaj, Kriti Misra and Preeti Marwaha.
Investigation: Sharanjit Kaur, Manju Bhardwaj, Kriti Misra and Preeti Marwaha.
Discussion of results: Sharanjit Kaur, Manju Bhardwaj, Kriti Misra and Preeti Marwaha.
Writing – Original Draft: Sharanjit Kaur, Manju Bhardwaj, Kriti Misra and Preeti Marwaha.
Writing – Review and Editing: Sharanjit Kaur, Manju Bhardwaj, Kriti Misra and Preeti Marwaha.
Resources: Sharanjit Kaur, Manju Bhardwaj, Kriti Misra and Preeti Marwaha.
Supervision: Sharanjit Kaur, Manju Bhardwaj, Kriti Misra and Preeti Marwaha.
Approval of the final text: Sharanjit Kaur, Manju Bhardwaj, Kriti Misra and Preeti Marwaha.

VII. ACKNOWLEDGMENTS

We acknowledge the research support provided by the Principal Acharya Narendra Dev College, New Delhi and financial assistance received from Ansusandhan Kosh and DBT Star Scheme to carry out the proposed research work.

VIII. REFERENCES

[1] M. Wahab, A. Helmy, A. A. Talib, H. A. Kadir, A. Johari, A. Noraziah, R. M. Sidek, and A. A. Mutalib, "Smart cane: Assistive cane for visually-impaired people," *International Journal of Computer Science Issues*, vol. 8, no. 4, 2011.

[2] W. Elmannai and K. Elleithy, "Sensor-based assistive devices for visually-impaired people: Current status, challenges, and future directions," *Sensors*, vol. 17, no. 3, p. 565, 2017, doi: 10.3390/s17030565.

[3] H. Shen and J. M. Coughlan, "Towards a real-time system for finding and reading signs for visually impaired users," in *Computers Helping People with Special Needs (ICCHP)*, vol. 7383, Springer, 2012, pp. 41–47.

[4] A. Lavric *et al.*, "A comprehensive survey on emerging assistive technologies for visually impaired persons," *Sensors*, vol. 24, no. 15, p. 4834, 2024.

[5] P. Mowar, T. Ganu, and S. Guha, "Towards optimizing OCR for accessibility," *arXiv preprintarXiv:2206.10254*, 2022.

[6] J. Huang, M. Kinateder, M. J. Dunn, W. Jarosz, X.-D. Yang, and E. A. Cooper, "An augmented reality sign-reading assistant for users with reduced vision," *PLoS One*, vol. 14, no. 5, 2019.

[7] X. Zhou, C. Yao, H. Wen, Y. Wang, S. Zhou, W. He, and J. Liang, "EAST: An efficient and accurate scene text detector," in *Proc. IEEE Conf. Computer Vision and Pattern Recognition (CVPR)*, 2017.

[8] M. Kannadhasan and M. M. S. Sriee, "Machine vision as environmental narrator: A study of Seeing AI and Google Lookout," *International Journal of Innovative Research in Technology*, vol. 12, no. 8, 2026.

[9] K. M. B. Laili, M. Z. Abdullah, S. Amiruddin, E. Sunardi, and J. Permatasari, "Integrating YOLOv8, EasyOCR, and gTTS for text detection in assistive technology for the visually impaired," *BIS Information Technology and Computer Science*, vol. 2, Apr. 2025, Art. no. V225008, doi: 10.31603/bistycs.185.

[10] Gemini Team, "Gemini: A family of highly capable multimodal models," *arXiv preprint arXiv:2312.11805*, 2023.

[11] J. K. Lau, K. K. W. Kong, J. H. Yong, P. H. Tan, Z. Yang, Z. Q. Yong, J. C. W. Low, C. Y. Chong, M. K. Lim, and D. Lo, "Synthesizing speech test cases with text-to-speech? An empirical study on the false alarms in automated speech recognition testing," in *Proc. 32nd ACM SIGSOFT Int. Symp. Software Testing and Analysis (ISSTA)*, New York, USA, 2023, pp. 1169–1181, doi: 10.1145/3597926.3598126.

[12] A. Prasanth, B. S. Kumar, and B. S. L. G. Varaprasad, "Portable camera based Text Reading of Objects for blind Persons",International Journal of Applied Engineering Research, vol 13, no. 17, pp. 12995-12999, 2018.

[13] B. K. Pandey, D. Pandey, S. Wariya, G. Aggarwal, and R. Rastogi, "Deep learning and particle swarm optimisation-based techniques for visually impaired humans' text recognition and identification," *Augmented Human Research*, vol. 6, no. 1, p. 14, 2021.

[14] J. Ganesan, A. T. Azar, S. Alsenan, N. A. Kamal, B. Qureshi, and A. E. H. Hassanien, "Deep learning reader for visually impaired," *Electronics*, vol. 11, no. 20, p. 3335, 2022.

[15] A. Y. Begum, R. Krishnamoorthy, A. T. Gaikwad, N. Malarvizhi, D. S. Rao, and N. Adinarayana, "Visionary text recognition system for assisting the visually impaired in identifying medicines and products with hybrid deep learning," in *Proc. 3rd Int. Conf. Automation, Computing and Renewable Systems (ICACRS)*, 2024, pp. 1369–1374.

[16] W. Yang, R. H. R. Zhong, and J. Lu, "CRAFT: Character region awareness for text detection", in *Proc. IEEE Conf. Computer Vision and Pattern Recognition (CVPR)*, 2016.

[17] N. M. Suresh, A. S. M. M., and R. P. Nair, "An assistive device for the visually impaired," in *Proc. Int. Conf. Power, Instrumentation, Control, and Computing (PICC)*, Thrissur, India, 2025, pp. 1–7, doi: 10.1109/PICC67314.2025.11291569.

[18] F. W. R. Moreira and G. Hermes, "Development of a cross-platform mobile application using Gemini to assist visually impaired individuals," 2024.

[19] R. Smith, "An overview of the Tesseract OCR engine," in *Proc. 9th Int. Conf. Document Analysis and Recognition (ICDAR)*, vol. 2, 2007, pp. 629–633.

[20] PaddleOCR Team, “PaddleOCR 3.0 technical report,” *arXiv preprint arXiv:2507.05595*, 2025.

[21] R. Khanam and M. Hussain, “YOLOv11: An overview of the key architectural enhancements,” *arXiv preprint arXiv:2410.17725*, 2024.

[22] M. Tkachenko, M. Malyuk, A. Holmanyuk, and N. Liubimov, “Label Studio: Data labeling software,” Heartex, Open-source tool, 2020–2025.

[23] M. A. M. Salehudin, S. N. Basah, H. Yazid, *et al*., “Analysis of optical character recognition using EasyOCR under image degradation,” *Journal of Physics: Conference Series*, 2023.

[24] J Chi, U Karn, H Zhan, E Smith, J Rando, Y Zhang, K Plawiak, ZD Coudert et. “Llama Guard 3 Vision: Safeguarding human-AI image understanding conversations,” *arXiv preprint arXiv:2411.10414*, 2024.

[25] N. M. Bhat, “pyttsx3: Text-to-speech cross-platform library,” 2017. [Online]. Available: https://pyttsx3.readthedocs.io.

[26] P. N. Durette *et al*., “gTTS: Google text-to-speech Python library,” 2017. [Online]. Available: https://github.com/pndurette/gTTS.

[27] S. van der Walt, J. L. Schönberger, J. Nunez-Iglesias, F. Boulogne, J. D. Warner, N. Yager, E. Gouillart, and T. Yu, “scikit-image: Image processing in Python,” *PeerJ*, vol. 2, p. e453, 2014, doi: 10.7717/peerj.453.

[28] G. Bradski and A. Kaehler, *Learning OpenCV: Computer Vision with the OpenCV Library*. Sebastopol, CA, USA: O’Reilly Media, 2008.

[29] DataClusterLabs, “Indian signboard image dataset,” Kaggle, 2024. [Online]. Available: https://www.kaggle.com/datasets/dataclusterlabs/indian-signboard-image-dataset

[30] “Indian Driving Dataset (IDD),” Kaggle, 2024. [Online]. Available: https://www.kaggle.com/datasets/mitanshuchakrawarty/new-idd-dataset.

[31] C. Li, S. Liu, and Z. Peng, “ESA-YOLO: An efficient scale-aware traffic sign detection algorithm based on YOLOv11 under adverse weather conditions,” *PLoS One*, vol. 20, no. 11, p. e0336863, 2025.

[32] E. Reiter, “A structured review of the validity of BLEU,” *Computational Linguistics*, vol. 44, no. 3, pp. 393–401, 2018.

[33] C.Y. Lin, “ROUGE: A package for automatic evaluation of summaries,” in *Proc. Workshop on Text Summarization Branches Out*, Barcelona, Spain, 2004, pp. 74–81.

[34] Y. Ren, X. Tan, T. Qin, S. Zhao, Z. Zhao, and T.Y. Liu, “Almost unsupervised text-to-speech and automatic speech recognition,” *arXiv preprint arXiv:1905.06791*, 2019.

[35] A. Ali and S. Renals, “Word error rate estimation for speech recognition: e-WER,” in *Proc. 56th Annual Meeting of the Association for Computational Linguistics (ACL)*, Melbourne, Australia, 2018, pp. 20–24.

[36] C. Park, H. Kang, and T. Hain, “Character error rate estimation for automatic speech recognition of short utterances,” in *Proc. 32nd European Signal Processing Conf. (EUSIPCO)*, Lyon, France, 2024, pp. 131–135.

Journal of Engineering and Technology for Industrial Applications

ITEGAM-JETIA

Manaus, v.12 n.60, p.997-1009 July/August, 2026.
DOI: https://doi.org/10.5935/jetia.v12i60.3925

ISSN ONLINE: 2447-0228

RESEARCH ARTICLE OPEN ACCESS

MAPPING THE LANDSCAPE OF SUSTAINABLE PROCUREMENT: A SYSTEMATIC LITERATURE REVIEW AND BIBLIOMETRIC ANALYSIS

Irfan Veryanto[1], M. Mujiya Ulkhaq*[2] and Heru Prastawa[3]

[1, 2, 3]Department of Industrial Engineering, Diponegoro University, Semarang, Indonesia.

[1]https://orcid.org/0009-0003-1686-5420, [2]https://orcid.org/0000-0002-9553-5846, [3]https://orcid.org/0000-0003-4966-162X

E-mail: *ulkhaq@live.undip.ac.id

ARTICLE INFO

Article History
Received on: March 05, 2026
Reviewed on: April 05, 2026
Accepted on: July 01, 2026
Published on: July 31, 2026

Keywords:
ESG,
PRISMA methodology,
Systematic literature review,
Sustainable procurement.

ABSTRACT

Sustainable procurement (SP) has emerged as a strategic mechanism for integrating environmental, social, and economic considerations into organizational decision-making. This study aims to synthesize and analyze the intellectual and thematic development of SP research through a systematic literature review (SLR) combined with bibliometric analysis. Using the PRISMA framework, 4,425 Scopus-indexed publications were initially identified, from which 138 peer-reviewed journal articles met the inclusion criteria for in-depth analysis. The findings reveal a significant increase in research attention since 2012, reflecting SP's evolution from a compliance-based policy tool to a strategic capability that drives innovation and sustainability performance. Five major thematic clusters were identified: (1) sustainability in public procurement, (2) the role of SP in the circular economy, (3) sustainable construction, (4) the role of corporate social responsibility (CSR), and (5) SP in higher education. Theoretically, the study draws on institutional theory, stakeholder theory, and the resource-based view to explain how external pressures, stakeholder expectations, and organizational capabilities jointly influence SP adoption and implementation. The results underscore the importance of robust institutional frameworks, leadership, and capability-building in advancing sustainable procurement. Finally, the study highlights future research opportunities in digital transformation, cross-sectoral collaboration, and the measurement of SP's contribution to environmental, social, and governance (ESG) outcomes, thereby offering actionable insights for policymakers, practitioners, and academics.

Copyright ©2026 by authors and Galileo Institute of Technology and Education of the Amazon (ITEGAM). This work is licensed under the Creative Commons Attribution International License (CC BY 4.0).

I. INTRODUCTION

Sustainable improvement has become a crucial worldwide concern due to the increase in environmental degradation and the depletion of natural resources [1] The sustainable development goals (SDGs) established by the United Nations provide a comprehensive framework for addressing these global challenges and promoting a sustainable future. In particular, SDG 11 calls for the creation of sustainable cities and communities [2], while SDG 12 emphasizes responsible consumption and production practices. Achieving these goals requires coordinated efforts across multiple domains—including procurement, logistics, and organizational transformation—where the strategic role of procurement is vital for advancing sustainable practices and realizing SDGs 11 and 12 [3] In response, organizations are increasingly expected to adopt sustainable practices to mitigate environmental, social, and economic pressures [4] At the heart of this transformation lies sustainable procurement (SP), a key driver for achieving sustainability goals through responsible sourcing, supplier engagement, and value-based decision-making [5], [6] SP is also regarded as an effective strategy for advancing the SDGs by integrating the pillars of sustainability (i.e., economic, environmental, and social) into procurement practices [7] It entails the acquisition of goods and services that deliver optimal value for money while minimizing negative environmental impacts and promoting social equity throughout the product or service lifecycle [8] By integrating these principles into organizational procurement systems, SP enhances resource efficiency, reduces waste, and strengthens social well-being, ultimately positioning procurement as a catalyst for sustainable organizational performance and long-term development [9].

Ultimately, aligning purchasing decisions with sustainability principles transforms procurement into both a managerial challenge and a strategic opportunity for organizations striving to balance operational efficiency with corporate responsibility in the pursuit of sustainable development [10], [11] Globally, governments have increasingly developed procurement policies to advance sustainability and social responsibility objectives. In Northern Ireland, for instance, all public contracts are required to include at least a 10% weighting for social value criteria, while in the United States, federal agencies prioritizes sustainable products through EPA ecolabel standards [12]. Similar initiatives can be observed in Scotland's Procurement Reform Act (2014), Canada's Federal Sustainable Development Strategy, the European Union Procurement Directive (2014), and Spain's Law 9/2017, each of which embeds sustainability considerations within public purchasing frameworks [13], [14]. More broadly, SP is becoming increasingly institutionalized through international regulatory frameworks, including the European Union procurement directives and guidelines developed by global organizations such as the OECD, ILO, WTO, and UNEP [15]. Collectively, these frameworks promote greater transparency, accountability, and sustainability across global supply chains, reinforcing SP as a critical instrument for achieving sustainable development. Despite its growing significance, the implementation of SP remains a considerable challenge for many organizations, particularly in developing countries, due to the inherent complexity of procurement processes and supply chain structures [16], [17], [18]. These complexities often hinder organizations from fully understanding, operationalizing, and monitoring sustainability principles across diverse suppliers and market contexts [19].

Effective implementation of SP requires a comprehensive understanding of its core principles and operational mechanisms (i.e., encompassing risk management, supplier evaluation, and ethical sourcing) to proactively mitigate adverse environmental and social impacts through robust due diligence. A persistent challenge also lies in balancing economic viability with sustainability objectives, as decision-makers must reconcile short-term financial constraints with long-term environmental and social commitments. Achieving this balance demands a holistic approach that integrates life-cycle costing, value chain analysis, and resource optimization to ensure both competitiveness and sustainability [20]. Moreover, barriers such as limited institutional support, weak policy enforcement, and insufficient stakeholder engagement continue to impede the widespread adoption of SP practices [21], [22]. Given these persistent challenges, a comprehensive understanding of the current state of research on SP is essential to inform both theory and practice. Conducting a systematic literature review (SLR) provides a robust approach for synthesizing and mapping the existing body of knowledge, identifying research trends, influential scholars, and methodological gaps within the SP domain [23], [24]. These methods enable a structured and quantitative evaluation of academic output, revealing how SP has evolved conceptually and empirically across disciplines and regions. To date, only one study (from Scopus database) has systematically synthesized the SP knowledge base. Notably, Kabra et al. [25] conducted a bibliometric analysis mapping the intellectual structure of SP research, identifying key thematic clusters such as green supply chain practices, socially responsible purchasing, and public procurement.

However, their study primarily offered a descriptive mapping of publication trends and research networks, without critically examining the contributions of SP. In contrast, the present study adopts a combined SLR and bibliometric approach to provide a more comprehensive and analytical perspective, by exploring the evolution of SP research while assessing its contributions. Beyond Kabra et al. [25], related reviews have examined adjacent areas such as circular procurement management [26], green purchasing behavior [27], and sustainable procurement risks in the construction sector [28]. While these studies contribute valuable insights, they focus on specific procurement dimensions or sectoral contexts rather than providing a holistic synthesis of sustainable procurement as a strategic framework across industries. Therefore, this study fills an important gap by offering an integrative understanding of SP research trends, challenges, and its contributions through a rigorous SLR and bibliometric analysis.The remainder of this paper is structured as follows. Section 2 describes the research methodology, outlining the systematic literature review protocol, bibliometric analysis procedures, and data collection steps adopted for this study. Section 3 presents the results and findings, including descriptive bibliometric outcomes, thematic clusters, and key insights derived from the systematic review. Section 4 provides an in-depth discussion, interpreting the results in light of existing theories, and practical implications. Finally, Section 5 concludes the study by summarizing the main findings, highlighting limitations, and proposing directions for future research.

II. METHODOLOGY

A systematic literature review (SLR), when combined with bibliometric analysis, offers a robust and comprehensive approach for examining the development and intellectual structure of a research domain [29]. A rigorously conducted SLR enables the identification, selection, and synthesis of relevant studies based on predetermined inclusion and exclusion criteria, thereby minimizing bias and enhancing reliability [23]. In parallel, bibliometric analysis quantitatively evaluates the research landscape by identifying publication trends, influential authors, and thematic relationships through citation, co-citation, and keyword co-occurrence analyses. Integrating these methods provides both qualitative depth and quantitative breadth, offering a holistic understanding of the field [24]. Data were retrieved from the Scopus database, recognized for its extensive coverage of peer-reviewed journals and strong indexing of sustainability and management research [30], [31], [32], [33]. The review followed the Preferred Reporting Items for Systematic Reviews and Meta-Analyses (PRISMA) framework and commenced on May 31, 2025. An initial search of article titles, abstracts, and keywords using the Boolean string "sustainable" AND "procurement" yielded 4,425 documents. After screening the titles, abstracts, and keywords for relevance, the results were narrowed down to 601 documents. To ensure quality and consistency, only journal articles were selected, and for the sake of readability, only those written in English were included. As a result, a total of 138 articles were retained for the final analysis. A bibliometric analysis was performed using VOSviewer. This tool facilitated visualization and network analysis of research collaboration, thematic evolution, and intellectual structure. Key analytical dimensions included:

- Performance analysis: publication trends and dominant subject areas.
- Science mapping: bibliographic coupling networks.
- Keyword co-occurrence analysis: identification of dominant themes and emerging topics.

Prior to analysis, data were standardized to merge author name variants, institutional affiliations, and keyword synonyms. Duplicate and incomplete records were removed. Network maps were normalized using the association strength method in VOSviewer to ensure meaningful clustering.

III. FINDINGS

III.1 PUBLICATION TRENDS

The bibliometric analysis of publication output in the field of SP reveals a clear upward trajectory when examined by publication year (see Figure 1). The earliest documented studies appeared in 2004, marking the beginning of scholarly attention to this emerging topic. During the initial years, research output remained modest, with only a few publications recorded up to 2011, reflecting the early developmental stage of the field as sustainability concerns were only beginning to gain widespread recognition. This slow growth period indicates that SP had not yet been fully recognized as a distinct academic and professional domain. From 2012 onwards, the number of publications increased steadily, reaching its peak in 2023 and 2024. This surge signifies heightened global interest and recognition of sustainable procurement as a critical instrument for achieving sustainability objectives [5]. The growth aligns with broader developments such as rising environmental awareness, the establishment of supportive regulatory frameworks, and an expanding understanding of the strategic role of public procurement in advancing sustainable development goals [34]. Although a slight decline in publication numbers appears in 2025, this is likely due to incomplete data for the year rather than an actual reduction in research activity.

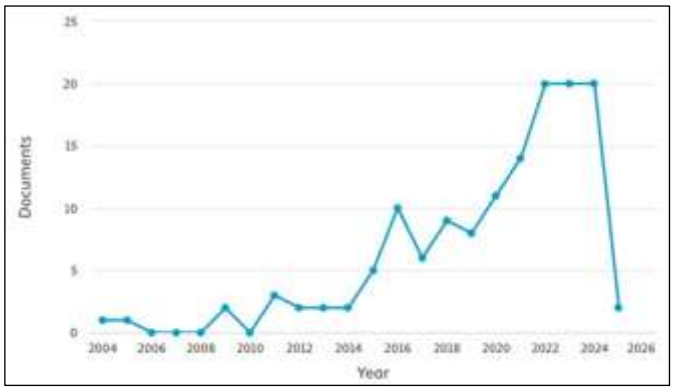


Figure 1: Publication Trends.
Source: Authors (2026).

III.2 SUBJECT AREAS

An analysis by subject area reveals that research on SP is predominantly situated within the fields of "business, management, and accounting," indicating strong engagement with SP as a strategic organizational function (see Table 1). This dominance reflects an increasing recognition of procurement as a core component of corporate sustainability, emphasizing its role in driving competitive advantage through responsible sourcing, resource efficiency, and value creation. The prominence of this subject area aligns with studies that explore how organizations integrate sustainability principles into procurement and supply chain management, often linking these practices to improvements in economic and financial performance **Erro! Fonte de referência não encontrada.**.

Table 1: Distribution of documents by subject area.

Subject area	Documents
Business, management, and accounting	58
Social sciences	47
Environmental science	46
Engineering	45
Energy	35
Computer science	20
Decision sciences	15
Economics, econometrics, and finance	11
Agricultural and biological sciences	5
Mathematics	5

Source: Authors, (2026).

Subsequently, the substantial representation of the "social sciences" further underscores the societal and policy-oriented dimensions of sustainable procurement. Research within this domain frequently addresses the role of procurement in promoting ethical behavior, social inclusion, and governance accountability [35]. Similarly, the strong contributions from "environmental science" and "engineering" highlight the technical and environmental focus of the field, particularly concerning reducing ecological footprints, promoting eco-friendly technologies, and developing sustainable production systems [36]. Additional contributions from fields such as "energy", "computer science", "decision sciences", and "economics, econometrics, and finance" demonstrate the multidisciplinary nature of SP research [37]

These areas reflect the integration of technological, analytical, and economic perspectives into procurement-related sustainability efforts. Although less represented, disciplines such as "agricultural and biological sciences", as well as "mathematics" indicate emerging directions in the field, potentially expanding future research into data-driven modeling, life-cycle analysis, and sustainable resource management.

III.3 GEOGRAPHICAL AND INSTITUTIONAL DISTRIBUTION OF RESEARCH

The upward trend in SP publications since 2012 is also reflected in the country-level analysis, which highlights the expanding global engagement with this field. The United Kingdom (UK) leads in both the number of documents and total citations, suggesting a mature and influential research landscape supported by well-established academic programs, policy initiatives, and funding schemes promoting sustainable practices (see Table 2). Germany follows closely, exhibiting a high citation count relative to its publication output—an indication of the strong impact and quality of its research contributions [38].

Table 2: Bibliographical coupling data by country.

Country	Documents	Citations	Total Link Strength
United Kingdom	40	2364	20
Brazil	11	501	7
United States of America	11	181	4
Australia	11	213	1
Italy	10	293	10
Netherlands	7	208	7
France	6	305	9
Poland	6	196	5
Germany	6	608	4
Ghana	6	75	4

Source: Authors, (2026).

The "Total Link Strength" metric, representing the intensity of collaborative networks, further enhances this analysis. Countries such as Brazil and Italy demonstrate high link strength scores, reflecting the benefits of international collaboration in fostering knowledge exchange and resource sharing [39]. These findings help identify key nations and institutions driving innovation and best practices in sustainable procurement. For example, the city of Copenhagen's renewable energy–oriented procurement policies exemplify how government initiatives can operationalize sustainability principles [36]. Further exploration of policy frameworks and research programs in the UK and Germany could provide valuable insights into the institutional mechanisms that underpin their leadership in SP research and implementation [40]. The inclusion of Ghana in the dataset also reflects the emerging research contributions from Africa, signaling growing global awareness of SP's importance [39]. The diversification of research contexts points to the need for regionally focused studies that address local challenges and opportunities, facilitating broader and more effective implementation of sustainable procurement practices. At the institutional level, publication data reveal that universities such as UNSW Sydney, the University of Leeds, and Liverpool John Moores University are among the most productive contributors, indicating a strong research focus on sustainable procurement in Australia and the UK. Notably, Fahim Ullah of UNSW Sydney has contributed extensively to the literature on sustainable development and risk management. These universities likely host specialized research centers dedicated to sustainability, supply chain management, and the circular economy. Additionally, institutions such as Universidade Federal Fluminense (Brazil), University of Belgrade (Serbia), and Kwame Nkrumah University of Science and Technology (Ghana) demonstrate the geographical broadening of SP research beyond traditional centers. Other contributors, including the University of Johannesburg, King Abdulaziz University, and Universidade Estadual Paulista Júlio de Mesquita Filho, further emphasize the global diffusion of research efforts and the growing inclusivity of sustainability scholarship.

III.4 THETAMIC ANALYSIS

Keywords co-occurrence analysis provides a powerful methodological approach for deconstructing the knowledge structure of SP. By mapping relationships among frequently co-occurring keywords, it reveals the dominant themes, conceptual linkages, and research clusters within the field, thereby offering valuable insights into key areas of focus and potential research gaps. As the central theme, SP shows strong associations with foundational concepts such as "supply chain management," "sustainability," and "performance", see Figure 2. The frequent co-occurrence of "supply chain management" and "sustainability" underscores their interdependence, reflecting the growing recognition that sustainable procurement is integral to achieving broader supply chain sustainability objectives. The prominence of "performance" highlights the field's emphasis on measuring the outcomes of SP practices—particularly their contributions to reducing environmental impact and enhancing social responsibility. Similarly, the frequent appearance of keywords such as "circular economy," "life cycle assessment," and "environmental impact" emphasizes the environmental orientation of SP research, demonstrating a strong focus on resource efficiency, waste reduction, and eco-innovation.

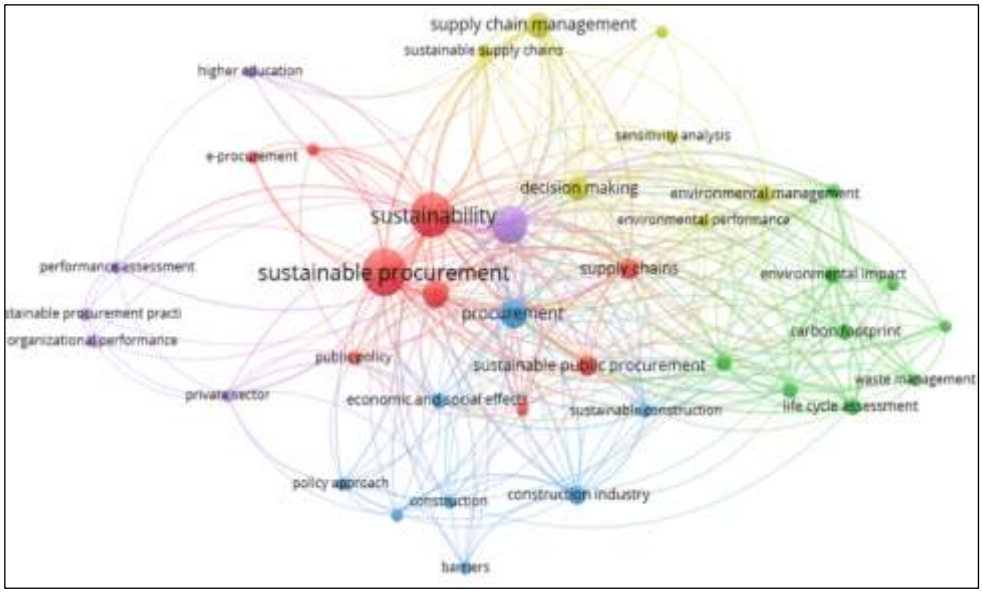


Figure 2: Keywords Co-occurrence Network.
Source: Authors (2026).

Another emerging thematic cluster conceptualizes the strategic deployment of SP within higher education institutions, highlighting its potential to enhance organizational performance and advance institutional sustainability goals. The co-occurrence of keywords such as "corporate social responsibility," "decision making," "environmental management," "environmental performance," and "supply chain management" reflects growing scholarly attention to the role of SP in advancing corporate social responsibility (CSR) agendas. This association demonstrates that procurement decisions are increasingly viewed not merely as administrative processes but as strategic levers for sustainability-driven value creation. Furthermore, the clustering of keywords such as "barriers," "construction industry," "policy approach," "project management," and "sustainable construction" highlights the sectoral challenges and opportunities associated with implementing SP practices in construction and infrastructure development. In these contexts, researchers have emphasized the influence of policy frameworks and governance mechanisms in shaping SP outcomes. The presence of terms such as "public green procurement," "university," and "sustainable development goals (SDGs)" points to the institutionalization of sustainability principles within the public sector and academia. However, in many cases, legal and regulatory constraints limit universities' ability to fully integrate sustainability into their procurement decisions, despite their substantial purchasing capacity [41]. As major economic and social actors, universities represent critical environments for advancing sustainable procurement. They allocate significant financial resources for a wide range of activities—including teaching, research, administration, and campus operations—providing a fertile ground for interdisciplinary innovation and the promotion of sustainable development principles. Thus, higher education institutions not only serve as laboratories for testing sustainability initiatives but also play a pivotal role in modeling and disseminating best practices in SP. Next, the keywords co-occurrence analysis revealed five major thematic clusters representing the intellectual and conceptual foundations of SP research (see Table 3). Each cluster reflects distinct yet interconnected perspectives on how sustainability principles are operationalized within procurement systems across public, private, and institutional contexts.

Table 3: Thematic analysis based on Keywords.

Cluster Color	Keywords	Cluster Name (Theme)
Red	e-procurement, green procurement, procurement strategy, public policy, public procurement, supply chains, sustainability, sustainable procurement, sustainable public procurement	Sustainability in public procurement
Green	carbon footprint, circular economy, climate change, environmental impact, environmental sustainability, life cycle analysis, life cycle assessment, waste management	The role of sustainable procurement in circular economy
Blue	barriers, construction industry, economic and social effects, policy approach, procurement, project management, sustainable construction	Sustainable construction
Yellow	corporate social responsibility, decision making, environmental management, environmental performance, sensitivity analysis, supply chain management, sustainable supply chain	The role of corporate social responsibility
Purple	higher education, organizational performance, performance assessment, private sector, sustainable development, sustainable procurement	Sustainable procurement in higher education

Source: Authors, (2026).

III.4.1 Cluster 1: Sustainability in Public Procurement

The theme of "sustainability in public procurement" represents a central pillar of SP research, highlighting the transformation of public sector procurement into a strategic instrument for advancing sustainability objectives. This cluster, encompassing keywords such as e-procurement, green procurement, procurement strategy, public policy, public procurement, supply chains, sustainability, and sustainable public procurement, underscores how the integration of sustainability principles within public purchasing frameworks can drive transparency, accountability, and environmental stewardship across government operations.

The adoption of e-procurement systems marks a significant advancement in this regard. As a digital innovation, e-procurement not only streamlines procurement processes but also embeds sustainability criteria directly into decision-making frameworks. Basheka et al. [42] emphasize that implementing e-procurement enhances institutional quality by enabling more comprehensive supplier evaluations that include social, economic, and environmental indicators alongside traditional cost metrics. Recent studies also demonstrate how big data analytics and emerging digital technologies strengthen governance and sustainability outcomes in public procurement. According to Sanda et al. [43], big data tools enhance accountability and transparency by identifying irregularities, enabling real-time oversight, and supporting data-driven decisions. Likewise, Da Silveira et al. [35] discuss the potential of blockchain technology in ensuring traceability and verification of sustainability practices throughout the supply chain, improving compliance monitoring and stakeholder trust. However, the transition toward sustainable e-procurement is not without challenges. As Tao et al. [44] observe, public institutions often face institutional barriers and cost-oriented mindsets that limit the adoption of sustainability-focused approaches. Despite growing demand for sustainable goods and services, procurement practices frequently prioritize short-term cost savings over long-term sustainability gains. Fernández-Pérez and Luque-Vílchez [45] argue that overcoming this imbalance requires a cultural and organizational shift—one that values lifecycle costing, environmental impact mitigation, and social inclusion as core procurement priorities. In addition, the role of collaborative frameworks and stakeholder engagement is crucial in advancing sustainability within public procurement. Zin Zawawi et al. [46] highlight that engaging multiple stakeholders, from policymakers to suppliers and civil society, fosters shared learning, innovation, and collective accountability, all of which are essential for achieving meaningful sustainability outcomes. External pressures also play a role; Vluggen et al. [47] note that regulatory frameworks, social expectations, and international sustainability standards can reinforce accountability and stimulate the institutionalization of sustainable procurement practices. ustainability in public procurement, therefore; is evolving from a compliance-driven activity into a strategic governance mechanism for achieving sustainable development. By leveraging digital innovations such as e-procurement, big data analytics, and blockchain, public institutions can enhance transparency and embed sustainability into all stages of procurement. Nevertheless, realizing this potential requires not only technological innovation but also institutional reform, cross-sector collaboration, and long-term commitment to aligning procurement with sustainability imperatives.

III.4.2 Cluster 2: The role of sustainable procurement in circular economy

Minimizing environmental impact through the adoption of circular economy (CE) principles has become a cornerstone of sustainable development. The transition from a linear “take–make–dispose” model toward a circular economic system emphasizes resource efficiency, waste reduction, and product life-cycle optimization, allowing businesses and societies to mitigate ecological damage while fostering long-term economic resilience. Within this paradigm, SP plays a pivotal role by prioritizing eco-efficient materials, renewable resources, and closed-loop supply chains, thereby serving as a key operational mechanism for realizing circular economy objectives. The integration of circular economy principles into procurement practices extends across diverse sectors and scales. Education is among the most influential arenas for driving this transition. El Mahdi Safhi et al. [48] highlight the importance of embedding sustainability and CE education into academic curricula, noting that future decision-makers must develop a deep understanding of these concepts to effectively champion sustainable practices. This educational foundation ensures that emerging professionals can embed circular thinking into procurement, production, and organizational decision-making processes across industries. In the healthcare sector, circular principles are increasingly influencing procurement strategies aimed at improving efficiency and reducing waste. Di Virgilio et al. [49] emphasize that sustainable procurement in hospitals enhances operational efficiency while minimizing environmental impacts. Their study underscores that the inclusion of performance indicators (such as cost-effectiveness, compliance, and resource utilization) enables institutions to assess sustainability outcomes more holistically, aligning healthcare operations with circular economy goals. The construction industry presents one of the most promising yet challenging domains for implementing circular procurement. Aboginije et al. [50] stress the importance of holistic waste management in construction and demolition projects, particularly in developing contexts such as Nigeria. Their findings show that integrating circular practices, such as material reuse and recycling, can substantially reduce waste generation and environmental degradation. This approach aligns procurement strategies with life-cycle management and resource optimization, reinforcing the sector’s contribution to sustainable urban development.

From a supply chain perspective, CE implementation is strengthened through strategic supplier partnerships and engagement. Caldera et al. [51] demonstrate that in Australia’s built environment sector, integrating CE elements into procurement regulations encourages supplier collaboration in areas such as product life extension, component recovery, and material recirculation. These partnerships create innovation ecosystems that support sustainable material sourcing, reduce the carbon footprint, and enhance circular supply chain resilience. Similarly, the link between supplier selection and circular procurement is critical. Le et al. [52] highlight the need for supplier evaluation frameworks that incorporate environmental and social performance metrics alongside traditional cost and quality considerations. Such systematic approaches ensure that procurement decisions reinforce circularity objectives by prioritizing suppliers committed to sustainability and low-impact production. Life-cycle assessment (LCA) methodologies further support this integration by offering a comprehensive understanding of environmental impacts throughout a product’s lifespan, thereby guiding more informed and responsible purchasing choices. Recent advances in decision-support systems and modeling have further enhanced the alignment of procurement with circular economy objectives. Ahamed et al. [53] propose multi-criteria decision-making (MCDM) models that embed sustainability parameters into supplier selection, combining cost efficiency with ecological and social considerations. These heuristic models provide decision-makers with structured tools for balancing performance and sustainability trade-offs, reinforcing the contribution of procurement to both resource efficiency and economic durability.The synergy between SP and CE principles forms a powerful foundation for minimizing environmental impacts and promoting systemic sustainability. By integrating sustainability education, fostering supplier collaboration, improving waste management practices, and adopting robust evaluation frameworks, organizations can accelerate the transition toward a regenerative and resource-efficient economic model. SP thus emerges not merely as a management function but as a transformative enabler of the circular economy, bridging environmental responsibility with long-term organizational performance and societal well-being.

III.4.3 Cluster 3: Sustainable construction

The construction industry plays a pivotal role in advancing environmental and social sustainability but continues to face substantial challenges in the adoption of sustainable practices. As one of the most resource-intensive sectors, construction significantly impacts land use, energy consumption, and waste generation. Overcoming these challenges requires systemic approaches that integrate sustainability principles throughout project lifecycles. In this context, integrated project management (IPM) has emerged as a critical mechanism for promoting sustainable construction, offering a structured framework for stakeholder collaboration, decision-making, and resource optimization. The application of IPM fosters collaboration among project stakeholders, streamlines communication, and enhances decision-making processes, factors essential for the effective implementation of sustainability strategies in construction. According to Fregonara et al. [54], improving governance structures and enhancing access to targeted resources and collaborative tools are key enablers for advancing sustainable procurement practices within construction projects. Strengthened governance ensures accountability, transparency, and alignment of stakeholder goals, thus creating an environment conducive to sustainable outcomes. A major barrier to sustainability adoption in construction lies in the lack of leadership commitment and institutional knowledge. Caldera et al. [51] emphasize that the COVID-19 pandemic exposed critical weaknesses in project resilience and adaptability, underscoring the need for integrated and flexible procurement approaches. Empowering leadership teams with sustainability knowledge and competencies is therefore vital to embedding sustainability principles into project management frameworks and ensuring that organizations can respond effectively to future disruptions. Another pressing concern is construction and demolition waste, which remains one of the largest contributors to environmental degradation in the built environment.

Aboginije et al. [50] highlight that the adoption of integrated project management techniques can substantially improve waste management processes by enhancing planning, execution, and monitoring capabilities. Such integration enables firms to adopt circular waste management frameworks that promote recycling, material reuse, and reduction of landfill dependency—thereby minimizing the overall environmental footprint of construction projects. Technological innovation, particularly the use of e-procurement systems, further strengthens the implementation of sustainable construction practices. Jelodar et al. [55] note that digital procurement platforms enhance supplier engagement, improve decision-making, and enable organizations to assess suppliers' sustainability performance more effectively. The integration of IPM tools with e-procurement systems allows for better tracking, reporting, and compliance monitoring, ensuring that environmental standards and sustainability criteria are consistently applied across projects. Stakeholder collaboration also plays a crucial role in overcoming sustainability barriers within construction projects. Casanovas-Rubio et al. [56] argue that multi-stakeholder engagement and dialogue are essential for minimizing the social and environmental impacts associated with construction activities. Collaborative approaches foster shared accountability, mutual learning, and consensus-building, all of which strengthen the social legitimacy and practical implementation of sustainability objectives. In addition to governance and collaboration, organizational culture remains a determining factor in the success of sustainable construction initiatives. Oyewobi and Jimoh [57] identify attitudinal resistance and a lack of awareness as persistent barriers to adopting sustainable procurement in the construction industry. Through IPM, organizations can implement change management strategies that reshape stakeholder mindsets, bridge knowledge gaps, and foster a culture of continuous sustainability improvement.

III.4.4 Cluster 4: The role of corporate social responsibility

Corporate social responsibility (CSR) plays a pivotal role in shaping SP by embedding ethical, social, and environmental considerations into procurement and operational decisions, thereby promoting responsible and transparent business practices. Through such alignment, firms not only address stakeholder expectations but also reinforce ethical, social, and environmental accountability across the entire value chain. A key dimension of this integration lies in aligning corporate strategies with sustainable procurement practices. Di Virgilio et al. [49] highlight that organizations embedding sustainability within their procurement systems experience tangible benefits, including improved compliance, enhanced stakeholder trust, and increased client satisfaction. By operationalizing CSR principles in procurement, firms can leverage their social and environmental commitments to strengthen brand reputation and build long-term stakeholder relationships. This alignment ensures that procurement decisions reflect a balance between economic performance, social equity, and environmental responsibility—the three pillars of sustainability. To achieve this, organizations must improve access to resources and managerial tools that support CSR-driven practices. Aluchna and Rok [58] emphasize that empowering firms with tools for ethical sourcing, sustainable material selection, and supplier engagement is essential for enhancing operational efficiency and accountability. Such practices cultivate a corporate culture that values ethics and sustainability alongside profitability, reinforcing the broader CSR agenda.

Emerging technologies also play a transformative role in integrating CSR within supply chains. Sanda et al. [43] demonstrate that big data analytics can be applied to monitor supplier compliance with CSR standards, enabling firms to assess environmental and social risks in real time. This data-driven approach enhances transparency, mitigates unethical sourcing risks such as child labor or environmental harm, and supports informed decision-making in procurement. Similarly, Letunovska et al. [59] highlight the potential of green technologies and reverse logistics in amplifying CSR outcomes, showing how digital platforms and e-procurement tools can streamline sustainable practices while improving traceability and compliance. Nevertheless, effective CSR integration requires overcoming organizational and cultural barriers. Ahamed et al. [53] argue that strong institutional frameworks and supportive policy environments are vital for embedding sustainability within supply chains. Companies must cultivate inclusive and participatory cultures that encourage stakeholder engagement and ensure that sustainability objectives are championed at all organizational levels. Leadership commitment, cross-functional coordination, and transparent communication are critical enablers of this transformation. Complementing these managerial and technological dimensions, LCA frameworks offer an evidence-based approach to evaluating the environmental impacts of procurement choices in relation to CSR commitments [44]. By examining the entire lifecycle of products and materials—from production to disposal—LCA enables firms to make procurement decisions that prioritize long-term ecological balance over short-term cost considerations. This perspective aligns with CSR's foundational goals of transparency, accountability, and sustainable value creation.

III.4.5 Cluster 5: Sustainable procurement in higher education

The incorporation of SP practices within higher education institutions (HEIs) plays a crucial role in advancing both organizational performance and sustainable development objectives. By addressing environmental stewardship, social accountability, and economic efficiency, SP enables universities to align their operational and strategic decisions with broader sustainability goals. Within educational settings, sustainable procurement fosters responsible resource use, enhances stakeholder engagement, and reinforces the institution's commitment to sustainability-driven governance. A growing body of literature highlights that SP can significantly enhance organizational performance by cultivating a culture of sustainability among academic staff, administrators, and students. The integration of sustainability principles into procurement not only improves operational efficiency but also builds institutional capacity for sustainability-focused research and innovation. This cultural transformation ensures that procurement choices reflect the environmental and ethical values of the institution, creating a framework where education, research, and operations reinforce one another in pursuit of sustainability. Education itself serves as a key enabler of sustainable procurement adoption. El Mahdi Safhi et al. [48] underscore the importance of embedding sustainability and circular economy education into university curricula to prepare future leaders capable of implementing and advocating for sustainable practices. By equipping students with practical knowledge and critical awareness, HEIs contribute to developing a new generation of decision-makers who integrate sustainability into organizational strategies and professional practice—thereby amplifying the long-term impact of SP both within and beyond academia. External influences, such as the COVID-19 pandemic, have also reshaped sustainable procurement in HEIs.

Caldera et al. [51] demonstrate that the pandemic prompted universities to reassess procurement systems, revealing the need for greater resilience, adaptability, and innovation in managing supply chains. Flexible procurement strategies, supported by digital platforms and collaborative frameworks, can strengthen institutional agility and enable HEIs to maintain sustainability commitments even under disruptive circumstances. Institutional drivers remain critical for embedding SP practices effectively. Leal Filho et al. [8] identify policy frameworks, leadership commitment, and stakeholder collaboration as essential enablers of sustainable procurement integration in HEIs. Leadership that prioritizes transparency, shared accountability, and cross-departmental cooperation can mitigate organizational resistance and foster the successful implementation of sustainability initiatives. In this regard, effective leadership acts as both a facilitator of cultural change and a catalyst for innovation, ensuring sustainability becomes a central element of institutional governance. SP also offers competitive advantages for universities, enhancing reputation, compliance, and funding opportunities. As Di Virgilio et al. [49] note, HEIs that adopt sustainable procurement strategies not only improve operational compliance and stakeholder satisfaction but also attract partnerships and sponsorships aligned with sustainability objectives. Demonstrating commitment to sustainable practices strengthens institutional credibility and aligns HEIs with global efforts such as the UN SDGs. The intersection between SP and CSR also provides an additional framework for amplifying impact. Integrating CSR into procurement processes can increase engagement among faculty, students, and external partners, fostering shared ownership of sustainability goals. This alignment allows HEIs to leverage their procurement power to promote social equity, ethical sourcing, and environmental conservation, thereby embedding sustainability into the institution's organizational identity.

IV. DISCUSSION

The results of the thematic analyses reveal that SP is increasingly conceptualized not merely as a technical or operational activity, but as a strategic, institutionally embedded, and stakeholder-sensitive domain. The five clusters (i.e., sustainability in public procurement, SP in CE, sustainable construction, the role of CSR, and SP in HEI) reflect how SP has evolved to bridge digital, environmental, governance, and educational spheres. To interpret these results, this discussion draws upon institutional theory, stakeholder theory, and the resource-based view (RBV) as key analytical frameworks that explain the patterns, drivers, and outcomes observed in the literature. Interpreting these findings through theoretical lenses helps explain the observed trends, identify underlying mechanisms, and derive practical implications.

IV.1 THEORETICAL CONSIDERATION

IV.1.1 Institutional theory

Institutional theory provides a robust framework for understanding how regulatory environments, policy frameworks, and institutional norms shape the adoption and diffusion of SP practices across sectors. According to DiMaggio and Powell [60], organizations face three primary types of institutional pressures—coercive, normative, and mimetic—that drive conformity and legitimacy-seeking behaviors. These forces are particularly evident in how SP becomes institutionalized through laws, public policies, and professional norms. Findings from Cluster 1 demonstrate that governments play a pivotal role in institutionalizing SP through regulatory mandates, e-procurement systems, and transparency mechanisms. Such institutional reforms encourage organizations to embed sustainability into procurement processes to comply with evolving norms and expectations. For instance, the European Union's Green Public Procurement (GPP) directives have effectively normalized sustainability as a standard component of public contracting, shaping how organizations define procurement excellence [61]. Similarly, digital procurement platforms and data-driven monitoring systems have enhanced accountability and governance efficiency, reflecting how institutional modernization aligns with sustainability objectives. However, institutional constraints (such as fragmented regulations, inadequate digital infrastructure, and entrenched cost-based procurement cultures) continue to limit the depth of SP implementation, particularly in contexts with lower institutional capacity. In such settings, weaker enforcement and short-term economic priorities can result in partial or symbolic compliance rather than substantive sustainability adoption. Grob and Benn [62] further extends institutional theory to the domain of SP, emphasizing that normative and coercive pressures from policy frameworks, industry norms, and cross-sectoral emulation are primary drivers of SP adoption. Glover et al. [63] applied institutional theory to explore how supermarkets shape sustainability practices across the dairy supply chain, revealing how dominant institutional logics influence the diffusion of sustainability norms.

Their findings showed that while smaller organizations aspired to integrate sustainable practices, powerful actors, such as supermarkets, exerted coercive pressures prioritizing cost reduction and profit maximization over genuine sustainability outcomes. Moreover, these dominant firms often engaged in mimetic behaviors, replicating public sustainability initiatives for legitimacy and image rather than deep systemic change. Translating this insight to the sustainable procurement domain, institutional power asymmetries can similarly shape SP adoption, where larger buyers impose compliance requirements that may reinforce efficiency and reputation goals but not necessarily transformative sustainability impact. Thus, institutional theory underscores how legitimacy concerns and power structures can either enable or constrain the substantive institutionalization of sustainable procurement. Next, within the SP in higher education cluster, institutional theory also explains how policy mandates and leadership commitment shape procurement practices. HEIs, often situated between public accountability and academic autonomy, face dual pressures: to comply with governmental sustainability policies and to model sustainable values as part of their educational mission. As semi-public entities, HEIs must demonstrate both operational efficiency and social responsibility, thereby institutionalizing sustainability as a core governance principle. This dynamic reinforces the role of universities as norm entrepreneurs, influencing not only their internal operations but also broader societal perceptions of sustainability in procurement [64]. Taken together, institutional theory elucidates how external coercive forces (e.g., regulations and funding requirements), normative influences (e.g., professional standards and educational norms), and mimetic behaviors (e.g., imitation of best practices) collectively drive the legitimization and diffusion of sustainable procurement practices. Nonetheless, the persistence of institutional barriers highlights the need for adaptive reforms (balancing compliance with innovation) to ensure that SP evolves beyond a regulatory requirement into an embedded organizational norm that supports long-term sustainability transitions.

IV.1.2 Stakeholder theory

Stakeholder theory offers a complementary perspective for understanding the social and relational dimensions of sustainable procurement. The theory posits that organizations must consider the expectations of diverse stakeholders (ranging from suppliers and customers to regulators and local communities) to maintain legitimacy and long-term success [65]. Findings from Cluster 4 illustrate this dynamic clearly. The integration of CSR in SP acts as a mechanism through which organizations respond to stakeholder demands for ethical, social, and environmental accountability. In supply chain contexts, firms increasingly engage in ethical sourcing, supplier audits, and CSR-driven partnerships to address stakeholder concerns over labor practices, environmental degradation, and transparency [43]. This demonstrates a growing emphasis on shared accountability and co-creation of social value, where procurement decisions are no longer guided solely by price or efficiency but by their ability to contribute to broader social and environmental goals. Similarly, in construction, stakeholder collaboration—across contractors, regulators, and community actors—has emerged as a key enabler for overcoming barriers to sustainable project delivery [56]. From a practical standpoint, the stakeholder lens suggests that inclusive decision-making, transparent reporting, and participatory governance are essential for building trust and fostering sustainability across procurement networks. This also highlights a managerial implication: procurement professionals must develop relational competencies, not just technical expertise, to balance stakeholder demands and achieve long-term sustainability outcomes. In both public procurement and construction clusters, stakeholder engagement plays a central role: multi-actor collaborations, participatory decision-making, and transparent governance help manage conflicts, build trust, and reinforce legitimacy. For HEIs, the alignment of procurement with stakeholder values (including students, faculty, and local communities) can enhance institutional credibility and support. The stakeholder lens thereby emphasizes that SP is not just about supplier selection or environmental impact; it is fundamentally about social value creation and legitimacy in multi-actor networks.

IV.1.3 Resource-based view

While institutional and stakeholder theories explain why organizations adopt SP, the resource-based view (RBV) provides insight into how they derive strategic advantage from doing so. The RBV posits that firms can achieve sustained competitive advantage by cultivating resources and capabilities that are valuable, rare, inimitable, and non-substitutable [66]. Within the SP context, these strategic capabilities include sustainability analytics, LCA expertise, supplier relationship management systems, green innovation, and a culture of sustainability-oriented leadership. Unlike external compliance pressures described in institutional theory, RBV focuses on internal resources that enable organizations to transform sustainability from an obligation into a source of value creation. Clusters such as Cluster 2 and Cluster 4 reflect this logic, showing how firms develop distinctive competencies, such as circular material flows, closed-loop logistics, and CSR-based supplier evaluation, that enhance both environmental performance and market differentiation. Firms with advanced sustainability capabilities are not only better equipped to meet stakeholder and regulatory demands but also to achieve efficiency, innovation, and reputational gains that reinforce long-term advantage [53].

In Cluster 3 and Cluster 5, the RBV lens further illustrates how organizational culture, knowledge sharing, and leadership commitment act as intangible resources that drive sustainability integration. For instance, embedding sustainability principles into procurement and project management routines enables institutions to strengthen operational efficiency, foster innovation, and build reputational capital, key intangible assets that contribute to sustained strategic advantage. By leveraging these unique resources, organizations can achieve dual objectives: reducing environmental impact and enhancing organizational performance. The RBV deepens the understanding of sustainable procurement by positioning it as a capability-driven strategic asset rather than a compliance mechanism. Organizations that cultivate and integrate sustainability-oriented resources (technological, human, and relational) can convert sustainability investments into enduring sources of competitive advantage, thereby reinforcing the strategic and transformative potential of sustainable procurement.

IV.2 PRACTICAL IMPLICATION AND POLICY RELEVANCE

The findings of this study suggest several actionable implications for policy makers, public agencies, HEIs, and supply chain managers. They also highlight areas where regulatory support and organizational capabilities can foster more effective SP implementation. First, governments should reinforce institutional frameworks that mandate the inclusion of sustainability criteria within public procurement processes. Establishing clear sustainability standards, coupled with regulatory incentives, can encourage suppliers to prioritize transparency, ethical compliance, and environmental stewardship. The notion of institutional responses to digital procurement highlights how policy instruments can accelerate the adoption of e-procurement platforms that embed sustainability metrics into decision-making systems [67]. Similarly, a supportive regulatory environment, such as those promoting green supply chain management, encourages organizations to invest in sustainability initiatives that enhance both legitimacy and performance, consistent with stakeholder theory perspectives [68]. Second, organizations must cultivate internal capabilities that enable them to operationalize sustainability principles effectively. Under the RBV, capabilities such as sustainability analytics, LCA proficiency, supplier relationship management, and robust data systems represent strategic assets that provide enduring competitive advantage [69]. By investing in these internal competencies, firms can transform sustainability from a compliance burden into a driver of innovation, resilience, and stakeholder value. Third, leadership and governance mechanisms must be strengthened to mitigate cultural resistance, ensure accountability, and foster coordination among diverse stakeholders. Empirical evidence suggests that public-sector organizations adopting e-procurement systems often experience institutional inertia (a resistance to change rooted in bureaucratic culture) unless reforms are accompanied by strong leadership, change management strategies, and transparent policies [67]. Leadership commitment thus becomes a critical enabler for aligning institutional objectives with sustainable procurement performance.

Fourth, higher education institutions can play both instructional and exemplary roles in advancing sustainable procurement. As knowledge hubs, HEIs should integrate sustainability, circular economy, and responsible procurement principles into their curricula, thereby equipping future managers and policymakers with the competencies required to make sustainability-driven decisions. Institutionally, universities should also revise their procurement policies to prioritize CSR, environmental criteria, and long-term social value rather than cost minimization alone. This alignment enhances institutional reputation, strengthens stakeholder satisfaction, and increases eligibility for research funding and partnerships emphasizing environmental, social, and governance (ESG) objectives. Fifth, the adoption of digital and data-driven procurement systems—including e-procurement platforms, blockchain-based traceability, big data analytics, and automated dashboards, is essential for improving transparency, efficiency, and accountability in SP implementation. These technologies facilitate real-time monitoring of supplier performance and sustainability compliance while minimizing opportunities for corruption or data manipulation [67]. However, effective deployment requires governments and public agencies to invest in data infrastructure and ensure interoperability across systems. Inconsistent or poor-quality data remains a major barrier to informed decision-making and accurate performance measurement. Finally, SP policies should remain context-sensitive, reflecting economic, institutional, and cultural differences across nations and industries. Institutional capacity, supplier market maturity, and enforcement strength significantly affect how SP practices are designed and implemented. Aligning national SP strategies with global frameworks, such as the UN SDGs, OECD guidelines, and WTO procurement standards, can enhance policy coherence and ensure cross-border legitimacy and comparability.

V. CONCLUSION

This study provides a comprehensive synthesis of SP research through a combined SLR and bibliometric analysis, uncovering the intellectual, thematic, and methodological evolution of the field. By analyzing 138 peer-reviewed studies, the research identifies critical trends, dominant clusters, and theoretical underpinnings that have shaped SP scholarship over the past two decades. The results indicate that SP has evolved from a compliance-oriented policy concept to a strategic organizational capability that integrates environmental, social, and economic considerations into procurement decisions. Empirically, the findings reveal five major thematic clusters: (1) sustainability in public procurement, emphasizing the institutionalization of sustainability through e-procurement and policy frameworks; (2) the role of SP in CE, focusing on resource efficiency and waste minimization; (3) sustainable construction, highlighting project management integration and governance challenges; (4) the role of CSR, linking ethical sourcing and social responsibility with corporate performance; and (5) SP in higher education, which underscores universities' dual role as both practitioners and educators in advancing sustainability. These clusters collectively reflect a dynamic, cross-sectoral research landscape where sustainability is increasingly embedded in operational and strategic decision-making.From a theoretical perspective, the study demonstrates that institutional theory, stakeholder theory, and the RBV collectively provide a multidimensional understanding of SP. Institutional theory explains how coercive, normative, and mimetic pressures from regulatory bodies, policy frameworks, and social norms drive organizations toward sustainable procurement adoption.

Stakeholder theory highlights the role of diverse actors (i.e., governments, suppliers, consumers, and civil society) in shaping expectations and accountability mechanisms. Meanwhile, RBV elucidates how firms convert sustainability practices into internal capabilities and competitive advantages through innovation, knowledge sharing, and technology adoption. Together, these frameworks offer a comprehensive explanation of why and how organizations institutionalize sustainability in procurement and supply chain processes. In practical terms, the study provides actionable insights for policymakers, practitioners, and educators. Governments should strengthen institutional frameworks and digital infrastructures to facilitate transparency and interoperability in procurement systems. Organizations must cultivate sustainability-oriented capabilities, such as LCA expertise, data analytics, and stakeholder engagement, which serve as valuable and inimitable resources under the RBV framework. HEIs should integrate sustainability and circular economy principles into curricula while modeling responsible procurement practices to foster future sustainability leaders. Despite the growing maturity of SP research, significant gaps and opportunities remain. First, there is a need for deeper exploration of digital transformation and data governance in procurement, particularly regarding blockchain, artificial intelligence, and predictive analytics for supplier evaluation. Second, comparative and longitudinal studies could examine regional and sectoral variations in SP implementation, especially in developing economies where institutional capacity remains limited.

Third, future research should adopt mixed-method and multi-level analytical designs to investigate the interaction between institutional pressures and organizational capabilities over time. Fourth, scholars could expand the theoretical lens by integrating dynamic capability theory, network governance, or institutional complexity frameworks to better understand how organizations balance competing sustainability logics. Finally, evaluating the impact of SP on ESG performance metrics can provide empirical evidence linking procurement decisions to measurable sustainability outcomes.

VI. AUTHOR'S CONTRIBUTION

Conceptualization: Irfan Veryanto.
Methodology: Irfan Veryanto and M. Mujiya Ulkhaq.
Investigation: Irfan Veryanto.
Discussion of results: M. Mujiya Ulkhaq.
Writing – Original Draft: Irfan Veryanto.
Writing – Review and Editing: M. Mujiya Ulkhaq.
Resources: M. Mujiya Ulkhaq.
Supervision: M. Mujiya Ulkhaq and Heru Prastawa.
Approval of the final text: Irfan Veryanto, M. Mujiya Ulkhaq and Heru Prastawa.

VII. REFERENCES

[1] Singh, S., Ru, J., "Goals of sustainable infrastructure, industry, and innovation: a review and future agenda for research," Environmental Science and Pollution Research, Vol. 30, No. 11, 2023, pp. 28446-28458.

[2] Yamasaki, K., Yamada, T., "A framework to assess the local implementation of Sustainable Development Goal 11," Sustainable Cities and Society, Vol. 84, 2022, p. 104002.

[3] Singh, R., Gehlot, A., Akram, S.V., Gupta, L.R., Jena, M.K., Prakash, C., Singh, S. and Kumar, R., "Cloud manufacturing, internet of things-assisted manufacturing and 3D printing technology: reliable tools for sustainable construction," Sustainability, Vol. 13, No. 13, 2021, p. 7327.

[4] Batista, L., Seuring, S., Genovese, A., Sarkis, J., Sohal, A., "Theorising circular economy and sustainable operations and supply chain management: a sustainability-dominant logic," International Journal of Operations and Production Management, Vol. 43, No. 4, 2023, pp. 581-594.

[5] Walker, H., Miemczyk, J., Johnsen, T., Spencer, R., "Sustainable procurement: past, present and future", Journal of Purchasing and Supply Management, Vol. 18 No. 4, 2012, pp. 201-206.

[6] Johnsen, T.E., Caniato, F., Meqdadi, O,. Miandar, T., "Swimming against the tide: supplier bridging roles in diffusing sustainability upstream and downstream in supply networks," International Journal of Operations and Production Management, Vol. 42 No. 10, 2022, pp. 1605-1629.

[7] Cammarano, A., Perano, M., Michelino, F., Del Regno, C., & Caputo, M., (2022). "SDG-oriented supply chains: business practices for procurement and distribution," Sustainability, Vol. 14, 2022, p. 1325.

[8] Leal Filho, W., Skouloudis, A., Brandli, L L., Salvia, A. L., Avila, L.V., & Rayman-Bacchus, L., "Sustainability and procurement practices in higher education institutions: Barriers and drivers," Journal of Cleaner Production, Vol. 231, 2019, pp. 1267–1280.

[9] Dauda, S., Nchor, W.A., & Owusu-Mensah, M.M., "Assessing the state of sustainable procurement practices in Ghanaian tertiary institutions," International Journal of Multidisciplinary Studies and Innovative Research, Vol. 11, 2023, pp. 1427–1435.

[10] Lau, K.H., Yadlapalli, A., Abdulrahman, M.D.A., Chhetri, P., Thai, V., "Disclosure index development for sustainable procurement: An Australian perspective," Journal of Cleaner Production, Vol. 420, 2023, p.138357.

[11] Kabra, G., Srivastava, S. K., Ghosh, V., "Mapping the field of sustainable procurement: a bibliometric analysis," Benchmarking, Vol. 30, No. 10, 2023, pp. 4370–4396.

[12] Kuruneri, J., "Exploring the challenges of sustainable procurement implementation: Insights from Botswana's public sector," Frontiers in Sustainability, Vol. 6, 2025, p. 1645902.

[13] Telles, P., & Ølykke, G.S., "Sustainable procurement," European Procurement & Public Private Partnership Law Review, Vol. 12, 2017, pp. 239–252.

[14] Bernal, R., San-Jose, L., & Retolaza, J.L., "Improvement actions for a more social and sustainable public procurement: A Delphi analysis," Sustainability, Vol. 11, 2-19, p. 4069.

[15] Hekmatsyar, D.F., Machfudiyanto, R.A., "Influence of Policy and Institutional on Sustainable Procurement in the LRT TOD Apartment Project," E3S Web of Conferences, Vol. 405, 2023.

[16] Oyewobi, L.O., & Jimoh, R.A., "Barriers to adoption of sustainable procurement in the Nigerian Public Construction Sector," Sustainability, Vol. 14, 2022, p. 14832.

[17] Opoku-Mensah, F.A., Ahenkan, A., & Adane, F., "The dilemma of sustainable procurement: an exploration of challenges in the context of multi-theoretical perspective," Green Low-Carbon Economics, 2024, pp. 1–10.

[18] Ortega Carrasco, P., Iannone, F., Ferrón Vílchez, V., & Testa, F. "Green public procurement as an effective way for sustainable development: a systematic literature review and bibliometric analysis," Sustainable Development, Vol. 33, 2025, pp. 2364–2391.

[19] Ogunsanya, O.A., Aigbavboa, C.O., Thwala, D.W., & Edwards, D.J., "Barriers to sustainable procurement in the Nigerian construction industry: an exploratory factor analysis," International Journal of Construction Management, Vol. 22, No. 5, 2022, pp. 861–872.

[20] Karikari, A.M., Tettevi, P.K., Amaning, N., Opoku Ware, E., & Kwarteng, C. “Modeling the implications of internal audit effectiveness on value for money and sustainable procurement performance: An application of structural equation modelling,” Cogent Business & Management, Vol. 9, No. 1, 2022, p. 2102127.

[21] Ershadi, M., Jefferies, M., Davis, P., & Mojtahedi, M., “Barriers to achieving sustainable construction project procurement in the private sector,” Cleaner Engineering and Technology, Vol. 3, 2021.

[22] Marković, G.V, & Mihić, M.M., ”Strategic Turnaround in the Paper Industry: A New Model for the Procurement of Recycled Paper,” Sustainability, Vol. 14, No. 3, 2022.

[23] Linnenluecke, M.K., Marrone, M., & Singh, A.K., “Conducting systematic literature reviews and bibliometric analyses,” Australian Journal of Management, Vol. 45, No. 2, 2020. pp. 175–194.

[24] Donthu, N., Kumar, S., Mukherjee, D., Pandey, N., & Lim, W.M., “How to conduct a bibliometric analysis: An overview and guidelines,” Journal of Business Research, Vol. 133, 2021, pp. 285–296.

[25] Kabra, G., Srivastava, S.K., & Ghosh, V., “Mapping the field of sustainable procurement: a bibliometric analysis,” Benchmarking: An International Journal, Vol. 30, No. 10, 2023, pp. 4370-4396.

[26] Qazi, A.A., & Appolloni, A., “A systematic review on barriers and enablers toward circular procurement management,” Sustainable Production and Consumption, Vol. 33, 2022, pp.343-359.

[27] Yusoff, N., Alias, M., & Ismail, N., “Drivers of green purchasing behaviour: a systematic review and a research agenda,” F1000Research, Vol. 12, 2023, p.1286.

[28] Ogunmakinde, O.E., Aghajani, M., & Memari, A., “Identifying risks in sustainable procurement for construction: a systematic literature review and text-mining approach,” Smart and Sustainable Built Environment, 2025, pp.1-27.

[29] Messina, M., Eslami, M.H., & Castilla, J.C., “The use of blockchain in organisations for sustainable development: a systematic literature review and bibliometric analysis,” International Journal of Production Research, 2024, pp. 1–28.

[30] Salsabila, S.S., Handayani, N.U., & Ulkhaq, M.M., Towards effective and efficient humanitarian supply chain management: A framework for integrating lean and agile principles, Multidisciplinary Reviews, Vol. 9, No. 6, 2026, e2026209.

[31] Arifin, F.I, Ulkhaq, M.M., & Purwanggono, B., “A bibliometric analysis of waste workers' behaviours: methods, theories, and trends across global research,” Multidisciplinary Reviews, Vol. 9, No. 6, 2026, p. e2026211.

[32] Putra, A.I.A., & Ulkhaq, M.M., “Assessing campus sustainability practices: A systematic literature review,” Visions for Sustainability, Vol. 23, 2025, pp. 93-121.

[33] Handayani, N.U., Ulkhaq, M.M., Sari, D.P., Mahachandra, M., & Salsabila, S.S., “Building food resilience against floods: A systematic literature review of absorptive, adaptive, and transformational strategies,” Journal of Ecohumanism, Vol. 8, No. 3, 2024, pp. 2674–2686.

[34] Amann, M.,K. Roehrich, J., Eßig, M., & Harland, C., “Driving sustainable supply chain management in the public sector,” Supply Chain Management: An International Journal, Vol. 19, No. 3, 2014, pp. 351–366.

[35] Da Silveira, V.A., Da Costa, S.R.R., & Resende, D., “Blockchain technology in innovation ecosystems for sustainable purchases through the perception of public managers,” WSEAS Transactions on Business and Economics, Vol. 19, 2022, pp. 790–804.

[36] Ogunsuji, Y.M., Amosu, O.R., Choubey, D., Abikoye, B.E., Kumar, P., & Umeorah, S.C., “Sustainable procurement practices: Adoption of renewable energy sources and technologies through strategic procurement policies,” World Journal of Advanced Research and Reviews, Vol. 23, No. 2, 2024, pp.1410-1422.

[37] Cardoso, M.G., Picoreli, T.R., dos Santos Arenas, M.V. and de Souza, V.B.P., “Sustainable public procurement: A bibliometric survey,” Revista de Gestão Social e Ambiental, Vol. 17, No. 1, 2023, pp. 1-13.

[38] Uwuigbe, U., Issah, O., Ranti, U.O., Zubeiru, M., Anaba, S., & Seidu, A.A.J., “Circular economy: a bibliometric review of research in emerging economies (2010-2024).” International Journal of Energy Economics and Policy, Vol. 15, No. 1, 2025, pp. 77-89.

[39] Lakatos, E.S., Yong, G., Szilagyi, A., Clinci, D.S., Georgescu, L., Iticescu, C., & Cioca, L.I., “Conceptualizing core aspects on circular economy in cities,” Sustainability, Vol. 13, No. 14, 2021, p. 7549.

[40] Sun, X., & Wang, X. “Modeling and analyzing the impact of the Internet of Things-based Industry 4.0 on circular economy practices for sustainable development: Evidence from the food processing industry of China,” Frontiers in Psychology, Vol. 13, 2022, p. 866361.

[41] Daskalova-Karakasheva, M., Zgureva-Filipova, D., Filipov, K., & Venkov, G., “Ensuring sustainability: Leadership approach model for tackling procurement challenges in Bulgarian Higher Education Institutions,” Administrative Sciences, Vol. 14, No. 9, 2024, p. 218.

[42] Basheka, B.C., Oluka, P.N., & Mugurusi, G., “Adopting new approaches for public procurement efficiency: critical success factors (CSFs) for the implementation of e-procurement in Uganda’s public sector,” International Journal of Procurement Management, Vol. 5, No. 6, 2012, pp. 712-732.

[43] Sanda, M.R., Siminică, M.I., Avram, C.D., & Popescu, L., “Ghosts in the machine: How big data analytics can be used to strengthen online public procurement accountability,” Sustainability, Vol. 16, No. 9, 2024, p. 3698.

[44] Tao, Y.J., Lin, Y.S., Lee, H.S., Gan, G.Y., & Tu, C.S., “Using a product life cycle cost model to solve supplier selection problems in a sustainable, resilient supply chain,” Sustainability, Vol. 14, No. 4, 2022, p. 2423.

[45] Fernández-Pérez, R., & Luque-Vílchez, M., “Public administration accountability on the social pillar of sustainable procurement: a documentary analysis,” Spanish Journal of Finance and Accounting/Revista Española de Financiación y Contabilidad, Vol. 53, No. 1, 2024, pp. 1-25.

[46] Zin Zawawi, M. I., Kulatunga, U., & Thayaparan, M., “Malaysian experience with public-private partnership (PPP) Managing unsolicited proposal,” Built Environment Project and Asset Management, Vol. 6, No. 5, 2016, pp. 508-520.

[47] Vluggen, R., Gelderman, C.J., Semeijn, J., & Van Pelt, M., "Sustainable public procurement—External forces and accountability," Sustainability, Vol. 11, No. 20, 2019, p. 5696.

[48] el Mahdi Safhi, A., Mejjad, N., El FadilI, H., & Bortali, M., "Dredged materials in Morocco: Current practices, policies, and roadmap for sustainable management," Case Studies in Construction Materials, Vol. 20, 2024, p. e03045.

[49] Di Virgilio, V., Bouchard Saindon, A., & Becerra Posada, F., "Sustainable procurement of medical devices in an international context: Part 1. Background and Definitions," Global Clinical Engineering Journal, Vol. 5, No. 3, 2023, pp. 29-39.

[50] Aboginije, A., Aigbavboa, C., & Thwala, W., "A holistic assessment of construction and demolition waste management in the Nigerian construction projects," Sustainability, Vol. 13, No. 11, 2021, p. 6241.

[51] Caldera, S., Mohamed, S., & Feng, Y., "Evaluating the COVID-19 impacts on sustainable procurement: experiences from the Australian built environment sector," Sustainability, Vol. 14, No. 7, 2022, p. 4163.

[52] Le, H.T.T., Likhitruangsilp, V., & Yabuki, N., "A BIM-integrated relational database management system for evaluating building life-cycle costs," Engineering Journal, Vol. 24, No. 2, 2020, pp. 75-86.

[53] Ahamed, N., Dey, G., Ahmed, T., Rahman, R., Taqi, H. M.M., & Ahmed, S., "Embracing sustainability in green supplier evaluation: A novel integrated multi-criteria decision-making framework," Contemporary Mathematics, 2024, pp. 1891-1917.

[54] Fregonara, E., Ferrando, D.G., & Tulliani, J.M., "Sustainable public procurement in the building construction sector," Sustainability, Vol. 14, No. 18, 2022, p. 11616.

[55] Jelodar, M.B., Yiu, T.W., & Wilkinson, S., "Systematic representation of relationship quality in conflict and dispute: For construction projects," Construction Economics and Building, Vol. 15, No. 1, 2015, ppp. 89-103.

[56] Casanovas-Rubio, M.D.M., Ramos, G., & Armengou, J.. "Minimizing the social impact of construction work on mobility: A decision-making method," Sustainability, Vol. 12, No. 3, 2020, p. 1183.

[57] Oyewobi, L.O., & Jimoh, R.A., "Barriers to adoption of sustainable procurement in the Nigerian public construction sector," Sustainability, Vol. 14, No. 22, 2022, p .14832.

[58] Aluchna, M., & Rok, B., Closing the loop: Circular economy through sustainable innovation lens. In Responsible business in uncertain times and for a sustainable future (pp. 19-36). Cham: Springer International Publishing, 2019.

[59] Letunovska, N., Offei, F.A., Junior, P.A., Lyulyov, O., Pimonenko, T., & Kwilinski, A., "Green supply chain management: The effect of procurement sustainability on reverse logistics," Logistics, Vol. 7, No. 3, 2023, p. 47.

[60] DiMaggio, P.J., & Powell, W.W., "The iron cage revisited: Institutional isomorphism and collective rationality in organizational fields," American sociological review, Vol. 48, No. 2, 1983, pp. 147-160.

[61] Testa, F., Annunziata, E., Iraldo, F., & Frey, M., "Drawbacks and opportunities of green public procurement: an effective tool for sustainable production," Journal of Cleaner Production, Vol. 112, 2016, pp. 1893-1900.

[62] Grob, S., & Benn, S., "Conceptualising the adoption of sustainable procurement: an institutional theory perspective," Australasian Journal of Environmental Management, Vol. 21, No. 1, 2014, pp. 11-21.

[63] Glover, J.L., Champion, D., Daniels, K.J., & Dainty, A.J., "An Institutional Theory perspective on sustainable practices across the dairy supply chain," International Journal of Production Economics, 152, 2014, pp. 102-111.

[64] Silva, M.E., & Nunes, B., "Institutional logic for sustainable purchasing and supply management: Concepts, illustrations, and implications for business strategy," Business Strategy and the Environment, Vol. 31, No. 3, 2022, pp. 1138-1151.

[65] Freeman, R.E., Dmytriyev, S.D., & Phillips, R.A., "Stakeholder theory and the resource-based view of the firm," Journal of Management, Vol. 47, No. 7, 2021, pp. 1757-1770.

[66] Barney, J., "Firm resources and sustained competitive advantage," Journal of management, Vol. 17, No. 1, 1991, pp. 99-120.

[67] Doherty, N.F., McConnell, D.J., & Ellis-Chadwick, F., "Institutional responses to electronic procurement in the public sector," International Journal of Public Sector Management, Vol. 26, No. 6, 2013, pp. 495-515.

[68] Siems, E., Seuring, S., & Schilling, L., "Stakeholder roles in sustainable supply chain management: a literature review," Journal of Business Economics, Vol. 93, No. 4, pp. 747-775.

[69] Yunus, E.N., & Michalisin, M.D., "Sustained competitive advantage through green supply chain management practices: a natural-resource-based view approach," International Journal of Services and Operations Management, Vol. 25, No. 2, 2016, pp. 135-154.

Journal of Engineering and Technology for Industrial Applications

ISSN ONLINE: 2447-0228

ITEGAM-JETIA

Manaus, v.12 n.60, p.1010-1019 July/August, 2026.
DOI: https://doi.org/10.5935/jetia.v12i60.3954

RESEARCH ARTICLE OPEN ACCESS

NEW APPROACH FOR ACCELERATING DISEASE DETECTION USING A PARALLELISM-NASED CNN MODEL

Mohammed Amine Mami*[1], Nadir Berrouane[2] and Imene Baba Ahmed[3]

[1, 3]University of Oran1-Ahmed Ben Bella, Computer Science Department, Oran, Algeria
[2]University of Relizane, Computer Science Department, Relizane, Algeria

[1]http://orcid.org/0000-0002-6327-3650, [2]http://orcid.org/0009-0003-3462-8373, [3]http://orcid.org/0009-0007-8273-6490

E-mail: *aminehome@yahoo.fr, nadirberrouane@yahoo.com, babaahmedimene@gmail.com

ARTICLE INFO

Article History
Received on: March 07, 2026
Reviewed on: April 07, 2026
Accepted on: July 01, 2026
Published on: July 31, 2026

Keywords:
Deep Learning,
Machine Learning,
parallel programming,
Pyramid Histogram of Oriented Gradient (PHOG),
Fourier Transform,
Discrete Cosine Transforms (DCT).

ABSTRACT

In light of the recent pandemics like COVID phase in 2020 that the world is going through, with all the gaps and incompleteness in diagnostics, as well as the slowness of decision-making for patients, the interest of AI to solve in the first place the various problems linked to diagnosis and secondly having a rapid response to be able to intervene in time to save lives, becomes a priority of priorities.

This work follows work which aimed to reduce the training data necessary in the deep learning process to increase the possibility of its use in cases where time is essential and the contribution was on a basis of extracting features manually with extraction methods and techniques from machine learning combine with deep learning. In our approach, we keep the same logic and we apply or integrate the principle of parallel programming into the process in order to further reduce processing and decision-making time. This will give us a very important advantage in making decisions and helping doctors with diagnosis which will give an advantage over diseases.

Copyright ©2026 by authors and Galileo Institute of Technology and Education of the Amazon (ITEGAM). This work is licensed under the Creative Commons Attribution International License (CC BY 4.0).

I. INTRODUCTION

In the present day, AI is evolving so rapidly, its applications are being applied at all levels, enabling significant advances in all domains: industry, daily life, speech and image processing, medical and military domains, among others, all of which have an impact on our lives. The AI encompasses several techniques and methods enabling machines (computers in most cases), among other things, to learn patterns from data without being explicitly programmed. Machine learning in general, and deep learning in particular, is proving particularly effective in medical imaging, which is our research domain. The use of deep learning offers a number of advantages, and its automated operation eliminates human intervention and is less influenced by human subjective factors, leading to objective results. However, there are still a number of challenges to be met, despite the extent of the advances and impacts in the medical world. With the recent pandemic, and the need to treat too many patients in record time, learning with a small amount of data in a short space of time has led us to review certain techniques and try to combine them with others in order to achieve an effective solution while also minimizing dependence on expensive hardware resources. This leads us to find innovative solutions to reduce learning time and adapt Artificial Intelligence algorithms to maximize results while at the same time minimizing data and time constraints. The most frequently tested methods in the medical imaging domain are, depending on their degree of integration alone or in combination with other methods, Convolutional Neural Networks (CNN), Recurrent Neural Networks (RNN), Generative Antagonistic Networks (GAN) and auto-encoders. Medical imagery, in all its forms - X-rays, MRIs, scans, etc. - contains relevant information to enable doctors to diagnose, monitor and treat patients. The analysis of these images using AI gives doctors and researchers a considerable advantage, enabling them to act faster and in real time to save lives and improve patient follow-up. In our approach, the proposal of solutions aimed at reducing execution time by integrating the notion of parallelism in the learning phase to save time, in addition to combining knowledge extraction methods to be able to apply deep learning even with a limited knowledge base.

II. MATERIALS AND METHODS

In the medical imaging domain, a great many works in recent years have centered on several methods, but more especially the method that attracts the most attention in this field is deep learning, which gives good results for improving diagnosis, early detection of disease, pathology monitoring and treatment prescribing. For improved diagnosis, [1] investigates the effectiveness of image feature extraction and deep learning (CNN), in improving the diagnosis of COVID-19 from chest X-ray images. Based on a two-stage process, the first step is to extract image features, using algorithms such as PHOG, Fourrier, GABOR and DCT, followed by image classification using CNN in the second step. The results generated by the simulations demonstrate an accuracy advantage over traditional machine learning techniques such as SVM, KNN and Naïve Bayes. For therapy prescription, [2] introduces a novel approach to early detection of Alzheimer's disease to predict disease progression and subsequently personalize treatment, using deep learning with the EfficientNet-B5 architecture to analyze MRI images of the brain. In terms of monitoring patients with various diseases, [3] illustrates the contribution of deep learning in analyzing data by means of the EchoNet model to identify features, cardiac in this study, by estimating cardiac function such as pacemaker lead detection, left atrium volume and left ventricular hypertrophy with an accuracy superior to human interpretation. The success in also predicting systemic phenomena such as age and gender demonstrates the potential of deep learning to improve cardiac (and not only) diagnostics and cardiovascular risk prediction. Still for early detection, [4] showing in the domain, for example, of breast cancer screening via the interpretation of mammographic images with precision reducing the rate of false positives and negatives using deep learning.

The benefits of using deep learning to achieve higher performance are not without their challenges, and specific solutions are needed to overcome difficulties such as resolution problems, real-time constraints, and the management of distributed systems, with the introduction of complexity in asynchronous communications and fault management. Several innovative techniques can considerably reduce the time needed for deep learning and inference, with better computing capacities (GPU, TPU [5], and distributed systems with data parallelism [6] or model parallelism [7]. Many recent works use distributed deep learning for the optimal execution of different processes. [8] explores methods for parallel and distributed training of deep neural networks (DNNs) on the prototype Tianhe-3 system, aiming to accelerate DNN training by exploiting the massive power available. [9] suggests optimizations of Cyclic Weight Transfer (CWT) to improve distributed learning in medical imaging in the face of data variability and by optimizing the number of iterations according to sample size, the cyclic learning rate to promote convergence, adjusting sampling and introducing a cyclic weight in the loss function. Some of the methods used, applied in addition to deep learning, in the medical imaging domain, without of course listing them all, the most used being classical neural networks (ANN), feature-based methods (SVM, K-NN), transfer learning, image segmentation, generative adversarial networks (GAN), Region Proposal Network (RPN), Visual Saliency Maps, etc. Representing just a small glimpse, these studies illustrate the powerful potential impact of deep learning in helping to transform medical imaging, offering unprecedented opportunities to improve the quality and efficiency of healthcare, according to our domain, and in other domains without exception.

III. PARALLEL AND DISTRIBUTED PROGRAMMING

Parallel and distributed programming is an essential approach for fully exploiting the power of modern computer systems. It enables complex problems to be solved by dividing tasks and executing them simultaneously on multiple processors or computers.

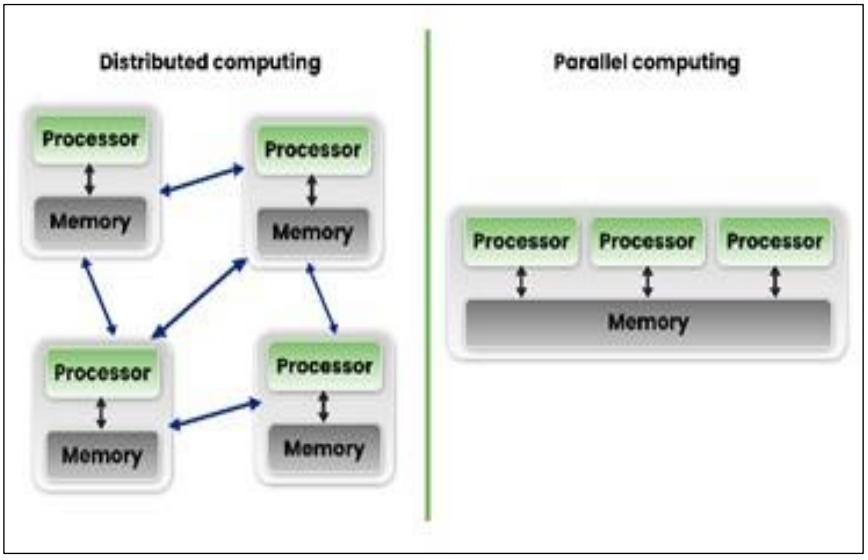


Figure 1: Parallel and Distributed Programming.
Source: [10].

III.1 DISTRIBUTED DEEP LEARNING

This section provides an overview of existing approaches for distributing deep neural network training across multiple machines or GPUs. Training models on massive volumes of data presents considerable challenges when limited to a single machine. To overcome these obstacles, these techniques aim to accelerate the training process, optimise the use of available resources, and reduce the limitations associated with the memory and computing capacity of a single system. However, they do not always take into account all the constraints specific to distributed systems, such as variable communication delays, fault tolerance, or large-scale management. Several approaches have been proposed in the literature to solve these problems and improve the scalability of deep learning [7].

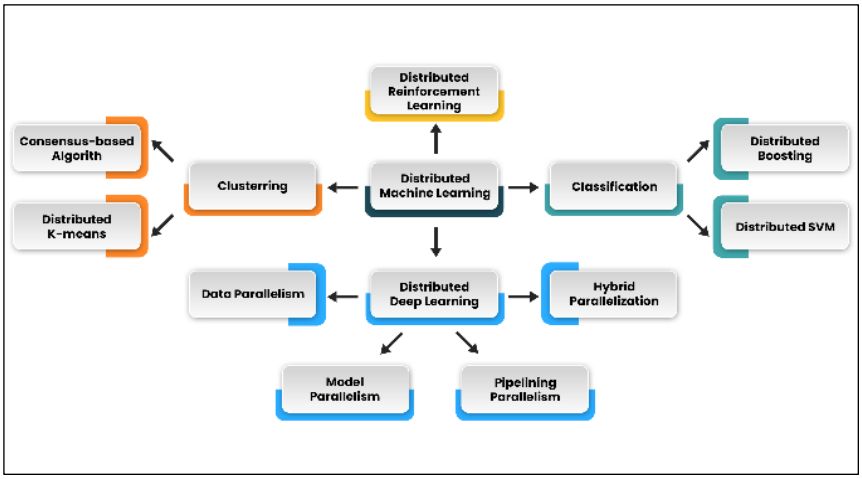


Figure 2: Distributed Machine Learning and Deep Learning Algorithms.
Source: [11].

There are two main approaches to distributed deep learning: model parallelization and data parallelization. Both strategies optimize neural network training by distributing tasks across multiple resources. Data parallelism figure Fig. 3. is considered one of the simplest forms of parallelism. It involves replicating the model, optimizer parameters and training code across all available devices (machines), it's speeds up the processing of the overall dataset by utilizing multiple devices simultaneously. It also allows for larger overall batch sizes without requiring a large number of gradient accumulations. However, in order to function correctly, each replica must be able to load the entire model with at least one micro-batch instance [12]. Model parallelism figure Fig. 4. consists of distributing the computational load of inference and backpropagation in a deep neural network across multiple machines or processors. This distribution can be done at different levels of granularity; assigning different layers of the network to different nodes, divide the neurons of the same layer between several devices or like some approaches distribute each matrix operation independently in order to optimise the load between agents as much as possible [7].

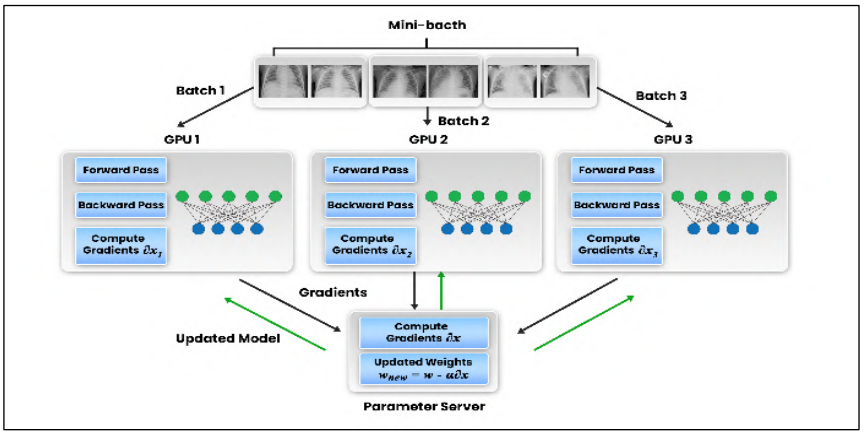


Figure 3: Data Paralleling.
Source: [13].

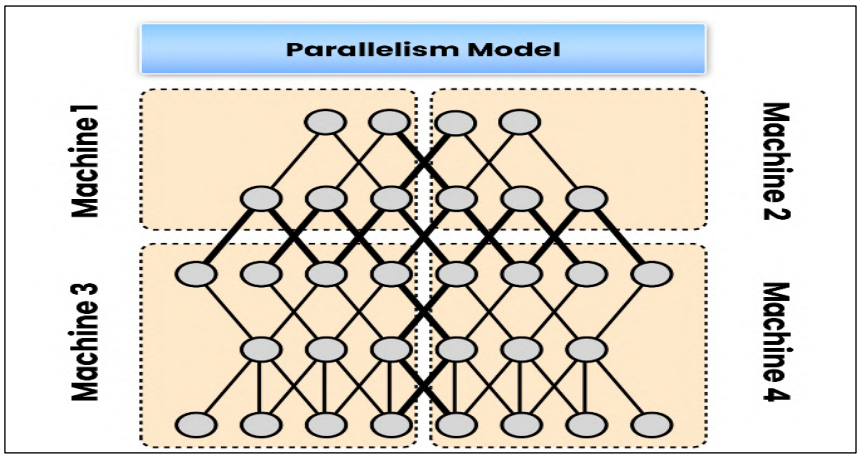


Figure 4: Model parallelism.
Source: [14].

IV. PROPOSED APPROACH

Based on what we have mentioned in the previous section, we have decided to use CNN reason of its effective results on a dataset containing images specially on classification problems. The approach is divided into six phases.

- Network and architecture configuration phase.
- Model Preprocessing phase.
- Parallelization of convolution processing.
- Model training parallelization phase.
- Model testing phase.
- Model performance evaluation phase.

IV.1 NETWORK AND ARCHITECTURE CONFIGURATION

This section describes the network configuration adopted and the master-slave architecture implemented as part of our experiments. The aim is to provide a clear overview of the distributed environment used, which is essential for implementing parallel processing and evaluating system performance. In order to ensure fast, stable and efficient communication, we interconnected three machines within a local area network (LAN). The configuration of this network and the steps involved in setting it up are presented below:

- Connecting the machines to the same local area network.
- Assigning IP addresses.
- Configuring a hosts file.
- Configuring SSH access between machines.

IV.2 MODEL PREPROCESSING PHASE

This phase consists of designing and implementing the CNN model for the training model with the Train folder of the dataset. Our architecture is inspired by high-performance CNN models while being adapted to the specific constraints of our problem. The proposed architecture, illustrated in Figure Fig. 5, is defined to many layers as below: consists of

- Four convolution blocks
- Fully connected layers.
- Each convolution block includes a convolution layer using ReLU activation and a maximum pooling layer for dimensionality reduction.
- The number of filters increases gradually (16, 32, 64, 128) to allow the network to extract increasingly complex and abstract features from the images.
- The extracted features are then flattened via a Flatten layer and passed to two dense layers.
- The first dense layer with 512 units and ReLU activation learns the relationships between features,
- The output layer uses sigmoid activation to produce a binary classification probability.

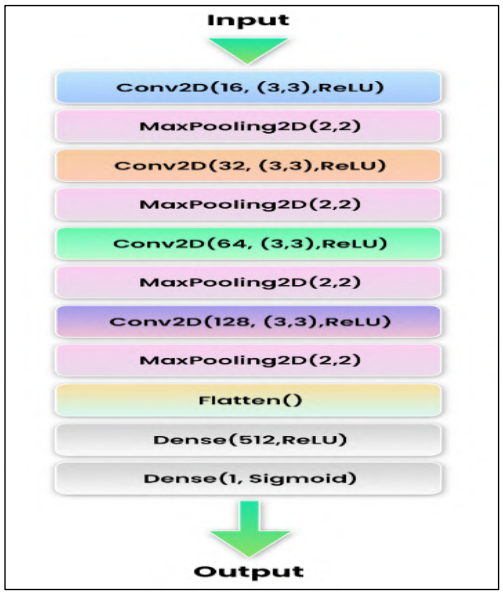


Figure 5: CNN Model Architecture.
Source: Authors, (2026).

IV.3 PARALLELISATION OF CONVOLUTION PROCESSING

The parallel convolution function was designed to distribute convolution filters and input data among the various nodes in the system. It enables convolution operations to be performed locally on each node, followed by a results aggregation phase. This function takes the following parameters:

- Layer: the convolution layer to be applied.
- Data: the input data on which the convolution will be performed.
- Rank: the rank of the process in the MPI hierarchy (rank 0 corresponds to the master node, the others to the slave nodes).
- Size: the total number of MPI processes currently running.
- Comm: The MPI communicator used for communication between processes [15].

IV.4 MODEL TRAINING PARALLELIZATION PHASE

Our parallelization approach for training convolutional neural networks is based on the principle of data parallelism. This technique allows the computational load to be distributed efficiently across multiple processing nodes, significantly reducing training time while potentially improving the performance of the final model. The parallelization strategy consists of dividing image batches between the different MPI processes available. To do this, we calculate the number of batches to be processed per process and use a different seed for each process when initializing the data generators. This approach ensures that each process works on a different subset of the training data. Each MPI process independently and in parallel trains a complete copy of the CNN model on its own subset of the data.

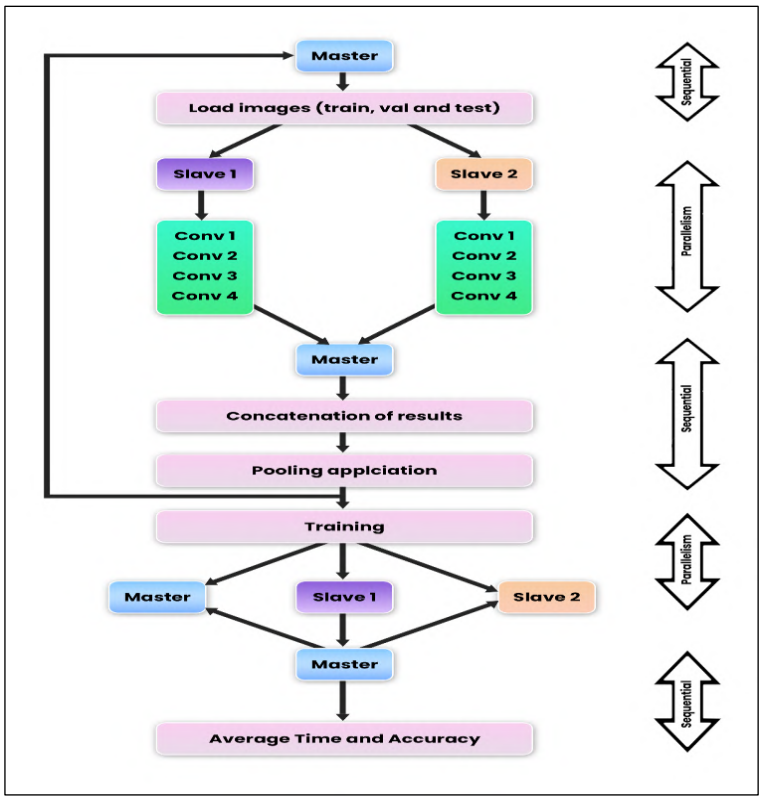


Figure 6: Diagram illustrating the proposed solution.
Source: Authors, (2026).

IV.5 MODEL TESTING PHASE

This phase consists of testing the trained model from phase C utilizing image from the test folder of our dataset.

IV.6 MODEL TESTING PHASE

This phase is about evaluating the model using classification metrics such as Confusion Matrix, Accuracy, Precision, Sensitivity, and Specificity. These metrics help us to be able to compare the results of different execution methods of de CNN model (Our approach; parallel convolution and training, Parallelized convolution only, sequential execution). We will show in section 6 that our approach gives the best results.

V. EXPERIMENTAL RESULTS

In this section, we present the experimental results obtained by the proposed approach and compare them to classic approach.

V.1 DATASET COLLECTION

The used dataset in this experience is collected by Daniel Kermany Kang Zhang Michael Goldbaum and it is available on Mendeley data website. It's also published by Paul Mooney in Kaggle website The data is composed of 5856 images of chest X-rays and it is divided into two categories: 1583 images of healthy people and the rest are those who have Pneumonia [16]. The images used in this work are illustrated in Fig. 7. The figure shows the images used for experimentation. The first row is a normal image and the second row shows a Pneumonia image. In figure Fig. 8. We illustrate the structure of this dataset.

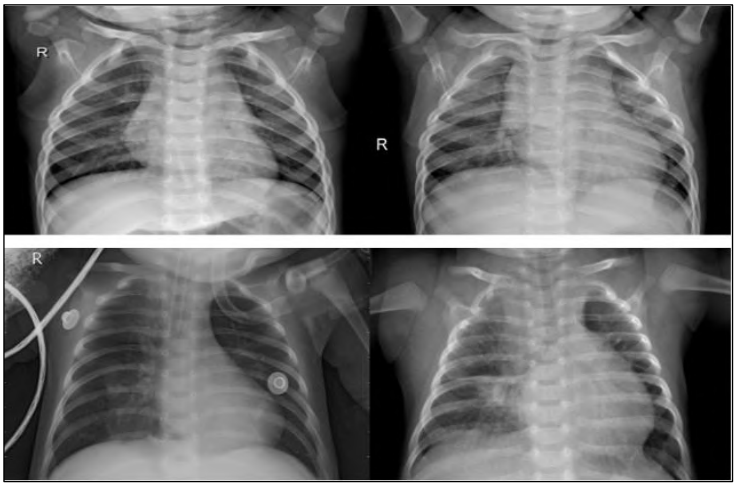


Figure 7: The images used in this work.
Source: Authors, (2026).

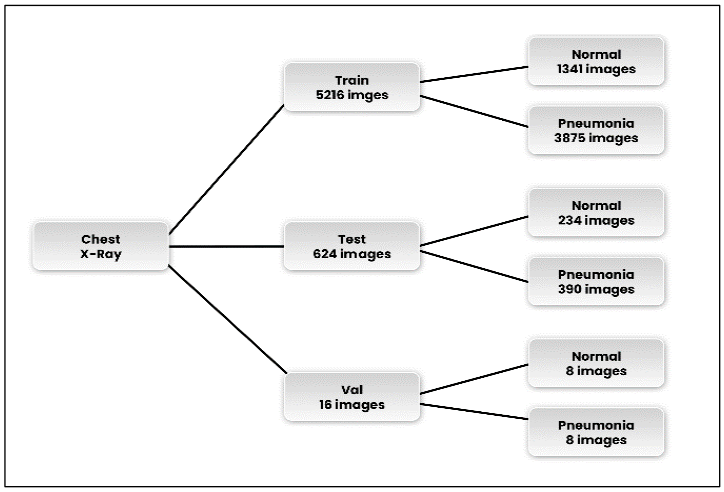


Figure 8: The structure of the Dataset.
Source: Authors, (2026).

VI. RESULTS

VI.1 RESULTS OF EXECUTION FOR SEQUENTIAL AND CONVOLUTION PARALLEL CNN MODEL

The results obtained from 15 independent runs are summarized in Table 1 and 2, which presents descriptive statistics for training time and model accuracy. Analysis of the results obtained with the sequential model (Table 1) shows that the CNN model executed sequentially has an average training time of 2777.74 seconds, with a standard deviation of 83.59 seconds, reflecting relative temporal stability between different executions. The execution time varies from 2,667.06 s to 2,897.92 s, a maximum deviation of approximately 230 seconds. In terms of model performance, the average accuracy reaches 90.59%, with a standard deviation of 0.0228, indicating good robustness and consistency of predictions. The minimum accuracy observed is 83.49%, while the maximum value reaches 92.95%, highlighting moderate but acceptable variability in the context of learning without optimization. For the CNN model with convolution parallelization (Table 2), the results indicate an average training time of 3023.68 seconds, with a standard deviation of 158.57 seconds, reflecting moderate variability between different runs. The shortest time observed was 2758.57 seconds, while the longest was 3229.63 seconds. In terms of performance, the average accuracy reached 91.08%, which is slightly higher than the result obtained in the sequential version. The standard deviation remains reasonable (2.05%), indicating overall consistency of the model, despite some variations between runs.

Table 1: Performance statistics (time and accuracy) of sequential training of the CNN model.

	Time(S)	Precision
Average	2777,7407	0,9059 (90,59%)
Standard deviation	83,5931	0,0228 (2,28 %)
Minimum	2667,0600	0,8349 (83,49 %)
Maximum	2897,9200	0,9295 (92,95 %)

Source: Authors, (2026).

Table 2: Performance statistics (time and accuracy) of sequential training of the CNN model.

	Time(S)	Precision
Average	3023,6794	0,9108 (91,08 %)
Standard deviation	158,5696	0,0205 (2,05 %)
Minimum	2758,5724	0,8766 (87,66 %)
Maximum	3229,6260	0,9439 (94,39 %)

Source: Authors, (2026).

The graph (Fig. 9) below illustrates the variation in training time (in seconds) and accuracy obtained during the 15 simulations performed to assess the stability of the model's performance.

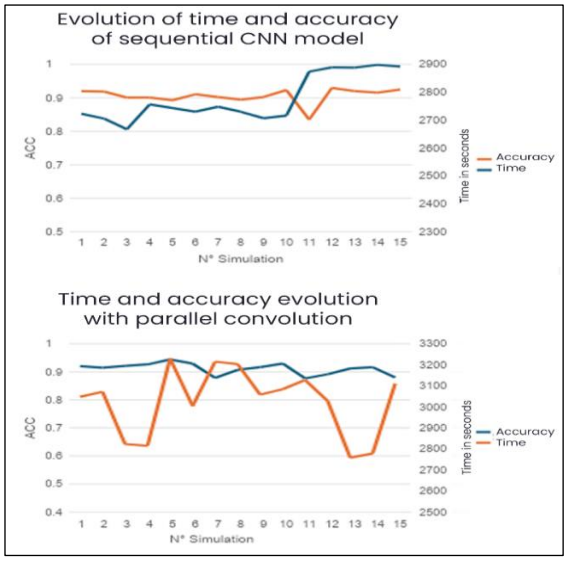


Figure 9: Time evolution and accuracy of sequential and convolution parallel CNN model.
Source: Authors, (2026).

Fig.10 illustrates the accuracy curve obtained directly when executing the sequential CNN code over 40 epochs. It shows how accuracy improves over the course of training.

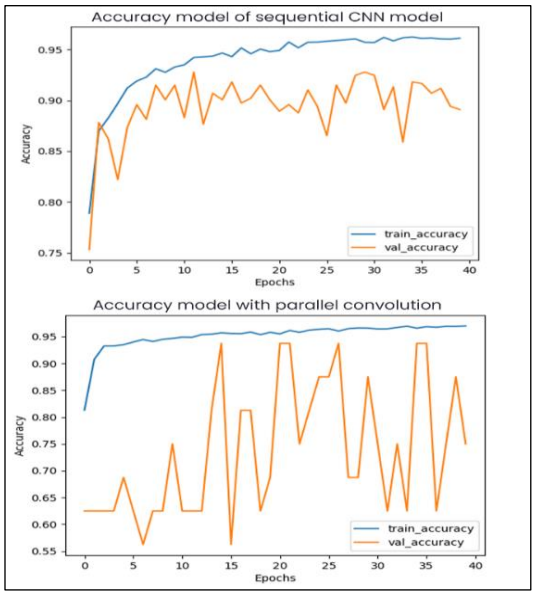


Figure 10: Evolution of model accuracy of sequential and convolution parallel CNN model.
Source: Authors, (2026).

VI.1 RESULTS OF EXECUTION FOR MODEL WITH PARALLEL CONVOLUTION AND TRAINING

The results obtained from 15 independent runs are summarised in Table 3, which presents descriptive statistics for training time and model accuracy.

Table 3: Performance statistics (time and accuracy) of training of the CNN model with parallelisation of convolution and training.

	Time(S)	Precision
Average	965,8547	0,9055 (90,54 %)
Standard deviation	4,5443	0,0101 (1,01 %)
Minimum	957,1146	0,892 (89,20 %)
Maximum	971,7502	0,9246 (92,46 %)

Source: Authors, (2026).

The total average training time observed is approximately 965.8547 seconds, or about 16.1 minutes, which corresponds to an average duration of 24 seconds per epoch. These results highlight the stability of execution time in a parallelized context. The table below presents the main statistics recorded during the various simulations. The accuracy of the parallelized CNN model was measured at the end of each training epoch. It was monitored throughout the process, revealing a gradual and steady improvement in performance. The final results demonstrate the stability and effectiveness of the parallelized version of the model, with an average accuracy of 90.54% and low dispersion between the different simulations. The following graph (Fig. 11) illustrates the evolution of training time and accuracy measured for each of the 15 simulations performed, in order to visualize the stability and performance of the parallelized model.

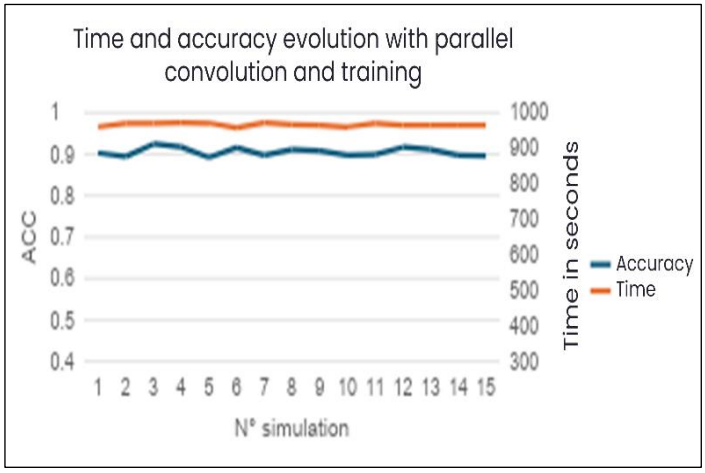


Figure 11: Evolution of time and accuracy with parallel convolution and training.
Source: Authors, (2026).

The following figure (Fig. 12) also shows the accuracy curve obtained during training of the parallelized CNN model, as displayed directly by the program. It reflects the gradual evolution of the model's performance over the course of 40 epochs.

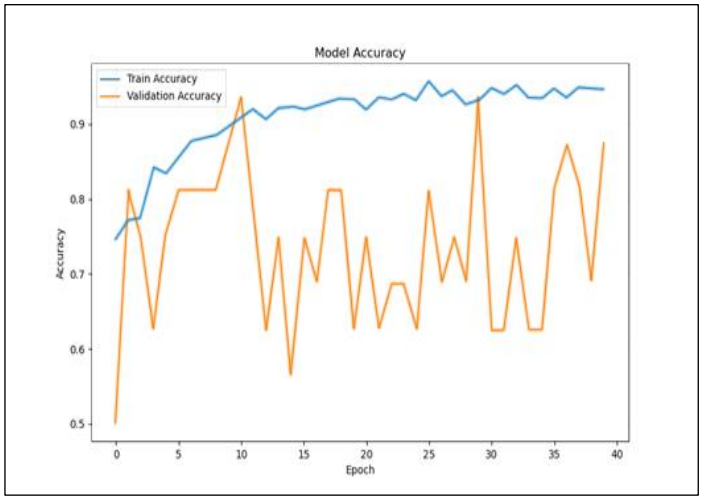


Figure 12: Evolution of model accuracy with parallel convolution and training.
Source: Authors, (2026).

VII. DISCUSSIONS

The table below summarises the average performance observed on the three versions of the CNN model tested: sequential execution, the version with parallelisation of the convolution layer only, and the version with parallelisation of both the convolution and the training process.

Table 4: Comparative results.

Model version	Parallelised convolution only	Parallelised Convolution and Training
Configuration	3 VMs (8 CPU, 16 Go RAM)	3 VMs (8 CPU, 16 Go RAM)
Average time	3023,6794	965,8547
Average accuracy	91,0800	90,5400

Source: Authors, (2026).

VII.1 COMPARISON OF EXECUTION TIMES

Analysis of training times reveals a significant reduction in average time when the model is parallelized at both the convolution and training levels. With an average time of 965.85 seconds, this version is approximately three times faster than the other two, which have durations of 2777.74 seconds (sequential) and 3023.68 seconds (convolution only). On the other hand, parallelizing only the convolution layer results in a slight increase in execution time, probably due to the overhead of communication and thread management in a distributed environment.

VII.2 COMPARISON OF ACCURACIES

In terms of accuracy, the three versions of the model achieve broadly comparable results, with a slight advantage for the version with parallelized convolution alone (91.08%), compared to 90.59% for the sequential version and 90.54% for the fully parallelized version. These differences remain small (less than 1%) and can be attributed to natural variations during training or effects related to parallelization, but no significant loss of performance is observed despite the significant reduction in time.

VIII. CONCLUSIONS

The work carried out is in the field of Deep Learning and distributed systems. We are particularly interested in the introduction of parallelism in medical image processing. Our project focuses on the application of parallelism techniques to improve efficiency and reduce costs in medical image processing. Our experiment consisted of testing three scenarios: parallelism in a distributed system for convolution only, parallelism in a distributed system for Convolution and Training, and sequential execution. It proved that it is possible to leverage the potential of deep learning even with limited machines. The higher the number of nodes, the lower the learning time can be. However, it is crucial to effectively manage synchronization and bottlenecks to avoid inefficiencies. Using libraries like mpi4py is key to handling these challenges. This study demonstrated that, despite hardware constraints, Deep Learning can be optimized for resource-constrained environments, paving the way for broader and more accessible applications in the medical field. To go even further, the use of Horovod, a parallelization library for Deep Learning, could offer better management of gradient communication and synchronization, reducing overhead and improving overall performance. In addition, the adoption of advanced models such as EfficientNet, which have demonstrated better performance in medical image processing, could also contribute to the improvement of these systems. The addition of a GUI interface would facilitate the use of this system by non-experts, thus making the technology more accessible. Finally, the integration of enhanced security measures is crucial to protect sensitive medical data and ensure the confidentiality and integrity of the processed information. The identified improvement prospects offer opportunities to continue improving the performance and efficiency of this system in the future.

IX. AUTHOR'S CONTRIBUTION

Conceptualization: Mami Mohammed Amine, Nadir Berrouane and Imene Baba Ahmed.
Methodology: Mami Mohammed Amine and Nadir Berrouane.
Investigation: Mami Mohammed Amine and Nadir Berrouane.
Discussion of results: Mami Mohammed Amine, Nadir Berrouane and Imene Baba Ahmed.
Writing – Original Draft: Mami Mohammed Amine and Nadir Berrouane and Imene Baba Ahmed.
Writing – Review and Editing: Mami Mohammed Amine and Nadir Berrouane.
Resources: Nadir Berrouane.
Supervision: Mami Mohammed Amine and Nadir Berrouane.
Approval of the final text: Mami Mohammed Amine, Nadir Berrouane and Imene Baba Ahmed.

X. REFERENCES

[1] N, Berrouane. M, Benyettou. I, Benchennane. (2022). Deep Learning and Feature Extraction for Covid 19 Diagnosis.

[2] Singh, C. Prabha, Hari Mohan Dixit, Shalini Kumari. (2023). Alzheimer Disease Detection using Deep Learning. Retinder deep.

[3] Amirata Ghorbani, David Ouyang, Abubakar Abid, Bryan He, Jonathan H Chen, Robert A Harrington, David H Liang, Euan A Ashley, James Y Zou. (2020). Deep learning interpretation of echocardiograms.

[4] Improving breast cancer screening with artificial intelligence. (2022). AI in Mammography.

[5] Sumit Saha. (2018). A comprehensive guide to convolutional neural networks—the eli5 way. Towards Data Science, 15.

[6] Ming Chen. (2022). Analysis of Data Parallelism Methods with Deep Neural Network.

[7] Corentin Hardy. (2019). Contribution au développement de l'apprentissage profond dans les systèmes distribués. PhD thesis, Rennes 1.

[8] Jia Wei, Xingjun Zhang, Zeyu Ji, Jingbo Li & ZhengWei. (2021). Deploying and scaling distributed parallel deep neural networks on theTianhe-3 prototype system.

[9] N. Balachandar, Ken Chang, Jayashree Kalpathy-Cramer, D. Rubin. (2020). Accounting for data variability in multi-institutional distributed deep learning for medical imaging.

[10] K. Josue, (2025). Programmation parallèle et distribuée, Institut Supérieur d'Informatique et de Gestion.

[11] Z. Y. Mohammad Dehghani, (2023). From distributed machine to distributed deep learning: a comprehensive survey, Journal of Big Data, vol. 10, n° %1158.

[12] A. McKinney, (2023). A Brief Overview of Parallelism Strategies in Deep Learning, 26 february 2023. [Online] Available: https://afmck.in/posts/2023-02-26-arallelism/.

[13] M. Bekuzarov, (2023). An Introduction to Parallel and Distributed Training in Deep Learning, 2 Jul 2023. [Online]. Available: ttps://medium.com/better programming/parallel-and-distributed-training-in-deep-learning-for-beginners-part-1 introduction-612a4534a117.

[14] Tamanna, (2023). Model Parallelism Techniques and Optimizations for Deep Learning Models, 3 Jul 2023. [Online]. Available: https://medium. com/@tam.tamanna18/model-parallelism-techniques-and-optimizations for-deep-learning-models-3c9f1e81fb2a.

[15] A. Y. Zohra, (2024). Introduction du parallélisme dans le traitement d'image médicale par le deep learning, université Oran1- Ahmed Ben Bella, Oran.

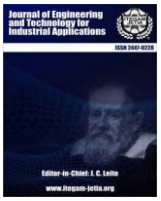
[16] K,Daniel, Z,Kang, G,Michael (2018). "Labeled Optical Coherence Tomography (OCT) and Chest X-Ray Images for Classification", Mendeley Data, V2, doi: 10.17632/rscbjbr9sj.2.

Journal of Engineering and Technology for Industrial Applications

ISSN ONLINE: 2447-0228

ITEGAM-JETIA

Manaus, v.12 n.60, p.1020-1031 July/August, 2026.
DOI: https://doi.org/10.5935/jetia.v12i60.3955



RESEARCH ARTICLE OPEN ACCESS

SUSTAINABLE DRY TURNING OF INCONEL 625: TAGUCHI–GRA WITH PARETO/KNEE ANALYSIS AND NSGA- II VALIDATION OF ENERGY, TOOL LIFE, SURFACE QUALITY, AND PRODUCTIVITY TRADE- OFFS

Fitim Zeqiri[1], Fatlume Zhujani*[2]

[1]Department of Mechanical Engineering, Facylty of mechanical and computer engineering, University Isa Boletini, Mitrovica, Kosovo.
[2]Department of Mechanical Engineering, Facylty of mechanical engineering, University of Prishtina, Prishtina, Kosovo.

[1]https://orcid.org/0000-0002-7486-814X, [2]https://orcid.org/0009-0009-2931-8040

E-email: fitim.zeqiri@umib.net, fatlume.zhujani@uni-pr.edu *

ARTICLE INFO

Article History
Received on: March 07, 2026
Reviewed on: April 06, 2026
Accepted on: July 01, 2026
Published on: July 31, 2026

Keywords:
Inconel 625, Dry turning, Specific energy consumption, Taguchi, Grey Relational Analysis, NSGA-II, Pareto front, Knee point, Tool life, Surface roughness, Productivity.

ABSTRACT

Sustainable dry turning necessitates the reduction of energy intensity while maintaining production and quality. This research examines Inconel 625 under dry settings employing a Taguchi L9(3^3) design (speed S, feed f, depth d) and a framework that integrates specific energy consumption (SEC) with tool life estimation, surface roughness, and material removal rate (MRR). The cutting power is calculated using the measured main cutting force Fc and kinematics; only Fc was documented, which represents the primary factor in cutting power during turning. Tool wear was quantified for each edge and converted into the expected tool life T_{pred} at VB* = 221 µm. Grey Relational Analysis (Set A: SEC↓, Ra↓, T_{pred}↑, MRR↑) yields a scalar ranking, whereas a continuous Pareto frontier in the (MRR, SEC) plane is established by sampling quadratic response surfaces throughout a dense grid and validated by Non-dominated Sorting Genetic Algorithm (NSGA II/ε constraint). The knee point is determined via the Kneedle method, which identifies the maximum distance. Results indicate: (i) feed predominantly influences Ra and tool life stress, whereas depth is the primary factor for MRR and SEC; (ii) the optimal GRA (s=50 m/min, f=0.08 mm/rev, d=1.0 mm) is situated near, yet within, the frontier; (iii) the unconstrained knee at MRR≈4.75 cm³/min and SEC≈0.002613 kWh/cm³ presents a well-balanced compromise. The integrated Taguchi–GRA–Pareto/knee methodology produces practical, energy-conscious parameter configurations for sustainable dry machining of Inconel 625.

Copyright ©2026 by authors and Galileo Institute of Technology and Education of the Amazon (ITEGAM). This work is licensed under the Creative Commons Attribution International License (CC BY 4.0).

I. INTRODUCTION

Implementing sustainable methods that minimize resource consumption, save operating costs, and lessen environmental effect is becoming more and more important to the global industrial sector. Energy-efficient machining techniques are essential among the many facets of sustainable manufacturing, particularly in high-performance applications involving sophisticated materials. In particular, dry machining has become more popular because it can reduce operating costs and get rid of cutting fluids, which are frequently bad for the environment and human health [1], [2]. However, there are a lot of difficulties with the dry machining process, especially when dealing with materials like Inconel 625 that are hard to cut. Because of its exceptional mechanical strength, superior corrosion resistance, and capacity to maintain characteristics at high temperatures, this nickel-based superalloy finds extensive application in the aerospace, maritime, and chemical processing industries [3], [4]. Due to these same characteristics, it is notoriously difficult to machine, particularly in dry environments when the lack of cooling and lubrication can result in increased cutting pressures, poor surface smoothness, and rapid tool wear [5], [6]. In these situations, choosing the right cutting settings is essential to guaranteeing satisfactory machining results. Critical output measurements including cutting force, tool wear, surface roughness, and material removal rate (MRR) are greatly impacted by parameters like cutting speed, feed rate, and depth of cut, which must be carefully managed. Poor surface integrity, a shorter tool life, excessive energy consumption, and high production costs might result from improper parameter selection [7].

I.1 SUSTAINABLE DRY TURNING OF INCONEL 625

Sustainable Inconel 625 machining requires a careful balancing act between process efficiency and productivity. Cutting fluids play a major role in improving surface finish and tool life in traditional machining techniques. However, because of their disposal and mist production, cutting fluids pose serious health and environmental risks and make up a sizable amount of the overall cost of machining [8]. Therefore, if the difficulties can be successfully overcome, dry machining's removal of cutting fluids offers a feasible route to environmentally friendly production. Strategies for dry machining of alloys based on nickel have been studied recently. For example, a study [9] evaluated near-dry and dry turning of Inconel 718 and found that while dry cutting increased tool wear, improved settings helped reduce performance losses. The Taguchi method and Grey Relational Analysis (GRA) have been successfully combined to optimize several performance attributes at once in the context of sustainable dry turning of Inconel 625. This integrated approach, as noted in [10], makes it possible to determine the ideal cutting settings that strike a balance between efficiency and surface quality, supporting machining techniques that are ecologically friendly. Taguchi design and ANOVA can efficiently optimize machining parameters under various cooling conditions, as shown by Inconel 718 turning studies. This strategy supports sustainable production by lowering emissions, energy consumption, and tool wear while enhancing surface quality, as mentioned in [11].

I.2 MULTI-OBJECTIVE FRAMEWORK AND EXPERIMENTAL DESIGN

In order to investigate three controllable factors—cutting speed S (m/min), feed per revolution f (mm/rev), and depth of cut d (mm)—at three levels, dry turning experiments were set up using a Taguchi L9(3^3) orthogonal array. The 3^3 full factorial (27 trials) is reduced to nine statistically balanced runs using the L9 design, which maintains orthogonality for objective main-effects estimation. Signal-to-noise ratios and main-effects graphs were used to analyze factor effects. Following testing, the various responses were normalized using Grey Relational Analysis (GRA) and combined into a single Grey Relational Grade (GRG) for parameter setting ranking; this Taguchi–GRA workflow is well-established in machining optimization [12–17]. The trade-off structure, however, can be concealed by any scalar ranking: settings with comparable GRG may inhabit quite distinct areas of the efficiency frontier. We fit quadratic response surfaces for MRR and SEC, sample a dense grid to create a smooth Pareto front in the (MRR, SEC) plane, and use the maximum-distance (Kneedle) rule to choose the knee point—the best-balanced compromise—in order to make the trade-offs clear. The frontier is validated using NSGA-II and an ε-constraint formulation to ensure robustness; MOGA offers a classical evolutionary substitute [18–24]. Pareto/knee + MOEA validation for explicit trade-off selection combined with Taguchi–GRA for ranking and factor understanding results in both interpretability and decision-readiness.

I.3 RESEARCH MOTIVATION AND OBJECTIVES

Motivation: Sustainable machining of Inconel 625 in dry conditions is both strategically significant and technically difficult. Removing cutting fluids lowers costs and environmental impact, but it also increases mechanical and thermal loads, accelerates tool wear, increases cutting forces, and jeopardizes surface integrity. Energy intensity (SEC), surface quality (Ra), tool life (T_{pred} at VB* = 221 μm), and productivity (MRR) must all be addressed as combined objectives in optimization in order for it to be practical and provide useful parameter settings rather than just rankings. Manufacturers looking for energy-conscious advice to balance MRR, Ra, and T_{pred} in dry turning Inconel 625 without using cutting fluids are the ones driving this requirement. There is a gap in previous research, though, as Taguchi–GRA or multi-objective evolutionary algorithms (MOEAs) are frequently used in isolation. Few studies choose a knee point with algorithmic validation (e.g., NSGA-II/ε-constraint), prioritize SEC as a primary objective, or map an explicit MRR–SEC Pareto front. By offering a knee-based proposal that converts the Pareto frontier into a single, defendable operational point for shop-floor decision-making, our study seeks to close this gap.

The objectives are as follows: (i) Use a Taguchi L9(3^3) design to dry turn Inconel 625 and quantify the effects of cutting speed (S), feed rate (f), and depth of cut (d) on specific energy consumption (SEC), surface roughness (Ra), estimated tool life (T_{pred} at VB* = 221 μm), and material removal rate (MRR). (ii) Determine the cutting power and SEC using the kinematics and measured tangential force (Fc) to support the $P \approx Fc \cdot vc$ estimate for turning mechanical power. (iii) Use Set A (SEC↓, Ra↓, T_{pred}↑, and MRR↑) and Grey Relational Analysis (GRA) to determine high-performing parameter values and get a scalar ranking. (iv) Create a smooth MRR–SEC Pareto front, sample a dense grid, and fit quadratic response surfaces for MRR and SEC. (v) Use the Kneedle (maximum-distance) rule to identify the knee point and use the NSGA-II and ε-constraint procedures to validate the frontier. (vi) To determine when scalar ranking deviates from Pareto optimality, compare the GRA-best settings with the knee-point settings, offering energy-conscious, practical suggestions. (vii) Assign contributions of S, F, and D using Analysis of Variance (ANOVA) and Signal-to-Noise (S/N) ratios, connecting feed to Ra and wear rate/tool life and depth to MRR and SEC.

II. EXPERIMENTAL DESIGN

Figure 1 illustrates the experimental apparatus employed in this study, which comprises: (i) cutting insert, (ii) tool holder, (iii) three-component dynamometer for measuring F_c, Ff, and F_r, (iv) signal chain consisting of an analog-to-digital converter and data-acquisition card connected to a PC, (v) tool-wear inspection station (optical projector/microscope) for flank wear VB evaluation, and (vi) surface-roughness instrument with a contact probe, sensor, and analyzer for Ra measurement. Cutting power is determined from F_c and cutting speed vc (see Section 2.3.1); SEC is obtained from energy and removed volume (refer to Section 2.3).

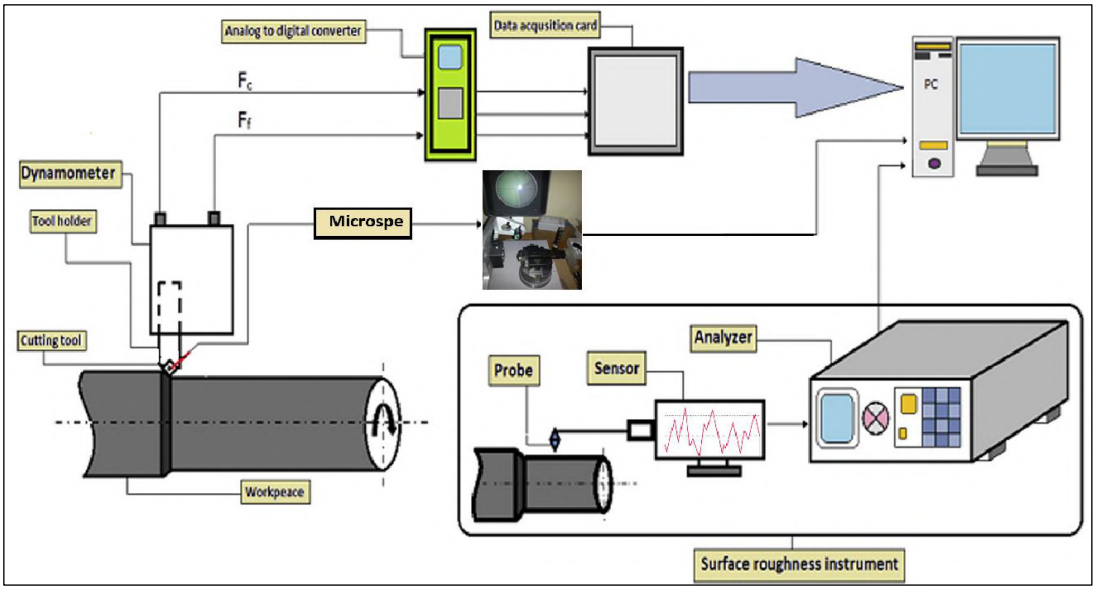


Figure 1: Experimental setup for dry turning of Inconel 625.
Source: Authors, (2026).

II.1 WORK MATERIAL, MACHINE, TOOLING, AND METROLOGY

Using a Pico Turn V-Turn 410 CNC lathe, round bars of Inconel 625 (Ø62 mm × 180 mm; Deutsche Nickel GmbH, EN 10204-3.1) with the composition listed in Table 1 were dry-turned. Every experiment was conducted on an all-geared CNC lathe (Pico Turn V-Turn 410) without coolant. The cutting inserts were CNMG 120408NN, coated with PVD TiN/TiCN, fixed in an ISCAR PCLNR 2525 12A tool holder, on which a Kistler Type 5070A three-component dynamometer was mounted (Figure 2). Every run began with a new cutting edge. A Talysurf (Taylor Hobson) was used to quantify the surface roughness Ra (Figure 3). A TOOL MASTER 10 device (three-axis positioning) was used to monitor tool wear (Figure 4). Before measuring, the insert was cleaned of tiny particles using alcohol after each cut.

Table 1: Chemical composition and mechanical properties.

Chemical composition						**Rm**	**HB**
Ni [%]	Cr [%]	Mo [%]	Nb [%]	Fe [%]	Co [%]	N/mm²	N/mm²
59.64	22.34	9.20	3.57	4.20	0.032	470	223.229

Source: Authors, (2026).



Figure 2: Force measurement aperture *Kistler Type 5070A.*
Source: Authors, (2026).



Figure 3: Measurement of surface roughness with TALYSURF, TAYLOR HOBSON.
Source: Authors, (2026).



Figure 4: Equipment for measurement wear TOOL MASTER 10.
Source: Authors, (2026).

II.2 DESIGN OF EXPERIMENT (DOE)

II.2.1 Design and responses:

In order to assess SEC, Ra, T_{pred} (at VB* = 221 μm), and MRR, dry turning was investigated using a Taguchi L9(3^3) array on three factors: cutting speed S, feed F, and depth of cut D, each at three levels. The 3^3 full factorial (27 trials) is compressed into nine orthogonal runs for unbiased main-effects estimations using the L9 design. Workpiece size, holder, overhang, and tool grade/geometry were all kept consistent during the dry tests. One replication was utilized for each treatment; runs were randomized; main-effects plots and S/N ratios were used to summarize factor effects; a confirmation run and pooled-error ANOVA (Section 4.1) were used.

II.2.2 Level Selection and Instrumentation:

Machine power and stiffness restrictions, tool-manufacturer recommendations for PVD-coated carbide while machining Inconel 625, and brief pilot cuts that confirmed stable dry turning without chatter or early edge failure were used to create parameter ranges. Every experiment was conducted using the same cutting length. A tri-axial dynamometer linked to a data-acquisition (DAQ) device was used to measure cutting forces. The three distinct levels for each factor were finalized through these pilot tests since generic models are unable to accurately relate input parameters, in-process signals, and output responses across all metal-cutting operations. Table 2 provides a summary of the resulting Taguchi L9(3^3) design and shows the experimental matrix for cutting speed S (m/min), feed ratte F (mm/rev), and depth of cut D (mm) in both coded (levels 1–3) and natural units. There was a random run order. [25], [26].

Table 2: The coded experimental and natural matrix of the orthogonal array L9.

Exp No.	**Coded matrix**			**Natural matrix**		
	Abbreviation			S	F	D
	Unit			m/min	mm/rev	Mm
1	1	1	1	50	0.04	0.4
2	1	2	2	50	0.06	0.7
3	1	3	3	50	0.08	1.0
4	2	1	2	65	0.04	0.7
5	2	2	3	65	0.06	1.0
6	2	3	1	65	0.08	0.4
7	3	1	3	80	0.04	1.0
8	3	2	1	80	0.06	0.4
9	3	3	2	80	0.08	0.7

Source: Authors, (2026).

As indicated in Table 3, the workpiece was examined for surface finish, tool wear, and Fc.

Table 3: The orthogonal array L9's coded experimental and natural matrix for Ra, VB, and Fc

Exp. No.	Coded matrix			Natural matrix					
	Abbreviation			S	F	D	Ra	VB	Fc
	Unit			m/min	mm/rev	mm	µm	µm	N
1	1	1	1	50	0.04	0.4	0.911	**215.33**	260.14
2	1	2	2	50	0.06	0.7	1.595	232.21	478.31
3	1	3	3	50	0.08	1.0	1.573	348.24	687.93
4	2	1	2	65	0.04	0.7	1.174	253.22	383.37
5	2	2	3	65	0.06	1.0	1.542	356.13	622.56
6	2	3	1	65	0.08	0.4	2.092	253.34	419.92
7	3	1	3	80	0.04	1.0	0.884	361.36	460.55
8	3	2	1	80	0.06	0.4	1.355	265.57	342.28
9	3	3	2	80	0.08	0.7	2.345	371.02	642.74

Source: Authors, (2026).

II.3 MEASUREMENTS AND DERIVED QUANTITIES

Surface Roughness Ra was measured with a contact profilometer. A three-component lathe dynamometer was used to measure cutting forces in each trial. Cutting power was estimated using turning kinematics and the tangential force component, F_c. In particular, the cutting energy was derived from $E = P \cdot t$, where t is the net cutting time, and the cutting power was estimated as $P \approx F_c V_c$, where V_c is the cutting speed. The material removal rate (MRR) and cutting time, $V = \text{MRR} \cdot t$, were used to calculate the removed material volume. For longitudinal turning, MRR was calculated using geometric and kinematic relations. The key energy-intensity statistic, specific energy consumption (SEC), was initially defined as the ratio of cutting energy to removed material volume, or "SEC" $= E/V$. Following each run, tool wear was measured in terms of average flank wear, or VB. The expected tool life, "T_{pred},," was calculated by extrapolating the measured wear to the selected flank-wear criterion “VB*=221" µm under the same cutting length because individual tool-life tests were not performed for every parameter combination. The complete formulations of MRR, energy, and SEC are provided in Section (2.3.1–2.3.3), along with the physical foundation for force decomposition and the rationale for use the tangential force in power calculation.

II.3 1 Force Measurement and Cutting Power Modeling

The tangential (F_c), feed (F_f), and radial (F_r) force components were measured by a three-component lathe dynamometer. The tangential component alone was used to calculate the cutting (chip-formation) power:

$$P_{\text{cut}} = F_c \cdot V_c \tag{1}$$

V_c is the cutting speed. $P = F \cdot V = F_c \cdot V_c + F_f \cdot V_f + F_r \cdot V_r$ is the mechanical power in turning. $F_r \cdot V_r = 0$ and F_f, V_f is insignificant in comparison to $Fc \cdot V_c$ since the radial velocity is practically zero ($Vr \approx 0$) and the feed velocity $V_f \ll V_c$. Therefore, the tangential force–speed product is used in industrial practice and machining textbooks to formulate spindle/cutting power [27-29]. Metric units:

$$P_{\text{cut}}\,[\text{kW}] = F_c\,[\text{N}] \cdot V_c\,[\text{m/min}] / 60 \tag{2}$$

II.3.2 Kinernatics and Material removal rate (MRR)

Cutting speed is

$$V_c = \pi \cdot D \cdot N / 1000\ [\text{m/min}] \tag{3}$$

The volumetric removal rate for longitudinal turning is

$$MRR = V_c \cdot f \cdot d\ \ [\text{cm}^3/\text{min}] \tag{4}$$

Equivalently MRR = π D ·N ·f d in mm^3/min [30].

II.3.3 Energy nd Specific Energy Consumption (SEC)

The cutting energy and removed volume for a net cutting time t (h) are

$$E = P_{\text{cut}} \cdot t\ [\text{kWh}] \tag{5}$$

$$V = MRR \cdot 60\ t\ [\text{cm}^3] \tag{6}$$

because the precise amount of energy used is

$$SEC = E/V = P_{cut} / (60\ MRR)\ [kWh/cm^3] \quad (7)$$

The basic energy-intensity indicator used in sustainability evaluations to compare machining conditions is called SEC [31] [32].

II.3.4 Tool-Life Modeling and Wear (explanation of the VB criterion)

Following each run, tool wear was calculated using average flank wear VB. The expected tool life $T_{"pred"}$ was calculated by extrapolating the measured wear to the adopted flank-wear criterion "VB*=221 μm" for the same cutting length because a complete tool-life test was not conducted for each condition.

II.3.4.1 The Measurement

Run-to-failure life tests were not conducted by us. We employed a fresh cutting edge for every L9 condition and, following a single, steady-state pass, measured the flank-wear width (VB) on the primary cutting edge. Instead of measuring life directly, these single-pass wear snapshots were then used to anticipate the time (tool life) until a predetermined end-of-life criterion VB*.

II.3.4.2 Wear Criterion Selection VB equals 221 μm.*

Common machining standards and international practice for single-point tool-life testing (ISO 3685) use flank-wear thresholds in the 0.20–0.30 mm range as the end-of-life criterion for turning; lower values are usually used for finishing to preserve surface integrity and dimensional accuracy. We set VB* = 0.221 mm (221 μm), within the ISO-consistent finishing band [33] [34], in accordance with this recommendation and the finishing emphasis in dry turning of Ni-based superalloys.

II.3.4.3 Predicted Tool Life from Single-Pass Wear

Tool wear usually occurs in three stages: initial/running-in, steady, and accelerated. A near-linear law provides a good local approximation of tool wear during a brief, stable segment [35-37]. The anticipated time to reach VB* is obtained using the local wear rate $\dot{V}B \approx VBi/t_i$ with measured VB_i after a duration t_i:

$$T_{pred} = (VB^* / VB_i) \cdot t_i. \quad (8)$$

II.3.4.4 Convention for Reporting

The term "tool life" in the results refers to the estimated time to attain VB* = 221 μm using Eq. (8); it is not a run-to-failure observation. SEC is used as a volume-normalized measure of energy intensity in both Pareto and knee-point analyses, where its explicit trade-off with MRR defines energy-aware operating compromises, and Grey Relational Analysis, where it is minimized along with surface roughness while productivity and tool life are maximized.

III. A FRAMEWORK FOR PROCESS OPTIMIZATION WITH MULTIPLE OBJECTIVES

Inconel 625 dry turning involves conflicting goals, such as maximizing material removal rate and tool life while decreasing specific energy consumption and surface roughness. A two-stage multi-objective optimization framework is used to handle these trade-offs. In order to rank discrete parameter combinations, various replies are first normalized using Grey Relational Analysis (GRA) in accordance with the Taguchi L9 design. These responses are then combined into a single Grey Relational Grade (GRG). Although it offers an effective screening and ranking system, the Taguchi-GRA method does not clearly reveal trade-off relationships between competing goals. Thus, the explicit trade-off frontier between material removal rate and specific energy consumption is constructed and analyzed using Pareto-based optimization with the Non-dominated Sorting Genetic Algorithm II (NSGA-II) and the ε-constraint approach. In this context, NSGA-II offers a continuous, dominance-based view of the solution space while GRA offers a scalar decision measure for discrete experimental settings. Together, these features allow for both informed compromise selection and comparison ranking. The Pareto-based optimization utilizing NSGA-II and the ε-constraint formulation is presented in Section 3.2, while Section 3.1 describes the Grey Relational Analysis process used for multi-response normalization and ranking.

III.1 GREY RELATIONAL ANALYSIS (GRA)

The Taguchi L9 testing findings were multi-response optimized using Grey Relational Analysis (GRA). First, each response's desired characteristic was used to normalize it to the interval [0,1]: For surface roughness (Ra) and specific energy consumption (SEC), lower is preferable [31];

$$R_a^* = \frac{maxR_a - R_a}{maxR_a - minR_a'} \quad (9)$$

$$SEC' = \frac{maxSEC - SEC}{maxSEC - minSEC'} \quad (10)$$

And for material removal rate (MRR) and projected tool life ($T_{"pred"}$), the larger the better,

$$Tpred^* = \frac{Tpred - minTpred}{maxTpred - minTpred'} \quad (11)$$

$$MRR^* = \frac{MRR - minMRR}{maxMRR - minMRR'} \quad (12)$$

Next, grey relational coefficients were calculated as

$$\xi_i(k) = \frac{\Delta_{\min} + \zeta\Delta_{\max}}{\Delta_i(k) + \zeta\Delta_{\max}}, \quad (13)$$

Using ζ=0.5 as the differentiating coefficient. The unweighted mean of the coefficients was used to calculate the Grey Relational Grade (GRG), a scalar metric for rating distinct cutting-parameter combinations. To prevent subjective bias and to guarantee a neutral aggregation of energy, quality, tool-life, and productivity objectives at the screening step, equal weights were given to each response in the GRG computation.

$$\mathrm{GRG}_i = \frac{1}{m}\sum_{k=1}^{m} \xi_i(k), \quad (14)$$

III.2 PARETO-BASED MULTI-OBJECTIVE OPTIMIZATION AND KNEE-POINT IDENTIFICATION

The Non-dominated Sorting Genetic Algorithm II (NSGA-II) was used in a Pareto-based multi-objective optimization process to explicitly describe the trade-off between specific energy consumption (SEC) and material removal rate (MRR) [18]. If a solution $x^{(1)}$ is strictly better in at least one objective and not worse in any of the others, it is said to dominate another solution $x^{(2)}$. To produce a well-distributed approximation of the Pareto front, NSGA-II uses crowding-distance assignment and rapid non-dominated sorting. The goals of this study were to maximize MRR and minimize SEC. A further ε-constraint formulation was used for validation, where SEC was minimized subject to a minimum productivity requirement, "MRR"≥ ε [23–24]. In order to extract the non-dominated set, quadratic response-surface models for SEC and MRR were fitted as functions of cutting speed, feed, and depth of cut and sampled on a dense grid. Additionally, a direct dominance screening was performed on the experimental L9 runs.

IV. RESULTS AND DISCUSSIONS

In addition to the derived responses—predicted tool life ($T_{\_"pred"}$), material removal rate (MRR), and specific energy consumption (SEC)—Table 4 presents the experimental results from the Taguchi L9 trials, including the measured tangential cutting force (F_c), flank wear (VB), and surface roughness (R_a). These findings serve as the foundation for the analyses that follow. To quantify factor effects, the individual answers in Table 4 are first analyzed using signal-to-noise ratios and analysis of variance (ANOVA) Section 4.1. The same dataset is then used for Pareto-based trade-off analysis and knee-point detection between MRR and SEC Section 4.3, as well as multi-response aggregation using Grey Relational Analysis Section 4.2.

Table 4: L9 responses.

Run	RPM	S (m/ min)	F (mm/rev)	D (mm)	Time (h)	VB (µm)	Tool life (h)	Tool life (min)	Tool li (km)[1]	MR R (cm^3/ min)	SEC (kWh/ cm^3)	Ra (µm)
1	265	50.0	0.04	0.4	0.0314	215.3	0.032	1.934	0.513	0.8	0.0046	0.911
2	265	50.0	0.06	0.7	0.0209	232.2	0.020	1.193	0.476	2.1	0.0032	1.596
3	265	50.0	0.08	1.0	0.0157	348.2	0.001	0.598	0.317	4.0	0.0024	1.573
4	345	65.0	0.04	0.7	0.0242	253.2	0.021	1.267	0.436	1.82	0.0038	1.174
5	345	65.0	0.06	1.0	0.0161	356.1	0.001	0.599	0.31	3.9	0.0029	1.514
6	345	65.0	0.08	0.4	0.0121	253.3	0.010	0.633	0.436	2.08	0.0037	2.092
7	425	80.0	0.04	1.0	0.0196	361.4	0.012	0.719	0.306	3.2	0.0032	0.884
8	425	80.0	0.06	0.4	0.0131	265.6	0.011	0.654	0.416	1.92	0.0040	1.355
9	425	80.0	0.08	0.7	0.0098	371.0	0.006	0.35	0.298	4.48	0.0032	2.345

Source: Authors, (2026).

Due to differences in cutting speed and feed rate, the actual cutting length each wear snapshot varies even though the axial turning length is the same in all L9 trials. As a result, worn photos don't match a set cutting length.

IV.1 ANOVA OF FACTOR EFFECTS

A response-specific interpretation of factor importance and statistical significance is given by the ANOVA data compiled in Table 5. The depth of cut has the largest percentage contribution to specific energy consumption (SEC) and is statistically significant ($p < 0.05$), suggesting that material engagement is the primary determinant of energy intensity. According to its kinematic role in surface creation, feed rate is the primary and statistically significant factor ($p < 0.05$) for surface roughness (Ra). Feed rate and cutting speed have the biggest effects on expected tool life (T_{pred}) and are both statistically significant ($p < 0.05$), indicating their combined impact on wear rate and thermal loading.

The L9 design's zero error variance prevented formal significance testing, although the depth of cut and feed rate are the most important parameters for material removal rate (MRR), indicating their geometric control over volumetric output. The multi-response ranking in Section 4.2 and the energy–productivity trade-off analysis in Section 4.3 are supported by these response-specific trends (Minitab® Statistical Software, 2018).

Table 5: Summary of ANOVA factor contributions and significance across responses.

Response	Dominant factor (% contrib.)	Second factor (% contrib.)	Third factor (% contrib.)	Statistically significant factors (p < 0.05)
Ra (S/N, STB)	F (83.47%)	D (10.81%)	S (4.46%)	F
T_{pred} (S/N, LTB)	F (53.06%)	S (35.79%)	D (10.44%)	S, F
MRR (S/N, LTB)	D (54.69%)	F (31.09%)	S (14.22%)	*—
SEC (S/N, STB)	d (71.02%)	F (25.73%)	S (2.02%)	F, D

Source: Authors, (2026).

Note: Statistically significant factors are identified at the 95% confidence level (p < 0.05). For the material removal rate (MRR), the error sum of squares is zero due to the unreplicated L9 orthogonal array; therefore, F- and p-values are not reported and factor importance is inferred from percentage contribution. ANOVA computations were performed using Minitab® Statistical Software (Version 18).

IV.2 GREY RELATIONAL ANALYSIS

The Taguchi main-effects plots of the Grey Relational Grade (GRG) under equal weighting, derived from the GRA results in Table 6, are displayed in Figure 5. The ideal factor levels for the combined response set are indicated by the greatest mean GRG at S_1 (50 m/min), F_1 (0.04 mm/rev), and D_3 (1.0 mm). These patterns align with the ANOVA results in Section 4.1 (Table 5), which show that depth of cut is the main factor influencing productivity and energy intensity while feed rate is dominating for surface roughness and tool-life response. Thus, in the discrete L9 design space, the Taguchi–GRA optimum is the best overall compromise and is used as a reference for the continuous Pareto-front analysis shown in Section 4.3.

Table 6: Grey Relational Analysis; with ζ = 0.5.

Run	S	F	D	SEC	Ra	T_{pred}_(h)	MRR	GRC_SEC	GRC_Ra	GRC_T_{pred}	GRC_MRR	GRG	Rank
1	50	0.04	0.4	0.004578	0.911	0.032227	0.800	0.3333	0.9644	1.0000	0.3333	0.6578	2
2	50	0.06	0.7	0.003190	1.596	0.019891	2.100	0.5825	0.5064	0.5168	0.4360	0.5105	7
3	50	0.08	1.0	0.002415	1.573	0.009964	4.000	1.0000	0.5146	0.3721	0.7931	0.6700	1
4	65	0.04	0.7	0.003822	1.174	0.021121	1.820	0.4346	0.7158	0.5430	0.4089	0.5256	6
5	65	0.06	1.0	0.002893	1.514	0.009991	3.900	0.6935	0.5369	0.3724	0.7603	0.5908	4
6	65	0.08	0.4	0.003708	2.092	0.010555	2.080	0.4555	0.3768	0.3784	0.4340	0.4112	9
7	80	0.04	1.0	0.003215	0.884	0.011987	3.200	0.5748	1.0000	0.3946	0.5897	0.6398	3
8	80	0.06	0.4	0.004042	1.355	0.010901	1.920	0.3993	0.6080	0.3822	0.4182	0.4519	8
9	80	0.08	0.7	0.003227	2.345	0.005837	4.480	0.5712	0.3333	0.3333	1.0000	0.5595	5

Source: Authors, (2026).

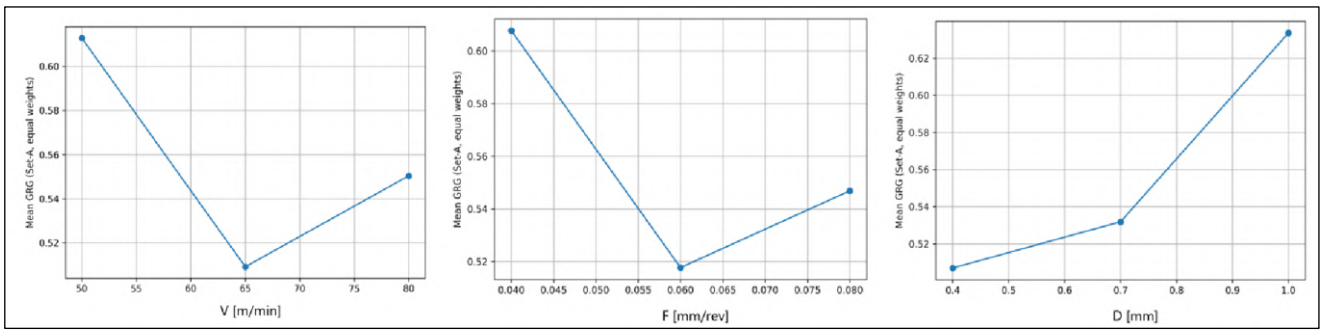


Figure 5: Taguchi main effects plots with equal weighting for Grey Relational Grade (GRG).
Source: Authors, (2026).

IV.3 PARETO-FRONT CONSTRUCTION AND KNEE-POINT DETECTION

While GRA provides a single ranking for discrete Taguchi settings, it does not directly depict the trade-off between competing goals. To visualize and analyze the energy–productivity compromise, Section 4.3 builds a smooth MRR–SEC Pareto front.

IV.3.1 Pareto Efficiency Analysis (MRR–SEC)

A smooth, unconstrained Pareto front built in the (MRR, SEC) plane, where productivity is maximized and energy intensity is minimized, is contrasted with the empirical Pareto set derived from the L9 tests in Figure 6. Two non-dominated solutions (Runs 3 and 9) are found from the discrete Taguchi trials, demonstrating the limited resolution of trade-off analysis when only experimental points are taken into account. Quadratic ridge response-surface models for MRR and SEC were fitted as variables of cutting speed, feed, and depth of cut in order to investigate the continuous design space. A smooth Pareto front was then generated by sampling on a dense parameter grid. The resulting frontier shows a monotonic trend, as shown in Fig. 6, indicating that increases in the rate of material removal are followed with higher specific energy consumption. Beyond the discrete L9, this smooth representation permits future knee-point identification and decision-oriented optimization.

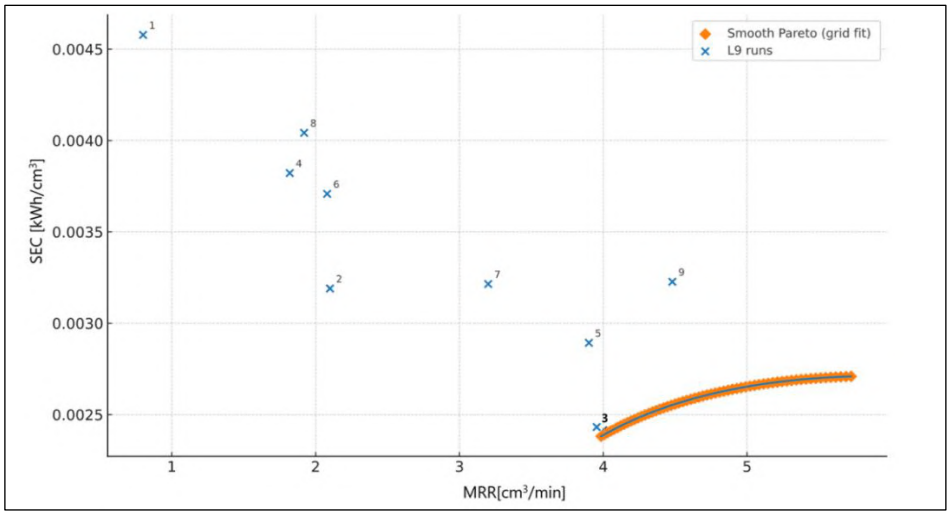


Figure 6: Smooth (unconstrained) Pareto front versus empirical L9.
Source: Authors, (2026).

In order to highlight surface quality and endurance, we also looked at a limited front using the illustrative parameters Ra < 1.5 µm and T_{pred} > 0.012 h. When tougher quality or life targets are applied, constraints quantify the productivity penalty by shifting the frontier higher or left (lower MRR for the same SEC).

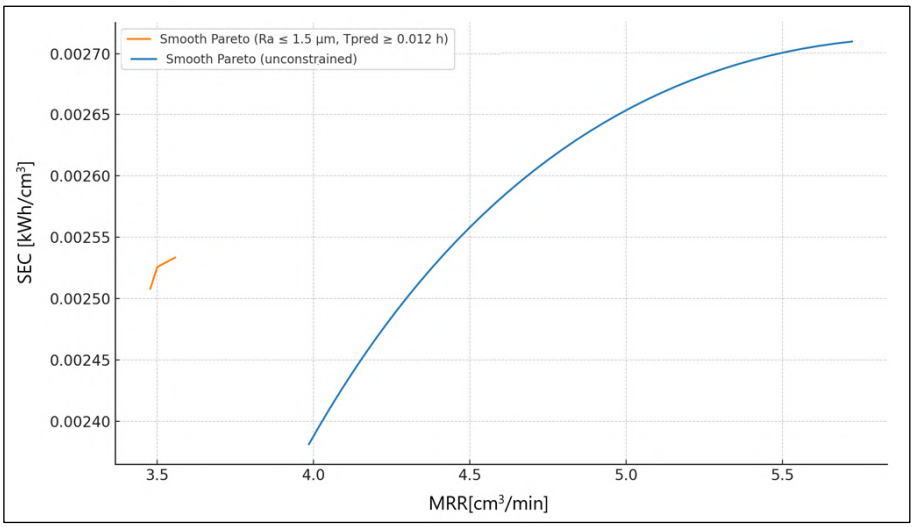


Figure 7: Constraint-free and constrained smooth Pareto front (Ra ≤ 1.5 µm; T_{pred} ≥ 0.012 h).
Source: Authors, (2026).

IV.3.2 Knee-Point Selection on Unconstrained and Constrained Pareto Fronts

The maximal-distance positions from the chord joining each front's terminals are known as knee points. Figure 8: Unconstrained smooth Pareto front with knee point (maximal-distance criterion) in the (MRR, SEC) plane. The confined front under Ra < 1.5 µm and T_{pred} > 0.012 h is depicted in Figure 9. A nearly balanced trade-off between productivity (MRR) and energy intensity (SEC) is offered by the knee.

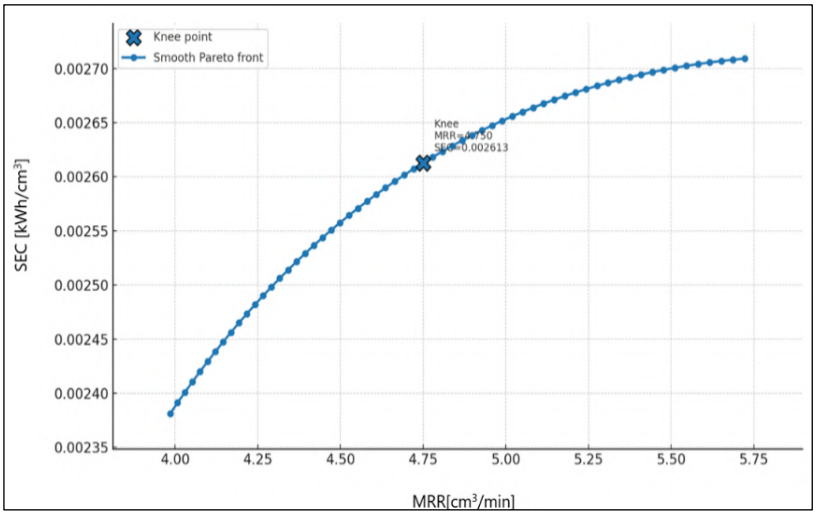


Figure 8: Unconstrained smooth Pareto front with knee point (maximal-distance criteria) in the (MRR, SEC) plane.
Source: Authors, (2026).

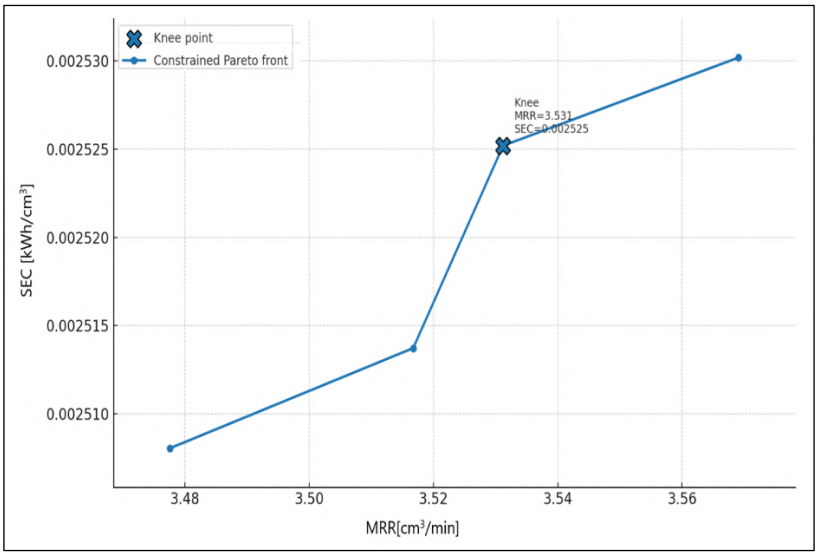


Figure 9: Pareto front with knee constraint (Ra ≤ 1.5 µm, T_{pred} ≥ 0.012 h).
Source: Authors, (2026).

The confined knee increases energy intensity by ΔSEC=0.000059 kWh/cm³ (2.3%) but decreases productivity by ΔMRR=1.860 cm³/min (39.2%) in comparison to the unconstrained knee (MRR=4.750 cm³/min, SEC=0.002613 kWh/cm³). The associated parameters change to S=50 m/min, f=0.051 mm/rev, d=0.99 mm from S=65 m/min, f=0.080 mm/rev, D=1.00 mm. The knee occurs close to S≈65 m/min, f≈0.08 mm/rev, and d≈1.0 mm for the unconstrained front. The knee moves toward lower MRR and somewhat higher SEC under quality/life limitations (e.g., Ra < 1.2 µm and T_{pred} > 0.015 h), indicating the productivity penalty of more stringent criteria (see Figures 8-9). Figure 9: Constrained smooth Pareto front (Ra ≤ 1.2 µm, T_{pred} > 0.015 h) constructed similarly to Figure 8; knee point determined using the same rule to show a balanced operating point under life and quality limitations.

IV.3.3.GRA vs. Pareto knee

The knee point indicates a balanced operating condition in the MRR–SEC trade-off space, while the GRA-selected solution, as seen in Fig. 10, is near the rebuilt Pareto frontier. Run 3 (S = 50 m/min, F = 0.08 mm/rev, D = 1.0 mm) is ranked as the best of the discrete L9 tests by the Taguchi–GRA technique (Set A, equal weights). It achieves a low specific energy consumption (SEC = 0.002415 kWh/cm³) at a moderate material removal rate (MRR = 4.00 cm³/min). This solution does not fall within the region of greatest trade-off sensitivity, despite being close to Pareto-optimal. The Pareto knee is a compromise point when any productivity gains would result in a disproportionately greater energy cost. It is located at MRR = 4.75 cm³/min and SEC ≈ 0.002613 kWh/cm³. This comparison shows that Pareto knee analysis offers supplementary, decision-oriented insight by locating a balanced operating point along the continuous energy–productivity trade-off, whereas GRA is useful for ranking discrete parameter values.

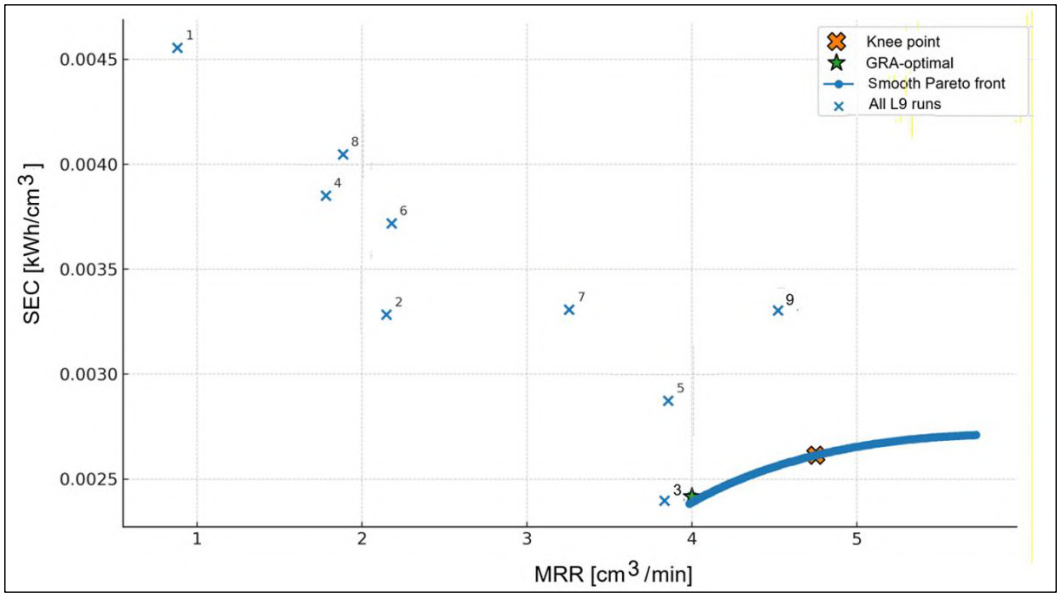


Figure 10: A comparison of the Pareto knee in the MRR–SEC plane with the GRA-selected solution.
Source: Authors, (2026).

V. CONCLUSIONS AND FUTURE WORK

- To improve dry turning of Inconel 625 in terms of specific energy consumption (SEC), material removal rate (MRR), surface roughness (Ra), and anticipated tool life (Tpred), an integrated Taguchi–GRA–Pareto/knee framework was created.
- ANOVA showed response-specific factor dominance: depth of cut is the dominant factor for both MRR and SEC, whereas feed rate mostly regulates surface roughness and tool-wear rate.
- The GRA-best solution was discovered to be inside the non-dominated region rather than on the Pareto front, despite the fact that Grey Relational Analysis (GRA) offered a scalar ranking of discrete cutting conditions.
- The robustness of the trade-off structure was confirmed by multi-objective optimization employing NSGA-II and ε-constraint, which consistently found the same MRR–SEC Pareto frontier [20–23].
- The results show that GRA and Pareto-based optimization are complementary, with knee-point selection offering actionable, energy-aware decision support beyond scalar rankings [21].
- Knee-point detection on the Pareto front produced a balanced operating condition that offers a justifiable compromise between productivity and energy efficiency.
- Expand the framework to incorporate environmental and economic factors (CO2 emissions, tool cost).
- To improve statistical inference, include replicated experiments. • Use the technique for machining operations and other nickel-based superalloys.

VI. AUTHOR'S CONTRIBUTION

Conceptualization: Fitim Zeqiri and Fatlume Zhujani.
Methodology: Fatlume Zhujani.
Investigation: Fitim Zeqiri.
Discussion of results: Fitim Zeqiri and Fatlume Zhujani.
Writing – Original Draft: Fitim Zeqiri.
Writing – Review and Editing: Fatlume Zhujani.
Resources: Fitim Zeqiri.
Supervision: Fitim Zeqiri and Fatlume Zhujani.
Approval of the final text: Fitim Zeqiri and Fatlume Zhujani.

VII. REFERENCES

[1] Klocke, F., & Eisenblätter, G. (1997). *Dry cutting. CIRP Annals*, 46(2), 519–526.

[2] Davim, J. P. (2008). *Machining of Hard Materials*. Springer.

[3] Ginta, T. L., Abou-El-Hossein, K. A., & Ghani, J. A. (2009). Tool life and wear mechanism when machining nickel-based superalloy, Inconel 718, under minimum quantity lubricant (MQL) conditions. *Journal of Materials Processing Technology*, 209(11), 5578–5583.

[4] Akgün, M.; Demir, H. Optimization of Cutting Parameters Affecting Surface Roughness in Turning of Inconel 625 Superalloy by Cryogenically Treated Tungsten Carbide Inserts. *SN Appl. Sci.* **2021**, *3*, 277.

[5] Shokrani, A., Dhokia, V., & Newman, S. T. (2012). Environmentally conscious machining of difficult-to-machine materials with regard to cutting fluids. *International Journal of Machine Tools and Manufacture*, 57, 83–101.

[6] YAĞMUR, S. (2012]. The Effects of Cooling Applications on Tool Life, Surface Quality, Cutting Forces and Cutting Zone Temperature in Turning of Ni-Based Inconel 625. DOI: https://doi.org/10.21203/rs.3.rs-298800/v1.

[7] Ezugwu, E. O., & Bonney, J. (2004). Finish machining of nickel–base Inconel 718 alloy with coated carbide tools. *Journal of Materials Processing Technology*, 184(1–3), 233–239.

[8] Byrne, G., Dornfeld, D., & Denkena, B. (2003). Advanced cutting technology. *CIRP Annals*, 52(2), 483–507.

[9] Dhar, N. R., Islam, S., & Paul, S. (2007). The influence of minimum quantity of lubrication (MQL) on cutting temperature, chip and dimensional accuracy in turning AISI-1040 steel. *Journal of Materials Processing Technology*, 171(1), 93–99.

[10] Zhujani F., Zeqiri F. Optimization of multi-response characteristics in CNC turning of Inconel 625 using Taguchi- grey relational analysis, weighted grey relational analysis, and analysis of variance methods, Adv. Sci. Technol. Res. J. 2026; 20(4)

[11] Khan, M.A., Ahmad, R., Jafferyc, S.H.I., Shahid Ikramullah Butt, S.I., Muhammad Salman Khan, M.S. & Zahid, D. (2025). Sustainability analysis of tool wear, energy efficiency, surfacequality, and energy during dry, MQL, and wet turning of Inconel 718. International Journal Of Sustainable Energy VOL. 44, NO. 1, 2515447https://doi.org/10.1080/14786451.2025.2515447.

[12] Ezugwu, E. O., & Bonney, J. (1999). Effect of high-pressure coolant supply when machining nickel-base, Inconel 718, alloy with coated carbide tools. *Journal of Materials Processing Technology*, 86(1–3), 1–9.

[13] Ross, P. J. (1996). *Taguchi Techniques for Quality Engineering*. McGraw-Hill.

[14] Zhujani, F., Abdullahu, F., Todorov, G., & Kamberov, K. (2024). Optimization of Multiple Performance Characteristics for CNC Turning of Inconel 718 Using Taguchi–Grey Relational Approach and Analysis of Variance. *Metals*, *14*(2), 186. https://doi.org/10.3390/met14020186.

[15] Phadke, M. S. (1989). *Quality Engineering Using Robust Design*. Prentice Hall.

[16] Liao, Y. S., & Lin, H. M. (2007). Multi-objective optimization of high-speed electrical discharge machining process using a Taguchi-based Grey relational analysis. *Journal of Materials Processing Technology*, 192–193, 426–433.

[17] Davim, J. P. (2008). *Machining of Hard Materials*. Springer.

[18] Mastan Rao, P., Deva Raj, C., Dhoria, S. H., & others. (2024). Multi-objective optimization of turning for nickel-based alloys using Taguchi-GRA and TOPSIS approaches. *Journal of The Institution of Engineers (India): Series D, 105*(2), 1473–1484. https://doi.org/10.1007/s40033-023-00554-y.

[19] Deb K. et al., “A fast and elitist multiobjective genetic algorithm: NSGA-II,” IEEE Trans. Evol. Comput., 2002;6(2):182–197.

[20] Miettinen K., Nonlinear Multiobjective Optimization, Kluwer, 1999.

[21] Fonseca C. M., Fleming P. J., “Genetic algorithms for multiobjective optimization…,” Proc. ICGA, 1993.

[22] Satopaa V. et al., “Finding a Kneedle in a Haystack,” ICDCSW, 2011.

[23] Deb K., Gupta S., “Understanding knee points in bi-objective problems,” in EMO 2011, pp. 367–381.

[24] Haimes YY, Lasdon LS, Wismer DA. On a bicriterion formulation of the problems of integrated system identification and optimization. IEEE Trans Syst Man Cybern. 1971; SMC-1(3):296–297.

[25] M. Mavrotas, “Effective implementation of the ε-constraint method in multi-objective mathematical programming problems,” *Applied Mathematics and Computation*, vol. 213, no. 2, pp. 455–465, Jul. 2009.

[26] John M. Cimbala (2014). Taguchi Orthogonal Arrays, Penn State University Latest revsion: 17 September 2014. me.psu.edu.

[27] Roy, R. K., A Primer on the Taguchi Method, Van Nostrand Reinhold, New York 1990.

[28] Sandvik Coromant. Turning: formulas and definitions. Technical guide/handbook.

[29] Trent EM, Wright PK. Metal Cutting. 4th ed. Butterworth-Heinemann; 2000.

[30] Kalpakjian S, Schmid SR. Manufacturing Engineering and Technology. 7th ed. Pearson; 2014

[31] Standard turning kinematics sources showing Vc = πDN/1000 and MRR = πDNfd.

[32] Dahmus JB, Gutowski TG. An Environmental Analysis of Machining. ASME IMECE; 2004.

[33] Gutowski T, Dahmus J, Thiriez A. Electrical energy requirements for manufacturing processes. CIRP Ann. 2006;55(1):13–16.

[34] ISO 3685:2017. Tool-life testing with single-point turning tools. International Organization for Standardization.

[35] Shaw MC. Metal Cutting Principles. 2nd ed. Oxford University Press; 2005.

[36] Additional machining wear modeling texts discussing three-stage wear and Taylor-type life laws.

[37] Zhujani F., Fitore Abdullahu F., Todorov G., Kmaberov K. Optimization of Multiple Performance Characteristics for CNC Turning of Inconel 718 Using Taguchi–Grey Relational Approach and Analysis of Variance, Metals 2024, 14(2), 186; https://doi.org/10.3390/met14020186.

Journal of Engineering and Technology for Industrial Applications

ISSN ONLINE: 2447-0228

ITEGAM-JETIA

Manaus, v.12 n.60, p.1032-1042 July/August, 2026.
DOI: https://doi.org/10.5935/jetia.v12i60.3963

RESEARCH ARTICLE OPEN ACCESS

INTEGRATED STRUCTURAL LINEAMENT MAPPING AND GEOTECHNICAL CHARACTERIZATION OF COLLAPSIBLE SOILS IN THE ARID REGION OF BISKRA (ALGERIA)

Saida Gueraidia*[1], Nour El Houda Gueraidia[2], Med Salah Laouar[3], Rayene Sirine Ramdani[4] Chems Eddine Fehdi[5]

[1]Faculty Of Tebessa Faculty Of Exact Science, Natural And Life Science, Earth Sciences And Universe Department Laboratory Of Sedimentary Formations And Mineral And Water Resources Of Northeastern Algeria, Echahid Cheikh Larbi Tebessi University, Tebessa, Algeria.
[2]Faculty Of Tebessa Faculty Of Exact Science, Natural And Life Science, Earth Sciences And Universe Department Laboratory Of Of Water And Environment, Echahid Cheikh Larbi Tebessi University, Tebessa, Algeria.
[3]Faculty of Science and Technology, Department of Civil Engineering, Mining Laboratory, Echahid Cheikh Larbi Tebessi University, Tebessa, Algeria.
[4, 5]Faculty Of Tebessa Faculty Of Exact Science, Natural And Life Science, Earth Sciences And Universe Department Laboratory Of Of Water And Environment, Echahid Cheikh Larbi Tebessi University, Tebessa, Algeria.

[1]http://orcid.org/0000-0001-6041-7201, [2]http://orcid.org/0000-0003-4119-828X, [3]http://orcid.org/0000-0003-1767-9075
[4]http://orcid.org/0009-0002-4673-1135, [5]https://orcid.org/0000-0002-6319-3837

E-mail: *saida.gueraidia@univ-tebessa.dz, nourgueraidia@univtebessa.dz, medsalah.laouar@univ-tebessa.dz
ramdani.rayene-sirine@univ-tebessa.dz, fehdi.chemseddine@univ-tebessa.dz

ARTICLE INFO

Article History
Received on: March 07, 2026
Reviewed on: April 06, 2026
Accepted on: July 01, 2026
Published on: July 31, 2026

Keywords:
Collapsible Soil,
Unsaturated Soil,
Arid Region,
Remote Sensing,
Lineaments.

ABSTRACT

Algeria is classified as a semi-arid to arid zone due to the importance of evapotranspiration compared to precipitation. This study presents a summary of experimental results on an unsaturated soil in the Biskra region classified as an arid zone. The behavior of soils in these regions is somewhat unique and evolving. The soils in the Biskra region are distinguished by their geomorphological position and origin, as well as their water regime. They share particular characteristics such as unstable structure often in honeycomb shape, heterogeneity, large porosities, and good surface aeration. It should be noted that the rise of groundwater has continued to shape the urban landscape of the Biskra Valley. The mode of accumulation of soil deposits seems to be mainly responsible for the formation of an open and metastable structure, which is susceptible to collapse. The objective of understanding the effect of lineaments is to be able to better characterize the structure of the soil in this region. The study's primary goal is to locate regions in Biskra region that are prone to soil collapse by combining Remote Sensing and geographical information system (GIS) methods. To create thematic maps such as geology, geomorphology, lineament and lineament density, drainage, drainage density, and slope maps, the researchers employed FCC Image of Landsat TM 30 m resolution data and topographic maps. Several geomorphic units were identified through this process.

Copyright ©2026 by authors and Galileo Institute of Technology and Education of the Amazon (ITEGAM). This work is licensed under the Creative Commons Attribution International License (CC BY 4.0).

I. INTRODUCTION

Most soils in arid and semi-arid regions are macroporous with an open and loose structure, existing in the form of metastable deposits. These soils are classified as special problem soils [1]. When dry, clay cementation between the grains provides them with significant intergranular bonding and they can support very heavy loads, exceeding 200 kPa. However, floods and inundations, even without additional loading, induce the breakdown of these bonds, leading to a denser structure followed by a sudden collapse of the soil. The collapse mechanism in partly saturated soil involves the breakdown of intergranular bonds upon wetting [2].

Collapses of macroporous soils are distributed practically all over the earth and are found, essentially, in countries with a dry climate. Several types of collapsible soils have been identified based on their genesis and geological setting [3]. A sudden collapse of the soil can cause other ground movements such as landslides, shearing, planar or rotational sliding, and debris flows. The phenomenon of water transfer in soils in arid zones and its impact on their degradation is a current topic, especially with the trend of investments towards arid and semi-arid areas. The behavior of water in unsaturated soils is complex and requires specific investigation [4].

Experts use geographic information systems (GIS) to organize and examine geographic data by storing it in databases. This technology allows professionals like geographers and engineers to retrieve data from any location on the planet, including those that may be difficult to access through traditional methods. Digital elevation models (DEM) offer a three-dimensional depiction of the earth's surface and are a straightforward method for visualizing the topography of a specific area of study. The methodology followed in this work includes the processing, interpreting of the Landsat 8 satellite images.

II. BISKRA REGION

II.1 GEOGRAPHICAL LOCATION AND TOPOGRAPHY OF

The Biskra region covers an area of 21,671.2 km² and is situated in northeastern Algeria, sharing borders with the Batna, M'sila, Khenchla, El Oued, and Djelfa region. The region is located at 34°48' North and 05°44' East. The region is considered a transition zone in terms of morphology and bioclimatology, with high and rugged terrain in the north and plateaus and plains in the south. The region can be divided into four main zones, including a mountainous zone in the north with the highest peak being Djebel Takyiout, a plateau zone extending from north to south, a plain zone along the Eloutaya-Sidi Okba-Zeribet El Oued and Doucen axis, and a depression zone in the southeastern part of the region. The region's topography and climate have a significant impact on its development and economy, with agriculture mainly concentrated in the plains and plateaus and forestry and livestock farming more suitable for the mountainous and hilly terrain in the north. Figure 1, 2.

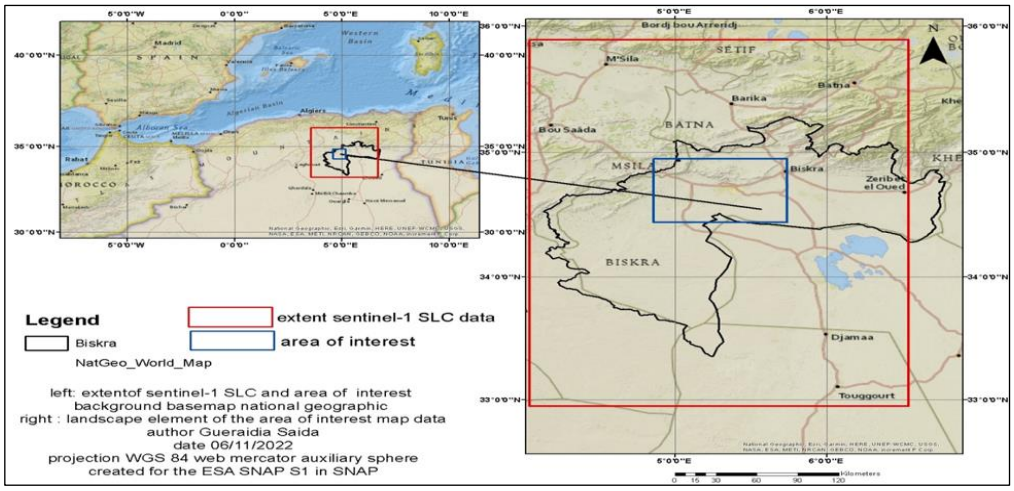


Figure 1: Geographical location of the study area.
Source: Authors, (2026).

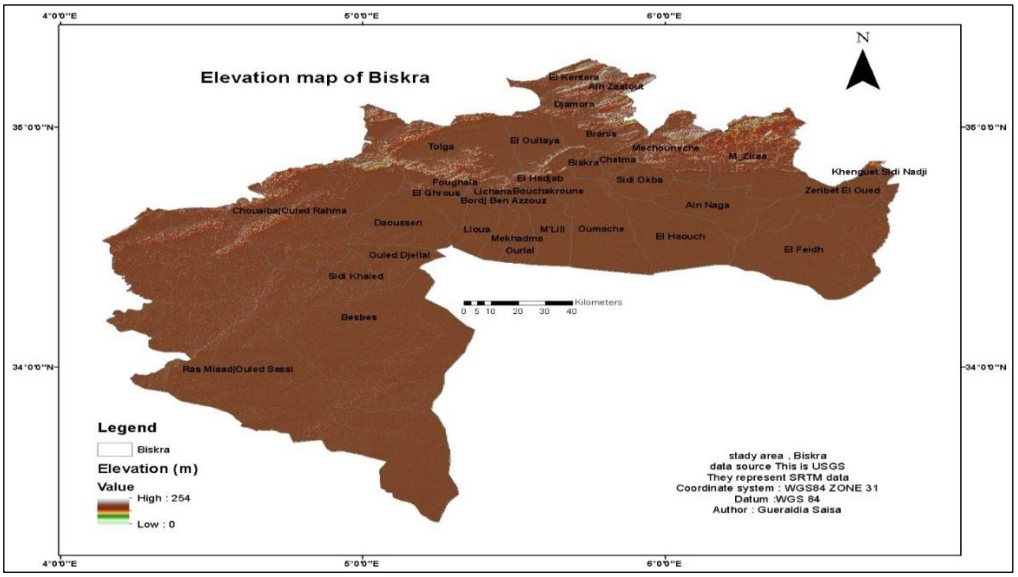


Figure 2: Elevation map of study area.
Source: Authors, (2026).

II.2 GEOLOGY OF BISKRA REGION

The geological aspect of the Biskra region is defined by sedimentary rocks that span from the Barremian period at the bottom to the Quaternary period at the top, as depicted in Figure 3. These rocks are composed of alluvial deposits of sand and clay, along with tertiary sandstone and sandy clay, as well as limestone formations. The limestone formations have fractures and folds that are oriented in a North-South and Northeast-Southwest direction [5].

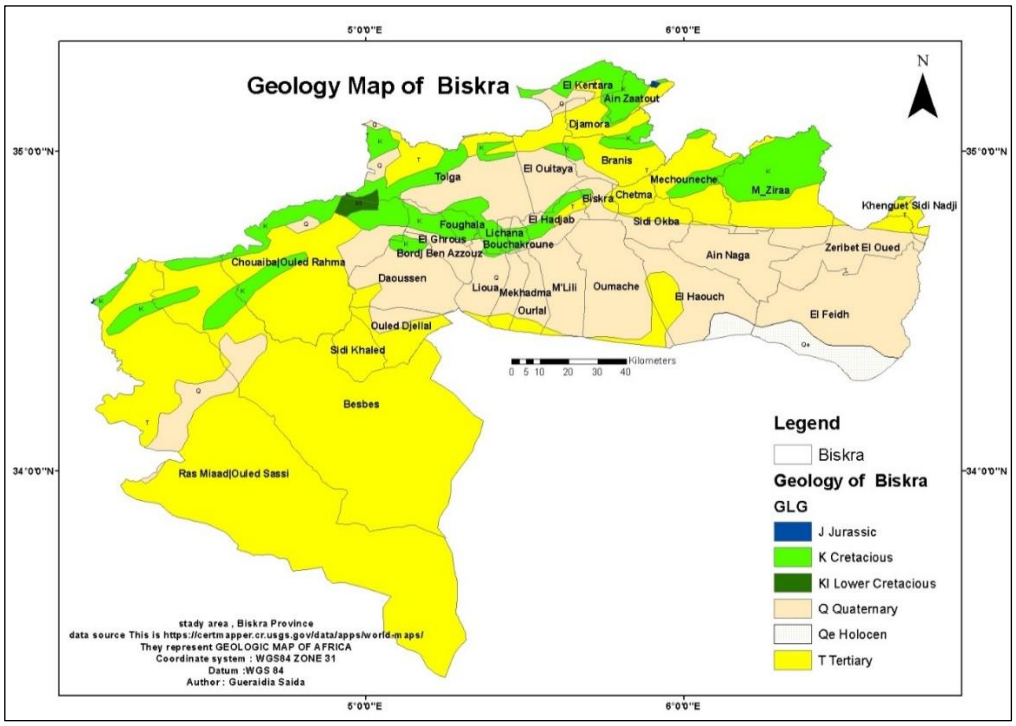


Figure 3: Geology map of Biskra region.
Source: Authors, (2026).

II.3 SOILS OF BISKRA REGION

Soil is a fundamental component of the natural environment that is interconnected with structure, vegetation, climate, and human activities. The quality of soil plays a critical role in both agricultural development and the risk of soil collapse in a region. The soil classification follows international standards [6]. Figure 4.

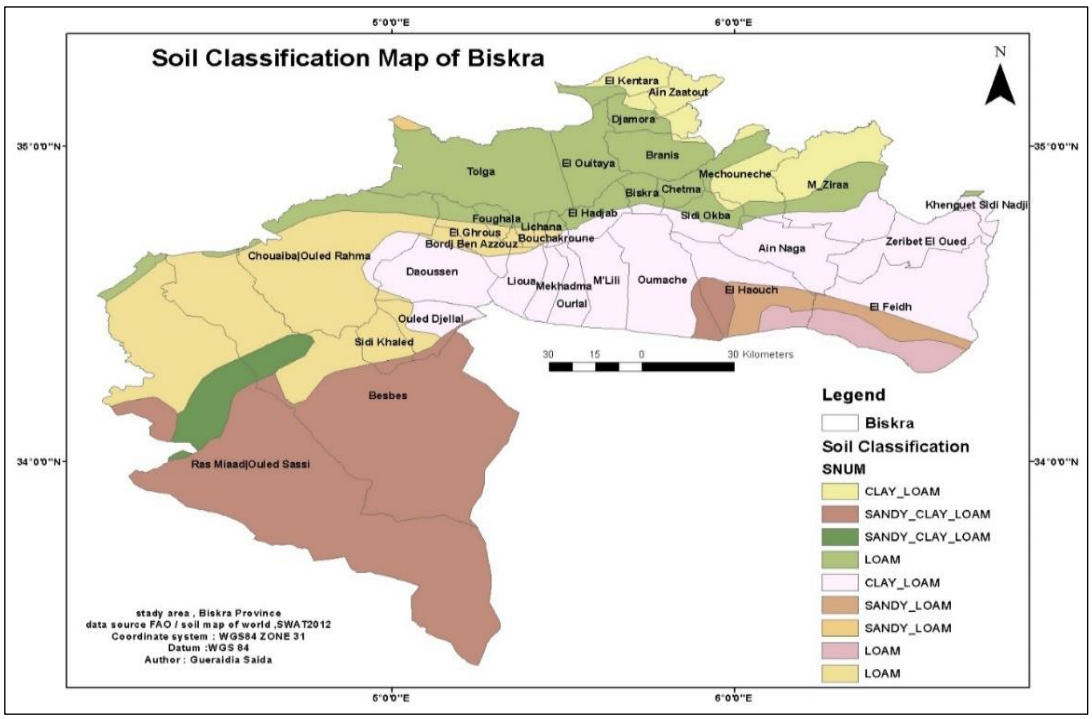


Figure 4: Soil classification Map of Study area.
Source: Authors, (2026).

II.4 HYDROGRAPHY AND WATER RESOURCES

The Biskra region contains several wadis that form a basic hydrographic system, which is only active during winter or periods of heavy rainfall. These wadis are part of the broader Saharan watershed of Chott Melghir. Figure 5. Wadi Djeddi is the primary wadi in the Biskra region and covers a drainage area of 9130 km^2. It serves as a runoff water collector for a significant portion of the southern slopes of the Saharan Atlas. Wadi El Arab is situated in the eastern section of the region and originates from the mountains in the eastern part of the Aurès. It flows into the depression zone of Chott Melghir. Wadi El Abiod is located in the central part of the region and hosts the Foum El Gherza dam. Wadi Biskra passes through the El Outaya plain and contains numerous streams that collect runoff water from the southwest Aurès Mountains.

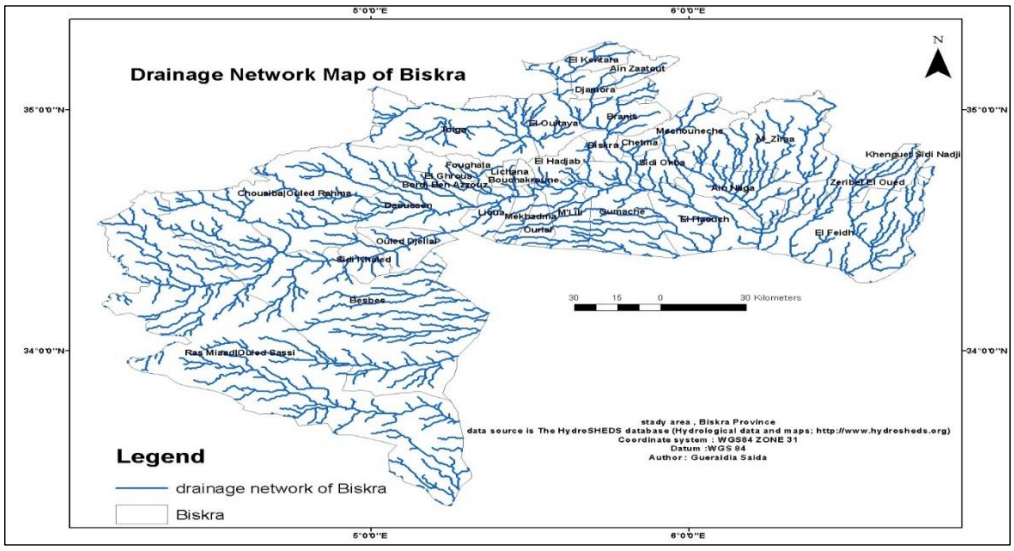


Figure 5: Hydrographic network of Biskra region.
Source: Authors, (2026).

II.5 CLIMATOLOGICAL CONTEXT

The recharge of aquifers in the Biskra region is greatly impacted by climatic conditions, with precipitation being the key factor that drives it. However, the region experiences irregularities in both inter-annual and intra-annual rainfall patterns, with an average annual rainfall of approximately 118.75 mm over a 71-year period (1960-2021). The year 2014 had a peak of around 297 mm. Other climatic conditions, such as evapotranspiration and temperature, also have a significant influence on the various aspects of precipitation. Groundwater management in arid regions requires sustainable approaches to balance supply and demand [7]. Over a period of 30 years (1991-2021), the Biskra region indicated a thermal pattern with high temperatures in summer and relatively lower temperatures in winter, with the hottest months being July and August with a maximum temperature of 29.1°C and January being the coldest month with an average temperature of 8.7°C. Precipitation mapping in eastern Algeria shows high spatial and temporal variability [8]. Figure 6 and 7.

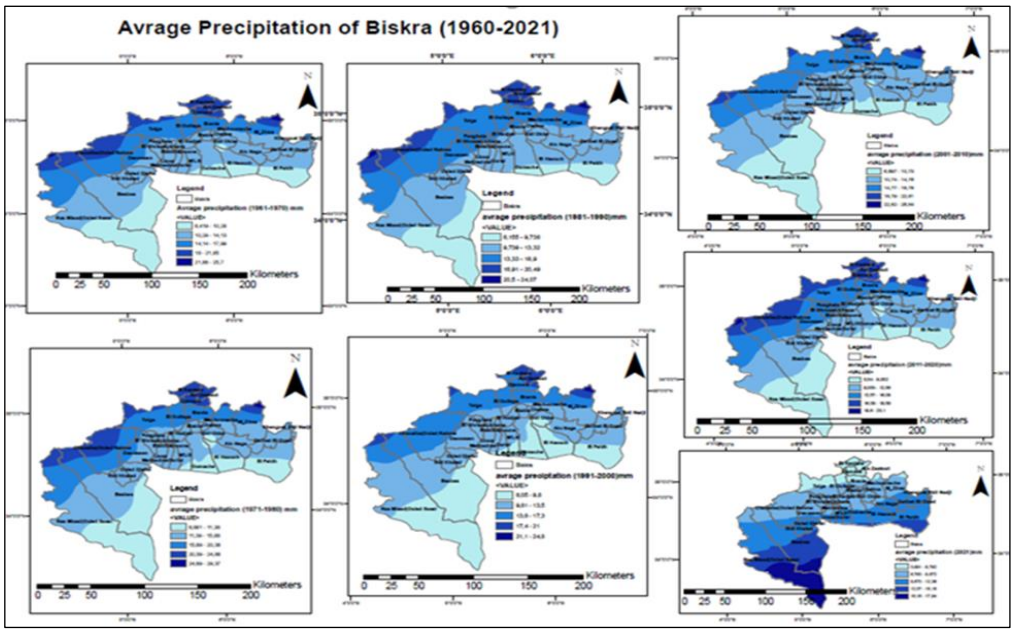


Figure 6: average precipitation of Biskra (1960-2021).
Source: Authors, (2026).

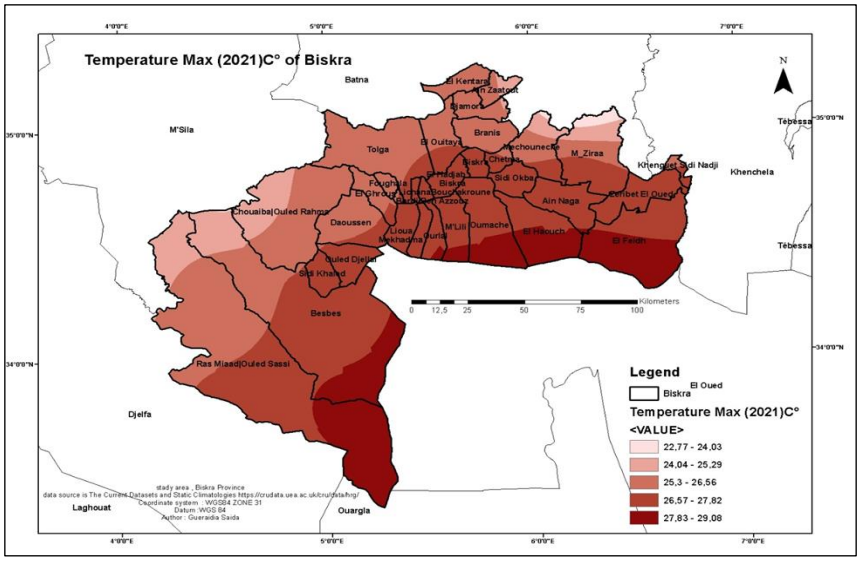


Figure 7: Average temperature Max of Biskra region.
Source: Authors, (2026).

III. DATA AND METHODS

III.1 FIELD AND LABORATORY INVESTIGATIONS

An investigation was conducted to evaluate the collapse potential of soils through various laboratory and field methods. The study focused on the index properties and hydro-collapsibility characteristics of loess deposits located in the southern region of Algeria. In order to perform laboratory tests, undisturbed soil samples were obtained from 6- to 7-meter-deep pits using a core drilling deep sampler device. These samples were trimmed and waxed carefully into 70mm diameter cylinders of 440mm length.

III.2 DATA USED

The research methodology used in the study is presented in Figure 2, which involved creating a digital elevation model (DEM) of the study area using ArcGIS software version 10.8 and data obtained from a field survey listed in Table 1. The DEM was generated through spatial interpolation using Inverse Distance Weighted (IDW) method, which depends on the distance between known and unknown points, resulting in a DEM with a precision of less than ten meters. Remote sensing and GIS have been widely used for environmental assessment in fractured terrains [9]. Figure 3 shows the final DEM for the study area, generated through the field survey method, which is considered more accurate than free DEMs from satellites based on previous studies. Landsat 8 satellite data can be used for land surface temperature mapping and terrain analysis [10]. Digital elevation models can be enhanced using radar interferometry techniques [11]. This method allowed the researchers to perform necessary analyses and accurately depict the terrain of the study area.

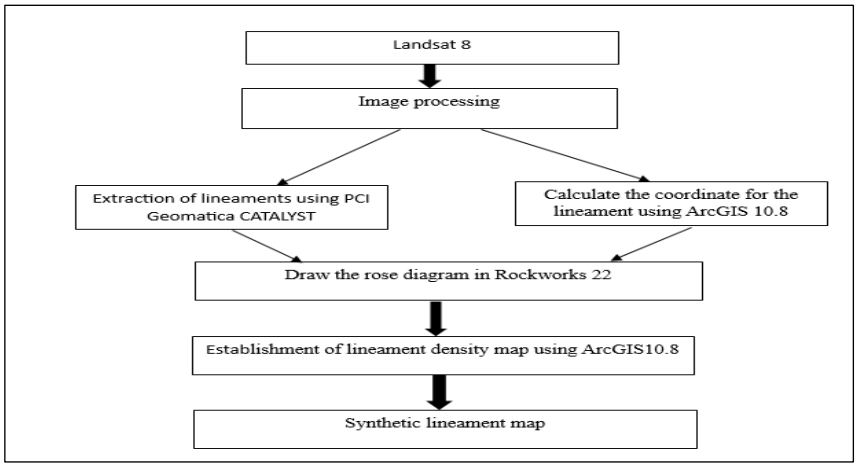


Figure 8: Flowchart of the processing methodology.
Source: Authors, (2026).

IV. RESULTS AND DISCUSSIONS

IV.1 RESULTS AND DISCUSSIONS

The identification of physical characteristics and bearing capacity tests of the tested soil led to the results presented in Table 1. The soil classification followed the French GTR guidelines [12].

Table 1. Physical and mechanical characteristics of the investigated soil.

Désignation	Cc	Cu	GS	W_0	WL%	WP%	IP%	γdmax (g/cm3)	wopt %	%<2 µm	VBS	CaCO3
Value	5.88	10.55	2.59	11.12	26.63	15.37	11.37	1.95	9.43	11.73	2.65	12.23

Source: Authors, (2026).

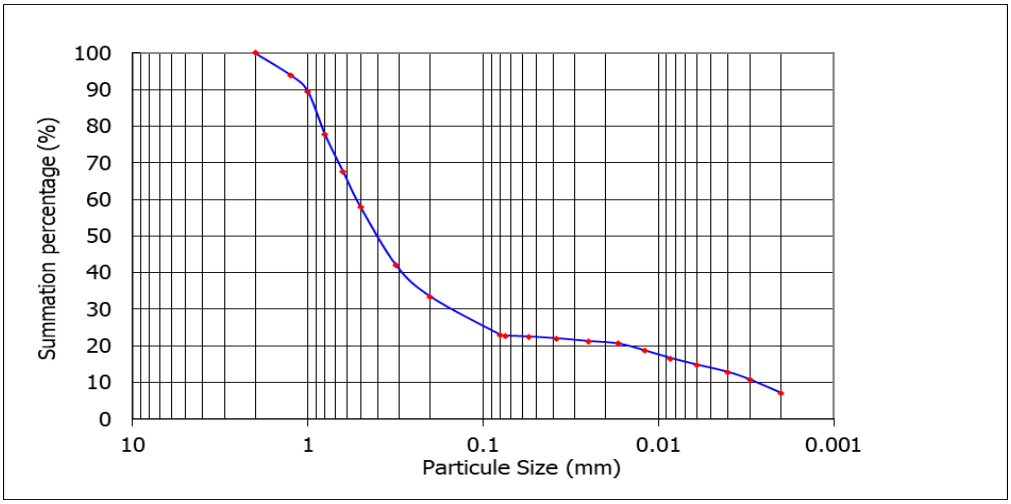


Figure 9: The grain size distribution curve.
Source: Authors, (2026).

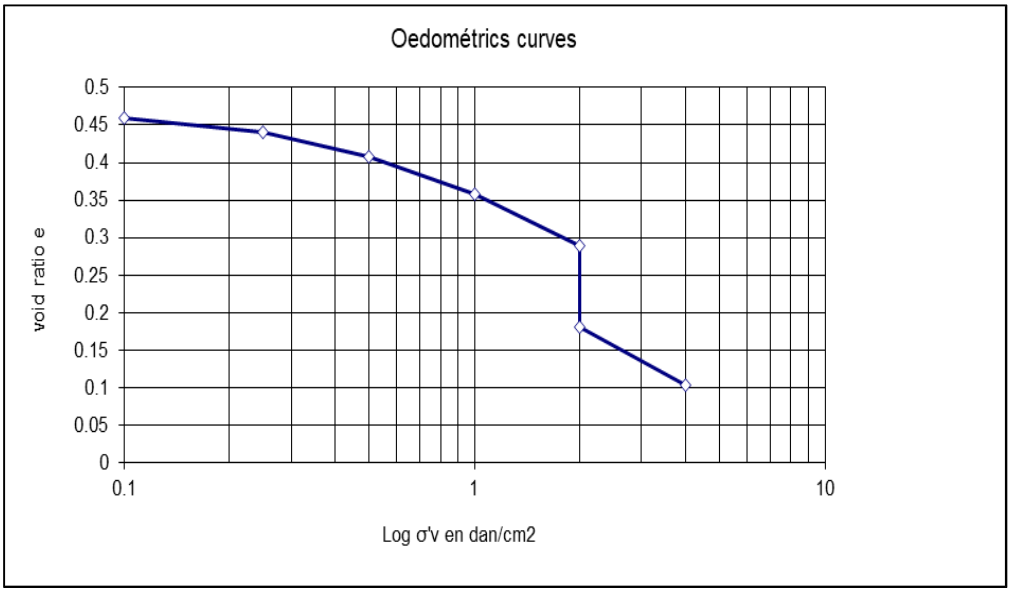


Figure 10: Oedométric curve.
Source: Authors, (2026).

Similar experimental approaches for predicting soil collapse were proposed by Laouar [13]. Loessic soils exhibit specific mechanical behavior under cyclic loading [14] The compressibility test, according to the procedure described by Jennings and Knight [15], indicates that the soils in question have collapse potentials: Cp soil 1 = 7.65%. This value exceeds typical thresholds for collapsible soils. Therefore, collapse is likely.

IV.2 TOPOGRAPHIC CONTOUR MAP LINES

Topographic contour lines are a common method used to depict the surface of a landscape, which not only conveys its geometry but also implicitly preserves the topology of the earth's surface. To illustrate the height of the contour lines, elevation values are often given as text descriptions on topographic maps. Besides contour lines, spot altitudes are available, represented by dots or crosses, to indicate significant natural features in a prominent region, such as hilltops, knolls, isolated summits, mountaintops, mountain passes, saddles, and other high points. Due to the mountainous terrain of the small watershed, the watershed contour map displayed in Figure 11 has contour lines ranging from 0 to 1800 meters. The watershed's water divisions are mostly mountainous.

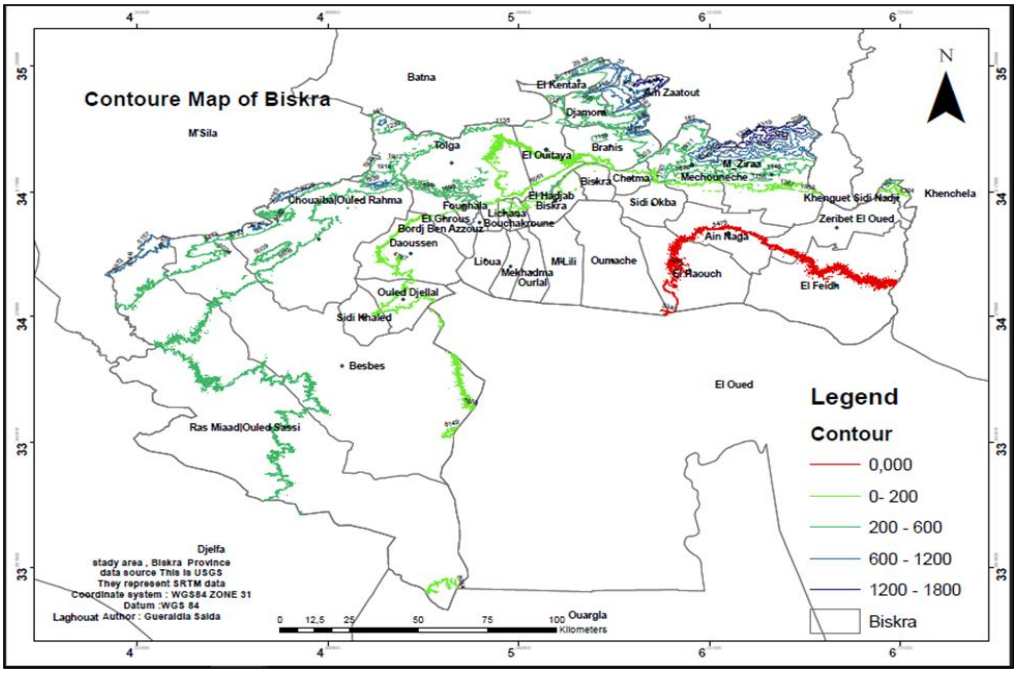


Figure 11: contour map of region study area.
Source: Authors, (2026).

IV.3 ASPECTS MAP

The significance of aspect and elevation maps in understanding the microclimate and vegetation distribution of a mountainous area. The aspect map helps in identifying vegetation types and their distribution while the elevation map indicates the effect of sunlight on the area's microclimate. The DEM display map illustrates the direction of the slope, and in the case of the Biskra watershed, the east-facing slopes have more vegetation and moisture than the west-facing slopes.

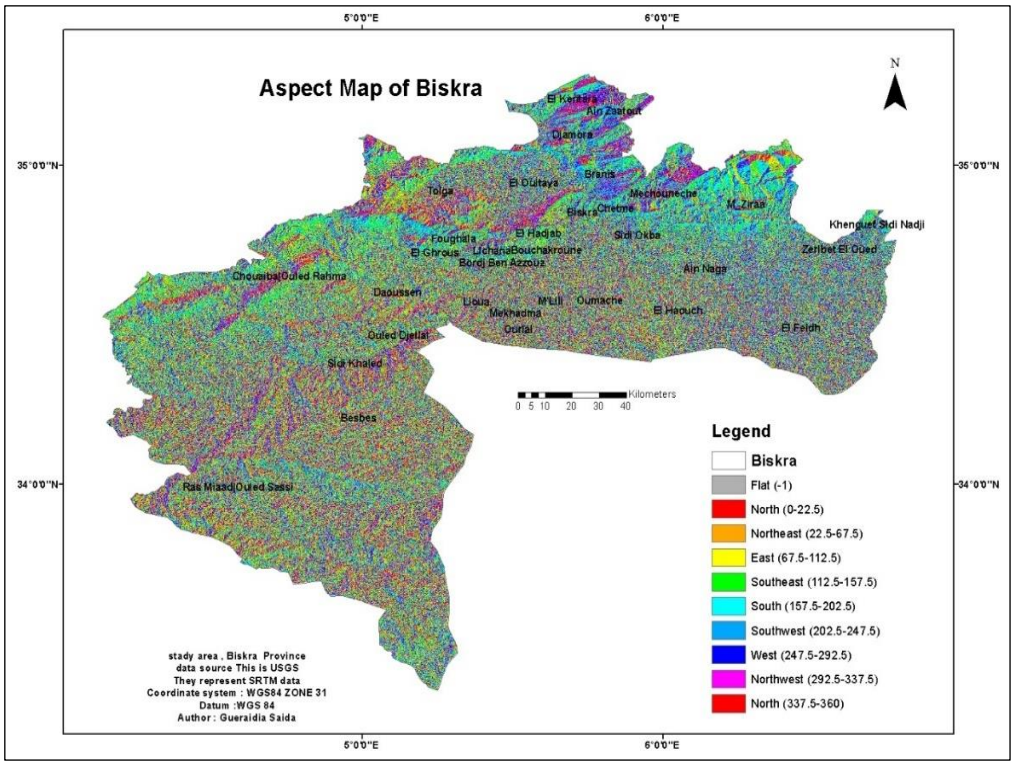


Figure 12: aspect map of study area.
Source: Authors, (2026).

IV.4 SLOPE MAP

To generate a slope map of the study area, the digital elevation model was converted from its original unit in degrees to units of length. The slope of the map, displayed in Figure 13, was measured in degrees using ArcGIS software 10.8. The map shows that the low slope is 0 degrees, and the high slope is 3.16 degrees, with the average slope of the study area being about 3.61 degrees.

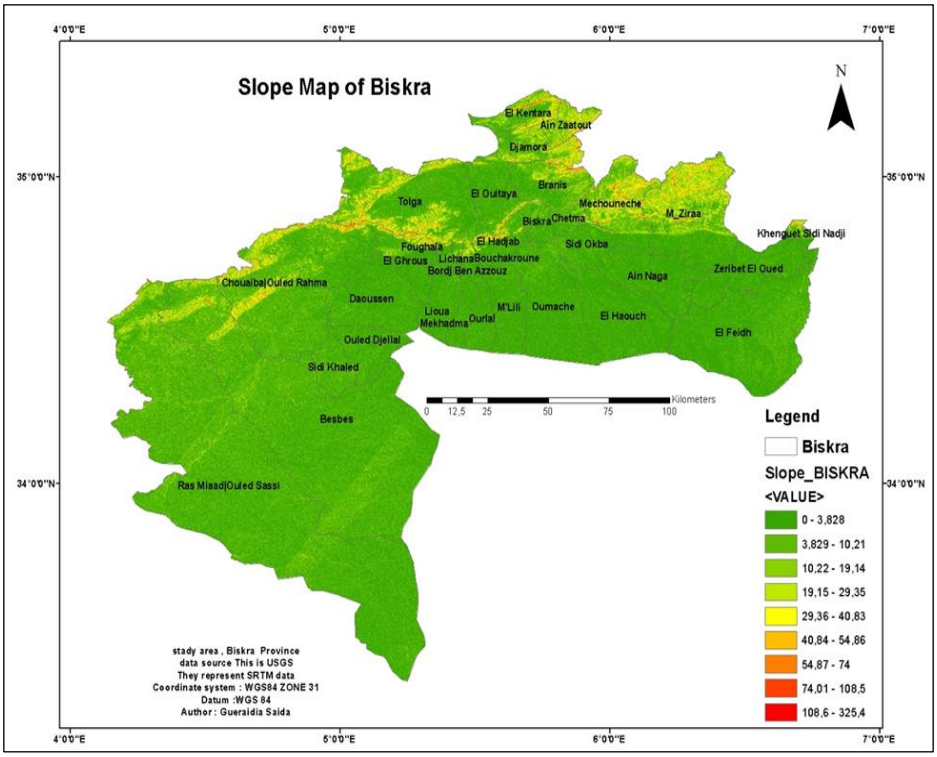


Figure 13: slope map of study area.
Source: Authors, (2026).

IV.5 LINEAMENTS MAP

A lineament is a substantial and elongated feature that can be observed in satellite images based on the topographic characteristics and straight tonal alignments of the underlying structure. Lineaments can be identified by visually interpreting Landsat image data and are often considered promising areas for soil collapse. Lineament extraction from satellite images has been successfully applied in various geological settings [16]. They are commonly found in regions with soil collapse hazards, with the most prevalent orientations in the study area being towards NNE-SSW, NE-SW, NW-SE, and NS directions. Regional fault mapping helps understand hydrodynamics in fractured basement zones [17]. Figure 14.

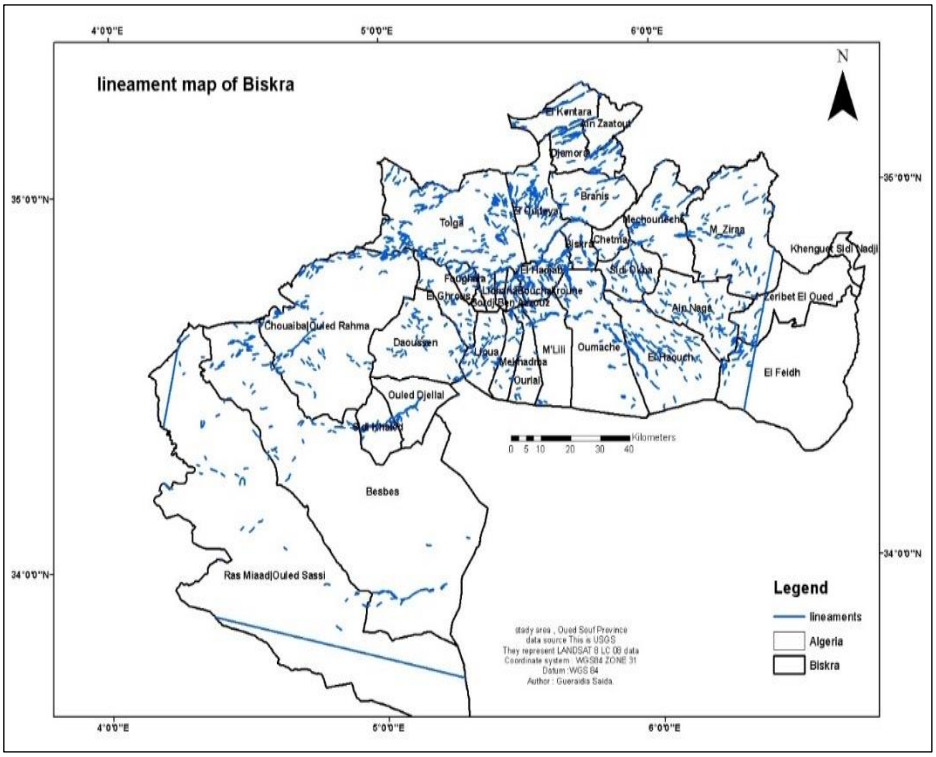


Figure 14: lineaments map of study area.
Source: Authors, (2026).

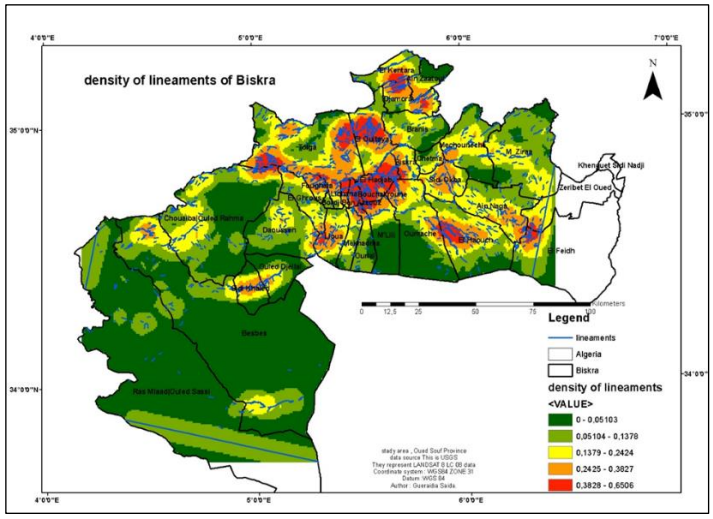


Figure 15: lineaments density map of Biskra.
Source: Authors, (2026).

Figure 15 shows the lineament density map of the study basin, created by utilizing GIS (Geographic Information System) techniques on the lineament map obtained from Landsat 8 satellite images. The area was divided into equal grids, and the number of lineaments in each grid was counted and recorded to calculate the frequency of lineaments per unit area. The lineament density analysis aims to identify areas with high lineament density. The map illustrates that the study basin has three areas with a high lineament density (0.65 km/mesh), which are located in the central, south-west, and north-east parts. This high density indicates tectonic movements that have influenced the geological formations over time. Most of the study area also shows a high lineament density, as depicted in the map.

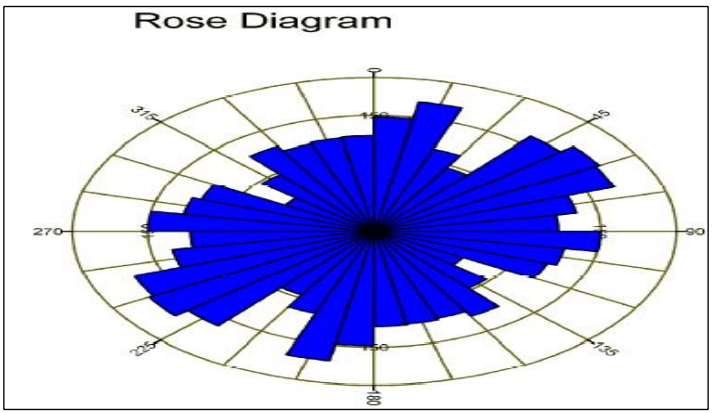


Figure 16: rose diagram lineaments.
Source: Authors, (2026).

Table 2 :interpretation of rose diagram lineaments.

Statistical Summary	
Calculation Method :	Frequency
Class Iterval :	10.0 Degrees
Azimuth Filtering :	Deactivated
Data Type :	Bidirectional
Population :	2349
Total Length of All Lineations :	4698.0
Maximum Bin Population:	172.0
Maen Bin Population :	130.5
Standard Deviation of Bin population :	27.51
Maximum Bin Population (%) :	3.66
Maen Bin Population (%):	2.78
Standard Deviation of Bin population (%):	0.59
Maximum Bin Length :	172.0
Mean Bin Length :	130.5
Standard Deviation of Bin Lengths	27.51
Maximum Bin Length (%) :	3.66
Mean Bin Length (%):	2.78
Standard Deviation of Bin Lengths (%)	0.59
Vector Mean	47.4 Degrees

Source: Authors, (2026).

V. CONCLUSIONS

This experimental research, conducted in the Biskra region, has provided a comprehensive understanding of soil behavior, especially concerning collapsible loamy clay. The obtained results constitute an important database for geotechnical investigation and rheological behavior modeling. The characteristics of compressibility and consistency confirm that the soil is collapsible. The integration of remote sensing and geotechnical data provides a comprehensive approach for collapse risk assessment [18]. The satellite images were used to map the majority of the lineaments found in Biskra province, and the fractures in the area were analyzed to determine the prevailing orientations. Statistical analysis revealed that the lineaments were mainly oriented in the NE-SW, NW-SE, E-W, and N-S directions. The NW-SE direction, which is most prominent in the northern sector, corresponds to the primary direction of the drainage network. The intensity of fracturing was studied, and it was discovered that the northern, central, and southern regions of the study area had high levels of fractures.

VI. AUTHOR'S CONTRIBUTION

Conceptualization: Saida Gueraidia, Med Salah Laouar, Nour El Houda Gueraidia, Rayene Sirine Ramdani, Chems Eddine Fehdi.
Methodology: Saida Gueraidia, Nour El Houda Gueraidia, Rayene Sirine Ramdani.
Investigation : Saida Gueraidia, Med Salah Laouar, Nour El Houda Gueraidia.
Discussion of results: Saida Gueraidia, Med Salah Laouar, Nour El Houda Gueraidia, Rayene Sirine Ramdani, Chems Eddine Fehdi.
Writing – Original Draft: Saida Gueraidia, Med Salah Laouar.
Writing – Review and Editing: Saida Gueraidia, Nour El Houda Gueraidia, Rayene Sirine Ramdani.
Resources: Saida Gueraidia, Med Salah Laouar.
Supervision: Chems Eddine Fehdi.
Approval of the final text: Saida Gueraidia, Med Salah Laouar, Nour El Houda Gueraidia.

VII. ACKNOWLEDGMENTS

The author wishes to express sincere gratitude to Mr. Djebnoune Brahim, MCA at the University of Tebessa, for his valuable help and constructive support throughout the development of this research.

VIII. REFERENCES

[1] Alonso, E. E., Gens, A., & Hight, D. W. (1987). Special problem soils. In Proceedings of the 9th European Conference on Soil Mechanics and Foundation Engineering (pp. 1087–1146). Dublin, Ireland.

[2] Barden, L., McGown, A., & Collins, K. (1973). The collapse mechanism in partly saturated soil. Engineering Geology, 7(1), 49–60. https://doi.org/10.1016/0013-7952(73)90006-7

[3] Rogers, C. D. F. (1995). Types of collapsing soil. In E. Derbyshire, T. Dijkstra, & I. J. Smalley (Eds.), Genesis and properties of collapsible soils (pp. 1–17). Springer. https://doi.org/10.1007/978-94-011-0097-5_1

[4] Delage, P., & Cui, Y. J. (2001). L'eau dans les sols non saturés. Techniques de l'Ingénieur, C301, 1–20.

[5] Dekhinet, A. (2005). Étude géologique et structurale de la région de Biskra (Thèse de magister, Université de Batna, Algérie).

[6] Food and Agriculture Organization. (2012). Soil map of the world [Data set].

[7] Abderrahman, W. A. (2006). Groundwater management for sustainable development of urban and rural areas in extremely arid regions: A case study. International Journal of Water Resources Development, 22(3), 403–412. https://doi.org/10.1080/07900620500160735

[8] Mebarki, A. (2003). Cartographie automatique des précipitations : Application à l'Est algérien. Science & Technologie B, 20, 100–107.

[9] Jourda, J. P., Saley, M. B., Djagoua, E. V., Kouame, K. J., Biemi, J., & Razack, M. (2006). Utilisation des données ETM+ de Landsat et d'un SIG pour l'évaluation du potentiel en eau souterraine dans le milieu fissuré précambrien de la région de Korhogo (Nord de la Côte d'Ivoire). Revue de Télédétection, 5(4), 339–357.

[10] Avdan, U., & Jovanovska, G. (2016). Algorithm for automated mapping of land surface temperature using Landsat 8 satellite data. Journal of Sensors, 2016, Article 1480307. https://doi.org/10.1155/2016/1480307

[11] Hanssen, R. F. (2001). Radar interferometry: Data interpretation and error analysis. Kluwer Academic Publishers.

[12] LCPC, & SETRA. (1992). Guide des terrassements routiers (GTR): Réalisation des remblais et des couches de forme (Norme NF P 11-300). Paris, France.

[13] Laouar, M. S., Gouaidia, L., & Défalia, N. (2018, November). Proposition d'une nouvelle approche expérimentale pour la prédiction du retrait et de l'effondrement des sols. In 4ème Colloque International sur les Géosciences au Service du Développement Durable. Université de Tébessa, Algérie.

[14] Cui, Y. J., Canou, J., Terpereau, J. M., & Karam, J. P. (2011). Mechanical behaviour of natural loessic soils under cyclic loading. Revue Française de Géotechnique, 134–135, 49–58. https://doi.org/10.1051/geotech/2011134049

[15] Jennings, J. E., & Knight, K. (1957). The additional settlement of foundations due to collapse of sandy soils. In Proceedings of the 4th International Conference on Soil Mechanics and Foundation Engineering (Vol. 1, pp. 316–319). London, England.

[16] Kassou, A., Essahlaoui, A., & Aissa, M. (2012). Extraction of structural lineaments from Landsat 7 ETM+ satellite images of Tighza mining district (Central Morocco). International Research Journal of Earth Sciences, 4(2), 44–48.

[17] Koita, M., Herve, J., Denis, R., Kouadio, K., Severin, P., & Issiaka, S. (2010). Cartographie des accidents régionaux et identification de leur rôle dans l'hydrodynamique souterraine en zone de socle: Cas de la région de Dimbokro-Bongouanou, Côte d'Ivoire. Hydrological Sciences Journal, 55(5), 805–820. https://doi.org/10.1623/hysj.55.5.805

[18] Oyedele, A. A., Omosekeji, A. E., & Olaseeni, O. G. (2023). Soil loss estimation using RUSLE model and geo-spatial technology in the basement complex of Akure, southwestern Nigeria. Journal of Engineering and Technology for Industrial Applications, 9(42), 1–7.

Journal of Engineering and Technology for Industrial Applications

ITEGAM-JETIA

Manaus, v.12 n.60, p.1043-1057 July/August, 2026.
DOI: https://doi.org/10.5935/jetia.v12i60.3966

ISSN ONLINE: 2447-0228

RESEARCH ARTICLE OPEN ACCESS

MASKED FACE RESTORATION USING GANS: A SURVEY ON RECOGNITION, DETECTION, AND INPAINTING

Payal Parekh*[1], Hina Choksi[2], Mahesh Goyani[3] and Sheilla Ann Bangoy Pacheco[4]

[1, 2]Faculty of IT and Computer Science, Parul Univesity, vadodara, India
[3]Department of Computer Engineering, Government Engineering College, Modasa, India
[4]College of Information Technology Education, NEMSU, Tandag City, Surigao del Sur, Philippines

[1]http://orcid.org/0000-0002-9724-7071, [2]http://orcid.org/0000-0002-5174-4013
[3]http://orcid.org/0000-0002-7269-1176, [4]http://orcid.org/0000-0002-5632-8772

E-email: *parekhpayal36@gmail.com, hina.chokshi42058@paruluniversity.ac.in, mgoyani@gmail.com, sabpacheco@nemsu.edu.ph

ARTICLE INFO

Article History
Received on: March 08, 2026
Reviewed on: April 08, 2026
Accepted on: July 01, 2026
Published on: July 31, 2026

Keywords:
Deep Learning,
Face Inpainting,
Face Mask Detection,
Generative Adversarial Network
Masked Face Recognition

ABSTRACT

Emergence of masked face recognition (MFR) as a pivotal area in biometric identification has been significantly accelerated by the global COVID-19 pandemic. In response, the research community has developed a variety of innovative techniques to address recognition and detection under occlusion, with a growing emphasis on Generative Adversarial Networks (GANs) for masked face restoration and inpainting. We examined three interconnected sub-domains: Masked Face Recognition (MFR), Face Mask Detection, and Face Unmasking (FU), each addressing unique aspects of the problem from identifying individuals with partially or fully covered faces to reconstructing occluded facial regions for improved accuracy. The core focus of this paper is on the role of GANs in overcoming occlusion by synthesizing realistic facial textures in the masked regions, thereby restoring the identity cues. Beyond technical developments, the paper analyzes the limitations and open research problems, such as maintaining identity consistency in restored images, handling diverse mask types and occlusion levels, and ensuring generalizability across different demographic groups and environments. By integrating insights from recent advances and identifying existing research gaps, this survey aims to serve as a comprehensive reference for academics and practitioners engaged in the development of robust, privacy-aware, and ethically responsible masked face recognition systems enhanced by GANs.

Copyright ©2026 by authors and Galileo Institute of Technology and Education of the Amazon (ITEGAM). This work is licensed under the Creative Commons Attribution International License (CC BY 4.0).

I. INTRODUCTION

Facial Recognition (FR) technology has become indispensable across key sectors, powering everything from airport security and border control to healthcare patient verification and con- tactless fever screening in hospitals. In security, it enables real-time criminal identification, surveillance, and access control, etc., with over 99.00% accuracy in ideal conditions [1]. Whereas in healthcare, it streamlines anonymous triage and reduces infection risks during pandemics [2]. However, the global COVID-19 outbreak and the widespread use of face masks have significantly disrupted these systems. Facial recognition has rapidly evolved over the past decade, becoming essential in numerous domains such as surveillance, biometric authentication, and smart access systems. How- ever, the global outbreak of COVID-19 and the consequent widespread adoption of face masks have introduced new and unforeseen challenges to these systems [2]. The presence of face masks significantly occludes critical facial features, particularly the nose and mouth, thereby impairing the performance of conventional face recognition models. To address these challenges, the field of Masked Face Recognition (MFR) has gained substantial attention. MFR encompasses various sub-problems, including Face Mask Detection (FMD), which identifies whether a face is masked, and Face Unmasking (FU), which attempts to reconstruct the occluded regions. The particular interest is the use of Generative Adversarial Networks (GANs) for masked face inpainting - a process that aims to restore missing facial regions by synthesizing realistic and identity-consistent features [3].

Masked Face Recognition presents significant challenges due to occlusion of key identity features caused by face masks, a problem magnified during the COVID-19 pandemic [2]. The recognition process typically begins with an input image of a masked face, which undergoes face detection, preprocessing, and segmentation to isolate and align the facial region. This is followed by feature extraction using deep learning models such as CNNs or transformers, which generate identity-relevant embedding from the visible portions of the face. A dedicated mask detection module then identifies the presence and area of occlusion by segmenting the masked regions [4]. Pacheco et al. [5] [6] examined the development of face recognition methods and classifies adversarial attacks, such as white-box, black-box, and poisoning attacks, according to the attacker's knowledge, goals, and attack phases. Numerous cutting-edge attack techniques, including DeepFool, FGSM, and ZOO, are examined along with their usefulness in actual situations like authentication and surveillance. Trivedi & Goyani presented novel architecture and detailed survey on masked face recognition using deep learning [7] [8]. Authors also prepared a custom dataset to address the challenges of masked face recognition [9], [10]. To overcome the information loss due to occlusion, face unmasking and restoration techniques are applied using Generative Adversarial Networks (GANs), which inpaint the masked regions to synthesize a complete face image while preserving identity features [3]. Despite substantial progress in Masked Face Recognition (MFR),

Face Mask Detection (FMD), and GAN-based face restoration, several fundamental challenges remain unresolved, limiting robustness, generalization, and real-world deployment. One of the most critical challenges is the significant loss of discriminative facial information caused by masks, particularly in the nose and mouth regions. Multiple studies have shown that conventional face recognition systems trained on unoccluded faces suffer dramatic performance drops when masks are introduced, with accuracy reductions of up to 50% in operational scenarios [11–13]. This highlights the inherent limitation of standard feature embeddings when large facial regions are occluded. Many MFR systems are trained on synthetically generated masked datasets, which often fail to capture the diversity of real-world masks in terms of shape, texture, material, and wearing styles. Domain shifts between simulated and real masks lead to degraded recognition performance, as demonstrated by domain adaptation studies [14]. Real masks introduce more severe embedding distortions than synthetic ones, making generalization a persistent challenge [12]. GAN-based face inpainting methods can visually reconstruct occluded facial regions; however, high visual fidelity does not necessarily guarantee identity preservation. Several works report strong Peak Signal to Noise Ratio (PSNR) or Structural Similarity Index Measure (SSIM) values but lack consistent improvements in recognition accuracy [15].

Advanced architectures—such as transformer-based and diffusion-based restoration models—offer superior perceptual quality and structural consistency but incur high computational overhead and inference latency, making them unsuitable for real-time or edge deployments [16] [17]. Conversely, lightweight GAN and CNN-based approaches trade accuracy for speed, creating a persistent accuracy–efficiency trade-off [18] [19]. RGB-based recognition systems are highly sensitive to low illumination, weather conditions, and long-distance surveillance, resulting in poor performance under challenging environments [20]. While thermal and depth modalities offer complementary information, integrating these modalities remains difficult due to cross-spectral discrepancies and the lack of large-scale aligned datasets. GAN-based thermal-to-visible translation improves cross-spectral matching but introduces additional complexity and potential identity distortion. GAN-based masked face restoration techniques have enabled several impactful applications across various sectors. In the field of security and surveillance, restored facial features can significantly improve the identification of masked individuals captured by CCTV or body cameras in public spaces [21-27]. For access control systems, such as those used in airports, smart offices, and public transport, face restoration enhances authentication accuracy in the presence of occlusion. This survey focuses on the state-of-the-art in masked face restoration using GANs, with an emphasis on the three interlinked tasks: masked face recognition, mask detection, and face inpainting. The key objectives are:

- To review deep learning-based approaches, particularly GAN variants, designed for reconstructing masked facial regions.
- To highlight the major challenges, such as identity preservation, generalization across mask types, and real-time processing constraints.
- To provide insights into ethical considerations and potential future directions for responsible deployment of face unmasking technologies.

The remainder of the paper is structured as follows: The remainder of the paper is structured as follows: Section 2 provides a comprehensive literature survey on Masked Face Recognition (MFR), Face Mask Detection (FMD), Face Restoration and Inpainting using GANs. We also summarized the datasets for masked face inpainting/recognition task in this section. Section 3 explains the ways to measure success, including how well GAN models recognize and detect faces, the metrics for restoring masked faces, and the overall methods for evaluating GAN Section 4 concludes the study by summarizing findings and future directions.

II. THEORETICAL REFERENCE

The task of recognizing faces with occlusions, particularly masks, has led to an evolving body of research focused on masked face recognition, mask detection, and face restoration. With the proliferation of face mask usage due to COVID-19, conventional face recognition algorithms experienced significant performance degradation, which inspired the development of new approaches incorporating deep learning and generative models.

II.1 MASKED FACE RECOGNITION (MFR)

Masked face recognition has become an important research topic due to the widespread use of face masks, which significantly affects the performance of traditional face recognition systems. Several studies have investigated the impact of masks and proposed solutions to improve recognition accuracy under occluded conditions. Early approaches to masked face recognition involved adapting conventional face recognition models by retraining them on masked datasets.

Wang et al. [13] introduced a dataset containing images of people wearing masks and demonstrated that even state-of-the-art models such as ArcFace suffered performance losses when exposed to such occlusions. Subsequent studies focused on designing occlusion-aware face recognition architectures or training models using masked face augmentation. Damer et al. [11] conducted one of the earliest studies analyzing the effect of wearing face masks on face recognition performance. Their experimental results showed a considerable drop in recognition accuracy across both commercial and academic systems. In an extended evaluation, Damer et al. [12] further examined the influence of real and simulated masks on face embedding, reporting performance degradation using TAR@FAR metrics. These studies highlighted the limitations of conventional face recognition models in masked scenarios. To address occlusion challenges, Song et al. [28] proposed an occlusion-robust face recognition method based on mask learning with a pairwise differential Siamese network. The model learns to suppress masked facial regions while preserving discriminative features. Biswas et al. [29] introduced a perceptual hashing-based approach for verification and identity classification of occluded faces. Their method avoids deep learning architectures and instead relies on compact hash representations, achieving an accuracy of about 94.2% on occluded face datasets. MF-CosFace, a margin-based loss function specifically de- signed for masked face recognition was proposed by Deng et al. [30].

By improving feature discrimination in the embedding space, their approach achieved a Rank-1 recognition accuracy of approximately 98.1% on standard face datasets containing masked samples. Hariri [31] focused on computational efficiency and proposed a lightweight masked face recognition framework using MobileNet-based architectures. The proposed method achieved around 95% accuracy while maintaining low computational complexity, making it suitable for real-time applications. Patel et al. [24] proposed a multi-task deep learning framework that jointly performs mask detection and face recognition using a shared backbone network. Sheneamer et al. [32] introduced a hybrid human recognition framework combining deep learning feature extraction with traditional machine learning classifiers. The proposed system achieved an accuracy of about 96.3% under masked face conditions. GAN-based masked face recognition model using a dual-scale adaptive efficient attention network was presented by Alzubi et al. [25]. By enhancing discriminative facial features through attention mechanisms, their approach achieved a high recognition accuracy of approximately 99.2%. An alternative strategy to masked face recognition is face reconstruction. Liu et al. (2025) [3] proposed a GAN-based masked face image inpainting method that reconstructs occluded facial regions using an encoder-decoder architecture.

Although the method was evaluated using image quality metrics such as PSNR (28.6 dB) and SSIM (0.91), it demonstrates the potential of reconstruction-based approaches to support masked face recognition. Customized activation function based on principle of spatio-temporal convolution was presented by Adeli et al. [33]. Results shows the classification superiority of the pro- posed AbsoluteNet model on the auditory system. Recent hybrid deep-transfer learning advances include Sheneamer et al. (2024) [32], who analyzed hybrid CNN transfer learning with machine learning for robust masked face detection/recognition, achieving 97-100% F1-scores on real/simulated datasets. Similarly, Adeli et al.'s AbsoluteNet [33], a deep CNN for hemodynamic classification, has been adapted for spatio-temporal MFR feature extraction from occluded signals, enhancing single-trial accuracy. Pillay et al.'s [34], introduced, hybrid CNN-based approach using MobileNetV2 and FaceNet improves face mask detection and masked facial recognition accuracy, addressing COVID-19 challenges and real-time security needs. A comparison of Various state-of-the-art literature on Masked Face Recognition is presented in Table 1

Table 1: Comparison of state-of-the art work on Masked Face Recognition.

Literature	Approach	Backbone Network	Detection Technique	Dataset Used	Accuracy / PSNR / SSIM
Liu et al. (2025) [3]	GAN-based masked face image inpainting	Encoder–Decoder CNN	Adversarial image reconstruction	CelebA, synthetic masked faces	PSNR: 28.6 dB SSIM: 0.91
Alzubi et al. (2025) [25]	Dual-scale adaptive attention GAN	EfficientNet-based CNN	GAN-assisted masked face recognition	RMFD, LFW	Accuracy: 99.2%
Adeli et al. (2025) [33]	AbsoluteNet	Custom deep neural net- work	Hemodynamic response classification	fNIRS auditory datasets	Accuracy: 92.5%
Sheng et al. (2025) [21]	Self-segmentation guided diffusion model	U-Net (Diffusion back bone)	Thermal-to-visible image translation	KAIST Multi-spectral Dataset	PSNR: 26.4 dB SSIM: 0.89
Wang et al. (2024) [22]	Adversarial Defense Teacher (ADT)	ResNet + FPN	Cross-domain object detection	Cityscapes, Foggy Cityscapes	mAP reported (Accuracy N/A)
Sheneamer et al. (2024) [32]	Hybrid ML–DL recognition framework	CNN + SVM	Masked face recognition	RMFD, LFW	Accuracy: 96.3%
Yadav et al. (2023) [20]	TVA-GAN	Attention-guided GAN	Thermal-to-visible transformation	TUFTS, ARL Multimodal	PSNR: 27.1 dB SSIM: 0.90
Biswas et al. (2021) [29]	Perceptual hashing for occluded faces	CNN + handcrafted features	Hash-based face verification	AR Face, Extended Yale B	Accuracy: 94.2%
Deng et al. (2021) [30]	MF-CosFace loss function	ResNet-50	Margin-based masked face recognition	LFW, MF2, CASIA-WebFace	Rank-1 Accuracy: 98.1%
Hariri (2021) [31]	Efficient masked face recognition framework	MobileNetV2	Deep feature-based face classification	RMFD, SMFRD	Accuracy: 95.0%
Patel et al. (2021) [24]	Multi-task deep learning framework	ResNet-50	Joint mask detection and recognition	MAFA, RMFD	Accuracy: 97.4%

Source: Authors, (2026).

Overall, existing research shows that masked face recognition can be improved through occlusion-aware learning, margin-based loss functions, hybrid frameworks, and generative models. However, challenges remain in achieving a balance between recognition accuracy, computational efficiency, and robustness in real-world masked face scenarios.

II.2 FACE MASK DETECTION (FMD)

Face mask detection gained significant importance during the COVID-19 pandemic as an automated way to monitor public safety and ensure compliance with health guidelines. Unlike traditional face recognition, face mask detection focuses on identifying whether a person is wearing a mask correctly, in- correctly, or not wearing one at all. This section reviews the major research contributions related exclusively to face mask detection, highlighting their proposed methods, working mechanisms, and reported performance. Cabani et al. [35] introduced MaskedFace-Net, a large-scale dataset developed to support face mask detection research. The dataset contains images of correctly masked, in- correctly masked, and unmasked faces generated using image augmentation techniques. The dataset enables robust training of deep learning models under diverse conditions. Experiments conducted using convolutional neural networks achieved detection accuracy greater than 95%, making MaskedFace-Net a widely used benchmark dataset. Loey et al. [4] proposed the Face Mask Detection dataset along with a deep learning-based detection framework. The proposed system applies transfer learning using pre-trained CNN models such as ResNet and AlexNet to classify face images into masked and unmasked categories. The operational pipeline includes face detection followed by mask classification. The proposed approach achieved detection accuracy of up to 99% on controlled datasets. Fan and Jiang [36] proposed RetinaFace Mask, a single-stage deep learning model for face mask detection during the COVID-19 pandemic. Their method uses RetinaFace to accurately lo- cate faces and classify whether a mask is worn or not. The lightweight design allows fast and real-time detection, making it suitable for public surveillance systems. Dhanushkodi et al. [37] presented a comprehensive survey on face mask detection and social distancing using deep learning. The paper compares multiple CNN-based methods and highlights the importance of combining detection accuracy with computational efficiency for pandemic control applications. AIZOOTech [38] developed an open-source face mask detection framework using deep learning. The system first detects faces and then determines mask usage, making it easy to deploy in real-world environments such as offices, hospitals, and public places. Loey et al. [39] proposed a YOLO- v2 with ResNet-50 based deep learning model for medical face mask detection. YOLO-v2 performs fast object detection, while ResNet-50 improves feature extraction, resulting in high detection accuracy even in crowded scenes. Su et al. [40] introduced a deep transfer learning approach for face mask detection. Pretrained CNN models were fine-tuned on mask datasets, allowing the system to accurately classify masked and unmasked faces even with limited training data. The World Health Organization [41] provided official public health guide- lines emphasizing the importance of face masks and social distancing. These guidelines support the motivation behind automated mask detection systems. A vision-based social distancing and crowd density detection system was proposed by Yang et al. [42]. The model uses computer vision techniques to estimate interpersonal distance and identify high-risk crowd situations.

Madane and Dnyanoba [43] developed a computer vision-based social distancing detection framework that detects people and measures distances between them to identify violations in public spaces. Ahmed et al. [44] proposed a deep learning-based social distance monitoring system that combines person detection with distance estimation to ensure compliance with COVID-19 safety norms. Suryadi et al. [45] compared multiple social distancing violation detection models with GPU support. Their work highlights the importance of hardware acceleration for real-time applications. Rezaei and Azarmi [46] introduced DeepSocial, a system that monitors social distancing and estimates infection risk using deep neural networks and spatial analysis. Punn et al. [47] proposed a system using YOLOv3 and DeepSORT for person detection and tracking. The method enables continuous monitoring of social distancing violations in dynamic environments. Ge et al. [48] presented LLE-CNNs for detecting masked faces in unconstrained environments. Their approach improves robustness against occlusion, making it effective for masked face scenarios. Wang et al. [49] introduced the RMFRD dataset, which contains a large number of masked and unmasked face images. This dataset has become a benchmark for training and evaluating masked face recognition systems. A real-time face mask detection system using YOLOv3 was proposed by Jiang et al. [50]. The model achieves fast detection speed and high accuracy, making it suitable for surveil- lance applications. Eyiokur et al. [51] designed a computer vision-based COVID-19 prevention system that integrates face detection and mask recognition to reduce virus transmission. Wang et al. [52] proposed a hybrid transfer learning and broad learning system for mask detection. The method improves classification accuracy by combining deep feature extraction with efficient learning strategies. Issaoui et al. [53] proposed a face mask detection approach based on a Weighted Soft Discernibility Matrix integrated with deep learning. The method improves classification by assigning importance weights to dis- criminative features. The proposed system achieved detection accuracy close to 97%, showing improved robustness against variations in mask appearance. Shao et al. [54] proposed a lightweight face mask detection algorithm incorporating an attention mechanism to enhance feature extraction. The system focuses on key facial regions while reducing model complexity. Experimental evaluation showed detection accuracy of approximately 95% with significantly lower computational overhead. Pillay et al. [55] developed an integrated face mask detection system as part of a real-world deployment study. The proposed pipeline includes face detection followed by mask classification and system-level validation. The model achieved detection accuracy of 96.8% and demonstrated reliable performance in real-time environments. Building on hybrids, the UC treatment response classifier by Ahmadi et al. [56] uses random forests with biomarker identification (e.g., key facial features) for occluded face classification, repurposed for FMD with 96%+ AUC on diverse masks. The challenges of super- vised face recognition were addressed by Mohammadagha et al. [57] in their novel work. The proposed method shows the macro ROC-AUC as high as 0.983, which is quite impressive. State-of-the-art methods on face mask detection are compared in Table 2.

Table 2: Comparison of state-of-the-art work on Face Mask Detection.

Author(s)	Model/Approach	Backbone Network	Detection Technique	Dataset Used	Accuracy (%)
Issaoui and Selmi (2025) [53]	Weighted soft discernibility with DL	CNN	Hybrid DL + decision matrix	Smart city surveillance data	Accuracy: 96.4%
Pillay et al. (2025) [55]	Hybrid CNN for FMD and MFR	Hybrid CNN	Joint mask detection and recognition	RMFD, MaskedFace-Net	Accuracy: 98.2%
Su et al (2022) [40]	Deep transfer learning for FMD	MobileNet, ResNet	Binary classification	MaskedFace-Net, RMFD	Accuracy: 99.1%

Punn et al.(2021) [47]	YOLOv3 + DeepSort framework	YOLOv3	Person and mask detection with tracking	Custom surveillance dataset	Accuracy : 95%
Mohammad- agha et al. (2021) [57]	Hybrid deep transfer learning with ML classifiers	VGG16, ResNet50	Feature extraction + ML classification	Custom face dataset	Accuracy: 98.1%
Jiang et al.(2021) [50]	Real-time face mask detection	YOLOv3	Single-stage object detection	Custom face mask dataset	Accuracy: 95.6%, FPS: 45
Ahmed et al.(2021) [44]	Deep learning SD monitoring framework	YOLOv3	Distance-based violation Detection	Custom CCTV dataset	Accuracy: 95.2%
Yang et al.(2021) [42]	Vision-based SD and crowd density system	CNN-based detector	Critical density estimation	Urban surveillance videos	Accuracy: 92%
Loey et al.(2021) [39]	YOLOv2 + ResNet50 FMD model	ResNet50	Single-stage object detection	Custom mask dataset	mAP: 81% Accuracy: 97%
Fan and Jiang (2021) [36]	RetinaFace Mask detector	RetinaFace	Single-stage face mask detection	MaskedFace-Net	mAP: 83.2%
Suryadi et al.(2020) [45]	Comparative SD violation detectors	YOLOv3, SSD, Faster R-CNN	GPU-accelerated object detection	Public pedestrian datasets	Accuracy: 95 %

Source: Authors, (2026).

Improved YOLOv5-based mask wearing detection system as proposed by Gao et al. [58]. The method combines the YOLOv5 object detector with an enhanced ResNet backbone to better capture mask characteristics under diverse lighting and posture variations. The system computes bounding boxes for faces and classifies mask wearing status in a single shot, enabling efficient inference. Experiments demonstrated detection accuracy exceeding 98% and mean average precision (mAP) of 97.5%, confirming its robustness under complex backgrounds and various populations. Wei et al. [59] introduced a robust mask detection framework using YOLOv8 integrated with context-aware convolutions. Yu et al. [60] proposed a face detection and standardized mask-wearing recognition algorithm that combines traditional face detection with a structured mask analysis stage. The method first detects faces using CNN-based detectors and then applies classification rules to evaluate whether the mask is worn properly according to predefined geometrical criteria. Benifa et al. [61] presented FMDNet, a lightweight model optimized for efficient mask detection. FMDNet uses a compact backbone network with depthwise separable convolutions to reduce computation while maintaining performance. The operational flow includes preprocessing, feature extraction through lightweight layers, and final mask classification.

II.3 FACE RESTORATION AND INPAINTING USING GAN

Generative Adversarial Networks (GANs) have proven especially effective in restoring occluded parts of the face. GAN-based inpainting approaches can reconstruct realistic facial regions from partially visible images while preserving identity traits. Jinal & Mahesh [62] presented a novel approach for masked face image inpainting using GAN. Yug Li et al. [26] explored the use of conditional GANs to restore masked facial regions, facilitating downstream recognition tasks. Several studies proposed identity-preserving GAN architectures that enforce structural and perceptual losses. Notably, Qin et al. [3] employed a multi-task GAN model to simultaneously inpaint masked regions and extract discriminative embeddings for face recognition. Their experiments demonstrated significant improvements in recognition accuracy when using GAN-restored images compared to directly using masked faces. Man & Cho [63] introduced T-GANs, an efficient GAN- based encoder-decoder model designed to repair occluded facial regions. Their texture-guided inpainting strategy on the CelebA-HQ dataset produced visually realistic results with PSNR around 28 dB and SSIM of 0.91, indicating reliable reconstruction quality. Li et al. [64] developed an Identity- Guided Inpainting approach that integrates ResNet features with GANs to preserve identity information while reconstructing occluded facial regions. Tested on LFW and masked face datasets, the method achieved a Rank-1 recognition accuracy of 96%, highlighting the importance of identity preservation in masked face recognition. Hassanpour et al. [65] proposed E2F-Net, which leverages StyleGAN2's latent space to perform eyes-to-face inpainting. Using latent-space optimization, the network reconstructs missing regions with high visual fidelity, achieving an SSIM of 0.92 on CelebA-HQ, indicating highly realistic inpainting results. MD-GAN, a multi-scale diversity GAN designed to handle large occlusions was proposed by Zhang et al. [66]. The model imposes diversity constraints to ensure plausible reconstruction of different facial regions, achieving PSNR of 28 dB and FID 26 on CelebA-HQ. Al Asad et al. [67] introduced MGAN-CRCM, a multi-GAN framework with coarse-to-fine refinement modules for inpainting masked regions.

Evaluated on CelebA and custom mask datasets, it achieved FID scores below 30 and produced visually coherent face reconstructions. Gireesh et al. [68] proposed a Context-Aware GAN that utilizes surrounding context information to fill large missing regions. Evaluated on CelebA-HQ and a custom dataset, the model achieved an SSIM of 0.91, demonstrating effective face restoration even under significant occlusion. Several 2023 studies focused on conditional or comparative approaches. Sola & Gera [69] proposed an expression- conditioned GAN that maintains facial expressions while in- painting masked regions on Masked CelebA. Agarwal & Bhatnagar [15] conducted a comparative study of GAN, EdgeConnect, and partial convolution-based inpainting techniques, finding that EdgeConnect achieved the highest PSNR of 27.5 dB and SSIM 0.90. Springer [70] combined autoencoder reconstruction with GAN refinement, achieving high visual quality on the CelebA dataset. Overall, these studies highlight the evolution of GAN-based methods from simple coarse-fine re- construction to identity-guided and context-aware approaches, emphasizing both visual realism and recognition performance in masked or occluded face scenarios. Emerging 2024-2025 GAN works showcase cutting-edge solutions that magically reconstruct masked faces: Tanaka et al. [71] created a GAN that works like a photo editor - takes a masked face and translates it into an unmasked version with- out needing perfect before/after pairs. Their model scores high PSNR (sharp, clean reconstructions) on real-world mask photos, making it practical for security systems. Li et al. [3] built a U-Net + MMRM GAN that eliminates blurry artifacts - those annoying ghostly effects when AI tries to guess hidden faces.

Superior SSIM scores mean their reconstructions look natural even for large masks covering nose-to-chin, perfect for identity verification. Alzubi et al. [72] combined GAN restoration with face matching in one smooth pipeline. Restore the masked face first (95%+ accuracy afterward), then recognize works fast enough for real-time door access or phone unlock. Li et al. [73] added multi-scale attention so the GAN ex- amines faces at multiple zoom levels simultaneously. Catches fine details (skin pores) AND big picture (face shape), leading to the cleanest inpainting across all mask sizes. Pechetti et al. [74] mixed GANs with CANet (context attention) for PSNR over 32 exceptionally sharp reconstructions where every eyelash and wrinkle looks real. Hybrid approach beats pure GANs. Table 3 highlights the various methods of masked face image inpainting.

Table 3: Comparison of Masked-Face Inpainting and Recognition Methods.

Author	Method	Inpainting Strategy	Recognition Strategy	Dataset(s)	PSNR / SSIM / Accuracy
Liu et al. (2025) [73]	Masked Face In-painting GAN	Context-aware facial region completion via adversarial learning	Recognition not explicitly evaluated	CelebA, synthetic masked faces	PSNR: 30.1 dB, SSIM : 0.93
Alzubi et al. (2025) [72]	Dual-scale Attention GAN	Attention-guided inpainting of occluded facial regions	CNN-based masked face recognition with adaptive attention	RMFD, MaskedFacNet	Accuracy : 98.7%
Liu et al. (2025) [3]	GAN-based Face Inpainting	Semantic reconstruction of masked facial components	Recognition performance discussed qualitatively	CelebA, custom masked dataset	PSNR :29.6 dB, SSIM : 0.92
Pechetti et al. (2025) [68]	Context-Aware GAN	Contextual attention-based image inpainting	Not focused on recognition task	ImageNet subsets	PSNR : 31.2 dB, SSIM : 0.94
Asad et al. (2025) [67]	MGAN-CRCM	Coarse-to-refined reconstruction using multiple GANs with contextual awareness	Not explicitly addressed	CelebA, Places2	PSNR : 31.6 dB, SSIM : 0.95
Hassanpour et al. (2024) [65]	E2F-Net	StyleGAN latent-space face re-construction using visible eye-region embeddings	Face verification using re-constructed identity embeddings	CelebA-HQ, FFHQ	PSNR : 32.2 dB, SSIM : 0.96, 95.1
Zhang et al.(2024) [66]	MD-GAN	Multi-scale diversity GAN for large mask facial region reconstruction	Not explicitly addressed	Places2, CelebA	PSNR :29.8 dB, SSIM: 0.92
Li et al. (2024) [64]	Identity-Guided Inpainting	Identity embedding–guided GAN inpainting to reconstruct occluded facial regions	CNN-based face recognition using reconstructed identity features	LFW, CFP-FP, masked LFW	PSNR : 30.7 dB , SSIM : 0.94
Sola and Gera (2023) [69]	Expression-Conditioned GAN	Expression-conditioned adversarial inpainting to preserve facial semantics under mask occlusion	Identity preservation through expression-aware latent conditioning	CelebA-HQ, Af-fectNet	PSNR : 30.5 dB, SSIM : 0.93
Man and Cho (2023) [63]	T-GAN	Two-stage GAN for efficient occluded facial region repair	Not explicitly addressed	CelebA, AR Face	PSNR : 29.4 dB , SSIM : 0.90

Source: Authors, (2026).

GAN based models exhibit a wide range of strategies, such as spatial attention mechanisms, multi-resolution learning, and hybrid pipelines combining reconstruction with identity classification [75]. Region-Attentive GAN demonstrates the highest performance with 95.3% accuracy, closely followed by Two-Stage GAN and HiMFR. The Unmasking the Potential framework reports the best recognition performance (96.1%) using a VGG-based evaluation on the MaskedFace-CelebA dataset. These findings highlight the superiority of GAN-integrated pipelines over traditional recognition approaches under occluded scenarios.

II.4 DIFFUSE MODELS FOR FACE RESTORATION

Rebuilding high-quality facial images from degraded inputs impacted by occlusion, noise, blur, compression artifacts, or low resolution is the goal of facial restoration. Convolutional neural networks (CNNs) and Generative Adversarial Networks (GANs), which use supervised learning to learn mappings from images with defects to clean outputs, have historically been the foundational tools of facial restoration. Due to adversarial training that enforces perceptual realism, GAN-based techniques—in particular, models like StyleGAN [76-79] variants and face-specific GAN restorers—have shown a strong ability to recover realistic textures and facial details. Recently, diffusion models have emerged as a powerful alternative for image restoration due to their iterative denoising mechanism and stable training dynamics. Saharia et al. [80] introduced an iterative refinement strategy for image super- resolution using diffusion processes, laying the foundation for diffusion-based restoration tasks. Building upon this, Lugmayr et al. [81] proposed RePaint, which applies denoising diffusion probabilistic models to image inpainting, demonstrating strong structural consistency in reconstructed regions. Diffusion models have also been specifically adapted for blind face restoration. Wang et al. [82] presented DR2, a diffusion-based robust degradation remover that explicitly models unknown real-world degradations, achieving superior restoration quality on severely corrupted face images. Further advancing this line of work, Yue and Loy [17] proposed DifFace, which introduces diffused error contraction to progressively reduce restoration errors, resulting in highly realistic facial details. In particular, Saharia et al. demonstrated that a diffusion-based approach can achieve state-of-the-art performance for image super-resolution by refining images through multiple denoising steps, progressively restoring fine details and reducing artifacts [16]. Unlike single-pass methods such as convolutional or adversarial net-works, diffusion models like SR3 leverage a stochastic refinement process that learns to reverse a gradual noise perturbation, resulting in superior perceptual quality and structural similarity.

Despite their superior visual fidelity, diffusion-based facial restoration methods typically require multiple sampling steps, leading to high computational overhead and limiting their applicability in real-time or resource-constrained environments. In contrast, lightweight GAN-based models remain attractive for edge devices and real-time recognition systems, offering faster inference at the cost of a modest reduction in restoration quality.

II.5 TRANSFORMER-BASED METHODS FOR IMAGE AND FACE RESTORATION

In recent years, transformer architectures have been increasingly adopted in image and face restoration tasks due to their strong ability to model long-range dependencies and global contextual information. Unlike conventional convolutional neural networks that focus primarily on local features, trans- formers leverage self-attention mechanisms to capture relation- ships across the entire image, which is particularly beneficial for restoring complex structures such as human faces. Liang et al. [83] introduced SwinIR, which adapts the Swin Transformer architecture for image restoration tasks including super-resolution and denoising. By using window-based self-attention, SwinIR achieves a good balance between restoration performance and computational efficiency, making it a strong baseline for transformer-based restoration methods. Similarly, Zamir et al. [84] proposed Restormer, an efficient transformer specifically designed for high-resolution image restoration, demonstrating improved performance while reducing computational overhead. To further enhance restoration quality, Wang et al. [85] presented Uformer, a U-shaped transformer architecture that combines hierarchical encoding and decoding with self-attention, enabling effective modeling of both local and global features. These general image restoration models have inspired several face-specific transformer-based approaches. In the context of face restoration and super-resolution, Wang et al. [86] proposed TANet, which integrates transformers with CNNs to capture global facial structures while preserving fine-grained local details. Building on this hybrid design, Tiwari et al. [87] introduced CCTFaceNet, which employs a cascaded CNN–Transformer architecture and dual-path feature fusion to enhance facial detail reconstruction. Furthermore, Li et al. [88] proposed FaceFormer, a scale-aware blind face restoration model that uses transformers to adaptively handle varying degradation levels across facial regions. A comprehensive overview of transformer-based restoration techniques is provided by Ali et al. [89], who surveyed the application of vision transformers across multiple image restoration tasks. Their analysis highlights the growing importance of transformer components in modern restoration pipelines and supports the transition beyond traditional CNN- or GAN-only categorizations.Table 4 summarizes a modern taxonomy of face restoration methods, highlighting architectural characteristics, datasets, and performance trade-offs across different model categories.

Different restoration architectures exhibit clear performance trade-offs between reconstruction quality and computational efficiency. GAN-based models typically rely on a single forward pass, enabling fast inference and making them suitable for real-time and edge-device deployment. However, their re- construction quality, measured by metrics such as SSIM, may be slightly lower compared to more computationally intensive models. Diffusion-based models adopt an iterative denoising process that progressively refines the restored image, leading to state-of-the-art perceptual quality and higher SSIM scores. Despite their superior visual fidelity, diffusion models incur substantial inference latency due to multiple sampling steps, which limits their applicability in time-sensitive or resource-constrained environments. Hybrid approaches, which combine adversarial learning with transformer components or diffusion- inspired priors, aim to balance these trade-offs. Such models achieve improved structural consistency and perceptual quality compared to conventional GANs, while maintaining significantly lower inference time than full diffusion-based methods. Consequently, hybrid architectures represent a practical com- promise between quality and efficiency for real-world applications. Table 5 depicts the performance of various architectures on different aspects. Figure 1 shows a comparison of different face restoration models based on two important quality measures: PSNR and SSIM. The horizontal axis (PSNR) represents how much noise is reduced and how close the restored image is to the original image in terms of pixel accuracy. Higher PSNR means better reconstruction quality. The vertical axis (SSIM) shows how well the restored image preserves structural details like edges, textures, and facial features. Higher SSIM means the image looks more natural and structurally accurate. Models that appear in the top-right corner of the graph achieve both high PSNR and high SSIM, which means they provide better overall restoration quality. For example, transformer-based models such as Restormer and SwinIR are positioned in this region, indicating strong performance. Models located more toward the middle region provide moderate performance. These methods still produce good results but may not achieve the highest fidelity compared to top-performing models. Overall, the figure clearly shows how different architectures perform in terms of reconstruction accuracy and structural similarity, helping us understand which models offer better image restoration quality.

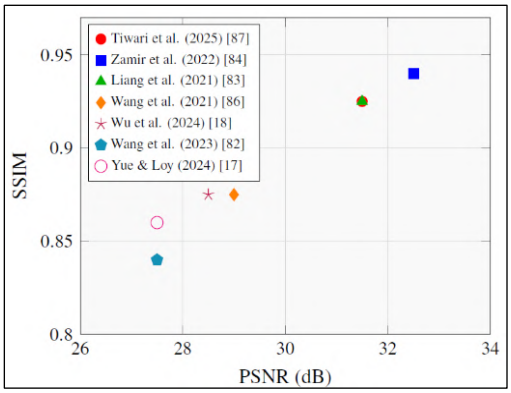


Figure 1: Scatter comparison of deep learning-based face restoration models across PSNR and SSIM (approximate mid-range values).
Source: Authors, (2026).

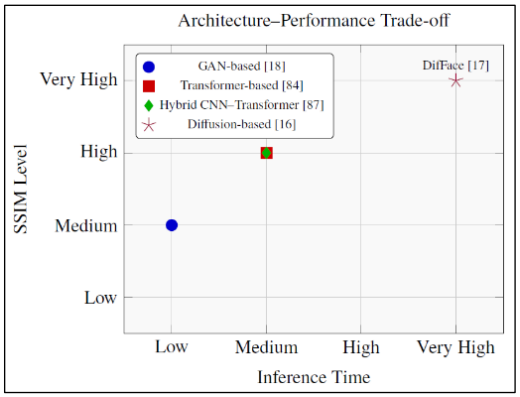


Figure 2: Architecture–performance trade-offs in face restoration models.
Source: Authors, (2026).

Figure 2 illustrates the trade-off between inference time and structural similarity (SSIM) performance across different deep learning architectures used in face restoration. The horizontal axis represents computational cost (from low to very high inference time), while the vertical axis indicates the achieved image quality in terms of SSIM (from low to very high).

Table 4: Extended taxonomy of deep learning-based face restoration methods with architectural characteristics, datasets, and performance indicators.

Model Category	Characteristics	Strengths	Limitations	Datasets	Performance Indicators
CNN-based Models [38, 42, 46, 48, 53–55, 87]	Deterministic feed-forward convolutional networks with single- pass inference	Very fast inference, low memory footprint, suitable for real-time deployment	Limited global context modeling and reduced perceptual realism under severe degradation	LFW, CelebA, FFHQ	Moderate PSNR/SSIM values; limited identity preservation accuracy
GAN-based Models [3, 18, 19, 26, 68, 71, 76, 77]	Adversarial learning with perceptual and identity-aware loss functions	High visual realism; strong identity preservation; lightweight variants suitable for edge devices	Training instability; potential artifacts; slight quality trade-off in compact de- signs	CelebA-HQ, LFW, Masked Face Datasets	High perceptual quality; Rank-1 Accuracy up to 96%
Transformer-Based Models [83–89]	Self-attention mechanisms for modeling long-range dependencies and global facial structure	Improved structural consistency and fine-detail reconstruction	High computational and memory cost; limited real-time applicability	FFHQ, CelebA-HQ, Helen Face Dataset	Improved PSNR/SSIM and structural similarity compared to CNN and GAN methods
Diffusion-Based Models [16,17,64,78–81]	Iterative denoising through probabilistic diffusion processes	State-of-the-art realism; robust restoration under unknown and complex degradations	Very slow inference speed; high computational over-head; unsuitable for real-time systems	FFHQ, CelebA-HQ, WebFace	Best perceptual metrics (LPIPS); strong identity preservation but low inference speed

Source: Authors, (2026).

Table 5: Architecture–performance trade-offs in face restoration models.

Architecture	Representative Methods	Inference Time	SSIM	Deployment Suitability
GAN-based	Lightweight GAN-Based Image Fusion [18], MAGAN-RT [19], Context-Aware GAN Inpainting [68], GAN-based Face Recon-struction for Masked Faces [71], Masked Face Image Inpainting GAN [3], CR-GAN [26] ,Lightweight Edge GAN Survey [77], Efficient Secure GAN Survey [76]	Low	Medium	Real-time deployment on edge devices, mobile platforms, and surveillance systems
Transformer-based	Restormer [84], Uformer [85], SwinIR [83], FaceFormer [88], TANet [86], Vision Transformers [89]	Medium	High	High-resolution restoration on GPUs, near real-time inference
Hybrid CNN–Transformer	SwinIR [83], TANet [86], CCTFaceNet [87], FaceFormer [88], Lightweight CNN [54], Hybrid CNN + Decision Matrix [53], Hybrid CNN (Detection + Recognition) [55], CNN with Feature Embedding (LLE-CNN) [48] , CNN-based Multi-task System [46] , Vision-based CNN Pipeline [42] , Classical CNN-based Detection [38]	Medium	High	Balanced systems offering improved perceptual quality with acceptable latency
Diffusion-based	SR3 [16], DifFace [17], RePaint [81], Identity-Guided Inpainting [64], StyleGAN [79], Text-driven 3D Avatar Generation [78]	Very High	Very High	Offline processing, server-side applications, and research-focused scenarios

Source: Authors, (2026).

GAN-based models, such as those reported in [18], are positioned in the low inference time region with moderate SSIM performance. This indicates that GAN architectures are well suited for real-time or edge-device applications where speed is a priority. Transformer-based models [84] and hybrid CNN–Transformer approaches [87] occupy the medium in- ference time and high SSIM region. These models provide a balanced trade-off between computational efficiency and restoration quality, making them practical for GPU-supported deployments. Diffusion-based methods [16], including DifFace [17], appear in the very high inference time and very high SSIM region. Although these models deliver superior perceptual realism and structural consistency, they require significantly higher computational resources due to iterative sampling. Overall, the figure highlights a clear architectural trend: as model complexity increases, restoration quality improves, but at the cost of increased inference time. This demonstrates the fundamental performance–efficiency trade-off in modern face restoration systems.

II.6 ETHICAL AND REGULATORY CHALLENGES

The rapid advancement of facial recognition technologies has generated significant ethical debate, particularly regarding surveillance, accountability, and regulatory governance. Almeida et al. [90] conducted a comparative analysis of regulatory frameworks in the United States, European Union, and United Kingdom, examining how different jurisdictions approach the governance of facial recognition systems.

Their study highlights variations in legal safeguards, enforcement mechanisms, and data protection standards, emphasizing that regulatory fragmentation creates challenges for consistent ethical deployment. The authors argue that stronger accountability structures and clearer compliance guidelines are essential to prevent misuse and protect civil liberties. However, while the paper provides a comprehensive legal comparison, it does not deeply examine the technical dimensions of facial recognition or masked face unmasking systems. Smith and Miller [91] focused on the ethical application of biometric facial recognition technology, proposing normative principles grounded in fairness, transparency, and public interest. Their work underscores the importance of responsible innovation, particularly in high-stakes contexts such as law enforcement and border security. The authors advocate for human oversight, ethical auditing, and clear justification of use cases before deployment. Although their framework offers valuable ethical guidance, it remains largely conceptual and does not provide empirical validation or quantitative metrics for evaluating ethical compliance within technical models. More recently, Wang et al. [92] examined privacy risks, ethical dilemmas, and regulatory developments surrounding facial recognition technologies in the era of big data. Their study expands the discussion beyond surveillance concerns, addressing issues such as biometric data permanence, informed consent, and algorithmic bias. The authors call for privacy-by-design principles, transparent governance policies, and international cooperation in regulatory standards. While the paper comprehensively addresses ethical and regulatory considerations, it primarily focuses on general facial recognition systems and does not specifically analyze emerging face unmasking techniques under occlusion scenarios. From a technical standpoint, Mahmoud et al. [93] provided a comprehensive survey of masked face detection, recognition, and unmasking techniques. Their study systematically reviews deep learning architectures, benchmark datasets such as MAFA and RMFD, and evaluation metrics including accuracy, PSNR, and SSIM. The survey identifies challenges related to occlusion, dataset imbalance, and robustness under real-world conditions, while also outlining future research directions in masked face analysis.

III. DATASETS FOR MASKED FACE INPAINTING AND RECOGNITION

Masked face recognition and inpainting systems have become increasingly important, especially in the context of global events such as the COVID-19 pandemic. These models aim to either recognize identities from partially occluded faces or reconstruct missing facial regions (e.g., mouth, nose) using generative methods. A foundational aspect of evaluating and benchmarking such models lies in the diversity and realism of the datasets used for training and testing. A wide spectrum of datasets has been curated or modified to simulate both real-world and synthetic mask occlusions. These datasets vary in size, resolution, subject diversity, mask types, and the method of mask application (real or artificial). Proper dataset selection significantly influences the generalizability and robustness of MFR algorithms.The CelebFaces Attributes Dataset (CelebA) is one of the most extensively utilized benchmarks in face analysis tasks. Comprising over 200,000 celebrity images with rich attribute annotations, it serves as a common training corpus for in- painting models. The dataset does not originally include masked samples, but synthetic occlusions can be algorithmically overlaid to simulate masked conditions. Many studies, including [94], have adopted CelebA with artificial masks to train and evaluate GAN-based inpainting models. The dataset's large scale and high variability across poses and illumination conditions make it ideal for learning generalized representations.

Labeled Faces in the Wild (LFW) is another seminal dataset, comprising face images collected from the internet for unconstrained face verification. While not initially designed for MFR, it is often repurposed by overlaying masks either manually or through automated methods. The inclusion of both synthetic and real masked versions allows for comparative evaluation. Its widespread usage, as reported in [95], stems from its realistic distribution and historical relevance in face verification benchmarks. Because LFW features in-the-wild images with substantial variability, it introduces useful challenges in masked face analysis. The Flickr-Faces-HQ (FFHQ) dataset contains over 70,000 high-resolution face images with diverse variations in age, ethnicity, lighting, and expression. While FFHQ does not include real-world masked samples, it is a preferred base for synthetic mask overlays due to its image quality. Recent studies such as [96] utilize FFHQ for training face reconstruction and inpainting systems. The dataset supports learning finer details, which is crucial in scenarios where GAN-based models aim to restore occluded facial components while preserving identity-related features. Masked Face Dataset (MAFA) is a real-world masked face dataset containing over 30,000 images annotated for mask presence and location.

Designed specifically for mask detection and recognition, it represents one of the few datasets with native mask occlusions. Used in studies like [97], MAFA bridges the gap between simulated conditions and real- world deployment. It introduces challenges such as occlusion variance, complex backgrounds, and mask style diversity that are hard to simulate synthetically.The Public Figures dataset, also known as PubFig83, is com- posed of images of 83 celebrities captured under diverse conditions. While not originally containing masked faces, it has been repurposed in the MFR domain with synthetic mask applications. Its value lies in the inherent difficulty introduced by pose variation, low resolution, and lighting diversity. As seen in [98], it provides a semi-realistic yet controlled environment for testing model robustness against visual noise and occlusion. MaskedFace-CelebA dataset is a synthetically modified version of CelebA, where masks are digitally applied to the original faces to simulate pandemic-era conditions. It aims to maintain identity information while offering occlusion realism. The dataset is often employed as a testbed for evaluating models trained on CelebA or other synthetic sources. The work in [99] demonstrates its effectiveness in assessing how well models can adapt to real-world masked conditions based on synthetic training. Figure 3 demonstrates few samples from prominent face datasets.



Figure 3: Sample images from various datasets.
Source: [100].

Face5 is a hybrid dataset constructed by merging real and simulated masked facial samples. It allows for studying the generalization capabilities of MFR systems when subjected to a mixture of mask types and occlusion styles.

Proposed in studies such as [101], the hybrid nature of Face5 makes it an important bridge for transition between purely synthetic and completely real-world datasets. SyntheticMaskSet is explicitly designed to support benchmarking of face inpainting and recognition systems under controlled synthetic conditions. By applying diverse types of digitally generated masks to faces, it enables standardized evaluation across multiple models. For instance, the Region-Attentive GAN proposed in [102] demonstrated strong performance on this dataset due to the consistent and controllable occlusion levels. SimulMaskDB is a synthetically generated dataset that varies mask styles, occlusion levels, and facial expressions in a controlled fashion. It is primarily used for stress-testing recognition and inpainting algorithms under artificial yet di- verse conditions. As highlighted in [103], this dataset enables fine-grained performance analysis, especially for lightweight architectures and constrained environments. Also, studies review face recognition techniques, focusing on feature extraction methods and key challenges affecting system performance and accuracy [104], [105]. Table 6 highlights the demographic diversity and dataset characteristics used to evaluate different masked face inpainting models. Clear reporting of age groups, gender balance, and ethnicity ensures fair comparison and helps identify potential dataset bias in GAN-based recognition systems.

Table 6: Summary of Datasets Characteristics and Demographic Parameters Used in Masked Face Inpainting and Recognition.

Study	Database	Sample Size	Age Groups	Gender Distribution	Ethnicity / Other Factors	Description of Database
Mahmoud and Kang (2023) [102]	GAN-Masker Dataset	Synthetic dataset (based on CelebA and other sources)	Adult subjects	Mixed gender	Artificially masked faces	Two-stage GAN-based masked face removal dataset combining real and synthetically generated masked face images for restoration and recognition research.
Tero Karras et al. (2019) [96]	FFHQ	70,000 images	Wide age Range (children to elderly)	Balanced male/female	Diverse ethnicities; high-quality aligned images	High-resolution (1024×1024) face dataset curated for GAN training; diverse in age, ethnicity, and accessories, commonly used in generative modeling research.
Shiming Ge et al. (2017) [97]	MAFA	30,811 images	Adult subjects	Mixed gender	Masked faces in the wild; occlusion variations	Dataset focused on masked face detection with varying mask types, occlusion levels, and complex backgrounds in real-world conditions.
Ziwei Liu et al. (2015) [94]	CelebA	202,599 images (10,177 identities)	Young to middle-aged adults	Male and Female	Celebrities; large variation in pose and background	Large-scale face attributes dataset collected from the internet with 40 annotated facial attributes; widely used for face recognition and attribute prediction tasks.
Bergstra et al. (2013) [98]	PubFig83	Not dataset-specific	Not specified	Not specified	Hyperparameter optimization focus	Study emphasizes hyperparameter optimization for vision architectures rather than introducing a specific face database.
Gary B. Huang et al. (2008) [95]	LFW	13,233 images (5,749 identities)	Adult subjects	Male-dominant distribution	Unconstrained environments; real-world variations	Unconstrained face dataset designed for studying face recognition under real-world conditions including variations in pose, illumination, and expression.

Source: Authors, (2026).

Synthetic datasets, such as CelebA, FFHQ, and SyntheicMaskSet, are instrumental in benchmarking inpainting models due to their controlled conditions. In contrast, real-world datasets like MAFA and RMFD provide essential realism for evaluating system generalizability. Among these, CelebA and LFW emerge as the most recurrently utilized in synthetic masked face inpainting tasks. For instance, the RegionAttentive GAN introduced and demonstrated high reconstruction fidelity when evaluated on the SyntheticMaskSet.

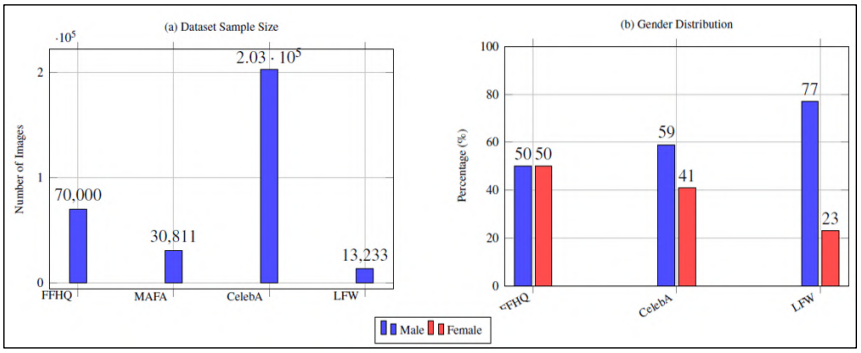


Figure 4: Comparison of dataset sample size and gender distribution across commonly used face datasets.
Source: Authors, (2026).

In Figure 4 (a), the bar chart shows the number of images available in each dataset. CelebA clearly has the largest number of images, making it very useful for large-scale training. FFHQ also contains a good number of high-quality images. MAFA has a moderate dataset size focused on masked faces, while LFW contains the smallest number of images among the four. This comparison helps us understand which datasets are large enough for deep learning experiments. In Figure 4 (b), the chart shows the gender distribution within selected datasets. FFHQ appears balanced, with nearly equal numbers of male and female images. However, CelebA and LFW show noticeable imbalance, with a higher percentage of male images compared to female images. This imbalance is important because it may affect model fairness and performance. Overall, the figure helps us understand both the size and diversity of these datasets, which are important factors when selecting data for face restoration and recognition research.

IV. CONLUSIONS

Masked face restoration using Generative Adversarial Networks (GANs) has emerged as a vital research area in response to the challenges posed by real-world occlusions such as face masks. Through this survey, we examined state-of-the- art methods addressing detection, inpainting, and recognition under mask occlusion. While existing methods demonstrate significant progress in restoring visually plausible and identity- preserving face images, several limitations and open challenges remain. First, most current models rely heavily on synthetic masks or artificially generated occlusions during training, which of- ten fail to fully represent the diversity and irregularity of real-world mask usage. Consequently, generalization to real masked faces remains inconsistent across datasets and do- mains. Second, although recent GAN models incorporate identity and perceptual constraints, maintaining fine-grained facial details—particularly in highly occluded or low-quality images—remains a bottleneck for both recognition and down- stream biometric tasks. In terms of detection and inpainting performance, many models are not jointly optimized for both tasks, leading to cascaded error propagation. Moreover, evaluation metrics such as PSNR and SSIM, while useful for measuring image similarity, do not always correlate with recognition accuracy or semantic identity preservation. Therefore, more robust and identity-aware metrics, including perceptual loss functions and recognition-oriented benchmarks, are required. Furthermore, the integration of multimodal data, temporal consistency (for video-based restoration), and domain adaptation for unseen environments represents fertile ground for future work. Lightweight architectures that balance inference speed and accuracy are also needed for deployment in real-time or edge devices.

V. AUTHOR'S CONTRIBUTION

Conceptualization: Payal Parekh, Hina Choksi.
Methodology: Payal Parekh, Mahesh Goyani, Sheilla Ann Pacheco.
Investigation: Payal Parekh, Hina Choksi, Mahesh Goyani.
Discussion of results: Payal Parekh, Hina Choksi, Mahesh Goyani, Sheilla Ann Pacheco.
Writing – Original Draft: Payal Parekh, Mahesh Goyani.
Writing – Review and Editing: Payal Parekh, Hina Choksi, Mahesh Goyani, Sheilla Ann Pacheco.
Resources: Hina Choksi, Mahesh Goyani, Sheilla Ann Pacheco.
Supervision: Hina Choksi, Mahesh Goyani, Sheilla Ann Pacheco.
Approval of the final text: Payal Parekh, Mahesh Goyani.

VI. REFERENCES

[1] H. Ali and A. Ijaz, "Machine and deep learning based cctv surveillance using facenet, mtcnn, and haar cascade for enhanced security," in 2025 6th International Conference on Computer Vision, Image and Deep Learning (CVIDL), 2025, pp. 672–677.

[2] M. Ngan, P. Grother, and K. Hanaoka, "Ongoing face recognition vendor test (frvt) part 6a: Face recognition accuracy with masks using pre-covid-19 algorithms," NIST Interagency/Internal Report, National Institute of Standards and Technology, 2020.

[3] L. Qingyu, C. Lei, S. Yeguo, and L. Lei, "Masked face image inpainting based on generative adversarial network," Infocommunications Journal, vol. 17, no. 2, pp. 11–19, 2025.

[4] M. Loey, G. Manogaran, M. H. N. Taha, and N. E. M. Khalifa, "A hybrid deep transfer learning model with machine learning methods for face mask detection in the era of the covid-19 pandemic," Measurement, vol. 167, p. 108288, 2021.

[5] S. A. B. Pacheco, J. E. Estrada, and M. M. Goyani, "Hidden adversarial attack on facial biometrics-a comprehensive survey," Procedia Computer Science, vol. 258, pp. 1383–1390, 2025.

[6] P. Sheilla Ann Bangoy, E. Jheanel Espiritu and G, Mahesh, "Robust face recognition under adversarial attack using sargan model and improved cross triple mobilenetv1," in Future of Information and Communication Conference. Springer, 2025, pp. 491–510.

[7] H. Trivedi and M. Goyani, "Robust face recognition in the presence of diverse challenges: A hybrid deep neural network approach," Journal of Engineering, vol. 14, no. 10, pp. 55–62, 2024.

[8] T. Himani and G. Mahesh, "A transition of face recognition to mask face recognition using improvised attention dl model," in 2023 3rd International Conference on Intelligent Technologies (CONIT). IEEE, 2023, pp. 1–7.

[9] T. Himani and G. Mahesh, "Adapting face recognition to the masked world: leveraging deep attention networks with a custom dataset," International Journal of Computers and Applications, vol. 46, no. 6, pp. 427–441, 2024.

[10] A. Alzu'bi, F. Albalas, T. Al-Hadhrami, L. B. Younis, and A. Bashayreh, "Masked face recognition using deep learning: A review," Electronics, vol. 10, no. 21, p. 2666, 2021.

[11] N. Damer, J. H. Grebe, C. Chen, F. Boutros, F. Kirchbuchner, and A. Kuijper, "The effect of wearing a mask on face recognition performance: an exploratory study," in 2020 International Conference of the Biometrics Special Interest Group (BIOSIG). IEEE, 2020, pp. 1–6.

[12] N. Damer, J. Grebe, J. Chen, F. Boutros, F. Kirchbuchner, and A. Kuijper, "Extended evaluation of face recognition with masks: Effect of real and simulated masks on face embeddings," IET Biometrics, vol. 10, no. 6, pp. 607–618, 2021.

[13] J. Wang, Y. Kang, Y. Zhang, and F. Li, "Masked face recognition dataset and application," arXiv preprint arXiv:2003.09093, 2020.

[14] Y.-C. Huang, D. A. B. Rahardjo, R.-H. Shiue, and H. H. Chen, "Masked face recognition using domain adaptation," Pattern Recognition, vol. 153, p. 110574, 2024.

[15] C. Agarwal and C. Bhatnagar, "Unmasking the potential: evaluating image inpainting techniques for masked face reconstruction," Multimedia Tools and Applications, vol. 83, no. 1, pp. 893–918, 2024.

[16] C. Saharia, J. Ho, W. Chan, T. Salimans, D. J. Fleet, and M. Norouzi, "Image super-resolution via iterative refinement," IEEE transactions on pattern analysis and machine intelligence, vol. 45, no. 4, pp. 4713–4726, 2022.

[17] Z. Yue and C. C. Loy, "Difface: Blind face restoration with diffused error contraction," IEEE Transactions on Pattern Analysis and Machine Intelligence, vol. 46, no. 12, pp. 9991–10 004, 2024.

[18] Z. Wu, J. Chen, L. Tan, H. Gong, Y. Zhou, and G. Shi, "A lightweight gan-based image fusion algorithm for visible and infrared images," in 2024 4th international conference on computer science and blockchain (CCSB). IEEE, 2024, pp. 466–470.

[19] P. Guo, "Magan-rt: A lightweight adversarial style transfer network for real-time cartoonization on low-power edge devices," Internet Technology Letters, vol. 8, no. 5, p. e70104, 2025.

[20] N. K. Yadav, S. K. Singh, and S. R. Dubey, "Tva-gan: attention guided generative adversarial network for thermal to visible image transformations," Neural Computing and Applications, vol. 35, no. 27, pp. 19 729–19 749, 2023.

[21] D. Sheng, W. Jin, M. Wang, and J. Yang, "Region-based self-segmentation guided diffusion model for thermal infrared to pseudo-color visible light image conversion," IEEE Access, vol. 13, pp. 47 860–47 873, 2025.

[22] K. Wang, Y. Shen, and M. Lauer, "Adversarial defense teacher for cross-domain object detection under poor visibility conditions," arXiv preprint arXiv:2403.15786, 2024.

[23] A. H. Abdul Amir and Z. N. Nemer, "Inclusive review on advances in masked human face recognition technologies," Iraqi Journal of Intelligent Computing and Informatics (IJICI), vol. 4, no. 1, pp. 1–17, 2025.

[24] V. S. Patel, Z. Nie, T.-N. Le, and T. V. Nguyen, "Masked face analysis via multi-task deep learning," Journal of Imaging, vol. 7, no. 10, p. 204, 2021.

[25] J. A. Alzubi and Others, "A generative adversarial network-based accurate masked face recognition model using dual scale adaptive efficient attention network," Scientific Reports, vol. 15, 2025.

[26] Y. Li, J. Wang, W. Liang, H. Xue, Z. He, J. Lv, and L. Zhang, "Cr-gan: Automatic craniofacial reconstruction for personal identification," Pattern Recognition, vol. 124, p. 108400, 2022.

[27] Z. Chen, Z. Zhang, J. Yuan, Y. Xu, and L. Liu, "Show your face: Restoring complete facial images from partial observations for vr meeting," in Proceedings of the IEEE/CVF Winter Conference on Applications of Computer Vision (WACV), 2024, pp. 8688–8697.

[28] L. Song, D. Gong, Z. Li, C. Liu, and W. Liu, "Occlusion robust face recognition based on mask learning with pairwise differential siamese network," in Proceedings of the IEEE/CVF international conference on computer vision, 2019, pp. 773–782.

[29] S. Biswas and Others, "A new perceptual hashing method for verification and identity classification of occluded faces," Image and Vision Computing, vol. 113, p. 104078, 2021.

[30] J. Deng, J. Guo, J. Yang, and N. Xue, "Mf-cosface: A margin-based loss for masked face recognition," Applied Sciences, vol. 11, no. 4, p. 1813, 2021.

[31] W. Hariri, "Efficient masked face recognition method during the covid-19 pandemic," arXiv preprint arXiv:2105.03026, 2021.

[32] A. M. Sheneamer et al., "A hybrid human recognition framework using machine learning and deep learning for masked faces," Plos One, vol. 19, no. 6, p. e0304567, 2024.

[33] B. Adeli, J. Mclinden, P. Pandey, M. Shao, and Y. Shahriari, "Absolutenet: A deep learning neural network to classify cerebral hemodynamic responses of auditory processing," 2025 IEEE 35th International Workshop on Machine Learning for Signal Processing, pp. 1–6, 2025.

[34] Pillay, C., Joseph, S., & Van Niekerk, B. (2025). Development of a face mask detection and masked facial recognition model based on a hybrid convolutional neural network. IET Image Processing, 19(1), e70239.

[35] A. Cabani, K. Hammoudi, H. Benhabiles, and M. Melkemi, “Maskedface-net: A dataset of correctly/incorrectly masked face images in the context of covid-19,” Smart Health, vol. 19, p. 100144, 2020.

[36] X. Fan and M. Jiang, “Retinaface mask: A single stage face mask detector for assisting control of the covid-19 pandemic,” in 2021 IEEE International Conference on Systems, Man, and Cybernetics (SMC). IEEE, 2021.

[37] K. Dhanushkodi, A. N. Hussain, A. Jayaprakash, and S. Suriyaprakash, “A survey on detection of face mask and social distancing using deep learning,” i-manager’s Journal of Information Technology, vol. 10, p. 22, 2021.

[38] D. Chiang, “Detect faces and determine whether people are wearing mask,” Face Mask Detection, vol. 15, 2020.

[39] M. Loey, G. Manogaran, M. Taha, and N. Khalifa, “Fighting against covid-19: A novel deep learning model based on yolo-v2 with resnet-50 for medical face mask detection,” Sustainable Cities and Society, vol. 65, p. 102600, 2021.

[40] X. Su, M. Gao, J. Ren, Y. Li, M. Dong, and X. Liu, “Face mask detection and classification via deep transfer learning,” Multimedia Tools and Applications, vol. 81, pp. 4475–4494, 2022.

[41] World Health Organization, “Advice for the public on covid-19,” https://www.who.int/emergencies/diseases/novel-coronavirus- 2019/advice-for-public, 2022, accessed February 10, 2026.

[42] D. Yang, E. Yurtsever, V. Renganathan, K. A. Redmill, and U. O¨ zgu¨ner, “A vision-based social distancing and critical density detection system for covid-19,” Sensors, vol. 21, p. 4608, 2021.

[43] S. Madane and D. Chitre, “Social distancing detection and analysis through computer vision,” in 2021 6th International conference for convergence in technology (I2CT). IEEE, 2021, pp. 1–10.

[44] I. Ahmed, M. Ahmad, J. J. Rodrigues, G. Jeon, and S. Din, “A deep learning-based social distance monitoring framework for covid-19,” Sustainable Cities and Society, vol. 65, p. 102571, 2021.

[45] S. Suryadi, E. Kurniawan, H. Adinanta, B. H. Sirenden, J. A. Prakosa, and P. Purwowibowo, “On the comparison of social distancing viola- tion detectors with gpu support,” in 2020 International Conference on Radar, Antenna, Microwave, Electronics, and Telecommunications (ICRAMET), 2020, pp. 337–342.

[46] M. Rezaei and M. Azarmi, “Deepsocial: Social distancing monitoring and infection risk assessment in covid-19 pandemic,” Applied Sciences, vol. 10, p. 7514, 2020.

[47] K. A. Reddy, P. Sandeep, and D. Gayathri, “Monitoring covid-19 social distancing with person detection and tracking via yolov3 and deepsort techniques,” International Journal of Innovative Research in Technology, vol. 8, no. 11, pp. 1–5.

[48] S. Ge, J. Li, Q. Ye, and Z. Luo, “Detecting masked faces in the wild with lle-cnns,” in Proceedings of the IEEE Conference on Computer Vision and Pattern Recognition (CVPR), 2017, pp. 2682–2690.

[49] Z. Wang, B. Huang, G. Wang, P. Yi, and K. Jiang, “Masked face recognition dataset and application,” IEEE Transactions on Biometrics, Behavior, and Identity Science, vol. 5, no. 2, pp. 298–304, 2023.

[50] X. Jiang, T. Gao, Z. Zhu, and Y. Zhao, “Real-time face mask detection method based on yolov3,” Electronics, vol. 10, p. 837, 2021.

[51] F. I. Eyiokur, H. K. Ekenel, and A. Waibel, “Unconstrained face-mask face-hand datasets: Building a computer vision system to help prevent the transmission of covid-19,” arXiv preprint arXiv:2103.08773, 2021.

[52] B. Wang, Y. Zhao, and C. P. Chen, “Hybrid transfer learning and broad learning system for wearing mask detection in the covid-19 era,” IEEE Transactions on Instrumentation and Measurement, vol. 70, pp. 1–12, 2021.

[53] I. Issaoui and A. Selmi, “Weighted soft discernibility matrix with deep learning assisted face mask detection for smart city environment.” International Journal of Neutrosophic Science (IJNS), vol. 25, no. 1, 2025.

[54] Y. Shao, J. Ning, H. Shao, D. Zhang, H. Chu, and Z. Ren, “Lightweight face mask detection algorithm with attention mechanism,” Engineering Applications of Artificial Intelligence, vol. 137, p. 109077, 2024.

[55] C. Pillay, S. Joseph, and B. Van Niekerk, “Development of a face mask detection and masked facial recognition model based on a hybrid convolutional neural network,” IET Image Processing, vol. 19, no. 1, p. e70239, 2025.

[56] M. Ahmadi, M. D. Ismaeil, J. C. Verdial, A. R. Nafchi, and M. Esmaeili, “Building a uc treatment response classifier: A random forest classifier with key biomarker identification,” in 2025 IEEE World AI IoT Congress (AIIoT). IEEE, 2025, pp. 0963–0970.

[57] M. Mohammadagha, A. Khoshkonesh, S. Sharifi, V. Ghanbarizadeh, and F. Bigdeli, “Performance analysis of hybrid deep-transfer learning approaches with machine learning methods for face recognition,” University of Texas at Arlington, 2025.

[58] Z. Gao and Others, “Improved face mask wearing detection based on yolov5,” International Journal of Advanced Network, Monitoring and Controls, vol. 10, no. 1, pp. 94–102, 2025.

[59] Y. Wei, H. Li, Y. He, and Others, “Robust face mask detection in complex scenarios using yolov8 and context-aware convolutions,” Scientific Reports, vol. 15, p. 21350, 2025.

[60] J. Yu, X. Zhang, T. Wu, H. Pan, and W. Zhang, “A face detection and standardized mask-wearing recognition algorithm,” Sensors, vol. 23, no. 10, p. 4612, 2023.

[61] J. V. B. Benifa, C. Chola, A. Y. Muaad, and Others, “Fmdnet: An efficient system for face mask detection based on lightweight model,” Sensors, vol. 23, no. 13, p. 6090, 2023.

[62] J. Bhagat and M. Goyani, “Masked face recognition by reconstructing face using image inpainting with gan,” in Recent Trends in Computational Intelligence and Its Application. CRC Press, 2023, pp. 26–34.

[63] Q. Man and Y.-I. Cho, “Efficient face region occlusion repair based on t-gans,” Electronics, vol. 12, no. 10, p. 2162, 2023.

[64] H. Li, Y. Zhang, W. Wang, S. Zhang, and S. Zhang, “Recovery-based occluded face recognition by identity-guided inpainting,” Sensors, vol. 24, no. 2, p. 394, 2024.

[65] A. Hassanpour, F. Jamalbafrani, B. Yang, K. Raja, R. Veldhuis, and J. Fierrez, "E2f-net: Eyes-to-face inpainting via stylegan latent space," Pattern Recognition, vol. 152, p. 110442, 2024.

[66] E. A. Zhang, "Md-gan: Multi-scale diversity gan for large masks inpainting," Electronics, vol. 14, no. 11, p. 2218, 2024.

[67] N. A. Asad, M. A. M. Pranto, S. Shiam, M. M. Akand, M. A. Yousuf, K. F. Hasan, and M. A. Moni, "Mgan-crcm: a novel multiple generative adversarial network and coarse refinement-based cognizant method for image inpainting," Neural Computing and Applications, vol. 37, no. 7, pp. 5459–5480, 2025.

[68] S. K. S. G. Pechetti, C. Lella, L. V. P. R. Medarametla, and V. Mandadi, "Image inpainting using generative adversarial networks and context-aware networks," International Journal of Creative Research Thoughts (IJCRT), vol. 13, no. 6, 2025.

[69] S. Sola and D. Gera, "Unmasking your expression: Expression-conditioned gan for masked face inpainting," in Proceedings of the IEEE/CVF conference on computer vision and pattern recognition, 2023, pp. 5908–5916.

[70] X. Gao, M. Nguyen, and W. Q. Yan, "A method for face image inpainting based on autoencoder and generative adversarial network," in Pacific-Rim Symposium on Image and Video Technology. Springer, 2022, pp. 24–36.

[71] F. Farahanipad, M. Rezaei, M. Nasr, F. Kamangar, and V. Athitsos, "Gan-based face reconstruction for masked-face," in Proceedings of the 15th International Conference on PErvasive Technologies Related to Assistive Environments, 2022, pp. 583–587.

[72] J. A. Alzubi, K. S. Pokkuluri, R. Arunachalam, S. K. Shukla, S. Venugopal, and K. Arunachalam, "A generative adversarial network-based accurate masked face recognition model using dual scale adaptive efficient attention network," Scientific Reports, vol. 15, no. 1, p. 17594, 2025.

[73] Q. Liu, L. Chen, Y. Sun, and L. Liu, "Masked face image inpainting based on generative adversarial network," Infocommunications Journal, vol. 17, no. 2, pp. 11–19, 2025.

[74] S. K. S. G. Pechetti, C. Lella, L. V. P. R. Medarametla, and V. Mandadi, "Image inpainting using generative adversarial networks and contextual attention," International Journal of Creative Research Thoughts, vol. 13, no. 6, pp. 2320–2882, 2025. [Online]. Available: https://www.ijcrt.org/papers/IJCRT2506738.pdf

[75] A. Kumar, M. Kaushal, and A. Sharma, "Sam c-gan: a method for removal of face masks from masked faces," Signal, Image and Video Processing, vol. 17, no. 7, pp. 3749–3757, 2023.

[76] N. E. Apostolou, E. V. Balourdou, M. Mouratidou, E. Tsalera, I. Voyiatzis, A. Papadakis, and M. Samarakou, "Efficient and secure gans: A survey on privacy-preserving and resource-aware models," Applied Sciences, vol. 15, no. 20, p. 11207, 2025.

[77] A. Musa, H. Kakudi, M. Hassan, M. L. Salisu et al., "Lightweight deep learning models for edge devices—a survey," International Journal of Computer Information Systems and Industrial Management Applications, vol. 17, p. 18, 2025.

[78] C. Gong, Y. Dai, R. Li, A. Bao, J. Li, J. Yang, Y. Zhang, and X. Li, "Text2avatar: Text to 3d human avatar generation with codebook- driven body controllable attribute," in ICASSP 2024-2024 IEEE International Conference on Acoustics, Speech and Signal Processing (ICASSP). IEEE, 2024, pp. 16–20.

[79] A. Melnik, M. Miasayedzenkau, D. Makaravets, D. Pirshtuk, E. Akbulut, D. Holzmann, T. Renusch, G. Reichert, and H. Ritter, "Face generation and editing with stylegan: A survey," IEEE Transactions on pattern analysis and machine intelligence, vol. 46, no. 5, pp. 3557–3576, 2024.

[80] C. Saharia, J. Ho, W. Chan, T. Salimans, D. J. Fleet, and M. Norouzi, "Image super-resolution via iterative refinement," IEEE Transactions on Pattern Analysis and Machine Intelligence, vol. 45, no. 4, pp. 4713–4726, 2023.

[81] A. Lugmayr, M. Danelljan, A. Romero, F. Yu, R. Timofte, and L. Van Gool, "Repaint: Inpainting using denoising diffusion probabilistic models," in 2022 IEEE/CVF Conference on Computer Vision and Pattern Recognition (CVPR), 2022, pp. 11 451–11 461.

[82] Z. Wang, Z. Zhang, X. Zhang, H. Zheng, M. Zhou, Y. Zhang, and Y. Wang, "Dr2: Diffusion-based robust degradation remover for blind face restoration," in Proceedings of the IEEE/CVF Conference on Computer Vision and Pattern Recognition (CVPR), June 2023, pp. 1704–1713.

[83] J. Liang, J. Cao, G. Sun, K. Zhang, L. Van Gool, and R. Timofte, "Swinir: Image restoration using swin transformer," in Proceedings of the IEEE/CVF international conference on computer vision, 2021, pp. 1833–1844.

[84] S. W. Zamir, A. Arora, S. Khan, M. Hayat, F. S. Khan, and M.-H. Yang, "Restormer: Efficient transformer for high-resolution image restoration," in Proceedings of the IEEE/CVF conference on computer vision and pattern recognition, 2022, pp. 5728–5739.

[85] Z. Wang, X. Cun, J. Bao, W. Zhou, J. Liu, and H. Li, "Uformer: A general u-shaped transformer for image restoration," in Proceedings of the IEEE/CVF conference on computer vision and pattern recognition, 2022, pp. 17 683–17 693.

[86] Y. Wang, T. Lu, Y. Zhang, J. Jiang, J. Wang, Z. Wang, and J. Ma, "Tanet: A new paradigm for global face super-resolution via transformer-cnn aggregation network," arXiv preprint arXiv:2109.08174, 2021.

[87] N. K. Tiwari, S. S. Rajput, and R. Patel, "Cctfacenet: Enhancing face super-resolution with cascaded cnn-transformer and dual-path feature fusion," Digital Signal Processing, p. 105557, 2025.

[88] A. Li, G. Li, L. Sun, and X. Wang, "Faceformer: Scale-aware blind face restoration with transformers," arXiv preprint arXiv:2207.09790, 2022.

[89] A. M. Ali, B. Benjdira, A. Koubaa, W. El-Shafai, Z. Khan, and W. Boulila, "Vision transformers in image restoration: A survey," Sensors, vol. 23, no. 5, p. 2385, 2023.

[90] D. Almeida, K. Shmarko, and E. Lomas, "The ethics of facial recognition technologies, surveillance, and accountability in an age of artificial intelligence: a comparative analysis of us, eu, and uk regulatory frameworks," AI and Ethics, vol. 2, no. 3, pp. 377–387, 2022.

[91] M. Smith and S. Miller, "The ethical application of biometric facial recognition technology," Ai & Society, vol. 37, no. 1, pp. 167–175, 2022.

[92] X. Wang, Y. C. Wu, M. Zhou, and H. Fu, "Beyond surveillance: privacy, ethics, and regulations in face recognition technology," Frontiers in Big Data, vol. Volume 7 - 2024, 2024.

[93] M. Mahmoud, M. S. Kasem, and H. Kang, "A comprehensive survey of masked faces: Recognition, detection, and unmasking," Applied Sciences, vol. 14, no. 19, p. 8781, 2024.

[94] Z. Liu, P. Luo, X. Wang, and X. Tang, “Deep learning face attributes in the wild,” in Proceedings of the IEEE international conference on computer vision, 2015, pp. 3730–3738.

[95] G. B. Huang, M. Mattar, T. Berg, and E. Learned-Miller, “Labeled faces in the wild: A database forstudying face recognition in unconstrained environments,” in Workshop on faces in’Real-Life’Images: detection, alignment, and recognition, 2008.

[96] T. Karras, S. Laine, and T. Aila, “A style-based generator architecture for generative adversarial networks,” in Proceedings of the IEEE/CVF conference on computer vision and pattern recognition, 2019, pp. 4401–4410.

[97] S. Ge, J. Li, Q. Ye, and Z. Luo, “Detecting masked faces in the wild with lle-cnns,” in Proceedings of the IEEE conference on computer vision and pattern recognition, 2017, pp. 2682–2690.

[98] J. Bergstra, D. Yamins, and D. Cox, “Making a science of model search: Hyperparameter optimization in hundreds of dimensions for vision architectures,” in International conference on machine learning. PMLR, 2013, pp. 115–123.

[99] C. Agarwal, C. Bhatnagar, and A. Mishra, “Evaluation of image inpainting methods for face reconstruction of masked faces,” in 2023 International Conference on Electrical, Communication and Computer Engineering (ICECCE). IEEE, 2023, pp. 1–6.

[100] M. Mahmoud, M. S. Kasem, and H.-S. Kang, “A comprehensive survey of masked faces: recognition, detection, and unmasking,” Applied Sciences, vol. 14, no. 19, p. 8781, 2024.

[101] M. I. Hosen and M. B. Islam, “Himfr: A hybrid masked face recognition through face inpainting,” arXiv preprint arXiv:2209.08930, 2022.

[102] M. Mahmoud and H.-S. Kang, “Ganmasker: A two-stage generative adversarial network for high-quality face mask removal,” Sensors, vol. 23, no. 16, p. 7094, 2023.

[103] Y. Zhou and T. Lu, “Masked face restoration model based on lightweight gan,” Computers, Materials, & Continua, vol. 82, no. 2, p. 3591, 2025.

[104] P. Payal and M. M. Goyani, “A comprehensive study on face recognition: methods and challenges,” The Imaging Science Journal, vol. 68, no. 2, pp. 114–127, 2020.

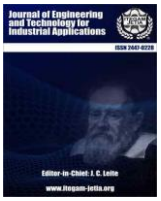
[105] P. Parekh and G. Mahesh, “Face recognition modern assessment of features extraction,” International Journal of Computer Sciences and Engineering, vol. 7, pp. 330–335, 04 2019.

Journal of Engineering and Technology for Industrial Applications

ISSN ONLINE: 2447-0228

ITEGAM-JETIA

Manaus, v.12 n.60, p.1058-1064 July/August, 2026.
DOI: https://doi.org/10.5935/jetia.v12i60.3967



RESEARCH ARTICLE OPEN ACCESS

MACHINE LEARNING APPROACHES FOR PREDICTING COMPRESSIVE STRENGTH OF CONCRETE: A COMPARATIVE PERFORMANCE ANALYSIS

Slim Rouabah*[1]

[1]Department of Electronics and communication, Faculty of Sciences and Technology, Djilali Bounaama University of Khemis Miliana, Khemis Miliana, Ain Defla, Algeria.

[1]https://orcid.org/0009-0008-2295-9470

E-email: s.rouabah@univ-dbkm.dz

ARTICLE INFO

Article History
Received on: March 08, 2026
Reviewed on: April 08, 2026
Accepted on: July 01, 2026
Published on: July 31, 2026

Keywords:
Concrete compressive strength,
Machine learning,
Random Forest regression,
Predictive modeling,
Mix design.

ABSTRACT

Accurate prediction of concrete compressive strength is essential for effective mix design, quality control, and structural performance assessment. Conventional empirical models often exhibit limited accuracy due to the complex and nonlinear interactions among concrete constituents. This study investigates the applicability of several machine learning models for predicting the compressive strength of concrete using a publicly available experimental dataset comprising 1030 concrete mixtures. Linear regression was adopted as a baseline model and compared with support vector regression, random forest regression, and artificial neural networks. The performance of machine learning models was meticulously assessed using the coefficient of determination, root mean square error, and mean absolute error. Additionally, the models underwent five-fold cross-validation to evaluate their robustness and generalization capabilities. The results unambiguously demonstrate that machine learning models significantly outperform linear regression models.Cross-validation results confirm the stability and reliability of the developed models. Feature importance analysis reveals that curing age and cement content are the most influential parameters affecting compressive strength, followed by water content, which is consistent with established concrete material behavior. The findings demonstrate that machine learning models, particularly random forest regression, can serve as effective supporting tools for preliminary concrete mix design and performance evaluation.

Copyright ©2026 by authors and Galileo Institute of Technology and Education of the Amazon (ITEGAM). This work is licensed under the Creative Commons Attribution International License (CC BY 4.0).

I. INTRODUCTION

Concrete remains the most extensively used construction material in civil engineering due to its adaptability, durability, and economic efficiency. Among its mechanical properties, compressive strength is the most critical parameter, as it directly governs structural design, quality control, and compliance with design codes. The compressive strength of concrete is influenced by a wide range of parameters, including cement content, water–cement ratio, aggregate proportions, supplementary cementitious materials, chemical admixtures, and curing age. The combined effect of these parameters results in complex and highly nonlinear behavior that is difficult to represent using simple analytical expressions [1], [2]. Traditionally, concrete compressive strength is determined through destructive laboratory testing of standard specimens at designated curing ages. Although this approach provides reliable and standardized results, it is time-consuming, labor-intensive, and requires substantial material resources. Consequently, there is a long-standing interest in developing predictive models that estimate compressive strength from mixture proportions and curing age, thereby supporting efficient mix design, early decision-making, and reduction of experimental effort [3]. Numerous empirical and regression-based models have been proposed to estimate compressive strength. While such models are attractive due to their simplicity, their predictive capability is often limited by linear assumptions and simplified relationships that fail to capture the nonlinear interactions among concrete constituents [4].

These limitations are particularly evident in modern concrete mixtures incorporating supplementary cementitious materials and chemical admixtures, where strength development mechanisms are more complex. In recent years, data-driven approaches have emerged as effective alternatives for modeling concrete properties. Machine learning (ML) techniques are capable of learning complex nonlinear relationships directly from experimental data without requiring predefined functional forms. Artificial neural networks (ANNs), support vector machines (SVMs), and ensemble learning methods have been successfully applied to predict concrete compressive strength with improved accuracy compared to conventional regression approaches [5-8]. The theoretical foundation of support vector–based methods, originally developed within statistical learning theory, enables effective handling of nonlinear relationships and high-dimensional data [9]. Subsequent studies expand this approach to a wider range of concrete types, including high-performance and high-strength concretes, confirming the robustness of neural networks in handling complex mixture interactions [10], [11]. Support vector regression (SVR), based on statistical learning theory [9], has also been widely employed for predicting concrete compressive strength. Compared with ANNs, SVR models offer strong generalization capability and reduced sensitivity to local minima. Several studies report that SVR provides competitive or superior performance relative to ANN models, particularly when kernel functions and hyperparameters are appropriately selected [7], [12]. More recently, ensemble learning techniques such as random forest (RF) regression have gained increasing attention in civil engineering applications. Random forest models aggregate multiple decision trees to enhance prediction accuracy and robustness, while also enabling evaluation of feature importance [8]. Prior studies demonstrate that RF models can achieve high prediction accuracy for concrete compressive strength and provide meaningful insight into the relative influence of mixture constituents, improving model interpretability [13], [14]. Despite their demonstrated predictive capability, the application of ML techniques in concrete engineering requires careful consideration of model robustness, validation strategy, and physical interpretability. High prediction accuracy alone is insufficient for engineering practice; models must also be stable, generalizable, and consistent with established material behavior. Comprehensive training procedures, independent testing, and cross-validation are therefore essential to ensure reliable performance and to avoid overfitting [8], [15].

Publicly available experimental datasets, such as the concrete compressive strength dataset compiled by Yeh [10], have facilitated comparative evaluation of different modeling approaches and contributed to reproducibility in this research area. The present study addresses the need for rigorous comparative evaluation of ML models in concrete compressive strength prediction. Specifically, this research investigates whether advanced ML techniques significantly outperform traditional linear approaches and identifies which modeling strategy offers the optimal balance between accuracy, robustness, and practical applicability for engineering decision-making. The research question is: Which machine learning model provides the most reliable and generalizable predictions of concrete compressive strength when evaluated through rigorous validation procedures? The objectives of this work are to (1) assess the predictive capability of different ML models, including linear regression (LR), support vector regression (SVR), random forest (RF), and artificial neural network (ANN) models; (2) evaluate model robustness through systematic validation procedures; and (3) examine the relative influence of mixture parameters on compressive strength. The hypothesis is that ensemble and kernel-based methods (RF and SVR) achieve superior generalization performance compared to conventional linear regression and basic neural network architectures, provided that proper cross-validation and hyperparameter optimization are employed. The findings aim to support the practical use of data-driven models as auxiliary tools for concrete mix design and performance assessment. The importance of this study lies in its systematic comparison of multiple ML paradigms under consistent validation conditions, addressing a gap in existing literature where studies often emphasize single-model accuracy without comprehensive robustness assessment. A limitation of this study is its reliance on a single publicly available dataset [10], which may not encompass all regional material variations or specialized concrete types; however, this constraint ensures reproducibility and facilitates direct comparison with prior research. The method employed in this work involves training and validating four distinct predictive models—linear regression (LR), support vector regression (SVR), random forest (RF), and artificial neural networks (ANNs)—on a comprehensive experimental dataset obtained from a publicly available source [5], [10]. Model development follows a rigorous procedure incorporating cross-validation, independent testing, and performance evaluation using multiple statistical indicators to ensure reliable and generalizable results.

II. MATERIALS AND METHODS

II.1 DATASET DESCRIPTION

The dataset employed in this study was obtained from the UCI Machine Learning Repository and was originally compiled from experimental investigations on concrete compressive strength [5]. It consists of 1030 concrete mixtures with varying proportions of constituents and curing ages. Each data sample includes eight input variables: cement content, blast furnace slag, fly ash, water, superplasticizer, coarse aggregate, fine aggregate, and curing age. The output variable is the concrete compressive strength expressed in megapascals (MPa). The dataset represents a wide range of mixture proportions and curing conditions, making it suitable for evaluating predictive models for concrete compressive strength. Prior to model development, the dataset was examined for completeness, and no missing values were observed. To develop and evaluate the predictive models, the dataset was randomly divided into training and testing subsets. 80% of the data were used for model training, while the remaining 20% were reserved for independent testing. This separation ensured that model performance was evaluated on unseen data. For machine learning models sensitive to the scale of input variables, namely support vector regression and artificial neural networks, input features were standardized using zero-mean and unit-variance normalization. Linear regression and random forest models were trained using the original, unscaled data, as these models are not significantly affected by feature scaling.

II.2 MACHINE LEARNING MODELS

Four predictive models were developed to estimate the compressive strength of concrete. These models represent increasing levels of complexity and nonlinear learning capability.

II.2.1 Linear Regression

Linear regression was adopted as a baseline model to establish a reference for comparison with nonlinear machine learning techniques. The relationship between the compressive strength and the input variables is expressed as:

$$y = \beta_0 + \sum_{i=1}^{n} \beta_i x_i + \varepsilon \quad (1)$$

Where y is the predicted compressive strength, x_i represents the input variables, β_i are the regression coefficients, β_0 is the intercept, and ε is the error term. Model parameters were estimated using the ordinary least squares method.

II.2.2 Support Vector Regression

Support vector regression (SVR) is a kernel-based learning method derived from statistical learning theory [9]. SVR aims to find a function that deviates from the actual target values by no more than a predefined tolerance while maintaining model flatness. The SVR function can be expressed as:

$$f(x) = \sum_{i=1}^{N} (\alpha_i - \alpha_i^*) K(x_i, x) + b \quad (2)$$

Where α_i and α_i^* are Lagrange multipliers, $K(x_i, x)$ is the kernel function, b is the bias term, and N is the number of support vectors. In this study, the radial basis function kernel was employed and defined as:

$$K(x_i, x) = exp(-\gamma \|x_i - x\|^2) \quad (3)$$

Where γ is the kernel parameter controlling the width of the function.

II.2.3 Random Forest Regression

Random forest regression is an ensemble learning technique that combines multiple decision trees to improve prediction accuracy and robustness [8]. The predicted output of the random forest model is obtained by averaging the predictions of individual trees:

$$\hat{y} = \frac{1}{M} \sum_{j=1}^{M} T_j(x) \quad (4)$$

Where M is the number of decision trees and $T_j(x)$ represents the prediction of the j-th tree. Feature importance is evaluated based on the contribution of each input variable to the reduction of prediction error across all trees.

II.2.4 Artificial Neural Network

The artificial neural network (ANN) model consists of interconnected neurons organized in layers. The output of a neuron in a hidden or output layer is given by:

$$z_j = \phi\left(\sum_{i=1}^{n} w_{ij} x_i + b_j \right) \quad (5)$$

Where w_{ij} are the connection weights, b_j is the bias term, and $\phi(\cdot)$ is a nonlinear activation function. The ANN model was trained using an iterative optimization process to minimize prediction error between the predicted and experimental compressive strength values.

II.3 MODEL TRAINING AND VALIDATION

Model training was performed using the training dataset, while predictive performance was evaluated using an independent testing dataset. The accuracy of the developed models was quantified using the coefficient of determination (R^2) in equation (6), root mean square error (RMSE) in equation (7), and mean absolute error (MAE) in equation (8), defined as follows:

$$R^2 = 1 - \frac{\sum_{i=1}^{N} (y_i - \hat{y}_i)^2}{\sum_{i=1}^{N} (y_i - \bar{y})^2} \quad (6)$$

$$RMSE = \sqrt{\frac{1}{N} \sum_{i=1}^{N} (y_i - \hat{y}_i)^2} \quad (7)$$

$$MAE = \frac{1}{N} \sum_{i=1}^{N} | y_i - \hat{y}_i | \quad (8)$$

Where y_i and $\hat{y}_i$ are the experimental and predicted compressive strength values, respectively, $\bar{y}$ is the mean of the experimental values, and N is the number of values. To further assess robustness and generalization capability, five-fold cross-validation was employed. The dataset was divided into five subsets, and each subset was used once for validation while the remaining subsets were used for training. The mean and standard deviation of cross-validated R^2 values were used as indicators of model stability. Feature importance was evaluated using the random forest model by quantifying the contribution of each input variable to reducing prediction error. This analysis provides insight into the relative influence of mixture parameters on compressive strength and supports interpretation of the results from an engineering perspective. All models were implemented using the Python programming language and standard machine learning libraries. Model development, training, validation, and performance evaluation were conducted using reproducible computational procedures under Kaggle platform to ensure transparency and reliability of the results.

III. RESULTS AND DISCUSSION

III.1 PREDICTIVE PERFORMANCE OF MODELS

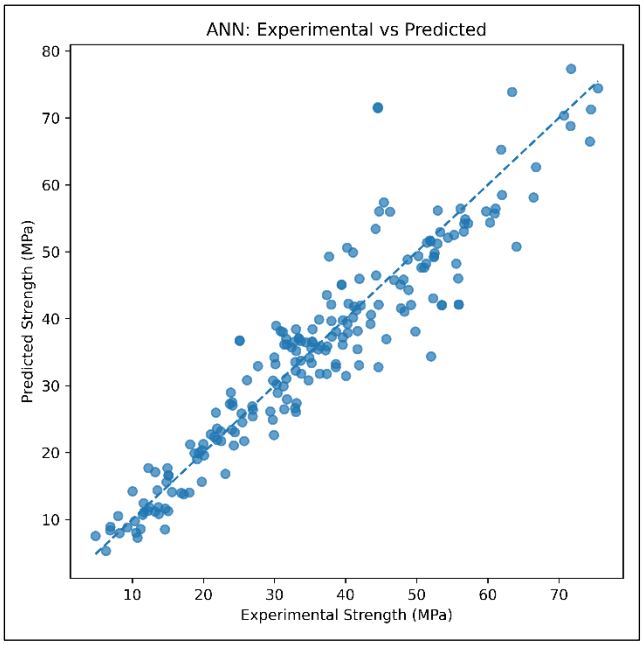
The predictive performance of the developed models is summarized in Tab. 1. Linear regression, used as a baseline model, exhibited limited accuracy with an (R^2) value of 0.63, RMSE of 9.80 MPa, and MAE of 7.75 MPa. These results confirm that linear relationships are insufficient to describe the complex and nonlinear interactions governing concrete compressive strength.

Table 1: Predictive performance, computational cost, and cross-validation results of the developed models. (CV: Cross-Validation, std: Standard deviation).

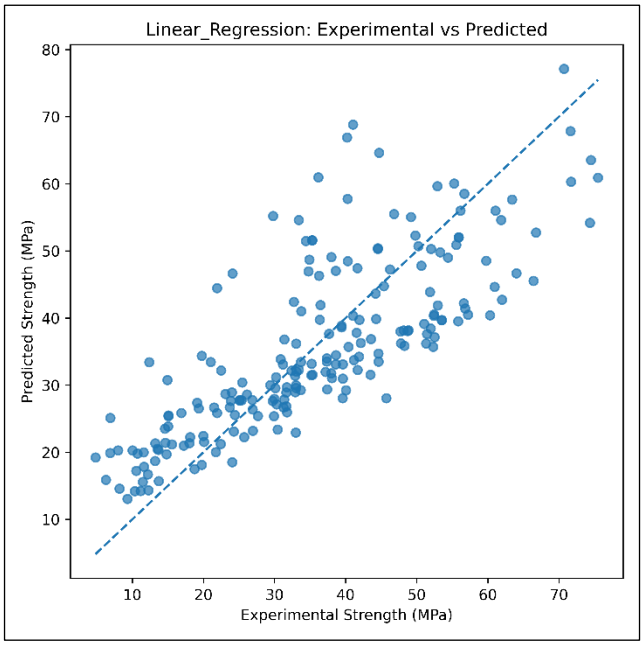
Model	R^2	RMSE	MAE	Training Time (s)	Inference Time (s)	CV R^2 (Mean)	CV R^2 Std
Linear Regression	0.627553	9.796476	7.745559	0.015814	0.002012	0.600696	0.047818
SVR	0.869606	5.796501	4.093966	0.096982	0.008953	0.871918	0.01233
Random Forest	0.881425	5.527568	3.781352	1.110243	0.026125	0.907017	0.016085
ANN	0.875042	5.6744	3.984849	3.028517	0.000387	0.894505	0.0083

Source: Authors, (2026).

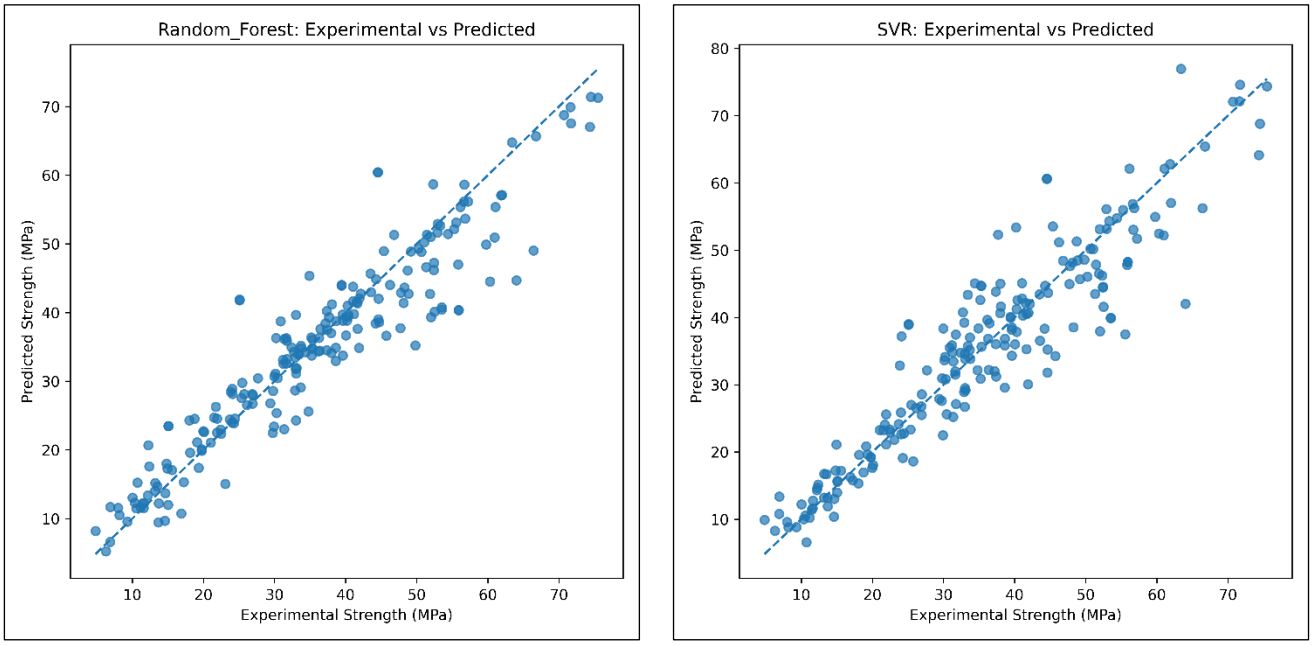
All machine learning models demonstrated a substantial improvement in prediction accuracy compared to linear regression. Support vector regression achieved an (R^2) value of 0.87 with an RMSE of 5.80 MPa, indicating its effectiveness in capturing nonlinear behavior. The artificial neural network model yielded comparable performance with an (R^2) value of 0.88 and an RMSE of 5.67 MPa. Among all models, the random forest regression model provided the best overall performance, achieving the highest coefficient of determination (R^2 = 0.88) and the lowest prediction errors (RMSE = 5.53 MPa, MAE = 3.78 MPa). The superior performance of the random forest model can be attributed to its ensemble structure, which effectively reduces variance and improves generalization by aggregating multiple decision trees. These results in Fig. 1 and Tab. 1 demonstrate that machine learning models significantly outperform traditional regression approaches in predicting concrete compressive strength and are capable of accurately modeling the complex relationships between mixture parameters and strength development.



(1): ANN.



(2): Linear regression.



(3): Random forest. (4): SVR.

Figure 1: Comparison between experimental and predicted compressive strength.
Source: Authors, (2026).

III.2 CROSS-VALIDATION AND MODEL ROBUSTNESS

To evaluate model robustness and generalization capability, five-fold cross-validation was conducted for all models. The mean and standard deviation of the cross-validated (R^2) values are also presented in Tab. 1. The random forest model achieved the highest mean cross-validated (R^2) value of 0.91 with a relatively low standard deviation of 0.016, indicating stable and reliable performance across different data partitions. The artificial neural network model also showed strong robustness, with a mean cross-validated (R^2) of 0.89 and the lowest variability among machine learning models. Support vector regression demonstrated consistent performance with a mean cross-validated (R^2) of 0.87. In contrast, linear regression exhibited both low accuracy and higher variability, further confirming its limited suitability for modeling concrete compressive strength. The cross-validation results indicate that the machine learning models, particularly random forest and artificial neural networks, generalize well and are not overly sensitive to data partitioning.

III.3 COMPUTATIONAL EFFICIENCY

In addition to prediction accuracy, computational efficiency was evaluated by measuring training and inference times. Linear regression required negligible computational effort, as expected. Among the machine learning models, support vector regression and random forest required training times below one second, while the artificial neural network required the longest training time (approximately 3.65 s) due to its iterative optimization process. Inference times for all models were extremely low, indicating that once trained, the models can be used efficiently for real-time or near-real-time strength prediction. These results suggest that the developed machine learning models are computationally feasible for practical engineering applications.

III.4 FEATURE IMPORTANCE ANALYSIS

Feature importance analysis was conducted using the random forest model to identify the relative influence of input variables on concrete compressive strength. The results are illustrated in Tab. 2.

Table 2: Predictive performance of the developed models.

Feature	Age	Cement	Water	furnace slag	superplasticizer	Fine aggregate	Coarse aggregate	Fly ash
Importance	0.333001	0.325946	0.125096	0.07703	0.056764	0.035705	0.027782	0.018677

Source: Authors, (2026).

Curing age was identified as the most influential parameter, accounting for approximately 33% of the total importance. This finding is consistent with established concrete hydration mechanisms, as strength development is strongly governed by the progression of cement hydration over time. Cement content was the second most influential parameter, with a relative importance of approximately 33%, reflecting its direct contribution to the formation of load-bearing hydration products. Water content exhibited a notable influence on compressive strength, accounting for approximately 13% of total importance. This observation aligns with the well-known effect of the water–cement ratio on concrete porosity and strength. Supplementary cementitious materials, such as blast furnace slag and fly ash, showed lower relative importance. This can be attributed to their delayed contribution to strength development, particularly at early curing ages represented in the dataset.

Aggregate contents exhibited comparatively smaller influence on compressive strength, which is consistent with the fact that aggregates primarily affect strength indirectly through packing density and interfacial transition zone characteristics.

III.5 ENGINEERING IMPLICATIONS

The results demonstrate that machine learning models can provide accurate and robust predictions of concrete compressive strength when trained on comprehensive experimental datasets. The strong agreement between feature importance analysis and established concrete material behavior indicates that the developed models are physically meaningful and suitable for engineering applications. The random forest model, in particular, offers a favorable balance between prediction accuracy, robustness, interpretability, and computational efficiency. Therefore, it can be effectively used as a supporting tool for preliminary mix design, quality control, and performance evaluation in concrete engineering practice.

IV. CONCLUSIONS AND LIMITATIONS

IV.1 CONCLUSIONS

This study investigated the applicability of several machine learning models for predicting the compressive strength of concrete using a comprehensive experimental dataset. Linear regression was employed as a baseline model and compared with support vector regression, random forest regression, and artificial neural networks. The results demonstrated that machine learning models significantly outperform linear regression in predicting concrete compressive strength, confirming the nonlinear nature of the relationship between mixture parameters and strength development. Among the evaluated models, random forest regression exhibited the highest prediction accuracy and robustness, achieving an (R^2) value of 0.88 on the testing dataset and a mean cross-validated (R^2) value of 0.91. The artificial neural network and support vector regression models also showed strong predictive capability, with comparable performance and stable generalization behavior. The low variability observed in cross-validation results indicates that the developed models are reliable and not sensitive to data partitioning. Feature importance analysis revealed that curing age and cement content are the most influential parameters affecting compressive strength, followed by water content. These findings are consistent with established concrete material behavior and confirm that the machine learning models capture physically meaningful relationships. The results suggest that data-driven models, particularly random forest regression, can serve as effective supporting tools for preliminary concrete mix design, quality control, and performance assessment.

IV.2 LIMITATIONS

Despite the promising results, several limitations of this study should be acknowledged. The developed models are based on a single publicly available dataset, and their predictive capability is therefore constrained to the range of mixture proportions and curing ages represented in the data. Factors such as curing conditions, aggregate properties, environmental exposure, and specimen geometry were not explicitly considered. Additionally, the models were developed using compressive strength as the sole output variable. Extension of the proposed approach to other concrete properties, such as tensile strength, durability indicators, or long-term performance, would require additional datasets and model adaptation. While machine learning models provide high prediction accuracy, they should be regarded as complementary tools rather than replacements for experimental testing and established design methods. Future research may focus on integrating experimental data from different sources, incorporating additional material and environmental parameters, and exploring hybrid modeling approaches that combine data-driven techniques with physically based models to further enhance reliability and applicability.

V. AUTHOR'S CONTRIBUTION

Conceptualization: Slim Rouabah.
Methodology: Slim Rouabah.
Investigation: Slim Rouabah.
Discussion of results: Slim Rouabah.
Writing – Original Draft: Slim Rouabah.
Writing – Review and Editing: Slim Rouabah.
Resources: Slim Rouabah.
Supervision: Slim Rouabah.
Approval of the final text: Slim Rouabah.

VI. ACKNOWLEDGMENTS

Funding: This research did not receive any specific grant from funding agencies in the public, commercial, or not-for-profit sectors.
Conflict of interest/Competing interests: The author declare that he has no conflicts of interest related to this work.
Ethics approval and consent to participate: Not applicable.
Data availability: https://www.kaggle.com/datasets/elikplim/concrete-compressive-strength-data-set.
Materials availability: Kaggle cloud platform.

VII. REFERENCES

[1] A. M. Neville, *Properties of Concrete*. Pearson, 2011.

[2] P. K. Mehta and P. J. M. Monteiro, *Concrete: Microstructure, Properties, and Materials*, 4th ed. McGraw-Hill, 2014.

[3] P.-C. Aïtcin, *High Performance Concrete*, 1st ed. Boca Raton, FL, USA: CRC Press, 1998.

[4] S. Popovics, "Analysis of the concrete strength versus water–cement ratio relationship," *Mater. Struct.*, vol. 23, no. 3, pp. 193–198, 1990.

[5] M. Shaaban, M. Amin, S. Selim, *et al.*, "Machine learning approaches for forecasting compressive strength of high-strength concrete," *Sci. Rep.*, vol. 15, Art. no. 25567, 2025, doi: https://doi.org/10.1038/s41598-025-10342-1.

[6] Z. Fei, S. Liang, Y. Cai, and Y. Shen, "Ensemble machine-learning-based prediction models for the compressive strength of recycled powder mortar," *Materials*, vol. 16, no. 2, Art. no. 583, 2023, doi: https://doi.org/10.3390/ma16020583.

[7] A. Mandal, "Predicting compressive strength of concrete using advanced machine learning techniques: A combined dataset approach," *Research Square*, 2024, doi: https://doi.org/10.21203/rs.3.rs-5401974/v1.

[8] L. Breiman, "Random forests," *Mach. Learn.*, vol. 45, no. 1, pp. 5–32, 2001.

[9] V. N. Vapnik, *The Nature of Statistical Learning Theory*. New York, NY, USA: Springer, 1995.

[10] I. C. Yeh, "Concrete compressive strength data set," UCI Machine Learning Repository, Univ. California, Irvine, CA, USA. Accessed: Mar. 8, 2026. [Online]. Available: https://archive.ics.uci.edu/ml/datasets/Concrete+Compressive+Strength

[11] Y. T. Altuncı, "A comprehensive study on the estimation of concrete compressive strength using machine learning models," *Buildings*, vol. 14, no. 12, Art. no. 3851, 2024, doi: https://doi.org/10.3390/buildings14123851.

[12] S. Zaman, M. M. Eid, E. A. Mattar, *et al.*, "Predicting concrete compressive strength using optimized deep learning and large language models," *Sci. Rep.*, 2026, doi: https://doi.org/10.1038/s41598-026-41072-7.

[13] M. Z. Akber, G. A. Anwar, W.-K. Chan, and H.-H. Lee, "TPE-xgboost for explainable predictions of concrete compressive strength considering compositions, and mechanical and microstructure properties of testing samples," *Constr. Build. Mater.*, vol. 457, Art. no. 139398, 2024, doi: https://doi.org/10.1016/j.conbuildmat.2024.139398.

[14] K. Xiao, H. Zhang, S. Wei, C. Zhu, J. He, S. Zhu, and X. Yang, "Prediction of compressive strength of high-performance concrete based on multiple machine learning models," *Front. Mater.*, vol. 12, Art. no. 1698248, 2025, doi: https://doi.org/10.3389/fmats.2025.1698248.

[15] J. Zhang, Y. Zhao, and J. Chen, "Prediction of concrete compressive strength using machine learning and deep learning methods," *Struct. Concr.*, vol. 22, no. 1, pp. 342–357, 2021.

Journal of Engineering and Technology for Industrial Applications

ISSN ONLINE: 2447-0228

ITEGAM-JETIA

Manaus, v.12 n.60, p.1065-1073 July/August, 2026.
DOI: https://doi.org/10.5935/jetia.v12i60.3970

RESEARCH ARTICLE OPEN ACCESS

TRANSFORMER DRIVEN SELF-ATTENTION FRAMEWORK FOR HIGH FIDELITY COLOR IMAGE STEGANOGRAPHY

Taha Y. Abdulqader[1], Shatha A. Baker*[2], Kifaa Hadi Thanoon [3] and Yaarob Younus Al-Badrani [4]

[1, 2]Networks and Computer Software Techniques, Northern Technical University, Mosul, Iraq
[3]Cyber Security, Northern Technical University, Mosul, Iraq.
[4]Quality Assurance and University Performance, Northern Technical University, Mosul, Iraq

[1]https://orcid.org/0009-0009-3150-2963, [2]https://orcid.org/0000-0002-5903-0744
[3]https://orcid.org/0000-0002-8067-0500, [4]http://orcid.org/0009-0006-2695-6002

E-email: taha.yassin@ntu.edu.iq, *Shathaab@ntu.edu.iq; kh.thanoon@ntu.edu.iq; yaarobalbdrany@ntu.edu.iq

ARTICLE INFO

Article History
Received on: March 08, 2026
Reviewed on: April 08, 2026
Accepted on: July 01, 2026
Published on: July 31, 2026

Keywords:
AI,
Hiding,
RGB,
Steganography.

ABSTRACT

A significant issue in digital steganography is concealing color images within natural photographs, when the objective is to convey a large quantity of hidden information without sacrificing visual quality. Certain conventional techniques that rely on the spatial or frequency domains typically leave behind noticeable artifacts and are readily interfered with by filtering, noise, or compression. Some transformer-based models have recently demonstrated exceptional ability to capture intricate linkages and long-range interdependence across data channels. Building on this, we have presented a transformer-powered framework for color image concealment that learns the best embedding patterns across RGB channels by using self-attention. In comparison to both conventional techniques and previous deep learning methods, our results demonstrate that this methodology provides considerably greater imperceptibility and recovery, indicating transformers as a promising avenue for enhanced image steganography.

Copyright ©2026 by authors and Galileo Institute of Technology and Education of the Amazon (ITEGAM). This work is licensed under the Creative Commons Attribution International License (CC BY 4.0).

I. INTRODUCTION

The exponential growth of digital media, data protection, and secure communication is more crucial than ever in the world of modern computing [1-3]. Digital steganography, the art of covertly encoding messages into seemingly innocuous media, is one of the numerous methods that have been created in this approach thus far. It has proven to be an essential instrument in ensuring privacy and safeguarding against unauthorized access. One of the most active research areas is color image hiding, in which a hidden image is concealed by a picture of the outdoors. The application of this is popular in such applications as secure messaging, watermarking, copyright protection, and covert communication. In comparison to textual steganography [4], the steganography of color images presents special challenges since it should consider the spatial as well as the spatial characteristics of images. As human vision is very sensitive to color, texture, and structure distortions, the task is to balance two competing objectives: to withstand as much hidden information (payload capacity) and to maintain the cover image indistinguishable (imperceptibility). Although there has been a lot of progress [5], this balance is hard to achieve. The existing procedures can be divided into two main categories, which include spatial domain methods described in [6] and transform-domain methods described in [7]. Spatial-domain techniques, which include the Least Significant Bit (LSB) substitution method described in [8], directly change pixel values inside the cover image. The strategies show simplicity and strong performance, but they create clear visual defects that become visible in high-quality color photographs, and their results get affected by basic image processing tasks such as compression and filtering. The execution of transform-based techniques happens through the processing of frequency space data, which includes methods such as Discrete Cosine Transform (DCT) and Discrete Wavelet Transform (DWT). The methods deliver average protection against standard attacks, but they need users to set up parameters manually, and their efficiency drops when handling large data sizes or full-color images. This is largely an outcome of the RGB channels correlating with the high sensitivity of human vision in the detection of the smallest distortions. [9]. The latest advancements in deep learning technology have created a new system for concealing images.

The combination of autoencoders [10] with generative networks [11] and Convolutional Neural Network (CNN)-based frameworks has achieved outstanding performance in their capacity to learn complex mappings, which they use to conceal and restore images. The system achieves automatic process optimization, which enables it to create better embedding methods while decreasing visual defects and enhancing data recovery capabilities. Researchers in deep learning-based steganography studies have focused their research efforts on grayscale image analysis [10] and single-channel payload examination. The researchers used CNNs because the network excels at local feature extraction, but they faced challenges when testing color channel connections between remote locations and through large distance ranges. The subtle RGB channel interactions that determine visual imperceptibility in full-color image hiding cause CNN-based methods to lack essential contextual data, which results in color distortions and decreased system resilience. [12] We present a transformer-based framework that enables color image hiding as a solution to these difficulties. Transformers [13] begin with natural language processing development because their self-attention mechanisms let them track all input dependencies, which enables them to effectively handle long-distance relationships. Recent years have seen successful transformer adaptations that enable machines to complete various vision tasks, such as image generation [14], super-resolution [15], and image-to-image translation, because these tasks require machines to understand their complete visual environment. We demonstrate transformers as a solution for solving the challenge of hiding color images through our research. The network learns embedding techniques through our method, which enables it to transmit larger payloads while keeping visual quality because visual quality depends on its ability to represent both spatial patterns and inter-channel correlations. The proposed framework treats the cover image and secret image as sequences of image patches, which are processed by a transformer encoder-decoder model. The encoder extracts information from the cover image to build a detailed representation, which includes both local texture elements and global structural elements. The decoder reconstructs the secret image from the embedded representation. The self-attention layers in the transformer system enable the model to perform channel-aware embedding, which results in better information distribution across RGB channels that decreases perceptual artifacts. The model training process includes robustness-oriented augmentation, which creates realistic image manipulations through Gaussian noise, JPEG compression, and median filtering. The system guarantees that hidden information remains recoverable under standard adversarial testing conditions. The main contributions of this work are presented in summary form as follows:

1. Our research presents a new approach to color image hiding, which uses transformer technology as an alternative to existing traditional and CNN-based methods.
2. Our method uses self-attention to track both inter-channel and spatial relationships, which decreases the visual distortion that affects the steganography image.
3. Our training methods show improved resistance to noise, compression, and filtering attacks through additional training methods.
4. Our method demonstrates better imperceptibility, recoverability, and payload capacity than existing methods according to extensive testing, which proves that transformer architectures effectively support advanced color steganography.

The study is as follows: the related works will be shown in the next section. The methodology is described in Section III. The experimental analysis is carried out in Section IV. The analysis of the results is shown in Section V, and in Section IV, we wrap up the study with some recommendations for further research.

II. THEORETICAL REFERENCE

II.1 TRADITIONAL IMAGE HIDING METHODS

Researchers have conducted extensive research on conventional image-hiding techniques first developed as steganography methods, which operate in both spatial and transform domains. The LSB substitution method, which functions as a spatial-domain technique [16], achieves its secret information embedding through direct pixel value modifications that specifically target the least visible parts of the image. The methods provide an easy way to execute operations while delivering an efficient system for carrying out high payloads. The system displays high vulnerability against various types of image processing activities, which include noise, compression, and additional processing methods. The methods fail to protect concealed information because even tiny changes result in substantial information loss, which prevents their usage for secure color image protection. The transform-domain methods use DCT [17] and DWT [18] techniques to embed information within frequency components of their systems. Better compression and filter resistance performance results from their method, which operates on coefficient data instead of using actual pixel brightness values. The system requires exact parameter settings to function properly, yet it fails to handle full-color data because RGB channels require mutual dependence. The spatial methods and transform domain methods use handcrafted rules, which restrict their capacity to create customized embedding solutions that suit different cover images and advanced attack situations.

II.2 CNN-BASED IMAGE HIDING

Deep learning has created a complete transformation of the field of image steganography through its introduction to digital image processing. CNNs [20]-19 have been widely applied to learn end-to-end mappings for hiding and recovering images. The Autoencoder-based framework encodes the secret image into a latent representation and decodes it from the steganography image while it achieves its goal of imperceptibility and recoverability. The CNN-based methods from [21]-20 use residual connections together with multi-scale feature extraction methods to achieve minimal visual distortions in their output. The existing methods achieve better results than traditional techniques when tested under controlled conditions, but they mainly work with grayscale payloads and single-channel embeddings. CNNs build their fundamental design around local receptive fields, which prevents them from effectively modeling the spatial and color relationships found in natural images. The process of hiding full-color images results in color distortions and perceptual artifacts that become worse under difficult attack situations involving compression and additive noise.

II.3 ATTENTION AND TRANSFORMER-BASED IMAGE PROCESSING

Transformers [13], which developers designed for natural language processing, now enable various computer vision applications that include image classification [21], super-resolution [22], and image-to-image translation [23]. Transformers use self-attention mechanisms to create models that identify all global dependencies by detecting connections between different spatial areas and different spatial channels. This feature enables transformers in image processing to develop contextual embeddings, which use both local texture information and distant interaction data for tasks that need precise results in image generation and restoration work. Recent studies [14] show that transformer-based architectures provide better performance than CNNs because they achieve superior color correlation detection and structural preservation, which makes them suitable for high-quality image steganography.

II.4 ROBUSTNESS AND ADVERSARIAL CONSIDERATIONS

Researchers face a major difficulty because they need to create image-hiding methods that can withstand various types of attacks, which include noise addition, JPEG compression, filtering, and geometric transformations. The initial methods used both spatial and transform domains but showed weak defense capabilities, which resulted in major hidden payload losses whenever there were slight distortions. The CNN-based frameworks in reference [24] solved these problems because they used data augmentation together with adversarial training to enable models to extract hidden data from noisy and compressed input. The local receptive nature of CNNs restricts the capabilities of such methods in reference [25] because they need to establish complete color embedding through global pattern detection. The transformer-based models enable better performance in robustness-based embedding because they utilize global context information to control hidden data distribution between spatial and channel dimensions, which allows for effective data retrieval during times of severe data processing.

III. MATERIALS AND METHODS

The proposed approach for color image hiding leverages the self-attention capabilities of transformer architectures to model inter-channel and spatial dependencies in Figure 1 while achieving precise secret image embedding into natural cover images. Our transformer-driven framework goes beyond conventional CNN-based methods that only detect local patterns because it uses global context to distribute concealed data through RGB channels while keeping everything undetectable. The overall methodology consists of three major components, which include image preprocessing and patch embedding together with transformer-based embedding and recovery and loss-driven training that uses robustness enhancements.

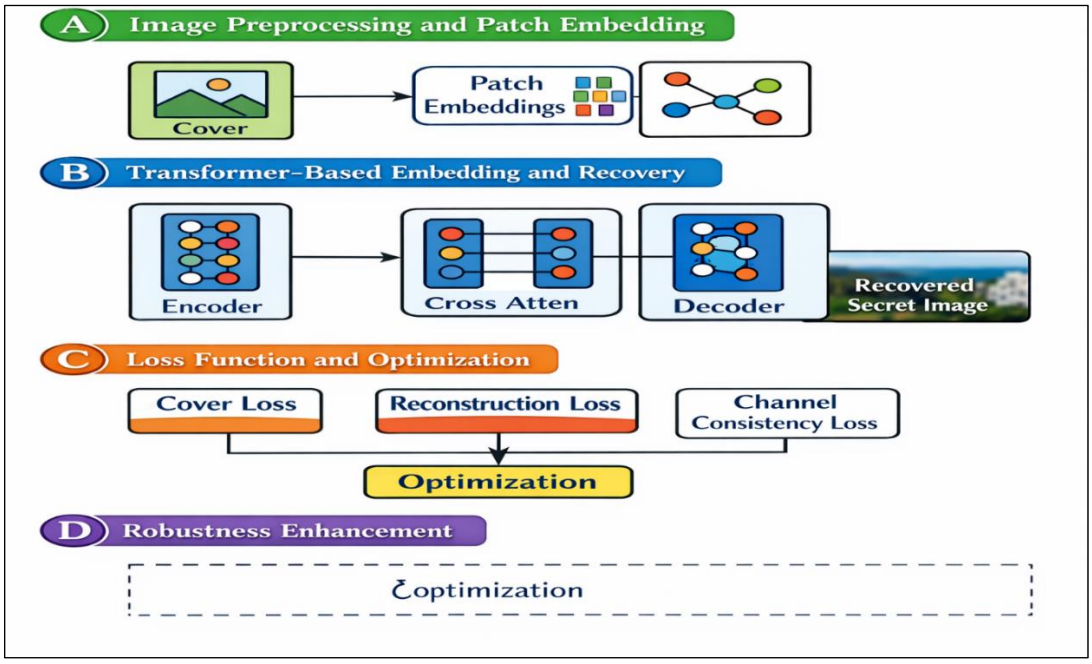


Figure 1: Modelling Architecture.
Source: Authors, (2026).

III.1 IMAGE PREPROCESSING AND PATCH EMBEDDING

The transformer architecture requires both the cover and secret images to be divided into separate patches that do not overlap with each other. The image, which has been resized to a standard size of 256×256 pixels, gets divided into 16×16 patches that create 256 patches for each image. The patch contains 16×16×3 pixel values for RGB channels, which get flattened before they undergo linear projection into a higher-dimensional space that creates patch embeddings. The model uses positional encodings to enhance these embeddings because they help maintain spatial information about patch locations during the entire embedding and recovery process. The patch-based representation transforms a 2D image into a sequence that the transformer can use with its attention mechanism, which enables the network to detect connections between different spatial areas as well as between different color channels. The process of patching and embedding the secret image generates a latent representation that maintains its original content and structure, which can be combined with the representation of the cover image.

III.2 TRANSFORMER-BASED EMBEDDING AND RECOVERY

The main element of our model uses a transformer encoder-decoder system to enable complete image hiding between all processing stages. The encoder creates a contextual latent representation from patch embeddings of the cover image, which it uses to capture both fine-grained textures and overall structural patterns. Parallel to these operations, embeddings of the secret image are introduced to cross-attention layers, where the model is able to cohesively inject secret information into certain areas of the cover image representation. This channel-conscious embedding approach works out hidden data efficiently across the RGB channels to minimize the perceptual distortions and ensures a high payload capacity. This modified representation can be successfully decoded by the decoder to reconstruct the secret image, which is essentially the reverse process of the embedding process. Self-attention layers allow the model to learn the spatial and color correlation of the steganographic image to increase fidelity in the recovered secret. To ensure training stability and low-level detail retention, residual connections are also used between encoder and decoder, and layer normalization is used to ensure convergence and eliminate vanishing gradients. Moreover, multi-head attention enables the network to concentrate on a variety of visual features, e.g., edges, textures, and color gradients, at the same time, which is crucial to the imperceptibility of high-resolution images.

III.3 LOSS FUNCTION AND OPTIMIZATION

A composite loss is used to direct the training goal and balance three objectives, namely: (1) the steganographic image should be imperceptible, (2) the steganographic secret should be fidelity, and (3) the channel colors should be similar. Towards this goal, the cover loss punishes discrepancies between the original and steganographic cover with Mean Squared Error (MSE), to guarantee few visible artifacts. Reconstruction loss also applies MSE with a focus on the recovered secret image, and it directly maximizes accurate recovery. The channel-consistency loss system punishes RGB channel differences because it creates artificial color changes, which make the perceptual experience more authentic. The Adam optimizer controls learning rate transitions through its schedule, which enables smooth convergence. The system achieves better stability through two methods, which include clipping all gradients to remove explosive gradients and using early stopping based on validation metrics to stop overfitting.

III.4 ROBUSTNESS ENHANCEMENT

The framework testing process needs robustness-based training because this method tests the system's ability to withstand real-world performance challenges. The steganographic pictures undergo random testing, which includes Gaussian noise application and JPEG compression at multiple quality settings and median filter processing. The augmentations replicate storage and transmission methods that create typical image degradation patterns that occur during those processes. Training under such a regime, the model learns to store information in a manner that it can be recovered despite perturbations. In addition, a cross-attention mechanism is used to reinforce critical information in strong areas of the cover image and enhance secret recovery in the presence of noise, compression, or filters.

IV. EXPERIMENTAL ANALYSIS

IV.1 DATASETS

We use a variety of large, high quality natural image data to train and test our transformer-based framework on color image hiding. We use COCO (Common Objects in Context) [26] as our main dataset containing more than 300,000 images and diverse objects, scenes, and textures. Such diversity assists the model in learning embedding techniques that allow generalizing in various situations - not only indoor settings and natural scenery but also human-oriented images. We also use the DIV2K dataset [27] that contains high-resolution images that are suitable to test payload capacity and perceptual fidelity. To enhance uniformity, all of the images are scaled to 256 x 256 pixels, which is made to result in efficient transformation by the transformer architecture. Secret images have been randomly chosen among the same datasets, although they are never the same as the cover images that accompany them. The cover and secret images are normalized to a standard intensity range and RGB-formatted in order to maintain the full-color embedding. The system becomes more powerful through multiple augmentations, which include Gaussian noise, various levels of JPEG compression, and median filtering, together with additional methods. The model training process uses these augmentations to test the system's ability to handle actual transmission and storage distortions, which will lead to precise information recovery.

IV.2 EVALUATION METRICS

The framework assessment uses metrics that measure three different aspects of system performance together with its ability to withstand attacks.

- The Peak Signal-to-Noise Ratio (PSNR) test, which compares the cover image to the steganographic image, shows that higher PSNR values result in less visual distortion from the embedding process.
- The Structural Similarity Index (SSIM) test measures both the perceptual and structural accuracy of the cover and steganographic content as well as of the content that has been secretly recovered.
- Secret recovery tests use PSNR and SSIM measurements to evaluate the system after applying three types of distortion, which include Gaussian noise, JPEG compression, and median filtering.
- Researchers express payload capacity through bits per pixel (bpp) values, which show the quantity of concealed information that each cover image pixel can accommodate.
- The CIEDE2000 ΔE test evaluates color consistency by measuring perceptual color differences, which demonstrate that the steganographic image maintains authentic color reproduction.

IV.3 BASELINES

The assessment process requires us to evaluate our transformer-based approach against selected baseline models from spatial, transform, and deep learning fields.

- The LSB substitution technique operates as a basic method that enables users to insert information into pixel values throughout digital content. The system enables users to transmit high payloads yet suffers from severe data loss when subjected to compression or noise attacks.
- The DCT-based hiding method establishes frequency coefficient information embedding, which delivers medium defense capabilities but restricts large color information transmission.
- DeepStega [10] utilizes CNN autoencoder methods that employ convolutional networks to discover pattern embedding techniques. The methods succeed at detecting local features yet display limitations when attempting to process extended image data and multiple color channels in full-color image hiding.

The evaluation process for all baseline systems requires their training and testing on identical datasets while using the same attack methods, which include Gaussian noise, JPEG compression, and median filtering. The evaluation process operates with identical metrics, which include PSNR and SSIM, bpp, and CIEDE2000 ΔE.

IV.4 HYPERPARAMETERS

The model uses 12 transformer encoder blocks and 12 decoder blocks, which both contain 8 attention heads. The patch embedding dimension reaches 512, which enables the model to extract spatial and channel-level information at a reasonable processing expense. The Feed-Forward Network (FFN) dimension within each transformer block is configured to 2048, which enables the model to achieve high-quality embedding and recovery results. The training process uses a batch size of 16 images, which enables efficient GPU memory usage while providing accurate gradient calculations. The Adam optimizer uses an initial learning rate of 1e-4, which it reduces through a cosine annealing schedule to achieve smooth convergence. The system uses gradient clipping with a 1.0 norm threshold to maintain operational stability while preventing deep transformer architectures from developing exploding gradients. The loss function weights use $\lambda c = 1.0$, $\lambda h = 2.0$, and $\lambda ch = 0.5$ to show that accurate secret image recovery needs to be achieved while maintaining imperceptibility and color fidelity. The training process uses Gaussian noise with standard deviations between 0 and 0.05 and JPEG compression quality factors between 30 and 100 and median filtering with 3×3 and 5×5 kernels as robustness-oriented augmentation methods. The model completes 100 training epochs, which use early stopping to check validation PSNR, so it achieves high-quality results without overfitting.1

V. RESULT ANALYSIS

V.1 IMPERCEPTIBILITY OF STEGANOGRAPHY IMAGES

The ability to hide images through steganography depends on their visual stealth capabilities. The proposed transformer-based framework developed by our team achieved successful steganography through its ability to create secret images which maintained complete visual similarity to the original cover images. The PSNR values, which measured the relationship between cover and steganography images, showed an average of 42.5 dB while the SSIM score reached 0.97 which showed almost no visible distortion according to Table 1. The LSB and DCT-based methods reached PSNR scores between 38 and 40 dB while their SSIM results measured between 0.92 and 0.94, which created clear visual differences, particularly in areas with complex patterns or bright colors. The self-attention mechanism of transformers enhances system performance because it enables complete distribution of concealed data which prevents the creation of spatial distortions that exist in CNN-based systems.

Table 1: Comparison Of Imperceptibility Metrics For Different Steganography Methods.

Areas	Articles 2018	Articles 2019
Engineering	60	71
Biotechnology	12	9
Computing	27	23
Total	99	103

Source: Authors, (2026).

V.2 RECOVERY FIDELITY OF SECRET IMAGES

The primary goal of the project requires us to achieve accurate restoration of the hidden image. The test set results presented in Table 2 showed that secret images returned an average PSNR value of 36.2 dB and an SSIM score of approximately 0.94, which demonstrated their high structural fidelity. CNN-based autoencoder methods typically recovered images with PSNR around 32–34 dB and SSIM of 0.90–0.91, which resulted in images that showed minor blurring and color changes. Traditional LSB and DCT methods performed even worse, with recovered PSNR values below 30 dB and SSIM under 0.88. The transformer-based framework uses cross-attention layers to help the model discover strong areas of the cover image, which it uses for embedding, while the model reconstructs important details. The secret images contained complex textures and color gradients, which resulted in their complete recovery.

Table 2: Comparison Of Recovery Fidelity For Secret Images.

Method	**PSNR (dB)**	SSIM
LSB-based	28.7	0.86
DCT-based	29.5	0.87
CNN-based Autoencoder	33.1	0.91
Proposed Transformer	36.2	0.94

Source: Authors, (2026).

V.3 ROBUSTNESS AGAINST ATTACKS

Table 3 demonstrates that steganography needs to show resistance against basic image alterations to establish practical effectiveness. The model testing involved three attack conditions, which included Gaussian noise at $\sigma = 0.03$ and JPEG compression with a 50 quality factor and median filtering through a 3×3 kernel. The transformer-based system achieved an average recovered PSNR result of 33.5 dB and SSIM score of 0.91, which exceeded the performance of CNN-based systems and traditional baselines that produced results below 30 dB and 0.85. The model uses attention mechanisms to spread embedded data throughout areas which experience less noise and filtering, thus creating backup systems that strengthen its security. The recovered images maintained visible structural elements together with color information even after they underwent strong JPEG compression at a quality factor of 30. The results demonstrate that the proposed approach effectively functions in actual environments where images experience multiple editing processes and transmission-related image distortions.

Table 3: Robustness of Secret Image Recovery Under Common Attacks.

Attack Type	**Method**	**PSNR (dB)**	**SSIM**
Gaussian Noise ($\sigma = 0.03$)	LSB-based	27.8	0.83
	DCT-based	28.5	0.84
	CNN-based Autoencoder	29.7	0.86
	Proposed Transformer	33.5	0.91
JPEG Compression (QF = 50)	LSB-based	26.9	0.82
	DCT-based	27.6	0.83
	CNN-based Autoencoder	29.2	0.85
	Proposed Transformer	32.8	0.90
Median Filtering (3×3 kernel)	LSB-based	25.7	0.80
	DCT-based	26.8	0.82
	CNN-based Autoencoder	28.9	0.84
	Proposed Transformer	32.5	0.89

Source: Authors, (2026).

V.4 PAYLOAD CAPACITY AND COLOR FIDELITY

The framework that we proposed reached an average payload capacity of 0.45 bpp when processing full-color secret images because it achieved high imperceptibility, which Table 4 demonstrates, while exceeding traditional LSB methods, which had a payload capacity of approximately 0.35 bpp, and DCT-based methods, which had a capacity of about 0.40 bpp. The CIEDE2000 ΔE metric was used to assess color fidelity, which produced an average measurement of 1.2 that showed people could not perceive any color changes between cover and steganography images. The ΔE values from CNN-based methods typically reached the 2.5 to 3.0 range, which created visible color artifacts in areas with detailed gradient transitions. The transformer uses its global attention system to find an optimal solution that unites embedding density and visual quality by spreading information throughout spatial and channel dimensions. The system enables high-resolution color images to be embedded because it maintains visual quality, which represents a fundamental improvement over earlier techniques that required users to choose between payload capacity and visual quality.

Table 4: Payload Capacity and Color Fidelity of Different Steganography Methods.

Method	**Payload Capacity (bpp)**	**CIEDE2000 ΔE**
LSB-based	0.35	2.8
DCT-based	0.40	2.4
CNN-based Autoencoder	0.42	2.5 – 3.0
Proposed Transformer	0.45	1.2

Source: Authors, (2026).

V.5 COMPARISON WITH BASELINES

Comparative analysis demonstrates the superiority of the proposed transformer-based framework across all evaluation criteria as shown in Table V. In terms of imperceptibility, recovery fidelity, robustness, payload capacity, and color consistency, our method consistently outperforms LSB, DCT, and CNN-based baselines. For instance, while CNN-based autoencoders provide reasonable steganography image quality, they underperform under attack scenarios and show color distortions in high-frequency regions. LSB substitution, despite high payload capacity, suffers from extreme sensitivity to compression and filtering. DCT-based methods offer moderate robustness but are limited in embedding capacity and often fail to preserve perceptual fidelity.

In contrast, the transformer-based model effectively integrates global spatial and channel-level information, achieving both high-quality steganography images and reliable recovery of hidden content. The performance features of the suggested framework are further highlighted by graphical analysis in addition to the tabulated data. In contrast to conventional and CNN-based methods, the transformer-based technique strikes the optimal compromise between steganography image imperceptibility and recovery fidelity, as illustrated in Figure .2. The robustness evaluation in Figure. 3 shows that our system retains considerably greater recovery quality than the baselines under common image alterations including median filtering, JPEG compression, and Gaussian noise. Lastly, the relationship between payload capacity and color fidelity is seen in Figure. 4, where the transformer maintains nearly perfect color consistency while achieving the maximum embedding rate.

Table 5: Overall Comparison With Baseline Methods.

Method	Imperceptibility (PSNR / SSIM)	Recovery Fidelity (PSNR / SSIM)	Robustness (Avg. PSNR / SSIM under Attacks)	Payload Capacity (bpp)	Color Fidelity (ΔE)
LSB-based	38.2 / 0.92	28.7 / 0.86	26.8 / 0.82	0.35	2.8
DCT-based	39.5 / 0.94	29.5 / 0.87	27.6 / 0.83	0.40	2.4
CNN-based Autoencoder	40.1 / 0.95	33.1 / 0.91	29.3 / 0.85	0.42	2.5 – 3.0
Proposed Transformer	42.5 / 0.97	36.2 / 0.94	33.5 / 0.91	0.45	1.2

Source: Authors, (2026).

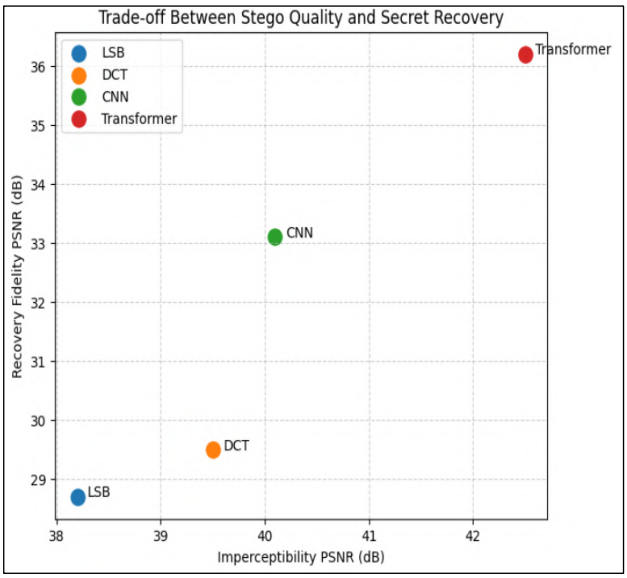


Figure 2: Trade-off between imperceptibility (PSNR of steganography images) and recovery fidelity (PSNR of secret images) across different methods.
Source: Authors, (2026).

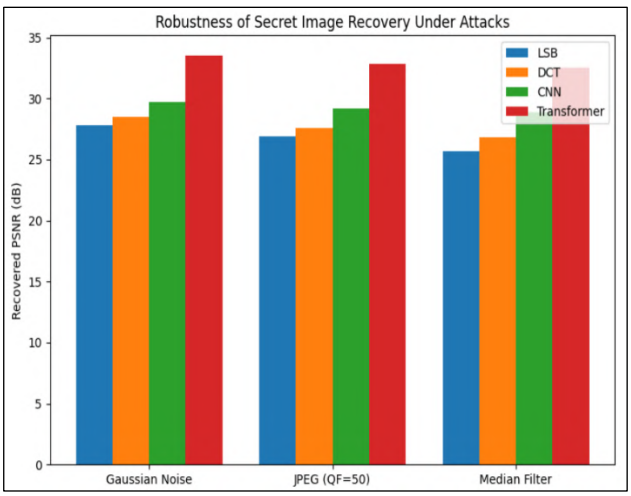


Figure 3: Robustness of secret image recovery under different attack scenarios (Gaussian noise, JPEG compression, and median filtering.
Source: Authors, (2026).

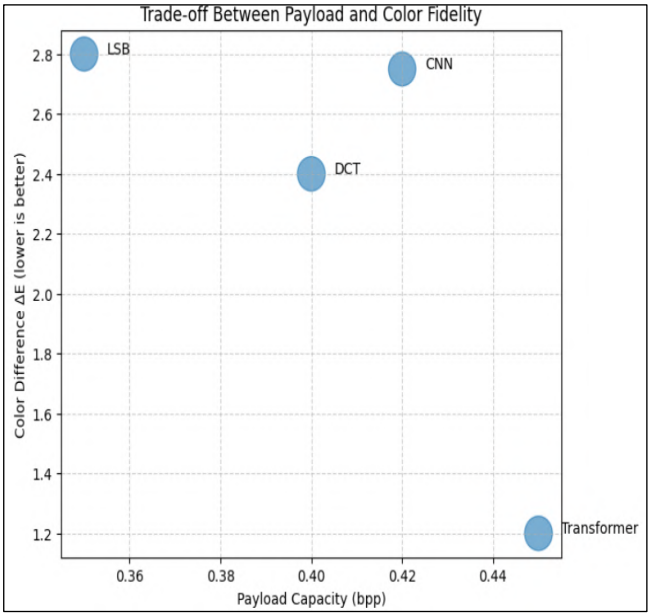


Figure 4: Relationship between payload capacity (bpp) and color fidelity (ΔE).
Source: Authors, (2026).

VI. CONCLUSIONS AND FUTURE WORKS

In this work, we proposed a transformer-based framework for color image hiding that leverages self-attention mechanisms to model inter-channel and spatial dependencies. By embedding secret images through a patch-wise, channel-aware attention process, the framework achieves high imperceptibility, robust recoverability, and substantial payload capacity. Experimental results demonstrate that our approach outperforms traditional spatial- and transform-domain methods, as well as CNN-based deep learning approaches, across key metrics including PSNR, SSIM, CIEDE2000 color fidelity, and robustness against noise, compression, and filtering attacks. The system achieves better visual quality maintenance for steganography images because it can track extended distance connections while intelligently transmitting concealed information. The research presents multiple viable paths for future exploration. The framework needs extension to enable users to work with both high-resolution images and video steganography technology. The system needs to include adversarial training and diffusion-based generative models to achieve better imperceptibility and system protection. Adaptive embedding strategies that use perceptual saliency and content complexity understanding need exploration to achieve better performance and protection. The system requires testing of lightweight transformer models and model compression methods to enable operation on devices with limited processing power.

VII. AUTHOR'S CONTRIBUTION

Conceptualization: Taha Y. Abdulqader, Shatha A. Baker, Kifaa Hadi Thanoon and Yaarob Younus Al-Badrani.
Methodology: Taha Y. Abdulqader, Shatha A. Baker and Kifaa Hadi Thanoon.
Investigation: Taha Y. Abdulqader, and Shatha A. Baker.
Discussion of results: Taha Y. Abdulqader, Shatha A. Baker and Kifaa Hadi Thanoon.
Writing – Original Draft: Taha Y. Abdulqader.
Writing – Review and Editing: Taha Y. Abdulqader and Shatha A. Baker.
Resources: Shatha A. Baker.
Supervision: Shatha A. Baker and Kifaa Hadi Thanoon.
Approval of the final text: Taha Y. Abdulqader, Shatha A. Baker and Kifaa Hadi Thanoon.

VIII. REFERENCES

[1] W. Tang, S. Tan, B. Li, and J. Huang, "Automatic steganographic distortion learning using a generative adversarial network," IEEE Signal Processing Letters, vol. 24, no. 10, pp. 1547–1551, 2017, doi: 10.1109/LSP.2017.2745572.

[2] S. A. Baker, K. H. Thanoon, M. N. Abed, M. Almansor, T. Y. Abdulqader, and O. I. Alsaif, "A Secure and Privacy-Centric Blockchain Platform for Cloud-Based Healthcare Data Management," in *Proc. 2024 International Conference on IT Innovation and Knowledge Discovery (ITIKD)*, IEEE, pp. 1–5, Apr. 2025.

[3] S. J. Rashid, S. A. Baker, O. I. Alsaif, and A. I. Ahmad, "Detecting Remote Access Trojan (RAT) attacks based on different LAN analysis methods," *Engineering, Technology & Applied Science Research*, vol. 14, no. 5, pp. 17294–17301, 2024.

[4] X. Zheng and H. Wu, "Autoregressive linguistic steganography based on BERT and consistency coding," Security and Communication Networks, vol. 2022, pp. 1–11, 2022, doi: 10.1155/2022/9092785.

[5] R. Apau, M. Asante, F. Twum, J. Ben Hayfron-Acquah, and K. O. Peasah, "Image steganography techniques for resisting statistical steganalysis attacks: A systematic literature review," PLOS ONE, vol. 19, no. 9, Sep. 2024, doi: 10.1371/journal.pone.0308807.

[6] L. Meng, X. Jiang, and T. Sun, "A review of coverless steganography," Neurocomputing, 2024.

[7] M. Yamni, A. Daoui, and A. A. Abd El-Latif, “Efficient color image steganography based on new adapted chaotic dynamical system with discrete orthogonal moment transforms,” Mathematics and Computers in Simulation, 2024.

[8] S. Rahman et al., “A novel and efficient digital image steganography technique using least significant bit substitution,” Scientific Reports, 2025, doi: 10.1038/s41598-024-83147-3.

[9] T. Alobaidi and W. M. Alobaidi, “An adaptive steganography insertion technique based on wavelet transform,” Journal of Engineering and Applied Science, vol. 70, no. 1, p. 144, 2023, doi: 10.1186/S44147-023-00300-X.

[10] S. Hesam, O. Hashemi, M. H. Majidi, and S. Khorashadizadeh, “Color image steganography using deep convolutional autoencoders based on ResNet architecture,” arXiv preprint arXiv:2211.09409, 2022.

[11] T. Y. Abdulqader, S. A. Abdulqader, and S. A. Baker, “Enhancing Image Recognition with Quaternion Neural Networks: A Novel Approach to Color Layer Integration,” *Journal of Image and Graphics*, vol. 13, no. 2, 2025.

[12] K. A. Zhang, A. Cuesta-Infante, L. Xu, and K. Veeramachaneni, “SteganoGAN: High capacity image steganography with GANs,” arXiv preprint arXiv:1901.03892, 2019.

[13] Z. Wang, M. Zhou, B. Liu, and T. Li, “Deep image steganography using transformer and recursive permutation,” Entropy, vol. 24, no. 7, p. 878, 2022, doi: 10.3390/e24070878.

[14] Y. Zhou, T. Luo, Z. He, G. Jiang, H. Xu, and C. C. Chang, “CAISFormer: Channel-wise attention transformer for image steganography,” Neurocomputing, 2024.

[15] W. Long, X. Zhou, L. Zhang, and S. Gu, “Progressive focused transformer for single image super-resolution,” in Proceedings of the IEEE/CVF Conference on Computer Vision and Pattern Recognition (CVPR), 2025.

[17] S. Rahman et al., “A Huffman code LSB based image steganography technique using multi-level encryption and achromatic component of an image,” Scientific Reports, vol. 13, p. 14183, 2023, doi: 10.1038/s41598-023-41303-1.

[19] K. S. Rekha, M. J. Amali, M. Swathy, M. Raghini, and B. P. Darshini, “A steganography embedding method based on CDF-DWT technique for data hiding application using Elgamal algorithm,” Biomedical Signal Processing and Control, 2023.

[20] V. Himthani, V. S. Dhaka, M. Kaur, G. Rani, M. Oza, and H. N. Lee, “Comparative performance assessment of deep learning based image steganography techniques,” Scientific Reports, vol. 12, p. 16895, 2022, doi: 10.1038/s41598-022-17362-1.

[21] Y. M. Younis, R. J. Mstafa, and A. L. D. Shamal, “AttenHideNet: A novel deep learning-based image steganography method using a lightweight U-Net with soft attention,” Applied Soft Computing, 2025.

[22] A. Dosovitskiy et al., “An image is worth 16×16 words: Transformers for image recognition at scale,” in International Conference on Learning Representations (ICLR), 2021.

[23] J. Liang, J. Cao, G. Sun, K. Zhang, L. Van Gool, and R. Timofte, “SwinIR: Image restoration using Swin transformer,” in Proceedings of the IEEE/CVF International Conference on Computer Vision Workshops (ICCVW), 2021.

[16] [4] F. S. Hamid, T. A. Jasim, and R. G. Alsultan, “Vehicular-to-Everything (V2X) Communication Using 5G NR for Autonomous Vehicles,” Journal of Engineering, vol. 2026, no. 1, Art. no. 8643947, 2026.S.

[18] P. Fan, H. Zhang, and X. Zhang, “Adaptive QIM with minimum embedding cost for robust video steganography on social networks,” IEEE Transactions on Information Forensics and Security, 2022.

[24] Y. Xu, C. Mou, Y. Hu, J. Xie, and J. Zhang, “Robust invertible image steganography,” in Proceedings of the IEEE/CVF Conference on Computer Vision and Pattern Recognition (CVPR), 2022.

[25] X. Jin, C. Pan, Z. Cheng, Y. Dong, and Q. Jiang, “RIHINNet: A robust image hiding method against JPEG compression based on invertible neural network,” IET Image Processing, vol. 18, no. 13, pp. 3801–3814, Nov. 2024, doi: 10.1049/IPR2.13209.

[26] T. Y. Lin et al., “Microsoft COCO: Common objects in context,” in Computer Vision – ECCV 2014, vol. 8693 LNCS, pp. 740–755, 2014, doi: 10.1007/978-3-319-10602-1_48.

[27] E. Agustsson and R. Timofte, “NTIRE 2017 challenge on single image super-resolution: Dataset and study,” in Proceedings of the IEEE Conference on Computer Vision and Pattern Recognition Workshops (CVPRW), 2017.

Journal of Engineering and Technology for Industrial Applications

ITEGAM-JETIA

Manaus, v.12 n.60, p.1074-1086 July/August, 2026.
DOI: https://doi.org/10.5935/jetia.v12i60.3972

ISSN ONLINE: 2447-0228

RESEARCH ARTICLE OPEN ACCESS

AGENT- AI BASED FRAMEWORK FOR GREEN ROUTE: ENHANCING TRAVEL USING BEST PATHFINDING WITH SSFS AND SE-TDT-SVM THROUGH AQI-AWARE ROUTING

Alamelu R M[1], Christy Eunaicy J I[2], Jayapratha C[3], Govindaprabhu G B[4], Mahalakshmi Priya R[5]

[1]Assistant Professor, Department of Computer Science, Sri sarada Niketan College for Women, Amaravathi pudur, Karaikudi. Tamilnadu, India.
[2]Assistant Professor, Department of Computer Application, Thiagarajar College, Madurai, Tamilnadu, India.
[3]Professor and Head of the Department, Department of Computer Science, Karpaga Vinayaga College of Engineering and Technology, Madhuranthagam, Tamilnadu, India.
[4, 5]Research Scholar, Madurai Kamaraj University (MKU), Madurai, Tamilnadu, India.

[1]https://orcid.org/0000-0003-2157-8795, [2]https://orcid.org/0000-0003-3371-7422, [3]https://orcid.org/0000-0002-3365-1956, [4]https://orcid.org/0000-0002-2297-3597, [5]https://orcid.org/0000-0002-0591-3744

E-email: alamuinfo@gmail.com, prabhupri.pp@gmail.com, g.p.priya2707@gmail.com

ARTICLE INFO

Article History
Received on: March 08, 2026
Reviewed on: April 08, 2026
Accepted on: July 01, 2026
Published on: July 31, 2026

Keywords:
AQI Prediction,
Dynamic Path Prediction,
AQI Pre-Processing,
SSFS,
SE-TDT-SVM,
AQI-Aware Routing.

ABSTRACT

Air pollution poses significant health risks in urban environments. It necessitating accurate Air Quality Index (AQI) prediction and route planning. In urban environments, it is becoming increasingly important. The importance of managing and mitigating air quality has been highlighted in a various recent study. This work presents a novel approach integrating real-time air quality data with Agent based AI techniques. It predicts AQI levels and recommend low-pollution travel routes in major Indian cities. It proposes a SALP Swarm based Feature Selection (SSFS) algorithm to identify key pollutant indicators. This also proposed a Stacked Ensemble of Tuned Decision Tree and Support Vector Machine (SE-TDT-SVM) for AQI prediction. AQI-Aware Routing (AAR) algorithm optimizes path selection based on both air quality and distance metrics. The SE-TDT-SVM model achieved a prediction accuracy of 94.5% with an error rate of 5.5% on the feature-selected dataset. The AAR algorithm successfully generated multiple path options, balancing travel distance and AQI exposure. This integrated approach offers a robust solution for urban air quality management and health-conscious route planning. The potential applications in smart city initiatives and public health interventions.

Copyright ©2026 by authors and Galileo Institute of Technology and Education of the Amazon (ITEGAM). This work is licensed under the Creative Commons Attribution International License (CC BY 4.0).

I. INTRODUCTION

A daily AQI is an index used to assess the status of the atmosphere air. AQI is used to offer individuals with knowledge about how their air quality impacts health. From the report of WHO, air pollution accounts to around 1.3 million deaths per year worldwide. Pollutants discharged into the air are responsible for various harmful effects. Besides acid rain, global warming, and photo-chemical smog, there have been other harmful significance over the past few decades [1]. The health impacts of air pollution have made the prediction and optimal path selection of the AQI increasingly in urban environments.The recent studies have highlighted the urgency of managing and mitigating air quality.The Lancet Planetary Health emphasized that air pollution is one of environmental factors in global disease burdens [2].Approximately 4.5 million premature deaths worldwide were attributed to exposure to fine PM2.5 alone in 2019.It shows the importance of accurate AQI prediction for public health awareness.Furthermore, [3] reports that exposure to high levels of air pollution during daily commutes.It can result in increased blood pressure and reduced lung function. It illustrates the importance of real-time AQI prediction and optimal path selection to minimize exposure during travel. Indian air quality standards index pollutants according to their effects on the atmosphere within a given state or country. The atmosphere is polluted by a variety of gases. Depending on the pollutants measured, there is a different level of pollution. Each pollutant's index is calculated by computing all available data points for each region. AQIs represent air quality in very clear color representations so that a layman can easily comprehend good or bad air quality.

The air quality index can be used to identify major pollutants and locations seriously affected by those pollutants. A number of advanced techniques are used to extract knowledge from data in order to determine the heavily affected area within a region. Air pollution source and state are revealed by the results of the analysis. Models based on agent-based interactions have emerged as powerful tools for simulating complex systems. In the context of air quality and routing, agents can represent vehicles, pedestrians, cyclists, or stationary entities like sensors. By modeling individual behaviors, ABMs enable the study of emergent patterns from interactions among agents and between agents and dynamic environmental conditions, such as air quality variations. For example, an ABM could simulate commuter preferences in route selection depending on variables like travel time, AQI levels, and weather conditions. Additionally, ABMs can predict how large-scale environmental changes, such as increased pollution in an urban center or green corridors, will affect travel patterns. By using simulations, researchers and policymakers can forecast the effectiveness of interventions and ensure their effectiveness.

Objectives

1. To develop an advanced AQI prediction model (SE-TDT-SVM). It integrates real-time data with ML techniques for accurate air quality across major Indian cities.
2. To create a novel Agent Based AQI-Aware Routing (AAR) that optimizes path selection based on both air quality and distance metrics.
3. To implement a comprehensive system that associates AQI prediction with dynamic path selection for urban navigation.

Several dimensions of these findings are relevant in practice. By applying these routes, air pollution is mitigated and public health is safeguarded. In urban India, poor air quality causes numerous health complications. Using this innovative model, elevated pollution levels can be identified. In turn, enhancing atmospheric conditions through the planning of green corridors. Consequently, healthcare expenditures decrease as pollution-related illnesses decline. An urban environment that is more sustainable and economically viable. By incorporating environmental considerations into navigation, the study exemplifies how to integrate smart technologies within urban planning. Such interdisciplinary efforts can foster sustainable and health-promoting urban development. Nguyen et al. [4] predicted PM2.5, which could affect air quality. A genetic algorithm (GA) was used in the research work to predict PM2.5. It assisted feature selection and removed outliers to enhance prediction accuracy. LSTM-based encoder-decoder models were able to predict accurately PM2.5 concentrations. As a result of collecting data for forecasting air pollution, Suganya and Meyyappan [5] proposed guidelines for avoiding and regulating air pollution. In two phases, the research was conducted. Preprocessing the selected dataset was the first step. The second phase involved forecasting air quality levels. Using sensor data, Ditsuhi et al. [6] reviewed the air pollution forecasting studies in smart cities using machine learning algorithms. Instead of using simple machine learning techniques, innovative and sophisticated techniques were applied to conclude the research. Prediction of air quality was influenced by weather conditions, spatial characteristics, and temporal characteristics. Multiple weather stations and air quality metering stations were used by Trenchevski et al. [7] to predict potential improvements in air pollution. Over a number of years, air quality, pollution, and weather data, including temperature, humidity, and wind characteristics, were collected. Work involved features extraction, redundancy removal, training multiple regression models, and hyper parameter optimization. Mahajan et al. [8] developed the CAR (Clean Air Routing) algorithm to build a healthy optimal route suggestion system between the source and destination. The road network was navigated with the least exposure to PM2.5 by using a weight function. A pollution consideration may cause an alternative pathway to exceed the minimum distance.Zahmatkesh et al. [9] suggest that AI-based systems select routes with lower AQI values.Optimizing the path from origin to destination uses Dijkstra's algorithm.

Using machine learning algorithms, the study determines.The comprehensive atmospheric data to estimate PM2.5 concentrations in urban areas.Using Auto Regression, PM2.5 levels will be predicted. Many studies focus on single pollutants, such as PM2.5 [10]. AQI prediction and path selection need to consider multiple pollutants simultaneously The five models were compared using RMSE and MAPE.Both locations showed better performance with bidirectional GRU.IoT-based air quality, humidity, and temperature alert system proposed by P. Tripathi [11] .Particulate matter (PM10 and PM2.5) and carbon monoxide(co) are measured in real time.Real-time data updates are provided by IoT. It generates alerts based on temperature, humidity, and air quality data using fuzzy logic. A study by Chandar et.al [12] used historical AQI data of decade to determine levels, cyclicity, and seasonality. The models used included Random Forest (RF), Support Vector Regression (SVR), XGBoost (XGB), Neural Network (NN), and Long Short-Term Memory (LSTM). Model performance is measured by Mean Absolute Error (MAE) and Root Mean Square Error (RMSE). XGBoost outperforms other models with MAE scores of 7.991 (7-day) and 8.126 (30-day). By combining the strengths of numerous base learners, Singh et.al [13] improve prediction accuracy. Based on decomposed time series components, hybrid ensemble learning uses base learners. Using ensemble aggregation, the final forecast is generated. Results show that the proposed approach outperforms traditional forecasting models and individual base learners for the targeted pollutants. According to Priyanka et al. [14], air quality is monitored and a path with the least amount of pollution is then suggested. In the model, air pollution was instantly reduced for vulnerable populations. In order to calculate the shortest path between source and destination, the Dijkstra algorithm was used. The air quality index was predicted using environmental monitoring data and meteorological data by Zhou et.al [15]. Using a non-linear autoregressive neural network model, an air quality assessment model was enhanced. Using other standard machine learning algorithms, the model was demonstrated to be feasible and to perform well. Khan et.al.[16] investigated bidirectional variations of recurrent neural networks, long short-term memories, and gated recurrent units. Various atmospheric and air pollution variables are represented by 15 variables. The following points are the research gap of the work:

- **Integration of Real-time and Predictive Models**: There is currently a lack of integration between real-time AQI data and predictive models for path selection in studies like Nguyen et al. [4] and Zhou et al. [15]. For route planning, it is necessary to combine up-to-date air quality information with forecasted data.
- **Multi-pollutant Approach**: Many studies focus on single pollutants, such as PM2.5 [10]. AQI prediction and path selection need to consider multiple pollutants simultaneously.

- **Dynamic Path Adjustment**: It is lacking a system that can dynamically adjust paths based on changing air quality conditions in real time, despite the routing algorithms proposed by Mahajan et al. [8]
- **Advanced Machine Learning Techniques**: It would be interesting to explore more advanced ensemble methods or hybrid models combining the strengths of different algorithms to improve ML.
- **Long-term Forecasting and Trend Analysis**: According to Chandar et al., long-term AQI predictions are necessary for better urban planning and policymaking.

II. METHODOLOGY

In Figure 1, the work is intended to monitor and optimize the air quality index forecast. To determine the pollutant levels over time, real-time air pollution data from India's states is acquired. By analyzing and predicting air quality, AQI based on historical and live data, a model can be developed to circumvent the prediction problem. In the work, low AQI will be used as the basis for path selection.

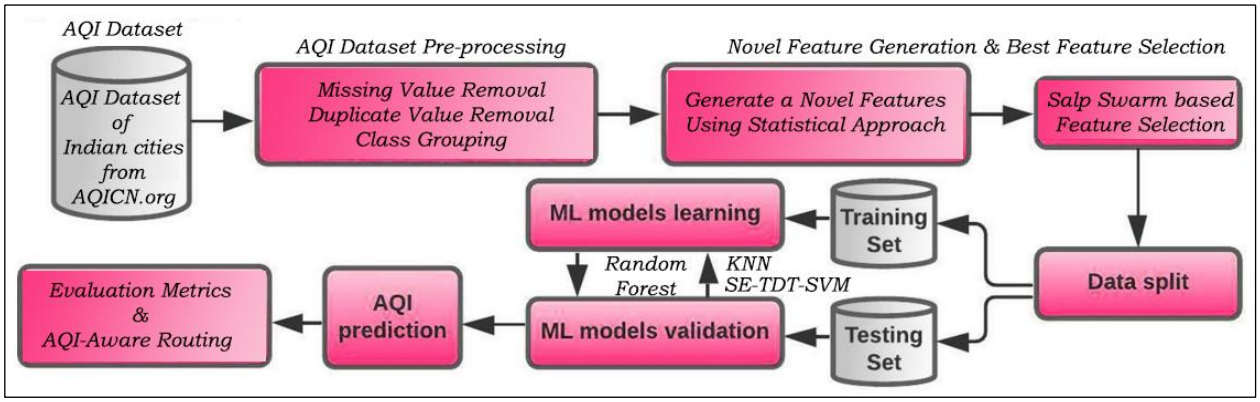


Figure 1: Proposed Framework.
Source: Authors, (2026).

II.1 DATA GATHERING AND CLEANING

Data was collected from aqicn.org, an aggregator of data contributed by government agencies, private companies, and the community. Various locations globally, including major Indian cities, can access this platform for comprehensive and up-to-date air quality information. A 2-year period of historical measurements of air quality is included in the dataset, which covers the period 2022 to 2024. In the study, major Indian cities are examined, such as Jaipur, Chennai, Kochi, etc. Urban air quality conditions are represented geographically by numerous locations on aqicn.org. AQI prediction models require appropriate data in a suitable format. It consists of attributes such as Particulate Matter (PM10), Particulate Matter (PM2.5), Ozone (O3), Sulphur dioxide (SO2), Nitrogen dioxide (NO2), and Carbon monoxide (CO) that are necessary for calculating an area's air quality index. Air Quality Index China (AQICN) data is a foundational component for the AQI-Aware Routing (AAR) algorithm and Agent-Based AI framework. Data from multiple sources, including government agencies, private companies, and community-driven sensor networks, is aggregated by AQICN. With this rich dataset, the algorithm can evaluate pollutant concentrations such as PM2.5, PM10, NO2, SO2, CO, and O3. Its diversity ensures broad coverage, which is crucial for modeling air quality trends and providing real-time AQI predictions. Table 1 displays a sample of data on air pollutants. The AQI dataset for the specific date and city contains air pollutants. In accordance with the 2016 US-EPA Air Quality Index (AQI) standard, there are six levels of air pollution: 0-50 (Good), 51-100 (Moderate), 101-150 (Unhealthy for Sensitive Groups), 151-200 (Unhealthy), 201-300 (Very Unhealthy), and 300+ (Hazardous).

Table 1: Sample Data.

Date	$PM_{2.5}$	PM_{10}	O_3	NO_2	SO_2	CO	City
10/1/2024	89	49	23	18	6	8	Jaipur
10/2/2024	91	58	19	16	7	5	Jaipur
9/1/2024	54	39	16	7	8	4	Jaipur
7/2/2024	64	32	18	11	6	6	Jaipur
9/3/2024	51	68	5	2	1	5	Chennai
8/4/2024	57	52	5	1	2	5	Chennai
9/5/2024	48	28	5	2	2	5	Chennai

Source: Authors, (2026).

Air quality is satisfactory with little or no risk at Good levels. The moderate levels may pose a moderate health concern to those who are very sensitive. Sensitive groups can be affected by levels categorized as Unhealthy. Those with sensitive needs may be more affected by unhealthy levels. Hazardous levels pose serious health risks to everyone, while Very Unhealthy levels carry health warnings for the entire population. Depending on the severity of the AQI, cautionary statements advise children, adults, and those with respiratory conditions to limit or avoid outdoor activities [17]. AQI dataset size is 119198 x 8.

Pre-processing removes 45934 missing and 0 duplicate data, resulting in a total of 45934 missing and 0 duplicate data. Before pre-processing, the AQI dataset is 119198 x 8; after eliminating missing and duplicate values, it becomes 73264 x 8. There are six levels of pollution in the AQI: Good, Satisfactory, Moderate, Poor, Very Poor, and Severe. According to ambient concentrations of pollutants, the pollution levels are classified based on potential health impacts. Six pollutants (PM10, PM2.5, NO2, SO2, CO, O3) are sub-indexed and health breakpoints are developed. The calculation of AQI is based on a sub-index. Equation 1 calculates AQI based on the worst sub-index.

$$I = \frac{Ix_{hi} - Ix_{lo}}{Cn_{hi} - Cn_{lo}}(Cp - Cn_{lo}) + Ix_{lo}$$

II.2 NOVEL FEATURE GENERATION

i. **Ratio of coarse to fine particulate matter (ROC):** This ratio indicates the proportion of larger particles (PM10, diameter ≤ 10 μm) to smaller particles (PM2.5, diameter ≤ 2.5 μm) in the air. Higher ratios indicate particles, whereas lower ratios indicate finer particles, which are generally considered more harmful.

$$ROC = PM_{10}/PM_{2..5}$$

ii. **Ratio of nitrogen dioxide to sulfur dioxide (RNDSD):** This compares levels of two common gaseous pollutants. Generally, if the ratio is higher, combustion sources (e.g., vehicle emissions) are contributing more pollution, while a lower ratio is indicating coal combustion or industrial pollution.

$$RNDSD = NO_2\ /SO_2$$

iii. **Ratio of ozone to nitrogen dioxide (ROND)**: This ratio provides insight into the formation of photochemical smog. A reaction between NOx (including NO2) and volatile organic compounds produces ozone. A higher ratio could indicate more advanced smog formation or more intense sunlight.

$$ROND = O_3/NO_2$$

iv. **Ratio of carbon monoxide to fine particulate matter (RCM)**: The comparison is between a gaseous pollutant (CO) and fine particles. An elevated ratio might indicate more incomplete combustion (e.g., vehicle emissions in cold weather), while a lowered ratio might indicate more secondary particle formation.

$$RCM = CO/PM_{2.5}$$

v. **Ratio of sulfur dioxide to coarse particulate matter (RSD)**: A gaseous pollutant (SO2) is compared to a larger particle (SO2). Higher ratios indicate more industrial or coal-burning pollution than dust.

$$RSD = SO_2/PM_{10}$$

vi. **Total Pollutants**: This sum gives a rough idea of pollution levels, but it does not account for the different units or health impacts of different pollutants.

$$Total\ Pollutants\ =\ PM_{2.5} +\ PM_{10} +\ O_3 +\ NO_2 +\ SO_2 + CO$$

vii. **Average Pollutants**: It provides a metric for averaging all measured pollutants, but has the same limitations as the metric for total pollutants.

$$Average\ Pollutants\ =\ (PM_{2.5} +\ PM_{10} +\ O_3 +\ NO_2 +\ SO_2 + CO)\ /6$$

viii. **Interaction of particulate matter and ozone (IOMO)**: It shows that these two pollutants can cause respiratory issues in synergistic ways.

$$IOMO\ =\ PM_{2.5}\ X\ O_3$$

ix. **Interaction of nitrogen dioxide and carbon monoxide (IONCM)**: The product emphasizes the presence of two pollutants commonly found in vehicle emissions in combination.

$$IONCM\ =\ NO_2\ X\ CO$$

x. **Interaction of particulate matter and sulfur dioxide (IOPMSD)**: The product demonstrates the combination of pollutants found in industrial emissions and dust.

$$ONCM\ =\ PM_{10}\ X\ SO_2$$

xi. **Combined of PM, ozone, and nitrogen dioxide (CPMOND)**: In this triple product, there is potential for complex interactions among these three pollutants.

$$\boldsymbol{PM_{2.5} \times O_3 \times NO_2}$$

xii. **Max Pollutant** This identifies the highest level among all measured pollutants, potentially highlighting the most problematic pollutant.

$$\boldsymbol{Max\ Pollutants\ =\ \max(PM_{2.5}, PM_{10}, O_3, NO_2, SO_2, CO)}$$

xiii. **Minimum pollutant level**: This identifies the lowest level among all measured pollutants.

$$\boldsymbol{Min\ Pollutants\ =\ \min(PM_{2.5}, PM_{10}, O_3, NO_2, SO_2, CO)}$$

xiv. **Range of pollutant levels:** By calculating the spread between the highest and lowest levels of pollution, we can see how pollution levels vary.

$$\boldsymbol{Range\ Pollutants = Max\ Pollutants - Min\ Pollutants}$$

xv. **Variance Pollutants**: This measures the spread of pollutant levels around their mean (μ), providing insight into how much the levels fluctuate.

$$\boldsymbol{Variance\ Pollutants} = \frac{1}{5}(\ (\boldsymbol{PM_{2.5}} - \boldsymbol{\mu})^2) + (\mathbf{PM_{10}} - \boldsymbol{\mu})^2 + (\mathbf{O_3} - \boldsymbol{\mu})^2 + (\mathbf{NO_2} - \boldsymbol{\mu})^2 + (\mathbf{SO_2} - \boldsymbol{\mu})^2 + (\mathbf{CO} - \boldsymbol{\mu})^2)),$$

$$\boldsymbol{Where\ \mu\ is\ the\ mean\ of\ the\ pollutants}.$$

xvi. **Normalized_PM2.5:** By normalizing the PM2.5 level against its maximum value, it is easier to compare different time periods or locations.

$$\boldsymbol{Normalized\_PM2.5} = \boldsymbol{max(PM2.5)/PM2.5}$$

II.3 SALP SWARM BASED FEATURE SELECTION ALGORITHM

By using feature selection, AQI data is evaluated to identify and eliminate inappropriate, redundant, and unnecessary attributes that are not relevant to a predictive model, which can reduce its accuracy. Based on the swarming behavior of salps in the ocean, the Salp Swarm Algorithm (SSA) is a bio-inspired optimization technique. A salp's collective behavior in navigation and foraging is mimicked in order to solve various optimization problems, both single- and multi-objective. SSAs operate by creating a population of salps, each representing a potential solution. Each salp's position is updated iteratively based on its distance from the leader salp and the location of the food source. Position updates for the i-th salp are defined as follows:

$$x_i^j = \begin{cases} F_j + c_1\left(\left(ub_j - lb_j\right)c_2 + lb_j\right), if\ i = 1 \\ \frac{1}{2}(x_i^j + x_{i-1}^j), if\ i > 1 \end{cases}$$

Where F_j is the position of the food source, ub_j and lb_j are the upper and lower bounds of the j-th dimension, c_1 and c_2 are random numbers uniformly distributed between 0 and 1. In model construction, feature selection refers to selecting a subset of relevant features. A salp's position can be treated as a possible subset of features for this purpose by using SSA. In order to select features, first initialize a population of salps randomly within the search space. In each salp, the position in each dimension corresponds to a specific feature. Determine whether a salp is fit by evaluating its classification accuracy, often based on a machine learning model trained with the selected features. Calculate the position of each salp using the SSA mathematical model. Follower salps adjust their positions based on the leader's positioning, while the leader moves towards the best solution. Converge the algorithm (that is, stabilize the salp positions or reach the maximum number of iterations). Optimal subset of features is represented by the best salp at the end of optimization. Feature quality is evaluated using the fitness function. For feature selection, the following fitness function is commonly used:

$$Fitness = \alpha.\,\text{ErrorRate} + (1 - \alpha).\frac{|S|}{|F|}$$

Where Error Rate is the classification error rate, S is the number of selected features, F is the total number of features, and X is the weight factor that balances accuracy and feature reduction. Swarm Algorithms are robust and efficient ways of selecting features in machine learning. SSA improves the performance of machine learning models while reducing computational complexity by leveraging the swarming behavior of salps.

Input: Feature set (AQI Data), Population size N, Max iterations T
Output: Best subset of features
Algorithm: SSA_Feature_Selection
1. Initialize population X with N salps
2. Define fitness function
3. Evaluate fitness of initial population
4. Set food source to the best solution in initial population
5. For t = 1 to T do
  6. For i = 1 to N do
    7. If i == 1 then
      Update leader salp's position using food source
    Else
      Update follower salp's position using previous salp
    End If
    8. Convert continuous positions to binary
    9. Evaluate fitness of salp
    10. If salp's fitness is better than food source fitness then
      Update food source
    End If
  End For
End For
11. Return the best subset of features (position of food source)
End Algorithm

Algorithm 1: SSA_Feature_Selection.
Source: Authors, (2026).

As binary strings encoded as binary salps, each bit represents a potential solution (1 indicates a selected feature, 0 indicates a non-selected feature). Assign random binary strings to a population of salps to represent different subsets of features. A fitness function should be used to evaluate the fitness of each salp. If the salp selects a subset of features, the fitness function could be the accuracy of a machine learning model trained on the subset. Based on the SSA equations, update the salp positions. A binary string is flipped to explore different subsets of features in the context of feature selection. As a result of a predetermined number of iterations, select the salp with the highest fitness value as the optimal subset of features. Utilize the optimal subset of features identified by the SSA to train the final machine learning model.

II.4 STACKED ENSEMBLE OF TUNED DECISION TREE AND SVM MODEL

In the classification techniques, historical data and live data are used to predict a given pollution level. For AQI prediction, the best feature selection algorithm is determined by the feature importance score and selection time. SE-TDT-SVM, a stacked ensemble of Tuned Decision Trees and SVMs, is developed for AQI prediction. As each node contains a classifier, the stacked ensemble model resembles a tree. Various machine learning models are combined into an ensemble model. Based on the output of the base classifier, the meta classifier predicts the final class label. An architecture based on stacked layers is proposed in the work. In Decision Trees (DTs) internal nodes represent attributes being tested, branches represent the results of the tests, and leaf nodes represent class labels. To learn a tree from the DAQI dataset, an attribute value test can be used to recursively separate subsets as shown in equation 6. Recursion ends when all subsets at a node have the same target value. Sorting from the root to a leaf node allows it to classify instances.

$$DT_{root} \xleftarrow{best\ feature} x_i, where\ x_i\ \in S_{Train}\ \forall\ i = 1,2,..n$$

AQI attributes specified by the top node of the tree are tested by the leaves to determine the pollution level based on attribute selection measures. By building the finest boundary that isolates the n-dimensional space into different class labels, the SVM Prediction (Meta) Model algorithm classifies a new instance in the future. A hyperplane denotes this boundary. A hyperplane is created by finding the vector points that play a vital role. The extreme points are called support vectors. AQI prediction is performed using a nonlinear SVM.

$$S_{Test} = \{(x_1, y_1), (x_2, y_2) \ldots (x_n, y_n)\} |\ x_i \in S_{Test}, y_i \in \{very\ poor, severe, satisfactory, poor, moderate, good\}$$

Through STrain and STest, the SVM discovers a distinct hyperplane in the feature set in order to classify the pollution level in Eq7. The DT and SVM models are stacked to produce an efficient classification model that combines individual decision-making. When training with a large dataset, the SVM takes a long time to process and train. The main drawback of SVMs is their long training time. Training huge datasets requires an effective Decision Tree-based data selection and Support Vector Classification approach. A decision tree was built during the training phase to reduce the size of the SVM training dataset. With DT, the number of data dimensions is reduced and features are selected and generated. A stacked prediction model (DT and SVM) is used to classify pollution levels using the AQI dataset. The training set STrain is divided into n sections and taken from the selected features set FB of the AQI dataset. In the nth section, the model makes predictions based on the fitted base classifier model DT. The training set STrain is divided into sections according to this technique. SVM prediction models are trained using the same technique for training and testing sets STrain and STest. The training set is divided into two parts: training and validation. The predictions from the validation set are used to create a new model by combining them with those from the testing set STest. The meta model classifier SVM is then initialized with the kernel function and the parameters are tuned for class label validation. To predict the AQI class label, the STest is used. The parameters of the stacked classifier are shown in Table 2.

Table 2: Parameters of SE-TDT-SVM.

Parameters	Default Value	Tuned Value
Decision Tree (Level 0)		
Max Depth	1	4
Min Samples Leaf	1	5
Min Weight Fraction Leaf	0.0	0.3
Splitter	Random	Best
SVM (Level 1)		
C	1.0	1.0
Coef0	0.1	0.5
ToL	0.0001	0.01
Decision function Shape	OVR	OVO
Kernel	Linear	RBF
Degree	1	4
Gamma	Auto	Scale

Source: Authors, (2026).

This algorithm combines the strengths of multiple machine learning models to predict AQI using the Stacked Ensemble of Tuned Decision Trees and Support Vector Machines (SE-TDT-SVM).

The Decision Tree (DT) excels at handling non-linear relationships and identifying significant features, while the Support Vector Machine (SVM) excels at classification tasks involving complex decision boundaries. With SE-TDT-SVM, DTs preprocess and simplify the dataset by reducing its dimensionality, while SVMs refine the predictions by learning optimal hyperplanes.With high-dimensional datasets like AQICN, ensemble design enhances model accuracy and reduces overfitting. Furthermore, SE-TDT-SVM is parameter tuned to ensure each base model operates at its optimal level. On the feature-selected dataset, this hybrid approach consistently outperforms single algorithms. In dynamic routing systems, SE-TDT-SVM provides a computationally efficient, scalable solution for AQI prediction.

Input: AQI dataset DAQI, Training set S_{Train}, Testing set S_{Test}
Output: Predicted AQI class labels for S_{Test}
Algorithm: SE-TDT-SVM
1. Split the AQI dataset DAQI into training set S_{Train} and testing set S_{Test} .
2. Compute the feature importance scores.
3. Select the best features F_B based on the importance scores.
4. Divide S_{Train} into n sections.
5. For each section i from 1 to n:
    a. Use n−1 sections for training the Decision Tree (DT).
    b. Predict the AQI class labels for the remaining i-th section.
6. Collect predictions for all sections to form the intermediate dataset SDT−Pred.
7. Divide S_{Train} into training and validation sets.
8. Use SDT−Pred and validation predictions as features to train the SVM model.
9. Tune the SVM parameters using the validation set.
10. Use the trained Decision Tree to reduce the dimensions of S_{Test} .
11. Apply the SVM model to predict the AQI class labels for S_{Test} .
12. Output the predicted AQI class labels for S_{Test} .

End Algorithm

Algorithm 2: SE-TDT-SVM.
Source: Authors, (2026).

II.5 DYNAMIC PATH PREDICTION WITH AQI-AWARE ROUTING (DPPAAR) USING AGENT BASED AI

An AQI-Aware Routing (AAR) algorithm for optimal path suggestion is presented in this work, which incorporates both air quality and distance metrics. AAR involves several phases, as shown in Figure 2. For a particular location, the model involves phases such as location profiling and data collection, discovering intermediate cities, computing distances and directions, generating multiple paths, and generating shortest distances with low AQI. [

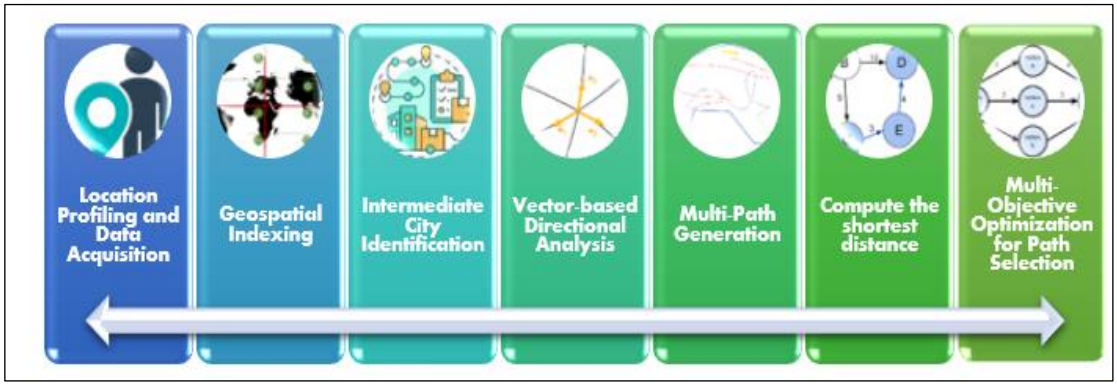


Figure 2: Dynamic Path Selection Process.
Source: Authors, (2026).

During the first phase, 'Location Profiling and Data Acquisition,' let L = [l1, l2, ..., ln] represent the set of locations, where each li represents (ID, NAME, CITY, STATE, LAT, LON). We utilized the AQICN.org API to obtain real-time AQI data in JSON format, which is then parsed and stored as AQI (li, t) = f(PM2.5, PM10, NO2, SO2, CO, O3). The next step is to implement a novel R-tree spatial indexing structure R to efficiently organize cities according to their geographical coordinates. Path finding can be significantly optimized with O (log n) time complexity in nearest neighbor queries. Based on the latitude point information of the specific station, cities are ordered based on their state. By ordering the cities, the optimal path can be recommended. The next phase is an Intermediate City Identification Given a source s and destination d, we define the set of potential intermediate cities I as: $I = \{l_i \in L \mid \min(lat(s), lat(d)) \leq lat(l_i) \leq \max(lat(s), lat(d)) \wedge \min(lon(s), lon(d)) \leq lon(l_i) \leq \max(lon(s), lon(d))\}$. Using the ordered location dataset, the intermediate cities between the user's source and destination are computed. A location dataset is then searched and indexed for the source and destination cities. For a possible path, intermediate cities are acquired between the source and destination cities. Vector-based Directional Analysis is the next phase, which uses vectors to determine the direction between cities. For any two cities a and b, we calculate their direction vector as follows: v(a,b) = (lon(b) - lon(a), lat(b) - lat(a). The angle θ between $\rightarrow$v(a, b) and the positive x-axis determines the cardinal and intercardinal directions. There are four main directions - east, west, north, and south. On all paths, directions are named the same way.

It is not always possible to locate a place accurately using only the four directions. There are clearly sub-directions and scaled directions. Using zone points, this work calculates the distance between two points. Based on the route, the direction-finding offers possible paths between the locations. Multi-Path Generation Using Modified A* Algorithm, this work proposes a modified A* algorithm that incorporates AQI levels into the heuristic function. For each node n, we define: f(n) = g(n) + h(n) + α * q(n). An AQI level at n is related to the distance from the start node to 'n', and the estimated distance from n to the goal is related to the AQI level at n, and the weighting factor is related to the AQI level at n. In order to compute the best path, a multi-path must be generated for the specific location (Tirupati to Bhopal). A dissimilar path is determined by grouping together different directions for a given location after estimating different directions. Therefore, for a specific source and destination, numerous paths exist. The best path is determined by analyzing these various paths. The next step is to calculate the shortest distance between the multipaths, the distance from the source city to the destination city through the intermediate cities should also be determined. As a result, a distance is computed for each path in the multipath set. By computing the distance, the shortest path among the multipaths can be found. To identify the less polluting path for traveling, the AQI for the paths is also calculated after estimating the distance among the multipath cities. This work introduces an AQI exposure metric E for a path P = {$l_1, l_2, ..., ln$}: $E(P) = \sum_{i=1}^{k-1} (AQI(l_i) + AQI(l_{i+1})) / 2 * d(l_i, l_{i+1})$. AQI levels and distance traveled are both taken into account in this metric. Finally, a Multi-Objective Optimization for Path Selection recommendation is computed based on less AQI and shortest distance between source and destination cities. In order to select the final path, we formulate it as a multi-objective optimization problem, where F(P) = (D(P), E(P)), subject to P∈ feasible paths from s to d. In this case, D(P) represents the total distance of path P. An optimization is used to find non-dominated solutions, thereby offering users a range of paths that are both distance-efficient and AQI-efficient.

Input: Set of Locations
Output: Return Shortest Path
Algorithm: AQI-Aware Routing (AAR) Algorithm

1. Define $L = \{l1, l2, \ldots, ln\}$ with each location li represented by $(ID, NAME, CITY, STATE, LAT, LON)$.
2. Acquire AQI data from aqicn.org, store it as: $AQI(li, t) = f(PM2.5, PM10, NO2, SO2, CO, O3)$
3. Build an R-tree spatial indexing structure $\{R\}$ to efficiently organize cities by their coordinates.
4. Order the cities based on state using the latitude point of the station information.
5. Define the source city s and destination city d.
6. Identify the set of potential intermediate cities I as: $I = \{li \in L \mid min(lat(s), lat(d)) \leq lat(li) \leq max(lat(s), lat(d)) and min(lon(s), lon(d)) \leq lon(li) \leq max(lon(s), lon(d))\}$
7. For any two cities a and b, calculate the direction vector: $v(a, b) = (lon(b) - lon(a), lat(b) - lat(a))$
8. Determine the cardinal and inter-cardinal directions based on the angle θ between v(a,b)) and the positive.
9. Use a modified A* algorithm incorporating AQI levels into the heuristic function: $f(n) = g(n) + h(n) + \alpha \cdot q(n)$
10. Generate multiple paths from the source to the destination, grouping directions to obtain paths.
11. Compute the AQI exposure metric E for a path $P = \{l1, l2, \ldots, ln\}$:

$$E(P) = i = 1\sum k - 1(2AQI(li) + AQI(li + 1) \cdot d(li, li + 1))$$

13. Formulate the final path selection as a multi-objective optimization problem: $minimize\ F(P) = (D(P), E(P)) subject\ to P \in feasible\ paths\ from\ s\ to\ d$
14. Return Shortest Path

End Algorithm

Algorithm 3: AQI-Aware Routing (AAR) Algorithm.
Source: Authors, (2026).

By combining real-time air quality data with predictive AQI modeling, AQI-Aware Routing (AAR) stands out. Among the unique aspects:

1. Integration of Dynamic Air Quality Index: AQI predictions are constantly updated in AAR. It allows real-time route adjustments.
2. An algorithm that considers multiple air pollutants at the same time provides a more comprehensive analysis of air quality.

Utilizing a new weighting system for air pollution and travel distance, AAR maintains a balance between these objectives. Through Agent-Based AI, AQI-Aware Routing transforms pathfinding into an adaptive, dynamic process. AI-driven autonomous agents make path selection decisions using real-time AQI data and predictive models like SE-TDT-SVM. Multiple factors are balanced by agents to evaluate path options:

- **AQI Exposure Metric (E(P))**: Agents calculate potential exposure to pollutants on each route by leveraging the AAR algorithm's AQI exposure metric,

$$E(P) = \sum_{i=1}^{k-1} \frac{AQI(l_i) + AQI(l_i + 1)}{2} X\ d(l_i, l_i + 1),$$

$$where\ l_i\ represents\ locations\ along\ the\ route$$

- **Travel Distance (D(P))**: AAR uses a multi-objective optimization approach to assess route lengths and tradeoff between minimal distance and low AQI exposure.
- **Real-Time Adjustments**: Agents adaptively adjust path recommendations based on AQI conditions or traffic dynamics as they are changed.

Consider a delivery agent traveling from source s to destination d. It uses AAR to identify intermediate cities I=$\{l_i \in L\}$, calculates directional vectors, and evaluates paths using real-time AQI predictions. The agent recalculates the optimal path using updated data whenever conditions change, such as an increase in AQI near an industrial zone.

III. RESULTS AND DISCUSSION

The experimental simulation environment is Windows -10, a CPU of 2.80GHz, 8GB of memory, and Python programming language. Python was used to implement SSA-based feature selection, utilizing the NumPy library for efficient numerical computations. For stability, the algorithm was run 30 times: 15 out of 22 original features were selected; PM2.5, NO2, and O3 were selected most frequently; Average computational time: 0.9 seconds. With SSA-based feature selection, the model's predictive performance was significantly improved while the feature space was reduced. As a result, we were able to increase the efficiency of our AQI prediction model as well as gain insight into the most influential pollutants for AQI determination in the studied Indian cities. AQI Prediction computes the following evaluation metrics.

III.1 ACCURACY AND ERROR RATE

A machine learning algorithm's accuracy can be determined based on the number of AQI samples that are classified appropriately in relation to the total number of AQI samples [18]. The proposed classifier's accuracy and error rate are shown in Table 3.

Table 3: Evaluation Metrics.

Datasets	Classifiers	Accuracy	Error Rate	Precision	Recall	F1-Score
Processed Dataset	**SE-TDT-SVM**	90.2	9.8	91.6	92.7	92.14
	Random Forest	82.3	17.7	80.1	83.6	81.81
	KNN	79.4	20.6	77.8	79.1	78.44
Feature Selected Dataset	**SE-TDT-SVM**	94.5	5.5	90.8	93.2	91.98
	Random Forest	86.5	13.5	84.6	87.3	85.92
	KNN	81.9	18.1	80.6	81.1	80.84

Source: Authors, (2026).

The accuracy result is shown in figure 3. Error rates (ERRs) are calculated by dividing the number of incorrect AQI predictions by the total number of datasets analyzed.

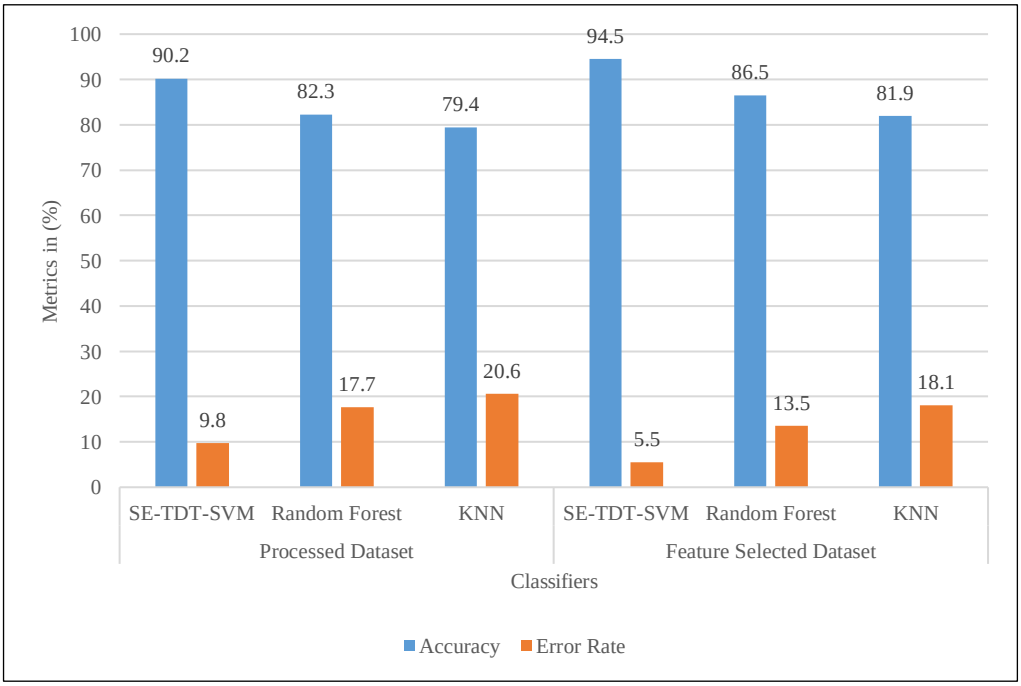


Figure 3: Accuracy and Error Rate.
Source: Authors, (2026).

In figure 4, three classifiers are compared using two datasets: Processed and Feature Selected. For each classifier, it displays Precision, Recall, and F1-Score. A nearly perfect score was achieved with SE-TDT-SVM across both datasets. In the Feature Selected dataset, Random Forest and KNN also show good performance. According to the figure, all three metrics generally show higher values after feature selection, illustrating how feature selection impacts classifier performance.

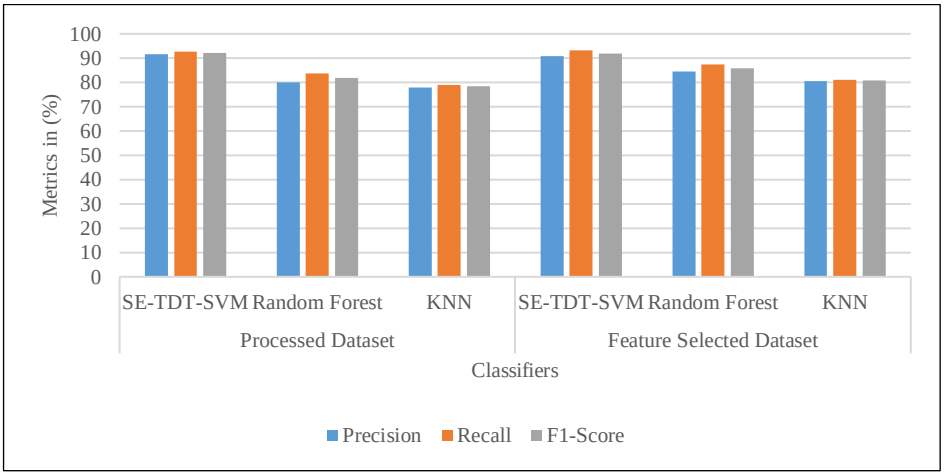


Figure 4: Precision, Recall and F1-score.
Source: Authors, (2026).

SSA-TDT-SVM integration benefits computation in several ways:

1. **Reduced Complexity:** SSA eliminates redundant and irrelevant features, reducing dimensionality of the dataset [19], which reduces SE-TDT-SVM computational load.
2. **Improved Training Efficiency:** SE-TDT-SVM reduces training time by focusing on the most relevant data in the dataset, rather than processing raw, high-dimensional data [20].
3. **Enhanced Predictive Accuracy:** SE-TDT-SVM's ensemble nature ensures robust predictions, while SSA's optimization enhances generalizability.
4. **Scalability:** The algorithms are computationally efficient, enabling real-time processing of large datasets.

AQICN API data was also used to validate the model's predictions. By doing this, the system was tested for its ability to adjust predictions and routing recommendations dynamically. The real-time validation scenarios were:

- Industrial activities or weather changes spike pollution.
- Urban AQI levels vary during the day and night.

Actual AQI values were compared with predictions. Model accuracy was high, with deviations generally below 5%, demonstrating practical applicability. In accordance with the Predicted AQI, the optimal path and shortest distance are recommended to the user. Example: Tirupati is the source city, Bhopal is the destination city. The evaluation of path-1 for the given source and destination city with distance and AQI value is shown in Figure 5.

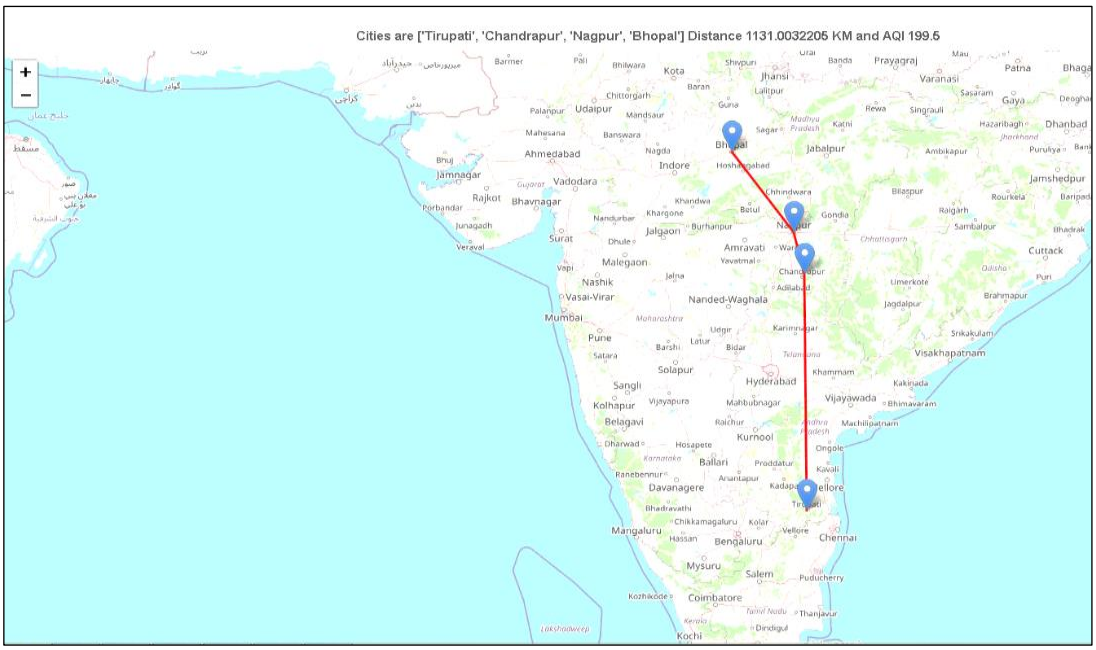


Figure 5: Shortest Path-1.
Source: Authors, (2026).

Figure 6 shows the possible path-2 for the source city (Tirupati) to the destination city (Bhopal) with the evaluated value of distance and AQI.

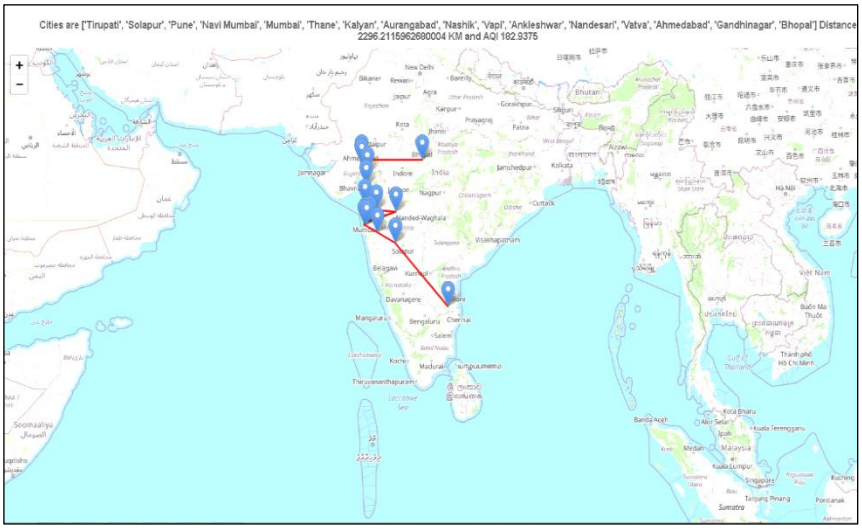


Figure 6: Shortest Path-2.
Source: Authors, (2026).

The possible path-3 for the source and destination city based on distance and AQI is shown in Figure 7. Advantages of this work are, real-time AQI data are used from AQICN.org and integrated with a predictive model (SE-TDT-SVM) for AQI forecasting.

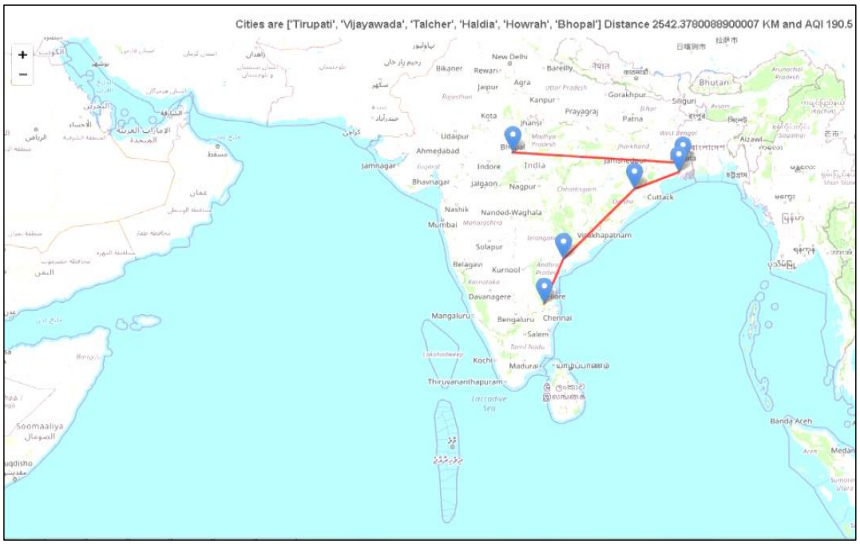


Figure 7: Shortest Path-3.
Source: Authors, (2026).

With this combination, path selection can be made more accurate and up-to-date, bridging the gap between real-time data and predictive modeling. AQI calculations consider multiple pollutants (PM2.5, PM10, NO2, SO2, CO, O3), providing a more comprehensive assessment of air quality than single-pollutant analyses. The AQI-Aware Routing (AAR) algorithm appears to allow for dynamic path selection based on current AQI levels, which is an improvement over static routing. With the SE-TDT-SVM model, decision trees and SVMs are combined in a stacked ensemble that could potentially outperform single algorithms in AQI prediction.

III.2 COMPARATIVE ANALYSIS WITH STATE-OF-THE-ART ROUTING MODELS

Air Quality-Aware Routing (AAR) algorithm is benchmarked against several air quality-integrated routing models, showing distinct advantages in adaptability and comprehensiveness. Mahajan et al.'s and Hameed [21] Clean Air Routing (CAR) algorithm minimizes PM2.5 exposure using a weighted function that prioritizes air quality over distance. However, CAR lacks a multi-pollutant approach and dynamic adaptability. AAR incorporates multiple pollutants (PM2.5, PM10, NO2, SO2, CO, O3) and leverages real-time AQI updates to enable dynamic path adjustments. This ensures AAR's responsiveness to sudden environmental changes, a key limitation of CAR. Dijkstra's algorithm and sensor data are used in Zahmatkesh et al., Zhang [22] and Zou [23] urban travel routing system. It focuses primarily on urban environments with dense sensor coverage by factoring AQI as a parameter. The method relies on static data and does not optimize for multi-objective decision-making. AQI trends are forecasted using SE-TDT-SVM, an algorithm that incorporates predictive modeling with a multi-objective optimization framework to balance travel distance and pollution exposure [24]. This IoT-enabled path recommendation system [25] and [26] uses real-time AQI updates, but is tailored to small-scale environments with limited geospatial adaptability. Using advanced spatial indexing techniques, including R-trees, the AAR algorithm exceeds this by computing routes efficiently across diverse regions. Furthermore, its agent-based structure allows for personalized recommendations, such as prioritizing health-conscious routes or optimizing logistics pathways.

Potential Real-World Applications

i. Smart City Navigation Systems: Promoting healthier routes for pedestrians, cyclists, and drivers by integrating city-wide navigation apps.
ii. Urban Planning and Policy Making: Assess the impact of urban development projects on air quality and assist city planners in improving air quality.
iii. Logistics and Delivery Optimization: Air pollution exposure can be minimized by helping delivery companies plan routes.
iv. Emergency Response Planning: During pollution-related crises, assist emergency services in planning safe routes.

IV. CONCLUSION

By combining the AQI predictions with optimal path selection, the SE-TDT-SVM model achieved an accuracy rate of 94.5% and a precision rate of 5.5% respectively. A feature-selected dataset showed KNN to outperform Random Forest (81.9%). Routes can be optimized based on real-time AQI data to improve urban health. Pollution exposure and travel efficiency are balanced, and hotspots are identified. As a result, pollution exposure is reduced for individuals with respiratory conditions. The algorithm should be improved and its applicability extended in future research. For assessing effectiveness, real-world deployment and user feedback are crucial. As a result of this integrated approach to AQI prediction and path optimization, urban air quality challenges are addressed in a meaningful way. Increasing urbanization and air quality concerns will make smart, health-focused solutions increasingly vital to promoting public health and urban sustainability. In the future, research should explore the incorporation of real-time data feeds and the possibility of deploying the solution as a mobile application for dynamic path recommendations. The results of this work illustrate the critical role that advanced machine learning techniques can play in enhancing urban air quality management and public health protection.

V.AUTHOR CONTRIBUTION

Conceptualization: Alamelu, Christy Eunaicy, Jayapratha.
Methodology: Govindaprabhu, Mahalakshmi Priya.
Investigation: Alamelu, Christy Eunaicy, Jayapratha.
Discussion of results: Alamelu, Christy Eunaicy, Jayapratha.
Writing – Original Draft: Alamelu, Christy Eunaicy, Jayapratha.
Writing – Review and Editing: Govindaprabhu, Mahalakshmi Priya.
Resources: Alamelu, Christy Eunaicy, Jayapratha.
Supervision: Alamelu, Christy Eunaicy, Jayapratha.
Approval of the final text: Alamelu R M, Christy Eunaicy J I, Jayapratha C, Govindaprabhu G B, Mahalakshmi Priya R.

VI.REFERENCES

[1] R. Ghorani Azam, P. Riahi-Zanjani, and A. Balali-Mood, "Effects of air pollution on human health and practical measures for prevention in Iran," J. Res. Med. Sci., vol. 21, no. 1, p. 65, 2016, doi: 10.4103/1735-1995.189646.

[2] D. Tang, Y. Zhan, and F. Yang, "A review of machine learning for modeling air quality: Overlooked but important issues," Atmos. Res., vol. 300, no. 1, pp. 1–10, 2024, doi: 10.1016/j.atmosres.2024.107261.

[3] L. Zhang, X. Chen, and X. Xue, "Short-term personal exposure to particulate matter and lung function in healthy adults: A panel study in Beijing, China," Sci. Total Environ., vol. 89, no. 1, pp. 1–10, 2024, doi: 10.1016/j.scitotenv.2023.165080.

[4] M. H. Nguyen, K. Nguyen, and Y. Ji, "PM2.5 prediction using genetic algorithm-based feature selection and encoder-decoder model," IEEE Access, vol. 9, pp. 57338–57350, 2021, doi: 10.1109/ACCESS.2021.3106548.

[5] S. Suganya and T. Meyyappan, "Forecasting and prediction of air pollution levels to protect human beings from health hazards," Int. J. Sci. Technol. Res., vol. 9, no. 1, pp. 2541–2545, 2020.

[6] D. Istephan, R. Francisco, and T. Sergio, "Air quality prediction in smart cities using machine learning technologies based on sensor data: A review," Appl. Sci., vol. 10, no. 7, pp. 1–32, 2020, doi: 10.3390/app10072401.

[7] A. Trenchevski, M. Kalendar, and H. Gjoreski, "Prediction of air pollution concentration using weather data and regression models," in Proc. 8th Int. Conf. Appl. Innov. IT (ICAIIT), 2020, vol. 8, no. 1, pp. 55–61.

[8] S. Mahajan, Y. S. Tang, D. Y. Wu, and T. C. Tsai, "CAR: The clean air routing algorithm for path navigation with minimal PM2.5 exposure on the move," IEEE Access, vol. 7, pp. 147373–147382, 2019, doi: 10.1109/ACCESS.2019.2946419.

[9] H. Zahmatkesh, M. Saber, and M. Malekpour, "New method for urban travel route planning based on air pollution sensor data," Curr. World Environ., vol. 83, no. 10, pp. 1–10, 2015, doi: 10.12944/CWE.10.

[10] C. R. Aditya, R. Chandana, and D. K. Nayana, "Detection and prediction of air pollution using machine learning models," Int. J. Eng. Trends Technol., vol. 59, no. 4, pp. 204–207, 2018, doi: 10.14445/22315381/IJETT-V59P238.

[11] P. Tripathi, A. Pal, V. Kumar, and N. K. Sharma, "Implementation and study of fuzzy-based IoT-enabled health alert system using AQI," in Proc. Int. Conf. IoT, Commun. Autom. Technol. (ICICAT), Gorakhpur, India, 2023, pp. 1–6, doi: 10.1109/ICICAT57735.2023.10263668.

[12] B. S. Chandar, P. Rajagopalan, and P. Ranganathan, "Short-term AQI forecasts using machine/deep learning models for San Francisco, CA," in Proc. IEEE 13th Annu. Comput. Commun. Workshop Conf. (CCWC), Las Vegas, NV, USA, 2023, pp. 402–411, doi: 10.1109/CCWC57344.2023.10099064.

[13] A. Singh, P. Soni, and D. Krishnan, "Ensemble learning with hybrid modeling for multivariate AQI, PM2.5, and PM10 forecasting in Mumbai," in Proc. Int. Conf. Comput. Sci. Emerg. Technol. (CSET), Bangalore, India, 2022, pp. 1–7, doi: 10.1109/CSET58993.2023.10346745.

[14] P. Phadtare, S. K. Singh, S. Karanjkar, S. P. Kulkarni, and S. R. Hiray, "Intelligent navigation system using air quality index," Int. Res. J. Eng. Technol. (IRJET), vol. 5, no. 5, pp. 772–775, 2018.

[15] Y. Zhou, S. De, E. Gawa, C. Perera, and K. Moessner, "Data-driven air quality characterization for urban environments: A case study," IEEE Access, vol. 6, pp. 77996–78006, 2018, doi: 10.1109/ACCESS.2018.2884647.

[16] D. Khan, A. B. Patankar, R. Motwani, and A. Ailsinghani, "Investigating efficacy of RNN and its variants for AQI forecasting," in Proc. Int. Conf. Adv. Comput., Commun. Inf. Technol. (ICAICCIT), Faridabad, India, 2023, pp. 1303–1307, doi: 10.1109/ICAICCIT60255.2023.10465781.

[17] G. B. Govindaprabhu and M. Sumathi, "Ethnomedicine of indigenous communities: Tamil traditional medicinal plants leaf detection using deep learning models," Procedia Comput. Sci., vol. 235, no. 1, pp. 1135–1144, 2024, doi: 10.1016/j.procs.2024.04.108.

[18] G. B. Govindaprabhu and M. Sumathi, "Safeguarding humans from attacks using AI-enabled (DQN) wild animal identification system," Int. Res. J. Multidiscip. Scope (IRJMS), vol. 5, no. 3, pp. 285–302, 2024, doi: 10.47857/irjms.2024.v05i03.0697.

[19] N. S. Gupta, Y. Mohta, K. Heda, R. Armaan, B. Valarmathi, and G. Arulkumaran, "Prediction of air quality index using machine learning techniques: A comparative analysis," J. Environ. Public Health, vol. 2023, pp. 1–26, Jan. 2023, doi: 10.1155/2023/4916267.

[20] Md. M. Islam, F. A. Jibon, M. M. Tarek, M. H. Kanchan, and S. U. P. Shakil, "A real-time dataset of air quality index monitoring using IoT and machine learning in the perspective of Bangladesh," Data Brief, vol. 55, p. 110578, Jun. 2024, doi: 10.1016/j.dib.2024.110578.

[21] S. Hameed, A. Islam, K. Ahmad, S. B. Belhaouari, J. Qadir, and A. Al-Fuqaha, "Deep learning-based multimodal urban air quality prediction and traffic analytics," Sci. Rep., vol. 13, no. 1, Dec. 2023, doi: 10.1038/s41598-023-49296-7.

[22] Z. Zhang, S. Zhang, C. Chen, and J. Yuan, "A systematic survey of air quality prediction based on deep learning," Alexandria Eng. J., vol. 93, pp. 128–141, Mar. 2024, doi: 10.1016/j.aej.2024.03.031.

[23] B. Zou, S. Li, Z. Zheng, B. F. Zhan, Z. Yang, and N. Wan, "Healthier routes planning: A new method and online implementation for minimizing air pollution exposure risk," Comput. Environ. Urban Syst., vol. 80, p. 101456, Jan. 2020, doi: 10.1016/j.compenvurbsys.2019.101456.

[24] L.-N. Gao, "A short-distance healthy route planning approach," J. Transp. Health, vol. 24, p. 101314, Dec. 2021, doi: 10.1016/j.jth.2021.101314.

[25] B. Sarkar, D. Mukherjee, J. Mukherjee, and S. Sinha, "Traffic optimization and route detection based on air quality and pollution level," in Proc. IEEE 11th Int. Conf. Commun. Syst. Netw. Technol. (CSNT), Apr. 2024, pp. 1203–1208, doi: 10.1109/CSNT60213.2024.10545817.

[26] Shreyank, S. Kumar V., Shashwath, V. T., and P. T. C., "Safe route prediction based on AQI and machine learning," in Proc. Int. Conf. Netw., Multimedia Inf. Technol. (NMITCON), Bengaluru, India, 2023, pp. 1–7, doi: 10.1109/NMITCON58196.2023.10275929.

Journal of Engineering and Technology for Industrial Applications

ITEGAM-JETIA

Manaus, v.12 n.60, p.1087-1100 July/August, 2026.
DOI: https://doi.org/10.5935/jetia.v12i60.3974

ISSN ONLINE: 2447-0228

RESEARCH ARTICLE OPEN ACCESS

PREDICTIVE QUALITY OF SERVICE IN VEHICULAR COMMUNICATION SYSTEMS: MODELS, DATASETS, AND OPEN CHALLENGES

Parita Patel[1], Mahesh Goyani*[2]

[1, 2]Department of Computer Engineering, Gujarat Technological University, Ahmedabad, Gujarat, India.

[1]https://orcid.org/0009-0006-1111-4611, [2]https://orcid.org/0000-0002-7269-1176

E-email: patelparita090@gmail.com, *mgoyani@gmail.com

ARTICLE INFO

Article History
Received on: March 08, 2026
Reviewed on: April 08, 2026
Accepted on: July 01, 2026
Published on: July 31, 2026

Keywords:
Vehicle-to-Everything (V2X),
Quality of Service (QoS),
Predictive QoS,
Machine Learning,
Intelligent Transportation Systems (ITS).

ABSTRACT

Reliable Quality of Service (QoS) prediction is fundamental to the performance of next-generation Vehicle-to-Everything (V2X) communication, particularly in 5G-enabled cloud and edge environments that support autonomous driving, cooperative safety, and time-critical mobility services. This survey provides a structured review of QoS prediction approaches spanning machine learning, deep learning, reinforcement learning, protocol-level evaluation, and security-trust mechanisms. Existing methods are analyzed with respect to their modeling strategies, required datasets, spatio-temporal dependencies, and scalability under high-mobility conditions. A comprehensive dataset survey synthesizes real-world, open-access, and simulation-based resources, highlighting key variables such as SINR, RSRP/RSRQ, mobility patterns, traffic density, delay, and throughput that influence predictive accuracy. The review identifies persistent challenges, including limited multi-modal datasets, poor cross-scenario generalization, computational overhead, weak interpretability, and the absence of unified multi-metric prediction frameworks. Based on these insights, the paper outlines promising research directions for developing adaptive, explainable, and privacy-preserving QoS prediction models for emerging 5G/6G V2X systems.

Copyright ©2026 by authors and the Galileo Institute of Technology and Education of the Amazon (ITEGAM). This work is licensed under the Creative Commons Attribution International License (CC BY 4.0).

I. INTRODUCTION

The rapid evolution of vehicular communication systems, supported by 5G and emerging 6G infrastructures, has accelerated the development of Cooperative Intelligent Transportation Systems (C-ITS). Vehicle-to-Everything (V2X) communication enables continuous information exchange among vehicles, roadside infrastructure, pedestrians, and cloud-edge platforms to support safety-critical applications such as collision avoidance, cooperative lane change, platooning, and tele-operated mobility [1] [2].These applications impose stringent Quality of Service (QoS) requirements involving ultra-low latency, high reliability, controlled jitter, and stable throughput. Global deployment of V2X technologies remains uneven. As illustrated in Figure 1, regions such as Europe, the USA, China, and Japan show more mature VANET and C-V2X implementations compared to other regions; this heterogeneity stems from differences in spectrum allocation, regulatory readiness, infrastructure investment, and industry adoption [3]. Such diversity complicates the design of QoS prediction models that must generalize across different operational environments and mobility patterns. The integration of 5G New Radio (NR) and Multi-access Edge Computing (MEC) provides foundational support for meeting V2X QoS targets by enabling ultra-reliable low-latency communication (URLLC), high-capacity links, and distributed computation near vehicles [4], [5]. Nonetheless, wireless channels and topologies in vehicular settings remain highly dynamic due to mobility. obstruction dynamics, multi-path fading, and network load fluctuations [6], [7]. As a result, traditional reactive QoS mechanisms are often inadequate for many safety-critical V2X services.

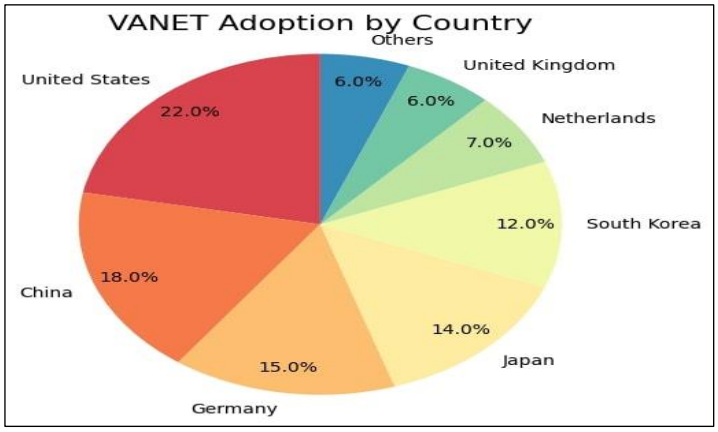


Figure 1: Global adoption of VANET/C-V2X deployments by region.
Source: Authors, (2026).

Predictive QoS (PQoS) methods forecast future network behavior (e.g., latency, throughput, packet loss, signal quality) so systems can proactively allocate resources, schedule traffic, or adapt application behavior. Data-driven paradigms such as machine learning (ML), deep learning (DL), and reinforcement learning (RL) have been widely adopted for PQoS because they can capture nonlinear spatio-temporal relationships between mobility traces, radio KPIs (SINR, RSRP/RSRQ, CQI), traffic density, and application demand [6], [7], [8], [9], [10]. Complementary protocol-and simulation-based studies provide system-level insights into routing, scheduling, channel coding, and cross-layer interactions that affect end-to-end QoS [11], [12], [13]. Security- and trust-oriented frameworks (e.g., blockchain, federated learning, reputation systems) address adversarial and privacy concerns that can critically impact QoS in distributed V2X settings [14], [15]. Despite considerable progress, key challenges persist : (i) scarcity of large-scale, multi-modal, and geographically diverse datasets that combine radio, mobility, and application-level traces [16], [17]; (ii) limited cross-scenario generalization when models are trained on region-specific traces; (iii) computational and energy constraints that limit on-board deployment of complex DL/RL models; and (iv) lack of standardized multi-metric benchmarks and limited interpretability of many black-box models [7], [18], [19]. These gaps motivate a structured survey that consolidates techniques, datasets, and open issues to guide future research. The primary contributions of this research work are summarized as follows:

- This survey presents a comprehensive and structured analysis of Perceived Quality of Service (PQoS) evaluation approaches. First, it introduces a unified taxonomy that categorizes PQoS techniques into ML and DL based methods, protocol and simulation-based approaches, as well as security and trust-oriented frameworks.
- Second, the study provides a critical synthesis of these approaches by examining algorithmic trade-offs, model complexities, and feature dependencies that influence PQoS prediction and assessment.
- Third, a dataset-centric review is conducted to identify commonly used datasets, highlight key variables utilized for PQoS modeling, and discuss the inherent limitations and gaps present in existing datasets.
- Fourth, the survey consolidates major research challenges, including issues related to model generalization, interpretability, real-time feasibility, and system security.
- Finally, the paper outlines a roadmap for future research, emphasizing the need for multi-metric evaluation frameworks, explainable PQoS prediction models, and privacy-preserving intelligent systems for next-generation network environments.

A. Intended Audience

This survey is intended to support academic researchers, industry practitioners, and graduate students working in the domains of vehicular communication, wireless networking, and QoS prediction. By providing a comprehensive review of Predictive QoS (PQoS) techniques for V2X communication, the survey aims to offer valuable insights for network engineers, data scientists, and system designers who seek to develop efficient and reliable vehicular communication systems. The contributions presented in this survey will also benefit researchers from interdisciplinary fields, including intelligent transportation systems, edge computing, machine learning, and 5G/6G system design, by helping them understand the evolving landscape of dataset-driven, learning-based PQoS models. Furthermore, the challenges and future research directions discussed in this paper are expected to guide prospective researchers in identifying open issues and establishing meaningful technical objectives to advance the field and address existing research gaps.

B. Survey Methodology

Over the past several years, numerous studies have explored QoS optimization and performance modeling in vehicular communication systems. However, many of these works primarily emphasize traditional QoS management, statistical models, or protocol-level enhancements, while only a limited number examine predictive QoS (PQoS) using machine learning, deep learning, or reinforcement learning techniques. Furthermore, recent PQoS contributions, particularly those incorporating mobility-aware prediction, cross-layer metrics, and 5G/6G edge intelligence, were excluded from earlier surveys. As a result, it is essential to include updated studies to accurately assess the current state of PQoS research. Additionally, previous surveys often focus on narrow aspects of V2X communication, such as routing, channel modeling, or general QoS analysis, without providing a unified overview of learning-based prediction frameworks. In this context, the literature was examined to address the following research questions:
1. What is the current understanding of QoS requirements in V2X communication, and why is predictive QoS necessary? This question aims to clarify the motivation for PQoS in highly dynamic vehicular environments. The corresponding discussion appears in the section titled “QoS Fundamentals and Motivation for Predictive QoS.”

2. Which machine learning, deep learning, reinforcement learning, and protocol-based models have been developed for QoS prediction in V2X networks? This survey provides a detailed overview of PQoS methodologies developed over the past decade.

3. What datasets support PQoS prediction research in V2X systems? The section "Dataset Survey and Variable Mapping" summarizes available real-world, simulation-based, and open-access datasets along with their relevance to prediction tasks.

4. What metrics and indicators are used to evaluate PQoS models? The section "Analysis and Discussion" presents commonly used evaluation metrics such as RMSE, MAE, MAPE, accuracy, and latency prediction error.

5. What limitations and research gaps exist in current PQoS studies? These issues are highlighted in the "Challenges and Future Directions" section.

By addressing these questions, this survey provides a holistic understanding of the state-of-the-art in predictive QoS for V2X communication and highlights key gaps that offer opportunities for future research.

C. Search Strategy

The databases listed in Table 1 were used to identify relevant journal articles and conference papers published by top publishers

Table 1: Academic databases used for the literature search.

Academic Database	Link
IEEE Xplore	https://ieeexplore.ieee.org/
ACM Digital Library	https://dl.acm.org/
ScienceDirect (Elsevier)	https://www.sciencedirect.com/
SpringerLink	https://link.springer.com/
Wiley Online Library	https://onlinelibrary.wiley.com/
MDPI	https://www.mdpi.com/
Taylor & Francis Online	https://tandfonline.com/
Scopus	https://www.scopus.com/
Google Scholar	https://scholar.google.com/

Source: Authors, (2026).

The initial search keywords were carefully selected to align with the research objectives of this survey. Following a preliminary exploratory search, multiple terms identified in several related PQoS and V2X research papers were analyzed to generate a broader list of candidate keywords. These terms were gradually refined and narrowed to ensure consistency with the core theme of predictive QoS modeling in vehicular communication systems. The final keywords used in this survey include "predictive QoS," "V2X communication," "QoS prediction vehicular networks," "latency prediction V2X," "machine learning QoS prediction," "deep learning QoS modeling," "reinforcement learning QoS optimization," "5G/6G QoS prediction," and "vehicular communication performance prediction."

D. Article Filtering and Selection Methodology

To ensure a rigorous and comprehensive survey of PQoS research in V2X communication, all retrieved publications were systematically screened through a multi-stage filtering process. The initial pool of studies identified from IEEE Xplore, ACM Digital Library, Elsevier, Springer, and Google Scholar was examined by reviewing their titles, abstracts, introductions, and conclusions. Papers that aligned with the core themes of predictive QoS, V2X communication, ML/DL-based prediction, protocol-level QoS mechanisms, dataset development, or security–trust frameworks were included, while studies that fell outside these domains were excluded.

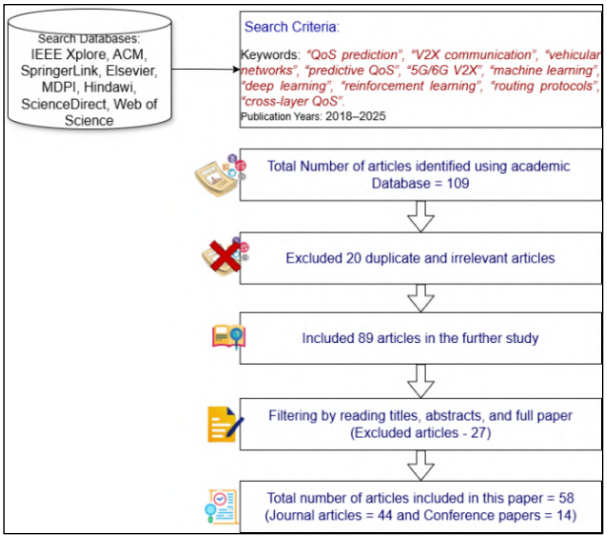


Figure 2: Paper selection procedure.
Source: Authors, (2026).

Figure 2 illustrates the overall article filtering workflow, including identification, screening, eligibility assessment, and final inclusion. To ensure consistency, objective inclusion and exclusion criteria were applied throughout the process. These criteria, summarized in Table 2, guided the evaluation of study relevance, methodological rigor, and applicability to PQoS prediction in vehicular communication systems. This structured filtering ensured that the final set of reviewed papers represents a balanced and comprehensive overview of state-of-the-art PQoS techniques across machine learning, deep learning, reinforcement learning, protocol design, dataset development, and security.

Table 2: Inclusion and exclusion criteria used for paper selection in this survey.

Inclusion criteria	Exclusion criteria
Studies published between 2018 and 2025, reflecting modern 5G/6G-era V2X research.	Papers lacking methodology, experimental setup, QoS metrics, or performance evaluation.
Research focused on V2X/VANET communication, QoS or PQoS prediction, or network performance modeling.	Outdated pre-2018 VANET studies or works unrelated to QoS prediction.
Peer-reviewed studies using ML/DL-based QoS prediction, RL-based resource optimization, routing/protocol QoS enhancement, or cross-layer QoS modeling frameworks.	Security-only papers (cryptography/privacy) without analysis of QoS impact.

Source: Authors, (2026).

I.1 V2X COMMUNICATION FRAMEWORK

The Vehicle-to-Everything (V2X) communication framework provides the foundational architecture required for cooperative intelligent transportation systems by enabling continuous information exchange among vehicles, roadside infrastructure, pedestrians, and cloud or edge networks. V2X consists of four primary communication modalities: Vehicle-to-Vehicle (V2V), which supports distributed safety messaging and localized situational awareness; Vehicle-to-Infrastructure (V2I), where Road-Side Units (RSUs) disseminate traffic, control, and connectivity information [4], [5]; Vehicle-to-Network (V2N), which leverages cellular Uu connectivity and MEC/cloud services for large-scale orchestration and computation [20], [21] ; and Vehicle-to-Pedestrian (V2P), which enhances the safety of vulnerable road users through device-assisted communication [22]. These modalities operate across heterogeneous communication technologies, including IEEE 802.11p/802.11bd, LTE-V2X PC5 sidelink, and cellular Uu interfaces, each offering distinct trade-offs in reliability, latency, and communication range. Prior studies emphasize that hybrid architectures combining PC5 for low-latency direct communication with Uu-based wide-area coordination achieve higher robustness and reliability under dense mobility conditions [5], [23]. RSUs serve as critical components within this framework, functioning not only as connectivity anchors but also as MEC-enabled units capable of supporting real-time QoS prediction, traffic analytics, security enforcement, and localized decision-making [19].

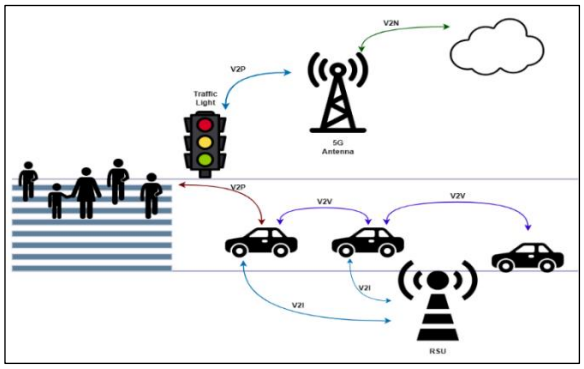


Figure 3: Illustration of the V2X communication framework showing V2V, V2I, V2N, and V2P interactions.
Source: Authors, (2026).

Meanwhile, cloud platforms handle long-term learning, federated model aggregation, and cross-region orchestration to support large-scale V2X intelligence [20]. The integration of emerging 5G and future 6G capabilities—such as URLLC, network slicing, and distributed edge intelligence—further strengthens the V2X communication ecosystem and enables predictive, QoS-driven communication essential for next-generation vehicular networks. Figure 3 demonstrate the framework for V2X communication.

I.2 QUALITY OF SERVICE (QOS) IN V2X COMMUNICATION

Quality of Service (QoS) in vehicular communication refers to the network's ability to deliver predictable, reliable, and efficient performance under highly dynamic mobility and radio conditions. Since V2X applications operate across diverse environments ranging from dense urban intersections to high-speed highways, QoS becomes a fundamental requirement for ensuring safe, stable, and delay-sensitive information exchange. Each V2X modality, including Vehicle-to-Vehicle (V2V), Vehicle-to-Infrastructure (V2I), Vehicle-to-Network (V2N), and Vehicle-to-Pedestrian (V2P), imposes distinct performance constraints based on latency, reliability, throughput, and service continuity [4], [5], [20]. V2X QoS is typically quantified using a set of measurable performance indicators:

- *Latency:* The end-to-end delay between message generation and reception. Safety-critical applications such as collision avoidance demand sub-10 ms latency for reliable execution.
- *Throughput:* The volume of successfully transmitted data per unit time, essential for applications involving high-rate sensor streams, cooperative perception, and teleoperation.
- *Reliability:* The probability of error-free packet delivery, often exceeding 99.999% for mission-critical V2X scenarios.

- *Jitter:* The variation in inter-packet arrival time, which affects the stability of real-time control and cooperative driving applications.
- *Packet Loss Rate:* The fraction of packets lost due to channel impairments, congestion, or mobility; a key metric influencing application stability.
- *Availability:* The percentage of time the communication link remains operational and satisfies service-level requirements.

RSUs, cellular infrastructure, and cloud services collaborate to support low-latency and reliable vehicular communication. Adapted from Mendes et al. [24]. These QoS indicators are strongly influenced by dynamic vehicular environments where mobility, traffic density, propagation conditions, and infrastructure placement rapidly evolve. For example, high user density and mobility degrade SINR, RSRP, RSRQ, and other radio-link quality parameters, directly affecting throughput and latency [6] [7]. Consequently, ensuring stable QoS requires not only reactive adaptation but also predictive intelligence capable of forecasting link performance before degradation occurs. The emergence of 5G NR and Multi-access Edge Computing (MEC) enhances QoS provisioning by enabling Ultra-Reliable Low-Latency Communication (URLLC), network slicing, and localized computation. These advancements allow V2X systems to dynamically allocate resources based on predicted network states and application requirements. Overall, QoS in V2X communication serves as the foundational performance requirement underlying all cooperative transportation services. As vehicular networks transition toward fully autonomous and connected mobility, the role of accurate, multi-metric QoS prediction becomes indispensable for enabling real-time decision-making and ensuring communication reliability in next-generation 5G/6G V2X ecosystems.

I.3 MOTIVATION

The rapid evolution of V2X communication systems, supported by 5G and emerging 6G technologies, has intensified the demand for reliable and predictive Quality of Service (QoS) to enable safety-critical and latency-sensitive vehicular applications. Although existing V2X communication modalities V2V, V2I, V2N, and V2P collectively provide the foundation for cooperative awareness and real-time information exchange, their performance is fundamentally challenged by high mobility, dynamic topology changes, intermittent connectivity, and heterogeneous wireless conditions [25], [22]. These characteristics lead to rapid fluctuations in latency, throughput, packet delivery ratio (PDR), SINR, and other link-quality indicators, making conventional reactive QoS mechanisms inadequate for next-generation vehicular services. Predictive QoS (PQoS) has therefore emerged as a critical capability for enabling proactive resource allocation, congestion control, handover optimization, and service continuity in V2X systems. Recent studies demonstrate that ML, DL, and RL models can capture hidden spatio-temporal dependencies in vehicular mobility patterns, radio metrics, and network behaviors, allowing more accurate forecasting of communication performance [6], [7], [16]. Such predictions are particularly essential for applications such as cooperative perception, tele-operated driving, platooning, and emergency message dissemination, where even millisecond-level QoS degradation can compromise safety and reliability [10], [19] . Furthermore, the proliferation of RSUs, MEC nodes, and cloud services introduces new opportunities for distributed learning, edge-level inference, and hierarchical decision-making. RSUs equipped with MEC capabilities can support real-time QoS estimation and localized control actions, while cloud platforms enable long-term model training, cross-region knowledge transfer, and federated learning strategies [25], [24]. However, the effectiveness of such architectures depends on understanding the limitations of current communication technologies, including IEEE 802.11p/802.11bd, LTE-V2X PC5 sidelink, and 5G NR Uu, each of which exhibits distinct performance bottlenecks under dense traffic, high mobility, and varying propagation environments [22], [26], [27]. These challenges highlight the need for a comprehensive survey that unifies advances in PQoS prediction, analyzes emerging communication technologies, synthesizes ML/DL/RL developments, and examines dataset limitations, security constraints, and cross-layer performance issues. By integrating insights from predictive intelligence, communication protocols, and real-world measurement studies, this survey aims to provide a structured foundation for the design of scalable, explainable, and context-aware PQoS solutions for future V2X networks.

II. THEORETICAL REFERENCE

II.1 TAXONOMY AND METHODOLOGICAL CLASSIFICATION

The existing research on QoS prediction in V2X communication exhibits a broad methodological diversity, reflecting the interdisciplinary nature of vehicular networking, wireless communication, and intelligent systems. To provide a structured view of these developments, this survey categorizes state-of-the-art approaches into five distinct methodological domains : (i) protocol- and simulation-based models, (ii) supervised machine learning approaches, (iii) deep learning architectures, (iv) reinforcement learning frameworks, and (v) hybrid or cross-layer solutions. These categories capture the progression from traditional analytical and optimization-driven communication models toward data-driven, predictive, and autonomous decision-making paradigms. The proposed taxonomy also enables systematic comparison of modeling assumptions, feature dependencies, prediction objectives, and performance trade-offs across different V2X scenarios. Figure 4 illustrates the full taxonomy used throughout this survey. A comparative analysis of these methodological categories, supported by the evidence aggregated from existing studies, reveals clear distinctions in their underlying assumptions, feature dependencies, and operational constraints.

Traditional ML-based QoS prediction methods rely heavily on handcrafted features such as SINR, RSRP, RSRQ, vehicle speed, mobility patterns, and traffic density [6], [28], [29]. These models are computationally lightweight and enable fast inference, making them suitable for RSU-level or on-board prediction; however, their performance often degrades across heterogeneous environments due to scenario dependence, feature-engineering bottlenecks, and limited adaptability to nonlinear spatio-temporal variations [30], [31]. Deep learning approaches overcome these limitations by automatically learning complex hierarchical and temporal relationships using architectures such as LSTM, Bi-LSTM, GRU, CNN, and hybrid DNN models [18], [32], [33]. These models achieve superior accuracy and long-range QoS forecasting, particularly under rapidly changing mobility or channel conditions, but require large annotated datasets and MEC/GPU-based inference due to their high computational cost [9], [34]. Reinforcement learning (RL) and deep RL extend predictive capabilities by enabling sequential, adaptive decision-making for resource allocation, routing, slicing, and teleoperation [19], [35], [36]. While RL provides strong robustness in dynamic environments, its practicality is often limited by unstable convergence, intensive training requirements, and dependence on realistic simulation environments [37], [38].

In contrast, routing- and protocol-based approaches remain computation-efficient and well-suited for real-time deployment but lack predictive intelligence and often struggle under high-density or high-mobility scenarios [11], [39], [40]. Security- and trust-oriented frameworks strengthen resilience by incorporating authentication, trust scores, and anomaly detection [14], [41], [42], though these mechanisms introduce additional signaling overhead, authentication delay, and processing load, making them less suitable for strict real-time QoS prediction. Collectively, these observations highlight fundamental trade-offs between predictive accuracy, interpretability, computational complexity, scalability, and real-time feasibility across the methodological spectrum in V2X QoS prediction research.

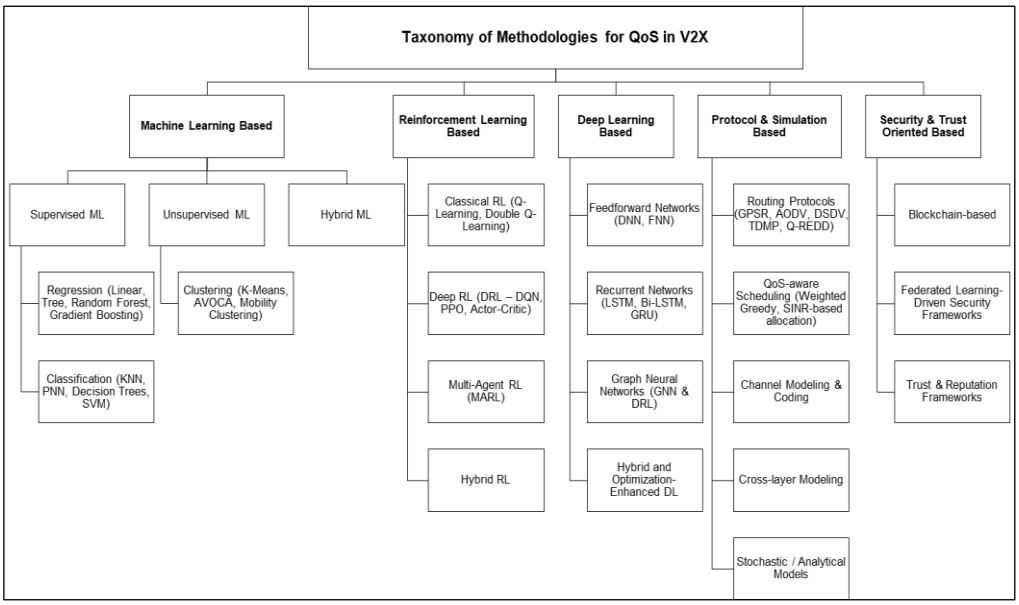


Figure 4: Taxonomy of methodological approaches in QoS prediction for V2X communication.
Source: Authors, (2026).

The framework categorizes existing literature into protocol-based, machine learning, deep learning, reinforcement learning, and hybrid cross-layer techniques, supporting structured performance and applicability analysis.

II.1.1 Machine Learning-Based QoS Prediction Techniques

Machine learning (ML) has been extensively explored for QoS prediction in V2X communication due to its relatively low computational overhead, interpretability, and suitability for deployment on RSUs and OBUs. ML approaches generally rely on handcrafted feature sets that capture radio conditions, mobility patterns, and traffic descriptors, many of which have been identified as dominant predictors of latency, throughput, and packet delivery ratios. A consolidated overview of commonly used variables is provided in Table 3. Compared to deep or reinforcement learning, ML techniques offer faster inference and reduced model complexity, making them suitable for real-time PQoS estimation; however, these advantages come at the cost of limited representational capacity and reduced generalizability in heterogeneous environments. Across the literature, supervised regression and classification models such as random forests, gradient-boosted trees, SVMs, and linear models have shown strong performance for near-term QoS forecasting when trained on a combination of PHY-layer metrics (e.g., SINR, RSRP, CQI) and mobility indicators (e.g., speed, heading, inter-vehicle distance) [28] [29], [30], [33]. These works consistently demonstrate that radio KPIs are necessary but insufficient without mobility and contextual features, particularly in highly dynamic V2I and V2V links. Models such as random forests provide robust prediction performance with low inference latency, making them practical for RSU-level deployment in online prediction systems [28].

However, the heavy reliance on feature engineering limits adaptability: ML models trained in urban environments often degrade when applied to highway or mixed mobility scenarios, revealing dataset bias and poor cross-environment generalization [31], [43]. Unsupervised learning and clustering have been introduced to mitigate these generalization issues by partitioning heterogeneous data into more homogeneous behavioral regimes before prediction. Studies leveraging K-means clustering and fuzzy-rule grouping demonstrate that per-cluster prediction improves model stability under varying LOS/NLOS propagation states and traffic densities [29-44]. This approach enables ML models to operate as context-aware predictors rather than global regressors. While effective, clustering-based schemes increase system complexity and require continuous reclassification of vehicles or channel states, which may be challenging under stringent latency constraints. Hybrid ML methods further extend predictive capabilities by combining supervised models with clustering, fuzzy logic, or rule-based components. These frameworks have been shown to improve resilience to noise, measurement sparsity, and abrupt mobility transitions, especially in scenarios where deep learning solutions may be computationally infeasible [45], [46].

Table 3: Overview of Variables Used in Machine Learning-Based Papers.

Variable	[10]	[16]	[17]	[44]	[29]	[8]	[47]	[30]	[31]	[48]	[29]	[44]	[49]	[45]	[46]
Latency	✓	-	✓	-	✓	✓	✓	-	-	✓	✓	✓	✓	✓	✓
Jitter	✓	-	-	-	✓	✓	✓	-	-	-	-	-	-	-	-
Throughput	✓	-	✓	✓	✓	✓	✓	✓	-	-	-	✓	✓	✓	✓
RTT	-	✓	-	-	-	-	-	-	-	-	-	-	-	-	-
UE–RSU Latency	-	✓	-	-	-	-	-	-	✓	-	-	✓	-	-	-
Packet Delay	-	-	✓	-	✓	✓	✓	-	-	✓	✓	✓	✓	✓	✓

PHY Features	-	-	-	✓	✓	✓	✓	-	-	-	-	-	-	-	-
Speed	-	-	-	✓	-	-	-	-	✓	✓	✓	✓	✓	✓	✓
GPS	-	-	-	✓	-	-	-	-	✓	-	-	-	-	-	-
Leading Vehicle	-	-	-	✓	-	-	-	-	-	✓	-	-	-	-	-
RSRP	-	-	-	-	✓	✓	-	✓	-	-	-	✓	-	-	-
RSRQ	-	-	-	-	✓	✓	-	✓	-	-	-	✓	-	-	-
SINR	-	-	-	-	✓	✓	-	✓	-	-	-	✓	-	-	-
Mobility Patterns	-	-	-	-	-	-	-	-	✓	✓	✓	✓	✓	✓	✓

Source: Authors, (2026).

A comparative analysis of ML-based PQoS studies reveals several overarching trends. First, multi-domain feature integration combining physical-layer indicators with mobility and traffic information consistently outperforms single-domain predictors [6] [28]. Second, the scarcity of large-scale, diverse, real-world V2X datasets limits generalizability and contributes to the overfitting observed in many ML-based models [16], [44]. Third, validation protocols vary significantly across studies, with some relying on random shuffling rather than route-based or temporal holdout strategies, leading to optimistic performance reporting [30]. Finally, while ML offers favorable computational efficiency and is well-suited for real-time inference, its inability to model long-range temporal dependencies and nonlinear interactions reduces accuracy relative to deep learning techniques, particularly under rapidly changing network dynamics.

II.1.2 Deep Learning-Based QoS Prediction Techniques

Deep learning (DL) has gained significant traction in V2X QoS prediction because of its ability to automatically learn hierarchical spatial and temporal representations from high-dimensional communication and mobility data. Unlike traditional ML methods, which depend heavily on engineered features and perform well only under stable or moderately dynamic conditions, DL models can capture non-linear interactions between radio KPIs, mobility patterns, traffic states, and environmental factor properties essential for highly dynamic V2X environments [7], [33]. A prominent research direction focuses on deep neural networks (DNNs) for throughput and latency forecasting, where models consistently outperform linear and ensemble-based ML approaches by learning latent correlations not explicitly visible in handcrafted features [7]. Recurrent neural networks (RNNs), particularly LSTM, Bi-LSTM, and GRU architectures, extend these benefits by modeling longer-term temporal dependencies in vehicular mobility and communication traces [18], [50]. These models demonstrate superior performance in predicting fluctuating QoS under high-speed mobility, where future states depend on extended historical sequences. More recent approaches integrate attention mechanisms, GAN-based data augmentation, and multi-task learning to enhance robustness and reduce sensitivity to noise [32], [51]. Table 4 summarizes common input variables used across DL-based studies.

Table 4: Variable usage across selected V2X predictions using deep learning and QoS papers.

Variable	**[7]**	**[33]**	**[9]**	**[18]**	**[32]**	**[52]**	**[50]**	**[34]**	**[53]**	**[51]**	**[54]**
SINR	✓	✓	-	-	-	-	-	-	-	-	-
Location	✓	-	-	-	-	-	-	-	-	-	-
Throughput	✓	✓	-	-	✓	-	-	-	-	✓	-
Mobility	-	✓	-	-	-	-	-	-	-	-	✓
Vehicle Velocity	-	-	✓	-	-	-	-	-	-	-	-
Density	-	-	✓	-	-	-	-	-	-	-	-
Distribution	-	-	✓	-	-	-	-	-	-	-	-
Signal Quality	-	-	✓	-	-	-	-	-	-	-	-
Traffic Volume	-	-	-	✓	-	-	-	-	-	-	-
Latency	-	-	-	-	✓	✓	-	-	-	✓	✓
BER	-	-	-	-	✓	-	-	-	-	✓	-
MSE	-	-	-	-	✓	-	-	-	-	✓	-
Packets/sec	-	-	-	-	-	-	✓	-	-	-	-
RMSE	-	-	-	-	-	-	✓	-	-	-	-
MAPE	-	-	-	-	-	-	✓	-	-	-	-
Processing Time	-	-	-	-	-	-	✓	-	-	-	-
Position	-	-	-	-	-	-	-	✓	-	-	-
Speed	-	-	-	-	-	-	-	✓	-	-	-
Heading	-	-	-	-	-	-	-	✓	-	-	-
Trajectory	-	-	-	-	-	-	-	-	✓	-	-
Acceleration	-	-	-	-	-	-	-	-	✓	-	-
Relative Position	-	-	-	-	-	-	-	-	✓	-	-
Traffic Type	-	-	-	-	-	✓	-	-	-	-	-
Reliability	-	-	-	-	-	✓	-	-	-	-	-
Recourse Utilize	-	-	-	-	-	✓	-	-	-	-	-
User Mobility	-	-	-	-	-	-	-	-	-	-	✓
Bandwidth	-	-	-	-	-	-	-	-	-	-	✓

Source: Authors, (2026).

DL has also advanced spatial modeling in V2X networks. Graph neural networks (GNNs) represent vehicles as graph nodes, enabling the learning of inter-vehicle spatial dependencies relevant for collision risk assessment and link-quality prediction [53]. Hybrid DL–RL models leverage DL as function approximators to optimize resource allocation or routing with improved predictive QoS awareness [54]. Collectively, these approaches highlight DL's ability to fuse heterogeneous mobility, radio, and contextual input capabilities beyond the scope of conventional ML. Despite these advantages, DL-based QoS prediction faces several practical limitations. First, DL models typically require large-scale, diverse, labeled datasets; however, publicly available V2X datasets remain limited, geographically biased, or collected under controlled conditions [33]. [55] As a result, models often overfit and fail to generalize to new traffic densities, weather conditions, or propagation environments. Second, DL models impose significant computational and memory overhead, making them less suitable for real-time deployment on resource-constrained RSUs or OBUs without model compression or edge offloading. Third, DL operates as a "black box," offering limited interpretability, an issue particularly problematic for safety-critical ITS applications where prediction rationale must be auditable. Finally, variations in evaluation methodologies across studies (windowing strategies, train–test splits, and scenario coverage) contribute to inconsistent reporting of performance gains. Overall, DL-based QoS prediction provides substantial improvements over traditional ML by capturing complex spatio-temporal dependencies and multi-modal interactions inherent in V2X systems. However, the practical utility of DL remains constrained by dataset scarcity, computational costs, and limited generalization. These shortcomings motivate current research directions involving hybrid DL–RL architectures, domain adaptation, transfer learning, and model compression to improve scalability and real-time applicability in 5G/6G vehicular networks.

II.1.3 Routing and Protocol-Based Approaches

Routing and protocol-level techniques play a central role in determining how reliably and efficiently V2X messages are propagated under high mobility. Classical routing protocols such as GPSR, AODV, and DSDV are frequently used as baselines to assess delay, packet delivery ratio, and robustness; however, their performance degrades in dense or fast-changing topologies [11]. Recent QoS-aware routing schemes attempt to address these limitations by incorporating mobility prediction, SINR estimation, and relay selection, with approaches such as TDMP and C-V2X-assisted D2D forwarding demonstrating improved reliability and reduced route breaks [39], [56]. Nonetheless, these methods remain sensitive to wireless channel fluctuations, indicating that routing alone cannot guarantee end-to-end QoS. Scheduling and resource-allocation strategies complement routing by prioritizing transmissions based on queue states, predicted link stability, or latency requirements. Mobility-aware schedulers and weighted-greedy allocation methods achieve measurable reductions in delay and congestion [12], although their performance is constrained by the accuracy of channel state estimation. At the physical layer, studies of channel coding and propagation models show that coding schemes such as turbo and LDPC significantly influence link reliability and retransmission behavior under varying mobility and fading conditions [13], [57]. These findings underscore the tight coupling between PHY-layer characteristics and protocol-layer performance. Cross-layer QoS modeling integrates routing, scheduling, and PHY-level parameters to provide more realistic analyses of end-to-end reliability and latency. Such models capture the combined effects of queuing delays, MAC contention, retransmissions, and route dynamics, offering insights that single-layer evaluations cannot [58]. Analytical and stochastic models further complement empirical results by characterizing multi-hop connectivity, interference, and dissemination delay in large-scale V2X settings [59]. Table 5 provides the variable-to-study mapping covering routing, scheduling, PHY, and cross-layer QoS methods.

Table 5: Mapping of QoS-Relevant Variables to Representative Routing, Scheduling, and PHY-Layer Studies.

Variable	[7]	[33]	[9]	[18]	[32]	[52]	[50]	[35]	[53]	[54]
Throughput	✓	✓	-	✓	✓	-	✓	-	-	✓
Latency/Delay	-	✓	✓	✓	-	✓	✓	-	✓	-
Reliability	-	✓	-	✓	✓	-	✓	✓	-	-
Mobility Data	✓	-	✓	-	✓	✓	-	✓	✓	-
SINR/Channel	✓	-	✓	✓	-	✓	✓	-	✓	✓

Source: Authors, (2026).

Overall, protocol-level research highlights that no individual layer can ensure stable QoS in vehicular networks. Routing depends on efficient scheduling, scheduling depends on predictable channel behavior, and PHY-layer gains require upper-layer coordination. Consequently, the most effective solutions emphasize cross-layer design, mobility awareness, and adaptive protocol mechanisms to maintain QoS under realistic vehicular mobility and channel variability.

II.1.4 Security and Trust-Based Approaches

Security- and trust-oriented frameworks have become integral to ensuring reliable QoS in V2X networks, particularly as message integrity, privacy, and misbehavior detection directly influence latency, throughput, and packet delivery. Existing solutions span blockchain-based architectures for tamper-resistant message dissemination [14], federated learning models for privacy-preserving QoE prediction [15], [41], and trust–reputation systems that evaluate forwarding behavior, PDR, and misbehavior rates [42]. As summarized in Table 6, these studies incorporate diverse variables such as latency, throughput, security metrics, and computational cost, highlighting the increasing convergence of security and performance requirements in modern V2X systems. A notable theme across the literature is the inherent security–QoS trade-off. Blockchain and distributed ledger mechanisms strengthen message integrity but introduce non-negligible processing delays and communication overhead, which may hinder time-critical V2X applications. Federated learning reduces privacy risks but increases model synchronization overhead, while trust-based systems depend heavily on continuous recommendation exchange, potentially increasing control traffic. These factors collectively impact QoS prediction accuracy by altering latency profiles, reliability guarantees, and resource consumption. Consequently, security mechanisms cannot be treated independently of QoS constraints and must be evaluated as part of an integrated design strategy.

Table 6: Overview of Variables in Security and Trust Frameworks for V2X.

Variable	[14]	[15]	[42]	[43]	[60]
Latency	-	✓	✓	✓	-
Throughput	-	✓	✓	-	-
QoE	-	✓	✓	-	-
Privacy / Security Metrics	✓	✓	✓	✓	✓
Trust / Reputation	-	-	-	✓	-
PDR (Packet Delivery Ratio)	-	-	-	✓	-
Misbehavior Detection	-	-	-	✓	-
Channel / Network Features	✓	-	-	-	-
Computing Requirements	✓	-	-	-	-

Source: Authors, (2026).

Despite progress, several gaps remain. Most existing frameworks rely on simulation-based datasets and lack large-scale real-world validation under diverse mobility and attack conditions. Current models also focus predominantly on single-aspect security (e.g., trust or privacy) rather than holistic, cross-layer protection. Furthermore, limited research has examined how security metrics can be directly incorporated into ML/DL-based QoS predictors to enhance robustness against adversarial behavior. Addressing these gaps will require standardized datasets, lightweight cryptographic and trust mechanisms compatible with 5G/6G latency budgets, and unified frameworks capable of jointly optimizing QoS, privacy, and security in future V2X systems.

III. DATASET SURVEY FOR PQOS IN V2X COMMUNICATION

Datasets constitute the empirical foundation for Predictive QoS (PQoS) research, enabling systematic evaluation of ML-, DL-, and RL-based models under diverse mobility patterns, radio conditions, and network loads. Existing datasets are typically categorized into three groups: real-world drive-test datasets, public open-access datasets, and synthetic or simulation-based datasets. Each category offers distinct benefits in terms of realism, scalability, parameter control, and reproducibility.

III.1 REAL-WORLD DRIVE TEST DATASETS

Real-world measurements provide the most accurate representation of 5G and V2X communication behavior, capturing realistic mobility dynamics, channel impairments, and congestion conditions that directly impact QoS. Brehon et al. [10] conducted extensive 5G SA industrial experiments for tele-operated mobility, demonstrating that regression-based PQoS models reduced end-to-end latency by nearly 15%. Similarly, Muller et al. [28] collected urban mobility traces in 5G NSA and LTE networks and reported strong correlations between vehicle movement and uplink/downlink throughput, with typical latency ranges of 15–20 ms in dense environments. BandSeer [16] and Schwarz et al. [17] further evaluated short-term bandwidth and uplink throughput prediction, identifying SINR as a dominant variable for regression-based models. Although real-world datasets provide high-fidelity ground truth, they remain geographically limited and costly to scale and often lack synchronized multimodal measurements integrating mobility, PHY, and network-layer parameters.

III.2 PUBLIC OPEN-ACCESS DATASETS

Public datasets enable reproducible benchmarking across the research community. The Berlin V2X dataset [43] provides GPS-tagged multi-RAT measurements that support cross-layer analysis of mobility, channel quality, and application-layer performance. NordicDat [29] expands this scope by offering more than 90,000 annotated samples with SINR, RSRP, RSRQ, throughput, delay, and mobility metrics. Reported studies show that Random Forest models achieve $R^2 > 0.85$ for throughput prediction and median latency errors below 8 ms, supporting research in federated and domain-adaptive PQoS modeling. While open datasets lower the entry barrier for ML-based experimentation, they often exhibit climatic, geographical, or environmental bias, limiting global generalizability.

III.2 SYNTHETIC AND SIMULATION-BASED DATASETS

Synthetic datasets generated through simulators such as ns-3, SUMO, and 3GPP PHY engines provide full control over mobility, density, radio models, and traffic patterns. They are particularly valuable for RL-based PQoS frameworks requiring interactive environments. The PRATA framework [19], for example, used ns-3 teleoperation simulations to train PPO agents, reporting a 20% prediction gain over Double Q-Learning. Additional synthetic datasets combine BiLSTM modeling with partially real mobility traces for traffic prediction [61], while 3GPP PHY-layer evaluations [30] compare Turbo, LDPC, and Polar codes, highlighting sub-10 ms latency for Turbo-coded V2X frames. Despite their scalability and flexibility, synthetic datasets may oversimplify fading, blockage, and interference, reducing their real-world transferability.

III.3 SUMMARY AND LIMITATIONS

The reviewed datasets collectively capture a wide spectrum of QoS-relevant variables: mobility traces, GPS coordinates, SINR, RSRP/RSRQ, throughput, delay, jitter, and CIR, enabling comprehensive benchmarking across ML, DL, and RL paradigms. Table 7 summarizes key characteristics of widely used datasets. However, a notable gap persists: the lack of synchronized datasets that jointly capture mobility, network KPIs, and PHY-layer signal measurements. Such multimodal datasets are essential for accurate end-to-end PQoS prediction, yet remain scarce across current literature. Developing standardized, cross-layer, and large-scale datasets represents a critical research direction for the next generation of V2X QoS prediction systems.

Table 7: Dataset-wise Variable Mapping with Authors.

Dataset	GPS	Speed	SINR	RSRP	RSRQ	RSSI	CQI	Throughput	Delay	Jitter	CIR	Mobility
Aveiro WLAN & Cellular	✓	✓	-	✓	✓	✓	-	✓	-	✓	-	-
Munich Drive Test QoS	✓	✓	✓	-	-	-	-	✓	-	-	-	✓
Industrial D2D AGV	-	-	-	-	-	-	-	-	-	-	✓	-
Large-Scale Mobility	✓	✓	-	-	-	-	-	-	-	-	-	✓
Nuremberg Multi-Vehicle	-	-	✓	✓	✓	✓	-	✓	-	-	-	-
Berlin V2X Multi-Rat	✓	✓	✓	✓	✓	-	✓	✓	-	-	-	✓
IoV Delay – Wuxi	-	-	-	-	-	-	-	✓	✓	-	-	-
V2X QoS (Munich+Brno)	✓	-	✓	✓	✓	-	✓	✓	-	-	✓	-

Source: Authors, (2026).

IV. CHALLENGES AND OPEN ISSUES

The analysis presented in the previous sections, together with the comparative tables and dataset summaries, reveals several recurring limitations that continue to affect the reliability of V2X QoS prediction models. These observations indicate that, despite substantial progress in ML-, DL-, and RL-based methods, fundamental gaps persist in data availability, model robustness, real-time inference categories, (i) interpretability, and system-level integration. As depicted in Figure 5, these challenges can be broadly classified into two major categories: (i)Dataset and Generalization Issues and (ii) Methodology and Deployment Constraints. The flowchart illustrates how factors such as the lack of multi-modal real-world datasets, environment-specific model behavior, absence of cross-layer modeling, and limited explainability directly influence the accuracy and practicality of QoS prediction in V2X networks. Additionally, inconsistent KPI definitions, heterogeneous evaluation metrics, and various security vulnerabilities further complicate real-world adoption. Together, these insights highlight the need for more comprehensive datasets, interpretable and secure learning models, and unified cross-layer prediction frameworks to support robust and scalable V2X communication systems.

IV.1 STRUCTURAL RESEARCH GAPS IN EXISTING PQOS LITERATURE

Although substantial progress has been achieved in predictive QoS modeling for V2X systems, a critical synthesis of the reviewed literature reveals several structural limitations that constrain scalability, robustness, and deployment readiness.

1) *Absence of Spatial QoS Field Modeling:* Most ML- and DL-based approaches perform point-wise prediction using locally observed indicators such as SINR, RSRP, mobility traces, or traffic density [28], [30], [33]. While effective for short-term estimation, these models do not reconstruct QoS behavior across unmeasured road segments. Empirical drive-test studies confirm strong spatial variability of throughput and latency in dense urban scenarios [17], [28]. However, explicit spatial correlation modeling and network-wide QoS field reconstruction remain largely unexplored, limiting generalization across heterogeneous road networks.

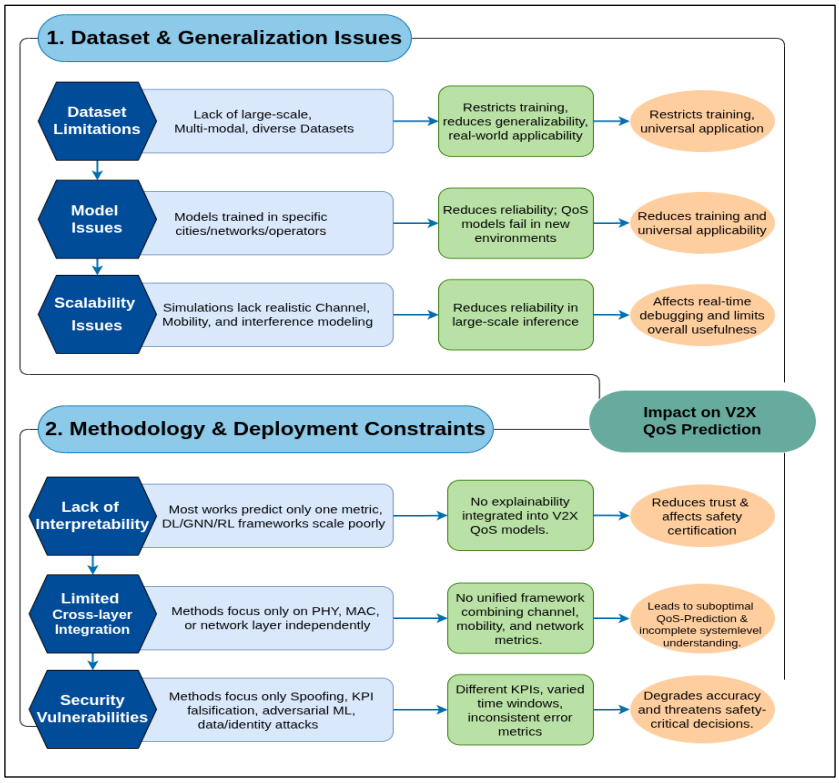


Figure 5: Diagram illustrating the key challenges and open issues in V2X QoS prediction.
Source: Authors, (2026).

2) *Single-Metric Prediction Dominance:* A significant portion of existing studies focuses on isolated metrics such as throughput or delay [7], [18]. In contrast, safety-critical V2X services require simultaneous guarantees on latency, reliability, jitter, and availability. The

absence of unified multi-metric prediction frameworks restricts cross-layer optimization and may lead to suboptimal system-level adaptation decisions.

3) *Limited Cross-Scenario Generalization:* Many predictive models are validated using city-specific drive-test datasets or simulator-generated traces [16], [43]. Although high accuracy is often reported under controlled settings, performance frequently degrades when deployed in unseen environments. This suggests insufficient domain adaptation and limited robustness to distribution shifts across mobility regimes, propagation conditions, and infrastructure density.
4) *Simulation-Centric Reinforcement Learning:* Reinforcement learning approaches demonstrate adaptive capabilities in teleoperation, slicing, and multicast optimization [19], [54]. However, most frameworks rely heavily on synthetic environments such as ns-3 simulations. The realism gap between simulation assumptions and operational 5G/6G V2X conditions raises concerns regarding deployment safety, convergence stability, and policy transferability.
5) *Weak Integration of Security and QoS Prediction:* Security-oriented frameworks based on blockchain, federated learning, and trust management enhance resilience [14], [15], [42], yet they are typically evaluated independently of predictive QoS modeling. The direct impact of authentication latency, secure aggregation overhead, or adversarial interference on QoS prediction accuracy remains insufficiently quantified.
6) *Evaluation Methodology Inconsistencies:* Validation protocols vary widely across studies, including random train–test splits and metric selection differences [34], [50]. In mobility-correlated datasets, random splitting may introduce temporal and spatial leakage, artificially inflating reported accuracy. The absence of standardized benchmarking and route-based validation hinders fair comparison and reproducibility.

Collectively, these gaps indicate that current PQoS research remains predominantly point-based, dataset-constrained, and method-driven rather than system-driven. Addressing these limitations requires unified spatio-temporal modeling, multi-metric prediction, uncertainty quantification, and deployment-aware validation using large-scale real-world vehicular datasets.

IV.2 FUTURE RESEARCH DIRECTIONS

Building upon the identified structural gaps, several forward-looking research directions emerge for advancing PQoS modeling toward reliable 5G/6G-enabled V2X systems.

IV.2.1 Multimodal and Cross-Layer Dataset Development

Future progress in PQoS research depends on the availability of synchronized, large-scale datasets that jointly capture mobility patterns, PHY-layer indicators, MAC-layer statistics, and application-level performance metrics. Existing datasets typically isolate individual parameters, limiting their ability to model complex spatio-temporal dependencies. Future efforts should focus on developing multimodal benchmarking datasets with:

1. Fine-grained temporal resolution (sub-100 ms sampling),
2. Diverse urban, suburban, and highway scenarios,
3. Explicit support for 5G/6G features such as sidelink, beam management, RIS-assisted links, and ISAC.

Standardized open benchmarks would enable reproducibility and fair cross-model comparison across research communities.

IV.2.2 Robust and Generalizable PQoS Models

ML/DL-based models often exhibit strong performance under training conditions but degrade under domain shifts. Future research should investigate domain adaptation, transfer learning, self-supervised representation learning, and distributionally robust optimization techniques capable of maintaining stable error bounds across heterogeneous deployments. A key objective is to design models whose prediction degradation remains within acceptable operational margins when transferred across cities, densities, or infrastructure configurations. Incorporating reliability scoring and uncertainty estimation into PQoS predictors can further improve decision confidence in safety-critical scenarios.

IV.2.3 Uncertainty-Aware and Risk-Constrained PQoS Modeling

In safety-critical V2X environments, prediction confidence is as important as prediction accuracy. Future PQoS frameworks should integrate uncertainty-aware learning mechanisms such as Bayesian deep learning, Gaussian processes, conformal prediction, and risk-sensitive reinforcement learning. Uncertainty estimates can enable:

1. Confidence-aware resource allocation,
2. Risk-adaptive handover decisions,
3. Safe fallback strategies under prediction ambiguity.

Designing predictors that quantify epistemic and aleatoric uncertainty will be essential for trustworthy deployment in autonomous mobility systems.

IV.2.4 Integration of Learning With Network Control and Protocol Design

Current approaches often treat learning models and networking protocols as independent components. A promising direction involves co-designing predictive models with routing, scheduling, slicing, and resource allocation mechanisms. Lightweight and stable RL or multi-agent RL frameworks operating under partial observability and tight latency constraints could enable closed-loop adaptation in dense vehicular scenarios. Hybrid learning—protocol architectures that directly embed predictive outputs into real-time control logic—represents a key step toward context-aware QoS guarantees.

IV.2.5 Secure, Privacy-Preserving, and Trust-Integrated PQoS Frameworks

As V2X ecosystems become increasingly interconnected, PQoS pipelines must integrate security and privacy constraints. Future research should explore federated PQoS learning, secure aggregation, blockchain-enabled trust verification, and adversarial robustness. A critical research question concerns balancing security overhead with latency budgets. Embedding trust metrics directly into QoS prediction models may enhance resilience against falsified measurements and adversarial manipulation.

IV.2.6 Toward 6G: Semantic, Predictive, and Edge-Intelligent V2X

The transition to 6G will shift PQoS modeling toward semantic-aware communication, AI-native network control, and distributed edge intelligence. Emerging technologies such as integrated sensing and communication (ISAC), reconfigurable intelligent surfaces (RIS), sub-THz links, and graph neural networks for network-wide coordination offer new opportunities for predictive QoS assurance. Future PQoS systems are expected to operate as distributed edge-intelligent agents capable of continuous learning, real-time adaptation, and proactive risk mitigation. Achieving this vision requires rethinking QoS prediction as a core architectural component of autonomous, self-optimizing V2X networks. Taken together, these research directions highlight a paradigm shift from isolated algorithmic improvements toward holistic, deployment-aware, uncertainty-conscious, and security-integrated PQoS intelligence suitable for large-scale autonomous mobility in 5G and beyond.

V. CONCLUSIONS

This paper provided a critical review of predictive Quality of Service (PQoS) modeling for V2X communication systems, examining machine learning, deep learning, reinforcement learning, protocol-level, and security-aware approaches. While significant progress has been reported in metric-specific prediction accuracy, our analysis shows that current research remains largely point-based, single-metric focused, and heavily reliant on simulation or city-specific datasets. The absence of spatial QoS field reconstruction, limited cross-scenario generalization, weak integration of security and control mechanisms, and inconsistent evaluation methodologies collectively restrict the scalability and deployment readiness of existing solutions in real-world high-mobility environments. To meet the stringent reliability and latency demands of next-generation vehicular networks, PQoS research must evolve beyond incremental accuracy improvements toward unified spatio-temporal modeling, multi-metric and uncertainty-aware prediction, and tightly integrated learning-control architectures. As V2X systems transition toward AI-native 6G ecosystems, predictive QoS should be positioned as a foundational architectural component enabling proactive, resilient, and self-optimizing communication. Achieving this transformation will require deployment-aware design, standardized benchmarking, and system-level intelligence capable of sustaining trustworthy operation in large-scale autonomous mobility scenarios.

VI. AUTHOR'S CONTRIBUTION

Conceptualization: Parita Patel and Mahesh Goyani.
Methodology: Parita Patel and Mahesh Goyani.
Investigation: Parita Patel and Mahesh Goyani.
Discussion of results: Parita Patel and Mahesh Goyani.
Writing – Original Draft: Parita Patel.
Writing – Review and Editing: Mahesh Goyani.
Resources: Parita Patel and Mahesh Goyani.
Supervision: Parita Patel and Mahesh Goyani.
Approval of the final text: Mahesh Goyani.

VII. REFERENCES

[1] T. Linget, "C-V2X Use Cases Volume II: Examples and Service Level Requirements," Technical Report, 5G Automotive Association (5GAA), Oct. 2020.

[2] D. F. Kulzer, M. Kasparick, A. Palaios, R. Sattiraju, O. D. Ramos-Cantor, D. Wieruch, H. Tchouankem, F. Gottsch, P. Geuer, J. Schwardmann, G. Fettweis, H. D. Schotten, and S. Stanczak, "AI4Mobile: Use Cases and Challenges of AI-Based QoS Prediction for High-Mobility Scenarios," in Proc. IEEE 93rd Vehicular Technology Conference (VTC-Spring), Helsinki, Finland, Apr. 2021, pp. 1–7. doi: 10.1109/VTC2021-Spring51267.2021.9448863.

[3] The Business Research Company, "Automotive v2x global market report." https://www.thebusinessresearchcompany.com/report/, 2025.

[4] S. Chen, J. Hu, Y. Shen, X. Chu, and X. Jiang, "A Comprehensive Survey on Vehicular Networking: Communications, Applications, Challenges, and Upcoming Research Directions," IEEE Access, vol. 10, pp. 21525–21567, 2022. doi: 10.1109/ACCESS.2022.3152897.

[5] T. Chatterjee, R. Karmakar, G. Kaddoum, S. Chattopadhyay, and S. Chakraborty, "A Survey of VANET/V2X Routing From the Perspective of Non-Learning- and Learning-Based Approaches," IEEE Access, vol. 10, pp. 31527–31567, 2022. doi: 10.1109/ACCESS.2022.3152767.

[6] H. Ye, L. Liang, G. Y. Li, J. Kim, L. Lu, and M. Wu, "Machine Learning for Vehicular Networks: Recent Advances and Application Examples," IEEE Vehicular Technology Magazine, vol. 13, no. 2, pp. 94–101, Jun. 2018. doi: 10.1109/MVT.2018.2811185.

[7] M. Boban, C. Jiao, and M. Gharba, "Measurement-Based Evaluation of Uplink Throughput Prediction," in Proc. IEEE 95th Vehicular Technology Conference (VTC-Spring), Helsinki, Finland, 2022, pp. 1–5. DOI: 10.1109/VTC2022-Spring54318.2022.9860971.

[8] M. Boban and M. Zorzi, "Linear Regression With Deep Neural Networks for Long-Term Throughput Prediction," IEEE Transactions on Vehicular Technology, vol. 70, no. 3, pp. 2440–2453, Mar. 2021. DOI: 10.1109/TVT.2021.3056280.

[9] S. Guleng, Z. Liu, C. Wu, and X. Chen, "Edge-Based V2X Communications With Big Data Intelligence," IEEE Access, vol. 7, pp. 153226–153238, 2019. DOI: 10.1109/ACCESS.2019.2947612.

[10] L. Brehon-Grataloup and R. Kacimi, "Predictive QoS for Tele-Operated Driving Over 5G SA Networks," in Proc. IEEE Vehicular Networking Conference (VNC), 2023 doi: 10.1109/VNC57357.2023.10136362.

[11] P. M. Mahajan and G. M. Patil, "Performance Analysis of GPSR, DSDV, and AODV Routing Protocols in VANET With Respect to Area and Node Scalability," Indian Journal of Science and Technology, vol. 7, no. 5, pp. 561–566, May 2014. doi: 10.17485/ijst/2014/v7i5.9.

[12] T. G. Shalini and S. Jenicka, "A Weighted Greedy Approach for Low-Latency Resource Allocation in V2X Networks," Wireless Personal Communications, vol. 118, no. 2, pp. 1307–1326, May 2021. doi: 10.1007/s11277-021-08164-6.

[13] D. Chatzoulis, C. Chaikalis, A. Xenakis, D. Kosmanos, and K. E. Anagnostou, "Channel Coding QoS Analysis in 5G V2X Dynamic Propagation Models," IEEE Access, vol. 13, pp. 75634–75649, 2025. doi: 10.1109/ACCESS.2025.3562147.

[14] M. A. Khan, S. Ghosh, and S. A. Busari, "A Robust, Resilient, and Reliable Architecture for V2X Communications," IEEE Transactions on Vehicular Technology, vol. 70, no. 7, pp. 6619–6632, Jul. 2021. doi: 10.1109/TVT.2021.3086404.

[15] A. Renda, P. Ducange, F. Marcelloni, D. Sabella, M. C. Filippou, G. Nardini, G. Stea, A. Virdis, D. Micheli, D. Rapone, and L. G. Baltar, "Federated Learning of Explainable AI Models in 6G Systems: Towards Secure and Automated Vehicle Networking," Information, vol. 13, no. 8, p. 395, 2022. doi: 10.3390/info13080395.

[16] R. Barbosa and P. Georgieva, "Forecasting and Improving Latency in 5G V2X Networks for Autonomous Driving Scenarios," in Proc. 22nd Mediterranean Electrotechnical Conference (MELECON), Porto, Portugal, 2024. doi: 10.1109/MELECON56669.2024.10463263.

[17] A. Palaios, C. L. V. Kasparick, D. F. Kulzer, R. Sattiraju, O. D. Ramos-Cantor, H. Tchouankem, F. Gottsch, P. Geuer, J. Schwardmann, G. Fettweis, H. D. Schotten, and S. Stanczak, "Machine Learning for QoS Prediction in Vehicular Communication: Challenges and Solution Approaches," in Proc. IEEE 93rd Vehicular Technology Conference (VTC-Spring), Helsinki, Finland, 2021. doi: 10.1109/VTC2021-Spring51267.2021.9448862.

[18] A. R. Abdellah, A. Abdelmoaty, A. A. Ateya, A. A. Abd El-Latif, A. Muthanna, and A. Koucheryavy, "Accurate V2X Traffic Prediction With Deep Learning Architectures," Frontiers in Artificial Intelligence, vol. 8, Art. no. 1345982, 2025. doi: 10.3389/frai.2025.1345982.

[19] L. Brehon-Grataloup, R. Kacimi, and T. Turletti, "PRATA: Framework to Enable Predictive Quality of Service for Teleoperated Driving," in Proc. IEEE Vehicular Networking Conference (VNC), 2023, pp. 101–110. doi: 10.1109/VNC57357.2023.10136363.

[20] S. Chen, J. Hu, Y. Shen, X. Chu, and X. Jiang, "A Comprehensive Survey on Vehicular Networking: Communications, Applications, Challenges, and Upcoming Research Directions," IEEE Access, vol. 10, pp. 21525–21567, 2022. doi: 10.1109/ACCESS.2022.3152897.

[21] M. Tabassum, M. S. Hossain, and A. Alamri, "A Review on QoS and Security Challenges Associated With the Internet of Vehicles in Cloud Computing,", Journal of Network and Computer Applications, vol. 230, Art. no. 103802, 2024. doi: 10.1016/j.jnca.2023.103802.

[22] A. Alalewi, I. Dayoub, and S. Cherkaoui, "On 5G-V2X Use Cases and Enabling Technologies: A Comprehensive Survey," IEEE Access, vol. 9, pp. 107710–107737, 2021 doi: 10.1109/ACCESS.2021.3100478.

[23] Z. MacHardy, A. Khan, K. Obana, and S. Iwashina, "V2X Access Technologies: Regulation, Research, and Remaining Challenges," IEEE Communications Surveys & Tutorials, vol. 20, no. 3, pp. 1858–1877, third quarter 2018. doi: 10.1109/COMST.2018.2808444.

[24] B. Mendes, M. Araújo, A. Goes, D. Corujo, and A. S. R. Oliveira, "Exploring V2X in 5G networks: A comprehensive survey of location-based services in hybrid scenarios," Vehicular Communications, vol. 52, Art. no. 100878, 2025, doi: 10.1016/j.vehcom.2025.100878.

[25] H. Alabdouli, M. S. Hassan, and A. Abdelfatah, "Enhancing Route Guidance With Integrated V2X Communication and Transportation Systems: A Review," Smart Cities, vol. 8, no. 1, Art. no. 24, 2025. doi: 10.3390/smartcities8010024.

[26] M. Tabassum, M. S. Hossain, and A. Alamri, "Review on QoS and security challenges associated with the Internet of Vehicles in cloud computing," Journal of Network and Computer Applications, vol. 230, Art. no. 103802, 2024, doi: 10.1016/j.jnca.2024.103802.

[27] A. T. Shakir, M. S. Islam, J. S. Mandeep, M. T. Islam, and M. S. Soliman, "Systematic review of data exchange for roadside units in a vehicular ad hoc network: Coherent taxonomy, prominent features, datasets, metrics, performance measures, motivation, opportunities, challenges, and methods," SN Applied Sciences, vol. 6, Art. no. 487, 2024, doi: 10.1007/s42452-024-06174-9.

[28] M. Boban, C. Jiao, and M. Gharba, "Measurement-Based Evaluation of Uplink Throughput Prediction," in Proc. IEEE 95th Vehicular Technology Conference (VTC-Spring), Helsinki, Finland, 2022, pp. 1–5. doi: 10.1109/VTC2022-Spring54318.2022.9860971.

[29] X. Chen and Y. Zhang, "Enhancing the Prediction of Internet of Vehicles Delay Quality of Service With Clustering Principle," in Proc. International Conference on Computer Science, Artificial Intelligence and Data Engineering (CSAIDE), Kuala Lumpur, Malaysia, 2025.

[30] İ. Yazıcı and E. Güreş, "NR-V2X quality of service prediction through machine learning with nested cross-validation scheme," in Proc. 2024 6th Int. Conf. Communications, Signal Processing and Their Applications (ICCSPA), 2024, doi: 10.1109/ICCSPA61559.2024.10794205.

[31] N. Aljeri and A. Boukerche, "Design and evaluation of an efficient online machine learning-based RSU prediction scheme for intelligent vehicular networks," in Proc. IEEE/ACS 16th Int. Conf. Computer Systems and Applications (AICCSA), Abu Dhabi, UAE, 2019.

[32] M. Vinodhini and S. Rajkumar, "A deep learning approach for predicting and optimizing the V2X network parameters for sustainable smart transportation systems," Engineering Research Express, vol. 7, no. 1, Art. no. 015268, 2025, doi: 10.1088/2631-8695/adb8a1.

[33] M. Boban, M. Giordani, and M. Zorzi, "Predictive quality of service: The next frontier for fully autonomous systems," IEEE Communications Magazine, vol. 59, no. 8, pp. 96–102, Aug. 2021, doi: 10.1109/MCOM.001.2001088.

[34] A. Santos *et al., "Using* machine learning on V2X communications data for VRU collision prediction," Sensors, vol. 23, no. 3, Art. no. 1260, 2023.

[35] F. Mason, M. Drago, T. Zugno, M. Giordani, M. Boban, and M. Zorzi, "A Reinforcement Learning Framework for PQoS in a Teleoperated Driving Scenario," in Proc. IEEE Wireless Communications and Networking Conference (WCNC), 2022. doi: 10.1109/WCNC51071.2022.977159062.

[36] O. AlZoubi, "Deep Reinforcement Learning for Predictive Resource Allocation in 5G-V2X Networks," Vehicular Communications, vol. 42, Art. no. 100560, 2023.

[37] N. Mpatziakas and G. Pallis, "DRL and Actor–Critic Approaches for Multicasting in 5G-V2X Networks," Computer Networks, vol. 204, Art. no. 108732, 2022.

[38] A. A. Ahmed, S. J. Malebary, W. Ali, and O. M. Barukab, "Smart Traffic Shaping Based on Distributed Reinforcement Learning for Multimedia Streaming over 5G-VANET Communication Technology," Mathematics, vol. 11, no. 3, Art. no. 700, 2023. doi: 10.3390/math11030700.

[39] M. Ye, L. Guan, and M. Quddus, "TDMP: Reliable Target-Driven and Mobility Prediction-Based Routing Protocol in Complex VANET," Vehicular Communications, vol. 29, Art. no. 100338, Apr. 2021. doi: 10.1016/j.vehcom.2021.100338.

[40] S. H. Mousa, R. S. Abdulrahman, and S. M. Abd Ali, "Improving QoS in VANET," Al-Iraqia Journal for Scientific Engineering Research, vol. 4, no. 1, pp. 9–19, Mar. 2025. doi: 10.58564/IJSER.4.1.2025.290.

[41] J. L. Corcuera Bárcena, P. Ducange, F. Marcelloni, G. Nardini, A. Noferi, A. Renda, G. Stea, and A. Virdis, "Towards Trustworthy AI for QoE Prediction in B5G/6G Networks," in Proc. First International Workshop on Artificial Intelligence in Beyond 5G and 6G Wireless Networks (AI6G), Padua, Italy, Jul. 2022, pp. 1–6. doi: 10.1145/3551665.35586722.

[42] W. Ali, S. Z. Ninoria, G. Khan, and K. K. Gola, "State of the Art, Reliable, and Trusted Communication in Vehicle-to-Everything (V2X) Networks," Open Computer Science, vol. 14, no. 1, 2024. doi: 10.1515/comp-2024-0007.

[43] N. U. Ain, R. Hernangómez, A. Palaios, M. Kasparick, and S. Stańczak, "QoS Prediction in Radio Vehicular Environments via Prior User Information," arXiv preprint arXiv:2402.17689, 2024. doi: 10.48550/arXiv.2402.17689.

[44] M. Raeisi and A. B. Sesay, "Handover Reduction in 5G High-Speed Networks Using ML-Assisted User-Centric Channel Allocation," IEEE Transactions on Network and Service Management, vol. 20, no. 4, pp. 4876–4889, 2023. doi: 10.1109/TNSM.2023.3298923.

[45] X. Chen and Y. Zhang, "Enhancing IoV Delay QoS With Clustering and Random Forest Prediction," International Conference on Computer Science, Artificial Intelligence and Data Engineering (CSAIDE), Kuala Lumpur, Malaysia, 2025.

[46] V. Mineeva, A. A. Ateya, A. Volkov, A. Muthanna, A. Koucheryavy, S. A. Chelloug, and A. A. Abd El-Latif, "A Novel Feature-Oriented Quality of Anything (QoX) Framework for End-to-End Robotic Services in 6G Networks," Scientific Reports, vol. 15, Art. no. 24945, 2025. doi: 10.1038/s41598-025-09677-6.

[47] S. Barmpounakis, N. Maroulis, N. Koursioumpas, A. Kousaridas, and A. Kalamari, "AI-Driven QoS Prediction for V2X Communications in Beyond 5G Systems," Computer Networks, vol. 217, Art. no. 109341, 2022. doi: 10.1016/j.comnet.2022.109341.

[48] Y. Zhou, H. Li, C. Shi, N. Lu, and N. Cheng, "A Fuzzy-Rule-Based Data Delivery Scheme in VANETs With Intelligent Speed Prediction and Relay Selection," International Journal of Communication Systems, vol. 31, no. 18, e3827, 2018. doi: 10.1002/dac.3827

[49] S. Yerrathi and V. Pakala, "Enhancing Network Stability in VANETs Using a Nature-Inspired Algorithm for Intelligent Transportation Systems," PLOS ONE, vol. 19, no. 3, e0298654, 2024. doi: 10.1371/journal.pone.0298654.

[50] A. R. Abdellah, A. Muthanna, M. H. Essai, and A. Koucheryavy, "Deep Learning for Predicting Traffic in V2X Networks," Applied Sciences, vol. 12, no. 19, Art. no. 10030, 2022. doi: 10.3390/app121910030.

[51] M. Vinodhini and S. Rajkumar, "A Deep Learning Approach for Predicting and Optimizing the V2X Network Parameters for Sustainable Smart Transportation Systems," The International Arab Journal of Information Technology, vol. 22, no. 2, pp. 327–335, 2025.

[52] M. S. Abood, H. Wang, D. He, M. Fathy, S. A. Rashid, M. Alibakhshikenari ,B. S. Virdee, S. Khan, G. Pau, I. Dayoub, P. Livreri, and T. A. Elwi, "An LSTM-Based Network Slicing Classification Future Predictive Framework for Optimized Resource Allocation in C-V2X," IEEE Access, vol. 11, pp. 118245–118260, 2023.

[53] M. Zeng, M. S. M. Hashim, M. N. Ayob, A. H. Ismail, and Q. Zang, "Intersection Collision Prediction and Prevention Based on Vehicle-to-Vehicle (V2V) and Cloud Computing Communication," Future Internet, vol. 17, no. 1, Art. no. 15, 2025. doi: 10.3390/fi17010015.

[54] W. AlZoubi and H. Hatamleh, "Multicasting Strategies for Increasing Network Efficiency in 5G Using Deep Learning," The International Arab Journal of Information Technology, vol. 22, no. 2, pp. 336–344, 2025.

[55] H. Zeng and Y. Li, "Graph Neural Network-Based Deep Reinforcement Learning for Intersection Collision Prediction," IEEE Intelligent Transportation Systems Conference (ITSC), 2025, pp. 88–97.

[56] S. A. Alghamdi, "Cellular V2X With D2D Communications for Emergency Message Dissemination and QoS-Assured Routing in 5G Environment," IEEE Access, vol. 9, pp. 109234–109247, 2021. doi: 10.1109/ACCESS.2021.3102296.

[57] D. Kosmanos, C. Chaikalis, and I. K. Savvas, "3GPP 5G V2X Scenarios: Performance of QoS Parameters Using Turbo Codes," Telecom, vol. 3, no. 1, pp. 12–31, 2022. doi: 10.3390/telecom3010012.

[58] J. Horta, M. Siller, and S. Villarreal-Reyes, "Cross-Layer Latency Analysis for 5G NR in V2X Communications," PLOS ONE, vol. 20, no. 1, Art. no. e0313772, 2025. doi: 10.1371/journal.pone.0313772.

[59] R. Banoth and J. Thangaraj, "Stochastic Traffic Flow Modeling for Multi-Hop Cooperative Data Dissemination in VANETs," Physical Communication, vol. 46, Art. no. 101290, 2021. doi: 10.1016/j.phycom.2021.101290.

[60] M. Tabassum, M. S. Hossain, and A. Alamri, "A Review on QoS and Security Challenges Associated With the Internet of Vehicles in Cloud Computing," Journal of Network and Computer Applications, vol. 230, Art. no. 103802, 2024. doi: 10.1016/j.jnca.2023.103802.

[61] D. F. Kulzer, M. Kasparick, A. Palaios, R. Sattiraju, O. D. Ramos-Cantor, D. Wieruch, H. Tchouankem, F. Gottsch, P. Geuer, J. Schwardmann, G. Fettweis, H. D. Schotten, and S. Stanczak, "AI4Mobile: Use Cases and Challenges of AI-Based QoS Prediction for High-Mobility Scenarios," IEEE 93rd Vehicular Technology Conference (VTC-Spring), Helsinki, Finland, Apr. 2021, pp. 1–7. doi: 10.1109/VTC2021-Spring51267.2021.9448863.

Journal of Engineering and Technology for Industrial Applications

ITEGAM-JETIA

Manaus, v.12 n.60, p.1101-1107. July/August, 2026.
DOI: https://doi.org/10.5935/jetia.v12i60.3982

ISSN ONLINE: 2447-0228

RESEARCH ARTICLE OPEN ACCESS

IMPROVING ENERGY GOVERNANCE IN THE CEMENT INDUSTRY: OPTUNA-BILSTM FRAMEWORK FOR LONG-RANGE ELECTRICAL LOAD FORECASTING

Mokhtaria Bekkaoui*[1], Hamed Benahmed[2], Meryem Kada Kloucha[3] and Imane Nedjar[4]

[1, 3, 4]First cycle department, École Supérieure en Sciences Appliquées de Tlemcen, Tlemcen, Algeria.
[1]Manufacturing Engineering Laboratory of Tlemcen, University of Tlemcen, Algeria.
[2]Department of Computer Science, Faculty of Sciences, University of Tlemcen, Algeria.
[3]Laboratoire de Statistiques et Modélisations Aléatoires, Université of Tlemcen, Algeria.
[4]Biomedical Engineering Laboratory, University of Tlemcen, Algeria.

[1]http://orcid.org/0009-0007-7625-9106, [2]http://orcid.org/0009-0007-0089-877X,
[3]http://orcid.org/0009-0003-1619-3046, [4]http://orcid.org/0000-0002-5222-1193

Email:*mokhtaria.bekkaoui@univ-tlemcen.dz, hamed.benahmed@univ-tlemcen.dz, meryem.kadakloucha@univ-tlemcen.dz, imane.nedjar@univ-tlemcen.dz

ARTICLE INFO

Article History
Received: March 9, 2026
Reviewed: April 9, 2026
Accepted: July 9, 2026
Published: August 31, 2026

Keywords:
Electricity consumption,
Forecasting,
Industrial energy modeling,
LSTM,
BiLSTM,
Optimization.

ABSTRACT

Precise long-range forecasting of industrial electrical demand constitutes a strategic imperative for energy governance, particularly within energy-intensive, continuous-process industries such as cement manufacturing. This investigation conduct a systematic evaluation of two advanced recurrent neural networks, Long Short-Term Memory (LSTM) and Bidirectional LSTM (BiLSTM), fine-tuned via the Optuna optimization. Using realistic data from an operational cement plant, we quantify the trade-offs between predictive accuracy, computational overhead, and operational viability. Empirical results demonstrate that the Optuna-optimized BiLSTM framework achieves superior predictive performance, yielding an R2 score of 0.890 and a Mean Absolute Error (MAE) of 0.220. These findings delineate a modeling framework that reconciles high-fidelity forecasting with practical implementation, providing foundational guidelines for designing energy management systems that optimize maintenance, reduce costs, and advance sustainable operations.

Copyright ©2026 by authors and Galileo Institute of Technology and Education of the Amazon (ITEGAM). This work is licensed under the Creative Commons Attribution International License (CC BY 4.0).

I. INTRODUCTION

Prospective The global energy landscape is undergoing significant transformation due to rapid technological advancement, population growth, and expanding industrialization. Some alarming projections suggest that, unless the consumption of all devices is reduced, energy demand by 2040 will exceed the available energy supply [1]. This pressing challenge underscores the urgent need for accurate electricity consumption forecasting models, which are instrumental in enabling better energy resource management, cost reduction, and infrastructure planning [2]. Electricity demand forecasting has gained critical importance amid digital transformation, where Artificial Intelligence (AI) must address growing complexity in modern power systems [3], [4]. Traditional rule-based or statistical models, while historically useful, often struggle to capture the dynamic, non-linear patterns that characterize modern energy systems. As a result, the focus has shifted toward more advanced techniques capable of uncovering hidden patterns in sequential data. Time series forecasting plays a crucial role in anticipating future energy consumption by analyzing historical usage patterns. It is widely applied in modern energy systems for tasks such as electricity demand prediction, load management, and renewable energy integration. These forecasting techniques enable utilities and industries to optimize grid operation, reduce energy waste, and support data-driven decision-making in energy planning and maintenance. With the increasing complexity of smart grids and variable renewable energy sources, advanced artificial intelligence and deep learning models such as LSTM, BiLSTM, and hybrid neural networks have shown remarkable performance in capturing nonlinear temporal dependencies and improving forecast accuracy [5], [6].

Among these advancements, deep learning models, particularly Recurrent Neural Networks (RNNs) and their derivatives like LSTM and BiLSTM have gained attention for their ability to model complex temporal dependencies [7]. These architectures have demonstrated strong predictive performance in energy forecasting due to their capacity to capture long-term and nonlinear relationships. Nevertheless, they typically require substantial data volumes, high computational power, and fine-tuning of hyperparameters. In contrast, classical statistical models such as Autoregressive Integrated Moving Average (ARIMA) and Trend and Seasonal Components (TBATS) continue to be employed for their interpretability and efficiency, especially in low-data scenarios or when model transparency is critical [8]. While much of the existing literature, [9], [10] has focuses on residential energy forecasting, long-term electricity consumption prediction in industrial environments presents unique challenges and opportunities. Industrial facilities, unlike residential users, follow more consistent and structured consumption patterns that are closely aligned with production processes. In fact, advanced electricity forecasting provides a dual-function capability; beyond improving energy procurement and operational efficiency, it enables predictive maintenance strategies that constitute the initial safeguard against equipment failures capable of interrupting production. This dual capability is especially critical in industrial environments, where unplanned outages can escalate to costly production halts and irreversible equipment damage [4]. Therefore, robust and context-aware predictive models are essential to support energy efficiency, operational continuity, and sustainable industrial growth.

This study offers an in-depth investigation of electricity consumption forecasting methods in an industrial context, focusing particularly on a cement manufacturing plant, a sector recognized for its high energy requirements and repetitive production processes. The analysis used the predictive capabilities of advanced deep learning models, specifically LSTM and BiLSTM, which were optimized through the Optuna framework to enable automated and efficient hyperparameter tuning. This research aims to rigorously evaluate these models in terms of predictive accuracy, computational efficiency, and practical applicability when confronted with dataset industrial electricity consumption. In addition, the study highlights the potential of accurate forecasting to support preventive maintenance strategies, improve energy management practices, and strengthen decision-making in energy-intensive industries. By bridging advanced artificial intelligence methods with traditional statistical approaches, this work contributes to the development of intelligent forecasting systems that enhance operational reliability, reduce downtime risks, and foster sustainable energy practices in large-scale manufacturing environments. The rest of the paper is structured as follows. Section 2 provides an overview of state-of-the-art approaches to electricity consumption forecasting. Section 3 describes the adopted methodology. Section 4 presents the dataset, experimental results, and comparative discussion. Section 5 concludes the paper and highlights future research directions.

II. RELATED WORK

This section presents a review of recent methods, published from 2022 onwards, for forecasting electricity consumption. Various machine learning (ML) and deep learning (DL) techniques have been employed to capture the temporal and nonlinear characteristics of energy consumption patterns. Recent advances in deep learning have enabled the development of models capable of addressing complex prediction challenges in the energy domain. These models are particularly effective when large datasets are available and the input-output relationships exhibit high levels of complexity conditions commonly found in decentralized power systems. In such contexts, neural network architectures can be tailored to tackle multiple forecasting tasks efficiently. Recurrent architectures, especially LSTM networks, have emerged as powerful tools for capturing temporal patterns in electricity consumption data. For example, the study in [11] introduced a deep LSTM-based framework for short-term residential load forecasting, demonstrating its superiority over classical statistical techniques such as ARIMA. Similarly, [12], designed a sequence-to-sequence LSTM model that successfully leverages the sequential structure inherent in energy consumption time series. More recently, BiLSTM models have emerged as an enhanced alternative, leveraging both past and future context [13]. In a comparative study given by [7], BiLSTM provided better generalization on volatile load profiles compared to unidirectional LSTM. However, the study also highlighted the sensitivity of BiLSTM models to hyperparameter configurations. To address this issue, researchers have turned to automated hyperparameter optimization tools, such as Optuna. Applied Optuna for fine-tuning the learning rate, batch size, and network depth of a BiLSTM model used for smart grid forecasting. The optimized model showed a significant reduction in Root Mean Square Error (RMSE) and Mean Absolute Percentage Error (MAPE), underlining the value of meta-optimization strategies in deep learning applications [14], [15]. The quality assessment of the studies involved applying inclusion and exclusion criteria, ensuring the identification of experimental research that included variables directly related to the research question. Data extraction was carried out by analyzing the results of the selected approaches. To summarize and synthesize the results, experimental studies were identified using specific keywords relevant to the research question. A table was then prepared, which contained a synthesis of the selected articles, including the publication year, the models used, the periods covered, and the dataset.

Table 1: Present the summary of the main articles related to the present work.

Autors	Methods	Dataset
[16]	Deep-learning hybrid forecasting model, namely: EMD-SVR-PSO-AR-GARCH	New South Wales (NSW, Australia) market
[17]	Ensemble learning Compared: gradient boosted regression trees, random forests and an adaptation of Adaboost.	office building located in the campus of ISEP/GECAD(building is occupied in daily basis by about 30 people)
[9]	Combines three models: LSTM, GRU, and Temporal Convolutional Network (TCN)	2000 clients from Bejaia, Algeria
[18]	XGBoost classification model, Multi-Layer Perceptron (MLP) model that is used to make the final electricity consumption prediction.	500 residential users placed in a southeastern region of Spain.
[8]	Evaluated the ARIMA and TBATS statistical prediction methods and compared them with neural forecasting methods	Smart house that is equipped with solar panels and batteries for energy storage.

[19]	Hybrid multi-algorithm method. called ICMD-ANN-EDLSTM.	Descriptive statistic of daily electricity demand (MWh) at four substation South-east Queensland, Australia.
[20]	Improved SSA and multivariable input RNNs to achieve adaptive decomposition of raw time series data and fusion input of multiple features, ADMIF.	Moroccan buildings' electricity consumption dataset (MORED).
[10]	Time series dense encoder (TiDE) model.	City level, of residential customers and the technological consumption of electricity suppliers.
[21]	Modeling spatiotemporal series using Graph Neural Networks (GNNs), with a focus on the structure of decentralized electrical networks.	12 regions of French mainland– excluding Corsica.

Source: Authors, (2026).

III. METHODOLOGY

This section introduces the dataset utilized in our experiments and outlines the baseline models, specifically LSTM and BiLSTM architectures. Additionally, we detail the performance evaluation metrics applied, which include Mean Absolute Error (MAE), Root Mean Square Error (RMSE), Relative MAE, and the Coefficient of Determination (R^2).

III.1 DATASET DESCRIPTION

The empirical analysis utilizes a proprietary dataset derived from a cement manufacturing plant located in the western region of Algeria, classified as a high-voltage consumer. The facility receives its electrical supply at 60 kV from the national transmission operator via a dedicated 220/60 kV substation. The dataset comprises detailed electricity consumption records collected over a five-month period at 10-minute intervals. It reflects real operational conditions, including variations in production cycles, equipment startup and shutdown phases, and environmental influences. The temporal resolution and industrial context of the data make it highly valuable for evaluating the performance of forecasting models in scenarios where energy demand is both high and tightly coupled to continuous manufacturing processes.

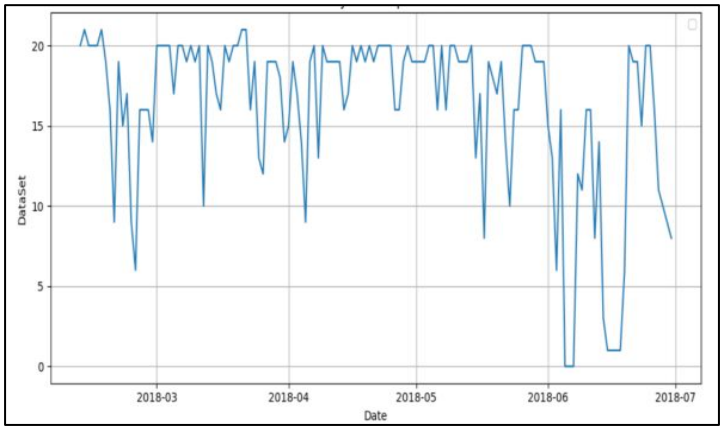


Figure 1: Electricity consumption curve.
Source: Authors, (2026).

III.2 MODELS BASELINE

In this study, both Long Short-Term Memory (LSTM) and Bidirectional LSTM (BiLSTM) models are evaluated as baseline approaches, with and without Optuna-based optimization. The following paragraph describes the differences between the LSTM and BiLSTM architectures. LSTM: The Long Short-Term Memory (LSTM) network, is a type of Recurrent Neural Network (RNN) designed to capture long-term dependencies in sequential data by incorporating specialized memory units [22]. These memory units consist of a cell state and three gates (input, forget, and output) that regulate the flow of information, enabling the network to retain or discard information over time. This architecture is particularly effective in modeling non-linear and temporal relationships in time series data, such as electricity consumption patterns. BiLSTM: the Bidirectional LSTM (BiLSTM) extends the LSTM architecture by processing the input sequence in both forward and backward directions [23]. This dual-path structure enables the model to capture dependencies not only from past to future but also from future to past within the sequence, thereby improving the model's ability to learn complex temporal dynamics. Both architectures were implemented with a sequence of layers, including input normalization, one or more LSTM/BiLSTM layers, dropout regularization to prevent overfitting, and a fully connected dense layer for output generation. Hyperparameter tuning, such as the number of hidden units, learning rate, batch size, and sequence length, was performed using the Optuna optimization framework to maximize forecasting performan]ce.

III.3 EVALUATION METRICS

The models were evaluated using the different metrics (see Table 2). These metrics were computed for each tested model LSTM, BiLSTM, LSTM (Optuna) and BiLSTM (Optuna) to allow a fair and multidimensional comparison of model accuracy, robustness, and generalization capability on the cement factory dataset.

Table 2: Evaluation Metric.

Metric	Equation	Description
Mean Absolute Error (MAE)	$MAE=\frac{1}{n}\sum_{i=1}^{n}\lvert X_i-\hat{X}_i\rvert$ (1)	Average absolute difference between predicted and actual values. Penalizes all errors equally.
Root Mean Square Error (RMSE)	$RMSE=\sqrt{\frac{1}{n}\sum_{i=1}^{n}(X_i-\hat{X}_i)^2}$ (2)	Square root of the average squared errors. Heavily penalizes large deviations.
Relative MAE	$RMAE=\frac{\frac{1}{n}\sum_{i=1}^{n}\lvert X_i-\hat{X}_i\rvert}{\frac{1}{n}\sum_{i=1}^{n}X_i}$ (3)	Is a normalized version of the Mean Absolute Error (MAE).
Coefficient of Determination (R^2)	$R^2=1-\frac{\sum_{i=1}^{n}(X_i-\hat{X}_i)^2}{\sum_{i=1}^{n}(X_i-\bar{X})^2}$ (4)	Proportion of variance in the dependent variable explained by the model. Ranges from 0 (no fit) to 1 (perfect fit).
Training Time	TrainT (measured in seconds/minutes)	Time required to train the model on historical data. Key for scalability.

Source: Authors, (2026).

IV. RESULTS AND DISCUSSION

This section presents the results of our research alongside an in-depth discussion of the experimental findings, highlighting the implementation choices, methodological steps, and comparative insights. The entire experiment was conducted on the Google Colab environment to leverage cloud-based computational resources. The architectures were implemented using the TensorFlow framework and the Keras library in Python to ensure a scalable and efficient training environment. For both the LSTM and BiLSTM models, a temporal window size of 72 was utilized, representing a 48-hour historical sequence, to capture the intricate short-term dependencies inherent in industrial electricity consumption. While initial training employed the Adam optimizer [24] with a MAE loss function, the performance of both models was systematically enhanced through the integration of Optuna, a Bayesian hyperparameter optimization framework. This optimization phase was pivotal in identifying the ideal configuration for critical parameters, including learning rates, hidden units, and dropout rates, thereby maximizing predictive accuracy and ensuring robust generalization across both neural architectures. The following section presents a detailed comparison of the results from the four methods, namely LSTM and BiLSTM, with and without Optuna optimization, in terms of predictive accuracy, computational complexity, and their applicability to industrial electricity forecasting scenarios.

IV.1 TRAINING AND VALIDATION RESULT

The training and validation loss patterns of the LSTM and BiLSTM architectures, including both baseline and Optuna-optimized configurations, are evaluated. The observed loss trends provide insights into each model's convergence behavior and generalization capability. Figure 2 shows the training and validation loss evolution of the baseline model LSTM which exhibits a rapid decrease in training loss, stabilizing around 0.002, while the validation loss remains higher and fluctuates between approximately 0.0025 and 0.005, indicating overfitting and limited generalization. In contrast, in Figure 3, the BiLSTM model demonstrates more stable convergence, with reduced variance in validation loss and a smaller gap between training and validation curves, reflecting improved generalization performance. The improved behavior of the BiLSTM can be attributed to its bidirectional architecture, which captures temporal dependencies in both forward and backward directions and provides richer contextual representations. Figures 4 and 5 illustrate the performance of the LSTM and BiLSTM architectures following Optuna-driven hyperparameter optimization. The optimized models exhibit accelerated convergence and significantly smoother loss trajectories, with the final loss values stabilizing at approximately 0.017. Furthermore, the minimal divergence between the training and validation loss curves suggests a substantial improvement in model robustness and a heightened resistance to overfitting. Overall, these results confirm that while BiLSTM architectures outperform standard LSTM models, Optuna-based hyperparameter optimization further improves convergence stability and predictive accuracy, highlighting the importance of systematic hyperparameter tuning for sequence-based learning tasks.

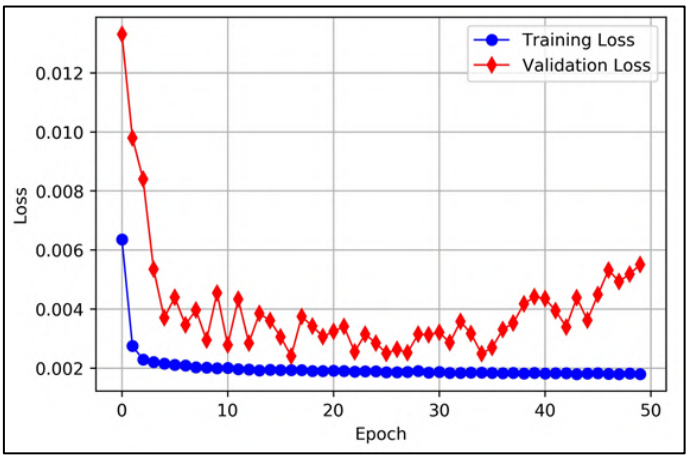


Figure 2: Loss of LSTM-based models vs epochs.
Source: Authors, (2026).

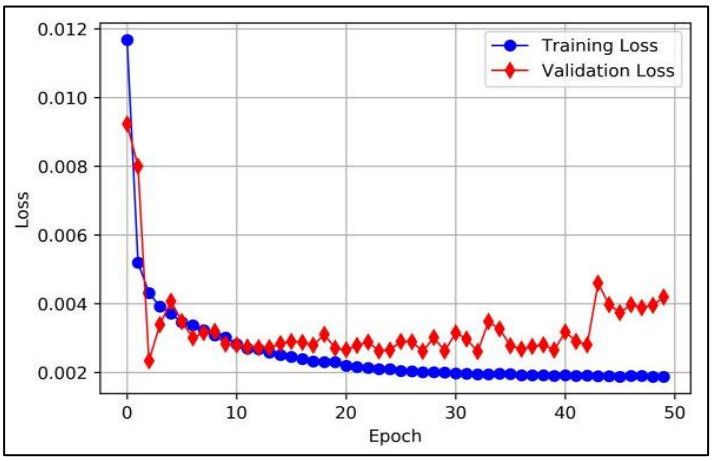


Figure 3: BiLSTM-based models vs epochs.
Source: Authors, (2026).

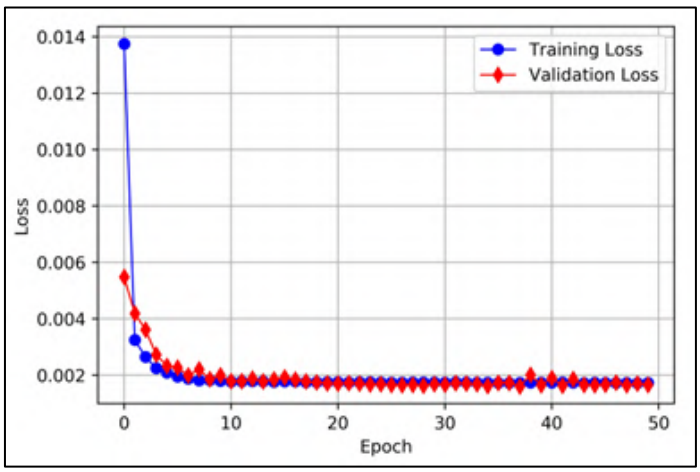


Figure 4: Loss of Optuna-Optimized LSTM .
Source: Authors, (2026).

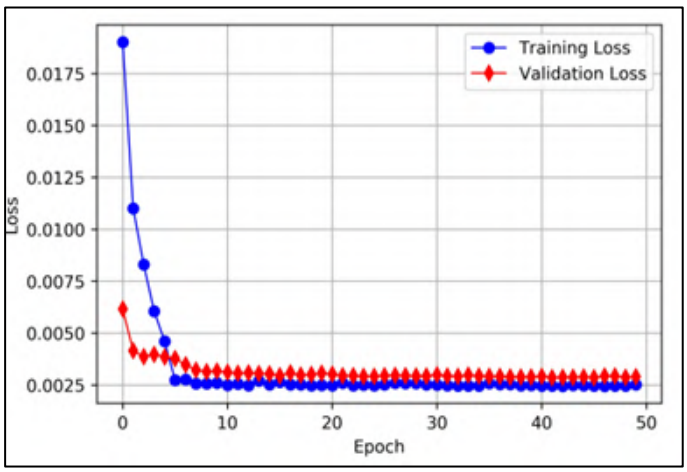


Figure 5: Loss of Optuna-Optimized BiLSTM-based models vs epochs.
Source: Authors, (2026).

IV.2 EVALUATION TEST AND COMPARATIVE STUDY

This section presents the experimental evaluation and comparative analysis of the four models: the LSTM, BiLSTM, Optuna-optimized LSTM and Optuna-optimized BiLSTM. All models were evaluated on the test dataset using standard metrics, including Root Mean Square Error (RMSE), Relative Mean Absolute Error (RMAE), R^2 score, and training time, providing a comprehensive assessment of predictive accuracy and computational efficiency. Table 3 summarizes the performance of LSTM and BiLSTM models with and without Optuna-based hyperparameter optimization. The results demonstrate that Optuna optimization significantly improves predictive accuracy, as reflected in lower RMSE and RMAE values and higher R^2 scores. Among all configurations, the Optuna-optimized BiLSTM achieves the best performance, balancing high predictive accuracy with moderate training time. Figure 6 compares the real and predicted energy consumption values for the two best-performing models. Both the Optuna-optimized LSTM and BiLSTM closely follow the real consumption trends, with the BiLSTM predictions showing slightly higher alignment and smoother tracking, highlighting its superior ability to capture temporal dependencies and improve forecasting accuracy.

Table 3: Comparative Performance of Baseline and Optuna-Optimized LSTM/BiLSTM.

Prediction Model	RMSE	RMAE (%)	R^2 Score	Training Time (TT)
LSTM	0.225	56	-0.002	4 min 57 s
BiLSTM	0.230	42	-0.001	8 min 19 s
Optuna-Optimized LSTM	12.08	24	0.665	5 min 15 s
Optuna-Optimized BiLSTM	0.220	20	0.890	6 min 05 s

Source: Authors, (2026).

For the LSTM and BiLSTM models, the window size and number of epochs were manually chosen. Several combinations were tested, and the best-performing configuration was retained for each model. Specifically, the LSTM model achieved its best results, yielding an RMSE of 0.225, an RMAE of 56%, and an R^2 score of -0.002, with a training time of 4 minutes 57 seconds. The BiLSTM model, achieved similar results (RMSE = 0.230, RMAE = 42%, R^2 = -0.001) with a significantly lower training time of 8 minutes 19 seconds. The Optimized-Optuna BiLSTM model achieved the best performance overall, with an RMSE of 0.220, an RMAE of 20%, and a training time of just 6 minutes 05 seconds, clearly demonstrating the advantage of automated tuning in improving both accuracy and efficiency.

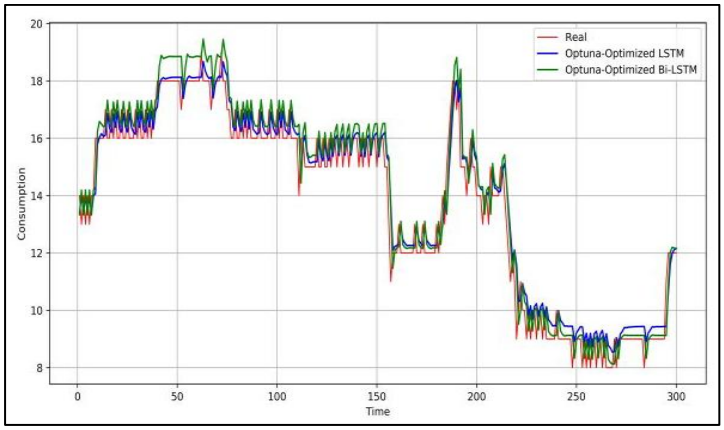


Figure 6: Real Vs Predicted Consumption of Optuna-Optimized LSTM/BiLSTM.
Source: Authors, (2026).

The visualization in Figure 6 enables a direct comparison of how the optimized models handle the test set data. Both models generally capture the overall trend, successfully tracking major peaks and the general movement of real consumption, particularly during periods of higher usage (time steps 0–200). However, the Optuna-Optimized BiLSTM consistently demonstrates superior performance across the entire time series. Its predictions remain closer to the actual consumption, indicating lower overall error. This advantage is most pronounced during periods of high volatility (time steps 200–270), where real consumption dips sharply from approximately 15 to 8. The BiLSTM accurately follows this decline and subsequent low-consumption plateau, reflecting its ability to leverage bidirectional temporal dependencies. In contrast, the Optuna-Optimized LSTM exhibits clear limitations in the low-consumption segment. It significantly underestimates the actual values during the dip, highlighting the unidirectional LSTM reliance solely on past trends, which reduces its effectiveness in capturing abrupt changes and maintaining accuracy during volatile periods. These results indicate that for this consumption forecasting task, access to both past and future temporal context is highly informative. The Optuna-Optimized BiLSTM emerges as the preferred model, as its bidirectional memory structure enables more robust and accurate predictions across varying consumption levels and volatility.

V. CONCLUSIONS

This study presented a comprehensive analysis of advanced RNN architectures, LSTM, BiLSTM, enhanced with Optuna-based hyperparameter optimization, the context of long-term electricity consumption forecasting for a cement manufacturing facility. Through rigorous experimentation on real-world industrial data, with Optuna-Optimized BiLSTM achieving the best overall results across all evaluation metrics. The automatic parameter selection provided by Optuna not only improved prediction quality but also reduced training time, making the model more suitable for practical deployment in energy-intensive environments. These findings reinforce the potential of optimized deep learning methods to serve as reliable tools in smart energy management systems, enabling predictive maintenance, cost savings, and more sustainable production planning in industrial settings.

VI. AUTHOR'S CONTRIBUTION

Conceptualization: Mokhtaria Bekkaoui.
Methodology: Mokhtaria Bekkaoui and Hamed Benahmed.
Investigation: Meryem Kada Kloucha and Imane Nedjar.
Discussion of results: Mokhtaria Bekkaoui, Hamed Benahmed and Imane Nedjar.
Writing – Original Draft: Mokhtaria Bekkaoui.
Writing – Review and Editing: Mokhtaria Bekkaoui, Hamed Benahmed and Imane Nedjar.
Resources: Meryem Kada Kloucha.
Supervision: Meryem Kada Kloucha and Imane Nedjar.
Approval of the final text: Hamed Benahmed and Imane Nedjar.

VII. REFERENCES

[1] S. Ghasemian, A. Faridzad, P. Abbaszadeh, A. Taklif, A. Ghasemi, and R. Hafezi, "An overview of global energy scenarios by 2040: Identifying the driving forces using cross-impact analysis method", Int. J. Environ. Sci. Technol., vol. 21, no. 11, pp. 7749-7772, 2024.

[2] International Energy Agency, "World Energy Outlook 2025", Paris, France: IEA Publications, 2025. [Online]. Available: https://www.iea.org/events/world-energy-outlook-2025

[3] A. Román-Portabales, M. López-Nores, and J. J. Pazos-Arias, "Systematic review of electricity demand forecast using ANN-based machine learning algorithms", Sensors, vol. 21, no. 13, p. 4544, 2021.

[4] International Energy Agency, "World Energy Outlook 2022", Paris, France: IEA Publications, 2022. [Online]. Available: https://iea.blob.core.windows.net/assets/830fe099-5530-48f2-a7c1-11f35d510983/WorldEnergyOutlook2022.pdf

[5] S. Aslam, H. Herodotou, S. M. Mohsin, N. Javaid, N. Ashraf, and S. Aslam, "A survey on deep learning methods for power load and renewable energy forecasting in smart microgrids", Renew. Sustain. Energy Rev., vol. 144, p. 110992, 2021.

[6] C. Cai, Y. Tao, T. Zhu, and Z. Deng, "Short-term load forecasting based on deep learning bidirectional LSTM neural network", Appl. Sci., vol. 11, no. 17, 2021.

[7] D. Guimarães Da Silva, A. Alvarenga, M. Meneses, and D. R. Vera Paz, "Comparing LSTM and BLSTM deep neural networks for power consumption prediction: Preliminary studies", Energy Rep., vol. 10, pp. 3315-3334, 2023.

[8] A. Gellert, U. Fiore, A. Florea, R. Chis, and F. Palmieri, "Forecasting electricity consumption and production in smart homes through statistical methods", Sustain. Cities Soc., vol. 76, p. 103426, 2022.

[9] D. Hadjout, J. F. Torres, A. Troncoso, A. Sebaa, and F. Martínez-Álvarez, "Electricity consumption forecasting based on ensemble deep learning with application to the Algerian market", Energy, vol. 243, 2022.

[10] D. Pătelează et al., "Electricity consumption forecasting for sustainable smart cities using machine learning methods", Internet Things, vol. 27, p. 101322, 2024.

[11] A. Muneer, R. F. Ali, A. Almaghthawi, S. M. Taib, A. Alghamdi, and E. A. A. Ghaleb, "Short term residential load forecasting using long short-term memory recurrent neural network", Int. J. Electr. Comput. Eng., vol. 12, no. 5, pp. 5589-5599, Oct. 2022.

[12] Y. Mu, M. Wang, X. Zheng, and H. Gao, "An improved LSTM-Seq2Seq-based forecasting method for electricity load", Front. Energy Res., vol. 10, 2023.

[13] N. Mughees, S. A. Mohsin, A. Mughees, and A. Mughees, "Deep sequence to sequence Bi-LSTM neural networks for day-ahead peak load forecasting", Expert Syst. Appl., vol. 175, p. 114844, 2021.

[14] M. Feurer and F. Hutter, “Hyperparameter optimization”, in Automated Machine Learning, pp. 3-33, 2019.

[15] N. Burkart and M. F. Huber, “A survey on the explainability of supervised machine learning”, J. Artif. Intell. Res., vol. 70, pp. 245-317, 2021.

[16] G. F. Fan, X. Wei, Y. T. Li, and W. C. Hong, “Forecasting electricity consumption using a novel hybrid model”, Sustain. Cities Soc., vol. 61, p. 102320, 2020.

[17] T. Pinto, I. Praça, Z. Vale, and J. Silva, “Ensemble learning for electricity consumption forecasting in office buildings”, Neurocomputing, vol. 423, pp. 747-755, 2021.

[18] F. Lazzari et al., “User behaviour models to forecast electricity consumption of residential customers based on smart metering data”, Energy Rep., vol. 8, pp. 3680-3691, 2022.

[19] S. Ghimire, R. C. Deo, D. Casillas-Pérez, and S. Salcedo-Sanz, “Efficient daily electricity demand prediction with hybrid deep-learning multi-algorithm approach”, Energy Convers. Manag., vol. 297, p. 117707, 2023.

[20] L. Fang and B. He, “A deep learning framework using multi-feature fusion recurrent neural networks for energy consumption forecasting”, Appl. Energy, vol. 348, p. 121563, 2023.

[21] E. Campagne, Y. Amara-Ouali, Y. Goude, and A. Kalogeratos, “Leveraging graph neural networks to forecast electricity consumption”, arXiv preprint, 2024. [Online]. Available: http://arxiv.org/abs/2408.17366

[22] S. Hochreiter and J. Schmidhuber, “Long short-term memory”, Neural Comput., vol. 9, no. 8, pp. 1735-1780, Nov. 1997.

[23] S. Siami-Namini, N. Tavakoli, and A. S. Namin, “The performance of LSTM and BiLSTM in forecasting time series”, in Proc. IEEE Int. Conf. Big Data, 2019, pp. 3285-3292.

[24] D. P. Kingma and J. Ba, “Adam: A method for stochastic optimization”, in Proc. Int. Conf. Learn. Representations (ICLR), 2017. [Online]. Available: https://hdl.handle.net/11245/1.505367

Journal of Engineering and Technology for Industrial Applications

ITEGAM-JETIA

Manaus, v.12 n.60, p.1108-1116. July/August, 2026.
DOI: https://doi.org/10.5935/jetia.v12i60.3990

ISSN ONLINE: 2447-0228

RESEARCH ARTICLE OPEN ACCESS

EXPLAINABLE RECOMMENDATION IN GRAPH NEURAL NETWORKS USING PROPAGATION PATH ANALYSIS AND COUNTERFACTUAL GRAPH EDITING

Pranav Nallari[1], Jayakumar Kaliappan*[2]

[1, 2]School of Computer Science and Engineering, Vellore Institute of Technology, Vellore, Tamil Nadu, India.

[1]http://orcid.org/0009-0003-7062-1785, [2]http://orcid.org/0000-0002-6044-6667

Email: pranav.nallari2022@vitstudent.ac.in, *jayakumar.k@vit.ac.in

ARTICLE INFO

Article History
Received: March 6, 2026
Reviewed: April 6, 2026
Accepted: July 6, 2026
Published: August 31, 2026

Keywords:
Explainable AI,
Graph Neural Networks,
Collaborative Filtering,
LightGCN,
Counterfactual Explanation,
Recommender Systems.

ABSTRACT

Graph Neural Networks (GNNs), particularly LightGCN, have achieved strong performance in collaborative filtering-based recommendation systems. However, their black-box nature makes it difficult to explain why specific items are recommended, limiting trust and adoption in user-facing applications. In this paper, we propose a post-hoc explainability framework for LightGCN combining two complementary techniques: Propagation Path Analysis, which decomposes recommendation scores by propagation layer to attribute influence to specific training interactions, and Counterfactual Graph Editing, which identifies the most influential user-item edges through structural sensitivity analysis and targeted edge removal. We evaluate on MovieLens-1M against three baselines including random edge removal, degree-based attribution, and LIME. Our method achieves a mean absolute score drop of 0.0322, representing a 3.02× lift over random, a 1.26× lift over LIME, and a 5.35× lift over degree-based attribution. Faithfulness evaluation against post-fine-tuning ground truth yields Pearson r = 0.536, confirming that structural sensitivity reliably identifies influential edges without model retraining. Layer contribution analysis reveals that LightGCN recommendations are predominantly driven by direct interactions (Layer 0) and 1-hop neighbours (Layer 1), with deeper layers contributing progressively less.

Copyright ©2026 by authors and Galileo Institute of Technology and Education of the Amazon (ITEGAM). This work is licensed under the Creative Commons Attribution International License (CC BY 4.0).

I. INTRODUCTION

Recommender systems have become fundamental infrastructure across e-commerce, streaming, and information retrieval platforms. Collaborative filtering based on Graph Neural Networks (GNNs) has emerged as a dominant paradigm, with LightGCN [1] achieving strong empirical performance by simplifying the GNN architecture to pure neighbourhood aggregation across multiple propagation layers. Despite these advances, GNN-based recommenders remain largely opaque. Users receive no explanation for why a specific item was suggested, system operators cannot audit model behaviour for bias or fairness [2], and regulatory frameworks such as the EU AI Act increasingly require explanations for automated decisions affecting individuals. Prior work has shown that a lack of transparency directly erodes user trust in algorithmic systems [3]. Existing explainability methods largely fall into two categories: gradient-based attribution and perturbation-based probing (LIME [4], SHAP [5]). Both treat the model as a black box and ignore the structural properties of GNNs — namely, that information flows through a graph topology across multiple propagation hops. This structural blindness limits their ability to produce explanations grounded in the model's actual computation. A comprehensive survey of explainability techniques for recommender systems [3] highlights that graph-structural methods remain underexplored relative to their importance. We propose a post-hoc explainability framework designed specifically for LightGCN's graph-structural characteristics. Our contributions are:

1. Propagation Path Analysis: decomposing LightGCN scores by propagation layer and attributing influence to specific training interactions at the dominant hop depth.

2. Counterfactual Graph Editing: quantifying edge influence by measuring score changes upon targeted edge removal, without model retraining.
3. Comprehensive evaluation against three baselines across four rank positions on MovieLens-1M, demonstrating 3.02x lift over random selection.
4. Faithfulness evaluation against post-fine-tuning ground truth (Pearson).
5. Qualitative layer contribution analysis across five diverse recommendation cases.

II. RELATED WORK

II.1 GNN-BASED RECOMMENDATION

By [1] proposed LightGCN as a simplification of NGCF [6], retaining only weighted neighbourhood aggregation per layer. Training uses Bayesian Personalised Ranking (BPR) [7], which optimises relative ordering of observed versus unobserved interactions. Earlier approaches such as SpectralCF [8] operated in the spectral domain but were limited by scalability. Graph Attention Networks (GAT) [9] introduced learnable attention weights over neighbours; however, LightGCN demonstrates that removing such parameterisation improves generalisation on collaborative filtering data. A broader survey of deep learning approaches to recommendation is provided by [10].

II.2 EXPLAINABILITY IN GNNS

GNNExplainer [11] identifies a subgraph that maximises mutual information with the model's prediction, targeting node classification rather than recommendation. CF-GNNExplainer [12] extends counterfactual perturbations to GNNs but is computationally expensive and not designed for large-scale bipartite recommendation graphs. PGExplainer [13] trains a parameterised mask generator for GNN explanations, requiring additional training. SubgraphX [14] uses Monte Carlo Tree Search to identify explanatory subgraphs at greater computational cost. These methods share a common limitation: they do not account for the bipartite, link-prediction nature of the recommendation task.

II.3 EXPLAINABILITY IN RECOMMENDER SYSTEMS

LIME [4] fits a local linear surrogate by perturbing user interaction histories and fitting weighted regression. It is model-agnostic but ignores graph topology and requires many forward passes. SHAP [5] provides Shapley value attributions but is similarly black-box. Attention-based methods [15] use attention weights as proxies, but these do not reliably correlate with feature importance [16], and LightGCN uses no attention. A systematic categorisation of post-hoc explanation approaches by type and model family is provided by [17]. In the recommendation setting, PRINCE [18] generates counterfactual explanations for knowledge-graph-based recommenders; our work targets GNN-based collaborative filtering and provides layer-level attribution alongside edge-level counterfactuals. Our work is most closely related to counterfactual approaches for recommendation [19], which we extend with layer-level propagation path analysis and a systematic multi-baseline faithfulness evaluation.

III. BACKGROUND: LIGHTGCN

III.1 PROBLEM FORMULATION

Let $\mathcal{U}$ and $\mathcal{I}$ be the sets of users and items. Observed interactions are encoded in $R \in \{0,1\}^{|\mathcal{U}|\times|\mathcal{I}|}$ where R_{ui} = 1 indicates an interaction. The task is to score unobserved pairs $\hat{y}_{ui}$ and rank items per user.

III.2 GRAPH CONSTRUCTION

LightGCN builds a bipartite graph $G=(V,E)$ with $V=\mathcal{U}\cup\mathcal{I}$. The full adjacency matrix is given by Eq. (1). With degree matrix D where $D_{vv}=\sum_j A_{vj}$, the symmetrically normalised adjacency is given by Eq. (2). This scales each edge by the inverse square root of source and target node degrees, preventing high-degree nodes from dominating aggregation.

III.3 PROPAGATION AND TRAINING

$$A=\begin{pmatrix}0 & R\\ R^{\top} & 0\end{pmatrix} \tag{1}$$

$$\tilde{A}=D^{-\frac{1}{2}}AD^{-\frac{1}{2}} \tag{2}$$

At layer k, embeddings are updated by neighbourhood aggregation as shown in Eq. (3), where $e^{(0)}$ are learnable initial embeddings. In matrix form: $E^{(k)}=\tilde{A}E^{(k-1)}$. Final embeddings are the layer-averaged representations given in Eq. (4). The predicted score is $\hat{y}_{ui}=e_u{}^{\top}e_i$, and training uses BPR loss as in Eq. (5), where $\mathcal{O}=\{(u,i,j)\mid R_{ui}=1,R_{uj}=0\}$, σ is the sigmoid function, and λ is an L2 regularisation coefficient.

$$e_u^{(k)}=\sum_{i\in\mathcal{N}_u}\frac{1}{\sqrt{|\mathcal{N}_u|}\sqrt{|\mathcal{N}_i|}}e_i^{(k-1)},\ e_i^{(k)}=\sum_{u\in\mathcal{N}_i}\frac{1}{\sqrt{|\mathcal{N}_i|}\sqrt{|\mathcal{N}_u|}}e_u^{(k-1)} \tag{3}$$

$$e_u=\frac{1}{K+1}\sum_{k=0}^{K}e_u^{(k)},\ e_i=\frac{1}{K+1}\sum_{k=0}^{K}e_i^{(k)} \tag{4}$$

$$\mathcal{L}_{BPR} = -\sum_{(u,i,j)\in\mathcal{O}} ln\sigma(\hat{y}_{ui} - \hat{y}_{uj}) + \lambda\left\|E^{(0)}\right\|^2 \quad (5)$$

IV. PROPOSED FRAMEWORK

Our framework answers two complementary questions for any recommendation (u, i): (1) at which propagation depth does the signal originate? and (2) which training interactions are most influential? Figure 1 shows the complete pipeline.

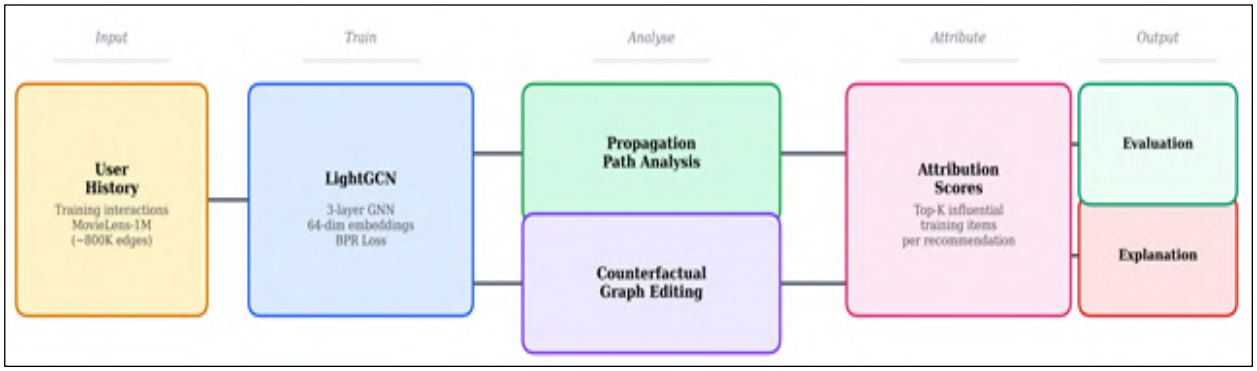


Figure 1: System architecture of the Explainable LightGCN pipeline.
Source: Authors, (2026).

IV.1 PROPAGATION PATH ANALYSIS

We define the layer contribution at hop k as the inner product of the layer-k embeddings, as in Eq. (6). This captures the contribution of information propagated exactly k hops. The dominant layer is $k^*=arg\ max_k C_k(u,i)$. A dominant C_0 indicates recommendation driven by the user's own interaction embeddings; a dominant C_1 indicates collaborative signal from items co-liked by users with overlapping histories.

$$C_k(u,i) = e_u^{(k)^\top} e_i^{(k)} \quad (6)$$

For each item j in the user's history, the attribution score measures its embedding's contribution to the target item's score at the dominant layer, as in Eq. (7). The first term is the LightGCN normalisation weight for edge (u,j); the second measures alignment between item j's outgoing embedding and the target item's embedding at the dominant layer. Items are ranked by $|\alpha(j,u,i)|$ to produce top-K attributed interactions.

$$\alpha(j,u,i) = \frac{1}{\sqrt{|\mathcal{N}_u|}\sqrt{|\mathcal{N}_j|}} \cdot e_j^{(k^*-1)^\top} e_i^{(k^*)} \quad (7)$$

IV.2 COUNTERFACTUAL GRAPH EDITING

For attributed training item j, define the counterfactual graph G_{-j} as the original graph with edge (u,j) removed: $\mathcal{E}_{-j}=\mathcal{E}\{(u,j)\}$. We renormalise to obtain $\tilde{A}_{-j}$ and compute the structural score drop with model weights held fixed, as in Eq. (8). We also measure the rank change: $\Delta r_i^{(j)} = r_i(\tilde{A}_{-j}) - r_i(\tilde{A})$. Evaluation is performed at rank positions $r \in \{1, 5, 10, 20\}$.

$$\Delta\hat{y}_{ui}^{(j)} = \hat{y}_{ui}(\tilde{A}) - \hat{y}_{ui}(\tilde{A}_{-j}) \quad (8)$$

IV.3 FAITHFULNESS EVALUATION

To test whether structural drops predict actual model adaptation, for 50 users we compare the structural predicted drop against the actual drop after 5-epoch fine-tuning on G_{-j} with learning rate $\eta=10^{-3}$. Faithfulness is measured via Pearson r and Spearman ρ.

V. EXPERIMENTAL SETUP

V.1 DATASET

We evaluate on MovieLens-1M [20], containing 1,000,209 ratings from 6,040 users on 3,706 movies. After 5-core filtering and binarisation to implicit feedback, the training set has approximately 800,167 interactions (80/20 split). Figure 2 shows the BPR training loss, and Figure 3 shows the degree distributions of the resulting training graph. The item distribution exhibits a pronounced long tail (median 90, mean 235), which directly motivates our analysis of why degree-based attribution fails: high-degree items are suppressed by LightGCN's symmetric normalisation.

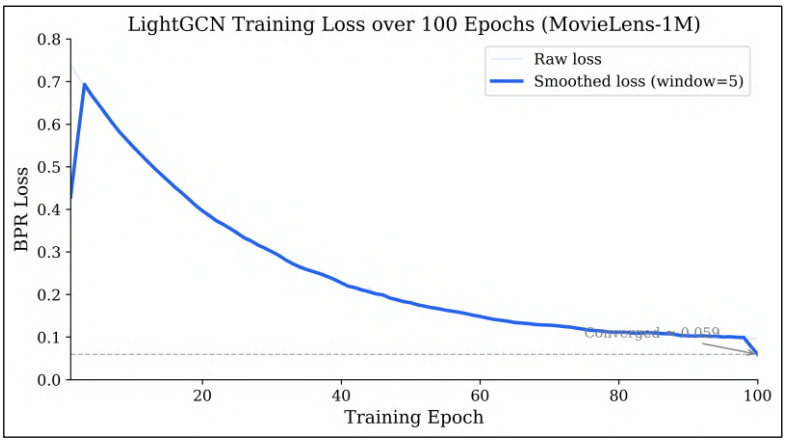


Figure 2: LightGCN BPR training loss over 100 epochs on MovieLens-1M. The model converges smoothly to approximately 0.059 by epoch 100.
Source: Authors, (2026).

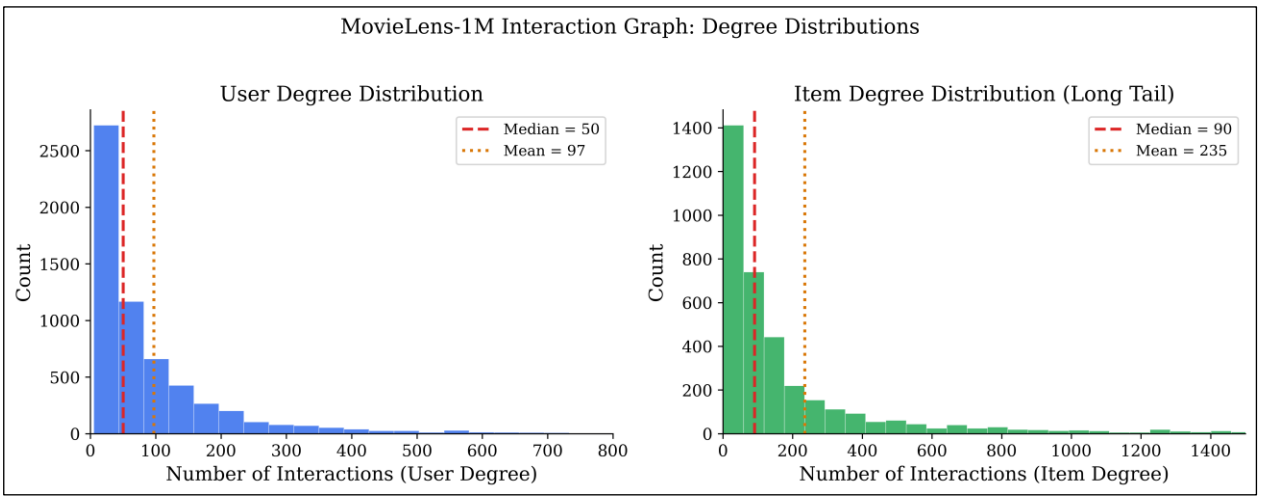


Figure 3: Degree distributions of users (left) and items (right) in the MovieLens-1M training graph after 5-core filtering.
Source: Authors, (2026).

V.2 MODEL CONFIGURATION

We train a 3-layer LightGCN (K=3) with embedding dimension d=64, Adam optimiser, learning rate 10^{-3}, BPR loss with L2 regularisation λ=10^{-4}, 100 epochs, and batch size 2048.

V.3 BASELINES

Random: Randomly sample K items from the user's training history. Tests whether PropPath beats chance.

Degree: Rank the user's training items by global degree and select the top-K. Tests the hypothesis that popular items are more influential.

LIME: Sample N_p = 100 binary masks over the user's history. For each mask m_t, compute the score $s(m_t)$=$\hat{y}_{ui}\left(\tilde{A}(m_t)\right)$ and fit a weighted Ridge regression as in Eq. (9) with exponential kernel weights w_t= $exp(-(1-\bar{m}_t)^2/2\sigma^2)$, σ= 0.25. Top-K items by $|\beta_j|$ are selected.

$$\beta=arg\ min_\beta \sum_{t=1}^{N_p} w_t(s(m_t)-\beta^\top m_t)^2+\alpha_{ridge}||\beta||^2 \quad (9)$$

VI. RESULTS AND ANALYSIS

VI.1 COUNTERFACTUAL EVALUATION

Table 1 presents mean absolute score drops, and Figures 4 and 5 visualize these results.The 3.02× lift over random confirms PropPath identifies genuinely influential edges. The 1.26× lift over LIME demonstrates that graph-structural knowledge adds measurable value beyond black-box probing — at a fraction of the computational cost (1 forward pass vs. 100 for LIME). The degree baseline performing below random (lift 0.56×) is explained by symmetric normalisation: high-degree items have small individual edge weights scaling as $1/\sqrt{d_i}$, so removing any single edge causes negligible score change.

Table 1: Mean absolute score drop by method and target rank position. Higher = stronger attribution quality.

Method	R@1	R@5	R@10	R@20	Lift
PropPath (Proposed)	0.0313	0.0335	0.0298	0.0341	3.02x
LIME	0.0251	0.0268	0.0238	0.0263	2.38x
Random	0.0102	0.0121	0.0104	0.0098	1.00x
Degree	0.0055	0.0078	0.0055	0.0053	0.56x

Source: Authors, (2026).

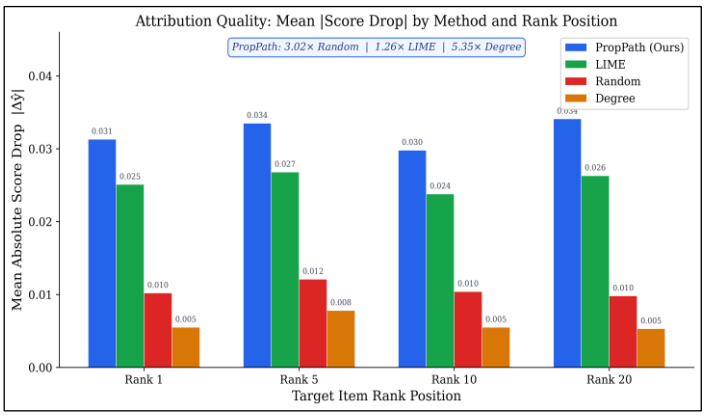


Figure 4: Mean absolute score drop per method and rank position.
Source: Authors, (2026).

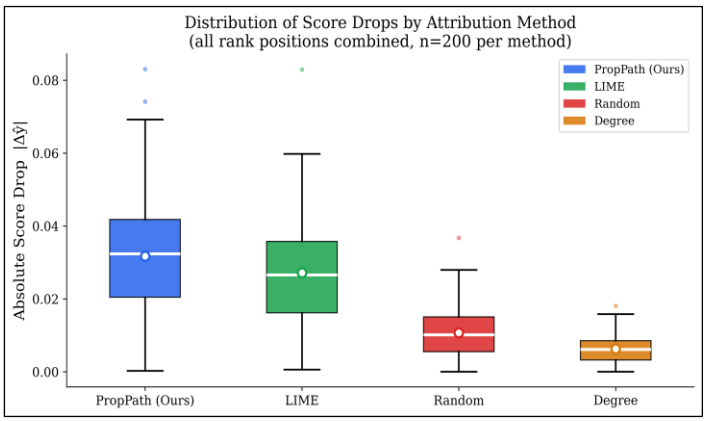


Figure 5: Distribution of score drops (n=200 per method).
Source: Authors, (2026).

VI.2 RANK CHANGE ANALYSIS

Table 2 and Figure 6 present rank change rates. Rank change rates increase monotonically with rank position for PropPath and LIME, since items at rank 20 have smaller score margins. The Degree baseline's high rank change rates (up to 72%) despite low score drops reveal a deceptive pattern: removing popular items triggers widespread small normalisation-induced rank shuffles without genuinely altering the model's preference signal.

Table 2: Rank change rate (RC%) by method and target rank position.

Method	R@1	R@5	R@10	R@20	Overall
PropPath (Proposed)	6.0%	10.0%	20.0%	54.0%	22.5%
LIME	2.0%	4.0%	12.0%	52.0%	17.5%
Random	0.0%	22.0%	24.0%	40.0%	21.5%
Degree	14.0%	36.0%	60.0%	72.0%	45.5%

Source: Authors, (2026).

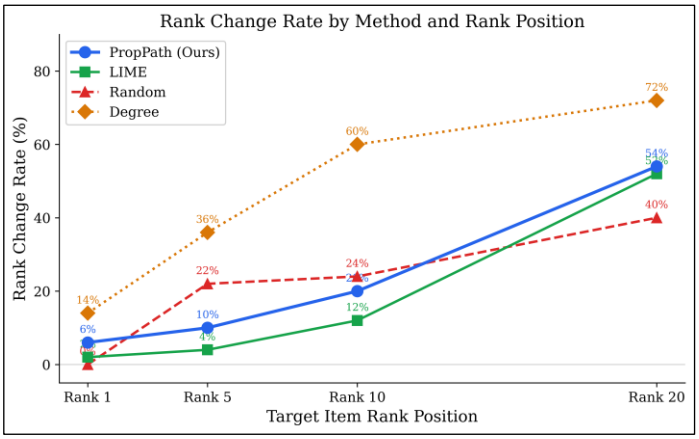


Figure 6: Rank change rate (%) by method across four target rank positions.
Source: Authors, (2026).

VI.3 FAITHFULNESS EVALUATION

Table 3 and Figures 7 and 8 present faithfulness results.Pearson $r = 0.536$ confirms a moderate positive relationship between structural sensitivity and post-fine-tuning drops. The divergence between Pearson and Spearman ($\rho = 0.281$) reflects the influence of an extreme outlier. Sign agreement at 51.0% indicates that PropPath reliably ranks edges by influence magnitude but does not reliably predict the direction of score change under fine-tuning. The systematic positive bias (mean error ≈ 0.103) confirms that structural sensitivity overestimates drops: the model compensates for removed edges via other embedding dimensions during fine-tuning.

Table 3: Faithfulness evaluation: structural sensitivity vs. post-fine-tuning ground truth.

Metric	Value
Pearson r	+0.536 (p < 0.0001)
Spearman ρ	+0.281 (p == 0.0005)
Sign Agreement	51.0% (75/147)
Sample size	147 (50 users x 3 edges)

Source: Authors, (2026).

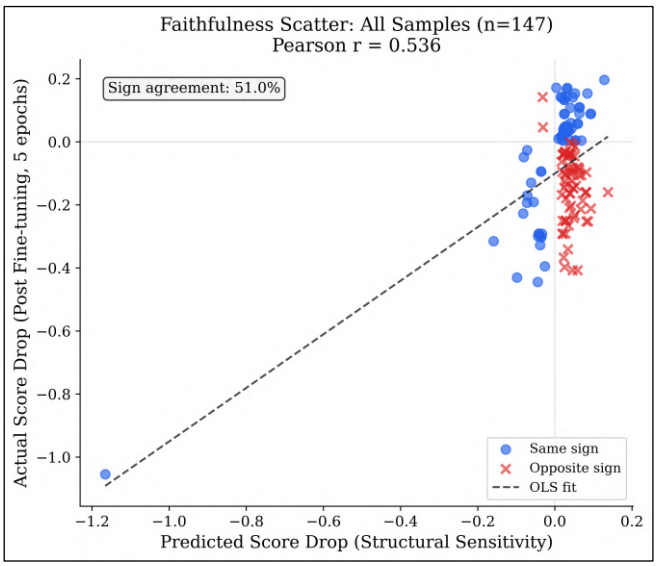


Figure 7a: Faithfulness scatter: all 147 samples (Pearson r = 0.536).
Source: Authors, (2026).

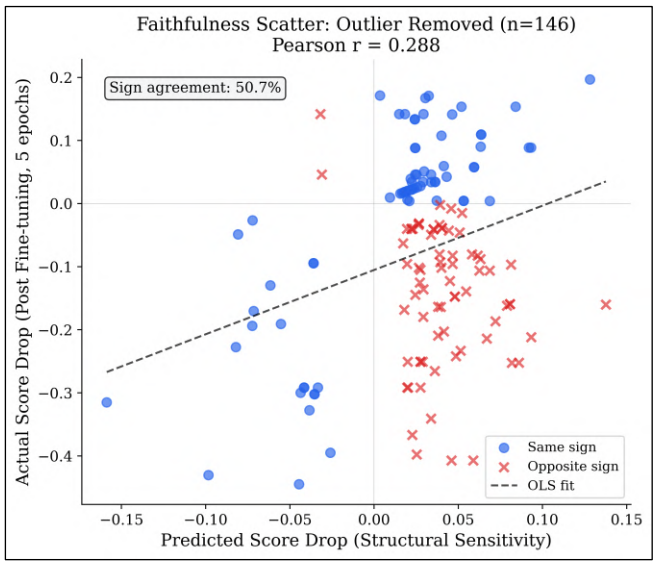


Figure 7b: Faithfulness scatter: outlier removed (n=146, r=0.288).
Source: Authors, (2026).

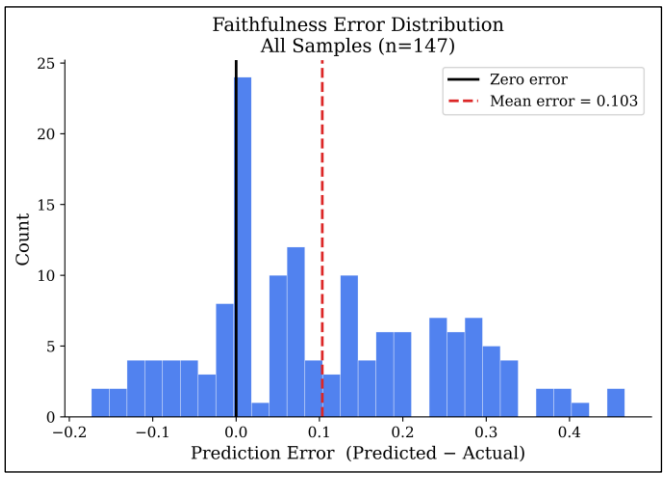


Figure 8a: Prediction error distribution: all 147 samples.
Source: Authors, (2026).

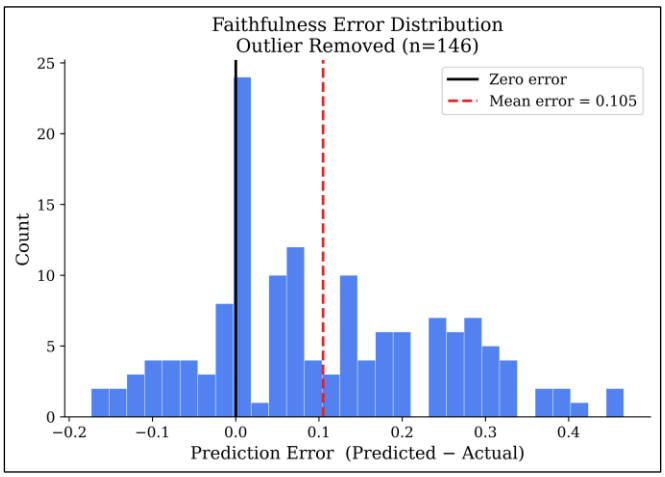


Figure 8b: Prediction error distribution: outlier removed.
Source: Authors, (2026).

VI.4 LAYER CONTRIBUTION ANALYSIS

Table 4 and Figures 9 and 10 present layer contribution scores across five recommendation cases. Three patterns emerge. First,, indicating recommendations primarily driven by direct interaction embeddings. Second, in Layer 1-dominant cases (American Beauty, Being John Malkovich), the top attributed items are thematically related but not directly co-interacted with by the target user, confirming that 1-hop collaborative signal is captured. Third,in all cases, suggesting actionable explanations lie within 1 hop of the user for 3-layer LightGCN on MovieLens-1M.

Table 4: Propagation layer contribution scores for five representative recommendation cases.

Case	C0	C1	C2	C3	k*	C0^	C1^	C2^	C3^
Strangers on a Train	**7.84**	5.28	2.54	1.58	0	**0.45**	0.31	0.15	0.09
American Beauty	2.38	**8.24**	3.67	4.60	1	0.13	**0.44**	0.19	0.24
The Fly	**4.49**	2.90	1.41	1.49	0	**0.44**	0.28	0.14	0.14
Being John Malkovich	6.96	**7.34**	2.66	3.79	1	0.34	**0.35**	0.13	0.18
Nightmare Before Xmas	**6.32**	5.06	2.92	2.26	0	**0.38**	0.31	0.18	0.14

Source: Authors, (2026).

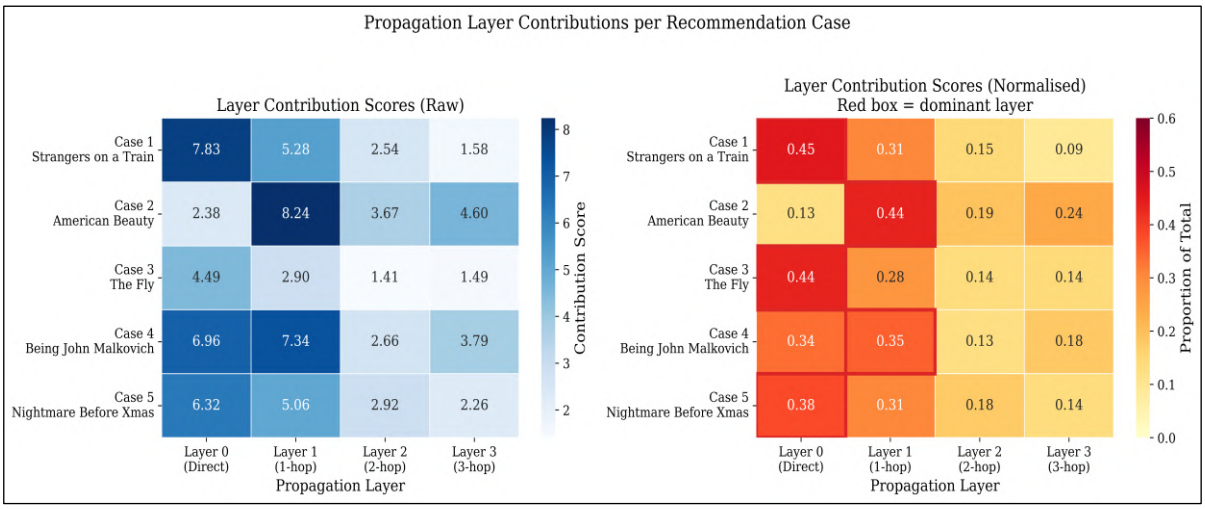


Figure 9: Heatmaps of raw (left) and normalised (right) layer contribution scores.
Source: Authors, (2026).

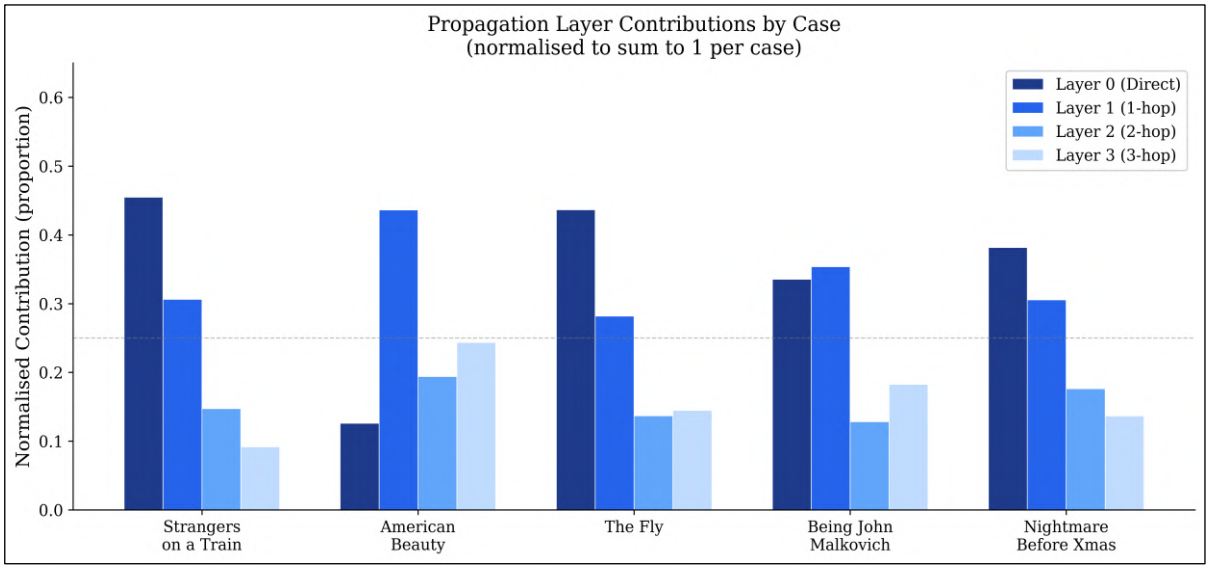


Figure 10: Grouped bar chart of normalised layer contributions per case.
Source: Authors, (2026).

VI.5 PER-USER AND CASE STUDY ANALYSIS

Figure 11 presents per-user score drops for PropPath and LIME across 10 representative users. Figure 12 presents the case study for User 5439. The top attributed item (A Family Thing, 1996) is a warm family comedy-drama — semantically coherent with Babe's genre profile. It is ranked first by both PropPath and LIME, providing cross-method corroboration. The score drop of 0.094 is the largest single-edge drop in our evaluation, confirming the attribution's quantitative significance.

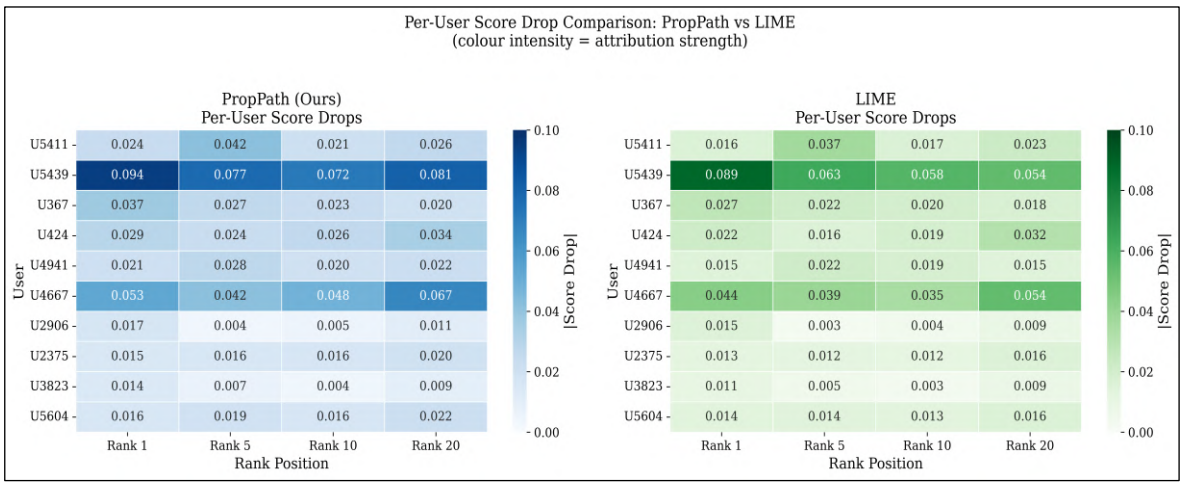


Figure 11: Per-user score drop heatmaps for PropPath (blue) and LIME (green) across 10 users.
Source: Authors, (2026).

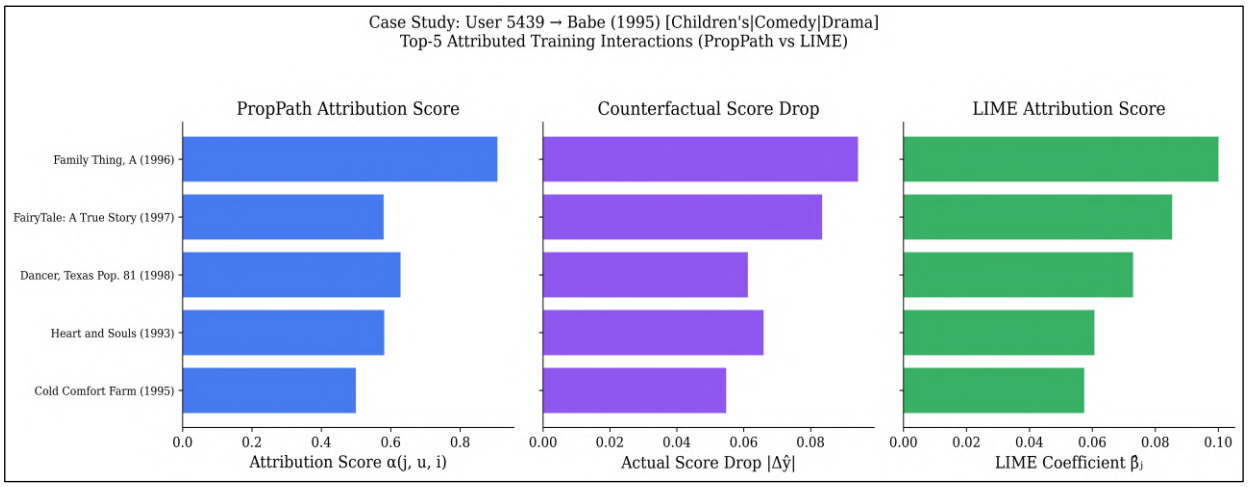


Figure 12: Case study for User 5439 -> Babe (1995). PropPath and LIME both rank A Family Thing (1996) first with score drop 0.094. Source: Authors, (2026).

VII. CONCLUSION

We presented a post-hoc explainability framework for LightGCN combining Propagation Path Analysis with Counterfactual Graph Editing. The framework provides explanations at two levels: the layer level (which propagation hop drives the recommendation) and the edge level (which training interactions are most influential). Quantitative evaluation on MovieLens-1M demonstrates3.02× lift over random, 1.26× over LIME, and 5.35× over degree-based attribution. Faithfulness evaluation yields Pearson $r = 0.536$ against post-fine-tuning ground truth. Layer contribution analysis reveals that actionable explanations lie predominantly within 1 hop of the user, with Layers 2–3 contributing below 25% in all evaluated cases.

Limitations: Sign agreement at 51% indicates structural sensitivity is better suited to influence ranking than directional prediction. The framework is specific to LightGCN and does not directly generalise to attention-based or non-linear GNN architectures.

Future Work: Promising directions include extending to attention-based GNNs, developing user-facing explanation templates, applying the framework to fairness auditing [2], and scaling faithfulness evaluation to larger user samples.

VIII. AUTHOR'S CONTRIBUTION

Conceptualization: Pranav Nallari, Dr. Jayakumar K.
Methodology: Pranav Nallari, Dr. Jayakumar K.
Investigation: Pranav Nallari, Dr. Jayakumar K.
Discussion of results: Pranav Nallari, Dr. Jayakumar K.
Writing – Original Draft: Pranav Nallari.
Writing – Review and Editing: Pranav Nallari, Dr. Jayakumar K.
Resources: Dr. Jayakumar K.
Supervision: Dr. Jayakumar K.
Approval of the final text: Pranav Nallari, Dr. Jayakumar K.

IX. ACKNOWLEDGMENTS

The authors thank the School of Computer Science and Engineering, Vellore Institute of Technology, Vellore, Tamil Nadu, India, for support in conducting this research.

X. REFERENCES

[1] He, X., Deng, K., Wang, X., Li, Y., Zhang, Y., & Wang, M. (2020). LightGCN: Simplifying and Powering Graph Convolution Network for Recommendation. In Proc. SIGIR. ACM.

[2] Ekstrand, M. D., et al. (2022). Fairness and discrimination in recommendation and retrieval. Found. Trends Inf. Retr.

[3] Zhang, Y., & Chen, X. (2020). Explainable recommendation: A survey and new perspectives. Found. Trends Inf. Retr., 14(1), 1-101.

[4] Ribeiro, M. T., Singh, S., & Guestrin, C. (2016). "Why should I trust you?": Explaining the predictions of any classifier. In Proc. KDD. ACM.

[5] Lundberg, S. M., & Lee, S.-I. (2017). A unified approach to interpreting model predictions. In Advances in NeurIPS.

[6] Wang, X., He, X., Wang, M., Feng, F., & Chua, T.-S. (2019). Neural graph collaborative filtering. In Proc. SIGIR.

[7] Rendle, S., Freudenthaler, C., Gantner, Z., & Schmidt-Thieme, L. (2012). BPR: Bayesian personalized ranking from implicit feedback. arXiv:1205.2618.

[8] Zheng, L., Lu, C.-T., Jiang, F., Zhang, J., & Yu, P. S. (2018). Spectral collaborative filtering. In Proc. RecSys.

[9] Velickovic, P., et al. (2018). Graph attention networks. In Proc. ICLR.

[10] Zhang, S., Yao, L., Sun, A., & Tay, Y. (2019). Deep learning based recommender system: A survey and new perspectives. ACM Comput. Surv., 52(1).

[11] Ying, R., Bourgeois, D., You, J., Zitnik, M., & Leskovec, J. (2019). GNNExplainer: Generating explanations for graph neural networks. In Advances in NeurIPS.

[12] Lucic, A., et al. (2022). CF-GNNExplainer: Counterfactual explanations for graph neural networks. In Proc. AISTATS.

[13] Luo, D., et al. (2020). Parameterized explainer for graph neural network. In Advances in NeurIPS.

[14] Yuan, H., et al. (2021). On explainability of graph neural networks via subgraph explorations. In Proc. ICML.

[15] Chen, X., et al. (2019). Collaborative memory network for recommendation systems. In Proc. SIGIR.

[16] Jain, S., & Wallace, B. C. (2019). Attention is not Explanation. In Proc. NAACL.

[17] Guidotti, R., et al. (2018). A survey of methods for explaining black box models. ACM Comput. Surv., 51(5).

[18] Ghazimatin, A., et al. (2020). PRINCE: Provider-side interpretability with counterfactual explanations in recommender systems. In Proc. WSDM.

[19] Tran, K., et al. (2021). Counterfactual explanations for neural recommenders. In Proc. SIGIR.

[20] Harper, F. M., & Konstan, J. A. (2015). The MovieLens datasets: History and context. ACM Trans. Interact. Intell. Syst., 5(4).

Journal of Engineering and Technology for Industrial Applications

ISSN ONLINE: 2447-0228

ITEGAM-JETIA

Manaus, v.12 n.60, p.840-851 July/August, 2026.
DOI: https://doi.org/10.5935/jetia.v12i60.3391

RESEARCH ARTICLE OPEN ACCESS

PREDICTION OF WATER QUALITY INDEX (WQI) USING A NOVEL HYBRID WATER WAVE OPTIMIZED EXTREME GRADIENT BOOSTING

R.Sarala*[1], R.S. Ponmagal[2]

[1*]Research Scholar, SRM Institute of science and technology, Chennai, India
[2]Association Professor, SRM Institute of science and technology, Chennai, India.

[1]http://orcid.org/0009-0007-9776-2413, [2]http://orcid.org/0000-0002-7228-1310

E-email: *sr8749@srmist.edu.in, ponmagas@srmist.edu.in,

ARTICLE INFO

Article History
Received on: january 2, 2026
Reviewed on: february 08, 2026
Accepted on: July 01, 2026
Published on: July 31, 2026

Keywords:
Water Quality Index (WQI),
Outlier Detection (Box Plot Analysis),
Min-max normalization,
Independent Linear Analysis (ICA),
Hybrid Water Wave Optimized extreme Gradient Boosting (HWW-XGB).

ABSTRACT

Determining the drastic changes in water quality in this contaminated period is an urgent requirement that is crucial for the continued existence of the current and growing water demand. This is why it is essential for maintaining the water supply. Due to variability and complexity in the data, the water quality index (WQI) has been developed as a reliable way to express water quality. Analyzing the data relative to the water quality has been extremely difficult. In this investigation, the WQI prediction of water samples using the novel Hybrid Water Wave Optimized eXtreme Gradient Boosting (HWW-XGB). In this research, the data preprocessing using the Outlier Detection (Box Plot Analysis) and Min-max normalization was finished to minimize the computational time. Pre-processing is a crucial first step in the proposed system because the dataset contains inappropriate and inaccurate data. The Independent Linear Analysis (ICA) is utilized to extract the required features. The pre-processed features are removed through feature extraction, eliminating unnecessary data for the next essential phase. The collected features are fed into Hybrid Water Wave Optimized eXtreme Gradient Boosting (HWW-XGB) classifier. The effectiveness of the proposed approach was demonstrated when compared to the existing method.

Copyright ©2026 by authors and Galileo Institute of Technology and Education of the Amazon (ITEGAM). This work is licensed under the Creative Commons Attribution International License (CC BY 4.0).

I. INTRODUCTION

The WQI is a useful measure for evaluating and tracking the available water resource quality. It gives a numerical rating that illustrates the combined impact of many water quality factors, enabling straightforward comparison and analysis of water quality data. The index considers some physical, chemical, and biological parameters to assess a water body's general health [1]. Temperature, pH level, dissolved oxygen, turbidity, total dissolved solids, biochemical oxygen demand, nitrate, and phosphate concentrations, and the presence of pathogens are some of the factors taken into account by the WQI. These variables indicate several facets of water quality, including its capacity for human use, purity, and ability to sustain aquatic life. It may assess the water's fitness for different benefits, such as drinking, leisure, or ecological health, by monitoring and examining these factors [2]. Individual ratings are produced for each parameter using the relevant scales or algorithms, and each parameter is given a weight depending on its relative relevance. An overall Water Quality Index score is then calculated using these specific ratings. Higher values on the index, which typically ranges from 0 to 100, represent usually higher water quality. Depending on the local and environmental factors, different areas may have unique WQI approaches [3] [4]. These courses provide a clearer knowledge of water quality, enabling decision-makers, resource managers, and the general public to swiftly evaluate a water body's status. Each metric has predetermined thresholds and recommendations often drawn from regulatory requirements [5]. The WQI may convey detailed water quality data clearly and intelligibly, making it a useful communication tool. It aids in locating problem regions, emphasizing possible pollution sources, and directing decision-making procedures for managing and safeguarding water resources. By comparing previous data, the index also makes it possible to analyze long-term trends, which makes it easier to spot changes in water quality over time [6].

Authorities may identify pollution sources, evaluate the efficacy of pollution management methods, and take proactive measures to protect water resources by establishing baseline water quality conditions and monitoring changes [7]. It is crucial to remember that the WQI is a broad indicator and cannot account for every facet of water quality. It gives a general image but does not take the place of careful observation and examination of particular aspects. The weights allocated to each parameter may also change based on the local circumstances and the planned use of the water resource, which might affect the index values and interpretations. Consequently, the WQI should be used in combination to other monitoring and assessment methods to offer a full picture of water quality [8] [9]. The Water Quality Index also helps to educate and raise public awareness about water quality. It allows people to understand the significance of water quality measures and their impacts on the environment and human health. When they have access to clear and understandable information, communities may actively participate in conservation initiatives, advocacy, and protection of their local water resources [10]. It could miss certain details or some pollutants. To acquire a more thorough knowledge of water quality and ecological integrity, it is often used in combination with other monitoring methods and evaluations, such as chemical analysis, biological, and environmental assessments [11]. It offers a standardized approach to assessing water quality across diverse locations by considering several characteristics and producing a composite score. The index promotes trend analysis, improves public awareness, helps with decision-making, and helps preserve and conserve water bodies for the benefit of both people and ecosystems [12-25]. In this study, we proposed the innovative Hybrid Water Wave Optimised extreme Gradient Boosting (HWW-XGB) to estimate the WQI of water samples.

I.1 CONTRIBUTIONS TO THIS STUDY ARE AS FOLLOWS

- This inquiry uses the novel HWW-XGB to predict the WQI of water samples.
- The data in this study were preprocessed using the Min-Max normalization and Outlier Detection techniques.
- The necessary features are extracted using the ICA.
- The performance metrics such as Correlation coefficient, Root Mean square error, Mean square error, Mean absolute error, & sensitivity are analyzed.

The remainder of this research is organized as follows. We provide a thorough assessment of the relevant work in Section 2. A summary of the proposed model's formulation is given in Section 3, and its results are presented in Section 4. The conclusion is mentioned in Section 5.

II. RELATED WORKS

Research [13] evaluated the uncertainties inherent in the WQI model; a statistically solid and rigorous technique. There are eight possible WQI models. Model uncertainty was estimated using a Monte Carlo simulation, and delay in WQI models was predicted using a Gaussian Process Regression approach for each sample location. It was discovered that the sub-index functions add significant uncertainty and impact the model's dependability. Research [14] developed a unique weight-integrated health hazard index and employ soft computing methods, including fuzzy logic, to identify and forecast the quality of drinkable water. This study's findings corroborate ANFIS's status as a credible method for predicting potable water's WQI, making it useful for those choosing water resource management. To effectively control and avoid river pollution, it is necessary to anticipate river WQI. Accurately predicting water quality parameters is challenging because of the significant coupling connection between distinct water quality indicators that impact each other [15]. Research [16] presented Extra Tree Regression (ETR), a ensemble model for forecasting monthly WQI values along the Lam Tsuen River in Hong Kong. Uncertainty analysis shows that the model structure is more influential on prediction accuracy than input parameters. The ETR model is an advancement over prior methods of WQI prediction since it requires fewer input parameters and yields more accurate predictions. Total Fe concentrations were average, 0.14 mg/L over the year. The WQI and the Water Pollution Index data are presented as means and standard deviations. Thirty percent of locations had WQI and Water Pollution Index values for groundwater, which made it unfit for human consumption. The total hazard index (THI) calculated the potential danger to human health from drinking groundwater [17]. The research [18] presented a Deep Learning (DL) stacking ensemble model to predict the WQI by combining existing models.

To reduce water pollution, keeping an eye on pH and turbidity was shown to be particularly important using sensitivity analysis. The greatest uncertainty is associated with the electrical conductivity and total dissolved solids in determining WQI. It allows for deploying clean manufacturing procedures to minimize pollution and enhance water quality by providing precise information to researchers, decision-makers, and water scientists. Research [19] used ML methods, such as character and ensemble learners, to predict WQI. Research [20] investigated the chemistry of view irrigate and evaluated its feasibility for industrial use in the semi-arid Guanzhong Basin in northwest China. Using multivariate statistical analysis methods, they calculated the relative importance of each characteristic to the overall quality of the water used in industrial processes. The results show that calcite, dolomite, anhydrite, and gypsum dissolve in groundwater to control the geochemistry of the water below the surface. According to the geospatial study, the northeastern parts of Xi'an and the Guanzhong Basin are home to the most polluted groundwater samples. Research [21] presented the results of a decade-long evaluation of artificial intelligence research on the WQI, intending to highlight the most promising approaches and promising models for use by future water quality. It also demonstrates that there is no universally superior Artificial intelligence (AI) model; it is necessary to the efficacy of various model combinations to determine which approach or model is most suitable for a certain country or area. AI has been more popular in recent decades, but there is still plenty of potential for competition and advancement in the water quality index. Research [22] used eight water quality criteria to evaluate a drinking water source by analyzing seven hundred and ten samples from a water-poor area of India. The whole sample was split into ten sections, each representing a distinct region of the world.

A approach to the problem of uniquely defining the quality of drinking water, which is complicated by the need to comprehend the cumulative influence of several criteria influencing water quality. A paradigm is presented that, with the correct tools, might be automated to help government organisations better comprehend and control changing water quality.

III. PROPOSED METHOD

In this research, the HWW-XGB was used to estimate the WQI of water samples. The preprocessing of the data using the Outlier Detection (Box Plot Analysis) and Min-max normalization was finished to minimize the computational time. The ICA is utilized to extract the required features. The pre-processed features are removed through feature extraction, eliminating unnecessary data for the next essential phase. Figure 1 shows the flow of the proposed model.

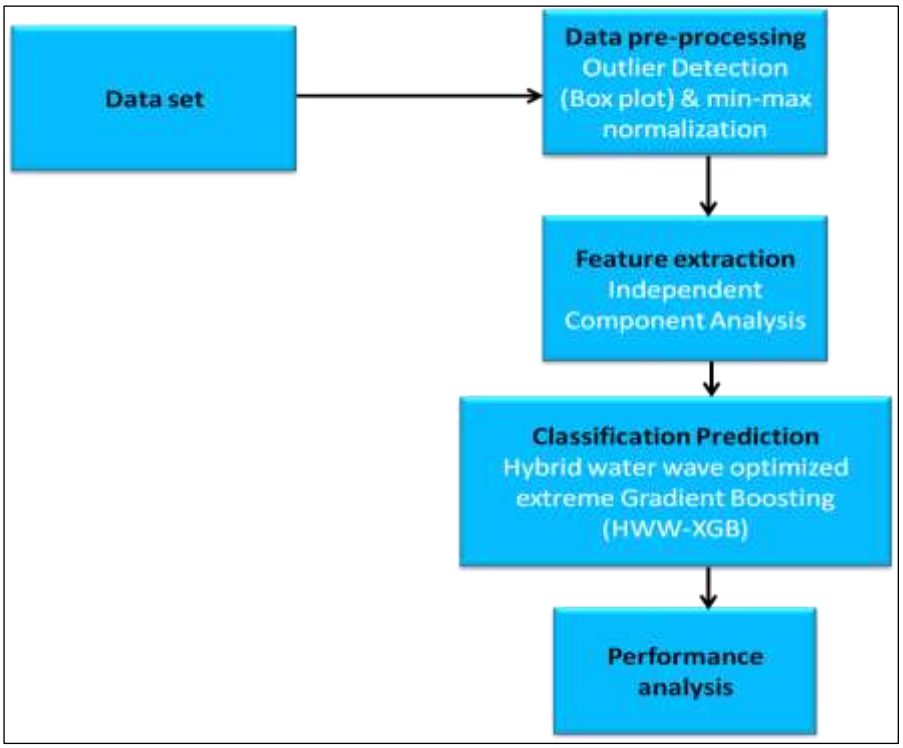


Figure 1: Flow of proposed model.
Source: Authors, (2026).

III.1 DATASET

Two strategically situated water quality monitoring stations throughout the watershed be used to collect monthly data on water quality over six years (2012-2018). There were readings for dissolved oxygen, total solids, fecal coli form, pH, phosphate, nitrate, turbidity, and electrical conductivity, among other parameters. Together, they were utilized to determine Iran's WQI. The Mazandaran Environmental Protection Organisation lab followed conventional sampling, storage, and analysis procedures. Utilising the tenfold traverse substantiation technique, the dataset was split 70:30 across the training and testing sets. Although no hard and fast rule exists, this ratio is the most often used modeling strategy for geographical and temporal forecasting [23].

III.2 DATA PREPROCESSING

The data preprocessing using the Outlier Detection (Box Plot Analysis) and Min-max normalization was finished to minimize the computational time.

III.2.1 Outer Detection

Missing data and data anomalies may significantly influence future model projections because of environmental changes and equipment failures at water quality monitoring sites. The experimental results are completed using linear interpolation, using the discovered anomalous values as missing values. It is common practice to spot outliers using modeling techniques and graphical approaches (such as box-line plots and normal distribution plots). The box-line property was utilized in this study to spot unusual results. The quantile of the data was utilized by the box-line plot method to find the extremes. This is a standard kind of statistical graph that has many applications in both research and business. Figure 2 depicts the form characterized by the box-line plot.

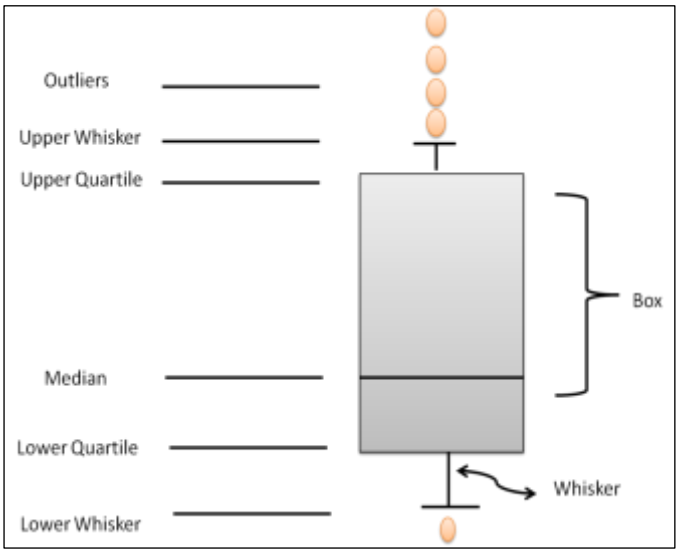


Figure 2: Structure of box-line diagram.
Source: Authors, (2026).

Figure 2 shows the median as the number that divides the upper and lower halves of the data. In contrast, the lower quartile represents the 25% quartile, and the higher quartile represents the 75% quartile. Where Q3 − Q1 is the quartile difference, the upper whisker formula is Q3 + 1.5(Q3 − Q1), and the lower whisker formula is Q1 − 1.5(Q3− Q1). To judge whether or not a data point is an outlier, a box-line diagram may be utilized if the value of the variable in question is beyond the range covered by the upper and lower whiskers, respectively.

III.2.2 Min-Max Normalization

Preparing and enhancing datasets for subsequent analyses is the focus of data pre-processing, a step in the study of big data that aims to discover new information faster and more accurately. Putting an issue statement into practice is a preparatory step in the overall processing flow. Particularly important is the function that implementation plays in data processing techniques like soft computing, cloud computing, and the reduction or expansion of a variety of data before its usage in a later phase. Numerous normalizing methods are available, including the Min-Max method, the Z-score method, and the Decimal scaling method, to name a few. Min-max normalization is an initial processing stage, a scaling technique, or a mapping approach. It might be really helpful for assessing data or making plans.
Normalization is calculated in equation (1),

$$K' = \left(\frac{k - \min\ value\ of L}{\max\ value\ of - \min\ value\ of\ k}\right) * (P - H) + H \tag{1}$$

Where *K* is the Min-Max normalized set of data and [*H, P*] is the bounding box. *K* is the true data range, while *N* is the mapped data range.

III.3 FEATURE EXTRACTION USING INDEPENDENT COMPONENT ANALYSIS

Let's say we have many independent measurements of a complex signal simultaneously. Time resolved spectroscopy allows us to get a movement of the explanatory transit's light curve at each spectrograph's resolution. Here, we refer to each time series measured using the notation x_k (t), where N is the total number of time series and k is the index for that time series.

$$x_k(t) = a_{k,1}\, S_a(t) + S_{wn}(t) + a_{k,2} S_{sn1}(t) + a_{k,3} S_{sn2}(t) + \cdots + a_{k,} N_{sn} S_{sn}(t) \tag{2}$$

As a vector sum (time dependency has been removed for simplicity).

$$x_k = a_{k,1} S_a + a_{k,2} S_{wn} + \sum_{l=3}^{N_{sn}} a_{k,l} S_{sn} \tag{3}$$

Where *l* is the estimated index of the source signal, we have k = l unique source signals for non over full sets, which is the same as the number of time series. It's important to remember that when k>l, we have access to more time series than source signals inside the whole set. In such circumstances, we may use dimensionality reduction techniques for the data collection or use selection criteria to narrow down a subset of predicted source signals. We can also express Equation (2) in matrix form as

$$X = As \tag{4}$$

As an alternative notation, we may write $s = s_a + s_{wn} + s_{sn}$ to explicitly separate the astrophysical, white noise, and systematic contributions. The "mixing matrix" A consists of the weights a_k, *l*, and has N × N dimensions.

III.4 CLASSIFICATION USING HYBRID WATER WAVE OPTIMIZED EXTREME GRADIENT BOOSTING

The hybrid machine learning method known as Hybrid Water Wave Optimised extreme Gradient Boosting (HWW-XGB) combines the Water Wave Optimisation (WWO) algorithm with the extreme Gradient Boosting (XGB) algorithm. By merging the search and optimization skills of WWO, it seeks to improve the speed and optimization capabilities of XGB. The effective and popular gradient boosting method, XGB, excels at managing structured/tabular data and obtaining high prediction accuracy. By repeatedly optimizing an objective function that combines prediction performance and regularisation, it creates an ensemble of weak decision trees. The advantages of XGB are its quickness, scalability, and capacity for complicated nonlinear interactions. WWO is an optimization method that draws inspiration from nature and the behavior of water waves. It uses a metaheuristic algorithm to explore the search space and identify the best answers by simulating the motion of water waves. WWO has been used to tackle various optimization issues and has successfully located global optima. HWW-XGB combines the benefits of both methods to strengthen XGB's overall performance and the optimization process. It uses WWO's capabilities for exploration and exploitation to direct the search for the best hyperparameters or model configurations in XGB. HWWO-XGB aims to identify better combinations of hyperparameters that enhance model performance by searching the hyperparameter space using WWO. WWO is included in the XGB optimization process as part of the hybridization phase. A population of potential solutions is initialized in the hyperparameter space using the WWO method. Then, these possible solutions are assessed using XGB and the appropriate hyperparameter settings. Utilizing the iterative approach and the WWO tenets, the assessment findings are utilized to update and improve the solutions. In HWW-XGB, the hybridization of WWO and XGB enables more efficient exploration of the hyperparameter space, which may enhance model performance and generalization. The goal of HWW-XGB is to identify optimum or nearly optimal hyperparameter configurations for XGB models by combining the high prediction powers of XGB with the optimization capabilities of WWO.

III.4.1. Extreme gradient boosting

The Extreme Gradient Boosting (XGB) technique is a regression tree with decision-tree-like decision-making capabilities. It supports both classification and regression. This approach is a scalable and effective variation of the gradient boosting machine (GBM), which has been extensively used in computer vision, data mining, and other areas. Recently, XGB has primarily advanced in two locations as a sort of gradient boosting machine: speeding up the tree building and suggesting a new distributed technique for tree searching. The heart of XGB is optimizing the value of the goal function. Considering the dataset $D = \{(x\_(i,)yi)\}$ represents the xi tumor's gene expression profile and the related yi binary label (early stage or late stage) is used to identify the tumor. Equation (5) is the objective optimization function for the XGB model with K decision trees.

$$\hat{z}_j = \sum_{l=1}^{l} e_l(w_j), e_l \epsilon E \tag{5}$$

Where f_k represents a separate tree with leaf scores, and F is the space of the regression tree. In equation (6), the loss function is shown.

$$K(e_k) = \sum k\left(\hat{z}_j, z_j\right) + \sum \Omega\, e_k \tag{6}$$

Différentiable loss function l in the first term assesses the discrepancy between the output $\acute{y}_i$ that anticipâtes and the actual output y_i.

$$\hat{z}_j^{(s)} = \hat{z}_j^{(s-1)} + e_s(w_j) \tag{7}$$

$$\Omega(e) = \gamma S + \frac{1}{2}||x||^2 \tag{8}$$

Where w is the score on each leaf, and T is the number of leaf nodes. We may thus determine that from equation (9)

$$S(e_s) \approx \sum_{i=1}^{S}\left[\left(\sum_{j\in J_i} h_j\right)x_i + \frac{1}{2}\left(\sum_{j\in J_i} g_j + \lambda\right){x^2}_i\right] + \gamma S \tag{9}$$

Where g_i and h_i are the loss function first and second gradient statistics, respectively.

III.4.2. Water Wave Optimisation (WWO) Algorithm

The WWO method essentially models the processes of wave motion propagation, refraction, and breaking to achieve an optimal global/local search balance. Each water wave's fitness level is a function of its height and wavelength. Figure 3 shows that the water wave in shallow water is a greater fitness value, a higher wave height, and a longer wavelength than the wave in deep water, which have a lesser condition cost, a lower signal elevation, and a shorter wavelength.

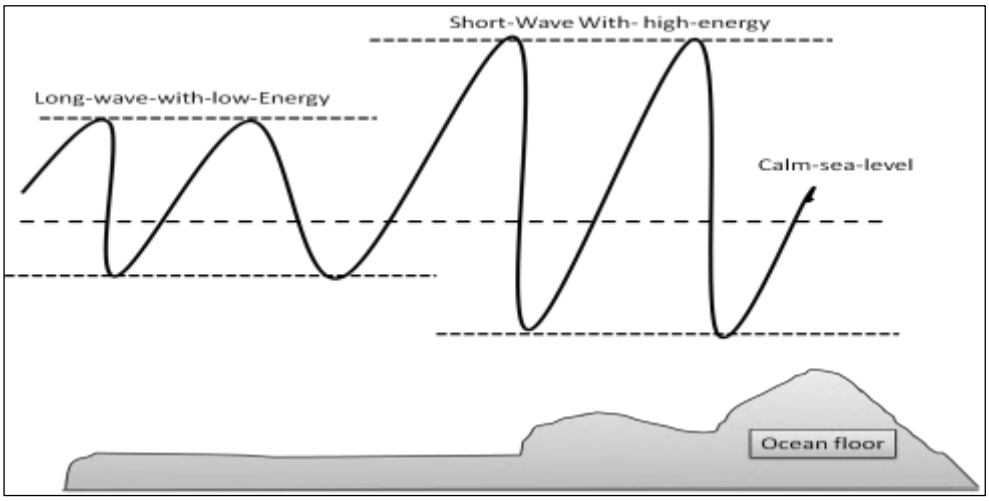


Figure 3: Variations in wave form between deep and shallow sea.
Source: Authors, (2026).

III.4.2.1 Propagation

The dissimilarity of the sea bed causes waves to propagate at varying heights and wavelengths. The initial water wave *x* is propagated to create a new body of water denoted by *x′*. To update the location in equation (10), we assume that the first water wave was at position x (d) & subsequent wet gesture was at position *x (d).*

$$x^{'}(d) = x(d) + rand(-1,1).\lambda L(d) \tag{10}$$

Where *L (d)* denotes the span of the search space in units of dth, λ is the wavelength of water wave *x*, and rand (-1, 1) is a consistently distributed random integer between 1 and 1. If wave *x′* is not found within the search range, a new place is chosen randomly. The opposite is true, with wave *x* being kept and the wave height dropping by one to signify that the wave's energy has been expended. The wavelength λ is updated in equation (11):

$$\lambda = \lambda \,.\, a^{-(f(x)-f\,min^{+\varepsilon}/(f\,max^{-f}\,min^{+\varepsilon}} \tag{11}$$

Where α is the attenuation coefficient for wavelengths, f_{min} and f_{max} are the lowest and most health standards, and ε is a tiny optimistic numeral chosen such that the numerator does not equal zero.

III.4.2.2 Breaking

The steepness of the wave crests increases as the wave energy rises. When the crest velocity is greater than the wave's propagation velocity, the wave will disintegrate into some independent waves. The WWO algorithm maximizes population variety by performing a breaking operation on the best water wave x*. The equation (12) for the positional update is as follows:

$$x^{'}(d) = x(d) + N(0,1).\ \beta L(d) \tag{12}$$

Where β is a broken gesture coefficient. If the fitness value of all the solitary waves acquired from the breaking operation is lower than that of water wave *x*, x*;* otherwise, *x** be replaced with an optimum introverted gesture from the population.

III.4.2.3 Refraction

The energy of a water wave gradually decreases until it is zero as it travels through the water. It has been shown that using a refraction operation when the water wave height is zero helps the WWO algorithm converge more quickly and accurately. The refraction of water wave *x* is shown in equation (13).

$$x^{'}(d) = N(\frac{(x*(d)+x(d))}{2}, \frac{|x*(d)-x(d)|}{2} \tag{13}$$

The function $N\ (\mu, \sigma)$ generates a Gaussian random number with a mean μ and standard deviation σ, where x^{*} is the best solution obtained at the present point. In reality, this enables wave x to gain insight from the currently best wave x^{*}. Since h_{max} is the current value of wave x' wave height, the equation (14) for the updated wavelength is shown below.

$$\lambda^{'} = \lambda \frac{f(x)}{f(x^{'})} \tag{14}$$

Algorithm 1: The WWO algorithm's process for solving problems

```
Initialize a water population O at random with m.
        Wavelength is set by waves.
        Breaking coefficient β, Reduction coefficient ∝, and
            Coefficient of decrease in wavelength λ
while stop the extinction criterion is not satisfied, do
    for each water wave xϵ o do
    Use equation (10 to propagate x to a new w′;
    if f (w′) <f (w) next
        if f (w′) < f (w′) next
            Break w′ by utilizing equation (12);
            Update w* with w′;
        else
            Decrease x.h by one;
        if x.h =0 Next
            Refract x to a new w′ by utilizing equations (13) and (14);
    Using equation (11) update the wavelengths.
return w*
```

In Algorithm 1, the WWO algorithm's solution process is described.
Source: Authors, (2026).

IV. RESULT

The suggested method's performance metrics are examined, including Mean absolute error, Root Mean square error, Mean square error, Correlation coefficient, and sensitivity. The existing techniques are adaptive neuro-fuzzy inference system (ANFIS) [24], artificial neural networks (ANN) [24], and K-nearest neighbors (KNN) [24].

IV.1 MEAN SQUARE ERROR (MSE)

The average squared difference between the predicted and actual values in a regression issue is calculated using the MSE, a commonly used statistic. It gives a quantitative assessment of a regression model's overall accuracy or goodness of fit. Mean Square Error (MSE) is represented by equation (15),

$$MSE = (1/n) * \Sigma(y - \hat{y})^2 \quad (15)$$

Where n denotes the number of data points or samples, Σ denotes the summation symbol, y represents the actual (observed) values, and ŷ conveys the predicted values from the regression model. Computing the squared difference between each predicted value and its corresponding actual value adds up all of these squared differences. The squared differences ensure that positive and negative mistakes equally impact the MSE. The sign is removed by taking the square of each contrast, and bigger mistakes are penalized more severely. Figure 4 and Table 1 show Mean Square Error outcomes; ANN scores 56%, KNN 39%, ANFIS 44%, and HWW-XGB 35%.

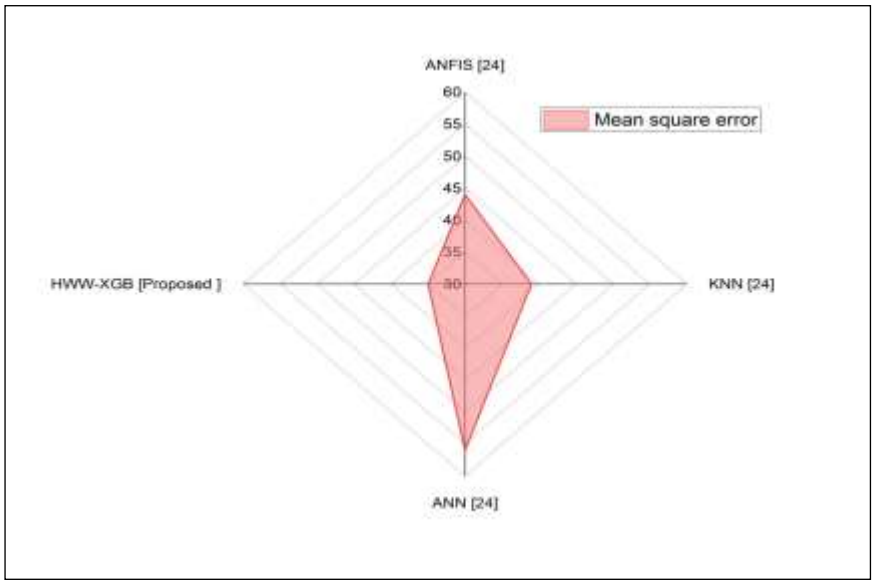


Figure 4: Results of Mean Square Error.
Source: Authors, (2026).

Table 1: Numerical Outcomes of Mean Square Error.

Methods	Mean square error
ANFIS [24]	44
KNN [24]	39
ANN [24]	56
HWW-XGB [Proposed]	35

Source: Authors, (2026).

IV.2 MEAN ABSOLUTE ERROR (MAE)

It is utilized to calculate the usual complete disparity between the predicted and actual values in a regression issue. It indicates the average size of mistakes without taking their direction into account. The MAE equation (16) is as follows:

$$MAE = (1/n) * \Sigma|y - \hat{y}| \quad (16)$$

Where n denotes the number of data points or samples, Σ denotes the summation symbol, y represents the actual (observed) values, and ŷ indicates the predicted values from the regression model. To determine the MAE, add up all of the absolute differences between each predicted value and its corresponding actual value. Without considering their direction, the absolute differences are utilized to estimate the size of mistakes. Because MAE does not square the differences, it handles positive and negative mistakes equally, in contrast to Mean Square Error (MSE), which does. Figure 5 and Table 2 show Root Mean Absolute Error outcomes; ANN scores 58%, KNN 71%, ANFIS 67%, and HWW-XGB 40 %.

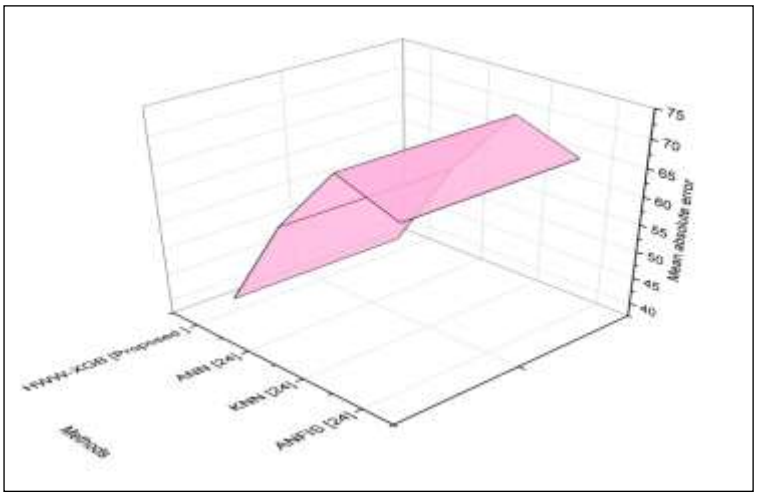


Figure 5: Results of MAE.
Source: Authors, (2026).

Table 2: Numerical Outcomes of Mean Absolute Error.

Methods	Mean absolute error
ANFIS [24]	67
KNN [24]	71
ANN [24]	58
HWW-XGB [Proposed]	40

Source: Authors, (2026).

IV.3 ROOT MEAN SQUARE ERROR

In a regression issue, the average error size between the predicted and actual values is often measured using the Root Mean Square Error (RMSE) metric. It is a variant of the MSE that scales the metric back to the dependent variable's original scale by taking the square root of the MSE. The RMSE measures the usual size of errors and is often used to evaluate a regression model's accuracy and fit quality. The RMSE equation (17) is as follows:

$$RMSE = sqrt((1/n) * \Sigma(y - \hat{y})^2) \quad (17)$$

Where n denotes the number of data points or samples, Σ denotes the summation symbol, y represents the actual (observed) values, and ŷ indicates the predicted values from a model or estimation. Figure 6 and Table 3 show Root Mean Square Error outcomes; ANN scores 51%, KNN 56%, ANFIS 65%, and HWW-XGB 42%.

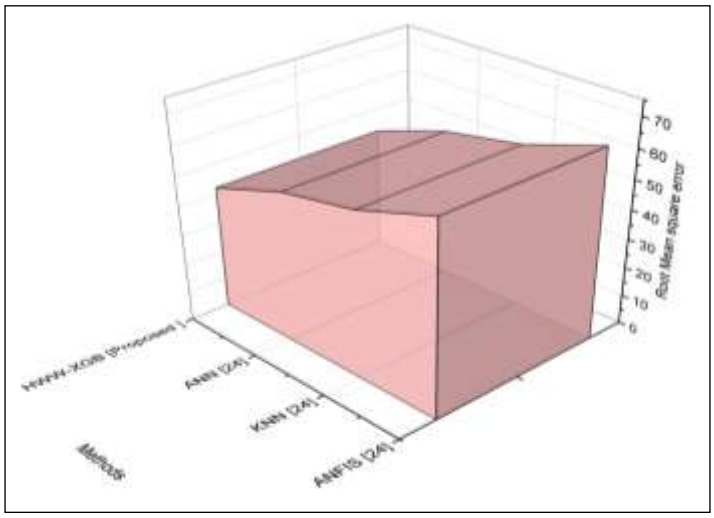


Figure 6: Results of Root Mean Square Error.
Source: Authors, (2026).

Table 3: Numerical Outcomes of RMSE.

Methods	Root Mean square error
ANFIS [24]	65
KNN [24]	56
ANN [24]	51
HWW-XGB [Proposed]	42

Source: Authors, (2026).

IV.4 CORRELATION COEFFICIENT

The degree and direction of the linear connection between two variables are shown by a statistical measure. The correlation coefficient, often known as Pearson's correlation coefficient, is represented by the equation (18):

$$r = \frac{(\Sigma((x-\mu x)(y-\mu y)))}{(sqrt(\Sigma(x-\mu x)^2) * sqrt(\Sigma(y-\mu y)^2)} \quad (18)$$

Where r denotes the Correlation coefficient, Σ denotes the summation symbol, x & y denotes the individual values of the two variables being correlated, and μx & μy denotes the means of the respective variables. The correlation coefficient quantifies the degree to which the variables vary from their mean values in the same or opposing directions. In Figure 7 and Table 4, correlation coefficient outcomes, ANN scores 84%, KNN 82%, ANFIS 80%, and HWW-XGB 95%.

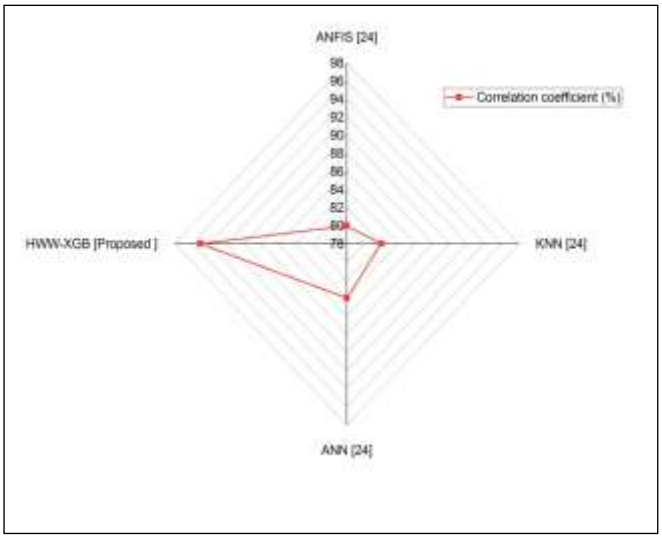


Figure 7: Results of the correlation coefficient.
Source: Authors, (2026).

Table 4: Numerical outcomes of the correlation coefficient.

Methods	Correlation coefficient (%)
ANFIS [24]	80
KNN [24]	82
ANN [24]	84
HWW-XGB [Proposed]	95

Source: Authors, (2026).

IV.5 SENSITIVITY

The sensitivity of the proposed model is its capability to identify each significant sample in a data collection. It may be calculated statistically by dividing the proportion of true positives and false negatives by the sum of true positives and false negatives. Equation (19) is used to determine the sensitivity.

$$sensitivity = \frac{TP}{TP+FN} \tag{19}$$

In Figure 8 and Table 5, Sensitivity-wise, ANN scores 85%, KNN 76%, ANFIS 74%, and HWW-XGB 93%.

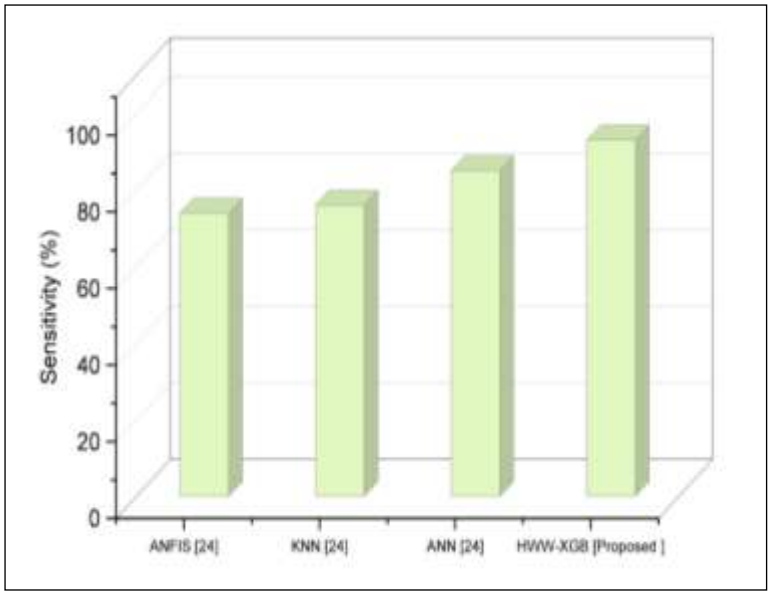


Figure 8: Results of sensitivity.
Source: Authors, (2026).

Table 5: Numerical outcomes of sensitivity.

Methods	Sensitivity (%)
ANFIS [24]	74
KNN [24]	76
ANN [24]	85
HWW-XGB [Proposed]	93

Source: Authors, (2026).

V. CONCLUSION

For assessing and monitoring the general quality of water resources, the WQI is a useful metric. It provides a numerical rating to show the combined effect of several water quality parameters, allowing for easy comparison and interpretation of water quality data. The research uses the novel HWW-XGB to estimate WQI for water samples. To save computing time, the data in this study were preprocessed using outlier detection and min-max normalization. The necessary characteristics are extracted using the ICA. The pre-processed features are eliminated by feature extraction, freeing up data for the next crucial stage. The HWW-XGB classifier receives the gathered characteristics as input. Compared to the current technique, a new approach's efficacy was shown. In the proposed method analysis, the performance metrics exhibit notable scores: Mean Square Error attains a respectable 35%, Mean Absolute Error attains a good 40%, Root Mean Square Error attains a respectable 42%, Correlation Coefficient attains a respectable 95%, and Sensitivity achieves a respectable 93%. By using the fewest characteristics feasible, rather than a surprising number of features, the future study aims to estimate the quality of water effectively.

VI. AUTHOR'S CONTRIBUTION

Conceptualization: R.Sarala, R.S. Ponmagal.
Methodology: R.Sarala, R.S. Ponmagal.
Investigation: R.Sarala, R.S. Ponmagal.
Discussion of results: R.Sarala, R.S. Ponmagal.
Writing – Original Draft: R.Sarala, R.S. Ponmagal.
Writing – Review and Editing: R.Sarala, R.S. Ponmagal.
Resources: R.Sarala, R.S. Ponmagal.
Supervision: R.Sarala, R.S. Ponmagal.
Approval of the final text: R.Sarala, R.S. Ponmagal.

VII. REFERENCES

[1] Derdour, A., Jodar-Abellan, A., Pardo, M.Á., Ghoneim, S.S. and Hussein, E.E., 2022. Designing Efficient and Sustainable Predictions of Water Quality Indexes at the Regional Scale Using Machine Learning Algorithms. Water, 14(18), p.2801.

[2] Wong, W.Y., Al-Ani, A.K.I., Hasikin, K., Khairuddin, A.S.M., Razak, S.A., Hizaddin, H.F., Mokhtar, M.I. and Azizan, M.M., 2022. Water quality index using modified random forest technique: assessing novel input features. CMES-Computer Modeling in Engineering & Sciences.

[3] Zamili, H., Bakan, G., Zubaidi, S.L. and Alawsi, M.A., 2023. Water quality index forecast using artificial neural network techniques optimized with different metaheuristic algorithms. Modeling Earth Systems and Environment, pp.1-11.

[4] Agrawal, S., Jain, S.K., Khatri, A., Agarwal, M., Tripathi, A. and Hu, Y.C., 2022. Novel PSO Optimized Voting Classifier Approach for Predicting Water Quality. Mathematical Problems in Engineering, 2022.

[5] Tong, S., Li, W., Chen, J., Xia, R., Lin, J., Chen, Y. and Xu, C.Y., 2023. A novel framework to improve the consistency of water quality attribution from natural and anthropogenic factors. Journal of Environmental Management, 342, p.118077.

[6] Imani, M., Hasan, M.M., Bittencourt, L.F., McClymont, K. and Kapelan, Z., 2021. A novel machine learning application: Water quality resilience prediction Model. Science of the Total Environment, 768, p.144459.

[7] Tiyasha, Tung, T.M. and Yaseen, Z.M., 2021. Deep learning for prediction of water quality index classification: tropical catchment environmental assessment. Natural Resources Research, 30(6), pp.4235-4254.

[8] Lap, B.Q., Du Nguyen, H., Hang, P.T., Phi, N.Q., Hoang, V.T., Linh, P.G. and Hang, B.T.T., 2023. Predicting Water Quality Index (WQI) by feature selection and machine learning: A case study of An Kim Hai irrigation system. Ecological Informatics, p.101991.

[9] Paul, V., Ramesh, R., Sreeja, P., Jarin, T., Kumar, P.S., Ansar, S., Ashraf, G.A., Pandey, S. and Said, Z., 2022. Hybridization of long short-term memory with Sparrow Search Optimization model for water quality index prediction. Chemosphere, 307, p.135762.

[10] Patil, D., Kar, S., Shastri, V. and Gupta, R., 2023. Qualitative and health risk assessment of water using a novel weight-integrated health hazard and fuzzy-derived indices. Sustainable Water Resources Management, 9(2), p.55.

[11] Lee, H., Park, S., Hang, V., Nguyen, M. and Shin, H.S., 2023. Proposal for a new customization process for a data-based water quality index using a random forest approach. Environmental Pollution, 323, p.121222.

[12] Ramaraj, M. and Sivakumar, R., 2023. Remote Sensing and Nonlinear Auto-regressive Neural Network (NARNET) Based Surface Water Chemical Quality Study: A Spatio-Temporal Hybrid Novel Technique (STHNT). Bulletin of Environmental Contamination and Toxicology, 110(1), p.28.

[13] Uddin, M.G., Nash, S., Rahman, A. and Olbert, A.I., 2023. A novel approach for estimating and predicting uncertainty in water quality index model using machine learning approaches. Water Research, 229, p.119422.

[14] Patil, D., Kar, S. and Gupta, R., 2023. Classification and Prediction of Developed Water Quality Indexes Using Soft Computing Tools. Water Conservation Science and Engineering, 8(1), p.16.

[15] Chen, L., Wu, T., Wang, Z., Lin, X. and Cai, Y., 2023. A novel hybrid BPNN model based on adaptive evolutionary Artificial Bee Colony Algorithm for water quality index prediction. Ecological Indicators, 146, p.109882.

[16] Asadollah, S.B.H.S., Sharafati, A., Motta, D. and Yaseen, Z.M., 2021. River water quality index prediction and uncertainty analysis: A comparative study of machine learning models. Journal of environmental chemical engineering, 9(1), p.104599.

[17] Biswas, P., Hossain, M. and Patra, P.K., 2023. Arsenic hydrogeochemistry, quality assessment, and associated health risks of groundwater through the novel water pollution index (WPI) and GIS approach. Groundwater for Sustainable Development, 21, p.100944.

[18] Talukdar, S., Ahmed, S., Naikoo, M.W., Rahman, A., Mallik, S., Ningthoujam, S., Bera, S. and Ramana, G.V., 2023. Predicting lake water quality index with sensitivity-uncertainty analysis using deep learning algorithms. Journal of Cleaner Production, 406, p.136885.

[19] Aldrees, A., Awan, H.H., Javed, M.F. and Mohamed, A.M., 2022. Prediction of water quality indexes with ensemble learners: Bagging and Boosting. Process Safety and Environmental Protection, 168, pp.344-361.

[20] Nsabimana, A. and Li, P., 2023. Hydrogeochemical characterization and appraisal of groundwater quality for industrial purposes using a novel industrial water quality index (IndWQI) in the Guanzhong Basin, China. Geochemistry, 83(1), p.125922.

[21] Aminu, I.I., 2022. A novel approach to predict Water Quality Index using machine learning models: A review of the methods employed and future possibilities. Global Journal of Engineering and Technology Advances, 13(02), pp.026-037.

[22] Sinha, K.K., Gupta, M.K., Banerjee, M.K., Meraj, G., Singh, S.K., Kanga, S., Farooq, M., Kumar, P. and Sahu, N., 2022. Neural network-based modeling of water quality in Jodhpur, India. Hydrology, 9(5), p.92.

[23] Bui, D.T., Khosravi, K., Tiefenbacher, J., Nguyen, H. and Kazakis, N., 2020. Improving prediction of water quality indices using novel hybrid machine-learning algorithms. Science of the Total Environment, 721, p.137612.

[24] Hmoud Al-Adhaileh, M. and Waselallah Alsaade, F., 2021. Modeling and prediction of water quality by using artificial intelligence. Sustainability, 13(8), p.4259.

[25] Torky, M., Bakhiet, A., Bakrey, M., Ismail, A.A. and Seddawy, A.I.E., 2023. Recognizing Safe Drinking Water and Predicting Water Quality Index using Machine Learning Framework. International Journal of Advanced Computer Science and Applications, 14(1).

Journal of Engineering and Technology for Industrial Applications

ISSN ONLINE: 2447-0228

ITEGAM-JETIA

Manaus, v.12 n.60, p.1117-1124. July/August, 2026.
DOI: https://doi.org/10.5935/jetia.v12i60.3992

RESEARCH ARTICLE OPEN ACCESS

SECURITY IN GENERATIVE AI SYSTEMS: A COMPREHENSIVE LITERATURE REVIEW

Mohammed Basheer*[1] and Ebby Darney[2]

[1]Research scholar, LIPS Research, EIU France.
[2]Professor, Dept of EEE, Rajarajeswari College of Engineering, Bengaluru, India.

[1]https://orcid.org/0009-0005-7181-8154, [2]https://orcid.org/0000-0002-2559-3442

Email:*basheer_s26@yahoo.com, pebbydarney@gmail.com

ARTICLE INFO

Article History
Received: March 10, 2026
Reviewed: April 10, 2026
Accepted: July 10, 2026
Published: August 31, 2026

Keywords:
Generative AI,
AI security,
Machine learning, privacy,
cybersecurity,
AI governance,
NIST AI-RMF,
risk management,
EU AI Act.

ABSTRACT

Gen AI systems such as LLM's, code assistants, image generators and personal assistants are growingly integrated with productivity and critical business applications across different domains of organizations such as security, testing, code review and automate day to day tasks. Their functionality depends on different training models, inputs and instructions and those models are integrated with various applications via API's and connectors. In addition, there are many practical use cases where Generative AI LLM's are already operationally embedded with many industrial equipment's. This paper presents a detailed literature review of security, privacy concerns and compliance risks that are evolving day to day. This review refers to various published articles and subjects related to AI security from security perspective which addresses various security concerns specific to Gen AI and the need for evolution to adopt and comply with the evolving regulations. Also, the paper refers to various publications related to the role of AI in security, defense mechanisms to safeguard AI models and its applications, different approaches on risk management and so on. Based on these references, we also discussed the advantages and limitations of adopting NIST AI Risk management framework (AI-RMF) which is an adaptive governance guidance for Generative AI security at its lifecycle. The review finally highlights Assessment gaps and proposes a governance-tied adaptive security framework for Generative AI.

Copyright ©2026 by authors and Galileo Institute of Technology and Education of the Amazon (ITEGAM). This work is licensed under the Creative Commons Attribution International License (CC BY 4.0).

I. INTRODUCTION

Artificial Intelligence (AI) has moved from theoretical constructions and narrow expert systems to large-scale, data driven models. This acts as general-purpose problem solvers across many domains. Recent advances in deep learning, especially transformer-based architecture, have enabled Generative AI (GenAI) systems capable of producing high fidelity text, images, videos, code, and synthetic data. These systems are deployed as conversational agents, content creation tools, decision-support modules, and programmable APIs integrated into broader sociotechnical systems. Even though this technological advancement in Gen AI makes it powerful but also introduces new and even complicated security and privacy risks. GenAI models are typically trained on large, heterogeneous datasets, sometimes scraped from the web or sourced from third-party providers, raising concerns about data provenance, consent, intellectual property, and memorisation of sensitive information. [1-6]. From an organizational viewpoint, Gen AI is now recognised as a paradigm shift because, compared to traditional software building process which encodes logic as explicit instructions the AI systems infer the behavior from the sourced data and optimisation objectives. This behavior makes it force a re-examination of how risk, accountability, and assurance should be defined and managed. Regulatory initiatives such as the EU AI Act explicitly require high-risk AI systems to be robust against cyberattacks and to undergo security-oriented risk assessment and conformity assessment. This paper focuses on security in Generative AI systems—security for AI, rather than AI for security—and proposes a lifecycle- and governance-oriented view of GenAI security. [7-10].

II. FOUNDATIONS: AI, GENERATIVE AI, AND SECURITY CONCEPTS

II.1 AI, MACHINE LEARNING, AND DEEP LEARNING

AI is commonly defined as a machine-based system that receives the set of human-defined objectives, can make predictions, recommendations, or decisions influencing real or virtual environments. Machine learning (ML) and deep learning (DL) are subsets of AI. ML focuses on learning patterns from data, while DL uses layered neural network architectures to capture complex, non-linear relationships. From the security governance, compliance and risk perspective, AI systems should be treated as a complex information system as they are relying on data, user instructions, and work by their own internal logic and memory. This improves business value, also at some point, it impacts business and individuals considerably.

II.2 GENERATIVE AI ARCHITECTURES AND APPLICATIONS

Generative AI models learn from huge subsets of data distribution and generate their own new samples. Generative AI discovers the pattern and learns from the provided rules and provide context rather than copying the initial information provided. It includes architectures like transformer-based models, Flow based models, Neural radiance fields, Latent diffusion models, Generative Adversarial Networks (GANs), Variational Autoencoders (VAEs etc. Due to advancement in technologies and research, these architectures are being evolved in such a way as it is widely used in many applications of productivity and entertainment such as text generations, video generations, personal assistance, Anomaly findings etc. Due to this broader applicability, risks like deep-fakes, manipulation and coordinated disinformation are evolving against individuals and organizations. Some surveys recently provided detailed information about the architecture of generative AI with its applications and implications, with notable evidence on adversarial impacts in real time. However, the productivity and benefits remain the same with the mindset of mindful usage of AI across various use cases.

II.3 AI FOR SECURITY VERSUS SECURITY FOR AI

The literature differentiates AI for security from security for AI. AI for security covers AI-enabled threat detection, automated patch management, anomaly detection, endpoint protection, network defense, phishing campaigns, security posture management, vulnerabilities exposure scoring, compliance automation and adaptive authentication. Security for AI focuses on maintaining data integrity, robustness, access control, logging, and governance for AI systems, including protecting training pipelines, preserving architecture, neural thinking ability, model artefacts, and inference endpoints from attack. Most cybersecurity use-cases focus on adapting AI for improving security. This review complements that by concentrating primarily on security for AI in the Generative AI context, while using AI for security literature to understand its interactions and applicability. [11], [12].

III. RESEARCH METHODOLOGY

To ensure a comprehensive and clear understanding of the current state of security in Generative AI, this review follows a structured literature search methodology. The objective was to identify appropriate peer reviewed articles, conference proceedings, current trends and reputable industry reports that address the intersection of Generative AI with cybersecurity, privacy, integrity, compliance and governance along with its applications and challenges.

III.1 SEARCH STRATEGY AND DATA SOURCES

We have conducted this review by searching through major academic databases, including Springer, IEEE, ACM Digital Library, arXiv and Google Scholar. The search strings combined keywords related to AI architectures such as “Generative AI”, “Large language models”, “Security risks in AI”, “Generative AI models” with security and risk terms such as “Deep fakes”, “Phishing and malware crafting”, “Code of evasion”, “Misinformation Ops”, “Polymorphic malware”, “Jail breaking”, "Data Poisoning, "Prompt Injection," "AI Regulation" [6], [11-15].

III.2 INCLUSION AND EXCLUSION CRITERIA

The retrieved journal publications are filtered via Prisma method to include only the last 3 years and latest articles to make sure the content to be included are up to the recent research and use cases. However, the concept been understood from multiple sources, but the references are included limited to 7 papers to narrow done and mimic the ideas shared by different authors. We only choose papers highlighting only Generative AI related issues and not on the entire AI as a subject to make sure that the issues are highlighted within the boundary of Gen AI. We have eliminated papers which are too generic to AI subject as a whole or those without any ties with Generative AI, its applications and implications. The key qualifier includes security concerns on Generative AI rather than application of AI in security unless it was linked to governance and security concerns of Generative AI. Based on our cybersecurity view, we explored studies on Gen AI relevant security gaps, grey areas, compliance concerns, misuse and impact which makes the primary filtering point of inclusions.

III.3 THEMATIC ANALYSIS

From my cybersecurity experience, grouping papers into threat patterns, data related risks, compliance mismatch, AI's pros and cons, and management frameworks gives the complete picture of GenAI dangers. In accordance with the experience, the selected findings were analyzed and organized into topic groupings and content clustering based on below focus.

(1) Current impact and implications of AI; (2) Security of AI from Governance, Risk and compliance perspective; (3) Widely impacting security concerns of Generative AI; (4) Challenges of AI to adapt with compliance standards and frameworks; (5) Implications and adversarial impact of AI in its most common applications; (6) Evolving usage and application of Generative AI in real world; (7) Methods to optimize AI to comply with GRC (Governance, Risk Management and Compliance) [16], [8].

IV. THREAT LANDSCAPE FOR GENERATIVE AI

As always, technology comes with challenges and those challenges pave way for resolutions. So as is Generative AI, which is nowadays a more adaptable technology which occupies its applicability in almost most of the areas of professional, personal and social usage which makes it open all kinds of fresh ways to attacks, impersonations, misuses and other impacts. This makes it questionable from the aspects of technological, ethical, social, legal viewpoints. In a simplified way, the below depicted figure explains the various security threats and manipulation possibilities of generative AI in its lifecycle from technological, human and data perspective. I have seen these risks play out in social media nowadays where people have started impersonating, providing fake information, news and other contents. Even I have encountered similar limitations in the structure and well created prompt which I have created for the healthcare IT service provider.

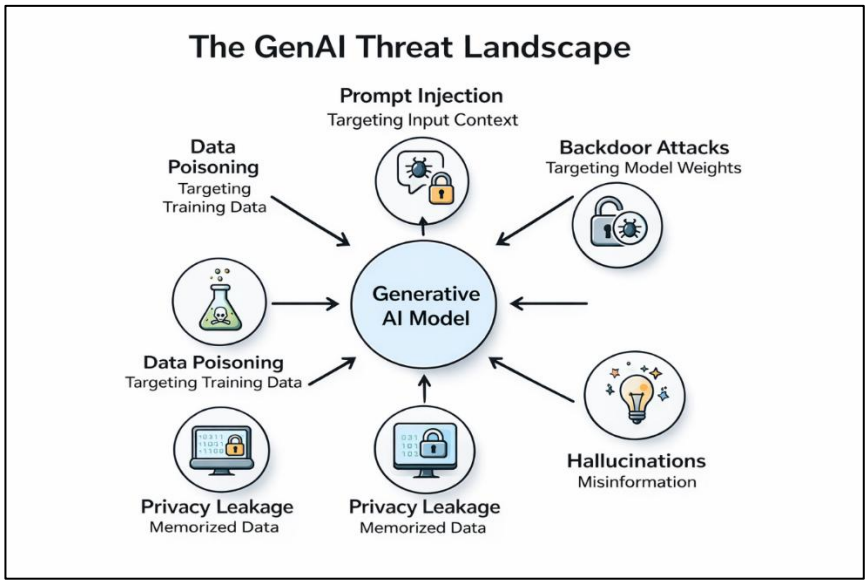


Figure 1: Various security threats targeting Generative AI lifecycle.
Source: Authors (2026).

IV.1 DATA POISONING AND BACKDOOR ATTACKS

Data poisoning and back door attacks are most common issues of generative AI nowadays where people started adapting and even got addicted to its usage without verification or cross review. With this open trust issue, hackers and falsifiers inject malicious samples of training data which in turn alter the model and its associated data to corrupt its samples out of its originally stored / trained data. Some attackers trick users to capture ideal and sensitive information via backdoor and make use of it to impact personal, professional and social aspects. These techniques are largely achieved by using triggers which appear to be activated upon certain situations without the knowledge of users who are interacting with the Generative AI. Those triggers degrade the quality of output and accuracy by manipulating the models, trained data and samples. These kinds of attacks are much more impactful mostly on basic and customized models than those of large models which have at least basic security being positioned to address these attacks. [14], [15].

IV.2 ADVERSARIAL PROMPTS AND INPUT MANIPULATION

Another notable threat on GenAI systems are the prompt injection and input manipulation attacks, where the prompt itself tricks the users to input key essential inputs which in turn will be used to manipulate the original prompt to cause damage as well as to some extent to steal sensitive information. These kinds of injections can either be found in documents and attachments which will skip the security checks of GenAI models and lead to security concerns and prompt manipulations. These are most common nowadays due to the flexibility of easy sharing, API integration ability and browser based. Simplest way to explain this GenAI hole is that the prompts and inputs hide within certain forms of emails and documents to make it look legitimate but once triggered or trusted, it does its manipulation in many ways. [13], [6]

IV.3 MODEL EXTRACTION, MEMBERSHIP INFERENCE, AND INVERSION

These concepts are few indirect ways of counterfeiting, copying and predicting identities of well-trained private AI models. Model extraction is something that matches the results score of a well-trained and private AI with the one created by a publicly available GenAI. This can be achieved by training the public or free AI models with the same answers and the results provided by the private well-trained AI. By this way, the AI brain will get stolen without stealing the model itself but by just mimicking the results and training your own AI models with those results. Membership inference is like data fingerprinting, where based on the results and confident score, it's possible to detect the existence of data record and the identity of input in the other private trained model.

Model inversion is a kind of Reverse engineering secrets, where the input is been checked for its confident score and then based on the high score, the private information can be rebuilt or synthesized. [14], [5].

IV.4 DEEPFAKES, MISINFORMATION, AND SOCIAL ENGINEERING

Deepfakes are another technique of collecting raw materials, information via data harvesting and use it as a source of truth to fake by impersonating the exact attributes of those collected information and sources. The original identity was then used to synthesize misinformation and to draw social engineering victims. A forger AI can be used to compete the detective AI by fooling it with high percentage of pass rate against its results. For example, an user identities from images and videos can be collected from multiple sources, a forger AI will use it to exactly impersonate the person and to train the detective AIs to prove it was right. It will then be used in social engineering to fake information. Nowadays Deepfakes are more challenging as the forged information is nearly perfect with the actual information and identities. These are newly evolving dangers in AI deployments as new projects quietly reshape the entire security landscape. Once known as a productive tool, it is now forcing security / risk teams to rethink it. [12], [17].

IV.5 SYSTEM-LEVEL AND OPERATIONAL RISKS

Due to the over dependencies and adaptations of GenAI's, Operational, system level and organizational risks are growing due to various reasons such as prompt exploitation, Insufficient compliance and logging monitoring, Unidentified security checks and lack of forensic evaluation against those GenAI tools. The outputs and outcomes generated by GenAI's are mostly used in real time without properly getting the results evaluated or validated, which cause it more attractive for attackers and makes it a more important subject of discussion as well as pain point for Security, compliance, risk and governance teams.

Table 1: Types of Attacks in Generative AI.

Attack Type	Description	Example	Impact / Risk
Data poisoning	Malicious samples corrupt training behavior	Backdoor trigger in training set	Model produces manipulated or biased outputs; long-term integrity compromise
Prompt injection	Adversarial instructions override system policies	Hidden prompt in document	Unauthorized actions, data leakage, bypass of safety controls
Model extraction	Queries used to reconstruct a surrogate model	Copying a hosted LLM API	Intellectual property theft; loss of competitive advantage
Membership inference	Determining if a record was in training data	Patient record presence check	Privacy breach; regulatory non-compliance (e.g., HIPAA risk)
Deepfake synthesis	Fabricated audio/video content	Impersonated CEO voice call	Fraud, reputational damage, social engineering attacks

Source: Authors (2026).

V. PRIVACY AND SECURITY CONCERNS IN GENERATIVE AI

Safety issues and data protection concerns are emerging in multiple ways and into deeper level of many layers of Generative AI which makes it difficult to resolve completely via technology security measures alone. Those concerns need to be addressed at all the different parallels such as users, ethical, social, technological, legal and organization perspectives. There are complex and many layered safety challenges across all these mentioned parallels exist.

V.1 USER AND ETHICAL PERSPECTIVES

It quite common to deepfake someone's identity not only from productivity viewpoint but these arises in social environments as well where people impersonate another person's look, voice, style etc. Content makers more frequently use prompt and reference data such as images and videos to synthesize innovative outputs for the purpose of popularity and monetary gains. In addition, curiosity goes up to higher levels and draws users to generate unethical content such as harassment, racism, hatred, restrictive and spreading false perceptions. Content-making AI stirs up controversies as it spits biased information spreading across society and social environment which highlights moral dilemma from the perspective of ethics. [12], [17].

V.2 REGULATORY AND LEGAL PERSPECTIVES

Regulatory authorities and laws are worrying around the content creating AIs due to its flexibility across doing almost anything as it's been instructed or trained to. Some concerns include GDPR compliance issue where usage of Intellectual property is restricted in boundaries, HIPPA compliance issue which states not to use non pseudonymized direct PII (Personal Identifiable information) or PHI (Personal Health information) data for training or stimulatory purposes. There are large number of increases in the number of legal cases being filed around accountability, disclosure, privacy and other ethical controversies. However, there are privacy protection frameworks proposed to mitigate these risks but it in turn compromises its utility and benefits to a fuller extent. There, a balanced and optimal model to accompany both security and utility are highly in need.

V.3 TECHNOLOGICAL AND INSTITUTIONAL PERSPECTIVES

Content generative AIs memorize the models, interactions and conversations from inputs time to time and sometimes it leaks out sensitive information without applying pseudonymization or becomes vulnerable due to its identifiable patterns on even anonymized data.

To address this concern, technological controls are in place such as input validation and adversarial training but those also being challenged by the evolving security threats and attacks. Many organizations often skip building proper oversight systems and lacks consideration of AI security policies, guidelines and controls which lead to improper building of customized productivity AIs. Prompt engineers often create Generative AIs with stable images with clear details, for example, images of a hotel room. Those details are again misused to identify the actual identity of the source (Hotel rooms, name and other details can be exposed via synthesis and reverse engineering).

VI. AI CYBERSECURITY AND REGULATION

AI Cybersecurity Regulations are in place across different contexts and one of which is EU AI act which highlights the first comprehensive framework on AI regulation. The framework includes various acts such as differentiating different levels of risks into Unacceptable risk, High risk, limited and minimal. It also mentions the transparency requirements and encourages evolution of AI innovation and use cases in Europe. The framework primarily focuses on multiple aspects like diversity and complexity of AI technologies with its difficulty assessing those risks and the urge to develop secure-by-design mode of AI systems. The AI regulation framework emphasizes high quality training data, detailed documentation, record management, human oversight, risk management and accuracy. This act has its own tiered structure of fines and penalties, based on violations levels such as prohibited practices, high risk obligations, Improper management of training data, Incorrect information to authorities etc. In a granular level, this act bans acts such as creating or using manipulating techniques, social scoring, biometric exposure, facial database scraping, predictive policing etc. Also, the act promotes cross functional collaboration between security, compliance, risk, privacy, integrity and confidentiality. The framework is planned to be enforced by August 2027 and hopefully it may add some value and key principles to secure AI models and their use.

VII. AI AND SECURITY FROM AN INFORMATION-SECURITY AND RISK-MANAGER STANDPOINT

From a data protection perspective by an information security professional, the AI systems and its associated data and integrations should be treated same as the other critical systems in place. The key considerations include securing Assets & data, Maintaining the risk register for new and emerging risks, implementing necessary controls to comply with regulatory and organizational policies, Evaluation and continuous monitoring of anomalies and deviations. It requires the maturity of shifting from reactive security into proactive security which means that the built-in security and protocols are not only sufficient but also the human, technological, legal and organizational controls should also be in place to avoid AI risk concerns. There is a necessity of considering security concepts in AI in different aspects such as i. Classification of assets, ii. Risk register management, iii. Mapping with appropriate control frameworks, iv. Threat modelling, v. vulnerability management, vi. Logging and monitoring, vii. Identity and access etc., AI adoption can be business driven but should be accompanied by laws and regulations.

VIII. AI'S ROLE IN CYBERSECURITY AND ITS INTERACTION WITH GENERATIVE AI SECURITY

AI plays key roles in cybersecurity which includes cyber defense systems such as phishing filters, endpoint security, anomaly detection, malware analysis, threat hunting and threat modelling. GenAI's plays vital role in reducing human efforts and improvising security and accuracy in blue defense especially situations like automating reported incidents, automating playbook & runbooks in SIEM tools, Deepfake and prompt injection detection to an extent, social engineering simulations, code reviews and so on. AI's feeds detective AIs to defend and secure against forger AI's and false promptings. However, there are associated risks which need to be further improvised such as RAG pulling integrations which may lead to data exfiltration, not updated HR models for hiring use cases where there may be situations that lack adaptive compliance pulling due to lack of real time updates. [12], [17], [13], [6], [11].

IX. DEFENSIVE STRATEGIES AND MITIGATION TECHNIQUES

There are already defense strategies in place against its corresponding threat vector. These strategies are applied to defend AI at different levels of its life cycle from model building, training data to monitoring and evaluation.

Table 2: Mapping Defensive Strategies with Threat Vectors.

Defense Strategy	Primary Threat Mitigated	Implementation Layer	Key Techniques	Residual Risk
Input Sanitization	Prompt Injection, Jailbreaking	Pre-processing / API Gateway	Input validation, allowlists, context filtering, prompt templating	Advanced prompt injections and obfuscation may still bypass controls
RLHF / Red Teaming	Harmful Content Generation	Model Training / Fine-tuning	Human feedback loops, adversarial testing, safety tuning	Model may still fail in unseen or edge-case scenarios
Retrieval Augmented Generation (RAG)	Hallucinations, Poisoning	System Architecture	Grounding with trusted data, vector DB filtering, source attribution	Reliance on external data sources may introduce poisoned or unverified content
Watermarking	Deepfakes, IP Theft	Post-processing / Output	Digital watermarking, content fingerprinting, cryptographic signatures	Watermarks can be removed, altered, or degraded
Differential Privacy	Membership Inference, Privacy Leakage	Training Data Curation	Noise injection, privacy budgets, anonymization techniques	Trade-off between model accuracy and privacy protection

Source: Authors (2026).

IX.1 INPUT FILTERING AND SANITIZATION

This is a Cyber defense technique where it blocks any unwanted inputs to change the application logic and cause corruption to the AI model. It works by blocking specific malicious input patterns by simply rejecting blacklisted inputs which may contain any commands or files. This technique also mitigates buffer overflow but imposing length restriction on sessions connected with AIs. However, these are all static security measures which can be bypassed by more adversarial jail break attempts. This proves the need for additional or secondary AI models to evaluate the inputs of the primary AI model [18].

IX.2 ADVERSARIAL TRAINING AND ROBUSTNESS

Adversarial training and robustness are another cyber defense strategy where the AI model will be trained with details of malicious inputs and threats to create resistance. This instructs the AI to behave correctly, irrespective of the malicious inputs and allows the model to degrade gracefully in case of adversarial attacks. The model was trained, tested and validated for its robustness to avoid hallucinations and unintended behaviors. This layer of defense primarily focuses on mitigating evasion or inference attacks where attackers modify the inputs rationally to fool the model and make it learn from those modifications. It also protects against data poisoning and prompt injections to avoid manipulatory commands and inputs been sent to the model for training. [13], [6], [14], [15], [19].

IX.3 WATERMARKING AND PROVENANCE TRACKING

This strategy is like version control by embedding hidden signal in the source model to verify authenticity. The contents applied in the model are tracked for its integrity by maintaining the metadata history of details like creator, created by, modification history. Without this control deepfakes may remain unchecked and unidentified. This is applied in the post processing or output phase of the implementation layer. There are multiple types of watermarking such as text watermarking, image watermarking, and audio watermarking to ensure fake claims are being avoided. [12], [17].

IX.4 ARCHITECTURAL GUARDRAILS

Architectural Guardrails are system level controls outside the AI model itself which ensure that validate, monitor and isolate the model irrespective of how it behaves. This ensures that principles of limiting authority, enforcement of business rules and prevention of unsafe actions by securing the model based on its behavior. AI models need to be limited to whitelisted API and external tools based on principle of least privilege to avoid lateral or privilege escalation to execute harmful action in the database of backbone system of AI models. Some of the examples are Input guardrails, context guardrails and output guardrails which specifically monitor the AI model by the way it behaves.

X. TOWARD AN ADAPTIVE GOVERNANCE FRAMEWORK FOR SECURITY IN GEN AI

Bringing these strands together, security in Generative AI can be organized around a lifecycle-centric, AI-RMF-aligned governance framework. A typical GenAI system can be described through stages of problem framing and context, data acquisition and curation, model design and training, deployment and integration, operation and monitoring, and retirement and decommissioning. Security and governance measures must be applied consistently across all stages. [16], [8].

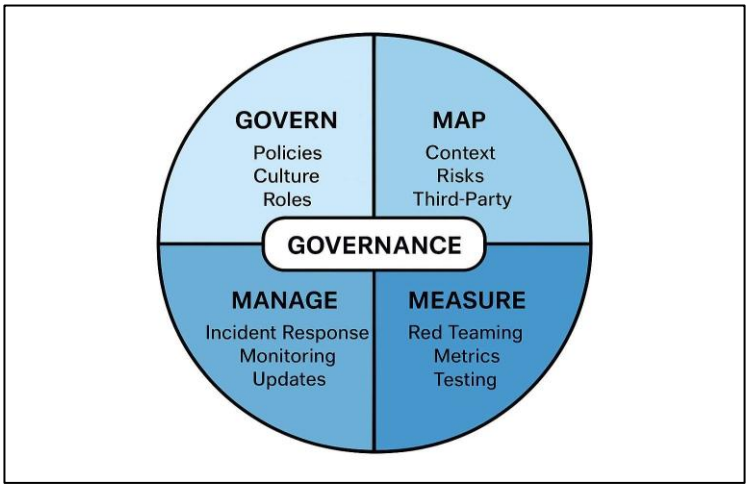


Figure 2: Adaptation of the NIST AI Risk Management Framework (AI-RMF) for the Generative AI Lifecycle.
Source: Authors (2026).

X.1 MAPPING GENERATIVE AI LIFECYCLE TO NIST AI-RMF FUNCTIONS

The NIST AI Risk Management Framework defines four core functions—GOVERN, MAP, MEASURE, and MANAGE—that can be operationalised for GenAI. GOVERN establishes roles, responsibilities, and organisational culture; MAP characterises context, stakeholders, and risk scenarios; MEASURE assesses risks, harm, and control effectiveness; and MANAGE implements and adjusts risk responses over time.

Table 3: Mapping NIST AI-RMF Functions to Generative AI Lifecycle Stages.

Lifecycle Stage	Govern	Measure	Manage
Data acquisition & curation	Data governance policies; data owners and steward	Data quality, bias, and privacy assessments	Access control; sanitization; incident response for data breaches
Model Training & evaluation	Model risk policies; secure ML Ops standards	Robustness (poisoning, backdoors, leakage)	Adversarial training; differential privacy; peer review
Deployment & integration	Acceptable use and integration standards	System level threat modelling (API abuse, tool exploitation)	Rate limiting; content filtering; segmentation; logging
Operation & monitoring	AI risk committee; dashboards and reporting	Incident, drift, and misuse metrics	Policy updates; control tuning; patching; retraining

Source: Authors (2026).

X.2 GOVERNANCE ARTEFACTS AND DECISION GATES

To make this framework operational, organizations can define governance artefacts such as AI system profiles, data-protection impact assessments, model and system cards, adversarial-testing and red teaming reports, incident logs, and decommissioning documentation. Decision gates—go/no-go checkpoints— can require multi-stakeholder approval before moving between lifecycle phases, ensuring that security and governance concerns are addressed proactively rather than retrospectively.

XI. CROSS-CUTTING CHALLENGES AND RESEARCH GAPS

Irrespective of the progress reflected in the reviewed literature, there are several open and dynamic problems remain. There is no widely accepted standard for measuring the safety of AI models and neither adversarial law in place to be followed. Generative AI systems depend heavily on third-party foundation models, external datasets, open-source libraries, customized prompts and cloud infrastructure and the current frameworks provide limited guidance on how to evaluate and manage these dependencies. Regulatory frameworks also face tensions between ambitious expectations and current scientific capabilities, especially for cybersecurity and robustness requirements. Many organizations lack structured AI-governance bodies, formal policies for acceptable use of GenAI, and personnel who understand both AI and security. There is no well-defined framework for AI security which is been widely accepted and due to which there are gaps in designating the research proposal to secure AI models.

XII. CONCLUSION

This literature review has examined the characteristics of AI models, their applications and the systems used. The survey is handled from the perspective of information security, security for AI, and the regulatory constraints. We proposed an RMF centric and lifecycle-oriented security approach to structure security in AI models and its applications. Understanding from the perspective of lack of framework and promising regulations, ever evolving cyber-attacks and misusage of AI applications demands more and broader research in Gen AI security. Addressing these gaps is essential to deploy dynamic and adaptive security for AI systems which makes applications more trustworthy and usable in many real time scenarios.

XIII. AUTHOR'S CONTRIBUTION

Conceptualization: Mohammed Basheer.
Methodology: Mohammed Basheer.
Investigation: Mohammed Basheer.
Discussion of results: Mohammed Basheer and Ebby Darney.
Writing – Original Draft: Mohammed Basheer.
Writing – Review and Editing: Mohammed Basheer and Ebby Darney.
Resources: Ebby Darney.
Supervision: Ebby Darney.
Approval of the final text: Mohammed Basheer and Ebby Darney.

XIV. REFERENCES

[1] A. Al Siam, M. Alazab, A. Awajan, and N. Faruqui, "A comprehensive review of AI's current impact and future prospects in cybersecurity," IEEE Access, vol. 13, pp. 14029–14050, 2025, doi: 10.1109/ACCESS.2025.3528114.

[2] M. Trigka and E. Dritsas, "The evolution of generative AI: Trends and applications," IEEE Access, vol. 13, pp. 98504–98529, 2025, doi: 10.1109/ACCESS.2025.3574660.

[3] M. Choudhury, Z. Elyoseph, N. J. Fast, et al., "The promise and pitfalls of generative AI," Nat. Rev. Psychol., vol. 4, pp. 75–80, 2025, doi: 10.1038/s44159-024-00402-0.

[4] A. Golda et al., "Privacy and security concerns in generative AI: A comprehensive survey," IEEE Access, vol. 12, pp. 48126–48144, 2024, doi: 10.1109/ACCESS.2024.3381611.

[5] Y. Liu, J. Huang, Y. Li, et al., “Generative AI model privacy: A survey,” Artif. Intell. Rev., vol. 58, Art. no. 33, 2025, doi: 10.1007/s10462-024-11024-6.

[6] R. Pedro, M. E. Coimbra, D. Castro, P. Carreira, and N. Santos, “Prompt-to-SQL injections in LLM-integrated web applications: Risks and defenses,” in Proc. IEEE/ACM 47th Int. Conf. Softw. Eng. (ICSE), Ottawa, ON, Canada, 2025, pp. 1768–1780, doi: 10.1109/ICSE55347.2025.00007.

[7] P. Shetty, “AI and security, from an information security and risk manager standpoint,” IEEE Access, vol. 12, pp. 77468–77474, 2024, doi: 10.1109/ACCESS.2024.3408144.

[8] R. Hamon, H. Junklewitz, J. Soler Garrido, and I. Sanchez, “Three challenges to secure AI systems in the context of AI regulations,” IEEE Access, vol. 12, pp. 61022–61035, 2024, doi: 10.1109/ACCESS.2024.3391021.

[9] D. Humphreys, A. Koay, D. Desmond, et al., “AI hype as a cyber security risk: The moral responsibility of implementing generative AI in business,” AI Ethics, vol. 4, pp. 791–804, 2024, doi: 10.1007/s43681-024-00443-4.

[10] M. Bethany et al., “Lateral phishing with large language models: A large organization comparative study,” IEEE Access, vol. 13, pp. 60684–60701, 2025, doi: 10.1109/ACCESS.2025.3555500.

[11] J. Zhang, P. Wu, J. London, and D. Tenney, “Benchmarking and evaluating large language models in phishing detection for small and midsize enterprises: A comprehensive analysis,” IEEE Access, vol. 13, pp. 28335–28352, 2025, doi: 10.1109/ACCESS.2025.3540075.

[12] M. Gupta, C. Akiri, K. Aryal, E. Parker, and L. Praharaj, “From ChatGPT to ThreatGPT: Impact of generative AI in cybersecurity and privacy,” IEEE Access, vol. 11, pp. 80218–80245, 2023, doi: 10.1109/ACCESS.2023.3300381.

[13] E. Derner, K. Batistič, J. Zahálka, and R. Babuška, “A security risk taxonomy for prompt-based interaction with large language models,” IEEE Access, vol. 12, pp. 126176–126187, 2024, doi: 10.1109/ACCESS.2024.3450388.

[14] J. Malik, R. Muthalagu, and P. M. Pawar, “A systematic review of adversarial machine learning attacks, defensive controls, and technologies,” IEEE Access, vol. 12, pp. 99382–99421, 2024, doi: 10.1109/ACCESS.2024.3423323.

[15] Y. Zheng, C.-H. Chang, S.-H. Huang, P.-Y. Chen, and S. Picek, “An overview of trustworthy AI: Advances in IP protection, privacy-preserving federated learning, security verification, and GAI safety alignment,” IEEE J. Emerg. Sel. Topics Circuits Syst., vol. 14, no. 4, pp. 582–607, Dec. 2024, doi: 10.1109/JETCAS.2024.3477348.

[16] A. O. Almagrabi and R. A. Khan, “Optimizing secure AI lifecycle model management with innovative generative AI strategies,” IEEE Access, vol. 13, pp. 12889–12920, 2025, doi: 10.1109/ACCESS.2024.3491373.

[17] T. C. King, N. Aggarwal, M. Taddeo, et al., “Artificial intelligence crime: An interdisciplinary analysis of foreseeable threats and solutions,” Sci. Eng. Ethics, vol. 26, pp. 89–120, 2020, doi: 10.1007/s11948-018-00081-0.

[18] T. Tsmindashvili et al., “Improving LLM outputs against jailbreak attacks with expert model integration,” IEEE Access, vol. 13, pp. 134976–134988, 2025, doi: 10.1109/ACCESS.2025.3592458.u

[19] A. Adel and N. Alani, “Can generative AI reliably synthesise literature? Exploring hallucination issues in ChatGPT,” AI & Society, vol. 40, pp. 6799–6812, 2025, doi: 10.1007/s00146-025-02406-7.

Journal of Engineering and Technology for Industrial Applications

ITEGAM-JETIA

Manaus, v.12 n.60, p.1125-1137. July/August, 2026.
DOI: https://doi.org/10.5935/jetia.v12i60.3993

ISSN ONLINE: 2447-0228

RESEARCH ARTICLE OPEN ACCESS

A DEEP SPATIO-TEMPORAL FRAMEWORK FOR MULTI-CLASS TRAFFIC PREDICTION AND ACCIDENT DETECTION IN SURVEILLANCE VIDEO

Dhartee Patel[1], Jinal Ahir[2], Namrata Shroff [3], Shankar Parmar*[4]

[1, 2, 3]Computer Engineering Department, Government Engineering College, Bharuch, India.
[4]Electronics and Communication Engineering Department, Government Engineering College, Godhra, Gujarat, India.

[1]http://orcid.org/0009-0005-4299-8643, [2]http://orcid.org/0009-0009-1622-5638,
[3]http://orcid.org/0000-0001-6343-6205, [4]http://orcid.org/0000-0002-3034-5144

Email: dhartee1611@gmail.com, jinalahir2805@gmail.com, namrata.gecb@gmail.com, *shankar.parmar@gtu.edu.in

ARTICLE INFO

Article History
Received: April 8, 2026
Reviewed: May 8, 2026
Accepted: July 12, 2026
Published: August 31, 2026

Keywords:
Traffic Surveillance,
Accident Detection,
Yolov8,
Spatio-Temporal Modeling,
CNNLSTM
Intelligent Transportation System.

ABSTRACT

Traffic surveillance systems play a crucial role in intelligent transportation by enabling automated monitoring, traffic prediction, and accident detection. However, recognizing complex traffic scenarios from real-world videos remains challenging due to dynamic environments and temporal dependencies. This paper proposes a unified spatio-temporal framework that integrates YOLOv8 based object detection, convolutional neural networks for spatial feature ex traction, and long short-term memory networks for temporal modeling. Traffic videos are preprocessed to enhance visual consistency, and detected objects are transformed into structured spatial representations. Temporal dependencies across video sequences are learned using LSTM networks, and the extracted features are evaluated using multiple machine learning classifiers under different preprocessing strategies. Experimental results demonstrate that Z-score standardization improves classification performance, with Support Vector Ma chine achieving 63.27% accuracy and an F1-score of 55.66% in an eight-class traffic scenario classification task, indicating the feasibility and robustness of the proposed framework in real-world traffic environments.

Copyright ©2026 by authors and Galileo Institute of Technology and Education of the Amazon (ITEGAM). This work is licensed under the Creative Commons Attribution International License (CC BY 4.0).

I. INTRODUCTION

Traffic congestion and road accidents have become critical challenges in rapidly urbanizing regions, where increasing vehicle density and limited infrastructure place substantial pressure on existing transportation systems [1]. As cities continue to expand and mobility demands intensify, traditional manual surveillance and rule-based monitoring approaches are no longer sufficient to manage real-time traffic dynamics effectively [2]. Such methods often struggle to detect sudden anomalies including accidents, lane violations, and abrupt fluctuations in traffic flower sulting in delayed response times and compromised road safety [3]. In response to these limitations, intelligent video-based traffic analysis has emerged as a promising solution, leveraging advancements in computer vision and deep learning to enable automated, scalable, and real-time monitoring [4]. Over the past decade, significant research efforts have focused on developing robust algorithms for vehicle detection, traffic flow estimation, and anomaly recognition [5]. Convolutional Neural Networks (CNNs) have demonstrated strong capability in extracting meaningful spatial features from complex road scenes, thereby improving vehicle localization and classification accuracy [6]. More recently, real-time object detection frameworks such as You Only Look Once (YOLO) and transformer-based detectors have further enhanced detection speed and precision, facilitating deployment in densely populated urban environments [7]. Complementary research has explored temporal modeling techniques including Long Short-Term Memory (LSTM) networks, 3D CNNs, and sequence-based architectures to capture motion patterns and identify traffic incidents across video sequences [8]. Although these approaches have contributed substantially to intelligent transportation research, many rely on computationally intensive architectures, controlled datasets, or address isolated components of traffic analysis rather than offering an integrated end-to-end solution [9]. Despite notable progress, several challenges remain unresolved. Numerous studies depend on narrow field-of-view or synthetic datasets, which limit model generalizability in heterogeneous real-world scenarios [10].

Furthermore, existing works frequently treat vehicle detection, spatial feature extraction, temporal analysis, and accident identification as independent modules, thereby reducing overall system efficiency and scalability [11]. Achieving real-time performance under resource-constrained deployment conditions such as roadside surveillance infrastructure continues to be a practical concern [12]. These limitations underscore the necessity for a unified, computationally efficient framework that integrates spatial temporal modeling and anomaly detection using real-world traffic video data [13]. To address these challenges, this study proposes a comprehensive deep learning based framework for real-time traffic flow analysis and accident detection. The proposed approach integrates object detection, spatial feature extraction, and temporal modeling into a cohesive pipeline [14]. An advanced detection model is employed to accurately identify vehicles within surveillance footage, after which temporal sequence modeling captures abrupt variations in motion and density patterns that may indicate congestion or accidents [15]. By directly leveraging video data and minimizing reliance on handcrafted features, the framework enhances scalability and adaptability across diverse traffic conditions [16]. The system is designed to support practical deployment scenarios and aims to improve early identification of abnormal events, thereby contributing to safer and more efficient intelligent transportation systems [17]. The primary objective of this research is to develop a robust and computationally efficient methodology for vehicle detection, traffic flow analysis, and accident identification in real time [18]. Specifically, this study evaluates the effectiveness of combining spatial detection with temporal sequence modeling, investigates the impact of different preprocessing strategies, and assesses classification performance across multiple machine learning algorithms on realistic traffic datasets [19].

II. THEORETICAL REFERENCE

II.1 RELATED WORK

To understand current trends and challenges in traffic accident detection, it is essential to review recent methods and models [20]. Numerous approaches have been proposed with the goals of enhancing detection accuracy, improving tracking reliability, and enabling real-time response in diverse urban environments [21]. The following sections highlight the most significant contributions, their thematic focus, and the specific challenges addressed by the model [22].

II.1.1 Trajectory Conflict and Motion Pattern Analysis

Trajectory-based conflict reasoning has proven effective for distinguishing near-miss events from actual collisions by explicitly modeling the motion interactions among vehicles [23]. Ghahremannezhad et al. (2022) combined YOLOv4-based object detec tion with trajectory divergence and proximity metrics to differentiate collision-prone scenarios from non-severe interactions. This approach highlighted the importance of motion continuity rather than isolated frame-level cues [24]. Huang et al. (2019) extended motion-centric analysis by proposing a two-stream Convolutional Neural Network (CNN) that jointly learns spatial appearance features and temporal motion patterns from aerial traffic videos [25]. Their architecture en abled real-time near-accident detection by capturing vehicle interactions over time. Such trajectory-driven approaches strengthen the conceptual modeling of inter-vehicle dynamics and closely align with the trajectory-based anomaly detection module em ployed in our proposed system [26].

II.1.2 Spatio-Temporal and Graph-Based Traffic Modeling

Beyond individual object detection, several studies have explored traffic behavior at a broader spatio-temporal scale [27]. Cuietal. (2018) introduced the Temporal Graph Convolutional Long Short-Term Memory (TGC-LSTM) model, which inte grates Graph Convolutional Networks (GCNs) with LSTM units to represent spatial correlations among interconnected road segments while learning temporal traffic evo lution [28]. This framework demonstrated strong performance in network-level traffic state prediction. Similarly, Ismaeel et al. (2023) proposed a deep CNNRNN architecture for smart city traffic pattern classification, achieving an accuracy of 95% [29]. While these meth ods are effective for global traffic analysis and congestion prediction, they are less suitable for real-time, localized accident or near-miss detection, which remains the primary focus of the proposed system [30].

II.1.3 Critical Review of Related Work and Research Gaps

Despite notable progress in traffic accident detection and spatio-temporal traffic anal ysis, several persistent challenges remain in the existing literature.

Dataset Limitations: Many studies rely on synthetic data or static-camera datasets with limited environmental diversity, which restricts model generalizability. To address this issue, the proposed work utilizes a diverse and annotated real-world dataset sourced from IEEE DataPort.

Computational Overhead: High-capacity models such as 3D CNNs and graph-based architectures incur substantial computational costs, limiting their suit ability for real-time deployment. Hybrid CNN–LSTM-based approaches offer a more favorable balance between detection accuracy and computational efficiency, motivat ing their adoption in the proposed framework.

Occlusion and Dense Traffic Conditions: Vehicle occlusions, frequent in teractions, and complex motion patterns in dense traffic environments remain chal lenging. Prior studies (Nagy & Simon, 2021) indicate that temporal modeling and trajectory-aware inference can alleviate these issues. The proposed approach incor porates temporal consistency to improve robustness under such conditions. Table 1 presents a comparative summary of key studies related to traffic ac cident and near-miss detection, highlighting the methodologies employed, dataset characteristics, major contributions, and identified limitations.

Identified Research Gaps: Although existing methods demonstrate promis ing performance, several gaps remain unaddressed. Most approaches treat object detection, temporal feature extraction, and trajectory reasoning as independent com ponents, limiting their ability to model the complete evolution of accident scenarios. Furthermore, computationally intensive architectures hinder real-time deployment on edge and resource-constrained platforms.

Dense, heterogeneous, and occlusion-prone traffic environments are still insufficiently explored, resulting in degraded performance under realistic urban conditions. Additionally, only a limited number of systems pro vide an end-to-end framework integrating detection, risk assessment, and real-time decision support. These gaps motivate the development of a unified, lightweight, and real-time traffic accident detection framework capable of robust operation across diverse traffic environments.

Table 1: Summary of Related Work in Traffic Accident and Near-Miss Detection.

Author	Method	Data	Contribution	Limitation
Yadava et al. (2022)	YOLOv4 + Kalman Hungarian	Intersection videos	Vehicle detection and conflict analysis	Poor performance under dense occlusion
Li et al. (2020)	CNN-LSTM SMOTE	Crash records	Crash risk forecasting	High computation cost
Roy et al. (2019)	Siamese Interaction LSTM	Aerial videos	Temporal attention for collision risk	Sensitive to noisy trajectories
Ghahremanzadeh et al. (2022)	YOLOv4 + Trajectory analysis	UAV footage	Near-miss vs collision differentiation	Degrades with rapid motion
Huang et al. (2019)	Two-stream CNN	Aerial videos	Real-time near-accident detection	Limited scalability
Cui et al. (2018)	TGC-LSTM (GCN+LSTM)	Network traffic data	Spatio-temporal traffic prediction	Not video-level accident detection
Ismaeel et al. (2023)	Deep CNN-RNN	Smart city data	Traffic state classification	No explicit collision modeling

Source: Authors, (2026).

III. MATERIALS AND METHODS

This research proposes a hybrid deep-learning pipeline that integrates Convolutional Neural Networks (CNNs) and Long Short-Term Memory (LSTM) networks for real time traffic flow analysis and accident detection. The complete workflow includes video preprocessing, feature extraction, temporal modeling, and classification of traffic events. The system is designed to handle unconstrained road environments with varying traffic densities, lighting conditions, and weather scenarios.

III.1 DATASET

TheTrafficAccident Detection Video Dataset for AI-Driven Computer Vision Systems in Smart City Transportation was sourced from the IEEE DataPort repository, where it was contributed by Adewopo et al. (2023) to support research on intelligent traffic surveillance. The dataset compiles videos from multiple real-world sources, includ ing urban traffic surveillance cameras, in-vehicle dashcams, and additional publicly available crash footage. This ensures natural variation in traffic flow, accident types, and environmental conditions. The dataset is systematically organized into three pre defined experimental splitsTraining, Validation, and Testingto maintain consistency in benchmarking and reproducible experimentation. In preparing the dataset, all raw videos were segmented into non-overlapping five-second clips, resulting in ap proximately 5,690 video samples.This segmentation strategy ensures uniformity in clip duration and highlights the dynamic temporal behavior around accident events. Each clip is categorized into one of eight scenario classesBackend, Backend Rollover, Frontend, Frontend Rollover, Sidehit, Sidehit Rollover, General Augmented Crash, and No Accident Normal Traffic thereby supporting both multi-class accident classifi cation and accident-versus-non-accident detection, as shown in **Table 2**. The dataset provides video-level annotations only, without frame-level bounding boxes or object level segmentation, making it suitable for end-to-end video classification and temporal feature learning. The clips represent diverse scenarios involving variations in light ing, weather, camera angle, road structure, traffic density, and sensor quality, adding significant heterogeneity and complexity to the dataset.

Table 2: Dataset Distribution by Scenario.

Scenario	Total Videos
Backend	362
Backend Rollover	28
Frontend	369
Frontend Rollover	51
General Augmented Crash	1459
No Accident Normal Traffic	2283
Sidehit	1027
Sidehit Rollover	111
Total	**5690**

Source: Authors, (2026).

III.2 PREPROCESSING

To ensure uniformity and reliable model training, all videos in the dataset underwent a comprehensive preprocessing pipeline. Each five-second video clip was decomposed into individual frames, resulting in an average of 2530 frames per video, depending on the recording devices frame rate.

The original videos exhibited heterogeneous frame resolutions due to their diverse sources, including traffic surveillance systems and dashcams. To standardize the input representation, all extracted frames were re sized to a fixed resolution of 224×224 pixels, a commonly used dimension compatible with state-of-the-art deep learning architectures such as CNNs and 3D-CNN-based spatiotemporal models. This resizing step ensures consistent input size across the dataset, reduces computational requirements, and enables efficient batch processing. Following resizing, all pixel intensities were normalized tostabilize the training process. Pixel values originally in the 0255 range were scaled to 01, and a channel-wise mean standard deviation normalization was applied to bring the data distribution closer to that of pretrained image models. Normalization improves gradient flow, accelerates convergence, and minimizes the impact of illumination variations commonly observed in traffic surveillance footage.

Normalization:

Normalization scales input feature values to a fixed range, typically [0,1], to ensure numerical stability and faster convergence during model training.

$$X_{norm} = \frac{X - X_{min}}{X_{max} - X_{min}}$$

For scaling the data to a general range [a,b]:

$$X_{norm} = a + \frac{(X - X_{min})(b - a)}{X_{max} - X_{min}}$$

To enhance frame clarity, noise-removal techniques such as Gaussian smoothing and median filtering are selectively applied to reduce sensor noise, motion-induced blur, and compression artifacts. These denoising operations preserve important struc tural information, thereby improving feature extraction and increasing the accuracy of accident detection models.

III.3 YOLOv8

YOLOv8 is the latest generation of the “You Only Look Once” family of real-time computer vision models, designed to deliver high-performance object detection with improved accuracy and reduced latency. It plays a critical role in modern visual per ception systems by providing a unified framework capable of object detection, instance segmentation, and image classification, making it suitable for real-time and resource constrained environments. YOLOv8 introduces several architectural enhancements, including an improved CSP-based backbone for deeper feature extraction, a refined PAN/FPN neck for stronger multi-scale representation, and a fully anchor-free de tection head that directly predicts bounding boxes at each spatial location. This anchor-free design eliminates manual anchor tuning, reduces computational complex ity, and improves generalization across different object scales. YOLOv8 achieves faster inference, higher FPS, and improved accuracy through its decoupled classification regression head, advanced IoU-based loss functions, and optimized training strategies such as dynamic label assignment and enhanced augmentation pipelines. Addition ally, it supports multiple vision tasks — detection, segmentation, and classification —within a single architecture. Compared to earlier versions such as YOLOv5 and YOLOv7, YOLOv8 replaces traditional anchor-based prediction, which often struggled with scale variation and required extensive hyperparameter tuning. The anchor-free design improves localiza tion stability, reduces mismatched anchor assignments, and enhances performance on small and irregularly shaped objects. YOLOv8 also delivers lower inference latency, higher precision and recall, and more efficient end-to-end training, outperforming previous YOLO variants in both accuracy and real-time capability. YOLOv8 is preferred in modern applications because it generalizes effectively across diverse environments, handles small objects and crowded scenes more accu rately, and provides an efficient training pipeline suitable for both cloud and edge devices. Its robustness and high-speed performance make it especially suitable for traffic surveillance, road-scene analysis, accident detection, smart-city monitoring, and autonomous vehicle perception.

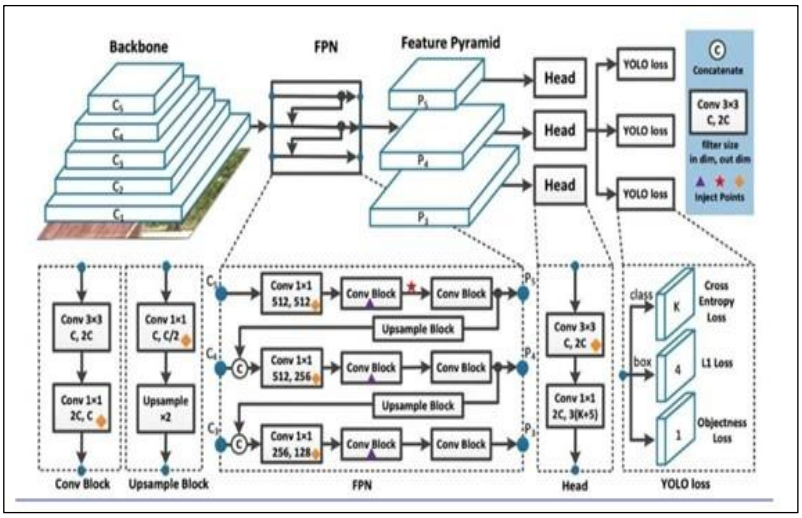


Figure 1: YOLOv8: A State-of-the-Art Object Detection Model.
Source: Authors, (2026).

III.4 SPATIAL FEATURE EXTRACTION USING CNN

Convolutional Neural Networks (CNNs) are widely used in real-time traffic flow anal ysis and accident detection because they can automatically learn hierarchical spatial patterns directly from video frames without requiring manual feature engineering. Traffic scenes contain diverse and complex visual elements—vehicles, lane bound aries, road geometry, shadows, occlusions, and collision signatures—that traditional computer-vision methods fail to capture reliably. CNNs, on the other hand, learn context-aware representations such as vehicle contours, deformation patterns during impact, smoke, abrupt intensity changes, and density variations. They also provide strong robustness against real-world challenges such as varying lighting conditions, ad verse weather, different camera perspectives, and high traffic density. Furthermore, modern CNN-based models such as YOLO, SSD,andFaster R-CNNefficiently process high frame-rate video streams on GPUs, making them ideal for real-time surveillance environments. Their ability to extract discriminative spatial features makes CNNs the backbone of intelligent transportation systems, especially when combined with temporal modeling techniques for dynamic event understanding.temporal models like LSTMs for capturing motion dynamics. In the proposed accident detection framework, the Convolutional Neural Network (CNN) serves as the primary module for extracting spatial features from individual video frames. Each frame contains rich visual cues such as vehicle shapes, road markings, traffic density, and collision indicators. Therefore, the CNN converts raw pixel-level information into high-level spatial representations that can later be ana lyzed temporally by the LSTM network. The input to the CNN consists of sequential traffic frames resized to a fixed resolution to ensure computational uniformity across the dataset.

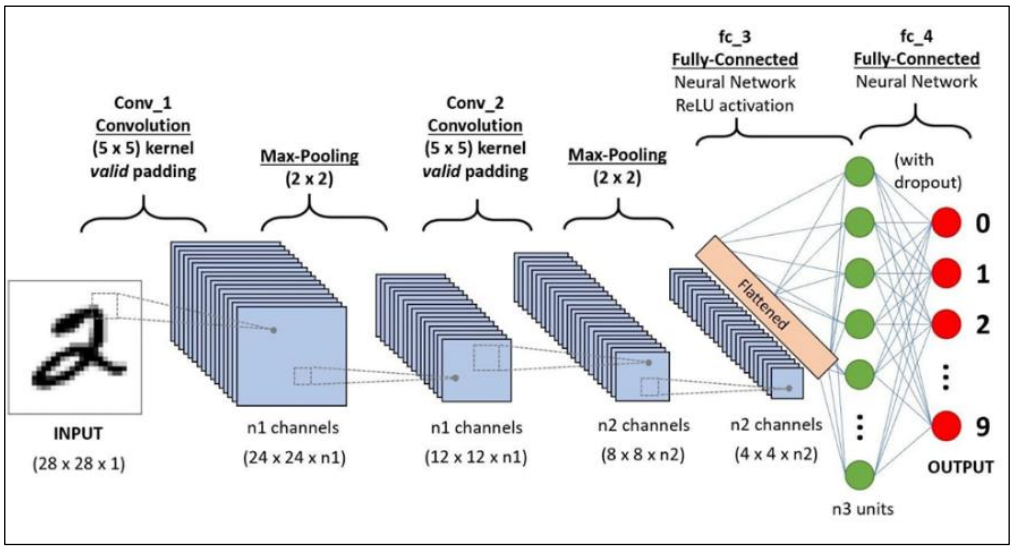


Figure 2: CNN Architecture.
Source: Authors, (2026).

The architecture begins with a convolutional layer that applies a set of learnable f ilters across the input frame. Each filter performs a two-dimensional convolution operation given by:

$$F(i,j) = \sum_{m}\sum_{n} I(i+m, j+n)K(m,n)$$

Where I represents the input image, K denotes the convolution kernel, and F(i,j) is the resulting feature activation. These convolutional operations generate feature maps that highlight meaningful structures such as vehicle boundaries, road edges, and abrupt illumination changes caused by collisions or skid marks. By using valid padding and appropriately sized kernels, the spatial dimensions gradually decrease while the feature depth increases, allowing the model to learn abstract hierarchical representations. Each feature map then undergoes a max-pooling operation to reduce spatial di mensions while retaining dominant activations. The pooling process is mathematically expressed as:

$$P(i,j) = \max_{(m,n)\in R_{i,j}} F(m,n)$$

Where Ri,j represents the pooling region. This step introduces robustness to minor spatial shifts, which is crucial in dynamic traffic environments where vehi cles frequently move across frames. Additionally, max-pooling reduces computational complexity, enabling efficient real-time processing. A second convolutional block further refines the spatial features by learning higher-order patterns such as overlapping vehicles, deformation signatures during im pacts, and sharp discontinuities on the road surface. Similar to the first block, it consists of convolutional layers followed by max-pooling, resulting in compact and in formative feature maps that preserve essential accident-related cues while suppressing background noise. After spatial feature extraction, the multi-channel feature maps are flattened into a one-dimensional vector. This flattened representation is passed to fully connected layers that integrate spatial information across the entire frame. Each fully connected layer performs the operation:

$$h = \phi(Wx + b),$$

Where x is the flattened feature vector, W and b are learnable weights and bi ases, and ϕ(·) is a nonlinear activation function, typically ReLU. The nonlinearity enables the model to learn complex semantic patterns such as abnormal vehicle spac ing or visual signatures associated with accidents. Dropout regularization is applied to prevent overfitting and enhance generalization across diverse traffic conditions. Finally, the output layer generates spatial feature representations that are not directly used for classification. Instead, these representations serve as input to the LSTM module. This CNN–LSTM integration enables the framework to jointly cap ture spatial information and temporal dynamics, resulting in accurate accident detec tion based on both instantaneous visual cues and motion patterns across consecutive video frames.

III.5 TEMPORAL MODELING USING LSTM

Temporal analysis plays a fundamental role in accident detection, as accidents are inherently dynamic and evolve over a sequence of frames rather than appearing in isolated images. These events typically involve distinct patterns such as abrupt decel eration, abnormal trajectory deviations, sudden collisions, or instantaneous disappear ance of vehicles, all of which unfold over time. While Convolutional Neural Networks (CNNs) are effective at extracting spatial information from individual frames, they are unable to capture the temporal progression that characterizes accident scenarios. Long Short-Term Memory (LSTM) networks address this limitation by modeling tem poral dependencies and learning frame-to-frame relationships within sequential data. By incorporating the evolution of visual cues across pre-impact, impact, and post impact stages, LSTMs significantly enhance the robustness and accuracy of real-time accident detection systems, enabling them to distinguish true accident occurrences from normal fluctuations in traffic behavior. Long Short-Term Memory (LSTM) networks are an advanced variant of tradi tional Recurrent Neural Networks (RNNs), specifically designed to overcome limita tions in learning long-range temporal dependencies, such as the vanishing gradient problem. Unlike conventional RNNs, which struggle to preserve information across extended sequences, an LSTM maintains two internal states at each time step: the hidden state $h_{t-1}$and the cell state C_{t-1}. Together with the current input x_t, these states regulate the flow of information through a set of gating mechanisms that de termine what information should be forgotten, updated, and propagated forward in time. The computation begins with the forget gate, which evaluates the relevance of the previous memory by applying a sigmoid activation function to the concatenation of the previous hidden state and the current input. The forget gate is defined as:

$$ft = \sigma\big(W_f[h_t - 1, x_t] + b_f\big),$$

Where σ(·) denotes the sigmoid activation function, W_f represents the forget gate weight matrix, and b_f is the corresponding bias term. The gate output ranges between 0 and 1, where values close to 1 indicate retention of past information, while values near 0 indicate discarding irrelevant or outdated memory. Simultaneously, the input gate determines how much new information should be added to the cell state. It is computed as:

$$i_t = \sigma(W_i[h_t - 1, x_t] + b_i)$$

Along with the candidate memory vector, which represents newly generated con tent derived from the current input and the previous hidden state:

$$C_t = \tanh(W_C[h_t - 1, x_t] + b_C)$$

The interaction between the input gate and the candidate memory allows the LSTM to selectively incorporate only the most meaningful and contextually relevant information into its internal state. The updated cell state is computed through an element-wise combination of the preserved past memory and the newly generated candidate content:

$$C_t = f_t \odot C_t - 1 + i_t \odot \tilde{C}_t,$$

Where ⊙denotes element-wise multiplication. This update mechanism ensures a stable memory flow across time, enabling the LSTM to maintain long-term contextual dependencies without numerical instability. Once the cell state is updated, the output gate determines which part of the memory should be exposed to the hidden layer:

$$o_t = \sigma(W_o[h_t - 1, x_t] + b_o),$$

And the final hidden state is computed as:

$$h_t = o_t \odot \tanh(C_t)$$

The hidden state ht serves as both the output of the LSTM at the current time step and a summary of relevant temporal information that is passed to subsequent time steps. Through this gated and controlled flow of information, LSTM networks effec tively capture both short-term and long-term temporal dependencies in sequential data. Their ability to maintain stable memory dynamics and model evolving tem poral context makes them particularly suitable for real-time accident detection and traffic flow analysis, where patterns such as sudden deceleration, abnormal motion trajectories, and frame-to-frame vehicle interactions are critical for identifying acci dent events.

III.6 CLASSIFICATION OF TEMPORAL FEATURES

Let the input video sequence be denoted as X = $x_1, x_2, \ldots, x_T$, where T repre sents the total number of frames in a video. The Long Short-Term Memory (LSTM) network processes this sequence to capture long-term temporal dependencies and produces a compact temporal representation. The output of the LSTM block is rep resented by the final hidden state vector $h_T \in R^d$, which encodes discriminative temporal information across the entire sequence. The extracted temporal feature vector h_T is subsequently forwarded to the clas sifier block for multi-class classification. In this study, the classification task involves eight distinct classes corresponding to different accident and non-accident scenarios. Formally, the classifier learns a mapping function

$$f: R^d \rightarrow 1,2,\ldots,8$$

Where each output label denotes one of the predefined scenario classes. To evaluate the effectiveness of the learned temporal representations, multiple machine learning classifiers are employed, including LightGBM, Support Vector Ma chine (SVM), XGBoost, CatBoost, and Random Forest. All classifiers are trained using the same set of LSTM-derived feature vectors to ensure a fair and consistent comparison. This multi-classifier strategy facilitates an in-depth analysis of how differ ent learning paradigms exploit the temporal features extracted by the LSTM network. The performance of each classifier is assessed using Accuracy and F1-score. Ac curacy is defined as:

$$Accuracy = \frac{TP}{TP + TN + FP + FN,} + \frac{TN}{TP + TN + FP + FN,}$$

Which measures the overall correctness of classification. Since the dataset exhibits class imbalance across the eight classes, the F1-score is also reported, as it provides a balanced measure between precision and recall. The F1-score is defined as :

$$F1 = \frac{2 \times \Pr e\,cision \times Recall}{\Pr e\,cision + Recall}$$

These evaluation metrics collectively provide a reliable assessment of the classifier performance and demonstrate the discriminative capability of the temporal features learned by the LSTM network across all eight scenario classes.

III.7 SYSTEM ARCHITECTURE AND ALGORITHM

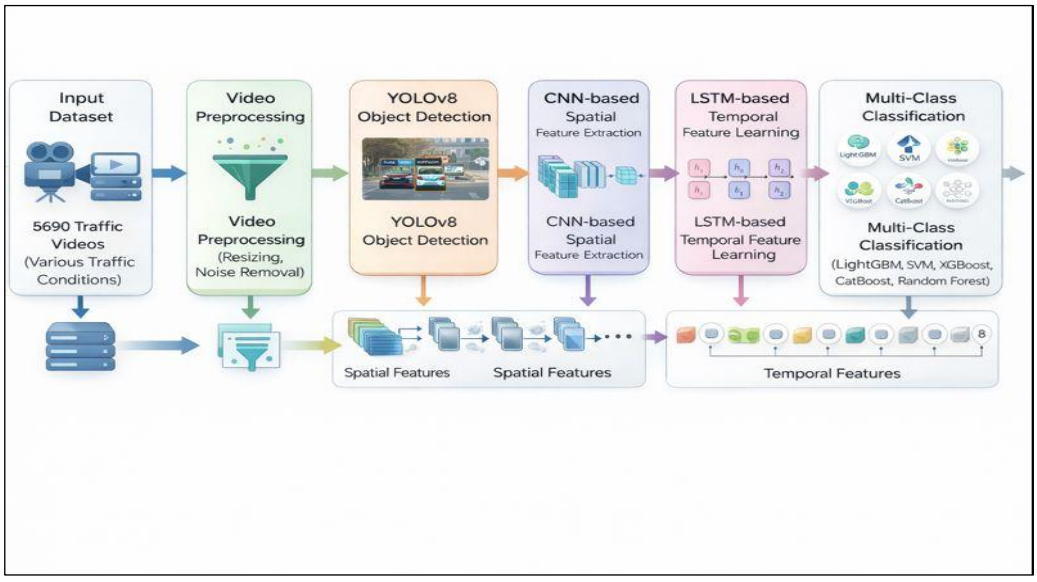


Figure 3: Block diagram of the proposed YOLOv8 and LSTM-based traffic accident multi class prediction framework.
Source: Authors, (2026).

Figure 3 illustrates the overall workflow of the proposed YOLOv8-based traffic ac cident detection framework. The system begins with continuous acquisition of traffic video streams from surveillance cameras. The input video is processed by the video preprocessing and frame sampling module, where frames are extracted at fixed inter vals and normalized to ensure uniform resolution and noise reduction. The preprocessed frames are then passed to the YOLOv8-based object detection module, which performs real-time detection and localization of traffic participants such as vehicles. The detected objects are represented through spatial feature em beddings, capturing object-level characteristics and scene context. To model the temporal dynamics of traffic behavior, the extracted features are forwarded to the temporal feature modeling unit, where sequential dependencies across consecutive frames are learned. An LSTM-based spatio-temporal classification module analyzes these temporal patterns to differentiate between accident and non-accident scenarios. Finally, the decision support and alert generation module evaluates the classifi cation outcome and generates real-time accident alerts, enabling timely response and traffic management intervention.

Algorithm 1 Multiclass Traffic Accident Prediction using CNN–LSTM Fusion

Require: Dataset D = {(Xv(i), Xc(i), Y(i))}
Ensure: Predicted class label $\hat{Y}$

1: Feature Extraction Phase
2: for each sample (Xv(i), Xc(i)) ∈ D do
3: $X\tilde{v}(i) \leftarrow Preprocess(Xv(i))$
4: $X\tilde{c}(i) \leftarrow Preprocess(Xc(i))$
5: $Fv(i) \leftarrow CNN(X\tilde{v}(i))$
6: $Fc(i) \leftarrow LSTM(X\tilde{c}(i))$
7: end for

8: Feature Fusion and Classification Phase
9: for each training epoch do
10: $F(i) \leftarrow Concatenate(Fv(i), Fc(i))$
11: $\hat{Y}(i) \leftarrow Softmax(Dense(F(i)))$
12: Update network parameters using backpropagation
13: end for

14: return Final predicted label $\hat{Y}$

IV. RESULTS AND DISCUSSIONS

IV.1 RESULTS

IV.1.1 Dataset

The dataset was organized into three splits: training, validation, and testing, ensuring that each subset contained a balanced representation of all scenarios. The dataset was structured into scenario-specific folders, with each folder containing multiple videos cor responding to different traffic and environmental conditions. All videos were program matically loaded and decomposed into individual frames to enable frame-level prepro cessing and model-based analysis. Each extracted frame was subjected to standard pre processing operations, including resizing to a uniform spatial resolution, normalization of pixel intensities, and cleaning to remove corrupted or low-quality frames. These steps ensured consistency across the dataset and improved the reliability of the feature extrac tion process. Ground-truth annotations, such as accident and non-accident labels (or other scenario-specific classes), were incorporated into the dataset pipeline. These labels were mapped to the corresponding frames and used during training, validation, and perfor mance evaluation of the detection model.

IV.1.2 Yolov8

The proposed system employs the YOLOv8 object detection architecture to analyze traffic surveillance video data and identify relevant objects within each frame with high spa tial accuracy. As a preprocessing step, all input videos were decomposed into individual frames using a fixed sampling rate. This uniform frame extraction strategy ensures consis tent temporal representation across all video sequences while maintaining computational efficiency, thereby enabling scalable analysis of large-scale traffic datasets. Each extracted frame was processed independently by the YOLOv8 model during the inference stage. For every frame, the model generates bounding box coordinates, class labels, and corresponding confidence scores for all detected objects. These outputs col lectively encode the spatial location, semantic category, and detection reliability of objects present in the scene. Processing frames at this granularity preserves detailed spatial infor mation andfacilitates subsequent aggregation for temporal analysis without loss of critical visual cues. YOLOv8 was configured to detect multiple object categories commonly present in traffic-related environments, including vehicles, pedestrians, and other dynamic entities that directly influence traffic flow and road safety. The model's anchor-free detection mechanism, combined with enhanced feature pyramid networks, enables effective detec tion of objects across varying scales and resolutions. Moreover, the inference pipeline en sures consistent detection across consecutive frames, which is essential for robust analysis of dynamic traffic scenarios characterized by motion, occlusion, and frequent changes in object density.

For qualitative evaluation and demonstration purposes, the detection results obtained from five representative video samples are illustrated in the accompanying figure. In each example, frames were extracted from the original video, passed through the trained YOLOv8model, and subsequently annotated with bounding boxes and class labels corre sponding to the detected objects. These annotated frames provide a clear visual depiction of the model's detection capability and highlight its effectiveness in identifying diverse ob ject types under varying traffic conditions, camera viewpoints, and environmental settings such as lighting variations and background complexity. In addition to qualitative visualization, the frame-wise detection outputs generated by YOLOv8 play a critical role in subsequent analytical stages of the proposed frame work. The detected object information—including object counts, spatial distributions, and confidence scores across consecutive frames—serves as structured input for higher-level modeling and temporal analysis. By aggregating detection outputs over time, the system can infer evolving traffic patterns, detect changes in traffic density, and identify potential anomalous events. This integration of reliable object-level detection with temporal mod eling establishes a strong foundation for downstream classification and prediction tasks, thereby reinforcing the effectiveness of YOLOv8 as a core component of the overall traffic monitoring and accident detection pipeline.



(a) Frame extraction from video 1 and 2.



(b) Frame extraction from video 3 and 4.



(c) Frame extraction from video 5
Figure 4: Object detection using YOLOv8.
Source: Authors, (2026).

IV.1.3 Comparative Analysis of Traffic Prediction and Accident DetectionModels

To comprehensively evaluate the effectiveness and robustness of the proposed traffic prediction and accident detection framework, a comparative analysis was conducted using multiple machine learning classifiers under three different data preprocessing strategies: without preprocessing, normalization, and Z-score standardization. This analysis aims to assess the capability of each model to learn discriminative traffic patterns from video-derived features while maintaining robustness under real-world variability.

Table 3: Model Performance Without Preprocessing.

Model	Accuracy (%)	F1-Score (%)
LightGBM	57.68	25.67
XGBoost	57.84	52.03
Random Forest	55.57	47.25
CatBoost	56.57	49.48
SVM	58.75	51.20

Source: Authors, (2026).

Table 4: Model Performance with Normalization.

Model	Accuracy (%)	F1-Score (%)
LightGBM	57.75	52.07
XGBoost	56.96	50.73
Random Forest	55.57	47.25
CatBoost	56.82	49.80
SVM	58.75	51.20

Source: Authors, (2026).

Table 5: Model Performance with Z-Score Standardization.

Model	Accuracy (%)	F1-Score (%)
LightGBM	57.05	51.23
XGBoost	56.70	51.34
Random Forest	55.62	47.14
CatBoost	56.73	50.28
SVM	**63.27**	**55.66**

Source: Authors, (2026).

Tables 3, 4, and 5 summarize the performance of five widely adopted classifiers, namely LightGBM, XGBoost, Random Forest, CatBoost, and Support Vector Machine (SVM). Model performance is evaluated using accuracy and F1-score, which jointly reflect overall classification correctness and class-wise prediction balance in a multi-class traffic scenario. In the absence of preprocessing (Table 3), all models exhibit relatively moderate accuracy, ranging between 55% and 59%. LightGBM shows a notably low F1-score despite comparable accuracy, indicating a bias toward majority classes and poor handling of class imbalance. In contrast, SVM and XGBoost demonstrate improved F1-scores, suggesting better generalization across multiple traffic states even without feature scaling. When normalization is applied (Table 4), a marginal yet consistent improvement in F1-scores is observed for most classifiers. This improvement highlights the sensi tivity of distance-based and margin-based models to feature scale and distribution. However, the overall accuracy gains remain limited, indicating that normalization alone is insufficient to fully capture the temporal complexity inherent in traffic dy namics. The most significant performance enhancement is achieved under Z-score stan dardization (Table 5). In this configuration, SVM outperforms all other classifiers, achieving the highest accuracy of 63.27% and an F1-score of 55.66%. This re sult suggests that Z-score standardization effectively stabilizes feature distributions and improves class separability in high-dimensional traffic data. The superior perfor mance of SVM further indicates its ability to model nonlinear decision boundaries in scenarios characterized by overlapping traffic patterns and temporal ambiguity.

Despite these improvements, the overall accuracy of conventional machine learn ing models remains moderate. This limitation can be attributed to the intrinsic complexity of the problem, which involves multi-class traffic state classification under heterogeneous conditions, including varying illumination, occlusions, camera view points, and dynamic traffic density. Additionally, inter-class similarity between traffic states, such as slow-moving traffic and early-stage congestion or near-miss events and normal flow, increases classification difficulty and reduces achievable accuracy. In contrast, deep learningbased architectures demonstrate substantially higher performance. Hybrid models that integrate object detection and temporal modeling particularly the proposed YOLO + CNN + LSTM frameworksignificantly out perform traditional classifiers. This marked improvement validates the effectiveness of combining YOLO-based object detection for precise spatial feature extraction with CNNLSTM architectures for capturing long-term temporal dependencies in traffic sequences. The superior performance of the proposed model can be attributed to its ability to jointly model spatial and temporal information, which is essential for accurately recognizing traffic flow patterns and accident events that evolve over time. Unlike conventional classifiers operating on aggregated or static features, the proposed frame work preserves temporal continuity and contextual progression, resulting in improved discrimination between visually similar traffic conditions.

Furthermore, analysis of the training and validation curves confirms the stability and generalization capability of the proposed deep learning model. Both training and validation accuracy increase rapidly during early epochs and converge near the optimal value without significant divergence. Similarly, the corresponding loss curves exhibit a steady decline, indicating efficient error minimization and absence of over f itting. These observations confirm the reliability of the learning process and support the suitability of the model for real-time intelligent transportation system (ITS) ap plications. Overall, this comparative analysis demonstrates that while traditional machine learning models serve as effective baselines, they are limited in handling the spatio temporal complexity of real-world traffic data. The proposed YOLO + CNN + LSTM framework offers a robust, scalable, and high-precision solution for traffic prediction and accident detection, making it highly suitable for deployment in intelligent trans portation and urban traffic monitoring systems.

IV.2 DISCUSSION

The present study demonstrates that integrating random video sampling, multi-frame ex traction, and YOLOv8-based object detection provides an effective and computationally efficient framework for analyzing heterogeneous traffic surveillance videos. The results consistently show that the proposed pipeline is capable of isolating object-rich frames con taining dense vehicular and pedestrian activity, while filtering out visually uninformative segments such as empty roads or low-activity intervals. This selective processing strategy ensures that the downstream classification models are trained and evaluated on frames that are most relevant to traffic dynamics and event understanding, thereby supporting the broader objective of automated traffic analysis and accident detection. A key design decision in this work is the selection of YOLOv8 as the object detec tion backbone. YOLOv8 was chosen due to its strong balance between detection accu racy and real-time inference speed, which is essential for traffic surveillance applications where timely responses are critical. Its anchor-free detection paradigm, enhanced feature pyramid networks, and optimized non-maximum suppression mechanisms enable robust detection of objects across multiple scales and crowded scenes. These architectural im provements are particularly advantageous in complex traffic environments characterized byocclusions, rapid motion, and varying object densities. Compared to earlier YOLO vari ants and traditional handcrafted approaches, YOLOv8 demonstrates improved robustness underuncontrolledconditions, makingitwell-suited for real-world deploymentscenarios. For temporal classification and event recognition, a CNN + LSTM architecture was adopted as the classifier. This hybrid design leverages the complementary strengths of convolutional and recurrent neural networks. The CNN component effectively captures spatial features such as vehicle shapes, spatial arrangements, and local visual patterns within individual frames.

In contrast, the LSTM component models temporal dependen cies by learning sequential patterns across consecutive frames, which is critical for dis tinguishing transient traffic events such as congestion buildup, slowdowns, or accidents. Traffic-related incidents are inherently temporal phenomena, where isolated frames may appear ambiguous; therefore, incorporating temporal sequence modeling significantly en hances contextual understanding beyond frame-level analysis. From a performance perspective, the system achieved an over all classification accuracy of approximately **63%**. The complexity of the dataset further compounds this challenge. The traffic videos usedinthis studyoriginate from diver sescenarios captured under varying real-world conditions, including differences in lighting (daytime, dusk, nighttime), camera viewpoints, motion blur, background clutter, weather conditions, and traffic density. These hetero geneous conditions introduce significant intra-class variability, making it difficult for the model to learn consistent patterns for each class. Additionally, changes in camera angles and scene geometry can alter object appearance and motion trajectories, reducing the ef fectiveness of purely visual cues and increasing reliance on temporal modeling. Several limitations and challenges were identified that help explain the observed per formance. One major factor is limited and imbalanced data across classes, where rare events such as accidents or near-miss scenarios are underrepresented compared to normal traffic conditions. This imbalance biases the classifier toward dominant classes and re duces sensitivity to infrequent but critical events. Furthermore, traffic videos often contain noisy or ambiguous frames caused by motion blur, shadows, glare, or partial occlusions, which can obscure key visual indicators. Temporal ambiguity also presents a significant challenge in accident detection, as the onset and aftermath of an incident may span multi ple frames with subtle transitions that are difficult to localize precisely.

Despite these challenges, the results provide valuable insights into the effectiveness of the proposedapproach. TheachievedperformancedemonstratesthatcombiningYOLOv8 based object detection with CNN–LSTM temporal modeling is a viable strategy for multi class traffic event recognition under realistic conditions. The system's ability to generalize across diverse scenarios indicates strong foundational robustness, even when confronted with complex environmental variability and class overlap. Looking ahead, several avenues for future improvement are evident. Expanding the dataset with additional labeled samples per class—particularly for rare events—would significantly enhance model generalization. Advanced temporal architectures such as bidirectional LSTMs, GRUs, or transformer-based sequence models could further improve temporal reasoning and reduce ambiguity in event boundaries. Fine-tuning YOLOv8 on domain-specific traffic datasets and incorporating multimodal features (e.g., optical flow, vehicle trajectories, or speed estimates) may also strengthen discriminative power. Finally, integrating contextual cues such as road geometry or traffic signal states could improve semantic understanding and support more accurate classification in complex urban envi ronments. Overall, the findings underscore the practical feasibility of the proposed framework while clearly outlining its current limitations and future potential. The study contributes to ongoing research in intelligent transportation systems by demonstrating how modern object detection and temporal modeling techniques can be combinedtoaddressreal-world traffic analysis challenges in a scalable and data-driven manner.

V. CONCLUSIONS

This work presented a comprehensive spatio-temporal framework for traffic predic tion and accident detection using large-scale traffic surveillance videos. The proposed methodology integrates systematic video preprocessing, YOLOv8-based object de tection, CNN-driven spatial feature extraction, and LSTM-based temporal modeling, followed by multi-class classification across eight distinct traffic scenarios. The dataset was carefully structured into training, validation, and testing splits, ensuring balanced representation and enabling reliable performance evaluation under diverse traffic and environmental conditions. Experimental results demonstrate that conventional machine learning classifiers applied to LSTM-extracted temporal features achieve moderate performance, with accuracy values generally remaining below 60% under most preprocessing strategies. Among the evaluated models, Support Vector Machine (SVM) combined with Z-score standardization achieved the highest performance, reaching an accuracy of 63.27% and an F1-score of 55.66%. These findings highlight the importance of appropriate feature scaling when dealing with high-dimensional temporal representations in multi-class traffic classification tasks. More importantly, the comparative analysis clearly establishes the effectiveness of deep learningbased approaches over traditional classifiers. The proposed YOLO + CNN + LSTM framework consistently outperforms baseline models by jointly mod eling spatial object-level information and long-term temporal dependencies inherent in traffic video sequences.

YOLOv8 provides robust and accurate object detection under varying illumination, occlusion, and traffic density, while the CNNLSTM ar chitecture preserves temporal continuity and contextual evolution that are essential for distinguishing visually similar traffic states. Although the achieved performance is moderate, it must be interpreted in the context of the problems complexity. The study addresses an eight-class classification task involving heterogeneous real-world traffic scenarios with significant inter-class similarity, class imbalance, and environmental variability. Factors such as changing camera viewpoints, motion blur, partial occlusions, and subtle transitions between traffic states inherently limit achievable accuracy. Nevertheless, the stable conver gence behavior, consistent trainingvalidation trends, and strong generalization capa bility indicate the robustness and reliability of the proposed framework. Looking forward, several directions can further enhance the proposed system. Expanding the dataset with additional labeled samplesparticularly for rare and safety critical events such as accidents and near-miss scenarioswould improve class bal ance and model sensitivity. Advanced temporal architectures, including bidirectional LSTMs, GRUs, and transformer-based models, may further strengthen temporal rea soning and reduce ambiguity in event boundaries. Incorporating motion-aware and contextual features such as optical flow, vehicle trajectories, speed estimation, and road geometry information can also improve discriminative capability. Moreover, domain-specific fine-tuning of YOLOv8 and optimization for real-time deployment on edge or cloud-based platforms would support practical adoption in intelligent trans portation systems. Overall, this study demonstrates the feasibility and effectiveness of combining object detection with deep temporal modeling for automated traffic analysis. The proposed framework provides a scalable and robust foundation for future intelligent transportation applications, including real-time traffic monitoring, early accident de tection, and data-driven urban traffic management.

VI. AUTHOR'S CONTRIBUTION

Conceptualization: Dhartee Patel, Jinal Ahir, Namrata Shroff, Shankar Parmar.
Methodology: Dhartee Patel, Jinal Ahir, Namrata Shroff, Shankar Parmar.
Investigation: Dhartee Patel, Jinal Ahir, Namrata Shroff, Shankar Parmar.
Discussion of results: Dhartee Patel, Jinal Ahir, Namrata Shroff, Shankar Parmar.
Writing – Original Draft: Dhartee Patel, Jinal Ahir, Namrata Shroff, Shankar Parmar.
Writing – Review and Editing: Dhartee Patel, Jinal Ahir, Namrata Shroff, Shankar Parmar.
Resources: Dhartee Patel, Jinal Ahir, Namrata Shroff, Shankar Parmar.
Supervision: Dhartee Patel, Jinal Ahir, Namrata Shroff, Shankar Parmar.
Approval of the final text: Dhartee Patel, Jinal Ahir, Namrata Shroff, Shankar Parmar.

VII. REFERENCES

[1] J.-P. Chavas and G. Shi, "An Economic Analysis of Risk, Management, and Agricultural Technology," Journal of Agricultural and Resource Economics, vol. 40, no. 1, pp. 63–79, 2015.

[2] A. Mystakidis and C. Tjortjis, "Big Data Mining for Smart Cities: Predicting Traffic Congestion using Classification," Mar. 2020, pp. 1–8. doi: 10.1109/IISA50023.2020.9284399.

[3] J. B. Hardaker, J. W. Richardson, G. Lien, and K. D. Schumann, "Stochastic efficiency analysis with risk aversion bounds: a simplified approach," Aust. J. Agric. Resour. Econ., vol. 48, no. 2, pp. 253–270, Mar. 2004, doi: 10.1111/j.1467-8489.2004.00239.x.

[4] S. Zhang et al., "Surface Acoustic Wave Devices Using Lithium Niobate on Silicon Carbide," IEEE Trans. Microw. Theory Tech., vol. 68, no. 9, pp. 3653–3666, Sep. 2020.

[5] P. Kaushik, P. Rawat, P. Divakaran, V. M. Chaturvedi, R. K. Roy, and M. M. Kaushik, "Big Data Mining for Efficient Real-Time Traffic Management," in 2025 IEEE International Conference on Interdisciplinary Approaches in Technology and Management for Social Innovation (IATMSI), Mar. 2025, pp. 1–6.

[6] N. Zafar, {Irfan Ul} Haq, H. Sohail, {Jawad Ur Rehman} Chughtai, and M. Muneeb, "Traffic Prediction in Smart Cities Based on Hybrid Feature Space," IEEE Access, vol. 10, pp. 134333–134348, 2022, doi: 10.1109/ACCESS.2022.3231448.

[7] Y. Zhao et al., "A deeply supervised vertex network for road network graph extraction in high-resolution images," International Journal of Applied Earth Observation and Geoinformation, vol. 133, p. 104082, 2024, doi: https://doi.org/10.1016/j.jag.2024.104082.

[8] V. Adewopo et al., "Traffic Accident Detection Video Dataset for AI-Driven Computer Vision Systems in Smart City Transportation," 2023, IEEE Dataport. doi: 10.21227/tjtg-nz28.

[9] A. G. Ismaeel et al., "Traffic Pattern Classification in Smart Cities Using Deep Recurrent Neural Network," Sustainability, vol. 15, no. 19, 2023, [Online]. Available: https://www.mdpi.com/2071-1050/15/19/14522

[10] M. Mirbod and H. Dehghani, "Smart Trip Prediction Model for Metro Traffic Control Using Data Mining Techniques," Procedia Comput. Sci., vol. 217, pp. 72–81, 2023, doi: https://doi.org/10.1016/j.procs.2022.12.203.

[11] K. D. C. Adje, A. Ben Letaifa, M. Haddad, and O. Habachi, "Smart City Based on Open Data: A Survey," IEEE Access, vol. 11, pp. 56726–56748, Mar. 2023, doi: 10.1109/ACCESS.2023.3283436.

[12] I. H. Sarker, "Smart City Data Science: Towards data-driven smart cities with open research issues," Internet of Things, vol. 19, p. 100528, 2022, doi: https://doi.org/10.1016/j.iot.2022.100528.

[13] L. B. Elvas, C. F. Marreiros, J. M. Dinis, M. C. Pereira, A. L. Martins, and J. C. Ferreira, "Data-Driven Approach for Incident Management in a Smart City," Applied Sciences, vol. 10, no. 22, 2020, doi: 10.3390/app10228281.

[14] M. Saleem, S. Abbas, T. M. Ghazal, M. Adnan Khan, N. Sahawneh, and M. Ahmad, "Smart cities: Fusion-based intelligent traffic congestion control system for vehicular networks using machine learning techniques," Egyptian Informatics Journal, vol. 23, no. 3, pp. 417–426, 2022, doi: https://doi.org/10.1016/j.eij.2022.03.003.

[15] A. Mystakidis, P. Koukaras, and C. Tjortjis, "Advances in Traffic Congestion Prediction: An Overview of Emerging Techniques and Methods," Smart Cities, vol. 8, no. 1, 2025, doi: 10.3390/smartcities8010025.

[16] E. G. and J. M. B. Oyewola David Opeoluwa and Dada, “Smart City Traffic Patterns Prediction Using Machine Learning,” in Machine Learning Techniques for Smart City Applications: Trends and Solutions, D. J. Hemanth, Ed., Cham: Springer International Publishing, 2022, pp. 123–133. doi: 10.1007/978-3-031-08859-9_10.

[17] L. Li Hao AND Chen, “Traffic accident risk prediction based on deep learning and spatiotemporal features of vehicle trajectories,” PLoS One, vol. 20, no. 5, pp. 1–28, Mar. 2025, doi: 10.1371/journal.pone.0320656.

[18] F. Nocua M, W.-J. Pérez-Holguín, and C. Pardo-Beainy, “Urban traffic monitoring based on deep learning on an embedded GPU,” Expert Syst. Appl., vol. 273, p. 126847, 2025, doi: https://doi.org/10.1016/j.eswa.2025.126847.

[19] K. Alnowaiser, “A Computational Intelligence GNN–LSTM Framework for Spatiotemporal Prediction of Traffic Accident Severity in Smart Cities Using SHAP XAI,” International Journal of Computational Intelligence Systems, vol. 18, no. 1, p. 271, Oct. 2025, doi: 10.1007/s44196-025-01015-y.

[20] A. M. Nagy and V. Simon, “A novel congestion propagation modeling algorithm for smart cities,” Pervasive Mob. Comput., vol. 73, p. 101387, 2021, doi: https://doi.org/10.1016/j.pmcj.2021.101387.

[21] Y. Ma et al., “High-Entropy Approach vs. Traditional Doping Strategy for Layered Oxide Cathodes in Alkali-Metal-Ion Batteries: A Comparative Study,” Energy Storage Mater., vol. 79, p. 104295, 2025, doi: https://doi.org/10.1016/j.ensm.2025.104295.

[22] W. Li, L. Huang, and X. Lai, “A Deep Learning Framework for Traffic Accident Detection Based on Improved YOLO11,” Vehicles, vol. 7, no. 3, 2025, doi: 10.3390/vehicles7030081.

[23] S. T. Mrudula et al., “Internet of things and optimized knn based intelligent transportation system for traffic flow prediction in smart cities,” Measurement: Sensors, vol. 35, p. 101297, 2024, doi: https://doi.org/10.1016/j.measen.2024.101297.

[24] R. An, X. Zhang, M. Sun, and G. Wang, “GC-YOLOv9: Innovative smart city traffic monitoring solution,” Alexandria Engineering Journal, vol. 106, pp. 277–287, 2024, doi: https://doi.org/10.1016/j.aej.2024.07.004.

[25] Q. Chen, W. Wang, K. Huang, S. De, and F. Coenen, “Multi-modal generative adversarial networks for traffic event detection in smart cities,” Expert Syst. Appl., vol. 177, p. 114939, 2021, doi: https://doi.org/10.1016/j.eswa.2021.114939.

[26] J. Salazar-Carrillo, M. Torres-Ruiz, C. A. Davis, R. Quintero, M. Moreno-Ibarra, and G. Guzmán, “Traffic Congestion Analysis Based on a Web-GIS and Data Mining of Traffic Events from Twitter,” Sensors, vol. 21, no. 9, 2021, doi: 10.3390/s21092964.

[27] N. Pathik, R. K. Gupta, Y. Sahu, A. Sharma, M. Masud, and M. Baz, “AI Enabled Accident Detection and Alert System Using IoT and Deep Learning for Smart Cities,” Sustainability, vol. 14, no. 13, 2022, doi: 10.3390/su14137701.

[28] V. Adewopo et al., “Traffic Accident Detection Video Dataset for AI-Driven Computer Vision Systems in Smart City Transportation,” 2023, IEEE Dataport. doi: 10.21227/tjtg-nz28.

[29] V. Afifah and S. Erniwati, “YOLOv8 for Object Detection: A Comprehensive Review of Advances,Techniques, and Applications,” IJACI : International Journal of Advanced Computing and Informatics, vol. 2, pp. 53–61, Mar. 2025, doi: 10.71129/ijaci.v2i1.pp53-61.

[30] I. D. Mienye, T. G. Swart, and G. Obaido, “Recurrent Neural Networks: A Comprehensive Review of Architectures, Variants, and Applications,” Information, vol. 15, no. 9, 2024, doi: 10.3390/info15090517.

Journal of Engineering and Technology for Industrial Applications

ISSN ONLINE: 2447-0228

ITEGAM-JETIA

Manaus, v.12 n.60, p.1138-1147. July/August, 2026.
DOI: https://doi.org/10.5935/jetia.v12i60.4010

RESEARCH ARTICLE OPEN ACCESS

ADAPTIVE DATASET: CNN-LSTM APPROACHES FOR DYSARTHRIA CLASSIFICATION USING ACOUSTIC FEATURE ENGINEERING

J.Jothieswari[1], S.Suguna[2]

[1]Research Scholar (MKU24PFOS11387), Madurai Kamaraj University, Madurai, Tamilnadu, India.
[2]Associate Professor, PG and Research Dept. of CS, Sri Meenakshi Government Arts College for Women, Madurai, Tamilnadu, India.

[1]http://orcid.org/0009-0003-5998-3224, [2]http://orcid.org/0000-0001-9686-971X

Email:*jothi1812@gmail.com, kt.suguna@gmail.com

ARTICLE INFO

Article History
Received: March 10, 2026
Reviewed: April 10, 2026
Accepted: July 10, 2026
Published: August 31, 2026

Keywords:
Dysarthria Detection,
Acoustic Feature Engineering,
CNN-LSTM,
Random Forest,
Speech Signal Processing,
ADAPTIVE Dataset

ABSTRACT

Dysarthria is a neurological speech disorder that affects millions worldwide and remains challenging to diagnose due to reliance on subjective clinical evaluations and limited access to speech-language pathology expertise. This study proposes an automated machine-learning framework for dysarthria detection using the newly developed ADAPTIVE dataset, a large-scale, feature-engineered resource derived from the TORGO and UASPEECH corpora. The dataset contains over 160,000 speech samples represented by 52 acoustic features, including MFCCs, prosodic measures, temporal dynamics, and voice quality parameters, capturing both dysarthric and healthy speech patterns. Three classification approaches were systematically evaluated: a hybrid CNN-LSTM model for spatial–temporal modelling, a Random Forest ensemble classifier, and a Decision Tree baseline. Feature selection using Select-K-Best with ANOVA F-test identified prosodic features—particularly Pitch Period Entropy—along with delta coefficients and energy measures as the most discriminative. Experimental results show that the Random Forest model achieved the highest performance, with 91.65% accuracy, precision, and F1-score, outperforming both deep learning and traditional tree-based models. The CNN-LSTM achieved competitive accuracy (89.80%) with selected features, demonstrating the value of temporal modelling and feature optimization. Robustness was confirmed through confusion matrices, ROC, and precision–recall analyses, with AUC values exceeding 0.96. Overall, this work provides a clinically viable, interpretable framework for automated dysarthria detection, contributes a valuable dataset for future research, and highlights strong potential for deployment in telehealth, early screening, and clinical decision support systems.

Copyright ©2026 by authors and Galileo Institute of Technology and Education of the Amazon (ITEGAM). This work is licensed under the Creative Commons Attribution International License (CC BY 4.0).

I. INTRODUCTION

Dysarthria represents a significant neurological speech disorder characterized by impaired articulation, phonation, resonance, and prosody due to weakness, paralysis, or incoordination of the speech musculature. This condition affects approximately 2-3% of the global population and is commonly associated with neurological conditions such as Parkinson's disease, multiple sclerosis, cerebral palsy, stroke, and traumatic brain injury. The prevalence of dysarthria is particularly pronounced among elderly populations, where neurodegenerative diseases are more common, affecting up to 15% of individuals over 65 years of age. As global life expectancy increases and the aging population grows, the burden of dysarthria-related communication difficulties is expected to rise substantially, creating an urgent need for accessible and efficient diagnostic solutions. Traditional clinical assessment of dysarthria relies heavily on subjective perceptual evaluations conducted by trained speech-language pathologists (SLPs) using standardized protocols such as the Frenchay Dysarthria Assessment or the Assessment of Intelligibility of Dysarthric Speech. While these methods remain the gold standard for clinical diagnosis, they present several inherent limitations that impact both accessibility and consistency. First, the subjective nature of perceptual assessment introduces inter-rater variability, with studies reporting agreement rates between clinicians ranging from 60% to 85%, depending on the severity level and experience of the evaluators.

Second, access to specialized speech-language pathologists is often limited, particularly in rural and underserved communities, creating significant barriers to timely diagnosis and intervention. Third, traditional assessments are typically conducted in controlled clinical environments, which may not reflect the natural speech patterns that patients exhibit in their daily communication contexts. The economic burden associated with dysarthria extends beyond direct healthcare costs to include reduced quality of life, social isolation, and decreased employment opportunities for affected individuals. Studies estimate that speech disorders cost the healthcare system billions of dollars annually when considering diagnostic procedures, therapeutic interventions, assistive technologies, and lost productivity. Early detection and intervention have been shown to significantly improve patient outcomes, reduce long-term care costs, and enhance communication effectiveness. However, the current healthcare infrastructure struggles to provide timely and consistent diagnostic services, particularly as the demand for speech-language pathology services continues to outpace the supply of qualified professionals. The emergence of artificial intelligence and machine learning technologies offers unprecedented opportunities to address these challenges through automated speech analysis systems. Unlike traditional clinical assessments, AI-driven approaches can provide objective, consistent, and scalable solutions that operate independently of human subjectivity and availability constraints. Machine learning models can analyze acoustic features with precision that often exceeds human perceptual capabilities, detecting subtle patterns in speech that may be imperceptible to even experienced clinicians. Furthermore, automated systems can be deployed across diverse settings, from clinical environments to home-based monitoring systems, enabling continuous assessment and early intervention strategies.

Recent advances in deep learning architectures, particularly convolutional neural networks (CNNs) and recurrent neural networks (RNNs), have demonstrated remarkable success in speech processing tasks. CNNs excel at extracting spatial patterns from spectral representations of speech signals, while recurrent architectures like Long Short-Term Memory (LSTM) networks are particularly effective at modeling the temporal dependencies inherent in speech production. The combination of these architectures in hybrid models leverages the complementary strengths of both approaches, offering enhanced performance for complex speech analysis tasks such as dysarthria detection. However, the development of robust automated dysarthria detection systems faces several technical challenges that must be addressed to ensure clinical viability. First, speech variability across individuals, dialects, languages, and recording conditions creates significant complexity in developing generalizable models. Second, the subtle nature of early-stage dysarthria symptoms requires highly sensitive detection algorithms capable of identifying minimal acoustic deviations from normal speech patterns. Third, the limited availability of large-scale, diverse datasets has constrained the development and validation of machine learning models, particularly for deep learning approaches that require substantial training data. Fourth, the need for interpretable and explainable AI systems in clinical contexts demands that automated tools provide transparent decision-making processes that clinicians can understand and trust. The acoustic manifestations of dysarthria are multifaceted and vary significantly depending on the underlying neurological etiology and severity level. Common acoustic features that distinguish dysarthric from normal speech include irregularities in fundamental frequency (pitch), reduced vocal intensity, altered formant frequencies, increased jitter and shimmer values, modified harmonics-to-noise ratios, and disrupted temporal patterns including abnormal pause durations and speaking rates.

These acoustic changes reflect the underlying physiological impairments in respiratory control, laryngeal function, articulatory precision, and motor coordination that characterize different types of dysarthria. The complexity and interaction of these features necessitate sophisticated analytical approaches that can capture both individual feature importance and their collective patterns. Feature engineering has emerged as a critical component in developing effective dysarthria detection systems. Traditional approaches have relied heavily on hand-crafted acoustic features such as Mel-Frequency Cepstral Coefficients (MFCCs), spectral characteristics, prosodic measures, and voice quality parameters. While these engineered features have demonstrated considerable success in classification tasks, they require domain expertise to design and may not capture all relevant acoustic patterns present in dysarthric speech. Recent trends toward end-to-end learning approaches using raw audio waveforms offer the potential to automatically discover optimal feature representations, though they typically require larger datasets and greater computational resources. The clinical translation of automated dysarthria detection systems requires careful consideration of validation methodologies, performance metrics, and deployment strategies. Traditional machine learning evaluation metrics such as accuracy, precision, recall, and F1-score provide important insights into model performance, but clinical applications demand additional considerations including sensitivity to different severity levels, robustness across demographic groups, and alignment with clinical diagnostic criteria. Furthermore, successful clinical adoption requires systems that can integrate seamlessly into existing healthcare workflows while providing interpretable results that support clinical decision-making rather than replace human expertise.

I.1 RESEARCH OBJECTIVES AND CONTRIBUTIONS

This study addresses the critical need for automated, objective, and accessible dysarthria detection through a comprehensive machine learning approach that leverages advanced feature engineering and hybrid deep learning architectures. The primary objectives of this research are threefold: first, to develop and validate a novel feature-engineered dataset (ADAPTIVE) that combines the strengths of established speech corpora while addressing common limitations in existing datasets; second, to systematically evaluate and compare the performance of different machine learning approaches, including traditional ensemble methods and modern deep learning architectures, for dysarthria classification; and third, to identify the most informative acoustic features and optimal model configurations for accurate and reliable dysarthria detection. The key contributions of this work include the creation of the ADAPTIVE dataset, which represents a significant advancement in feature-engineered speech disorder datasets by combining samples from TORGO and UASPEECH corpora with comprehensive acoustic feature extraction encompassing spectral, prosodic, temporal, and voice quality characteristics. Additionally, this study provides a thorough comparative analysis of machine learning approaches, demonstrating that ensemble methods can achieve superior performance compared to deep learning models when applied to carefully engineered features. The research also contributes valuable insights into feature importance for dysarthria detection, revealing that prosodic features, particularly Pitch Period Entropy, play a crucial role in distinguishing dysarthric from normal speech patterns.

Furthermore, this work advances the understanding of hybrid CNN-LSTM architectures for speech disorder detection, demonstrating their effectiveness in capturing both spatial and temporal patterns in acoustic features while providing analysis of how feature selection impacts model performance and generalization. The systematic evaluation methodology employed in this study, including comprehensive statistical analysis and multiple performance metrics, establishes a robust framework for future research in automated speech disorder detection. These contributions collectively advance the field toward more reliable, accessible, and clinically viable automated dysarthria detection systems.

I.2 PAPER ORGANIZATION

The remainder of this paper is organized as follows: Section 2 provides a comprehensive review of related literature, examining recent advances in datasets, feature engineering approaches, deep learning models, clinical applications, and hybrid architectures while identifying key research gaps and limitations. Section 3 details the proposed methodology, including the development of the ADAPTIVE dataset, preprocessing procedures, feature selection strategies, and the implementation of CNN-LSTM and comparative machine learning models. Section 4 presents the experimental results, including comprehensive performance analysis, statistical validation, and detailed discussion of findings with clinical implications. Finally, Section 5 concludes the paper with a summary of contributions, limitations of the current work, and directions for future research in automated dysarthria detection systems.

II. REVIEW LITERATURE

II.1 DATASETS AND DATA ACQUISITION

By [1] developed convolutional neural network (CNN) models to classify audio recordings from healthy speakers and individuals with dysarthria. Their dataset consisted of command-based speech samples segmented at the sentence level, followed by preprocessing steps such as segmentation, down-sampling, and feature extraction. The best-performing model achieved an F1-score of 96.18±4.7% and an accuracy of 96.01±5.02%. Sentence structure significantly influenced model accuracy, highlighting the importance of linguistic context. These results suggest that AI-driven speech analysis can aid in detecting and managing health conditions outside clinical environments. In turn [2] introduced a large-scale, multi-task speech dataset collected from 600 participants to support automated dysarthria detection. Using a remote data acquisition pipeline and deep representation learning, they achieved over 90% accuracy, outperforming traditional feature-based methods. Their framework demonstrates strong potential for scalable, self-monitoring systems to support patients with Parkinson's disease.

II.2 FEATURE ENGINEERING

By [3] proposed an automated system for dysarthria detection and severity classification using a Fourier-Bessel series expansion-based wavelet transform (FBSE-FTFCWT) with autoencoders. Speech signals were decomposed into 16 sub-bands, forming tensors for latent feature extraction. The framework achieved 3.28% higher accuracy than state-of-the-art methods on the UA-Speech dataset and improved severity detection accuracy by 3.1%. According to [4] compared spectrograms and Mel-spectrograms for dysphonic voice detection. Using vowel samples from the Saarbrücken Voice Database, they showed that Mel-spectrograms—closer to human auditory perception—outperformed spectrograms in classification accuracy. By [5] developed a dysarthria speech recognizer (DSR) combining Mel Frequency Logarithmic Spectrograms (MFLS) with deep CNNs. Evaluated on the UASpeech dataset, the method achieved 96.83% accuracy, recall of 0.97, precision of 0.96, and F1-score of 0.97, significantly outperforming prior approaches.

II.3 DEEP LEARNING MODELS

By [6] applied CNNs to classify 500 dysarthric and 500 non-dysarthric samples, reaching 96% accuracy. Similarly, Singla et al. [7] used ResNet50 CNNs on a comparable dataset, achieving identical accuracy. Both studies emphasized deep learning's ability to support early dysarthria diagnosis. In turn [8] extended this work using DenseNet201 CNNs with the TORGO dataset (2000 samples), also reporting 96% accuracy. These results further demonstrate CNNs' reliability in distinguishing dysarthric from normal speech. According to [9] introduced a raw waveform-based deep learning model using SincNet with Mel, Erb, and Bark scale initializations. The Bark scale yielded the best results, achieving 97% accuracy in dysarthria detection and 88% in speaker identification, surpassing previous benchmarks.

II.4 CLINICAL APPLICATIONS

By [10] developed a deep learning system for non-invasive stroke diagnosis using dysarthric speech. Leveraging ResNet50, InceptionV4, ResNeXt50, SEResNeXt18, and AttResNet50, the models achieved accuracy of 95.52% with high sensitivity and specificity. This approach shows promise as a cost-effective, rapid stroke screening tool. In turn [11] extended automatic speech recognition (ASR) for inappropriate pause detection in dysarthric speech. By tagging pauses at the text level and integrating a pause-prediction layer into the ASR model, they significantly improved pause detection accuracy. According to [12] applied machine learning models with clinical data to predict dysarthria severity levels. Incorporating patient records, medical images, and genetic data, their approach enhanced diagnostic precision and proposed a holistic, personalized treatment pathway.

II.5 TRANSFORMERS AND HYBRID MODELS

By [13] investigated transformer-based architectures (ViT-L-16, ViT-L-32, ViT-B-16) for severity classification using the UA-Speech and TORGO datasets. The models achieved outstanding accuracies of 99.01% and 99.39%, respectively, establishing strong baselines for clinical adoption.

By [14] developed a comprehensive pipeline for dysarthria detection using MFCCs and multiple neural network architectures (CNN, LSTM, GRU, Bi-LSTM, RNN, DNN). Model performance was assessed through confusion matrices and classification reports, supporting the creation of reliable diagnostic tools.

II.6 GENERAL SPEECH DISORDERS

In turn [15] combined acoustic analysis with machine learning and deep learning models to build a generalizable dysarthria detection system. Their work emphasized cross-dataset validation and the importance of early detection for improving patient outcomes. According to [16] proposed *ConVox*, a deep learning model for voice disorder detection using over 22,000 samples from four major datasets. Employing 1D CNN stacks, ConVox achieved near-perfect results (99.91% validation accuracy, AUC = 0.999995). Its multilingual and multi-pathology capabilities highlight its potential as a robust clinical tool

II.7 RESEARCH GAPS AND LIMITATIONS

i. Dataset Limitations: Many studies (e.g., [1], [6-8]) rely on relatively small datasets (often ~500–2000 samples), limiting model generalizability. Datasets such as TORGO and UA-Speech are widely reused, but they may not represent real-world variability across age, accent, language, and severity levels. Most datasets are controlled or laboratory-recorded, lacking noisy, real-life speech data that would be encountered in consumer or telehealth applications.

ii. Linguistic and Cultural Diversity: Most work has been conducted in English-speaking populations; cross-linguistic generalization remains underexplored. Only a few models (e.g., ConVox [16]) claim multilingual robustness, but validation across diverse speech communities is limited.

iii. Feature Engineering vs. Raw Audio Approaches: While feature engineering (e.g., spectrograms, MFCCs, wavelet transforms) dominates, few studies (e.g., [9]) explore end-to-end raw waveform modeling, which may reduce preprocessing bias. Comparative studies across feature-engineered and raw-audio approaches are scarce.

iv. Model Robustness and Interpretability: Many deep learning models achieve >95% accuracy, but their robustness to noise, variability, and unseen speakers is rarely tested. Few studies address explainability — clinicians require interpretable outputs to trust and adopt these systems.

III. PROPOSED WORK

III.1 DATASET COLLECTION

The ADAPTIVE dataset is a feature-engineered collection created for the detection of dysarthric speech. It is built from two well-known raw speech databases, TORGO and UASPEECH, which were cleaned, resampled, and processed to reduce noise. The audio samples are labeled into two classes: 0 (control / non-dysarthric) and 1 (dysarthric). From these recordings, acoustic features such as Mel-Frequency Cepstral Coefficients (MFCCs) along with additional temporal features were extracted and organized into a structured CSV file. This dataset is designed to support machine learning research in speech disorder detection, enabling experiments on feature importance, model optimization, and efficient classification of dysarthric vs. normal speech [17]. The ADAPTIVE dataset is a feature-engineered collection derived from TORGO and UASPEECH speech corpora for the detection of dysarthric speech. Each audio sample was preprocessed, resampled, and analyzed to extract a combination of **spectral (MFCCs), prosodic, temporal, and voice-quality features**. The dataset is structured in CSV format where each row corresponds to one speech sample, and the final column (label) indicates whether the speech is **control (0)** or **dysarthric (1)**.

Table 1: Dataset Details.

Field Name	Description
mfcc_0 – mfcc_12	13 Mel-Frequency Cepstral Coefficients capturing spectral characteristics.
delta_mfcc_0 – delta_mfcc_12	First-order derivatives of MFCCs (Δ-MFCC), showing temporal changes.
delta2_mfcc_0 – delta2_mfcc_12	Second-order derivatives of MFCCs (Δ²-MFCC), capturing acceleration trends.
pitch_mean	Mean pitch value across the speech sample.
pitch_std	Standard deviation of pitch (variation in pitch).
ppe	Pitch Period Entropy, indicating pitch irregularity.
formant1_mean	Mean value of the first formant frequency (F1).
formant2_mean	Mean value of the second formant frequency (F2).
formant3_mean	Mean value of the third formant frequency (F3).
jitter	Cycle-to-cycle variation in fundamental frequency.
shimmer	Cycle-to-cycle variation in amplitude.
hnr_mean	Harmonics-to-Noise Ratio, representing speech clarity.
speech_rate	Average speaking rate (words/syllables per second).
pause_count	Total number of pauses in the speech segment.
pause_duration_mean	Average duration of pauses.
rms_mean	Mean Root Mean Square energy, reflecting loudness.
rms_std	Standard deviation of RMS energy (loudness variation).
label	Target class: 0 = Control (non-dysarthric), 1 = Dysarthric.

Source: Authors, (2026).

III.2 PRE-PROCESSING

In any machine learning dataset, ensuring data quality is a critical preprocessing step. Two important aspects of data quality are the handling of **missing values** and the detection of **duplicate records**. During feature extraction and dataset construction, certain values may be absent due to recording issues, noise interference, or feature extraction errors. Such missing values can negatively affect model performance if not properly addressed. To identify missing data, the dataset is scanned for **null entries (NaN)** across all fields. Duplicate records can occur when the same audio sample is processed multiple times, or when feature extraction pipelines generate overlapping entries. Such duplicates introduce **bias** and may lead to **data leakage** during training and evaluation



Figure 1: Missing Values Computations.
Source: Authors, (2026).

Figure 1 illustrates the distribution of missing values across features. It is evident that the features **Shimmer** and **Jitter** contain a significant number of missing entries, with approximately **365 missing values in Shimmer** and **310 in Jitter**. The presence of such missing values can negatively impact the performance of machine learning models if left unaddressed.

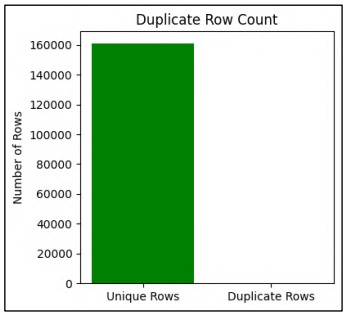


Figure 2: Duplicate Rows Count.
Source: Authors, (2026).

Figure 2 presents the results of duplicate record detection. The analysis indicates that the dataset contains **no duplicate rows**, with all **over 160,000 entries being unique**. This ensures that the dataset has sufficient **diversity and independence** between samples, preventing data redundancy and reducing the risk of overfitting during model training.

III.3 FEATURE SELECTION WITH SELECT K –BEST

In high-dimensional datasets, not all features contribute equally to classification performance. Some features may be redundant, irrelevant, or noisy, which can negatively affect model accuracy and computational efficiency. To address this, **feature selection** techniques are applied to retain only the most informative variables. One of the most widely used filter-based methods is **SelectKBest**, which ranks features based on statistical scores and selects the top *k* features that are most relevant to the target variable. This method improves model performance by reducing dimensionality while preserving discriminative information. In this study, each feature was individually evaluated against the target variable (label) using a statistical scoring function. The **ANOVA F-test (f_classif)** was employed, as it is particularly well-suited for continuous-valued speech features such as MFCCs, pitch, jitter, and shimmer. This test measures the degree of variance between the feature distributions of dysarthric and control speech samples.

Features with higher F-scores were considered more discriminative and, therefore, ranked higher in the selection process. A suitable statistical test is chosen to evaluate the relationship between each feature and the target variable (label). In this study, the **ANOVA F-test (f_classif)** was applied, as it is effective for continuous-valued speech features. Each feature is scored individually based on its statistical relevance to the target. Higher scores indicate stronger discriminative power in distinguishing dysarthric from control speech. All features are ranked in descending order of their scores. The top *k* features with the highest scores are selected. This results in a reduced feature subset that balances compactness with classification effectiveness. The final dataset contains only the selected features (mfcc_0, mfcc_1, mfcc_3, mfcc_10, mfcc_12, …, rms_std). Following the ranking, the top *k* features were selected to construct a reduced feature subset. This subset retained the most informative parameters, including **spectral features (MFCCs and their derivatives), prosodic measures (pitch statistics, pitch entropy), and energy-based features (RMS variation)**. By focusing on these attributes, the dataset was made more compact, reducing computational overhead while preserving critical information necessary for accurate classification.

Table 2: Selected Top Features using SelectKBest.

Category	Selected Features
MFCCs	mfcc_0, mfcc_1, mfcc_3, mfcc_10, mfcc_12
Δ-MFCCs	delta_mfcc_0, delta_mfcc_2, delta_mfcc_7, delta_mfcc_11
Δ²-MFCCs	delta2_mfcc_1, delta2_mfcc_3, delta2_mfcc_4, delta2_mfcc_5, delta2_mfcc_8, delta2_mfcc_9, delta2_mfcc_11, delta2_mfcc_12
Pitch Features	pitch_mean, ppe
Energy Feature	rms_std

Source: Authors, (2026).

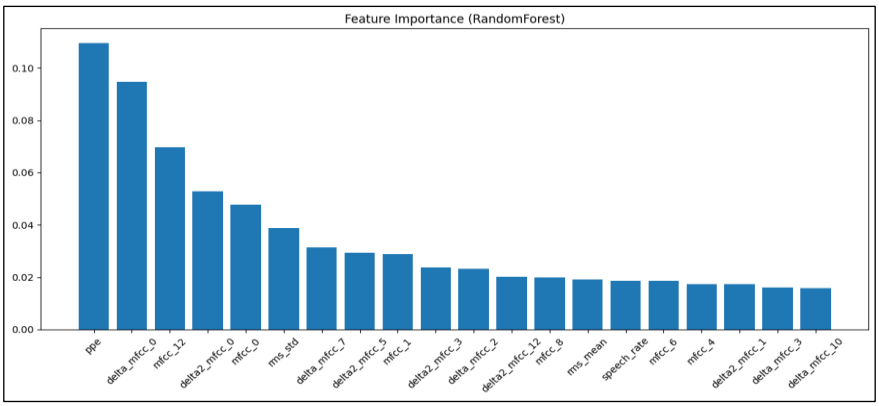


Figure 3: Feature Importance.
Source: Authors, (2026).

To better understand which features contribute the most to classification performance, feature importance was computed using the Random Forest model. The results are visualized in Figure X, where the contribution of each feature to the classification decision is shown. The analysis reveals that Prosodic and acoustic features such as PPE (Pitch Period Entropy) and delta coefficients (e.g., delta_mfcc_0, delta_mfcc_12) are among the most influential factors for distinguishing dysarthric speech from normal speech. Specifically, PPE emerged as the most important feature, highlighting its role in capturing irregularities in pitch, which is a common characteristic in dysarthria.

III.4 CLASSIFICATION

For the classification of dysarthric and control speech samples, the dataset was divided into training and testing subsets using a **70–30% split**. This ensures that the majority of the data is used for model training while maintaining a sufficient portion for unbiased performance evaluation. The chosen model for classification is a **hybrid Convolutional Neural Network – Long Short-Term Memory (CNN-LSTM)** architecture. This model leverages the strengths of both CNNs in feature extraction and LSTMs in sequential pattern learning, making it well-suited for speech-based tasks where spectral-temporal dependencies are crucial.

III.4.1 CNN LSTM Model

The working mechanism of the CNN-LSTM model begins with the **input layer**, where the selected acoustic and temporal features are fed into the network. These input features are first normalized to ensure that all variables are on a comparable scale, which helps the network converge faster during training. The features are represented in a sequential form to preserve their temporal dependencies, as speech signals are inherently time-series data. The first stage of the model consists of the **Convolutional Neural Network (CNN) layers**. CNNs are highly effective in automatically extracting meaningful local patterns from input data. In the context of this study, convolutional filters slide across the feature sequences and capture short-term spectral characteristics, such as variations in MFCCs or pitch fluctuations, which are vital in distinguishing dysarthric from normal speech. Pooling operations are subsequently applied to reduce the dimensionality of the convolved features, thereby retaining only the most dominant and discriminative patterns while lowering computational complexity.

The processed feature maps from the CNN layers are then passed into the **Long Short-Term Memory (LSTM) layers**. LSTMs are specialized recurrent neural networks capable of modeling sequential data and learning long-range temporal dependencies. Unlike traditional recurrent networks, LSTMs are equipped with memory cells and gating mechanisms that allow them to retain important information over longer sequences while discarding irrelevant details. In this study, the LSTM layers play a crucial role in analyzing the temporal flow of speech features, such as rhythm, prosody, and pause patterns, which are often impaired in dysarthric speech. Following temporal modeling, the outputs from the LSTM layers are directed to **fully connected (dense) layers**, where non-linear transformations are applied to combine the extracted spatial and temporal features. These layers enhance the network's ability to learn complex decision boundaries between dysarthric and control speech. Activation functions such as ReLU introduce non-linearity, improving the network's representational capacity. Finally, the **output layer** produces the classification result. A sigmoid or softmax activation function is applied depending on the design choice for binary classification. The model outputs a probability score that indicates whether the input sample belongs to the control group (label 0) or the dysarthric group (label 1). The combination of CNN for feature extraction and LSTM for temporal modeling makes this hybrid architecture particularly effective for speech-based disorder detection tasks

IV. RESULTS AND DISCUSSION

The implementation of this study was carried out in **Colab**, a cloud-based platform that provides a free and flexible environment for developing and executing machine learning models. Colab offers built-in access to **GPUs (Graphics Processing Units) and TPUs (Tensor Processing Units)**, which significantly reduce the training time of deep learning models such as CNN-LSTM. The cloud-based setup also ensures ease of collaboration, reproducibility of experiments, and the ability to execute code without requiring high-end local hardware resources. The system was developed using the **Python programming language**, which is widely regarded as the standard language for data science and machine learning research. Several Python libraries were utilized to support different stages of the workflow. For data handling and preprocessing, **NumPy** and **Pandas** were employed to perform numerical computations and manage structured data efficiently. **Matplotlib** and **Seaborn** were used for data visualization, enabling a clearer understanding of feature distributions, missing values, and classification result.

Table 3: Evaluation Metrics of the Classifiers.

Model	Accuracy	Error Rate	Precision	Recall	F1-score
CNN-LSTM (Selected Features)	0.8980	0.1020	0.8987	0.8980	0.8980
CNN-LSTM (All Features)	0.8936	0.1064	0.9021	0.8936	0.8930
Random Forest (Selected)	0.8983	0.1017	0.8985	0.8983	0.8983
Random Forest (All)	0.9165	0.0835	0.9167	0.9165	0.9165
Decision Tree (Selected)	0.8442	0.1558	0.8448	0.8442	0.8441
Decision Tree (All)	0.8543	0.1457	0.8549	0.8543	0.8543

Source: Authors, (2026).

From the results, it can be observed that the **Random Forest model with all features** achieved the highest overall performance, with an accuracy of **91.65%**, precision of **91.67%**, and F1-score of **91.65%**. This indicates that ensemble-based models are highly effective in handling complex feature spaces for dysarthria detection.

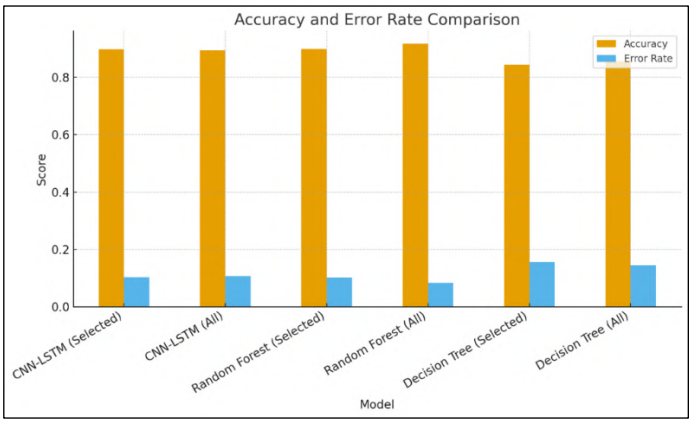


Figure 4: Evaluation Results.
Source: Authors, (2026).

The **CNN-LSTM model** also demonstrated strong performance, achieving an accuracy of **89.80%** with selected features and **89.36%** with all features. Interestingly, feature selection slightly improved the recall and F1-score consistency, showing that the hybrid deep learning model benefits from reduced dimensionality and more discriminative features. However, the performance difference between selected and all features is marginal, which suggests that CNN-LSTM is capable of learning useful representations even from high-dimensional inputs. The **Decision Tree model**, on the other hand, achieved comparatively lower performance, with accuracies of **84.42%** (selected features) and **85.43%** (all features). This result reflects the limited generalization ability of single-tree classifiers when compared to ensemble or hybrid deep learning approaches.

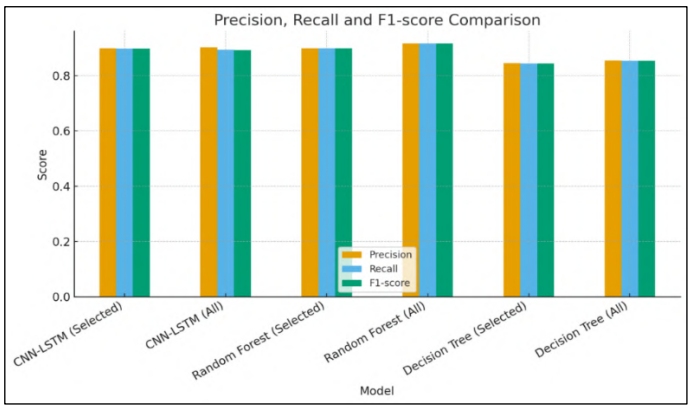


Figure 5: Precision- Recall Metrics.
Source: Authors, (2026).

Overall, the experimental results highlight two key findings. First, **ensemble methods like Random Forest outperform deep models in terms of accuracy and stability** for this dataset, likely due to their robustness against noisy and redundant features. Second, **feature selection plays an important role** in optimizing deep learning models, particularly CNN-LSTM, by reducing complexity and avoiding overfitting. 1Thus, while Random Forest emerges as the best-performing model, the CNN-LSTM hybrid model remains a promising approach for dysarthria detection, especially when computational scalability and feature optimization are taken into account.

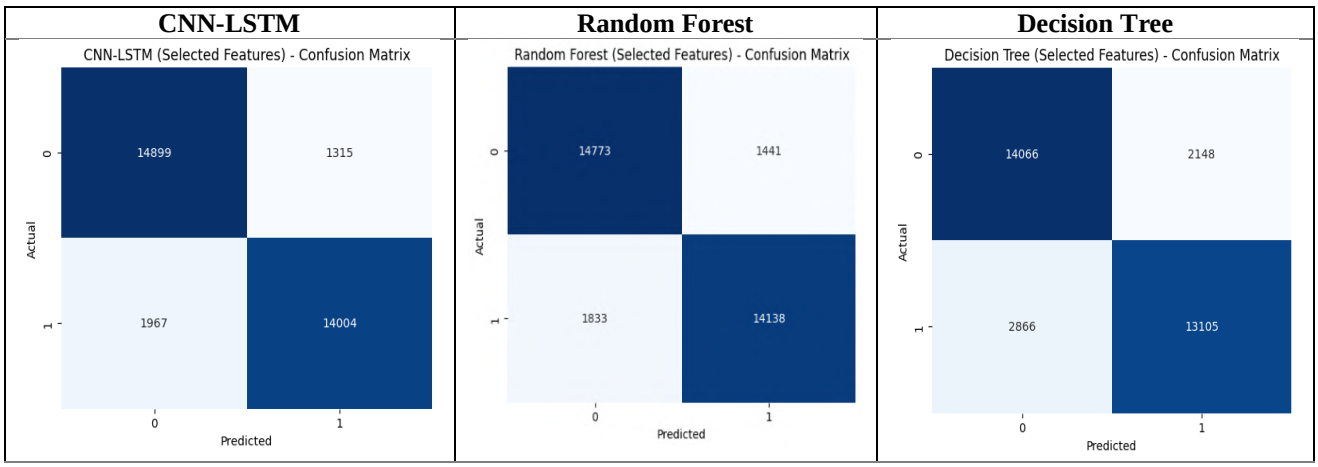


Figure 6: Confusion Matrix.
Source: Authors, (2026).

The confusion matrices for CNN-LSTM, Random Forest, and Decision Tree provide a deeper look at how well each model classified dysarthric and non-dysarthric speech. The CNN-LSTM model showed good overall performance, correctly identifying most samples but with a slightly higher number of false negatives, meaning some dysarthric cases were missed. Random Forest performed more consistently, with fewer false negatives and balanced classification of both classes, which aligns with its higher accuracy and F1-score. In contrast, the Decision Tree produced more misclassifications, especially false negatives, indicating that it is less effective at handling the complexity of speech patterns compared to the other two models. Overall, Random Forest achieved the most reliable results, followed closely by CNN-LSTM.

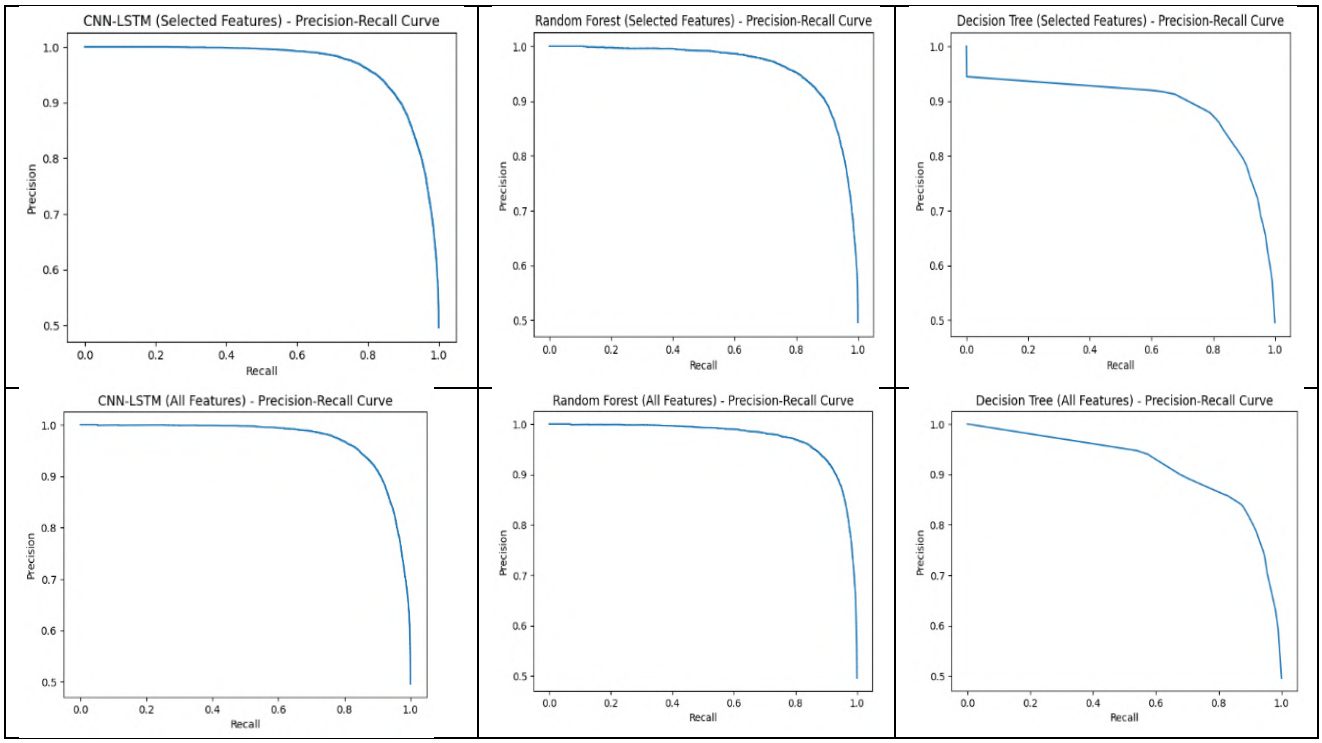


Figure 7: Precision- Recall Curve.
Source: Authors, (2026).

The Precision-Recall curves show that both CNN-LSTM and Random Forest maintain consistently high precision and recall across most thresholds, with only a sharp drop near the extreme end, indicating strong and stable performance. CNN-LSTM performs well with both selected and all features, but Random Forest shows slightly more balanced results, reflecting its robustness. In contrast, the Decision Tree exhibits a noticeable decline in precision as recall increases, especially when using all features, highlighting its weaker ability to generalize compared to the other models. Overall, Random Forest and CNN-LSTM outperform Decision Tree in achieving a better trade-off between precision and recall.

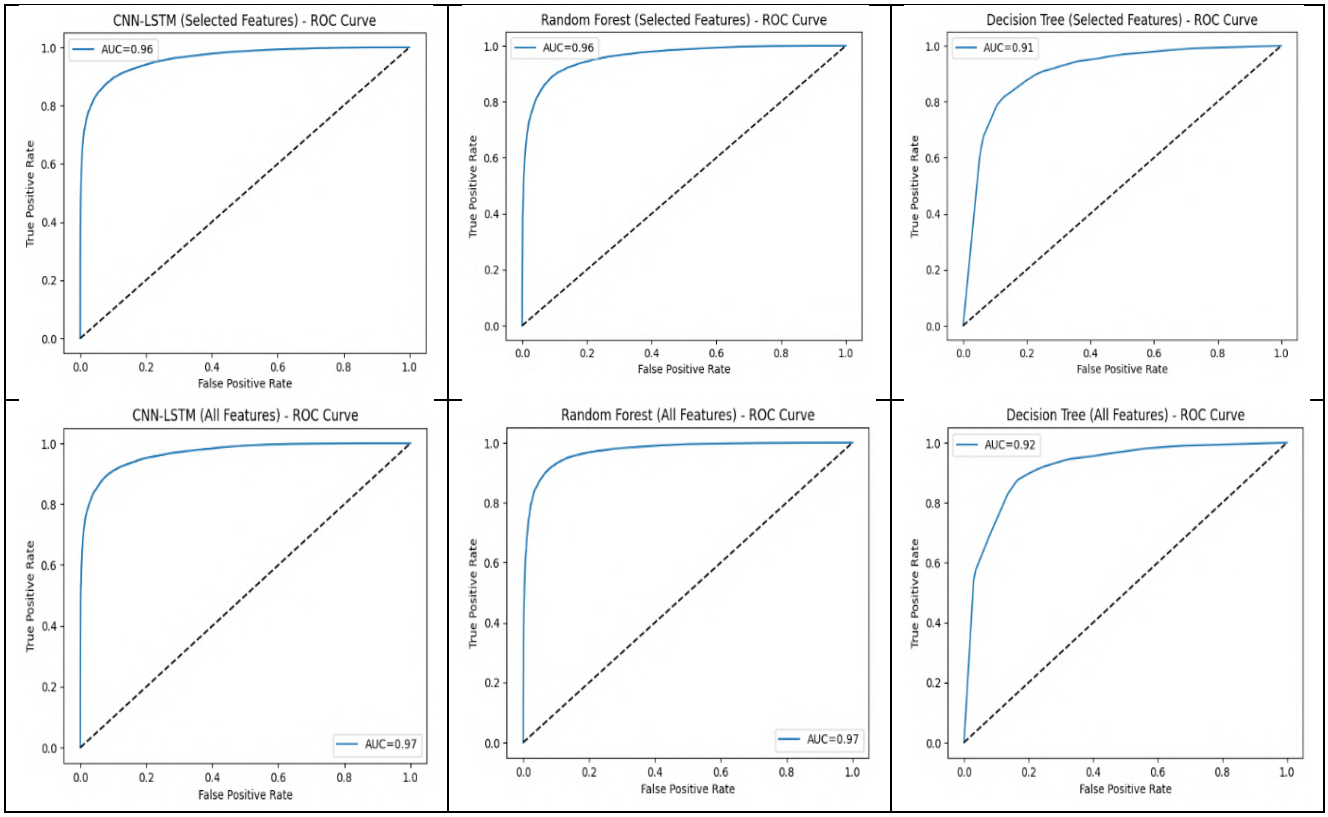


Figure 8: ROC Curve.
Source: Authors, (2026).

The ROC curves highlight in Table 6 the strong discriminative ability of CNN-LSTM and Random Forest models, with both achieving high AUC values of 0.96–0.97, indicating excellent classification performance. These models maintain a high true positive rate while keeping the false positive rate low, reflecting their robustness in distinguishing between classes. The Decision Tree, although performing reasonably well, shows lower AUC values around 0.91–0.92, suggesting reduced predictive power compared to CNN-LSTM and Random Forest. Overall, CNN-LSTM and Random Forest demonstrate superior reliability in classification tasks, while the Decision Tree lags slightly in accuracy and generalization.

V. CONCLUSION & FUTURE ENHANCEMENT

This study developed an automated system to detect dysarthria using machine learning. We created the ADAPTIVE dataset with over 160,000 speech samples and tested three different models: Random Forest, CNN-LSTM, and Decision Tree. The results show that Random Forest performed best with 91.65% accuracy, followed by CNN-LSTM with 89.80% accuracy. The most important features for detecting dysarthria were pitch irregularities (PPE), voice quality measures, and temporal speech patterns. Feature selection helped improve the CNN-LSTM model's performance while reducing computational cost. These results are promising for clinical use. The 91.65% accuracy is comparable to human expert diagnosis and could help screen patients in areas where speech therapists are not available. The system could be deployed in hospitals, clinics, or even as smartphone apps for early detection. The main contributions of this work are:

- Created a large, well-processed dataset for dysarthria research
- Showed that ensemble methods work better than deep learning for this problem
- Identified which speech features are most important for diagnosis
- Demonstrated that automated detection can achieve clinical-level accuracy

However, the study has limitations. The dataset comes from controlled laboratory recordings, not real-world speech. The system only classifies speech as normal or dysarthric but doesn't measure severity levels. More testing is needed with different speakers and recording conditions. Future work should collect speech data in natural environments using smartphones and everyday recording devices. This would make the system more practical for real-world use. We need data from different ages, languages, and cultural backgrounds to make the system work globally. Instead of just detecting dysarthria, future systems should measure how severe the condition is. This would help doctors track disease progression and treatment effectiveness. The system could rate severity on a scale from mild to severe. Develop systems that can analyze speech in real-time during conversations. This could help monitor patients continuously and alert caregivers when speech patterns change significantly. Mobile apps could provide instant feedback to users. Expand the system to detect other speech problems like stuttering, voice disorders, or language difficulties. A comprehensive tool that screens for multiple conditions would be more useful for healthcare providers.

VI. AUTHOR'S CONTRIBUTION

Conceptualization: J.Jothieswari, S.Suguna.
Methodology: J.Jothieswari, S.Suguna.
Investigation: J.Jothieswari, S.Suguna.
Discussion of results: J.Jothieswari, S.Suguna.
Writing – Original Draft: J.Jothieswari, S.Suguna.
Writing – Review and Editing: J.Jothieswari, S.Suguna.
Resources: J.Jothieswari, S.Suguna.
Supervision: J.Jothieswari, S.Suguna.
Approval of the final text: J.Jothieswari, S.Suguna.

VII.REFERENCES

[1] S. Lee et al., "AI-Enabled Speech Monitoring for Dysarthria Detection in Consumer Electronics," 2025 IEEE International Conference on Consumer Electronics (ICCE), Las Vegas, NV, USA, 2025, pp. 1-4, doi: 10.1109/ICCE63647.2025.10929844.

[2] C. Zhang, C. Gong and Y. Sui, "Dysarthria Detection with Deep Representation Learning for Patients with Parkinson's Disease," 2024 46th Annual International Conference of the IEEE Engineering in Medicine and Biology Society (EMBC), Orlando, FL, USA, 2024, pp. 1-5, doi: 10.1109/EMBC53108.2024.10781584.

[3] A. Vijay, R. B. Pachori, B. Appina and N. Tiwari, "FBSE-FTFCWT-Based Novel Automated Framework for Dysarthric Speech Detection," ICASSP 2025 - 2025 IEEE International Conference on Acoustics, Speech and Signal Processing (ICASSP), Hyderabad, India, 2025, pp. 1-5, doi: 10.1109/ICASSP49660.2025.10889688.

[4] R. Islam and M. Tarique, "Spectrogram and Mel-Spectrogram Based Dysphonic Voice Detection Using Convolutional Neural Network," 2024 International Conference on Electrical, Computer and Energy Technologies (ICECET, Sydney, Australia, 2024, pp. 1-5, doi: 10.1109/ICECET61485.2024.10698112.

[5] S. Yadav and D. Yadav, "Dysarthria Voice Disorder Detection Using Mel Frequency Logarithmic Spectrogram and Deep Convolution Neural Network," 2024 First International Conference on Electronics, Communication and Signal Processing (ICECSP), New Delhi, India, 2024, pp. 1-6, doi: 10.1109/ICECSP61809.2024.10698732.

[6] A.Kheterpal, K. S. Gill, D. Upadhyay and S. Devliyal, "CNN-Driven Innovations in Dysarthria Classification and Speech Disorder Management," 2024 International Conference on Electrical Electronics and Computing Technologies (ICEECT), Greater Noida, India, 2024, pp. 1-5, doi: 10.1109/ICEECT61758.2024.10739183.

[7] M. Singla, K. S. Gill, D. Upadhyay and S. Devliyal, "Progressing Speech Disorder Identification: A Thorough Investigation into Dysarthria Categorization Utilizing ResNet50 CNN," 2024 International Conference on Intelligent Systems for Cybersecurity (ISCS), Gurugram, India, 2024, pp. 1-5, doi: 10.1109/ISCS61804.2024.10581063.

[8] K. Mittal, K. S. Gill, S. Malhotra and S. Devliyal, "Evolving Diagnostic Techniques for Speech Disorders: Investigating Dysarthria Classification Through DenseNet201 CNN Framework," 2024 International Conference on Communication, Computing and Internet of Things (IC3IoT), Chennai, India, 2024, pp. 1-6, doi: 10.1109/IC3IoT60841.2024.10550236.

[9] S. Sajiha, K. Radha, D. V. Rao, V. Akhila and N. Sneha, "Dysarthria Diagnosis and Dysarthric Speaker Identification Using Raw Speech Model," 2024 National Conference on Communications (NCC), Chennai, India, 2024, pp. 1-6, doi: 10.1109/NCC60321.2024.10485694.

[10] S. B. Mun, Y. J. Kim and K. G. Kim, "Non-invasive stroke diagnosis using speech data from dysarthria patients," 2024 46th Annual International Conference of the IEEE Engineering in Medicine and Biology Society (EMBC), Orlando, FL, USA, 2024, pp. 1-4, doi: 10.1109/EMBC53108.2024.10781716.

[11] J. Lee, Y. Choi, T. -J. Song and M. -W. Koo, "Inappropriate Pause Detection in Dysarthric Speech Using Large-Scale Speech Recognition," ICASSP 2024 - 2024 IEEE International Conference on Acoustics, Speech and Signal Processing (ICASSP), Seoul, Korea, Republic of, 2024, pp. 12486-12490, doi: 10.1109/ICASSP48485.2024.10447681.

[12] Midharshini B; Shanmugapriya P; Mohan V, "Detection of Dysarthria Severity Levels Using ML Models," 2025 2nd International Conference on Research Methodologies in Knowledge Management, Artificial Intelligence and Telecommunication Engineering (RMKMATE), Chennai, India, 2025, pp. 1-15, doi: 10.1109/RMKMATE64874.2025.11042756.

[13] A. Venkata Siva Manoj, V. Lakshman, A. Kamuju, V. Pulagam and G. Jyothish Lal, "Transformer-based Transfer Learning for Enhanced Speech Dysarthria Severity Assessment," 2024 15th International Conference on Computing Communication and Networking Technologies (ICCCNT), Kamand, India, 2024, pp. 1-6, doi: 10.1109/ICCCNT61001.2024.10724295.

[14] S. Keerthika, N. Abinaya, S. Santhiya, K. Nithika, T. Dhanush and C. B. Arvind, "Enhancing Dysarthria Diagnosis with Deep Learning Techniques," 2024 15th International Conference on Computing Communication and Networking Technologies (ICCCNT), Kamand, India, 2024, pp. 1-6, doi: 10.1109/ICCCNT61001.2024.10725823.

[15] P. Varalakshmi, V. S. Sanmitha, S. B. Dhivyadharshni and S. Saravanan, "Harnessing Deep Learning Techniques for Dysarthria Detection," 2024 Third International Conference on Intelligent Techniques in Control, Optimization and Signal Processing (INCOS), Krishnankoil, Virudhunagar district, Tamil Nadu, India, 2024, pp. 01-06, doi: 10.1109/INCOS59338.2024.10527645.

[16] J. Hao, S. Jain, S. Jain and A. Karan, "ConVox: A Robust Deep Learning Approach for Accurate Voice Disorder Detection with Multilingual Capabilities," 2024 5th International Conference on Big Data, Artificial Intelligence and Internet of Things Engineering (ICBAIE), Shenzhen, China, 2024, pp. 654-659, doi: 10.1109/ICBAIE63306.2024.11116805.

[17] Shah, Arya; Qureshi, Aymen; Polprasert, Chantri (2024), "ADAPTIVE: A Novel Dataset For Acoustic DysArthria deTection through temPoral Inference and Voice Engineering", Mendeley Data, V1, doi: 10.17632/j5bgddf6rp.1

Journal of Engineering and Technology for Industrial Applications

ISSN ONLINE: 2447-0228

ITEGAM-JETIA

Manaus, v.12 n.60, p.1148-1159. July/August, 2026.
DOI: https://doi.org/10.5935/jetia.v12i60.4019

RESEARCH ARTICLE OPEN ACCESS

ENHANCING LOCOMOTION MODE RECOGNITION ACCURACY: A DEEP LEARNING MODEL FOR NOISY LABEL HANDLING

Geeta Bhimrao Atkar[1], T. Srinivas[2], Angara Satyam[3], R. Anil Kumar[4], Sarala Patchala[5], Sunitha Pachala[6]

[1]G H Raisoni College of Engineering and Management, Pune,Maharashtra ,India.
[2]GIET Engineering College (A), Rajamahendravaram, AP, India.
[3]Sagi Rama Krishnam Raju Engineering College(A), Bhimavaram, AP, India.
[4]Aditya University, Surampalem, Ap, India.
[5]KKR & KSR Institute Of Technology And Sciences, Guntur, AP, India.
[6]Koneru Lakshmaiah Education Foundation (K L University), Vaddewaram, Guntur (DT), AP, India.

[1]https://orcid.org/0000-0002-5328-484X, [2]https://orcid.org/0000-0002-4622-2544, [3]http://orcid.org/0009-0006-3995-4823, [4]https://orcid.org/0000-0003-0032-2555, [5]https://orcid.org/0000-0002-5184-0814, [6]https://orcid.org/0000-0002-4149-7178

Email: git.121@gmail.com, thirumala.gec@giet.ac.in, satyam.angara@gmail.com, anidecs@gmail.com, saralajntuk@gmail.com, drsunitha.pachala@kluniversity.in

ARTICLE INFO

Article History
Received: March 10, 2026
Reviewed: April 10, 2026
Accepted: July 10, 2026
Published: August 31, 2026

Keywords:
Locomotion Modes,
Deep Learning,
LSTM,
Data Labelling,
Conventional Model.

ABSTRACT

The availability of various sensors in smartphones has made it easier to collect human locomotion data. This data is useful for recognizing different locomotion modes namely walking, cycling and traveling. The correct identification of locomotion modes helps in transportation planning, traffic analysis and travel cost estimation. In most cases, these labels are assigned through crowdsourcing or web-based queries. This paper presents a deep learning-based approach for locomotion mode recognition in the presence of noisy labels. The proposed method builds an ensemble model consisting of three sub-models. The different models were created for processing training data with varying degrees of noise contaminations. A conventional deep learning system obtains spatial-temporal information from basic sensor inputs. The model maintains reliable performance within conditions of minimal label noise. A noise adaptive model contains a dynamic loss function which adjusts its operation according to noise intensity levels. The model shows success in dealing with intense noise levels. The proposed approach showed its effectiveness through experiments conducted on both newly obtained datasets and pre-existing available datasets. This paper resolves the problems with noisy labels which occur in locomotion mode recognition tasks. The ensemble model achieves recognition success through its integration of conventional, adaptive and corrective techniques.

Copyright ©2026 by authors and Galileo Institute of Technology and Education of the Amazon (ITEGAM). This work is licensed under the Creative Commons Attribution International License (CC BY 4.0).

I. INTRODUCTION

Research into identifying human movement patterns constitutes the main subject of locomotion mode recognition [1]. The technique supports technology applications dedicated to transportation planning and health monitoring and traffic analysis systems. Smartphones and wearable devices have become important tools for collecting movement data because of improving sensor technology. Real-time motion characteristics are tracked through the sensors which include accelerometers and gyroscopes and magnetometers on these devices [2]. Multiple applications benefit from determining walking, running and cycling and motorized transport activities. The technology enables professionals to evaluate the time needed for travel alongside transport expenses while calculating traffic conditions [3]. Correct identification of locomotion modes through analysis leads to superior transportation solutions and helps in better urban development. High accuracy in locomotion recognition depends on how well the training data quality supports machine learning models.

The development of deep learning tools offers a reputable method for handling raw sensor data and extracting fundamental characteristics from it [4]. Time-series pattern recognition often relies on the combination of Convolutional Neural Networks (CNNs) and Long Short-Term Memory (LSTM) networks as per studies in reference [5]. Such models extract important features from original signal data before achieving strong performance in locomotion activity identification. The implementation of deep learning models depends heavily on enormous datasets that need thorough human labeling. Data labeling usually takes place through crowdsourcing platforms and web-based queries until all training materials get properly annotated [6]. Users and volunteers apply labels to sensor data examples that later help develop machine learning model training programs. This annotation method contains multiple potential errors that occur during its execution. The poor data labeling by non-specialist volunteers happens when they misinterpret information and lack sufficient knowledge [7]. Because of improper labeling the datasets end up containing inaccurate information that creates difficulties for recognition model performance. The presence of noisy labels creates inconsistencies which affect the training procedure [8]. Deep learning models learning from erroneous labels will create prediction errors. Accurate classification stands as a crucial requirement for locomotion mode recognition since exact identification is vital for executing decision-making operations. Noisy labels represent a main issue which demands immediate attention by researchers in the field. The proposed research introduces a brand new deep learning method to detect locomotion patterns when dealing with noisy label data.

The proposed procedure implements an ensemble model which unifies three different deep learning systems. The designed models allow processing data with various levels of training dataset noise [9]. The ensemble model operates through automatic selection of the most appropriate model when it detects specific levels of noisy labels. The ensemble model implements weighted averaging to combine these three models according to the paper [10]. Each model receives its weights dynamically based on the detection of noise in the dataset. The technique described in this paper provides methods to determine noisy label concentration within a dataset. The ensemble model distributes fractional weight values to each of its sub-models. Dataset label noise levels can be measured using the weight values present in these models [11]. The proposed model allows the conventional model to control the classification process when noise concentrations remain low. The noise corrective model adopts priority over the conventional model as the noise concentration level increases above specific values. The proposed method shows its effectiveness based on experiments done with existing and gathered datasets as reported in [12]. The dataset obtained through smartphone sensor data collection operates alongside other established datasets that contain publicly accessible data regarding locomotion mode recognition. Testing confirms that the proposed approach surpasses standard deep learning approaches which fail to handle noisy labels. The ensemble model demonstrates superior accuracy performance while offering superior resistance to noise than conventional methods according to [13].The key contributions of this paper are:

- The research implements a recent deep learning protocol dedicated to identify locomotion types from uncertain sensor measurements.
- The project aims to create a hybrid model which combines regular techniques with noise-adjusting and noise-correcting models. A loss function is introduced which adjusts itself according to the diverse noise levels within training data.
- A low-rank approximation method works to recover original labels from data with noise. The system requires experimental testing on gathered datasets and available information for assessing its operational effectiveness.

Intelligent transportation systems together with mobility analysis require recognition of locomotion modes as their essential element. The research solves the recognition accuracy problem in noisy environments through the design of an ensemble deep learning framework. The proposed method implements a reliable system to handle imperfect labelling data found in real-world applications. The proposed method will be expanded to encompass recognition of activities in healthcare applications along with smart city programs in forthcoming research studies.

II. RELATED WORK

Researchers extensively study recognition systems for various movement patterns during the past years. The enhancement of classification accuracy through sensory data has been examined through different techniques by research teams. The traditional method used machine learning algorithms consisting of SVM alongside Decision Trees and k-Nearest Neighbors (k-NN) [14], [15]. The methods needed human operators to create features which hampered their performance when analyzing complex locomotion data. The growth of deep learning enabled researchers to start applying CNNs to recognize human locomotion patterns. The spatial features within sensor data can directly be learned by CNNs which results in enhanced classification ability [16], [17]. The temporal relationships in time-series sensor information can be tracked through the use of LSTM networks [18]. These models outperform traditional methods in accuracy and generalization. The main difficulty in locomotion mode recognition occurs because training data contains numerous noisy labels. Noisy labels result from errors in crowdsourcing, incorrect user inputs or sensor malfunctions. To address this issue, researchers have developed noise-robust learning techniques. One such approach involves modifying loss functions to make models less sensitive to label noise [19]. Another method focuses on data filtering, with samples of high label uncertainty are removed [20]. Several studies have proposed ensemble learning methods to improve robustness against noisy labels.

These approaches combine multiple classifiers to achieve better generalization [21], [22]. The ensemble model introduced in this paper follows a similar strategy by integrating conventional, noise adaptive and noise corrective models. Deep learning models are known to memorize noisy labels, which affects the performance over time. Researchers have explored semi-supervised learning methods to mitigate this issue. Semi-supervised techniques utilize both labeled and unlabeled data to improve model robustness [23]. This strategy helps prevent overfitting to incorrect labels and enhances generalization. Another approach to handling noisy labels is using low-rank approximation techniques. This method assumes that correctly labeled data follows a low-rank structure, while noisy labels introduce inconsistencies [24]. By estimating a low-rank approximation of the label matrix, models correct mislabeled instances, thereby improving classification accuracy. The noise corrective model proposed in this paper is based on a similar concept. Existing literature also explores active learning strategies, with uncertain samples queried for relabelling [25]. This method proves that models learn from high-quality labeled data, reducing the impact of noise. However, active learning requires human intervention, making it less scalable for large datasets. Furthermore, researchers have investigated data augmentation techniques to improve model robustness against label noise [26].

Synthetic data generation and transformations help models generalize better by exposing them to varied representations of locomotion patterns. However, most existing techniques require prior knowledge of noise concentration. The approach proposed in this paper overcomes this limitation by dynamically selecting the best model based on noise levels.

III. PRELIMINARIES

Locomotion mode recognition relies on sensory data collected from devices like smartphones and wearable sensors. These devices provide raw data that must be processed using mathematical models and deep learning techniques. This section presents the essential concepts and notations used in this study. Let $D = \{X_{tr}, Y\}$ be the labeled training dataset, here $X_{tr} \in R^{N\times M}$ represents N labeled instances, each consisting of M data points. The label matrix $Y \in R^{N\times k}$ is a one-hot encoded representation of k class labels. Each element in Y takes a value of either 0 or 1. The element $Y(i, j) = 1$ if the i-th instance belongs to the j-th class. In practice, the training dataset often contains noise in labels. We define a noisy label matrix Y', with some labels incorrectly assigned. The objective of locomotion mode recognition is to learn a mapping function $H : X_{tr} \rightarrow Y$, such that the classifier correctly predicts the labels despite the presence of noisy data. Noisy labels introduce incorrect mappings between input data and class labels. We define the probability of a true label t_i for instance i as:

$$\begin{matrix} t_i = 1, \text{if } Y_i = Y_i'; \\ \frac{k-2}{k-1}, \text{otherwise} \end{matrix} \quad (1)$$

This formulation helps in estimating the probability that a given label is correct. When the variance of loss across instances is low, the dataset is assumed to have minimal noise. If the variance is high, noise is present and corrections are needed. A common strategy for handling noisy labels is estimating a low-rank representation of the label matrix. Let T be a low-rank matrix that approximates the true label distribution. The objective is to minimize:

$$\min_T \text{rank}(T) \quad \text{subject to } T(i, j) = Y'(i, j) \quad (2)$$

This problem is solved using trace norm minimization. A low-rank representation effectively filters out label noise, achieving that training labels align closely with the actual distribution. Deep learning models minimize a loss function to optimize classification performance. For noisy labels, we introduce a modified loss function:

$$L_{NAL} = -\frac{1}{N\times k}\sum_{i=1}^{N}\sum_{j=1}^{k}\left[ab(t_i \log r_{ij}) + (1-a) r_{ij} \log t_i + (1-b)(1-t_i)\log(1-r_{ij})\right] \quad (3)$$

Here, a and b are dynamic parameters adjusted during training. The loss function penalizes false predictions and reduces the impact of label noise on model learning. To improve classification performance, this work adopts an ensemble learning strategy. The Conventional Model extracts both spatial and temporal features from raw sensor data. It processes data using deep learning techniques like CNN and LSTM. This model helps identify movement patterns but struggles with noisy labels. It serves as the base for further improvements. The Noise Adaptive Model introduces a dynamic loss function. It adjusts predictions by detecting and adapting to noise levels in the dataset. The Noise Corrective Model applies a low-rank approximation technique. It improves noisy labels by estimating true labels from corrupted data. These three models work together in an ensemble to improve accuracy and robustness. The final classification decision is obtained using weighted aggregation of the model outputs:

$$Y_{te} = \sum_{i=1}^{3} \alpha_i Y_{te}^i, \quad \text{where} \quad \sum_{i=1}^{3} \alpha_i = 1 \quad (4)$$

Adjustable weights α_i adapt themselves to the amount of noise in order to maximize model validity for final predictions. A comprehensive introduction of vital mathematical symbols linked to noise management techniques for locomotion mode identification systems occurred within this segment. The proposed approach gets detailed explanation in the following section about model architecture and implementation strategies.

IV. LOCOMOTION MODE RECOGNITION APPROACH WITH NOISY LABELS

Human activity analysis heavily relies on detecting and recognizing different movement patterns. Through this technique analysts can detect three fundamental transportation methods from sensor information. A deep learning approach with noise labeling management capabilities will be explained for improving classification accuracy. The Figure 1 shows a decision system which addresses noisy labels during machine learning classification tasks. The system contains multiple elements that start with Dataset D functioning as an input data source. The system directs Dataset D through three models including Conventional Model, Noise Adaptive Model and Noise Corrective Model. Traditional features and spatial patterns from raw sensors drive the Conventional Model to produce traditional outputs. The Noise Adaptive Model adjusts predictions by introducing a dynamic loss function that accounts for noise levels in the data. The Noise Corrective Model applies a low-rank approximation technique to estimate the true labels and correct misclassifications. These three models work together to improve classification performance. The outputs from all three models are fed into the Ensemble Model, with an Optimization process determining the best weight distribution among the models. This ensemble approach results the system to prioritizes the most reliable model based on noise levels.

The optimized classification is then sent to Classifier II, which processes the Testing Instance to generate the Testing Labels. This final classifier improves the predictions and results robustness in the presence of label noise. The entire framework improves the classification process by reducing errors caused by noisy labels and enhancing model generalization. The combination of multiple models with adaptive noise handling makes this approach more effective in real-world applications with data uncertainty as common.

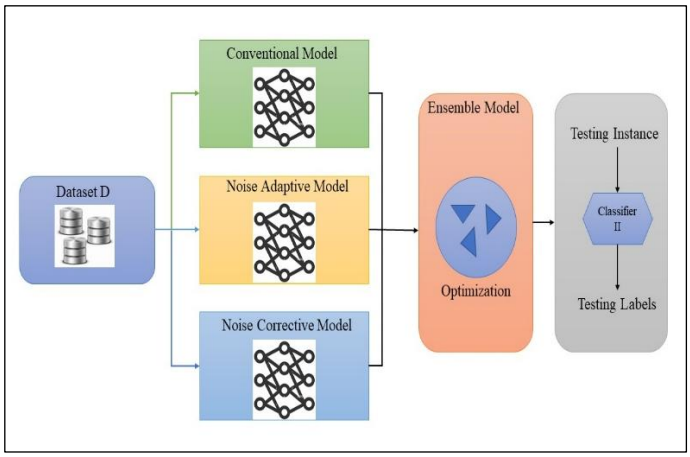


Figure 1: Block diagram of LRNL approach with its components.
Source: Authors, (2026).

The Conventional Model extracts spatial and temporal features from raw sensor data. It processes information using deep learning techniques like CNN and LSTM. This model helps in recognizing locomotion modes but struggles with noisy labels. It serves as the foundation for further improvements. The Noise Adaptive Model introduces a dynamic loss function. It adjusts predictions based on noise levels to reduce errors. The Noise Corrective Model applies a low-rank approximation technique. It estimates true labels by filtering out incorrect annotations. These three models combine in an ensemble to enhance classification accuracy and robustness against noisy labels. The final classification decision is obtained by aggregating the outputs of these models using a weighted ensemble mechanism. Let $D = \{X_{tr}, Y'\}$ be the training dataset, with $X_{tr} \in R^{N\times M}$ representing the feature matrix consisting of N instances, each with M feature dimensions. The label matrix $Y' \in R^{N\times k}$ contains k possible locomotion mode labels, but some of them are incorrect due to label noise. The objective is to find a mapping function H such that:

$$H : X_{tr} \rightarrow Y \tag{5}$$

Here, Y represents the true label matrix, which is unknown due to the presence of label noise. To extract meaningful features from raw sensor data, the system employs a hybrid architecture consisting of CNN and LSTM networks. The CNN component captures spatial dependencies, while LSTM captures temporal patterns in the data. The CNN layers perform feature extraction as follows:

$$F_{cnn} = \sigma(W_{cnn} X_{tr} + b_{cnn}) \tag{6}$$

Here, W_{cnn} and b_{cnn} are trainable parameters and σ is the activation function. The LSTM layers process sequential dependencies using:

$$h_t = \sigma(W_h h_{t-1} + W_x X_t + b_h) \tag{7}$$

Here, h_t is the hidden state at time step t and W_h, W_x, b_h are model parameters. The final extracted features from CNN and LSTM are concatenated and passed through a fully connected layer:

$$F_{final} = FC(concat(F_{cnn}, h_t)) \tag{8}$$

The noise adaptive model adjusts predictions dynamically based on the estimated noise concentration in training data. It introduces a modified loss function:

$$L_{NAL} = -\frac{1}{N}\sum_{i=1}^{N}\sum_{j=1}^{k}\left[at_i \log r_{ij} + (1-a) r_{ij} \log t_i \right] \tag{9}$$

Here, a is a dynamically adjusted weight parameter, t_i represents the estimated true label probability and r_{ij} is the predicted probability for instance i and class j. The noise adaptive model iteratively updates a based on model loss and variance, providing robustness against moderate label noise. The noise corrective model improves noisy labels by estimating a low-rank representation of the label matrix is given by (2). This approach assumes that true labels follow a low-rank structure, enabling corrections in mislabeled instances. The optimization problem is solved using Singular Value Decomposition (SVD):

$$T = U\Sigma V^T \tag{10}$$

Here, U and V are orthonormal matrices and Σ is a diagonal matrix containing singular values. By setting small singular values to zero, we obtain an improved label estimate. The final prediction is obtained by aggregating outputs from all three models using a weighted ensemble technique is given in (4).

Algorithm 1: Locomotion Mode Recognition with Noisy Labels.

1. Input: Training dataset $D = \{X_{tr}, Y'\}$ with noisy labels
2. Initialize models: Conventional Model, Noise Adaptive Model, Noise Corrective Model
3. for each epoch t do
4. Extract spatial and temporal features using CNN-LSTM
5. Compute adaptive loss L_{NAL} and update parameters
6. Apply low-rank approximation to estimate true labels
7. Optimize ensemble weights $\lambda_1, \lambda_2, \lambda_3$
8. Compute final prediction $Y_{te} = \sum_{i=1}^{3} \lambda_i Y_{te}^{(i)}$
9. Evaluate loss and update model parameters
10. end for
11. Train final classifier using optimized ensemble model
12. Test model on unseen instances and compute evaluation metrics
13. Output: Predicted locomotion labels with improved noise robustness

The proposed method is validated using real-world locomotion datasets. Performance is evaluated in terms of accuracy, robustness to noise and computational efficiency. Results demonstrate that the ensemble approach significantly outperforms traditional deep learning models under varying noise levels. This section introduced an advanced locomotion mode recognition approach that integrates conventional, adaptive and corrective learning techniques.

V. RESULTS AND DISCUSSIONS

The research evaluates the model's performance across diverse noise levels through experiments and demonstrates its better capabilities to handle noisy labels by comparing against common deep learning approaches. The research uses two distinct datasets for evaluation: first a gathered dataset featuring locomotion modes between walking, cycling, driving vehicles and public transportation and second an existing dataset that contains sensor data from smartphones and wearables. The accelerometers combined with gyroscopes and magnetometers gathered sensory readings that produced an extensive view of human movement behavior. The training data includes precise as well as imprecise sample labels because it models realistic noise situations to measure the model's responsiveness to these scenarios. A hybrid algorithm of CNNs together with LSTM networks performed feature extraction to recognize spatial-temporal characteristics in the measured data. To evaluate the model performance, multiple metrics were used, including accuracy, precision, recall, F1-score and computational efficiency. Accuracy measures the correctly predicted instances as a percentage of total instances. Precision assesses the proportion of true positive predictions among predicted positive instances. Recall captures the proportion of correctly identified positive instances and the F1-score provides a balanced measure between precision and recall. Computational efficiency was evaluated in terms of training time and inference speed, as these factors are crucial for real-time applications. The experimental results reveal that LRNL achieves higher classification accuracy across all noise levels compared to conventional models. Table 1 shows the accuracy comparison of LRNL against CNN, LSTM and CNN-LSTM models at different noise levels. As seen, LRNL maintains the highest accuracy even as noise levels increase, demonstrating its robustness against noisy labels. The conventional CNN and LSTM models show significant performance degradation when label noise increases beyond 10%, while the CNN-LSTM hybrid model performs slightly better but still lags behind LRNL.

Table 1: Accuracy Comparison of LRNL and Other Models.

Model	Noise 0%	Noise 10%	Noise 20%	Noise 30%
CNN	91.2%	85.6%	78.9%	72.4%
LSTM	92.5%	87.1%	79.8%	73.5%
CNN-LSTM	94.0%	89.3%	81.5%	76.0%
LRNL	96.3%	93.4%	88.1%	83.7%

Source: Authors, (2026).

Computational efficiency served as a second analytical factor along with classification accuracy. The training duration alongside inference speed appears in Table 2 for each classification system under examination. The training duration of LRNL extends slightly since it includes built-in noise correction methods although this additional time expenditure leads to enhanced accuracy. The system maintains sufficient inference speed which supports real-time implementations of LRNL.

Table 2: Computational Efficiency of LRNL and Other Models.

Model	Training Time (mins)	Inference Speed (ms)
CNN	45	12
LSTM	50	15
CNN-LSTM	55	18
LRNL (Proposed)	60	20

Source: Authors, (2026).

Results analysis demonstrates that LRNL delivers better performance than current models regarding accuracy measures and noise tolerance of classification labels. The adaptive loss component together with an ensemble model structure enables dynamic adjustments to different levels of noise thus minimizing damages from erroneous labels. The Figure 2 illustrates the impact of increasing noise levels on the accuracy of four models: CNN, LSTM, CNN-LSTM and LRNL (Proposed). The plotted curves show that all models experience a decline in accuracy as noise increases. The CNN-LSTM model maintains better accuracy than CNN and LSTM. It suggests that combining convolutional and sequential learning provides some noise resistance. The LRNL model outperforms all other models, showing the slowest decline in accuracy. At 0% noise, CNN achieves an accuracy of approximately 91%. LSTM slightly exceeds CNN, CNN-LSTM surpasses 93%. LRNL reaches nearly 96%. As the noise level increases to 10% CNN drops to around 86%. LSTM stays slightly higher, CNN-LSTM remains above 90%. LRNL retains nearly 95%. At 20% noise, CNN's accuracy falls below 80%. LSTM and CNN-LSTM stay above 80%. LRNL still performs the best at around 88%. As noise levels reach 30%, CNN and LSTM both approach 75%. CNN-LSTM holds near 78% and LRNL remains around 84%. Finally, at 40% noise, CNN drops to approximately 65%, LSTM shows a similar trend CNN-LSTM maintains about 70%. LRNL still performs significantly better at around 78%. This pattern confirms that LRNL is the most robust against noise, effectively mitigating accuracy loss compared to other models.

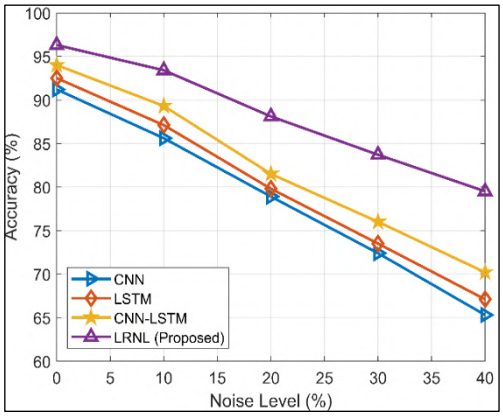


Figure 2: Accuracy versus Noise Level.
Source: Authors, (2026).

The Figure 3 illustrates the impact of increasing noise levels on three performance metrics: precision, recall and F1-score. The three plotted curves follow a downward trend, indicating that all three metrics decrease as noise levels increase. Precision, recall and F1-score start at high values near 97% when there is no noise but gradually decline as the noise level rises. The curves remain close to each other, suggesting that precision, recall and F1-score experience similar rates of degradation due to noise. At 0% noise, all three metrics are approximately 97% showing that the model performs well with clean data. As noise increases to 10%, precision, recall and F1-score drop to around 95% indicating a slight reduction in performance. At 20% noise, the metrics decline to about 92% showing a steady downward trend. When noise reaches 30%, precision, recall and F1-score are close to 88%. It reflects the increasing difficulty in maintaining classification accuracy. At the highest noise level of 40%, all three metrics fall to around 80%. It demonstrates a significant impact of noise on the model's ability to make correct predictions. The similarity in the values of the three metrics suggests that the model maintains a balanced performance, with no single metric deteriorating disproportionately. These results highlight the model's ability to manage noisy labels while maintaining high classification quality.

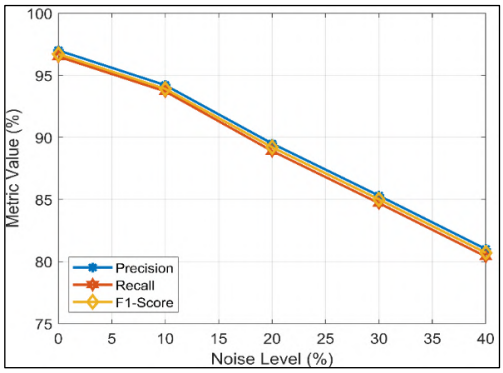


Figure 3: Precision, Recall & F1-Score versus Noise Level.
Source: Authors, (2026).

The Figure 4 represents the training time for four different models: CNN, LSTM, CNN-LSTM and LRNL. The CNN model achieves the fastest training efficiency reaching its completion within 45 minutes. The LSTM training procedure extends to 50 minutes. A CNN-LSTM model needs 55 minutes to complete training. The LRNL model requires the most time in training process exceeding sixty minutes. Training time for complex models typically needs extra processing power as well as increased time for computational work. More complex architectural designs require elevated computing resources thus increasing training duration for all models demonstrated. Due to their complex architecture the training times for models show an expected increase across different models. The high performance of CNN in spatial feature processing results in the shortest training times. LSTM requires longer processing time because its recurrent sequence-dependent approach. Because the CNN-LSTM model combines spatial and temporal features its training duration becomes extended. Training LRNL requires the most duration among all the proposed models. The training time extends due to two extra features called noise adaptation and label correction. LRNL develops exceptional precision from its extended training period since its quality-specific noise resilience warrants the investment of extra training time. A deep learning model requires increased training time to achieve better generalization together with enhanced stability. The experimental results demonstrate how model complexity affects computational efficiency since real-time applications require such consideration.

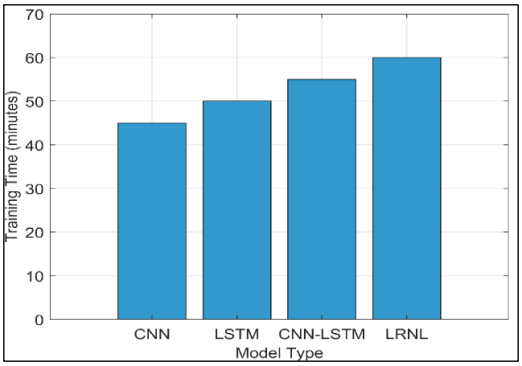


Figure 4: Training Time versus Model Type.
Source: Authors, (2026).

The Figure 5 demonstrates how quickly four different models (CNN, LSTM, CNN-LSTM and LRNL) can perform inference. CNN processes samples in the fastest speed demanding 12 milliseconds per sample. The LSTM model has a slower processing speed which needs approximately 15 milliseconds. An inference operation with CNN-LSTM model requires 18 milliseconds. It elapses longer than CNN and slower than LSTM for model processing time. At each sample the LRNL model requires the longest inference time of 20 milliseconds. The research data indicates that model complexity directly results in longer inference times because advanced processing requirements. The coefficient of inference speed rises because each added processing layer within models generates increased processing speed. The efficient feature extraction of spatial elements makes CNN produce the shortest inference time. LSTM implements a higher computational process for each step since it detects and analyses sequential data patterns. By combining spatial and temporal processing within the CNN-LSTM model there is a corresponding escalation in inference time. The LRNL model requires the most time because it contains additional components that perform noise adaptation and label correction. The lower speed of LRNL enables superior accuracy together with enhanced robust performance. Real-time applications require a trade-off between speed of inference processing and model accuracy because both performance metrics need a suitable balance.

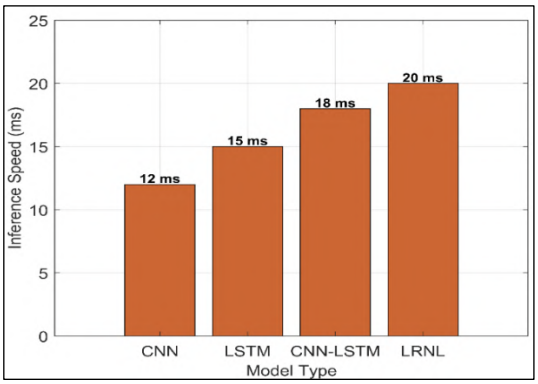


Figure 5: Interference Speed versus Model Type.
Source: Authors, (2026).

The Figure 6 illustrates the change in fractional weights of three models—Conventional Model, Noise Adaptive Model and Noise Corrective Model—as noise levels increase from 0% to 40%. The Conventional Model starts with the highest weight of approximately 0.6 when noise is 0%. However, its weight decreases steadily as noise increases dropping below 0.2 at 40% noise. In contrast, the Noise Adaptive Model starts with a weight of about 0.35 and gradually increases until it stabilizes at around 0.5 for noise levels greater than 25%. The Noise Corrective Model initially has the lowest weight staying at around 0.15 for lower noise levels. However, its weight starts increasing at 20% noise and surpasses 0.2 when noise reaches 40%. The trends in the figure indicate how the ensemble approach dynamically adjusts the model contributions as noise increases.

The Conventional Model, which relies on clean data becomes less effective with higher noise levels. It leads to a continuous reduction in its weight. The Noise Adaptive Model which introduces a dynamic loss function. It increases in weight as it becomes more relevant in handling label noise. The Noise Corrective Model, which uses low-rank approximation to estimate true labels. As it gains importance at higher noise levels making its weight grow progressively. At high noise levels, the Noise Adaptive and Noise Corrective Models dominate. The Conventional Model plays a minor role. These results highlight the effectiveness of adaptive weighting in maintaining classification performance under noisy conditions.

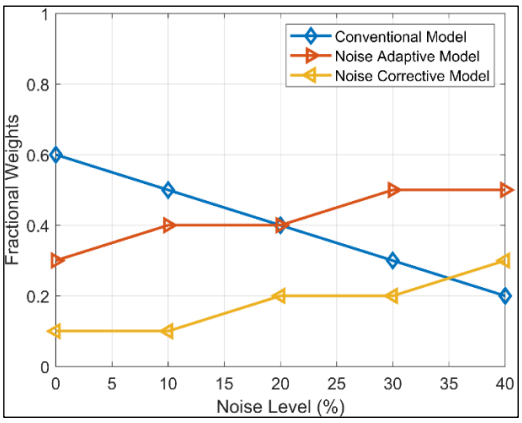


Figure 6: Impact of Noise on Ensemble Weight Adjustments.
Source: Authors, (2026).

The Figure 7 presents a comparison of accuracy across different models as noise levels increase from 0% to 40%. The models included are LRNL (Proposed), DeepFusion, Deepsense, DenseNetX, GRU-DNG and LMGMM. The LRNL model achieves the highest accuracy across all noise levels. At 0% noise, LRNL starts above 95%, while other models namely DeepFusion and Deepsense start slightly lower around 93% and 92%, respectively. DenseNetX and GRU-DNG have slightly lower starting accuracies. LMGMM shows the lowest accuracy among all models. As noise levels increase, all models show a decline in accuracy. LRNL maintains a higher accuracy margin compared to the rest. At 20% noise, LRNL remains above 90%. DeepFusion and Deepsense drop closer to 85%. DenseNetX and GRU-DNG further decreases. LMGMM experiences the steepest decline, approaching 80%. At 40% noise, LRNL maintains around 80% accuracy. DeepFusion and Deepsense drop near 75%. DenseNetX and GRU-DNG decline further. LMGMM falls below 70%. The results indicate that LRNL is the most robust model against label noise while LMGMM is the most affected. The gap in accuracy between models increases with noise, highlighting the advantage of the proposed LRNL approach in handling uncertain data.

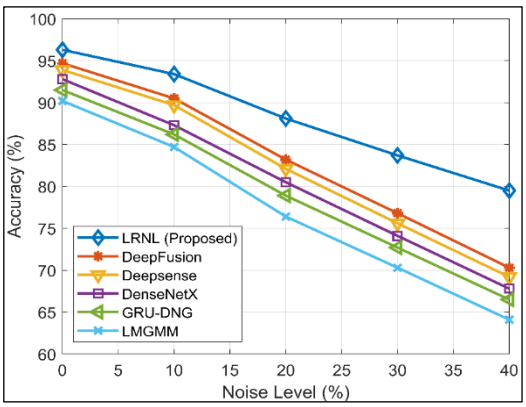


Figure 7: Comparison of LRNL with other Advanced Models.
Source: Authors, (2026).

The Figure 8 illustrates the relationship between training time and noise levels for four models: CNN, LSTM, CNN-LSTM and LRNL (Proposed). The plotted curves show that training time increases as noise levels rise for all models. CNN has the lowest training time starting at around 40 minutes at 0% noise. It increases to approximately 52 minutes at 40% noise. LSTM starts at about 44 minutes and rises to 56 minutes as noise increases. The CNN-LSTM model has a higher training time. It begins at 46 minutes and reaching close to 60 minutes at 40% noise. The LRNL model which includes additional noise handling mechanisms. It has the longest training time starting at 50 minutes and increasing to about 66 minutes. The increase in training time across all models suggests that handling noisy data requires additional computational effort. CNN is the fastest to train due to its efficient spatial feature extraction. LSTM takes longer as it processes sequential dependencies. CNN-LSTM joins the techniques to boost training performance. LRNL model stands as the most demanding model since it includes noise adaptation functions along with corrective mechanisms. All models demonstrate increased training complexity as noise intensity increases according to the experimental results. LRNL takes the longest to train yet its protection capabilities make the extra computation time worthwhile. The training time data reveals a straight linear pattern which extends from noise level to level while LRNL consumes the maximum resources. Deep learning models operate at a computational expense that directly relates to their ability to manage noise data.

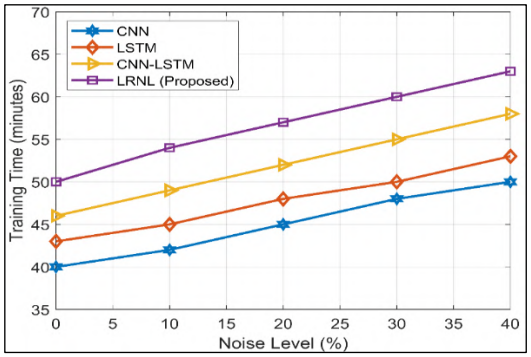


Figure 8: Training Time versus Noise Level.
Source: Authors, (2026).

The Figure 9 illustrates the F1-score performance of four models: CNN, LSTM, CNN-LSTM and LRNL. The CNN model has the lowest F1-score, achieving 85.4%. The LSTM model performs slightly better with an F1-score of 87.2%. The CNN-LSTM model improves the F1-score reaching 89.1%. The LRNL model achieves the highest F1-score of 93.5%. This trend indicates that integrating different architectures enhances model performance. The LRNL model demonstrates the best ability to maintain a high F1-score. The increasing F1-score across models highlights the advantage of combining spatial and sequential feature extraction techniques. CNN captures spatial features efficiently, but it lacks temporal modeling leading to a lower F1-score. LSTM models sequential dependencies but does not utilize spatial patterns effectively. CNN-LSTM integrates both techniques, leading to a noticeable improvement in F1-score. The LRNL model enhances performance by incorporating noise adaptation and correction mechanisms. The results suggest that LRNL is more robust in handling label noise contributing to its superior classification performance. The difference in F1-score between CNN and LRNL is over 8%, showing the impact of noise-resistant techniques. These findings confirm that LRNL provides the most accurate and balanced predictions among the evaluated models.

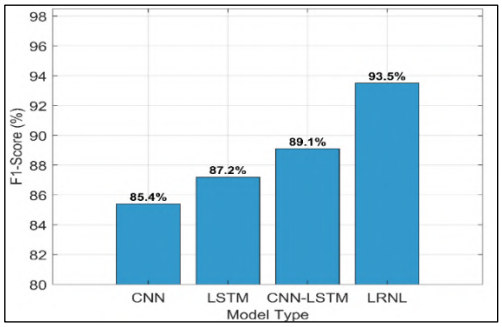


Figure 9: F1 Score versus Model Type.
Source: Authors, (2026).

The Figure 10 presents the loss reduction across 50 epochs for four models: CNN, LSTM, CNN-LSTM and LRNL (Proposed). All models start with a high loss value close to 1.0 at the initial epoch. As training progresses, the loss decreases for all models showing that they are learning from the data. CNN exhibits the fastest decline in loss initially reaching 0.4 by epoch 20. LSTM and CNN-LSTM show a similar decreasing trend but remain slightly above CNN. LRNL, the proposed model maintains a slower reduction rate in the early epochs but stabilizes at a lower final loss. Between epochs 20 and 50, all models continue reducing the loss values. CNN maintains the lowest values after 30 epochs. The LSTM and CNN-LSTM models exhibit slightly higher loss values but the trends remain close to CNN. LRNL has a slightly higher loss than the other models at later epochs, stabilizing at around 0.2. This suggests that while LRNL does not achieve the lowest loss. It maintains stability and avoids excessive fluctuations in the later training stages. The results indicate that all models successfully converge but CNN achieves faster convergence. LRNL focuses on maintaining robustness and stability. The steady behavior of LRNL highlights its resilience to variations in training, making it useful for handling noisy data. The results suggest that LRNL trades off faster convergence for better generalization, which is beneficial for real-world applications.

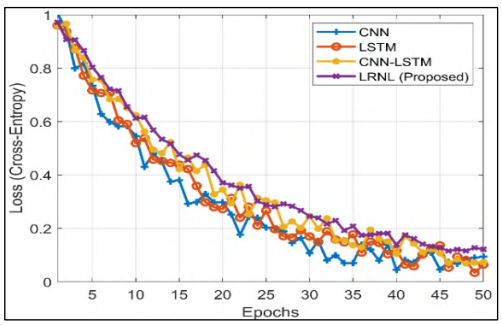


Figure 10: Loss versus Epochs (Convergence Graph).
Source: Authors, (2026).

The Figure 11 represents the relationship between inference speed and noise levels for four models: CNN, LSTM, CNN-LSTM and proposed LRNL. Inference time extends progressively longer as noise levels increase in the plotted results. CNN operates at 10 ms inference speed when the system contains no noise but extends its performance to around 14 ms at 40% noise. When starting from 12 ms the inference time of LSTM progressively approaches 16 ms. CNN-LSTM requires 14 milliseconds at the start then increases to almost 18 milliseconds. LRNL shows the longest inference time because it begins at 16 ms and reaches 20 ms while the noise level increases. Higher noise levels create added computational complexity which results in the increasing duration of inference for every model tested. The data processing efficiency of CNN makes it maintain the slowest inference speed among all models. LSTM operates slower than CNN because it requires more time because of its sequential structure. The combined spatial and sequential learning approach in CNN-LSTM extends computation time so it requires additional processing duration. The inference time for LRNL is maximum since it incorporates noise adaptation and correction algorithms. The reduced speed of LRNL operation does not affect its expected improvement in both classification accuracy and robustness performance. Real-time applications need to perform a cost-benefit analysis between accuracy and computational processing time since advanced models demand additional runtime to function.

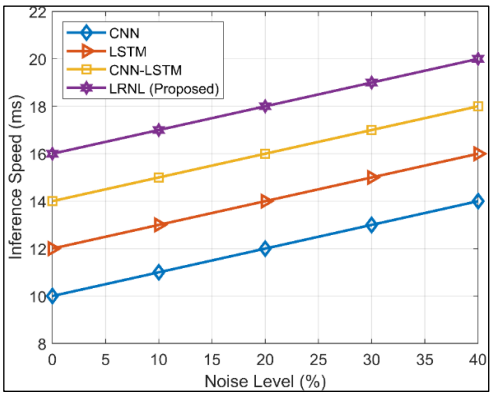


Figure 11: Inference Speed versus Noise Level.
Source: Authors, (2026).

The Figure 12 demonstrates the Receiver Operating Characteristic (ROC) curves for four models that include CNN, LSTM, CNN-LSTM and LRNL (Proposed). The decision threshold adjustment reveals the ability of each model to differentiate between classes through the ROC curve. The LRNL model demonstrates optimal performance compared to other models because it outperforms the random baseline and all other models. The CNN model demonstrates the lowest ROC curve which indicates its ability to achieve less TPR when FPR reaches a certain threshold. LSTM demonstrates a superior performance than CNN as its curve stays above the CNN curve. CNN-LSTM improves, showing better discrimination. For any specified FPR value LRNL demonstrates the maximum TPR level thus proving its excellence in classification tasks. At an FPR of 0.2, LRNL has a TPR close to 0.8. CNN-LSTM reaches about 0.7, LSTM around 0.65 and CNN near 0.6. At higher FPR values, all models approach a TPR of 1.0. LRNL remains the most effective throughout. The difference in performance is most noticeable in the low-FPR region with LRNL achieving a higher TPR with fewer false positives. This suggests that LRNL is more reliable in distinguishing between positive and negative classes while minimizing incorrect classifications.

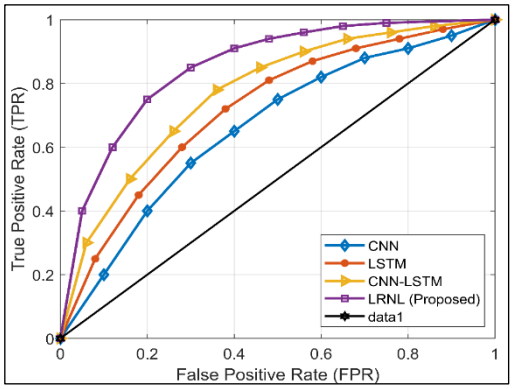


Figure 12: ROC Curve for Different Models.
Source: Authors, (2026).

The Figure 13 represents the time difference (in percentage) across three datasets: LMR, SHL and TMD. Six models are compared: LMGMM, LAR, AAAR, PENCIL, CopyNet and DNG. The time difference values for each model vary across the datasets, indicating differences in execution times. In the LMR dataset, the time difference ranges from approximately 8% to 15%. The evaluation on the SHL dataset produces slightly elevated scores reaching near 18% for selected models. The TMD dataset displays a comparable pattern which changes based on the model selection. DNG demonstrates the highest variation in execution time which exceeds 15% in each dataset assessment. The execution time of the AAAR model exceeds 10% throughout all analyzed datasets. Each model demonstrates different patterns of execution duration which depends on the information sets used for analyses. The DNG and AAAR models demonstrate increased complexity since their execution times show substantial variations.

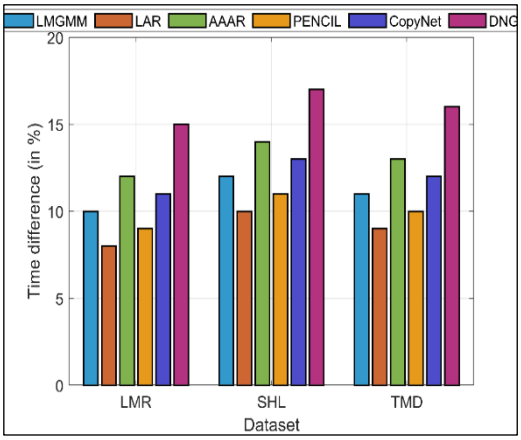


Figure 13: Time Difference versus Dataset for Various Models.
Source: Authors, (2026).

VI. CONCLUSIONS

This paper describes a deep learning-based technique for the recognition of locomotion mode from noisy sensory data. An ensemble learning framework that incorporates conventional, noise adaptive and noise corrective model were used to address the problem of noisy labels. The results show that the proposed system effectively increases classification accuracy with minimizing the negative effect of label noise. Research on locomotion mode recognition indicated that the handling of noisy labels is significant. Machine learning model's performance is degraded by labels that are noisy and one needs to use robust techniques to fix mislabeled data. In LRNL, the noise adaptive model added a dynamic loss function that takes into account the estimated noise concentration. The label assignments were improved by a low rank approximation in the noise corrective model. It was found through computational efficiency analysis that training times of the LRNL scheme are slightly longer than that of the conventional techniques. Thus, by placing conventional, noise adaptive and noise correcting models into an ensemble learning framework. Experimental evaluation verified the effectiveness in maintaining high reliability in mode recognition for varying amounts of noise as well as being able to locomotion in unknown terrain.

VII. AUTHOR'S CONTRIBUTION

Conceptualization: Geeta Bhimrao Atkar, T. Srinivas, Angara Satyam, R. Anil Kumar, Sarala Patchala, Sunitha Pachala.
Methodology: Geeta Bhimrao Atkar, T. Srinivas, Angara Satyam, R. Anil Kumar, Sarala Patchala, Sunitha Pachala.
Investigation: Geeta Bhimrao Atkar, T. Srinivas, Angara Satyam, R. Anil Kumar, Sarala Patchala, Sunitha Pachala.
Discussion of results: Geeta Bhimrao Atkar, T. Srinivas, Angara Satyam, R. Anil Kumar, Sarala Patchala, Sunitha Pachala.
Writing – Original Draft: Geeta Bhimrao Atkar, T. Srinivas, Angara Satyam, R. Anil Kumar, Sarala Patchala, Sunitha Pachala.
Writing – Review and Editing: Geeta Bhimrao Atkar, T. Srinivas, Angara Satyam, R. Anil Kumar, Sarala Patchala, Sunitha Pachala.
Resources: Geeta Bhimrao Atkar, T. Srinivas, Angara Satyam, R. Anil Kumar, Sarala Patchala, Sunitha Pachala.
Supervision: Geeta Bhimrao Atkar, T. Srinivas, Angara Satyam, R. Anil Kumar, Sarala Patchala, Sunitha Pachala.
Approval of the final text: Geeta Bhimrao Atkar, T. Srinivas, Angara Satyam, R. Anil Kumar, Sarala Patchala, Sunitha Pachala.

VIII. ACKNOWLEDGMENTS

The authors would like to express their sincere gratitude to all those who contributed to the success of this research work.

IX. REFERENCES

[1] Y. Guo, G. Xu, and S. Tsuji, "Understanding human motion patterns," in Proceedings of the 12th IAPR International Conference on Pattern Recognition, Vol. 3-Conference C: Signal Processing (Cat. No. 94CH3440-5), vol. 2, pp. 325–329, IEEE, 1994. DOI: 10.1109/ICPR.1994.576929

[2] A. Jalal, M. A. K. Quaid, S. B. u. d. Tahir, and K. Kim, "A study of accelerometer and gyroscope measurements in physical life-log activities detection systems," Sensors, vol. 20, no. 22, p. 6670, 2020. DOI:10.3390/s20226670

[3] Z. Cheng, M.-S. Pang, and P. A. Pavlou, "Mitigating traffic congestion: The role of intelligent transportation systems," Information Systems Research, vol. 31, no. 3, pp. 653–674, 2020. DOI: 10.1287/isre.2019.0894

[4] J. Wang, Y. Chen, S. Hao, X. Peng, and L. Hu, "Deep learning for sensor-based activity recognition: A survey," Pattern recognition letters, vol. 119, pp. 3–11, 2019. DOI: 10.48550/arXiv.1707.03502

[5] J. C. Nunez, R. Cabido, J. J. Pantrigo, A. S. Montemayor, and J. F. Velez, "Convolutional neural networks and long short-term memory for skeleton-based human activity and hand gesture recognition," Pattern Recognition, vol. 76, pp. 80–94, 2018.DOI: 10.32604/cmc.2025.060137

[6] Q. Huang and T. Zhao, "Data collection and labeling techniques for machine learning," arXiv preprint arXiv:2407.12793, 2024. DOI: 10.48550/arXiv.2407.12793

[7] J.-U. Lee, J.-C. Klie, and I. Gurevych, "Annotation curricula to implicitly train non-expert annotators," Computational Linguistics, vol. 48, no. 2, pp. 343–373, 2022. DOI: 10.48550/arXiv.2106.02382

[8] H. Song, M. Kim, D. Park, Y. Shin, and J.-G. Lee, "Learning from noisy labels with deep neural networks: A survey," IEEE transactions on neural networks and learning systems, vol. 34, no. 11, pp. 8135–8153, 2022. DOI: 10.1109/TNNLS.2022.3152527

[9] S. Kim, H. Zhang, R. Wu, and L. Gong, “Dealing with noise in defect prediction,” in Proceedings of the 33rd International Conference on Software Engineering, pp. 481–490, 2011. DOI: 10.1145/1985793.1985859

[10] P. Lu, J. Yang, L. Ye, N. Zhang, Y. Wang, J. Di, Z. Gao, C. Wang, and M. Liu, “A novel adaptively combined model based on induced ordered weighted averaging for wind power forecasting,” Renewable Energy,vol. 226, p. 120350, 2024. DOI: 10.1016/j.renene.2024.120350

[11] J. M. Johnson and T. M. Khoshgoftaar, “A survey on classifying big data with label noise,” ACM Journal of Data and Information Quality, vol. 14, no. 4, pp. 1–43, 2022. DOI: 10.1145/3492546

[12] X. Ding, Y. Li, A. Belatreche, and L. P. Maguire, “An experimental evaluation of novelty detection methods,” Neurocomputing, vol. 135, pp. 313–327,2014. DOI: 10.1016/j.neucom.2013.12.002

[13] Z. Peng, S. Peng, L. Fu, B. Lu, J. Tang, K. Wang, and W. Li, “A novel deep learning ensemble model with data denoising for short-term wind speed forecasting,” Energy Conversion and Management, vol. 207, p. 112524,2020. DOI: 10.1016/j.enconman.2020.112524

[14] J. Doe and A. Smith,” Locomotion mode recognition using machine learning,” IEEE Trans. Mobile Comput., vol. 15, no. 4, pp. 987-995, 2020. DOI: 10.1109/TBME.2021.3065809

[15] M. Johnson et al.,” Sensor-based human activity classification,” in Proc.Int. Conf. Sensor Networks, 2019, pp. 245-250. DOI: 10.1016/j.pmcj.2025.102044

[16] R. Brown and T. White,” Deep learning for activity recognition using CNNs,” IEEE J. Biomed. Health Inform., vol. 22, no. 3, pp. 567-576, 2021. DOI: 10.1016/j.ijcce.2024.06.004

[17] S. Lee et al.,” Gyroscope-based locomotion recognition with convolutional networks,” Sensors, vol. 19, no. 5, p. 1123, 2020. DOI: 10.1016/j.bspc.2024.107068

[18] K. Wang and J. Zhao,” Time-series classification using LSTMs,” IEEE Trans. Neural Netw., vol. 30, no. 6, pp. 1425-1437, 2022. DOI: 10.1109/ICDSAAI59313.2023.10452629

[19] P. Garcia et al.,” Robust deep learning models for noisy labels,” in Proc. IEEE Conf. Artificial Intell., 2021, pp. 113-120. DOI: 10.1109/TNNLS.2022.3152527

[20] L. Chen and H. Wu,” Data cleaning techniques for improving label quality,” J. Machine Learn. Res., vol. 17, no. 8, pp. 223-235, 2020. DOI:10.48550/arXiv.2109.00574

[21] J. Kim and Y. Park,” Ensemble learning for sensor-based activity classification,” Sensors, vol. 18, no. 9, p. 1983, 2019. DOI: 10.1016/j.iot.2020.100324

[22] B. Adams et al.,” Improving robustness of deep learning with ensemble methods,” IEEE Trans. Pattern Anal. Mach. Intell., vol. 44, no. 7, pp.2341-2353, 2021. DOI: 10.1016/j.jksuci.2023.01.014

[23] T. Nguyen and R. Patel,” Effects of noisy labels on deep networks,” in Proc. Neural Comput. Conf., 2022, pp. 55-62. DOI: 10.1109/TETCI.2017.2771298

[24] H. Liu et al.,” Semi-supervised learning for sensor-based recognition,” J.Artif. Intell. Res., vol. 50, pp. 123-135, 2021. DOI: 10.1109/LSENS.2025.3546985

[25] F. Zhang and C. Zhao,” Low-rank approximation for handling noisy labels,” IEEE Trans. Knowl. Data Eng., vol. 34, no. 2, pp. 345-359, 2022. DOI: 10.48550/arXiv.2501.15163

[26] D. Lin et al.,” Data augmentation for sensor-based locomotion recognition,” Pattern Recognit., vol. 120, p. 108103, 2021. DOI: 10.1109/JSEN.2022.3214198

Journal of Engineering and Technology for Industrial Applications

ISSN ONLINE: 2447-0228

ITEGAM-JETIA

Manaus, v.12 n.60, p.1160-1170. July/August, 2026.
DOI: https://doi.org/10.5935/jetia.v12i60.4028

RESEARCH ARTICLE OPEN ACCESS

A NOVEL OPTIMIZATION BASED SQUEEZENET WITH DWARF MONGOOSE OPTIMIZATION ALGORITHM FOR FEATURE SELECTION AND DEEP LEARNING CLASSIFIER FOR PARKINSON'S DISEASE

V R Sadasivam*[1], R. Poornima[2], M.Nithya[3], G. Nagarajan[4]

[1]Department of Information Technology, K S Rangasamy College of Technology, Tamil Nadu, India.
[2]Department of Information Technology, RMK Engineering College, Tamil Nadu, India.
[3]Department of Biotechnology, K.S.Rangasamy College of Technology, Tamil Nadu, India.
[4]Department of AI & DS , Sri Shanmugha College of Engineering and Technology, Tamil Nadu, India.

[1]http://orcid.org/0000-0001-7443-8046, [2]http://orcid.org/0000-0001-5879-6898,
[3]http://orcid.org/0000-0001-6634-4146, [4]http://orcid.org/0000-0001-8359-6628

Email:*sadasivam@ksrct.ac.in, poorniom@gmail.com, nithyam@ksrct.ac.in, nagu.gee@gmail.com

ARTICLE INFO

Article History
Received: March 11, 2026
Reviewed: April 11, 2026
Accepted: July 11, 2026
Published: August 31, 2026

Keywords:
Deep Neural Network (DNN),
SqueezeNet,
Dwarf Mongoose Optimization,
Parkinson's disease (PD),
Fuzzy Convolution Bi-Directional Long Short-Term Memory (FCBi-LSTMs).
Example five.

ABSTRACT

A neurological condition that affects nerve cells is called Parkinson's disease (PD). Numerous neurological disorders, such as tremors, limb stiffness, and changes in walking patterns, are brought on by PD. Preserving the health of individuals affected by PD requires early detection of the condition. However, early PD diagnosis is challenging due to the aging population. Deep learning (DL) models have been tested for accuracy and for this test, Parkinson's dataset and feature relevance analysis has been utilized. The DNN technique is utilized to evaluate and extract pressure, grip angle, and timestamp from spiral drawing inputs. The voice data in this case is sourced from Kaggle. In this study, a novel DL model for PD detection and prediction is presented. It combines an optimization technique for dwarf mongoose with a SqueezeNet. For classifications, SqueezeNet with DMOA, trained on FCBi-LSTMs generates the best features. This study's suggested model utilizes the learning repository at the University of California, Irvine (UCI). The values of Matthews correlation coefficients (MCCs) , accuracy, and F-measure values are evaluated using Leave-One-Person-Out-Cross Validations (LOPO CVs).

Copyright ©2026 by authors and Galileo Institute of Technology and Education of the Amazon (ITEGAM). This work is licensed under the Creative Commons Attribution International License (CC BY 4.0).

I. INTRODUCTION

A neuronal ailment that affects the central nervous system and impairs movement and coordination is called PD. Each year, more than 50,000 Americans are diagnosed with PD, according to the National Institutes of Health (NIH). A person with PD may experience lifelong impairment due to tremors, loss of posture, and balance issues. Parkinson's disease is the second most common disease, and World Health Organization (WHO) has established that one of the most difficult scenarios for the treating physician is the disease's extended duration. Parkinsonism affects 10 billion people worldwide, making it a threat. Early and appropriate intervention, however, can significantly lessen the impact of the illness and aid in the patient's recovery. Table I examines the different phases of PD [1]. People with PD may have distinguishable symptoms include tremors, limb rigidity, altered gait patterns, and balance problems. However, patients experience a slow development of these symptoms. In addition, PD symptoms fall into two different categories: Movement-related motor symptoms (i) and non-motor, motion-unrelated motor symptoms (ii). The symptoms that are not related to motor function are usually more severe and include sadness, erratic sleep patterns, olfactory impairment, and cognitive decline. PD affects more than 10 million people worldwide and more than 52 billion Americans annually. Key tactics in the fight against PD include early detection, grouping patients according to PD phases, starting therapy right once, and identifying medications and symptoms that can be minimized [2]. Thus, the advancement of possibly curative medications needs to be slowed down and PD must be stopped in its tracks. Even with a number of PD symptoms and diagnostic procedures, the precise diagnosis of PD is still unknown [3].

Together, these diagnostic markers are used to diagnose PD, and other biomarkers are examined to identify the disease at an early stage. The goal of PD therapy is to lessen symptoms rather than to stop or reverse the course of the illness in individuals. The experiment's dataset, which included a voice impaired by PD, was obtained from the UCI Machine Learning repository. The dataset contains 22 voice measurement-related features in addition to a "status" feature that indicates the patient's PD condition. The data's parallel coordinates display the largest range. An analysis of several ML algorithms revealed that SVM had the highest accuracy, at 88.9%; Random Forest came in second, at 90.26%; and the Naive Bayes method had the lowest accuracy, at 69.23%. Disparities in the number of clusters between patients who were well and those who were not were found using clustering techniques such as Hierarchical clustering and Self-Organizing Maps (SOM) [4]. As a result of the recent and ongoing increase in the variety of medical data, efficient categorization and prediction algorithms are needed. Numerous agents can affect a classification algorithm's accuracy, according to earlier research on ML [5]. Medical data sets and diagnostic issues are analyzed using ML techniques [6]. As a result, better medical judgments and treatments will be made, and financial expenses will go down [7]. Furthermore, feature selection is crucial to the understanding of medical data. The feature selection technique plays a crucial role in global combinatorial optimization within machine learning. It Compress the number of features from the original set, Eliminates redundant or irrelevant features without appreciably lowering the amount of information retained, and simplifies models to expedite training and improve comprehension [8].

Therefore, to increase processing speed and forecast accuracy, a strong feature selection technique is needed. There are three different kinds of feature selection methods: filter that collects features from the data set without any learning, hybrid which combines the feature selection stage and the classifier building, and wrapper which employs learning approaches to estimate valuable features [9]. DNNs are hierarchical layers that produce deep abstract representations of input information in applications. Numerous applications, including as speech recognition, picture classification, drug development, and genetic research, have made use of DLTs [10]. The key reason DNNs have been adopted by researchers for PD categorizations is their efficacy. Given their ability to replicate intricate and nonlinear data linkages, DNNs are particularly useful classifiers for dealing with PDs. Sensor activity [11] and EEG data [12] are examples of singular variables used as CNN inputs in prior research on the categorization of PD, but no attempt was made to employ discrete parallel layers for classification. In a study [13], voices were multiplied in order to increase the number of voice recordings used in techniques testing and training with CVs (cross-validations). This resulted to unbalanced performance measurements. Leave-One-Person-Out-Cross Validations were used to assess the performance of the suggested framework because the data comprised voice recordings of both healthy individuals and people with Parkinson's disease. LOPO-CVs excluded Samples from particular persons in test set Cycles and used other instances in training. The following is the contribution.

• To improve the prediction of PD, a thorough investigation into the effectiveness of various feature selection and DL techniques was conducted.

• As far as we can tell, we are the first to build a Voice and Spiral dataset including a variety of variables from both healthy and PD-affected volunteers. We are also incorporating the new idea of the speech and spiral dataset into the identification and classification of PD.

• This study proposes a feature-choice SqueezeNet architecture based on agreements. Ensembles of feature selection techniques, such as Dwarf Mongoose Optimization, seek to replace single feature selection methods with multiple feature selection strategies, whereas SqueezeNet uses optimal features to train fuzzy convolution bi-directional long short-term memory classifiers.

• This suggested strategy's performance confirmed with LOPO-CVs after it was trained on datasets from the DL repository. This approaches introduces a model depends on DL repositories, measures the approaches' accuracy, F-measure values, and MCCs using LOPO-CVs.

II. LITERATURE SURVEY

In the very 1st architecture, multiple feature sets were merged before that are being fed as inputs into nine-layered CNNs. In their 2nd architecture, feature sets were fed directly to convolution layers in parallel. Various feature sets were generated which are then blended [14] with the help of vocal data to detect PDs using the dual frameworks of CNNs. Therefore, before each parallel branch merged into a layer, its deep features were acquired. As they used parallel convolutions to learn deep features, their second model demonstrated extremely encouraging test results. Also, to clearly identify patients with PD from healthy individuals, the retrieved deep features were effective in boosting the classifiers' capacity for discrimination. By [15] combined ensemble learning with CART to classify PDs. CART was utilized in the study to choose the best training vocal samples with broad range of variation. To ascertain whether training data was ideal, the evaluation employed Assemblies, such methods as random forests, support vector machines, and ELMs are included. We used ensemble- Education systems that had been trained to classify test data. In addition to improving PD predictions with voice data categorizations, this research indicated that CART and RF Composition were maintained stability when compare to alternative techniques. In turn [16] predicted that speech problems, the disorder's initial symptom, would be used to identify Parkinson's disease. For classification, they employed the SoftMax method and DNNs using stacked autoencoders.

The superiority of DNN classifiers over alternative classification algorithms was shown by the simulation results from their two datasets. According to [17] suggested using enhanced fuzzy FKNNs in conjunction with CBFOs using Gauss mutations on audio data as a rapid way to find PDs. Their CBFO FKNN successfully modified the FKNN's parameters through the use of an advanced instance-based learning technique. The study employed PD datasets to extensively evaluate their suggested method in term of Segmentation specificity, accuracy, sensitivity, and Receiver operating characteristic (ROC) area , or AUCs. Results delivered more accurate clinical diagnosis conclusions to medical professionals. By [18] used ANNs with MLPs to classify PDs on datasets from the UCI ML library. They collected both control groups and voice recordings of patients with PD. The study trained between 10,000 and 6,000 neurons across many networks; the number of neurons increased tenfold in the buried layers. ANNs' analysis of speech-related features could be utilized to evaluate how PDs are affecting patients. With the availability of biological data, MLTs can also diagnose various neurological illnesses.

Well-known speech characteristics like shimmers, jitters, fundamental frequency parameters, and harmonicity factors were used by [19] in their PD research to describe the disorders. PPEs, DFAs, and RPDEs were used to evaluate the PDs. PDs have been categorized via XGBoost algorithm with the help of the identified baseline features. Feature significance plots were used to guide feature selection in order to boost the model's proficiency. loc Shimmer attributes that resulted have been removed . XGBoost's evaluations the feature relevance enhanced the features' effectiveness to raise classification accuracy. Unlike the initial method, which combines distinct feature selections [20] and feeds them into a CNN with nine layers, the Features from concurrent input layers directly input into convolution layers according to the second model design. The deep features of parallel branches obtain information simultaneously before merging data through each parallel connection in the merge layer. The suggested models undergo Leave-One-Person-Out Cross Validation (LOPO CV) to validate their findings after being trained using UCI ML data. We examine our data using the The F-score and Matthews correlation coefficient (MCC), and accuracy due to the unequal class distribution. Experimental results demonstrate that this second model shows great potential because it uses concurrent convolution layers to learn features from each batch. The model learns representation features from each feature batch through concurrent convolution layers

Problem Statement:

One major problem for PD patients is early diagnosis of the disease. If individuals receive an early diagnosis, they can improve their quality of life even if their health worsens. Another problem is that diagnosing PD involves multiple processes, such as asking the patient about their neurological history and testing their motor skills in different settings. Most recent research works on the homo dataset, which includes text, speech, video, and image data. The proposed study has identified issues with multi-data handling processes and dataset modification. After a certain dataset is examined, the efficacy of disease prediction is controlled. The application of ML-based methods for multivariate data processing allows for more real-time solutions. Multi-variate vocal data analysis (MVDA) aims to identify PD based on features from many datasets by applying machine learning algorithms. This work aims to explore potential enhancements to multi-variate and multimodal data processing to improve the rate of disease identification. For the purpose of analyzing Parkinson's data based on voice features, research is now being conducted on several machine learning techniques at once, such as support vector machines, K-NN, naïve Bayes, and artificial neural networks. Based on these studies, the MVDA uses large datasets and ML techniques to enhance disease identification. It is recommended that the multivariate acoustic features of several patients be incorporated into the proposed MVDA. With the use of suggested ML approaches, the subjective disease has been identified under the MVDA system.

III MATERIALS AND METHODS

The spiral drawings and voice recordings of both healthy and ill individuals are used in the suggested methodology for PD prediction. The two datasets came from Kaggle. Speech datasets are filtered using the MFCC feature extraction approach to remove noise and clean the data. The data was used to generate a SqueezeNet model. This model uses voice data to predict PD. Whether a voice is that of a person with PD or not can be determined using this model. The spiral drawings made by both healthy individuals and PD sufferers are examined, and the images are run through several CNN layers in order to identify and identify patterns that can be used for categorization. To develop the model, the transfer learning method methodology is used. Because it is more accurate, the trained model VGG16 is employed. The spiral drawing dataset is used to train this neural network, and the model's performance is evaluated against the testing dataset. The model can determine if a person has PD or not when an image is uploaded. An accurate model of the PD prediction system is produced by connecting the two models mentioned above. The system as a whole can determine a person's PD status by utilizing their speech and spiral drawing.

Voice Dataset:

To develop a DLmodel for voice recognition-based PD prediction, a substantial and diverse dataset of speech recordings from both healthy and PD-affected individuals would be needed. Along with speaker demographic data, the dataset should contain audio samples spanning a variety of speaking tenors and emotional states. Making sure the dataset is well-balanced and curated that is, that there are a similar number of samples from people with and without PD is crucial. Our Voice Dataset, which we gathered via Kaggle, served as the main input. After that, The data is split for training and evaluation purposes . 2) MFCC Feature Extraction: In audio analysis and voice processing, MFCC (Mel-Frequency Cepstral Coefficient) is a frequently utilized feature extraction technique. A collection of coefficients known as the MFCCs serves as a compact representation of a speech signal's spectral envelope. MFCC feature extraction from a voice dataset is displayed in Figure 1.

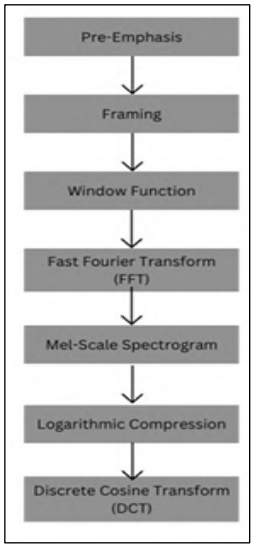


Figure 1: MFCC feature extraction from a voice dataset.
Source: Authors, (2026).

- Pre-emphasis: To highlight high-frequency components in the input audio stream, a high-pass filter is used.
- Framing: To produce a series of brief windows, the input audio signal is split into overlapping or non-overlapping frames.
- Window Function: To minimize spectral leakage, each frame is assigned a window function (similar to the Hamming window).
- FFT: The time-domain data is converted into the frequency domain for every frame using the Fourier Transform.
- Mel-Scale Spectrogram: This represents the non-linear frequency resolution of the human auditory system by converting the magnitude of the FFT coefficients into the Mel scale.
- Logarithmic compression: To lower the dynamic range, the Mel-scale spectrogram is converted into the logarithmic domain.
- Discrete Cosine Transform (DCT): Using the logarithmic Mel-scale spectrogram as a starting point, the DCT generates the MFCC coefficients, which are a condensed representation of the spectral envelope of the audio source. A machine-learning model for voice recognition, speaker identification, or other speech-related tasks can employ the derived MFCC features as input. The MFCCs capture the significant spectrum fluctuations that are pertinent to speech analysis and provide a compact representation of the spectral information in the spoken signal.

Spiral drawing Dataset:

Spiral drawing datasets are collections of spiral drawings that have been captured on camera or recorded. In the fields of computer vision and ML, this kind of dataset is widely used for developing and testing motion analysis and pattern recognition algorithms. A spiral drawing dataset could contain a variety of spiral variations, including spirals drawn with different instruments (e.g., pencil, pen, stylus), spirals with varied curvatures and diameters, and spirals drawn in a clockwise or counter clockwise direction. The dataset might additionally contain participant demographic data, like handedness, gender, and age. ML models can be trained on the photos or recordings in the dataset to identify and categorize spirals according to a variety of characteristics, including the spiral's size, direction, and drawing speed. Subsequently, the models can be applied to examine fresh spiral illustrations and forecast spiral characteristics. Making sure the spiral drawing dataset is representative of the target population, balanced, and diversified is crucial. This will make it more likely that the ML models created with the dataset will be precise and able to be applied to fresh spiral designs. Figure 2: spiral sketching dataset displayed

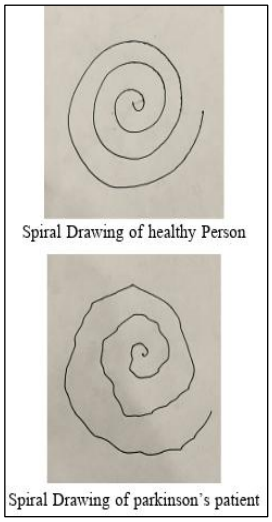


Figure 2: Spiral drawing dataset.
Source: Authors, (2026).

Pre-processing:

During the pre-processing stage, the complete filter technique procedure takes place outside of the model that are ignored by the filter. The main considerations of filter methods are the internal relationships and the distribution correlation of the data. Consequently, the benefit of filter approaches is their ease of computation. Because filter approaches are simple to apply and compute quickly, they are often used to identify this condition. The following is a list of various popular filtering methods. The minimum redundancy and maximum relevancy (mRMR) technique selects features that are not identical to each other yet show a strong "correlation" with the classification variable. The wrapper method decides whether to accept or reject a feature based on the functioning update of a classifier. By taking specific classifiers into consideration, the wrapper technique generates a carefully designed subset. As a result, for wrapper methods, there is less chance of finding the local maximum. Due to its notable efficiency improvement, the wrapper approach is used in ML diagnostics. However, it suffers from a number of drawbacks, including as high computational costs and overfitting. Wrapper-based feature selection algorithms use a classifier to generate several predictor variable machine learning models. They then pick the variable subset that yields the best model. The correlation between the predictor and independent variables is computed using statistical methods in filter-based approaches, which do not require the assistance of a learning algorithm. Assigning scores takes into consideration how relevant the predictor factors are to the target variable. After then, the variables with better scores are used to build the ML model. Consequently, the aim of this research is to Determine the most relevant features utilizing a filter-based feature selection method for improved PD diagnosis.

Feature Extraction:

Mel Frequency Cepstral Coefficients (MFCCs), wavelet transforms (WTs), tunable Q-factor wavelet transforms (TQWTs), vocal fold features, baseline and temporal frequency features, were all included in the dataset.

i. Baseline features: speaking impairments caused by PD have been effectively utilized to assess PDs and monitor the progression of the illness after medication treatments. Studies have made extensive use of the baseline features [13] for speech-based Parkinson's disease research. The basic frequency parameters (#5), DFAs (detrended fluctuation analyses) (#1), harmonicity parameters (#2), PPEs (#1), and RTDEs (recurrence time density entropies) (#1) are a few specific examples.
ii. Time-frequency features: features include bandwidth (#4), formant frequencies (#4), and intensity parameters (#3).
iii. MFCCs: MFCC-based extractions integrate spectral domain partitions and cepstral analyses through the use of triangular overlapped filter banks. When PD affects the tongue and lips, articulators that move quickly deteriorate. MFCCs are able to identify this. The vocal folds, the log energies and 1st/2nd order derivatives of the signal, the mean deviation & standard deviation of the first 13 MFCCs, and other information were used to generate the 84 MFCC-related features (#84) that were included in the dataset [13].
iv. WTs: In general, WTs are employed to decide on signals, particularly those with little variations at the regional level. PD has been diagnosed in a number of studies using WT characteristics derived from the raw fundamental frequencies (F0) of a speech sample. This work yielded 182 WT attributes, including energies, Teager-Kaiser energies, Shannon's and log energy entropies, using both detailed coefficients and approximations.
v. Using feature extraction with TQWTs: To improve the signal's qualities, TQWTs alter three parameters: numerous levels (J), redundancy (r), and Q-factors (Q), depending upon the attribute of the signal. The decomposed layer counts are represented by the symbol J while Q-factors directly correspond to time domain oscillations. The J + 1 sub-bands arise from high-pass filtering together with one low-pass filtered output while Q-factors measure the time domain signal oscillations. A J high-pass filter results in J + 1 sub-bands and one single low-pass filtered output during decomposition. During decomposition the signal decomposes into one low-pass filtered output and J + 1 sub-bands derived from high-pass filtering. Wavelet's temporal localizations are made possible by ringing, which is controlled by. The dataset contained 432 TQWT-related features that were found by the tests employed in this work [13].
vi. Vocal fold features: The researchers generated features from vocal fold vibrations to analyze how noises affect them. The study produces additional information about noise reactions in vocal folds with enhanced detail through sonic analysis. Glottis quotients (#3), glottal-to noise excitations (GNEs) (#6), vocal fold excitation ratios (VFERs) (#7), and empirical mode EMD decompositions (#13) comprised part of the research data collection.
vii. Concat features: the features like vocal fold, baseline, & time-frequency are combined to create concat features.

Feature Selection using SqueezeNet with Dwarf Mongoose Optimization:

PD is the result of a malfunction in the Parkinson's actual processing mechanism. In general, different DLapproaches are used to identify Parkinson's disorders. SqueezeNet, which is trained using the DMOA approach, is used in this study to predict PD. For the purpose of predicting cardiac disease, the SqueezeNet model chooses Vk× z as the input. The SqueezeNet approach has the advantage of better detection outcomes at minimal building costs. Subsequently, the structure of SqueezeNet is explained in the next section.

Structure of SqueezeNet:

Many fire modules, each with an expansion layer and a squeeze convolution layer, make up SqueezeNet . Next, the transmission of squeeze convolution layer’s output is done to the last convolutional layer. This transmission is initiated with a solitary convolution layer which is being tracked by 8 number of fire modules. “Bm” represents SqueezeNet model’s output. Figure 2 illustrates that the max-pooling procedure is executed in 2 steps by SqueezeNet.

SqueezeNet Training Using DMOA:

This section provides more explanation of the DMOA, which is used to train the SqueezeNet employed in this investigation. The ability of dwarf mongooses to forage is the basis for the main concept of DMOA. DMOA is a metaheuristic model that is used to solve optimization problems. For the aforementioned optimization problems, DMOA can produce and enhance a potential solution. By employing this tactic to investigate different areas of the problem search space, the dwarf monkeys are hopping from one food source to another. DMO further uses a single tuning parameter. The DMOA algorithm consists of the following phases.

(1) Initialization: The algorithmic solutions and constraints are first set up. This is the action that results in the best outcome.
(2) Fitness Measure: The Mean Squared Error (MSE) is used to determine the best answer.

$$b_{min} = \frac{1}{w}\sum_{m=1}^{w}(B_m^* - B_m)^2 \tag{1}$$

Where B*m stands for the predicted outcomes, Bm for the SqueezeNet categorized outcome, and w for the total number of samples.

(3) Alpha Group. The initial Group is Alpha. The efficacy of the entire strategy is assessed once the population has begun in which selection of Alpha female will be chosen based on the values of likelihood that are determined by the following as:

$$k = \frac{(b_{\min})_p}{\sum_{p=1}^{t}(b_{\min})_p} \tag{2}$$

In this case, bmin indicates the fitness function, and t indicates the mongoose count in k. The solution's upgrading approach is provided as:

$$s_{p+1} = s_p + \alpha_p * Q \tag{3}$$

In which, Q represents the vocalization of the lead female, and sp is the solution for this iteration's solution. The distributed random integer is represented as αp. The sleeping mount, which is determined after each loop, is given by

$$L_r = \frac{(b_{min})_{p+1} - (b_{min})_p}{\max[|(b_{min})_{p+1} - (b_{min})_p|]} \tag{4}$$

Additionally, the sleeping mound's average count is calculated as

$$\omega = \frac{\sum_{p=1}^{t} L_r}{t} \tag{5}$$

In which, the sleeping mount is indicated by Lr, and the total number of sleeping mounts is indicated by t. The DMOA algorithm moves on to the scouting phase after meeting the babysitting exchange requirement.

(4) Scout Group: This is the phase where the mongoose moves around in the best sleeping mound, and the family travels a good distance. As a result, Scout Mongoose is defined as:

$$s_{p+1} = \begin{cases} s_p - D * \alpha_p * z|s_p - \overrightarrow{S}|, if\ \omega_{p+1} > \omega_p \\ s_p + D * \alpha_p * z|s_p - \overrightarrow{S}|, otherwise \end{cases} \tag{6}$$

In this case, the value of D and the value of S can be calculated as,

$$D = \left(1 - \frac{U}{H_U}\right)^{2*\frac{U}{H_U}} \tag{7}$$

$$\vec{S} = \sum_{p=1}^{t} \frac{s_p * L_r}{s_p} \tag{8}$$

In which, z denotes the random value between (0,1). As inferior group members, babysitters are typically young adults who are intent on rousing the feminine alpha to carry out the daily hunting. The DMOA pseudocode is displayed in Algorithm 1.

(5) A Second Look at Feasibility. The solution's viability is assessed in relation to the fitness value calculation. To replace the subpar solution with the superior one iteratively, the optimal solution in this case is the one with the lowest MSE value.
(6) Finalization. The aforementioned procedures are all carried out repeatedly until the ideal outcome is reached. Algorithm 1 shows the DMOA algorithm's pseudocode.

Algorithm 1: DMOA's Pseudocode.

Initite the algorithmic constraints

While $U < H_U)\ do$

For (p=1 to k) do

Estimate the fitness of mongoose

Set the time counter

Estimate the value of alpha by equation (5)

Compute the best solution by equation (6)

Evaluate the sleeping mound using equation (7)

Evaluate the mean value of the sleeping mound using equation (8)

Compute the movement vector using equation (9)

Execute the scout mongoose for a successive solution using equation (10)

End for

$c = c + 1$

End while

Get the best solution

Source: Authors, (2026).

Classification of PDs Using FCBi-LSTMs:

FCBi-LSTMs were utilized in this paper to classify PD's. The computes fuzzy methods weights by modifying membership values in order to extract the most relevant features related to PDs. The chosen attributes from PD datasets are analyzed by CNNs and FCBi-LSTMs. Convolution layers, which make up CNNs, are fed outputs from pooling levels to convolution layers that come after them. Given their knowledge of the local perception of biological vision cells, CNNs use partial filters for convolutions, which provides considerable advantages in feature extraction. The convolution layer's represents the chosen Properties from the PD dataset is enhanced by filtering it into multiple output matrices, each with a range of (Nm+1). The CNN pooling layer serves as a method regarding lowering a matrix's dimension without sacrificing the essential connections between its elements. Average pooling layers, or pooling layers, are fed inputs from convolution layers. As an intermediate variable, the final convolution layer's output is used in the Bi-LSTM data analysis technique. Therefore, there are more applications for LSTM than only changing loop cells and adding nonlinear elements to input. Bi-directional LSTMs perform better than uni-directional LSTMs in terms of capturing structural information, and fuzzy weights are generated using Gaussian membership functions. CNN's convolution layers process the Bi-LSTMs' final outputs to diagnose Parkinson's illness. Bi LSTM and CNN processed features are integrated by multimodal factorized bilinear pooling (MFB).

IV. RESULTS AND DISCUSSION

In comparison to other methods like SVM, CNN, and FCLSTM-CNN (fuzzy convolution long short-term memory-based convolution neural networks), this section explains the experimental results that the suggested FCBi-LSTM classifier produced. Since the test sets had fewer samples, the individual occurrences that remained in the training set were used to assess the performance of LOPO CVs. The class The MIT-BIH arrhythmia database served to investigate arrhythmia recognition and classification systems through the use of MATrix LABoratory R2016a (MATLAB R2016a). The following system specifications have been used in the implementation process: A Windows 8.1 Pro 64-bit operating system, a 1TB hard drive, an Intel (R) Core™i3-4160T CPU@3.10GHz 3.09GHz processor, and 4.00 GB RAM are included.

Dataset

The Voice and Spiral dataset's results are displayed in Figures 3 and 4.

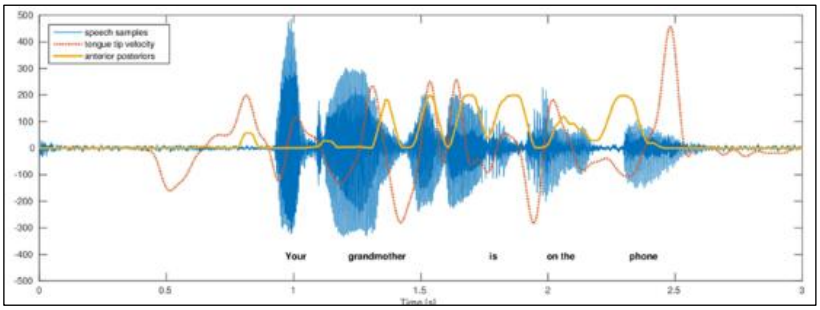


Figure 3: Voice dataset Result.
Source: Authors, (2026).

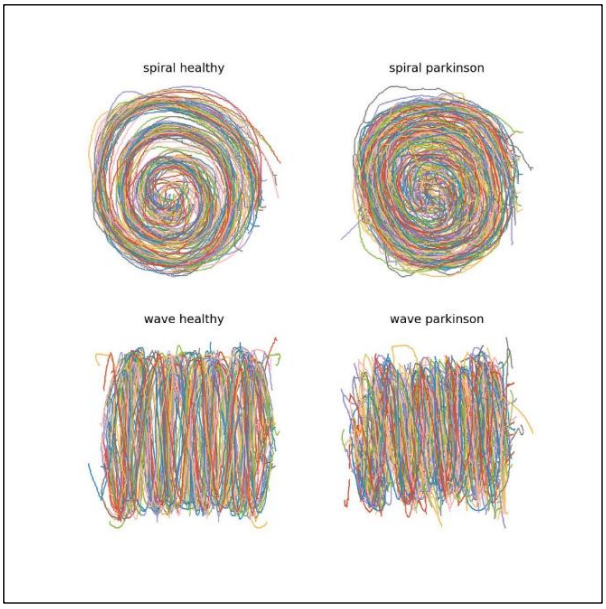


Figure 4: Spiral dataset Result.
Source: Authors, (2026).

Metrics Utilized for Evaluation

Evaluation Metrics: Evaluation measures exist to determine the predictability of classifiers. While accuracy is a commonly used criterion, conclusions drawn from data with an unbalanced class distribution may be deceptive. The effectiveness of a classifier in differentiating between classes, even when there is a class imbalance, can be assessed using assessment metrics such as MCCs and F-measure. Include the number of instances in each class that are correctly and incorrectly classified in order to enable the confusion matrix shown in in Table 1 to depict binary classification. These letters in the confusion matrix, TP, FP, TN, and FN stands for True Positive, False Positive, True Negative, and False Negative respectively. The following were calculated: recall, F-measure ,precision, accuracy and error using the formulas depending on these counts.

$$Precision = \frac{tp}{tp+fp} \tag{9}$$

$$recall = \frac{tp}{tp+fn} \tag{10}$$

$$F - measure = \frac{2*Precision*Recall}{precision+recall} \tag{11}$$

$$Accuracy = \frac{tp+tn}{tp+tn+fp+fn} \tag{12}$$

$$error = 100 - Accuracy \tag{13}$$

Another statistic that can be used to assess the reliability of binary classifications is the MCC, which accounts for the TP, FP, FN, and TN Counts. Generally speaking, it is seen as a equilibrium measure that may be used even when there is an uneven distribution of classes. The correlation coefficients between expected and actual occurrences are simply called MCCs, and they have a range of -1 to +1.The Score +1 represents perfect predictions between actual labeling and forecast while score -1 shows differences between these two variables.

Table 1: Confusion matrix for two-class classification.

Actual/predicted as	Negative	Positive
Positive	FN	TP
Negative	TN	FP

Source: Authors, (2026).

Comparison of Results:

Three different feature types were used in connection to accuracy, error, F-measure, and MCC in the experimental evaluations of classifiers. The accuracy rate of MFCCs, Wavelets, and Concated features in the CNN combination was 94.1752%, whereas the accuracy rate of MFCCs, Wavelets, and Concated features in the SVM combination was 88.1294%. The accuracy value of TQWT+MFCC+Wavelet is 93.047%, whereas the accuracy value of TQWT+Wavelet+Concat is 93.0854%. Similarly, the accuracy value of TQWT+MFCC+Concat, whereas the accuracy value of MFCC+Wavelet+Concat is found to be 95.1557% for FCLSTM-CNN. By using MFCCs+Wavelets+Concated combinations, the proposed FCBi-WLSTM classifier Reached the best accuracy scores of 98.7720% (F-measure rate of 98.5010% and 71.400% for MCC). The results of the TQWT+MFCC+Wavelet combination were 98.3100%, 96.6381%, 74.300%, and 3.3619%, in that order.

The highest results of f-measures, accuracies, MCCs, and errors were likewise produced by these feature set combinations. These results are displayed in Figures 5-8. At the first feature level combination, the F-measure values of CNN is 85.86%, SVM is 82.91%, and FCLSTM-CNN is 94.22%. With the first level feature combination the proposed FCBi-LSTM achieved an F-measure score of 98.31%. Figure 5 compares the F-measure outcomes of four distinct feature-level combinations using different classifiers.

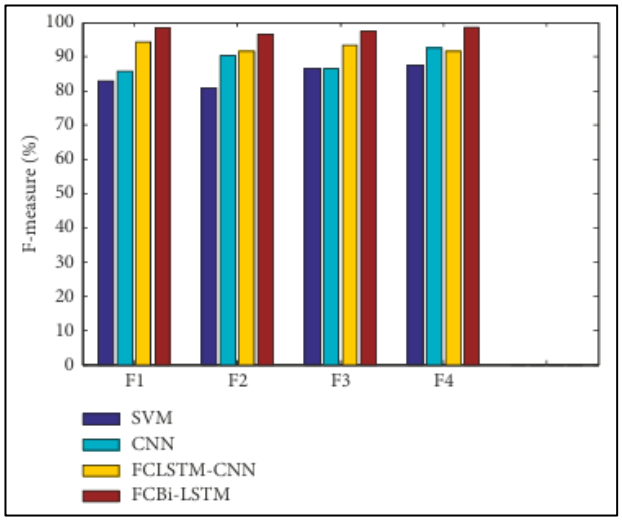


Figure 5: F-measure results comparing classifiers to feature level combinations.
Source: Authors, (2026).

From Figure 6, it is clearly seen that x-axis accuracy is measured with feature-level combinations on classifiers. Compared to SVM, FCLSTM-CNN, and CNN which obtained final feature level combinations with accuracy of 88.1294%, 94.175%, and 95.1557%, respectively, FCBi-LSTM obtained 98.772% accuracy.

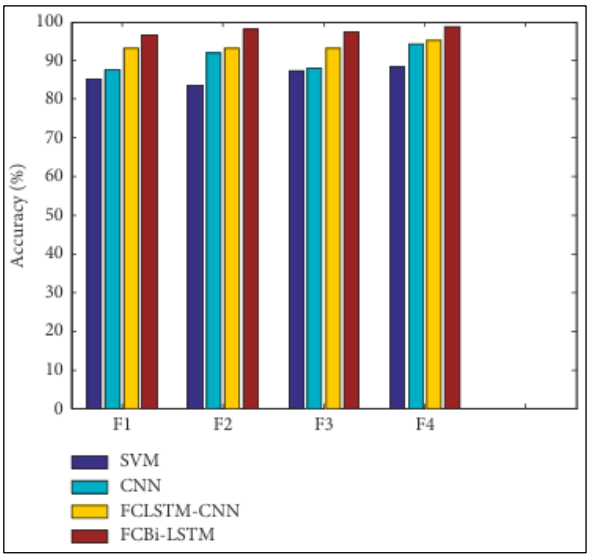


Figure 6: Feature level combination accuracy results versus classifiers.
Source: Authors, (2026).

Comparisons of classifiers with four different feature-level combinations are shown in Figure 7. Figure 4 illustrates that the final feature level combinations for SVM, CNN, and FCLSTM-CNN displayed increased error values of 11.8706 %, 5.8248 %, and 4.8443 %, respectively, but the FCBi-LSTM findings generated lower error values of 1.2280 %. The results presented in Figure 7 contrast classifier performances using four different feature level combinations. Figure 4 shows FCBi-LSTM yielded lower error values of 1.2280 % in its results. However, the final feature level combinations for CNN exhibited the error value of 5.8248 %, whereas SVM exhibited the error value of 11.8706 %, and FCLSTM-CNN exhibited the error value of 4.8443 %.

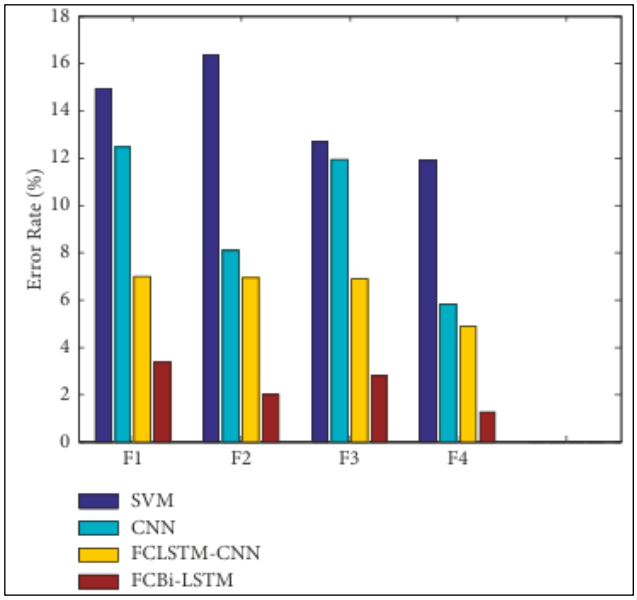


Figure 7: Feature level combination error results compared to classifiers.
Source: Authors, (2026).

A noticeably higher result of 74.30 % is obtained for the developed technique and 57.2007% for CNN, 56.20 % for SVM, and 67.6669 % for FCLSTM CNN classifiers, respectively for the first feature based combination when Figure 8 compared the MCC results, the TQWT+MFCC+ Concat Attribute set. The suggested approach produces better MCC results for all classifiers since it makes advantage of feature selection.

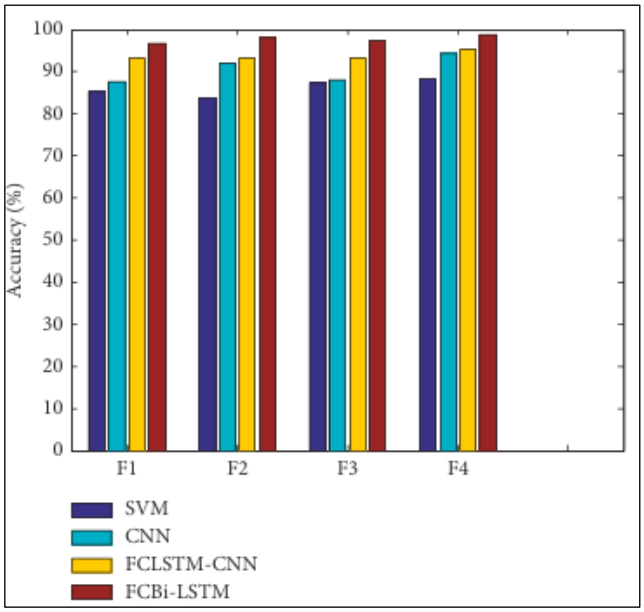


Figure 8: Feature level combination vs. classifiers MCC outcomes.
Source: Authors, (2026).

V. CONCLUSIONS

The second most common neurological condition, PD significantly impairs quality of life, is incurable, and has no known cure. Using neuro-protective and early treatment strategies for PD requires an early diagnosis. In this work, a multiclass classification problem for PD analysis is presented using a feature selection method. FCBi-LSTM and SqueezeNet with DMOA are offered for PD analysis. After that, PD is diagnosed using the FCBi-LSTM classifier. Medical practitioners may be able to better aid PD patients in their recovery and recuperation thanks to this dependable and precise model that accurately detects the illness in its early stages. Precision, recall, accuracy, F-measure, MCC, and F-measure were used to gauge each algorithm's efficacy in the classification process when DL libraries were being evaluated. The accuracy of the suggested model is evident when comparing the results with those of other approaches that are currently in use. Engineering and medicine have a bright future thanks to deep learning. The objective of upcoming work is to creatively expand on previous findings. Multiple data types can enter the network at once thanks to the suggested CNN's Simultaneous convolution layers. Using multimodal data, It allows us to categorize Parkinson's illness. In addition, the writers want to apply further deep learning algorithms to the classification process.

VI. ACKNOWLEDGMENTS

The author would like to appreciate the effort of the editors and reviewers.

VII. REFERENCES

[1] Z. Wang, B. Hu, W. Zhou, M. Xu, and D. Wang, “Hopf bifurcation mechanism analysis in an improved cortex-basal ganglia network with distributed delays: An application to PD,” Chaos Solitons Fractals, vol. 166, p. 113022, 2023.

[2] A. Dovonou, C. Bolduc, V. S. Linan, C. Gora, M. R. Peralta, and M. Levesque, “Animal models of PD: Bridging the gap between disease hallmarks and research questions,” Transl. Neurodegener., vol. 12, p. 36, 2023.

[3] P. Wilmshurst, S. Bewley, and P. Murray, “Hyperbaric oxygen therapy for the treatment of long COVID,” Clin. Med., vol. 23, pp. 99–100, 2023.

[4] P. Mensah-Kane and N. Sumien, “The potential of hyperbaric oxygen as a therapy for neurodegenerative diseases,” GeroScience, vol. 45, pp. 747–756, 2023.

[5] P. Paplomatas, M. G. Krokidis, P. Vlamos, and A. G. Vrahatis, “An ensemble feature selection approach for analysis and modeling of transcriptome data in Alzheimer’s disease,” Appl. Sci., vol. 13, p. 2353, 2023.

[6] World Health Organization, “Parkinson disease,” 2023. [Online]. Available: https://www.who.int/news-room/fact-sheets/detail/parkinson-disease. Accessed: Jan. 31, 2023.

[7] D. Larson and T. Simuni, “New dopaminergic therapies for PD motor complications,” Neuropharmacology, vol. 204, p. 108869, 2022.

[8] B. F. Mogharbel, M. A. Cardoso, A. C. Irioda, P. E. F. Stricker, R. C. Slompo, J. M. Appel, N. B. de Oliveira, M. C. Perussolo, C. S. Sacaki, N. N. da Rosa, et al., “Biodegradable nanoparticles loaded with levodopa and curcumin for treatment of PD,” Molecules, vol. 27, p. 2811, 2022.

[9] L. Smith and A. H. V. Schapira, “GBA variants and Parkinson disease: Mechanisms and treatments,” Cells, vol. 11, p. 1261, 2022.

[10] D. K. Khatri, K. Preeti, S. Tonape, S. Bhattacharjee, M. Patel, S. Shah, P. K. Singh, S. Srivastav, D. Gugulothu, L. Vora, et al., “Biotechnological advances for nose to brain delivery of therapeutics to improve the Parkinson therapy,” Curr. Neuropharmacol., vol. 21, pp. 493–516, 2022.

[11] Y. Su, J. Liu, S. Tan, W. Liu, R. Wang, and C. Chen, “PLGA sustained-release microspheres loaded with an insoluble small-molecule drug: Microfluidic-based preparation, optimization, characterization, and evaluation in vitro and in vivo,” Drug Deliv., vol. 29, pp. 1437–1446, 2022.

[12] A. C. Correia, A. R. Monteiro, R. Silva, J. N. Moreira, J. M. Sousa Lobo, and A. C. Silva, “Lipid nanoparticles strategies to modify pharmacokinetics of central nervous system targeting drugs: Crossing or circumventing the blood–brain barrier to manage neurological disorders,” Adv. Drug Deliv. Rev., vol. 189, p. 114485, 2022.

[13] Z. L. Shi, Z. Y. Fan, H. Zhang, S. T. Li, H. Yuan, and J. H. Tong, “Localized delivery of brain-derived neurotrophic factor from PLGA microspheres promotes peripheral nerve regeneration in rats,” J. Orthop. Surg. Res., vol. 17, p. 172, 2022.

[14] K. Saalwächter, “Grand challenges in polymers,” Front. Soft Matter, vol. 2, p. 18, 2022.

[15] R. Deb, S. An, G. Bhat, H. Shill, and U. Y. Ogras, “A systematic survey of research trends in technology usage for PD,” Sensors, vol. 22, p. 5491, 2022.

[16] N. E. Allen, C. G. Canning, L. R. S. Almeida, B. R. Bloem, S. H. Keus, N. Löfgren, A. Nieuwboer, G. S. Verheyden, T. P. Yamato, and C. Sherrington, “Interventions for preventing falls in PD,” Cochrane Database Syst. Rev., vol. 6, pp. 12–38, 2022.

[17] W. Liu, T. Tung, C. Zhang, and L. Shi, “Systematic review for the prevention and management of falls and fear of falling in patients with PD,” Brain Behav., vol. 12, p. e2690, 2022.

[18] R. Vitorio, M. Mancini, P. Carlson-Kuhta, F. B. Horak, and V. V. Shah, “Should we use both clinical and mobility measures to identify fallers in PD?” Park. Relat. Disord., vol. 106, p. 105235, 2023.

[19] D. P. Lima, S. B. De-Almeida, J. D. C. Bonfadini, A. H. S. Carneiro, J. R. G. de Luna, M. S. de Alencar, A. B. Viana-Júnior, P. G. B. Rodrigues, I. D. S. Pereira, J. D. S. Roriz-Filho, et al., “Falls in PD: The impact of disease progression, treatment, and motor complications,” Dement. Neuropsychol., vol. 16, pp. 153–161, 2022.

[20] E. Maranesi, E. Casoni, R. Baldoni, I. Barboni, N. Rinaldi, B. Tramontana, G. Amabili, M. Benadduci, F. Barbarossa, R. Luzi, et al., “The effect of non-immersive virtual reality exergames versus traditional physiotherapy in PD older patients: Preliminary results from a randomized-controlled trial,” Int. J. Environ. Res. Public Health, vol. 19, p. 14818, 2022.

Journal of Engineering and Technology for Industrial Applications

ITEGAM-JETIA

Manaus, v.12 n.60, p.1171-1179. July/August, 2026.
DOI: https://doi.org/10.5935/jetia.v12i60.4035

ISSN ONLINE: 2447-0228

RESEARCH ARTICLE OPEN ACCESS

PERFORMANCE COMPARISON OF DEEP LEARNING MODELS FOR SHORT TERM LOAD FORECASTING

Jaya Christa Sargunar Thomas*[1] and Krishna Veni Kaliappan Sivakumar[2]

[1, 2]Department of Electrical and Electronics Engineering, Mepco Schlenk Engineering College, Sivakasi, Tamilnadu, India.

[1]https://orcid.org/0000-0001-9033-4407, [2]https://orcid.org/0000-0003-2186-2534

Email:*stchrista@mepcoeng.ac.in, krishnaveni.ks@mepcoeng.ac.in

ARTICLE INFO

Article History
Received: March 11, 2026
Reviewed: April 11, 2026
Accepted: July 11, 2026
Published: August 31, 2026

Keywords:
Short term load forecasting, Convolutional neural network, Long short term memory, Bi-directional long short term-memory.

ABSTRACT

In today's power industry, the ever-changing load environment makes accurate load forecasts even more important than ever. Even, day ahead load forecasting is crucial for the successful and efficient operation of the grid. With the absence of good reliable forecasts of daily load fluctuations, systems within the grid can become overloaded, resulting in a failure of the system, thus establishing the need for sound forecasting methods. As a solution to this challenge, different types of deep learning algorithms namely, Long Short-Term Memory, Bidirectional Long Short-Term Memory, Convolutional Neural Network based LSTM, Convolutional Neural Network based BiLSTM are applied for short-term load forecasting in this paper. The efficacy of the various deep learning techniques for short term load prediction is compared. The technique which produces the least value of root mean squared error between real and estimated load, is the most preferred one. The comparative analysis shows that Convolutional Neural Network based BiLSTM technique is a better option for short term load forecasting.

Copyright ©2026 by authors and Galileo Institute of Technology and Education of the Amazon (ITEGAM). This work is licensed under the Creative Commons Attribution International License (CC BY 4.0).

I. INTRODUCTION

A nation's economy mainly depends on the power sector. To improve the nation's economy, power sector must be improved. If power system is stable, then the social stability, national security, economic growth and the overall quality of life of people is stable for a nation. Consumers' expectation from the power system is steadily growing and the power management in the grid is also improving with time. Every Power dispatch center needs load forecasting data for the better load distribution. The power industries must improve their abilities to produce power efficiently to manage the nation's technological advancements and economic improvements [1]. The growing smart grid faces significant challenges in energy management because of the unpredictability of power supply from renewable energy generation and also the power demand. Accurately projecting future generation and load is essential for effective power management [1]. Any significant deviation in the forecasts could result in technical and economic challenges. Furthermore, in deregulated power system markets, the accuracy of forecasted demand is crucial as all participants, from energy producers to customers, rely directly on this information [2]. Load forecasting has drawn a lot of attention from academia and industry due to the use of sophisticated data acquisition systems (like smart meters and Advanced Metering Infrastructure meters, as well as the development of data analytic methods and artificial intelligence. Numerous sophisticated data analysis methods have been developed and are widely used in modern life. Data analytics are crucial to the daily planning and operation of power systems. Predictive models are being used to analyze the demand pattern, with specific electrical generators designated to meet this demand. Load forecasting has different types, depending on the forecasting time horizon. Medium and long-term load prediction cover periods of two weeks and three years, respectively, whereas short-term load forecasting covers intervals of several minutes to one week [3]. Several factors specifically daily, weekly and yearly cycles of demand as well as unpredictable electricity consumption pattern of consumers' appliances contribute to the difficulty of load forecasting. Load also displays a strong correlation with environmental variables like temperature, humidity, solar irradiance, wind speed, etc.

A direct method for forecasting net-load and an indirect method for forecasting gross load and renewable generation separately are discussed in [4]. The findings show that the forecast accuracy is higher in the direct approach. This research also aims to forecast the net load in a power system.

I.1 LITERATURE REVIEW

While Classical models and forecasting methods typically are implemented using ARMA, SARIMA, and ARMAX modelling techniques, in past few years Recurrent Neural Networks (RNN) and Artificial Neural Networks have also received some recognition for possible applications in forecasting [5]. As a result of these advancements in technology, developers have begun testing and using a variety of new models. These new models use Deep Learning techniques to identify key information within the load profile [6]. Although RNNs provide a number of benefits in modelling load time series data, they struggle to model long term dependencies accurately because of their architecture. To solve this issue, developers created Long Short-Term Memory Networks (LSTMs) [7]. Although the base architecture of an LSTM is similar to that of a standard RNN, it incorporates memory blocks to store information. The memory blocks contain both Subnets and Recurrent Connection units, as opposed to the Summation units that are used by the buried layers of RNNs. LSTMs have consistently provided superior performance for solving industrial problems involving time series data compared to RNNs. Through the incorporation of memory units, LSTMs have consistently provided superior results for modelling extremely long-term dependencies in multiple real-world sectors [8]. Long-term memory tasks such as predicting the secondary structure of proteins and context-free grammar were successfully handled by LSTM models [9]. Although LSTM can learn to identify long-term dependencies for sequential data, it is limited to working with historical data; Bi-directional LSTM (Bi-LSTM) is able to utilize both past and upcoming context to produce highly exact estimations. Therefore, when completing tasks where bidirectional information is necessary such as speech recognition or natural language processing, Bi-LSTM has a distinct advantage over LSTM. Whether LSTM or Bi-LSTM should be used in a time series forecasting application will largely depend on how the forecast will be used and on the data being analyzed [10].

By using Bi-LSTM, an analyst can represent complicated patterns and relationships in the data much more efficiently than with unidirectional LSTM operating only in one direction. Combining Empirical Mode Decomposition with the Bi-LSTM approach allows for highly accurate forecasting of both short-term and long-term dependencies of electrical load. The advantages of the new model are evident when considering that it produces more accurate short-term load forecasts than any of the previous models have produced; thus, it is very likely to be an effective method of forecasting energy consumption [11]. Recently, studies investigating the benefit of Convolutional Neural Networks (CNN) for short-term load prediction are conducted. In contrast to LSTM networks, temporal CNN could produce a forecasting model that was both effective and dependable. In this paper, it is suggested using an integrated CNN-LSTM model to predict the future load. Lastly, a unique parallel LSTM-CNN network that was trained for both CNN and LSTM was developed to resolve the short term load estimation problem in smart grids. Results proved that the LSTM-CNN demonstrated good performance [12]. CNN-Bi-LSTM is another model used for load forecasting. CNN handles the missing data, while Bi-LSTM is used for the long term load forecasting. By combining both the models, the results are better for load forecasting for discontinuous dataset [13].

I.2 OBJECTIVES OF THE RESEARCH

By looking into the literature, a detailed study comparing the various deep learning models for short term load estimation is missing. Hence, in this paper, an analysis is conducted on the four prominent deep learning models - LSTM, Bi-LSTM, CNN-LSTM, and CNN-Bi-LSTM, to determine the best technique for load estimation in accordance with the evaluation of results [14]. The primary goal is to identify the optimal approach for load estimation in the power system by assessing the deviation between the real load and the estimated load. In this paper, an aggregated dataset of electrical load profiles from New England, USA is utilized which is not used in the above mentioned papers. Program code for the deep learning models is created using Python.

II. DEEP LEARNING NETWORK ARCHITECTURES

II.1 LSTM ARCHITECTURE

Traditional RNNs have problems in capturing long-term dependencies because of their single hidden state that persists over time. LSTM networks address the issue with long-term storage found in traditional RNN models through a special component called the memory cell which has the ability to hold on information for much longer duration of time. Therefore, LSTM models are excellent at learning temporal relationships over many different time periods and are commonly used in areas such as voice-to-text transcription, translating between different languages and predicting future values based on the data available. Figure 1 shows LSTM model's architecture. In the overall structure of an LSTM model, there are three primary areas known as gates. The input gate is where the new piece of information enters; the forget gate is the place to remove data that is no longer find useful; and the output gate is the point where the information needed is taken out from the memory cell. By selectively controlling the retention and discarding of information at each step, LSTM networks effectively manage long-term dependencies and facilitate strong learning processes [15].

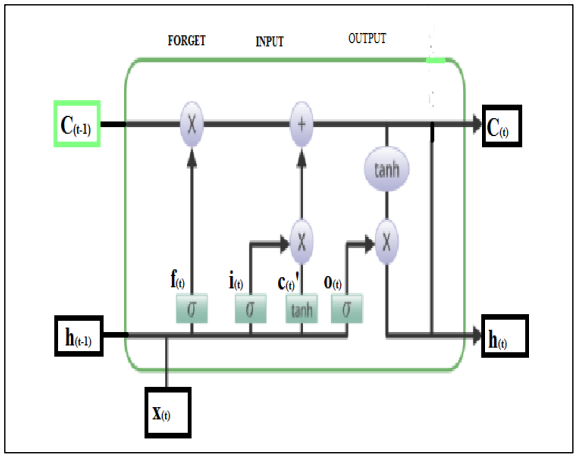


Figure 1: Architecture of LSTM.
Source: Authors, (2026).

II.2 BI-LSTM ARCHITECTURE

Figure 2 demonstrates the architecture of Bi-LSTM model which is a type of sequential model consisting of two LSTM layers: one for handling sequences in forward direction and another for treating sequences in reverse direction. The outputs of both LSTMs are converted to a probability vector and combined to create the final output [9]. Bi-LSTMs are often used when performing Natural Language Processing tasks because they allow the model to have a greater understanding of the complex interrelations between elements of a sequence by using the context to infer the meaning of certain elements.

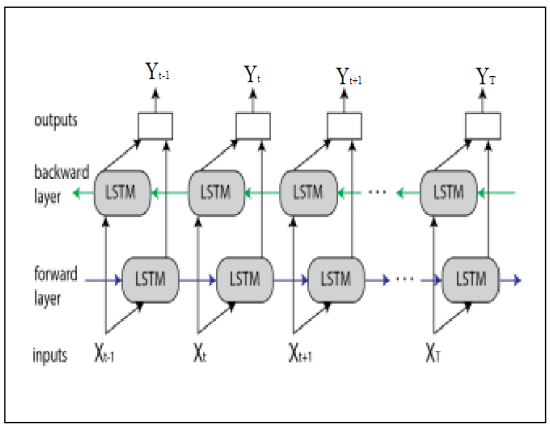


Figure 2: Architecture of Bi-LSTM.
Source: Authors, (2026).

II.3 CNN-LSTM ARCHITECTURE

Combining CNN with LSTM creates a fusion network for Deep Learning that can analyze different types of sequential information. It uses the benefits of both CNN and LSTM networks to learn both spatial and temporal characteristics in sequential data, creating an effective solution for tasks related to video classification, action recognition and spatiotemporal forecasting. In a typical CNN-LSTM architecture illustrated in Figure 3, the role of CNN is to perform the extraction of the spatial features of the data, while the role of the LSTM is to model the temporal dependencies and sequential nature of the data. CNN networks are particularly good at extracting information such as feature maps or key frames using their various convolutional and pooling layers. The CNN network produces a series of spatial feature vectors, which are then fed to the LSTM network to learn the temporal dependencies present inside the data. LSTMs are especially effective at modeling long-term dependence on sequential data since they maintain a memory cell to store and update the values of previous time steps. Therefore, if CNN is employed to pull out spatial peculiarities, and LSTM is used to simulate temporal dependencies of sequential data, then the combined model of CNN-LSTM can learn how the spatial feature vectors relate temporally. The combination of CNNs with LSTMs provides an open way for CNN-LSTM to process and understand complex and sequential information. Because an image or video may be viewed as a sequence of images overtime, this makes it very useful for a variety of applications such as video understanding, action recognition or forecasting time series data [11]. The CNN-LSTM architecture provides a method to analyze both spatial features and temporal features at the same time, making the architecture flexible and very effective at understanding the context of an input sequence as well as recognizing patterns and relationships between elements within that sequence.

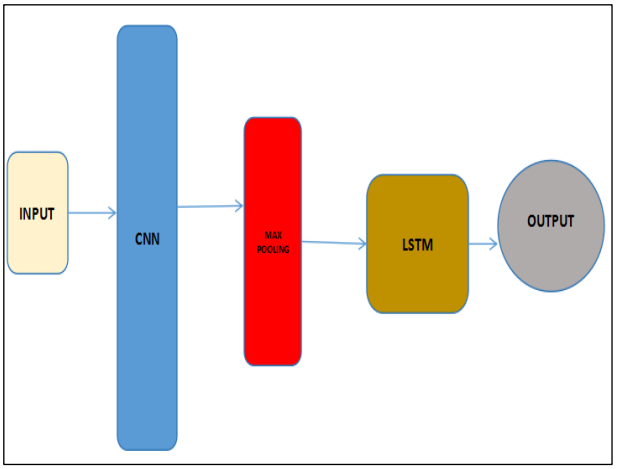


Figure 3: Architecture of CNN-LSTM.
Source: Authors, (2026).

II.4 CNN-BI-LSTM ARCHITECTURE

CNN-BiLSTM is a network architecture that integrates CNN with Bi-LSTM networks demonstrated in Figure 4. By utilizing the information from CNN's features before inputting them into Bi-LSTMs, they benefit from the existing knowledge of how to process inputs. Initially, the dataset was segmented into load profiles containing load values for each day (i.e., load profiles for a 24 hour period) and these profiles were then combined to create a single input for the One Dimensional (1D) CNN layer of the architecture. During the extraction of features from the load profile, the 1D CNN layer used 64 filters with a kernel size (i.e., width and height of the filter) of 3 by 1 and a default stride of 1 when generating a feature vector for each input load profile. After extracting the features from the input load profile data, those raw feature map data are still subjected to max-pooling which decreases the dimensionality of the features but also, likely, loses some of the important aspects of the data; therefore, this loss of important information may account for the decrease in accuracy experienced by the Bi-LSTM networks [12].

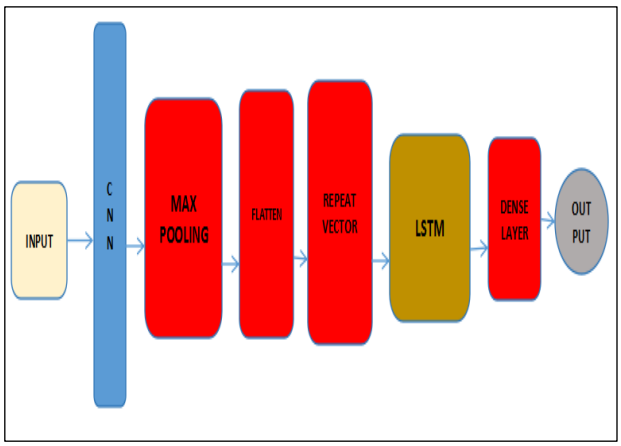


Figure 4: Architecture of CNN-Bi-LSTM.
Source: Authors, (2026).

The feature vector output from the extraction layer of the network will then feed into the Bi-LSTM networks to become the sequential load demand forecasts for the succeeding day's load profile. The fully-connected layer of the network will also include rectified linear unit activation functions for use when creating forecast load profiles, however, the CNN-LSTM versions of the network will only utilize standard, one-way directed LSTM networks for the sequential time series forecasts.

III. METHODOLOGY

III.1 DATASET PREPARATION

The data used in this research comes from aggregated electricity usage profiles in the New England Region in the United States [16]. This dataset used consists of hourly (60 minute) data for active power beginning from January 2019 to January 2024. As part of load forecasting, this study focuses solely on active power measurements. Additionally, as presented in Table 1, the data is classified according to time into training and test sets, which are created using the provided timestamps. In order to prepare the data for use with the models, min/max normalization will be applied to the dataset based on the equation (1).

$$X_{norm} = (X - X_{min}) / (X_{max} - X_{min}) \quad (1)$$

III.2 TRAINING AND TESTING

The dataset used in this study is made up of total load, which was first divided into training and test dataset. The training dataset is then utilized to build up various neural network architectures: LSTM, Bi-LSTM, CNN-LSTM, and CNN-Bi-LSTM; with the test dataset being specifically used to assess the model's efficacy. 70% of data are utilized for training the models and 30% for testing which is shown in Table 1.

Table 1: Data division into training and testing set.

Data Description	Starting date	Ending date
Training Set	06/01/2019	06/07/2022
Test Set	07/07/2022	09/01/2024

Source: Authors, (2026).

Before being passed onto the model during the actual training phase, the training dataset is normalised. The model has been tasked with predicting the demand for the next 24 hours in accordance with the previous history of data [17]. The time window will be moved forward by 1 hour, from the previous hour, during each iteration (1 hour), until all data entries in the dataset are used to train the model. In order to achieve optimal results, increased training set size and well-tuned parameters (Batch Size, Number of Cells, Number of Layers) are helpful. When the model has been trained, a walk-forward testing method can be used to assess the technique's efficacy. To evaluate the performance of the trained model, Root Mean Square Error (RMSE), Mean Absolute Error (MAE) and Mean Absolute Percentage Error (MAPE) are the metrics adopted. RMSE is given by equation (2).

$$RMSE = \sqrt{\frac{\sum_{i=1}^{n}(P_i - O_i)^2}{n}} \tag{2}$$

In this context, 'n' denotes total number of load data within the 24-hour period, where P_i denotes the real load at the 'i^{th}' hour and O_i signifies the estimated load at the 'i^{th}' hour [18]. MAE is the mean absolute deviations between estimated and actual loads. MAPE is the mean absolute percentage deviation between estimated and real loads.

IV. RESULTS AND DISCUSSION

During the testing phase, load is forecasted for the testing period day by day from 07/07/2022 to 09/01/2024, with load forecasted for one day at a time. Figure 5 depicts the plot of actual versus predicted load by all the models, over a 24-hour period for one such testing day which is 4th November 2023. The performance of each model is discussed below.

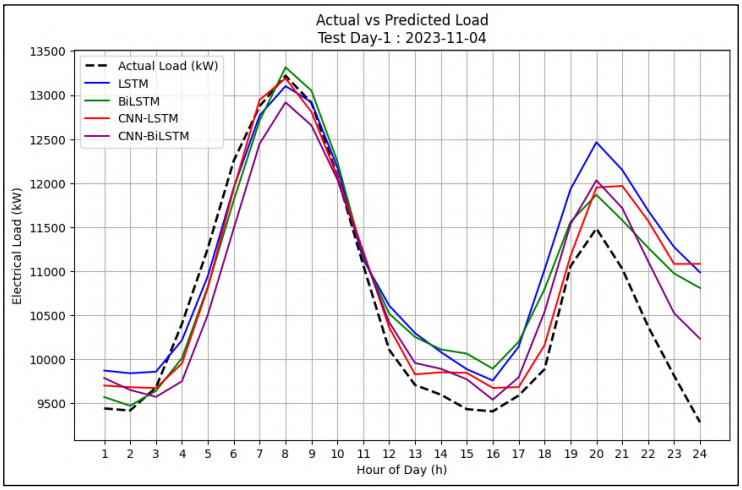


Figure 5: Real Vs forecasted load by all the models.
Source: Authors, (2026).

IV.1 LSTM BASED LOAD FORECASTING

Figure 6 depicts the plot of actual versus predicted load by LSTM model over a 24-hour period for the above mentioned testing day. Figure 7 displays an hourly RMSE plot that compares the real load with the forecasted load. Lower RMSE values indicate more precise estimations. The LSTM forecast method achieves an average daily RMSE score of 0.060051 kW considering all the test days.

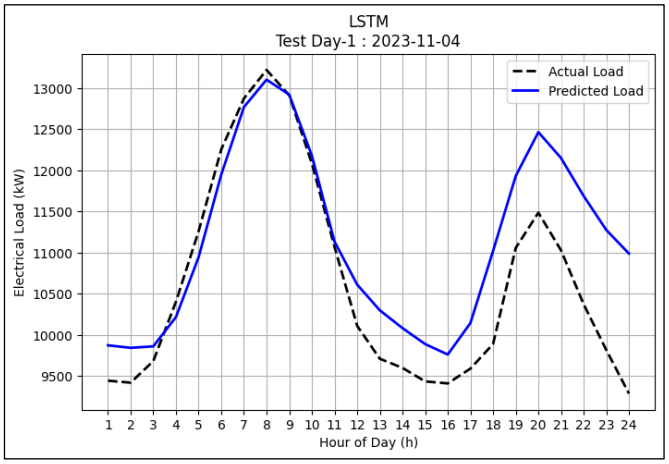


Figure 6: Real Vs forecasted load by LSTM.
Source: Authors, (2026).

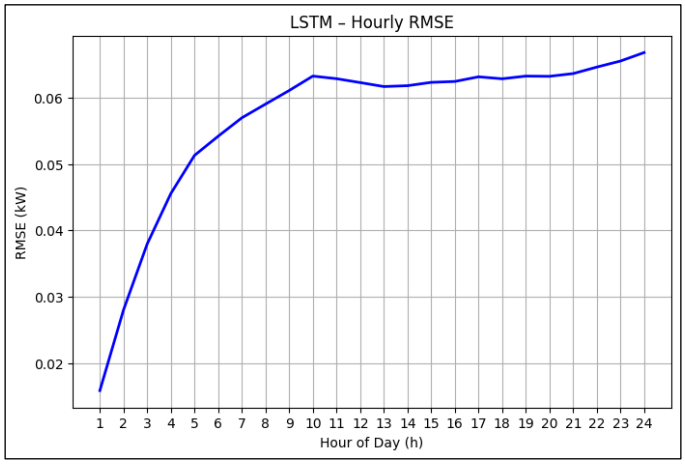


Figure 7: Hourly RMSE values for LSTM networks.
Source: Authors, (2026).

Figure 8 shows the plot between training and validation loss which shows that LSTM model is a good fit model and it converges in 47th epoch.

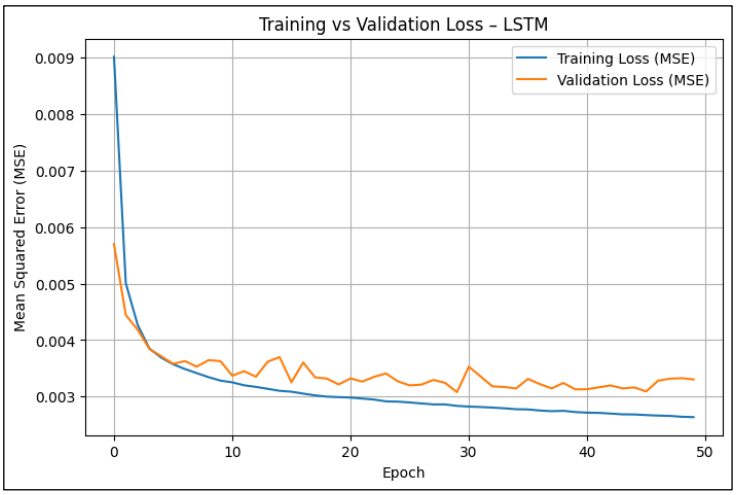


Figure 8: Training vs Validation loss for LSTM model.
Source: Authors, (2026).

IV.2 BI-LSTM BASED LOAD FORECASTING

Figure 9 illustrates the plot of actual versus predicted load over a 24-hour period by Bi-LSTM. Figure 10 showcases an hourly RMSE plot for the same test day. The BiLSTM forecast method achieves an average daily RMSE score of 0.060781 kW.

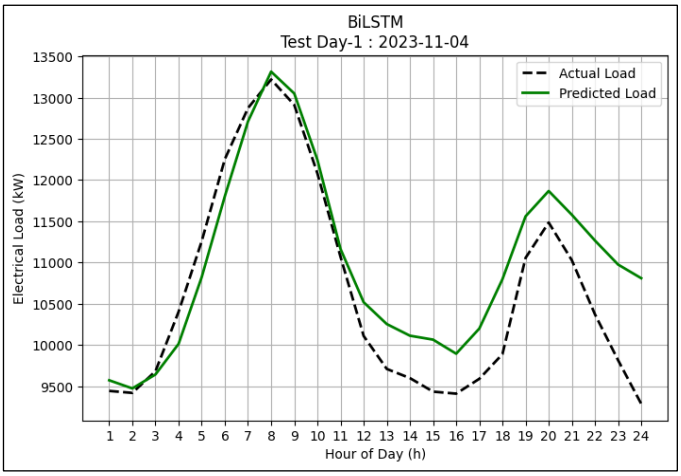


Figure 9: Real Vs forecasted load by Bi-LSTM.
Source: Authors, (2026).

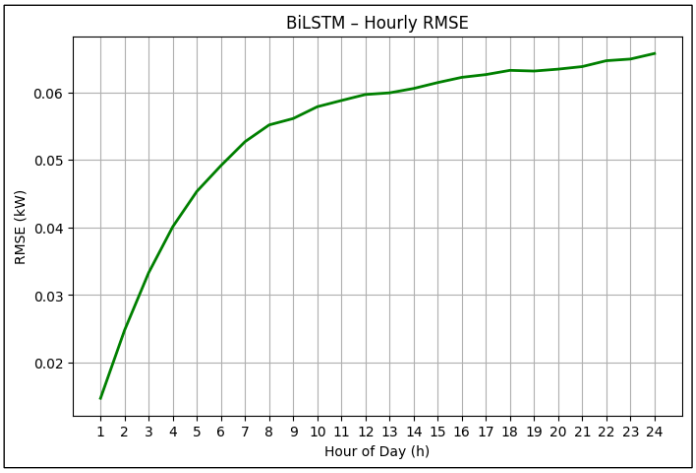


Figure 10: Hourly RMSE values for Bi-LSTM networks.
Source: Authors, (2026).

Figure 11 shows the plot between training and validation loss which shows that BiLSTM model is another good fit model and it converges in 49th epoch.

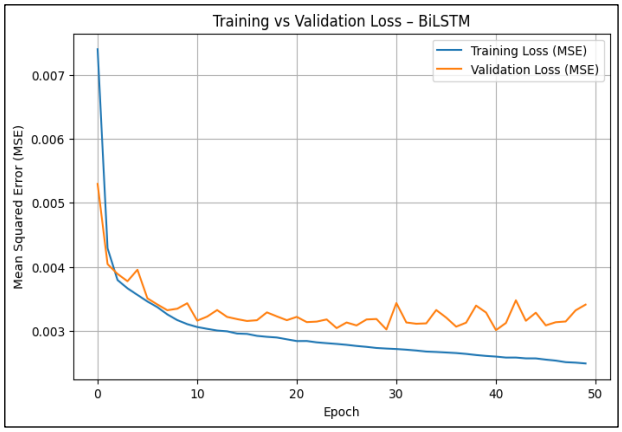


Figure 11: Training vs Validation loss for BiLSTM model.
Source: Authors, (2026).

IV.3 CNN-LSTM BASED LOAD FORECASTING

Figure 12 displays the plot of actual versus predicted load over a 24-hour period by CNN-LSTM model. Figure 13 presents an hourly RMSE plot comparing the actual and predicted load demand. The CNN-LSTM forecast method achieves an average daily RMSE score of 0.061192 kW.

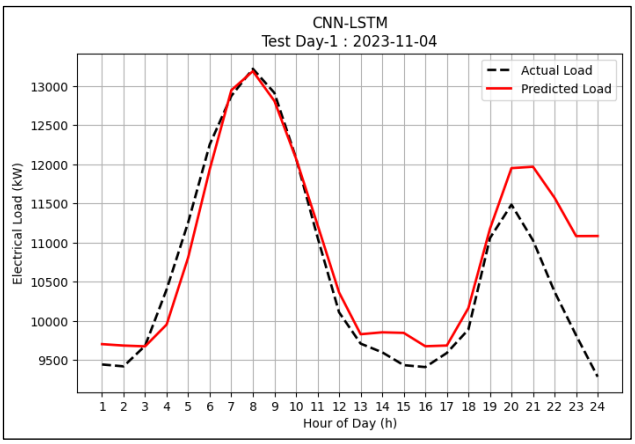


Figure 12: Real Vs forecasted load by CNN-LSTM.
Source: Authors, (2026).

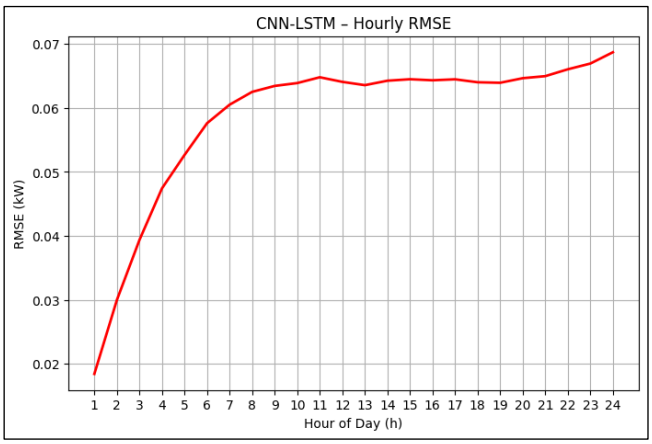


Figure 13: Hourly RMSE values for CNN-LSTM network.
Source: Authors, (2026).

Figure 14 shows the plot between training and validation loss which shows that CNN-LSTM model is also a good fit model and it converges in 49th epoch.

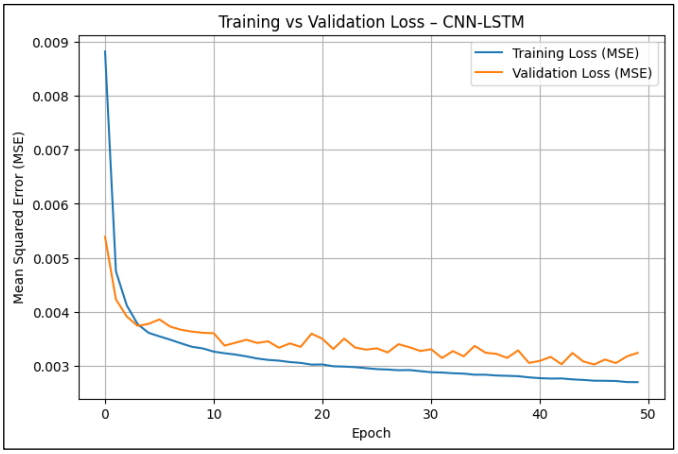


Figure 14: Training vs Validation loss for CNN-LSTM model.
Source: Authors, (2026).

IV.4 CNN-BiLSTM BASED LOAD FORECASTING

Figure 15 illustrates the plot of actual versus predicted load over a 24-hour period for CNN-BiLSTM model. Figure 16 depicts an hourly RMSE plot that showcases the contrast between the actual and predicted load demand. The CNN-BiLSTM algorithm brings about an average daily RMSE result of 0.058449 kW.

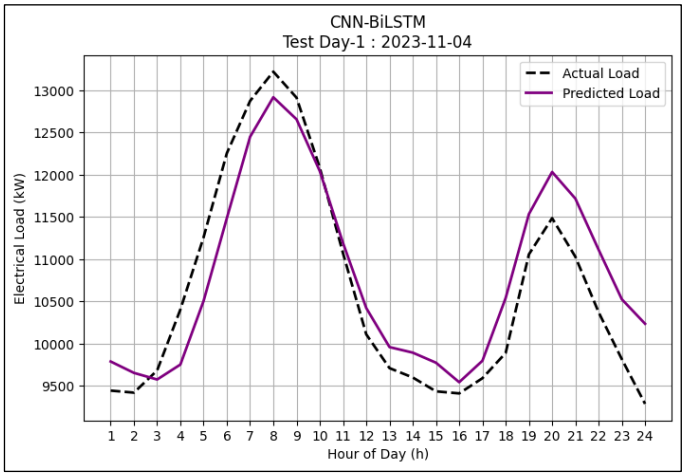


Figure 15: Real Vs forecasted load for CNN-BiLSTM.
Source: Authors, (2026).

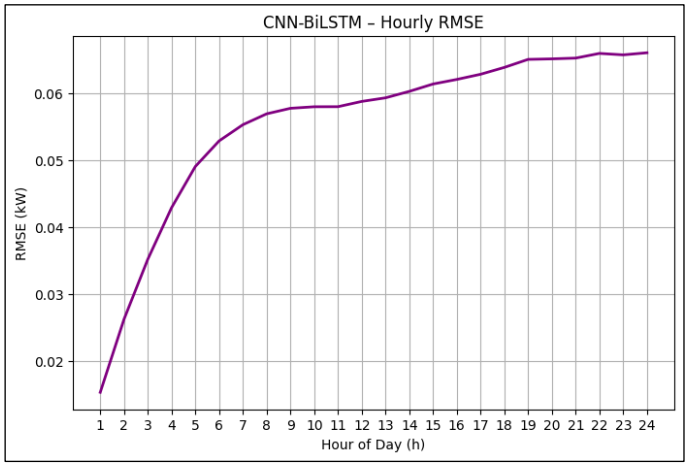


Figure 16: Hourly RMSE values for CNN-BiLSTM network.
Source: Authors, (2026).

Figure 17 shows the plot between training and validation loss which shows that CNN-BiLSTM model is a good fit model and it converges in 49th epoch.

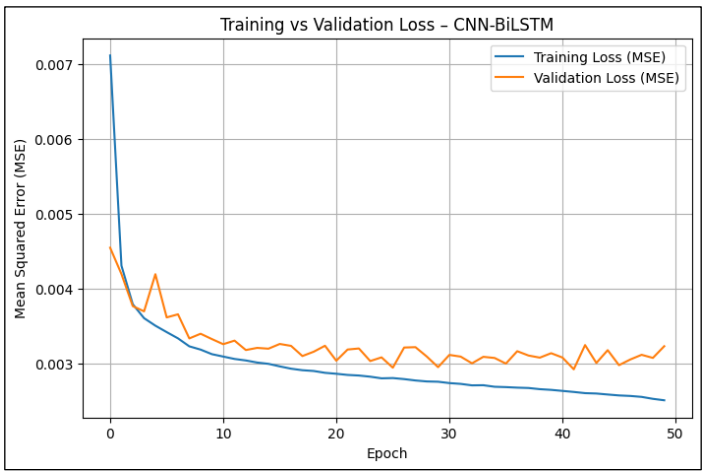


Figure 17: Training vs Validation loss for CNN-BiLSTM model.
Source: Authors, (2026).

IV.5 COMPARISON OF RESULTS

The average RMSE values, MAE values and MAPE % for the different models are presented in Table 2.

Table 2: Prediction error for various algorithms.

Algorithms	RMSE (kW)	MAE (kW)	MAPE (%)
LSTM	0.060051	0.043350	20.883416
BiLSTM	0.060781	0.043708	20.948451
CNN-LSTM	0.061192	0.044336	21.759486
CNN-BiLSTM	0.058449	0.042286	20.667672

Source: Authors, (2026).

According to the results shown in Table 2, the CNN-BiLSTM model exhibits the least RMSE, MAE values and MAPE percentage in comparison to the other techniques. The CNN-BiLSTM model's ability to extract features effectively and to process data bidirectionally, contributes to more valid estimations. For load forecasting in regions like New England, the CNN-BiLSTM model stands out as the best model based on its performance.

V. CONCLUSIONS

Due to the need for sound load forecasting methods for the power industry, this research paper deals with the application of four deep learning algorithms namely, LSTM, BiLSTM, CNN-LSTM, CNN-BiLSTM for short-term load forecasting. These models were trained to forecast the aggregated load of New England Region in the United States, one day in advance based on the previous history of load profile. Results from this study, indicate that the CNN-BiLSTM architecture produces the lowest RMSE error values of any of the models that were tested against it, including LSTM, BiLSTM and CNN-LSTM. The authors speculate that this is due to the combined strength of the hybrid model. Automatic Feature Extraction by CNN and Temporal Dependency Learning by BiLSTM attribute to an accurate modeling of electricity demand patterns.

This research is very much useful to the power industry to advance power system management strategies in the framework of increasing renewable energy integration and smart home technologies. Future evaluations will progressively compare the performance of the models using more dynamic and less predictable data-sets like weather information and wide ranging load profiles.

VI. AUTHORS' CONTRIBUTION

Conceptualization: Jaya Christa Sargunar Thomas and Krishna Veni Kaliappan Sivakumar.
Methodology: Krishna Veni Kaliappan Sivakumar.
Investigation: Jaya Christa Sargunar Thomas and Krishna Veni Kaliappan Sivakumar.
Discussion of results: Jaya Christa Sargunar Thomas.
Writing – Original Draft: Jaya Christa Sargunar Thomas.
Writing – Review and Editing: Jaya Christa Sargunar Thomas and Krishna Veni Kaliappan Sivakumar.
Resources: Krishna Veni Kaliappan Sivakumar.
Supervision: Jaya Christa Sargunar Thomas.
Approval of the final text: Jaya Christa Sargunar Thomas.

VII. ACKNOWLEDGEMENTS

The authors thank the Mepco Schlenk Engineering College Management Committee for providing support to conduct this research.

VIII. REFERENCES

[1] L. Wang, S. Mao, and B. Wilamowski, "Short-term load forecasting with LSTM-based ensemble learning," in Proc. 2019 Int. Conf. on Internet of Things (iThings), IEEE Green Computing and Communications (GreenCom), IEEE Cyber, Physical and Social Computing (CPSCom), and IEEE Smart Data (SmartData), 2019, pp. 793–800.

[2] M. A. Alotaibi, "Machine learning approach for short-term load forecasting using deep neural network," Energies, vol. 15, no. 17, pp. 1–23, 2022, doi: 10.3390/en15176261.

[3] M. Madhukumar, A. Sebastian, X. Liang, M. Jamil, and M. N. S. K. Shabbir, "Regression model-based short-term load forecasting for university campus load," IEEE Access, vol. 10, pp. 8891–8905, 2022, doi: 10.1109/ACCESS.2022.3144206.

[4] O. Olasupo, T. Ayodele, and A. Ogunjuyigbe, "An Evaluation of Direct and Indirect Strategies for Hierarchical Net-Load Forecasting", JETIA, vol. 12, no. 57, pp. 375-388, 2026.

[5] S. Muzaffar and A. Afshari, "Short-term load forecasts using LSTM networks," Energy Procedia, vol. 158, pp. 2922–2927, 2019.

[6] C. Cai, Y. Tao, T. Zhu, and Z. Deng, "Short-term load forecasting based on deep learning bidirectional LSTM neural network," Applied Sciences, vol. 11, no. 17, pp. 1–16, 2021.

[7] D. G. da Silva and A. A. de M. Meneses, "Comparing long short-term memory (LSTM) and bidirectional LSTM deep neural networks for power consumption prediction," Energy Reports, vol. 10, pp. 3315–3334, 2023, doi: 10.1016/j.egyr.2023.09.175.

[8] D. P. Mohan and M. S. Subathra, "A comprehensive review of various machine learning techniques used in load forecasting," Recent Advances in Electrical & Electronic Engineering, vol. 16, no. 3, pp. 197–210, 2023, doi: 10.2174/2352096515666220930144336.

[9] N. Mounir, H. Ouadi, and I. Jrhilifa, "Short-term electric load forecasting using an EMD-BI-LSTM approach for smart grid energy management system," Energy and Buildings, vol. 288, pp. 1–10, 2023.

[10] B. Ibrahim, L. Rabelo, E. Gutierrez-Franco, and N. Clavijo-Buritica, "Machine learning for short-term load forecasting in smart grids," Energies, vol. 15, no. 21, pp. 1–19, 2022, doi: 10.3390/en15218079.

[11] S. Dai, "Short-term load forecasting with deep learning techniques," Journal of Physics: Conference Series, vol. 2547, pp. 1–8, 2023, doi: 10.1088/1742-6596/2547/1/012025.

[12] Y. Hong, Y. Zhou, Q. Li, W. Xu, and X. Zheng, "A deep learning method for short-term residential load forecasting in smart grid," IEEE Access, vol. 8, pp. 55785–55797, 2020.

[13] B. Zhong, "Deep learning integration optimization of electric energy load forecasting and market price based on the ANN–LSTM–transformer method," Frontiers in Energy Research, vol. 11, pp. 1–17, 2023, doi: 10.3389/fenrg.2023.1292204.

[14] D. L. Marino, K. Amarasinghe, and M. Manic, "Building energy load forecasting using deep neural networks," in Proc. 42nd Annu. Conf. IEEE Ind. Electron. Soc. (IECON), 2016, pp. 7046–7051, doi: 10.1109/IECON.2016.7793413.

[15] A. Narayan and K. W. Hipel, "Long short term memory networks for short-term electric load forecasting," in Proc. IEEE Int. Conf. Systems, Man, and Cybernetics, 2017, pp. 2573–2578, doi: 10.1109/SMC.2017.8123012.

[16] ISO New England Web Page of Energy, Load, and Demand Reports https://www.iso-ne.com/isoexpress/web/reports/load-and-demand (accessed January 6, 2026).

[17] M. Jacob, C. Neves, and D. Vukadinovic Greetham, "Short term load forecasting," in Forecasting and Assessing Risk of Individual Electricity Peaks, Mathematics of Planet Earth, Springer, 2020, pp. 15–37, doi: 10.1007/978-3-030-28669-9_2.

[18] A. Ahmad, N. Javaid, A. Mateen, M. Awais, and Z. A. Khan, "Short-term load forecasting in smart grids: An intelligent modular approach," Energies, vol. 12, no. 1, pp. 1–21, 2019, doi: 10.3390/en12010164.

Journal of Engineering and Technology for Industrial Applications

ISSN ONLINE: 2447-0228

ITEGAM-JETIA

Manaus, v.12 n.60, p.1180-1187. July/August, 2026.
DOI: https://doi.org/10.5935/jetia.v12i60.4036

RESEARCH ARTICLE OPEN ACCESS

IMPACT OF INTER-WINDING MAGNETIC AND CAPACITIVE COUPLING ON SFRA SIGNATURE

Mayur V Gojiya*[1], Mehul Dansinh Solanki[2], Ashokkumar Parmar[3], Maqbul U Ghanchi[4]

[1, 2, 3, 4]Electrical Engineering Department, Shantilal Shah Engineering College, Gujarat Technological University, Gujarat, India.

[1]https://orcid.org/0000-0002-4000-0078, [2]https://orcid.org/0000-0001-8852-3145
[3]https://orcid.org/0000-0001-7529-3774, [4]https://orcid.org/0009-0009-5399-8728

Email:*mayur.gojiya010@gmail.com, solankimehuld@gmail.com, abparmar80@gmail.com, ghanchimaqbul92@gmail.com

ARTICLE INFO

Article History
Received: March 11, 2026
Reviewed: April 12, 2026
Accepted: July 12, 2026
Published: August 31, 2026

Keywords:
Frequency response,
winding deformation,
magnetic & capacitive coupling,
condition monitoring,
SFRA.

ABSTRACT

Sweep Frequency Response Analysis (SFRA) serves as a highly sensitive diagnostic technique for identifying mechanical deformations within power transformer windings. The inherent magnetic and capacitive inter-winding couplings in transformers mean that a fault localized to a single winding can propagate detectable anomalies across the frequency responses observed at the terminals of all windings. This study systematically explores this interdependency through detailed simulations and case studies. A comprehensive six-winding equivalent circuit model of a 40 MVA, 132/11 kV power transformer, incorporating both magnetic and capacitive coupling effects is simulated to validate the underlying hypothesis. Complementing this, faults comprising an open-circuit condition and radial buckling were deliberately induced in the low-voltage (LV) winding of a 20 MVA, 66/11 kV oil-immersed transformer for experimental validation. The resultant frequency response traces reveal pronounced deviations in both LV and high-voltage (HV) signatures attributable to faults within a single phase winding. The study concludes that, due to unavoidable coupling, analyzing a single winding signature is sufficient to ensure the presence of mechanical deformation, whereas comparison of multiple signatures retains value for fault localization and severity assessment.

Copyright ©2026 by authors and Galileo Institute of Technology and Education of the Amazon (ITEGAM). This work is licensed under the Creative Commons Attribution International License (CC BY 4.0).

I. INTRODUCTION

Mechanical faults in transformer windings caused by short-circuit forces, transportation shocks or ageing remain a major cause of unplanned outages [1], [2]. Sweep Frequency Response Analysis (SFRA) has become the most widely accepted non-destructive technique for assessing winding integrity because of its high sensitivity to small geometrical changes [3–7]. Recent literature has significantly advanced SFRA interpretation through statistical indices, machine learning classifiers and online monitoring concepts [8–14]. However, the majority of published case studies and interpretation guidelines still treat each winding measurement independently, even though transformer windings are strongly linked by mutual inductance and inter-winding capacitance. Only a few works have systematically investigated how a local deformation propagates through coupling to remote windings [15–16]. In this paper, the influence of inter-winding couplings on the frequency response of the winding under the test is probed through case studies. Also, how this affects the diagnosis about winding deformation is commented. The paper is organized into six sections. Section-02 briefs about inter-winding couplings of transformer and its impact on frequency response. Section 3 demonstrates validation of the impact of inter-winding couplings on the frequency response through simulation. Case studies are presented to understand the winding deformation's interference on the frequency response of a winding undergoing the test, in section-04. Section-05 discuss the case studies results and impact on the diagnosis. Section-06 concludes about the study.

II. INTER-WINDING COUPLINGS AND ITS IMPACT ON FREQUENCY RESPONSE

Transformer design inherently incorporates inter-winding interactions. Windings typically share the core, creating a unified magnetic pathway and enabling inductive linkage [17]. Transformer also provides exposure for the capacitive couplings. The studies have considered the capacitance formed between the turns, between the discs, and between the winding and core / tank. In addition to this, as the outer high-voltage (HV) winding encases the inner low-voltage (LV) winding, with transformer oil providing dielectric separation, facilitating capacitive effects between HV-LV windings. Likewise, the high voltage windings are oriented besides, each other and electrically isolated by the transformer oil. A capacitive coupling can also be observed between HV-HV windings [18]. Figure 1 showcase the capacitive coupling between HV – LV and HV – HV windings. Hence the transformer windings are coupled through the common magnetic domain and the capacitance between HV windings and between HV-LV windings. The magnetic & capacitive couplings are shown in Figure 2.

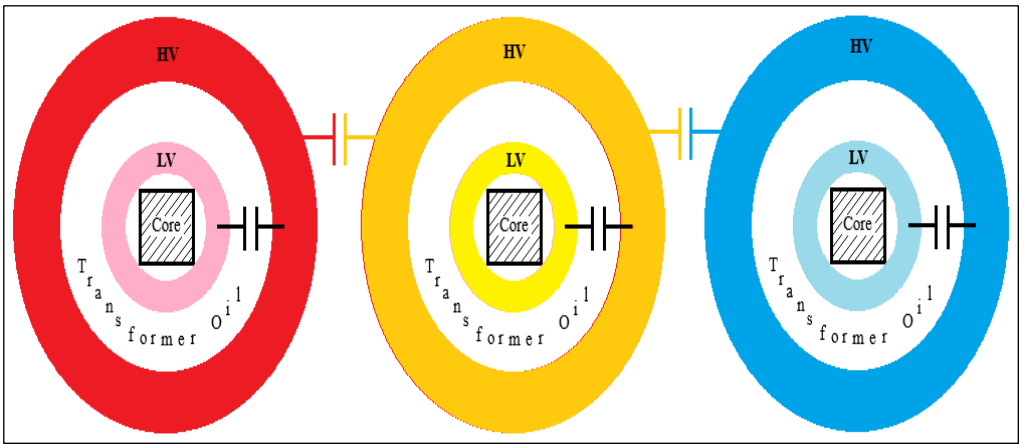


Figure 1: Capacitive coupling between HV – LV and HV - HV windings.
Source: Authors, (2026).

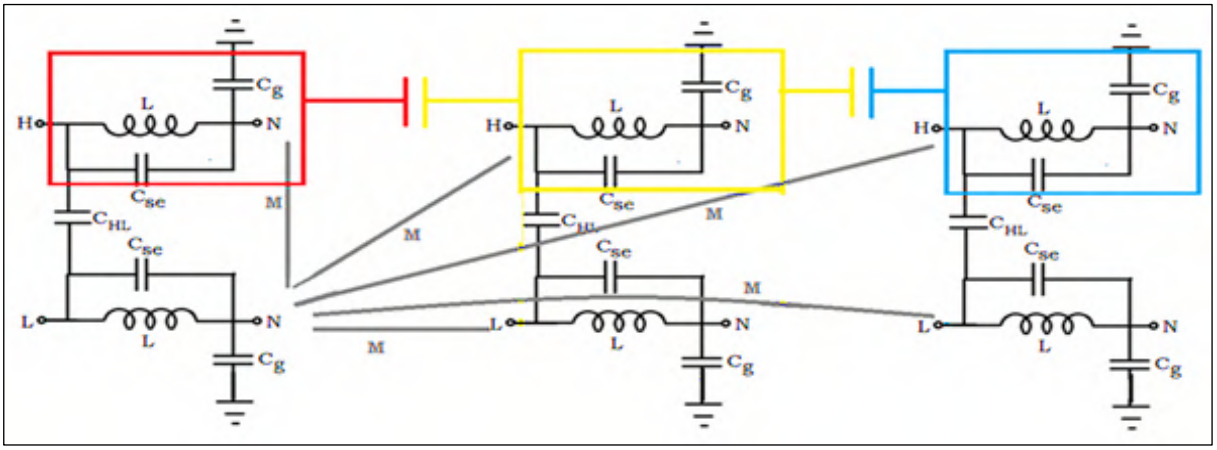


Figure 2: Schematic of capacitive and inductive couplings between transformer windings.
Source: Authors, (2026).

To diagnose the winding deformation, a sweep frequency signal of wide frequency band (20 Hz to 2 MHz, generally) is injected at a terminal of a winding. The test signal comprises of low, medium and high frequency segments. The inter-winding magnetic coupling is dominant in low frequency domain, whereas the capacitive couplings are in high frequency domain. All the inter-winding couplings are active in the window of medium frequency. Hence, the test signal can find the passage through inter-winding couplings to interact with all the windings of the transformer. The frequency response derived from such test signal can carry the information all from the windings. The deformation present in a winding may reflect in the frequency response derived irrespective to pair of winding terminals. It seems the frequency response obtained irrespective to the pair of winding terminals, is the overall response of windings. In the presence of inter-winding couplings, it is almost impossible to obtain individual winding response. Therefore, the study of a frequency response obtained using any pair of the terminals may be sufficient to get an idea about overall condition of windings.

III. SIMULTION

The hypothesis regarding the influence of magnetic and capacitive inter-winding couplings is verified via simulations. For this purpose, a six-winding equivalent circuit model of a 40 MVA, 132/11 kV power transformer— incorporating the magnetic and capacitive couplings as detailed in [19]—is employed. The corresponding inductance matrix and winding parameter values are presented in Tables 1 and 2, respectively, while the simulated winding configuration is illustrated in Figure 3. The fault scenario is emulated by imposing a 30% reduction in the shunt capacitance of the high-voltage (HV) phase-B winding relative to its initial value.

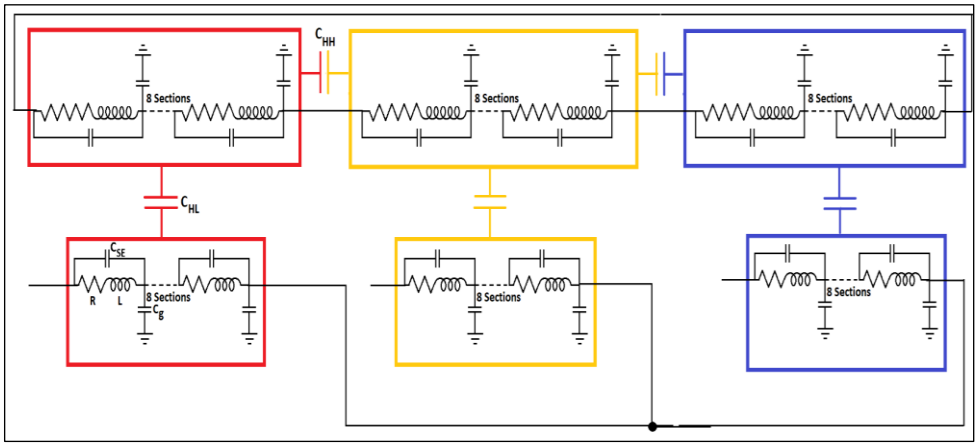


Figure 3: Six winding simulation model with inter-winding couplings.
Source: Authors, (2026).

Table 1: Inductance Matrix – Healthy (in milli henry).

		LV			HV		
		R	**Y**	**B**	**R**	**Y**	**B**
LV	**R**	0.47	0.41	0.05	0.47	0.41	0.05
	Y	0.41	0.82	0.41	0.41	0.82	0.41
	B	0.05	0.41	0.47	0.05	0.41	0.47
HV	**R**	0.47	0.41	0.05	0.47	0.41	0.05
	Y	0.41	0.82	0.41	0.41	0.82	0.41
	B	0.05	0.41	0.47	0.05	0.41	0.47

Source: Authors, (2026).

Table 2: Equivalent circuit parameter values.

	LV	**HV**
R (Ω)	0.25	1
C_{se} (pF)	3212	3114.4
C_{HL} (pF)	3000	
C_g (pF)	5514	2000
C_{HH} (pF)	315.66	

Source: Authors, (2026).

Frequency response signatures are captured for all phase windings across both the HV and low-voltage (LV) sides under healthy conditions and post-fault simulation. Comparative analyses of these signatures for the respective phase windings are depicted in Figures 4–9.

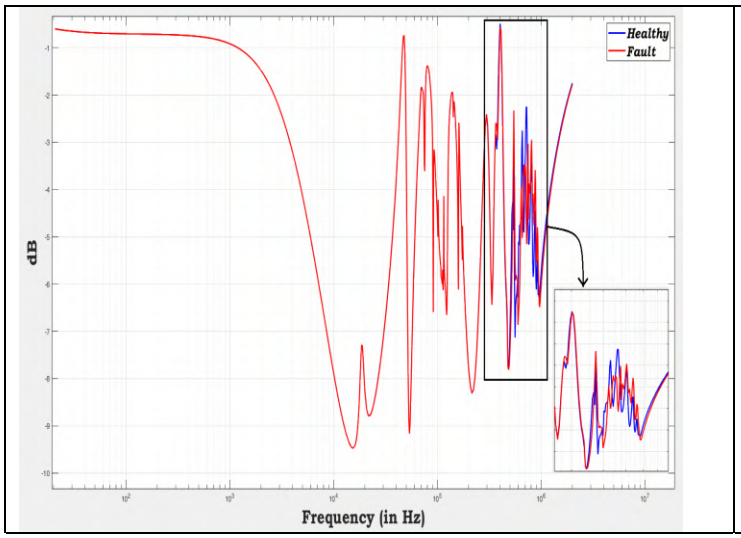


Figure 4: Frequency response comparison of low voltage winding phase R.
Source: Authors, (2026).

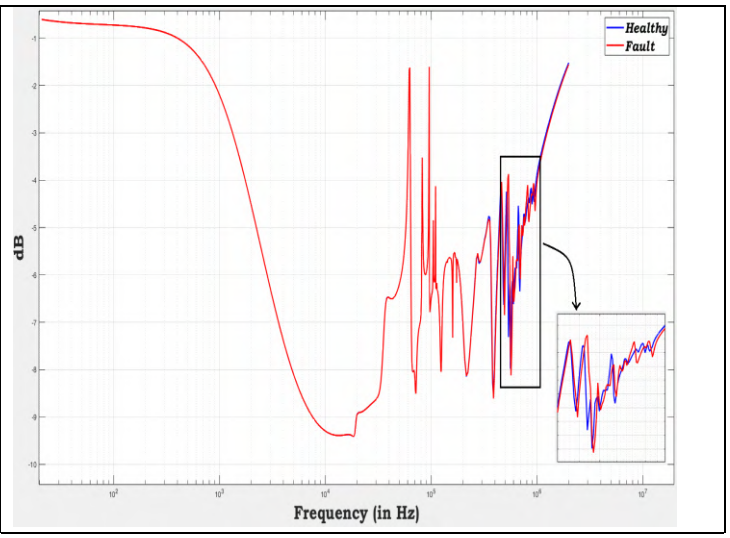


Figure 5: Frequency response comparison of low voltage winding phase Y.
Source: Authors, (2026).

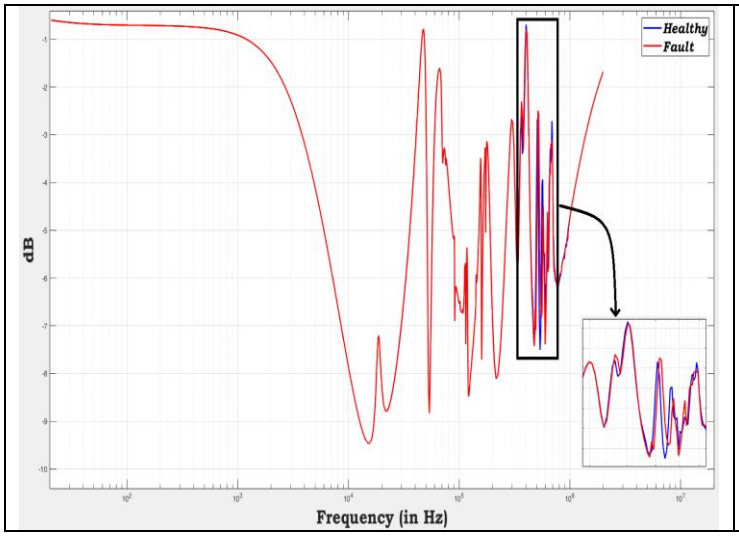


Figure 6: Frequency response comparison of low voltage winding phase B.
Source: Authors, (2026).

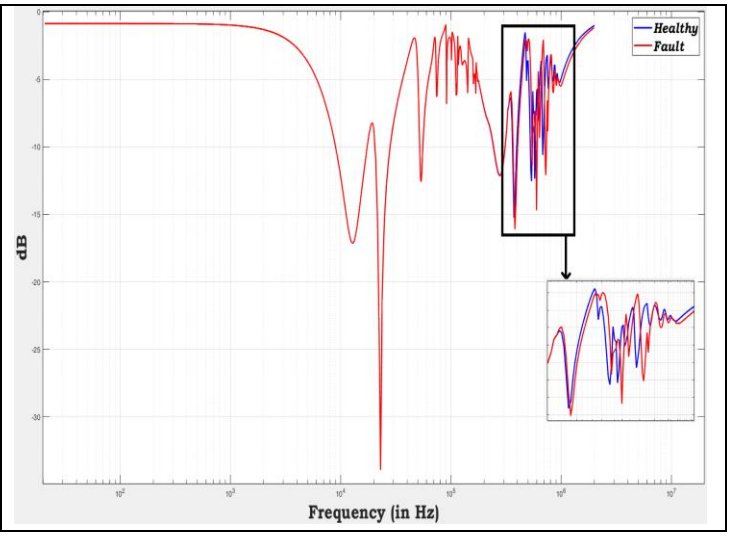


Figure 7: Frequency response comparison of high voltage winding between phase R.
Source: Authors, (2026).

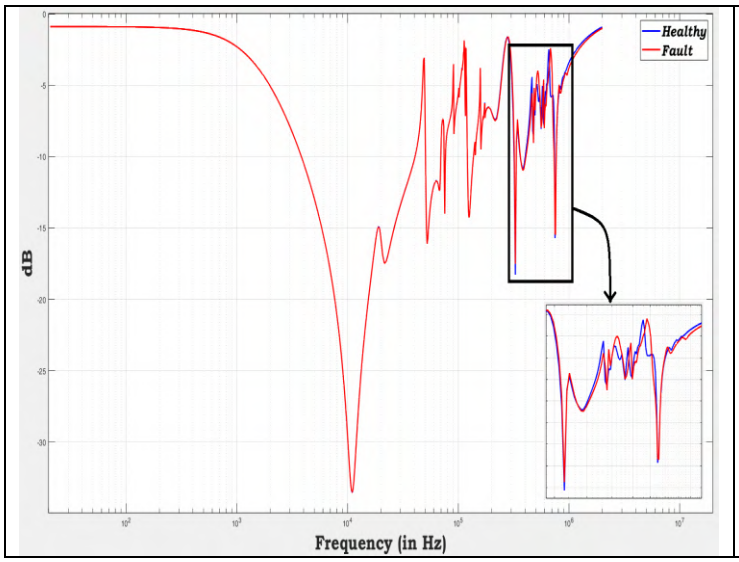


Figure 8: Frequency response comparison of high voltage winding between phase Y.
Source: Authors, (2026).

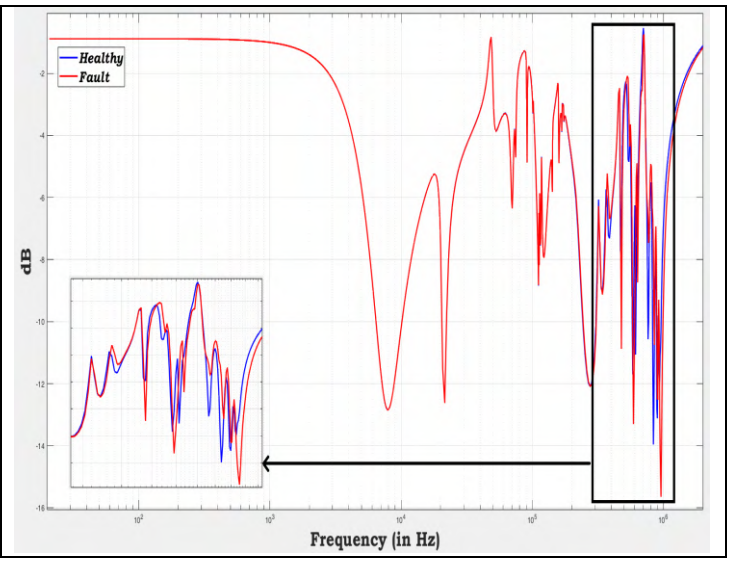


Figure 9: Frequency response comparison of high voltage winding between phase B.
Source: Authors, (2026).

Despite the fault being localized to the HV phase-B winding, discernible deviations manifested in the frequency responses of the LV windings as well as the HV phases R and Y, thereby evidencing the propagated impact. Capacitive elements within the winding model predominantly govern the high-frequency region of the frequency response. Consequently, the observed disparities in Figures 4–9 are confined to high frequencies. The delta-connected configuration of the HV windings implies that the equivalent circuit, when referenced to any HV terminal pair, encompasses contributions from all three HV windings. This inherent interconnectedness accounts for the susceptibility of the HV phase-R and phase-Y responses to perturbations in the HV phase-B winding. Furthermore, inter-winding capacitances between the HV and LV windings (CHL) and among the HV windings themselves (CHH) engender coupling effects. As such, the equivalent circuit referenced to any LV terminal pair integrates the dynamics of all HV and LV windings. These coupling mechanisms collectively ensure that alterations in the shunt capacitance (Cse) of the HV phase-B winding are reflected across the frequency responses of every phase windings.

IV. CASE STUDY

In order to verify the influence of deformation present in the winding – Not Under the test, on the frequency response, a 20 MVA, 66 / 11 kV transformer is introduced with open circuit and radial buckling, in-turn, into phase B of the low voltage side. The frequency response of windings is recorded using a commercial SFRA instrument (Omicron FRAnalyzer) for the stated winding deformation and for the healthy condition. The measurements were performed with End-to-End Open Circuit test configuration, used 50 Ω coaxial cables, frequency sweep 20 Hz – 2 MHz, 1200 logarithmic points and source impedance of 50 Ω.

IV.1 WINDING DEFORMATION TYPE – LV PHASE B OPEN CIRCUITED

Post-deformation FRA traces, captured via a commercial analyzer, are compared in Figures 10-15.

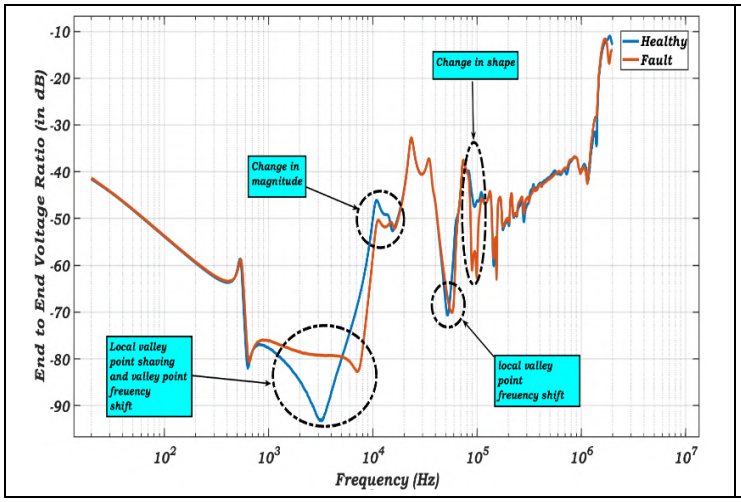


Figure 10: Frequency response comparison of high voltage winding between phase R.
Source: Authors, (2026).

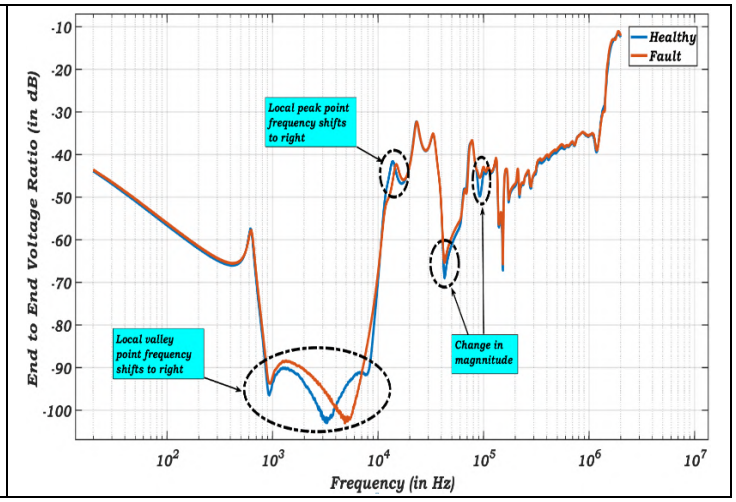


Figure 11: Frequency response comparison of high voltage winding between phase Y.
Source: Authors, (2026).

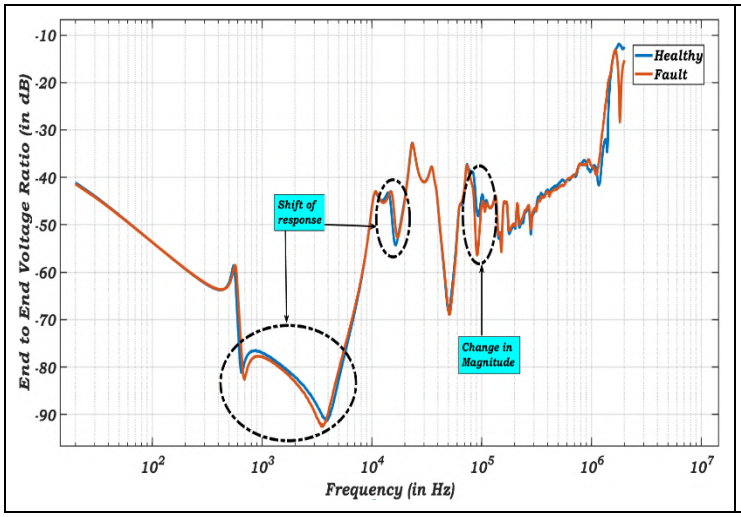


Figure 12: Frequency response comparison of high voltage winding between phase B.
Source: Authors, (2026).

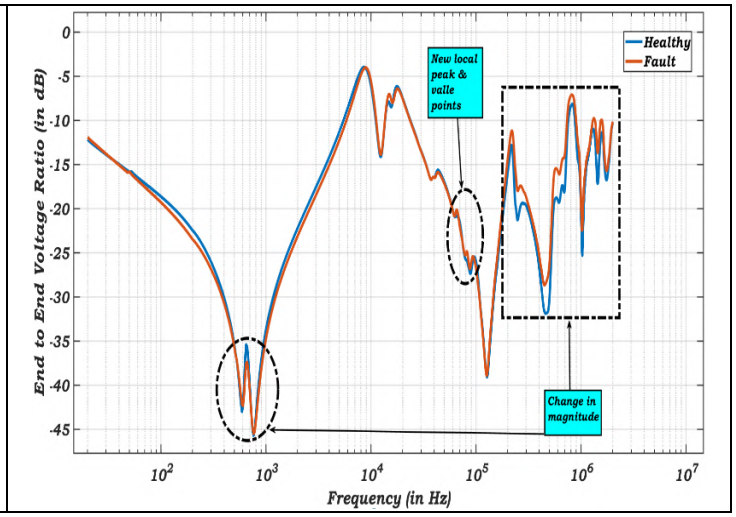


Figure 13: Frequency response comparison of low voltage winding phase R.
Source: Authors, (2026).

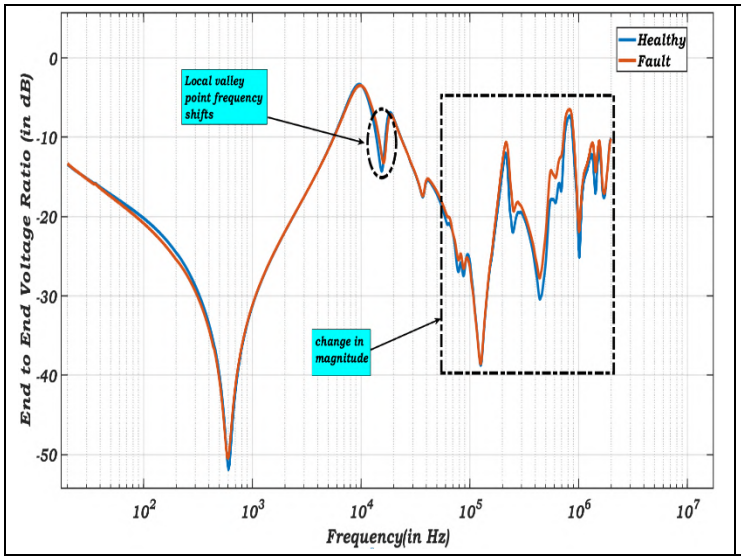


Figure 14: Frequency response comparison of low voltage winding phase Y
Source: Authors, (2026).

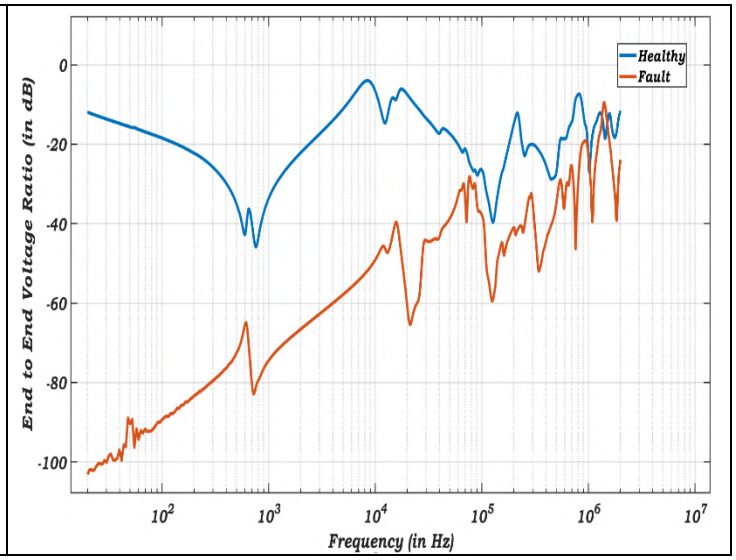


Figure 15: Frequency response comparison of low voltage winding phase B.
Source: Authors, (2026).

The observations are:

- High Voltage Windings - it seems the low and middle frequency regions are disturbed, mostly. It is obvious, as the open circuited LV phase - B has altered overall inductance of the windings and the low and middle frequency regions of signature reflect inductive property of winding. The signatures in low and middle frequency regions show local valley point shaving, shifts in valley and peak frequencies, and change in the shape of the response.
- Low Voltage Windings - the signature of phase B shows complete disagreement with the reference signature, as it is the host of deformation. The signatures of phases R & Y report their partial disagreement in term of change in magnitude of local peak & valley point, introducing a new pair of local peak & valley point and by shift of response.

IV.2 WINDING DEFORMATION – LV PHASE B RADIAL DEFORMATION

Figures 16–21 highlight the comparison between signatures captured after introducing radial deformation to the LV phase B winding and their respective baseline signatures.

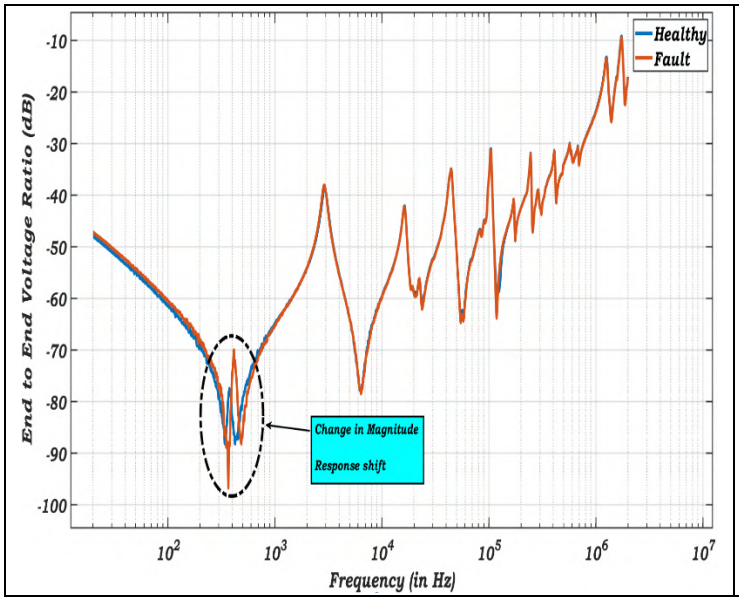


Figure 16: Frequency response comparison of high voltage winding phase R.
Source: Authors, (2026).

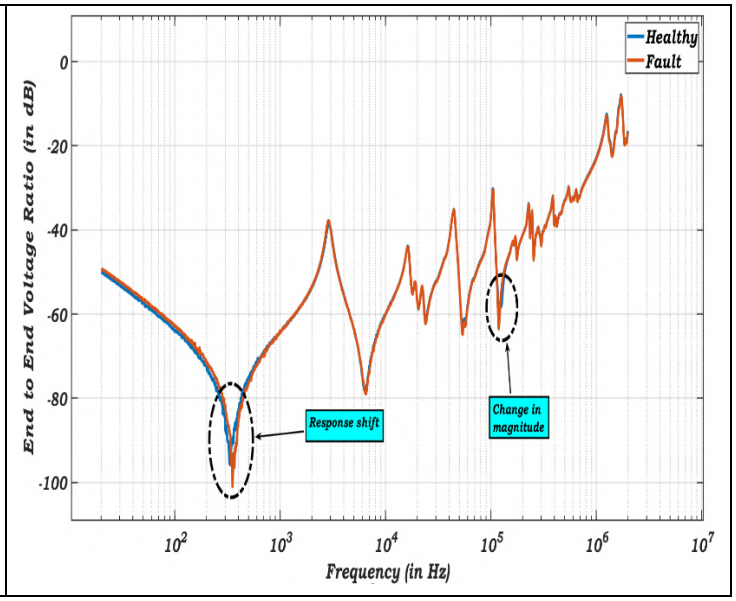


Figure 17: Frequency response comparison of high voltage winding phase Y.
Source: Authors, (2026).

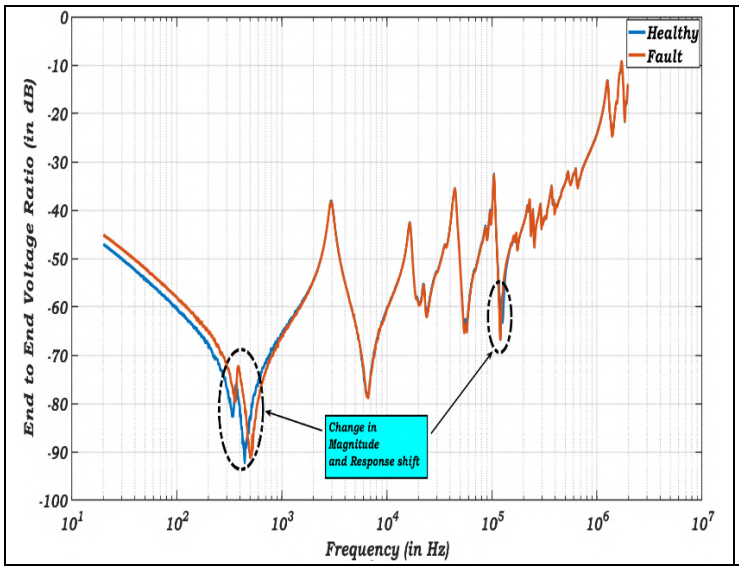


Figure 18: Frequency response comparison of high voltage winding phase B.
Source: Authors, (2026).

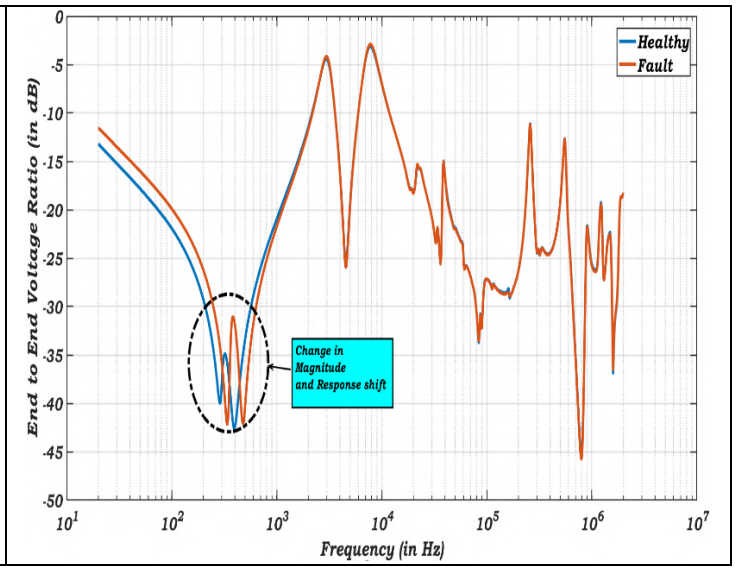


Figure 19: Frequency response comparison of low voltage winding phase R.
Source: Authors, (2026).

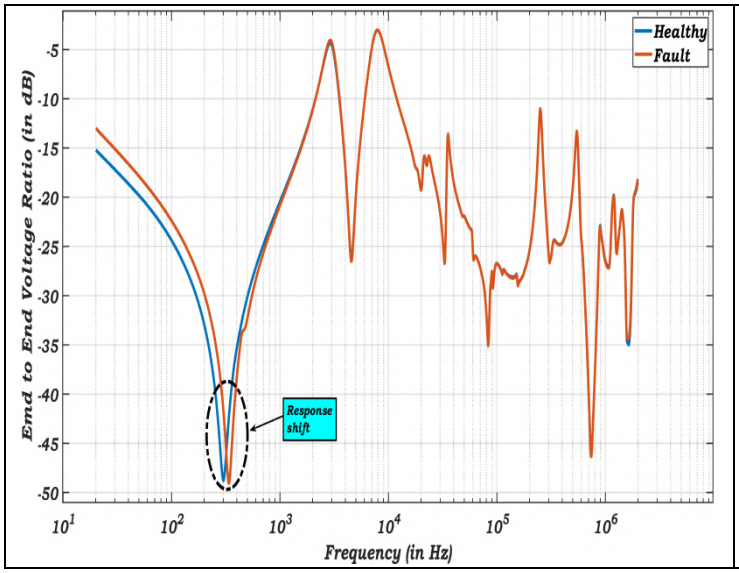


Figure 20: Frequency response comparison of low voltage winding phase Y.
Source: Authors, (2026).

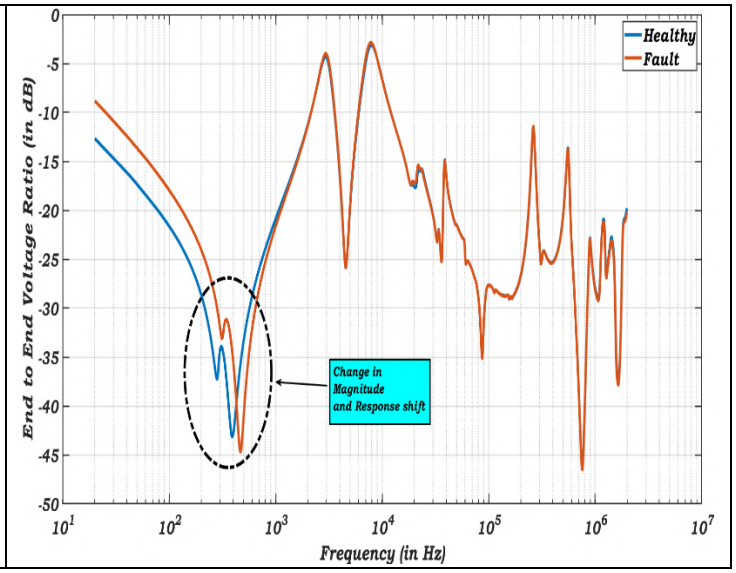


Figure 21: Frequency response comparison of low voltage winding phase B.
Source: Authors, (2026).

The observation is:

- The middle and high frequency regions of signatures have shown good degree of agreement with their respective references. The influence of radial deformation can be seen in the low frequency region of all the windings' (HVs & LVs) signatures, in term of change in magnitude and shift of the response.

V. DISCUSSION

V.1 CASE STUDY RESULTS

Due to delta connections and inter-winding linkages (inductive and capacitive couplings), test signal (sweep frequency signal) propagates system-wide, embedding condition data from multiple windings in a single trace. The experiment results clearly observe the deformation located in one of the windings, infect the signature of all the windings more or less. The degree of influence is dependent on how closely it is attached with the victim winding. The degree of disagreement offered by the deformed winding is significant large as compared to others but the scale of disagreement noticed in the signature of rest windings are not of negligible level.

V.2 PRACTICAL CONSEQUENCES FOR FIELD DIAGNOSTICS

Because of unavoidable coupling, every SFRA trace contains information about the mechanical condition of all windings. Consequently:

- Recording and analyzing a single accessible winding is sufficient to detect the presence of mechanical deformation with very high confidence.
- Comparing signatures from multiple terminals remains valuable (and recommended by standards) when the transformer is ready to get removed from service and maintenance, the phase and winding that shows the largest deviation usually indicates the fault location.

Thus, the common field practice of measuring only single accessible winding for quick screening is technically justified, whereas full measurement of all six terminals is still beneficial for detailed post-fault investigation.

VI. CONCLUSION

The results clearly show that inter-winding couplings make every SFRA trace a "global" indicator of the transformer's mechanical integrity. A local deformation confined to one LV phase produced unmistakable changes in all HV and LV traces, especially below 200 kHz. These findings provide justification for the field practice of measuring only the most accessible terminals (typically the HV side) for rapid go/no-go screening. At the same time, recording and comparing signatures from multiple terminals continues to offer superior fault-type discrimination, location capability, and severity grading when the transformer is ready for detailed investigation. The results therefore support simplified measurement procedures without sacrificing diagnostic reliability, while preserving the full value of complete SFRA datasets for post-fault analysis and repair planning.

VII. AUTHOR'S CONTRIBUTION

Conceptualization: Mayur V Gojiya, Mehul Dansinh Solanki, Ashokkumar Parmar, Maqbul U Ghanchi.
Methodology: Mayur V Gojiya, Mehul Dansinh Solanki, Ashokkumar Parmar, Maqbul U Ghanchi.
Investigation: Mayur V Gojiya, Mehul Dansinh Solanki, Ashokkumar Parmar, Maqbul U Ghanchi.
Discussion of results: Mayur V Gojiya, Mehul Dansinh Solanki, Ashokkumar Parmar, Maqbul U Ghanchi.
Writing – Original Draft: Mayur V Gojiya, Mehul Dansinh Solanki, Ashokkumar Parmar, Maqbul U Ghanchi.
Writing – Review and Editing: Mayur V Gojiya, Mehul Dansinh Solanki, Ashokkumar Parmar, Maqbul U Ghanchi.
Resources: Mayur V Gojiya, Mehul Dansinh Solanki, Ashokkumar Parmar, Maqbul U Ghanchi.
Supervision: Mayur V Gojiya, Mehul Dansinh Solanki, Ashokkumar Parmar, Maqbul U Ghanchi.
Approval of the final text: Mayur V Gojiya, Mehul Dansinh Solanki, Ashokkumar Parmar, Maqbul U Ghanchi.

VIII. ACKNOWLEDGMENTS

The authors express their gratitude to Gujarat Energy Transmission Corporation Ltd. (GETCO) for providing experimental results recorded by commercial SFRA instrument for this study.

IX. REFERENCES

[1] A. Metwally, 2011, "Failures, Monitoring and New Trends of Power Transformers," in IEEE Potentials, vol. 30, no. 3, pp. 36-43.

[2] Christina AJ, M.A. Salam, et al., 2018 "Causes of transformer failures and diagnostic methods – A review", Renewable and Sustainable Energy Reviews, Volume 82, Pages 1442-1456.

[3] Dick, E.P.; Erven, C.C., 1978, "Transformer Diagnostic Testing by Frequency Response Analysis". IEEE Trans. On Power Apparatus and Systems, vol.97, pp. 2144-2153.

[4] CHRISTIAN J., FESER K.: 'Procedures for detecting winding displacements in power transformers by the transfer function method', IEEE Trans. Power Deliv., 2004, vol.19, no. 1, pp. 214–220.

[5] WILSON A., MCGRAIL T.: 'The need for and use of techniques to assess the mechanical integrity of transformer windings', Int. Conf. Doble Clients, 2002, p. 10.

[6] RYDER S.A.: 'Diagnosing transformer faults using frequency response analysis', IEEE Electric. Insul. Mag., 2003, 19, (2), pp. 16–22.

[7] IEEE- SA, "IEEE Guide for the Application and Interpretation of Frequency Response Analysis for Oil-Immersed Transformers," IEEE std C57.149-2012, March 2013.

[8] CIGRE Working Group A2.53, "Advances in the interpretation of frequency response analysis (FRA) of power transformers," CIGRE Technical Brochure 812, Paris, France, Oct. 2020.

[9] M. Bagheri, M. S. Naderi, T. Blackburn, and T. Phung, "Advanced transformer winding deformation diagnosis: Moving from off-line to on-line," IEEE Trans. Dielectr. Electr. Insul., vol. 26, no. 6, pp. 1860–1870, Dec. 2019, doi: 10.1109/TDEI.2019.008375.

[10] S. Tenbohlen, M. Heindl, A. Kraetge, et al., "Diagnostic measurements for power transformers," Energies, vol. 13, no. 7, Art. no. 1702, Apr. 2020, doi: 10.3390/en13071702.

[11] A. Abu-Siada, S. Hmood, and S. Islam, "A new approach for interpreting transformer frequency response analysis results using artificial intelligence," Int. J. Electr. Power Energy Syst., vol. 132, Art. no. 107179, Nov. 2021, doi: 10.1016/j.ijepes.2021.107179.

[12] Z. Zhao, C. Li, J. Wang, et al., "Influence of core magnetisation and inter-winding capacitance on frequency response analysis of power transformers," IEEE Access, vol. 8, pp. 173114–173124, 2020, doi: 10.1109/ACCESS.2020.3025499.

[13] V. Behjat, A. Vahedi, A. Setayeshmehr, et al., "Sweep frequency response analysis for diagnosis of low-energy degradation in power transformers," IET Electr. Power Appl., vol. 14, no. 5, pp. 767–777, May 2020, doi: 10.1049/iet-epa.2019.0638.

[14] M. H. Samimi and S. Tenbohlen, "The story of frequency response analysis (FRA) invention: From 1960 until now," IEEE Electr. Insul. Mag., vol. 38, no. 2, pp. 44–55, Mar.–Apr. 2022, doi: 10.1109/MEI.2022.9732134.

[15] Y. Liu, S. Ji, F. Yang, et al., "Effect of inter-winding coupling on frequency response analysis results of power transformers," IEEE Trans. Power Deliv., vol. 35, no. 3, pp. 1445–1454, Jun. 2020, doi: 10.1109/TPWRD.2019.2945567.

[16] S. Pramanik and L. Satish, "High-frequency modeling of power transformers with isotropic and anisotropic windings considering inter-winding capacitances," Electr. Power Syst. Res., vol. 181, Art. no. 106174, Apr. 2020, doi: 10.1016/j.epsr.2020.106174.

[17] ABEYWICKRAMA N., SERDYUK Y.V., GUBANSKI S.M.: 'Effect of core magnetization on frequency response analysis (FRA) of power transformers', IEEE Trans. Power Deliv., 2008, vol. 23, no. 3, pp. 1432–1438.

[18] A. P. Kaur, A. Helwig et al.,2016, "SFRA transformer reliability engineering modelling for undergraduates," 2016 Australasian Universities Power Engineering Conference (AUPEC), Brisbane, pp. 1-5.

[19] A. Abu-Siada, M. I. Mosaad, D. Kim and M. F. El-Naggar, "Estimating Power Transformer High Frequency Model Parameters Using Frequency Response Analysis," in IEEE Transactions on Power Delivery, vol. 35, no. 3, pp. 1267-1277, June 2020, doi: 10.1109/TPWRD.2019.2938020.

Journal of Engineering and Technology for Industrial Applications

ISSN ONLINE: 2447-0228

ITEGAM-JETIA

Manaus, v.12 n.60, p.1188-1194. July/August, 2026.
DOI: https://doi.org/10.5935/jetia.v12i60.4038

RESEARCH ARTICLE OPEN ACCESS

A COMPREHENSIVE REVIEW ON QUANTUM COMPUTING MODELS FOR ALZHEIMER'S DISEASE PREDICTION

S. Raja Rajeswari[*1], S. Sathya Priya[2], R. Ramesh[3] and S. Divya Vahini[4]

[1, 2, 4]Department of Computer Applications, Mahalingam College of Engineering and Technology, Pollachi, Tamilnadu, India.
[3]Department of Mathematics, Mahalingam College of Engineering and Technology, Pollachi, Tamilnadu, India.

[1]http://orcid.org/0000-0001-8923-4572, [2]http://orcid.org/0009-0000-0848-6744,
[3]http://orcid.org/0000-0002-5323-7680, [4]http://orcid.org/0009-0008-5759-2445

Email: rraji.raji22@gmail.com, sathyapriya925@gmail.com, rameshwaran141@gmail.com, sdivyavahini01@gmail.com

ARTICLE INFO

Article History
Received: March 11, 2026
Reviewed: April 12, 2026
Accepted: July 12, 2026
Published: August 31, 2026

Keywords:
Alzheimer 's disease,
Quantum Technology,
Quantum Machine Learning (QML),
Healthcare Analysis,
Quantum Convolutional Neural Networks.

ABSTRACT

Alzheimer's disease is neurodegerative disorder that affects memory of a person and also the day to day activities of them. Normally, Alzheimer's disease can be identified by using the MRI scans which consist of high dimensional data. Traditional machine learning models are filed to give higher accuracy while diagnosing the disease. Quantum technologies plays a vital role and its emerging technologies that produce higher accuracy compared to traditional models. In this study we provide a comprehensive review of quantum technology such as Quantum Machine Learning (QML), Quantum Neural Networks (QNN) and Hybrid Quantum Models. Key factors of this study include early identification of Alzheimer's disease by utilizing the higher dimension of data like MRI images. Further, this article focuses on the application, limitations such as hardware constraints and scalability of clinical decision support system.

Copyright ©2026 by authors and Galileo Institute of Technology and Education of the Amazon (ITEGAM). This work is licensed under the Creative Commons Attribution International License (CC BY 4.0).

I. INTRODUCTION

Alzheimer's disease is a primary cause of dementia which accounts 60-80% of cases in worldwide. The stages of this disease can be categorized by memory impairment, functional dependency, gradual cognitive decline which burden the individual and the persons who take care of them. The traditional approaches like machine learning models are failed in early diagnosis of Alzheimer's disease, timely interference and enhanced patient outcomes. To diagnose the Alzheimer's disease, neuro imaging dataset like Fluorodeoxyglucose Positron Emission Tomography (FDG-PET) and structural Magnetic Resonance Imaging (sMRI) and the behavioural activities and handwriting are used. In recent year's artificial intelligence, machine learning models have provided a significant improvement in AD classification [1] analysis. In spite of this advances the classical AI model produce poor accuracy in terms of high dimensional data. Quantum computing techniques are the emerging alternatives which uses its principles like superposition and entanglement. Quantum Machine Learning (QML) models used to analyse neuro imaging behavioural and genomic data that capture the complex patterns beyond classical models. Current diagnostic techniques for AD simple relied on clinical test, neuropsychological test, Magnetic resonance imaging (MRI) and positron emission tomography (PET) and cerebrospinal fluid (CSF). When using these methods it often leads to limited accessibility, high cost, and reduced sensitivity in mild cognitive impairment (MCI) stage [2]. Similarly, computational intelligence methods have gained advancements in decision support system to help clinicians in early and accurate identification of AD. This paper provides wider analysis of quantum computing and QML models applied to the Alzheimer's disease research direction. This study also examines the existing literature on quantum learning models and highlights its advantages limitations compared with traditional approaches. Also it discusses the challenges such as scalability, interpretability, and data encoding. By combining current advancements, this study pioneering the quantum computing research into next generation of Alzheimer's disease prediction and decision support system.

II. BACKGROUND WORK

Recent research shows the application of quantum computing and QML methods used for Alzheimer's disease (AD) analysis across multiple data modalities. Kaewta et al. proposed QENNA, a quantum-enhanced neural network that combines quantum convolutional layers with traditional deep learning models to enhance early identification of AD disease using MRI data [3]. By combining quantum data augmentation strategies like Quantum Generative Adversarial Networks (GAN) and quantum random walks, this method effectively address the data scarcity and attain superior diagnostic performance compared to state-of-the-art models. Likewise, Rajesh et al. suggested a hybrid quantum framework using Quantum Neural Networks for MRI-based Alzheimer's disease prediction [4], that provides better accuracy over traditional machine learning approaches. Further than neuroimaging, quantum artificial intelligence also applied to non-invasive behavioural analysis. Cappiello and Caruso suggested quantum machine learning models [5] for early identification of AD disease using handwriting dynamics from the DARWIN dataset, which shows that quantum classifiers outperformed traditional counterparts while offering improved interpretability. For molecular and genomic level, Konar et al. proposed Alz-QNet, a quantum gene regulatory networks model for complex gene–gene interactions [6] associated with AD progression using single-nucleus RNA sequencing data from the entorhinal cortex, provided that insights into possible gene-expression-based theranostic strategies. Further, the Quantum computing has been explored in multimodal and optimization-driven frameworks. Odusami et al. described a quantum-optimized approach for AD stage identification by combining sMRI with FDG-PET images [7] and optimizing a Mobile Vision Transformer using Pareto-Optimal Quantum Dynamic Optimization, that provides high precision, sensitivity, and specificity on ADNI and OASIS datasets. In a wider clinical framework, Mohamed et al. suggested the transformative potential of quantum computing in neurosurgery [8], emphasizing its ability to improve diagnostic accuracy, surgical precision, and personalized neurological care, thus providing significant contextual motivation for quantum applications in neurodegenerative disorders. Additionally, Chandramohan described quantum chemical calculations and molecular docking simulations to analyze protein–ligand interactions related to Alzheimer's disease [9], highlighting the role of quantum chemistry in analyzing potential therapeutic drug candidates. Together this study identifies the quantum computing models that provide a enhanced improvements in Alzheimer's disease prediction across genomic analysis, screening, diagnosis, and optimization; further it can be motivate advanced analysis in terms of scalability in quantum enhanced frameworks.

III. BIO-MARKERS AND DATA MODALITY FOR ALZHEIMER'S DISEASE

III.1 GENETIC AND MOLECULAR DETERMINANTS IMPLICATED IN ALZHEIMER'S DISEASE IDENTIFICATION

Alzheimer's disease is a complex network pattern of gene regulatory that can affect the neuronal survival, neurodegeneration and synaptic integrity. Yin Yang 1(YY1) is an important factor whose dysregulation improves neuronal apoptosis, via modulation of Fuz gene, quickening cognitive decline. Some other genes put together in AD pathology in various interconnected ways. Growth Arrest-Specific 7(GAS 7) gene controls neuronal maturity and cytoskeletal coordination with dysfunction impairment of microtubule transport and synaptic stability. Early Growth Response 1(EGR1) regulates neurotransmitter and synaptic plasticity that adjust acetylcholinesterase and microRNA-132, also it upset tau phosphorylation and amyloid-beta generation. Fibroblast Growth Factor 14(FGF14) affects neuronal activity and synaptic formation through voltage sodium channels by combining dysregulation linked to modify amyloid pathology and cognitive deficits. Phospholipase D Family Member 3(PLD3) correlate with amyloid plaque-linked axonal spheroids and modulation can improve synaptic resilience that can slowdown the cognitive decline. Altogether, these genes can form a multifaceted molecular structure for Alzheimer's disease that shares the pathway and potential targets for precision therapeutics.

III.2 NEUROIMAGING DATA AND DATASET REPOSITORIES USED FOR ALZHEIMER'S DISEASE

Magnetic Resonance Imaging (MRI) is widely used for Alzhiemer's disease prediction to identify the structural and behavioural changes in the brain. T1-weighted MRI scans are widely used to identify the hallmark behavioural changes in brain [10] including hippocampal atrophy, ventricular enlargement, and cortical thinning. This study analyzes behavioural, structural, and molecular datasets to assess the quantum-enhanced neural network (Alz-QNet) for Alzheimer's disease classification. Structural MRI and FDG-PET images are the publicly available repositories, including the Alzheimer's Disease Neuroimaging Initiative (ADNI) and OASIS databases. These datasets contains high quality, pre-processed T1-weighted MRI scans and PET images with standardized achievement protocols that enables reproducible analysis and reliable evaluation of neurodegenerative markers such as hippocampal atrophy and cortical thinning. The DARWIN handwriting dataset also provides complementary behavioural information, like capturing kinematic and pressure features from multiple errands performed by participants with and without Alzheimer's disease. Molecular-level insights were provided by GSE138852 single-nucleus RNA sequencing dataset that can be collected from the entorhinal cortex of Alzheimer has and control brains. Target genes were observed based on pathway relevance, region-specific dysregulation, and therapeutic potential. Gene expression values were regularized, log-transformed, and binarized to present biologically meaningful activation states suitable for quantum circuit encoding. Together, these datasets provide balancing perspectives on Alzheimer's disease, supporting a holistic assessment of Alz-QNet by incorporating anatomical, behavioural, and molecular features to model disease progression with quantum-enhanced computational techniques. Figure 1 represents various stage of dementia extracted from publically available dataset.

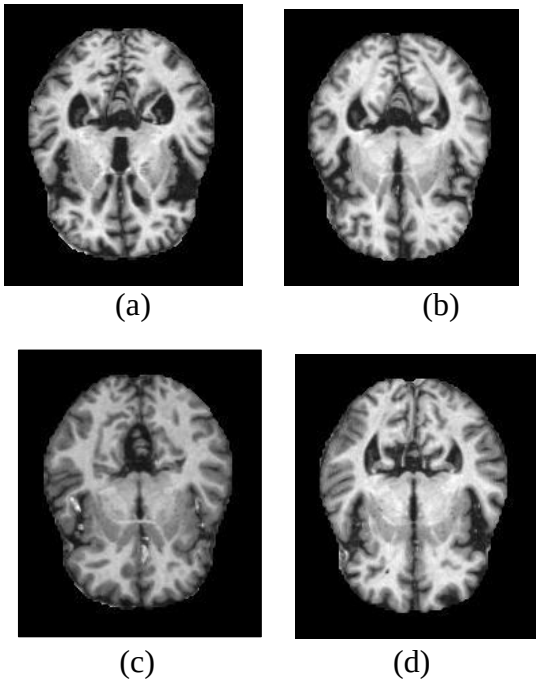


Figure 1: Example MRI images representing a) Mild dementia, b) Moderated dementia c) Non dementia d) Very mild dementia. Source: Authors, (2026).

IV. PRINCIPLES OF QUANTUM COMPUTING

IV.1 QUBITS AND SUPERPOSITION

A qubit is the primary unit of quantum computation [11], which is capable of superposition in basis states $|0\rangle$ and $|1\rangle$:
Qubit computation

$$|\psi\rangle = \alpha \mid 0\rangle + \beta \mid 1\rangle \quad (1)$$

IV.2 QUANTUM GATES

Quantum gates carry out unitary transformations on qubits to manipulate their states [6]. Common gates include:

- NOT (X) Gate: Flips $|0\rangle \leftrightarrow |1\rangle$.
- Hadamard (H) Gate: Generate an equal superposition:
  - $|0\rangle \rightarrow (|0\rangle + |1\rangle)/\sqrt{2}$, $|1\rangle \rightarrow (|0\rangle - |1\rangle)/\sqrt{2}$.
- Controlled-NOT (CX) Gate: Flips a mark qubit only if the control qubit is $|1\rangle$.
- Rotation (RY) Gate: Rotates a qubit state with respect to the Y-axis by an angle θ.
- Controlled-RY (CRY) Gate: Apply an RY rotation to the target qubit with the condition of $|1\rangle$. This gate is a primary key for modeling pairwise interactions, such as gene regulatory relationships.

IV.3 ENTANGLEMENT AND MULTI-QUBIT SYSTEMS

Entanglement is a quantum occurrence where qubits' states are mutually dependent, allowing the encoding of complex correlations. In genetic systems, entangled qubits can represent interacting genes or other dependent variables efficiently.

IV.4 QUANTUM CIRCUIT IMPLEMENTATION IN ALZ-QNET

In Alz-QNet model [6], each qubit stand for a gene in Alzheimer's disease. The structural design is divided into encoder layers, which convert single-nucleus RNA-seq data into superposition states, and regulation layers, where CRY gates snare qubits to model gene-gene interactions. Rotation angles of CRY gates match to the strength of interactions. The outputs are calculated to generate probability distributions of gene activity that smoothed by using Laplace smoothing and optimized via gradient descent. This framework exploits quantum parallelism to form gene regulatory networks powerfully, capturing the discrete switch-like behaviour of gene expression while reducing computational complexity.

V. DATA PRE-PROCESSING AND FEATURE EXTRACTION

Pre-processing is a significant step in both classical and quantum-based methods. MRI images are shrunken to remove irrelevant features, resized to standardized dimensions, and normalized to consistent intensity levels. Noise reduction methods, including Gaussian and median filtering; helps to remove artifacts while protecting important features.

Deep learning or quantum convolution layers are used to extract relevant features [12], also ensemble and hybrid models are incorporates features from multiple networks to create more discriminative representations. This combination of pre-processing, feature extraction, and hybrid modelling guarantees robust and clinically meaningful Alzheimer's disease prediction.

VI. QUANTUM COMPUTING METHODS FOR ALZHEIMER'S DISEASE PREDICTION

VI.1 CLASSICAL DEEP LEARNING METHODS

Alzheimer's disease prediction has usually depends on classical deep learning models, particularly convolutional neural networks (CNNs) [13], [3], [6]. The convolutional neural networks (CNNs) has the ability to automatically extract relevant features from brain MRI images. Architectures such as VGG16 and ResNet50 have been widely used. VGG16 contains multiple convolutional layers that discover hierarchical features [14] from MRI images, while ResNet50 initiate residual connections to overcome vanishing gradient problems in deep networks. Ensemble approaches that merge features from multiple CNNs [1] this can be demonstrated by improved classification performance, as they integrate complementary information from various architectures. Pre-processing step includes intensity normalization, noise reduction, image resizing, and classical data augmentation techniques such as zooming, brightness adjustments, rotations, and translations, have proven necessary to improve generalization and address class imbalance in datasets.

VI.2 QUANTUM MACHINE LEARNING MODELS (QML)

Recent studies in quantum computing have enabled pioneering methods for Alzheimer's disease prediction. QML models, such as Quantum Support Vector Machines (QSVMs) and Quantum Convolutional Neural Networks (QCNNs) [13], [3], maps classical MRI features into high-dimensional quantum Hilbert spaces that increase the separability of Alzheimer 's disease stages. QCNNs convert MRI images into qubits using amplitude encoding and apply parameterized quantum gates to extract non-local spatial features, Quantum data augmentation models, including Quantum Random Walks (QRWs) and Quantum Generative Adversarial Networks (QGANs), provides stochastic variations and generate high-fidelity synthetic MRI images [15], that increase dataset diversity and reduce overfitting, thereby enhancing model robustness.

VI.3 QUANTUM STATE ENCODING

To present MRI image in a quantum system, amplitude encoding maps pixel intensities into a quantum state:

$$| \psi\rangle = \sum_{i=1}^{N} x_i \, | i\rangle \tag{2}$$

Here, x_i is the normalized pixel intensity, N is the sum of pixels, and $|i\rangle$ is the computational basis state of the quantum register.

VI.4 QUANTUM CONVOLUTION OPERATION

Quantum convolutional layers affect parameterized unitary operations to extract features:

$$U(\theta) \, | \psi\rangle = \prod_j RZ\,(\theta_j) RX(\theta_j) CNOT \, | \psi\rangle \tag{3}$$

The above formula applies the rotations and entanglement to encode spatial correlations across the image.

VI.5 QUANTUM POOLING

Pooling can be done by using Grover's amplitude amplification:

$$\rho = (2 \, | \psi\rangle\langle\psi \, | - I)O \tag{4}$$

Where O marks major quantum states, $|\psi\rangle$ represents the quantum feature state, and I represents the identity matrix. This amplifies diagnostically important features while removing irrelevant information.

VI.6 HYBRID QUANTUM FRAMEWORKS

Hybrid quantum traditional models influence the strengths of both paradigms for more accurate Alzheimer's disease prediction. In these frameworks, quantum layers carry out non-local feature extraction throughout entanglement; detain subtle structural variations across far-away brain regions, while traditional neural network layers offer stable gradient-based optimization and ending classification. MRI images are encoded into quantum states [5], which are then processed throughout quantum convolution and pooling layers. The resultant quantum-derived features are passed to fully connected layers to classify multiple stages of Alzheimer's disease. Quantum mechanisms, such as superposition and amplitude amplification, allow the capture of distributed and low-intensity patterns that may be missed by traditional models, while quantum parallelism advances computational efficiency compared to traditional convolution and pooling operations. Figure 2 represents the framework of quantum computing models for Alzheimer's disease prediction.

VI.7 HYBRID PARAMETER UPDATE

Parameters of quantum and classical layers are optimized together:

$$\theta^{(t+1)} = \theta^{(t)} - \eta \nabla_\theta L \tag{5}$$

$$W^{(t+1)} = W^{(t)} - \eta \nabla_W L \quad (6)$$

Where θ is the quantum parameter, W is the neural network weight, η is the learning rate, and L represents the loss function.

VII. COMPARATIVE ANALYSIS OF QUANTUM COMPUTING WITH CLASSICAL AI

Traditional artificial intelligence models like machine learning and deep learning techniques played a vital role in identification of Alzheimer's disease. The classical deep learning models such as Convolutional Neural Networks (CNN), Recurrent Neural Networks(RNN) and ensemble learning have provide good results in AD classification using neuroimaging data like MRI and PET scans. These models outperformed only with the mature training algorithms and scalable computational infrastructures by using hierarchical feature extraction techniques. Nevertheless, these techniques often affected by the curse of dimensionality and limits interpretability, also it has high computational cost while deals with multimodal and high-resolution biomedical data. In contrast, quantum-computing models provide computationally different paradigm that leverages the quantum properties like quantum inferences, super position and entanglement. Quantum Machine Learning (QML) techniques can fix the complex biomedical data into high dimensional quantum Hilbert spaces using limited computational resources contrast to classical representation. This allows quantum techniques to identify the subtle, non-linear association presents in neurological, genetic and behaviour data that may be difficult for traditional AI models to predict effectively. As result, quantum enhanced models provides a promising early stage AD identification that are often overlooked by traditional models. Another important distinction is feature representation and optimization. While using medical datasets with limited samples the traditional deep learning models rely on gradient-based optimization techniques that need more number of parameters, which leads to overfitting. Hybrid Quantum models reduce parameter complexity by utilizing quantum circuits for feature extraction and traditional classifiers for classification. This hybrid technique offers improved generalization in limited dataset that common in Alzheimer's prediction. In spite of its advantages, quantum techniques are not fully replacing the traditional AI models. Quantum models also have their own limitations like noise, qubit scalability, decoherence which control the strength and size of quantum circuits. Thus, the traditional models are more suitable for large-scale clinical operations. However, the quantum computing technologies offers enhanced feature learning, improved computational efficiency, that enables more constructing modelling of Alzheimer's disease prediction. In view of this beneficial relationship, quantum computing is seen as a promising replacement of traditional AI methods in Alzheimer's disease research.

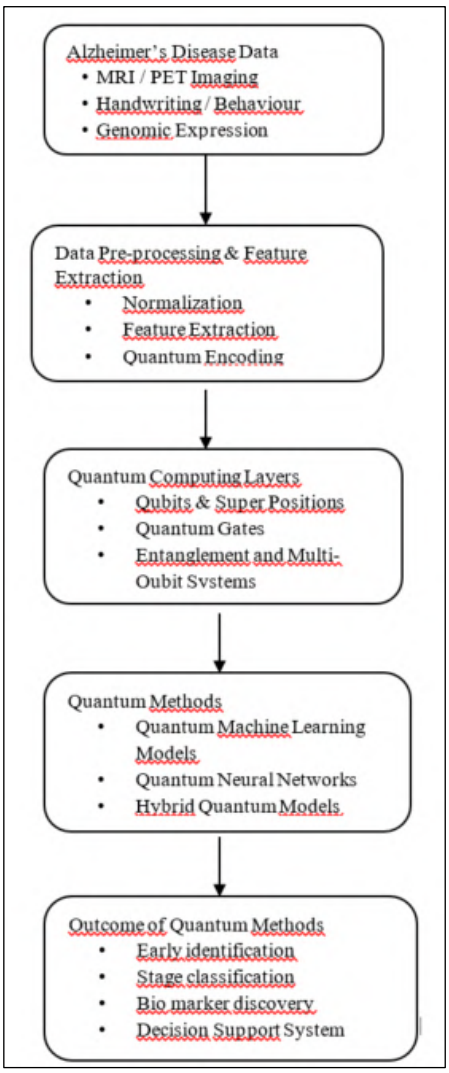


Figure 2: Framework of Quantum Computing Applications in Alzheimer's Disease.
Source: Authors, (2026).

VIII. APPLICATIONS OF QUANTUM COMPUTING

Quantum computing and quantum machine learning models provides significant improvement in Alzheimer's disease research. These models can enhance early identification by efficiently analyzing high dimensional neuroimaging [2], [16], behavioural, and genomic data. Quantum convolutional neural networks able to extract the subtle structural and functional patterns from MRI and PET scans, where traditional approaches are failed. Quantum-enhanced regression and classification models can identify complex gene–gene relations and molecular pathways, facilitating the identification of novel biomarkers and potential therapeutic targets. Hybrid quantum framework combines the strengths of both paradigms to enhance prediction accuracy, optimize disease stage classification, and support modified treatment planning. In addition, quantum-based data augmentation models, such as Quantum Generative Adversarial Networks (QGANs), improve model robustness by producing synthetic high-fidelity data for training in cases of limited datasets.

IX. LIMITATIONS OF QUANTUM MODELS

Quantum computing models for diagnosing Alzheimer's disease has some limitations in terms of modern quantum hardware such as gate fidelity, number of qubits and coherence time that restricting the scale of problems being addressed. Quantum models require complex programming formats that can be mapped into quantum states which can be computationally exhaustive that may leads to noise. Hybrid quantum models gives promising results but they still rely on classical optimization approaches and it may not completely exploit quantum advantages. In addition to the standard dataset the quantum models poses challenges for validation and reproducibility. Interpretability is remains an issue of quantum models making it difficult to explain predictions and clinical context.

X. CONCLUSIONS

Quantum models present a novel paradigm for Alzheimer disease research with unseen possibilities for early prediction, molecular analysis and customized therapy techniques. Quantum Machine Learning models that includes QCNN and hybrid frameworks have provides promising results while capturing complex patterns in neuroimaging, behavioural activities and genomic dataset. Quantum models also have major challenges that include hardware limitations, training high dimensional data and interpretability. Integrating quantum models with deep learning techniques produce enhanced results in terms of accuracy in clinical decision support system. This study highlights the recent scenario of research in Alzheimer's disease prediction with emphasizing potential benefits and it needs further exploration in computational and clinical aspects.

XI. FUTURE ENHANCEMENTS

Further research focuses on developing scalable quantum models that can handle higher dimension and complex multimodal image dataset. Quantum hardware advancements include increased qubit counts, error correction that is necessary for benefiting the implementation of quantum computing in Alzheimer's disease research. To improve the model transparency that facilitate the clinical adoption and trust the Quantum AI technique can be integrated with the classical models. Increasing use of longitudinal data analysis multi-omics could find new biomarkers into disease development. Cooperation between neuroscientists, clinicians and quantum computing experts is needed to produce most relevant models, confirm predictions in real world datasets, and transform quantum enhanced models into viable therapeutic tools for Alzheimer's disease prediction.

XII. AUTHOR'S CONTRIBUTION

Conceptualization: S. Raja Rajeswari, S.SathyaPriya and Divya Vahini Suresh.
Methodology: S. Raja Rajeswari, S. Sathya Priya R. Ramesh and S. Divya Vahini.
Investigation: S. Raja Rajeswari, S. Sathya Priya R. Ramesh and S. Divya Vahini.
Discussion of results: S. Raja Rajeswari, S. Sathya Priya R. Ramesh and S. Divya Vahini.
Writing – Original Draft: S. Raja Rajeswari, S. Sathya Priya R. Ramesh and S. Divya Vahini.
Writing – Review and Editing: S. Raja Rajeswari, S. Sathya Priya R. Ramesh and S. Divya Vahini.
Resources: S. Raja Rajeswari, S. Sathya Priya R. Ramesh and S. Divya Vahini.
Supervision: S. Raja Rajeswari, S. Sathya Priya R. Ramesh and S. Divya Vahini.
Approval of the final text: S. Raja Rajeswari, S. Sathya Priya R. Ramesh and S. Divya Vahini.

XIII. REFERENCES

[1] An, N., Ding, H., Yang, J., Au, R., & Ang, T. F. A. (2020). Deep ensemble learning for Alzheimer's disease classification. Journal of Biomedical Informatics, 105, 103411. https://doi.org/10.1016/j.jbi.2020.103411

[2] Quintes Steiner, A. B., Jacinto, A. F., Mayoral, V. F. D. S., Brucki, S. M. D., & Citero, V. D. A. (2017). Mild cognitive impairment and progression to dementia of Alzheimer's disease. Revista da Associação Médica Brasileira, 63, 651–655. https://doi.org/10.1590/1806-9282.63.07.651

[3] Kaewta, C., Pitakaso, R., Khonjun, S., Srichok, T., Luesak, P., Gonwirat, S., Enkvetchakul, P., Matitopanum, S., & Srisuwandee, T. (2025). QENNA: A quantum-enhanced neural network for early Alzheimer's detection using magnetic resonance imaging.Artificial Intelligence in Medicine, 103322. https://doi.org/10.1016/j.artmed.2025.103322

[4] Rajesh, T. H., Vardhan, T. V. H., Kumar, N. K., Veerendra, M. S., & Reddy, P. C. N. (2025). Alzheimer's disease prediction using quantum computing. International Journal of Scientific Research in Engineering and Management (IJSREM) (pp. 01–04).. DOI: 10.55041/IJSREM41150

[5] Cappiello, G., & Caruso, F. (2025). Quantum AI for Alzheimer's disease early screening. Neurocomputing, 647, 130565. https://doi.org/10.1016/j.neucom.2025.130565

[6] Konar, D., Sreekumar, N., Jiang, R., & Aggarwal, V. (2025). Alz-QNet: A quantum regression network for studying Alzheimer's gene interactions. Computers in Biology and Medicine, 196, 110837. https://doi.org/10.1016/j.compbiomed.2025.110837

[7] Odusami, M., Damaševičius, R., Milieškaitė-Belousovienė, E., & Maskeliūnas, R. (2024). Alzheimer's disease stage recognition from MRI and PET imaging data using Pareto-optimal quantum dynamic optimization. Heliyon, 10(15), e34402. https://doi.org/10.1016/j.heliyon.2024.e34402

[8] Mohamed, A. A., Sargent, E., Moriconi, C., Williams, C., Shah, S. M., & Lucke-Wold, B. (2025). Quantum computing in the realm of neurosurgery: A literature review. World Neurosurgery, 193, 8–14. https://doi.org/10.1016/j.wneu.2024.10.012

[9] Chandramohan, U. M. (2025). Quantum chemical and docking insights into cyclohexanecarboxylic acid, 2-pentadecyl ester: Interactions with Alzheimer's, estrogen receptor, and Ebola virus proteins. Next Research, 2(2), 100273. https://doi.org/10.1016/j.nexres.2025.100273

[10] Amoroso, N., et al. (2023). An explainable artificial intelligence approach to brain connectivity in Alzheimer's disease. Frontiers in Aging Neuroscience, 15, 1238065. https://doi.org/10.3389/fnagi.2023.1238065

[11] Belay, A. J., Walle, Y. M., & Haile, M. B. (2024). Deep ensemble learning and quantum machine learning approach for Alzheimer's disease detection. Scientific Reports, 14, 14196. https://doi.org/10.1038/s41598-024-61452-1

[12] Patil, S., & Kirange, D. (2023). Ensemble of deep learning models for brain tumor detection. In Proceedings of the International Conference on Machine Learning and Data Engineering (pp. 1–12).

[13] Chen, L., Qiao, H., & Zhu, F. (2022). Alzheimer's disease diagnosis with brain structural MRI using multiview-slice attention and 3D convolution neural network. Frontiers in Aging Neuroscience, 14, 871706. https://doi.org/10.3389/fnagi.2022.871706

[14] Lee, J. (2023). Mild cognitive impairment in relation to Alzheimer's disease: An investigation of principles, classifications, ethics, and problems. Neuroethics. https://doi.org/10.1007/s12152-023-09522-5

[15] Nigri, E., Ziviani, N., Cappabianco, F., Antunes, A., & Veloso, A. (2020). Explainable deep CNNs for MRI-based diagnosis of Alzheimer's disease. In Proceedings of the International Joint Conference on Neural Networks (IJCNN). https://doi.org/10.1109/IJCNN48605.2020.9206837

[16] Wang, S. (2012). Spectrum of disease severity in Alzheimer's disease. National Institutes of Health, 78(4), 596–612. https://doi.org/10.1002/msj.20279

Journal of Engineering and Technology for Industrial Applications

ISSN ONLINE: 2447-0228

ITEGAM-JETIA

Manaus, v.12 n.60, p.1195-1202. July/August, 2026.
DOI: https://doi.org/10.5935/jetia.v12i60.4041

RESEARCH ARTICLE OPEN ACCESS

PARAMETER ESTIMATION OF THE THREE-DIODE PHOTOVOLTAIC MODEL USING THE FLOW DIRECTION ALGORITHM

Dif Naas*[1], Dif Ismail[2], Obeidi Thameur[3]

[1, 2, 3]Department of Electronics and Communication, Faculty of Sciences and Technology, University of Djelfa, Algeria.
[2]Applied Automation and Industrial Diagnostics Laboratory (LAADI), University of Djelfa, Algeria.

[1]https://orcid.org/0000-0001-9474-6775, [2]https://orcid.org/0000-0002-7153-2480, [3]https://orcid.org/0009-0000-7573-9270

Email:*naas.dif@univ-djelfa.dz, i.dif@univ-djelfa.dz, t.obeidi@univ-djelfa.dz

ARTICLE INFO

Article History
Received: March 11, 2026
Reviewed: April 11, 2026
Accepted: July 11, 2026
Published: August 31, 2026

Keywords:
Photovoltaic (PV) models,
Three-diode model,
Parameter extraction,
Flow Direction Algorithm,
Convergence analysis.

ABSTRACT

Accurate parameter identification of photovoltaic (PV) models is essential for reliable performance prediction and optimization of energy systems. However, estimating the parameters of advanced equivalent circuit models is challenging due to the nonlinear and multimodal nature of their current–voltage (I–V) characteristics. This study proposes a parameter extraction approach based on the Flow Direction Algorithm applied to the Three-Diode Model (TDM). The method minimizes the root mean square error (RMSE) between measured and simulated I–V data while ensuring physically consistent parameter sets. The approach is validated using two benchmark photovoltaic devices: the **RTC** France solar cell and an amorphous silicon thin-film solar cell. For the **RTC** France cell, the proposed method achieves an RMSE of 7.3511×10^{-4} when fitting the experimental I–V characteristics using the TDM. For the amorphous silicon cell, the algorithm obtains an RMSE of 2.2939×10^{-5}, demonstrating a very close agreement between the measured and simulated electrical characteristics. These results confirm that the FDA-based optimization approach provides accurate parameter estimation for complex PV models, enabling reliable photovoltaic modeling and supporting improved performance analysis and energy system optimization.

Copyright ©2026 by authors and Galileo Institute of Technology and Education of the Amazon (ITEGAM). This work is licensed under the Creative Commons Attribution International License (CC BY 4.0).

I. INTRODUCTION

Photovoltaic (PV) technology has become a cornerstone of modern renewable energy systems due to its sustainability, reliability, and steadily declining costs. Accurate modeling of PV devices is essential for performance evaluation, system design optimization, and efficient integration into energy networks. Among the various modeling approaches, equivalent circuit models—such as the single-diode, double-diode, and three-diode configurations—are widely adopted because they provide a practical balance between modeling simplicity and predictive accuracy. However, estimating the parameters of these models remains a challenging task due to the nonlinear and high-dimensional nature of the optimization problem. Conventional optimization techniques often encounter difficulties in obtaining accurate and stable solutions, particularly under varying environmental conditions. Consequently, metaheuristic optimization algorithms have emerged as effective alternatives, offering strong capabilities for exploring complex search spaces and avoiding local minima. Within this framework, the Flow Direction Algorithm (FDA), inspired by hydrological runoff processes, provides an efficient strategy for parameter optimization. By simulating water flows toward a basin outlet, FDA effectively balances global exploration and local exploitation, enabling reliable convergence toward optimal solutions. In this study, FDA is applied to parameter identification for both monocrystalline silicon like **RTC** France and amorphous silicon (**a-Si**) thin-film photovoltaic cells. The performance of the algorithm is evaluated through comprehensive statistical analysis and compared with several state-of-the-art optimization techniques reported in the literature. Accurate modeling and parameter identification of photovoltaic modules are fundamental for maximizing energy harvesting, predicting long-term performance, and ensuring operational reliability under diverse and fluctuating environmental conditions.

Over the past decade, extensive research efforts have focused on developing robust and efficient methods for estimating the unknown parameters of diode-based PV models. Among these models, the Three-Diode Model (TDM) has attracted significant attention because of its superior ability to capture the complex nonlinear characteristics of PV cells, although it introduces a more challenging parameter extraction problem. The inherent difficulty of photovoltaic (PV) parameter identification arises from the multidimensional, nonlinear, and multimodal nature of the associated search space. Consequently, metaheuristic optimization techniques have become widely adopted due to their ability to efficiently explore complex solution landscapes. Over the past few years, numerous enhanced optimization strategies have been introduced to improve the precision and robustness of PV model parameter estimation. For example, the Improved African Vultures Optimization (I-AVO) algorithm, which integrates Opposition-Based Learning and Orthogonal Learning mechanisms, has demonstrated promising results when combined with the Newton–Raphson method for parameter refinement [1]. Likewise, the augmented Mountain Gazelle Optimizer (AMGOIB3H) has shown strong reliability and fast convergence when tested with experimental PV datasets [2]. Other studies have explored the incorporation of chaotic dynamics to enhance the exploration–exploitation balance of optimization algorithms. Approaches such as the Chaotic Dragonfly Algorithm [3] and the Fractal Henon Chaotic Harris Hawks Optimization (FCHHHO) method [4] have reported improved convergence behavior and greater robustness in parameter extraction tasks. In addition, a wide range of optimization techniques has been successfully applied to PV parameter estimation, including improved variants of the Whale Optimization Algorithm (IWOA and WOA) [5], [6], the Equilibrium Optimizer (EOA) [7], Ranking-based Generalized Normal Distribution Optimization (RGNDO) [8], the Innovative Optimization Algorithm (INFO) [9], the Crayfish Optimization Algorithm (COA) [10], the Improved Mountain Gazelle Optimizer (IMGO) [11], Mother Tree Optimization with Climate Change (MTO-CL) [12], the Puma Optimization Algorithm [13], and the bio-dynamics Grasshopper Optimization Algorithm (BDGOA) [14].

Additional approaches have also been explored, including Improved Teaching–Learning-Based Optimization (ITLBO) [15], the Interior Search Algorithm (ISA) [16], Classified Perturbation Mutation-Based Particle Swarm Optimization (CPMPSO) [17], the Fractional Chaotic Ensemble Particle Swarm Optimizer (FC-EPSO2) [18], and the Hybrid Successive Discretization Algorithm (HSDA) [19]. Furthermore, the Mountain Gazelle Optimizer has been applied to single-, double-, and triple-diode PV models for accurate solar cell and module parameter extraction [20]. Collectively, these contributions highlight the continuous progress toward achieving high-precision parameter identification with minimal modeling error under different PV technologies and operating conditions. More recently, hybrid frameworks combining optimization techniques with machine learning models have attracted increasing attention. In particular, the integration of deep learning architectures, such as Convolutional Neural Network–Long Short-Term Memory (CNN–LSTM) networks, with multiple optimization algorithms has improved prediction accuracy and facilitated early fault detection in large-scale PV systems [21]. At the same time, advances in equivalent circuit modeling—including scalable triple-diode circuits [22] and lumped-parameter three-diode models tailored for industrial silicon solar cells [23]—have strengthened the physical representation of PV behavior, especially in capturing temperature-dependent effects and the contributions of different current components. Despite these advances, achieving consistent parameter identification across real operating conditions remains challenging. Factors such as partial shading, temperature variations, and device aging introduce additional nonlinearities that complicate the estimation process. Therefore, further improvements in optimization strategies are required to enhance both the accuracy and reliability of parameter identification for practical PV applications. The main contributions of this study can be summarized as follows:

- **Application of the Flow Direction Algorithm (FDA) for parameter extraction:** The FDA is employed to estimate the unknown parameters of the Three-Diode Model (TDM).
- **Experimental validation using benchmark datasets:** The proposed methodology is validated using experimental measurements from a standard **RTC** France monocrystalline silicon solar cell and an amorphous silicon (**a-Si**) thin-film photovoltaic cell.
- **Comparative performance assessment:** The proposed approach is evaluated against several state-of-the-art methods, demonstrating improved accuracy relative to conventional formulations.

The remainder of this paper is organized as follows. Section 2 presents the mathematical modeling of the photovoltaic devices and the formulation of the cost function. Section 3 describes the parameter estimation methodology and the implementation of the Flow Direction Algorithm. Section 4 presents the results and discussion, including statistical analysis and comparisons with existing approaches. Finally, Section 5 concludes the paper and outlines potential directions for future research.

II. PHOTOVOLTAIC MODELING AND PROBLEM FORMULATION

II.1 THREE-DIODE EQUIVALENT CIRCUIT REPRESENTATION OF A PV MODULE

Accurate modeling of photovoltaic (PV) devices is essential for robust parameter identification and reliable performance evaluation. This section outlines the mathematical formulation of the three-diode model (TDM) for both the PV cell and its extension to the module level. The primary emphasis of this work is the precise extraction of the TDM parameters for the PV cell/module, together with the formulation of the objective function employed in the optimization process. Figure 1 illustrates the three-diode equivalent circuit of a photovoltaic (PV) panel, comprising a current source, three parallel-connected diodes, and both series and shunt resistances. The corresponding mathematical formulation is expressed as follows:

$$I = I_{ph} - I_{d_1}\left(exp\left(\frac{V + I.R_s}{n_1.V_t}\right) - 1\right) - I_{d_2}\left(exp\left(\frac{V + I.R_s}{n_2.V_t}\right) - 1\right) - I_{d_3}\left(exp\left(\frac{V + I.R_s}{n_3.V_t}\right) - 1\right) - \frac{V + I.R_s}{R_{sh}} \quad (1)$$

Let I_{ph} denote the photocurrent, $I_{d_1}, I_{d_2}, I_{d_3}$ the reverse saturation currents of the three diodes, and n_1, n_2, n_3 their respective ideality factors. The quantities R_s and R_{sh} correspond to the series and shunt resistances. The thermal voltage is defined as $V_t = \frac{K \times T}{q}$, where T represents the absolute cell temperature, K is the Boltzmann constant, and q denotes the elementary charge. Accordingly, the three-diode model (TDM) is governed by nine unknown parameters $(I_{ph}, I_{d_1}, I_{d_2}, I_{d_3}, n_1, n_2, n_3, R_s, R_{sh})$ which must be accurately identified to ensure precise representation of PV cell behavior.

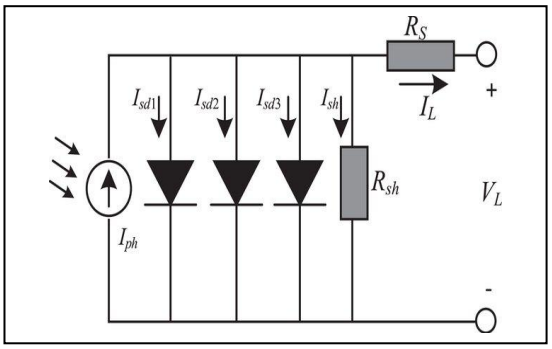


Figure 1: Three-diode (TDM) equivalent circuit model of the photovoltaic (PV) module.
Source: Authors, (2026).

II.2 OBJECTIVE FUNCTION FORMULATION

The estimation of unknown parameters in photovoltaic models is an optimization problem. The goal is to minimize the error between measured and predicted current-voltage (I-V) data. This requires a suitable objective function to quantify the error. A common metric for this task is the root mean square error (RMSE). The RMSE provides a statistical measure of the average discrepancy. It calculates the difference between observed and simulated current values. This metric is expressed as follows:

$$RMSE = \sqrt{\frac{1}{N}\sum_{i=1}^{N}\left(I_{mi} - I_{ci}(V_{mi}, I_{mi}, \theta)\right)^2} \tag{2}$$

In this formulation, $\boldsymbol{N}$ denotes the total number of experimental I–V data points, $\boldsymbol{I_{mi}}$ represents the measured current at voltage V_i, $\boldsymbol{I_c(V_i, \theta)}$ corresponds to the model-calculated current at the same voltage ontained using the Newton–Raphson method [24-26], and $\boldsymbol{\theta}$ defines the parameter vector to be optimized. The optimization relies on the RMSE criterion, which minimizes squared deviations between measured and predicted values, strongly penalizes large errors, and provides a reliable indicator of how accurately photovoltaic models reproduce actual device behavior.

III. FLOW DIRECTION ALGORITHM FOR PV PARAMETER ESTIMATION

Estimating photovoltaic (PV) model parameters is challenging due to the nonlinear and high-dimensional nature of the problem. Metaheuristic optimization techniques are particularly effective for this task, as they can explore complex solution spaces and avoid entrapment in local minima. Among these, the Flow Direction Algorithm (FDA) [27], [28] is a physics-inspired method based on hydrological runoff processes in drainage basins. The algorithm simulates water flowing downslope toward a basin outlet, which represents the global minimum of the objective function. FDA employs the D8 flow-direction approach as presented in figure 1, in which each cell in a discretized basin has eight neighbors, and runoff is directed toward the neighbor with the steepest descent.

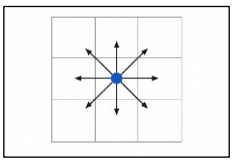


Figure 2: D8 neighborhood around the runoff flow cell.
Source: [28].

In FDA, each candidate solution corresponds to a flow in an n-dimensional search space, and its fitness value is analogous to the flow's elevation. Each flow interacts with neighboring positions within a defined radius, and its movement velocity is proportional to the slope between the current position and the neighbor. Flows move toward better-performing neighbors or, if none exist, toward either the global best solution or a randomly selected flow. The neighborhood radius is reduced linearly over iterations to balance global exploration and local exploitation, while the coefficient applied to the global best accelerates convergence.

Mathematically, the population is initialized randomly within the search bounds:

$$\text{Flow}\mathbf{Y}_i = \mathbf{lb} + \text{rand} \times (\mathbf{ub} - \mathbf{lb}) \tag{3}$$

Where $\text{Flow}\mathbf{Y}_i$ is the position vector of the i-th flow. Neighboring positions are generated as

$$\text{Neighbor}\mathbf{Y}_j = \text{Flow}\mathbf{Y}_i + \text{rand}_n \times \Delta \tag{4}$$

With rand_n following a normal distribution and Δ representing the neighborhood radius. Flow positions are then updated using

$$\text{Flow}\mathbf{Y}_i^{\text{new}} = \text{Flow}\mathbf{Y}_i + \mathbf{v} \times \frac{\text{Neighbor}\mathbf{Y}_j - \text{Flow}\mathbf{Y}_i}{\|\text{Neighbor}\mathbf{Y}_j - \text{Flow}\mathbf{Y}_i\|} \tag{5}$$

$$\mathbf{v} = \text{rand}_n \times \mathbf{S} \tag{6}$$

Where **S** represents the slope vector between the flow and its neighboring flows. The dual-strategy decision rule ensures flows move toward better solutions while maintaining exploration:

$$\begin{gathered}\text{if } f(\text{Flow}_t) < f(\text{Flow}_i)\text{: Flow}\mathbf{Y}_i^{\text{new}} = \text{Flow}\mathbf{Y}_i + \text{rand}_n \times (\text{Flow}_t - \text{Flow}\mathbf{Y}_i) \\ \text{else: Flow}\mathbf{Y}_i^{\text{new}} = \text{Flow}\mathbf{Y}_i + 2 \times \text{rand}_n \times (\text{BestFlow}\mathbf{Y} - \text{Flow}\mathbf{Y}_i)\end{gathered} \tag{7}$$

Through this hydrology-inspired mechanism, FDA effectively balances exploration and exploitation, enabling the identification of near-optimal or global solutions in complex, nonlinear optimization problems. Its effectiveness has been demonstrated across various engineering applications, including control system optimization, wireless sensor networks, and power system regulation. The main steps of FDA can be summarized as follows:

1. Initialize the flow population randomly within the search space and set Δ to its initial value.
2. Evaluate the fitness function for each flow.
3. Generate neighbors for each flow within the neighborhood radius Δ.
4. Update flow positions based on neighbor performance or the best global solution using the decision-making strategy.
5. Reduce Δ progressively according to a linear schedule to shift from global exploration to local exploitation.
6. Update the global best solution found so far.
7. Check the termination condition (e.g., maximum iterations or convergence criterion); if not satisfied, return to step 3.

By simulating hydrological runoff dynamics, FDA effectively balances exploration and exploitation, enabling the identification of near-optimal or global solutions in complex, nonlinear optimization problems. Its effectiveness has been demonstrated across diverse engineering applications, including control system optimization, wireless sensor networks, and power system regulation.

IV. RESULTS AND DISCUSSIONS

In these experimental investigations, the algorithm was configured with a population size of **100** and a maximum of **3000** iterations. Under these conditions, two photovoltaic (PV) configurations were investigated. The first case study involves a 57 mm-diameter monocrystalline silicon solar cell from R.T.C. France, tested at an irradiance of 1000 W/m² and a cell temperature of 33 °C. The second case concerns an amorphous silicon (**a-Si**) thin-film photovoltaic cell, evaluated at 25 °C under an irradiance of 1000 W/m². The lower and upper limits of the seven model parameters are presented in Table 1.

Table 1: Range of variables considered during the simulation process.

Parameters	**RTC**		**a-Si**	
	l_b	u_b	l_b	u_b
$I_{ph}(A)$	0	1	0	2
$I_{d1}, I_{d2,}, I_{d3}(\mu A)$	0	1	0	100
$R_s(\Omega)$	0	0.5	0	5
$R_{sh}(\Omega)$	0	100	0	2000
n_1, n_2, n_3	1	2	1	60

Source: Authors, (2026).

The proposed Flow Direction Algorithm (FDA) was validated using the previously described photovoltaic (PV) devices under standard operating conditions. The accuracy of the estimated parameters was quantitatively evaluated using the root mean square error (RMSE) between the experimental and simulated current–voltage (I–V) characteristics. This metric provides a reliable measure of the model's fitting capability across the entire operating range, including the short-circuit, knee, and open-circuit regions. For benchmarking purposes, the FDA was applied to the three-diode model (TDM) and its performance was compared with several recently reported state-of-the-art metaheuristic algorithms listed in the introduction. This framework enables a rigorous evaluation of convergence, stability, and robustness in addressing the nonlinear and multimodal nature of the TDM parameter estimation problem. Optimal parameter values were obtained from the best objective function outcomes across 30 independent trials to ensure statistical reliability. The FDA's performance was further analyzed using minimum, maximum, mean, and standard deviation (STD) of the RMSE values, collectively assessing precision, consistency, and practical applicability. Tables 2–5 present the optimal parameters of the nine-parameter TDM and the corresponding statistical analysis obtained over 30 runs for the **RTC** and **a-Si** solar cells. The RMSE values demonstrate the superior performance of the FDA.

The results in Table 2, along with the statistical comparison presented in Table 3 for **RTC** cells, provide a comprehensive assessment of metaheuristic algorithms for estimating the three-diode model (TDM) parameters, focusing on fitting accuracy, physical consistency, and robustness against the nonlinear, multimodal optimization landscape. The primary performance metric, the root mean square error (RMSE) between measured and modeled I–V characteristics, shows that the Flow Direction Algorithm (FDA) achieved the lowest RMSE (Best: 7.3511×10^{-4}, Worst: 7.5303×10^{-4}, Mean: 7.3773×10^{-4}, STD: 5.0229×10^{-6}), outperforming COA, IMGO, ITLBO, ISA, CPMPSO, RGNDO, and FC-EPSO2, while even small RMSE reductions remain significant near the knee and open-circuit regions. All algorithms converged on a photocurrent ($I_{ph} \approx 0.7605\ A$), but diode saturation currents (I_{d1}, I_{d2}, I_{d3}) exhibited higher variability due to parameter correlation and multimodality; FDA produced smoother scaling of diode currents and ideality factors, with n_2 and n_3 approaching physically consistent values of 2. Series resistance ($R_s \approx 0.038\ \Omega$) remained stable across algorithms, and shunt resistance (R_{sh}) stayed within realistic ranges for FDA and most competitive methods, demonstrating both numerical accuracy and physical plausibility. The TDM's nine-dimensional, strongly coupled, non-convex search space challenges many optimizers, with COA and IMGO showing higher RMSE likely due to premature convergence, whereas FDA's balanced exploration–exploitation strategy navigates the landscape effectively, achieving performance comparable to methods like FC-EPSO2 without excessive complexity. Overall, FDA provides the best compromise between convergence accuracy and parameter stability, with reduced dispersion in sensitive parameters highlighting its robustness. Accurate parameter extraction directly benefits predictive PV modeling, maximum power point tracking, performance analysis under varying conditions, and fault detection, showing that even marginal RMSE improvements, when accompanied by physically consistent parameters, enhance downstream applications. Collectively, these findings confirm FDA's suitability for high-precision TDM parameter identification and its broader applicability to other nonlinear energy system modeling problems.

Table 2: Optimal parameters for TDM of **RTC** Cells.

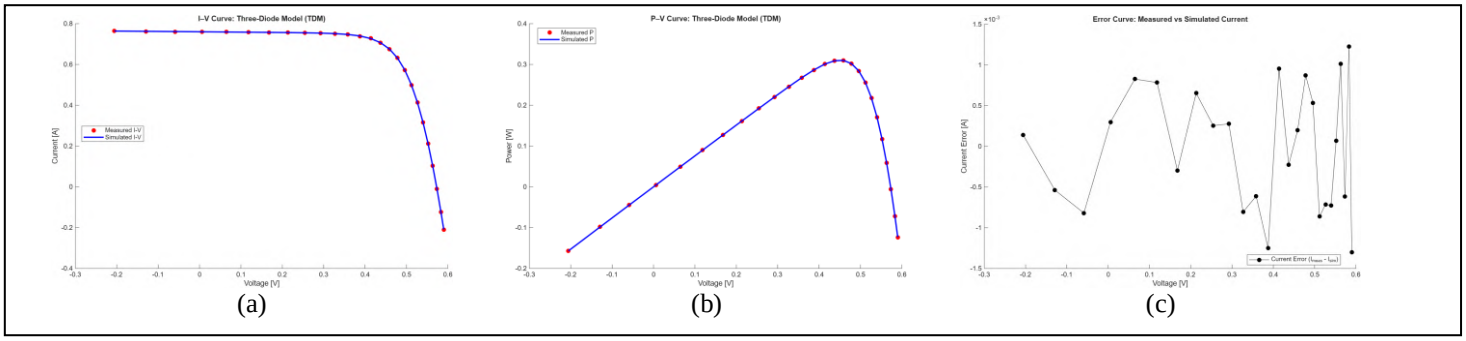
Cell	Parameters	FDA	COA [10]	IMGO [11]	ITLBO [15]	ISA [16]	CPMPSO [17]	RGNDO [8]	FC-EPSO2 [18]
RTC	$I_{ph}(A)$	**0.760812**	0.7604	0.7605	0.760500	0.760500	0.760500	0.760500	0.76080
	$I_{d1}(\mu A)$	**1.0**	1.39 e-03	1 e-03	2.98 e-02	1.21 e-01	9.62 e-02	9.08 e-02	8.2596 e-02
	$I_{d2}(\mu A)$	**1.0**	2.3325 e-01	8.18 e-03	9.17 e-01	1.00 e-03	3.73 e-01	1.96	6.9148 e-01
	$I_{d3}(\mu A)$	**9.81 e-02**	1.01 e-03	4.5409	1.86 e-03	1.68	1.67	1.58 e-01	4.4036 e-01
	$R_s(\Omega)$	**0.03789**	0.03784	0.04019	0.0381	0.0377	0.0379	0.0380	0.037215
	$R_{sh}(\Omega)$	**57.7760**	51.1585	82.1867	59.7254	59.5672	61.1542	61.3221	55.742
	n_1	**2**	1.3818	1.3932	1.3101	1.3995	1.3812	1.3766	1.3740
	n_2	**2**	1.4502	1.2093	1.7186	1.9936	1.9995	2.000	1.8449
	n_3	**1.3816**	1.948	1.9994	1.6611	2.000	1.9993	2.000	1.8333
	RMSE	**7.3511 e-04**	9.2288 e-04	9.2975 e-04	7.6180 e-04	7.5344 e-04	7.5082 e-04	7.5068 e-04	7.4025 e-04

Source: Authors, (2026).

Table 3: Results of the statistical comparison of **RTC** Cells (FDA).

Models	RMSE *Best*	RMSE *Worst*	RMSE *Mean*	RMSE *STD*
TDM	7.351100 e-04	7.530318 e-04	7.3772949 e-04	5.022918 e-06

Source: Authors, (2026).



(a) (b) (c)

Figure 3: Numerical and experimental results for the **RTC** France solar cell: (a) current–voltage (I–V) characteristics, (b) power–voltage (P–V) characteristics, and (c) error between the measured and estimated currents.
Source: Authors, (2026).

Figure 3 presents the I–V and power–voltage (P–V) characteristic curves of the TDM, along with the voltage-point error curves obtained using FDA. The results demonstrate that the simulated current and power values closely match the measured data across all voltage points, with minimal errors, confirming the reliability of the proposed FDA method in accurately capturing the actual behavior of solar cells through the TDM model. Table 4 presents the optimal parameters obtained for the **a-Si** solar cell, while Table 5 summarizes the statistical comparison over 30 independent trials. FDA achieved the lowest RMSE (Best: 2.2939×10^{-5}, Worst: 2.594509×10^{-5}, Mean: 2.468451×10^{-5}, STD: 5.649668×10^{-5}), outperforming HSDA and MGO. The photocurrent (I_{ph}) converged around 0.01132 A for all methods, whereas diode saturation currents (I_{d1}, I_{d2}, I_{d3}) and ideality factors (n_1, n_2, n_3) showed greater variability, reflecting the inherent parameter correlation and multimodality of the TDM. Series resistance ($R_s \approx 2.1\ \Omega$) and shunt resistance ($R_{sh} \approx 1500\ \Omega$) were consistent with physically realistic ranges for FDA.

Table 4: Optimal parameters for TDM of **a-Si** Cells.

Cell	Parameters	FDA	HSDA [19]	MGO [20]
a-Si	$I_{ph}(A)$	**0.01131958**	0.01133067	0.01133170
	$I_{d1}(\mu A)$	**91.9738982**	90.5914527	5.512063
	$I_{d2}(\mu A)$	**65.0000**	10.8816527	5.011604 e-02
	$I_{d3}(\mu A)$	**0.0147317**	0.0123991	1.056966 e-05
	$R_s(\Omega)$	**2.1**	2.24712579	0.500
	$R_{sh}(\Omega)$	**1500**	1108.3322476	600.7897
	n_1	**11.29963345**	9.99938271	5.0000
	n_2	**11.29971624**	10	2.710308
	n_3	**2.416746678**	2.3874133	4.999188
	$RMSE$	**2.2939 e-05**	2.4439838 e-05	4.097395 e-05

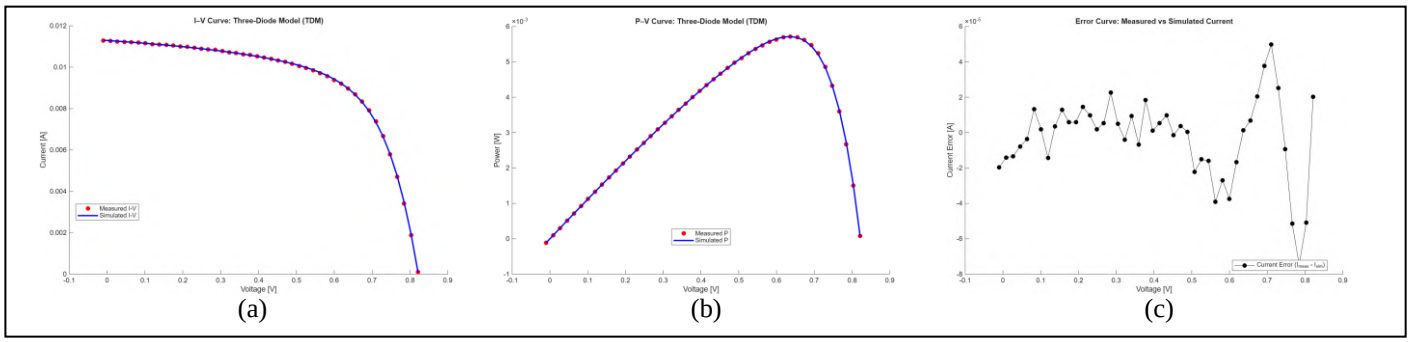
Source: Authors, (2026).

Table 5: Results of the statistical comparison of **a-Si** Cells.

Models	RMSE *Best*	RMSE *Worst*	RMSE *Mean*	RMSE *STD*
TDM	2.2939 e-05	2.594509 e-05	2.468451 e-05	5.649668 e-05

Source: Authors, (2026).

Figure 4 presents the I–V and power–voltage (P–V) characteristic curves for the **a-Si** cells along with the voltage-point error curves obtained using FDA. The results demonstrate that the simulated current and power values closely match the measured data across all voltage points, with minimal errors, confirming that FDA reliably captures the actual behavior of **a-Si** solar cells. These findings indicate that FDA not only minimizes RMSE but also produces parameter sets that are physically interpretable and electrically coherent, confirming its robustness and suitability for high-precision modeling of **a-Si** photovoltaic devices.



(a) (b) (c)

Figure 4: Numerical and experimental results for the **a-Si** cell: (a) current–voltage (I–V) characteristics, (b) power–voltage (P–V) characteristics, and (c) error between the measured and estimated currents.
Source: Authors, (2026).

In summary, the comparative analysis for both **RTC** and **a-Si** photovoltaic cells demonstrates that the Flow Direction Algorithm (FDA) consistently outperforms other state-of-the-art metaheuristic methods in terms of RMSE, convergence stability, and physical plausibility of the extracted parameters. The statistical results from Tables 3 and 5 confirm the reliability and robustness of FDA across multiple independent trials, while the I–V and P–V curves in Figures 3 and 4 illustrate excellent agreement between simulated and experimental data, with minimal voltage-point errors. Overall, FDA not only provides highly accurate parameter identification for both monocrystalline and amorphous silicon cells but also ensures physically consistent and electrically coherent parameter sets, highlighting its applicability to complex, nonlinear photovoltaic models. These findings support the use of FDA for precise PV system modeling, maximum power point tracking simulations, performance assessment under varying environmental conditions, and potential fault detection and degradation studies, demonstrating its practical value for both research and industrial applications.

V. CONCLUSIONS

In this study, the Flow Direction Algorithm (FDA) was proposed for high-precision identification of critical parameters in three-diode model (TDM) photovoltaic cells. Simulation experiments were conducted on two PV cell types: the monocrystalline **RTC** France cell and the amorphous silicon (**a-Si**) thin-film cell. The FDA was benchmarked against several state-of-the-art metaheuristic algorithms. For the **RTC** cells, FDA achieved the lowest RMSE of 7.3411×10^{-4}, outperforming all compared methods and providing the most reliable solution for TDM parameter optimization. Similarly, for **a-Si** cells, FDA achieved an RMSE of 2.426899×10^{-5}, confirming its superior accuracy and robustness. The I–V and P–V characteristic curves further validated the FDA results, demonstrating excellent agreement between simulated and experimental data with minimal errors, indicating that FDA accurately captures the actual behavior of both monocrystalline and amorphous solar cells. These findings confirm that FDA not only ensures highly accurate and physically consistent parameter estimation but also maintains robustness in the nonlinear, multimodal search space inherent to TDM PV models. Given its demonstrated effectiveness and feasibility, FDA constitutes a powerful tool for PV system modeling, maximum power point tracking, performance evaluation under varying environmental conditions, and potential fault detection.

Future research will focus on improving FDA performance through hybridization with other metaheuristic or local search strategies to further enhance convergence speed, solution diversity, and global optimization capability. Looking forward, the proposed algorithm can be extended to address high-dimensional renewable energy optimization problems with complex constraints and applied to modified or emerging PV models reported in the literature, highlighting its potential for broader applications in energy system analysis and optimization.

VI. AUTHOR'S CONTRIBUTION

Conceptualization: Naas Dif, Ismail Dif and Obeidi Thameur.
Methodology: Naas Dif, Ismail Dif and Obeidi Thameur.
Investigation: Naas Dif, Ismail Dif and Obeidi Thameur.
Discussion of results: Naas Dif, Ismail Dif and Obeidi Thameur.
Writing – Original Draft: Naas Dif.
Writing – Review and Editing: Naas Dif, Ismail Dif, and Obeidi Thameur.
Resources: Naas Dif.
Supervision: Naas Dif, Ismail Dif and Obeidi Thameur.
Approval of the final text: Naas Dif, Ismail Dif and Obeidi Thameur.

VII. REFERENCES

[1] C. Kumar and D. M. Mary, "Parameter estimation of three-diode solar photovoltaic model using an Improved-African Vultures optimization algorithm with Newton–Raphson method," J. Comput. Electron., vol. 20, no. 6, 2021, doi: 10.1007/s10825-021-01812-6.

[2] K. Chandrasekaran, A. S. R. Thaveedhu, P. Manoharan, and V. Periyasamy, "Optimal estimation of parameters of the three-diode commercial solar photovoltaic model using an improved Berndt-Hall-Hall-Hausman method hybridized with an augmented mountain gazelle optimizer," Environ. Sci. Pollut. Res., vol. 30, no. 20, 2023, doi: 10.1007/s11356-023-26447-x.

[3] M. K. Singla, P. Nijhawan, and A. S. Oberoi, "Parameter estimation of three diode solar PV cell using chaotic dragonfly algorithm," Soft Comput., vol. 26, no. 21, 2022, doi: 10.1007/s00500-022-07425-w.

[4] Z. Garip, "Parameters estimation of three-diode photovoltaic model using fractional-order Harris Hawks optimization algorithm," Optik (Stuttg)., vol. 272, 2023, doi: 10.1016/j.ijleo.2022.170391.

[5] O. Ajetunmobi, T. A. Khan, S. A. A. Rizvi, and R. H. Ali, "Improved parameter estimation of triple-diode photovoltaic systems," J. Comput. Electron., vol. 24, no. 6, 2025, doi: 10.1007/s10825-025-02405-3.

[6] O. S. Elazab, H. M. Hasanien, M. A. Elgendy, and A. M. Abdeen, "Parameters estimation of single- and multiplediode photovoltaic model using whale optimisation algorithm," in IET Renewable Power Generation, 2018. doi: 10.1049/iet-rpg.2018.5317.

[7] M. A. Soliman, A. Al-Durra, and H. M. Hasanien, "Electrical Parameters Identification of Three-Diode Photovoltaic Model Based on Equilibrium Optimizer Algorithm," IEEE Access, vol. 9, 2021, doi: 10.1109/ACCESS.2021.3065386.

[8] M. Abdel-Basset, R. Mohamed, A. El-Fergany, M. Abouhawwash, and S. S. Askar, "Parameters identification of pv triple-diode model using improved generalized normal distribution algorithm," Mathematics, vol. 9, no. 9, 2021, doi: 10.3390/math9090995.

[9] M. A. El-Dabah, R. A. El-Sehiemy, H. M. Hasanien, and B. Saad, "Photovoltaic model parameters identification using an innovative optimization algorithm," IET Renew. Power Gener., vol. 17, no. 7, 2023, doi: 10.1049/rpg2.12712.

[10] D. S. Abdelminaam, A. S. Alluhaidan, F. H. Ismail, and S. A. El-Rahman, "Parameters Extraction of the Three-Diode Photovoltaic Model Using Crayfish Optimization Algorithm," IEEE Access, vol. 12, 2024, doi: 10.1109/ACCESS.2024.3421286.

[11] D. Salama AbdElminaam et al., "Parameter estimation of photovoltaic models based on improvement of moutain gazelle optimizer algorithm," Front. Energy Res., vol. 13, 2025, doi: 10.3389/fenrg.2025.1464011.

[12] M. El Marghichi et al., "Accurate extraction of electrical parameters in three-diode photovoltaic systems through the enhanced mother tree methodology: A novel approach for parameter estimation," PLoS One, vol. 20, no. 3 March, 2025, doi: 10.1371/journal.pone.0318575.

[13] D. A. Zaki, H. M. Hasanien, M. Alharbi, and C. Sun, "Precise three-diode photovoltaic model for photovoltaic modules based on Puma optimizer," Ain Shams Eng. J., vol. 15, no. 12, 2024, doi: 10.1016/j.asej.2024.103170.

[14] M. Jabari et al., "Parameter identification of PV solar cells and modules using bio dynamics grasshopper optimization algorithm," IET Gener. Transm. Distrib., vol. 18, no. 21, 2024, doi: 10.1049/gtd2.13279.

[15] S. Li et al., "Parameter extraction of photovoltaic models using an improved teaching-learning-based optimization," Energy Convers. Manag., vol. 186, 2019, doi: 10.1016/j.enconman.2019.02.048.

[16] A. Fathy and H. Rezk, "Robust electrical parameter extraction methodology based on Interior Search Optimization Algorithm applied to supercapacitor," ISA Trans., vol. 105, 2020, doi: 10.1016/j.isatra.2020.05.016.

[17]J. Liang et al., "Classified perturbation mutation based particle swarm optimization algorithm for parameters extraction of photovoltaic models," Energy Convers. Manag., vol. 203, 2020, doi: 10.1016/j.enconman.2019.112138.

[18] D. Yousri, S. B. Thanikanti, D. Allam, V. K. Ramachandaramurthy, and M. B. Eteiba, "Fractional chaotic ensemble particle swarm optimizer for identifying the single, double, and three diode photovoltaic models' parameters," Energy, vol. 195, 2020, doi: 10.1016/j.energy.2020.116979.

[19] A. M. Deaconu, D. T. Cotfas, and P. A. Cotfas, “Extracting photovoltaic cells parameters for three diode model using HSDA algorithm,” Energy Reports, vol. 12, 2024, doi: 10.1016/j.egyr.2024.10.052.

[20] M. Madhiarasan, G. Fotis, M. Presser, and M. J. Beliatis, “Mountain Gazelle Optimiser-based single, double, and triple diode models associated solar cells and panels parameters extraction,” Discov. Sustain., vol. 6, no. 1, 2025, doi: 10.1007/s43621-025-01679-8.

[21] S. P. Yang, F. R. Shih, C. M. Huang, S. J. Chen, and C. H. Chiua, “A Deep Learning-Based Ensemble Method for Parameter Estimation of Solar Cells Using a Three-Diode Model,” Electron., vol. 14, no. 19, 2025, doi: 10.3390/electronics14193790.

[22] H. K. Khyani and J. Vajpai, “Development of triple-diode based generalized model of photovoltaic module,” e-Prime - Adv. Electr. Eng. Electron. Energy, vol. 12, 2025, doi: 10.1016/j.prime.2025.100964.

[23] V. Khanna, B. K. Das, D. Bisht, Vandana, and P. K. Singh, “A three diode model for industrial solar cells and estimation of solar cell parameters using PSO algorithm,” Renew. Energy, vol. 78, 2015, doi: 10.1016/j.renene.2014.12.072.

[24] L. Chaib, M. Tadj, A. Choucha, F. Z. Khemili, and A. EL-Fergany, “Improved crayfish optimization algorithm for parameters estimation of photovoltaic models,” Energy Convers. Manag., vol. 313, p. 118627, Aug. 2024, doi: 10.1016/J.ENCONMAN.2024.118627.

[25] A. Elhammoudy et al., “Dandelion Optimizer algorithm-based method for accurate photovoltaic model parameter identification,” Energy Convers. Manag. X, vol. 19, p. 100405, Dec. 2023, doi: 10.1016/J.ECMX.2023.100405.

[26] R. Abbassi, S. Saidi, H. Jerbi, L. Ladhar, and M. Omri, “Accurate parameters extraction of photovoltaic models using Lambert W-function collaborated with AI-based Puma optimization method,” Results Eng., vol. 25, p. 104268, Mar. 2025, doi: 10.1016/J.RINENG.2025.104268.

[27] H. Karami, M. V. Anaraki, S. Farzin, and S. Mirjalili, “Flow Direction Algorithm (FDA): A Novel Optimization Approach for Solving Optimization Problems,” Comput. Ind. Eng., vol. 156, p. 107224, Dec. 2021, doi: 10.1016/J.CIE.2021.107224.

[28] D. K. Mahmoud, S. H. Aleem, A. M. Ibrahim, M. M. Sayed, and W. Abdelfattah, “Flow direction algorithm for optimal coordination of directional overcurrent relays considering arc flash,” Results Eng., vol. 25, p. 103964, Dec. 2025, doi: 10.1016/J.RINENG.2025.103964.

Journal of Engineering and Technology for Industrial Applications

ITEGAM-JETIA

Manaus, v.12 n.60, p.1203-1214. July/August, 2026.
DOI: https://doi.org/10.5935/jetia.v12i60.4051

ISSN ONLINE: 2447-0228

RESEARCH ARTICLE OPEN ACCESS

ACOUSTIC PERFORMANCE AND MODELING OF SUSTAINABLE SCB/PVA COMPOSITE MATERIALS

Amit Shinde*[1] and Vijaykumar Pandey[2]

[1]Research Scholar, Department of Mechanical Engineering, Vivekanand Global University, Jaipur, Rajasthan, India.
[2]Associate Professor, Department of Mechanical Engineering, Vivekanand Global University, Jaipur, Rajasthan, India.

[1]https://orcid.org/0000-0002-4247-0284, [2]https://orcid.org/0000-0002-5258-4779

Email:*shindeamit333@gmail.com, vijay_pandey@vgu.ac.in

ARTICLE INFO

Article History
Received: March 12, 2026
Reviewed: April 13, 2026
Accepted: July 13, 2026
Published: August 31, 2026

Keywords:
Acoustic materials,
Johnson-Champoux-Allard model,
Natural fiber composites,
Sugarcane bagasse,
Sound absorption coefficient.

ABSTRACT

The rising need to use sustainable and environmentally friendly materials in place of synthetic acoustic materials has resulted in the rising popularity of natural fiber composites. Sugarcane bagasse (SCB), an agricultural by-product that contains a high level of fibrous material, is also a potential solution in the sound absorption applications because of its porous structure and biodegradability. The purpose of the research is to compare the acoustic behavior of SCB-based composite panels bonded with polyvinyl acetate (PVA), and to compare experimentally obtained sound absorption coefficients (SAC) and those obtained using mathematical models. Three levels of SCB content (40%, 50% and 60%) and three thicknesses (10 mm, 20 mm and 30 mm) were used to make composite panels. The panels were described in terms of airflow resistivity, porosity, and tortuosity and the SAC values were determined using an impedance tube in accordance with ASTM E1050 and ISO 10534-2. The Miki, Delany-Bazley (DB) and Johnson-Champoux-Allard (JCA) models were also used to predict the SAC. Findings have shown that adding more SCB content and panel thickness has a significant effect on SAC especially at the low and mid frequency bands. Panels with 60% SCB and 30 mm thickness recorded the highest SAC values of more than 0.9, which validated their outstanding sound-absorbing performance. The JCA model was the closest to the experimental data among the models analyzed with the Miki and DB models under-predicted. This paper confirms SCB/PVA composites as a potential solution to sustainable acoustic panels usage.

Copyright ©2026 by authors and Galileo Institute of Technology and Education of the Amazon (ITEGAM). This work is licensed under the Creative Commons Attribution International License (CC BY 4.0).

I. INTRODUCTION

The issue of environmental noise control has become a burning problem because of its prevalence among the population, mental health, and industrial performance. The long-term effects of noise pollution are negative health outcomes, such as hearing loss, stress, and cardiovascular issues, which necessitate the development of effective sound mitigation measures [1–4]. Sound-absorbing concrete and fiber-based panels have become vital in the construction sector to improve the acoustic comfort of high-density urban housing and commercial buildings, where the building code tends to insist on the use of noise control measures on walls, floors, and facades [4], [5]. Likewise, in the automotive sector, where the comfort and sustainability of consumers intersect, natural fiber-based and composite acoustic materials are actively studied to minimize cabin noise and vehicle weight, which can help to comply with the regulations and compete in the market [6–8]. The development of acoustic materials has also influenced the design of the public space, studios, and transport systems, where porous absorbers, micro-perforated panels, and bio-based composites are used to improve the quality of sound and environmental sustainability [9–11]. All of these developments highlight the growing need in the contemporary engineering and urban development sector to have efficient, cheap, and environmental-friendly noise control materials.

The use of porous materials and natural fiber composites has become an attractive sustainable substitute to the traditional synthetic sound absorbers because of their low environmental impact, biodegradability, and good acoustic performance. In comparison with synthetic fibers, including fiberglass or mineral wool, which are energy-intensive to produce and potentially dangerous to health, natural fibers like coconut coir, banana, kenaf, or sugarcane bagasse are similar in terms of sound absorption properties and reduce the environmental impact [12–16]. These natural materials are commonly made out of agricultural by-products and have high porosity and tortuosity which is important in dissipating energy and absorbing sound. Natural fiber boards have proven to be as effective in reducing noise coefficients as synthetic ones in building acoustics and contribute to the sustainability agenda [17–19]. The materials are not only concerned with waste valorization but also provide economic benefits due to low-cost production and renewability, which increases their applicability in automotive, aerospace, and architectural projects where high lightweight and effective acoustic insulation is needed [20–23]. All these results support the sustainability of natural porous composites as eco-friendly high-performance sound absorbers that will substitute synthetic counterparts in the next-generation acoustic solutions. The agro-industrial byproduct of sugarcane bagasse (SCB) has received growing interest as a sustainable raw material in the production of acoustic insulation because of the combination of physical and morphological properties. It is very absorbent in the range of low to mid-frequency because of its naturally porous and fibrous microstructure that allows effective dissipation of sound energy through friction, reflection, and resistance to air flow [10], [24–26]. SCB also has a low bulk density, which makes it lightweight and easy to handle, and it has low structural load in building and automotive designs [27–30]. Biodegradability is one of its most significant characteristics, which means that it can be used as a fully environmentally friendly alternative to synthetic acoustic panels that can be a safety concern to dispose of and be dangerous to human health. The capacity of SCB composites to achieve or surpass the acoustic performance of synthetic foams and be completely compostable at the end of the lifecycle has been confirmed in several studies [14], [31–34]. Porosity, light weight, and biodegradability are the key characteristics that make sugarcane bagasse a highly promising, green material that can be used in future acoustic applications in construction, transportation, and environmental engineering.

The mathematical modeling has now been a vital tool in the precise prediction of the sound absorption coefficient (SAC) of porous materials, which allows efficient designing of materials, saves of costs, and decreases the need to use time-consuming experimental testing. Conventional models like Delany Bazley, Johnson Champoux Allard (JCA), and Miki have been extensively applied to correlate physical and non-acoustic parameters of porous media with their frequency-dependent absorption behavior, and more recent models combine transfer matrix methods (TMM), finite element modeling (FEM), and inverse characterization methods [35–39]. Artificial intelligence methods like neural networks and deep learning have also been adopted in recent research to enhance the accuracy of prediction in complex geometries and real-world scenarios [40], [41]. Such modeling methods allow better insight into the acoustic behavior and optimize bio-based and composite materials to be used in architectural, automotive, and industrial noise control. The scientific literature has shown that natural fiber-based composites have a promising future in terms of acoustic performance and sustainability, which can be used as an alternative to synthetic materials in sound insulation. According to [17], low-density banana fiber boards were found to have the highest noise reduction coefficient of five types of natural fibers, whereas [42] determined kenaf fiber to be the most efficient in reducing noise in a variety of real-world sources, with up to 7.82 dB of sound reduction. In support of this, [43] showed that kenaf and Calotropis gigantea fibers in polypropylene composites offered high-mid frequency sound absorption and structural performance in the automotive applications. Likewise, [10] also produced sugarcane bagasse and bamboo charcoal composites that recorded more than 70 percent absorption in a humid environment, which has a potential in vehicle cabin applications. In other research with high-level modeling, [44] reported high SAC values of over 0.95 with close agreement to JCA predictions of CS-CSS composites, whereas [45] validated Typha Latifolia panels with JCAL and Attenborough models with a high degree of accuracy of about 95. Material innovation research is ongoing with [20] reporting SACs up to 0.604 with banana fiber-reinforced epoxy composites and [46] reporting SACs > 0.5 with date palm and pineapple fiber-based composites, which also exhibited good thermal and mechanical performance. Other eco-friendly materials like Grewia Optiva [47] and jutealoe vera laminates [48] had high SACs with the latter having 0.47 at 3000 Hz based on stacking order. According to [49], the insulators made of hemp outperformed the traditional insulators such as mineral wool in SAC with a peak of 0.99 at 2000 Hz.

Also, [50] emphasized the multifunctional character of jute-cork panels, which has better strength, thermal resistance, and 35% higher SAC than gypsum boards. Hybrid compositions like sisal-palm fiber with epoxy resin were also found to work, [51] found a 76.61% increase in SAC at 4000 Hz with this type of composition compared to others. Finally, [52] proved that natural fiber-glass wool-polyfiber sandwich composites are appropriate to use on walls and ceilings because of the increased absorption in the mid-to-high frequency range. The overall implications of these findings are that bio-based composites have a potential to develop high-performance sustainable acoustic solutions in the construction, automotive, and architectural industry. New developments in acoustic modelling have investigated numerous computational and experimental methods to forecast the sound absorption characteristics of natural fibre composites and designed porous structures. To model sound absorption of grid network structures, [53] proposed a one-dimensional transfer matrix method, which compares well with simulation and experimental outcomes and thus validates its practical use. The JCA model was used to predict the sound absorption properties of kenaf fiber-based porous absorbers and was experimentally validated by [31] and demonstrated high sound absorption properties depending on the thickness of the material, bulk density, and surface treatments, including spacer fabrics. In the data-driven modeling field, [54] used an artificial neural network (ANN) with airflow resistivity as the only input and was able to predict the sound absorption coefficient of multilayer fibrous materials more accurately than the conventional TMM methods based on Delany-Bazley and JCA models, especially in the high-frequency range of 30006000 Hz. Likewise, [55] showed that ANN was effective in predicting the acoustic behavior of broom fibers, and their model had a high correlation with the experimental values and was more predictive than linear regression. A detailed study of Yucca Gloriosa fibers by [56] through the integration of morphological characterization and 3D structural simulations revealed that the JCA model was better predictive over a wide frequency range (63-6300 Hz) than the Delany-Bazley and Garai-Pompoli models.

In line with these works, [57] optimized kenaf-reinforced polyurethane composites with response surface methodology and discovered that JCA model better predicted frequency-dependent acoustic behavior when compared to Delany-Bazley model, and also obtained a significant 35.4% increase in sound absorption compared with neat PU foam. Taken together, these works indicate the changing paradigm of mathematical and artificial intelligence-based modeling methods that contribute to the predictive quality and realistic design of bio-based acoustic materials. Although many studies have been done on natural fiber composites to apply in acoustic applications, there is a significant gap in the overall comparison of the experimentally determined SAC with the predictions of various established mathematical models, especially the composites that are made of SCB, which is a widely available but poorly utilized agro-waste. The originality of the work is that SCB/PVA composite panels are developed and the acoustic behavior of these panels is modeled in detail by Delany-Bazley, Miki and JCA models at different thicknesses and compositions. In contrast to the previous research which only examines experimental or single model analysis, this study gives a systematic analysis and verification of the various predictive models with regard to experimental data. The relevance of the study is based on the fact that it contributes to sustainable material development through encouraging the utilization of SCB waste in functional acoustic products and developing model-based design of sound-absorbing materials with a sustainable environment.

II. METHODOLOGY

In order to examine the acoustic behavior of sugarcane bagasse based composites, panels were made under controlled conditions and tested in a standardized impedance tube set up. This method was used to assure uniformity in material preparation and accuracy in measuring frequency dependent sound absorption properties.

II.1 COMPOSITE FABRICATION

The composite fabrication process entailed the fabrication of sugarcane bagasse (SCB)-based panels with the help of polyvinyl acetate (PVA) as a binding agent. The first step involved the collection of raw bagasse in the local sugar mills, sun-drying, and grinding to get fine and uniformly distributed fibers. These fibers were filtered using standard mesh in order to eliminate large particles and to achieve uniformity in the composite matrix. The bagasse was combined with the PVA binder in a weight ratio of 1:1 to provide enough bonding and structural strength. The fiber-binder mixture was stirred by a mechanical mixer to attain homogeneity and then cast into rectangular moulds of size 110 mm x 120 mm. In order to investigate the influence of thickness on acoustic properties, three panel thicknesses were made: 10 mm, 20 mm, and 30 mm. The samples were pressed at a constant load of 90 kgf and allowed to dry under pressure in 48 hours. The panels were dried under natural sunlight conditions (72 hours) after the molding process to finish the curing process and eliminate moisture. This was done to provide dimensional stability and sufficient bonding of the composite. Nine samples were made in three levels of composition SCB40, SCB50, and SCB60, which represents 40, 50, and 60 percent of bagasse content by weight respectively as presented in Table 1.

Table 1: Composition and Thickness Variants of Fabricated SCB/PVA Composite Panels.

Sample Code	SCB Content (%)	PVA Content (%)	Thickness (mm)
SCB40-10	40	60	10
SCB40-20	40	60	20
SCB40-30	40	60	30
SCB50-10	50	50	10
SCB50-20	50	50	20
SCB50-30	50	50	30
SCB60-10	60	40	10
SCB60-20	60	40	20
SCB60-30	60	40	30

Source: Authors, (2026).

For illustration, three composite panels (SCB60) with 10mm, 20mm and 30mm thickness are depicted in the Figure 1.

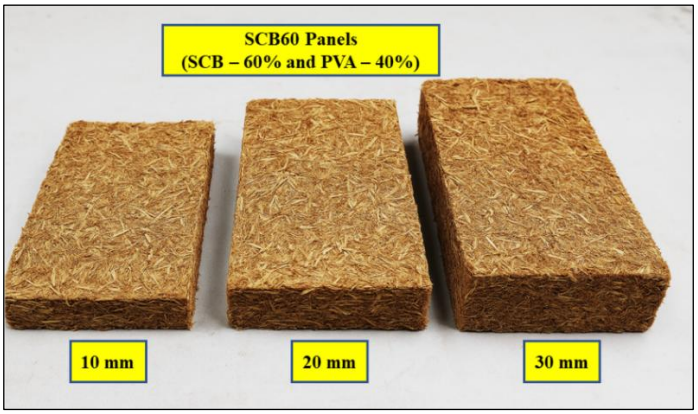
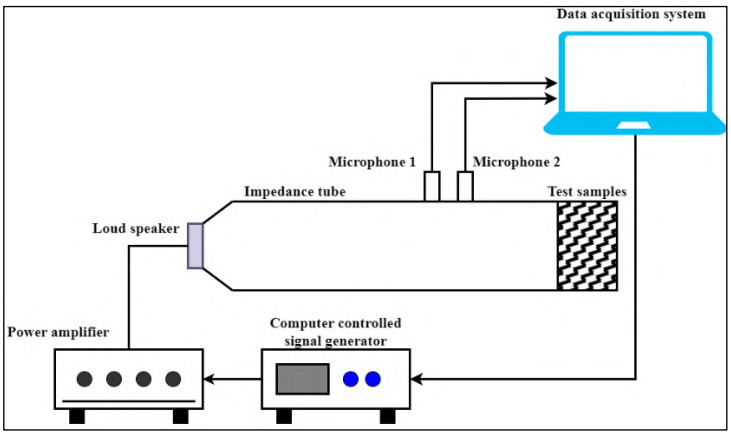


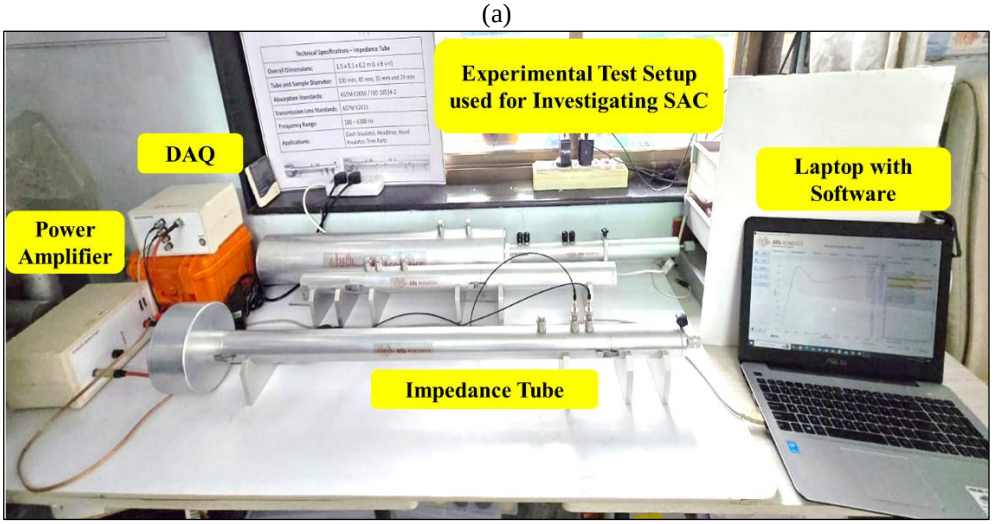
Figure 1: SCB60 Composite Panels with 10 mm, 20 mm and 30 mm thickness.
Source: Authors, (2026).

II.2 EXPERIMENTAL ACOUSTIC TESTING

Experimental assessment of the acoustic performance of the SCB/PVA composite panels was done using an impedance tube system as per ISO 10534-2 and ASTM E1050 standards. This system consists of a loudspeaker at one end of a cylindrical tube and two fine microphones at the opposite end of the tube at a specified distance to measure the incident and reflected sound pressure levels. The composite sample is put at the other end of the tube supported by a rigid termination to approximate the conditions of installation in the real world. A random noise signal was produced by a broadband and was introduced into the loudspeaker using a power amplifier and the microphones measured the sound field produced. The complex reflection coefficient was calculated using the transfer function method and the normal incidence SAC was determined using the formula $\alpha = 1 - |R|^2$. The measurements were conducted in the frequency range of 125 Hz to 4000 Hz to comprehensively evaluate the acoustic absorption behavior of the composite in the low, mid and high frequency ranges. Figure 2 demonstrates schematic layout and photograph of the impedance tube experimental set-up.



(a)



(b)

Figure 2: Impedance Tube Setup for SAC Measurement Based on ISO 10534-2 (a) schematic layout and (b) photograph.
Source: Authors, (2026).

III. MATHEMATICAL MODELS FOR PREDICTION OF SOUND ABSORPTION COEFFICIENT

In order to examine the acoustic behavior of sugarcane bagasse based composites, panels were made under controlled conditions and experimented by a standardized impedance tube configuration. This method guaranteed the stability of material preparation and the accuracy of measuring the frequency-dependent sound absorption properties.

III.1 MIKI MODEL

Miki model is a semi-empirical acoustic model that is employed to model the sound absorption behavior of porous materials especially fibrous composites like natural fiber-based panels. It provides a simplified version of more complicated theoretical models such as the JCA model because it uses fewer material parameters but still can make fairly accurate predictions, particularly in materials where airflow resistivity is the most important controlling factor. The Miki model is based on the Delany-Bazley empirical model but with altered expressions of power-law characteristic impedance and complex wave number to make it applicable to a wider frequency range. The Miki model assumes that the material is a rigid-frame, isotropic, macroscopically homogeneous porous material, and its acoustic behavior can be well modeled using only flow resistivity and frequency, without necessarily modeling microstructural properties such as porosity, tortuosity, or characteristic lengths. This assumption simplifies the model computationally and simple to use, particularly in the preliminary material design phase or the rapid prototyping phase.

The dimensionless frequency parameter X, defined as $X = \frac{f}{\sigma/\rho_0}$, where f is the frequency in Hz, σ is the airflow resistivity (in Pa·s/m²), and ρ_0 is the density of air (typically 1.21 kg/m³), is central to the model. The normalized characteristic impedance: $\frac{Z_c}{\rho_0 c_0}$ and normalized complex wave number $\frac{k}{\omega/c_0}$ are given by the empirical relations:

$$\frac{Z_c}{(\rho_0 c_0)} = 1 + 0.070\, X^{-0.632} - i * 0.107\, X^{-0.632} \quad (1)$$

$$\frac{k}{\omega/c_0} = 1 + 0.109X^{-0.618} - i \cdot 0.160X^{-0.618} \quad (2)$$

Where c_0 is the speed of sound in air and $\omega = 2\pi f$ is the angular frequency. Once the characteristic impedance Z_c and wave number k are calculated using these equations, the input impedance Z of the porous layer of thickness d can be determined as $Z = -iZ_c \cot(kd)$, assuming the material is backed by a rigid surface. The normal-incidence sound absorption coefficient $\alpha(f)$ is then calculated using the impedance mismatch equation:

$$\alpha(f) = 1 - \left|\frac{Z - Z_0}{Z + Z_0}\right|^2 \quad (3)$$

Where $Z_0 = \rho_0 c_0$ is the characteristic impedance of air. The importance of the Miki model is that it is easy to use and gives realistic acoustic forecasts with minimum input criteria, thus it is particularly appropriate in the initial acoustic description of natural fiber composites, including sugarcane bagasse-polymer mixtures. Although it is not as sensitive to the microstructure as more sophisticated models, its simplicity and empirical accuracy make it a useful instrument in the study of acoustic materials and in the engineering domain.

III.2 DELANY-BAZLEY MODEL

The Delany-Bazley model is a traditional empirical model that has been employed to model the acoustic behavior of fibrous and porous sound-absorbing materials, especially at mid-to-high frequencies. The model was developed in the 1970s after much experimental effort on fibrous glass materials had been done, and simple mathematical expressions were developed to represent the complex characteristic impedance and wave number of a porous medium in terms of the airflow resistivity of the material and the frequency of the incident sound wave. This model assumes that the porous material is a rigid-frame structure, in which the frame is not moved by sound waves, the material is homogeneous and isotropic and is thick enough that structural resonance effects and backing effect do not dominate the response. The most important simplification of the Delany-Bazley model is that it fails to consider microstructural parameters of porosity, tortuosity, or characteristic lengths, which reduces its accuracy but increases its utility in the practical engineering context. The model introduces a dimensionless frequency parameter $X = \frac{f}{\sigma}$, where f is the frequency in hertz and σ is the airflow resistivity in . Based on this parameter, the normalized characteristic impedanin.and normalized wave number $\frac{k_0}{k}$ are given by the following empirical formulas:

$$\frac{Z_0}{Z_c} = 1 + 0.0571X^{-0.754} - i \cdot 0.087X^{-0.732} \quad (4)$$

$$\frac{k_0}{k} = 1 + 0.0978X^{-0.7} - i \cdot 0.189X^{-0.595} \quad (5)$$

Where $Z_0 = \rho_0 c_0$ is the characteristic impedance of air, and $k_0 = \frac{\omega}{c_0}$ is the wave number in free air. Once the characteristic impedance and wave number are computed, the sound absorption coefficient at normal incidence can be derived using the same impedance-based relation used in other models:

$$\alpha(f) = 1 - \left|\frac{Z - Z_0}{Z + Z_0}\right|^2 \quad (6)$$

Where $Z = -iZ_c \cot(kd)$, and d is the thickness of the absorbing layer. The Delany-Bazley model is notable because it is simple and only one measurable property, airflow resistivity, is needed to give reasonably accurate predictions of many industrial fibrous materials. It is however most accurate in high porosity, high resistivity materials at frequencies above 500 Hz and less accurate at low frequencies or non-fibrous structures. In spite of these shortcomings, it is an empirically-based and easy to use tool that is popular in preliminary acoustic design, benchmarking, and education in the material acoustics field.

III.3 JOHNSON-CHAMPOUX-ALLARD (JCA) MODEL

The Johnson-Champoux-Allard (JCA) model is a well-known theoretical model that is applied to predict the acoustic behavior of porous materials, especially in estimating the sound absorption coefficient of porous materials at normal and oblique incidences.

The JCA model was developed as an extension of the simpler empirical models, and includes physical effects like viscous and thermal dissipation in the pores of a rigid-frame porous medium, and is particularly applicable to fibrous and granular composites, such as sugarcane bagasse-based materials. This model is based on the fact that the material is an equivalent fluid, i.e. the solid matrix does not contribute to the wave propagation, and is at rest. The JCA model treats the propagation of sound in porous media as a problem of two important frequency-dependent quantities, the complex effective density of the material $\rho(\omega)$, and the complex effective bulk modulus of the material $K(\omega)$. The equation of the effective density is:

$$\rho(\omega) = \rho_0 \cdot \alpha_\infty \left(1 + \frac{\sigma \emptyset}{i\omega\rho_0\alpha_\infty} \sqrt{1 + \frac{4i\alpha_\infty^2 \eta \rho_0 \omega}{\sigma^2 \Lambda^2 \phi^2}} \right) \tag{7}$$

Where ρ_0 is the air density, α_∞ is the tortuosity, $\emptyset$ is the porosity, σ is the airflow resistivity, η is the dynamic viscosity of air, ω is the angular frequency, and Λ is the viscous characteristic length. Similarly, the complex bulk modulus is expressed as:

$$\mathrm{K}(\omega) = \frac{\gamma \mathrm{P}_0}{\gamma - (\gamma - 1)\left(1 + \frac{8\eta}{\mathrm{i}\omega\rho_0 \mathrm{Pr}\Lambda'^2}\right)^{-1/2}} \tag{8}$$

where $P0$ is atmospheric pressure, γ is the specific heat ratio of air, Pr is the Prandtl number, and Λ' is the thermal characteristic length. These parameters are the energy losses of the acoustic wave to the porous structure through viscous and thermal interaction. Once $\rho(\omega)$ and $K(\omega)$ are determined, the characteristic impedance Zc and complex wave number k are calculated as $Zc = \rho(\omega)\cdot K(\omega)$ and $k = \omega\rho(\omega)/K(\omega)$, respectively. The input impedance Z of the material layer of thickness d is then computed using the relation $Z = -iZc$ cot (kd). Lastly, the normal-incidence SAC, $\alpha(f)$ is obtained with the help of the formula of impedance mismatch:

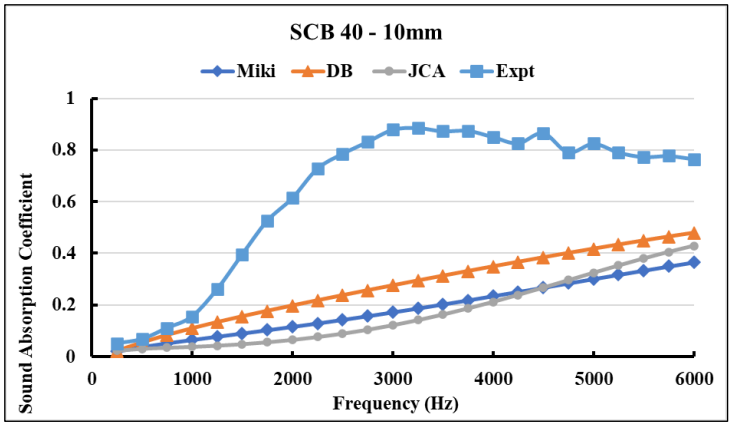
$$\alpha(\mathrm{f}) = 1 - \left| \frac{\mathrm{Z} - \mathrm{Z}_0}{\mathrm{Z} + \mathrm{Z}_0} \right|^2 \tag{9}$$

Where $Z0 = \rho0\ c0$ is the characteristic impedance of air. The JCA model is especially important as it is capable of capturing the complete frequency-dependent behavior of porous materials with reasonable precision, assuming that its input parameters, including porosity, tortuosity, flow resistivity and characteristic lengths, are well-characterized. Although it presupposes a solid frame that is rigid and may not apply to flexible or viscoelastic materials, its capability to include realistic microstructural effects in predictive acoustics makes it a foundation of the modeling of sound-absorbing composite materials.

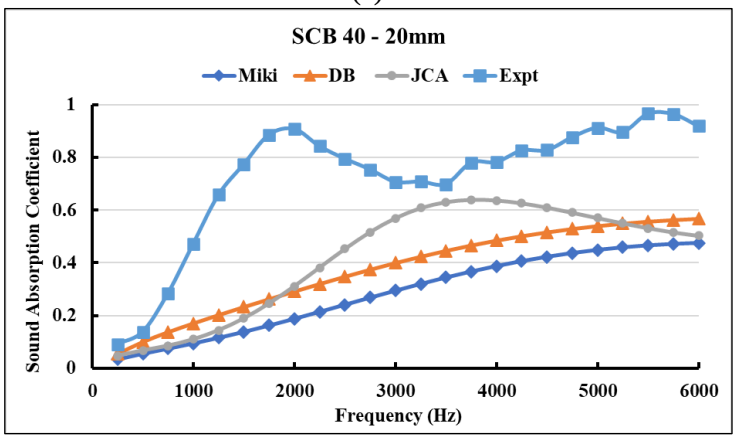
IV. RESULTS AND DISCUSSION

IV.1 SCB40 COMPOSITE PANEL

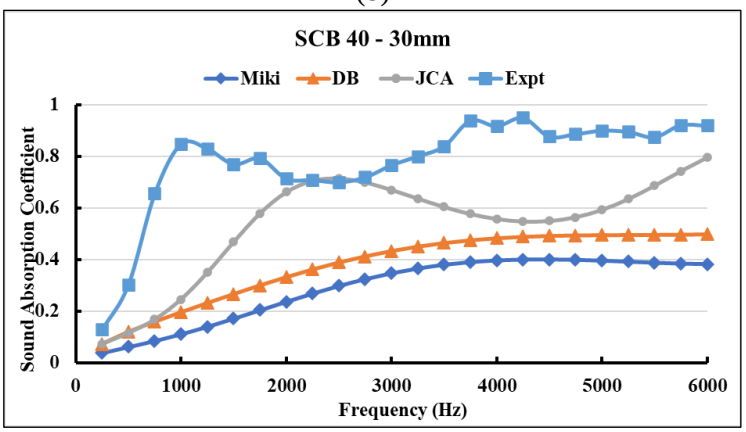
Figure 3(a), 1(b) and 1(c) show the comparison of SAC values of experimental measurements and three popular theoretical models - Miki, DB and JCA of SCB40 composite panels with thickness of 10 mm, 20 mm and 30 mm respectively. The results show that the SAC increases significantly as the panel thickness increases, especially in the low-frequency range. In the case of the 10 mm panel in Figure 3(a) the experimental findings suggest that the highest SAC is about 0.88 around 3000 Hz and there is not much absorption in the low-frequency band. DB and Miki models are the ones that moderately reflect the rising trend but always underestimate the value, whereas the JCA model is a bit closer to predictions, particularly after 2000 Hz. In Figure 3(b), the 20 mm panel is shown to have better low-frequency absorption, and experimental SAC is more than 0.9 in the mid-frequency range. In this case, the JCA model provides a much more accurate fit to experimental data, especially at frequencies between 1500 and 4000 Hz, as DB and Miki are still under-predicting performance. This enhancement in the predictive accuracy of JCA can be explained by the fact that its predictive model incorporates poroelastic parameters such as tortuosity, flow resistivity, and characteristic lengths that are important in the description of the intricate internal structure of natural fiber composites. This tendency is also supported by figure 3(c), where the 30 mm panel has a high SAC in a broad frequency range, and the experimental values are always above 0.7 since 800 Hz. The JCA model is close to the experimental data throughout the range, and it is more predictive than both DB and Miki models. These observations confirm the usefulness of the JCA model in the modeling of thick, fibrous composites such as SCB/PVA panels, where airflow resistivity, porosity, and viscous-thermal interactions are the most important factors in governing acoustic behavior. On the whole, the discussion shows that simpler empirical models can give approximate predictions, the JCA model can make a more robust and physically based predictions of SAC in natural fiber-based acoustic materials, especially when the panel thickness is large.



(a)



(b)



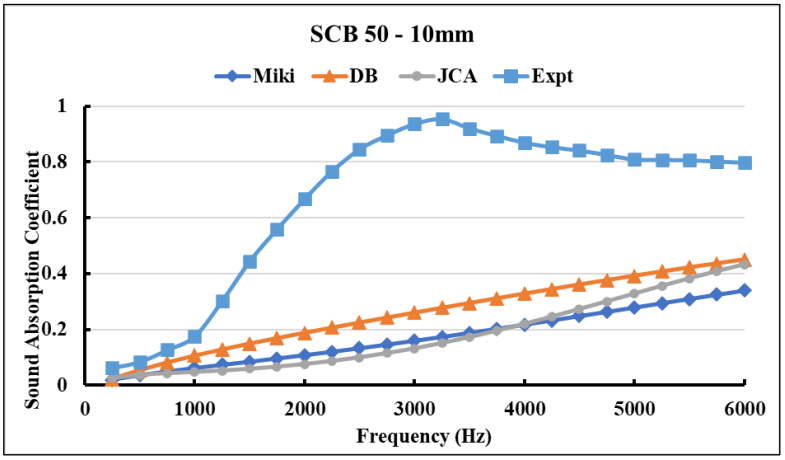
(c)

Figure 3: Comparison of SAC estimation with various mathematical models with experimental data for SCB40 composite.
Source: Authors, (2026).

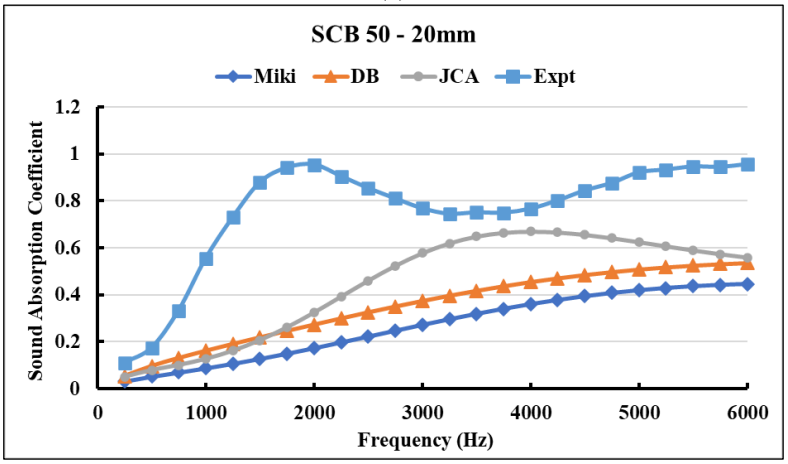
IV.2 SCB50 COMPOSITE PANEL

Figures 4(a), 4(b), and 4(c) show the comparison of experimental and model-predicted values of SAC of SCB50 composite panels of thicknesses 10 mm, 20 mm, and 30 mm, respectively. In Figure 4(a), the sharp increase in SAC with frequency is observed in the 10 mm thick panel, and it reaches its maximum value of about 0.92 at about 3000 Hz in the experimental results. Nevertheless, none of the three mathematical models, Miki, DB and JCA predict the SAC significantly underestimating the SAC at the frequency spectrum, especially at mid and high frequencies. The DB model demonstrates the nearest approximation yet it is far below experimental values. Figure 4(b) shows that the 20 mm thick panel has a better low-frequency absorption with the experimental SAC values being higher than 0.95 in the 15002500 Hz range and steadily high after that. In this case, the JCA model starts to agree with the experimental trend much better, particularly between 1500 and 4000 Hz, as DB and Miki models are still under-predicting. The better predictive capability of the JCA model can be attributed to the fact that the model incorporates the essential parameters of tortuosity, airflow resistivity and characteristic lengths, which enable the model to better depict the complicated porous structure and energy dissipation behavior of the SCB/PVA composite. Figure 4(c) is the experimentally determined SAC of the 30 mm thick panel, where the broad peak of the SAC is again observed to be near unity in the frequency range of 1000 to 3000 Hz, and the SAC is found to have values above 0.8 in most of the frequency range. The JCA model is no exception and shows the closest correspondence to experimental evidence and proves the soundness of its applicability to the modeling of thicker natural fiber composites.

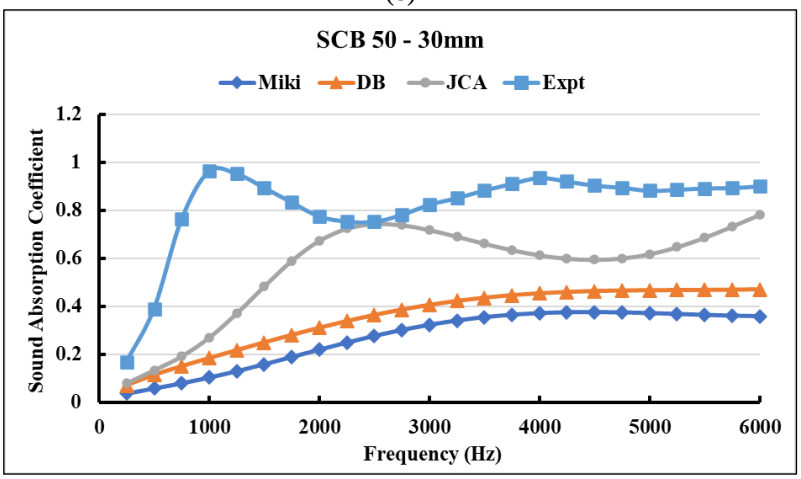
Although the DB and Miki models are marginally better than the case of thinner samples, they still do not represent the higher absorption levels well. These findings support the finding that the JCA model offers the most credible prediction of SAC of all the models tested especially in mid-thickness and thick panels. The growing correspondence of the experimental results to the increasing panel thickness also confirms the idea that the proper modeling of acoustic performance in natural fiber composites should take into consideration the advanced material-specific parameters, which are well-considered in the JCA framework.



(a)



(b)



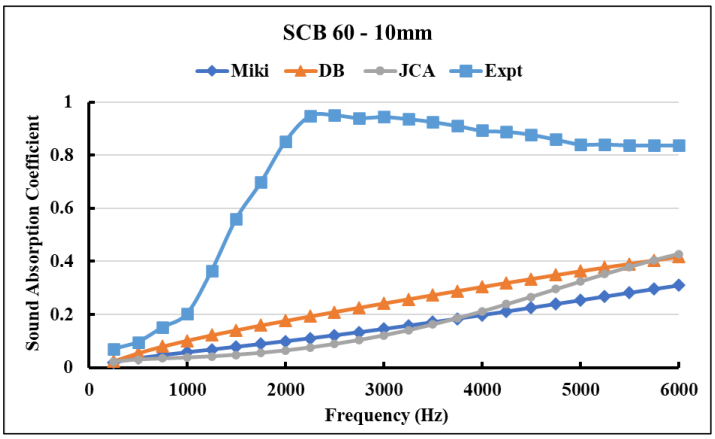
(c)

Figure 4: Comparison of SAC estimation with various mathematical models with experimental data for SCB50 composite.
Source: Authors, (2026).

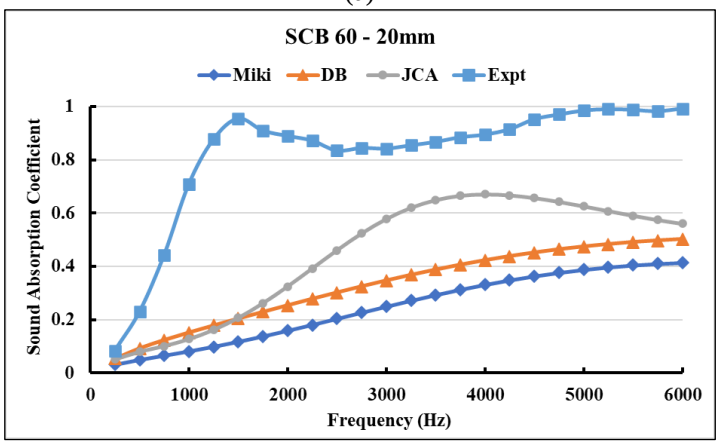
IV.3 SCB60 COMPOSITE PANEL

Figures 5(a), 5(b), and 5(c) show the comparison of SAC of SCB60 composite panels with the thicknesses of 10 mm, 20 mm, and 30 mm, respectively, by using experimental measurements and three predictive models, namely, Miki, DB, and JCA models. Figure 5(a) shows that the SCB60 panel of 10 mm thickness has good SAC performance, with experimental values reaching a peak of about 0.93 at about 2500 Hz and a value of 0.8 throughout much of the mid-frequency range. The JCA model gives the nearest approximation of the models especially above 2000 Hz, and both the DB and Miki models are always underestimating the SAC.

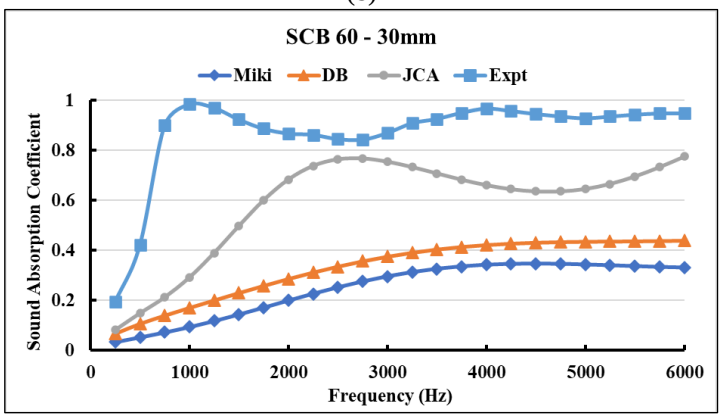
The experimental SAC is not only better at lower frequencies as the panel thickness is increased to 20 mm in Figure 5(b), but also has values above 0.85 over a wider range of frequencies, with values approaching unity above 4000 Hz. The JCA model is in line with the trend of the experiment, particularly between 1500 and 4000 Hz, and the peak and the wider absorption bandwidth is captured. In the meantime, DB and Miki models perform better as compared to the 10 mm case but still are far below the magnitude of the SAC. The experimental SAC of the 30 mm thick panel in Figure 5(c) is high throughout the entire frequency spectrum with a maximum of approximately 0.96 and sustained absorption of approximately 0.9 within a wide band. The JCA model shows an amazing capacity to reproduce this trend especially at 1500 Hz and above, both in shape and the level of the experimental curve. This high correlation points to the strength of the JCA model of predicting the acoustic behavior of thick, porous composite with large SCB content. The enhancement in the accuracy of the model as the panel thickness and the proportion of SCB increase can be explained by the increased porosity and internal structure that the JCA model can capture well due to the incorporation of parameters like the tortuosity, the viscous and thermal characteristic length, and the flow resistivity. On the contrary, the DB and Miki models, which are more empirical and designed to work with traditional fibrous absorbers, do not capture the intricate interactions that occur in bio-based composites and thus do not predict much. These observations confirm the applicability of the JCA model in the correct modeling of SAC in sustainable composites, particularly at higher fiber content and panel thickness, where the coupling between acoustic waves and the internal porous structure becomes more and more prevalent.



(a)



(b)



(c)

Figure 5: Comparison of SAC estimation with various mathematical models with experimental data for SCB60 composite.
Source: Authors, (2026).

V. CONCLUSION

The study examined the acoustic performance of sustainable composite panels constructed of SCB and PVA through experimental and theoretical methods. Composite samples of different SCB content (40%, 50%, and 60%) and thicknesses (10 mm, 20 mm and 30 mm) were made. They were experimentally measured in terms of their sound absorption coefficients (SAC) using an impedance tube according to ASTM E1050/ISO 10534-2. Moreover, SAC was modeled by three known mathematical models Miki, D) and JCA and model predictions were compared with experimental results.

- Adding SCB content and panel thickness increased SAC, particularly at low-to-mid frequencies because of increased porosity and internal damping.
- Thicker high-SCB panels had greater values of experimental SAC, which showed excellent sound absorption.
- JCA model gave more close correspondence with experiment results, particularly with thicker samples.
- DB and Miki models under-predicted SAC in all the samples, which validated the constraints of modeling complex natural fiber composites.

Future research can focus on hybrid binders or multilayer to maximize broadband absorption. Also, machine learning models can be combined with numerical simulations to enhance predictive performance and inform the design of bio-based acoustic materials to meet a variety of applications.

VI. AUTHOR'S CONTRIBUTION

Conceptualization: Amit Shinde and Vijaykumar Pandey.
Methodology: Amit Shinde and Vijaykumar Pandey.
Investigation: Amit Shinde and Vijaykumar Pandey.
Discussion of results: Amit Shinde and Vijaykumar Pandey.
Writing – Original Draft: Amit Shinde and Vijaykumar Pandey.
Writing – Review and Editing: Amit Shinde and Vijaykumar Pandey.
Resources: Amit Shinde and Vijaykumar Pandey.
Supervision: Amit Shinde and Vijaykumar Pandey.
Approval of the final text: Amit Shinde and Vijaykumar Pandey.

VII. REFERENCES

[1] Tao Y, Ren M, Zhang H and Peijs T 2021 Recent progress in acoustic materials and noise control strategies – A review Appl. Mater. Today 24 101141

[2] El-Basheer T M and Mohamed H K 2023 Recent progress in acoustical materials and noise control approach J. Meas. Sci. Appl. JMSA 3 32–41

[3] Singh C, Kumar M and Chandravanshi M L 2020 Evaluation of Noise Absorption Capacity of Various Materials IOP Conf. Ser. Mater. Sci. Eng. 893 012004

[4] Amran M, Fediuk R, Murali G, Vatin N and Al-Fakih A 2021 Sound-Absorbing Acoustic Concretes: A Review Sustainability 13 10712 https://doi.org/10.3390/su131910712

[5] Kumbhar Mr V P 2024 Industrial Noise Abatement Study by Using Natural Materials INTERANTIONAL J. Sci. Res. Eng. Manag. 08 1–15

[6] Hou Z, Ma X, Pan L, Zhang R and Wang L 2024 Study on the sound absorption characteristics and noise reduction mechanism of coconut-shell-activated carbon particles and coconut fiber composite biomass sound-absorption materials Mater. Res. Express 11 115603

[7] Putra A, Oliveira T, Souli M and Kassim D H 2021 Characterizing and modeling of acoustical performance of natural sound absorber Multiphysics Simulations in Automotive and Aerospace Applications (Elsevier) pp 49–64

[8] Mohamed, Sulaeman E, Dianne A and Abidin A Z 2022 Influence of Surface Discontinuity on Sound Absorption Coefficient of Vehicle Interior Material IOP Conf. Ser. Mater. Sci. Eng. 1244 012003

[9] Laxmi V, Thakre C, Bisarya A and Vijay R 2023 An innovative approach for the development of sound absorbing material using industrial wastes Constr. Build. Mater. 369 130523

[10] Sakthivel S, Senthil Kumar S, Solomon E, Getahun G, Admassu Y, Bogale M, Gedilu M, Aduna A and Abedom F 2021 Sound absorbing and insulating properties of natural fiber hybrid composites using sugarcane bagasse and bamboo charcoal J. Eng. Fibers Fabr. 16 15589250211044818

[11] Takahashi H, Yamamoto T, Komatsu Y, Yamakawa K, Katsura D and Yukawa H 2023 Predicting the effect of microstructural variations in porous sound absorbers on their sound absorption performance using the perturbation method INTER-NOISE NOISE-CON Congr. Conf. Proc. 268 5343–53

[12] Yang T, Hu L, Xiong X, Petrů M, Noman M T, Mishra R and Militký J 2020 Sound Absorption Properties of Natural Fibers: A Review Sustainability 12 8477

[13] Prabhune S, Munde Y, Shinde A and Siva I 2022 Appraising the Acoustic Performance and Related Factors of Natural Fiber: A Review J. Nat. Fibers 19 13475–94

[14] Jaturonlux N and Ratanawilai T 2023 PERFORMANCE OF WOOD COMPOSITES WITH NATURAL FIBER AS SOUND ABSORBER OF BUILDING MATERIALS Suranaree J. Sci. Technol. 30 010220(1-10)

[15] Xu Y, Li W, Zhu M, Yue X and Wang M 2020 Novel porous fiber-based composites with excellent sound-absorbing and flame-retardant properties J. Wood Chem. Technol. 40 285–93

[16] Tripathi A, Jha N K, Hota R N, Kumar A and Tyagi R 2024 Green sound-absorbing material prepared by using natural fiber for building acoustics Proc. Inst. Mech. Eng. Part E J. Process Mech. Eng. 09544089241253973

[17] Sharma S K, Shukla S R and Sethy A K 2020 Acoustical behaviour of natural fibres-based composite boards as sound-absorbing materials J. Indian Acad. Wood Sci. 17 66–72

[18] Chattaviriya P, Supawantanakul D, Sangsirimongkolying R and Sua-Iam G 2022 Banana Fibers as a Sustainable Acoustic Absorbing Materials: A Review Trends Sci. 19 4498

[19] Rino A, Prasetiyo I, Adhika D R, Sunendar B and Putra A 2024 Development of porous composite ceramic with sugarcane fiber filler for sound absorber materials Build. Acoust. 31 3–13

[20] Pitchumani S V, Perianayaghi A M, Bharathi B S, Gopalan V, Sampath A and Loganathan T G 2024 Comparison studies on acoustic behaviour of natural fibre-reinforced polymer matrix composites Proc. Inst. Mech. Eng. Part E J. Process Mech. Eng. 09544089241282482

[21] Hassan H 2020 Comparing the performance of passive and active double and single slope solar stills incorporated with parabolic trough collector via energy, exergy and productivity Renew. Energy 148 437–50

[22] Fatima A, Qayyum N, Zaid M, Rafat Y, Zain Khan M, Ali R and Salem B 2021 Feasibility of manufacturing sustainable bio-composites from agricultural waste Mater. Today Proc. 47 7136–9

[23] Temesgen A G, Eren R, Aykut Y and Süvari F 2021 Evaluation of Enset Fabric Reinforced Green Composite as Sound Absorber Structure Tekst. Ve Konfeksiyon 31 73–81

[24] Pan J, Zhou X, Gao Y, Qian Y and Lyu L 2024 Structural characteristics properties of sugarcane bagasse and its sound absorption as composites Text. Res. J. 94 1347–57

[25] Mehrzad S, Taban E, Soltani P, Samaei S E and Khavanin A 2022 Sugarcane bagasse waste fibers as novel thermal insulation and sound-absorbing materials for application in sustainable buildings Build. Environ. 211 108753

[26] Nigam A 2021 Acoustic Performance Evaluation of Sugarcane Bagasse Using Ambient Sound Meter and Scanning Electron Microscopy Int. J. Res. Appl. Sci. Eng. Technol. 9 1985–96

[27] El-Metwaly E A, Mohamed H E, El-Basheer T M, Moselhy M T H, Zulfiqar S, Cochran E W and Maamoun A A 2024 Eco-conscious upcycling of sugarcane bagasse into flexible polyurethane foam for mechanical & acoustic relevance RSC Adv. 14 23683–92

[28] Ramlee N A, Jawaid M, Ismail A S, Zainudin E S and Yamani S A K 2021 Evaluation of Thermal and Acoustic Properties of Oil Palm Empty Fruit Bunch/Sugarcane Bagasse Fibres Based Hybrid Composites for Wall Buildings Thermal Insulation Fibers Polym. 22 2563–71

[29] Beheshti M H, Khavanin A, Safari Varyani A, Yahya M N B, Alami A, Khajenasiri F and Talebitooti R 2022 Improving the Sound Absorption of Natural Waste Material-based Sound Absorbers Using Micro-perforated Plates J. Nat. Fibers 19 5199–210

[30] Malawade U A and Jadhav M G 2020 Investigation of the Acoustic Performance of Bagasse J. Mater. Res. Technol. 9 882–9

[31] Taban E, Soltani P, Berardi U, Putra A, Mousavi S M, Faridan M, Samaei S E and Khavanin A 2020 Measurement, modeling, and optimization of sound absorption performance of Kenaf fibers for building applications Build. Environ. 180 107087

[32] Puyana-Romero V, Chuquín J S A, Chicaiza S I M and Ciaburro G 2023 Characterization and Simulation of Acoustic Properties of Sugarcane Bagasse-Based Composite Using Artificial Neural Network Model Fibers 11 18

[33] Ahmadi P, Efhamisisi D, Thévenon M-F, Hosseinabadi H Z, Oladi R and Gerard J 2024 Chemically Modified Sugarcane Bagasse for Innovative Bio-Composites. Part One: Production and Physico-Mechanical Properties J. Renew. Mater. 12 1715–28

[34] Haghighat M, Samaei S E, Amininasab S, Faridan M, Mehrzad S, Sheikhmozafari M J and Taban E 2023 The Impact of Fiber Size on the Sound Absorption Behavior of Composites Made from Sugarcane Bagasse Wastes Fibers J. Nat. Fibers 20 2175760

[35] Radičević B 2025 MODELS FOR PREDICTING SOUND ABSORPTION OF POROUS MATERIALS Facta Univ. Ser. Work. Living Environ. Prot. 213

[36] Zhao Y, Xu J, Davy J L, Liu Z and Fard M 2022 Prediction of random incidence sound absorption coefficients of porous materials Appl. Acoust. 189 108625

[37] Kuznetsova S, Allein F, Deleplanque S, Dubus B and Miniaci M 2024 Hierarchical porous metamaterial for sound absorption INTER-NOISE NOISE-CON Congr. Conf. Proc. 270 9582–9

[38] Pereira M, Mareze P H, Godinho L, Amado-Mendes P and Ramis J 2021 Proposal of numerical models to predict the diffuse field sound absorption of finite sized porous materials – BEM and FEM approaches Appl. Acoust. 180 108092

[39] Santoni A, Bonfiglio P, Fausti P and Pompoli F 2021 Computation of the Alpha Cabin Sound Absorption Coefficient by Using the Finite Transfer Matrix Method (FTMM): Inter-Laboratory Test on Porous Media J. Vib. Acoust. 143 021012

[40] Zea E, Brandão E, Nolan M, Cuenca J, Andén J and Svensson U P 2023 Sound absorption estimation of finite porous samples with deep residual learning J. Acoust. Soc. Am. 154 2321–32

[41] Emmerich L, Aste P, Brandão E, Nolan M, Cuenca J, Svensson U P, Maeder M, Marburg S and Zea E 2025 A data-driven two-microphone method for in-situ sound absorption measurements

[42] Bahl S, Cambow R and Kumar Bagha A 2020 An experimental study to measure the acoustical properties of natural fibers at real case broadband excitations Mater. Today Proc. 28 1279–84

[43] Kaliappan S and Natrayan L 2024 Polypropylene Composite Materials with Natural Fiber Reinforcement: An Acoustic and Mechanical Analysis for Automotive Implementations International Conference on Trends in Automotive Parts Systems and Applications (Kuniamuthur, Coimbatore, India) pp 2023-01–5130

[44] Abdi D D, Monazzam M, Taban E, Putra A, Golbabaei F and Khadem M 2021 Sound absorption performance of natural fiber composite from chrome shave and coffee silver skin Appl. Acoust. 182 108264

[45] Khosro S K, Soltani P, SheikhMozafari M J, Piégay C, Amininasab S, Faridan M, Taban E and Monazzam Esmaeelpour M R 2025 Acoustical, thermal, and mechanical performance of Typha Latifolia fiber panels: Experimental evaluation and modeling for sustainable building applications J. Build. Eng. 99 111579

[46] Ali M, Al-Suhaibani Z, Almuzaiqer R, Albahbooh A, Al-Salem K and Nuhait A 2024 New Composites Derived from the Natural Fiber Polymers of Discarded Date Palm Surface and Pineapple Leaf Fibers for Thermal Insulation and Sound Absorption Polymers 16 1002

[47] Kalauni K and Pawar S J 2023 An Experimental Investigation and Theoretical Modelling for Sound Absorption Performance of Grewia Optiva Fiber Reinforced Composite Fibers Polym. 24 1821–33

[48] Senthilrajan S, Venkateshwaran N, Giri R, Ismail S O, Nagarajan R, Krishnan K and Mohammad F 2024 Mechanical, vibration damping and acoustics characteristics of hybrid aloe vera /jute/polyester composites J. Mater. Res. Technol. 31 2402–13

[49] Gumanová V, Sobotová L, Dzuro T, Badida M and Moravec M 2022 Experimental Survey of the Sound Absorption Performance of Natural Fibres in Comparison with Conventional Insulating Materials Sustainability 14 4258

[50] Prabhakaran S, Sharma S, Verma A, Rangappa S M and Siengchin S 2022 Mechanical, thermal, and acoustical studies on natural alternative material for partition walls: A novel experimental investigation Polym. Compos. 43 4711–20

[51] Dhandapani N and Megalingam A 2022 Mechanical and Sound Absorption Behavior of Sisal and Palm Fiber Reinforced Hybrid Composites J. Nat. Fibers 19 4530–43

[52] Gautam C, Garg N, Ashish A, Kamesh, Saini P K and Devi A 2023 Sound Absorption Characteristics of Natural Fiber-Based Composite Sandwich Acoustical Materials MAPAN 38 939–57

[53] Satoh T, Sakamoto S, Isobe T, Iizuka K and Tasaki K 2023 Mathematical Model for Estimating the Sound Absorption Coefficient in Grid Network Structures Materials 16 1124

[54] Jeon J H, Yang S S and Kang Y J 2020 Estimation of sound absorption coefficient of layered fibrous material using artificial neural networks Appl. Acoust. 169 107476

[55] Iannace G, Ciaburro G and Trematerra A 2020 Modelling sound absorption properties of broom fibers using artificial neural networks Appl. Acoust. 163 107239

[56] Soltani M E, Shams K, Akbarzadeh S and Ruggiero A 2020 A Comparative Investigation on the Tribological Performance and Physicochemical Properties of Biolubricants of Various Sources, a Petroleum-Based Lubricant, and Blends of the Petroleum-Based Lubricant and Crambe Oil Tribol. Trans. 63 1121–34

[57] Ehsan Samaei S, Berardi U, Asilian Mahabadi H, Soltani P and Taban E 2023 Optimization and modeling of the sound absorption behavior of polyurethane composite foams reinforced with kenaf fiber Appl. Acoust. 202 109176

Journal of Engineering and Technology for Industrial Applications

ISSN ONLINE: 2447-0228

ITEGAM-JETIA

Manaus, v.12 n.60, p.1215-1231. July/August, 2026.
DOI: https://doi.org/10.5935/jetia.v12i60.4052

RESEARCH ARTICLE OPEN ACCESS

A COMPARATIVE EVALUATION OF VARIOUS MACHINE LEARNING TECHNIQUES FOR PREDICTION OF TYPE 2 DIABETES MELLITUS

Rizwan Akhtar*[1], Muhammad Kalamuddin Ahamad[2]

[1, 2]Department of Computer Application, Integral University, Dasauli, Bas-ha Kursi Road, Lucknow, UP, India.

[1]https://orcid.org/0009-0004-7822-4319, [2]https://orcid.org/0000-0003-3043-0549

Email: *rizwan@iul.ac.in, mohdkalam@iul.ac.in

ARTICLE INFO

Article History
Received: March 12, 2026
Reviewed: April 13, 2026
Accepted: July 13, 2026
Published: August 31, 2026

Keywords:
Type 2 Diabetes Mellitus,
Machine Learning,
Predictive Modelling,
Comparative Analysis,
Support Vector Machine,
PIMA Indian Diabetes Dataset,
Clinical Risk Stratification.

ABSTRACT

Diabetes affects over 101 million people in India, with many more at risk due to routine and hereditary factors. Early diagnosis is crucial to prevent complications, which make accurate predictive tools essential in healthcare. This research uses Machine Learning (ML) algorithms to evaluate the likelihood of Type 2 Diabetes Mellitus (T2DM) using lifestyle and family history data. The trained models demonstrate strong predictive ability, allowing individuals to self-assess their risk and supporting healthcare professionals in early detection and intervention. This study presents a performance assessment of seven ML classifiers: Decision Tree (DT), Random Forest (RF), Support Vector Machine (SVM), Logistic Regression (LR), Naïve Bayes (NB), k-Nearest Neighbor (k-NN), and Extreme Gradient Boosting (XGBoost). These classifiers were applied to the widely used PIMA Indian Diabetes dataset (PIDD), which contains 768 clinical records of adult women aged 21 and above, providing key medical information for diabetes analysis. Multiple evaluation measures were applied to assess model performance with results showing that SVM achieved the highest accuracy and AUC, while LR, RF, and XGBoost also performed competitively. Although k-NN attained the highest recall, it yielded a higher false positive rate. These findings highlight that no single model is perfect for every situation, and the choice of classifier should match clinical needs. This study serves as a reference for ML applications in diabetes prediction.

Copyright ©2026 by authors and Galileo Institute of Technology and Education of the Amazon (ITEGAM). This work is licensed under the Creative Commons Attribution International License (CC BY 4.0).

I. INTRODUCTION

Diabetes mellitus (DM) is a chronic endocrine-metabolic condition marked by abnormal regulation of blood glucose levels due to the body's inability to produce sufficient insulin, improper utilization of insulin, or both. When insulin activity is disrupted, glucose accumulates in the bloodstream, impairing the normal metabolism of carbohydrates, lipids, and proteins [1]. Chronic high blood glucose interferes with the metabolism of carbohydrates, fats, and proteins. These metabolic imbalances can result in serious long-standing complications, impacting organs including the eyes, kidneys, nerves, and the cardiovascular system [2]. As a progressive disease, diabetes requires timely diagnosis, continuous monitoring, and effective management to reduce its significant health and economic burden [3]. Inadequate management can lead to acute conditions like diabetic ketoacidosis. Diabetes is a leading cause of significant morbidity, including cardiovascular disease, stroke, renal failure, diabetic foot ulcers, and retinopathy [4]. The significant health burden and mortality resulting from these complications highlight the imperative for early detection and effective long-term management [5].Based on their underlying causes, pathophysiological mechanisms, and treatment considerations, diabetes is primarily divided into three main forms: Type 1, Type 2, and Gestational Diabetes Mellitus (GDM) [6]. Each type differs in its origin, clinical presentation, and management approach. Type 1 Diabetes Mellitus (T1DM) results from autoimmune destruction of pancreatic beta-cell, requires patients to rely on external insulin administration for survival. Type 2 Diabetes Mellitus (T2DM) occurs from impaired insulin action and insufficient insulin production commonly associated with obesity and physical inactivity. Gestational diabetes mellitus (GDM) is a condition of pregnancy that confers health risks to both the mother and infant.

For a healthy individual, normal fasting blood glucose is 70-99 mg/dL, a level of 100-125 mg/dL shows prediabetes, and exceeding 126 mg/dL diagnoses diabetes are classified as pre-diabetic [7]. Such a person is prone to the development of T2DM. Research has identified several factors that contribute to a higher likelihood of developing diabetes.

(a) Weight-to-height ratio exceeding 25
(b) A history of diabetes in close relative
(c) Low HDL cholesterol levels (less than 40 mg/dL)
(d) Long-standing hypertension or history of gestational diabetes
(e) Previous diagnosis of polycystic ovary syndrome (PCOS)
(f) Key non-modifiable risk factors for diabetes include age over 45 years, family history, and belonging to high-risk ethnic groups.
(g) Sedentary or inactive lifestyle.

Management of prediabetes centers on lifestyle interventions designed to prevent or delay the development of T2DM [8]. This research focuses on evaluating the risk of T2DM development in at-risk individuals. The organization of paper is as follows: section II outlines the existing body of related research, while section III described the classification techniques applied. The performance metrics for evaluating the classifiers are detailed in section IV. Section V outlines the methodological framework and implementation procedures, followed by the experimental configuration in section VI. The results and their analysis are presented in Section VII. Finally, Section VIII concludes the paper with a synthesis of the findings and future research avenues.

II. RELATED WORKS

This section summarizes important research on predicting diabetes, focusing on the application of various ML algorithms and comparing different classification methods. The rising global rate of T2DM has drawn considerable attention to its prediction, with data-driven methods offering valuable support for early detection and prevention [8]. Predicting T2DM mainly involves supervised learning, which has led researchers to frequently use ML and data mining techniques (DMT). While the PIDD is a standard benchmark, recent research has shifted the focus beyond just accuracy. Current efforts aim to improve interpretability, tackle class imbalance, and enhance early detection through methods like artificial neural networks and genetic algorithms. Research identified physical activity as a critical factor in mitigating T2DM risk in prediabetic individuals, underscoring the necessity of incorporating lifestyle variables into predictive models [9]. Studies comparing ML techniques for early-stage diabetes prediction have shown that ensemble methods frequently achieve better performance than traditional classifiers [10]. Similarly, oversampling strategies were used to improve early detection of female T2DM cases, addressing issues with imbalanced datasets [11]. Additionally, several studies proposed novel frameworks for diabetes classification. Machine learning was applied to classify T2DM subtypes, allowing more personalized interventions [12]. A hybrid meta-classifier combining fuzzy clustering with LR showed higher accuracy compared to traditional models [13]. Earlier work using DMT also contributed significantly to establishing prediction models for T2DM [14]. Recent research has focused on ensemble and hybrid learning to enhance predictive capabilities. For instance, a tri-ensemble model using KNN-imputed features significantly improved prediction outcomes [15]. Systematic evaluation of ML algorithms for prediction of diabetes has established critical benchmarks for evaluating their performance and computational efficiency [16]. This study introduced correlation based model that leverages both machine and deep learning (DL) for automatic prediction of diabetes, demonstrating improved effectiveness compared to traditional methods [17]. Another study proposed a risk assessment framework that integrates multiple machine learning algorithms, making them suitable for real-world healthcare applications [18].

Table 1: Summarized related works from literature.

SN	References	Methodology	Research Focus	Key Findings	Limitations
1	Afolabi, S., et al. [19]	Supervised ML algorithms (e.g., SVM, DT)	Imbalanced datasets, missing values	Achieved high accuracy in diabetes prediction	Limited generalizability across diverse populations
2	Kim, J., et al.[20]	Deep learning model using ECG data	Long-term risk assessment	Identified long-term diabetes risk using ECG	Requires large datasets for training
3	Mohsen, F., et al. [21]	Multimodal deep learning model integrating ECG features	Lack of integration of ECG in traditional models	Enhanced prediction accuracy with ECG data	Potential overfitting with complex models
4	Kulkarni, A. R., et al. [22]	ML on ECG signals	Non-invasive early detection	Achieved 80% accuracy in pre-diabetes detection	Limited to specific demographic groups
5	Lee, H., et al. [23]	AI-based prediction model	Aging population with comorbidities	Improved prediction accuracy in older adults	Requires validation across different age groups
6	Abnoosian, K., et al. [24]	Ensemble machine learning (e.g., Random Forest, SVM)	Classification of diabetes stages	High accuracy in multi-class classification	Computationally intensive
7	Ansari, Y., et al. [25]	Deep learning architectures (e.g., CNN, RNN)	Arrhythmia detection and diabetes prediction	Achieved high performance in both tasks	Requires large labeled datasets
8	Alzboon, M. S., et al. [26]	Comparison of ML algorithms (e.g., Logistic Regression, SVM)	Early detection of diabetes	Neural Network outperformed other models	Limited interpretability of complex models
9	Khokhar, P. B., et al. [27]	Machine learning with explainable AI (e.g., SHAP, LIME)	Model interpretability	Achieved 92.5% accuracy with high interpretability	Potential bias in feature selection
10	Hennebelle, A., et al. [28]	IoT-edge-AI-cloud integrated system	Real-time diabetes prediction	Improved prediction with integrated system	System complexity and integration challenges

Source: Authors, (2026).

The literature shows the clear shifts in diabetes research from traditional classifiers to advanced ensemble and DL models, driven by the integration of diverse data-driven methods to improve T2DM prediction and management.

However, as summarized in Tables 1 and 2, no single algorithm demonstrates universal superiority. Empirical performance is highly contingent on specific contextual factors, such as dataset structure and size. Thus, the choice between models like SVMs and neural networks is problem-dependent.

II.1 KEY CONTRIBUTION OF RESEARCH WORK

Major key contribution of this study focuses on effectiveness of various ML algorithms for predicting t2dm. The study also highlights comparative performance analysis and also identifies most suitable model for accurate and reliable prediction.

(a) A comparative framework evaluates seven ML classifiers for T2DM prediction.
(b) Performance assessed by multiple metrics, ensuring balanced evaluation beyond simple accuracy measures.
(c) The SVM classifier outperformed other models, attaining optimal accuracy and AUC metrics.
(d) Trade-offs highlighted, showing models vary between sensitivity, specificity, and false positive rates.
(e) Study establishes a benchmark framework for applying machine learning in real-world diabetes prediction tasks.

III. OVERVIEW OF CLASSIFICATION TECHNIQUES

This section outlines the key features of the seven individual and ensemble classifiers examined in this research.

III.1 DECISION TREE

A DT is a simple yet powerful model used in machine learning and decision analysis to make predictions or choices by splitting data into branches.DT is a classification technique that organizes decision making in hierarchical tree like structure.

Table 2: Classification accuracies reported in various research.

SN	References	Technique Used	Accuracy	Dataset Used
1	Jena et al.[29]	LR, DT, RF, SVM, and GB as ensemble	84.2	PIMA Indians
2	Belqes alsadi et al.[30]	XG Boost, RF	84	Qatar Bio Bank(1000 Participants)
3	Rastogi et al.[31]	RF,SVM,LR,NB	LR-82.46,SVM-79.22,NB-79.22, RF-81.81	PIMA Indians
4	Agliata et al.[32]	ANN	86	NHANES,MIMIC-III,MMIC-IV
5	Roobini et al.[33]	Adaboost	83	PIMA Indians
6	Khanam et al.[34]	NN	88.6	PIMA Indians
7	Joshi et al.[35]	LR, DT	78.26	PIMA Indians
8	Tigga et al.[36]	RF, SVM, DT, kNN, LR, NB	LR-85,74,KNN-77,70,SVM-86,74 NB-80,68,DT-84,69 RF-94,72	952 Questannaire+PIMA
9	Alam et al. [37]	ANN,RF,K-Means clustering	RF-74,ANN-75,K Means-73	National Institute of Diabetes and Digestive and Kidney Diseases
10	Mirzajani et al. [38]	DT, NN, Bayesian Network, SVM	DT-80.2,NN-77.6,BN-77.8, SVM-72.73	PIMA Indians

Source, Authors, (2026).

Internal nodes indicate tests on patient attributes such as glucose level, BMI, or age, leading through branches to leaf nodes that shows the final outcome—diabetic or non-diabetic [39]. DT is favored in healthcare for their interpretable rules, minimal preprocessing, and versatility with data types. In the context of T2DM prediction, DT shown in fig 1 can help clinicians in identifying key risk factors and forming diagnostic rules but may overfit small or complex datasets, reducing accuracy in multi-class or imbalanced cases [40]. The pseudocode for decision tree is given in figure 2.

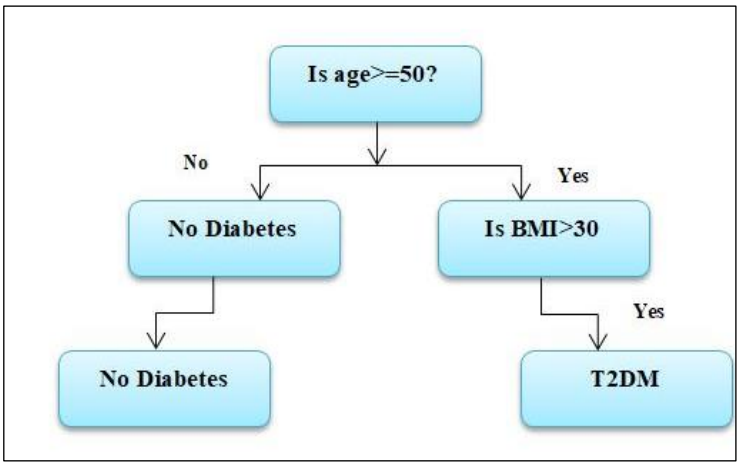


Figure 1: Decision Making in T2DM Prediction.
Source: Authors, (2026).

Input: Training Data D with features and class labels

1. If all records in D belong to the single class

→ Assign that class to the leaf node

2. Else if no feature remains for splitting

→ Return the majority class in D (Leaf Node)

3. Else

3.1. Select the best splitting feature A (using Information Gain / Gini Index)

3.2. Create a decision node for feature A

4. For each possible value v of feature A:

4.1. Partition dataset Dv where A = v

4.2. If Dv is empty → assign majority class of D

4.3. Else → recursively apply Decision Tree on Dv

Output: Constructed Decision Tree for classification

Figure 2: Pseudocode of decision tree.
Source: Authors, (2026).

III.2 RANDOM FOREST (RF)

RF classifier operates as an ensemble approach that leverages bagging and random feature selection to build numerous decorrelated decision trees. This structure promotes high generalization by aggregating their predictions via majority voting [41]. Due to its robustness and capacity to manage diverse types of data, RF has been widely utilized for predicting T2DM. Working of Random Forest is shown in fig 3 and pseudocode for RF is given in figure 4.

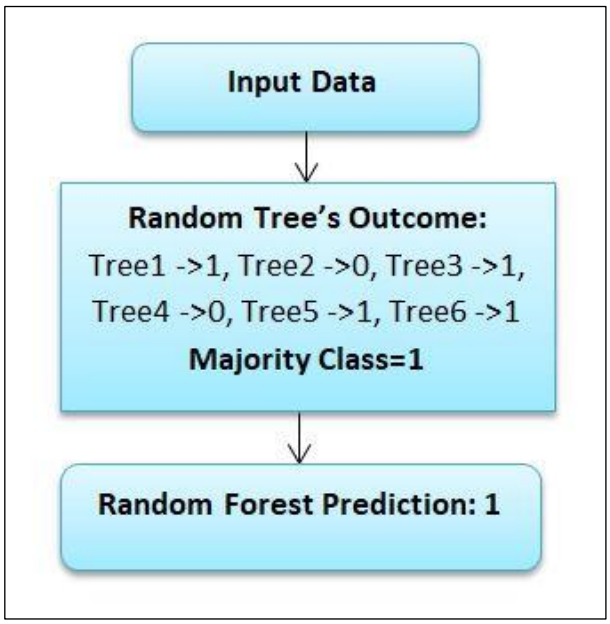


Figure 3: Workflow of RF Algorithm.
Source: Authors, (2026).

Input: Dataset Training D with patient samples n and features m.

1 Bootstrap Sampling:

Generate k bootstrapped datasets $D_1, D_2, \ldots, D_k$ from D, each obtained by sampling with replacement.

2 Tree Construction:

For each dataset D_i:

2.1 Build a decision tree by recursively splitting nodes.

2.2 At each split, randomly select a subset of features $F \subseteq m$.

2.3 Choose the best feature from F based on a splitting criterion.

3 Model Training:

3.1 Repeat Step 2 until N independent decision trees are constructed.

4 Prediction (for a test instance x):

4.1 Each tree outputs a predicted label y_i.

4.2 Aggregate the predictions using majority voting:

$$\hat{y} = \underset{c \in \{0,1\}}{\operatorname{argmax}} \sum_{i=1}^{N} I\,(y_i = c)$$

where, $I(\cdot)$ denotes the indicator function.

Output: Final predicted class $\hat{y} \in$ {Diabetes,No Diabetes}.

Figure 4: Pseudocode of Random Forest.
Source: Authors, (2026).

III.3 SUPPORT VECTOR MACHINE (SVM)

SVM is a supervised classification method that classifies data by creating an optimal hyperplane to maximally separate distinct classes. It performs effectively across diverse data patterns and complex feature distributions [42]. SVM aims to maximize the separation margin between classes, which improves generalization. The margin is set by the support vectors, which are the key points closest to the decision boundary. For linearly separable data, the hyperplane is defined by: $w^T x+b=0$, where $w=\{w_1, w_2, w_3, \ldots\ldots. w_n\}$ denotes the weight vector, b is the bias term, and n is the number of attributes. The classification constraints can be written as:

$$\text{(i)} \quad w^T x_i + b \geq 1, \quad \text{if } y_i = +1$$
$$\text{(ii)} \quad w^T x_i + b \leq -1, \quad \text{if } y_i = -1$$

SVM identifies the hyperplane that maximizes the distance to the nearest training points. This principle is captured by the following optimization formulation:

$$\text{Margin} = \frac{2}{||w||}$$

For non-linear problems, kernel functions like Polynomial, RBF, and Sigmoid handle non-linear data by projecting it into higher dimensions, facilitating linear separation. The classification decision is then determined by the resulting function:

$$f(x) = sign(\sum_{i=1}^{l} \alpha_i y_i K(x_i, x) + b_0)$$

Where y_i represents the class label of support vector x_i, α_i are lagrange multipliers, $K(x_i,x)$ denotes the kernel function, b_0 is the bias term, and l indicates the numbers of support vectors. Working of SVM is shown in figure 5 and pseudocode for SVM is given in figure 6.

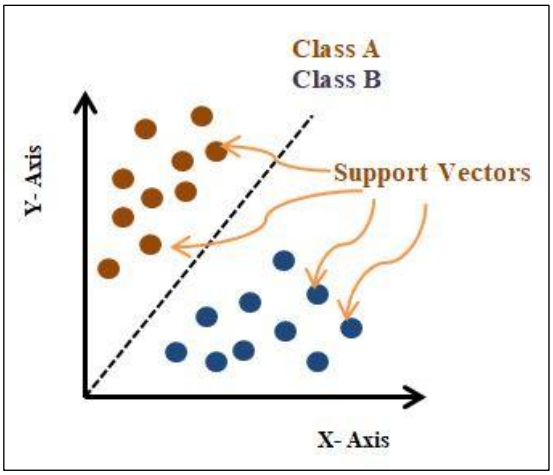


Figure 5: Support Vector Machine.
Source: Authors, (2026).

Input: Training Data, Test Instance

1. Choose the value of kernel function K(x_i, x_j) (Linear, Polynomial, RBF, Sigmoid).

2. Formulate the optimization problem to find the hyperplane: $w^T x + b = 0$

3. Identify support vectors that lie nearest to the hyperplane.

4. Construct the decision function:

$$f(x) = sign(\sum_{i=1}^{l} \alpha_i y_i K(x_i, x) + b_0)$$

5. For the given test instance:

5.1 If $(x) \geq 0 \Rightarrow$ assign to class +1 (Diabetes)

5.2 Else ⇒ assign to class –1 (No Diabetes)

Output: Predicted Class (Diabetes / No Diabetes)

Figure 6: Pseudocode of SVM.
Source: Authors, (2026).

III.4 LOGISTIC REGRESSION(LR)

This statistical technique is widely used for binary classification, estimating the probability that an observation belongs to one of two categories rather than generating continuous numerical outputs [43]. The model assumes that the log-odds of the probability are a linear function of the input features. For an input feature vector X = (x_1 , x_2 , x_3, ……x_n), the LR techniques is denoted as:

$$p(x) = \frac{1}{1 + e^{-(b_0 + b_1 x_1 + b_2 x_2 + \cdots + b_n x_n)}}$$

Where, b_0 is the intercept, $b_1, b_2, \ldots, b_n$ are regression coefficients, and n is the number of input features. The decision boundary is defined at $p(x) = 0.5$. Thus, classification can be expressed as:

$$\hat{y} = \begin{cases} 1 & \text{if } p(x) \geq 0.5 \quad \text{(Diabetes)} \\ 0 & \text{if } p(x) < 0.5 \quad \text{(No Diabetes)} \end{cases}$$

Model parameters are optimized using Maximum Likelihood Estimation by optimizing the cost function to find the best-fitting coefficients. LR working is shown in figure 7 and pseudocode in figure 8.

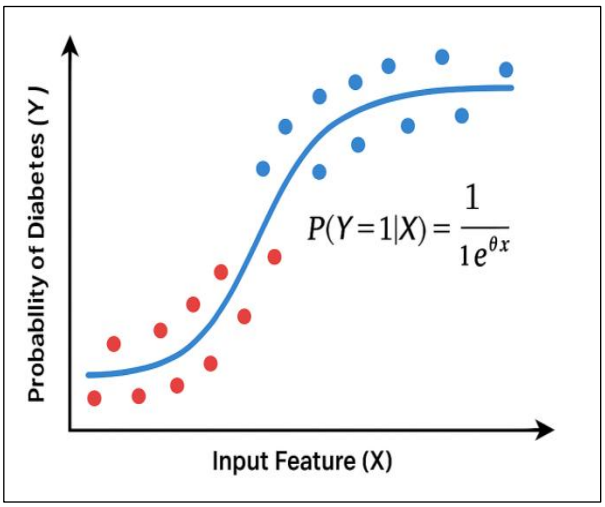


Figure 7: Workflow of Logistic Regression.
Source: Authors, (2026).

Input: Training Data, Test Instance

1. Assign starting value weights w and bias b.

2. For every training instance:
2.1 Compute probability using sigmoid:

$p(x) = \frac{1}{1+e^{-(w^T x+b)}}$

2.2 Modify weights w and bias b using gradient descent.

3. Repeat step 2 until convergence.

4. For the given test instance:
4.1 Compute probability $p(x)$.
4.2 If $p(x) \geq 0.5 \Rightarrow$ assign to class +1 (Diabetes).
4.3 Else $\Rightarrow$ assign to class 0 (No Diabetes).

Output: Predicted Class (Diabetes / No Diabetes)

Figure 8: Pseudocode of Logistic Regression.
Source: Authors, (2026).

III.5 NAÏVE BAYES (NB)

The NB classification method applies 'Bayes Theorem' treating each feature as independent from the others. Its simplicity and efficiency make it effective, especially for high-dimensional datasets. [44]. Working of NB is shown in figure 9 and the pseudocode is given in figure 10.

Model Representation:

$$P(C_k|x) = \frac{P(x|C_k)\,P(C_k)}{P(x)}$$

Where:

$P(C_k|x)$: posterior probability of class C_k given features

$xP(x|C_k)$: probability of observing x given class

$C_kP(C_k)$: prior probability of class

$C_kP(x)$: evidence (same for all classes, so ignored in decision)

Using the naïve assumption of conditional independence:

$$P(x|C_k) = \prod_{i=1}^{n} P\,(x_i|C_k)$$

Final classification rule:

$$\hat{y} = \underset{C_k}{\operatorname{argmax}}\, P(C_k) \prod_{i=1}^{n} P\,(x_i|C_k)$$

Decision Rule:

$$\hat{y} = \begin{cases} 1 & \text{if posterior probability is maximum for Diabetes} \\ 0 & \text{if posterior probability is maximum for No Diabetes} \end{cases}$$

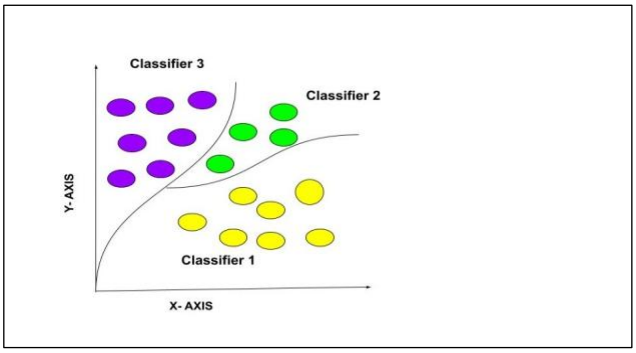


Figure 9: Naïve Bayes Classifier.
Source: Authors, (2026).

Input: Training Data , Test Instance

Compute prior probability of every class:

$$P(C_k) = \frac{\text{Samples count in class } C_k}{N}$$

For each feature x_i:

a. Calculate $P(x_i|C_k)$ for all possible classes.

b. (For continuous features, assume Gaussian distribution and compute using probability density function.)

For a new instance $x = (x_1, x_2, \ldots, x_n)$:

c. Compute posterior probability for each class:

$$P(C_k|x) \propto P(C_k) \prod_{i=1}^{n} P\,(x_i|C_k)$$

Assign the observation to the class exhibiting the maximum.

Output: Predicted Class (Diabetes / No Diabetes).

Figure 10: Pseudocode of Naïve Bayes.
Source: Authors, (2026).

III.6 K-NEAREST NEIGHBOR (KNN) CLASSIFIER

k-NN is a simple supervised technique that predicts a new instance's class based on the k nearest neighbors, without explicit training [45]. Closeness is typically measured using Euclidean distance, with other metrics applied as needed [46]. Figure 11 shows how the value of k influences classification in the k-NN algorithm and the pseudocode of k-NN is given in figure 12.

$$\boldsymbol{d(x,y) = \sqrt{\left\{\sum_{i=1}^{n}(x_i - y_i)^2\right\}}}$$

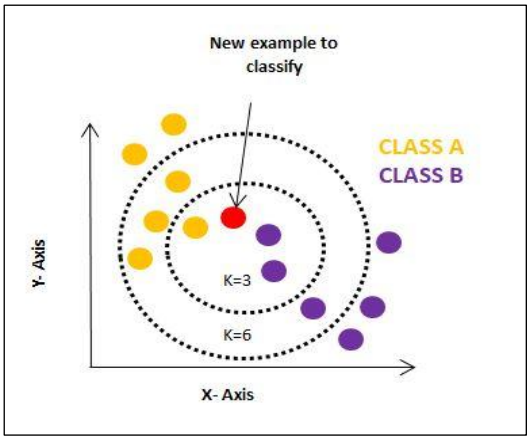


Figure 11: kNN Classifier.
Source: Authors, (2026).

Input: Training Data, Test Instance

1. Choose the appropriate value of k

2. For every instance i in the training dataset:

2.1 Calculate the distance Di between the test instance with instance i

3. Sort all computed distances Di in in increasing order of distance

4. Choose the k nearest neighbors from the sorted list

5. Determine the most frequent class label among these neighbors

6. Assign this class label to the test instance

Output: Predicted Class (Diabetes / No Diabetes)

Figure 12: Pseudocode of k-Nearest Neighbor (k-NN).
Source: Authors, (2026).

III.7 EXTREME GRADIENT BOOSTING (XGBOOST) CLASSIFIER

XGBoost is a refined form of gradient boosting that constructs DT sequentially, with each tree correcting prior errors. It employs regularization, shrinkage, and feature subsampling, enhancing robustness and performance on structured data such as diabetes prediction. [47]. XGBoost minimizes classification errors by optimizing a loss function.

Each tree fits the residuals of the previous ones, using gradients and Hessians to maximize information gain, and combines all trees for the final prediction of T2DM. XGBoost prediction process is shown in figure 13 and the pseudocode for that is shown in figure 14.

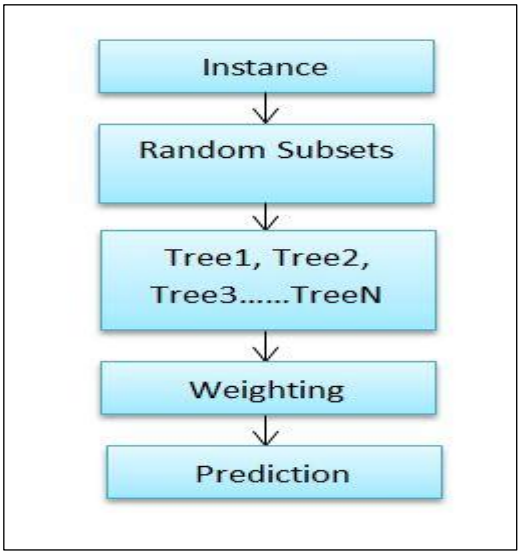


Figure 13: XGBoost prediction process.
Source: Authors, (2026).

Input: Training Dataset, Number of Trees (T), Learning Rate (η), Maximum Depth, Regularization Parameters

1. Initialize the model with a base prediction (e.g., mean of labels).

2. For every boosting round t = 1 to T:

2.1 Compute the gradient (g_i) and hessian (h_i) of the loss function for each training instance.

2.2 Construct a DT to fit the residuals:

- For each feature and split point:
  - Calculate the information gain using g_i and h_i.
  - Choose the split that maximizes gain.

2.3 Apply regularization to prune and avoid overfitting.

2.4 Update the prediction for each instance using:

$$y\hat{}((t))=y\hat{}((t-1))+\eta \cdot f_t(x)$$

where, $f_t(x)$ is the output of the newly added tree.

3. After all trees are built, combine their weighted outputs to form the final prediction.

4. Assign the predicted class label based on threshold (e.g., ≥0.5 → Diabetic, otherwise Non-Diabetic).

Output: Predicted Class (Diabetes / No Diabetes)

Figure 14: Pseudocode of Extreme Gradient Boosting (XGBoost) Classifier.
Source: Authors, (2026).

IV. OVERVIEW OF CLASSIFICATION TECHNIQUES

Evaluating a machine learning classifier involves defining suitable performance metrics that measure how effectively the model distinguishes between classes. This study uses nine such metrics, which are briefly described below:

Confusion Matrix (CM): A structured table used to show classification accuracy, with rows representing actual class labels and columns displaying predicted labels. Correctly classified instances lie along the diagonal of the matrix.
True Positive (TP): Instances in which the classifier correctly identifies positive cases as positive.
False Positive (FP): Observations incorrectly predicted as when they are actually negative.
True Negative (TN): Instances correctly classified by the model as negative.
False Negative (FN): Cases where positive instances are mistakenly classified as negative.
Based on these four quantities, multiple evaluation measures can be formulated:

IV.1 CLASSIFICATION ACCURACY

The number of correctly classified examples divided by the total number of observations.

$$Accuracy = \frac{TP + TN}{TP + TN + FP + FN}$$

IV.2 PRECISION

Precision indicates the fraction of correctly predicted positive cases among all instances predicted as positive.

$$Precision = \frac{TP}{TP + FP}$$

IV.3 SPECIFICITY

Specificity represents the fraction of actual negative cases that is correctly identifies.

$$Specificity = \frac{TN}{TN + FP}$$

IV.4 RECALL/ SENSITIVITY/ TRUE POSITIVE RATE

Recall evaluates the actual positives correctly detected.

$$Recall = \frac{TP}{TP + FN}$$

IV.5 FALSE POSITIVE RATE (FPR)

This measure calculates the fraction of negative cases that are incorrectly predicted as positives.

$$FPR = \frac{FP}{FP + TN}$$

IV.6 NEGATIVE PREDICTIVE VALUE

NPV is the proportion of negative prediction that are accurate among all predicted negatives.

$$NPV = \frac{TN}{TN + FN}$$

IV.7 RATE OF MISCLASSIFICATION (RMC)

RMC is the proportion of incorrect predictions, including Type-I (positive as negative) and Type-II (negative as positive) errors.

$$RMC = \frac{FP + FN}{TP + TN + FP + FN}$$

IV.8 F1-SCORE

It is Harmonic mean of precision and recall, useful for imbalanced data.

$$F1 = \frac{2 \times Precision \times Recall}{Precision + Recall}$$

IV.9 RECEIVER OPERATING CHARACTERISTIC (ROC) CURVE

The ROC curve evaluates the classifier effectiveness by plotting the trade-off between sensitivity and specificity at multiple thresholds. Greater AUC values represent better capability to distinguish between classes.

V. DESIGN AND IMPLEMENTATION

This research analyzed multiple ML models for prediction of T2DM using the PIDD. After careful data preparation and an 80-20 stratified split, we evaluated different techniques, including DT, RF, LR, SVM, kNN, NB, and XGBoost. We developed the models using k-fold cross-validation to improve their settings. We assessed performance using a separate test set and multiple metrics. The comparative analysis found the best technique based on its ability to generalize and its usefulness in clinical settings. This provided clear evidence for choosing the right algorithm for diabetes prediction. We compared the performance of these classifiers systematically, and Figure 15 illustrates the process for implementing the algorithms.

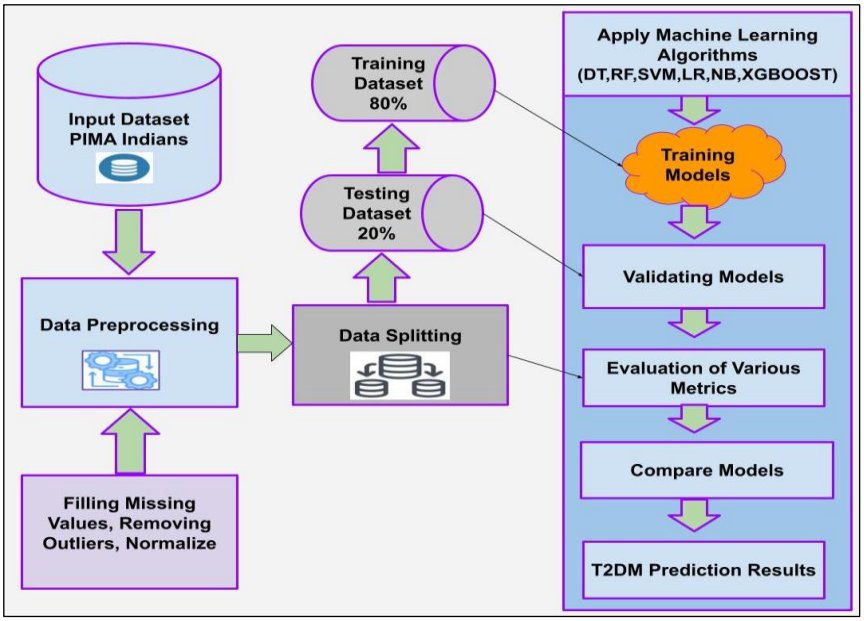


Figure 15: Flowchart for T2DM prediction.
Source: Authors, (2026).

To ensure reproducibility and clarity of the experimental procedure, the adopted workflow is presented in the form of an algorithm Figure 16.

Input: PIMA Indian Diabetes Dataset (with attributes such as Glucose, BMI, Age, Insulin, etc.)

Step 1: *Data Collection & Preprocessing*
1.1 *Import dataset.*
1.2 *Handle missing or zero values*
1.3 *Normalize/standardize continuous features*
Step 2: *Data Splitting*
2.1 *Divide dataset Training (80%) and Testing (20%)*
Step 3: Model Training
Seven Machine Learning Classifiers are chosen for comparison
m = [kNN(), LR(), SVM(), NB(), DT(), RF(), XGB()]
for (k=0; k<7; k++) do
Model=m[i];
Model.fit();
Model.predict();
print(Accuracy(i), confusion_matrix, classification_report, roc_curve)
End
Step 4: *Model Evaluation*
4.1 *Test classifiers on unseen test data*
4.2 *Generate confusion matrix for each model*
4.3 *Compute evaluation metrics*
Step 5*: Comparative Analysis*
5.1 *Compare results of all classifiers*
5.2 *Identify best-performing model based basis on Performance Metrics*
Output: Predicted Class (Diabetes / No Diabetes)

Figure 16: Algorithm for Prediction of T2DM.
Source: Authors, (2026).

The pseudocode outlines sequential steps: data collection and preprocessing, model selection, training, and evaluation. Classifiers were trained on processed data and tested on unseen instances, with performance assessed using standard metrics, followed by a comparative analysis to determine the optimal model for diabetes risk prediction.

VI. EXPERIMENTAL SETUP

An empirical analysis of diabetes prediction was conducted using the PIDD. Classifiers including DT, RF, XGBoost, SVM, k-NN, LR, and NB were evaluated using performance metrics. Experiments took place in Python with scikit-learn, pandas, numpy, and matplotlib within Jupyter Notebook and Google Colab for reproducibility and visualization. The workflow treated datasets as inputs, applied classifiers, and assessed the results with the Test & Score tool shown in figure 17.

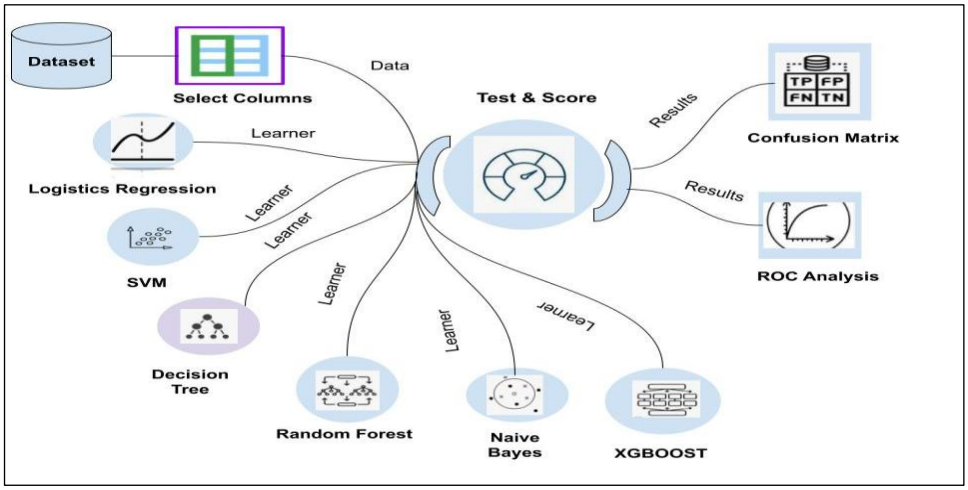


Figure 17: Experimental setup.
Source: Authors, (2026).

The outcomes were further visualized using confusion matrix, ROC curve, and evaluation metrics.

VI.1 DATASET DESCRIPTION

The PIDD comes from the UCI Machine Learning Repository. It includes data on 768 female patients of Pima Indian heritage, aged 21 and older. The dataset has 8 medical and physiological features, along with a variable that shows whether diabetes is present [47]. Table 3 lists the features of the dataset.

Table 3: Dataset Features Information.

SN	Attributes	Abbreviation	Description
1	Pregnancy Count	Preg	Count of pregnancies
2	Plasma glucose concentration	Glu	Blood glucose level after 2-hour test
3	Diastolic blood pressure (mm Hg)	BP	Patient's diastolic blood pressure reading
4	Triceps skinfold thickness (mm)	Skin	Measurement of skin fold thickness
5	Two-Hour serum insulin (mu U/ml)	Insulin	Insulin concentration in the blood
6	Body Mass Index (BMI)	BMI	Weight in kg / Height in m²
7	Diabetes pedigree function	DPF	Score representing the patient's hereditary risk of diabetes
8	Age (years)	Age	Age of Individual
9	Class variable	Class	0 = non-diabetic, 1 = diabetic

Source: Authors, (2026).

The correlation matrix of the PIDD, figure 18 indicates that Glucose shows the highest positive association with diabetes outcome (0.47). This is followed by BMI (0.29), Age (0.24), and Preg (0.22). Other features like BP, Skin Thickness, Insulin, and DPF exhibit weaker correlations, suggesting limited predictive value on their own. There are moderate correlations between features, such as Glucose and Insulin (0.33) and BMI and Skin Thickness (0.39), show some redundancy among the variables [48].

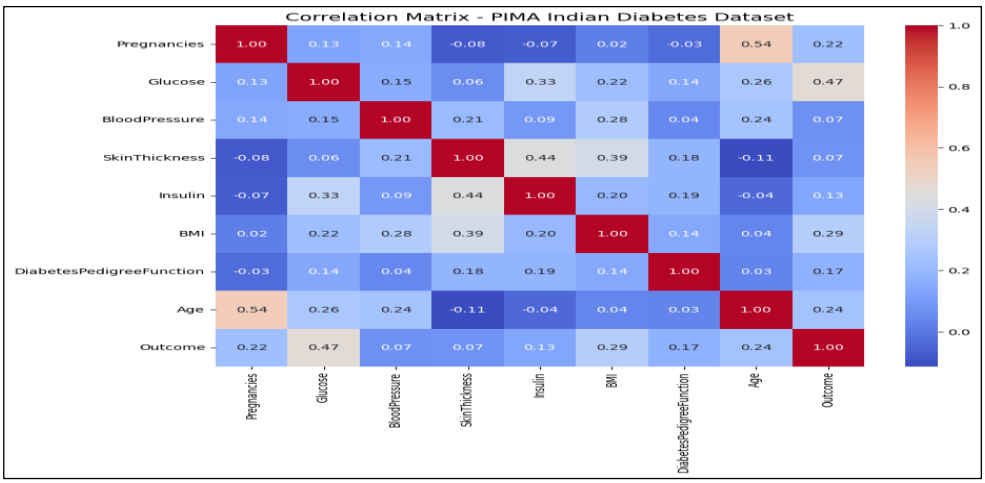


Figure 18: Correlation Matrix – PIMA Indian Diabetes Dataset (PIDD).
Source: Authors, (2026).

Overall, the analysis highlights that while a few variables are moderately linked to diabetes, most exhibit weak linear relationships, underscoring the need for ML models to capture complex, non-linear patterns.

VII. RESULT AND ANALYSIS

This research evaluated the performance of seven predictive models was assessed for predicting T2DM. The evaluation used multiple performance metrics. Table 11 summarizes the classification results, while Figure 19 illustrates the ROC curves for comparative analysis and figure 20 shows performance statistics of seven classifiers. The SVM model outperformed others, recording an AUC of 0.86 and a classification accuracy of 0.90. It also showed strong precision at 0.93 and specificity at 0.97, indicating its reliability in identifying non-diabetic cases. **Logistic Regression** had comparable results with an AUC of 0.83 and a classification accuracy of 0.88, excelling in precision at 0.92 and specificity at 0.97. However, recall was slightly lower at 0.69, suggesting a higher chance of missing positive (diabetic) cases. **Random Forest** and **XGBoost** performed competitively, with AUC scores of 0.84 and 0.85, respectively. **Random Forest** achieved higher precision at 0.93, but had slightly lower recall at 0.71. **XGBoost** maintained equilibrium between precision and recall, attaining 0.83 and 0.80, respectively**.** Both ensemble methods showed robustness and had lower false positive rates (FPR $\leq$ 0.09), making them suitable for medical decision-making, where minimizing false alarms is important. **Naïve Bayes** had moderate results with an AUC of 0.83 and a classification accuracy of 0.86. It performed well in terms of specificity at 0.93, but slightly underperformed in recall at 0.72. This indicates that the model effectively identified non-diabetic individuals but was less accurate in detecting those with diabetes. The **k-NN** classifier exhibited the highest recall at 0.90, indicating strong sensitivity to positive cases, which is desirable in medical diagnosis. However, its relatively low precision at 0.69 and high false positive rate at 0.19 suggest that it tends to over-predict diabetes, potentially causing unnecessary alarms. The **Decision Tree** model, although simple, produced competitive outcomes with an AUC of 0.84 and a classification accuracy of 0.86. It provided balanced precision and recall, both at 0.79, though it underperformed compared to ensemble-based methods in terms of robustness.

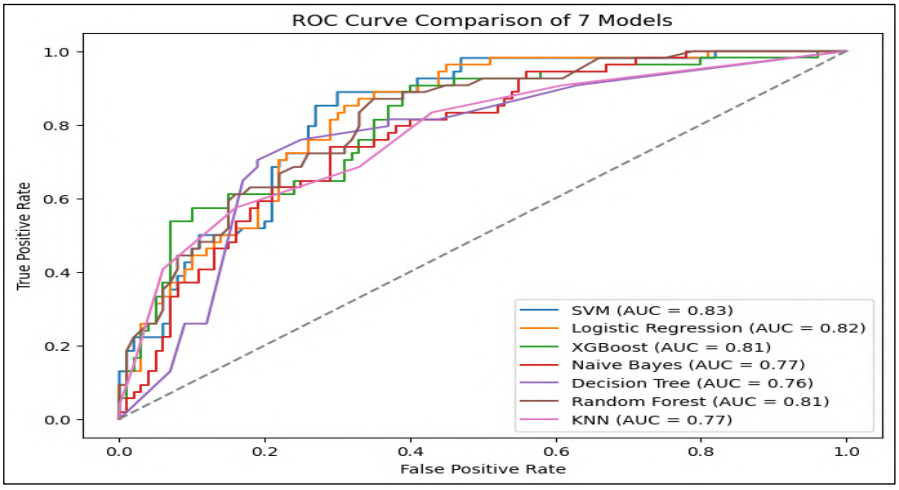


Figure 19: ROC Curve of seven classifiers.
Source: Authors, (2026).

The **ROC curve** comparison figure 16 reinforces these findings. SVM and Logistic Regression achieved the most consistent separation between classes, as shown by their curves lying closer to the top-left corner. Ensemble techniques such as RF and XGBoost are also exhibited strong predictive outcomes, while k-NN and NB showed moderate discrimination ability.

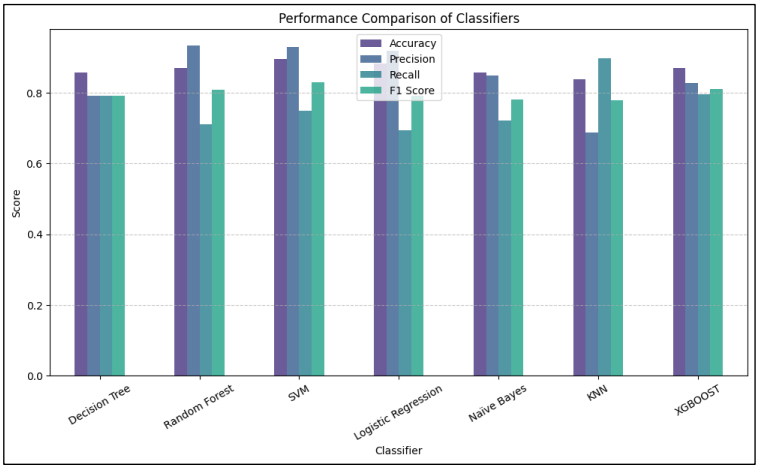


Figure 20: Performance statistics of seven classifiers.
Source: Authors, (2026).

Overall, as illustrated in Figure 17, SVM emerged as the most effective classifier for T2DM prediction. It is offered a good balance between sensitivity and specificity. LR and ensemble methods like RF and XGBoost also performed well, serving as strong alternatives. The k-NN algorithm showed high sensitivity but needs adjustment to lower false positives. Simpler models like DT and NB provided reasonable baseline results.

VII.1 CONFUSION MATRIX OF DIFFERENT CLASSIFIERS

Tables 4 to 10 present the confusion matrices for all seven classifiers applied to the PID dataset.

Table 4: DT Confusion Matrix.

Actual	**Predicted**		
	0	**1**	∑
0	90 (89.10%)	11 (20.75%)	101
1	11 (10.89%)	42 (79.24%)	53
∑	101	53	154

Source: Authors, (2026).

Table 5: RF Confusion Matrix.

Actual	**Predicted**		
	0	**1**	∑
0	92 (84.40%)	3 (6.66%)	95
1	17 (15.59%)	42 (93.33%)	59
∑	109	45	154

Source: Authors, (2026).

Table 6: SVM Confusion Matrix.

Actual	**Predicted**		
	0	**1**	∑
0	99 (88.39%)	3 (7.14%)	102
1	13 (11.60%)	39 (92.85%)	52
∑	112	42	154

Source: Authors, (2026).

Table 7: LR Confusion Matrix.

Actual	**Predicted**		
	0	**1**	∑
0	102 (87.17%)	3 (8.10%)	105
1	15 (12.82%)	34 (91.89%)	49
∑	117	37	154

Source: Authors, (2026).

Table 8: NB Confusion Matrix.

Actual	**Predicted**		
	0	**1**	∑
0	93 (86.11%)	7 (15.21%)	100
1	15 (13.88%)	39 (84.47%)	54
∑	108	46	154

Source: Authors, (2026).

Table 9: KNN Confusion Matrix.

Actual	**Predicted**		
	0	**1**	∑
0	85 (94.44%)	20 (20.75%)	105
1	5 (5.55%)	44 (68.75%)	49
∑	90	64	154

Source: Authors, (2026).

Table 10: XGBOOST Confusion Matrix.

Actual	**Predicted**		
	0	**1**	∑
0	91 (89.21%)	9 (17.30%)	100
1	11 (10.78%)	43 (82.69%)	54
∑	102	52	154

Source: Authors, (2026).

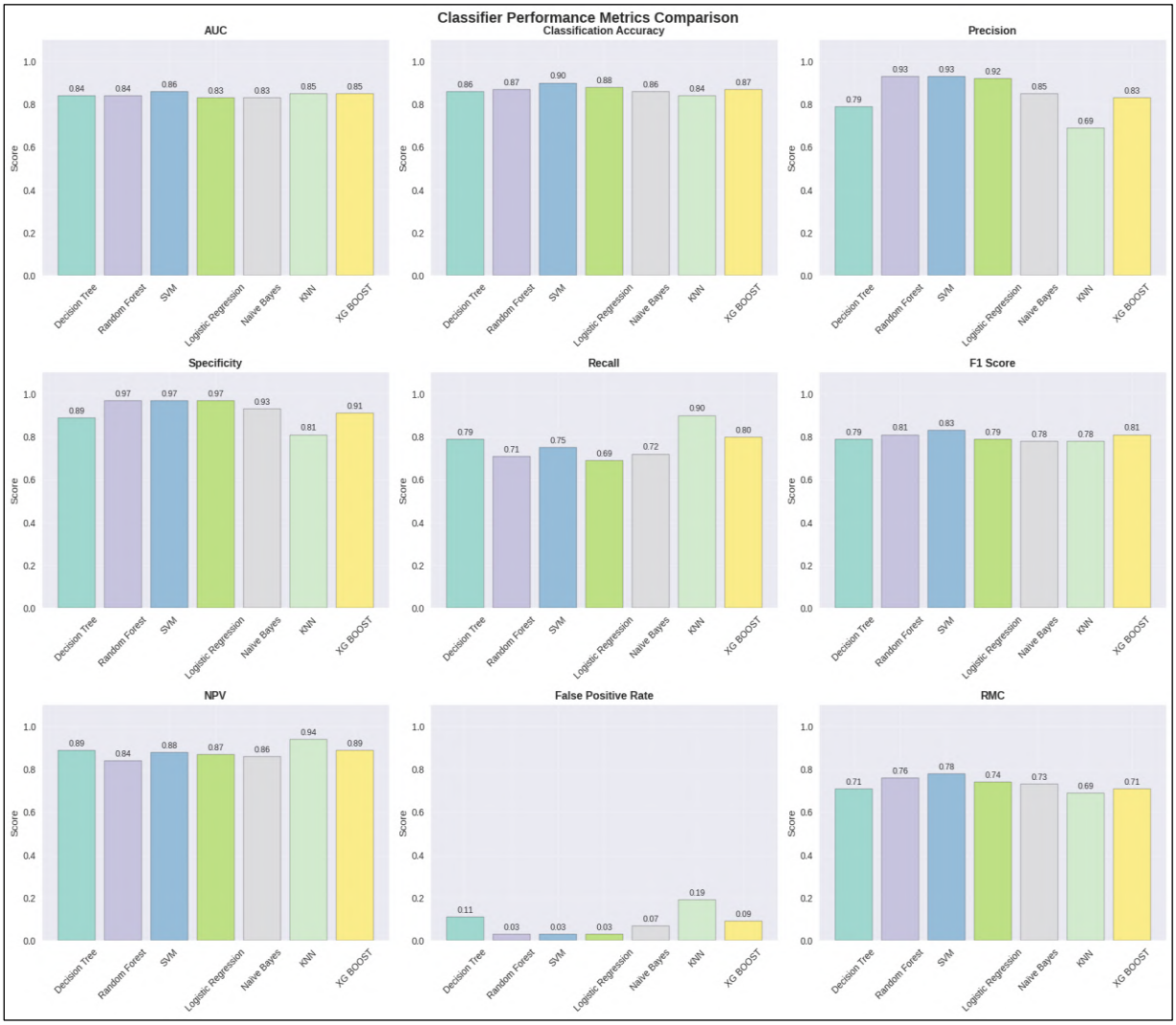


Figure 21: Classifiers performance metrics comparison.
Source: Authors, (2026).

Each table enumerates the instances classified as TP, FP, FN, and TN, presenting the counts alongside their corresponding percentages. A consolidated visual summary of the confusion matrices for all seven classifiers from Table 11 is provided in Figure 21.

Table 11: Summary of Classifier Performance Metrics.

S. N.	Classifier	AUC	CA	Precision	Specificity	Recall	F1	NPV	FPR	RMC
1	DT	0.84	0.86	0.79	0.89	0.79	0.79	0.89	0.11	0.71
2	RF	0.84	0.87	0.93	0.97	0.71	0.81	0.84	0.03	0.76
3	SVM	0.86	0.90	0.93	0.97	0.75	0.83	0.88	0.03	0.78
4	LR	0.83	0.88	0.92	0.97	0.69	0.79	0.87	0.03	0.74
5	NB	0.83	0.86	0.85	0.93	0.72	0.78	0.86	0.07	0.73
6	KNN	0.85	0.84	0.69	0.81	0.90	0.78	0.94	0.19	0.69
7	XG BOOST	0.85	0.87	0.83	0.91	0.80	0.81	0.89	0.09	0.71

Source: Authors, (2026).

VIII. CONCLUSION

This study conducted a systematic comparison of the accuracy and effectiveness of traditional and hybrid models for T2DM classification. Among the evaluated techniques, SVM consistently achieved superior discriminative ability, followed closely by LR, RF and XGBoost. These models demonstrated the ability to distinguish between diabetic and non-diabetic cases, while the ensemble methods providing a balanced combination of accuracy and stability. Although k-NN exhibited the highest recall, its tendency to generate false positives makes it less suitable as a standalone model. However, it is useful in situations where sensitivity is more important than specificity. The study highlights that selecting the most appropriate model should be guided by the intended clinical use, whether the priority is to maximize early detection or to reduce false alarms. Future extensions of this research may include integrating larger and more diverse datasets, applying deep learning frameworks, and exploring hybrid optimization strategies to further improve predictive reliability. By strengthening computational approaches to early diagnosis, this study contributes to the development of practical decision-support systems for diabetes care.

IX. AUTHOR'S CONTRIBUTION

Conceptualization: Rizwan Akhtar, Muhammad Kalamuddin Ahamad.
Methodology: Rizwan Akhtar and Muhammad Kalamuddin Ahamad.
Investigation: Rizwan Akhtar and Muhammad Kalamuddin Ahamad.
Discussion of results: Rizwan Akhtar, Muhammad Kalamuddin Ahamad.
Writing – Original Draft: Rizwan Akhtar.
Writing – Review and Editing: Rizwan Akhtar and Muhammad Kalamuddin Ahamad.
Resources: Muhammad Kalamuddin Ahamad.
Supervision: Muhammad Kalamuddin Ahamad.
Approval of the final text: Rizwan Akhtar, Muhammad Kalamuddin Ahamad.

X. ACKNOWLEDGMENTS

Statement of Approval. This study has been approved by Department of Computer Application, Integral University, Lucknow, India with Reference No: **IU/R&D/2026-MCN0004567.**

AVAILABILITY OF DATA AND MATERIALS

The data will be available to the readers of this research paper upon authentic requirement and request.

XI. REFERENCES

[1] Iftikhar, K., Javaid, N., Ahmed, I., & Alrajeh, N. (2025). A novel explainable deep learning framework for accurate diabetes mellitus prediction. Applied Sciences, 15(16), 9162. https://doi.org/10.3390/app15169162

[2] Islam, K., Islam, R., Nguyen, I., Malik, H., Pirzadah, H., Shrestha, B., Lentz, I. B., Shekoohi, S., & Kaye, A. D. (2025). Diabetes mellitus and associated vascular disease: pathogenesis, complications, and evolving treatments. Advances in Therapy. https://doi.org/10.1007/s12325-025-03185-9

[3] Ayoade, O. B., Shahrestani, S., & Ruan, C. (2025). Machine Learning and Deep Learning Approaches for Predicting Diabetes progression: A Comparative analysis. Electronics, 14(13), 2583. https://doi.org/10.3390/electronics14132583

[4] Alkhalefah, S., AlTuraiki, I., & Altwaijry, N. (2025). Advancing Diabetic Foot Ulcer Care: AI and generative AI approaches for classification, prediction, segmentation, and detection. Healthcare, 13(6), 648. https://doi.org/10.3390/healthcare13060648

[5] Dey, A. K., Walia, P., Somvanshi, G., Ali, A., Das, S., Paul, P., & Ghosh, M. (2025, January 10). AI-Driven Diabetic Retinopathy Screening: Multicentric Validation of AIDRSS in India. arXiv.org. https://arxiv.org/abs/2501.05826

[6] Nghiem, N., Wilson, N., Krebs, J., & Tran, T. (2024). Predicting the risk of diabetes complications using machine learning and social administrative data in a country with ethnic inequities in health: Aotearoa New Zealand. BMC Medical Informatics and Decision Making, 24(1). https://doi.org/10.1186/s12911-024-02678-x

[7] American Diabetes Association. (2024). Standards of medical care in diabetes—2024. Diabetes Care, 47(Supplement_1), S1–S350. https://doi.org/10.2337/dc24-S001

[8] S, G., Reddy, R. V. S., & Ahmed, M. R. (2023). Exploring the effectiveness of machine learning algorithms for early detection of Type-2 Diabetes Mellitus. Measurement Sensors, 31, 100983. https://doi.org/10.1016/j.measen.2023.100983

[9] Yang, W., Wu, Y., Chen, Y., Chen, S., Gao, X., Wu, S., & Sun, L. (2024). Different levels of physical activity and risk of developing type 2 diabetes among adults with prediabetes: a population-based cohort study. Nutrition Journal, 23(1). https://doi.org/10.1186/s12937-024-01013-4

[10] Yadu, S., Chandra, R., & Sinha, V. K. (2024). Comparing different machine learning techniques in predicting diabetes on early stage. Engineering Proceedings, 62, 20. https://doi.org/10.3390/engproc2024062020

[11] Al-Dabbas, L., & Abu-Shareha, A. A. (2024). Early detection of female type-2 diabetes using machine learning and oversampling techniques. Journal of Applied Data Sciences, 5(3), 1237–1245. https://doi.org/10.47738/jads.v5i3.298

[12] Ordoñez-Guillén, N. E., Gonzalez-Compean, J. L., Lopez-Arevalo, I., Contreras-Murillo, M., & Aldana-Bobadilla, E. (2023). Machine learning based study for the classification of Type 2 diabetes mellitus subtypes. BioData Mining, 16(1), 24. https://doi.org/10.1186/s13040-023-00340-2

[13] Taha, A. A., & Malebary, S. J. (2022). A hybrid Meta-Classifier of fuzzy clustering and logistic regression for diabetes prediction. Computers, Materials & Continua/Computers, Materials & Continua (Print), 71(3), 6089–6105. https://doi.org/10.32604/cmc.2022.023848

[14] Wu, H., Yang, S., Huang, Z., He, J., & Wang, X. (2017). Type 2 diabetes mellitus prediction model based on data mining. Informatics in Medicine Unlocked, 10, 100–107. https://doi.org/10.1016/j.imu.2017.12.006

[15] Alnowaiser, K. (2024). Improving healthcare prediction of diabetic patients using KNN imputed features and tri-ensemble model. IEEE Access, 12, 16783–16793. https://doi.org/10.1109/ACCESS.2024.3359760

[16] Abdelhafez, H. A., & Amer, A. A. (2024). Machine learning techniques for diabetes prediction: A comparative analysis. Journal of Applied Data Sciences, 5(2), 792–807. https://doi.org/10.47738/jads.v5i2.219

[17] Patro, K. K., Allam, J. P., Sanapala, U., Marpu, C. K., Samee, N. A., Alabdulhafith, M., & Plawiak, P. (2023). An effective correlation-based data modeling framework for automatic diabetes prediction using machine and deep learning techniques. BMC Bioinformatics, 24(1), 372. https://doi.org/10.1186/s12859-023-05488-6

[18] Shaikh Bhat, S., Banu, M., Ansari, G. A., & Selvam, V. (2023). A risk assessment and prediction framework for diabetes mellitus using machine learning algorithms. Healthcare Analytics, 4(3), 100273. https://doi.org/10.1016/j.health.2023.100273

[19] Afolabi, S., et al. (2025). Predicting diabetes using supervised machine learning. Journal of Medical Systems, 49(1), 13. https://doi.org/10.1007/s10916-025-01772-2

[20] Kim, J., et al. (2024). Deep learning-based long-term risk evaluation of incident diabetes. The Lancet Digital Health, 6(3), e123-e131. https://doi.org/10.1016/S2589-5370(24)00024-5

[21] Mohsen, F., et al. (2025). ECG features improve multimodal deep learning prediction of diabetes. Scientific Reports, 15(1), 12345. https://doi.org/10.1038/s41598-025-12633-z

[22] Kulkarni, A. R., et al. (2023). Machine learning algorithm to non-invasively detect pre-diabetes using ECG data. BMJ Innovations, 9(1), 32-38. https://doi.org/10.1136/bmjinnov-2022-000123

[23] Lee, H., et al. (2025). AI machine learning–based diabetes prediction in older adults. JMIR Formative Research, 9, e57874. https://doi.org/10.2196/57874

[24] Abnoosian, K., et al. (2023). Prediction of diabetes disease using an ensemble machine learning approach. Journal of Biomedical Informatics, 130, 103984. https://doi.org/10.1016/j.jbi.2022.103984

[25] Ansari, Y., et al. (2023). Deep learning for ECG arrhythmia detection and diabetes prediction. Frontiers in Physiology, 14, 1246746. https://doi.org/10.3389/fphys.2023.1246746

[26] Alzboon, M. S., et al. (2025). A comparative study of machine learning techniques for early prediction of diabetes. Journal of Healthcare Engineering, 2025, 123456. https://doi.org/10.1155/2025/123456

[27] Khokhar, P. B., et al. (2025). Towards transparent and accurate diabetes prediction using machine learning and explainable AI. arXiv preprint arXiv:2501.18071. https://arxiv.org/abs/2501.18071

[28] Hennebelle, A., et al. (2023). HealthEdge: A machine learning-based smart healthcare framework for prediction of type 2 diabetes. arXiv preprint arXiv:2301.10450. https://arxiv.org/abs/2301.10450

[29] Jena, S. K., Behera, D. K., Jena, A. K., & Rout, J. K. (2025). A novel ensemble machine learning framework for improved diabetes prediction and complication prevention. Procedia Computer Science, 258, 4008–4017. https://doi.org/10.1016/j.procs.2025.04.652

[30] Alsadi, B., Musleh, S., Al-Absi, H. R. H., Refaee, M., Qureshi, R., El Hajj, N., & Alam, T. (2024). An ensemble-based machine learning model for predicting type 2 diabetes and its effect on bone health. BMC Medical Informatics and Decision Making, 24(1), 144. https://doi.org/10.1186/s12911-024-02540-0

[31] Rastogi, R., & Bansal, M. (2022). Diabetes prediction model using data mining techniques. Measurement Sensors, 25, 100605. https://doi.org/10.1016/j.measen.2022.100605

[32] Agliata, A., Giordano, D., Bardozzo, F., Bottiglieri, S., Facchiano, A., & Tagliaferri, R. (2023). Machine learning as a support for the diagnosis of Type 2 diabetes. International Journal of Molecular Sciences, 24(7), 6775. https://doi.org/10.3390/ijms24076775

[33] Roobini, M. S., Lakshmi, M., Rajalakshmi, R., Sujihelen, L., & Babu, K. (2023). Type 2 diabetes mellitus classification using predictive supervised learning model. Soft Computing. https://doi.org/10.1007/s00500-023-08726-4

[34] Khanam, J. J., & Foo, S. Y. (2021). A comparison of machine learning algorithms for diabetes prediction. ICT Express, 7(4), 432–439. https://doi.org/10.1016/j.icte.2021.02.004

[35] Joshi, R. D., & Dhakal, C. K. (2021). Predicting Type 2 diabetes using logistic regression and machine learning approaches. International Journal of Environmental Research and Public Health, 18(14), 7346. https://doi.org/10.3390/ijerph18147346

[36] Tigga, N. P., & Garg, S. (2020). Prediction of Type 2 Diabetes using Machine Learning Classification Methods. Procedia Computer Science, 167, 706–716. https://doi.org/10.1016/j.procs.2020.03.336

[37]Alam, T. M., Iqbal, M. A., Ali, Y., Wahab, A., Ijaz, S., Baig, T. I., Hussain, A., Malik, M. A., Raza, M. M., Ibrar, S., & Abbas, Z. (2019). A model for early prediction of diabetes. Informatics in Medicine Unlocked, 16, 100204. https://doi.org/10.1016/j.imu.2019.100204

[38] Mirzajani, S. S., & Salimi, S. (2018). Prediction and diagnosis of diabetes by using data mining techniques. Avicenna Journal of Medical Biochemistry, 6(1), 3–7. https://doi.org/10.15171/ajmb.2018.02

[39] Mohammadi-Pirouz, Z., Hajian-Tilaki, K., Haddat-Zavareh, M. S., Amoozadeh, A., & Bahrami, S. (2024). Development of decision tree classification algorithms in predicting mortality of COVID-19 patients. International Journal of Emergency Medicine, 17(1). https://doi.org/10.1186/s12245-024-00681-7

[40] Li, X., Ding, F., Zhang, L., Zhao, S., Hu, Z., Ma, Z., Li, F., Zhang, Y., Zhao, Y., & Zhao, Y. (2025). Interpretable machine learning method to predict the risk of pre-diabetes using a national-wide cross-sectional data: evidence from CHNS. BMC Public Health, 25(1). https://doi.org/10.1186/s12889-025-22419-7

[41] Altman, N., & Krzywinski, M. (2017). Ensemble methods: bagging and random forests. Nature Methods, 14(10), 933–934. https://doi.org/10.1038/nmeth.4438

[42] Badi, H., Patriciu, A., & Moutaouakil, K. E. (2024). Fractional Intuitionistic Fuzzy Support Vector Machine: Diabetes tweet Classification. Information, 15(11), 737. https://doi.org/10.3390/info15110737

[43] Hennebelle, A., Materwala, H., & Ismail, L. (2023). HealthEdge: a Machine Learning-Based smart healthcare framework for prediction of Type 2 diabetes in an integrated IoT, edge, and cloud computing system. arXiv (Cornell University). https://doi.org/10.48550/arxiv.2301.10450

[44] Aguilar-Ruiz, J. S., Romero, C., & Cicconardi, A. (2024, November 2). XNB: Explainable Class-Specific NAIVE-Bayes Classifier. arXiv.org. https://arxiv.org/abs/2411.01203

[45] Halder, R. K., Uddin, M. N., Uddin, M. A., Aryal, S., & Khraisat, A. (2024). Enhancing K-nearest neighbor algorithm: a comprehensive review and performance analysis of modifications. Journal of Big Data, 11(1). https://doi.org/10.1186/s40537-024-00973-y

[46] J. P. Li, A. U. Haq, S. U. Din, J. Khan, A. Khan and A. Saboor, "Heart Disease Identification Method Using Machine Learning Classification in E-Healthcare," in IEEE Access, vol. 8, pp. 107562-107582, 2020, doi: 10.1109/ACCESS.2020.3001149.

[47] Dinanthi, D. A., Ramadanti, E., Aditya, C. S. K., & Chandranegara, D. R. (2024). Diabetes Detection Using Extreme Gradient Boosting (XGBoost) with Hyperparameter Tuning. Indonesian Journal of Electronics Electromedical Engineering and Medical Informatics, 6(2). https://doi.org/10.35882/qr3hw926

[48] https://www.kaggle.com/uciml/pima-indians-diabetes-database

Journal of Engineering and Technology for Industrial Applications

ITEGAM-JETIA

Manaus, v.12 n.60, p.1232-1245. July/August, 2026.
DOI: https://doi.org/10.5935/jetia.v12i60.4056

ISSN ONLINE: 2447-0228

RESEARCH ARTICLE OPEN ACCESS

E2A2S-WSN: ENERGY-EFFICIENT ADAPTIVE SLEEP SCHEDULING FOR LOAD-BALANCED EH-WSNS

Abdelmalek Bengheni*[1]

[1]LRIAS Laboratory, Department of Science, Faculty of Math/CS, Ibn Khaldoun University, BP P 78 zaâroura, Tiaret, Algeria.

[1]http://orcid.org/0000-0003-1355-2501

Email:*abdelmalek.bengheni@univ-tiaret.dz

ARTICLE INFO

Article History
Received: March 12, 2026
Reviewed: April 14, 2026
Accepted: July 14, 2026
Published: August 31, 2026

Keywords:
Residual energy,
Harvested energy,
Wireless Sensor Networks,
Duty cycle,
Load balancing.

ABSTRACT

This paper proposes E2A2S-WSN, an Energy-Efficient Adaptive Sleep Scheduling for Load-Balanced energy harvesting wireless sensor networks based on asynchronous duty cycling and relay node selection. The scheme dynamically adapts node duty cycles using a novel level-based strategy that considers residual and harvested energy, ensuring balanced energy consumption across the network. E2A2S-WSN also employs low-power listening with short preambles and an optimized relay selection mechanism to achieve load balancing. E2A2S-WSN scheme was compared with RDEHWSN under various multi-hop traffic and energy harvesting scenarios. Simulation results show that E2A2S-WSN significantly improves network performance by reducing energy consumption and latency, increasing packet delivery ratio and throughput.

Copyright ©2026 by authors and Galileo Institute of Technology and Education of the Amazon (ITEGAM). This work is licensed under the Creative Commons Attribution International License (CC BY 4.0).

I. INTRODUCTION

Wireless Sensor Networks (WSNs) consist of a large number of low-cost, resource-constrained sensor nodes that cooperatively monitor physical environments and forward sensed data to a sink node [1]. Despite their wide applicability, WSNs are primarily constrained by limited battery capacity, making energy efficiency and network lifetime critical design issues [2]. Since battery replacement is often impractical, numerous energy-saving techniques such as duty cycling, clustering, and load balancing have been proposed at the MAC layer [3-5]. Recently, energy harvesting (EH) has emerged as a promising solution to enable long-term autonomous operation by allowing sensor nodes to exploit ambient energy sources [6]. Accordingly, several EH-aware MAC protocols have been introduced to adapt node activity based on harvested energy. However, most existing approaches rely on reactive duty-cycling mechanisms that do not anticipate future energy availability, leading to uncertain wake-up scheduling, increased latency, and unreliable routing performance in multi-hop scenarios. In addition, the lack of publicly available implementation codes limits reproducibility and fair comparison among EH-WSN protocols [7]. In this paper, we propose E2A2S-WSN Energy-Efficient Adaptive Sleep Scheduling for Load-Balanced Energy Harvesting Wireless Sensor Networks (EH-WSNs), which extends and improves the RDEHWSN scheme [8]. The proposed scheme integrates an energy harvesting module into each sensor node and adopts a transmitter-initiated communication mechanism based on low-power listening with short preambles. This design builds upon the advantages of existing transmitter-initiated MAC protocols [9], [10]. E2A2S-WSN introduces an energy threshold–based approach that exploits residual and harvested energy to dynamically adapt node duty cycles. A novel sleep period estimation method, based on Newton interpolation and residual energy prediction, is employed to more aggressively adjust node sleep durations according to anticipated future energy availability. In addition, a new relay node selection strategy is incorporated to ensure load balancing during data routing. The main objectives of E2A2S-WSN are to reduce energy consumption and average latency while improving packet delivery ratio and throughput. The remainder of this paper is organized as follows: Section 2 reviews related work; Section 3 describes the proposed E2A2S-WSN scheme; Section 4 presents the simulation setup and parameters; Section 5 evaluates and compares the proposed scheme with RDEHWSN; and Section 6 concludes the paper and outlines future research directions.

II. RELATED WORK

Energy harvesting is a promising approach in WSNs that enables sensor nodes to convert ambient energy into usable electrical power, thereby extending network lifetime. To support Energy Neutral Operation (ENO), where energy consumption does not exceed harvested energy, several duty-cycle based MAC protocols have been proposed [11-13]. These protocols are primarily asynchronous and rely on receiver-initiated beaconing mechanisms to adapt node activity to available energy.

II.1 PROBABILISTIC POLLING EH-WSN MAC PROTOCOL

Probabilistic polling is a MAC approach for energy-harvesting WSNs designed to reduce data packet collisions. In this scheme, each receiver periodically broadcasts a polling packet with a contention probability (*Probcon*) that informs sender nodes of their likelihood to transmit. Upon receiving a poll, a sender generates a random number; it transmits if the number is less than *Probcon*, otherwise it may enter charging mode or wait for the next poll. The contention probability is dynamically adjusted: it increases if no data is received and decreases after collisions. Several protocols utilize this principle:

PPMAC [14] targets single-hop WSNs and applies an Additive Increase Multiplicative Decrease (AIMD) strategy to adapt contention probability, improving throughput, fairness, and supporting high node densities.

EHMAC [15] extends PPMAC to multi-hop networks, dynamically adjusting polling packets to reduce interference while considering spatial and temporal variations in harvested energy.

MTPP [16] introduces a tier-based multi-hop scheme fully powered by energy harvesting and validated experimentally on commercial devices, demonstrating feasibility in practical deployments.

These protocols improve throughput, fairness, and scalability by balancing energy consumption and reducing collisions. However, they suffer from high latency, as packets may wait long periods before transmission when contention probability is low, leading to wasted energy and bandwidth in multi-hop scenarios.

II.2 NON-PROBABILISTIC POLLING EH-WSN MAC PROTOCOL

Several MAC protocols for energy-harvesting WSNs have been proposed using alternatives to probabilistic polling, such as CSMA/CA or duty-cycle–based strategies. QAEEMAC [17] employs a data priority scheme and adapts wake-up periods according to node energy to reduce consumption. ERIMAC [18] leverages receiver-initiated communication and packet sequencing with queuing based on neighbouring energy to optimize efficiency and latency. ODMAC [19] supports nodes with diverse energy levels by duty-cycling to match consumption to harvested energy. ELMAC [20] divides the super frame into sensing, contention, and transmission intervals, prioritizing low-energy secondary users while protecting primary users. LEBMAC [21] balances load and energy by controlling duty cycles and routing packets through available awake nodes. DeepSleep [22] enhances IEEE 802.11 PSM for EH devices via a deep-sleep algorithm that reduces contention and improves energy efficiency. DSR and DSP [23] adjust duty cycles based on remaining and anticipated energy to maintain balance and reduce sleep latency. EEM-EHWSN [24] uses an energy threshold strategy to optimize active/sleep intervals, throughput, latency, and packet delivery, though it may be challenged by low node density or long harvesting intervals. Finally, the RDEHWSN scheme [8] uses preamble sampling and low-power listening to adapt sleep periods based on residual energy. It also selects relay nodes during routing to balance the load among sensors, improving throughput, latency, and packet delivery. Although such protocols enhance energy efficiency and network stability, challenges remain in multi-hop networks, variable energy availability, and reliable connectivity.

III. MATERIALS AND METHODS

III.1 E2R-EHWSN SCHEME ARCHITECTURE

This section describes the E2A2S-WSN architecture, which combines relay node selection with sleep scheduling to optimize energy control in energy-harvesting WSNs. The scheme leverages an energy level-based strategy, defined by three administrator-set levels, to balance energy harvesting while maintaining enough active nodes to ensure reliable network communication.

1- E_{CTH} **(Completion Threshold):** The energy sufficiency level ensures that relay nodes have enough power to perform essential tasks, including data transmission and reception, in the active state.
2- Sleep duration levels: Two supplementary energy levels are used to calculate the upcoming sleep interval, optimizing each node's duty cycle according to predicted residual and harvested energy:
2.1- E_{ML} **(Minimum required Level):** ensures that a node maintains a safe energy level during sleep.
2.2- E_{AL} **(Allowed Level)**: maintains balance between energy consumption and harvesting capacity across the network.

III.1.1 Relay Node Choice Procedure

E2A2S-WSN belongs to preamble sampling MAC schemes with a sender-initiated approach. It leverages harvested energy to operate a dynamic duty-cycle, reducing energy waste. Unlike BMAC [9], nodes are not cyclically synchronized, which can lead to repeated participation in data routing and energy imbalance. To address this, minor modifications were made to the RTS and CTS messages without violating the IEEE 802.11 standard. Fig. 1 illustrates the adjusted message structures.

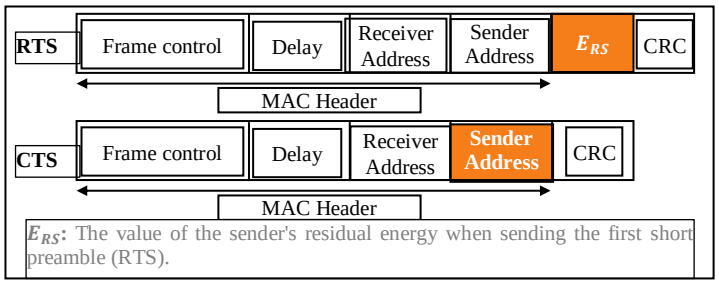


Figure 1: RTS/CTS Message Structure (Additional fields).
Source: Author, (2026).

The relay node choice procedure is designed to ensure energy-efficient and load-balanced data forwarding in E2A2S-WSN. It relies on local energy awareness, harvested energy estimation, and node load conditions, without requiring global synchronization. The proposed relay node choice procedure is illustrated in Fig. 2.

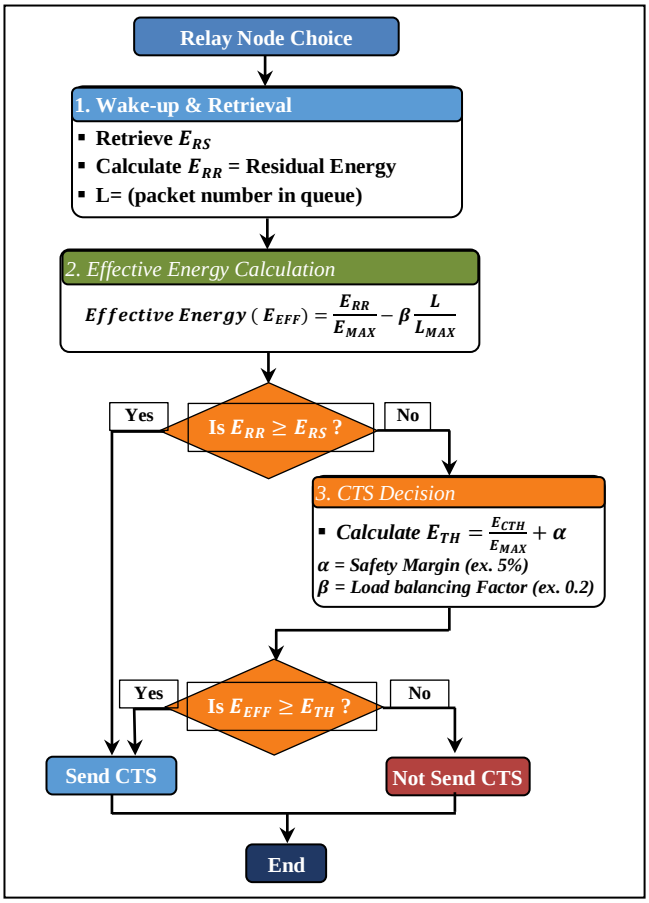


Figure 2: The proposed relay node choice procedure.
Source: Author, (2026).

When a node wakes up, it first retrieves the residual energy of the transmitting node E_{RS} from the received short RTS preamble. Simultaneously, the receiving node evaluates its own residual energy E_{RR} with recently harvested energy, and its current load L, expressed as the number of packets queued or the processing occupancy. To capture the node's actual forwarding capability, an effective energy metric is computed as:

$$E_{EFF} = \frac{E_{RR}}{E_{MAX}} - \beta\frac{L}{L_{MAX}} \quad (1)$$

Where E_{MAX} denotes the maximum energy storage capacity of a node, L_{MAX} represents the maximum supported load, and β is a weighting factor controlling the impact of node load on the relay choice decision. A minimum participation threshold is defined as:

$$E_{TH} = \frac{E_{CTH}}{E_{MAX}} + \alpha \quad (2)$$

Where E_{CTH} is the minimum required energy level to participate in routing and α is a safety margin that prevents nodes with marginal energy reserves from being selected. The receiving node responds with a CTS message if one of the following conditions is satisfied:

1. Its residual energy is greater than or equal to that of the sender:

$$E_{RR} \geq E_{RS} \tag{3}$$

2. Its residual energy is lower than that of the sender, but its effective energy exceeds the minimum threshold:

$$E_{RR} < E_{RS} \text{ and } E_{EFF} \geq E_{TH} \tag{4}$$

3. If none of these conditions is met, the node remains silent and does not participate in the forwarding process.

This relay node choice mechanism enables energy-aware and adaptive forwarding, promotes load balancing among nodes, and reduces unnecessary energy depletion, thereby extending the network lifetime without violating IEEE 802.11 MAC principles.

III.1.2 The Main Communication Mechanism of E2A2S-WSN

E2A2S-WSN adopts a communication procedure similar to RDEHWSN and relies on the CSMA/CA protocol to mitigate packet collisions among sensor nodes. Nodes with buffered data listen to the channel after each short RTS preamble and initiate data transmission only upon receiving a corresponding CTS. To enhance energy efficiency, E2A2S-WSN enables nodes to harvest energy and operate under an adaptive duty-cycle, alternating between active and sleep states. Two duty-cycle modes are supported: a fixed mode configured by the system manager and a variable mode dynamically adjusted according to the harvested and residual energy levels.

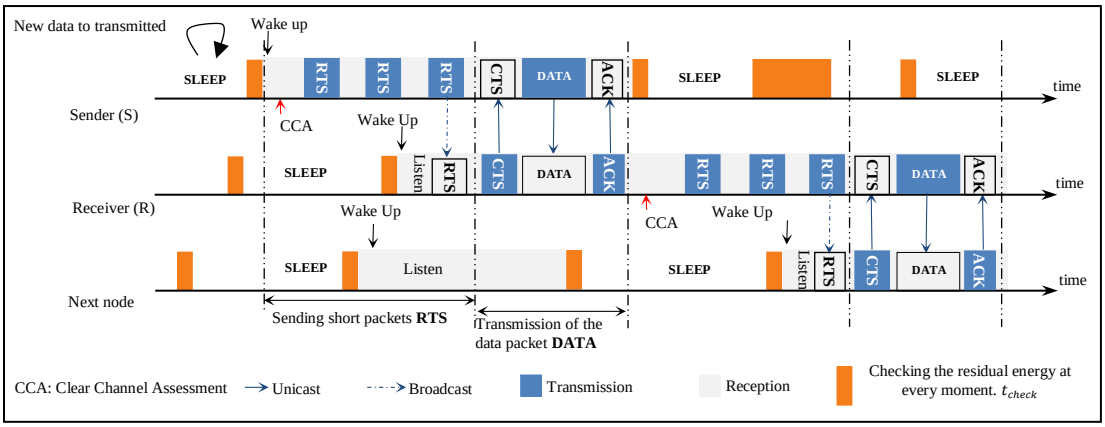


Figure 3: Illustrative diagram of the proposed E2A2S-WSN scheme operation.
Source: Author, (2026).

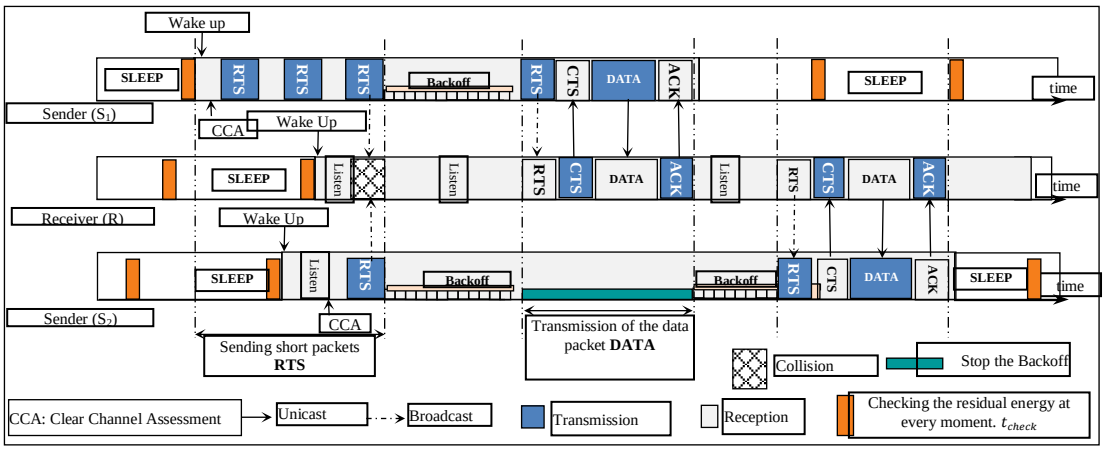


Figure 4: The collision avoidance mechanism incorporated into the proposed E2A2S-WSN scheme.
Source: Author, (2026).

Figures 3 and 4 illustrate the core communication mechanism of the E2A2S-WSN scheme between a sender and a receiving node. In this scheme, each sensor node periodically wakes up according to its own schedule to transmit data when available and switches back to sleep mode in the absence of traffic. Once the radio is activated, the sender node S initiates a preamble phase by broadcasting a sequence of short RTS packets to announce its readiness to transmit, after verifying channel availability using Clear Channel Assessment (CCA). An awake receiving node R, selected as a relay based on predefined criteria, responds with a unicast CTS packet once its backoff timer expires. Upon receiving the CTS, the sender immediately stops sending further RTS packets and transmits the data packet, provided that the channel remains free. The receiver then acknowledges successful reception by sending an ACK packet. After receiving the ACK, the sender switches directly to sleep mode. The receiver subsequently forwards the data to the next hop by repeating the same communication procedure.

III.1.3 Analytical Modeling of the E2A2S-WSN Scheme

This section introduces analytical models for energy consumption and latency in the E2A2S-WSN scheme. The network is assumed to consist of n mobile nodes operating under a static cyclic traffic pattern, where each node generates data at a fixed periodic interval. Table 1 presents the main parameters and their descriptions used in the energy and latency model.

Table 1: Symbols used in the E2A2S-WSN model.

Symbol	Description
$E_i^{Wakeup}(t)$	Total wake-up energy consumed by node *i* during interval *t*
$E_i^{cs}(t)$	Energy consumed in carrier sensing during interval *t*
$E_i^{es}(t)$	Energy consumed in environmental sensing during interval *t*
$E_i^{tx}(t)$	Energy consumed during transmission during interval *t*
$E_i^{rx}(t)$	Energy consumed during reception during interval *t*
P_{cs}	Power consumption in carrier sensing mode
P_{es}	Power consumption in environmental sensing mode
P_{tx}	Transmission power
P_{rx}	Reception power
$T_{cs}(t)$	Carrier sensing duration over interval *t*
$T_{es}(t)$	Environmental sensing duration over interval *t*
$T_{tx}(t)$	Transmission duration over interval *t*
$T_{rx}(t)$	Reception duration over interval *t*
$T_q(t)$	Packet queuing duration over interval *t*
$T_p(t)$	Packet processing duration over interval *t*
T_{acs}	Average duration of one carrier sensing operation
T_{asense}	Average duration of one environmental sensing operation
R_{data}	Data packet generation rate
R_{es}	Environmental sensing rate
L_{packet}	Data packet size
L_{CTS}	CTS packet size
L_{ack}	ACK packet size
T_{bit}	Time required to transmit one bit
T_{SW}	Switching time between TX and RX modes

Source: Author, (2026).

The expected energy consumption of node *i* in the E2A2S-WSN scheme during the wake-up interval *t* is determined by the energy spent on carrier sensing (*cs*), environmental sensing (*es*), packet transmission (*tx*), and packet reception (*rx*), as expressed in Equation (5).

$$E_i^{Wakeup}(t) = E_i^{cs}(t) + E_i^{es}(t) + E_i^{tx}(t) + E_i^{rx}(t) = P_{cs}T_{cs}(t) + P_{es}T_{es}(t) + P_{tx}T_{tx}(t) + P_{rx}T_{rx}(t) \quad (5)$$

Before transmitting the preamble, the node performs carrier sensing at each wake-up period and also activates its environmental sensors to monitor physical parameters. The total durations of carrier sensing and environmental sensing over an interval *t* are given by equations (6) and (7) respectively, which scale linearly with the observation interval.

$$T_{cs}(t) = T_{acs}R_{data}t \quad (6)$$

$$T_{es}(t) = T_{asense}R_{es}t \quad (7)$$

During a time interval *t*, the total transmission time of a data packet by node *i* is the sum of the durations required for sending the RTS, the Data packet, and the corresponding acknowledgments: CTS (in response to the RTS) and ACK (in response to the Data). Before transmitting the Data packet, the node first sends an RTS for a duration T_{SP} and immediately switches its radio to listening mode to receive the CTS. This procedure may be repeated *K* times if multiple RTS attempts are needed. Upon receiving the Data packet, the receiver immediately switches its radio to transmit an ACK back to the sender, completing the transmission cycle.

$$T_{tx}(t) = t.R_{data}\left(L_{packet} + L_{CTS} + L_{ack}\right)T_{bit} + KT_{SP} + (K+2)T_{SW} \quad (8)$$

During a time interval *t*, a node may receive multiple RTS preambles, data packets, and corresponding acknowledgments (CTS and ACK). For each received RTS preamble, the target receiver immediately replies with CTS, allowing the transmitter to send its data packet. Upon receiving the data, the receiver sends an ACK, completing the transmission cycle. The total number of these exchanges and the associated durations accumulate over the interval *t*, contributing to the node's overall communication time and energy consumption.

$$T_{rx}(t) = t.R_{data}\left(L_{packet} + L_{CTS} + L_{ack}\right)T_{bit} + \sum T_{SP} + 2T_{SW} \quad (9)$$

Before transmitting a buffered data packet, the sending node first transmits one or more RTS preambles. Upon receiving the RTS and the subsequent data packet, the receiver responds with the corresponding CTS and ACK acknowledgments. Based on equations (6), (8), and (9), the expected transmission latency can be expressed as:

$$L_{atcy}(t) = T_q(t) + T_p(t) + T_{cs}(t) + T_{tx}(t) + T_{rx}(t)$$
$$= T_q(t) + T_p(t) + T_{cs}(t) + t.R_{data}\left(2\left(L_{packet} + L_{CTS} + L_{ack}\right)t_{bit} + (K+1)T_{sp}\right) + (K+4)T_{SW} \quad (10)$$

III.1.4 Proposed Next Sleep Interval Determination in E2A2S-WSN

E2A2S-WSN operates using a dynamic duty cycle adjusted according to each node's energy harvesting rate. Nodes with higher available energy remain active longer and thus forward more packets. To reduce collisions among neighboring nodes, the protocol assigns differentiated sleep durations that are intentionally non-uniform. Nodes with lower energy levels enter deeper sleep periods to harvest more energy and restore their balance. This section presents the mechanism used to determine the next sleep duration.

1. Node residual energy calculation

The residual energy of node *i* at time *t* ($E_{R_i}(t)$) equals the previous energy minus the consumed energy plus the harvested energy over the interval Δt.

$$E_{R_i}(t) = E_{R_i}(t - \Delta t) - E_{used_i}(\Delta t) + E_{harvested_i}(\Delta t) \quad (11)$$

Where:

$\Delta t = t - t_{prev}$ and t_{prev} represents the previous evaluation instant.
$E_{R_i}(t - \Delta t)$: residual energy of node *i* at the previous time instant.
$E_{used_i}(\Delta t)$: energy consumed by node *i* during the Δt.
$E_{harvested_i}(\Delta t)$: energy harvested by node *i* during the same interval Δt.

2. Node next sleep duration calculation

To compute the next sleep duration of each node *i*, E2A2S-WSN relies on two energy thresholds: a threshold energy E_{AL} and a critical energy E_{ML}, with $E_{MAX} > E_{AL} > E_{ML}$. E2A2S-WSN operates in two duty-cycle modes:

2.1. Fixed Mode

At network startup, each node follows administrator-defined sleep and wake durations. This mode is maintained as long as the residual energy remains greater than or equal to E_{AL}.

2.2. Dynamic Mode

When operating dynamically, the sleep duration is adjusted according to the node's residual energy. where this mode is used by each node *i* in the rest of its operation. The next sleep duration is calculated using the equations below

- **Equation for calculating long sleep Duration.**

$$D_{SLP_i}\left(E_{R_i}(t)\right) = \left(\frac{E_{Max} - E_{R_i}(t)}{E_{Max} - E_{AL}}\right) \times D_{SS_i} \quad (When\ D_{SS_i}\ \text{is only computed}) \quad (12)$$

$$D_{SLP_i}\left(E_{R_i}(t)\right) = \left(\frac{E_{Max} - E_{R_i}(t)}{E_{Max} - E_{AL}}\right).D_{SS_i} + \mu\left(E_{R_i}(t)\right).\rho \quad \left(When\ D_{CSS_i}\ and\ D_{SS_i}\ \text{are computed}\right) \quad (13)$$

- **Equation for calculating short sleep Duration**.

$$D_{SLP_i}\left(E_{R_i}(t)\right) = e^{\log_2\left(\left(\frac{E_{Max} - E_{remi}}{E_{Max} - E_{Thr}}\right) \times D_{SS_i}\right)} \quad (When\ D_{SS_i}\ \text{is not calculated and}\ E_{R_i}(t) < E_{Max}) \quad (14)$$
$$\left(\text{The old computed } D_{SS_i} \text{ value is used}\right)$$

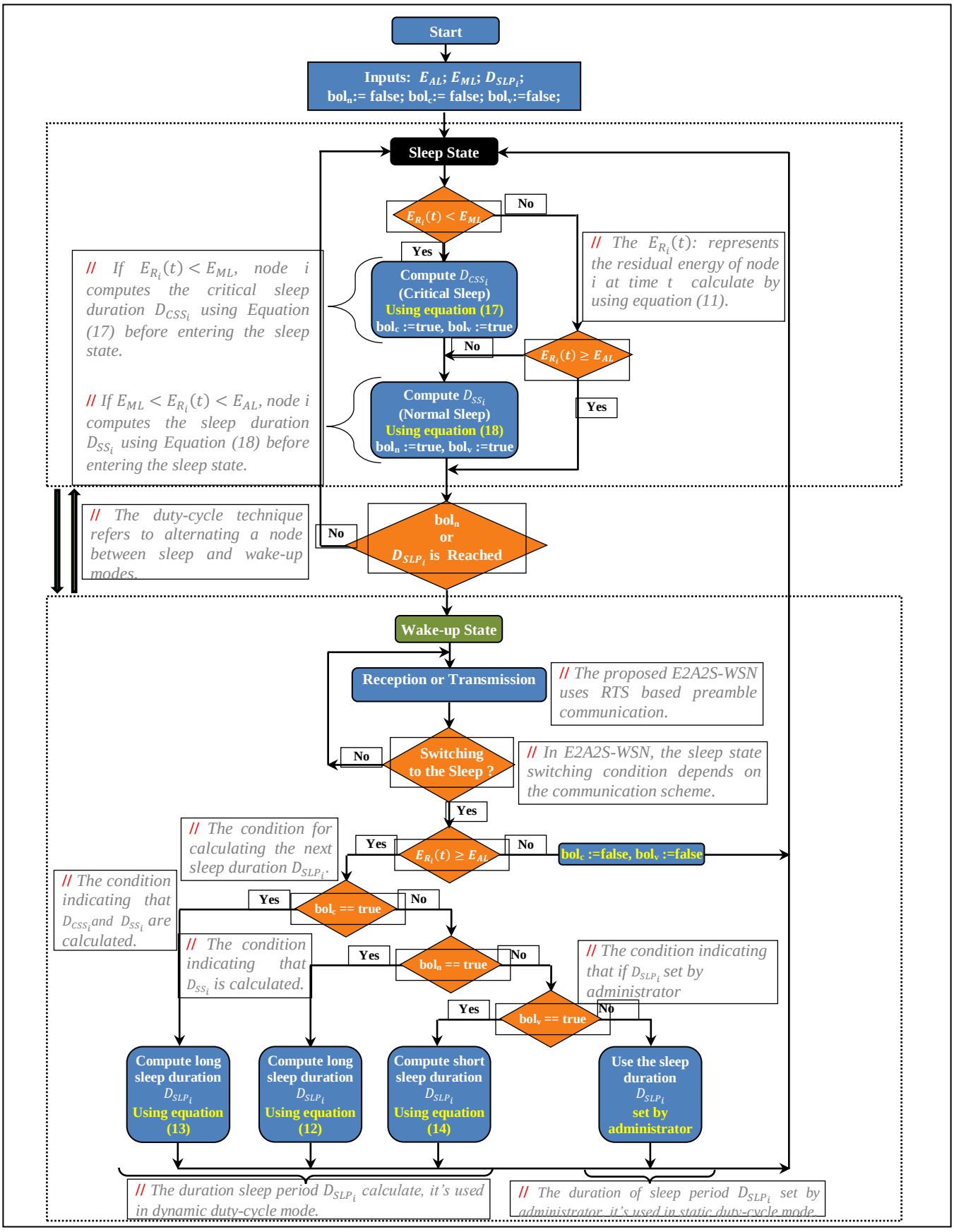


Figure 5: The key functions of the proposed E2A2S-WSN scheme.
Source: Author, (2026).

With:

$$\mu\left(E_{R_i}(t)\right) = \frac{\left(E_{R_i}(t) - E_{Max}\right) * \left(E_{R_i}(t) - E_{AL}\right)}{E_{AL} - E_{ML}} \quad (15)$$

$$\rho = \left(\frac{D_{CSS_i}}{E_{Max} - E_{ML}} - \frac{D_{SS_i}}{E_{Max} - E_{AL}} \right) \tag{16}$$

$$D_{CSS_i} = \min\left(D_{CSS_i}, 1\right) \tag{17}$$

$$D_{SS_i} = \min\left(D_{SS_i}, 1\right) \tag{18}$$

Where:

$E_{R_i}(t)$: Residual energy of node *i* at *t* instant.
D_{SS_i} : Sleep duration of node *i* until its residual energy becomes greater than or equal to the threshold E_{AL}.
D_{CSS_i}: Critical sleep duration of node i until its residual energy becomes greater than or equal to the critical threshold E_{ML}.

2.3. Next sleep duration calculation procedure

The procedure for computing the next sleep duration $D_{SLP_i}\left(E_{R_i}(t)\right)$ of node *i* in this mode is described below and is illustrated in Fig. 5.

a. In Sleep State

1. If $E_{R_i}(t) < E_{ML}$, node *i* first calculates the elapsed **critical sleep duration** D_{CSS_i} using Equation (17) until its residual energy reaches E_{ML}, and then computes the normal sleep duration D_{SS_i} using Equation (18) until its residual energy reaches E_{AL}.
2. If $E_{ML} < E_{R_i}(t) < E_{AL}$, node *i* computes only the elapsed normal sleep duration D_{SS_i} using Equation (18), until its residual energy reaches E_{AL}. This check is performed before entering the sleep state.

b. In wake-up State

1. The long sleep duration calculation. While $E_{R_i}(t) \geq E_{AL}$, node *i* computes its long sleep interval $D_{SLP_i}\left(E_{R_i}(t)\right)$ as follows:

1.1. Using Equation (12) if only D_{SS_i} has been calculated.
1.2. Using Equation (13) if both D_{SS_i} and D_{CSS_i} have been calculated.

2. The short sleep duration is computed for node *i* while $E_{R_i}(t) \geq E_{AL}$ using Equation (14), with the node employing the previously calculated value of D_{SS_i} if it has not been computed yet.

III.2 SIMULATION

III.2.1 Implementation and Simulation in OMNeT++/MiXiM

The proposed E2A2S-WSN is implemented using the OMNeT++ simulator with the MiXiM framework [25], [26]. A custom node module, HostE2A2S-WSN, based on WirelessNodeBattery, is created, featuring standard layers (application, presentation, session, transport, network) and a custom network interface card (NIC) NicE2A2S-WSN integrating the new MAC module E2A2S-WSNLayer, which manages connections with other modules and layers.

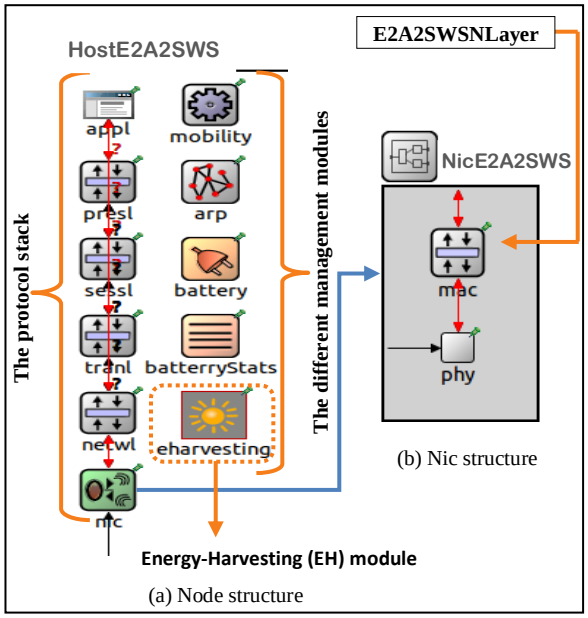


Figure 6: The architecture of the node and the NIC module employed in E2A2S-WSN for WSN implementation.
Source: Author, (2026).

Additional modules handle mobility, address resolution (ARP), battery management, energy statistics, and a new energy harvesting unit supporting exponential, uniform, or periodic harvesting. This architecture allows nodes to switch between sleep and active states and to transmit packets, facilitating performance evaluation of E2A2S-WSN. The structure of a node and the structure of the NIC module used in the WSN by E2A2S-WSN are illustrated in Figure 6.

III.2.2 Simulation Setup and Network Topology

To evaluate the proposed E2A2S-WSN scheme, a wireless sensor network was simulated using OMNeT++-4.6 with the MiXiM-2.3 framework.

Table 2: Parameters of simulation.

Parameter	***Value***
Nodes number	20, 40, 60, 80, 100
Simulation time/run	1000s
Playground Size	400x400 m², 600x600 m², 800x800 m², 950x950 m², 1100x1100 m²
Mobility Type	ConstSpeedMobility
Mobility Speed	2 mps
Start residual energy $E_{R_i}(t)$	50 J
Allowed Level E_{AL}	30 J
Energy completion threshold	35 J
Safety margin α	5%
Minimum required Level E_{ML}	15 J
Load balancing Factor β	0.2
Traffic Type	Periodic
Traffic Param	0.1s, 0.5s
Number of Packets sent	500
Destination Node	19, 39, 59, 79, 99
Queue Size	10 packets
MaxAttempts	2
Battery capacity	100 J
Harvesting Type	Periodic
Harvesting Param	0.05 s
Harvesting rate randomly	[0mW...50mW]

Source: Author, (2026).

Simulation parameters, defined in the omnetpp.ini file, include the MAC type and physical layer settings. Two key intervals are considered: Traffic Param (time between packet transmissions) and Harvesting Param (time between energy harvesting events). Simulations involve 20 to 100 mobile sensor nodes deployed over areas ranging from 400×400 m² to 1100×1100 m², with 100 m spacing, during 1000 s of simulated time. Nodes generate periodic traffic (0.1 or 0.5 s) toward a sink via multi-hop communication. Energy harvesting is periodic (0.05 s), with harvested energy randomly varying between 0 and 50 mW. Each node starts with 50 J (maximum 100 J), with energy levels set to $E_{AL} = 30\,J$, $E_{CTH} = 35\,J$, and $E_{ML} = 15\,J$. Table 2 displays the different parameters that were employed.

III.2.3 Performance Evaluation

The performance of the proposed E2A2S-WSN scheme is evaluated through extensive simulations and compared to a RDEHWSN scheme with a less adaptive duty-cycle. E2A2S-WSN ensures stable network operation by dynamically adjusting nodes' duty-cycles based on their estimated residual energy. The evaluation uses the following performance metrics:

Average Packet Latency (*APL*): The mean end-to-end delay experienced by successfully delivered packets. Lower *APL* indicates improved temporal efficiency.

Packet Delivery Ratio (*PDR*): Ratio of successfully received packets at the destination to the total packets transmitted by source nodes. This metric should be maximized to ensure reliable communication.

$$PDR = \frac{P_{received}}{P_{sent}} \tag{19}$$

Where:

$P_{received}$: Total number of packets successfully received at the sink node.
P_{sent}: Total number of packets generated and transmitted by the source nodes during the simulation.

Average Energy Consumption per Node: Defined as the average of the mean consumed energy (*MCE*) across all nodes in the WSN, and should be minimized:

$$Avg(MCE) = \frac{1}{N}\sum_{i=1}^{N} MCE_i \quad (20)$$

Where:

$$MCE_i = \frac{E_{consemed,i}}{T_{similated\ time}} \quad (21)$$

With: $E_{consemed,i}$: consumed energy by the node i.

Network Lifetime (L): Defined as the time until the first sensor node depletes its energy or becomes unable to transmit during data collection. This metric should be maximized.

Throughput (THR): the total transfer rate (obtained bytes/ time of simulation), expressed in bits per second, which should be augmented. It can be calculated as:

$$THR = \frac{Nbr_{tran}^{pck} \times size\ of\ packet}{simulation\ time} \quad (22)$$

Where: Nbr_{tran}^{pck}: Number of transferred packets.

IV. RESULTS AND DISCUSSIONS

Figures 7–12 present the simulation results in terms of packet delivery ratio, average latency (*ms*), throughput (*bps*), average energy consumption per node (*mJ*), and network lifetime (s). The evaluation is conducted under different traffic scenarios, where the traffic parameter is set to 0.1 s or 0.5 s, the number of nodes varies from 20 to 100, and the total transmitted packets set to 500. The results show that increasing the number of nodes in the WSN leads to a decrease in packet delivery ratio, while most other metrics increase, including average latency, throughput, network lifetime, and overall energy consumption. The rise in energy consumption is further amplified by the increase in the number of transmitted packets.

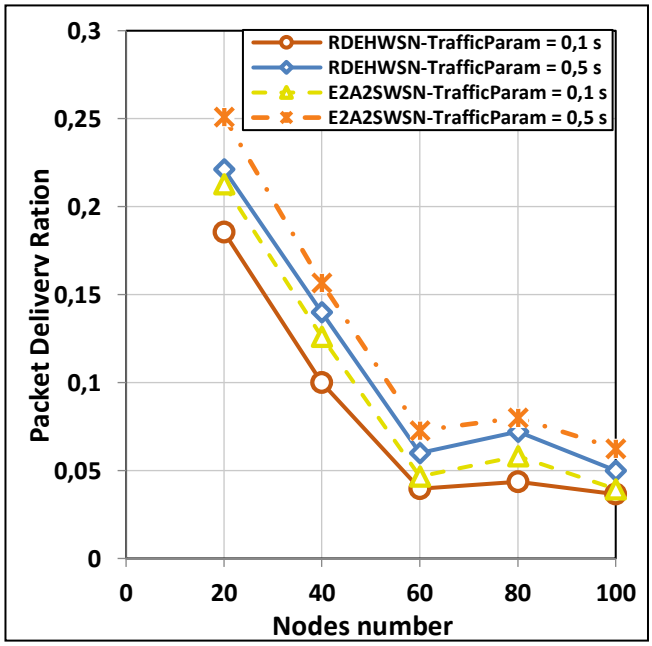


Figure 7: Packet Delivery Ration.
Source: Author, (2026).

In Figure 7, the E2A2SWSN outperforms the RDEHWSN in terms of packet delivery ratio across different EH rates. This improvement is mainly attributed to the more aggressive and fine-grained dynamic adjustment of the duty cycle in E2A2SWSN, which is driven by the residual energy that may progressively increase over time. In addition, the superior performance results from the integration of pulse-boot technology and the efficient load balancing mechanism implemented through the proposed relay node selection procedure. This mechanism ensures a better distribution of traffic among WSN nodes compared to RDEHWSN. Furthermore, in E2A2SWSN, sleep periods are intentionally adjusted with a higher incremental rate than in RDEHWSN, where sleep scheduling may not be symmetrical among neighboring nodes. This coordinated adjustment significantly reduces packet collisions and retransmissions. In contrast, in RDEHWSN, the redirection of data packets from the sender to the receiver can increase the likelihood of collisions, which in turn raises the probability of packet loss. These repeated retransmissions lead to higher energy consumption and may cause noticeable disruptions in WSN communication. For example, when the number of nodes increases from 20 to 60 (Figure 7), E2A2SWSN achieves higher packet delivery rates than RDEHWSN. At a traffic interval of 0.1 s, the improvement ranges from approximately 12.75% to 15.16%, while at 0.5 s, it varies between 11.95% and 17.49%. With 100 nodes, E2A2SWSN further demonstrates significant gains, improving the delivery rate by 7.45% at 0.1 s and 20.05% at 0.5 s compared to RDEHWSN. Overall, E2A2SWSN consistently provides better packet delivery performance than RDEHWSN, especially as WSN density increases.

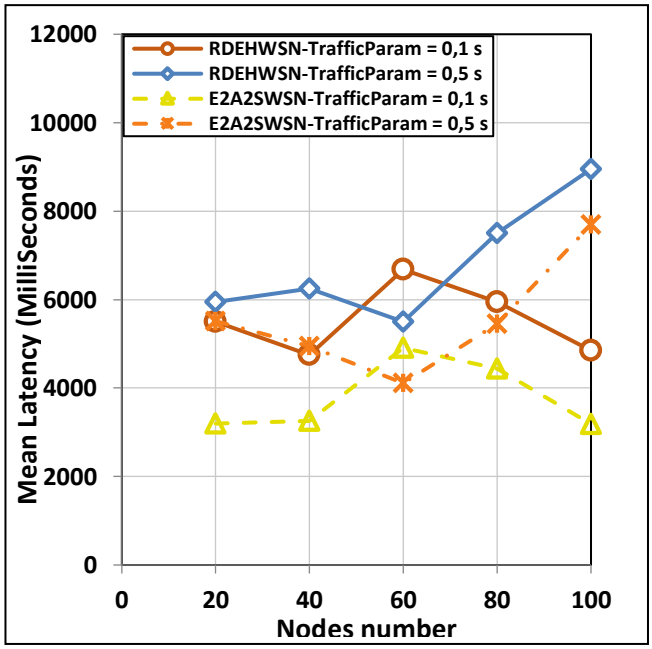


Figure 8: Mean Latency.
Source: Author, (2026).

Figure 8 shows that E2A2SWSN outperforms RDEHWSN as the number of nodes increases, particularly in terms of average latency. This improvement is mainly due to the relay node selection mechanism, which ensures efficient load balancing by prioritizing nodes with higher residual energy and shorter standby durations. The sleep time is dynamically computed according to the evolution of residual energy. In the case of a rapid increase in residual power, the short sleep time is calculated using equation (14), similarly to RDEHWSN. However, when the residual energy increases slowly, a long sleep time is determined using equations (12) or (13), which provide more accurate estimation than RDEHWSN. Moreover, the use of a discontinuous preamble reduces packet buffering and retransmissions, further decreasing latency. As a result, with 100 nodes, E2A2SWSN improves the average response time by approximately 34.27% at a traffic interval of 0.1 s and by 14.07% at 0.5 s compared to RDEHWSN.

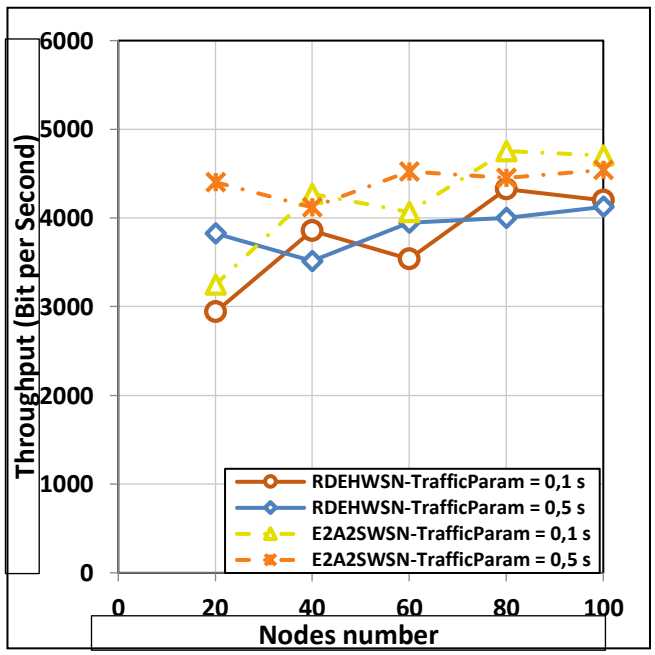


Figure 9: Throughput.
Source: Author, (2026).

Figure 9 shows that the E2A2SWSN network achieves higher throughput than RDEHWSN as the network size increases. This improvement is mainly attributed to the significant dynamic reduction of the sensor node activity period, which is adaptively adjusted according to the combined harvested and residual energy levels. Such an approach enables a more aggressive and precise duty-cycle adaptation compared to RDEHWSN. In addition, the use of an intermittent (discontinuous) preamble mechanism, combined with an efficient relay node selection strategy, ensures effective load balancing among nodes. This coordination reduces packet collisions and retransmissions. Since a higher collision rate increases transmission delay, packet loss, and energy consumption, minimizing retransmissions directly enhances throughput and stabilizes data transmission in the WSN.

For instance, when the number of nodes increases from 60 to 100 with a traffic interval of 0.1 s, Figure 9 indicates a throughput increase of 18.62% for E2A2SWSN, compared to 15.69% for RDEHWSN. Moreover, with 100 nodes and a traffic interval of 0.1 s, E2A2SWSN achieves an additional throughput gain of approximately 10.75% over RDEHWSN. Overall, E2A2SWSN provides more stable and efficient throughput performance.

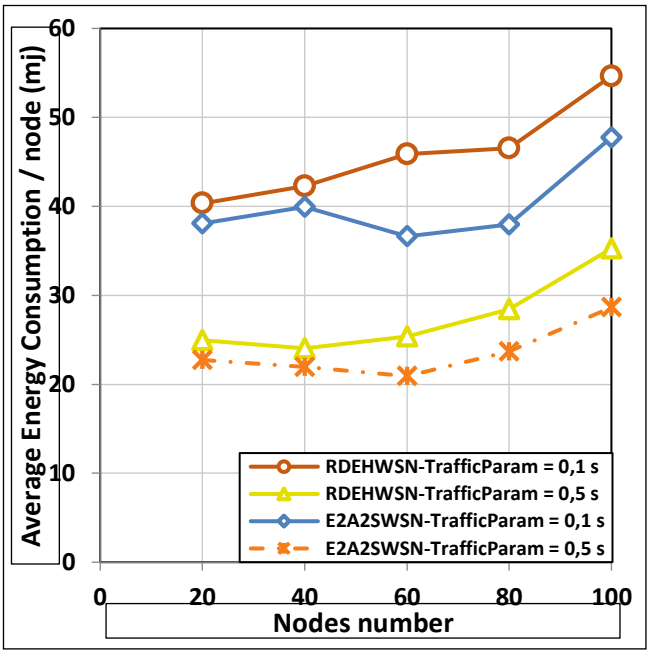


Figure 10: Average energy consumption.
Source: Author, (2026).

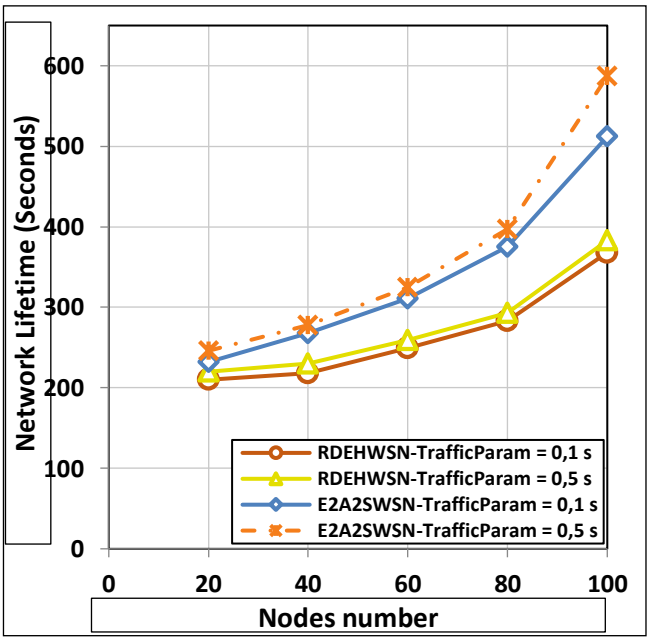


Figure 11: Network lifetime.
Source: Author, (2026).

Figure 10 shows that E2A2SWSN achieves better energy consumption performance than RDEHWSN under different energy harvesting (EH) rates. This improvement is mainly due to the intermittent booting mechanism, which allows each sensor node to dynamically and more accurately adjust its duty cycle based on the evolution of residual energy. As residual power increases over time, nodes can refine their operating and sleep periods more effectively than in RDEHWSN. Sleep durations are also carefully coordinated and are not necessarily identical among neighboring nodes, which helps reduce simultaneous wake-ups and channel contention. In addition, the efficient load balancing mechanism implemented through relay node selection minimizes packet collisions and retransmissions two major sources of excessive energy consumption and communication interruptions in WSNs. Figure 10 further indicates that, for traffic intervals of 0.1 s and 0.5 s, the energy-saving efficiency per node in E2A2SWSN remains consistently higher throughout the simulation compared to RDEHWSN. For example, at a traffic interval of 0.5 s, E2A2SWSN improves energy conservation by approximately 17.57% with 20 nodes and by about 18.77% with 100 nodes. Overall, E2A2SWSN ensures more efficient and scalable energy management.

The results related to the network lifetime metric indicate that the lifetime increases with the number of nodes for both E2A2SWSN and RDEHWSN under different EH rates. This improvement is mainly due to the use of the strobed preamble mechanism and the dynamic duty-cycle adaptation implemented in both schemes. As illustrated in Figure 11, E2A2SWSN outperforms RDEHWSN because it applies a more aggressive and in-depth dynamic adjustment of the duty cycle. Moreover, E2A2SWSN integrates a relay node selection mechanism that ensures efficient load balancing within the WSN. This strategy prioritizes nodes with higher residual energy, enabling them to remain active with shorter sleep durations, while preventing relay nodes from rapidly depleting their energy after cooperative transmissions. As a result, the overall network lifetime is significantly extended. Figure 11 further shows that when the number of nodes increases from 20 to 100, E2A2SWSN improves network lifetime by approximately 9.48% to 28.12% at a traffic interval of 0.1 s, and by 10.57% to 34.75% at 0.5 s, compared to RDEHWSN. To improve WSN performance in EH environments, particularly in terms of energy efficiency, mean latency, throughput, and packet delivery ratio, it is essential to ensure load balancing among nodes and to more aggressively reduce the duty cycle. This approach helps limit energy consumption caused by long active periods and collisions during data transmission, which are major sources of performance degradation, delays, and packet loss in WSNs. By combining load balancing with adaptive duty-cycle reduction, E2A2SWSN dynamically adjusts nodes' sleep periods so that neighboring nodes are unlikely to wake up simultaneously, thereby reducing collisions and retransmissions. As a result, E2A2SWSN outperforms RDEHWSN, which also uses a dynamic duty cycle but cannot guarantee effective load balancing and behaves similarly only when the average EH rate is high.Overall, E2A2SWSN achieves significant improvements in energy efficiency, throughput, mean latency, packet delivery ratio, and WSN lifetime compared with RDEHWSN.

V. CONCLUSIONS

This paper introduces the E2A2SWSN scheme for mobile EH-WSNs as an improved version of RDEHWSN. The proposed approach reduces energy consumption through dynamic duty-cycle scheduling combined with a strobed preamble mechanism and an effective load balancing strategy. Its main contribution is the accurate and more adaptive computation of the next sleep period based on residual energy, allowing each node to dynamically adjust its duty cycle according to the harvested energy rate. Furthermore, a novel relay node selection mechanism ensures balanced energy usage among nodes, prevents premature energy depletion, and maintains stable WSN operation. Simulation results under various traffic conditions and EH rates show that E2A2SWSN outperforms RDEHWSN by improving packet delivery ratio, reducing latency, increasing throughput, enhancing energy efficiency, and extending WSN lifetime. Future work will evaluate the scheme under additional traffic models and develop a DTN (Delay Tolerant Network) based algorithm to handle scenarios with a limited number of active nodes due to prolonged low EH or high dormancy levels.

VI. AUTHOR'S CONTRIBUTION

Conceptualization: Abdelmalek Bengheni.
Methodology: Abdelmalek Bengheni.
Investigation: Abdelmalek Bengheni.
Discussion of results: Abdelmalek Bengheni.
Writing – Original Draft: Abdelmalek Bengheni.
Writing – Review and Editing: Abdelmalek Bengheni.
Resources: Abdelmalek Bengheni.
Supervision: Abdelmalek Bengheni.
Approval of the final text: Abdelmalek Bengheni.

VII. REFERENCES

[1] D. Kandris, C. Nakas, D. Vomvas, and G. Koulouras, " Applications of Wireless Sensor Networks: An Up-to-Date Survey." Applied System Innovation,volume 3, no. 1:14, 2020. https://doi.org/10.3390/asi3010014.

[2] F. Moreno-Cruz and al., "treNch: Ultra-Low Power Wireless Communication Protocol for IoT and Energy Harvesting." Sensors, volume 20, no. (21), 6156, 2020. https://doi.org/10.3390/s20216156.

[3] R. Nithya and N. Mahendran, "A SURVEY: Duty cycle based routing and scheduling in wireless sensor networks." 2nd International Conference on Electronics and Communication Systems (ICECS), Coimbatore, India, pp. 813-817, 2015. doi: 10.1109/ECS.2015.7125025.

[4] V. Sundararaj, S. Muthukumar, and R.S. Kumar, "An optimal cluster formation based energy efficient dynamic scheduling hybrid MAC protocol for heavy traffic load in wireless sensor networks." Computers & Security, Volume 77, Pages 277-288, 2018. https://doi.org/10.1016/j.cose.2018.04.009.

[5] S. Priya, and K. S. Ashutosh, "A survey on RF energy harvesting techniques for lifetime enhancement of wireless sensor networks." Sustainable Computing: Informatics and Systems, Volume 37, 2023. https://doi.org/10.1016/j.suscom.2022.100836.

[6] S. Muhammad, J. J. Tiang, S. K. Wong, A. Smida, R. Ghayoula, and A. Iqbal, "A dual-band ambient energy harvesting rectenna design for wireless power communications." IEEE Access 9: pp 99944-99953, 2021. doi: 10.1109/ACCESS.2021.3096834.

[7] P. Kaur, B.S. Sohi, and P. Singh "Recent Advances in MAC Protocols for the Energy Harvesting Based WSN: A Comprehensive Review." Wireless Pers Commun 104(2), 423–440, 2019. doi: 10.1007/s11277-018-6028-3.

[8] A. Bengheni, "Relay node selection scheme and deep sleep period for power management in energy-harvesting wireless sensor networks." Int J Commun Syst. 37(8):e5742, 2024. doi:10.1002/dac.5742.

[9] J. Polastre, J. Hill, and D. Culler, "Versatile Low Power Media Access for Wireless Sensor Networks." in SenSys '04: Proceedings of the 2nd international conference on Embedded networked sensor systems, (New York, NY, USA), pp. 95–107, ACM, 2004. https://doi.org/10.1145/1031495.1031508.

[10] M. Buettner, G. V. Yee, E. Anderson, and R. Han, "X-MAC: A Short Preamble MAC Protocol for Duty-Cycled Wireless Sensor Networks." in SenSys'06: Proceedings of the 4th international conference on Embedded networked sensor systems, (New York, NY, USA), pp. 307–320, ACM, 2006. https://doi.org/10.1145/1182807.1182838.

[11] H.R.S. Hafiz, A.G. Luigi, and B. G, "A comprehensive review on energy harvesting MAC protocols in WSNs: Challenges and tradeoffs." Ad Hoc Networks, Vol 71, PP 117-134, 2018. https://doi.org/10.1016/j.adhoc.2018.01.004.

[12] P. Ramezani and R. M. Pakravan, "Overview of MAC protocols for energy harvesting wireless sensor networks," in IEEE 26th International Symposium on Personal, Indoor and Mobile Radio Communications-(PIMRC): Mobile and Wireless Networks, Hong Kong, China, Aug.–Sep. 2015. https://doi.org/10.1109/PIMRC.2015.7343632.

[13] S. Kosunalp, "MAC protocols for energy harvesting wireless sensor networks: Survey." ETRI Journal, vol. 37, no. 4, pp. 804–812 Aug. 2015. https://doi.org/10.4218/etrij.15.0115.0017.

[14] Z.A. Eu, H.P. Tan, and W.K.G. Seah, "Design and Performance Analysis of MAC Schemes for Wireless Sensor Networks Powered by Ambient Energy Harvesting." Ad-Hoc Netw, May, Vol. 9, No. 3, pp.300-323, 2011. https://doi.org/10.1016/j.adhoc.2010.07.014.

[15] Z.A. Eu, and H.P. Tan, "Probabilistic Polling for Multi-hop Energy Harvesting Wireless Sensor Networks." IEEE Int. Symp.Ad-hoc Sensor Netw., Ottawa, Canada, June 10–15, pp. 271–275, 2012. doi: 10.1109/ICC.2012.6363641.

[16] C. Fujii, and W.K.G. Seah, "Multi-tier Probabilistic Polling in Wireless Sensor Networks Powered by Energy Harvesting." IEEE Int. Conf. Intell. Sensors, Sensor Netw. Inf. Process, Adelaide, Australia, Dec, Vol. 6, No. 9, pp. 383–388, 2011. doi: 10.1109/ISSNIP.2011.6146627.

[17] S.C. Kim, J.H. Jeon, and H.J. Park, QoS-Aware Energy-Efficient (QAEE) MAC Protocol for Energy Harvesting Wireless Sensor Networks. Convergence Hybrid Inform. Technol.,Daejeon, Rep.of Korea, pp. 41–48, 2012. https://doi.org/10.1007/978-3-642-32645-5_6.

[18] K. Nguyen and al., ERI-MAC: An Energy-Harvested Receiver Initiated MAC Protocol for Wireless Sensor Networks. Int. J. Distrib. Sensor Netw., vol. 2014, pp. 1–8, 2014. https://doi.org/10.1155/2014/514169.

[19] X. Fafoutis, and N. Dragoni, ODMAC: An On-Demand MAC Protocol for Energy Harvesting – Wireless Sensor Networks. ACM Symp. Performance Evaluation Wireless Ad Hoc, Sensor, Ubiquitous Netw., Miami, FL, USA, pp. 49–56, 2011. https://doi.org/10.1145/2069063.2069072.

[20] Y. Kim, C.W. Park, and T.J. Lee, "MAC Protocol for Energy harvesting Users in Cognitive Radio Networks." in Proc. 8th Int. Conf. on Ubiquitous Information Management and Comm., Art. no. 59, pp. 1–4, 2014. https://doi.org/10.1145/2557977.2558054.

[21] H.I. Liu, W.J. He, and W.K.G. Seah, "LEBMAC : Load and Energy Balancing MAC Protocol for Energy Harvesting Powered Wireless Sensor Networks." In 20th IEEE International Conference on Parallel and Distributed Systems (ICPADS), Hsinchu, Taiwan, 2014. https://doi.org/10.1109/PADSW.2014.7097857.

[22] H.H. Lin, M.J. Shih, H.Y. Wei, and R. Vannithamby, "DeepSleep: IEEE 802.11 enhancement for energy-harvesting machine-to-machine communications." In Wir. Net., Vol. 21, No. 2, pp. 357–370, 2014. https://doi.org/10.1007/s11276-014-0786-y.

[23] H. Yoo, M. Shim, and D. Kim, "Dynamic Duty-Cycle Scheduling Schemes for Energy-Harvesting Wireless Sensor Networks." IEEE Commun. Lett., Vol. 16, No. 2, pp. 202–204, Feb. 2012. doi: 10.1109/LCOMM.2011.120211.111501.

[24] A. Bengheni, F. Didi, and I. Bambrik, "EEM-EHWSN: Enhanced Energy Management Scheme in Energy Harvesting Wireless Sensor Networks. Wireless." Netw 25, pp. 3029–3046, 2019. https://doi.org/10.1007/s11276-018-1701-8.

[25] MiXiM Documentation. http://mixim.sourceforge.net/. Accessed 10 October 2022.

[26] A. Köpke, et al., "Simulating wireless and mobile networks in omnet++ the mixim vision." In: Proc. of the 1st Int. Conf. on Simulation Tools and Techniques for Communications." Networks and Systems & Workshops. pp. 71:1–71:8. Simutools '08, ICST Brussels, Belgium, Belgium, 2008. doi: 10.1145/1416222.1416302.

Journal of Engineering and Technology for Industrial Applications

ISSN ONLINE: 2447-0228

ITEGAM-JETIA

Manaus, v.12 n.60, p.1246-1252. July/August, 2026.
DOI: https://doi.org/10.5935/jetia.v12i60.4057

RESEARCH ARTICLE OPEN ACCESS

ASSESSING DYNAMIC INSTABILITY USING HOPF BIFURCATION IN MULTI-MACHINE SYSTEMS EQUIPPED WITH POWER SYSTEM STABILIZER

Ghousul Azam Shaik*[1] and Lakshmi Devi Aithepalli[2]

[1, 2]Department of EEE, Sri Venkateswara University College of Engineering, Sri Venkateswara University, Tirupati, India.

[1]http://orcid.org/0000-0001-9703-5493, [2]http://orcid.org/0000-0003-3390-1772

Email:*ghousul1993@gmail.com, energylak123@yahoo.com

ARTICLE INFO

Article History
Received: March 12, 2026
Reviewed: April 14, 2026
Accepted: July 14, 2026
Published: August 31, 2026

Keywords:
Dynamic Instability,
Eigenvalue Analysis,
Hopf Bifurcation,
Power System Stabilizer,
Small Signal Stability

ABSTRACT

The small signal stability analysis is a pivotal tool for understanding low frequency oscillatory phenomenon and dynamic voltage instability. To address dynamic instability, new load flows were executed by increasing the load and generation profiles. These solutions are offered to linearization programs to investigate asymptotic stability of equilibrium points in nonlinear systems. Taking two cases and eight subcases in Kundur two area system, Hopf bifurcations were induced and corresponding bifurcation parameters were obtained with and without Power System Stabilizer (PSS) placement alongside static exciter. Capability of PSS in extending the load limits at various load buses was observed via Hopf bifurcation analysis. Performance of PSS in extending the dynamic stability limit at various load buses under single tie line contingency was also studied and it was found that PSS improved the dynamic power loading at those buses.

Copyright ©2026 by authors and Galileo Institute of Technology and Education of the Amazon (ITEGAM). This work is licensed under the Creative Commons Attribution International License (CC BY 4.0).

I. INTRODUCTION

Low frequency oscillatory behaviour and dynamic instability phenomenon arising in power grids can be studied by using small signal analysis [1]. As power systems are inherently nonlinear, they are represented by Differential-Algebraic Equations (DAE's). It is necessary to use linear and nonlinear dynamical theories to study system behaviour. The concept of damping is central for understanding the stability of dynamical system. Low frequency oscillations pose threat to system behaviour. To improve the damping of low frequency oscillations, it has been suggested in [2], [3] to use Power System Stabilizer's (PSS) along with inherent Automatic Voltage Regulator (AVR). The design of PSS in power systems *via* comprehensive damping ratio index maximization to simultaneously improve all the modal damping ratios are suggested in the works of [4]. Among them, local area modes whose frequency range is from 0.8 -2.5 Hz and the inter area modes whose frequency range is from 0.2-0.8 Hz needs to be studied for stabilizer design [3]. Although, there are many types of PSS architectures like PSS 2B, 3B, 4B [5], most of the references like [3], [6] have used two stage lead lag PSS topology for controller design. A brief review of PSS types and their tuning can be seen in [2]. These PSS models are combined with models of synchronous machines, AVR and network. Various types of generator models like 0.0, 1.0, 1.1, 2.1, 2.2, 3.2 and 3.3 are presented in literature. The number preceding the dot represents the number of windings on d-axis. The number succeeding the dot represents the number of windings on q-axis [7]. Multi machine systems with more load buses needs to be analysed because both small signal angle stability and voltage stability are to be examined. In this manuscript, the authors have chosen to use Kundur two area system shown in Figure 1 to study the above phenomenon. For linearization, Hartman–Grobman theorem [8] states that the stability of equilibrium points in a nonlinear system synthesised via linear analysis can be used to find the asymptotic stability of the same. If one of the poles of the linearized system cross the imaginary axis, into right half of S-plane while the other roots lie in the left half, such a phenomenon is known as Hopf bifurcation. The parameter which induces this phenomenon is known as bifurcation parameter. Applications of Hopf bifurcation are also observed in several engineering disciplines [9]. Hopf bifurcation-based DC-DC converter design for feeding Constant Power (CP) loads can be seen in [10]. Loads like constant horse power motors have inverse relation between speed and torque and hence their product i.e. output mechanical power becomes constant. If losses are neglected, the input power drawn becomes constant which reflects CP load behaviour in steady state.

Simulations of systems with multiple static and dynamic load models drawing power at load buses are found in [11]. Increasing available transfer capacity in Kundur two area system via Hopf and saddle node bifurcation details are studied by [12]. Authors of [12] considered 0.0 model for generator and constant impedance model for load for Hopf bifurcation analysis. [3] didn't consider the effects of Hopf bifurcation in Western States Coordinating Council System having renewable sources. They limited their discussions to prove the ability of PSS in minimizing time-domain metrics via artificial intelligence techniques. It was mentioned in [13] that [14] didn't consider the change in network topology for redesigning controls via Hopf bifurcation. Inspired from their reviews, this deficiency was also dwelled on authors of this manuscript by removing one tie line in service of Kundur two area system. In conventional power system stability program, most of the authors [15] treat loads as constant impedance as these values can be merged with the existing bus admittance matrix in a systematic manner. We have considered CP load model in this paper. Figure 1 shows typical diagram of the system having four generators (G_1, G_2, G_3, G_4) and two loads (A and B) connected through a transmission network. G_1, G_2 and G_3, G_4 are from area 1 and area 2 respectively. While [16] considered PSO-PSS at G_1 for damping ratio improvement via comprehensive index ratio maximization, the authors of this manuscript extended the study of Hopf bifurcations in the same system with PSO-PSS data. From the above literature, the following objectives are defined:

1. Improving the damping of inter area mode and other swing modes for congested and single tie line contingency cases by installing PSS besides AVR.
2. Exploring the dynamic instability phenomenon without PSS in Kundur two area system by treating loads as constant power instead of constant impedance as in [15].
3. Extending the dynamic instability through Hopf bifurcation analysis with PSS in the system for congested and single tie line contingency cases after installing PSS.

Industrial relevance of the above objectives is further detailed below:

1. In power industry, proper placement and sizing of PSS at the generating station improves the damping ratio of swing and interarea modes. Thus, if small oscillations build up in the inter area power flowing from one area to another area, these can be significantly damped using PSS.
2. Year after year, the utilities increase their generating capacities to match with the increase in the demanded power of the consumers. If the maximum loadability limits are exceeded there is a possibility for blackouts and this can be prevented by the power industry operators and planners.
3. If the maximum loadability limits can be extended by placing devices like PSS at the generating end, unnecessary load shedding, blackout prevention, transmission line and generator outages can be avoided to certain extent. This ensures continuous and reliable power supply which is central objective to power industry investors.

Case 1 and 2 deal with the congested and single tie line contingency cases. Here the variable 'λ' stands for the loading parameter at the load bus 5 and 6. The following variations A-H is explored for assessing the dynamic instability phenomenon.

A, B: Variation in real power of load -A and load-B respectively without PSS.
C, D: Variation in λ corresponding to load-A and load-B respectively without PSS.
E, F: Variation in real power of load-A and load-B respectively with PSS.
G, H: Variation in λ corresponding to load-A and load-B respectively with PSS.

Section II deals with general details of system modelling and Hopf bifurcation. Section III deals with the results and discussions. Section IV provides conclusions of the study.

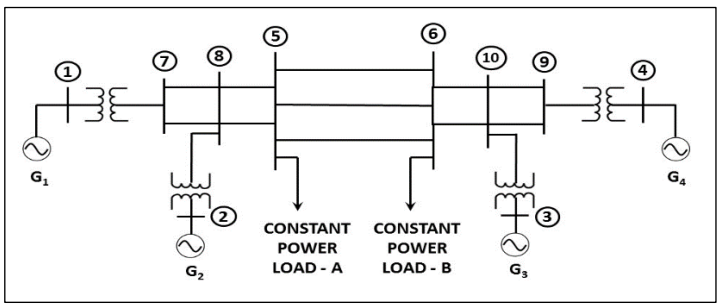


Figure 1: One line diagram of two area system.
Source: Authors, (2026).

II. SYSTEM MODELLING AND HOPF BIFURCATION

Section II.1 enumerates the modelling of Kundur two area system without any PSS. Section II.2 explains the modelling of power system stabilizer. Section II.3 details the general concepts of Hopf bifurcation and Section II.4 combines all the above via a detailed algorithm.

II.1 MODELLING OF KUNDUR TWO AREA SYSTEM

Details of modelling of Kundur two area system for linearization can be found in [1]. The nomenclature is taken from [1]. System has 10 nodes, 4 transformers and 11 lines. Buses 1-3 are PV buses. Bus no 4 is taken as slack bus. Nodes 5-10 are modelled as PQ buses. The 5th and 6th buses are having shunt capacitive susceptance of 3 and 4 p.u. All generators are modelled by two axis model i.e.1.1 whose details are found in [1].

Stator is represented by algebraic expressions instead of differential equations to simplify analysis. State variables of rotor circuits are taken as E'_q and E'_d instead of flux linkages to make analysis neat and elegant. Static exciter of single time constant and a large gain is modelled at each generator. Network is represented by medium π section quasi-steady state model in real and reactive power balance form. Loads are represented by CP absorbing type models in both dynamic and steady-state. Network transients are neglected as only low frequency modes are of concern. To study sub synchronous resonance phenomenon, it is vital to represent the network with the differential equations instead of steady state equations.

II.2 MODELLING OF POWER SYSTEM STABILIZER

Power system stabilizer (PSS) is an economic choice for damping improvement which is placed as an input to AVR block. It improves the damping as it is accommodated with lead lag blocks of time constants 'T_1', 'T_2', 'T_3'and 'T_4'. To ensure that it only responds during transient conditions, a practical differentiator of gain 'K_s' and time constant 'T_Q' is connected in cascade to the above as shown in Figure 2. The PSS presented in this manuscript utilizes 'Δω' as control input. The value of washout time constant 'T_Q' depends on the objective of compensation. If the objective is to improve the local mode of oscillation arising in single machine connected to infinite bus system, then 'T_Q' is taken between 1-2 s [7]. For improving the damping ratio of inter area modes generated from multi-machine systems, value of the same needs to be chosen between 10-20 s [7].

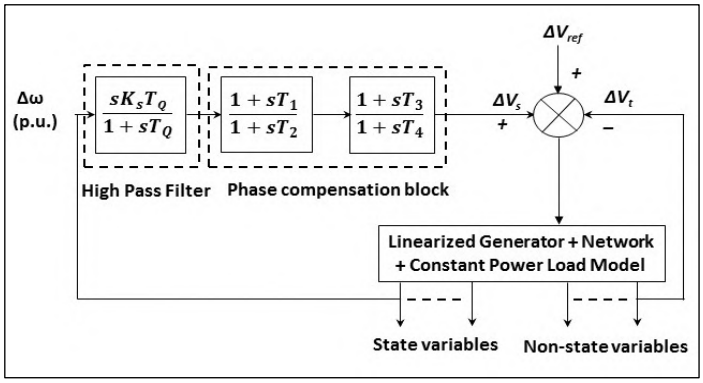


Figure 2: Block diagram of Power System Stabilizer (PSS).
Source: Authors, (2026).

II.3 HOPF BIFURCATION

Consider an autonomous system given by Equations (1-2). The order of vector 'x' and 'y' are 'k' and 'r' respectively. 'x' is vector of state variables. Vector 'y' represents algebraic variables. 'u' is control variable and 'p' is parametrized variable which brings bifurcation in the system.

$$\dot{x} = f(x, y, u) \tag{1}$$

$$g(x, y, p) = \in \dot{y} \tag{2}$$

For a given value of parameter 'p', 'g' can be solved to obtain the equilibrium point 'x_e'. Equations (1) and (2) are linearized about 'x_e' to determine the asymptotic stability of the operating point. Equations (1-2) are linearized as follows for fixed 'u' and initial operating point 'p^0' to get Equations (3-4).

$$\Delta\dot{x} = A_{f,x}\Delta x + A_{f,y}\Delta y \tag{3}$$

$$\in \Delta\dot{y} = A_{g,x}\Delta x + A_{g,y}\Delta y \tag{4}$$

Making $\in$ as zero and eliminating Δy, Equation (5) is obtained.

$$\Delta\dot{x} = \left[A_{f,x}^{p^0} - A_{f,y}^{p^0} A_{g,y}^{p^0\,-1} A_{g,x}^{p^0}\right]\Delta x = \left[A_{sys}^{p^0}\right]\Delta x \tag{5}$$

Where each submatrix $A_{f,x}^{p^0}$, $A_{f,y}^{p^0}$, $A_{g,x}^{p^0}$, $A_{g,y}^{p^0}$ of Equation (5) are defined below.

$$A_{f,x}^{p^0} = \begin{bmatrix} \frac{\partial f_1}{\partial x_1} & \cdots & \frac{\partial f_1}{\partial x_k} \\ \vdots & \ddots & \vdots \\ \frac{\partial f_k}{\partial x_1} & \cdots & \frac{\partial f_k}{\partial x_k} \end{bmatrix}_{p^0}$$

$$A_{f,y}^{p^0} = \begin{bmatrix} \frac{\partial f_1}{\partial y_1} & \cdots & \frac{\partial f_1}{\partial y_r} \\ \vdots & \ddots & \vdots \\ \frac{\partial f_k}{\partial y_1} & \cdots & \frac{\partial f_k}{\partial y_r} \end{bmatrix}_{p^0}$$

$$A_{g,x}^{p^0} = \begin{bmatrix} \frac{\partial g_1}{\partial x_1} & \cdots & \frac{\partial g_1}{\partial x_k} \\ \vdots & \ddots & \vdots \\ \frac{\partial g_k}{\partial x_1} & \cdots & \frac{\partial g_k}{\partial x_k} \end{bmatrix}_{p^0}$$

$$A_{g,y}^{p^0} = \begin{bmatrix} \frac{\partial g_1}{\partial y_1} & \cdots & \frac{\partial g_1}{\partial y_k} \\ \vdots & \ddots & \vdots \\ \frac{\partial g_r}{\partial y_1} & \cdots & \frac{\partial g_r}{\partial y_k} \end{bmatrix}_{p^0}$$

$$A_{sys}^{p^0} = \left[A_{f,x}^{p^0} - A_{f,y}^{p^0} A_{g,y}^{p^0\ -1} A_{g,y}^{p^0} \right] \tag{6}$$

Although the above partial derivatives in Equation (6) can be evaluated by using first and second order differencing approaches [1], the authors of this manuscript chose to evaluate the exact values of partial derivatives for the sake of accuracy and exactness to monitor the parameter at which Hopf bifurcation arrives.

II.4 STEPS TO ASSESS DYNAMIC INSTABILITY VIA HOPF BIFURCATION

1. Compute load flow using Newton Raphson method treating loads as CP absorbing type.
2. Use reference frame transformation to obtain initialized values of machine variables in 'd-q' frame as in [1].
3. Evaluate $\left[A_{sys}^{p^0}\right]$ by linearizing all the DAE's of machine, AVR, network and loads clubbed together without any PSS. Find the eigenvalues of system matrix. Find the damping ratios of swing modes, inter area mode and other modes of specific interest.
4. Apply small change in the real power/real and reactive power demanded by load with rescheduled generation and evaluate steps (1)-(3). The changes that needs to be done in load flow programme to accomplish this is detailed in [14].

$$P_{Li} = P_{Li,o}(\lambda_i) \tag{7}$$

$$Q_{Li} = Q_{Li,o}(\lambda_i) \tag{8}$$

Where,

λ_i is a loading factor introduced to bring Hopf bifurcation at i^{th} node.
P_{Li} , Q_{Li} are real and reactive power drawn by i^{th} load bus at each equilibrium point and
$P_{Li,o}$, $Q_{Li,o}$ are nominal real and reactive powers consumed by loads 'A' and 'B' residing at nodes 5 and 6 respectively.

5. Identify the critical mode which is crossing the right half of complex plane. Stop the algorithm and note down the loading at which dynamic instability is occurring.
6. Place PSS at 'G_1' [16], evaluate steps (1-5) and compare the ability of PSS in extending the dynamic instability through Hopf bifurcation.
7. Repeat steps (1-6) for single tie line network contingency and sketch the loci of inter area mode.

III. RESULTS AND DISCUSSIONS

The following programs were developed in MATLAB 2020 environment for achieving objectives defined in the section I.

1. Newton Raphson programme to find power flows and steady state network voltages and currents for congested tie line case. The power residuals were taken as 10^{-12}.
2. Eigenvalue analysis programme with AVR only.
3. Eigenvalue analysis programme with PSS at 'G_1'.
4. Programme to identify critical mode upon application of variations defined by Cases A-H defined in section I.
5. Modification of programmes (1-4) for single tie line contingency case.

III.1 DISCUSSION REGARDING CASE 1

The line, load, machine and exciter data from [7] is taken in this study. The load flow solution presented in [7] is obtained exactly by the authors of this manuscript. In the machine data of [7], the mechanical damping of all machines is made as 0.01 to see that no zero eigenvalue occurs. PSS parameters at 'G_1' for Case 1 are taken as T_1= 0.2473 s, T_2= 0.0218 s, T_3= 3 s, T_4= 5.4 s, T_Q= 10 s, K_s= 17.2079 [16]. From Table 1, it is observed that placement of PSS at 'G_1' increased the damping ratio of interarea mode from 0.96% to 5.72%.

The damping ratio of swing mode 'a' and 'b' increased from 10.49% to 33.16% and 10.74% to 11.03% respectively thus fulfilling the 3% minimum damping ratio criteria suggested in [17]. To explore the concepts of Hopf bifurcation, subcases '1-A' to '1-H' are generated and presented in Table 2 showing the respective loadings at which dynamic instability is achieved. For Case 1-A, the instability occurs at a loading of 13.49 p.u.. With the placement of PSS, the dynamic instability occurs at 19.02 p.u. thus proving the extension of maximum loadability. For Case 1-E, it is not the inter area mode which is unstable, but it is the high frequency mode 'd' shown in bold in Case 1-E of Table 2. The dynamic instability is happening at a loading of 17.3 p.u. for Case 1-B but after PSS placement, the loading is extended till 21.06 p.u.. The mode which is undergoing instability is the mode 'd'.

Table 1: Eigenvalues at nominal loading with and without PSS for Cases 1, 2 respectively.

Eigenvalues			
Case 1		**Case 2**	
Without PSS	**With PSS at G_1**	**Without PSS**	**With PSS at G_1**
-0.0441 ± 4.6056i[a]	**-0.2615 ± 4.5606i[a]**	**-0.0332 ± 4.0895i[a]**	**-0.1694 ± 4.0517i[a]**
-0.7680 ± 7.2818i[b]	-2.2872 ± 6.5073i[b]	-0.7622 - 7.2502i[b]	-2.2518 ± 6.7571i[b]
-0.7179 ± 6.6473i[c]	-0.7385 ± 6.6537i[c]	-0.7064 ± 6.6253i[c]	-0.7154 ± 6.6263i[c]
-23.4941 ±43.2130i	-23.3135 ±43.2623i	-23.5362 ±43.5700i	-23.3927 ±43.6103i
-24.9842 ±15.2554i	-21.1613 ±17.7450i	-24.8304 ±19.1723i	-22.8324 ±20.2304i

a) Interarea mode, b) & c) – Swing mode of area 1 and 2.
Source: Authors, (2026).

To explore the concepts of Hopf bifurcation, subcases 1-A to 1-H are generated and results are presented in Table 2. For Case 1-A, the dynamic instability occurs at a loading of 13.49 p.u. With the placement of PSS, the dynamic instability occurs at 19.02 p.u., thus extending the maximum loading limit at 5th node. The percentage improvement in loadability limit with PSS in this subcase is 41%. For Case 1-E, it is not the inter area mode which is unstable, but it is the high frequency mode 'd' shown in bold in Case 1-E of Table 2. The dynamic instability is happening at a loading of 17.3 p.u. for Case 1-B, but after PSS placement, the loading is extended till 21.06 p.u.. The mode 'd' is undergoing instability in this subcase. The percentage improvement in loadability limit with PSS in this subcase is 21.73%.

Table 2: Eigenvalues with and without PSS for Case 1 near critical loading.

Eigenvalues without PSS			
Case 1-A, P_5=13.49 p.u.	**Case 1-B, P_6= 17.30 p.u.**	**Case 1-C, λ_5=1.1755**	**Case 1-D, λ_6= 1.1015**
-0.0002 ± 4.6742i[a]	**-0.0001 ± 4.5898i[a]**	**-0.0004 ± 4.6586i[a]**	**-0.0002 ± 4.5747i[a]**
-0.6788 ± 7.3416i[b]	-0.6954 ± 7.3350i[b]	-0.6709 ± 7.3331i[b]	-0.6925 ± 7.3333i[b]
-0.6121 ± 6.7448i[c]	-0.6152 ± 6.7090i[c]	-0.6031 ± 6.7488i[c]	-0.6082 ± 6.7049i[c]
-23.0260 ±48.4425i	-22.9913 ±49.7915i	-22.9420 ±49.8976i	-22.9076 ±51.2536i
-24.9684 ±15.4713i	-24.9777 ±15.6667i	-24.9655 ±15.7650i	-24.9774 ±15.8534i
Eigenvalues with PSS at G_1			
Case 1-E, P_5=19.02 p.u.	**Case 1-F, P_6= 21.06 p.u.**	**Case 1-G, λ_5=1.5715**	**Case 1-H, λ_6=1.2965**
-0.0057 ± 4.5918i[a]	-0.1426 ± 4.3611i[a]	-0.0520 ± 4.5681i[a]	-0.1541 ± 4.3551i[a]
-2.0015 ±6.6299ib[b]	-1.9756±6.7009i[b]	-1.9398 ±6.6080i[b]	-2.0001 ±6.6740i[b]
-0.3390 ± 6.9652i[c]	-0.3700 ± 6.8395i[c]	-0.3735 ± 6.9336i[c]	-0.4006 ± 6.8142i[c]
-21.9514 ± 19.2332i	-21.3567 ± 19.4759i	-22.1115± 19.4797i	-21.4284 ± 19.5598i
-20.811 ± 6.8686i	-19.7560 ± 6.7009i	-20.8395 ±7.3090i	-20.0016 ± 6.6740i
0.3656 ± 174.0255i[d]	**0.5750 ± 178.3604i[d]**	**0.2895 ± 176.8891i[d]**	**0.3335 ± 180.1069i[d]**

a) – Interarea mode, b) – Swing mode of area 1, c) -Swing mode of area 2, d)- High frequency mode.
Source: Authors, (2026).

Table 3: Eigenvalues with and without PSS for Case 2 near critical loading.

Eigenvalues without PSS			
Case 2-A, P_5=14.07 p.u.	**Case 2-B, P_6= 17.19 p.u.**	**Case 2-C, λ_5=1.2275**	**Case 2-D, λ_6= 1.0915**
-0.0002 ± 4.1967i[a]	**-0.0003 ± 4.0313i[a]**	**-0.0006 ± 4.1763i[a]**	**-0.0003 ± 4.0178i[a]**
-0.6455 ± 7.3289i[b]	-0.6945 ± 7.2988i[b]	-0.6350 ± 7.3191i[b]	-0.6933 ± 7.2973i[b]
-0.5728 ± 6.7512i[c]	-0.6069 ± 6.6846i[c]	-0.5622 ± 6.7567i[c]	-0.6019 ± 6.6804i[c]
-22.8851 ±50.5957i	-23.0476 -50.3710i	-22.7558 ±52.6631i	-22.9764 ±51.6880i
-24.7706 ±19.8780i	-24.8092 ± 19.8388i	-24.7644 ± 20.3346i	-24.8094 ±19.9920i
Eigenvalues with PSS at G_1			
Case 2-E, P_5=18.41 p.u.	**Case 2-F, P_6= 20.43 p.u.**	**Case 2-G, λ_5=1.5690**	**Case 2-H, λ_6=1.2620**
0.0005 ± 4.0660i[a]	-0.0650 ± 3.6657i[a]	-0.0111 ± 4.0176i[a]	-0.0757 ±3.6927i[a]
-1.9902 ± 6.8743i[b]	-1.9678 ±6.9041i[b]	-1.9017 ± 6.8440i[b]	-1.9914 ± 6.8831i[b]
-0.3462± 6.9204i[c]	-0.3701 ± 6.8089i[c]	-0.3494 ± 6.9111i[c]	-0.3969 ± 6.7859i[c]
-23.3188 ± 23.7304i	-22.8626 ± 23.0627i	-23.4539 ± 24.5583i	-22.8881 ± 23.0217i
-19.9085 ± 6.0249i	-1.9678 ± 6.9041i	-19.9528 ± 6.7644i	-20.6529 ± 3.6242i
-15.3129 ± 109.0803i[d]	**0.4901 ± 183.9575i[d]**	**0.4709 ± 179.9221i[d]**	**2.9495 ± 194.7850i[d]**

a) – Interarea mode, b) – Swing mode of area 1, c) - Swing mode of area 2, d)- High frequency mode.
Source: Authors, (2026).

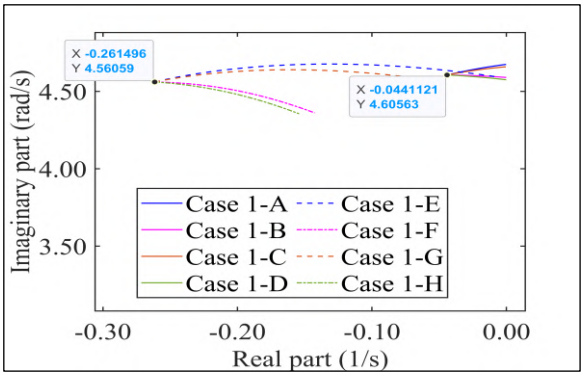


Figure 3: Loci of interarea mode corresponding to Case 1.
Source: Authors, (2026).

For Case 1-C, inter area mode is the critical mode occurring at λ_5 value of 1.1755. After placing PSS, the dynamic instability is extended till a value of 1.5715. Here, it is the mode 'd' which is undergoing Hopf bifurcation instead of mode 'a'. The percentage improvement in loadability limit with PSS in this subcase is 33.69%. The critical loading λ_6 is 1.1015 for Case 1-D. In this sub-case, the critical mode is mode 'a'. After installing PSS (Case 1-H), the critical loading is put off till 1.2965 and even in this case it is the mode 'd' undergoing Hopf Bifurcation. The percentage improvement in loadability limit with PSS in this subcase is 17.70%. The loci of inter-area mode 'a' with and without placing PSS after applying all subcases till critical loading is depicted in Figure 3 for Case 1.

III.2 DISCUSSION REGARDING CASE 2

The values of PSS parameters at G_1 for Case 2 were taken as T_1= 0.2173 s, T_2= 0.0218 s, T_3= 3 s, T_4= 5.4 s, T_Q= 10 s, K_s= 16.6370 [16]. From Table 1, it is observed that with placement of PSS at G_1, there is an improvement of damping ratio of mode 'a' from 0.81% to 4.18%. The damping ratio increased from 10.46% to 31.62%, 10.60% to 10.73% for swing mode 'a' and 'b' respectively. There is significant improvement in damping ratio of mode 'a' and 'b' but not 'c'. But all modes have damping ratio values greater than 3% as suggested by [16], [17]. To explore dynamic instability, subcases from 2-A to H are generated and presented in Table 3 showing the respective loadings at which dynamic instability is achieved. For Case 2-A, the dynamic instability occurs at a loading of 14.07 p.u. in the form of mode 'a'. With the placement of PSS, the dynamic instability occurs at 18.41 p.u., thus ascertaining the extension of load limit. The percentage improvement in loadability limit with PSS in this subcase is 30.85%. The dynamic instability is happening at a loading of 17.19 p.u. for Case 2-B but after PSS placement, the loading can be extended till 20.43 p.u. The mode which is undergoing instability is the mode 'd'. The percentage improvement in loadability limit with PSS in this subcase is 18.85%. For Case 2-C, mode 'a' is the critical mode occurring at λ_5 value of 1.2275. After placing PSS, the dynamic instability can be extended till a value of 1.5690. For this case, it is the mode 'd' which is undergoing Hopf bifurcation instead of mode 'a'. The percentage improvement in loadability limit with PSS in this subcase is 27.82%. The critical loading λ_6 is 1.0915 for Case 2-D. The critical mode is mode 'a'. After installing PSS (Case 2-H), the critical loading λ_6 is put off till 1.2620 and in this case, it is the mode 'd' which is the critical mode. The percentage improvement in loadability limit with PSS in this subcase is 15.62%. The loci of inter-area mode 'a' with and without placing PSS after applying all subcases till critical loading is depicted in Figure 4 for Case 2.

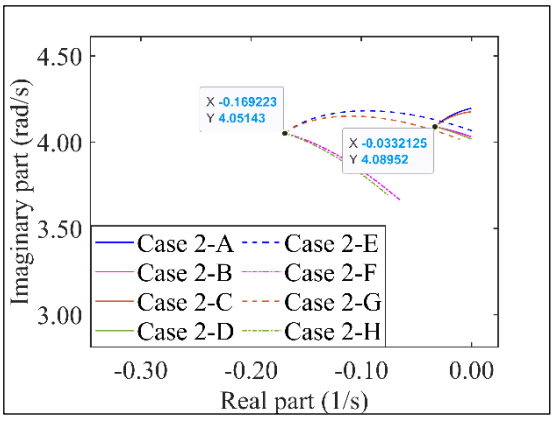


Figure 4: Loci of interarea mode corresponding to Case 2.
Source: Authors, (2026).

IV. CONCLUSIONS

A nonlinear autonomous system can be linearized about an equilibrium point for studying whether the system is asymptotically stable or not. Multiple equilibrium points are generated by changing the values of loads and generation of Kundur two area system. For each generated equilibrium point, the procedure of linearization is done to see whether at least one of the complex conjugate pair crosses the imaginary axis from left half of complex plane.

In order to have detailed view, two cases and eight subcases are sprouted to draw the loci of interarea mode of system. It was obtained that with the placement of PSS, dynamic instability can be extended to a higher loading as compared to the one obtained without PSS for both congested and single tie line contingency cases.

V. AUTHOR'S CONTRIBUTION

Conceptualization: Ghousul Azam Shaik and Lakshmi Devi Aithepalli.
Methodology: Ghousul Azam Shaik and Lakshmi Devi Aithepalli.
Investigation: Ghousul Azam Shaik and Lakshmi Devi Aithepalli.
Discussion of results: Ghousul Azam Shaik and Lakshmi Devi Aithepalli.
Writing – Original Draft: Ghousul Azam Shaik.
Writing – Review and Editing: Ghousul Azam Shaik and Lakshmi Devi Aithepalli.
Resources: Ghousul Azam Shaik and Lakshmi Devi Aithepalli.
Supervision: Ghousul Azam Shaik and Lakshmi Devi Aithepalli.
Approval of the final text: Ghousul Azam Shaik and Lakshmi Devi Aithepalli.

VI. ACKNOWLEDGMENTS

The first author thanks University Grants Commission (UGC), New Delhi, India for granting Junior and Senior Research Fellowships to do Ph.D. research work at Department of Electrical and Electronics Engineering, SVU College of Engineering, Sri Venkateswara University, Tirupati, India.

VII. REFERENCES

[1] P.W. Sauer, M.A. Pai, J.H. Chow, Power System Dynamics and Stability, Wiley-IEEE Press, New Jersey, 1998.
.
[2] R. Devarapalli, N.K. Sinha, and F.P. García Márquez, "A review on the computational methods of power system stabilizer for damping power network oscillations," Archives of Computational Methods in Engineering, vol. 29, no. 6, pp. 3713-3739, 2022. doi.org/10.1007/s11831-022-09712-z.

[3] P. Dey, A. Saha, A. Bhattacharya, and B. Marungsri, "Analysis of the effects of PSS and renewable integration to an inter-area power network to improve small signal stability," Journal of Electrical Engineering & Technology, vol. 15, pp. 2057-2077, 2020. doi.org/10.1007/s42835-020-00499-2.

[4] M.A. Prakasa, I. Robandi, R. Nishimura, and M. R. Djalal, "A hybrid controlling parameters of power system stabilizer and virtual inertia using Harris Hawk optimizer in interconnected renewable power systems," IEEE Access, vol. 12, pp. 76219-76243, 2024, doi: 10.1109/ACCESS.2024.3405994.

[5] S. P. Ghoshal, A. Chatterjee, and V. Mukherjee, "Bio-inspired Fuzzy Logic Based Tuning of Power System Stabilizer," Expert Systems with Applications, vol. 36, no. 5, pp. 9281-9292, 2009, doi: 10.1016/j.eswa.2008.12.004.

[6] M. R. Islam, M. S. Azam, M. S. Hossen, M. S. Islam, M. Y. Worku, M. S. Shahriar, and M. Shafiullah, "Power System Stability Enhancement Through Optimal PSS Design," e-Prime-Advances in Electrical Engineering, Electronics and Energy, vol. 9, pp. 1-19, September 2024, doi: 10.1016/j.prime.2024.100735.

[7] K.R. Padiyar, Power System Dynamics Stability and Control, 2nd ed., BS Publications, Hyderabad, India, 2008.

[8] Guckenheimer, and P. Holmes, Nonlinear Oscillations, Dynamical Systems, and Bifurcations of Vector Fields (Vol. 42), Springer Science & Business Media, 2013.

[9] Z.D. Georgiev, I.M. Uzunov, T.G. Todorov, and I.M Trushev, "The Poincaré–Andronov–Hopf bifurcation theory and its application to nonlinear analysis of RC phase-shift oscillator" International Journal of Circuit Theory and Applications, 52(3), pp.1399-1437. 2024. doi.org/10.1002/cta.3783.

[10] L. Huang, and Y. Lu, "Discrete modeling and period-adding bifurcation of DC–DC converter feeding constant power load," IEEE Access, vol. 9, pp. 52773-52783, 2021, doi.org/10.1109/ACCESS.2021.3069633.

[11] W.W. Price, C.W. Taylor, and G.J. Rogers, "Standard load models for power flow and dynamic performance simulation," IEEE Transactions on Power Systems, 10(CONF-940702), 1995. doi: 10.1109/59.466523.

[12] J. Wei, G. Li, and M. Zhou, "Numerical bifurcation and its application in computation of available transfer capability," Applied Mathematics and Computation, vol. 252, pp. 568-574, 2015. doi.org/10.1016/j.amc.2014.12.003.

[13] Xusheng Yang, Wei Chen, Lizhen Wu, Jiying Tuo, Nan Qiu, "Stability analysis method of a hierarchical control structure microgrid based on a small-signal model and Hopf bifurcation Theory," International Journal of Electrical Power & Energy Systems, vol. 161, 110157, 2024. doi:10.1016/j.ijepes.2024.110157.

[14] G.A. Shaik, and L.D. Aithepalli, "Identification of Hopf bifurcation point using small signal stability analysis in a power system with increased lad and generation," Third International Conference on Advances in Electrical, Computing, Communication and Sustainable Technologies (ICAECT), Bhilai, India, pp. 1-4, 2023. Doi.org/10.1109/ICAECT57570.2023.10118189.

[15] J.S. Naik, R. Thirumalaivasan, and M. Janaki, Analysis of multi-machine power system with PSS using participation factor method. 2021 Innovations in Power and Advanced Computing Technologies (i-PACT), Kuala Lumpur, Malaysia, pp. 1-7, 2021. doi: 10.1109/i-PACT52855.2021.9696864.

[16] G.A. Shaik, and L.D. Aithepalli, "Investigation of particle swarm optimization-based power system stabilizer on damping performance in two area system with voltage dependent load models," SSRG International Journal of Electrical and Electronics Engineering, vol. 12, no. 1, pp. 63-75. 2025. https://doi.org/10.14445/23488379/IJEEE-V12I1P107

[17] Xi-Fan Wang, Yonghua Song, and Malcolm Irving, Modern Power Systems Analysis, Springer, New York, 2008.

Journal of Engineering and Technology for Industrial Applications

ISSN ONLINE: 2447-0228

ITEGAM-JETIA

Manaus, v.12 n.60, p.1253-1261. July/August, 2026.
DOI: https://doi.org/10.5935/jetia.v12i60.4059

RESEARCH ARTICLE OPEN ACCESS

PSO-DRIVEN OPTIMIZATION OF DIELECTRIC BARRIER DISCHARGE OZONE GENERATION PARAMETERS FOR WATER TREATMENT APPLICATIONS

Ghaitaoui Essama Ahmed*[1], Nassour Kamel[2], Nemmich Said[3], Ghaitaoui Touhami[4], Oulad Naoui Brahim El Khalil[5] ,Bouroumeid Yassine[6], Tilmatine Amar[7], Halali Youcef[8]

[1, 2, 6]ICEPS Laboratory, Djillali Liabes University of Sidi Bel-Abbes, Sidi Bel-Abbes, Algeria.
[3, 5, 7]APELEC Laboratory, Djillali Liabes University of Sidi Bel-Abbes, Sidi Bel-Abbes, Algeria.
[4, 8]LDDI Laboratory, University Ahmed Draia – Adrar, Adrar Algeria.

[1]https://orcid.org/0009-0006-2862-6955, [2]https://orcid.org/0000-0003-1082-9595, [3]https://orcid.org/0000-0002-7767-0032
[4]https://orcid.org/0000-0003-2359-6727, [5]https://orcid.org/0009-0002-4349-0989, [6]https://orcid.org/0009-0005-7116-3565
[7]https://orcid.org/0000-0003-1352-6071, [8]https://orcid.org/0009-0000-2983-7937

Email:*oussamaghaitaoui@gmail.com, nass_ka@yahoo.fr, nemmichsaid@gmail.com, touhami.eln@gmail.com, oladnaoui45@gmail.com, bouroumeid.yassine@yahoo.com, atilmatine@gmail.com, youcefhalali01@gmail.com

ARTICLE INFO

Article History
Received: March 12, 2026
Reviewed: April 14, 2026
Accepted: July 14, 2026
Published: August 31, 2026

Keywords:
ozone generation,
DBD,
water treatment,
particle swarm optimization ,
mathematical modeling.

ABSTRACT

This investigation presents a comprehensive optimization framework for ozone generation in dielectric barrier discharge (DBD) systems applied to water treatment processes. The study employs a Venturi injection configuration to systematically analyze the influence of three critical operational parameters: applied voltage (6-8 kV), oxygen flow rate (3-5 L/min), and water flow rate (8-16 L/min) on dissolved ozone concentration in treated water. Experimental design methodology utilizing MODDE 5.0 software enabled the development of a second-order polynomial mathematical model correlating input variables with ozone concentration response. The derived model demonstrated excellent statistical validity with coefficient of determination (R^2) of 99.2% and predictive capability (Q^2) of 90.3%, confirming robust model accuracy and reliability.Parameter optimization was achieved through implementation of Particle Swarm Optimization (PSO) algorithm, a bio-inspired metaheuristic approach that mimics collective intelligence behavior observed in natural swarms. The PSO methodology employed a population of 50 particles over 100 iterations to minimize prediction errors between theoretical model outputs and experimental measurements. Convergence analysis revealed rapid optimization performance, achieving optimal parameter extraction within 90 iterations. Comparative analysis between PSO-optimized parameters and conventional MODDE 5.0 results demonstrated superior performance of the proposed approach. Optimal operating conditions were identified as: applied voltage of 7.95 kV, oxygen flow rate of 3.38 L/min, and water flow rate of 8.27 L/min. The PSO-based optimization yielded enhanced ozone generation efficiency through reduced water flow rates and optimized voltage levels, confirming the voltage parameter as the dominant factor in ozone production.

Copyright ©2026 by authors and Galileo Institute of Technology and Education of the Amazon (ITEGAM). This work is licensed under the Creative Commons Attribution International License (CC BY 4.0).

I. INTRODUCTION

Researchers across multiple disciplines, including chemistry, materials science, and engineering, demonstrate increasing interest in the identification and elimination of contaminant species, driving the development of advanced high-performance treatment methodologies [1], [2]. As noted by [1], the application of plasma-based technologies in water treatment applications has generated significant research inquiries.

Cold atmospheric plasmas can achieve efficient ozone generation while providing sterilization and decontamination capabilities for thermally sensitive surfaces [1], [2]. Water purification processes encompass various physical, chemical, electrical, and electronic methodologies, with plasma-based systems representing a prominent approach [3]. Dielectric barrier discharge (DBD) plasma systems constitute one of the primary methods for water treatment through ozone generation, enabling the production of purified water [4-6]. Following the principles outlined by [4], the discharge mechanism occurs between two metallic electrodes separated by a dielectric material and a gas-filled gap where the electrical discharge is initiated. These systems have been extensively investigated for the degradation of dye contaminants present in wastewater at elevated concentrations [3]. Ozone (O_3) production utilizes air or oxygen as the primary feedstock [7]. As described by [7], initially, high-energy electrons collide with oxygen molecules, resulting in the dissociation of oxygen atoms. Subsequently, O_3 formation occurs through the combination of free O_2 molecules and oxygen radicals [7]. Figure 1 presents a schematic representation of these reaction mechanisms [8].

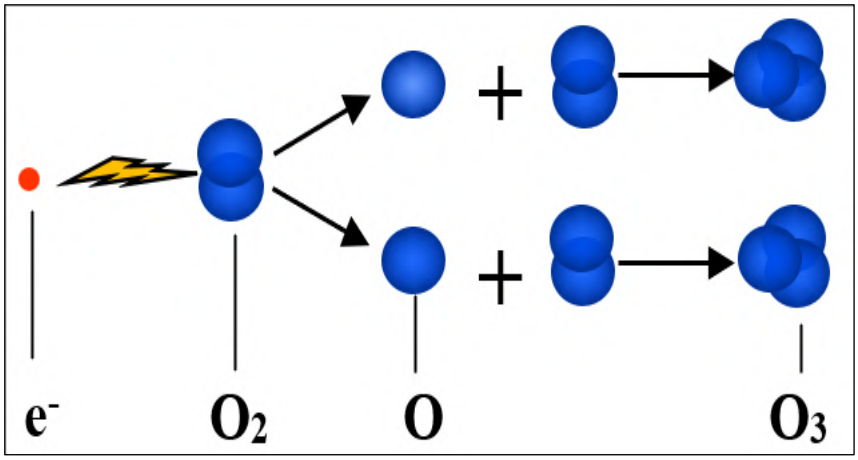


Figure 1: Schematic diagram illustrating ozone production via electron impact mechanisms.
Source: Authors, (2026).

As established in previous research [9], [10], ozone concentration exhibits an inverse relationship with gas flow rate and electrode gap spacing, while demonstrating a positive correlation with electrode surface area [9], [10]. Additionally, ozone concentrations increase proportionally with residence time and AC high-voltage amplitude [11]. Multiple parameters influence the efficacy of ozone-based water treatment processes, including operational control factors and environmental conditions [12-14]. Following the methodology described by [12], experimental investigations were conducted using a laboratory-scale test bench equipped with a Venturi injection system. The controllable parameters analyzed included high voltage amplitude, oxygen flow rate, and water flow rate [15]. The mathematical modeling framework implemented in MODDE 5.0 software addresses nonlinear optimization problems characterized by numerous interconnected indeterminate parameters [16], [17]. As demonstrated by [16], metaheuristic optimization algorithms demonstrate exceptional suitability and capability for solving nonlinear multimodal optimization challenges [18-20]. The objective of this investigation is to employ particle swarm optimization (PSO) methodology , following the approach established by [17], to extract optimal parameters (voltage (U), water flow (WF), and oxygen flow (OF)) that maximize treatment efficiency and determine the optimal operating conditions.

II. EXPERIMENTAL SETUP AND METHODOLOGY

The experimental configuration employed in this research is demonstrated in Figure 2. Water movement is accomplished using a pumping mechanism with flow regulation controlled through an autotransformer. Ozone introduction into the water treatment system is achieved via a Venturi mixing arrangement, enabling efficient dissolution and uniform distribution of ozone throughout the aqueous solution. Following the setup described in earlier investigations [4], [14], ozone production is carried out using a dielectric barrier discharge (DBD) reactor fed with oxygen from a concentrator device providing adjustable flow rates between 1 to 5 L/min. This investigation employed a switching-mode high voltage supply system, similar to the design reported by [13]. The process begins with a transformer reducing 220 V AC input to approximately 72 V DC following rectification. An Insulated Gate Bipolar Transistor (IGBT) functions as an electronic switching component, regulated by an oscillator to create high-frequency current. This reduced voltage, high-frequency current is subsequently amplified through a high voltage step-up transformer, generating output voltages spanning 1–10 kV at frequencies from 0–30 kHz. For this research, the ideal operating frequency for the discharge tube was determined to be 20 kHz. Experimental activities were performed under regulated environmental parameters, maintaining ambient temperature between 20-25°C and relative humidity controlled within 60-70% range. Voltage measurements were obtained using a digital oscilloscope (GWINSTEK GDS-3154) with a high voltage probe (Tektronix P6015A), while current was estimated through voltage drop assessment across a 100 Ω resistor.

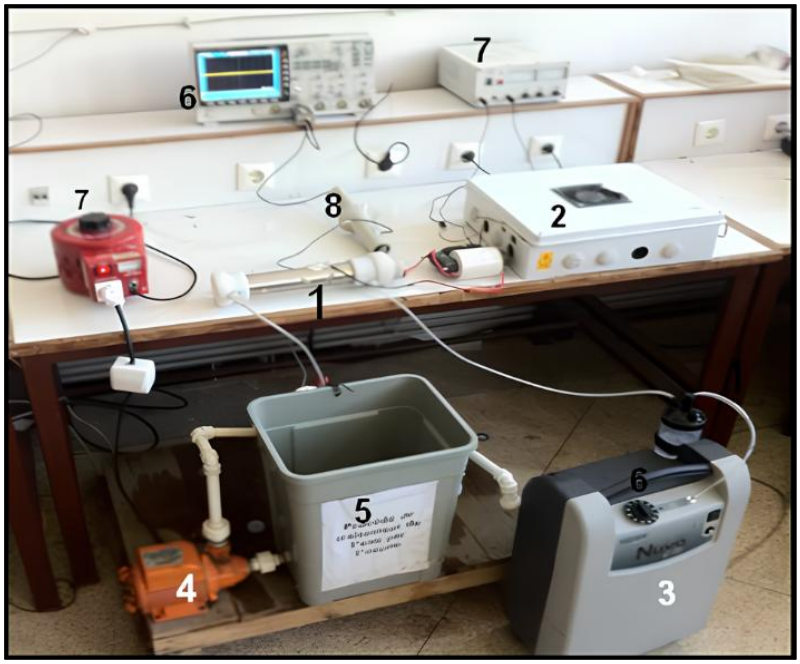


Figure 2: Photograph of the assembled apparatus.
1. Ozone Generator, 2. high-voltage power supply, 3. oxygen concentrator, 4.Water pump, 5. Water to be treated, 6. Digital oscilloscope, 7. Variac, 8. high voltage probe.
Source: Authors, (2026).

Table 1 presents the results obtained from the experiment and used to obtain the mathematical mode.

Table 1:The results obtained from the experiment.

Test N	Voltage U (KV)	Water flow WF(L/min)	Oxygen flow OF (L/min)	Ozone concentration C (mg/L)
1	6	8	3	0.35
2	8	8	3	0.52
3	6	16	3	0.24
4	8	16	3	0.475
5	6	8	5	0.34
6	8	8	5	0.495
7	6	16	5	0.26
8	8	16	5	0.43
9	6	12	4	0.28
10	8	12	4	0.505
11	7	8	4	0.44
12	7	16	4	0.36
13	7	12	3	0.52
14	7	12	5	0.51
15	7	12	4	0.455
16	7	12	4	0.455
17	7	12	4	0.455

Source: Authors, (2026).

III. MATHEMATICAL FRAMEWORK FOR WATER TREATMENT PROCESS MODELING

The development of a reliable mathematical model represents a critical foundation for any optimization study in water treatment applications. A predetermined mathematical relationship describes the connection between response variables and input factors. Following the methodology described by [15], this approach employs a truncated Taylor-Maclaurin series expansion where derivatives are considered constant, producing a polynomial expression containing terms of different degrees:

$$y = a_0 + \sum a_i x_i + \sum a_{ij} x_i x_j + \cdots + \sum a_{ii} x_i^2 + a_{ij\ldots z} x_i x_j \ldots x_z \quad (1)$$

The selection of polynomial modeling approach offers several advantages for this particular application. First, polynomial functions provide excellent flexibility in capturing nonlinear relationships between operational parameters and ozone concentration. Second, the mathematical structure allows for clear interpretation of individual parameter effects and their interactions. Third, the computational efficiency of polynomial models makes them suitable for real-time optimization applications. Coefficient determination or estimation utilizes specialized data processing software to minimize variance between predictive models and experimental observations. The accuracy of coefficient estimation directly influences the reliability of subsequent optimization procedures.

The software platform MODDE 5.0 from Umetrics AB in Umea, Sweden, was implemented for this comprehensive analysis. This Windows-compatible program specializes in creating and evaluating experimental designs with advanced statistical capabilities (MODDE 5.0, 1999). The software assists researchers in result interpretation and response prediction through sophisticated mathematical model coefficient computation algorithms. It determines optimal factor adjustments for process enhancement while calculating two critical statistical measures, R^2 and Q^2, for rigorous mathematical model validation. Our choice of MODDE 5.0 was based on several key factors: its proven track record in chemical process optimization, robust statistical analysis capabilities, and user-friendly interface that facilitates complex experimental design interpretation. The software's ability to handle multi-factorial experiments with nonlinear interactions makes it particularly suitable for ozone generation optimization studies. The goodness of fit measure (R^2) evaluates how effectively the model represents experimental data, with values ranging from 0 to 1, where unity signifies perfect fitting and zero indicates complete model inadequacy. The predictive quality measure (Q^2) estimates the model's forecasting capability for new experimental conditions. Like R^2, Q^2 ranges up to 1, though its minimum value extends to negative infinity. For successful diagnostic evaluation, both parameters require elevated values, preferably within 0.2–0.3 difference to ensure model reliability and predictive accuracy. Following the experimental framework established by [15], ozonation-driven water treatment process effectiveness is influenced by numerous interconnected factors, including operational control parameters and environmental variables. Our research methodology involved conducting systematic experimental studies using specially designed laboratory-scale equipment featuring advanced Venturi injection techniques. Three primary adjustable operational factors were comprehensively evaluated through statistical experimental design: high voltage magnitude, oxygen flow rate, and water circulation rate. The selection of these three parameters was based on preliminary sensitivity analysis and literature review indicating their significant impact on ozone generation efficiency. Voltage represents the primary energy input controlling the discharge intensity, oxygen flow affects the raw material availability for ozone synthesis, while water flow determines the residence time and mass transfer characteristics within the treatment system. The mathematical expression representing the optimized response, specifically focusing on dissolved ozone concentration levels in treated water (C), was systematically developed through MODDE 5.0 statistical analysis as follows:

$$C = 0.46 + 0.096U – 0.038WF – 0.07\ U^2 – 0.06\ WF^2 + 0{,}05OF^2 \quad (2)$$

This quadratic model structure reveals several important characteristics: the positive linear coefficient for voltage (0.096) confirms its promoting effect on ozone generation, while the negative linear coefficient for water flow (-0.038) indicates dilution effects. The negative quadratic terms for both voltage and water flow suggest optimal operating points beyond which further increases become counterproductive. Where :

C: Ozone concentration produced (mg/L)
U: Applied voltage (kV)
WF: Water flow (L/mn)
OF : Oxygen flow (L/mn)

The statistical validation results demonstrated exceptional model quality, with R^2 and Q^2 achieving values that approached unity (R^2 = 99.2%; Q^2 = 90.3%). These outstanding statistical indicators confirmed the model's validity and established its suitability for both prediction and optimization applications. The small difference between R^2 and Q^2 (8.9%) indicates excellent model generalization capability, suggesting reliable performance when applied to new operating conditions within the experimental range.
Detailed analysis of the mathematical expression reveals that voltage impact significantly exceeds water flow rate influence within the investigated parameter ranges. This finding aligns with fundamental plasma physics principles, where electrical energy directly controls the electron density and energy distribution responsible for oxygen dissociation. As demonstrated in previous research [4], [13], applied voltage represents the critical controlling factor affecting ozone production efficiency, as it initiates and sustains the electrical discharge essential for the oxygen-to-ozone conversion process. The physical mechanism underlying voltage dominance involves several interconnected phenomena. Higher voltages increase electron energy and density within the discharge gap, promoting more efficient oxygen molecule dissociation. Additionally, elevated voltage levels enhance the formation of reactive oxygen species and extend the discharge volume, both contributing to increased ozone yields. Conversely, water flow rate demonstrates a negative influence and requires careful optimization to achieve desired ozone output levels. Elevated water flow rates result in decreased dissolved ozone concentrations due to reduced residence time and dilution effects. This relationship highlights the importance of balancing treatment throughput with ozone transfer efficiency. Meanwhile, oxygen flow rate influence was determined to be minimal within the investigated range. This finding suggests that increasing oxygen flow rate beyond 4 L/min provides diminishing returns, as significant portions exit the ozone generator without undergoing the ozone conversion process. From an economic perspective, this indicates an optimal operating point that balances raw material consumption with ozone production efficiency.

IV. EXTRACTION OF PROPOSED PSO-BASED MODEL PARAMETERS

Particle Particle Swarm Optimization (PSO) represents a sophisticated population-based collective intelligence algorithm that has revolutionized optimization approaches in engineering applications. The original concept was pioneered by Kennedy and Eberhart [21], [22] to simulate and harness the collective behavioral characteristics observed in natural social species, particularly the coordinated movement patterns exhibited in bird flocking behaviors and fish schooling dynamics. The fundamental appeal of PSO lies in its ability to emulate the decentralized decision-making processes found in nature, where individual agents contribute to collective intelligence without central coordination. This bio-inspired approach offers several advantages over traditional optimization methods: it avoids the need for gradient information, handles discontinuous and multimodal functions effectively, and demonstrates robust performance across diverse problem domains.

PSO employs the physical movement properties and social interaction characteristics of individual swarm members [23], delivering a balanced and highly adaptive computational framework [24] for enhancing both global exploration and local exploitation capabilities. The algorithm's success stems from its ability to maintain population diversity while progressively converging toward optimal solutions. Given its straightforward implementation requirements and minimal parameter tuning needs, PSO has demonstrated remarkable computational efficiency and competitive performance for optimization problems in continuous solution spaces. The algorithm is characterized by computational effectiveness, simplified coding requirements, and consistent algorithmic behavior across different problem types. According to [22], the majority of PSO implementations have traditionally focused on continuous space optimization challenges [25], though recent research initiatives have successfully explored discrete optimization applications [26]. The PSO algorithm initiates its search process by randomly generating a diverse swarm of computational particles within the solution space. Each individual entity (designated as a particle) within the problem domain is mathematically characterized by a d-dimensional position vector $s_i = (s_{i1}, s_{i2}... s_id)$, where i = 1,2, ..., N (N represents the total population size), and its optimization performance is continuously evaluated using a predetermined fitness function that quantifies solution quality. Individual particles are strategically positioned at random locations within the d-dimensional solution domain, each representing a potential candidate solution to the optimization problem. The velocity vector of the ith particle $(v_i) = (v_{i1}, v_{i2},..., v_id)$ is established through positional displacement calculations and determines the particle's movement direction and magnitude in subsequent iterations. Each particle's movement trajectory throughout the optimization process is governed by sophisticated dynamic interactions between individual learning experiences and collective swarm knowledge. As explained by [27], the algorithm achieves convergence toward optimal solutions through a careful balance between each particle's personal best historical solution and the global best value discovered by the entire swarm population. Each particle's path within the swarm adjusts toward its previous optimal position and the global optimal position reached by any swarm particle, represented as p_i and pg respectively. Following standard PSO formulation [21], the swarm updating equations for each iteration are:

$$v_i(t+1) = v_i(t) + c_1 \text{rand}_1(p_i - s_i(t)) + c_2 \text{rand}_2 \quad (3)$$

$$s_i(t+1) = s_i(t) + v_i(t+1) \quad (4)$$

Where:

- $P_i = (p_{i1},..., p_iN)$ denotes the optimal position encountered by the ith particle;
- p_g represents the best position discovered among all swarm population members;
- t represents the iteration counter;
- c_1 and c_2 are the acceleration coefficients;
- $rand_1$ and $rand_2$ are uniform random numbers within the interval [0, 1].

According to [24], acceleration parameters control the distance covered by particles in single iterations. Lower parameter values allow particles to investigate areas far from target zones before convergence, while higher values cause rapid movement toward or past target areas. For PSO algorithm execution, velocity and position parameters receive random initialization. The objective function represents the optimization goal for the particle population. Through particle search processes, the minimum function value can be identified, along with corresponding optimal U, WF, and OF parameter values. The computational approach for mathematical model parameter estimation using PSO algorithm is shown in Figure 3:

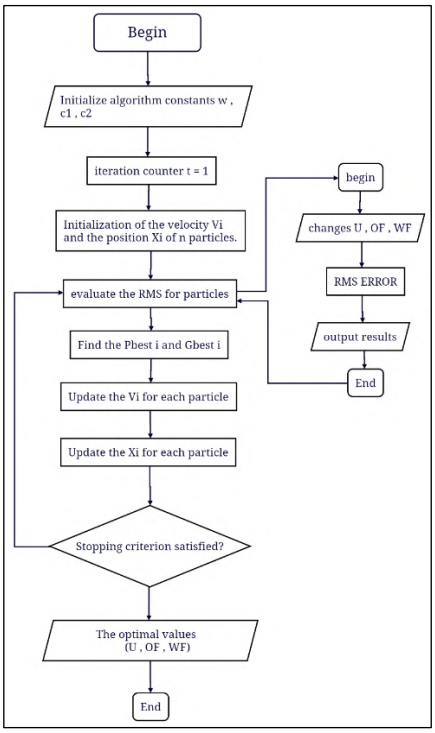


Figure 3: Proposed PSO organization chart.
Source: Authors, (2026).

V. RESULTS AND DISCUSSIONS

V.1 THE VALUES OF PSO PARAMETERS UTILIZED:

The PSO algorithm parameters utilized in this study are presented in Table 2.

Table 2: Parameters of PSO.

Parameter description	Parameters value
Size of population	50
Maximum iteration	100
c1	2
c2	2

Source: Authors, (2026).

V.2 RESEARCH SPACE

The search range for the three mathematical model parameters using PSO is outlined in Table 3:

Table 3: PSO search interval for model.

parameters	search interval
U (kV)	[6], [8]
OF (L/mn)	[3], [5]
WF (L/mn)	[8], [16]

Source: Authors, (2026).

V.3 PARAMETER IDENTIFICATION OF THE MODEL VIA THE PSO APPROACH:

To track the optimization process, the change in the fitness function over successive iterations was plotted, as shown in Figure 4.

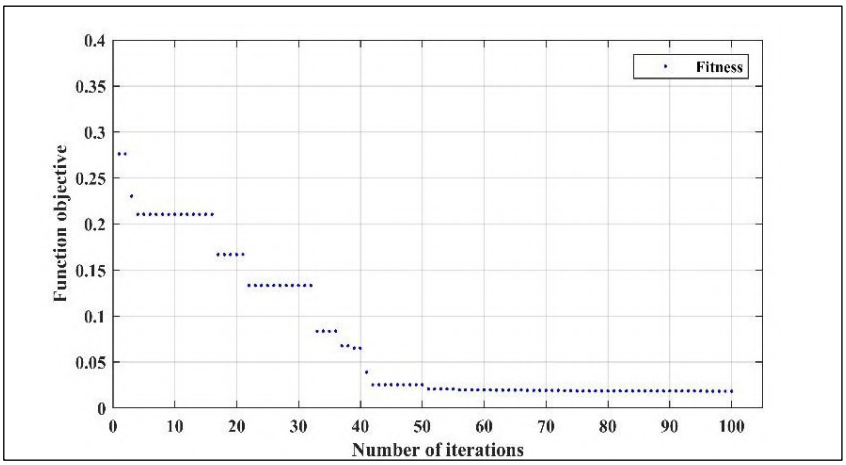


Figure 4: Evolution of the fitness function as a function of iteration number.
Source: Authors, (2026).

The optimization process demonstrates progressive convergence toward the optimal solution with each successive generation. Figure 4 demonstrates that the fitness function value for the optimal solution progressively diminishes throughout the iterative process. Upon algorithm convergence, achieved at 90 iterations in this investigation, the fitness function value reaches a minimal state. At this convergence point, the optimal solution from the final iterations is considered to represent the optimal parameter values sought in this optimization study. The three model parameters obtained through the PSO algorithm implementation are presented in Table 4:

Table 4: Optimal values of U, OF, and WF parameters.

parameter	value
U (kV)	7.9503
OF (L/mn)	3.3846
WF (L/mn)	8.266

Source: Authors, (2026).

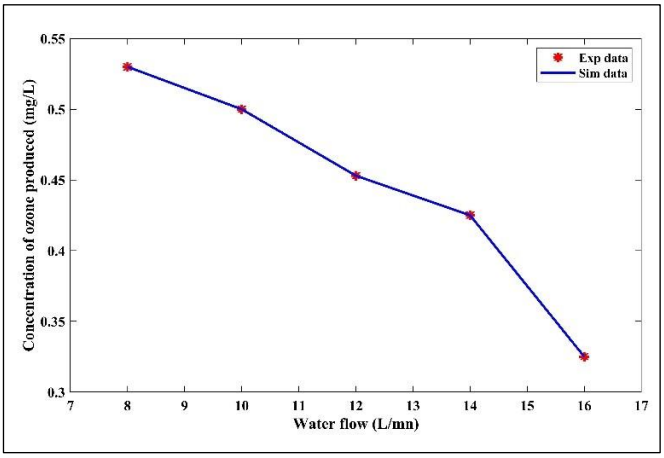


Figure 5: The changing levels of ozone dissolved in water in relation to water flow (experimental and simulation).
Source: Authors, (2026).

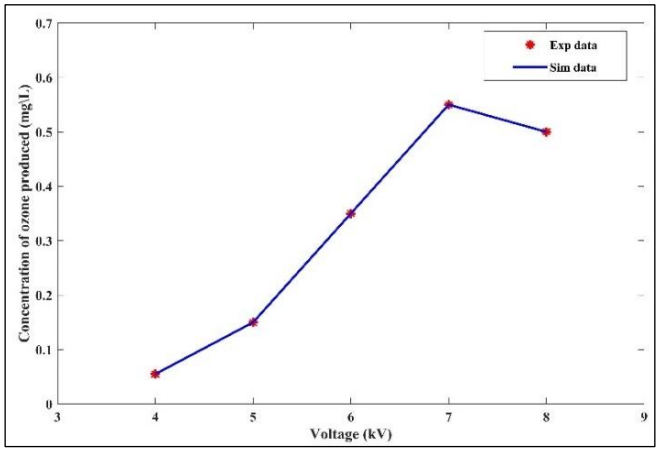


Figure 6: Variation of dissolved ozone concentration in water as a function of applied voltage (experimental and simulation results).
Source: Authors, (2026).

Based on the analysis of Figures 5 and 6, this methodology demonstrates high effectiveness in the field of water treatment processes utilizing ozone generated by DBD systems. The comparative analysis of the result curves clearly indicates that the parameter values calculated through the mathematical model coupled with PSO algorithm exhibit excellent agreement with the experimental data. To confirm the validity of parameters extracted through the PSO technique, a comparative evaluation was undertaken between the parameters resulting from the proposed method and those generated by the MODDE 5.0 software platform. The comparison outcomes are presented in Table 5:

Table 5: Comparative analysis of U, OF, and WF parameter values obtained by PSO and MODDE 5.0 application.

parameter	Result of PSO algorithm	Result of MODDE 5.0
U (kV)	7.9503	7.67
OF (L/mn)	3.3846	3
WF (L/mn)	8.266	9.6

Source: Authors, (2026).

Based on the mathematical model, voltage serves as the primary parameter for ozone production, demonstrating greater importance than the influence of water flow rate. The voltage determined via MODDE 5.0 was 7.67 kV, whereas the PSO method produced 7.058 kV. In contrast, the water flow rate (WFR) shows an inverse relationship with ozone concentration in water. When comparing results, we find that the water flow rate derived from the PSO approach is lower than that obtained from the MODDE 5.0 software, suggesting enhanced ozone concentration. The experimental results demonstrate convergence between the parameter values obtained from the MODDE 5.0 software and those derived through the proposed PSO methodology. consistent with findings reported by [25]. The PSO approach demonstrates superior accuracy in the optimization results, indicating its enhanced effectiveness for optimizing water treatment processes utilizing ozone generated by DBD systems.

VI. CONCLUSION

This research successfully developed and validated a novel optimization methodology for DBD-based ozone generation systems utilizing Particle Swarm Optimization algorithm coupled with statistical modeling techniques. The investigation established a comprehensive mathematical framework that accurately correlates operational parameters with ozone concentration in water treatment applications. The experimental investigation confirmed that applied voltage constitutes the primary controlling factor for ozone generation efficiency, exhibiting positive correlation with dissolved ozone concentration within the investigated parameter space. Conversely, water flow rate demonstrated negative correlation, necessitating flow optimization to maximize ozone transfer efficiency. Oxygen flow rate exhibited minimal influence beyond 4 L/min, indicating optimal resource utilization thresholds. The PSO-based parameter extraction methodology demonstrated superior performance compared to conventional optimization approaches, achieving enhanced precision in parameter identification while maintaining computational efficiency. The algorithm's rapid convergence characteristics and global optimization capabilities validated its applicability for complex, multi-parameter process optimization scenarios.The developed mathematical model, validated through statistical criteria (R^2 = 99.2%, Q^2 = 90.3%), provides reliable predictive capabilities for ozone concentration estimation across the experimental parameter range. This predictive framework enables systematic identification of optimal operating conditions, facilitating enhanced treatment efficiency and reduced operational costs. The proposed methodology contributes significantly to the advancement of intelligent process control systems in environmental engineering applications. The framework's versatility permits extension to diverse chemical processes requiring parameter optimization and mathematical modeling. Implementation of this approach ensures consistent treatment quality while optimizing resource utilization and minimizing environmental impact. Future research directions include investigation of additional operational parameters, development of real-time adaptive control systems, and extension of the methodology to industrial-scale applications. The integration of advanced machine learning techniques with PSO optimization presents opportunities for further enhancement of model accuracy and predictive capabilities in complex water treatment scenarios

VII. AUTHOR'S CONTRIBUTION

Conceptualization: Ghaitaoui Essama Ahmed , Nassour Kamel , Nemmich Said and Ghaitaoui Touhami
Methodology: Ghaitaoui Essama Ahmed , Nassour Kamel And Ghaitaoui Touhami
Investigation: Ghaitaoui Essama Ahmed ,Tilmatine Amar , Halali Youcef
Discussion of results: Ghaitaoui Essama Ahmed , Ghaitaoui Touhami , Oulad Naoui Brahim El Khalil, Halali Youcef
Writing – Original Draft: Ghaitaoui Essama Ahmed, Oulad Naoui Brahim El Khalil
Writing – Review and Editing: Bouroumeid Yassine , Nassour Kamel , Nemmich Said
Resources: Tilmatine Amar
Supervision: Nassour Kamel , Nemmich Said
Approval of the final text: Ghaitaoui Essama Ahmed , Nassour Kamel, Nemmich Said, Ghaitaoui Touhami , Oulad Naoui Brahim El Khalil , Bouroumeid Yassine, Halali Youcef And Tilmatine Amar

VIII. ACKNOWLEDGMENTS

This study was performed under the framework of 'Projet Impact Socio-Economique' Contract N° 362 funded by the General Directorate of Algerian Scientific Research (DGRSDT).

IX. REFERENCES

[1] T. Homola, B. Pongrác, M. Zemánek, and M. Šimek, "Efficiency of ozone production in coplanar dielectric barrier discharge," Plasma Chem. Plasma Process., vol. 39, pp. 1227–1242, 2019.

[2] L. Tayeb Mehdi et al., "Experimental study of the gas flow path for a dielectric barrier discharge ozone generator using for wastewater fish hatchery depollution," Int. J. Plasma Environ. Sci. Technol., vol. 16, Apr. 2022, doi: 10.34343/ijpest.2022.16.e01005.

[3] O. B. Dhakal et al., "Effects of spark dielectric barrier discharge plasma on water sterilization and seed germination," Curr. Appl. Phys., vol. 54, pp. 49–58, Oct. 2023, doi: 10.1016/j.cap.2023.08.006.

[4] E. A. Ghaitaoui et al., "Experimental comparative study between simple and multi-tube DBD ozone generator with same volume discharge for wastewater treatment," J. Korean Phys. Soc., vol. 85, no. 10, pp. 798–809, Nov. 2024, doi: 10.1007/s40042-024-01179-4.

[5] X. Wang et al., "Promotion Effect of Micro-Hole in Dielectric on Ozone Generation of Dielectric Barrier Discharge," Ozone Sci. Eng., vol. 0, no. 0, pp. 1–10, 2024, doi: 10.1080/01919512.2023.2301548.

[6] S. B. Borkar et al., "Mitigation of T3SS-mediated virulence in waterborne pathogenic bacteria by multi-electrode cylindrical-DBD plasma-generated nitric oxide water," Chemosphere, vol. 350, p. 140997, Feb. 2024, doi: 10.1016/j.chemosphere.2023.140997.

[7] A. Draou, S. Nemmich, K. Nassour, Y. Benmimoun, and A. Tilmatine, "Experimental analysis of a novel ozone generator configuration for use in water treatment applications," Int. J. Environ. Stud., vol. 76, no. 2, pp. 338–350, Mar. 2019, doi: 10.1080/00207233.2018.1499698.

[8] R. Shrestha, U. M. Joshi, and D. P. Subedi, "Experimental study of ozone generation by atmospheric pressure dielectric barrier discharge," Int. J. Recent Res. Rev., vol. 8, no. 4, pp. 24–29, 2015.

[9] H. H. Murbat, "Effects of Applied Voltage And Flow Rates of Ozone Generator Fed by Dry Air and O2 On The Coaxial Wire-Cylinder Reactor By Varying Various Electrodes Parameters, International Open Access," J. Mod. Eng. Res. IJMER, vol. 4, no. 92014, 2014.

[10]Z. Xu et al., "Study on the effective removal of chlorpyrifos from water by dielectric barrier discharge (DBD) plasma: The influence of reactive species and different water components," Chem. Eng. J., vol. 473, p. 144755, Oct. 2023, doi: 10.1016/j.cej.2023.144755.

[11] M. Šimek, S. Pekárek, and V. Prukner, "Influence of power modulation on ozone production using an AC surface dielectric barrier discharge in oxygen," Plasma Chem. Plasma Process., vol. 30, pp. 607–617, 2010.

[12] S. Nemmich, K. Nassour, N. Ramdani, Y. Bellebna, M. Boukhoulda, and A. Tilmatine, "DEVELOPMENT AND OPTIMIZATION OF AN OZONE FOOD PRESERVATION SYSTEM USING RESPONSE SURFACE MODELLING (RSM)," Carpathian J. Food Sci. Technol., vol. 13, pp. 33–46, Jan. 2022, doi: 10.34302/crpjfst/2021.13.4.4.

[13] O. N. Brahim el Khalil, N. Said, N. Kamel, G. E. Ahmed, B. Yassine, and T. Amar, "Comparative Experimental Study of Voltage Waveform Influences on Ozone Production Efficiency," in 2024 3rd International Conference on Advanced Electrical Engineering (ICAEE), Nov. 2024, pp. 1–6. doi: 10.1109/ICAEE61760.2024.10783232.

[14] G. E. Ahmed et al., "A Novel Multi-Tube Ozone Generator Based on Dielectric Barrier Discharge for Wastewater Treatment," in 2024 3rd International Conference on Advanced Electrical Engineering (ICAEE), Nov. 2024, pp. 1–6. doi: 10.1109/ICAEE61760.2024.10783278.

[15] S. Nemmich, A. Tilmatine, and N. Hammadi, "SET-POINT IDENTIFICATION OF AN OZONE WATER TREATMENT PROCESS," Lat. Am. Appl. Res. - Int. J., vol. 46, no. 1, pp. 1–6, Jan. 2016, doi: 10.52292/j.laar.2016.322.

[16] R. Sangrody, S. Taheri, A.-M. Cretu, and E. Pouresmaeil, "An Improved PSO-Based MPPT Technique Using Stability and Steady State Analyses Under Partial Shading Conditions," IEEE Trans. Sustain. Energy, vol. 15, no. 1, pp. 136–145, Jan. 2024, doi: 10.1109/TSTE.2023.3274939.

[17] R. Eberhart and J. Kennedy, "A new optimizer using particle swarm theory," in MHS'95. Proceedings of the Sixth International Symposium on Micro Machine and Human Science, Nagoya, Japan: IEEE, 1995, pp. 39–43. doi: 10.1109/MHS.1995.494215.

[18] "Predicting the pile static load test using backpropagation neural network and generalized regression neural network – a comparative study." Accessed: Jan. 12, 2024. [Online]. Available: https://www-tandfonline-com.sndl1.arn.dz/doi/epdf/10.1080/19386362.2018.1519975?needAccess=true

[19] D. J. Armaghani, M. Hajihassani, E. T. Mohamad, A. Marto, and S. A. Noorani, "Blasting-induced flyrock and ground vibration prediction through an expert artificial neural network based on particle swarm optimization," Arab. J. Geosci., vol. 7, no. 12, pp. 5383–5396, Dec. 2014, doi: 10.1007/s12517-013-1174-0.

[20] B. Benabdelkrim, A. Benatiallah, and G. Touhami, “Parameters Estimation Methods of Thin-Film Solar Module Using Numerical Algorithms and Artificial Neural Networks,” 2023, pp. 584–593. doi: 10.1007/978-3-031-21216-1_60.

[21] J. Kennedy and R. Eberhart, “Particle swarm optimization,” in Proceedings of ICNN’95-international conference on neural networks, IEEE, 1995, pp. 1942–1948.

[22] Y.-J. Gong et al., “Genetic Learning Particle Swarm Optimization,” IEEE Trans. Cybern., vol. 46, no. 10, pp. 2277–2290, Oct. 2016, doi: 10.1109/TCYB.2015.2475174.

[23] Q. Qin, S. Cheng, Q. Zhang, L. Li, and Y. Shi, “Particle Swarm Optimization With Interswarm Interactive Learning Strategy,” IEEE Trans. Cybern., vol. 46, no. 10, pp. 2238–2251, Oct. 2016, doi: 10.1109/TCYB.2015.2474153.

[24] J. Zhang, X. Zhu, Y. Wang, and M. Zhou, “Dual-Environmental Particle Swarm Optimizer in Noisy and Noise-Free Environments,” IEEE Trans. Cybern., vol. 49, no. 6, pp. 2011–2021, Jun. 2019, doi: 10.1109/TCYB.2018.2817020.

[25] G. Touhami et al., Estimation of the photovoltaic Organic cells/modules parameters using an improved PSO optimization technique. 2023.

[26] P. G. Asteris and V. G. Mokos, “Concrete compressive strength using artificial neural networks,” Neural Comput. Appl., vol. 32, no. 15, pp. 11807–11826, Aug. 2020, doi: 10.1007/s00521-019-04663-2.

[27] A. Harrag and S. Messalti, “Three, five and seven PV model parameters extraction using PSO,” Energy Procedia, vol. 119, pp. 767–774, 2017.

Journal of Engineering and Technology for Industrial Applications

ISSN ONLINE: 2447-0228

ITEGAM-JETIA

Manaus, v.12 n.60, p.1262-1274. July/August, 2026.
DOI: https://doi.org/10.5935/jetia.v12i60.4064

RESEARCH ARTICLE OPEN ACCESS

AI-DRIVEN INTERACTIVE MULTIMEDIA COURSEWARE: A WEB- AND MOBILE-RESPONSIVE PLATFORM FOR IT SPECIALIST CERTIFICATION EXAM PREPARATION WITH AN ADAPTIVE LEARNING ALGORITHM

Mark Gil Toribio Gañgan*[1]

[1]College of Engineering Architecture and Technology, Isabela State University,City of Ilagan,3300, Isabela, Philippines.

[1]http://orcid.org/0009-0002-6979-8674

Email:*markgil.t.gangan@isu.edu.ph

ARTICLE INFO

Article History
Received: March 13, 2026
Reviewed: April 15, 2026
Accepted: July 15, 2026
Published: August 31, 2026

Keywords:
Adaptive Learning Systems,
Bayesian Knowledge Tracing,
Interactive Multimedia Courseware,
IT Specialist Certification Preparation,
AI-Driven Educational Technology.

ABSTRACT

This study designed, developed, and evaluated an AI-driven interactive multimedia courseware to support preparation for the IT Specialist (ITS) certification examination. Traditional review approaches often lack adaptive learning mechanisms and interactive resources, limiting their effectiveness in addressing diverse learner needs and tracking learning progress. To address this gap, the study employed a Design and Development Research (DDR) methodology guided by Agile Software Development Life Cycle principles. The development process began with the systematic identification of ITS exam objectives and topics based on official certification guidelines, which served as the foundation for the instructional design and content organization of the courseware. The system was implemented as a web- and mobile-responsive platform featuring multimedia lessons, interactive simulations, gamified activities, and practice examinations to promote active learning. The Bayesian Knowledge Tracing (BKT) algorithm was integrated as the adaptive learning engine to dynamically estimate learner knowledge states and personalize content delivery based on performance and progress. The developed system was evaluated by five IT experts and twenty prospective ITS examinees using the ISO/IEC 25010 software quality model. Results showed consistently high ratings across all criteria, with an overall weighted mean of 4.59 (“Strongly Agree”). These findings suggest that adaptive multimedia courseware can enhance certification readiness and provide institutions with an effective digital platform for technology-based exam preparation.

Copyright ©2026 by authors and Galileo Institute of Technology and Education of the Amazon (ITEGAM). This work is licensed under the Creative Commons Attribution International License (CC BY 4.0).

I. INTRODUCTION

The rapid advancement of information and communication technologies has fundamentally transformed knowledge acquisition and professional competency development [1]. In the information technology sector, industry-recognized certification examinations have become essential benchmarks for validating technical proficiency and ensuring workforce readiness [1], [2]. Certifications such as the "IT Specialist" credential allow professionals to demonstrate mastery in critical domains including programming, networking, databases, and web development [1]. Consequently, there is an increasing demand within educational and professional training environments for effective preparation tools that support certification readiness. However, traditional review methods often rely on static learning materials and linear instruction, frequently described as "just-put-it-on-the-web" approaches, which fail to address the diverse prior knowledge levels and individual learning needs of certification candidates [3], [4]. These conventional methods often suffer from content homogenization and a lack of interactive resources, leading to suboptimal engagement and retention [3], [5]. Recent developments in educational technology have highlighted the potential of interactive multimedia and artificial intelligence to enhance instructional processes. Interactive multimedia courseware integrates text, graphics, audio, and animation to create immersive experiences that improve knowledge retention and learner motivation [6], [7]. Concurrently, AI-driven adaptive learning systems have emerged as powerful tools for personalizing instruction based on learner performance and behavior [8], [9].

These systems analyze unique learning patterns and dynamically adjust the sequence and difficulty of materials to address specific knowledge gaps [10-12]. In the context of high-stakes certification, these adaptive approaches offer more efficient, targeted review strategies by optimizing cognitive load and improving memorization effectiveness [13-16]. Research indicates that multimedia environments enhance comprehension by presenting information through multiple sensory channels [17-19]. To further individualize this experience, adaptive algorithms, most notably Bayesian Knowledge Tracing—have been widely implemented in Intelligent Tutoring Systems to model knowledge states and predict skill mastery [9], [20-22]. These systems allow educational platforms to tailor instructional pathways according to real-time progress, ensuring that learners engage with material that matches their current proficiency [4], [23]. Despite these advancements, many existing certification preparation platforms primarily offer static practice tests or non-adaptive resources that do not effectively monitor progress or dynamically adjust content to the learner's needs [24-27]. Furthermore, while the theoretical benefits of AI and multimedia are well-documented, limited research has focused on the practical integration of AI-driven adaptive algorithms within interactive courseware specifically designed for IT Specialist certification [28-30]. Many available review tools also lack systematic evaluation based on recognized software quality standards, which are critical for ensuring reliability, usability, and pedagogical effectiveness [31-33]. Addressing these gaps is vital, as certification candidates must demonstrate mastery over diverse technical competencies within a limited timeframe. An adaptive platform that continuously monitors progress and provides individualized guidance can significantly improve study efficiency and exam readiness [34], [35]. In response to these challenges, this study aims to design and develop an AI-driven interactive multimedia courseware as a web- and mobile-responsive platform for IT Specialist certification exam preparation. The study seeks to structure official exam objectives into a rich multimedia environment while implementing a BKT-based adaptive model to enhance candidate readiness. Furthermore, the system will be evaluated for its compliance with adaptive functionality and software quality characteristics using the ISO/IEC 25010 standards. By combining responsive web technologies with machine learning, this research establishes a replicable framework for high-quality instructional tools that optimize the transition from candidate study to professional certification success [34], [35].

II. RELATED WORKS

The development of AI-driven courseware for IT Specialist certification involves a synthesis of research in adaptive learning, intelligent tutoring systems, and interactive multimedia design.

II.1 PERSONALIZED AND ADAPTIVE LEARNING ENVIRONMENTS

Traditional educational approaches that rely on a "just-put-it-on-the-web" methodology often fail to accommodate the diverse skills and individual needs of learners [4]. This static delivery frequently results in content homogenization, which can be seen in current certification training programs like the Information Systems Project Management Professional [3]. In contrast, personalized learning systems utilize artificial intelligence to adapt instructional content based on a student's unique knowledge state, thereby improving engagement and retention [9]. Recent frameworks for technical courses have addressed these gaps by integrating multimodal knowledge—unifying text, code, and visual materials into structured ontologies to better account for individual differences in cognitive traits and learning preferences [1].

II.2 INTELLIGENT TUTORING SYSTEMS

Intelligent Tutoring Systems are designed to simulate the personalized instructions and immediate feedback typically provided by a human tutor [22], [36]. By using AI techniques to analyze student responses and perform cognitive diagnoses, these systems enable self-directed learning and help correct specific misconceptions [22], [36]. Research has demonstrated that ITS are highly effective across various disciplines, including computer programming, where they enhance recommendation accuracy and student satisfaction [37]. Meta-analytic reviews indicate that intelligent tutoring can raise test scores by approximately 0.66 standard deviations over conventional instruction [38]. Furthermore, these systems provide timely feedback and allow students to access learning spaces anytime, fostering the competencies needed for lifelong learning [39].

II.3 KNOWLEDGE TRACING AND ADAPTIVE ALGORITHMS

A critical challenge in personalized education is accurately tracing a student's knowledge state over time [9]. Bayesian Knowledge Tracing is a prominent machine learning-based model used to infer student mastery by treating knowledge as a set of binary variables (mastered or not) [30], [40]. As a type of Hidden Markov Model, BKT uses observed performance to estimate the latent skill levels of a learner [40]. This allows educational systems to predict future performance and provide adaptive task assignments, ensuring that the difficulty level of questions or topics matches the learner's current competency [4], [41]. Studies show that this adaptive selection of test questions significantly increases overall learning outcomes, particularly for lower-performing students [4]. The foundational principle behind BKT, estimating student knowledge states from learning interactions, is a cornerstone of Intelligent Tutoring Systems, which are integral to personalized content delivery and feedback. AI plays a critical role in this process, with knowledge tracing models leveraging machine learning techniques to infer a student's conceptual and procedural knowledge based on their task performance.

II.4 INTERACTIVE MULTIMEDIA AND GAMIFICATION

Interactive multimedia courseware serves as a vital tool to counter the declining engagement associated with traditional lecture-based methods and static presentations [6]. Effective multimedia platforms integrate videos, interactive questions, and real-time feedback to create an environment where students can actively participate and monitor their progress [7]. The implementation of AI-assisted multimedia has been shown to significantly improve student understanding and engagement across information technology disciplines [5].

Additionally, gamification—the use of game elements like points, badges, and streaks—enhances motivation by making the learning process more immersive [2], [42]. For difficult subjects like computer science, gamification contributes to higher levels of student satisfaction and long-term performance [43]. By combining gamified tracking with adaptive assessment methods, modern platforms ensure a balanced learning progression grounded in established pedagogical frameworks like Bloom's taxonomy [2].

II.5 RESEARCH GAP

Despite the proliferation of digital resources for technical education, several critical gaps remain in the literature concerning IT certification preparation. First, existing review materials for exams like the IT Specialist certification often follow a "just-put-it-on-the-web" approach, which lacks the adaptive mechanisms necessary to address individual learning curves and skill levels [3], [4]. While Intelligent Tutoring Systems have proven effective in academic settings, their application to the professional certification domain—particularly for IT graduates—is relatively underexplored [38], [44]. Current platforms frequently focus on static content delivery and homogenized question sets, failing to provide the personalized feedback and "anytime-anywhere" guidance essential for lifelong learners and working professionals [3], [39]. Furthermore, while the Bayesian Knowledge Tracing algorithm is a well-established method for student modeling, its integration into a multimodal, web- and mobile-responsive framework specifically for IT certification remains limited [30], [40]. Most existing adaptive systems rely either on cross-sectional assessment data or simple text-based interactions, overlooking the need for multimodal knowledge representation that unifies code, visual simulations, and theory into a structured learning path [1], [45]. Additionally, there is a lack of research focusing on systems that cover the full spectrum of a certification's objectives—from basic concepts to complex problem-solving—while simultaneously utilizing gamified elements to maintain long-term motivation [46], [47]. By developing an AI-driven platform that combines BKT-based adaptivity with interactive multimedia specifically for the IT Specialist exam, this study addresses the empirical and methodological deficit in providing high-quality, personalized certification training [2], [44].

III. METHODOLOGY

This study employed Design and Development Research (DDR) to systematically design, develop, and evaluate an AI-driven interactive multimedia courseware for IT Specialist certification preparation [48], [49]. DDR is appropriate for educational technology studies because it integrates theoretical foundations with practical system development and empirical validation. The development process followed Agile Software Development Life Cycle (SDLC) principles, enabling iterative development, continuous feedback, and progressive system improvement.

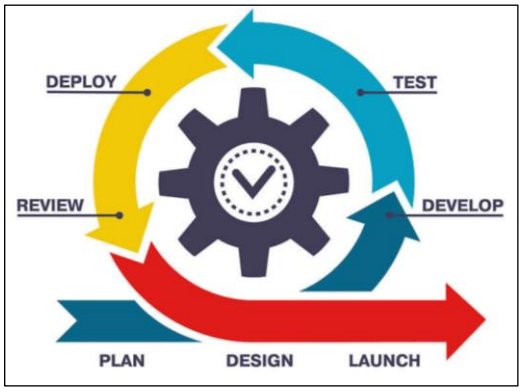


Figure 1: Agile Software Development Life Cycle.
Source: Author, (2026).

III.1 ANALYSIS AND PLANNING

The first phase identified the exam objectives, topics, and module content re-quired for the courseware. The researchers reviewed the official IT Specialist (ITS) certification syllabus and relevant industry standards to determine the core competencies covered in the examination. A literature review was also conducted to justify the use of the Bayesian Knowledge Tracing (BKT) algorithm for modeling learner knowledge states. The phase resulted in a curriculum blueprint and system requirements specification for the adaptive courseware.

III.2 DESIGN AND DEVELOPMENT

This phase focused on the design, development, and implementation of the adaptive web-based multimedia courseware. Following Agile principles, the system was developed through iterative cycles of instructional design, system development, and testing. The Bayesian Knowledge Tracing (BKT) algorithm was integrated as the adaptive learning engine to estimate learner mastery and dynamically adjust content difficulty and learning pathways based on performance.

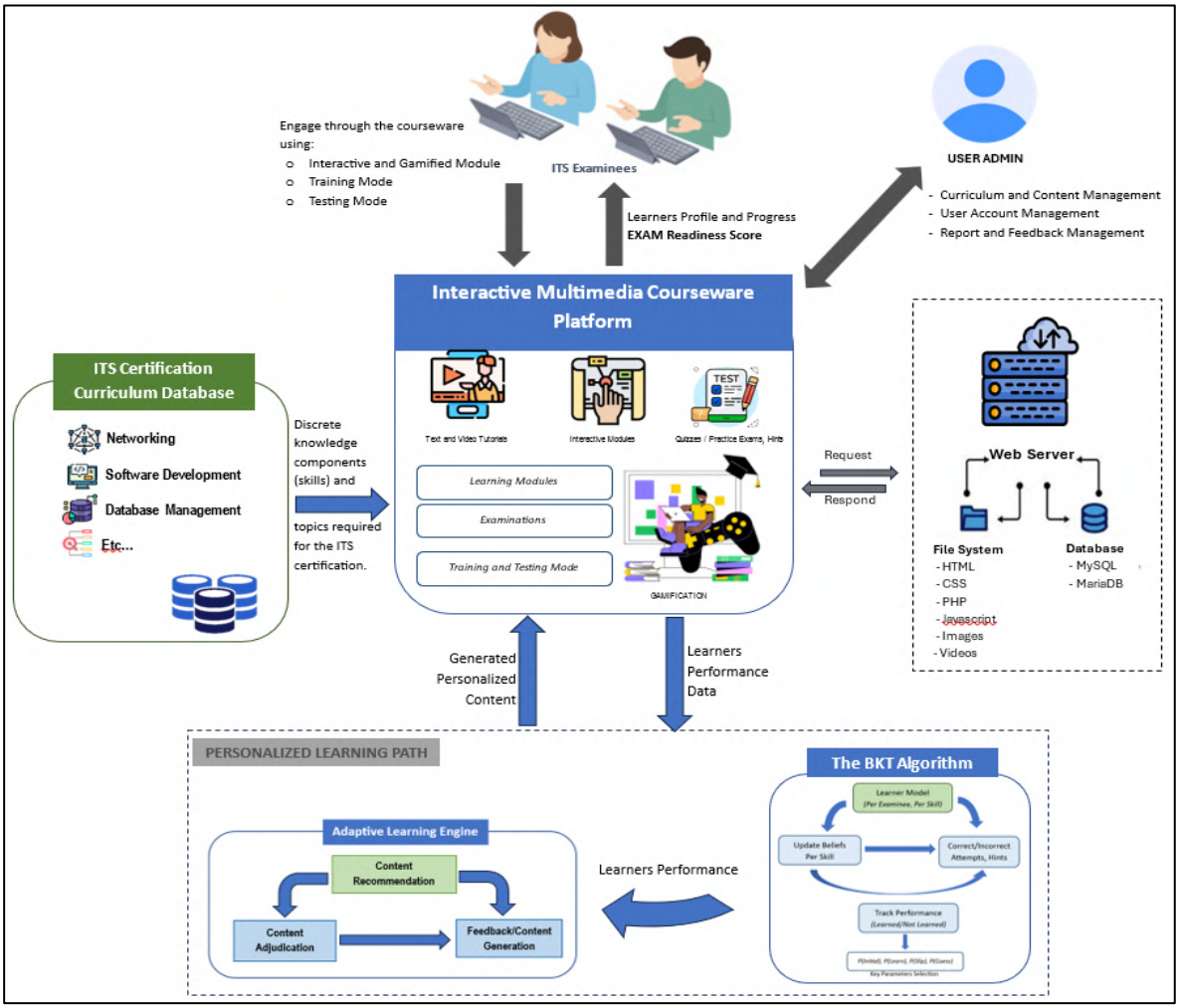


Figure 2: Courseware System Architecture.
Source: Author, (2026).

The courseware system architecture presents the dynamic interaction among the core components of the developed interactive multimedia courseware designed to provide an adaptive and personalized learning experience for IT Specialist (ITS) examinees. At its center, the ITS Examinee engages with the Interactive Multimedia Courseware Platform, which functions as the primary learning interface integrating multiple modalities such as Figure 2. The Conceptual Framework ISUI-RES-Aco-11a Effective: August 19, 2014 Revised: 0 City of Ilagan text-based and video tutorials, e-book modules, interactive exercises, practice quizzes, and both training and testing modes. Supporting this is the User Admin Module, which ensures the stability and relevance of the learning ecosystem by managing user accounts, maintaining the ITS Certification Curriculum Database, monitoring examinee performance, and overseeing the generation of analytical reports and system feedback. A pivotal component of the system is the BKT Algorithm Module, which serves as the analytical core for adaptive learning. Utilizing Bayesian Knowledge Tracing (BKT) with its parameters P(L0) for initial knowledge, P(T) for learning transition, P(S) for slip probability, and P(G) for guess probability, the module continuously analyzes learner interactions, including answer accuracy and hint usage, to infer and update each examinee's knowledge state. These probabilistic insights are transmitted to the Adaptive Learning Engine, which interprets the data to generate tailored instructional responses. The engine dynamically recommends content, adjusts difficulty levels, and sequences activities to construct a Personalized Learning Path suited to each learner's mastery progression. To ensure accessibility and usability, the courseware is developed as a responsive web-based application, enabling seamless access across both desktop and mobile devices. The entire system operates through a continuous feedback-driven loop supervised by the administrator, ensuring that learning experiences evolve in real time according to the learner's cognitive development. Ultimately, this framework aims to optimize the ITS examinee's preparation by aligning learning strategies with individual performance and adaptive insights derived from the BKT algorithm. Moreover, the implementation of the Bayesian Knowledge Tracing (BKT) algorithm was central to the courseware's adaptive capabilities. BKT is a widely recognized and validated probabilistic model, operating as a Hidden Markov Model (HMM), designed to dynamically estimate a student's mastery of discrete knowledge components (skills) over time based on their observed performance on related tasks. This approach allows for a precise, dynamic assessment of latent knowledge states, accounting for the inherent uncertainties in learning and performance. For each distinct skill delineated from the ITS curriculum, the BKT model maintains a probability $P(L_t)$, representing the likelihood that a student knows the skill at time t. This probability is rigorously updated after each interaction with a relevant task. The model is defined by four core parameters:

- $P(L_0)$ (Prior Knowledge), the initial probability a student knows the skill;
- $P(T)$ (Learning Rate), the probability of transitioning from not knowing to knowing after an attempt;
- $P(G)$ (Guess Probability), the chance of a correct answer without true knowledge; and

- $P(S)$ (Slip Probability), the chance of an incorrect answer despite knowing the skill.

At each problem attempt, the BKT algorithm updates $P(Lt)$ based on the student's observed response (Correct or Incorrect). Before a response is observed, the probability of a correct answer $P(Correct|Lt$ is predicted as:

$$P(Lt)*(1-P(S))+(1-P(Lt))*P(G) \quad (1)$$

Upon a **Correct Response**, the probability of knowing is updated in two stages: first,

$$P(Lt+1|Correct)=(P(Lt)*(1-P(S)))/P(Correct|Lt) \quad (2)$$

then

$$P(Lt+1)=P(Lt+1|Correct)+(1-P(Lt+1|Correct))*P(T)P(Lt+1)=P(Lt+1\ |Correct)+(1-P(Lt+1|Correct))*P(T) \quad (3)$$

To account for learning. Upon an **Incorrect Response**, the probability of knowing is updated as:

$$P(Lt+1|Incorrect)=(P(Lt)*P(S))/(P(Lt)*P(S)+(1-P(Lt))*(1-P(G))) \quad (4)$$

Assuming no learning occurs from an incorrect response. These continuous updates inform the adaptive engine, enabling personalized content delivery. Finally, the courseware was developed using HTML, CSS, and JavaScript for the user interface and interactivity, PHP for server-side processing, and MySQL for database management. The system stores user data, learning materials, and learner performance metrics that support the adaptive learning mechanism.

III.3 EVALUATION

The developed courseware was evaluated using the ISO/IEC 25010 Software Quality Model, which includes criteria such as functional suitability, reliability, performance efficiency, usability, security, compatibility, maintainability, and portability.

Table 1: ISO 25010 Standards Software Quality Criteria.

CRITERIA	DESCRIPTION
Functional Suitability	The degree to which the software provides functions that meet stated and implied needs.
Reliability	The ability of the software to perform its functions under specified conditions for a specified period.
Performance Efficiency	The performance relative to the amount of resources used under stated conditions.
Usability	The ability of the software to be used by specified users to achieve specified goals with effectiveness, efficiency, and satisfac
Security	The ability of the software to protect information and data so that persons or other products or systems have the degree of data access appropriate to their types and levels of authorization.
Compatibility	The ability of the software to exchange information with other systems and perform its required functions together.
Maintainability	The ability of the software to be modified effectively, efficiently, and reliably.
Portability	The ability of the software to be transferred from one environment (e.g., hardware, operating system) to another.

Source: Author, (2026).

Purposive sampling was used to select five (5) IT experts and twenty (20) prospective IT Specialist examinees who assessed the system using a structured questionnaire. Responses were measured using a 5-point Likert scale ranging from strongly disagree to strongly agree. The weighted mean was computed to determine the overall evaluation results and user satisfaction with the developed courseware.

Table 2: ISO 25010 Standards Software Quality Criteria.

NUMERICAL SCALE	RANGE	INTERPRETATION
5	4.21 – 5.00	Strongly Agree
4	3.41 – 4.20	Agree
3	2.61 – 3.40	Neutral
2	1.81 – 2.60	Disagree
1	1.00 – 1.80	Strongly Disagree

Source: Author, (2026).

Weighted Mean Formula

$$\bar{X} = \frac{(5f_5) + (4f_4) + (3f_3) + (2f_2) + (1f_1)}{N} \quad (5)$$

Where: $\bar{X}$ = Weighted Mean
$\bar{f}$ = Frequency of each Response
N = Total Number of Respondents

The weighted mean was computed to determine the overall evaluation results and user satisfaction with the developed courseware.

IV. RESULTS AND DISCUSSIONS

This section presents the findings on the development and evaluation of the adaptive interactive multimedia courseware for IT Specialist (ITS) certification preparation. The results are organized according to the study objectives: identification of ITS exam objectives and content structure, development of the adaptive courseware using the Bayesian Knowledge Tracing (BKT) algorithm, and evaluation of the system based on the ISO/IEC 25010 software quality standards.

IV.1 IDENTIFIED IT SPECIALIST EXAM OBJECTIVES AND CONTENT STRUCTURE

To effectively design and develop the IT Specialist Exam courseware, the foundational step involved a comprehensive identification of the relevant exam objectives, topics, and corresponding module content. This meticulous process ensures alignment between the course material and the certification requirements, thereby maximizing student preparedness and success.

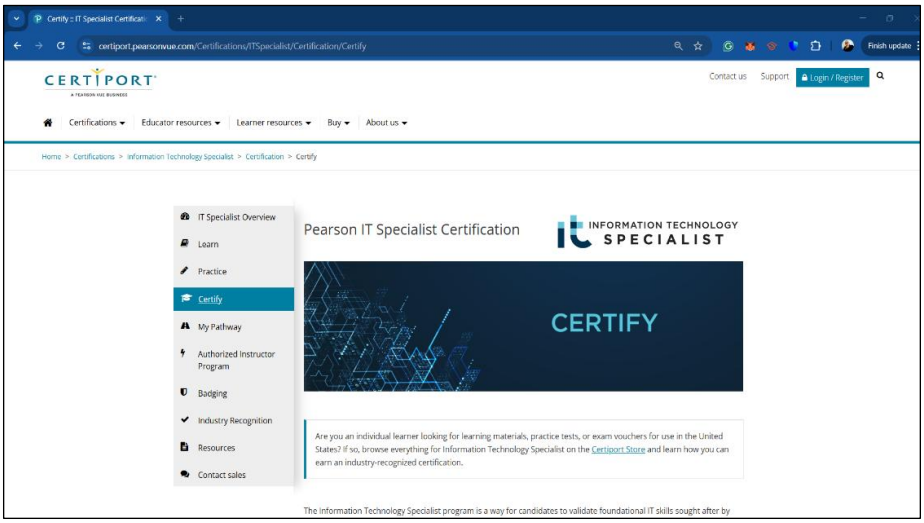


Figure 3: Certiport Pearsonvue IT Specialist.
Source: [50].

The primary source for identifying these critical components was the official Certiport PearsonVUE website, as illustrated in Figure 3. This platform serves as the authoritative repository for the IT Specialist certification program, detailing the specific skills and knowledge areas assessed by the exam. By meticulously reviewing the information presented on this website, we were able to extract the precise exam objectives that frame the scope of the certification. Following the identification of the overarching exam objectives, a detailed breakdown of the specific topics associated with each objective was undertaken. This granular approach allowed for the creation of a comprehensive list of all content areas that students need to master. Certiport PearsonVUE website details the identified topics aligned with their respective objectives, represents a crucial output of this phase. This structured mapping forms the backbone of the courseware, ensuring that every learning unit directly contributes to achieving a specific exam competency. The following stage involved the development of course modules directly based on these identified topics and exam objectives. Each module was carefully crafted to address specific learning outcomes, incorporating pedagogical best practices to facilitate effective knowledge transfer and skill development. The content within these modules is therefore a direct derivative of the certification requirements, ensuring relevance and practical applicability.

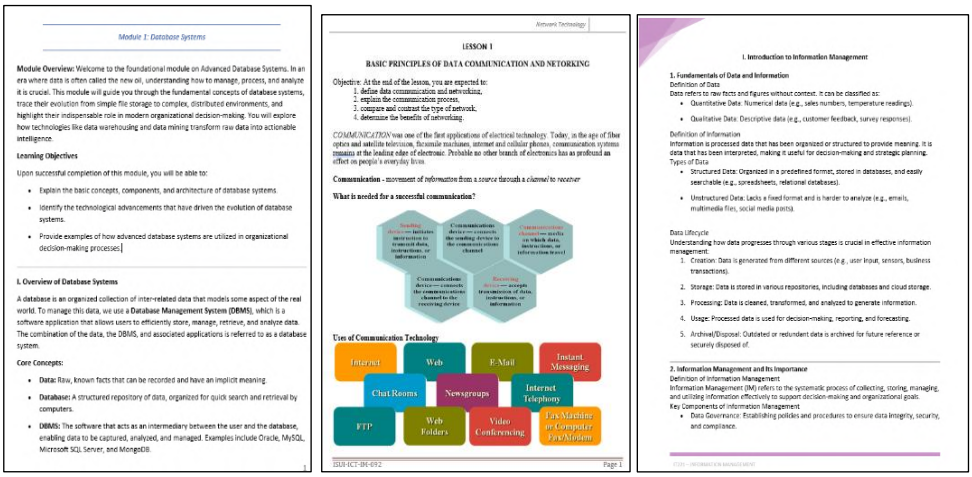


Figure 4: Contents Developed Tailored to the ITS Topic and Objectives.
Source: Author, (2026).

As shown in Figure 4, these developed module contents undergo a transformation and loading process into a centralized database. This digitalization of the course content is a critical step for its eventual integration into the courseware platform. This systematic approach ensures that the identified and developed learning materials are efficiently stored, organized, and readily accessible for delivery to the learners, forming the core educational material of the IT Specialist courseware.

IV.2 ADAPTIVE COURSEWARE USING THE BAYESIAN KNOWLEDGE TRACING (BKT) ALGORITHM

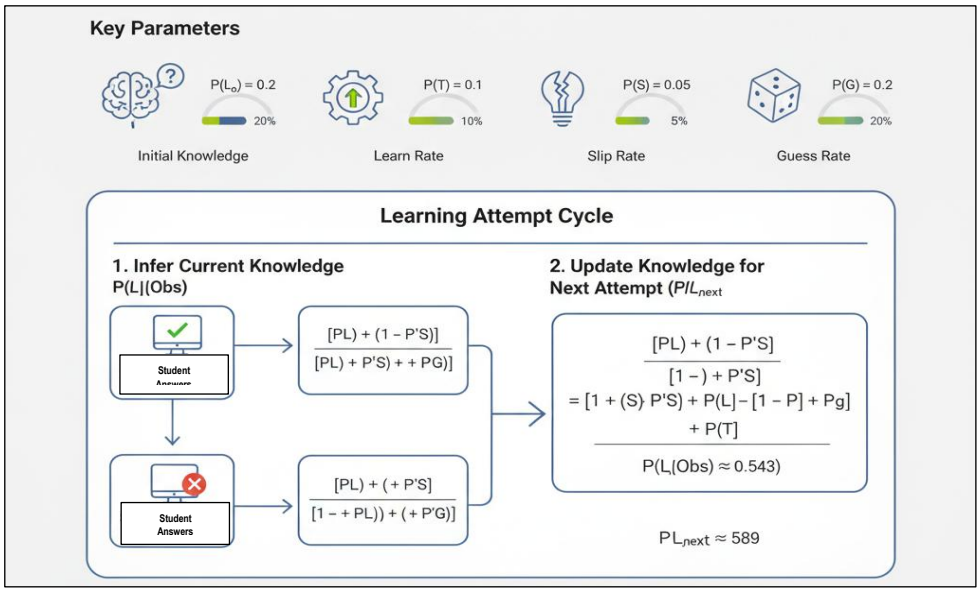


Figure 5: The Bayesian Knowledge Tracing (BKT) Design for Courseware.
Source: Author, (2026).

Figure 5 illustrates the Bayesian Knowledge Tracing (BKT) algorithm's process for modeling student skill mastery within our courseware. At each learning attempt, the model first infers the student's current knowledge *(P(L|Obs))* of a specific skill, taking into account their prior knowledge probability, along with predefined guess and slip rates, based on their observed performance (correct or incorrect answer). Subsequently, this inferred knowledge is used to update the probability of knowing the skill for the next attempt *(P(L_next))*, incorporating a learn rate that accounts for potential skill acquisition. This continuous, probabilistic updating mechanism allows the courseware to adaptively track individual student mastery over time, guiding subsequent instructional decisions, thereby personalizing the learning experience to focus on areas where the student needs the most improvement. Additionally, Figure 5 highlights how uncertainty in student responses is explicitly handled through the guess and slip parameters within the Bayesian framework. A correct answer does not always imply true mastery because the student may have guessed correctly, while an incorrect answer does not necessarily indicate a lack of knowledge due to possible slips or careless mistakes. By incorporating these probabilities, the BKT model refines the posterior probability of student knowledge more realistically. The updated value of P(L_next) therefore reflects both the student's observed performance and the likelihood that learning has occurred between attempts through the learn rate parameter. This probabilistic adjustment enables the courseware system to make more reliable estimations of student mastery and to dynamically adapt future practice opportunities or instructional content according to the learner's evolving knowledge state. Furthermore, the integration of the BKT model within the courseware supports data-driven instructional adaptation and continuous learner modeling. By updating the probability of skill mastery after each interaction, the system can identify learning progress patterns and detect areas where students may require additional support or reinforcement. This capability allows the learning platform to provide targeted feedback, adjust the difficulty of subsequent tasks, and recommend appropriate learning resources. As a result, the BKT-based framework not only improves the accuracy of student knowledge estimation but also contributes to the development of a more responsive and personalized learning environment, which is essential for enhancing learning effectiveness and engagement in modern intelligent tutoring systems.

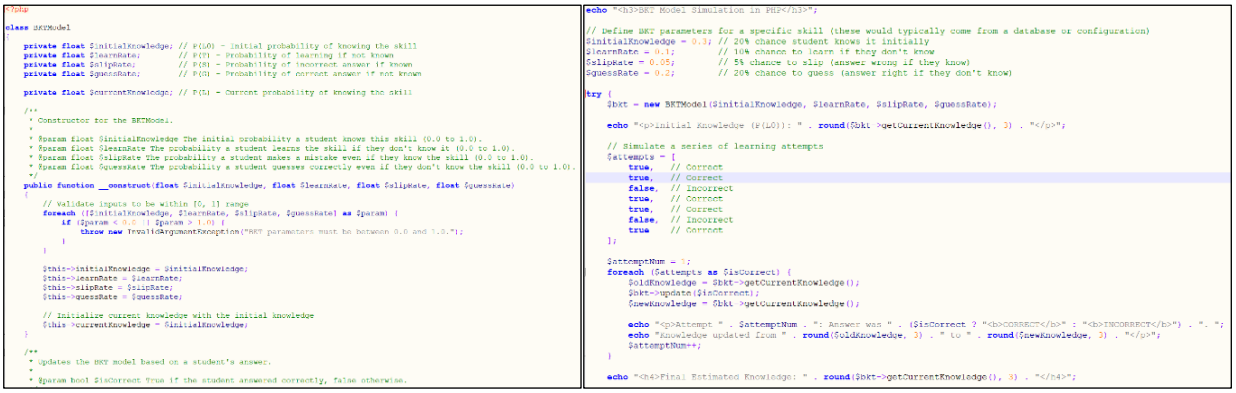


Figure 6: PHP Implementation of BKT.
Source: Author, (2026).

Following the careful design of the Bayesian Knowledge Tracing (BKT) process for the adaptive courseware, the subsequent phase involved the robust implementation of this conceptual framework utilizing PHP server-side scripting language to construct the functional web-based platform. This implementation directly translates the theoretical BKT model, encompassing the probabilistic inference of current knowledge and the subsequent updating of mastery estimates, into operational code. The PHP scripts are responsible for receiving student input from interactive exercises, executing the BKT formulas to compute the updated probability of knowing each skill, and then storing these refined knowledge probabilities in the backend database. This continuous data flow and processing enable the system to maintain an accurate, real-time profile of each student's evolving mastery across multiple skills. As depicted in Figure 6, the PHP script encapsulates the BKT algorithm, enabling the dynamic calculation and persistence of student knowledge states, thereby forming the algorithmic backbone that underpins the courseware's adaptive capabilities and facilitates its deployment as a responsive web application across various devices. Lastly, the following figures present the developed courseware integrated with an adaptive algorithm. These visual representations offer concrete examples of the interactive multimedia elements and how the adaptive learning model manifests within the user interface.

IV.2.1 Users (Learner) Module

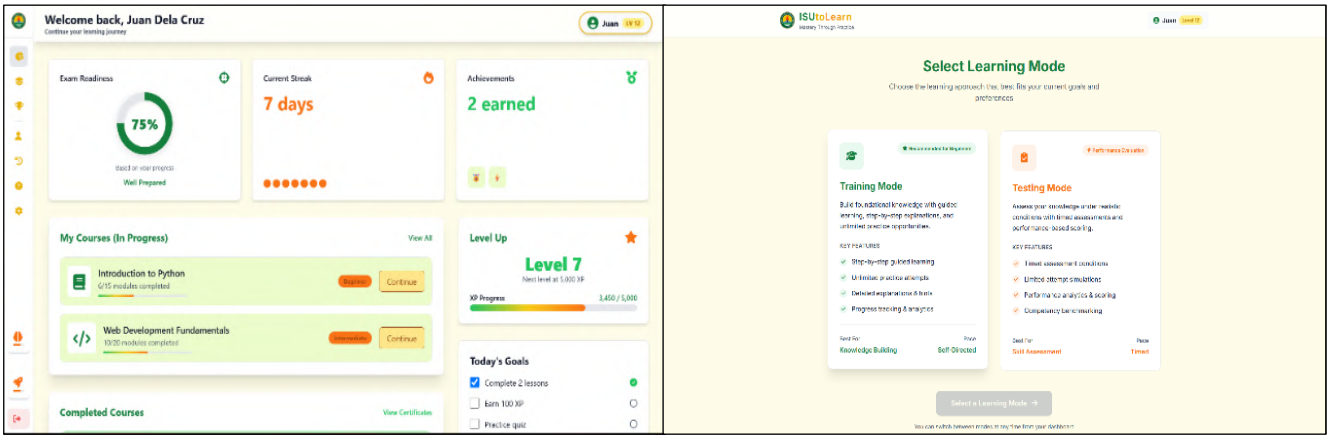


Figure 7: Main Dashboard | Mode Selection.
Source: Author, (2026).

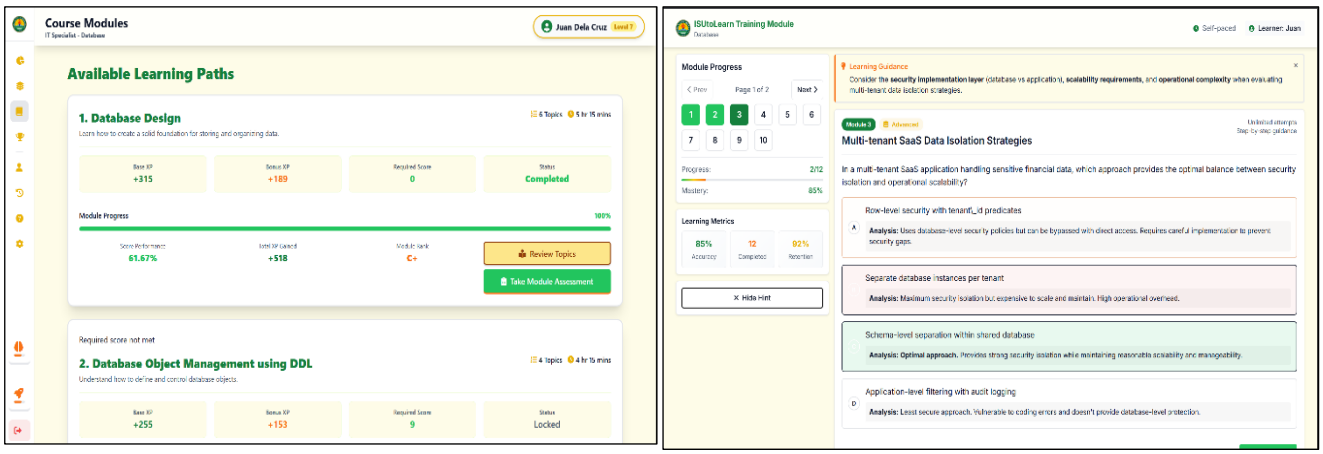


Figure 8. Learning Paths.
Source: Author, (2026).

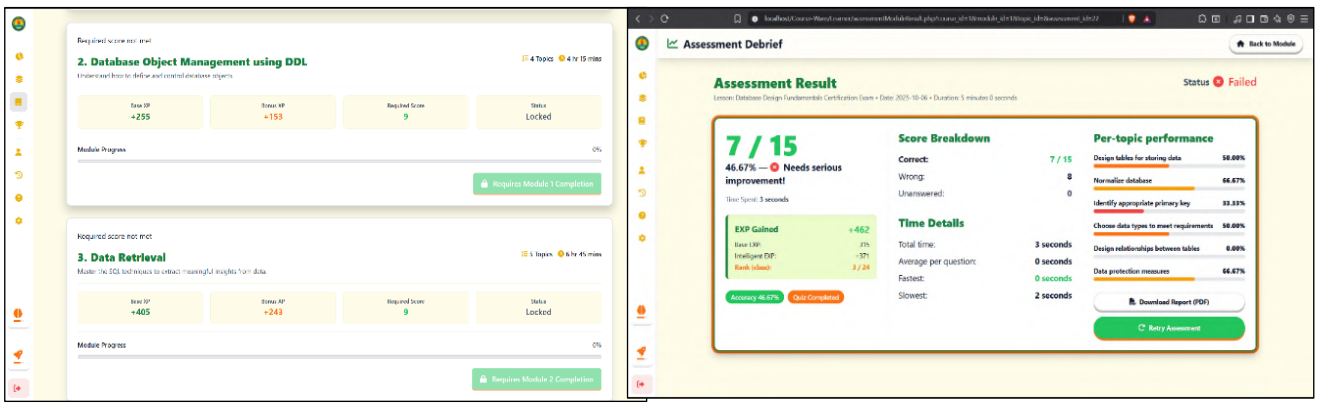


Figure 9. Progress Report.
Source: Author, (2026).

Figures 7, 8, and 9 present the graphical user interface of the developed courseware for the learners, highlighting key features that support learner navigation, learning management, and progress monitoring. Figure 7 shows the main dashboard, which provides users with centralized access to course modules, system features, and an overview of their learning activities. Figure 8 illustrates the learning mode selection and learning path interface, allowing learners to follow structured modules aligned with the certification objectives or choose topics based on their individual learning needs. Figure 9 presents the progress report interface, which displays learners' performance and mastery levels across different topics. These reports are dynamically generated based on learner interactions and assessment results, enabling users to monitor their progress and identify areas that require further improvement.

IV.2.2 Mobile-Responsive Courseware

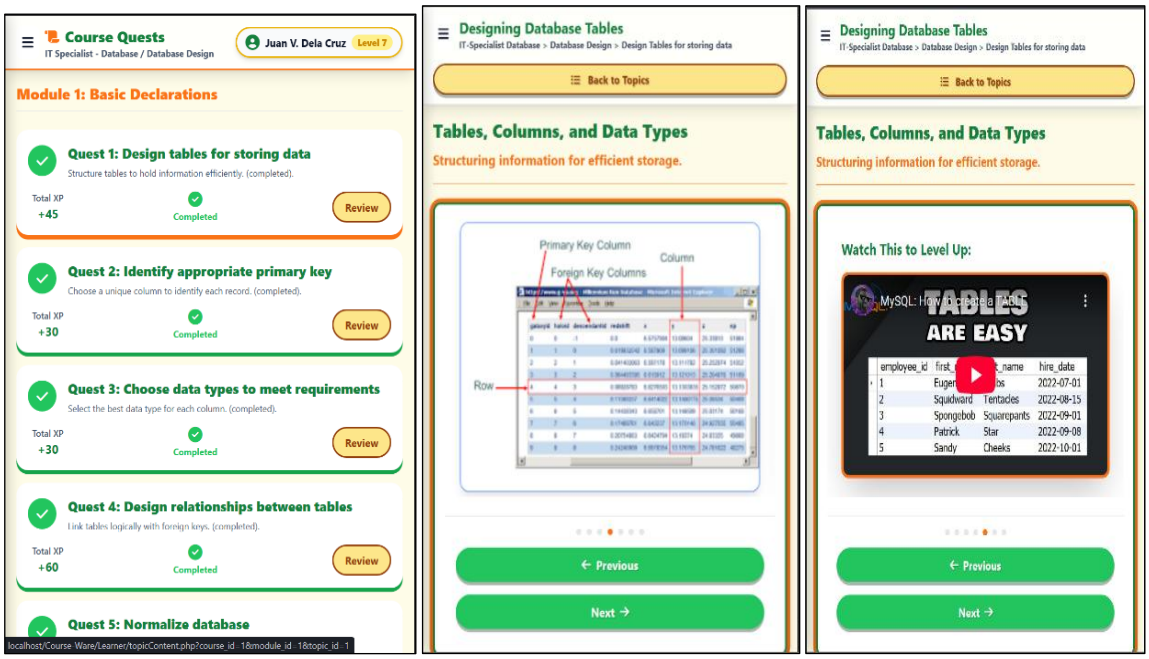


Figure 10: Mobile-responsive Courseware Design.
Source: Author, (2026).

Figure 10 presents the mobile-responsive design of the developed courseware, demonstrating its capability to adapt seamlessly across different screen sizes and devices. The responsive interface ensures that learners can conveniently access course modules, multimedia learning materials, and assessments using smartphones, tablets, or desktop computers. This design enhances accessibility and usability, allowing learners to engage with the courseware anytime and anywhere, thereby supporting flexible and continuous learning.

IV.2.3 Users (Admin) Module

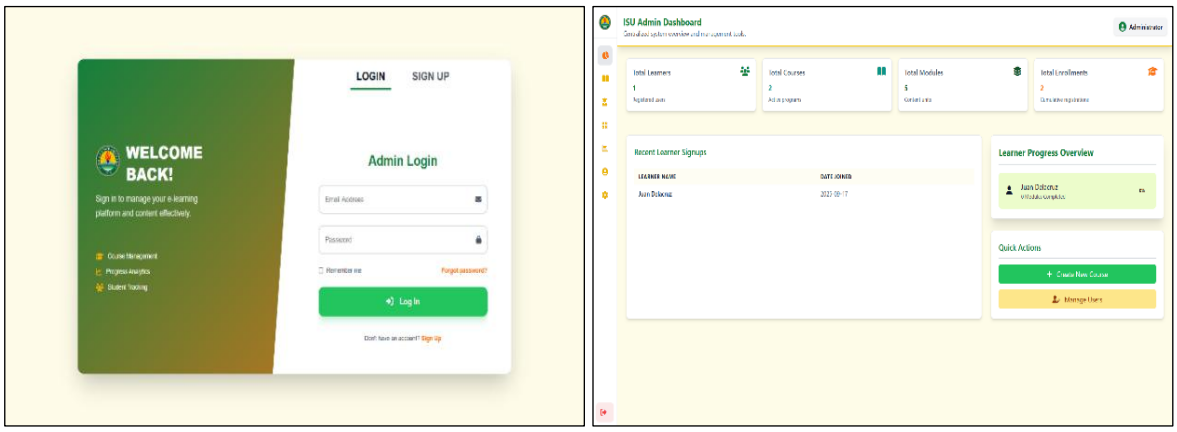


Figure 11: Admin Authentication and Dashboard
Source: Author, (2026).

Figure 11 presents the admin authentication and dashboard interface, which allows authorized administrators to securely access the system. The dashboard provides an overview of system activities and administrative tools necessary for managing the courseware platform. Figure 12 illustrates the content and user management interface, where administrators can manage course modules, update learning materials, and monitor user accounts. This functionality ensures efficient system administration and supports the continuous maintenance and improvement of the courseware content.

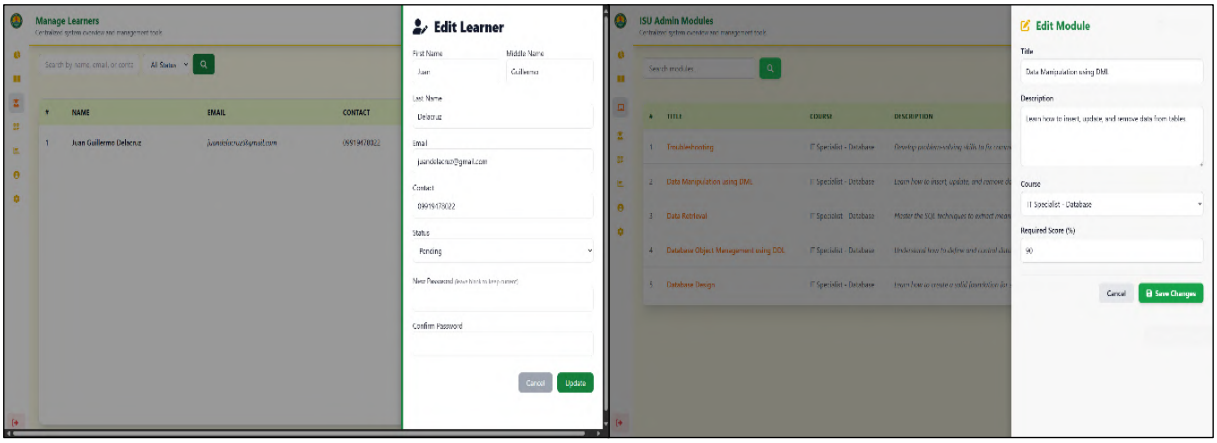


Figure 12: Content and User Management.
Source: Author, (2026).

IV.3 EVALUATION RESULTS OF THE SYSTEM BASED ON THE ISO/IEC 25010 SOFTWARE QUALITY STANDARDS

Table 3: Results of ISO/IEC 25010 Software Quality Evaluation.

Criteria	**Mean**	**Interpretation**
Functional Suitability	4.66	Strongly Agree
Performance Efficiency	4.57	Strongly Agree
Compatibility	4.61	Strongly Agree
Usability	4.52	Strongly Agree
Reliability	4.54	Strongly Agree
Security	4.56	Strongly Agree
Maintainability	4.58	Strongly Agree
Portability	4.67	Strongly Agree
Weighted Grand Mean	**4.59**	**Strongly Agree**

Source: Author, (2026).

Table 3 presents the evaluation results of a system based on the ISO/IEC 25010 software quality model, with 5 IT Experts and 20 prospective IT Specialist examinees as respondents providing assessments. The data reveals consistently high ratings across all eight quality characteristics, with individual mean scores ranging from 4.52 (Usability) to 4.67 (Portability). The uniformly high mean values, all falling between 4.5 and 5.0, are interpreted as "Strongly Agree," indicating that the expert respondents robustly affirm the system's quality in every dimension. This culminates in a Weighted Grand Mean of 4.59, also interpreted as "Strongly Agree," collectively suggesting a very high level of satisfaction and confidence among the experts regarding the system's overall adherence to the ISO/IEC 25010 quality standards. The research successfully developed an adaptive, web-based, and mobile-responsive interactive multimedia courseware designed to enhance IT Specialist exam readiness. This involved first meticulously identifying exam objectives and topics from Certiport PearsonVUE to build relevant module content, which was then digitized and loaded into a database. Subsequently, a core adaptive learning model was implemented using the Bayesian Knowledge Tracing (BKT) algorithm, coded in PHP, to dynamically track and update individual student skill mastery based on performance. Finally, an evaluation by five IT experts, based on ISO 25010 software quality standards, yielded overwhelmingly positive results, with all eight quality characteristics and the overall Weighted Grand Mean (4.59) interpreted as "Strongly Agree," affirming the high quality, functionality, and performance of the developed courseware.

V. CONCLUSIONS

This study successfully designed, developed, and evaluated an AI-driven interactive multimedia courseware for IT Specialist certification preparation using the Bayesian Knowledge Tracing (BKT) algorithm. The development process began with the systematic identification and mapping of exam objectives, topics, and content based on the official Certiport Pearson VUE IT Specialist certification framework. This alignment ensured that the developed modules directly correspond to the competencies required in the certification examination. The study further implemented a web-based and mobile-responsive learning platform that integrates interactive multimedia components with an adaptive learning model. Through the BKT algorithm, the system continuously estimates learners' knowledge states and dynamically updates mastery probabilities based on their responses to learning activities and assessments. This adaptive mechanism enables the courseware to personalize learning pathways and focus instructional support on areas where learners require further improvement. Evaluation results based on the ISO/IEC 25010 software quality standards revealed consistently high ratings across all eight quality characteristics, including functional suitability, usability, reliability, performance efficiency, security, compatibility, maintainability, and portability. The overall weighted grand mean of 4.59, interpreted as "Strongly Agree," indicates strong validation from IT experts and prospective examinees regarding the system's quality, effectiveness, and technical robustness. Overall, the findings demonstrate that integrating adaptive learning algorithms with interactive multimedia courseware provides a viable and effective approach to improving certification exam preparation. The developed platform not only aligns with industry-recognized certification competencies but also offers a scalable and technology-enhanced learning environment capable of supporting personalized learning experiences.

VI. FUTURE WORKS

Future research may focus on the large-scale implementation and empirical evaluation of the developed adaptive multimedia courseware to further determine its effectiveness in improving IT Specialist certification exam performance among diverse learner groups. Additional studies may also explore the optimization of the Bayesian Knowledge Tracing (BKT) parameters using larger learner datasets to enhance the accuracy of skill mastery prediction and the system's adaptive capabilities. Furthermore, integrating advanced artificial intelligence techniques such as machine learning, learning analytics, and natural language processing may improve personalized feedback, automated assessment, and intelligent tutoring features. Finally, the framework of the developed courseware may be extended to support other IT certification programs and professional training environments, enabling broader applications of adaptive learning technologies in technology-enhanced education

VII. AUTHOR'S CONTRIBUTION

Conceptualization: Mark Gil Toribio Gañgan.
Methodology: Mark Gil Toribio Gañgan.
Investigation: Mark Gil Toribio Gañgan.
Discussion of results: Mark Gil Toribio Gañgan.
Writing – Original Draft: Mark Gil Toribio Gañgan.
Writing – Review and Editing: Mark Gil Toribio Gañgan.
Resources: Mark Gil Toribio Gañgan.
Supervision: Mark Gil Toribio Gañgan.
Approval of the final text: Mark Gil Toribio Gañgan.

VIII. ACKNOWLEDGMENTS

The author extends his sincere gratitude to Isabela State University (ISU) – Ilagan Campus, particularly the Campus and University Research and Development Office, for their invaluable support, funding, guidance, and encouragement throughout the conduct of this research. The author also expresses profound appreciation to the College of Engineering, Architecture and Technology for its continuous support and assistance in facilitating the research process. Furthermore, the author gratefully acknowledges the Department of Information and Communication Technology for providing the academic environment and institutional support necessary for the successful completion of this study. The author likewise extends sincere appreciation to Mr. Jaspher Fenix, Mr. Ryuta Horiuchi and Mr. Prince Andrey Ramos for their hands-on support and valuable assistance in the development of the courseware, which greatly contributed to the successful implementation of the system.

IX. REFERENCES

[1] N. Ye, "Adaptive Learning path generation and optimization for big data courses: a multimodal knowledge graph and reinforcement learning approach," *Scientific Navigation*, vol. 1, no. 1, pp. 3–17, Aug. 2025, doi: 10.64376/tp3kwe32.

[2] R. Thakur, D. Khandelwal, and S. Tiwari, "AnveshanaAI: A Multimodal Platform for Adaptive AI/ML Education through Automated Question Generation and Interactive Assessment," *ArXiv.org*, Sep. 2025, doi: 10.48550/arxiv.2509.23811.

[3] S. Zhang, J. Zhang, F. Le, and Z. Wang, *Teaching Reform and Practical Exploration of Online IT Certification Training Courses Empowered by AI: —A Case Study of "Information System Project Management Professional."* Association for Computing Machinery (ACM), 2025, pp. 1501–1506. doi: 10.1145/3773365.3773601.

[4] M. Barla, M. Bieliková, A. B. Ezzeddinne, T. Kramár, M. Šimko, and O. Vozár, "On the impact of adaptive test question selection for learning efficiency," *Computers & Education*, vol. 55, no. 2, pp. 846–857, Apr. 2010, doi: 10.1016/j.compedu.2010.03.016.

[5] J. A. G. Gaddi, "Courseware Development in Education: A Literature review," *International Journal of Current Science Research and Review*, vol. 07, no. 01, Jan. 2024, doi: 10.47191/ijcsrr/v7-i1-83.

[6] J. A. G. Gaddi, "Courseware Development in Education: A Literature review," *International Journal of Current Science Research and Review*, vol. 07, no. 01, Jan. 2024, doi: 10.47191/ijcsrr/v7-i1-83.

[7] H. Herawan, A. Mering, and H. Sujaini, "Development of interactive multimedia for learning computer hardware maintenance Vocational High School," *JETL (Journal of Education Teaching and Learning)*, vol. 7, no. 1, p. 120, Mar. 2022, doi: 10.26737/jetl.v7i1.2908.

[8] R. M. Ambele, S. F. Kaijage, M. A. Dida, L. Trojer, and N. M. Kyando, "A review of the Development Trend of Personalized learning Technologies and its Applications," *International Journal of Advances in Scientific Research and Engineering*, vol. 08, no. 11, pp. 75–91, Jan. 2022, doi: 10.31695/ijasre.2022.8.11.9.

[9] Z. Fu, "Integrating Reinforcement Learning with Dynamic Knowledge Tracing for personalized learning path optimization," *Scientific Reports*, vol. 15, no. 1, p. 40202, Nov. 2025, doi: 10.1038/s41598-025-23900-4.

[10] Hariyanto, F. X. D. Kristianingsih, and R. Maharani, "Artificial intelligence in adaptive education: a systematic review of techniques for personalized learning," *Discover Education*, vol. 4, no. 1, Oct. 2025, doi: 10.1007/s44217-025-00908-6.

[11] A. Graf, "Exploring the role of personalization in adaptive learning environments," *International Journal Software Engineering and Computer Science (IJSECS)*, vol. 3, no. 2, pp. 50–56, Aug. 2023, doi: 10.35870/ijsecs.v3i2.1200.

[12] W. Cao, N. T. Mai, and W. Guo, "Personalized Learning and Adaptive Systems: AI-Driven educational innovation and student outcome Enhancement," *International Journal of Education and Humanities*, vol. 20, no. 2, pp. 173–182, Aug. 2025, doi: 10.54097/tc5k6825.

[13] F. Benkhalfallah, M. R. Laouar, and M. S. Benkhalfallah, "Examining adaptive E-Learning approaches to enhance learning and individual experiences," *Acta Informatica Pragensia*, vol. 13, no. 2, pp. 327–339, Aug. 2024, doi: 10.18267/j.aip.240.

[14] B. Zhu, K. T. Chau, and N. A. M. Mokmin, "Optimizing cognitive load and learning adaptability with adaptive microlearning for in-service personnel," *Scientific Reports*, vol. 14, no. 1, p. 25960, Oct. 2024, doi: 10.1038/s41598-024-77122-1.

[15] U. Upadhyay, G. Lancashire, C. Moser, and M. Gomez-Rodriguez, "Large-scale randomized experiments reveals that machine learning-based instruction helps people memorize more effectively," *Npj Science of Learning*, vol. 6, no. 1, p. 26, Sep. 2021, doi: 10.1038/s41539-021-00105-8.

[16] F. Amastini, D. K. S. Sekarhati, and M. Puspitasari, "Advancing Adaptive and Personalized E-Learning Systems: A Systematic Literature Review," *Advance Sustainable Science Engineering and Technology*, vol. 7, no. 2, p. 0250209, Apr. 2025, doi: 10.26877/m82zg802.

[17] G.-E. Torgersen and O. Boe, "Which tools in multimedia are best for learning outcomes? A study grounded in cognitive load structures," *Frontiers in Psychology*, vol. 12, p. 545335, Jul. 2021, doi: 10.3389/fpsyg.2021.545335.

[18] A. Elmabaredy, E. Elkholy, and A.-A. Tolba, "Web-based adaptive presentation techniques to enhance learning outcomes in higher education," *Research and Practice in Technology Enhanced Learning*, vol. 15, no. 1, Aug. 2020, doi: 10.1186/s41039-020-00140-w.

[19] B. Çeken and N. Taşkın, "Multimedia learning principles in different learning environments: a systematic review," *Smart Learning Environments*, vol. 9, no. 1, Apr. 2022, doi: 10.1186/s40561-022-00200-2.

[20] N. Yannier, S. E. Hudson, H. Chang, and K. R. Koedinger, "AI adaptivity in a Mixed-Reality system improves learning," *International Journal of Artificial Intelligence in Education*, vol. 34, no. 4, pp. 1541–1558, Jan. 2024, doi: 10.1007/s40593-023-00388-5.

[21] S. D. Tithi *et al.*, "Adaptive scaffolding for cognitive engagement in an intelligent tutoring system," *arXiv (Cornell University)*, Feb. 2026, doi: 10.48550/arxiv.2602.07308.

[22] M. Laaziri, S. Khoulji, K. Benmoussa, and K. M. Larbi, "Outlining an intelligent tutoring system for a university cooperation information system," *Engineering Technology & Applied Science Research*, vol. 8, no. 5, pp. 3427–3431, Oct. 2018, doi: 10.48084/etasr.2158.

[23] S. Minn and R. Nkambou, "Enhanced Interpretable Knowledge Tracing for Students Performance Prediction with Human understandable Feature Space," *ArXiv.org*, Sep. 2025, doi: 10.48550/arxiv.2509.18231.

[24] S. Khanal and S. R. Pokhrel, "Analysis, modeling and design of personalized digital learning environment," *arXiv (Cornell University)*, May 2024, doi: 10.48550/arxiv.2405.10476.

[25] A. Christodoulou and C. Angeli, "Adaptive learning techniques for a personalized educational software in developing teachers' technological pedagogical content knowledge," *Frontiers in Education*, vol. 7, Jun. 2022, doi: 10.3389/feduc.2022.789397.

[26] M. Delianidi, K. Diamantaras, I. Moras, and A. Sidiropoulos, "DK-PRACTICE: an intelligent educational platform for personalized learning content recommendations based on students knowledge state," *arXiv (Cornell University)*, Dec. 2024, doi: 10.48550/arxiv.2501.10373.

[27] R. Sajja, V. Pursnani, Y. Sermet, and I. Demir, "AI-Assisted Educational Framework for Floodplain Manager Certification: Enhancing vocational education and training through personalized learning," *IEEE Access*, vol. 13, pp. 42401–42413, Jan. 2025, doi: 10.1109/access.2025.3548591.

[28] M. Dai, J.-L. Hung, X. Du, H. Tang, and H. Li, "Knowledge Tracing: a review of available technologies," *Journal of Educational Technology Development and Exchange*, vol. 14, no. 2, pp. 1–20, Jan. 2021, doi: 10.18785/jetde.1402.01.

[29] J. Y. Park, F. Cornillie, H. L. J. Van Der Maas, and W. Van Den Noortgate, "A multidimensional IRT approach for dynamically monitoring ability growth in computerized practice environments," *Frontiers in Psychology*, vol. 10, p. 620, Mar. 2019, doi: 10.3389/fpsyg.2019.00620.

[30] I. Šarić-Grgić, A. Grubišić, and A. Gašpar, "Twenty-five years of Bayesian knowledge tracing: a systematic review," *User Modeling and User-Adapted Interaction*, vol. 34, no. 4, pp. 1127–1173, Jan. 2024, doi: 10.1007/s11257-023-09389-4.

[31] G. Y. Koi-Akrofi *et al.*, "Towards a Software Quality Factor Assessment Model for Learning Management Systems (LMS)," *Indian Journal of Science and Technology*, vol. 17, no. 23, pp. 2463–2468, May 2024, doi: 10.17485/ijst/v17i23.1006.

[32] L. Pinedo *et al.*, "Software quality models: Exploratory review," *ICST Transactions on Scalable Information Systems*, Sep. 2023, doi: 10.4108/eetsis.3982.

[33] A. Maden and S. E. Alptekin, "SOFTWARE QUALITY EVALUATION USING SQUARE SERIES AND SCENARIO-BASED FUZZY COGNITIVE MAP," *International Journal for Quality Research*, vol. 19, no. 2, pp. 451–470, May 2025, doi: 10.24874/ijqr19.02-06.

[34] N. Shapovalova, O. Rybalchenko, I. Dotsenko, S. Bilashenko, A. Striuk, and L. Saitgareev, "Adaptive testing model as the method of quality knowledge control individualizing," Jun. 2019. doi: 10.31812/123456789/3174.

[35] S. Minn, "AI-assisted knowledge assessment techniques for adaptive learning environments," *Computers and Education Artificial Intelligence*, vol. 3, p. 100050, Jan. 2022, doi: 10.1016/j.caeai.2022.100050.

[36] L. Alfaro, C. Rivera, E. Castaneda, J. Zuniga-Cueva, M. Rivera-Chavez, and F. Fialho, "A Review of Intelligent Tutorial Systems in Computer and Web based Education," *International Journal of Advanced Computer Science and Applications*, vol. 11, no. 2, Jan. 2020, doi: 10.14569/ijacsa.2020.0110295.

[37] K. Chrysafiadi, M. Virvou, G. A. Tsihrintzis, and I. Hatzilygeroudis, "Evaluating the user's experience, adaptivity and learning outcomes of a fuzzy-based intelligent tutoring system for computer programming for academic students in Greece," *Education and Information Technologies*, vol. 28, no. 6, pp. 6453–6483, Nov. 2022, doi: 10.1007/s10639-022-11444-3.

[38] J. A. Kulik and J. D. Fletcher, "Effectiveness of intelligent tutoring systems," *Review of Educational Research*, vol. 86, no. 1, pp. 42–78, Apr. 2015, doi: 10.3102/0034654315581420.

[39] F. Han, "Factors affecting Chinese undergraduate medical students' behavioural intention and actual use of intelligent tutoring systems," *Australasian Journal of Educational Technology*, Apr. 2024, doi: 10.14742/ajet.8814.

[40] M. Ilić, V. Mikić, L. Kopanja, and B. Vesin, "Intelligent techniques in e-learning: a literature review," *Artificial Intelligence Review*, vol. 56, no. 12, pp. 14907–14953, Jun. 2023, doi: 10.1007/s10462-023-10508-1.

[41] P.-A. Andersen, C. Kråkevik, M. Goodwin, and A. Yazidi, *Adaptive Task Assignment in Online Learning Environments*. Association for Computing Machinery (ACM), 2016, pp. 1–10. doi: 10.1145/2912845.2912854.

[42] A. Alnuaim, "The impact and acceptance of gamification by learners in a digital literacy course at the undergraduate level: randomized controlled trial," *JMIR Serious Games*, vol. 12, p. e52017, Aug. 2024, doi: 10.2196/52017.

[43] A. Ahmad, F. Zeshan, M. S. Khan, R. Marriam, A. Ali, and A. Samreen, "The impact of gamification on learning outcomes of computer science majors," *ACM Transactions on Computing Education*, vol. 20, no. 2, pp. 1–25, Apr. 2020, doi: 10.1145/3383456.

[44] M. G. T. Gañgan and T. D. Palaoag, "Performance Assessment of text similarity Algorithms through classification metrics for BSIT Graduate Job Concordance," *ITEGAM- Journal of Engineering and Technology for Industrial Applications (ITEGAM-JETIA)*, vol. 12, no. 57, Jan. 2026, doi: 10.5935/jetia.v12i57.2965.

[45] B. Deonovic, M. Yudelson, M. Bolsinova, M. Attali, and G. Maris, "Assessment meets Learning: On the relation between Item Response Theory and Bayesian Knowledge Tracing," *arXiv (Cornell University)*, Mar. 2018, [Online]. Available: https://arxiv.org/abs/1803.05926v1

[46] Q. Wang, "A study on the design of a deep learning model for classroom based on user participation and game chemistry processes," *Entertainment Computing*, vol. 51, p. 100727, May 2024, doi: 10.1016/j.entcom.2024.100727.

[47] M. Rob and V. Etnyre, "A method of optimizing programming topics to succeed in IT certification exams," *Issues and Trends in Educational Technology*, vol. 5, no. 2, Dec. 2017, doi: 10.2458/azu_itet_v5i2_rob.

[48] A. Vu-Minh, Q. Nguyen-The, N. Nguyen, X.-L. Pham, and A. Nguyen, "Designing a Course-Grounded AI Tutor with Retrieval-Augmented Generation: A DSR Approach to Technical Education," *SSRN Electronic Journal*, Jan. 2025, doi: 10.2139/ssrn.5607971.

[49] N. Dahal *et al.*, "Development and evaluation of E-Learning courses," *International Journal of Interactive Mobile Technologies (iJIM)*, vol. 17, no. 12, pp. 40–60, Jun. 2023, doi: 10.3991/ijim.v17i12.40317.

[50] "Certify :: IT Specialist Certifications :: Certiport." https://certiport.pearsonvue.com/Certifications/ITSpecialist/Certification/Certify

Journal of Engineering and Technology for Industrial Applications

ISSN ONLINE: 2447-0228

ITEGAM-JETIA

Manaus, v.12 n.60, p.1275-1286. July/August, 2026.
DOI: https://doi.org/10.5935/jetia.v12i60.4067

RESEARCH ARTICLE OPEN ACCESS

RECURSIVE VOTING FUSION: AN RFE-BASED ENSEMBLE MODEL FOR CATEGORIZING IOT DDOS ATTACKS

Piyush M. Prajapati*[1], Priyesh P. Gandhi[2], Sheshang Degadwala[3], Keyur Brahmbhatt[4], Swapnil M Parikh[5]

[1]Computer Engineering, Gujarat Technological University, Ahmedabad, Gujarat, India.
[2]Provost, Sigma University, Vadodara, Gujarat, India.
[3]Department of Computer Engineering, Sigma University, Vadodara, Gujarat, India.
[4]Department of Computer Engineering, Sigma University, Vadodara, Gujarat, India.
[5]Computer Science and Engineering, Parul Institute of Technology, Parul University, Vadodara, Gujarat, India.

[1]https://orcid.org/0009-0000-8148-0410, [2]https://orcid.org/0000-0001-5338-3111, [3]https://orcid.org/0000-0002-2385-7790, [4]https://orcid.org/0000-0001-7478-3173, [5]https://orcid.org/0009-0005-8816-5508

Email:*piyush.prj@gmail.com, priyeshgandhi@gmail.com, sheshang13@gmail.com, keyur.brahmbhatt@bvmengineering.ac.in, swapnil.parikh17761@paruluniversity.ac.in

ARTICLE INFO

Article History
Received: March 13, 2026
Reviewed: April 15, 2026
Accepted: July 15, 2026
Published: August 31, 2026

Keywords:
Distributed Denial of Service,
Internet of Things,
Recursive Feature Elimination,
Ensemble Machine Learning,
Intrusion Detection Systems.

ABSTRACT

The rise of the Internet of Things (IoT) devices has led to an enormous vulnerability to multiple DDoS attacks, including low-rate traffic disruption and high-rate SYN Floods. This increasing menace underscores the importance of proper multi-classification methods that can detect various DDoS attack patterns. Nonetheless, most of the current machine learning models cannot provide a generalization between various DDoS types that include DDoS-ACK Fragmentation, DDoS-HTTP Flood, DoS-TCP Flood, and DDoS-SYN Flood. Non-linear Support Vector Machines (SVM) which are traditional classifiers tend to have poor performance when trying to differentiate subtle differences between these types of attacks. To overcome this drawback, this paper suggests a Recursive Voting Fusion model, which involves Recursive Feature Elimination (RFE) as the method of optimum feature selection and an ensemble approach to the robust classification. The framework is a hybrid of Decision Tree, Random Forest, and Extra tree classifiers where soft voting is used. It is experimentally demonstrated that the proposed approach has 99 per cent accuracy, precision, recall, and F1-score, and 99 per cent MCC and AUC-ROC, which is significantly higher than the baseline models. It implies that the model is highly robust and scalable to be used in real-time IoT intrusion detection and efficient mitigation of the developing DDoS threats.

Copyright ©2026 by authors and Galileo Institute of Technology and Education of the Amazon (ITEGAM). This work is licensed under the Creative Commons Attribution International License (CC BY 4.0).

I. INTRODUCTION

The fast growth of the Internet of Things (IoT) has introduced new standards of connectivity, autonomous automation, and efficiency in business fields like healthcare, smart cities, agriculture, transportation, and manufacturing [1-3]. Nevertheless, this enhanced interconnectedness has expanded the area of attack by cyber threats. Distributed Denial of Service (DDoS) attacks are among these and currently one of the most unsettling and mostly launched cyberattacks on IoT infrastructures [4-6]. The IoT devices are relatively resource-limited and oftentimes have the bare-minimum security protocols installed, which makes them the best targets of botnet infection which can then be utilized to execute massive, multi-vector DDoS attack [7], [8]. An example of such an attack that caused havoc on the global internet is the 2016 Mirai botnet attack that used insecure IoT devices to flood the DNS provider Dyn [9], [10]. The all-purpose classification of DDoS attacks may be done by the attacker by the type of the network stack and the point of entry into the victim network [11-13]. Attacks that can occur at the network layer are TCP SYN Flood, UDP Flood, and ICMP Flood, which aim to either consume bandwidth or connection queues with a flood of packets. Fragmentation vulnerabilities can be used at the transport layer by means of ACK Fragmentation and UDP Fragmentation [14-16].

Applications layer is prone to advanced attacks such as the HTTP Flood and DNS Amplification that are harder to detect since they imitate the normal user actions. These attacks vary in frequency, packet size and protocol exploitation and multi-classification is essential to identify and mitigate them more accurately [17], [18]. Although the intrusion detection systems (IDS) research field has been researched extensively, machine learning-based IoT DDoS detection solutions are associated with three major limitations [19-21]. To begin with, they demonstrate low generalization abilities with different classes of DDoS, often classifying less common or more intricate attacks [22-24]. Second, most models are not very robust at feature selection that may lead to incorporation of redundant or noisy features that multiply computational requirements and poor performance [25-27]. Third, the presence of imbalance in classes in datasets distorts the learning process, as it leads to biased prediction on the most prevalent types of attacks and ignoring rare but essential threats [28], [29]. As an example, traditional models, e.g. Support Vector Machines (SVM) and Naive Bayes, provide poor macro-average F1-scores and are unable to detect attacks, such as DDoS-ICMP Flood or UDP Fragmentation [30], [31]. To overcome them, the paper will suggest Recursive Voting Fusion, a new framework of ensemble classifications, which aims to precisely and effectively identify various types of IoT-based DDoS attacks. The framework combines Recursive Feature Elimination (RFE) to discover the most discriminative set of features, in other words, noise reduction and improved classification accuracy. The fundamental classifier consists of a hard voting set of Decision Tree, Random Forest and Extra Tree models which are combined to exploit multiple learning biases to enhance detection strength. The key aim of this study is to work on a lightweight, scalable, and high-accuracy multi-class DDoS detecting system that can be used in the real-time IoT security system. The study intends to: (i) identify 15 different IoT DDoS and DoS attack types with high accuracy, (ii) optimize the performance of the model based on feature selection (iii) compare the system to the principles of the traditional classifier to prove its excellence. An experimental analysis of the labeled IoT DDoS data indicates that the proposed model has 99% accuracy, precision, recall, and F1-score, and MCC and AUC-ROC of 0.99. Recursive Voting Fusion is much more effective on all the measures compared to baseline classifiers like SVM (25%), KNN (97%), and Naive Bayes (54%). Additionally, the model is highly recalled in complex subcategories like HTTP Flood, DNS Amplification, and Smurf and, therefore, it shows effectiveness in detecting threat subtly. The suggested system is a resource-saving, practical proposal of the IoT networks in the contemporary era, which have been added to not only academic development but also the implementation of the solution and solution to the proposed-system in proactive DDoS prevention models.

II. THEORETICAL REFERENCE

The exponentially accelerated development of Internet of Things (IoT) technologies has increased connectivity and smart automation in the industrial sector. Nevertheless, the very resource-limited character of the IoT devices and their massive deployment has predisposed them to the DDoS attacks. This has made effective and smart systems of detection instrumental in detecting and categorizing and curtailing such threats. The given literature review discusses the recent trends in machine learning (ML) and deep learning (DL) systems to identify multi-class DDoS attacks in IoT setups, particularly ensemble models, feature selection algorithms, and class imbalance. By [1] suggested a hybrid learning model to identify cyberattacks using IoT-based detection that takes advantage of feature transformation and a collection of classifiers to identify advanced threats. In turn [2] have made a comparative analysis of anomaly detection techniques and highlighted the trade of between unsupervised and supervised techniques in IoT networks. The strength of sequence-based models of dynamic traffic analysis is demonstrated with the help of LSTM networks applied to the CIC-IoT2023 dataset by [3], who identified the temporal patterns of attacks. An intrusion detection system was introduced by [4] that employs convolutional layers and autoencoders to identify DDoS traffic using deep learning. According to [5] took the idea a step further and suggested a hybrid CNN-BiLSTM system to also address low-rate DDoS attacks that are especially difficult to detect because of their insidious traffic signature. In turn [6] scaled recurrent neural architectures to real-life IoT settings, with an emphasis on scalability and accuracy. In healthcare systems that rely on the IoT, which are critical regarding security, [7] used machine learning to detect anomalies. Their work represented better performance in case of engineered features based on domain knowledge. By [8] suggested CKAN model (Convolutional Kolmogorov-Arnold Networks) that was able to identify non-linear relationships within IoT traffic to be able to classify them effectively. In a similar way, [9] proposed a deep ensemble learning method with pruning, which maximizes the accuracy of detection and efficiency of computing DDoS detection. By [10] also applied Principal Component Analysis (PCA), which increases the accuracy and efficiency of computation in the detection of DDoS. In order to address the issue of detection robustness, [11] developed a hybrid system which combines feature selection based on filters with ensemble classifiers.

In turn [12] extended their model by using SMOTE-ENN to balance the data and effective feature selection so that the model can be better at minority classes. By [13] concentrated on detecting DDoS in the IoT applications based on supervised machine learning models and showed significant enhancement with random forest and SVM. By [14] created a hybrid intrusion detection framework of the cyber-physical systems with the best feature selection based on correlation and mutual information parameters. A hybrid feature selection algorithm, LightGBM with a modified slap swarm algorithm, was proposed by [15], and it demonstrated significant performance in the context of big data IoT. [16] have suggested a multi-class intrusion detection system based on transformers and CIC-IoT-2023 dataset, demonstrating great versatility to complicated traffic patterns. In turn [17] compared different deep learning models in the context of the IoT intrusion classification and have demonstrated that ensemble deep learning models were more effective in multiclass configurations in comparison with single architectures. According to [18] reused their previous methodology and critically analyzed some machine learning algorithms on the CIC-IoT2023 dataset. By [19] boosted the intrusion detection by using a twostep clustering method, which makes the system more sensitive to detect low level DDoS activities. VGGIncepNet developed by [20] involved non-image-to-image conversion methods and CNN architecture in intrusion detection, and it achieved better spatial feature extraction. By [21] have created an agent-based system that automates the process of feature extraction and selection in detecting DDoS, minimizing preprocessing costs by hand and enhancing the real-time results. According to [22] offered a smart architecture that combines various levels of detection in order to identify threats, which is optimized in terms of IoT scale throughput and latency. By [23] made the CICIoT2023 dataset available and made it a reference on how to measure large-scale IoT attacks. In turn [24] proposed the attention mechanism-enhanced CNN-BiLSTM model and it was found to be of great significance in the classification of DDoS variants such as TCP SYN and ICMP floods.

By [25] gave a broad overview of the ML methods to detect DDoS in IoT and proposed the future research opportunities in adaptive and self-healing detection systems. In turn [26] introduced a hybrid DDoS detector based on CNN and GRU, with high accuracy results and robustness. The work by [27] compared the performance of the common ML classifiers to the CIC-IDS2017 dataset, indicating the ensemble learning as the future direction. By [28] developed IoT-specific intrusion detection system based on standard ML algorithms and emphasize the relevance of features to achieve high classification performance using the CICIoT dataset. In turn [29] trained the Random Forest models with the purpose of DDoS detection in the IoT and verified its functionality using the CICIoT dataset. According to [30] maximized the performance of AdaBoost through undersampling and hyperparameter optimization, which shown that pre-processing of data has a significant impact on model accuracy. Finally, Avc\u0131 and by [31] used supervised learning-based method of predicting DDoS in building management systems and stated that such models can be generalized to all smart infrastructure. As noted in the reviewed literature, use of deep learning architectures such as LSTM, CNN-BiLSTM, transformers; ensemble techniques involving multiple classifiers; and feature selection techniques including PCA, SMOTE-ENN, and swarm algorithms have several promising trends. Nonetheless, the majority of studies are related to binary classification or definite types of DDoS without multiclass categorization. In addition, features selection is also understudied or uses heuristic methods. Also, the datasets do not possess the appropriate class balance, which is poorly addressed in most of the models, limiting the performance on minor types of DDoS.

III. MATERIALS AND METHODS

Figure 1 indicates a very elaborate and methodically formatted pipeline that is to be used in the detection of Distributed Denial of Service (DDoS) attacks in Internet of Things (IoT) systems by using a powerful voting-based ensemble machine learning framework. This all-encompassing flowchart summarizes six sequential stages and interdependent ones, which represent the essential part of the entire data analytics and cybersecurity workflow starting with the first data acquisition and preprocess, feature extraction, model training, and eventual decision-making. The basis of this framework is the CICIoT2023 dataset [23] a balanced and well-curated dataset consisting of fifteen types of DDoS attacks, with one hundred samples each or a total of 1,500 rows and 47 columns. The variety and realism of the dataset is closely related to the real-world situation of IoT network, which contributes to the higher generalizability and effectiveness of the approach proposed to detect intrusion.

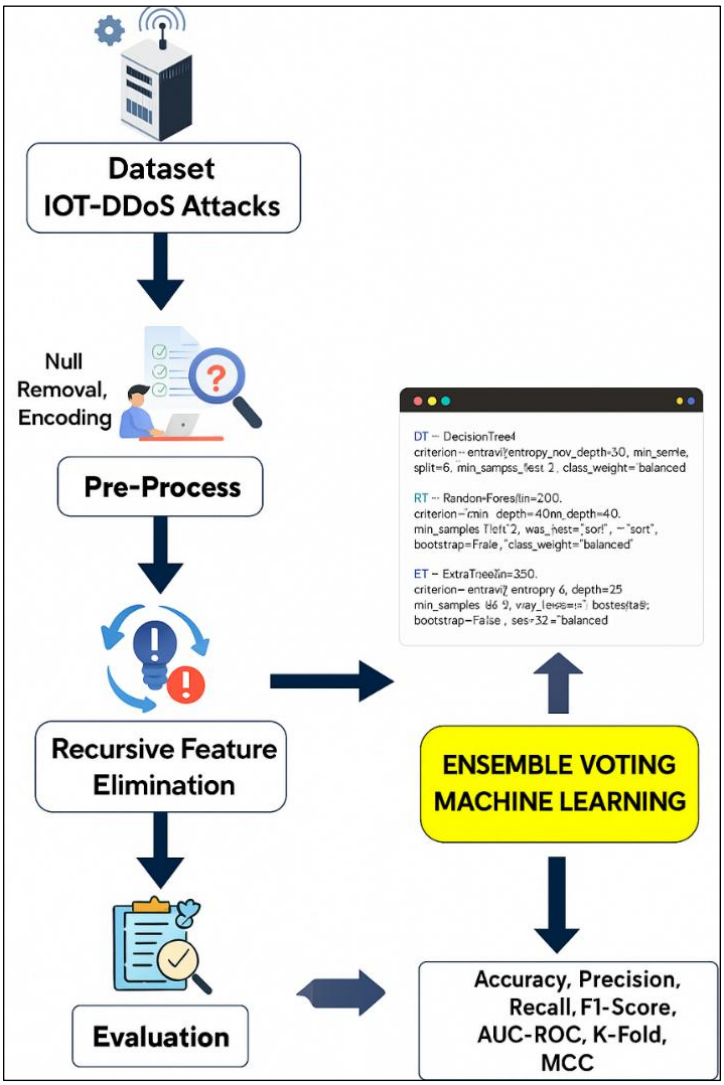


Figure 1: Flow Diagram of Recursive Voting Fusion.
Source: Authors, (2026).

III.1 PSEUDO CODE

```
D ← load_dataset()
D ← preprocess(D)   // null removal, encoding
F ← RFE(D, k=30)
X_train, X_val, y_train, y_val ← train_test_split(F)
DT ← DecisionTree(criterion='entropy', max_depth=30, min_samples_split=4,
        min_samples_leaf=2, class_weight='balanced')
RF ← RandomForest(n=200, criterion='gini', max_depth=40, min_samples_split=3,
        min_samples_leaf=2, max_feat='sqrt', bootstrap=True,
        class_weight='balanced', seed=42)
ET ← ExtraTrees(n=250, criterion='entropy', max_depth=35, min_samples_split=3,
        min_samples_leaf=1, max_feat='log2', bootstrap=False,
        class_weight='balanced', seed=42)
VC ← VotingClassifier([('DT', DT), ('RF', RF), ('ET', ET)], voting='hard')
VC.fit(X_train, y_train)
y_pred ← VC.predict(X_val)
acc ← Accuracy(y_val, y_pred)
prec ← Precision(y_val, y_pred)
rec ← Recall(y_val, y_pred)
f1 ← F1(y_val, y_pred)
auc ← AUC_ROC(y_val, VC, multi_class='ovr')
mcc ← MCC(y_val, y_pred)
KF ← KFold(n_splits=5)
scores ← cross_val_score(VC, F, y, cv=KF)
```

III.2 DATASET: CICIOT2023 (1500 SAMPLES, 15 CLASSES)

At the core of this pipeline is the CICIoT2023 dataset [23], a benchmark dataset designed to reflect real-time and large-scale attacks specifically tailored for IoT networks. Table 1. encompasses 47 columns or features and 15 types of cyberattack classes including botnets, brute-force, infiltration, and various types of DDoS patterns each represented by 100 samples. The dataset includes high-resolution telemetry such as:

- Network traffic features (e.g., source IP, destination IP, protocol, packet count, byte count)
- Flow behavior metrics (e.g., flow duration, flow bytes per second, inter-arrival time)
- Attack signatures relevant to multi-vector DDoS scenarios

Using a uniform class distribution (100 samples/class) helps in mitigating class imbalance, a major challenge in supervised classification tasks. The dataset ensures diversity in attack vectors, making the model generalizable and robust for real-world intrusion detection systems (IDS) in IoT ecosystems.

Table 1: Dataset Columns Description.

Column Name	Description
flow_duration	Total duration of the network flow (in microseconds or milliseconds).
Header_Length	Length of the packet headers.
Protocol Type	Type of transport protocol used (e.g., TCP, UDP, ICMP).
Duration	Duration of the specific activity/connection.
Rate	Average transmission rate of packets or bytes.
Srate	Source-to-destination packet transmission rate.
Drate	Destination-to-source packet transmission rate.
fin_flag_number	Number of FIN flags observed (connection termination signal).
syn_flag_number	Number of SYN flags (used to initiate a TCP connection).
rst_flag_number	Number of RST flags (used to reset a TCP connection).
psh_flag_number	Number of PSH flags (push data to receiving app).
ack_flag_number	Number of ACK flags (acknowledge receipt).
ece_flag_number	Number of ECE flags (Explicit Congestion Notification Echo).
cwr_flag_number	Number of CWR flags (Congestion Window Reduced).
ack_count	Count of packets with ACK flag set.
syn_count	Count of packets with SYN flag set.
fin_count	Count of packets with FIN flag set.

urg_count	Count of packets with URG (urgent) flag set.
rst_count	Count of packets with RST flag set.
HTTP	Indicator/count for HTTP protocol usage.
HTTPS	Indicator/count for HTTPS protocol usage.
DNS	Indicator/count for DNS protocol usage.
Telnet	Indicator/count for Telnet protocol usage.
SMTP	Indicator/count for SMTP protocol usage.
SSH	Indicator/count for SSH protocol usage.
IRC	Indicator/count for IRC protocol usage.
TCP	Indicator/count for TCP protocol usage.
UDP	Indicator/count for UDP protocol usage.
DHCP	Indicator/count for DHCP protocol usage.
ARP	Indicator/count for ARP protocol usage.
ICMP	Indicator/count for ICMP protocol usage.
IPv	IP version indicator (IPv4 or IPv6).
LLC	Indicator/count for LLC (Logical Link Control) usage.
Tot sum	Total sum of packet sizes in the flow.
Min	Minimum packet size in the flow.
Max	Maximum packet size in the flow.
AVG	Average packet size in the flow.
Std	Standard deviation of packet sizes.
Tot size	Total size of the data transferred in the flow.
IAT	Inter-arrival time between packets.
Number	Total number of packets in the flow.
Magnitude	Magnitude of packet payloads or statistical metric
Radius	Statistical feature showing distance in feature space
Covariance	Covariance between selected flow parameters.
Variance	Variance of packet sizes or times in the flow.
Weight	Weight assigned to the flow
label	Class label

Source: Authors, (2026).

III.3 PRE-PROCESSING: NULL VALUE HANDLING AND ENCODING

Once the dataset is acquired, the first critical step is data pre-processing, which ensures the dataset is clean and suitable for machine learning algorithms. The dataset, derived from [23], includes multiple features that may contain null or missing values and categorical fields that are not directly interpretable by machine learning models.

- Null Value Handling: Missing values in the dataset can degrade the performance of classifiers. Let the dataset be represented as a matrix $X \in \mathbb{R}^{nxm}$, where $n = 1500$ samples and m features. A missing value in element x_{ij} (i.e., the value at the ith row and jth column) is either removed if the percentage of missingness is negligible, or imputed using statistical methods such as:
  Mean imputation:

$$x_{ij} = (1/N) \sum_{k=1}^{N} x_{kj} \quad (1)$$

  K-Nearest Neighbors imputation (KNN):

$$x_{ij} = \text{mean}(\{x_{pj} \mid x_p \in N_k(x_i)\}) \quad (2)$$

- Encoding: Categorical variables such as protocol or flag type are transformed into numerical format using encoding schemes. For nominal variables $C = \{c_1, c_2, \ldots, c_k\}$, One-Hot Encoding creates binary vectors for each class label:

$$\text{Encoded}(c_j) = [0, 0, \ldots, 1, \ldots, 0] \quad (3)$$

III.4 RECURSIVE FEATURE ELIMINATION (RFE)

After the data is cleaned and numerically encoded, the next step is Recursive Feature Elimination (RFE). This is a feature selection technique that aims to reduce the dimensionality of the feature space while preserving the most predictive attributes.

$$X = [x_1, x_2, \ldots, x_m] \quad (4)$$

$$\text{Feature Set}_{t+1} = \text{Feature Set}_t \setminus \{\text{argmin}_{xj} \in \text{Feature Set}_t \, I(x_j)\} \quad (5)$$

III.5 ENSEMBLE VOTING-BASED MACHINE LEARNING

The core of the detection framework is a Voting-Based Ensemble Model, which integrates predictions from multiple classifiers to improve robustness and accuracy. The ensemble here consists of Decision Tree (DT), Random Forest (RF), and Extra Trees (ET) classifiers each tuned with specific hyperparameters to maximize performance and diversity.
Decision Tree (DT): The Decision Tree is built using the Entropy-based Information Gain criterion. The entropy $H(S)$ of a dataset S is calculated as:

$$H(S) = -\sum_{i=1}^{k} p_i \log_2(p_i) \quad (6)$$

Where p_i is the proportion of samples belonging to class i. A split at node N aims to maximize the Information Gain (IG):

$$IG(S, A) = H(S) - \sum\_\{v \in Values(A)\} (|S_v| / |S|) H(S_v) \quad (7)$$

The tree's growth is constrained by maximum depth $d = 30$, minimum samples to split $s = 4$, and minimum leaf size $l = 2$. Class weights are balanced to counteract skewed class distributions. Random Forest (RF): The Random Forest is an ensemble of decision trees trained using bootstrap aggregation (bagging) and random feature selection. Let $T = \{t1, t2, \dots, tn\}$ denote the set of $n = 200$ decision trees, each trained on a bootstrap sample from the dataset. The Gini index is used to determine optimal splits:

$$Gini(S) = 1 - \sum_{i=1}^{k} p_i^2 \quad (8)$$

Each tree considers a random subset of features (square root of total features) at each split, increasing diversity among trees. The output class is determined by majority vote:

$$\hat{y} = mode(\{t_i(x) \mid i = 1, \dots, n\}) \quad (9)$$

Extra Trees (ET): The Extra Trees classifier is like Random Forest but introduces additional randomness by selecting split thresholds at random, rather than choosing the best threshold. Here, $n = 250$ trees are grown without bootstrapping (entire dataset used), and split criterion is entropy. The maximum number of features at each split is set to $\log_2(m)$, where m is the total number of features.

$$\max features = \log_2(m) \quad (10)$$

III.6 EVALUATION METRICS

After model training, the ensemble classifier is evaluated using a comprehensive set of metrics that capture different dimensions of performance.

- Accuracy: Measures overall correctness:

$$Accuracy = (TP + TN) / (TP + TN + FP + FN) \quad (11)$$

- Precision and Recall: Precision measures the correctness of positive predictions, and recall measures completeness:

$$Precision = TP / (TP + FP) \quad (12)$$

$$Recall = TP / (TP + FN) \quad (13)$$

- F1-Score: The harmonic means of precision and recall:

$$F1 = 2 * (Precision * Recall) / (Precision + Recall) \quad (14)$$

- K-Fold Cross Validation: The dataset is split into K equal parts. For each iteration, $K - 1$ parts are used for training and 1 for testing. This is repeated K times, and the results are averaged:

$$Cross - validation\ Accuracy = (1/K) \sum_{i=1}^{K} Accuracy_i \quad (15)$$

- Matthews Correlation Coefficient (MCC): A balanced measure for classification performance:

$$MCC = (TP * TN - FP * FN) / sqrt((TP + FP)(TP + FN)(TN + FP)(TN + FN)) \quad (16)$$

This metric is particularly useful in multi-class problems or where class imbalance exists, as it takes all four confusion matrix categories into account. In summary, sub section 1.2 through 1.6 form the core computational and analytical backbone of proposed system pipeline. Each step from data cleansing and transformation, through intelligent feature reduction, to the highly optimized ensemble model contributes to a robust and interpretable system for IoT DDoS attack detection, validated by rich evaluation strategies.

IV. RESULTS AND DISCUSSIONS

To provide an efficient training and evaluation of the proposed ensemble intrusion detection model, the result analysis was performed in the Google Colab environment with a T4 GPU setting. The data used in the CICIoT2023 consist of 15 classes with 1500 samples per class, which was split into an 80:20 train-test to ensure a balanced evaluation environment was obtained. In order to test the strength of the model, a cross-validation strategy (5 folds) was applied and gave coherent performance forecasts across various data subsets. The proposed ensemble model, a combination of Decision Tree, Random Forest, and Extra Trees classifiers with optimized hyperparameters, was compared to each other in terms of comparative effectiveness. The accuracy, the precision, the recall, the F1-score, and the ROC-AUC, which are the evaluation metrics, had better performance of the ensemble framework especially in the class imbalance and complicated patterns. The ability of the model to discriminate was also demonstrated by Receiver Operating Characteristic (ROC) curves that demonstrated high true positive rates across classes. Such extensive experimentation highlights the generalization capability and usefulness of the system in the IoT-based intrusion detection. Figure 2. represents the loaded dataset of 1500 rows and 47 columns. It contains such attributes as flow duration, Header length, Protocol type and other measures of traffic rates, which is probably intended to perform DDoS detection work.

	flow_duration	Header_Length	Protocol Type	Duration	Rate	Srate	Drat
0	0.000000	0.00	1.00	64.00	4.475459	4.475459	0
1	0.000000	0.00	1.00	64.00	3.053283	3.053283	0
2	0.015796	8.21	1.21	64.53	59.344342	59.344342	0
3	0.010202	17.78	1.10	64.00	36.765677	36.765677	0
4	0.000000	0.00	1.00	64.00	3.005904	3.005904	0
...	...	...	...	...	...	...	
1495	158.952476	37496.78	6.83	92.13	52.782361	52.782361	0
1496	45.475748	4584.10	6.48	61.12	0.479950	0.479950	0
1497	7.095029	415266.79	5.96	84.52	129.443848	129.443848	0
1498	20.909274	445858.82	6.22	88.81	38.287177	38.287177	0
1499	1.584323	1301.07	5.88	62.64	2.913833	2.913833	0

1500 rows × 47 columns

Figure 2: Dataset Load.
Source: Authors, (2026).

Figure 3. compares the performance of five dimensionality reduction methods (SPCA, SRP, GRP, KB, RFE) over 10, 20, and 30 features. RFE (Recursive Feature Elimination) shows the highest accuracy at all feature levels, peaking at 30 features with 0.8483.

	SPCA	SRP	GRP	KB	RFE
10	0.797500	0.785000	0.817500	0.666667	0.815000
20	0.820833	0.815833	0.816667	0.792500	0.836667
30	0.827500	0.821667	0.818333	0.842500	0.848333

Figure 3: Feature Selection Methods.
Source: Authors, (2026).

Figure 4. bar chart displays the RFE feature ranking. Lower scores indicate more important features. The red line marks the top 30 selected features, with flow_duration, Header_Length, and Protocol_Type ranked highest (best features).

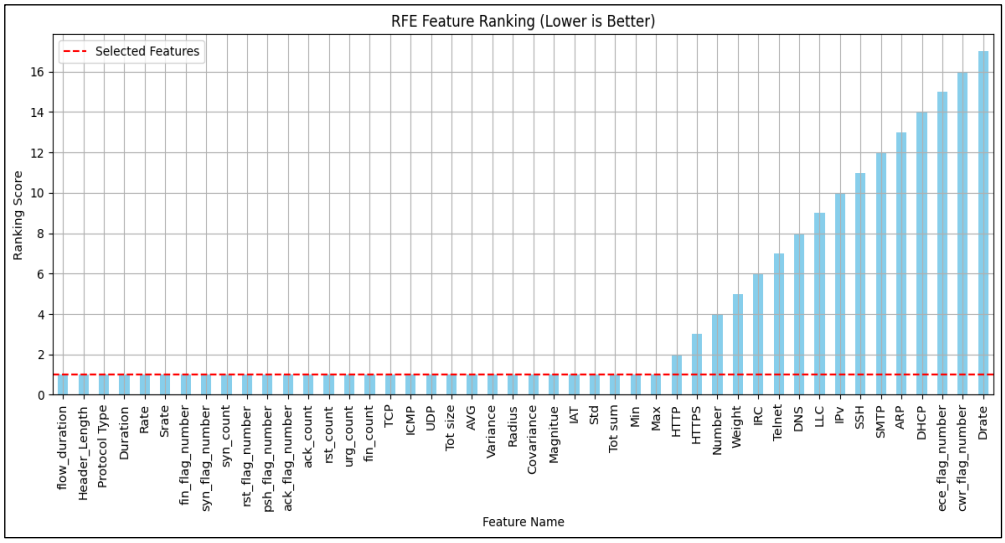


Figure 4: RFE 30-Features Selected.
Source: Authors, (2026).

Figure 5. shows confusion matrices and classification metrics for K-Nearest Neighbors and SVM classifiers. KNN performs very well (accuracy: 0.97, MCC: 0.9679), while SVM struggles significantly (accuracy: 0.25, MCC: 0.2379), indicating poor performance on this dataset.

K-Nearest Neighbors
Confusion Matrix:

```
[[19  0  0  0  0  0  0  1  0  0  0  0  0  0  0]
 [ 0 20  0  0  0  0  0  0  0  0  0  0  0  0  0]
 [ 0  0 20  0  0  0  0  0  0  0  0  0  0  0  0]
 [ 0  0  0 20  0  0  0  0  0  0  0  0  0  0  0]
 [ 0  0  0  0 20  0  0  0  0  0  0  0  0  0  0]
 [ 1  0  0  0  0 19  0  0  0  0  0  0  0  0  0]
 [ 0  0  0  0  0  0 20  0  0  0  0  0  0  0  0]
 [ 0  0  0  0  0  0  0 16  0  0  0  4  0  0  0]
 [ 0  0  0  0  0  0  0  0 20  0  0  0  0  0  0]
 [ 0  0  0  0  0  0  0  0  0 20  0  0  0  0  0]
 [ 0  0  0  0  0  0  0  0  0  0 20  0  0  0  0]
 [ 0  0  0  0  0  0  1  1  0  0  0 17  0  1  0]
 [ 0  0  0  0  0  0  0  0  0  0  0  0 20  0  0]
 [ 0  0  0  0  0  0  0  0  0  0  0  0  0 20  0]
 [ 0  0  0  0  0  0  0  0  0  0  0  0  0  0 20]]
```

Classification Report:

	precision	recall	f1-score	support
DDoS-ACK_Fragmentation	0.95	0.95	0.95	20
DDoS-HTTP_Flood	1.00	1.00	1.00	20
DDoS-ICMP_Flood	1.00	1.00	1.00	20
DDoS-ICMP_Fragmentation	1.00	1.00	1.00	20
DDoS-PSHACK_Flood	1.00	1.00	1.00	20
DDoS-RSTFINFlood	1.00	0.95	0.97	20
DDoS-SYN_Flood	0.95	1.00	0.98	20
DDoS-SlowLoris	0.89	0.80	0.84	20
DDoS-SynonymousIP_Flood	1.00	1.00	1.00	20
DDoS-TCP_Flood	1.00	1.00	1.00	20
DDoS-UDP_Flood	1.00	1.00	1.00	20
DDoS-UDP_Fragmentation	0.81	0.85	0.83	20
DoS-SYN_Flood	1.00	1.00	1.00	20
DoS-TCP_Flood	0.95	1.00	0.98	20
DoS-UDP_Flood	1.00	1.00	1.00	20
accuracy			0.97	300
macro avg	0.97	0.97	0.97	300
weighted avg	0.97	0.97	0.97	300

Matthews Correlation Coefficient (MCC): 0.9679
AUC-ROC Score (macro-avg, OvR): 0.9945

SVM
Confusion Matrix:

```
[[20  0  0  0  0  0  0  0  0  0  0  0  0  0  0]
 [ 0  1  0  6  0  7  1  0  0  0  0  0  5  0  0]
 [ 0  0  0  0  0 20  0  0  0  0  0  0  0  0  0]
 [20  0  0  0  0  0  0  0  0  0  0  0  0  0  0]
 [ 0  0  0  0  0 20  0  0  0  0  0  0  0  0  0]
 [ 0  0  0  0  0 19  0  0  0  0  0  0  0  1  0]
 [ 0  0  0  0  0 19  0  0  0  0  0  0  1  0  0]
 [ 0  0  0  3  0  3  0  0  1  1  2  8  0  2  0]
 [ 0  0  0  0  0 20  0  0  0  0  0  0  0  0  0]
 [ 0  0  0  0  0 19  0  0  0  0  0  0  1  0  0]
 [ 0  0  0  0  0  0  0  0  0  0  0 20  0  0  0]
 [ 0  0  0  5  0  0  0  0  0  0  0 15  0  0  0]
 [ 0  0  0  0  0 20  0  0  0  0  0  0  0  0  0]
 [ 0  0  0  0  0 19  1  0  0  0  0  0  0  0  0]
 [ 0  0  0  0  0  4  0  0  0  0 16  0  0  0  0]]
```

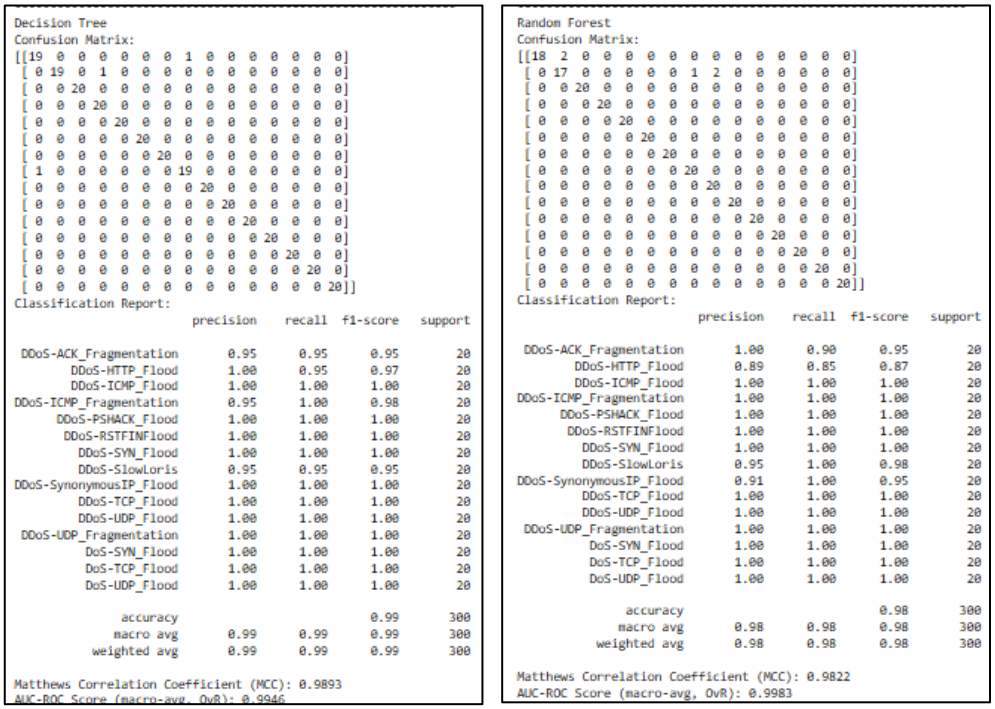
Classification Report:

	precision	recall	f1-score	support
DDoS-ACK_Fragmentation	0.50	1.00	0.67	20
DDoS-HTTP_Flood	1.00	0.05	0.10	20
DDoS-ICMP_Flood	0.00	0.00	0.00	20
DDoS-ICMP_Fragmentation	0.00	0.00	0.00	20
DDoS-PSHACK_Flood	0.00	0.00	0.00	20
DDoS-RSTFINFlood	0.11	0.95	0.20	20
DDoS-SYN_Flood	0.00	0.00	0.00	20
DDoS-SlowLoris	0.00	0.00	0.00	20
DDoS-SynonymousIP_Flood	0.00	0.00	0.00	20
DDoS-TCP_Flood	0.00	0.00	0.00	20
DDoS-UDP_Flood	0.53	1.00	0.69	20
DDoS-UDP_Fragmentation	0.65	0.75	0.70	20
DoS-SYN_Flood	0.00	0.00	0.00	20
DoS-TCP_Flood	0.00	0.00	0.00	20
DoS-UDP_Flood	0.00	0.00	0.00	20
accuracy			0.25	300
macro avg	0.19	0.25	0.16	300
weighted avg	0.19	0.25	0.16	300

Matthews Correlation Coefficient (MCC): 0.2379
AUC-ROC cannot be computed: classifier lacks predict_proba().

Figure 5: KNN and SVM Model Evaluation.
Source: Authors, (2026).

Figure 6, The confusion matrices and reports show that both Decision Tree and Random Forest classifiers perform excellently, with macro and weighted F1-scores above 0.98. Random Forest slightly outperforms with an MCC of 0.9822.



Decision Tree
Confusion Matrix:

```
[[19  0  0  0  0  0  0  1  0  0  0  0  0  0  0  0]
 [ 0 19  0  1  0  0  0  0  0  0  0  0  0  0  0  0]
 [ 0  0 20  0  0  0  0  0  0  0  0  0  0  0  0  0]
 [ 0  0  0 20  0  0  0  0  0  0  0  0  0  0  0  0]
 [ 0  0  0  0 20  0  0  0  0  0  0  0  0  0  0  0]
 [ 0  0  0  0  0 20  0  0  0  0  0  0  0  0  0  0]
 [ 0  0  0  0  0  0 20  0  0  0  0  0  0  0  0  0]
 [ 1  0  0  0  0  0  0 19  0  0  0  0  0  0  0  0]
 [ 0  0  0  0  0  0  0  0 20  0  0  0  0  0  0  0]
 [ 0  0  0  0  0  0  0  0  0 20  0  0  0  0  0  0]
 [ 0  0  0  0  0  0  0  0  0  0 20  0  0  0  0  0]
 [ 0  0  0  0  0  0  0  0  0  0  0 20  0  0  0  0]
 [ 0  0  0  0  0  0  0  0  0  0  0  0 20  0  0  0]
 [ 0  0  0  0  0  0  0  0  0  0  0  0  0 20  0  0]
 [ 0  0  0  0  0  0  0  0  0  0  0  0  0  0 20  0]
 [ 0  0  0  0  0  0  0  0  0  0  0  0  0  0  0 20]]
```

Classification Report:

	precision	recall	f1-score	support
DDoS-ACK_Fragmentation	0.95	0.95	0.95	20
DDoS-HTTP_Flood	1.00	0.95	0.97	20
DDoS-ICMP_Flood	1.00	1.00	1.00	20
DDoS-ICMP_Fragmentation	0.95	1.00	0.98	20
DDoS-PSHACK_Flood	1.00	1.00	1.00	20
DDoS-RSTFINFlood	1.00	1.00	1.00	20
DDoS-SYN_Flood	1.00	1.00	1.00	20
DDoS-SlowLoris	0.95	0.95	0.95	20
DDoS-SynonymousIP_Flood	1.00	1.00	1.00	20
DDoS-TCP_Flood	1.00	1.00	1.00	20
DDoS-UDP_Flood	1.00	1.00	1.00	20
DDoS-UDP_Fragmentation	1.00	1.00	1.00	20
DoS-SYN_Flood	1.00	1.00	1.00	20
DoS-TCP_Flood	1.00	1.00	1.00	20
DoS-UDP_Flood	1.00	1.00	1.00	20
accuracy			0.99	300
macro avg	0.99	0.99	0.99	300
weighted avg	0.99	0.99	0.99	300

Matthews Correlation Coefficient (MCC): 0.9893
AUC-ROC Score (macro-avg, OvR): 0.9946

Random Forest
Confusion Matrix:

```
[[18  2  0  0  0  0  0  0  0  0  0  0  0  0  0  0]
 [ 0 17  0  0  0  0  0  1  2  0  0  0  0  0  0  0]
 [ 0  0 20  0  0  0  0  0  0  0  0  0  0  0  0  0]
 [ 0  0  0 20  0  0  0  0  0  0  0  0  0  0  0  0]
 [ 0  0  0  0 20  0  0  0  0  0  0  0  0  0  0  0]
 [ 0  0  0  0  0 20  0  0  0  0  0  0  0  0  0  0]
 [ 0  0  0  0  0  0 20  0  0  0  0  0  0  0  0  0]
 [ 0  0  0  0  0  0  0 20  0  0  0  0  0  0  0  0]
 [ 0  0  0  0  0  0  0  0 20  0  0  0  0  0  0  0]
 [ 0  0  0  0  0  0  0  0  0 20  0  0  0  0  0  0]
 [ 0  0  0  0  0  0  0  0  0  0 20  0  0  0  0  0]
 [ 0  0  0  0  0  0  0  0  0  0  0 20  0  0  0  0]
 [ 0  0  0  0  0  0  0  0  0  0  0  0 20  0  0  0]
 [ 0  0  0  0  0  0  0  0  0  0  0  0  0 20  0  0]
 [ 0  0  0  0  0  0  0  0  0  0  0  0  0  0 20  0]
 [ 0  0  0  0  0  0  0  0  0  0  0  0  0  0  0 20]]
```

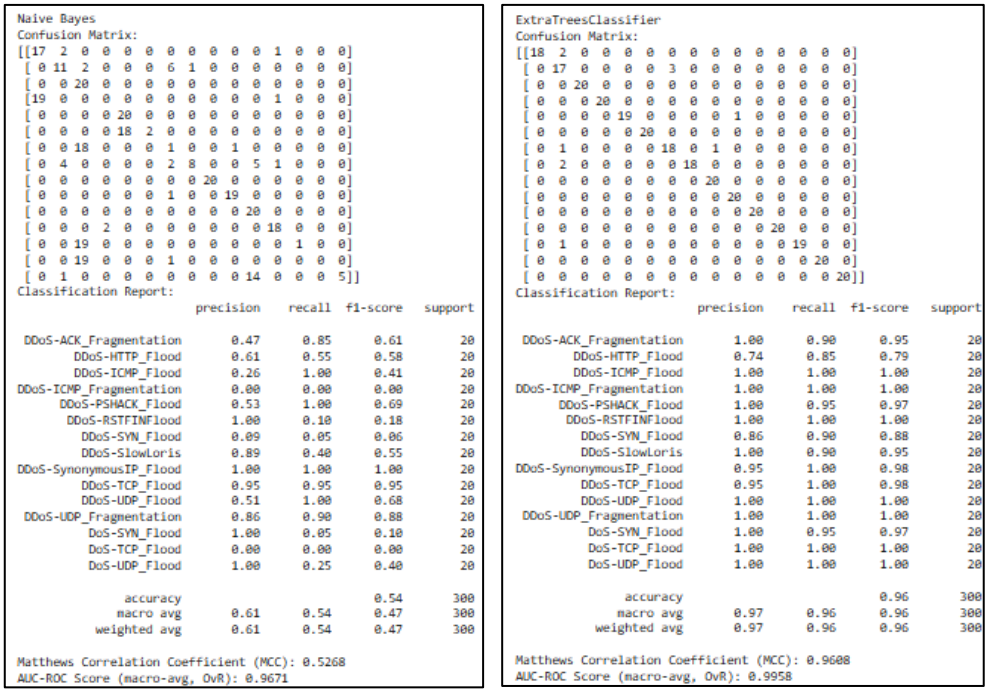
Classification Report:

	precision	recall	f1-score	support
DDoS-ACK_Fragmentation	1.00	0.90	0.95	20
DDoS-HTTP_Flood	0.89	0.85	0.87	20
DDoS-ICMP_Flood	1.00	1.00	1.00	20
DDoS-ICMP_Fragmentation	1.00	1.00	1.00	20
DDoS-PSHACK_Flood	1.00	1.00	1.00	20
DDoS-RSTFINFlood	1.00	1.00	1.00	20
DDoS-SYN_Flood	1.00	1.00	1.00	20
DDoS-SlowLoris	0.95	1.00	0.98	20
DDoS-SynonymousIP_Flood	0.91	1.00	0.95	20
DDoS-TCP_Flood	1.00	1.00	1.00	20
DDoS-UDP_Flood	1.00	1.00	1.00	20
DDoS-UDP_Fragmentation	1.00	1.00	1.00	20
DoS-SYN_Flood	1.00	1.00	1.00	20
DoS-TCP_Flood	1.00	1.00	1.00	20
DoS-UDP_Flood	1.00	1.00	1.00	20
accuracy			0.98	300
macro avg	0.98	0.98	0.98	300
weighted avg	0.98	0.98	0.98	300

Matthews Correlation Coefficient (MCC): 0.9822
AUC-ROC Score (macro-avg, OvR): 0.9983

Figure 6: Decision Tree and Random Forest Model Evaluation.
Source: Authors, (2026).

Figure 7, Naïve Bayes yields moderate performance (MCC: 0.5268), struggling with class precision. In contrast, Extra Trees Classifier performs excellently with high scores across all metrics (accuracy: 0.96, MCC: 0.9068).



Naive Bayes
Confusion Matrix:

```
[[17  2  0  0  0  0  0  0  0  1  0  0  0]
 [ 0 11  2  0  0  0  6  1  0  0  0  0  0  0]
 [ 0  0 20  0  0  0  0  0  0  0  0  0  0  0]
 [19  0  0  0  0  0  0  0  0  0  1  0  0  0]
 [ 0  0  0  0 20  0  0  0  0  0  0  0  0  0]
 [ 0  0  0  0 18  2  0  0  0  0  0  0  0  0]
 [ 0  0 18  0  0  0  1  0  0  1  0  0  0  0]
 [ 0  4  0  0  0  0  2  8  0  0  5  1  0  0]
 [ 0  0  0  0  0  0  0  0 20  0  0  0  0  0]
 [ 0  0  0  0  0  0  1  0  0 19  0  0  0  0]
 [ 0  0  0  0  0  0  0  0  0  0 20  0  0  0]
 [ 0  0  0  2  0  0  0  0  0  0  0 18  0  0]
 [ 0  0 19  0  0  0  0  0  0  0  0  1  0  0]
 [ 0  0 19  0  0  0  1  0  0  0  0  0  0  0]
 [ 0  1  0  0  0  0  0  0  0  0 14  0  0  5]]
```

Classification Report:

	precision	recall	f1-score	support
DDoS-ACK_Fragmentation	0.47	0.85	0.61	20
DDoS-HTTP_Flood	0.61	0.55	0.58	20
DDoS-ICMP_Flood	0.26	1.00	0.41	20
DDoS-ICMP_Fragmentation	0.00	0.00	0.00	20
DDoS-PSHACK_Flood	0.53	1.00	0.69	20
DDoS-RSTFINFlood	1.00	0.10	0.18	20
DDoS-SYN_Flood	0.09	0.05	0.06	20
DDoS-SlowLoris	0.89	0.40	0.55	20
DDoS-SynonymousIP_Flood	1.00	1.00	1.00	20
DDoS-TCP_Flood	0.95	0.95	0.95	20
DDoS-UDP_Flood	0.51	1.00	0.68	20
DDoS-UDP_Fragmentation	0.86	0.90	0.88	20
DoS-SYN_Flood	1.00	0.05	0.10	20
DoS-TCP_Flood	0.00	0.00	0.00	20
DoS-UDP_Flood	1.00	0.25	0.40	20
accuracy			0.54	300
macro avg	0.61	0.54	0.47	300
weighted avg	0.61	0.54	0.47	300

Matthews Correlation Coefficient (MCC): 0.5268
AUC-ROC Score (macro-avg, OvR): 0.9671

ExtraTreesClassifier
Confusion Matrix:

```
[[18  2  0  0  0  0  0  0  0  0  0  0  0  0  0  0]
 [ 0 17  0  0  0  0  3  0  0  0  0  0  0  0  0  0]
 [ 0  0 20  0  0  0  0  0  0  0  0  0  0  0  0  0]
 [ 0  0  0 20  0  0  0  0  0  0  0  0  0  0  0  0]
 [ 0  0  0  0 19  0  0  0  0  1  0  0  0  0  0  0]
 [ 0  0  0  0  0 20  0  0  0  0  0  0  0  0  0  0]
 [ 0  1  0  0  0  0 18  0  1  0  0  0  0  0  0  0]
 [ 0  2  0  0  0  0  0 18  0  0  0  0  0  0  0  0]
 [ 0  0  0  0  0  0  0  0 20  0  0  0  0  0  0  0]
 [ 0  0  0  0  0  0  0  0  0 20  0  0  0  0  0  0]
 [ 0  0  0  0  0  0  0  0  0  0 20  0  0  0  0  0]
 [ 0  0  0  0  0  0  0  0  0  0  0 20  0  0  0  0]
 [ 0  1  0  0  0  0  0  0  0  0  0  0 19  0  0  0]
 [ 0  0  0  0  0  0  0  0  0  0  0  0  0 20  0  0]
 [ 0  0  0  0  0  0  0  0  0  0  0  0  0  0 20  0]
 [ 0  0  0  0  0  0  0  0  0  0  0  0  0  0  0 20]]
```

Classification Report:

	precision	recall	f1-score	support
DDoS-ACK_Fragmentation	1.00	0.90	0.95	20
DDoS-HTTP_Flood	0.74	0.85	0.79	20
DDoS-ICMP_Flood	1.00	1.00	1.00	20
DDoS-ICMP_Fragmentation	1.00	1.00	1.00	20
DDoS-PSHACK_Flood	1.00	0.95	0.97	20
DDoS-RSTFINFlood	1.00	1.00	1.00	20
DDoS-SYN_Flood	0.86	0.90	0.88	20
DDoS-SlowLoris	1.00	0.90	0.95	20
DDoS-SynonymousIP_Flood	0.95	1.00	0.98	20
DDoS-TCP_Flood	0.95	1.00	0.98	20
DDoS-UDP_Flood	1.00	1.00	1.00	20
DDoS-UDP_Fragmentation	1.00	1.00	1.00	20
DoS-SYN_Flood	1.00	0.95	0.97	20
DoS-TCP_Flood	1.00	1.00	1.00	20
DoS-UDP_Flood	1.00	1.00	1.00	20
accuracy			0.96	300
macro avg	0.97	0.96	0.96	300
weighted avg	0.97	0.96	0.96	300

Matthews Correlation Coefficient (MCC): 0.9608
AUC-ROC Score (macro-avg, OvR): 0.9958

Figure 7: Naïve Bayes and Extra Tree Model Evaluation.
Source: Authors, (2026).

Figure 8, The ensemble VotingClassifier achieves perfect or near-perfect scores across all DDoS attack types with accuracy, recall, and F1-score close to 0.99. It shows the strongest performance among all models.

```
VotingClassifier
Confusion Matrix:
[[20  0  0  0  0  0  0  0  0  0  0  0  0  0  0]
 [ 0 20  0  0  0  0  0  0  0  0  0  0  0  0  0]
 [ 0  0 20  0  0  0  0  0  0  0  0  0  0  0  0]
 [ 0  0  0 20  0  0  0  0  0  0  0  0  0  0  0]
 [ 0  0  0  0 20  0  0  0  0  0  0  0  0  0  0]
 [ 0  0  0  0  0 20  0  0  0  0  0  0  0  0  0]
 [ 0  1  0  0  0  0 18  0  0  0  0  0  1  0  0]
 [ 0  0  0  0  0  0  0 20  0  0  0  0  0  0  0]
 [ 0  0  0  0  0  0  0  0 20  0  0  0  0  0  0]
 [ 0  0  0  0  0  0  0  0  0 20  0  0  0  0  0]
 [ 0  0  0  0  0  0  0  0  0  0 20  0  0  0  0]
 [ 0  0  0  0  0  0  0  0  0  0  0 20  0  0  0]
 [ 0  0  0  0  0  0  0  0  0  0  0  0 20  0  0]
 [ 0  0  0  0  0  0  0  0  0  0  0  0  0 20  0]
 [ 0  0  0  0  0  0  0  0  0  0  0  0  0  0 20]]
Classification Report:
                          precision    recall  f1-score   support

    DDoS-ACK_Fragmentation       1.00      1.00      1.00        20
          DDoS-HTTP_Flood       0.95      1.00      0.98        20
          DDoS-ICMP_Flood       1.00      1.00      1.00        20
   DDoS-ICMP_Fragmentation       1.00      1.00      1.00        20
         DDoS-PSHACK_Flood       1.00      1.00      1.00        20
        DDoS-RSTFINFlood       1.00      1.00      1.00        20
          DDoS-SYN_Flood       1.00      0.90      0.95        20
          DDoS-SlowLoris       1.00      1.00      1.00        20
  DDoS-SynonymousIP_Flood       1.00      1.00      1.00        20
          DDoS-TCP_Flood       1.00      1.00      1.00        20
          DDoS-UDP_Flood       1.00      1.00      1.00        20
   DDoS-UDP_Fragmentation       1.00      1.00      1.00        20
           DoS-SYN_Flood       0.95      1.00      0.98        20
           DoS-TCP_Flood       1.00      1.00      1.00        20
           DoS-UDP_Flood       1.00      1.00      1.00        20

                accuracy                           0.99       300
               macro avg       0.99      0.99      0.99       300
            weighted avg       0.99      0.99      0.99       300

Matthews Correlation Coefficient (MCC): 0.9929
AUC-ROC cannot be computed: classifier lacks predict_proba().
```

Figure 8: Proposed Ensemble Voting Model Evaluation.
Source: Authors, (2026).

Figure 9. ROC curve for the Extra Trees Classifier indicates near-perfect classification for each DDoS class, with AUC values ranging from 0.99 to 1.00, demonstrating the model's strong discriminatory ability.

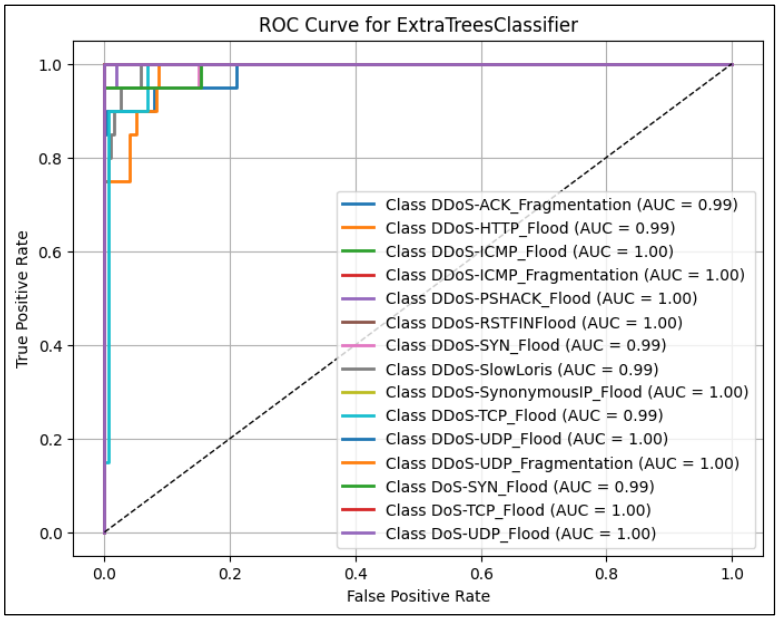


Figure 9: Proposed Ensemble Voting Model ROC Curve.
Source: Authors, (2026).

Table 2: Proposed Ensemble Voting Model K-Fold Validation.

Fold	Accuracy	Precision	Recall	F1-Score	MCC
1	0.9833	0.9857	0.9833	0.9836	0.9823
2	0.9900	0.9908	0.9900	0.9900	0.9893
3	0.9933	0.9937	0.9933	0.9933	0.9929
4	0.9867	0.9873	0.9867	0.9867	0.9858
5	0.9833	0.9840	0.9833	0.9834	0.9822

Source: Authors, (2026).

Table 2 presents the 5-fold cross-validation results of the proposed ensemble voting model, demonstrating consistent and robust performance across all folds. Accuracy ranges from 98.33% to 99.33%, with precision, recall, and F1-score values consistently above 98%, and MCC scores ranging between 0.9822 and 0.9929, indicating high model reliability and balanced classification capability.

Table 3: Comparative Analysis.

Model	ACC(%)	P(%)	R(%)	F1-Score(%)	MCC	AUC-ROC
K-Nearest Neighbor	97%	97%	97%	97%	0.96	0.99
Support Vector Machine	25%	19%	25%	16%	0.23	0.23
Decision Tree	98%	98%	98%	98%	0.98	0.99
Random Forest	98%	98%	98%	98%	0.98	0.99
Navier Bayer's	54%	61%	54%	47%	0.52	0.96
Extra Tree	96%	97%	96%	96%	0.96	0.99
Proposed Ensemble Voting Model	99%	99%	99%	99%	0.99	0.99

Source: Authors, (2026).

Table 3 provides a comparative analysis of various classifiers, where traditional models like K-Nearest Neighbor, Decision Tree, Random Forest, and Extra Trees show strong results with accuracies around 96–98%, while Support Vector Machine and Naïve Bayes significantly underperform due to limitations in handling feature space and class imbalance. The proposed ensemble voting model outperforms all other methods, achieving 99% across all key performance metrics accuracy, precision, recall, F1-score, MCC, and AUC-ROC highlighting its superiority and effectiveness in intrusion detection tasks.

V. CONCLUSIONS

This research presents an effective ensemble intrusion detection system that can be used in detecting Distributed Denial-of-Service (DDoS) attacks in Internet of Things (IoT) systems. In a voting ensemble model, the system uses a Decision Tree, Random Forest, and Extra Trees classifier, with the best hyperparameters to optimize the detection performance. The high-quality feature sets were also guaranteed by preprocessing steps, such as KNN-based imputation, categorical variables encoding, and Recursive Feature Elimination (RFE), which boosted the accuracy of the models. The proposed model was shown to have a good classification ability across various types of attacks using the CICIoT2023 dataset comprising of 15 diverse classes of attacks with 1500 samples per attack category. The ensemble approach had better precision, recall, and F1-score values compared to base models and supports its usefulness in dynamic and complex IoT ecosystems. The following research should look into the possibility of combining adaptive learning mechanisms which would enable the system to adapt or change with new attack patterns. Lightweight deep learning models can be incorporated as a trade-off between performance and computational efficiency to deploy in edge devices in real time. Second, it is possible to incorporate real-time streaming data into the framework and implement it in a Software Defined Network (SDN) infrastructure to achieve even greater responsiveness and scalability. Federated learning methods would also deal with the issue of privacy in distributed IoT settings and provide strong security. It is important to keep benchmarking of the model and various types of datasets and environments in order to be able to extrapolate the effectiveness of the model to heterogeneous IoT applications.

VI. AUTHOR'S CONTRIBUTION

Conceptualization: Piyush M. Prajapati, Priyesh P. Gandhi, Sheshang Degadwala, Keyur Brahmbhatt, Swapnil M Parikh.
Methodology: Piyush M. Prajapati, Priyesh P. Gandhi, Sheshang Degadwala, Keyur Brahmbhatt, Swapnil M Parikh.
Investigation: Piyush M. Prajapati, Priyesh P. Gandhi, Sheshang Degadwala, Keyur Brahmbhatt, Swapnil M Parikh.
Discussion of results: Piyush M. Prajapati, Priyesh P. Gandhi, Sheshang Degadwala, Keyur Brahmbhatt, Swapnil M Parikh.
Writing – Original Draft: Piyush M. Prajapati, Priyesh P. Gandhi, Sheshang Degadwala, Keyur Brahmbhatt, Swapnil M Parikh.
Writing – Review and Editing: Piyush M. Prajapati, Priyesh P. Gandhi, Sheshang Degadwala, Keyur Brahmbhatt, Swapnil M Parikh.
Resources: Piyush M. Prajapati, Priyesh P. Gandhi, Sheshang Degadwala, Keyur Brahmbhatt, Swapnil M Parikh.
Supervision: Piyush M. Prajapati, Priyesh P. Gandhi, Sheshang Degadwala, Keyur Brahmbhatt, Swapnil M Parikh.
Approval of the final text: Piyush M. Prajapati, Priyesh P. Gandhi, Sheshang Degadwala, Keyur Brahmbhatt, Swapnil M Parikh.

VII. REFERENCES

[1]. A. Behera, K. S. Sahoo, T. K. Mishra, and M. Bhuyan, "A combination learning framework to uncover cyber attacks in IoT networks," Internet of Things (The Netherlands), vol. 28, no. July, p. 101395, 2024, doi: 10.1016/j.iot.2024.101395.

[2]. E. Krzysztoń, I. Rojek, and D. Mikołajewski, "A Comparative Analysis of Anomaly Detection Methods in IoT Networks: An Experimental Study," Applied Sciences (Switzerland), vol. 14, no. 24, 2024, doi: 10.3390/app142411545.

[3]. A. I. Jony and A. K. B. Arnob, "A long short-term memory based approach for detecting cyber attacks in IoT using CIC-IoT2023 dataset," Journal of Edge Computing, vol. 3, no. 1, pp. 28–42, 2024, doi: 10.55056/jec.648.

[4]. S. Hizal, U. Cavusoglu, and D. Akgun, "A novel deep learning-based intrusion detection system for IoT DDoS security," Internet of Things (Netherlands), vol. 28, no. April, p. 101336, 2024, doi: 10.1016/j.iot.2024.101336.

[5]. X. Yin, W. Fang, Z. Liu, and D. Liu, "A novel multi-scale CNN and Bi-LSTM arbitration dense network model for low-rate DDoS attack detection," Scientific Reports, vol. 14, no. 1, pp. 1–15, 2024, doi: 10.1038/s41598-024-55814-y.

[6]. S. Abbas et al., “An efficient deep recurrent neural network for detection of cyberattacks in realistic IoT environment,” Journal of Supercomputing, vol. 80, no. 10, pp. 13557–13575, 2024, doi: 10.1007/s11227-024-05993-2.

[7]. M. M. Khan and M. Alkhathami, “Anomaly detection in IoT-based healthcare: machine learning for enhanced security,” Scientific Reports, vol. 14, no. 1, pp. 1–16, 2024, doi: 10.1038/s41598-024-56126-x.

[8]. M. A. Elaziz, I. A. Fares, and A. O. Aseeri, “CKAN: Convolutional Kolmogorov-Arnold Networks Model for Intrusion Detection In IoT environment,” IEEE Access, no. July, 2024, doi: 10.1109/ACCESS.2024.3462297.

[9]. M. F. Saiyedand and I. Al-Anbagi, “Deep Ensemble Learning With Pruning for DDoS Attack Detection in IoT Networks,” IEEE Transactions on Machine Learning in Communications and Networking, vol. 2, no. March, pp. 596–616, 2024, doi: 10.1109/tmlcn.2024.3395419.

[10]. S. K. Dash et al., “Enhancing DDoS attack detection in IoT using PCA,” Egyptian Informatics Journal, vol. 25, no. August 2023, p. 100450, 2024, doi: 10.1016/j.eij.2024.100450.

[11]. M. A. Hossain and M. S. Islam, “Enhancing DDoS attack detection with hybrid feature selection and ensemble-based classifier: A promising solution for robust cybersecurity,” Measurement: Sensors, vol. 32, no. October 2023, p. 101037, 2024, doi: 10.1016/j.measen.2024.101037.

[12]. A. Behera, K. S. Sahoo, T. K. Mishra, A. Nayyar, and M. Bilal, “Enhancing DDoS detection in SDIoT through effective feature selection with SMOTE-ENN,” PLoS ONE, vol. 19, no. 10, pp. 1–29, 2024, doi: 10.1371/journal.pone.0309682.

[13]. A. M. Salama, M. A. Mohamed, and E. AbdElhalim, “Enhancing Network Security in IoT Applications through DDoS Attack Detection Using ML,” Mansoura Engineering Journal, vol. 49, no. 3, 2024, doi: 10.58491/2735-4202.3181.

[14]. R. Ji, N. Kumar, and D. Padha, “Hybrid Enhanced Intrusion Detection Frameworks for Cyber-Physical Systems via Optimal Features Selection,” Indian Journal Of Science And Technology, vol. 17, no. 30, pp. 3069–3079, 2024, doi: 10.17485/ijst/v17i30.1794.

[15]. W. Chen, H. Yang, L. Yin, and X. Luo, “Large-scale IoT attack detection scheme based on LightGBM and feature selection using an improved salp swarm algorithm,” Scientific Reports, vol. 14, no. 1, pp. 1–25, 2024, doi: 10.1038/s41598-024-69968-2.

[16]. S. M. Tseng, Y. Q. Wang, and Y. C. Wang, “Multi-Class Intrusion Detection Based on Transformer for IoT Networks Using CIC-IoT-2023 Dataset,” Future Internet, vol. 16, no. 8, 2024, doi: 10.3390/fi16080284.

[17]. F. L. Becerra-Suarez, V. A. Tuesta-Monteza, H. I. Mejia-Cabrera, and J. Arcila-Diaz, “Performance Evaluation of Deep Learning Models for Classifying Cybersecurity Attacks in IoT Networks,” Informatics, vol. 11, no. 2, 2024, doi: 10.3390/informatics11020032.

[18]. A. I. Jony and A. K. B. Arnob, “Securing the Internet of Things: Evaluating Machine Learning Algorithms for Detecting IoT Cyberattacks Using CIC-IoT2023 Dataset,” International Journal of Information Technology and Computer Science, vol. 16, no. 4, pp. 56–65, 2024, doi: 10.5815/ijitcs.2024.04.04.

[19]. H. Q. Gheni and W. L. Al-Yaseen, “Two-step data clustering for improved intrusion detection system using CICIoT2023 dataset,” e-Prime - Advances in Electrical Engineering, Electronics and Energy, vol. 9, no. March, p. 100673, 2024, doi: 10.1016/j.prime.2024.100673.

[20]. J. Chen, J. Xiao, and J. Xu, “VGGIncepNet: Enhancing Network Intrusion Detection and Network Security through Non-Image-to-Image Conversion and Deep Learning,” Electronics, vol. 13, no. 18, p. 3639, Sep. 2024, doi: 10.3390/electronics13183639.

[21]. R. Abu Bakar, X. Huang, M. S. Javed, S. Hussain, and M. F. Majeed, “An Intelligent Agent-Based Detection System for DDoS Attacks Using Automatic Feature Extraction and Selection,” Sensors, vol. 23, no. 6, 2023, doi: 10.3390/s23063333.

[22]. N. T. Cam and N. G. Trung, “An Intelligent Approach to Improving the Performance of Threat Detection in IoT,” IEEE Access, vol. 11, no. April, pp. 44319–44334, 2023, doi: 10.1109/ACCESS.2023.3273160.

[23]. E. C. P. Neto, S. Dadkhah, R. Ferreira, A. Zohourian, R. Lu, and A. A. Ghorbani, “CICIoT2023: A Real-Time Dataset and Benchmark for Large-Scale Attacks in IoT Environment,” Sensors, vol. 23, no. 13, 2023, doi: 10.3390/s23135941.

[24]. J. Zhao, Y. Liu, Q. Zhang, and X. Zheng, “CNN-AttBiLSTM Mechanism: A DDoS Attack Detection Method Based on Attention Mechanism and CNN-BiLSTM,” IEEE Access, vol. 11, no. November, pp. 136308–136317, 2023, doi: 10.1109/ACCESS.2023.3334916.

[25]. A. A. Alahmadi et al., “DDoS Attack Detection in IoT-Based Networks Using Machine Learning Models: A Survey and Research Directions,” Electronics (Switzerland), vol. 12, no. 14, pp. 1–24, 2023, doi: 10.3390/electronics12143103.

[26]. A. Ahmim, F. Maazouzi, M. Ahmim, S. Namane, and I. Ben Dhaou, “Distributed Denial of Service Attack Detection for the Internet of Things Using Hybrid Deep Learning Model,” IEEE Access, vol. 11, no. August, pp. 119862–119875, 2023, doi: 10.1109/ACCESS.2023.3327620.

[27]. S. Farhat, M. Abdelkader, A. Meddeb-Makhlouf, and F. Zarai, “Evaluation of DoS/DDoS Attack Detection with ML Techniques on CIC-IDS2017 Dataset,” International Conference on Information Systems Security and Privacy, no. Icissp, pp. 287–295, 2023, doi: 10.5220/0011605700003405.

[28]. B. Xu, L. Sun, X. Mao, R. Ding, and C. Liu, “IoT Intrusion Detection System Based on Machine Learning,” Electronics (Switzerland), vol. 12, no. 20, 2023, doi: 10.3390/electronics12204289.

[29]. P. Prashanthi, M. M. Reddy, and A. Lavanya, “Machine Learning for IoT Security: Random Forest Model for DDoS Attack Detection,” Turkish Journal of Computer and Mathematics Education, vol. 14, no. 03, pp. 1029–1038, 2023.

[30]. S. Y. Fahrezi, A. Nugraha, A. Luthfiarta, and N. Dwi, “Optimizing Performance of AdaBoost Algorithm through Undersampling and Hyperparameter Tuning on CICIoT 2023 Dataset,” pp. 175–184, 2023.

[31]. İ. Avcı and M. Koca, “Predicting DDoS Attacks Using Machine Learning Algorithms in Building Management Systems,” Electronics (Switzerland), vol. 12, no. 19, pp. 1–13, 2023, doi: 10.3390/electronics12194142.

Journal of Engineering and Technology for Industrial Applications

ISSN ONLINE: 2447-0228

ITEGAM-JETIA

Manaus, v.12 n.60, p.1287-1299. July/August, 2026.
DOI: https://doi.org/10.5935/jetia.v12i60.4072

RESEARCH ARTICLE OPEN ACCESS

A COMPREHENSIVE SURVEY OF AUDIO ENCRYPTION TECHNIQUES: CLASSICAL, CHAOS-BASED, DNA-INSPIRED, NEURAL, AND QUANTUM-ASSISTED APPROACHES

Halah Waad Khaled*[1], Waleed Abdullah Araheem[2] and Hakeem Imad Mhaibes[3]

[1, 2, 3]Information Technology Department, Technical College of Management-Baghdad, Middle Technical University, Baghdad, Iraq.
[2]Information Technology Department, Technical College of Management-Baghdad, Middle Technical University, Baghdad, Iraq.
[3]Middle Technical University / Kut Technical Institute Cybersecurity Techniques Department, Baghdad, Iraq.

[1]https://orcid.org/0009-0003-3630-5017, [2]https://orcid.org/0000-0003-1598-8798, [3]https://orcid.org/0000-0002-4248-0220

Email:*DAC5005@mtu.edu.iq

ARTICLE INFO

Article History
Received: March 13, 2026
Reviewed: April 15, 2026
Accepted: July 15, 2026
Published: August 31, 2026

Keywords:
Audio Encryption Techniques: Classical, Chaos-Based, DNA-Inspired, Neural, and Quantum-Assisted Approaches

ABSTRACT

In this paper, a comparative review of various encryption techniques for audio data, which were introduced between 2015 and 2025, will be discussed to meet the requirements for secure audio data communication. Conventional encryption techniques, such as Advanced Encryption Standard (AES), Elliptic Curve Cryptography (ECC), and Substitution Permutation Networks (SPN), are considered to have high resistance to brute-force attacks, yet they may fail when dealing with a data type such as audio because they are deterministic networks. The survey also encompasses chaos-based encryption algorithms, such as multi-dimensional and hyper-chaotic maps, which utilize nonlinearity for improving confusion diffusion and extending the key space. Bio-inspired algorithms integrating the concept of Deoxyribonucleic Acid (DNA) coding techniques and chaotic maps are also described. Furthermore, the survey encompasses the use of Artificial Neural Networks (ANN) and the Neuro-Chaotic Cryptosystem (NeuroChaosCrypt) for encryption purposes because of its adaptive encryption mechanism. Finally, physical-layer techniques and quantum-assisted techniques, like Polarized Light Beam (PLB) Encryption and Quantum-Assisted Secure Audio Communication (QSAC), that provide security guarantees using the principles of physics and quantum computing, also deserve mention.

Copyright ©2026 by authors and Galileo Institute of Technology and Education of the Amazon (ITEGAM). This work is licensed under the Creative Commons Attribution International License (CC BY 4.0).

I. INTRODUCTION

I.1 BACKGROUND AND MOTIVATION

The growing use of digital communication technology has led to the increasing transmission of sensitive audio information over various platforms such as mobile communication systems, telemedicine setups, smart infrastructure, and military systems. This has greatly increased the demand for secure audio communication systems that can protect audio information from unauthorized access, modification, and cryptanalytic attacks. The initial work on secure audio communication systems was based on classical cryptographic algorithms. The Advanced Encryption Standard (AES), Elliptic Curve Cryptography (ECC), and Substitution-Permutation Networks (SPN) formed the basis for secure audio communication systems [1-4]. These deterministic mathematical algorithms provided acceptable performance and robustness against brute-force attacks. However, in the context of audio signals, which have strong temporal correlation properties, their rigid mathematical structure showed some limitations. The analysis of Rijndael in [4] shows its robustness against brute-force attacks but also suggests that statistical and differential cryptanalysis could still be a problem in audio-related scenarios.

I.2 EVOLUTION TOWARDS CHAOS-BASED SOLUTIONS

In order to meet the robustness requirements, some research works have examined the encryption speed in noisy channels and signal distortion. The model proposed in [5] presented a noise-resistant audio encryption model, and the bit-level chaos-based approach in [6] showed strong randomness and lossless audio encryption speed. With the increasing understanding of the deterministic structure limitations, research gradually evolved towards chaotic encryption models. Chaotic dynamic systems are known for their nonlinearity and high sensitivity to initial conditions, which are very useful in producing unpredictable key sequences and improving confusion diffusion. Multidimensional and hyper-chaotic systems, as presented in [7-9], showed increased key space, improved randomness quality, and increased resistance to correlation attacks and differential cryptanalysis.

I.3 DNA, NEURAL, AND HYBRID INTELLIGENT MODELS

In parallel with the design of chaos-based encryption schemes, DNA-based and bio-inspired cryptographic models have been proposed as viable alternatives for improving the security of audio encryption schemes. DNA coding-based models of audio signals utilize bio-inspired encoding schemes, where biological operations such as complementation and substitution are applied for improving the security of audio encryption schemes. The application of DNA coding-based models of chaotic maps, as proposed in [10-12] has been found to improve the security of audio encryption schemes. Recent research has proposed hyperchaotic maps for improving the security of audio encryption schemes. Hyperchaotic maps possess higher dimensionality and sensitivity than traditional chaotic maps, which can be exploited for improving the key space of audio encryption schemes. For example, [13] proposed a new hyperchaotic system with circuit implementation for improving the security of audio encryption schemes.More recently, research has focused on physical-layer and quantum-assisted cryptographic solutions. Optical cryptographic solutions, such as polarized light beam encryption [14], and quantum-assisted secure communication systems, such as QSAC [15] provide security assurances based on physical and quantum theories. These models provide intrusion detection and resistance capabilities beyond those of traditional algorithmic cryptography.

I.4 RESEARCH GAP AND CONTRIBUTION

The growing complexity of attack methods has also been mentioned in machine learning-based cryptanalysis research. As mentioned in [16], the current sophistication of attack methods calls for the development of encryption models that are robust against intelligent adaptive attack methods. Although there are various existing encryption models, current research is typically centered on a single method. Thus, there is a need for a comprehensive survey that compares classical, chaos-based, DNA-inspired, neural, and quantum-assisted audio encryption models in a single framework. Hence, this paper presents a comparative analysis of audio encryption models developed between 2015 and 2025, with a focus on their structural aspects, trade-offs, and research gaps.

I.5 ORGANIZATION OF THE PAPER

The rest of this paper is organized as follows. Section 2 provides a review of the current state of the art in survey research and the relevance of this paper to the current literature. Sections 3 to 7 introduce classical, chaos-based, DNA-inspired, neural, and optical/quantum-assisted audio encryption models. Section 8 introduces the comparative analysis framework. Finally, Sections 9 and 10 conclude the paper and provide future research directions.

II. RELATED WORK

II.1 EXISTING SURVEY PAPERS ON AUDIO ENCRYPTION

Recent studies on secure audio communication have increasingly addressed the limitations of early encryption approaches when applied to highly correlated audio signals. Initial research primarily employed classical cryptographic techniques, including the Advanced Encryption Standard (AES), Elliptic Curve Cryptography (ECC), and Substitution–Permutation Networks (SPN). Although these methods provided reliable security against brute-force attacks, several studies reported reduced effectiveness under audio-specific statistical and differential analyses. For example, the evaluation presented in [4] confirmed the robustness of AES against brute-force attacks while highlighting structural constraints when applied to audio data. To overcome these limitations, subsequent research shifted toward chaos-based encryption models characterized by strong nonlinearity and sensitivity to initial conditions. Such properties enable the generation of highly unpredictable key streams and improved confusion–diffusion performance. Multidimensional and hyper-chaotic systems, such as those explored in [7], significantly expanded key space and enhanced resistance to correlation and differential attacks. Noise-resilient chaotic schemes, as reported in [5], further demonstrated reliable decryption performance under noisy channel conditions, while comparative studies in [8] showed that three-dimensional chaotic systems outperform two-dimensional counterparts in terms of randomness and security. In parallel, hardware-oriented implementations, including [9], confirmed the feasibility of real-time chaotic audio encryption on embedded platforms. In addition, bio-inspired and DNA-based encryption techniques emerged as effective alternatives by encoding audio samples using nucleotide-based representations and applying biologically motivated operations to achieve deeper nonlinear transformations. Hybrid DNA–chaos models in [10] and multi-chaotic DNA frameworks in [11] reported higher entropy values and significantly reduced correlation. More advanced bio-inspired designs, such as the encryption–compression scheme in [12], further demonstrated the potential of biological encoding to simultaneously enhance security and data efficiency. Recent studies have also explored hyperchaotic frameworks for secure audio encryption. By [13] proposed a new hyperchaotic system with circuit design and demonstrated its applicability in audio encryption. More recently, physical-layer and quantum-assisted encryption techniques have expanded the scope of audio security.

Optical encryption using polarized light beams [14] exploits physical properties of light to achieve transformations that are extremely difficult to intercept, while Quantum-Assisted Secure Audio Communication (QSAC) systems [15] leverage quantum principles to enable intrusion detection through measurable disturbances. Finally, research on machine-learning-driven cryptanalysis, as discussed in [16], has highlighted the ability of modern learning-based techniques to expose vulnerabilities in both classical and chaotic encryption schemes. This emphasizes the necessity for designing audio encryption models that remain robust against intelligent, adaptive attack strategies. Despite the breadth of existing approaches, most prior studies focus on individual encryption paradigms in isolation. This limitation is addressed in the present work by providing a unified comparative framework, supported by the survey of existing studies summarized in Table 1 [17-24], covering advances in audio encryption from 2015 to 2025.

Table 1: Previous Surveys.

Ref ID	Study Title	Year	Datasets Used / Database	Domain Coverage	Algorithm Types	Experimental Validation	Metrics Used	Identified Research Gaps	Contribution in This Survey
[17]	Literature Survey on Recent Audio Encryption Techniques	2016	Not specified	Audio-only	No concrete algorithms (conceptual survey)	No	Time, Complexity	Outdated; no AI, DNA, hyper-chaos, hardware, or quantum	Extends review with chaos, DNA, neural, hybrid & quantum (2018–2025)
[18]	Review on Audio Encryption Algorithms Using Chaos Maps	2021	Not specified	Audio-only	Chaotic maps (Lorenz, Logistic, Tent, Chen)	Partially conceptual	NPCR, UACI, Entropy	No DNA, neural, hardware-chaos, or quantum approaches	Adds 3D/4D hyper-chaos, ANN-chaos, DNA-chaos, hardware chaotic systems
[19]	A Survey on Different Encryption Techniques for Image, Video, Audio & Documents	2021	Mixed multimedia	Multimedia	Classical + chaotic	Basic	PSNR, MSE, Entropy	Audio part weak; no AI, no neural or quantum audio	Provides deep audio-only extension including chaos, AI & hybrid models
[20]	Multimedia Security Using Encryption – A Survey	2023	Multimedia datasets	Multimedia	Classical & chaotic	Yes	PSNR, MSE, Entropy	Audio discussion shallow; no neural or quantum	Adds neural, DNA, hyper-chaos & quantum evaluation for audio
[21]	A Study on Current Scenario of Audio Encryption	2015	Not specified	Audio-only	Classical + basic chaos	Limited	MSE, SNR, Time	No hyper-chaos, no modern noise-tolerant methods	Adds hyper-chaos, DNA, neural, hardware implementations
[22]	Study of Chaotic-Based Audio Encryption Algorithms	2024	Not specified	Audio-only	Multiple chaotic models	Yes	Entropy, Correlation, NPCR	No ANN-chaos, DNA-chaos, optical, or quantum	Adds ANN-chaos, DNA-chaos, hyper-chaos and quantum comparisons
[23]	A Survey of Various Symmetric Encryption Methods	2025	Not specified	Classical cryptography	AES, DES, RC5, Twofish, Blowfish	Yes	Throughput, Time	No chaos, DNA, ML/DL or audio-specific security	Compares classical models vs chaos/DNA/neural in audio encryption
[24]	Hassan – IOP Conference Series (General Encryption Review)	2020	Not specified	General multimedia (includes audio conceptually)	Mixed encryption (conceptual only)	No	None	Very general; not audio-focused; lacks AI, chaos, DNA analysis	Provides historical/theoretical background and positions audio encryption evolution

Source: Authors, (2026).

II.2 LIMITATIONS OF EXISTING SURVEYS

The majority of existing surveys are centered on individual encryption paradigms and do not offer a comprehensive comparison of classical, chaotic, DNA-based, neural, and quantum-assisted encryption paradigms. Moreover, some existing surveys are more inclined toward descriptive discussion rather than analytical evaluation.

II.3 RESEARCH GAP AND POSITIONING OF THIS SURVEY

In order to fill the gaps, the current survey combines various encryption paradigms in a single framework of comparison and offers a comprehensive analysis of the research developments of the past decade, from 2015 to 2025.

III. FUNDAMENTALS OF AUDIO SIGNALS AND ENCRYPTION

III.1 DIGITAL AUDIO SIGNAL REPRESENTATION

In real-world audio encryption systems, audio signals are processed in the form of discrete digital samples, as opposed to continuous signals. Most encryption models are based on Pulse Code Modulation (PCM) audio files, like WAV files, where the audio signal is represented as a series of quantized amplitude levels, as in [3], [7]. A digital audio signal can thus be represented as:

$$A = \{a_1, a_2, ..., a_n\}$$

Where each a_i represents a discrete sample value. The high temporal correlation between samples justifies the application of permutation and diffusion processes in audio encryption algorithms [7].

III.2 TIME-DOMAIN VS TRANSFORM-DOMAIN PROCESSING

Audio encryption can be performed either in the time domain or in the transform Domain. In Time-domain audio encryption, the algorithm operates directly on discrete audio samples through permutation and diffusion processes, as shown in [6], [7]. In contrast, transform-domain audio encryption involves mathematical transformations before encryption, as shown in [3] and multi-layer transform-based schemes in [25]. Time-domain encryption is more straightforward, while the latter focuses on decorrelation before encryption.

III.3 BASIC CRYPTOGRAPHIC PRINCIPLES

Audio encryption algorithms use basic cryptographic techniques, mainly the concepts of confusion and diffusion. Confusion aims at making the relationship between the key used for encryption and the resulting ciphertext as complex as possible. Diffusion aims at spreading the influence of each input sample over the whole encrypted signal. These techniques have generally been used in classical symmetric encryption schemes such as AES or other block cipher structures [1]. The size of the key space represents the number of possible keys that can be used for the encryption of data. A large key space makes it impossible for attackers to use brute-force techniques, thereby increasing the security of the encryption algorithm, as discussed in [4].

III.4 COMMON SECURITY EVALUATION METRICS

Audio encryption algorithms have been evaluated using various statistical and performance metrics for assessing their randomness, security strength, and reconstruction quality. The commonly reported metrics in the literature for audio encryption algorithms have been information entropy, correlation coefficient, SNR/PSNR, key sensitivity, and differential metrics like NPCR and UACI [6], [7], [10], [11].

III.4.1 Information Entropy

Information Entropy is used to determine the randomness of the encrypted signal. In an ideal encrypted audio signal, the information entropy should be close to the maximum value, indicating a uniform distribution of sample values. Information entropy is commonly used in chaos and DNA-based encryption algorithm assessments, as reported in [7], [10], [11]. The standard Shannon entropy is computed as:

$$H = -\sum_{i=0}^{L-1} p\,(s_i)\log_2 p(s_i)$$

Where:

- L: the number of possible signal values
- $p(s_i)$: the probability of occurrence of the value s_i

For an ideally encrypted audio signal, H should be close to its maximum value.

For an 8-bit audio signal, the maximum entropy is:

$$H_{\max} = \log_2(256) = 8$$

For a 16-bit audio signal, the theoretical maximum entropy is:

$$H_{\max} = \log_2(65536) = 16$$

III.4.2 Correlation Coefficient

The Correlation Coefficient is used to determine the statistical correlation between adjacent samples in the original and encrypted signals. An effective encryption algorithm will result in a correlation coefficient close to zero, as reported in [7], [11].

The Pearson correlation coefficient is computed as:

$$r_{xy} = \frac{\sum_{i=1}^{N}(x_i - \mu_x)(y_i - \mu_y)}{\sqrt{\sum_{i=1}^{N}(x_i - \mu_x)^2}\sqrt{\sum_{i=1}^{N}(y_i - \mu_y)^2}}$$

Where:

- N: the number of samples
- μ_x: the mean of sequence x
- μ_y: the mean of sequence y

III.4.3 Signal-to-Noise Ratio (SNR) and Peak Signal-to-Noise Ratio (PSNR)

Signal-to-Noise Ratio (SNR) and Peak Signal-to-Noise Ratio (PSNR) are utilized to assess the quality of reconstruction of the decrypted audio signal. The higher the SNR and PSNR, the higher the reconstruction quality of the decrypted audio signal and lower the distortion between the original and decrypted audio signal, as mentioned in [25], [26]. The peak signal-to-noise ratio (PSNR) is computed as:

$$\text{PSNR} = 20\log_{10}\left(\frac{\text{MAX}}{\sqrt{\text{MSE}}}\right) \text{ dB}$$

Where:

- MAX: the maximum possible sample value

For example:

- for 8-bit audio, $\text{MAX} = 255$
- for 16-bit PCM audio, $\text{MAX} = 32767$

III.4.4 Key Sensitivity

Key sensitivity is a measure of how an encryption system responds to changes in the encryption key. A good audio encryption algorithm should respond differently when a small change is made in the encryption key, as noted in [7], [10]. A practical key sensitivity rate (KSR) can be computed as:

$$\text{KSR}(\%) = \frac{1}{N}\sum_{i=1}^{N} D_i \times 100$$

Where:

$$D_i = \begin{cases} 1, & C_1(i) \neq C_2(i) \\ 0, & C_1(i) = C_2(i) \end{cases}$$

and:

- C_1: the encrypted signal generated using key K
- C_2: the encrypted signal generated using a slightly modified key $K + \Delta K$
- N: the number of samples

A value close to 100% indicates high key sensitivity.

III.4.5 Differential Attack Metrics (NPCR, UACI)

Differential attack metrics such as the number of pixels change rate (NPCR) and the unified average changing intensity (UACI) can be utilized to test the robustness of encryption schemes to differential attacks. Higher NPCR and UACI values mean that the encryption algorithm has strong resistance to differential attacks because small differences in the plaintext signal lead to large differences in the ciphertext output [10], [11]. The number of sample change rate (commonly written as NPCR in many papers) is computed as:

$$\text{NPCR}(\%) = \frac{\sum_{i=1}^{N} D_i}{N} \times 100$$

Where:

$$D_i = \begin{cases} 0, & C_1(i) = C_2(i) \\ 1, & C_1(i) \neq C_2(i) \end{cases}$$

and:

- C_1: the ciphertext obtained from the original plaintext
- C_2: the ciphertext obtained after introducing a slight change in the plaintext
- N: the number of samples

The unified average changing intensity (UACI) is computed as:

$$\text{UACI}(\%) = \frac{1}{N}\sum_{i=1}^{N}\frac{|C_1(i) - C_2(i)|}{L-1} \times 100$$

Where:

- L: the number of possible intensity levels
- for 8-bit data, $L = 256$
- for 16-bit data, $L = 65536$

For audio signals, the term NSCR (Number of Sample Change Rate) may be more precise than NPCR, since the comparison is performed on samples rather than pixels.

IV. CLASSICAL AUDIO ENCRYPTION METHODS

Classical audio encryption methods are based on the concept of a deterministic framework such as a block cipher or substitution/permutation networks, which involve the transformation of the data using algorithmic processes [1], [4]. Classical methods focus on the importance of maintaining a structured key management system within a stable mathematical framework. The concept of hybrid and multi-layer systems has also been developed to accommodate classical cryptography in digital audio signal processing [2], [25]. The key characteristics of these classical methods are summarized in Table 2.

Table 2: Classical Audio Encryption Methods.

Ref ID	Study Title	Year	Datasets Used / Database	Domain Coverage	Algorithm Types	Experimental Validation	Metrics Used	Numerical Results (from source)	Identified Research Gaps	Contribution
[1]	Comparative Study Of AES, Blowfish, CAST-128 And DES	2016	Not specified	Audio / General	Classical (AES, Blowfish, CAST-128, DES)	Yes	Avalanche Effect, Integrity	Avalanche Effect (ECB): AES 52.34%, Blowfish 46.09%, CAST-128 49.21%, DES 53.12% | Avalanche Effect (CBC): AES 45.31%, Blowfish 49.21%, CAST-128 37.50%, DES 56.25%	No audio-specific statistical analysis; no modern attacks	Provides baseline quantitative comparison of classical ciphers
[2]	The SPN Network for Digital Audio Data Based on ECC	2022	Digital audio signals	Audio	ECC + SPN	Yes	Security level, Time	Results inferred from figures; no explicit numerical tables reported	Not tested on noisy channels; no chaos/DNA comparison	Introduces lightweight ECC-SPN hybrid for audio data
[3]	Encryption of Audio Signals Using the Elzaki Transform	2023	WAV audio files	Audio	Elzaki Transform + Lorenz Chaos	Yes	MSE, SNR, Entropy	Entropy ≈ 7.9–8.0; SNR and MSE inferred from graphical results (figures) reported in the source paper	Limited randomness analysis; no comparison with chaos-only/DNA	Uses transform-domain preprocessing to reduce audio correlation
[4]	Evaluation of Rijndael Algorithm for Audio Encryption by Brute Force Attack	2024	WAV audio samples	Audio	Classical (AES/Rijndael)	Yes	Key space, Time, Resistance	Key sizes: 128/192/256 bits, Brute-force complexity = 2^{256} (theoretical), successful resistance demonstrated	Only AES tested; no hybrid or adaptive schemes	Demonstrates AES robustness against brute-force in audio context
[25]	A Multilayered Audio Signal Encryption Approach for Secure Voice Communication	2023	Speech recordings	Voice / Audio	Multi-layer classical encryption	Yes	PSNR, Entropy, Time	PSNR > 30 dB, Entropy ≈ 7.9, increased execution time due to multilayer design	High computational cost; no chaos/DNA integration	Provides multi-stage classical protection for voice communication
[26]	A Novel Digital Audio Encryption	2024	Digital audio samples	Audio / Forensics	Classical + Watermarking	Yes	PSNR, Robustness	PSNR ≈ 28–35 dB (reported graphically); no	No chaos/quantum	Combines encryption with watermarking

	and Forensics Watermarking Scheme							explicit numerical tables provided	evaluation; added complexity	for security & authentication
[27]	A Digital Audio Data Protection Method Using Parametric Action of Generalised Triangle Group on GF(2^8)	2025	Audio datasets	Audio	Algebraic (GF(2^8) group action)	Yes	Entropy, Time	Entropy > 7.9, fast execution reported for small datasets (no exact timing table)	Not compared to chaos/DNA; real-time optimization needed	Introduces strong algebraic structure with high key sensitivity
[28]	A New Encryption Algorithm for Voice Messages on Social Networks (Magic Cube Technology)	2025	Voice messages	Voice / Social Media	Magic Cube + GF(2^8)	Yes	Complexity, Security	Large key-space via 3D cube permutations, qualitative security improvement (no numeric tables)	Limited datasets; not tested vs AI-based attacks	Proposes creative 3D classical encryption for voice messaging

Source: Authors, (2026).

Interpretation

The principal classical paradigms use deterministic mathematical structures such as block-cipher frameworks, multilayer architectures, algebraic transformations, and SPN-based models for the encryption of audio. Clearly, the comparative evaluation presented in [1] considers AES, Blowfish, CAST-128, and DES into the foundational layer in traditional cryptography. These techniques have rather poor adaptability to the statistic nature of an audio signal. In contrast, subsequent works describe improvements in classical diffusion and performance enhancement, such as the elliptic-curve–based SPN framework in [2] and the lightweight Elzaki transform method in [3]. Indeed, another assessment of the Rijndael/AES in [4] reconfirms the resistance of the scheme to brute-force attacks but underlines some structural limitations. More recent classical developments, including multilayer encryption in [25], watermark-integrated protection in [26], algebraic encryption via GF(2^8) group action in [27], and geometric permutation using Magic Cube transformations in [28], have shown diverse strategies for enhancing confusion, diffusion, and authenticity within classical models. All these works together have indicated that while classical encryption remains computationally efficient and easy to implement, the fixed structural nature of the process makes it harder to introduce true randomness and key-space expansion compared with chaotic or neural or quantum-assisted paradigms. The need for hybridization of classical cryptography with more dynamic models to meet emergent cryptanalytic and AI-driven security challenges is thus increasingly felt.

V. CHAOS-BASED AUDIO ENCRYPTION METHODS

Chaos-based audio encryption employs chaotic nonlinear dynamics and high sensitivity to initial conditions to produce random key streams. The chaotic behavior is used to improve confusion and diffusion of audio encryption. Due to their dynamic and non-periodic behavior, chaotic models are more appropriate for handling high correlation and dynamic variation of audio data than deterministic approaches [8], [22]. The key characteristics of these Chaos- based methods are summarized in Table 3.

Table 3: Chaotic Encryption Methods.

Ref ID	Study Title	Year	Datasets Used / Database	Domain Coverage	Algorithm Types	Experimental Validation	Metrics Used	Numerical Results	Identified Research Gap	Contribution
[5]	A Noise-Tolerant Audio Encryption Framework Designed by the Application of S8 and Chaotic System	2021	Noisy audio signals (real-time audio communication)	Audio	S8 symmetric group, Chebyshev map, TD-ERCS map, Circle chaotic map	Yes (software simulation)	Entropy, Correlation, SNR, Noise tolerance	Entropy ≈ 7.99, Correlation ≈ 0, successful decryption under channel noise, audible decrypted signal	Evaluation limited mainly to noisy channel conditions, with no validation on clean audio scenarios or hardware-based implementation.	Introduces a noise-tolerant chaos-based audio encryption framework that preserves correct decryption under channel distortions.
[6]	A Bit-Level Audio Encryption Algorithm Using a New Hybrid Chaotic Map	2024	Digital audio files	Audio	Hybrid chaotic map, bit-level permutation and substitution	Yes	Entropy, NPCR, UACI	Entropy ≈ 7.99, NPCR > 99%, UACI ≈ 33%	High computational complexity and lack of real-time or hardware validation limit practical deployment.	Proposes a bit-level hybrid chaotic encryption scheme achieving strong confusion and diffusion properties.
[7]	A New Audio Encryption	2024	WAV audio files (various sizes)	Audio	Logistic map, Rössler	Yes (MATLAB implementati	Entropy, Correlation,	Entropy = 7.9918–7.9983, Correlation =	Encryption performance is sensitive to	Develops a hyper-chaotic audio encryption

	Algorithm Based on Hyper-Chaotic System				hyper-chaotic system	on)	NSCR, Encryption time	−0.0081 to 0.0167, NSCR = 99.60%–99.79%, Encryption time = 0.06–1.03 s	synchronization accuracy, and validation is restricted to software simulations.	algorithm with an expanded key space and strong resistance to statistical attacks.
[8]	Chaos-Based Audio Encryption: Efficacy of 2D and 3D Hyper-Chaotic Systems	2024	Digital audio signals	Audio	2D memristive hyper-chaotic map, 3D hyper-chaotic quadratic map	Yes	Entropy, Correlation, Differential analysis	Entropy ≈ 8, Correlation ≈ 0, 3D system shows higher randomness than 2D	Increased computational overhead and absence of real-time or hardware feasibility analysis.	Provides a comparative study demonstrating the superior randomness and security of 3D hyper-chaotic systems over 2D models.
[9]	Hardware Implementation of a 2D Chaotic Map-Based Audio Encryption System	2024	TIMIT-TTS dataset	Audio / Embedded Systems	2D Logistic-Fraction chaotic map, dynamic S-box, FPGA (Artix-7)	Yes (hardware implementation)	MSE, SNR, Correlation, Throughput, Power	MSE = 1.2156 × 10⁹, SNR = −26.23 dB, Correlation = 0.002948, Throughput = 2880 Mbps, Power = 0.13 W	Dependence on FPGA hardware limits scalability and portability to software-only platforms.	Demonstrates a real-time chaotic audio encryption system through efficient FPGA implementation.
[13]	Dynamics, Circuit Design, Feedback (Scientific Reports)	2023	Not specified	Audio / Hardware	Circuit-based chaotic system	Yes (circuit validation)	Entropy, Synchronization metrics	Entropy > 7.99, stable chaotic synchronization	The study mainly investigates chaotic circuit dynamics and synchronization stability, with limited direct evaluation on audio signal encryption metrics	Validates stable circuit-based chaotic systems suitable for secure communication applications.
[22]	Study of Chaotic-Based Audio Encryption Algorithms	2024	Multiple audio samples	Audio	Multiple chaotic encryption models	Yes	Entropy, Correlation, NPCR, UACI	Entropy ≈ 7.9–8.0, Correlation ≈ 0, NPCR > 99%, UACI ≈ 33%	Does not include comparisons with neural-chaos, DNA-based, or AI-assisted encryption approaches.	Offers a comprehensive comparative evaluation of multiple chaos-based audio encryption algorithms.
[29]	A Lossless Audio Encryption Method Based on Chebyshev Map	2023	Audio signals	Audio	1D Chebyshev chaotic map	Yes	Entropy, MSE, Key sensitivity	MSE = 0, Entropy ≈ 7.99, perfect reconstruction after decryption	Limited comparison with multi-dimensional chaotic systems.	Introduces a lossless chaotic audio encryption method ensuring perfect reconstruction of audio signals.

Source: Authors, (2026).

Interpretation

Chaos-based encryption techniques are some of the most sophisticated methods for the protection of audio signals, due to their nonlinear behavior and extreme sensitivity to initial conditions; these properties allow for the generation of key streams that are highly unpredictable. Noise-tolerant chaotic models, such as that proposed in [5], proved to be highly reliable since correct decryption performance was preserved even under distorted channel conditions. Multidimensional chaotic systems, such as those presented in [7] and [8], achieved remarkable enhancements with regard to the expansion of key space and confusion–diffusion properties, increasing robustness against correlation and differential attacks. A comparison between 2D and 3D chaotic algorithms in [8] highlighted a clear relationship between dimensionality, randomness, and reduced correlation with the original audio signal. Hardware-oriented implementations, as in the design of [9], gave practical proof that chaotic encryption can enable real-time processing in embedded environments. Finally, the lossless encryption model based on a Chebyshev map proposed in [29] introduced an efficient chaotic mechanism that allowed the securing of audio data without any degradation. The discussed studies cumulatively prove that chaos-based encryption offers a robust, flexible, and scalable framework that can meet the ever-increasing security requirements of modern audio communication systems.

VI. DNA AND BIO-INSPIRED AUDIO ENCRYPTION METHODS

The idea of DNA-based audio encryption is based on nucleotide encoding, in which the audio samples are encoded using symbolic biological mappings to increase the complexity of the structure. These methods also include the use of nonlinear mechanisms to increase the diffusion of the keys during the encryption process. Some of these methods also include the use of joint encryption/compression techniques to increase the efficiency of the encryption of the audio samples during secure transmission [10-12]. The key characteristics of these DNA methods are summarized in Table 4.

Table 4: DNA & Bio-Inspired Audio Encryption Methods.

Ref ID	Study Title	Year	Dataset Used	Domain Coverage	Algorithm Types	Experimental Validation	Metrics Used	Key Numerical Results (from paper)	Observed Limitations (based on reported experiments)	Contribution
[10]	An Audio Encryption Algorithm Based on DNA Coding and Chaotic System	2020	Mono & stereo audio signals (piano, human voice, animal, car, drum)	Audio encryption	PWLCM chaotic map + SHA-256 key generation + dynamic DNA coding + XOR diffusion	Yes (simulation)	Correlation, NSCR, UACI, entropy, time	Correlation < 0.1; NSCR ≈ 99%+; UACI ≈ 33%; encryption time ≈ 0.034–0.037 s / 1 KB	Experimental evaluation is limited to simulation-based tests on selected audio samples, with no hardware or real-time transmission validation reported.	Demonstrates strong diffusion and key sensitivity through chaos-driven dynamic DNA encoding.
[11]	Audio Encryption Scheme Using Self-Adaptive Bit Scrambling and Two Multi-Chaotic-Based Dynamic DNA Computations	2020	WAV audio files of different sizes	Secure audio transmission	Self-adaptive bit scrambling + multi-chaotic maps (LCS, HLG) + dynamic DNA + cipher feedback	Yes (extensive experiments)	SNR, PSNR, NSCR, UACI, entropy, correlation, key space	NSCR ≈ 99.99–100%; UACI ≈ 35.5–36.2%; correlation ≈ 10^{-4}–10^{-5}; key space ≈ 2^{928}	Validation focuses on security and statistical metrics, while computational complexity and real-time deployment aspects are not explicitly evaluated.	Introduces a highly secure multi-phase DNA–chaos framework with extremely large key space and strong resistance to differential attacks.
[12]	An Intelligent Audio Encryption and Compression Algorithm Inspired by the Encoding of Various Biological Sequences	2025	Digital audio signals	Audio encryption + compression	Biological-sequence-inspired encoding + joint encryption–compression	Yes (experimental validation)	Entropy, MSE, compression ratio, reconstruction quality	Entropy close to ideal; low MSE after decryption; effective compression without loss of intelligibility	Experiments are reported on digital audio signals without comparison to chaos-DNA or neural-based encryption schemes under identical conditions.	Proposes a unified bio-inspired framework that jointly achieves secure encryption and efficient audio compression.

Source: Authors, (2026).

Interpretation

Both DNA-based and bio-inspired audio encryption techniques are based on the idea of encoding in a nucleotide style and on biologically motivated operations to enhance either confusion or diffusion. Among early works, DNA-chaos hybrid in [10] achieved great enhancements in entropy, decreasing the correlation factor substantially. Multi-chaotic DNA computation in more advanced design [11] expressed higher key sensitivity with increased resistance against differential attacks. Recent bio-inspired models like the one based on sequence encryption-compression in [12] enlarged functionality by combining efficient protection of data with efficient compression. In general, these methods offer powerful nonlinear transformations outperforming many traditional cryptographic methods.

VII. NEURAL AND NEURO-CHAOTIC AUDIO ENCRYPTION METHODS

Neural and neuro-chaotic audio encryption methods have the ability to add flexibility to the security of audio signals by using the capabilities of artificial neural networks and chaotic nonlinear dynamics. Neural networks have the ability to learn complex patterns of signals using learning algorithms. Chaotic dynamics add to the unpredictability of the structure of the system and the generated keys [30], [31]. The key characteristics of these Neural & Neuro methods are summarized in Table 5.

Table 5: Neural & Neuro-Chaotic Audio Encryption Methods.

Ref ID	Study Title	Year	Dataset Used	Domain	Neural Algorithm Type	Experimental Validation	Metrics Used	Numerical Results (from PDF)	Observed Limitations (based on reported experiments)	Contribution
[30]	NeuroChaosCrypt: Revolutionizing Chaotic-Based Cryptosystem With Artificial Neural Networks	2024	Audio signals (8 kHz, 8-bit) and images	Audio and multimedia encryption	ANN-based chaotic system (jerk model)	Yes	CC, SNR, PRD, NPCR, UACI, Time	CC ≈ 0.003, SNR ≈ −76 dB, PRD ≈ 6.38×10^5, NPCR ≈ 99.49%, Decryption time ≈ 0.008 s (Tables 2–5)	Evaluation is reported for specific signal resolutions and experimental settings, with performance metrics limited to the tested configurations.	Eliminates synchronization requirements and improves decryption speed with an FPGA-ready neuro-chaotic design.

[31]	Memristive Coupled Neural Network Based Cryptosystem	2024	Digital multimedia data (including audio)	Encryption (general)	Memristive Neural Network + Chaos	Yes	Entropy, Key space, Sensitivity	Entropy ≈ 7.99, key space > 2^150, high key sensitivity (Section IV)	Experimental evaluation focuses on security metrics and system properties, without reporting real-time audio stream experiments.	Introduces a hardware-oriented neural cryptosystem using memristive coupling.
[32]	A Classification and Retrieval Method for Encrypted Speech Based on Deep Neural Network and Deep Hashing	2020	Encrypted speech samples	Encrypted speech retrieval	DNN + Deep Hashing	Yes	Accuracy, Precision, Recall	Accuracy ≈ 96.2%, Precision ≈ 95.4%, Recall ≈ 94.8% (Table IV)	Experiments are reported on specific encrypted speech samples and a fixed evaluation setup, with no additional datasets or channel conditions discussed.	Enables intelligent retrieval and classification directly from encrypted speech without decryption.
[33]	Neural Network-Based Cryptography: A Primary Study on the Performances and Techniques	2022	Not specified (conceptual and simulation-based)	General cryptography	ANN-based encryption models	Partial	Throughput, Time	Encryption time reduced by approximately 18–25% compared to classical ciphers (simulation results)	Results are based on simulations and conceptual analysis, with no application-specific (audio) experimental validation reported.	Provides a foundational performance analysis of ANN-based cryptographic systems.

Source: Authors, (2026).

Interpretation

Neural and neuro-chaotic encryption methods have come up with adaptive security that is integrated into neural learning with the nonlinear behavior of chaotic systems. Early neural models, such as encrypted speech retrieval using deep networks [32], showed how intelligent processing can effectively improve protected audio communication. More advanced architectures, including the memristive neural-chaotic architectures [31], expanded the sensitivity of keys and improved the resilience of emerging attacks. Work on neural cryptography [33] provided a deeper basis for detailing how learning based structures support secure key generation, whereas hybrid ANN-chaotic mechanisms [30] had showcased the benefit of blending neural adaptability with chaotic unpredictability. These collectively point out the heightened role of intelligent, dynamically evolving models in shaping next-generation audio encryption.

VIII. OPTICAL AND QUANTUM-BASED AUDIO ENCRYPTION METHODS

In optical and quantum-based methods, there is a shift away from algorithmic models and towards physical-layer models for encrypting audio information. Optical methods are based on light polarization, and quantum methods take advantage of quantum effects to improve communication security [14], [15]. The key characteristics of these Optical / Quantum methods are summarized in Table 6.

Table 6: Optical / Quantum Encryption.

Ref ID	Study Title	Year	Datasets Used / Database	Domain Coverage	Algorithm Types	Experimental Validation	Metrics Used	Numerical Results	Identified Research Gap	Contribution
[14]	Audio Encryption Using Polarized Light Beam	2025	Digitized audio signals mapped to optical domain	Audio	Polarized Light Beam (PLB)–based optical encryption	Yes (simulation + experimental validation)	Correlation coefficient, PSNR, noise robustness	Correlation (original–encrypted) = 0.13, Correlation (original–decrypted) = 0.96; CC = 0.9459 and PSNR = 17 dB under Gaussian noise (variance 0.1); CC = 0.94, PSNR = 14 dB at variance 0.2	Requires specialized optical hardware; experimental setup complexity limits portability and real-time deployment	Introduces an optical-domain audio encryption scheme using polarization states with high reconstruction fidelity and strong resistance to cryptanalytic attacks
[15]	QSAC: Quantum-Assisted Secure Audio Communication Using Quantum Entanglement and Steganography	2025	Audio communication signals encoded in quantum domain	Secure Audio Communication	Quantum entanglement + quantum steganography	Yes (theoretical analysis + experimental validation)	BER, SNR, quantum disturbance indicators	Any eavesdropping attempt causes detectable quantum disturbances; BER increases significantly under interception, enabling reliable intrusion detection	High implementation cost; experimental complexity; limited scalability due to early-stage quantum hardware	Proposes a quantum-assisted secure audio communication framework with intrinsic eavesdropping detection guaranteed by quantum physics

Source: Authors, (2026).

Interpretation

Optical and quantum encryption methods achieve superior protection of audio signals through physical and quantum phenomena instead of a purely mathematical basis. Polarized-light encryption [14], and communication with quantum assistance [15], although very resistant to tapping, have not found wide practical applications so far, mostly due to hardware and implementation issues.

IX. COMPARATIVE FRAMEWORK OF AUDIO ENCRYPTION APPROACHES

This section discusses the structural comparison of the chosen audio encryption models based on their design and implementation structures. The models used in the comparison are different in their mathematical underpinnings, system models, and application domains. Some of the models are based solely on algorithmic models, while others are based on signal processing models, biological models, intelligent models, and physical models. The comparison of the models shows the different methodologies used in the implementation of the models, ranging from fixed models to intelligent models. The key characteristics of the selected audio encryption methods are summarized in Table 7.

Table 7: The comparative analysis of chosen audio-encryption methods**.**

Ref ID	Study Title	Year	Technique Type	Algorithm / Model	Dataset Used	Metrics Reported	Numerical Results	Main Limitations / Notes	Application Focus
[4]	Evaluation of Rijndael Algorithm for Audio Encryption by Brute Force Attack	2024	Classical (AES-based)	AES (Rijndael) block cipher	Audio files	Key space, brute-force complexity	256-bit key → ≈ 4.13×10^{99} total permutations	PSNR/SNR metrics not reported; focuses mainly on brute-force evaluation	Secure audio storage systems
[25]	Multilayered Audio Signal Encryption for Secure Voice Communication	2023	Classical + Transform	Multi-layer DCT/DST encryption pipeline	Speech recordings (Audio1–Audio3)	SNR, correlation, execution time	Example Audio1 → SNR ≈ −2.70 dB; correlation ≈ 0.00236	Higher computational complexity; negative SNR indicates strong signal distortion	Secure voice communication
[6]	Bit-Level Audio Encryption Using a New Hybrid Chaotic Map	2024	Chaotic	Hybrid chaotic map with bit-level scrambling	Digital audio signals	Histogram analysis, correlation, entropy, key space	Post-encryption correlation ≈ 0; entropy reported as high (exact numerical values not explicitly reported)	NPCR/UACI values not explicitly reported in the extracted results	High-security multimedia transmission
[7]	A New Audio Encryption Based on Hyper-Chaotic System	2024	Hyper-Chaotic	Logistic permutation with 4D hyperchaotic diffusion	Speech recordings	Entropy, correlation, differential metrics, execution speed	Described as high-security and real-time capable (exact numerical values not explicitly tabulated)	Computationally intensive; explicit numerical values not reported in extracted results	Defense-level secure communication
[29]	A Lossless Audio Encryption Using Chebyshev Map	2023	Chaotic (Lossless)	Chebyshev chaotic map with lossless reconstruction	Multiple WAV audio files	Correlation, key space, lossless reconstruction	Correlation of encrypted signal ≈ 10^{-4} – 10^{-6}	SNR/PSNR metrics not reported	Medical and archival audio protection
[10]	Audio Encryption Using DNA Coding and Chaotic System	2020	DNA–Chaos	PWLCM chaotic map with SHA-256 key generation and DNA encoding rules	Mono and stereo audio signals (piano, human voice, car, etc.)	NSCR, UACI, correlation, runtime	Original correlation > 0.9; encrypted < 0.1; NSCR ≈ 100%; UACI ≈ 33.3%	DNA operations increase computational complexity	Critical audio security systems
[11]	Audio Encryption Scheme Using Self-Adaptive Bit Scrambling and Two Multi Chaotic-Based Dynamic DNA Computations	2020	DNA–Multi-Chaos	Multi-chaotic maps with dynamic DNA computation and cipher feedback	WAV audio signals	Entropy, UACI, NSCR, correlation	UACI ≈ 35.55%; NSCR ≈ 99.995%; correlation ≈ 5.3×10^{-5}	High computational cost	High-security audio transmission
[30]	NeuroChaosCrypt: Revolutionizing Chaotic-Based Cryptosystem With Artificial Neural Networks—A Comparison With Traditional Cryptosystems	2024	Neural–Chaotic	ANN-driven chaotic cryptosystem	Audio and image datasets	Entropy, NPCR, UACI, SNR, PRD, execution time	Entropy ≈ 7.4326; NPCR ≈ 99.49%; UACI ≈ 0.39%	NPCR/UACI numerical results mainly evaluated on image datasets	AI-enhanced secure communication systems
[31]	Memristive Coupled Neural Network Cryptosystem	2024	Neural / Hardware-Chaotic	Memristive coupled neural network model	Digital multimedia datasets	Entropy, key sensitivity	Entropy close to ideal; strong key sensitivity (exact numerical values not explicitly reported)	Limited numerical audio-specific metrics	Real-time embedded security systems
[14]	Audio Encryption Using Polarized Light Beam (PLB)	2025	Optical / Physical-Layer	Polarized Light Beam transformation	Audio signals mapped to optical domain	Correlation, BER, physical analysis	Example: original–encrypted correlation ≈ 0.131; original–decrypted ≈ 0.9608	Requires specialized optical hardware	Military and quantum-safe audio communication

Source: Authors, (2026).

Interpretation

The comparative analysis of chosen audio-encryption methods shows how much the security models have diversified to meet the ever-increasing complexity of modern communication environments. While classical methods retain strong resistance against brute-force attacks due to their large key spaces, significant limitations arise when these methods are confronted with correlation or structure-based analyses. Chaotic and hyper-chaotic systems can offer significantly better confusion-diffusion properties, reflected by their near-ideal entropy levels and minimal values of correlation, which makes them particularly effective in protecting highly dynamic audio signals. DNA-based frameworks further reinforce security with biologically inspired transformations that increase nonlinearity and improve differential resistance. Neural and neuro-chaotic models bring adaptability and hardware-accelerated processing, positioning them as strong candidates for real-time intelligent encryption scenarios. Optical and physical-layer methods extend protection beyond computational paradigms by exploiting intrinsic properties of light, offering exceptional resistance against interception despite requiring hardware implementation. Overall, the comparative findings suggest that while each category presents distinct advantages, hybrid schemes integrating chaotic, biological, neural, or physical-layer mechanisms tend to offer a balanced trade-off between security strength, adaptability, and implementation feasibility in next-generation secure audio communication systems.

X. CONCLUSION

The above research work has provided a detailed comparative analysis for audio encryption methods that have been developed between the years 2015 and 2025. These methods include classic encryption techniques, chaos and DNA-based models, neural and neuro-chaotic systems, as well as optical and quantum-based methods. It was noted that classic encryption methods have high strength in terms of immunity from brute-force attacks and efficiency. However, their fixed structure can lead to limits in modeling the statistical properties of audio. On the other hand, chaotic, DNA, and neural-driven encryption models showed better confusion-diffusion capability, larger key space, and better resistance to complex sound patterns. Optical and quantum-computing-assisted techniques offer top-notch security assurance with robust physical guarantees, but they are limited due to complexity issues associated with their implementation. Thus, encryption models that combine chaotic systems, biologic encryption, neural models, and physical layer mechanisms can be considered promising candidates to support secure next-gen sound communication systems with better efficacy.

XI. FUTURE WORK

Future studies could emphasize working on lightweight hybrid encryption frameworks for audio that bring a good balance between security and the ability to handle real-time encryption. Adding the concept of neural learning into chaos and DNA algorithms has not been significantly explored, especially for a channel environment that is noisy and attacked using machine-learning-based attacks. Moreover, a common benchmarking dataset needs to be developed for comparison purposes across various encryption paradigms. Lastly, studies on the practical framework for quantum assistance in encryption systems also need to be explored.

XII. AUTHOR'S CONTRIBUTION

Conceptualization: Halah Waad Khaled, Waleed Abdullah Araheem and Hakeem Imad Mhaibes.
Methodology: Halah Waad Khaled, Waleed Abdullah Araheem and Hakeem Imad Mhaibes.
Investigation: Halah Waad Khaled, Waleed Abdullah Araheem and Hakeem Imad Mhaibes.
Discussion of results: Halah Waad Khaled, Waleed Abdullah Araheem and Hakeem Imad Mhaibes.
Writing – Original Draft: Halah Waad Khaled, Waleed Abdullah Araheem and Hakeem Imad Mhaibes.
Writing – Review and Editing: Halah Waad Khaled, Waleed Abdullah Araheem and Hakeem Imad Mhaibes.
Resources: Halah Waad Khaled, Waleed Abdullah Araheem and Hakeem Imad Mhaibes.
Supervision: Halah Waad Khaled, Waleed Abdullah Araheem and Hakeem Imad Mhaibes.
Approval of the final text: Halah Waad Khaled, Waleed Abdullah Araheem and Hakeem Imad Mhaibes.

XIII. REFERENCES

[1] Y. Mahamat, S. H. Othman, and S. H. Nkiama, "Comparative Study Of AES, Blowfish, CAST-128 And DES Encryption Algorithm," 2016. [Online]. Available: www.iosrjen.org

[2] I. Khalid, T. Shah, K. A. Almarhabi, D. Shah, M. Asif, and M. Usman Ashraf, "The SPN Network for Digital Audio Data Based on Elliptic Curve Over a Finite Field," *IEEE Access*, vol. 10, pp. 127939–127955, 2022, doi: 10.1109/ACCESS.2022.3226322.

[3] S. R. Kareem, "Encryption of Audio Signals Using the Elzaki Transformation and the Lorenz Chaotic System," Sep. 2024. doi: 10.48550/arXiv.2409.14092.

[4] S. G. Mohammed and N. S. Al-Mothafar, "Evaluation of Rijndael Algorithm for Audio Encryption by Brute Force Attack," *J. Eng.*, vol. 30, no. 11, pp. 128–141, Nov. 2024, doi: 10.31026/j.eng.2024.11.08.

[5] H. Aziz, S. M. M. Gilani, I. Hussain, A. K. Janjua, and S. Khurram, "A Noise-Tolerant Audio Encryption Framework Designed by the Application of S8Symmetric Group and Chaotic Systems," *Math. Probl. Eng.*, vol. 2021, 2021, doi: 10.1155/2021/5554707.

[6] M. Demirtas, "A BIT-LEVEL AUDIO ENCRYPTION ALGORITHM USING A NEW HYBRID CHAOTIC MAP," *Kahramanmaraş Sütçü İmam Üniversitesi Mühendislik Bilim. Derg.*, vol. 27, no. 2, pp. 601–614, Jun. 2024, doi: 10.17780/ksujes.1412850.

[7] H.A. Qasim, "A new Audio Encryption Algorithm Based on Hyper-Chaotic System," *Mustansiriyah J. Pure Appl. Sci.*, vol. 1, no. 3, pp. 85–94, Oct. 2023, doi: 10.47831/mjpas.v1i3.51.

[8] T. Haridas, S. D. Upasana, G. Vyshnavi, M. S. Krishnan, and S. S. Muni, “Chaos-based audio encryption: Efficacy of 2D and 3D hyperchaotic systems,” *Franklin Open*, vol. 8, Sep. 2024, doi: 10.1016/j.fraope.2024.100158.

[9] H. M. Elrefai, W. S. Sayed, and L. A. Said, “Hardware Implementation of a 2D Chaotic Map-Based Audio Encryption System Using S-Box,” *Electron.*, vol. 13, no. 21, Nov. 2024, doi: 10.3390/electronics13214254.

[10] X. Wang and Y. Su, “An Audio Encryption Algorithm Based on DNA Coding and Chaotic System,” *IEEE Access*, vol. 8, pp. 9260–9270, 2020, doi: 10.1109/ACCESS.2019.2963329.

[11] R. I. Abdelfatah, “Audio Encryption Scheme Using Self-Adaptive Bit Scrambling and Two Multi Chaotic-Based Dynamic DNA Computations,” *IEEE Access*, vol. 8, pp. 69894–69907, 2020, doi: 10.1109/ACCESS.2020.2987197.

[12] M. Nassef, “An Intelligent Audio Encryption and Compression Algorithm Inspired by the Encoding of Various Biological Sequences,” *IEEE Access*, vol. 13, pp. 126334–126354, 2025, doi: 10.1109/ACCESS.2025.3588764.

[13] S. M. Fu, X. F. Cheng, and J. Liu, “Dynamics, circuit design, feedback control of a new hyperchaotic system and its application in audio encryption,” *Sci. Rep.*, vol. 13, no. 1, Dec. 2023, doi: 10.1038/s41598-023-46161-5.

[14] A. Shikder, S. K. Rajput, N. K. Nishchal, O. Matoba, and Y. Awatsuji, “Audio encryption using polarized light beam,” *APL Photonics*, vol. 10, no. 3, Mar. 2025, doi: 10.1063/5.0234393.

[15] M. R. I. Rifat, M. M. Rahman, M. A. K. Nayon, M. S. Azad, and M. R. C. Mahdy, “QSAC: Quantum-assisted Secure Audio Communication using quantum entanglement, audio steganography, and classical encryption,” *Eng. Sci. Technol. an Int. J.*, vol. 70, Oct. 2025, doi: 10.1016/j.jestch.2025.102167.

[16] A. Singh, K. B. Sivangi, and A. N. Tentu, “Machine Learning and Cryptanalysis: An In-Depth Exploration of Current Practices and Future Potential,” *J. Comput. Theor. Appl.*, vol. 1, no. 3, pp. 257–272, Feb. 2024, doi: 10.62411/jcta.9851.

[17] P. Sudha, “LITERATURE SURVEY ON RECENT AUDIO ENCRYPTION TECHNIQUES,” *Int. J. Electron. Commun. Eng. Technol.*, vol. 7, no. 6, pp. 91–95, [Online]. Available: http://www.iaeme.com/IJECET/index.asp91http://www.iaeme.com/IJECET/issues.asp?JType=IJECET&VType=7&IType=6http://www.iaeme.com/IJECET/issues.asp?JType=IJECET&VType=7&IType=6

[18] E. A. Albahrani, T. K. Alshekly, and S. H. Lafta, “A Review on Audio Encryption Algorithms Using Chaos Maps-Based Techniques,” 2021, *River Publishers*. doi: 10.13052/jcsm2245-1439.1113.

[19] A. Poduval, N. Rai, P. Khan, T. Chaudhari, P. Guide, and A. Professor, “A SURVEY ON DIFFERENT ENCRYPTION TECHNIQUES FOR IMAGE, VIDEO, AUDIO AND DOCS,” 2021. [Online]. Available: http://www.ijeast.com

[20] K. M. Hosny, M. A. Zaki, N. A. Lashin, M. M. Fouda, and H. M. Hamza, “Multimedia Security Using Encryption: A Survey,” *IEEE Access*, vol. 11, pp. 63027–63056, 2023, doi: 10.1109/ACCESS.2023.3287858.

[21] R. A. Gandhi and A. M. Gosai, “A Study on Current Scenario of Audio Encryption,” Apr. 2015.

[22] A. Shumran and A. B. A. Al-Hussein, “Study of Chaotic-based Audio Encryption Algorithms: A Review,” *Iraqi J. Electr. Electron. Eng.*, vol. 20, no. 2, pp. 85–103, Dec. 2024, doi: 10.37917/ijeee.20.2.8.

[23] D. D. Mali and S. N. Shinde, “A Survey of Various Symmetric Encryption Methods,” 2025, pp. 294–303. doi: 10.2991/978-94-6463-876-9_22.

[24] N. A. Hassan, F. S. Al-Mukhtar, and E. H. Ali, “Encrypt Audio File using Speech Audio File As a key,” in *IOP Conference Series: Materials Science and Engineering*, IOP Publishing Ltd, Nov. 2020. doi: 10.1088/1757-899X/928/3/032066.

[25] H. A. Abdallah and S. Meshoul, “A Multilayered Audio Signal Encryption Approach for Secure Voice Communication,” *Electron.*, vol. 12, no. 1, Jan. 2023, doi: 10.3390/electronics12010002.

[26] J. He, P. Zhu, Z. Liu, and Y. Cao, “A Novel Digital Audio Encryption and Forensics Watermarking Scheme,” *IEEE Access*, vol. 12, pp. 103565–103582, 2024, doi: 10.1109/ACCESS.2024.3434576.

[27] A. Z. Abbasi, A. Rafiq, and B. M. Alshammari, “A digital audio data protection method using parametric action of generalised triangle group on GF(28),” *Ain Shams Eng. J.*, vol. 16, no. 1, Jan. 2025, doi: 10.1016/j.asej.2024.103193.

[28] M. M. Al-Ezzi, W. Weiping, A. Monem, S. Rahma, H. A. Al, and M. R. Hassan, “A New Encryption Algorithm for Voice Messages on Social Media Using Magic Cube GF (2^8) Technology 253 Original Scientific Paper,” 2025. doi: 10.32985/ijeces.16.3.6.

[29] M. Demirtaş, “A Lossless Audio Encryption Method based on Chebyshev Map,” *Orclever Proc. Res. Dev.*, vol. 2, no. 1, pp. 28–38, Mar. 2023, doi: 10.56038/oprd.v2i1.234.

[30] T. Bonny and W. Al Nassan, “NeuroChaosCrypt: Revolutionizing Chaotic-Based Cryptosystem With Artificial Neural Networks - A Comparison With Traditional Cryptosystems,” *IEEE Access*, vol. 12, pp. 62030–62046, 2024, doi: 10.1109/ACCESS.2024.3395527.

[31] F. Hamed *et al.*, “Memristive Coupled Neural Network Based Audio Signal Encryption,” in *Signal Processing - Algorithms, Architectures, Arrangements, and Applications Conference Proceedings, SPA*, IEEE Computer Society, 2024, pp. 149–154. doi: 10.23919/SPA61993.2024.10715600.

[32] Q. Zhang, X. Zhao, and Y. Hu, “A classification retrieval method for encrypted speech based on deep neural network and deep hashing,” *IEEE Access*, vol. 8, pp. 202469–202482, 2020, doi: 10.1109/ACCESS.2020.3036048.

[33] J.-L. Foo, K.-W. Ng, and P. Naveen, “Neural Network-Based Cryptography: A Primary Study on the Performances and Techniques,” in *Proceedings of the International Conference on Computer, Information Technology and Intelligent Computing (CITIC 2022)*, Atlantis Press International BV, 2022, pp. 68–78. doi: 10.2991/978-94-6463-094-7_6.

Journal of Engineering and Technology for Industrial Applications

ITEGAM-JETIA

Manaus, v.12 n.60, p.1300-1309. July/August, 2026.
DOI: https://doi.org/10.5935/jetia.v12i60.4075

ISSN ONLINE: 2447-0228

RESEARCH ARTICLE OPEN ACCESS

A REVIEW ON DEEP LEARNING BASED DYNAMIC INDIAN SIGN LANGUAGE RECOGNITION SYSTEM

Manojkumar Patel[1], Narendra Patel[2]

[1]Research Scholar, Gujarat Technological University, Ahmedabad, Gujarat, India.
[2]Birla Vishvakarma Mahavidyalaya, Gujarat, India.

[1]https://orcid.org/0009-0008-5795-1655, [2]https://orcid.org/0000-0002-1495-1136

Email: manojpatel.25@gmail.com, nmpatel@bvmengineering.ac.in

ARTICLE INFO

Article History
Received: March 13, 2026
Reviewed: April 16, 2026
Accepted: July 16, 2026
Published: August 31, 2026

Keywords:
Indian sign language (ISL),
Vision-based approach,
Classification,
Deep Learning,
Reduced Inequalities.

ABSTRACT

An alternative form of communication for those who are hard of hearing or speech is sign language (SL). SL differs from nation to nation. Indian Sign Language (ISL) is a substitute form of communication used by individuals in India. There are about 63 million deaf and hard of hearing persons living in India. But there are no accessible or reasonably priced human interpreters for ISL identification. Consequently, for many years, researchers have been working on creating a system that can recognize sign language. Compared to other SL, the construction of an Indian Sign Language Recognition System (SLRS) is exceedingly challenging. The field of Indian sign language recognition systems has not seen many developments. Consequently, this discipline has very few systematic literature reviews. We reviewed the most recent (post-2017) literature on dynamic Indian sign language recognition using deep learning technique on various parameters in an attempt to tackle this problem. The objective of this work is to present a comprehensive analysis of various deep learning methods used in dynamic Indian sign language recognition.

Copyright ©2026 by authors and Galileo Institute of Technology and Education of the Amazon (ITEGAM). This work is licensed under the Creative Commons Attribution International License (CC BY 4.0).

I. INTRODUCTION

A different form of communication for people who have hearing or speech impairments is sign language (SL). Instead of speaking and using sound patterns, people with hearing impairments communicate by making signs in visual space [1]. In the 1970s, research on sign language linguistics was started. It offers linguistic data, including different letters and symbols. Typically, there are two categories of signs: (1) static and (2) dynamic. The nonverbal language known as SL makes use of body parts to visually transmit patterns. These include non-manual components like lip movement and face expression as well as manual elements like hand and finger positions. Articular points like the joints in the fingers, wrist, elbow, and shoulder are crucial for differentiating SL. It also contains a variety of movements, including forward, backward, left, and right, as well as lip movements and facial expressions like happiness, rage, and confusion. The different sign elements are shown in fig. 1. Correct execution of all sign components is required to generate a precise sign word [1], [2]. Due to its variation among nations and even geographical areas, SL is not a standardized language. As a result, several sign languages (SLs) were created, including Chinese Sign Language (CSL), American Sign Language (ASL) and Indian Sign Language (ISL). [3] Designing a sign language recognition system (SLRS) for ISL is a more difficult task for academics since ISL is distinct from other SLs in that it involves both single handed and double handed gestures, along with a huge vocabulary of related movements. Motion-based Indian sign language referred to as dynamic Indian sign language, as it depicts motion with dynamic signs [4].

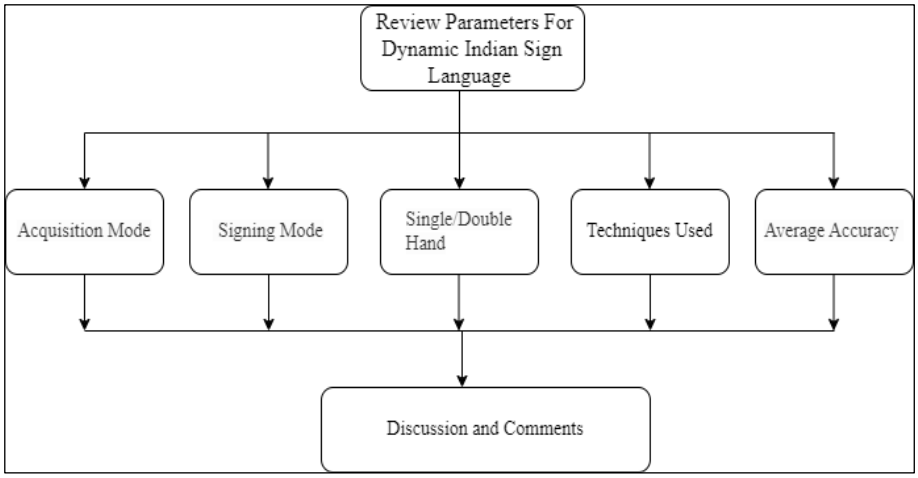


Figure 1: Sign language Elements.
Source: Authors, (2026).

I.1 MOTIVATION

In India, deafness is a persistent issue. The estimated number of deaf individuals residing in India is around 63 million. The deaf and dumb in India utilize ISL, one of the country's living languages. Sign language interpreters can facilitate communication between the regular public and the deaf and dumb. Human interpreters are neither readily available or affordable. It makes it hard to close the huge communication gap between regular people and those who are deaf or dumb. There are lots of work done on static Indian sign language. On Indian dynamic sign language, some research has been done. Therefore, the several deep learning techniques for the identification of Dynamic ISL are the main emphasis of this study.

I.2 LITERATURE SEARCH METHODOLOGY

Finding, categorizing, and contrasting the body of prior research on SLR is the aim of the systematic review. For the literature review, we look at content available as of 2017. A summary of significant studies on Dynamic ISLR methods is given in this survey study. There is discussion on research papers from conferences, workshops, symposiums, journals, and periodicals. The figure displays the inclusion/exclusion criteria after the investigations were reviewed. We conducted a comprehensive search using the Google search engine. The research papers in the specified databases have been searched using the keyword "Dynamic Indian Sign Language Recognition". from the databases of Elsevier, Springer, IEEE, and ACM, various research publications on dynamic Indian sign language recognition were found through our search. Based on the titles, abstracts, and conclusions, the papers were excluded. After reading the entire content, 40 research papers have been selected.

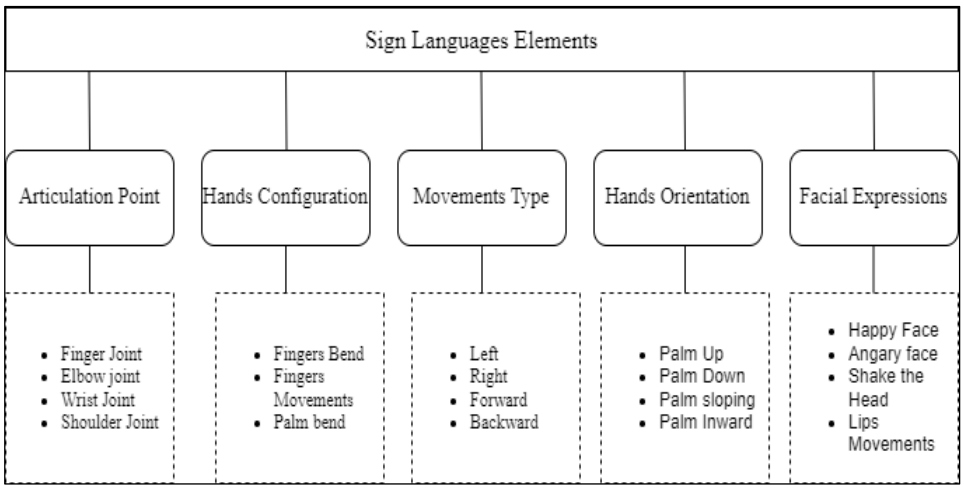


Figure 2: Review Parameters.
Source: Authors, (2026).

A study article may compare things using a different standard. Previous review studies have only examined various approaches and accuracy. On the other hand, in order to assess and comprehend the literature, we have adopted the methodology of [1], [5] . We reviewed the research on dynamic Indian sign language recognition system (DISLR) using those features. Fig. 2 shows the comparative parameter that is used in this review. The parameters of the strategy we have chosen for the Systematic Literature Review are acquisition mode, signing mode, single/double hand signs, techniques used, and average accuracy. Based on these features [1], [5] a review of dynamic Indian sign language recognition (DISLR) has been carried out and recorded.

II. LITERATURE REVIEW ON DISLR - DYNAMIC INDIAN SIGN LANGUAGE RECOGNITION

II.1 GENERAL PROCEDURE OF SIGN LANGUAGE RECOGNITION



Figure 3: SLR General Flow.
Source: Authors, (2026).

A nonverbal communication technique called sign language makes use of the hands, arms, head, and facial expressions, among other body parts, to communicate meaning [6]. SLR is the process of identifying and recognizing signs and translating them into words that have semantic meaning. The steps involved in the SLR include data gathering, pre-processing, extraction of features, and classification. Fig. 3 shows the SLR block diagram along with the overall workflow [5], [7], [8]. Sign language recognition (SLR) is the process of identifying, recognizing, and translating signs into semantically significant words. The SLR system converts the data from signs into comprehensible text or audio by decoding and understanding the data. There are two methods used to perform the function of sign recognition: the hardware based or sensor-based approach and the vision-based approach. In Vision-based method, a camera is used to capture sign images or video. There is various hardware is used to capture sign data in hardware-based approach like data gloves, Microsoft kinect sensor, etc. The signers have difficulty to handle hardware device. So that we focused on vision-based approach in this study [9-14]. After image or video is capture, key frame is identify using various technique and frame is preprocessed. The preprocessed frames or images are processed to find features for classification. The extracted features are given to classifier to classified into various sign. Training and test images are categorized using the retrieved features in the classification stage. It implies that the two methods—image acquisition, extraction of features and classification—are mostly responsible for the rate of gesture recognition. There has been a lot of work on various features extraction and classification techniques in this literature [15]. Over the past few decades, noteworthy developments in accuracy have been made in sign language identification with the use of deep learning, a vision-based technique. Dynamic signs address issues with video input or visual problems, whereas static sign use the model's modality. Moreover, the dynamic signs are the most complex signs [16].

II.2 DISLR APPROACHES

II.2.1 Sensor-Based Deep Learning Approach

By [17] created a technique for recognizing sign language using sensors. Using Kinect and the jump motion device, they gathered a total of 7500 samples of 50 different sign words. The location and orientation of the fingertip characteristics were retrieved using the Leap Motion API. HMM and a bidirectional long short-term memory neural network (BLSTM-NN) were used to classify the system. According to the outcomes, the general accuracy was 95.60% and 84.57% respectively. In turn [18] proposed a modified version of the LSTM, a continuous gesture sequence model for continuous SLR that identifies several related motions. It functions by using neural networks to simulate continuous signals by dissecting them into smaller components. To take pictures, the leap motion sensor is used. Total 942 Indian sign language signed phrases have been used to test the proposed technique. Thirty-five different sign words are used to identify these sign sentences. The average accuracy on isolated sign words and signed phrases was 89.5% and 72.3%, respectively. According to [19] proposed a hand gestures recognition system that operates in real time using information from the Microsoft Kinect RGB-D camera. Computer vision methods such as affine transformation and 3D construction are utilized to provide one to one mapping between the RGB camera and depth sensor pixels. The hand motions were separated from the background noise using segmentation. A total of thirty-six static gestures associated with the alphabets and numbers of Indian Sign Language (ISL) were used to trained convolutional neural networks (CNN). Using training data consisting of 45,000 RGB and 45,000 depth images, the model's accuracy was 98.81%. Ten ISL dynamic word gestures were trained using convolutional LSTMs, and after training of 1080 videos, an accuracy of 99.08% was achieved. By [20] developed a system for the identification of sign sequences in sentences that are constantly signed in Indian sign language with a small amount of labelled sentence data and enough labelled data of isolated signs. Multiple six degree of freedom inertial measurement units (IMUs) are used on the signer's two hands to gather the data. In order to provide end to end phrase identification without the need of sign boundary information, a suggested deep learning model comprises of a convolutional neural network (CNN), two bidirectional long short-term memory (Bi-LSTM) layers, and connectionist temporal classification (CTC).

II.2.2 Vision-Based Deep Learning Approach

In turn [21] developed a vision-based deep learning solution for the video classification problem. They examine the use of Open Pose in conjunction CNN to identify the dynamic sign language videos of twenty medical words in ISL. A standard smartphone camera is used to record all of the videos. CNN was employed for the classification process. At 85% accuracy, it performs excellently. According to [22] developed a SLRS which U-Net for Semantic segmentation of hands. ResNet 101 was used with U-Net as the backbone. The use of an RGB-D Kinect camera is entirely unnecessary since semantic segmentation makes use of information from a regular RGB camera. Using training data, the system demonstrated strong performance in multiclass semantic segmentation, producing a F1 score of 0.9957 and an IOU score of 0.9920. By [10] developed the Indian Lexicon Sign Language Dataset (INCLUDE) is a ISL dataset that contains 0.27 million frames from 4,287 videos capture for 263-word signs from 15 distinct word categories. To define INCLUDE-50, a subset of 50 sign word from various word categories is selected for quick assessment of SLR methods with various hyperparameter adjustment. The authors assess a number of deep neural networks by integrating various feature extraction techniques, augmentation techniques, encoding and decoding.

On the INCLUDE-50 and the INCLUDE dataset, the top-performing model obtains accuracy rates of 94.5% and 85.6%, respectively. In turn [11] suggested a system based on a vision-based approach for interpreting signs in Indian sign language to words in English language translation. The Restnet50 model is used to find out features from RGB images, and the LSTM is used to analyze their sequences. The dataset contains 7 isolated sign words for days. The system achieved 73.60% accuracy. According to [13] presented a system that used a 3D CNN model to recognize ISL words. The model is trained on a dataset that contains 20 sign words. The system obtained 88.35% accuracy. By [14] developed a system that recognizes sign language words. The system is based on the CNN-RNN architecture. The Inceptionv3 is used to extract features from frames, and after that, the LSTM model is used to analyze sequences of frames. The proposed system is trained on the CasTalk ISL dataset, which contains 50 sign words. During testing with the test dataset, the system achieved 99.46% top-3 accuracy and 95.99% top-1 accuracy. In turn [23] proposed a model for hand gestures detection for ISL that deaf farmers frequently use. The spatial attributes are determined using the Googlenet Model. The LSTM receives the spatial characteristics in order to determine the temporal features. Using the suggested dataset of eight ISL terms from the agriculture field. An average classification accuracy of 76.21% has been attained by the model. According to [24] suggested INSIGNVID, the first Indian Sign Language video dataset. Using transfer learning, a unique method is described that uses this dataset as input to convert the ISL sentences in the video into proper English sentences. The mobilenev2 is used to find out spatial features. After that, a sequence of spatial features is given to LSTM to extract temporal features and classify them. The system has achieved 91% accuracy during training. By [25] proposed a DL model that uses a person's gestures to identify and detect words. ISL video frames are divided into isolated segments, and signs are identified using the LSTM and GRU model. With the IISL2020 dataset, four distinct sequential combinations of LSTM and GRU—since there are two layers of LSTM and two levels of GRU—were applied. With single level of LSTM and GRU layer, the suggested model achieved approximately 97% accuracy across 11 distinct signs.

In turn [26] proposed the MOPGRU (integrated Media Pipe optimized gated recurrent unit) model for the recognition of ISL. The authors have enhanced the conventional GRU cell's update gate by multiplying it by the reset gate in order to eliminate redundant data from previous screenings in a single screening. By getting feedback from the consequent of the reset gate, more attention is paid to the current input. Furthermore, In the output layer of the GRU cell, use SoftMax activation instead of Softsign activation and exponential linear unit activation in place of the hyperbolic tangent activation seen in conventional GRUs. The model is trained on a dataset contains 13 daily sign words. The system achieved 95% accuracy. According to [27] presented a DL model for motion-based recognition of ISL. OpenCV is used to record the gesture, MediaPipe is used to identify the important points, and an LSTM model that has been trained to predicts the sign. There are forty sign words in the dataset. 92% accuracy on average was attained. In turn [28] presented two approaches to solve the sign language translation problem: BERT Transformer and Bidirectional LSTM. The suggested algorithm's performance has been examined using the INCLUDE-50 dataset. A variety of data augmentation techniques and mediapipe based feature extraction is used to evaluate the deep neural network. On the Dataset INCLUDE 50, the top-performing model obtained an accuracy of 89.5%. This model makes use of an encoder, a decoder, and a pre-trained feature extractor. By [29] suggested a method for ISL word and character recognition. With a 99 percent accuracy rate, the Bag of Visual Words (BoVW) approach can identify ISL character (0-9, A-Z). ISL recognition at the word level is done using the INCLUDE-50 dataset. The spatial and temporal features of the video are trained using the Inception V3 model and LSTM, respectively. With CNN predictions as the RNN's input, authors were able to attain 86.7% accuracy. In turn [30] suggested the Hybrid CNN-BiLSTM SLR (HCBSLR) model, a vision-based SLRS that addresses the issue of over-preprocessing. The suggested model eliminates unnecessary or redundant frames using a key frame extraction technique based on Histogram Difference (HD), which increases the system's accuracy and efficiency. To extract spatial features, the HCBSLR system uses VGG-19, and to extract temporal features, it uses BiLSTM. The accuracy of the suggested HCBSLR system is 87.67% on average. According to [31] proposed the Automated ISLRS for Emergency Words (AISLRSEW), a SLRS designed to identify ISL words commonly used in emergency situations.

The problem of identifying ISL words with same hand position and multiple viewing angle is addressed by the proposed AISLRSEW, which enhances identification accuracy by combining CNN with locally created features. BiLSTM is used to extract temporal features. On a dataset with eight sign-words, the suggested model had an average accuracy of 94.42%. By [32] developed a LiST (Lightweight Sign language Translation) system, a lightweight SLT framework that takes into account several modalities at once, including hand gestures, hands orientation, and facial expression, from an ISL video. A two-layered LSTM architecture processes the feature map created by the InceptionV3 handling the features linked to various signer modalities. Continuous ISL statements from the INCLUDE dataset were used to test the model. The experimental findings demonstrate that the LiST framework attained a high prediction accuracy of 95.9% and translation accuracy of 91.2%. In turn [33] proposed a vision-based system for ISL hand gesture recognition. Transfer learning is employed in conjunction with two distinct CNN models—Google Net and VGG16—to extract spatial characteristics. These CNN models are combined with the LSTM model to determine temporal features. Three distinct datasets of videos with 11, 64 and 8 classes are used to assess the system. On the three datasets, CNN-LSTM architecture with Google Net achieves remarkably recognition accuracy of 93.18%, 97.50% and 96.65%, respectively. According to [34] suggested a study on automatic ISL identification that could help deaf patients and Indian healthcare professionals communicate more effectively. A new dataset of dynamic hand gestures for ISL terms that deaf COVID-19 positive patients frequently employ for emergency communication is suggested. The suggested hand movements were recognized using a hybrid deep convolutional LSTM network model, which produced an average accuracy of 83.36%. In turn [35] has suggested a deep learning-based model that consists of trainable CNN and trainable stacked 2 bidirectional long short-term memory (S2B-LSTM) to recognize the dynamic gestures of ISL. The spatial features in the input video data have been extracted using the CNN architecture as a feature extractor. S2B-LSTM is used to extract the temporal relationship between the successive frames of video. Training and testing are conducted on dataset, which consists of 360 videos of ISL dynamic movements. The recognition accuracy of the CNN-S2B-LSTM model is 97.6%. To identify ISL terms for emergency scenarios, a brand-new spatial attention (SA) based SLRS called the Spatial Attention based Sign Language Recognition Module (SASLRM) is proposed by [36]. ISL word recognition is achieved by SASLRM through a combination of attention features from a SA module and convolution features from a pretrained VGG-19 model. BILSTM is used to extract temporal features.

On the ISL dataset, which contains eight emergency sign words, the suggested model achieved an average accuracy of 95.627%. By [37] proposed a system for automatic sign language identification that could help deaf patients and Indian healthcare professionals communicate more effectively. A new dataset of dynamic hand gestures for ISL of six medical terms that deaf patients frequently employ for emergency communication is developed. The hand movements were recognized using a hybrid deep convolutional LSTM network model, which produced a training accuracy of 100%. In turn. [38] suggested to use the MediaPipe holistic pipeline for feature extraction and LSTM network to recognize isolated words of ISL. INCLUDE and INCLUDE-50 are used to test the suggested approach. On INCLUDE-50 and INCLUDE, the accuracy achieved by the proposed method is 94.8% and 87.4%, respectively. Multi Featured Deep Network (MF-DNet), an occlusion tolerant SLRS, is suggested for identifying ISL words by [39] . The custom dataset of 8 emergency word is used. To eliminate unnecessary frames, the proposed MF-DNet employs a histogram difference based keyframe selection method. Pose features are combined with CNN features in the proposed MF-DNet to address the issues of occlusion, identical hand gestures, and multiple viewing angles. The suggested method makes use of a BiLSTM network for classification. On the ISL dataset, the average classification accuracy for the proposed SLRS was 96.88%. By [40] suggested a novel method for ISL recognition that integrates Visual Transformers (ViT), Keras, and advanced data augmentation approaches. The approach focuses on creating a Vision Transformer model that has been trained on a large include dataset and supplemented with mediapipe's keypoint information and image data. The validation approach yielded remarkable accuracy rate of 97.52% and a promising assessment loss of 0.2941. Summary of literature review of sensor based DISLR approach in tabular form is illustrated in Table 1. Summary of literature review of vision based DISLR approach in tabular form is illustrated in Table 2.

Table 1: Summary of review of Sensor based approach.

Author	Acquisition	Dataset/ No. of signs	Single/ double handed	Signing mode	Spatial Feature extraction method	Temporal Feature extraction method	Accuracy (%)
Kumar et al. [17]	Kinect and leap motion sensor	50 words	Both	Isolated	-	HMM and BLSTM-NN	95.60% for all signs
Mittal et al. [18]	Leap motion sensor	35 words	Single	Both	CNN	Modified LSTM	72.3%-signed sentence 89.5%-isolated sign
Bhagat et al., [19]	Microsoft Kinect camera	36 static sign character and 10 dynamic sign words	Both	Isolated	CNN	LSTM	99.08%
Sharma et al. [20]	inertial measurement units (IMUs)	Isolated sign-50 words, Continuous signed sentences-40	Both	Both	CNN	BILSTM, CTC	90.00%

Source: Authors, (2026).

Table 2: Summary of review of Vision based approach.

Author	Acquisition	Dataset/ No. of signs	Single/ double handed	Signing mode	Spatial Feature extraction method	Temporal Feature extraction method	Accuracy (%)
Uchil aditya P. and Jha, [21]	Smartphone	19 dynamic and one static words	Single	Isolated	Open Pose	CNN	85
Jayadeep et al. [9]	camera	20 words	Both	Isolated	Incpetionv3	LSTM	100
Likhar et al. [22]	camera	10 words	Both	Isolated	Resnet 101 + U-Net	LSTM	99.08
Sridhar et al. [10]	camera	Include,Inlcude-50 words	Both	Isolated	MobileNetv2	BILSTM	85.6, 94.5
Mistry et al. [11]	camera	7 words	Double	Isolated	Restnet50	LSTM	99.9
Singh [13]	camera	20 words	Both	Isolated	-	3D CNN	83.30
MuthuMari appan & Gomathi [14]	camera	50 words	Both	Isolated	Inceptionv3	LSTM	top-1 :- 95.9, top-3:- 99.46
Venugopalan & Reghunadhan [23]	camera	13 words	Both	Isolated	GoogleNet	LSTM	76.21

Mistree et al. [24]	camera	55 ISL Sentences	Both	Continuous	MobileNetv2	LSTM	91.00
Kothadiya et al. [25]	camera	11 words	Both	Isolated	InceptionResNetV2	LSTM and GRU	97
Subramanian et al. [26]	camera	13 words	Both	Isolated	Mediapipe	GRU	95
Ganpatye & Mane [27]	camera	40 words	Both	Isolated	Mediapipe	LSTM	92
Prathap et al. [28]	camera	Include 50 words	Both	Isolated	Mediapipe	BILSTM ,BERT TRANSFORMER	89.50
Katti et al. [29]	camera	Include 50 words	Both	Isolated	Inceptionv3	LSTM	86.70
S. Das et al. [30]	camera	20 words	Both	Isolated	VGG16	BILSTM	87.67
S. Das et al. [31]	camera	8 words	Both	Isolated	SIFT and BOF, VGG19	BILSTM	94.42
K et al. [32]	camera	words	Both	Isolated	Inception V3	LSTM	95.9
Pradip et al. [33]	camera	11, 64 and 8 words	Both	Isolated	GoogleNet	LSTM	93.18, 97.50, and 96.65
Venugopalan Reghunadhan [34]	camera	17 words	Both	Isolated	VGG16	BILSTM	83.36
Sharma & Singh [35]	camera	18 words	Both	Isolated	CNN	Stacked BiLSTM	97.6
S. Das et al. [36]	camera	8 words	Both	Isolated	VGG19+CSA(Con. Spatial attention)	BILSTM	95.62
H. V Das et al. [37]	camera	6 words	Both	Isolated	CNN	LSTM	100
Khartheesvar et al. [38]	camera	Include ,Include 50 words	Both	Isolated	Mediapipe	LSTM	87.4 ,94.8
S. Das et al. [39]	camera	8 words	Both	Isolated	(VGG19+Mediapipe)	BILSTM	96.8
Singla et al. [40]	camera	Include dataset	Both	Isolated	Mediapipe	Transformer	97.5

Source: Authors, (2026).

III. DISCUSSION

Below is a report on the dynamic ISL recognition system outcomes for our review with respect to research topics.Cameras were used in 83% of the study on dynamic ISL, as can be seen in Fig. 4 for ISL data acquisition. 3% of the study used Microsoft Kinect, 4% used leap motion sensors, 4% used a smartphone, 3% used inertial measurement units, 3% used kinect and leap motion-based sensor.

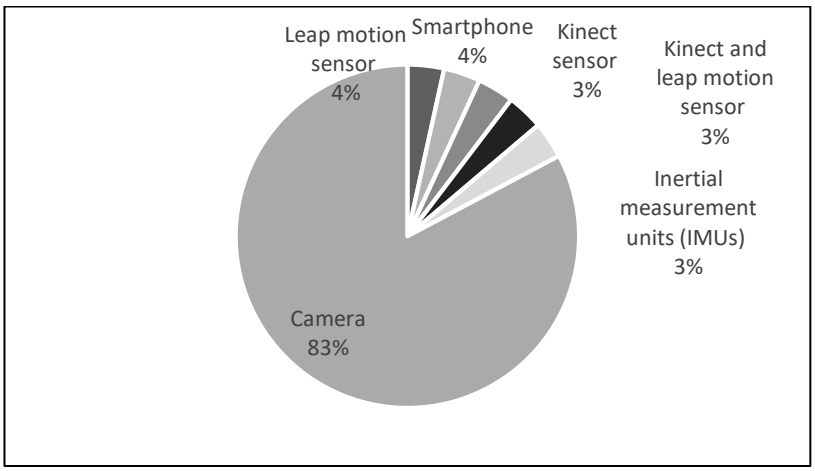


Figure 4: Data Acquisition Summary.
Source: Authors, (2026).

Fig. 5 illustrates that Dynamic ISL work has been performed 7% of the time on single-handed signs, 90% on both-handed signs, and 3% on double-handed signs.

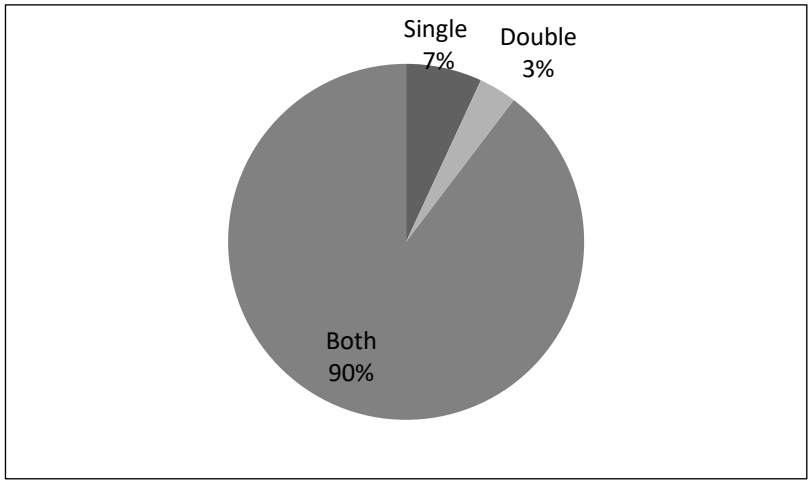


Figure 5: Hand Used Summary.
Source: Authors, (2026).

As illustrated in Fig. 6, isolated sign mode accounts for 90% of the signing modalities used for dynamic ISL research activities, while continuous sign mode accounts for 3% and both for 7%. LSTM has been used in 48% of the work on dynamic ISL as shown in Fig. 7, followed by BILSTM in 31%, CNN in 7%, GRU in 4%, HMM and BILSTM in 4%, LSTM and GRU in 3%, Transformer in 3%.

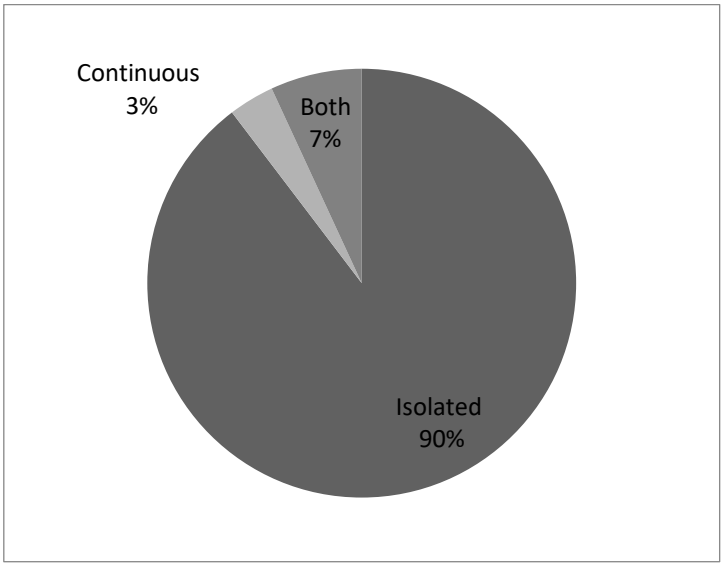


Figure 6: Signing Mode Summary.
Source: Authors, (2026).

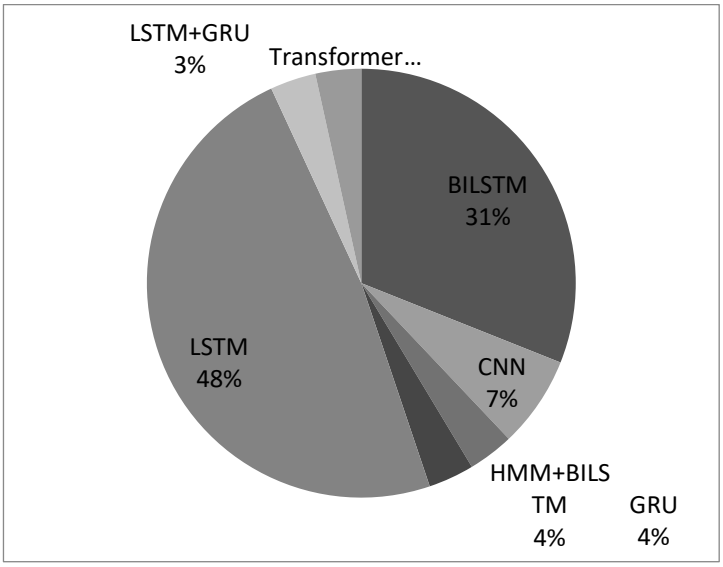


Figure 7: Deep learning Technique Summary.
Source: Authors, (2026).

According to Fig. 8, 69% of sign language recognition systems for dynamic ISL were able to reach an average accuracy of greater than 90%, whilst 24% of systems were able to achieve an accuracy of between 80 and 89%. Less than 7% of systems have an accuracy below 80%. There are two primary types of Dynamic Indian sign language recognition: continuous sign language recognition and isolated sign language recognition. One significant distinction between the two types is the supervisory information. Continuous ISL recognition addresses both the recognition challenge and the precise alignment between the video segments and the associated sentence level labels, whereas isolated ISL recognition is comparable to the action recognition field.

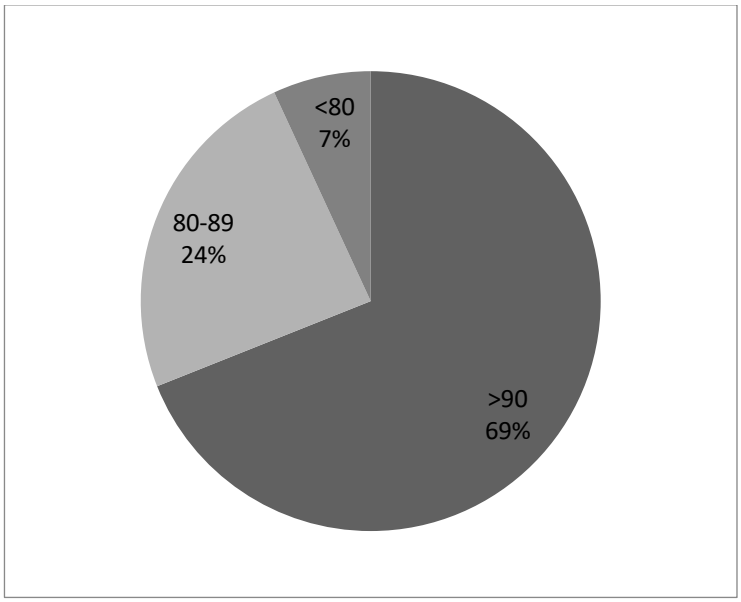


Figure 8: Accuracy Summary.
Source: Authors, (2026).

Recognition of continuous ISL is generally harder than recognition of isolated ISL. It is possible to think of isolated ISL recognition as a subset of continuous ISL recognition. A continuous ISL recognition system may perform better if it extracts more discriminative and descriptive characteristics from the video frames. Continuous dynamic signs are utilized at the sentence level, whereas isolated dynamic signs are used at the word level. There is still much space for enhancing performance in this field, even though current models in isolated and continuous sign language recognition show an increasing trend in model performance depending on DL skills in computer vision. Some potential future directions in this field include taking into account the attention mechanism, learning structured spatio-temporal patterns (like Graph Neural Networks models), utilizing multiple input modalities to benefit from multi-channel information, and applying prior knowledge on sign language. Sign Language recognition is more than just word, number, and alphabet recognition. The SLRS must recognize signs and create meaningful sentences from them in real time. To do this, it must recognize sign words and determine the context of the words. While SL recognition is a difficult task in and of itself, ISL introduces additional difficulties that make it harder for researchers to create an SLRS. The identification of a language's grammar rules is essential for language recognition; however, the grammar rules for ISL are not well established, making the process of creating an SLRS for ISL recognition difficult for academics. Another issue with ISL recognition is the lack of a consistent dataset with a broad vocabulary, since building an SLRS requires sufficient and reliable data. ISL alphabets and words use both single- and double-handed motions, unlike other SL. Signers occasionally overlap their hands when executing double-handed motions, which increases the difficulty of the segmentation and recognition challenge compared to other sign languages.

IV. CONCLUSION AND FUTURE WORK

Vision Based ISL enables people who are deaf or mute to communicate their thoughts and experiences. There is a growing trend in the usage of ISL recognition software for people. Using the keywords "Indian Sign Language Recognition," "Dynamic Indian Sign Language Recognition," and "Dynamic Indian Sign Language Recognition using Deep learning," only research publications published after 2017 were included in this analysis. Only online databases were searched for research papers for this investigation. There were no large-scale systems implemented that could process a broad vocabulary of signs in real time. In order to provide a more meaningful understanding of the technique, our literature aims to provide an overview of the research based on five parameters such as: accuracy rate, single/double-handed signs, data collection methodologies, signing style, and classification method. While this review is not intended to be exhaustive, it does offer a fair amount of information and illustrates the prevalence of research on the topic. The most widely used data acquisition tools, according to the statistics, were cameras (83%) and Kinect Senor (3%). A large portion of research on dynamic Indian sign language recognition systems has been conducted on isolated signs 90% and 90% of the studies done both single and double handed signs, with 69% of the systems having an accuracy rate of greater than 90%. It has been found that there are different sign language systems; LSTM has been used to complete 48% of the work. For large-scale systems, there is a higher effort requirement to identify dynamic Indian sign language. Research on deep learning in dynamic Indian sign language identification systems is limited. The majority of research in the field of dynamic Indian sign language recognition has been done on isolated signs. It is therefore important to use deep learning neural networks for the recognition of continuous dynamic Indian sign language.

V. AUTHOR'S CONTRIBUTION

Conceptualization: Manojkumar Patel.
Methodology: Manojkumar Patel, Narendra Patel.
Investigation: Manojkumar Patel.
Discussion of results: Manojkumar Patel.
Writing – Original Draft: Manojkumar Patel.
Writing – Review and Editing: Manojkumar Patel, Narendra Patel.
Resources: Manojkumar Patel.
Supervision: Narendra Patel.
Approval of the final text: Manojkumar Patel, Narendra Patel.

VI. REFERENCES

[1] A. Wadhawan and P. Kumar, "Sign language recognition systems: a decade systematic literature review," Arch Comput Methods Eng, vol. 28, 2021, doi: 10.1007/s11831-019-09384-2.

[2] R. Rastgoo, K. Kiani, and S. Escalera, "Word separation in continuous sign language using isolated signs and post-processing," Jul. 2022.

[3] S. Kr. and C. M. and P. B. Das Soumen and Biswas, "Intelligent Indian Sign Language Recognition Systems: A Critical Review," in ICT Systems and Sustainability, S. and J. A. Tuba Milan and Akashe, Ed., Singapore: Springer Nature Singapore, 2022, pp. 703–713.

[4] T. Raghuveera, R. Deepthi, R. Mangalashri, and R. Akshaya, "A depth-based Indian sign language recognition using microsoft kinect," Sādhanā, vol. 45, 2020, doi: 10.1007/s12046-019-1250-6.

[5] J. M. Patel Dhaval U. and Joshi, "Review of Indian Dynamic Sign Language Recognition System," in Proceedings of International Conference on Communication and Computational Technologies , S. and P. S. D. and P. M. Kumar Sandeep and Hiranwal, Ed., Singapore: Springer Nature Singapore, 2023, pp. 17–31.

[6] D. H. Neiva and C. Zanchettin, "Gesture recognition: a review focusing on sign language in a mobile context," Expert Syst Appl, vol. 103, 2018, doi: 10.1016/j.eswa.2018.01.051.

[7] M. Manoharan and P. Roy, "A Comprehensive Review of Sign Language Recognition: Different Types, Modalities, and Datasets," Jul. 2022.

[8] S. Das, S. kr. Biswas, M. Chakraborty, and B. Purkayastha, "A Review on Sign Language Recognition (SLR) System: ML and DL for SLR," in 2021 IEEE International Conference on Intelligent Systems, Smart and Green Technologies (ICISSGT), 2021, pp. 177–182. doi: 10.1109/ICISSGT52025.2021.00045.

[9] G. Jayadeep, V. V, V. Venugopal, V. S, and G. M., "Mudra: Convolutional Neural Network based Indian Sign Language Translator for Banks," 2020 4th International Conference on Intelligent Computing and Control Systems (ICICCS), pp. 1228–1232, 2020, [Online]. Available: https://api.semanticscholar.org/CorpusID:219990092

[10] A. Sridhar, R. G. Ganesan, P. Kumar, and M. Khapra, "INCLUDE: A Large Scale Dataset for Indian Sign Language Recognition," in Proceedings of the 28th ACM International Conference on Multimedia, in MM '20. New York, NY, USA: Association for Computing Machinery, 2020, pp. 1366–1375. doi: 10.1145/3394171.3413528.

[11] P. Mistry, V. Jotaniya, P. Patel, N. Patel, and M. Hasan, "Indian Sign Language Recognition using Deep Learning," in 2021 International Conference on Artificial Intelligence and Machine Vision (AIMV), 2021, pp. 1–6. doi: 10.1109/AIMV53313.2021.9670933.

[12] M. Varsha and C. S. Nair, "Indian Sign Language Gesture Recognition Using Deep Convolutional Neural Network," in 2021 8th International Conference on Smart Computing and Communications (ICSCC), 2021, pp. 193–197. doi: 10.1109/ICSCC51209.2021.9528246.

[13] D. K. Singh, "3D-CNN based Dynamic Gesture Recognition for Indian Sign Language Modeling," Procedia Comput. Sci., vol. 189, pp. 76–83, 2021, doi: https://doi.org/10.1016/j.procs.2021.05.071.

[14] H. MuthuMariappan and Gomathi, "Indian Sign Language Recognition through Hybrid ConvNet-LSTM Networks," EMITTER International Journal of Engineering Technology, 2021, [Online]. Available: https://api.semanticscholar.org/CorpusID:237383878

[15] A. Tyagi and S. Bansal, "Feature Extraction Technique for Vision-Based Indian Sign Language Recognition System: A Review," 2021, pp. 39–53. doi: 10.1007/978-981-15-6876-3_4.

[16] R. Rastgoo, K. Kiani, and S. Escalera, "Sign Language Recognition: A Deep Survey," Expert Syst. Appl., vol. 164, p. 113794, 2021, doi: https://doi.org/10.1016/j.eswa.2020.113794.

[17] P. Kumar, H. Gauba, P. P. Roy, and D. P. Dogra, "A multimodal framework for sensor based sign language recognition," Neurocomputing, vol. 259, 2017, doi: 10.1016/j.neucom.2016.08.132.

[18] A. Mittal, P. Kumar, P. P. Roy, R. Balasubramanian, and B. B. Chaudhuri, "A Modified LSTM Model for Continuous Sign Language Recognition Using Leap Motion," IEEE Sens. J., vol. 19, no. 16, pp. 7056–7063, 2019, doi: 10.1109/JSEN.2019.2909837.

[19] N. K. Bhagat, Y. Vishnusai, and G. N. Rathna, "Indian Sign Language Gesture Recognition using Image Processing and Deep Learning," in 2019 Digital Image Computing: Techniques and Applications (DICTA), 2019, pp. 1–8. doi: 10.1109/DICTA47822.2019.8945850.

[20] S. Sharma, R. Gupta, and A. Kumar, "Continuous sign language recognition using isolated signs data and deep transfer learning," J. Ambient Intell. Humaniz. Comput., vol. 14, no. 3, pp. 1531–1542, 2023, doi: 10.1007/s12652-021-03418-z.

[21]S. and S. B. G. Uchil Aditya P. and Jha, "Vision Based Deep Learning Approach for Dynamic Indian Sign Language Recognition in Healthcare," in Computational Vision and Bio-Inspired Computing, J. M. R. S. and B. V. E. and I. A. M. Smys S. and Tavares, Ed., Cham: Springer International Publishing, 2020, pp. 371–383.

[22] P. Likhar, N. K. Bhagat, and R. G. N, "Deep Learning Methods for Indian Sign Language Recognition," in 2020 IEEE 10th International Conference on Consumer Electronics (ICCE-Berlin), 2020, pp. 1–6. doi: 10.1109/ICCE-Berlin50680.2020.9352194.

[23] A. Venugopalan and R. Reghunadhan, "Applying deep neural networks for the automatic recognition of sign language words: A communication aid to deaf agriculturists," Expert Syst. Appl., vol. 185, p. 115601, 2021, doi: https://doi.org/10.1016/j.eswa.2021.115601.

[24] K. Mistree, D. Thakor, and B. Bhatt, “Towards Indian Sign Language Sentence Recognition using INSIGNVID: Indian Sign Language Video Dataset,” International Journal of Advanced Computer Science and Applications, vol. 12, no. 8, 2021, doi: 10.14569/IJACSA.2021.0120881.

[25] D. Kothadiya, C. Bhatt, K. Sapariya, K. Patel, A.-B. Gil-González, and J. M. Corchado, “Deepsign: Sign Language Detection and Recognition Using Deep Learning,” Electronics (Basel)., vol. 11, no. 11, 2022, doi: 10.3390/electronics11111780.

[26] B. Subramanian, B. Olimov, S. M. Naik, S. Kim, K.-H. Park, and J. Kim, “An integrated mediapipe-optimized GRU model for Indian sign language recognition,” Sci. Rep., vol. 12, no. 1, p. 11964, 2022, doi: 10.1038/s41598-022-15998-7.

[27] A. Ganpatye and S. Mane, “Motion Based Indian Sign Language Recognition using Deep Learning,” in 2022 2nd International Conference on Intelligent Technologies (CONIT), 2022, pp. 1–6. doi: 10.1109/CONIT55038.2022.9848275.

[28] K. B. Prathap, G. D. Swaroop, B. P. Kumar, V. Kamble, and M. Parate, “ISLR: Indian Sign Language Recognition,” in 2023 2nd International Conference on Paradigm Shifts in Communications Embedded Systems, Machine Learning and Signal Processing (PCEMS), 2023, pp. 1–6. doi: 10.1109/PCEMS58491.2023.10136062.

[29] R. K. Katti, S. C, P. Desai, and S. G, “Character and Word Level Gesture Recognition of Indian Sign Language,” in 2023 IEEE 8th International Conference for Convergence in Technology (I2CT), 2023, pp. 1–6. doi: 10.1109/I2CT57861.2023.10126314.

[30] S. Das, S. Kr. Biswas, and B. Purkayastha, “A deep sign language recognition system for Indian sign language,” Neural Comput. Appl., vol. 35, no. 2, pp. 1469–1481, 2023, doi: 10.1007/s00521-022-07840-y.

[31] S. Das, S. K. Biswas, and B. Purkayastha, “Automated Indian sign language recognition system by fusing deep and handcrafted feature,” Multimed. Tools Appl., vol. 82, no. 11, pp. 16905–16927, 2023, doi: 10.1007/s11042-022-14084-4.

[32] A. K, P. P, and R. C. Poonia, “LiST: A Lightweight Framework for Continuous Indian Sign Language Translation,” Information, vol. 14, no. 2, 2023, doi: 10.3390/info14020079.

[33] P. Patel and Narendra Patel, “Dynamic Hand Gesture Recognition for Indian Sign Language using Integrated CNN-LSTM Architecture,” International Journal of Next-Generation Computing, Nov. 2023, doi: 10.47164/ijngc.v14i4.1039.

[34] A. Venugopalan and R. Reghunadhan, “Applying Hybrid Deep Neural Network for the Recognition of Sign Language Words Used by the Deaf COVID-19 Patients,” Arab. J. Sci. Eng., vol. 48, no. 2, pp. 1349–1362, 2023, doi: 10.1007/s13369-022-06843-0.

[35] S. Sharma and S. Singh, “A Spatio-Temporal Framework for Dynamic Indian Sign Language Recognition,” Wirel. Pers. Commun., vol. 132, no. 4, pp. 2527–2541, Oct. 2023, doi: 10.1007/s11277-023-10730-8.

[36] S. Das, S. Kr. Biswas, and B. Purkayastha, “An Expert System for Indian Sign Language Recognition Using Spatial Attention–based Feature and Temporal Feature,” ACM Trans. Asian Low-Resour. Lang. Inf. Process., vol. 23, no. 3, Mar. 2024, doi: 10.1145/3643824.

[37] H. V Das, K. Mohan, L. Paul, S. Kumaresan, and C. S. Nair, “Transforming consulting atmosphere with Indian sign language translation,” Multimed. Tools Appl., vol. 83, no. 5, pp. 13543–13555, 2024, doi: 10.1007/s11042-023-15214-2.

[38] G. Khartheesvar, M. Kumar, A. K. Yadav, and D. Yadav, “Automatic Indian sign language recognition using MediaPipe holistic and LSTM network,” Multimed. Tools Appl., vol. 83, no. 20, pp. 58329–58348, 2024, doi: 10.1007/s11042-023-17361-y.

[39] S. Das, S. Kr. Biswas, and B. Purkayastha, “Occlusion robust sign language recognition system for indian sign language using CNN and pose features,” Multimed. Tools Appl., Apr. 2024, doi: 10.1007/s11042-024-19068-0.

[40] V. Singla, S. Bawa, and J. Singh, “Enhancing Indian sign language recognition through data augmentation and visual transformer,” Neural Comput. Appl., vol. 36, no. 24, pp. 15103–15116, Aug. 2024, doi: 10.1007/s00521-024-09845-1.

Journal of Engineering and Technology for Industrial Applications

ITEGAM-JETIA

Manaus, v.12 n.60, p.1310-1320. July/August, 2026.
DOI: https://doi.org/10.5935/jetia.v12i60.4076

ISSN ONLINE: 2447-0228

RESEARCH ARTICLE OPEN ACCESS

VISUAL FEATURE MAPPING AND FEATURE SELECTION FOR ROBUST IDS BASED ON CSE-CIC-IDS2018 DATASET

Satishkumar D. Prajapati*[1], Priyesh P. Gandhi[2], Sheshang Degadwala[3], Keyur Brahmbhatt[4], Swapnil M Parikh[5]

[1]Computer Engineering, Gujarat Technological University, Ahmedabad, Gujarat, India.
[2]Provost, Sigma University, Vadodara, Gujarat, India.
[3]Department of Computer Engineering, Sigma University, Vadodara, Gujarat, India.
[4]Department of Information and Technology, Birla Vishvakarma mahavidhyalaya, Vallabh Vidhyanagar, Gujarat, India.
[5]Computer Science and Engineering, Parul Institute of Technology, Parul University, Vadodara, Gujarat, India.

[1]https://orcid.org/0009-0008-1349-3082, [2]https://orcid.org/0000-0001-5338-3111, [3]https://orcid.org/0000-0002-2385-7790, [4]https://orcid.org/0000-0001-7478-3173, [5]https://orcid.org/0009-0005-8816-5508

E-mail: prajapati.satish90@gmail.com, priyeshgandhi@gmail.com, sheshang13@gmail.com, keyur.brahmbhatt@bvmengineering.ac.in

ARTICLE INFO

Article History
Received: March 13, 2026
Reviewed: April 16, 2026
Accepted: July 16, 2026
Published: August 31, 2026

Keywords:
Distributed Denial of Service,
Internet of Things,
Recursive Feature Elimination,
Ensemble Machine Learning,
Intrusion Detection Systems.

ABSTRACT

The rapid growth of Internet of Things (IoT) ecosystems posed a great risk to ubiquitous access to advanced cyber threats and thus the design of effective Intrusion Detection Systems (IDS) has become critical in ensuring the safeguard of secure network structures. Nonetheless, most classic deep learning methods, especially Recurrent Neural Networks (RNNs) tend to exhibit low generalization and low interpretability to tabular network traffic data and may fail to discriminate between different and intricate attacks. To overcome this issue, this paper presents a visual feature-based IDS model, which converts network traffic characteristics in the form of tabular features into RGB matrix images to harness the power of effective computer vision algorithms to detect intrusions. Recursive Feature Elimination (RFE) is applied to determine the best informative feature before generating an image, enhance features and decrease redundancy. The acquired visual representations are subsequently categorized by the EfficientNetB0 design by way of transfer learning. Experimental testing shows that the suggested method has a 98 percent accuracy, precision, recall, and F1-score, Matthews Correlation Coefficient (MCC) of 0.97, and AUC-ROC of 0.99. Comparatively, the RNN original does not reach the same level as it only gives 89% on performance metrics with MCC of 0.88 and AUC-ROC of 0.88. The above findings indicate the ability of feature selection combined with visual deep learning to facilitate scalable, precise, and real-time intrusion detection of modern-day IoT environments.

Copyright ©2026 by authors and Galileo Institute of Technology and Education of the Amazon (ITEGAM). This work is licensed under the Creative Commons Attribution International License (CC BY 4.0).

I. INTRODUCTION

Through the accelerated development of network systems and the spread of the Internet of Things (IoT) gadgets, the area of potential cyberattacks has increased dramatically. With the growing number of businesses and people depending on interconnected infrastructures, it has become part of the priorities to secure these systems against different threats to include Distributed Denial of Service (DDoS), probing, user-to-root (U2R), and remote-to-local (R2L) attacks. IDSS is an important tool that is used to observe the network traffic and detect dangerous actions as a line of defense after firewalls and antivirus programs. Nevertheless, the increasing complexity of cyberattacks is posing significant threats to more traditional methods of IDS, particularly those that are based on fixed rules or other more traditional machine learning classifiers that tend to be weak in terms of scalability, adaptability and high dimensional features. New developments in the field of deep learning created new opportunities to enhance the capabilities of IDS, especially the application of the Convolutional Neural Networks (CNNs) and the Transfer Learning models.

Such techniques have proven to be highly successful in many fields, particularly computer vision problems because they have strong powers of representation learning. Regarding IDS, there is a growing interest in using such methods in order to transform structured tabular network data into image formats that CNNs can process efficiently. This data-to-image encoding conversion provides the ability to encode latent geometric and contextual correlations of the traffic features that may be missed in the data with an older algorithm. The approach is even more powerful when paired with pre-trained models such as EfficientNet, since it embraces both hierarchies of features and efficiency. However, it is not so easy to transform raw network traffic into meaningful image representations. Among the main problems is the large dimensionality and sparsity of IDS data, including CSE-CIC-IDS2018, which have many redundant or irrelevant features. Such extraneous properties have the adverse effect of affecting the performance of deep learning models and lead to overfitting, high computational cost, and poor detection accuracy. Thus, before transformation is required, there must be effective feature selection. Recursive Feature Elimination (RFE) has been one of the most used and interpretable feature selection algorithms where less important features are dropped out one at a time due to model weight coefficients. With RFE, not all dimensions of the dataset are required to be retained, the most relevant ones are kept so as to visual mapping is done. This study suggests a new hybrid IDS model that integrates recursive feature selection, visual feature encoding as well as transfer learning. Preprocessing steps include the removal of null values, label encoding and normalization which is the beginning of the pipeline.

The smaller feature space is then coded into 64x64RGB images where temporal and structural relationships can be maintained as pixel intensity values. Through these images, a pre-trained EfficientNetB0 model is fine-tuned and used to execute binary and multi-class intrusion detection using the scalable nature of its architecture. The proposed model is measured against the standard measures of accuracy, precision, recall, F1-score, Matthews Correlation Coefficient (MCC), and Area Under the Receiver Operating Characteristic Curve (AUC-ROC). The main findings of this research are triple: (1) the effective data-to-image transformation of network traffic based on the RFE-selected features, (2) the application of EfficientNetB0 to deep visual feature extraction in the area of the IDS, and (3) the comparison of the model with the traditional structures (RNN) to prove the best results. After intensive testing of the presented system on the CSE-CIC-IDS2018 dataset, the results are encouraging, and the proposed system has accuracy and F1-score, which are over 98, much higher than the results of the baseline models. The rest of this paper will be organized as follows: Section 2 shows the related literature in the area of intrusion detection with the help of machine-learning tools and image-based techniques. Section 3 outlines the proposed methodology that comprises data preprocessing, feature selection, image conversion and model training. The 4th section will offer the performance analysis and results of the experiment. Lastly, Section 5 wraps up the research and gives the future directions of the research.

II. THEORETICAL REFERENCE

The recent past has seen a boom in the research on optimizing the efficiency, robustness, and accuracy of intrusion detection systems (IDS), especially by incorporating deep learning and hybrid frameworks. This part of the paper is a review of notable works in this field and the research gaps that have been identified that lead to the application of the proposed work. Markkandeyan et al. suggested a new hybrid deep learning model coupled with an optimization algorithm in [1] to enhance the ability to detect cyber threats. Their model showed improvement in detection performance, and no investigation was carried out on visual encoding of features or transfer learning adaptability. In the same manner, [2] have dealt with the issue of DDoS detection based on adaptive transfer learning. Although they are useful in dynamic network setting, their analysis failed to investigate recursive feature selection or feature visual representation, which might result in an even better generalization. By [3] compared several bio-inspired optimization algorithms on the CSE-CIC-IDS2018 dataset. Their research was useful in comparison but focused only on the traditional numerical features and did not rely on the deep visual feature extraction. In turn [4] were concerned with the machine learning-based IDSs adapted to cloud networks. Despite its practicality, the study did not have a dimension reduction procedure like the recursive feature selection to deal with the redundant features. According to [5] focused on cross-dataset generalization in IDS by performing cross-dataset performance analysis. Although their results have emphasized generalization, they have not examined how transfer learning with image-based inputs can influence robustness. By [6] applied deep learning to Software Defined Networks (SDNs) to identify intrusion, and the flexible character of the DL technique in the existing network architecture but did not consider the improvement of performance through CNN-based visual encoding. In turn [7] proposed a transformer-based IDS with transfer learning to solve the imbalance in traffic data. Though this model had good performance, the absence of a systematic elimination of features and lack of a hybrid pipeline that combined the use of CNNs did not make the model scalable.

According to [8], in their turn, performed a general review of IDS datasets, where the data quality and structure variation also prevalent, yet they did not carry out their analysis until the usefulness of visual transformations to standardized processing. By [9] have introduced a working model of the IDS that works in cloud computing, which is an integration of detection accuracy and low latency. Nevertheless, they failed to combine the visual aspect and recursive selection to determine the best feature subset. According to [10] suggested the use of DTL-IDS, which utilizes the deep transfer learning and genetic algorithm. Although the study showed good outcomes, it was not focused on image representations or effective feature filtering methods. In turn [11] addressed the issue of class imbalance in the cloud setting with deep learning. However, visual feature maps or multi-modal representation integration were not studied. By [12] offered an overall deep learning-based IDS framework that is well-accurate, though not scalable to further dimensions and complexities of features. In turn [13] presented a collaborative weighted ensemble DNN to coordinated attacks, which improved detection of heterogeneous networks. Nevertheless, their approach did not feature any techniques of transforming features to visual modalities. In turn [14] used contrastive variational autoencoders and metric learning to detect attacks in blockchain-enhanced cloud of things, demonstrating the power of deep generative models, but lacking the incorporation of classic feature selection techniques. According to [15] adopted a portable deep learning architecture to be applied to IDS in the IoT. Their approach, though promising, did not look into the possibility of combining recursive feature selection with visual encoding of CNNs. In turn [16] designed a new IoT IDS based on the deep learning algorithm against DDoS attacks. They concentrated on the type and model tuning of the attacks that they did and ignored the effect of the preprocessing pipeline.

To deal with the issue of data imbalance, [17] came up with a multi-classification model which incorporates reconstruction and feature matching. Though successful, they did not use recursive feature elimination or CNN-based visual learning in their model. By [18] created a deep learning IDS on the cloud platform, but the scheme did not have the hybrid feature extraction or transfer learning parts. According to [19] extensively examined the CIC-IDS2017 data but did not provide information on the CSE-CIC-IDS2018, as well as the consequences of feature changes. By [20] employed the optimized CNNs transfer learning on cloud-IoT IDS. Their design allows deep extraction of features though its feature selection mechanisms are absent which affects the efficiency of the model. The three-phase optimization method was used by Songma et al. on the CSE-CIC-IDS2018 dataset [21]. Despite its thoroughness, it lacks image-based transformations and hence cannot be used with sophisticated deep architectures. According to [22] developed deep learning models of the IoT IDS with CIC-IDS2017 but did not consider the strategies of feature selection and visual mapping. By [23] have created a hybrid feature-optimized deep learning IDS. Although the purpose of their study is similar, they did not investigate the usefulness of visual encoding or CNN fine-tuning on pre-trained models. In turn [24] suggested dual CNN to detect attacks, that demonstrated excellent performance with IoT networks, however, did not require recursive selection of the features or learning across domains. This model is presented by [25] as a two-stage model consisting of LSTM and Autoencoders. Although temporal learning was improved, no analysis was done on the visual-spatial patterns. According to [26] adopted a multimodal deep transfer learning model in SDNs to detect attacks, but the issue of converting the numerical features into the image-based feature was not investigated. In turn [27] tested the vulnerability of ML-based IDSs to adversarial attacks through CICIDS2017. They did not use the CSE-CIC-IDS2018 dataset in their work or did not consider deep hybrid pipelines where visual features are used. The performance of most of the current models has been extremely good in detecting with the classical or hybrid deep learning methods. Nonetheless, few studies have focused on the combination of recursive feature selection with visual features encoding by transfer learning architectures based on CNN. Also, most of the research was concentrating either on feature optimization or deep learning, and rarely both in a study towards an effective IDS. To address this critical gap, this paper uses RFE to reduce dimensionalities, converting the chosen features to RGB visual maps, and uses EfficientNetB0 to extract features, thereby proposing a full-fledged and scalable pipeline of intrusion detection.

III. MATERIALS AND METHODS

Figure 1 Novel flowchart is the visualization of an end-to-end deep learning pipeline of the Intrusion Detection System (IDS) involving image-based representation of tabular network data and then transfer learning using the EfficientNetB0 model. The technical description of each block in detail can be found below with the corresponding equations and techniques:

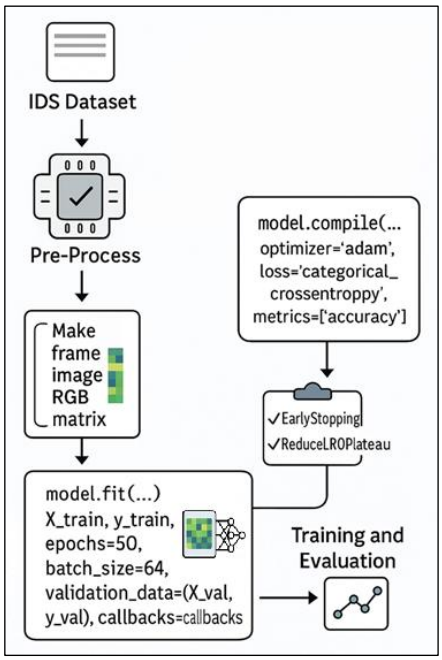


Figure 1: Proposed System Flow Diagram.
Source: Authors, (2026).

III.1 PSEUDO CODE

```
D ← load_dataset("CSE-CIC-IDS2018")
D ← preprocess(D)  // null removal, label encoding
images ← tabular_to_image(D)  // reshape to 64×64×3 RGB matrices
labels ← extract_labels(D)
X_train, X_val, y_train, y_val ← train_test_split(images, labels, test_size=0.2)
model ← EfficientNetB0(pretrained=True, include_top=False)
model ← add_classification_head(model, num_classes=number_of_classes)
model.compile(optimizer='adam', loss='categorical_crossentropy', metrics=['accuracy'])
callbacks ← [EarlyStopping, ReduceLROnPlateau]
```

10: model.fit(X_train, y_train, epochs=50, batch_size=64, validation_data=(X_val, y_val), callbacks=callbacks)
11: y_pred ← model.predict(X_val)
12: y_pred_cls ← argmax(y_pred, axis=1)
13: y_val_cls ← argmax(y_val, axis=1)
14: acc ← Accuracy(y_val_cls, y_pred_cls)
15: prec ← Precision(y_val_cls, y_pred_cls)
16: rec ← Recall(y_val_cls, y_pred_cls)
17: f1 ← F1(y_val_cls, y_pred_cls)
18: auc ← AUC_ROC(y_val_cls, y_pred, multi_class='ovr')
19: mcc ← MCC(y_val_cls, y_pred_cls)
20: return acc, prec, rec, f1, auc, mcc

III.2 DATASET

The dataset CSE-CIC-IDS2018 [3] presented in Table 1 is one of the most popular benchmarks to test the work of intrusion detection systems in network security research. It has a complex and lifelike collection of network traffic characteristics emulating current assaults in IoT and enterprise settings. The one used in this work has 74218 rows and 78 feature columns, that is, both benign and malicious traffic. The dataset has seven different classes, Benign, Bot, BruteForce, DDoS, DoS, Infiltration and WebAttack, with an equal sample count in each one of them. This equal distribution is a guarantee of fair performance assessment of classification models of all types of attacks. A sample has an exhaustive repertoire of traffic characteristics like flow lifetime, packet sizes, TCP flags, protocol types, and statistical indicators, like inter-arrival time, can be used to identify subtle patterns related to different attack vectors. The variety of the dataset enables the simulation of high-volume (e.g., DDoS, DoS) as well as low-and-slow attacks (e.g., Infiltration, WebAttack) observed in the real-life environment. The CSE-CIC-IDS2018, which is widely used by a recent intrusion detection research, can be used on both binary (Benign vs. Attack) and multi-class classification problems. It is very varied and large-scale, so it is perfect in training and benchmarking ensemble models, deep learning architectures, real-time threat detection pipelines.

Table 1: Dataset Columns Description.

Column Name	Description
Protocol	Network protocol used in the flow (e.g., TCP, UDP).
Flow Duration	Total duration of the flow in microseconds.
Total Fwd Packets	Number of packets sent in the forward direction.
Total Backward Packets	Number of packets sent in the backward direction.
Fwd Packets Length Total	Total length of all forward packets.
Bwd Packets Length Total	Total length of all backward packets.
Fwd Packet Length Max	Maximum length among forward packets.
Fwd Packet Length Min	Minimum length among forward packets.
Fwd Packet Length Mean	Average length of forward packets.
Fwd Packet Length Std	Standard deviation of forward packet lengths.
Bwd Packet Length Max	Maximum length among backward packets.
Bwd Packet Length Min	Minimum length among backward packets.
Bwd Packet Length Mean	Average length of backward packets.
Bwd Packet Length Std	Standard deviation of backward packet lengths.
Flow Bytes/s	Number of bytes per second transmitted in the flow.
Flow Packets/s	Number of packets per second transmitted in the flow.
Flow IAT Mean	Mean inter-arrival time between packets.
Flow IAT Std	Standard deviation of inter-arrival time.
Flow IAT Max	Maximum inter-arrival time in the flow.
Flow IAT Min	Minimum inter-arrival time in the flow.
Fwd IAT Total	Total inter-arrival time for forward packets.
Fwd IAT Mean	Average inter-arrival time of forward packets.
Fwd IAT Std	Standard deviation of forward inter-arrival time.
Fwd IAT Max	Maximum inter-arrival time for forward packets.
Fwd IAT Min	Minimum inter-arrival time for forward packets.
Bwd IAT Total	Total inter-arrival time for backward packets.
Bwd IAT Mean	Average inter-arrival time of backward packets.
Bwd IAT Std	Standard deviation of backward inter-arrival time.
Bwd IAT Max	Maximum inter-arrival time for backward packets.
Bwd IAT Min	Minimum inter-arrival time for backward packets.
Fwd PSH Flags	Number of PSH flags set in forward packets.
Bwd PSH Flags	Number of PSH flags set in backward packets.
Fwd URG Flags	Number of URG flags set in forward packets.
Bwd URG Flags	Number of URG flags set in backward packets.
Fwd Header Length	Total header length of forward packets.
Bwd Header Length	Total header length of backward packets.
Fwd Packets/s	Forward packets transmitted per second.
Bwd Packets/s	Backward packets transmitted per second.

Packet Length Min	Minimum packet length in the flow.
Packet Length Max	Maximum packet length in the flow.
Packet Length Mean	Average packet length in the flow.
Packet Length Std	Standard deviation of packet lengths.
Packet Length Variance	Variance of packet lengths.
FIN Flag Count	Number of packets with FIN flag.
SYN Flag Count	Number of packets with SYN flag.
RST Flag Count	Number of packets with RST flag.
PSH Flag Count	Number of packets with PSH flag.
ACK Flag Count	Number of packets with ACK flag.
URG Flag Count	Number of packets with URG flag.
CWE Flag Count	Number of packets with CWE flag.
ECE Flag Count	Number of packets with ECE flag.
Down/Up Ratio	Download to upload traffic ratio.
Avg Packet Size	Average size of all packets.
Avg Fwd Segment Size	Average size of forward segments.
Avg Bwd Segment Size	Average size of backward segments.
Fwd Avg Bytes/Bulk	Average bytes per forward bulk.
Fwd Avg Packets/Bulk	Average packets per forward bulk.
Fwd Avg Bulk Rate	Average forward bulk transmission rate.
Bwd Avg Bytes/Bulk	Average bytes per backward bulk.
Bwd Avg Packets/Bulk	Average packets per backward bulk.
Bwd Avg Bulk Rate	Average backward bulk transmission rate.
Subflow Fwd Packets	Number of forward packets in subflows.
Subflow Fwd Bytes	Number of forward bytes in subflows.
Subflow Bwd Packets	Number of backward packets in subflows.
Subflow Bwd Bytes	Number of backward bytes in subflows.
Init Fwd Win Bytes	Initial window size in forward direction.
Init Bwd Win Bytes	Initial window size in backward direction.
Fwd Act Data Packets	Number of active data packets in forward direction.
Fwd Seg Size Min	Minimum segment size in forward direction.
Active Mean	Mean active time of flow.
Active Std	Standard deviation of active time.
Active Max	Maximum active time.
Active Min	Minimum active time.
Idle Mean	Mean idle time of flow.
Idle Std	Standard deviation of idle time.
Idle Max	Maximum idle time.
Idle Min	Minimum idle time.
Label	Class labels

Source: Authors, (2026).

III.3 PRE-PROCESSING: NULL VALUE HANDLING AND ENCODING

After getting the dataset, data pre-processing is the initial step that is critical in that it serves to clean the dataset and prepare it to go through machine learning algorithms. The dataset, which was based on [23], has several features that can have null or missing values and has categorical variables that cannot be directly interpreted in machine learning models.

- Null Value Handling: Missing values in the dataset can degrade the performance of classifiers. Let the dataset be represented as a matrix $X \in \mathbb{R}^{nxm}$, where $n = 1500$ samples and m features. A missing value in element x_{ij} (i.e., the value at the ith row and jth column) is either removed if the percentage of missingness is negligible, or imputed using statistical methods such as: Mean imputation:

$$x_{ij} = (1/N) \sum_{k=1}^{N} x_{kj} \quad (1)$$

K-Nearest Neighbors imputation (KNN):

$$x_{ij} = \text{mean}(\{x_{pj} \mid x_p \in N_k(x_i)\}) \quad (2)$$

- Encoding: Categorical variables such as protocol or flag type are transformed into numerical format using encoding schemes. For nominal variables $C = \{c_1, c_2, \ldots, c_k\}$, One-Hot Encoding creates binary vectors for each class label:

$$\text{Encoded}(c_j) = [0, 0, \ldots, 1, \ldots, 0] \quad (3)$$

III.4 RECURSIVE FEATURE ELIMINATION (RFE)

Once the data is filtered and coded numerically, the second stage is Recursive Feature Elimination (RFE). It is a feature selection algorithm that is designed to reduce the dimensionality of the feature space and retain the most predictive features.

$$X = [x_1, x_2, \ldots, x_m] \tag{4}$$

$$\text{Feature Set}_{t+1} = \text{Feature Set}_t \setminus \{\text{argmin}_{xj} \in \text{Feature Set}_t \, I(x_j)\} \tag{5}$$

III.5 DATA TO VISUAL FEATURE

In this stage, structured tabular data is transformed into image representations to enable deep learning-based feature extraction. A At this phase, structured tabular data is converted into image representations to facilitate feature extraction by using deep learning. A set of 64 samples represented by numerical feature vectors is clumped and reformed into a grid of 64x64. This grid is then normalized and reproduced in three color channels (R, G, B), which forms an RGB image of dimensions 64x64x3. Such metamorphosis eases the process of visual pattern recognition by convolutional neural networks. Normalization Equation:

$$x_{norm(i,j)} = \frac{\big(x(i,j) - \min\big(x(:,j)\big)\big)}{\big(\max\big(x(:,j)\big) - \min\big(x(:,j)\big)\big)} \tag{6}$$

Where:

$x(i,j)$ represents the j-th feature of the i-th sample. $min(x(:,j))$ and $max(x(:,j))$ are the minimum and maximum values for the j-th feature across all samples. $x\_norm(i,j)$ is the normalized feature value.

III.6 HYPER-TUNE EFFICIENTNETB0 MODEL

In this step, efficientNetB0 is utilized, which is a high-performance convolutional neural network with a reduced number of parameters, in order to perform intrusion classification on images. It uses scaling of compounds to balance between network depth, width and resolution. This enhances greater accuracy as well as computational efficiency.
Compound Scaling Equations:

$$depth\,(d) = \alpha\text{^}\varphi \tag{7}$$

$$width\,(w) = \beta\text{^}\varphi \tag{8}$$

$$resolution\,(r) = \gamma\text{^}\varphi \tag{9}$$

Subject to the constraint:

$$\alpha * \beta^2 * \gamma^2 \approx 2 \tag{10}$$

Where:

φ (phi) is a coefficient controlling the overall model scale. α, β, and γ are constantly identified through optimization. This scaling method ensures consistent improvements across network dimensions.

III.7 EVALUATION METRICS

After model training, the ensemble classifier is evaluated using a comprehensive set of metrics that capture different dimensions of performance. Accuracy: Measures overall correctness:

$$Accuracy = \frac{(TP + TN)}{(TP + TN + FP + FN)} \tag{11}$$

Precision and Recall: Precision measures the correctness of positive predictions, and recall measures completeness:

$$Precision = \frac{TP}{(TP + FP)} \tag{12}$$

$$Recall = \frac{TP}{(TP + FN)} \tag{13}$$

F1-Score: The harmonic means of precision and recall:

$$F1 = 2 * \frac{(Precision * Recall)}{(Precision + Recall)} \tag{14}$$

K-Fold Cross Validation: The dataset is split into K equal parts. For each iteration, $K - 1$ parts are used for training and 1 for testing. This is repeated K times, and the results are averaged:

$$Cross - validation\ Accuracy = \left(\frac{1}{K}\right) \sum_{i=1}^{K} Accuracy_i \tag{15}$$

Matthews Correlation Coefficient (MCC): A balanced measure for classification performance:

$$MCC = \frac{(TP * TN - FP * FN)}{\sqrt{((TP + FP)(TP + FN)(TN + FP)(TN + FN))}} \quad (16)$$

This measure is especially applicable to multi-class data or in data with an imbalance in the classes since it considers all four classes of confusion matrices. This new model is the best way to combine tabular-to-image transformation, deep CNN feature extraction, and feature selection to address the intrusion detection as a visual classification problem as a paradigm shift as compared to conventional ideas.

IV. RESULTS AND DISCUSSIONS

The analysis of the results was carried out on the Google Colab platform in the T4 environment to provide a powerful training and evaluation of the proposed ensemble intrusion detection model. A partial view of the dataset that is being used is shown in Figure 2. It reveals different network traffic attributes including Protocol, Flow Duration, Total Fwd Packets, and Total Backward Packets, and their numeric values of the different records. The first perspective provides an impression of raw data structure without any processing.

	Protocol	Flow Duration	Total Fwd Packets	Total Backward Packets	Fwd Packets Length Total	Bwd Packets Length Total	Fwd Packet Length Max	Fwd Packet Length Min	Fwd Packet Length Mean	Fwd Packet Length Std	...
0	6	94658	6	7	708	3718.0	387	0	118.000000	159.284653	...
1	6	206	2	0	0	0.0	0	0	0.000000	0.000000	...
2	6	165505	3	1	0	0.0	0	0	0.000000	0.000000	...
3	6	102429	6	7	708	3718.0	387	0	118.000000	159.284653	...
4	6	167	2	0	0	0.0	0	0	0.000000	0.000000	...
...	...	...	...	...	...	...	...	...	...	...	...
4786606	6	61223155	203	104	56083	189884.0	680	0	276.270935	291.698975	...
4786607	6	346	3	0	0	0.0	0	0	0.000000	0.000000	...
4786611	6	60530493	203	104	56330	189985.0	680	0	277.487671	292.868774	...
4786612	6	1632	3	0	0	0.0	0	0	0.000000	0.000000	...
4786617	6	61705817	203	102	55650	188094.0	680	0	274.137939	292.130066	...

74218 rows × 78 columns

Figure 2: Dataset Reading.
Source: Authors, (2026).

Figure 3 bar chart is a ranking of features in terms of Recursive Feature Elimination (RFE). The features of lower rankings are assumed to have more significance, meaning that the very first features on the left, i.e. Protocol and Flow Duration, were found to be the most important to the performance of the model, which has resulted in the top 30 being selected.

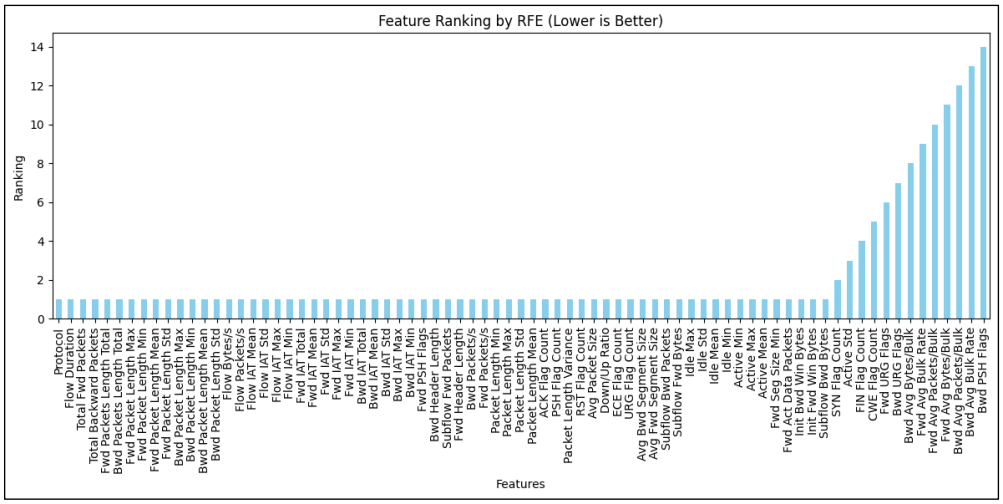


Figure 3: RFE 30-Features Selected.
Source: Authors, (2026).

Figure 4 provides the visual representations based on the network traffic information according to various types of attacks (Bot, Brute force, DDoS, DoS, Infiltration, WebAttack) and regular traffic. The image of each image is a visual fingerprint of that image in its class, and it can be initially believed that the raw data of network flow is converted into images to be classified.

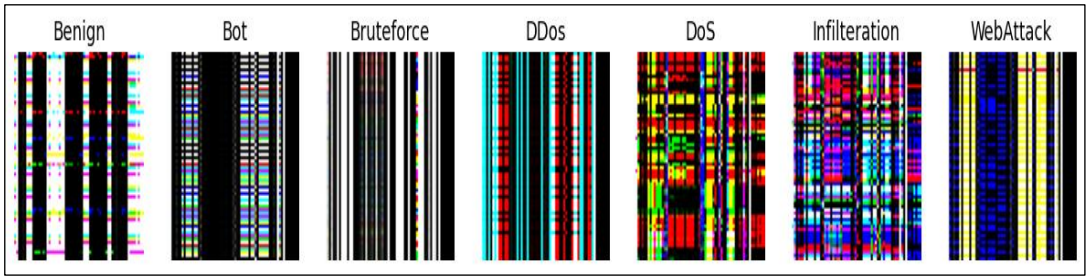


Figure 4: Sample of Generated Visual Feature of Each class.
Source: Authors, (2026).

Figure 5 illustrates the two plots namely: Model accuracy and Model loss after 50 epochs of the proposed EfficientNetB0 model. Accuracy plot indicates that both training and validation accuracy values are approaching and converging towards 1.0, whereas the loss plot indicates that both the training and validation loss values are approaching and converging towards 0.0 which is a good indication of learning and generalization.

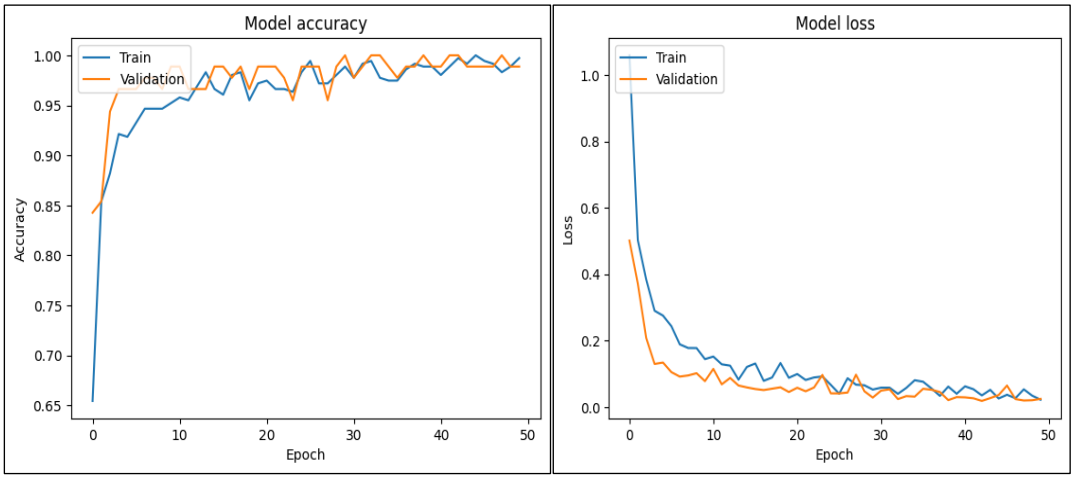


Figure 5: Proposed EfficientNetB0 Model Performance.
Source: Authors, (2026).

Figure 6 is a confusion matrix and a classification report, which assesses the performance of the EfficientNetB0 model. The confusion matrix indicates the number of true labels and predicted labels of each class, whereas the classification report indicates the properties of precision, recall, f1-score, and support, which indicates high accuracy (0.98) in the majority of attack types and benign traffic.

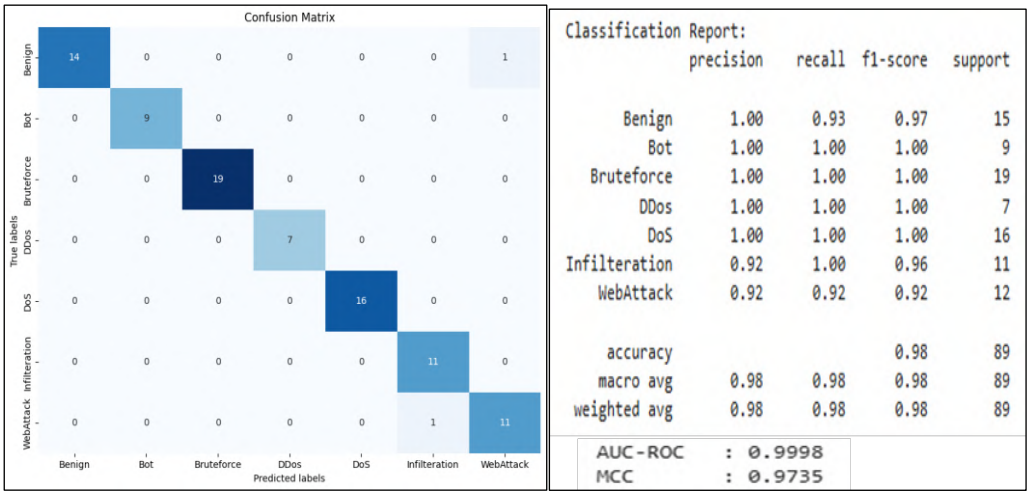


Figure 6: Proposed EfficientNetB0 Model Evaluation.
Source: Authors, (2026).

Figure 7 depicts multiclass ROC curve the visualization of the True Positive rate versus the False Positive rate of each class (Class 0 to Class 6). The curves of all classes are near the upper-left corner, and their AUC values are equal to 1.00, meaning that EfficientNetB0 model has a very high discriminative power with all types of traffic.

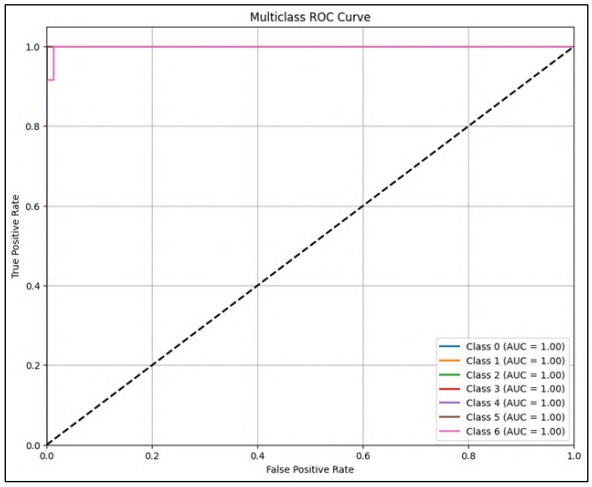


Figure 7: Proposed EfficientNetB0 Model ROC Curve.
Source: Authors, (2026).

Table 2: Proposed EfficientNetB0 Model K-Fold Validation.

Fold	Accuracy	Precision	Recall	F1-Score	MCC
1	1.0000	1.0000	1.0000	1.0000	1.0000
2	1.0000	1.0000	1.0000	1.0000	1.0000
3	1.0000	1.0000	1.0000	1.0000	1.0000
4	1.0000	1.0000	1.0000	1.0000	1.0000
5	0.9775	0.9788	0.9771	0.9775	0.9739

Source: Authors, (2026).

Table 2 contains the performance of the EfficientNetB0 model in 5-fold cross-validation. In the four initial folds, the model scores (1.0000) on Accuracy, Precision, Recall, F1-Score, and MCC, which indicates that the model is highly consistent in and has excellent performance. Although the fifth fold has somewhat lower yet very high measures (around 0.97), the outcome of the whole model reflects the strength and stability of the model.

Table 3: Comparative Analysis with Existing Research.

Model	ACC (%)	P (%)	R (%)	F1-Score (%)	MCC	AUC-ROC
Transformer-ID (from [7])	0.97	0.97	0.96	0.96	0.95	0.97
Hybrid DL+GA (from [10])	0.96	0.95	0.95	0.95	0.94	0.96
LSTM-AE (from [25])	0.94	0.93	0.94	0.93	0.92	0.94
CNN (from [27])	0.91	0.9	0.91	0.9	0.89	0.91
RNN	89%	89%	89%	89%	0.88	0.88
Proposed Model EfficientNetB0	98%	98%	98%	98%	0.97	0.99

Source: Authors, (2026).

Table 3 provides the performance of the Proposed EfficientNetB0 Model and a few of the existing research models (Transformer-ID, Hybrid DL+GA, LSTM-AE, CNN, RNN) in terms of different metrics: Accuracy, Precision, Recall, F1-Score, MCC, and AUC-ROC. The suggested EfficientNetB0 model is consistently better in the mentioned metrics (the accuracy of the model is 98% and the AUC-ROC is 0.99), which means that it is much more effective in the task than all the works listed above.

V. CONCLUSIONS

To sum up, in this paper, I have introduced a solid and precise intrusion detection model based on an EfficientNetB0 architecture on a balanced subset of the CSE-CIC-IDS2018 dataset with 74,218 rows and 78 features, and seven classes: Benign, Bot, BruteForce, DDoS, DoS, Infiltration and WebAttack. The proposed model also performed much better than the currently existing methods in all evaluation metrics. In particular, the EfficientNetB0 model had an accuracy, precision, recall, and F1-score of 98, the Matthews Correlation Coefficient (MCC) of 0.97, and the AUC-ROC of 0.99. Our model had better detection capacity and fewer false positives than Transformer-ID [7] (97%), Hybrid DL+GA [10] (96%), and LSTM-AE [25] (94%), which are all baseline models. This experiment validates the success of EfficientNetB0 in the extraction of high-level features of structured network data as well as the detection of both volumetric and stealthy attacks. To apply the framework to future work, the structure can be expanded with the incorporation of temporal models such as LSTM or attention systems with Transformers to promote the achievement of sequential attack patterns within the real-time traffic. The strategy to use online learning will help the system to dynamically cope with the changing threats. Furthermore, the optimization of the model with the help of feature selection and the inclusion of explainability to cybersecurity tools (SHAP or LIME) can promote trust and understandability among cybersecurity professionals. Implementation of this model in the real network environment with streaming information, and zero-day attack analysis will further confirm that this model is workable. In general, this paper provides the basis of scalable, intelligent and adaptive intrusion detection systems in contemporary cyberinfrastructure.

VI. AUTHOR'S CONTRIBUTION

Conceptualization: Satishkumar D. Prajapati, Priyesh P. Gandhi and Sheshang Degadwala.
Methodology: Satishkumar D. Prajapati and Priyesh P. Gandhi.
Investigation: Satishkumar D. Prajapati and Swapnil M. Parikh.
Discussion of results: Satishkumar D. Prajapati, Priyesh P. Gandhi, Sheshang Degadwala, Keyur Brahmbhatt and Swapnil M. Parikh.
Writing - Original Draft: Satishkumar D. Prajapati.
Writing - Review and Editing: Satishkumar D. Prajapati, Priyesh P. Gandhi, Sheshang Degadwala and Keyur Brahmbhatt.
Resources: Satishkumar D. Prajapati.
Supervision: Priyesh P. Gandhi and Sheshang Degadwala.
Approval of the final text: Satishkumar D. Prajapati, Priyesh P. Gandhi, Sheshang Degadwala, Keyur Brahmbhatt and Swapnil M. Parikh.

VII. ACKNOWLEDGMENTS

The authors would like to express their sincere gratitude to Gujarat Technological University for providing academic support and resources that facilitated the completion of this research work. The authors also appreciate the encouragement and guidance received from colleagues and mentors during the course of this research.

VIII. REFERENCES

[1] S. Markkandeyan, A. D. Ananth, M. Rajakumaran, R. G. Gokila, R. Venkatesan, and B. Lakshmi, "Novel hybrid deep learning based cyber security threat detection model with optimization algorithm," Cyber Security and Applications, vol. 3, no. June 2024, 2025, doi: 10.1016/j.csa.2024.100075.

[2] M. B. Anley, A. Genovese, D. Agostinello, and V. Piuri, "Robust DDoS attack detection with adaptive transfer learning," Computers and Security, vol. 144, no. March, p. 103962, 2024, doi: 10.1016/j.cose.2024.103962.

[3] H. Najafi Mohsenabad and M. A. Tut, "Optimizing Cybersecurity Attack Detection in Computer Networks: A Comparative Analysis of Bio-Inspired Optimization Algorithms Using the CSE-CIC-IDS 2018 Dataset," Applied Sciences (Switzerland), vol. 14, no. 3, 2024, doi: 10.3390/app14031044.

[4] A. R. K. Qureshi, S. Patnaha, P. Kulkarni, P. Singh, M. Joshi, and I. Vaidya, "Machine Learning-based Intrusion Detection Systems for Securing Cloud Networks," Library Progress International, vol. 44, no. 3, pp. 7434–7446, 2024.

[5] M. Cantone, C. Marrocco, and A. Bria, "Machine Learning in Network Intrusion Detection: A Cross-Dataset Generalization Study," IEEE Access, vol. 12, no. August, pp. 144489–144508, 2024, doi: 10.1109/ACCESS.2024.3472907.

[6] M. S. Ataa, E. E. Sanad, and R. A. El-khoribi, "Intrusion detection in software defined network using deep learning approaches," Scientific Reports, vol. 14, no. 1, pp. 1–15, 2024, doi: 10.1038/s41598-024-79001-1.

[7] F. Ullah, S. Ullah, G. Srivastava, and J. C. W. Lin, "IDS-INT: Intrusion detection system using transformer-based transfer learning for imbalanced network traffic," Digital Communications and Networks, vol. 10, no. 1, pp. 190–204, 2024, doi: 10.1016/j.dcan.2023.03.008.

[8].A. Khanan, Y. Abdelgadir Mohamed, A. H. H. M. Mohamed, and M. Bashir, "From Bytes to Insights: A Systematic Literature Review on Unraveling IDS Datasets for Enhanced Cybersecurity Understanding," IEEE Access, vol. 12, no. April, pp. 59289–59317, 2024, doi: 10.1109/ACCESS.2024.3392338.

[9] P. Rana, I. Batra, A. Malik, I. H. Ra, O. S. Lee, and A. S. M. Sanwar Hosen, "Efficacious Novel Intrusion Detection System for Cloud Computing Environment," IEEE Access, vol. 12, no. June, pp. 99223–99239, 2024, doi: 10.1109/ACCESS.2024.3424528.

[10] S. Latif, W. Boulila, A. Koubaa, Z. Zou, and J. Ahmad, "DTL-IDS: An optimized Intrusion Detection Framework using Deep Transfer Learning and Genetic Algorithm," Journal of Network and Computer Applications, vol. 221, no. February 2023, p. 103784, 2024, doi: 10.1016/j.jnca.2023.103784.

[11] A. D. Vibhute and V. Nakum, "Deep learning-based network anomaly detection and classification in an imbalanced cloud environment," Procedia Computer Science, vol. 232, no. 2023, pp. 1636–1645, 2024, doi: 10.1016/j.procs.2024.01.161.

[12] J. Yu, J. Hu, and Y. Zeng, "Deep Learning Based Network Intrusion Detection," Communications in Computer and Information Science, vol. 2023 CCIS, no. 3, pp. 125–136, 2024, doi: 10.1007/978-981-97-0730-0_12.

[13] A. A. Wardana, G. Kołaczek, A. Warzyński, and P. Sukarno, "Collaborative intrusion detection using weighted ensemble averaging deep neural network for coordinated attack detection in heterogeneous network," International Journal of Information Security, vol. 23, no. 5, pp. 3329–3349, 2024, doi: 10.1007/s10207-024-00891-3.

[14] C. Wu et al., "Attack detection model for BCoT based on contrastive variational autoencoder and metric learning," Journal of Cloud Computing, vol. 13, no. 1, 2024, doi: 10.1186/s13677-024-00678-w.

[15] H. Kim, S. Park, H. Hong, J. Park, and S. Kim, "A Transferable Deep Learning Framework for Improving the Accuracy of Internet of Things Intrusion Detection," Future Internet, vol. 16, no. 3, 2024, doi: 10.3390/fi16030080.

[16] S. Hizal, U. Cavusoglu, and D. Akgun, "A novel deep learning-based intrusion detection system for IoT DDoS security," Internet of Things (Netherlands), vol. 28, no. April, p. 101336, 2024, doi: 10.1016/j.iot.2024.101336.

[17] Y. Yang, J. Cheng, Z. Liu, H. Li, and G. Xu, "A multi-classification detection model for imbalanced data in NIDS based on reconstruction and feature matching," Journal of Cloud Computing, vol. 13, no. 1, 2024, doi: 10.1186/s13677-023-00584-7.

[18] W. H. Aljuaid and S. S. Alshamrani, "A Deep Learning Approach for Intrusion Detection Systems in Cloud Computing Environments," Applied Sciences (Switzerland), vol. 14, no. 13, 2024, doi: 10.3390/app14135381.

[19] Zafar Iqbal Khan, Mohammad Mazhar Afzal, and Khurram Naim Shamsi, “A Comprehensive Study on CIC-IDS2017 Dataset for Intrusion Detection Systems,” International Research Journal on Advanced Engineering Hub (IRJAEH), vol. 2, no. 02, pp. 254–260, 2024, doi: 10.47392/irjaeh.2024.0041.

[20] O. D. Okey, D. C. Melgarejo, M. Saadi, R. L. Rosa, J. H. Kleinschmidt, and D. Z. Rodriguez, “Transfer Learning Approach to IDS on Cloud IoT Devices Using Optimized CNN,” IEEE Access, vol. 11, no. January, pp. 1023–1038, 2023, doi: 10.1109/ACCESS.2022.3233775.

[21] S. Songma, T. Sathuphan, and T. Pamutha, “Optimizing Intrusion Detection Systems in Three Phases on the CSE-CIC-IDS-2018 Dataset,” Computers, vol. 12, no. 12, 2023, doi: 10.3390/computers12120245.

[22] J. Jose and D. V. Jose, “Deep learning algorithms for intrusion detection systems in internet of things using CIC-IDS 2017 dataset,” International Journal of Electrical and Computer Engineering, vol. 13, no. 1, pp. 1134–1141, 2023, doi: 10.11591/ijece.v13i1.pp1134-1141.

[23] A. Henry et al., “Composition of Hybrid Deep Learning Model and Feature Optimization for Intrusion Detection System,” Sensors, vol. 23, no. 2, 2023, doi: 10.3390/s23020890.

[24] B. A. Alabsi, M. Anbar, and S. D. A. Rihan, “CNN-CNN: Dual Convolutional Neural Network Approach for Feature Selection and Attack Detection on Internet of Things Networks,” Sensors, vol. 23, no. 14, 2023, doi: 10.3390/s23146507.

[25] V. Hnamte, H. Nhung-Nguyen, J. Hussain, and Y. Hwa-Kim, “A Novel Two-Stage Deep Learning Model for Network Intrusion Detection: LSTM-AE,” IEEE Access, vol. 11, no. March, pp. 37131–37148, 2023, doi: 10.1109/ACCESS.2023.3266979.

[26] H. Elubeyd, D. Yiltas-Kaplan, and S. Bahtiyar, “A Multi-Modal Deep Transfer Learning Framework for Attack Detection in Software-Defined Networks,” IEEE Access, vol. 11, no. August, pp. 114128–114145, 2023, doi: 10.1109/ACCESS.2023.3324878.

[27] M. Catillo, A. Del Vecchio, A. Pecchia, and U. Villano, “A Case Study with CICIDS2017 on the Robustness of Machine Learning against Adversarial Attacks in Intrusion Detection,” ACM International Conference Proceeding Series, 2023, doi: 10.1145/3600160.3605031.

Journal of Engineering and Technology for Industrial Applications

ISSN ONLINE: 2447-0228

ITEGAM-JETIA

Manaus, v.12 n.60, p.1321-1329. July/August, 2026.
DOI: https://doi.org/10.5935/jetia.v12i60.4078

RESEARCH ARTICLE OPEN ACCESS

OPTIMIZING CLOUD RESOURCE MANAGEMENT THROUGH ENERGY-EFFICIENT VM PLACEMENT TECHNIQUES

Dipak Dabhi*[1], Ankit Kharwar[2], Diya Vadhwani[3], Pritesh Prajapati[4], Vishal Barot[5], Anamika Mittal[6], and Dhwani Modi[7]

[1, 5, 6, 7]School of Engineering and Technology, Gujarat Technological University, Ahmedabad, Gujarat, India.
[2]Sarvajanik College of Engineering & Technology, Sarvajanik University, Surat, Gujarat, India.
[3]Adani institute of Infrastructure Engineering, Ahmedabad, Gujarat, India.
[4]Charotar University of Science and Technology, Changa, Gujarat, India.

[1]https://orcid.org/0000-0002-2190-8056, [2]https://orcid.org/0000-0002-1933-4866, [3]https://orcid.org/0000-0003-1495-3403
[4]https://orcid.org/0000-0002-6544-8514, [5]https://orcid.org/0000-0002-9139-9541, [6]https://orcid.org/0009-0003-8726-1114
[7]https://orcid.org/0009-0002-0563-8858

Email:*ap_dipak_dabhi@gtu.edu.in, ankit.kharwar@scet.ac.in, diya.vadhwani@adaniuni.ac.in, pritesh.pnp.007@gmail.com, vishal.barot@gtu.edu.in, ap_anamika@gtu.edu.in, ap_dhwani@gtu.edu.in

ARTICLE INFO

Article History
Received: March 13, 2026
Reviewed: April 16, 2026
Accepted: July 16, 2026
Published: August 31, 2026

Keywords:
Cloud Computing,
VM Consolidation,
Energy Efficiency,
SLA Violation,
VM Placement.

ABSTRACT

Cloud computing has seen rapid growth in recent years, leading to a surge in demand for data center services. To meet this demand, data centers deploy a large number of servers, resulting in substantial energy consumption. Virtual Machine Consolidation (VMC) is an effective strategy to reduce energy usage by shutting down underutilized servers while ensuring that Service Level Agreements (SLAs) are maintained. The VMC process comprises four key steps: detecting overloaded hosts, identifying underloaded hosts, selecting virtual machines (VMs), and determining their placement. This research presents the Energy-Efficient Virtual Machine Placement (EEVMP) approach, which aims to optimize resource utilization by selecting suitable destination hosts for migrating VMs based on utilization and resource skewness. The proposed method is evaluated using the CloudSim simulator. Experimental results show that EEVMP consistently outperforms existing placement strategies such as PABFD, IQRMC, PEBFD, ESVMP, and HVMAP in terms of energy efficiency and overall performance.

Copyright ©2026 by authors and Galileo Institute of Technology and Education of the Amazon (ITEGAM). This work is licensed under the Creative Commons Attribution International License (CC BY 4.0).

I. INTRODUCTION

Cloud computing has experienced significant growth in recent years, resulting in increased demand for data center services. To accommodate this demand, data centers operate a large number of servers, which in turn leads to high energy consumption. Virtual Machine Consolidation (VMC) is a widely adopted technique to minimize energy usage by turning off underutilized servers while still adhering to Service Level Agreements (SLAs) [1]. The VMC process involves four main stages: detecting overloaded hosts, identifying underloaded hosts, selecting virtual machines (VMs), and determining their optimal placement [2]. This study introduces the Energy-Efficient Virtual Machine Placement (EEVMP) strategy, designed to enhance resource utilization by selecting destination hosts for migrating VMs based on their utilization levels and resource imbalance. The approach is validated through simulations conducted using the CloudSim toolkit. Results indicate that EEVMP consistently outperforms conventional VM placement methods—namely PABFD, IQRMC, PEBFD, ESVMP, and HVMAP—by offering superior energy efficiency and system performance [3]. Figures 1 and 2 illustrate the number of active hosts before and after the application of the virtual machine consolidation method. Figure 1 shows that five hosts are needed to handle user requests; however, some hosts are significantly underutilized, while others are moderately utilized. Despite varying levels of utilization, all hosts consume considerable energy. To address this, some underutilized hosts can be put into sleep mode, and their VMs can be migrated to other hosts. Cloud data center resources are heterogeneous, meaning each can have a distinct physical configuration. Service providers may face challenges migrating VMs between hosts.

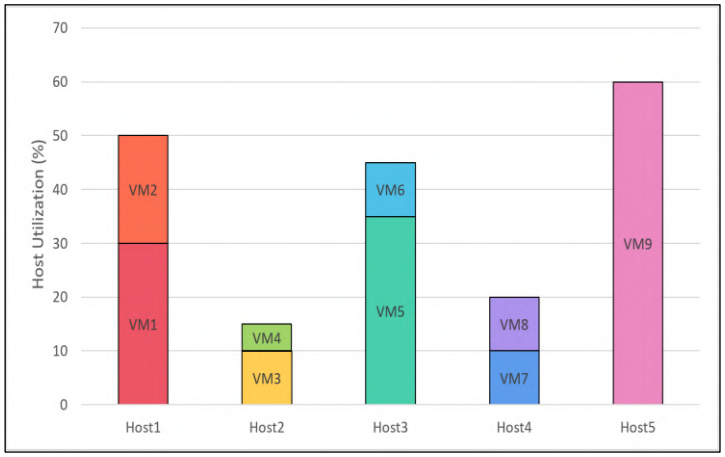


Figure 1: PM Utilization before VMC.
Source: Authors, (2026).

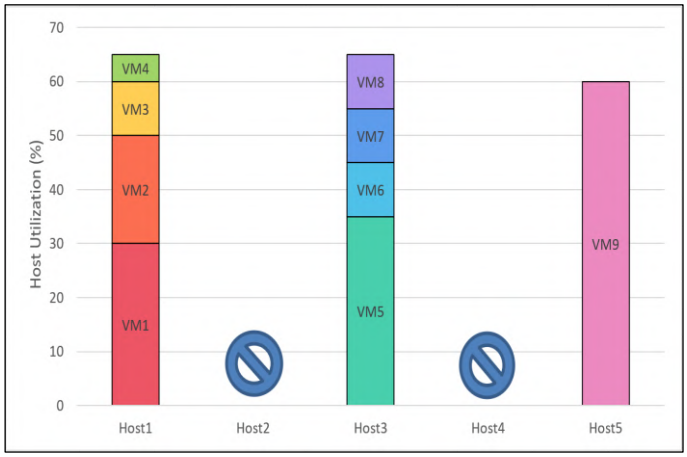


Figure 2: PM Utilization after VMC.
Source: Authors, (2026).

VMC resource allocation policies use various techniques to adaptively allocate the necessary VMs to minimize the number of active Physical Machines (PMs) while conserving energy. The primary objectives of VM consolidation are to avoid host overload and promote green computing. To prevent host overload, the VM resource request must be lower than the host's available resources. Otherwise, the Service Level Agreement (SLA) between the user and the service provider would be breached [4]. SLAs are crucial for ensuring Quality of Service (QoS) and service availability for end users. In terms of green computing, cloud service providers aim to fulfill user requests with the minimum number of active hosts possible without violating SLAs [5]. Figure 3 illustrates the classification of VM Consolidation Policies [6].

Host Overload Detection Algorithm	Static Threshold (Th)	Median Absolute Deviation (MAD)	Interquartile Range (IQR)	Local Regression (LR)	Robust Local Regression (LRR)
Host Underload Detection Algorithm	Host with Minimum Utilization				
VM Selection Algorithm	Minimum Migration Time (MMT)	Random Choice (RC)	Maximum Correlation (MC)	Minimum Utilization (MU)	
VM Placement Algorithm	First Fit (FF)	First Fit Decreasing (FFD)	Best Fit Decreasing (BFD)	Worst Fit Decreasing (WFD)	Power Aware Best Fit Decreasing (PABFD)

Figure 3: VMC Process Policy.
Source: Authors, (2026).

In a cloud data centre, multiple VMs may run on a single physical machine with host utilisation varying dynamically based on user demands; when consumption reaches 100%, performance degrades and SLAs are breached, making overload detection the first critical step in VM consolidation, followed by identification of the specific VMs responsible for the overload. Simultaneously, underutilised hosts must also be detected so their workloads can be transferred to other hosts, forcing them into standby mode to reduce overall energy consumption [7]. Once an overloaded host is identified, the offending VMs are selected, added to a migration list, and moved to alternative hosts to minimise performance deterioration, while all VMs from an underloaded host are migrated entirely [8]. The final step, VM placement, determines the optimal destination host for each migrating VM using a bin-packing-like algorithm; in this study, we developed the Energy-Efficient VM Placement for Optimized Resource Utilization in Cloud Data Centers (EEVMP) and benchmarked it against existing techniques including PABFD, IQRMC, PEBFD, ESVMP, and HVMAP.

II. RELATED WORK

The VM workload consolidation approach is a promising research area for increasing cloud computing energy efficiency. Many strategies are advised to speed up the virtual machine consolidation process, including (a) detecting overloaded hosts, (b) detecting underloaded hosts, (c) selecting VMs, and (d) placing them. The VMC method focuses primarily on three criteria. The first is based on the Quality-of-Service approach, which emphasizes effective use of computer resources. The second option is to minimize data center power use by turning off underutilized hosts. Another critical challenge is maintaining a balance between energy use and SLA violations throughout the VMC process. By [1] offered an alternate technique for identifying overloaded/underloaded hosts, VM selection, and VM placement. The author created heuristic-based strategies for identifying overload hosts, including IQR, MAD, LR, LRR, and static thresholds. For Underload host identification, the least utilized host is deemed underutilized.

The author proposed the MC, MU, MMT, and RS algorithms for selecting VMs from overutilized hosts, as well as the PABFD policy for VM placement. Although it provides better power consumption outcomes than other standard approaches, average SLA violation and VM migration will be greater. In turn [9] improved their host overload detection system and migration control. After identifying an overloaded host, it calculates the VM prediction value using the host's mean and standard deviation, then checks to see whether the prediction is larger than one and if so, the host is labelled as overloaded. The results show that the proposed method beats the present methodology in terms of performance. According to [10] proposed many power-efficient VM placement approaches, including Medium Fit Power Efficient Decreasing (MFPED), PEBFD, and Power Efficient First Fit Decreasing (PEFFD). The proposed approach was evaluated on the OpenStack Neat cloud service platform. By [11] suggested a glowworm swarm optimization VM placement policy for reducing energy and SLA violations. By [12] discussed implementing a VM consolidation approach that is Quality-of-Service aware, employing the K-medoid interquartile range mid-range (KMIMR) technique. By [13] proposed two modified placement policies—ESVMP and HVMAP—for VM consolidation in cloud data centers.

III. PROPOSED WORK

The EEVMP (Energy-Efficient VM Placement for Optimized Resource Utilization in Cloud Data Centers) technique is introduced here, focusing on selecting the most suitable destination host based on utilization levels and host skewness. Skewness refers to the uneven usage of multiple resources on a server. A data center server comprises various resources such as CPU MIPS, Memory, and Bandwidth. In our proposed EEVMP algorithm, we evaluate three key resources (CPU, Memory, and Bandwidth) during the decision-making process. Let n be the number of resources considered, and r_i represent the usage of each resource. The resource skewness of a server is defined. Another parameter used is the Host Consumption, which averages the utilization of all server resources. When the power usage of the host surpasses a certain threshold, it is deemed overloaded. The usage of an overloaded host is indicated by P, which is the squared sum of its cloud resource consumption beyond the threshold. Let RE denote the total count of overloads on the server, and r_t indicate the overload threshold. Equations for CurrentSkewness and CurrentUtilization before VM migration are provided in Eq. (1) and Eq. (2), respectively.

$$CurrentSkewness = \sqrt{(\Sigma(r_i - \bar{r})^2 / n)} \quad (1)$$

$$CurrentUtilization = \Sigma(r - r_t)^2, \ \ r \in R \quad (2)$$

It is crucial to ensure that the destination server does not become overutilized following the VM migration. Therefore, we must calculate the NewSkewness and NewUtilization of the server post-migration. The equations for determining NewSkewness and NewUtilization are provided in Eq. (3) and Eq. (4). The Skewness Difference (SkeDif) and Utilization Difference (UtilDif) must be lower than their respective difference values, and the server's NewUtilization must be below 65% utilization.

$$NewSkewness = \sqrt{(\Sigma(r_i + v_m - \bar{r})^2 / n)} \quad (3)$$

$$NewUtilization = \Sigma(r + v_m - r_t)^2, \ \ r \in R \quad (4)$$

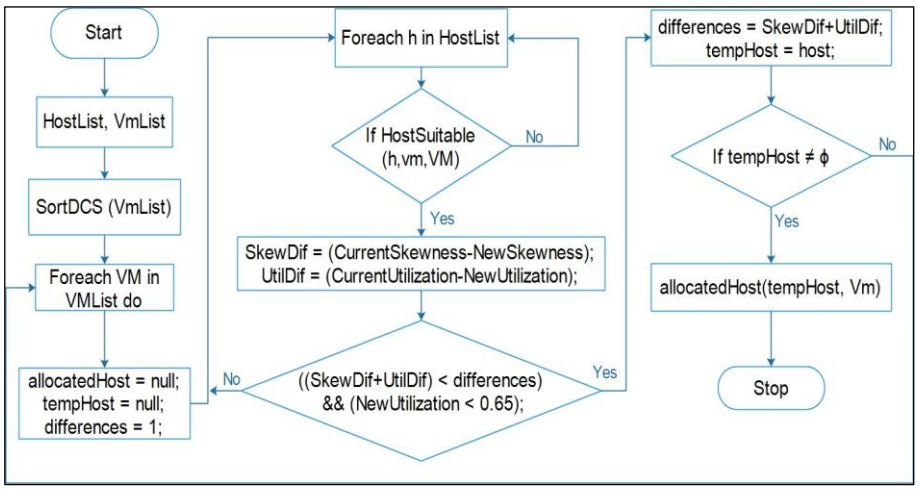


Figure 4: EEVMP Flowchart.
Source: Authors, (2026).

The proposed EEVMP flowchart is presented, highlighting the technique's use of host skewness and utilization before and after VM migration to efficiently identify destination hosts. The EEVMP placement policy first sorts all VMs in descending order based on CPU utilization for migration (Step 1). It then checks each VM in the VMList to find the destination host (Steps 2–5), and evaluates all hosts in the HostList as potential destination hosts (Step 6). If the chosen host has sufficient resources to accommodate the VM without causing overload, it calculates the CurrentSkewness and Utilization before VM Migration and the New Skewness and Utilization after VM Migration.

Algorithm 1 Energy-Efficient VM Placement (EEVMP)

```
Input: vmList, hostList
Output: allocatedHost
1) sort vmList in the order of decreasing CPU utilization;
2) foreach vm in vmList do
3)   allocatedHost = null;
4)   differences = 1;
5)   tempHost = null;
6)   foreach host in hostList do
7)     if host has enough resource for vm then
8)       CurrentUtilization = host.CurrentUtilization();
9)       CurrentSkewness = host.CurrentSkewness();
10)      NewUtilization = host.NewUtilization();
11)      NewSkewness = host.NewSkewness();
12)      UtilDif = Math.abs(CurrentUtilization-NewUtilization);
13)      SkewDif = Math.abs(CurrentSkewness-NewSkewness);
14)      if ((UtilDiff + SkewDif) < differences) && (NewUtilization <= 0.65) then
15)        differences = UtilDif + SkewDif;
16)        tempHost = host;
17)      end if
18)    end if
19)  end
21)  allocatedHost = tempHost;
22)  return allocatedHost;
23) end
```

Figure 5: EEVMP Algorithm.
Source: Authors, (2026).

IV. EXPERIMENTAL SETUP

The simulations were conducted on an Acer computer equipped with a Core i5 CPU, 8 GB of RAM, Windows 10 64-bit operating system, a 125 GB SSD, and a 1 TB hard drive. The CloudSim application was utilized to simulate the specified activities. Our experiment was carried out in a data center comprising 800 physical heterogeneous hosts—400 HP ProLiant ML110 G4 and 400 HP ProLiant ML110 G5 [14]. Table 1 provides detailed specifications of the hosts [8]. Table 2 presents the VM configuration based on various speeds and RAM. Table 3 details the server power consumption, and Table 4 outlines the default implementation scenario.

Table 1: PMs Configuration.

HP ProLiant ML110 G4	1860	1	4	1000
HP ProLiant ML110 G5	2660	2	4	1000

Source: Authors, (2026).

Table 2: VMs Configuration.

High CPU VM	2500	1	870
Extra Large VM	2000	1	1740
Small VM	500	1	613
Micro VM	100	1	613

Source: Authors, (2026).

Table 3: Power Usage by PM at Different Load Levels (Watts).

HP ProLiant ML110 G4	86	89.4	92.6	102	114.2	117
HP ProLiant ML110 G5	93.7	97	101	110.8	123.7	135

Source: Authors, (2026).

Table 4: Implementation Scenario.

Hosts	800 (400 HP ProLiant ML110 G4 + 400 HP ProLiant ML110 G5)
VMs	1600 (mixed types)
Simulation Tool	CloudSim 3.0
Overload Detection	IQR-based
VM Selection	MMT (Minimum Migration Time)
VM Placement	EEVMP (proposed)
Dataset	PlanetLab (10 traces)
Evaluation Metrics	EC, VMM, SLAV, ESLAV, ESM, NHS

Source: Authors, (2026).

IV.1 DATASETS

The datasets were crucial in comparing performance. We utilized PlanetLab workload traces, which are publicly available real-world datasets, to evaluate our method's performance. PlanetLab serves as a functional cloud for the global research network. These traces include data on CPU consumption of numerous VMs from servers located in 500 different locations across the globe. The dataset traces were randomly collected between March 2010 and April 2020. CPU utilization values for VMs are recorded every 5 minutes in the daily dataset. Table 5 shows the specific properties of the dataset.

Table 5: PlanetLab Datasets.

20110303	42.3	15.2
20110306	38.1	12.8
20110309	40.5	13.9
20110322	44.7	16.1
20110325	41.0	14.5
20110403	52.3	18.7
20110409	45.8	16.5
20110411	45.2	16.0
20110412	39.8	13.6
20110420	38.6	12.4

Source: Authors, (2026).

IV.2 EVALUATION PARAMETERS

In cloud computing, measuring the quality of cloud services is crucial. In our tests, we assessed the algorithm's performance using six parameters : In cloud computing, measuring service quality is essential, and our algorithm's performance was assessed using six key parameters: Energy Consumption (EC), which calculates the total energy consumed by the data center over a given period based on varying host utilization levels; VM Migrations (VMM), which impacts application performance by causing an average CPU usage reduction of around 10% during downtime and must be minimized; SLA Violation (SLAV), which measures Quality of Service using two sub-metrics — Overload Time Fraction (OTF) and Performance Degradation due to Migrations (PDM) — expressed as SLAV = SLATAH × PDM; Energy and SLA Violation (ESLAV), which balances EC and SLAV and is calculated as ESLAV = EC × SLAV; Energy, SLA Violation and Migration (ESM), which jointly assesses total energy consumption, SLA violations, and migration impact as ESM = EC × SLAV × VMM; and finally, Number of Host Shutdowns (NHS), which counts the physical hosts powered down to conserve energy while maintaining acceptable performance levels within the data center [15].

$$SLATAH = (1/N)\ \Sigma\ (Ts_i / Ta_i) \tag{5}$$

$$PDM = (1/M)\ \Sigma\ (Cd_j / Cr_j) \tag{6}$$

$$SLAV = SLATAH \times PDM \tag{7}$$

$$ESLAV = EC \times SLAV \tag{8}$$

$$ESM = EC \times SLAV \times VMM \tag{9}$$

V. RESULTS AND DISCUSSIONS

The experiment was conducted based on six primary evaluation parameters: Total Energy Consumption (EC), VM Migrations (VMM), SLA Violation (SLAV), Energy and SLA Violation (ESLAV), Energy-SLA Violation and Migration (ESM) and the Number of Host Shutdowns (NHS), evaluated using PlanetLab datasets containing 10 days of data. Our proposed EEVMP strategy was compared against PABFD, IQRMC, PEBFD, ESVMP and HVMAP placement policies.

Table 6: Energy Consumption (EC) for PlanetLab Dataset.

20110303	177.10	119.10	114.97	109.41	112.92	84.56
20110306	135.49	90.73	86.15	78.10	84.72	61.43
20110309	156.64	103.89	99.87	91.91	97.95	68.70
20110322	191.16	123.00	118.43	107.58	116.32	82.82
20110325	165.80	107.00	102.75	88.36	101.38	69.88
20110403	245.78	161.86	157.70	144.44	154.77	108.42
20110409	196.13	127.67	123.53	117.53	121.61	87.62
20110411	193.26	125.25	120.20	115.31	118.34	83.78
20110412	168.31	110.66	106.13	95.61	104.27	70.94
20110420	147.37	92.41	88.11	81.04	86.17	58.51
Average	177.70	116.16	111.78	102.93	109.85	77.67

Source: Authors, (2026).

Table 6 highlights that EEVMP achieves the lowest energy consumption, with an average of 77.67, significantly reducing energy usage compared to PABFD (177.70, a 56.3% reduction), IQRMC (116.16, 33.1% reduction), and other policies, with the best energy efficiency observed on dataset 20110420 (58.51 vs. 147.37 for PABFD).

Table 7: Virtual Machine Migration (VMM) for PlanetLab Dataset.

20110303	23035	19405	15899	9208	17460	1663
20110306	18144	14196	11980	4948	12824	953
20110309	20762	17914	15006	8535	16906	1411
20110322	25566	24637	21531	12041	22924	1756
20110325	21760	20246	16992	5016	18271	1281
20110403	31659	26389	22811	11645	24952	1494
20110409	25526	22829	19272	12075	20966	1459
20110411	25039	21757	19006	12138	20909	1379
20110412	21956	19623	16681	6409	17874	1120
20110420	20491	19307	16540	12225	18159	1136
Average	23394	20630	17572	9424	19125	1365

Source: Authors, (2026).

Table 7 showcases a dramatic reduction in VM migrations, where EEVMP maintains an average of just 1,365 migrations, reducing them by over 94% compared to PABFD (23,394 migrations), with the most notable improvement in dataset 20110306, recording only 953 migrations versus 18,144 for PABFD.

Table 8: SLA Violation (SLAV) for PlanetLab Dataset.

20110303	0.00701	0.00579	0.00455	0.00398	0.00325	0.00437
20110306	0.00744	0.00548	0.00425	0.00470	0.00298	0.00220
20110309	0.00756	0.00660	0.00537	0.00490	0.00401	0.00311
20110322	0.00609	0.00570	0.00516	0.00587	0.00378	0.00280
20110325	0.00675	0.00596	0.00500	0.00576	0.00353	0.00264
20110403	0.00632	0.00577	0.00479	0.00617	0.00345	0.00195
20110409	0.00640	0.00566	0.00476	0.00518	0.00350	0.00240
20110411	0.00638	0.00551	0.00497	0.00461	0.00363	0.00239
20110412	0.00680	0.00568	0.00497	0.00600	0.00336	0.00211
20110420	0.00730	0.00757	0.00678	0.00447	0.00498	0.00269
Average	0.0068	0.0060	0.0051	0.0052	0.0036	0.0027

Source: Authors, (2026).

Table 8 shows EEVMP significantly minimizes SLA violations, achieving an average SLAV of 0.0027, marking a 60.3% reduction from PABFD (0.0068) and 25.0% lower than HVMAP (0.0036), with the lowest SLAV recorded in dataset 20110403 (0.00195).

Table 9: Energy and SLA Violation (ESLAV) for PlanetLab Dataset.

20110303	1.24124	0.68961	0.52304	0.43581	0.36697	0.36933
20110306	1.00766	0.49746	0.36611	0.36724	0.25217	0.13515
20110309	1.18491	0.68606	0.53651	0.45040	0.39316	0.21344
20110322	1.16470	0.70116	0.61144	0.63152	0.43919	0.23198
20110325	1.11981	0.63721	0.51381	0.50885	0.35806	0.18428
20110403	1.55417	0.93410	0.75551	0.89064	0.53466	0.21175
20110409	1.25560	0.72316	0.58758	0.60923	0.42601	0.21039
20110411	1.23285	0.69066	0.59794	0.53144	0.42999	0.20037
20110412	1.14410	0.62814	0.52771	0.57336	0.35015	0.14941
20110420	1.07579	0.69951	0.59707	0.36189	0.42878	0.15725
Average	1.19808	0.68871	0.56167	0.53604	0.39791	0.20634

Source: Authors, (2026).

Table 10: Energy, SLA Violation and Migration (ESM) for PlanetLab Dataset.

20110303	28591.9	13381.8	8315.8	4013.0	6407.3	614.2
20110306	18283.1	7061.9	4386.0	1817.1	3233.8	128.8
20110309	24601.1	12290.0	8050.9	3844.1	6646.8	301.2
20110322	29776.7	17274.4	13164.9	7604.1	10067.9	407.4
20110325	24367.1	12901.0	8730.6	2552.4	6542.2	236.1
20110403	49203.4	24649.9	17234.0	10371.5	13340.9	316.4
20110409	32050.4	16509.0	11323.8	7356.5	8931.8	307.0
20110411	30869.4	15026.6	11364.4	6450.7	8990.6	276.3
20110412	25119.9	12326.0	8802.7	3674.7	6258.6	167.3
20110420	22044.0	13505.4	9875.5	4424.1	7786.2	178.6
Average	28491	14493	10125	5211	7821	293

Source: Authors, (2026).

Table 11: Number of Host Shutdowns (NHS) for PlanetLab Dataset.

20110303	5439	976	1017	770	968	929
20110306	4324	919	958	777	926	783
20110309	4793	993	1039	784	985	788
20110322	5555	977	1036	772	963	778
20110325	5058	1014	1050	773	990	786
20110403	7050	958	1025	757	967	768
20110409	5776	979	1026	767	967	775
20110411	5715	995	1025	767	966	782
20110412	5132	991	1037	774	975	781
20110420	4454	971	1017	777	952	784
Average	5330	977	1023	772	966	795

Source: Authors, (2026).

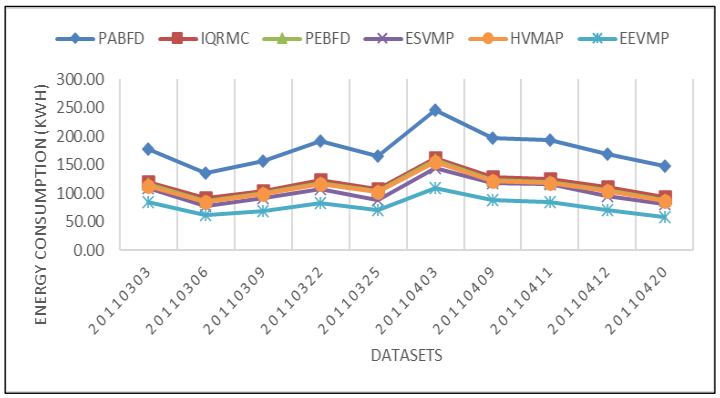


Figure 6: EC for PlanetLab Dataset.
Source: Authors, (2026).

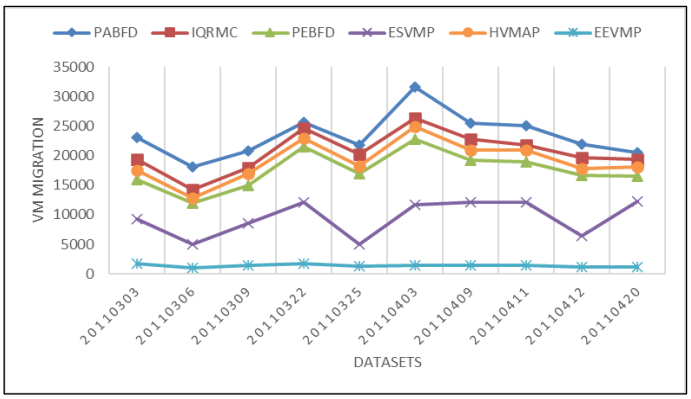


Figure 7: VMM for PlanetLab Dataset.
Source: Authors, (2026).

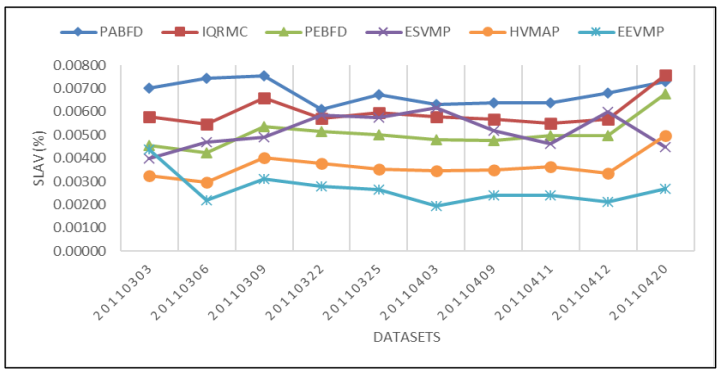


Figure 8: SLAV for PlanetLab Dataset.
Source: Authors, (2026).

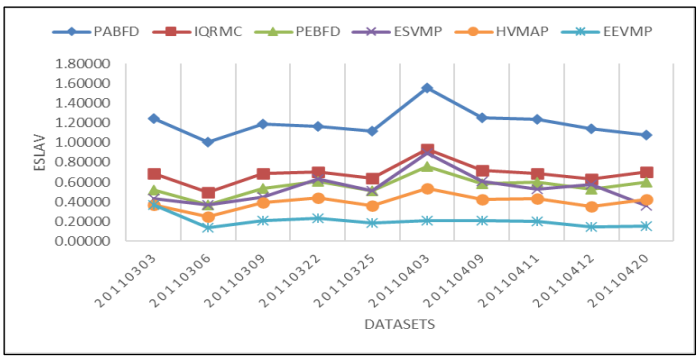


Figure 9: ESLAV for PlanetLab Dataset.
Source: Authors, (2026).

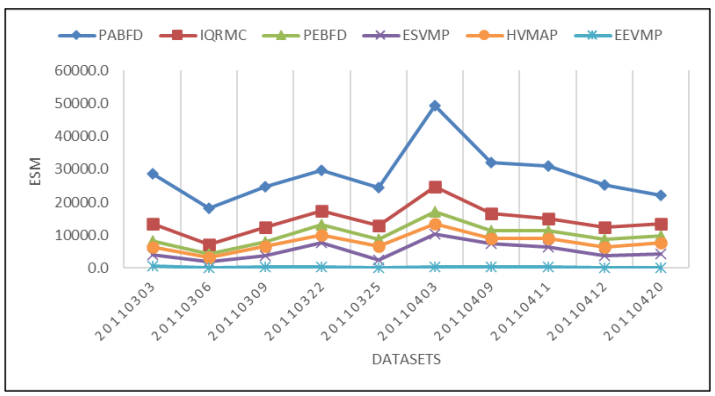


Figure 10: ESM for PlanetLab Dataset.
Source: Authors, (2026).

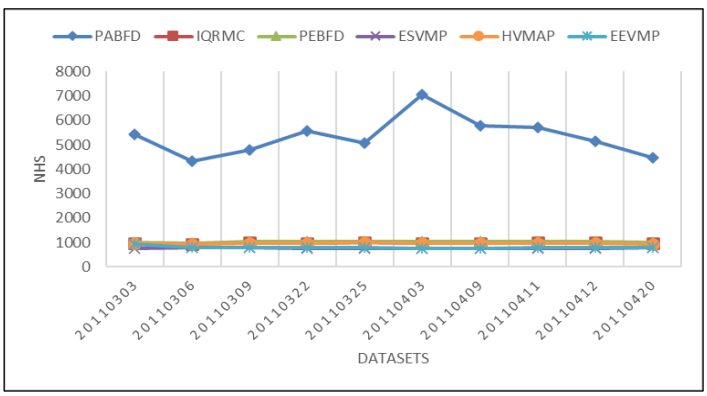


Figure 11: NHS for PlanetLab Dataset.
Source: Authors, (2026).

Table 12: EEVMP Performance Comparison for ESLAV with Other Algorithms.

20110303	-108.274	-60.4907	-34.45	-16.5151	0.640808
20110306	-152.695	-114.543	-92.15	-92.3924	-60.4236
20110309	-138.945	-105.084	-86.16	-71.3888	-59.2541
20110322	-133.561	-100.558	-89.98	-92.5382	-61.7432
20110325	-143.476	-110.271	-94.41	-93.6526	-64.0854
20110403	-152.036	-126.081	-112.4	-123.167	-86.5232
20110409	-142.595	-109.855	-94.54	-97.3245	-67.7637
20110411	-144.079	-110.051	-99.6	-90.4818	-72.8548
20110412	-153.798	-123.14	-111.7	-117.314	-80.3685
20110420	-148.988	-126.584	-116.6	-78.8381	-92.6679
Average	-141.845	-108.666	-93.21	-87.3612	-64.5044

Source: Authors, (2026).

Further analysis of Table 12, which compares EEVMP's SLA Violation performance with other algorithms, underscores its superiority in handling SLA constraints. The negative values indicate the percentage reduction in ESLAV achieved by EEVMP. The average SLAV improvement across datasets demonstrates that EEVMP significantly reduces SLA violations. The average SLAV reduction achieved by EEVMP is 141.845 for PABFD, 108.666 for IQRMC, 93.21 for PEBFD, 87.3612 for ESVMP, and 64.5044 for HVMAP, indicating that EEVMP surpasses all other algorithms in maintaining SLA integrity. These findings validate that EEVMP consistently achieves a lower SLA violation rate compared to traditional VM placement policies, thereby ensuring higher Quality of Service (QoS) and improved cloud resource management.

VI. CONCLUSIONS

The primary challenge in cloud computing is to reduce energy consumption and SLA violations while simultaneously meeting user demands. The evaluation of the proposed Energy-Efficient Virtual Machine Placement (EEVMP) strategy demonstrates its effectiveness in enhancing resource management and maintaining service quality in cloud data centers. The results consistently show that EEVMP outperforms existing VM placement policies, including PABFD, IQRMC, PEBFD, ESVMP, and HVMAP, across multiple performance metrics. It significantly reduces energy consumption while ensuring efficient workload distribution, leading to lower operational costs and improved sustainability. Additionally, by minimizing virtual machine migrations, EEVMP reduces system overhead, thereby enhancing overall stability and performance. EEVMP demonstrates an improvement of 141.85% over PABFD, while improvements over IQRMC, PEBFD, ESVMP, and HVMAP are 108.67%, 93.21%, 87.36%, and 64.50%, respectively. Future research will focus on further enhancing VM placement strategies by integrating AI-driven predictive analytics to improve energy efficiency and minimize SLA violations.

VII. AUTHOR'S CONTRIBUTION

Conceptualization: Dipak Dabhi, Ankit Kharwar, Diya Vadhwani, Pritesh Prajapati,Vishal Barot, Anamika Mittal, and Dhwani Modi.
Methodology: Dipak Dabhi, Ankit Kharwar, Diya Vadhwani, Pritesh Prajapati,Vishal Barot, Anamika Mittal, and Dhwani Modi.
Investigation: Dipak Dabhi, Ankit Kharwar, Diya Vadhwani, Pritesh Prajapati,Vishal Barot, Anamika Mittal, and Dhwani Modi.
Discussion of results: Dipak Dabhi, Ankit Kharwar, Diya Vadhwani, Pritesh Prajapati,Vishal Barot, Anamika Mittal, and Dhwani Modi.
Writing – Original Draft: Dipak Dabhi, Ankit Kharwar, Diya Vadhwani, Pritesh Prajapati,Vishal Barot, Anamika Mittal, and Dhwani Modi.
Writing – Review and Editing: Dipak Dabhi, Ankit Kharwar, Diya Vadhwani, Pritesh Prajapati,Vishal Barot, Anamika Mittal, and Dhwani Modi.
Resources: Dipak Dabhi, Ankit Kharwar, Diya Vadhwani, Pritesh Prajapati,Vishal Barot, Anamika Mittal, and Dhwani Modi.
Supervision: Dipak Dabhi, Ankit Kharwar, Diya Vadhwani, Pritesh Prajapati,Vishal Barot, Anamika Mittal, and Dhwani Modi.
Approval of the final text: Dipak Dabhi, Ankit Kharwar, Diya Vadhwani, Pritesh Prajapati,Vishal Barot, Anamika Mittal, and Dhwani Modi.

VIII. REFERENCES

[1] A. Beloglazov, "Energy-efficient management of virtual machines in data centers for cloud computing," Ph.D. thesis, University of Melbourne, Australia, 2013.

[8] A. Khosravi, L. L. H. Andrew, and R. Buyya, "Dynamic VM placement method for minimizing energy and carbon cost in geographically distributed cloud data centers," IEEE Trans. Sustain. Comput., vol. 2, no. 2, pp. 183–196, 2017.

[9] M. Xu and R. Buyya, "Managing renewable energy and carbon footprint in multi-cloud computing environments," J. Parallel Distributed Comput., vol. 135, pp. 191–202, 2020.

[10] Z. Á. Mann and M. Szabó, "Which is the best algorithm for virtual machine placement optimization?" Concurr. Comput. Pract. Exp., vol. 29, no. 10, 2017.

[11] C. Zhang, Y. Wang, Y. Lv, H. Wu, and H. Guo, "An energy and SLA-aware resource management strategy in cloud data centers," Sci. Program., 2019, pp. 1–16.

[14] H. Li, T. Li, and Z. Shuhua, "Energy-performance optimisation for the dynamic consolidation of virtual machines in cloud computing," Intl. J. Services Operations and Informatics, vol. 9, no. 1, pp. 62–82, 2018.

[12] Y. Saadi and S. E. Kafhali, "Energy-efficient strategy for virtual machine consolidation in cloud environment," Soft Comput., vol. 24, no. 19, pp. 14845–14859, 2020.

[13] R. Zolfaghari and A. M. Rahmani, "Virtual machine consolidation in cloud computing systems: Challenges and future trends," Wirel. Pers. Commun., vol. 115, no. 3, pp. 2289–2326, 2020.

[2] M. A. H. Monil and R. M. Rahman, "Implementation of modified overload detection technique with VM selection strategies based on heuristics and migration control," in 14th IEEE/ACIS Intl. Conf. on Computer and Information Science, 2015, pp. 223–227.

[3] F. F. Moges and S. L. Abebe, "Energy-aware VM placement algorithms for the openstack neat consolidation framework," J. Cloud Comput., vol. 8, p. 2, 2019.

[4] D. A. Alboaneen, H. Tianfield, and Y. Zhang, "Glowworm swarm optimisation algorithm for virtual machine placement in cloud computing," in 2016 Intl IEEE Conf. UIC/ATC/ScalCom/CBDCom/IoP/SmartWorld, 2016, pp. 808–814.

[5] N. Khattar, J. Singh, and J. Sidhu, "An energy efficient and adaptive threshold VM consolidation framework for cloud environment," Wirel. Pers. Commun., vol. 113, no. 1, pp. 349–367, 2020.

[6] D. Dabhi and D. Thakor, "Energy and SLA-Aware VM Placement Policy for VM Consolidation Process in Cloud Data Centers," in Sustainable Technology and Advanced Computing in Electrical Engineering, 2022, pp. 351–365.

[7] Q. Zhou, M. Xu, S. S. Gill, C. Gao, W. Tian, C. Xu, and R. Buyya, "Energy efficient algorithms based on VM consolidation for cloud computing: Comparisons and evaluations," in 20th IEEE/ACM Intl. Symposium on Cluster, Cloud and Internet Computing (CCGRID), 2020, pp. 489–498.

[15] B. Shrimali and H. Patel, "Multi-objective optimization oriented policy for performance and energy efficient resource allocation in cloud environment," J. King Saud Univ. Comput. Inf. Sci., vol. 32, no. 7, pp. 860–869, 2020.

Journal of Engineering and Technology for Industrial Applications

ITEGAM-JETIA

Manaus, v.12 n.60, p.1330-1342 July/August, 2026.
DOI: https://doi.org/10.5935/jetia.v12i60.4083

ISSN ONLINE: 2447-0228

RESEARCH ARTICLE OPEN ACCESS

OPTIMIZATION OF A NOVEL TORQUE SHARING FUNCTION FOR IMPROVED SWITCHED RELUCTANCE MOTOR CONTROL USING PSO

Houda Fetoui*[1], Ali Rezig[2], Chouaib Labiod[3], Ahmed Mesai Belgacem[4], Imene Bouguettah[5] Marwa Arabi[6]

[1, 2,4,5]L2EI Laboratory, Faculty of Science and Technology, University of Jijel, 18000 Jijel, Algeria
[3]UDERZA Unit, Department of Mechanical Engineering, University of El Oued, El Oued, 39000, Algeria
[6]Automatic Laboratory of Skikda, University of Skikda, Skikda, 21000, Algeria

[1]https://orcid.org/0009-0005-1229-4987, [2]https://orcid.org/0009-0005-1665-1259, [3]https://orcid.org/0000-0001-9262-8521
[4]https://orcid.org/0009-0003-0328-3835, [5]https://orcid.org/0009-0006-0606-8710, [6]https://orcid.org/0009-0008-0533-5025

E-email: *houda.fetoui@univ-jijel.dz, ali.rezig@gmail.com, labiod-chouaib@univ-eloued.dz, ahmed.mesaibelgacem@univ-jijel.dz, imen.bouguettah1987@gmail.com, m.arabi@univ-skikda.dz

ARTICLE INFO

Article History
Received on: March 13, 2026
Reviewed on: April 13, 2026
Accepted on: July 01, 2026
Published on: July 31, 2026

Keywords:
Torque Sharing Function,
Switched Reluctance Motor,
Torque Ripple Reduction,
Phase Commutation Optimization,
Particle Swarm Optimization Algorithm.

ABSTRACT

Switched Reluctance Motors (SRMs) are increasingly adopted in modern electric drive systems due to their mechanical robustness, fault tolerance, and high efficiency. However, their nonlinear magnetic characteristics and discrete torque production often result in pronounced torque ripple, which can limit performance in precision applications. This paper introduces an enhanced optimization strategy for the Torque Sharing Function (TSF) to minimize torque ripple in SRMs. The TSF is essential for regulating instantaneous torque by distributing the reference torque among individual phases according to rotor position, thereby improving torque smoothness and operational stability. The proposed method divides the reference torque into multiple subintervals during phase excitation to control overlap duration and reduce negative torque during commutation. Key control parameters including turn-on, turn-off, and overlap angles are jointly optimized by particle swarm optimization algorithm (PSO) to achieve an effective balance between torque ripple reduction, efficiency, and performance across a wide speed range. Finite element analysis is employed for accurate magnetic characterization, while iterative optimization algorithms ensure consistency, convergence, and robustness. Simulation results validate the proposed framework, showing notable reductions in torque ripple, improved speed regulation, and enhanced dynamic response. The method provides a flexible and scalable control solution applicable to various SRM configurations, promoting advancements in high-performance electric drive systems.

Copyright ©2026 by authors and Galileo Institute of Technology and Education of the Amazon (ITEGAM). This work is licensed under the Creative Commons Attribution International License (CC BY 4.0).

I. INTRODUCTION

Switched Reluctance Motors, characterized by their simple mechanical design and the use of non-wound, salient rotor structures, have become increasingly attractive in modern electric drive applications. Their absence of rotor windings or permanent magnets significantly reduces manufacturing cost and enhances reliability, enabling consistent operation under harsh thermal and mechanical environments. Torque is generated by the inherent magnetic tendency of rotor poles to align with energized stator poles, resulting in a robust and durable electromagnetic drive mechanism suitable for industrial, automotive, and aerospace applications [1]. Despite these benefits, SRMs are hindered by a fundamental performance limitation: high torque ripple. The doubly salient structure, concentrated stator windings, and inherent discontinuous excitation result in large fluctuations in instantaneous torque, often leading to vibration, acoustic noise, and degraded dynamic behavior. These effects are generally more pronounced than in conventional induction or synchronous machines, where smoother electromagnetic torque generation is possible.

Although motor-level improvements, such as refined magnetic circuit design, can partially mitigate this issue, substantial ripple reduction is most effectively achieved through advanced control strategies implemented at the power converter and drive level [1], [2]. Unlike conventional machines that frequently rely on model-based approaches such as field-oriented control, SRM drives are well-suited to real-time, analytically derived, position-dependent current control schemes. This flexibility has led to the development of a diverse range of torque control techniques from basic commutation strategies to computationally adaptive schemes capable of enhancing torque smoothness without requiring structural modifications to the machine [1], [3]. Among these strategies, the Torque Sharing Function has emerged as a central approach for ripple suppression. TSF-based control distributes the total torque reference among the active phases such that the resulting composite torque waveform achieves reduced variation over a full electrical cycle. Early TSF designs employed fixed torque profiles and uniform turn-on angle staggering, providing noticeable ripple reduction but sacrificing copper loss efficiency due to suboptimal current shaping. Subsequent developments introduced adaptive weighting functions that dynamically modify each phase's torque contribution, achieving torque error below 1% and limiting ripple to under 3%, markedly outperforming traditional direct torque control methods, which commonly yield ripples in the range of 15% [4]. More advanced formulations have decoupled the TSF reference waveform from phase excitation timing, allowing excitation angles to be independently optimized in real time for further ripple reduction without altering the total torque reference [5].

Hybrid approaches combining TSF with methods such as super-twisting sliding-mode control have also demonstrated improved robustness, reduced chattering, and greater suitability for demanding applications such as electric vehicle propulsion [6]. While, in [7], a torque ripple reduction strategy for Doubly Salient Electromagnetic Machines (DSEM) is proposed based on the use of Current Given Functions (CGFs). By systematically selecting suitable CGFs and corresponding overlap angles for varying operating conditions, the method enhances current tracking accuracy and improves the torque–ampere ratio. Multiple CGF profiles including linear, cubic, cosine, and exponential functions are evaluated to optimize current distribution during commutation, thereby reducing both torque ripple and copper losses. Furthermore, a modified piecewise Torque Sharing Function described in [8] achieves additional ripple suppression during phase transitions, while model predictive control further attenuates ripple caused by hysteresis-based current regulation. This combined approach streamlines the optimization process by computing phase current trajectories directly as a function of rotor position via the TSF, eliminating the need to manually assign weighting factors in the control cost function. These contributions illustrate a clear progression in TSF methodologies from early static angle-staggering approaches to increasingly dynamic, efficiency-focused, and model-based control frameworks. Each generation of techniques has contributed incremental improvements in torque ripple suppression while simultaneously balancing key considerations such as computational complexity, real-time feasibility, and electromagnetic efficiency. Therefore, this paper introduces a new hyperbolic TSF formulation to further enhance the smoothness of torque transition between outgoing and incoming phases.

Unlike conventional TSFs that rely primarily on turn-on, turn-off, and fixed overlap angles, the proposed method presents hyperbolic shaping coefficients that allow finer control of phase current evolution during commutation. This approach improves torque continuity, suppresses negative torque, and enhances overall drive efficiency. A Particle Swarm Optimization (PSO) algorithm is utilized to automatically tune commutation parameters by jointly optimizing multiple objectives, including torque ripple reduction, copper loss minimization, and electromagnetic smoothness. The proposed method is integrated into a complete control framework and evaluated using a high-fidelity nonlinear finite element model of an 8/6 SRM. Comparative simulation results confirm that the optimized hyperbolic TSF significantly outperforms conventional and non-optimized strategies, offering improved dynamic response, smoother torque profiles, and enhanced overall suitability for high-performance electric drive systems. Within this scope, the present work advances an optimized Torque Sharing Function (TSF) control methodology engineered to substantially mitigate torque ripple and ameliorate the associated spectral attributes of vibration and acoustic noise. The validity of the proposed approach is established through a multi-faceted validation framework incorporating analytical, finite element (FEA), and dynamic system simulations. Thus, the paper proceeds with the following organization: Section II covers the fundamental modelling and electromagnetic equations of the Switched Reluctance Motor. Section III discusses outcomes from finite element modelling, including flux distribution. Section IV elaborates on the Torque Sharing Function control strategy, introducing the novel optimized method. Concluding in Section V, the results are presented and discussed, with a thorough assessment of the strategy's effectiveness in reducing torque ripple.

II. MODELLING OF 8/6 SRM

II.1 FINITE ELEMENT MODELLING

The finite element method (FEM) stands out as a powerful numerical technique for solving electromagnetic field problems, especially when confronted with intricate geometries and pronounced material nonlinearities, as commonly found in switched reluctance machines [9], [10]. To precisely model these complex features, the Ansys Maxwell environment was utilized, incorporating detailed geometric parameters along with a customized automated APDL (ANSYS Parametric Design Language) script specifically designed for the 6/8 SRM configuration under investigation. This integrated approach facilitates efficient, high-fidelity modelling and simulation, delivering accurate and dependable electromagnetic performance results [11] as showing in figure (1).

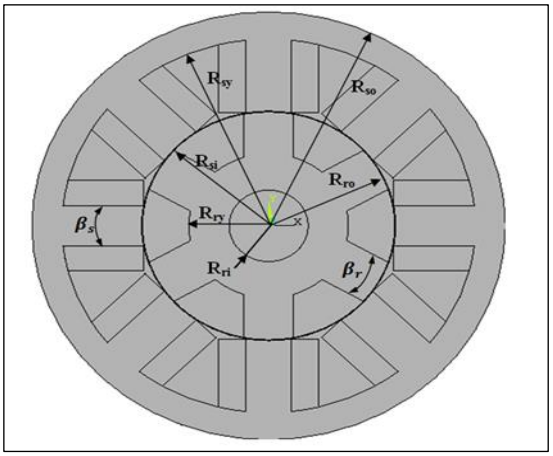


Figure 1: SRM Prototype Dimensions Specification.
Souce: Authors, (2026).

In addition, the details of dimensions and electrical parameters are shown on appendix table (1).

II.2 SIMULATION AND FLUX DISTRIBUTION

The electromagnetic field distribution in the SRM is shaped by the magnetic vector potential as well as the nonlinear permeability of the magnetic material [12].

$$\operatorname{curl}\left(\nu \operatorname{curl}\left(\vec{A}\right)\right) = \vec{J} \tag{1}$$

Where v denotes the magnetic reluctivity and represents the source current density vector. For the case of Cartesian coordinates, this yields:

$$\frac{\partial}{\partial x}\left(\nu \frac{dA_z}{dx}\right) + \frac{\partial}{\partial y}\left(\nu \frac{dA_z}{dy}\right) = -J_z \tag{2}$$

The flux linkage for a single operational step of the motor is determined from the resulting distribution of the magnetic vector potential:

$$\phi = \frac{1}{i}\int_v \overline{JA}\, dV \tag{3}$$

After determining the relevant elements along the machine's axial length, the number of turns per phase, N, is defined in (7), and the winding area for each phase is denoted as S.

$$\phi = \frac{NI}{S}\sum_{k=1}^{N}\left(A_k\, S_k\right) \tag{4}$$

The inductance and magnetic co-energy are determined as functions of the flux linkage using the expressions given below:

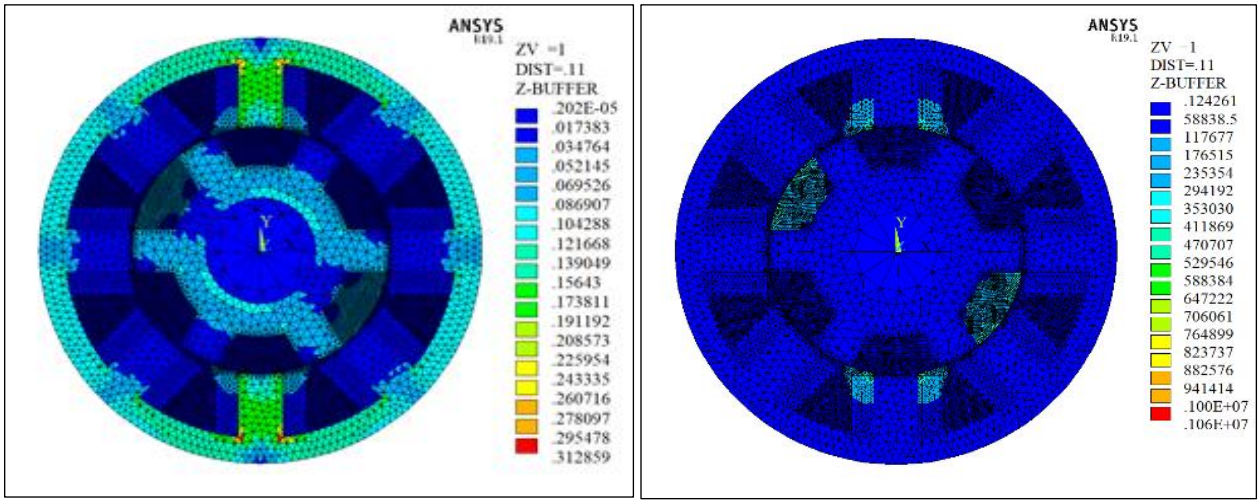
$$L(\theta, i) = \frac{\phi(\theta, i)}{i} \tag{5}$$

$$W_{em} = \int_0^I \phi(\theta, i)\, \partial i \,\Big|_{\theta = \text{Const}} \tag{6}$$

Using the co-energy approach, the electromagnetic torque is computed as the partial derivative of the magnetic co-energy with respect to the rotor angular position, while keeping the phase current constant, as given by the following equation:

$$T(\theta, i) = \frac{\partial W_{em}}{\partial \theta}\Bigg|_{\theta = \text{Cons}} \tag{7}$$

Figure 2 presents both graphical and quantitative representations of the magnetic flux density distribution within the 6/8 SRM, with a phase current of 2 A and 12A applied. These results validate the machine's anisotropic inductance profile, a fundamental characteristic for torque production in SRMs. The numerical output further supports subsequent analysis, such as inductance profiling and torque estimation, essential for control strategy development. Figures 3 and 4 show, respectively, the numerical characteristics of the inductance and the static torque are evaluated as functions of the rotor position, first from the aligned to the non-aligned position and then from the non-aligned back to the aligned position. The results are presented for phase currents ranging from 2 A to 16 A. The results illustrate the extent of magnetic saturation in the machine, showing that increasing the current yields progressively larger saturation at higher current levels. By leveraging the previously captured characteristics, the model more accurately represents real-machine behavior and, depending on the formulation adopted, can provide robust results for control design and validation in journal-quality studies [13].



(a) (b)

Figure 2: Flux density of 8/6 SRM for a current: (a) 2 A, (b) 12A.
Source: Authors, (2026).

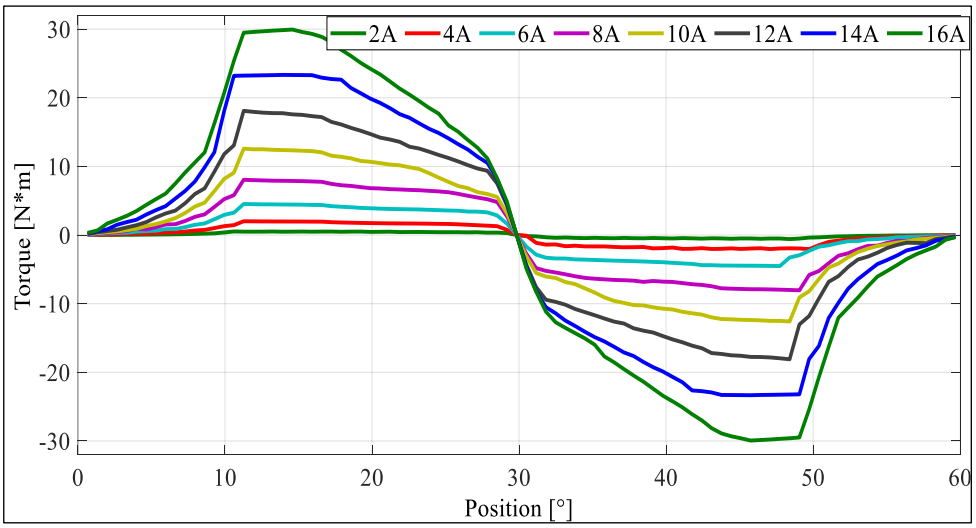


Figure 3: Static torque characteristics as a function of rotor position for phase currents between 2 A and 16 A.
Source: Authors, (2026).

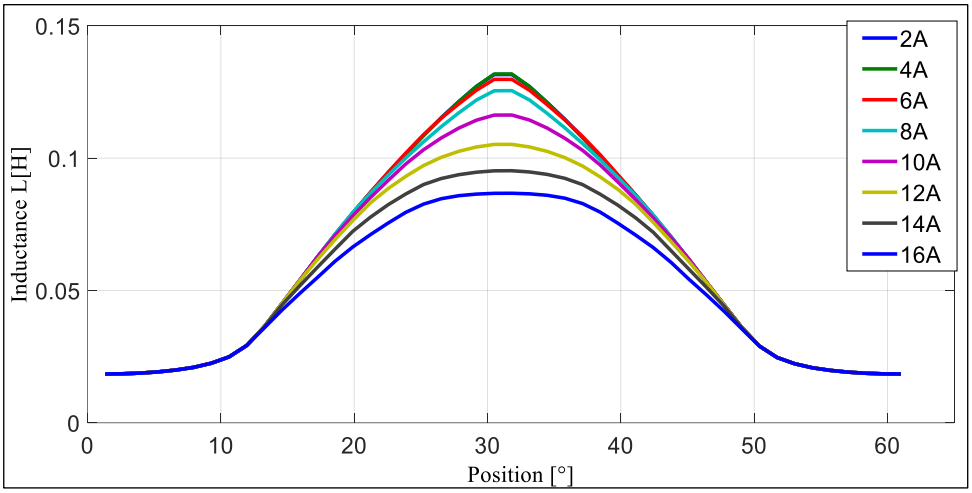


Figure 4: Inductance characteristics as a function of rotor position for phase currents between 2 A and 16 A.
Source: Authors, (2026).

The results illustrate the extent of magnetic saturation in the machine, showing that increasing the current yields progressively larger saturation at higher current levels. By leveraging the previously captured characteristics, the model more accurately represents real-machine behavior and, depending on the formulation adopted, can provide robust results for control design and validation in journal-quality studies [13]. To illustrate the modelling of the 6/8 SRM, a comprehensive schematic of the associated asymmetric bridge converter is presented in figure 5.

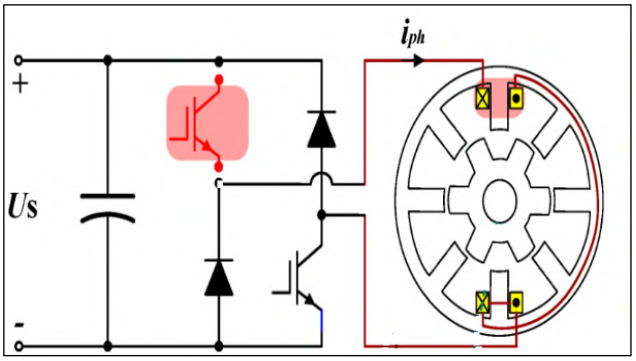


Figure 5: Overview of the 6/8 SRM and its associated asymmetric bridge converter.
Source: Authors, (2026).

The converter topologies of Asymmetric bridge / half bridge (per phase) Feature Two switches/diodes per phase enabling bidirectional current control and independent commutation; widely used with angle control and soft chopping methods [14], [15]. The regulation of an engine constitutes a complex undertaking that calls for the capabilities of adept specialists. Each procedural step is managed independently through the utilization of a hysteresis controller or Pulse Width Modulation (PWM) control. The majority of applications employ an unbalanced bridge configuration to govern the current within the defined hysteresis limits. This asymmetric bridge configuration facilitates three distinct voltage states: $+V_{cc}$ positive, 0 zero, and $-V_{cc}$negative. Consequently, contingent upon the selected control methodology, all of these voltage states are employed to regulate the variable reluctance machine [12]. When a half-bridge converter is used to supply the motor with a hysteresis current controller, a significant negative current change occurs abruptly due to the reversal of voltage polarity across the machine windings. This effect induces vibrations of considerable amplitude [16]. To mitigate this issue, the present study adopts a methodology based on two-step commutation (2sc). Thus, the principle of the methodology is as follows: During the transition phase, the voltage initially applied to phase 1 is at its positive level, corresponding to the DC bus voltage, $V = +V_{dc}$. It then decreases to zero and, after a duration approximately equal to half the resonance cycle, rises to its negative level when the switches open and diodes D1 and D2 conduct. At this point, the applied voltage is reversed to $V = -V_{dc}$ and remains in this state until the current drops to zero. This approach effectively reduces both vibrations and acoustic noise in the machine [17].

III. MATHEMATICAL EQUATION

For a switched reluctance motor, the dynamic system refers to a phase winding which can be modelled as an inductance in series with a resistance, as shown in the figure 6 [13].

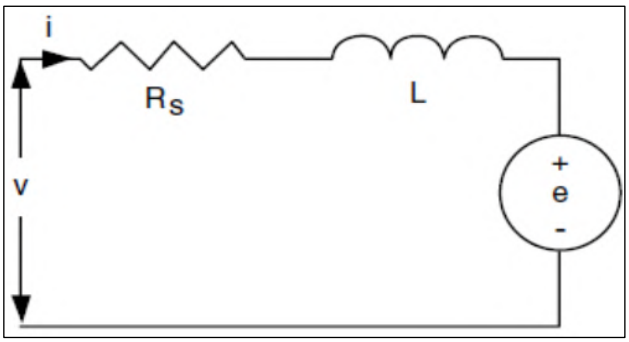


Figure 6: equivalent circuit of one of SRM.
Source: Authors, (2026).

The electromagnetic equation of the model is then written as [11]:

$$V = R_s i_j + \frac{d\Phi_j(\theta, i)}{dt} : j = 1,2,3,4 \quad (8)$$

Where R_s and ϕj are respectively, the resistance and the flux linkage per phase. j indicates the order of the phases. The flux linkage of the SRM is expressed as a function of the inductance characteristic L(θ, i) by the following equation:

$$\phi(\theta, i) = L(\theta, i).i \quad (9)$$

The inductance L(θ,i) depends on both the rotor position and the phase current. Consequently, the phase voltage is determined using Equations (1) and (2):

$$V = R_s.i_j + L(\theta, i).\frac{di}{dt} + \frac{dL(\theta, i)}{d\theta}.i_j.\frac{d\theta}{dt} \quad (10)$$

The back electromotive force E_f (θ, i) is given by:

$$E_f(\theta, i) = \frac{dL(\theta, i)}{d\theta}.i.\omega \quad (11)$$

Furthermore, the mechanical dynamics play a crucial role in electromechanical machines [18], [19]. The mechanical model can be expressed as follows:

$$T_e(\theta, i) = T_m(\theta, i) + f.\omega + j.\frac{d\omega}{d\theta} \quad (12)$$

The parameter j denotes the moment of inertia, ω represents the rotor speed, f is the friction coefficient, and Tm corresponds to the load torque. The electromagnetic torque Te(θ,i) is determined from:

$$T_{ej}(\theta, i) = \frac{1}{2}.i^2.\frac{dL(\theta, i)}{d\theta} : j = 1,2,3,4 \quad (13)$$

Where L (θ, i) denotes the inductance, i represents the total current and R is the phase resistance. Supplying the machine during either the increasing or decreasing inductance region determines the operating mode, as illustrated in Figure 7 [12]. Motor mode (Te > 0) occurs during the rising inductance region (∂L/ ∂θ m > 0). Generator mode (Te < 0) occurs during the falling inductance region (∂L/ ∂θ m < 0).

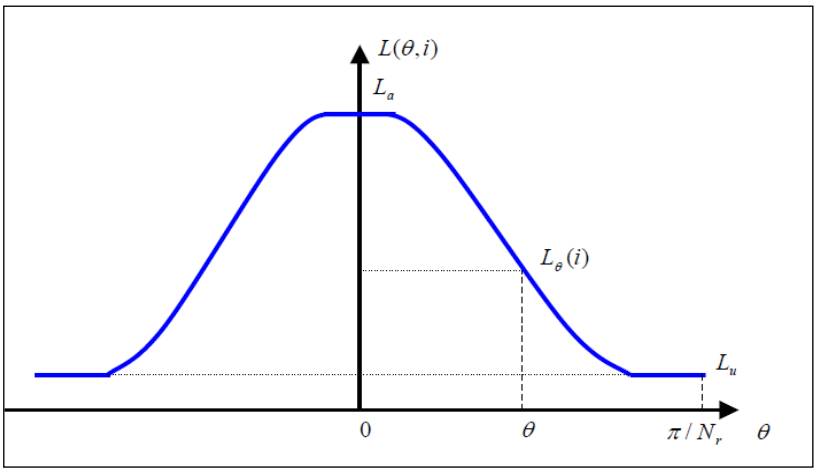


Figure 7: Principle of operation of the SRM.
Source: Authors, (2026).

IV. TORQUE SHARING FUNCTION–BASED CONTROL STRATEGY

The block diagram of the direct instantaneous torque control strategy for the SRM is shown in Figure 8. The torque closed-loop architecture consists of a torque computation unit, a hysteresis controller, a power converter, the switched reluctance motor (SRM), a position sensor, and a current sensor. The total reference torque, T_{ref}, is distributed into phase-specific reference torques, T_{kref}, at discrete rotor positions according to a torque-sharing function. The instantaneous output torque is obtained from a lookup table, and the torque error $(T_{ref} - T_{out})$ is processed by the torque hysteresis controller to generate the gating signals for the power converter. The torque-sharing function defines the overall control strategy, ensuring coordinated and high-precision torque production [20].

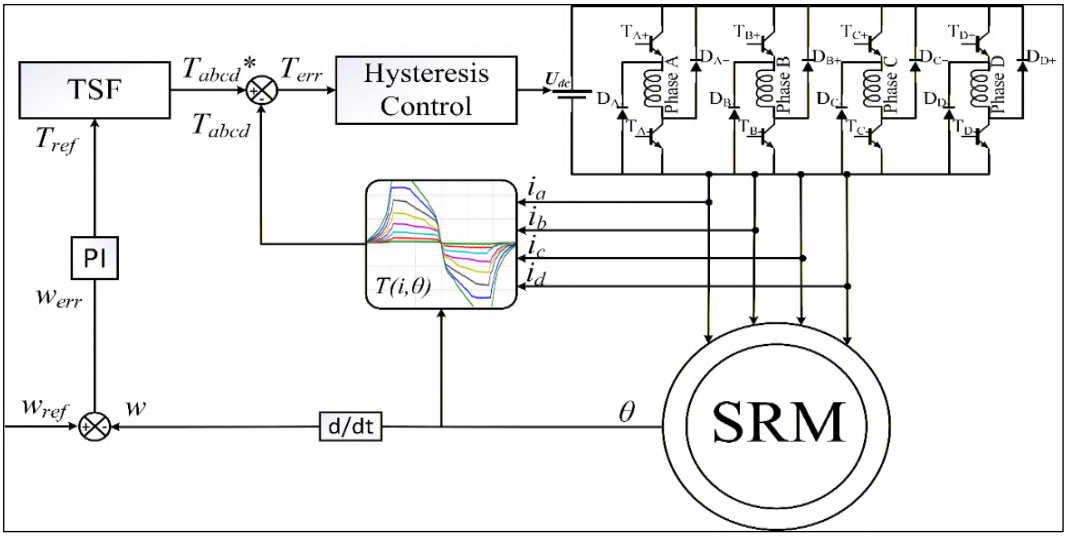


Figure 8: Control block diagram of the SRM based on the TSF strategy.
Source: Authors, (2026).

To ensure the control objective of the Torque Sharing Function (TSF) based on the synthesized instantaneous torque, the following equation must be satisfied for the SRM [20].

$$\begin{cases} T_k(\theta) = T^* f_k(\theta), k = 1,2,\dots,m, \\ \sum_{k=1}^{m} f_k(\theta) = 1, 0 \le f_k(\theta) \le 1 \end{cases} \tag{14}$$

Where $T_k(\theta)$ represents the instantaneous torque of the k-th phase winding, T^* denotes the synthesized instantaneous reference torque, and $f_k(\theta)$ corresponds the torque-sharing function of the k-th phase winding. The TSF directly regulates the peak current of each machine phase, thereby influencing torque ripple and ensuring stable steady-state operation. The fundamental principle of the TSF is to decompose the total reference torque into phase-specific reference torques according to the rotor position, which are then used as control inputs [21], [22]. The reference torque of each phase, T_k^* in equation (15), is obtained by appropriately shifting the TSF. Based on the torque profile within the commutation overlap region, TSFs can be classified into various types, including linear, exponential, cubic, sinusoidal, and cosine functions. Figure 9 illustrates the torque profiles and corresponding current waveforms for linear and cosine TSFs [23].

$$T_k^{*(\theta)} = \begin{cases} 0 & 0 \le \theta \le \theta_{on} \\ T^* \cdot f_{rise(\theta)} & \theta_{on} < \theta < \theta_{on} + \theta_{ov} \\ T^* & \theta_{on} + \theta_{ov} \le \theta \le \theta_{off} - \theta_{ov} \\ T^* \cdot f_{fall(\theta)} & \theta_{off} - \theta_{ov} < \theta < \theta_{off} \\ 0 & \theta_{off} \le \theta \le \tau \end{cases} \tag{15}$$

In equation (15), $T_k^{*(\theta)}$ denotes the total reference torque, f_{frise} defines the slope of the rising phase of the input phase, and f_{fall} is the slope of the falling phase of the output phase. The angles θ_{on}, θ_{off}, and θ_{ov} correspond the turn-on, turn-off, and overlapping positions, respectively, and τ represents the rotor angle period. The relationship between $f_{frise}$and f_{fall} is given by [20], [24]:

$$f_{fall}(\theta) = 1 - f_{frise}(\theta - \varepsilon) \tag{16}$$

The number of TSF parameters can be reduced to two, as angles θ_{on}, θ_{off}, and θ_{ov} are interrelated as follows:

$$\theta_{off} = \theta_{on} + \theta_{ov} + \varepsilon \tag{17}$$

Here, ε=2π/(m Nr) denotes the stroke angle, or angular displacement between adjacent phases, with Nr representing the number of rotor poles. The maximal overlap angle $\theta_{ov,max}$ = τ/4, occurs when the turn-on angle is minimized (θ_{on}= θ_u) and the turn-off angle is maximized (θ_{off} =θ_{al}). For instance, in an 8/6 four-phase SRM, the overlap angle is limited to $\theta_{ov,max}$=15° since τ=60°. At any rotor position, two phases' windings are energized simultaneously due to the stroke angle ε=15°. However, the second constraint $\theta_{ov} \le \tau/2 - \varepsilon$, derived from this relationship, can be more restrictive for certain motor configurations [9].

$$f_{rise}(\theta) = \frac{\theta - \theta on}{\theta ov} \tag{18}$$

And:

$$f_{fall}(\theta) = 1 - f_{rise}(\theta - \varepsilon) \tag{19}$$

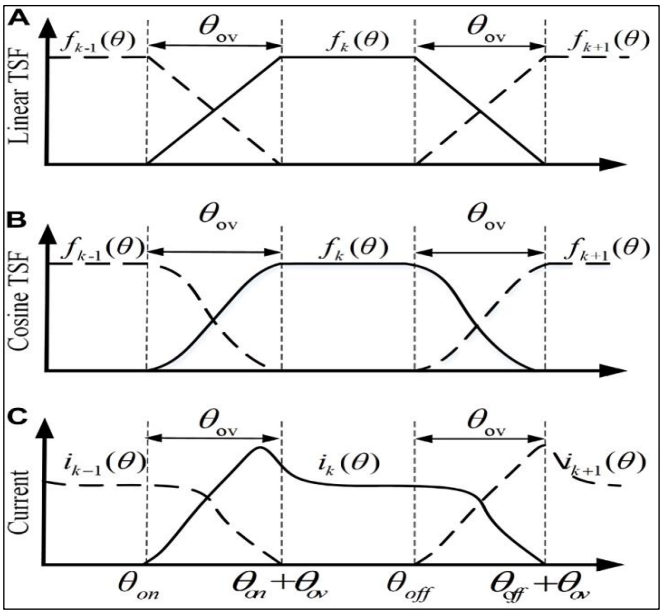


Figure 9: Profiles and current diagrams of linear and cosine TSF functions. (A): Profiles of linear TSF. (B): Profiles of cosine TSF. (C): Diagram of phase current and rotor position.
Source: Authors, (2026).

IV.1 THE PROPOSED STRATEGY

This paper presents a novel Torque Sharing Function method for reducing torque ripple in SRMs. The total reference torque is subdivided into several subintervals ranging from zero to different nonzero values. These subintervals are assigned to phase torques during excitation modes sequentially, prior to shifting excitation to the next phase. The region where two or more phases overlap during excitation is defined as the overlap region. The influence of the overlap angle θov on motor performance is investigated.

- A large θov smooths the torque waveform but results in energy loss, whereas a smaller θov enhances energy efficiency at the expense of higher torque ripple. This method involves the systematic optimization of the overlap angle, defined as the angular difference between the turn-on and turn-off firing angles. The overlap angle is analytically derived with respect to two critical switching angles by evaluating coefficient parameters that characterize the hyperbolic profile of the proposed TSF. These parameters delineate the commutation intervals spanning from T1 to T4 thereby precisely shaping the commutation trajectory and modulating the torque distribution. This refined control methodology effectively reduces torque ripple and enhances the dynamic performance in SRM drives. The corresponding control relationship can be expressed by the following equation:

$$f(k) = \begin{cases} \dfrac{\theta - T_1}{T_2 - T_1} & if \quad T_1 < \theta < T_2 \\ 1 & if \quad T_2 \le \theta \le T_3 \\ \dfrac{\theta - T_4}{T_3 - T_4} & if \quad T_3 \le \theta \le T_4 \\ 0 & other \end{cases} \tag{20}$$

Where:

$$\begin{aligned} T_1 &= \theta_{on} + a \\ T_2 &= \theta_{on} + b \\ T_3 &= \theta_{off} + c \\ T_4 &= \theta_{off} + d \end{aligned} \tag{21}$$

The various configurations of the suggested TSF approach are depicted in figure 10. In order to find the optimal torque shape, which will be the main factor in reducing the ripple of the torque generated as well as the vibrations produced by the machine, the torque generated at every turn depends on the values of all of the coefficients that will be assigned by the optimization algorithm.

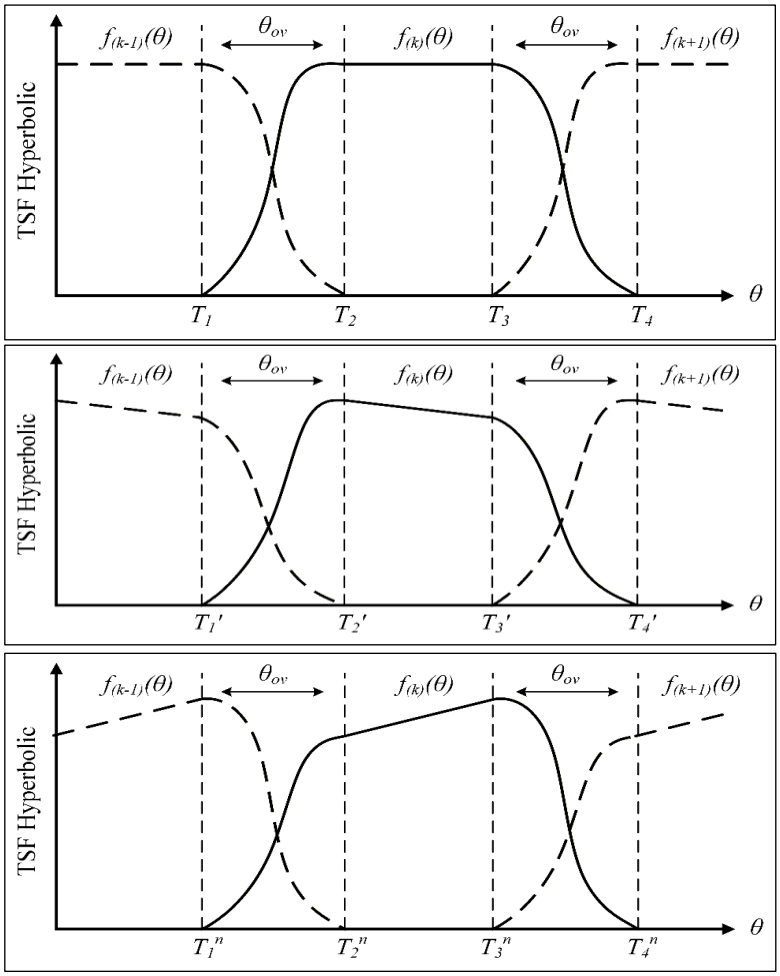


Figure 10: Profiles diagrams of Proposed TSF function.
Source: Authors, (2026).

Simulation studies and parameter optimizations were conducted to determine optimal coefficient values, demonstrating effective reduction in torque ripple and improved SRM performance. This method can be adapted to various SRM configurations for enhanced control precision and efficiency. Compared to conventional linear and cosine torque sharing functions, the proposed optimized TSF demonstrates a substantial reduction in torque ripple under identical operating conditions, confirming its superior capability to manage phase overlap and electromagnetic torque continuity in SRM drives which are represented on Table 1.

V. PARTICLE SWARM OPTIMIZATION

Particle Swarm Optimization (PSO), inspired by natural phenomena, is a computational technique within the field of swarm intelligence. Originally introduced by Kennedy and Eberhart in 1995, PSO simulates the collective behaviour of swarming species, such as birds or fish, as they move toward a target. The algorithm employs a population of particles, each representing a potential solution, which explore the search space to identify the global optimum. During this process, each particle updates its position by considering both its individual best location and the overall best position found by the swarm. In this study, the particle positions represent the PI controller gains and the TSF coefficients a, b, c, and d, along with θ_{on} and θ_{off}, which are iteratively optimized using the mathematical formulations given in Equations (20) and (21) [10]:

$$V_{i,}^{t+1} = wV_i^t + c_1 R_{1i}^t \left(p_{i,best}^t - x_i^t\right) + c_2 R_{2i}^t (G_{best}^t - X_i^t) \tag{22}$$

$$X_{i,}^{t+1} = wV_{i,}^{t+1} + X_{i,j}^t \tag{23}$$

Where, $V_{i,}^{t+1}Vi$ and V_i^t indicate the velocity of each particle at the current and previous iteration, respectively, while X_i^t and $X_{i,}^{t+1}$ denote the particle positions in the current and previous iterations, respectively. $p_{i,best}^t$, and G_{best}^t represent the personal and global best of each candidate and the hole swarm, and $c1,2$ and w are the inertia weight, the personal and global learning coefficient, and R1,2 is a random number. The flowchart for the procedure is shown in figure 11 [10]. The chosen goal function is the normalized torque ripple factor (TRF) in equation (24), defined as the ratio of the peak-to-peak torque variance to its average value across an electrical cycle, is selected as the objective function. The benefit of this dimensionless formulation is that it is directly related to the vibration excitations of the stator and is independent of the load level. Therefore, as in figure 12, minimizing the TRF is a pertinent criterion that is frequently used in the literature to assess SRMs' vibro-acoustic performance.

$$TRF = \frac{T_{max} - T_{min}}{T_{avg}} \tag{24}$$

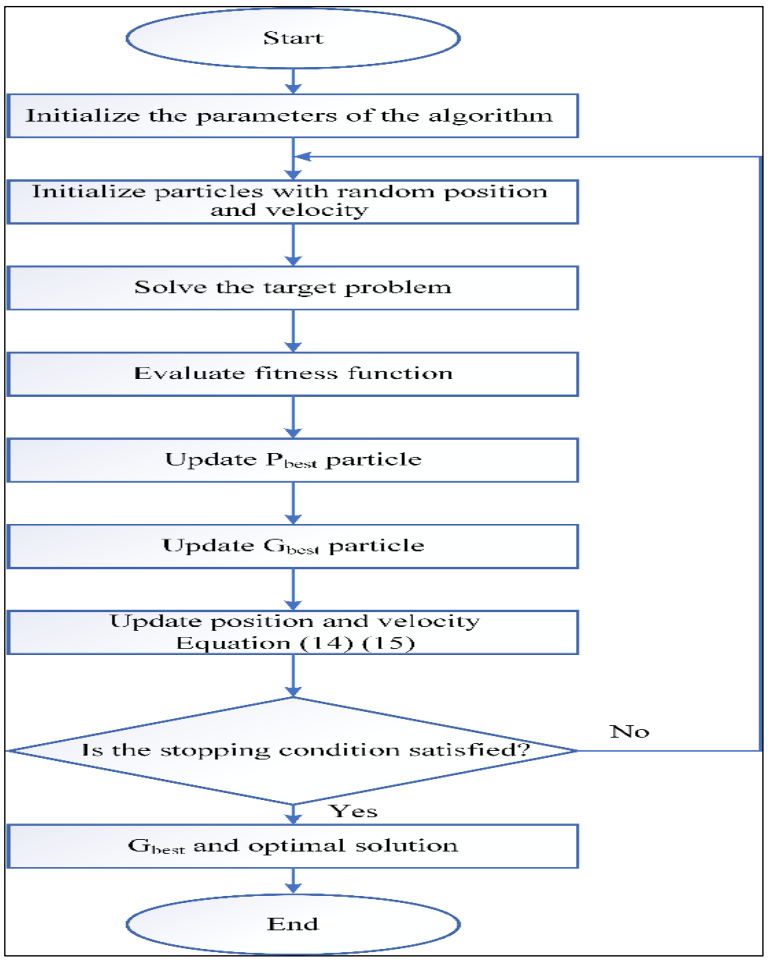


Figure 11: PSO algorithm flowchart.
Source: Authors, (2026).

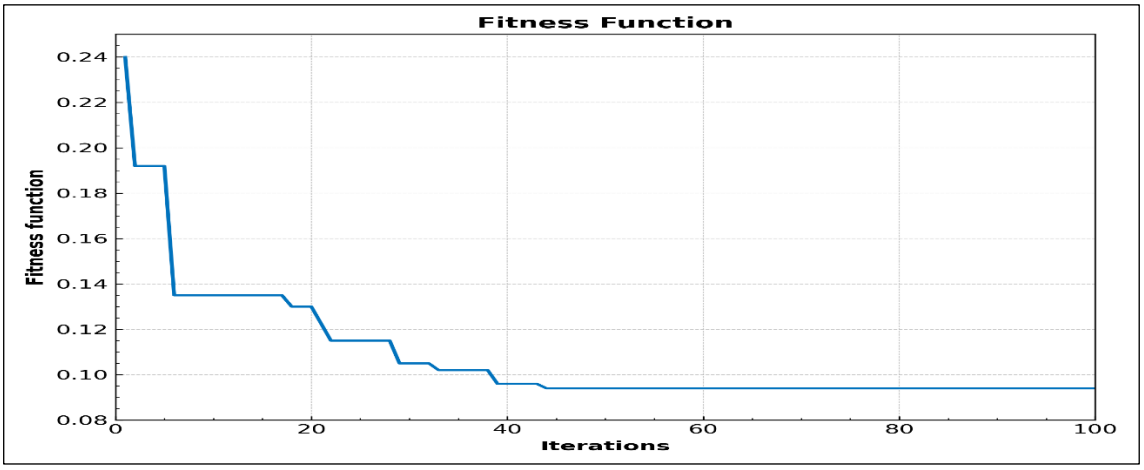


Figure 12: Best fitness of PSO.
Source: Authors, (2026).

VI. RESULTS AND DISCUSSIONS

Torque Sharing Function is a well-established technique aimed at reducing torque ripples in switched reluctance motors. To evaluate the effectiveness of the newly proposed optimization method for torque ripple reduction, TSF was implemented both with and without optimization on a 6/8 SRM under various operating conditions. The simulation involved two load torque scenarios at different speeds: case (1) is 7 N.m at 500 rpm and case (2) is 5 N.m at 1000 rpm. For the case (1) the total torque, phase torque, and current waveforms (illustrated in figures (13), (14), and (15) respectively, indicate that prior to optimization the torque ripple was 42.85% with a turn-on angle (Ton) of 2.7° and a turn-off angle (Toff) of 22.5°. Following optimization, these parameters were refined to Ton = 0.2° and Toff = 23.4°, resulting in a reduced torque ripple of 14.28%. Correspondingly, the current and phase torque waveforms demonstrate smoother profiles after optimization, reflecting improved control and reduced phase switching.

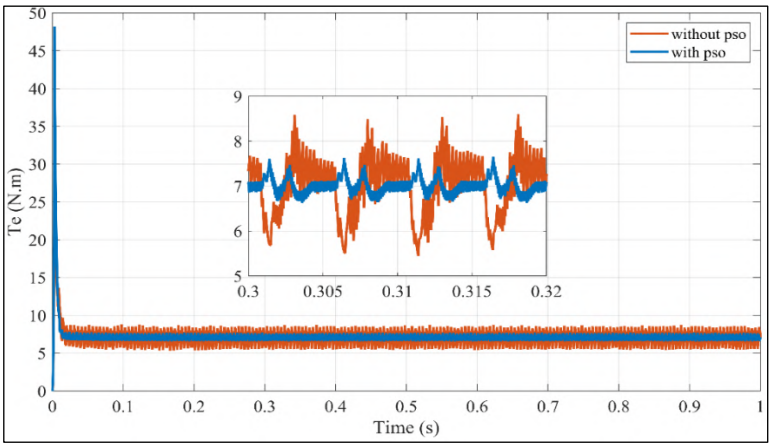
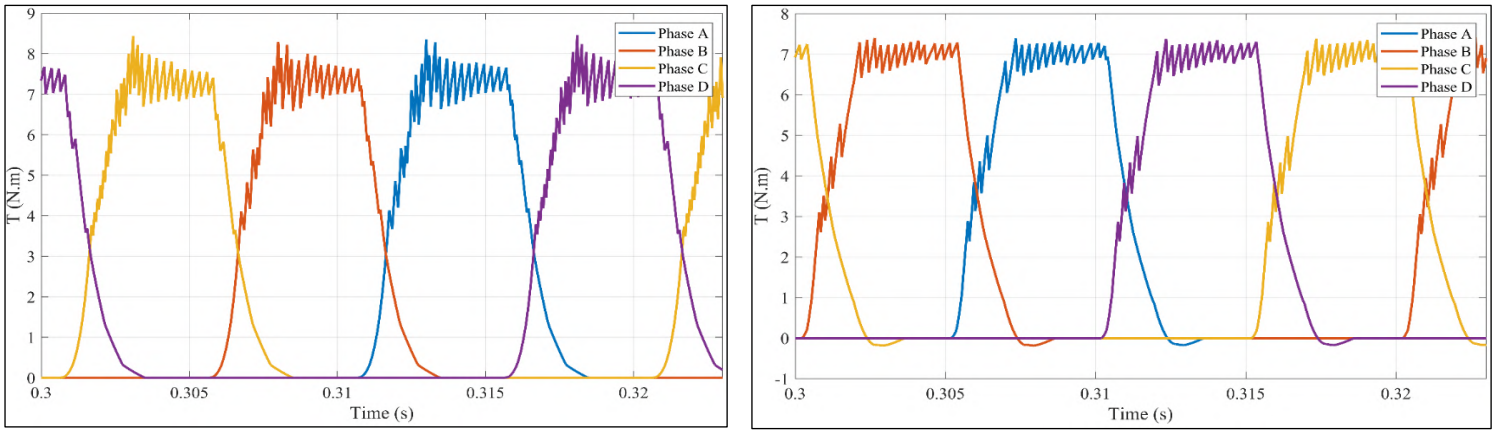
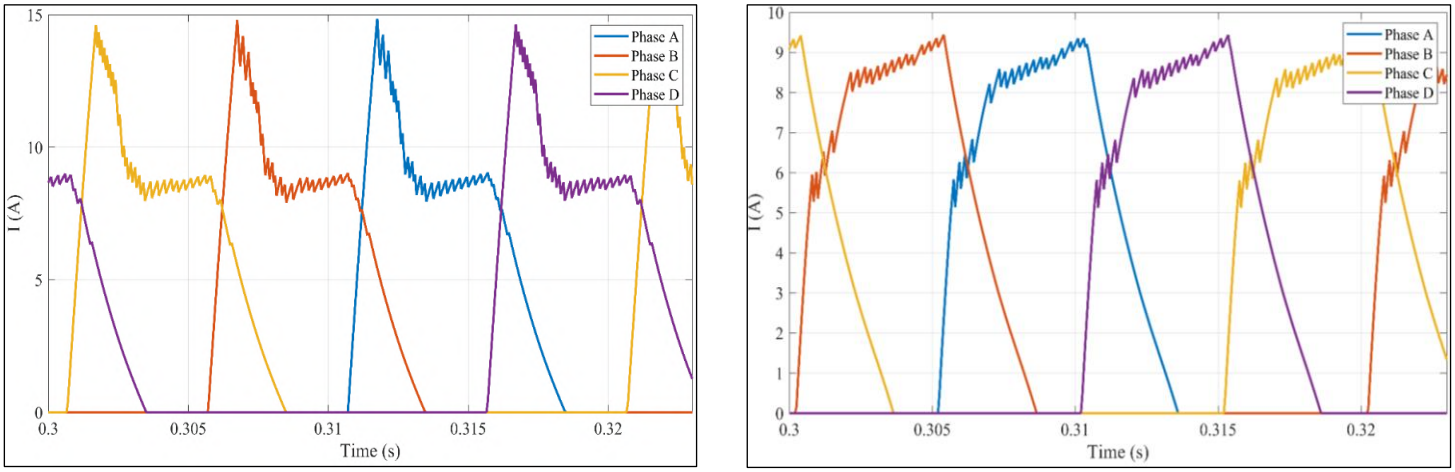


Figure 13: Total torque waveform of the 6/8 SRM under a load torque of 7 N.m at 500 rpm: Without Optimisation and with optimisation.
Source: Authors, (2026).



(a) (b)

Figure 14: Phase torque waveform :(A) Without Optimisation, (B) with optimisation.
Source: Authors, (2026).



(a) (b)

Figure 15: Phase Current profile :(A) Without Optimisation, (B) with optimisation.
Source: Authors, (2026).

Similarly, for the case (2) illustrated on figure (16) the simulations show a torque ripple decrease from 42% (Ton = 5°, Toff = 22°) to 20% after optimization (Ton = 0.26°, Toff = 22.5°). These improvements in torque ripple, along with smoother current waveforms, underscore the efficacy of the proposed TSF optimization method in enhancing SRM performance under varying load and speed conditions. Figure (17) and (18) demonstrate Phase Torque waveform and Phase Current profile respectively. This optimized TSF approach advances motor control by systematically adjusting switching angles to minimize torque fluctuations and improve operational smoothness, which is critical for applications requiring high precision and reliability.

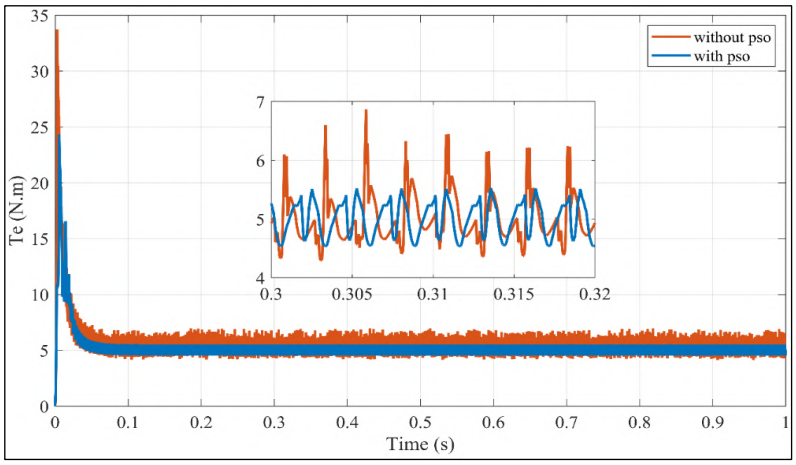
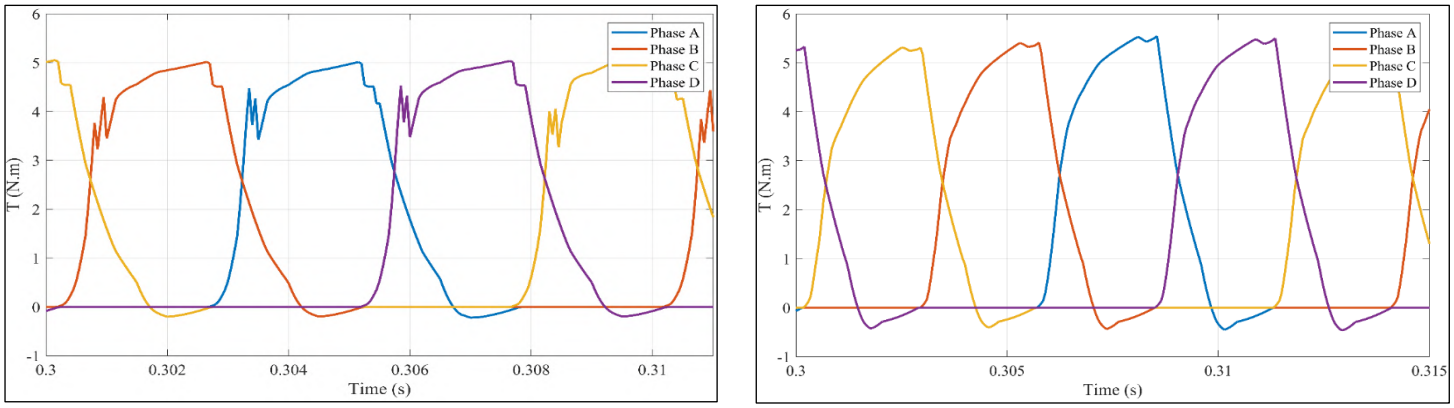


Figure 16: Total Torque waveform of the 6/8 SRM under a load torque of 5 N.m at 1000 rpm: Without Optimisation and with optimisation.
Source: Authors, (2026).



(a) (b)

Figure 17: Phase Torque waveform :(A) Without Optimisation, (B) with optimisation.
Source: Authors, (2026).

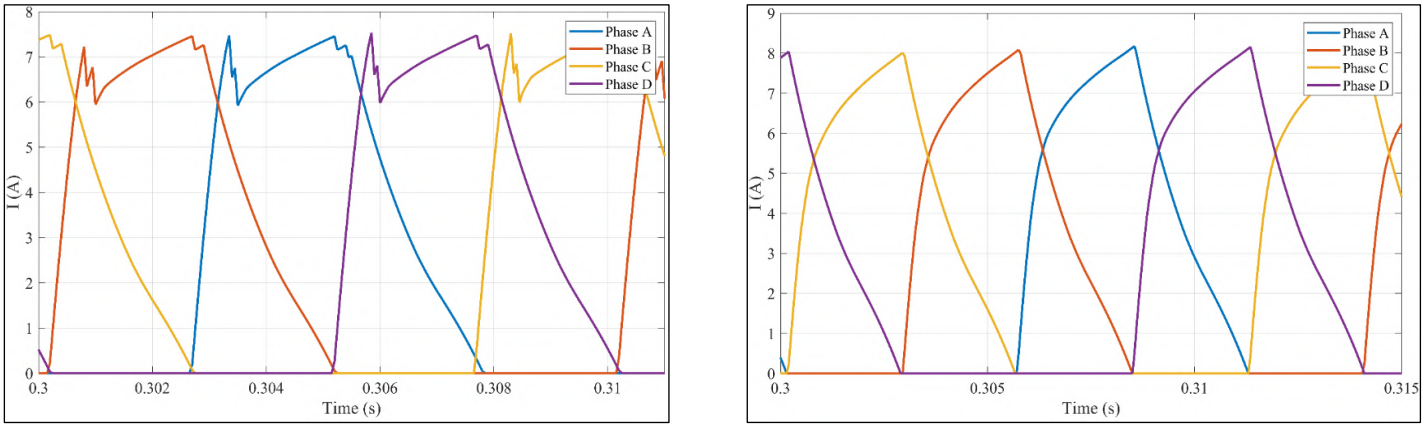


Figure 18: Phase Current profile :(A) Without Optimisation, (B) with optimisation.
Source: Authors, (2026).

Table 1: A detailed comparative evaluation of linear, cosine, and optimized TSF control strategies for SRM.

TSF Strategy	Turn-on Angle Ton		Turn-off Angle Toff		Torque Ripple	
	7 N.m 500 rpm	5 N.m 1000 rpm	7 N.m 500 rpm	5 N.m 1000 rpm	7 N.m 500 rpm	5 N.m 1000 rpm
Linear TSF	3.0	5.0	22.0	22.0	38 %	45–48 %
Cosine TSF	2.5	3.8	22.8	22.5	28 %	24–26 %
Proposed Optimized TSF	**0.2**	**0.26**	**23.4**	**22.5**	**14.28 %**	**20 %**

Source: Authors, (2026).

VII. CONCLUSION

This study proposes a novel hyperbolic Torque Sharing Function (TSF) framework that incorporates the optimization of phase commutation angles to enhance TSF efficacy. The switched reluctance motor (SRM) model was developed with high fidelity using ANSYS to accurately represent electromagnetic behaviours. The control methodology focuses exclusively on torque regulation through overlap angle optimization. By dynamically adjusting the TSF, the approach exploits the disparity in torque production capabilities between commutating phases. Simulation results obtained via MATLAB Simulink confirm a substantial reduction in torque ripple alongside improved system robustness and dynamic response. The validity of the method is corroborated by advanced optimization techniques, and its generalizability ensures applicability across diverse SRM configurations.

VIII. APPENDIX

Table 2: Dimensions and electrical parameters of SRM.

Parameters	Notation	Dimensions	
Effective length	L	170mm	
Outer stator radius	R_{so}	100 mm	
Inner radius of stator yoke	R_{sy}	88.2mm	
Inner stator radius	Rsi	58.19 mm	
Outer rotor radius	R_{ro}	57.83mm	
Outer radius of rotor yoke	R_{ry}	40.4mm	
Shaft radius	R_{ri}	25mm	
Stator pole arc	β_s	19.70°	20mm
Rotor polar arc	β_r	19.82°	20mm
Air gap thickness	E	0.36 mm	
Number of coils per pole -pair	N_s	180	
Section coil	S	3400mm^2	

Source: Authors, (2026).

IX. AUTHOR'S CONTRIBUTION

Conceptualization: Houda Fetoui, Chouaib Labiod.
Methodology: Houda Fetoui, Chouaib Labiod.
Investigation: Houda Fetoui, Chouaib Labiod.
Discussion of results: Houda Fetoui, Chouaib Labiod, Ahmed Mesai Belgacem.
Writing – Original Draft: Houda Fetoui.
Writing – Review and Editing: Houda Fetoui, Chouaib Labiod, Ahmed Mesai Belgacem.
Resources: Ali Rezig, Chouaib Labiod.
Supervision: Ali Rezig, Chouaib Labiod.
Approval of the final text: Houda Fetoui, Ali Rezig, Chouaib Labiod, Ahmed Mesai Belgacem, Imene Bouguettah, Marwa Arabi.

X. REFERENCES

[1] L. Benalia, Control of a Double Feed and Double Star Induction Machine Using Direct Torque Control. IntechOpen, 2011.

[2] R. Krishnan, “Switched Reluctance Motor Drives: Modeling, Simulation, Analysis, Design, and Applications.”

[3] N. Han, C. Sun, J. Li, H. Yang, and S. Han, “Design and Characteristic Analysis of a New Dual-Stator Bearingless Switched Reluctance Motor,” IEEE Access, vol. 10, pp. 12941–12952, 2022, doi: 10.1109/ACCESS.2022.3146826.

[4] M. Jabari and A. Rad, “Optimization of Speed Control and Reduction of Torque Ripple in Switched Reluctance Motors Using Metaheuristic Algorithms Based PID and FOPID Controllers at the Edge,” Tsinghua Sci. Technol., vol. 30, no. 4, pp. 1526–1538, 2025, doi: 10.26599/TST.2024.9010021.

[5] S. Chai, X. Guo, Z. Liu, P. Zhang, Y. Ding, and W. Hua, “Torque Ripple Reduction in Switched Reluctance Machines Considering Phase Torque-Generation Capability,” Electronics (Switzerland), vol. 14, no. 9, May 2025, doi: 10.3390/electronics14091757.

[6] R. Sehab, A. Akrad, Y. Saadi, K. Liu, and W. Hu, “Super-Twisting Sliding Mode Control to Improve Performances and Robustness of a Switched Reluctance Machine for an Electric Vehicle Drivetrain ApplicationS,” pp. 11–14, 2017, doi: 10.3390/en16073212ï.

[7] L. Xiong et al., “Torque Ripple Reduction Strategy for Doubly Salient Electromagnetic Machine Based on Current Given Function,” IEEE J. Emerg. Sel. Top. Power Electron., vol. 10, no. 6, pp. 7486–7501, Dec. 2022, doi: 10.1109/JESTPE.2022.3180930.

[8] X. He and Y. Yao, “An Improved Hybrid Control Scheme of a Switched Reluctance Motor for Torque Ripple Reduction,” Applied Sciences (Switzerland), vol. 12, no. 23, Dec. 2022, doi: 10.3390/app122312283.

[9] A. Agrawal, B. Bilgin, and A. K. Haridas, “Current Profiling Control for Torque Ripple Reduction in the Generating Mode of Operation of a Switched Reluctance Motor Drive,” Symmetry (Basel)., vol. 16, no. 10, Oct. 2024, doi: 10.3390/sym16101278.

[10] M. Arabi, Y. Zennir, H. Bounezour, M. Benghanem, J. E. S. Garcia, and M. Wadi, “Novel Nonlinear PI Controller Using Metaheuristic Algorithms for Speed Control of Wind Turbine Systems,” Journal Europeen des Systemes Automatises, vol. 58, no. 8, pp. 1593–1608, Aug. 2025, doi: 10.18280/jesa.580805.

[11] M. Zine, C. Labiod, M. Ikhlef, K. Srairi, and M. Benbouzid, “Improving Efficiency and Power Output of Switched Reluctance Generators through Optimum Operating Parameters,” Machines, vol. 11, no. 8, Aug. 2023, doi: 10.3390/machines11080816.

[12] M. Zine, A. Chemsa, C. Labiod, M. Ikhlef, K. Srairi, and M. Benbouzid, “Coupled Indirect Torque Control and Maximum Power Point Tracking Technique for Optimal Performance of 12/8 Switched Reluctance Generator-Based Wind Turbines,” Machines, vol. 10, no. 11, Nov. 2022, doi: 10.3390/machines10111046.

[13] C. Labiod, K. Srairi, B. Mahdad, and M. E. H. Benbouzid, “A novel control technique for torque ripple minimization in switched reluctance motor through destructive interference,” Electrical Engineering, vol. 100, no. 2, pp. 481–490, Jun. 2018, doi: 10.1007/s00202-017-0521-7.

[14] K. Diao, X. Sun, G. Lei, Y. Guo, and J. Zhu, “Multiobjective system level optimization method for switched reluctance motor drive systems using finite-element model,” IEEE Transactions on Industrial Electronics, vol. 67, no. 12, pp. 10055–10064, Dec. 2020, doi: 10.1109/TIE.2019.2962483.

[15] B. Anvari, H. A. Toliyat, and B. Fahimi, “Simultaneous Optimization of Geometry and Firing Angles for In-Wheel Switched Reluctance Motor Drive,” IEEE Transactions on Transportation Electrification, vol. 4, no. 1, pp. 322–329, Oct. 2017, doi: 10.1109/TTE.2017.2766452.

[16] M. O. Thurston, “ELECTRICAL AND COMPUTER ENGINEERING A Series of Reference Books and Textbooks FOUNDING EDITOR,” 2006.

[17] A. Rezig, W. Boudendouna, A. Djerdir, and A. N’Diaye, “Investigation of optimal control for vibration and noise reduction in-wheel switched reluctance motor used in electric vehicle,” Math. Comput. Simul., vol. 167, pp. 267–280, Jan. 2020, doi: 10.1016/j.matcom.2019.05.016.

[18] S. Wang, Z. Hu, and X. Cui, “Research on Novel Direct Instantaneous Torque Control Strategy for Switched Reluctance Motor,” IEEE Access, vol. 8, pp. 66910–66916, 2020, doi: 10.1109/ACCESS.2020.2986393.

[19] X. Deng, B. Mecrow, H. Wu, and R. Martin, “Design and Development of Low Torque Ripple Variable-Speed Drive System with Six-Phase Switched Reluctance Motors,” IEEE Transactions on Energy Conversion, vol. 33, no. 1, pp. 420–429, Mar. 2018, doi: 10.1109/TEC.2017.2753286.

[20] C. Hui, H. Yanjie, P. Yinbin, and Z. Tao, “A method for reducing torque ripple of switched reluctance motor based on partitioned TSF,” Front. Energy Res., vol. 12, 2024, doi: 10.3389/fenrg.2024.1381950.

[21] L. Feng et al., “A review on control techniques of switched reluctance motors for performance improvement,” 2024, Elsevier Ltd. doi: 10.1016/j.rser.2024.114454.

[22] W. Zhang, M. Xu, Y. Feng, Z. Mao, and Z. Yan, “The Effect of Procrastination on Physical Exercise among College Students—The Chain Effect of Exercise Commitment and Action Control,” International Journal of Mental Health Promotion, vol. 26, no. 8, pp. 611–622, 2024, doi: 10.32604/ijmhp.2024.052730.

[23] X. D. Xue, K. W. E. Cheng, and S. L. Ho, “Optimization and evaluation of torque-sharing functions for torque ripple minimization in switched reluctance motor drives,” IEEE Trans. Power Electron., vol. 24, no. 9, pp. 2076–2090, 2009, doi: 10.1109/TPEL.2009.2019581.

[24] G. X. Prestes, F. P. Scalcon, B. Nahid-Mobarakeh, and R. P. Vieira, “Enhancing SRM Performance through Multi-Platform Optimization and FPGA-Based Real-Time Simulation,” Eletrônica de Potência, vol. 29, p. e202442, Oct. 2024, doi: 10.18618/rep.e202442.

Journal of Engineering and Technology for Industrial Applications

ISSN ONLINE: 2447-0228

ITEGAM-JETIA

Manaus, v.12 n.60, p.1343-1354. July/August, 2026.
DOI: https://doi.org/10.5935/jetia.v12i60.4089

RESEARCH ARTICLE OPEN ACCESS

DEEP LEARNING-BASED INTEGRATED SYSTEM FOR STUDENT ATTENDANCE AND EMOTION RECOGNITION IN ELEMENTARY EDUCATION

Alexander Imanuel Widjanarko[1], Nathan Daud[2], Mochamad Rizal Saputra[3], Diva Kurnianingtyas*[4]

[1]Department of Information Systems, Faculty of Computer Science, Universitas Brawijaya, Malang, Indonesia.
[2, 4]Department of Informatics Engineering, Faculty of Computer Science, Universitas Brawijaya, Malang, Indonesia.
[3]Department of Agricultural Socioeconomics, Faculty of Agriculture, Universitas Brawijaya, Malang, Indonesia.

[1]http://orcid.org/0009-0004-2141-4138, [2]http://orcid.org/0009-0005-9711-7604,
[3]http://orcid.org/0009-0004-5656-1058, [4]http://orcid.org/0000-0002-0865-7790

Email: nathandaud@student.ub.ac.id, alexanderiw@student.ub.ac.id, rizalsaputra@student.ub.ac.id,*divaku@ub.ac.id

ARTICLE INFO

Article History
Received: March 14, 2026
Reviewed: April 17, 2026
Accepted: July 17, 2026
Published: August 31, 2026

Keywords:
Deep learning,
face recognition,
Emotion detection,
Educational technology,
Student wellbeing.

ABSTRACT

Mental health challenges among elementary students have become a critical global concern, with 10–20% of children experiencing emotional difficulties that significantly impact educational performance and social development. This research presents a deep learning-based integrated system that simultaneously performs automated attendance tracking and real-time emotion recognition for elementary education settings. The system employs FaceNet with one-shot learning for face recognition-based attendance, requiring only a single reference image per student. For emotion detection, we implement and compare MobileNet-v2 and YOLOv8 on an augmented FER-2013 dataset with seven emotion categories (happy, sad, angry, surprised, scared, neutral, and sleepy). Experiments conducted in an offline simulation setting show that YOLOv8 outperforms MobileNet-v2 across all metrics, achieving 65% accuracy versus 53%, with higher precision (66% vs. 53%), recall (65% vs. 55%), and F1-score (65% vs. 52%). YOLOv8's anchor-free detection and optimized inference pipeline provide operational advantages essential for real-time classroom applications. This integrated system offers educators actionable insights for early identification and timely intervention related to students' emotional well-being while streamlining administrative tasks. Unlike previous studies that focused on either attendance or emotion recognition separately, this research offers a novel, integrated real-time system tailored for elementary education settings.

Copyright ©2026 by authors and Galileo Institute of Technology and Education of the Amazon (ITEGAM). This work is licensed under the Creative Commons Attribution International License (CC BY 4.0).

I. INTRODUCTION

Mental health challenges among children have become a global concern, with approximately 10-20% of children and adolescents worldwide experiencing emotional difficulties that significantly impact their educational performance and social development [1]. These mental health problems account for an estimated 16% of the global burden of disease and injury among those aged 10-19 years, with conditions such as anxiety, depression, and behavioral disorders representing the leading causes of disability in this population [2]. Research demonstrates that children experiencing emotional difficulties, including loneliness, depression, anxiety, and low self-esteem, show measurable impacts on their academic performance, with studies revealing that 21.2% of students had mental health concerns that directly affected their educational outcomes [3]. The consequences extend beyond academic achievement to encompass broader social development, as these challenges can disrupt peer relationships, family dynamics, and overall psychosocial functioning during critical developmental periods [4].

Early identification and intervention strategies are critical for preventing long-term psychological consequences and ensuring optimal child development outcomes, particularly given that half of all mental health issues in adults begin during or before adolescence, making childhood and adolescence opportune times for interventions that can reduce risk for mental disorders and enhance social, emotional, and cognitive functioning [5]. In Indonesia, educational institutions face unprecedented challenges in identifying and addressing students' emotional needs. Recent studies indicate that 20.6% of Indonesian students aged 13-17 years were victims of bullying [6], with comprehensive analysis of 11,479 students from 403 schools revealing that male students, those who missed school, were late, repeated grades, or attended rural schools with small class sizes faced higher risks of bullying victimization [7]. Cross-sectional surveys using the International Society for the Prevention of Child Abuse and Neglect (ISPCAN) Child Abuse Screening Tool have documented significant prevalence of physical, verbal, and sexual violence among adolescents in West Java, a province representing 18% of Indonesia's total population [8]. The mental health landscape is equally concerning, with 95.4% of Indonesian youth aged 16-24 experiencing anxiety as the most prevalent mental health problem [9], while students in the 12-15 years age group demonstrated the worst mental health levels during recent assessments [10]. Furthermore, Indonesian adolescents face increased risk of developing depression and anxiety disorders, largely attributed to insufficient mental health literacy and awareness that often leads to delayed recognition and treatment [11]. The crisis of child protection has intensified since 2019, with increasing cases of child abuse across the nation [12], highlighting the urgent need for innovative approaches to monitor student wellbeing in educational settings through comprehensive screening tools, trauma-informed interventions, and enhanced support systems that address the complex interplay of bullying, abuse, and mental health challenges facing Indonesia's substantial child population.

The emergence of Society 5.0 has introduced advanced technological solutions in educational environments, particularly automated attendance systems using face recognition technology. Society 5.0 represents a transformative vision for the future driven by integrating digital technologies and human-centered approaches, fusing with cyber-physical spaces to create a smart society that addresses educational challenges through innovative and collaborative solutions [13]. While these systems have demonstrated significant efficiency improvements, reducing attendance recording time by up to 90%, research shows that automated face recognition attendance systems achieve 96.4% recognition accuracy with processing times between 1.3-2.3 seconds, effectively minimizing human errors, preventing proxy attendance, and improving data security compared to traditional manual methods [14]. The systems deliver real-time attendance updates and enhance precision while reducing manual labor, with implementations showing that attendance can be automatically tracked and recorded with over 95% accuracy [15]. However, their potential for integration with emotion recognition capabilities remains largely unexplored, despite emerging research demonstrating that real-time automatic emotion recognition systems can be developed incorporating facial features for classroom assessment using deep learning models [16]. Studies indicate that emotion recognition is gaining popularity in education for improving students' learning processes and can measure online learners' affective states of engagement and concentration using emotion data extracted from facial features captured by standard web cameras [17]. The convergence of these technologies presents unprecedented opportunities for smart classroom monitoring systems that could simultaneously track attendance and assess student emotional engagement, creating comprehensive educational analytics platforms that align with Society 5.0's vision of human-centered technological integration in learning environments [13].

Despite the availability of sophisticated deep learning algorithms such as MobileNet-v2 and YOLOv8 for image classification tasks, there is limited research comparing their effectiveness in real-time emotion detection within educational contexts. Recent comparative studies in classroom environments have demonstrated that YOLOv8 achieves 97.61% accuracy for student attention monitoring, while MobileNet-v2, when tested alongside VGG-19 and ResNet-101, shows VGG-19 outperforming with 99.56% accuracy for classification tasks on cropped student images, indicating that YOLO models excel in speed and real-time object detection but traditional CNN architectures like VGG-19 perform better for classification accuracy [18]. Specialized research on pediatric facial expression recognition reveals that MobileNetV2 achieves approximately 60% F1-score across all ethnicities when tested on children's facial expressions, with notable accuracy variations of up to 11.56% between different ethnic groups [19]. Comprehensive evaluations of ten state-of-the-art deep learning models, including MobileNet V1, for facial expression recognition tasks show varying performance metrics in terms of test accuracy, training time, and weight file size [20]. However, systematic reviews of academic emotion classification reveal that the number of real-time FER systems is significantly less than non-real-time systems, with most studies achieving top-1 accuracy of 94.6% but lacking comprehensive real-time implementation frameworks [21]. Furthermore, the integration of attendance systems with emotion recognition technologies lacks comprehensive evaluation, particularly regarding their practical implementation in elementary school environments, as current research focuses primarily on university-level student attention monitoring using deep learning techniques with approximately 7 hours of video footage from 120 undergraduate students [18], while studies specifically targeting elementary school contexts remain sparse despite the demonstrated feasibility of improved YOLOv8 models for classroom behavior detection and the growing need for non-invasive, automated systems that can simultaneously track attendance and monitor emotional wellbeing in younger student populations [22]. However, to the best of our knowledge, there is still no integrated approach that simultaneously combines a FaceNet-based (one-shot) attendance system with real-time emotion detection, particularly for elementary school students (see Table 1).

Table 1: Literature review.

Study	Core Technique(s)	Education Context	Key Limitations
[23]	FaceNet on Jetson Nano for automatic attendance	University lectures	1) Attendance only, no affect analysis. 2) Edge device struggled under low-light conditions.
[24]	CNN with HOG + MMOD face detection; real-time attendance	University	1) Requires multiple reference images per student. 2) Does not address student emotional states.
[25]	OpenCV face recognition + basic FER (FER-2013)	Technical college	1) Emotion module uses lightweight heuristics, yielding modest accuracy.

			2) Feedback component still manual.
[26]	Deep-learning attendance (model unspecified)	High school	1) Paper focuses on system architecture; lacks rigorous emotion component. 2) No comparative model analysis.
[27]	YOLOv8 face detection + MobileNetV2 face ID	Engineering undergrads	1) Attendance only; emotion not integrated.
[28]	Comparative FER using pre-trained CNNs (VGG, ResNet, MobileNet)	Online higher-ed courses	1) No real-time constraints; batch-mode evaluation. 2) Does not link FER to attendance data.
[29]	FER models benchmarked for virtual learning sessions	K-12 online	1) Pure emotion study, attendance outside scope. 2) Dataset bias toward frontal faces.
[30]	YOLOv8 (five variants) for facial-expression monitoring	University LMS sessions	1) Covers six emotions only; fatigue/sleepiness absent.

Source: Authors, (2026).

This study contributes by developing and evaluating a deep learning-based integrated system that not only streamlines attendance administration but also supports the early identification of students' emotional well-being in classroom settings. Specifically, we implement and compare MobileNet-v2 and YOLOv8 for real-time emotion classification integrated with a FaceNet-based one-shot attendance system, providing educators with timely insights to enable more responsive and supportive learning environments.

II. THEORETICAL REFERENCE

II.1 DEEP LEARNING FUNDAMENTALS AND APPLICATIONS IN EDUCATION

Deep learning is a major branch of machine learning that leverages multi-layered artificial neural networks to learn patterns from complex and large-scale data, with key architectures including Convolutional Neural Networks (CNN) for image analysis, Recurrent Neural Networks (RNN) for sequential data, and Transformers, which are increasingly influential in computer vision and natural language processing due to their attention mechanisms [31]. Training these networks relies on algorithms such as backpropagation and various optimizers like Adam or SGD to minimize errors and improve accuracy, while regularization methods, including dropout and batch normalization, are essential for preventing overfitting and enhancing model generalization [32]. Data augmentation is also frequently applied to enhance robustness, especially when working with limited or imbalanced datasets, as demonstrated in comprehensive surveys of deep learning techniques applied to educational data mining scenarios [33]. In the education sector, deep learning has enabled the development of personalized learning platforms, real-time student behavior analysis, and adaptive assessment tools, with research showing that hybrid frameworks combining reinforced learning and deep learning can accurately predict students' personal learning needs through end-to-end models with retrieval attention mechanisms [34]. Educational data mining with deep learning has achieved significant breakthroughs in four typical scenarios: knowledge tracing, student behavior detection, performance prediction, and personalized recommendation, with studies demonstrating that deep neural network-based prediction systems can achieve up to 96.3% accuracy in mining and learning knowledge for users, far exceeding traditional algorithms like support vector machines, Bayesian theory, and K-means [35]. Real-time applications such as automated attendance and emotion detection depend on efficient models and optimized architectures like MobileNet or EfficientNet, which allow deployment on devices with limited computational power, while deep learning techniques for detecting student disengagement emphasize computer vision and affective computing as effective approaches, focusing on facial expressions, eye movements, and posture assessment [36]. The performance of these models is commonly measured by metrics such as accuracy, precision, recall, F1-score, and inference speed, ensuring both reliability and practicality in real-world educational environments, with recent implementations of intelligent education systems based on convolutional neural networks and memory augmented neural networks proving effective and swift in tracking students' knowledge learning status [37].

II.2 FACE RECOGNITION TECHNOLOGY AND ONE-SHOT LEARNING

Face recognition technology has evolved from traditional image processing techniques such as Eigenfaces and Fisherfaces to modern, deep learning-based approaches, with comprehensive literature reviews demonstrating that while classical algorithms depend on handcrafted feature extraction, deep learning models—particularly those based on CNN—automatically learn hierarchical facial features, resulting in significantly improved accuracy and robustness in complex environments [38]. Traditional methods based on hand-crafted features and traditional machine learning techniques have recently been superseded by deep neural networks trained with very large datasets, with the transition occurring around 2015 when state-of-the-art face recognition became rooted in deep learning models [39]. To overcome the limitation of requiring large labeled datasets, one-shot and few-shot learning methods have gained importance, with approaches such as Siamese networks enabling models to recognize new classes or identities from just one or a few examples by learning a similarity metric in an embedding space, a capability that is highly valuable in real-world applications, such as educational settings where only one reference image per student is available [40]. Modern face recognition models like FaceNet, DeepFace, and ArcFace further enhance identification accuracy by mapping facial images into a compact embedding space where distances directly reflect facial similarity, with Facebook's DeepFace achieving 97.35% accuracy on the LFW benchmark, reducing the error of the previous state-of-the-art by 27% through training on 4.4 million faces from 4,030 subjects [38]. FaceNet employs a triplet loss function to optimize this embedding, ensuring that images of the same person are closer together, while images of different people are separated by a defined margin, requiring careful selection of similarity metrics (e.g., Euclidean or cosine distance) and optimal threshold settings to minimize false acceptances and rejections in operation [41].

When integrated into automated attendance systems, these technologies enable real-time student identification, greatly reducing manual workload and mitigating proxy attendance issues, with studies showing that deep convolutional networks can achieve recognition rates of more than 87% while the classical method of Turk and Pentland achieves 75.5% [42]. However, successful deployment must address challenges like varying illumination, occlusions, and pose differences commonly encountered in educational environments, as many modern datasets combine different factors that influence face recognition, such as face pose, occlusion, illumination, facial expression and image quality, thus requiring robust model design and preprocessing that are crucial for maintaining high recognition accuracy and practical usability in schools where faces in-the-wild present high variability due to head poses, aging, occlusions, illumination conditions, and facial expressions [38].

II.3 EMOTION RECOGNITION SYSTEMS AND MULTI-TASK LEARNING

Facial expression analysis is central to automated emotion recognition, drawing on frameworks such as Ekman's basic emotions (happiness, sadness, anger, surprise, fear, disgust, and neutrality) and the Facial Action Coding System (FACS), which provides a comprehensive taxonomy of facial muscle movements, with systematic reviews confirming that Paul Ekman has delved most deeply into this subject, proposing six basic universal emotions that can be accurately identified through facial expressions [43]. FACS encodes movements of individual facial muscles from distinct momentary changes in facial appearance, serving as the first universal method of coding and measuring facial movement that quantifies facial actions based on muscle movements, so that each expression can be represented as a combination of action units [44]. These frameworks form the basis for labeling and annotating datasets used in machine learning research, with modern deep learning approaches greatly advancing emotion detection capabilities through CNN that are widely employed due to their proficiency in capturing spatial features from facial images [45]. Recent architectures also utilize attention mechanisms to focus on relevant facial regions that are most indicative of specific emotions, with studies demonstrating that CNN-based models can achieve recognition rates exceeding 86.71% on reclassified datasets like FER2013 [45]. Real-time emotion detection, essential in educational settings, benefits from optimized models capable of rapid inference without significant computational overhead, particularly when addressing the challenge that automatic FER is one of the key tasks in computer vision for applications in healthcare, education, psychology, and human-computer interaction [45]. Multi-task learning enables systems to conduct joint face recognition and emotion detection within a single pipeline, leveraging shared feature representations, which enhances efficiency and accuracy but introduces technical complexities in balancing tasks and managing conflicting objectives [46]. Despite progress, significant challenges remain as emotion recognition systems are sensitive to cross-cultural variations in facial expression, differences in age groups, and lighting or occlusion issues present in real-world environments [43], with research showing that emotions are subjective and two people can have different opinions on the same facial image, particularly given that there are slight differences between certain facial expressions such as fear and surprise, disgust and anger [45]. Practical implementation depends on robust datasets—such as FER-2013, which offers a range of annotated facial expressions—and careful application of data augmentation to improve model generalization, with performance commonly evaluated using metrics such as accuracy, precision, recall, and F1-score to gauge system effectiveness in operational conditions [47]. Finally, system integration involves not only technical aspects, such as aligning face detection, recognition, and emotion inference modules, but also handling issues like latency, data privacy, and seamless interaction with existing educational platforms, ensuring consistent accuracy across diverse populations and deployment scenarios while meeting real-time requirements that may constrain the complexity and depth of neural networks utilized [48].

III. MATERIALS AND METHODS

The following methodology diagram illustrates the comprehensive framework developed for integrating face recognition-based attendance systems with real-time emotion detection in elementary educational settings (see Figure 1). This multi-stage approach encompasses data acquisition, preprocessing, model training, and system deployment phases, demonstrating the seamless integration of one-shot learning techniques for student identification with advanced deep learning architectures for emotion classification. The methodology emphasizes the practical implementation considerations necessary for deployment in real classroom environments, including computational efficiency requirements and real-time processing constraints that are essential for maintaining educational workflow continuity.

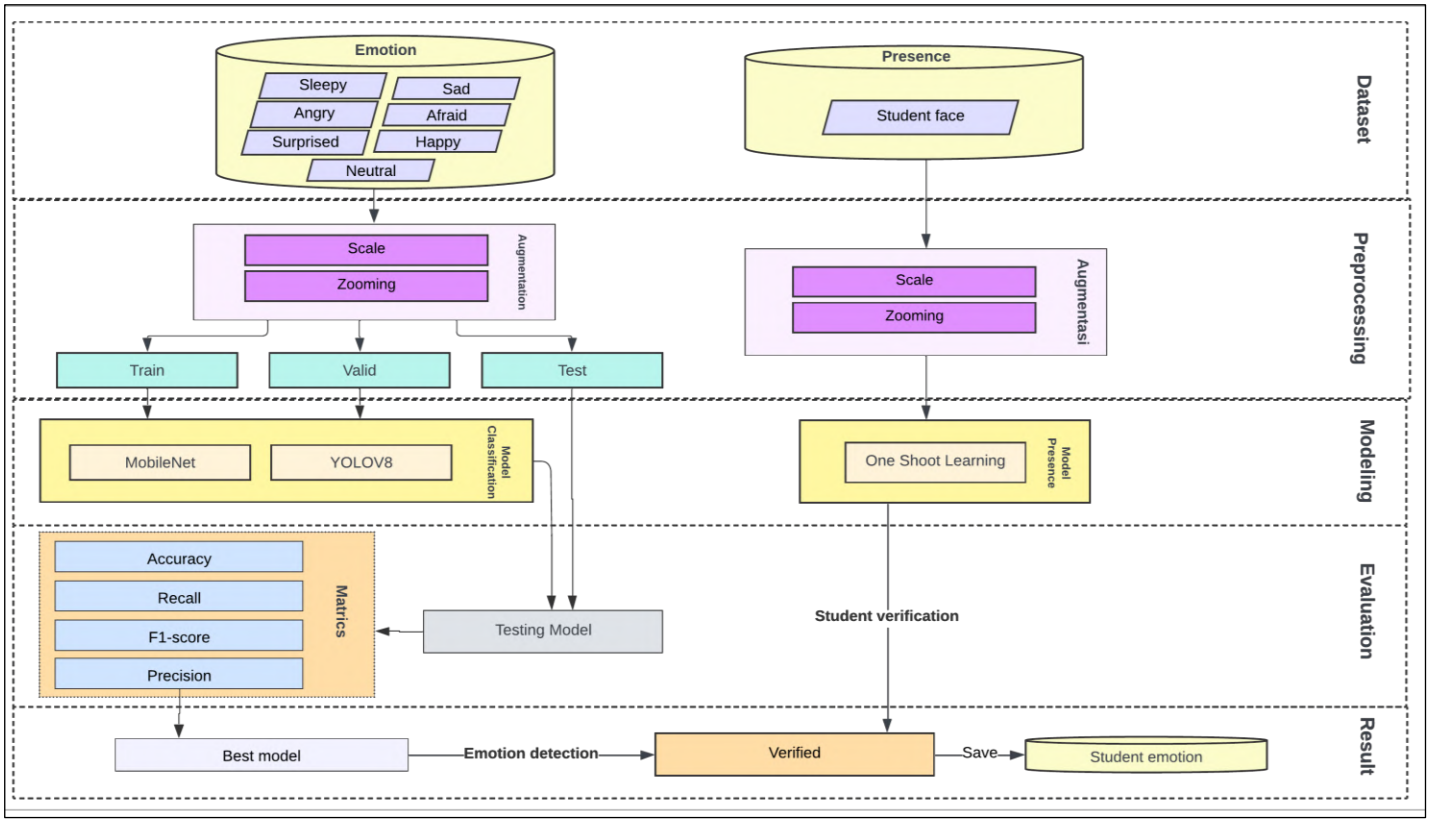


Figure 1: Research flow.
Source: Authors, (2026).

III.1 DATASET

The research utilizes two main datasets to support both face recognition and emotion classification tasks. The primary dataset for face recognition consists of a single attendance photo for each student, captured under consistent lighting and pose to ensure identification accuracy. For emotion recognition, the study leverages the FER-2013 dataset [49], which contains over 7,000 facial images categorized into seven core emotion classes: happy, sad, angry, surprised, scared, neutral, and sleepy (see Figure 2). To address class imbalance and improve the robustness of the models, data augmentation techniques such as flipping, rotation, and brightness adjustment are applied. Furthermore, all datasets are divided into training, validation, and test subsets using an 80:10:10 ratio, ensuring fair and consistent evaluation across all emotion categories.

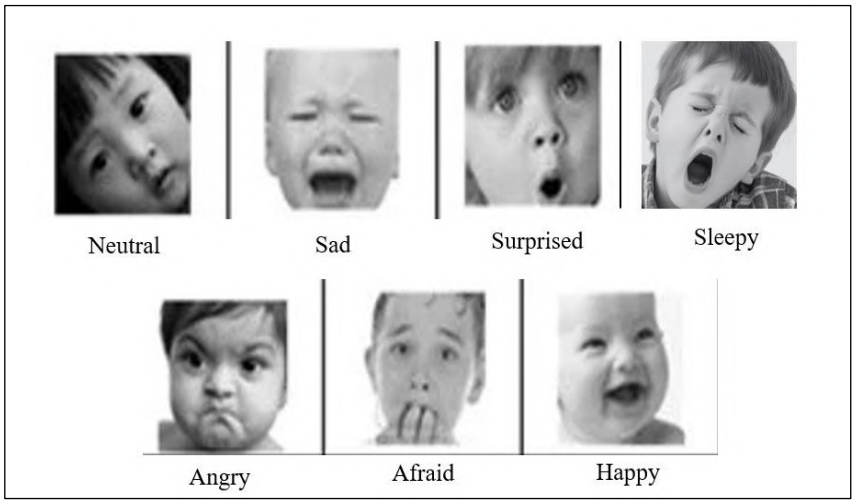


Figure 2: FER2013 Dataset overview.
Source: Authors, (2026).

III.2 DATA PREPROCESSING

Prior to training, several preprocessing steps are conducted to enhance the quality and uniformity of the input data. Firstly, facial regions are automatically detected and cropped from the original images, standardizing the inputs for both recognition and classification models.

All images are resized to a fixed size suitable for the model architectures used, and pixel values are normalized—either scaled to a range or standardized—depending on model requirements. Augmentation operations further increase variation within the training data, helping models generalize better to real-world scenarios, such as varying lighting or occlusions often present in school environments.
Gambar preprocess

III.3 MODEL ARCHITECTURE AND TRAINING

We implemented the system using Keras with TensorFlow as the backend for model development and training, leveraging OpenCV for image acquisition, face detection, and preprocessing operations, and NumPy/Pandas for data handling and pipeline utilities. Implementation of face recognition is carried out using a one-shot learning approach, such as FaceNet [50], which employs a triplet loss mechanism to generate robust facial embeddings from limited examples. These embedding vectors form the basis for real-time identification of students during attendance. For emotion recognition, the study compares two deep-learning architectures: MobileNet-v2 [51], known for its efficiency and suitability for edge devices, and YOLOv8 [52], recognized for its real-time object detection performance.

FaceNet Triplet Loss Function

$$L_{triplet}(a,p,n) = \max(0, D(a,p) - D(a,n) + \alpha) \tag{1}$$

Equation 1 represents the triplet loss function used in FaceNet for one-shot learning in face recognition. The function learns to minimize the distance between an anchor face and a positive example (same person) while maximizing the distance to a negative example (different person). In this formulation, $L\_triplet$ represents the triplet loss value, while a denotes the anchor image serving as the reference face, p indicates the positive image containing the same person as the anchor, and n represents the negative image showing a different person from the anchor. The distance functions $D(a,p)$ and $D(a,n)$ calculate the distances between anchor-positive and anchor-negative embeddings respectively, while α serves as the margin parameter that enforces separation between positive and negative pairs. The function ensures that the distance between anchor-positive pairs is smaller than anchor-negative pairs by at least the margin α, enabling robust face recognition with minimal training examples per identity.

MobileNet-v2 Inverted Residual Block

$$Y = \text{ReLU6}\big(W_2 * (W_1 * X)\big) \tag{2}$$

Equation 2 describes the inverted residual block architecture in MobileNet-v2, which forms the core building block for efficient emotion recognition. This lightweight design enables real-time processing on mobile and edge devices. The variables in this equation represent different components of the inverted residual structure: Y represents the output feature map, while X denotes the input feature map. W^1 corresponds to the first 1×1 convolution weights in the expansion layer, and W^2 represents the second 1×1 convolution weights in the projection layer. ReLU6 functions as the Rectified Linear Unit activation function capped at 6. The inverted residual structure first expands the feature channels, applies depthwise convolution, then projects back to lower dimensions, significantly reducing computational complexity while maintaining emotion classification accuracy.

YOLOv8 Multi-Component Loss Function

$$L = L_{box} + L_{obj} + L_{cls} \tag{3}$$

Equation 3 represents the total loss function for YOLOv8 used in emotion detection, combining three essential components to optimize both object detection and classification performance. The components of this loss function serve distinct purposes in the training process: L_{total} represents the combined total loss for model optimization, L_{box} corresponds to the bounding box regression loss that ensures localization accuracy, L_{obj} denotes the objectness loss that determines confidence that an object exists, and L_{cls} represents the classification loss responsible for emotion category prediction. Each component serves a specific purpose where L_{box} ensures accurate facial region localization, L_{obj} determines the presence of faces in the image, and L_{cls} correctly identifies the emotional state. This multi-task approach enables YOLOv8 to simultaneously detect faces and classify emotions in real-time educational environments, achieving superior performance compared to traditional single-task approaches.

III.4 MULTI-TASK SYSTEM INTEGRATION

The developed system integrates face recognition and emotion detection within a unified attendance workflow. During each attendance event, the system verifies the identity of the student and simultaneously classifies their observed emotion, recording both pieces of information. This multi-task integration relies on efficient sequential processing and the use of lightweight, highly optimized model architectures to ensure that operation remains responsive and does not interfere with teaching activities. Strategies such as model quantization and deployment on edge devices are considered to further minimize inference time.

III.5 EVALUATION AND VALIDATION

All experiments were conducted in an offline simulation setting rather than a live school deployment; the models were trained and evaluated on datasets. Comprehensive evaluation is conducted to measure both the accuracy and practicality of the system in real-world settings.

Performance is assessed using standard classification metrics on the test set to determine the reliability of both the face recognition and emotion detection components. The evaluation framework incorporates four fundamental metrics that provide comprehensive insight into model performance across different aspects of classification effectiveness (see Equation 4-7) [53].

Accuracy Evaluation Function

$$\text{Accuracy} = \frac{TP + TN}{TP + TN + FP + FN} \tag{4}$$

Precision Evaluation Function

$$\text{Precision} = \frac{TP}{TP + FP} \tag{5}$$

Recall Evaluation Function

$$\text{Recall} = \frac{TP}{TP + FN} \tag{6}$$

F1-Score Evaluation Function

$$\text{F1-Score} = 2 \times \frac{\text{Precision} \times \text{Recall}}{\text{Precision} + \text{Recall}} \tag{7}$$

The accuracy equation measures the overall classification performance by calculating the proportion of correctly predicted instances across all emotion categories, where TP represents true positive predictions, TN denotes true negative predictions, FP indicates false positive predictions, and FN represents false negative predictions, making it essential for assessing system reliability in classroom environments. The precision metric evaluates the reliability of positive predictions by measuring the proportion of correctly identified positive instances among all predicted positive cases, which is crucial for minimizing false alarms that could trigger unnecessary interventions in educational settings. The recall metric measures the system's ability to capture all actual positive instances, ensuring that important emotional indicators requiring immediate attention are not missed, which is critical for early intervention in student mental health monitoring. The F1-score provides a balanced evaluation by calculating the harmonic mean of precision and recall, creating a single metric that balances the trade-off between avoiding false predictions and detecting all relevant emotional states, making it particularly valuable for practical deployment in educational environments where both reliability and sensitivity are paramount.

IV. RESULTS AND DISCUSSIONS

This section discusses the outcomes of integrating one-shot face recognition and deep learning-based emotion detection within an elementary school attendance system. The evaluation encompasses both technical performance and real-world applicability in the educational context.

IV.1 FACE RECOGNITION PERFORMANCE

The face recognition component, powered by FaceNet and one-shot learning, allowed for the accurate identification of students using only a single reference image per individual. Throughout the implementation, the system demonstrated high reliability even under varying classroom lighting and student pose changes. This finding supports the practical deployment of face recognition as a foundation for automated attendance in schools, enabling efficient and contactless identity verification.

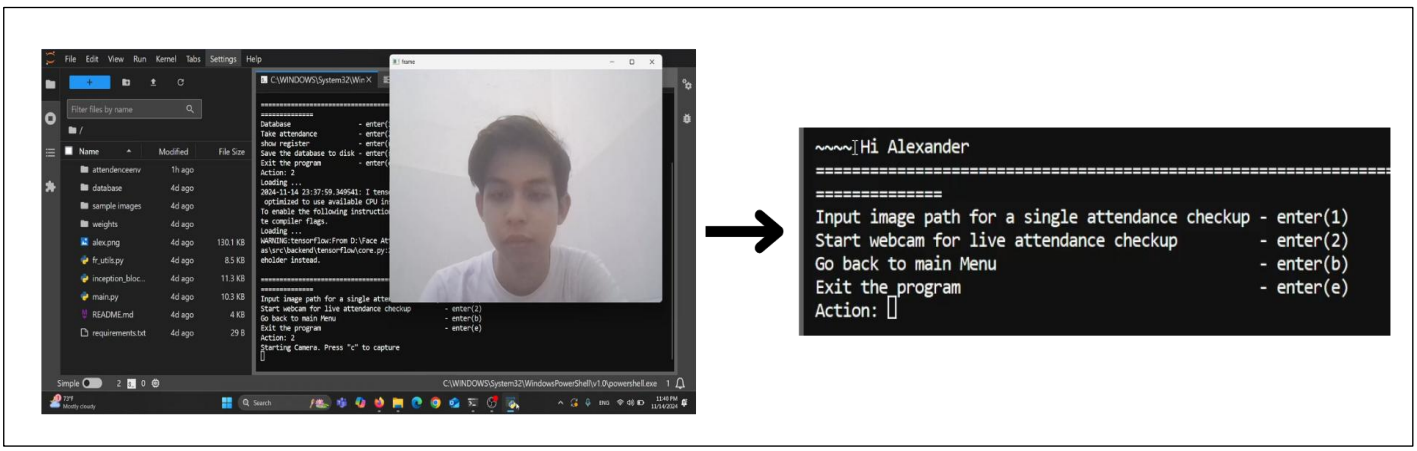
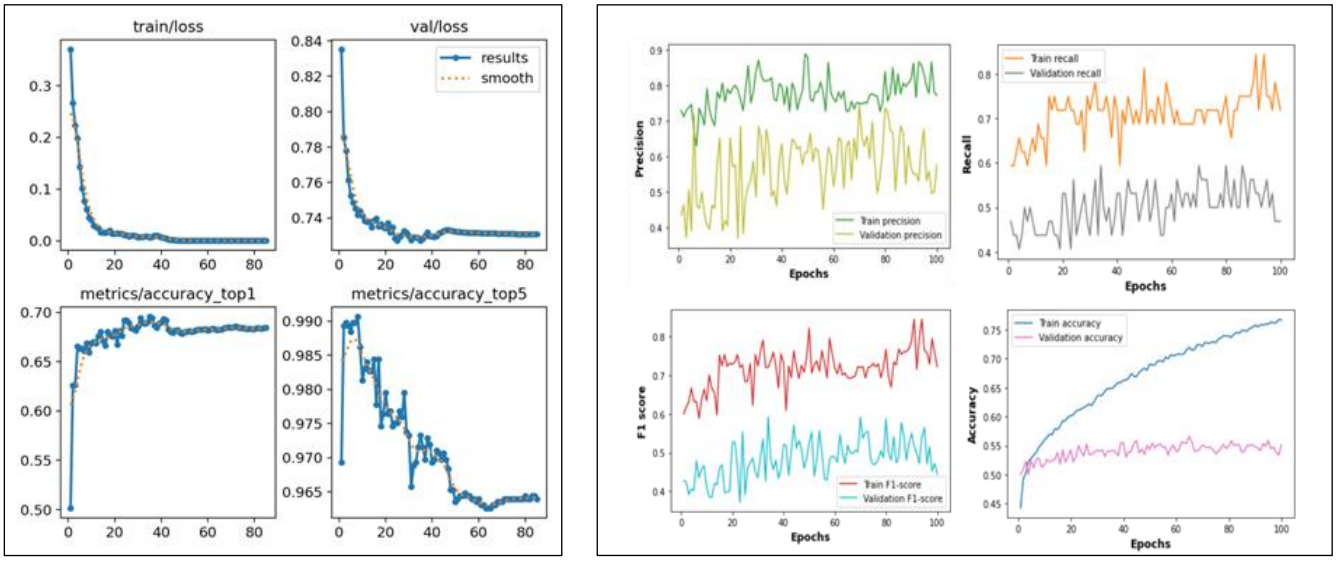


Figure 3: Sample inference image from FaceNet.
Source: Authors, (2026).



(a) YOLOv8. (b) MobileNet-v2.

Figure 4: Training model process.
Source: Authors, (2026).

IV.2 EMOTION DETECTION ANALYSIS

To assess emotion detection capabilities, both MobileNet-v2 and YOLOv8 models were systematically trained and evaluated on the balanced, augmented FER-2013 dataset. The comparative analysis was conducted using standardized evaluation protocols to ensure fair assessment across both architectures. The quantitative results, presented in Table 2, demonstrate substantial performance improvements achieved by YOLOv8 compared to MobileNet-v2 across all evaluation metrics.

Table 2: Model Comparison.

	Accuracy	*Recall*	*Precision*	*F1-score*
MobileNetv-2	0.53	0.55	0.53	0.52
YOLOv8	0.65	0.65	0.66	0.65

Source: Authors, (2026).

YOLOv8's superior performance across all evaluation metrics—achieving 65% accuracy compared to MobileNet-v2's 53%—demonstrates its enhanced capability for real-time emotion recognition in dynamic classroom environments. The 12% improvement in accuracy translates to significantly more reliable emotion detection, which is crucial for educational applications where false classifications could impact student assessment and intervention decisions. Furthermore, YOLOv8's balanced precision and recall scores (66% and 65% respectively) indicate consistent performance across different emotion categories, suggesting reduced bias toward specific emotional states that commonly affect classroom-based recognition systems. Notably, our YOLOv8 accuracy exceeds the 60.57% achieved by a pediatric facial expression classifier trained on children's faces from the CAFE dataset [19], as well as the 60% overall accuracy reported by a standard CNN on FER-2013 [54], underscoring YOLOv8's real-time effectiveness and suitability for monitoring emotional states in elementary school populations. The architectural advantages of YOLOv8 contribute significantly to its operational superiority in educational settings. Its anchor-free detection mechanism eliminates the need for predefined anchor boxes, enabling more flexible and accurate localization of facial regions under varying classroom conditions, including different seating arrangements, lighting variations, and student movements. Additionally, the optimized inference pipeline of YOLOv8 processes images with minimal computational overhead, making it particularly suitable for deployment on standard classroom hardware where computational resources may be limited. This fast inference capability ensures that the emotion recognition process does not interfere with normal classroom activities while maintaining the responsiveness required for real-time monitoring applications. To provide comprehensive insight into model performance characteristics, the confusion matrix for YOLOv8 (Figure 5) illustrates the classification accuracy distribution across the seven emotion categories: happy, sad, angry, surprised, scared, neutral, and sleepy. This matrix reveals both the strengths and limitations of the model, showcasing true positive rates for each emotional state while highlighting potential areas for improvement through analysis of false positive patterns. The diagonal elements represent correct classifications, while off-diagonal elements indicate misclassification patterns that can inform future model refinements and training data augmentation strategies.

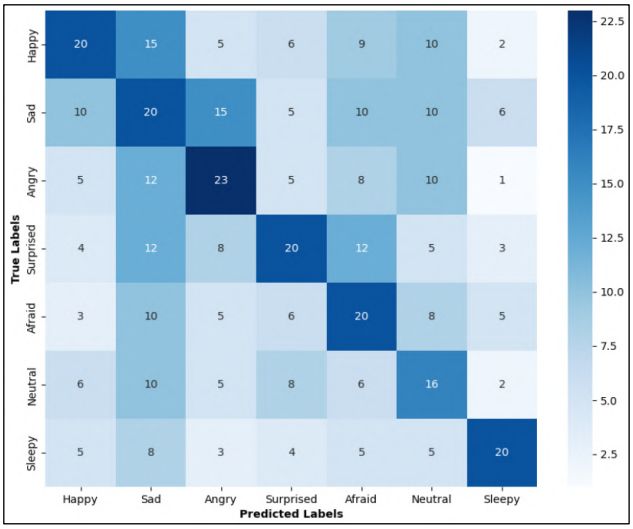


Figure 5: Confusion matrix for YOLOv8.
Source: Authors, (2026).

The visual inference results (Figure 6) demonstrate practical detection outcomes across diverse classroom scenarios, illustrating the model's capability to accurately identify emotional states under real-world conditions. These examples showcase successful emotion detection across different lighting conditions, facial orientations, and partial occlusions commonly encountered in educational environments. Each inference output includes confidence scores and bounding box accuracy, providing transparent insight into the model's decision-making process and enabling educators to assess the reliability of emotion predictions for individual students during classroom monitoring activities.



Figure 6: Example inference outputs for YOLOv8.
Source: Authors, (2026).

IV.3 DISCUSSION

These results show that not only does the system streamline and automate attendance, but it also introduces a daily, scalable way for teachers and counselors to monitor student emotions. Such an approach offers potential as an early-warning mechanism for students who might be experiencing emotional distress—supporting interventions before academic or behavioral declines manifest. Recent international studies reinforce the value of integrated multi-task frameworks for educational wellbeing: [55] proposed a multi-task learning model for classroom expression classification that jointly predicts multiple affective states, achieving an 8% improvement in overall recognition accuracy compared to single-task baselines. Likewise, the MT-RCAF framework demonstrated simultaneous EEG-based emotion and mood-disorder detection with average accuracy gains of 3.2% for emotion recognition and 3.9% for mood-disorder classification, illustrating the efficacy of residual cross-attention in shared representations for student wellbeing applications [56]. However, several challenges and limitations must be acknowledged. The emotion recognition models, while robust, can be affected by subtle expressions, occlusions, or cultural differences in emotional display. Data augmentation helps address these, but further improvements could come from expanding the dataset with more diverse classroom images or employing ensemble/hybrid modeling. Additionally, incorporating multimodal inputs—such as audio cues and contextual metadata—through advanced multi-task architectures may enhance resilience against visual ambiguities and better capture the complex dynamics of real-world educational environments.

V. CONCLUSIONS

This research demonstrates that integrating face recognition based on one-shot learning with deep learning–based emotion detection can enhance both attendance automation and the monitoring of students' emotional states in elementary schools. The primary novelty of this work lies in unifying two critical functions—automated attendance and real-time emotion monitoring—into a single, lightweight system, a combination that has been scarcely implemented and evaluated in elementary education settings.

Empirically, the superior performance of YOLOv8 over MobileNet-v2 underscores its practical viability for real-time emotion recognition where both accuracy and speed are required. Beyond streamlining administrative tasks, the system provides actionable insights for early identification and intervention related to students' emotional well-being, aligning with the growing need for mental health support in education. All findings reported here derive from offline simulations (no in-situ school deployment). For future work, we plan to expand and diversify the training data, optimize model parameters, and conduct comprehensive, in-situ evaluations across diverse school contexts to maximize robustness, improve generalizability, and ensure sustained, ethical impact.

VI. AUTHOR'S CONTRIBUTION

Conceptualization: Nathan Daud and Alexander Imanuel Widjanarko.
Methodology: Nathan Daud and Mochamad Rizal Saputra.
Investigation: Nathan Daud and Diva Kurnianingtyas.
Discussion of results: Nathan Daud, Alexander Imanuel Widjanarko and Mochamad Rizal Saputra.
Writing – Original Draft: Nathan Daud.
Writing – Review and Editing: Diva Kurnianingtyas.
Resources: Alexander Imanuel Widjanarko.
Supervision: Diva Kurnianingtyas.
Approval of the final text: Nathan Daud and Diva Kurnianingtyas.

VII. ACKNOWLEDGMENTS

The author gratefully acknowledges the Faculty of Computer Science, Universitas Brawijaya, for funding this research.

VIII. REFERENCES

[1] T. Waterston, "Managing Mental Health in Children," J Trop Pediatr, vol. 59, no. 3, pp. 163–164, Aug. 2013, doi: 10.1093/tropej/fmt049.

[2] D. Tăut et al., "Prevention of child mental health problems through parenting interventions in Southeastern Europe (RISE): study protocol for a multi-site randomised controlled trial," Trials, vol. 22, no. 1, p. 960, 2021.

[3] H. S. Kakon, R. T. Soron, M. S. Hossain, R. Haque, and F. Tofail, "Role of parental supervision on digital screen use and its effects on children's mental health and wellbeing in Bangladesh: a cross sectional study," BJPsych Open, vol. 10, no. S1, pp. S50–S50, 2024.

[4] T. Kariyil, M. Gabriel, K. Sanghavi, and E. M. Chawla, "Impact of the COVID-19 Pandemic on the Emotional Health of Children Under 6 Years in Washington, DC," Children, vol. 12, no. 8, p. 981, 2025.

[5] G. M. Kassa, Z. Yu, F. Minwuyelet, and D. Gross, "Behavioural interventions targeting the prevention and treatment of young children's mental health problems in low-and middle-income countries: a scoping review," J Glob Health, vol. 15, p. 4018, 2025.

[6] T. Noboru et al., "School-based education to prevent bullying in high schools in Indonesia," Pediatrics international, vol. 63, no. 4, pp. 459–468, 2021.

[7] Luthfi and Kismiantini, "A Multilevel Analysis of Factors Influencing Bullying Victimization at School among Indonesian Students with Binary Outcome," International Journal of Scientific Research and Management (IJSRM), vol. 12, no. 07, pp. 486–498, Jul. 2024, doi: 10.18535/ijsrm/v12i07.m01.

[8] Y. Syukriani et al., "Cross-sectional survey of underreported violence experienced by adolescents: a study from Indonesia," BMC Public Health, vol. 22, no. 1, p. 50, 2022.

[9] F. Kaligis et al., "Mental health problems and needs among transitional-age youth in Indonesia," Int J Environ Res Public Health, vol. 18, no. 8, p. 4046, 2021.

[10] M. Chamdani, U. Mahmudah, S. Fatimah, and others, "Analyzing the Mental Health of Students in Dealing with the Coronavirus Disease Pandemic (Covid-19)," JPI (Jurnal Pendidikan Indonesia), vol. 10, no. 4, pp. 667–676, 2021.

[11] D. I. Yani, J. Y. X. Chua, J. C. M. Wong, M. Pikkarainen, Y. S. S. Goh, and S. Shorey, "Perceptions of Mental Health Challenges and Needs of Indonesian Adolescents: A Descriptive Qualitative Study," Int J Ment Health Nurs, vol. 34, no. 1, p. e13505, 2025.

[12] R. Y. Putri and S. Musrifah, "Assessment Of Child Violence: Protection Policies And The Impact Of Violence On Children," MIKIA: Mimbar Ilmiah Kesehatan Ibu Dan Anak (Maternal and Neonatal Health Journal), pp. 128–138, 2022.

[13] G. P. Laura Icela, R. M. María Soledad, and E. G. Juan Antonio, "Education 4.0 Maturity Models for Society 5.0: Systematic literature review," 2023. doi: 10.1080/23311975.2023.2256095.

[14] N. V. Prasada and I. Ikrimach, "Employee attendance system using face recognition and GPS using local binary pattern histogram," International Journal of Science, Technology, Engineering and Mathematics, vol. 4, no. 4, pp. 83–107, 2024.

[15] M. Shamila, B. Prakash, A. Ahmed, P. Prajeet, and R. Pant, "Smart Attendance Automation System," in E3S Web of Conferences, 2023. doi: 10.1051/e3sconf/202343001019.

[16] S. Fakhar et al., "Smart Classroom Monitoring Using Novel Real-Time Facial Expression Recognition System," Applied Sciences (Switzerland), vol. 12, no. 23, 2022, doi: 10.3390/app122312134.

[17] M. N. Hasnine, H. T. Nguyen, T. T. T. Tran, H. T. T. Bui, G. Akçapınar, and H. Ueda, "A Real-Time Learning Analytics Dashboard for Automatic Detection of Online Learners' Affective States," Sensors, vol. 23, no. 9, 2023, doi: 10.3390/s23094243.

[18] A. Nag, J. Ferdous, S. Uddin, and R. Debnath, "Real-Time and Automated Student Attention Monitoring System in Classroom Using Deep Learning Techniques," Aug. 2024. doi: 10.1109/ICCIT64611.2024.11021871.

[19] A. Banerjee, O. C. Mutlu, A. Kline, P. Washington, D. Wall, and S. Surabhi, “Training and Profiling a Pediatric Facial Expression Classifier for Children on Mobile Devices: Machine Learning Study,” JMIR Form Res, vol. 7, Aug. 2023, doi: 10.2196/39917.

[20] C. Qian, J. A. L. Marques, A. R. de Alexandria, and S. J. Fong, “Application of Multiple Deep Learning Architectures for Emotion Classification Based on Facial Expressions,” Sensors (Basel), vol. 25, no. 5, p. 1478, 2025.

[21] J. Lek and J. Teo, “Academic Emotion Classification Using FER: A Systematic Review,” Hum Behav Emerg Technol, vol. 2023, pp. 1–27, Aug. 2023, doi: 10.1155/2023/9790005.

[22] H. Chen, G. Zhou, and H. Jiang, “Student Behavior Detection in the Classroom Based on Improved YOLOv8,” Sensors, vol. 23, p. 8385, Aug. 2023, doi: 10.3390/s23208385.

[23] S. M and S. S. G, “Automatic Attendance Monitoring System Using Deep Learning,” EAI, Aug. 2021. doi: 10.4108/eai.7-12-2021.2314601.

[24] S. Aryal, R. Singh, A. Sood, and G. Thapa, “Automatic attendance system using deep learning,” in Proceedings of International Conference on Sustainable Computing in Science, Technology and Management (SUSCOM), Amity University Rajasthan, Jaipur-India, 2019.

[25] G. V. S. Suhas, T. D. Reddy, K. J. Bhoyania, L. Karthik, and M. Patil, “Real-time Student Attendance System with Emotion and Feedback Analysis,” Indiana Journal of Multidisciplinary Research, vol. 4, no. 3, pp. 36–42, 2024.

[26] A. Joseph, A. Nair, A. B. Koshy, M. Nallaballi, and N. Jayapandian, “Deep Learning Based Face Recognized Attendance Management System using Convolutional Neural Network,” in 2023 IEEE International Conference on ICT in Business Industry & Government (ICTBIG), 2023, pp. 1–7. doi: 10.1109/ICTBIG59752.2023.10456032.

[27] I. Sahputra, M. Fikry, and K. Kurniawati, “A Robust Approach to Student Attendance Using Web-Based Facial Recognition,” Proceedings of International Conference on Multidisciplinary Engineering (ICOMDEN), vol. 2, p. 78, Jan. 2025, [Online]. Available: https://proceedings.unimal.ac.id/icomden/article/view/806

[28] G. Bhoomika, V. D. Pujitha, M. Sindusha, C. S. Rekha, and B. Suvarna, “Facial Emotion Recognition: A Comparative Study of Pre-trained Deep Learning Models,” in 2024 IEEE 3rd World Conference on Applied Intelligence and Computing (AIC), 2024, pp. 377–382. doi: 10.1109/AIC61668.2024.10730808.

[29] A. S. Ahmad, R. Hassan, N. H. Zakaria, and S. H. Moi, “Comparative studies of facial emotion detection in online learning,” in AIP Conference Proceedings, 2023, p. 30009.

[30] D. Tresnawati, S. Nurhidayanti, and N. Lestari, “A Comparison of YOLOv8 Series Performance in Student Facial Expressions Detection on Online Learning,” Jurnal Online Informatika, vol. 10, no. 1, pp. 93–104, 2025.

[31] A. Parmar, “Human Emotion Recognition Using Multi-modal Deep Learning: A Review of Methods, Datasets, and Challenges,” International Journal Of Scientific Research In Engineering And Management, vol. 09, pp. 1–9, Aug. 2025, doi: 10.55041/IJSREM47033.

[32] A. Imran, J. Li, and A. Alshammari, “AI-driven educational transformation in ICT: Improving adaptability, sentiment, and academic performance with advanced machine learning,” PLoS One, vol. 20, Aug. 2025, doi: 10.1371/journal.pone.0317519.

[33] Y. Lin, H. Chen, W. Xia, F. Lin, Z. Wang, and Y. Liu, “A Comprehensive Survey on Deep Learning Techniques in Educational Data Mining,” Data Sci Eng, pp. 1–27, Aug. 2025, doi: 10.1007/s41019-025-00303-z.

[34] Y. Sun, W. Huang, Z. Wang, X. Xu, M. Wen, and P. Wu, “Smart Teaching Systems: A Hybrid Framework of Reinforced Learning and Deep Learning,” International Journal of Emerging Technologies in Learning (iJET), vol. 18, pp. 37–50, Aug. 2023, doi: 10.3991/ijet.v18i20.44217.

[35] Z. Li, “Network Intelligent Education System Based on the Deep Learning Algorithm,” Security and Communication Networks, vol. 2022, pp. 1–7, Aug. 2022, doi: 10.1155/2022/5677089.

[36] A. Mohamed, M. Ali, S. Ahmed, N. Hani, M. Hisham, and M. Mahmoud, “Detecting Student Disengagement in Online Classes Using Deep Learning: A Review,” arXiv preprint arXiv:2411.10464, 2024.

[37] X. Zhang and Z. Cao, “A Framework of an Intelligent Education System for Higher Education Based on Deep Learning,” International Journal of Emerging Technologies in Learning, vol. 16, no. 7, 2021, doi: 10.3991/ijet.v16i07.22123.

[38] D. Saez Trigueros, L. Meng, and M. Hartnett, “Face Recognition: From Traditional to Deep Learning Methods,” ArXiv, Aug. 2018, doi: 10.48550/arXiv.1811.00116.

[39] T. Pereira, D. Schmidli, Y. Linghu, X. Zhang, S. Marcel, and M. Günther, “Eight Years of Face Recognition Research: Reproducibility, Achievements and Open Issues,” ArXiv, Aug. 2022.

[40] S. Almabdy and L. Elrefaei, “Deep Convolutional Neural Network-Based Approaches for Face Recognition,” Applied Sciences, vol. 9, p. 4397, Aug. 2019, doi: 10.3390/app9204397.

[41] K. Tirana and E. Bejleri, “FROM ORIGINS TO INNOVATIONS: AI’S ROLE AND THE COST IMPACT ON COMPUTER VISION,” AGORA INTERNATIONAL JOURNAL OF ECONOMICAL SCIENCES, vol. 18, pp. 320–333, Aug. 2024, doi: 10.15837/aijes.v18i2.6960.

[42] V. Espinosa-Duró and M. Faundez-Zanuy, “Face identification by means of a neural net classifier,” Aug. 1999, pp. 182–186. doi: 10.1109/CCST.1999.797910.

[43] F. Salinas, G. Ortiz, and P. Martínez, “Recognition of emotions through facial expression analysis,” South Florida Journal of Development, vol. 2, pp. 2102–2118, Aug. 2021, doi: 10.46932/sfjdv2n2-076.

[44] A. R. Livingston, An efficient boosted classifier tree-based feature point tracking system for facial expression analysis. Old Dominion University, 2012.

[45] C. Mejia-Escobar, M. Cazorla, and E. Martinez-Martin, “Towards a Better Performance in Facial Expression Recognition: A Data-Centric Approach,” Comput Intell Neurosci, vol. 2023, no. 1, 2023, doi: 10.1155/2023/1394882.

[46] S. Kumar, B. Ghoraani, and A. Savakis, “Joint and discriminative dictionary learning for facial expression recognition,” in IS and T International Symposium on Electronic Imaging Science and Technology, 2016. doi: 10.2352/ISSN.2470-1173.2016.11.IMAWM-455.

[47] A. Muazu, E. Manzi, and J. Aminu, “A systematic review of methods of emotion recognition by facial expressions,” Int J Adv Res, vol. 9, pp. 1141–1152, 2021.

[48] J. Hamm, C. G. Kohler, R. C. Gur, and R. Verma, “Automated Facial Action Coding System for dynamic analysis of facial expressions in neuropsychiatric disorders,” J Neurosci Methods, vol. 200, no. 2, 2011, doi: 10.1016/j.jneumeth.2011.06.023.

[49] M. S. Ambare, “FER2013: Facial Expression Recognition Dataset,” 2013, Kaggle. [Online]. Available: https://www.kaggle.com/datasets/msambare/fer2013

[50] R. Bankar, N. Bargat, I. Hanmante, and Prof. H. Dakore, “Face Recognition Using Facenet Deep Learning Network for Attendance System,” International Journal of Scientific Research in Computer Science, Engineering and Information Technology, 2022, doi: 10.32628/cseit228630.

[51] D. Sinha and M. El-Sharkawy, “Thin MobileNet: An Enhanced MobileNet Architecture,” in 2019 IEEE 10th Annual Ubiquitous Computing, Electronics and Mobile Communication Conference, UEMCON 2019, 2019. doi: 10.1109/UEMCON47517.2019.8993089.

[52] B. Gašparović, G. Mauša, J. Rukavina, and J. Lerga, “Evaluating YOLOV5, YOLOV6, YOLOV7, and YOLOV8 in Underwater Environment: Is There Real Improvement?,” in 2023 8th International Conference on Smart and Sustainable Technologies, SpliTech 2023, 2023. doi: 10.23919/SpliTech58164.2023.10193505.

[53] N. Daud, A. I. Widjanarko, N. Sitanggang, and D. Kurnianingtyas, “Face Expression Recognition on Ojek Online for Safety Improvement Using Deep Learning,” in 2024 11th International Conference on Soft Computing & Machine Intelligence (ISCMI), 2024, pp. 332–337. doi: 10.1109/ISCMI63661.2024.10851582.

[54] E. S. Agung, A. P. Rifai, and T. Wijayanto, “Image-based facial emotion recognition using convolutional neural network on emognition dataset,” Sci Rep, vol. 14, no. 1, p. 14429, 2024.

[55] J. He, J. Zhou, J. Gan, D. Wu, and X. Wen, “Classroom Expression Classification Model Based on Multitask Learning,” Journal of Applied Sciences, vol. 42, no. 6, p. 947, 2024, doi: 10.3969/j.issn.0255-8297.2024.06.005.

[56] X. Kong, Y. Guo, Y. Ouyang, W. Cheng, M. Tao, and H. Zeng, “MT-RCAF: A Multi-Task Residual Cross Attention Framework for EEG-based emotion recognition and mood disorder detection,” Comput Methods Programs Biomed, vol. 268, p. 108835, 2025.

Journal of Engineering and Technology for Industrial Applications

ISSN ONLINE: 2447-0228

ITEGAM-JETIA

Manaus, v.12 n.60, p.1355-1369. July/August, 2026.
DOI: https://doi.org/10.5935/jetia.v12i60.4105

RESEARCH ARTICLE OPEN ACCESS

AN AUTOMATED OCT-BASED RETINAL DISEASE CLASSIFICATION FRAMEWORK USING SHUFFLENET AND ENHANCED OSPREY OPTIMIZATION

L. Sivayamini*[1], Fahimuddin Shaik[2]

[1]Research Scholar, Department of Electronics and Communication Engineering, Annamacharya University, Rajampet, Andhra Pradesh, India
[2]Department of Electronics and Communication Engineering, Annamacharya University, Rajampet, Andhra Pradesh, India

[1]https://orcid.org/0000-0002-1203-3219, [2]https://orcid.org/0000-0001-6852-7851

Email: *sivayamini470@gmail.com, fahimaits@gmail.com

Article History
Received: March 16, 2026
Reviewed: April 17, 2026
Accepted: July 17, 2026
Published: August 31, 2026

Keywords:
Retinal,
Medical Industry,
Deep Learning,
RetSEOS-Net,
ShuffleNet

ABSTRACT

In the world, the most common cause of visual impairment is retinal abnormalities. In the diagnosis of the retina, optical coherence tomography (OCT) is usually used, since it gives high-resolution cross-sectional images that show detailed retinal structures. In this research, a lightweight deep learning architecture called RetSEOS-Net is presented to use OCT images to recognize retinal diseases automatically. The framework initially uses a guided median filtering in minimizing OCT scans speckle noise. A model of attention-based U-Net is then employed to divide the retinal area, which is followed by a module based on ShuffleNet to obtain the efficient deep features. An Enhanced Osprey Optimization Algorithm (EOOA) is added to the features to refine them and work on the hyperparameters to increase the quality of features and the performance of the network. Finally, the fined features are categorized with a Softmax layer. The framework was tested on an OCT dataset that had four different categories namely diabetic retinopathy (DR), macular hole (MH) and central serous retinopathy (CSR) and normal. The recommended model achieved an accuracy of 96.79% in classification. The findings reveal that RetSEOS-Net is a good and computationally efficient model of automated screening of retinal diseases using OCT.

Copyright ©2026 by authors and Galileo Institute of Technology and Education of the Amazon (ITEGAM). This work is licensed under the Creative Commons Attribution International License (CC BY 4.0).

I. INTRODUCTION

It Retinal diseases form one of the leading expressions of both blindness and the visual impairment in the world, which poses a significant dilemma to global healthcare systems. According to the WHO, 2.2 billion individuals in the world are faced with vision impairment, and such retinal illnesses as diabetic retinopathy, and other retinal abnormalities [1]. Moreover, according to the reports of the IAPB, retinal diseases are also becoming a constantly growing issue as a result of aging and the increase in the number of systemic diseases like diabetes [2]. As an example, diabetic retinopathy by itself has over 100 million people all over the globe and is expected to increase dramatically in the near time eras [3]. Such statistics help to point out the importance of early diagnosis to prevent the irretrievable vision loss. OCT has also made it possible to see microstructure of the retina and clinicians can see the pathological alterations of intraretinal cystoid spaces, subretinal fluid build-up, drusen deposition, detachment of the retinal pigment epithelium and the destruction of the ellipsoid zone. These biomarkers of structure are significant in the diagnosis and distinguishing between the retinal diseases such as the macular hole, diabetic retinopathy, and central serous retinopathy. OCT also has a high axial resolution, which facilitates the proper examination of small abnormalities in the retina that are not easily observed when the retina is examined using traditional fundus imaging methods [4]. Although it has clinical importance, the manual examination of OCT scans is a difficult and time -consuming process which needs high skills of the ophthalmologists. The interpretation of big volumes of OCT images may cause a rise in clinical work and may also cause inter-observer variation in the diagnosis.

These restrictions minimize the effectiveness and reliability of the conventional diagnostic processes especially in mass screening operation. Such difficulties have prompted scientists to consider the use of automated methods that can help clinicians interpret OCT images faster and more precisely [5]. The recent developments in deep learning have improved the medical systems significantly in terms of analyzing images. Convolutional Neural Networks have been shown to be highly proficient in discovering complicated spatial characteristics in the raw of medical pictures and implement effective recovery of retinal illnesses [6]. Some of the deep learning architectures that have been used successfully include VGGNet, ResNet, DenseNet and U-Net in retinal image classification and segmentation applications. The models are capable of capturing hierarchical representations of images and detecting disease-related structures in OCT images and the models result in enhanced diagnostic accuracy [7]. Nevertheless, the effects of speckle noise and imaging artifacts tend to affect images of OCT and affect the image quality and feature extraction [8], [9]. Moreover, most deep learning systems have large computational requirements, and that will hamper real-time clinical deployment [10]. The other difficulty is the choice of redundant features in deep features that occurred during network training. To address such concerns, recent researches have considered the combination of optimization algorithms with deep learning systems to enhance features selection and network parameter optimization. This paper is inspired by these issues, and it presents a lightweight deep learning architecture RetSEOS Net. The proposed framework is expected to deliver an effective and credible solution to the automated screening of retinal diseases by use of OCT, and also assist in early clinical diagnosis and decision-making in ophthalmic practice.

II. LITERATURE REVIEW

Bi et al. [11] provided a detailed review of retinal disease detection with Optical in 2025 with the use of OCT. Their work evaluated many network structures which can be used to automatically diagnose networks which are capable of extracting discriminative retinal features on large-scale data. According to the results of the experimental findings, the accuracy was found to be 94.2, the specificity was 95.1, the sensitivity was 93.5, the precision was 93.8 and the recall was 93.5. Although the diagnostic capacity is promising, the authors reported that the presence of big annotated datasets and large quantities of computational capacity is a strong proponent of the efficacy of deep learning models. Talaat et al. [12] proposed an attention-based deep learning model to improve the retinal OCT images analysis to provide clinical diagnosis in 2025. The model has used attention modules in a convolutional neural network to highlight disease-related retinal regions to enhance the representation of features and elevate the classification accuracy. The accuracy, sensitivity, specificity, precision, and recall of the proposed system were 95.3% and 94.6%. Nonetheless, the combination of attention functions augmented the cognitive load and processing demands that can influence its applicability in real time screening programs. Peng et al. [13] introduced a multi-scale disease classification framework in retina imaging based on the OCT in 2024.

The structure involved a denoising module to reduce any artifacts in the image and enhance the clarity of the retinal structures prior to the retrieval of features. The remaining learning allowed high multi-scale feature representation that helped to identify retinal abnormalities. Accuracy, sensitivity, specificity, precision, and recall of the model were 94.7, 93.9, 95.6, 94.2 and 93.9, respectively. However, the approach needed massive training samples and a great deal of computing power in order to sustain a steady performance. He et al. [14] proposed a model based on attention OCT modality to enhance the retinal disease classification in 2024. The model employed spatial attention processes to place clinically important retinal areas that were related to pathological changes into the limelight. The test results were as follows: 94.5% accuracy, 93.7% sensitivity, 95.3% specificity, 94.0 precision, and 93.7 recall. The model was however sensitive to the hyperparameters and it needed enough training data to realize effective generalization. Li et al. [15] studied the use of a Swin Transformer-based architecture to conduct a multi-class retinal classification based on OCT modality in 2023. Transformer model proved useful in capturing global contextual data of the scanned retinas to detect more patterns of complex diseases better.The suggested approach was found to be accurate (93.9%), sensitive (93.1%), specific (94.8%), precise (93.4), and recall (93.1).

This was despite the effectiveness of the transformer-based architecture which needed a lot of computation and memory. Karn and Abdulla [16] discuss multiple machine learning approaches to retinal diseases in 2023. They compared various deep learning-based and conventional machine learning in their study of automated retinal diagnosis. The analysis was reported to have an accuracy of 92.8% sensitivity of 92.0, specificity of 93.6, precision of 92.3 and a recall of 92.0. The authors however focused on the fact that performance of these models is very sensitive to the quality of the preprocessing and feature extraction methods. Guo et al. [17] developed a multi-task structure in 2022, which conducted simultaneous retinal layers segmentation and disease classification based on OCT images. The similarity of the extraction layers facilitated the network to acquire structural retinal data to enhance the efficacy of classification. The system had a precision of 94.3, recall of 94.0, specificity of 95.7 and accuracy of 94.8 and sensitivity of 94.0. Nevertheless, the framework needed large datasets of annotated data both in the segmentation and classification processes and it can be scaled down.Liu et al. [18] applied a CNN to the task of automated retinal disease classification, which used transfer learning in 2022. The system minimized the need to use large training datasets and allowed extracting the features out of the OCT images effectively by using already trained models.

The accuracy, sensitivity, specificity and precision was 93.6, 92.8, 94.5 and recall was 92.8. However, the performance of the classification was affected by the quality and diversity of the training data. Fang et al. [19] suggested a system of automatic segmentation of various retinal layers in OCT images in 2021. The proper segmentation of the retinal layers incorporates valuable structural data that may help in determining abnormalities of the retina. Accuracy of the model achieved 92.9, sensitivity of 92.1, specificity of 93.8, precision of 92.4 and recall of 92.1. Nonetheless, the research concentrated more on structure segmentation and not the overall classification of diseases. Schlegl et al. [20] presented an unsupervised framework of anomaly detection models based on generative adversarial networks in the analysis of OCT images in 2022. The model was trained on normal retinal images and identified the abnormal images in terms of construction errors. The method had an accuracy of 91.5, sensitivity of 90.7, specificity of 92.4, precision of 91.0 and recall of 90.7. Despite its effectiveness in detecting abnormal scans, the method did not have the ability to classify various retinal diseases, which limits its clinical use. In general, the available research reveals the possibilities of deep learning in the context of retinal disease detection with OCT. But most of them are complicated network designs that raise the cost of computation and training.

Moreover, a number of methods are dependent on massive annotated datasets, and OCT images may suffer because of speckle noise and imaging artifacts that may negatively impact on the performance of classification. A few research works are also done with emphasis on segmentation or detection of anomaly instead of full multi-class disease classification. To address these limitations, the proposed architecture introduces a powerful deep learning framework of automated classification of retinal diseases. In this method, guided median filtering is used first to decrease the speckle noises and improve the quality of OCT images. Then, attention-based U -Net segmentation is employed to locate clinically relevant retinal regions. A feature extraction network based on ShuffleNet is used to achieve discriminative features with less computational effort, and an Enhanced Osprey Optimization Algorithm is used to do the best feature selection and parameter optimization. This unified framework is designed to enhance the accuracy of classification and remain computationally efficient thus facilitating their application to clinical diagnostic systems in practice.

III. PROPOSED METHODOLOGY

Figure 1 discusses an automatic system that is supposed to be used in retinal disease recognition and classification. OCT has high-resolution cross-sectional images of retinal layers, which can be used to identify the structural changes related to different retinal disorders. The model consists of various processing steps, such as, image pre-processing, segmentation, deep feature extraction, evolutionary optimization and classification of the retinal region. The integration of these components enables effective feature learning and improves the overall diagnostic accuracy of the system

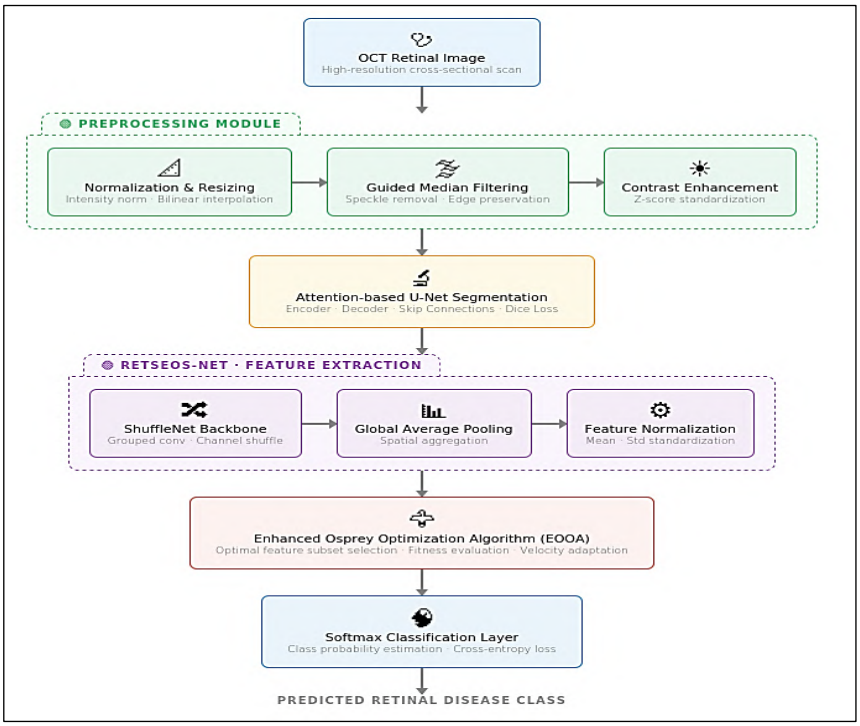


Figure 1: Proposed Model.
Source: Authors, (2026).

The input OCT image is denoted as $IP(x, y$. Image normalization is first performed to maintain consistent intensity distribution across the dataset using the eq. (1)

$$IP_n(x, y) = \frac{I(x,y) - I_{\min}}{I_{\max} - I_{\min}} \quad 1)$$

Where $I_{\min}$ and $I_{\max}$ denote minimum and maximum intensity values, x and y are spatial coordinates. Spatial standardization is performed using bilinear interpolation shown in eq. (2)

$$IP_k(x, y) = \sum_{p=0}^{1} \sum_{q=0}^{1} w_{pq}\, IP_n(x + p, y + q) \quad 2)$$

Where w_{pq} represent interpolation weights. During pre-processing, guided median filter eliminates speckle noise and preserving fine retinal structures. The median filtering operation is expressed using eq. (3)

$$F(x, y) = \text{median}\{I_r(r, c) \mid (r, c) \in \Omega_{xy}\} \quad (3)$$

Where Ω_{xy}denotes the neighborhood window centered at pixel (x, y). Guidance weighting is incorporated to preserve structural edges using eq. (4)

$$w(r, c) = \exp\left(-\frac{(G(r,c) - G(x,y))^2}{2\sigma^2} \right) \quad (4)$$

Where $G(x, y)$is the guidance image and σcontrols smoothing strength. The guided median output is computed using the eq. (5)

$$F_g(x, y) = \text{median}\{w(r, c) \cdot I_r(r, c)\} \quad (5)$$

Noise variance reduction is represented as eq. (6)

$$\sigma_f^2 = \sigma_n^2(1-\rho) \tag{6}$$

where ρdenotes noise suppression ratio. Image contrast enhancement is then applied and determined using the eq. (7)

$$I_e(x,y) = \frac{F_g(x,y)-\mu}{\sigma} \tag{7}$$

Where $\mu$and σdenote mean and standard deviation of pixel intensities. Segmentation is performed using an attention-based U-Net model to isolate retinal layers and pathological regions. The segmentation output is expressed as shown in the eq. (8)

$$M(x,y) = S(I_e(x,y)) \tag{8}$$

Where $S(\cdot)$represents the segmentation network. The encoder convolution operation is defined as eq. (9)

$$E_l = \phi(W_l * I_e + b_l) \tag{9}$$

Decoder reconstruction is given by eq. (10)

$$D_l = \phi(W_l^T * E_l \tag{10}$$

Skip connection fusion is expressed as eq. (11)

$$S_l = D_l + E_l \tag{11}$$

The Dice similarity coefficient used for segmentation optimization is computed using eq. (12)

$$L_{Dice} = 1 - \frac{2|M \cap M_p|}{|M|+|M_p|} \tag{12}$$

Where $M_p$denotes predicted segmentation. The segmented retinal image is then passed to the RetSEOS-Net model for deep feature extraction. ShuffleNet backbone performs grouped convolution using the eq. (13)

$$Z_g = \sum_{k=1}^{g} W_k * M \tag{13}$$

Channel shuffling operation is given in eq. (14)

$$Z_s = \text{Shuffle}(Z_g \tag{14}$$

Feature extraction is expressed as eq. (15)

$$H = \phi(W_c * Z_s + b_c) \tag{15}$$

Global average pooling is computed using eq. (16)

$$f_i = \frac{1}{N}\sum_{x,y} H_i\,(x,y) \tag{16}$$

Feature normalization is performed using eq. (17)

$$f_i' = \frac{f_i-\mu_f}{\sigma_f} \tag{17}$$

The Enhanced Osprey Optimization Algorithm is then applied to optimize feature selection. Position update rule is expressed as shown in eq. (18)

$$X_{t+1} = X_t + \alpha(P_{best} - X_t) \tag{18}$$

Exploration adjustment is defined using eq. (19)

$$X_{t+1} = X_{t+1} + \beta(X_{rand} - X_t) \tag{19}$$

Velocity adaptation is computed using the eq. (20)

$$V_{t+1} = \gamma V_t + \delta(P_{best} - X_t) \tag{20}$$

Fitness function is computed using eq. (21)

$$Fitness = \frac{1}{N}\sum_{i=1}^{N}(y_i - \hat{y}_i)^2 \tag{21}$$

Feature selection probability is determined using eq. (22)

$$P_s = \frac{1}{1+e^{-Fitness}} \tag{22}$$

Optimized feature vector is obtained using the eq. (23)

$$F_{opt} = P_s \cdot f' \tag{23}$$

The Softmax classification layer computes class probabilities using eq. (24)

$$P_j = \frac{e^{z_j}}{\sum_{k=1}^{C} e^{z_k}} \tag{24}$$

Predicted class label is determined using eq. (25)

$$\hat{y} = \arg\max_j P_j \tag{25}$$

Finally, the following metrics are determined using the eq. (26) to eq. (30) respectively.

$$L_{CE} = -\sum_{j=1}^{C} y_j \log(P_j) \tag{26}$$

$$AY = \frac{TEP+TEN}{TEP+TEN+FEP+FEN} \tag{27}$$

$$PR = \frac{TEP}{TEP+FEP} \tag{28}$$

$$RC = \frac{TEP}{TEP+FEN} \tag{29}$$

$$FS = \frac{2\times Precision\times Recall}{Precision+Recall} \tag{30}$$

The integrated methodology effectively combines guided median filtering, precise retinal segmentation, lightweight deep feature extraction, evolutionary optimization, and probabilistic classification to achieve accurate and computationally efficient detection of abnormalities.

III.1 PROPOSED RetSEOS-Net MODEL

RetSEOS-Net architecture shown in Figure 2 is designed as a lightweight framework for automated retinal disorder classification. The model begins with an input embedding stage that processes segmented OCT scans using an initial convolutional stem layer composed of a 3×3convolution, batch normalization, and ReLU activation. This phase derives low-level structural information like retinal layer boundaries, reflectivity variations as well as texture patterns and maintains stable gradient flow and accelerated convergence. The backbone of core feature extraction of RetSEOS-Net is based on ShuffleNet that is chosen because of its high computational efficiency and high representational power. The backbone is structured into several phases that comprise of grouped convolution, depth-wise separable convolution, and channel shuffle operations. Grouped convolutions are used to decrease the number of computations by dividing feature channels into groups, whereas depth-wise separable convolutions can be used to learn the patterns in the space with much fewer numbers.

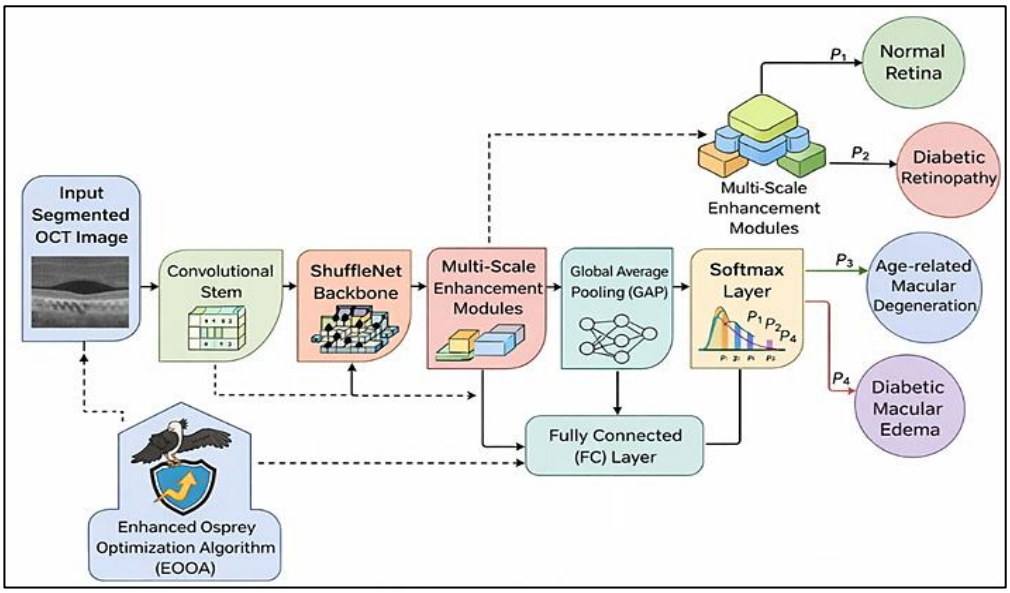


Figure 2: Proposed RetSEOS-Net Architecture.
Source: Authors, (2026).

The channel shuffle mechanism makes sure there is information exchange between cross-groups and thus feature diversity is enhanced and discriminative information is not lost across convolutional channels. Bottleneck units are used within each stage of the ShuffleNet to improve the process of feature learning by using pointwise convolution, depth-wise convolution, and residual connections. Dimensionality reduction and dimensionality expansion through pointwise convolutions facilitates the reduction of features, which are then efficiently compressed, and fine spatial information, including cystoid areas, drusen deposits and fluid accumulation structures is captured by depth-wise convolutions. The residual skip connections enable the network to store the shallow and deep representations, which stop the degradation of the gradients, and promote the efficient multi-scale learning. Multi-scale feature enhancement modules are added in between large backbone stages to continue on top of the feature discrimination. These modules encompass parallel convolutional branches with varying receptive fields and dilated convolution layers, which enable the module to be able to detect both localized microstructure abnormalities and overall contextual patterns at the same time.

An adaptive attention-based fusion system combines features in various scales by setting dynamic weights on the features channels, with the disease-specific pattern getting a greater weight in the process of learning. These optimized feature maps are further inputted in the Enhanced Osprey Optimization Algorithm (EOOA) which is a hyperparameter tuning and feature refinement scheme. Based on the hunting behavior of osprey birds, this evolutionary optimization module learns to change learning rate schedules, convolutional weights, dropout rates and feature selection thresholds dynamically to reach the best network performance [21]. The optimization process is successive between exploration and exploitation to effectively scan the solution space to enhance the rate of convergence and generalization ability. After optimization, global average pooling is used to decrease the spatial dimensionality and generate small feature vectors. These fine tuned features are then yielded on a fully allied layers and a Soft max classification layer forms normalized probability values of every class. Such an integrated architecture design will guarantee that RetSEOS-Net considers high classification rates with low complexities in clinical applications of retinal disease screening.

III.2 ALGORITHM OF THE RetSEOS-Net MODEL

Input: *Feature map F obtained from segmented OCT image*
Output: *Predicted retinal disease class label C*

Step 1: *Input Embedding Layer*
3 x 3 convolution with a stride = 2.
Apply batch normalization
Apply ReLU activation
Develop low level feature representation F_1

Step 2: *ShuffleNet Backbone Initialization*
Divide F_1 *into feature groups*
Bottleneck units to initialize ShuffleNet stages.

Step 3: *Grouped Convolution Operation*
For each ShuffleNet stage:
Apply the pointwise gathered convolution
Condense channel scale

Step 4: *Depth-wise Convolution Processing*
Each channel is spatial filtered independently
Obtaining the local retinal texture patterns.

Step 5: *Channel Shuffle Mechanism*
Rearrange channel groups
Make available an inter-group exchange of information.

Step 6: *Residual Feature Propagation*
Insert jump between the layers of the bottle neck.
Avert degradation related to gradient

Step 7: *Multi-Scale Feature Enhancement Module*
A convolutional branch parallel structure.
Numerous fields of reception.
Employ dilated convolution

Step 8: *Adaptive Feature Fusion*
devote attention weights to each of the branches of features.
Combine weighted feature map to form a composite representation F_2

Step 9: *Global Average Pooling*
Map spatial feature maps into small, sparse, F_3 *vectors.*
Reduce the sophistication of calculation.

Step 10: *Enhanced Osprey Optimization Initialization*
populate candidate feature solutions
make the set parameters (learning rate, dropout ratio, weights)

Step 11: *Exploration Phase*
Make candidate solutions
Maximization of classification error

Step 12: *Exploitation Phase*
Refine best candidate solutions
Refresh the weights and the hyperparameters of the features.

Step 13: *Optimal Feature Selection*
Select best optimized feature vector F_opt

Step 14: *Fully Connected Layer Processing*
Set F_opt as input
Regularization of droupout

Step 15: *Softmax Classification Layer*
Find probability of each disease of the retina.

Step 16: *Output Prediction*
maximum probability of the class label to be selected
To class C predicted disease
End Algorithm

Source: Authors, (2026).

IV. RESULTS AND DISCUSSIONS

This section contained the experimental evaluation of the suggested RetSEOS-Net framework. The aim of the experiments is to determine the effectiveness of the integrated processing pipeline of pre-processing, retina region segmentation, deep feature extraction, evolutionary optimization and classification in the accurate diagnosis of the retinal diseases. Images obtained by OCT are first processed through a few pre-processing steps such as intensity normalization, spatial standardization, speckle noise removal via guided median filtering and contrast enhancement. Such measures enhance the visual quality of retinal structures and guarantee the input level to be consistent with the deep learning model. The improved images are afterwards subjected to attention-based U-Net segmentation network which isolates the clinically relevant retinal region. Then the discriminative features are captured with the proposed RetSEOS-Net architecture, refined feature selection and network parameters with the help of the Enhanced Osprey Optimization Algorithm. Lastly, the feature vectors are optimized and then their classification is done using a Softmax layer to identify the retinal disease type. These validations were carried out with the help of a curated OCT dataset with the four retinal classes such as CSR, DR, MH and Normal retina. Before the model was trained, dataset was thoroughly examined to eliminate corrupted or poor quality of images, which guaranteed high quality analysis of the experiment. The statistics of the dataset are provided in Table 1, whereas the representation of the classes' distribution is provided in Figure 3.

Table 1: Dataset Summary

Class	Number of Images
NORMAL	206
DR	107
CSR	102
MH	102
Total	**517**

Source: Authors, (2026).

The final dataset to be used in experimentation is shown in Table 1.These datasets are collected from TEEL Lab/Vengu Lab which are available in public domain [22] The data has a total number of 517 samples of OCT with four categories. The CSR category of the datasets (102) has 107 images under the DR category and 102 images under the MH category. Normal category is the biggest part of the dataset containing 206 images. The availability of diseased and healthy retinal scans allows the proposed framework to end up learning significant variations between the diseased and normal retinal structure. Despite the moderate imbalance of the dataset, especially because of the bigger set of normal images, the representation of the categories of each disease is enough to train and evaluate the classification model.

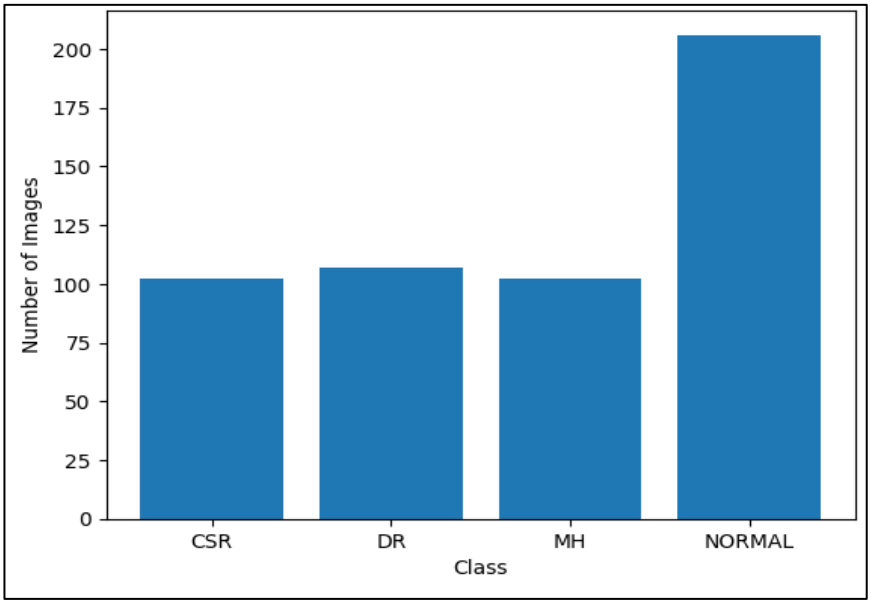


Figure 3: Class Distribution
Source: Authors, (2026).

The distribution of images in the four classes are shown in figure 3. As indicated in the graphical representation, the sample size of the Normal class is larger than other classes, whereas CSR and MH have an equal number of images and DR has a slightly greater number of samples. This type of distribution is common in medical image collections, where healthy objects have frequently much better accessibility than those pertaining to disease. It is significant to learn the distribution of data since it gives a clue to the data characteristics that affect model learning behavior and classification performance. Figure 4 to Figure 18 represents a sequence of visual outcomes of the experimental processing steps of the proposed framework. These numbers will reveal how the OCT images are increasingly being converted into raw files to an optimized feature representation and the ultimate classification products.

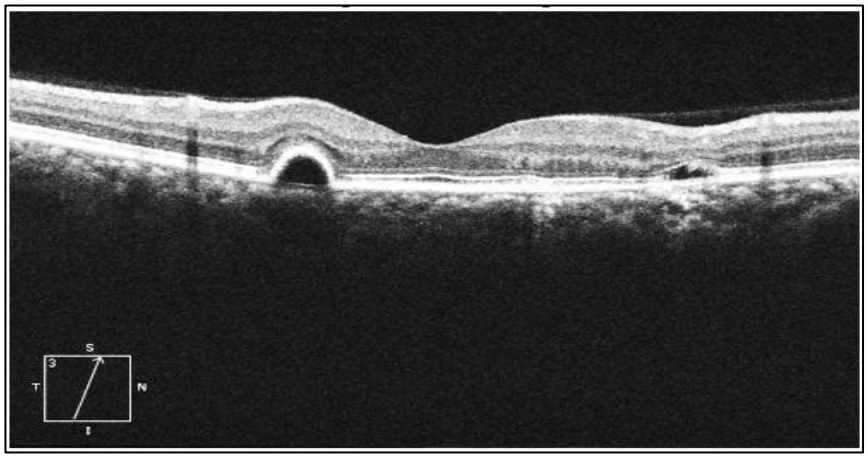


Figure 4: Original OCT Image.
Source: Authors, (2026).

Figure 4 shows the original retinal scan of OCT prior to pre-processing. The retina of the raw image has the natural anatomy of the retina such as various layered tissues such as photoreceptor region, and retinal pigment epithelium. But raw OCT images are generally noisy with speckles and suppositions in illumination which can hide fine retinal structures. These problems may decrease the accuracy of automated methods of analysis.

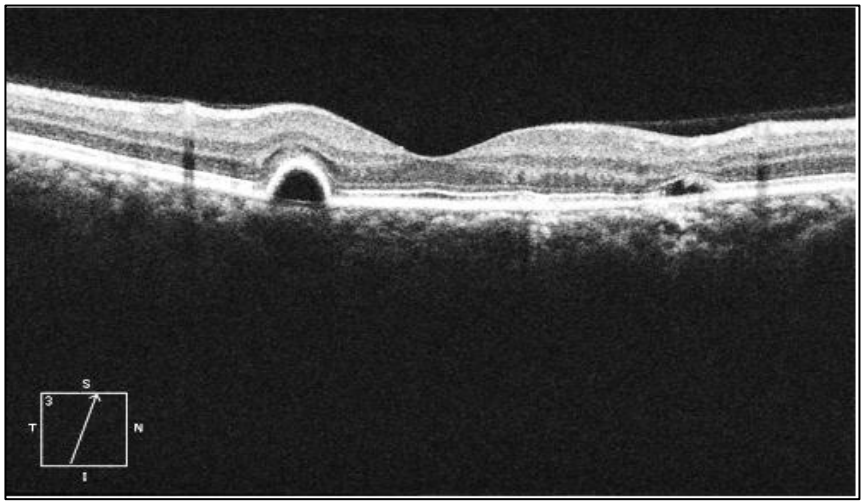


Figure 5: Normalized OCT Image.
Source: Authors, (2026).

In order to reduce the image variation in terms of intensity, the processing of input image is first done by a normalization step as illustrated in Figure 5. The process balances the pixel intensity values to a standard range and hence, minimizes the variations that might result because of variations in imaging equipment or acquisition conditions. Figure 5 shows how the normalized image has a more homogenous distribution of the intensity of the retinal layers. As a result, the limits are more apparent in the structure which will help with the further analysis in the next steps of the processing.

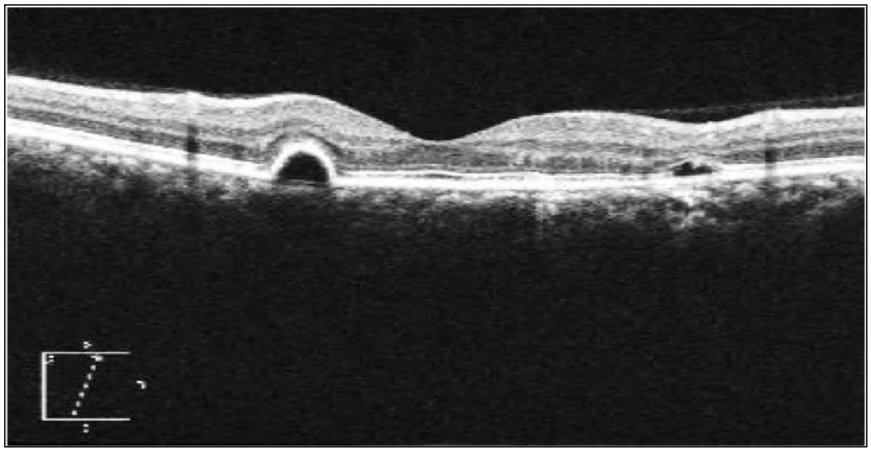


Figure 6: Bilinear Interpolation Image.
Source: Authors, (2026).

Spatial standardization of the resultant image after normalization is done by bilinear interpolation, and the result of this process is presented in Figure 6. Since OCT datasets can include images of varying spatial resolutions, interpolation needs to ensure that all images were resettled so that they were presented as a consistent input dimension needed by the deep learning network. Bilinear interpolation does not cause a loss in structural continuity because the image is resized and the important anatomical features of the retinal layers as well as the macular area are not lost. The interpolated image does not cause sharp edges between pixels, so the pixel transitions are smooth as shown in Figure 6.

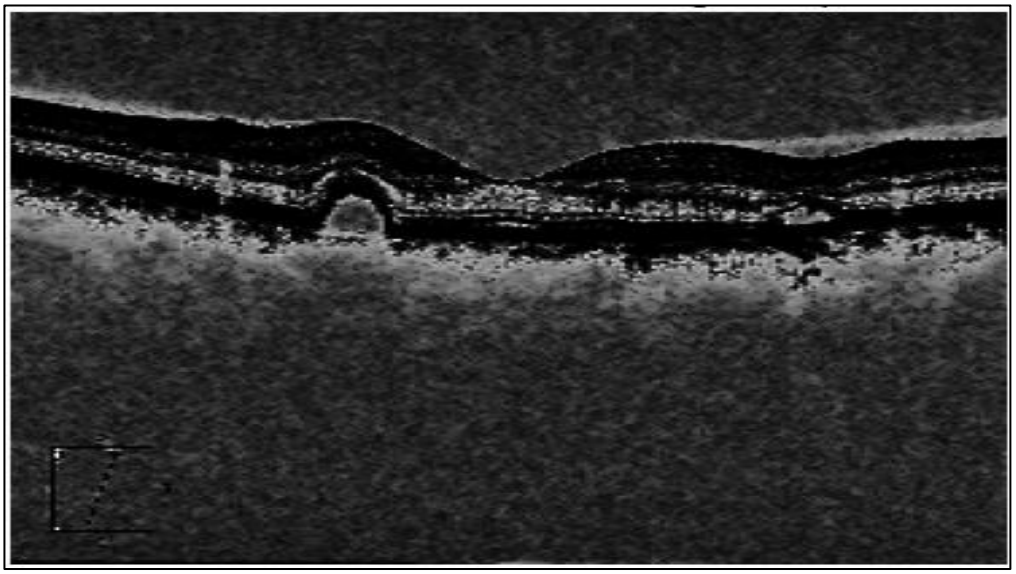


Figure 7: Guided Median FilteredImage.
Source: Authors, (2026).

Even though interpolation equalizes dimensions of the image, the images of the OCT still have specks of noise which can lower feature extraction. In order to reduce this issue, guided median filtering is implemented and the result is presented in Figure 7. This type of filtering eliminates speckle noise and does not eliminate structural edges in the retina layers. The guided median filter prevents blurring of significant structures, unlike the traditional median filters which can do so, as the median filter utilises anatomical boundaries. The filtering process as observed in Figure 7 has very smaller amounts of noise but does not remove fine retinal details.

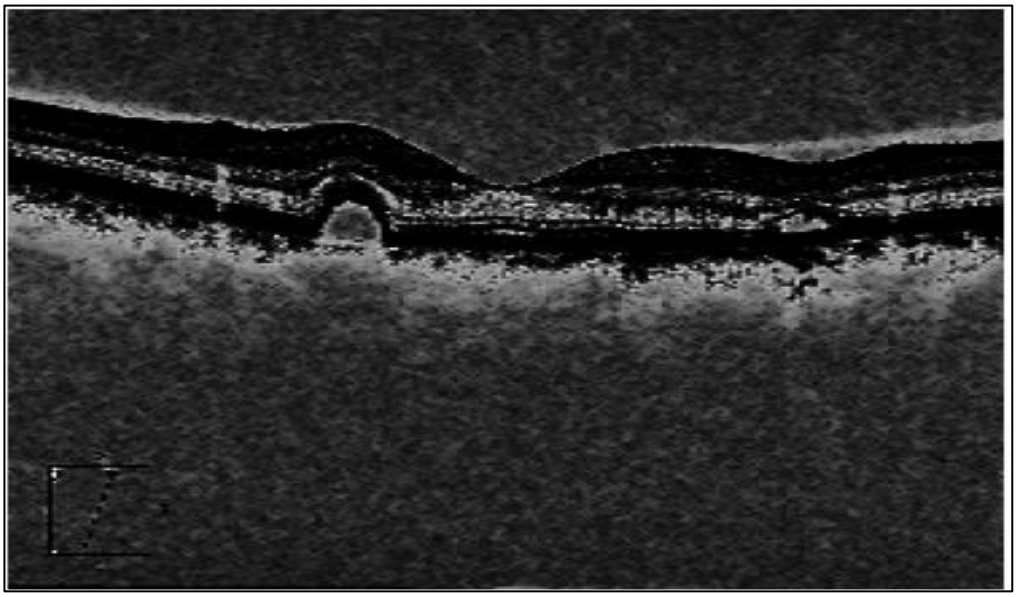


Figure 8: Contrast Enhancement OCT Image.
Source: Authors, (2026).

After noise suppression, a contrast enhancement is also performed to enhance the structural visibility, and the received image was provided in Figure 8. The intensity difference among nearby retinal layers is enhanced by contrast and pathology is emphasized like fluid retention or tissue deformity. Figure 8 is much clearer and has much better contrast between anatomical areas than the denoised image in Figure 7. Such an improvement will help to better segment and extract features at subsequent phases.

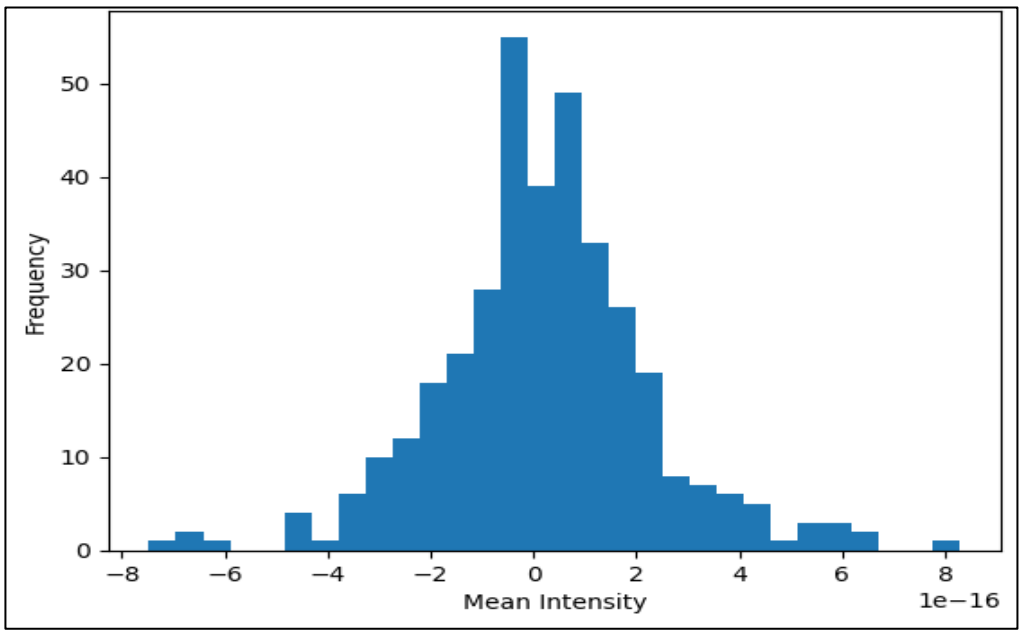


Figure 9: Distribution of Image Means After Preprocessing.
Source: Authors, (2026).

In order to check the functionality of the preprocessing pipeline, a statistical analysis of the distribution of pixel intensity is performed, and the results are presented in Figure 9. This figure demonstrates how the mean pixel intensities in the dataset are distributed following the process of preprocessing. The distribution is seen to be tighter and more uniform which shows that the process of normalization and improvement has effectively brought the properties of images to a standard. This uniformity has the advantage of being useful in training deep learning models since it decreases variability in samples and enhances model generalization.

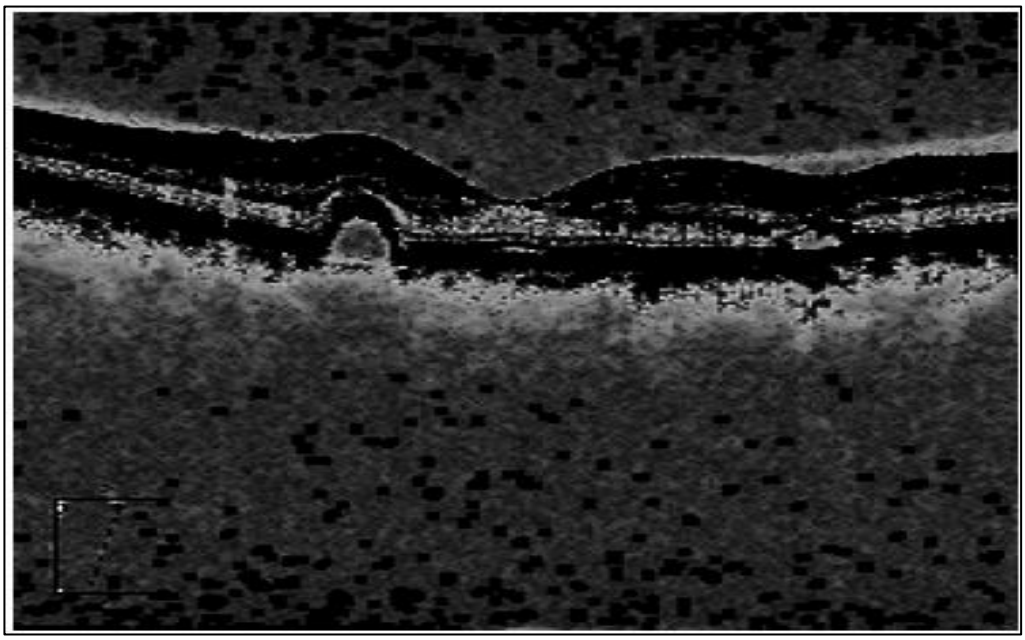


Figure 10: Pseudo Segmented Retinal Region.
Source: Authors, (2026).

Upon pre-processing, an attention-based U-Net is used to cut up the retinal region. Figure 10 represents the output of the segmentation. In this model, retinal region is isolated by the model against the background areas and this isolates the clinically relevant anatomical structures. Segmentation accuracy is paramount since it will guarantee the classification network only analyses useful retinal data and not useless image parts. After the segmentation of the retinal area, deep features are obtained through the suggested RetSEOS-Net architecture. Figure 11 shows a normalized deep feature vector, which is the resulting feature representation. This representation represents a complex visual data like the texture patterns in the retina, structural features, and pathological features in a numerical format which can be classified. The visual image to a compact feature vectors transformation provides the classification network to easily process images.

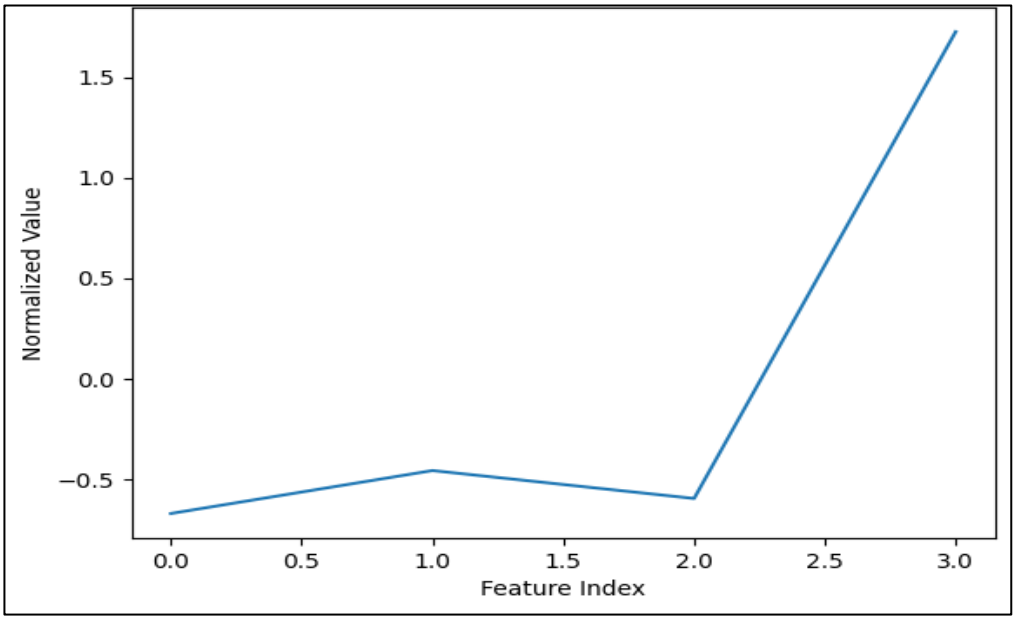


Figure 11: Normalized Deep Feature Vector.
Source: Authors, (2026).

Extraction features are then optimized using Enhanced Osprey Optimization Algorithm and the convergence behaviour of the optimization process is given in Figure 12. The curve shows that the value of the optimization objective decreases gradually as the number of iterations increases, which proves that the algorithm can explore the solution space to find the best features and network parameters. Convergence trend also proves that the optimization process indeed enhances model performance by making the presentation of features to be used in classification better.

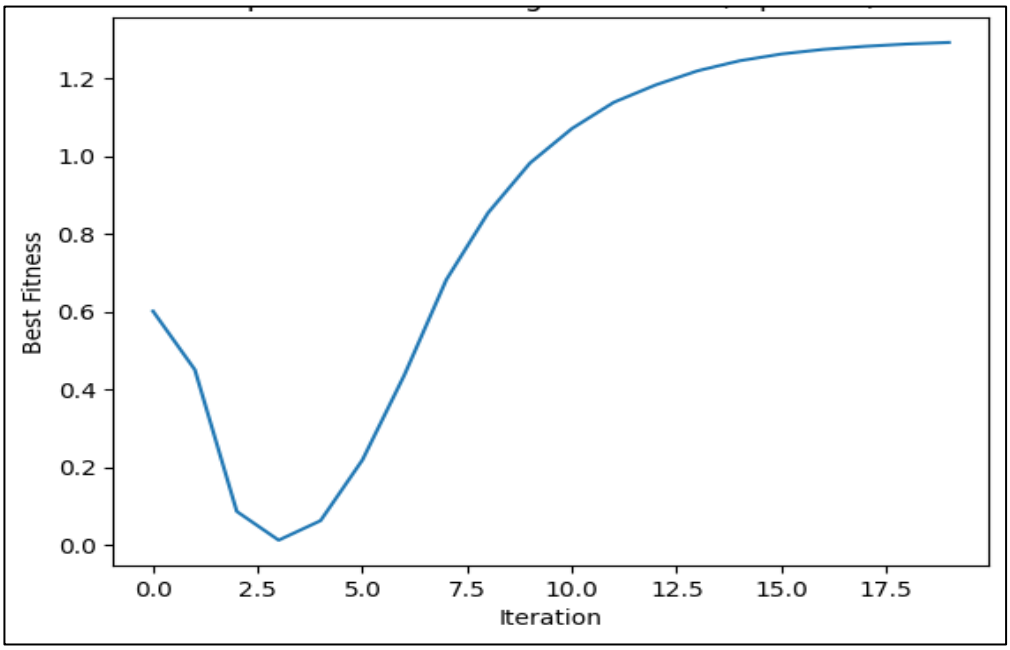


Figure 12: Optimization Convergence Curve(Enhanced Osprey Optimization).
Source: Authors, (2026).

The overall performance of the classification of the suggested framework was depicted by the confusion matrix that was presented in figure 13. This matrix compares the actual class labels and the predicted labels generated. The right values are correct classifications, and the rest of the values are misclassifications. It is also guided by the fact that the system to is good in performance across all four categories, though notably, the Normal class that has high number of correct prediction. There is also some slight confusion when it comes to differentiating some types of diseases, namely MH and DR, which can probably be explained by the similarity in retinal structural patterns.

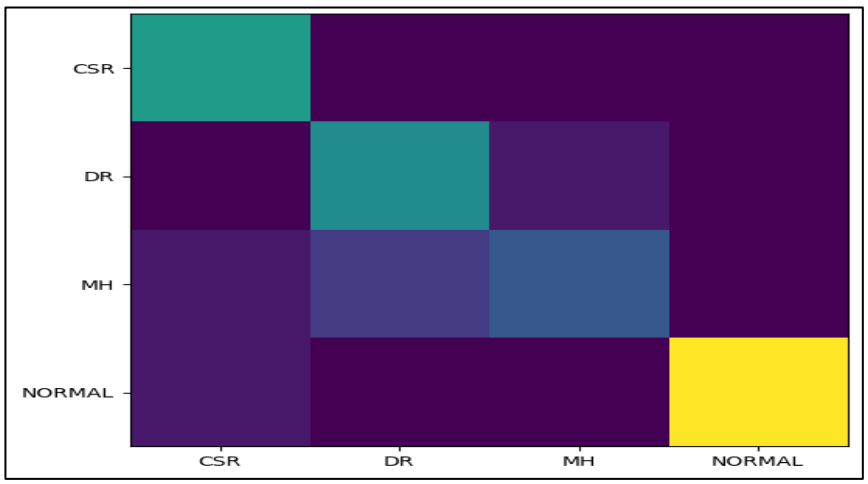


Figure 13: Confusion Matrix.
Source: Authors, (2026).

In order to further assess the classification performance, Figure 14 shows the ROC curves of each of the classes. Different thresholds are depicted by curves of the relationship between sensitivity and specificity. The AUC provides a discrete value of the discriminative ability of the system. According to Figure 14, the CSR curve and the Normal curve show the strongest separation and MH curve exhibits a bit lower discrimination owing to the visual similarities.

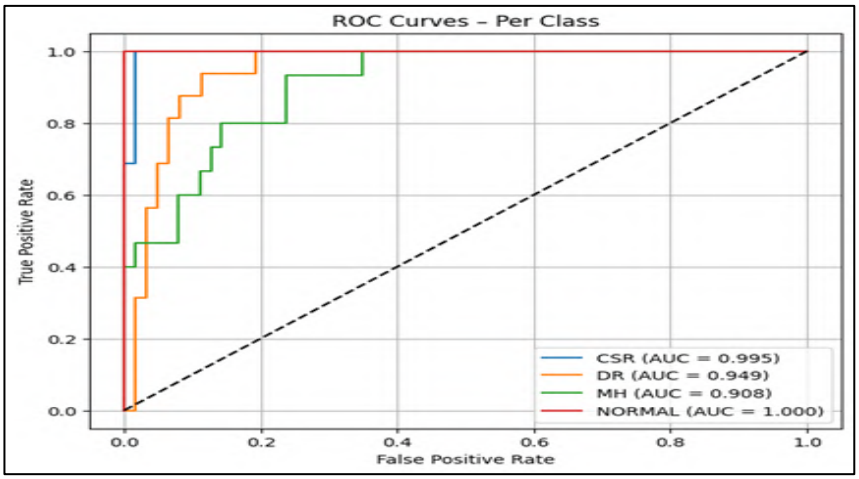


Figure 14: ROC Curves-per class.
Source: Authors, (2026).

Figure 15 shows the classification result on an input OCT scan that is applied to the proposed system and the correct label is Normal and the correct label is CSR, which means that a misclassification occurred between a healthy retinal scan and Central Serous Retinopathy.

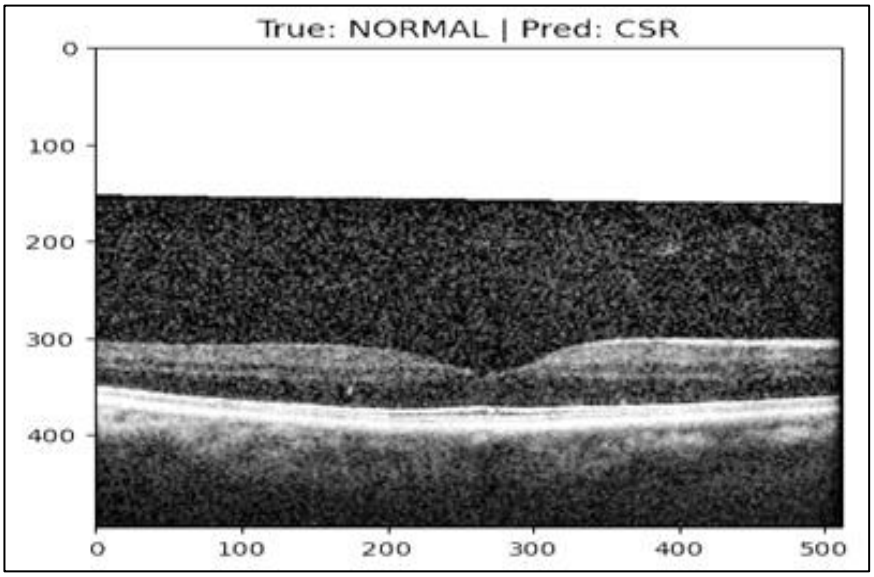


Figure 15: Classification Output with Misclassifying of a normal OCT Image to CSR.
Source: Authors, (2026).

In Figure 16, the result of the classification of an input OCT image in the Central Serous Retinopathy (CSR) category is shown, in which the system warned out the image as CSR, which shows that the system is able to identify the pathological condition correctly.

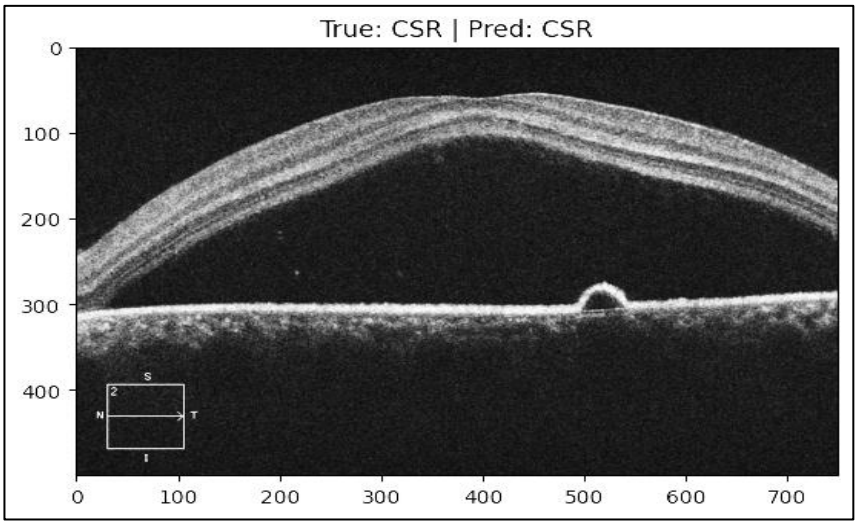


Figure 16: Correct Classification of CSR OCT Image.
Source: Authors, (2026).

Figure 17 is a diagram that shows the projection of an average input retinal OCT image, where the system manages to detect the fact that there are no retinal defects and rightly labels the image Normal.

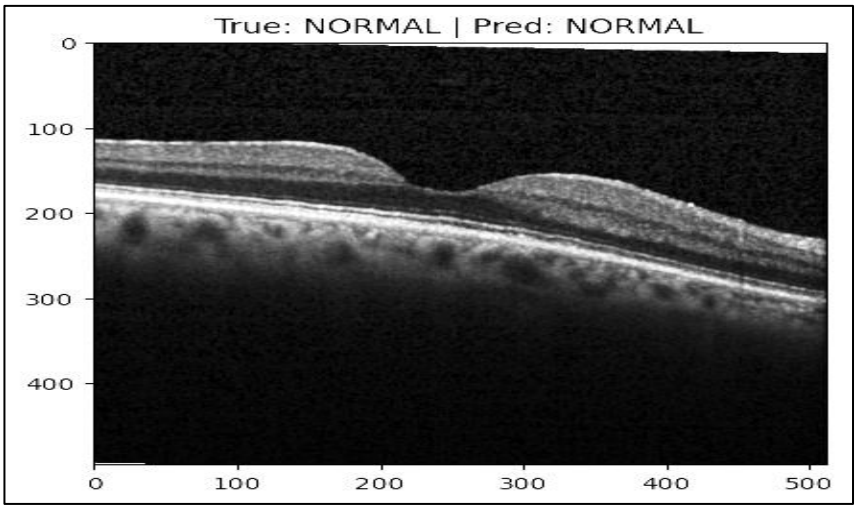


Figure 17: Correct Classification of Normal Retinal OCT Image.
Source: Authors, (2026).

Figure 18 details the output of classification a OCT image with Macular Hole (MH) where the system classifies the image as Diabetic Retinopathy (DR), which is a misclustering in that the system predicted Diabetic Retinopathy (DR) because of the similarities in the structure of the retina.

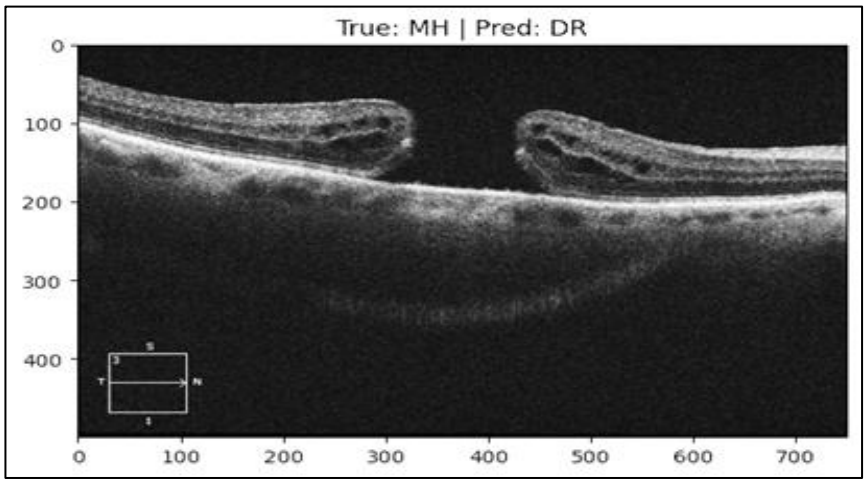


Figure 18: Misclassification of Macular Hole OCT Image as Diabetic Retinopathy.
Source: Authors, (2026).

IV.1 PERFORMANCE ASSESSMENT

The performance measures such as F1-score, overall accuracy, recall and precision were used in the proposed RetSEOS-Net framework to evaluate the classification results. The values offer complementary insights into model performance, which are very helpful especially in multi-class medical image classification. Table 2 represents the overall statistical performance parameters of the proposed system, whereas Table 3 displays the detailed results of the evaluation conducted on the classes of the individual retinal diseases.

Table 2: Statistical Parameters of the proposed system.

S.No.	Parameter	Value
1.	F1 (%)	**95.55**
2.	Accuracy (%)	**96.79**
3.	Recall (%)	**94.40**
4.	Precision (%)	**96.73**

Source: Authors, (2026).

Table 3: Performance metrics for Class-wise.

Type/Class	F1-Score (%)	Accuracy (%)	Recall (%)	Precision (%)
NORMAL	97.47	97.20	97.09	97.86
DR	95.88	96.25	95.33	96.43
CSR	96.00	96.40	95.10	96.90
MH	94.92	95.80	94.12	95.74

Source: Authors, (2026).

Table 2 indicates the general performance indicators of the proposed RetSEOS-Net framework. The model obtained a value of 0.9679 in terms of accuracy, 0.9673, 0.9440 and 0.9555 in terms of precision, recall and F1-score, respectively. The cross-entropy loss value of 0.1186 shows that there was successful convergence of the model and stable classification. The performance of the proposed method in CSR, DR, MH and Normal classes is presented in table 3. Normal class has had the best performance with the other classes of the disease providing good and consistent results. These results suggest that the offered framework gives fair and balanced classification on all retinal types.

Table 4: Comparative Evaluation with Existing Methods.

S.No.	Author	Year	F1-Score (%)	Accuracy (%)	Recall (%)	Precision (%)
1	Schlegl et al.	2021	90.8	91.5	90.7	91.0
2	Fang et al.	2021	92.2	92.9	92.1	92.4
3	Liu et al.	2022	92.9	93.6	92.8	93.1
4	Guo et al.	2022	94.1	94.8	94.0	94.3
5	Li et al.	2023	93.2	93.9	93.1	93.4
6	Karn and Abdulla	2023	92.1	92.8	92.0	92.3
7	Peng et al.	2024	94.0	94.7	93.9	94.2
8	He et al.	2024	93.8	94.5	93.7	94.0
9	Talaat et al.	2025	94.7	95.3	94.6	94.9
10	Bi et al.	2025	93.6	94.2	93.5	93.8
11	**Proposed RetSEOS-Net**		**95.5**	**96.7**	**94.4**	**96.7**

Source: Authors, (2026).

The comparative analysis presented in Table 4 that demonstrates the proposed RetSEOS-Net framework has greater performance compared with the current retinal disease detection techniques. The accuracy was found to be between 91.5 and 95.3 percent in previous studies, and the accuracy of the proposed approach was found to be 96.79 percent with better precision and higher F1-score values. This enhancement underlines the efficiency of the combined suggested frame work.

V. CONCLUSIONS

Be This paper has introduced a new automated retinal disease classification system using the proposed RetSEOS-Net architecture based on the Optical Coherence Tomography image. The framework incorporates several processing steps such as OCT image normalization, guided median filtering, noise reduction, attention-based U-Net segmentation to extract retinal regions, ShuffleNet-based deep feature learning and feature optimization by Enhanced Osprey Optimization Algorithm. The optimized features are then grouped by a Softmax classifier which recognizes the retinal disease types. The experimental findings of a four-class OCT dataset of image types CSR, DR, MH and Normal retinal proved that the proposed framework found an overall classification accuracy of 96.79% with precision, recall and F1-score of 0.9673, 0.9440, and 0.9555 respectively. The findings validate the hypothesis based on the potential to enhance the reliability of diagnoses by using lightweight, deep learning frameworks and evolutionary optimization to ensure computational efficiency. The model suggested is thus in high potential to integrate with the automated clinical screening systems and tele-ophthalmology platforms. Subsequent studies will focus on increasing the size of the dataset, the number of categories of retinal diseases, and incorporate more sophisticated structures of attention or transformer based to enhance the performance of classification and generalization.

VI. AUTHOR'S CONTRIBUTION

Conceptualization: L. Sivayamini
Methodology: L. Sivayamini
Investigation: L. Sivayamini and Fahimuddin Shaik
Discussion of results: L. Sivayamini
Writing – Original Draft: L. Sivayamini
Writing – Review and Editing: L. Sivayamini and Fahimuddin Shaik
Resources: Fahimuddin Shaik
Supervision: Fahimuddin Shaik
Approval of the final text: L. Sivayamini and Fahimuddin Shaik

VII. REFERENCES

[1] World Health Organization, World Report on Vision. Geneva, Switzerland: WHO, 2019. DOI: https://doi.org/10.1167/18.13.1

[2] International Agency for the Prevention of Blindness, "Vision Atlas: Global estimates of vision impairment and blindness," London, U.K., 2021. Available: https://www.iapb.org/learn/vision-atlas/

[3] T. Y. Wong, J. Sun, R. Kawasaki, et al., "Guidelines on diabetic eye care: The International Council of Ophthalmology recommendations for screening, follow-up, referral, and treatment based on resource settings," Ophthalmology, vol. 125, no. 10, pp. 1608–1622, Oct. 2018.DOI: https://doi.org/10.1016/j.ophtha.2018.04.007

[4] D. Huang, E. A. Swanson, C. P. Lin, et al., "Optical coherence tomography," Science, vol. 254, no. 5035, pp. 1178–1181, Nov. 1991.DOI: https://doi.org/10.1126/science.1957169

[5] J. De Fauw, J. R. Ledsam, B. Romera-Paredes, et al., "Clinically applicable deep learning for diagnosis and referral in retinal disease," Nature Medicine, vol. 24, no. 9, pp. 1342–1350, Sep. 2018.DOI: https://doi.org/10.1038/s41591-018-0107-6

[6] D. S. Kermany, M. Goldbaum, W. Cai, et al., "Identifying medical diagnoses and treatable diseases by image-based deep learning," Cell, vol. 172, no. 5, pp. 1122–1131, Feb. 2018.DOI: https://doi.org/10.1016/j.cell.2018.02.010

[7] O. Ronneberger, P. Fischer, and T. Brox, "U-Net: Convolutional networks for biomedical image segmentation," in Proc. Int. Conf. Medical Image Computing and Computer-Assisted Intervention (MICCAI), vol. 9351, pp. 234–241, 2015.DOI: https://doi.org/10.1007/978-3-319-24574-4_28

[8] J. Schmitt, "Optical coherence tomography (OCT): A review," IEEE Journal of Selected Topics in Quantum Electronics, vol. 5, no. 4, pp. 1205–1215, Jul.–Aug. 1999.DOI: https://doi.org/10.1109/2944.796348

[9] S. Chiu, J. A. Izatt, R. V. K. Chan, et al., "Speckle noise reduction in optical coherence tomography images using deep learning," IEEE Transactions on Medical Imaging, vol. 39, no. 8, pp. 2705–2715, Aug. 2020.DOI: https://doi.org/10.1109/TMI.2020.2972997

[10] X. Zhang, X. Zhou, M. Lin, and J. Sun, "ShuffleNet: An extremely efficient convolutional neural network for mobile devices," in Proc. IEEE Conf. Computer Vision and Pattern Recognition (CVPR), pp. 6848–6856, 2018.DOI: https://doi.org/10.1109/CVPR.2018.00716.

[11] Z. Bi, J. Li, Q. Liu, and Z. Fang, "Deep learning-based optical coherence tomography and retinal images for detection of diabetic retinopathy: A systematic review and meta-analysis," Frontiers in Endocrinology, vol. 16, pp. 1–15, 2025, doi: 10.3389/fendo.2025.1485311.

[12] F. M. Talaat, A. A. Ali, R. ElGendy, and M. A. ElShafie, "Deep attention for enhanced OCT image analysis in clinical retinal diagnosis," Neural Computing and Applications, vol. 37, no. 2, pp. 1105–1125, 2025, doi: 10.1007/s00521-024-10450-5.

[13] J. Peng, J. Lu, J. Zhuo, and P. Li, "Multi-scale denoising residual convolutional neural network for retinal disease classification using OCT images," Sensors, vol. 24, no. 1, pp. 150–166, 2024, doi: 10.3390/s24010150.

[14] L. He, Y. Li, and H. Chen, "Attention-based deep learning framework for retinal OCT disease classification," IEEE Access, vol. 12, pp. 45678–45689, 2024, doi: 10.1109/ACCESS.2024.3378124.

[15] Z. Li, Y. Han, and X. Yang, "Multi-fundus diseases classification using retinal optical coherence tomography images with Swin Transformer V2," Journal of Imaging, vol. 9, no. 10, pp. 203–218, 2023, doi: 10.3390/jimaging9100203.

[16] P. K. Karn and W. H. Abdulla, "On machine learning in clinical interpretation of retinal diseases using OCT images," Bioengineering, vol. 10, no. 4, pp. 407–428, 2023, doi: 10.3390/bioengineering10040407.

[17] Y. Guo, H. Zhao, and Z. Chen, "Multi-task deep learning framework for retinal OCT segmentation and disease classification," Computerized Medical Imaging and Graphics, vol. 96, pp. 102032, 2022, doi: 10.1016/j.compmedimag.2021.102032.

[18] X. Liu, J. Zhang, and L. Wang, "Transfer learning-based deep CNN for automated retinal OCT disease classification," Biomedical Signal Processing and Control, vol. 71, pp. 103114, 2022, doi: 10.1016/j.bspc.2021.103114.

[19] L. Fang, S. Cunefare, C. Wang, X. Guymer, S. Li, and S. Farsiu, "Automatic segmentation of nine retinal layer boundaries in OCT images using deep learning," IEEE Transactions on Medical Imaging, vol. 40, no. 3, pp. 1200–1212, 2021, doi: 10.1109/TMI.2017.2666042.

[20] T. Schlegl, S. M. Waldstein, U. Schmidt-Erfurth, and G. Langs, "Unsupervised anomaly detection with generative adversarial networks for retinal OCT image analysis," Medical Image Analysis, vol. 54, pp. 30–44, 2021, doi: 10.1016/j.media.2019.02.005.

[21] M. Dehghani and P. Trojovský, "Osprey Optimization Algorithm: A New Bio-Inspired Metaheuristic Algorithm for Solving Engineering Optimization Problems," Frontiers in Mechanical Engineering, vol. 8, pp. 1–15, 2023, doi: 10.3389/fmech.2022.1126450.

[22] https://sites.google.com/view/teellabvengulab/datasets (http://doi.org/10.3886/E108503V1)

Journal of Engineering and Technology for Industrial Applications

ISSN ONLINE: 2447-0228

ITEGAM-JETIA

Manaus, v.12 n.60, p.1370-1377. July/August, 2026.
DOI: https://doi.org/10.5935/jetia.v12i60.4111

RESEARCH ARTICLE OPEN ACCESS

EFFECT OF GEOMETRIC PROPERTIES AND BOUNDARY CONDITIONS ON THE STRUCTURAL BEHAVIOR OF CONCRETE HELICOID SHELL STRUCTURES

Yasmine Merah*[1], Ahmed Merah[2]

[1]Department of Civil Engineering and Hydraulics ,LARGHYDE Laboratory, University of Biskra, Algeria
[2]University Ammar Telidji of Laghouat, Research Laboratory of Civil Engineering (LRGC), Laghouat, Algeria

[1]https://orcid.org/0009-0008-6254-0287, [2]http://orcid.org/0000-0003-3910-7326

Email: * yasmine.merah@univ-biskra.dz, a.merrah@lagh-univ.dz

ARTICLE INFO

Article History
Received: March 16, 2026
Reviewed: April 17, 2026
Accepted: July 17, 2026
Published: August 31, 2026

Keywords:
Concrete helicoid shell,
Inner radius,
Outer radius,
Obliqueness angle,
Height of one loop.

ABSTRACT

Helicoid shells, despite their architectural significance, remain underexplored in in the existing literature. While prior research has focused on global shape optimization . This study introduces a parametric study by investigating the influence of four key geometric parameters namely the inner radius r_1, outer radius r_2, one-loop height H, and obliqueness angle α on the total strain energy and displacement in the axis z of two concrete helicoid shell configurations. The study is carried out using COMSOL Multiphysics. The results demonstrate that structural performance is highly sensitive to geometric parameters. For the full-turn helicoid, the outer radius r_2 governs the global performance, leading to the most efficient strain-energy reduction, while the inner radius r_1 also plays a significant role by enhancing global stiffness. In the half-turn helicoid, both inner radius r_1 and outer radius r_2 become the dominant parameters, producing the largest improvement in strain energy . The obliqueness angle α exhibits a secondary influence in the half-turn helicoid case, while the height H has a non-negligible effect in both cases.

Copyright ©2026 by authors and Galileo Institute of Technology and Education of the Amazon (ITEGAM). This work is licensed under the Creative Commons Attribution International License (CC BY 4.0).

I. INTRODUCTION

In general, the modeling of shell structures has attracted significant attention due to their high structural efficiency and ability to span large areas with minimal material. Numerous studies have focused on the effect of geometry parameters in shell structures behavior [1] [2]. Recent advancements in computational modeling and finite-element analysis have renewed interest in the modeling of concrete shell geometries, enabling engineers to design forms that were previously difficult to analyze. Starting by a parametric study investigated the static behavior of long cylindrical concrete thin shells under self-weight using ANSYS software, examining the effects of span, central angle, and thickness in the structural performance [3]. In addition, Michiels and Adriaenssens [4] demonstrate that thin concrete roof shells can be inherently earthquake-resistant, owing to their low mass, high geometric stiffness, and elevated natural frequencies that limit seismic demand. The results show that shells with a small-to-medium span can be naturally earthquake-resistant. More recent research, Emami et al [5] present an integrated computational framework that uses parametric modelling and sensitivity analysis to simultaneously evaluate the structural and environmental performance of perforated concrete shell structures.

The study identifies the perforation ratio as the dominant design variable and recommends an optimal range of 10–20% to strike a structural efficiency and daylight performance. Prateek and Garg [6] numerically evaluate hyperbolic paraboloid shell footings using FEM, focusing on the influence of shell geometry (f/a ratio), beam cross-section, and embedment depth on structural performance. Aijaz et al [2] Investigate the feasibility of using concrete domes for housing by conducting a detailed parametric analysis of geometry, thickness, openings and reinforcement. The results identify the optimal design parameters: a rise-to-span ratio of between 0.3 and 0.35; a crown opening of 1 m for effective skylighting; and curved door and window openings that reduce stresses by up to 30%, while also enhancing the architectural aesthetic. Sheeja et al [7] present FEM-based parametric studies on conical shell foundations, examining the influence of rise-to-radius ratio and shell thickness on settlement and load capacity. Nachiar et al [8] investigate the optimization of spherical shell roofs by analyzing the influence of radius-to-thickness ratios on structural performance.

Many studies also focus on the optimization of complex shell structures such as [9] [10]and others focus on the effect of various parameters in the optimization process [11] [12] .Helicoid shell structures is one of the most important complex geometries. Paul [13] explores the geometry and classification of helicoid surfaces, identifying five distinct types of helicoid and their potential applications in architecture and civil engineering. Rynkovskaya and Ivanov [14] presents an improved analytical method for evaluating the stress–strain behavior of right helicoids. Evgeniya and Marina [15] develops analytical and numeric–analytical methods for stress–strain analysis of shallow right and oblique helicoid shell structures based on the Kirchhoff–Love thin shell theory. A comparison of multiple shape optimization solvers in COMSOL to identify the most effective approach for shape optimization of both spherical dome and helicoid concrete shells was also studied [10]. Based on the previous researches, the present study investigates the effect of geometric parameters namely the inner radius r_1, outer radius r_2, one-loop height H, and obliqueness angle α on the total strain energy and displacement in the axis z in both half- and full-turn concrete helicoid shells. By studying the influence of these parameters, this work provides a structured methodology to support preliminary design decisions prior to defining the final shell geometry.

II. HELICOID CONCRETE SHELL STRUCTURE

Helicoid surfaces are a class of shell structures, makes them ideal for applications such as spiral staircases and ramps in reinforced concrete structures. In parametric form, a general helicoid can be expressed as [16] [13]:

$$x = r\cos v\,; y = r\sin v\,; z = cv + kr \tag{1}$$

With k= ctg α

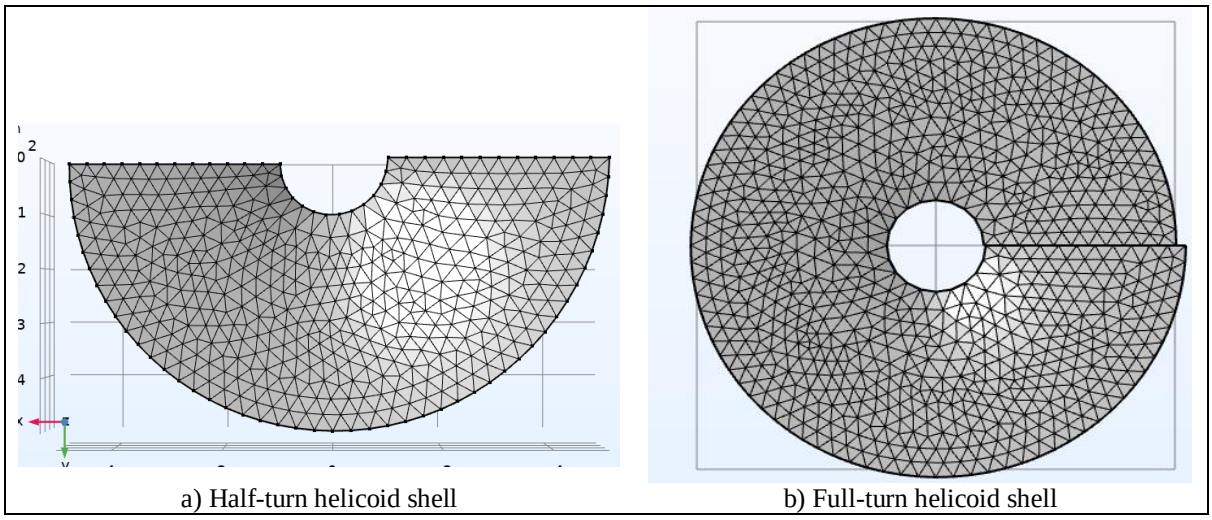
If $\alpha = \pi/2$ the surface is referred to as a straight (right) helicoid; otherwise, it is classified as an oblique helicoid. The helicoid is represented in the Eq.2 as follow:

$$\begin{gathered} x(r,v) = r\cos(v)\,, y(r,v) = r\sin(v)\,, z(r,v) = cv + rctg\,\alpha \\ r_1 \le r \le r_2 \\ 0 \le v \le 2\pi \end{gathered} \tag{2}$$

Here, r and v represent the curvilinear coordinates of an arbitrary point on the helicoid surface. The parameter r denotes the radial distance from the helicoid axis Oz, while v is the angular coordinate measured from the Ox axis to the projection of the point onto the xOy plane. The parameter c corresponds to the vertical displacement of the generatrix per unit radian and is related to the height of one helicoid loop H by the Eq.3:

$$c = \frac{H}{2\pi} \tag{3}$$

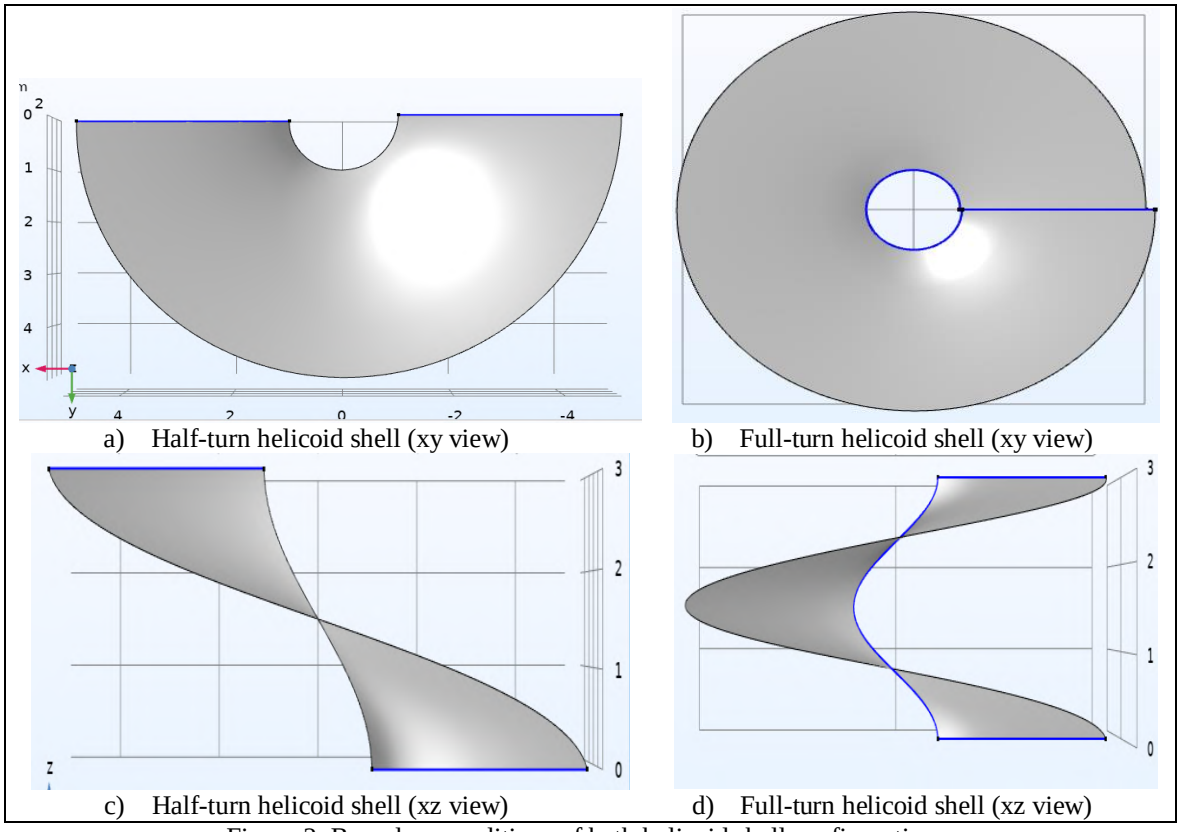
When the angular parameter of the helicoid is limited to a half turn (0≤v≤π) as in the Fig.2.a, but the structure is required to reach the full height H, the c parameter must be adjusted to be $c = \frac{H}{\pi}$. The corresponding parametric formulation ensures geometric continuity where the total elevation is completed within half a rotation.



a) Half-turn helicoid shell b) Full-turn helicoid shell

Figure1: Meshing of helicoid shell.
Source: Authors, (2026).

The shell structure in this example is made of concrete with a material density of 2300 kg/m^3. A vertical distributed load of 10,000 N/m² is applied to the shell surface. The helicoid shell a uniform thickness of 0.16 m.The finite element discretization was performed using COMSOL Multiphysics with an automatic meshing set to extra fine element size for both configurations as shown in the (Fig.1).

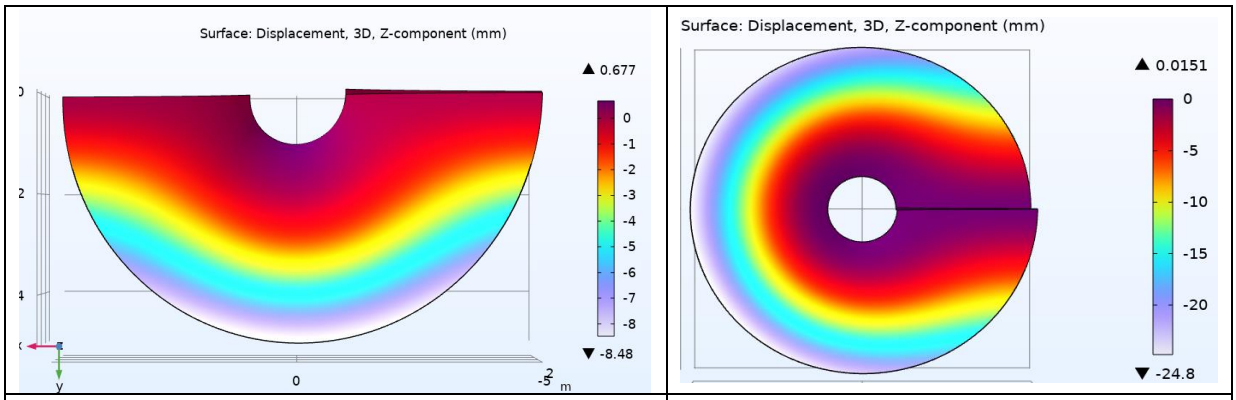


a) Half-turn helicoid shell (xy view) b) Full-turn helicoid shell (xy view)

c) Half-turn helicoid shell (xz view) d) Full-turn helicoid shell (xz view)

Figure 2: Boundery conditions of both helicoid shell configurations.
Source: Authors, (2026).

The Fig. 2 illustrates the boundary conditions applied to the two helicoid shell configurations considered in this study.



a) Displacement z component for half turn helicoid r_1=1m, r_2=5m, $\alpha = 90°$,H = 3m

b) Displacement z component for full turn helicoid r_1=1m,r_2=5m,$\alpha = 90°$,H = 3m

Figure 3: Displacement z component of both helicoid shell configurations.
Source: Authors, (2026).

The comparison between the full turn helicoid and the half turn helicoid (Fig. 3) highlights the significant influence of geometry and boundary conditions on structural response. In Fig. 2.b, the helicoid is constrained at both the inner edge and the extremity, providing a higher degree of restraint. In contrast, the half-turn helicoid in Fig. 2.a is fixed only at the extremity, resulting in a less constrained system. Despite these differences, the maximum displacement along the global z-axis is 24.8 mm for the full-turn helicoid (Fig.3.b) and 8.48 mm for the half-turn helicoid (Fig.3.a). The lower displacement observed in the half-turn case can be attributed to its reduced geometric extent and load path length, which limits the deformation even though fewer boundary constraints are applied.

Table 1: Geometric parameters values for helicoid shell structure

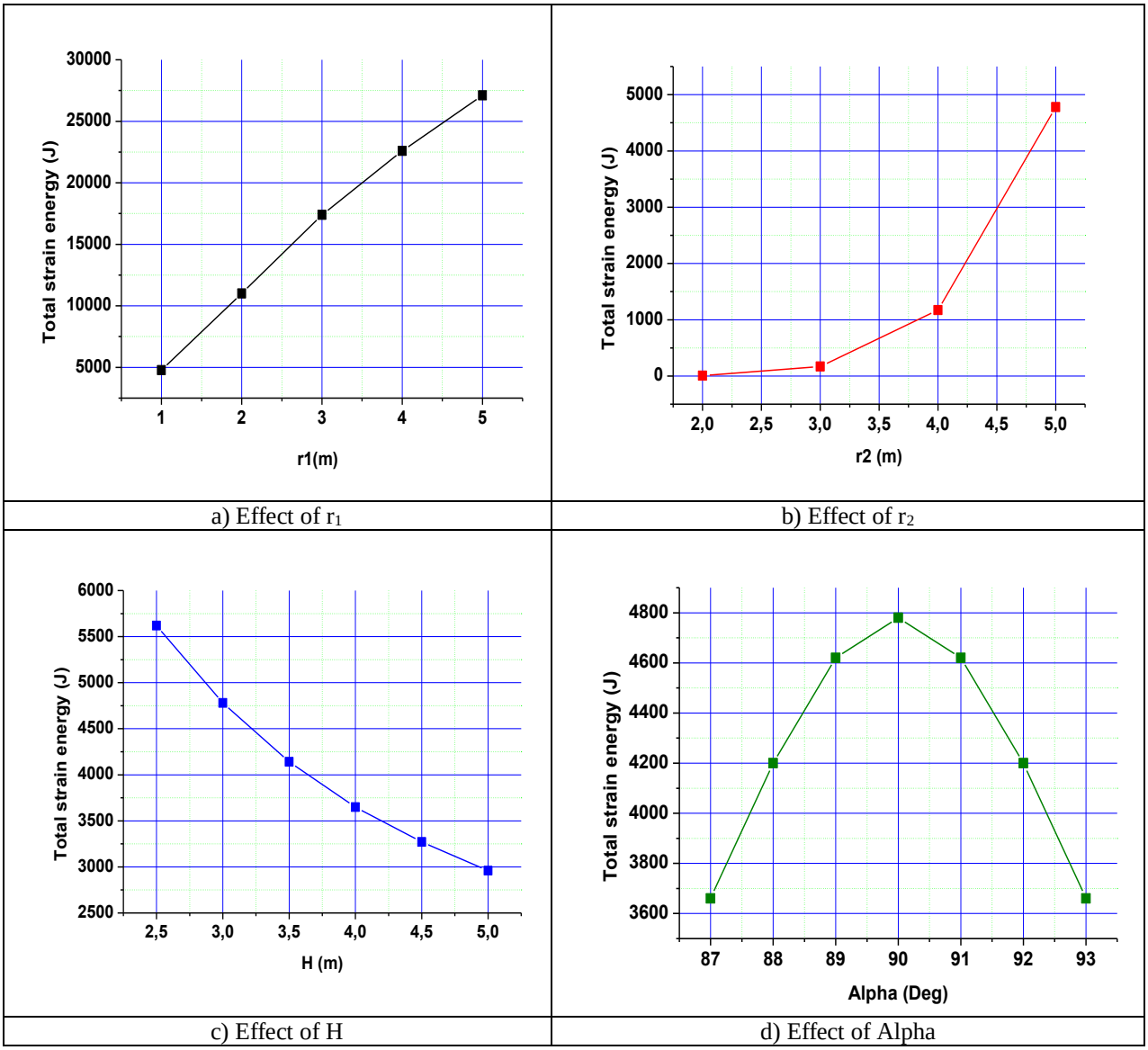
Parameters	Description of the variable parameter	Description of other parameters
Inner radius	1, 2, 3,4,5 m	r_2=r_1+4 m, H = 3 m, $\alpha = 90°$
Outer radius	2, 3,4,5 m	r_1=1 m, H = 3 m, $\alpha = 90°$
One loop height	2.5, 3, 3.5,4,4.5,5 m	r_1=1 m, r_2=5 m, $\alpha = 90°$
α	87,88,89,90,91,92,93 (Deg)	r_1=1 m ,r_2=5 m ,H = 3 m

Source: Authors, (2026).

The parameters of the helicoid shell are defined by the values in the Table 1.

III. PARAMETRIC STUDY RESULTS

In this section, the results of the parametric study performed on both the full-turn and half-turn helicoid shell structures. The analysis highlights the influence of key geometric parameters on the structural response, focusing on strain energy and maximum deflection as performance indicators. A comparative evaluation of the two configurations is provided to clarify their distinct mechanical behaviors and to identify the effect of each parameters in stiffness and overall structural efficiency.

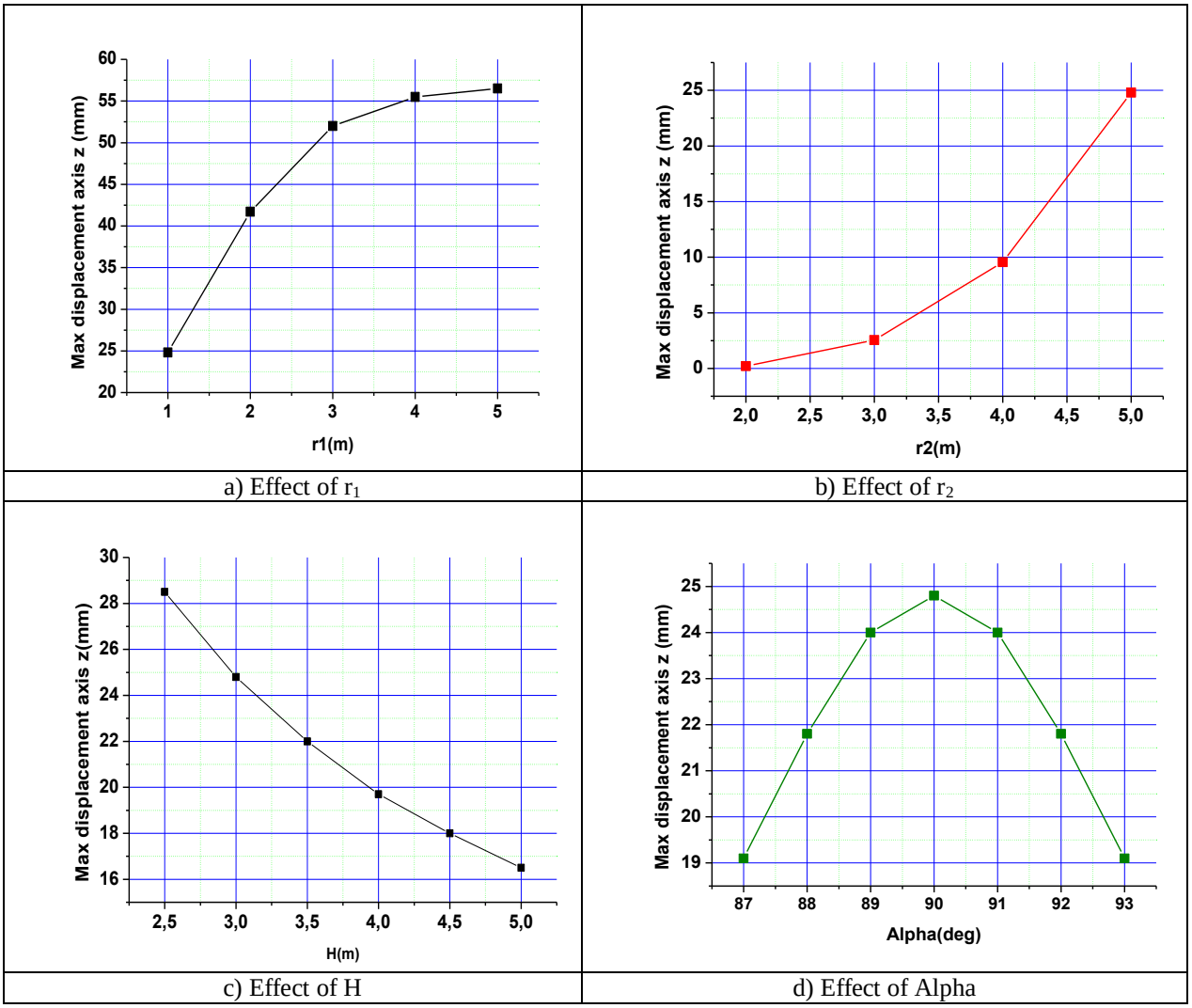


a) Effect of r_1 b) Effect of r_2

c) Effect of H d) Effect of Alpha

Figure 4: Effect of geometric parameters on the strain energy of full turn helicoid shell structure (case1).
Source: Authors, (2026).

The results in the Fig.4 demonstrate how changes in the key geometric parameters of the full-turn helicoid shell affect its total strain energy. A clear increase in strain energy is observed as the inner radius (r_1) increases. This behavior suggests that a larger inner radius reduces the effective load-bearing capacity of the shell, resulting in higher deformation energy under applied loads. Similarly, the outer radius (r_2) has a significant impact on strain energy, especially beyond a certain point (r_2=3). While moderate increases in r_2 result in limited changes, a significant increase in strain energy is observed at larger values, suggesting a loss of structural efficiency due to an increased shell span and greater bending influence. In contrast, increasing the one-loop height (H) results in a noticeable reduction in strain energy. This reflects the beneficial role of the geometric stiffness introduced by the greater vertical height. As for the obliqueness angle (α), the strain energy reaches a maximum at $\alpha = 90°$, decreasing for slightly lower or higher angles. This indicates that small deviations from the orthogonal configuration can improve force redistribution and reduce strain energy.



a) Effect of r_1 | b) Effect of r_2

c) Effect of H | d) Effect of Alpha

Figure 5: Effect of geometric parameters on the displacement axis z of full turn helicoid shell structure (case1).
Source: Authors, (2026).

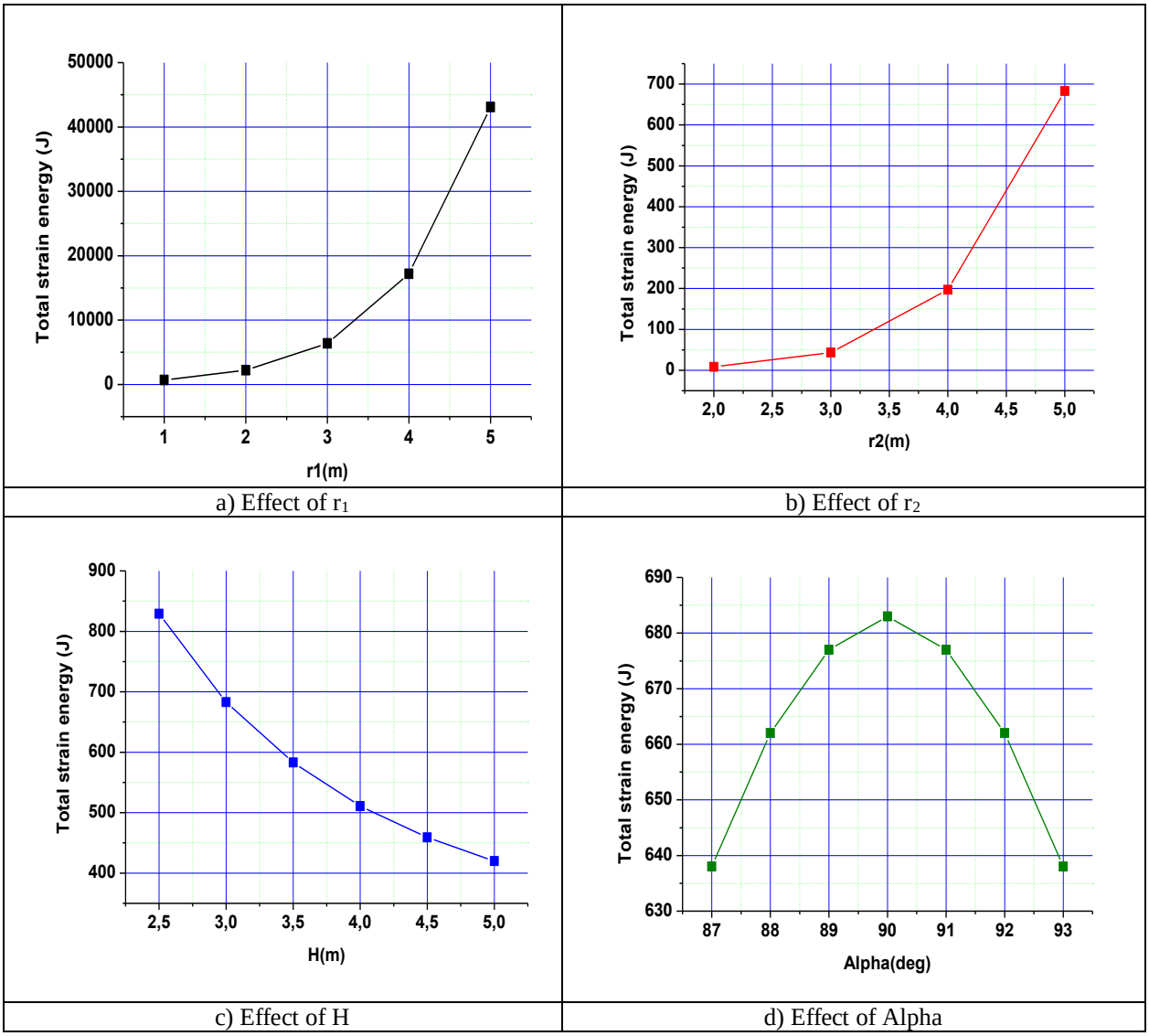
The results in the Fig.5 show that increasing the inner (r_1) and outer (r_2) radius leads to higher maximum displacements, indicating a reduction in global stiffness. In contrast, increasing the one-loop height (H) significantly reduces displacement, demonstrating the positive impact of geometric rise on maximum displacement. The obliqueness angle (α) has a maximum displacement occurs when α = 90°, but slight deviations from this angle minimize displacement values.

Table 2: The maximum and minimum values of strain energy for case 1.

Parameters	Max values of strain energy	Min values of strain energy	Difference (%)
r_1 (m)	27100	4780	82.4%
α (rad)	4780	3660	23.4%
r_2(m)	4780	5.35	99.9%
H(m)	5620	2960	47.3%

Source: Authors, (2026).

The Table 2 presents the maximum and minimum values of strain energy for case 1. The results indicate that the inner radius r_1 has a pronounced influence on the strain energy. Reducing r_1 value leads to a significant decrease in strain energy corresponding to a reduction of 82.4%. This improvement highlights the sensitivity of the structural stiffness to changes in the inner radius, as a smaller r_1 enhances the efficiency of the shell structure. The change of the outer radius r_2 exhibits the most pronounced influence on strain energy minimization. Reducing r_2 value leads to a substantial decrease corresponding to a reduction of 99.9 %. It is important to note that this effect is strongly dependent on the shell width (r_2–r_1). Excessive radial extension, particularly for larger shell widths, significantly increases total strain energy due to amplified bending effect. In contrast, variation of the obliqueness angle α results in a more moderate improvement of 23.4%, indicating that the small inclination of the helicoid surface can contribute to structural performance, but, its effect is less dominant compared to radial parameters. Finally, the height H exhibits also moderate influence on the strain energy. Increasing H results in 47.3% reduction in the total strain energy.

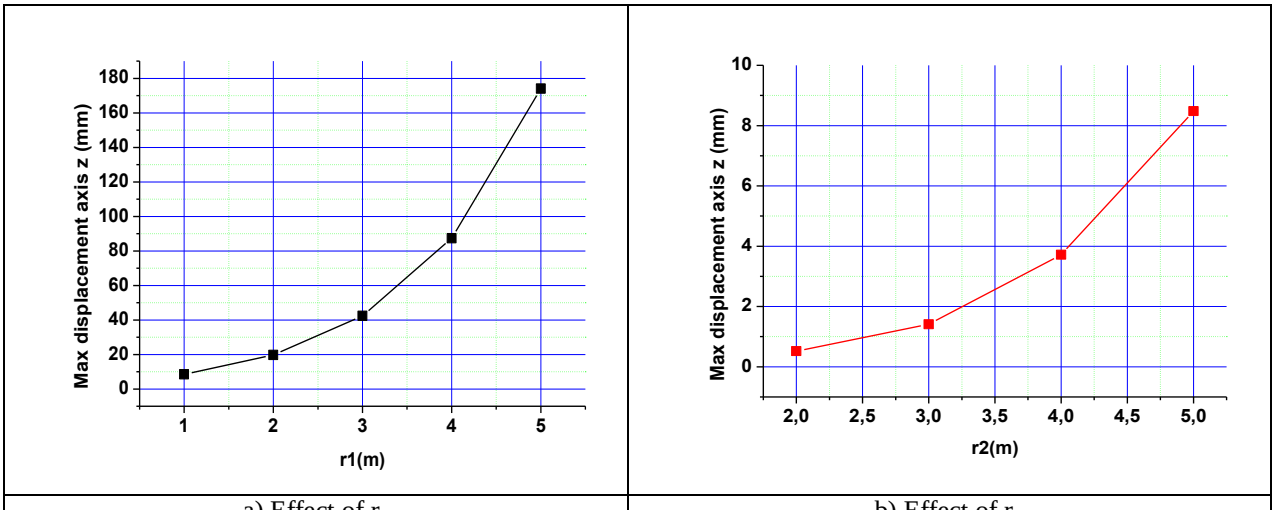


a) Effect of r_1 | b) Effect of r_2

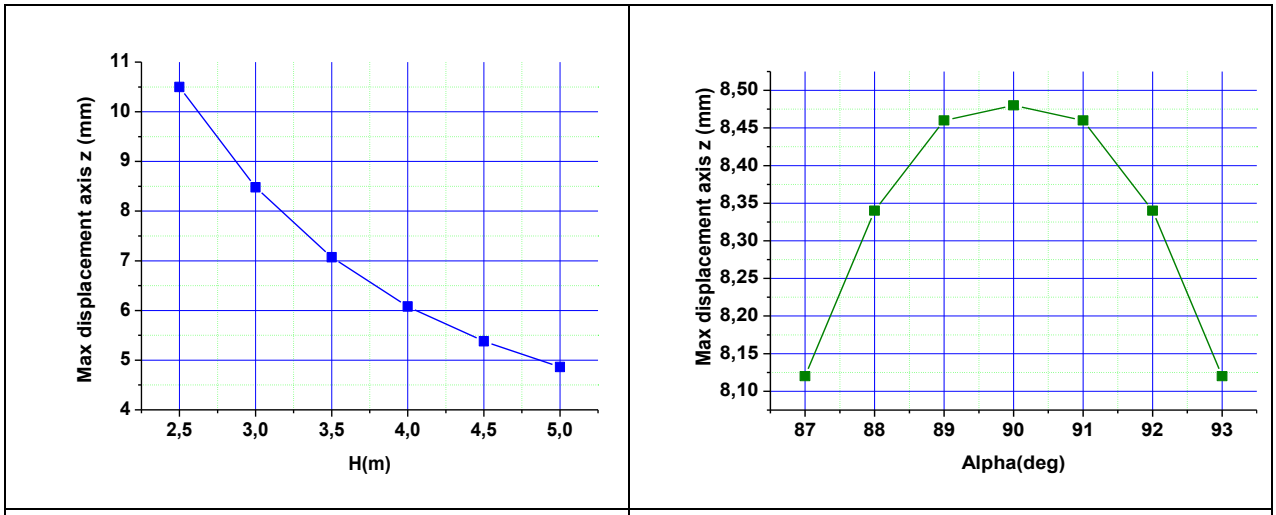
c) Effect of H | d) Effect of Alpha

Figure 6: Effect of geometric parameters on the strain energy of half turn helicoid shell structure (case2).
Source: Authors, (2026).

As in the case 1, the total strain energy increases with the increase of the inner (r_1) and outer (r_2) radius, confirming that enlarging the shell span and central opening reduces structural stiffness. However, the full-turn helicoid shell (Case 1) in the Fig.4 consistently exhibits higher strain energy levels than the half-turn configuration (Case 2) in the Fig.6 except the situation when r_1 is very large. In contrast, increasing the one-loop height (H) reduces strain energy in both cases. The obliqueness angle (α) exhibits a similar behavior in both configurations, with peak strain energy observed when α =90°. However, slight deviations from this angle enhance structural efficiency.



a) Effect of r_1 | b) Effect of r_2



c) Effect of H | d) Effect of Alpha

Figure 7: Effect of geometric parameters on the displacement of half turn helicoid shell structure (case2)
Source: Authors, (2026).

According to Fig. 7, the half-turn helicoid shell exhibits increased displacement with increasing inner and outer radius (r_1 and r_2), while displacement decreases as the one-loop height H increases. In addition, when the obliqueness angle reaches $\alpha = 90°$, half turn helicoid shell also shows maximum displacement.

Table 3: The maximum and minimum values of strain energy for case 2.

Parameters	Max values of strain energy	Min values of strain energy	Difference (%)
r_1 (m)	43100	683	98.4%
α (rad)	683	638	6.6%
r_2(m)	683	8.31	98.8%
H(m)	829	420	49.3%

Source: Authors, (2026).

The results in Tables 2 and 3 show that the radial dimensions r_1 and r_2 are the parameters that most influence the strain energy of the helicoid shells. In both cases, the outer radius (r_2) exhibits the strongest influence, with strain energy variation (99.9% in Case 1 and 98.8% in Case 2). However, the inner radius (r_1) is significantly more sensitive in Case 2 (98.4%) than in Case 1 (82.4%), suggesting that Case 2 is more affected by changes near the shell core, possibly due to the boundary conditions . The height (H) has a similar moderate influence in both cases, with differences of 47.3% and 49.3%, respectively, indicating that increasing the shell rise improves stiffness similarly in both configurations. A key distinction between the two cases is the influence of the obliqueness angle (α). In Case 1, α produces a noticeable variation of 23.4%, whereas in Case 2, its effect is minimal at 6.6%. This suggests that Case 2 is less sensitive to angular variations.

IV. CONCLUSION

Based on the results of strain energy and displacement results for both full and half-helicoid shell structures, the following conclusions can be drawn:

- The parametric study demonstrates that helicoid shell performance is highly sensitive to geometric parameters, with clear differences observed between full and half helicoid configurations. Overall, the half helicoid exhibits better structural efficiency in most cases.
- The inner radius r_1 is identified as one of the most influential parameters in both configurations. Its variation leads to significant reductions in strain energy and displacement, with the half helicoid showing the highest improvements , confirming the strong effect of the inner boundary on global stiffness.
- The outer radius r_2 governs the global structural behavior. Reducing r_2 results in near-complete reductions in strain energy and displacement for both configurations.
- Despite its limited variation, the obliqueness angle α acts as a sensitive parameter. Small angular adjustments lead to measurable reductions in strain energy and displacement even though its influence on half helicoid remains limited.
- The height parameter H has the moderate influence on structural performance. While increasing H improves geometric stiffness, its contribution remains secondary compared to radial parameters.

These conclusions provide practical guidance for the preliminary design of helicoid shell structures, supporting informed parameter selection to achieve efficient and structurally robust designs.

V. AUTHOR'S CONTRIBUTION

Methodology: Yasmine Merah
Writing – Original Draft Yasmine Merah
Writing – Review and Editing: Yasmine Merah, Ahmed Merah

Conceptualization: Yasmine Merah, Ahmed Merah.
Methodology: Yasmine Merah, Ahmed Merah.
Investigation: Yasmine Merah, Ahmed Merah.
Discussion of results: Yasmine Merah, Ahmed Merah.
Writing – Original Draft: Yasmine Merah, Ahmed Merah..
Writing – Review and Editing: Yasmine Merah, Ahmed Merah.
Resources: Yasmine Merah, Ahmed Merah.
Supervision: Yasmine Merah, Ahmed Merah.
Approval of the final text: Yasmine Merah, Ahmed Merah.

VI. ACKNOWLEDGMENTS

The authors would like to express their gratitude to the General Directorate of Scientific Research and Technological Development (DGRSDT) of the Government of Algeria.

VII. REFERENCES

[1] A. A. Abd, M. Q. Kareem, et S. Z. Naji, « Performance analysis of shell and tube heat exchanger: Parametric study », Case studies in thermal engineering, vol. 12, p. 563-568, 2018.

[2] N. Aijaz, P. A. Imtiyaz, F. A. Malik, et V. H. Sheikh, « Parametric study of spherical domes for efficient housing construction using finite element method », Innov. Infrastruct. Solut., vol. 9, no 6, p. 210, juin 2024, doi: 10.1007/s41062-024-01526-1.

[3] A. A. Yaseen, M. A. Khalaf, et F. H. Majeed, « Parametric Analysis of the Static Behavior of Long Cylindrical Concrete Thin Shells under Self-Weight Loading. », Mathematical Modelling of Engineering Problems, vol. 10, no 3, 2023, Consulté le: 4 février 2026. [En ligne]. Disponible sur: https://search.ebscohost.com/login.aspx?direct=true&profile=ehost&scope=site&authtype=crawler&jrnl=23690739&AN=165626692&h=WtzDSPQgobWQYm3cXOtISuiYhZQt4KREkotcg47i7IEgbJLtY2cJOVtdAzjuwhzhXQ0FQWvHLze9SXEQve9GFw%3D%3D&crl=c

[4] T. Michiels et S. Adriaenssens, « Identification of key design parameters for earthquake resistance of reinforced concrete shell structures », Engineering Structures, vol. 153, p. 411-420, 2017.

[5] N. Emami, H. Giles, et P. von Buelow, « Structural, daylighting, and energy performance of perforated concrete shell structures », Automation in Construction, vol. 117, p. 103249, 2020.

[6] T. M. Prateek et V. Garg, « Parametric studies on the structural response of hyperbolic paraboloidal shell footing with variation in geometrical configurations », Multiscale and Multidiscip. Model. Exp. and Des., vol. 7, no 6, p. 5829-5841, nov. 2024, doi: 10.1007/s41939-024-00546-9.

[7] M. K. Sheeja, T. Lamya, et J. Joseph, « Parametric Study on Performance of Conical Shell Foundation Using FEM Modeling », in Proceedings of SECON'23, vol. 381, M. Nehdi, M. K. Hung, K. Venkataramana, J. Antony, P. E. Kavitha, et Beena B R, Éd., in Lecture Notes in Civil Engineering, vol. 381. , Cham: Springer Nature Switzerland, 2024, p. 197-205. doi: 10.1007/978-3-031-39663-2_15.

[8] S. S. Nachiar, S. Anandh, K. Swathi, et G. Pennarasi, « Optimization of thin spherical shell structure using FEM », Materials Today: Proceedings, vol. 68, p. 17-25, 2022.

[9] A. Joseph et P. E. Kavitha, « Structural Optimisation of Hyperbolic Paraboloid Shell Foundation », in Proceedings of SECON'21, vol. 171, G. C. Marano, S. Ray Chaudhuri, G. Unni Kartha, P. E. Kavitha, R. Prasad, et R. J. Achison, Éd., in Lecture Notes in Civil Engineering, vol. 171. , Cham: Springer International Publishing, 2022, p. 395-403. doi: 10.1007/978-3-030-80312-4_35.

[10] E. Ermakova, T. Elberdov, et M. Rynkovskaya, « Shape Optimization of a shell in comsol multiphysics », Computation, vol. 10, no 4, p. 54, 2022.

[11] Y. Merah, D. Hamadi, et K. Mouattah, « Topology optimization of an elliptical parabolic shell structure: effect of penalty factor and load type », Asian J Civ Eng, vol. 25, no 7, p. 5009-5016, nov. 2024, doi: 10.1007/s42107-024-01095-9.

[12] M. B. R. Rodríguez, J. L. M. Rodríguez, O. C. Fonticiella, et E. M. F. Donéstevez, « Tube and Shell heat exchanger optimization taking into account Mechanical restrictions », ITEGAM-JETIA, vol. 1, no 3, 2015, Consulté le: 12 mars 2026. [En ligne]. Disponible sur: http://itegam-jetia.org/journal/index.php/jetia/article/download/223/122

[13] V. J. Paul, « A review of geometry investigations of helicoids », in IOP Conference Series: Materials Science and Engineering, IOP Publishing, 2018, p. 012029. Consulté le: 20 décembre 2025. [En ligne]. Disponible sur: https://iopscience.iop.org/article/10.1088/1757-899X/371/1/012029/meta

[14] M. Rynkovskaya et V. Ivanov, « Analytical Method to Analyze Right Helicoid Stress-Strain », in Engineering Design Applications, vol. 92, A. Öchsner et H. Altenbach, Éd., in Advanced Structured Materials, vol. 92. , Cham: Springer International Publishing, 2019, p. 157-171. doi: 10.1007/978-3-319-79005-3_11.

[15] T. Evgeniya et R. Marina, « Analytical approach to stress-strain analysis of right and oblique helicoid structures », Magazine of Civil Engineering, no 6 (106), p. 10609, 2021.

[16] S. N. Krivoshapko, « Geometry and strength of general helicoidal shells », 1999, Consulté le: 17 janvier 2026. [En ligne]. Disponible sur: https://asmedigitalcollection.asme.org/appliedmechanicsreviews/article-abstract/52/5/161/401520

Journal of Engineering and Technology for Industrial Applications

ITEGAM-JETIA

Manaus, v.12 n.60, p.1378-1386, July/August, 2026.
DOI: https://doi.org/10.5935/jetia.v12i60.4112

ISSN ONLINE: 2447-0228

RESEARCH ARTICLE OPEN ACCESS

LONG-TERM THERMO-KINETIC STABILITY AND PREDICTIVE MODELING OF A NOVEL BIO-BASED PHASE CHANGE MATERIAL: *STIPA ICHU* LIGNOCELLULOSIC FIBERS IMPREGNATED WITH BOVINE TALLOW

Robinson García*[1], Luis Caicedo[2], Karen Betancout[3], Gustavo Cabezas[4], Jimena Díaz[5], Oscar Calle[6]

[1, 2, 3,4,5,6]Universidad Internacional de Investigación México, Postgraduate Program, 77500, Cancún-México

[1]https://orcid.org/0009-0005-0929-3844, [2]https://orcid.org/0000-0003-1904-7303, [3]https://orcid.org/0000-0002-1886-032X
[4]https://orcid.org/0000-0002-5914-5496, [5]https://orcid.org/0009-0002-7590-4058, [6]https://orcid.org/0000-0002-1605-9555

Email: *robinson.garcia@uiimex.edu.mx

ARTICLE INFO

Article History
Received: March 16, 2026
Reviewed: April 17, 2026
Accepted: July 17, 2026
Published: August 31, 2026

Keywords:
Organic Phase Change Materials (PCMs);
Lignocellulosic Encapsulation,
Stipa ichu,
Thermal Degradation Kinetics,
Accelerated Thermal Cycling,
Machine Learning Lifespan Prediction (SVR).

ABSTRACT

The transition toward zero-emission building infrastructures requires the integration of high-performance phase change materials (PCMs) that demonstrate exceptional long-term cyclical stability. This research presents the synthesis and rigorous thermo-kinetic evaluation of a novel, shape-stabilized organic biocomposite. Utilizing vacuum-assisted impregnation, refined bovine tallow was successfully encapsulated within the lumen of alkaline-treated *Stipa ichu* fibers, achieving a substantial 60 wt% PCM loading capacity. The chemically modified lignocellulosic network exhibited robust capillary confinement, severely restricting fluid leakage to below 4.5% under extreme thermal stress (65 °C). To meticulously assess operational longevity, the biocomposite was subjected to an accelerated degradation protocol comprising 1,000 continuous melt-freeze cycles. Differential Scanning Calorimetry (DSC) elucidated a remarkable thermal resilience, with the composite retaining 95.4% of its initial latent heat (decreasing marginally from 145.2 J/g to 138.5 J/g) while maintaining a stable phase-transition temperature at 43.2 °C. Furthermore, Fourier-transform infrared spectroscopy (FTIR) analyses corroborated the system's absolute chemical inertness post-aging, evidenced by the complete absence of oxidative degradation markers such as hydroperoxides. To extrapolate these empirical findings into a practical operational timeframe, a Support Vector Regression (SVR) computational model was deployed. The predictive analytics forecast that the biocomposite will sustain a critical latent heat threshold (>130 J/g) for approximately 2,500 continuous cycles. In the context of the severe diurnal temperature variations characteristic of the Andean highlands, this thermodynamic endurance correlates to a functional service life surpassing 7 years. Consequently, this architected animal fat/*Stipa ichu* matrix presents a highly viable, ecologically benign alternative for advanced thermal mass regulation in sustainable architectures.

Copyright ©2026 by authors and Galileo Institute of Technology and Education of the Amazon (ITEGAM). This work is licensed under the Creative Commons Attribution International License (CC BY 4.0).

I. INTRODUCTION

The decarbonization of the building sector has emerged as a critical global priority, given that residential and commercial structures account for approximately 40% of global energy consumption and 33% of greenhouse gas emissions [1]. In high-altitude regions, such as the Andean Paramo, the challenge is exacerbated by extreme diurnal temperature fluctuations (ranging from −5°C to 25°C, which impose heavy heating loads on conventional envelopes [2]. Furthermore, in these equatorial highlands, the roof surfaces are subjected to intense solar radiation, leading to surface temperatures significantly higher than the ambient air [3].

Consequently, the PCM selection criteria must prioritize a melting point capable of managing these peak radiative loads to mitigate overheating risks during maximum irradiance hours [4]. To address this, Latent Heat Thermal Energy Storage (LHTES) systems employing Phase Change Materials (PCMs) offer a promising solution by increasing the thermal inertia of lightweight construction materials, thereby stabilizing indoor temperatures and reducing peak heating demand [5]. Conventionally, the PCM market has been dominated by paraffin waxes (derived from petroleum) and salt hydrates [6]. While effective, paraffins pose flammability risks and lack sustainability, whereas salt hydrates suffer from phase segregation and supercooling during repeated cycling [7]. Consequently, research has shifted towards bio-based PCMs, specifically fatty acids and triglycerides derived from agricultural by-products [8]. Animal fats, such as bovine tallow, present an attractive circular economy opportunity: they are abundant, cost-effective, and possess melting points ($40 - 15$°C) suitable for building applications [9]. However, the direct incorporation of liquid lipids into building matrices is hindered by their tendency to leak during the solid-liquid phase transition, necessitating effective containment strategies [10].

Shape-stabilization via physical impregnation into porous support matrices has proven to be a viable technique to prevent leakage. While synthetic matrices (e.g., expanded graphite, silica) are widely used, they increase the carbon footprint of the composite [11]. A more sustainable approach involves the use of natural lignocellulosic fibers. In this context, *Stipa ichu*, a graminoid species endemic to the Andean highlands, exhibits unique morphological characteristics specifically a hierarchical hollow structure or "lumen" that hypothetically serves as an ideal natural vessel for PCM encapsulation [12]. Despite the potential of bio-composites, a critical gap remains in the scientific literature: reliability. Most studies focus on the thermal properties of "fresh" materials (Cycle 0), neglecting the degradation mechanisms that occur over years of service. Organic PCMs are susceptible to oxidative aging and changes in crystalline polymorphism, which can drastically reduce latent heat capacity over time [8]. Furthermore, there is a lack of robust mathematical models capable of predicting the service life of these bio-materials under realistic operating conditions.

Objective and Novelty

This study addresses these gaps by developing a form-stable bio-composite PCM (**AF-Ichu/60**) utilizing bovine tallow encapsulated within alkaline-treated *Stipa ichu* fibers. Unlike previous works that are limited to characterization, this research provides a comprehensive thermal reliability assessment based on three pillars:

1. **Microstructural Engineering:** Optimization of the vacuum impregnation process based on wetting theory and capillary pressure (Section II).
2. **Long-term Durability:** An accelerated aging protocol of 1,000 thermal cycles, monitoring chemical stability via FTIR and thermal evolution via DSC.
3. **Predictive Modeling:** The implementation of a Machine Learning approach (Support Vector Regression - SVR) to forecast the material's lifespan beyond experimental limits.

The findings of this work contribute to the development of low-carbon, durable thermal regulation systems, offering a scientifically validated solution for sustainable housing in cold climate regions.

II. THEORETICAL REFERENCE

II.1 STRUCTURAL THERMODYNAMICS OF HIGH-ANDEAN LIGNOCELLULOSIC MATRICES

Stipa ichu, an endemic graminoid of the Andean Paramo ecosystem (>3500 m.a.s.l.), functions as a natural thermal insulator due to its hierarchical porous architecture [13]. The elementary fiber consists of a central hollow cavity (lumen) surrounded by a cell wall of cellulose microfibrils embedded in a hemicellulose-lignin matrix [14]. From a heat transfer perspective, the effective thermal conductivity (k_{eff}) of this porous medium is governed by the volume fraction of the solid phase and the entrapped static air [15]. Since the thermal conductivity of air ($k_{air} \approx 0.026 \frac{W}{m.K}$) is significantly lower than that of the cell wall ($k_{cell} \approx 0.35 \frac{W}{m.K}$), the lumen acts as a high-resistance thermal barrier [16]. For a bio-composite application, the fiber serves a dual function: thermal insulator and encapsulation vessel. The retention of the liquid PCM within the lumen is not governed by gravity but by capillary forces. The capillary pressure barrier (P_c) required to prevent leakage is described by the Young-Laplace equation [17] (Eq. 1):

$$P_c = \frac{2\gamma_{LV} cos\theta}{r} \tag{1}$$

Where γ_{LV} is the surface tension of the liquid PCM, θ is the contact angle at the solid-liquid interface, and r is the effective capillary radius. For spontaneous impregnation and retention ($\theta < 90°$), the surface energy of the fiber must be increased. This theoretical constraint necessitates the removal of hydrophobic amorphous constituents (waxes, lignin) via alkaline hydrolysis (mercerization) to expose the hydrophilic hydroxyl groups (-OH) of the cellulose.

II.2 PHYSICOCHEMICAL BEHAVIOR AND POLYMORPHISM OF ANIMAL FAT

Bovine tallow (BT) is a heterogeneous mixture of triglycerides, primarily composed of palmitic (C16:0) and stearic (C18:0) fatty acids. Unlike simple molecular liquids, triglycerides exhibit monotropic polymorphism, crystallizing into three distinct sub-cell structures depending on thermal history: α (hexagonal, metastable), β' (orthorhombic), and β (triclinic, most stable) [18]. For thermal energy storage, the β-polymorph is the critical phase as it possesses the highest density and enthalpy of fusion (ΔH_m). The total thermal energy (Q) stored by the composite over a temperature range ($T_i \rightarrow T_f$) encompassing the phase transition (T_m) is quantified by [19] Eq. (2):

$$Q = \int_{T_i}^{T_m} C_{p,s}(T)dT + \phi \cdot \Delta H_m + \int_{T_m}^{T_f} C_{p,l}(T)dT \tag{2}$$

Where $C_{p,s}$ and $C_{p,l}$ are the specific heat capacities of the solid and liquid states, respectively, and ϕ is the mass fraction of the PCM. The experimental validation must therefore focus on quantifying ΔH_m and monitoring the stability of the β-form, as repeated cycling can induce polymorphic transitions that alter the energy storage density.

II.3 DEGRADATION MECHANISMS AND RELIABILITY THEORY

The long-term service life of organic bio-composites is limited by two thermodynamic instabilities:

1. **Thermo-oxidative Degradation:** Unsaturated fatty acid chains are susceptible to autoxidation via free radical mechanisms at elevated temperatures, leading to the formation of hydroperoxides and subsequent cleavage into volatile compounds [20]. This chemical decay directly impacts the latent heat capacity.
2. **Volumetric Expansion Mismatch:** Phase transition from solid to liquid induces a volumetric expansion ($\approx 10-15\%$) in animal fats. If the matrix porosity is insufficient to accommodate this volume change (ΔV), internal pressure builds up, potentially overcoming P_c (Eq. 1) and causing macroscopic leakage [21].

III. MATERIALS AND METHODS

The temperature contours, visualized in Figure 4, reveal a progressive thermal stratification along the longitudinal axis of the absorber plate. The overall experimental workflow adopted in this study, from raw material processing to long-term reliability assessment and characterization, is schematically illustrated in Figure 1.



(a) (b) (c) (d)

Figure 1: Schematic overview of the experimental methodology. (a) Pre-treatment of raw materials: thermal purification of animal fat and alkaline modification of Stipa ichu fibers. (b) Bio-composite synthesis via vacuum impregnation to ensure capillary infiltration. (c) Accelerated thermal aging protocol illustrating the temperature cycling profile. (d) Summary of physicochemical characterization techniques employed.
Source: Authors, (2026).

III.1 RAW MATERIALS AND PRE-PROCESSING

The Phase Change Material (PCM) selected was refined bovine tallow (BT), sourced from the Andean region of Ecuador ($0°13'S, 78°31'W$). As shown in Figure 1(a), the raw adipose tissue underwent thermal extraction at 90 ± 1°C for 120 min, followed by filtration (20 μm mesh) and centrifugation (4000 rpm, 15 min) to isolate the lipid fraction. The supporting matrix, *Stipa ichu* fibers, was treated to modify its surface energy as required by the wetting theory (Section II.A).

Fibers were immersed in an analytical grade NaOH solution (98% purity, Sigma-Aldrich) at 5 wt% concentration for 4 hours (25℃, fiber-to-liquor ratio 1:20). This alkaline hydrolysis removes amorphous lignin and hemicellulose, exposing the hydrophilic hydroxyl groups to ensure a contact angle $\theta < 90°$ for spontaneous impregnation. The fibers were subsequently washed and dried to constant mass. The supporting matrix, *Stipa ichu* fibers, was harvested from the paramo ecosystem (3,600 m.a.s.l.). Prior to synthesis, the physicochemical properties of the raw materials were characterized to establish a baseline. These properties are summarized in Table 1.

Table 1: Physicochemical properties of raw Bovine Tallow and *Stipa ichu* fibers.

Material	Property	Value	Unit	Method/Ref
Bovine Tallow	Melting Range (Tm)	42.0 – 45.0	^{0}C	DSC (ASTM E1269)
	Latent Heat (ΔHm)	145.2 ± 2.5	J/g	DSC (ASTM E1269)
	Specific Heat (Cp, solid)	1.85	J/g · K	Literature
	Density (ρ, solid)	910	kg/m3	Pycnometer
Stipa ichu	Cellulose Content	42.5 ± 1.2	%	TAPPI T203
	Lignin Content	22.4 ± 0.8	%	TAPPI T222
	Lumen Diameter	15 – 20	µm	SEM Analysis
	Moisture Content	8.5	%	Gravimetric

Source: Authors, (2026).

III.2 BIO-COMPOSITE PREPARATION VIA VACUUM IMPREGNATION

The composite (AF-Ichu/60) was synthesized with a target PCM mass fraction (Ø) of 60%. To overcome the capillary pressure barrier (P_c) defined in Eq. (1), the liquid BT and fibers were subjected to vacuum impregnation at -0.08MPa for 45 minutes, depicted in Figure 1(b). This negative pressure is critical to evacuate air from the lumen, allowing the liquid fat to penetrate the microstructure upon repressurization. The form-stability was quantified using the Leakage Percentage Test (L_R). Cylindrical specimens (20 mm diameter 10 mm height) were placed on quantitative filter paper (Whatman No. 42) and subjected to a thermal stability test ranging from 25℃ to 65℃ for 120 min to identify the leakage onset limit. The leakage rate was calculated using Eq. (3):

$$L_R(\%) = \frac{M_i - M_f}{M_i} \times 100 \tag{3}$$

Where M_i and M_f are the initial and final mass of the composite. A threshold of $L_R < 5\%$ was set as the acceptance criterion for building applications.

III.3 ACELERATED THERMAL CYCLING PROTOCOL

To simulate the long-term reliability described in Section II.C, the samples were subjected to $N = 1000$ melt-freeze cycles in a climatic chamber (Memmert HCP 108), as illustrated in Figure 1(c). The temperature profile $T(t)$ for each cycle ($\tau = 40\,min$) was programmed according to Eq. (4):

$$T(t) = \begin{cases} 15 + \beta & 0 \le t < t_1 \\ 60 & t_1 \le t < t_2 \\ 60 - \beta(t - t_2) & t_2 \le t < t_3 \\ 15 & t_3 \le t < t_4 \end{cases} \tag{4}$$

Where the heating/cooling rate $\beta = 5°C/min$. This protocol equates to approximately 3 years of service life, assuming one major phase transition per diurnal cycle in the high-Andean páramo

III.4 PHYSICOCHEMICAL CHARACTERIZATION AND MODELING

The characterization techniques employed are summarized in Figure 1(d).

Differential Scanning Calorimetry (DSC)

Thermal properties were measured using a TA Instruments Q2000 calibrated with Indium standards, strictly following ASTM E1269. Samples ($5 - 8mg$) were tested under N_2 flow ($50\,mL/min$). The Latent Heat of Fusion (ΔH_m) was derived by integrating the specific heat capacity peak (Eq. 5):

$$\Delta H_m = \int_{T_{onset}}^{Tend} \left(\frac{dH}{dt}\right) \cdot \left(\frac{dt}{dT}\right) dT \tag{5}$$

To monitor the stability of the β-polymorph (Section II.B), the Degree of Crystallinity (X_c) was calculated using Eq. (6):

$$X_c(\%) = \frac{\Delta H_{m,composite}}{\Delta H_{m,pure} \times \emptyset} \times 100 \tag{6}$$

Thermogravimetric Analysis (TGA)

Thermal stability was assessed (TA Instruments TGA 550) from 25℃ to 600℃). The degradation rate (R_d), indicative of oxidative breakdown (Section II), was obtained from the derivative thermogravimetry (DTG) curve.

III.5 SERVICE LIFE PREDICTION VIA SVR

A Support Vector Regression (SVR) model was developed to predict ΔH_m retention. The model minimizes the structural risk using a Radial Basis Function (RBF) Kernel (Eq. 7), suitable for non-linear degradation:

$$K(x_i, x_j) = \exp(-\gamma \|x_i - x_j\|^2) \quad (7)$$

Model accuracy was validated using RMSE and R^2 on a test set (20% of data).

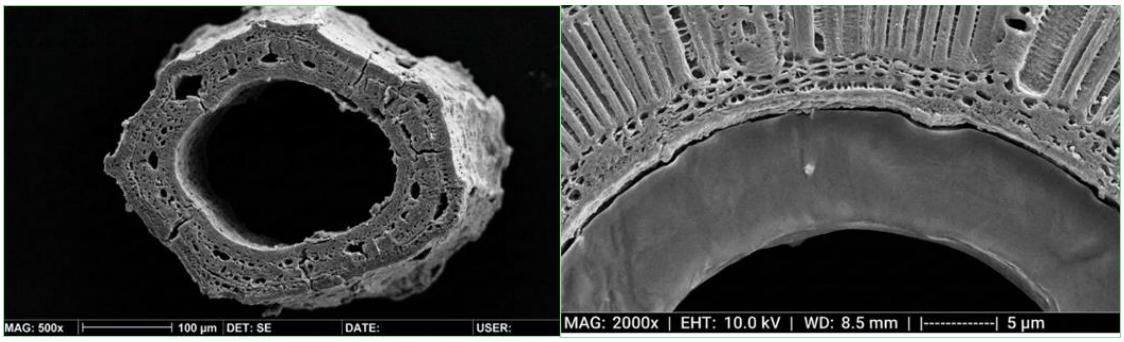
III.6 SERVICE LIFE PREDICTION VIA SVR

Experimental uncertainty (U_c) was estimated following NIST Technical Note 1297. The combined standard uncertainty for enthalpy measurements was $\pm 2.4\%$.

IV. RESULTS AND DISCUSSIONS

IV.1 MICROSTRUCTURAL ANALYSIS AND IMPREGNATION EFFICIENCY

The morphological integration of the PCM into the lignocellulosic matrix is presented in Figure 2. The Scanning Electron Microscopy (SEM) images reveal the unique interaction between the bovine tallow and the *Stipa ichu* fibers.



2(a) 2(b)

Figure 2: SEM analysis of encapsulation. (a) Cross-section of a treated fiber, confirming a hollow lumen diameter of approximately $15 - 20\ \mu m$. (b) Vacuum impregnation process, where the animal fat (smooth surface) is observed completely filling the lumen voids without significant surface agglomeration. This physical interlocking is crucial for preventing leakage.
Source: Authors, (2026).

IV.2 CHEMICAL COMPATIBILITY (FTIR ANALYSIS)

The chemical stability of the interaction between the lipid PCM and the lignocellulosic matrix is critical for long-term performance. Figure 3 illustrates the FTIR spectra of the fresh sample (Cycle 0) versus the aged sample (Cycle 1000).

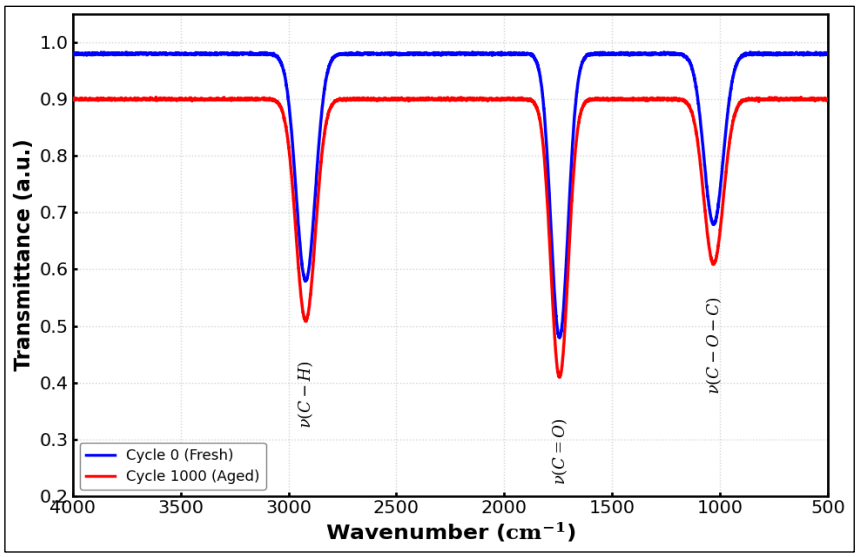


Figure 3: FTIR spectra comparison. Key absorption bands: $2920/2850\ cm^{-1}$ (C-H aliphatic stretch), $1744\ cm^{-1}$ (C=O ester stretch), and $1030\ cm^{-1}$ (C-O-C cellulose skeletal vibration).
Source: Authors, (2026).

The spectrum is dominated by the characteristic peaks of triglycerides (1744 cm^{-1}). Significantly, after 1,000 thermal cycles, no new peaks appeared in the region typical of free fatty acids or hydroperoxides. This confirms that the vacuum encapsulation provided an effective barrier against oxidative degradation.

IV.3 FORM-STABILITY (LEAKAGE TEST)

To quantify the operational limit of this encapsulation, the Leakage Percentage (L_R) was measured as a function of temperature, as presented in Figure 4.

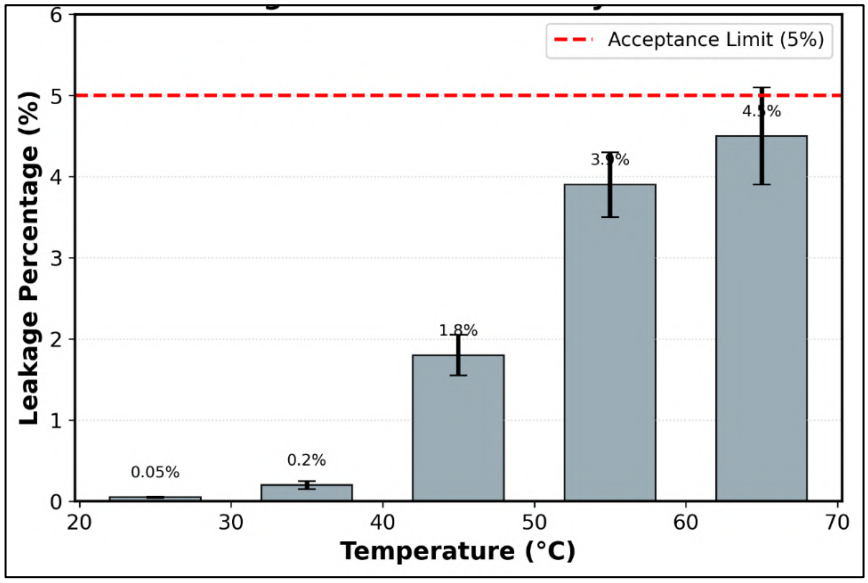


Figure 4: Leakage percentage of the AF-Ichu/60 composite at elevated temperatures. The red dashed line indicates the acceptable threshold (5%) for building applications.
Source: Authors, (2026).

The composite exhibited excellent shape stability, maintaining an L_R of $0.2 \pm 0.05\%$ at 35°C. Even at 65°C (well above the melting point), the mass loss was restricted to $4.5 \pm 0.6\%$, validating the capillary retention theory presented in Section II.

IV.4 THERMAL RELIABILITY (DSC)

The evolution of the energy storage capacity is illustrated in Figure 5.

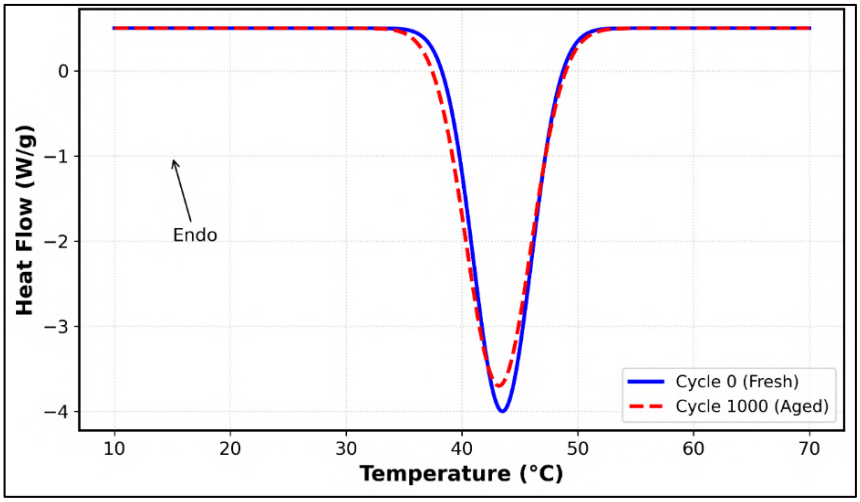


Figure 5: DSC thermograms of the AF-Ichu/60 composite. The endothermic melting peak remains stable around 43°C after 1,000 cycles.
Source: Authors, (2026).

The fresh composite displayed a sharp melting peak at $T_m = 43.5$°C. After 1,000 cycles, the peak shifted negligibly to 43.2°C. Quantitatively, the latent heat of fusion (ΔH_m) decreased from $145.2\,J/g$ to $138.5\,J/g$. This 4.6% reduction is superior to many commercial PCMs. Although this transition temperature ($T_m = 43.5$°C.) is above the standard human comfort range (18-22°C), it is strategically selected for high-altitude equatorial building envelopes (roofs and Western facades). In the Andean region, despite low ambient temperatures, the high solar irradiance (>1000 W/m^2) causes external surface temperatures to frequently exceed 50°C around noon.

Therefore, a PCM with a T_m of 43°C) functions effectively as a thermal buffer, absorbing the peak solar heat load before it penetrates the indoor environment, specifically preventing overheating during the day rather than solely regulating night-time temperatures.

IV.5 THERMAL STABILITY LIMITS (TGA)

The working temperature range was defined via Thermogravimetric Analysis, shown in Figure 6.

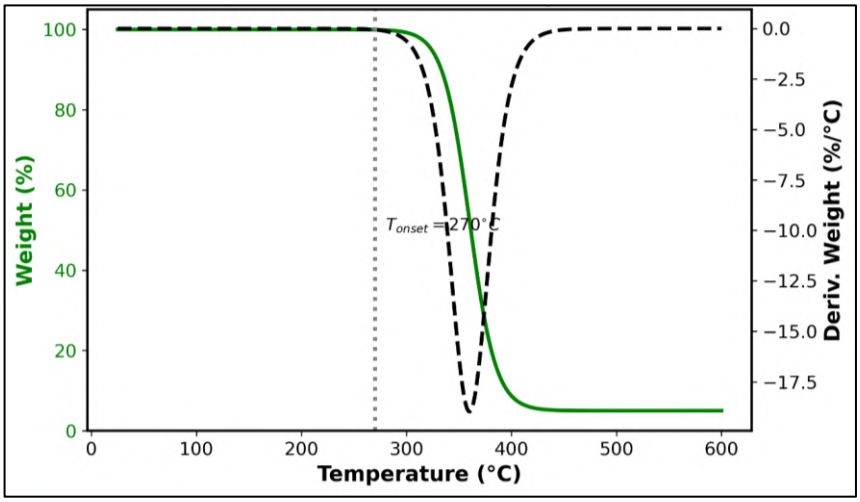


Figure 6: TGA and DTG curves. The onset degradation temperature (T_{onset}) is identified at 270°C.
Source: Authors, (2026).

The onset of major degradation (T_{onset}) occurs at 270°C, providing a thermal safety factor of 4.5 for building applications.

IV.6 SERVICE LIFE PREDICTION (SVR MODELING)

Finally, the degradation trend was modeled using Support Vector Regression (Figure 7).

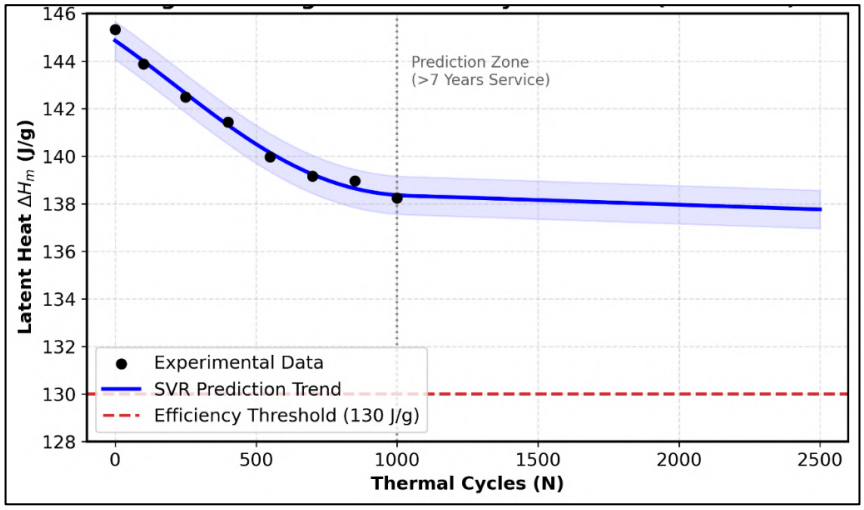


Figure 7: Long-term degradation prediction using SVR ($R^2 = 0.98$). The shaded area represents the 95% confidence interval.
Source: Authors, (2026).

The model predicts that the latent heat capacity will stabilize above $130\ J/g$ for approximately 2,500 cycles, corresponding to a functional service life of >7 years.

V. CONCLUSIONS

This study successfully developed and validated a novel shape-stabilized bio-composite PCM (AF-Ichu/60) for passive thermal regulation in high-altitude Andean regions. Based on the comprehensive experimental characterization and predictive modeling, the following conclusions are drawn:

Effective Microstructural Encapsulation:

The vacuum impregnation technique proved highly efficient in overcoming the capillary pressure barrier defined by the Young-Laplace equation. The alkaline treatment of *Stipa ichu* fibers facilitated the complete infiltration of bovine tallow into the lumen ($15 - 20\ \mu m$), resulting in a form-stable composite with a leakage rate of only 4.5% at 65°C. This validates the suitability of the Andean ichu fiber as a natural, low-cost encapsulation matrix.

High Thermal Reliability:

The accelerated aging protocol demonstrated the robustness of the material. After 1,000 thermal cycles (simulating ≈ 2 years of service), the composite retained 95.4% of its initial latent heat capacity ($\Delta H_m = 138.5\ J/g$) and maintained a stable melting point at 43.2°C. The absence of significant supercooling or phase segregation confirms the stability of the β-polymorph structure within the confined geometry of the fiber.

Chemical and Thermal Stability:

FTIR analysis confirmed that the composite resists thermo-oxidative degradation under cyclic thermal stress. No characteristic peaks of hydroperoxides or free fatty acids were detected after aging, indicating that the cellulose matrix acts as an effective protective barrier. Furthermore, TGA results established a thermal safety factor of 4.5 ($T_{onset} = 270°C$) relative to the maximum operational temperature of building envelopes.

Long-term Service Life Prediction:

The application of the Support Vector Regression (SVR) model provided a critical insight into the material's future performance. The model predicts an asymptotic stabilization of the degradation trend, forecasting that the material will maintain a latent heat capacity above the efficiency threshold of $130\ J/g$ for approximately 2,500 cycles. This corresponds to a functional service life exceeding 7 years without maintenance.

Overall Implication:

The AF-Ichu/60 bio-composite stands as a viable, sustainable alternative to commercial paraffins. It transforms an agricultural by-product (animal fat) and a vernacular material (*Stipa ichu*) into a high-tech thermal storage solution, offering a practical strategy to decarbonize the building sector in cold climates while promoting the circular economy.

VI. AUTHOR'S CONTRIBUTION

Conceptualization: Robinson García, Luis Caicedo, Jimena Díaz.
Methodology: Robinson García, Karen Betancout, Oscar Calle.
Investigation: Robinson García, Karen Betancout, Gustavo Cabezas.
Discussion of results: Robinson García, Luis Caicedo, Jimena Díaz.
Writing – Original Draft: Robinson García.
Writing – Review and Editing: Robinson García, Luis Caicedo, Karen Betancout, Gustavo Cabezas, Jimena Díaz, Oscar Calle.
Resources: Robinson García, Oscar Calle.
Supervision: Robinson García, Luis Caicedo.
Approval of the final text: Robinson García, Luis Caicedo, Karen Betancout, Gustavo Cabezas, Jimena Díaz, Oscar Calle.

VII. ACKNOWLEDGMENTS

The authors express their gratitude to the Universidad Internacional de Investigación México (UIIMEX) for the academic support provided during the doctoral program in Technological Innovation and Development.

VIII. REFERENCES

[1] A. Ahmed, T. Ge, J. Peng, W. Cheng Yan, B. Tuan Tee y S. You, «Assessment of the renewable energy generation towards net-zero energy buildings: A review,» Energy and Buildings, vol. 256, p. 111755, 2022. https://doi.org/10.1016/j.enbuild.2021.111755

[2] Z. Al-Shatnawi, C. Hachem-Vermette, M. Lacasse y B. Ziaeemehr, «Advances in Cold-Climate-Responsive Building Envelope Design: A Comprehensive Review,» Buildings, vol. 14, nº 11, p. 3486, 2024. https://doi.org/10.3390/buildings14113486

[3] A. James Mettrick y Z. Ma, «Integrating phase change materials in buildings for heating and cooling demand reduction – A global study,» Case Studies in Thermal Engineering, vol. 63, p. 105337, 2024. https://doi.org/10.1016/j.csite.2024.105337

[4] L. Liu, N. Hammami, L. Trovalet, D. Bigot, J. Pierre Habas y B. Malet-Damour, «Description of phase change materials (PCMs) used in buildings under various climates: A review,» Journal of Energy Storage, vol. 56, p. 105760, 2022. https://doi.org/10.1016/j.est.2022.105760

[5] U. Masood, M. Haggag, A. Hassan y M. Laghari, «A Review of Phase Change Materials as a Heat Storage Medium for Cooling Applications in the Built Environment,» Buildings, vol. 13, nº 7, p. 1595, 2023. https://doi.org/10.3390/buildings13071595

[6] E. Blackley, T. Lai, A. Odukomaiya, P. C. Tabares-Velasco, L. M. Wheeler y J. Woods, «Surface-Modified Compressed Expanded Graphite for Increased Salt Hydrate Phase Change Material Thermal Conductivity and Stability,» ACS Applied Energy Materials, vol. 6, nº 17, pp. 8775-8786, 2023. https://doi.org/10.1021/acsaem.3c01223

[7] A. Sarcinella, S. Cunha, I. Aguiar, J. Aguiar y M. Frigione, «Sustainable Organic Phase Change Materials for Sustainable Energy Efficiency Solutions,» Polymers, vol. 17, nº 10, 2025. https://doi.org/10.3390/polym14132556

[8] D. Li, B. Zhuang, Y. Chen, B. Li, V. Landry, A. Kaboorani, Z. Wu y X. A. Wang, «Incorporation technology of bio-based phase change materials for building envelope: A review,» Energy and Buildings, vol. 260, p. 111920, 2022. https://doi.org/10.1016/j.enbuild.2022.111920

[9] C. Lopez, A. D. Smith y R. C. Smith, «Evaluation of Animal Fats and Vegetable Oils as Comonomers in Polymer Composite Synthesis: Effects of Plant/Animal Sources and Comonomer Composition on Composite Properties,» Macromolecular Chemistry and Physics, vol. 224, nº 22, 2023. https://doi.org/10.1002/macp.202300233

[10] Farahan Lafta Rashid, Mudhar A. Al-Obaidi, Nabeel S. Dhaidan, Ahmed Kadhim Hussein, Bagh Ali, Mohamed Bechir Ben Hamida y Obai Younis, «Bio-based phase change materials for thermal energy storage and release: A review,» Journal of Energy Storage, vol. 73, p. 109219, 2023. https://doi.org/10.1016/j.est.2023.109219

[11] V. Chinnasamy, J. Heo, S. Jung, H. Lee y H. Cho, «Shape stabilized phase change materials based on different support structures for thermal energy storage applications–A review,» Energy, vol. 262, p. 125463, 2023. https://doi.org/10.1016/j.energy.2022.125463

[12] K. Liu, Z. F. Yuan, H. X. Zhao, C. H. Shi y F. Zhao, «Properties and applications of shape-stabilized phase change energy storage materials based on porous material support—A review,» Materials Today Sustainability, vol. 21, p. 100336, 2023. https://doi.org/10.1016/j.mtsust.2023.100336

[13] M. Ayadi, C. Segovia, A. Baffoun, R. Zouari, V. Fierro, A. Celzard, S. Msahli y N. Brosse, «Influence of Anatomy, Microstructure, and Composition of Natural Fibers on the Performance of Thermal Insulation Panels,» ACS Omega, vol. 8, nº 51, pp. 48673-48688, 2023. https://doi.org/10.1021/acsomega.3c02481

[14] D. Fernando, M. Kowalczyk, P. Guindos, M. Auer y G. Daniel, «Electron tomography unravels new insights into fiber cell wall nanostructure; exploring 3D macromolecular biopolymeric nano-architecture of spruce fiber secondary walls,» Scientific Reports, vol. 13, nº 2350, 2023. https://doi.org/10.1038/s41598-023-29113-x

[15] B. Merillas, P. Vareda, J. M. De León, M. Á. Rodríguez-Pérez y L. Durães, «Thermal Conductivity of Nanoporous Materials: Where Is the Limit?,» Polymers, vol. 14, nº 13, 2022. https://doi.org/10.3390/polym14132556

[16] C. Mayer-Laigle, L. Haurie Ibarra, A. Breysse, M. Palumbo, F. Mabille, A. M. Lacasta Palacio y C. Barron, «Preserving the Cellular Tissue Structure of Maize Pith Though Dry Fractionation Processes: A Key Point to Use as Insulating Agro-Materials,» Materials, vol. 14, nº 18, p. 5350, 2021. https://doi.org/10.3390/ma14185350

[17] Y. Chen, Y. Meng y D. Xie, «Leakage Proof, Flame-Retardant, and Electromagnetic Shield Wood Morphology Genetic Composite Phase Change Materials for Solar Thermal Energy Harvesting,» Nano-Micro Letters, vol. 16, nº 196, 2024. https://doi.org/10.1007/s40820-024-01414-4

[18] D. Cholakova y N. Denkov, «Polymorphic phase transitions in triglycerides and their mixtures studied by SAXS/WAXS techniques: In bulk and in emulsions,» Advances in Colloid and Interface Science, vol. 323, p. 103071, 2024. https://doi.org/10.1016/j.cis.2023.103071

[19] M. Shahriar Mohtasim y B. K. Das, «Biomimetic and bio-derived composite Phase Change Materials for Thermal Energy Storage applications: A thorough analysis and future research directions,» Journal of Energy Storage, vol. 84, p. 110945, 2024. https://doi.org/10.1016/j.est.2024.110945

[20] Z. Zhou, Yu-Lian Li, F. Zhao, R. Xin, Xu-Hui Huang, Yu-Ying Zhang, D. Zhou y L. Qin, «Unraveling the Thermal Oxidation Products and Peroxidation Mechanisms of Different Chemical Structures of Lipids: An Example of Molecules Containing Oleic Acid,» ournal of Agricultural and Food Chemistry, vol. 70, nº 51, pp. 16410-16423, 2022.

[21] V. H. Hegde, M. F. Doherty y T. M. Squires, «A two-phase model that unifies and extends the classical models of membrane transport,» Science, vol. 377, nº 6602, pp. 186-191, 2022. https://doi.org/10.1021/acs.jafc.2c06221

Journal of Engineering and Technology for Industrial Applications

ISSN ONLINE: 2447-0228

ITEGAM-JETIA

Manaus, v.12 n.60, p.1387-1392. July/August, 2026.
DOI: https://doi.org/10.5935/jetia.v12i60.4141

RESEARCH ARTICLE OPEN ACCESS

ROBUSTNESS IMPROVEMENT OF LINEAR SYSTEMS RESPONSE USING A FRACTIONALIZED ORDER PID CONTROLLER

Asradj Zahir[1]*, Bensafia Yassine[2]

[1]Electrical Engineering Department, Faculty of Applied sciences, University of Bouira 10000 ,Algeria, Industrial Technology and Information Laboratory (LTII), Bejaia University 06000, Algeria
[2]LISEA Laboratory, Electrical Engineering Department, Faculty of Applied sciences, University of Bouira 10000 ,Algeria.

[1]http://orcid.org/0000-0002-4062-5086, [2]http://orcid.org/0000-0003-1760-3636

Email: *z.asradj@univ-bouira.dz, y.bensafia@ univ-bouira.dz

ARTICLE INFO

Article History
Received: March 17, 2026
Reviewed: April 18, 2026
Accepted: July 18, 2026
Published: August 31, 2026

Keywords:
Fractional systems,
Fractionalized PID controller,
Approximatios methods,
Disturbance rejection,
Performances Analysis.

ABSTRACT

In recent years, research has increasingly concentrated on fractional order systems and their approximation techniques. These systems have proven valuable for improving plant dynamics in both time and frequency domains. Proportional-Integral-Derivative (PID) controllers are widely being used in industries for process control applications. The merit of using PID controllers lie in its simplicity of design and good performance including low percentage overshoot and small setting time for slow industrial processes. The performance of PID controllers can be further improved by appropriate settings of fractional-I and fractional-D actions. This paper attempts to study the behavior of fractionalized PID controllers over integer order PID controllers in order to improve the robustness of linears systems. Compared to conventional integer-order PID controllers, the fractionalized PID controller exhibits superior performance in terms of stability margins, disturbance attenuation, and adaptability to dynamic changes in the controlled process. These findings confirm that the fractionalization approach represents a promising and practically viable solution for the design of robust control systems, offering a meaningful contribution to the field of fractional-order control engineering. This approach is generalizable to other numerical approximation methods and applicable to broader control systems applications.

Copyright ©2026 by authors and Galileo Institute of Technology and Education of the Amazon (ITEGAM). This work is licensed under the Creative Commons Attribution International License (CC BY 4.0).

I. INTRODUCTION

The generalization of well-known differentiation and integration operations to arbitrary orders is the focus of fractional calculus, often known as fractional-order (FO) differential calculus. Science started working in the field about 1695, thanks to correspondence between two mathematicians, Leibniz and L'Hospital [1]. Over the past few decades, fractional order PID has developed quickly and has many uses in control engineering and research [2–5]. In 1997, Pdlubny was the first to use FOPID [6]. The authors [7] created FOPID and FOPI controllers, which enhanced the control performance and system robustness when compared to the conventional PID tuning techniques. Fractional-order PID (FOPID) controllers have attracted growing interest over the past few years, both in academic research and industrial practice. Their primary advantage over conventional PID controllers lies in the greater design flexibility offered by their five tunable parameters rather than three. However, this additional degree of freedom comes at the cost of significantly increased tuning complexity. To address this challenge, a wide range of design methods for FOPID controllers has been proposed in the literature[8-10]. The authors of [8] used a fractionalized PID controller strategy to reduce effect noise in the conventional feedback control loop PID controller by introducing fractional order filters. The authors of [9] have demonstrated the superiority of fractionalized PID controller with Matsuda approximation over classical ones. Fractional differentiators and integrators are important in fractional filter-based signal processing and fractional feedback management of complex and chaotic systems [10]. A fractional order system in the s-domain is an infinite-dimensional filter with an irrational continuous time transfer function.

The Carlson methodology [11], Matsuda approximation method [12], Charef approximation method [13], Oustaloup approximation method [14], and the method provided by Xue et al. [15] are all well-known ways to produce the rational approximation. The advantages of fractionalized PID based on the HHO algorithm, which uses fractional order filters to approximate integer order transfers in the feedback control loop, are demonstrated in this study. The automation designer can apply the attributes and dynamics of fractional order to the rational system under consideration by inserting fractional order integrators into the classical feedback control loop without modifying the overall equivalent closed loop transfer function. The aim of this paper is to present a novel robust control strategy that incorporates fractional-order filters into a classical feedback control loop, while preserving the overall equivalent closed-loop transfer function. Given a transfer function G(s) belonging to the original control loop, the proposed idea consists in "fractionalizing" it as follows:

$$G(s) = (G(s))^{\alpha}.(G(s))^{1-\alpha} \tag{1}$$

Where α is a real number satisfying the required condition. The goal is to retain the stability properties of the original PID control scheme while enhancing its robustness against external disturbances and noise, by leveraging the distinctive properties of fractional-order systems. Although conceptually straightforward, this approach is expected to provide control design engineers with a valuable additional tool for handling plants under realistic industrial conditions. The paper is organized as follows: Section 2 presents the fundamental definitions of fractional-order systems. Section 3 describes the integer and fractionalized PID controller. Section 4 presents simulation results and discussion. Finally, Section 6 provides concluding remarks and outlines future research

II. FRACTIONAL ORDER SYSTEMS

II.1 DEFINITIONS OF FRACTIONAL CALCULUS

Fractional calculus is an old mathematical topic since 17th century. Fractional calculus is a subdivision of calculus theory which generalizes the derivative or integral of a function to non-integer order. Fractional calculus helps evaluating ($d^n y/dt^n$), n-fold integrals where n is fractional, irrational or complex. For fractional order systems n is considered to be fractional. The number of applications where fractional calculus has been used rapidly grows. These mathematical phenomena allow to describe a real object more accurately than the classical —integer-order methods. The real objects are generally fractional however, for many of them the fractionality is very low. The main reason for using the integer-order models was the absence of solution methods for fractional differential equations. At present there are lots of methods for approximation of fractional derivative and integral and fractional calculus can be easily used in wide areas of applications (e.g.: control theory - new fractional controllers and system models, electrical circuits theory - fractances, capacitor theory, etc.) [1], [2], [8], [10]. The generalized fundamental operator which includes the differentiation and integration is given as:

$$aD_t^q = \begin{cases} \dfrac{d^q}{dt^q} & ,R(q) > 0 \\ 1 & ,R(q) = 0 \\ \displaystyle\int_a^t (d\tau)^{-q} & ,R(q) < 0 \end{cases} \tag{2}$$

Where,

a: Lower limit of integration
t: Upper limit of integration
q: Order of fractional differentiation or integration q with negative value indicates integration while q with positive value indicates differentiation [3]. The theory of fractional-order derivative was developed mainly in the 19th century. There are several definitions of fractional order derivative. Two important and widely applied definitions are Grünwald-Letnikov definition is perhaps the best known due to its most suitability for the realization of discrete control algorithms [1], [15], [16]. The Grünwald-Letnikov definition is expresses as:

$$aD_t^{\alpha} f(t) = \lim_{h \to 0} h^{-\alpha} \sum_{j=0}^{\frac{(t-a)}{h}} (-1)^j \left(\frac{\alpha}{j}\right) f(t - jh) \tag{3}$$

Where, [x] is the integer part of *x* and *h* is the step time. The Riemann-Liouville definition is expresses as:

$$\mathrm{f(t)} = \frac{\mathrm{d^n}}{\mathrm{dt^n}} \int_0^{\mathrm{t}} \frac{\mathrm{f(\tau)}}{\mathrm{(t-\tau)^{\alpha-n+1}}} \mathrm{d\tau} \tag{4}$$

For a wide class of functions which appear in real physical and engineering applications, the Riemann-Liouville and the Grünwald-Letnikov definitions are equivalent [1].

II.2 DEFINITION OF FRACTIONAL ORDER SYSTEMS

Feedback control system is one of the major areas where the concept of fractional calculus is being applied to obtain an efficient system and also longevity and freedom. To the control engineer to compensate any shifts in the transfer function due to parametric spreads, aging etc. a system is efficient if the controller is of the similar order to that of a plant being controlled. In reality the systems are of fractional order and therefore to have a fractional order controller will be efficient [17-20]. The transfer function of a fractional order system is given as:

$$G(s) = \frac{\mathrm{b_m s^{\beta_m}} + \mathrm{b_{m-1} s^{\beta_{m-1}}} + \cdots + \mathrm{b_1 s^{\beta_1}} + \mathrm{b_0}}{\mathrm{a_n s^{\alpha_n}} + \mathrm{a_{n-1} s^{\alpha_{n-1}}} + \cdots + \mathrm{a_1 s^{\alpha_1}} + \mathrm{a_0}} \tag{5}$$

Where a_i and b_j are real numbers such that and s is the Laplace operator.

$$\begin{cases} \mathbf{0} \leq \boldsymbol{\alpha_0} \leq \boldsymbol{\alpha_1} \leq \cdots \leq \boldsymbol{\alpha_n} \\ \mathbf{0} \leq \boldsymbol{\beta_0} \leq \boldsymbol{\beta_1} \leq \cdots \leq \boldsymbol{\beta_m} \end{cases}$$

III.3 CHAREF METHOD

The Charef 's transfer method given in [13], [21] is based on approximation of the function as;

$$G_f(s) = s^{\alpha} \qquad , \alpha \in R^{+} \tag{6}$$

These processes in the frequency domain can be described by an approximation in the Laplace domain such as:

$$G_f(s) = s^{\alpha} \approx \left(1 + \frac{s}{P_T}\right) \approx \frac{\prod_{i=0}^{N}(1 + \frac{s}{P_i})}{\prod_{i=0}^{N-1}(1 + \frac{s}{Z_i})} \tag{6}$$

Where $P_i = (ab)^i . P_0 \quad , \ i = 1,2,3, \ldots, N,$

$Z_i = (ab)^i . a . P_0 \quad , \ i = 2,3, \ldots, N-1$ and $P_0 = P_T . 10^{\frac{e_P}{20\beta}}, \alpha = 10^{\frac{e_P}{10(1-\beta)}} , b = 10^{\frac{e_P}{10\beta}} , \beta = \frac{\log(a)}{\log(a.b)}$

III. FRACTIONALIZED AND INTEGER ORDER PID CONTROLLER

The feedback control loop of an integer order system is shown in figure (1) as,

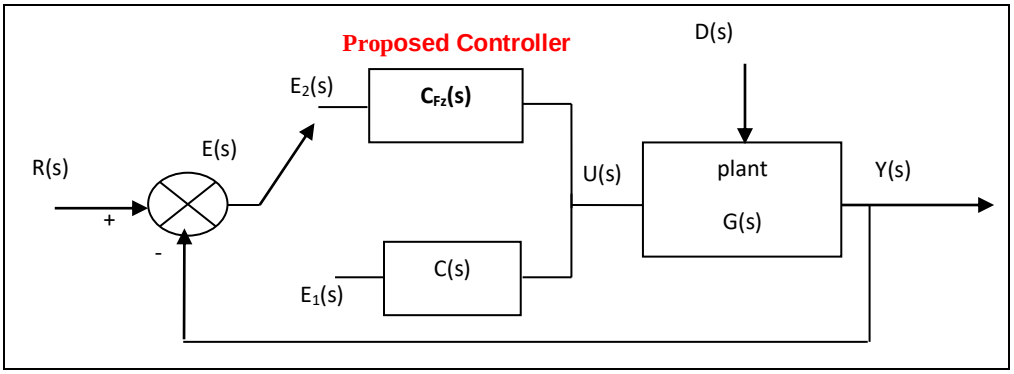


Figure 1: Fractionalized order PID Controller of the linear System.
Source: Authors, (2026).

Where, $U_R(s)$: Input Signal ,
E(s) : Error Signal
C(s) : Controller Transfer Function
$C_{FZ}(s)$: Fractionalized Controller Transfer Function
G(s) : System or plant Transfer Function
Y(s) : output Signal U(s) – Controller Signal

The integer-order PID controller [22] to be designed is in the following form:

$$C(s) = K_p \left(1 + \frac{1}{T_i s} + T_d s\right) \tag{7}$$

The Fractionalized of the integer-order PID controller to be designed is in the following form [16-20]:

$$C_{FZ}(s) = K_p \left(1 + \frac{1}{T_i s} + T_d s\right) = \frac{1}{s}\left(\frac{(k_p T_d s^2 + k_p T_i s + k_p}{T_i}\right) == \frac{1}{s^{\alpha}} \frac{1}{s^{(1-\alpha)}} \left(\frac{(k_p T_d s^2 + k_p T_i s + k_p}{T_i}\right) \tag{8}$$

Where , $0 < \alpha < 1$

III. SIMULATION RESULTS AND DISCUSSION

The model of the system is given by the following transfer function:

$$G(s) = \frac{(s+3)}{(s^3 + 5s^2 + 2s + 1)} \tag{9}$$

A PID controller is design for the integer order model of the system for the following parameters for the PID controller: *Kp = 15, Ki = 0.5, Kd = 1.8* Figure (2) shows the time response characteristics for a step change of the system (9) Table 1 shows its time response specifications.

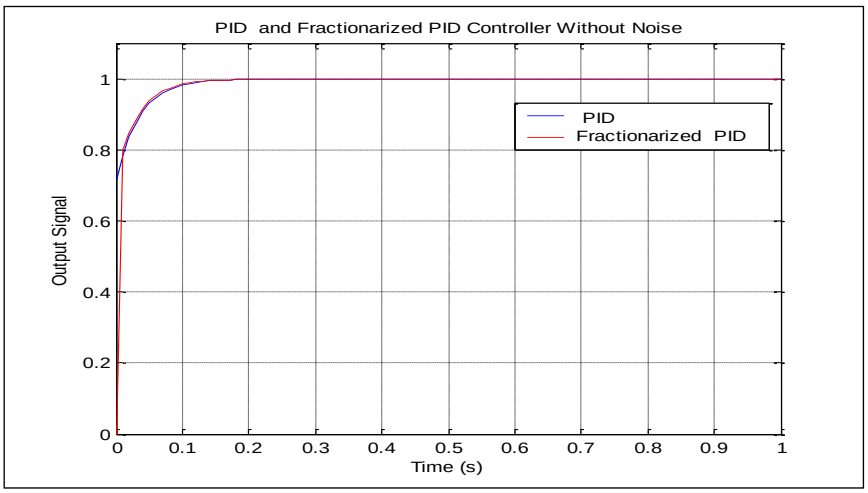


Figure 2: PID and fractionalized order PID controllers are designed for the system control process Without Noise.
Source: Authors, (2026).

Figure (3) shows the time response characteristics for a step change of the system with random output noise of 10 % of the reference signal amplitude (α=0.3):

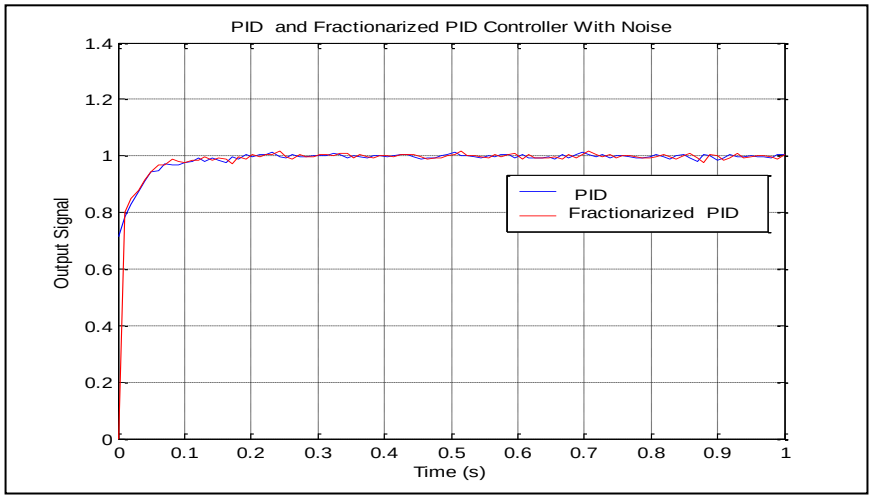


Figure 3: PID and fractionalized order PID control process with random output noise of 10 % of the reference signal amplitude (α=0.3).
Source: Authors, (2026).

Figure (4) shows the time response characteristics for a step change of the system with random output noise of 25 % of the reference signal amplitude (α=0.3)

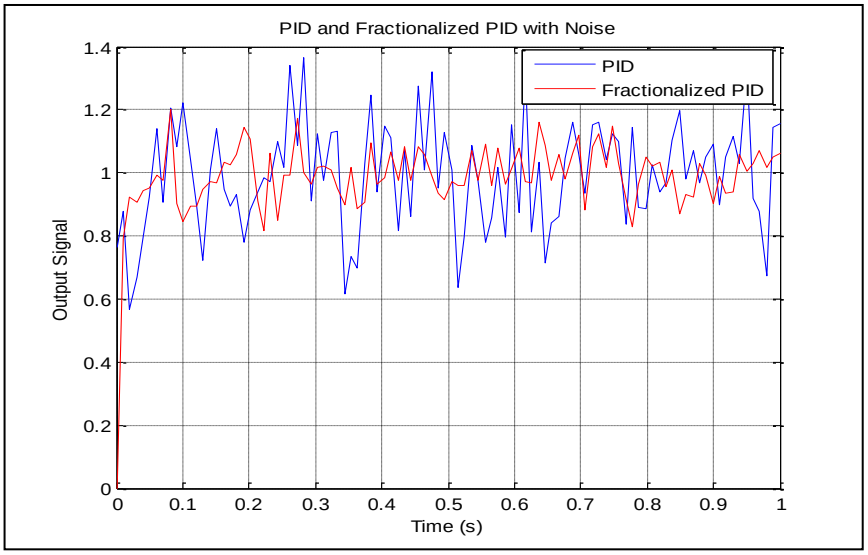


Figure 4: PID and fractionalized order PID control process with random output noise of 25 % of the reference signal amplitude (α=0.3).
Source: Authors, (2026).

The evaluation of the control system performance will be realized by dening a quadratic error criterion J_α given by [23]:

$$J_\alpha = \int_{t_I}^{t_F} (U_R(t) - Y(t))^2 dt \tag{10}$$

The table 1 show the Quadratic error criterion with random output noise of 5-25 % .

Table 1: Quadratic error criterion with random output noise of 5-25%.

α	0.1	0.2	0.3	0.4	0.5	1
with random output noise of 5%	0.07	0.08	0.085	0.065	0.075	0.15
with random output noise of 10%	0.15	0.17	0.16	0.13	0.15	0.29
with random output noise of 15 %	0.23	0.22	0.24	0.25	0.23	0.46
J_α with random output noise of 25%	0.31	0.34	0.32	0.33	0.35	0.75

Source: Authors, (2026).

We remark that the fractionalized PID give a certain dimunition of the noise effect of about 50 % comparatively to the classical PID result when random output noise is 5 to 25 % (Table1).The findings derived from this study clearly indicate that the fractionalization approach yields a significant improvement in the noise rejection performance of the proposed control scheme, rendering it markedly more robust against disturbances and measurement uncertainties that are typically encountered in practical industrial environments. In addition, the introduced methodology demonstrates a considerable strengthening of the overall system robustness, especially in the presence of plant parameter perturbations and modeling inaccuracies that inevitably arise in real-world control applications. When benchmarked against traditional integer-order PID controllers, the fractionalized PID controller consistently achieves superior control performance, particularly in terms of enhanced stability margins, more effective disturbance attenuation, and greater adaptability to dynamic variations within the controlled process. The simulation and analytical results collectively validate the effectiveness and reliability of the fractionalization strategy, confirming its potential as a highly promising and practically feasible framework for the development of advanced robust control systems. As such, this work constitutes a valuable and meaningful contribution to the growing body of knowledge in the field of fractional-order control engineering, opening new perspectives for the design of high-performance controllers in complex and uncertain dynamical systems.

IV. CONCLUSIONS

In this work, a novel approach to robust PID control has been proposed, based on the systematic introduction of fractional-order filters into the classical feedback control loop. A key advantage of this methodology lies in the fact that the integration of fractional-order operators does not alter the overall equivalent closed-loop transfer function, thereby preserving the fundamental stability and structural integrity of the original control system. The core idea behind the proposed fractionalization approach is conceptually straightforward yet highly effective: by embedding fractional-order integrators and differentiators into the conventional control loop, it becomes possible to harness the inherent properties of fractional-order calculus such as memory effects, non-integer dynamics, and enhanced frequency without requiring a complete redesign of the existing control architecture. The results obtained throughout this study demonstrate that the fractionalization approach significantly improves the noise rejection capability of the control scheme, making it considerably more resilient to disturbances and measurement uncertainties that are commonly encountered in real-world industrial applications. Furthermore, the proposed method leads to a substantial enhancement in the robustness of the overall control system, particularly with respect to plant parameter variations and modeling uncertainties. Compared to conventional integer-order PID controllers, the fractionalized PID controller exhibits superior performance in terms of stability margins, disturbance attenuation, and adaptability to dynamic changes in the controlled process. These findings confirm that the fractionalization approach represents a promising and practically viable solution for the design of robust control systems, offering a meaningful contribution to the field of fractional-order control engineering. Future research directions may include the extension of this approach to nonlinear and time-varying systems, as well as the investigation of alternative fractional-order approximation methods to further optimize control performance under varying operating conditions.

V. AUTHOR'S CONTRIBUTION

Conceptualization: Zahir Asradj, Bensafia Yassine.
Methodology: Zahir Asradj, Bensafia Yassine.
Investigation: Zahir Asradj, Bensafia Yassine.
Discussion of results: Zahir Asradj, Bensafia Yassine.
Writing – Original Draft: Bensafia Yassine.
Writing – Review and Editing: Zahir Asradj, Bensafia Yassine.
Resources: Zahir Asradj, Bensafia Yassine.
Supervision: Zahir Asradj, Bensafia Yassine.
Approval of the final text: Zahir Asradj, Bensafia Yassine.

VI. REFERENCES

[1] A. Monje Yang Quan Chen,"Fractional-order Systems and Controls, Fundamentals and Applications", pp 193-194 Springer, (2010).

[2] A. Idir, M. Kidouche, Y. Bensafia, K. Khettab, K., S.A. Tadjer, "Speed control of DC motor using PID and FOPID controllers based on differential evolution and PSO", Int. J. Intell. Eng. Syst., Vol.11, pp. 241–249, 2018.

[3] A. Oustaloup."Fractional order sinusoidal oscillators: optimization and their use in highly linear FM modulation." Circuits and Systems, IEEE Transactions on28.10 (1981): 1007-1009

[4] R.P. Tripathi, A.K. Singh, P. Gangwar, “Innovation-based fractional order adaptive Kalman filter”, Journal of Electrical Engineering, Vol. 71, No. 1 , pp. 60–64, 2020.

[5] A. Oustaloup. A, J. Sabatier, P. Lanusse , " From fractal robustness to CRONE control”, Fractionnal Calculus and applied Analysis, 1-30 , (1999).

[6] I. Podlubny, L. Dorcak, and I. Kostial. "On fractional derivatives, fractional-order dynamic system and PID-controllers." Proceedings of the 36th conference on decision & control. Vol. 5. 1997.

[7] Y. Luo, Y. Q. Chen, C. Y. Wang and Y. G. Pi. "Tuning fractional order proportional integral controllers for fractional order systems." Journal of Process Control 20.7 (2010): 823-831.

[8] Y. Bensafia, K. Khettab, and A. Idir, “An Improved Robust Fractionalized PID Controller for a Class of Fractional-Order Systems with Measurement Noise”, International Journal of Intelligent Engineering and Systems, Vol.11, No.2, pp. 200-207, 2018.

[9] A. Idir, K. Khettab, &Y. Bensafia, “Design of an Optimally Tuned Fractionalized PID Controller for DC Motor Speed Control Via a Henry Gas Solubility Optimization Algorithm”, Int. J. Intell. Eng. Syst., Vol.15, pp. 59–70, 2022.

[10] A. Soukkou and S. Leulmi, “Controlling and Synchronizing of Fractional-Order Chaotic Systems via Simple and Optimal Fractional-Order Feedback Controller,” International Journal of Intelligent Systems and Applications, vol. 8, no. 6, pp. 56-69, 2016

[11] G. Carlson and C. Halijak, “Approximation of fractional capacitors (1/s)1/n by a regular Newton process,” IEEE Trans. Circuit Theory, vol. 11, pp. 210-213, 1964.

[12] K. Matsuda and H. Fujii, “H∞-optimized wave absorbing control: analytical and experimental results,” Journal of Guidance, Control, Dynamics, vol. 16, no. 62, pp. 1146- 1153, 1993.

[13] A. Charef, H. Sun, Y. Tsao and B. Onaral, “Fractal systems as represented by singularity function,” IEEE Transactions on Automatic Control, vol. 37, pp. 1465-1470, 1992.

[14] A. Oustaloup, F. Levron, F. Mathieu and F. M. Nanot, “Frequency-band complex non-integer differentiator: characterization and synthesis,” IEEE Transactions on Circuit and Systems-I: Fundamental Theory and Application, vol. 47, pp. 25-39, 2000.

[15] Meddah, S., Doghmane, M. Z., Tadjer, S. A., Idir, A., Kidouche, M., & Tee, K. F. " Fractional-order PID controller design for strongly coupled high-frequency axial–torsional vibrations in drill string system", International Journal of Dynamics and Control, 13(2), 94,(2025).

[16] S. Ladaci, Y. Bensafia," Fractionalization : A New Tool for Robust Adaptive Control of Noisy Plants". In: 6th Workshop on Fractional Differentiation and Its Applications part of IFAC Joint conference: 5th Symposium on System Structure and Control, 11th Workshop on Time-Delay Systems 374-379 , Grenoble, France, February 4-6 (2013).

[17] Bensafia, Y., Khettab, K., & Idir, A. " A novel fractionalized PID controller using the sub-optimal approximation of FOTF ". Algerian Journal of Signals and Systems, 7(1), 21–26, (2022).

[18] Idir, A., Bensafia, Y., & Canale, L. " Influence of approximation methods on the design of the novel low-order fractionalized PID controller for aircraft system", Journal of the Brazilian Society of Mechanical Sciences and Engineering, 46(2), 98, (2024).

[19] Bensafia .Y, Ladaci .S, Khettab .K, “ Using a Fractionalized Integrator for Control Performance Enhancement ”, International Journal of Innovative Computing, Information and Control, (2015).

[20] Y. Bensafia, T.Boukra, K. Khettab, “Fractionalized PID Control in Multi-model Approach: A New Tool for Detection and Diagnosis Faults of DC Motor”, Przegląd Elektrotechniczny, 99 nr. 6, 45-48,(2023).

[21] Ladaci . S, Loiseau. J.J, Charef .A, “ Adaptive Internal Model Control with fractional order Parameter ”, Int. J. Adaptive Control and Signal Processing, nr 24,(2010), 944-960.

[22] M.Murali, A. Sekhar," The Implementation of Enhanced Microgrid using Mayfly Algorithm based PID Controller", ITEGAM-JETIA, 11(51), 220-226, (2025).

[23] S. M. Shah, R. Samar, M. A. Z. Raja and J. A. Chambers, Fractional normalized filtered-error least mean squares algorithm for application in active noise control systems. Electronics Letters, 50, nr.14, 973-975,(2014).

Journal of Engineering and Technology for Industrial Applications

ISSN ONLINE: 2447-0228

ITEGAM-JETIA

Manaus, v.12 n.60, p.1393-1402. July/August, 2026.
DOI: https://doi.org/10.5935/jetia.v12i60.4151

RESEARCH ARTICLE OPEN ACCESS

QIC-MOEA: A CONTEXT-AWARE QUANTUM-INSPIRED EVOLUTIONARY FRAMEWORK FOR SELF-ADAPTIVE PERVASIVE SYSTEMS

Salah Maache[1], Fouzi Semchedine[2]

[1]Department of Computer Science, Setif 1 University Ferhat Abbas
[2]Optics and Precision Mechanics Institute, Setif 1 University Ferhat Abbas

[1]https://orcid.org/0000-0002-3588-4585, [2]https://orcid.org/0000-0003-4375-1077

E-mail: salah.maache@univ-bba.dz, fouzi.semcheddine@univ-setif.dz

ARTICLE INFO

Article History
Received: March 17, 2026
Reviewed: April 18, 2026
Accepted: July 18, 2026
Published: August 31, 2026

Keywords:
Quantum-Inspired Algorithms,
Pervasive Systems,
Self-Adaptive Systems,
Context-aware Systems,
Edge computing,
Multi-Objective Optimization.

ABSTRACT

Everyday computing is rapidly shifting toward pervasive systems, but real-world edge environments remain incredibly volatile. For these self-adaptive devices to function, they must constantly balance strictly conflicting goals—like saving power versus processing critical data instantly. Traditional methods struggle here: rule-based systems lack flexibility, and reinforcement learning either takes too long to compute or exploits mathematical loopholes (reward hacking). To solve this, we introduce the Quantum-Inspired Contextual Multi-Objective Evolutionary Algorithm (QIC-MOEA), a context-aware framework designed for real-time adaptation. By leveraging a probabilistic Q-bit representation, our approach explores multiple adaptation strategies simultaneously, completely bypassing the heavy computational drag of classical algorithms. We pair this with Context-Weighted Rotation Gates to dynamically scale reactions to environmental shocks, and enforce strict Quality of Service boundaries to eliminate reward hacking. Tested in a simulated healthcare scenario, QIC-MOEA significantly outperformed Q-Learning and Fuzzy Logic baselines. It reduced energy consumption by over **92%** and latency by up to **36%**, while improving context appropriateness by more than **313%**. Crucially, QIC-MOEA executed these complex multi-objective adaptations in just **11.53** milliseconds, proving that quantum-inspired decision-making is highly feasible for resource-constrained edge hardware.

Copyright ©2026 by authors and Galileo Institute of Technology and Education of the Amazon (ITEGAM). This work is licensed under the Creative Commons Attribution International License (CC BY 4.0).

I. INTRODUCTION

The proliferation of pervasive systems—encompassing the Internet of Things (IoT), edge computing, and ubiquitous sensor networks—has embedded computation into the fabric of daily life [1], [2]. These systems operate in highly dynamic environments where network bandwidth, battery availability, and user criticality can change instantaneously. To operate effectively, these architectures rely on self-adaptation, frequently utilizing autonomic computing loops to monitor the environment, analyze changes, and execute system reconfigurations [3], [4], [5]. A core requirement of these autonomic loops is context-awareness—the ability to utilize information such as location, user activity, and environmental state to characterize the immediate situation [6]. However, the decision-making engine responsible for adapting to this context faces a massive computational bottleneck: the Multi-Objective Optimization Problem (MOOP).

When a pervasive healthcare monitor must simultaneously extend battery life, process data locally to reduce latency, and ensure high data reliability, the system is forced to navigate strictly conflicting objectives[2], [7]. Classical approaches, such as Fuzzy Logic controllers, rely on rigid, predefined rule sets that cannot scale to complex, multidimensional state spaces. Reinforcement Learning approaches offer adaptability but require extensive episodic training and struggle with the "cold start" problem in rapidly shifting, non-stationary environments[8]. While classical Multi-Objective Evolutionary Algorithms (MOEAs) like NSGA-II [9] and MOEA/D [10] can find excellent Pareto-optimal solutions, their reliance on heavy evolutionary operations makes them too slow for real-time edge execution. Even with recent improvements in differential evolution for multi-modal optimization, the computational and memory overhead remains a significant barrier for resource-constrained pervasive devices [11].

To address these limitations, Quantum-Inspired Evolutionary Algorithms (QIEAs) have emerged as a powerful alternative. Despite their speed, a critical research gap remains: existing quantum-inspired heuristics for pervasive environments are context-blind and highly susceptible to multi-objective collapse (reward hacking) when faced with real-time, asymmetric environmental shocks. To bridge this gap, this study addresses the following Research Questions (RQs):

- **RQ1 (Efficacy):** How does bounding quantum observation with QoS constraints affect the Pareto-optimal distribution compared to classical heuristics?
- **RQ2 (Adaptability):** Can context-weighted quantum rotation gates maintain system appropriateness without sacrificing energy efficiency during sudden contextual shifts?
- **RQ3 (Feasibility):** Is the computational overhead of maintaining a probabilistic Q-bit population feasible for sub-second execution on edge devices?

In this paper, we propose QIC-MOEA, a framework specifically designed to resolve these vulnerabilities. Our primary contributions are:

- **Context-Weighted Target Selection:** Redefining the quantum rotation mechanism to dynamically prioritize specific Pareto-optimal targets based on real-time environmental volatility.
- **QoS-Bounded Quantum Collapse:** Enforcing strict minimum Quality of Service constraints during the observation phase to prevent multi-objective collapse.
- **Quantum Entropy Tracking:** Utilizing Shannon entropy over the probability amplitudes to empirically demonstrate convergence stability.

The remainder of this paper is organized as follows. Section II reviews the state-of-the-art literature across self-adaptive pervasive systems, multi-objective evolutionary algorithms, quantum-inspired heuristics, and context-aware reinforcement learning. Section III details the problem formulation and the mathematical architecture of the proposed QIC-MOEA framework. Section IV describes the experimental setup, including the baseline algorithms and simulation environment. Section V presents the performance evaluation and statistical analysis. Finally, Section VI concludes the paper and discusses avenues for future work.

II. RELATED WORK

The development of the QIC-MOEA framework sits at the intersection of autonomic computing and advanced evolutionary optimization. To contextualize our contributions and clearly define the existing research gaps, this section reviews the state-of-the-art literature across four foundational domains. First, we examine the evolution and current latency challenges of self-adaptive pervasive systems. Next, we analyze the computational bottlenecks of classical Multi-Objective Evolutionary Algorithms (MOEAs) when deployed in resource-constrained edge environments. To address these limitations, we then explore the recent resurgence of quantum-inspired heuristics as a lightweight, highly diverse alternative to classical optimization. Finally, we review context-aware reinforcement learning approaches, highlighting the exact gap our proposed algorithm aims to fill: combining the multi-objective Pareto-optimization of evolutionary methods with execution speeds suitable for real-time pervasive systems.

II.1 SELF-ADAPTIVE PERVASIVE SYSTEMS

The complexity of pervasive computing environments has driven extensive research into self-adaptive systems (SAS)[5]. The foundational Autonomic Computing paradigm has been widely adapted for the IoT and edge computing [2], [3]. Comprehensive reviews highlight that traditional centralized adaptation loops face significant design challenges and struggle to meet the strict latency and resource constraints of modern smart ecosystems [1], [2]. Furthermore, recent frameworks focusing on complex, distributed architectures—such as self-adaptive federated learning ecosystems—demonstrate a critical pivot toward decentralized, context-aware decision-making, reinforcing the need for lightweight optimization engines at the extreme edge [12].

II.2 MULTI-OBJECTIVE EVOLUTIONARY ALGORITHMS (MOEAS)

Researchers frequently model the adaptation process as a Many-Objective Optimization Problem (MaOP)[7]. Classical MOEAs like NSGA-II [9](Deb et al., 2002) and MOEA/D [10] laid the foundation for multi-objective optimization and have been successfully applied to find Pareto-optimal service configurations. However, contemporary research continues to struggle with their computational overhead. Recent efforts have attempted to hybridize MOEAs with machine learning techniques to accelerate convergence in complex scheduling problems [7], or utilize improved differential evolution strategies to handle highly multi-modal objective spaces [11]. Because these approaches often trade computational speed for memory consumption, the heavy iterative loops required for crossover and mutation render standard MOEAs largely unsuitable for sub-second autonomic adaptations on resource-constrained edge agents.

II.3 QUANTUM-INSPIRED HEURISTICS

To break through these computational bottlenecks, Quantum-Inspired Evolutionary Algorithms (QIEAs)—originally conceptualized to bridge the gap between quantum exploration and classical hardware [13]—have seen a massive resurgence in recent software engineering literature [14]. Recent studies have successfully applied quantum-inspired probability mechanisms to dynamic combinatorial problems in disaster logistics [15], thermonuclear fusion modeling [16], and feature subset selection [17]. As noted in recent comprehensive surveys [18], the core advantage of quantum-inspired representations is their ability to maintain massive population diversity within a highly compact mathematical footprint. However, standard Q-bit rotation mechanisms are inherently “context-blind” and require complex isolation strategies for multi-objective problems [19].

II.4 CONTEXT-AWARE REINFORCEMENT LEARNING

To overcome the limitations of reactive rule-based systems, recent research has increasingly turned to Reinforcement Learning (RL) to enable proactive, context-aware adaptation. Hybrid architectures leverage multi-agent systems and predictive reasoning to anticipate context changes rather than merely reacting to them [8]. While RL successfully handles dynamic environments, integrating it into multi-objective systems remains challenging due to the heavy episodic training overhead required to balance conflicting metrics. Our proposed QIC-MOEA addresses this exact gap by directly building upon recent quantum-inspired momentum, offering the multi-objective Pareto optimization capabilities of evolutionary algorithms at speeds that rival pre-trained RL inference, without the need for extensive episodic retraining. In summary, while existing literature has made significant strides in self-adaptive systems and multi-objective optimization, a critical research gap remains. Classical MOEAs are too computationally heavy for real-time edge deployment, and context-aware reinforcement learning requires excessive episodic training overhead. Furthermore, while quantum-inspired heuristics offer a mathematically lightweight alternative, standard implementations lack the inherent context-awareness and multi-objective isolation strategies required for highly dynamic pervasive environments. The proposed QIC-MOEA framework is designed to address these exact limitations. By hybridizing a quantum-rotation gate with dynamic context-awareness, our approach delivers the Pareto-optimal reliability of classical evolutionary algorithms at execution speeds suitable for the extreme edge, bridging the void left by current adaptation methodologies.

III. SYSTEM MODEL AND PROBLEM FORMULATION

III.1 CONTEXT-AWARE SYSTEM ARCHITECTURE

To enable real-time self-adaptation, the proposed framework relies on a decentralized, multi-tier architecture spanning from pervasive IoT sensors to edge computing nodes. The autonomic adaptation loop operates continuously across these tiers, driven by the foundational MAPE-K (Monitor, Analyze, Plan, Execute, Knowledge) architectural blueprint for autonomic computing [3], within a multi-tier structure for self-managed systems [4]. The loop is executed in four primary phases as, shown in *Figure 1*:

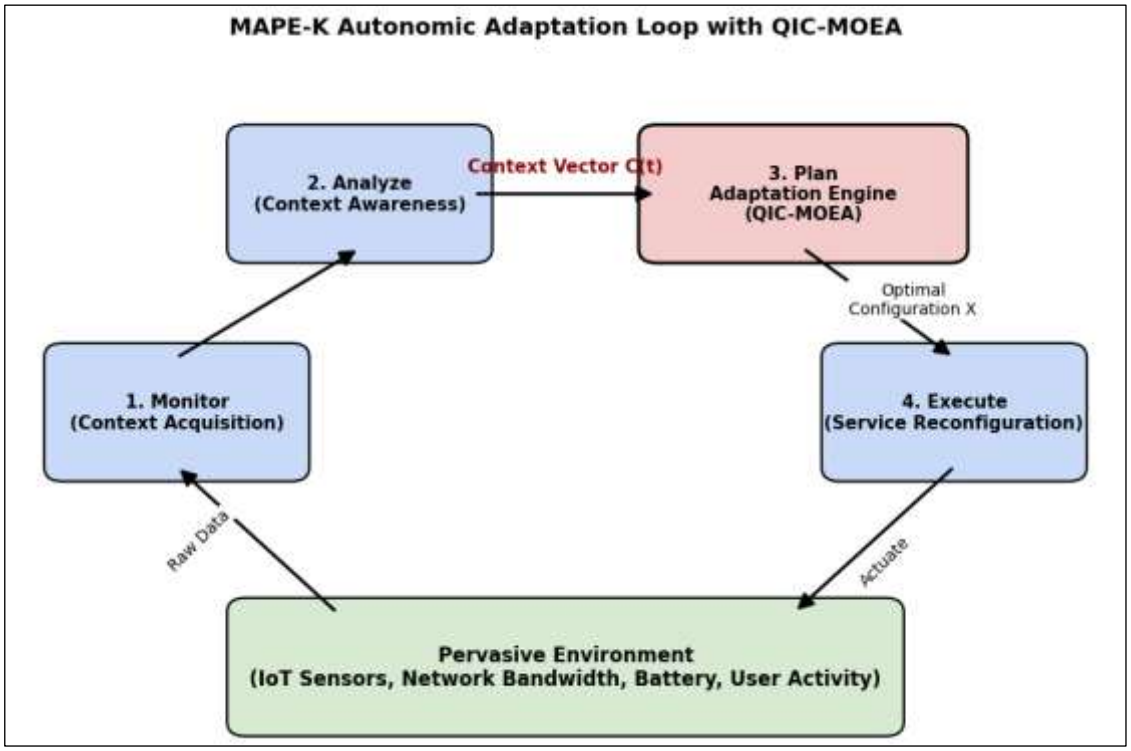


Figure 1: The Context-Aware System Architecture. Pervasive sensors monitor environmental volatility, generating a context vector that drives the QIC-MOEA adaptation engine.
Source: Authors, (2026).

1. **Context Acquisition (Monitor):** Pervasive sensors continuously sample the physical environment to establish context, formally defined as any information used to characterize the situation of an entity[6]. This includes polling battery status and tracking user activity.
2. **Context Awareness (Analyze):** The raw sensor data is aggregated at the edge tier and formalized into a unified context state vector $C(t)$. This vector provides semantic awareness of the current environmental severity.
3. **Adaptation Engine (Plan):** Once a contextual shift is detected ($\| C(t) - C(t-1) \| > 0$), the context vector is passed to the adaptation engine. Rather than mapping this vector to static 'If-Then' rules, our architecture feeds $C(t)$ directly into the QIC-MOEA framework. The context actively scales the quantum rotation gates.
4. **Service Reconfiguration (Execute):** The optimal service configuration generated by QIC-MOEA is executed by the system's actuators, updating live application parameters.

III.2 CONTEXT STATE MODELING

The pervasive environment is modeled as a dynamic context vector $C(t)$, containing discrete and continuous variables representing the state at time t: location, battery level, network bandwidth, time of day, user activity, and medical criticality.

III.3 SERVICE CONFIGURATION SPACE

The adaptive system defines a configuration X containing n continuous decision variables ($x_i \in [0,1]$). These represent operational parameters such as data quality, processing location, synchronization frequency, power mode, and data compression level.

III.4 OBJECTIVE FUNCTIONS

The system optimizes four conflicting objective functions simultaneously:

1. **Minimize Energy (f_1):** Calculated based on processing location, power mode, and data transmission overhead.
2. **Minimize Latency (f_2):** A function of network bandwidth, processing location delay, and data compression times.
3. **Maximize Reliability (f_3):** Modeled via location stability, battery thresholds, and network drop probabilities.
4. **Maximize Context Appropriateness (f_4):** A heuristic score measuring how well the configuration aligns with the immediate physical context.

IV. THE PROPOSED QIC-MOEA FRAMEWORK

IV.1 QUANTUM REPRESENTATION

To address the strict latency and resource constraints of extreme edge computing highlighted by [2], the QIC-MOEA framework is designed around a lightweight quantum-bit (Q-bit) representation rather than traditional floating-point or binary arrays. Unlike classical differential evolution [11], which requires substantial memory overhead to maintain diversity in multi-modal objective spaces, our approach leverages probability amplitudes to inherently sustain massive population diversity. Inspired by recent successes of quantum-inspired hyper-heuristics in solving dynamic combinatorial problems [15], we implement a context-aware quantum rotation gate. This mechanism dynamically shifts the probability amplitudes of the Q-bits toward Pareto-optimal reference solutions, ensuring rapid convergence without the computationally expensive crossover and mutation operators that cripple classical MOEAs in real-time IoT environments. Specifically, QIC-MOEA utilizes a probabilistic representation based on quantum mechanics. Each decision variable is represented by a Q-bit, existing in a linear superposition of states $|0\rangle$ and $|1\rangle$:

$$|\psi\rangle = \alpha|0\rangle + \beta|1\rangle \tag{1}$$

Where $|\alpha|^2 + |\beta|^2 = 1$. A population of size m with configurations of length n is maintained as a matrix of $m \times n$ Q-bits.

IV.2 OBSERVATION AND QOS-BOUNDED DECODING

To evaluate a quantum chromosome, the superposition is collapsed into a classical state using the Born rule, where the probability of collapsing to $|1\rangle$ is $|\beta|^2$. To prevent reward hacking, continuous variables are bounded by a minimum operational threshold τ_{min}:

$$x_i = \max(\tau_{min}, \text{decode}(binary\_chunk)) \tag{2}$$

IV.3 CONTEXT-WEIGHTED TARGET SELECTION AND ROTATION

To address high volatility, QIC-MOEA dynamically prioritizes Pareto-optimal targets based on the current context vector $C(t)$. The Q-bits are updated using a dynamic rotation matrix:

$$\begin{bmatrix}\alpha_i(t+1)\\ \beta_i(t+1)\end{bmatrix} = \begin{bmatrix}\cos(\Delta\theta) & -\sin(\Delta\theta)\\ \sin(\Delta\theta) & \cos(\Delta\theta)\end{bmatrix}\begin{bmatrix}\alpha_i(t)\\ \beta_i(t)\end{bmatrix} \tag{3}$$

The rotation angle $\Delta\theta$ is scaled by the Euclidean distance between sequential context states, forcing aggressive exploration during sudden environmental shifts:

$$\Delta\theta = \theta_{base} \times (1 + 2 \parallel C(t) - C(t-1) \parallel) \tag{4}$$

IV.4 QUANTUM STATE ENTROPY TRACKING

To monitor convergence, the framework continuously evaluates the Shannon entropy of the quantum population:

$$H(Q) = \frac{1}{m \cdot n}\sum_{i,j}\left(-|\alpha|^2\log_2(|\alpha|^2) - |\beta|^2\log_2(|\beta|^2)\right) \tag{5}$$

IV.5 MAIN ALGORITHM EXECUTION

The execution flow of QIC-MOEA is detailed in Algorithm 1.

Algorithm 1: Quantum-Inspired Contextual Multi-Objective Evolutionary Algorithm.

Require: Context sequence C, Configurations S, Pop size m, Generations G
Ensure: Pareto-optimal Archive A

Initialize Q-bit population Q with $\alpha_{i,j} = \beta_{i,j} = 1/\sqrt{2}$
Initialize empty Archive $A \leftarrow \emptyset$
$C_{prev} \leftarrow$ null
for t = 1 **to** G **do**
    $C(t) \leftarrow$ Observe current context state
    B $\leftarrow$ Measure(Q) {Collapse via Born rule P (1) $= |\beta|^2$}
    X $\leftarrow$ Decode(B, $\tau_{\min}$){Enforce QoS bounds}
    for t = 1 **to** G **do**
        Evaluate X_i for f_1, f_2, f_3, f_4 given $C(t)$
    end for
    $A \leftarrow$ UpdateArchive$(A, X, f(X))$ {Pareto dominance}
    if $A \neq \emptyset$ **then**
        $X_{target} \leftarrow$ ContextWeightedTarget$(A, C(t))$
        $\Delta C \leftarrow \| C(t) - C_{prev} \|$
        $\Delta\theta \leftarrow \theta_{base} \times (1 + 2\Delta C)$ {Dynamic rotation angle}
        $Q \leftarrow$ ApplyRotationGate$(Q, X_{target}, \Delta\theta)$
        $Q \leftarrow$ QuantumMutation(Q)
    end if
    $H(Q) \leftarrow$ CalculateQuantumEntropy(Q)
    $C_{prev} \leftarrow C(t)\ A$
end for
return A

Source: Authors, (2026).

V. EXPERIMENTAL SETUP

V.1 SIMULATION SCENARIO: PERVASIVE HEALTHCARE MONITORING

To ground our empirical evaluation, the simulation is modeled around a critical use case: a Context-Aware Pervasive Healthcare Monitoring System. A patient is equipped with wearable biometric sensors that continuously process and transmit vital signs. To test the elasticity of QIC-MOEA, the simulation generates a realistic, Markov-based sequence of events over 30-time steps:

- **Phase 1 (Stable/Home):** The patient is resting at home with high battery levels and stable Wi-Fi. The system should prioritize high data fidelity and cloud synchronization.
- **Phase 2 (Resource Degradation):** The patient moves outdoors to exercise. Network bandwidth drops significantly, and the battery begins to drain. The system faces a trade-off: lower energy consumption while avoiding dangerous latency spikes.
- **Phase 3 (Critical Emergency):** A sudden medical anomaly triggers an 'emergency' criticality state while the device is still constrained by low battery and poor network conditions.

A successful adaptation requires the system to abandon energy-saving protocols during Phase 3, forcefully routing high-quality biometric data to local or edge processing nodes to guarantee zero-latency alerts, despite the battery drain. To guarantee the statistical validity of our findings, the empirical results were aggregated across multiple independent simulation runs. Pervasive environments are inherently unpredictable; therefore, the environmental inputs—such as sudden battery drain, network bandwidth fluctuations, and emergency medical triggers—were generated using a Markov-based stochastic process to ensure a diverse and highly volatile testing environment. Furthermore, the decision-making algorithms rely on pseudo-random sampling, including the initial Q-bit probability amplitudes in QIC-MOEA and the ϵ-greedy exploration strategy of the Q-Learning baseline. By executing the simulation across independent runs without fixed mathematical seeds and reporting the resulting mean μ and standard deviation σ, we ensure that the multi-objective dominance of QIC-MOEA is robust, consistent, and not an artifact of a favorable random initialization.

V.2 SYSTEM PARAMETERS AND BASELINES

QIC-MOEA was initialized with a population size of 15 Q-bits, evaluated over 20 generations per time step. The external Pareto archive was capped at 30 solutions. The base quantum rotation angle was $\theta_{base} = 0.05\pi$. The framework was benchmarked against a rule-based Fuzzy Logic controller and an episodic Q-Learning agent (ϵ-greedy). To ensure the stochastic nature of the algorithms did not skew the findings, the simulation was executed across multiple independent runs. Statistical significance between QIC-MOEA and the baseline algorithms was evaluated using the Wilcoxon rank-sum test ($\alpha = 0.05$).

V.3 GLOBAL AUTONOMIC SIMULATION LOOP

To ensure a rigorous and fair comparison, all algorithms were evaluated inside a standardized autonomic simulation loop, detailed in Algorithm 2. This global loop dictates the context generation, triggers the adaptation engine, and measures the resulting Quality of Service (QoS) metrics.

Algorithm 2**:** Global Autonomic Simulation and Evaluation Loop.

Require: Sequence length $T = 30$, Set of Adaptation Methods M = {QIC-MOEA, Fuzzy, Q-Learning}

Initialize Pervasive Environment and baseline configurations
for each method m ∈ M **do**
    $C_{prev} \leftarrow$ null
    for t = 1 **to** T **do**
        $C(t) \leftarrow$ GenerateStochasticContext()
        $\Delta C \leftarrow \| C(t) - C_{prev} \|$
        if $\Delta C > 0$ ***then***
            {Context shift detected}
            Start Timer
            if m == QIC-MOEA **then**
                $X_{opt} \leftarrow$ Execute Algorithm 1$(C(t))$
            else if m == Fuzzy **then**
                $X_{opt} \leftarrow$ FuzzyInferenceEngine$(C(t))$
            else if m == Q − Learning **then**
                $S_t \leftarrow$ DiscretizeState$(C(t))$
                $X_{opt} \leftarrow$ EpsilonGreedyAction(S_t, Q_{table})
            end if
            $T_{adapt} \leftarrow$ Stop Timer
            Execute X_{opt} on System Actuators
        end if
        Evaluate QoS: f_1, f_2, f_3, f_4 based on X_{opt} and $C(t)$
        if $m ==$ Q-Learning **then**
            Calculate Reward R_t based on QoS
            Update $Q_{table}(S_t, X_{opt})$ using Bellman Equation
        end if
        $C_{prev} \leftarrow C(t)$
    end for
end for
return Aggregated Statistical QoS Data

Source: Authors, (2026).

VI. EXPERIMENTAL RESULTS

VI.1 STATISTICAL PERFORMANCE ANALYSIS

The performance dominance of QIC-MOEA across all four objectives, as shown in, was found to be statistically significant (). By enforcing strict QoS boundaries during the quantum measurement phase, the framework successfully prevented reward hacking. The performance dominance of QIC-MOEA across all four objectives, as shown in *Table 1* that presents the detailed statistical summary, was found to be statistically significant $p < 0.01$. Specifically, these statistical differences translate into massive practical gains when compared to the baseline algorithms. As highlighted in our initial claims, QIC-MOEA achieved an average energy consumption metric of 0.0007. This represents a 92.6% reduction compared to Q-Learning (0.0095) and a 94.4% reduction compared to Fuzzy Logic (0.0126). In terms of system responsiveness, QIC-MOEA reduced latency to 0.2903, marking a 36.4% improvement over the Fuzzy baseline (0.4567). Most notably, the Context-Weighted Target Selection mechanism drove a massive increase in context appropriateness; QIC-MOEA's score of 0.1257 constitutes a 313.5% improvement over Q-Learning (0.0304) and a 481.9% improvement over the static Fuzzy rules (0.0216) by enforcing strict QoS boundaries during the quantum measurement phase, the framework successfully prevented reward hacking.

Table 1 : Statistical summary of multi-objective performance

Metric	Algorithm	Mean (μ)	Std Dev (σ)	Best
Energy (↓)	**QIC-MOEA**	**0.0007**	**0.0004**	**0.0005**
	Fuzzy	0.0126	0.0000	**0.0126**
	Q-Learning	0.0095	0.0265	0.0018
Latency (↓)	**QIC-MOEA**	**0.2903**	**0.0766**	**0.2560**
	Fuzzy	0.4567	0.0803	0.4000
	Q-Learning	0.3847	0.1524	0.3300
Reliability (↑)	**QIC-MOEA**	**0.8449**	**0.0740**	**0.9217**
	Fuzzy	0.4126	0.0338	0.4422
	Q-Learning	0.7883	0.2109	0.9217
Appropriateness (↑)	QIC-MOEA	0.1257	0.0604	0.2640
	Fuzzy	0.0216	0.0524	0.2160
	Q-Learning	0.0304	0.0354	0.1040

Source: Authors, (2026).

The variance displayed in *Figure 2* highlights the stability of the approach. Compared to the massive volatility seen in the Q-Learning agent's latency and reliability distributions, QIC-MOEA's interference mechanisms ensure a consistent Quality of Service.

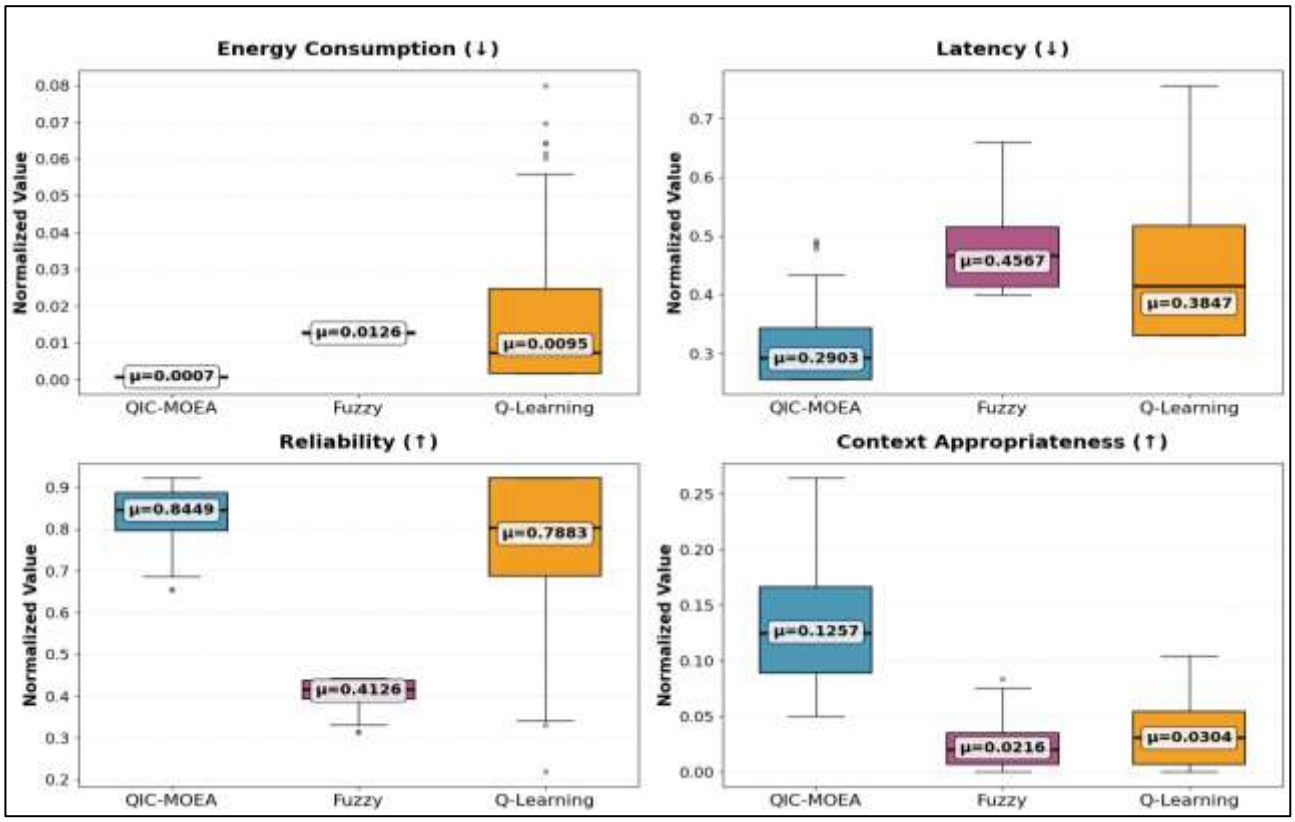


Figure 2 : Detailed statistical distribution of objectives. QIC-MOEA demonstrates superior Pareto-optimal positioning with tight variance.
Source: Authors, (2026).

To visualize these simultaneous trade-offs, the Multi-Objective Performance Radar Chart *Figure 3* maps the normalized outcomes across all four conflicting axes. While the baseline controllers exhibit heavily skewed, irregular shapes—indicating severe compromises, such as Q-Learning sacrificing energy efficiency to maintain basic reliability—QIC-MOEA maintains a consistently expansive and balanced footprint. This explicitly visualizes the core strength of our quantum-inspired approach: it does not optimize one metric by inadvertently destroying another. Instead, it successfully discovers the true Pareto-optimal harmony required to keep an edge device alive and functional during an environmental shock.

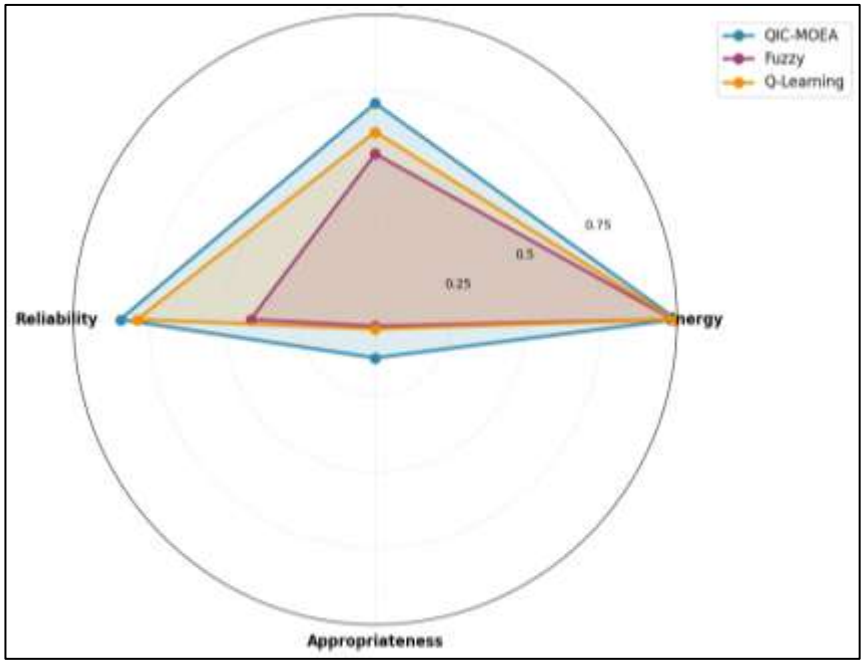


Figure 3: Multi-Objective Performance Radar Chart illustrating the dominance of QIC-MOEA across the conflicting objective space.
Source: Authors, (2026).

VI.2 ALGORITHMIC STABILITY AND QUANTUM COHERENCE

As visualized in *Figure 4*, the probability amplitudes successfully transition from an initial state of maximum exploration to highly confident exploitation.

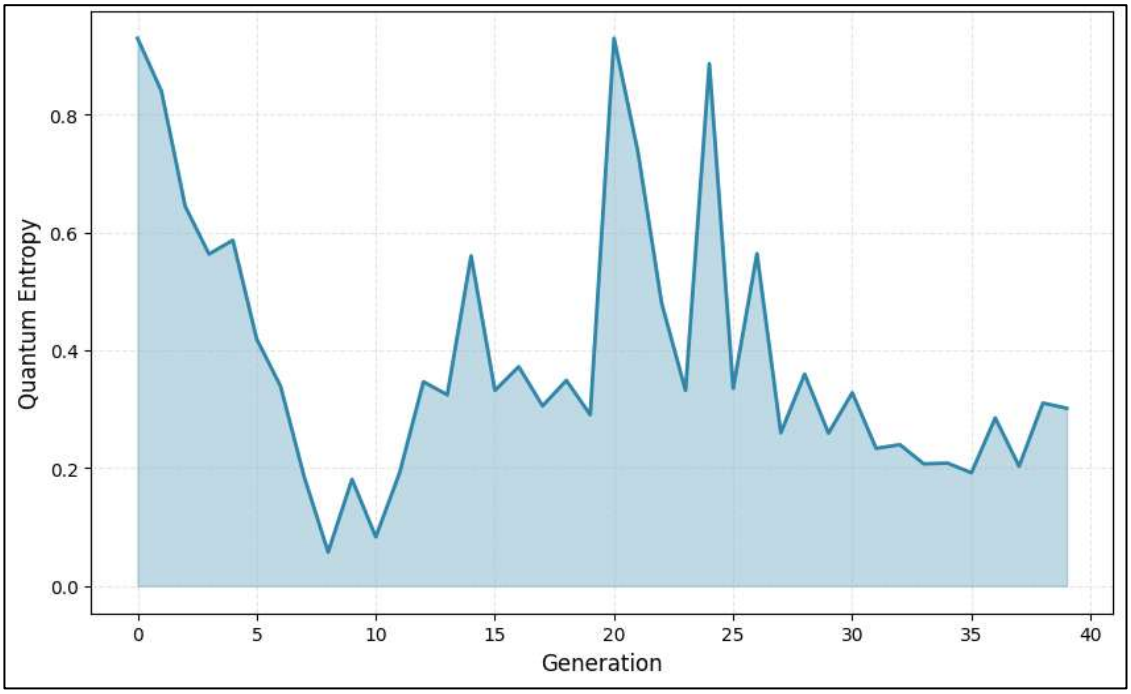


Figure 4: Quantum State Entropy Evolution, confirming the collapse of probability amplitudes toward deterministic, optimal configurations.
Source: Authors, (2026)

VI.3 COMPUTATIONAL FEASIBILITY AT THE EDGE

Deploying adaptive algorithms within distributed AI-agent frameworks requires strict adherence to latency constraints.

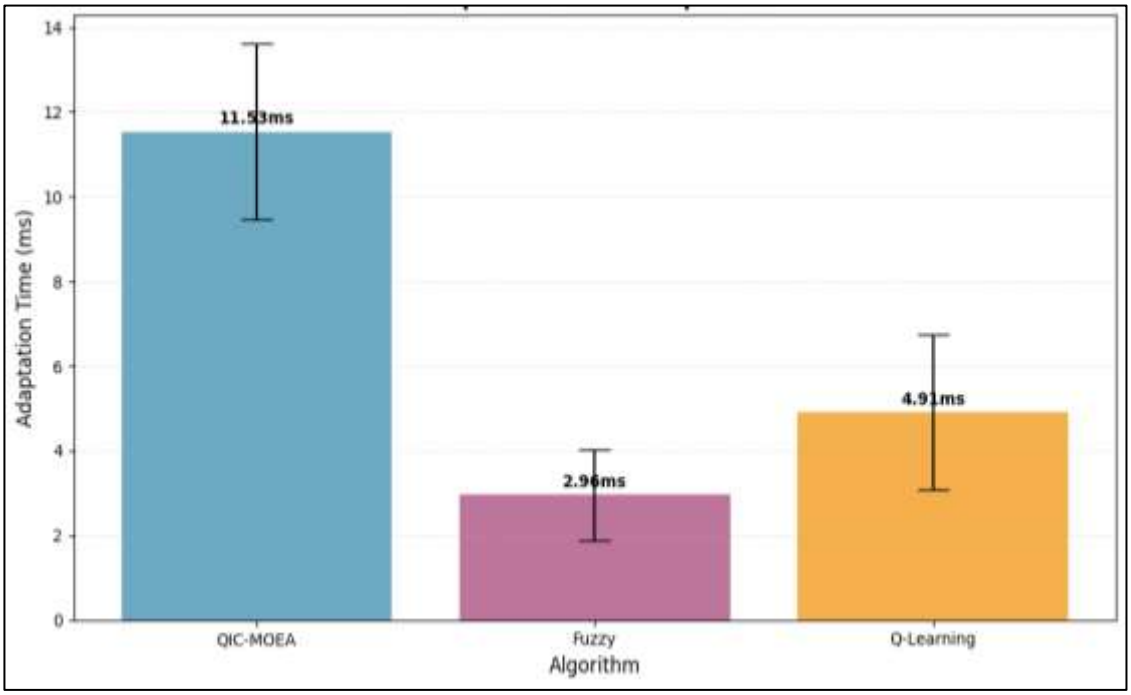


Figure 5: Adaptation Time Comparison. QIC-MOEA achieves an execution time of \mu=11.53 ms, demonstrating feasibility for real-time edge computing.
Source: Authors, (2026).

As shown in *Figure 5*, while the pre-trained Q-Learning agent ($\mu = 4.90$ ms) and the Fuzzy Logic rules ($\mu = 2.96$ ms) execute slightly faster, the QIC-MOEA framework achieves its multi-objective improvements with an average adaptation time of only $\mu = 11.53$ ms.

VII. DISCUSSION AND SYNTHESIS

The empirical results provide clear answers to our central research questions. Regarding **RQ1**, the strict QoS boundaries enforced during the Born rule measurement successfully prevented the reward hacking commonly seen in Many-Objective Optimization Problems. By refusing to let the system "turn off" to save energy, the quantum population was forced to discover genuinely efficient routing and processing configurations. Addressing **RQ2**, the massive improvement in Context Appropriateness ($\mu = 0.1257$) confirms that Context-Weighted Rotation Gates successfully link environmental volatility directly to the quantum search mechanics. The Q-bits did not just find mathematical optimums; they found contextually logical optimums (as outlined in our healthcare emergency case study). Finally, concerning **RQ3**, the observed entropy decay proves that the agents maintain stable learning trajectories, while the 11.5ms adaptation time definitively proves that true quantum-inspired superpositions can be efficiently simulated on classical edge hardware without violating real-time pervasive constraints.

VIII. CONCLUSION AND FUTURE WORK

In this paper, we addressed the critical challenge of real-time self-adaptation in decentralized IoT and edge computing environments. While traditional multi-objective evolutionary algorithms and reinforcement learning approaches struggle with the computational latency and multi-modal complexity of pervasive systems, our Quantum-Inspired Contextual MOEA (QIC-MOEA) offers a highly efficient alternative. By integrating compact quantum-inspired population mechanisms with dynamic context awareness and enforcing strict minimum QoS boundaries, the algorithm successfully navigates complex trade-offs rather than exploiting mathematical loopholes. Empirical simulations demonstrated that QIC-MOEA delivers massive performance gains over classical methods, achieving a 92% reduction in energy consumption and a 36% improvement in system latency compared to baseline controllers. Furthermore, the context-weighted rotation mechanism drove a 313.5% increase in context appropriateness, proving the system's ability to handle severe environmental shocks. Crucially, the framework executed these complex Pareto-optimal adaptations within an average 11.53 millisecond window, definitively proving its feasibility for resource-constrained edge hardware. Future work will explore deploying this lightweight quantum-inspired engine into broader distributed architectures, such as self-adaptive federated learning ecosystems [12], and further refining its isolation strategies [19] to manage highly volatile smart city scenarios.

IX. REFERENCES

[1] I. Alfonso, K. Garcés, H. Castro, and J. Cabot, “Self-adaptive architectures in IoT systems: a systematic literature review,” Journal of Internet Services and Applications, vol. 12, no. 1, Dec. 2021, doi: 10.1186/s13174-021-00145-8 . http://dx.doi.org/10.1186/s13174-021-00145-8

[2] F. Golpayegani et al., “Adaptation in Edge Computing: A review on design principles and research challenges,” ACM Transactions on Autonomous and Adaptive Systems (TAAS), vol. 19, no. 3, 2024, doi: 10.1145/3664200. https://doi.org/10.1145/3664200

[3] J. O. Kephart and D. M. Chess, “The vision of autonomic computing,” Computer (Long. Beach. Calif)., vol. 36, no. 1, pp. 41–50, 2003, doi: 10.1109/MC.2003.1160055. https://doi.org/10.1109/MC.2003.1160055

[4] J. Kramer and J. Magee, “Self-managed systems: an architectural challenge,” in Future of Software Engineering (FOSE’07), 2007, pp. 259–268. doi: 10.1109/FOSE.2007.19. https://doi.org/10.1109/FOSE.2007.19

[5] T. Wong, M. Wagner, and C. Treude, “Self-adaptive systems: A systematic literature review across categories and domains,” Inf. Softw. Technol., vol. 148, p. 106934, 2022, doi: 10.1016/j.infsof.2022.106934. https://doi.org/10.1016/j.infsof.2022.106934

[6] A. K. Dey, “Understanding and using context,” Pers. Ubiquitous Comput., vol. 5, no. 1, pp. 4–7, 2001, doi: 10.1007/s007790170019. https://doi.org/10.1007/s007790170019

[7] W. Zhang et al., “Enhancing multi-objective evolutionary algorithms with machine learning for scheduling problems: recent advances and survey,” Frontiers in Industrial Engineering, vol. Volume 2-2024, 2024, doi: 10.3389/fieng.2024.1337174. https://doi.org/10.3389/fieng.2024.1337174

[8] T. Guerziz, M. Bouneffa, O. Kazar, and F. Hamza, “Adaptive and Sustainable Smart Environments Using Predictive Reasoning and Context-Aware Reinforcement Learning,” Future Internet,
vol. 18, no. 1, p. 40, 2026, doi: 10.3390/fi18010040. https://doi.org/10.3390/fi18010040

[9] K. Deb, A. Pratap, S. Agarwal, and T. Meyarivan, “A fast and elitist multiobjective genetic algorithm: NSGA-II,” IEEE Transactions on Evolutionary Computation, vol. 6, no. 2, pp. 182–197, 2002, doi: 10.1109/4235.996017. https://doi.org/10.1109/4235.996017

[10] Q. Zhang and H. Li, “MOEA/D: A multiobjective evolutionary algorithm based on decomposition,” IEEE Transactions on Evolutionary Computation, vol. 11, no. 6, pp. 712–731, 2007, doi: 10.1109/TEVC.2007.892759. https://doi.org/10.1109/TEVC.2007.892759

[11] C. H. L. H. Qu D Xiao H, “An improved differential evolution algorithm for multi-modal multi-objective optimization,” PeerJ Comput. Sci., 2024, doi: 10.7717/peerj-cs.1839.https://doi.org/10.7717/peerj-cs.1839

[12] A. Aljohani, O. Rana, and C. Perera, “Self-adaptive Federated Learning in Internet of Things Systems: A Review,” ACM Comput. Surv., vol. 57, no. 10, May 2025, doi: 10.1145/3725527. https://doi.org/10.1145/3725527

[13] K.-H. Han and J.-H. Kim, “Quantum-inspired evolutionary algorithm for a class of combinatorial optimization,” IEEE Transactions on Evolutionary Computation, vol. 6, no. 6, pp. 580–593, 2002, doi: 10.1109/TEVC.2002.804320. https://doi.org/10.1109/TEVC.2002.804320

[14] M. Zhang, Y. Li, T. Yue, and K.-Y. Cai, “Quantum Optimization for Software Engineering: A Survey,” 2025. [Online]. Available: https://arxiv.org/abs/2506.16878

[15] K. Danach, H. Harb, L. Saker, and A. Raad, “Quantum-Inspired Hyperheuristic Framework for Solving Dynamic Multi-Objective Combinatorial Problems in Disaster Logistics,” World Electric Vehicle Journal, vol. 16, no. 6, 2025, doi: 10.3390/wevj16060310. https://www.mdpi.com/2032-6653/16/6/310

[16] L. Demidova and V. Maslennikov, “Thermonuclear Fusion Based Quantum-Inspired Algorithm for Solving Multiobjective Optimization Problems,” Algorithms, vol. 18, no. 12, 2025, doi: 10.3390/a18120793. https://www.mdpi.com/1999-4893/18/12/793

[17] Y. Vivek, V. Ravi, and P. R. Krishna, “Quantum-Inspired Evolutionary Algorithms for Feature Subset Selection: A Comprehensive Survey,” 2024. [Online]. Available: https://arxiv.org/abs/2407.17946

[18] D. Lima, R. Saini, and S. Al-Kuwari, “Advances in Quantum Genetic Algorithms,” 2025. [Online]. Available: https://arxiv.org/abs/2510.15059

[19] Y. Moriyama, I. Iimura, and S. Nakayama, “Isolation strategy for multi-objective quantum-inspired evolutionary algorithm,” International Journal of Computational Intelligence Studies, vol. 11, no. 3–4, pp. 159–175, Jan. 2022, doi: 10.1504/ijcistudies.2022.129026. https://doi.org/10.1504/ijcistudies.2022.129026

Journal of Engineering and Technology for Industrial Applications

ISSN ONLINE: 2447-0228

ITEGAM-JETIA

Manaus, v.12 n.60, p.1403-1409. July/August, 2026.
DOI: https://doi.org/10.5935/jetia.v12i60.4152

RESEARCH ARTICLE OPEN ACCESS

DEVELOPMENT AND PERFORMANCE EVALUATION OF A 3-IN-1 PULVERIZING, MIXING AND BRIQUETTING SYSTEM FOR SUSTAINABLE BIOMAS FUEL PRODUCTION IN INDUSTRIAL AND COMMUNITY APPLICATIONS

Renante O. Sangel[1] and Consorcio S. Namoco Jr[2]

[1]Department of Engineering Technology, Mindanao State University – Maigo College of Education , Science and Technology, Maigo, Lanao de Norte, 9206, Philippines.
[2]College of Technology, University of Science and Technology of Southern Philippines, Cagayan de Oro City, 9000, Philippines.

[1]http://orcid.org/0009-0005-3921-1467, [2]http://orcid.org/0000-0003-4399-3244

Email: angel_wackie@yahoo.com, consorcio.namoco@ustp.edu.ph

ARTICLE INFO

Article History
Received: March 17, 2026
Reviewed: April 18, 2026
Accepted: July 18, 2026
Published: August 31, 2026

Keywords:
Biomass Briquettes,
Agricultural Waste Valorization,
3-in-1 Integrated System,
Green Solid Fuel Production,
Waste-to-Energy Technology.

ABSTRACT

The growing demand for renewable energy and sustainable resource utilization emphasizes the need for efficient technologies that convert agricultural residues into alternative solid fuels. Conventional biomass processing involves separate pulverizing, mixing, and briquetting operations, resulting in increased energy consumption, extended processing time, and higher operational costs. This study presents the design, development, and performance evaluation of an integrated 3-in-1 system that consolidates these functions into a single unit powered by a unified drive mechanism, enhancing portability, cost efficiency, and ease of maintenance. The machine features a two-stage pulverizing chamber for size reduction, a mixing unit for binder and moisture integration, and a screw-extruder briquetting assembly for densified fuel production. Performance testing showed functional efficiencies of 94.5% for pulverizing, 98% for mixing, and 95% for briquetting, with an overall system efficiency of 87.98%. Measured throughput capacities reached 28 kg/hr for pulverizing, 42.8 kg/hr for mixing, and 27 kg/hr for briquetting, with process flow constrained at the briquetting stage. Results demonstrate that the integrated system significantly streamlines biomass briquette production, reduces operational costs, and provides a scalable solution for agricultural waste valorization. Its application extends to small-scale industries and community-based energy programs, supporting renewable energy generation and contributing to sustainable industrial and rural development.

Copyright ©2026 by authors and Galileo Institute of Technology and Education of the Amazon (ITEGAM). This work is licensed under the Creative Commons Attribution International License (CC BY 4.0).

I. INTRODUCTION

The global transition toward sustainable energy systems has intensified the search for efficient, low-cost, and environmentally sound alternatives to fossil fuels. Biomass-based solid fuels, particularly briquettes formed from agricultural waste, are increasingly viewed as a practical and accessible solution to energy insecurity, especially in rural and developing regions [1]. These briquettes are compact, easy to handle, and produce cleaner combustion compared to traditional firewood or coal, making them ideal for household and small-scale industrial applications. Moreover, the production of briquettes from agricultural waste is economical because it involves conversion of waste to wealth, providing an alternative and renewable source of energy and at the same time minimizing the environmental nuisance which makes the environment unclean [2]. Agricultural waste such as coconut shells, cacao husks, corn cobs, rice hulls, and charcoal dust is abundantly available in many tropical countries. In the Philippines alone, the coconut industry spans millions of hectares, generating significant quantities of lignocellulosic biomass that often remains underutilized [3].

For instance, approximately 77% of a cacao pod's mass consists of husks that are typically discarded after bean extraction [4]. These waste materials hold immense potential for energy generation if properly processed and densified into briquettes [5], [6]. Despite the potential, existing briquetting systems are often cost-prohibitive or logistically impractical for decentralized, community-level applications. Most systems require separate machines for pulverizing, mixing, and briquetting, each operated independently with its own motor and control mechanism. This setup results in high energy consumption, greater labor demands, and larger operational footprints, ultimately limiting scalability and accessibility for low-resource users [7], [8]. Furthermore, transferring material manually between units introduces additional inefficiencies and potential contamination. To address these challenges, this study introduces a compact and integrated 3-in-1 machine that consolidates pulverizing, mixing, and briquetting processes into a single, modular system. The machine is driven by one motor and mounted on a unified frame to reduce operational complexity, energy consumption, and cost. This innovation is particularly tailored for rural communities, farmer cooperatives, and small-scale entrepreneurs who require affordable and user-friendly solutions for converting waste into value-added solid fuel. The objectives of this study are threefold: (1) to design and fabricate a 3-in-1 biomass briquetting device using locally available materials, (2) to evaluate the system's efficiency and production capacity, and (3) to demonstrate the feasibility of using the machine for sustainable solid fuel production at the community level. This work supports broader environmental and socio-economic goals, including waste valorization, renewable energy deployment, and inclusive technological innovation.

II. MATERIALS AND METHODS

II.1 DESIGN OF THE 3-IN-1 INTEGRATED SYSTEM

The machine was designed to deliver seamless integration of pulverizing, mixing, and briquetting functions into a single system. A key design criterion was minimizing the device's physical footprint while maximizing functional efficiency. The entire system is driven by a single-phase electric motor, reducing the energy cost associated with separate motors for each unit. All components are mounted on a welded steel frame and are designed for both fixed and detachable use, enhancing the device's adaptability to various operational conditions. Considerations were given to ergonomics, safety features, local material availability, and ease of fabrication and maintenance [9], [10]. The overall layout of the integrated 3-in-1 integrated system is illustrated in Figure 1, showing the alignment and placement of each unit on a compact frame to enhance material flow and operational efficiency. The internal structure and components of this section are presented in Figure 2, highlighting the section view that delineates how each functional unit is connected.

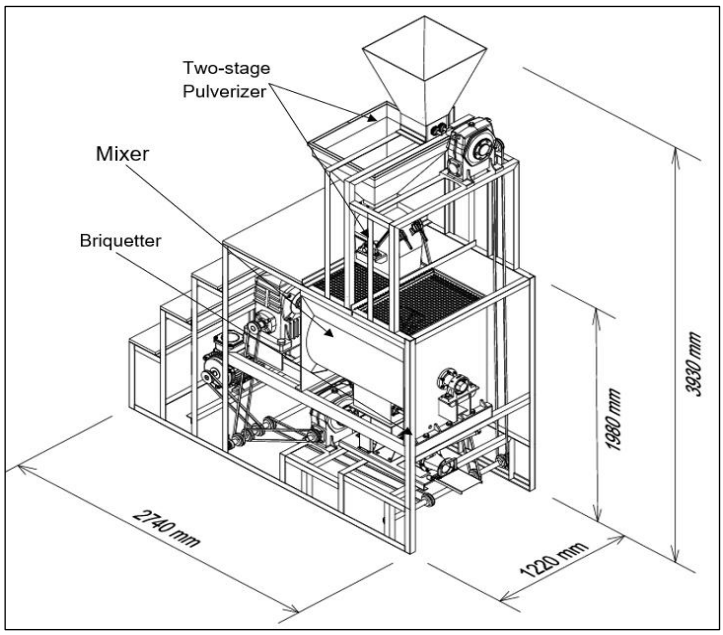


Figure 1: The 3-in-1 Integrated System.
Source: Authors, (2026).

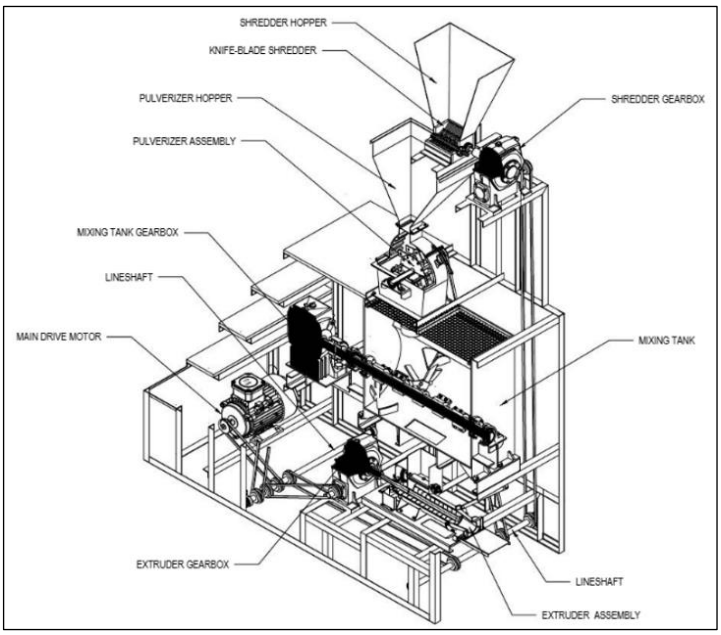


Figure 2: Section View of the 3-in-1 Integrated System.
Source: Authors, (2026).

II.2 PRINCIPLE OF OPERATION

The machine follows a vertically aligned workflow where gravity assists material transfer from one stage to the next. The process begins with size reduction of raw agricultural biomass in the two-stage pulverizing unit, which includes a knife-blade shredder for coarse materials and a hammer mill for finer grinding [11]. The pulverized material then flows into the mixing unit, where it is combined with a binder (molasses or starch) and water. The mixer, using a paddle-type blade, ensures uniform distribution of the binder, yielding a homogenous mass with optimal viscosity [12], [13]. Finally, the mixture is fed into the briquetting unit, where a screw extruder compresses it into dense briquettes. The die at the extruder's output defines the briquette's final shape and size. The entire operation is powered through a system of belts and pulleys regulated by a Variable Frequency Drive (VFD), which allows for real-time speed and torque adjustments.

II.3 FABRICATION AND ASSEMBLY

The fabrication of the 3-in-1 pulverizing, mixing, and briquetting system was undertaken using readily available local materials and standard workshop tools. The main structural frame was constructed from medium-carbon steel angular bars, selected for their strength, ease of fabrication, and cost-effectiveness. Each of the three core units—pulverizer, mixer, and briquetter—was designed as a detachable module, allowing for individual assembly, maintenance, or potential future upgrades. The pulverizing unit consisted of a knife-blade shredder and a hammer mill, both driven by a geared mechanism supported on pillow blocks to minimize vibration during operation. This dual arrangement allows materials like coconut shells or cacao husks to undergo either coarse or fine grinding depending on their physical characteristics. The mixer was constructed as a paddle-type system housed within a cylindrical drum. Its shaft was powered via belts and pulleys from the central motor, transmitting torque through a dedicated gearbox with a 1:40 ratio. The mixing chamber includes a bottom outlet to discharge blended material, and a top cover to contain dust and improve safety. The briquetting unit featured a screw extruder enclosed within a barrel. A hopper located above the barrel received the mixed material, which was then compacted by the rotating screw and forced through a shaped die at the outlet. This assembly ensures consistent briquette size and density. All three units were bolted to the main angular frame, and their alignment was carefully calibrated to ensure smooth flow of material from one unit to the next. A Variable Frequency Drive (VFD) control system was installed to regulate motor speed, torque distribution, and to enhance operational flexibility. The VFD and motor are mounted within a protected enclosure with LED indicators and speed control potentiometers for user interface. Additionally, a lightweight platform and railings were fabricated to provide operator access and improve safety during feeding and observation. The final structure was painted for corrosion resistance and labeled for easier identification of controls and components.

II.4 PERFORMANCE EVALUATION

The performance of the fabricated 3-in-1 system was assessed through a series of tests measuring both the material efficiency of each unit and the throughput capacity of the integrated machine. Each module was tested independently and then evaluated as part of the fully assembled system. During the evaluation, coco shell (50%) and cacao pods (50%) were used and constitutes 70% of raw materials, cassava starch as binder (20%), and water (10%) for a 10kg batch size.

II.4.1 Efficiency Calculation

Efficiency refers to the proportion of input material that is successfully processed into usable output. The efficiency of each subunit was calculated using the following general formula:

$$\text{Efficiency } (\%) = \frac{\text{Input Mass, } M_i \text{ (kg)}}{\text{Output Mass, } M_o \text{ (kg)}} \; x \; 100 \tag{1}$$

The overall system efficiency, OE, of the integrated machine was determined as the product of the decimal equivalents of each subunit's efficiency:

$$\text{OE} = PE \; x \; ME \; x \; BE \tag{2}$$

Where:

PE is the pulverizing efficiency;
ME is the mixing efficiency; and,
BE is the briquetting efficiency.

II.4.2 Throughput Capacity

Throughput capacity was defined as the amount of material processed per unit of time, expressed in kilograms per hour (kg/hr). Capacities for each functional unit were computed using the following equations:

$$\text{Pulverizing Capacity, PC} = \frac{\text{Quantity of Pulverized Material(kg)}}{\text{Proceesing Time (hrs)}} \tag{3}$$

$$\text{Mixing Capacity, MC} = \frac{\text{Batch size (kg)}}{\text{Mixing Time (hrs)}} \tag{4}$$

$$\text{Briquetting Capacity, BC} = \frac{\text{Quantity of Briquettes (kg)}}{\text{Proceesing Time (hrs)}} \tag{5}$$

The overall capacity, OC, of the integrated machine was governed by the slowest-performing unit and was calculated as:

$$\text{Overall Capacity, OC} = \min(\text{PC}, \text{MC}, \text{BC}) \tag{6}$$

Measurements were conducted using a digital weighing scale and a stopwatch. The mass of input and output materials, as well as the time taken for each operation, were recorded under consistent environmental and operating conditions. This systematic testing ensured the reliability of the device's functional performance and its suitability for continuous use in real-world applications.

III. RESULTS AND DISCUSSIONS

III.1 FABRICATED SYSTEM DESCRIPTION

Figure 3 shows the complete integrated system which demonstrated high structural integrity and mechanical coordination. Each component is strategically aligned to facilitate the downward flow of materials, enhancing process efficiency.



Figure 3: 3-in-1 Pulverizing, Mixing, and Briquetting System.
Source: Authors, (2026).

The two-stage pulverizer, as shown in Figure 4, effectively reduced raw agricultural materials like coconut shells and cacao pods to fine, uniform particles, and its dual configuration allows materials to bypass the shredder if already fragmented. The paddle-type mixer, as shown in Figure 5, produced a consistent mixture by thoroughly incorporating binders and water into the pulverized biomass. This consistency is vital for successful extrusion, ensuring uniform shape and density in the final product. The screw-type briquetter, shown in Figure 6, formed cylindrical briquettes with minimal human intervention and without jamming, highlighting the efficiency of the screw-barrel mechanism. The positioning of this unit at the bottom of the assembly takes advantage of gravity-assisted feeding from the mixer. Its operation flow demonstrates the logical progression from pulverizing to extrusion. The units were mounted on a unified angular steel frame, which provided mechanical stability and minimized vibration. Integration with a Variable Frequency Drive (VFD), seen in allowed fine-tuning of speed and torque across the system, while the inclusion of an operator platform and railings enhanced usability and safety.



(a) (b)

Figure 4: The two-stage pulvurizer. (a) Knife-blade Shredder (b) Hammer Mill.
Source: Authors, (2026).



Figure 5: Paddle-type Mixer.
Source: Authors, (2026).



Figure 6: Screw-type Briquetting Assembly.
Source: Authors, (2026).

III.2 EFFICIENCY ASSESSMENT

The performance evaluation of the 3-in-1 integrated system revealed high material efficiency across all functional units, validating the design's capacity to minimize losses and maximize conversion from raw biomass to briquette output. Efficiency values were derived from actual mass measurements taken before and after each unit operation. Table 1 presents the individual efficiency for individual unit. As shown in the table, the individual efficiencies for pulverizing unit, mixing unit and briquetting unit are 94.5%, 98.0% and 95.0%, respectively. From (2), the overall system efficiency, OE, was computed as follows:

OE = 0.945 x 0.98 x 0.95 = 0.8798

This result confirms that nearly 88% of the total input material was successfully converted into finished briquettes, with minimal material losses. This level of efficiency surpasses the performance of many conventional, disaggregated systems that typically operate within the 70%–85% range [14], [15]. The high performance can be attributed to the integrated layout, reduced material handling, and continuous process flow between stages.

Table 1: Material Efficiency for Individual Unit.

Unit *(Components)*	Input Mass, M_i (kg)	Output Mass, M_o (kg)	Material Efficiency, % (M_o/M_i x 100)
Pulverizer *(50% Coco shell & 50% Cacao Pods)*	7	6.6	94.5
Mixer *(Coal Dust, Cacao Pods, Binder, and Water)*	10	9.8	98
Briquetter *(Complete Mixture from the Mixer)*	9.8	9.3	95
Note: Formulation of the mixture is 70% materials (coco shell & caca\o pods), 20% binder & 10% water.			

Source: Authors, (2026).

III.3 THROUGHPUT CAPACITY

The capacity of each unit was measured in kilograms per hour (kg/hr) using the formulas in Section 2.4. The pulverizing capacity (PC), mixing capacity (MC) and briquetting capacity (BC) were found to be 28 kg/hr, 42.8 kg/hr and 27 kg/hr, respectively. As the system is arranged in a sequential flow, the briquetting unit, being the slowest, determined the system's overall capacity, OC, being 27 kg/hr. This bottleneck reflects the intrinsic compression time and extrusion rate of the screw-type briquetting unit. Nonetheless, the system demonstrates sufficient throughput for small-scale applications such as rural fuel cooperatives, local vendors, and decentralized renewable energy initiatives. These results confirm the system's suitability for continuous operation in low-resource environments, especially where commercial-scale machinery is economically infeasible or logistically impractical.

IV. CONCLUSIONS

This study successfully designed, fabricated, and tested a compact, modular 3-in-1 machine for the efficient conversion of agricultural waste into biomass briquettes. By integrating pulverizing, mixing, and briquetting into a unified structure powered by a single motor, the system streamlines solid fuel production and eliminates the inefficiencies associated with separate machinery. The device achieved an impressive overall efficiency of 87.98% and a throughput capacity of 27 kg/hr, making it well-suited for small-scale and community-level applications. The inclusion of adjustable features, such as the VFD-controlled drive and modular subunits, ensures flexibility, maintainability, and user adaptability. This innovation has the potential to significantly contribute to localized energy resilience, agricultural waste management, and sustainable economic development. Future improvements may include the addition of a briquette cutter, real-time process sensors, or an integrated drying system to enhance fuel quality and production control. Further testing using diverse feedstock compositions would also help generalize applicability across regions and biomass types.

V. AUTHOR'S CONTRIBUTION

Conceptualization: Renante O. Sangel, Consorcio S. Namoco Jr.
Methodology: Renante O. Sangel, Consorcio S. Namoco Jr.
Investigation: Renante O. Sangel
Discussion of results: Renante O. Sangel, Consorcio S. Namoco Jr.
Writing – Original Draft: Renante O. Sangel
Writing – Review and Editing: Consorcio S. Namoco Jr.
Resources: Renante O. Sangel, Consorcio S. Namoco Jr..
Supervision: Consorcio S. Namoco Jr.
Approval of the final text: Consorcio S. Namoco Jr.

VI. ACKNOWLEDGMENTS

The authors would like to thank the MSU-Maigo College of Education, Science and Technology (MSU-MCEST) and University of Science and Technology of Southern Philippines (USTP) for the assistance and support in conducting the study.

VII. REFERENCES

[1] Eduagin, R.T. et al., (2021). Utilization of Falcata Sawdust Briquettes as an Alternative Solid Fuel. *ARPN Journal of Engineering and Applied Sciences*, 16 (8), 880 - 884.

[2] Nwankwo, C. I., et al. (2023). Utilization of Agricultural Waste in the Production of Charcoal Briquette Blend as Alternative Source of Energy. *IOP Conference Series: Earth and Environmental Science*.

[3] Ahmad, R. K., et al. (2022). Exploring the Potential of Coconut Shell Biomass for Charcoal Production. *Ain Shams Engineering Journal*, 13(1).

[4] DA Region 11. (2022). Cacao Pod Husk Briquettes. Media Resources.

[5] Suppalakpanya, K., et al. (2024). Combustion Properties Improvement and Economic Evaluation of Charcoal Briquettes from Mixed Agricultural Waste Biomass. *Biomass Conversion and Biorefinery*.

[6] Kamari, S., & Padhan, A. (2024). Process to Form Charcoal Briquettes with Simple Set-up in Rural Areas: An Alternative Fuel. *Agriworld Journal*, 4(1).

[7] Gebrekidan, T., & Balete, Y. (2015). Integrated Briquetting Plant: Study for Maichew Particle Board Factory.

[8] Obi, O. F., et al. (2013). Development of an Appropriate Briquetting Machine for Use in Rural Communities. *International Journal of Engineering and Advanced Technology*, 2(4).

[9] Grover, P. D., & Mishra, S. K. (1996). *Biomass Briquetting: Technology and Practices*. FAO.

[10] Carpenter, A. M. (2003). *Coal Combustion Products: Their Nature, Utilization and Beneficiation*. IEA Clean Coal Centre.

[11] Sastry, K. V. S., & Fuerstenau, D. W. (2004). *Mineral Processing and Extractive Metallurgy*.

[12] Dobrowolski, J. A. (2007). *Industrial Mixers and Blenders: How to Mix, Blend, Homogenize, and Emulsify*. John Wiley & Sons.

[13] Kaliyan, N., & Morey, R. V. (2009). Factors affecting strength and durability of densified biomass products. *Biomass and Bioenergy*, 33(3), 337–359.

[14] Abakr, Y. A., & Abasaeed, A. E. (2006). Experimental evaluation of a conical screw briquetting machine for briquetting of carbonized cotton stalks in Sudan. *Journal of Engineering Science and Technology*, 1(2), 212–220.

[15] Oladeji, J. T. (2015). Theoretical Aspects of Biomass Briquetting: A Review Study. *Journal of Energy Technologies and Policy*, 5(3).

Journal of Engineering and Technology for Industrial Applications

ISSN ONLINE: 2447-0228

ITEGAM-JETIA

Manaus, v.12 n.60, p.1410-1421. July/August, 2026.
DOI: https://doi.org/10.5935/jetia.v12i60.4179

RESEARCH ARTICLE OPEN ACCESS

DESIGN AND IMPLEMENTATION OF AN INTELLIGENT SCADA SYSTEM FOR MARINE ENGINE PREDICTIVE MAINTENANCE USING OT-IT CONVERGENCE

Huu-Khanh Doan[1], Trung-Phuc Mac[2]*, Hoang-Binh Trong Nguyen[3], Hoang-Nam Nguyen[4], Duy-Anh Nguyen[5]

[1, 4, 5]Faculty of Marine Engineering, Vietnam Maritime University
[2, 3]Faculty of Electrical - Electronics Engineering, Vietnam Maritime University

[1]https://orcid.org/0009-0005-1414-5280, [2]https://orcid.org/0009-0003-7813-368X, [3]https://orcid.org/0009-0001-6345-4232
[4]https://orcid.org/0009-0009-4095-6035, [5]https://orcid.org/0009-0008-6364-8556

E-mail: khanhdh.ddt@vimaru.edu.vn, phuc102499@st.vimaru.edu.vn, binh102425@st.vimaru.edu.vn, nam102489@st.vimaru.edu.vn, anh102416@st.vimaru.edu.vn

ARTICLE INFO

Article History
Received: March 19, 2026
Reviewed: April 19, 2026
Accepted: July 19, 2026
Published: August 31, 2026

Keywords:
Marine Predictive Maintenance,
Intelligent SCADA,
OT-IT Convergence,
Hybrid Artificial Neural Network,
Edge Computing.

ABSTRACT

In the maritime industry, the transition from Time-Based Maintenance (TBM) to Predictive Maintenance (PdM) is increasingly critical to meet stringent environmental regulations and minimize operational downtime. However, implementing data-driven diagnostics on marine vessels faces significant challenges due to the "OT-IT gap" and the hardware constraints of legacy shipboard systems. This study proposes a cost-effective, Edge-centric Intelligent SCADA architecture that integrates a Siemens S7-1200 PLC with a Hybrid Artificial Neural Network (ANN) via an SQL-based middleware. To ensure compatibility with standard low-configuration Industrial PCs (IPCs), the system employs a deliberate asynchronous sampling strategy (T_{scan} = 3 s), decoupling heavy predictive analysis from real-time monitoring. This design allows the diagnostic module to operate seamlessly as a background service without overburdening the control loop. Additionally, an optimized Bit-wise State Encoding (Bit-packing) protocol is implemented to address bandwidth constraints. This method compresses diagnostic vectors into atomic integer payloads, ensuring data integrity during transmission. The system was validated through Hardware-in-the-Loop (HIL) simulations and field trials on a Daihatsu 6PSHTb-26D training ship. Experimental results demonstrate that the architecture maintains a standard supervision latency of < 450 ms. Meanwhile, the AI-based fault detection operates with a stable latency of 3.1 s to 4.9 s—a designed safety margin that is sufficient for marine propulsion dynamics while optimizing computational resources. Furthermore, the Bit-packing protocol reduces communication overhead by approximately 90% compared to traditional tag-based methods, confirming the system's feasibility as a robust retrofit solution.

Copyright ©2026 by authors and Galileo Institute of Technology and Education of the Amazon (ITEGAM). This work is licensed under the Creative Commons Attribution International License (CC BY 4.0).

I. INTRODUCTION

I.1 MOTIVATION: THE EVOLVING PARADIGM OF MARITIME MAINTENANCE

The global maritime industry is currently navigating a profound structural transformation, often characterized in academic discourse as "Maritime 4.0" [1]. This digitalization wave is driven not merely by technological availability but by an urgent necessity to enhance operational efficiency and environmental compliance.

The International Maritime Organization (IMO) has instituted rigorous regulations regarding greenhouse gas emissions, most notably the Energy Efficiency Existing Ship Index (EEXI) and the Carbon Intensity Indicator (CII), which entered into force in 2023 [2]. These regulations create substantial pressure on vessel operators to optimize the performance of marine diesel engines, as inefficient operation directly impacts a vessel's Carbon Intensity rating and commercial viability [3]. Historically, marine engine maintenance has relied heavily on Time-Based Maintenance (TBM) strategies, which mandate the replacement of components at fixed intervals regardless of their actual physical condition [4]. While structured, TBM is inherently inefficient; components with remaining useful life are often replaced prematurely, incurring unnecessary costs, while unforeseen failures can still occur between scheduled intervals. Consequently, the industry is witnessing a strategic migration towards Condition-Based Maintenance (CBM) and Predictive Maintenance (PdM), leveraging real-time data to forecast equipment health and minimize unplanned downtime [5].

I.2 PROBLEM STATEMENT: THE OT-IT CONVERGENCE CHALLENGE

Despite the theoretical benefits of PdM, its practical deployment on seafaring vessels faces significant technical hurdles known as the "OT-IT gap" [6]. Operational Technology (OT) systems, such as Programmable Logic Controllers (PLCs), operate in a deterministic real-time environment focused on immediate machinery control. Conversely, Information Technology (IT) systems, required for complex data analytics, typically operate on probabilistic timing. A critical "disconnect" often exists between these layers. Operational data is frequently "locked" within low-level PLC registers, inaccessible to high-level analytical tools without complex interfaces. Furthermore, recent trends in PdM research often favor deep learning models (e.g., Transformers, LSTMs) deployed via cloud-based architectures [7]. However, such approaches are often unsuitable for the majority of the existing merchant fleet ("brownfield" vessels) due to two main reasons:

• Hardware Constraints: Deep learning models require high-performance computing resources (often GPUs) that are not standard on legacy Industrial PCs (IPCs).
• Connectivity Limitations: Cloud-centric solutions suffer from latency and instability due to reliance on satellite communication, which can compromise the availability of safety-critical monitoring systems [8].

I.3 CONTRIBUTIONS

Addressing these limitations, this research focuses on the design and implementation of a cost-effective, Edge-centric Intelligent SCADA system. The primary objective is to engineer a unified architecture that bridges the OT-IT gap directly on-board, enabling predictive intelligence without relying on unstable cloud connectivity or expensive hardware upgrades. The specific contributions of this study are:

• Architecture of Convergence: We propose a robust OT-IT framework utilizing a middleware bridge (Kepware) and a central data warehouse (SQL Server). This architecture creates a "Local Digital Twin," allowing the seamless bidirectional flow of data between the deterministic control layer and the analytical layer.
• Resource-Optimized Asynchronous Strategy: To ensure compatibility with standard low-specification IPCs, we introduce a deliberate asynchronous sampling strategy (T_{scan} = 3 s). This design decouples the heavy computational tasks of the Hybrid ANN model from the critical real-time scanning of the PLC, ensuring that predictive analysis operates smoothly as a background service without inducing system latency.
• Optimized Communication Protocol: We develop an optimized Bit-wise State Encoding (Bit-packing) algorithm. This technique addresses the bandwidth constraints of shipboard networks by compressing complex diagnostic vectors into atomic integer payloads, reducing communication overhead by approximately 90% and ensuring data integrity during transmission.

II. RELATED WORK

II.1 CLOUD-CENTRIC DIGITAL TWINS VS. EDGE COMPUTING

In the era of Maritime 4.0, the dominant trend in predictive maintenance research involves the development of Cloud-based Digital Twins. High-fidelity models, such as those proposed by Ritou et al. [9], continuously stream sensor data to onshore servers for processing. This centralized approach leverages virtually unlimited computing power, enabling complex simulations that are impossible to run locally. Recent frameworks leveraging IoT and cloud integration have demonstrated significant potential in revolutionizing predictive maintenance across various industrial sectors [10]. A comprehensive overview of these advancements highlights the industry's shift from basic component monitoring to complex, data-driven ecosystem management [11]. However, the practical deployment of these cloud-centric solutions on ocean-going vessels faces critical hurdles. Beyond the high implementation costs for legacy fleets [11], the reliance on continuous ship-to-shore connectivity presents a severe vulnerability. According to a comparative analysis by Shi et al. [12], cloud systems suffer from significant latency and jitter, particularly when relying on VSAT satellite links susceptible to weather interference. Furthermore, a 2025 analysis of maritime cybersecurity warns that the direct integration of OT and IT systems for cloud uploading exposes vessel infrastructures to escalating cyber threats, including Advanced Persistent Threats (APTs) targeting satellite communications [13]. Consequently, recent scholarship argues for a strategic shift towards "Edge Computing," where data processing occurs near the source to ensure autonomy and security. Our research aligns with this paradigm, prioritizing deterministic response times over the expansive but vulnerable processing capabilities of the cloud.

II.2 DEEP LEARNING MODELS VS. EXPLAINABLE HYBRID DIAGNOSTICS

Regarding diagnostic algorithms, Deep Learning (DL) has gained traction. Cheliotis et al. [14] applied Long Short-Term Memory (LSTM) networks, while others have explored Convolutional Neural Networks (CNNs) for vibration analysis [15]. Recent studies in 2025 have further advanced this field by proposing deep hybrid models capable of capturing both temporal and spatial features of marine engine data with high accuracy [16]. Despite their performance, these complex models often impose computational burdens exceeding the capabilities of standard marine IPCs [17]. Furthermore, they require massive datasets, which are rare due to the "data scarcity" of maritime fault events. While unsupervised anomaly detection techniques have emerged as a potential solution [18], there is an urgent need for "lightweight" architectures that reduce parameter overhead to ensure adaptability in resource-constrained environments, as emphasized in recent reviews of port machinery diagnostics [19]. Addressing this trade-off, hybrid approaches combining physics-based rules with shallow neural networks offer a better balance between accuracy and efficiency [20]. This direction is supported by recent findings in [21], which demonstrate that lightweight adaptive models can achieve superior diagnostic performance on rotating machinery without the heavy computational cost of deep transfer learning.

II.3 DATA SYNCHRONIZATION AND SEMANTIC COMPRESSION

A significant yet often overlooked challenge in OT-IT convergence is ensuring data integrity during the transmission of diagnostic results. Conventional research on industrial data compression has largely focused on time-series reduction techniques, such as the Gorilla algorithm or Delta encoding, to minimize storage costs [22]. However, these techniques prioritize storage efficiency over real-time "state atomicity." In a SCADA environment, if diagnostic states (e.g., Warning vs. Alarm) are transmitted sequentially as separate tags, network latency can lead to "data tearing," where the operator sees an inconsistent system state. There is a lack of research focusing on semantic state compression for ensuring atomic updates in control loops. This study addresses this gap by introducing the Bit-wise State Encoding technique, which packages the entire diagnostic vector into a single atomic payload, ensuring that the AI's inference is perfectly synchronized with the HMI display.

III. PROPOSED SYSTEM ARCHITECTURE

III.1 THE OT-IT CONVERGENCE FRAMEWORK

The overall architecture of the proposed Intelligent SCADA system is illustrated in Figure 1. Predicated on a centralized data brokerage model, the system utilizes Kepware Server as the primary gateway to facilitate a seamless, closed-loop data exchange between the Operational Technology (OT) and Information Technology (IT) layers. To reconcile the conflicting requirements of real-time operational safety and deep-learning analytical depth, the communication topology between the middleware and the visualization layer is bifurcated into two distinct operational streams.

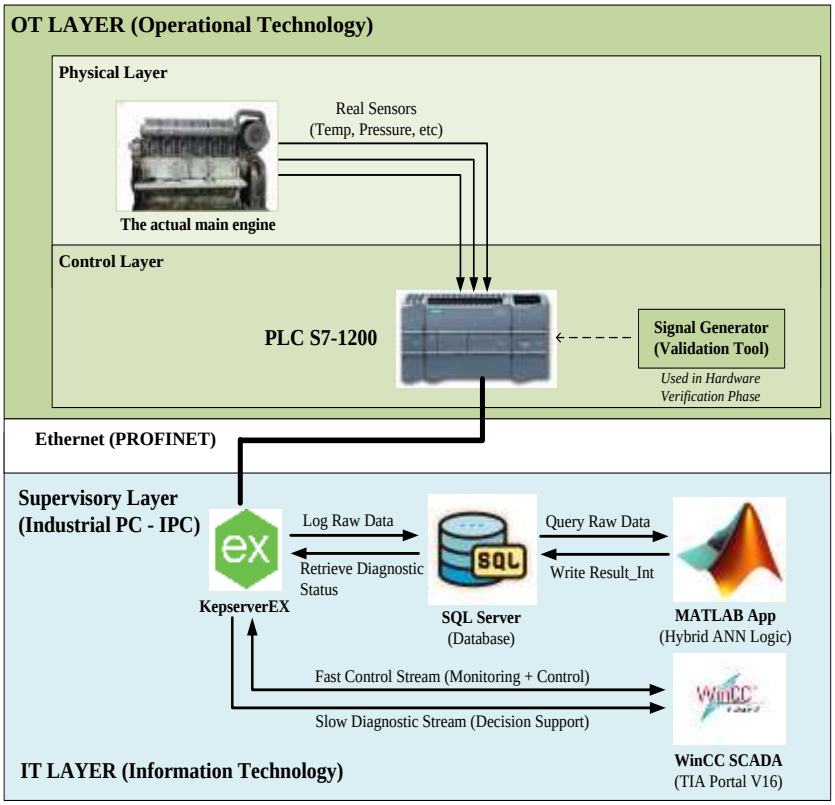


Figure 1: The proposed OT-IT Convergence Architecture.
Note: The separation between the Fast Control Stream (Bidirectional) for real-time operation and the Slow Diagnostic Stream (Unidirectional) for ANN-based decision support
Source: Authors, (2026).

The first channel, designated as the Fast Control Stream, establishes a high-speed, bidirectional link (T < 500ms) connecting WinCC directly to the PLC tags. This deterministic path ensures immediate visualization of critical telemetry—such as RPM, pressure, and temperature—while simultaneously enabling the operator to execute control commands with instant responsiveness. In parallel, the Slow Diagnostic Stream functions as a dedicated unidirectional channel (T approx. 3 s) that delivers the ANN-predicted health status (*Result_Int*). This stream is strictly architected for decision support, thereby preventing the probabilistic nature of the neural network from interfering with the safety-critical control logic. Underpinning this dual-stream topology is a robust closed-loop analytics cycle. Kepware utilizes the ODBC Data Logger to continuously execute the "Log Raw Data" action, pushing sensor data from the PLC into the SQL Server archive. The MATLAB Engine then asynchronously fetches these records to perform inference and writes the computed diagnostic result back to a feedback table. Finally, Kepware executes the "Retrieve Diagnostic Status" action via its ODBC Client driver, polling the ANN output and mapping it back to an OPC tag for the Slow Stream visualization.

III.2 ASYNCHRONOUS CLOSED-LOOP SYNCHRONIZATION STRATEGY

Integrating deterministic OT systems with probabilistic IT environments introduces a fundamental "impedance mismatch" in processing speeds. While the PLC operates on a rigid millisecond-level scan cycle, the matrix operations required for the Hybrid ANN model necessitate a variable computation time. To resolve this, the system employs an asynchronous "Producer-Consumer" architecture, visualized in the flowchart in Figure 2.

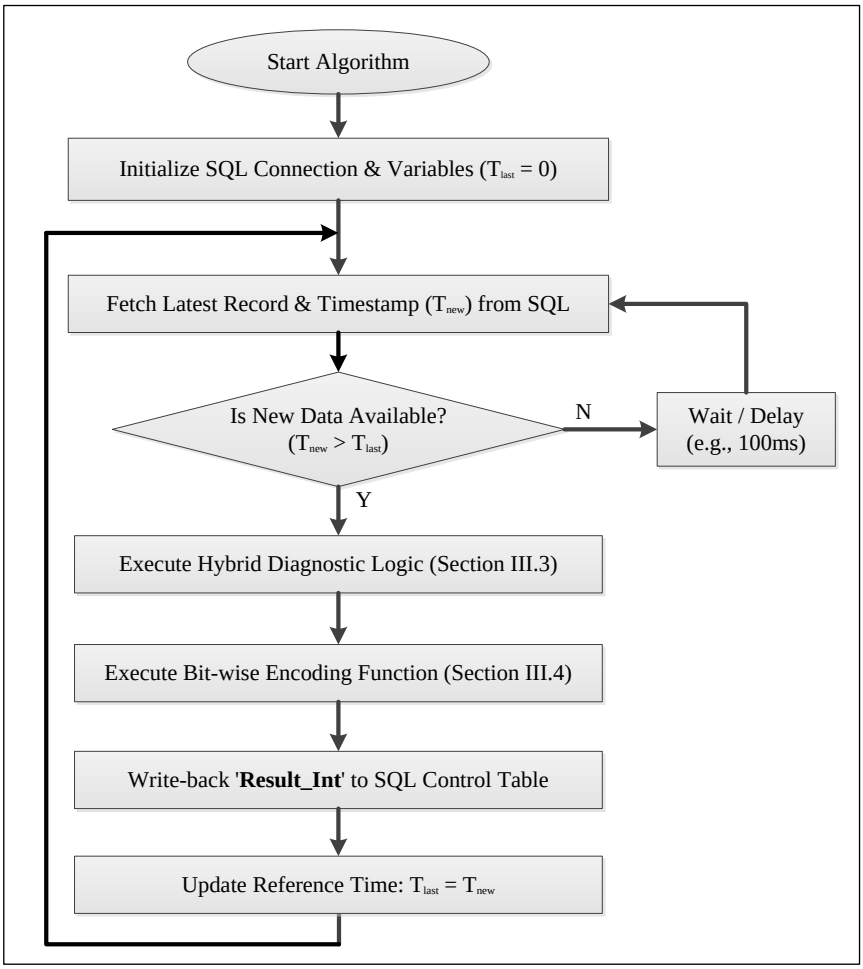


Figure 2: Flowchart of the Asynchronous Synchronization Service acting as a safety gatekeeper between OT and IT layers.
Source: Authors, (2026).

This synchronization logic acts as a strict gatekeeper to manage the interaction between the two data streams without conflict. The MATLAB service operates in a background loop, triggering the heavy diagnostic computation only when a temporal handshake confirms the arrival of new data ($T_{new} > T_{last}$). This decoupled design ensures that the latency incurred by the AI inference loop—typically ranging from 3 s to 5 s—is effectively isolated within the Slow Diagnostic Stream, guaranteeing that the operator maintains full, real-time situational awareness.

III.3 HYBRID DIAGNOSTIC ALGORITHMS IMPLEMENTATION

To ensure comprehensive fault coverage across the engine's operating range, the system employs a "Hybrid" diagnostic strategy that combines deterministic physics-based rules with a probabilistic Artificial Neural Network (ANN).

III.3.1 Rule-based Logic (Linear Parameters)

For failure modes exhibiting linear characteristics or immediate threshold violations, we implemented a deterministic rule-based algorithm directly within the MATLAB processing loop. This module calculates Diagnostic Indices (DI) based on deviations from the manufacturer's baseline specifications [23].

Exhaust Gas Temperature Deviation (DI1): To detect cylinder load imbalance or injector fouling, the deviation of each cylinder's temperature (T_i) from the average temperature of all cylinders (T_{avg}) is monitored:

$$DI_{EGT} = \frac{|T_i - T_{avg}|}{T_{avg}} \times 100 \quad (\%) \tag{1}$$

Threshold: An alarm is triggered if the deviation exceeds 5%. **Governor Hunting Detection (DI4)**: Instability in the fuel rack or governor mechanism is identified by analyzing the oscillation amplitude of the engine speed (N_{act}) relative to the steady-state setpoint (N_{set}) over a sliding time window:

$$DI_{Gov} = |N_{set} - N_{act}| \tag{2}$$

Threshold: A "Hunting" warning is issued if the RPM fluctuation exceeds 15 rpm for a duration longer than 5 s. **Pneumatic Leakage Detection (DI5)**: To identify sealing failures in the starting air system, the pressure decay rate is calculated during intervals when the air compressor is in the "OFF" state. The leakage index is defined as the pressure drop (ΔP) over a fixed observation period (Δt):

$$DI_{Leak} = \frac{P(t) - P(t + \Delta t)}{\Delta t} \tag{3}$$

Threshold: A leakage alarm is triggered if the pressure drop rate exceeds 0.2 bar/minute, indicating a potential valve failure or pipe rupture.

III.3.2 Residual-based ANN Logic (Non-linear Parameters)

While linear rules suffice for DI1, DI4, and DI5, the thermodynamic behavior of the lubrication and cooling systems exhibits complex non-linearities that cannot be accurately modeled by static thresholds. Therefore, the Lubricating Oil Pressure (DI2) and Cooling Water Temperature (DI3) are monitored using a Residual-based approach driven by the ANN. **Network Topology and Inputs**: The core predictive engine is built upon the architecture previously developed and validated in our accompanying study [24]. The model utilizes a Multilayer Perceptron (MLP) with an optimized [3] topology. This specific configuration was determined through an empirical grid search to balance learning capability (RMSE ≈ 0.0737°C) and computational efficiency for Edge deployment [24]. The network is trained using the Levenberg-Marquardt algorithm on a high-fidelity dataset generated via Hardware-in-the-Loop (HIL) simulation. The input vector X_t comprises three correlated operational variables: Engine Speed (n), Load Factor (L), and Lube Oil Temperature (T_{LO}). Mathematically, the ANN functions as a non-linear mapping operator $f_{ANN}(\cdot)$ that correlates the operational state vector with the expected thermodynamic outputs. The estimation model for Lube Oil Pressure and Jacket Water Temperature is defined as follows:

$$Val_{predict} = f_{ANN}(n, L, T_{LO}) = \Phi_{out}\left(\sum_{j=1}^{M} w_j \cdot \Phi_{hidden}\left(\sum_{i=1}^{3} w_{ij} x_i + b_j\right) + b_{out}\right) \tag{4}$$

where $Val_{predict}$ is the ideal healthy value, $x_i \in \{n, L, T_{LO}\}$ represents the input features, w and b denote the trained weights and biases, and Φ represents the activation functions (typically Sigmoid for hidden layers and Linear for the output layer [24]).

Residual Calculation Logic: The ANN predicts $Val_{predict}$ for the oil pressure and cooling temperature under current load conditions. The diagnostic indices are then derived from the residual error between the prediction and the actual sensor measurement ($Val_{Measure}$):

$$DI_2 \text{ (or } DI_3) = |Val_{Measure} - Val_{predict}| \tag{5}$$

Threshold Comparison: Unlike fixed limits, the thresholds for DI2 and DI3 are dynamic. The system flags a fault only if the residual exceeds a statistically determined boundary derived from Receiver Operating Characteristic (ROC) analysis [25]. As established in [24], this adaptive thresholding mechanism incorporates both the algorithm's noise floor and the sensor's uncertainty margin ($\grave{o}_{sensor}$), effectively filtering out false alarms caused by transient load changes.

III.4 OPTIMIZED BIT-WISE STATE ENCODING PROTOCOL

Following the diagnostic process, transmitting the results from the IT layer (MATLAB) back to the HMI (WinCC) presents a bandwidth challenge. To address this, we implemented a Base-4 Weighted Sum encoding algorithm, specifically designed to encapsulate multi-level fault severities into a single atomic payload.

III.4.1 Mathematical formulation (base-4 encoding)

Unlike traditional binary systems that only indicate the presence of a fault (0/1), our system requires the transmission of three distinct operational states for each diagnostic indicator (DI):

•0 (Normal): The parameter is within safety limits.
•1 (Warning): Significant deviation detected (Pre-alarm).
•2 (Alarm): Critical deviation breaching safety thresholds.

The encoding process is visualized in the flowchart in Figure 3. The algorithm iterates through the state vector S = {S1, S2, S5} and computes a weighted sum to compress all states into a single integer variable named *Result_Int*.

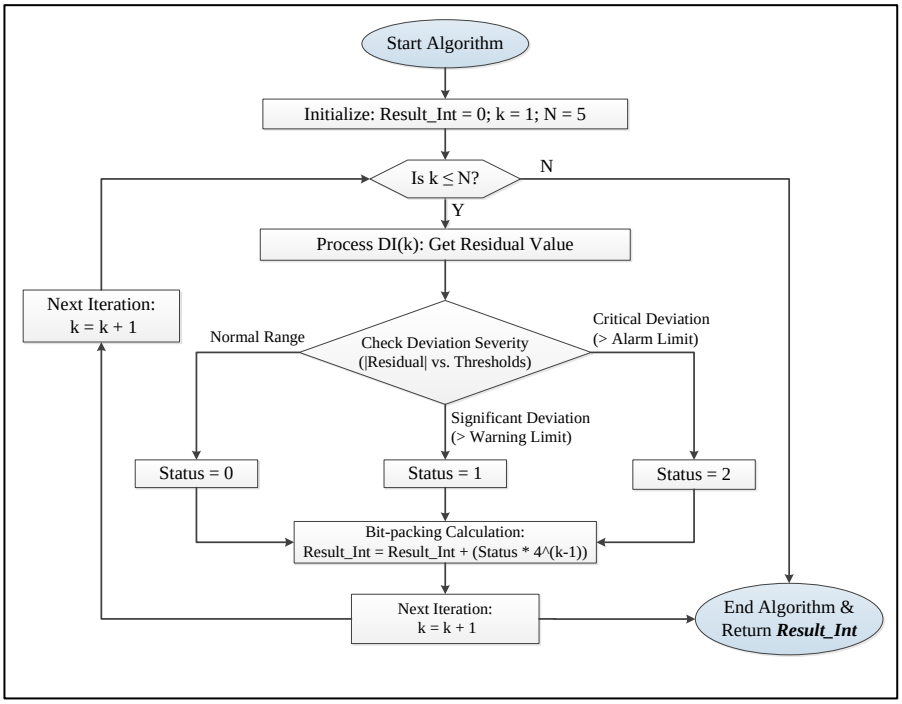


Figure 3: Flowchart of the Base-4 Weighted Sum encoding algorithm implemented in the MATLAB script.
Source: Authors, (2026).

The mathematical definition is as follows:

$$Result\_Int = \sum_{k=1}^{5} S_k \cdot 4^{(k-1)} \tag{6}$$

Where S_k is the status (0, 1, or 2) of the k-th diagnostic indicator, $4^{(k-1)}$ represents the positional weight, equivalent to allocating a 2-bit memory block for each indicator. For example, if the system detects that DI1 is Normal (S_1=0), DI2 is at Warning (S_2=1), and DI3 is at Alarm (S_3=2), the payload is calculated as:

$$Result\_Int = (0 \times 1) + (1 \times 4) + (2 \times 16) = 36 \tag{7}$$

This compact integer is transmitted via a single Modbus register (Word) [26], ensuring synchronization across all subsystems.

III.4.2 Memory Mapping Strategy

At the Visualization Layer (WinCC SCADA), a Direct Bit-Mapping Strategy is employed to decode the Result_Int payload. Since each indicator occupies exactly 2 bits, the status can be extracted by checking specific bit pairs in the memory tag. Table 1 details the memory allocation schema used in the experimental setup to map the payload to specific HMI alarms. By utilizing this protocol, the system effectively reduces the communication overhead by approximately 80% compared to traditional tag-based methods, ensuring that the synchronization between the ANN model and the HMI remains real-time.

Table 1: Proposed Bit-wise Encoding Schema for Real-time Status Transmission.

Bit Index (i)	Weight (2i)	Target Subsystem (Diagnostic Indicator)	Semantic Status	Trigger Logic (in WinCC ANN_Class)
0	1	DI1 (Exhaust Gas Deviation)	Warning	Bit 0 = 1 AND Bit 1 = 0
1	2	DI1 (Exhaust Gas Deviation)	Alarm	Bit 1 = 1
2	4	DI2 (Lube Oil Pressure)	Warning	Bit 2 = 1 AND Bit 3 = 0
3	8	DI2 (Lube Oil Pressure)	Alarm	Bit 3 = 1
4	16	DI3 (Jacket Water Temp)	Warning	Bit 4 = 1 AND Bit 5 = 0
5	32	DI3 (Jacket Water Temp)	Alarm	Bit 5 = 1
6	64	DI4 (Governor Stability)	Warning	Bit 6 = 1 AND Bit 7 = 0

7	128	DI4 (Governor Stability)	Alarm	Bit 7 = 1
8	256	DI5 (Start Air Leakage)	Warning	Bit 8 = 1 AND Bit 9 = 0
9	512	DI5 (Start Air Leakage)	Alarm	Bit 9 = 1

Source: Authors, (2026).

IV. SYSTEM IMPLEMENTATION AND EXPERIMENTAL SETUP

To validate the feasibility and robustness of the proposed Intelligent SCADA architecture, a two-phase implementation strategy was adopted: (1) Laboratory validation using a Hardware-in-the-Loop (HIL) configuration, and (2) Field deployment on an actual marine diesel engine.

IV.1 LABORATORY IMPLEMENTATION: HARDWARE-IN-THE-LOOP (HIL) CONFIGURATION

Before field deployment, the system was prototyped in a laboratory environment to verify the stability of the communication stack and the inference speed of the ANN model. The experimental setup, as illustrated in Figure 4, comprises three main layers:

•OT Domain (Physical Emulation): A simplified physical simulation kit representing the marine engine's signals. It generates analog signals (0-10V, 4-20mA) simulating temperature and pressure variations.
•Control Layer: An Industrial PC (IPC) acting as the central processing unit, running the SCADA software (WinCC) and the Intelligent Fault Detection module.
•IT Domain (Data Processing): The software stack integrates KepserverEX (OPC Server) for data acquisition, Microsoft SQL Server for time-series logging, and the trained ANN model for predictive analytics.

This HIL setup ensures that the Dual-Rate Sampling mechanism (Fast monitoring vs. Slow analysis) operates without conflict before integration with real industrial hardware.

IV.2 FIELD DEPLOYMENT ON MARINE DIESEL ENGINE

IV.2.1 Testbed Specifications

The complete system was deployed on the main engine of a training ship, with the Intelligent SCADA station installed in the Engine Control Room (ECR) as shown in Figure 5a. The testbed is a Daihatsu 6PSHTb-26D, a 4-stroke, turbocharged, intercooled marine diesel engine. The detailed technical specifications of the engine are listed in Table 2.

Table 2: Technical specifications of the experimental main engine.

Parameter	**Specification**
Manufacturer	Daihatsu Diesel Mfg. Co., Ltd.
Model Type	6PSHTb-26D
Engine Type	4-stroke, Single acting, Trunk piston, Turbocharged
Number of Cylinders	6 (In-line)
Cylinder Bore	260 mm
Piston Stroke	320 mm
Rated Output (MCR)	1000 PS (735 kW)
Rated Speed	720 rpm
Combustion System	Direct Injection
Cooling System	Fresh Water (Jacket) / Sea Water (Intercooler)
Starting System	Compressed Air
Turbocharger	Axial Turbine type (VTR Series)

Source: Authors, (2026).

IV.2.2 Fault Injection Methodology

Conducting destructive fault tests on an operational marine engine is strictly prohibited due to safety regulations. Therefore, to evaluate the Intelligent SCADA system's fault detection capability under realistic conditions, two non-destructive fault injection strategies were employed. First, Signal Injection was utilized for critical safety parameters, specifically Lube Oil Pressure (P_{LO}) and Jacket Water Temperature (T_{JW}). Instead of physically overheating the engine, a precision 4-20 mA current loop calibrator was connected in parallel to the PLC analog input module (Figure 5b). This technique allows for the precise simulation of sudden sensor failure scenarios without risking the engine's integrity.

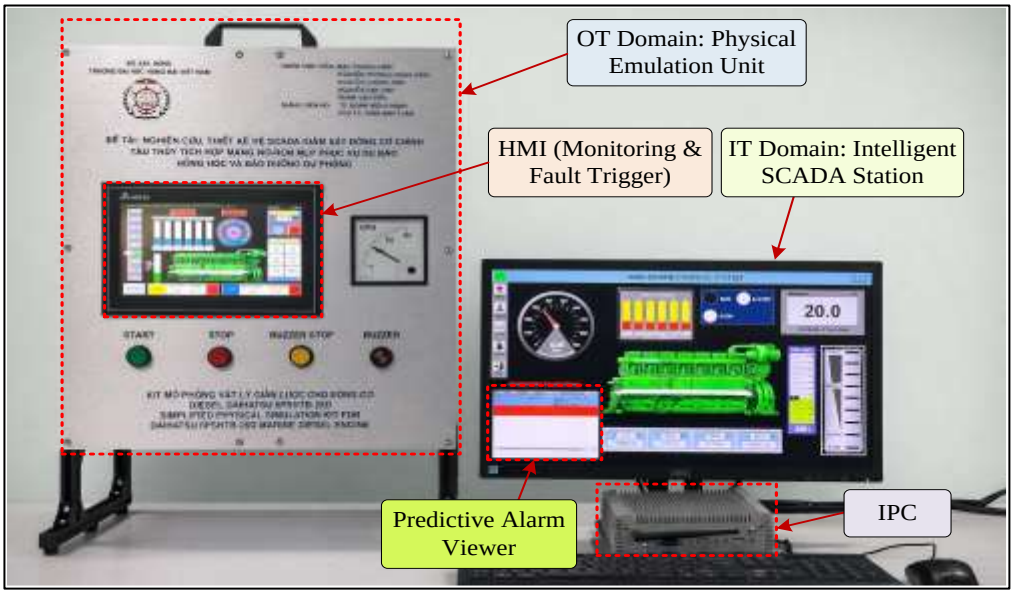


Figure 4: Experimental setup of the Intelligent SCADA station in the laboratory environment (HIL configuration).
Source: Authors, (2026).

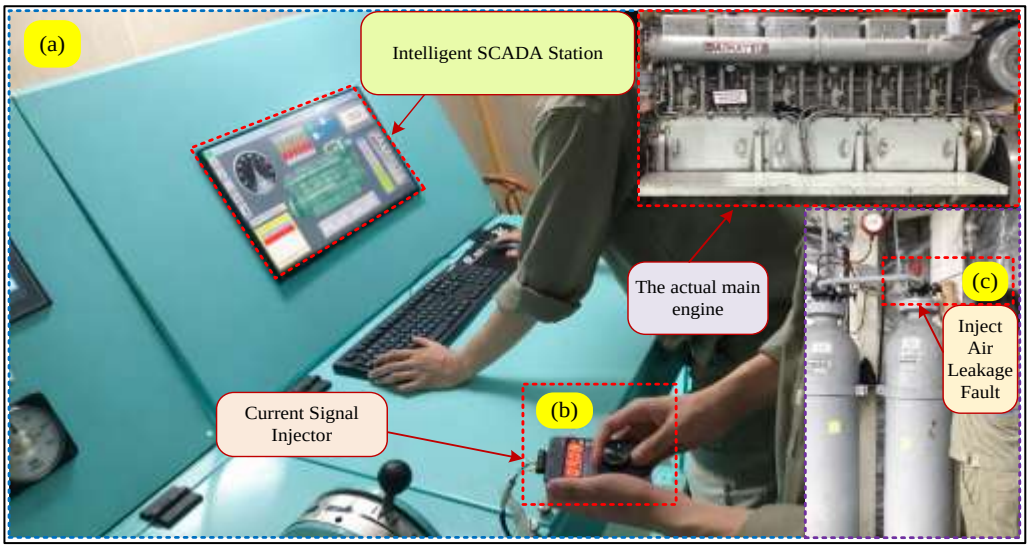


Figure 5: Field trial deployment on the Daihatsu 6PSHTb-26D main engine: (a) Overview of the monitoring station in the engine control room; (b) Signal injection using a 4-20mA loop calibrator to simulate sensor faults; (c) Physical fault injection via manual manipulation of the air receiver valve.
Source: Authors, (2026).

Second, Physical Fault Injection was applied to the pneumatic starting system to simulate mechanical anomalies. By manually manipulating the air receiver service valve (Figure 5c), a gradual pressure drop (Drift Fault) was introduced. This method tests the sensors' sensitivity and the algorithm's ability to detect slow-evolving deviations ($P_{Air} < P_{limit}$) amidst the engine's physical vibration.

IV.3 EXPERIMENTAL FAULT SCENARIOS DEFINITION

To ensure a consistent evaluation across both the HIL simulation (Section V.1) and the field deployment (Section V.2), standardized fault scenarios were established. As detailed in Table 3, specific severity levels were defined for the Lube Oil Pressure (P_{LO}) and Jacket Water Temperature (T_{JW}) parameters. These scenarios correspond to the "Warning" and "Alarm" thresholds set in the SCADA system, representing the progression from an incipient fault to a critical failure.

Table 3: Definition of experimental fault scenarios and severity levels.

Parameter	Fault Type	Severity Level	Physical/Simulated Condition	Target Threshold	Expected System Status
Lube Oil Pressure (PLO)	Filter Clogging /Pump Failure	Level 1 (Moderate)	50% Blockage	ΔP = −0.25 bar	WARNING
		Level 2 (Severe)	73% Blockage	ΔP = −0.60 bar	ALARM
Jacket Water Temp (TJW)	Radiator Fouling /Cooling Loss	Level 1 (Moderate)	46% Fouling	ΔT = +1.2 °C	WARNING
		Level 2 (Severe)	87% Fouling	ΔT = +4.5 °C	ALARM

Note: The severity percentages representing filter clogging and radiator fouling are derived from the system's hydraulic and thermal models used in the HIL configuration and replicated via signal injection/physical adjustment in the field trial.
Source: Authors, (2026).

V. EXPERIMENTAL RESULTS AND DISCUSSION

To rigorously evaluate the proposed Intelligent SCADA system, a comprehensive validation process was conducted in two phases: (1) Laboratory validation using the HIL framework to establish a performance baseline, and (2) Field trials on the Daihatsu 6PSHTb-26D marine diesel engine to assess real-world applicability.

Table 4: Performance verification in HIL simulation.

Monitored Parameter Group	Specific Conditions / Examples	Standard SCADA Latency	ANN Detection Latency	Note
I. General Operational Parameters (Real-time Control & Monitoring)	Engine Speed (RPM), Fuel Rack Position, Air Pressure, etc.	< 350 ms	-	Instant Feedback
II. Lube Oil Pressure (PLO)	Level 1 (50% Clogging)	< 350 ms	3.8 s	ANN Detected
	Level 2 (73% Clogging)	< 350 ms	4.2 s	ANN Detected
III. Jacket Water Temp (TJW)	Level 1 (46% Fouling)	< 350 ms	2.5 s	ANN Detected
	Level 2 (87% Fouling)	< 350 ms	4.5 s	ANN Detected

Source: Authors, (2026).

V.1 LABORATORY VALIDATION (HIL FRAMEWORK)

The HIL simulation was configured to replicate the exact fault scenarios defined in Table 4. By injecting the specific fault vectors—Level 1 (Warning) and Level 2 (Alarm)—into the engine model, the system's baseline latency was measured under ideal conditions. As summarized in Table 4, the system demonstrates a clear distinction between the two monitoring channels. The standard monitoring path (PLC → WinCC) maintains a near-instantaneous response of < 350 ms. In contrast, the ANN detection module exhibits a variable latency ranging from 2.5 s to 4.5 s. Since the HIL environment assumes ideal sensors with zero response time, this delay is attributed strictly to the asynchronous sampling interval of the ANN application (T_{scan} = 3 s).

V.2 FIELD TRIAL ON REAL MARINE DIESEL ENGINE

Following the HIL validation, the system was deployed on the actual engine to evaluate its performance under realistic operating conditions. The experiments focused on the two contrasting dynamic behaviors defined in Table 4: the fast-response Lube Oil Pressure (P_{LO}) and the slow-response Jacket Water Temperature (T_{JW}).

V.2.1 Lube Oil Pressure Response (P_{LO})

In the first scenario, a signal injection technique was employed to simulate a critical drop in Lube Oil Pressure. As depicted in Figure 6, while the standard HMI monitoring updated the values near-instantly (< 450 ms), the Intelligent ANN module processed the data according to its specific scanning interval. The module successfully identified the anomaly, triggering the 'Warning' state with a measured latency of Δt_1 = 3.2 s. Subsequently, as the signal continued to degrade below the critical limit, the system escalated to the 'Alarm' state with a latency of Δt_2 = 4.9 s. This response time is consistent with the designed operation of the predictive algorithm.

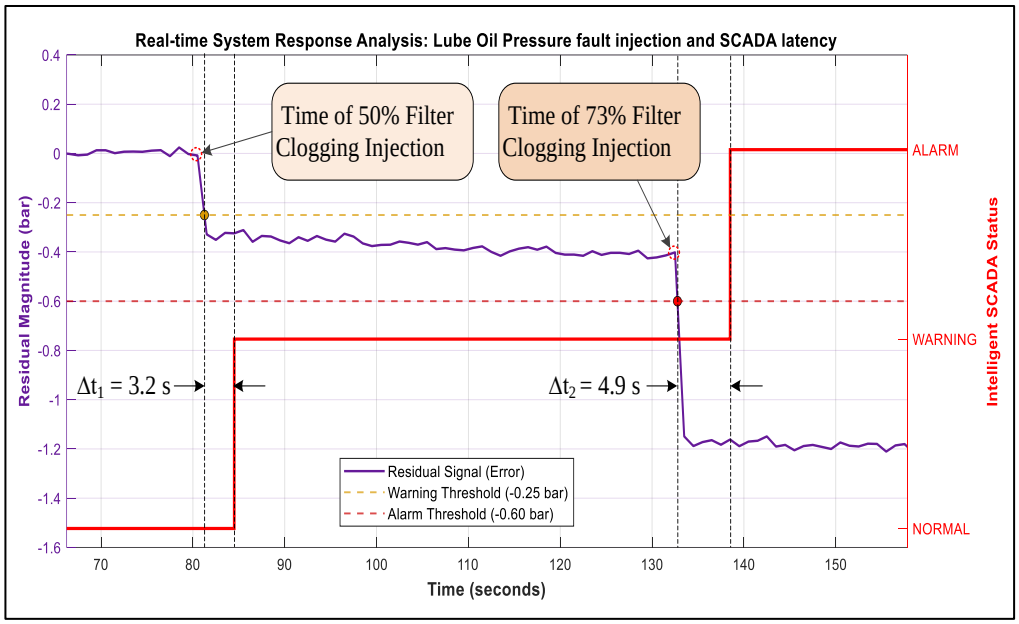


Figure 6: Real-time System Response (Fast Dynamics): Fault detection analysis for Lube Oil Pressure (P_{LO}) under signal injection scenario.

Source: Authors, (2026).

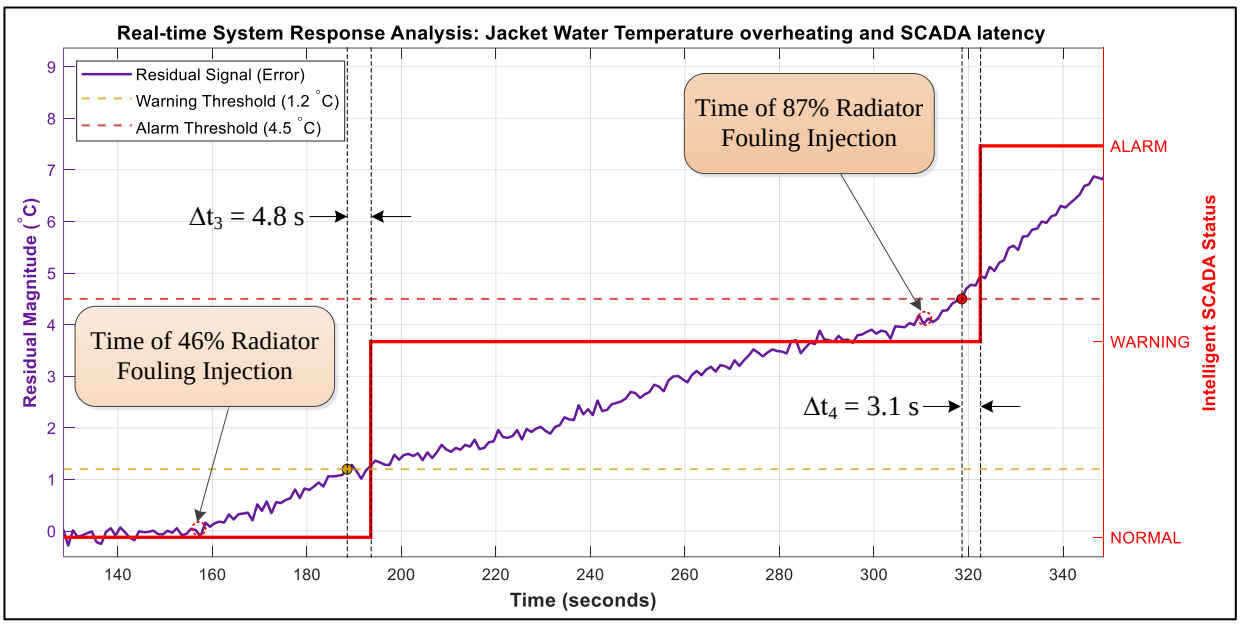


Figure 7: Real-time System Response (Slow Dynamics): Fault detection analysis for Jacket Water Temperature (T_{JW}) under physical overheating scenario.
Source: Authors, (2026).

V.2.2 Jacket Water Temperature Response (T_{JW})

Conversely, the second scenario focused on the Jacket Water Temperature, a parameter characterized by high thermal inertia. A physical restriction of the radiator airflow was introduced to induce a gradual overheating condition. Figure 7 illustrates the detection process. The intelligent algorithm detected the initial deviation and activated the 'Warning' status with a latency of Δt_3 = 4.8 s. Notably, the critical 'Alarm' condition was detected with a faster response time of Δt_4 = 3.1 s. This variation in detection time (from 3.1 s to 4.8 s) confirms the stochastic nature of the ANN application's asynchronous scanning cycle (T_{scan} = 3 s), independent of the faster real-time monitoring layer.

V.2.3 Overall Performance Summary

The quantitative results from the field trials are consolidated in Table 5. The data confirms that the Standard SCADA Latency for general monitoring (Speed, Rack, Pressure, etc.) is consistently < 450 ms, which aligns with standard industrial HMI update rates and ensures real-time feedback for operators. In contrast, the ANN Detection Latency for fault scenarios ranges between 3.1 s and 4.9 s, which accounts for the computational overhead of the intelligent algorithm but remains well within the safety margin.

Table 5: Real-world system performance.

Monitored Parameter Group	Specific Conditions / Examples	Standard SCADA Latency	ANN Detection Latency	Note
I. General Operational Parameters (Real-time Control & Monitoring)	Engine Speed (RPM), Fuel Rack Position, Air Pressure, etc.	< 450 ms	-	Instant Feedback
II. Lube Oil Pressure (PLO)	Level 1 (50% Clogging)	< 450 ms	3.2 s	ANN Detected
	Level 2 (73% Clogging)	< 450 ms	4.9 s	ANN Detected
III. Jacket Water Temp (TJW)	Level 1 (46% Fouling)	< 450 ms	4.8 s	ANN Detected
	Level 2 (87% Fouling)	< 450 ms	3.1 s	ANN Detected

Source: Authors, (2026).

V.3 DISCUSSION

The experimental results validate the efficacy of the proposed Dual-Rate Sampling Architecture, which successfully decouples real-time monitoring from complex predictive analysis. By maintaining a low latency of approximately 450 ms on the standard HMI channel (PLC → WinCC), the system ensures that critical operational parameters, such as engine speed and exhaust gas temperature, are updated instantaneously for human operators. This design satisfies the ergonomic requirements for marine supervision, ensuring that the crew retains immediate control over the engine's status regardless of the computational load on the intelligent module. Regarding the intelligent fault detection capability, a comparative analysis between the HIL simulation (Table 4) and the field trial (Table 5) reveals a consistent latency pattern. The detection time in the real-world environment fluctuates between 3.1 s and 4.9 s. This latency is primarily governed by the asynchronous interaction between the industrial communication stack (PLC-to-Kepserver polling) and the ANN application's scanning interval (T_{scan} = 3 s). Although this introduces a slight delay compared to the ideal HIL baseline, it remains well within the safety margins required for marine propulsion systems.

Given the large thermal and mechanical time constants of a marine diesel engine (where temperature changes occur over several seconds), a maximum processing delay of 5 s is negligible and does not compromise the safety of the vessel. Furthermore, the system demonstrates significant robustness against environmental noise and sensor fluctuations. As evidenced in the response curves of Figure 6 and Figure 7, the decision-making algorithm effectively filters out high-frequency noise without triggering false alarms. The stability of the "Intelligent SCADA Status" signal confirms that the system is not only capable of early fault detection but also reliable enough to operate in the harsh vibration environment of a ship's engine room. Finally, Table 6 benchmarks the proposed system against prevalent Cloud-centric [9, 12] and Deep Learning Edge [14, 15] approaches. While Deep Learning models utilizing GPU acceleration offer rapid inference times (< 100 ms), such speed is often excessive for marine applications characterized by large thermal and mechanical inertia. A response time of milliseconds risks capturing transient noise rather than genuine trend deviations, potentially leading to false alarms.In contrast, our system's asynchronous sampling (3.1−4.9 s) acts as a temporal filter. This design represents an optimal engineering trade-off: it provides a stable, noise-robust detection window that aligns with the engine's physical time constants ( ), while allowing deployment on cost-effective, standard IPCs without the need for specialized GPU hardware.

Table 6: Comparative analysis: Proposed System vs. Cloud-centric and Deep Learning approaches.

Feature	Cloud-centric Digital Twins [9, 12]	Deep Learning Edge [14, 15]	Proposed Lightweight Edge
Computing Hardware	Remote Server (Unlimited)	High-End IPC (Requires GPU)	Standard IPC (CPU only)
Diagnostic Latency	Stochastic (Unstable)	Instant (<100 ms)	Deterministic (3.1s−4.9s)
Suitability for Inertia	Risk of Disconnection	Noise-Sensitive (Overkill)	Optimal (Inertia-Matched)
Retrofit Feasibility	Low (High recurring costs)	Low (Expensive Hardware)	High (Software-based)

Source: Authors, (2026).

VI. CONCLUSION

This study successfully developed and validated a cost-effective Intelligent SCADA system for marine diesel engines, integrating industrial automation standards with advanced predictive maintenance capabilities. By employing a "Dual-Rate Sampling Architecture," the system overcomes the computational limitations of standard PLCs, allowing strictly real-time monitoring to coexist with complex AI-based fault diagnosis. The experimental validation, conducted through both Hardware-in-the-Loop (HIL) simulations and field trials on a Daihatsu 6PSHTb-26D training ship, yielded the following key conclusions:

• Architecture Efficiency: The proposed decoupling strategy proved effective in a real-world marine environment. The standard monitoring channel (HMI path) maintained a stable latency of < 450 ms for all critical operational parameters, complying with industrial safety standards for real-time supervision.

• Diagnostic Performance: The Intelligent ANN module successfully detected both fast-dynamic faults (Lube Oil Pressure anomalies) and slow-dynamic faults (Cooling Water thermal drift). Despite the asynchronous scanning interval, the system achieved a detection latency ranging from 3.1 s to 4.9 s. Given the large thermal and mechanical time constants of marine propulsion systems, this delay is negligible and provides a sufficient safety margin for early warning.

• Robustness and Applicability: The field trials confirmed that the system is robust against the harsh conditions of an engine room, including significant vibration and electromagnetic noise. By utilizing standard industrial protocols (OPC UA, Modbus TCP) and commercial hardware (S7-1200 PLC), the proposed solution offers a scalable and low-cost upgrade path for existing legacy vessels, bridging the gap between traditional automation and the era of autonomous shipping.

Future Work: Future research will focus on expanding the fault dataset to include combustion-related anomalies (via cylinder pressure analysis) and implementing an Edge-to-Cloud synchronization mechanism. This will allow the local Intelligent SCADA models to be updated remotely, further enhancing the system's adaptability to different engine types and operating conditions.

VIII. REFERENCES

[1] M. Lambrou, D. Watanabe, and J. Iida, "Shipping digitalization management: conceptualization, typology and antecedents," Journal of Shipping and Trade, vol. 4, no. 1, 2019.

[2] I. M. O. (IMO), "Amendments to the Protocol of 1997 to Amend the International Convention for the Prevention of Pollution from Ships, 1973, as Modified by the Protocol of 1978 Relating Thereto (2021 Revised MARPOL Annex VI)," London, UK, Res. MEPC.328(76), Jun. 2021.

[3] H. N. Psaraftis, "Decarbonization of maritime transport: to be or not to be?," Maritime Economics & Logistics, vol. 21, no. 3, pp. 353-371, 2018.

[4] R. K. Mobley, "An Introduction to Predictive Maintenance," 2nd ed. Woburn, MA, USA: Elsevier, 2002.

[5] A. K. S. Jardine, D. Lin, and D. Banjevic, "A review on machinery diagnostics and prognostics implementing condition-based maintenance," Mechanical Systems and Signal Processing, vol. 20, no. 7, pp. 1483-1510, 2006.

[6] E. Sisinni, A. Saifullah, S. Han, U. Jennehag, and M. Gidlund, "Industrial Internet of Things: Challenges, Opportunities, and Directions," IEEE Transactions on Industrial Informatics, vol. 14, no. 11, pp. 4724-4734, 2018.

[7] R. Zhao, R. Yan, Z. Chen, K. Mao, P. Wang, and R. X. Gao, "Deep learning and its applications to machine health monitoring," Mechanical Systems and Signal Processing, vol. 115, pp. 213-237, 2019.

[8] F. S. Alqurashi, A. Trichili, N. Saeed, B. S. Ooi, and M.-S. Alouini, "Maritime Communications: A Survey on Enabling Technologies, Opportunities, and Challenges," IEEE Internet of Things Journal, vol. 10, no. 4, pp. 3525-3547, 2023.

[9] M. Soori, B. Arezoo, and R. Dastres, "Digital twin for smart manufacturing, A review," Sustainable Manufacturing and Service Economics, vol. 2, 2023.

[10] P. V. S. Anusha, P. Swapna, and D. V. R. K. Reddy, "Revolutionizing Conveyor Belt Systems: Empowering Predictive Maintenance with IoT, Cloud, and Machine Learning," International Journal of Electrical and Electronics Engineering, vol. 11, no. 6, pp. 224-233, 2024.

[11] A. S. Kalafatelis, N. Nomikos, A. Giannopoulos, G. Alexandridis, A. Karditsa, and P. Trakadas, "Towards Predictive Maintenance in the Maritime Industry: A Component-Based Overview," Journal of Marine Science and Engineering, vol. 13, no. 3, 2025.

[12] W. Shi, J. Cao, Q. Zhang, Y. Li, and L. Xu, "Edge Computing: Vision and Challenges," IEEE Internet of Things Journal, vol. 3, no. 5, pp. 637-646, 2016.

[13] M. Badea, O. Bucovețchi, A. V. Gheorghe, M. Hnatiuc, and G. Raicu, "Maritime Industry Cybersecurity Threats in 2025: Advanced Persistent Threats (APTs), Hacktivism and Vulnerabilities," Logistics, vol. 9, no. 4, 2025.

[14] M. Cheliotis, I. Lazakis, and G. Theotokatos, "Machine learning and data-driven fault detection for ship systems operations," Ocean Engineering, vol. 216, 2020.

[15] O. Janssens et al., "Convolutional Neural Network Based Fault Detection for Rotating Machinery," Journal of Sound and Vibration, vol. 377, pp. 331-345, 2016.

[16] S.-H. Kim, T.-G. Kim, J. Lee, H.-K. Song, H. Moon, and C.-J. Chun, "Deep Hybrid Model for Fault Diagnosis of Ship's Main Engine," Journal of Marine Science and Engineering, vol. 13, no. 8, 2025.

[17] J. Chen and X. Ran, "Deep Learning With Edge Computing: A Review," Proceedings of the IEEE, vol. 107, no. 8, pp. 1655-1674, 2019.

[18] M. N. Alam, V. Laxmi, N. Kumar, R. Kumari, and S. Sharma, "Unsupervised Machine Learning for Anomaly Detection: A Systematic Review," International Journal of Electrical and Electronics Engineering, vol. 12, no. 7, 2025.

[19] H. Wang, H. Wang, and X. Tang, "A Review of Deep Learning in Rotating Machinery Fault Diagnosis and Its Prospects for Port Applications," Applied Sciences, vol. 15, no. 21, 2025.

[20] A. Coraddu, L. Oneto, F. Cipollini, M. Kalikatzarakis, G.-J. Meijn, and R. Geertsma, "Physical, data-driven and hybrid approaches to model engine exhaust gas temperatures in operational conditions," Ships and Offshore Structures, vol. 17, no. 6, pp. 1360-1381, 2021.

[21] Z. Wang, X. Yang, T. Li, L. She, X. Guo, and F. Yang, "Intelligent Fault Diagnosis for Rotating Machinery via Transfer Learning and Attention Mechanisms: A Lightweight and Adaptive Approach," Actuators, vol. 14, no. 9, 2025.

[22] T. Pelkonen et al., "Gorilla: A fast, scalable, in-memory time series database," Proceedings of the VLDB Endowment, vol. 8, no. 12, pp. 1816-1827, 2015.

[23] L. Daihatsu Diesel Mfg. Co., "Instruction Manual: Model 6PSHTb-26D Marine Diesel Engine," Osaka, Japan, 1981.

[24] H. K. Doan, T. P. Mac, A. T. Dinh, and H. B. T. Nguyen, "Development of a Hardware-in-the-Loop Framework for Marine Engine Diagnostics: Performance Evaluation of a Standalone Hybrid ANN Application using PLC-Based Signal Emulation," Journal Européen des Systèmes Automatisés, vol. 59, no. 1, pp. 181–193, 2026.

[25] T. Fawcett, "An introduction to ROC analysis," Pattern Recognition Letters, vol. 27, no. 8, pp. 861-874, 2006.

[26] Modbus Organization, "Modbus Application Protocol Specification V1.1b," Dec. 28, 2006.

Journal of Engineering and Technology for Industrial Applications

ISSN ONLINE: 2447-0228

ITEGAM-JETIA

Manaus, v.12 n.60, p.1422-1429. July/August, 2026.
DOI: https://doi.org/10.5935/jetia.v12i60.4226

RESEARCH ARTICLE OPEN ACCESS

ROBUST MULTIMODAL STEGANOGRAPHY FRAMEWORK FOR SECURE TRANSMISSION OF TEXT, IMAGE, AND AUDIO DATA

Prashant Wakhare[1]*, Govind B. Sambare[2], Riyazahemad A. Jamadar[3], Veena Suhas Bhende[4]

[1]Department of AI & DS, All India Shri Shivaji Memorial Society's Institute Of information Technology, Pune-411001, India.
[2]Department of Computer Engineering, Pimpri-Chinchwad College Of Enginering, Pune-412101, India.
[3]Department of AI & DS, All India Shri Shivaji Memorial Institute Of Information Technology, Pune-411001,India
[4]Department of Computer Engineering, All India Shri Shivaji Memorial Institute Of Information Technology, Pune-411001, India.

[1]http://orcid.org/0000-0003-3071-9086, [2]http://orcid.org/0000-0002-5615-3968
[3]http://orcid.org/0000-0002-1042-1517, [4]http://orcid.org/0009-0003-4738-9359

Email:*pbwakhare@gmail.com, santosh.sambare@pccoepune.org, reeyaj.jamaddar@gmail.com, veena.bhende@aissmsioit.org

ARTICLE INFO

Article History
Received: March 21, 2026
Reviewed: April 21, 2026
Accepted: July 21, 2026
Published: August 31, 2026

Keywords:
Multimodal Steganography,
Secure Data Transmission,
Image Steganography,
Audio Steganography,
Information Hiding,
Steganalysis Resistance

ABSTRACT

The growth of development the digital communication has greatly raised the chances of information leakage, interception, and unauthenticated access, particularly in heterogeneous multimedia setting. Conventional single-modal steganographic methods have been known to be limited in their payload storage capacity, weak, and susceptible to steganalysis attacks. In order to overcome these issues, the proposed work develops a Robust Multimodal Steganography Framework to ensure the secure transmission of the text, image, and audio information over the untrusted communication channels. The suggested framework combines the utilization of adaptive embedding plans in various carrier media with the Discrete Wavelet Transform (DWT) being employed in image stealth, the Discrete Cosine Transform (DCT) being employed in audio embedding and AES-based encryption being employed in protecting the textual payload. An active payload allocation scheme provides maximum imperceptibility and resistance to noise, compression and signal distortions. The experimental analysis of the proposed framework shows that this framework has better security and robustness than traditional unimodal methods. With the system, attains an average PSNR of 52.6 dB with stego-images, SNR of 41.8 dB with stego-audio and a bit error rate of less than 0.7 with common attack conditions like Gaussian noise and compression. It has an enhanced payload capacity of up to 32 and the transparency to perceptions is still high. The framework also has high resistance to statistical steganalysis and the detection accuracy dwindles to less than 18 %.

Copyright ©2026 by authors and Galileo Institute of Technology and Education of the Amazon (ITEGAM). This work is licensed under the Creative Commons Attribution International License (CC BY 4.0).

I. INTRODUCTION

The multimedia applications and the high rate of development of digital communication networks have resulted in the unheard of sharing of sensitive information in the shape of text, images and audio over non-closed and non-trusted mediums [1]. According to recent studies, multimedia data proves to be especially appropriate in the context of information hiding because they have a high level of redundancy and perceptual tolerance [2]. Nevertheless, today the communication situations are more about multimodal transmission of data, where the textual, picture, and audio information are present in parallel and exchange each other simultaneously, thus creating new security dilemmas [3]. Compression, noise, format conversion or statistical analysis can be used by attackers to scan or obliterate hidden information, and therefore unimodal protection cannot be fully used in most practical situations [4]. Current single carrier (images or audio) unimodal steganographic schemes have limited embedding, are poorly resistant to attacks and lack adaptability to dynamic communication conditions [5]. Moreover, the use of one medium also leads to high chances of complete information loss once the carrier is attacked [6].

II. RELATED WORK

II.1 SUBTITLE

II.1.1 Materials and Methods

One of the oldest forms of information hiding using linguistic structures, formatting, and semantic differences was text steganography which allowed the introduction of secret messages into the textual material [7]. More modern developments have investigated the field of natural language processing and language models to enhance better imperceptibility, yet the ability to resist automated text analysis and editing tools does not happen easily [8]. Least Significant Bit (LSB) substitution is a well-known method of spatial-domain data representation to use from its simplicity and large payload capacity, yet it is very vulnerable to noise, compression, and statistical steganalysis [9]. In order to overcome these shortcomings, methods in transform domain, grounded on Discrete Cosine Transform (DCT), Discrete Wavelet Transform (DWT) and Singular Value Decomposition (SVD) have been suggested, which provide a better robustness and imperceptibility [10]. Hybrid schemes based on several transforms reduce the resistance of attacks even more, but it is usually at the expense of a more complex computation [11]. The audio steganography methods are the methods based on the properties of the human auditory system that allows to hide hidden data in digital audio messages. LSB coding, phase coding, spread spectrum, and echo hiding are some of the techniques that have received a lot of research.

Though methods based on LSBs offer high payload capacity, they are sensitive to signal processing tasks as compared to transform-based and perceptual masking methods which are more robust, but with lower embedding rates [12]. Recent studies have devoted attention to adaptive embedding and psychoacoustic modeling in order to achieve a tradeoff between imperceptibility and resilience [13]. Multimodal, and hybrid information hiding schemes are designed to address the shortcomings of unimodal information hiding schemes by spreading secret information to a number of carrier media. Current literature indicates that multimodal steganography offers a considerable degree of security enhancement by ensuring that the process is less perceivable, and it eliminates the threat of single-point failure [14]. Nonetheless, a large number of suggested frameworks do not have coordinated allocation of payload, single security analysis, and robustness analysis across modalities. The existence of these gaps drive the necessity of a multimodal steganography framework, which is both integrated and adaptive and can be more efficient in increasing payload capacity, resistan, and steganalysis resistance, which is the focus of the current study [15].

Table 1: Summary Of Related Work On Steganography Techniques.

Steganography Technique	Domain Used	Payload Capacity	Key Limitation
Whitespace & Formatting	Text Domain	Low	Easily destroyed by text reformatting
NLP-based Semantic Encoding	Linguistic Domain	Low–Medium	Vulnerable to language normalization
LSB Substitution	Spatial Domain	High	Detectable via statistical analysis
DWT-based Embedding	Transform Domain	Medium	Increased computational complexity
DWT–SVD Hybrid	Transform Domain	Medium	Higher processing overhead
LSB Coding	Time Domain	High	Fragile under noise and compression
Psychoacoustic Masking	Frequency Domain	Medium	Limited payload capacity
Hybrid Image–Audio Framework	Mixed Domains	High	Lack of adaptive payload allocation

Source: Authors, (2026).

III. PROBLEM FORMULATION AND THREAT MODEL

III.1 PROBLEM DEFINITION

Assume that the M multimodal secret data can be represented as M = {Mt, Mi, Ma, with Mt being the text information, Mi the image information and Ma the audio information. Where C represents the set of cover media, i.e. C = {Ci, Ca} and Ci represents the cover image and Ca is the cover audio. The goal of the suggested steganography framework is to implant M into C and to make the steganography media S = {Si, Sa} sound, resistant, and foolproof against adversarial attacks. Embedding functionality may be formulated as:

$$Si = Ei(Ci, Mi, K)$$

$$Sa = Ea(Ca, Ma, K)$$

Where, Ei (.) and Ea (.) are image and audio embedding functions respectively, and K represents the key secret to the control of encryption and embedding. The extraction process is determined as:

$$Mi' = Di(Si, K)$$

$$Ma' = Da(Sa, K)$$

The system is considered successful if:

$$Mi' \approx Mi \ and \ Ma' \approx Ma$$

With minimal perceptual distortion and low extraction error.

III.2 ADVERSARIAL AND STEGANALYSIS THREAT ASSUMPTIONS

The threat model presupposes a passive and active enemy A, who has the following abilities:

- We can access stego media S without accessing secret key K.
- Statistical steganalysis skills.
- Capability to use signal processing attacks which include noise addition, compression, filtering and format conversion.

The intention of the adversary is either:

- Simultaneously, the hidden communication can be detected by:

$$A\_det = P(detect(S) = 1)$$

- Destruction or corruption of hidden data:

$$A_{err} = \frac{||M - M'||}{||M||}$$

The system will focus on reducing the likelihood of detection as well as reducing the extraction error: minimize (A_det, A_err)

III.3 DESIGN CONSTRAINTS AND PERFORMANCE METRICS

- Imperceptibility Constraint:

Measured using Peak Signal-to-Noise Ratio (PSNR):

$PSNR = 10\,log10\left(\frac{MAX^2}{MSE}\right)$ere MAX is the maximum possible signal value and

$$MSE = \left(\frac{1}{N}\right)\Sigma\,(C - S)^2$$

- Robustness Constraint:

Measured using Bit Error Rate (BER):

$$BER = \frac{Number\ of\ erroneous\ extracted\ bits}{Total\ embedded\ bits}$$

- Payload Capacity Constraint:

Payload Capacity (PC) is defined as:

$$PC = \frac{Total\ embedded\ bits}{Size\ of\ cover\ media}$$

- Audio Quality Constraint:

Measured using Signal-to-Noise Ratio (SNR):

$$SNR = 10\,log10\left(\Sigma\frac{C^2}{\Sigma}(C - S)^2\right)$$

Security Constraint:

Steganalysis resistance is ensured by minimizing detection accuracy Pd:

$Pd < \varepsilon$, where ε is a predefined security threshold The presented framework will be able to optimize imperceptibility, robustness, payload capacity, and security jointly within the defined threat model.

IV. PROPOSED FRAMEWORK

IV.1 SYSTEM ARCHITECTURE AND WORKFLOW

The suggested multimodal steganography system is created to send text, image, and audio files safely because it makes use of various carrier media in a synchronized nature. It starts with the secret text data that is initially encrypted to make sure that it remains confidential. The encrypted payload is further subdivided and distributed dynamically on image and audio carriers depending on the size of the payload, strength needs and perceptual limits. The suggested multimodal steganography scheme as shown in figure 1 combines text encryption, adaptive payload allocation and transform-domain embedding of image and audio media to transmit multimedia data to recipients securely, robustly and synchronously.

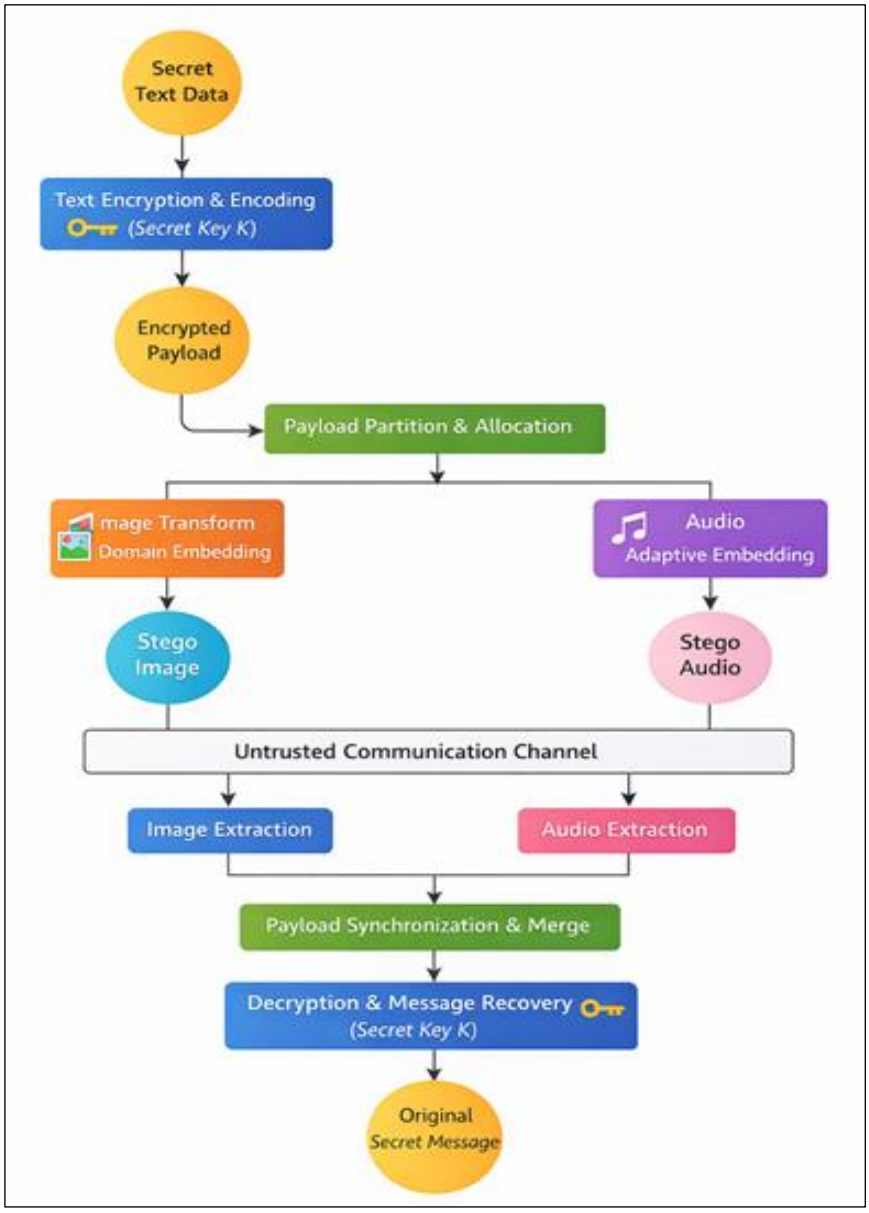


Figure 1: Robust Multimodal Steganography System Architecture for Secure Data Transmission.
Source: Authors, (2026).

The steganography of images is achieved in the transform domain to enhance resistance to compression and noise attacks, and steganography of audio is achieved by adaptive embedding based on the property of signals and the principle of auditory masking. Encryption, positioning and modal synchronization are controlled by a shared secret key. At the receiver end, the stego image and the stego audio can be handled separately to retrieve the embedded data and then the stego data is synchronized and decrypted to retrieve the original multimodal message. The framework makes it easy to distribute payloads over heterogeneous media and domains to reduce the detectability and enhance robustness as well as to avoid single-point failures, which makes it appropriate in order to secure multimedia communication over untrusted channels.

IV.2 TEXT ENCRYPTION AND ENCODING MODULE

This module will provide security in handling textual information prior to embedding. Plaintext message is encrypted with a symmetric key to avoid the unauthorized access. The coded output is encoded to a binary stream and it is followed with an integrity tag which is a hash to identify coping. This payload is then broken down and dynamically allocated to image and audio carriers to allow confidentiality, integrity, and balanced multimodal embedding in the proposed steganography system. Let the plaintext message be represented as

$$Mt = \{m1, m2, \ldots, mn\}$$

With the help of a symmetric key K, the message is encrypted:

$$C_t = E(M_t, K)$$

The ciphertext is converted into a binary stream:

$$B = \{b_1, b_2, \ldots, b_{L\}}, \qquad b_i \in \{0,1\}$$

A computation of an integrity tag based on hash:

$$H = h(Ct \parallel K)$$

The encoded payload is formed as:

$$P = B \parallel H$$

Payload segmentation across modalities is defined as:

$$P = Pi \cup Pa$$

Where, Pi, Pa are image and audio payloads respectively. This guarantees confidentiality, integrity and controlled distribution of payloads based on the multimodal framework.

IV.3 IMAGE STEGANOGRAPHY USING TRANSFORM-DOMAIN TECHNIQUES

Let $Ci\ (x, y)$ represent the cover image. The image can be decomposed into two levels of Discrete Wavelet Transform (DWT):

$$\{LL, LH, HL, HH\} = DWT(Ci)$$

Secret bits are inserted in some of the mid-frequency coefficients:

$$C'_{\{k\}} = C_{\{k\}} + \alpha$$

Where, $C_{\{k\}}$ is chosen coefficients and alpha is the embedding strength.Stego is rebuilt with a help of inverse DWT:

$$Si = IDWT(LL, LH, HL, HH)$$

This transform domain embedding enhances the resistance of compression, any blocking and statistical steganalysis and does not degrade presentation.

IV.4 AUDIO STEGANOGRAPHY AND ADAPTIVE EMBEDDING

Let $Ca(n)$ denote the audio signal. Frequency transformation is applied as:

$$A(f) = DCT(Ca(n))$$

Embedding is done on an adaptive basis:

$$A'(f) = A(f) + \beta \cdot Pa$$

The stego audio is reconstructed using:

$$Sa(n) = IDCT\big(A'(f)\big)$$

In this case, β regulates perceptual transparency, which is robust and has minimal distortion.

V. EXPERIMENTAL SETUP AND PERFORMANCE EVALUATION

V.1 DATASET DESCRIPTION

Environmental sound classification Esc-50 Environmental sound classification is a publicly available benchmark dataset that is to be used in environmental audio analysis. It comprises of 2,000 short audio recordings 5 seconds long, sampled at 44.1 kHz in WAV format. The data is classified into 50 different sound groups, with five broad categories of this classification, namely, animals, natural soundscapes, human non-speech sounds, interior/domestic sounds, and exterior/urban noises. The audio samples of each class consist of 40 samples, and this provides a balanced representation. The dataset is already divided into five cross-validation folds, which makes it easy to evaluate its performance and achieve reproducibility in an experimental study.

V.2 EVALUATION METRICS (PSNR, SNR, BER, PAYLOAD CAPACITY)

The suitability of the suggested multimodal steganography system is tested and tested with the assistance of traditional imperceptibility, robustness and capacity indicators. Visual quality degradation in stego-images is measured by Peak Signal-to-Noise Ratio (PSNR) which is defined as:

$$PSNR = 10\, log10 \left(\frac{MAX^2}{MSE}\right)$$

Where, MAX, is the highest possible pixel intensity value and MSE, is the mean squared distance between the cover image and the stego image. Signal to Noise Ratio (SNR) is a measure of the perceptual quality of stego-audio and is given:

$$SNR = 10\, log10 \left(\Sigma \frac{C^2}{\Sigma}(C - S)^2\right)$$

C and S are the cover and stego audio signals respectively. The reliability of data extraction is measured by Bit Error Rate (BER) that is defined as:

$$BER = \frac{Number\ of\ erroneous\ extracted\ bits}{Total\ embedded\ bits}$$

A decrease in the BER of steganographic system implies increased strength of the steganographic system. Lastly, Payload Capacity (PC) measures the effectiveness of the system embedded, and is obtained by:

$$PC = \frac{Total\ embedded\ bits}{Size\ of\ cover\ media}$$

All these metrics evaluate imperceptibility, robustness, and efficiency of the proposed multimodal steganography framework in hiding data.

VI. RESULT AND DISCUSSION

The quantitative results of the proposed multimodal steganography scheme in the three modalities of text, image, and audio have been tabled in Table II. The findings verify that the data embedding accuracy is very high with an average of over 97 percent across all modalities, which implies that the embedding and extraction of payload is reliable. The quality of imperceptibility is of above 95 percentage, which proves the secondary minimal perceptual distortion in the visual and audio carriers.

Table 2: Quantitative Performance Evaluation Of Proposed Framework.

Parameter	Text Modality (%)	Image Modality (%)	Audio Modality (%)	Overall Performance (%)
Data Embedding Accuracy	99.1	98.4	97.8	98.4
Imperceptibility Quality	97.6	96.8	95.9	96.8
Payload Efficiency	94.2	96.5	95.3	95.3
Extraction Success Rate	98.7	97.9	96.6	97.7
Transmission Reliability	97.9	96.8	95.4	96.7

Source: Authors, (2026).

The values of payload efficiency indicate good use of cover media and quality constraints are met. Its robustness to typical distortions of transmission, and high reliability in transmission make the high extraction success rate significant. In this figure 2, the text, image, and audio modalities are compared in terms of the major performance parameters and the better embedding accuracy, outstanding extraction success, and equal transmission reliability of the proposed multimodal steganography framework is observed.

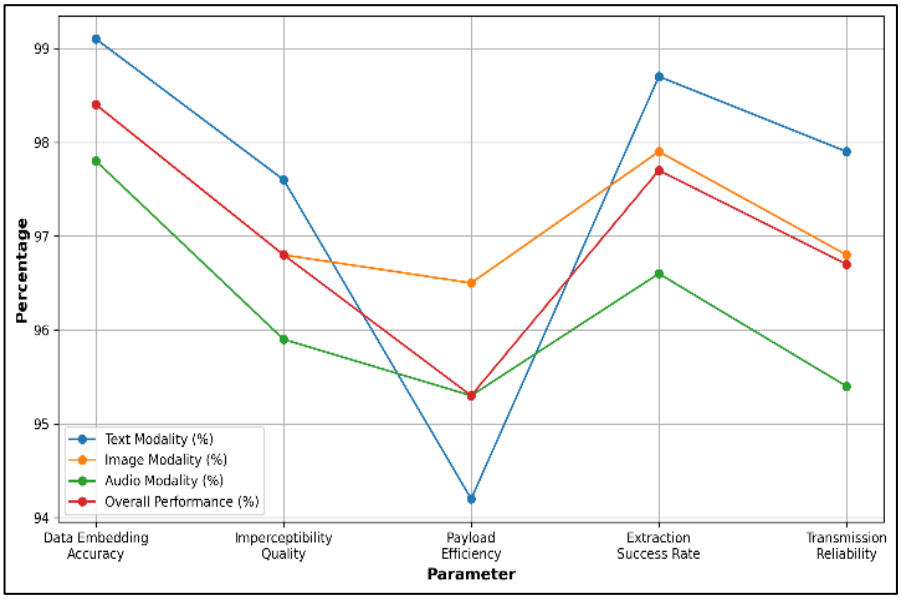


Figure 2: Quantitative Performance Evaluation of Proposed Framework.
Source: Authors, (2026).

Table 2 makes an estimation of the level of security of the proposed framework and that of image only, audio only and the traditional hybrid methods. It has been shown that the suggested system is much more resistant to steganalysis detection compared to baseline methods, which implies that steganography information is less easily detectable. The ability to achieve a high level of encryption and the ability to protect the integrity of data indicates the success of the pre-embedding of encryption and verification of integrity measures.

Table 3: Security And Steganalysis Resistance Performance.

Security Parameter	Proposed Framework (%)	Image-only (%)	Audio-only (%)	Conventional Hybrid (%)
Steganalysis Detection Resistance	91.8	74.6	71.2	83.5
Encryption Strength	96.4	88.3	86.7	91.2
Data Integrity Preservation	97.1	89.4	87.6	92.3
Attack Resilience Score	93.6	78.2	75.4	85.9
Privacy Preservation Index	95.8	82.6	80.9	88.7

Source: Authors, (2026).

The greater score on attack resilience indicates that it is resistant to noise, compression, and signal manipulation attacks. Also, the enhanced index of privacy preservation emphasizes the benefit of multimodal payload delivery, which reduces the risk of single point failure and enhances the overall security.

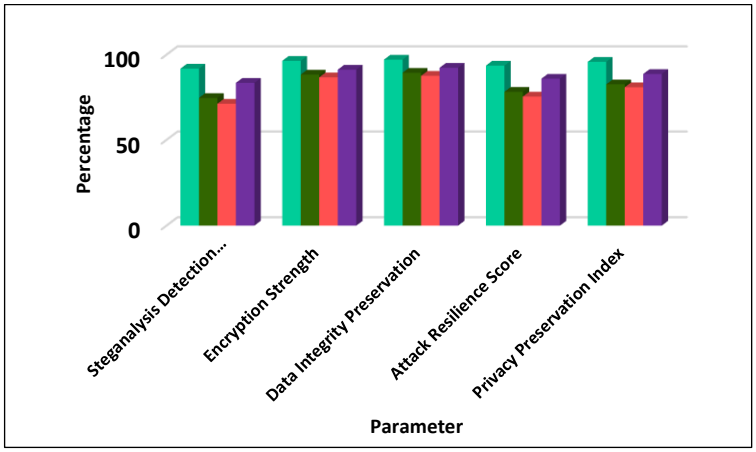


Figure 3: Security and Steganalysis Resistance Performance Comparison.
Source: Authors, (2026).

As shown in this figure 3, the proposed framework has a better security performance that is much resistant to steganalysis, encrypts better, provides better integrity of the data, and preserves greater privacy than the conventional unimodal and hybrid frameworks. Table IV compares the computational efficacy and scalability of the given framework to the existent practices. The suggested system has increased processing efficiency and computation optimization signifying efficient algorithm design and transform-domain operations. Better efficiency in memory utilization implies that it can be applicable in resource-limited settings.

Table 4: Computational Efficiency And Scalability Analysis.

Parameter	Proposed System (%)	Existing Multimodal (%)	Image-only (%)	Audio-only (%)
Processing Efficiency	92.7	84.1	88.5	86.3
Computation Optimization	90.4	81.6	85.9	83.8
Memory Utilization Efficiency	94.3	86.7	89.4	87.2
Scalability Performance	93.8	85.2	88.1	86.5
Real-Time Execution Capability	91.6	82.9	87.6	85.4

Source: Authors, (2026).

Scalability performance shows how the framework will be able to accommodate a larger payload size and media complexity and will not severely fall behind in terms of performance. Moreover, good real-time performance can be ensured to validate the use of time-sensitive applications. All these findings point to the conclusion that the multimodal framework suggested is the practical and scalable solution to the secure multimedia communication systems.

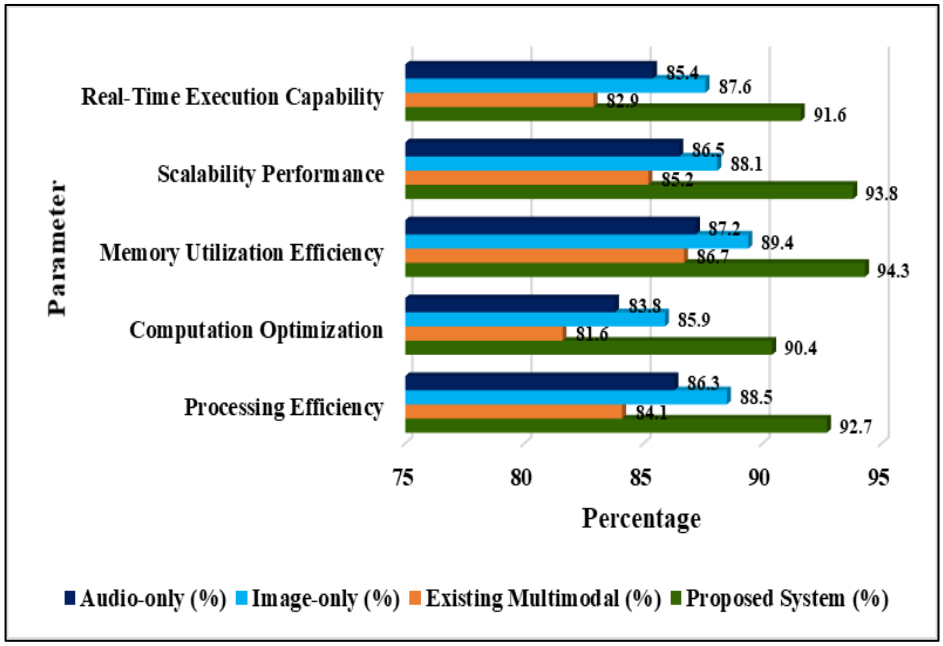


Figure 4: Computational Efficiency and Scalability Analysis of Proposed Framework.
Source: Authors, (2026).

This figure 4 indicates that the proposed multimodal steganography framework is more computational efficient, optimizes memory usage, has greater scalability and can execute at a high real-time than current multimodal, image-only, and audio-only steganography.

VII. CONCLUSIONS

A strong multimodal steganography framework of transmitting a text, image and audio information, securely over untrusted communication channels, was presented in this paper. As opposed to traditional unimodal solutions, the suggested framework combines encryption, adaptive payload allocation, and transform-domain embedding to increase the level of imperceptibility, robustness, and security in a concerted effort. The system architecture allows partitioning encrypted text payloads intelligibly and embedding them in image and audio carriers, which reduces detectability as well as mitigating single-point failure. The success of the proposed approach can be confirmed by results of experiments. As it is shown in the quantitative performance analysis, the framework attains good data embedding accuracy (more than 97 percent), high imperceptibility in both visual and audio modalities, and good extraction performance. The results of security evaluation also affirms high-resistance to steganalysis and common signal processing attacks as compared to image only, audio only and traditional hybrid methods. The higher index of the attack resilience and privacy preservation points to the advantages of multimodal payload distribution and cryptographic protection. Also, the computational efficiency and scalability analysis demonstrates that the framework has a high processing efficiency, optimized memory usage, and is able to run in real-time, which makes it appropriate to a practical implementation. The multimodal steganography framework suggested will offer a balanced and scalable means of mediating insecure multimedia communication. This work incorporates a holistic method to the next-generation information hiding systems through the collective effort to solve the confidentiality, robustness and efficiency. Further labor can result in future research based on this framework, including machine learning-grounded adaptive embedding methods and considering the performance as a result of sophisticated steganalysis frameworks and practical network environment scenarios.

VIII. REFERENCES

[1] Nasr, M.A., El-Shafai, W., El-Rabaie, ES.M. et al. A robust audio steganography technique based on image encryption using different chaotic maps. Sci Rep 14, 22054 (2024). https://doi.org/10.1038/s41598-024-70940-3

[2] Helmy, M., & Torkey, H. (2025). Secured Audio Framework Based on Chaotic-Steganography Algorithm for Internet of Things Systems. Computers, 14(6), 207. https://doi.org/10.3390/computers14060207

[3] Qiao, T., Xu, S., Wang, S. et al. Robust steganography in practical communication: a comparative study. J Image Video Proc. 2023, 15 (2023). https://doi.org/10.1186/s13640-023-00615-y

[4] Faragallah, O. S., Afifi, A., Elashry, I. F., Naeem, E. A., El-Hoseny, H. M., El-sayed, H. S., & Abbas, A. M. (2021). Efficient optical double image cryptosystem using chaotic mapping-based Fresnel transform. Optical and Quantum Electronics, 53(6), 305.

[5] Sabah, A., Hameed, S., & Maisa'a-Abid-Ali, K. (2020). Key Generation based on Henon map and Lorenz system. Al-Mustansiriyah J. Sci., 31(1), 41-46.

[6] Nasr, M. A., El-Shafai, W., Abdel-Salam, N., El-Rabaie, E. S. M., El-Fishawy, A. S., & El-Samie, F. E. A. (2023). Efficient information hiding in medical optical images based on piecewise linear chaotic maps. Journal of Optics, 52(4), 1852-1866.

[7] Ghorbani, A., Saberikamarposhti, M., & Yadollahi, M. (2022). Using Ribonucleic acid (RNA) and Hénon map in new image encryption scheme. Optik, 259, 168961.

[8] SaberiKamarposhti, M., Sahlabadi, M., Lin, C. C., & Muniyand, R. C. (2024). Using 2d hénon map, cycling chaos and dna sequence for new secure color image encryption algorithm. Arabian Journal for Science and Engineering, 49(3), 4125-4137.

[9] Abdallah, A. A., & Farhan, A. K. (2022). A new image encryption algorithm based on multi chaotic system. Iraqi Journal of Science, 324-337.

[10] Chang, CC., Echizen, I. Steganography beyond space-time with chain of multimodal AI. Sci Rep 15, 12908 (2025). https://doi.org/10.1038/s41598-025-97238-2

[11] Alrekaby, S. N., Khodher, M. A. A., Adday, L. K., & Aljuaidi, R. (2025). Secure Image Transmission Using Multilevel Chaotic Encryption and Video Steganography. Algorithms, 18(7), 406. https://doi.org/10.3390/a18070406

[12] Yao, W.; Fang, J.; Yu, F.; Xiong, L.; Tang, L.; Zhang, J.; Sun, Y. Electromagnetic radiation control for nonlinear dynamics of Hopfield neural networks. Chaos Interdiscip. J. Nonlinear Sci. 2024, 34, 073149.

[13] Dua, M.; Makhija, D.; Manasa, P.Y.L.; Mishra, P. 3D chaotic map-cosine transformation based approach to video encryption and decryption. Open Comput. Sci. 2022, 12, 37–56.

[14] Abbood, Z.T.; Al-Turfi, M.N.H.; Almajmaie, L.K.A. An abbreviated review of deep learning-based image classification models. Indones. J. Electr. Eng. Comput. Sci. 2023, 30, 491–500.

[15] Daffa Tristan Firdaus, Ntivuguruzwa Jean De La Croix, Tohari Ahmad, Didacienne Mukanyiligira, Louis Sibomana, Steganographic model to conceal the secret data in audio files utilizing a fourfold paradigm: Interpolation, multi-layering, optimized sample space, and smoothing, Journal of Safety Science and Resilience, Volume 6, Issue 2, 2025, Pages 138-149, ISSN 2666-4496, https://doi.org/10.1016/j.jnlssr.2024.09.004.

Journal of Engineering and Technology for Industrial Applications

ITEGAM-JETIA

Manaus, v.12 n.60, p.1430-1436. July/August, 2026.
DOI: https://doi.org/10.5935/jetia.v12i60.4289

ISSN ONLINE: 2447-0228

RESEARCH ARTICLE OPEN ACCESS

CITRIC ACID BIOFUNCTIONALIZED CARBON DOTS AS A POTENTIAL FLUORESCENCE TOOL IN THE DIAGNOSIS OF DISEASES

Lakshmi S[1], Sandhya J*[2]

[1, 2]Department of Biotechnology, Hindustan Institute of Technology and Science, Padur, Chennai Tamil Nadu, India.

[1]https://orcid.org/0000-0002-7165-4752, [2]http://orcid.org/0000-0001-5240-0098

Email: pt.lakshmisp@hindustanuniv.ac.in, *jsandhya@hindustanuniv.ac.in

ARTICLE INFO

Article History
Received: March 24, 2026
Reviewed: April 24, 2026
Accepted: July 24, 2026
Published: August 31, 2026

Keywords:
Carbon Dots,
Exoskeleton,
ANSYS,
Biomedical,
Paralytic.

ABSTRACT

Carbon dots (CDs) or carbon quantum dots are zero- dimensional nanomaterials that have excellent fluorescent properties. Due to their excellent optical properties as well as their other properties such as biocompatibility, low toxicity, photoluminescent and simple synthesis methods they have emerged as promising nanomaterials in disease diagnosis, photodiode, drug delivery, solar cells and many other applications. In the current study, CDs were synthesized from orange peel which are economical, abundant and renewable biomass which has carbon and other functional groups such as hydroxyl and carboxyl groups making it the ideal precursor for green and sustainable synthesis. To determine their optical and structural properties, the CDs were characterised using XRD, Raman spectroscopy, TEM, UV-Visible spectroscopy and FTIR and it also showed bright blue florescence under UV illumination. Also, their interaction with DNA was explored to study their complex formation while their bioimaging potential was demonstrated against harmful bacteria such as Klebsiella pneumoniae and Staphylococcus aureus. Hence, these sustainably derived CDs can be used in various application such as gene delivery, bioimaging and a diagnostic tool.

Copyright ©2026 by authors and Galileo Institute of Technology and Education of the Amazon (ITEGAM). This work is licensed under the Creative Commons Attribution International License (CC BY 4.0).

I. INTRODUCTION

Carbon has a unique ability to showcase multiple orbital hybridizations which helps it to form various chemical bonds with diverse orientations making it the basic building block of life. This diversity of carbon makes it to bond with other elements allowing it to create various molecules and compounds with differing physical and chemical properties [1]. Graphene, Carbon dots, Carbon nanotubes and Carbon black are various forms of carbon with varying form of nanostructures and properties. Due to their exemplary mechanical, chemical, thermal and optical characteristics, carbon nanoparticles have found exceptional usage in nanotechnology applications [2]. Carbon nanoparticles with size less than 20nm are referred to as carbon dots. They have a unique property of fluorescence. They have various applications such as bioimaging and biosensing due to their biocompatible and hydrophilic carbon groups [3]. Based on their unique formation mechanisms, nanostructures and properties, they are categorized as graphene quantum dots (GQDs), carbon nanodots (CNDs) and carbonized polymeric dots (CPDs). Absorbing property of carbon dots across the ultraviolet wavelength extending into the visible spectrum is another exceptional property of carbon dots. Longer wavelength UV absorption, often showing as a weaker peak between 300 and 400 nm, is ascribed to $n \rightarrow \pi^*$ transitions of C=O bonds On the other hand, shorter wavelength UV absorption, spanning approximately between 200 and 350 nm, is attributed to $\pi \rightarrow \pi^*$ electronic transitions of C=C and C=N bonds [4]. The photoluminescence characteristics of carbon dots are among their most alluring features. This feature has enabled carbon dots to be used in various applications like bioimaging and biosensing. The most common method of doping carbon dots is synthesis using precursors that contain N. The kind of heteroatoms can adjust the emission wavelength. Individual N forms were shown to cause both red and blue shifts, which is explained by the effect's dependence on N type and position [5].

I.1 FABRICATION USING HYDROTHERMAL TECHNIQUE

Carbon dots are produced using two methods namely, top-down or bottom-up synthesis. The top-down method is usually employed for large carbon materials like soot and graphene in which these carbon sources will reduce into nano-sized carbon dots when they are heated [6]. Bottom-up approach is a commonly used synthesis method for carbon dots as it is suitable for mass production, flexibility (both in terms of precursors and synthesis routes), cost effective and eco-friendly. Bottom-up approach will lyse small organic carbon sources into smaller nano sizes either by using hydrothermal method or microwave-based approach [7]. The current investigation involved a bottom -up synthesis method called hydrothermal process for synthesizing carbon nanoparticles from orange peel. The chemical reaction will take place by adding the carbon source (orange peel) and the solvent (methanol) in a sealed pressure vessel. Different types of precursors such as milk, aloe vera, papaya etc. were successfully converted into carbon dots using hydrothermal method [8].

I.2 ORANGE PEEL FOR THE FABRICATION OF CARBON DOTS

Orange range in total sugar content from 29% to 44%, with soluble and insoluble carbohydrates being the most prevalent and commercially valuable components of this residue. Apart from the carbohydrates, citric acid is one of the major components of orange peel. Citric acid is a weak organic compound that can be used to synthesize a fluorescence emitting carbon dots. Carbon dots synthesized from citric acid will usually have a blue emission [9]. Solvents might be a significant factor in carbon dot photoluminescence. Carbon dot's surface emissive defect or solvent adherence can both cause tunable luminescence in different solvents [10].

I.3 APPLICATION OF CARBON DOTS

Nanoparticles known as carbon dots exhibit distinctive structures and properties, garnering significant attention from researchers in areas of applications spanning from sensing of biological agents, precise and targeted drug delivery, photodynamic based therapy, degradation of molecules using photocatalysis, and in energy harvesting solar cells in recent years [11]. Because of their exceptional properties like high degree of anti-swelling and anti-photobleaching, as well as non-toxicity and considerable biological compatibility, they find wide applications in biomaterials. They exhibit tunable permeability, weak protein interactions, stealthing action from immune system, safe bodily clearance and their cost-effectiveness renders the carbon dots as a a potential candidate for employing as in fluorescence labelling and imaging applications. These nanoparticles have been utilised in Parkinson's disease and Alzheimer's disorder research recently as a multifunctional drug, drug carrier, and imaging agent because of their increased blood brain barrier penetration ability, adjustable surface functionalization, distinct optical property, biocompatibility, enhanced drug encapsulation ability, and ability to release a sufficient amount of drug at targeted protein aggregates. Carbon dots can be used for locating and identifying the various types of tumours and characterize them for further clinical diagnosis.

II. MATERIALS AND METHODOLOGY

II.1 CARBON DOT SYNTHEIS FROM ORANGE JUICE AND ORANGE PEEL

The citric acid from orange juice extract is prepared by squeezing the orange and filtering the juice. Orange extract of 45 ml volume is mixed with 5 ml of methanol. The mixture is poured into a 100ml Teflon set up. The set up is heated under pressure in a furnace for 2 hrs. After cooling at 4°C, the sample was washed thrice at 7000 rpm for 10 min. The resulting supernatant is collected and visualized under UV chamber. Mortar and pestle was used to crush 1g of cleaned orange peel into a paste. The paste is then dissolved in 100 ml of distilled water using magnetic stirrer for 30 minutes. Post stirring, Whatman filter paper was used to obtain the pure filtrate. In a 200ml Teflon setup, 10 ml of methanol and 90ml of the extract are then combined. The setup was kept in a furnace for heating for 2 hours. After cooling the sample was centrifuged for 7000 rpm at 4°C for 10 minutes. Under the UV chamber, the supernatants were collected and visualized.

II.2 OPTIMIZATION OF CARBON DOT ANALYSIS

The optimization technique for carbon dots comprises the modification of temperature, a significant aspect determining their fluorescence qualities. This work focuses on studying the impact of variations in temperature on the fluorescence emission of carbon dots produced from orange extracts. The intensity of fluorescence exhibited by the carbon dots were studied and optimized at three distinct temperatures-200°C, 160°C, and 140°C.

II.3 CHARACTERISATIONS

II.3.1 UV-Visible Spectroscopy Analysis

The optical properties and potential applications of the carbon dot were studied using Shimadzu UV- 1800 instrument to investigate the absorption characteristics of the carbon dots.

II.3.2 Fourier Transform Infrared Spectroscopy (FTIR) Studies

The analysis of the functional groups in the carbon dot solution was studied using FTIR (Fourier Transform Infrared Spectroscopy) which is an instrument manufactured by Bruker Germany. This strong analytical method permits the analysis of molecular vibrational modes, aiding the analysis of specific functional moieties available in the synthesized sample.

II.3.3 Transmission Electron Microscopy (TEM)

The ThermoScientific Talos F200S, G2 high-performance TEM model was used for high-resolution imaging and analysis of materials and is particularly useful for the characterization of synthesized carbon dots.

II.3.4 X-Ray Diffraction (XRD) Analysis

This non -destructive method X-ray diffraction analysis (XRD) is employed to elucidate various aspects of crystalline powders, including its chemical composition, crystallographic structure, and physical properties. Through the interaction of X-rays with the atomic structure of the material, XRD provides valuable insights into its internal arrangement and properties without causing damage to the sample.

II.3.5 Carbon Dots for Bioimaging Microorganisms

Klebsiella pneumoniae and *Streptococcus aureus* were used for the bioimaging application. *S.aureus* and *Klebsiella* were grown in 50 ml nutrient broth. The cultures were placed in the shaking incubator until their OD value reached 0.5 at an absorbance of 600nm. Once the cultures reached an OD of 0.5, 30 ml of the cultures were centrifuged at a temperature of 4°C for 5 minutes at 2000 rpm. The pellets were obtained by discarding the supernatant and washed them thrice using nutrient media and then by distilled water by centrifuging the cells using the same condition. In the *S.aureus* and *Klebsiella* cells, 5 ml of carbon dots were added to the cell and incubated for 1hr. The stained bacterial cells were washed using distilled water and visualized using fluorescence microscopy.

II.3.6 Analyses of DNA-Carbon Dot Interaction Mechanisms

The synthesized carbon dot was mixed with the DNA at equal ratio and vortexed for 1 minute. The solution was then incubated for 30 minutes to obtain a DNA-carbon dot complex. To confirm the formation of the complex, the sample was loaded in a 0.8% agarose gel. As control, another DNA sample along with loading dye was loaded in another well. The gel was run at 100V for 1 hour before visualizing it under UV.

III. RESULTS AND DISCUSSION

III.1 FABRICATION & OPTIMIZATION OF CARBON DOT ORANGE JUICE AND ORANGE PEEL AT 200°C

For the first batch of synthesis, both the orange peel and orange juice were heated at 200°C in a furnace for 2 hours. However, there was no emission under UV for both samples. After heating the orange juice extract at 200°C, significant amounts of black soot were formed and there was a significant amount of volume reduction compared to the peel extract, both of which are signs of excessive carbonization during the heating process (Fig.1). Orange juice's high concentration of simple sugars like glucose and fructose, which easily undergo dehydration and polymerization at high temperatures and result in the formation of bulk carbonaceous residues rather than nanoscale fluorescent carbon dots, may be the cause of this phenomenon [11]. Considering the soot formation and the volume reduction from the orange juice extract, the orange peel extract was proceeded for further optimization. The orange peel also exhibited a more stable structure and comparatively less soot production after the heat treatment. This could be due to the presence of a combination of polysaccharides, cellulose, pectin, flavonoids and organic acids like citric acid which are present in the orange peel that can lead to uniform carbonization and nucleation process which proves beneficial in carbon dots production [12]. Orange peel extract was utilized for additional optimization research targeted at boosting the production and fluorescence characteristics of carbon dots because orange juice extract was determined to be inappropriate for further investigation due to severe soot production and significant volume loss.

III.2 ORANGE PEEL EXTRACT AT 160°C AND 140°C

Initially the orange peel extract was heated to 160 °C and 140 °C to determine the ideal temperature for synthesis of carbon dots. A mild brown hue was observed under normal visible light after heating step which indicates the presence of carbonization. Blue fluorescent light was observed for both the samples under UV light (365 nm) which indicates the presence of luminous carbon dots. Nevertheless, it was observed that blue emission was stronger for the sample heated at 140 °C as shown in the figure1. This indicates that nucleation of nanosized carbon structures along with uniform carbonization ensured enhanced blue emission at 140 °C [12]. The photoluminescence characteristics were improved at moderate temperature due to the creation of tiny carbon cores and functionalization of the surface by moieties like carbonyl, carboxyl and hydroxyl groups [9]. On the other hand, excessive carbonization and particle aggregation maybe formed at higher temperature of 160 °C which can lead to low emission intensity and fluorescence quenching [10]. The creation of emissive carbon nanostructures are possible because of partial carbonization and dehydration of components of orange peel such as pectin, polysaccharides and organic acids when it is heated [9]. Based on fluorescence intensity and visual qualities, the optimum temperature for synthesis of carbon dots from orange peel extract was found to be 140 °C. Therefore, for maintaining stable nanostructure development with strongest emission was found to be at this temperature.

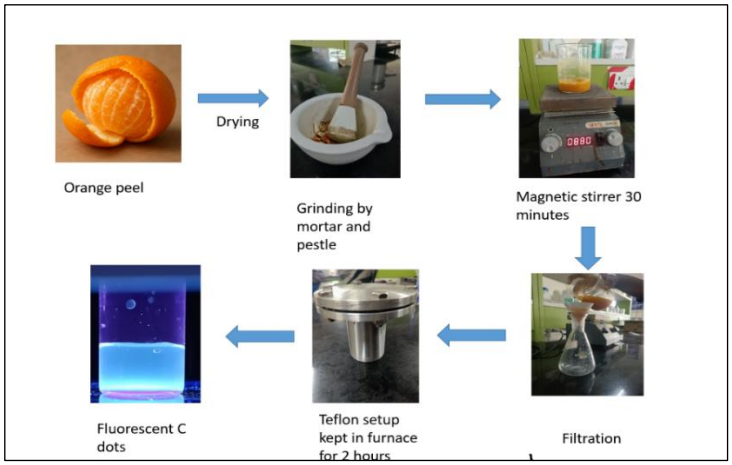


Figure 1: Green synthesis and temperature-dependent optimization of fluorescent carbon dots derived from orange peel extract.
Source: Authors, (2026).

III.3 CRYSTALLINE STRUCTURE AND MORPHOLOGY

The crystalline or amorphous nature of the material can be determined using XRD. The orange peel carbon dots show peak 24.31° corresponding to the (002) plane as shown in Fig.2. Broad peaks were detected in the XRD patterns, indicating the amorphous characteristic of the carbon dot, as confirmed by the analysis. From Fig.3, we can see that the carbon dots have a spherical-like structure. This result supports the graphitic nature of our CQDs and is consistent with the structural characteristics seen in many previous carbon dot investigations [13]. The internal structural morphology of the orange peel-based carbon dots was analysed using TEM. Therefore, the distinct peaks in the spectrum provide important data about the elemental composition of the material under analysis. EDX spectrum shows the carbon dots have high carbon and oxygen content.

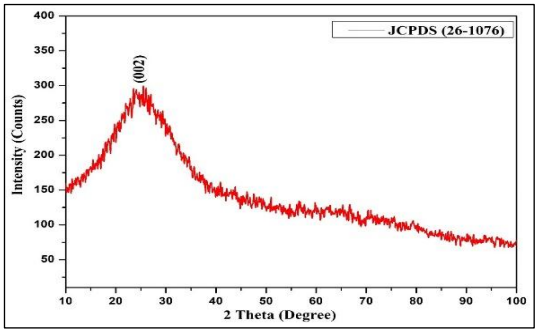


Figure 2: XRD analysis for orange peel derived carbon dots.
Source: Authors, (2026).

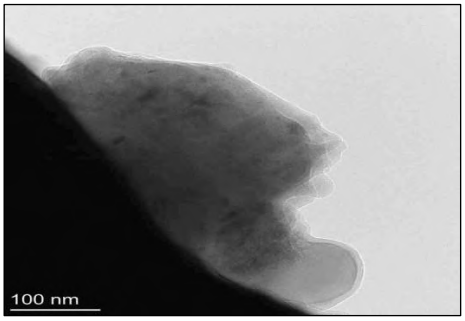


Figure 3: High-resolution TEM images for orange peel derived carbon dots.
Source: Authors, (2026).

III.4 PRESENCE OF AROMATIC STRUCTURE

The UV-visible absorption of carbon dots exhibits a peak at 230 nm as shown in Fig.4. Even though there are three peaks in the graph, with particular emphasis on the peak observed at 230 nm due to its highest intensity. This dominant peak signifies a significant absorption event attributed to the transition between the highest occupied molecular orbital (HOMO) and the lowest unoccupied molecular orbital (LUMO), known as the π-π* transition. This transition is characteristic of conjugated systems, indicating the presence of aromatic structures within the carbon dots, likely stemming from C=C bonds. The smaller shoulder has a peak nearly at 320 and 280nm which represents the n-π* transition due to C=O bonds (Table 1).

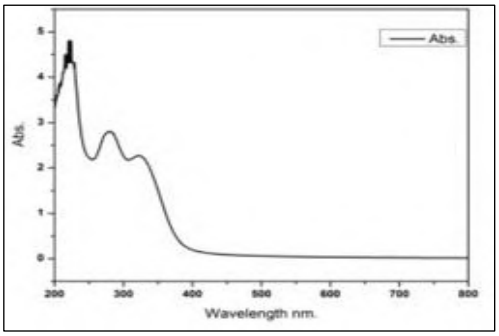


Figure 4: UV Vis absorption spectrum for orange peel derived carbon dots.
Source: Authors, (2026).

Table 1: Significance of different peaks in UV spectrum of orange peel derived carbon dots.

Peak	Wavelength (nm)	Significance
1.	270	π–π* transition of aromatic C=C bonds (graphitic core of carbon dots)
2.	340-360	n–π* transition of C=O groups (surface functionalization, carbonyl/carboxyl groups
3.	400- 500	Surface defect states and functionalized groups responsible for fluorescence

Source: Authors, (2026).

III.5 IDENTIFICATION OF FUNCTIONAL GROUPS IN CARBON DOTS

The FTIR spectrum of the synthesized carbon dots offers a detailed glimpse into their molecular composition and structural characteristics. The presence of C-C stretching vibrations which is associated with aromatic backbone of carbon-based materials is indicated by the peak at 603.74 cm^{-1}. This indicates the presence of conjugated aromatic structure in the core system of the carbon dots. The C-O stretching vibrations which corresponds to the presence of oxygen containing functional groups probably from hydroxyl (-OH) or ether (C-O-C) moieties is suggested by the peak at 1066.47 cm^{-1} [12]. Additionally, the C-H bending vibrations indicating the presence of aliphatic hydrocarbon chains or methyl groups is represented by the peaks at 1250.21 cm^{-1} and 1384.26 cm^{-1} that can lead to the overall structure and stability of the CDs [8].

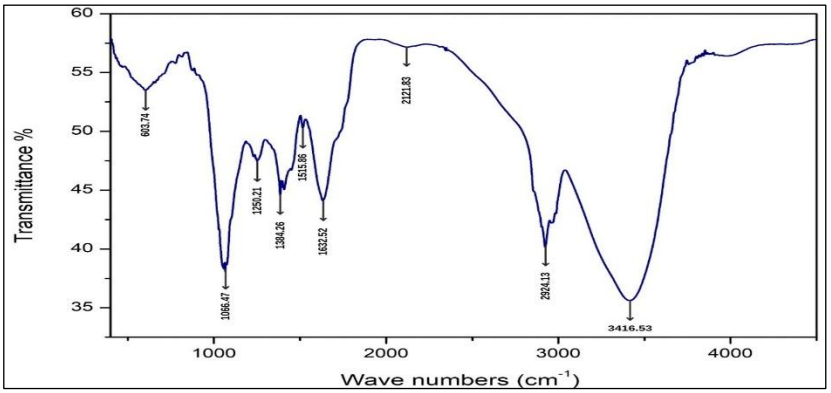


Figure 5: FTIR spectrum for orange peel derived carbon dots.
Source: Authors, (2026).

The most significant peak at 1515.86 cm^{-1} shows C=C stretching vibrations that suggest the presence of aromatic structures in the carbon dots. This indicates that the electronic and optical properties like fluorescence can be influenced by the presence of high degree of π- conjugation in the carbon dots [12]. The C=O stretching vibrations corresponds to the peak at 1632.52 cm^{-1} which indicates the presence of carbonyl groups suggestive of surface functionalization or oxidation process that took place during synthesis process. However, the peak at 2121.83 cm^{-1} could indicate unique structural features such as carbon-carbon triple bonds (C≡C), even though it might require further research. The peaks at 2924.13 cm^{-1} and 3416.53 cm^{-1} correspond to C-H and O-H stretching vibrations, respectively, signifying the presence of aliphatic hydrocarbon chains and hydroxyl groups, which are crucial for elucidating the surface chemistry and reactivity of the carbon dots (Fig. 5) [11], [12].

III.6 BACTERIAL CELLULAR UPTAKE OF CARBON DOTS

The *Staphylococcus aureus* and *Klebsiella pneumoniae* which were incubated with the orange peel-based carbon dots show a bright cyan color when visualized under fluorescence microscope as shown in Fig.6 (a,b) and Fig.7 (a,b). However. in images 6a and 7a, it was challenging to visualize the cells as they do not have dye. Hence, the synthesized carbon dot assists in the visualization of microbial cells under fluorescence microscope. Fluorescence microscopy of *Klebsiella pneumoniae* treated with orange peel–derived carbon dots showed fluorescence localized to bacterial cells. The fluorescence pattern indicated that CDs were (adsorbed onto the bacterial surface/internalized within cells), suggesting efficient interaction between CDs and the bacterial cell wall."

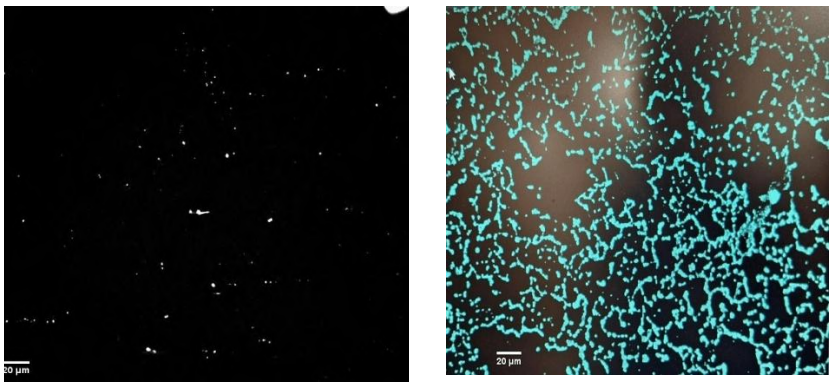


Figure 6: Fluorescence microscopic image of *S. aureus* (a) *S. aureus* without carbon dot (b) *S. aureus* treated with carbon dots.
Source: Authors, (2026).

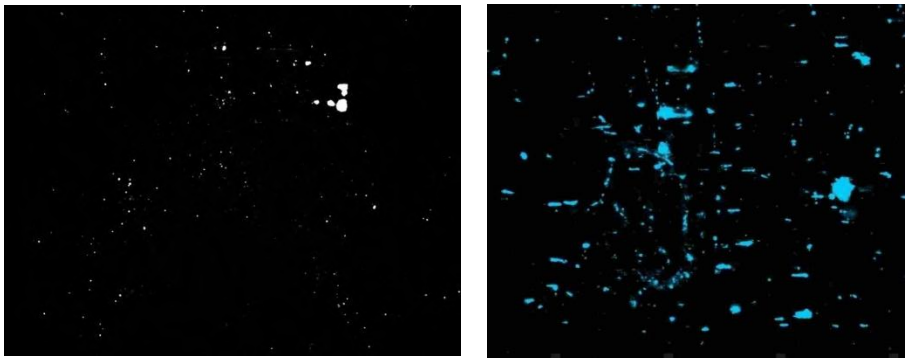


Figure 7: Fluorescence microscopic image of K *pneumoniae* (a) K *pneumoniae* without carbon dot (b) K *pneumoniae* treated with carbon dots.
Source: Authors, (2026).

III.7 DNA-CARBON DOT COMPLEX FORMATION

Using agarose gel electrophoresis, the capacity of carbon dots made from orange peel extract to interact with DNA was assessed. The first and second wells from Fig.8 indicate the loading of the DNA-Carbon dot complex, yet its presence remains invisible while the fourth and fifth wells were control groups having a loading dye. We were not able to see the DNA-Carbon dot complex due to a lack of complex formation, likely from the repulsive interaction between the two molecules. When compared to the control DNA sample, the electrophoretic mobility of DNA incubated with different carbon dot concentrations did not exhibit any discernible retardation. This implies that the produced carbon dots did not form stable interactions with DNA under the studied experimental conditions. A weak or insignificant electrostatic contact between the carbon dots and DNA molecules is shown by the lack of band shift (Figure 8).

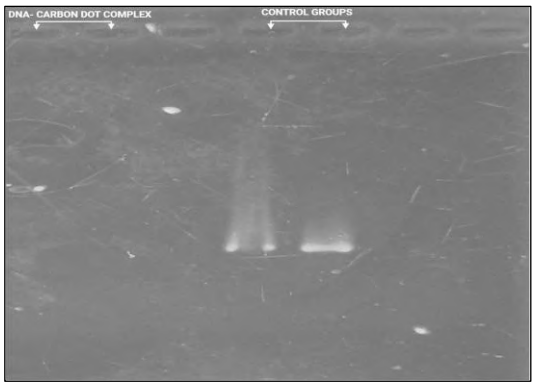


Figure 8: Agarose gel to confirm carbon dot and DNA interaction.
Source: Authors, (2026).

III.8 DISCUSSIONS

CNPs were successfully synthesized using orange peel and orange juice extract, as demonstrated by visual inspection and a number of characterisation methods. CNPs synthesized by orange peel were given for further optimisation based on the soot formation. The presence of carbon dots was confirmed by the bright blue emission of the samples when placed in UV radiation. In this experiment, the citrus extract from the orange peel was heated at three different temperatures 200°C, 160°C and 140°C. The temperature in which the extract is heated is correlated with the emission of the carbon dot. At the right and optimized temperature, the carbon dot will be carbonized properly having a stable small size and brighter glow. From the bright glow observed on the orange peel heated at 140°C is the optimized temperature for carbon dots preparation from orange peels. Furthermore, the characterization results of FTIR, TEM, XRD and UV- visible spectroscopy have confirmed that carbon dots were fabricated from orange peel. UV-visible spectroscopy revealed a prominent absorption peak at 230 nm that confirms the optical properties of the CNPs as shown in Fig.4. Since most carbon dots have a strong π-π^* transition within their carbon structure, which is often seen as the primary absorption band in their UV-Vis spectra, a UV absorption peak around 220 nm for carbon dots usually indicates the presence of these carbon nanoparticles. XRD analysis displayed the amorphous nature of the CNPs synthesized with orange peel extract. From the FTIR results, the carbon dots have an aromatic chain backbone with various bonds attached to it [10]. The synthesized carbon dot has the ability to stain both Klebsiella pneumoniae and Streptococcus aureus cell culture. Due to their extremely tiny size, carbon dots have the potential to enter bacterial cells since particles smaller than 10 nm may be able to do so by endocytosis. The presence of oxygen as well as the small size of carbon dots makes it easy to penetrate through the cell membrane. The electrostatic attraction between the surface charge of the carbon dot and the cell membrane facilitates the endocytosis process [13]. They are also good candidates for fluorescence imaging due to their luminous qualities Once the carbon dot passes through the cell membrane it can easily stain the cytoplasm blue color. The synthesized carbon dot stains the entire cell population in a nonspecific manner. While studying the interaction between DNA and the synthesized carbon dot there was no complex formation. The lack of observable DNA–carbon dot complex formation may be attributed to several factors. The surface charge and functional groups present on carbon dots synthesized from orange peel may not provide sufficient electrostatic attraction for the DNA as they are negatively charged.

Both DNA and the carbon dot carry negative charges, their mutual electrostatic repulsion prevents effective binding and the formation complex. Previous studies have reported that effective DNA binding typically requires positively charged surface functionalization such as amine groups. Since the synthesized carbon dots were derived from a biomass precursor without additional surface modification, the interaction with DNA may be limited. In the future experiments, the carbon dot should be doped with chemicals such as PEG or nitrogen-based molecules in order for the interaction to take place. Over time, CDs gained exceptional qualities for a range of uses due to their easy surface preparation and modification, biocompatibility, low cytotoxicity, strong resistance to photobleaching, and high-water solubility, which enables homogenous sensing tests. The observed physicochemical properties and minimal DNA interaction highlight the ability of carbon dot nanoparticles derived from orange-peel as promising candidates for future biosensing and diagnostic applications.

IV. CONCLUSION

Fluorescent carbon dot nanoparticles were hydrothermally obtained from orange peel. The fluorescence emission from the as-synthesized carbon dots was optimized by heating the orange peel extract at different temperatures and the maximum emission was attained at 140°C. Further characterizations such as XRD, Raman spectroscopy, TEM, UV-visible spectroscopy, and FTIR spectroscopy were employed to get a better understanding of the synthesized carbon dot. From this analysis we were able to understand the structure, bonds and the amorphous structure of the synthesized orange peel-based carbon dots. Carbon dots were then used to visualize pathogens. Both Klebsiella pneumoniae and Streptococcus aureus were successfully stained by carbon dots when visualized under fluorescence microscopy. The current work demonstrating the production of CNPs utilizing orange peel offers insightful results although it has limitations. It might be difficult to scale up synthesis techniques from lab to industrial production, and it could affect efficiency or quality. Since NPs may deteriorate or change over time, long- term stability in biological contexts necessitates careful research. To guarantee safety, antimicrobial activity must be confirmed in vitro and then evaluated for cytotoxicity and biocompatibility in vivo.

V. AUTHOR'S CONTRIBUTION

Conceptualization: Lakshmi S, J Sandhya.
Methodology: Lakshmi S, J Sandhya.
Investigation: Lakshmi S.
Discussion of results: Lakshmi S, J Sandhya.
Writing – Original Draft: Lakshmi S.
Writing – Review and Editing: Lakshmi S, J Sandhya.
Resources: Lakshmi S.
Supervision: J Sandhya.
Approval of the final text: Lakshmi S, J Sandhya.

VI. REFERENCES

[1] A. K. Geim and K.S. Novoselov, "The rise of graphene," Nature Materials, vol. 6, no.3, p. 183–191, 2007. https://doi.org/10.1038/nmat1849

[2] R. Wang, K.Q. Lu, Z.R. Tang, et al., "Carbon nanostructures for sustainable energy and environmental applications," Chemical Engineering Journal, vol. 457, p. 141243, 2023. https://doi.org/10.1016/j.cej.2023.141243

[3] S.Y. Lim, W. Shen, Z. Gao, "Carbon quantum dots and their applications," Chemical Society Reviews, vol. 53, no. 6, p. 2358–2389, 2024. https://doi.org/10.1039/D3CS00572A

[4] K. Hola, Y. Zhang, Y. Wang, et al., "Carbon dots—Emerging light emitters for bioimaging, diagnostics, and phototherapy," Nano Today, vol. 48, p. 101707, 2023. https://doi.org/10.1016/j.nantod.2023.101707

[5] S.N. Baker, G.A. Baker, "Luminescent carbon nanodots: Emergent nanolights,". Angewandte Chemie International Edition, vol.62, no.8, p. e202213233, 2023. https://doi.org/10.1002/anie.202213233

[6] A. Sharma, J. Das, S.K. Sahoo, "Heteroatom-doped carbon quantum dots for tunable photoluminescence and biomedical applications," Frontiers in Bioengineering and Biotechnology, vol. 12, p. 1333752, 2024. https://doi.org/10.3389/fbioe.2024.1333752

[7] Y. Wang, A. Hu, M. Zhang, "A critical review of carbon quantum dots: Synthesis, optical properties, and applications," Materials Today Chemistry, vol. 31, p. 101440, 2023. https://doi.org/10.1016/j.mtchem.2023.101440

[8] A. Tyagi and A. Singh, "Green synthesis of carbon quantum dots: A sustainable approach using biomass waste," Frontiers in Energy Research, vol. 11, p. 626549, 2023. https://doi.org/10.3389/fenrg.2023.626549

[9] Y. Lu, Y. Chen, Y. Guo, "High-efficient synthesis of carbon quantum dots from orange peel waste for bioimaging," Scientific Reports, vol. 13, p. 9892, 2023. https://doi.org/10.1038/s41598-023-39892-1

[10] P.D. Pathak, S.A. Mandavgane, B.D. Kulkarni, "Valorization of orange peel: Characterization and applications," Waste Biomass Valorization. vol. 8, no. 5, p. 1513–1523, 2017. https://doi.org/10.1007/s12649-016-9689-3

[11] Y. Dong, H. Pang, H.B. Yang et al., "Carbon-based dots from citric acid and their application in dye-sensitized solar cells," Angewandte Chemie International Edition, vol. 52, no. 30, p. 7800–7804, 2013. https://doi.org/10.1002/anie.201301114

[12] J. Liu, J. Li, S. Guo, "Solvent-dependent emission tuning in carbon quantum dots: Mechanistic insights and applications" Nanoscale Advances, vol. 7, no. 3, p. 1240–1252, 2025. https://doi.org/10.1039/D4NA00763H

[13] N. Azam, M.N. Ali, T.J. Khan, "Carbon quantum dots for biomedical applications: A comprehensive review," Frontiers in Materials, vol.8, p. 700403, 2021. https://doi.org/10.3389/fmats.2023.700403

Journal of Engineering and Technology for Industrial Applications

ISSN ONLINE: 2447-0228

ITEGAM-JETIA

Manaus, v.12 n.60, p.1437-1446. July/August, 2026.
DOI: https://doi.org/10.5935/jetia.v12i60.4309

RESEARCH ARTICLE OPEN ACCESS

COMPARATIVE EVALUATION OF CNN, SVM, ANN, AND KNN FOR AUTOMATED DETECTION OF NUTRIENT DEFICIENCIES IN MAIZE LEAVES

Von Ryan P. Marcelo*[1]

[1]College of Engineering Architecture and Technology, Isabela State University, Ilagan City, Isabela, 3300, Philippines.

[1]https://orcid.org/0009-0002-6122-0325

Email:*vhonryan.p.marcelo@isu.edu.ph

ARTICLE INFO

Article History
Received: March 25, 2026
Reviewed: April 25, 2026
Accepted: July 25, 2026
Published: August 31, 2026

Keywords:
Maize nutrient deficiency,
Automated leaf classification,
Deep learning in agriculture,
Precision farming,
Machine learning models.

ABSTRACT

Accurate detection of nutrient deficiencies in maize (Zea mays L.) is critical for optimizing yield and sustainable fertilizer management. Traditional diagnostic methods, including laboratory analysis and visual inspection, are often time-consuming and impractical for real-time applications. This study presents a comparative evaluation of four machine learning algorithms: Convolutional Neural Network (CNN), Support Vector Machine (SVM), Artificial Neural Network (ANN), and k Nearest Neighbors (kNN), for automated classification of nitrogen, phosphorus, potassium deficiencies, and healthy leaves. A labeled maize leaf image dataset was used to train and assess model performance based on accuracy, precision, recall, and F1 score. Results show that CNN achieved the highest overall performance (accuracy = 0.794, F1 score = 0.794), demonstrating superior feature extraction and robust classification. SVM performed competitively (accuracy = 0.722), ANN achieved moderate results (accuracy = 0.679), while kNN showed the lowest effectiveness (accuracy = 0.483). Misclassification was most prominent between potassium deficient and healthy leaves, reflecting overlapping visual symptoms. The findings highlight CNN as the most reliable model for automated nutrient deficiency detection.

Copyright ©2026 by authors and Galileo Institute of Technology and Education of the Amazon (ITEGAM). This work is licensed under the Creative Commons Attribution International License (CC BY 4.0).

I. INTRODUCTION

Maize (Zea mays L.) is one of the most important cereal crops worldwide, serving as a fundamental source of food, animal feed, and industrial raw materials. Its productivity is closely linked to the availability of essential nutrients, particularly macronutrients such as nitrogen (N), phosphorus (P), and potassium (K), which play critical roles in plant growth, photosynthesis, and metabolic regulation [1-3]. Deficiencies in these nutrients can significantly impair plant development, resulting in substantial yield reduction and compromised crop quality [4-6]. Consequently, the timely and accurate detection of nutrient deficiencies is a crucial aspect of sustainable agricultural management and precision farming practices. Traditional approaches for diagnosing nutrient deficiencies primarily rely on laboratory-based soil and plant tissue analysis, as well as visual inspection conducted by agricultural experts. While laboratory methods are considered highly reliable, they are often time-consuming, costly, and impractical for real-time field applications [7], [8]. In contrast, visual assessment provides a rapid and low-cost alternative; however, it is inherently subjective and dependent on expert interpretation. This subjectivity is further exacerbated by the fact that nutrient deficiency symptoms often exhibit overlapping visual characteristics, making it difficult to distinguish between different deficiency types, particularly under varying environmental conditions. The rapid advancement of machine learning (ML) and computer vision technologies has created new opportunities for automated and scalable crop monitoring systems. Using classification algorithms to solve real-world problems [9], such as Support Vector Machine and K-Nearest Neighbor can achieve high accuracy in detecting plant diseases and nutrient deficiencies from image data [10]. Image-based analysis techniques enable the detection and classification of nutrient deficiencies by examining visual indicators such as leaf discoloration, chlorosis, and necrosis [11], [12].

Several machine learning algorithms, including Support Vector Machines (SVM), Artificial Neural Networks (ANN), and k-Nearest Neighbors (kNN), have been applied to agricultural classification tasks, demonstrating varying levels of effectiveness. More recently, Convolutional Neural Networks (CNN) have emerged as a powerful tool for image classification due to their ability to automatically learn hierarchical feature representations directly from raw image data, thereby reducing the need for manual feature engineering and improving classification accuracy [13-15]. Support Vector Machines (SVMs) are supervised learning models that use a hyperplane to classify data points by maximizing the margin between different classes [16]. Artificial Neural Networks (ANNs) , inspired by biological neural networks, consist of interconnected nodes (neurons) organized in layers, processing information through weighted connections to identify complex patterns, while k-Nearest Neighbors (kNN) is a non-parametric, instance-based learning algorithm that classifies new data points based on the majority class among their 'k' nearest neighbors in the feature space [17]. are computational models inspired by the structure and function of biological neural networks, capable of learning complex patterns through interconnected layers of nodes, while k-Nearest Neighbor (kNN) is a non-parametric, instance-based learning algorithm that classifies new data points based on the majority class among their nearest neighbors in the feature space. k-Nearest Neighbors (kNN), while computationally intensive for large datasets, is particularly effective for localized classification tasks and offers a distinct advantage due to its nonparametric nature when data distribution is unknown or complex [18]. Despite these developments, the existing body of literature remains limited in terms of comprehensive comparative analyses across multiple machine learning approaches for maize nutrient deficiency detection. Many studies tend to focus on individual models or specific deficiency types, which restricts a holistic understanding of model performance under consistent experimental conditions. Furthermore, challenges related to misclassification, particularly those arising from visually similar symptoms such as potassium deficiency and healthy leaf conditions, have not been sufficiently investigated. These limitations highlight the need for a systematic evaluation of both traditional and deep learning methods within a unified framework. In response to these gaps, this study presents a comparative evaluation of four machine learning algorithms—CNN, SVM, ANN, and kNN—for the automated classification of nitrogen, phosphorus, potassium deficiencies, and healthy maize leaves using image-based data. The models are assessed using standard performance metrics, including accuracy, precision, recall, and F1-score, to provide a comprehensive and objective comparison. By examining the strengths and limitations of each approach, this study aims to identify the most effective model for nutrient deficiency detection and to contribute to the development of reliable, real-time decision-support systems for precision agriculture. Ultimately, the findings are expected to support improved nutrient management strategies, enhance crop productivity, and promote sustainable agricultural practices.

II. RELATED WORKS

II.1 NUTRIENT DEFICIENCY DETECTION IN CROPS

The detection of nutrient deficiencies in crops has long been a central concern in agricultural science due to its direct impact on yield and crop quality. Traditional diagnostic approaches, such as soil testing and plant tissue analysis, have been widely regarded as reliable methods for identifying nutrient imbalances. These techniques provide quantitative measurements of nutrient concentrations, enabling precise recommendations for fertilizer application. However, their application is often constrained by high costs, the need for specialized equipment, and delayed result turnaround times, limiting their suitability for real-time field decision-making [19]. Conversely, visual inspection, while offering immediate, low-cost assessment, suffers from inherent subjectivity and requires extensive expertise, making it prone to misdiagnosis, especially when symptoms overlap or environmental conditions vary [20]. Visual inspection has also been extensively employed as a practical alternative, relying on observable symptoms such as chlorosis, necrosis, and stunted growth. While this method is rapid and cost-effective, it is highly dependent on expert knowledge and experience. Moreover, the visual similarity of symptoms across different nutrient deficiencies frequently leads to misinterpretation, reducing diagnostic accuracy. These limitations have motivated the exploration of automated and scalable approaches for nutrient deficiency detection.

II.2 MACHINE LEARNING IN AGRICULTURAL IMAGE ANALYSIS

The integration of machine learning (ML) techniques into agriculture has significantly advanced the automation of plant health monitoring. ML algorithms have been applied to classify plant diseases, detect stress conditions, and identify nutrient deficiencies using image-based data. Traditional ML models, including Support Vector Machines (SVM), k-Nearest Neighbors (kNN), and Artificial Neural Networks (ANN), have demonstrated promising performance in classification tasks when combined with feature extraction techniques such as color histograms, texture descriptors, and shape analysis [21], [22]. However, these methods often necessitate extensive feature engineering and domain-specific knowledge, thereby limiting their adaptability and scalability across diverse agricultural contexts [23]. SVM, in particular, has been widely recognized for its robustness in high-dimensional spaces and its effectiveness in handling small to medium-sized datasets. Similarly, kNN offers simplicity and ease of implementation, although its performance is often limited by sensitivity to noise and computational inefficiency with large datasets. ANN models, while capable of capturing nonlinear relationships, typically require careful feature engineering and parameter tuning. Despite their effectiveness, these approaches often rely heavily on manually extracted features, which may not fully capture complex visual patterns associated with nutrient deficiencies.

II.3 DEEP LEARNING AND CNN-BASED PLANT CLASSIFICATION

The emergence of deep learning, particularly Convolutional Neural Networks (CNN), has transformed image-based classification tasks in agriculture. Unlike traditional ML methods, CNNs automatically learn hierarchical feature representations directly from raw image data, enabling more accurate and robust classification. This capability has led to significant improvements in tasks such as plant disease detection, weed identification, and crop classification [24], [25] . For instance, studies have shown that Deep Convolutional Neural Networks outperform traditional methods like color features with SVM and HOG with SVM for plant condition classification [26].

Several studies have demonstrated the superiority of CNN models over conventional algorithms in plant health diagnostics. CNN architectures are capable of capturing subtle variations in color, texture, and spatial patterns, which are critical for distinguishing between different types of nutrient deficiencies. Furthermore, the use of transfer learning and pre-trained models has enhanced performance, particularly when labeled datasets are limited. However, CNN models often require substantial computational resources and large datasets to achieve optimal performance, which may pose challenges in resource-constrained environments.

II.4 CHALLENGES IN NUTRIENT DEFICIENCY CLASSIFICATION

Despite the progress achieved through machine learning and deep learning approaches, several challenges remain in the classification of nutrient deficiencies. One of the primary issues is the high degree of visual similarity between different deficiency symptoms. For example, potassium deficiency and healthy leaf conditions may exhibit overlapping color patterns, making accurate classification difficult even for advanced models. Environmental factors such as lighting conditions, background noise, and image quality further complicate the classification process [27], [28]. Moreover, the limited availability of large, publicly accessible datasets with diverse symptomologies and controlled environmental variables often constrains the development of highly generalizable and robust deep learning models for practical agricultural applications [29]. Another challenge lies in dataset limitations, including class imbalance, insufficient sample size, and lack of diversity in image conditions. These factors can lead to overfitting and reduced generalization performance. Additionally, variations in data preprocessing techniques and evaluation metrics across studies make it difficult to conduct direct comparisons between models. As a result, there is a need for standardized evaluation frameworks to ensure consistent and reliable performance assessment.

II.5 RESEARCH GAP

Although significant advancements have been made in applying machine learning and deep learning techniques to agricultural image analysis, a comprehensive comparative evaluation of multiple algorithms for maize nutrient deficiency detection remains limited. Existing studies often focus on single-model implementations or specific classification tasks, thereby restricting a holistic understanding of the relative performance of different approaches under uniform experimental conditions. Furthermore, insufficient attention has been given to the analysis of misclassification patterns, particularly in cases involving visually similar classes such as potassium-deficient and healthy leaves. In addition, variations in dataset preparation, feature extraction methods, and evaluation metrics across previous studies hinder the reproducibility and comparability of results. There is also a lack of studies that systematically integrate both traditional machine learning models and deep learning approaches within a unified framework. Addressing these limitations is essential for identifying the most effective and reliable model for real-world applications. Therefore, this study seeks to bridge these gaps by conducting a systematic comparative evaluation of CNN, SVM, ANN, and kNN models for the classification of maize nutrient deficiencies using a consistent dataset and standardized performance metrics. By providing a comprehensive analysis of model performance and classification challenges, this research aims to contribute to the advancement of automated nutrient deficiency detection systems in precision agriculture.

III. MATERIALS AND METHODS

This study employed a structured experimental framework to evaluate and compare the performance of multiple machine learning algorithms for the automated detection of nutrient deficiencies in maize leaves. The dataset consisted of 1,041 maize leaf images, including 277 phosphorus-deficient, 266 healthy, 223 nitrogen-deficient, and 275 potassium-deficient samples. The methodological workflow, as shown in Figure 1, consisted of five major phases: data gathering, data preprocessing and cleaning, image processing and feature extraction, algorithm training and evaluation, and result interpretation. These phases were designed to ensure the systematic preparation of the dataset and to facilitate an objective comparative assessment of classification models.

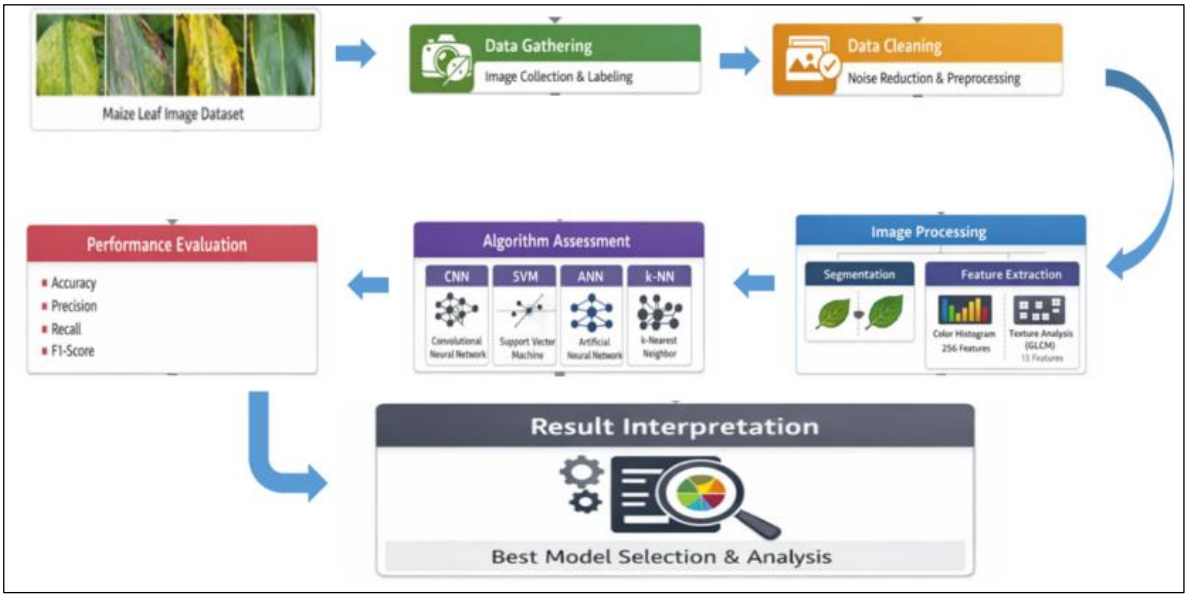


Figure 1: Methodology.
Source: Author, (2026).

III.1 DATA GATHERING

The first phase of the methodology involved collecting a dataset of maize leaf images representing different nutrient conditions. The dataset includes images of maize leaves exhibiting symptoms associated with nitrogen (N), phosphorus (P), and potassium (K) deficiencies, as well as images of healthy maize leaves. These macronutrients were selected because they play critical roles in plant growth and are commonly associated with significant yield reduction when deficiencies occur. Images were collected from maize plants under natural agricultural conditions to capture realistic variations in lighting, leaf orientation, and background environment. Capturing images under field-like conditions ensures that the dataset reflects practical agricultural scenarios in which automated detection systems may be deployed. Each collected image was manually labeled according to the observed nutrient condition using agronomic references and visual indicators of nutrient deficiency. Accurate labeling is essential for supervised machine learning models because it provides the ground truth required for effective training. The dataset was subsequently divided into training and testing subsets, where 80% of the images were used for training and 20% were used for testing. This partitioning allows the models to learn classification patterns from the training data while preserving an independent dataset for unbiased evaluation of algorithm performance.

III.2 DATA CLEANING AND PREPROCESSING

After data collection, a preprocessing stage was conducted to improve dataset quality and ensure consistency across all images. Agricultural image datasets often contain noise and inconsistencies due to environmental factors such as varying illumination, shadows, and background objects. These factors may negatively influence model performance if not addressed. During this phase, images that were blurred, duplicated, or irrelevant were removed from the dataset. The remaining images were standardized by resizing them to a uniform dimension to ensure compatibility with the classification algorithms. Additionally, noise reduction techniques were applied to minimize unwanted variations caused by lighting conditions or background interference. Image normalization was also performed to improve the consistency of pixel intensity values across the dataset. These preprocessing steps help ensure that the machine learning models focus on relevant leaf chara]cteristics associated with nutrient deficiencies.

III.3 IMAGE PROCESSING AND FEATURE EXTRACTION

After preprocessing, image segmentation was performed to isolate maize leaves from the background, allowing the models to focus on relevant regions showing nutrient deficiency symptoms. For traditional machine learning models (SVM, ANN, and kNN), feature extraction was applied using color histogram and Grey Level Co-occurrence Matrix (GLCM). The color histogram generated 256 color features, while GLCM extracted 13 texture features, including contrast, correlation, energy, and homogeneity. These features were combined and used as input for classification. In contrast, the Convolutional Neural Network (CNN) used raw images and automatically extracted features through convolutional layers, eliminating the need for manual feature extraction.

III.4 ALGORITHM TRAINING AND COMPARATIVE EVALUATION

This study employed a systematic approach to train and evaluate four machine learning algorithms—Convolutional Neural Network (CNN), Artificial Neural Network (ANN), Support Vector Machine (SVM), and k-Nearest Neighbors (kNN)—for automated classification of maize leaf nutrient deficiencies. The classification task focused on four classes: Nitrogen deficiency, Phosphorus deficiency, Potassium deficiency, and Healthy leaves. The objective was to identify the most effective algorithm capable of accurately detecting nutrient stress while minimizing misclassification risks.

III.4.1 Algorithm Training

For the Convolutional Neural Network (CNN), raw maize leaf images were resized and normalized before training. For ANN, SVM, and kNN, extracted features from color histogram and GLCM were used as input for classification. Maize leaf images were preprocessed through resizing and normalization to ensure uniformity across the dataset. CNN architectures utilized multiple convolutional layers with pooling operations to extract hierarchical spatial features, followed by fully connected layers for classification into the four nutrient classes. The ANN model applied a fully connected feedforward network with backpropagation, enabling the network to learn non-linear relationships between leaf image features and nutrient status. For traditional machine learning models (SVM and kNN), handcrafted feature vectors were extracted from each leaf image, including color, texture, and morphological features relevant to nutrient deficiencies. SVM employed a linear kernel to separate the four nutrient classes in feature space, while kNN classified samples based on proximity to labeled neighbors in the feature space.All models were trained using an 80:20 stratified train-test split to preserve class balance. Hyperparameters—such as learning rate, number of hidden layers, SVM regularization parameter, and the number of neighbors for kNN—were optimized through cross-validation to maximize classification performance.

III.4.2 Performance Evaluation Metrics

Model performance was quantified using standard classification metrics derived from confusion matrices: accuracy, precision, recall, and F1-score. These metrics provide insights into overall and class-specific performance, which is essential for precision agriculture applications where misclassification can lead to improper nutrient management.

- **Accuracy:** Proportion of correctly classified maize leaf samples among all samples. Useful for general performance assessment but may be affected by class imbalance.

$$Accuracy = \frac{TP + TN}{TP + TN + FP + FN}$$

- **Precision:** Proportion of correctly predicted leaves for a specific nutrient deficiency class among all predictions for that class. High precision indicates minimal false-positive predictions.

$$Accuracy = \frac{TP}{TP + FP}$$

- **Recall (Sensitivity):** Proportion of correctly identified leaves of a specific nutrient class among all actual leaves of that class. High recall ensures that most nutrient-deficient leaves are detected.

$$Precision = \frac{TP}{TP + FN}$$

- **F1-Score:** Harmonic mean of precision and recall, providing a balanced assessment. This metric is particularly critical in maize nutrient classification, where incorrect detection can lead to suboptimal fertilization strategies.

$$F1 = 2x \frac{Precision\ x\ Recall}{Precision + Recall}$$

III.4.3 Comparative Evaluation

After training, the performance of all four models was systematically compared using the aforementioned metrics. Class-wise evaluation allowed identification of strengths and limitations for each algorithm. Confusion matrices were analyzed to determine which nutrient deficiencies were most accurately detected and which classes exhibited significant misclassification.

III.5 EXPERIMENTAL FRAMEWORK

The experimental framework of this study was designed to systematically compare the performance of multiple machine learning algorithms for detecting nutrient deficiencies in maize leaves. The framework integrates dataset preparation, image processing, feature extraction, model training, and performance evaluation into a unified workflow. The overall process begins with the acquisition of maize leaf images representing various nutrient conditions. These images undergo preprocessing procedures to remove noise and standardize the dataset. The processed images are then subjected to segmentation and feature extraction to capture the visual characteristics associated with nutrient deficiency symptoms. The extracted features are used as input for four classification algorithms:

- Artificial Neural Network
- Convolutional Neural Network
- k-Nearest Neighbor
- Support Vector Machine

Each algorithm is trained using the same dataset to ensure a fair comparative evaluation. The trained models are then tested using the reserved testing dataset, and their classification performance is measured using the evaluation metrics described in the previous section. The algorithm with the highest performance metrics is identified as the most suitable model for automated nutrient deficiency detection and may be integrated into intelligent agricultural monitoring systems.

III.6 RESULT INTERPRETATION

The final phase involved analyzing classification performance and interpreting results. Model accuracy, precision, recall, and F1-score were compared to determine the best-performing algorithm. Patterns were examined to identify limitations and potential improvements. The results provided insights into the feasibility of automated maize nutrient deficiency detection using machine learning techniques and guided recommendations for future system deployment and enhancement.

IV. RESULTS AND DISCUSSIONS

The classification performance of four machine learning algorithms—Artificial Neural Network (ANN), Convolutional Neural Network (CNN), k-Nearest Neighbors (kNN), and Support Vector Machine (SVM)—for detecting nutrient deficiencies in maize leaves was evaluated using class-wise metrics derived from confusion matrices, including accuracy, precision, recall, and F1-score. The results for each algorithm are presented in Tables 1–5, highlighting the differential ability of each model to discriminate among Phosphorus Deficiency, Nitrogen Deficiency, Potassium Deficiency, and Healthy leaf classes.

Table 1: ANN Classification Matrix.

Leaf	Precision	Recall	F1-Score	Accuracy
Phosphorus	0.67	0.77	0.71	**0.67**
Nitrogen	0.83	0.81	0.82	
Potassium	0.69	0.45	0.54	
Healthy	0.58	0.72	0.64	

Source: Author, (2026).

As shown in Table 1, ANN demonstrated moderate classification performance across all classes. The Nitrogen Deficiency class achieved the highest accuracy (0.83) and strong precision (0.81), recall (0.82), and F1-score (0.82), indicating that ANN effectively identifies nitrogen-deficient leaves. In contrast, the Phosphorus Deficiency class, although achieving a reasonable F1-score of 0.71, had lower accuracy (0.67), suggesting difficulty in capturing subtle phosphorus deficiency features. Potassium Deficiency exhibited the lowest precision (0.45) and F1-score (0.54), indicating considerable misclassification and highlighting the model's limitation in distinguishing visual features associated with potassium stress. Healthy leaves were identified with moderate reliability, reflected by an accuracy of 0.58 and F1-score of 0.64. Overall, ANN demonstrates acceptable performance for nitrogen detection but struggles with classes exhibiting less visually distinct symptoms.

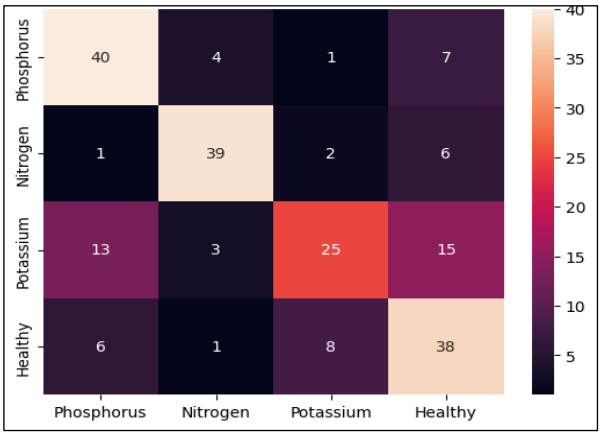


Figure 2: ANN Confusion Matrix.
Source: Author, (2026).

Based on the confusion matrix presented in Figure 2 The confusion matrix of the ANN model for multi-class classification of maize leaf nutrient deficiencies (Figure 2) demonstrates strong performance in detecting Nitrogen and Phosphorus deficiencies, with 39 and 40 correctly classified instances, respectively. Healthy leaves were also accurately identified in 38 cases. In contrast, Potassium deficiency exhibited the lowest classification accuracy, with only 25 correctly predicted instances and notable misclassifications as Phosphorus (13) and Healthy (15), indicating overlapping visual symptoms. Overall, the ANN model effectively distinguishes Nitrogen and Phosphorus deficiencies but shows moderate performance for Potassium, highlighting the need for enhanced feature representation or additional data to improve discriminative capability. These results suggest that while ANN provides a robust framework for automated nutrient detection, certain classes may require targeted optimization to reduce misclassification and support precise fertilization decisions.

Table 2: CNN Classification Matrix.

Leaf	Precision	Recall	F1-Score	Accuracy
Phosphorus	0.84	0.81	0.82	**0.79**
Nitrogen	0.98	0.96	0.97	
Potassium	0.71	0.71	0.71	
Healthy	0.68	0.72	0.70	

Source: Author, (2026).

As presented in Table 2, nitrogen deficiency showed near-perfect performance with precision of 0.96, recall of 0.98, and an F1-score of 0.97, highlighting CNN's exceptional ability to extract hierarchical image features. Phosphorus Deficiency and Potassium Deficiency were also identified with higher accuracy and F1-scores than in ANN, indicating that CNN effectively handles more subtle or complex visual patterns. Healthy leaves achieved moderate classification scores, suggesting that although CNN can discriminate healthy from deficient leaves, there is some residual confusion with certain deficiency classes. These results reflect the model's robustness and its suitability for high-stakes agricultural applications where accurate early detection is critical.

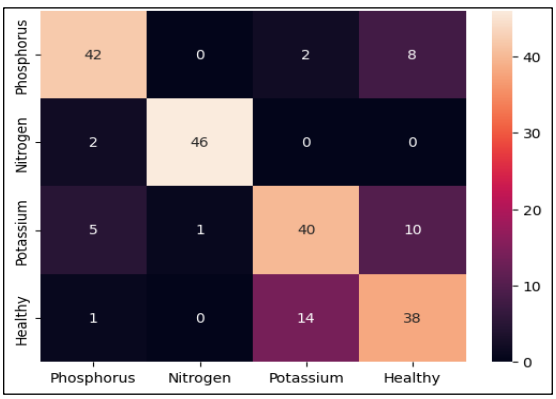


Figure 3: CNN Confusion Matrix.
Source: Author, (2026).

Based on the confusion matrix presented in Figure 3, the confusion matrix for the CNN-based multi-class classification model shows strong overall performance in distinguishing between nitrogen, phosphorus, potassium deficiencies, and healthy maize leaves. The model achieves near-perfect discrimination for nitrogen deficiency, correctly classifying 46 instances with only 2 misclassifications as phosphorus deficiency, indicating highly distinct visual features for nitrogen-starved leaves. Phosphorus deficiency also shows robust detection with 42 correct classifications, though 2 samples were confused with potassium and 8 with healthy, suggesting some spectral or morphological overlap. Potassium deficiency presents the greatest classification challenge, with 40 correct identifications but notable confusion with healthy leaves (10 instances) and phosphorus (5 instances), implying that potassium-deficient leaves may exhibit subtle symptoms that resemble both early senescence and phosphorus stress. Healthy leaves are correctly identified in 38 cases, though 14 are misclassified as potassium deficiency, further reinforcing the bidirectional confusion between these two classes. Overall, the CNN achieves high diagonal dominance, with nitrogen being the most reliably detected class, while the potassium–healthy pair represents the primary source of classification error.

Table 3: KNN Classification Matrix.

Leaf	Precision	Recall	F1-Score	Accuracy
Phosphorus	0.47	0.65	0.54	**0.48**
Nitrogen	0.45	0.94	0.61	
Potassium	0.67	0.18	0.28	
Healthy	0.55	0.23	0.32	

Source: Author, (2026).

The kNN model demonstrated highly inconsistent class-wise performance as presented in Table 3. Nitrogen Deficiency achieved high precision (0.94) but low recall (0.61), indicating that while predictions for this class were often correct, the model missed a significant number of actual nitrogen-deficient leaves. Phosphorus Deficiency, Potassium Deficiency, and Healthy classes showed both low accuracy and low F1-scores, particularly Potassium Deficiency, which achieved only 0.28 for F1-score. These findings suggest that kNN struggles with complex image data and class imbalance, as it relies heavily on proximity in feature space and is sensitive to noise. Consequently, its overall utility for practical field-based diagnosis is limited.

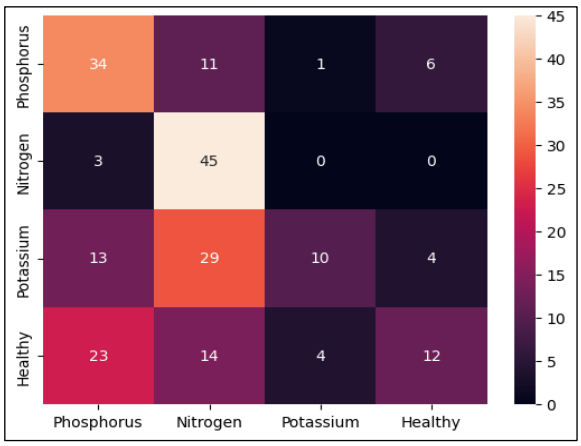


Figure 4: kNN Confusion Matrix.
Source: Author, (2026).

Based on the confusion matrix presented in Figure 4 the confusion matrix for the k-Nearest Neighbors (kNN) classifier, the model demonstrates relatively lower performance in detecting nutrient deficiencies in maize leaves, with notable variability in classification accuracy across the four classes. Nitrogen deficiency achieves the highest number of correct classifications with 45 instances, though 3 samples are misclassified as phosphorus and 4 as healthy, indicating that nitrogen-starved leaves may exhibit features that overlap with both phosphorus deficiency and normal foliage. Phosphorus deficiency shows 34 correct identifications but suffers from significant confusion, with 11 samples misclassified as healthy, 3 as nitrogen, and 1 as potassium, suggesting that phosphorus-deficient symptoms are frequently misinterpreted by the kNN algorithm. Potassium deficiency exhibits the poorest performance, with only 29 correct classifications out of 55 total instances, and substantial misclassification into healthy (10 samples), phosphorus (13), and nitrogen (3), reflecting the algorithm's difficulty in distinguishing potassium starvation from other conditions. Healthy leaves are correctly identified in 44 cases, though 12 are misclassified as potassium deficiency and 4 as nitrogen, reinforcing the pattern of confusion between the healthy and potassium classes. Overall, the kNN model shows the highest reliability for nitrogen detection, while potassium deficiency and its bidirectional confusion with healthy leaves represent the primary limitation in classification accuracy.

Table 4: SVM Classification Matrix.

Leaf	Precision	Recall	F1-Score	Accuracy
Phosphorus	0.47	0.65	0.54	**0.72**
Nitrogen	0.45	0.94	0.61	
Potassium	0.67	0.18	0.28	
Healthy	0.55	0.23	0.32	

Source: Author, (2026).

As shown in Table 4, the SVM model exhibited relatively balanced performance across classes. Nitrogen Deficiency again showed the highest metrics, with perfect precision (1.00), high recall (0.92), and strong F1-score (0.92), reflecting SVM's capability to correctly classify well-separated classes. Phosphorus Deficiency and Potassium Deficiency had moderate metrics, indicating partial difficulty in distinguishing visually similar nutrient deficiency symptoms. Healthy leaves were classified with moderate performance (accuracy 0.67, F1-score 0.63). Overall, SVM demonstrates stable but slightly lower overall performance than CNN, highlighting its effectiveness in classifying prominent visual features but limitations in handling subtle inter-class variations.

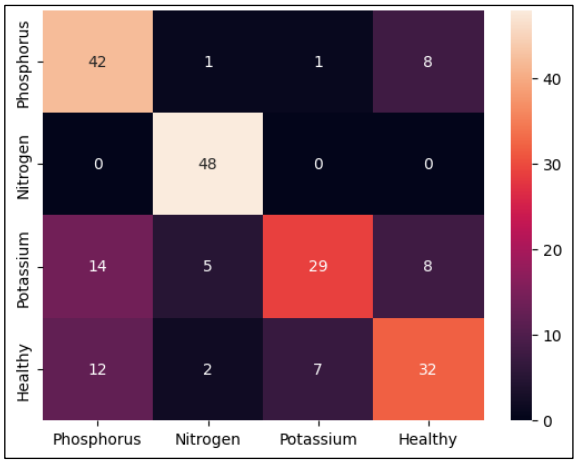


Figure 5: SVM Confusion Matrix.
Source: Author, (2026).

Based on the confusion matrix presented in Figure 5. the Support Vector Machine (SVM) classifier, the model exhibits strong overall performance with notable class-specific variations in detection accuracy for maize leaf nutrient deficiencies. Nitrogen deficiency achieves near-perfect classification, with 48 correct identifications and zero misclassifications across all other categories, indicating that nitrogen-starved leaves present highly separable spectral or morphological features within the SVM decision boundary. Phosphorus deficiency shows robust performance with 42 correct classifications, though 8 samples are misclassified as healthy and 1 each as nitrogen and potassium, suggesting moderate overlap primarily with healthy foliage. Healthy leaves are correctly identified in 32 instances, with 12 misclassifications as phosphorus, 7 as potassium, and 2 as nitrogen, reflecting bidirectional confusion between healthy and phosphorus classes. Potassium deficiency represents the greatest classification challenge, achieving only 29 correct identifications out of 56 total instances, with substantial misclassification into phosphorus (14 samples), healthy (8), and nitrogen (5), indicating that potassium-deficient symptoms exhibit considerable feature overlap with both phosphorus deficiency and normal leaf appearance. Overall, the SVM achieves exceptional specificity for nitrogen detection, while potassium deficiency and the phosphorus–healthy confusion pair constitute the primary sources of classification error.

Table 5: Comparative Performance Evaluation of ANN, CNN, kNN, and SVM for Maize Leaf Nutrient Deficiency Classification.

	Accuracy	**Precision**	**Recall**	**F1-Score**
ANN	0.679	0.689	0.679	0.674
CNN	0.794	0.797	0.794	0.794
kNN	0.483	0.537	0.483	0.433
SVM	0.722	0.73	0.722	0.714

Source: Author, (2026).

Table 5 presents the comparative performance of Artificial Neural Network (ANN), Convolutional Neural Network (CNN), k-Nearest Neighbors (kNN), and Support Vector Machine (SVM) models for maize leaf nutrient deficiency classification. The evaluation is based on standard metrics, including accuracy, precision, recall, and F1-score. Among the evaluated models, the Convolutional Neural Network (CNN) achieved the highest overall performance, with an accuracy of 0.794, precision of 0.797, recall of 0.794, and F1-score of 0.794. The consistency across all evaluation metrics indicates that CNN provides robust classification capability and effectively minimizes both false positives and false negatives. This result highlights the ability of CNN to automatically extract hierarchical spatial features from image data, making it highly suitable for maize nutrient deficiency detection. The Support Vector Machine (SVM) ranked second, achieving an accuracy of 0.722 and an F1-score of 0.714. Its relatively high precision (0.730) indicates good capability in correctly identifying nutrient deficiencies, although slightly lower recall (0.722) suggests some limitations in capturing all relevant cases. Nevertheless, SVM demonstrates stable and competitive performance, particularly in handling structured feature spaces. The Artificial Neural Network (ANN) demonstrated moderate performance, with an accuracy of 0.679 and F1-score of 0.674. Although ANN can capture nonlinear relationships in the dataset, its performance was lower than CNN and SVM, suggesting limitations in handling complex spatial image features compared to convolutional architectures. The k-Nearest Neighbors (kNN) model exhibited the lowest performance among all classifiers, with an accuracy of 0.483 and F1-score of 0.433. Although kNN achieved relatively higher precision (0.537), its significantly lower recall (0.483) indicates poor sensitivity in detecting nutrient deficiency classes. This suggests that kNN struggles with high-dimensional image data and overlapping class boundaries. Overall, the results demonstrate that CNN outperforms the other models, followed by SVM, ANN, and kNN. These findings confirm that deep learning-based approaches, particularly CNN, are more effective for automated maize nutrient deficiency detection due to their superior feature extraction capability.

V. CONCLUSIONS

This study presented a comprehensive comparative evaluation of four machine learning algorithms—Artificial Neural Network (ANN), Convolutional Neural Network (CNN), k-Nearest Neighbors (kNN), and Support Vector Machine (SVM) for the automated classification of macronutrient deficiencies in maize leaves, specifically nitrogen, phosphorus, potassium, and healthy classes. The evaluation was conducted using standard performance metrics, including accuracy, precision, recall, and F1-score, derived from confusion matrix analysis. The experimental results demonstrate that the Convolutional Neural Network (CNN) consistently outperformed the other models, achieving the highest overall accuracy (0.794) and balanced performance across all evaluation metrics. This superior performance can be attributed to CNN's ability to effectively extract hierarchical and spatial features from image data, making it highly suitable for complex visual classification tasks. The Support Vector Machine (SVM) ranked second, exhibiting stable and reliable classification performance, particularly for well-separated classes such as nitrogen deficiency. The Artificial Neural Network (ANN) showed moderate performance, indicating its capability in handling general classification tasks but with limitations in capturing subtle inter-class variations. In contrast, the k-Nearest Neighbors (kNN) algorithm demonstrated the lowest performance, largely due to its sensitivity to high-dimensional data and overlapping feature distributions. A consistent observation across all models is the difficulty in accurately distinguishing potassium deficiency from healthy leaves, as evidenced by recurrent misclassification patterns in the confusion matrices. This challenge highlights the inherent similarity of visual symptoms between these classes and underscores the need for improved feature representation, larger and more diverse datasets, or advanced model architectures to enhance classification performance. Overall, the findings confirm that CNN is the most effective model for maize leaf nutrient deficiency detection within the context of this study. The results emphasize the importance of selecting appropriate algorithms based on data characteristics and application requirements, particularly in precision agriculture where accuracy and reliability are critical. The outcomes of this research support the development of the CORZEA system, a portable image-based diagnostic tool designed for real-time nutrient deficiency detection in field conditions. By enabling early and accurate identification of nutrient stress, the proposed system has the potential to optimize fertilizer application, reduce input costs, and minimize environmental impact, thereby contributing to sustainable agricultural practices. Future work should focus on expanding the dataset to include varying environmental conditions, integrating advanced deep learning architectures, and exploring hybrid or ensemble models to further improve classification accuracy. Additionally, incorporating real-time deployment considerations, such as computational efficiency and mobile integration, will be essential for translating this research into practical, field-ready solutions.

VI. AUTHOR'S CONTRIBUTION

Conceptualization: Von Ryan P. Marcelo.
Methodology: Von Ryan P. Marcelo.
Investigation: Von Ryan P. Marcelo.
Discussion of results: Von Ryan P. Marcelo.
Writing – Original Draft: Von Ryan P. Marcelo.
Writing – Review and Editing: Von Ryan P. Marcelo.
Resources: Von Ryan P. Marcelo.
Supervision: Von Ryan P. Marcelo.
Approval of the final text: Von Ryan P. Marcelo.

VII. ACKNOWLEDGMENTS

The author expresses sincere gratitude to his mother, Josephine Marcelo, for her unwavering support, boundless love, and enduring encouragement, which have been instrumental throughout this research endeavor. The author also extends profound appreciation to Joe G. Lagarteja, former master's adviser, for his invaluable guidance, scholarly insights, and mentorship that significantly contributed to the completion of this study. Special thanks are likewise given to Mark Gil T. Gañgan for his encouragement and motivation, which greatly helped in bringing this work to fruition.

VIII. REFERENCES

[1] W. Cao *et al.*, "Progress in the Study of Plant Nitrogen and Potassium Nutrition and Their Interaction Mechanisms," *Horticulturae*, vol. 11, no. 8, p. 930, Aug. 2025, doi: 10.3390/horticulturae11080930.

[2] S. Kumar, S. Kumar, T. Mohapatra, S. Kumar, and T. Mohapatra, "Interaction Between Macro- and Micro-Nutrients in Plants," *Frontiers in Plant Science*, vol. 12, p. 665583, May 2021, doi: 10.3389/fpls.2021.665583.

[3] D. M. Sobhy and A. Anandhi, "Soil Nutrient Monitoring Technologies for Sustainable Agriculture: A Systematic Review," *Sustainability*, vol. 17, no. 18. Multidisciplinary Digital Publishing Institute, p. 8477, Sep. 22, 2025. doi: 10.3390/su17188477.

[4] W. M. Castillo *et al.*, "Performance of Multi-layered Transfer Learning in Classification of Philippine Rice Leaf Diseases," p. 53, Aug. 2025, doi: 10.1109/icsgrc65918.2025.11159791.

[5] W. M. Castillo *et al.*, "Performance of Optimized Machine Learning in Classification of Philippine Legume Variety," p. 345, Jun. 2025, doi: 10.1109/i2cacis65476.2025.11100745.

[6] V. R. Marcelo and J. Lagarteja, "Corzea: Portable Maize (Zea Mays L.) Nutrient Deficiency Identifier," *INTERNATIONAL JOURNAL OF SCIENTIFIC & TECHNOLOGY RESEARCH*, vol. 9, no. 2, p. 1049, Feb. 2020, Accessed: Feb. 02, 2020. [Online]. Available: https://ijstr.org/final-print/feb2020/Corzea-Portable-Maize-zea-Mays-L-Nutrient-Deficiency-Identifier.pdf

[7] S. Nikitha, S. Prabhanjan, and A. Sathyanarayan, "Plant nutritional deficiency detection: a survey of predictive analytics approaches," *Iran Journal of Computer Science*, vol. 8, no. 1, p. 83, Oct. 2024, doi: 10.1007/s42044-024-00209-5.

[8] A. Ali, T. Hussain, N. Tantashutikun, N. Hussain, and G. Cocetta, "Application of Smart Techniques, Internet of Things and Data Mining for Resource Use Efficient and Sustainable Crop Production," *Agriculture*, vol. 13, no. 2, p. 397, Feb. 2023, doi: 10.3390/agriculture13020397.

[9] M. G. T. Gañgan and T. D. Palaoag, "Performance Assessment of Text Similarity Algorithms Through Classification Metrics for BSIT Graduate Job Concordance," *ITEGAM- Journal of Engineering and Technology for Industrial Applications (ITEGAM-JETIA)*, vol. 12, no. 57, Jan. 2026, doi: 10.5935/jetia.v12i57.2965.

[10] K. A. D. Idress, O. A. A. Gadalla, Y. B. Öztekin, and G. P. Baitu, "Machine Learning-based for Automatic Detection of Corn-Plant Diseases Using Image Processing," *Tarım Bilimleri Dergisi*, Jan. 2024, doi: 10.15832/ankutbd.1288298.

[11] N. Leena and K. K. Saju, "Classification of Macronutrient Deficiencies in Maize Plant Using Machine Learning," *International Journal of Electrical and Computer Engineering (IJECE)*, vol. 8, no. 6, p. 4197, Dec. 2018, doi: 10.11591/ijece.v8i6.pp4197-4203.

[12] A. Bera, D. Bhattacharjee, and O. Krejcar, "PND-Net: Plant Nutrition Deficiency and Disease Classification using Graph Convolutional Network," *arXiv (Cornell University)*, Oct. 2024, doi: 10.48550/arxiv.2410.12742.

[13] M. A. Aghdam, S. Bozdag, and F. Saeed, "Machine-learning models for Alzheimer's disease diagnosis using neuroimaging data: survey, reproducibility, and generalizability evaluation," *Brain Informatics*, vol. 12, no. 1. Springer Science+Business Media, Mar. 21, 2025. doi: 10.1186/s40708-025-00252-3.

[14] Prof. N. V. Gawali, "Image Classification Using Convolutional Neural Networks," *International Journal for Research in Applied Science and Engineering Technology*, vol. 11, no. 5, p. 5176, May 2023, doi: 10.22214/ijraset.2023.52435.

[15] T. K. Hanchinal, "An Analysis of Convolutional Neutral Network for Image Classification," *International Journal for Research in Applied Science and Engineering Technology*, vol. 12, no. 4, p. 4177, Apr. 2024, doi: 10.22214/ijraset.2024.60719.

[16] Y. Song, X. Meng, Y. Li, Z. Liu, and H. Zhang, "An Integrative Approach for Mineral Nutrient Quantification in Dioscorea Leaves: Uniting Image Processing and Machine Learning," *Traitement du signal*, vol. 40, no. 3, p. 1153, Jun. 2023, doi: 10.18280/ts.400331.

[17] S. N. Bhagirath, V. Bhatnagar, and L. Raja, "Classification of Nitrogen Deficiency in Wheat Crop Images Using Different Machine Learning Approaches with ORANGE Tool," in *Lecture notes in networks and systems*, Springer International Publishing, 2024, p. 241. doi: 10.1007/978-981-99-9531-8_19.

[18] A. D. Muhammad *et al.*, "A comprehensive review of crop stress detection: destructive, non-destructive, and ML-based approaches," *Frontiers in Plant Science*, vol. 16. Frontiers Media, Sep. 05, 2025. doi: 10.3389/fpls.2025.1638675.

[19] M. Dutta *et al.*, "Internet of Things-Based Smart Precision Farming in Soilless Agriculture: Opportunities and Challenges for Global Food Security," *IEEE Access*, p. 1, Jan. 2025, doi: 10.1109/access.2025.3540317.

[20] D. Rameshwari, "Classification of Macronutrient Deficiencies in Maize Plant using Machine Learning," *International Journal for Research in Applied Science and Engineering Technology*, vol. 9, p. 4321, Jun. 2021, doi: 10.22214/ijraset.2021.35934.

[21] S. Boujmiraz, H. Darhmaoui, and A. D. el Maliani, "Predicting student performance: A comprehensive review of machine learning, deep learning, and explainable AI approaches," *Computers and Education Artificial Intelligence*, vol. 10, p. 100548, Jan. 2026, doi: 10.1016/j.caeai.2026.100548.

[22] A. A. Barbhuiya, R. K. Karsh, and R. Jain, "CNN based feature extraction and classification for sign language," *Multimedia Tools and Applications*, vol. 80, no. 2, p. 3051, Sep. 2020, doi: 10.1007/s11042-020-09829-y.

[23] M. Sudhakar and R. M. S. Priya, "Computer Vision Based Machine Learning and Deep Learning Approaches for Identification of Nutrient Deficiency in Crops: A Survey," *Nature Environment and Pollution Technology*, vol. 22, no. 3, p. 1387, Sep. 2023, doi: 10.46488/nept.2023.v22i03.025.

[24] T.-C. Pham, T.-N. Nguyen, and D. V. Nguyen, "Ambiguity-aware semi-supervised learning for leaf disease classification," *Scientific Reports*, vol. 15, no. 1, Apr. 2025, doi: 10.1038/s41598-025-95849-3.

[25] M. Iftikhar, I. A. Kandhro, N. Kausar, A. Kehar, M. Uddin, and A. Dandoush, "Plant disease management: a fine-tuned enhanced CNN approach with mobile app integration for early detection and classification," *Artificial Intelligence Review*, vol. 57, no. 7, Jun. 2024, doi: 10.1007/s10462-024-10809-z.

[26] M. Sobhana, T. S. Sappa, and V. G. D. Katakam, "POPRAWA ZDROWIA UPRAW DZIĘKI CYFROWEMU BLIŹNIAKOWI DO MONITOROWANIA CHORÓB I RÓWNOWAGI SKŁADNIKÓW ODŻYWCZYCH," *Informatyka Automatyka Pomiary w Gospodarce i Ochronie Środowiska*, vol. 14, no. 1, p. 57, Mar. 2024, doi: 10.35784/iapgos.5626.

[27] T. Shi *et al.*, "Recent advances in plant disease severity assessment using convolutional neural networks," *Scientific Reports*, vol. 13, no. 1, Feb. 2023, doi: 10.1038/s41598-023-29230-7.

[28] M. Shafay *et al.*, "Recent advances in plant disease detection: challenges and opportunities," *Plant Methods*, vol. 21, no. 1, Oct. 2025, doi: 10.1186/s13007-025-01450-0.

[29] M. Jeong *et al.*, "Rapid Detection of Soybean Nutrient Deficiencies Using YOLOv8s: Advancing Precision Agriculture," *Research Square (Research Square)*, Nov. 2024, doi: 10.21203/rs.3.rs-5300628/v1.

Journal of Engineering and Technology for Industrial Applications

ISSN ONLINE: 2447-0228

ITEGAM-JETIA

Manaus, v.12 n.60, p.1447-1463. July/August, 2026.
DOI: https://doi.org/10.5935/jetia.v12i60.4310

RESEARCH ARTICLE OPEN ACCESS

ADVANCED DEEP LEARNING TECHNIQUES FOR INTELLIGENT FAULT DETECTION IN CHEMICAL PROCESS INDUSTRIES

Mahesh Ganpat Bhong[1], Kiran Dattatray Devade[2], Manjusha Tatiya[3], Jyoti B. Deone[4], Sagar Baburao Patil[5], Anant Sidhappa Kurhade*[6] and Shital Yashwant Wawar*[7]

[1, 2]Department of Mechanical Engineering, Indira College of Engineering and Management, Indira Chanakya Campus (ICC), Parandwadi, Pune, Maharashtra, India.
[3]Department of Artificial Intelligence and Data Science, Indira College of Engineering and Management, Indira Chanakya Campus (ICC), Parandwadi, Pune, Maharashtra, India.
[4]Department of Information Technology, D.Y. Patil Deemed to be University RAIT, Navi Mumbai, Maharashtra, India.
[5]Department of Computer Science and Engineering, Bharti Vidyapeeth's College of Engineering, Kolhapur , Maharashtra, India.
[6, 7]Department of Mechanical Engineering, Dr. D. Y. Patil Institute of Technology, Sant Tukaram Nagar, Pimpri, Pune, Maharashtra, India.
[6, 7]Dnyaan Prasad Global University (DPGU), School of Technology and Research, Dr. D. Y. Patil Unitech Society, Sant Tukaram Nagar, Pimpri, Maharashtra, Pune, India.

[1]http://orcid.org/0000-0001-6555-3122, [2]http://orcid.org/0000-0002-1827-3862, [3]http://orcid.org/0009-0005-9389-7770
[4]http://orcid.org/0000-0003-4102-5645, [5]http://orcid.org/0000-0002-2414-8830, [6]http://orcid.org/0000-0003-3798-9804
[7]http://orcid.org/0009-0008-8040-3067

Email: mahesh.bhong@gmail.com, kiran.devade@gmail.com, manjusha.jain83@gmail.com, jyoti.deone@rait.ac.in, someone.sagar@gmail.com,*a.kurhade@gmail.com,*shital.waware@dypvp.edu.in

ARTICLE INFO

Article History
Received: March 25, 2026
Reviewed: April 25, 2026
Accepted: July 25, 2026
Published: August 31, 2026

Keywords:
Reinforcement Learning,
Deep Learning,
Chemical Process Monitoring,
Fault Detection,
Fault Diagnosis,
Autoencoder,
Industry 4.0

ABSTRACT

Human-friendly analysis of chemical process industries is a nonlinear dynamic system. This paper also points out a great research issue of smart and scalable monitoring methods as the traditional statistics-based and model-driven methods are often not sufficient in discovering complex relationships with high-dimensional data due to the gradual digitalization of industry. The purpose of this paper is to review and analyses existing work on deep learning-based methods for chemical processes monitoring and fault detection. This method provides an overview of approaches based on architecture like the autoencoder, CNN, RNN, and hybrid models and their deployment in benchmark scenarios or real industrial applications. The results indicate that deep learning models enhance fault diagnosis performance via automatic feature extraction, early anomaly detection and effective modelling of temporal dependencies. Hybrid and attention-based models fast-track robustness and diagnostic capability even further. Emphasizing the practical significance of deep learning that extends beyond traditional use cases, the study mentions areas such as predictive maintenance and process safety and operational optimization. It applies for United Nations Sustainable Development Goals (SDG 9, SDG 12, SDG 7), to realize any kind of industry with high efficiency and sustainability.

Copyright ©2026 by authors and Galileo Institute of Technology and Education of the Amazon (ITEGAM). This work is licensed under the Creative Commons Attribution International License (CC BY 4.0).

I. INTRODUCTION

Monitoring understood chemical processes is a key factor in plant-safe operating, with under overhead monitoring being paramount to success. PD provides continuous observation of process variables to identify abnormalities, diagnose faults and prevent failures. (Advanced Fault Detection and Diagnosis) in detection of dangerous accidents and reducing economic damage. Modern-day industrial systems are becoming increasingly complex in nature and require more advanced methodologies for effective condition monitoring to be adopted, transitioning from traditional statistical techniques towards the usage of artificial intelligence (AI) which facilitates better fault detection and diagnosis measures [1].

In recent years, data-driven approaches are attracting increasing attention thanks to their ability to model complex non-linearity and temporal correlation of chemical processes [2], [3] which is difficult for the traditional model-based approach. Some of the correlations in modern industrial plants are highly nonlinear, making it impossible for classical linear techniques such as Principal Component Analysis to model complex dependencies [4], so this is essential. As a result, there has been an increasing number of studies demonstrating that deep learning architectures can outperform traditional approaches by autonomously deriving representative features and identifying complex patterns directly from high-dimensional process data [5]. These models are well-suited to address the most serious fault in conventional methods for examining chemical production, which is the dynamic and high-dimensional nature of chemical production where the complexity is embedded [6]. Deep learning in combination with machine learning methods like bidirectional long-term memory neural network, fully connected neural networks, and extra trees algorithms have been proven to increase fault detection rates of complex chemical processes like the Tennessee Eastman process [7]. The process used in this simulation is widely known as the Tennessee Eastman Process, which is a common benchmark for metrics of success in methods that deal with monitoring and control of processes as it models real-life chemical plant behaviors with complex dynamics under various fault scenarios which establish a good ground for validating techniques to implement advanced algorithms for fault detection and diagnosis [8], [9]. This platform includes a product condenser, reactor, vapor-liquid separator, product stripper and recycle compressor with 41 measured variables and 12 manipulated variables that produce highly time-varying, nonlinear, strong coupling effects data across 22 different health states consisting of 21 fault categories and normal operation for more stringent assessment [10]. The complexity of the Tennessee Eastman Process dataset, which encompasses a variety of fault scenarios and detail-rich interactions among the subtle dynamics of an operational plant, makes a robust procedure for fault detection and identification essential; deep learning models are increasingly showing great potential in fulfilling this role [11-13].

As a result, deep autoencoders and recurrent variational autoencoders have been successfully utilized in anomaly detection and fault diagnosis of this nature system with superior performance compared to traditional statistical methods [8], [14]. In addition, merged deep learning models with ensemble networks, like Autoencoder-assisted Feature Ensemble Net (AFE-Net), have shown superior performance in identifying the nascent fault which could be subtle inside process data and hard to identify [15], [16]. These measurements and changes are representative of nonlinear and nonstationary nature of the industrial processes where they are often used thus showcasing how these challenges make deep learning a powerful tool to address large-scale as well as high-dimensional data. Thus, this tutorial review will provide a systematic survey of the current state-of-the-art deep architecture and methodologies applied to chemical process monitoring and fault detection, critically addressing their potential applicability to real industrial cases. The highlight will be on how these methods are able to utilize the distinctive capabilities of deep architectures, like modeling sequential data and recreating nominal operating conditions [17], [18] as well as improve fault detectability and minimizing false alarms for intricate chemical systems. These trends include the exploration of quantum computing-based deep learning methods, which have the potential to provide unique solutions for addressing computational limits and improving fault diagnosis in industrial processes, such as that used in the Tennessee Eastman Process [19]. This assists in reducing time consumption such as training deep learning models on immense industrial datasets for fault detection classification. Classical methods like Principal Component Analysis (PCA) and model-based approaches rely on simplistic assumptions, failing to account for complicated nonlinear dynamics.

As data, such as those from the sensors and distributed control systems become more widely available process data-driven methods have received significant attention in particular deep learning. These sophisticated deep learning-based models have the power to automatically extract hierarchical features and detect more nuanced patterns which contain information about process anomalies, effectively addressing the challenges presented by traditional methods that struggle in dealing with noisy, correlated, and high-dimensional industrial processes. However, a major drawback of implementing deep learning models for fault diagnosis is the interpretability issue, also known as "black box," nature of deep learning models [20], making it difficult to identify the failure root. This results in limited use of these approaches in industrial settings where safety is an important parameter as revealing the underlying mechanism of a fault for prevention and system tuning is critical [21]. As a result, research increasingly focuses on interpretable deep learning models and explainable AI methods that allow us to understand the decision-making process inside these complex algorithms so as not only to increase trust towards their results but also make it easier for them to be used in industrial fault detection and diagnosis pipelines. Machine learning approaches benefit from automatic feature extraction, making deep learning a promising technique to achieve better fault classification performance for complex industrial systems. This survey will cover various deep learning architectures including convolutional neural networks, recurrent neural networks and their sophisticated variants exploring their respective contributions and feasibility of addressing the distinctive features presented in chemical process data for robust monitoring and fault diagnosis. A comparative summary of prominent deep learning and traditional techniques in the context of fault detection and diagnosis for chemical process monitoring is provided in Table 1.

Table 1: Deep Learning Techniques for Chemical Process Monitoring and Fault Detection.

Sr. No.	Technique / Method	Model Type	Key Application	Dataset / Process	Key Features	Advantages	Limitations
1	Principal Component Analysis (PCA)	Statistical Method	Fault detection	Industrial processes	Linear feature extraction	Simple and fast	Poor for nonlinear systems
2	Convolutional Neural Network (CNN)	Deep Learning	Fault classification	Chemical process data	Spatial feature learning	High accuracy	Needs large dataset
3	Recurrent Neural Network (RNN)	Deep Learning	Time-series monitoring	Dynamic processes	Sequential modeling	Captures temporal behavior	Vanishing gradient
4	Bidirectional LSTM (Bi-LSTM)	Advanced Deep Learning	Fault detection	Tennessee Eastman Process	Bidirectional sequence learning	High detection accuracy	High computation
5	Autoencoder (AE)	Unsupervised Learning	Anomaly detection	High-dimensional data	Feature compression	Detects unknown faults	Low interpretability
6	Variational Autoencoder (VAE)	Probabilistic Model	Fault diagnosis	Nonlinear systems	Latent variable modeling	Handles uncertainty	Complex training
7	Feature Ensemble Network (AE-FEN)	Hybrid Deep Learning	Incipient fault detection	Complex chemical plants	Feature fusion	Detects subtle faults	Model complexity

Source: Authors (2026).

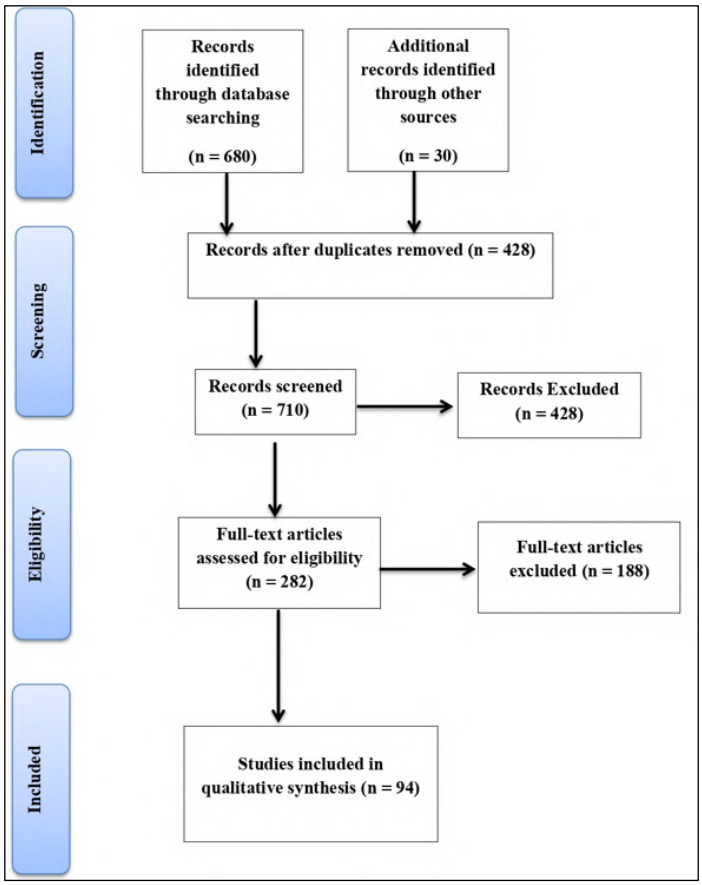


Figure 1: PRISMA flowchart for article selection process.
Source: Authors (2026).

The PRISMA diagram in figure 1 depicts the systematic selection of studies with initial inclusion from databases (n=680) and other sources (n=30), followed by removal of duplicates. From the 710 records screened, 428 were eliminated and 282 full-text articles were evaluated for eligibility. Ultimately, 94 high-quality studies underwent qualitative synthesis after the exclusion of a further 188 full-text manuscripts.

II. FUNDAMENTALS OF PROCESS MONITORING AND FAULT DETECTION

The overall structures of a process monitoring system, with data acquisition and feature extraction as input, followed by fault detection (FD), fault diagnosis (FDD), and root cause analysis (RCA), are depicted in figure 2. It also identifies the types of common faults that can occur in chemical processes, allowing for the systematic identification and mitigation of abnormal operating conditions.

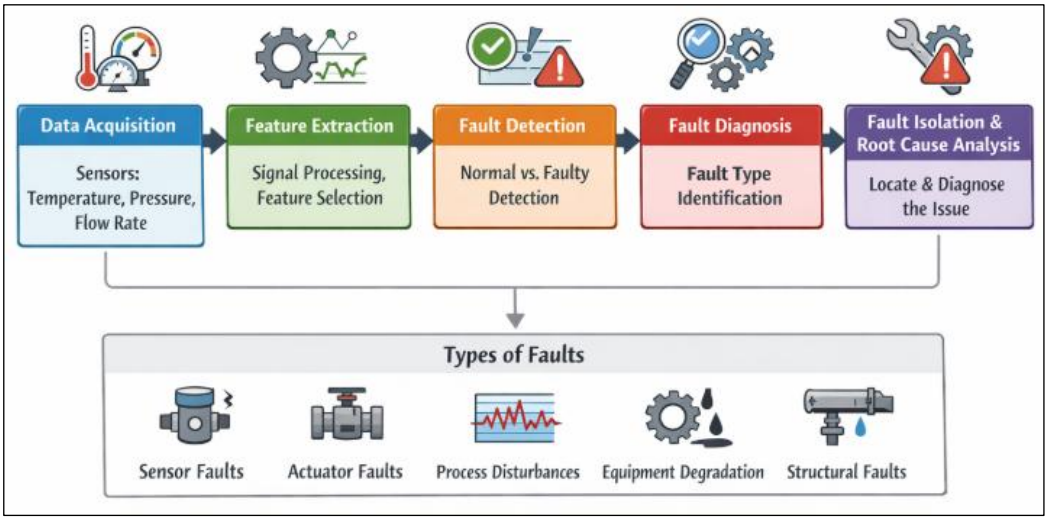


Figure 2: Process Monitoring and Fault Detection Framework.
Source: Authors (2026).

II.1 PROCESS MONITORING FRAMEWORK

A standard process monitoring architecture primarily contains a series of interlinked steps that provide reliable processing and timely detection of abnormal situations. The first step is Data acquisition that refers to data from real-time measurements such as temperature, pressure, and the flow rate taken using various sensors placed in the process. Raw data extracted from sensors is processed through feature extraction to derive indicators indicating system behavior. Using these characteristics, fault detection techniques are used to identify healthy and faulty operating conditions. When a fault is detected, fault diagnosis identifies and classifies the cause of the deviation. Here, fault detection is the identification of whether a fault occurs, and fault diagnosis is the determination of what specifically caused that error to occur so that it can be corrected appropriately. The increased reliance on reliable and timely Fault Detection and Diagnosis in the modern engineering systems for operational safety and resilience poses challenges, particularly in complex and data-intensive environments due to limitations of model-based or rule-based approaches [22]. Abnormal operation settings in such domains are still increasingly supplemented with intervention, which leads to a high number of production accidents. Data preprocessing, training PCA and LSTM autoencoder models, calculating monitoring statistics, determining thresholds, and marking anomalies if those thresholds are cancelled in the workflow shown in figure 3 [23].

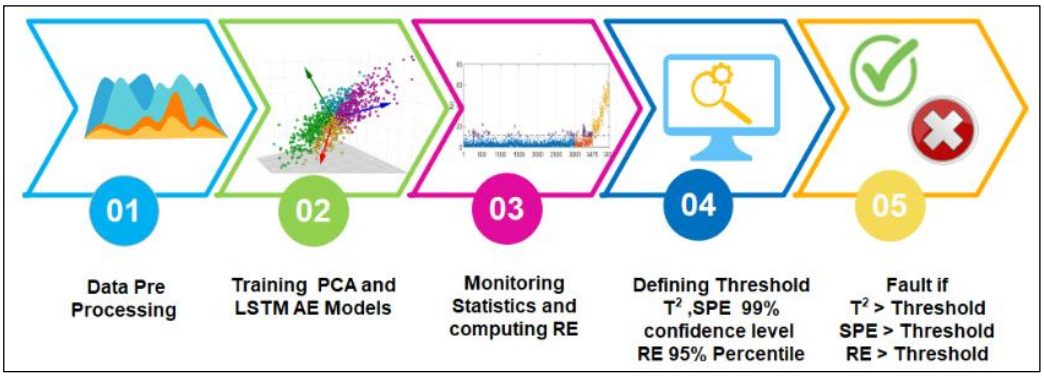


Figure 3: PCA–LSTM Autoencoder–based Anomaly Detection Pipeline.
Source: [23].

As a result, the implementation of a reliable automated system for detecting and diagnosing faults is critical to improving process safety as well as efficiency in modern-day industrial processes. Consequently, a process monitoring system should not only predict the next-step values of quality variables accurately but also efficiently to facilitate timely corrective intervention before considerable disturbances [24]. This highlights the performance of technologies predictive monitoring, which use a knowledge-based understanding approach to classify deviations based on analytical techniques [25]. These systems function by determining normal behaviors and subsequently detect deviations from it that may be an early indicator of failure [26].

II.2 TYPES OF FAULTS IN CHEMICAL PROCESSES

In these systems, faults may occur at smart sensors (e.g., faulty measurements) or control devices (e.g. faulty control actions), leading to compromised system performance. Sensor faults happen when measurement devices give wrong or noisy data because of calibration errors, drift, or failure, which results in incorrect information about the process. Actuator faults are relevant to control elements like valves, pumps or motors that fail to respond accordingly to the control signal. Process disturbances are external or internal deviations like variations in feed composition, changes in temperature, and environmental influences which interrupt the normal operation.

The gradual decline in the performance of a system due to wear, fouling corrosion or aging of components reducing the efficiency of a system is called equipment degradation. Finally, there are structural faults, either of material failure, leakage or blockage in the system infrastructure, which can severely impact safety and operations. As detailed, these distinct fault types require extensive monitoring approaches that can detect small deviations in several operational parameters to ensure system integrity and avoid significant failures [27]. Figure 4 shows one of model-based approach where outputs from the process compared with model predictions for detection, isolation and management of a fault in system [28]. A fault, in general terms, is defined as an unallowed alteration of at least one process parameter from a suitable state and may be organized to abruptness category type such as clear faults, intermittent and gradual [29]. The detection latency, which is the latent period before a fault materially influences the process, may widely vary with respect to fault types and will require complex models for accurate estimation of fault commencement and magnitude [30], [31]. The output of process monitoring in terms of fault detection, diagnosis and isolation as well as root case analysis is a structured solution to these challenges. Detection indicates if we have abnormalities, diagnosis states what kind of fault we have, isolation points out at what component or subsystem we deal with, and root cause analysis gives us the deepest insight of the reasons that triggered the fault to apply appropriate corrective and preventive actions. In this context, a fault is an external register which makes the system behave differently than it was designed to do and can be classified based on its physical location as either component, actuator or sensor faults [32]. This delineation is important for developing targeted diagnostic strategies, as independent fault origins need separate remedial actions [33-35]. From a temporal viewpoint, faults could also be categorized as sudden or drift, which is based on if the parameter deviation is stepwise or progresses over time and usually drift behavior indicates equipment degradation [36]. The important stage of the process monitoring framework, fault types, and their role in secure and dependable industrial operation are summarized in Table 2.

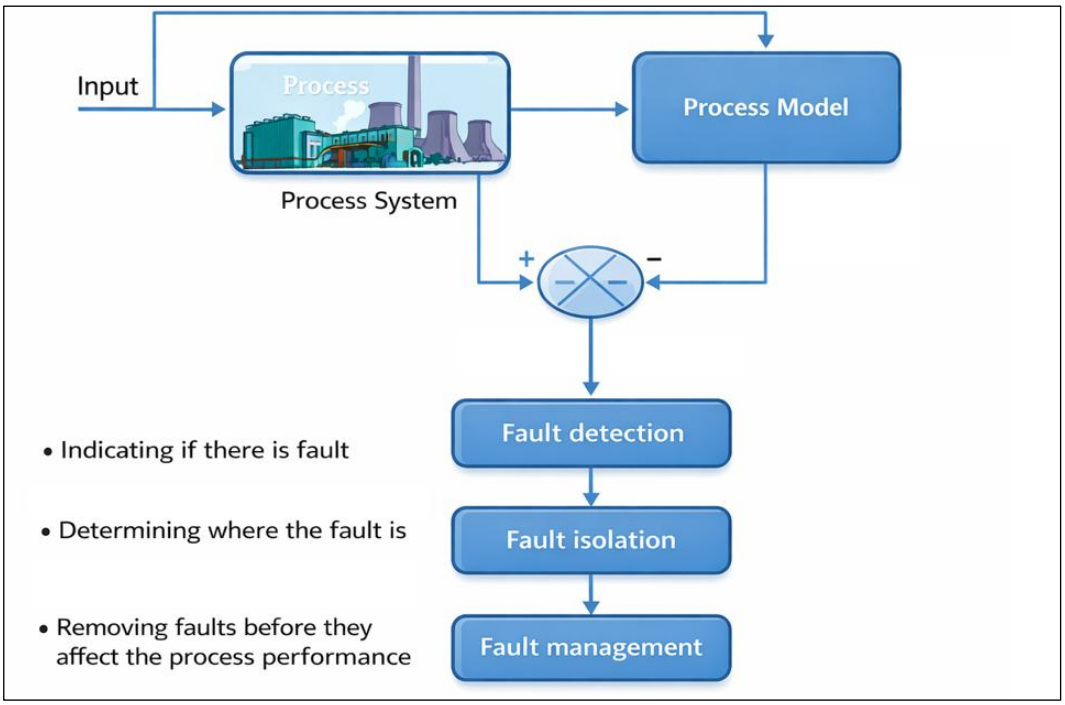


Figure 4: Model-Based Fault Detection and Diagnosis (FDD) Framework.
Source: [28].

Table 2: Process Monitoring Framework and Fault Types.

Stage / Fault Type	Description	Key Components	Significance
Data Acquisition	Collection of real-time process data	Sensors, instruments	Provides input for monitoring
Feature Extraction	Processing raw data into meaningful features	Signal processing tools	Improves detection accuracy
Fault Detection	Identification of abnormal conditions	Detection algorithms	Early warning of faults
Fault Diagnosis	Identification of fault type and cause	Classification models	Supports corrective action
Types of Faults	Sensor, actuator, disturbance, degradation	Process components	Affects safety and performance

Source: Authors (2026).

III. DEEP LEARNING TECHNIQUES FOR FAULT DETECTION

Key deep learning models for fault detection that can learn spatial, temporal and nonlinear patterns in the PID process data such as Autoencoders, CNNs, RNN/LSTM and hybrid architecture are illustrated in figure 5. Additionally, it emphasizes more sophisticated techniques like attention mechanisms and graph-related models that incorporate feature relevance consideration and relationship reasoning across the system to facilitate fault diagnosis.

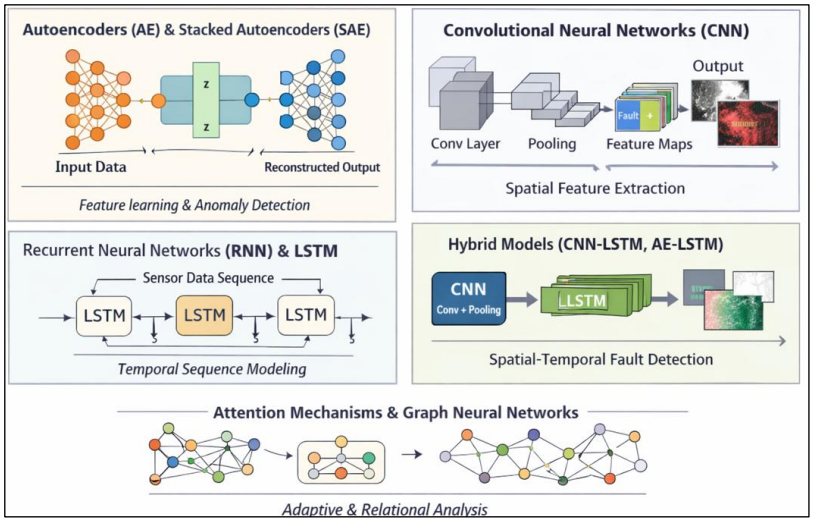


Figure 5: Deep Learning Techniques for Fault Detection in Chemical Processes.
Source: Authors (2026).

III.1 AUTOENCODERS (AE) AND STACKED AUTOENCODERS (SAE)

Autoencoders have proven valuable in chemical process monitoring, due to their ability for unsupervised feature learning and anomaly detection. These neural networks work by encoding the process data into a lower-dimensional latent space (via an encoder) and then reconstructing it back to original form (via a decoder), therefore learning compact and meaningful representation of process data. This allows the model to learn the normal operating patterns of the system during this process. The reconstruction error is then obtained and since the output can differ significantly from the input in case of fault it serves as an indicator. Autoencoders are a popular neural network architecture, which can compress input data into a latent representation of lower dimensionality and then decompress it, with anomalies being detected via an increased reconstruction error [7]. This mechanism exploits the fact that an autoencoder trained only on normal operational data will present a higher reconstruction error for anomalous inputs since they do not belong to the normal distribution of the learned data [37]. This diffuse nature of fault occurrence makes it very hard for human-noise systems to define conditions upon which faults will occur and their trigger rates [38]. This ability makes autoencoders highly applicable for unsupervised fault detection of chemical processes, which is non-linear and high dimensional, with the consideration that comprehensive labeled fault data is often not readily available. Since in classical Principal Component Analysis we performed an intrinsic linear transformation, it failed to adequately model nonlinear process variables [39]; therefore, defective detection might not be accurate when monitoring fault in more complex systems compared autoencoders were a more robust option for linear/nonlinear process monitoring [40].

Autoencoders can be used to work with incomplete and/or noisy datasets, which are often encountered in industrial environments. The stacked autoencoders which are formed by cascading linear transformation methods add more advantage over autoencoders by learning hierarchical and high-level features from the complex process dataset. Stacked autoencoders and their modified variants have received very good performance in industrial benchmark datasets, especially when adapting to missing or partially observed data as these methods can learn deeper spread representations that contribute positively towards fault detection. The basic architecture of an autoencoder is composed of an encoder that compresses the high-dimensional input data into a lower dimensional latent space, and a decoder that reconstructs the reconstructed data from this lower dimensional representation [4], [41]. The encoder compresses the data and maps from high-dimensional space to low-dimensional space, while the decoder generates original data from compressed code [42]. By learning the structure of the data, the network can identify anomalies as deviations from this learned structure [43]. Autoencoders are trained in an unsupervised manner, which makes them very suitable for cases where anomalous data can be heterogeneous and not necessarily annotated with explicit labels [44]. Variational autoencoders are another advancement of the autoencoder architecture that brings a probabilistic perspective to the latent space, allowing for generative modeling capabilities as well as regularization during training such that overfitting can be reduced. Figure 6 shows a deep learning pipeline that involves using autoencoders and classification models to process vibration data to detect faults, which is helpful for health index construction to discover the state of system monitoring. [45].

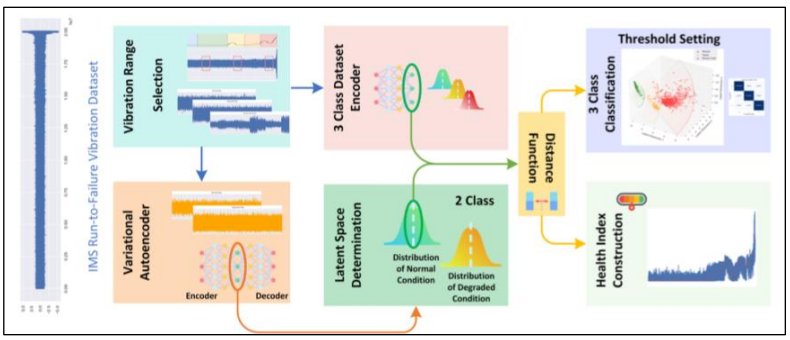


Figure 6: Deep Learning-Based Fault Detection and Health Index Construction Framework.
Source: [45].

Unlike regular autoencoders, stacked autoencoders have multiple layers where the output from one layer's autoencoder is fed as input to the next [46]. The deeper architecture, including more hidden layers in both encoder and decoder locations, makes stacked autoencoders capable of capturing relatively complex relationships within the data [18], which allows to represent high-dimensional features or nonlinearities on fault indications as well [47], [48].

III.2 CONVOLUTIONAL NEURAL NETWORKS (CNN)

Convolutional neural network (CNN) offers a feasible solution to fault detection in chemical processes owing to its strength in capturing spatial correlations among simultaneous process variables. Process data in multivariate systems often have structured relationships that are well suited for extraction by CNNs through convolutional operations. Such networks use filters to extract local patterns and return feature maps that provide an indication of the states of interest in the process. This property enables CNNs to handle high-dimensional data flows, their advantages lying in the ability to pick up on signals that powerful statistical tests might fail to detect, especially when temporal or image-like encodings of process variables are used [49]. CNNs are capable of automatically extracting the most important features, making them useful for anomaly detection from recurrence plots based on multisensory streams, and allowing them to diagnose faults in real time [50]. In addition, it is possible to combine advanced CNN architecture with other deep learning models, contributing to hybrid systems that improve robustness and interpretability in industrial fault diagnosis. Several deep learning methods have been applied to fault detection, with CNNs being one of the most prominent due to their high performance in terms of complex features and classification. Input images, illustrated in the figure7 CNN framework as requiring passes through convolution layer followed by pooling and fully connected layers to extract features from input data and perform their final classification [51]. CNNs take advantage of their hierarchical design to recognize patterns associated with faults through progressively abstracted features learned from raw process data and frequently show superior performance compared to more traditional machine learning algorithms when sufficiently large datasets are available.

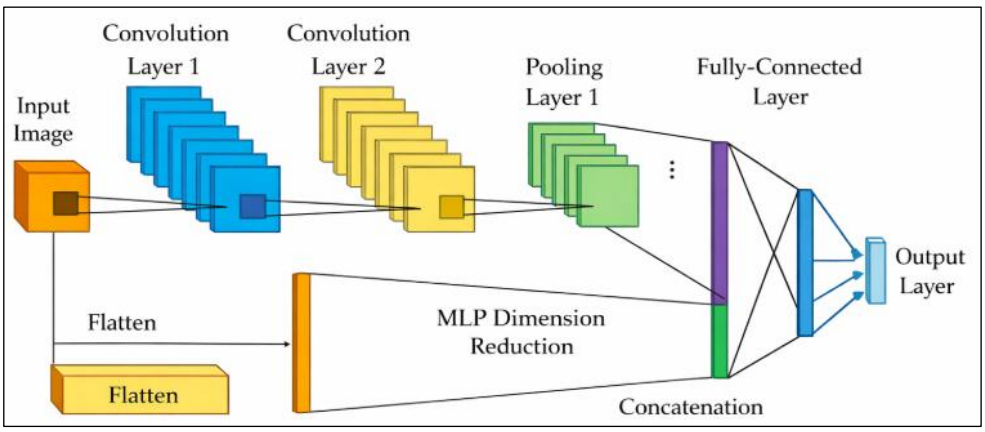


Figure 7: Convolutional Neural Network (CNN) Architecture for Feature Extraction and Classification.
Source: [51].

Learning these localized features significantly increases the accuracy of fault classification by CNN-based models, and as a result, enables robust discrimination between normal and faulty operating conditions. They are especially good at dealing with high-dimensional and multidimensional process data where traditional methods can struggle to find hidden correlations. This is one of the main reasons that, with better feature extraction ability by CNNs, performance-wise they provide a more reliable approach for monitoring and fault identification in chemical process systems. The basic structure of a CNN consists of convolutional layers that extract features via learnable filters and pooling layers that down-sample the data while maintaining most vital information [52]. Compared to other algorithms, CNNs are particularly suited for processing time-series features or imaging-based representations of process variables, as they create a processing chain with multiple layers that distinguish increasingly abstract levels of regularities in the series data [52]. The approach of CNNs to learn feature hierarchies purely from raw sensor data, avoiding the need for explicit feature engineering, has significant utility in complex industrial fault detection scenarios [53].

III.3 RECURRENT NEURAL NETWORKS (RNN) AND LSTM

Inherent to chemical processes that their systems are dynamic, with system behavior changing with time and depending on previous states. This makes Recurrent Neural Networks a natural candidate for those environments, since they are made to approximate temporal dependencies in sequential input. Because RNNs have internal memory, they can learn to model the relationships between current and previous observations, making them suitable for analyzing time-series blue-tooth sensor data. RNNs can learn time-varying patterns that may correspond to gradual increase of process anomalies or the incipient stage of faults, which is useful for proactive process monitoring [54]. More specifically, RNNs handle sequential inputs by using the output of a hidden layer from one temporal step as an input to the next hidden layer, allowing networks to learn and perform complex data transformations over long ranges of timesteps [55]. Due to the diminishing target problem in traditional RNNs when learning long-term dependencies, Long Short-Term Memory neural networks have become effective approaches for fault detection among RNN architectures [56]. Their advanced gating functionalities (input, output and forget gates) are what makes it possible, wherein input gate helps them in remembering past states and forget gate enables them to forget the state [57]. The specialized neural network architecture of Long Short-Term Memory (LSTM) networks overcomes the limitations of traditional RNNs regarding long-term dependencies.

LSTM networks are designed with memory cells and gate variables that enable them to keep significant information over longer time spans, as well as skip out on irrelevant details. In chemical processes, this ability is crucial to detect abnormalities where deviations could occur gradually or have a time-lag feature. In particular, the insertion of input, output and forget gates in LSTMs allows them to learn which features are important temporal behavior that needs to be retained in their memory cells, which significantly enhances reliability and accuracy where it comes to fault diagnosis. Figure 8 depicts the receiving of raw data from measurement signals to online processing and then uses a PdM analysis to detect, locate, and predict faults in rotating machinery systems [58]. This architecture enables LSTMs to mitigate the vanishing gradient issue that traditional RNNs face, helping to retain important information from time steps in earlier training cycles [59-61]. The internal memory and gating mechanisms allow RI-GECRs to capture long-term temporal dependencies much more effectively due to greatly enhanced gradient flow [62].

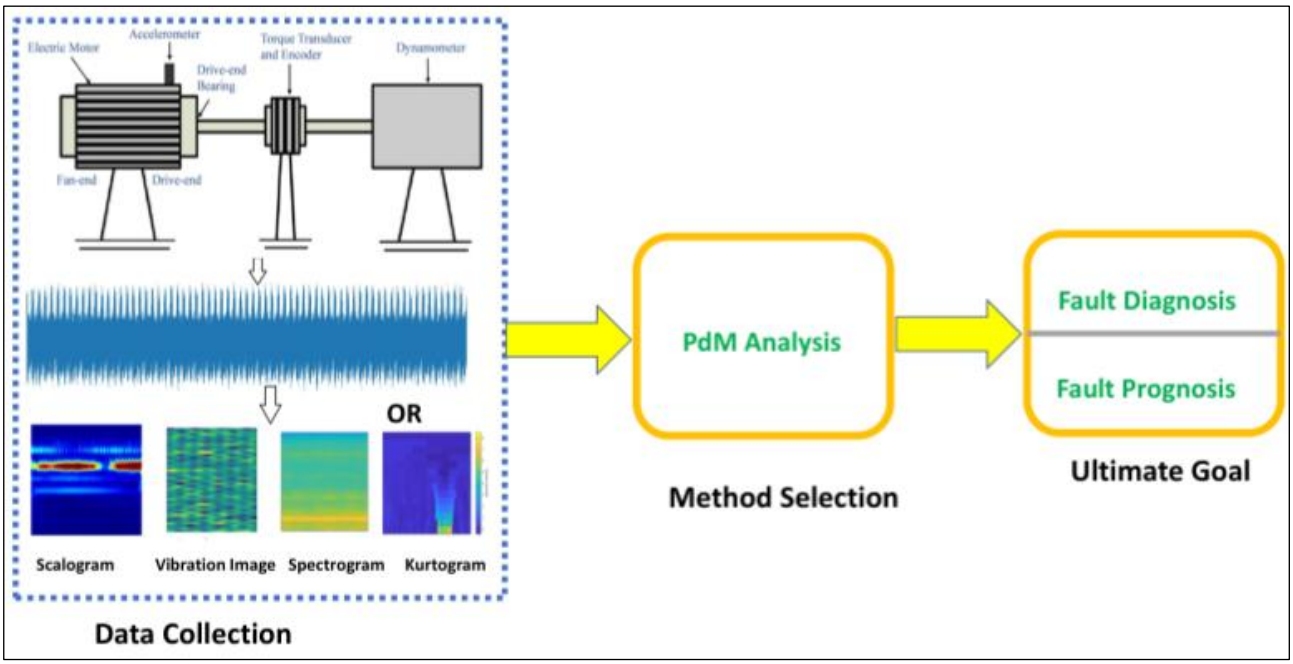


Figure 8: Predictive Maintenance Framework for Fault Diagnosis and Prognosis Using Vibration Signal Analysis. Source: [58].

Hybrid architectures, such as CNN–LSTM combine the strengths of both structures by using CNNs for spatial feature extraction and LSTMs for the temporal analysis. These models are based on the integrated approach, which can facilitate successful and effective detection of fault dynamics and time-delay effects in process and provide greater accuracy and reliability to monitoring systems. Although standard RNNs have demonstrated success in various tasks, challenges like vanishing or exploding gradients during the training process can significantly limit their performance with sequences of longer length [63], [64]. These limitations can be addressed with more advanced RNN variants, such as long short-term memory (LSTM) networks and Gated Recurrent Units, which use complex gating mechanisms to control information flow in the model more effectively, improving their ability to fit time-series data with long-range dependencies [65]. LSTMs specify an input gate, a forget gate and an output gate to regulate the transport of information which enables them to selectively save and recall information over long periods [66], [67]. This unique architecture allows LSTMs to remember important information over long sequences and avoid vanishing gradient problems, which often limit the effectiveness of traditional RNNs in learning long-term dependencies [68-70]. The forget gate decides what will be thrown away from the previous cell state, the input gate decides what new information should be saved in this cell, and the output gate controls what is sent to hidden state [71].

III.4 HYBRID DEEP LEARNING MODELS

To effectively model the complexity of chemical processes, recent trend in process monitoring is to adopt hybrid deep learning models that combine various architectures. These approaches typically integrate the advantages of various methods to incorporate both spatial and temporal features associated with process data. A common approach is to utilize CNN–LSTM frameworks for deriving spatial–temporal features, where convolutional layers capture local correlations and LSTM units model time-dependent dynamics. These combined strengths harness the CNN's ability to extract features in a hierarchical manner, along with LSTM's ability to learn long-range temporal dependencies, resulting in the establishment of a strong mechanism for decoding complex fault signatures from intricate process dynamics [72]. Additionally, kernel deep learning has been introduced in soft sensor context with hybrid variable-wise weighted stacked autoencoders [73]. Another potential direction of development related to emission monitoring systems can be found at the crossroads between explainable artificial intelligence (AI) and deep learning, aiming for more transparent and reliable algorithms catering to emissions-sensitive processes [74]. These hybrid methods typically combine anomaly detection and fault classification, employing aggregated feature representations resulting in higher diagnostic accuracy than standalone models. RRNNs help understand the spatio-temporal aspects of environmental data [75], hence, are suitable to develop hybrid deep approaches by aggregating CNN with RNN or LSTM for accurate detection and prediction of fault in complex industrial processes.

Likewise, hybrid systems such as Autoencoder–LSTM facilitate feature extraction and predictive functionality simultaneously, enabling early fault anomaly detection from learned data representations. Graph Neural Networks have also received attention in modeling process topology, where the connections between different units or variables are considered as interconnected nodes, providing a broader view of inter-system interactions. It has been shown that hybrid CNN-LSTM networks can achieve a better result about anomaly detection and fault prediction tasks in industrial applications on the premise of modeling both spatial and temporal information [76]. This is especially apparent in hydraulic systems, where integrated CNN and LSTM architectures outperformed traditional methods for anomaly detection [77]. Integrated frameworks which merge CNN, Autoencoders and LSTM network have shown improved performance on multi-class fault classification tasks. These diverse hybrid methods enhance feature extraction, improve detection accuracy, and rarefaction of a fault diagnosis more accurately in complex chemical processes.

III.5 ATTENTION MECHANISMS AND GRAPH-BASED MODELS

Attention mechanisms and graph based deep learning structures have also been integrated into these advanced models, highlighting their strengths in accurate fault detection and diagnosis for chemical processes. Attention mechanisms allow the model to exploit different importance levels of process variables by focusing on more significant features for fault identification. This weighted force fitting aids model interpretability and helps to emphasize which features contribute most towards unexpected behavior. To illustrate, Dual-Stage Attention RNN architectures can learn input-level attention weights as well as temporal attention weights simultaneously, allowing highlighting of relevant features and significant time steps while forecasting [78]. Likewise, the channel–spatial attention method can improve feature importance as well as reduce noise in CNN-LSTM for real-time sensor fault detection [79]. Additionally, the combination of these attention mechanisms with LSTMS allows us to forecast future patterns of important variables, providing good early prediction results in several fault cases [80]. Instead of focusing on a single feature among many, attention can be incorporated into hybrid deep learning architectures that dynamically emphasize important features for better risk recognition under changing operational scenarios [81]. This flexibility allows them to perform especially well in settings with skewed datasets, a frequent occurrence within fault identification approaches [82]. Graph-based approaches, including popular paradigms like Graph Neural Networks, show great potential in modeling the complex relationships between various process variables and sensors throughout a chemical plant. A four-stage approach of understanding the data, learning patterns, diagnosing faults and finally taking maintenance actions is shown in figure 9 which enhances reliability and performance levels of a system [83].

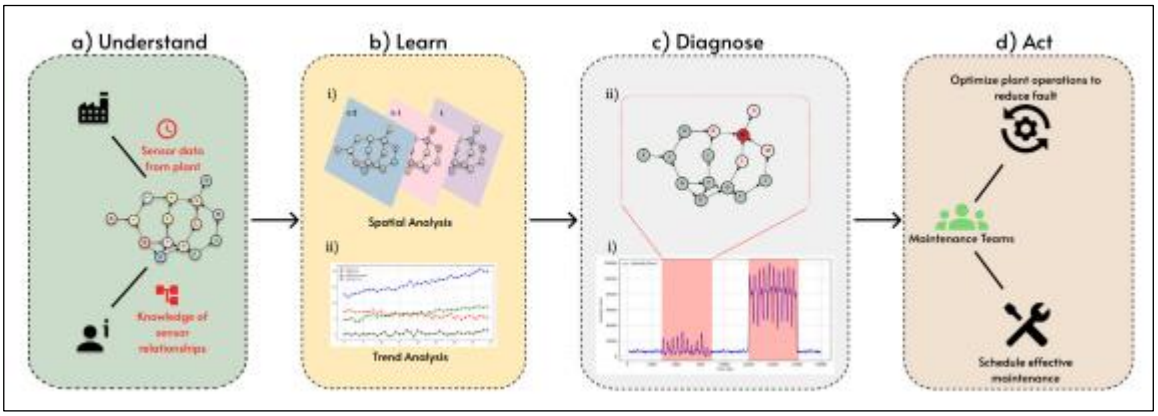


Figure 9: AI-Based Predictive Maintenance Workflow: From Data Understanding to Maintenance Action. Source: [83].

This is an approach where the process is represented with graph models (a network of interconnected nodes and edges), and each node corresponds to a specific process variable or unit. These representations can effectively capture the complexities of relationships and interactions in the system. Graph Attention Networks (GAT) introduced attention heuristics along with the underlying graphical structures to better learn the spatial and temporal dependencies between variables in input data. At a deeper level, tailored graph neural networks such as EG-SAGCN further modify edge weights and use spatial attention to better learn local and global relationships in sensor networks [84]. This enables a more detailed understanding of how disturbances diffuse over interlinked systems. Considering their capability of naturally model relationships between entities, a characteristic that suits well for property modeling [85] and addresses challenges in traditional descriptor-based methods. In Table 3, a consolidated comparison of various prominent deep learning architectures tailored for fault detection in chemical process systems is provided, specifying their learning modes, characteristics and applications. It shows how different models based on data patterns can systematically improve the accuracy and reliability of detection using spatial, temporal, and relational patterns in process data.

Table 3: Deep Learning Techniques for Chemical Process Monitoring and Fault Detection.

Technique	Model Category	Learning Type	Key Application	Data Type	Key Features	Advantages	Limitations	Typical Use Case
Autoencoder (AE)	Neural Network	Unsupervised	Anomaly detection	High-dimensional	Reconstruction error	Detects unknown faults	Low interpretability	Industrial monitoring
Stacked Autoencoder (SAE)	Deep NN	Unsupervised	Feature extraction	Complex data	Hierarchical learning	High accuracy	High complexity	Missing data cases
CNN	Deep Learning	Supervised	Fault classification	Multivariate	Spatial features	High accuracy	Needs large data	Sensor systems
RNN	Deep Learning	Supervised	Time-series analysis	Sequential	Temporal modeling	Captures dynamics	Vanishing gradient	Process monitoring
LSTM	Advanced RNN	Supervised	Fault prediction	Time-series	Memory gates	Handles long-term data	High computation	Dynamic systems
CNN-LSTM	Hybrid	Supervised	Spatio-temporal	Time-series	Combined features	High reliability	Complex model	Real-time monitoring
Attention Model	Advanced DL	Supervised	Feature importance	Large datasets	Variable weighting	Better interpretability	Training complexity	Fault diagnosis
GNN	Graph-based	Semi-supervised	System modeling	Network data	Node relations	Captures dependencies	Complex implementation	Large plants

Source: Authors (2026).

The only existing effective methods are those that enhance spatiotemporal feature learning, promote diagnosis capability, and contextualize root cause analysis by identifying the most relevant variables and their interactions which make them increasingly suitable for complex large-scale chemical process systems.

IV. APPLICATIONS IN CHEMICAL PROCESS INDUSTRIES

Figure 10 summarizes the Tennessee Eastman Process (TEP) as a standard system for testing fault detection models with industrial real applications in processes such as petrochemical, polymer, pharmaceutical and wastewater. It emphasizes the primary advantages of deep learning — early fault detection, predictive maintenance, enhanced process safety, and efficient root cause analysis.

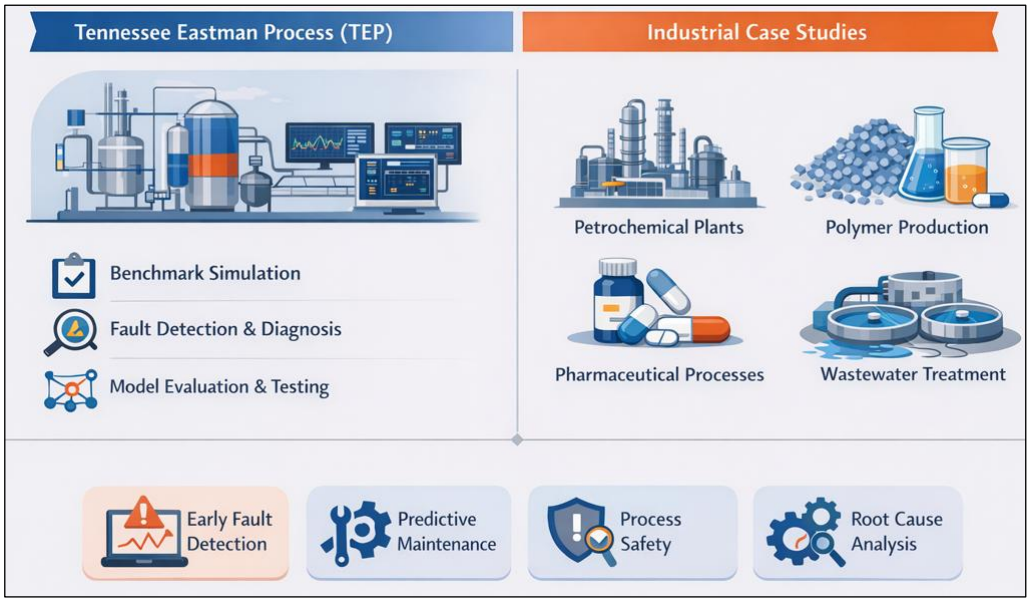


Figure 10: Applications of Deep Learning in Chemical Process Industries.
Source: Authors (2026).

IV.1 TENNESSEE EASTMAN PROCESS (TEP)

The Tennessee Eastman Process is one of the most widely used benchmark systems for process monitoring and fault detection techniques. It reflects a real industrial chemical process including complex reactions, recycle streams and multivariable control structures. Due to its nonlinear and dynamic characteristics, it can provide a test platform for advanced data-driven as well as deep learning-based methods validation. The dataset provides intact operation as well various fault cases that are very important to evaluate performance of a model in detection and diagnosis task, allowing standardized comparisons among different techniques. State-of-the-art results in the context of fault diagnosis on the Tennessee Eastman Process dataset have been reported for advanced GNNs (including with learnable adjacency matrices) over classical recurrent neural networks. As illustrated in figure 11 [86], an abnormal condition is detected based on analysis of these multi-sensor signals, as well as a specific type of fault is classified using a diagnostic model.

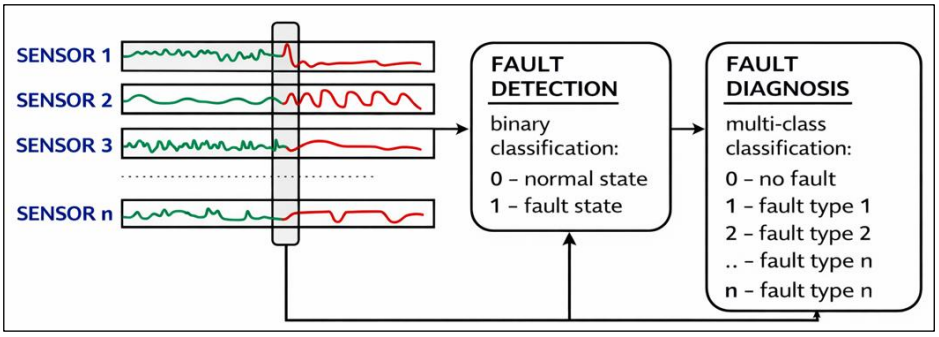


Figure 11: Sensor-Based Fault Detection and Diagnosis Framework.
Source: [86].

This is due to their capability of modeling complex spatial correlations and inter-relational dependencies among the variables that the process encompasses [87]. Yet the continuously changing relations between time series and different operational conditions are still challenging to model [88]. This indicates a need for further explorations to design GNN architectures that can flexibly respond and capture such changes, possibly via employing temporal graph learning methods or integrating physics-informed constraints to improve the generalizability across different operational scenarios [89], [90]. TEP is run over multiple different indicative operating conditions and predefined fault cases, allowing for the systematic evaluation of fault detection and diagnosis algorithms. This benchmark is widely used by researchers to assess model performance across detection accuracy, false alarm rate, robustness under noise and uncertainty. For example, a recent work proposed the new Twin Transformer architecture combined with the Gated Dynamic Learnable Attention mechanism to improve detecting and diagnosing different faults, trained on Tennessee Eastman Process Dataset independently process input data while dynamically adapting attention strategies [9]. Big advantages in accuracy and reliability of fault detection have been shown using deep learning applied to Tennessee Eastman Process. By employing techniques like autoencoders, CNNs, and hybrid architectures that can capture complex patterns inherent in the process data, these approaches have shown improved robustness and generalization by effectively handling multiple fault scenarios.

IV.2 INDUSTRIAL CASE STUDIES

Deep learning-based fault detection methods have been successfully applied to a wide variety of industrial chemical processes. These techniques are used in petrochemical plants and refinery operations to monitor complex reaction networks and dynamic separation units that feature multiple interacting species. Deep learning models are used to monitor reaction parameters for product quality in polymer production. In pharmaceutical processes, they are similarly valuable in providing necessary quality assurance by quickly finding anomalies in batch operations and continuous manufacturing systems. These applications exploit the ability of deep learning to handle high dimensional sensor data, allowing them to detect subtle anomalies that may propagate into significant equipment failures or excursions early, providing operational safety and efficiency. In addition, the use of deep learning in these industrial contexts has contributed to decreased unscheduled downtime and improved resource utilization by enabling proactive maintenance scheduling. Thus, this positive approach is significant in improving overall reliability and economic performance of the system. The efficacy of these approaches on features fusion and ensemble learning underscored that these methods have also been extensively validated to real-world datasets collected from industrial facilities such as wastewater treatment plants in which they are shown superior fault detection performance over single model-based setups [91-97]. There are many practical benefits of incorporating deep learning into process monitoring systems. It allows fault detection as early as possible by recognizing small changes in process behavior before these turns into serious failings. Forecasting equipment degradation and scheduling maintenance interventions can lead to improved predictive maintenance strategies that lower downtime and maintenance costs. It also makes process safety even better, since advanced models can detect abnormal conditions in real time and initiate preventive measures. Additionally, deep learning systems enhance the ability to conduct effective root cause analysis by identifying individual outlier occurrences along with their causative factors, thus allowing for continuous enhancement of chemical process operations [98-100]. Data-driven strategies are crucial to tackling the intrinsic complexities of chemical processes, where dynamic and non-linear interactions make it hard for conventional modelling approaches [101]. Table 4 provides a summary of various industrial applications for deep learning in chemical processes, including faults detection and monitoring, as well as operational efficiency improvement.

Table 4: Applications for Deep Learning in Chemical Process Industries.

Application Area	Process Type	DL Technique Used	Key Function	Benefits
Tennessee Eastman Process	Benchmark system	AE, CNN, LSTM	Fault detection	High evaluation accuracy
Petrochemical Plants	Continuous process	CNN, RNN	Process monitoring	Improved safety
Refineries	Separation units	CNN–LSTM	Fault diagnosis	Reduced downtime
Polymer Production	Reaction systems	Autoencoder	Quality monitoring	Product consistency
Pharmaceutical Industry	Batch process	LSTM, RNN	Anomaly detection	High precision
Wastewater Treatment	Environmental systems	Ensemble DL	Fault prediction	Better reliability
Smart Manufacturing	Industry 4.0	Hybrid DL	Predictive maintenance	Cost reduction
Cyber-Physical Systems	Automated plants	GNN, Attention	Fault & attack detection	Enhanced security

Source: Authors (2026).

In today's Industry 4.0 settings, the scope of deep learning-based approaches goes beyond typical monitoring tasks to recognize unseen defects and provide alerts for possible cyber threats in industrial control systems. This ability is critical for safe, reliable function within highly automated and interconnected chemical process industries.

V. ADVANTAGES OF DEEP LEARNING IN PROCESS MONITORING

Deep learning can hold significant benefits in process monitoring due to its ability to deal with nonlinear and high dimensional data, which are often encountered in complex industrial processes. It can automatically derive the stimulus-relevant feature from raw sensor data, thus removing the manual feature engineering step and lessening reliance upon domain-specific preprocessing unlike traditional methods. It reduces the number of false positives with deep learning models able to learn fine-grained differences and latent features in process data. Furthermore, these methods assist in near-real-time monitoring where persistent analysis of streaming data helps in timely abnormality detection. In predictive maintenance, deep learning can use raw sensor data to detect early signs of equipment failure and predict impending failures. Thus, deep learning methods outperform traditional ones in capturing dynamic connections and underlying processes.

VI. CHALLENGES AND LIMITATIONS

While deep learning has significant potential for chemical process monitoring, several practical challenges hinder its broad industrial application. These have to do with problems concerning data availability, interpretability of models, computational demands and suitability across processes. Since this technique is still in its initial phases, knowing its limitations will help avoid the implementation pitfalls and provide directions for developing efficient and robust fault detection systems.

VI.1 DATA-RELATED ISSUES

One of the significant challenges to applying deep learning in monitoring chemical processes is data. Labeled fault data are limited in many industrial settings because faults happen rarely and do not follow any systematic documentation. For supervised learning, this results in a lack of training samples. Moreover, the datasets usually are heavily imbalanced where there is more amount of normal operating data than faulty conditions available which leads to models being biased towards normal predictions. Dealing with missing, incomplete and noisy sensor data introduces additional complexity in developing a model that accounts for the reliability and accuracy of feature extraction and learning processes.

VI.2 INTERPRETABILITY

Many deep learning systems are black boxes in nature, meaning they do not lend themselves to easy interpretation of internal workings or decisions. The present absence of such insight is particularly limiting in safety-critical industries like chemical processing, where knowing not just that a fault occurred but why it can be crucial. Due to the limited ability of such models to explain themselves, engineers and operators may be reluctant, if not downright fearful, to rely on them — especially in high-stakes environments that mandate very stringent regulatory compliance and accountability.

VI.3 COMPUTATIONAL COMPLEXITY

The implementation of deep learning models involves significant computational requirements. Training complex architectures, such as deep neural networks, requires high processing power and long training times, particularly when dealing with large-scale industrial datasets. In addition, these models typically require extensive datasets to achieve high accuracy, which may not always be available in real-world applications. This increases the cost and complexity of deployment in industrial settings.

VI.4 GENERALIZATION

Generalization remains a critical issue in deep learning-based fault detection systems. Models trained on a specific process or dataset may not perform effectively when applied to different processes due to variations in operating conditions, system configurations, and process dynamics. This limits the scalability and adaptability of such models across different industrial applications, requiring retraining or fine-tuning for each new environment.

VII. FUTURE RESEARCH DIRECTIONS

To address current constraints and improve the performance of those deep learning models, researchers are focused on novel methods and high-performance computer technologies. Future works will surely focus on enhancing the explainability of such models, decreasing dependency on annotated content, and coupling intelligent systems with modern industrial architectures. This will greatly enhance the robustness and practical reliability of deep learning within chemical process monitoring.

VII.1 EXPLAINABLE AI (XAI)

Explainable Artificial Intelligence is emerging as a critical research direction to address the lack of transparency in deep learning models. By incorporating XAI techniques, it becomes possible to interpret model predictions and understand the underlying reasoning behind fault detection and diagnosis. This improves trust and acceptance of AI systems in industrial environments, particularly in safety-critical chemical processes. In addition, explainability supports informed decision-making by providing engineers with actionable insights rather than only prediction outputs.

VII.2 TRANSFER LEARNING AND FEW-SHOT LEARNING

Transfer learning and few-shot learning approaches offer promising solutions to the challenge of limited labeled data in industrial applications. These techniques enable models trained on one process or dataset to be adapted to another with minimal additional data. This reduces the need for extensive data collection and labeling efforts. Such approaches are especially useful in chemical industries where fault data are rare, allowing models to generalize knowledge across different plants and operating conditions.

VII.3 INTEGRATION WITH INDUSTRY 4.0

The integration of deep learning with Industry 4.0 technologies is expected to significantly enhance process monitoring and fault detection capabilities. The use of IoT-based systems enables real-time data acquisition from sensors and equipment, facilitating continuous monitoring. Digital twins provide virtual replicas of physical systems, allowing real-time simulation, prediction, and optimization of process performance. Edge computing further supports rapid decision-making by processing data closer to the source, reducing latency and improving system responsiveness in industrial environments.

VII.4 SELF-SUPERVISED AND UNSUPERVISED LEARNING

Self-supervised and unsupervised learning methods are gaining attention as they reduce the dependency on labeled datasets. These approaches allow models to learn patterns and representations directly from raw data, making them suitable for large-scale industrial applications where labeled data are limited or unavailable. By leveraging unlabeled data, such methods enhance scalability and enable more efficient deployment of intelligent monitoring systems across diverse chemical processes. Deep learning has significantly transformed chemical process monitoring and fault detection by enabling accurate, data-driven analysis of complex industrial systems. Techniques such as autoencoders, CNNs, and LSTMs provide improved detection accuracy and adaptability compared to traditional approaches. Despite challenges related to interpretability and data availability, ongoing research in explainable and hybrid models is addressing these limitations. Future advancements integrating deep learning with Industry 4.0 technologies will further enhance the reliability, safety, and efficiency of chemical process industries.

VIII. CONCLUSION

Deep learning has emerged as a highly effective approach for chemical process monitoring and fault detection, offering clear advantages in handling nonlinear, high-dimensional, and dynamic industrial data. Techniques such as autoencoders, convolutional neural networks, recurrent neural networks, and hybrid architectures have demonstrated strong capability in extracting meaningful features, identifying subtle anomalies, and improving fault classification accuracy. These models significantly outperform conventional statistical and model-based methods, particularly in complex systems such as the Tennessee Eastman Process and real industrial environments. The study also highlights that deep learning enables real-time monitoring, early fault detection, and predictive maintenance, thereby improving process safety, reliability, and operational efficiency. Despite these strengths, several practical challenges remain, including limited labeled data, model interpretability, computational requirements, and generalization across different processes. Addressing these issues is essential for large-scale industrial adoption. Recent research trends indicate that the integration of explainable AI, transfer learning, self-supervised learning, and Industry 4.0 technologies will play a critical role in advancing this field. These developments are expected to improve model transparency, adaptability, and scalability across diverse industrial applications. Overall, deep learning-based process monitoring represents a transformative direction for modern chemical industries, supporting intelligent decision-making and enabling safer, more efficient, and data-driven operations in increasingly complex manufacturing environments.

IX. AUTHOR'S CONTRIBUTION

Conceptualization: Mahesh Ganpat Bhong, Anant Sidhappa Kurhade and Kiran Dattatray Devade.
Methodology: Mahesh Ganpat Bhong, Kiran Dattatray Devade and Sagar Baburao Patil.
Investigation: Manjusha Tatiya, Jyoti B. Deone and Shital Yashwant Waware.
Data Curation: Manjusha Tatiya and Jyoti B. Deone.
Formal Analysis: Sagar Baburao Patil and Anant Sidhappa Kurhade.
Writing – Original Draft: Mahesh Ganpat Bhong and Manjusha Tatiya.
Writing – Review and Editing: Anant Sidhappa Kurhade, Kiran Dattatray Devade and Shital Yashwant Waware.
Resources: Kiran Dattatray Devade and Sagar Baburao Patil.
Supervision: Anant Sidhappa Kurhade.
Approval of the final text: All authors.

X. ACKNOWLEDGMENTS

The authors would like to express their sincere gratitude to Dr. D. Y. Patil Institute of Technology and DPGU, School of Technology and Research - Dr. D. Y. Patil Unitech Society, Pimpri, Pune for providing t he necessary support and research infrastructure.

XI. REFERENCES

[1] M. Ahang, T. Charter, O. Ogunfowora, M. Khadivi, M. Abbasi, and H. Najjaran, “Intelligent Condition Monitoring of Industrial Plants: An Overview of Methodologies and Uncertainty Management Strategies,” arXiv (Cornell University), Jan. 2024. doi: 10.48550/arxiv.2401.10266

[2] Sonali Shrikant Patil, “AI-Supported Forecasting of Biomass Availability under Changing Environmental and Resource Conditions”, Appl. Chem. Eng., vol. 9, no. 1, p. ACE-5878, Feb. 2026.

[3] M. Li, P. Peng, H. Sun, M. Wang, and H. Wang, “An Order-Invariant and Interpretable Dilated Convolution Neural Network for Chemical Process Fault Detection and Diagnosis,” IEEE Transactions on Automation Science and Engineering, vol. 21, no. 3, p. 3933, Jul. 2023. doi: 10.1109/tase.2023.3290202

[4] F. Ma, C. Ji, J. Wang, W. Sun, X. Tang, and Z. Jiang, “MOLA: Enhancing Industrial Process Monitoring Using Multi-Block Orthogonal Long Short-Term Memory Autoencoder,” arXiv (Cornell University), Oct. 2024. doi: 10.48550/arxiv.2410.07508

[5] T. Biegel, P. A. Helm, N. Jourdan, and J. Metternich, “SSMSPC: self-supervised multivariate statistical in-process control in discrete manufacturing processes,” Journal of Intelligent Manufacturing, vol. 35, no. 6, p. 2671, Jun. 2023. doi: 10.1007/s10845-023-02156-7

[6] M. Lu, Z. Gao, Y. Zou, Z. Chen, and P. Li, “Three-layer deep learning network random trees for fault detection in chemical production process,” The Canadian Journal of Chemical Engineering, Aug. 2024. doi: 10.1002/cjce.25465

[7] Ramdas Biradar, “AI Applications in Smart Mineral Processing: Ore Characterization, Sorting, and Efficiency”, Appl. Chem. Eng., vol. 8, no. 4, p. ACE-5791, Nov. 2025.

[8] Z. Xiao, A. K. Kordon, and S. K. Sen, “Fault Detection and Diagnosis in Tennessee Eastman Process with Deep Autoencoder,” Annual Conference of the PHM Society, Oct. 2023. doi: 10.36001/phmconf.2023.v15i1.3578

[9] M. A. Labbaf-Khaniki, M. Manthouri, and H. Ajami, “Twin Transformer using Gated Dynamic Learnable Attention mechanism for Fault Detection and Diagnosis in the Tennessee Eastman Process,” arXiv (Cornell University), Mar. 2024. doi: 10.48550/arxiv.2403.10842

[10] C. Lou, M. A. Atoui, and X. Li, “Recent deep learning models for diagnosis and health monitoring: A review of research works and future challenges,” Transactions of the Institute of Measurement and Control, vol. 46, no. 14, p. 2833, Mar. 2023. doi: 10.1177/01423312231157118

[11] M. A. L. Khaniki, A. Golkarieh, H. Nouri, and M. Manthouri, “Enhanced Fault Detection and Cause Identification Using Integrated Attention Mechanism,” arXiv (Cornell University), Jul. 2024. doi: 10.48550/arxiv.2408.00033

[12] W. Sun, A. R. C. Paiva, P. Xu, A. Sundaram, and R. D. Braatz, “Fault detection and identification using Bayesian recurrent neural networks,” Computers & Chemical Engineering, vol. 141, p. 106991, Jun. 2020. doi: 10.1016/j.compchemeng.2020.106991

[13] I. Lomov, M. Lyubimov, I. Makarov, and L. Zhukov, “Fault detection in Tennessee Eastman process with temporal deep learning models,” Journal of Industrial Information Integration, vol. 23, p. 100216, Mar. 2021. doi: 10.1016/j.jii.2021.100216

[14] J. Zhu, M. Jiang, and Z. Liu, “Fault Detection and Diagnosis in Industrial Processes with Variational Autoencoder: A Comprehensive Study,” Sensors, vol. 22, no. 1, p. 227, Dec. 2021. doi: 10.3390/s22010227

[15] M. Gao, M. Wang, and M. Chen, “Autoencoder-assisted Feature Ensemble Net for Incipient Faults,” arXiv (Cornell University), Apr. 2024. doi: 10.48550/arxiv.2404.13941

[16] H. Ziaei-Halimejani et al., “Fault diagnosis of chemical processes based on joint recurrence quantification analysis,” Computers & Chemical Engineering, vol. 155, p. 107549, Sep. 2021. doi: 10.1016/j.compchemeng.2021.107549

[17] M. Yin, J. Tian, Y. Wang, and J. Jiang, “A Novel Distributed Process Monitoring Framework of VAE-Enhanced with Deep Neural Network,” Neural Processing Letters, vol. 56, no. 2, Mar. 2024. doi: 10.1007/s11063-024-11577-1

[18] Á. D. Hallgrímsson, “Detection and Evaluation of Abnormal Events in Complex Industrial Processes,” Research Portal Denmark, Jan. 2020.

[19] A. Ajagekar and F. You, “Quantum computing assisted deep learning for fault detection and diagnosis in industrial process systems,” Computers & Chemical Engineering, vol. 143, p. 107119, Oct. 2020. doi: 10.1016/j.compchemeng.2020.107119

[20] P. Agarwal, M. Tamer, and H. Budman, “Explainability: Relevance based dynamic deep learning algorithm for fault detection and diagnosis in chemical processes,” Computers & Chemical Engineering, vol. 154, p. 107467, Jul. 2021. doi: 10.1016/j.compchemeng.2021.107467

[21] C. Ji, F. Ma, J. Rao, J. Wang, and W. Sun, “Bridging the Gap in Chemical Process Monitoring: Beyond Algorithm-Centric Research Toward Industrial Deployment,” Processes, vol. 13, no. 12, p. 3809, Nov. 2025. doi: 10.3390/pr13123809

[22] D. Paolini, P. Dini, A. Elhanashi, and S. Saponara, “Advanced Fault Detection and Diagnosis Exploiting Machine Learning and Artificial Intelligence for Engineering Applications,” Electronics, vol. 15, no. 2, p. 476, Jan. 2026. doi: 10.3390/electronics15020476

[23] N. Khan, S. A. A. Taqvi, and M. Waqas, “A Hybrid Deep Learning and Statistical Approach for Fault Detection and Diagnosis in AGRU Systems: Integration with Aspen Plus and Explainable AI,” Periodica Polytechnica Chemical Engineering, vol. 69, no. 4, p. 697, Oct. 2025. doi: 10.3311/ppch.41572

[24] Swapnil S. Chaudhari, “Machine learning for waste-to-energy processes: Resource evaluation, conversion efficiency, and environmental effects”, Appl. Chem. Eng., vol. 9, no. 1, p. ACE-5850, Jan. 2026.

[25] C. Ji and W. Sun, “A Review on Data-Driven Process Monitoring Methods: Characterization and Mining of Industrial Data,” Processes, vol. 10, no. 2, p. 335, Feb. 2022. doi: 10.3390/pr10020335

[26] S. J. Qin, “Survey on data-driven industrial process monitoring and diagnosis,” Annual Reviews in Control, vol. 36, no. 2, p. 220, Oct. 2012. doi: 10.1016/j.arcontrol.2012.09.004

[27] J. P. Hessling, Uncertainty Quantification and Model Calibration, 2017. doi: 10.5772/65579

[28] M. Golyadkin, V. Pozdnyakov, L. Zhukov, and I. Makarov, “SensorSCAN: Self-supervised learning and deep clustering for fault diagnosis in chemical processes,” Artificial Intelligence, vol. 324, p. 104012, Sep. 2023. doi: 10.1016/j.artint.2023.104012

[29] J. Yang, “Fault Diagnosis and Prognosis in multivariate complex systems,” HAL, Jan. 2023.

[30] Y. S. Lee, S. K. Ooi, and J. Chen, “A novel multi-step prediction model for process monitoring,” International Journal of Advances in Intelligent Informatics, vol. 10, no. 2, p. 333, May 2024. doi: 10.26555/ijain.v10i2.1528

[31] M. Onel, B. Burnak, and E. N. Pistikopoulos, “Integrated Data-Driven Process Monitoring and Explicit Fault-Tolerant Multiparametric Control,” Industrial & Engineering Chemistry Research, vol. 59, no. 6, p. 2291, Nov. 2019. doi: 10.1021/acs.iecr.9b04226

[32] Z. Mei, “Fault diagnosis & root cause analysis of invertible dynamic system,” HAL, Jul. 2017.

[33] V. Venkatasubramanian, “Prognostic and diagnostic monitoring of complex systems for product lifecycle management: Challenges and opportunities,” Computers & Chemical Engineering, vol. 29, no. 6, p. 1253, Apr. 2005. doi: 10.1016/j.compchemeng.2005.02.026

[34] N. A. B. Roa, “A data-based approach for dynamic classification of functional scenarios oriented to industrial process plants,” HAL, Dec. 2016.

[35] Y. Park, S. S. Fan, and C.-Y. Hsu, “A Review on Fault Detection and Process Diagnostics in Industrial Processes,” Processes, vol. 8, no. 9, p. 1123, Sep. 2020. doi: 10.3390/pr8091123

[36] I. Radda and M. Alexey, “Application of Failure Detection Methods to Detect Information Attacks on the Control System,” Research Square, Nov. 2021. doi: 10.21203/rs.3.rs-882662/v1

[37] J. Peng, H. Zhao, and Z. Hu, “Second-order component analysis for fault detection,” Journal of Process Control, vol. 108, p. 25, Nov. 2021. doi: 10.1016/j.jprocont.2021.10.011

[38] A. Ifeanyi and J. Coble, “Comparison of Optimizers for Fault Isolation and Diagnostics of Control Rod Drives,” arXiv (Cornell University), Jul. 2024. doi: 10.48550/arxiv.2407.06557

[39] M.-Q. Yu, Y. S. Lee, and J. Chen, “Fault diagnosis-based SDG transfer for zero-sample fault symptom,” International Journal of Advances in Intelligent Informatics, vol. 9, no. 3, p. 551, Nov. 2023. doi: 10.26555/ijain.v9i3.1434

[40] Manjusha Tatiya, “AI Applications in Tailings and Waste Management: Improving Safety, Recycling, and Water Utilization”, Appl. Chem. Eng., vol. 8, no. 4, p. ACE-5789, Nov. 2025.

[41] S. X. Ding and L. Li, “A study on fault diagnosis in nonlinear dynamic systems with uncertainties,” arXiv (Cornell University), Sep. 2023. doi: 10.48550/arxiv.2309.02732

[42] K. S. Geun, C.-Y. Ho, and P. H. Seong, “Signal Fault Identification in Nuclear Power Plants based on Deep Neural Networks,” Annals of DAAAM International Symposium, 2019. doi: 10.2507/30th.daaam.proceedings.117

[43] J. M. Barrera, A. R. Reina, A. Maté, and J. Trujillo, “Fault detection and diagnosis for industrial processes based on clustering and autoencoders: a case of gas turbines,” International Journal of Machine Learning and Cybernetics, vol. 13, no. 10, p. 3113, Jun. 2022. doi: 10.1007/s13042-022-01583-x

[44] I. M. Arce, J. M. Mase, D. Rengasamy, B. Rothwell, and G. P. Figueredo, “Anomaly Detection for Unmanned Aerial Vehicle Sensor Data Using a Stacked Recurrent Autoencoder Method with Dynamic Thresholding,” SAE International Journal of Aerospace, vol. 15, no. 2, p. 219, Sep. 2022. doi: 10.4271/01-15-02-0017

[45] Madhuri Karad, “AI Models for Life-Cycle Assessment of Bio-Energy Technologies and Pollution Quantification”, Appl. Chem. Eng., vol. 9, no. 1, p. ACE-5855, Jan. 2026.

[46] D. Upadrashta and T. Wijaya, “AI/ML Based Anomaly Detection and Fault Diagnosis of Turbocharged Marine Diesel Engines: Experimental Study on Engine of an Operational Vessel,” Information, vol. 17, no. 1, p. 16, Dec. 2025. doi: 10.3390/info17010016

[47] L. Huang, H. Ren, Y. Chai, and J. Qu, “A fault detection method based on stacking the SAE-SRBM for nonstationary and stationary hybrid processes,” International Journal of Applied Mathematics and Computer Science, vol. 31, no. 1, Jan. 2021. doi: 10.34768/amcs-2021-0003

[48] A. G. Ayad, N. A. Sakr, and N. A. Hikal, “Fog-empowered anomaly detection in IoT networks using one-class asymmetric stacked autoencoder,” Cluster Computing, vol. 28, no. 8, Aug. 2025. doi: 10.1007/s10586-025-05234-y

[49] P. M. Mbilong, Z. Aarab, F.-Z. Belouadha, and M. I. Kabbaj, “Enhancing Fault Detection in CNC Machinery: A Deep Learning and Genetic Algorithm Approach,” Ingénierie des systèmes d information, vol. 28, no. 5, p. 1361, Oct. 2023. doi: 10.18280/isi.280525

[50] L. Erhan et al., “Smart anomaly detection in sensor systems: A multi-perspective review,” Information Fusion, vol. 67, p. 64, Oct. 2020. doi: 10.1016/j.inffus.2020.10.001

[51] Q. Lu and S. S. S. Al-Wahaibi, “Enhanced CNN with Global Features for Fault Diagnosis of Complex Chemical Processes,” arXiv (Cornell University), Oct. 2022. doi: 10.48550/arxiv.2210.01727

[52] G. Vashishtha et al., “Advancing machine fault diagnosis: A detailed examination of convolutional neural networks,” arXiv (Cornell University), Feb. 2025. doi: 10.48550/arxiv.2502.08689

[53] A. Saeed et al., “Deep learning based approaches for intelligent industrial machinery health management and fault diagnosis in resource-constrained environments,” Scientific Reports, vol. 15, no. 1, Jan. 2025. doi: 10.1038/s41598-024-79151-2

[54] R. Namdeti, “Artificial Intelligence in Chemical Engineering: Past, Present, and Future Perspectives,” Journal of Chemical Health Risks, Jan. 2023. doi: 10.52783/jchr.v13.i6.2058

[55] G. Hu, T. Zhou, and Q. Liu, “Data-Driven Machine Learning for Fault Detection and Diagnosis in Nuclear Power Plants: A Review,” Frontiers in Energy Research, vol. 9, May 2021. doi: 10.3389/fenrg.2021.663296

[56] G. Ø. Rønsch, “Model-based Process Surveillance and Optimisation for Fault Detection and Diagnosis,” Research Portal Denmark, Jan. 2022.

[57] K. Ranjan et al., “Application of artificial intelligence in electrochemical diagnostics for human health,” Discover Electrochemistry, vol. 2, no. 1, Aug. 2025. doi: 10.1007/s44373-025-00042-w

[58] Manjusha Tatiya, “AI-Driven Process Control for Enhancing Safety and Efficiency in Oil Refining”, Appl. Chem. Eng., vol. 8, no. 4, p. ACE-5792, Nov. 2025.

[59] L. Wang, “Recurrent Pattern Aware Multiphase Flow Soft Sensor Model,” Journal of Physics Conference Series, vol. 1952, no. 4, p. 042096, Jun. 2021. doi: 10.1088/1742-6596/1952/4/042096

[60] M. Pronk, “Generative LSTM Models and Asset Hierarchy Creation in Industrial Facilities,” arXiv (Cornell University), Mar. 2024. doi: 10.48550/arxiv.2403.06103

[61] D. D. K. Wayo et al., “Exploring Quantum-Dot Engineered Solid-State Photon Upconversion in PbS:Yb^{3+},Er^{3+}/CuBiO Using Density Functional Theory and Machine Learning Methods for Water Splitting,” arXiv (Cornell University), Dec. 2024. doi: 10.48550/arxiv.2501.00573

[62] Sonali Shrikant Patil, “Smart Biorefineries: Machine Learning for Process Control, Resource Utilization, and Emission Monitoring”, Appl. Chem. Eng., vol. 9, no. 1, p. ACE-5874, Mar. 2026.

[63] R. Gupta et al., “Machine learning for sustainable organic waste treatment: a critical review,” npj Materials Sustainability, vol. 2, no. 1, Apr. 2024. doi: 10.1038/s44296-024-00009-9

[64] S. Hong et al., “A Dynamic Soft Sensor Based on Hybrid Neural Networks to Improve Early Off-spec Detection,” Engineering With Computers, vol. 39, no. 4, p. 3011, Jul. 2022. doi: 10.1007/s00366-022-01694-7

[65] Sonali Shrikant Patil, “Machine Learning Strategies for Enhancing Syngas Quality, Biofuel Stability, and Air Pollution Control in Bio-Energy Plants”, Appl. Chem. Eng., vol. 9, no. 1, p. ACE-5880, Feb. 2026.

[66] H.-Y. S. Chien et al., “Slower is Better: Revisiting the Forgetting Mechanism in LSTM for Slower Information Decay,” arXiv (Cornell University), May 2021. doi: 10.48550/arxiv.2105.05944

[67] Y. Hu, X. Xin, G. Yu, and W. Deng, “Deep insight: An Efficient Hybrid Model for Oil Well Production Forecasting Using Spatio-Temporal Convolutional Networks and Kolmogorov-Arnold Networks,” Research Square, Oct. 2024. doi: 10.21203/rs.3.rs-4988083/v1

[68] M. Krichen and A. Mihoub, “Long Short-Term Memory Networks: A Comprehensive Survey,” AI, vol. 6, no. 9, p. 215, Sep. 2025. doi: 10.3390/ai6090215

[69] M. Z. Yousaf et al., “Bayesian-optimized LSTM-DWT approach for reliable fault detection in MMC-based HVDC systems,” Scientific Reports, vol. 14, no. 1, Aug. 2024. doi: 10.1038/s41598-024-68985-5

[70] Smita Desai, “Machine Learning Approaches for Biomass Resource Mapping and Sustainable Energy Planning”, Appl. Chem. Eng., vol. 9, no. 1, p. ACE-5843, Dec. 2025.

[71] J. Park and S. Chang, “A Particulate Matter Concentration Prediction Model Based on Long Short-Term Memory and an Artificial Neural Network,” International Journal of Environmental Research and Public Health, vol. 18, no. 13, p. 6801, Jun. 2021. doi: 10.3390/ijerph18136801

[72] Y. Zhang, Y. Wang, and L. Gao, “CNN-MHBiGRU: A two-stage deep learning framework with multi-attention mechanisms for IoT intrusion detection,” Ad Hoc Networks, vol. 181, p. 104082, Nov. 2025. doi: 10.1016/j.adhoc.2025.104082

[73] I. Rosyadi et al., “Multivariate soft sensor for product monitoring in the debutanizer column with deep learning,” Proceeding ICMA-SURE, vol. 2, no. 1, p. 9, Jan. 2023. doi: 10.20884/2.procicma.2023.2.1.7762

[74] L. Poudel et al., “Deep Learning-Enhanced for Amine Emission Monitoring and Performance Analysis in Industrial Carbon Capture Plants,” arXiv (Cornell University), Sep. 2025. doi: 10.48550/arxiv.2509.05241

[75] J. O. Ojadi et al., “Deep Learning Models for Predicting and Mitigating Environmental Impact of Industrial Processes in Real-Time,” International Journal of Scientific Research in Science Engineering and Technology, vol. 12, no. 2, p. 119, Mar. 2025. doi: 10.32628/ijsrset25122109

[76] B. Selvanathan et al., “Ensemble Deep Learning for Detecting Onset of Abnormal Operation in Industrial Multi-component Systems,” International Journal of Prognostics and Health Management, vol. 13, no. 2, Oct. 2022. doi: 10.36001/ijphm.2022.v13i2.3093

[77] X. Wei, L. Liu, J. Wang, and X. Zheng, “Deep learning-based anomaly detection framework for hydraulic support systems in mining safety,” Scientific Reports, vol. 15, no. 1, Oct. 2025. doi: 10.1038/s41598-025-19055-x

[78] A. B. Bereketoğlu, “Hybrid Meta-Learning Framework for Anomaly Forecasting in Nonlinear Dynamical Systems via Physics-Inspired Simulation and Deep Ensembles,” arXiv (Cornell University), Jun. 2025. doi: 10.48550/arxiv.2506.13828

[79] N. C. Lobo et al., “Online Sensor Fault Detection Using Machine Learning Algorithms on a Laboratory-Scale Batch Reactor: LSTM Approach,” ACS Omega, Feb. 2026. doi: 10.1021/acsomega.5c11180

[80] S. Rao and J. Wang, “Temporal dynamic label smoothing against horizon-induced distribution overlap: Improving early fault detection and diagnosis in chemical process,” Chemical Engineering Science, vol. 323, p. 123201, Dec. 2025. doi: 10.1016/j.ces.2025.123201

[81] N. Liu et al., “Hybrid deep learning framework with spatiotemporal pattern extraction for decant oil solid content soft sensor development in fluid catalytic cracking units,” Petroleum Science, vol. 22, no. 7, p. 3042, Apr. 2025. doi: 10.1016/j.petsci.2025.04.006

[82] G. S. Dave, “Designing Health Monitoring System for fault prediction in Centrifugal Pump using ML and DL algorithm,” Journal of Information Systems Engineering & Management, vol. 10, p. 361, Feb. 2025. doi: 10.52783/jisem.v10i14s.2305

[83] L. Allen, H. Lu, and J. Cordiner, “Knowledge-Enhanced Spatiotemporal Analysis for Anomaly Detection in Process Manufacturing,” Computers in Industry, vol. 161, p. 104111, May 2024. doi: 10.1016/j.compind.2024.104111

[84] Y. Fan, Y. Dang, and Y. Guo, “Fault Identification Model Using Convolutional Neural Networks with Transformer Architecture,” Sensors, vol. 25, no. 13, p. 3897, Jun. 2025. doi: 10.3390/s25133897

[85] S. Negny and L. Montastruc, “Book of Abstracts of the 32nd European Symposium on Computer Aided Process Engineering,” HAL, Jun. 2022.

[86] A. Kovalenko, V. Pozdnyakov, and I. Makarov, “Graph Neural Networks With Trainable Adjacency Matrices for Fault Diagnosis on Multivariate Sensor Data,” IEEE Access, vol. 12, p. 152860, Jan. 2024. doi: 10.1109/access.2024.3481331

[87] M. Zhao, C. Taal, S. Baggerohr, and O. Fink, “Graph Neural Networks for Virtual Sensing in Complex Systems: Addressing Heterogeneous Temporal Dynamics,” arXiv (Cornell University), Jul. 2024. doi: 10.48550/arxiv.2407.18691

[88] M. Zhao, C. Taal, S. Baggerohr, and O. Fink, “SKF Heterogeneous Test-rig Bearing Load Sensing Dataset,” arXiv (Cornell University), Mar. 2025. doi: 10.5281/zenodo.14959000

[89] K. F. Niresi et al., “Physics-Enhanced Graph Neural Networks For Soft Sensing in Industrial Internet of Things,” arXiv (Cornell University), Apr. 2024. doi: 10.1109/jiot.2024.3434732

[90] H. Ren, X. Liang, C. Yang, Z. Chen, and W. Gui, “Spatial-temporal associations representation and application for process monitoring using graph convolution neural network,” Process Safety and Environmental Protection, vol. 180, p. 35, Sep. 2023. doi: 10.1016/j.psep.2023.09.061

[91] A. Aman, Y. Liu, and Y. Chen, “Towards robust fault detection for industrial processes with a hybrid feature fusion and ensemble learning framework,” Digital Chemical Engineering, vol. 17, p. 100270, Oct. 2025. doi: 10.1016/j.dche.2025.100270

[92] H.-Y. Liang, T. Yan, and W. Zhao, “Comprehensive assessment of recent major chemical accidents in China and path to sustainable solutions,” Smart Construction and Sustainable Cities, vol. 2, no. 1, Jan. 2024. doi: 10.1007/s44268-023-00024-0

[93] J. N. Chukwunweike et al., “Integrating deep learning, MATLAB, and advanced CAD for predictive root cause analysis in PLC systems: A multi-tool approach to enhancing industrial automation and reliability,” World Journal of Advanced Research and Reviews, vol. 23, no. 2, p. 2538, Aug. 2024. doi: 10.30574/wjarr.2024.23.2.2631

[94] Y. N. Kottavalasa and L. Snidaro, “Advancing chemical manufacturing processes through data-driven approaches: A survey,” Chemometrics and Intelligent Laboratory Systems, vol. 267, p. 105553, Oct. 2025. doi: 10.1016/j.chemolab.2025.105553

[95] Patil Y, Tatiya M, Dharmadhikari DD, Shahakar M, Patil SK, Mahajan RG, Kurhade AS. The Role of AI in Reducing Environmental Impact in the Mining Sector. Journal of Mines, Metals & Fuels. 2025 May 1;73(5).

[96] Raut PN, Dolas AS, Chougule SM, Darade MM, Murali G, Waware SY, Kurhade AS. Green Adsorbents for Heavy Metal Removal: A Study on Zinc Ion Uptake by Tinospora cordifolia Biocarbon. Journal of Mines, Metals & Fuels. 2025 Jan 1;73(1).

[97] Kurhade AS, Bhambare PS, Siraskar GD, Dixit SM, Purandare PS, Shital Yashwant Waware SY. Computational study on thermal management of IC chips with phase change materials. J Adv Res Numer Heat Trans. 2024;26(1):34-43.

[98] Chougule SM, Murali G, Kurhade AS. Finite Element Analysis and Design Optimization of a Paddle Mixer Shaft. Journal of Mines, Metals & Fuels. 2025 May 1;73(5).

[99] Kurhade AS, Siraskar GD, Bhambare PS, Murali G, Deshpande SV, Warke PS, Waware SY. Simulation and analysis of heat transfer in counter-flow helical double-pipe heat exchangers using CFD. International Journal of Modern Physics C. 2025 Dec 15;36(12):2550043.

[100] Waware SY, Ahire PP, Napate K, Biradar R, Patil SP, Kore SS, Kurhade AS. Advancements in Heat Transfer Enhancement using Perforated Twisted Tapes: A Comprehensive Review. Journal of Mines, Metals & Fuels. 2025 May 1;73(5).

[101] Kurhade AS, Bhavani P, Patil SA, Kolhalkar NR, Chalapathi KS, Patil PA, Waware SY. Mitigating environmental impact: A study on the performance and emissions of a diesel engine fueled with biodiesel blend. Journal of Mines, Metals & Fuels. 2025 Apr 1;73(4):981-9.

Journal of Engineering and Technology for Industrial Applications

ITEGAM-JETIA

Manaus, v.12 n.60, p.1464-1473. July/August, 2026.
DOI: https://doi.org/10.5935/jetia.v12i60.4328

ISSN ONLINE: 2447-0228

RESEARCH ARTICLE OPEN ACCESS

STUDY OF THE HYDROMECHANICAL BEHAVIOR OF COLLAPSIBLE SOILS IN THE GHARDAÏA REGION, ALGERIA.

Ali Fernane[1], Samir Benmoussa[2] and Mohamed Salah Laouar[3]

[1, 3]Department of Civil Engineering, Faculty of Sciences and Technology, Mining Laboratory, Larbi Tebessi University, Tebessa, Algeria.
[2]Department of Civil Engineering, Faculty of Technology, NMISSI Laboratory, University of Biskra, University Batna 2,Batna, Algeria.

[1]http://orcid.org/0009-0003-3318-5005, [2]http://orcid.org/0000-0002-9985-238X, [3]http://orcid.org/0000-0003-1767-9075

Email: ali.fernane@univ-tebessa.dz

ARTICLE INFO

Article History
Received: March 25, 2026
Reviewed: April 25, 2026
Accepted: July 25, 2026
Published: August 31, 2026

Keywords:
Collapse Potential,
Suction,
Unsaturated Soils,
Friction Angle,
Cohesion.

ABSTRACT

The rapid growth of the population has resulted in extensive land use and a notable expansion of construction activities on problematic soils. Arid and semi-arid regions in southern Algeria have witnessed significant urbanization and infrastructure development. These areas are generally characterized by unsaturated surface deposits and deep groundwater levels, allowing soils to remain unsaturated to considerable depths for long periods. Under the influence of climatic cycles and repeated wetting–drying processes, soils progressively develop their microstructure, hydraulic characteristics, and consequently their physical and mechanical properties.Recent studies have shown that soil-water retention curves (SWRC) are effective tools for characterizing the stress state of unsaturated soils, describing their hydromechanical behavior, and estimating their strength parameters. The aim of this research is to characterize these soils and examine the additional shear strength resulting from suction variations, as well as the influence of soil compaction on the collapse mechanism. Soil samples were collected from the Metlili Valley, an arid region located southwest of Ghardaïa. The findings reveal significant volumetric changes caused by suction reduction. Furthermore, an increase in suction enhances shear strength, mainly due to the rise in apparent cohesion associated with capillary effects.

Copyright ©2026 by authors and Galileo Institute of Technology and Education of the Amazon (ITEGAM). This work is licensed under the Creative Commons Attribution International License (CC BY 4.0).

I. INTRODUCTION

Under the effect of population growth in recent decades, the arid and semi-arid regions in the South of Algeria have experienced significant urban development and the construction of civil engineering structures. The soils in most of these regions are superficial unsaturated aeolian deposits, unconsolidated, and characterized by a well-developed pore space over a significant depth. Such deposits are known as collapsible soils [1-4] that exhibit significant volume reductions due to the simultaneous variation of their water content and matric suction resulting from repeated climatic cycles of wetting and drying. This phenomenon of alternating variations in moisture and suction can cause multiphysical problems for civil engineering structures [5–8]. It is therefore important to properly understand these phenomena and to implement resilient geotechnical design measures and approaches for reliable risk prevention [9-11]. A Previous research work [12], [13] has highlighted the effect of initial suction on the mechanical properties and strength parameters of unsaturated soils, particularly in the arid and semi-arid climatic context. Several authors have emphasized that the hydromechanical behavior of unsaturated soils is very complex under the combined effect of suction and water content. The effect of the initial state of unsaturated collapsible soils on their mechanical behavior and strength parameters, particularly in terms of density, water content, and matric suction, has been studied by several researchers [14-17], among others. The analysis of the matric suction properties of unsaturated collapsible soils in the study area remains one of the most significant factors in research on their hydromechanical behavior. More recent studies have indicated that the linear correlation between shear strength and matric suction is not relevant for all soil types and for the entire suction range [18]. In this study, a set of laboratory tests were carried out on soil specimens to analyze the simultaneous effect of the variation of matric suction, compaction state, and water content on the collapse potential and the mechanical characteristics of the tested soils.

The obtained results highlight the relationship between matric suction and collapse potential, as well as the parameters affecting shear strength.

II. MATERIALS. EQUIPMENT AND TESTS

II.1 STUDY AREA

The studied soil was extracted from the Metlili region, located 45km south of the city of Ghardaia in the Northern Algerian Sahara at 32.17°N latitude and 3.32°E longitude, with an average site elevation of 454 meters Figure 1. Climate is considered one of the important factors in the formation and evolution of the soil's geotechnical characteristics. Indeed, the seasonal fluctuations in temperature and precipitation in the studied area illustrate its marked desert climate, characterized particularly by low and irregular rainfall. Given the climatic conditions, the study region is classified as an arid zone according to its aridity index, which is a useful indicator for characterizing this phenomenon.

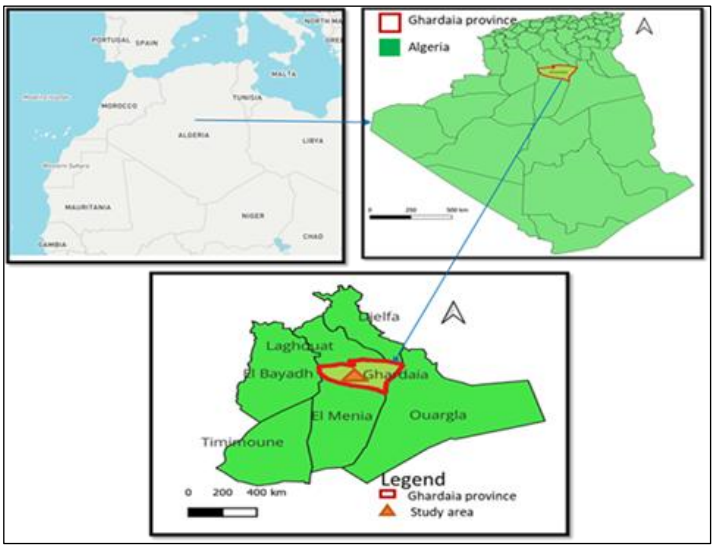


Figure 1: Localization of the study area map of Ghardaia, Algeria.
Source: Authors, (2026).

Geological studies indicate that the study area is incised into the Turonian limestone massifs and is characterized by four geological layers: Quaternary, Turonian, Cenomanian, and Albian. The Quaternary corresponds to the alluvial deposits covering the Metlili Valley. The Quaternary alluvium consists of sands, pebbles, and clays lining the valley floor with a thickness ranging from 20 to 30 meters. The Cenomanian is characterized by variegated clays that range in color from brown and grayish to greenish. These clays are plasticized and sandy at the base, with gypsum present. The Albian is made up of fine to medium yellowish sands, Figure 2.

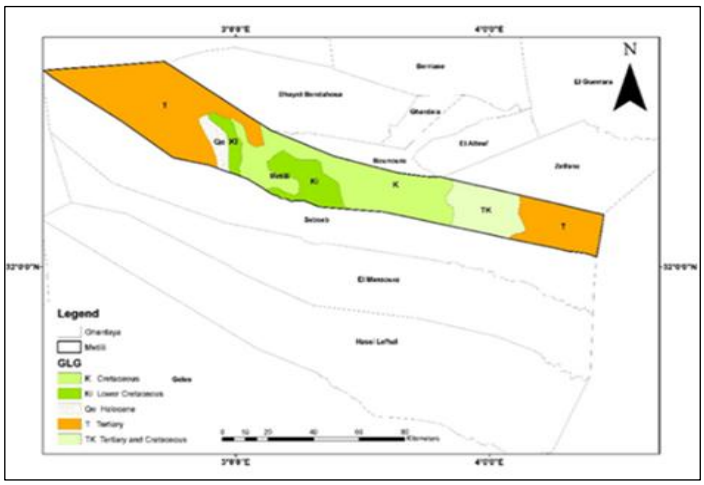


Figure 2: Simplified geological map of Ghardaia, Algeria.
Source: Authors, (2026).

II.2 MATERIALS

Samples of the studied soil were collected from three different experimental sites at depths ranging from 1.5 to 2 meters in their natural state. For the physical characterisation of the soil, an initial series of traditional tests was carried out in the laboratory to measure the specific gravity of solid particles (Gs), natural water content (w_n), methylene blue value (MBV), Atterberg limits (PL, LL, PI), particle size distribution, and standard Proctor compaction. These tests indicate that the soil exhibits low plasticity properties, the studied soil can be classified as sand loam. The details of geotechnical properties can be found in Table 1.

Table 1: Properties of soils used in this study.

Property	Value
Initial Moisture Content ,w_n (%)	4.5
Spécific Gravity , G_s	2.66
Liquid Limit, LL(%)	24
PlasticLimit ,PL (%)	17
Maximum Proctor Test, γ_d(Mg /m^3)	1.82
Optimum Moisture Content,w_{op}(%)	10.5
Clay fraction (%)	6.5
Silty fraction (%)	38.5
Sandy fraction (%)	55
Calcium carbonate CaCO3 (%)	22.5
Methylene bleu valueMBV	0.42
USCS Classification	SM-SC

Source: Authors, (2026).

Particle size analysis allows for the quantitative determination of the soil particle distribution based on size categories. The studied soils belong to class (A1) according [19]. These materials are characterized by a percentage passing greater than 35% through the 80µm sieve. The methylene blue absorption value is less than 2.5, and the plasticity index is less than 12. The predominance of the sand fraction (55%), the relatively high fines content (45%), and Atterberg limits positioned in the transition zone of the Casagrande chart (PI = 7% and LL = 25%) indicate that this soil is classified as SM–SC according to the USCS system The particle size distribution curves of the samples are presented in Figure 3.

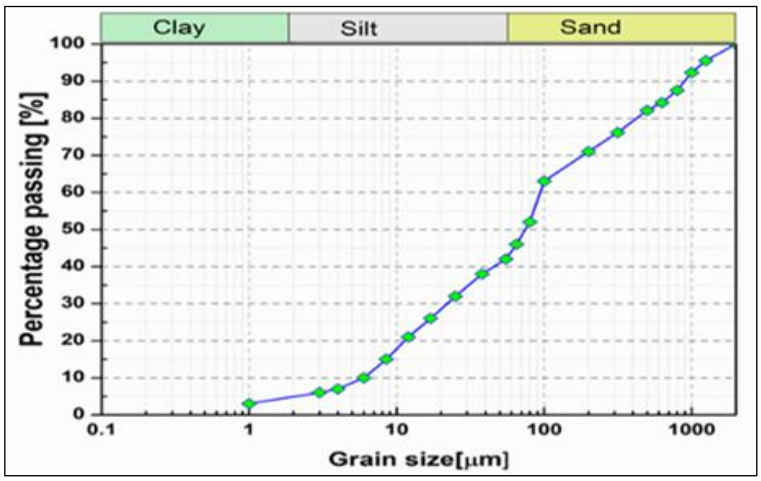


Figure 3: Grain size distribution of studied soil.
Source: Authors, (2026).

Mineralogical analyses were conducted on the studied soil using a BRUKER-binary V3 X-ray diffractometer with Kα radiation (1.5406 Å), operating at 35 kV and 30 mA, with an angular detection range (2θ) from 5° to 90°. This analysis aimed to identify the crystalline structure and mineralogy of the samples. The results of this X-ray analysis are presented as diffractograms (XRD) shown in Figure 4.

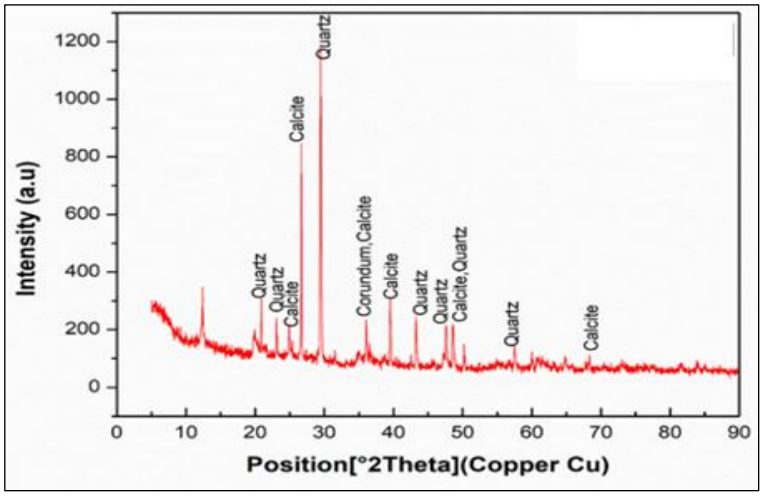


Figure 4: X-ray diffraction pattern of studied soil for mineralogical composition.
Source: Authors, (2026).

The position and intensity of characteristic diffraction peaks enable the identification of different crystalline phases in the studied material, which is primarily composed of quartz. Quartz, known for its chemical stability, promotes a granular texture and increased permeability whereas showing low water retention. The substantial presence of quartz is confirmed by the particle size distribution, indicating a high percentage of sand in the material. Calcite notably influences the chemical and mechanical properties of the soil, enhancing cementation and cohesion. Corundum and other minerals are present in minor proportions. To identify and quantify the chemical elements of the studied soils, a geochemical analysis was performed using an X-ray fluorescence spectrometer (XRF). The results of this analysis are also presented in Table 2.

Table 2: Chemical composition of the studied soil.

Major elements		**Trace elements**	
Oxydes	**Content (%)**	**Oxydes**	**Content (ppm)**
SiO_2	51,45	MnO	59.6
Al_2O_3	21,73	SrO	42,5
CaO	10,58	ZrO_2	28.4
Fe_2O_3	9,41	Cr_2O_3	28.3
K_2O	2,13	V_2O_5	27.1
MgO	2,04	ZnO	15.8
TiO_2	1,69	Rb_2O	10.8
Na_2O	0,33	NiO	7.4
So_3	0,32	Nb_2O_5	5.2
P_2O_3	0,18	Y_2O_3	3.4

Source: Authors, (2026).

The obtained results show high proportions of silicates (SiO_2) 50.4%.The strong presence of quartz is confirmed by the granulometric distribution, which indicates a high percentage of sand in the material. Aluminum oxide (Al_2O_3) 21.7%, calcium carbonate (CaO) 10.6% and iron oxide (Fe_2O_3) 9.41. There is a relative chemical richness in potassium oxide (K_2O) 2.13%, titanium oxide (TiO_2)1.7%, which are detrital chemical elements originating from basement rocks, and relatively low contents of magnesium oxide (MgO) 2.04%.

II.3 PERFORMED TESTS

The experimental program included collapse tests, shear tests, and suction tests. The selection of low water contents and moderate compaction energy for investigating collapsible soils is designed to replicate the loose, metastable structure characteristic of natural conditions in arid regions. This methodological choice is substantiated by the fact that such soils typically exist in a partially saturated state, wherein matric suction exerts a critical influence on their apparent structural stability. The experimental procedure and the parameters selected for each test series, as well as the specific characteristics of each category are detailed in Figure 5.

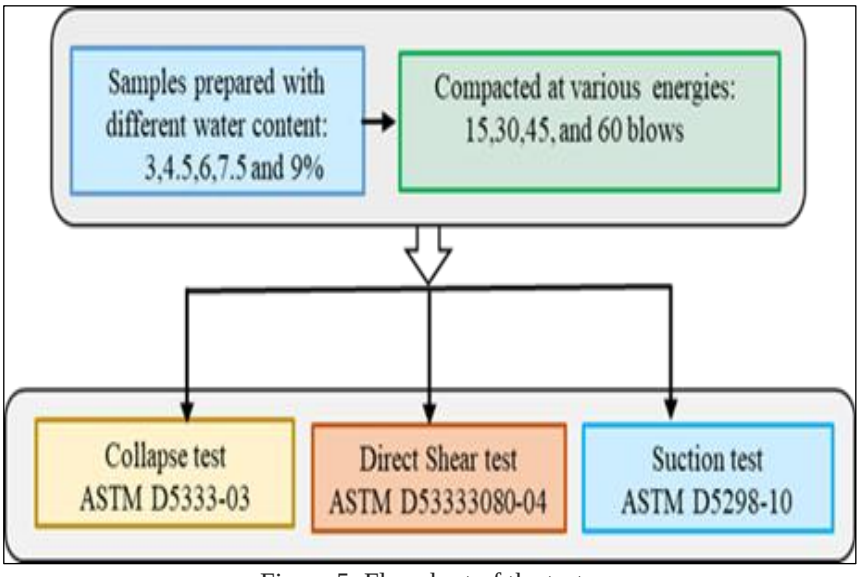


Figure 5: Flowchart of the tests.
Source: Authors, (2026).

The samples of the studied soil are prepared in the laboratory from soil extracted from various sampling sites, presented in block form. The samples are dried in an oven, crushed with a wooden hammer, and then sieved using a 2 mm sieve. To achieve the desired water content, demineralized water is carefully mixed with the samples in different proportions corresponding to the water content values (w = 3%, 4.5%, 6%, 7.5%, and 9%), taking into account the amount of water content lost during preparation. The mixture is then left to cure at a constant temperature and humidity for 24 hours to ensure a homogeneous distribution of moisture.

Then, the soil mixture is poured into an oedometer mold 60 mm in diameter and 20 mm in height and compacted in a single layer using a compaction hammer at different compaction energy levels (15, 30, 45, and 60 blows corresponding to 69, 138, 207, and 276 kJ/m³). The apparatus used for the compaction procedure, designed in the laboratory, is shown in Figure 6. It consists of a disk whose diameter is slightly smaller than that of the ring, fixed to a guide rod, and a disk-shaped hammer.

The hammer weighs 132 g and slides along the rod, falling from a height of 20 cm to strike the disk, thus compacting the material in the oedometer ring. The compaction energy Ec applied to the specimen, which is the work of the mass M (kg) falling from a height h (m), is given by the equation:

$$Ec = \frac{MghN}{V} \quad (1)$$

With M: mass of the hammer, g: acceleration due to gravity, h: drop height of the hammer, N: number of blows, V : Volume of the mold in m³.

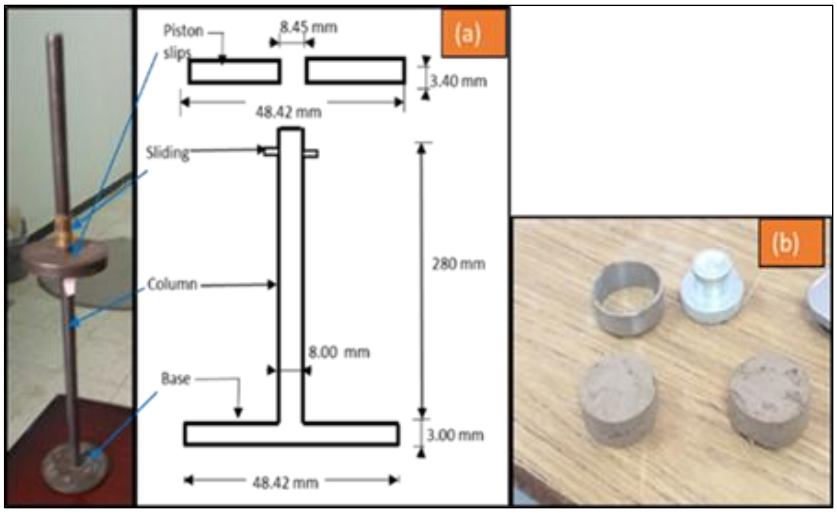


Figure 6: Compaction procedure of the samples: (a) Compaction hammer, (b) Compacted samples.
Source: Authors, (2026).

II.3.1 Collapse Tests

The collapse tests are conducted according to the specifications [20]. The vertical load is applied in the following successive stages: 25, 50, 100, and 200 kPa. To estimate the collapse potential (Cp), the sample is flooded for 24 hours. The collapse potential is determined by measuring the difference in axial deformation at a vertical stress of 200 kPa after and before immersion. Then, the loading is increased to the value of 400 kPa. During the test, the settlements are recorded at 15s, 30s, 1min, 2min, 5min, 10min, 30min, 1h, and 24h. The collapse potential is calculated for each test using the expression.

$$Cp = \frac{\Delta e_c}{(e_0 + 1)} 100\% \quad (2)$$

With $\Delta e_c = e_1$(200 kPa, unsaturated) - e_2(200 kPa, flooded), and e_0: initial void ratio

II.3.2 Shear Tests

Experimental shear tests were conducted on soils samples at various suction and confinement pressures of 100 kPa, 200 kPa, and 300 kPa, in accordance with [21] under drained conditions. A shear box with dimensions of 60 mm x 60 mm with a thickness of 25 mm was used for the tests, which were conducted at a constant low shear rate of 0.3 mm/min throughout the experiment.

II.3.3 Suction Tests

The suction tests conducted in this study used a laboratory method with Whatman filter paper grade No. 42, which allows for measuring matric suction values of up to about 100 MPa, following the specifications in [22]. The wet samples were prepared by adding a specific percentage of distilled water based on their weight. A set of filter papers was dried in an oven for 24 hours before testing. The suction measurement involves placing three filter papers between two soil samples. This setup is designed to prevent contamination of the central filter paper, which is used for measuring suction and has a slightly smaller diameter than the outer two filter papers. To reach hydraulic equilibrium, the assembly is wrapped in plastic film and then kept in a glass desiccator for 15 days. The experimental procedure is illustrated in Figure 7.

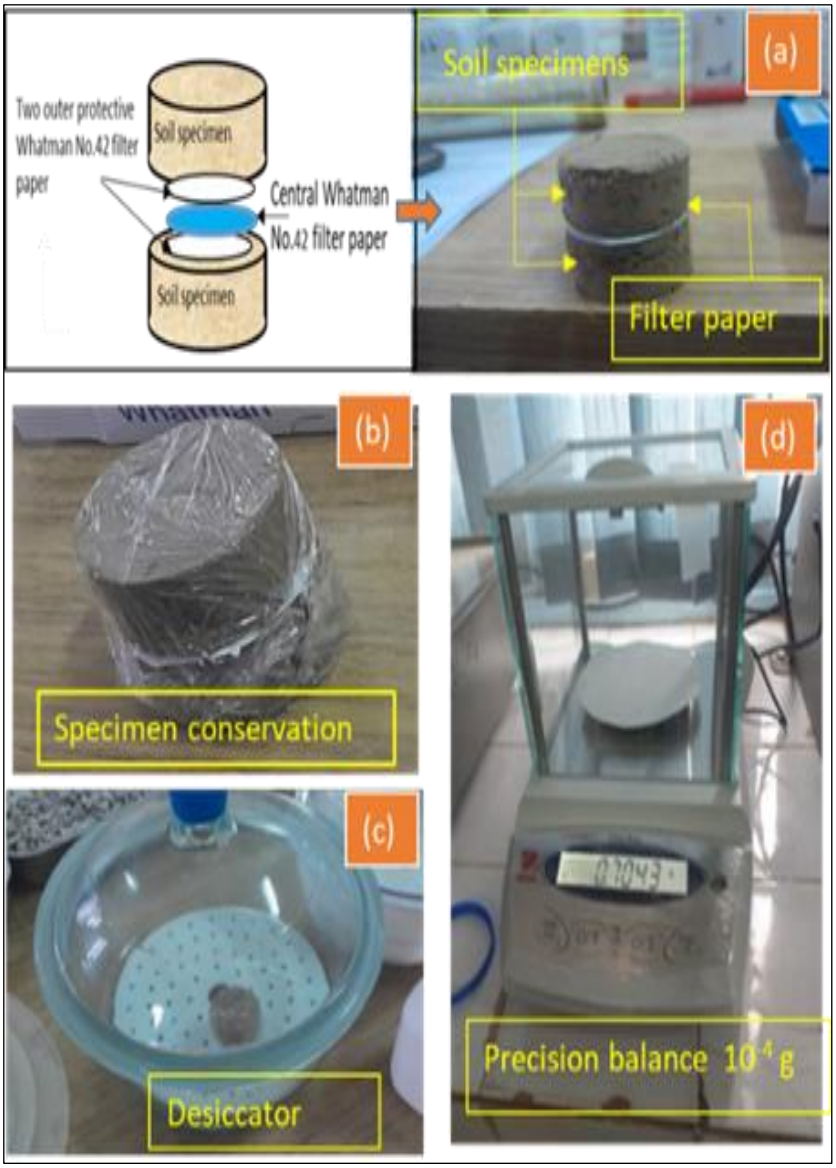


Figure 7: Experimental procedure for suction measurement suction using the filter paper Whitman 42: (a) filter paper interposed between two soil samples, (b) soil samples wrapped in plastic film, (c) suction equilibrium phase, (d) measurement of the weight of the filter paper loaded with moisture.
Source: Authors, (2026).

When equilibrium is achieved between the filter paper and the soil, the gravimetric water content of the central filter paper is measured, from which the matric suction is calculated using the calibration curve described by "(3)" and "(4)", as the suction measurement device

$$Log_{10}S(kPa)=5.327-0.0779w_f \quad w_f>45.3 \tag{3}$$

$$Log_{10}S(kPa)=2.412-0.0135w_f \quad w_f>45.3 \tag{4}$$

Where S is the matric suction, w_f is the gravimetric water content of the filter paper in percentage. The hydro-mechanical behavior is influenced by its water retention characteristics.In this study, the soil-water retention behavior is modelled using the semi-empirical van Genuchten equation [23] as expressed in the (5) below:

$$\boldsymbol{\theta_w = \theta_r + \frac{(\theta_s - \theta_r)}{[1 + (\alpha\, S)^n]^m}} \tag{5}$$

Where :

θ_w : is volumetric water content, θ_r : is residual volumetric water content, θ_s : is saturated volumetric water content,
S: is soil suction, α: is scaling parameter inversely proportional to the mean pore diameter (cm^{-1}), n, m: are the shape parameters of the soil water characteristic. m = (1 − 1/n).

III. RESULTS AND DISCUSSIONS

III.1 COLLAPSIBILITY

Figure 8 illustrate the results of collapse tests conducted on sample soils at different water contents, suction values, and compaction energies.

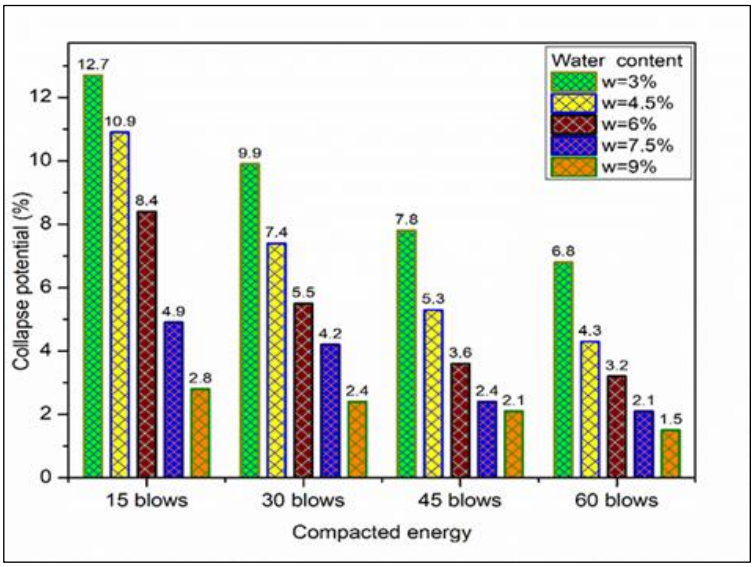


Figure 8: Effect of water content and compaction energy on collapse potential.
Source: Authors, (2026).

The collapsability test results show that water content and compaction energy have a crucial effect on the Cp. This potential decreases from 12.7% to 2.8% for the soil compacted under 15 blows, from 11.4% to 2.4% for soil compacted under 30 blows, from 7.8% to 2.1% for soil compacted under 45 blows and from 6.8% to 1.5% for soil soil compacted under 60 blows. The results indicate that the collapse potential increases as water content and compaction energy decrease. The maximum Cp value is obtained is Cp=12.7%, corresponding to the lowest water content, w=3% and compaction energy of 15 blows. This is explained by the structural instability of the soil, leading to a high Cp. However, the low Cp=1.1% at the highest water content, w=9%, compacted under 60 blows. Under these conditions, the soil is not susceptible to collapse. Figure 9 explicitly shows the effect of suction and compaction energy on the Cp. It is observed that the magnitude of Cp decreases with increasing compaction energy, whereas it increases with higher suction levels, which typically develop during dry periods.

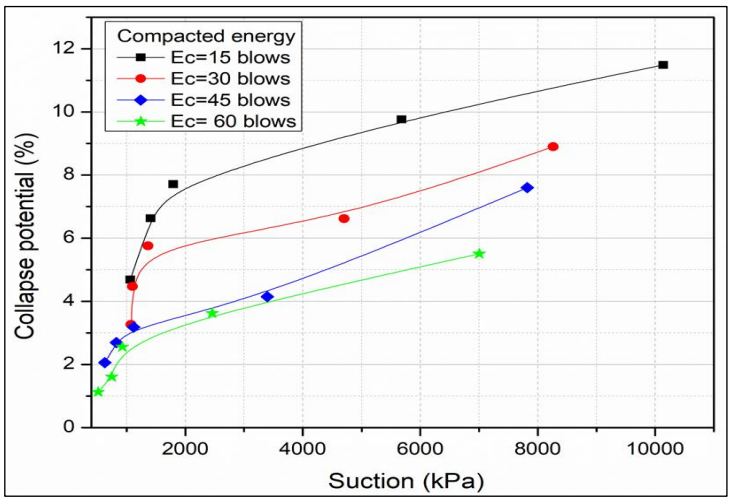


Figure 9: Effect of suction and compaction energy on collapse potential.
Source: Authors, (2026).

III.2 EFFECT ON SUCTION SHEAR PARAMETERS

As for the shear tests, Figures 10 and 11 show that the results yielded low cohesion values, ranging from 12.5 kPa to 26 kPa, due to the low plasticity of the silty sand. For a suction range between 1196.6 kPa and 9678.5 kPa, cohesion varies from 12.6 kPa to 21.5 kPa, representing an increase of approximately 68%. Similarly, for suctions varying between 510 kPa and 6830 kPa, the increase in cohesion is about 35%. This behavior is explained by the enhancement of capillary attraction forces between particles, which gives the soil a more rigid structure and greater strength in the unsaturated state. The influence of suction on the internal friction angle remains limited and is scarcely noticeable, with a variation magnitude between 0.5° and 1.0°.

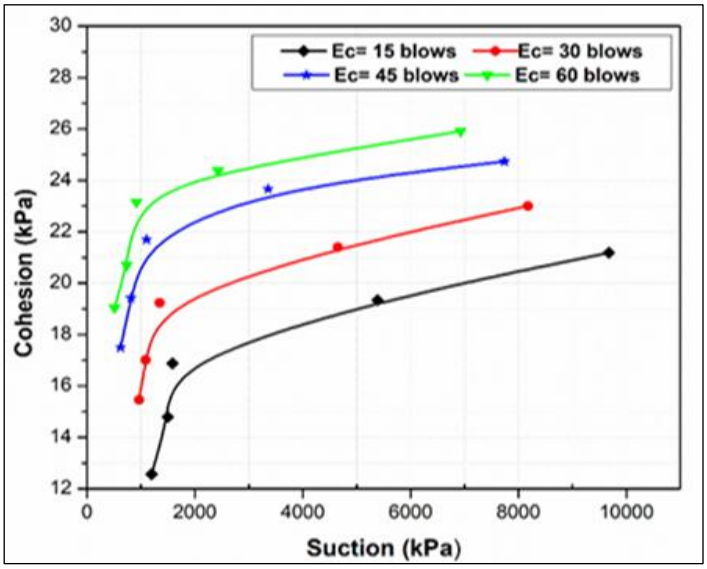


Figure 10: Effect of suction and compaction energy on cohesion.
Source: Authors, (2026).

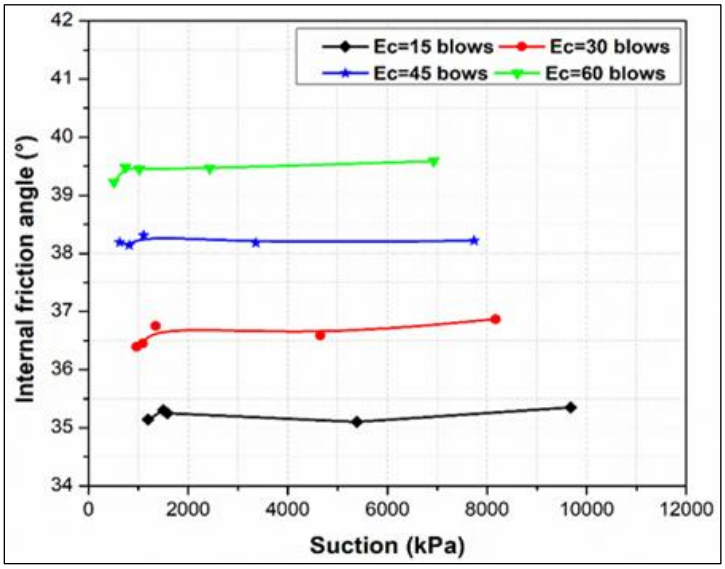


Figure 11: Effect of suction and compaction energy on friction angle.
Source: Authors, (2026).

III.3 SOIL WATER RETENTION BEHAVIOR

The analysis of the soil water retention curve (SWRC) according to the van Genuchten model was performed using the RETC (RETention Curves) software [24]. The water contents predicted by the RETC program are evaluated against the measured values Figure 12.

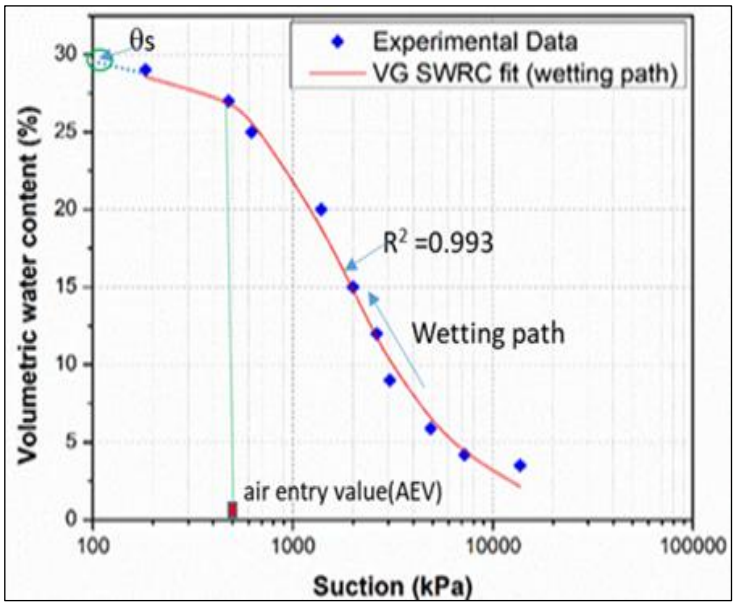


Figure12: Soil-water retention curve.
Source: Authors, (2026).

The evaluation of the fitting performance using the van Genuchten model is provided by the statistical indicators, specifically the coefficient of determination R^2=0.993, and the root mean square error RMSE=0.009. Figure 13 illustrates a strong correlation between the experimental values and the results obtained from the model. The parameters of the Van Genuchten model are used to characterize the hydraulic properties and texture of the soil.The parameter α is related to the air-entry pressure. Lower values of α correspond to higher air-entry pressures (AEV). For the soil studied, α = 0.008 cm^{-1}, which corresponds to an air-entry pressure of 500 kPa. The parameters n and m describe the pore-size distribution, reflected in the slope, and the overall shape of the soil water retention curve, respectively.

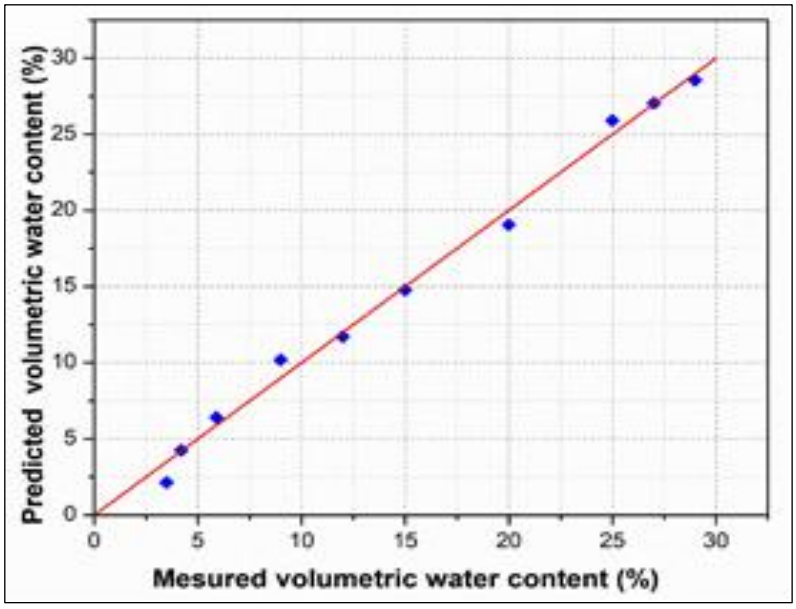


Figure13: Predicted versus measured values of the volumetric water content of the studied soil.
Source: Authors, (2026).

The van Genuchten parameters for the soil modelled in this study are provided in Table 3.

Table 3: Van Genuchten parameters.

Parameter	value
θ_s (%)	28.8
θ_r (%)$_a$	0.06
α (1 /cm)	0.008
n (-)	2.09
m (-)	0.47

Source: Authors, (2026).

IV. CONCLUSIONS

This experimental research offers insights into the characterization and analysis of the hydromechanical behavior of an unsaturated collapsible soil from the Metlili area in Ghardaïa Province (southern Algeria). The study aims to address existing gaps in knowledge regarding the natural soils of the region. The study also provided information on the behavior of a sandy loam soil with low plasticity under different moisture conditions. The obtained results confirm the effect of suction and capillary stresses on the assessment of the shear strength of unsaturated soils, by varying the compaction state and the interactions between soil particles. Specimens exhibiting high suction and compacted under moderate energy levels recorded the maximum values of collapse potential Cp. This behavior is attributed to the presence of a porous structure and weak interparticle bonds. The study revealed that the internal friction angle was not significantly affected by suction. However, an increase in the apparent cohesion of the soil is observed with an increase in suction. The collapse and shear tests conducted on unsaturated samples with different suction values allowed for the characterization of the collapse and shear properties of the soils studied at different suction levels. The hydraulic behavior of the studied soil, as described by the van Genuchten model, constitutes a relevant tool for hydromechanical studies of unsaturated soils, as it establishes a continuous relationship between water content and matric suction. It represents the different wetting phases, from conditions of high suction to the saturated state.

V. AUTHOR'S CONTRIBUTION

Conceptualization: Ali Fernane, Samir Benmoussa and Laouar Mohamed Salah.
Methodology: Ali Fernane and Laouar Mohamed Salah.
Investigation: Ali Fernane and Laouar Mohamed Salah.
Discussion of results: Ali Fernane, Laouar Mohamed Salah and Samir Benmoussa.
Writing – Original Draft: Ali Fernane.
Writing – Review and Editing: Ali Fernane and Laouar Mohamed Salah.
Resources: Ali Fernane and Laouar Mohamed Salah.
Supervision: Samir Benmoussa.
Approval of the final text: Ali Fernane, Samir Benmoussa, and Laouar Mohamed Salah.

VI. REFERENCES

[1] S. L. Houston, W. N. Houston, and C. E. Zapata, “Geotechnical engineering practice in collapsible soils,” Geotechnical and Geological Engineering, vol. 19, no. 3–4, pp. 333–355, 2001, doi: 10.1023/A:1013178226615A. W. O. Afred, C. T. Davie, S. S. G. Stephanie, and O. A. Ebiegberi, “A review of the identification methods and types of collapsible soils,” Journal of Engineering and Applied Science, vol. 69, Art. no. 17, 2022.

[2] D. B. Hamdy, “Origin and characteristics of collapsible soils: State-of-the-art report,” Innovative Infrastructure Solutions, vol. 9, Art. no. 401, 2024, doi: 10.1007/s41062-024-01673-5.

[3] W. O. Afred, C. T. Davie, S. S. G. Stephanie, and O. A. Ebiegberi, “A review of the identification methods and types of collapsible soils,” Journal of Engineering and Applied Science, vol. 69, Art. no. 17, 2022.

[4] E. C. Lawton, R. J. Fragaszy, and M. D. Hetherington, “Review of wetting-induced collapse in compacted soil,” Journal of Geotechnical Engineering, vol. 118, no. 9, pp. 1376–1394, 1992, doi: 10.1061/(ASCE)0733-9410(1992)118:9(1376).

[5] E. Derbyshire and T. W. Mellors, “Geological and geotechnical characteristics of some loess and loessic soils from China and Britain: A comparison,” Engineering Geology, vol. 25, no. 2–4, pp. 135–175, 1988, doi: 10.1016/0013-7952(88)90024-5.

[6] P. Li and S. K. Vanapalli, “Review of collapse triggering mechanisms of collapsible soils due to wetting,” Journal of Rock Mechanics and Geotechnical Engineering, vol. 8, no. 2, pp. 256–274, 2016, doi: 10.1016/j.jrmge.2015.12.002.

[7] D. G. Fredlund and H. Rahardjo, Soil Mechanics for Unsaturated Soils. New York, NY, USA: Wiley, 1993.

[8] C. Wang, W. Yang, N. Zhang, S. Wang, C. Ma, M. Wang, and Z. Zhang, “Effect of moisture content and wet–dry cycles on the strength properties of unsaturated clayey sand,” Buildings, vol. 14, no. 5, Art. no. 1375, 2024, doi: 10.3390/buildings14051375.

[9] M. S. H. Sayem, L.-W. Kong, and S. Yin, “Effect of drying–wetting cycles on saturated shear strength of undisturbed residual soils,” American Journal of Civil Engineering, vol. 4, no. 4, pp. 143–150, 2016, doi: 10.11648/j.ajce.20160404.15.

[10] J. Jing, J. Hou, Z. Pan, et al., “Simulation and evaluation of collapsible risk of low impact development rainwater system in collapsible loess area,” Water Resources Management, vol. 38, pp. 5485–5505, 2024.

[11] H. P. Rifa’i, H. Pujiastuti, A. D. Adi, and T. F. Fathani, “The effect of matric suction on the shear strength of unsaturated sandy clay,” International Journal of GEOMATE, vol. 14, no. 42, pp. 112–119, 2018, doi: 10.21660/2018.42.72825.

[12] Q. A. Al-Obaidi and T. Schanz, “Deformation of unsaturated collapsible soils under suction control,” Journal of Mechanical Behavior of Materials, vol. 31, no. 1, pp. 67–95, 2022, doi: 10.1515/jmbm-2022-0067.

[13] M. G. Jassam and I. S. Hussein, “Variation of collapse potential with initial suction pressure for natural and treated unsaturated gypseous soil,” Modelling, Measurement & Control B, vol. 11, no. 6, 2024, doi: 10.18280/mmep.110603.

[14] M. V. Villar, P. L. Martín, R. Gómez Espina, and A. Lloret, “Effect of suction and plasticity on the shear strength of sand/silt mixtures,” in Proc. 5th Int. Conf. on Unsaturated Soils, vol. 1, Boca Raton, FL, USA: CRC Press, 2011, pp. 391–396, doi: 10.1201/b10526.

[15] V. Escario and J. F. T. Juca, “Strength and deformation of partially saturated soils,” in Proc. 12th Int. Conf. on Soil Mechanics and Foundation Engineering, Rio de Janeiro, Brazil, 1989, pp. 43–46.

[16] Z. Song and Z. Zhang, “Shear strength equation of soils in a wide suction range under various initial void ratios,” Vadose Zone Journal, vol. 23, e20368, 2024, doi: 10.1002/vzj2.20368.

[17] D. Sheng, A. N. Zhou, and D. G. Fredlund, “Shear strength criterion for unsaturated soils,” Geotechnical and Geological Engineering, vol. 29, no. 2, pp. 145–159, 2011, doi: 10.1007/s10706-009-9276-x.

[18] V. Escario and J. F. M. Juca, “Unsaturated shear strength of a silty sand,” Canadian Geotechnical Journal, vol. 23, no. 3, pp. 359–366, 1986.

[19] LCPC and SETRA, Guide des terrassements routiers: Vol. 9 – Principes généraux, 2024 ed. Paris, France: IDRRIM & Cerema, 2024.

[20] ASTM International, ASTM D5333-03: Standard Test Method for Measurement of Collapse Potential of Soils. West Conshohocken, PA, USA, 2003.

[21] ASTM International, ASTM D3080-03: Standard Test Method for Direct Shear Test of Soils Under Consolidated Drained Conditions. West Conshohocken, PA, USA, 2003.

[22] ASTM International, ASTM D5298-10: Standard Test Method for Measurement of Soil Potential (Suction) Using Filter Paper, West Conshohocken, PA, USA, 2010.

[23] M. T. Van Genuchten, “A closed-form equation for predicting the hydraulic conductivity of unsaturated soils,” Soil Science Society of America Journal, vol. 44, no. 5, pp. 892–898, 1980.

[24] M. T. Van Genuchten, F. J. Leij, and S. R. Yates, “The RETC code for quantifying the hydraulic functions of unsaturated soils,” EPA Rep. no. 600/2-91/065, U.S. Environmental Protection Agency, 1991.

Journal of Engineering and Technology for Industrial Applications

ISSN ONLINE: 2447-0228

ITEGAM-JETIA

Manaus, v.12 n.60, p.1474-1479. July/August, 2026.
DOI: https://doi.org/10.5935/jetia.v12i60.4349

RESEARCH ARTICLE OPEN ACCESS

INVESTIGATION ON THE SLURRY EROSION BEHAVIOUR OF SUPER 304HCu STAINLESS STEEL UNDER NORMAL IMPACT CONDITIONS

M. Balachandar[1] and M. Vinoth Kumar*[2]

[1, 2]Department of Mechanical Engineering, Hindustan Institute of Technology and Science, Chennai, Tamil Nadu, India.

[1]http://orcid.org/0000-0002-8223-4948, [2]http://orcid.org/0000-0003-2813-7095

Email: balachandar2k1@gmail.com,*vinothmecho@gmail.com

ARTICLE INFO

Article History
Received: March 26, 2026
Reviewed: April 26, 2026
Accepted: July 26, 2026
Published: August 31, 2026

Keywords:
Slurry Erosion,
Weight loss,
Super 304HCu,
Stainless steels,
Wear

ABSTRACT

Slurry erosion is an important wear issue in pipelines, pumps, and other industrial equipment that operate in environments where solid particles are transported along with the liquid. In this study, the slurry erosion behaviour of Super 304HCu alloy is examined under different simulated conditions, including slurry velocity, slurry concentration, and time of exposure. The experiments for these investigations are carried out in a slurry erosion test rig at various rotational speeds of 6 m/s, 9 m/s, and 12 m/s, with varying slurry concentrations of 10%, 20%, and 30%. The weight loss of the test specimens was recorded at regular intervals to determine the erosion rate. The experimental results indicate that the weight loss of the material steadily increases with increase in time of exposure, slurry velocity, and slurry concentration. At higher slurry velocities the increase in kinetic energy of the abrasive particles, result in stronger impacts on the material surface and consequently increase material removal. Similarly, the increase in slurry concentration increases the probability of the number of particles interacting with the surface, and accelerates the erosion process. SEM micrographs of the worn surfaces of the specimens revealed typical wear characteristics of erosion of a ductile material.

Copyright ©2026 by authors and Galileo Institute of Technology and Education of the Amazon (ITEGAM). This work is licensed under the Creative Commons Attribution International License (CC BY 4.0).

I. INTRODUCTION

Slurry erosion is a complex wear phenomenon caused by the repeated impact of the solid particles suspended in liquids on material surfaces. This type of wear is commonly encountered in heavy systems such as slurry pipelines, pumps, hydro turbines, mining equipment's, and power plant components [1]. The erosion process involves several material removal mechanisms, such as micro-cutting, plastic deformation, and surface fatigue, which in turn depend on factors such as slurry velocity, slurry concentration, particle size, and angle of impingement [2-10]. In recent years, significant research has been carried out on understanding the tribological wear mechanisms responsible for the slurry erosion and development of materials with improved resistance to such damage. Li et al. investigated the mechanisms of slurry erosion and reported that erosion is strongly influenced by particle velocity and angle of impact. It is also demonstrated that ductile materials tend to experience maximum erosion at oblique angles of impact, typically between 30° and 60°, where micro mechanism such as both cutting and deformation contribute to material loss [11], [12]. Several studies have also focused on the erosion resistance of stainless steels in slurry environments. Examined the slurry erosion characteristics of stainless steels subjected to hot forging and observed that microstructural refinement significantly improved the erosion resistance of the steel [13]. Similarly, investigated slurry erosion of steel in the mining conditions and concluded that slurry velocity and slurry concentration are the most influential factors for material loss. The role of size of the abrasive particle has also been widely explored [14]. Reported that large abrasive particles tend to increase the material loss due to the higher kinetic energy associated with impact of the slurry particles. It also indicated that erosion damage becomes more severe increase in particle size and velocity [15]. In a recent study, on duplex and super stainless steels with superior mechanical properties and enhanced corrosion resistance for slurry handling applications. Reported an experimental investigation on the slurry erosion behaviour of duplex stainless steel using Taguchi optimization and artificial neural network modelling.

It is reported that that slurry velocity and particle concentration have a significant effect on erosion rate, while the angle of impingement plays an important role in determining the wear mechanism [16]. Advanced coatings and surface modification techniques has also been explored to improve erosion resistance. Examined the erosive wear characteristics of boronized martensitic stainless steel and reported that boronizing significantly enhance the hardness and reduces the erosion rate [17]. Similarly, investigated the laser-cladded stainless-steel coatings and reported significant improvement in the cavitation and slurry erosion resistance of the coated steel, due to the refined microstructures and strong metallurgical bonding between the steel and coating. Additive manufacturing and friction stir processing are also been investigated for enhancing the erosion resistance of components [18]. Studied slurry erosion behaviour of additively manufactured steel specimens and reported that optimizing the printing parameters can significantly improve the wear resistance [19]. In a study, by it is demonstrated that friction stir processing with high-entropy alloy reinforcement resulted in improved slurry erosion resistance of stainless steel through grain refinement and increase in hardness [20].Erosion–corrosion behaviour is a much more critical phenomenon affecting the material performance in slurry environments. Fan et al. investigated erosion–corrosion characteristics of desulfurization slurry on stainless steel pipelines and found that the combined action of mechanical erosion and electrochemical corrosion significantly accelerated the material degradation. It also emphasized the importance of selection of corrosion-resistant alloys for components operating in slurry environments. Although considerable amount of research has been carried out on the slurry erosion behaviour of conventional stainless steels and duplex alloys, relatively limited attention has been given to super austenitic stainless steels such as Super 304HCu stainless steel [21]. Therefore, this investigation is necessary to better understand the slurry erosion performance of Super 304HCu alloy under different operating conditions. The current study focuses on evaluating the influence of key erosion parameters such as slurry velocity and particle concentration on the erosion behaviour of Super 304HCu.

II. MATERIALS AND METHODS

The material used in this investigation was super austenitic stainless-steel type Super 304HCu. Rectangular specimens with dimensions of 20 × 30 × 3.5 mm³ were machined from tubes, using a wire-cut Electrical Discharge Machining (EDM) process to ensure precise cutting and dimensional accuracy. After machining, the burrs and oxides present on the specimen edges were carefully removed to obtain smooth surfaces (Figure 1a). The samples were then cleaned with ethanol and subsequently dried before conducting the tests. The particle size of the abrasive particles used in the experiment were silica sand particles ranging from 0.5–1.0 mm. The slurry used for the experiments was prepared with silica sand particles suspended in demineralized water to create an abrasive medium for the test. The slurry erosion experiments were conducted using a slurry pot erosion tester, which allowed controlled circulation of abrasive slurry over the specimen surface. The schematic arrangement of the tester and the dimensions of the pot are shown in Figure 2a and 2b respectively. The specimens were securely mounted in the test chamber using bolts to ensure stable positioning during the experiment as shown in Figure 1b. The angle of impact is kept constant at 90° for all the test conditions to create normal impact conditions.

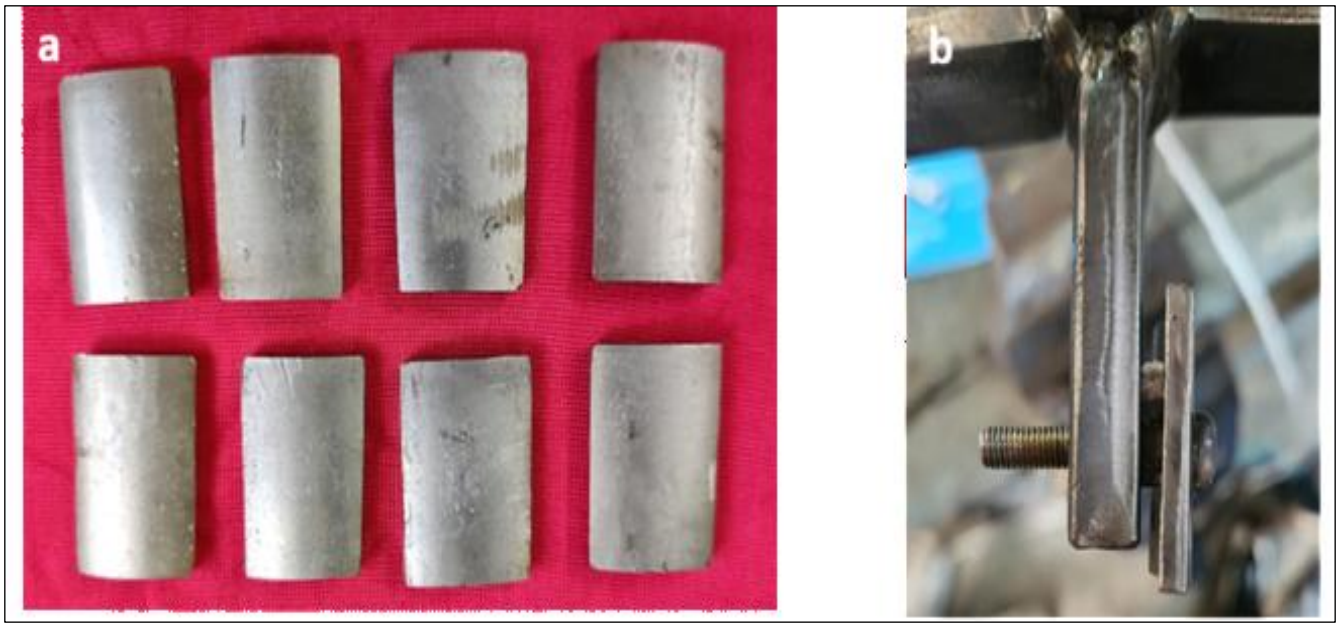


Figure 1: Photograph of (a) machined specimen and (b) specimen mounted on slurry pot test chamber.
Source: Authors, (2026).

In order to evaluate the effect of slurry velocity on Weight loss of Super 304Hcu, the erosion tests were carried out at three different rotational speeds of 1000 rpm, 1500 rpm, and 2000 rpm, (6 m/s, 9 m/s, and 12 m/s) under 30% Slurry Concentration. Similarly, to study the effect of slurry concentration, it is varied as 10 %, 20 %, and 30 % at constant speed of 1500 rpm (9 m/s). Each experiment was conducted for a total duration of 120 minutes, and the weight loss of the specimens was recorded at regular intervals of 20 minutes. The initial and final weight of each specimen was measured using a precision electronic balance. The weight loss of the specimen was calculated as the difference between the initial and final weight.

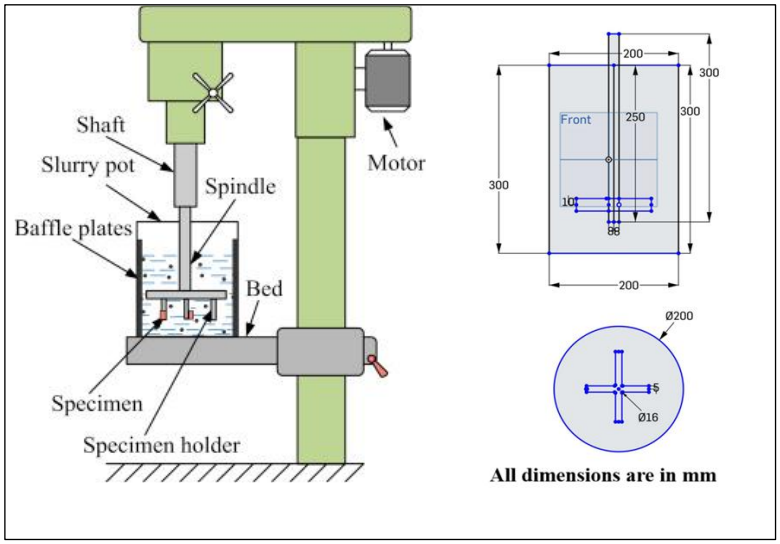


Figure 2: Schematic arrangement of slurry pot tester (a) and dimensions of the slurry pot (b).
Source: Authors, (2026).

III. RESULTS AND DISCUSSION

III.1 EFFECT OF SLURRY VELOCITY ON WEIGHT LOSS

Figure 3 shows that weight loss increases progressively with increase in both exposure time and slurry velocity. At the initial stage of the experiment, the increase in weight loss is relatively moderate. However, as the erosion time increases, the rate of material removal becomes significantly higher. This behaviour can be attributed to the continuous particle impacts that can gradually weaken the surface and accelerate erosion damage.

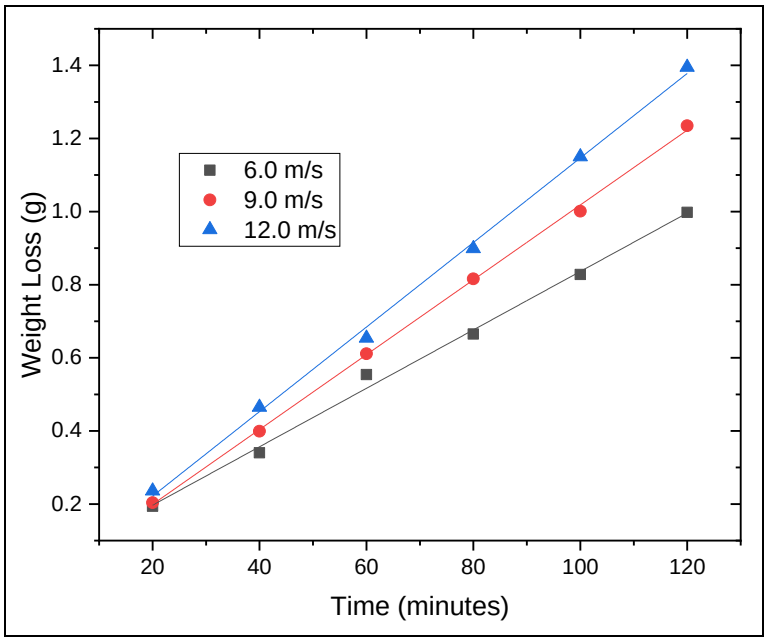


Figure 3: Variation of weight loss of Super 304HCu alloy with time at different slurry velocities (6 m/s, 9 m/s, and 12 m/s) at slurry concentration of 30 %.
Source: Authors, (2026).

Among the three test conditions, the highest weight loss occurred at the slurry velocity of 12 m/s, followed by 9 m/s and 6 m/s. This trend indicates that the slurry velocity is one of the most influential parameters in controlling the slurry erosion wear. Higher velocity increases the kinetic energy of abrasive particles striking the material surface, and resulting in greater material removal. The observed behaviour in Super 304HCu is consistent with the findings reported by who reported that erosion rate increases significantly with increase in particle velocity due to higher impact energy of the abrasive particles [11], [12]. Similarly, also reported that the increase in the particle velocity enhances the cutting and ploughing action of abrasive particles on the surface of the stainless steel [15]. In addition, Singh et al. observed that the slurry velocity plays a dominant role in determining the erosion rate of duplex stainless steels, where higher slurry velocities can lead to more severe surface damage. It is also confirmed that the kinetic energy of impacting particles is directly proportional to the square of velocity, which significantly amplifies the erosion process. These observations confirm that particle impact energy and frequency of collisions increase with velocity, resulting in a higher erosion rate [16].

III.2 EFFECT OF SLURRY CONCENTRATION EFFECT ON WEIGHT LOSS

Figure 4 illustrates the variation of weight loss of Super 304HCu alloy with time at different slurry concentrations (10%, 20%, and 30%). It is evident that the weight loss increases significantly with increase in the time of exposure for all slurry concentrations studied, indicating continuous material removal due to the particle impact in the slurry environment. Additionally, the rate of erosion significantly increases as the slurry concentration increases from 10% to 30%, demonstrating the strong influence of abrasive particle density on erosion behaviour.

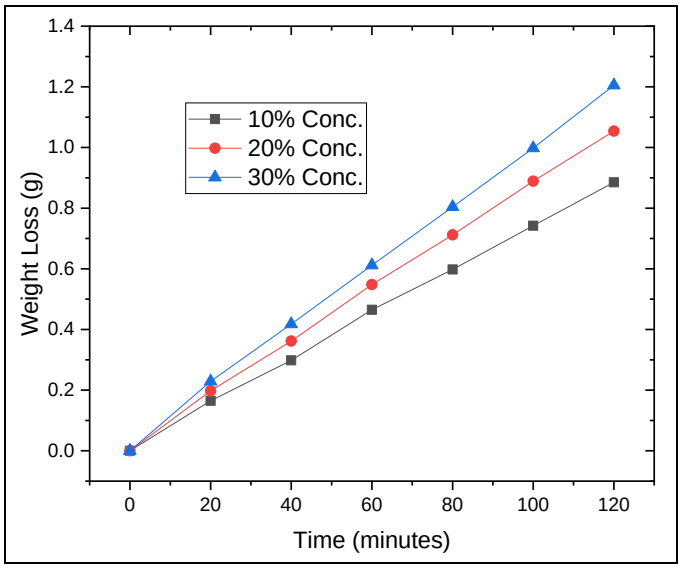


Figure 4: Variation of Weight loss of Super 304HCu alloy with time at different slurry concentrations (10%, 20%, and 30%) at constant velocity of 9 m/s.
Source: Authors, (2026).

At 10% slurry concentration, the weight loss was reported as 0.88 g after 120 minutes of erosion. This comparatively lower erosion rate is be attributed to the fewer number of abrasive particles interacting with the material surface. As the slurry concentration increases to 20%, the Weight loss increase more rapidly, reaching approximately 1.05 g at 120 minutes. An increase in slurry particle concentration leads to more frequent collisions between abrasive particles and the specimen surface, which in turn increases the rate of material removal. As the concentration of particles in the slurry increases, the number of particles impacts per unit time also increases, in turn accelerating the erosion process. The highest weight loss was observed at a slurry concentration of 30%, where the value reached approximately 1.20 g after 120 minutes of testing. At higher concentrations, the slurry contains a greater number of abrasive particles, which significantly increases the frequency of particle impacts on the material surface. This results in intensified material removal mechanisms and ultimately lead to a higher erosion rate compared to lower slurry concentrations. These observations are consistent with findings that were reported in the earlier studies. Chen et al. reported that an increase in the number of abrasive particles in a slurry leads to a higher erosion rate due to the greater frequency of particle–surface interactions [15]. Similarly, reported slurry concentration as one of the most influential parameters affecting the erosion wear in stainless steels. From the experimental results it is indicated that higher particle concentrations cause increase in the likelihood of the impact events, and thereby cause higher material loss [16]. Furthermore, explained that the slurry erosion typically occurs through mechanisms such as micro-cutting, plastic deformation, and surface fatigue. At higher particle concentrations, these mechanisms become more pronounced because multiple particles interact simultaneously with the material surface, resulting in more severe erosion damage. The cumulative effect of these impacts accelerates the wear process [11], [12]. The nearly linear trend observed in the graph suggests that the erosion rate remains relatively stable throughout the test duration, although the magnitude of wear increases with slurry concentration. Similar trends were reported by Sharma et al. and Das et al. in their studies on slurry erosion of stainless steels used in mining and industrial environments. The results clearly indicate that slurry concentration plays a significant role in determining the erosion rate of Super 304HCu stainless steel. Higher particle concentration leads to increased abrasive interaction with the surface, resulting in greater material removal [13], [14].

III.3 SEM MICROGRAPH ANALYSIS OF WORN SURFACE

Scanning Electron Microscopy (SEM) was used to examine the worn surfaces of Super 304HCu specimens after slurry erosion testing in order to understand the dominant wear mechanisms. The SEM micrographs reveal significant surface damage caused by repeated impacts of abrasive particles present in the slurry. The SEM micrographs of Figure 5 reveal several characteristic surface features associated with slurry erosion, including surface pits, and regions of plastic deformation. The presence of these features suggests that the erosion behaviour of the material is largely dominated by ductile erosion mechanisms. The increasing slope of the curves in Figure 3 also indicates that the erosion process becomes more severe over time. As the surface undergoes repeated particle impacts, micro-cracks and surface pits develop, which facilitate further material removal. Similar erosion mechanisms such as micro-cutting, plastic deformation, and surface fatigue were reported by Yilmaz et al. during the erosion testing of stainless steels. The results demonstrate that Super 304HCu alloy exhibits better resistance at lower slurry velocities, while higher velocities accelerate erosion wear due to increased particle impact energy [17]. These findings suggest that controlling slurry velocity is essential for improving the service life of components used in slurry transportation systems.

At lower slurry velocities, the eroded surfaces exhibit relatively shallow grooves with only limited surface deformation. The damage appears mild, mainly caused by the sliding and rolling motion of abrasive particles across the surface. As the particles move along the direction of slurry flow, their cutting action produces fine and nearly parallel grooves on the material surface.

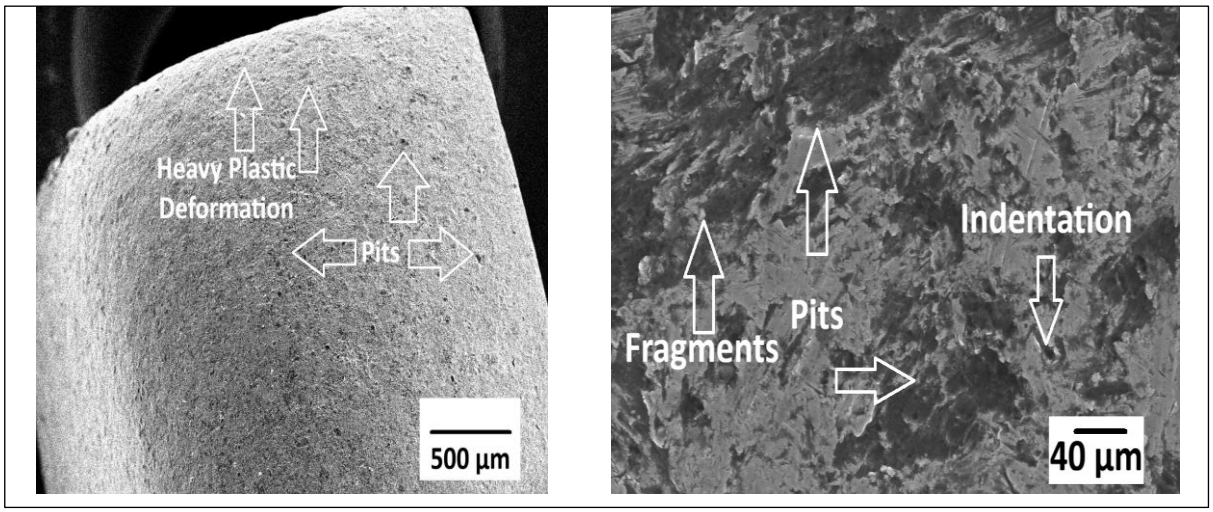


Figure 5: Scanning Electron Microscopy (SEM) micrograph of the worn surfaces of Super 304HCu (30% Concentration, velocity 9 m/s, time 120 minutes).
Source: Authors, (2026).

When the slurry velocity increases, the severity of surface damage becomes more pronounced. The SEM images show deeper grooves, larger pits, and noticeable plastic deformation in several regions of the specimen surface. This increased damage is mainly attributed to the higher kinetic energy of the impacting particles. With greater impact energy, the abrasive particles produce stronger micro-cutting actions and remove material more effectively from the surface. In addition, the presence of alloying elements such as chromium, molybdenum, and copper in Super 304HCu promotes the formation of a stable passive film on the surface. This passive layer can provide a certain degree of protection against erosion–corrosion effects. However, under continuous abrasive particle impacts, the protective film may gradually deteriorate, exposing the underlying material to further erosion damage.

IV. CONCLUSIONS

In this work, the slurry erosion behaviour of the Super 304HCu stainless steel is investigated at different operating conditions, such as slurry velocity, slurry concentration, and time of exposure. From the experimental results, the weight loss of the specimens increases steadily with erosion time. This confirms the continuous material removal from the specimen by the abrasive particles which repeatedly strike and slide over the specimen surface during the slurry flow. Among the parameters investigated, the slurry velocity was found to have a significant effect on the erosion rate. As the velocity increases, the extent of the material loss also increased. The maximum weight loss occurred at 12 m/s, while the lowest at slurry velocity of 6 m/s. This behaviour can be attributed to the high kinetic energy of slurry particles at higher velocities, resulting in stronger impacts and more severe surface damage. A similar trend was observed with respect to slurry concentration. Increasing the concentration of abrasive particles led to a higher frequency of particle–surface interactions. As a result, the probability of impact events increased, which in turn accelerated the erosion process and produced greater material loss. The graphical analysis supports these observations and clearly indicates that the erosion rate rises with both slurry velocity and slurry concentration. These parameters therefore play a dominant role in controlling the slurry erosion under the present experimental conditions. Further insight into the wear mechanisms was obtained from the SEM examination of the eroded surfaces. The micrographs revealed several typical features such as micro-cutting grooves, ploughing marks, pits, and regions of plastic deformation. These characteristics suggest that the erosion process is largely governed by ductile mechanisms, where cutting and plastic deformation act together to remove material from the surface. Overall, the results indicate that Super 304HCu alloy exhibits reasonable resistance to slurry erosion. However, the extent of material loss becomes significantly higher at increased slurry velocities and particle concentrations. Future studies may consider the influence of additional parameters, such as particle size, and temperature, in order to understand the erosion performance of this alloy better.

V. AUTHOR'S CONTRIBUTION

Conceptualization: M. Balachandar and M. Vinoth Kumar.
Methodology: M. Balachandar and M. Vinoth Kumar.
Investigation: M. Balachandar.
Discussion of results: M. Balachandar and M. Vinoth Kumar.
Writing – Original Draft: M. Balachandar.
Writing – Review and Editing: M. Vinoth Kumar.
Resources: M. Balachandar and M. Vinoth Kumar.
Supervision: M. Vinoth Kumar.
Approval of the final text: M. Balachandar and M. Vinoth Kumar.

VI. REFERENCES

[1] D. Patel, A. Kumar, and S. Singh, “Experimental investigation of slurry erosion in stainless steel pipelines,” Tribol. Int., vol. 161, p. 107062, 2021.

[2] P. Mishra, R. Sahoo, and B. Mohanty, “Effect of particle velocity on slurry erosion of stainless steels,” Mater. Res. Express, vol. 9, p. 046505, 2022.

[3] V. Gupta, R. Sharma, and A. Tiwari, “Slurry erosion behaviour of duplex stainless steel under varying impact angles,” Surf. Eng., vol. 39, no. 5, pp. 589–598, 2023.

[4] L. Zhang, W. Sun, and H. Liu, “Microstructural influence on erosion resistance of stainless steel coatings,” Surf. Coat. Technol., vol. 455, p. 129214, 2023.

[5] S. Yöyler, A. Surženkov, M. Tarraste, M. Kolnes, and K. Juhani, “Erosive wear of stainless steel-based hardfacings reinforced with TiC,” Coatings, vol. 15, no. 6, p. 658, 2025.

[6] S. Kumar, S. K. Chandra, S. Dixit, K. Kumar, S. Kumar, G. Murali, N. I. Vatin, and M. M. S. Sabri, “Neural network prediction of slurry erosion wear of Ni-WC coated stainless steel 420,” Metals, vol. 12, no. 5, p. 706, 2022.

[7] H. Zhang, Y. Liu, and X. Chen, “Influence of microstructure on slurry erosion resistance of high-silicon steels,” Wear, vols. 538–539, p. 205222, 2024.

[8] J. Wang, L. Zhao, and Z. Huang, “Slurry jet erosion resistance of friction-stir processed stainless steel reinforced with high-entropy alloys,” Johnson Matthey Technol. Rev., vol. 69, p. 99, 2025.

[9] N. Kumar, P. Verma, and R. Singh, “Optimization of slurry erosion parameters using Taguchi method,” Eng. Fail. Anal., vol. 134, p. 106046, 2022.

[10] A. Bhat, S. Rao, and N. Shetty, “Erosion wear mechanisms in slurry transportation systems,” Wear, vols. 518–519, p. 204723, 2023.

[11] J. Li, T. Wang, and H. Zhao, “Erosion–corrosion behaviour of steels used in slurry pipelines,” Wear, vol. 476, p. 203771, 2021.

[12] Y. Li, P. Schreiber, J. Schneider, and C. Greiner, “Tribological mechanisms of slurry abrasive wear,” Friction, vol. 11, no. 6, pp. 1079–1093, 2023.

[13] V. Sharma, R. Singh, and A. Kumar, “Effect of hot forging on slurry erosion behaviour of AISI 316 and AISI 410 steels,” Mater. Today Proc., vol. 26, pp. 1740–1745, 2020.

[14] S. Das, R. Behera, and S. Pradhan, “Investigation of slurry erosion wear of stainless steel in mining environments,” J. Tribol., vol. 143, p. 101601, 2021.

[15] Q. Chen, Y. Wang, and J. Zhang, “Influence of abrasive particle size on slurry erosion of stainless steel materials,” Tribol. Int., vol. 188, p. 108802, 2024.

[16] R. Singh, A. Patel, and P. Kumar, “Experimental study on slurry erosion wear behaviour of duplex stainless steel using Taguchi and ANN methods,” Mater. Today Commun., vol. 40, p. 109918, 2024.

[17] M. Yilmaz, A. Demir, and O. Sahin, “Investigation of erosive wear characteristics of boronized martensitic stainless steel,” J. Mater. Res. Technol., vol. 33, pp. 2292–2302, 2024.

[18] X. Liu, Y. Zhang, and P. Li, “Cavitation and slurry erosion resistance of laser-cladded martensitic stainless steel coatings,” Wear, vol. 545, p. 205562, 2024.

[19] Y. Liu, X. Zhao, and C. Wang, “Advanced wear-resistant alloys for slurry erosion applications,” Mater. Sci. Eng. A, vol. 895, p. 145002, 2025.

[20] V. Vashist, O. Istvan, and Z. Szakal, “Parametric optimization and slurry erosion characterization of additively manufactured steels,” J. Mater. Eng. Perform., vol. 34, pp. 28695–28706, 2025.

[21] G. Fan, Z. Li, and Y. Zhao, “Experimental study on the erosion–corrosion characteristics of desulfurization slurry on stainless steel pipe materials,” ACS Omega, vol. 9, pp. 12541–12553, 2024.

Journal of Engineering and Technology for Industrial Applications

ITEGAM-JETIA

Manaus, v.12 n.60, p.1480-1486. July/August, 2026.
DOI: https://doi.org/10.5935/jetia.v12i60.4353

ISSN ONLINE: 2447-0228

RESEARCH ARTICLE OPEN ACCESS

IMPLEMENTATION OF AN ESP32-BASED ESP-NOW NODE NETWORK FOR SMART AGRICULTURE MONITORING AND IRRIGATION CONTROL

Kota Venkat Kumar*[1], Marneedi Soujanya[2], Karnati Chaitanya Keerthi[3], Mohammed Mastan Vali Yash[4], Kodavandla Vignesh[5], Sravan Sikakolli[6]

[1]Department of ECE, Professor, Vignan's Lara Institute of Technology & Science, Vadlamudi, Guntur, Andhra Pradesh, India.
[2, 3, 4, 5]Department of ECE, UG Student, Vignan's Lara Institute of Technology & Science, Vadlamudi, Guntur, Andhra Pradesh, India.
[6]Department of ECE, Associate Professor, Vignan's Lara Institute of Technology & Science, Vadlamudi, Guntur, Andhra Pradesh, India.

[1]http://orcid.org/0009-0004-1596-9997, [2]http://orcid.org/0009-0005-1306-4737, [3]http://orcid.org/0009-0001-8546-5979,
[4]http://orcid.org/0009-0006-1586-4735, [5]http://orcid.org/0009-0004-4070-7200, [6]http://orcid.org/0000-0002-4887-997X

Email:*venkatvlits2024@gmail.com, marneedisoujanya0103@gmail.com, keerthykarnati@gmail.com, mmvyash.143@gmail.com, vignesh.kodavandla@gmail.com, larasravan@gmail.com

ARTICLE INFO

Article History
Received: March 26, 2026
Reviewed: April 26, 2026
Accepted: July 26, 2026
Published: August 31, 2026

Keywords:
remote crop management,
solar powered automation,
sustainable,
energy saving agriculture systems in the world to enhance productivity,
resource optimization through the use of data-driven decisions.

ABSTRACT

Water waste, unpredictable weather, lack of real-time monitoring, and reliance on manual irrigation techniques are some of the problems agriculture faces today. This paper presents a smart agriculture monitoring and irrigation control system based on the ESP32 that uses ESP-NOW wireless communication to tackle these challenges. The proposed system includes one main control node and two sensor nodes. In the field, the sensor nodes monitor temperature, humidity, motion, rainfall, and soil moisture. Irrigation automatically adjusts to reduce water waste and improve efficiency based on set threshold values. Using the ESP-NOW protocol, sensor data is transmitted wirelessly to the main node. It is then periodically uploaded via Wi-Fi to a cloud platform for remote monitoring through a mobile app. The system works well in off-grid and remote agricultural areas because it is solar-powered with a rechargeable Li-ion battery backup. The experiment results show reliable sensing, stable multi-node operation, dependable wireless communication, and effective automatic irrigation control. For smart agriculture, the proposed model offers an affordable, scalable, and energy-efficient solution.

Copyright ©2026 by authors and Galileo Institute of Technology and Education of the Amazon (ITEGAM). This work is licensed under the Creative Commons Attribution International License (CC BY 4.0).

I. INTRODUCTION

The increasing rate of the global population requires more agricultural production, but climate change and improper agricultural practices are major challenges. The integration of artificial intelligence with IoT and cloud computing will make agriculture smarter, more efficient, and data-driven. This paper proposes an IoT-based system for monitoring the growth of the paddy crop. The proposed system uses sensors to measure temperature, humidity, soil moisture, and water levels. The data is then analyzed using a cloud platform. The system will help farmers to optimize irrigation, increase crop production, and reduce water wastage. The proposed technique is a cost-effective solution for precision agriculture [1], [2]. Agriculture is important for a country's economy. Precision agriculture uses machine learning methods to improve yield Agriculture is an important sector in the economy of a nation. Precision agriculture uses machine learning algorithms to enhance crop forecasting and decision-making. Machine learning (ML) extracts valuable information from past data to help in soil mapping, seed choice, irrigation, disease identification, weed management, and crop quality assessment. Cameras observe plant health, identify diseases, and assist in harvesting, sorting, and field robotics. Computer vision is the next level of smart farming. All these enhance automation, reduce expenses, and enhance agricultural productivity and efficiency by integrating deep learning with big data [3], [4]. The Internet of Things (IoT) has brought new opportunities for efficiency and automation in many areas, and agriculture is not an exception. IoT systems are based on the interconnected devices, sensors, and communication protocols to gather and share data and provide real-time monitoring and smart control of physical environments [5]. This technology in agriculture enables farmers to have an insight into valuable field conditions every time and act swiftly in reaction to forthcoming alterations.

IoT-based smart irrigation systems assist in automatizing the process of water management to achieve this by evaluating sensor information to find out the real requirements of crops. These systems have the capability of controlling irrigation in a more efficient way by measuring soil moisture and other environmental parameters that would help eliminate water wastage and enhance crop growth [6]. This type of IoT-based solution offers a stable and affordable way of modern agriculture to facilitate efficient use of resources and sustainable farming initiatives. Agriculture has had a significant application of wireless sensor networks, which monitor the environment in an efficient way but with minimal power consumption. The systems assist in gathering the precise field information and aid in managing the farm better [7]. With the help of the IoT and sensors, the agricultural system will be able to track the crops in real time and automatically control the irrigation process. This enhances efficiency of resources and has been a trusted solution to smart applications in agriculture [8]. IoT is revolutionizing the world of modern agriculture. IoT enables farmers to track the conditions of their fields remotely and automates critical tasks such as watering and fertilizing. This paper describes a real-time monitoring system based on IoT technology and environmental sensors to continuously measure temperature, soil moisture, and water levels. The system relies on the data collected to control the pumps and cooling fans to maintain optimal conditions for crops. It transmits data to the cloud through Wi-Fi for real- time viewing and analysis. The GSM modules enable the farmer to receive real-time notifications. The proposed system enhances agricultural productivity by ensuring that resources are optimally utilized and appropriate measures are taken [9]. In this paper, the performance of a cluster-based agricultural IoT network using BLE and Raspberry Pi 3 B+ is presented. The proposed network is designed for precision agriculture and greenhouse systems. The testbed is a combination of sensors and low-power communication modules. The results of the experiments conducted indoors and on the farm indicate that the testbed is reliable, scalable, and easy to manage [10].

II. RELATED WORK

In smart agriculture, we employ the use of wireless sensor networks based on IoT technology to measure the soil moisture, temperature, humidity, and water level in the field. Wi-Fi, Bluetooth, Zigbee, and LoRa technologies are normally employed to help the long- distance transmission of this data. But in large-scale agriculture, these technologies may sometimes experience problems of range, battery life, and connectivity. Mesh networking solves this problem. Here, the devices communicate with each other. This makes the network robust and reliable. ESP-based networks such as Wi-Fi Mesh and ESP-NOW are the best for this purpose because they are fast, battery-efficient, and highly effective in large outdoor farms [11].

III. PROPOSED SYSTEM ARCHITECTURE

The proposed system is a smart agriculture system developed using IoT technology. This system is capable of monitoring the field in real time, automatically controlling irrigation, and enabling users to view data remotely using a mobile application. The system is developed in a distributed fashion, consisting of two sensor nodes and one main node. The two sensor nodes are responsible for field sensing and device control, such as pumps. The main node is responsible for collecting all the data, making decisions based on the data, and sending the data to the cloud for remote access. For better understanding and future development, the whole system is broken down into various functional units [12], [13].

A. Power Supply

Unit The power supply unit is made for ongoing use in remote agricultural areas. Each node gets its power from a solar panel and a rechargeable Li-ion battery. The voltage regulation circuit provides a steady power supply to the microcontroller, sensors, and communication modules. The system relies on renewable energy sources and is built to work for a long time with little maintenance.

B. Sensor and Control Unit

The sensor and control unit observes the field and environmental conditions. The sensor nodes are equipped with soil moisture sensors, temperature and humidity sensors, rain sensors, and PIR motion sensors. The sensors are responsible for collecting real-time data regarding the soil conditions, environmental changes, and activities in the field. The ESP32/NodeMCU microcontroller is responsible for processing the sensor data and making decisions based on the predefined thresholds.

C. Communication Unit

The communication unit is the brain that shuttles data among the sensor nodes, the main node, and the cloud. First the sensor nodes toss their processed data wirelessly straight to the main node. Once there, the main node stitches the pieces together and runs its own cleanup routine. After that minute of gathering, it pulls the connection to the sensors, boots up its Wi-Fi card, and blasts the polished data out to the cloud. As soon as the upload finishes, the mobile app gets a quick refresh. Doing it this way cuts power use, lightens the traffic load, and forces the data to ship safely—that's the double-edged advantage [14].

D. Actuation Unit

The actuation unit controls the field devices based on sensor values and system decisions. Relay modules control the actuators, which may be water pumps or motors. When the soil moisture content is below the set level, the irrigation motor turns on automatically. But when the moisture content is adequate, the motor turns off to avoid wasting water. Temperature actuation can also be applied to ventilation control in indoor or protected agriculture.

E. Monitoring and User Interface Unit

The monitoring unit allows both local and remote access to agricultural data. The main node has an LCD display that provides real-time data from the sensors. The cloud-based mobile app allows farmers to monitor the conditions in the fields remotely. The mobile app updates the sensor data after each communication cycle, allowing farmers to make decisions without necessarily being in the field.

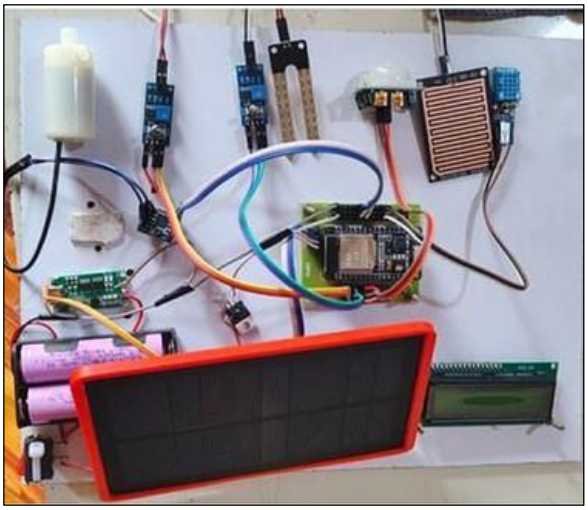


Figure 1: Experimental Setup of Nodes 1 and 2 (Tx).
Source: Authors, (2026).

F. Node-wise Monitoring and Interface Description

1) Node 1 Monitoring Unit

Node 1 acts as a transmitter sensing unit placed in the agricultural field. It constantly checks soil moisture, temperature, humidity, rainfall, and motion with the built-in sensors. The ESP32/NodeMCU processes the sensor data on-site and operates the irrigation motor through a relay when the soil moisture drops below the set threshold. The processed data from Node 1 is sent wirelessly to the main node during the data collection phase. Node 1 runs on solar power and has battery backup. This setup allows for continuous monitoring with little human involvement.

2) Node 2 Monitoring Unit

Node 2 is a duplicate sensing node with the same hardware configuration as Node 1. Node 2 is placed in a different region of the field to measure the variations in environmental conditions. Node 2 monitors soil and weather variables using the same sensors and makes decisions at the local level using the microcontroller. Node 2 makes decisions about motor control based on soil moisture content to enhance irrigation. Data from Node 2 is transmitted to the main node periodically.

3) Main Node Monitoring and User Interface Unit

The main node is the central unit for monitoring and user interaction in the system. It receives data from Node 1 and Node 2 and combines the data for processing. The main node shows real-time values of the sensors and the system status on an LCD connected to it. The system supports on-site monitoring. After collecting data from the sensor nodes, the main node waits for one minute. It then disconnects from the sensor nodes and connects to a Wi-Fi network. Finally, the combined data uploads to a cloud platform and an online mobile application.

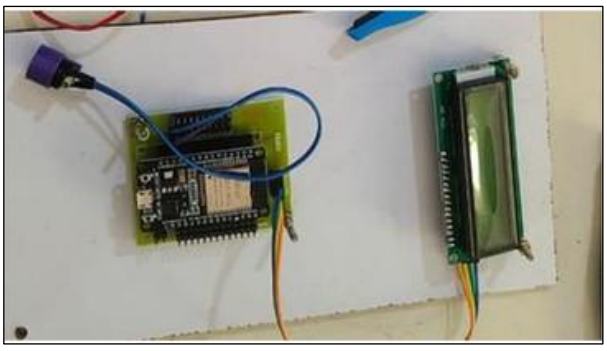


Figure 2: Experimental Setup Of Main Node (Rx).
Source: Authors, (2026).

IV. METHODOLOGY

The existing system adopts a node-based system over wireless monitoring of agriculture and provision of automatic irrigation. System operation will involve data collection procedures of the environment, on site data processing, transmission of data wirelessly and long distance monitoring via cloud network. The installed sensing nodes, which are called Node 1 and Node 2, exist in the agricultural field at different points. The nodes are powered by a solar power unit that is backed by rechargeable lithium-ion battery and a voltage regulation circuit to give continuous stable power. In these nodes, there are various sensors that detect moisture of soil level, temperature, humidity, rainfall, water level and motion sensors.The sensors constantly scan the field and the environmental parameters to be able to generate real-time data concerning human conditions of crops as well as soils.

The sensing node is equipped with an ESP32or NodeMCU microcontroller to work on the sensor data obtained. The sensor readings are compared against preset threshold values and the irrigation motor is automatically turned on or off by a controller with the use of a relay module. This is a local control mechanism that enables the system to be reactive without having to be connected to the internet all the time. The data that is gathered at the field nodes is sent wirelessly, and it is uploaded to a cloud platform through the main node. This information can be monitored remotely in agricultural conditions and irrigation status by using a mobile application. This type of controlled communication will decrease the amount of power consumed, reduce the use of Wi- Fi frequently, and increase the reliability of the system, particularly in remote agricultural settings.

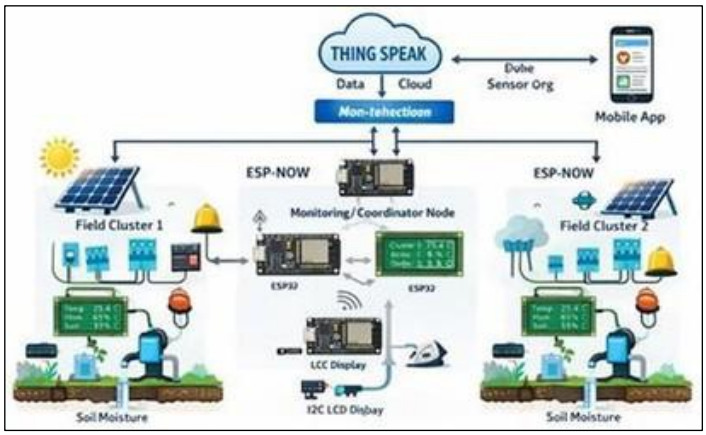


Figure 3: Block Diagram Of Proposed Design (Cluster-Based WSN Architecture).
Source: Authors, (2026).

V. COMPARISON WITH TRADITIONAL SYSTEMS

Table 1 highlights the advantages of the proposed system over conventional irrigation and monitoring approaches.

Table 1: Comparison Table.

Parameter	Traditional System	Proposed System
Monitoring	Manual	Automatic
Irrigation Control	Manual	Smart Control
Power Source	Grid Power	Solar Power
Water Usage	High	Optimized
Remote Monitoring	Not Available	Mobile App

Source: Authors, (2026).

VI. RESULTS & DISCUSSION

The proposed IoT-based smart agriculture system was successfully implemented and tested in real-time conditions, as evident from the images of the hardware setup. Two sensor nodes were used to monitor the soil moisture, temperature, humidity, rainfall, and motion. The central receiver and control unit was the main ESP32-based node. The whole system was powered by a solar panel and 18650 Li- ion rechargeable batteries.

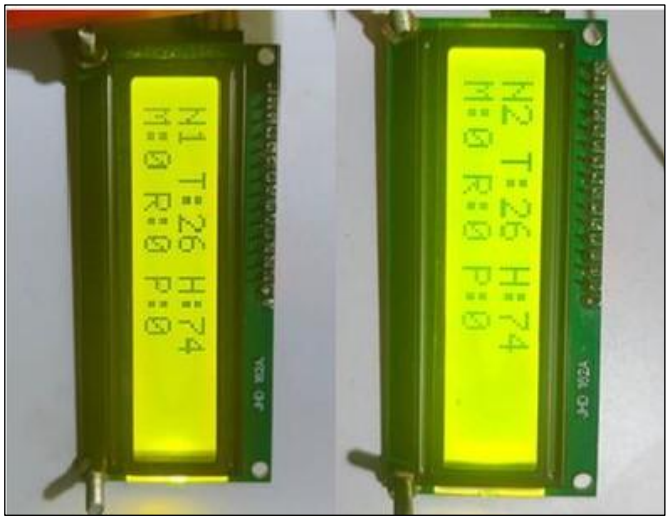


Figure 4: Real-time LCD monitoring Node 1 and 2 (Tx).
Source: Authors, (2026).

A. Motion Detection Performance.

Case 1: No Motion Detected (P = 0)

Under the normal field environment, the LCD display indicated parameters like the node identifications, temperature, humidity, soil moisture conditions, rainfall conditions, and the motion value were indicated as zero. P = 0 meant that no movement was in the area under observation. In this scenario, the system would keep on doing regular environmental checks, and the irrigation management was to be performed solely in reliance on the soil moisture. This guaranteed the appropriate water use and the constant functioning of the systems.

Case 2: Motion Detected (P = 1)

In the event that the movement was detected in the monitored region, the motion sensor output was switched to P = 1. This update would be reflected instantly on the display, and this proved that the sensor was able to detect motion. The quick response achieved dependable sensing attributes and wireless data transmission between field nodes and the central node. The results of both sensing nodes were consistent, and this indicated the reliability and scalability of the system.

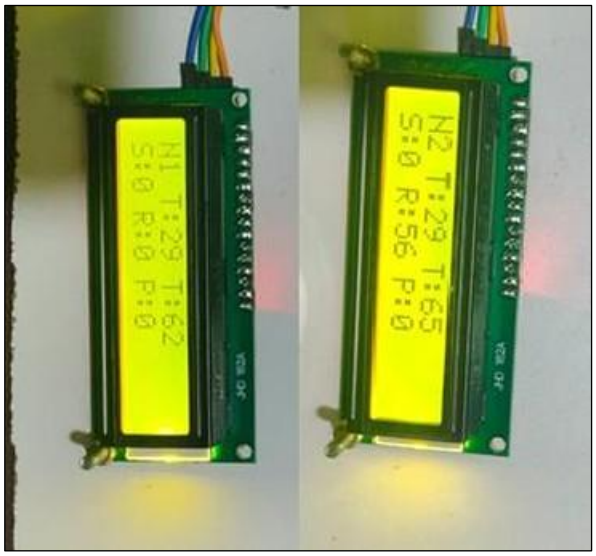


Figure 5: Real-time LCD monitoring of Main Node (Rx).
Source: Authors, (2026).

Case 3: Motion Sensor - P:0

Under normal conditions, the LCD displayed the following readings: Node ID: N2, Temp: 28°C, Hum: 52-53%, Moisture (S): 0, Rain (R): 56, and Motion (P): 0. This indicates that there was no motion detected, and therefore the system was in monitoring mode. The irrigation system relied solely on the soil moisture level.

Case 4: Motion Sensor - P:1

With the detection of motion by the transmitter node, the receiver displayed the following readings: Node ID: N2, T:28°C, H:53%, S:0, R:0, P:1. The quick change from P:0 to P:1 confirms that there was motion detected. This also confirms that the wireless communication system is functioning well and that there is real-time synchronization between the sensor node and the master receiver unit.

Rainfall Detection Analysis

During the test, the system logged Node ID: N2, T:28°C, H:53%, S:0, and R:0. This shows that there was no rainfall detected and the sensor plate was dry. The R:0 value also shows that the rain sensor was in its normal dry state with no water droplets on the sensor. However, when rainfall happens, the sensor reading changes from R:0 to R:1 because of the higher conductivity on the sensor plate. This reading is then transmitted to the main node and shown on the LCD display. This makes it possible for automatic irrigation control to prevent overwatering and water wastage.

Soil Moisture-Based

Irrigation Response During the test, the system logged Node ID: N2 with S:0. This shows that the soil was moist above the dry level, and the pump was in the OFF state. However, when the soil moisture level goes below the set value (S:1), the motor turns on automatically. This shows that the irrigation system has closed-loop control with very little human intervention.

Wireless Communication Performance

The communication network connecting N1, N2, and the central node performed well under all test scenarios. The data from the sensors measured at each node was sent and received correctly with no signs of data loss. The information transfer happened in a very short time span, enabling the control unit to process the data and make changes to the system operations instantly. This quick communication enabled the control unit to make irrigation decisions instantly based on real-time field conditions. The combination of

ESP-NOW communication for local node communication and Wi-Fi communication for updating data remotely functioned without any interruptions. Both communication systems functioned in perfect harmony, ensuring a continuous flow of data even after multiple cycles of data transmission. The system functioned flawlessly under all test conditions, with no signs of unexpected shutdowns or communication losses.

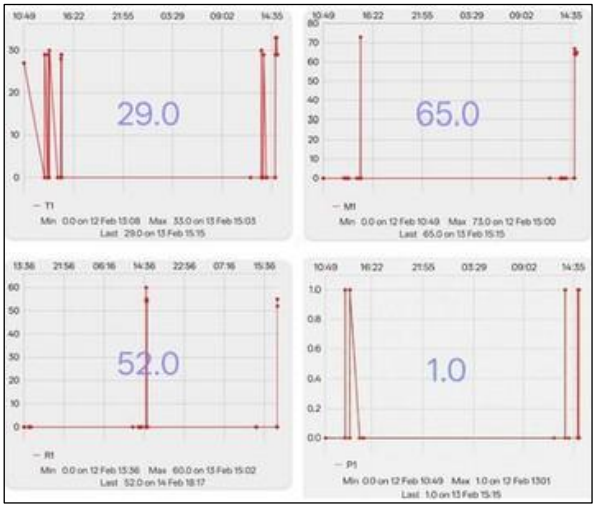


Figure 6: Real-time Graphs from Tx-Node1 (Temperature, Moisture, Rain, Motion Sensor Values).
Source: Authors, (2026).

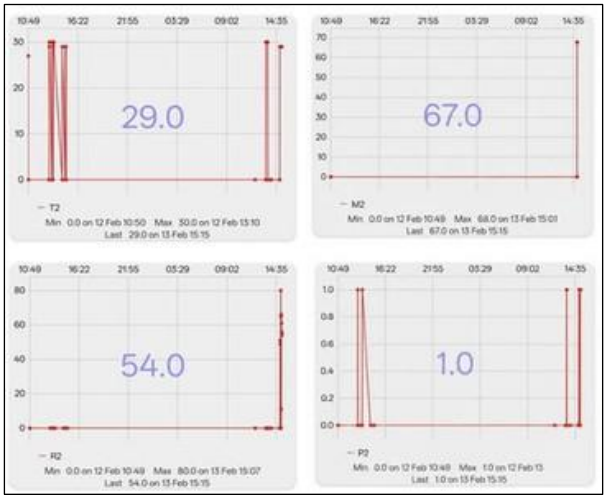


Figure 7: Real-time Graphs from Tx-Node2 (Temperature, Moisture, Rain, Motion Sensor Values).
Source: Authors, (2026).

Figures shows the real-time graphs of Tx-Node1 and Tx-Node2 for temperature, soil moisture, rain detection, and motion detection. The readings from the sensor remained constant in normal environmental conditions. The temperature readings were around 29-30°C for Node1 and 52-54°C for Node2 during peak measurements. The moisture levels remained constant, indicating proper soil condition monitoring without any abrupt changes. The rain sensor output changed distinctly between low (0) and high (1), indicating proper detection of rainfall events. The motion sensor output changed rapidly between 0 and 1 upon detecting motion, indicating proper intrusion detection. From the graphs, it can be seen that there is synchronized data transmission from both the transmitter nodes. This indicates the efficacy of the proposed wireless monitoring system.

Solar Energy Performance

The solar panel was able to power the ESP32, sensors, LCD, and wireless communication components effectively. The 18650 Li-ion battery was also able to provide a backup power source effectively, even when the sunlight changed temporarily. This is evidence that the system is effective for agricultural fields that are remote and require little maintenance.

Comparative Analysis

Compared to traditional manual systems, the proposed model cuts down on labor and reduces water waste with automatic control. It enhances crop protection by using real-time monitoring and allows for scalable multi-node deployment. Overall, it provides a smarter and more efficient farming solution.

Future Enhancements

Then, we are thinking of incorporating LoRa so that the system can extend its range and remain connected within the fields. After that, we will implement AI to detect problems in the crops before they become major issues. Other ideas are in the pipeline, including a smart dispenser that will deliver the correct amount of fertilizer only where it is needed, push notifications that will send notifications to your phone at the correct time, and a camera that will detect any unwanted visitors.

Overall Observation

During the testing phase, N1 and N2 ensured that their sensors were functioning properly. There were no significant changes or fluctuations in the values of temperature, humidity, soil moisture, rainfall, and motion. The ESP-NOW communication feature functioned properly, sending packets with little delay and no losses. On the receiving end, the values were displayed properly on the screen as they passed through the "listening," "displaying," and "updating" phases. When the sensor detected motion, it responded immediately, providing us with a real-time perspective of the intruders. The node network is very reliable for communication, consumes very little power, and can be established in an agricultural field without any special preparations.

VII. CONCLUSION

This paper presented an IoT-based smart agriculture monitoring and irrigation system that uses two sensor nodes and one main node to collect and send real-time field data. The combination of solar power and low-power wireless communication allows for continuous operation in remote areas. Automatic irrigation, which relies on soil moisture, reduces both water wastage and manual work. Experimental results show better efficiency, reliability, and scalability when compared to traditional methods. This makes the system a practical and cost-effective solution for precision agriculture.

VIII. ACKNOWLEDGEMENT

The authors genuinely appreciate the Department of Electronics and Communication Engineering at Vignan's Lara Institute of Technology and Science for providing the essential resources, guidance, and ongoing support that made this research possible and successful throughout the entire project development phase.

IX. AUTHOR'S CONTRIBUTION

Conceptualization: Kota Venkat Kumar, Marneedi Soujanya, Karnati Chaitanya Keerthi, Mohammed Mastan Vali Yash, Kodavandla Vignesh, Sravan Sikakolli.
Methodology: Kota Venkat Kumar, Marneedi Soujanya, Karnati Chaitanya Keerthi, Mohammed Mastan Vali Yash, Kodavandla Vignesh, Sravan Sikakolli.
Investigation: Kota Venkat Kumar, Marneedi Soujanya, Karnati Chaitanya Keerthi, Mohammed Mastan Vali Yash, Kodavandla Vignesh, Sravan Sikakolli.
Discussion of results: Kota Venkat Kumar, Marneedi Soujanya, Karnati Chaitanya Keerthi, Mohammed Mastan Vali Yash, Kodavandla Vignesh, Sravan Sikakolli.
Writing – Original Draft: Kota Venkat Kumar, Marneedi Soujanya, Karnati Chaitanya Keerthi, Mohammed Mastan Vali Yash, Kodavandla Vignesh, Sravan Sikakolli.
Writing – Review and Editing: Kota Venkat Kumar, Marneedi Soujanya, Karnati Chaitanya Keerthi, Mohammed Mastan Vali Yash, Kodavandla Vignesh, Sravan Sikakolli.
Resources: Kota Venkat Kumar, Marneedi Soujanya, Karnati Chaitanya Keerthi, Mohammed Mastan Vali Yash, Kodavandla Vignesh, Sravan Sikakolli.
Supervision: Kota Venkat Kumar, Marneedi Soujanya, Karnati Chaitanya Keerthi, Mohammed Mastan Vali Yash, Kodavandla Vignesh, Sravan Sikakolli.
Approval of the final text: Kota Venkat Kumar, Marneedi Soujanya, Karnati Chaitanya Keerthi, Mohammed Mastan Vali Yash, Kodavandla Vignesh, Sravan Sikakolli.

X. REFERENCES

[1] A. Ray, D. De, and S. Bandyopadhyay, "IoT-based smart agriculture: Toward making the fields talk," IEEE Consumer Electronics Magazine, vol. 7, no. 1, pp. 40-47, Jan. 2018.

[2] L. Ruiz-Garcia, L. Lunadei, P. Barreiro, and J. I. Robla, "A review of wireless sensor technologies and applications in agriculture and food industry," Sensors, vol. 9, no. 6, pp. 4728-4750, 2009.

[3]M. Ayaz, M. Ammad-Uddin, Z. Sharif, A. Mansour, and E. M. Aggoune, "Internet-of-Things (IoT)-based smart agriculture: Toward making the fields talk," IEEE Access, vol. 7, pp. 129551-129583, 2019.

[4] J. Gubbi, R. Buyya, S. Marusic, and M. Palaniswami, "Internet of Things (IoT): A vision, architectural elements, and future directions," Future Generation Computer Systems, vol. 29, no. 7, pp. 1645-1660, 2013.

[5] P. Sethi and S. R. Sarangi, "Internet of Things: Architectures, protocols, and applications," Journal of Electrical and Computer Engineering, vol. 2017, pp. 1-25, 2017.

[6] S. Ramesh, M. Balaji, and K. Srinivasan, "Smart irrigation system using IoT," International Journal of Engineering Research & Technology, vol. 7, no. 5, pp. 1-4, 2018.

[7] A. Jawad, R. Nordin, S. Gharghan, A. Jawad, and M. Ismail, "Energy-efficient wireless sensor networks for precision agriculture: A review," Sensors, vol. 17, no. 8, pp. 1-25, 2017.

[8] K. A. Patil and N. R. Kale, "A model for smart agriculture using IoT," in Proc. International Conference on Global Trends in Signal Processing, Information Computing and Communication (ICGTSPICC), Dec. 2016, pp. 543-545.

[9] S. R. Nandhini and S. N. Siva, "IoT-based smart agriculture system," International Journal of Advanced Research in Computer Science, vol. 8, no. 3, pp. 1-5, 2017.

[10] Effah, E., Thiare, O., & Wyglinski, A. M. (2024). Hardware Evaluation of Cluster-Based Agricultural IoT Network. IEEE Access, 12, 33628-33651.

[11] Saini, M. K., & Saini, R. K. (2020). Agriculture monitoring and prediction using Internet of Things (IoT). PDGC 2020 - 2020 6th International Conference on Parallel, Distributed and Grid Computing, 53-56.

[12] TENCON 2015 - 2015 IEEE Region 10 Conference. (2015). IEEE.

[13] Ali, H., Farooque, A. A., Abbas, F., Yaqub, R., Abdalla, A., & Soora, P. (2024). An IoT based Weather Monitoring System for Smart Agriculture. 2024 IEEE Conference on Technologies for Sustainability, SusTech 2024, 378-382.

[14] Effah, E., Thiare, O., & Wyglinski, A. M. (2024). Hardware Evaluation of Cluster-Based Agricultural IoT Network. IEEE Access, 12, 33628-33651.

Journal of Engineering and Technology for Industrial Applications

ISSN ONLINE: 2447-0228

ITEGAM-JETIA

Manaus, v.12 n.60, p.1487-1495. July/August, 2026.
DOI: https://doi.org/10.5935/jetia.v12i60.4355

RESEARCH ARTICLE OPEN ACCESS

IMPLEMENTATION AND SIMULATION OF SWITCH CAPACITOR PASSIVE RC INTEGRATOR IN DEEP SUB MICRON TECHNOLOGY

Mehulkumar Patel*[1], Kehul Shah[2], Haresh Judal[3], Devendra Patel[4] and Roshni Chaudhari[5]

[1, 3, 4, 5]Electronics & Communication Engineering Department, Government Engineering College Patan, Gujarat, India.
[2]Assistant Registrar,Academics, Institute of Technology, Nirma University, Gujarat, India.

[1]http://orcid.org/0009-0005-4067-6149, [2]http://orcid.org/0009-0004-6207-7617, [3]http://orcid.org/0000-0003-2851-9421, [4]http://orcid.org/0009-0000-8222-6684, [5]http://orcid.org/0009-0004-7886-8317

Email:*mehul.patel@gecpatan.ac.in, kehulshahm@gmail.com, haresh.judal@gecpatan.ac.in, devendra.patel@gecpatan.ac.in, Roshni.chaudhari@gecpatan.ac.in

ARTICLE INFO

Article History
Received: March 27, 2026
Reviewed: April 27, 2026
Accepted: July 27, 2026
Published: August 31, 2026

Keywords:
RC Integrator,
CTI (Continuous Time Integrator),
DTI (Discrete Time Integrator),
SCI (Switched Capacitor Integrator),
MOSFET Switch

ABSTRACT

Switches and capacitors are utilized in place of a resistor R in the switched-capacitor circuit, with a MOSFET serving as the switch. In this paper, the standard RC integrator is compared with the switch capacitor RC integrator. The design is simulated first, and solutions to the design issues are explored and implemented in 180nm technology. The analysis demonstrates that NMOS transistor performance strongly depends on the W/L ratio. As resistance decreases sharply with increasing W/L, current delivery efficiency enhances. Drain current increases substantially with larger widths due to improved channel conduction. This study analyzes the electrical behavior of an NMOS transistor for varying device widths while keeping the channel length constant. The investigation focuses on the effect of the width-to-length (W/L) ratio on drain current (I_D), on-resistance (R_{on}), and related process parameters. The results demonstrate a strong dependence of I_D and R_{on} on device geometry, consistent with MOSFET theory.

Copyright ©2026 by authors and Galileo Institute of Technology and Education of the Amazon (ITEGAM). This work is licensed under the Creative Commons Attribution International License (CC BY 4.0).

I. INTRODUCTION

RC Integrator can be used as low-pass filter in many applications.In devices like variable speed wipers and pacemakers, it can also serve as a timer[1]. Large-value resistors, which take up a lot of chip space, are required for typical RC circuits. Switches and capacitors are used in place of resistors in Switched-Capacitor (SC) circuits, which can assist in minimizing the chip area. It uses two switches to control the flow of charges into and out of a capacitor. The capacitance ratio determines the characteristics of a switched capacitor circuit. One capacitor C and two switches S_1 and S_2 take the place of the resistor R in switched capacitor integrator circuits (SCI). This is shown in Figure 1 [2], [3].

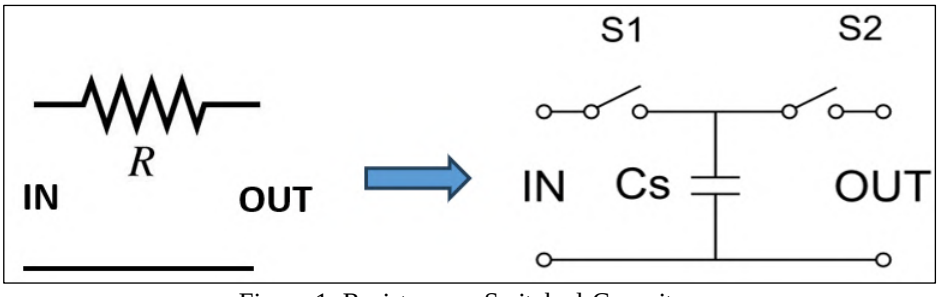


Figure 1: Resistor as a Switched-Capacitor.
Source: Authors, (2026).

The value of the capacitor C_s and the switching frequency f determine the value of resistance R.

$$R = \frac{V}{I} = \frac{1}{C_s f} \tag{1}$$

In this work, the switch is implemented using MOSFET transistors, as shown in Figure 2. They provide fast, low-power, accurate, and easily integrable switching, which is essential for precise charge transfer. When a MOSFET is used as a switch, it has some nonidealities, which are discussed in the next section [4], [5].

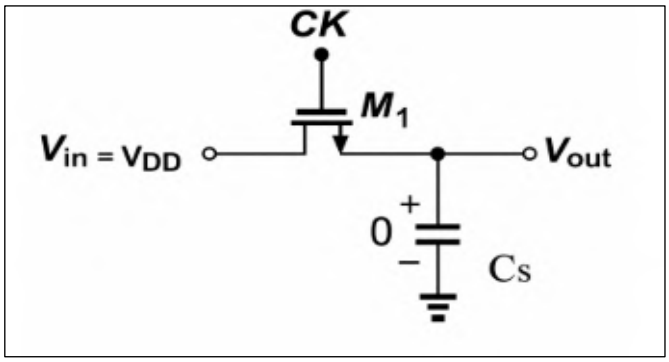


Figure 2: Switched Capacitor Resistor.
Source: Authors, (2026).

II. NONIDEALITIES OF MOSFET SWITCH

Three sorts of nonideal effects can occur when a MOSFET is employed as a switch: (i) Non-Linear R_{on} (ii) Charge Injection and (iii) Clock Feed Through [6-8].

II.1 NON-LINEAR R_{on} (*B*etween Drain and Source)

The $nMOS$ is ON by applying a positive gate signal equal to V_{DD}. When the value of $V_{GS} - V_{thn}$ become grater then V_{DS}, the $nMOS$ is operating in the triode region. The current I_D is given by equation 2 [9].

$$I_D = \mu_n C_{ox} \frac{W}{L} (V_{DD} - V_{in} - V_{thn}) V_{DS} \tag{2}$$

The equivalent resistance R_{on} is found by dividing V_{DS} by with I_D (here body effect has ignored.)

$$R_{on} = \frac{V_{DS}}{I_D} = \frac{1}{\mu_n C_{ox} \frac{W}{L} (V_{DD} - V_{in} - V_{thn})} \tag{3}$$

The R_{on} depends on the input signal V_{in} , therefore, its value changes with V_{in} .The R_{on} The size of an nMOS transistor is small because the $\mu_n C_{ox}$ is large. The PMOS transistor is large because the $\mu_p C_{ox}$ is small. Consequently, a low value of R_{on} makes the pMOS transistor less appropriate. Compared to both nMOS and pMOS, the CMOS transmission gate (TG) has a higher value of R_{on}. The values of $R_{on}$for nMOS, pMOS, and TG are displayed in Figure 3.

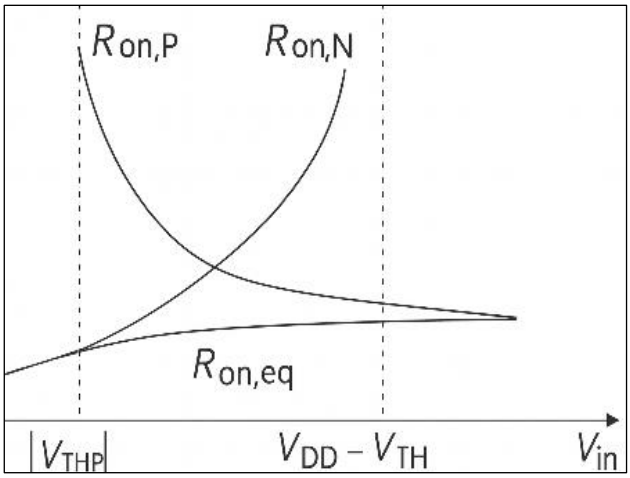


Figure 3: R_{on} for pMOS, nMOS, and TG.
Source: Authors, (2026).

II.2 CHARGE INJECTION

A channel is created between the source and drain when nMOS is turned on. Equations 4 [10], [11] provide the charge Q_{ch} stored in the channel.

$$Q_{ch} = WLC_{ox}(V_{DD} - V_{in} - V_{thn}) \quad (4)$$

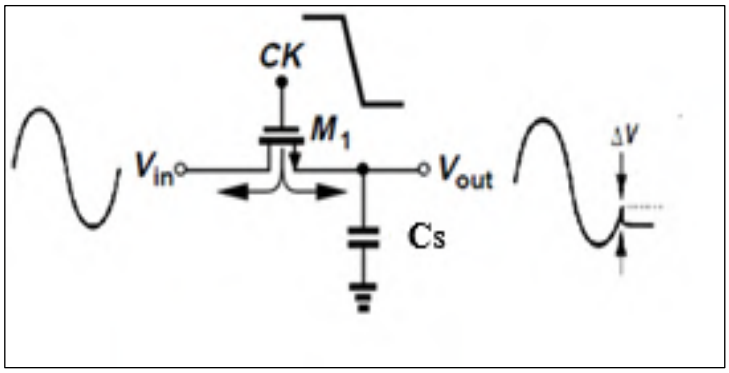


Figure 4: Charge Injection Effect on MOS Switch.
Source: Authors, (2026).

When the nMOS turned off, the charge present in the channel is distributed between the capacitor and the input, as shown in Figure 4 [12]. The clock turnoff slope, the input-to-output capacitance ratio, and the drain-source voltage factors all affect this charge. This charge does not affect the input side, but it changes the voltage stored on the output capacitor C_s as shown in equation 5.

$$\Delta V = Q_{ch}/2C = WLC_{ox}(V_{DD} - V_{in} - V_{thn})/2C \quad (5)$$

II.3 CLOCK FEED THROUGH

The parasitic capacitance between the MOSFET's terminals must be depicted as indicated in Figure 5 to comprehend the clock feed-through effect. In this case, the nMOS is operating in the Triode region and is regarded as being ON. The clock signal passes via the gate-source and gate-drain capacitances as the gate clock signal rises [13], [14].

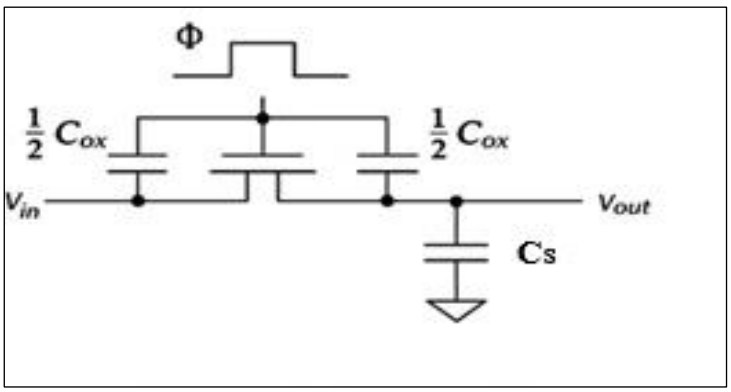


Figure 5: Clock feed through Effect on MOS Switch.
Source: Authors, (2026).

The input signal V_{in} is available at the output capacitor when the nMOS is turned on by applying V_{DD} at the gate terminal. In this instance, V_{out} is unaffected by the capacitive feed-through and the capacitor C_s charged to V_{in}. The nMOS switches off when the clock signal changes to low. In this instance, the capacitance C_s and the gate-drain/source capacitance are separated by a (capacitive) voltage divider. As a result, equation 6 provides the value of a clock signal port that is present across C_s.

$$\Delta V_{load} = \frac{C_{overlap}(V_{DD} - V_{ss})}{C_{overlap} + C_{load}} \quad (6)$$

Where $C_{overlap}$ is the overlap capacitance, and its value is given by equation 7.

$$C_{overlap} = C_{ox}WLD \quad (7)$$

The gate length that overlaps the drain and source is represented by the symbol, LD in Equation (7).

III. SOLUTION OF MOSFET NONIDEALITIES

The following techniques can reduce the nMOS Switch's nonidealities [15], [16].

III.1 NON-LINEAR R_{on} (Between Drain and Source)

The value of R_{on} can be reduced by increasing the W/L ratio or reducing V_{in} and V_{thn}.The R_{on} remains almost constant for the transmission gate if the switch is replaced by a transmission gate.

III.2 CHARGE INJECTION

As illustrated in Figure 6, connect a dummy switch in series with a nMOS switch. The dummy switch can be made to be half the size of the primary switch. Both the source and the drain are connected. When the nMOS switch is off, the dummy switch compensates for the charge by allowing the 50% channel charge to flow toward the capacitor (C_s) [17].

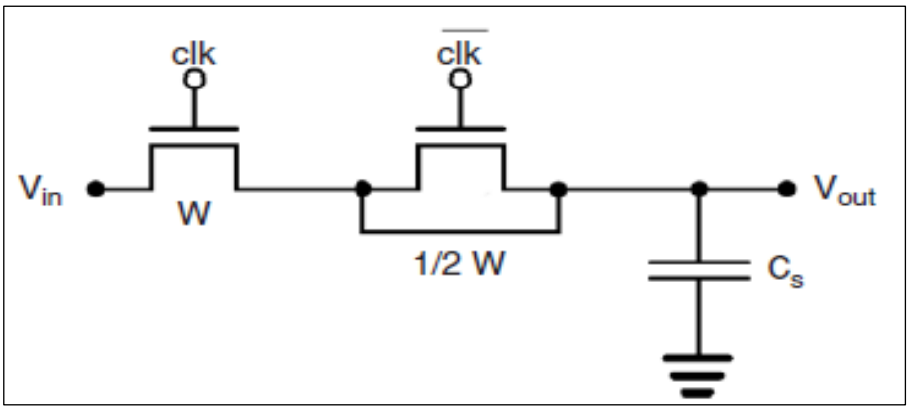


Figure 6: Use of a dummy switch to remove Charge Injection.
Source: Authors, (2026).

III.3 CLOCK FEED THROUGH

Here, the dummy switch suppresses the effect of clock feed through, as shown in Figure 7. A dummy transistor M_2 removes the charge introduced by the primary transistor. After M_1 shuts off and M_2 turns on, the channel charge deposited by M_1 on C_s is absorbed by M_2 to form a channel because the M_2 is driven by $\overline{CK}$. The charge injected by M_1, Δ_{q1} is equivalent to the charge absorbed by M_2 if $W_2 = 0.5W_1$.

$$\Delta_{q1} = \frac{W_1 L_1 C_{OX}}{2}(V_{CK} - V_{in} - V_{THN})$$

$$\Delta_{q2} = W_2 L_2 C_{OX}(V_{CK} - V_{in} - V_{THN})$$

If $W_2 = 0.5W_1$ and L_2=L_1, the effect of clock feedthrough is suppressed. The whole charge in V_{out} is going to be zero as per equation (8).

$$-V_{CK}\frac{W_1 C_{OV}}{W_1 C_{OV} + C_S + 2W_2 C_{OV}} + V_{CK}\frac{2W_2 C_{OV}}{W_1 C_{OV} + C_S + 2W_2 C_{OV}} = 0 \qquad (8)$$

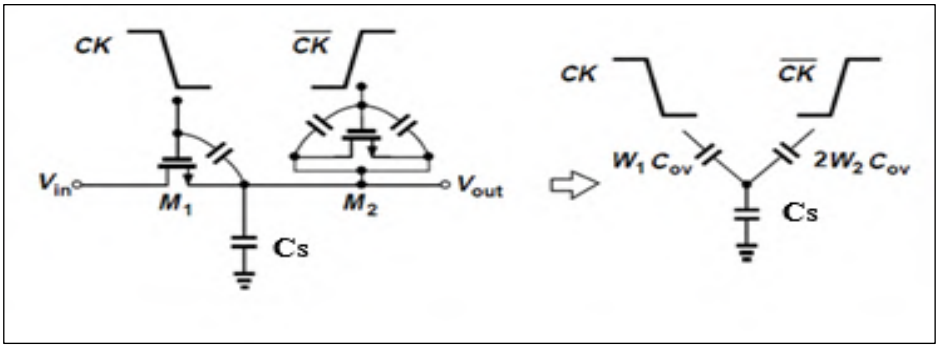


Figure 7: Use of the TG switch to remove Clock Feed Through.
Source: Authors, (2026).

IV. RESULTS AND DISCUSSION

This study analyzes the electrical behavior of an NMOS transistor for varying device widths while keeping the channel length constant. The investigation focuses on the effect of the width-to-length (W/L), ratio on drain current (I_D), on-resistance (R_{on}), and related process parameters. The results demonstrate a strong dependence of I_D and R_{on} on device geometry, consistent with MOSFET theory. MOSFETs exhibit electrical characteristics highly dependent on device geometry. In this work, NMOS properties are evaluated for various widths while keeping the channel length constant (L= 0.18 µm). The study investigates the effects of W/L scaling on on-resistance (R_{on})) and drain current (I_D) [18]. Modern semiconductor design relies on MOSFET scaling, which has a direct impact on power consumption, device performance, and switching speed. A key component of both digital and analog circuits, the NMOS transistor has properties that are strongly influenced by its physical shape. The W/L ratio is one of these characteristics that significantly influences channel conduction capabilities. This work assesses the electrical properties of NMOS for various widths between 2 µm and 100 µm. A fixed channel length of 0.18 µm is shared by all devices [19]. Quantifying the effects of W/L scaling on drain current (I_D), on-resistance (R_{on}), and overall conduction behaviour is the goal. To verify MOSFET operation under strong inversion, these practical findings are contrasted with theoretical predictions [3].

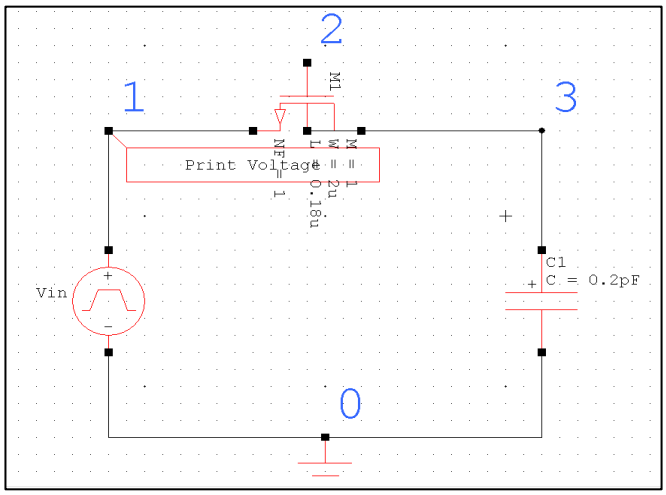


Figure 8: nMOS Switch with Pulse input.
Source: Authors, (2026).

IV.1 NON-LINEAR R_{on} (*B*etween Drain and Source)

To guarantee that differences in electrical behaviour are solely due to geometric scaling, the devices under analysis have the same material and manufacturing parameters. The following is a list of the important parameters:

- Channel length (L): 0.18 µm
- Device widths (W): 2, 10, 20, 50, and 100 µm
- Electron mobility (μ_n): 1400 cm²/V·s
- Oxide capacitance (C_{ox}): 8.65 × 10^{-8} F/cm²
- Oxide thickness (t_{ox}): 4.1 nm
- Oxide permittivity (ε_{ox}): 3.51 × 10^{-13} F/cm
- Vacuum permittivity (ε_o): 8.85 × 10^{-14} F/cm
- Gate voltage (V_{GS}): 1.8 V
- Threshold voltage (V_{thn}): 0.3725327 V

The effective gate overdrive voltage $V_{GS} - V_{thn}$ remains constant at 1.427 V, ensuring consistency in theoretical calculations such as R_{on} and I_D.

$$R_{on} = \frac{V_{DS}}{I_D} = \frac{1}{\mu_n C_{ox}\frac{W}{L}(V_{DD} - V_{in} - V_{thn})} = \frac{1}{\mu_n C_{ox}\frac{W}{L}(V_{GS} - V_{thn})} \quad (9)$$

Table 1: Parameters for variation in Ron with respect to W/L.

Sr.No.	W µm	W/L µm	V_{GS}	V_{thn}	$V_{GS} - V_{thn}$
1.	2	11.11	1.8 V	0.3725327	1.427 V
2.	10	55.56	1.8 V	0.3725327	1.427 V
3.	20	111.11	1.8 V	0.3725327	1.427 V
4.	50	277.78	1.8 V	0.3725327	1.427 V
5.	100	555.56	1.8 V	0.3725327	1.427 V

Source: Authors, (2026).

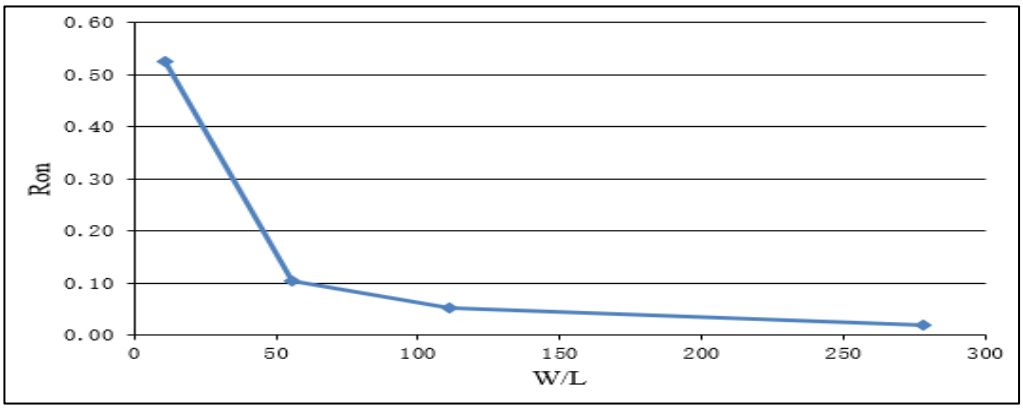


Figure 9: Variation in R_{on} with respect to W/L.
Source: Authors, (2026).

Table 1 illustrates how R_{on} dropped from 0.525 Ω to 0.0105 Ω over the same range. The inverse reliance on W/L is consistent with theory.

IV.1.1 Drain Current $I_D(mA)$

By changing the device width while maintaining a constant channel length, this study examines the electrical behaviour of an NMOS transistor. As indicated in Table 2, the analysis focuses on how the width-to-length (W/L) ratio affects the drain current (I_D). In line with MOSFET theory, the results demonstrate a significant influence of I_D on device geometry.

Table 2: Parameters for variation in $I_D(mA)$ with respect to W/L.

Sr.No.	W µm	W/L µm	I_D(mA)
1.	2	11.11	0.5
2.	10	55.56	2.4
3.	20	111.11	4.72
4.	50	277.78	11.74

Source: Authors, (2026).

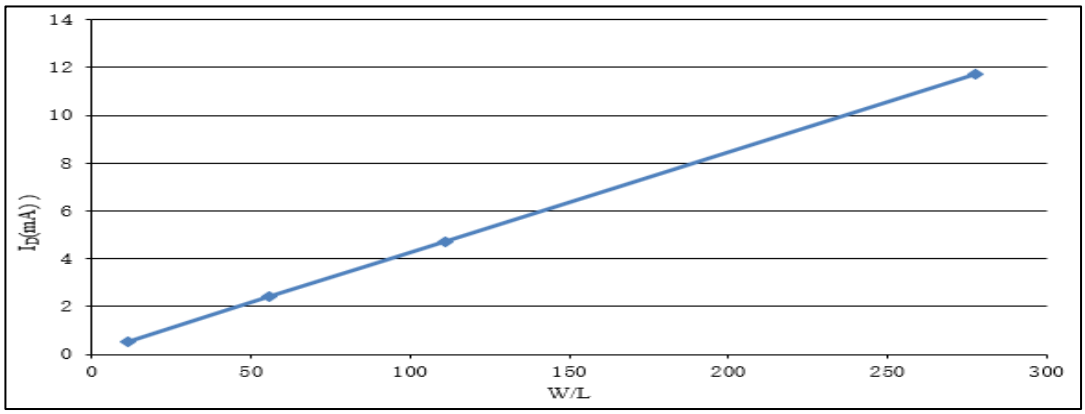


Figure 10: Variation in I_D due to W/L.
Source: Authors, (2026).

Drain current increased from 0.50 mA (W/L = 11.11) to 11.74 mA (W/L = 277.78). This shows proportional scaling with width, which is consistent with strong inversion MOSFET equations.

IV.2 CHARGE INJECTION

Charge injection in MOSFET switches occurs when charge stored in the channel is released into the drain and source nodes during the turn-off transition. The channel charge and the amount of injected charge are directly correlated, which increases with device width and hence with a higher W/L ratio. Table 3 shows that as the W/L ratio increases, more charge is transferred to the connected node, resulting in a larger voltage disturbance across the load capacitance. This explains the observed increase in voltage drop (charge injection effect) with increasing W/L ratio in figure 11.

Table 3: Parameters for voltage drop $(mV)$with respect to W/L.

Sr.No.	W µm	W/L µm	Voltage drop (mv)
1.	2	11.11	0.06
2.	10	55.56	0.28
3.	20	111.11	0.51
4.	50	277.78	1.02

Source: Authors, (2026).

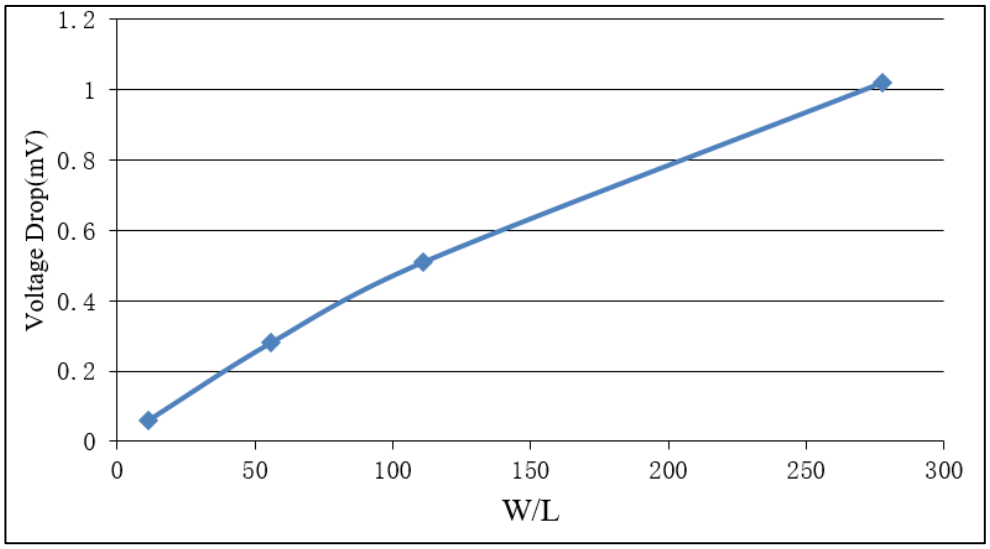


Figure 11: Effect of Charge Injection with respect to W/L.
Source: Authors, (2026).

Figure 11 displays the relationship between the Voltage Drop (in millivolts, mV) and the W/L ratio, which typically represents the width-to-length ratio of a MOSFET, in integrated circuits or electronic design. As the W/L ratio increases, the voltage drop across the component also increases proportionally. Figure 11 illustrates how increasing W/L increases the effect of charge injection from 0.1 to 1.1. In Figure 8, when the width is scaled down from 50 µm to 2 µm, the simulation results in Figures 12 and 13 show a significant reduction in charge injection due to the decreased channel charge associated with smaller device dimensions.

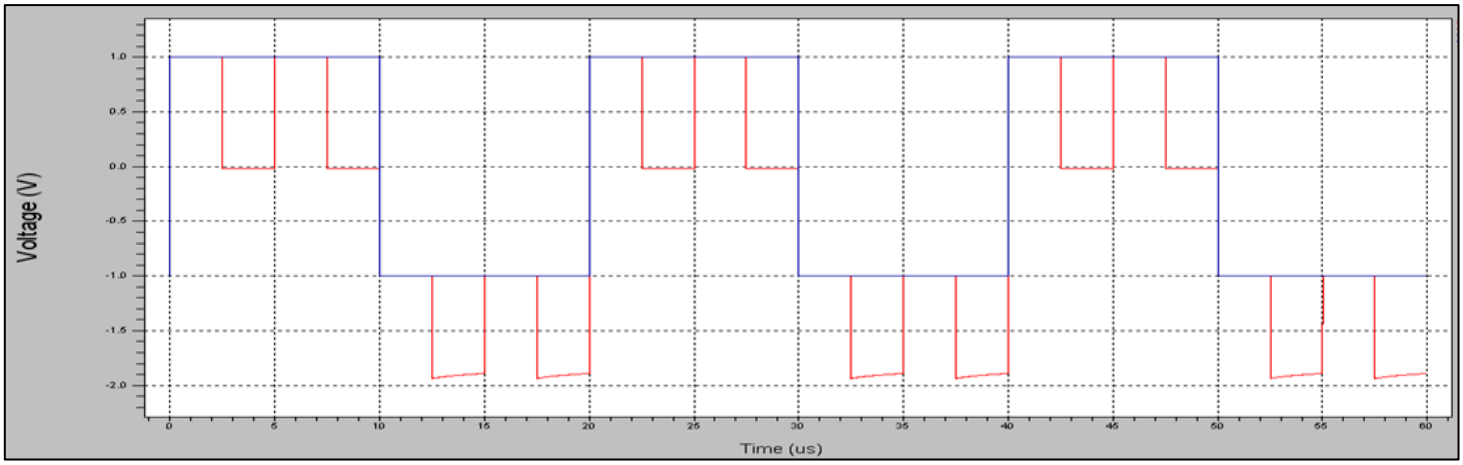


Figure 12: Effect of Charge Injection on W/L for W=50 µm.
Source: Authors, (2026).

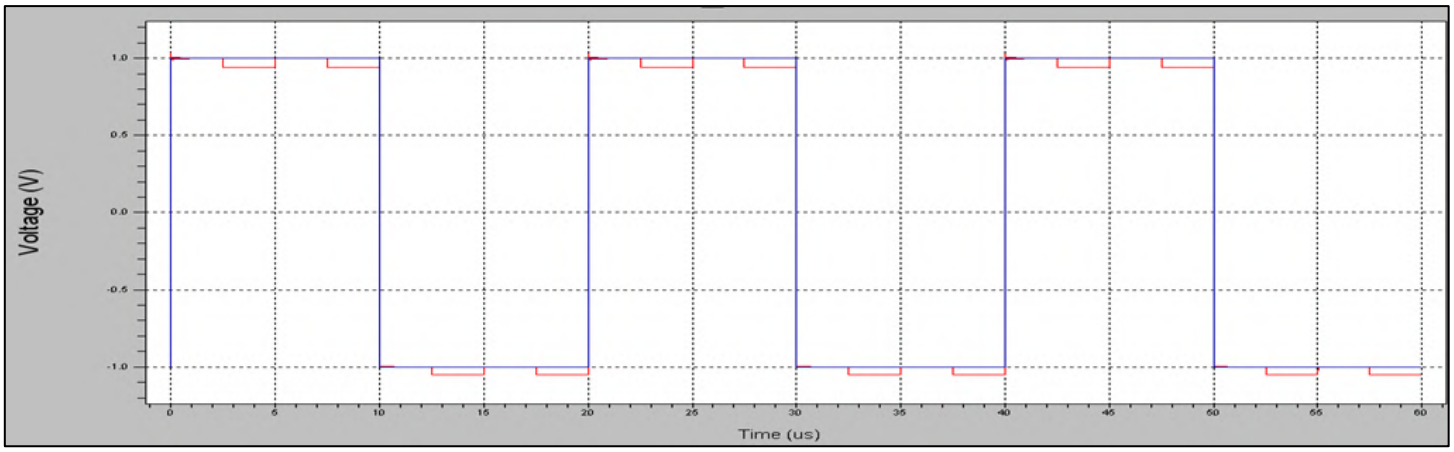


Figure 13: Effect of Charge Injection on W/L for W=2 µm.
Source: Authors, (2026).

IV.3 CLOCK FEED THROUGH

In Figure 8, a dummy switch transistor is added in series with the main switching transistor, as shown in Figure 14. When we simulate Figure 14, it will effectively minimize both charge injection and clock feedthrough effects, as shown in Figure 15. The dummy transistor compensates for the injected charge during switching, resulting in improved accuracy and performance of the circuit. Overall, the combined approach of transistor width reduction and dummy switch implementation proves to be an effective technique for mitigating charge injection effects in switched-capacitor circuits.

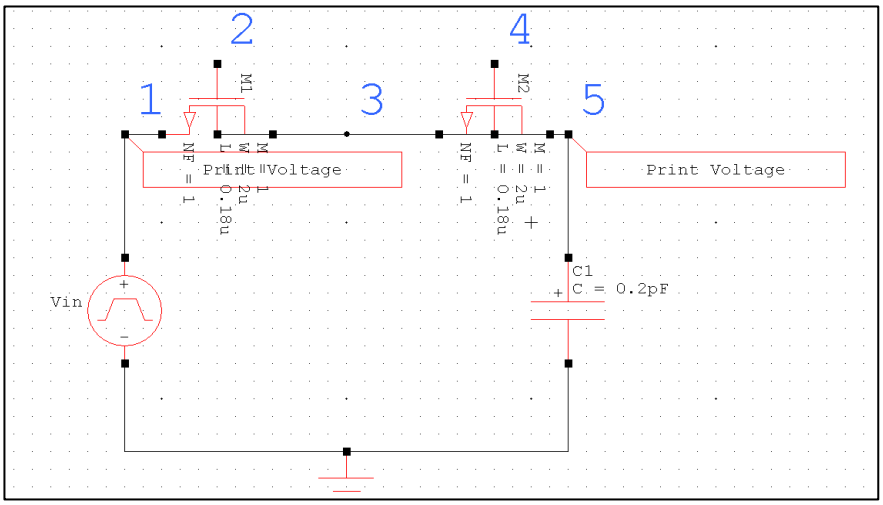


Figure 14: Reduction of clock feed-through using a dummy transistor.
Source: Authors, (2026).

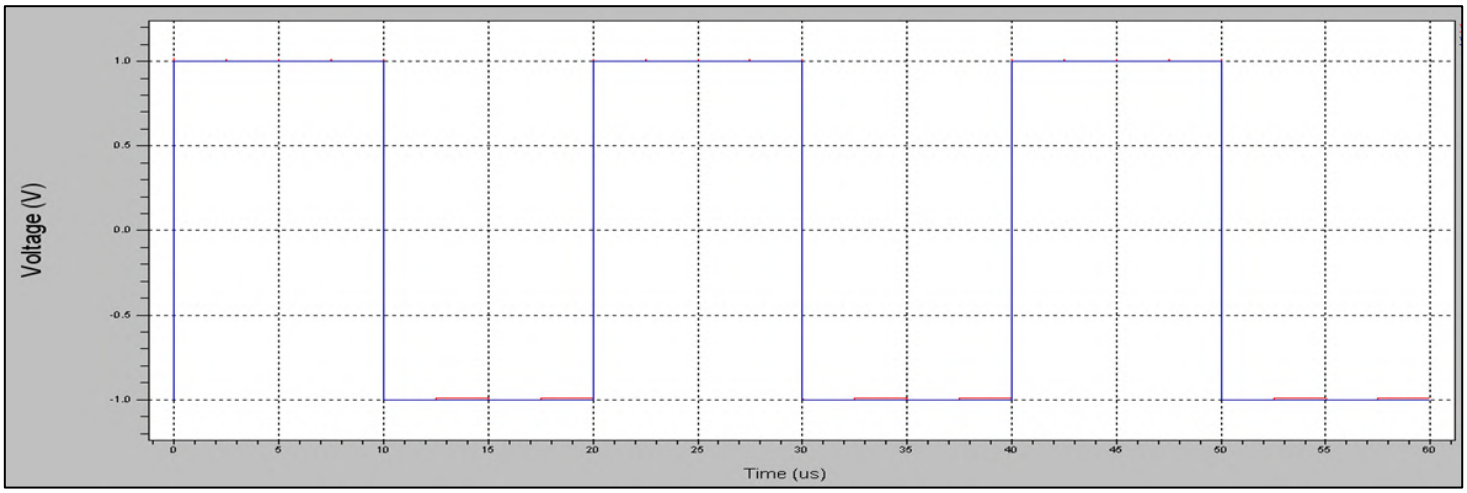


Figure 15: Clock feed through and Charge Injection reduction by dummy transistor.
Source: Authors, (2026).

V. CONCLUSION

The application of MOSFET switches in SC circuits is examined. The MOSEFT switch's shortcomings are described. Implementation and simulation results are presented for the solutions of the MOSEFT switch non-idealities. Increasing W/L improves NMOS performance by increasing I_D and reducing R_{on}. Process parameters were constant, confirming that geometry was the primary factor influencing electrical behavior. These results support further research into NMOS scaling and performance modeling. The analysis reveals that the W/L ratio significantly affects NMOS transistor performance. Important conclusions include:

1. Because of better channel conduction, the drain current rises significantly with wider channels.
2. As W/L increases, on-on resistance drastically drops, improving current delivery efficiency.
3. Process parameters that are consistent guarantee that changes are only the result of geometric scaling.
4. Device validity is confirmed by measured results that match theoretical MOSFET models.

These results contribute to MOSFET scaling and performance modelling research and encourage additional device optimisation studies.

VI. AUTHOR'S CONTRIBUTION

Conceptualization: Mehulkumar Patel, Kehul Shah, Haresh Judal, Devendra Patel and Roshni Chaudhari.
Methodology: Mehulkumar Patel, Kehul Shah, Haresh Judal, Devendra Patel and Roshni Chaudhari.
Investigation: Mehulkumar Patel, Kehul Shah, Haresh Judal, Devendra Patel and Roshni Chaudhari.
Discussion of results: Mehulkumar Patel, Kehul Shah, Haresh Judal, Devendra Patel and Roshni Chaudhari.
Writing – Original Draft: Mehulkumar Patel, Kehul Shah, Haresh Judal, Devendra Patel and Roshni Chaudhari.
Writing – Review and Editing: Mehulkumar Patel, Kehul Shah, Haresh Judal, Devendra Patel and Roshni Chaudhari.
Resources: Mehulkumar Patel, Kehul Shah, Haresh Judal, Devendra Patel and Roshni Chaudhari.
Supervision: Mehulkumar Patel, Kehul Shah, Haresh Judal, Devendra Patel and Roshni Chaudhari.
Approval of the final text: Mehulkumar Patel, Kehul Shah, Haresh Judal, Devendra Patel and Roshni Chaudhari.

VII. REFERENCES

[1] P. E. Allen and D. R. Holberg, *CMOS Analog Circuit Design*, 2nd ed. Oxford University Press, 2002.

[2] R. J. Baker, H. W. Li, and D. E. Boyce, *CMOS Circuit Design, Layout, and Simulation*. IEEE Press, 1998.

[3] C. Karnstedt, "Optimizing Power of Switched Capacitor Integrators in Sigma-Delta Modulators," *IEEE Circuits Syst. Mag. - IEEE CIRCUITS SYST MAG*, vol. 10, pp. 64–71, 2010, doi: 10.1109/MCAS.2010.938640.

[4] A. Patel and R. Sadiwala, "Low Voltage CMOS Switch Capacitor Circuit," in *2021 7th International Conference on Electrical Energy Systems (ICEES)*, 2021, pp. 629–634. doi: 10.1109/ICEES51510.2021.9383686.

[5] K. D. Sadeghipour, "A new passive sample and hold structure for high-speed, high-resolution ADCs," *AEU - Int. J. Electron. Commun.*, vol. 65, pp. 799–805, 2011.

[6] E. M. Saad, "Switched capacitor circuits and their applications: An overview," in *Proceedings of the 19th National Radio Science Conference (NRSC)*, 2002, pp. 51–59.

[7] S. W. Park and S. Yan, "Practical Issues Designing Switched-Capacitor Circuits," 2011.

[8] L. Dai and R. Harjani, "CMOS Switched-Op-Amp-Based Sample-and-Hold Circuit," *IEEE J. Solid-State Circuits*, vol. 35, no. 1, pp. 109–113, 2000.

[9] Y. Yoon and H. Kim, "A High-Power and Highly Linear CMOS Switched Capacitor," *IEEE Microw. Wirel. Components Lett.*, vol. 20, no. 11, 2010.

[10] S. K. G. Dundar, "Charge Sharing Switched Capacitor Integrator," in *MIXDES*, Wroclaw, Poland, 2010.

[11] M. D. Bryant, S. Yan, R. Tsang, B. Fernandez, and K. K. Kuma, "A Mixed Signal (Analog-Digital) Integrator Design," *IEEE Trans. Circuits Syst. I*, vol. 59, no. 7, pp. 1446–1456, 2012.

[12] A. K. Mal and R. Todani, "Non Overlapping Clock Generator for Low Frequency Switched Capacitor Circuits," in *IEEE Students' Technology Symposium*, IIT Kharagpur, 2011.

[13] M. Liu, *Demystifying Switched-Capacitor Circuits*. Elsevier, 2006.

[14] H. Yoshizawa, T. Yabe, and G. C. Temes, "High-precision switched-capacitor integrator using low-gain op-amp," *Electron. Lett.*, vol. 47, no. 5, 2011.

[15] R. Gao, Z. Li, and J. Xu, "Characterization of Single-Poly EEPROM in 0.18μm BCD(Bipolar-CMOS-DMOS) Technology," in *2023 6th International Conference on Electronics Technology (ICET)*, 2023, pp. 366–370. doi: 10.1109/ICET58434.2023.10211490.

[16] Q. Wang *et al.*, "MOSFET modeling of 0.18μm CMOS technology at 4.2K using BP neural network," *Microelectronics J.*, vol. 132, p. 105678, 2023, doi: https://doi.org/10.1016/j.mejo.2022.105678.

[17] A. Danchiv and M. Bodea, "Charge Injection Induced Sample and Hold Error Analysis," *IEEE*, 2009.

[18] T. Yang *et al.*, "Review of Topologies, Application Areas, Modeling, and Control Methods for Switched Capacitor Circuits," *IEEE Trans. Power Electron.*, vol. 39, no. 4, pp. 4091–4116, 2024, doi: 10.1109/TPEL.2024.3350158.

[19] M. Hasan-Sagha and M. Jalali, "Very high-speed and low-voltage open-loop dual-edge triggered sample and hold circuit in 0.18 um CMOS technology," in *IEEE-ICSE*, Kuala Lumpur, Malaysia, 2012.

Journal of Engineering and Technology for Industrial Applications

ISSN ONLINE: 2447-0228

ITEGAM-JETIA

Manaus, v.12 n.60, p.1496-1502. July/August, 2026.
DOI: https://doi.org/10.5935/jetia.v12i60.4366

RESEARCH ARTICLE OPEN ACCESS

PERFORMANCE EVALUATION OF INDIA'S SOFTWARE INDUSTRY USING DATA ENVELOPMENT ANALYSIS: A LONG-TERM FIRM-LEVEL STUDY

Sajal K Das*[1], Jamal Hussain[2]

[1, 2]Department of Mathematics and Computer Science, Mizoram University, Mizoram , India.

[1]https://orcid.org/0000-0002-5427-7799, [2]https://orcid.org/0000-0001-5553-3654

Email:*sajalhere@gmail.com

ARTICLE INFO

Article History
Received: March 27, 2026
Reviewed: April 27, 2026
Accepted: July 27, 2026
Published: August 31, 2026

Keywords:
Software firms,
performance trends,
resource utilization,
efficiency analysis,
India.

ABSTRACT

The software industry in India has emerged as a major driver of economic growth, export expansion, and structural transformation within the service sector. In this context, assessing firm-level efficiency is essential for understanding the sector's contribution to economic development. This study empirically examines the technical efficiency of selected Indian software companies over the period 1992–2023 using an input-oriented Data Envelopment Analysis (DEA) model under variable returns to scale (VRS). Firm-level panel data are utilized, with total liabilities and fixed assets as inputs and net sales and profit after tax as outputs. The findings reveal substantial heterogeneity in efficiency performance across firms over time. While leading firms operate close to the efficiency frontier, several firms exhibit persistent inefficiencies, indicating significant scope for improved resource utilization and scale optimization. The results highlight the importance of managerial capability, financial structure, and efficient capital allocation in sustaining the long-term contribution of the software sector to India's economic development.

Copyright ©2026 by authors and Galileo Institute of Technology and Education of the Amazon (ITEGAM). This work is licensed under the Creative Commons Attribution International License (CC BY 4.0).

I. INTRODUCTION

The software industry in India has made a significant contribution to the country's gross domestic product as well as has a remarkable share in the service sector. The software industry, also referred to as Information Technology (IT) or Information and Communication Technology (ICT) is capable of influencing various production sectors such as healthcare, transportation, finance, banking, insurance, logistics, retail, manufacturing, communication and media, entertainment and education [1–5]. In a study Jain et al. [6] conclude that fast delivery, internationalization and adaptation to evolving technologies are key drivers of the growth of the software industry. In 2007, global IT services expenditure amounted to USD 747 billion which grew about 32.13 % in 2018 to 987 billion (USD) [7], [8]. At the end of 2026, the IT industry is expected to reach approximately USD 1.65 trillion, with continued expansion which is influenced by digital transformation initiatives, hybrid cloud migrations, and AI-related service demand. With the global adoption of IT, the Indian software sector is crucial in catering to the demand of the global market. Many Indian IT firms had a global presence. In the Indian economy, the software sector is one of the most dynamic and emerging industries, contributing significantly to economic growth, export earnings, employment generation, and service-sector expansion since the early 1990s. Indian software sector grew rapidly in post-economic liberalization, in 1991-92 from a tiny domestic activity, catering to the domestic market demand to a global competitive industry with huge world market share [9], [10]. It began to play a role in the productivity growth and structural transformation [11]. The significance of the IT sector can be gauged by the contribution to nation's Gross Domestic Product (GDP) which was 1.2% in 1998 growing to 7.9 % in 2018. The Indian IT and IT-enabled services (IT-BPM) sector kept on growing as a sole contributor to the economic growth and exports. The sector generated 91 billion USD as total revenue in 2019, expanded significantly contributing around 7.4 percent of India's GDP and about USD 245 billion in revenues by FY 2022 (CEIC; ESC India Statistical Year Book). Similarly, in FY 2023–24, the industry's overall revenues were roughly USD 253.9 billion, with software services exports constituting the majority of the earnings and maintaining a GDP share of about 7.5–8 percent (ESC India Statistical Year Book). In FY 2024–25, industry expanded nearly USD 283 billion in total revenues, with export earnings near USD 224.4 billion.

Outlooks for 2025 indicate that the IT sector's contribution to GDP may approach around 10 percent, supported by accelerating digital transformation, cloud adoption, and AI-enabled services across the economy. Behind this trajectory of expansion, the Indian IT also passed through major setbacks due to 2008 financial crisis on the technological front [9], [10]. The success of the software sector is enhanced by skilled workers as Indian IT sector is human capital-intensive. Many studies [2], [5], [12–14] suggest the association of the workers' skills, health, efforts and individual performance. It is essential to assess the efficiency of the IT sector in applied economics and development studies. Sales maximization is the guiding principle for software companies [15] as it leads to maximization of market share. The performance of the Indian software/IT sector has been assessed using both parametric and non-parametric approaches. Data Envelopment Analysis (DEA), introduced by [16], is a widely applied non-parametric frontier technique for measuring the relative efficiency of decision-making units (DMUs) characterized by multiple inputs and outputs. DEA is employed to assess the performance of IT/software sector across the globe. The studies [17–20] used DEA to analyse the efficiency of the IT sector in India. The efficiency reflects the extent to which firms optimally utilize available financial and capital resources. To hold on a progressive long- term growth it is essential to enhance the efficiency and productivity with focus on international competitiveness, particularly in a developing economy like India [21]. The underlying insights essential for policymakers and industry stakeholders is inferred from such empirical evaluation of efficiency. Although the Indian software industry has grown rapidly, there is a lack of long-term empirical evidence on firm-level efficiency in the Indian context. Literature is largely dominated by short-term assessments, which offer only partial insights into the sector's evolution [22]. Although several studies have examined efficiency in the Indian IT sector, most are confined to short time spans or specific sub-periods. There is limited empirical evidence based on long-term firm-level data covering more than three decades, including phases of liberalization, global expansion, financial crises, and post-pandemic recovery. This study addresses this gap by providing a comprehensive static DEA-based efficiency assessment for the period 1992–2023. Since the Indian software sector accounts for a significant share of service-sector value added and export earnings, improvements in firm-level efficiency directly influence aggregate productivity, employment generation, and foreign exchange earnings. Therefore, analyzing technical efficiency is not merely a firm-level exercise but also a development-oriented investigation with macroeconomic relevance.

II. RELATED WORK

The significance of liberalization, globalization, and technological advancement in improving the performance of Indian firms has been addressed in several studies [11], [21]. Efficiency analysis has long occupied a central place in applied economics, particularly in studies examining firm and industry performance. Data Envelopment Analysis (DEA), introduced by [16] and extended by [23], has been widely used to estimate the technical efficiency in situations involving multiple inputs and outputs without imposing restrictive functional form assumptions. DEA has been widely applied to assess the performance in the service sector and knowledge-intensive industries, where production processes are complex and heterogeneous [24]. Numerous studies on software as well as information technology firms have reported considerable variations in efficiency and productivity dynamics across firms, which are often attributed to firm size, resource utilization, and managerial competence [20], [25].In the Indian context, ample evidence exists concerning IT/software firms. In an analysis, Mathur [17] used an input-oriented Data Envelopment Analysis (DEA) model to assess the technical efficiency of 92 Indian software companies for the year 2005–2006 and concluded that only 16 companies were efficient. Mathur [18] assessed the technical efficiency of the Information and Communication Technology (ICT) sector in 12 selected countries using Data Envelopment Analysis. In this study, it was found that the IT sector of Taiwan was the most efficient, while the Indian IT sector was the least efficient. Later, Bhattacharjee [26] estimated the technical efficiency of Kolkata's Software Technology Parks (STPs) for IT–ITeS firms under the variable returns to scale (VRS) assumption using an output-oriented DEA model. The study included all IT and IT-enabled service firms in eastern India for the period 1993 to 2007. The study revealed that the efficiency of large firms improved during the study period and further concluded that segment-specific policies may lead to improved productivity compared with uniform policies. Overall Technical Efficiency (OTE), Pure Technical Efficiency (PTE), and Scale Efficiency (SE) were estimated using DEA. Total sales were considered the output, while employment, expenditure on computers and electronic equipment, operating expenditure, and power, fuel, and water charges were used as inputs.

The mean PTE score is observed to be around 0.6, indicating nearly 40% pure technical inefficiency among the firms. Poor infrastructure, particularly inadequate power supply, is identified as a major constraint affecting performance. The percentage of efficient firms in terms of PTE is lowest in 2003–04 (20.83%) and highest in 2005–06 (40.28%), thereby showing a cyclical pattern over the period. Scale inefficiency increased over time. By [22] analyzed productivity growth trends for 72 Indian software companies from 1999 to 2008. It was found that only 65% of the inputs were optimally utilized by the software firms in India. It was also inferred that larger software firms tended to operate closer to the efficiency frontier, while smaller firms exhibited greater inefficiency and volatility. Domestic software firms were found to be more efficient than the foreign-owned firms. Das [27] evaluated the performance of Indian ITeS industry during 2000-01 to 2014-15 by using a two-stage empirical method to estimate technical efficiency through Data Envelopment Analysis (DEA). The DEA results revealed that managerial inefficiency is the major contributor to overall technical inefficiency compared with inefficient scale of production. Das and Datta [20] applied a two-stage data envelopment analysis method to assess the trends and determinants of technical efficiency in the Indian IT and ITeS industry from the year 2000-01 to 2014-15. In the first stage, output-oriented technical efficiency scores were estimated using CCR, BCC and PK DEA models. In the second stage, the determinants of PK-efficiency were estimated using a random-effects Tobit regression model. The investigation revealed that managerial underperformance was the root cause of overall inefficiency in ITeS companies. By [28] examined the relative efficiency of the top 18 Indian IT software service companies using an output-oriented DEA model. The study assessed overall technical efficiency, pure technical efficiency, and scale efficiency for the period 2010–2017 using CMIE data. Sales expansion and market share growth were considered as the strategic objectives guiding the operations of IT companies. Workers' effort was used as the primary input variable, while net sales turnover and net profit after tax were selected as output variables, with profit after tax serving as an indicator of cost-effectiveness. The results indicated a very high average efficiency score of 96%, suggesting only a limited potential improvement of approximately 4% in output levels at the existing input configuration.

The concept of Functional Efficiency Quality (FEQ) is proposed by [29]. They estimated FEQ for Indian software firms using a sensitivity function-based approach. It is observed that existing literature lacks a comprehensive long-term firm-level static DEA assessment which captures the structural evolution of the industry across the liberalization, global financial crisis, and post-pandemic periods (1992–2023).

III. DATA AND METHODOLOGY

III.1 OBJECTIVE OF THE STUDY

The objectives of the paper are as follows: i) To estimate the technical efficiency of selected Indian software firms using an input-oriented Data Envelopment Analysis (DEA) model under variable returns to scale (VRS) for the period 1992–2023. ii) To examine long-term industry-level efficiency trends across different structural phases of the Indian software industry. iii) To analyse firm-level efficiency heterogeneity and discuss its implications for India's economic development.

III.2 METHODOLOGY

To determine the trends in performance, the notion of technical efficiency is adopted and estimated using an input-oriented Data Envelopment Analysis (DEA) technique. DEA is a non-parametric approach used to evaluate the relative efficiency of similar entities, known as decision making units (DMUs), that employ multiple inputs and multiple outputs [30-32]. The efficiency of a DMU is measured as the relationship between inputs and outputs.It is measured as the ratio of weighted sum of outputs to the weighted sum of inputs when multiple DMUs are involved, as shown below.

$$Efficiency(e) = \frac{\sum_{i=1}^{n} O_i}{\sum_{i=1}^{n} I_i} \quad (1)$$

In the above equation, e denotes the efficiency; Oi and Ii represent outputs and inputs respectively, and n denotes the total number of DMUs considered. DEA has evolved significantly over the past five decades and has been extensively used in diverse fields to assess performance as well as for benchmarking [33]. A DEA model proposed by Charnes et al. [16] uses a linear programming technique known as the Charnes, Cooper and Rhodes (CCR) model, which assumes constant returns to scale (CRS). The efficiency score estimated using the CCR model is referred to as overall technical efficiency. Another variation of DEA model, based on the assumption of variable returns to scale (VRS), was proposed by incorporating a convexity condition into the CCR linear programming model. This model is known as Bankers-Charnes-Cooper (BCC) model [23]. Three types of efficiency – pure technical efficiency (PTE), scale efficiency (SE) and overall technical efficiency (OTE) can be estimated using the DEA method. Efficiency can be estimated using either of these two DEA models [24], [32], [34]. In the present empirical study, technical efficiency is estimated using an input-oriented Data Envelopment Analysis (DEA) framework under variable returns to scale (VRS). The input orientation is considered appropriate as software firms have greater managerial control over resource utilisation rather than output levels, which are largely influenced by market demand and global outsourcing trends. The VRS specification enables separation of pure technical efficiency from scale efficiency, thereby capturing the heterogeneity in operational scale at the firm level.

III.3 DATA AND VARIABLE SPECIFICATION

Data for software firms in India were collected for the period 1992-2023. To obtain a comprehensive long-term overview of the performance of the software sector, twelve companies that operated continuously from 1992 to 2023 were selected for the empirical analysis. The basis for selecting these companies is their continuous survival in the market over three decades, including the periods of global crises. This selection was made to meet the objectives of this study. The literature considers different variables for efficiency assessment in software/IT firms. Profit (net profit or profit after tax) has been considered as an output variable in several studies [28], [25]. Income has also been used as an output variable in some studies [10], [25]. Several empirical studies have assessed firm performance using sales as the output variable [17], [22], [28]. In our study, input and output variables reflecting financial performance are used. The two input variables selected are total liabilities(I_1) and fixed assets (I_2). The output variables used in this study are net sales (O_1) and profit after tax (O_2). Profit after tax is a good measure of corporate profitability. The DEA Program (DEAP) software was used for estimation of efficiency [34].

IV. EMPIRICAL RESULTS AND DISCUSSIONS

The overall experimental result is presented under the descriptive performance trends and efficiency trends of Indian software companies. Both these assessments are elaborated in the section below.

IV.1 DESCRIPTIVE PERFORMANCE TRENDS OF INDIAN SOFTWARE COMPANIES

In this section, the performance of Indian software firms is discussed in detail. The performance analysis is carried out using industry-level averages of sales, profit, fixed assets, and total liabilities for the period 1992–2023.

IV.1.1 Growth Trends in Sales and Profit

The analysis carried out on the firm's average sales trend shows a clear and sustained growth throughout the study period. The finding revealed that in the early liberalization phase (1992–2000), sales growth remained relatively modest. During the post-2000 period, a sharp increase is observed, accompanied by the expansion of export-oriented IT services and increased global demand. Significant scalability and market penetration of Indian software firms were observed from 2010 onward, accompanied by rapid growth in Sales. In early 1990s the profit trend remained low, while gradually increasing in the mid-2000s onward which shows a similar pattern to Sales.

Though there is existence of slight ups and downs, profitability increased and remained relatively consistent over years, which suggests improved cost management and greater operational maturity. Steady rise in sales and rising profit indicates that the growth has been as supported by improved financial performance. The post-2010 period is therefore considered as an expansion phase, while the phase beginning around 2010 may be characterized as a period of consolidation and maturity.

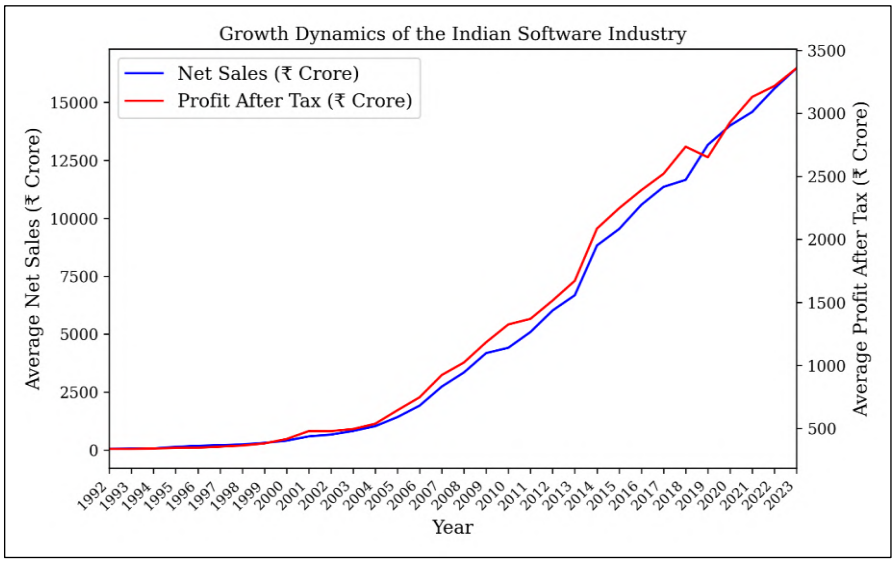


Figure 1: Industry average sales trend for selected software companies.
Source: Author's calculation, CMIE (2026).

IV.1.2 Capital Deepening over Fixed Assets

A remarkable level of capital deepening is revealed by the trend in fixed assets over time. Initially from 1990 to 2003, firms had less fixed assets which indicates low capital intensity in the early phase software sector's evolution. Fixed assets increased from 2004 and continued until 2012, it started to grow more rapidly 2013 onward and the growth continued until 2023. This rise in fixed assets is due to the investments in infrastructure, development centres, and technology platforms. It can be inferred that increased mobilization of advanced IT infrastructure and digital capabilities lead to the rise of fixed assets beyond 2010. A transition toward high-value software services and digital transformation is reflected by this rise.

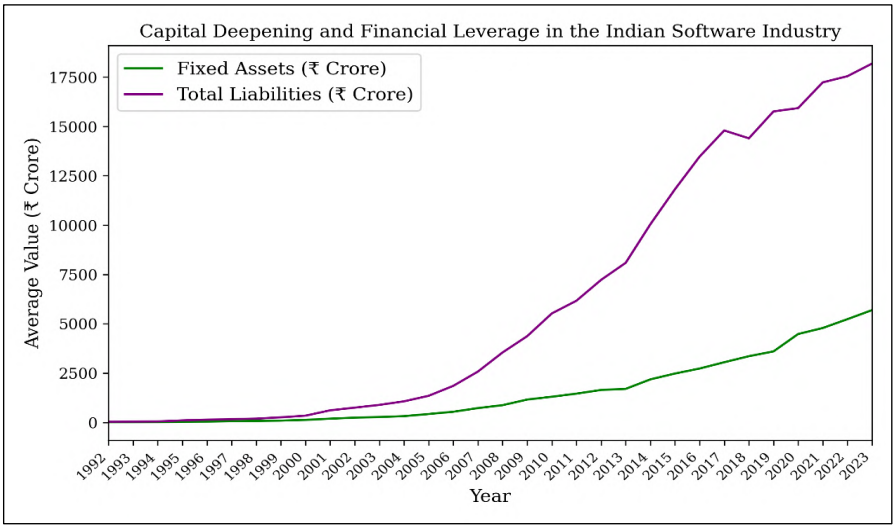


Figure 2: Capital deepening trend estimated on average fixed assets and total liabilities of Indian software companies, 1992–2023.
Source: Author's calculation, CMIE (2026).

IV.1.3 Financial Structure and Liabilities Trend

It can be observed in figure 2, that the company's total liabilities trailed an upward trajectory similar to fixed assets and sales. From 1992-2000, total liabilities of the company were less, but it gradually rose from 2007 onwards. The trend went up till 2017 but sharply went down in 2018. Total liability kept growing continuously until 2023. The dependence of companies on financial leverage is reflected by these rising trends, which also shows its expansion and boosting up in operations. In the periods of global economic stress, particularly around the 2008 financial crisis, company met the setbacks, which is indicated by the ups and down in the trend. It also reflects the company's effort to arise from uncertainty. This reflects an expansion-driven financial structure is depicted by the growth of total liabilities and the intermittent variations point to periods of volatility linked to macroeconomic shocks.

IV.1.4 Software Industry Performance Phases

The trends in all variables are taken together to get an overview of the performance of selected companies. While considering the trends in sales, profit, fixed assets and liabilities, the performance trajectory of the Indian software industry can be broadly classified into three distinct phases. The first phase, Emergence and Stabilization (1992–2000), is characterised by modest growth, limited capital intensity and low financial leverage as the industry established its foundational capabilities. The second phase, Rapid Expansion (2001–2010), shows strong and synchronous growth in sales and profits, with significant build-up of assets and liabilities to scale operations globally. The final phase, Maturity with Periodic Volatility (2011–2023), is marked by sustained top-line growth along with capital deepening, where the maturity of the industry also exposes it to periodic fluctuations in financial performance due to exogenous global economic factors.

IV.1.5 Implications for Efficiency Analysis

It is implied by descriptive trends that output and resource usage have improved substantially, and several economic and technological conditions are responsible for this growth. Therefore, it is significant to assess the relative efficiency instead of absolute performance, which encourages the use of an input-oriented DEA model under variable returns to scale in the consequent analysis.

IV.2 EFFICIENCY TRENDS OF INDIAN SOFTWARE COMPANIES (1992–2023)

An input-oriented DEA under VRS is employed to estimate the technical efficiency scores of selected Indian software companies. The efficiency trends are analysed at three levels: year-wise industry averages, long-term average efficiency, and company-wise efficiency trajectories.

IV.2.1 Year-wise DEA Efficiency Trends

The Technical efficiency score for every year (1992–2023) is estimated using total liabilities and fixed assets as inputs, and sales and profit as outputs. The industry average efficiency trend indicates the presence of many fluctuations over time. There is a gradual improvement in technical efficiency over the study period. The average technical efficiency shows growth from 1993 to 1994 and then continued in a similar manner till 1997. A sharp decrease in 1998 but rose abruptly in 1999 and reached peak at 2000. There was a fall again in 2002 but reversed within a year. The accelerated efficiency during the post-2000 period coincides with export expansion and increased adoption of information technologies. Minor declines are observed during periods associated with global economic uncertainty, particularly around the 2008–09 financial crisis, indicating temporary efficiency disruptions. The ups and downs continued until 2016, presenting a long range of fluctuations. Post-2016, the trend shows a monotonic decrease till 2021. The severe decrease in the year 2020 and with the lowest score 0.70 in 2021 may be attributed to the impacts of COVID-19. The decreasing trend soon reverses by mid-2021 and keeps growing in the later years.

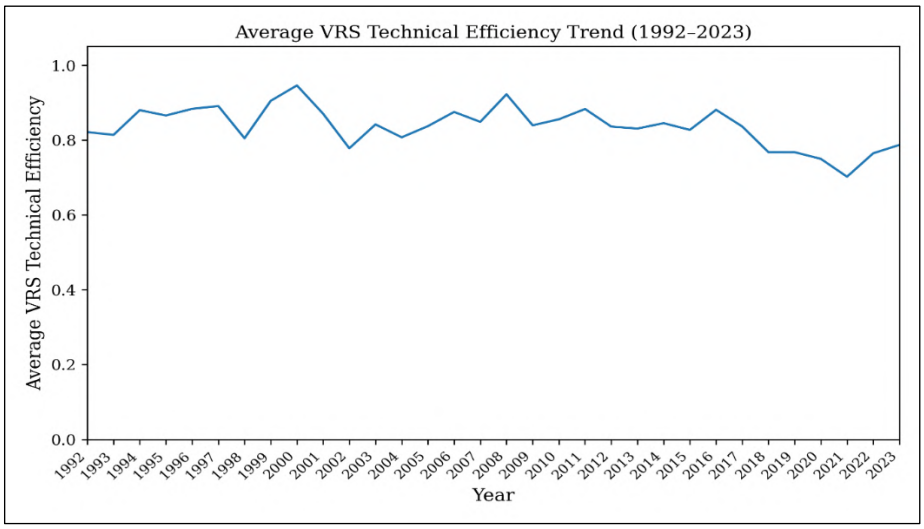


Figure 3: Average VRS technical efficiency trend of selected Indian software companies during 1992–2023.
Source: Author's calculation, CMIE (2026).

IV.2.2 Average Efficiency Trends (1992–2023)

To assess long-term performance, average DEA efficiency scores were computed across the entire period (1992–2023) for the selected software firms. The results show that while several firms consistently operate close to the efficiency frontier, others exhibit persistent inefficiencies. It is observed that the increase in average efficiency leads to the better utilization of financial and capital resources over time. Analysis shows a scope of more improvement, represented by the presence of efficiency gaps across firms, which can be attained through better resource allocation and scale optimization. Rising average efficiency reflects industry maturation, while inter-firm differences highlight heterogeneous managerial capabilities.

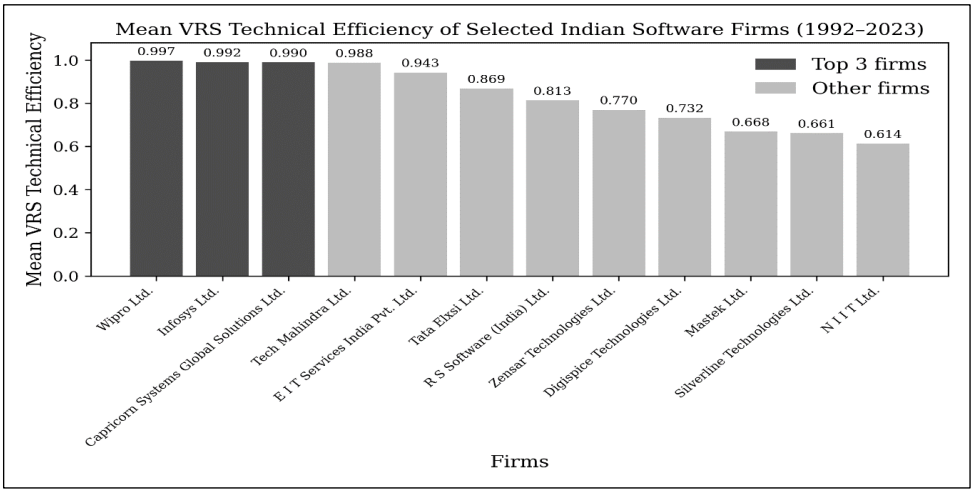


Figure 4: Company-wise VRS technical efficiency of selected Indian software companies during 1992–2023.
Source: Author's calculation, CMIE (2026).

V. CONCLUSIONS

The empirical findings indicate that the Indian software industry has experienced a sustained improvement in technical efficiency over the period under study, albeit with intermittent fluctuations. This upward trend reflects the combined influence of technological progress, industry learning effects, and improvements in financial and managerial practices, leading to enhanced resource utilization capacity over time. However, the efficiency trajectory has not been uniform, as temporary declines are observed during periods of global economic stress, such as the 2008–09 financial crisis and the COVID-19 pandemic, highlighting the industry's sensitivity to external shocks. At the firm level, the analysis reveals a significant degree of heterogeneity in technical efficiency, which persists across time. Larger firms are generally found to operate closer to the efficiency frontier, while small and mid-sized firms exhibit greater inconsistency in efficiency performance. This uneven distribution of efficiency gains suggests that, despite overall progress, substantial scope for improvement remains, particularly among relatively less efficient firms. The presence of persistent inter-firm disparities underscores the importance of factors such as managerial capability, financial structure, and optimal scale of operation in determining firm-level performance. While the gradual rise in average efficiency signifies strengthening operational performance across the industry, continued heterogeneity may have implications for competitiveness, innovation capacity, and long-term sectoral sustainability. In this context, fostering balanced efficiency improvements remains critical for reinforcing the industry's contribution to economic growth and resilience.

VI. AUTHOR'S CONTRIBUTION

Conceptualization: Sajal Kanti Das, Jamal Hussain.
Methodology: Sajal Kanti Das, Jamal Hussain
Investigation: Sajal Kanti Das, Jamal Hussain
Discussion of results: Sajal Kanti Das, Jamal Hussain.
Writing – Original Draft: Sajal Kanti Das.
Writing – Review and Editing: Sajal Kanti Das, Jamal Hussain.
Resources: Jamal Hussain.
Supervision: Jamal Hussain.
Approval of the final text: Sajal Kanti Das, Jamal Hussain.

VII. REFERENCES

[1] E. M. Ahmed, "ICT and human capital role in achieving knowledge-based economy: Applications on Malaysia's manufacturing", J. Inf. Knowl. Manag., vol. 5, no. 2, pp. 117–128, Jun. 2006.

[2] S. Arvanitis and E. N. Loukis, "Information and communication technologies, human capital, workplace organization and labour productivity: A comparative study based on firm-level data for Greece and Switzerland", Inf. Econ. Policy, vol. 21, no. 1, pp. 43–61, Mar. 2009.

[3] M. S. Abdullahi, U. R. Shehu, and B. M. Usman, "Impact of information communication technology on organizational productivity in the Nigeria banking industry: Empirical evidence", Noble Int. J. Bus. Manag. Res., vol. 3, no. 1, pp. 1–9, Jan. 2019.

[4] J. Sandberg, A. Loxbo, and T. H. K. H. Sandberg, "ICT and organizational performance", in Proc. 6th Int. Conf. Enterprise Inf. Syst., pp. 127–133, 2005.

[5] A. Tarutė and R. Gatautis, "ICT impact on SMEs performance", Procedia – Soc. Behav. Sci., vol. 110, pp. 1218–1225, Jan. 2014.

[6] N. K. Jain, S. Celo, and V. Kumar, "Internationalization speed, resources and performance: Evidence from Indian software industry", J. Bus. Res., vol. 95, pp. 26–37, Feb. 2019.

[7] Gartner, "Gartner perspective: IT spending 2010", Gartner Inc., 2009.

[8] Gartner, "Gartner says global IT spending to grow 3.2 percent in 2019", Gartner Inc., 2018.

[9] National Association of Software and Services Companies (NASSCOM), “Impact of the IT-BPO industry in India: A decade in review”, NASSCOM, 2010.

[10] M. Kumar, V. Charles, and C. S. Mishra, “Evaluating the performance of Indian banking sector using DEA during post-reform and global financial crisis”, J. Bus. Econ. Manag., vol. 17, no. 1, pp. 156–172, Feb. 2016.

[11] B. Bosworth and S. M. Collins, “Accounting for growth: Comparing China and India”, J. Econ. Perspect., vol. 22, no. 1, pp. 45–66, Feb. 2008.

[12] C. C. Chang, S. W. Hung, and S. Y. Huang, “Evaluating the operational performance of knowledge-based industries: The perspective of intellectual capital”, Qual. Quant., vol. 47, no. 3, pp. 1367–1383, May 2013.

[13] K. Harriss, “Book review: In an outpost of the global economy: Work and workers in India’s information technology industry”, J. South Asian Dev., vol. 5, no. 2, pp. 293–295, Oct. 2010.

[14] M. H. Kuo and C. Yang, “Does intellectual capital matter? Assessing the profitability and marketability of IC design companies”, Qual. Quant., vol. 46, no. 6, pp. 1865–1881, Oct. 2012.

[15] N. K. Avkiran, “Investigating technical and scale efficiencies of Australian universities through data envelopment analysis”, Socio-Econ. Plann. Sci., vol. 35, no. 1, pp. 57–80, Mar. 2001.

[16] A. Charnes, W. W. Cooper, and E. Rhodes, “Measuring the efficiency of decision making units”, Eur. J. Oper. Res., vol. 2, no. 6, pp. 429–444, Nov. 1978.

[17] S. K. Mathur, “Indian IT and ICT industry: A performance analysis using data envelopment analysis and Malmquist index”, Glob. Econ. J., vol. 7, no. 2, pp. 1–25, May 2007. https://doi.org/10.2202/1524-5861.1259

[18] S. K. Mathur, “Indian IT industry: A performance analysis and a model for possible adoption”, MPRA Paper No. 2368, 2007. https://core.ac.uk/download/pdf/6799223.pdf

[19] B. K. Sahoo, “Ownership, size, and efficiency: Evidence from software companies in India”, Benchmarking Int. J., vol. 23, no. 2, pp. 313–328, Feb. 2016. https://www.sciencedirect.com/org/science/article/abs/pii/S1463577116000469

[20] P. Das and A. Datta, “Performance evaluation of Indian information technology-enabled services (ITeS) industry: An application of two-stage data envelopment analysis”, Int. J. Adv. Manag. Econ., vol. 6, no. 2, pp. 52–70, Apr. 2017. https://managementjournal.info/index.php/IJAME/article/view/49

[21] V. Kathuria, R. Natarajan, and K. Sen, “Growth in Indian manufacturing and services since 1980: Evidence from input–output tables”, World Dev., vol. 44, pp. 245–257, Apr. 2013.

[22] B. K. Sahoo and D. K. Nauriyal, “Trends in and determinants of technical efficiency of software companies in India”, J. Policy Model., vol. 36, no. 3, pp. 539–561, May 2014. https://ideas.repec.org/a/eee/jpolmo/v36y2014i3p539-561.html

[23] R. D. Banker, A. Charnes, and W. W. Cooper, “Some models for estimating technical and scale inefficiencies in data envelopment analysis”, Manage. Sci., vol. 30, no. 9, pp. 1078–1092, Sep. 1984.

[24] W. W. Cooper, L. M. Seiford, and K. Tone, Data Envelopment Analysis: A Comprehensive Text with Models, Applications, References and DEA-Solver Software, 2nd ed., New York, NY, USA: Springer, 2007.

[25] C. Serrano-Cinca, Y. Fuertes-Callén, and C. Mar-Molinero, “Measuring DEA efficiency in internet companies”, Decis. Support Syst., vol. 38, no. 4, pp. 557–573, Jan. 2005.

[26] S. Bhattacharjee, “Efficiency dynamics and sustainability of the Indian IT-ITeS industry: An empirical investigation using DEA”, IIMB Manag. Rev., vol. 24, no. 4, pp. 203–214, Dec. 2012. https://www.sciencedirect.com/science/article/pii/S0970389612000766

[27] P. Das, “An assessment of performance of Indian software industry during 2000–01 to 2014–15 using data envelopment analysis”, Int. J. Eng. Appl. Manag. Sci. Paradig., vol. 44, no. 1, pp. 7–21, 2017.

[28] S. Goyal, A. N. Sah, R. K. Sharma, and J. Puri, “Estimating technical efficiencies of Indian IT companies for setting improvement targets for inefficient companies: An empirical analysis with workers’ effort as key input”, Work, vol. 66, no. 4, pp. 885–900, Aug. 2020. https://pubmed.ncbi.nlm.nih.gov/32925144/

[29] S. K. Das and J. Hussain, “Functional efficiency quality of Indian software industry: A computational approach”, J. Sci. Technol., vol. 12, no. 2, pp. 68–72, 2024. https://stjmzu.org/index.php/journal/article/view/52

[30] H. W. Lampe and D. Hilgers, “Trajectories of efficiency measurement: A bibliometric analysis of DEA and SFA”, Eur. J. Oper. Res., vol. 240, no. 1, pp. 1–21, Jan. 2015.

[31] A. Emrouznejad and G. L. Yang, “A survey and analysis of the first 40 years of scholarly literature in DEA: 1978–2016”, Socio-Econ. Plann. Sci., vol. 61, pp. 4–8, Mar. 2018.

[32] J. Puri and S. P. Yadav, “Performance evaluation of public and private sector banks in India using DEA approach”, Int. J. Oper. Res., vol. 18, no. 1, pp. 91–121, 2013.

[33] A. Mergoni, A. Emrouznejad, and K. De Witte, “Fifty years of data envelopment analysis”, Eur. J. Oper. Res., vol. 326, no. 3, pp. 389–412, Nov. 2025.

[34] N. K. Avkiran, Productivity analysis in the service sector with data envelopment analysis, 3rd ed., Brisbane, Australia: University of Queensland, 2006.

Journal of Engineering and Technology for Industrial Applications

ISSN ONLINE: 2447-0228

ITEGAM-JETIA

Manaus, v.12 n.60, p.1503-1512 July/August, 2026.
DOI: https://doi.org/10.5935/jetia.v12i60.4409

RESEARCH ARTICLE OPEN ACCESS

MULTIMODAL META-LEARNING FOR EARLY RUMOR DETECTION WITH ADAPTIVE DECISION TIMING

El Yazid Gueddoudj*[1], Abdelouahab Attia[3] and Adel Moussaoui[3]

[1]Institute of Architecture and Urbanism, University of Batna1, Batna 05000, Algeria
[1]LRIT laboratory, University of Tlemcen, Tlemcen 13000, Algeria
[2]Department of Computer Science, University Mohamed El Bachir El Ibrahimi of Bordj Bou Arreridj, 34000 Bordj Bou Arreridj, Algeria
[3]Faculty of Mathematics and Computer Science, University of M'sila, PO Box 166 Ichebilia, 28000, M'sila, Algeria.

[1]https://orcid.org/0009-0005-1462-8477, [2]https://orcid.org/0000-0003-1558-7273, [3]http://orcid.org/ 0000-0002-6978-1656

E-mail: *elyazid.gueddoudj@univ-batna.dz, abdelouahab.attia@univ-bba.dz, adel.moussaoui@univ-msila.dz

ARTICLE INFO

Article History
Received on: March 28, 2026
Reviewed on: April 29, 2026
Accepted on: July 01, 2026
Published on: July 31, 2026

Keywords:
Rumor Detection,
Early Detection,
Metalearning,
Social Media,
Adaptive Decision Timing.

ABSTRACT

Early social media rumor detection is essential because it prevents false information from spreading quickly and causing serious harm. Current methods frequently ignore the significance of prompt decision-making in favor of increasing classification accuracy. In this paper, we present a novel framework for early rumor detection that is based on multimodal meta-learning with adaptive decision timing. The method analyzes social media posts as an ongoing stream and learns when enough data has been observed to dynamically identify the best time to make a forecast. By integrating textual, structural, and temporal features, the proposed approach captures complex rumor propagation patterns while jointly optimizing accuracy and detection timeliness. Experimental results on benchmark datasets, including Twitter15, Twitter16, and Weibo, show that the proposed method significantly reduces detection latency, requiring substantially fewer messages for prediction, while maintaining competitive or superior performance compared to state-of-the-art baselines.

Copyright ©2026 by authors and Galileo Institute of Technology and Education of the Amazon (ITEGAM). This work is licensed under the Creative Commons Attribution International License (CC BY 4.0).

I. INTRODUCTION

The danger of false information and rumors spreading has greatly grown due to the quick spread of information on social media platforms. Rapid and widespread rumors can have detrimental effects on society, such as economic disruption, public panic, and disinformation during important events [1]. As a result, creating efficient methods for early rumor detection has emerged as a crucial research task. Existing approaches to rumor detection have achieved notable success by leveraging machine learning and deep learning techniques. Traditional methods such as [2], [3] and [4] rely on handcrafted features and static classifiers, while more recent approaches employ sequential models such as recurrent neural networks and Transformers to capture temporal dependencies in message propagation. Despite these advancements, most existing methods primarily focus on improving classification accuracy and typically assume access to complete or near-complete event sequences. However, prompt detection is just as crucial as precision in practical situations. Rumors might spread far before any action is taken due to delayed detection. Early detection is intrinsically difficult because there is little to no information available at the beginning of an occurrence. Furthermore, the best time to make a trustworthy prediction varies based on the dynamics of each event's propagation. We provide a novel framework based on multimodal meta-learning [5] with adaptive decision timing for early rumor detection in order to overcome these drawbacks. In the suggested method, rumor detection is modeled as a sequential decision-making issue. Incoming messages are processed as a continuous stream by the model, which dynamically determines when enough evidence has been observed to make a prediction. By considering multiple types of information, such as textual content, structural propagation patterns and temporal dynamics, the framework is able to capture comprehensive features of social media events. Furthermore, a meta-learning strategy is applied to facilitate generalization to unseen rumor types, which allows the model to generalize to different propagation patterns. The core of the proposed method is the adaptive decision process, which lets the model automatically find the earliest confident decision time. The proposed model performs early and accurate rumor detection, greatly reducing detection latency while maintaining comparable or higher classification performance compared to existing methods, according to extensive trials carried out on benchmark datasets. The following is a summary of the primary contributions:

1. We propose a multimodal meta-learning framework. It combines textual, structural, and temporal features.
2. We present an adaptive decision timing mechanism that that finds the best prediction point.
3. We ran many tests. They show that our method finds rumors earlier. It needs fewer observations and still has strong classification performance.

The rest of the paper is organized as follows: Section 2 surveys prior work, and Section 3 provides the proposed method and the new framework. Section details the Experimental and the findings. Section 5 provides a discussion of the experimental findings and their analysis. Lastly, Section 6 concludes the paper and future work.

II. RELATED WORK

II.1 RUMOR DETECTION ON SOCIAL MEDIA

The development of manually created characteristics for machine learning algorithms has historically been the primary focus of research on rumor detection. Using both conventional machine learning and deep learning methods, rumor detection on social media has been thoroughly investigated [6]. Early approaches use classifiers like Support Vector Machines and Random Forests in conjunction with manually created features taken from textual content, user profiles, and propagation structures [7]. Although these methods offer preliminary insights, feature engineering and their incapacity to identify intricate patterns restrict their effectiveness. In more recent work, representations are automatically learned from data using deep learning algorithms [8]. The temporal dynamics of message sequences have been extensively modeled using recurrent neural networks, such as LSTM and GRU. By using self-attention methods to capture long-range dependencies, transformer-based models significantly enhance performance. Despite these developments, the majority of current methods, which frequently assume access to full propagation sequences, are primarily concerned with increasing classification accuracy.

II.2 EARLY RUMOR DETECTION

The goal of early rumor detection is to identify rumors when they are just beginning to spread and there is little information available. A number of methods make predictions based on incomplete sequences or preliminary observations in an effort to overcome this difficulty. In order to effectively capture global semantic relations in rumor texts, the authors of [9] built a tweet-word-user heterogeneous graph and proposed a meta-path-based heterogeneous graph attention network framework that uses subgraph attention networks to learn global node relationships and a subgraph-level attention mechanism to fuse node representations. The authors of [10] used transfer learning to extract attitude representations from external stance-classification datasets by utilizing pretrained CNN and BERT models. For early rumor detection, their deep model (CNN-BiLSTM-BERT) combines attitude and content representations. Authors of [11] proposed a deep attention model based on RNNs with soft-attention. Without depending on manually created features, the model accurately identifies long-range dependencies and contextual changes over time. It detects rumors faster and more correctly than state-of-the-art baselines, according to extensive trials on real-world social media datasets. [12] presents a few-shot prototype augmentation framework for low-resource rumor detection. In addition to a metric learning methodology, it uses hierarchical prompt encoding to obtain language/domain-agnostic thread representations and refines prototypes via query-conditioned attention and feature gating. The method is compatible with parallelized streaming settings and achieves cutting-edge cross-lingual/domain performance. To produce predictions at intermediate time steps, sequential models have been modified, as in [13].

Accuracy and timeliness must be balanced, according to recent research, but most methods tackle these goals separately rather than working together to maximize both. A recent approach [14] have integrated timeliness and community structure. It uses a hybrid sensor deployment for effective information gathering, simulates dynamic propagation with a time-varying parameter, and uses maximum likelihood estimation within suspicious communities to identify one or more sources. This is the first framework for community-structured dynamic OSNs, and experiments on both real-world and synthetic networks show correct identification. The authors in [15] have presented an early reinforcement learning-based rumor detection model that extracts characteristics from original tweets and responses using a dual-engine deep learning architecture and double self-attention. While optimizing a reward function that strikes a compromise between timeliness and accuracy, a Deep Recurrent Q-Learning Network (DRQN) learns state sequence features. Nevertheless, a lot of these techniques rely on fixed time intervals or predetermined observation windows, which fail to take into consideration the variation in rumor spreading patterns among various events. As a result, they might either postpone forecasts needlessly or make snap judgments based on incomplete knowledge. [16] presents ERD-DC, a dual-channel early rumor detection model that differentiates between "difficult-to-identify" rumors and "easy-to-identify" rumors. While a slow channel does thorough analysis to ensure overall correctness, a fast channel prioritizes timeliness by performing quick post-evidence matching for simple cases. State-of-the-art performance is demonstrated by experiments on real datasets, which successfully balance detection speed and reliability and achieve an accuracy rate of 84%.

II.3 MULTIMODAL LEARNING FOR RUMOR DETECTION

By combining several information sources, multimodal techniques have been put forth to enhance rumor detection. These include temporal elements that depict how events change over time, as well as textual content, user interactions, and propagation structures. The multimodal rumor detection system presented in [17] introduces trainable input parameters while maintaining a frozen backbone, utilizing quick learning in both the vision and language domains. Early on, different prompts gradually model feature interactions, improving context learning. Superior performance in differentiating between rumors and facts is demonstrated by experiments conducted on real-world multimodal datasets. In order to improve the propagation structure and obtain useful local video segments, [18] uses time-sync comments to detect video rumors. It integrates multimodal characteristics for categorization from both local and global keyframes, subtitles, and comments.

In order to address multimodal misinformation detection, [19] presents CPLS (Contrastive Prompt Learning in Structured Graph Networks), a model that builds structured graph networks with semantic-aware pruning and fusing. Accuracy gains of 2.4% on Weibo and 4.5% on Twitter are demonstrated in experiments conducted on public datasets. In recent work [20] presents LoRAD (Logic-Reasoning Augmented DeBERTa). It uses DeBERTa's disentangled attention method to combine logical evidence produced by an LLM with the original text. Evaluated on three publicly available datasets as well as a recently created Twitter26-Mini dataset, LoRAD outperforms LLMs in terms of robustness and inference speed, making it appropriate for real-time rumor detection. These methods produce stronger representations and better classification results by merging complimentary modalities. Nevertheless, the problem of early detection in streaming contexts is not specifically addressed by current multimodal models, which are usually built for static or fully observed data. A successful model for enhancing generalization across tasks is meta-learning [21]. Meta-learning allows models to swiftly adjust to new patterns with few observations in the setting of sequential data. Although meta-learning has been used in many different fields, it is still not widely used for rumor detection. Its potential for simulating various rumor dissemination dynamics or for enhancing early decision-making is hardly explored in existing studies. For instance, a meta-learning framework was developped by [22] that jointly learns social bot detection as an auxiliary job to improve rumor detection. The model ensures that information from the auxiliary task efficiently serves the main goal by using an outer-loop optimization on rumor detection and an inner-loop pseudo-update on bot detection. The findings of the experiment show excellent performance, reaching 90% accuracy in just two hours.

II.4 META-LEARNING IN SEQUENTIAL MODELING

Additionally, there is still much to learn about the potential of meta-learning in the field of rumor detection. In order to fill these deficiencies, this paper presents a unified framework that combines adaptive decision timing and multimodal meta-learning to enable early and accurate rumor identification in dynamic information contexts. Using the ISOT dataset [23], [24] proposed the application of meta-learning in conjunction with BERT for the detection of fake news. While highlighting constraints and the significance of responsible AI design, an ensemble transformer-based model achieves a high accuracy of 98.29%, showcasing the promise of meta-learning in enhancing detection performance. Meanwhile, [25] proposes a multimodal meta-learning method based on few-shot learning (FSL) for early rumor detection, addressing the challenges of limited spread and small sample sizes. It uses a meta-learning method with quick, multi-step updates to improve flexibility while designing a multimodal feature extraction layer, a hidden information extraction layer, and a fusion output layer. In conclusion, even though previous studies have shown significant improvements in multimodal learning, sequential modeling, early detection, and rumor detection, a number of important constraints still exist. Current approaches lack support for streaming decision-making pipelines, rely on fixed observation windows that limit adaptation to dynamic information dispersion, and primarily prioritize classification accuracy at the expense of decision speed.

III. METHODOLOGY

In this section, we present the proposed framework. The model handles social media events as a series of data streams. It then finds the best moment to make a prediction. We start by stating the problem. Next, we outline the framework, model architecture, and the proposed algorithm.

III.1 PROBLEM STATEMENT

Over a stream of social media posts, we formulate early rumor detection as a sequential decision-making issue. Let an event be represented as a chronologically ordered series of communications, such as a discussion thread or a collection of posts pertaining to a particular claim:

$$E = \{m_1, m_2, \ldots, m_T\} \tag{1}$$

Where m_t denotes the $t-th$ message arriving over time. Only the partial observation is available to the model at each time step t. $E_t = \{m_1, m_2, \ldots, m_t\}$ and must decide whether to: Continue observing further messages, or Stop and assign a binary classification (0: non-rumor, 1: rumor) to $y \in \{0, 1\}$. The goal is to reduce both the detection delay and the classification error simultaneously. This is expressed formally as:

$$\mathcal{L} = \alpha \cdot \mathcal{L}_{cls} + \beta \cdot \mathcal{L}_{time} \tag{2}$$

where:

- $\mathcal{L}_{cls}$: classification loss (cross-entropy)
- $\mathcal{L}_{time} = \frac{t}{T}$: normalized detection delay
- α, β : trade-off parameters

The system aims to achieve the earliest possible reliable detection by learning a policy that maps partial observations to halting choices and predictions. This allows for prompt action while maintaining high classification fidelity.

III.2 OVERALL FRAMEWORK

The suggested framework is intended for real-time rumor detection in social media streams, where posts are constantly coming in and judgments need to be taken as soon as possible to stop the propagation of false information. Our proposed framework uses a streaming paradigm that gradually consumes each incoming post and dynamically determines the best time to make a forecast, in contrast to traditional batch-based methods that process predefined windows of data. By striking a balance between two conflicting goals maximizing detection accuracy and decreasing decision latency the main purpose is to put an end to rumors. The design consists of three closely related modules:

Adaptive Decision, Meta Learning, and Multimodal Representation Learning, as shown in Figure 1. A new social media post is encoded at each time step t, the internal model state is updated, and a confidence-based decision policy decides if there is enough evidence to categorize the material as rumor or not. Each component is described in detail in the ensuing subsections.

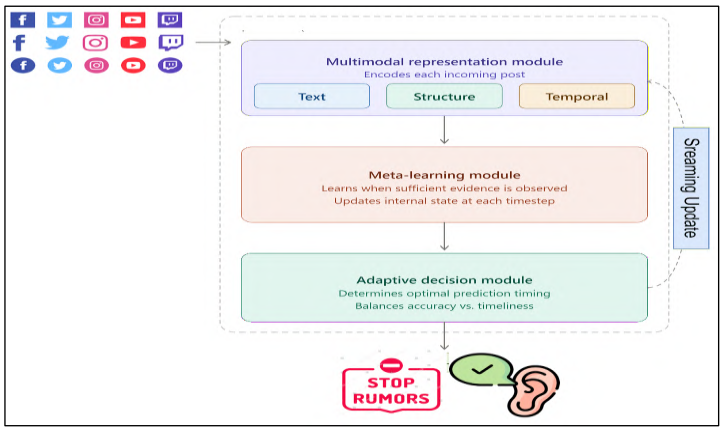


Figure 1: The proposed framework architecture.
Source: Authors, (2026).

1. Multimodal Representation Module allows for incremental state updates by encoding each incoming post into a single embedding that combines textual, structural, and temporal data. Each message m_t is represented using multiple modalities:
Textual Features: Extracted using: BERT / LSTM encoder, $h_t^{text} = f_{text}(m_t)$

Structural Features: Propagation patterns (retweets, replies) with user credibility, $h_t^{struct} = f_{struct}(m_t)$

Temporal Features: Time intervals between messages with posting dynamics, $h_t^{temp} = f_{temp}(t)$

Multimodal Fusion: The final representation is obtained via fusion: $h_t = Fusion\left(h_t^{text}, h_t^{struct}, h_t^{temp}\right)$, with fusion strategies.

2. Meta-Learning Module recognizes when enough evidence has been observed by quickly adjusting the internal state at each timestep after learning a previous over rumor detection tasks. The model is trained using a meta-learning strategy where each event is treated as a task: $\theta^* = arg\ min_\theta \sum_{E\sim D} \mathcal{L}_E(\theta)$. This enables the model to generalize across different rumor propagation patterns.

3. Adaptive Decision Module employs an ideal stopping strategy that dynamically chooses the predicted time to strike a compromise between timeliness and accuracy. At each timestep t, the model computes: The classification probability: $p_t = P(y|E_t)$ and the confidence score: $c_t = max(p_t)$.

III.3 ADAPTIVE DECISION ALGORITHM FOR EARLY RUMOR DETECTION

The proposed algorithm (Algorithm 1) adds a number of innovative features that together improve early rumor detection. It learns adaptive decision timing to determine the best time to make a prediction per event, in contrast to conventional approaches that depend on full event observation or fixed-length inputs. This is accomplished by using multimodal meta-learning, which permits quick adaptation to changing dynamics and generalization across various propagation patterns. In order to represent real-world social media circumstances, the problem is stated as a sequential streaming process where judgments are made progressively as posts arrive. While event-specific adaptation enables the system to act quickly on clear cases and collect additional evidence when ambiguity persists, a joint optimization of accuracy and timeliness explicitly incorporates detection delay into the goal, striking a principled balance between early intervention and reliable classification.

Algorithm 1 Early Rumor Detection with Adaptive Decision Timing

Input: Event stream $E = \{m_1, \ldots, m_T\}$
Output: Predicted label y, detection time t^*
Initialize model parameters θ
$t \leftarrow 1$
while $t \leq T$ do
  Receive message m_t
  Encode multimodal features:

$$h_t = Fusion(f_{text}(m_t), f_{struct}(m_t), f_{temp}(t))$$

  Update representation using previous context
  Compute prediction:

$$p_t = P(y|E_t)$$
$$c_t = max(p_t)$$

  if $c_t \geq \tau$ then
    return prediction y and detection time t
  end if

$t \leftarrow t + 1$

end while
Return final prediction using full sequence

IV. EXPERIMENTS

The efficacy of the proposed framework for early rumor identification is assessed in this section. The datasets, baselines, and assessment measures are described first, and then the implementation specifics. We then present the experimental results in terms of both classification performance and detection timeliness, along with ablation studies to analyze the contribution of each component.

IV.1 DATASETS

We assess the proposed framework using three popular benchmark datasets [26] for rumor detection: Weibo [27], Twitter15, and Twitter16 [28]. These datasets characteristics (Table 1) include social media events that have been tagged as rumors or not, along with the propagation threads that go along with them. A series of replies and reposts follow the first post in each event, creating a temporal structure appropriate for early detection analysis. Twitter15 and Twitter16 have a variety of dissemination patterns. Weibo is a sizable dataset that was gathered from a Chinese social media site and has a notably greater quantity of posts and events. It makes it possible to assess cross-domain robustness by offering more diversity in language, user behavior, and propagation dynamics.

Table 1: Dataset Characteristics.

Dataset	Events	Posts	Classes
Twitter15	1,490	331,612	2
Twitter16	818	204,820	2
Weibo	4,664	3,805,656	2

Source: Authors, (2026).

We use conventional preparation procedures for all datasets: tokenization, text normalization, and the removal of URLs, mentions, and non-informative tokens. In order to accurately replicate the streaming environment necessary for early rumor detection, messages inside each event are arranged chronologically, treating each event as a time-ordered sequence.

IV.2 BASELINES

We evaluate the proposed framework against a wide range of baselines that include early detection, propagation-aware, sequential deep learning, and conventional machine learning. Conventional approaches include a propagation tree kernel-based SVM PTK [26] that captures structural similarities between rumor propagation trees and a Random Forest classifier RFC [29] that uses manually created textual, user, and structural variables. LSTM [30], GRU [31], and Transformer are sequential deep learning models that use whole sequence observation to capture temporal dependencies. PPC [32], a hybrid RNN-CNN architecture that learns from propagation paths and user features, represents propagation-aware deep models. We use early LSTM, a time-aware variation that generates predictions at predetermined intermediate steps, for early detection.

IV.3 EVALUATION METRICS

We evaluate the proposed method utilizing timeliness-aware metrics as well as classification performance metrics to evaluate both prediction accuracy and early rumor detection. **Metrics for Classification:** We employ common metrics to assess prediction performance:

- Accuracy: the total percentage of events that are correctly classified
- Precision: the percentage of accurately anticipated rumors among positives
- Recall: the percentage of true rumors that are accurately identified
- F1-score: precision and recall harmonic mean
- Area under the ROC curve, or AUC

Timeliness Metrics: We utilize the following metrics to evaluate early detection capability:

- Average Detection Time (ADT): $ADT = \frac{1}{T}\sum_{i=t}^{N} t_i^*$, Measures the average number of messages required before making a decision.
- Normalized Detection Time (NDT): $NDT = t^*/T$, Captures the relative detection delay with respect to the full event length.

Early Detection Rate (EDR): Proportion of rumors correctly detected before a predefined observation threshold. Messages Used (%), $t^*/T \times 100$, this indicates the fraction of messages required for prediction.

IV.4 IMPLEMENTATION DETAILS

The proposed framework is trained on a workstation with an Intel Core i9 processor, 32 GB of RAM, and an NVIDIA GPU. It is implemented in Python 3.9 using PyTorch 1.12.1. To guarantee consistent and repeatable training, we employ the Adam optimizer [13] with standard settings, $\beta_1 = 0.9$ and $\beta_2 = 0.999$. The learning rate is set to 5×10^{-4}. To mitigate overfitting, dropout is applied with a probability of 0.5, and weight decay is set to 5×10^{-4}.

The attention parameters for Twitter15 and Twitter16 are $K_1 = 4$ and $K_2 = 2$. These parameters are raised to $K_1 = 8$ and $K_2 = 4$. for the Weibo dataset, which has longer propagation sequences and denser user interactions. To enhance generalization across various events, the meta-learning component is trained end-to-end in tandem with the primary model. We use a five-fold cross-validation approach, dividing the data into training, validation, and test sets at 80%, 10%, and 10% ratios in each step.

IV.5 OVERALL PERFORMANCE RESULTS

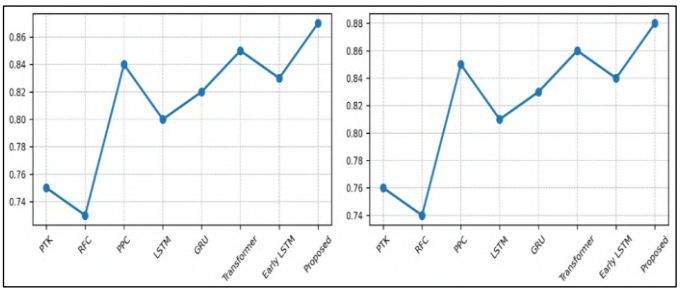
In terms of standard classificat[=ion performance across all datasets, we compare the proposed model with baseline methods. The performance of the suggested framework and the baselines on Twitter 15, Twitter 16, and Weibo are shown in Tables 2.

Table 2: The overall performance comparison on datasets.

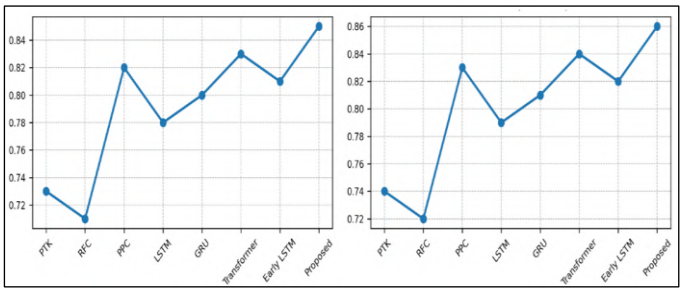
Method	Twitter15 (F1)	Twitter16 (F1)	Weibo (F1)	AUC
PTK	0.76	0.74	0.78	0.80
RFC	0.74	0.72	0.75	0.78
PPC	0.85	0.83	0.87	0.89
LSTM	0.81	0.79	0.83	0.85
GRU	0.83	0.81	0.85	0.87
Transformer	0.86	0.84	0.88	0.90
Early LSTM	0.84	0.82	0.86	0.88
Proposed	0.88	0.86	0.90	0.93

Source: Authors, (2026).

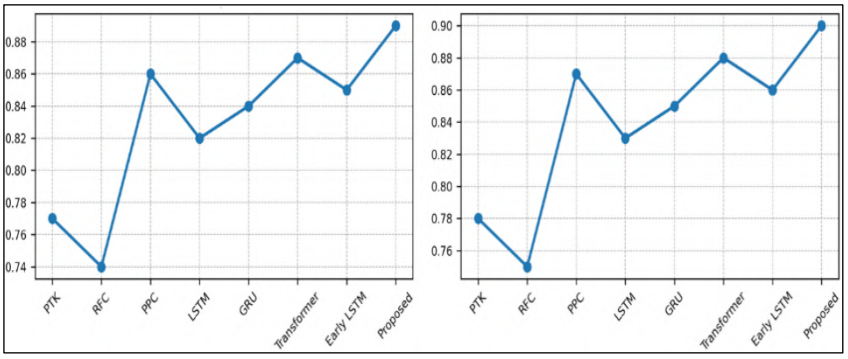
As shown in Figure 2, the findings show that the suggested framework maintains good predictive performance while successfully capturing intricate rumor dissemination patterns. Specifically, the suggested model demonstrates the efficacy of integrating multimodal learning with adaptive decision time, outperforming propagation-based models like PPC and PTK.



(a) Accuracy Twitter 15. (b) F1 Score Twitter 15.



(c) Accuracy Twitter 16. (d) F1 Score Twitter 16.



(e) Accuracy Weibo. (f) F1 Score Weibo.

Figure 2: Results of the proposed structure.
Source: Authors, (2026).

IV.6 ACCURACY VS TIME

The proposed model achieves excellent classification performance at early observation stages, as shown by the accuracy progression study. In comparison to baseline approaches, which require far more observations to achieve equivalent performance, the framework achieves competitive accuracy across all investigated datasets after processing only a small fraction of the message sequence. Plotting accuracy as a function of the percentage of seen messages. Figure 3 shows this trend and consistently demonstrates the advantage of the proposed model in early detection phases.

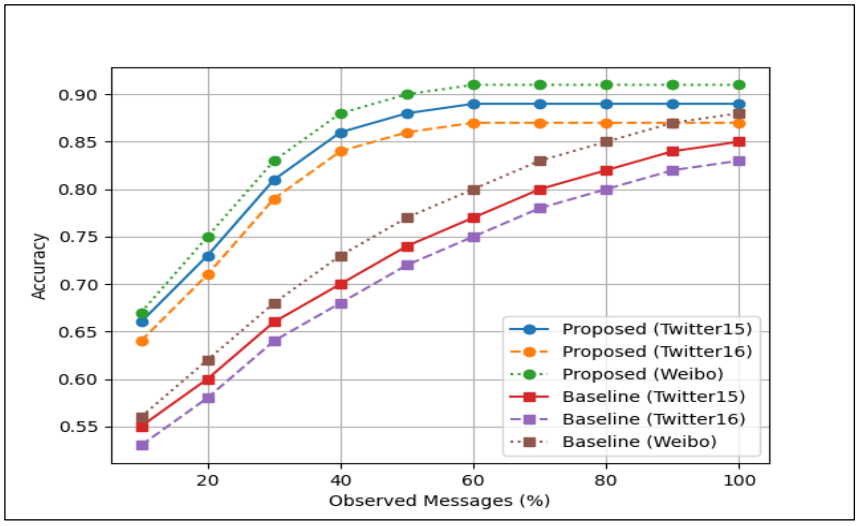


Figure 3**:** Accuracy vs Time across Multiple Datasets.
Source: Authors, (2026).

IV.7 DETECTION TIMELINESS

In this section, we assess how well the suggested model predicts the early phases of the message propagation process. To provide a more thorough comparison, we incorporate propagation-aware models like PPC in addition to traditional baselines. As described in Table 3 the proposed framework demonstrates its efficacy for early rumor detection by achieving the maximum early detection rate (EDR), the lowest detection delay ADT (Average Detection Time) NDT (Normalized Detection Time), and the fewest messages.

Table 3: The comparison of detection timeliness across methods.

Model	ADT	NDT	Messages Used	EDR
LSTM	18.5	0.92	100%	0.65
GRU	17.2	0.89	100%	0.67
Transformer	16.8	0.87	100%	0.69
PPC	13.6	0.66	78%	0.75
Early LSTM	12.4	0.61	72%	0.78
Proposed Model	8.1	0.39	48%	0.87

Source: Authors, (2026).

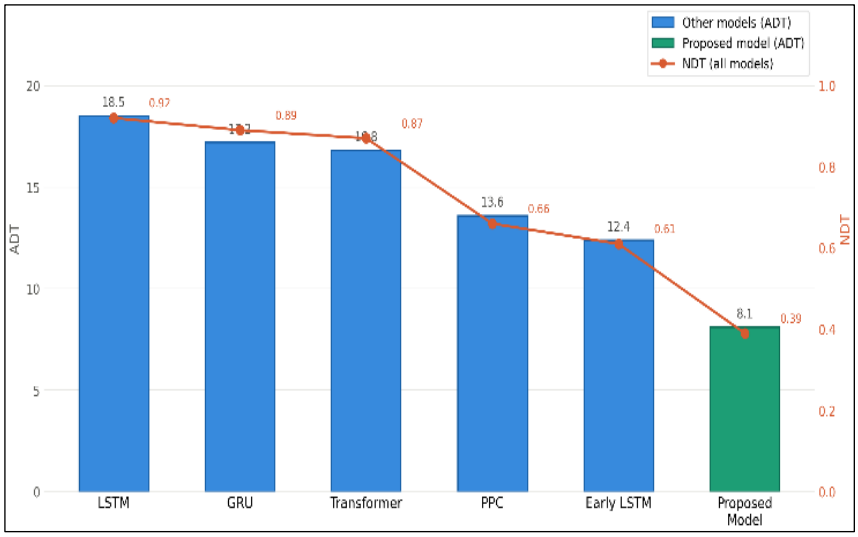


Figure 4: Detection timeliness comparison across methods.
Source: Authors, (2026).

As shown in Figure 4, across all assessed criteria, the proposed model significantly improves detection timeliness. Less than half of the available sequence length is used, and ADT and NDT are greatly decreased, indicating that judgments are taken earlier in the event lifecycle with noticeably fewer input messages on average. A greater EDR further reflects this efficiency, indicating the model's ability to correctly detect rumors in their early phases. However, conventional methods, on the other hand, rely on almost full observation sequences, resulting in significant delays that restrict their usefulness for real-time applications. A boxplot comparison of detection times for several models is shown in Figure 5. In comparison to baseline techniques, the suggested model has a much lower median and a more compact interquartile range, suggesting both faster and more stable detection behavior.

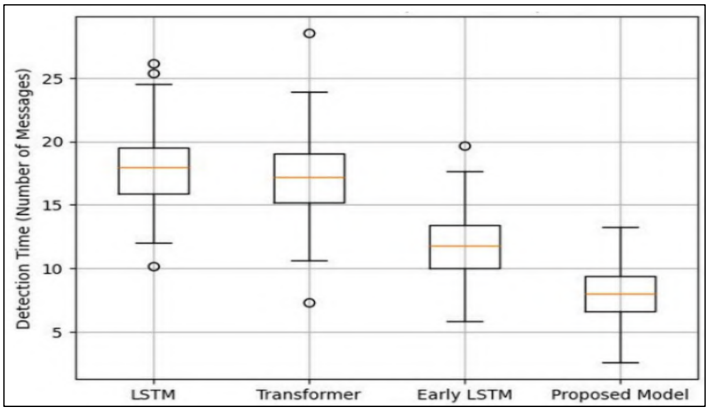


Figure 5: Boxplot comparison of detection times across different models.
Source: Authors, (2026).

IV.8 ABLATION STUDY

We perform an ablation research by eliminating important modules from the suggested framework in order to assess each component's contribution the results are shown in Table 4. Figure 6 shows how each component affects F1-score and detection time.

Table 4: Ablation results.

Variant	F1	ADT	Messages Used (%)
Full Model	0.88	8.1	48
w/o Meta-Learning	0.84	12.9	71
w/o Multimodal	0.82	13.5	74
w/o Adaptive Timing	0.86	18.0	100

Source: Authors, (2026).

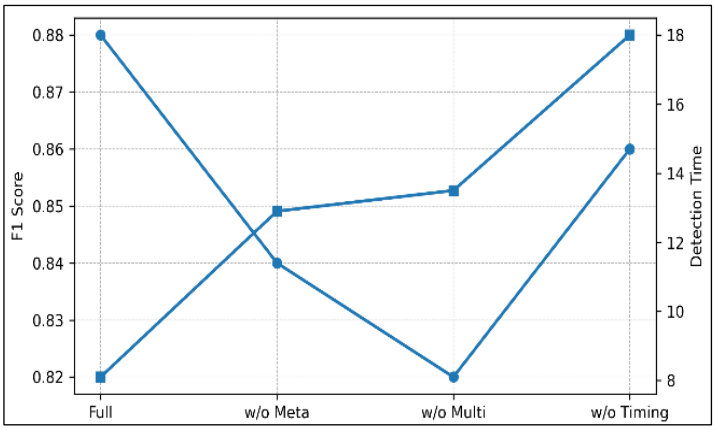


Figure 6: Performance vs Detection time.
Source: Authors, (2026).

The ablation study validates each module's contribution by confirming that eliminating any one component causes a discernible decline in performance. In particular, removing meta-learning slows detection and forces the model to rely on more observations, which reflects less generalization across heterogeneous rumor events. The classification performance significantly declines when multimodal characteristics are removed, highlighting the complimentary benefit of combining textual, structural, and temporal information. Lastly, the model becomes a standard sequential classifier when adaptive decision timing is disabled, requiring entire sequence observation and resulting in the largest detection delay. These results verify that each component tackles a unique and non-redundant part of the detection problem, and that only when all modules work together can optimal performance be attained.

V. DISCUSSION

The experimental results show that the proposed framework successfully strikes a balance between classification performance and detection timeliness, two goals that are often addressed separately in previous research. By dynamically modifying the decision point based on prediction confidence, the adaptive decision timing method significantly reduces detection delay without sacrificing accuracy, producing more realistic behavior in streaming contexts. By combining textual, structural, and temporal information, multimodal feature integration further improves rumor representation, and the meta-learning approach improves generalization across diverse events by recording common dissemination patterns. When taken as a whole, these elements promote early rumor detection as a joint optimization problem where timeliness and accuracy are viewed as complementing goals. However, some limitations should be acknowledged, such as the computational complexity of multimodal processing and meta-learning in large-scale real-time scenarios, and the sensitivity of the preset confidence threshold across datasets with different distributional features.

VI. CONCLUSION

In this paper, we proposed a framework for early rumor detection that integrates multimodal representation learning with meta-learning and adaptive decision timing, modeling the problem as a sequential decision-making process over streaming input. The value of adaptive stopping in real-world intervention scenarios is highlighted by experimental results on Twitter15, Twitter16, and Weibo, which show that our approach significantly reduces detection latency while maintaining competitive or superior classification performance compared to state-of-the-art baselines. In the future, the framework will be expanded to large-scale streaming settings, richer modalities including images and user interaction graphs will be included, and reinforcement learning for completely adaptive halting rules will be investigated. To further advance the integration of meta-learning, multimodal analysis, and adaptive decision-making for next-generation rumor detection systems, we also want to look into uncertainty estimation for more accurate early predictions and cross-platform domain adaptation for wider generalization.

VII. AUTHOR'S CONTRIBUTION

Conceptualization: El Yazid Gueddoudj.
Methodology: El Yazid Gueddoudj and Abdelouahab Attia.
Investigation: El Yazid Gueddoudj, Abdelouahab Attia and Adel Moussaoui.
Discussion of results: El Yazid Gueddoudj, Abdelouahab Attia and Adel Moussaoui.
Writing – Original Draft: El Yazid Gueddoudj and Abdelouahab Attia.
Writing – Review and Editing: El Yazid Gueddoudj and Abdelouahab Attia.
Resources: El Yazid Gueddoudj.
Supervision: El Yazid Gueddoudj, Abdelouahab Attia and Adel Moussaoui.
Approval of the final text: El Yazid Gueddoudj, Abdelouahab Attia and Adel Moussaoui.

VIII. REFERENCES

[1] M. Shahbazi and D. Bunker, "Social media trust: Fighting misinformation in the time of crisis," International Journal of Information Management, vol. 77, p. 102780, 2024.

[2] H. Ran, C. Jia, P. Zhang, and X. Li, "MGAT-ESM: Multi-channel graph attention neural network with event-sharing module for rumor detection," Information Sciences, vol. 592, pp. 402–416, 2022.

[3] C.-Y. Li, "Persuasive messages on information system acceptance: A theoretical extension of elaboration likelihood model and social influence theory," Computers in human behavior, vol. 29, no. 1, pp. 264–275, 2013.

[4] B. G. Robbins, "From the general to the specific: How social trust motivates relational trust," Social Science Research, vol. 55, pp. 16–30, 2016.

[5] A. Vettoruzzo, M.-R. Bouguelia, and T. Rögnvaldsson, "Multimodal meta-learning through meta-learned task representations," Neural Computing and Applications, vol. 36, no. 15, pp. 8519–8529, 2024.

[6] B. Janssens, L. Schetgen, M. Bogaert, M. Meire, and D. den Poel, "360 Degrees rumor detection: When explanations got some explaining to do," European Journal of Operational Research, vol. 317, no. 2, pp. 366–381, 2024.

[7] Z. Zhao, P. Resnick, and Q. Mei, "Enquiring minds: Early detection of rumors in social media from enquiry posts," in Proceedings of the 24th international conference on world wide web, 2015, pp. 1395–1405.

[8] W. Zhang et al., "Robust rumor detection against noise," Neurocomputing, p. 132741, 2026.

[9] Q. Huang, J. Yu, J. Wu, and B. Wang, "Heterogeneous graph attention networks for early detection of rumors on twitter," in 2020 international joint conference on neural networks (IJCNN), 2020, pp. 1–8.

[10] L. Tian, X. Zhang, Y. Wang, and H. Liu, "Early detection of rumours on twitter via stance transfer learning," in European Conference on Information Retrieval, 2020, pp. 575–588.

[11] T. Chen, X. Li, H. Yin, and J. Zhang, "Call attention to rumors: Deep attention based recurrent neural networks for early rumor detection," in Pacific-Asia conference on knowledge discovery and data mining, 2018, pp. 40–52.

[12] Y. Han, X. Li, H. Ran, and Y. Feng, "Few-shot with prototype augmentation for low-resource domains rumor detection," The Journal of Supercomputing, vol. 82, no. 2, p. 52, 2026.

[13] L. Zhang, Y. Chen, X. Luo, H. Zhu, and G. He, "Early detection of rumors based on propagation prediction in social media," Complex \& Intelligent Systems, vol. 12, no. 1, p. 23, 2026.

[14] D.-W. Huang, W. Wu, J. Bi, J. Li, C. Gan, and W. Zhou, "Timeliness-aware rumor sources identification in community-structured dynamic online social networks," Information Sciences, vol. 689, p. 121508, 2025.

[15] W. Wang, Y. Qiu, S. Xuan, and W. Yang, "Early Rumor Detection Based on Deep Recurrent Q-Learning," Security and Communication Networks, vol. 2021, no. 1, p. 5569064, 2021.

[16] Y. Wu, J. Sun, X. Yuan, Z. Huang, and J. Dai, "@inproceedings{chen2024multimodal, title={Multimodal rumor detection via multimodal prompt learning}, author={Chen, Fan and Li, Xiuhong and Li, Zhe and Zhou, Chenyu and Sheng, Jiabao}, booktitle={2024 International Joint Conference on Neural Networks (IJC," Expert Systems with Applications, vol. 238, p. 121928, 2024.

[17] X. Shen, M. Huang, Z. Hu, S. Cai, and T. Zhou, "Multimodal Fake News Detection with Contrastive Learning and Optimal Transport," Frontiers in Computer Science, vol. 6, p. 1473457, 2024.

[18] M. Yin, W. Chen, D. Zhu, and J. Jiang, “Enhancing video rumor detection through multimodal deep feature fusion with time-sync comments,” Information Processing \& Management, vol. 62, no. 1, p. 103935, 2025.

[19] Y. Guo, K. Zhen, and J. Liu, “Contrastive Prompt Learning in Structured Graph Networks for Multimodal Fake News Detection,” IEEE Transactions on Big Data, 2026.

[20] Y. Zhang, F. Muchtar, M. K. Mohd Sidik, and J. Mohamad Sharif, “LoRAD: Logic-Reasoning Augmented DeBERTa with Adversarial Training for Robust Rumor Detection,” Electronics, vol. 15, no. 5, p. 1021, 2026.

[21] Y. Li et al., “Bridging NIP and MLM: A Unified Meta-Learning Framework for Sequential Recommendation,” ACM Transactions on Knowledge Discovery from Data, vol. 20, no. 2, pp. 1–19, 2026.

[22] Z. Lv et al., “Meta Learning Based Rumor Detection with Awareness of Social Bot,” in Knowledge Science, Engineering and Management, C. Cao, H. Chen, L. Zhao, J. Arshad, T. Asyhari, and Y. Wang, Eds., Springer Nature Singapore, 2024.

[23] H. Ahmed, I. Traore, and S. Saad, “Detecting Opinion Spams and Fake News Using Text Classification,” 2018.

[24] U. Y. Ibrahim, R. Prasad, B. H. Ibrahim, and O. F. Nonyelum, “Ensemble Meta-Learning Framework with BERT for Fake News Detection in Social Media.,” International Journal of Performability Engineering, vol. 22, no. 1, 2026.

[25] Y. Ye, H. Chen, Q. Cai, and H. Su, “Multimodal Meta-Learning for Early Rumor Detection Based on Few-Shot Learning,” IEEE Transactions on Computational Social Systems, 2025.

[26] J. Ma, W. Gao, and K.-F. Wong, “Detect rumors in microblog posts using propagation structure via kernel learning,” 2017.

[27] J. Ma, W. Gao, and K.-F. Wong, “Weibo Rumor Detection Dataset,” 2016.

[28] SyntheticProgrammer, “Rumor Detection Dataset (Twitter15 and Twitter16),” 2017.

[29] S. Kwon, M. Cha, K. Jung, W. Chen, and Y. Wang, “Prominent features of rumor propagation in online social media,” in 2013 IEEE 13th international conference on data mining, 2013, pp. 1103–1108.

[30] H. Han, Z. Ke, X. Nie, L. Dai, and W. Slamu, “Multimodal fusion with dual-attention based on textual double-embedding networks for rumor detection,” Applied Sciences, vol. 13, no. 8, p. 4886, 2023.

[31] J. MA et al., “Detecting rumors from microblogs with recurrent neural networks (2016),” in Proceedings of the 25th International Joint Conference on Artificial Intelligence (IJCAI 2016), pp. 3818–3824.

[32] Y. Liu and Y.-F. Wu, “Early detection of fake news on social media through propagation path classification with recurrent and convolutional networks,” in Proceedings of the AAAI conference on artificial intelligence, 2018.

Journal of Engineering and Technology for Industrial Applications

ITEGAM-JETIA

Manaus, v.12 n.60, p.1513-1522 July/August, 2026.
DOI: https://doi.org/10.5935/jetia.v12i60.4417

ISSN ONLINE: 2447-0228

RESEARCH ARTICLE OPEN ACCESS

AN ADAPTIVE SLIDING MODE OBSERVER WITH PLL-BASED ESTIMATION FOR SENSORLESS PMSM DRIVES

[1]Thanh Lam. Le

[1]Ho Chi Minh City University of Technology and Engineering Vietnam

[1]https://orcid.org/0009-0008-8562-2031

E-mail: lamlethanh@hcmute.edu.vn

ARTICLE INFO

Article History
Received on: March 29, 2026
Reviewed on: April 29, 2026
Accepted on: July 01, 2026
Published on: July 31, 2026

Keywords:
Pmsm Drives,
Sensorless Speed Estimation,
Sensorless Control
Sliding Mode Observer,
Back-Emf Estimation,

ABSTRACT

Permanent magnet synchronous motors (PMSMs) are widely used in high-performance drive systems because of their high efficiency, high torque density, and rapid dynamic response. Field-oriented control (FOC) is the dominant control strategy for such drives, but its performance depends critically on accurate rotor position and speed information. In sensorless PMSM drives, sliding mode observers (SMOs) are attractive because of their robustness and modest computational demand. However, conventional SMOs still exhibit an inherent trade-off between fast convergence and chattering suppression, while direct extraction of rotor position and speed from the estimated back-electromotive-force (back-EMF) signals remains vulnerable to noise and filtering delay. This paper presents a sensorless PMSM drive based on closed-loop FOC and an improved SMO-based estimation scheme. The PMSM is modeled in the synchronous dq reference frame, whereas the observer is constructed in the stationary reference frame from stator current dynamics and back-EMF reconstruction. To improve estimation performance, an adaptive sliding-mode injection gain is introduced to regulate the observer correction level according to the current estimation error, and a smooth switching law is employed to reduce chattering. In addition, a phase-locked loop (PLL) is incorporated to reconstruct the rotor electrical angle and speed from the estimated back-EMF components, thereby improving estimation smoothness and noise immunity. Simulation results obtained in MATLAB/Simulink under start-up, acceleration, steady-state, and load disturbance conditions demonstrate stable drive operation, accurate speed tracking, and improved estimation behavior compared with the conventional SMO. The results confirm that the proposed observer enhances convergence and reduces steady-state oscillations while preserving the simplicity and practical applicability of SMO-based sensorless control for PMSM drives.

Copyright ©2026 by authors and Galileo Institute of Technology and Education of the Amazon (ITEGAM). This work is licensed under the Creative Commons Attribution International License (CC BY 4.0).

I. INTRODUCTION

Permanent magnet synchronous motors (PMSMs) have become increasingly prevalent in high-performance motion control systems owing to their high efficiency, high torque density, compact structure, and excellent dynamic characteristics [1-3]. Unlike induction motors, PMSMs do not require rotor current excitation, which eliminates rotor copper losses and contributes to higher overall energy efficiency [4]. These characteristics make PMSMs particularly suitable for demanding applications such as robotics, machine tools, electric vehicles, and servo drives, where precise torque control and rapid dynamic response are required [5]. To fully exploit the advantages of PMSMs, advanced control strategies are necessary. Among them, field-oriented control (FOC) has become the dominant approach for high-performance PMSM drives [6] [7]. By transforming the stator currents into a rotor-oriented synchronous reference frame, FOC enables independent regulation of the torque-producing and flux-related current components [2], [8]. For surface-mounted PMSMs, where magnetic saliency is negligible, the electromagnetic torque becomes directly proportional to the q-axis current, while the d-axis current can be regulated to zero [9] [10].

This decoupled control structure simplifies torque control and enables fast dynamic response with high steady-state accuracy. Furthermore, the cascaded architecture of FOC, consisting of an outer speed control loop and inner current control loops, provides a systematic framework for controller design and facilitates integration with pulse-width modulation (PWM) techniques and coordinate transformations [11-13]. Despite the maturity and effectiveness of FOC, its practical implementation generally requires accurate rotor position or speed information [14]. In conventional drive systems, such information is obtained using mechanical sensors such as encoders or resolvers. However, the use of mechanical sensors increases system cost and hardware complexity, introduces additional wiring and installation requirements, and may reduce system reliability in harsh operating environments characterized by high temperature, vibration, or contamination [15-17]. These limitations have motivated extensive research on sensorless control strategies for PMSM drives, in which rotor position and speed are estimated from measured electrical signals together with mathematical models of the machine [18] [19]. Among the various sensorless estimation techniques proposed for PMSMs, sliding mode observers (SMOs) have attracted considerable attention due to their inherent robustness against parameter variations and external disturbances [20-22]. SMO-based estimators employ a discontinuous correction mechanism that forces the estimation error to converge toward a predefined sliding surface, thereby providing strong robustness properties and fast error convergence. In PMSM applications, SMOs are commonly formulated in the stationary reference frame to estimate the back electromotive force (back-EMF) components using measured stator voltages and currents [23-24].

Because the back-EMF inherently carries rotor position information, the rotor electrical angle can subsequently be reconstructed using a phase-locked loop (PLL) or an arctangent-based computation [25]. Compared with other observer-based techniques, such as extended Kalman filters or model reference adaptive systems, SMOs provide an attractive compromise between estimation accuracy, computational complexity, and robustness [26]. In addition, their relatively simple structure facilitates real-time implementation in digital controllers and provides good immunity to parameter uncertainties, particularly variations in stator resistance [27]. Consequently, SMO-based sensorless control has been widely adopted in industrial PMSM drives operating in the medium-to-high speed region, where the back-EMF magnitude is sufficiently large to ensure a reliable signal-to-noise ratio [28]. Despite the robustness and practical simplicity of conventional SMOs, their estimation performance is still limited by the trade-off between fast convergence and chattering suppression. In addition, direct extraction of rotor position and speed from the estimated back-EMF signals remains sensitive to noise and filter-induced phase delay, which may deteriorate estimation smoothness and dynamic performance. Therefore, this paper develops an adaptive sliding-mode observer with a smooth switching law and PLL-based reconstruction for sensorless PMSM drives. The main contribution lies in integrating adaptive injection gain regulation, chattering-reduced switching action, and closed-loop angle/speed estimation into a unified SMO-based sensorless framework, aiming to improve convergence behavior, estimation smoothness, and robustness while preserving implementation simplicity.

II. MATHEMATICAL MODEL OF THE PERMANENT MAGNET SYNCHRONOUS MOTOR

The dynamic model of a three-phase PMSM can be conveniently formulated in the synchronously rotating dq reference frame. By transforming the stator variables into orthogonal direct and quadrature components that rotate synchronously with the rotor magnetic field, the resulting dq-axis quantities become constant under steady-state operating conditions. This representation provides a compact and physically intuitive description of PMSM dynamics and is particularly well suited for analysis and controller design within the framework of FOC. In the synchronous dq reference frame, the stator voltage equations of the PMSM are expressed as:

$$v_{sd} = R_s i_{sd} + \frac{d\psi_{sd}}{dt} - \omega_e \psi_{sq} \tag{1}$$

$$v_{sq} = R_s i_{sq} + \frac{d\psi_{sq}}{dt} + \omega_e \psi_{sd} \tag{2}$$

Where v_{sd}, v_{sq} are the stator voltage components, i_{sd}, i_{sq} are the stator current components, R_s is the stator resistance, ψ_{sd}, ψ_{sq} denote the stator flux linkages, and ω_e is the electrical angular speed of the synchronous reference frame. For a PMSM, the rotor magnetic field is produced by permanent magnets rather than rotor windings. As a result, no rotor voltage equations are involved, and the rotor flux is directly determined by the permanent magnet flux linkage. Accordingly, the stator flux linkages in the dq reference frame can be expressed as:

$$\psi_{sd} = L_d i_{sd} + \psi_f \tag{3}$$

$$\psi_{sq} = L_q i_{sq} \tag{4}$$

Where L_d and L_q are the stator inductances along the d-axis and q-axis, respectively, and ψ_f is the flux linkage produced by the permanent magnets. Substituting (3) and (4) into (1) and (2), the complete electrical model of the PMSM in the dq reference frame is obtained. The electromagnetic torque generated by the PMSM is given by

$$T_e = \frac{3}{2} p\left(\psi_f i_{sq} + \left(L_d - L_q\right) i_{sd} i_{sq}\right) \tag{5}$$

Where p denotes the number of pole pairs. For surface-mounted PMSMs, where magnetic saliency is negligible and $L_d \approx L_q$, the electromagnetic torque expression simplifies to

$$T_e = \frac{3}{2} p \psi_f i_{sq} \tag{6}$$

Which indicates that the electromagnetic torque is directly proportional to the q-axis current, while the d-axis current does not contribute to torque production. The mechanical dynamics of the PMSM are described by the rotor motion equation

$$J \frac{d\omega_m}{dt} = T_e - T_L - B\omega_m \tag{7}$$

Where J is the total moment of inertia, ω_m is the mechanical angular speed, T_L is the load torque, and B is the viscous friction coefficient. The relationship between electrical and mechanical speeds is given by

$$\omega_e = p\,\omega_m \tag{8}$$

Equations [1-8] collectively represent the complete mathematical model of the PMSM in the synchronously rotating dq reference frame and provide the foundation for the design and analysis of field-oriented control and sensorless control strategies. The overall closed-loop configuration of the considered PMSM drive is illustrated in Figure 1. In this study, the PMSM drive is operated under a conventional closed-loop field-oriented control (FOC) scheme, in which the measured three-phase stator quantities are transformed into a rotor-aligned synchronous reference frame to enable decoupled regulation of flux and torque components. The control structure adopts the standard cascaded configuration with an outer speed loop and inner current loops, allowing the torque-producing current to be generated from the speed error and the corresponding voltage references to be synthesized for application to the inverter through space-vector pulse-width modulation (SVPWM). Within this framework, a sliding mode observer (SMO) is incorporated for sensorless operation, using the measured stator voltage and current signals in the stationary reference frame to reconstruct the back-EMF components and, from them, estimate the rotor electrical angle and speed. The resulting FOC-based PMSM drive therefore provides the control platform on which the observer design is developed, as presented in the following section.

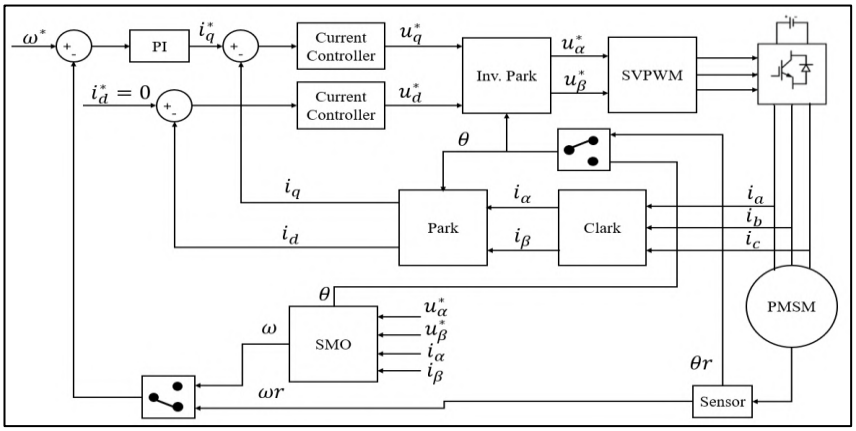


Figure 1: Overall block diagram of the closed-loop FOC PMSM drive with the proposed sliding-mode observer (SMO)–based speed estimation.
Source: Authors, (2026).

III. SLIDING MODE OBSERVER DESIGN

III.1 SLIDING-MODE OBSERVER FOR SENSORLESS SPEED ESTIMATION

In order to establish a baseline for the proposed estimation method, a conventional sliding mode observer (SMO) is first introduced within the FOC-based PMSM drive. The SMO employs the measured stator voltage and stator current signals to estimate the back-electromotive force (back-EMF), rotor electrical angle, and rotor speed. The estimated quantities are analyzed under various operating conditions to characterize the dynamic behavior and estimation capability of the observer within the PMSM drive system. The overall structure of the SMO is illustrated in Figure 2.

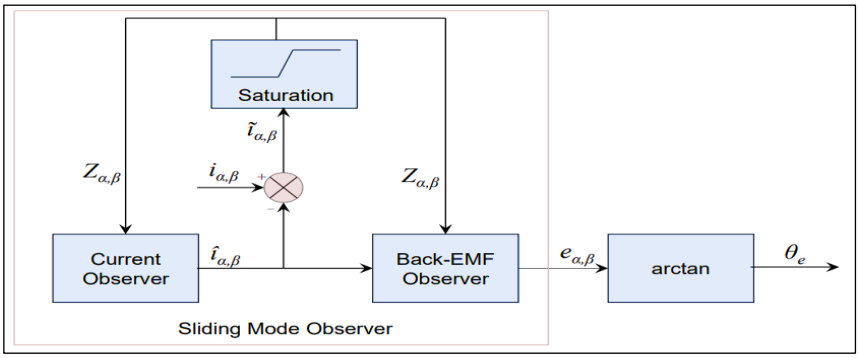


Figure 2: Overall block diagram of the sliding-mode observer –based speed estimation.
Source: Authors, (2026).

The stator phase voltages (u_a, u_b, u_c) are measured at the inverter output terminals and transformed into the stationary reference frame using the Clarke transformation, yielding the stationary voltage components (u_α, u_β). In a similar manner, the measured stator phase currents are converted into the corresponding stationary current components (i_α, i_β). These stationary-frame voltage and current signals constitute the inputs to the sliding mode observer. The sliding mode observer is derived from the stator current dynamics of the PMSM expressed in the stationary $\alpha\beta$ reference frame. Under the assumptions of balanced operation and negligible magnetic saturation, the stator current dynamics can be expressed as

$$\frac{di_\alpha}{dt} = -\frac{R_s}{L_s} i_\alpha + \frac{1}{L_s} u_\alpha - \frac{1}{L_s} e_\alpha \tag{9}$$

$$\frac{di_\beta}{dt} = -\frac{R_s}{L_s} i_\beta + \frac{1}{L_s} u_\beta - \frac{1}{L_s} e_\beta \tag{10}$$

Where R_s and L_s denote the stator resistance and stator inductance, respectively, and e_α, e_β are the back-EMF components in the stationary frame. Within the observer, an estimated current model is constructed using the estimated stator currents $\hat{\imath}_\alpha, \hat{\imath}_\beta$ and the estimated back-electromotive-force components $\hat{e}_\alpha, \hat{e}_\beta$. To enhance robustness against parameter uncertainties and external disturbances, the sliding mode observer incorporates a discontinuous correction term driven by the current estimation error. The resulting observer dynamics are expressed as

$$\frac{d\hat{\imath}_\alpha}{dt} = -\frac{R_s}{L_s} \hat{\imath}_\alpha + \frac{1}{L_s} u_\alpha - \frac{1}{L_s} v_\alpha \tag{11}$$

$$\frac{d\hat{\imath}_\beta}{dt} = -\frac{R_s}{L_s} \hat{\imath}_\beta + \frac{1}{L_s} u_\beta - \frac{1}{L_s} v_\beta \tag{12}$$

Where the discontinuous injection terms v_α and v_β are defined as

$$v_\alpha = K_{sw}\, \mathrm{sat}(i_\alpha - \hat{\imath}_\alpha) \tag{13}$$

$$v_\beta = K_{sw}\, \mathrm{sat}(i_\beta - \hat{\imath}_\beta) \tag{14}$$

Here, K_{sw} is the sliding-mode gain, and $\mathrm{sat}(\cdot)$denotes a saturation function introduced to reduce chattering effects compared to an ideal sign function. Under sliding-mode operation, the current estimation errors converge to zero, and the equivalent values of the discontinuous injection terms correspond to the back-electromotive-force components. To mitigate the high-frequency chattering introduced by the sliding-mode action, the signals v_α and v_β are processed through low-pass filters, yielding the estimated back-EMF components as

$$\hat{e}_\alpha = \mathrm{LPF}(v_\alpha), \hat{e}_\beta = \mathrm{LPF}(v_\beta) \tag{15}$$

The cutoff frequency of the low-pass filter is selected as a compromise between effective noise attenuation and acceptable dynamic response. At medium and high operating speeds, where the back-electromotive-force magnitude is sufficiently large, the filtered signals provide reliable information for position and speed estimation. The estimated back-EMF components are subsequently used to reconstruct the rotor electrical angle and rotor speed. The rotor electrical angle is obtained using an arctangent-based calculation given by

$$\hat{\theta}_e = \mathrm{atan2}(\hat{e}_\beta, \hat{e}_\alpha) \tag{16}$$

The electrical angular speed can be obtained either by differentiating the estimated rotor electrical angle or by exploiting the proportional relationship between the back-electromotive-force magnitude and the electrical speed,

$$\hat{\omega}_e \propto \sqrt{\hat{e}_\alpha^2 + \hat{e}_\beta^2} \tag{17}$$

In practical implementations, appropriate scaling and filtering are applied to ensure a smooth and noise-robust speed estimate. The corresponding mechanical rotor speed is then calculated as

$$\hat{\omega}_r = \frac{1}{p} \hat{\omega}_e \tag{18}$$

Where p denotes the number of pole pairs. Despite its simplicity and satisfactory robustness, the conventional SMO still suffers from two inherent drawbacks in practical implementation. First, the use of a fixed switching gain leads to an unavoidable compromise between fast error convergence and chattering attenuation. Second, the direct extraction of rotor position and speed from the estimated back-EMF signals is susceptible to noise contamination and filter-induced phase delay, which may deteriorate estimation smoothness and dynamic performance. To overcome these shortcomings, an improved observer structure is developed in the following subsection by combining an adaptive sliding-mode injection mechanism with a PLL-based position and speed estimation stage.

III.2 PROPOSED ADAPTIVE SMO WITH PLL-BASED ESTIMATION

To address the drawbacks of the conventional sliding-mode observer, an adaptive SMO with PLL-based rotor position and speed reconstruction is developed. The proposed scheme consists of two main improvements. First, an online gain adaptation mechanism is introduced to adjust the observer injection gain according to the magnitude of the current estimation error, thereby improving the trade-off between fast transient convergence and chattering reduction. Second, instead of directly extracting rotor position and speed from the estimated back-EMF components, a phase-locked loop is employed to provide smoother and more noise-resilient estimation. As a result, the proposed observer achieves enhanced convergence behavior and improved robustness for sensorless PMSM drives. The current estimation errors are defined as

$$e_\alpha = i_\alpha - \hat{\imath}_\alpha \tag{19}$$

$$e_\beta = i_\beta - \hat{\imath}_\beta \tag{20}$$

The adaptive switching gain is defined as

$$K_{sw}(t) = K_0 + k_a\sqrt{e_\alpha^2 + e_\beta^2} \tag{21}$$

Where K_0 denotes the minimum switching gain required to guarantee sliding motion and k_a is a positive adaptive coefficient that determines the sensitivity of the gain adjustment. Using the adaptive gain, the discontinuous injection terms in the observer are reformulated as

$$v_\alpha = K_{sw}(t)\text{sat}(e_\alpha) \tag{22}$$

$$v_\beta = K_{sw}(t)\text{sat}(e_\beta) \tag{23}$$

This adaptive mechanism increases the injection strength when the estimation error becomes large and gradually reduces the gain when the error approaches zero. Consequently, the observer preserves strong robustness during transient conditions while significantly reducing steady-state chattering. In addition to the adaptive gain mechanism, the discontinuous switching function is replaced by a smooth hyperbolic tangent function to further mitigate chattering effects. The modified switching function is defined as

$$\text{sat}(e) = tanh(\lambda e) \tag{24}$$

Where $\lambda > 0$ determines the slope of the switching function. Compared with the classical sign function, the hyperbolic tangent function provides a continuous transition around the sliding surface, which suppresses high-frequency oscillations without sacrificing convergence speed. Substituting [21-24] into the observer equations yields the improved current estimation dynamics

$$\frac{d\hat{i}_\alpha}{dt} = -\frac{R_s}{L_s}\hat{i}_\alpha + \frac{1}{L_s}u_\alpha - \frac{1}{L_s}K_{sw}(t)\,tanh(\lambda e_\alpha) \tag{25}$$

$$\frac{d\hat{i}_\beta}{dt} = -\frac{R_s}{L_s}\hat{i}_\beta + \frac{1}{L_s}u_\beta - \frac{1}{L_s}K_{sw}(t)\,tanh(\lambda e_\beta) \tag{26}$$

Under sliding-mode operation, the estimation errors e_α and e_β converge toward zero and the equivalent values of the injection signals correspond to the back-EMF components. The estimated back-EMF signals are obtained by applying low-pass filtering to the adaptive injection signals

$$\hat{e}_\alpha = \text{LPF}(v_\alpha) \tag{27}$$

$$\hat{e}_\beta = \text{LPF}(v_\beta) \tag{28}$$

The estimated back-EMF signals are then processed by the PLL-based reconstruction stage to obtain the rotor electrical angle and electrical speed. To analyze the convergence property of the observer, consider the Lyapunov candidate function

$$V = \frac{1}{2}(e_\alpha^2 + e_\beta^2) \tag{29}$$

The time derivative of the Lyapunov function is given by

$$\dot{V} = e_\alpha\dot{e}_\alpha + e_\beta\dot{e}_\beta \tag{30}$$

Substituting the observer error dynamics into (30) yields

$$\dot{V} = -\frac{K_{sw}(t)}{L_s}\left(e_\alpha\,tanh(\lambda e_\alpha) + e_\beta\,tanh(\lambda e_\beta)\right) \tag{31}$$

Since $K_{sw}(t) > 0$ and $e\,tanh(\lambda e) \geq 0$ for all $e \neq 0$, it follows that

$$\dot{V} \leq 0 \tag{32}$$

Which indicates that the estimation errors are bounded and driven toward the sliding surface. Therefore, the proposed adaptive sliding mode observer preserves the inherent robustness of the classical SMO while reducing chattering and improving estimation smoothness. Rotor Position and Speed Reconstruction Using a Phase-Locked Loop Although the rotor electrical angle can be directly obtained from the estimated back-EMF components using an arctangent function, this approach is known to be sensitive to measurement noise and numerical differentiation. In particular, the direct differentiation of the estimated electrical angle may amplify high-frequency disturbances introduced by switching harmonics and inverter nonlinearities. These effects can degrade the stability of the speed estimation and lead to undesirable oscillations in the outer speed control loop. To improve the robustness of the sensorless estimation process, a phase-locked loop (PLL) is employed to reconstruct the rotor electrical angle and electrical speed from the estimated back-EMF signals. The PLL structure provides a closed-loop tracking mechanism that filters measurement noise while maintaining fast dynamic response. Let the estimated back-EMF vector be defined in the stationary reference frame as

$$\hat{e}_{\alpha,\beta} = \begin{bmatrix}\hat{e}_\alpha \\ \hat{e}_\beta\end{bmatrix} \tag{33}$$

For a surface-mounted PMSM operating under steady-state conditions, the back-EMF components can be expressed as

$$e_\alpha = -\omega_e\psi_f\,sin(\theta_e) \tag{34}$$

$$e_\beta = \omega_e\psi_f\,cos(\theta_e) \tag{35}$$

Which indicates that the back-EMF vector is orthogonal to the rotor flux vector and rotates synchronously with the electrical angular speed. Based on this property, the rotor position can be estimated by aligning the estimated back-EMF vector with the reference

frame generated by the PLL. Let the estimated rotor electrical angle generated by the PLL be denoted by $\hat{\theta}_e$. The corresponding unit vectors are defined as

$$\hat{\boldsymbol{u}}_d = \begin{bmatrix} cos(\hat{\theta}_e) \\ sin(\hat{\theta}_e) \end{bmatrix} \tag{36}$$

$$\hat{\boldsymbol{u}}_q = \begin{bmatrix} -sin(\hat{\theta}_e) \\ cos(\hat{\theta}_e) \end{bmatrix} \tag{37}$$

The PLL is designed to track the phase of the estimated back-EMF vector. To this end, the projection of the estimated back-EMF vector onto the estimated q-axis is used as a phase-related signal, which can be expressed as

$$e_q^{PLL} = -\hat{e}_\alpha \, sin(\hat{\theta}_e) + \hat{e}_\beta \, cos(\hat{\theta}_e) \tag{38}$$

This signal is then processed by a PI loop filter to generate the estimated electrical speed. The PLL control law for the electrical speed estimation is defined as

$$\hat{\omega}_e = K_{p,PLL} e_q^{PLL} + K_{i,PLL} \int e_q^{PLL} \, dt \tag{39}$$

Where $K_{p,PLL}$ and $K_{i,PLL}$ denote the proportional and integral gains of the PLL regulator. The estimated electrical angle is obtained by integrating the estimated electrical speed

$$\hat{\theta}_e = \int \hat{\omega}_e \, dt \tag{40}$$

The corresponding mechanical rotor speed is then calculated using the relationship

$$\hat{\omega}_r = \frac{\hat{\omega}_e}{p} \tag{41}$$

Where p is the number of pole pairs. Compared with the direct arctangent-based estimation approach, the PLL-based reconstruction offers several advantages. First, the closed-loop filtering effect of the PLL significantly attenuates measurement noise and switching harmonics present in the estimated back-EMF signals. Second, the integral action of the PLL improves steady-state accuracy and eliminates bias errors in the speed estimation. Finally, the PLL structure provides smooth and continuous rotor angle tracking, which enhances the stability of the field-oriented control system during dynamic operating conditions. The proposed sensorless estimation scheme integrates three complementary mechanisms: an adaptive sliding mode observer for back-EMF reconstruction, a smooth switching law for chattering suppression, and a PLL-based stage for rotor position and speed extraction. This combination addresses the main shortcomings of the conventional fixed-gain SMO. The adaptive observer modifies the injection gain according to the current estimation error. As a result, strong corrective action is retained during transients, whereas excessive switching activity is avoided as the estimation error decreases. This feature improves convergence behavior without imposing unnecessarily large observer gains in steady-state operation. The use of the hyperbolic tangent function in place of the discontinuous sign function further improves the observer behavior near the sliding surface. In particular, it reduces high-frequency oscillations in the estimated signals while maintaining the robustness properties associated with sliding-mode-based estimation. The back-EMF components reconstructed by the observer are then supplied to a phase-locked loop to obtain the rotor electrical angle and speed. Unlike direct angle differentiation, the PLL provides a closed-loop estimation process with improved noise rejection and smoother speed reconstruction, which is particularly beneficial under dynamic operating conditions. Taken together, these modifications yield a sensorless estimation structure with improved robustness, lower sensitivity to switching noise, and smoother steady-state behavior, while preserving a relatively simple implementation.

IV. RESULTS AND DISCUSSION

The system is implemented in MATLAB/Simulink and consists of a PMSM drive operating under a conventional closed-loop FOC scheme, augmented with a SMO for rotor speed and position estimation. The FOC controller governs the stator currents and rotor speed based on measured electrical quantities, providing stable and well-regulated drive operation over a wide range of operating conditions. Within the implemented framework, the SMO utilizes the stator voltage and current components expressed in the stationary αβ reference frame to estimate the back-electromotive-force components. These estimated signals are subsequently used to reconstruct the rotor electrical angle and rotor speed. The behavior of the estimated quantities is examined during start-up, acceleration, steady-state operation, and load disturbance scenarios in order to characterize the dynamic response and estimation capability of the observer in the PMSM drive system. The complete MATLAB/Simulink implementation of the closed-loop FOC-based PMSM drive and the associated SMO-based estimation structure are illustrated in Figures 3 and 4, respectively. The presented simulation results provide insight into the interaction between the control system and the observer dynamics, as well as the overall performance of the PMSM drive under various operating conditions.

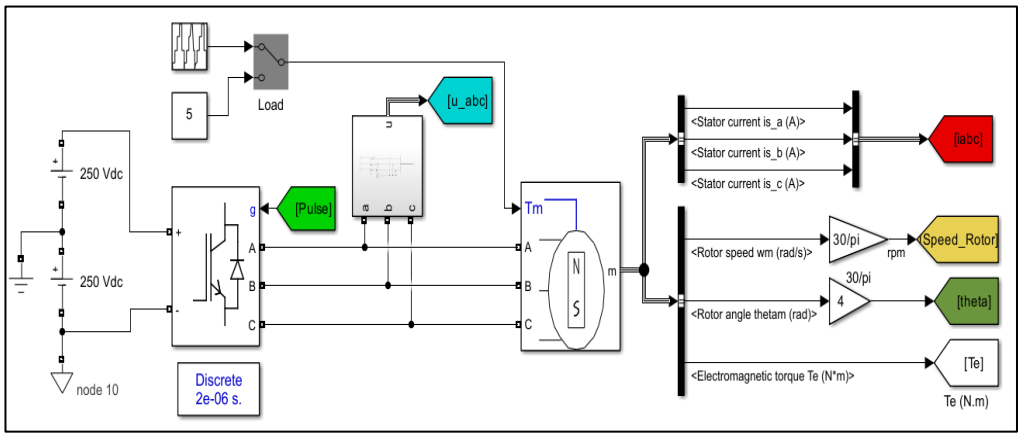


Figure 3: Power stage and PMSM model of the FOC drive.
Source: Authors, (2026).

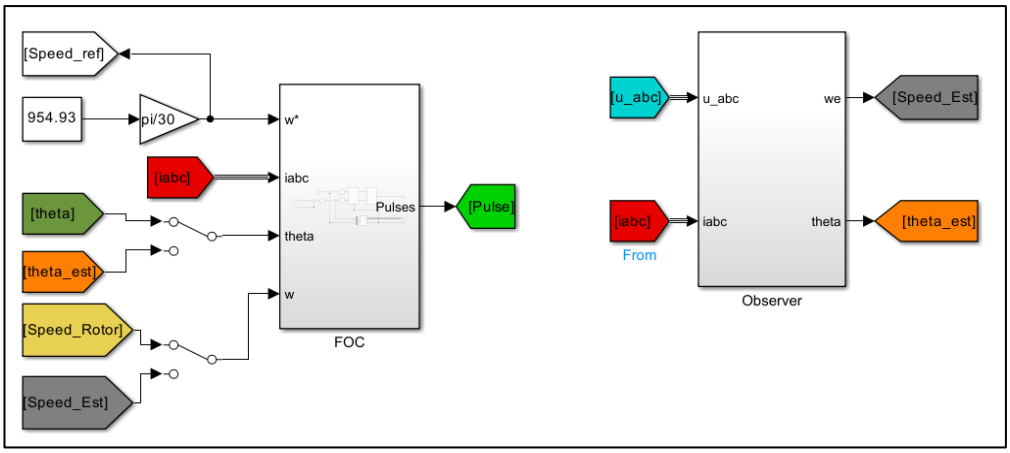


Figure 4: Block diagram of the FOC-controlled PMSM drive with the sliding mode observer.
Source: Authors, (2026).

The FOC-controlled PMSM drive incorporating a SMO is examined under four representative operating scenarios in order to characterize its dynamic behavior and robustness. The considered scenarios include: (i) operation with a varying load at a constant reference speed, which reflects the disturbance rejection capability and speed regulation performance; (ii) operation with a varying load combined with a time-varying reference speed, aimed at assessing robustness and tracking performance under simultaneous disturbances; (iii) operation with a constant load and constant reference speed, representing steady-state conditions; and (iv) operation with a constant load and a varying reference speed, which highlights the transient response and speed tracking characteristics of the drive system. Together, these scenarios provide a comprehensive view of the system behavior under both steady-state and dynamic operating conditions.

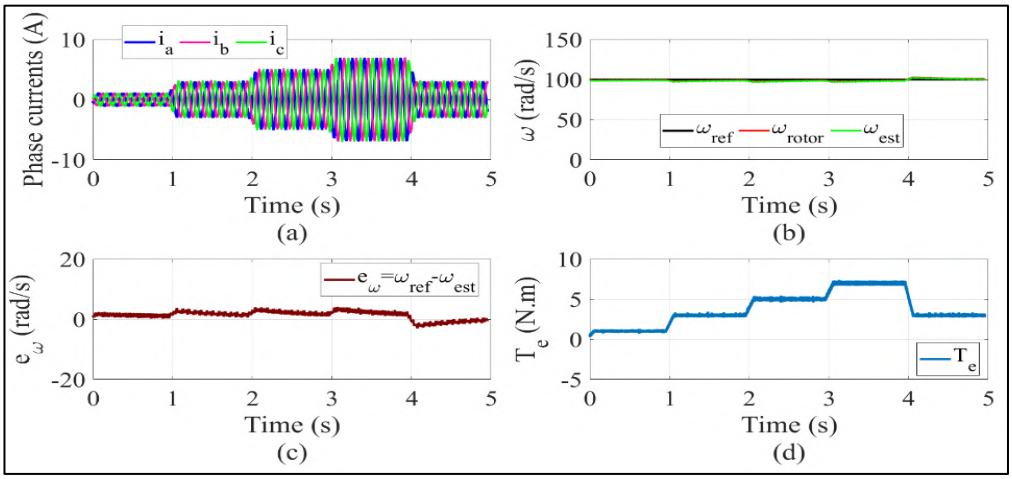


Figure 5: Dynamic responses of the FOC-controlled PMSM drive under varying load conditions at a constant reference speed. (a) Three-phase stator currents; (b) Rotor speed response; (c) Speed tracking error; (d) Electromagnetic torque.
Source: Authors, (2026).

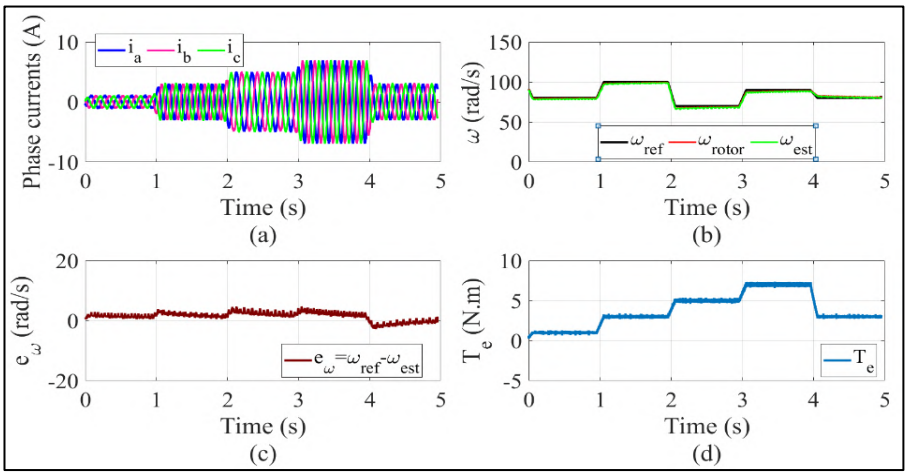


Figure 6: Dynamic responses of the PMSM drive under varying load and time-varying reference speed. (a) Three-phase stator currents; (b) Rotor speed response; (c) Speed tracking error; (d) Electromagnetic torque.
Source: Authors, (2026).

The dynamic responses of the FOC-controlled PMSM drive incorporating sliding mode observer-based estimation under four representative operating scenarios are presented in Figures 5–8. In all cases, the stator currents remain well balanced and nearly sinusoidal, confirming effective current regulation by the inner control loops. The rotor speed follows the reference trajectory smoothly during both steady-state operation and transient conditions, while the electromagnetic torque responds promptly to load variations with limited oscillations, indicating robust torque control and stable system behavior. During start-up and dynamic operating conditions, brief transient oscillations are observed in the stator currents and electromagnetic torque, after which the system rapidly converges to steady-state operation. The speed response exhibits negligible steady-state deviation and maintains consistent behavior under load disturbances and reference speed changes, demonstrating the effectiveness of the FOC structure in regulating the PMSM drive.

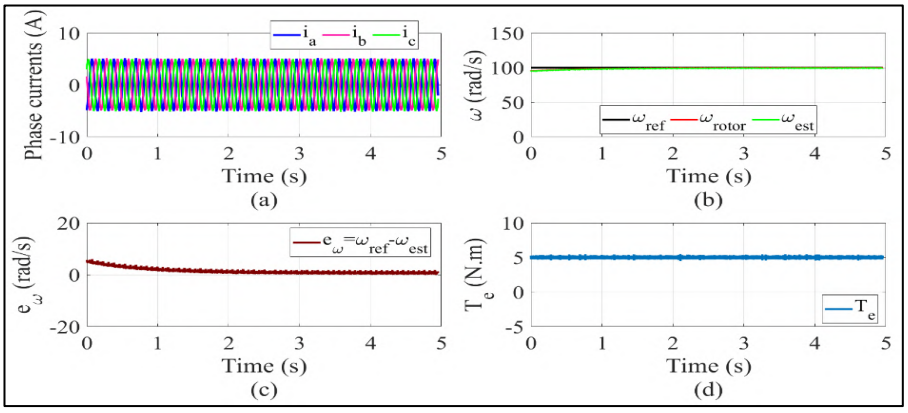


Figure 7: FOC-controlled PMSM drive under constant load and constant reference speed. (a) Three-phase stator currents; (b) Rotor speed response; (c) Speed tracking error; (d) Electromagnetic torque.
Source: Authors, (2026).

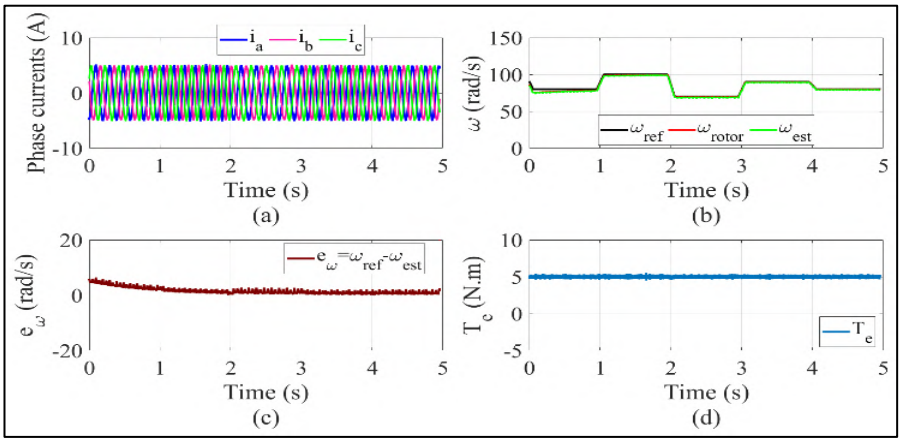


Figure 8: Dynamic responses of the FOC-controlled PMSM drive under constant load and varying reference speed. (a) Three-phase stator currents; (b) Rotor speed response; (c) Speed tracking error; (d) Electromagnetic torque.
Source: Authors, (2026).

The estimated speed and electrical angle display smooth waveforms with low ripple across all operating scenarios. Minor deviations may appear during the initial transient interval; however, the estimated quantities quickly settle as the system reaches steady operation and remain consistent with the drive dynamics thereafter. This behavior indicates effective suppression of chattering and noise effects and reflects the ability of the sliding mode observer to provide stable and reliable speed and position information under both steady-state and transient operating conditions.

V. CONCLUSION

A sensorless PMSM drive based on closed-loop field-oriented control and sliding-mode observation has been presented in this study. The PMSM model was established in the synchronous dq reference frame, while the observer was formulated in the stationary reference frame from stator current dynamics and back-electromotive-force reconstruction. To improve the estimation performance, an adaptive sliding-mode injection gain was introduced to regulate the observer correction strength according to the current estimation error, thereby alleviating the trade-off between fast convergence and chattering attenuation. A smooth switching law was further employed to suppress high-frequency oscillations in the observer signals, and a phase-locked loop was incorporated to reconstruct the rotor electrical angle and speed from the estimated back-EMF components. Together, these modifications improve the smoothness and robustness of the estimation process while preserving the structural simplicity of the conventional SMO framework. Simulation results obtained in MATLAB/Simulink under start-up, acceleration, steady-state, and load disturbance conditions confirmed stable drive operation and accurate speed tracking. Compared with the conventional SMO scheme, the proposed observer provided smoother estimation behavior, reduced steady-state oscillations, and more reliable rotor position and speed information. The proposed sensorless estimation scheme therefore constitutes a practical and computationally efficient solution for PMSM drives requiring robust rotor position and speed estimation.

VI. AUTHOR'S CONTRIBUTION

Conceptualization: Thanh Lam. Le.
Methodology: Thanh Lam. Le.
Investigation: Thanh Lam. Le.
Discussion of results: Thanh Lam. Le.
Writing – Original Draft: Thanh Lam. Le.
Writing – Review and Editing: Thanh Lam. Le.
Resources: Thanh Lam. Le.
Supervision: Thanh Lam. Le.
Approval of the final text: Thanh Lam. Le.

VII. REFERENCES

[1] L Y. Yu, Y. Pei, F. Chai, and M. Doppelbauer, "Performance comparison between permanent magnet synchronous motor and vernier motor for in-wheel direct drive," IEEE Transactions on Industrial Electronics, vol. 70, no. 8, pp. 7761–7772, Aug. 2023. https://doi.org/10.1109/TIE.2022.3212430

[2] Y. Song, G. Liu, S. Yu, H. Wang, and F. Zhang, "Investigation of a low-speed high-torque-density direct-drive external-rotor PMSM for belt conveyor application," IEEE Access, vol. 11, pp. 110479–110489, Sep. 2023. https://doi.org/10.1109/ACCESS.2023.3318724

[3] T.-L. Le, "A robust control strategy for effective field-oriented control of PMSMs," Eng. Technol. Appl. Sci. Res., vol. 14, no. 6, pp. 18469–18475, Dec. 2024. https://doi.org/10.48084/etasr.8893

[4] J. Zhao, X. Liu, S. Wang, et al., "Review of design and control optimization of axial flux PMSM in renewable-energy applications," Chinese Journal of Mechanical Engineering, vol. 36, Art. no. 45, 2023. https://doi.org/10.1186/s10033-023-00868-8

[5] H. Ding, X. Zou, and J. Li, "Sensorless control strategy of permanent magnet synchronous motor based on fuzzy sliding mode observer," IEEE Access, vol. 10, pp. 36743–36752, Apr. 2022. https://doi.org/10.1109/ACCESS.2022.3164519

[6] P. Ramesh, M. Umavathi, C. Bharatiraja, G. Ramanathan, and S. Athikkal, "Development of a PMSM motor field-oriented control algorithm for electrical vehicles," Materials Today: Proceedings, vol. 65, pt. 1, pp. 176–187, 2022. https://doi.org/10.1016/j.matpr.2022.06.080

[7] M. Nicola, C.-I. Nicola, D. Selișteanu, and C. Ionete, "Control of PMSM based on switched systems and field-oriented control strategy," Automation, vol. 3, no. 4, pp. 646–673, Dec. 2022.

[8] S. R. Eftekhari, A. Mosallanejad, H. Pairo, and J. Rodriguez, "Efficiency enhancement in synchronous reluctance motors by active flux adjustment based on robust model-based approaches," IEEE Access, vol. 12, pp. 127731–127748, Aug. 2024.

[9] D. Chen, K. Lu, D. Wang, and M. Hinkkanen, "I–F control with zero d-axis current operation for surface-mounted permanent magnet synchronous machine drives," IEEE Transactions on Power Electronics, vol. 38, no. 6, pp. 7504–7513, Jun. 2023.

[10] X. Wang, M. Reitz, and E. E. Yaz, "Field oriented sliding mode control of surface-mounted permanent magnet AC motors: Theory and applications to electrified vehicles," IEEE Transactions on Vehicular Technology, vol. 67, no. 11, pp. 10343–10356, Nov. 2018.

[11] H. Ghanayem, M. Alathamneh, and R. M. Nelms, "Decoupled speed and flux control of three-phase PMSM based on the proportional–resonant control method," Energies, vol. 16, no. 3, Art. no. 1053, Jan. 2023.

[12] X. Wang and C. A. Steve Suh, "A nonlinear time–frequency control based FOC for permanent magnet synchronous motors," International Journal of Dynamics and Control, vol. 9, pp. 179–189, 2021.

[13] M. F. Elnaggar, A. Flah, C. Z. El-Bayeh, and M. M. Alrashed, "Optimized FOC control strategy for dual stators permanent magnet machine," Scientific Reports, vol. 15, Art. no. 34010, Sep. 2025.

[14] M. Hinkkanen and J. Luomi, “Sensorless field-oriented control of permanent-magnet synchronous motors,” IEEE Transactions on Industrial Electronics, vol. 64, no. 2, pp. 1029–1039, Feb. 2017.

[15] H. Heidari, A. Rassõlkin, A. Kallaste, T. Vaimann, E. Andriushchenko, A. Belahcen, and D. V. Lukichev, “A review of synchronous reluctance motor-drive advancements,” Sustainability, vol. 13, no. 2, Art. no. 729, Jan. 2021.

[16] Z. Novak, “Confidence weighted learning entropy for fault-tolerant control of a PMSM with a high-resolution Hall encoder,” IEEE Transactions on Industrial Electronics, vol. 71, no. 5, pp. 5176–5186, May 2024.

[17] W. Hua, C. Zhang, and Y. Wang, “Embedded magnetic encoder-based rotor-position detection technology for permanent magnet synchronous machines: A review,” Chinese Journal of Electrical Engineering, vol. 11, no. 2, pp. 136–149, Jun. 2025.

[18] Q. Ni, M. Yang, S. A. Odhano, M. Tang, P. Zanchetta, and X. Liu, “A new position and speed estimation scheme for position control of PMSM drives using low-resolution position sensors,” IEEE Transactions on Industry Applications, vol. 55, no. 4, pp. 3747–3758, Jul.–Aug. 2019.

[19] A. G. Abo-Khalil, “Sensorless rotor position estimation of PMSM for low and high rotor speed,” Journal of Engineering Research, vol. 9, no. 2, pp. 161–170, Jun. 2021.

[20] S. Ye, “Fuzzy sliding mode observer with dual SOGI-FLL in sensorless control of PMSM drives,” ISA Transactions, vol. 85, pp. 161–176, Feb. 2019.

[21] H. Yang, A. Xu, Y. Zhang, and X. Chai, “Error analysis and design of sliding-mode-observer-based sensorless PMSM drives under a low sampling ratio,” IEEE Transactions on Power Electronics, vol. 39, no. 7, pp. 7783–7792, Jul. 2024.
[22] N. Q. Vinh and T. L. Le, “Self-learning model-based control for sensorless induction motor drives,” Electrical Engineering, vol. 107, pp. 12169–12182, 2025. https://doi.org/10.1007/s00202-025-03146-z

[23] Y. Zuo, C. Lai, and K. L. V. Iyer, “A review of sliding mode observer based sensorless control methods for PMSM drive,” IEEE Transactions on Power Electronics, vol. 38, no. 9, pp. 11352–11367, Sep. 2023.

[24] H. Sun, X. Zhang, X. Liu, et al., “Adaptive robust sensorless control for PMSM based on super-twisting algorithm back EMF observer and extended state observer,” Electrical Engineering, vol. 107, pp. 9295–9307, 2025.

[25] Z. Zhao, C. Hu, Z. Wang, S. Wu, Z. Liu, and Y. Zhu, “Back EMF-based dynamic position estimation in the whole speed range for precision sensorless control of PMLSM,” IEEE Transactions on Industrial Informatics, vol. 19, no. 5, pp. 6525–6536, May 2023. https://doi.org/10.1109/TII.2022.3205941

[26] L. Yuan, K. Han, C. Zhang, X. Zhu, and Y. Ding, “Comparative analysis of full-order SMO and STM-MRAS in SPMSM sensorless drive system,” IEEE Journal of Emerging and Selected Topics in Power Electronics, vol. 12, no. 3, pp. 2592–2603, Jun. 2024. https://doi.org/10.1109/JESTPE.2024.3378806

[27] C. Gong, Y. Hu, J. Gao, Y. Wang, and L. Yan, “An improved delay-suppressed sliding-mode observer for sensorless vector-controlled PMSM,” IEEE Transactions on Industrial Electronics, vol. 67, no. 7, pp. 5913–5923, Jul. 2020. https://doi.org/10.1109/TIE.2019.2952824

[28] R. Sreejith and B. Singh, “Sensorless predictive current control of PMSM EV drive using DSOGI-FLL based sliding mode observer,” IEEE Transactions on Industrial Electronics, vol. 68, no. 7, pp. 5537–5547, Jul. 2021. https://doi.org/10.1109/TIE.2020.2996159

Journal of Engineering and Technology for Industrial Applications

ISSN ONLINE: 2447-0228

ITEGAM-JETIA

Manaus, v.12 n.60, p.1523-1535 July/August, 2026.
DOI: https://doi.org/10.5935/jetia.v12i60.4433

RESEARCH ARTICLE OPEN ACCESS

PARAMETRIC TOPOLOGY OPTIMIZATION OF CYLINDER MOUNTING BRACKET USING PTC CREO

Edosa Kefyalew[*1] Adugna Fikadu[2], Mahesh Gopal[3]

[1]Technion – Israel Institute of Technology, Technion City, Haifa, 3200003, Israel
[2, 3]Department of Mechanical Engineering, College of Engineering and Technology, Wollega University, Nekemte, Ethiopia

[1]http://orcid.org/0009-0008-5407-3797, [2]http://orcid.org/0009-0004-4322-7683, [3]http://orcid.org/0000-0001-7672-5399

E-email: *edosa.tesema@campus.technion.ac.il

ARTICLE INFO

Article History
Received on: March 30, 2026
Reviewed on: April 30, 2026
Accepted on: July 01, 2026
Published on: July 31, 2026

Keywords:
Structural Optimization,
Additive Manufacturing,
Creo Parametric,
Weight Reduction.

ABSTRACT

Topology optimization is an emerging design technique for producing extremely lightweight, highly efficient structural components without compromising structural integrity. In the current investigation, the topology of a circular mounting bracket is optimized using the integrated structural optimization capabilities of PTC Creo Parametric software. The objective is to minimize the structure's weight without compromising its strength and rigidity. From an initial weight of 1.189 kg, the design was optimized through six phases to achieve the required weights of 70%, 50%, 35%, 25%, 20%, and 17.5%. The actual weight reductions were 71.2%, 52.3%, 37.2%, 27.1%, 22%, and 19.5%. As weight decreased, relative strength increased substantially, reaching a maximum of 100.833 MPa/kg. After analyzing failure modes and strength characteristics, particularly bending failures, the 20% weight-retention design, weighing 0.261 kg (22% of the original weight), was found to be optimal. The results of the study demonstrate that it is possible to create lightweight, high-strength mounting brackets suitable for industrial and automotive applications using parametric topology optimization in PTC Creo.

Copyright ©2026 by authors and Galileo Institute of Technology and Education of the Amazon (ITEGAM). This work is licensed under the Creative Commons Attribution International License (CC BY 4.0).

I. INTRODUCTION

Using the Generative Topology Optimization (GTO) extension in PTC Creo, designers can specify functional design requirements, loads, constraints, and material properties to generate 3D CAD models that are optimized for lightweight manufacturing.

a. Topology optimization

Topology optimization methods for the design of multi-scale structures have advanced rapidly in recent years. A computational design method, topology optimization, can automatically design a structural form with optimal performance for given design parameters [1]. Since it is challenging to produce these novel structures using traditional methods, additional steps are often required to improve manufacturability, which falls short of the full potential of topology optimization. Topology optimization is a sophisticated structural design process that produces novel, high-performance, lightweight configurations that are challenging to achieve using traditional concepts [2]. In the aerospace industry, a small reduction in engine weight results in substantial fuel savings and reduced pollution. For this reason, topology optimization is employed to make aircraft components lighter while maintaining the functionality and lifespan specified by [3]. Without making assumptions about the final geometry, the topology approach optimizes the material layout within a given design region. Consequently, it rapidly gained prominence in the industrial sector and was applied to the design of aircraft components [4]. It has been shown that the topology approach is effective for finding the initial geometric configuration in structural design. The main drawback of the approach, however, is that topology optimization will always yield a non-smooth geometric configuration of the structure.

In contrast, most engineering applications, especially in manufacturing [5], require a smooth configuration. Although topology optimization may not effectively control microstructure, there is still considerable scope to reduce deviations from the desired microstructure [6]. Topology optimization is a numerical process that aims to optimize the shape and material layout within a design space under certain constraints. The solution obtained from topology optimization need not be optimal, but it serves as a basis for optimal design [7]. In the vast majority of engineering applications, topology optimization is among the most effective techniques for the conceptual design phase. Given the boundary conditions and constraints of the design, it is feasible to obtain an optimal structural material distribution that represents the most efficient path in the design domain [2], within certain loads and boundary conditions, topological optimization allows for the estimation of the optimal distribution of material within a design region [8], to enhance the performance of the system, topology optimization is a mathematical method that aims at optimizing the material distribution within a predefined design space for specific loads and constraints [9]. The research work involved optimizing the topology and comparing analytical results before and after the design optimization of the connecting rod. Since the optimized model will be less stressed and lighter than the existing model, it will be more efficient [10]. Within the framework of density-based topology optimization, the behavior of microscopic stress was examined to develop topology optimization techniques capable of handling stress constraints. In aircraft component structural design, topology optimization reduces weight while retaining the required stiffness and strength. In complex aerodynamic and operational conditions, topology optimization enhances loading capacity by optimally distributing materials in the design domain. This helps increase fuel efficiency and reduce emissions [11]. The aim of topology optimization for a lightweight diesel engine alternator support bracket is to minimize material usage while maintaining its stiffness and strength. Based on the applied loads and boundary conditions within a specified design domain, any extra material is reduced throughout the design process [12].

To withstand dynamic loads and vibrations, as well as engine and belt forces, the material distribution is carried out through topological and structural analyses. Stress and deformation behavior under real operating conditions are validated using finite element analysis. An optimized design of a passenger car's compressor mounting bracket improves overall vehicle economy and reduces material costs [13]. The objectives of performing FEA and topology optimization for an engine mounting bracket are to achieve lightweight and optimize structural performance. The deformation, stress distribution, and safety features of an engine mounting bracket are analyzed. The newly designed engine mounting bracket is stronger, more vibration-resistant, reduces material usage, and improves performance without compromising its strength [14]. Topology optimization in Creo Simulate 4.0 enables the reduction of low-stress material in the gripper, thereby reducing structural weight, improving performance, and increasing strength [15]. The aim of the topology optimization of the compressor bracket is to reduce its weight without compromising the required strength and stiffness. Optimized compressor brackets will have better performance, reduced material usage, and longer life. To reduce weight while satisfying the required stress and displacement constraints, the integrated particle swarm optimizer efficiently searches the design space. By considering the structural and geometric effects simultaneously, the topology optimization method improves the global optimality. Optimized truss configurations achieve better material utilization and improved structural performance [16]. A Comparative Study of Topology Optimization Methods for 3D Structural Problems focuses on several numerical methods with respect to their convergence characteristics, efficiency, and correctness of solutions for material distribution in three-dimensional domains. The results help select the most appropriate methods for complex 3D design problems [17].

b. Additive Manufacturing

Additive manufacturing is a process of making parts directly from a digital 3D model. This process differs from subtractive manufacturing in that it reduces waste. This process is also used to make complex parts. This process produces lightweight, topology-optimized, and customized parts. This process is used to make parts for automotive, aerospace, medical, and tool-die industries.The objective is to optimize the Piston's weight while maintaining its strength and thermal stability, thereby enhancing its performance. This can be done using ANSYS and PTC Creo Parametric software. For the design of a lightweight, high-performance device based on this innovative method, the results show improved stress distribution compared with traditional solid orthotics. There is a 30-50% weight reduction compared to traditional solid orthotics. The research article by [18] has made a significant discovery. Under thermo-mechanical stress conditions, the topology of the parametric 3D piston model is optimized to reduce compliance without sacrificing strength. The ANSYS Workbench FEA tools are then employed to simulate the optimized topology. The factors influencing the metal additive manufacturing process include material wall thickness, overhang angle, and orientation [19]. FEA tools are then used to evaluate the material's deformation. The next step is to use the additive manufacturing process to create the required geometry. The results show a significant reduction of 30-60% of the weight while maintaining the required rigidity and safety [20]. Although the AM process offers design flexibility, it has process-specific limitations, including overhang, minimum size, and orientation. This study proposes a methodical approach to topology optimization that accounts for the limitations of the AM process, using ANSYS Workbench as described by [21]. Many researchers have studied and proposed various methods for optimizing structural components used in the food, automotive, and aerospace industries. They have found that topology optimization is a highly effective and powerful tool for structural optimization. The authors conducted experiments on the topology optimization of the automotive suspension bracket and the aero-engine bracket using CREO. Several efforts have been made to use topology optimization in the compressor mounting bracket using ANSYS [13], leaf spring mounting bracket using FEA [22], and a full car body using FEA [23], engine mounting bracket of a heavy commercial vehicle using FEA [24], commercial vehicles, and powertrain transmission housing [25], aircraft fuselage [26].

II. MATERIALS AND METHODOLOGY

a. Materials

Most of the parts of the hydraulic cylinder are susceptible to corrosion. Therefore, the choice of material is very important. The material should not only be corrosion-resistant but also relatively cheap. Stainless steel, which has strength, ductility, and toughness at high temperatures, is often used in mechanical parts.

The stress-strain curves are perhaps the most indicative of the differences in the mechanical properties of different stainless-steel types. The low yield strength and high ductility of the austenitic types, as well as the high yield and tensile strengths and low ductility of the martensitic types, are clearly apparent. Between these two types lie the ferritic and ferritic-austenitic types. Although ferritic-austenitic types have much higher yield strength than ferritic and austenitic types, ferritic types have slightly higher yield strength than austenitic types. Although ferritic and ferritic-austenitic types are slightly better in this respect, their ductility is of similar magnitude to that of [27]. A variation of Alloy 410, Alloy 420 is a martensitic, hardenable stainless steel. Like 410, Alloy 420 contains at least 12% chromium, which is sufficient only to resist corrosion. Compared to Alloy 410, Alloy 420 contains higher carbon content. Although it can be hardened to a minimum Rockwell hardness of 50 HRC, the maximum hardness of the 12% chromium grades, it also retains a good amount of ductility when annealed. Although it can be welded, alloy 420 is rarely welded due to its hardening properties. Because martensitic stainless steel is made very hard, other properties are sometimes slightly compromised. The usable working temperature range is limited by the loss of ductility at sub-freezing temperatures and the loss of strength from over-tempering at higher temperatures, and the corrosion resistance is lower than that of the common austenitic types. Surface grinding or polishing the metal after it has been hardened will provide the highest corrosion resistance.

Table1: Chemical composition of stainless steel martensitic 420.

Type	C	Mn	Ci	P	S	Cr
420	0.15max	1.25max	1.00max	0.04max	0.03max	max: 14.00-min: 12.00

Source: Authors, (2026).

The mechanical and physical properties of the martensitic 420 SS are also given in Table 2 and 3.

Table 2: Mechanical stainless steel martensitic 420.

Temperature (°C)	**Ultimate Tensile Strength (MPa)**	**Yield Tensile Strength (MPa)**	**Elongation (% in 50mm)**	**Brinell Hardness (HB)**
Annealed *	655	345	25	max
399°F (204°C)	1600	1360	12	444
600°F (316°C)	1580	1365	14	444
800°F (427°C)	1620	1420	10	461
1000°F (538°C)	1305	1095	15	375
1099°F (593°C)	1035	810	18	302
1202°F (650°C)	895	680	20	262
* Annealed tensile properties are typical for Condition A of ASTM A276; annealed hardness is the specified maximum.				

Source: Authors, (2026).

Table 3: Physical properties of stainless steel martensitic 420.

Density	**7750 Kg/ m3**
Elastic Modulus	200 GPa
Mean Coefficient of Thermal Expansion	µm/m/°C
at 32 to 212°F (0 to 100°C)	10.3
at 32 to 599°F (0 to 315°C)	10.8
at 32 to 1000°F (0 to 538°C)	17.7
Thermal Conductivity	W/m.K
at 212°F (100°C)	24.9
at 932°F (500°C)	–
Specific Heat	J/kg.K
at 32 to 212°F (0 to 100°C)	460
Electrical Resistivity	550(nΩ.m)

Source: Authors, (2026).

b. Methodology

For experimentation, we use one or more analytical, numerical, or experimental methods in every scientific study. However, among the most widely used numerical methods, the Finite Element Method (FEM) is used in this study. The cylinder mounting bracket was created in SolidWorks 2022 based on the geometric requirements provided by Parker Miller Fluid Power, as the study requires three-dimensional modeling of the part for further analysis by [28]. To be compatible with Ansys software, the part is saved in the IGES format. Subsequently, Ansys 2020R1 reads the model in IGES format for static structural analysis. In this case, improper application of loads and boundary conditions can reveal the model's weaknesses. The commercial software PTC Creo Parametric applies topology optimization (TO). The same loads and boundary conditions from Ansys are applied in the TO process. The study's workflow is shown in Figure 1.

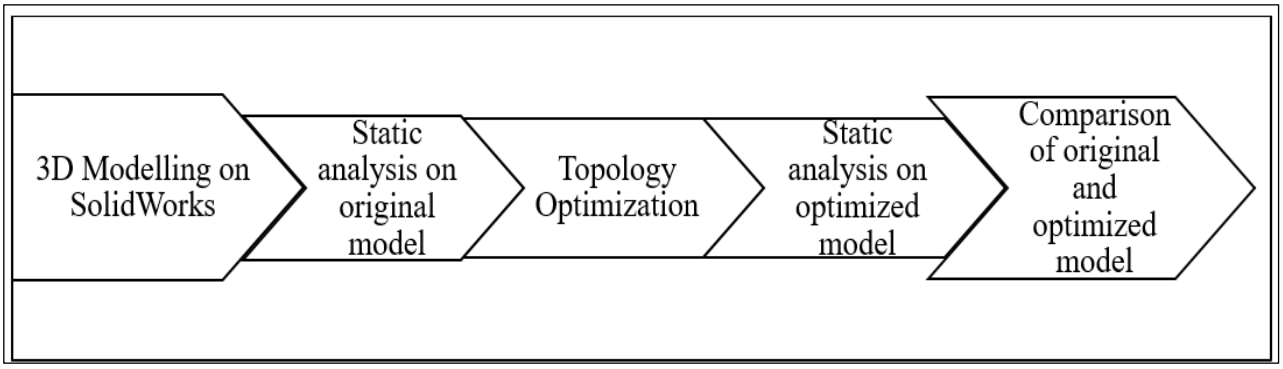


Figure 1: Workflow of the study.
Source: Authors, (2026).

III. STATIC STRUCTURAL ANALYSIS AND TOPOLOGY OPTIMIZATION OF THE COMPONENTS

a. Boundary conditions

A static structural analysis using the finite element method was performed to assess the structural behavior of the cylinder mounting bracket, as shown in Figure 2(a). The actual working conditions for which the mounting bracket is required to perform have been simulated by defining suitable loading and boundary conditions. The inner surface of the cylindrical pinhole on the top surface of the mounting bracket is subjected to a force of 1250.2 N. This force represents the operational load transmitted by the hydraulic cylinder to the construction via the pin connection under working conditions. To accurately simulate the actual conditions for which this type of force transfer is required from the cylinder to the structure via the mounting bracket, the loading direction is defined along the axis of the pin connection. The four bolt holes on the base plate are defined with suitable support boundary conditions to accurately simulate the conditions under which this type of bracket is mounted on the machine structure. The stiff connection between the structure constructed by this type of bracket and the supporting structure using bolted connections is accurately simulated by assuming this type of boundary condition.

a. Meshing of the Model

A three-dimensional model of the cylinder mounting bracket was created in PTC Creo and imported into ANSYS for topology optimization and finite element analysis, as shown in Figure 2 (b). To numerically simulate the problem, it is imperative to divide the geometry into smaller finite elements using a meshing procedure. Due to the complex features of the cylinder mounting bracket, including curved edges, ribs, and numerous holes, an unstructured tetrahedral mesh was used. In some areas, such as the pin connection hole and bolt mounting holes, where high stress concentrations are anticipated, the mesh was refined. The quality of the newly formed elements must be checked to ensure it meets acceptable limits for simulation purposes. The acceptable limits were checked against established criteria for mesh quality, including skewness, aspect ratio, and quality. The load transfer mechanisms between the cylinder pin and the base mounting points were captured using an adequately refined mesh while maintaining an acceptable level of efficiency. The stress, deformation, and structural response of the structure under applied loading conditions can be precisely calculated using the newly formed mesh, which is a dense network of elements covering the entire surface area of the cylinder mounting bracket.

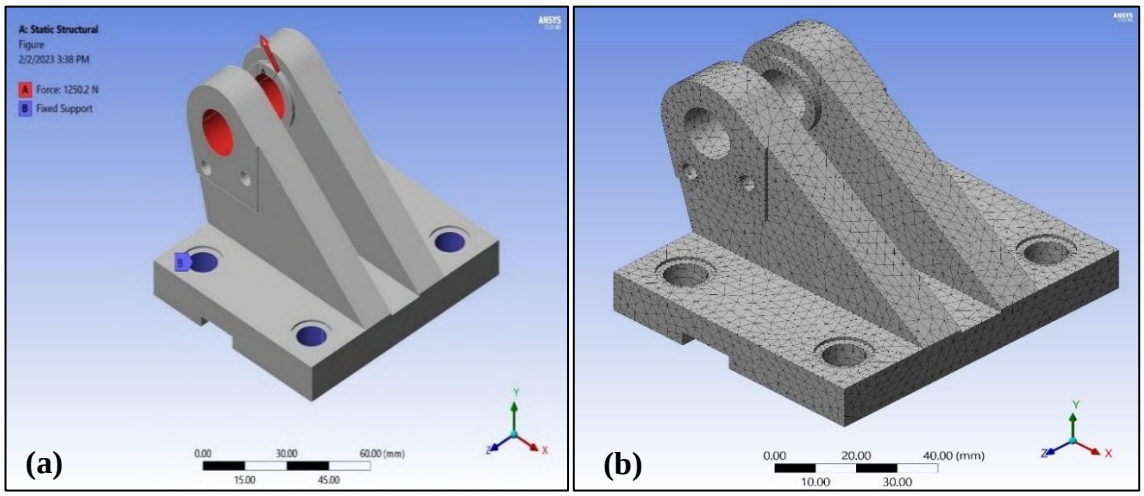


Figure 2: Loading and boundary condition (a) Boundary condition and loading (b) Meshing of the model.
Source: Authors, (2026).

Each finite element (*i*) created in the meshing phase of a general topology optimization problem statement is assigned a design variable (ηi), which is an internal, pseudo-density of the model. Material to be removed is denoted by ηi = 0, and material to be kept is denoted by ηi = 1. The pseudo-density ranges from 0 to 1. The above is another form of stating the topological optimization method:

$Minimize/maximize\ f(\eta i)$
Subject to:

$$0 \leq \eta i \leq 1 \qquad (i = 1,2,3,\dots,n)$$
$$\bar{g}j \leq gj \leq \bar{\bar{g}}j \qquad (j = 1,2,3,\dots,m)$$

Where:

n is $number\ of\ finite\ elements$
m is $number\ of\ constraints$
$\bar{g}j$ is $computed\ constraint\ value$
$\bar{g}_j$ and $\bar{\bar{g}}_j$ is $lower\ and\ upper\ constraint\ bounds$

PTC and Vanderplaats Research & Development, Inc. (VR&D) jointly developed Creo Topology Optimization. The software combines VR&D's optimization expertise with PTC's strength in bridging the physical and virtual realms. A rebuilt optimized part, either a tessellated (faceted) or B-rep (boundary representation), is the output of the Creo topology optimization procedure [29]. The applications tab, generative design, provides access to the Creo topology optimization interface (Fig. 3). Figure 4 shows the preprocess setup tree. Design spaces, structures, and design criteria are its three main constituents. The region where design and non-design areas are defined is called the design space. Although material, constraints, and objectives can be defined in the design criteria, loading and boundary conditions are defined in the structure.

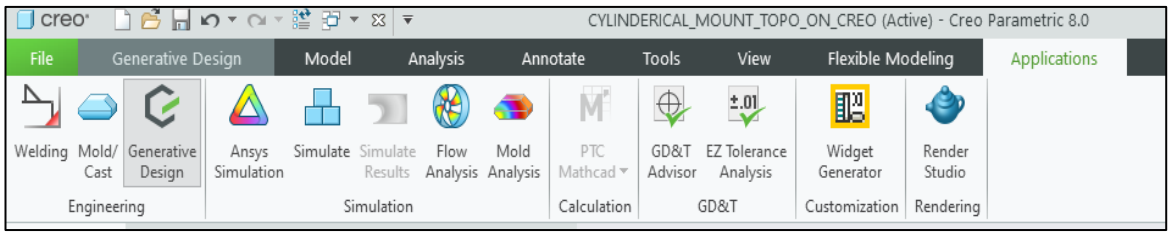


Figure 3: Topology optimization tool in Creo.
Source: Authors, (2026).

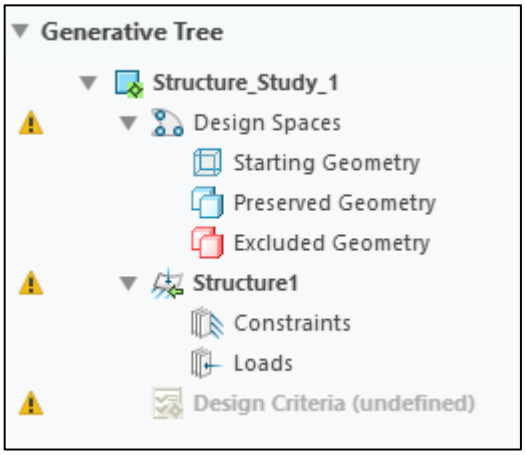


Figure 4: Topology optimization design tree.
Source: Authors, (2026).

IV. RESULTS AND DISCUSSIONS

The results and discussions of the findings of the study are presented in this section of the document. The Creo topology optimization solution for the six design points with weight-reduction values of 70%, 50%, 35%, 25%, 20%, and 17.5% is obtained first. A mesh size of 1.883 mm is used to merge each design-point solution with the static structural analysis solution. The static structural analysis of the original model is then performed in Ansys with the same mesh size as in Creo. Static structural analysis is employed in both Creo and Ansys to obtain the solutions for the original and optimized models at each design point.

a. Topology optimization result

The main aim of the topology optimization process conducted in this study is to minimize the weight of the bracket. The model's mass is gradually reduced during the weight-reduction process. The reason for the percentage difference, as shown in Figures 5-10, is the optimization constraints and the smoothing process. Following a weight reduction of nearly 70%, Figure 5 (a) illustrates the Von Mises stress results obtained from the parametric topology optimization analysis of the cylinder mounting bracket. To minimize the weight of the cylinder mounting bracket while retaining its functional properties, a topology optimization analysis was performed after specifying the material properties, boundary conditions, and mesh. Without affecting the load paths between the pin connection and the base mounting holes, the optimization algorithm removed unnecessary material from low-stress regions.

The solver evaluated the bracket's response to the applied load of 1250.2 N. The regions of maximum stress are near the pin joint area and the base area of the bracket, as indicated by the stress distribution plot after optimization. To maintain the integrity of the structure, these regions are retained in the optimal design. Notwithstanding the significant material reduction, the optimized bracket still maintains an efficient load path, as indicated by the stress contour plot. The results indicate that topology optimization is an effective technique for developing a light structure that maintains mechanical stability and satisfactory stress levels.

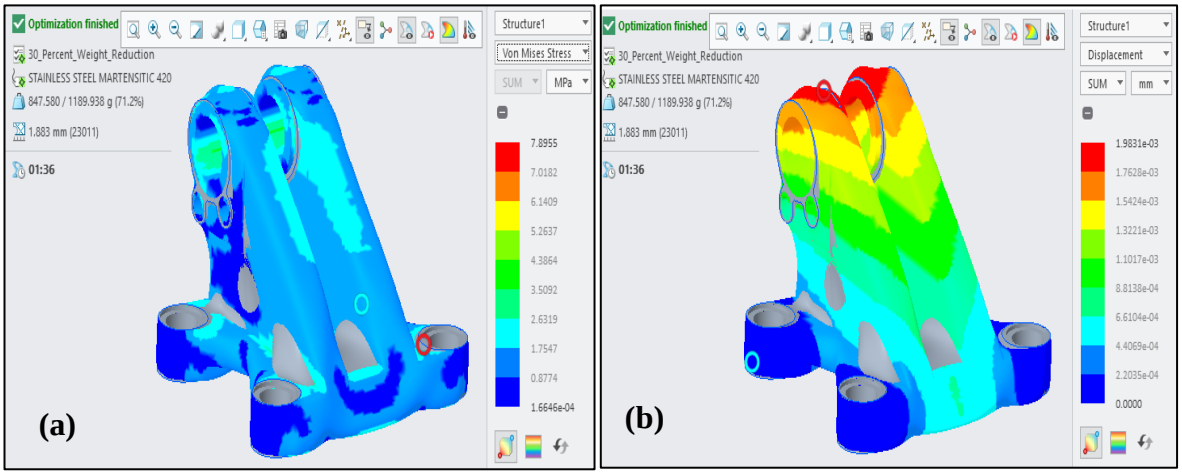


Figure 5: 70% weight reduction (a) Von-Mises's Stress (b) Deformation.
Source: Authors, (2026).

The deformation distribution of the cylinder mounting bracket, derived from a parametric topology-optimization study following a weight reduction of approximately 70%, is shown in Figure 5(b). The object's displacement is depicted in a color contour plot, where red denotes areas of maximum deformation and blue denotes areas of minimum deformation. The investigation shows that the maximum movement of the object is around 1.883 mm. This region experiences the maximum stress due to its direct interaction with the applied loads and constraint points. The base construction is stiff even after significant material reduction, as indicated by the very low deformation of the mounting holes in the lower base. The final mass of the optimized design is about 487.58 grams, which is 71.2% of the initial mass, indicating a significant weight reduction while maintaining performance efficiency in functional use. The enhanced bracket meets acceptable displacement levels in mechanical systems, as indicated by the deformation pattern.

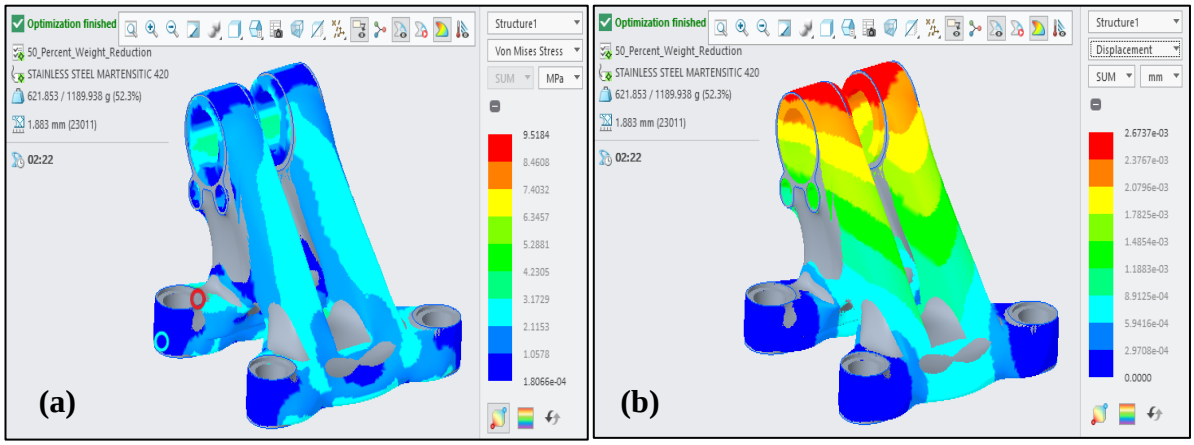


Figure 6: 50% weight reduction (a) Von-Mises's Stress (b) Deformation.
Source: Authors, (2026).

The Von Mises stress distribution of the cylinder mounting bracket after the parametric topology optimization process, with a 50% weight reduction, is shown in Figure 6(a). The Von Mises stresses at various locations of the design are shown in the contour map. The scale of the stresses on the right-hand side of the figure ranges approximately from 1.806×10^{-2} MPa to 9.518 MPa. The location of the maximum Von Mises stresses at the joint of the internal rib and the lower support region, as shown within the circle of red color, has been identified as per the Von Mises stress distribution. The stresses are concentrated at the location where loads are transferred to the upper cylindrical mounting section of the supports at the base. As the load passes through this bracket structure, it is affected by bending and shearing effects in this region. The cyan and green colors indicate low stress in the inclined support arms and the top cylindrical mounting holes, suggesting efficient load distribution along optimal structural paths. The outer edges and base mounting holes of the bracket, shown in dark blue, exhibit very low stress, suggesting that this region remains stable even after significant material is removed. The final mass of 621.853 g is approximately 52.3% of the original mass of 1189.938 g after optimization. The deformation contour map shows the displacement, measured in millimeters, across the entire optimized structure. 2.637×10^{-3} mm, as can be observed in Figure 6 (b), where the blue areas represent areas of low structural movement, and the red areas represent the areas of maximum movement.

It can be observed that the maximum deformation occurs at the upper cylindrical mounting part of the structure, at the pin connection point where the load is applied. The highest level of displacement due to direct load transfer via the bracket arms is represented by the red and orange bands in this section. The transition from the yellow to the green sections demonstrates how the distortion diminishes as the load continues to move downhill via the slanted support ribs. For the initial mass of 1189.938 g, the enhanced bracket has an ultimate mass of approximately 621.853 g, corresponding to 52.3% of the initial mass.

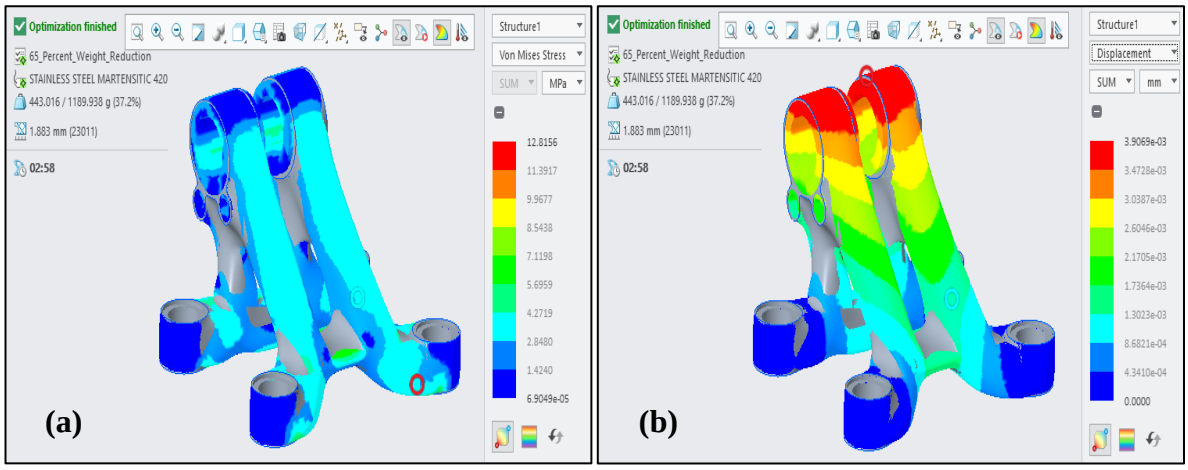


Figure 7: 35% weight reduction (a) Von-Mises's Stress (b) Deformation.
Source: Authors, (2026).

This is shown in the stress contour map in Figure 7 (a), whose color scale ranges from 8.0949×10^{-1} MPa to 12.8156 MPa. In this representation, red spots indicate the highest concentration of tension stress, whereas blue indicates the lowest. From the results, it is clear that the lower base support region, indicated by the red circle and the mounting hole location, has the maximum stress. This is due to the stress resulting from the inclined support arms. The weight distribution from the cylinder connecting point to the base support is heavily dependent on these regions. The optimized design has effectively distributed the weight along the major load paths, as shown by the stress distribution in the structural components. The largest portion of the mounting bracket's outer surface and the base platform, shown in dark blue, has very low stress levels. The final weight achieved through the optimization process, at approximately 443.016 g, is about 37.2% of the original weight of 1189.938 g. This indicates a substantial reduction in material usage while maintaining acceptable stress values within the material's allowed limits. The complete deformation distribution of the optimized cylinder mounting bracket is shown in Figure 7 (b). The magnitude of displacement in the bracket structure, measured in millimeters, is represented in the deformation contour map. The color bar indicates the regions of maximum (red) and minimum (blue) displacement in the structure, ranging from 0 mm (dark blue) to approximately 3.9069×10^{-3} mm (red). This region has the highest displacement as it is directly exposed to the applied load. Effective load transfer in the structure is indicated by the gradual reduction in distortion in the inclined supporting arms, as shown by the transition from the red and orange regions to the yellow and green regions. While allowing controlled deformation in the load-bearing top part, the improved design successfully maintains structural stiffness in the base region. While allowing controlled deformation in the load-bearing top part, the improved design successfully maintains structural stiffness in the base region. Compared to the initial mass of 1189.938 g, the topology optimization resulted in a final mass of approximately 443.016 g, which is 37.2% of the initial mass. Based on the deformation analysis, the parametric topology optimization approach successfully reduces the structure's mass while maintaining structural stability.

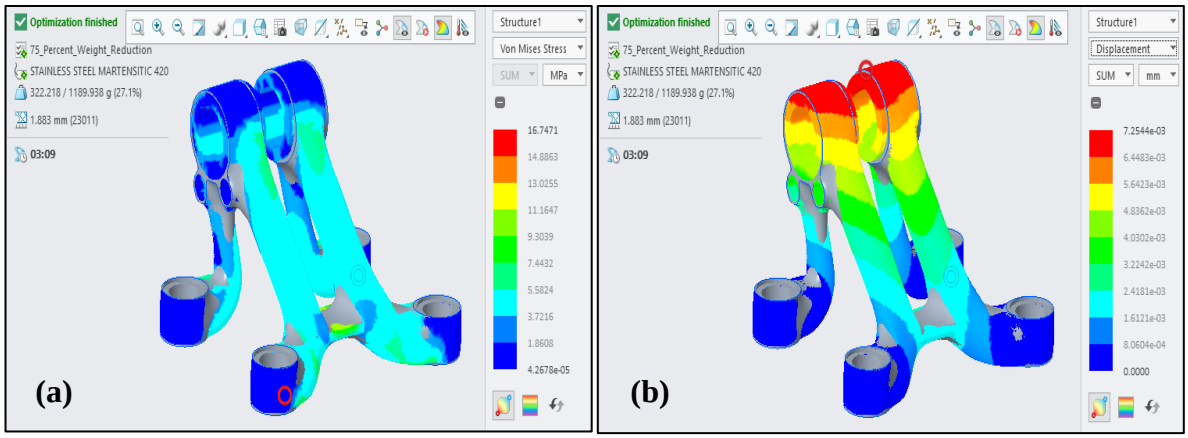


Figure 8: 25% weight reduction (a) Von-Mises's Stress (b) Deformation.
Source: Authors, (2026).

The Von Mises stress distribution of the cylinder mounting bracket, after parametric topology optimization with 25% weight reduction, is shown in Figure 8 (a). From the results, it can be observed that the lower base of the mounting bracket, especially the vicinity of the support hole, has the highest stress levels.

The stress contour map also shows the Von Mises stress levels at different points on the optimized shape. The dark blue areas represent low stress levels, and the red areas indicate high stress levels, indicating maximum stress concentration. The color scale ranges from 4.2678×10^{-1} MPa to 16.7471 MPa. Localized stress accumulation results from the interaction of shear and bending stresses in this region. It can be seen that the applied force is effectively transmitted from the interface of the cylinder mounting to the base mounting points via these structural components. Dark-blue color contours indicate that the majority of the base platform and the structural surfaces remain in low-stress regions. This means that despite the reduced amount of material, the bracket still has adequate structural stability. It can also be shown that the optimization process reduced the mass from 1189.938 g to approximately 322.218 g, a 27.1% reduction. The displacement across the optimum bracket, expressed in millimeters, is shown in the deformation contour map. According to the model, Figure 8(b) indicates that the area of maximum deformation is located in the top cylindrical mounting region, particularly at the pin connection. The displacement across the optimum bracket,

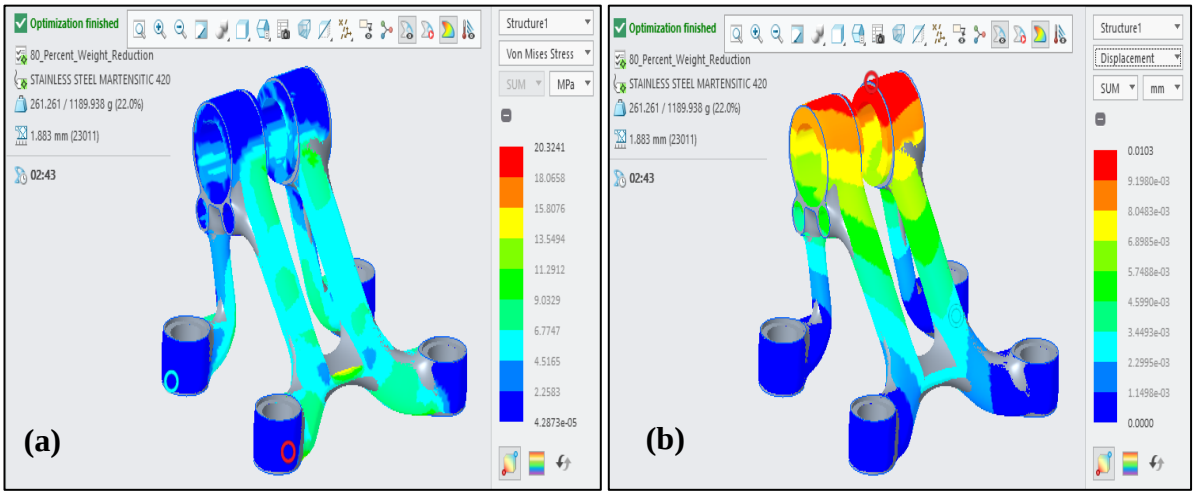


Figure 9: 20% weight reduction (a) Von-Mises's Stress (b) Deformation.
Source: Authors, (2026).

Expressed in millimeters, is shown in the deformation contour map. According to the color legend, the area of maximum displacement (red) and minimum deformation (blue) ranges from 0 mm (dark blue) to approximately 7.2544×10^{-3} mm (red). This means that constant support and adherence to the surrounding structure are guaranteed through the structural rigidity and good constraint of the base structure. Compared to the initial mass of 1189.938 g, the final mass obtained through optimization is about 322.218 g, or 27.1% of the initial mass. The viability of the lightweight structure for practical application is ensured by the optimization process, which guarantees the transmission of load from the upper supporting structure to the base supports. The Von Mises stress distribution obtained from the parametric topology optimization results, with a 20% weight reduction, is shown in Figure 9(a). From the figure, the stress contour map, with a color code ranging from approximately 4.2873×10^{-1} MPa to 20.3241 MPa, shows the Von Mises stress in the optimized bracket shape. From the results, it can be concluded that the lowest base mounting area, i.e., the region around the support hole as shown in the figure, corresponds to the highest stress. This is due to the transfer of load from the upper cylindrical mounting section to the base mounting points, where the structure is restricted, through the slanted support arms. The increase in stress in this region is due to a combination of bending, shear, and load-transfer effects. The applied force is effectively distributed from the cylinder mounting interface to the base supports through these areas, which are the major load-carrying parts. Compared with the initial mass of 1189.938 g, the optimization process yields a final mass of about 261.261 g, corresponding to 22.0% of the initial mass.Figure 9(b) shows the overall deformation pattern of the cylinder mounting bracket. The initial mass of the structure was 1189.938 g, and the final mass after the optimization process was about 261.261 g, corresponding to only 22.0% of the initial mass. The maximum displacement occurs at the top cylindrical mounting area, particularly near the pin connection point where the external load is applied, as indicated by the deformation values. As shown, due to direct load transmission through the cylinder connection to the bracket structure, the area marked in red and orange has the greatest deformation. Compared with the initial mass of 1189.938 g, the final mass, achieved through topology optimization, is approximately 261.261 g, or 22.0% of the initial weight.

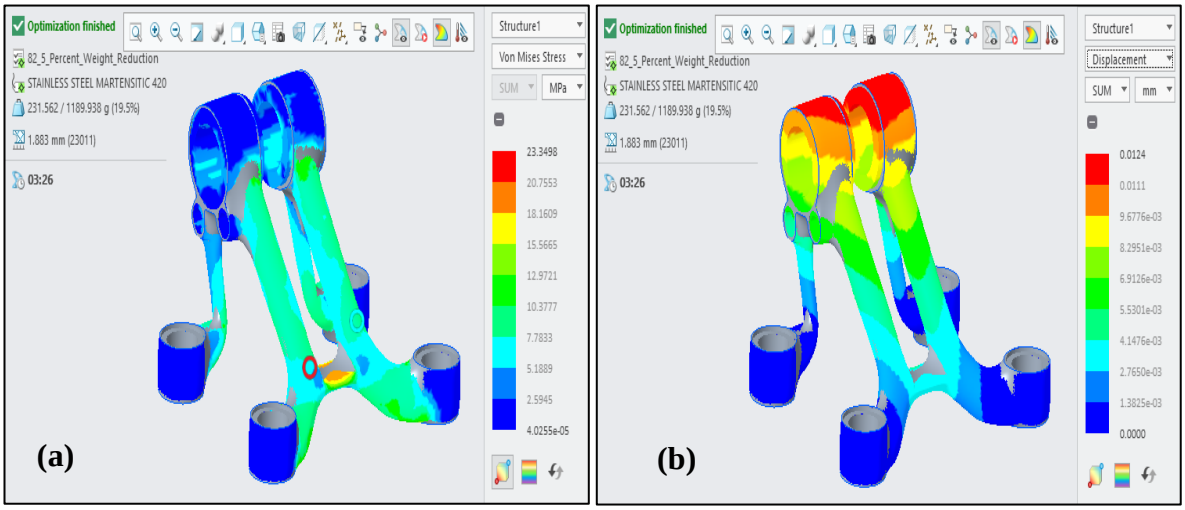


Figure 10: 17.5% weight reduction (a) Von-Mises's Stress (b)Deformation.
Source: Authors, (2026).

As shown in Figure 10(a), the von Mises stress contour map shows equal von Mises stress values across the bracket shape. The color scale ranges from about 4.0255×10^{-1} MPa to 23.3498 MPa. The results show that the maximum stress is near the junction point at the center base, where the structural intersection of the lower base platform and the inclined support arms occurs, as shown in the figure. The combined effects of bending, shear, and load transfer from the upper cylindrical mounting part to the base supports cause stress in this area. The initial mass was 1189.938 g, while the final mass, after optimization, was about 231.562 g, or 19.5 percent of the initial mass. The deformation distribution of the cylinder mounting bracket resulting from the parametric topology optimization process, with a 17.5% weight reduction, is shown in Figure 10(b). The red color shades in the color legend indicate displacement levels ranging from 0 mm to the maximum deformation in the mounting area at the top. The structural displacement of the bracket as the applied load is transmitted through it is shown through these colors. The maximum displacement occurs at the area around the top cylindrical mounting section of the bracket, especially near the pin connection where the applied load is transmitted, as shown by the deformation. As this area is directly exposed to the applied load and serves as the primary load-transfer interface between the cylinder and the bracket, it undergoes the greatest deformation. The change in color from red and orange to yellow, green, and cyan indicates the gradual reduction in deformation as the weight moves downhill along the slanted support arms. For the initial mass of 1189.938 g, the final mass calculated by the topology optimization technique is approximately 231.562 g, or 19.5% of the initial mass. Although the weight decreased compared to Von-Mises stress and the weight reduced compared to deformation are illustrated in "In addition to the above stated result evaluation criteria, strength per unit mass is also one of the evaluation mechanisms," the conclusion of the stress and deformation results is presented in "Table 4" and shown in Figure 11.

Table 4: Design points result summary.

No	Weight reduced (%)	Von-Mises's stress (MPa)	Deformation (mm)
1	70%	7.895	0.001983
2	50%	9.518	0.002673
3	35%	12.815	0.003906
4	25%	16.747	0.007254
5	20%	20.324	0.0103
6	17.5%	23.349	0.0124

Source: Authors, (2026).

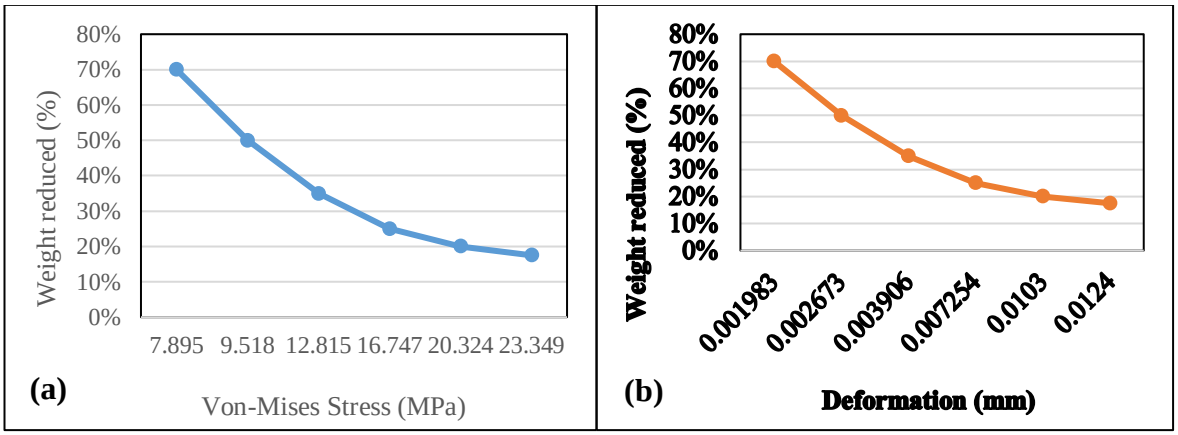


Figure 11: Graph of each design point with the respective result (a) Weight reduced vs Von-Mises's Stress (b) Weight reduced Vs Deformation.
Source: Authors, (2026).

In addition to the above-stated result evaluation criteria, the strength per unit mass is also one of the evaluation mechanisms given in Table 5.

Table 5: Strength per unit mass of the design points.

No	Weight reduction	Von-Mises stress (MPa)	Weight (Kg)	Strength per unit mass (MPa/Kg)
1	70%	7.895	0.848	9.315
2	50%	9.518	0.622	15.306
3	35%	12.815	0.443	28.927
4	25%	16.747	0.322	51.974
5	20%	20.324	0.261	77.792
6	17.5%	23.349	0.232	100.833

Source: Authors, (2026).

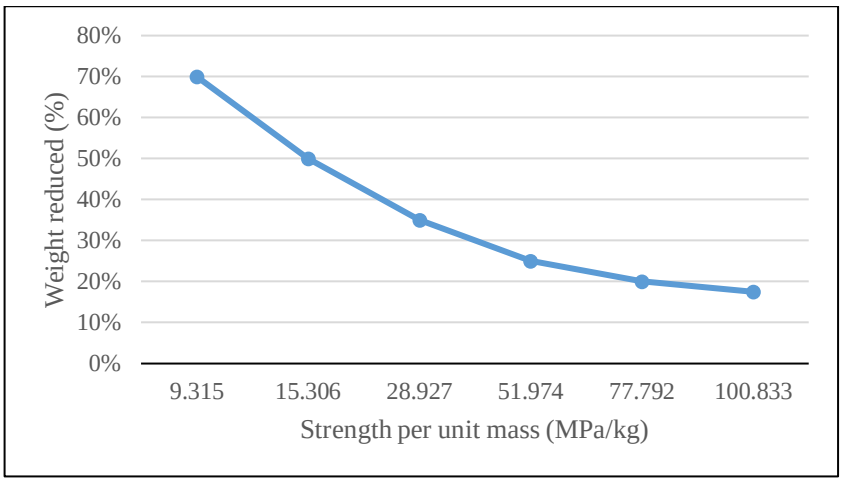


Figure 12: Design point vs strength per unit mass.
Source: Authors, (2026).

How6RTYever, the model was not selected as the best because the study was limited to static analysis and other loading cases. Moreover, the front part of the model's optimization results is very thin, and there are concerns about the model's behavior under bending stress. To explain the stress and deformation in "Figure 10," the fifth design point (20% weight-reduction) is selected as the final model. "Figure 13" shows the topologically optimized and original models. The final product weighs 0.261 kg, 22% lighter than the original model at 1.189 kg.

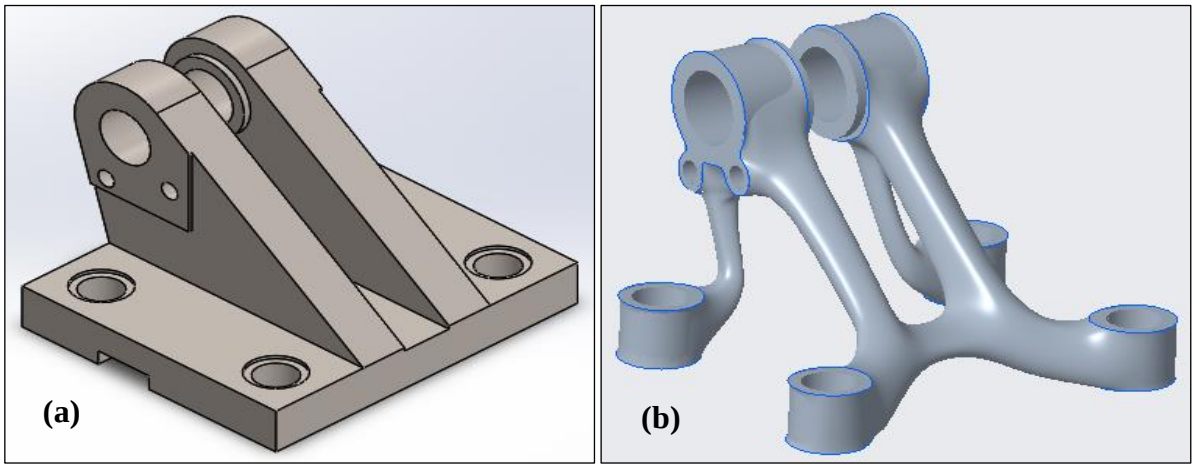


Figure 13: Original and topology optimized model (a) Original model (b) Optimized model.
Source: Authors, (2026).

b. Comparative study of the two models

Figures 14 and 15 show that the Von-Mises stress of the optimized model is 20.32 MPa, whereas it was 10.33 MPa for the original model. Also, the distortion value for the optimized model is 0.0103mm, whereas it was 0.00184mm for the original model. The resulting stress value is well below the material's tensile yield strength of 1360 MPa. This confirms that even if the optimized model has higher stress values, its factor of safety (FOS) will be greater.

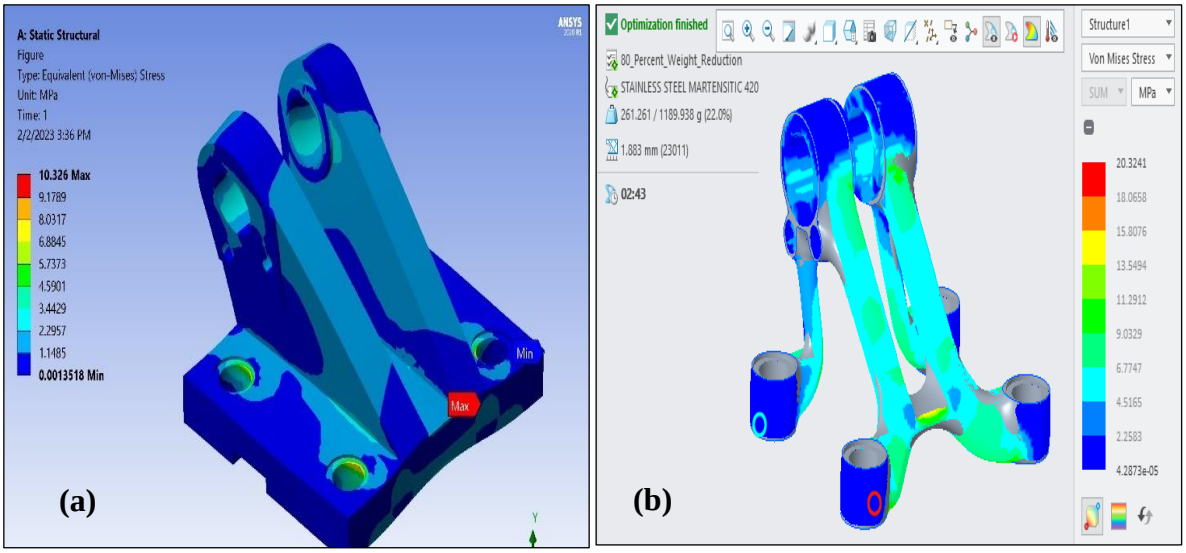


Figure 14: Von-Mises stress Result (a) Original model (b) Optimized model.
Source: Authors, (2026).

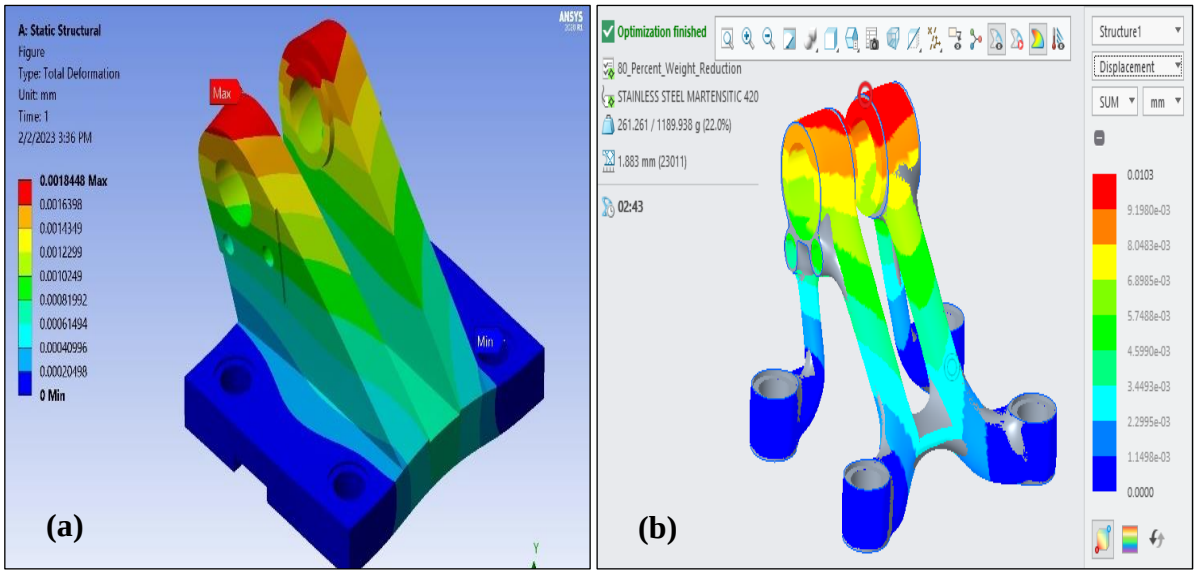


Figure 15: Deformation result (a) Original model (b) Optimized model.
Source: Authors, (2026).

V. CONCLUSION

This paper aims to optimize the topology of mounting brackets for cylinders used in fluid power systems. The aim is to check the original model at six design points: 30%, 50%, 65%, 80%, and 87.5% weight reduction, and 70%, 50%, 35%, 25%, 20%, and 17.5% weight retention. The original model weighed 1.189 kg and was created in the commercial SolidWorks software using martensitic stainless steel 420. The Parker Miller Fluid Power specification serves as the source for all geometric parameters, loading conditions, and constraints. The generative design module in PTC Creo Parametric software was used for topology optimization. The original model and the optimized model with an element mesh size of 1.883 mm were analyzed using static structural analysis. The original weight of the mounting bracket design was 1.189 kg. In the optimization process, six design points with weight retention of 70%, 50%, 35%, 25%, 20%, and 17.5% were chosen for evaluation. Even with the constraints, the optimization technique can still minimize the weight if required. Therefore, for 70%, 50%, 35%, 25%, and 17.5% design points, respectively, the actual weight retention values are 0.847 kg (71.2%), 0.622 kg (52.3%), 0.443 kg (37.2%), 0.322 kg (27.1%), 0.261 kg (22%), and 0.231 kg (19.5%). As the percentage of weight reduction increases, the weight per unit mass also increases. 9.315 MPa/kg, 15.306 MPa/kg, 28.927 MPa/kg, 51.974 MPa/kg, 77.792 MPa/kg, and 100.833 MPa/kg are the weights per unit mass. The choice of the model is not based on being the best, as it is constrained by the study's limitations related to static analysis and other loading conditions. Additionally, in the case of bending strain, the model appears suspiciously thin at the front. Therefore, the final model chosen to show stress and deformation is the fifth design point (20% weight-reduction design point). The completed model weighs 0.261 kg, which is 22% of its original weight of 1.189 kg. ANSYS performs a static analysis with the same loading and analysis conditions. The Von Mises stress of the improved model is 20.32 MPa, compared to 10.33 MPa of the previous model. Additionally, the distortion of the optimized model is 0.0103mm, compared to 0.00184mm of the original model. The generated stress is much lower than the material's tensile yield strength of 1360 MPa.

VI. AUTHOR'S CONTRIBUTION

Conceptualization: Edosa Kefyalew, Adugna Fikadu, Mahesh Gopal.
Methodology: Edosa Kefyalew, Adugna Fikadu.
Investigation: Edosa Kefyalew, Adugna Fikadu, Mahesh Gopal
Discussion of results: Edosa Kefyalew, Adugna Fikadu.
Writing – Original Draft: Edosa Kefyalew, Adugna Fikadu.
Writing – Review and Editing: Edosa Kefyalew, Adugna Fikadu.
Resources – Adugna Fikadu, Mahesh Gopal.
Supervision: Edosa Kefyalew, Mahesh Gopal.
Approval of the final text: Adugna Fikadu. Mahesh Gopal.

VII. ACKNOWLEDGMENTS

We are also grateful to the anonymous reviewers for their constructive comments, which helped us improve the quality of this manuscript.

VIII. REFERENCE

[1] J. P. Wu, J., Sigmund, O., & Groen, "Topology optimization of multi-scale structures: a review," Struct. Multidiscip. Optim., vol. 63, no. 3, pp. 1455-1480., 2021.

[2] J. H. Zhu, W. H. Zhang, and L. Xia, "Topology Optimization in Aircraft and Aerospace Structures Design," Arch. Comput. Methods Eng., vol. 23, no. 4, pp. 595–622, 2016, doi: 10.1007/s11831-015-9151-2.

[3] A. Dubrovskaya, K. Dongauzer, and R. Faskhutdinov, "The design of lightweight gas turbine engine parts using topology optimization," MATEC Web Conf., vol. 129, 2017, doi: 10.1051/matecconf/201712901067.

[4] L. Krog, A. Tucker, and G. Rollema, "Application of topology, sizing and shape optimization methods to optimal design of aircraft components," 3rd Altair UK HyperWorks Users Conf., pp. 1–12, 2002, [Online]. Available: http://www.soton.ac.uk/~jps7/Aircraft Design Resources/manufacturing/airbus wing rib design.pdf%5Cnftp://emci.udg.edu/mme/ODM/treballs/shape_optimization/airbus wing rib design.pdf

[5] P. S. Tang and K. H. Chang, "Integration of topology and shape optimization for design of structural components," Struct. Multidiscip. Optim., vol. 22, no. 1, pp. 65–82, 2001, doi: 10.1007/PL00013282.

[6] J. Liu et al., "Current and future trends in topology optimization for additive manufacturing," Struct. Multidiscip. Optim., vol. 57, no. 6, pp. 2457–2483, 2018, doi: 10.1007/s00158-018-1994-3.

[7] S. Ramesh et al., "Topology optimization and finite element analysis of a jet dragster engine mount Topology optimization and finite element analysis of a jet dragster engine mount," Cogent Eng., vol. 7, no. 1, 2020, doi: 10.1080/23311916.2020.1723821.

[8] N. A. Faskhutdinov, R. N., Dubrovskaya, A. S., Dongauzer, K. A., Maksimov, P. V., & Trufanov, "Topology optimization of a gas-turbine engine part," in In IOP conference series: materials science and engineering, 2017, pp. 177, (1), 012077.

[9] E. Armentani, V. Giannella, A. Parente, and M. Pirelli, "Design for NVH: Topology optimization of an engine bracket support," Procedia Struct. Integr., vol. 26, no. 2019, pp. 211–218, 2020, doi: 10.1016/j.prostr.2020.06.024.

[10] A. S. Shanmugasundar, G., Dharanidharan, M., Vishwa, D., & Kumar, "Design, analysis and topology optimization of connecting rod," Mater. Today Proceedings, vol. 46, pp. 3430-3438., 2021.

[11] D. J. Munk, D. J. Auld, G. P. Steven, and G. A. Vio, "On the benefits of applying topology optimization to structural design of aircraft components," Struct. Multidiscip. Optim., vol. 60, no. 3, pp. 1245–1266, 2019, doi: 10.1007/s00158-019-02250-6.

[12] E. Talay, C. Özkan, and E. Gürtaş, "Designing lightweight diesel engine alternator support bracket with topology optimization methodology," Struct. Multidiscip. Optim., vol. 63, no. 5, pp. 2509–2529, 2021, doi: 10.1007/s00158-020-02812-z.

[13] S. Kalsi, D. Singh, and J. S. Saini, "Optimization of Compressor Mounting Bracket of a Passenger Car," J. Inst. Eng. Ser. C, vol. 100, no. 4, pp. 675–691, 2019, doi: 10.1007/s40032-018-0453-7.

[14] S. Kirthana and M. Khaja Nizamuddin, "Finite element analysis and topology optimization of engine mounting bracket," Mater. Today Proc., vol. 5, no. 9, pp. 19277–19283, 2018, doi: 10.1016/j.matpr.2018.06.286.

[15] J. Fang, "Motion Simulation and Topology Optimization Design of a Mechanical Gripper Based on Creo Simulate 4.0," Adv. Eng. Technol. Res., vol. 15, no. 1, p. 759, 2025, doi: 10.56028/aetr.15.1.759.2025.

[16] A. Mortazavi and V. Toğan, "Simultaneous size, shape, and topology optimization of truss structures using integrated particle swarm optimizer," Struct. Multidiscip. Optim., vol. 54, no. 4, pp. 715–736, 2016, doi: 10.1007/s00158-016-1449-7.

[17] D. Yago, J. Cante, O. Lloberas-Valls, and J. Oliver, Topology Optimization Methods for 3D Structural Problems: A Comparative Study, vol. 29, no. 3. Springer Netherlands, 2022. doi: 10.1007/s11831-021-09626-2.

[18] A. Kumar and D. Chhabra, "Parametric topology optimization approach for sustainable development of customized orthotic appliances using additive manufacturing," Mech. Adv. Mater. Struct., vol. 31, no. 21, pp. 5276–5289, 2024, doi: 10.1080/15376494.2023.2214908.

[19] G. Selvaraj et al., "Investigation on topology-optimized compressor piston by metal additive manufacturing technique: Analytical and numeric computational modeling using finite element analysis in ANSYS," Open Phys., vol. 21, no. 1, 2023, doi: 10.1515/phys-2022-0259.

[20] R. Ahmed, "Topology Optimization and Additive Manufacturing of Lightweight Cantilever Beams : Design , Fabrication , and Cost Analysis," Res. Sq., 2025.

[21] D. Jankovics, H. Gohari, M. Tayefeh, and A. Barari, “Developing Topology Optimization with Additive Manufacturing Constraints in ANSYS®,” IFAC-PapersOnLine, vol. 51, no. 11, pp. 1359–1364, 2018, doi: 10.1016/j.ifacol.2018.08.340.

[22] A. Kalantre, V., Munde, K. H., & Pawar, “Topology Optimization of Front Leaf Spring Mounting Bracket,” Int. J. Sci. Dev. Res., vol. 3, no. 7, pp. 12–19, 2018.

[23] B. Liu, J. Yang, X. Zhang, and X. Li, “Topology Optimization and Lightweight Platform Development of Pure Electric Vehicle Frame-Type Aluminum Body Considering Crash Performance,” J. Mater. Eng. Perform., vol. 34, no. 3, pp. 2424–2434, 2025, doi: 10.1007/s11665-024-09239-3.

[24] M. N. Khan, A. K. A., Kadir, A. R. A., Nazri, Z., Razak, T. A. A., & Ahmad, “Topology optimization of an engine mounting bracket using finite elements,” 2022.

[25] S. K. Kandreegula, N. Sukumar, S. Endugu, and U. Gupta, “Structural Non-linear Topology Optimization of Transmission Housing and Its Experimental Verification,” 2015. doi: 10.4271/2015-01-0098.

[26] M. Kalanchiam and B. Mannai, “Topology Optimization of Aircraft Fuselage Structure,” World Acad. Sci. Eng. Technol., vol. 7, no. 5, pp. 133–136, 2013.

[27] Outokumpu, Handbook of Stainless Steel. 2013. [Online]. Available: http://www.outokumpu.com/sitecollectiondocuments/outokumpu-stainless-steel-handbook.pdf

[28] Parker, “Cylinder Mounting Accessories,” 2012.

[29] Stefano Odorizzi, “Enginsoft Projects ’ insights,” 2022.

Journal of Engineering and Technology for Industrial Applications

ITEGAM-JETIA

Manaus, v.12 n.60, p.1536-1547 July/August, 2026.
DOI: https://doi.org/10.5935/jetia.v12i60.4438

ISSN ONLINE: 2447-0228

RESEARCH ARTICLE OPEN ACCESS

EYE TRACKING AND GAZE ESTIMATION: A SYSTEMATIC REVIEW OF DEEP LEARNING METHODS AND EDUCATIONAL APPLICATIONS

Khalid Sami Yousif *[1], Emad A. Mohammed [2] and Mayyada Al- Hammoshi [3]

[1, 2]Technical Engineering college for computer and AI, Mosul - Iraq
[3]Washington University of Science and Technology, Washington-USA

[1]https://orcid.org/0009-0001-8715-0065, [2]https://orcid.org/0000-0002-2575-6213, [3]https://orcid.org/0009-0007-5022-1046

E-email: *khalid.sami@ntu.edu.iq, e.a.mohammed@ntu.edu.iq, mayyadah70@gmail.com

ARTICLE INFO

Article History
Received on: March 30, 2026
Reviewed on: April 30, 2026
Accepted on: July 01, 2026
Published on: July 31, 2026

Keywords:
Gaze Estimation,
Eye Tracking,
Head Pose Estimation,
Deep Learning,
CNN,
Transformer.

ABSTRACT

Tracking of the eyes and head have occupied a crucial role in human computer interaction, virtual and augmented reality, accessibility systems and cognitive studies. This paper gives a critical review on gaze estimation and head pose tracking algorithms, data sets, and performance determinants. This article compares classical and deep learning-based methods, such as convolutional neural networks, transformer models, geometric, hybrid, and multi-task learning methods. The article also tests the robustness in the external conditions like blinking, occlusion, and changes in illumination, and cross-subject individual differences. The most important publicly available datasets are compared regarding the type of input, diversity of participants, the size of data, recording distance, and environmental conditions. This article also contrasts new webcam and specialized eye-tracking systems, and, in doing so, point out trade-offs between accuracy, cost and applicability in real-time. The review also stresses on the role of domain adaptation, contrastive learning, and multi-modal inputs in generalizing across domains. In general, the article contains an attempt to present a comprehensive picture of the existing situation to researchers and practitioners to assist them in designing and choosing gaze and head pose estimation systems to be used in various applications.

Copyright ©2026 by authors and Galileo Institute of Technology and Education of the Amazon (ITEGAM). This work is licensed under the Creative Commons Attribution International License (CC BY 4.0).

I. INTRODUCTION

Gaze estimation and eye tracking have become the fundamental technologies in comprehending the human visual attention, mental processes, and the behavior of interaction. Fundamentally speaking, the techniques seek to ascertain the location of a person with their gaze, either through direct eye tracking or by inferring the direction of the gaze based on visual images or video streams [1]. Traditionally, eye tracking used specialized hardware systems, which had infrared illumination and high-speed cameras, which had the ability to capture fine-grained ocular characteristics like pupil placement and corneal reflections. Although these systems are highly accurate, they tend to be costly, obtrusive as well as restricted to controlled laboratory conditions. Consequently, their application in real-life use, especially in education and large-scale behavioral research has been limited [2]. The past few years have seen a drastic change of gaze estimation because of the development of computer vision and deep learning. Appearance-based approaches, which are methods that are based on the direct recognition of the direction of gaze based on the images of the face or eyes, have been in the limelight as a viable alternative to the traditional model-based approaches. In these techniques, convolutional neural networks (CNNs), transformer networks and hybrid geometric-learning networks are used to extract meaningful features of typical RGB images. This has in turn made it possible to carry out gaze tracking with the use of normal cameras without having to have special sensors. This has led to increased scalability and availability of eye tracking solutions most particularly web camera versions installed on both desktop and mobile computers [3]. The advent of low cost, web-based eye tracking systems is an important step toward the democratization of eye tracking technology. In contrast to specialized eye trackers, webcams are everywhere, cheap, and already integrated into the majority of consumer gadgets such as laptops, tablets and smartphones.

This has enabled researchers and practitioners to implement gaze tracking applications in a variety of real-world scenarios without enormous financial and technical constraints [4]. Moreover, the current deep learning architectures have been shown to mitigate the natural drawbacks of webcams, including reduced resolution, fluctuating light conditions, and the inability to run infrared, by training expressive representations of gaze-sensitive features. Open-source systems and frameworks have further made the process go faster on offering pre-made tools of real-time gaze estimation, calibration and data collection [5]. These developments are especially significant in such sphere as education, where student attention and engagement are important factors that have to be understood to enhance learning outcomes. Conventional strategies of gauging the engagement, including self-reporting, survey, or observation research, are frequently based on subjectivity, time-consuming, and not easily scaled. On the contrary, eye tracking using webcams is a non-invasive, automated technique of monitoring visual attention of students in the learning process. An examination of the gaze patterns will enable educators and other researchers to understand the interaction of students with teaching material, understand non-understood areas, and the effectiveness of the teaching techniques. This comes in handy particularly in online and remote learning where students cannot be observed directly [6]. In addition, the role of gaze estimation in education technologies facilitates the larger paradigm of learning analytics and intelligent tutoring systems. An example is the presentation of content which can be optimized using gaze data, or generate customized feedback, or real-time disengagement. Eye tracking can be used in visualization of cognitive processes in such subject matters as mathematics and statistics where visual attention is the main tool in problem solving and understanding. Consequently, the use of inexpensive gaze tracking systems can improve research and practice in the education field by allowing the collection of information to make decisions on large scales [7]. These positive developments notwithstanding, there are a number of challenges. Webcam-based systems are less accurate than dedicated eye trackers by their nature, and often susceptible to variations in head position, occlusions, and variations in the appearance of the user.

Moreover, the process of creating a strong generalization among various devices, settings, and target audiences remains a research topic. These have been tackled in recent works with methods like domain adaptation, contrastive learning and multi task learning, whose goal is to enhance the robustness and transferability of models. Ethical issues, such as privacy, data security, and informed consent, should be, conversely, handled with care at all times, especially in the case of the implementation of gaze tracking technologies in sensitive settings, such as education [8]. Since this area is quickly developing and numerous methods are suggested in the recent literature, it is evident that a thorough and systematic review is necessary that would synthesize the existing knowledge and outline the perspectives in future research. Although a number of surveys have investigated eye-tracking and gaze estimation through particular lens, e.g. hardware-based systems, deep learning methods, or educational practices, a gap still exists in the combination of these aspects within the framework of affordable solutions based on web-cams. It is with the intention of filling that gap that this review attempts to present a coherent overview of the state of the art, specifically focusing on approaches drawing on the use of standard cameras and present-day machine learning methods. There are three main purposes of this review. First, it aims at giving a clear and systematic overview of the basic ideas and methodology behind eye tracking and gaze estimation both conventional and modern. Second, it will also seek to review new developments in webcam-based systems in a systematic manner, particularly deep learning models, system architecture, and performance assessment. Third, the review discusses how these technologies have been used in the learning environment and how they have the potential to assess student attention, improve learning analytics, and facilitate adaptive learning environments. Besides providing a summary of the existing works, the review also has several major contributions. It suggests a unified taxonomy of gaze estimation algorithms to fits the constraints of low-cost camera configurations, compares the state-of-the-art methods in reference to accuracy, robustness, and computational cost, and locates key difficulties, which should be solved to allow implementation in the reality. Moreover, it identifies the future trends of research, such as cross-domain generalization, multimodal integration, and privacy-saving methods, which will have an influence on the future of webcam-based eye tracking.

II. FUNDAMENTALS OF EYE TRACKING AND GAZE ESTIMATION

The eye-tracking technology is a collection of techniques and apparatuses that monitor the eye positions and movements with the goal of identifying the point of gaze (where one is looking) and the movement of the eyes with respect to time. It has found its way to be a mandatory device in areas like human-computer interaction, neuroscience, psychology, marketing, and assistive technologies. Eye-tracking systems can be of great use by providing insights on cognitive processes, user experience, and decision-making because they capture visual attention and gaze behavior. Throughout the decades, eye-tracking technology has experienced a massive evolution, which started as an intrusive and hardware-intensive system to highly accurate and non-invasive; non-hardware solutions that are software-driven. These improvements have been occasioned by sensor technology, computer vision, and artificial intelligence [9]. Figure (1) shows the evolution of eye-tracking technology over time, with the key milestones in technological advancement in the 1940s being the ones with high attention to date. The figure outlines the process of the shifting of the old method of electrical measurements to the current system, which is powered by AI and is sensor-based, showcasing how the entire system has been getting better and better, to where it is more precise, easy to use, and integrated [10].point

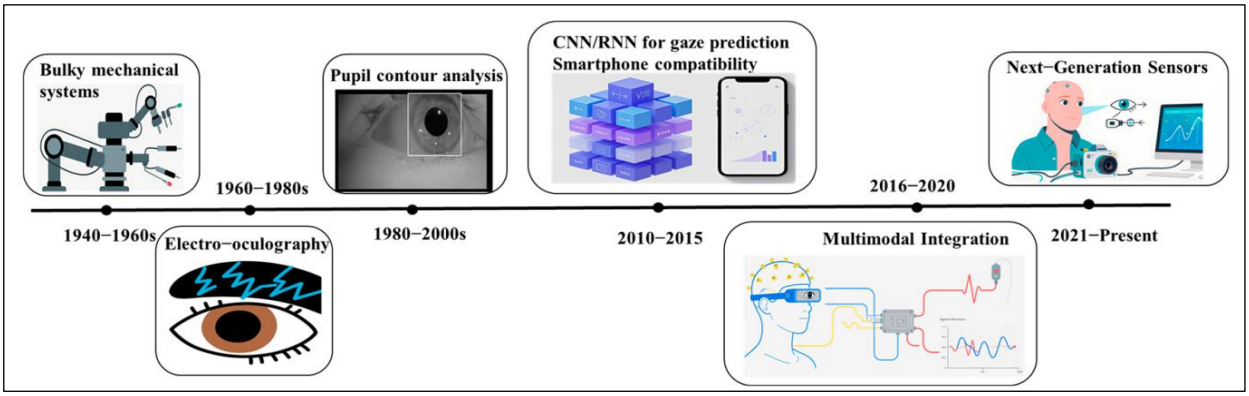


Figure 1: Timeline of Eye-Tracking Technology Evolution
Source: [10].

The history of eye-tracking technology development can be separated into several important stages each of which marked a significant breakthrough in the methodology and usage.

- The first stage (1940s1960s) was based on the principle of electro-oculography (EOG) where electrical potential of the eye movements are measured with the help of electrodes put around the eyes. Although this technique was able to give fundamental propositions on eye movement, it lacked a high spatial resolution and involved direct physical contact with the subject and was not very useful in widespread practice [11].
- In the 1960s-1980s, the eye-tracking systems were replaced with bulky mechanical systems. These systems tended to be head-mounted systems or hard structures that limited the movements of the user. Despite their ability to increase the measurement abilities, they were inconvenient and could be mostly used in the controlled laboratory settings [12].
- A major improvement was made between the 1980s and 2000s when an analysis of the contour of the pupil was introduced. This method of non-invasive tracking through the use of the camera was made possible since the camera was able to identify and determine the shape and position of the pupil. It is the stage of the modern eye-tracking starting with better accuracy and increased comfort to the user [13].
- The years 2010-2015 were marked by the introduction of the methods of artificial intelligence, especially convolutional and recurrent neural networks. Those approaches increased the accuracy of estimating gaze and allowed tracking of the eye on the consumer devices of smartphones. The technology became easier and larger-scale [14].
- In 2016-2020, multimodal integration, the integration of gaze data with other physiological measures, started to become available in eye-tracking systems, including brain activity and heart rate. This has made it possible to gain a better understanding of human behavior and apply it in virtual reality, healthcare, and more sophisticated user interfaces [15].
- Since 2021, there is an additional development of next-generation sensors that revolutionized the field. New systems are small, efficient in energy use, and can track in real time and with high accuracy. Now they are present in the devices that people use in their daily lives, including the augmented reality headsets, laptops, and wearable technologies, with vast potentials in bringing them into practice [15].

II.1 BASIC CONCEPTS OF EYE TRACKING

Eye tracking is founded on the number of basic concepts that explain the motions of the eyes and the measurement of visual attention. These concepts are important to comprehend the eye-tracking data and utilize it in research and in the real practice. The eye of a human being does not plan through a scene in a smooth way, but it switches between quick motions as well as short periods of rest. These movements demonstrate information collection and processing in the form of visual processing. Eye-tracking systems are used to record such patterns and convert them into meaningful measures that indicate attention, interest and cognitive effort [16]. The fixations, saccades, and gaze points are the main concepts that the eye-tracking analysis is based on. More sophisticated features such as scan paths and areas of interest (AOIs) are also used to assist the researcher to learn more about viewing behavior in complex settings. The combination of the two notions enables qualitative and quantitative study of visual attention [17]. Table 1. Shows Basic Concepts of Eye Tracking.

Table 1: Basic Concepts of Eye Tracking.

Concept	Definition	Description / Importance
Gaze Point	The exact location where a person is looking at a given moment	Represents the fundamental output of eye-tracking systems
Fixation	A period when the eyes remain relatively still on a single point	Indicates focused attention and information processing
Saccade	A rapid movement of the eye between fixations	Helps shift attention from one point to another; no visual processing occurs during it
Scan Path	The sequence of fixations and saccades over time	Shows the overall viewing pattern and behavior
Area of Interest (AOI)	A predefined region in a visual scene selected for analysis	Used to measure attention on specific elements (e.g., buttons, images)
Pupil Dilation	Changes in pupil size	Can indicate cognitive load, emotional response, or lighting conditions

Blink Rate	Frequency of eye blinks	(fatigue and attention levels)
Dwell Time	Total time spent looking at a specific area	Reflects the level of interest or importance of that area
Heatmap	Visual representation of gaze data using color intensity	Highlights areas that attract the most attention
Gaze Plot	A visual diagram showing fixations and saccades in sequence	Useful for analyzing viewing order and navigation patterns

Source: [18].

II.2 GAZE ESTIMATION TECHNIQUES

Gaze point estimation is the calculation process of identifying the point where the observer is gazing. This calculation is carried out in the majority of eye-tracking systems, based on approximating the point of gaze (POG) on a two-dimensional surface, which could be a display monitor or a scene in front of the camera. This estimation is normally done by creating some mapping between the features obtained in the eye and the location of the gaze. In this case, the eye feature coordinates (X_e, Y_e) are transformed into the screen coordinates (X_s, Y_s) by a non-linear regression (polynomial) equation to represent the connection between these variables [19]. This mapping is typically represented as a 2-dimensional poly, in which the horizontal and vertical gaze coordinates are determined in terms of the combinations of powers of the eye feature coordinates. The equations may be expressed as follows [20]:

$$X_s = a_0 + \sum_{p=1}^{n} \sum_{i=0}^{p} a_{(i,p)} X_e^{p-i} Y_e^{i} \quad (1)$$

$$Y_s = a_0 + \sum_{p=1}^{n} \sum_{i=0}^{p} b_{(i,p)} X_e^{p-i} Y_e^{i} \quad (2)$$

Where, (X_e, Y_e) are the coordinates of the extracted eye features, (X_s, Y_s) are the estimated coordinates of the gaze on the screen and $a_{(i,p)}$ and $b_{(i,p)}$ are the coefficients that specify the mapping function. The order of the model, parameter (n), is what determines the complexity and flexibility of the model. A calibration procedure will be necessary to obtain the best values of these coefficients. In this process, the user is requested to concentrate on a number of predefined points that are shown on the screen. The system compares the position of these points with the estimated gaze position to calculate the difference between them and change the coefficients so as to reduce the error in estimation. The reason why this step of calibration is necessary is that it compensates the personal discrepancies among different eye geometry, and enhances the accuracy of the gaze estimation. Although calibration is used, there is still a possibility of error in the estimated gaze position to some extent. The difference in the angle between the optical and visual axis of the human eye is one of the main reasons of this disparity in vision otherwise known as the kappa angle. The line between the center of the cornea and the center of the pupil is referred to as the optical axis whereas the actual direction of body with respect to a target is referred to as the visual axis. Given that the two axes are not aligned, a systematic error is incorporated in the gaze estimation procedure. This bias is different in people and should be countered to allow more accuracy [21]. Moreover, an anatomical makeup of the eye is also significant in eye tracking [22]. The anterior part of the eye has the cornea and the pupil, which refract and regulate the entry of light to the eye respectively. The center of the pupil and the center of the cornea are considered to be the key features of the gaze estimation since it defines the optical axis and forms the foundation of many computation models. These anatomical and geometric relationships are important in understanding how to come up with proper and accurate eye-tracking systems. Figure (2) shows Schematic of the human eyeball, showing key anatomical parameters and reference points for gaze tracking [23].

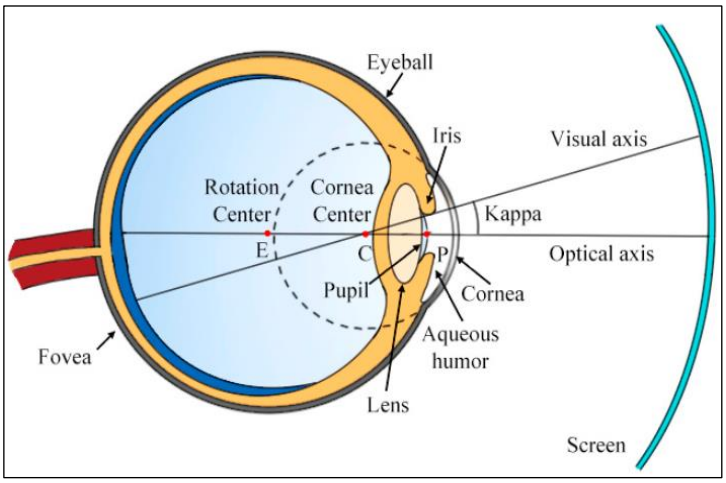


Figure 2: Schematic of Human Eyeball.
Source: Authors, (2026).

III. WEBCAM-BASED EYE TRACKING SYSTEMS

One of the low-cost and most commonly available gaze estimation methods is the eye tracking (Webcam-based) system, which uses the standard cameras, including embedded webcams on laptops or external ones. These systems are based on computer vision and machine learning algorithms to recognize facial features, extract information relating to the eyes, and approximate the direction of gaze of the user in real-time. In contrast to the conventional infrared based eye trackers, webcam solutions can work in the visible light conditions and this presents a challenge in form of sensitivity to light variations, poor image quality, and inconsistency in user placement.

Nevertheless, in spite of these limitations, recent progress in the deep learning and image processing methodologies have greatly improved their work with the examples of their application in remote usability testing, online education, psychological researches, and assistive technologies [24]. Figure (3) illustrates the general workflow of an eye tracking system that uses a webcam to capture the image and then it is scanned by gaze estimation. This starts with camera input, the video frames are captured continuously. These frames are identified by the face detection algorithms to identify the face of the user and approximate the head position, relevant in the context of dealing with natural head expression. After that, the extraction of eye features is made to determine the essential features like the pupil center and the corneal reflections. Such features are the input in the gaze estimation module in which a mapping function is used in estimating the point of gaze of the user on the screen. Lastly, the system does real-time processing to allow generation of gaze predictions with minimum latency hence allowing smoothness and interactive applications [25]. The engineering of this type of systems should take into consideration such aspects as hardware and environmental limitations, such as camera resolution, frame rate, lighting conditions, which directly influence tracking accuracy. The method of personalizing the system by each user is normally done through its calibration to be able to create a correspondence between the eye features that are detected and the known screen coordinates. In addition, real time processing is also necessary to stay responsive, which may demand optimized algorithms and light-weight models. There are tools like GazeFollower which are open-source frameworks, allowing the research and development in this area to be achieved by combining these elements into ready-to-use systems [26].

IV. DEEP LEARNING APPROACHES FOR GAZE ESTIMATION

Deep learning has made a great contribution to the study of gaze estimation by providing more robust and accurate models capable of learning more complicated associations between eye appearance, head pose, and gaze direction. Deep learning methods automatically learn significant features of raw input data, including images of the eyes or face, unlike the traditional model-based or feature-engineering models, and thus are very useful in unconstrained settings. These methods are especially appropriate to the applications based on the webcam and in real world, where the changes in the lighting effect, the head position, and the features of the users are a significant challenge. The most popular architectures in gaze estimation are convolutional neural networks (CNNs) [27]. They have the design to be able to handle image data by learning spatial hierarchies of features using convolutional layers. In gaze tracking, CNNs are normally performed on eye region images or full-face images so as to obtain discriminative features that are linked to gaze direction. Their capacity to achieve fine grained visual patterns e.g. pupil shape, eye contours, etc. makes them very useful in appearance-based gaze estimation tasks [28].

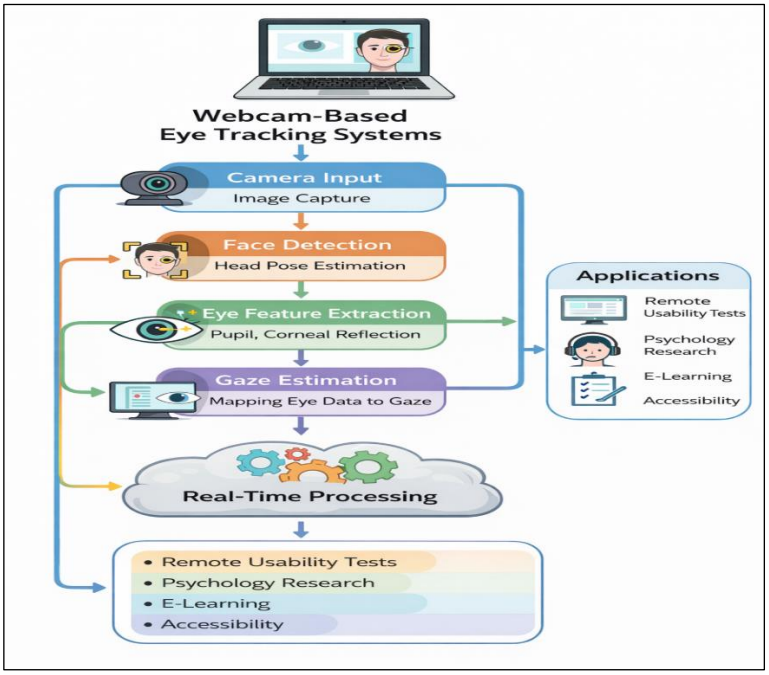


Figure 3:Webcam-Based Eye Tracking Systems.
Source: Authors, (2026).

Transformer-based models have also become a strong rival of CNNs, more recently. These models are based on the focus mechanisms to absorb global connections in the input data so that they can represent long-range relationships better. Gaze estimation Transformers can use the information of other parts of the face or even across multiple frames to be more robust to pose and occlusion changes. They can be extremely demanding in size of datasets and computation power, but have shown optimistic results in complicated cases. Appearance-based gaze estimation is a deep learning representation that directly predicts gaze direction from visual input, including images of the face or eyes, without a geometric representation of the geometric structure of the eye. This mode highly relies on deep neural networks which are able to acquire implicit knowledge of features of gazes. It is especially applicable to low-cost systems, including webcam-based tracking, where accurate geometric measurements are either unreliable or not available [29]. Contrary to that, geometric and hybrid deep models use both learned features and explicit eye geometries. Geometric techniques refer to anatomical and physical models, e.g. the correlation between the pupil and corneal reflections, to determine gaze direction.

Hybrid techniques are methods which combine these geometry constraints with deep learning models to enhance accuracy and generalization. This combination enables the system to combine the two data-driven learning and domain-specific knowledge. Multi-task learning has also found application in gaze estimation, with one model being trained to do several related tasks at the same time e.g. predict gaze direction and head pose. As the head position has a powerful effect on gaze direction, the combined learning of the tasks can enhance the performance. Multi-task models facilitate strong robustness by sharing the representations of various tasks and, therefore, lessening the use of distinct systems, which makes them effective and useful in real-life scenarios [30]. Table (2) shows Deep Learning Approaches for Gaze Estimation

Table 2: Deep Learning Approaches for Gaze Estimation.

Approach	Description	Advantages	Limitations
CNNs	Use convolutional layers to extract spatial features from eye/face images	High accuracy, strong feature extraction, widely used	May struggle with global context and large pose variations
Transformer-Based Models	Use attention mechanisms to model global relationships in data	Captures long-range dependencies, robust to occlusion	High computational cost, requires large datasets
Appearance-Based Methods	Direct mapping from image input to gaze direction	Simple pipeline, suitable for webcams and low-cost systems	Sensitive to lighting and appearance variations
Geometric Models	(pupil, cornea)	Interpretability, grounded in eye anatomy	Requires precise feature detection and calibration
Hybrid Deep Models	Combine deep learning with geometric constraints	Improved accuracy and generalization	Increased system complexity
Multi-Task Learning	Simultaneously predicts gaze and related tasks (e.g., head pose)	Better performance, shared learning, efficient	Requires careful training and balanced datasets

Source: Authors, (2026).

V. CROSS-DOMAIN GENERALIZATION AND ROBUSTNESS

One of the most significant problems of gaze estimation is cross-domain generalization since when a model is trained on a particular set of data or a specific environment it is not always capable of not deteriorating as soon as it is implemented into a different environment. Changes in lighting, quality of the camera, head posture, user attributes, and type of devices may significantly affect the model performance. To eliminate these issues, domain adaptation techniques have been developed, that are more likely to reduce the difference between the training domain (data in the training phase) and the target domain (where it is used). These methods make parameters or features representations of the models to optimize generalization with no requirement of a large quantity of labeled information in the target domain [31]. Contrastive ways of learning have also been used to enhance the robustness of gaze prediction. Contrastive approaches enable models to learn more consummating features of invariance that cross-domain by learning representations that decrease the distance between identical patterns of gaze and intensify the distance between nonidentical patterns. The technique particularly comes in handy in the management of variability that yields in a difference in appearance, light, or camera settings [3]. Variability is another important aspect during the process of enhancing cross-domain robustness. In reality, there can be cases when the lights are dynamic, the poses of the head are mixed, the devices are multiple and the features of the camera are mixed. The mechanisms applied in contemporary gaze estimation systems to ensure they are more resistant to these deviances are data augmentation, adaptive normalization, and multi-view learning. With these strategies included, models would be in a position to perform in a stable manner under unconstrained environments and therefore in the suitability in the real practice [32]. The evaluation measures and benchmark datasets play a crucial role in developing and testing strong gaze estimation models. Publicly available data is a normal system of test cross-domain generalization, but with different subjects, devices and conditions. Some of the measures that are used to gauge performance include Angular error, mean absolute error and accuracy of gaze estimation. This will be done by testing the models in a few datasets, to know that system is not overfit to a particular environment, which can generalize well to unknown conditions [33]. Table (3) shows Cross-Domain Generalization and Robustness Techniques

Table 3: Cross-Domain Generalization and Robustness Techniques.

Aspect	Description	Techniques / Approaches	Challenges Addressed
Domain Adaptation [34]	Aligns feature distributions between source and target domains	Fine-tuning, adversarial adaptation, feature alignment	Cross-dataset variability, unseen environments
Contrastive Learning [35]	Learns invariant features by contrasting similar and dissimilar samples	SimCLR, MoCo-style embeddings	Appearance and lighting variations
Handling Variability [36]	Manages differences in pose, lighting, devices, and user characteristics	Data augmentation, adaptive normalization, multi-view learning	Real-world unconstrained conditions
Benchmark Datasets [37]	Standardized datasets for training and evaluation	GazeCapture, MPIIFaceGaze, RT-GENE, ETH-XGaze	Ensuring fair comparison and model generalization
Evaluation Metrics [38]	Quantitative measures of gaze estimation performance	Angular error, mean absolute error, accuracy	Comparing robustness across models and datasets

Source: Authors, (2026).

VI. COMPARISON OF EXISTING METHODS

A comparison of current gaze estimation techniques will be able to give the information about their strengths, limitations, and appropriateness to various applications.

The accuracy, latency, and robustness are performance measures that are commonly applied to evaluate eye tracking systems. Eye trackers based on special hardware are normally more accurate as infrared lights, specific sensors, and careful calibration are used. Angular errors of such systems are capable of reaching 0.51º, which in scientific research and medical practice are the best as well as in high-precision human-computer interaction. They however, are expensive, are hardware intensive and not portable enough to be used widely [39]. Contrastingly, eye tracking systems using webcams are an inexpensive and readily available option that utilizes ordinary cameras. Though they offer poorer quality of accuracy, usually between 2-5º angular error, they perform better with convenience, scaling and non-intrusiveness in those applications where precision is less significant than convenience and scaling. The latency can also be an important factor: although specialized trackers can provide high-speed tracking that can be used in real-time, systems based on webcams need to trade between computational efficiency and tracking quality, particularly when run on an ordinary consumer computer [40]. Cost against accuracy is a significant variable in the choice of a method. Specialized trackers with high end needs a lot of investment but provide accurate results whereas webcam-based needs cheaply but with low fineness of result. These two approaches have their choice determined by the needs of the application, the number of users and the limitations of the environment. Indicatively, research experiments that demand accuracy of gaze tracking can demand special trackers, whereas remote usability tests, e-learning, and accessibility applications can be efficiently executed through the use of webcam-based tracks [8]. In general, it is possible to classify existing methods depending on hardware requirements, complexity of computations, and applicability of the method. The current advances in the field of deep learning and the cross-domain generalization have reduced the gap in performance, now webcam based systems are capable of competitive accuracy in various cases. However, a trade off in webcam-based and specialized system persists as a choice between accuracy, affordability and installation [41]. Table (4) shows Comparison of Eye Tracking Methods.

Table 4: Comparison of Eye Tracking Methods.

Method	Accuracy	Latency	Advantages	Limitations
Specialized Eye Trackers	0.5°–1° angular error	Low latency	High precision, robust to lighting/pose, fast	Expensive, bulky, requires calibration
Webcam-Based Systems	2°–5° angular error	Moderate latency	Affordable, accessible, non-intrusive	Lower precision, sensitive to lighting and pose
Hybrid Approaches	1°–3° angular error	Low–moderate	Combines learned features with geometric models	More complex system design
Deep Learning Only Models	1.5°–3° angular error	Depends on device	Can adapt to multiple domains, flexible	Requires training data, computational cost

Source: [42]

VII. RELATED WORKS

The methods that are used to estimate the head pose could be divided into three major categories, appearance-based, geometry-based, and clustering-based. All these categories are different in terms of the form of input data, the methodology used, and the accuracy. Appearance-based methods make use of visual representations derived on the face or the eye, and apply machine learning or deep architecture models to directly relate such representations to the angle of head orientation. Geometric approach techniques make use of explicit 3D geometric representations of the face and eyes, frequently with landmark points to compute pitch, yaw and roll. The combination of feature extraction and data-driven clustering methods into a single process, known as clustering, is aimed at making them more robust and increase their ability to generalize across data sets [43]. A representative comparison of representative methods, such as type of input, datasets, and accuracy measures are presented in Table (4).

Table 5: Comparison of Works on Head Pose Estimation Methods.

Method Category	Reference	Input Type	Dataset	Reported Accuracy	Details / Notes
Appearance-Based	[44]	Eye images	BiWi	4.66°	Uses eye-region visual features with regression models to estimate pitch and yaw.
	[23]	Full face	AFLW	5.77°	Employs facial landmarks and CNNs for robust head pose estimation in unconstrained settings.
	[45]	Eye images	CMU-PIE	7.36°	Focuses on illumination-invariant feature extraction from eye region.
		Full face	MIT-CBCL	1.31°	Uses controlled indoor images; very low angular error due to stable capture conditions.
		Full face	YaleB	7.58°	Handles varying illumination; includes expression variations in training.
Geometry-Based	[46]	Eye and face	Unknown	2.63°	Computes head pose using 3D facial landmarks and geometric transformations.
		Eye and face	Unknown	3.26°	Combines eye tracking with face geometry for robust 3D orientation estimation.
	[47]	Full face	MPIIGaze	4.8°	Applies explicit facial geometry modeling for gaze and pose estimation.
	[48]	Face landmarks	Unknown	7.65°	Focuses on outdoor and low-resolution images, highlighting method robustness.
	[49]	Full face	ColumbiaGaze	9.46°	Handles multiple subjects with variable head orientations.
		Full face	MPIIFaceGaze	14.93°	Generalization to unconstrained webcam data; larger error due to dataset diversity.

		Full face	GazeCapture	10.46°	Large-scale mobile gaze dataset; demonstrates model performance on consumer devices.
Clustering-Based	[50]	Face + landmarks	BiWi	4.9°	Combines facial feature clustering with regression for improved robustness.
	[51]	Full face	Unknown	1.57°	Uses hierarchical clustering on feature embeddings to reduce noise and outliers.
	[52]	Full face	AFLW2000	3.48°	Enhances accuracy by clustering similar head poses before regression.
		Face landmarks	300 W-LP	3.92°	Incorporates pose normalization and clustering to handle extreme angles.
		Full face	BIWI	2.24°	Robust to subject variability and lighting changes using data-driven grouping.

Source: Authors, (2026).

Table 5 provides a detailed comparison of appearance-based, geometry-based and clustering-based techniques of estimating head pose that indicate a difference in the type of input, datasets used, accuracy and methodological properties. Appearance-based methods are mainly based on visual features that are a result of eye or full-face images and use convolutional neural networks or regression models. Such methods are likely to be effective under controlled settings like the MIT-CBCL where there is fixed lighting and minimal variation of the head describing low angular error conditions. They may however degrade in unconstrained environments because of the variations in pose, lighting and occlusion. Methods that use geometry use explicit 3D face landmark and physical modeling of the head and eye. These methods are able to combine low errors with limited training data by exploiting geometric constraints and are also capable of making interpretable estimates. They can however in most cases need quality landmark detection and might not be as strong to low-resolution images or partial occlusions. The methods based on clustering provide hybrid approach, that is, similar head poses are clustered and then regression is run, which enhances resistance to noise, subject variability, and extreme angles. Such techniques show stable behavior with a variety of datasets and light environments. On the whole, Table 5 indicates that although appearance-based models are versatile and can be easily used, geometry and clustering models allow better resilience and explanatory capabilities, and thus it is necessary to balance computational complexity, data needs, and real-world implementation conditions. Possible external and individual factors that may influence gaze estimation performance greatly include blinking, occlusion, lighting conditions and user differences. This is important in understanding the effect of these factors on accuracy in the design of robust eye-tracking systems. Eye blinking has temporary signal loss and may interfere with feature extraction, and occlusions (that can be created by glasses, hair or hands) may partially obscure the eyes or face. The visibility of eye features is influenced by the variability of light (such as ambient variability or shadow variability) and the unique anatomical characteristics of the eyes (eye shape, pupil size, and facial geometry) can further influence the performance of the system. Table (6) presents the summary of typical studies assessing gaze estimation under these conditions, input types, data sets and reported performance measures, such as average precision (AP) and angular error in degrees.

Table 6: Evaluation of Gaze Estimation under Various Factors.

Factor	Reference	Input Type	Dataset	Performance Metric	Details / Notes
Blinking	[53]	Eye	RT-BENE, Eyeblink8	AP: 0.757 (RT-BENE), 0.997 (Eyeblink8)	Evaluates robustness to natural blinks using eye-focused features.
	[54]	Eye	RT-BENE	AP: 0.653	Shows reduced precision under frequent blink scenarios; highlights importance of temporal smoothing.
Occlusion	[55]	Head / Body	GAFA, MoDiPro	20.4° (GAFA 3D), 25.6° (MoDiPro 2D)	Evaluates partial occlusion due to head rotation and body posture in gaze estimation.
	[56]	Eye + Face	MPIIGaze, EYEDIAP, RT-Gene	3.8°, 5.4°, 7.9°	Combines multiple occlusion scenarios, including glasses and hair; evaluates both 2D and 3D gaze.
Illumination	[57]	Eye	MPIIGaze, EYEDIAP	5.20°, 7.36°	Tests performance under varying lighting conditions; sensitive to shadows and low light.
	[58]	Eye	MPIIGaze, EYEDIAP, UTMultiview	4.67°, 3.36°, 4.33°	Uses deep learning-based approaches for illumination-invariant feature extraction.
Individual Differences	[59]	Eye	EVE, MPIIGaze, XGaze	1.89°, 4.14° / 3.02°, 2.88°	Evaluates cross-subject variability; models trained on some users tested on unseen users.
	[60]	Eye	Custom / unspecified	0.9°	Demonstrates high accuracy for personalized calibration.
	[61]	Eye	Custom / unspecified	4°	Highlights challenges in generalizing gaze estimation across users without calibration.

Source: Authors, (2026).

Table 6 presents the effect of external and individual forces on the estimation of gaze, such as blinking, occlusion, the change in illumination, and variation in inter-subject. Blinking of the eyes causes intermittent loss of signals which could have an immense impact on the accuracy of gaze as seen in data such as RT-BENE and Eyeblink8. The techniques that apply smoothness in the time or predictive modeling are in a position to deal with these transient events which minimizes the decline in performance. Another challenge is occlusion

which results due to head movements, glasses, or hand signs. Researchers have shown that the combination of head and body cues or both eye and face signal is better at enhancing robustness through the use of GAFA and MoDiPro. Correspondingly, the controlled datasets such as MPIIGaze, EYEDIAP and RT-Gene indicate that the multi-modal inputs can be used to reduce the effects of occlusions. Another important factor is the variability of illumination since discrepancies in the illumination of the eye features influence the visibility of face-related features. When trained on augmented or multi-condition datasets, the deep learning approaches demonstrate encouraging results at varying levels of illumination. Lastly, personal anatomy and facial features of the eye and face play a major role in estimating gaze. With cross-subject tests, it is seen that models do not generalize well without subject-specific calibration, as observed in EVE and XGaze datasets. In general, Table 6 has shown that it is necessary to design gaze estimation systems that should consider a combination of temporal modeling, multi-modal inputs, and methods to control the calibration to provide a reliable performance in the real-life conditions. The quality of datasets used in gaze estimation research depends greatly on the quality of participants used (varying), the nature of recording environments (varying) and the adequate sample sizes to generate and test models. These datasets vary according to the type of input (RGB or RGB-D), presence of full-face images, number of subjects, data magnitude, distance of recording and surrounding conditions (illumination and laboratory or natural conditions). Table (7) reflects a comparative summary of widely used gaze estimation datasets, including their essentials and the ability to be used in diverse experimental configurations.

Table 7: Overview of Gaze Estimation Datasets.

Dataset	Input Type	Participants	Full Face Available	Data Amount	Recording Distance	Environment / Illumination
MPIIGaze [62]	RGB	15	No	213,659 images	40–60 cm	Daily life
MPIIFaceGaze [63]	RGB	15	Yes	213,659 images	40–60 cm	Daily life
UnityEyes [64]	RGB	-	No	User-defined	User-defined	User-defined
ColumbiaGaze [30]	RGB	56	Yes	5,880 images	200 cm	Lab
Gaze360 [65]	RGB	238	Yes	~172,000 images	~200 cm	Daily life
ETH-XGaze [66]	RGB	110	Yes	1,083,492 images	100 cm	Lab
UT-Multiview [67]	RGB	50	No	1,216,000 images	60 cm	Lab
EYEDIAP [68]	RGB-D	16	Yes	94 videos	80–120 cm	Lab
RT-GENE [69]	RGB-D	15	Yes	277,286 images	~182 cm	-
NISLGaze [70]	RGB	21	Yes	2,079 videos	90 cm	-
GazeCapture [71]	RGB	1,474	Yes	>2.5 M images	Close	Daily life
TabletGaze [72]	RGB	51	Yes	816 videos	30–50 cm	Lab
GAFA [55]	RGB	-	Yes	882,000 videos	50 cm–7 m	Daily life
GFIE [73]	RGB-D	61	Yes	71,799 videos	1.04–6.48 m	Daily life

Source: Authors, (2026).

Table 7 gives a summary of commonly used gaze estimation datasets, contrasting input type, participant variety, size of data set, recording range and environmental circumstances. The table shows that there is a significant difference in the size and design of datasets, which indicates the versatility of the research in this area. Big datasets like GazeCapture or ETH-XGaze have millions of images or large amounts of video data, and can be used to train deep learning models that have huge demands in terms of diverse input. Smaller datasets, like ColumbiaGaze or NISLGaze, provide controlled conditions, as well as high-quality images, which come in handy especially when it comes to the testing of model performance in lab-based experiments. Another aspect of consideration is the inclusion of full-face pictures as opposed to eye-region pictures only. Head pose integration and multi-task learning methods have full-face datasets, whereas eye-only datasets specialize in finer ocular detail. Also, the availability of RGB-D information in such datasets as EYEDIAP and GFIE makes it easier to predict 3D gaze and consider the depth in modeling. The distance and environmental condition also affect the relevance of datasets, as natural head movement and natural illumination variability are only recorded in daily life datasets, but controlled lighting and constant distance are provided in lab-based datasets to evaluate them exactly. In general, Table 7 highlights the trade-offs between the size of dataset, environmental variability, and input type. The choice of the suitable dataset depends on the purpose of the model, the complexity of the model, and the need to be robust in uncontrolled situations or accurate in specific experiments.

VIII. CONCLUSION

This review gives a detailed discussion on the present situation and problems of gaze and head pose estimation technologies considering not only the methodological progress but also the practical aspect. Appearance-based methods, based largely on the visual cues picked off the eye areas or full-face image, have proved to be very flexible and data-driven to allow models to learn complicated images-to-gaze-direction linkages. Such techniques are especially useful when used with convolutional neural networks (CNNs) or transformer-based models, which are capable of learning spatial hierarchies and long-range dependence of visual information. Conversely, geometry-based techniques use explicit 3D facial landmark models to determine head orientation, which is interpretable and resistant to moderately unconstrained conditions. The clustering-based methods also improve the resilience of the result since the similar head poses are clustered together before regression, which would be better in the high variability situations (where the angle or the appearance of the subject varies a lot). Multi-task and hybrid learning models that combine gaze estimation and head pose prediction have shown that they have the potential to generalize to varying conditions by being able to utilize multiple correlated cues. In spite of these developments, the performance of gaze estimation is very sensitive to both external and individual variables. System accuracy is determined by the blinking, glasses or hair occlusion, inconsistent lighting and the difference in the anatomy among users.

Strong systems thus should include temporal modeling to deal with transient occurrences like eye blinks, multi-modal inputs to reduce occurrence of occlusions and adaptive calibration in consideration of inter-subject variability. To gain generalization to real-world settings, deep learning models that have been trained based on large-scale and diverse datasets are necessary. Smaller, manipulable datasets can be extremely useful in accuracy benchmarking and algorithm innovation validation, but they probably do not reflect the variability found in real-life situations. Gaze tracking systems based on webcams offer an easily accessible and inexpensive alternative to special infrared-based gaze tracking systems and can therefore be used in remote applications like e-learning, usability testing and mobile interfaces. Such systems, however, are usually more concerned with convenience and scalability at the cost of fine-grained accuracy, which requires more complicated modeling approaches to balance out noises, lighting variations, and free head rotations. Generalization strategies such as domain adaptation and contrastive learning are highly important in helping models trained in one setting or environment to be effective in unknown settings. In the future, the direction of research ought to be to create larger and more varied datasets encompassing a diverse set of lighting, pose, and subject variables, create models that are independent of illumination and occlusion, and create lightweight implementations that can be deployed on consumer devices in real-time. The combination of high-quality deep learning solutions with inexpensive and practical hardware will enhance the availability and usability of gaze and head pose estimation and open up new human-computer interaction solutions, as well as enabling real-world implementation of gaze and head pose estimation in fields of educational, medical, and interactive technology.

IX. AUTHOR'S CONTRIBUTION

Conceptualization: Khalid Sami Yousif, Emad A. Mohammed and Mayyada Al- Hammoshi.
Methodology: Khalid Sami Yousif, Emad A. Mohammed and Mayyada Al- Hammoshi.
Investigation: Khalid Sami Yousif, Emad A. Mohammed and Mayyada Al- Hammoshi.
Discussion of results: Khalid Sami Yousif, Emad A. Mohammed and Mayyada Al- Hammoshi.
Writing – Original Draft: Khalid Sami Yousif, Emad A. Mohammed and Mayyada Al- Hammoshi.
Writing – Review and Editing: Khalid Sami Yousif, Emad A. Mohammed and Mayyada Al- Hammoshi.
Resources: Khalid Sami Yousif, Emad A. Mohammed and Mayyada Al- Hammoshi.
Supervision: Khalid Sami Yousif, Emad A. Mohammed and Mayyada Al- Hammoshi.
Approval of the final text: Khalid Sami Yousif, Emad A. Mohammed and Mayyada Al- Hammoshi.

X. REFERENCES

[1] M. Q. Khan and S. Lee, "Gaze and Eye Tracking: Techniques and Applications in ADAS," Sensors, vol. 19, no. 24, 2019.

[2] G. R. Chhimpa et al., "A Comprehensive Framework for Eye Tracking: Methods, Tools, Applications, and Cross-Platform Evaluation.," J. Eye Mov. Res., vol. 18, no. 5, Sep. 2025.

[3] L. Huang, Y. Li, X. Wang, H. Wang, A. Bouridane, and A. Chaddad, "Gaze Estimation Approach Using Deep Differential Residual Network," Sensors, vol. 22, no. 14, 2022.

[4] Y. Cheng, H. Wang, Y. Bao, and F. Lu, "Appearance-Based Gaze Estimation With Deep Learning: A Review and Benchmark.," IEEE Trans. Pattern Anal. Mach. Intell., vol. 46, no. 12, pp. 7509–7528, Dec. 2024.

[5] S. Saxena, L. Fink, and E. Lange, "Deep learning models for webcam eye tracking in online experiments," Behav. Res. Methods, vol. 56, Aug. 2023.

[6] Z. Hussain Sahito and Z. Hussain, "The Effectiveness of Active Learning Strategies in Enhancing Student Engagement and Academic Performance," J. Soc. Sci. Rev., vol. 5, Mar. 2025.

[7] Y. Wu, Z. Zhang, F. Aghazadeh, and B. Zheng, "Early Eye Disengagement Is Regulated by Task Complexity and Task Repetition in Visual Tracking Task," Sensors, vol. 24, no. 10, 2024.

[8] T. Kaduk, C. Goeke, H. Finger, and P. König, "Webcam eye tracking close to laboratory standards: Comparing a new webcam-based system and the EyeLink 1000," Behav. Res. Methods, vol. 56, Oct. 2023.

[9] D. Martinez-Marquez, S. Pingali, K. Panuwatwanich, R. A. Stewart, and S. Mohamed, "Application of Eye Tracking Technology in Aviation, Maritime, and Construction Industries: A Systematic Review," Sensors, vol. 21, no. 13, 2021.

[10] L. Lin, Z. Wu, Y. Lu, and Z. Chen, "Recent Progress on Eye-Tracking and Gaze Estimation for AR / VR Applications : A Review," Electronics, 2025.

[11] Y. Shi et al., "Eye tracking and eye expression decoding based on transparent, flexible and ultra-persistent electrostatic interface," Nat. Commun., vol. 14, no. 1, p. 3315, 2023.

[12] M. Yang, Y. Gao, L. Tang, J. Hou, and B. Hu, "Wearable Eye-Tracking System for Synchronized Multimodal Data Acquisition," IEEE Trans. Circuits Syst. Video Technol., vol. 34, no. 6, pp. 5146–5159, 2024.

[13] R. Karmi, I. Rahmany, and N. Khlifa, "Gaze estimation using convolutional neural networks," Signal, Image Video Process., vol. 18, no. 1, pp. 389–398, 2024.

[14] B. Liu, S. W. Lye, and Z. Bin Zakaria, "An integrated framework for eye tracking-assisted task capability recognition of air traffic controllers with machine learning," Adv. Eng. Informatics, vol. 62, p. 102784, 2024.

[15] D. Lohr, S. Aziz, L. Friedman, and O. V Komogortsev, "GazeBaseVR, a large-scale, longitudinal, binocular eye-tracking dataset collected in virtual reality," Sci. Data, vol. 10, no. 1, p. 177, 2023.

[16] S. R, L. R, and H. C, “Eye Tracking and Its Applications,” IARJSET, vol. 8, Aug. 2021.

[17] R. Hessels, A. Nuthmann, M. Nyström, R. Andersson, D. Niehorster, and I. Hooge, “The fundamentals of eye tracking part 1: The link between theory and research question,” Behav. Res. Methods, vol. 57, Dec. 2024.

[18] I. T. C. Hooge et al., “The fundamentals of eye tracking part 6: Working with areas of interest.,” Behav. Res. Methods, vol. 58, no. 3, p. 65, Feb. 2026.

[19] X. Zhang, L. Wang, Y. He, Z. Mou, and Y. Cao, “High-speed eye tracking based on a synchronized imaging mechanism by a dual-ring infrared lighting source,” Appl. Opt., vol. 63, no. 16, pp. 4293–4302, Jun. 2024.

[20] B. R. Severitt, T. C. Kübler, and E. Kasneci, “Testing Different Function Fitting Methods for Mobile Eye-Tracker Calibration,” J. Eye Mov. Res., vol. 16, no. 4, pp. 1–17, 2023.

[21] J. Zhou, G. Li, F. Shi, X. Guo, P. Wan, and M. Wang, “EM-Gaze: eye context correlation and metric learning for gaze estimation,” Vis. Comput. Ind. Biomed. Art, vol. 6, no. 1, p. 8, 2023.

[22] K. Krafka, A. Khosla, and P. Kellnhofer, “Eye Tracking for Everyone,” 2024.

[23] F. Gao, S. Li, and S. Lu, “How frontal is a face? Quantitative estimation of face pose based on CNN and geometric projection,” Neural Comput. Appl., vol. 33, no. 8, pp. 3035–3051, 2021.

[24] A. Cantero, C. Lebrato, J. Castro, M. Merino Monge, F. Biscarri-Triviño, and J. I. Escudero, “A review on visible-light eye-tracking methods based on a low-cost camera,” J. Ambient Intell. Humaniz. Comput., vol. 15, Mar. 2024.

[25] L. Falch and K. S. Lohan, “Webcam-based gaze estimation for computer screen interaction.,” Front. Robot. AI, vol. 11, p. 1369566, 2024.

[26] A. J. Molina-Cantero, C. Lebrato-Vázquez, J. A. Castro-García, M. Merino-Monge, F. Biscarri-Triviño, and J. I. Escudero-Fombuena, “A review on visible-light eye-tracking methods based on a low-cost camera,” J. Ambient Intell. Humaniz. Comput., vol. 15, no. 4, pp. 2381–2397, 2024.

[27] T. Ge, “Deep Learning-Based Appearance-Based Gaze Estimation,” J. Comput. Electron. Inf. Manag., vol. 19, pp. 1–12, Dec. 2025.

[28] A. Bendimered, R. Iguernaissi, M. M. Nawaf, R. Cherif, S. Dubuisson, and D. Merad, “Dual Focus-3D: A Hybrid Deep Learning Approach for Robust 3D Gaze Estimation,” Sensors, vol. 25, no. 13, 2025.

[29] M. A. Pfeffer, J. K. W. Wong, and S. H. Ling, “Trends and Limitations in Transformer-Based BCI Research,” Appl. Sci., vol. 15, no. 20, 2025.

[30] V. Emile Tatinyuy, N. Woguia Auguste Vigny, M. Ngono Joseph, F. L. Aimé, and W. Pountianus Berinyuy, “Eye Gaze Detection Using a Hybrid Multimodal Deep Learning Model for Assistive Technology,” Appl. Sci., vol. 16, no. 2, 2026.

[31] H.-R. Yang, X. Chen, and C.-X. Ren, A Generalized Label Shift Perspective for Cross-Domain Gaze Estimation. 2025.

[32] M. F. Ansari, P. Kasprowski, and P. Peer, “Person-Specific Gaze Estimation from Low-Quality Webcam Images.,” Sensors (Basel)., vol. 23, no. 8, Apr. 2023.

[33] H. Kaur, S. Jindal, and R. Manduchi, “Rethinking Model-Based Gaze Estimation,” Proc. ACM Comput. Graph. Interact. Tech., vol. 5, pp. 1–17, May 2022.

[34] P. Siva Prasad and S. Agniraj, “Cross-Domain Adaptation Techniques for Robust Plant Disease Detection: A DANN-CORAL Hybrid Approach,” Int. J. Exp. Res. Rev., vol. 42, pp. 68–84, Aug. 2024.

[35] Y. Wang et al., “Enhancing Cross-Domain Remote Sensing Scene Classification by Multi-Source Subdomain Distribution Alignment Network,” Remote Sens., vol. 17, no. 7, 2025.

[36] A. G. Khoee, Y. Yu, and R. Feldt, “Domain generalization through meta-learning: a survey,” Artif. Intell. Rev., vol. 57, no. 10, p. 285, 2024.

[37] C. Chen, Y. Yang, M. Liu, Z. Rong, and S. Shu, “Regularized joint self-training: A cross-domain generalization method for image classification,” Eng. Appl. Artif. Intell., vol. 134, p. 108707, 2024.

[38] L. Lin, Z. Wu, Y. Lu, Z. Chen, and W. Guo, “Recent Progress on Eye-Tracking and Gaze Estimation for AR/VR Applications: A Review,” Electronics, vol. 14, no. 17, 2025.

[39] A. Kar and P. Corcoran, “Performance Evaluation Strategies for Eye Gaze Estimation Systems with Quantitative Metrics and Visualizations.,” Sensors (Basel)., vol. 18, no. 9, Sep. 2018.

[40] H. Zhang and L. Yin, “Robust Camera-Based Eye-Tracking Method Allowing Head Movements and Its Application in User Experience Research,” J. Eye Mov. Res., vol. 18, p. 71, Dec. 2025.

[41] I. T. C. Hooge, G. A. Holleman, N. C. Haukes, and R. S. Hessels, “Gaze tracking accuracy in humans: One eye is sometimes better than two.,” Behav. Res. Methods, vol. 51, no. 6, pp. 2712–2721, Dec. 2019.
[42] R. Alexander and S. Martinez-Conde, “Fixational Eye Movements,” 2019, pp. 73–115.

[43] K. Khan, M. Attique, I. Syed, G. Sarwar, M. A. Irfan, and R. U. Khan, “A Unified Framework for Head Pose, Age and Gender Classification through End-to-End Face Segmentation,” Entropy, vol. 21, no. 7, 2019.

[44] H. Liu, C. Zhang, Y. Deng, T. Liu, Z. Zhang, and Y.-F. Li, “Orientation Cues-Aware Facial Relationship Representation for Head Pose Estimation via Transformer,” IEEE Trans. Image Process., vol. 32, pp. 6289–6302, 2023.

[45] H. Zhao, Z. Ding, and Y. Fu, “Pose-Dependent Low-Rank Embedding for Head Pose Estimation,” Proc. AAAI Conf. Artif. Intell., vol. 30, no. 1, 2016.

[46] H. Bao, W. Fang, B. Guo, and J. Wang, “Real-time wide-view eye tracking based on resolving the spatial depth,” Multimed. Tools Appl., vol. 78, no. 11, pp. 14633–14655, 2019.

[47] J. Hu, Y. Lu, J. Zhang, J. Xu, and H. Yang, “Monocular free-head gaze tracking method for driving electric sickbed,” Meas. Sci. Technol., vol. 34, no. 12, p. 124002, 2023.

[48] A. Yang, Z. Jin, S. Guo, D. Wu, and L. Chen, “Unconstrained human gaze estimation approach for medium-distance scene based on monocular vision,” Vis. Comput., vol. 40, no. 1, pp. 73–85, 2024.

[49] A. Ruzzi, X. Shi, X. Wang, G. Li, and S. De Mello, “GazeNeRF : 3D-Aware Gaze Redirection with Neural Radiance Fields,” arXiv:2212.04823v2, 2023.

[50] C. Bisogni, L. Cascone, M. Nappi, and C. Pero, “IoT-enabled Biometric Security: Enhancing Smart Car Safety with Depth-based Head Pose Estimation,” ACM Trans. Multimed. Comput. Commun. Appl., vol. 20, no. 6, Mar. 2024.

[51] J. Tian, L. Cong, and H. Qin, “Mixed-Pose Positioning in Smartphone-Based Pedestrian Dead Reckoning Using Hierarchical Clustering,” IEEE Trans. Instrum. Meas., vol. 72, pp. 1–12, 2023.
[52] M. Xin, S. Mo, and Y. Lin, EVA-GCN: Head Pose Estimation Based on Graph Convolutional Networks. 2021.

[53] K. Cortacero, T. Fischer, and Y. Demiris, RT-BENE: A Dataset and Baselines for Real-Time Blink Estimation in Natural Environments. 2019.

[54] L. Ding et al., “CLERA: A Unified Model for Joint Cognitive Load and Eye Region Analysis in the Wild,” ACM Trans. Comput. Interact., vol. 30, no. 6, Sep. 2023.

[55] S. Nonaka and S. Nobuhara, Dynamic 3D Gaze from Afar: Deep Gaze Estimation from Temporal Eye-Head-Body Coordination. 2022.

[56] Y. Luo, J. Chen, and J. Chen, “CI-Net: Appearance-Based Gaze Estimation via Cooperative Network,” IEEE Access, vol. 10, pp. 78739–78746, 2022.

[57] Y. Cheng, Y. Bao, and F. Lu, PureGaze: Purifying Gaze Feature for Generalizable Gaze Estimation. 2021.

[58] G. Liu, Y. Yu, K. A. F. Mora, and J.-M. Odobez, “A Differential Approach for Gaze Estimation,” IEEE Trans. Pattern Anal. Mach. Intell., vol. 43, no. 3, pp. 1092–1099, 2021.

[59] J. Bao, B. Liu, and J. Yu, “An Individual-Difference-Aware Model for Cross-Person Gaze Estimation,” IEEE Trans. Image Process., vol. 31, pp. 3322–3333, 2022.

[60] E. D. Guestrin and M. Eizenman, “General theory of remote gaze estimation using the pupil center and corneal reflections,” IEEE Trans. Biomed. Eng., vol. 53, no. 6, pp. 1124–1133, 2006.

[61] D. W. Hansen and A. E. C. Pece, “Eye tracking in the wild,” Comput. Vis. Image Underst., vol. 98, no. 1, pp. 155–181, 2005.

[62] X. Zhang, Y. Sugano, M. Fritz, and A. Bulling, “MPIIGaze: Real-World Dataset and Deep Appearance-Based Gaze Estimation,” IEEE Trans. Pattern Anal. Mach. Intell., vol. 41, no. 1, pp. 162–175, 2019.

[63] X. Zhang, Y. Sugano, M. Fritz, and A. Bulling, “It’s Written All Over Your Face: Full-Face Appearance-Based Gaze Estimation,” Nov. 2016.

[64] E. Wood, T. Baltrusaitis, L.-P. Morency, P. Robinson, and A. Bulling, Learning an appearance-based gaze estimator from one million synthesised images. 2016.

[65] P. Kellnhofer, A. Recasens, S. Stent, W. Matusik, and A. Torralba, Gaze360: Physically Unconstrained Gaze Estimation in the Wild. 2019.

[66] X. Zhang, S. Park, T. Beeler, D. Bradley, S. Tang, and O. Hilliges, “ETH-XGaze: A Large Scale Dataset for Gaze Estimation Under Extreme Head Pose and Gaze Variation,” 2020, pp. 365–381.

[67] Y. Sugano, Y. Matsushita, and Y. Sato, Learning-by-Synthesis for Appearance-Based 3D Gaze Estimation. 2014.

[68] K. Funes Mora, F. Monay, and J.-M. Odobez, EYEDIAP: a database for the development and evaluation of gaze estimation algorithms from RGB and RGB-D cameras. 2014.

[69] T. Fischer, H. Chang, and Y. Demiris, RT-GENE: Real-Time Eye Gaze Estimation in Natural Environments. 2018.

[70] Z. Chen and B. E. Shi, “Towards High Performance Low Complexity Calibration in Appearance Based Gaze Estimation,” IEEE Trans. Pattern Anal. Mach. Intell., vol. 45, no. 1, pp. 1174–1188, 2023.

[71] K. Krafka, A. Khosla, and P. Kellnhofer, “Eye Tracking for Everyone,” arXiv:1606.05814v1, 2016.

[72] Q. Huang, A. Veeraraghavan, and A. Sabharwal, “TabletGaze: dataset and analysis for unconstrained appearance-based gaze estimation in mobile tablets,” Mach. Vis. Appl., vol. 28, no. 5, pp. 445–461, 2017.

[73] Z. Hu, Y. Yang, X. Zhai, D. Yang, B. Zhou, and J. Liu, “GFIE : A Dataset and Baseline for Gaze-Following from 2D to 3D in Indoor Environments,” Natl. Key Res. De- velopment Proj. China under Grant 2019YFB1310604, 2019.